Proceedings of the
2016 Summer Biomechanics, Bioengineering and Biotransport Conference

This is an electronically searchable and linked version of the program.

Instructions for abstract search:
1) Click on abstract title in Session Listing

OR

2) Search by keyword or author using find option: [control] + F (PC)
[command ⌘] + F (Mac)

SB3C
biomechanics.
bioengineering.
biotransport.
SB3C.org

June 29 – July 2, 2016
National Harbor, Maryland

Permission to download, print, and photocopy a single, individual copy of any of the works contained in this file for personal use in research and/or educational pursuit is granted by the Organizing Committee for the 2016 Summer Biomechanics, Bioengineering, and Biotransport Conference. For other uses, contact the Organizing Committee for the 2016 Summer Biomechanics, Bioengineering, and Biotransport Conference.

ISBN: 978-0-692-71816-2

WEDNESDAY, JUNE 29	3:45pm - 5:15pm

Nano, Micro, and Multi-Scale Mechanics in Cell and Tissue Engineering — Wilson B

Session Chair: X. Sherry Liu, *University of Pennsylvania, PA, United States*
Session Co-Chair: Nadeen Chahine, *Feinstein Institute, NY, United States*

3:45PM **A Chemo-mechanical Model for Extracellular Matrix and Nuclear Rigidity Regulated Size of Focal Adhesion Plaques** SB³C2016-679
Xuan P. Cao[1], Yuan Lin[2], Tristan Driscoll[3], Janusz Franco-Barraza[4], Edna Cukierman[4], Robert Mauck[3], Vivek Shenoy[5], *[1]Materials Science and Engineering, University of Pennsylvania, Philadelphia, PA, United States, [2]Department of Mechanical Engineering, The University of Hong Kong, Hong Kong, Hong Kong, [3]Department of Bioengineering, University of Pennsylvania, Philadelphia, PA, United States, [4]Fox Chase Cancer Center, Philadelphia, PA, United States, [5]Department of Materials Science and Engineering, University of Pennsylvania, Philadelphia, PA, United States*

4:00PM **A Predictive Multiscale Model for Simulating Flow-Induced Platelet Activation: Correlating with In-Vitro Results** SB³C2016-690
Peng Zhang[1], Chao Gao[1], Jawaad Sheriff[1], Marvin J. Slepian[1, 2], Yuefan Deng[3], Danny Bluestein[1], *[1]Biomedical Engineering Department, Stony Brook University, Stony Brook, NY, United States, [2]Departments of Medicine and Biomedical Engineering, University of Arizona, Tucson, AZ, United States, [3]Applied Mathematics Department, Stony Brook University, Stony Brook, NY, United States*

4:15PM **Cell Organization Dictates Stress Generation in Tissue Engineered Cell Sheets** SB³C2016-665
Inge A. E. W. van Loosdregt[1], Patrick W. Alford[2], Cees W. J. Oomens[1], Sandra Loerakker[1], Carlijn V. C. Bouten[1], *[1]Biomedical Engineering, Eindhoven University of Technology, Eindhoven, Netherlands, [2]Biomedical Engineering, University of Minnesota, Minneapolis, MN, United States*

4:30PM **Impacts of Maturation on the Nanostructure and Nanomechanics of the Meniscus Extracellular Matrix** SB³C2016-948
Qing Li[1], Feini Qu[2, 3], Biao Han[1], Robert L. Mauck[2, 3], Lin Han[1], *[1]School of Biomedical Engineering, Science and Health Systems, Drexel University, Philadelphia, PA, United States, [2]McKay Orthopaedic Research Laboratory, University of Pennsylvania, Philadelphia, PA, United States, [3]Translational Musculoskeletal Research Center, Philadelphia Veterans Administration Medical Center, Philadelphia, PA, United States*

4:45PM **Linking Mitral Valve Interstitial Cell Deformation to Biosynthetic Response: Implications for Mitral Valve Repair** SB³C2016-802
Salma Ayoub[1], Chung-Hao Lee[1], Connor T. Hughes[1], Giovanni Ferrari[2], Michael S. Sacks[1], *[1]The University of Texas at Austin, Austin, TX, United States, [2]University of Pennsylvania, Philadelphia, PA, United States*

5:00PM **Mechanical Effects of Dynamic Binding between Tau Proteins on Microtubules during Axonal Injury** SB³C2016-111
Hossein Ahmadzadeh[1], Douglas Smith[2], Vivek Shenoy[3], *[1]University of Pennsylvania, Philadelphia, PA, United States, [2]Penn Center for Brain Injury and Repair and Department of Neurosurgery, University of Pennsylvania, Philadelphia, PA, United States, [3]Department of Materials Science and Engineering, University of Pennsylvania, Philadelphia, PA, United States*

WEDNESDAY, JUNE 29	3:45pm - 5:15pm

Modeling and Mechanosensitivity — Wilson C

Session Chair: Clark Hung, *Columbia, NY, United States*
Session Co-Chair: Malisa Sarntinoranont, *University of Florida, FL, United States*

3:45PM **Age-Related Differences in Human Dermal Fibroblast Mechanosensitivity to Hyaluronic Acid Dermal Filler** SB³C2016-877
Aribet M. De Jesus[1], Sathivel Chinnathambi[1], Mariam El-Hattab[1], Douglas K. Henstrom[2], Edward A. Sander[1], *[1]Department of Biomedical Engineering, University of Iowa, Iowa City, IA, United States, [2]Department of Otolaryngology - Head and Neck Surgery, University of Iowa, Iowa City, IA, United States*

Copyright 2016 The Organizing Committee for the 2016 Summer Biomechanics, Bioengineering and Biotransport Conference

4:00PM **A Comparison of Phenomenological and Thermodynamically Consistent Approaches to the Modelling of Cells Subjected to Dynamic Loading** SB³C2016-1113
Patrick McGarry[1], Vikram S. Deshpande[2], *[1]National University of Ireland Galway, Galway, Ireland, [2]University of Cambridge, Cambridge, United Kingdom*

4:15PM **Modeling the Gas Foaming Process for Expanding Electrospun Nano iber Membranes in the Third Dimension** SB³C2016-707
Zhuoran Li[1], Jingwei Xie[2], **Linxia Gu**[1], *[1]Dept. of Mechanical & Materials Engineering, University of Nebraska-Lincoln, lincoln, NE, United States, [2]Department of Surgery-Transplant and Holland Regenerative Medicine Program, University of Nebraska Medical Center, Omaha, NE, United States*

4:30PM **A Model for Biological Fibers Derived From Implicit Elasticity** SB³C2016-48
Alan D. Freed, *Mechanical Engineering, Texas A&M University, College Station, TX, United States*

4:45PM **Chemically Conjugated Growth Factors on Electrospun Biomimetic Scaffolds Enhance Cell Adhesion and Proliferation** SB³C2016-31
Hannah M. Pauly[1], Ketul C. Popat[1, 2], Nicholas J. Dunne[3, 4], Daniel J. Kelly[5], Tammy L. Haut Donahue[1, 2], *[1]School of Biomedical Engineering, Colorado State University, Fort Collins, CO, United States, [2]Mechanical Engineering, Colorado State University, Fort Collins, CO, United States, [3]School of Mechanical and Aerospace Engineering, Queens University of Belfast, Belfast, United Kingdom, [4]School of Mechanical and Manufacturing Engineering, Dublin City University, Dublin, Ireland, [5]Trinity Centre for Bioengineering, Trinity College, Dublin, Ireland*

5:00PM **Finite Element Modeling of Cell pH and Ca^{2+} Regulations for Chondrocytes with Mixture Theory** SB³C2016-854
Chieh (Jay) Hou[1], Eben G. Estell[2], Clark T. Hung[2], Gerard A. Ateshian[1], *[1]Mechanical Engineering, Columbia University, New York, NY, United States, [2]Biomedical Engineering, Columbia University, New York, NY, United States*

WEDNESDAY, JUNE 29 | 3:45pm - 5:15pm

Musculo-skeletal Soft Tissue Mechanics — Wilson D

Session Chair: Richard Debski, *University of Pittsburgh, PA, United States*
Session Co-Chair: Suzanne Maher, *Hospital for Special Surgery, NY, United States*

3:45PM **Block Co-Polymer Based Hydrogels for Meniscal Replacement** SB³C2016-36
Kristine M. Fischenich[1], Jackson T. Lewis[1], Travis S. Bailey[1, 2], Tammy L. Haut Donahue[1, 3], *[1]School of Biomedical Engineering, Colorado State University, Fort Collins, CO, United States, [2]Chemical and Biological Engineering, Colorado State University, Fort Collins, CO, United States, [3]Department of Mechanical Engineering, Colorado State University, Fort Collins, CO, United States*

4:00PM **Effects of Mechanical Load on Scaffold-Cartilage Integration: A Computationally Augmented Biological Model** SB³C2016-914
Supansa Yodmuang[1], Hongqiang Guo[1], Tony Chen[1], Caroline Brial[1], Peter A. Torzilli[2], Russell Warren[2], Suzanne Maher[1], *[1]Biomechanics, Hospital for Special Surgery, New York, NY, United States, [2]Tissue Engineering, Regeneration and Repair Program, Hospital for Special Surgery, New York, NY, United States*

4:15PM **Skeletal Muscle Permeability: Direct Experimental Evaluation and Modeling Implications** SB³C2016-103
Benjamin B. Wheatley[1], Gregory M. Odegard[2], Kenton R. Kaufman[3], **Tammy L. Haut Donahue**[1], *[1]Mechanical Engineering, Colorado State University, Fort Collins, CO, United States, [2]Mechanical Engineering-Engineering Mechanics, Michigan Technological University, Fort Collins, CO, United States, [3]Department of Orthopaedic Surgery, Mayo Clinic, Rochester, MN, United States*

4:30PM **Investigating Deep Pressure Induced Deep Tissue Injury Using MRI and 3D Finite Element Analaysis** SB³C2016-122
Willeke A. Traa[1], Mark C. van Turnhout[1], Jules L. Nelissen[1], Gustav J. Strijkers[2], Klaas Nicolay[1], Dan L. Bader[3], Cees W. J. Oomens[1], *[1]Department of Biomedical Engineering, University of Technology Eindhoven, Eindhoven, Netherlands, [2]Department of Biomedical Engineering and Physics, Amsterdam Medical Centre, Amsterdam, Netherlands, [3]Department of Health Sciences, University of Southampton, Southampton, United Kingdom*

4:45PM **Effects of Meniscal Transplantation on Knee Joint Contact Mechanics and PostOperative Articular Cartilage Imaging** SB³C2016-815
Hongsheng Wang, Matthew Koff, Hollis Potter, Scott Rodeo, **Suzanne A. Maher**, *Hospital for Special Surgery, New York City, NY, United States*

Copyright 2016 The Organizing Committee for the 2016 Summer Biomechanics, Bioengineering and Biotransport Conference

5:00PM **Site- and Force-dependent Strain Behavior in the Porcine Anterior Cruciate Ligament** SB³C2016-1040
Satoshi Yamakawa[1], Richard E. Debski[2], Hiromichi Fujie[1], *[1]Tokyo Metropolitan University, Hino, Japan, [2]University of Pittsburgh, Pittsburgh, PA, United States*

WEDNESDAY, JUNE 29 | 3:45pm - 5:15pm

Extracelluar Matrix Mechanics in Aneurysms — Annapolis 1

Session Chair: Ken Monson, *University of Utah, UT, United States*
Session Co-Chair: Shamik Bhattacharya, *St.Mary's University, TX, United States*

3:45PM **A Comparative Study of the Mechanical Response and Fiber Structure in an Elastase Induced Aneurysm Model in Rabbits and Human Cerebral Aneurysms** SB³C2016-1112
Chao Sang[1], Xinjie Duan[1], David F. Kallmes[2], Ram Kadirvel[2], Yonghong Ding[2], Daying Dai[2], Khaled M. Aziz[3], Juan R. Cebral[4], Anne M. Robertson[1], *[1]Mechanical Engineering and Materials Science, University of Pittsburgh, Pittsburgh, PA, United States, [2]Department of Radiology, Mayo Clinic, Rochester, MN, United States, [3]Department of Neurosurgery, Allegheny General Hospital, Pittsburgh, PA, United States, [4]Department of Bioengineering, George Mason University, Fairfax, VA, United States*

4:00PM **A Structural Finite Element Model for Lamellar Unit of Aortic Media Indicates Heterogeneous Stress Field After Collagen Recruitment** SB³C2016-676
James R. Thunes, Joseph Pichamuthu, Julie A. Phillippi, Thomas G. Gleason, David A. Vorp, Spandan Maiti, *Bioengineering, University of Pittsburgh, Pittsburgh, PA, United States*

4:15PM **Development and Evaluation of an Image Analysis Approach for the Study of Recurrence in Coil Embolized Cerebral Aneurysms** SB³C2016-166
Anna Schumacher[1], Luca Antiga[2], Tatiana Correa[1], David Hasan[3], Madhavan Raghavan[1], *[1]Biomedical Engineering, University of Iowa, Iowa City, IA, United States, [2]Orobix Srl, Bergamo, Italy, [3]Neurosurgery, University of Iowa, Iowa City, IA, United States*

4:30PM **Effect of Penta-galloyl Glucose on Murine AAA: Material Parameter Optimization and Finite Element Implementation** SB³C2016-791
Mirunalini Thirugnanasambandam[1], Dan Simionescu[2], Eugene Sprague[3], Beth Goins[4], Geoffrey D. Clarke[4], Hai-Chao Han[5], Krysta Amezcua[1], Oluwaseun R. Adeyinka[1], Ender Finol[1], *[1]Department of Biomedical Engineering, University of Texas at San Antonio, San Antonio, TX, United States, [2]Department of Bioengineering, Clemson University, Clemson, SC, United States, [3]Department of Medicine, University of Texas Health Science Center at San Antonio, San Antonio, TX, United States, [4]Department of Radiology, University of Texas Health Science Center at San Antonio, San Antonio, TX, United States, [5]Department of Mechanical Engineering, University of Texas at San Antonio, San Antonio, TX, United States*

4:45PM **Mechanical Behavior and Genetic Signaling in Aortic Aneurysms in Newborn Lysyl Oxidase Knockout Mice** SB³C2016-728
Marius C. Staiculescu[1], Robert Mecham[2], Jessica Wagenseil[1], *[1]Mechanical Engineering and Materials Science, Washington University, St. Louis, MO, United States, [2]Cell Biology, Washington University, St. Louis, MO, United States*

5:00PM **In Vitro Rupture Patterns of Ascending Thoracic Aortic Aneurysms** SB³C2016-607
Jia Lu[1], Yuanming Lu[1], Ambroise Duprey[2], Stéphane Avril[2], *[1]Mechanical and Industrial Engineering, The University of Iowa, Iowa City, IA, United States, [2]Ecole Nationale Suprieure des Mines, St. Étienne, France*

Copyright 2016 The Organizing Committee for the 2016 Summer Biomechanics, Bioengineering and Biotransport Conference

WEDNESDAY, JUNE 29	3:45pm - 5:15pm

Atherosclerosis — Annapolis 2

Session Chair: Frank Gijsen, *Erasmus University Rotterdam, Netherlands*
Session Co-Chair: David Vorp, *University of Pittsburgh, PA, United States*

3:45PM **Assessment of Analysis Methods to Evaluate the Association Between Wall Shear Stress and Coronary Artery Disease in the Clinical Setting** SB³C2016-1036
Lucas H. Timmins[1,2], David S. Molony[1,3], Parham Eshtehardi[3], Michael C. McDaniel[3], John N. Oshinski[1,2], Habib Samady[3], Don P. Giddens[1], *[1]Biomedical Engineering, Georgia Institute of Technology, Atlanta, GA, United States, [2]Radiology and Imaging Sciences, Emory University School of Medicine, Atlanta, GA, United States, [3]Medicine (Cardiology), Emory University School of Medicine, Atlanta, GA, United States*

4:00PM **Impact of Bi-Axial Shear on Atherogenic Gene Expression by Endothelial Cells** SB³C2016-87
Amlan Chakraborty[1], Sutirtha Chakraborty[2], Venkatakrishna R. Jala[2], Jonathan Thomas[2], **M. Keith Sharp**[2], R Eric Berson[2], Haribabu Bodduluri[2], *[1]Entegris, Inc, Franklin, MA, United States, [2]University of Louisville, Louisville, KY, United States*

4:15PM **Cap Inflammation Leads to Large Plaque Cap Stress Decrease and Strain Increase: MRI-PET/CT-Based FSI Modeling** SB³C2016-28
Dalin Tang[1,2], Chun Yang[1,3], Sarayu Huang[4], Venkatesh Mani[4], Zahi A. Fayad[4], *[1]WPI, Worcester, MA, United States, [2]Southeast University, Nanjing, China, [3]China Information Tech. Designing & Consulting Institute Co., Ltd., Beijing, China, [4]Translational and molecular imaging institute, New York, NY, United States*

4:30PM **MRI based Cap Thickness and Peak Cap Stress Prediction: Man Versus Machine** SB³C2016-782
Annette M. Kok[1], Aad van der Lugt[2], Antonius F. W. van der Steen[1], Jolanda J. Wentzel[1], Frank J. H. Gijsen[1], *[1]Biomedical Engineering, Erasmus MC, Rotterdam, Netherlands, [2]Radiology, Erasmus MC, Rotterdam, Netherlands*

4:45PM **The Relation Between Shear Stress Metrics and Atherosclerosis: a Follow-up Study in the Carotid Arteries of Atherosclerotic Mice** SB³C2016-39
David De Wilde[1], Bram Trachet[1,2], Guido R. Y. De Meyer[3], **Patrick Segers**[1], *[1]Ghent University, Ghent, Belgium, [2]Institute for Bioengineering, EPFL, Lausanne, Switzerland, [3]Division of Physiopharmacology, University of Antwerp, Antwerp, Belgium*

5:00PM **Effect of Stent Oversizing on In-stent Restenosis in the Second Part of the Popliteal Artery** SB³C2016-1132
Azadeh Lotfi[1], Tracie Barber[1], Anne Simmons[1], Ramon Varcoe[2], *[1]Mechanical and manufacturing Engineering, University of new South Wales, Sydney, Australia, [2]Department of Surgery, Prince of Wales Hospital, Sydney, Australia*

WEDNESDAY, JUNE 29	3:45pm - 5:15pm

Musculoskeletal System and Design — Azalea 2

Session Chair: Michele Grimm, *Wayne State, MI, United States*
Session Co-Chair: Brett Steineman, *Colorado State University, CO, United States*

3:45PM **Elucidating Mechanisms of Tendon Damage by Measuring Multiscale Unloaded Recovery following Tensile Loading** SB³C2016-800
Andrea H. Lee[1], Spencer E. Szczesny[2], Kristen L. Fetchko[1], Michael H. Santare[3], Dawn M. Elliott[1], *[1]Department of Biomedical Engineering, University of Delaware, Newark, DE, United States, [2]Department of Orthopaedic Surgery, University of Pennsylvania, Philadelphia, PA, United States, [3]Department of Mechanical Engineering, University of Delaware, Newark, DE, United States*

4:00PM **The Use of Individual Motion Units to Analyze In Vivo Total Thoracolumbar Motion in Healthy Older Adults** SB³C2016-717
Eileen S. Cadel[1], Sarah N. Galvis[1], William M. Eboch[2], Paul M. Arnold[3], Sara E. Wilson[2], Elizabeth A. Friis[2], *[1]Bioengineering Graduate Program, University of Kansas, Lawrence, KS, United States, [2]Mechanical Engineering, University of Kansas, Lawrence, KS, United States, [3]Department of Neurology, University of Kansas Medical Center, Kansas City, KS, United States*

Copyright 2016 The Organizing Committee for the 2016 Summer Biomechanics, Bioengineering and Biotransport Conference

4:15PM **Novel Instrumented Mouthguard Designs to Accurately Measure Head Kinematics for Traumatic Brain Injury** SB³C2016-696
Calvin Kuo[1], Lyndia C. Wu[2], David B. Camarillo[1, 2], *[1]Mechanical Engineering, Stanford University, Stanford, CA, United States, [2]Bioengineering, Stanford University, Stanford, CA, United States*

4:30PM **Effective Stiffnesses for the Human Buttocks and Thigh Regions Obtained Through in vivo Methods: Applications to Medical Seating** SB³C2016-124
Wu Pan, Zac Sadler, Lindsay Nault, Tamara Reid Bush, *Mechanical Engineering, Michigan State University, East Lansing, MI, United States*

4:45PM **Fatigue Testing of a Composite Meniscus Implant - What are the Limits?** SB³C2016-669
Jonathan J. Elsner[1], Maoz Shemesh[2], Adaya Shefy-Peleg[2], Eyal Zylberberg[2], Zahava Barkai[3], Eran Linder-Ganz[2], *[1]Research and Development, Active Implants, Cambridge, MA, United States, [2]Research and Development, Active Implants, Netanya, Israel, [3]Wolfson Applied Materials Research Center, Tel-Aviv University, Tel-Aviv, Israel*

5:00PM **Footwear Affects Muscle Activity during Ramp Walking** SB³C2016-685
Feng Wei, Andrew J. Crechiolo, Roger C. Haut, *Orthopaedic Biomechanics Laboratories, Michigan State University, East Lansing, MI, United States*

WEDNESDAY, JUNE 29 | 3:45pm - 5:15pm

Thermal Treatment and Hyperthermia — Azalea 3

Session Chair: Aili Zhang, *Shanghai Jiao Tong University, China*
Session Co-Chair: Zhenpeng Qin, *University of Texas at Dallas, TX, United States*

3:45PM **Development of a 3-D Whole Body Heat Transfer Model for Accurately Predicting Time of Death in Forensic Science** SB³C2016-149
Catherine Bartgis, Alexander LeBrun, Amirreza Saharkhiz, Ronghui Ma, **Liang Zhu**, *Mechanical Engineering, University of Maryland Baltimore County, Baltimore, MD, United States*

4:00PM **A Counterexample of Entropy-Enthalpy Compensation in Collagen Denaturation** SB³C2016-900
Neil T. Wright, *Mechanical Engineering, Michigan State University, East Lansing, MI, United States*

4:15PM **Contribution of Ultrasound Absorption in Nanoparticles for Hyperthermia Application** SB³C2016-765
Vishal Kumar[1], Surendra Devarakonda[2], Rupak K Banerjee[2], Ashok K Ganguli[1, 3], **Chandan Bera**[1], *[1]Institute of Nano Science and Technology, Mohali, India, [2]Mechanical and Materials Engineering Department, University of Cincinnati, Cincinnati, OH, United States, [3]Department of Chemistry, Indian Institute of Technology, Delhi, New Delhi, India*

4:30PM **Dynamic Bubble Formation in ADV Assisted HIFU with Preexisting Bubble Wall** SB³C2016-767
Ying Xin[1], **Aili Zhang**[1], Lisa X. Xu[1], Jeffery B. Fowlkes[2], *[1]Shanghai Jiao Tong University, Shanghai, China, [2]University of Michigan, Ann Arbor, MI, United States*

4:45PM **In Vitro and In Vivo Model for Assessing Irreversible Electroporation on Pancreatic Cancer** SB³C2016-770
Qi Shao[1], Connie Chung[1], Feng Liu[1], Kianna Elahi[2], Paolo Provenzano[2], Bruce Forsyth[3], John C. Bischof[1], *[1]Mechanical Engineering, University of Minnesota, Minneapolis, MN, United States, [2]Biomedical Engineering, University of Minnesota, Minneapolis, MN, United States, [3]Boston Scientific, Marlborough, MA, United States*

5:00PM **Nanosecond Protein Thermal Inactivation by Plasmonic Nanoparticle Laser Heating** SB³C2016-745
Peiyuan Kang, **Zhenpeng Qin**, *Mechanical Engineering, University of Texas at Dallas, Richardson, TX, United States*

Copyright 2016 The Organizing Committee for the 2016 Summer Biomechanics, Bioengineering and Biotransport Conference

THURSDAY, JUNE 30	8:00am - 9:30am

Engineering Translation: Disease Models and Outcomes — Wilson B

Session Chair: Sharan Ramaswamy, *Florida International University, FL, United States*
Session Co-Chair: Ozan Akkus, *Case Western Reserve University, OH, United States*

8:00AM **3D in vitro Platform to Isolate Dormancy Capable Cancer Cells** SB³C2016-740
Julian A. Preciado, Eduardo Retagui, Molly Lefebvre, Samira Azarin, Emil Lou, Alptekin Aksan, *Mechanical Engineering, University of Minnesota, Minneapolis, MN, United States*

8:15AM **Biomechanical Regulation of Angiogenesis by Cancer-Associated Fibroblasts** SB³C2016-97
M.K. Sewell-Loftin[1], Elizabeth L. Crist[1], B. Taylor Hughes[1], Samantha van Hove[2], Gregory D. Longmore[2, 3], Steven C. George[1], *[1]Department of Biomedical Engineering, Washington University in St. Louis, St. Louis, MO, United States, [2]Department of Cell Biology and Physiology, Washington University in St. Louis, St. Louis, MO, United States, [3]Department of Medicine, Oncology Division, Washington University in St. Louis, St. Louis, MO, United States*

8:30AM **Chondro-protective Effect of Zoledronate on In Situ Chondrocytes Damaged by Interleukin-1** SB³C2016-999
Mengxi Lv, Yilu Zhou, Shongshan Fan, Olivia Smith, Liyun Wang, X.Lucas Lu, *University of Delaware, Newark, DE, United States*

8:45AM **Photoclickable Peptide Microarrays for High Throughput Screening and Discovery in Regenerative Medicine and Disease Models** SB³C2016-1098
Michael L. Floren, *Department of Mechanical Engineering, University of Colorado Boulder, Boulder, CO, United States*

9:00AM **Characterization of Glioblastoma Growth Using Five Different Mathematical Models** SB³C2016-986
Mitra Shabanisamghabady, Martin L. Tanaka, *Engineering and Technology, Western Carolina University, Cullowhee, NC, United States*

9:15AM **Application of a Novel Biomechanical Fiber Model to Tissue Engineering for Improved Clinical Outcomes** SB³C2016-1055
Andrew B. Robbins[1], Silvia Minardi[2], Ennio Tasciotti[2], Alan D. Freed[3], Michael R. Moreno[3], *[1]Biomedical Engineering, Texas A&M University, College Station, TX, United States, [2]Methodist Research Hospital, Houston, TX, United States, [3]Mechanical Engineering, Texas A&M University, College Station, TX, United States*

THURSDAY, JUNE 30	8:00am - 9:30am

Design and Optimization of Cardiovascular Devices — Wilson C

Session Chair: Alan D. Freed, *Texas A&M University, TX, United States*
Session Co-Chair: Michael Moreno, *Texas A&M, TX, United States*

8:00AM **A Computational Framework for Optimization of Transcatheter Aortic Valve Leaflets** SB³C2016-993
Kyle E. Murdock[1], Kewei Li[2], Caitlin Martin[1], Wei Sun[1], *[1]Biomedical Engineering, Georgia Institute of Technology, Atlanta, GA, United States, [2]Biomedical Engineering, Graz University of Technology, Graz, Austria*

8:15AM **A Computational Investigation of the Positioning of Transcatheter Aortic Heart Valves to Enhance Long Term Performance** SB³C2016-773
Orla M. McGee, Paul S. Gunning, Laoise M. McNamara, *Biomedical Engineering, NUIGalway, Galway, Ireland*

8:30AM **Computational Modeling of Optimization of Drug-Eluting Stents Under Multiple Mechanical Criteria** SB³C2016-882
Francois P. M. Cornat, Franz Bozsak, Abdul I. Barakat, *Laboratoire d'hydrodynamique LadHyX, Ecole Polytechnique, Palaiseau cedex, France*

8:45AM **Development and Evaluation of an Arborizing Catheter for Convection Enhanced Delivery** SB³C2016-849
Egleide Y. Elenes[1], Christopher G. Rylander[2], *[1]Biomedical Engineering, The University of Texas at Austin, Austin, TX, United States, [2]Mechanical Engineering, The University of Texas at Austin, Austin, TX, United States*

Copyright 2016 The Organizing Committee for the 2016 Summer Biomechanics, Bioengineering and Biotransport Conference

9:00AM **A Virtual Coiling Algorithm to Simulate Endovascular Coil Deployment in Cerebral Aneurysm using Spring Based Geometric Constraint Model** SB³C2016-716
Rahul Sanal[1], Robert J. Damiano[1], Adnan H. Siddiqui[2], Jinhui Xu[3], Hui Meng[1], *[1]Department of Mechanical and Aerospace Engineering, State University of New York at Buffalo, Buffalo, NY, United States, [2]Department of Neurosurgery, State University of New York at Buffalo, Buffalo, NY, United States, [3]Department of Computer Science and Engineering, State University of New York at Buffalo, Buffalo, NY, United States*

9:15AM **Visco-Hyperelastic Modeling of the Penn State Pulsatile Pneumatic Pediatric VAD Membrane** SB³C2016-884
Bryan Good, Keefe Manning, *Bioengineering, The Pennsylvania State University, University Park, PA, United States*

THURSDAY, JUNE 30 | 8:00am - 9:30am

Injury: Brain I — Wilson D

Session Chair: Songbai Ji, *Dartmouth College, NH, United States*
Session Co-Chair: Reuben H. Kraft, *The Pennsylvania State University, PA, United States*

8:00AM **Modal Analysis of Human Brain Dynamics in Contact Sports** SB³C2016-1023
Mehmet Kurt, Kaveh Laksari, David B. Camarillo, *Bioengineering, Stanford University, Stanford, CA, United States*

8:15AM **Characterization of White Matter Using Asymmetric Indentation and Inverse Modeling in Large Strain** SB³C2016-53
Yuan Feng[1], Chung-Hao Lee[2], Lining Sun[1], Shengjun Fu[1], *[1]Mechanical and Electronic Engineering, Soochow University, Suzhou, China, [2]ICES, The University of Texas at Austin, Austin, TX, United States*

8:30AM **White Matter Injury Susceptibility Using Whole-brain Tractography: Concept Illustration** SB³C2016-69
Wei Zhao[1], James C. Ford[2], Thomas W. McAllister[3], Songbai Ji[1, 4], *[1]Thayer School of Engineering, Dartmouth College, Hanover, NH, United States, [2]Department of Psychiatry, Geisel School of Medicine, Dartmouth College, Hanover, NH, United States, [3]Department of Psychiatry, Indiana University School of Medicine, Indiana University, Indianapolis, IN, United States, [4]Department of Surgery and of Orthopaedic Surgery, Dartmouth College, Hanover, NH, United States*

8:45AM **A Bayesian Approach to Model Selection and Surrogate Modeling: Application to Traumatic Brain Injury Simulations** SB³C2016-1039
Sandeep Madireddy, **Kumar Vemaganti**, *Mechanical & Materials Engineering, University of Cincinnati, Cincinnati, OH, United States*

9:00AM **Subconcussive Head Impact Exposure for Concussed and Non-Concussed Division III College Football Athletes** SB³C2016-708
Alok S. Shah[1, 2], Brian D. Stemper[1, 2], James K. Murtha[1], Rachel A. Chiariello[1, 2], John R. Humm[1, 2], Ashley LaRoche[1], Michael McCrea[1, 2], *[1]Department of Neurosurgery, Medical College of Wisconsin, Milwaukee, WI, United States, [2]Neuroscience Research Center, Veterans Affairs Medical Center, Milwaukee, WI, United States*

9:15AM **Heterogeneity of Viscoelastic Behavior of Rat Brain** SB³C2016-1043
Soroush Assari, Golriz Kermani, Ali Hemmasizadeh, Mary F. Barbe, Kurosh Darvish, *Temple University, Philadelphia, PA, United States*

THURSDAY, JUNE 30 | 8:00am - 9:30am

ATH Plaque Imaging and Mechanics — Annapolis 1

Session Chair: Dalin Tang, *Worcester Polytechnic Institute, MA, United States*
Session Co-Chair: Lucas H. Timmins, *Georgia Institute of Technology, GA, United States*

8:00AM **A CT Based Model of the Fracture of Calcified Atherosclerotic Plaques** SB³C2016-1019
Brían L. O'Reilly, Patrick McGarry, Peter E. McHugh, *Biomedical Engineering, National University of Ireland, Galway, Ireland*

Copyright 2016 The Organizing Committee for the 2016 Summer Biomechanics, Bioengineering and Biotransport Conference

8:15AM **Characterization of Fracture Behavior of Human Atherosclerotic Fibrous Caps Using a Miniature Single Edge Notched Tensile Test** SB³C2016-610

Lindsey A. Davis[1], Samantha E. Stewart[1], Christopher G. Carsten[2], Bruce A. Snyder[2], Michael A. Sutton[1], Susan M. Lessner[1], *[1]University of South Carolina, Columbia, SC, United States, [2]Greenville Health System, Greenville, SC, United States*

8:30AM **Deployment and Degradation of a Bioresorbable Stent: a Coupled Computational Model Between Stent and Artery** SB³C2016-777

Johanne Mensah-Gourmel[1], François Cornat[1], Antoine Lafont[2], Abdul I. Barakat[1], *[1]Hydrodynamics Laboratory - Ecole Polytechnique, Palaiseau, France, [2]Georges Pompidou European Hospital - Cardiology department - APHP - Paris Descartes University, Paris, France*

8:45AM **Imaging and Quantifying the 3D Collagen Architecture in Atherosclerotic Plaques** SB³C2016-940

Ali C. Akyildiz[1], Lambert Speelman[1], Chen-Ket Chai[2], Cees Oomens[2], Gustav Strijkers[3], Frank Gijsen[1], *[1]Biomedical Engineering Department, Erasmus MC, Rotterdam, Netherlands, [2]Department of Biomedical Engineering, Eindhoven University of Technology, Eindhoven, Netherlands, [3]Department of Biomedical Engineering & Physics, University of Amsterdam, Amsterdam, Netherlands*

9:00AM **Loss of Elastic Fiber Integrity Due to Fibulin-5 Deficiency Alters Aortic Elasticity, Central Hemodynamics, and Cardiac Function** SB³C2016-167

Jacopo Ferruzzi[1, 2], Paolo Di Achille[2], Pradyumn Agarwal[3], Federica Cuomo[3], C. Alberto Figueroa[3], Jay D. Humphrey[2, 4], *[1]Boston University, Boston, MA, United States, [2]Department of Biomedical Engineering, Yale University, New Haven, CT, United States, [3]Department of Biomedical Engineering, University of Michigan, Ann Arbor, MI, United States, [4]Vascular Biology & Therapeutics Program, Yale School of Medicine, New Haven, CT, United States*

9:15AM **Effects of Opening Angle, Axial Stretch and Circumferential Shrinkage on Blood Vessel Stress and Strain Calculations** SB³C2016-581

Liang Wang[1], Jian Zhu[2], Akiko Maehara[3], Jie Zheng[4], Chun Yang[1, 5], David Muccigrosso[4], Gary S. Mintz[3], Dalin Tang[1, 6], *[1]Mathematical Department, Worcester Polytechnic Institute, Worcester, MA, United States, [2]Department of Cardiology, Zhongda Hosiptial, Southeast University, Nanjing, China, [3]The Cardiovascular Research Foundation, Columbia University, New York, NY, United States, [4]Mallinckrodt Institute of Radiology, Washington University, St. Louis, MO, United States, [5]Network Technology Research Institute, China United Network Comm. Co., Ltd., Beijing, China, [6]Department of Mathemtics, Southeast University, Nanjing, China*

THURSDAY, JUNE 30 | 8:00am - 9:30am

Aneurysm Biomechanics — Annapolis 2

Session Chair: Ender A. Finol, *University of Texas at San Antonio, TX, United States*
Session Co-Chair: Jessica Shang, *University of Rochester, NY, United States*

8:00AM **Prediction of Abdominal Aortic Aneurysm shape evolution using Gaussian Process Implicit Surfaces** SB³C2016-56

Huan N. Do[1], Jongeun Choi[1, 2], Seungik Baek[1], *[1]Mechanical Engineering, Michigan State University, East Lansing, MI, United States, [2]Department of Electrical and Computer Engineering, Michigan State University, East Lansing, MI, United States*

8:15AM **A New Approach for Abdominal Aortic Aneurysm Local Growth Quantification** SB³C2016-783

Eleni Metaxa[1], Iordan Iordanov[1], Emmanuel Maravelakis[2], **Yannis Papaharilaou**[1], *[1]Institute for Applied and Computational Mathematics, Foundation for Research and Technology - Hellas, Heraklion, Greece, [2](2)Department of Environmental and Natural Resources Engineering, Technological Educational Institute of Crete, Chania, Greece*

8:30AM **Novel Growth and Remodeling Mechanisms May Explain the Unique Expansion Patterns and Evolving Mechanical Behavior of Abdominal Aortic Aneurysms** SB³C2016-1052

John S. Wilson[1], Christian Cyron[2], Jay D. Humphrey[3], *[1]Radiology, Emory University, Atlanta, GA, United States, [2]Mechanical Engineering, Technical University of Munich, Garching, Germany, [3]Biomedical Engineering, Yale University, New Haven, CT, United States*

Copyright 2016 The Organizing Committee for the 2016 Summer Biomechanics, Bioengineering and Biotransport Conference

8:45AM **Intrasaccular Hemodynamics, Wall Inflammation and Degenerative Changes of Cerebral Aneurysm Wall** SB³C2016-132

Juan Cebral[1], Eliisa Ollikainen[2], BongJae Chung[1], Fernando Mut[1], Visa Sippola[2], Behdam Jahromi[2], Riikka Tulamo[2], Juha Hernesniemi[2], Mika Niemela[2], Anne Robertson[3], Juhana Frosen[2, 4], *[1]Bioengineering, George Mason University, Fairfax, VA, United States, [2]Neurosurgery, Biomedicum & Helsinki University Hospital, Helsinki, Finland, [3]Mechanical and Material Science & Bioengineering, University of Pittsburgh, Pittsburgh, PA, United States, [4]Neurocenter, Kuopio University Hospital, Kuopio, Finland*

9:00AM **Fluid-structure Interaction of a Ruptured Intracranial Aneurysm: Does Patient-specific Wall Thickness Matter?** SB³C2016-35

Philipp Berg[1], Samuel Voß[1], Sylvia Glaßer[2], Thomas Hoffmann[3], Simon Weigand[3], Gábor Janiga[1], *[1]Department of Fluid Dynamics and Technical Flows, University of Magdeburg, Magdeburg, Germany, [2]Department of Simulation and Graphics, University of Magdeburg, Magdeburg, Germany, [3]Department of Neuroradiology, University Hospital Magdeburg, Magdeburg, Germany*

9:15AM **Intra Aneurysmal Angiographic Analysis in Patients Towards Determination of Flow Diversion Efficacy** SB³C2016-1138

Ronak J. Dholakia, Chander Sadasivan, David J. Fiorella, Henry H. Woo, Baruch B. Lieber, *Neurological Surgery, Stony Brook University, Stony Brook, NY, United States*

THURSDAY, JUNE 30 | 8:00am - 9:30am

Computational Mechanics and Simulations — Azalea 2

Session Chair: Jonathan Vande Geest, *University of Pittsburgh, PA, United States*
Session Co-Chair: Andrew Feola, *Georgia Institute of Technology, A, United States*

8:00AM **Study of Two Arterial Wall Delamination Experiments** SB³C2016-635

Xiaochang Leng[1], Boran Zhou[2], Xiaomin Deng[1], Lindsey Davis[2, 3], Susan Lessner[2, 3], Michael Sutton[1, 2], Tarek Shazly[1, 2], *[1]Department of Mechanical Engineering, University of South Carolina, Columbia, SC, United States, [2]Biomedical Engineering Program, University of South Carolina, Columbia, SC, United States, [3]Department of Cell Biology & Anatomy, University of South Carolina, Columbia, SC, United States*

8:15AM **Individual-Specific Finite Element Model of the Rat Optic Nerve Head Under Elevated Intraocular Pressure Conditions** SB³C2016-107

Stephen A. Schwaner[1], Marta Pazos[2, 3], Hongli Yang[3], Elaine C. Johnson[4], John C. Morrison[4], Claude F. Burgoyne[3], C. Ross Ethier[1, 5], *[1]George W. Woodruff School of Mechanical Engineering, Georgia Institute of Technology, Atlanta, GA, United States, [2]Ophthalmology Department, Hospital de l'Esperanca-Parc de Salut Mar. Institute Mar d'Investigacions Mediques, Barcelona, Spain, [3]Devers Eye Institute, Optic Nerve Head Research Laboratory, Portland, OR, United States, [4]Casey Eye Institute, Oregon Health and Science University, Portland, OR, United States, [5]Coulter Department of Biomedical Engineering, Georgia Institute of Technology/Emory University, Atlanta, GA, United States*

8:30AM **Lamina Cribrosa Disinsertions as a Mechanoprotective Strategy** SB³C2016-786

Andrew P. Voorhees[1], Ning-Jiun Jan[1, 2], John G. Flanagan[3], Jeremy M. Sivak[4], Ian A. Sigal[1, 2], *[1]Ophthalmology, University of Pittsburgh, Pittsburgh, PA, United States, [2]Bioengineering, University of Pittsburgh, Pittsburgh, PA, United States, [3]Optometry and Vision Science, University of California Berkeley, Berkeley, CA, United States, [4]Ophthalmology and Vision Sciences, University of Toronto, Toronto, ON, Canada*

8:45AM **Magnetic Resonance Elastography of White Matter Brain Tissue Ex Vivo** SB³C2016-687

John L. Schmidt[1], Dennis J. Tweten[1], Andrew A. Badachhape[2], Ruth J. Okamoto[1], Joel R. Garbow[3], Philip V. Bayly[1, 2], *[1]Mechanical Engineering and Materials Science, Washington University, St. Louis, MO, United States, [2]Biomedical Engineering, Washington University, St. Louis, MO, United States, [3]Radiology, Washington University, St. Louis, MO, United States*

9:00AM **Numerical Constraint for Tracking Tagged Magnetic Resonance Images in Biomechanical Simulations** SB³C2016-1002

Arnold David Gomez[1], Deva Chan[2], Yuan-Chiao Lu[2], Dzung Pham[2], Philip Bayly[3], Jerry Prince[1], *[1]Electrical and Computer Engineering Department, Johns Hopkins University, Baltimore, MD, United States, [2]Center for Neuroscience and Regenerative Medicine, Henry Jackson Foundation, Bethesda, MD, United States, [3]Mechanical Engineering Department, Washington University in St. Louis, St. Louis, MO, United States*

Copyright 2016 The Organizing Committee for the 2016 Summer Biomechanics, Bioengineering and Biotransport Conference

9:15AM **A Parameterized Ultrasound-Based Finite Element Analysis of the Mechanical Environment of Pregnancy** SB³C2016-927

Andrea R. Westervelt[1], Michael Fernandez[1], Joy Vink[2], Chia-Ling Nhan-Chang[2], Miaoying Fan[2], Ronald J. Wapner[2], Michael House[3], Kristin M. Myers[1], *[1]Mechanical Engineering, Columbia University, New York, NY, United States, [2]Obstetrics and Gynecology Division of Maternal Fetal Medicine, Columbia University, New York, NY, United States, [3]Obstetrics and Gynecology Division of Maternal Fetal Medicine, Tufts Medical Center, Boston, MA, United States*

THURSDAY, JUNE 30 | 8:00am - 9:30am

Imaging and Modeling Physiological Microflows; Lymphatics, CSF, and Eyes — Azalea 3

Session Chair: James Moore, *Imperial College London, London, United Kingdom*
Session Co-Chair: Ryan Pedrigi, *University of Nebraska, NE, United States*

8:00AM **Contractile Activity in Branched Lymphatic Vessels** SB³C2016-1000

Samira Jamalian[1], Michael J. Davis[2], James E. Moore[1], *[1]Bioengineering, Imperial College London, London, United Kingdom, [2]University of Missouri School of Medicine, Columbia, MO, United States*

8:15AM **Investigation of the Pressure-length Relationship along a Lymphatic Chain with Modeling and Experiments** SB³C2016-828

Mohammad S. Razavi[1], Tyler S. Nelson[1], Rudolph L. Gleason[1, 2], **J. Brandon Dixon**[1, 2], *[1]Mechanical Engineering, Georgia Institute of Technology, Atlanta, GA, United States, [2]Biomedical Engineering, Georgia Tech and Emory University, Atlanta, GA, United States*

8:30AM **Assessment of 4D Flow Accuracy for Quantification of Cerebrospinal Fluid Dynamics in the Cervical Spine: Comparison of in vitro Measurements and Numerical Simulation** SB³C2016-789

Soroush Heidari Pahlavian[1], Francis Loth[1], Suraj Thyagaraj[1], Alexander Bunck[2], Daniel Giese[2], Bryn Martin[3], *[1]Department of Mechanical Engineering, The University of Akron, Akron, OH, United States, [2]Department of Radiology, University Hospital of Cologne, Cologne, Germany, [3]Department of Biological Engineering, The University of Idaho, Moscow, ID, United States*

8:45AM **Quantifying Cerebrospinal Fluid Dynamics Using Real-Time Phase Contrast MRI** SB³C2016-51

Selda Yildiz[1], John Oshinski[2], Karim G. Sabra[1], *[1]Woodruff School of Mechanical Engineering, Georgia Institute of Technology, Atlanta, GA, United States, [2]Radiology & Imaging Sciences and Biomedical Engineering, Emory University, Atlanta, GA, United States*

9:00AM **Aqueous Humor Flow in the Posterior Chamber of the Eye with Iridotomy** SB³C2016-129

Mariia Dvoriashyna[1], Rodolfo Repetto[1], Jennifer H. Tweedy[2], *[1]Department of Civil, Chemical and Environmantal Engineering, University of Genoa, Genoa, Italy, [2]Department of Bioengineering, Imperial College London, London, United Kingdom*

9:15AM **Rheological Characterization of an Embryo Culture Liquid and Implications for Culture in Microfuidic Devices** SB³C2016-678

Irene Nepita[1], Alberto Lagazzo[1], Stefano Barone[2], Giovanni Besio[1], **Alessandro Stocchino**[1], Rodolfo Repetto[1], *[1]Department of Civil, Chemical and Environmental Engineering, University of Genoa, Genoa, Italy, [2]Centro Procreazione Assistita, Ospedale della Versilia, Lido di Camaiore, Italy*

THURSDAY, JUNE 30 | 9:45am - 11:15am

Cardiovascular Cell and Tissue Engineering — Wilson B

Session Chair: Alisa Morss Clyne, *Drexel University, PA, United States*
Session Co-Chair: Pat Alford, *University of Minnesota, MN, United States*

9:45AM **Cardiac Contractility and Global Tissue Organization** SB³C2016-841

Meghan Knight, Nancy Drew, Linda McCarthy, **Anna Grosberg**, *UCIrvine, Irvine, CA, United States*

Copyright 2016 The Organizing Committee for the 2016 Summer Biomechanics, Bioengineering and Biotransport Conference

10:00AM **Comparison of In Vitro Endothelial Wound Healing in Bare Metal vs. Drug-Eluting Stents** SB³C2016-89
Elizabeth Antoine, Abdul Barakat, *Mechanics, Ecole Polytechnique, Palaiseau, France*

10:15AM **Direction-dependent Collagen Disruption in Overstretched Cerebral Arteries** SB³C2016-734
Matthew I. Converse[1], Justin T. Ingram[2], Raymond G. Walther[1], Kenneth L. Monson[3], *[1]Mechanical Engineering, University of Utah, Salt Lake City, UT, United States, [2]Bioengineering, University of Utah, Salt Lake City, UT, United States, [3]Mechanical Engineering; Bioengineering, University of Utah, Salt Lake City, UT, United States*

10:30AM **Shear Stress Maintains Endocardial Phenotype in Induced Pluripotent Stem Cell Derived Endocardial Cells** SB³C2016-758
Mark Vander Roest, Camryn Johnson, Scott Baldwin, W. David Merryman, *Vanderbilt University, Nashville, TN, United States*

10:45AM **TGF-Beta 1 and Adipose-derived Mesenchymal Stem Cell Secreted Factors Aid in the Organization of Deposited Elastin Within 3D Fibroblast and Smooth Muscle Cell Constructs** SB³C2016-1022
Aneesh Ramaswamy, Justin Weinbaum, David Vorp, *Bioengineering, University of Pittsburgh, Pittsburgh, PA, United States*

11:00AM **Valve Interstitial Cell Contractile Strength and Metabolic State are Dependent on its Shape** SB³C2016-686
Ngoc Lam, Timothy Muldoon, Narasimhan Rajaram, **Kartik Balachandran**, *University of Arkansas, Fayetteville, AR, United States*

THURSDAY, JUNE 30	**9:45am - 11:15am**

Safety and Biocompatibility in Medical Device Design — Wilson C

Session Chair: Lucas H. Timmins, *Georgia Institute of Technology, GA, United States*
Session Co-Chair: Michael Moreno, *Texas A&M, TX, United States*

9:45AM **Bearing Surface Damage Analysis of Anatomical and Reverse Total Shoulder Replacements: Retrieval Analysis Across Fixation Designs and UHMWPE Compositions** SB³C2016-1131
Louis G. Malito[1], Noah Bonnheim[1], Lulu Li[1], Taylor Lee[1], Steven Gunther[2], Tom Norris[3], Mike Ries[4], Lisa Pruitt[1], *[1]Mechanical Engineering, University of California, Berkeley, Berkeley, CA, United States, [2]Orthopedic Surgery, Martha Jefferson Hospital, Charlottesville, VA, United States, [3]San Francisco Shoulder, Elbow & Hand Clinic, San Francisco, CA, United States, [4]Tahoe Fracture and Orthopaedic Clinic, Carson City, NV, United States*

10:00AM **Wear Testing of an Innovative Design for Hip Resurfacing** SB³C2016-568
John B. Everingham, Jillian L. Helms, Kevin J. Warburton, Jeff Brourman, Steven Fox, Trevor J. Lujan, *Mechanical and Biomedical Engineering, Boise State University, Boise, ID, United States*

10:15AM **Evaluation of Laser Bacterial Anti-Fouling of Transparent Nanocrystalline Yttria-Stabilized-Zirconia Cranial Implant** SB³C2016-976
David L. Halaney, Yasaman Damestani, Natalie De Howitt, Javier E. Garay, Guillermo Aguilar, *Mechanical Engineering, University of California, Riverside, Riverside, CA, United States*

10:30AM **Polydopamine Based Insulating Coating for Shape Memory Alloy Biomedical Devices** SB³C2016-589
Mohammad Sahlabadi, Yao Zhao, Harold H Lee, Fei Ren, **Parsaoran Hutapea**, *Temple University, Philadelphia, PA, United States*

10:45AM **Addressing Iatrogenic Injury due to Traumatic Urethral Catheterisation** SB³C2016-831
Eoghan M. Cunnane[1], Niall F. Francis[2], Connor V. Cunnane[1], Rory O'C Mooney[1], John A. Thornhill[2], Michael T. Walsh[1], *[1]Mechanical, Aeronautical and Biomedical Engineering, University of Limerick, Limerick, Ireland, [2]Department of Urology, Tallaght Hospital, Dublin, Ireland*

11:00AM **Investigating the In Vitro and In Vivo Biocompatibility of a Novel Biodegradable Fe-316L Stent** SB³C2016-147
Jennifer Frattolin[1, 2], Richard Leask[3], Stephen Yue[4], Olivier F. Bertrand[1, 5], Rosaire Mongrain[1, 2], *[1]Department of Mechanical Engineering, McGill University, Montreal, QC, Canada, [2]Montreal Heart Institute, Montreal, QC, Canada, [3]Department of Chemical Engineering, McGill University, Montreal, QC, Canada, [4]Department of Mining and Materials Engineering, McGill University, Montreal, QC, Canada, [5]Interventional Cardiology Laboratories, Quebec Heart and Lung Institute, Laval University, Quebec City, QC, Canada*

Copyright 2016 The Organizing Committee for the 2016 Summer Biomechanics, Bioengineering and Biotransport Conference

THURSDAY, JUNE 30	9:45am - 11:15am

Injury: Brain II — Wilson D

Session Chair: Brittany Coats, *University of Utah, UT, United States*
Session Co-Chair: JiangYue Zhang, *Johns Hopkins, MD, United States*

9:45AM **In Situ Estimation of Axonal Injury Strain Thresholds Following Tissue-level Tensile Stretch** SB^{3}C2016-955
Sagar Singh[1], Assimina A. Pelegri[2], David I. Shreiber[1], *[1]Biomedical Engineering, Rutgers, The State University of New Jersey, Piscataway, NJ, United States, [2]Mechanical and Aerospace Engineering, Rutgers, The State University of New Jersey, Piscataway, NJ, United States*

10:00AM **Simulated Blast-Induced Cavitation: An Invitro Study** SB^{3}C2016-996
Saranya Canchi, Yu Hong, Karen Kelly, Michael A. King, Ghatu Subhash, Malisa Sarntinoranont, *University of Florida, Gainesville, FL, United States*

10:15AM **Bandwidth Requirements for Wearable Head Impact Sensors** SB^{3}C2016-602
Lyndia C. Wu, Kaveh Laksari, Calvin Kuo, David B. Camarillo, *Bioengineering, Stanford University, Stanford, CA, United States*

10:30AM **In-Situ Head Acceleration Measurements for Playground Impacts Relative to Head Injury Metrics** SB^{3}C2016-747
Eric A. Kennedy, Greg P. Danchik, Chris D. DiDomenico, *Biomedical Engineering, Bucknell University, Lewisburg, PA, United States*

10:45AM **Development of Finite Element-Based Injury Metrics for Head Injury Prediction** SB^{3}C2016-866
Derek A. Jones, Jillian E. Urban, Ashley A. Weaver, Joel D. Stitzel, *Biomedical Engineering, Wake Forest University School of Medicine, Winston-Salem, NC, United States*

11:00AM **Sex Differences in the Dynamic Brain Response to a Mild Angular Head Acceleration** SB^{3}C2016-743
Deva Chan[1], Andrew Knutsen[2], Yuan-Chiao Lu[1], Sarah Yang[1], Philip Bayly[3], John Butman[4], Dzung Pham[1], *[1]Center for Neuroscience and Regenerative Medicine, Henry M Jackson Foundation, Bethesda, MD, United States, [2]Institute for Defense Analyses, Alexandria, VA, United States, [3]Mechanical Engineering and Materials Science, Washington University of St. Louis, St. Louis, MO, United States, [4]Radiology and Imaging Sciences, National Institutes of Health Clinical Center, Bethesda, MD, United States*

THURSDAY, JUNE 30	9:45am - 11:15am

Mechanics of Heart Valves — Annapolis 1

Session Chair: Michael Sacks, *The University of Texas at Austin, TX, United States*
Session Chair: Lik Chuan Lee, *Michigan State University, MI, United States*

9:45AM **Age-Dependent Differences in Mechanical Properties of Chemically Treated Bovine Pericardium** SB^{3}C2016-1115
Andres D. Caballero, Fatiesa Sulejmani, Wei Sun, *The Wallace H. Coulter Department of Biomedical Engineering, Georgia Institute of Technology and Emory University, Atlanta, GA, United States*

10:00AM **Effects of Sagging Versus Stretched Leaflets on Bioprosthetic Heart Valve Durability** SB^{3}C2016-620
Nandini Duraiswamy[1], Parinaz Fathi[2], Stephen M. Retta[1], Jason D. Weaver[1], *[1]Center for Devices and Radiological Health, Food and Drug Administration, Silver Spring, MD, United States, [2]Oak Ridge Institute for Science & Education, Oak Ridge, TN, United States*

10:15AM **Stress-Relaxation Behaviors of Diseased Heart Valve Tissues** SB^{3}C2016-1093
Kaitlyn Barbour[1], Siyao Huang[2], **HY Shadow Huang**[2], *[1]Biomedical Eng., NC State, Raleigh, NC, United States, [2]Mechanical and Aerospace Eng., NC State, Raleigh, NC, United States*

Copyright 2016 The Organizing Committee for the 2016 Summer Biomechanics, Bioengineering and Biotransport Conference

10:30AM **Stress Fiber Contractile Behavior in Aortic Valve Interstitial Cells** SB³C2016-818
Yusuke Sakamoto[1], Rachel M. Buchanan[2], Johannah S. Adams[3], Farshid Guilak[4], Michael S. Sacks[1, 2], *[1]The Institute for Computational Engineering and Sciences, The University of Texas at Austin, Austin, TX, United States, [2]Department of Biomedical Engineering, The University of Texas at Austin, Austin, TX, United States, [3]Departments of Orthopaedic Surgery and Biomedical Engineering, Duke University, Durham, NC, United States, [4]Departments of Orthopaedic Surgery, Biomedical Engineering, and Developmental Biology, Washington University, St. Louis, St. Louis, MO, United States*

10:45AM **Design of a Novel In Vitro Simulation of a Dynamically Contracting Mitral Valve Annulus** SB³C2016-702
Thomas F. Easley, Charlie H. Bloodworth, Ajit P. Yoganathan, *Georgia Institute of Technology, Atlanta, GA, United States*

11:00AM **Novel Irreversible Chemistry Produces Structurally More Stable Tissue Based Biomaterials** SB³C2016-1049
Hobey Tam[1], Will Zhang[2], Daniel Infante[1], Nathaniel Parchment[1], Michael Sacks[2], Narendra Vyavahare[1], *[1]Bioengineering, Clemson University, Clemson, SC, United States, [2]Biomedical Engineering, University of Texas, Austin, Austin, TX, United States*

THURSDAY, JUNE 30 | 9:45am - 11:15pm

Cerebral Aneurysm — Annapolis 2

Session Chair: Kristian Valen-Sendstad, *Simula Research Laboratory, Lysaker, Norway*
Session Co-Chair: David Steinman, *University of Toronto, ON, Canada*

9:45AM **A Simple and Rational Approach to Outflow Conditions in Cerebrovascular CFD Models.** SB³C2016-1026
Christophe Chnafa[1], Kristian Valen-Sendstad[2], Olivier Brina[3], Vitor Mendes Pereira[4], David Steinman[1], *[1]Mechanical & Industrial Engineering, University of Toronto, Toronto, ON, Canada, [2]Simula Research Laboratory, Centre for Biomedical Computing, Lysaker, Norway, [3]Department of Medical Imaging, Toronto Western Hospital, Toronto, ON, Canada, [4]Toronto Western Hospital, Toronto, ON, Canada*

10:00AM **Non-newtonian versus Numerical Rheology: Practical Impact of Shear-thinning on the Prediction of Stable and Unstable Flows in Intracranial Aneurysms** SB³C2016-579
Owais Khan[1], David A. Steinman[1], Kristian Valen-Sendstad[2], *[1]Mechanical and Industrial Engineering, University of Toronto, Toronto, ON, Canada, [2]Simula Research Laboratory, Kristian Valen-Sendstad, Lysaker, Norway*

10:15AM **Numerical Modeling of Post-surgical Flow in Basilar Artery Aneurysms** SB³C2016-609
Alireza Vali[1], Michael Lawton[2], David Saloner[3], Vitaliy Rayz[1], *[1]Neurosurgery, Medical College of Wisconsin, Milwaukee, WI, United States, [2]Neurological Surgery, University of California San Francisco, San Francisco, CA, United States, [3]Radiology and Biomedical Imaging, University of California San Francisco, San Francisco, CA, United States*

10:30AM **Comparison of Flow Conditions in Aneurysms at the Basilar Tip and Internal Carotid Artery Terminus** SB³C2016-110
Ravi Doddasomayajula[1], BongJae Chung[1], Farid Hamzei-Sichani[2], Christopher Putman[3], Juan Cebral[1], *[1]George Mason University, Fairfax, VA, United States, [2]Mt. Sinai Hospital, New York, NY, United States, [3]Inova Fairfax Hospital, Falls Church, VA, United States*

10:45AM **Hemodynamics in Developing Stages of Cerebral Aneurysms Using Spectral-Element Simulations and Comparison with PIV Experiments** SB³C2016-1008
Tanvi K. Kaushik[1], Yulia T. Peet[1], Priya Nair[2], David H. Frakes[2], *[1]School for Engineering of Matter, Transport and Energy, Arizona State University, Tempe, AZ, United States, [2]School of Biological and Health Systems Engineering, Arizona State University, Tempe, AZ, United States*

11:00AM **Aneurysmal Flow Modifications by Coils and Flow Diverters and Long-Term Treatment Outcome** SB³C2016-1081
Robert J. Damiano[1], Nicole Varble[1], Rahul Sanal[1], Jason M. Davies[2], Adnan H. Siddiqui[2], Hui Meng[1], *[1]Mechanical and Aerospace Engineering, University at Buffalo, Buffalo, NY, United States, [2]Neurosurgery, University at Buffalo, Buffalo, NY, United States*

Copyright 2016 The Organizing Committee for the 2016 Summer Biomechanics, Bioengineering and Biotransport Conference

THURSDAY, JUNE 30	9:45am - 11:15am

Musculoskeletal Soft Tissue: Disc — Azalea 2

Session Chair: Amy Claeson, *University of Delaware, DE, United States*
Session Co-Chair: Grace D. O'Connell, *University of California, Berkeley, CA, United States*

9:45AM **Failure Properties of Annulus Fibrosus** SB³C2016-983
Noah Bonnheim, Benjamin Werbner, Grace O'Connell, *Mechanical Engineering, University of California, Berkeley, Berkeley, CA, United States*

10:00AM **A Probabilistic Finite Element Analysis of the Annulus Fibrosus Elastic Properties Influence on the Behavior of the Human L4-L5 and L5-S1 Segments** SB³C2016-127
Héctor E. Jaramillo[1], José J. García[2], *[1]Departamento de Energética y Mecánica, Universidad Autonoma De Occidente, Cali, Colombia, [2]Escuela de Ingeniería Civil y Geomática, Universidad Del Valle, Cali, Colombia*

10:15AM **A High Throughput Nucleus Pulposus Explant Culture System Preserves Tissue Integrity** SB³C2016-962
Timothy Jacobsen, Nadeen Chahine, *The Feinstein Institute for Medical Reseaerch, Manhasset, NY, United States*

10:30AM **Validation of a High Throughput Hydrostatic Pressure Bioreactor on the Nucleus Pulposus Biosynthesis** SB³C2016-1078
Bhranti Shah, Farzana Chowdhury, Nadeen Chahine, *Feinstein Institute for Medical Research, Manahasset, NY, United States*

10:45AM **Nucleotomy Alters Internal Strain Distribution of the Human Lumbar Intervertebral Disc** SB³C2016-1082
Amy A. Claeson[1], Brent L. Showalter[2], Edward J. Vresilovic[3], Alexander C. Wright[4], James C. Gee[4], Neil R. Malhotra[4], Dawn M. Elliott[1], *[1]Department of Biomedical Engineering, University of Delaware, Newark, DE, United States, [2]Department of Bioengineering, University of Pennsylvania, Philadelphia, PA, United States, [3]Department of Orthopaedics and Rehabilitation, Pennsylvania State University, Hershey, PA, United States, [4]Department of Radiology, University of Pennsylvania, Philadelphia, PA, United States*

11:00AM **Potential Involvement of Endplate Purinergic Signaling in Low Back Pain** SB³C2016-1117
Mary Boggs, John DeLucca, Dawn Elliot, Randall Duncan, *University of Delaware, Newark, DE, United States*

THURSDAY, JUNE 30	9:45am - 11:15am

Cryopreservation and Cryotherapy — Azalea 3

Session Chair: Nilay Chakraborty, *University of Michigan Dearborn, MI, United States*
Session Co-Chair: Sepideh Khoshnevis, *University of Texas at Austin, TX, United States*

9:45AM **Nanowarming of Arteris** SB³C2016-1089
Navid Manuchehrabadi, *University of Minnesota, Minneapolis, MN, United States*

10:00AM **Physiological Basis for Rational Cryotherapy Protocol Design** SB³C2016-737
Sepideh Khoshnevis[1], Robert M. Brothers[2], Kenneth R. Diller[1], *[1]University of Texas at Austin, Austin, TX, United States, [2]University of Texas at Arlington, Arlington, TX, United States*

10:15AM **Alginate Hydrogel Microencapsulation Inhibits Devitrification and Enables Large-volume Low-cpa Cell Vitrification** SB³C2016-582
Haishui Huang, *The Ohio State University, Columbus, OH, United States*

10:30AM **Development of an Isothermal Vitrification Matrix and Method for the Room Temperature Stabilization of Proteinaceous Cancer Biomarkers in Archival Human Sera** SB³C2016-839
Morwena J. Solivio, Goeun Heo, Alptekin Aksan, *Mechanical Engineering, University of Minnesota, Minneapolis, MN, United States*

10:45AM **Dynamic Vapor Sorption in Trehalose/salt Mixtures: Effect of Composition on Retention of the Amorphous State** SB³C2016-168
Gloria Elliott, Babak Bagheri, Lindong Weng, Matthew Van Vorst, *Department of Mechanical Engineering, UNC Charlotte, Charlotte, NC, United States*

Copyright 2016 The Organizing Committee for the 2016 Summer Biomechanics, Bioengineering and Biotransport Conference

11:00AM **A Raman Microspectroscopic Technique to Quantify Residual Water in Desiccated Samples** SB³C2016-876
Quinn Osgood, Jason Solocinski, **Nilay Chakraborty**, *Mechanical Engineering Department, University of Michigan Dearborn, Dearborn, MI, United States*

THURSDAY, JUNE 30 | 1:00pm - 3:15pm

Poster Session I — Biotransport Diagnostics and Therapeutics — Exhibit Hall A

1 **Probing the Interactions Between Mannobiose Molecules, Using Atomic Force Microscopy (afm).** SB³C2016-989
Komitige H. Perera, Saswati Basu, Preethii Chandran, *Biochemistry and Molecular Biology, Howard University, Washington, DC, United States*

2 **Increased Capture of Magnetic Microbeads Due to Switching of Electroosmotic Flow** SB³C2016-1067
Samuel A. Miller[1], William R. Heineman[2], Rupak K. Banerjee[1], *[1]Department of Mechanical and Materials Engineering, University of Cincinnati, Cincinnati, OH, United States, [2]Department of Chemistry, University of Cincinnati, Cincinnati, OH, United States*

3 **Evaluation of Sensitivity and Accuracy of Infrared Thermography for Melanoma Screening** SB³C2016-145
Yiyong Li[1], Alexander M. LeBrun[2], L. D. Timmie Topoleski[2], **Liang Zhu**[2], *[1]Mechanical Engineering, Beijing University of Aeronautics & Astronautics, Beijing, China, [2]Mechanical Engineering, University of Maryland Baltimore County, Baltimore, MD, United States*

4 **Validation of Image-assisted Modeling Approach to Design Heating Protocols in Magnetic Nanoparticle Hyperthermia** SB³C2016-24
Alexander M. LeBrun[1], Tejashree Joglekar[2], Charles Bieberich[2], Ronghui Ma[1], **Liang Zhu**[1], *[1]Mechanical Engineering, University of Maryland Baltimore County, Baltimore, MD, United States, [2]Biology, University of Maryland Baltimore County, Baltimore, MD, United States*

5 **Development and Characterization of Protein Nanoparticles Derived from Lung Extracellular Matrix** SB³C2016-682
Patrick A. Link[1], Sirish K. Desai[2], Nan Zhou[3], Da-Ren Chen[3], **Rebecca L. Heise**[1], *[1]Biomedical Engineering, VCU, Richmond, VA, United States, [2]J.R. Tucker High School, Richmond, VA, United States, [3]Mechanical and Nuclear Engineering, VCU, Richmond, VA, United States*

6 **Stiffness-Independent on-Chip Extraction of Cell-Laden Hydrogel Microcapsules from Oil Emulsion Into Aqueous Solution Based on Dielectrophoresis** SB³C2016-721
Mingrui Sun[1], Haishui Huang[2], Xiaoming He[1], *[1]Biomedical Engineering, The Ohio State University, Columbus, OH, United States, [2]Mechanical Engineering, The Ohio State University, Columbus, OH, United States*

7 **Point-of-Care Diagnosis by Nanoparticle Aggregation: Tuning the Sensitivity by Nanoparticle Size and Concentration** SB³C2016-1114
Peiyuan Kang, **Zhenpeng Qin**, *Mechanical Engineering, University of Texas at Dallas, Richardson, TX, United States*

THURSDAY, JUNE 30 | 1:00pm - 3:15pm

Poster Session I — Cancer and Tumor Microenvironments — Exhibit Hall A

8 **In vitro Testing of Hydrogel Delivery for Potential Treatment for Pancreatic Cancer Lesions** SB³C2016-1125
Thomas L. Merrill, *rowan university, Glassboro, NJ, United States*

9 **Effect on Oligosaccharide Grafting on the Polyelectrolyte and Protonation Dynamics of Polyethylenimine** SB³C2016-1018
Saswati Basu, Danielle N. Miller, Stacy N. Apugo, Preethi L. Chandran, *Chemical Engineering, Howard University, Washington, DC, United States*

10 **Enhanced Microwave Hyperthermia of Cancer Cells with Fullerene** SB³C2016-724
Mingrui Sun, Xiaoming He, *Biomedical Engineering, The Ohio State University, Columbus, OH, United States*

Copyright 2016 The Organizing Committee for the 2016 Summer Biomechanics, Bioengineering and Biotransport Conference

11 **Isolation of Rare Tumor Cells Using Adhesion Rolling in a Microfluidic Chip with Inclined Wavy Surfaces** SB³C2016-749
Shunqiang Wang[1], Roy Ghosh[1], Ran He[1], Jie Yang[2], Yaling Liu[1, 3], *[1]Department of Mechanical Engineering & Mechanics, Lehigh University, Bethlehem, PA, United States, [2]School of Mechanics and Engineering, Southwest Jiaotong University, Chengdu, China, [3]Bioengineering Department, Lehigh University, Bethlehem, PA, United States*

12 **Analyzing Effects of Chemotherapeutic Drugs for the Prevention of Chemotherapy-Induced Alopecia** SB³C2016-1060
Likitha Somasekhar, Kunal Mitra, Carlos Martino, *Biomedical Engineering, Florida Institute of Technology, melbourne, FL, United States*

13 **Relationship Between Mechanical Stiffness and Multiple Cancer Cell Proliferation and Morphology in 3D Encapsulated Gelatin Methacrylate Hydrogels** SB³C2016-605
Sean Hennigan[1], Susan A. Pomilla[2], Melissa A. DePrato[1], John R. Beliveau[1], **Jason W. Nichol**[2], *[1]Biology and Biotechnology, Endicott College, Beverly, MA, United States, [2]Bioengineering, Endicott College, Beverly, MA, United States*

14 **A 3D Model of Breast Tumor- Endothelial Cell Interactions** SB³C2016-792
Swathi Swaminathan[1], Olivia Ngo[2], Alisa Morss Clyne[3], *[1]Mechanical Engineering and Mechanics, Drexel University, Philadelphia, PA, United States, [2]Biomedical Engineering, Science and Health Systems, Drexel University, Philadelphia, PA, United States, [3]Mechanical Engineering and Mechanics/ Biomedical Engineering, Science and Health Systems, Drexel University, Philadelphia, PA, United States*

THURSDAY, JUNE 30 | 1:00pm - 3:15pm

Poster Session I — Bachelors Level Student Paper Competition I: Physiology & Diseases - Cellular & Tissue Mechanics - Biomaterial & Material Characterization — Exhibit Hall A

34 **Off-axis Biaxial Analysis of Synthetic Scaffolds for Hernia Repair** SB³C2016-587
Savannah Est[1, 2], Maddie Roen[1], Vivian Chi[2], Adrian Simien[2], Ryan Castile[1], Dominic Thompson[2], Corey R. Deeken[3], Spencer P. Lake[1], *[1]Department of Mechanical Engineering & Materials Science, Washington University in St. Louis, St. Louis, MO, United States, [2]Department of Surgery, Section Minimally Invasive Surgery, Washington University School of Medicine, St. Louis, MO, United States, [3]Covalent Bio, LLC, St. Louis, MO, United States*

35 **The Characterization of the Bone Marrow Mechanical Environment Using Poroelastic Models with Material Properties Determined From Micro-finite Element Modeling** SB³C2016-1057
Jason A. Shar[1], Thomas A. Metzger[2], Tyler Kreipke[2], Glen Neibur[2], Joshua Gargac[1], *[1]Engineering, University of Mount Union, Alliance, OH, United States, [2]AME, University of Notre Dame, Notre Dame, IN, United States*

36 **Anterolateral Capsule of the Knee Functions as a Sheet of Tissue based on Tissue Strain** SB³C2016-96
Stephanie L. Sexton[1], Daniel Guenther[2], Kevin Bell[1], Sebastian Irarrazaval[1], Ata Rahnemai-Azar[1], Freddie Fu[1], Volker Musahl[1], Richard Debski[1], *[1]University of Pittsburgh, Pittsburgh, PA, United States, [2]Hannover Medical School, Hannover, Germany*

37 **Methodology to Reduce Dimensional Variability in Tensile Testing of Soft Fibrous Tissue** SB³C2016-604
Madison E. Krentz, Jaremy J. Creechley, Trevor J. Lujan, *Mechanical and Biomedical Engineering, Boise State University, Boise, ID, United States*

38 **Ultrasound Measurement of Shape Change During In Vitro Inflation of an Arterial Bifurcation** SB³C2016-864
John P. Carruth, Ryan R. Mahutga, Christopher E. Korenczuk, Victor H. Barocas, *Biomedical Engineering, University of Minnesota - Twin Cities, Saint Paul, MN, United States*

39 **Three-Element Windkessel Model to Describe Pulmonary Vasculature Changes in Hypertensive Rat** SB³C2016-1031
Jesse W. Gerringer, Daniela Vélez-Rendon, Daniela Valdez-Jasso, *Bioengineering, University of Illinois at Chicago, Chicago, IL, United States*

Copyright 2016 The Organizing Committee for the 2016 Summer Biomechanics, Bioengineering and Biotransport Conference

40 **Analysis of the Effect of Saliva on the Degradation of Absorbable Sutures** SB³C2016-1075
Luke E. Riexinger[1], Jenna W. Briddell[2], Donna M. Ebenstein[1], *[1]Biomedical Engineering, Bucknell University, Lewisburg, PA, United States, [2]Otolaryngology, Geisinger Medical Center, Danville, PA, United States*

41 **Viscoelastic Properties of Human Patellar Tendons Measured Using Continuous Shear Wave Elastography** SB³C2016-606
Courtney T. Cox[1], Jennifer A. Zellers[1], Karin G. Silbernagel[1], Daniel H. Cortes[2], *[1]University of Delaware, Newark, DE, United States, [2]Penn State University, University Park, PA, United States*

42 **Determining Impedance in Pulmonary Vessels Using Four-Element Windkessel Models** SB³C2016-1133
Julie C. Wagner, Jesse W. Gerringer, Daniela Valdez-Jasso, *Bioengineering, University of Illinois - Chicago, Chicago, IL, United States*

43 **The Influence of Gel Stiffness on Growth Factor Gene Expression of Schwann Cells** SB³C2016-808
Carlisle R. DeJulius, Rebecca Kuntz Willits, *Department of Biomedical Engineering, The University of Akron, Akron, OH, United States*

THURSDAY, JUNE 30	**1:00pm - 3:15pm**

Poster Session I — Bachelors Level Student Paper Competition II: Imaging - Devices - Human Dynamics & Injury - Fluids & Microfluidics - Heat Transfer — Exhibit Hall A

44 **DTI Voxel-Wise Analysis of Mild TBI in Neonatal Pigs Following Non-Impact Head Rotation.** SB³C2016-941
Boston C. Terry[1], Gregory G. Scott[2], Osama Abdullah[1], Brittany Coats[2], *[1]Biomedical Engineering, University of Utah, Salt Lake City, UT, United States, [2]Mechanical Engineering, University of Utah, Salt Lake City, UT, United States*

45 **Characterizing a Novel Ex-Vivo Animal Knee Model: ACL Rupture and Meniscus Compressive Strength** SB³C2016-585
Nicole L. Zaino, Mark J. Hedgeland, Laurel Kuxhaus, Arthur J. Michalek, *Mechanical & Aeronautical Engineering, Clarkson University, Potsdam, NY, United States*

46 **Characterization of Particulate and Vapor Phase Nicotine in Electronic Cigarettes** SB³C2016-106
Mark C. Daley[1], James W. Baish[1], Dabrina D. Dutcher[2], Timothy M. Raymond[2], *[1]Biomedical Engineering, Bucknell Unviersity, Lewisburg, PA, United States, [2]Chemical Engineering, Bucknell Unviersity, Lewisburg, PA, United States*

47 **A Novel Imaging Technique to Quantify Surface Wear in Joint Replacement Devices** SB³C2016-583
Katherine Hollar[1], John Everingham[1], Jillian Helms[1], Daniel Ferguson[2], Trevor Lujan[1], *[1]Boise State University, Boise, ID, United States, [2]Global Inspection Solutions, Boise, ID, United States*

48 **Additive Manufacturing of Localized Microneedle Drug-Delivery System** SB³C2016-985
Sofia Chinchilla[1], Yangfeng Lu[1], Corey J. Schurko[1], Douglas C. Crowder[1], Bum-Joon Park[2], Jae-Won Choi[3], Yang H. Yun[1], *[1]Biomedical Engineering, University of Akron, Akron, OH, United States, [2]Molecular Biology, Pusan National University, Busan, Korea, Republic of, [3]Mechanical Engineering, University of Akron, Akron, OH, United States*

49 **Structural Interactions of the Vessel Wall and Stent Graft in Abdominal Aortic Aneurysm Treatment** SB³C2016-711
Ryan J. Pewowaruk, Victor H. Barocas, *Biomedical Engineering, University of Minnesota - Twin Cities, Minneapolis, MN, United States*

50 **A Flexible Method for Producing F.E.M. Analysis of Bone Using Open-Source Software** SB³C2016-967
Abhishektha Boppana[1], Ryan Sefcik[2], Jerry G. Myers[3], *[1]Biomedical Engineering, Case Western Reserve University, Cleveland, OH, United States, [2]Biochemistry, The Ohio State University, Columbus, OH, United States, [3]NASA Glenn Research Center, Cleveland, OH, United States*

51 **Investigation of Superposition in Microchannel Geometry for Inertial Particle Separation** SB³C2016-969
Utku M. Sonmez, Samir Jaber, Levent Trabzon, *Mechanical Engineering, Istanbul Technical University, İstanbul, Turkey*

Copyright 2016 The Organizing Committee for the 2016 Summer Biomechanics, Bioengineering and Biotransport Conference

52 **A Fluid Dynamics Analysis of the Manifestation of Ebstein's Anomaly in the Right Ventricle** SB³C2016-1140
Alyssa L. Niquette[1], Shelly Lo[1], Adam Shore[2], Vittoria Flamini[1], Puneet Bhatla[3], *[1]NYU Tandon School of Engineering, Brooklyn, NY, United States, [2]NYU Langone Medical Center, New York, NY, United States, [3]NYU Langone Medical Center, Brooklyn, NY, United States*

53 **Internal-External Rotation Axis Locates Laterally Outside of Stifle Joints in the Dog** SB³C2016-1017
Tetsuya Takagi[1], Nobuo Kanno[2], Masakazu Shimada[2], Yasushi Hara[2], Satoshi Yamakawa[1], Richard E. Debski[3], Glen A. Livesay[4], Hiromichi Fujie[1], *[1]Faculty of System Design, Tokyo Metropolitan University, Tokyo, Japan, [2]Division of Veterinary Surgery Department of Veterinary Science Faculty of Veterinary Medicine, Nippon Veterinary and Life Science University, Tokyo, Japan, [3]Bioengineering department Faculty of Engineering, University of Pittsburgh, Pittsburgh, PA, United States, [4]Department of Biology & Biomedical Engineering, Rose-Hulman Institute of Technology, Terre Haute, IN, United States*

THURSDAY, JUNE 30 | 1:00pm - 3:15pm

Poster Session I — Mechanotransduction and Sub-Cellular Biophysics — Exhibit Hall A

54 **Effect of Compaction on Stretch Sensitivity in Fibroblast-Populated Collagen Gels** SB³C2016-837
Kellen Chen, Jeffrey W. Holmes, *University of Virginia, Charlottesville, VA, United States*

55 **Role of P2r-er Ca2+ Signaling in Ca2+ Oscillations of In Situ Osteocytes in Response to Medium Intensity Focused Ultrasound** SB³C2016-1120
Minyi Hu, Jian Jiao, Daniel Gibbons, Yi-Xian Qin, *Stony Brook University, Stony Brook, NY, United States*

56 **Mechanical Trauma in Articular Cartilage Induces Rapid, Location-Dependent Chondrocyte Dysfunction** SB³C2016-819
Lena R. Bartell[1], Michelle M. Delco[2], Lawrence J. Bonassar[3], Itai Cohen[4], Lisa A. Fortier[2], *[1]School of Applied and Engineering Physics, Cornell University, Ithaca, NY, United States, [2]Department of Clinical Sciences, Cornell University, Ithaca, NY, United States, [3]Meinig School of Biomedical Engineering and Sibley School of Mechanical and Aerospace Engineering, Cornell University, Ithaca, NY, United States, [4]Department of Physics, Cornell University, Ithaca, NY, United States*

57 **A Study for the Effects of the Mechanical Trapping of the Nucleus on Cellular Events Using a Micropillar Substrate** SB³C2016-569
Kazuaki Nagayama, *Department of Intelligent Systems Engineering, Ibaraki University, Hitachi, Japan*

58 **A Cell Migration Model Integrating the Mechanical Stress Generation and Sensing with Biochemical Signals** SB³C2016-639
hongyan yuan[1], Kevin K. Parker[2], *[1]University of Rhode Island, kingston, RI, United States, [2]Harvard University, Cambridge, MA, United States*

59 **Disturbed Cyclical Stretch of Endothelial Cells Promotes Nuclear Expression of the Pro-Atherogenic Transcription Factor NF-kB** SB³C2016-677
Ryan M. Pedrigi, Konstantinos I. Papadimitriou, Avinash Kondiboyina, Sukhjinder Sidhu, James Chau, Emmanuel M. Drakakis, Rob Krams, *Bioengineering, Imperial College London, London, United Kingdom*

60 **ElectroMechanical Coupling Behavior of Endothelial Cells** SB³C2016-1077
Khashayar Teimoori[1], Richard Khalily[2], Ali M. Sadegh[3], Marom Bikson[2], *[1]Mechanical Engineering Department, The City College of the City University of New York, New York, NY, United States, [2]Biomedical Engineering Department, The City College of the City University of New York, New York, NY, United States, [3]Mechanical Engineering, The City College of the City University of New York, New York, NY, United States*

61 **Thermodynamic Fluctuations Determine the Kinetics of Swell-burst Cycles of Giant Unilamellar Vesicles Under Osmotic Stress** SB³C2016-1118
Morgan Chabanon[1], James Ho[2], Atul Parikh[3], **Padmini Rangamani**[1], *[1]UCSD, La Jolla, CA, United States, [2]NTU, Singapore, Singapore, [3]UC Davis, Davis, CA, United States*

Copyright 2016 The Organizing Committee for the 2016 Summer Biomechanics, Bioengineering and Biotransport Conference

62 **The Effect of Loading Frequency on Tenocyte Metabolism** SB³C2016-595
Chineye P. Udeze[1], Eleanor R. Jones[2], Graham P. Riley[2], Dylan Morrissey[3, 4], Hazel R. C. Screen[1], *[1]School of Engineering and Material Science, Queen Mary University of London, Mile End, United Kingdom, [2]University of East Anglia, Norwich, United Kingdom, [3]Sport and Exercise Medicine, Queen Mary University of London, London, United Kingdom, [4]Physiotherapy Department, Bart's Health NHS Trust, London, United Kingdom*

63 **Mild Traumatic Brain Injury Resulted in Increased Aquaporin-4 Expression - Relevance to Post-Injury Edema** SB³C2016-670
Nasya Sturdivant[1], Sean Smith[1], Syed Ali[2], Jeff Wolchok[1], Kartik Balachandran[1], *[1]University of Arkansas, Fayetteville, AR, United States, [2]National Center for Toxicological Research, Jefferson, AR, United States*

THURSDAY, JUNE 30 | 1:00pm - 3:15pm

Poster Session I — Nano, Micro, and Multi-Scale Mechanics — Exhibit Hall A

64 **A Mechanostatistical Model for the Rapid Assessment of Femoral Neck Cortical Fracture Risk** SB³C2016-164
Xiaoming Wang[1], Raj Das[2], Peter Hunter[1], Justin Fernandez[1, 3], *[1]Auckland Bioengineering Institute, The University of Auckland, Auckland, New Zealand, [2]Department of Mechanical Engineering, The University of Auckland, Auckland, New Zealand, [3]Department of Engineering Science, The University of Auckland, Auckland, New Zealand*

65 **ElectroMechanical Coupling Behavior of Axon Microtubules** SB³C2016-720
Khashayar Teimoori[1], Ali M. Sadegh[1], Marom Bikson[2], *[1]Mechanical Engineering Department, The City College of the City University of New York, New York, NY, United States, [2]Biomedical Engineering Department, The City College of the City University of New York, New York, NY, United States*

66 **On Mechanics and Structure of 3D Randomly Cross-linked Fibrous Networks** SB³C2016-779
Hamed Hatami-Marbini, *Mechanical & Industrial Engineering, University of Illinois at Chicago, Chicago, IL, United States*

67 **Detailed Finite Element Modeling of Fiber-reinforced Tissues** SB³C2016-755
Bo Yang, Minhao Zhou, Grace D. O'Connell, *Mechanical Engineering, University of California, Berkeley, CA, United States*

68 **Micro-Structurally Motivated Constitutive Model for Human Skin** SB³C2016-52
Sheng Chen[1], A. Ni Annaidh[2], Sara Roccabianca[1], *[1]Mechanical Engineering, MIchigan State University, East Lansing, MI, United States, [2]School of Mechanical & Materials Engineering, University College Dublin, Dublin, Ireland*

69 **Computational Modeling of the Arterial Wall Based on Layer-specific Histological Data** SB³C2016-58
Tao Jin, Ilinca Stanciulescu, *Civil and Environmental Engineering, Rice University, Houston, TX, United States*

70 **Implications of Desiccation Induced Microheterogeneity on Protein Stability** SB³C2016-577
Sampreeti Jena[1], Raj Suryanarayanan[2], Alptekin Aksan[1], *[1]Mechanical Engineering, University of Minnesota, Minneapolis, MN, United States, [2]Department of Pharmaceutics, University of Minnesota, Minneapolis, MN, United States*

71 **Multidomain Particle Dynamics Simulator Engine** SB³C2016-155
Vi Q. Ha, *Mechanical Engineering, Univesity of Connecticut, storrs, CT, United States*

72 **FiberFit: A Validated Software Application to Measure Fiber Organization in Soft Tissue** SB³C2016-863
Azamat Tulepbergenov, **Erica Morrill**, Christina Stender, Roshani Lamichhane, Raquel Brown, Trevor Lujan, *Boise State University, Boise, ID, United States*

73 **Nonlinear Bending Dynamics of a Semiflexible Filament in 3D Brownian Fluctuation** SB³C2016-958
Jyothirmai J. Simhadri, Preethi Chandran, *Chemical Engineering, Howard University, Washington, DC, United States*

74 **Strain Determination in the Osteocyte Lacunae Using Finite Element Analysis** SB³C2016-797
Ganesh Thiagarajan, *Civil and Mechanical Engineering, University of Missouri Kansas City, Kansas City, MO, United States*

Copyright 2016 The Organizing Committee for the 2016 Summer Biomechanics, Bioengineering and Biotransport Conference

THURSDAY, JUNE 30	1:00pm - 3:15pm

Poster Session I — Medical Devices — Exhibit Hall A

95 **Using An Electroactive Polymer, Dielectric Elastomer, for Making Implantable Blood Pump** SB³C2016-49
Sheldon Ho, Yoke Yin Foo, Hareesh Gobada, Phan Thien Nhan, Jian Zhu, Choon Hwai Yap, *NUS, Singapore, Singapore*

96 **A Novel Self-expandable Retractor for Neuroendoscopy.** SB³C2016-719
Yang Xia[1], Zhong You[1], Puneet Plaha[2], Jingxian Yang[3], *[1]Engineering Science, University of Oxford, OXFORD, United Kingdom, [2]Department of Neurosurgery, John Radcliffe Hospital, OXFORD, United Kingdom, [3]Department of Pharmacy, Liaoning University of Traditional Medicine, Dalian, China*

97 **Fold-and-Go Single Knee Scooter** SB³C2016-830
Kevin Mozurkewich, Nicholas Colarossi, Muntha Issa, *Lawrence Technological University, Livonia, MI, United States*

98 **Customizable Surface-Coating Method for Bioprosthetic Valve Biocompatibility** SB³C2016-870
Monica M. Fahrenholtz, K. Jane Grande-Allen, *Bioengineering, Rice University, Houston, TX, United States*

99 **Design Optimization of a Hyaluronan-based Drug-delivery Device to Improve Ocular Retention** SB³C2016-879
Jourdan Colter[1], Nathaniel Cady[2], Hee-Kyoung Lee[3], Brenda Mann[3], Barbara Wirostko[3], Brittany Coats[1], *[1]Mechanical Engineering, University of Utah, Salt Lake City, UT, United States, [2]Colleges of Nanoscale Science and Engineering, SUNY Polytechnic Institute, Albany, NY, United States, [3]Jade Therapeutics Inc., Salt Lake City, UT, United States*

100 **Hemodynamic Effects of Asynchronous Pumping of the Penn State Pulsatile Pneumatic Pediatric VAD** SB³C2016-889
Bryan Good, Keefe Manning, *Bioengineering, The Pennsylvania State University, University Park, PA, United States*

101 **Performance Evaluation of a Developed Acoustic Impedance Device in Tumor Screening** SB³C2016-890
Ali Mohammadabadi[1], Qimei Gu[1], Alexander LeBrun[1], Mohamed Younis[2], Liang Zhu[1], *[1]Mechanical Engineering, University of Maryland Baltimore County, Baltimore, MD, United States, [2]Computer Science and Electrical Engineering, University of Maryland Baltimore County, Baltimore, MD, United States*

102 **The Effect of Simulated Anatomical Constraints on Buckling Loads of Cardiac Leads** SB³C2016-906
Donna Walsh[1], Ashok Williams[1], Nandini Duraiswamy[1], Oleg Vesnovsky[1], L.D. Timmie Topoleski[1, 2], *[1]Food and Drug Administration, Silver Spring, MD, United States, [2]Department of Mechanical Engineering, University of Maryland, Baltimore County, Baltimore, MD, United States*

103 **Clot Integration Factor for In Vitro Quantification of Stent-Retriever Deployment using Cone-Beam Computed Tomography** SB³C2016-929
Kajo van der Marel[1], Olivia W. Brooks[1], Robert M. King[1], Ju-Yu Chueh[1], Miklos Marosfoi[1], Erin T. Langan[1], Sarena L. Carniato[2], Raul G. Nogueira[3], Ajay K. Wakhloo[1], Matthew J. Gounis[1], Ajit S. Puri[1], *[1]Department of Radiology, University of Massachusetts Medical School, Worcester, MA, United States, [2]PreClinical Science, Stryker Neurovascular, Fremont, CA, United States, [3]Department of Neurology, Emory University School of Medicine, Atlanta, GA, United States*

104 **Design of a Cardiovascular Flow Mimicking Pump** SB³C2016-1009
Chris F. Brake, **Clifton R. Johnston**, *Mechanical Engineering, Dalhousie University, Halifax, NS, Canada*

105 **Simulation of Centrifugal Pump Thrombosis In Vitro** SB³C2016-1024
Susan Hastings[1], Shriprasad Deshpande[2], Scott Wagoner[2], Kevin Maher[2], David Ku[1], *[1]Mechanical Engineering, Georgia Institute of Technology, ATLANTA, GA, United States, [2]Pediatrics, Emory University School of Medicine, ATLANTA, GA, United States*

106 **Investigation of Forces and Moments During Minimally Invasive Total Hip Arthroplasty and the Likelihood of Intraoperative Fracture** SB³C2016-1058
Pooyan Abbasi[1], Dustin Greenhill[2], Andrew Star[2], Kurosh Darvish[1], *[1]Temple University, Philadelphia, PA, United States, [2]Temple University Hospital, Philadelphia, PA, United States*

107 **Magnetically Levitated Shear Inducing Device for the Testing of Cell Fragility** SB³C2016-1094
Oyuna Myagmar, Ramnath Raghunaithan, **Steven W. Day**, *Rochester Institute of Technology, Rochester, NY, United States*

Copyright 2016 The Organizing Committee for the 2016 Summer Biomechanics, Bioengineering and Biotransport Conference

108 **Patient-Specific Assessment of Pre-TPVR Angioplasty Coronary Compression Using the Finite Element Method** SB³C2016-1139

Sara Amendola[1], Doff McElhinney[2], Puneet Bhatla[3], **Vittoria Flamini**[1], *[1]Mechanical and Aerospace, NYU Tandon School of Engineering, Brooklyn, NY, United States, [2]Medical Center, Stanford, Stanford, CA, United States, [3]Pediatrics, NYU Langone Medical Center, Brooklyn, NY, United States*

THURSDAY, JUNE 30 | 1:00pm - 3:15pm

Poster Session I — Atherosclerosis & Aneurysms — Exhibit Hall A

129 **Modification of a Parallel Plate Flow Chamber for Analysis of Endothelial Response to Disturbed Flow** SB³C2016-944

Jason M. Sedlak[1], Alisa Morss Clyne[2], *[1]Biomedical Engineering, Drexel University, Philadelphia, PA, United States, [2]Mechanical Engineering and Mechanics, Drexel University, Philadelphia, PA, United States*

130 **Wall Shear Stress and Combined VH-IVUS and OCT Analysis of Coronary Plaque Composition** SB³C2016-951

David Molony[1], Lucas Timmins[1], Udit Joshi[1], Yasir Bouchi[1], Bill Gogas[1], Habib Samady[1], Don Giddens[2], *[1]Emory University, Atlanta, GA, United States, [2]Georgia Institute of Technology, Atlanta, GA, United States*

131 **An Explorative CFD Study on Stenosis-induced Flow Instabilities in the Carotid Artery** SB³C2016-668

Viviana Mancini[1], Jan Vierendeels[2], Daniela Tommasin[1], Simon Shaw[3], Abigail Swillens[1], Awais Yousaf[4], Stephen E. Greenwald[4], *[1]IBiTech-bioMMeda, Ghent University, Ghent, Belgium, [2]Ghent University, Ghent, Belgium, [3]Brunel University, London, United Kingdom, [4]Queen Mary University of London, London, United Kingdom*

132 **Co-localizations and Correlations of Established and Emerging Indicators of Disturbed Wall Shear Stress at the Normal Carotid Bifurcation** SB³C2016-140

Diego Gallo[1], David A. Steinman[2], Morbiducci Umberto[1], *[1]Department of Mechanical and Aerospace Engineering, Politecnico di Torino, Turin, Italy, [2]Department of Mechanical & Industrial Engineering, University of Toronto, Toronto, ON, Canada*

133 **Longitudinal Study of Wall Shear Stress Over Atherosclerotic Plaques in Mice** SB³C2016-768

Ruoyu Xing, Astrid Moerman, Yanto Ridwan, Anton van der Steen, Frank Gijsen, Kim van der Heiden, *Erasmus MC, Rotterdam, Netherlands*

134 **Influence of Plaque Stifffness on Deformation and Flow of Arterial Stenosis Model for Percutaneous Transluminal Coronary Angioplasty** SB³C2016-658

Shunichi Kobayashi[1], Daiki Miyamoto[2], Hajime Kitami[1], *[1]Faculty of Textile Science and Technology, Shinshu University, Ueda, Japan, [2]Graduate School of Science and Technology, Shinshu University, Ueda, Japan*

135 **Effect of Deformation on Cerebral Aneurysm in Middle Cerebral Artery** SB³C2016-763

Suguru O. Omachi, Gaku Tanaka, Hao Liu, Ryuhei Yamaguchi, *Chiba University, Chiba, Japan*

136 **Numerical Simulation of Mechanics of Rupture in Abdominal Aortic Aneurysms Using Fluid-structure Interaction Methods** SB³C2016-980

Tejas Canchi[1, 2], Eddie Yin Kwee Ng[3], Esley Chin Hock Pwee[3], Dinesh Kumar Srinivasan[4], Sriram Narayanan[5], *[1]Lee Kong Chian School of Medicine, Nanyang Technological University, Singapore, Singapore, [2]Mechanical and Aerospace Engineering, Nanyang Technological University, Singapore, Singapore, [3]Mechanical and Aerospace Engineering, Nanyang Technological University, Singapore, Singapore, Singapore, [4]Lee Kong Chian School of Medicine, Nanyang Technological University, Singapore, Singapore, Singapore, [5]Department of General Surgery, Tan Tock Seng Hospital, Singapore, Singapore*

137 **How Sensitive are Hemodynamics in Intracranial Aneurysms to Different Blood Flow Waveforms?** SB³C2016-933

Michael J. Durka[1], Issac H. Wong[1], David F. Kallmes[2], Dario Pasalic[2], Juan R. Cebral[3], Pablo J. Blanco[4], Manoj Jagani[2], Anne M. Robertson[1], *[1]Department of Mechanical Engineering and Materials Science, University of Pittsburgh, Pittsburgh, PA, United States, [2]Mayo Clinic, Rochester, MN, United States, [3]Department of Bioengineering, George Mason University, Fairfax, VA, United States, [4]Laboratorio Nacional de Computacao Cientifica, Petropolis, Brazil*

Copyright 2016 The Organizing Committee for the 2016 Summer Biomechanics, Bioengineering and Biotransport Conference

138 **PCOM Aneurysms: Angio-Architecture, Hemodynamics and Geometry** SB³C2016-136
BongJae Chung[1], Ravi Doddasomayajula[1], Fernando Mut[1], Farid Hamzei-Sichani[2], Christopher Putman[3], Michael Pritz[1], Carlos Jimenez[4], Juan Cebral[1], *[1]Bioengineering & Krasnow Institute, George Mason University, Fairfax, VA, United States, [2]Interventional Neuroradiology, Mt. Sinai Hospital, New York, NY, United States, [3]Interventional Neuroradiology, Inova Fairfax Hospital, Falls Church, VA, United States, [4]Neurosurgery, University of Antioquia, Medellin, Colombia*

139 **Association of Hemodynamic Stresses with Thickness of Aneurysm Wall: A Case Study** SB³C2016-726
Hamidreza Rajabzadeh Oghaz[1], Jaco J. M. Zwanenburg[2], Hui Meng[1], *[1]University at Buffalo, Buffalo, NY, United States, [2]University Medical Center Utrecht, Utrecht, Netherlands*

140 **Comparison of Cerebral Aneurysm Flow Fields Obtained From Cfd And Dsa** SB³C2016-126
Juan Cebral[1], BongJae Chung[1], Fernando Mut[1], Fred van Nijnatten[2], Danny Ruijters[2], *[1]Bioengineering, George Mason University, Fairfax, VA, United States, [2]IGT Innovation, Philips Healthcare, Best, Netherlands*

141 **Objective Identification of the Yield Point from Tensile Testing of Aortic Tissues** SB³C2016-752
Madhavan L. Raghavan, Timothy K. Chung, Chaid D. Schwarz, *Biomedical Engineering, University of Iowa, Iowa City, IA, United States*

142 **Biomechanical Characterization of Six Murine Models of Thoracic Aortic Aneurysm and Dissection** SB³C2016-872
Chiara Bellini, Matthew R. Bersi, Jacopo Ferruzzi, Jay D. Humphrey, *Biomedical Engineering, Yale University, New Haven, CT, United States*

143 **A Novel Technique for Assessment of Mechanical Properties of Vascular Tissue** SB³C2016-662
Stefan Sanders, Frans van de Vosse, Marcel Rutten, *Eindhoven University of Technology, Eindhoven, Netherlands*

144 **Towards the Characterization of Carotid Plaque Tissue Toughness: Linking Mechanical Properties to Biological Content** SB³C2016-680
Hilary E. Barrett[1], Eoghan M. Cunnane[1], Eamon G. Kavanagh[2], Michael T. Walsh[1], *[1]Centre for Applied Biomedical Engineering (CABER) and Health Research Institute (HRI), University of Limerick, Limerick, Ireland, [2]Department of Vascular Surgery, University Hospital Limerick, Limerick, Ireland*

THURSDAY, JUNE 30	**1:00pm - 3:15pm**

Poster Session I — Cardiovascular Diagnostics and Devices — Exhibit Hall A

145 **Bifurcation Angle and Fractional Flow Reserve: A Multiscale Numerical Study of Coronary Bifurcation Lesions** SB³C2016-148
Catherine Pagiatakis[1, 2], Jean-Claude Tardif[2, 3], Philippe L. L'Allier[2, 4], **J. Frattolin**[2, 5], Rosaire Mongrain[1, 2], *[1]Mechanical Engineering, McGill University, Montreal, QC, Canada, [2]Montreal Heart Institute, Montreal, QC, Canada, [3]Faculty of Medicine, Université de Montréal, Montreal, QC, Canada, [4]Université de Montréal, Montreal, QC, Canada, [5]McGill University, Montreal, QC, Canada*

146 **Development of an Integrated Multi-Scale Simulation System with Multi-modal Data for Cerebral Circulation** SB³C2016-997
Marie Oshima[1], Zhao Zhang[2], Masaharu Kobayashi[1], Shigeki Yamada[3], Fuyou Liang[4], Shu Takagi[2], *[1]Interfaculty Intiative in Information Studies, The University of Tokyo, Tokyo, Japan, [2]Departoment of Mechanical Engineering, The University of Tokyo, Tokyo, Japan, [3]Department of Neurosurgery, Rakuwakai Otowa Hospital, Kyoto, Japan, [4]Department of Naval Architecutre and Ocean Engineering, Shanghai Jiao Tong University, Shanghai, China*

147 **Windkessel Approach for Blood Flow Responses: Application in Venous Ulcer Risk Assessment** SB³C2016-774
Wu Pan, Seungik Baek, Tamara Reid Bush, *Mechanical Engineering, Michigan State University, East Lansing, MI, United States*

148 **Patient-Specific CFD of Clinical Mitral Regurgitation as a Novel Method to Quantify Regurgitation Severity** SB³C2016-118
Muhammad Jamil[1], Kian Keong Poh[2], Choon Hwai Yap[1], *[1]Department of Biomedical Engineering, National University of Singapore, Singapore, Singapore, [2]Department of Medicine, Yong Loo Lin School of Medicine, National University of Singapore, Singapore, Singapore*

Copyright 2016 The Organizing Committee for the 2016 Summer Biomechanics, Bioengineering and Biotransport Conference

149 **Assessing Hemodynamic Response to Exercise for Patient with Left Ventricular Hypertrophy by Integrating Cardiovascular and Autonomic Nervous Systems** SB³C2016-93
Weiwei Jin[1], Fuyou Liang[2], Hao Liu[1, 2], *[1]Chiba University, Chiba, Japan, [2]Shanghai Jiao Tong University and Chiba University International Cooperative Research Center, Shanghai Jiao Tong University, Shanghai, China*

150 **Translating 4d-flow MRI to Clinical Practice** SB³C2016-1137
Kurt R. Sansom[1], Haining Liu[2], chun yuan[2], Alberto Aliseda[1], Gador Canton[2], *[1]Mechanical Engineering, University of Washington, WA, United States, [2]Vascular Imaging Laboratory, University of Washington, WA, United States*

151 **Patient-Specific Computational Fluid Dynamics Simulations of the Human Fetal Left Ventricle Based on 4D Clinical Ultrasound Imaging** SB³C2016-83
Changquan Lai[1], Guat Ling Lim[2], Muhammad Jamil[3], Citra Nurfarah Zaini Mattar[2], Arijit Biswas[2], **Choon Hwai Yap**[3], *[1]SIngapore MIT Alliance for Reseach and Technology, Singapore, Singapore, [2]Obstetrics and Gynecology, National University Hospital Systems, Singapore, Singapore, Singapore, [3]Biomedical Engineering, National University of Singapore, Singapore, Singapore*

152 **Impact of Idealized Versus Measured Velocity Profiles in Computational Models of Mass Transport in the Human Aorta** SB³C2016-593
Giuseppe De Nisco[1], Peng Zhang[2], Gianpaolo Usala[1], Diego Gallo[1], Xiao Liu[2], Xiaoyan Deng[2], Giovanna Rizzo[3], Umberto Morbiducci[1], *[1]Mechanical and Aerospace Engineering, Politecnico di Torino, Turin, Italy, [2]School of Biological Science and Medical Engineering, Beihang University, Beijing, China, [3]Research National Council, IBFM, Milan, Italy*

153 **Micro Matrix Encapsulation of Cell Aggregates for Injectable Delivery Augments Stem Cell Therapy of Myocardial Infarction** SB³C2016-731
Shuting zhao, Xiaoming He, *Biomedical Engineering, The ohio state university, Columbus, OH, United States*

THURSDAY, JUNE 30	**1:00pm - 3:15pm**

Poster Session I — Masters Level Student Paper Competition I: Physiology & Diseases - Cellular & Tissue Mechanics - Biomaterial & Material Characterization — Exhibit Hall A

188 **Early Production of Phospholipase A_2 Accompanies Spinal Neuroinflammation and Pain Following Nerve Root Compression** SB³C2016-641
Sonia Kartha, Jenell Smith, Beth Winkelstein, *University of Pennsylvania, Philadelphia, PA, United States*

189 **Disorganized Layers within an Otherwise Aligned Fibrous Network Preserve Bulk Mechanics and Promote Strain Reconstitution in the Context of Radial Tears** SB³C2016-873
Sonia Bansal[1, 2, 3], Niobra M. Keah[1, 3], Feini Qu[1, 3, 4], Spencer E. Szczesny[1, 3], Alexander L. Neuwirth[1, 3], Robert L. Mauck[1, 2, 3], Miltiadis H. Zgonis[1, 3], *[1]McKay Orthopaedic Research Laboratory, University of Pennsylvania, Philadelphia, PA, United States, [2]Department of Bioengineering, University of Pennsylvania, Philadelphia, PA, United States, [3]Translational Musculoskeletal Research Center, Philadelphia VA Medical Center, Philadelphia, PA, United States, [4]University of Pennsylvania, School of Veterinary Medicine, Philadelphia, PA, United States*

190 **Long-term Exposure to Buffer Solution Alters Tendon Structure and Mechanics -Implications for Fatigue Studies** SB³C2016-1037
Babak N. Safa[1, 2], Kyle D. Meadows[2], Spencer E. Szczesny[3], Dawn M. Elliott[2], *[1]Mechanical engineering, University of delaware, Newark, DE, United States, [2]Biomedical engineering, University of delaware, Newark, DE, United States, [3]Department of Orthopaedic Surgery, University of Pennsylvania, Philadelphia, PA, United States*

191 **Effect of Ablation Pattern on Mechanical Function in the Atrium: A Finite-Element Study** SB³C2016-592
Thien-Khoi N. Phung, Patrick T. Norton, John D. Ferguson, Jeffrey W. Holmes, *University of Virginia, Charlottesville, VA, United States*

192 **Effects of Reproduction and Lactation on Maternal Bone Tissue Mechanical Properties at Different Length Scales** SB³C2016-885
Yihan Li[1], Peng Guo[1], Wei-Ju Tseng[1], Chantal M. J. de Bakker[1], Prashant Chandrasekaran[2], Yonghoon Jeong[3], Do-Gyoon Kim[3], Lin Han[2], X. Sherry Liu[1], *[1]University of Pennsylvania, Philadelphia, PA, United States, [2]Drexel University, Philadelphia, PA, United States, [3]The Ohio State University, Columbus, OH, United States*

Copyright 2016 The Organizing Committee for the 2016 Summer Biomechanics, Bioengineering and Biotransport Conference

193 **Methods to Determine Right Ventricular Performance in a Rat Animal Model of Pulmonary Arterial Hypertension** SB³C2016-1046

Daniela M. Velez Rendon, Jesse Gerringer, Gizzel Gomez, Erica Pursell, Daniela Valdez-Jasso, *Bioengineering, University of Illinois at Chicago, Chicago, IL, United States*

194 **Surface Modification of Electrospun gelatin/fibrinogen Scaffolds to Encourage Endothelial Cell Function** SB³C2016-162

Catalina Ardila[1], David Maestas[2], Victoria Lundine[2], Marvin Slepian[3, 4], Jonathan Vande Geest[5], *[1]Graduate Interdisciplinary Program of Biomedical Engineering, The University of Arizona, Tucson, AZ, United States, [2]Biomedical Engineering, The University of Arizona, Tucson, AZ, United States, [3]Sarver Heart Center, The University of Arizona, Tucson, AZ, United States, [4]Interventional Cardiology, The University of Arizona, Tucson, AZ, United States, [5]Bioengineering, University of Pittsburgh, Pittsburgh, PA, United States*

195 **Swelling of Collagen-Hyaluronic Acid Co-Gels: An In Vitro Residual Stress Model** SB³C2016-942

David S. Nedrelow[1], Victor K. Lai[2], Spencer P. Lake[3], Bumjun Kim[1], Emily M. Weiss[1], Robert T. Tranquillo[4], Victor H. Barocas[1], *[1]Biomedical Engineering, University of Minnesota, Minneapolis, MN, United States, [2]Chemical Engineering, University of Minnesota, Duluth, MN, United States, [3]Mechanical Engineering and Materials Science, Washington University, St. Louis, MO, United States, [4]Chemical Engineering and Materials Science, University of Minnesota, Minneapolis, MN, United States*

196 **Longitudinal Assessment of Mouse Bone Microstructure by In Vivo µCT Imaging with Minimal Radiation Effects** SB³C2016-1035

Hongbo Zhao, Chih-Chiang Chang, Youwen Yang, Wei-Ju Tseng, Chantal M. J. de Bakker, X. Sherry Liu, *Department of Orthopaedic Surgery, University of Pennsylvania, Philadelphia, PA, United States*

197 **Pathological Engineering Study of Human Cerebral Aneurysms Three Dimensional Accumulation of Foam Cells Versus Hemodynamics** SB³C2016-1110

Kenta Suto[1], Takanobu Yagi[1, 2], Yasutaka Tobe[1], Takuma Murayoshi[1], Kiyofumi Takanishi[1], Mitsuo Umezu[1], Hirotaka Yoshida[3], Kazutoshi Nishitani[3], Yoshifumi Okada[3], Shigemi Kitahara[3], *[1]Center for Advanced Biomedical science (TWIns), Waseda University, Tokyo, Japan, [2](2)EBM corporation Ohmoriminami, Ohtaku, Tokyo, 143-0013 Japan, Tokyo, Japan, [3]Kitahara International Hospital Oowada-cho, Hachioji-shi, Tokyo Japan, Tokyo, Japan*

198 **Mathematical Modelling of Oxygen Transport in the Retina** SB³C2016-1007

Wouter J. Thijssen, Emilie Lunddahl, Andris Piebalgs, Xiao Y. Xu, *Chemical Engineering, Imperial College London, London, United Kingdom*

199 **Effect of Hydration on Intervertebral Disc Recovery** SB³C2016-754

Semih Bezci, Grace D. O'Connell, *Mechanical Engineering, University of California, Berkeley, Berkeley, CA, United States*

200 **The Role of IGF-1 in the Cytoskeletal Regulation of Gating of TRPV4 Channels in Articular Chondrocytes** SB³C2016-1101

Victor DeBarros[1], Joseph D. Gardinier[2], Lauren Hurd[3], Mary E. Boggs[1], Randall Duncan[4], *[1]Biological Sciences, University of Delaware, Newark, DE, United States, [2]Orthopedics/Bone and Joint Center, Henry Ford Health System, Detroit, MI, United States, [3]Molecular Diagnostics Laboratory, Nemours/AI duPont Hospital for Children, Wilmington, DE, United States, [4]Biological Sciences and Biomedical Engineering, University of Delaware, Newark, DE, United States*

201 **Image-based Analysis for Inverse Estimation of Muscle Fiber Forces in the Tongue** SB³C2016-1004

Narihiko Koike[1], Tsukasa Yoshinaga[1], Kazunori Nozaki[2], Satoshi Ii[1], Shigeo Wada[1], *[1]Osaka University, Toyonaka, Japan, [2]Osaka University Dental Hospital, Suita, Japan*

202 **Modeling the Viscoelastic Properties of Pulmonary Vessels in a Hypertensive Rat** SB³C2016-1020

Erica Pursell, Daniela Velez-Rendon, Daniela Valdez-Jasso, *University of Illinois at Chicago, Chicago, IL, United States*

203 **Biomechanical Consequences of Subchondral Bone Cysts - A Finite Element Analysis of the Equine Stifle Joint** SB³C2016-922

Lance F. Frazer[1], Kenneth Fischer[2], Elizabeth Santschi[3], *[1]Bioengineering, University of Kansas, Lawrence, KS, United States, [2]Mechanical Engineering, University of Kansas, Lawrence, KS, United States, [3]Clinical Sciences, Kansas State University, Manhattan, KS, United States*

Copyright 2016 The Organizing Committee for the 2016 Summer Biomechanics, Bioengineering and Biotransport Conference

204 **Confined Compression of a Hydrogel Composite for Nucleus Pulposus Tissue Engineering** SB³C2016-932
Thomas R. Christiani[1], Rachel Adams[2], Erin Signor[3], Alex Crudo[4], Patrick Myers[4], Dan Collins[4], Kathryn Wrinn[4], Michael Arigot[4], Alexandra Guido[4], Jennifer Vernengo[2], Jennifer Kadlowec[4], *[1]Biomedical Engineering, Rowan University, Glassboro, NJ, United States, [2]Chemical Engineering, Rowan University, Glassboro, NJ, United States, [3]Civil Engineering, Rowan University, Glassboro, NJ, United States, [4]Mechanical Engineering, Rowan University, Glassboro, NJ, United States*

205 **Flow Field Post-repair in Critical Aortic Valve Stenosis : Implications to Recurring Disease State** SB³C2016-909
Sana Nasim[1], Glenda Castellanos[1], Angie Estrada[1], Denise Medina[1], Makensley Lordeus[1], Lilliam Valdes-Cruz[2], Steven Bibevski[2], Frank Scholl[2], Benjamin Bosel[1], Arvind Agarwal[1], Sharan Ramaswamy[1], *[1]Florida International University, Miami, FL, United States, [2]Joe DiMaggio's Children's Hospital, Hollywood, FL, United States*

THURSDAY, JUNE 30 | 1:00pm - 3:15pm

Poster Session I — Masters Level Student Paper Competition II: Imaging - Devices - Human Dynamics & Injury - Fluids & Microfluidics - Heat Transfer — Exhibit Hall A

206 **Comprehensive Hemdodynamics of Living Donor Liver Transplant** SB³C2016-101
David R. Rutkowski[1, 2], Scott B. Reeder[2, 3, 4], Luis A. Fernandez[5], Alejandro Roldán-Alzate[1, 2], *[1]Mechanical Engineering, University of Wisconsin-Madison, Madison, WI, United States, [2]Radiology, University of Wisconsin-Madison, Madison, WI, United States, [3]Medical Physics, University of Wisconsin-Madison, Madison, WI, United States, [4]Biomedical Engineering, University of Wisconsin-Madison, Madison, WI, United States, [5]Surgery, UW Hospital and Clinincs, Madison, WI, United States*

207 **Patient Specific Computational Models to Optimize Surgical Correction for Flatfoot Deformity** SB³C2016-923
Brian A. Smith, Robert Adelaar, Jennifer Wayne, *Biomedical Engineering, Virginia Commonwealth University, Richmond, VA, United States*

208 **Determination of HIFU Induced Temperature Rise at Focal Location Using Numerical Approach** SB³C2016-1066
Sai Sameer Paruchuri[1], Surendra B. Devarakonda[1], Seyed Ahmad Reza Dibaji[1], Matthew R. Myers[2], Rupak K. Banerjee[1], *[1]Department of Mechanical Engineering, University of Cincinnati, Cincinnati, OH, United States, [2]Division of Applied Mechanics, Center for Devices and Radiological Health, US Food and Drug Administration, Cincinnati, OH, United States*

209 **Reproducibility of Mouse Trabecular Bone Microstructure at Multiple Skeletal Sites by In Vivo Micro Computed Tomography Imaging** SB³C2016-655
Chih-Chiang Chang[1], Hongbo Zhao[2], Youwen Yang[1], Chantal M. J. de Bakker[1], Wei-Ju Tseng[2], X. Sherry Liu[1], *[1]Bioengineering, University of Pennsylvania, Philadelphia, PA, United States, [2]University of Pennsylvania, Philadelphia, PA, United States*

210 **Patient Specific In Vitro Models for Hemodynamic Analysis of Congenital Heart Disease - Additive Manufacturing Approach** SB³C2016-757
Rafael Medero[1, 2], Sylvana García-Rodríguez[2], Christopher J. François[2], Alejandro Roldán-Alzate[1, 2], Petros V. Anagnostopoulos[3], *[1]Mechanical Engineering, University of Wisconsin-Madison, Madison, WI, United States, [2]Radiology, University of Wisconsin-Madison, Madison, WI, United States, [3]Pediatric Cardiothoracic Surgery, University of Wisconsin-Madison, Madison, WI, United States*

211 **Drill-Specific Head Impact Exposure in Youth Football Practice** SB³C2016-814
Eamon Campolettano, Steve Rowson, Stefan Duma, *Virginia Tech, Blacksburg, VA, United States*

212 **The Food and Drug Administration's Nozzle Benchmark: In Theory, There is No Difference Between Theory and Practise. But, in Practice, There is.** SB³C2016-580
Aslak Bergersen[1], Mikael Mortensen[2], Kristian Valen-Sendstad[1], *[1]Simula Research Laboratory, Lysaker, Norway, [2]Department of Mathematics, University of Oslo, Oslo, Norway*

213 **Laboratory Evaluation of Wearable Head Impact Sensors** SB³C2016-887
Abigail M. Tyson, Steven Rowson, Stefan M. Duma, *Biomedical Engineering and Mechanics, Virginia Tech, Blacksburg, VA, United States*

Copyright 2016 The Organizing Committee for the 2016 Summer Biomechanics, Bioengineering and Biotransport Conference

214 **Biomechanical Comparison of Youth and Adult Football Helmets: Standards Testing** SB³C2016-80
David W. Sproule, Steven Rowson, *Biomedical Engineering and Mechanics, Virginia Tech, Blacksburg, VA, United States*

215 **Investigation of Flow Instability with Vascular Geometry at the Bifurcation of Middle Cerebral Arteries From Healthy Volunteers** SB³C2016-1106
Takuma Murayoshi[1], Takanobu Yagi[1, 2], Yasutaka Tobe[1], Kenta Suto[1], Kiyofumi Alex Takanishi[1], Mitsuo Umezu[1], Hirotaka Yoshida[3], Kazutoshi Nishitani[3], Yoshifumi Okada[3], Shigemi Kitahara[3], *[1]Center for Advanced Biomedical science (TWIns), Waseda University, Tokyo, Japan, [2]EBM corporation, Tokyo, Japan, [3]Kitahara International Hospital, Tokyo, Japan*

216 **Performance of Three Variable-length Intramedullary Nails: The Effect of the Length-adjustment Mechanism** SB³C2016-627
Mark Hedgeland[1], Alexander Martin Clark[2], Laurel Kuxhaus[1], *[1]Clarkson University, Potsdam, NY, United States, [2]Canton-Potsdam Hospital, Potsdam, NY, United States*

217 **A Phenomenological Model of Damage and Recovery in the Intervertebral Disc of the Cervical Spine due to Cyclic Loading** SB³C2016-928
Shruti Motiwale[1], Xianlin Zhou[2], Reuben H. Kraft[1], *[1]Department of Mechanical and Nuclear Engineering, The Pennsylvania State University, University Park, PA, United States, [2]CFD Research Corporation, Huntsville, AL, United States*

218 **Study of the Consistency of Wall Shear Stress in Healthy Major Human Cerebral Arteries** SB³C2016-1034
Kiyofumi A. Takanishi[1], Takanobu Yagi[1], Takuma Murayoshi[1], Kenta Suto[1], Mitsuo Umezu[1], Hiroki Yoshida[2], Kazutoshi Nishitani[2], Yoshifumi Okada[2], Yoshimi Kitahara[2], Akihide Yamamoto[3], Hidehiro iida[3], Hiroharu Kataoka[3], *[1]Center for Advanced Biomedical Science (TWIns), Waseda University, Tokyo, Japan, [2]Kitahara International Hospital, Tokyo, Japan, [3]National cerebral and cardiovascular centre, Osaka, Japan*

219 **A Finite Element Analysis of Augmented Glenoid Components** SB³C2016-15
Nikolas K. Knowles, G. Daniel G. Langohr, Louis M. Ferreira, George S. Athwal, *Biomedical Engineering, The University of Western Ontario, London, ON, Canada*

220 **Development of a Novel Fistula Occlusion Device** SB³C2016-584
Alyssa K. Rollando[1], Sara E. Wilson[2], Stephen C. Waller[3], Richard Gilroy[4], James M. Stiles[5], *[1]Bioengineering Graduate Program, University of Kansas, Lawrence, KS, United States, [2]Department of Mechanical Engineering, University of Kansas, Lawrence, KS, United States, [3]Department of Internal Medicine, University of Kansas Medical Center, Kansas City, KS, United States, [4]Department of Gastroenterology, Hepatology and Motility, University of Kansas Medical Center, Kansas City, KS, United States, [5]Department of Electrical Engineering and Computer Science, University of Kansas, Lawrence, KS, United States*

THURSDAY, JUNE 30 | 1:00pm - 3:15pm

Poster Session I — Cardiovascular Tissue Mechanics — Exhibit Hall A

227 **The Effect of Electropotenital on Nitinol Fatigue Life** SB³C2016-626
Shiril Sivan[1, 2], Matthew A. Di Prima[1], Jason D. Weaver[1], *[1]CDRH OSEL DAM, FDA, Silver Spring, MD, United States, [2]Oak Ridge Institute of Science and Education, Oak Ridge, TN, United States*

228 **Right Ventricular Adaptation to Pressure Overload Conditions in Mice** SB³C2016-652
Tik Chee Cheng[1], Diana Tabima[1], Zhijie Wang[1], Tim Hacker[2], Naomi Chesler[1, 2], *[1]Biomedical Engineering, University of Wisconsin-Madison, Madison, WI, United States, [2]Medicine, University of Wisconsin-Madison, Madison, WI, United States*

229 **Measurement of Aortic Stent Graft Coefficients of Friction** SB³C2016-60
Matthew G. Doyle[1, 2], Michael Lancaster[1], Leonard W. Tse[2], Thomas L. Forbes[2], Cristina H. Amon[1, 3], *[1]Department of Mechanical and Industrial Engineering, University of Toronto, Toronto, ON, Canada, [2]Division of Vascular Surgery, University of Toronto, Toronto, ON, Canada, [3]Institute of Biomaterials and Biomedical Engineering, University of Toronto, Toronto, ON, Canada*

Copyright 2016 The Organizing Committee for the 2016 Summer Biomechanics, Bioengineering and Biotransport Conference

230 **Effect of Sodium Hypochlorite on the Fatigue Performance and Corrosion Resistance of Nitinol Wires** SB³C2016-622
Erick J. Gutierrez[1, 2], Srinidhi Nagaraja[1], Shiril Sivan[1, 2], Jason D. Weaver[1], Matthew Di Prima[1], *[1]Center for Devices and Radiological Health, U.S. Food and Drug Administration, Silver Spring, MD, United States, [2]Oak Ridge Institute for Science and Education, Oak Ridge, TN, United States*

231 **Integration of Opencascade and Improved Global Surface Interpolation Methods into Simvascular 2.0** SB³C2016-924
Adam R. Updegrove[1], Nathan M. Wilson[2], Shawn C. Shadden[1], *[1]Mechanical Engineering, University of California, Berkeley, Berkeley, CA, United States, [2]Open Source Medical Software Corporation, Santa Monica, CA, United States*

232 **Modelling the Evolution of Smooth Muscle Cell Stress Fibres following Stent Deployment in an Artery** SB³C2016-1065
Catherine A. O'Connor, Noel H. Reynolds, Patrick McGarry, *Biomedical Engineering, National University of Ireland, Galway, Galway, Ireland*

233 **Evaluating Left Ventricular Function Using Cardiac and Respiratory-Gated Volumetric Murine Ultrasound** SB³C2016-776
Arvin H. Soepriatna[1], Frederick W. Damen[1, 2], Pavlos P. Vlachos[1, 3], Craig J. Goergen[1], *[1]Weldon School of Biomedical Engineering, Purdue University, West Lafayette, IN, United States, [2]School of Medicine, Indiana University, Indianapolis, IN, United States, [3]Department of Mechanical Engineering, Purdue University, West Lafayette, IN, United States*

234 **Computational Analysis of Right-ventricular Fiber Distribution as a Compensatory Mechanism During Pressure Overload** SB³C2016-995
Arnold David Gomez[1], Huashan Zou[1], Osama M. Abdullah[1], Megan E. Bowen[2], Xiaoquing Liu[2], David A. Bull[2], Edward W. Hsu[1], Stephen H. McKellar[2], *[1]Bioengineering, University of Utah, Salt Lake City, UT, United States, [2]Division of Cardiothoracic Surgery, University of Utah, Salt Lake City, UT, United States*

235 **Image-Based Computational Modeling of the Ventricular Mechanics in Patients with Pulmonary Hypertension** SB³C2016-27
Ce Xi[1], Xiaodan Zhao[2], Liang Zhong[2], Martin Genet[3], Lik Chuan Lee[1], *[1]Michigan State Universiy, East lansing, MI, United States, [2]National Heart Center, Singapore, Singapore, [3]*École Polytechnique, Paris, France

236 **Comparison of Material Properties between the Main and Left Pulmonary Arteries of Congenital Heart Disease Subjects Using Cardiac Magnetic Resonance: A Feasibility Study** SB³C2016-990
Gavin A. D'Souza[1], Michael D. Taylor[2], Namheon Lee[2], Rupak K. Banerjee[1], *[1]Department of Mechanical and Materials Engineering, University of Cincinnati, Cincinnati, OH, United States, [2]The Heart Institute, Cincinnati Children's Hospital Medical Center, Cincinnati, OH, United States*

237 **Decreased Wall Shear Stress in Isolated Regions of the Pulmonary Endothelium Could Impact Pulmonary Vascular Dysfunction on a Global and Cellular Level in Pulmonary Hypertension** SB³C2016-875
Vitaly O. Kheyfets[1], Michal Schafer[1], Joyce D. Schroeder[1], Jamie Dunning[1], Chris Podgprski[2], James Browning[3], Jean Hertzberg[3], Kendall Hunter[1], Kern Buckner[2], Robin Shandas[1], Brett Fenster[2], *[1]Bioengineering/Medicine, University of Colorado Denver|Anschutz Medical Campus, Denver, CO, United States, [2]Cardiology, National Jewish Health, Denver, CO, United States, [3]Mechanical Engineering, University of Colorado Boulder, Boulder, CO, United States*

238 **In Vitro Studies on Native to Engineered Heart Valve Tissue Integration** SB³C2016-938
Kristin Comella, Danique Stewart, Sasmita Rath, Sharan Ramaswamy, *Biomedical Engineering, Florida International University, Miami, FL, United States*

239 **Mathematical Modeling of Fluid--Structure Interaction in Bioprosthetic Heart Valves: Numerical Approximation and Experimental Validation** SB³C2016-1069
David Kamensky[1], Ming-Chen Hsu[2], John G. Lesicko[1], Mitchell A. Katona[1], Jordan L. Graves[1], Samuel J. Petter[1], Thomas J. R. Hughes[1], Michael S. Sacks[1], *[1]Institute for Computational Engineering and Sciences, University of Texas at Austin, Austin, TX, United States, [2]Mechanical Engineering, Iowa State University, Ames, IA, United States*

240 **In-vivo Analysis and Residual Strains in Semilunar Heart Valves** SB³C2016-905
Ankush Aggarwal[1, 2], Alison Pouch[3], Eric Lai[3], John Lesicko[2], Joseph H. Gorman[3], Robert C. Gorman[3], Michael S. Sacks[2], *[1]Swansea University, Swansea, United Kingdom, [2]University of Texas at Austin, Austin, TX, United States, [3]University of Pennsylvania, Philadelphia, PA, United States*

Copyright 2016 The Organizing Committee for the 2016 Summer Biomechanics, Bioengineering and Biotransport Conference

241 **Multi-resolution Models of the Mitral Valve Leaflets for High Fidelity Biomechanical Simulations** SB³C2016-921
Amir H. Khalighi[1], Andrew Drach[2], Charles Bloodworth[3], Eric L. Pierce[3], Ajit P. Yoganathan[3], Robert C. Gorman[4], Joseph H. Gorman[4], Michael S. Sacks[5], *[1]Mechanical Engineering, University of Texas at Austin, Austin, TX, United States, [2]Instituite for Computational Engineering and Sciences, University of Texas at Austin, Austin, TX, United States, [3]Georgia Institute of Technology, Atlanta, GA, United States, [4]Gorman Cardiovascular Research Group, University of Pennsylvania, Philadelphia, PA, United States, [5]Biomedical Engineering, University of Texas at Austin, Austin, TX, United States*

242 **Determination of the Tensile Mechanical Properties of the Segmented Tricuspid Valve Annulus** SB³C2016-759
Fatima Al-Quaiti[1], Evelia Salinas[1], Lori Boies[1], Edward Sako[2], Shamik Bhattacharya[1], *[1]Engineering, St.Mary's University, San Antonio, TX, United States, [2]University of Texas Health Science Center at San Antonio, San Antonio, TX, United States*

243 **Inverse Modeling Based Estimation of In-vivo Stresses and Their Relation to Simulated Layer-specific Interstitial Cell Deformations in the Mitral Valve** SB³C2016-114
Chung-Hao Lee[1], Kristen Feaver[1], Will Zhang[1], Robert C. Gorman[2], Joseph H. Gorman[2], Michael S. Sacks[1], *[1]Institute for Computational Engineering and Sciences, Department of Biomedical Engineering, The University of Texas at Austin, Austin, TX, United States, [2]Gorman Cardiovascular Research Group, University of Pennsylvania, Philadelphia, PA, United States*

244 **Mitral Valve Leaflet Remodeling During Pregnancy: Implications for Modeling Valvular Adaptation** SB³C2016-803
Bruno V. Rego[1], Sarah M. Wells[2], Michael S. Sacks[1], *[1]Biomedical Engineering, The University of Texas at Austin, Austin, TX, United States, [2]Biomedical Engineering, Dalhousie University, Halifax, NS, Canada*

THURSDAY, JUNE 30 | 1:00pm - 3:15pm

Poster Session I | Injury | Exhibit Hall A

258 **Cervical Spine Forces and Disc Herniation Risk During Standardized Rear-End Impact Testing** SB³C2016-930
Keith Button, Stephanie Rossman, Brian Weaver, Steve Rundell, *Explico Engineering Company, Novi, MI, United States*

259 **Changes of Total Finger Forces Due to Emulating Finger Amputations Using a Cylinder Handle Device** SB³C2016-1085
Diego F. Villegas[1], Jorge H. Escobar[1], Ricardo A. Quiros[1], Edna R. Buitrago[2], Ivan D. Quintero[2], *[1]Mechanical Engineering Department, Universidad Industrial De Santader, Bucaramanga, Colombia, [2]School of Medicine, Universidad Industrial De Santader, Bucaramanga, Colombia*

260 **Biomechanical Properties of the Neonatal Brachial Plexus** SB³C2016-827
Anita Singh[1], Shania Shaji[1], Maria Delivoria[2], Malaeb Shadi[2], *[1]Biomedical Engineering, Widener, Chester, PA, United States, [2]Pediatrics, Obstet. & Gynecol., Drexel College of Medicine, Philadelphia, PA, United States*

261 **Pulmonary Contusion Modeling in Reconstructions of Frontal Motor Vehicle Collisions** SB³C2016-858
James P. Gaewsky, Derek A. Jones, Ashley A. Weaver, Joel D. Stitzel, *Center for Injury Biomechanics, Wake Forest University, Winston-Salem, NC, United States*

262 **Sensitive Injury Detection in the Cervical Spine Using Acoustic Emission** SB³C2016-1027
Jay K. Shridharani, Brian R. Bigler, Courtney A. Cox, Maria A. Ortiz-Paparoni, **Anna E. Knight**, Cameron R. 'Dale' Bass, *Biomedical Engineering, Duke University, Durham, NC, United States*

263 **Comparison of Computed Tomography Imaging Measurements to Created Injuries Under UBB Loading Conditions** SB³C2016-586
Nathanael P. Kuo, Christopher J. Dooley, Constantine K. Demetropoulos, Kyle A. Ott, Andrew C. Merkle, *Research and Exploratory Development Department, Johns Hopkins University Applied Physics Laboratory, Laurel, MD, United States*

264 **An Investigations of Human Long Bone Fracture Patterns During Traumatic Amputations From Moving Railroad Equipment** SB³C2016-1092
Brian T. Weaver[1, 2], Mark Davison[2], Steve Rundell[2], Eric Meyer[3], *[1]Orthopedics Biomechanics Laboratories, Michigan State University, East Lansing, MI, United States, [2]Explico Engineering Co., Novi, MI, United States, [3]Biomedical Engineering, Lawrence Technological University, East Lansing, MI, United States*

Copyright 2016 The Organizing Committee for the 2016 Summer Biomechanics, Bioengineering and Biotransport Conference

265 **Development of a Combat Helmet Suspension System Computational Model: Implications for Pad Design and Injury Outcome** SB³C2016-978
Connor Bradfield, Quang Luong, Brian DeVincentis, John Clark, Adam Golman, Catherine Carneal, *Johns Hopkins Applied Physics Lab, Laurel, MD, United States*

266 **Development and Parametric Study of a 3-year-old Child Abdominal Finite Element Model** SB³C2016-1014
Haiyan Li[1], Ruirui Lu[1], Shijie Ruan[1], Shihai Cui[1], Chunxiang Wang[2], *[1]Tianjin University of Science and Technology, Tianjin, China, [2]Tianjin Children's Hospital, Tianjin, China*

267 **Dynamic Bending Response of the Unrestrained Femur in Underbody Blast Loading** SB³C2016-1102
Joshua G. Chen, Gwansik Park, Edward M. Spratley, Robert S. Salzar, *Mechanical and Aerospace Engineering, University of Virginia, Charlottesville, VA, United States*

268 **Scaling between Human and Porcine Models for Traumatic Brain Injury** SB³C2016-154
Siddiq Qidwai[1], Robert Saunders[2], *[1]Multifunctional Materials Branch, Code 6350, US Naval Research Laboratory, Washington, DC, United States, [2]Leidos Corporation, Arlington, VA, United States*

269 **Validation of a Porcine Head and Upper Torso Model** SB³C2016-156
Robert Saunders[1], Siddiq Qidwai[2], *[1]Leidos Corporation, Arlington, VA, United States, [2]U.S. Naval Research Lab, Washington, DC, United States*

270 **The Effect of Limited Fractional Anisotropy Representation on Brain Injury Predictions** SB³C2016-157
Shankarjee Krishnamoorthi[1], **Siddiq Qidwai**[2], *[1]NRL/ASEE Postdoctoral Fellowship, US Naval Research Laboratory, Washington, DC, United States, [2]Multifunctional Materials Branch, US Naval Research Laboratory, Washington, DC, United States*

271 **Simple Geometric Scaling to Transform Cervical Spine Injury Criteria From Males to Females Adequate?** SB³C2016-907
Narayan Yoganandan[1], Frank Pintar[1], Cameron-Dale Bass[2], Maria Ortiz[2], Hattie Cutcliffe[2], Jonathan Rupp[3], Amanda Agnew[4], Ashley Weaver[5], Scott Gayzik[5], Liming Voo[6], *[1]Neurosurgery, Medical College of Wisconsin, Milwaukee, WI, United States, [2]Duke University, Durham, NC, United States, [3]University of Michigan, Ann Arbor, MI, United States, [4]Ohio State University, Columbus, OH, United States, [5]Wake Forest University School of Medicine, Winston-Salem, NC, United States, [6]John Hopkins University, Laurel, MD, United States*

272 **A Study on the Mechanical Response of the Human Head during Single-Collision Car Crashes using Finite Element Analysis** SB³C2016-979
Parker Berthelson, *Mississippi State University, Mississippi State, MS, United States*

273 **Computational Fluid Dynamics Predictions of Pressure Loading on the Human Head in a Laboratory-Based Blast Test Methodology** SB³C2016-1041
Rubbel Kumar[1], Catherine Carneal[1], Ashish Nedungadi[1], Marina Carboni[2], Jonathan Cyganik[2], Michael Maffeo[2], *[1]JHU/APL, Laurel, MD, United States, [2]NSRDEC, Natick, MA, United States*

274 **A Computational Model of the Eye for Primary Blast Injury** SB³C2016-709
Bahram Notghi[1], Rajneesh Bhardwaj[2], Thao D. Nguyen[1], *[1]Mechanical Engineering, John Hopkins University, Baltimore, MD, United States, [2]Department of Mechanical Engineering, Indian Institute of Technology Bombay, Powai, Mumbai, India*

275 **Sustained Presentation of Neurotrophic Cues Following Traumatic Brain Injury Through Matrix Immobilized BDNF Fragment Peptides** SB³C2016-738
Christopher J. Lowe, David I. Shreiber, *Biomedical Engineering, Rutgers, the State University of New Jersey, Piscataway, NJ, United States*

276 **Comparison of Validation Data for Finite Element Models of the Human Head** SB³C2016-1103
Logan E. Miller, *Biomedical Engineering, Virginia Tech-Wake Forest University School of Biomedical Engineering and Sciences, Winston-Salem, NC, United States*

277 **Uncertainty and Similarity in Brain Strains Resulting From Shape Variation in Head Rotational Velocity Profile** SB³C2016-68
Wei Zhao[1], Songbai Ji[1, 2], *[1]Thayer School of Engineering, Dartmouth College, Hanover, NH, United States, [2]Department of Surgery and of Orthopaedic Surgery, Dartmouth College, Hanover, NH, United States*

278 **Registration, Regional Identification and Transfer of Data From Mri Scans to Finite Element Models** SB³C2016-590
Shankarjee Krishnamoorthi, Siddiq Qidwai, *US Naval Research Laboratory, Washington, DC, United States*

Copyright 2016 The Organizing Committee for the 2016 Summer Biomechanics, Bioengineering and Biotransport Conference

THURSDAY, JUNE 30	3:15pm - 4:45pm

Musculoskeletal Tissue Engineering: Micro to Macro — Wilson B

Session Chair: Matt Fisher, *North Carolina State University, NC, United States*
Session Co-Chair: Mariana Kersh, *University of Illinois, Urbana, IL, United States*

3:15PM **Anchorage-Independent Priming Increases Chondrogenic Potential of Human Mesenchymal Stem Cells** SB³C2016-1005
Andrea R. Tan[1], Daniel S. Donovan[2], Gerard A. Ateshian[1], J. Chloe Bulinski[3], Clark T. Hung[1], *[1]Biomedical Engineering, Columbia University, New York, NY, United States, [2]Orthopedic Surgery, Mt. Sinai-Roosevelt, New York, NY, United States, [3]Biological Sciences, Columbia University, New York, NY, United States*

3:30PM **Mechanical Control of Endochondral Bone Regeneration by Engineered Chondrogenic Mesenchymal Condensates** SB³C2016-151
Anna M. McDermott[1], Samuel Herberg[2], Hope B. Pearson[1], Devon E. Mason[1], Eben Alsberg[2], **Joel B. Boerckel**[1], *[1]Aerospace and Mechanical Engineering, University of Notre Dame, Notre Dame, IN, United States, [2]Biomedical Engineering, Case Western Reserve University, Cleveland, OH, United States*

3:45PM **Tissue Engineering Platform for Molecular Manipulation of Tenogenesis** SB³C2016-612
Chun Chien[1], Brian Pryce[2], Sara F. Tufa[2], Douglas R. Keene[2], **Alice H. Huang**[1], *[1]Orthopaedics, Icahn School of Medicine at Mount Sinai, New York, NY, United States, [2]Shriners Hospital, Portland, OR, United States*

4:00PM **The Effect of Cell Density on Prestress Development in Engineered Microtissues** SB³C2016-120
Mathieu A. J. van Kelle, Sandra Loerakker, Carlijn V. C. Bouten, *Biomedical Engineering, Eindhoven University of Technology, Eindhoven, Netherlands*

4:15PM **Microfluidic-fabrication of Bundled Cellular Scaffolds by Phaseseparated Polymer Solution** SB³C2016-1032
Yukiko T. Matsunaga, *Institute of Industrial Science, The University of Tokyo, Tokyo, Japan*

4:30PM **Variations in the Relative Size of the Cruciate Ligaments and Menisci in the Porcine Stifle Joint throughout Skeletal Growth** SB³C2016-694
Stephanie G. Cone[1], Hope E. Piercy[1], Lynn A. Fordham[2], Jorge A. Piedrahita[3], Jeffrey T. Spang[4], Matthew B. Fisher[1, 4], *[1]Department of Biomedical Engineering, North Carolina State University and University of North Carolina - Chapel Hill, Raleigh, NC, United States, [2]Department of Radiology, University of North Carolina - Chapel Hill, Chapel Hill, NC, United States, [3]College of Veterinary Medicine, North Carolina State University, Raleigh, NC, United States, [4]Department of Orthopaedics, University of North Carolina - Chapel Hill, Chapel Hill, NC, United States*

THURSDAY, JUNE 30	3:15pm - 4:45pm

Reproductive Biomechanics — Wilson C

Session Chair: Kristin Myers, *Columbia University, NY, United States*
Session Co-Chair: Kristin Miller, *Tulane University, LA, United States*

3:15PM **Mechanical Properties of Pregnant Cervix from Mouse Models of Infection-Mediated and Hormone-Mediated Preterm Birth** SB³C2016-1011
Kyoko Yoshida[1], Alexandra Willcockson[2], Shanmugasundaram Nallasamy[2], Mala Mahendroo[2], Kristin Myers[1], *[1]Mechanical Engineering, Columbia University, New York, NY, United States, [2]Obstetrics and Gynecology, UT Southwestern Medical Center, Dallas, TX, United States*

3:30PM **Nonlinear Creep Behavior of Uterosacral and Cardinal Ligaments** SB³C2016-855
Adwoa Baah-Dwomoh, Ting Tan, Raffaella De Vita, *Virginia Tech, Blacksburg, VA, United States*

3:45PM **Exploring Differences in the Tensile Response of the Pregnant and Non-pregnant Mouse Cervix** SB³C2016-902
Carrie E. Barnum[1], Jennifer L. Fey[1], Brianne K. Connizzo[1, 2], Snehal S. Shetye[1], Michal A. Elovitz[3], Louis J. Soslowsky[1], *[1]McKay Orthopaedic Research Laboratory, University of Pennsylvania, Philadelphia, PA, United States, [2]Department of Biological Engineering, Massachusetts Institute of Technology, Boston, MA, United States, [3]Maternal and Child Health Research Program, Department OBGYN, University of Pennsylvania, Philadelphia, PA, United States*

Copyright 2016 The Organizing Committee for the 2016 Summer Biomechanics, Bioengineering and Biotransport Conference

4:00PM **Effect of Elastin Digestion on the Biaxial Mechanical Response of the Murine Vagina** SB³C2016-703
Katy M. Robison, Derek J. Bivona, Kristin S. Miller, *Biomedical Engineering, Tulane University, New Orleans, LA, United States*

4:15PM **How much Additional Maternal Spatial Capacity do Forceps Require When Delivering the Fetal Head During Vaginal Birth?** SB³C2016-775
Paige V. Tracy[1], John O. L. DeLancey[2], James A. Ashton-Miller[3], *[1]Biomedical Engineering, University of Michigan, Ann Arbor, MI, United States, [2]Obstetrics and Gynecology, University of Michigan, Ann Arbor, MI, United States, [3]Mechanical Engineering, Biomedical Engineering, University of Michigan, Ann Arbor, MI, United States*

4:30PM **Use Inverse Finite Element Method to Determine the Impairments in Pelvic Floor Support Structure in Women with Pelvic Organ Prolapse** SB³C2016-847
Mark T. Gordon[1], James A. Ashton-Miller[2], John O. L. DeLancey[3], Luyun L. Chen[2], *[1]Bioengineering and Mechanical Engineering, California Baptist University, Riverside, CA, United States, [2]Biomedical Engineering Department, University of Michigan, Ann Arbor, MI, United States, [3]Obstetrics and Gynecology Department, University of Michigan, Ann Arbor, MI, United States*

THURSDAY, JUNE 30 | 3:15pm - 4:45pm

Solid Mechanics: Growth and Remodeling — Wilson D

Session Chair: Sara Roccabianca, *Michigan State University, MI, United States*
Session Co-Chair: Lik Chuan Lee, *Michigan State University, MI, United States*

3:15PM **Adventitial Remodeling in Hypertension Leads to Aortic Maladaptation and Loss of Function** SB³C2016-840
Matthew R. Bersi[1], Chiara Bellini[1], Jing Wu[2], Kim R. C. Montaniel[2], David G. Harrison[2], Jay D. Humphrey[1], *[1]Biomedical Engineering, Yale University, New Haven, CT, United States, [2]Medicine and Pharmacology, Vanderbilt University, Nashville, TN, United States*

3:30PM **Effects of Hemodynamic Changes on the Developing Dorsal Aorta of the Chick Embryo** SB³C2016-99
Gabriela Espinosa, Larry Taber, **Jessica Wagenseil**, *Washington University in St. Louis, St. Louis, MO, United States*

3:45PM **Flow-Rate-Controlled Remodeling of Glomerular Capillaries** SB³C2016-829
Lazarina Gyoneva[1], **Daniel Goodman**[1], Yoav Segal[1, 2], Kevin D. Dorfman[1], Victor H. Barocas[1], *[1]University of Minnesota, Minneapolis, MN, United States, [2]VA Medical Center, Minneapolis, MN, United States*

4:00PM **A Comparison of Phenomenologic Growth Laws for Myocardial Hypertrophy** SB³C2016-161
Colleen M. Witzenburg, Jeffrey W. Holmes, *Biomedical Engineering, University of Virginia, Charlottesville, VA, United States*

4:15PM **Experimental Investigation of Functional Forms Required for Modeling Degrading Acellular Tissue Engineered Vascular Grafts in a Predictive Growth and Remodeling Framework** SB³C2016-780
Piyusha S. Gade[1], Keewon Lee[1], Blaise N. Pfaff[2], Yadong Wang[3], Anne M. Robertson[4], *[1]Department of Bioengineering, University of Pittsburgh, Pittsburgh, PA, United States, [2]Department of Chemical Engineering, Pennsylvania State University, Philadelphia, PA, United States, [3]Department of Bioengineering, Chemical and Petroleum Engineering, Surgery, University of Pittsburgh, Pittsburgh, PA, United States, [4]Department of Mechanical Engineering and Materials Science, Bioengineering, University of Pittsburgh, Pittsburgh, PA, United States*

4:30PM **Histological and Biomechanical analyses of Human Abdominal Aortic Aneurysms** SB³C2016-1044
Mirunalini Thirugnanasambandam[1], Karthik Mikkineni[2], Satish Muluk[2], Oluwaseun R. Adeyinka[1], Ender Finol[1], *[1]Department of Biomedical Engineering, University of Texas at San Antonio, San Antonio, TX, United States, [2]Division of Vascular Surgery, Allegheny Health Network, Pittsburgh, PA, United States*

Copyright 2016 The Organizing Committee for the 2016 Summer Biomechanics, Bioengineering and Biotransport Conference

THURSDAY, JUNE 30	3:15pm - 4:45pm

Characterization of Cardiovascular Tissues — Annapolis 1

Session Co-Chair: Jonathan Wenk, *University of Kentucky, KY, United States*
Session Co-Chair: Hai-Chao Han, *UTSA, San Antonio, TX, United States*

3:15PM **A Multi-Scale Mechanical and Cellular Argument for the Differential Performance of Coronary Artery Bypass Grafts** SB³C2016-937

David A. Prim[1], Boran Zhou[1], Laurel Carter[2], Vinal Menon[3], Jay Potts[3], Tarek Shazly[1], John F. Eberth[3], *[1]Biomedical Engineering, University of South Carolina, Columbia, SC, United States, [2]University of South Carolina School of Medicine, Columbia, SC, United States, [3]Cell Biology and Anatomy, University of South Carolina School of Medicine, Columbia, SC, United States*

3:30PM **Is There a Critical Time Point for Antihypertensive Treatment? Embryonic Antihypertensive Treatment Alters Arterial Stiffness in Elastin Haploinsufficient Mice** SB³C2016-982

Jungsil Kim[1], Victoria Le[2], Robert Mecham[3], Jessica Wagenseil[1], *[1]Mechanical Engineering & Materials Science, Washington University in St. Louis, St. Louis, MO, United States, [2]Biomedical Engineering, University of Texas, Austin, TX, United States, [3]Cell Biology & Physiology, Washington University in St. Louis, St. Louis, MO, United States*

3:45PM **Anatomically-driven Multiscale Model of Ascending Thoracic Aorta, with Application to Multidirectional Experiments** SB³C2016-917

Rohit Y. Dhume[1], Christopher E. Korenczuk[2], Victor H. Barocas[2], *[1]Department of Mechanical Engineering, University of Minnesota, Minneapolis, MN, United States, [2]Department of Biomedical Engineering, University of Minnesota, Minneapolis, MN, United States*

4:00PM **The Mitral Valve Chordae Tendineae: A Topological And Geometric Analysis** SB³C2016-852

Amir H. Khalighi[1], Andrew Drach[2], Charles Bloodworth[3], Eric L. Pierce[3], Ajit Yoganathan[3], Robert C. Gorman[4], Joseph H. Gorman[4], Michael S. Sacks[2], *[1]Mechanical Engineering, University of Texas at Austin, Austin, TX, United States, [2]University of Texas at Austin, Austin, TX, United States, [3]Georgia Institute of Technology, Atlanta, GA, United States, [4]University of Pennsylvania, Philadelphia, PA, United States*

4:15PM **Quantification of Biventricular Myocardial Strains from Cine Magnetic Resonance Images of Pulmonary Hypertensive Patients Using Hyperelastic Warping** SB³C2016-25

Ce Xi[1], Xiaodan Zhao[2], Liang Zhong[2], Martin Genet[3], Lik Chuan Lee[4], *[1]Michigan State Universiy, East lansing, MI, United States, [2]National Heart Center, Singapore, Singapore,* [3]École Polytechnique, Paris, France, *[4]Michigan State University, East Lansing, MI, United States*

4:30PM **A Novel Numerical-Experimental Inverse Modeling Approach to Investigate the Time-Evolving Three-Dimensional Mechanical Properties of Infarcted Myocardium** SB³C2016-735

David S. Li[1], João S. Soares[1], John G. Lesicko[1], Reza Avazmohammadi[1], Joseph H. Gorman[2], Robert C. Gorman[2], Michael S. Sacks[1], *[1]Biomedical Engineering, The University of Texas at Austin, Austin, TX, United States, [2]Perelman School of Medicine, University of Pennsylvania, Philadelphia, PA, United States*

THURSDAY, JUNE 30	3:15pm - 4:45pm

Physiological Valves — Annapolis 2

Session Chair: Michael Sacks, *University of Texas, Austin, TX, United States*
Session Co-Chair: Lakshmi P. D. Dasi, *Ohio State University, OH, United States*

3:15PM **Developing Computational Fluid-Structure Models for the Lymphatic Valve** SB³C2016-881

John T. Wilson[1], Lowell T. Edgar[1], Raoul van Loon[2], James E. Moore[1], *[1]Bioengineering, Imperial College London, London, United Kingdom, [2]Swansea University, Swansea, United Kingdom*

3:30PM **Blood Clotting Potential and Hemodynamic Analysis of a Superhydrophobic Bileaflet Mechanical Heart Valve** SB³C2016-901

David Bark[1], Hamed Vahabi[1], Hieu Bui[2], Sanli Movafaghi[1], Arun Kota[1], Ketul Popat[1], Lakshmi Prasad Dasi[1], *[1]Mechanical Engineering, Colorado State University, Fort Collins, CO, United States, [2]Biomedical Engineering, Colorado State University, Fort Collins, CO, United States*

Copyright 2016 The Organizing Committee for the 2016 Summer Biomechanics, Bioengineering and Biotransport Conference

3:45PM **FSI Simulation of Intraventricular Flow in a Patient-Specific Left Ventricular Model with both Mitral and Aortic Valves** SB³C2016-1121
Andres D. Caballero, Wenbin Mao, Wei Sun, *The Wallace H. Coulter Department of Biomedical Engineering, Georgia Institute of Technology and Emory University, Atlanta, GA, United States*

4:00PM **A Robust Framework for Building Attribute-Rich FE Models of Mitral Valve from Medical Images** SB³C2016-1003
Andrew Drach[1], Amir H. Khalighi[2], Robert C. Gorman[3], Joseph H. Gorman[3], Ajit P. Yoganathan[4], Michael S. Sacks[5], *[1]Institute for Computational Engineering and Sciences, The University of Texas at Austin, Austin, TX, United States, [2]Mechanical Engineering, The University of Texas at Austin, Austin, TX, United States, [3]Perelman School of Medicine, University of Pennsylvania, Philadelphia, PA, United States, [4]Cardiovascular Fluid Mechanics Laboratory, Georgia Institute of Technology, Atlanta, GA, United States, [5]Biomedical Engineering, The University of Texas at Austin, Austin, TX, United States*

4:15PM **Computational Assessment of Hemodynamic Parameters of Bicuspid Aortic Valve Aortopathy** SB³C2016-57
Kai Cao[1], **Philippe Sucosky**[2], *[1]Department of Aerospace and Mechanical Engineering, University of Notre Dame, Notre Dame, IN, United States, [2]Department of Mechanical and Materials Engineering, Wright State University, Dayton, OH, United States*

4:30PM **Importance of Including Papillary Muscles and Trabeculae in Cardiac Flow Simulations** SB³C2016-86
Jonas Lantz, Lilian Henriksson, Anders Persson, Matts Karlsson, Tino Ebbers, *Linkoping university, Linkoping, Sweden*

THURSDAY, JUNE 30 | 3:15pm - 4:45pm

Trends, Tips, and Tricks in Biomechanical Engineering Education — Azalea 2

Session Chair: Sarah Kieweg, *University of Kansas, KS, United States*
Session Co-Chair: Kristen Billiar, *Worcester Polytechnic Institute, MA, United States*

3:15PM **Student Learning of Biomechanics Topics by Embedding "Quantified Self" Motivated Problem Based Learning Modules in Biomedical Engineering Courses** SB³C2016-1116
Eric G. Meyer, Mansoor Nasir, *Biomedical Engineering, Lawrence Technological University, Southfield, MI, United States*

3:30PM **Introduction to Finite Element Modeling in a Guided Project-based Approach to Biomechanics Research** SB³C2016-992
Alexander Kotelsky, Amy L. Lerner, *Biomedical Engineering, University of Rochester, Rochester, NY, United States*

3:45PM **A New Educational Approach to Teaching Science and Engineering for K-12 Students** SB³C2016-860
Kritsakorn Chaumpanich[1], Michelle Johnson[2], Yingcai Xiao[1], Philip A. Allen[3], **Yang H. Yun**[4], *[1]Computer Science, Univeristy of Akron, Akron, OH, United States, [2]PLTW Biomedical Science, North High School, Akron, OH, United States, [3]Psychology, Univeristy of Akron, Akron, OH, United States, [4]Biomedical Engineering, Univeristy of Akron, Akron, OH, United States*

4:00PM **A Course in Maker Activities for a Master of Engineering in Design and Commercialization** SB³C2016-688
Brandon Kirkland, Ophelia Johnson, **Alan Eberhardt**, *UAB, Birmingham, AL, United States*

4:15PM **Best Practices in teaching biomechanics: Connecting Biomechanics Beyond the Classroom** SB³C2016-575
Laurel Kuxhaus, *Clarkson University, Potsdam, NY, United States*

4:30PM **When Theatre comes to Capstone Design: Oh How Creative They can Be...** SB³C2016-805
Ferris Pfeiffer[1], Suzanne Burgoyne[2], Rachel E. Bauer[2], *[1]Bioengineering/Orthopaedic Surgery, University of Missouri, Columbia, MO, United States, [2]Theatre, University of Missouri, Columbia, MO, United States*

Copyright 2016 The Organizing Committee for the 2016 Summer Biomechanics, Bioengineering and Biotransport Conference

THURSDAY, JUNE 30	3:15pm - 4:45pm

Cancer and Tumor Microenvironment — Azalea 3

Session Chair: Sihong Wang, *City College of New York, NY, United States*
Session Co-Chair: Hai Wang, *The Ohio State University, OH, United States*

3:15PM **Investigation of Biotransport in a Tumor with Non-Homogeneous Permeability Using a Non-Intrusive Polynomial Chaos Approach** SB³C2016-785
Miao Lu[1], Liang Zhu[1], Ronghui Ma[1], Maher Salloum[2], Meilin Yu[1], *[1]Mechanical Engineering, University of Maryland, Baltimore County, Baltimore, MD, United States, [2]Sandia National Labs, Livermore, CA, United States*

3:30PM **Adhesion and Invasion of Circulating Cancer Cells on Inflamed Endothelium** SB³C2016-848
Taylor J. Thompson, **Bumsoo Han**, *Mechanical Engineering, Purdue University, West Lafayette, IN, United States*

3:45PM **A Near Infrared Laser-activated "Nanobomb" for Breaking the Barriers to MicroRNA Delivery** SB³C2016-133
Hai Wang, Xiaoming He, *Biomedical Engineering, The Ohio State University, Columbus, OH, United States*

4:00PM **Conformal Nanoencapsulation of Allogeneic T Cells Mitigate Graft-versus-Host Disease but Retain Graft-versus-Leukemia Activity** SB³C2016-718
Shuting zhao, Xiaoming He, *Biomedical Engineering, The Ohio State University, Columbus, OH, United States*

4:15PM **Monitoring Tumor Response to Therapeutic TR4 Fusion Protein via in vivo Imaging** SB³C2016-67
Marianna Prokopi[1], Costas Pitsillides[2], Mahendra Deonarain[3], Konstantinos Kapnisis[2], Spyros Stylianou[4], George Kousparos[5], Christina Kousparou[1], **Andreas Anayiotos**[2], Agamemnon Epenetos[1], *[1]Trojantec Ltd, Nicosia, Cyprus, [2]Mechanical and Materials Science and Engineering, Cyprus University of Technology, Limassol, Cyprus, [3]ShyDen Biotechnology Ltd, Stevenage, Herts, United Kingdom, [4]Translational Genetics Team, The Cyprus Institute of Neurology & Genetics, Nicosia, Cyprus, [5]Frimley Park Hospital, NHS Foundation Trust, Surrey, United Kingdom*

4:30PM **Development of a Tissue Engineered 3D Microfluidic Tumor Platform to Study Nanoparticle Transport** SB³C2016-1100
Manasa Gadde[1], Matthew R. DeWitt[2], Marissa N. Rylander[3], *[1]Biomedical Engineering, University of Texas at Austin, Austin, TX, United States, [2]Virginia Tech-Wake Forest SBES, Virginia Tech, Blacksburg, VA, United States, [3]Mechanical Engineering, University of Texas at Austin, Austin, TX, United States*

FRIDAY, JULY 1	9:45am - 11:15am

PhD Competition: Signaling & Remodeling — Wilson B

Session Chair: Triantafyllos Stylianopolous, *University of Cyprus, Cyprus*
Session Co-Chair: Trevor Lujan, *Boise State, ID, United States*

9:45AM **Reproduction Induces Adaptation of the Maternal Skeleton and Alters Patterns of Postmenopausal Bone Loss** SB³C2016-138
Chantal M. J. de Bakker, Allison R. Altman-Singles, Wei-Ju Tseng, Laurel Leavitt, Connie Li, X. Sherry Liu, *Department of Orthopaedic Surgery, University of Pennsylvania, Philadelphia, PA, United States*

10:00AM **Local Changes to the Growth Plate in Response to Injury** SB³C2016-691
Lauren M. Mangano[1], Meghan E. Kupratis[1], Katie Li[1], Eric Rapp[2], Louis C. Gerstenfeld[3], Elise F. Morgan[1, 2, 3], *[1]Biomedical Engineering, Boston University, Boston, MA, United States, [2]Mechanical Engineering, Boston University, Boston, MA, United States, [3]Orthopaedic Surgery, Boston University, Boston, MA, United States*

10:15AM **Vascular Smooth Muscle Cell Mechano-Adaptation Laws** SB³C2016-159
Kerianne E. Steucke, Zaw Win, Emily E. Walsh, Taylor R. Stemler, Patrick W. Alford, *Biomedical Engineering, University of Minnesota, Minneapolis, MN, United States*

10:30AM **Cadherin-11 Excacerbates Maladaptive Remodeling After Myocardial Infarction** SB³C2016-1080
Alison Schroer, W. David Merryman, *Vanderbilt University, Nashville, TN, United States*

Copyright 2016 The Organizing Committee for the 2016 Summer Biomechanics, Bioengineering and Biotransport Conference

10:45AM **Positive and Negative Cues for Modulating Neurite Dynamics and Receptor Expression to Improve Peripheral Nerve Regeneration** SB³C2016-611

Melissa R. Wrobel, Harini G. Sundararaghavan, *Biomedical Engineering, Wayne State University, Detroit, MI, United States*

11:00AM **The RhoA/ROCK Pathway Mediates Nociceptive Signaling After Painful Ligament Loading** SB³C2016-32

Sijia Zhang, Beth Winkelstein, *University of Pennsylvania, Philadelphia, PA, United States*

FRIDAY, JULY 1 | 9:45am - 11:15am

PhD Competition: Mechanosensing & Mechanics — Wilson C

Session Chair: Corinne Henak, *Wisconsin, WI, United States*
Session Co-Chair: Andrew Kemper, *Virginia Tech, VA, United States*

9:45AM **Chondrocyte Death and Mitochondrial Dysfunction are Mediated by Cartilage Friction and Shear Strain** SB³C2016-807

Edward D. Bonnevie[1], Michelle L. Delco[2], Naveen Jasty[1], Lena R. Bartell[3], Lisa A. Fortier[2], Itai Cohen[3], Lawrence J. Bonassar[1, 4], *[1]Mechanical Engineering, Cornell University, Ithaca, NY, United States, [2]Comparative Biomedical Sciences, Cornell University, Ithaca, NY, United States, [3]Applied Engineering Physics, Cornell University, Ithaca, NY, United States, [4]Biomedical Engineering, Cornell University, Ithaca, NY, United States*

10:00AM **Direct Osmotic Pressure Measurements in Articular Cartilage Demonstrate Non-Ideal and Concentration-Dependent Phenomena** SB³C2016-1010

Brandon K. Zimmerman[1], Robert J. Nims[2], Clark T. Hung[2], Gerard A. Ateshian[1, 2], *[1]Mechanical Engineering, Columbia University, New York, NY, United States, [2]Biomedical Engineering, Columbia University, New York, NY, United States*

10:15AM **N-Cadherin Adhesive Interactions Modulate ECM Mechanosensing and Fate Commitment in Mesenchymal Stem Cells** SB³C2016-640

Brian D. Cosgrove[1, 2, 3], Keeley L. Mui[4], Tristan P. Driscoll[1, 2], Steven R. Caliari[1, 3], Richard K. Assoian[4], Jason A. Burdick[1, 3], Robert L. Mauck[1, 2, 3], *[1]Bioengineering, University of Pennsylvania, Philadelphia, PA, United States, [2]Orthopedic Surgery, University of Pennsylvania, Philadelphia, PA, United States, [3]Translational Musculoskeletal Research Center, Philadelphia VA Medical Center, Philadelphia, PA, United States, [4]Pharmacology, University of Pennsylvania, Philadelphia, PA, United States*

10:30AM **A Multiphysics Model of the Pacinian Corpuscle** SB³C2016-95

Julia C. Quindlen[1], Henryk K. Stolarski[2], Martha Flanders[3], Victor H. Barocas[1], *[1]Biomedical Engineering, University of Minnesota, Minneapolis, MN, United States, [2]Civil Engineering, University of Minnesota, Minneapolis, MN, United States, [3]Neuroscience, University of Minnesota, Minneapolis, MN, United States*

10:45AM **Molecular Level Detection and Quantification of Collagen Mechanical Damage Using Collagen Hybridizing Peptides** SB³C2016-809

Jared L. Zitnay[1, 2], Yang Li[1], Zhao Qin[3], Baptiste Depalle[3], Shawn P. Reese[1, 2], Markus J. Buehler[3], S. Michael Yu[1], Jeffrey A. Weiss[1, 2, 4], *[1]Bioengineering, University of Utah, Salt Lake City, UT, United States, [2]Scientific Computing and Imaging Institute, University of Utah, Salt Lake City, UT, United States, [3]Civil and Environmental Engineering, Massachusetts Institute of Technology, Cambridge, MA, United States, [4]Orthopaedics, University of Utah, Salt Lake City, UT, United States*

11:00AM **Collagen Degradation Alters Failure Properties & Matrix Reorganization During Tensile Loading** SB³C2016-92

Meagan Ita, Beth Winkelstein, *University of Pennsylvania, Philadelphia, PA, United States*

Copyright 2016 The Organizing Committee for the 2016 Summer Biomechanics, Bioengineering and Biotransport Conference

FRIDAY, JULY 1	9:45am - 11:15am

PhD Competition: Tissue Mechanics & Modeling — Wilson D

Session Chair: Roger Haut, *Michigan State University, MI, United States*
Session Co-Chair: Megan Killian, *University of Delaware, DE, United States*

9:45AM **Multiscale Mechanics of Human Supraspinatus Tendon in Shear after Proteoglycan Depletion** SB³C2016-72
Fei Fang[1], Spencer P. Lake[1, 2, 3], *[1]Mechanical Engineering & Materials Science, Washington University in St. Louis, St. Louis, MO, United States, [2]Department of Biomedical Engineering, Washington University in St. Louis, St. Louis, MO, United States, [3]Department of Orthopaedic Surgery, Washington University in St. Louis, St. Louis, MO, United States*

10:00AM **Subject-specific vs. Averaged Structural Models of the Collagen Network in the Lumbar Facet Capsular Ligament** SB³C2016-918
Vahhab Zarei[1], Amy A. Claeson[2], Chao Liu[2], Taner Akkin[2], Victor H. Barocas[2], *[1]Mechanical Engineering, University of Minnesota, Minneapolis, MN, United States, [2]Biomedical Engineering, University of Minnesota, Minneapolis, MN, United States*

10:15AM **Dynamic Imaging of Tendon Tissue Stress** SB³C2016-1042
Jack A. Martin[1], Alexander C. Ehlers[2], James R. Hermus[2], Matthew S. Allen[3], Daniel J. Segalman[3], Darryl G. Thelen[4], *[1]Materials Science Program, University of Wisconsin-Madison, Madison, WI, United States, [2]Department of Biomedical Engineering, University of Wisconsin-Madison, Madison, WI, United States, [3]Department of Engineering Physics, University of Wisconsin-Madison, Madison, WI, United States, [4]Department of Mechanical Engineering, University of Wisconsin-Madison, Madison, WI, United States*

10:30AM **Tsai-Hill Maximum-Work Theory as a Failure Criterion for Fibrous Biological Tissues** SB³C2016-689
Christopher E. Korenczuk, Victor H. Barocas, *Department of Biomedical Engineering, University of Minnesota, Minneapolis, MN, United States*

10:45AM **Remodeling by Fibroblasts Alters the Rate-dependent Mechanical Properties of Collagen** SB³C2016-894
Behzad Babaei[1], Ali Davarian[2], Kenneth M. Pryse[2], William B. McConnaughey[2], Elliot L. Elson[2], Guy M. Genin[1], *[1]Department of Mechanical Engineering & Materials Science, Washington University in St. Louis, St. Louis, MO, United States, [2]Department of Biochemistry & Molecular Biophysics, Washington University in St. Louis, St. Louis, MO, United States*

11:00AM **A Permanent Set Constitutive Model for Exogenously Cross-linked Collagenous Tissues** SB³C2016-954
Will Zhang[1], Hobey Tam[2], Wei Sun[3], Naren Vyavahare[2], Michael S. Sacks[1], *[1]Department of Biomedical Engineering, Institute for Computational Engineering and Sciences, The University of Texas at Austin, Austin, TX, United States, [2]Department of Bioengineering, Clemson University, Clemson, SC, United States, [3]Department of Biomedical Engineering, Georgia Institute of Technology, Atlanta, GA, United States*

FRIDAY, JULY 1	9:45am - 11:15am

PhD Competition: Biomechanics of Injury — Annapolis 1

Session Chair: Brittany Coats, *University of Utah, UT, United States*
Session Co-Chair: Lakiesha Williams, *MIssissippi State, MS, United States*

9:45AM **Coronal Head Rotation and Rapid Corpus Callosum Tract Strain in Sports-Related Mild Traumatic Brain Injury** SB³C2016-971
Fidel Hernandez[1], Chiara Giordano[2], Svein Kleiven[2], David Camarillo[1, 3], *[1]Department of Mechanical Engineering, Stanford University, Stanford, CA, United States, [2]Department of Neuronic Engineering, KTH Royal Institute of Technology, Stockholm, Sweden, [3]Department of Bioengineering, Stanford University, Stanford, CA, United States*

10:00AM **Differences in the Ability of Bicycle Helmets to Reduce Risk of Head Injury** SB³C2016-1090
Megan L. Bland, Steven Rowson, *Virginia Tech, Blacksburg, VA, United States*

10:15AM **Spatio-Temporal Quantification of Cartilage Structural Changes in a Murine Model of Post-Traumatic Osteoarthritis** SB³C2016-966
Michael A. David, Avery T. White, Rachael Pilachowski, Ryan C. Locke, Melanie K. Smith, Christopher Price, *Biomedical Engineering, University of Delaware, Newark, DE, United States*

Copyright 2016 The Organizing Committee for the 2016 Summer Biomechanics, Bioengineering and Biotransport Conference

10:30AM **Principal Component Analysis of Friction Force Hysteresis Curves for Detecting Fatigue Failure and Generating Frictional S-N Curves for Articular Cartilage** SB³C2016-1071

Krista M. Durney[1], Robert J. Nims[1], James F. Boorman-Padgett[2], Jason T. Suh[1], Hyeon Jin Koo[1], Polina V. Smirnova[1], Gregory T. Salamone[1], Brian K. Jones[2], Sevan R. Oungoulian[2], Clark T. Hung[1], Gerard A. Ateshian[1, 2], *[1]Biomedical Engineering, Columbia University, New York, NY, United States, [2]Mechanical Engineering, Columbia University, New York, NY, United States*

10:45AM **Experimental Biomechanics of the Anterior Cruciate Ligament: Hyperelasticity and Viscoelasticity** SB³C2016-1063

Kaitlyn Mallett[1], Ellen M. Arruda[2], *[1]Mechanical Engineering, University of Michigan, Ann Arbor, MI, United States, [2]Mechanical Engineering, Biomedical Engineering, Program in Macromolecular Science and Engineering, University of Michigan, Ann Arbor, MI, United States*

11:00AM **Alterations in the Anterior Capsule Correlate with Impaired Joint Mechanics in a Rat Elbow Model of Post-Traumatic Joint Stiffness** SB³C2016-618

Chelsey Dunham[1], Ryan Castile[1], Leesa Galatz[2], Spencer Lake[1], *[1]Washington University in St. Louis, St. Louis, MO, United States, [2]Mount Sinai, New York, NY, United States*

FRIDAY, JULY 1 | 9:45am - 11:15am

PhD Competition: Cardiac & Vascular — Annapolis 2

Session Chair: Daniela Valdez-Jasso, *UI Chicago, IL, United States*
Session Co-Chair: Will Richardson, *Clemson, SC, United States*

9:45AM **Cellular Architecture Dictates Anisotropic Mechanical Properties of Vascular Smooth Muscle Cells** SB³C2016-629

Zaw Win, Justin M. Buksa, Patrick W. Alford, *Biomedical Engineering, University of Minnesota, Minneapolis, MN, United States*

10:00AM **Analysis of Chromatin Mechanics During Cardiomyocyte Contraction Using Nuclear Spatial Strain Maps Reveals New Protective Mechanism** SB³C2016-751

Benjamin Seelbinder[1], Soham Ghosh[1], Sarah Calve[2], Corey P. Neu[1, 2], *[1]Mechanical Engineering, Universtiy of Colorado Boulder, Boulder, CO, United States, [2]Biomedical Engineering, Purdue University, West Lafayette, IN, United States*

10:15AM **Acute Effects of Cell Free Hemoglobin and Sickled Red Blood Cells on Pulmonary Vascular Impedance in Otherwise Healthy Mice** SB³C2016-772

David A. Schreier[1], Timothy Hacker[2], Diana Tabima[1], Naomi C. Chesler[1], *[1]Biomedical Engineering, University of Wisconsin-Madison, Madison, WI, United States, [2]Medicine, University of Wisconsin-Madison, Madison, WI, United States*

10:30AM **Virtual Evaluation of Surgical Revascularization Techniques in Coronary Artery Bypass Surgery** SB³C2016-904

Abhay B. Ramachandra[1, 2], Christopher Jensen[3], Andrew B. Goldstone[3], Joseph Y. Woo[3], Jack H. Boyd[3], Andrew Kahn[4], Alison Marsden[2], *[1]Department of Mechanical and Aerospace Engineering, University of California San Diego, La Jolla, CA, United States, [2]Institute for Computational and Mathematical Engineering, Department of Pediatric Cardiology, Stanford University, Stanford, CA, United States, [3]Department of Cardiothoracic Surgery, Stanford University, Stanford, CA, United States, [4]Department of Medicine, University of California San Diego, La Jolla, CA, United States*

10:45AM **Computation Investigation of Hydrogel Injection Characteristics for Myocardial Support** SB³C2016-94

Hua Wang[1], Christopher Rodell[2], Mandonna Lee[3], Neville Dusaj[4], Jason Burdick[2], Robert Gorman[3], Jonathan Wenk[1, 5], *[1]Department of Mechanical Engineering, University of Kentucky, Lexington, KY, United States, [2]Department of Bioengineering, University of Pennsylvania, Philadelphia, PA, United States, [3]Gorman Cardiovascular Research Group, University of Pennsylvania, Philadelphia, PA, United States, [4]Department of Chemistry and Physics, University of Pennsylvania, Philadelphia, PA, United States, [5]Department of Surgery, University of Kentucky, Lexington, KY, United States*

Copyright 2016 The Organizing Committee for the 2016 Summer Biomechanics, Bioengineering and Biotransport Conference

11:00AM **Contribution of Glycosaminoglycans to Extracellular Matrix Fiber Recruitment and Arterial Wall Mechanics** SB³C2016-104

Jeffrey Mattson[1], Raphaël Turcotte[2, 3], Yanhang Zhang[1, 2], *[1]Mechanical Engineering, Boston University, Boston, MA, United States, [2]Biomedical Engineering, Boston University, Boston, MA, United States, [3]Center for Systems Biology, Advanced Microscopy Program, Wellman Center for Photomedicine, Massachusetts General Hospital, Harvard Medical School, Boston, MA, United States*

FRIDAY, JULY 1	9:45am - 11:15am

Undergraduate Design Competition - Rehabilitation & Assistive Devices

Azalea 2

Session Chair: Tamara Bush, *Michigan State University, MI, United States*
Session Co-Chair: Nicole Corbiere, *Clarkson University, NY, United States*

9:45AM **Substitute Voice Production via a Mechanically-Driven Arti icial Larynx** SB³C2016-130

Michael R. Baldwin[1], Kateri A. Kaminski[1], Janet A. Hrdina[1], Evan T. Cody[2], Erik A. Gillespie[1], Tyler T. Tuttle[1], **Byron D. E. Erath**[1], *[1]Mechanical and Aeronautical Engineering, Clarkson University, Potsdam, NY, United States, [2]School of Business, Clarkson University, Potsdam, NY, United States*

10:00AM **Wireless Instrumented Cane** SB³C2016-1095

Me'Lanae Garrett[1], Binod Shilpakar[1], Joel A. Whitney[1], Jon T. E. Williams[1], Radhakrishnan Srinivasan[2], Lakiesha Williams[2], *[1]Agricultural and Biological Engineering, Mississippi State University, Starkville, MS, United States, [2]Agricultural and Biological Engineering, Mississippi State University, Mississippi State, MS, United States*

10:15AM **Intrahospital Assistive Transportation Device for Mechanically Ventilated Pediatric Patients** SB³C2016-1047

Allison Fetz, Elysia Masters, Ravi Patel, Ameen Ozrail, John Williams, Gary Bowlin, Maris Brown, *Biomedical Engineering, University of Memphis, Memphis, TN, United States*

10:30AM **Adaptable, Affordable, and Reusable Interim Prosthetic Leg Solution in Response to Recent Medicare Coverage Changes** SB³C2016-615

Jason A. Shar, Andrew M. Milhoan, Nathan F. Levengood, Joshua Gargac, Matthew Volansky, *Mechanical Engineering, University of Mount Union, Alliance, OH, United States*

10:45AM **Improved Ankle Foot Orthosis for Clubfoot Treatment** SB³C2016-574

Angela Guardia[1], Alissa Adams[1], Brianna Bruni-Bossio[1], Alberto Palomino[1], Rex Wu[1], Kajsa Duke[2], *[1]Mechanical Engineering, University of Alberta, Edmonton, AB, Canada, [2]Mechanical Engineering - Biomedical Option, University of Alberta, Edmonton, AB, Canada*

11:00AM **Reaching Aid for Spinal Fusion Recipients** SB³C2016-834

Bijal Patel, **Casey K. Schiner**, Celia M. Staniak, Maryssa Mercer, Michele Grimm, Brian Mundo, *Wayne State University, Detroit, MI, United States*

FRIDAY, JULY 1	9:45am - 11:15am

PhD Competition: Devices, Microfluidics and Sensing

Azalea 3

Session Chair: James Baish, *Bucknell University, PA, United States*
Session Co-Chair: Luke Herbertson, *FDA, DC, United States*

9:45AM **Programming 'On-Demand' Delivery From Mechanically-Activated Microcapsules** SB³C2016-134

Bhavana Mohanraj, Miju Kim, Daeyeon Lee, George R. Dodge, Robert L. Mauck, *University of Pennsylvania, Philadelphia, PA, United States*

10:00AM **Analysis of Cell Spreading on Micropatterned Substrates using a Thermodynamically Consistent Non-Local Active Formulation** SB³C2016-1015

Eoin McEvoy[1], Tommaso Ristori[2], Sandra Loerakker[2], Vikram S. Deshpande[3], Patrick McGarry[1], *[1]Biomedical Engineering, National University of Ireland Galway, Galway, Ireland, [2]Biomedical Engineering, Eindhoven University of Technology, Eindhoven, Netherlands, [3]Engineering, University of Cambridge, Cambridge, United Kingdom*

Copyright 2016 The Organizing Committee for the 2016 Summer Biomechanics, Bioengineering and Biotransport Conference

10:15AM **An Experimental Canine Patent Ductus Arteriosus Occluder Based on Shape Memory Polymer Foam in a Nitinol Cage** SB³C2016-21
Mark A. Wierzbicki, Bradley H. Due, Landon D. Nash, Brandis Keller, Sonya G. Gordon, Matthew W. Miller, Duncan J. Maitland, *Texas A&M University, College Station, TX, United States*

10:30AM **Microfluidics for the Study of Oxygen Gradients at the Maternal Fetal Interface** SB³C2016-794
Yassen Abbas[1, 2], Carolin Oefner[2, 3], Graham J. Burton[2, 4], Ashley Moffett[2, 3], Michelle L. Oyen[1, 2], *[1]Engineering, University of Cambridge, Cambridge, United Kingdom, [2]Centre for Trophoblast Research, University of Cambridge, Cambridge, United Kingdom, [3]Pathology, University of Cambridge, Cambridge, United Kingdom, [4]Department of Physiology, Development and Neuroscience, University of Cambridge, Cambridge, United Kingdom*

10:45AM **Thermal Contrast Amplification (TCA) Readers Improve the Limit of Detection for Influenza and Malaria Lateral Flow Assays** SB³C2016-1056
Yiru Wang[1], Zhenpeng Qin[1, 2], David Boulware[3], Iveth J. González[4], David Bell[3, 5], Warren Chan[6], Peter Chiodini[7], Roxanne Rees-Channer[7], John C. Bischof[1], *[1]Department of Mechanical Engineering, University of Minnesota - Twin Cities, Minneapolis, MN, United States, [2]University of Texas at Dallas, Richardson, TX, United States, [3]Department of Medicine Infectious Diseases and International Medicine, University of Minnesota - Twin Cities, Minneapolis, MN, United States, [4]Foundation for New Innovative Diagnosis, Geneva, Switzerland, [5]Global Good Fund, Bellevue, WA, United States, [6]Department of Chemistry, University of Toronto, Toronto, ON, Canada, [7]Hospital for Tropical Disease, University College London, London, United Kingdom*

11:00AM **Error and Uncertainty Quantification of a Commercial CFD Solver in an Intracranial Anenrusym** SB³C2016-1074
Nicole Varble[1, 2], Nikhil Paliwal[1, 2], Jianping Xiang[2, 3], Kristian Debus[4], Hui Meng[1, 2, 5], *[1]Mechanical and Aerospace Engineering, SUNY University at Buffalo, Buffalo, NY, United States, [2]Toshiba Stroke and Vascular Research Center, Buffalo, NY, United States, [3]Neurosurgery, SUNY University at Buffalo, Buffalo, NY, United States, [4]CD-adapco, Melville, NY, United States, [5]Biomedical Engineering, SUNY University at Buffalo, Buffalo, NY, United States*

FRIDAY, JULY 1 | 1:00pm - 3:15pm

Poster Session II — Thermal Treatment and Cryotherapy — Exhibit Hall A

15 **Blood Cooling Using Cryogenic Nitrogen** SB³C2016-638
Joseph Licwinko, Brian Dixon, *Mechanical Engineering, Rowan University, Glassboro, NJ, United States*

16 **Can We Use Apparent Thermal Conductivity to Include the Effect of Blood Perfusion? An Attempt to Predict Frozen Region During Cryosurgery** SB³C2016-766
Mohammed M. H. Shurrab, Haidong Wang, Takanobu Fukunaga, Kosaku Kurata, Hiroshi Takamatsu, *Mechanical Engineering, Kyushu University, Fukuoka, Japan*

17 **Development and Validation of a Brain Phantom for Therapeutic Cooling Devices** SB³C2016-1012
Ryan Packett[1], Philip Brown[1], Gautam Popli[2], Scott Gayzik[1], *[1]Biomedical Engineering, Wake Forest University, Winston Salem, NC, United States, [2]Neurosurgery, Wake Forest University, Winston Salem, NC, United States*

18 **Modulation of Ice Formation Characteristics Due to Addition of Trehalose in Cryoprotectant** SB³C2016-891
Jason Solocinski, Mian Wang, Quinn Osgood, **Nilay Chakraborty**, *Mechanical Engineering Department, University of Michigan Dearborn, Dearborn, MI, United States*

19 **A Novel Cryopreservation Approach Without Penetrating Cryoprotectants** SB³C2016-725
Haishui H. Huang, *The Ohio State University, Columbus, OH, United States*

20 **Enhancement of Cryopreservation outcome of Adipose Tissue Derived Stem Cells by Thermal Stress** SB³C2016-651
Mulla Shahensha Shaik, *Mechanical Engineering, Louisiana State University, Baton Rouge, LA, United States*

21 **Proliferation of Human Adipose Derived Stem Cells Cultured on Porous Poly (l-lactic Acid) Scaffolds Prepared by Thermally Controlled Methods** SB³C2016-43
Harish Chinnasami, Ram Devireddy, *Mechanical Engineering Department, Louisiana State University, Baton Rouge, LA, United States*

Copyright 2016 The Organizing Committee for the 2016 Summer Biomechanics, Bioengineering and Biotransport Conference

FRIDAY, JULY 1	1:00pm - 3:15pm

Poster Session II — Ocular and Optofluidics — Exhibit Hall A

22 **Study of Ganciclovir Permeability Through Bovine, Rabbit & Human Alzhemeir Ex-vivo Ocular Tissues** SB³C2016-1099
Anita Penkova[1, 2], Komsan Rattanakijsuntorn[1], Satwindar Sadhal[1, 2], *[1]University of Southern California, Los Angeles, CA, United States, [2]Saban Research Institute, Children's hospital Los Angeles, Los Angeles, CA, United States*

23 **Intraocular Pressure Measurement Through the Laser Induced Cavitation Bubbles Dynamics** SB³C2016-761
Luis F. Devia-Cruz, Santiago Camacho-López, *Optics, CICESE, Ensenada, Mexico*

24 **Fluid Displacement During Droplet Formation at Microfluidic Flow-focusing Junction at Microfluidic Flow-focusing Junction** SB³C2016-722
Haishui H. Huang, *The Ohio State University, Columbus, OH, United States*

25 **Role of Intracranial Pressure in Optic Nerve Head Biomechanics** SB³C2016-713
Yi Hua, *Dept. of Mechanical & Materials Engineering, University of Nebraska-Lincoln, Lincoln, NE, United States*

26 **Finite Element Model of Ocular Accommodation Mechanism Based on Lens Pre-Tensioning and Ciliary Muscle Contraction** SB³C2016-572
Katherine R. Knaus[1], AnnMarie Hipsley[2], Silvia S. Blemker[1], *[1]University of Virginia, Charlottesville, VA, United States, [2]Ace Vison Group Inc., Akron, OH, United States*

27 **Riboflavin/uva Collagen Cross-linking Effects on Tensile and Compressive Properties of the Cornea** SB³C2016-799
Hamed Hatami-Marbini, *Mechanical & Industrial Engineering, University of Illinois at Chicago, Chicago, IL, United States*

28 **Regional Variations in the Mechanical Strains of the Human Optic Nerve Head** SB³C2016-804
Dan Midgett[1], Mohak Patel[2], Mary Pease[3], Christian Franck[2], Harry Quigley[3], Vicky Nguyen[1], *[1]Mechanical Engineering, Johns Hopkins University, Baltimore, MD, United States, [2]Engineering, Brown University, Providence, RI, United States, [3]Ophthalmology, Johns Hopkins University, Baltimore, MD, United States*

29 **An Image-Based Inverse Finite Element Method to Determine the Mechanical Properties of Human Trabecular Meshwork** SB³C2016-984
Anup D. Pant[1], Lawrence Kagemann[2], Ian Sigal[2], Joel Schuman[2], Rouzbeh Amini[1], *[1]Biomedical Engineering, The University of Akron, Akron, OH, United States, [2]Department of Bioengineering, Department of Opthalmology, University of Pittsburg, Pittsburgh, PA, United States*

30 **3D Characterization of Corneal Deformation Using Ultrasound Speckle Tracking** SB³C2016-936
Keyton Clayson, Elias Pavlatos, Jun Liu, *The Ohio State University, Columbus, OH, United States*

31 **The Impact of Ocular Pressures, Material Properties and Geometry on Optic Nerve Head Deformation** SB³C2016-637
Andrew Feola[1], Jerry G. Myers[2], Julia Raykin[1], Emily S. Nelson[2], Brian Samuels[3], C. Ross Ethier[1], *[1]Department of Biomedical Engineering, Georgia Institute of Technology, Atlanta, GA, United States, [2]NASA Glenn Research Center, Cleveland, OH, United States, [3]Department of Ophthalmology, University of Alabama at Birmingham, Birmingham, AL, United States*

32 **Development of a Platform for Studying Astrocyte Mechanobiology: Compression of Astrocytes in 3D Collagen Gels** SB³C2016-868
John J. E. Mulvihill[1, 2], Lisa A. Schildmeyer[1], Julia Raykin[1], Eric J. Snider[1], Kavita Chinoy[1], Danny J. Kelly[2], C. Ross Ethier[1, 3], *[1]Wallace H. Coulter Dept. of Biomedical Engineering, Georgia Institute of Technology, Atlanta, GA, United States, [2]Mechanical and Manufacturing Engineering, Trinity College Dublin, Dublin, Ireland, [3]Atlanta VA Medical Center, Decatur, GA, United States*

33 **Characterization of the Mechanical Behavior of the Optic Nerve Sheath** SB³C2016-1054
Julia Raykin, Roy Wang, Taylor E. Forte, Andrew Feola, Brian Samuels, Jerry G. Myers, Emily S. Nelson, Rudy L. Gleason, C. Ross Ethier, *Georgia Institute of Technology, Atlanta, GA, United States*

Copyright 2016 The Organizing Committee for the 2016 Summer Biomechanics, Bioengineering and Biotransport Conference

FRIDAY, JULY 1	1:00pm - 3:15pm

Poster Session II — Cardiovascular Tissue Engineering — Exhibit Hall A

75 **Connexin 43 Stability and Gap Junction Channel Functionality: the Role of Heparan Sulphate** SB³C2016-642
Solomon Mensah, Homa Homayoni, Ming Cheng, Brian Plouffe, Eno E. Ebong, *Bioengineering, Northeastern University, Boston, MA, United States*

76 **Phenotypic Changes of Stromal Vascular Fraction Cells for Use in a Tissue Engineered Vascular Graft** SB³C2016-861
Darren G. Haskett, *Department of Surgery, University of Pittsburgh, Pittsburgh, PA, United States*

77 **Influence of Subarachnoid Hemorrhage Factors on Vascular Smooth Muscle Cell Functional Phenotype in the Development of Cerebral Vasospasm** SB³C2016-865
Eric S. Hald, Zaw Win, Justin Buksa, Connor Timm, Patrick W. Alford, *Biomedical Engineering, University of Minnesota, Minneapolis, MN, United States*

78 **Biomechanical Evaluation of Gelatin/Fibrinogen Electrospun Cylindrical Scaffolds Seeded with 3T3 Mouse Fibroblasts and Porcine Smooth Muscle Cells** SB³C2016-1064
Ehab Tamimi[1], Jamie L. Hernandez[2], Corina MacIsaac[2], Catalina Ardila[1], Jonathan P. Vande Geest[3], *[1]Graduate Interdisciplinary Program of Biomedical Engineering, University of Arizona, Tucson, AZ, United States, [2]Biomedical Engineering, University of Arizona, Tucson, AZ, United States, [3]Department of Bioengineering, University of Pittsburgh, Pittsburgh, PA, United States*

79 **Quantify Patient-specific Coronary Vessel Material Property and Its Impact on Plaque Stress/strain Calculations Using Cine Ivus and 3D Fsi Models** SB³C2016-644
Xiaoya Guo[1], Jian Zhu[2], Liang Wang[3], Akiko Maehara[4], Jie Zheng[5], Chun Yang[6], David Muccigrosso[5], Gary S. Mintz[4], Dalin Tang[3], *[1]Southeast University, Nanjing, China, [2]Zhongda Hospital, Southeast University, Nanjing, China, [3]Worcester Polytechnic Institute, Worcester, MA, United States, [4]Columbia University, New York, NY, United States, [5]Washington University, St. Louis, MO, United States, [6]China United Network Comm. Co. Ltd., Beijing, China*

80 **Modeling Active Contraction of Left Ventricle Using Different Zero-load Diastole and Systole Geometries** SB³C2016-54
Longling Fan[1], Jing Yao[2], Chun Yang[3], Di Xu[2], Dalin Tang[4], *[1]Southeast University, Nanjing, China, [2]First Affiliated Hospital of Nanjing Medical University, Nanjing, China, [3]China Information Tech. Designing & Consulting Institute Co., Ltd., Beijing, China, [4]Math Sciences Department Worcester Polytechnic Institute, Worcestor, MA, United States*

81 **A Model to Determine the Effect of Axial Stretch on Lumen Collapse of Arteries** SB³C2016-857
Fatemeh Fatemi Far, Hai Chao Han, *Mechanical Engineering, University of Texas at San Antonio, San Antonio, TX, United States*

82 **Inhomogeneity of the Material Properties of Thoracic Aorta in Three Dimensions** SB³C2016-1033
Golriz Kermani, Ali Hemmasizadeh, Soroush Assari, Michael Autieri, Kurosh Darvish, *Temple University, Philadelphia, PA, United States*

83 **Mechanics of Heart Tube Formation in Chick Embryo** SB³C2016-65
Hadi S. Hosseini[1], Larry A. Taber[2], *[1]BME/Physics, Washington University in Saint Louis, Saint Louis, MO, United States, [2]BME, Washington University in Saint Louis, Saint Louis, MO, United States*

84 **Myocardial Wall Stiffening in a Mouse Model of Persistent Truncus Arteriosus** SB³C2016-1061
Christine Miller Buffinton[1], Kerra R. Mercon[1], Alyssa K. Benjamin[2], Asena Abay[3], Elise M. Buffinton[4], Roberta K. Blaho[3], Ashley N. Firment[5], Anne M. Moon[5], *[1]Mechanical Engineering, Bucknell University, Lewisburg, PA, United States, [2]Biology, Bucknell University, Lewisburg, PA, United States, [3]Biomedical Engineering, Bucknell University, Lewisburg, PA, United States, [4]Civil and Environmental Engineering, Cornell University, Ithaca, NY, United States, [5]Weis Center for Research, Geisinger Medical Center, Danville, PA, United States*

85 **Using Patient-Specific MRI-Based Right Ventricle Models with Different Zero-Load Diastole and Systole Geometries for Better Stress and Strain Calculations and Post-Surgery Outcome Prediction** SB³C2016-29
Dalin Tang[1, 2], Pedro del Nido[3], Chun Yang[1, 4], Heng Zuo[1], Xueying Huang[1, 5], Rahul H. Rathod[3], Alexander Tang[3], Zheyang Wu[1], Kristen L. Billiar[1], Tal Geva[3], *[1]WPI, Worcester, MA, United States, [2]Southeast University, Nanjing, China, [3]Harvard Medical School, Boston, MA, United States, [4]China Information Tech. Designing & Consulting Institute Co., Ltd, Beijing, China, [5]Xiamen University, Xiamen, China*

Copyright 2016 The Organizing Committee for the 2016 Summer Biomechanics, Bioengineering and Biotransport Conference

FRIDAY, JULY 1	1:00pm - 3:15pm

Poster Session II — Tissue and Cellular Microenvironment — Exhibit Hall A

86 **Study on the Biosolubility of Calcined Bovine Bone Scaffold for Bone Tissue Engineering** SB³C2016-1141
Shigeo Tanaka[1], Naoki HIrooka[2], *[1]Institute of Science and Engineering, Kanazawa University, Kanazawa, Japan, [2]Graduate School of Natural Science and Technology, Kanazawa University, Kanazawa, Japan*

87 **Molecular Spectroscopic Identification of the Water Compartments in Cartilage** SB³C2016-78
Mustafa Unal, Ozan Akkus, *Case Western Reserve University, Cleveland, OH, United States*

88 **Modeling Calcium Transients in Human Pluripotent Stem Cell-Derived Cardiomyocytes** SB³C2016-1108
Kevin Beussman, Marita Rodriguez, Adam Rakla, Ashley Emery, Nathan Sniadecki, *Mechanical Engineering, University of Washington, Seattle, WA, United States*

89 **Polycaprolactone Fibrous Scaffolds to Navigate Neural Stem Cells** SB³C2016-880
Nastaran Hashemi, *Iowa State University, Ames, IA, United States*

90 **Effect of Shear Stress on Glucose Metabolism in Pulmonary Arterial Hypertension** SB³C2016-810
Sarah Basehore, Alisa Morss Clyne, *Biomedical Engineering, Drexel University, Philadelphia, PA, United States*

91 **Impact of Membrane Cholesterol in the Monocyte Adhesion Cascade** SB³C2016-714
Amit K. Saha[1], Pawel Osmulski[2], Anand K. Ramasubramanian[1], *[1]Biomedical Engineering, University of Texas at San Antonio, San antonio, TX, United States, [2]Molecular Medicine, University of Texas Health Science Center at San Antonio, San antonio, TX, United States*

92 **Endothelial Cell Glycocalyx Modulates Shear-induced Tubule Formation** SB³C2016-119
Ping Zhao, Xiao Liu, Xiaoyan Deng, *School of Biological Science and Medical Engineering, Beihang University, Beijing, China*

93 **Decellularized Extracellular Matrix Electrospun Scaffold for a Novel Airway Smooth Muscle Model** SB³C2016-824
Bethany M. Young[1], Bryan A. Blakeney[2], Gretchen E. Schreyak[1], Robert A. Pouliot[1], **Rebecca L. Heise**[1], *[1]Biomedical Engineering, VCU, Richmond, VA, United States, [2]Physiology and Biophysics, VCU, Richmond, VA, United States*

94 **Numerical Investigation of Cell Migration** SB³C2016-1126
Xiaowei Zeng, Liqiang Lin, *Mechanical Engineering, University of Texas at San Antonio, San Antonio, TX, United States*

FRIDAY, JULY 1	1:00pm - 3:15pm

Poster Session II — Human Dynamics and Rehabilitation — Exhibit Hall A

109 **Biomechanical Analysis of Kicks in Soccer and Kicks in Football** SB³C2016-617
Allison M. Gerren, Tori Breitenbach, Jacob Forstat, Jonathan Fox, Mohamed Samir Hefzy, *The University of Toledo, Toledo, OH, United States*

110 **Assessing Kinematics and Kinetics of FES-rowing** SB³C2016-897
Adina Draghici[1], Glen Picard[2], J. Andrew Taylor[2, 3], Sandra Shefelbine[1, 4], *[1]Bioengineering, Northeastern University, Boston, MA, United States, [2]Cardiovascular Research Laboratory, Spaulding Rehabilitation Hospital, Boston, MA, United States, [3]Physical Medicine and Rehabilitation, Harvard Medical School, Boston, MA, United States, [4]Mechanical and Industrial Engineering, Northeastern University, Boston, MA, United States*

111 **Utilizing Bandwidth to Quantify Human Torso Motor Control Capability** SB³C2016-915
Shahab Karimi[1], Martin L. Tanaka[1], N. Peter Reeves[2], Sudhir Kaul[1], *[1]Engineering and Technology, Western Carolina University, Cullowhee, NC, United States, [2]Osteopathic Surgical Specialty, Michigan State University, East Lansing, MI, United States*

112 **Building a Better Quarterback: Using Biomechanics to Optimize Throwing Mechanics** SB³C2016-1127
Hunter Storaci[1], Andrew Robbins[1], Michael R. Moreno[1, 2], *[1]Biomedical Engineering, Texas A&M University, College Station, TX, United States, [2]Mechanical Engineering, Texas A&M University, College Station, TX, United States*

Copyright 2016 The Organizing Committee for the 2016 Summer Biomechanics, Bioengineering and Biotransport Conference

113 **Design of an Affordable Outdoor Add-on to a Manual Wheelchair for Developing Countries** SB³C2016-645
Swostik Dash, Vivek Sarda, Ashish Sharma, **S. Sujatha**, *Mechanical Engineering, Indian Institute of Technology Madras, Chennai, India*

114 **Relationship Between Force Applied & Velocity of Contraction of Air Muscles.** SB³C2016-1122
Aniruddha Phatak, *Rochester Institute of Technology, Rochester, NY, United States*

115 **Comparison of Humeral Head Osteotomy using Anatomic and Guide-Assisted Cuts** SB³C2016-1070
Emily A. West[1, 2, 3], Nikolas K. Knowles[1, 2, 3], Louis M. Ferreira[1, 2, 3], George S. Athwal[2], *[1]Biomedical Engineering, Western University, London, ON, Canada, [2]Roth|McFarlene Hand and Upper Limb Center, London, ON, Canada, [3]Lawson Health Research Institute, London, ON, Canada*

116 **A Testing Protocol for Evaluating and Classifying Spinal Orthoses** SB³C2016-76
Denis J. DiAngelo, John C. Simmons, Daniel M. Wido, *Orthopaedic Surgery and Biomedical Engineering, The University of Tennessee Health Science Center, Memphis, TN, United States*

117 **A Novel Distractive and Mobility-Enabling Lumbar Spinal Orthosis** SB³C2016-733
Daniel C. Hillyard, **Denis J. DiAngelo**, *Department of Orthopaedic Surgery and Biomedical Engineering, The University of Tennessee Health Science Center, Memphis, TN, United States*

118 **The Biomechanical Effects of Strap Options on Scoliosis Bracing Mechanics** SB³C2016-965
Chloe L. Chung[1], Derek M. Kelly[2], Jack R. Steele[3], **Denis J. DiAngelo**[1], *[1]The Department of Orthopaedic Surgery and Biomedical Engineering, The University of Tennessee Health Science Center, Memphis, TN, United States, [2]The Department of Orthopaedics, Campbell Clinic Orthopaedics and Le Bonheur Children's Hospital, Memphis, TN, United States, [3]Center for Orthotics and Prosthetics, Inc., Memphis, TN, United States*

119 **A.R.K. Brace: and Active Rehabilitation Knee Brace** SB³C2016-859
Jarrel Bobb[1], Kelly Chickering[2], **Patrick Donohue**[2], Mac Gallagher[3], Shannon Hartzell[4], Cole Lipman[2], M. Jake Miorin[2], Kailan Ottaway[2], Alexander A. Brown[2], *[1]Biology, Lafayette College, Easton, PA, United States, [2]Mechanical Engineering, Lafayette College, Easton, PA, United States, [3]Economics, Lafayette College, Easton, PA, United States, [4]Neuroscience, Lafayette College, Easton, PA, United States*

120 **Cable Actuated 3D Printed Exoskeleton: for Restoration of Hand Motor Function in Stroke Affected Patients** SB³C2016-616
Aaron J. Brice[1], Muxi Li[1], Stéphane Magnan[1], Jin Wang[1], Tyler Friesen[1], Yongsheng Ma[2], Ahmed Qureshi[2], Jonathon Schofield[2], *[1]Mechanical Engineering, University of Alberta, Edmonton, AB, Canada, [2]Mechanical Engineering, University of Alberta, Spruce Grove, AB, Canada*

FRIDAY, JULY 1 | 1:00pm - 3:15pm

Poster Session II — Best Practices in Contemporary Biomechanical Engineering Education — Exhibit Hall A

121 **Enhancing Biomechanical Engineering Education Through Problem Based Learning** SB³C2016-1104
Alisa Morss Clyne, *Drexel University, Philadelphia, PA, United States*

122 **Project-based Biomechanics Laboratories: Theory and Practice** SB³C2016-1038
Kristen L. Billiar, Glenn R. Gaudette, *Biomedical Engineering, Worcester Polytechnic Institute, Worcester, MA, United States*

123 **Utilizing Problem-Based Learning to Teach Biomedical Engineering as a Chemical Engineering Elective** SB³C2016-684
Victor Lai, *Chemical Engineering, University of Minnesota - Duluth, Duluth, MN, United States*

124 **A Master of Engineerng in Design and Commercialization** SB³C2016-673
Alan Eberhardt, Brandon Kirkland, Ophelia Johnson, Joel Dobbs, Lee Moradi, *UAB, Birmingham, AL, United States*

125 **"Contemporary Issues in ... Bioengineering": A New Required Course Addressing Several Curricular Concerns** SB³C2016-826
Steven W. Day, Robert J. Stevens, *Rochester Institute of Technology, Rochester, NY, United States*

Copyright 2016 The Organizing Committee for the 2016 Summer Biomechanics, Bioengineering and Biotransport Conference

126 **Recruiting and Supporting Transfer students to Mechanical Engineering Program at UMBC** SB³C2016-23
Liang Zhu[1], Dwayne Arola[2], Anne Spence[1], Carlos Romero-Talamas[1], Charles Eggleton[1], *[1]Mechanical Engineering, University of Maryland Baltimore County, Baltimore, MD, United States, [2]Materials Science and Engineering, University of Washington, Seattle, WA, United States*

127 **Experiences with Introducing STEM Clubs to K-12 Students: Perils, Pitfalls, and Pearls of Wisdom?** SB³C2016-821
Ferris Pfeiffer, *Bioengineering/Orthopaedic Surgery, University of Missouri, Columbia, MO, United States*

128 **Audio Response System for Active Learning in a Large Lecture Class** SB³C2016-61
Craig J. Goergen, *Biomedical Engineering, Purdue University, West Lafeyette, IN, United States*

FRIDAY, JULY 1 | 1:00pm - 3:15pm

Poster Session II — Cardiovascular Fluid Mechanics — Exhibit Hall A

154 **Hemodynamic Modifications and its Association with Outcome in Intracranial Aneurysms Treated using Flow Diverters** SB³C2016-798
Nikhil Paliwal[1], Jason Davies[2], Adnan H. Siddiqui[2], Hui Meng[1], *[1]Mechanical and Aerospace Engineering, University at Buffalo, the State University of New York, Buffalo, NY, United States, [2]Neurosurgery, University at Buffalo, the State University of New York, Buffalo, NY, United States*

155 **Flow Diverting Characteristics of Endoluminal and Intrasaccular Devices: A Comparison** SB³C2016-143
Fernando Mut[1], Pedro Lylyk[2], David Kallmes[3], Juan Cebral[1], *[1]Bioengineering, George Mason University, Fairfax, VA, United States, [2]Interventional Neuroradiology, Instituto Clinico ENERI, Buenos Aires, Argentina, [3]Radiology, Mayo Clinic, Rochester, MN, United States*

156 **Computational Modeling of Coiled Cerebral Aneurysms: Comparing Homogeneous Porous Medium Against Micro-CT Reconstructed Coil Volume in Aneurysmal Sac Hemodynamics** SB³C2016-1029
Michael C. Barbour[1], Patrick McGah[1], Christian Geindreau[2], Sabine Rolland du Roscoat[2], Kurt Sansom[1], Venkat Keshav Chivukula[1], Ryan P. Morton[3], John D. Nerva[3], Basavaraj V. Ghodke[4], Laligam N. Sekhar[3], Michael R. Levitt[3], Louis J. Kim[3], Alberto Aliseda[1], *[1]Mechanical Engineering, University of Washington, Seattle, WA, United States, [2]3SR Universite Grenoble Alps, Grenoble, France, [3]Neurological Surgery, University of Washington, Seattle, WA, United States, [4]Radiology, Harborview Medical Center, Seattle, WA, United States*

157 **Numerical Modeling of Flow Diverter Stent in Giant Cerebral Aneurysm** SB³C2016-771
Augusto F. Sanches, Eva Gutheil, *University of Heidelberg, Heidelberg, Germany*

158 **The Quantification of Blood Flow Patterns Induced by Endovascular Stent Grafts: An Experimental Investigation of The Effects of Oversizing and Compliance** SB³C2016-867
Amanda Colella Centazzo, *Mechanical Engineering, Dalhousie University, Halifax, NS, Canada*

159 **The Quantification of Blood Flow Patterns Induced by Endovascular Stent Grafts: An Experimental Investigation of the Effects of Oversizing and Compliance** SB³C2016-1013
Amanda Colella-Centazzo, **Clifton R. Johnston**, *Mechanical Engineering, Dalhousie University, Halifax, NS, Canada*

160 **A Preliminary Study to Determine If Arteriovenous Fistula Configuration Generates Helical Flow and If Helical Flow is A SurrogateMarker of Exposure to Disturbed Shear** SB³C2016-871
Connor V. Cunnane[1], Leonard D. Browne[1], Stephen P. Broderick[1], Craig Dunlop[2], Graeme J. Houston[3], Michael T. Walsh[1], *[1]Mechanical Aeronautical and Biomedical Engineering Department, University of Limerick, Limerick, Ireland, [2]Vascular Flow Technologies, Dundee, United Kingdom, [3]Cardiovascular and Diabetes Medicine, University of Dundee, Dundee, United Kingdom*

161 **A Real-Time Programmable Pulsatile Flow Pump for In-Vitro Cardiovascular Experimentation** SB³C2016-998
Rahul Raj Mechoor, Tyler M. Schmidt, Ethan O. Kung, *Mechanical Engineering, Clemson University, Clemson, SC, United States*

Copyright 2016 The Organizing Committee for the 2016 Summer Biomechanics, Bioengineering and Biotransport Conference

162 **Evaluation of Pulsatile and Continuous Flow Ventricular Assist Device Implementation in the Single-Ventricle Circulation: A Lumped-Parameter Modeling Study** SB³C2016-672
Tyler M. Schmidt[1], David N. Rosenthal[2], Olaf Reinhartz[2], Alison L. Marsden[3], Ethan O. Kung[1], The Modeling of Congenital Hearts Alliance (MOCHA) Investigators[4], *[1]Department of Mechanical Engineering, Clemson University, Clemson, SC, United States, [2]School of Medicine, Stanford University, Stanford, CA, United States, [3]Department of Pediatrics, Stanford University, Stanford, CA, United States, [4]Institute of Cardiovascular Sciences, University College London, London, United Kingdom*

163 **Apical Inflow Cannula Angle and Left Ventricular Size Impact LVAD Thrombosis Risk** SB³C2016-836
Venkat Keshav Chivukula[1], Patrick McGah[1], Anthony R. Prisco[2], Jennifer A. Beckman[3], Guilherme J. M. Garcia[2], Claudius Mahr[3], Alberto Aliseda[1], *[1]Mechanical Engineering, University of Washington, Seattle, WA, United States, [2]Biotechnology and Bioengineering Center, Medical College of Wisconsin, Milwaukee, WI, United States, [3]Division of Cardiology, University of Washington, Seattle, WA, United States*

164 **Native Cardiac Output and Surgical Implantation Configuration May Influence LVAD Thrombosis Risk** SB³C2016-838
Venkat Keshav Chivukula[1], Patrick McGah[1], Anthony Prisco[2], Jennifer Beckman[3], Guilherme Garcia[2], Claudius Mahr[3], Alberto Aliseda[1], *[1]Mechanical Engineering, University of Washington, Seattle, WA, United States, [2]Biotechnology and Bioengineering Center, Medical College of Wisconsin, Milwaukee, WI, United States, [3]Division of Cardiology, University of Washington, Seattle, WA, United States*

FRIDAY, JULY 1 | 1:00pm - 3:15pm

Poster Session II | Respiratory | Exhibit Hall A

165 **Acoustic Visualisation of Flow-Sound in the Respiratory Airway** SB³C2016-1001
Gabriel Pramudita Saputra[1], Kazunori Nozaki[2], Satoshi Ii[1], Chizu Habukawa[3], Shigeo Wada[1], *[1]Department of Biomechanical Science and Engineering, Graduate School of Engineering Science Osaka University, Osaka, Japan, [2]Division of Dental Informatics, Osaka University Dental Hospital, Osaka, Japan, [3]Department of Pediatrics, Minami Wakayama Medical Center, Wakayama, Japan*

168 **Influence of Standardization of Airway Geometry on Airflow and Particle Transport** SB³C2016-169
Toshihiro Sera[1], Hiroaki Kuninaga[2], Kazuaki Fukasaku[3], Hideo Yokota[3], Masao Tanaka[2], *[1]Kyushu Univ., Fukuoka, Japan, [2]Osaka Univ., Toyonaka, Japan, [3]RIKEN, Wako, Japan*

169 **Investigating Force Transfer During Parturition Using Experimental and Computational Methods** SB³C2016-599
Alexa Baumer[1], Roseanna Pealatere[2], Lisa J. Fauci[2], Megan C. Leftwich[1], *[1]The George Washington University, Washington, DC, United States, [2]Tulane University, New Orleans, LA, United States*

170 **A Mathematical Model of Vitreoschisis** SB³C2016-692
Krystyna Isakova[1], Jan Oscar Pralits[2], Outi-Leena Tammisola[1], Rodolfo Repetto[2], *[1]Faculty of Engineering, University of Nottingham, Nottingham, United Kingdom, [2]Department of Civil, Chemical and Environmental Engineering, University of Genoa, Genoa, Italy*

171 **Digital Manufacturing and In Silico Modeling for Rational Design of Drug Delivery to the Central Nervous System** SB³C2016-953
Kevin Tangen[1], Ted Gabor[2], Lu Lu[2], Yayue Pan[2], Narasimhan Sriram[1], Andreas Linninger[1, 3], *[1]Bioengineering, University of Illinois at Chicago, Chicago, IL, United States, [2]Mechanical Engineering, University of Illinois at Chicago, Chicago, IL, United States, [3]Neurosurgery, University of Illinois at Chicago, Chicago, IL, United States*

172 **Integration of a Baroreflex Model into a Whole Body Physiology Engine** SB³C2016-888
Rachel B. Clipp, M. Cameron Thames, Jeffrey B. Webb, Rodney Metoyer, Zachary M. Swarm, Aaron M. Bray, *Applied Research Associates, Inc, Raleigh, NC, United States*

Copyright 2016 The Organizing Committee for the 2016 Summer Biomechanics, Bioengineering and Biotransport Conference

FRIDAY, JULY 1	1:00pm - 3:15pm

Poster Session II — Respiratory and Others Fluid Mechanics — Exhibit Hall A

173 **Aortic Regurgitation on Left Ventricular Diastolic Flow** SB³C2016-643
Ikechukwu (Ikay) Okafor[1], Vrishank Raghav[1], Gautam Kumar[2], Ajit Yoganathan[1], *[1]Georgia Institute of Technology, Atlanta, GA, United States, [2]Emory University, Atlanta, GA, United States*

174 **Computational Fluid Flow Modeling of a Pulmonary Vascular Phantom with Experimental Validation** SB³C2016-66
Alifer D. Bordones[1, 2], Matthew Leroux[1, 2], Vitaly O. Kheyfets[3], Ender A. Finol[1], *[1]Biomedical Engineering, University of Texas at San Antonio, San Antonio, TX, United States, [2]Graduate Program in Biomedical Engineering, University of Texas Health Science Center at San Antonio, San Antonio, TX, United States, [3]Bioengineering, University of Colorado Denver, Denver, CO, United States*

175 **Similarities and Differences Between Flow Mode of a Leukocyte and Circulating Tumor Cell in Microvessels** SB³C2016-742
Naoki Takeishi[1], Yohsuke Imai[2], Takami Yamaguchi[1], Takuji Ishikawa[2], *[1]Graduate School of Biomedical Engineering, Tohoku University, Sendai, Japan, [2]Division of Mechanical Engineering, Tohoku University, Sendai, Japan*

176 **Subject Specific Simulation of Entire Cerebral Arterial Tree: Implementation of Automatic Parametric Mesh Generation.** SB³C2016-171
Mahsa Ghaffari[1], Ben C. Schneller[1], Ali Alaraj[2], Andreas A. Linninger[1], *[1]Bioengineering, University of Illinois at Chicago, Chicago, IL, United States, [2]Department of Neurosurgery, University of Illinois at Chicago, Chicago, IL, United States*

177 **Hemodynamic Analysis on Correlations between Bicuspid Aortic Valve and Aneurysm Progression with an Integrated Model of Left Ventricle and Aorta** SB³C2016-1021
Takashi Fujiwara[1], Fuyou Liang[2], Koichi Sughimoto[3], Hao Liu[1], *[1]Graduate School of Engineering, Chiba University, Chiba, Japan, [2]School of Naval Architecture, Ocean & Civil Engineering, Shanghai Jiao Tong University, Shanghai, China, [3]Cardiovascular Surgery, Kitazato University Hospital, Kanagawa, Japan*

178 **Porcine Small Intestinal Submucosal Valve Dynamics in the Aortic Position** SB³C2016-856
Omkar V. Mankame[1], Makensley Lordeus[1], Lilliam Valdes-Cruz[2], Steven Bibevski[2], Frank Scholl[2], Sarah M. Bell[2], Ivan Baez[2], Sharan Ramaswamy[1], *[1]Biomedical Engineering, Florida International University, Miami, FL, United States, [2]Joe DiMaggio Children's Hospital, Memorial Regional Hospital, Hollywood, FL, United States*

179 **Comparison of Pediatric and Adult Blood Viscoelasticity** SB³C2016-88
M Keith Sharp[1], Mary E. Gregg[1], Guy Brock[2], George M. Pantalos[1], *[1]University of Louisville, Louisville, KY, United States, [2]Ohio State University, Columbus, OH, United States*

180 **Understanding the Fluid Mechanics of Aortic Regurgitation** SB³C2016-650
Samantha Houser[1], Ikechukwu Okafor[2], **Vrishank Raghav**[1], Ajit Yoganathan[1], *[1]Biomedical Engineering, Georgia Institute of Technology, Atlanta, GA, United States, [2]School of Chemical and Biomolecular Engineering, Georgia Institute of Technology, Atlanta, GA, United States*

181 **Abnormal Characteristics of Blood Flow in Human Left Atrium with Prior History of Embolic Stroke: Computational Fluid Dynamics Study** SB³C2016-659
Tomohiro Otani[1], Shigeo Wada[1], Hiroshi Ashikaga[2], *[1]Mechanical Science & Bioengineering, Osaka University, Toyonaka, Japan, [2]School of Medicine, Johns Hopkins University, Baltimore, MD, United States*

182 **Computational Modeling of Embolus Migration in the Human Inferior Vena Cava** SB³C2016-55
Kenneth I. Aycock[1], Robert L. Campbell[2], Brent A. Craven[3], Keefe B. Manning[1], *[1]Biomedical Engineering, The Pennsylvania State University, State College, PA, United States, [2]Mechanical and Nuclear Engineering, The Pennsylvania State University, State College, PA, United States, [3]Center for Devices and Radiological Health, U.S. Food and Drug Administration, State College, PA, United States*

183 **Shear Dependent Sickle Red Blood Cell Adhesion in Shear Gradient Hele Shaw Flow** SB³C2016-647
Erdem Kucukal, Umut A. Gurkan, *Mechanical and Aerospace Engineering, Case Western Reserve University, Cleveland, OH, United States*

184 **Velocity-Dilatation Formulation for Computational Fluid Dynamics in FEBio** SB³C2016-788
Gerard A. Ateshian[1], Jay J. Shim[1], Steve Maas[2], Jeffrey A. Weiss[2], *[1]Mechanical Engineering, Columbia University, New York, NY, United States, [2]Bioengineering, University of Utah, Salt Lake City, UT, United States*

Copyright 2016 The Organizing Committee for the 2016 Summer Biomechanics, Bioengineering and Biotransport Conference

185 **Production of Monodispere Silica Gel Microspheres for Bioencapsulation by Extrusion Into An Oil Crossflow** SB³C2016-653
Joey Benson[1], Lawrence Wackett[2, 3], Alptekin Aksan[1, 3], *[1]Department of Mechanical Engineering, University of Minnesota, Minneapolis, MN, United States, [2]Department of Biochemistry, Molecular Biology and Biophysics, University of Minnesota, Minneapolis, MN, United States, [3]BioTechnology Institute, University of Minnesota, St Paul, MN, United States*

186 **Bacterial Growth Inside Reversible Ca-alginate Beads Encapsulated in a Thin Silica Film** SB³C2016-853
Goeun Heo[1], Jonathan K. Sakkos[1], Sujin Yeom[2], Lawrence P. Wackett[2, 3], Alptekin Aksan[1, 3], *[1]Mechanical Engineering, University of Minnesota, Minneapolis, MN, United States, [2]Biochemistry, Molecular, Biology, and Biophysics, University of Minnesota, Minneapolis, MN, United States, [3]Biotechnology Institute, St Paul, MN, United States*

187 **Microbial Regeneration of Adsorbent Silica Gel for Sustainable Treatment of Environmental Pollutants** SB³C2016-608
Jonathan Sakkos[1], Lawrence P. Wackett[2], Alptekin Aksan[1], *[1]Mechanical Engineering, University of Minnesota, Minneapolis, MN, United States, [2]Biochemistry, Molecular Biology, and Biophysics, University of Minnesota, Minneapolis, MN, United States*

FRIDAY, JULY 1 | 1:00pm - 3:15pm

Poster Session II — Bone Mechanics — Exhibit Hall A

221 **Evaluation of BioDent Reference Point Indentation (RPI) Platform to Measure the Elastic Modulus in Mouse Bones** SB³C2016-795
Ganesh Thiagarajan, *Civil and Mechanical Engineering, University of Missouri Kansas City, Kansas City, MO, United States*

222 **Effects of Body Weight Supported Treadmill Training on Bone and Muscle Following Spinal Cord Injury** SB³C2016-910
Anita Singh[1], Bridgette Saverine[1], Gabrielle Gehron[1], Brittany King[2], Shania Shaji[1], Jennifer Kadlowec[2], *[1]Widener University, Chester, PA, United States, [2]Rowan University, Glassboro, NJ, United States*

223 **Orientation Dependent Strain Characterization of the Ultrastructure In Bone** SB³C2016-1136
Jitin S. Samuel, Xiaodu Wang, *University of Texas at San Antonio, San Antonio, TX, United States*

224 **A Coupled Reaction-Diffusion-Strain Model for Bone Growth in the Cranial Vault** SB³C2016-931
Chanyoung Lee, Reuben H. Kraft, *Department of Mechanical and Nuclear Engineering, Pennsylvania State University, University Park, PA, United States*

225 **Modeling Bone Formation with a Lab-on-a-Chip Platform** SB³C2016-63
Marnie M. Saunders, Spencer L. York, Estee L. George, Erica L. Grutkowski, Jennifer L. Smith, *Biomedical Engineering, The University of Akron, Akron, OH, United States*

226 **A Cellular Automata Model Verifying Osteoblastic Bone Formation In Vitro** SB³C2016-42
Estee L. George[1], Flora F. Opoku Asantewaa[2], Gabrielle K. Van Scoy[2], Alicia Prieto-Langarica[2], Marnie M. Saunders[1], *[1]The University of Akron, Akron, OH, United States, [2]Youngstown State University, Youngstown, OH, United States*

FRIDAY, JULY 1 | 1:00pm - 3:15pm

Poster Session II — Growth, Remodeling and Repair — Exhibit Hall A

245 **Acceleration of Critical Bone Defect Healing by Ultrasound Radiation Force in a Rat Tibial Model** SB³C2016-949
Yi-Xian Qin, Jingbo Liu, Tony Zhang, Xiaofei Li, *Biomedical Engineering, Stony Brook University, Stony Brook, NY, United States*

Copyright 2016 The Organizing Committee for the 2016 Summer Biomechanics, Bioengineering and Biotransport Conference

246 **A Novel Structural Constitutive Model for Passive Right Ventricular Myocardium: Toward An Understanding of Remodeling During Pulmonary Hypertension** SB³C2016-137
Reza Avazmohammadi, Michael S. Sacks, *Institute for Computational Engineering and Sciences, The University of Texas at Austin, Austin, TX, United States*

247 **Experimental Validation of a Subject-Specific Anisotropic Model of the Rotator Cuff to Predict Tear Propagation** SB³C2016-820
R. Matthew Miller[1], James Thunes[1], Volker Musahl[2], Spandan Maiti[1], Richard E. Debski[1], *[1]Bioengineering, University of Pittsburgh, Pittsburgh, PA, United States, [2]Orthopaedic Surgery, University of Pittsburgh, Pittsburgh, PA, United States*

248 **Kinematic Evidence of Ring Apophysis Fracture During Cyclic Loading Typical of ADLs** SB³C2016-623
Nicole C. Corbiere[1], Stacey L. Zeigler[2], Kathleen A. Issen[1], Arthur J. Michalek[1], Laurel Kuxhaus[1], *[1]Mechanical and Aeronautical Engineering, Clarkson University, Potsdam, NY, United States, [2]Physical Therapy, Clarkson University, Potsdam, NY, United States*

249 **Effective Remodeling of Wall Content in Cerebral Aneurysms** SB³C2016-1028
Xinjie Duan, *Mechanical Engineering and Material Science, University of Pittsburgh, Pittsburgh, PA, United States*

250 **Modeling Soft Tissue Damage and Failure Using a Hybrid Particle/Continuum Approach** SB³C2016-71
Manuel K. Rausch[1], George E. Karniadakis[2], Jay D. Humphrey[1], *[1]Biomedical Engineering, Yale University, New Haven, CT, United States, [2]Applied Mathematics, Brown University, Providence, RI, United States*

251 **Temporal Healing Response of Achilles Tendons in Rodents Following Injury Depends on Surgical Treatment and Return to Activity Time** SB³C2016-84
Benjamin R. Freedman, Tyler R. Morris, Nabeel S. Salka, Joshua A. Gordon, Adam M. Pardes, Corinne N. Riggin, Courtney A. Nuss, Jennica J. Tucker, Pankti R. Bhatt, George W. Fryhofer, Daniel C. Farber, Louis J. Soslowsky, *McKay Orthopaedic Research Laboratory, University of Pennsylvania, Philadelphia, PA, United States*

252 **A Theoretical Evaluation of Potential Strategies for Enhancing Cellular Anabolism in the Extracellular Matrix of the Invertertebral Disc** SB³C2016-98
Shihab Asfour[1], Juan Pablo de Rivero Vaccari[2], **Francesco Travascio**[1], *[1]Industrial Engineering, University of Miami, Coral Gables, FL, United States, [2]Neurosurgery, University of Miami, Miami, FL, United States*

253 **In-Vitro Model of Healing Ligament** SB³C2016-727
Stephanie M. F. Tuft, Julia T. Oxford, Erica E. Morrill, Raquel J. Brown, Trevor J. Lujan, *Biology, and Mechanical and Biomedical Engineering, Boise State University, Boise, ID, United States*

254 **Adipose-derived Mesenchymal Stem Cells Stimulate Elastin Production by Adult Human Smooth Muscle Cells in a 3D Fibrin Scaffold** SB³C2016-1119
Kory Blose, Justin Weinbaum, David Vorp, *Bioengineering, University of Pittsburgh, Pittsburgh, PA, United States*

255 **Effect of Three Dimensional Spheroid Culture on Bipotent Murine Liver Progenitor Cells** SB³C2016-165
Kenichiro Nishii, Erik Brodin, Taylor Renshaw, Rachael Weesner, **Jessica L. Sparks**, *Miami University, Oxford, OH, United States*

256 **Does Tissue Architecture Matter to Bulk Mechanics? Scrambled Embryos Suggest Not.** SB³C2016-862
Joseph H. Shawky, Lance A. Davidson, *Bioengineering, University of Pittsburgh, Pittsburgh, PA, United States*

257 **Urinary Bladder Structure Remodeling Study with Multiphoton Imaging** SB³C2016-1030
Fangzhou Cheng[1], Jack Hornsby[2], Donna Daly[3], Florenta Kullmann[1], Lori Birder[1], Anne Robertson[1], Mark Thompson[2], Paul Watton[3], *[1]University of Pittsburgh, Pittsburgh, PA, United States, [2]University of Oxford, Oxford, United Kingdom, [3]University of Sheffield, Sheffield, United Kingdom*

Copyright 2016 The Organizing Committee for the 2016 Summer Biomechanics, Bioengineering and Biotransport Conference

FRIDAY, JULY 1	1:00pm - 3:15pm

Poster Session II — Musculoskeletal Soft Tissue Mechanics — Exhibit Hall A

279 **The Contribution of Articular Cartilage Focal Defect Size and Location on Whole Knee Computational Models** SB³C2016-64
Benjamin C. Marchi, Rhima Coleman, Ellen M. Arruda, *Mechanical Engineering, University of Michigan, Ann Arbor, MI, United States*

280 **Determining the Relationship Between the Biomechanical and Biochemical Properties of Articular Cartilage Utilizing An Artificial Neural Network** SB³C2016-903
Joe T. Rexwinkle[1], Ferris Pfeiffer[2], Nikki Werner[3], Aaron M. Stoker[3], *[1]Mechanical Engineering, University of Missouri, Columbia, MO, United States, [2]Bioengineering/Orthopaedic Surgery, University of Missouri, Columbia, MO, United States, [3]Veterinary Medicine, University of Missouri, Columbia, MO, United States*

281 **Mechanical Properties of the Growth Plate in a Rat Model of Obesity** SB³C2016-926
Patrick Estep[1], Moriah Smoot[2], Shawn Gilbert[1], **Alan Eberhardt**[1], *[1]UAB, Birmingham, AL, United States, [2]University of Alabaama, Tuscaloosa, AL, United States*

282 **The Dynamics of Proteoglycan Loss in Articular Cartilage Following Mechanical Perturbation** SB³C2016-667
Lorenza Henao Murillo, Keita Ito, **Corrinus C. van Donkelaar**, *Biomedical Engineering, Eindhoven University of Technology, Eindhoven, Netherlands*

283 **Tribological Rehydration 2: Insights into the Mechanics of Cartilage Recovery** SB³C2016-163
David L. Burris[1], Axel Moore[2], *[1]Mechanical Engineering, University of Delaware, Newark, DE, United States, [2]Biomedial Engineering, University of Delaware, Newark, DE, United States*

284 **Smoking and Smoking Cessation: Implications on the Degeneration of the Intervertebral Disc** SB³C2016-741
Shady Elmasry[1], Shihab Asfour[1], Juan Pablo de Rivero Vaccari[2], Francesco Travascio[1], *[1]Industrial Engineering, University of Miami, Coral Gables, FL, United States, [2]Neurological Surgery, University of Miami, Miami, FL, United States*

285 **Biomechanics of Muscle Tendon Junction and Tendon Bone Insertions** SB³C2016-1073
Sandhya Chandrasekaran, Ashley Saltzman, **HY Shadow Huang**, *NC State, Raleigh, NC, United States*

286 **The Effect of Ligament Stiffness on Shoulder Cartilage Pressure and Kinematics** SB³C2016-844
Hafizur Rahman, Mariana E. Kersh, *Department of Mechanical Science and Engineering, University of Illinois at Urbana-Champaign, Urbana, IL, United States*

287 **Anterior Cruciate Ligament Femoral Entheseal Shape and Insertion Angle are Risk Factors for Injury** SB³C2016-160
Callan M. L. Luetkemeyer, Ellen M. Arruda, *Mechanical Engineering, University of Michigan, Ann Arbor, MI, United States*

288 **Uninjured Supraspinatus Tendons in Rodents Do Not Exhibit Different Material Properties Across Sex** SB³C2016-674
Kelsey A. Robinson, Adam M. Pardes, Benjamin R. Freedman, Louis J. Soslowsky, *Department of Orthopaedics, University of Pennsylvania, Philadelphia, PA, United States*

289 **Simvastatin Does Not Adversely Affect the Mechanical and Histological Properties of the Achilles Tendon in a Diet Induced Hypercholesterolemia Rat Model** SB³C2016-778
Daniel S. Choi, Jennica J. Tucker, Louis J. Soslowsky, *University of Pennsylvania, Philadelphia, PA, United States*

290 **The Response to Stress Deprivation Differs Between the Interfascicular and Fascicular Matrix of Tendon** SB³C2016-664
Daniel T. Rowson, Martin M. Knight, Hazel R. C. Screen, *School of Engineering and Materials Science, Institute of Bioengineering, London, United Kingdom*

291 **Overlap Between Anterior Cruciate Ligament and the Anterolateral Meniscal Root Insertions: A Scanning Microscopy Study** SB³C2016-105
Brett D. Steineman[1], Samuel G. Moulton[2], Tammy L. Haut Donahue[3], Chase S. Dean[2], Robert F. LaPrade[2, 4], *[1]School of Biomedical Engineering, Colorado State University, Fort Collins, CO, United States, [2]Steadman Philippon Research Institute, Vail, CO, United States, [3]Mechanical Engineering, Colorado State University, Fort Collins, CO, United States, [4]The Steadman Clinic, Vail, CO, United States*

Copyright 2016 The Organizing Committee for the 2016 Summer Biomechanics, Bioengineering and Biotransport Conference

292 **Correlation of Supraspinatus Tendon Degeneration and Quantitative Ultrasound Measures** SB³C2016-710
Gerald A. Ferrer[1], R. Matthew Miller[1], Masahito Yoshida[2], Amir A. Rahnemai-Azar[2], Volker Musahl[1, 2], Richard E. Debski[1, 2], *[1]Department of Bioengineering, University of Pittsburgh, Pittsburgh, PA, United States, [2]Department of Orthopaedic Surgery, University of Pittsburgh, Pittsburgh, PA, United States*

293 **Energy Storing and Positional Human Tendons: Mechanics and Changes with Ageing** SB³C2016-81
Dharmesh Patel[1], Ewa M. Spiesz[1], Chavaunne T. Thorpe[1], Helen L. Birch[2], Graham P. Riley[3], Peter D. Clegg[4], Hazel R. C. Screen[1], *[1]School of Engineering and Materials Science, Queen Mary University of London, London, United Kingdom, [2]Institute of Orthopaedics and Musculoskeletal Science, University College London, London, United Kingdom, [3]School of Biological Sciences, University of East Anglia, Norwich, United Kingdom, [4]Department of Musculoskeletal Biology, University of Liverpool, Liverpool, United Kingdom*

294 **Effect of Collagen Fibril Alignment on Viscoelastic Mechanical Properties of Ligament** SB³C2016-109
Erica E. Morrill[1], Christina J. Stender[1], Raquel J. Brown[2], Trevor J. Lujan[1], *[1]Mechanical and Biomedical Engineering, Boise State University, Boise, ID, United States, [2]Biomolecular Research Center, Boise State University, Boise, ID, United States*

295 **Sex Differences in Achilles Tendon Properties Three Weeks After Injury in Rats** SB³C2016-144
George W. Fryhofer, Benjamin R. Freedman, Adam M. Pardes, Cody D. Hillin, Louis J. Soslowsky, *McKay Orthopaedic Research Laboratory, University of Pennsylvania, Philadelphia, PA, United States*

296 **Differences Between the Mechanical and Microstructural Properties of the Human ACL and PCL** SB³C2016-628
Ryan Castile[1], Nathan Skelley[2], Jon Wright[3], Robert Brophy[2], Spencer Lake[1], *[1]Mechanical Engineering, Washington University in St. Louis, St. Louis, MO, United States, [2]Washington University in St. Louis, St. Louis, MO, United States, [3]Beaumont Health, Royal Oak, MI, United States*

297 **Consequences of Meniscus Cracks in Uniaxial Tension** SB³C2016-911
John M. Peloquin[1], Julia Pezick[2], Pranita Muralidhar[2], Michael H. Santare[3], Dawn M. Elliott[2], *[1]Department of Bioengineering, University of Pennsylvania, Philadelphia, PA, United States, [2]Department of Biomedical Engineering, University of Delaware, Newark, DE, United States, [3]Department of Mechanical Engineering, University of Delaware, Newark, DE, United States*

298 **Effect of Age on the Mechanical Properties of the Porcine Temporomandibular Joint Disc** SB³C2016-152
Jesse Lowe, Alejandro Almarza, *Bioengineering, University of Pittsburgh, Pittsburgh, PA, United States*

299 **In Situ Measurements of Hydraulic Permeability in Skeletal Muscles** SB³C2016-960
Michael Schenk, Lijian Peng, Xingyu Chen, **Shaopeng Pei**, X. Lucas Lu, Liyun Wang, *University of Delaware, Newark, DE, United States*

300 **Muscle Volume Prediction using Anthropometric Measurements and Population Derived Statistical Models** SB³C2016-117
Shasha Yeung, Justin Fernandez, Geoffery Handsfield, Cameron Walker, Thor Besier, Ju Zhang, *Auckland Bioengineering Institute, Auckland, New Zealand*

301 **Probing the Transition From Compaction to Fatigue in Human Articular Cartilage Under Cyclic Loading** SB³C2016-671
Jonathan T. Kaplan[1, 2], M. Hicham Drissi[3], Corey P. Neu[4], **David M. Pierce**[1], *[1]Mechanical Engineering/Biomedical Engineering/Mathematics, University of Connecticut, Storrs, CT, United States, [2]Biomechanics Research and Engineering, Natick Soldier RD&E Center, Natick, MA, United States, [3]Orthopaedic Surgery, University of Connecticut Health Center, Farmington, CT, United States, [4]Mechanical Engineering, University of Colorado, Boulder, CO, United States*

FRIDAY, JULY 1 | 1:00pm - 3:15pm

Poster Session II — Joint and Spine Biomechanics — Exhibit Hall A

302 **Post-Operative Complications of Computer Assisted Total Knee Arthroplasty in Osteoporotic Femurs and Tibias: A Finite Element Study** SB³C2016-1129
Ruth Solomon[1], Andrew Sori[1], Shihab Asfour[1], Loren Latta[2], Ali Alhandi[2], Francesco Travascio[1], *[1]Industrial Engineering, University of Miami, Coral Gables, FL, United States, [2]Max Biedermann Institute for Biomechanics, Miami Beach, FL, United States*

Copyright 2016 The Organizing Committee for the 2016 Summer Biomechanics, Bioengineering and Biotransport Conference

303 **Computational Analysis on Post-Fusion Effects of Hardware Preservation of Removal on Osteoporotic Proximal Tibia Cartilage and Subchondral Bone** SB³C2016-812

Andrew Sori[1], Ruth Solomon[1], Shihab Asfour[1], Ronald Lindsey[2], Ali Alhandi[3], Loren Latta[3], Francesco Travascio[1], *[1]Industrial Engineering, University of Miami, Coral Gables, FL, United States, [2]Orthopaedic Surgery, University of Texas Medical Brach, Galveston, TX, United States, [3]Max Biedermann Institute for Biomechanics, Miami Beach, FL, United States*

304 **Effects of Tibiofemoral Compression on ACL Forces and Knee Kinematics Under Combined Knee Loads** SB³C2016-630

Kent T. Yamaguchi, Daniel Boguszewski, Justin Mathew, Keith Markolf, David McAllister, *Orthopedic Surgery, University of California Los Angeles, Los Angeles, CA, United States*

305 **Development of Clinically Relevant Constraint Measurement Using Modified Total Knee Replacement Implants** SB³C2016-956

Scott N. Anderson[1], Peter S. Walker[2], Ryan T. Willing[1], *[1]Mechanical Engineering, Binghamton University, Binghamton, NY, United States, [2]Langone Medical Center, New York University, New York, NY, United States*

306 **Nonlinear Multifactorial Influence of Ligament Properties on Rotatory Knee Stability: Novel Application of Bayesian Sensitivity Analysis** SB³C2016-1128

Mohammad Kia[1], Po-Hsu Chen[2], Thomas L. Wickiewicz[3], Andrew D. Pearle[3], Thomas Santner[2], **Carl W. Imhauser**[1], *[1]Biomechanics, Hospital for Special Surgery, New York, NY, United States, [2]Statistics, The Ohio State University, Columbus, OH, United States, [3]Orthopaedic Surgery, Hospital for Special Surgery, New York, NY, United States*

307 **Generating a Subject-specific Musculoskeletal Model of the Knee Using Motion Capture Data and Medical Imaging** SB³C2016-576

Mousa Kazemi, *ABI, Auckland, New Zealand*

308 **Evaluation of a Displacement-Driven Model for Assessing Patellofemoral Joint Contact Mechanics** SB³C2016-46

Jonathan A. Gustafson, Kyle A. Berkow, Richard E. Debski, Shawn Farrokhi, *Bioengineering, University of Pittsburgh, Pittsburgh, PA, United States*

309 **Toward Patient-specific Computational Model of the Knee Joint** SB³C2016-90

Hongqiang Guo[1], Thomas Santner[2], Amy Lerner[3], Suzanne Maher[1], *[1]Hospital for Special Surgery, New York, NY, United States, [2]The Ohio State University, Columbus, OH, United States, [3]University of Rochester, Rochester, NY, United States*

310 **A Population Derived Mechanostatistical Model of the Human and Sheep Spine to Evaluate Spinal Fusion Implants** SB³C2016-654

Alex Swee, Vickie Shim, Justin Fernandez, *Auckland Bioengineering Institute, University of Auckland, Auckland City, New Zealand*

311 **Changes in Cervical Spine Intervertebral Disc Properties with Repetitive Axial Loading** SB³C2016-123

Brian D. Stemper[1, 2], Alok S. Shah[1, 2], Narayan Yoganandan[1, 2], Mingxin Zheng[3, 4], Brian Snyder[3, 4], *[1]Neurosurgery, Medical College of Wisconsin, Milwaukee, WI, United States, [2]Research Service, Zablocki VA Medical Center, Milwaukee, WI, United States, [3]Beth Israel Deaconess Medical Center, Boston, MA, United States, [4]Harvard Medical School, Boston, MA, United States*

312 **Treatment of Thoracolumbar Burst Fracture: A Biomechanical Analysis of Three Different Fixation Constructs** SB³C2016-746

Shady Elmasry[1], Shihab Asfour[1], Joseph Gjolaj[2], Loren Latta[3], Frank Eismont[2], Francesco Travascio[1], *[1]Industrial Engineering, University of Miami, Coral Gables, FL, United States, [2]Orthopaedic Surgery, University of Miami, Miami, FL, United States, [3]Max Biedermann Institute for Biomechanics, Miami Beach, FL, United States*

313 **Detecting Osteoporotic Vertebral Compression Fractures: BMD vs. Acoustic Emission Technique** SB³C2016-908

jihui li[1], Thomas Mazahery[1], Ronald Childs[1], Mark Theiss[1], Melanie Pham[2], *[1]Orthopaedics, Fairfax hospital, Falls Church, VA, United States, [2]Surgery, Eastern Virginia Medical School, Norfolk, VA, United States*

314 **Computer Simulation of Lumbar Flexion Shows In-Plane and Through-Plane Shear of the Facet Capsular Ligament** SB³C2016-22

Amy A. Claeson, Victor H. Barocas, *Biomedical Engineering, University of Minnesota, Minneapolis, MN, United States*

315 **Shape Optimization of Lumbar Intervertebral Cages Featuring Different Cross-Section Shapes** SB³C2016-634

Chaochao Zhou[1], Khalid Sethi[2], Ryan Willing[1], *[1]Department of Mechanical Engineering, Binghamton University, Binghamton, NY, United States, [2]Senecka Spine, Binghamton, NY, United States*

Copyright 2016 The Organizing Committee for the 2016 Summer Biomechanics, Bioengineering and Biotransport Conference

316 **A Comparison of Normal and Osteoarthritic Humeral Head Size and Morphology** SB³C2016-17
Nikolas K. Knowles[1], Michael J. Carroll[2], Louis M. Ferreira[1], Jay D. Keener[3], George S. Athwal[2], *[1]Biomedical Engineering, The University of Western Ontario, London, ON, Canada, [2]The University of Western Ontario, London, ON, Canada, [3]Washington University, St. Louis, MO, United States*

FRIDAY, JULY 1 | 1:00pm - 3:15pm

Poster Session II — Other Solid, Tissue, Cellular and Molecular Biomechanics — Exhibit Hall A

317 **Evaluation of Polymeric Scaffolds Using a Vertical Layered Coextrusion for Topical Drug Delivery Applications and Comparison with Electrostatic Spinning** SB³C2016-621
Mohammad Mofidfar, Eric Baer, Gary E. Wnek, *Macromolecular Science and Engineering, CWRU, Cleveland, OH, United States*

318 **Synthesis and Characterization of Mesopore Forsterite Powder for Biomedical Application** SB³C2016-1053
Seyed Mehdi Mirhadi[1], **Fariborz Tavangarian**[2], *[1]Shahreza Branch, Islamic Azad University, Isfahan, Iran, Islamic Republic of, [2]Morehead State Univeristy, Morehead, KY, United States*

319 **PLA/ PLGA-coated Chitosan Micro-implants for Sustained Release of Methotrexate to Treat Vitreo-retinal Diseases** SB³C2016-172
Soumyarwit Manna[1], Marwan F. Al-Rjoub[1], Anna Donnell[2], Necati Kaval[2], James J. Augsburger[3], Zelia M. Correa[3], Rupak Banerjee[1], *[1]Mechanical and Materials Engineering, University of Cincinnati, Cincinnati, OH, United States, [2]Chemistry, University of Cincinnati, Cincinnati, OH, United States, [3]Ophthalmology, University of Cincinnati, Cincinnati, OH, United States*

320 **Investigating Collagen Methacrylamide, a Photocrosslinkable, Thermoreversible, Collagen-Based Hydrogel, for Regenerative Medicine** SB³C2016-946
Kathryn E. Drzewiecki, Juilee N. Malavade, David I. Shreiber, *Biomedical Engineering, Rutgers, The State University of New Jersey, Piscataway, NJ, United States*

321 **Detection of SK Channels on Neuronal Axons of Skchannels on Neuronal Axons** SB³C2016-33
Krithika Abiraman, Anastasios V. Tzingounis, George Lykotrafitis, *Univeristy of Connecticut, Storrs, CT, United States*

322 **Emulation of Muscular Thin Film Deflection Using Thermal Contraction: Comparison of Constitutive Models** SB³C2016-813
Victoria A. Webster[1], Santiago G. Nieto[2], Anna Grosberg[3], Ozan Akkus[1], Hillel J. Chiel[4], Roger D. Quinn[1], *[1]Mechanical Engineering, Case Western Reserve University, Cleveland, OH, United States, [2]Biomedical Engineering, Case Western Reserve University, Cleveland, OH, United States, [3]Biomedical Engineering, University of California, Irvine, Irvine, CA, United States, [4]Biology, Case Western Reserve University, Cleveland, OH, United States*

323 **Simulation of Strain Induced Damage During Delivery** SB³C2016-633
Olivier Mayeur[1, 2], Estelle JeanDitGautier[3], Pauline Lecomte[1, 2], Jean-François Witz[4], Chrystele Rubod[2, 3], Michel Cosson[2, 5], **Mathias J. Brieu**[1, 2], *[1]MSO, Centrale Lille, Villeneuve D'Ascq, France, [2]Lml - fre 3723, CNRS, Villeneuve d'Ascq, France, [3]Hopital Jeanne de Flandre, CHR Lille, Lille, France, [4]LML - FRE 3723, CNRS, Villeneuve D'Ascq, France, [5]Hopital Jeanne de Flandre, CHR Lille, Villeneuve D'Ascq, France*

324 **Elastin Fiber Network in Porince Epicardium: 3D Viscualization and Quantification** SB³C2016-823
Xiaodan Shi, Bryn Brazile, David Lee, Sourav Patnaik, Jim Cooley, Raj Prabhu, Lakiesha Williams, Song Zhang, Jun Liao, *Mississippi State University, Mississippi State, MS, United States*

325 **Determining the Effect of Elastin Digestion on the Regional Biaxial Mechanical Properties of the Murine Cervix** SB³C2016-695
Victoria Morris, **Cassandra Conway**, Kristin Miller, *Biomedical Engineering, Tulane University, New Orleans, LA, United States*

326 **Viscosity is a Necessary Component of Mechanical Characterization of Biological Tissue** SB³C2016-935
Andres Rubiano[1], Daniel Delitto[2], Song Han[1], Steven Hughes[2], Chelsey S. Simmons[1, 3, 4], *[1]Mechanical and Aerospace Engineering, University of Florida, Gainesville, FL, United States, [2]Department of Surgery, University of Florida, Gainesville, FL, United States, [3]Biomedical Engineering, University of Florida, Gainesville, FL, United States, [4]Division of Cardiovascular Medicine, University of Florida, Gainesville, FL, United States*

Copyright 2016 The Organizing Committee for the 2016 Summer Biomechanics, Bioengineering and Biotransport Conference

327 **Quantification and Comparison of Mechanical Properties of the Urinary Bladder Wall** SB³C2016-934
Antonella Massafra, **Sara Roccabianca**, *Mechanical Engineering, Michigan State University, East Lansing, MI, United States*

328 **A Mechanical Analysis of Compressible Collagen Hydrogels** SB³C2016-1135
Brooks Lane[1], Tarek Shazly[1, 2], John Eberth[1, 3], *[1]Biomedical Engineering, University of South Carolina, Columbia, SC, United States, [2]Mechanical Engineering, University of South Carolina, Columbia, SC, United States, [3]Cell Biology and Anatomy, University of South Carolina, Columbia, SC, United States*

329 **Stochastic Head Morphology Description for Uncertainty Quantification of TBI Prediction** SB³C2016-591
Kirubel Teferra[1], Siddiq M. Qidwai[1], Shankarjee Krishnamoorthi[2], *[1]Multifunctional materials branch, Code 6353, Naval Research Laboratory, Washington DC, DC, United States, [2]NRL/ASEE Postdoctoral fellowship, Naval Research Laboratory, Washington DC, DC, United States*

330 **Characterization of the Failure Responses of Skin: Comparison of Uniaxial and Equibiaxial Planar Mechanics** SB³C2016-649
Samantha Schumm, Meagan Ita, Beth Winkelstein, *University of Pennsylvania, Philadelphia, PA, United States*

SATURDAY, JULY 2 | 11:45am - 1:15pm

Engineering the Cellular Microenvironment — Wilson B

Session Chair: Brendon Baker, *University of Michigan, MI, United States*
Session Co-Chair: Alice Huang, *Mount Sinai School of Medicine, NY, United States*

11:45AM **A Biomimetic Core-Shell Platform for Miniaturized 3D Cell and Tissue Engineering** SB³C2016-943
Pranay Agarwal, Jung K. Choi, Xiaoming He, *Biomedical Engineering, The Ohio State University, Columbus, OH, United States*

12:00PM **Differentiating Stem Cells Exhibit Molecular and Microenvironmental Heterogeneity at the Single Cell Level** SB³C2016-793
Claire M. McLeod[1, 2, 3], Allison J. Cote[1], Arjun Raj[1], Robert L. Mauck[1, 2, 3], *[1]Department of Bioengineering, University of Pennsylvania, Philadelphia, PA, United States, [2]Translational Musculoskeletal Research Center, Philadelphia VA Medical Center, Philadelphia, PA, United States, [3]Department of Orthopaedic Surgery, University of Pennsylvania, Philadelphia, PA, United States*

12:15PM **Anisotropically Stiff Micropillar Substrate for Controlling Cellular Alignment and Elongation** SB³C2016-750
Yunus Alapan[1], Mousa Younesi[1], Ozan Akkus[1, 2, 3], Umut A. Gurkan[1, 2, 3], *[1]Mechanical and Aerospace Engineering Department, Case Western Reserve University, Cleveland, OH, United States, [2]Biomedical Engineering Department, Case Western Reserve University, Cleveland, OH, United States, [3]Orthopaedics Department, Case Western Reserve University, Cleveland, OH, United States*

12:30PM **Non-swelling Micromolded Hydrogels Reveal That Matrix Degradability Controls Multicellularity of 3D Cell Invasion** SB³C2016-973
Brendon M. Baker[1], Britta Trappmann[1], Jason A. Burdick[2], Christopher S. Chen[1], *[1]Biomedical Engineering, Boston University, Boston, MA, United States, [2]Bioengineering, University of Pennsylvania, Philadelphia, PA, United States*

12:45PM **Schwann Cells Promote Penetration and Myelination of Regenerated Axons into Patterned Channels** SB³C2016-45
Chun Liu, **Christina Chan**, *Chemical Engineering and Materials Science, Michigan State University, East Lansing, MI, United States*

1:00PM **Tunable and Selective Nanofiber Degradation Regulates 3D Cell Migration** SB³C2016-631
Feini Qu[1, 2], Julianne L. Holloway[1, 2], Jason A. Burdick[1, 2], Robert Mauck[1, 2], *[1]University of Pennsylvania, Philadelphia, PA, United States, [2]Philadelphia VA Medical Center, Philadelphia, PA, United States*

Copyright 2016 The Organizing Committee for the 2016 Summer Biomechanics, Bioengineering and Biotransport Conference

SATURDAY, JULY 2	11:45am - 1:15pm

Upper and Lower Extremity Joint Mechanics — Wilson C

Session Chair: Ken Fischer, *University of Kansas, KS, United States*
Session Co-Chair: Justin Fernandez, *The University of Auckland, New Zealand*

11:45AM **Fibrin Glue Increases the Strength of Conduit-Assisted Digital Nerve Repairs** SB³C2016-912
Patrick J. Schimoler[1, 2], Jessica Childe[2], Steven Regal[2], Alexander Kharlamov[2], Peter Tang[2], Mark Carl Miller[1, 2], *[1]Mechanical Engineering and Materials Science, University of Pittsburgh, Pittsburgh, PA, United States, [2]Orthopaedic Surgery, Allegheny General Hospital, Pittsburgh, PA, United States*

12:00PM **The Effect of Lateralizing Joint Center of Rotation of Reverse Total Shoulder Arthroplasty on Adduction Range of Motion and Initial Implant Fixation: A Finite Element Study** SB³C2016-988
Josie Elwell[1], Joseph Choi[2], Ryan Willing[1], *[1]Binghamton University, Binghamton, NY, United States, [2]Guthrie Clinic, Sayre, PA, United States*

12:15PM **Premorbid Retroversion is Significantly Greater in Type B2 Glenoids** SB³C2016-16
Nikolas K. Knowles[1], Louis M. Ferreira[1], George S. Athwal[2], *[1]Biomedical Engineering, The University of Western Ontario, London, ON, Canada, [2]Surgery, The University of Western Ontario, London, ON, Canada*

12:30PM **Novel Method for Characterizing Loading Patterns of Knee Stabilizers Yields New Insight into the Function of the Anterolateral Ligament** SB³C2016-974
Robert N. Kent[1], Thomas L. Wickiewicz[2], Andrew D. Pearle[2], Carl W. Imhauser[1], *[1]Department of Biomechanics, Hospital for Special Surgery, New York, NY, United States, [2]Department of Orthopedic Surgery, Hospital for Special Surgery, New York, NY, United States*

12:45PM **Effects of Proximal Tibia Anterior Closing Wedge Osteotomy on ACL Force and Knee Kinematics** SB³C2016-75
Kent T. Yamaguchi[1], Daniel V. Boguszewski[1], Edward Cheung[1], Justin Mathew[2], Keith Markolf[1], David McAllister[1], Frank Petrigliano[1], *[1]Orthopedic Surgery, University of California Los Angeles, Los Angeles, CA, United States, [2]David Geffen School of Medicine, University of California Los Angeles, Los Angeles, CA, United States*

1:00PM **Virtual Design of Modular 3D Printed Ankle Foot Orthoses** SB³C2016-661
Alessio Ielapi[1], Benedict Verhegghe[1], Miguel Vermandel[2], Jan Patrick Deckers[2], Malcolm Forward[3], Egle Vasiliauskaite[3], Matthieu De Beule[1], *[1]IBiTech-bioMMeda, Gent University, Gent, Belgium, [2]V!GO N.V. / S.A., Wetteren, Belgium, [3]Gait & Movement Analysis Laboratory, University Hospital Ghent, Gent, Belgium*

SATURDAY, JULY 2	11:45am - 1:15pm

Musculoskeletal Soft Tissue: Cartilage — Wilson D

Session Chair: Jennifer Wayne, *Virginia Commonwealth University, VA, United States*
Session Co-Chair: David M. Pierce, *University of Connecticut, CT, United States*

11:45AM **Indispensable Roles of Decorin and Biglycan in Cartilage Mechanical Function During Maturation** SB³C2016-964
Basak Doyran[1], Qingmei Yao[2], Samuel J. Rozans[1], Qing Li[1], Marian F. Young[3], Renato V. Iozzo[4], David Birk[2], Lin Han[1], *[1]School of Biomedical Engineering, Science and Health Systems, Drexel Univeristy, Philadelphia, PA, United States, [2]Department of Molecular Pharmacology and Physiology, University of South Florida, Tampa, FL, United States, [3]Molecular Biology of Bones and Teeth Section, National Institutes of Health, Bethesda, MD, United States, [4]Department of Pathology, Anatomy and Cell Biology, Thomas Jefferson University, Philadelphia, PA, United States*

12:00PM **An Alternative Method to Characterize the Quasi-Static Material Properties of Murine Articular Cartilage** SB³C2016-744
Alexander Kotelsky, Chandler Woo, Mark R. Buckley, *Biomedical Engineering, University of Rochester, Rochester, NY, United States*

12:15PM **Bisphosphonate can Rescue the Damaged Articular Cartilage in vitro** SB³C2016-70
Yilu Zhou, Mengxi Lv, Marisa Bisram, Joshua Blotnick, Liyun Wang, X. Lucas Lu, *University of Delaware, Newark, DE, United States*

Copyright 2016 The Organizing Committee for the 2016 Summer Biomechanics, Bioengineering and Biotransport Conference

12:30PM **Tribological Rehydration I: A New Mechanism of Interstitial Fluid Recovery** SB³C2016-74
Axel Moore[1], David Burris[2], *[1]Biomedical Engineering, University of Delaware, Newark, DE, United States, [2]Mechanical Engineering, University of Delaware, Newark, DE, United States*

12:45PM **Mechanostatistical Cartilage Pellet Model to Evaluate Cartilage Growth in Scaffolds** SB³C2016-573
Christopher Miller, *Auckland Bioengineering institute, University of Auckland, Auckland, New Zealand*

1:00PM **Shear Testing of Human Articular Cartilage: Anistropy Apparent at Large But Not Small Shear Strains** SB³C2016-712
Franz S. Maier[1], M. Hicham Drissi[2], David M. Pierce[1], *[1]Mechanical Engineering/Biomedical Engineering/Mathematics, University of Connecticut, Storrs, CT, United States, [2]Orthopaedic Surgery, University of Connecticut Health Center, Farmington, CT, United States*

SATURDAY, JULY 2 | 11:45am - 1:15pm

Morphogenesis, Remodeling and Repair — Annapolis 1

Session Chair: Nandan L. Nerurkar, *Harvard Medical School, MA, United States*
Session Co-Chair: Lance Davidson, *University of Pittsburgh, PA, United States*

11:45AM **Mechanical Regulation of Cell Behaviors During Convergent Extension of the Xenopus laevis Neural Plate** SB³C2016-1105
Deepthi S. Vijayraghavan, Emily E. Kieffer, Joseph H. Shawky, Lance A. Davidson, *Bioengineering, University of Pittsburgh, Pittsburgh, PA, United States*

12:00PM **Meso-Scale Reorganization of Metabolic Brain Networks is Associated with Persistent Pain** SB³C2016-59
Megan Sperry, Sonia Kartha, Eric Granquist, Beth Winkelstein, *University of Pennsylvania, Philadelphia, PA, United States*

12:15PM **Molecular Control of Differential Growth During Looping of the Embryonic Small Intestine** SB³C2016-832
Nandan L. Nerurkar, Cliff Tabin, *Genetics, Harvard Medical School, Boston, MA, United States*

12:30PM **Optimization of In Vitro Endothelial Cell Self-Assembly for Millimeter Scale Vasculogenesis** SB³C2016-878
Joshua T. Morgan, Jasmine Shirazi, Erica M. Comber, Peter A. Sariano, Jason P. Gleghorn, *Biomedical Engineering, University of Delaware, Newark, DE, United States*

12:45PM **Structural Analysis of Early Embryonic Aortic Arch Morhphogenesis** SB³C2016-895
Seyedehsamaneh Lashkarinia, Senol Piskin, Selda Goktas, **Kerem Pekkan**, *Koc University, İstanbul, Turkey*

1:00PM **The Effect of Dynamic Stimulation on Joint Morphogenesis of the Embryonic Chick Knee Joint** SB³C2016-14
Vikesh V. Chandaria, Niamh C. Nowlan, *Bioengineering, Imperial College London, London, United Kingdom*

SATURDAY, JULY 2 | 11:45am - 1:15pm

Pediatric Cardiology and Embryology — Annapolis 2

Session Chair: Alison Marsden, *UC San Diego, CA, United States*
Session Co-Chair: Ethan Kung, *Clemson University, SC, United States*

11:45AM **Quantifying Circumferential and Wall Shear Stress in a Developing Embryonic Heart Using Non-invasive Techniques** SB³C2016-893
David Bark[1], Deborah Garrity[2], Lakshmi Prasad Dasi[1], *[1]Mechanical Engineering, Colorado State University, Fort Collins, CO, United States, [2]Biology, Colorado State University, Fort Collins, CO, United States*

12:00PM **Buckling Configurations of the Extracardiac Total Cavopulmonary Conduit** SB³C2016-883
Gokce Nur Oguz[1], Senol Piskin[1], Erhan Ermek[1], Naz Altekin[1], Ahmet Arnaz[2], Kerem Pekkan[1], *[1]Mechanical Engineering, Koc University, Istanbul, Turkey, [2]Cardiovascular Surgery, Acıbadem Bakırköy Hospital, Istanbul, Turkey*

Copyright 2016 The Organizing Committee for the 2016 Summer Biomechanics, Bioengineering and Biotransport Conference

12:15PM **In Vivo Measurements of Wall Shear Stress Environment in Fetus Umbilical Arteries and Veins** SB³C2016-34
Shier Nee Saw[1], Dawn Chia[2], Citra Nurfarah Zaini Mattar[2], Arijit Biswas[2], Choon Hwai Yap[1], *[1]Department of Biomedical Engineering, National University of Singapore, Singapore, Singapore, [2]Department of Obstetrics and Gynecology, National University of Singapore & National University Health Systems, Singapore, Singapore*

12:30PM **Coronary Circulation in an In Vitro Multi-scale Model of Norwood Circulation** SB³C2016-91
Lauren E. Carter, Tim Conover, Tian-qi Hang, Richard Figliola, *Mechanical Engineering, Clemson University, Clemson, SC, United States*

12:45PM **Implementation of the Assisted Bidirectional Glenn in an Idealized Single Ventricle Model** SB³C2016-1091
Jessica K. Shang[1], Mahdi Esmaily-Moghadam[2], Tigran Khalapyan[3], Richard Figliola[4], Olaf Reinhartz[3], Tain-Yen Hsia[5], Alison L. Marsden[1], *[1]Pediatrics, Stanford University, Stanford, CA, United States, [2]Center for Turbulence Research, Stanford University, Stanford, CA, United States, [3]Cardiothoracic Surgery, Stanford University, Stanford, CA, United States, [4]Mechanical Engineering, Clemson University, Clemson, SC, United States, [5]Cardiothoracic Surgery, Great Ormond Street Hospital, London, United Kingdom*

1:00PM **Computational Fluid Dynamics of Fetal Right Ventricle Based on Patient-specific Ultrasound Images** SB³C2016-85
Hadi Wiputra[1], Changquan Lai[1], R. Nivetha[1], Khong Chun Chua[1], Joel Heng[1], Guo Lan[1], Guat Ling Lim[2], Citra Nurfarah Zaini Mattar[2], Biswas Arijit[2], Hwa Liang Leo[1], Choon Hwai Yap[1], *[1]National University of Singapore, Singapore, Singapore, [2]Department of Obstetrics and Gynecology, National University Hospital Systems, Singapore, Singapore*

SATURDAY, JULY 2 | 11:45am - 1:15pm

Rehabilitation Devices, Modeling, and Control — Azalea 2

Session Chair: Ted Conway, *Florida Institute of Technology, FL, United States*
Session Co-Chair: Laurel Kuxhaus, *Clarkson University, NY, United States*

11:45AM **The Synergistic Use of Haptic Feedback with an EMG Controlled Transfemoral Powered-Knee Prosthesis** SB³C2016-596
J. Miles Canino, Kevin B. Fite, *Mechanical and Aeronautical Engineering, Clarkson University, Potsdam, NY, United States*

12:00PM **Functional Evaluation of Exoskeleton Control Strategies for Treating Crouch Gait in Cerebral Palsy** SB³C2016-816
Zachary F. Lerner, Diane L. Damiano, Thomas C. Bulea, *Rehabilitation Medicine Department, National Institutes of Health, Bethesda, MD, United States*

12:15PM **A Methodology for the Quantification of Upper Limb Prosthetic Socket Interface Mechanics** SB³C2016-37
Jonathon S. Schofield[1], Jason P. Carey[1], Paul D. Marasco[2], Jacqueline S. Hebert[3], *[1]Mechanical Engineering, University of Alberta, Edmonton, AB, Canada, [2]Biomedical Engineering, Cleveland Clinic, Cleveland, OH, United States, [3]Faculty of Medicine and Dentistry, University of Alberta, Edmonton, AB, Canada*

12:30PM **A Mechanical Analog Model of Adolescent Idiopathic Scoliosis** SB³C2016-963
Chloe L. Chung[1], Derek M. Kelly[2], Jack R. Steele[3], **Denis J. DiAngelo**[1], *[1]The Department of Orthopaedic Surgery and Biomedical Engineering, The University of Tennessee Health Science Center, Memphis, TN, United States, [2]The Department of Orthopaedics, Campbell Clinic Orthopaedics and Le Bonheur Children's Hospital, Memphis, TN, United States, [3]The Center for Orthotics and Prosthetics, Inc., Memphis, TN, United States*

12:45PM **Mapping Hand Dysfunction: A Model for Use in Rehabilitation** SB³C2016-843
Joshua P. Drost[1], Hyokyoung Hong[2], Tamara Reid Bush[1], *[1]Mechanical Engineering, Michigan State University, East Lansing, MI, United States, [2]Statistics and Probability, Michigan State University, East Lansing, MI, United States*

1:00PM **Kinematic Evaluation of a Wearable Soft Robotic System for Continuous Passive Motion in Post Stroke Hand Rehabilitation** SB³C2016-833
Rita M. Patterson[1], Nicoleta Bugnariu[2], Timothy Niacaris[3], Mahdi Haghshenas-Jaryani[4], Carrigan Wei[4], Caleb Nothnagle[4], Muthu Wijesundara[5], *[1]Family Medicine and Osteopathic Manipulative Medicine, University of North Texas Health Science Center, Fort Worth, TX, United States, [2]Physical Therapy, University of North Texas Health Science Center, Fort Worth, TX, United States, [3]Orthopaedic Surgery, University of North Texas Health Science Center, Fort Worth, TX, United States, [4]Research Institute, University of Texas At Arlington, Arlington, TX, United States, [5]Osteopathic Manipulative Medicine, University of North Texas Health Science Center, Fort Worth, TX, United States*

Copyright 2016 The Organizing Committee for the 2016 Summer Biomechanics, Bioengineering and Biotransport Conference

SATURDAY, JULY 2	11:45am - 1:15pm

Hemodynamic Flows and Devices — Azalea 3

Session Chair: Richard Figliola, *Clemson University, SC, United States*
Session Co-Chair: Brandon Dixon, *Georgia Tech, GA, United States*

11:45AM **Computational Assessment of the Effect of Arteriovenous Graft Flow Rate on Vascular Access Hemodynamics in a Novel Modular Anastomotic Valve Device** SB³C2016-597
Andrew McNally[1], A. George Akingba[2], Philippe Sucosky[3], *[1]University of Notre Dame, South Bend, IN, United States, [2]Indiana University - Purdue University of Indiana, Indianapolis, IN, United States, [3]Wright State University, Dayton, OH, United States*

12:00PM **Effect of Transcatheter Aortic Valve Positioning on Paravalvular Leakage: A Patient-Specific Numerical Model** SB³C2016-753
Matteo Bianchi, Ram P. Ghosh, Gil Marom, Danny Bluestein, *Biomedical Engineering, Stony Brook University, Stony Book, NY, United States*

12:15PM **Image-Based Simulations Show Significant Flow Fluctuations in a Normal Left Ventricle.** SB³C2016-131
Christophe Chnafa[1], Simon Mendez[2], Franck Nicoud[2], *[1]Mechanical & Industrial Engineering, University of Toronto, Toronto, ON, Canada, [2]IMAG, University of Montpellier, Montpellier, France*

12:30PM **Hemodynamic Regulation of Tie1 in Aortic Valve Endothelial Cells** SB³C2016-756
Camryn Johnson, W. David Merryman, *Vanderbilt University, Nashville, TN, United States*

12:45PM **Patient-Specific CFD Simulations of Intraventricular Haemodynamics Based on 3D Ultrasound Imaging.** SB³C2016-121
Alessandra M. Bavo[1], Alison M. Pouch[2], Joris Degroote[3], Jan Vierendeels[3], Joseph H. Gorman[2], Robert C. Gorman[2], Patrick Segers[1], *[1]ELIS department, Ibitech bioMMeda, Ghent University, Gent, Belgium, [2]Gorman Cardiovascular Research Group, University of Pennsylvania, Philadelphia, PA, United States, [3]Department of Flow, Heat and Combustion Mechanics, Ghent University, Gent, Belgium*

1:00PM **Flap Motion and Flow Reversal Vary with Number of Tears in an In Vitro Model of Descending Thoracic Aortic Dissection** SB³C2016-683
Joav Birjiniuk[1], Lucas H. Timmins[1, 2], Mark Young[3], John N. Oshinski[1, 2], Ravi K. Veeraswamy[4], David N. Ku[5], *[1]Biomedical Engineering, Georgia Institute of Technology, Atlanta, GA, United States, [2]Radiology, Emory University School of Medicine, Atlanta, GA, United States, [3]Cardiac and Vascular Group, Medtronic, Inc., Santa Rosa, CA, United States, [4]Division of Vascular Surgery, Department of Surgery, Emory University School of Medicine, Atlanta, GA, United States, [5]Mechanical Engineering, Georgia Institute of Technology, Atlanta, GA, United States*

SATURDAY, JULY 2	1:30pm - 3:00pm

Mechanotransduction and Sub-Cellular Biophysics — Wilson B

Session Chair: Toshiro Ohashi, *Hokkaido University, Sapporo, Japan*
Session Co-Chair: Joel B. Boerckel, *University of Notre Dame, IN, United States*

1:30PM **Changes in Nuclear Stiffness of Nesprin-1 Depleted Fibroblasts Exposed to Cyclic Stretching** SB³C2016-760
Naoya Sakamoto[1], Kiyomi Sadamoto[2], Mai Ogawa[2], Masaki Takeuchi[2], Noriyuki Kataoka[3], *[1]Department of Intelligent Mechanical Systems, Tokyo Metropolitan University, Tokyo, Japan, [2]Department of Medical Engineering, Kawasaki University of Medical Welfare, Okayama, Japan, [3]Department of Mechanical Engineering, Nihon University, Fukushima, Japan*

1:45PM **Deletion of Cadherin-11 Increases Smooth Muscle Actin Expression But Prevents Contraction in Valve Fibroblasts** SB³C2016-1088
Meghan Bowler, W. David Merryman, *Vanderbilt University, Nashville, TN, United States*

Copyright 2016 The Organizing Committee for the 2016 Summer Biomechanics, Bioengineering and Biotransport Conference

2:00PM **Matrix Stiffness Enhances Vasculogenesis Through Cytoskeletal Activation of YAP and TAZ Mediated Gene Expression** SB³C2016-822

Devon E. Mason[1], Sherry L. Voytik-Harbin[2], Mervin C. Yoder[3], Joel D. Boerckel[1], *[1]Aerospace and Mechanical Engineering, University of Notre Dame, Notre Dame, IN, United States, [2]Weldon School of Biomedical Engineering and Dept. of Basic Medical Sciences, Perdue University, West Lafayette, IN, United States, [3]Herman B Wells Center for Pediatric Research, Indiana University School of Medicine, Indianapolis, IN, United States*

2:15PM **Regulation of Valve Interstitial Cell Contractility and Metabolism by Mesoscale Architecture** SB³C2016-920

Ishita Tandon, Atefeh Razavi, Timothy Muldoon, Narasimhan Rajaram, Kartik Balachandran, *University of Arkansas, Fayetteville, AR, United States*

2:30PM **Strain-rate Dependent Mechanical Responses of the Aortic Valve Interstitial Cells** SB³C2016-950

Yusuke Sakamoto[1], Rachel M. Buchanan[2], Johannah S. Adams[3], Farshid Guilak[4], Michael S. Sacks[1, 2], *[1]The Institute for Computational Engineering and Sciences, The University of Texas at Austin, Austin, TX, United States, [2]Department of Biomedical Engineering, The University of Texas at Austin, Austin, TX, United States, [3](2) Departments of Orthopaedic Surgery and Biomedical Engineering, Duke University, Durham, NC, United States, [4]Departments of Orthopaedic Surgery, Biomedical Engineering, and Developmental Biology, Washington University, St. Louis, St. Louis, MO, United States*

2:45PM **Myosin II Mediated Cortical Contractility Regulates Nucleus Pulposus Cell Osmotic Properties and Morphology** SB³C2016-959

Timothy Jacobsen, Paula Hernandez, Nadeen Chahine, *The Feinstein Institute for Medical Reseaerch, Manhasset, NY, United States*

SATURDAY, JULY 2 | 1:30pm - 3:00pm

Celebration for Vijay Goel: Spine Biomechanics — Wilson C

Session Chair: Denis DiAngelo, *University of Tennessee, TN, United States*
Session Co-Chair: Francesco Travascio, *University of Miami, FL, United States*

1:30PM **The Effect of Degeneration on the Six Degree of Freedom Mechanical Properties of Human Spine Segments** SB³C2016-646

John J. Costi[1], Dhara Amin[1], Dana Sommerfeld[2], Isaac Lawless[1], Richard Stanley[1], Boyin Ding[3], *[1]School of Computer Science, Engineering and Mathematics, Flinders University, Adelaide, Australia, [2]Institute of Biomechanics, TUHH Hamburg University, Hamburg, Germany, [3]School of Mechanical Engineering, The University of Adelaide, Adelaide, Australia*

1:45PM **The Resonance of the Thoracic Spine Under Whole Body Vibration is Non-Linear & Depends on Acceleration: An in Vivo Study Using a Rat Model** SB³C2016-82

Timothy Holsgrove, Martha Zeeman, William Welch, Beth Winkelstein, *University of Pennsylvania, Philadelphia, PA, United States*

2:00PM **MRI Quantification of Human Spine Cartilage Endplate Geometry** SB³C2016-704

John DeLucca[1], John Peloquin[2], Lachlan Smith[2], Nichol Reisher[1], Alexander Wright[2], Edward Vresilovic[3], Dawn Elliott[1], *[1]University of Delaware, Newark, DE, United States, [2]University of Pennsylvania, Philadelphia, PA, United States, [3]Pennsylvania State University, Hershey, PA, United States*

2:15PM **Cervical Spinal Cord Stress: A Comprehensive Finite Element Model of the Cervical Spinal Cord** SB³C2016-698

Kirsten E. Stoner[1], Kingsely O. Abode-Iyamah[2], Douglas C. Fredericks[3], Matthew A. Howard[2], Nicole M. Grosland[1], *[1]Biomedical Engineering, University of Iowa, Iowa City, IA, United States, [2]Neurosurgery, University of Iowa, Iowa City, IA, United States, [3]Orthopaedics, University of Iowa, Iowa City, IA, United States*

2:30PM **Mechanisms of Cervical Spine Disc Injury Under Cyclic Loading: Experiments and Finite Element Analysis** SB³C2016-835

Sagar Umale[1], Narayan Yoganandan[1], Mike Arun[1], Brian Stemper[1], Brian Snyder[2], *[1]Neuroscience Research, Medical College of Wisconsin, Milwaukee, WI, United States, [2]Harvard Medical School, Beth Israel Deaconess Medical Center, Boston, MA, United States*

Copyright 2016 The Organizing Committee for the 2016 Summer Biomechanics, Bioengineering and Biotransport Conference

2:45PM **A Finite Element Analysis of the Occipitoatlantal Capsular Ligaments as the Primary Stabilizers of the Adult and Pediatric CraniocervicalJunction** SB³C2016-62

Rinchen Phuntsok[1], Benjamin Ellis[1], Douglas Brockmeyer[2], *[1]Department of Bioengineering, University of Utah, Salt Lake City, UT, United States, [2]School of Medicine, Pediatric Neurosurgery, University of Utah, Salt Lake City, UT, United States*

SATURDAY, JULY 2 | 1:30pm - 3:00pm

Bone Biomechanics — Wilson D

Session Chair: Mariana Kersh, *University of Illinois, Urbana, IL, United States*
Session Co-Chair: Eric Kennedy, *Bucknell University, PA, United States*

1:30PM **The Development of a "Fuzzy" Yield Envelope for Trabecular Porcine Skull Bone Using Numerical Simulations** SB³C2016-1050

Allison N. Ranslow, Reuben H. Kraft, *Mechanical and Nuclear Engineering, Penn State University, University Park, PA, United States*

1:45PM **Design of Fatigue Test for Ex-Vivo Mouse Vertebra** SB³C2016-1025

Megan M. Pendleton[1], Joshua S. Alwood[2], Grace D. O'Connell[1], Tony M. Keaveny[1], *[1]Mechanical Engineering, UC Berkeley, Berkeley, CA, United States, [2]Space Biosciences Division, NASA Ames Research Center, Moffett Field, CA, United States*

2:00PM **Electric Properties of Cortical Bone are Strong Predictors of Bone Mechanical Properties** SB³C2016-77

Mustafa Unal[1], Fatih Cingoz[2], Cevat Bagcioglu[2], Yilmaz Sozer[2], Ozan Akkus[1], *[1]Case Western Reserve University, Cleveland, OH, United States, [2]The University of Akron, Akron, OH, United States*

2:15PM **Diagnostic Potential of Kirschner (K-) Wire and Reference Probe Indentation for the Prediction of Bone Mineral Density (BMD)** SB³C2016-1076

Eric A. Kennedy[1], Sarah C. Denning[1], Donna M. Ebenstein[1], Thomas R. Bowen[2], *[1]Biomedical Engineering, Bucknell University, Lewisburg, PA, United States, [2]Orthopaedic Surgery, Geisinger Health System, Danville, PA, United States*

2:30PM **Bioinspired Simulation of Polycrystalline Materials** SB³C2016-1096

Liqiang Lin, Xiaodu Wang, xiaowei Zeng, *Mechanical Engineering, University of Texas at San Antonio, San Antonio, TX, United States*

2:45PM **Characteristic X-ray Diffraction Method for Mechanical Analysis of Mineral and Collagen Phases in Bone Tissue** SB³C2016-781

Masahiro Todoh, Shigeru Tadano, *Faculty of Engineering, Hokkaido University, Sapporo, Japan*

SATURDAY, JULY 2 | 1:30pm - 3:00pm

Solid Mechanics: Biomechanics of Injury — Annapolis 1

Session Chair: Ian A. Sigal, *University of Pittsburgh, PA, United States*
Session Co-Chair: Timothy P. Holsgrove, *University of Pennsylvania, PA, United States*

1:30PM **Quantitative Comparison of Human Body and ATD Occupant Models in US-NCAP Test Simulations** SB³C2016-975

Berkan Guleyupoglu, Bharath Koya, Matt Davis, Scott Gayzik, *Biomedical Engineering, Wake Forest University School of Medicine, Winston Salem, NC, United States*

1:45PM **Upper Cervical Spine Loading Simulating Low-Speed Collisions Significantly Increases Facet Strains Compared to Equivalent Quasistatic Loading** SB³C2016-115

Timothy Holsgrove, Nicolas Jaumard, Nina Zhu, Nicholas Stiansen, William Welch, Beth Winkelstein, *University of Pennsylvania, Philadelphia, PA, United States*

Copyright 2016 The Organizing Committee for the 2016 Summer Biomechanics, Bioengineering and Biotransport Conference

2:00PM **Injury-Based Advanced Automatic Crash Notification Algorithm Improves Motor Vehicle Crash Occupant Triage** SB³C2016-102
Samantha Schoell[1], Ashley Weaver[1], Jennifer Talton[2], Ryan Barnard[2], R. Shayn Martin[1], J. Wayne Meredith[1], Joel Stitzel[1], *[1]Wake Forest School of Medicine, Winston-Salem, NC, United States, [2]Division of Public Health Sciences, Wake Forest School of Medicine, Winston-Salem, NC, United States*

2:15PM **Damage Modeling of a Human Tibia and Fibula Fracture Caused by a Mixed Martial Arts Kick** SB³C2016-825
Andrew Lamont[1], **Vina L. Nguyen**[1, 2], Robbin Bertucci[1], Youssef Hammi[1], Mark F. Horstemeyer[1], Jun Liao[1, 2], Hongjoo Rhee[1], Lakiesha Williams[1, 2], Rajkumar Prabhu[1, 2], *[1]Center of Advanced Vehicular Systems, Mississippi State University, Starkville, MS, United States, [2]Department of Agricultural and Biological Engineering, Mississippi State University, Mississippi State, MS, United States*

2:30PM **Assessing the Ability of Hockey Helmets to Reduce Concussion Risk** SB³C2016-952
Bethany Rowson, Steven Rowson, Stefan M. Duma, *Biomedical Engineering and Mechanics, Virginia Tech, Blacksburg, VA, United States*

2:45PM **Foul Tip Attenuation of Baseball Catcher Masks Using Head Impact Metrics** SB³C2016-625
Christopher Eckersley, Hattie Cutcliffe, Jay Shridharani, Cameron 'Dale' Bass, Terrance White, *Biomedical Engineering, Duke University, Durham, NC, United States*

SATURDAY, JULY 2 | 1:30pm - 3:00pm

Thrombosis and Cardiac Flows — Annapolis 2

Session Chair: Keefe Manning, *Pennsylvania State University, PA, United States*
Session Co-Chair: Shawn Shadden, *UC Berkeley, CA, United States*

1:30PM **Coagulation Cascade Model Reduction Using a Genetic Algorithm** SB³C2016-113
Kirk B. Hansen, Shawn C. Shadden, *Mechanical Engineering, University of California, Berkeley, Berkeley, CA, United States*

1:45PM **Macroscopic Predictions of Thrombus Growth in a Three-Dimensional Backward-Facing Step** SB³C2016-108
Joshua O. Taylor, Steven Deutsch, **Keefe B. Manning**, *Biomedical Engineering, The Pennsylvania State University, University Park, PA, United States*

2:00PM **Distal Emboli Following Cover Assisted Thrombectomy** SB³C2016-892
Juyu Chueh, Ajit S. Puri, Matthew J. Gounis, *Radiology, University of Massachusetts Medical School, Worcester, MA, United States*

2:15PM **Towards Non-invasive, Computational Modeling of the Transport of Thrombo-emboli and Athero-emboli along Arteries** SB³C2016-970
Debanjan Mukherjee, Shawn C. Shadden, *U.C. Berkeley, Berkeley, CA, United States*

2:30PM **A Shape Optimization Approach Applied to Intraluminal Thrombus Deposition in Abdominal Aortic Aneurysms** SB³C2016-939
Paolo DiAchile[1], George Tellides[2], Jay D. Humphrey[1], *[1]Department of Biomedical Engineering, Yale University, New Haven, CT, United States, [2]Surgery, Yale School of Medicine, New Haven, CT, United States*

2:45PM **Predicting False Lumen Thrombosis in 3D Patient-Specific Models of Type B Aortic Dissection** SB³C2016-636
Claudia Menichini[1], Zhuo Cheng[1], Richard G. J. Gibbs[2], Xiao Y. Xu[1], *[1]Department of Chemical Engineering, Imperial College London, London, United Kingdom, [2]Department of Surgery and Cancer, St. Mary's Hospital, Imperial College NHS Trust, London, United Kingdom*

Copyright 2016 The Organizing Committee for the 2016 Summer Biomechanics, Bioengineering and Biotransport Conference

SATURDAY, JULY 2	1:30pm - 3:00pm

Human Dynamics of the Torso and Lower Extremities — Azalea 2

Session Chair: Joseph Iaquinto, *VA, Puget Sound, WA, United States*
Session Co-Chair: Tom Gardner, *Columbia University, NY, United States*

1:30PM **Muscle Activation in Cyclic Lifting with Trained Lumbar-Pelvic Coordination** SB³C2016-1086
Timothy D. Craig, Alice E. Riley, Neena K. Sharma, **Sara E. Wilson**, *Mechanical Engineering, University of Kansas, Lawrence, KS, United States*

1:45PM **The Determination of Free Torque on Athletic Turf Surfaces Using Insole Pressure Data** SB³C2016-1079
Brian T. Weaver[1, 2], Jerrod E. Braman[1], Roger C. Haut[1], *[1]Orthopedics Biomechanics Laboratories, Michigan State University, East Lansing, MI, United States, [2]Explico Engineering Co., Novi, MI, United States*

2:00PM **Knee and Ankle Biomechanics During Squatting with Heels On and Off the Ground, with and without Body Weight Shifting** SB³C2016-624
Jonathan Fox, Mohamed Samir Hefzy, Charles Armstrong, *The University of Toledo, Toledo, OH, United States*

2:15PM **A Method for Predicting Complete Ground Reaction Forces with Plantar Pressure Insoles during Level and Angled Walking** SB³C2016-851
Andrew J. Crechiolo, Feng Wei, Roger C. Haut, *Orthopaedic Biomechanics Laboratories, Michigan State University, East Lansing, MI, United States*

2:30PM **Knee Medial Tibial Cartilage Stress One and Five Years After Anterior Cruciate Ligament Reconstruction** SB³C2016-916
Ashutosh Khandha[1], Kurt Manal[2], Lynn Snyder-Mackler[3], Thomas S. Buchanan[4], *[1]Biomedical Engineering, University of Delaware, Newark, DE, United States, [2]Mechanical Engineering, University of Delaware, Newark, DE, United States, [3]Physical Therapy, University of Delaware, Newark, DE, United States, [4]Biomedical Engineering, Mechanical Engineering, University of Delaware, Newark, DE, United States*

2:45PM **The Effect of Soft Tissue Artifact on Kinematic Measurement - an Evaluation of Optical Marker Motion using Biplane Fluoroscopy.** SB³C2016-1097
Joseph M. Iaquinto[1], Matthew W. Kindig[1], David R. Haynor[2], William R. Ledoux[1], *[1]VA Puget Sound, Seattle, WA, United States, [2]University of Washington Medical Center, Seattle, WA, United States*

SATURDAY, JULY 2	1:30pm - 3:00pm

Hemodynamics, Lymphatics and Lung Therapy — Azalea 3

Session Chair: Nastaran Hashemi, *Iowa State University, IA, United States*
Session Co-Chair: Joshua Smith, *Lafayette College, LA, United States*

1:30PM **Cerebral Blood Flow Simulation for the Whole Mouse Brain** SB³C2016-1062
ben schneller[1], Mahsa Ghaffari[1], Sahar Ghanavati[2], john sled[2], andreas linninger[1], *[1]university of illinois at chicago, chicago, IL, United States, [2]University of Toronto, toronto, ON, Canada*

1:45PM **Directing Angiogenesis with Fluid Mechanics at Vessel Bifurcations** SB³C2016-1123
Ehsan Akbari, *Department of Mechanical and Aerospace Engineering, The Ohio State University, Columbus, OH, United States*

2:00PM **In Silico and In Vitro Modelling of Flow Behaviour in Lymphatic Vessels** SB³C2016-787
Sinéad T. Morley, David T. Newport, Michael T. Walsh, *MABE, University of Limerick, Limerick, Ireland*

2:15PM **Placenta-on-a-chip: A Novel Platform in Drug Testing and Toxicology Applications** SB³C2016-919
Nastaran Hashemi, *Iowa State University, Ames, IA, United States*

2:30PM **Preventing Upper Airway Collapse Using CPAP with and without Pressure Oscillations** SB³C2016-19
Ahmed M. Al-Jumaily, Sherif Ashaat, Loulin Huang, *Institute of Biomedical Technologies, Auckland University of Technology, Auckland, New Zealand*

Copyright 2016 The Organizing Committee for the 2016 Summer Biomechanics, Bioengineering and Biotransport Conference

2:45PM **Upper Airway Dynamic Characteristics in Healthy Subjects and OSA Patients** SB^{3}C2016-50
Sherif Ashaat, **Ahmed M. Al-Jumaily**, Loulin Huang, *Institute of Biomedical Technologies, Auckland University of Technology, Auckland, New Zealand*

SATURDAY, JULY 2 | 3:15pm - 4:45pm

Measuring and Modeling Cellular Phenomena — Wilson B

Session Chair: Lin H. Han, *Drexel University, PA, United States*
Session Co-Chair: Edward Guo, *Columbia University, NY, United States*

3:15PM **A Chemo-mechanical Free-energy-based Approach to Model Durotaxis and Extracellular Stiffness Dependent Contraction and Polarization of Cells** SB^{3}C2016-570
Vivek Shenoy, Hailong Wang, Xiao Wang, *Materials Science and Engineering, University of Pennsylvania, Philadelphia, PA, United States*

3:30PM **Disorder as a Biomechanical Pattern Forming Mechanism that Guides Symmetric Vertebrate Body Elongation** SB^{3}C2016-158
Dipjyoti Das[1], Thierry Emonet[2], **Scott Holley**[1], *[1]Molecular, Cellular and Developmental Biology, Yale University, New Haven, CT, United States, [2]Molecular, Cellular and Developmental Biology and Physics, Yale University, New Haven, CT, United States*

3:45PM **Real-time Monitoring of the Mechanical Properties of Engineered Tissues During Growth and Remodeling.** SB^{3}C2016-578
Pim J. A. Oomen[1, 2], Cees W. J. Oomens[1], Carlijn V. C. Bouten[1, 2], Sandra Loerakker[1, 2], *[1]Department of Biomedical Engineering, Eindhoven University of Technology, Eindhoven, Netherlands, [2]Institute for Complex Molecular Systems, Eindhoven University of Technology, Eindhoven, Netherlands*

4:00PM **Modulation of ICAM-4 Adhesion Receptors on SS-RBCs Revealed by Atomic Force Microscopy** SB^{3}C2016-73
Jing Zhang[1], Biree Andemariam[2], George Lykotrafitis[3], *[1]Mechanical Engineering, University of Connecticut, Storrs, CT, United States, [2]Adult Sickle Cell Center, University of Connecticut Health Center, Farmington, CT, United States, [3]Mechanical Engineering/biomedical Engineering, University of Connecticut, Storrs, CT, United States*

4:15PM **Surface Protrusion of Human Endothelial Cells: Experiment and Model** SB^{3}C2016-699
Jin-Yu Shao, Jin Hao, Yong Chen, *Washington University in St. Louis, Saint Louis, MO, United States*

4:30PM **Traction Force Measurement of Migrating Cells in Multichannel Micropillar Device** SB^{3}C2016-801
Toshiro Ohashi[1], Akito Sugawara[2], *[1]Faculty of Engineering, Hokkaido University, Sapporo, Japan, [2]Graduate School of Engineering, Hokkaido University, Sapporo, Japan*

SATURDAY, JULY 2 | 3:15pm - 4:45pm

Ocular Biomechanics — Wilson C

Session Chair: Ross Ethier, *Georgia Institute of Technology, GA, United States*
Session Co-Chair: Matthew Reilly, *Ohio State University, OH, United States*

3:15PM **Quantification of Scleral Stiffening in Rat Eyes as a Function of Glyceraldehyde Concentration and Age** SB^{3}C2016-736
Ian C. Campbell[1, 2], Bailey G. Hannon[3], A. Thomas Read[2], Joseph M. Sherwood[4], Pedro Gonzalez[5], C. Ross Ethier[1, 2, 3], *[1]Rehabilitation Research and Development, Atlanta VA Medical Center, Decatur, GA, United States, [2]Biomedical Engineering, Georgia Institute of Technology and Emory University, Atlanta, GA, United States, [3]Mechanical Engineering, Georgia Institute of Technology, Atlanta, GA, United States, [4]Bioengineering, Imperial College London, London, United Kingdom, [5]Ophthalmology, Duke University, Durham, NC, United States*

3:30PM **Measuring In-Vivo the Interplay Between Intraocular and Intracranial Pressure Effects on the Optic Nerve Head** SB^{3}C2016-701
Ian A. Sigal[1], Huong Tran[1], Alexandra Judisch[1], Bo Wang[1], Matthew A. Smith[1], Andrew Voorhees[1], Joel Schuman[1, 2], Gadi Wollstein[1], *[1]University of Pittsburgh, Pittsburgh, PA, United States, [2]New York University, New York, NY, United States*

Copyright 2016 The Organizing Committee for the 2016 Summer Biomechanics, Bioengineering and Biotransport Conference

3:45PM **An Innovative Method for Measuring Adhesion at the Vitreoretinal Interface** SB³C2016-1111
Christopher J. Creveling, *University of Utah, Salt Lake City, UT, United States*

4:00PM **IOP-Induced Strains in the Optic Nerve Head Using Ultrasound Speckle Tracking** SB³C2016-796
Elias Pavlatos[1], Xueliang Pan[1, 2], Richard T. Hart[1], Paul A. Weber[3], Jun Liu[1, 3], *[1]Department of Biomedical Engineering, The Ohio State University, Columbus, OH, United States, [2]Center for Biostatistics, The Ohio State University, Columbus, OH, United States, [3]Department of Ophthalmology, The Ohio State University, Columbus, OH, United States*

4:15PM **A Mathematical Model of Posterior Vitreous Detachment and Generation of Vitreoretinal Tractions** SB³C2016-663
Federica Di Michele[1], **Rodolfo Repetto**[2], Amabile Tatone[1], *[1]Department of Information Engineering, Computer Science and Mathematics, University of L'Aquila, L'Aquila, Italy, [2]Department of Civil, Chemical and Environmental Engineering, University of Genoa, Genoa, Italy*

4:30PM **Modelling Corneal Mechanical Behavior with a Biphasictransversely Isotropic Poroviscoelastic Constitutive Model** SB³C2016-619
Hamed Hatami-Marbini, *Mechanical & Industrial Engineering, University of Illinois at Chicago, Chicago, IL, United States*

SATURDAY, JULY 2	**3:15pm - 4:45pm**

Musculo-Skeletal Soft Tissue Mechanics: Ligament and Tendon — Wilson D

Session Chair: Spencer Lake, *Washington University, St. Louis, MO, United States*
Session Co-Chair: Victor Barocas, *University of Minnesota, MN, United States*

3:15PM **A Reactive Viscoelastic Continuum Damage Model for Tendon** SB³C2016-1107
Babak N. Safa[1, 2], Andrea H. Lee[2], Michael H. Santare[1], Dawn M. Elliott[2], *[1]Mechanical engineering, University of delaware, Newark, DE, United States, [2]Biomedical engineering, University of delaware, Newark, DE, United States*

3:30PM **Multiscale Regression Modeling in Mouse Supraspinatus Tendons Reveals Regional Contribution of Dynamic Processes to Structure-Function Relationships** SB³C2016-30
Brianne K. Connizzo[1], Sheila M. Adams[2], Thomas H. Adams[2], Abbas F. Jawad[3], David E. Birk[2], Louis J. Soslowsky[1], *[1]McKay Orthopaedic Research Laboratory, University of Pennsylvania, Philadelphia, PA, United States, [2]Department of Molecular Pharmacology & Physiology, University of South Florida, Tampa, FL, United States, [3]Department of Pediatrics, Perelman School of Medicine, University of Pennsylvania and Children's Hospital of Philadelphia, Philadelphia, PA, United States*

3:45PM **Localized Histological Differences in Tendon Degeneration Between Torn and Intact Supraspinatus Tendon** SB³C2016-817
R. Matthew Miller[1], Gerald A. Ferrer[1], Masahito Yoshida[2], Leanna Sullivan[1], James H-C Wang[2], Volker Musahl[2], Richard E. Debski[1], *[1]Bioengineering, University of Pittsburgh, Pittsburgh, PA, United States, [2]Orthopaedic Surgery, University of Pittsburgh, Pittsburgh, PA, United States*

4:00PM **Recovery of Functional Properties During Neonatal Tendon Regeneration** SB³C2016-112
Kristen Howell[1], Rebecca Bell[2], Sara F. Tufa[3], Douglas R. Keene[3], Nelly Andarawis-Puri[2], **Alice H. Huang**[1], *[1]Orthopaedics, Icahn School of Medicine at Mount Sinai, New York, NY, United States, [2]Cornell University, Ithaca, NY, United States, [3]Shriners Hospital, Portland, OR, United States*

4:15PM **Altered Mechanics of Supraspinatus Tendons from Elastin-Deficient Genetically-Modified Mice** SB³C2016-128
Fei Fang[1], Gabriela Espinosa[2], Lindsey Kahan[2], Robert P. Mecham[3], Spencer P. Lake[1, 2, 4], *[1]Mechanical Engineering & Materials Science, Washington University in St. Louis, St. Louis, MO, United States, [2]Department of Biomedical Engineering, Washington University in St. Louis, St. Louis, MO, United States, [3]Department of Cell Biology & Physiology, Washington University in St. Louis, St. Louis, MO, United States, [4]Department of Orthopaedic Surgery, Washington University in St. Louis, St. Louis, MO, United States*

Copyright 2016 The Organizing Committee for the 2016 Summer Biomechanics, Bioengineering and Biotransport Conference

4:30PM **Fascicles and the Interfascicular Matrix show Superior Fatigue Resistance in Energy Storing Tendons** SB³C2016-20
Chavaunne T. Thorpe[1], Graham P. Riley[2], Helen L. Birch[3], Peter D. Clegg[4], Hazel R. C. Screen[1], *[1]Institute of Bioengineering, Queen Mary University of London, London, United Kingdom, [2]School of Biological Sciences, University of East Anglia, Norwich, United Kingdom, [3]Institute of Orthopaedics and Musculoskeletal Science, University College London, London, United Kingdom, [4]Institute of Ageing and Chronic Disease, University of Liverpool, Liverpool, United Kingdom*

SATURDAY, JULY 2	3:15pm - 4:45pm

Military Injury — Annapolis 1

Session Chair: Liming Voo, *Johns Hopkins University Applied Physics Laboratory, MD, United States*
Session Co-Chair: Ali Sadegh, *City College of New York, NY, United States*

3:15PM **A Robust and Generalized Procedure for Generating Human Injury Probability Curves** SB³C2016-898
Narayan Yoganandan[1, 2], Scott Gayzik[3], Anjishnu Banerjee[4], Fang-Chi Hsu[3], Frank Pintar[1], Cameron-Dale Bass[5], Hattie Cutcliffe[5], Jonathan Rupp[6], Francesco Tenore[7], JiangYue Zhang[8], Liming Voo[9], *[1]Neurosurgery, Medical College of Wisconsin, Milwaukee, WI, United States, [2]Medical College of Wisconsin, Milwaukee, WI, United States, [3]Wake Forest University School of Medicine, Winston-Salem, NC, United States, [4]Biostatistics, Medical College of Wisconsin, Milwaukee, WI, United States, [5]Duke University, Durham, NC, United States, [6]University of Michigan, Ann Arbor, MI, United States, [7]Neurosurgery, John Hokins Universtiy, Laurel, MD, United States, [8]Johns Hopkins University, Laurel, MD, United States, [9]John Hopkins University, Laurel, MD, United States*

3:30PM **Similitude Assessment Method for Comparing PMHS Response Data from Impact Loading Across Multiple Test Devices** SB³C2016-846
Christopher J. Dooley[1], Francesco V. Tenore[1], Scott Gayzik[2], Andrew C. Merkle[1], *[1]Biomechanics and Injury Mitigation Systems, Johns Hopkins University Applied Physics Lab, Laurel, MD, United States, [2]School of Medicine, Wake Forest University, Winston-Salem, NC, United States*

3:45PM **Forces Applied to the Foot and Pelvis in High Rate Vertical Accelerative Loading** SB³C2016-896
Jonathan D. Rupp, Carl Miller, Lauren Zaseck, Nichole Ritchie, Anne Bonifas, Laura Slykhouse, Matthew P. Reed, *University of Michigan Transportation Research Institute, Ann Arbor, MI, United States*

4:00PM **Modeling and Sensitivity Analysis of the WIAMan ATD Head and Neck: A Finite Element Study** SB³C2016-748
Matthew L. Davis[1], Jeremy M. Schap[1], Michael P. Boyle[2], Robert S. Armiger[2], Mostafiz Chowdhury[3], F. Scott Gayzik[1], *[1]Biomedical Engineering, Wake Forest University School of Medicine, Winston Salem, NC, United States, [2]Johns Hopkins Applied Physics Laboratory, Laurel, MD, United States, [3]U.S. Army Research Laboratory, Aberdeen Proving Groung, MD, United States*

4:15PM **Effects of Seated Soldier Posture on Pelvic Force Transmissibility** SB³C2016-1006
Brandon J. Perry[1], Kyvory A. Henderson[1], Edward M. Spratley[1], JiangYue Zhang[2], Andrew C. Merkle[2], Robert S. Salzar[1], *[1]Mechanical and Aerospace Engineering, University of Virginia, Charlottesville, VA, United States, [2]Applied Physics Laboratory, Johns Hopkins University, Baltimore, MD, United States*

4:30PM **The Effect of Variability in Warfighter Population on Injury: A Modeling Study** SB³C2016-588
Shankarjee Krishnamoorthi, Amit Bagchi, Siddiq Qidwai, *US Naval Research Laboratory, Washington, DC, United States*

SATURDAY, JULY 2	3:15pm - 4:45pm

Cardiovascular Diagnostics and Imaging — Annapolis 2

Session Chair: Craig Goergen, *Purdue, IN, United States*
Session Co-Chair: Matt Gounis, *University of Massachusetts Medical Center, MA, United States*

3:15PM **Near-wall Stagnation in Large Arteries: Is Wall Shear Stress Magnitude Sufficient?** SB³C2016-739
Amirhossein Arzani[1], Alberto M. Gambaruto[2], Guoning Chen[3], Shawn C. Shadden[1], *[1]Mechanical Engineering, University of California, Berkeley, Berkeley, CA, United States, [2]Mechanical Engineering, University of Bristol, Bristol, United Kingdom, [3]Computer Science, University of Houston, Houston, TX, United States*

Copyright 2016 The Organizing Committee for the 2016 Summer Biomechanics, Bioengineering and Biotransport Conference

3:30PM **A Computational Study of the Effects of Age-Associated Regional Changes in Artery Mechanics on Systemic Hemodynamics** SB³C2016-972

Federica Cuomo[1], Sara Roccabianca[2], Desmond Dillon-Murphy[3], Nan Xiao[3], Jay D. Humphrey[4], C. Alberto Figueroa[5], *[1]Biomedical Engineering, University of Michigan, Ann Arbor, MI, United States, [2]Mechanical Engineering, Michigan State University, East Lansing, MI, United States, [3]King's College London, London, United Kingdom, [4]Yale University, New Haven, CT, United States, [5]University of Michigan, Ann Arbor, MI, United States*

3:45PM **Differences in Pelvic Blood Flow Mediate Differences in Abdominal Wall Shear Stress Between Men and Women** SB³C2016-1068

Elizabeth Iffrig, John N. Oshinski, William R. Taylor, *Emory University, Atlanta, GA, United States*

4:00PM **Automated Optimization Framework for Cardiovascular Flow Simulations** SB³C2016-977

Aekaansh Verma[1], Alison Marsden[2], *[1]Mechanical Engineering, Stanford Univesity, Stanford, CA, United States, [2]Department of Pediatrics, Stanford Univesity, Stanford, CA, United States*

4:15PM **Quantification of Distal Cerebral Vascular Bed Collateral Resistances Using 1D Hemodynamic Model and CT Perfusion** SB³C2016-991

Jeffrey Pyne[1], Jaiyoung Ryu[1], Jared Narvid[2], Shawn Shadden[1], *[1]University of California Berkeley, Berkeley, CA, United States, [2]University of San Francisco, San Francisco, CA, United States*

4:30PM **Validation and Uncertainty Analysis of a Clinical CFD Tool—AView—for Intracranial Aneurysm Flow Simulation** SB³C2016-1016

Xiang Jianping[1, 2, 3], Nikhil Paliwal[1, 3], Nicole Varble[1, 3], Adnan H. Siddiqui[2, 3], Hui Meng[1, 2, 3], *[1]Department of Aerospace and Mechanical Engineering, SUNY-BUFFALO, BUFFALO, NY, United States, [2]Department of Neurosurgery, SUNY-BUFFALO, Buffalo, NY, United States, [3]Toshiba Stroke and Vascular Research Center, SUNY-BUFFALO, Buffalo, NY, United States*

SATURDAY, JULY 2 | 3:15pm - 4:45pm

Biotransport at Multiple Scales — Azalea 2

Session Chair: Sati Sadhal, *University of Southern California, CA, United States*
Session Co-Chair: Anita Penkova, *University of Southern California, CA, United States*

3:15PM **Modeling and Optimization of Silica Gel Encapsulated Synergistic Bacteria** SB³C2016-150

Baris Ragip Mutlu, Jonathan Sakkos, Sujin Yeom, Lawrence Wackett, Alptekin Aksan, *University of Minnesota, Minneapolis, MN, United States*

3:30PM **Continuous on-Chip Human Cell Separation Based on Conductivity-Induced Dielectrophoresis with Self-Assembled Ionic Liquid Electrodes** SB³C2016-715

Mingrui Sun, Xiaoming He, *Biomedical Engineering, The Ohio State University, Columbus, OH, United States*

3:45PM **Microchip Electrophoresis Platform for Point-of-Care Diagnosis of Sickle Cell Disease** SB³C2016-603

Ryan Ung[1], Yunus Alapan[2], Muhammad N. Hasan[2], Megan Romelfanger[1], Tolulope Rosanwo[3], Asya Akkus[2], Mehmet Cakar[4], Kutay Icoz[4], Connie Piccone[3], Jane Little[3], **Umut A. Gurkan**[1, 2, 3], *[1]Biomedical Engineering Department, Case Western Reserve University, Cleveland, OH, United States, [2]Mechanical and Aerospace Engineering Department, Case Western Reserve University, Cleveland, OH, United States, [3]School of Medicine, Case Western Reserve University, Cleveland, OH, United States, [4]Abdullah Gul University, Kayseri, Turkey*

4:00PM **Direct Quantification of Solute Diffusivity in Porous, Viscoelastic Materials Using Correlation Spectroscopy** SB³C2016-1051

Janty Shoga, Christopher Price, *University of Delaware, Newark, DE, United States*

4:15PM **Quantitative Assessment of Intracellular Delivery of Membrane-Impermeable Macromolecules Using Cell Deformation** SB³C2016-660

Kosaku Kurata[1], Atsushi Kurogawa[2], Takanobu Fukunaga[1], Haidong Wang[1], Hiroshi Takamatsu[1], *[1]Department of Mechanical Engineering, Kyushu University, Fukuoka, Japan, [2]Graduate School of Engineering, Kyushu University, Fukuoka, Japan*

4:30PM **Study Vascular Permeability in a Microfluidic Device** SB³C2016-47

Yaling Liu, Chris Uhl, Salman Sohrab, *Lehigh University, Bethlehem, PA, United States*

Copyright 2016 The Organizing Committee for the 2016 Summer Biomechanics, Bioengineering and Biotransport Conference

SATURDAY, JULY 2	3:15pm - 4:45pm

Respiratory Fluid Mechanics — Azalea 3

Session Chair: Jessica Oakes, *Berkley, CA, United States*
Session Co-Chair: Barry Lieber, *Stonybrook, NY, United States*

3:15PM **Age Dependent Susceptibility to Inhaled Particles** SB^{3}C2016-968
Jessica M. Oakes[1, 2, 3], Irene E. Vignon-Clementel[2, 3], Céline Grandmont[2, 3], Shawn C. Shadden[1], *[1]Mechanical Engineering, University of California Berkeley, Berkeley, CA, United States, [2]INRIA de Paris, Paris, France, [3]Laboratoire Jacques-Louis Lions, UPMC Université Paris 6, Paris, France*

3:30PM **Effect of Inflow Boundary Condition on Nasal Transitional Flow** SB^{3}C2016-657
Shun Shimizu[1], **Takashi Sakamoto**[1], Shinya Kimura[1], Gaku Tanaka[1], Toshihiro Sera[2], Hideo Yokota[3], Kenji Ono[4], *[1]Graduate School of Engineering, Chiba University, Chiba, Japan, [2]Engineering, Kyushu University, Fukuoka, Japan, [3]Image Processing Research Team, RIKEN, Kobe, Japan, [4]Advanced Visualization Research Team, RIKEN, Kobe, Japan*

3:45PM **Morphological Measurement and the Oxygen Diffusion Analysis in Mouse Acinar Cluster Obtained From Micro-ct** SB^{3}C2016-769
Luosha Xiao[1], Toshihiro Sera[2], Kenichiro Koshiyama[1], **Shigeo Wada**[1], *[1]Osaka University, Osaka, Japan, [2]Kyushu University, Fukuoka, Japan*

4:00PM **Simulation of Airflow in Realistic Model Pulmonary Acinus** SB^{3}C2016-762
Yuri Inagaki[1], Keisuke Yamanaka[1], Gaku Tanaka[1], Toshihiro Sera[2], *[1]Mechanical Engineering, Chiba University, Chiba, Japan, [2]Mechanical Engineering, Kyushu University, Fukuoka, Japan*

4:15PM **In Vitro Characterization of Tracheal Pressures for Infant Nasal Airway Replicas Receiving High-flow Nasal Cannula Therapy** SB^{3}C2016-142
Douglas E. A. Rebstock[1], **Andrew R. Martin**[1], Georges Callibotte[2], Warren H. Finlay[1], Michelle L. Noga[3], Ira M. Katz[4], *[1]Mechanical Engineering, University of Alberta, Edmonton, AB, Canada, [2]Medical R&D, Air Liquide Santé International, Paris-Saclay Research Center, Les Loges-en-Josas, France, [3]Radiology and Diagnostic Imaging, University of Alberta, Edmonton, AB, Canada, [4]Medical R&D, Air Liquide Santé International, Paris-Saclay Research Center, Edmonton, AB, Canada*

4:30PM **Evaluation of Design Parameters for a Novel Personal Air Purification Method to Mitigate Particle Aspiration** SB^{3}C2016-1087
Christopher Idelson, Christopher Rylander, *Mechanical Engineering, The University of Texas at Austin, Austin, TX, United States*

Copyright 2016 The Organizing Committee for the 2016 Summer Biomechanics, Bioengineering and Biotransport Conference

Copyright 2016 The Organizing Committee for the 2016 Summer Biomechanics, Bioengineering and Biotransport Conference

SB^{3}C2016
Summer Biomechanics, Bioengineering and Biotransport Conference
June 29 –July 2, National Harbor, MD, USA
SB³C2016-14

THE EFFECT OF DYNAMIC STIMULATION ON JOINT MORPHOGENESIS OF THE EMBRYONIC CHICK KNEE JOINT

Vikesh V. Chandaria, Niamh C. Nowlan

Department of Bioengineering
Imperial College London
London, UK

INTRODUCTION

Evolution has generated joint shapes highly specialised for joint function. Alterations or abnormalities in joint shape development can therefore severely compromise this ability. Mechanical stimulation has been identified as a critical variable during joint morphogenesis from both clinical case studies and animal models [1, 2]. It has been shown that under immobilised conditions developing joints in the chick embryo become fused across the joint site and appear simplified and flattened [3, 4]. By manually moving developing knee joints *in vitro,* it was demonstrated that the effects of immobilisation could be countered [5]. However, how variations of applied mechanical stimulation affects joint shape development remains poorly understood.

In this study we focused on exploring the effect of magnitude of movement on joint morphogenesis. It was hypothesised that joint shape would be affected by mechanical stimulation in a dose-dependent manner and that an increase in stimulation magnitude would lead to a more physiological joint shape. A novel *in vitro* explant culture setup was created using a compression bioreactor to apply 3 magnitudes of flexion to the developing chick knee (stifle) joint. After six days, cultured joints were compared between groups to estimate the impact of the amount of movement experienced.

METHODS

Chick embryos were harvested after 7 days of incubation at 37^{o}C. Hind limbs were separated from the main body and the soft tissues removed. Hind limb explants were positioned into customised bioreactor chambers where they were cultured *in vitro* for the duration of the study.

Culture conditions were similar to those used for chick femur explants by Kanczler et al, [6]. Each chamber was filled with serum free basal culture media alpha-MEM and supplemented with 1% Antibiotic/Antimycotic and 100uM Ascorbic Acid leaving the explants at an air-liquid interface. The culture medium was replenished every 24 hours.

For each embryo harvested the right hind limb was exposed to dynamic stimulation and the left hind limb was cultured under static conditions. Dynamic explants were loaded in compression with a sinusoidal waveform at an average rate of 4 mm/s for 2 hours, 3 times per day over a culture period of 6 days. Three experiments were performed applying 9±2.9, 14±4.0 and 22±5.0 (mean±SD) degrees of knee flexion. Observations of chick motility *in ovo* report an approximate mean knee flexion of 12 degrees, therefore the experiments resembled reduced, physiological and over stimulated groups respectively [7].

Differences in joint shape were analysed using virtual 3D reconstructions created using optical projection tomography (OPT) [8]. Cultured explants were stained with Alcian Blue and prepared for imaging using protocols from Quintana and Sharpe [9]. Shape profiles of the distal femoral condyles and proximal fibula and tibia were traced from the 3D models of each explant. Static and dynamic groups were compared to identify shape differences. Measurements of rudiment length and anterior posterior joint region size were also compared for each group.

RESULTS

The major effect of dynamic stimulation as compared to static culture occurred in the medial side of the joint. Under dynamic conditions the anterior-posterior width of the medial condyle and tibia were significantly larger than those produced under static conditions for all groups. The medial condyle was curved towards the posterior direction and protruded lower and closer to the tibia under dynamic stimulation

Copyright 2016 The Organizing Committee for the 2016 Summer Biomechanics, Bioengineering and Biotransport Conference

conditions compared to the shape profiles of static joints (data not shown).

Evaluation of the 3D models of the knee joints from the 3 stimulated groups revealed that, at the maximum 22±5.0 degrees of flexion, fusion of the joint on the lateral side had occurred merging the femur and fibula (Figure 1). This was consistent for all explants in this group.

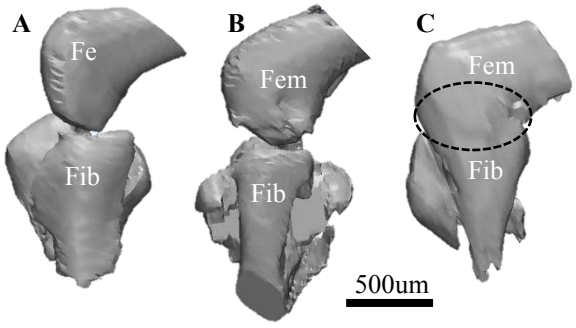

Figure 1: Lateral views of 3D knee joint models of explants cultured under A) reduced, B) physiological and C) over stimulated conditions. Dotted area indicates fusion between rudiments. Fem: Femur; Fib: Fibula

Outlines of the joint shape were overlaid to produce shape profile atlases for each group. The shape profiles of the lateral condyle, fibula and tibia did not show any obvious differences between the 3 magnitudes. The posterior curve of the medial condyle was seen in both the reduced and physiological groups but was absent in the over stimulated group (Figure 2). The migration of the medial condyle towards to the tibia in dynamic explants increased with the applied magnitude. However, the intercondylar fossa separating the two condyles was dramatically reduced in 3 out of 4 femora in the over stimulated group (Figure 2).

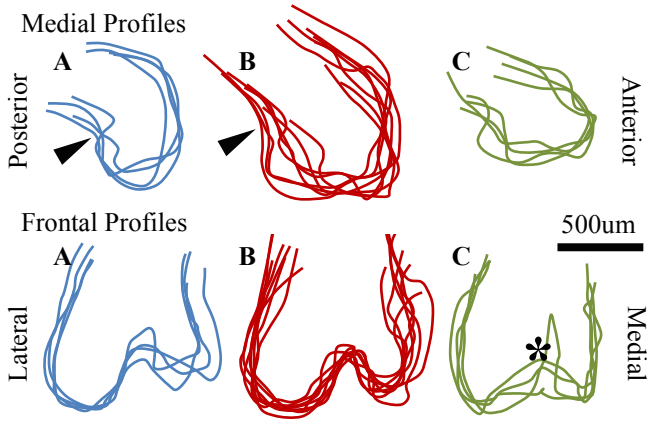

Figure 2: Shape profiles of the medial condyle of A) reduced B) physiological and C) over stimulated explants. Filled arrows illustrate the posterior bend; *indicated the missing intercondylar fossa.

Measurements were normalised for each group to their static controls to give the percentage difference caused by the applied stimulation. The percentage difference in rudiment length and joint region width compared to static explants increased with magnitude for all measurements made, with the exception of the lateral condyle which was smaller in dynamic joints compared to static explants for the reduced and physiological magnitudes (Figure 3).

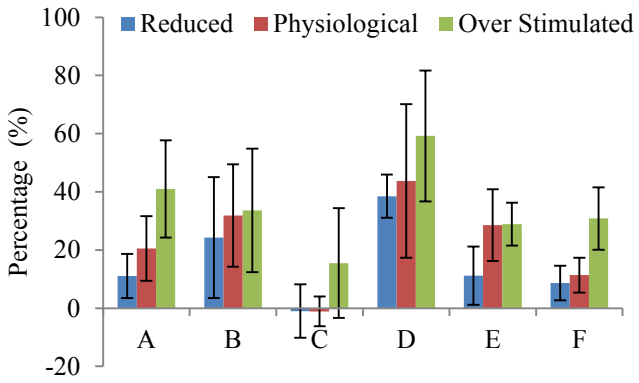

Figure 3: Percentage difference in A) Femoral length, B) Tibial Length, C) Lateral Condyle width, D) Medial Condyle width, C) Fibula width, E) Tibial width of dynamic joints compared with static controls. Error bars represent standard deviation.

DISCUSSION

This study has pioneered the exploration of how magnitude of movement affects prenatal joint shape development. After 7 days of incubation the lateral condyle is clearly distinguishable from the distal femur whereas the medial condyle has only slightly emerged [10]. Under normal circumstances this joint region would rapidly develop to create two equally sized femoral condyles as seen in mature joints. Therefore, it was expected that the medial condyle would produce major differences in our study. Our data supports this theory, that movement is necessary to signal the development of the medial condyle.

Although similar sized medial and lateral condyles were never achieved, the data revealed sensitivity to magnitude of movement. The under stimulated group produced smaller differences in size and a less prominent medial condyle suggesting reduced morphological progression compared to the average and over stimulated groups. The over stimulated group produced the largest differences in size; however the loss of the intercondylar fossa and simplified shape of the medial condyle implied too much stimulation could have had a negative influence on joint morphogenesis.

The data obtained in this study support our hypothesis of a dose-dependent relationship between joint shape and mechanical stimulation. These findings also demonstrate that this relationship is complex, and reveal the threshold above which dynamic stimulation is detrimental to the development of joint shape.

ACKNOWLEDGEMENTS

The work presented was supported by funding from the EU FP7 ERC Starting Grant 336306.

REFERENCES

1. Rodríguez, J., et al., Calcif Tissue Int, 1988. 43(6): p. 335-339. **2.** Nowlan, N.C., et al, Ann. N. Y. Acad. Sci., 2007. 1101(1): p. 389-411. **3.** Roddy, K.A., et al, PLoS ONE, 2011. 6(2). **4.** Drachman, D.B., et al, Dev Biol, 1966. 14(3): p. 401-420. **5.** Lelkes, G., J Embryol Exp Morphol, 1958. 6(2): p. 183-186. **6.** Kanczler, J.M., et al., Tissue Eng Part C: Methods, 2012. 18(10): p. 747-760. **7.** Watson, S.J., et al, J of Neurobiol, 1990. 21(4): p. 651-660. **8.** Sharpe, J., et al., Science, 2002. 296(5567): p. 541-545. **9.** Quintana, L., et al, Cold Spring Harb Protoc, 2011. 2011(6): p. pdb.top116. **10.** Roddy, K.A., et al., J Anat, 2009. 214(3): p. 374-387.

Copyright 2016 The Organizing Committee for the 2016 Summer Biomechanics, Bioengineering and Biotransport Conference

SB³C2016
Summer Biomechanics, Bioengineering and Biotransport Conference
June 29 –July 2, National Harbor, MD, USA
SB³C2016-15

A FINITE ELEMENT ANALYSIS OF AUGMENTED GLENOID COMPONENTS

Nikolas K. Knowles (1,2), G. Daniel G. Langohr (1,2), Louis M. Ferreira (1,2), George S. Athwal (2)

(1) Biomedical Engineering Department
The University of Western Ontario
London, ON, Canada

(2) Roth|McFarlane Hand and Upper Limb
Centre, St. Josephs Health Care
London, ON, Canada

INTRODUCTION

Osteoarthritis induced glenoid bone loss can be classified by two common morphological erosion patterns: symmetric and asymmetric. An asymmetrically eroded glenoid has a bi-concave articular morphology that is retroverted by the glenoid erosion. In symmetrically eroded glenoids requiring joint replacement, the articular surface is typically reamed to match the curvature of the implant for full backside contact. This method, when used on asymmetrically eroded glenoids to correct the version angle, is referred to as eccentric reaming; however, the bi-concave articular morphology of the asymmetric glenoid may require substantial bone removal to facilitate implantation of standard glenoid components at the desired version angle.[2,4] This pathoanatomy therefore presents a challenging scenario for joint replacement in these complex cases.

To address these challenges, augmented glenoid components correct version with reduced removal of anterior bone by precluding the need for eccentric reaming. These claims are supported by recent studies which suggest that augments preserve underlying bone by volume.[2,4] The backside geometry of these components includes a posterior-step or wedge that is oriented along the vertical centerline. However, this is not consistent with recent studies which have shown that asymmetrical bone loss is not purely posterior, but rather is oriented in the posteroinferior direction.[1,3,5] Thus, aligning an augmented component with the type B2 erosion line may reduce bone removal and produce more congruent backside-to-bone contact, but likely at the cost of component malrotation.

While augmented designs address some aspects of the articular morphology of asymmetrically eroded type B2 glenoids, the knowledge base surrounding component fixation and load transfer is still largely based on the biomechanics of standard components with symmetrical erosion. Thus, given that recent literature has revealed significant differences between symmetrically versus asymmetrically eroded glenoids, there is a corresponding lack of data pertaining to the biomechanics that may alter load transfer through the component to the underlying bone. This study used finite element analysis to characterize augmented glenoid components based on three clinically relevant designs and two proposed designs with augments rotated to match the orientation of asymmetrical erosion, as previously reported.[3] All augmented designs were tested under varying simulated net joint loading directions and magnitudes, in order to quantify bone displacements, as well as contact area, and micromotion, at the implant-bone interface.

METHODS

Five augmented glenoid component designs were modeled to assess varying backside geometries (Figure 1). All implants were based on averaged characteristics of commercially available augmented implants and were constructed as CAD models with identical peg sizes/locations, geometrical shape, and articular and backside curvatures. Augment sizes were chosen to fully correct acquired retroversion while minimizing anterior reaming. The selected augments were: 7 mm posterior/parametric-step, 35° posterior/parametric-wedge, and 16° full-wedge. A 1 mm cement mantle surrounded each peg for complete peg fixation. The scapular models were created from a patient with advanced asymmetric glenoid erosion. Bone was discretized using tetrahedral elements and a heterogeneous distribution of cancellous bone properties were assigned based on CT intensity. Cortical elements were assigned homogenous properties. Scapular models were constrained on the medial boarder under loading. Net load vectors were applied to the articular surface of the augmented component by a simulated humeral component with a 4 mm mismatch in curvature. Loads of 500, 750 and 1000 N were applied to the center of the glenoid component and then varied 6° in all directions surrounding the central

Copyright 2016 The Organizing Committee for the 2016 Summer Biomechanics, Bioengineering and Biotransport Conference

position, for a total of 27 loading conditions. The compressive contact area, global posterior bone displacement (Figure 1), and micromotion were measured.

RESULTS

Compressive contact area represents the area of load transfer from the implant to the bone and was found to increase linearly with applied load and as the net joint load vector moved from anterior to posterior. Global bone displacements in the posterior region were found to increase in the stepped implants for posterior and posterosuperior directed loads, but were found to be relatively uniform for all other load magnitudes/directions, and for all other implants. Micromotion at the bone-implant interface was greatest for all implants under posteriorly directed loads. For posterior loads, the posterior-wedged implant showed much greater micromotions compared to the other implants. Micromotions were lowest with centrally directed loads, and moderate under anterior loading.

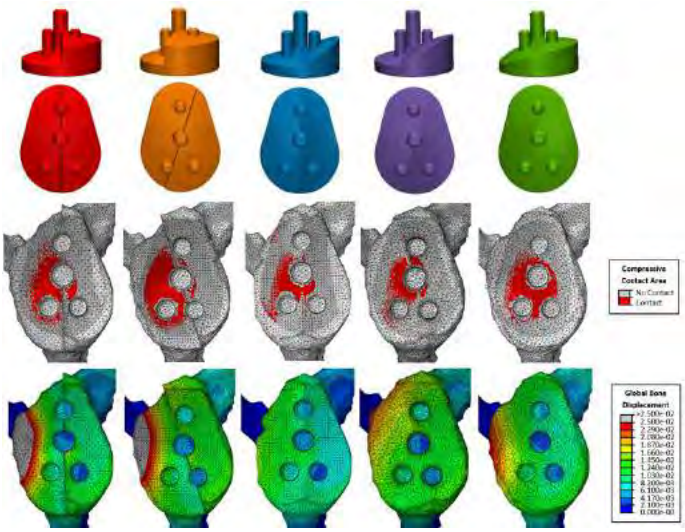

Figure 1: Finite element results for five augmented glenoid component designs – posterior-step (left column), parametric step (left-middle column), posterior-wedge (middle column), parametric-wedge (right-middle column) and full-wedge (right column). The compressive contact area represents the area of load transfer from the implant to the underlying bone. The global bone displacement is the magnitude of bone displacement in millimeters. Figures are for a 750 N compressive load directed six degrees posteroinferior in a right shoulder. Posterior is left, anterior is right for each glenoid.

DISCUSSION

This study addressed the under implant bone as the result of the biomechanical loading of augmented glenoid components under varying simulated joint loading. The loads chosen in this study represent the full range of net joint load vectors experienced *in-vivo.* The results suggest that compressive contact areas, global posterior bone displacements, and micromotion are largely a function of the magnitude and direction of the applied net joint load vector. The posterior-step implant showed relatively greater posterior bone displacement under posterior loading than the other two implants. This may be due to the increased bone removal required to facilitate the augmented component design. The wedged implants preserved more posterior bone, which likely decreased the global bone displacements observed in this region.

ACKNOWLEDGEMENTS

Nikolas K Knowles and G Daniel G Langohr are supported in part by the Natural Sciences and Engineering Research Council (NSERC) of Canada.

REFERENCES

1. Beuckelaers E, Jacxsens M, Van Tongel A, De Wilde LF. Three-dimensional computed tomography scan evaluation of the pattern of erosion in type B glenoids. J Shoulder Elbow Surg 2014;23(1):109–16.
2. Kersten AD, Flores-Hernandez C, Hoenecke HR, D'Lima DD. Posterior augmented glenoid designs preserve more bone in biconcave glenoids. J Shoulder Elbow Surg 2015;24(7):1135-1141.
3. Knowles NK, Keener J, Ferreira LF, Athwal GS. Quantification of the position, orientation, and surface area of bone loss in type B2 glenoids. J Shoulder Elbow Surg 2015;24(4):503-510
4. Knowles NK, Ferreira LM, Athwal GS. Augmented glenoid component designs for type B2 erosions : a computational comparison by volume of bone removal and quality of remaining bone. J Shoulder Elbow Surg 2015;24(8):1218-1226.
5. Terrier A, Ston J, Larrea X, Farron A. Measurements of three-dimensional glenoid erosion when planning the prosthetic replacement of osteoarthritic shoulders. Bone Joint J 2014;96-B(4):513–518.

Copyright 2016 The Organizing Committee for the 2016 Summer Biomechanics, Bioengineering and Biotransport Conference

SB³C2016
Summer Biomechanics, Bioengineering and Biotransport Conference
June 29 –July 2, National Harbor, MD, USA
SB³C2016-16

PREMORBID RETROVERSION IS SIGNIFICANETLY GREATER IN TYPE B2 GLENOIDS

Nikolas K. Knowles (1,2), Louis M. Ferreira (1,2), George S. Athwal (2)

(1) Biomedical Engineering Department
The University of Western Ontario
London, ON, Canada

(2) Roth|McFarlane Hand and Upper Limb
Centre, St. Josephs Health Care
London, ON, Canada

INTRODUCTION

Posterior glenoid erosion in osteoarthritis is believed to be initiated by posterior humeral head subluxation.[1] As the humeral head subluxates posteroinferiorly, it eccentrically erodes the posteroinferior aspect of the glenoid, leading to a bi-concave appearance. This pattern of erosion has been classified as a type B2 glenoid.[2] The aetiology of posterior glenohumeral instability and subluxation is unknown, and likely multifactorial. We postulate, based on clinical observations, that one possible factor in posteroinferior subluxation is greater than normal premorbid glenoid retroversion and inferior inclination.

The purpose of this study was to compare version and inclination of the anterior half of the glenoid in shoulders with type B2 osteoarthritis and age-appropriate normals (Figure 1). The objective was to determine whether type B2 glenoids exhibit greater retroversion or inferior inclination that may be causative factors in the development of posteroinferior subluxation. We hypothesized that type B2 glenoids would have greater anterior premorbid retroversion and inferior inclination, which may be contributing factors to posteroinferior humeral head subluxation.

METHODS

This study examined eighty scapulae, evenly distributed between two groups: osteoarthritis (OA) with type B2 glenoids and age-matched normals. The Walch type B2 OA group consisted of 15 left and 25 right shoulders (25 male, 15 female, mean age: 64±8 years), and the non-arthritic normal group consisted of 23 left and 17 right shoulders (25 male, 15 female, mean age: 68±16 years). Three-dimensional models of all shoulders were constructed from CT DICOM data. Points were placed on the anterior half of the glenoid articular surface, avoiding erosion, osteophytes and/or labrum calcification (Figure 2). A plane was fit to the set of points and custom code determined the version angle and inclination angle of the fit plane compared to the zero degree version plane – perpendicular to the validated scapular coronal plane. Interobserver reliability was used to validate anterior glenoid point selection by two observers using intraclass correlation coefficients (ICC) with a 2-way random effects model and absolute agreement (SPSS Statistics, IBM Software).

RESULTS

Comparing cohorts, the version of the anterior paleoglenoid region of type B2 glenoids (-14±6°) was significantly greater ($p<0.001$) than the anterior half of the non-arthritic normal glenoids (-5±5°). The statistical trends persisted when comparing males (n=25) and females (n=15) (males: B2 version = -15±6°; normal version = -6±6°, $p<0.001$) (females: B2 version = -11±5°; normal version =-5±5°, $p=0.004$).

There were no significant differences ($p=0.166$) in inclination angle between type B2 glenoids (0±6°) and non-arthritic normal glenoids (2±5°) when all shoulders were compared. This result persisted by sex (males: B2 inclination = 0±5°; normal inclination = 1±5°, $p=0.555$) (females: B2 inclination = 0±7°; normal inclination = 4±5°, $p=0.170$). Histograms illustrating the distribution of glenoid version and inclination are shown in figures 3 and 4, respectively.

Inter-observer reliability was excellent (ICC=0.954, 95% CI: 0.787 to 0.989) for version and excellent (ICC=0.938, 95% CI: 0.663 to 0.986) for inclination between the two observers.

Copyright 2016 The Organizing Committee for the 2016 Summer Biomechanics, Bioengineering and Biotransport Conference

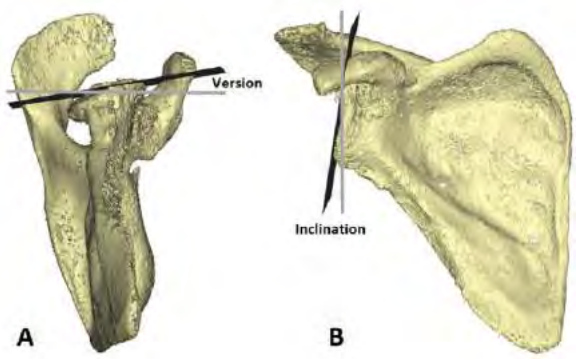

Figure 1: Inferior view of the zero degree version plane (grey) and plane fit to anterior points (black) used to determine the native anterior glenoid version angle or paleoglenoid version (A). Anterior view of the zero degree version plane (grey) and plane fit to anterior points (black) used to determine the native anterior glenoid inclination angle or paleoglenoid inclination (B). Note the difference between the paleoglenoid version and the eroded surface in this type B2 glenoid.

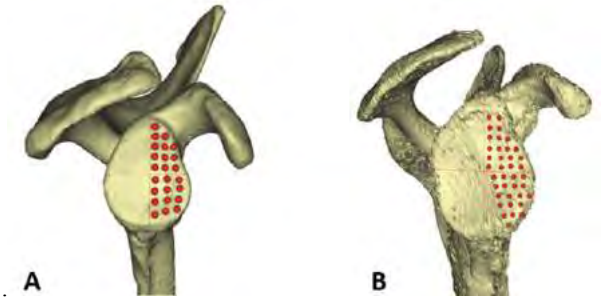

Figure 2: Points (red dots) placed on the anterior half of the glenoid used to calculate native anterior glenoid version and inclination. Point placement in a normal non-arthritic shoulder (A). Point placement on the paleoglenoid in a type B2 osteoarthritic patient (B). Note in the type B2 patient, points in the inferior region are placed to avoid erosion morphology.

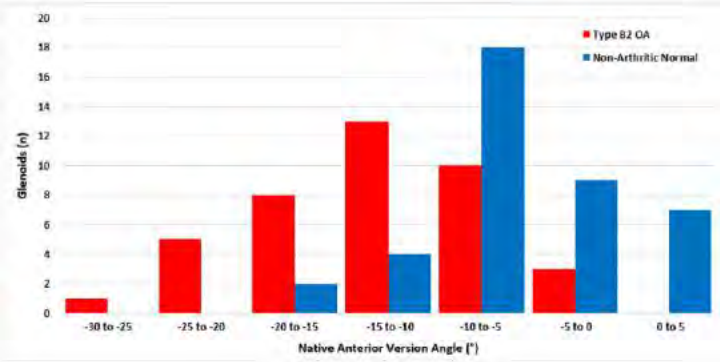

Figure 3: Distribution of the version angle of the anterior half of the glenoid. Negative values represent retroversion.

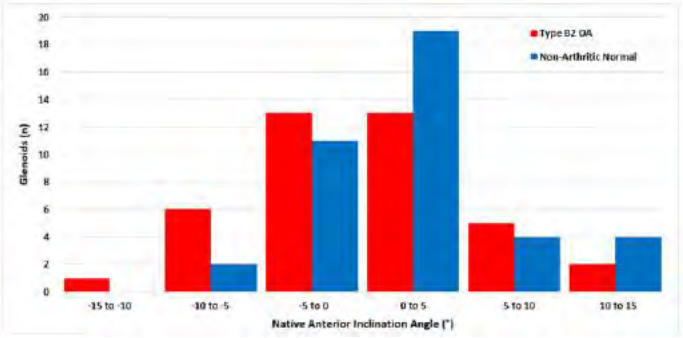

Figure 4: Distribution of the inclination angle of the anterior half of the glenoid. Negative values represent inferior inclination.

DISCUSSION

The results of this study suggest that patients who acquire posterior glenoid bone loss and associated retroversion, may have increased native glenoid retroversion when compared to non-arthritic normals. The anterior half of the glenoid in patients with type B2 glenoid erosion typically maintains articular cartilage, indicating that this region has not undergone bony erosion. Interestingly, there were no significant differences between glenoid inclination in the two groups. Assessing whether these similarities exist with larger cohort sizes may increase our understanding of the mechanisms of glenoid posterior erosion.

ACKNOWLEDGEMENTS

Nikolas K Knowles is supported in part by the Natural Sciences and Engineering Research Council (NSERC) of Canada.

REFERENCES

1. Kidder JF, Rouleau DM., Pons-Villanueva J, Dynamidis S, DeFranco MJ, Walch G. Humeral head posterior subluxation on CT scan: validation and comparison of 2 methods of measurement. Tech. Shoulder Elb Surg;11(3):72–76.
2. Walch G, Badet R, Boulahia A, Khoury A. Morphologic study of the glenoid in primary glenohumeral osteoarthritis. J Arthroplasty 1999;14(6):756-760.

Copyright 2016 The Organizing Committee for the 2016 Summer Biomechanics, Bioengineering and Biotransport Conference

SB³C2016
Summer Biomechanics, Bioengineering and Biotransport Conference
June 29 –July 2, National Harbor, MD, USA
SB³C2016-17

A COMPARISON OF NORMAL AND OSTEOARTHRITIC HUMERAL HEAD SIZE AND MORPHOLOGY

Nikolas K. Knowles (1,2), Michael J. Carroll (2), Louis M. Ferreira (1,2), Jay D. Keener (3), George S. Athwal (2)

(1) Biomedical Engineering Department
The University of Western Ontario
London, ON, Canada

(2) Roth|McFarlane Hand and Upper Limb Centre, St. Josephs Health Care
London, ON, Canada

(3) Washington University/Barnes-Jewish Hospital, St. Louis, MO, USA

INTRODUCTION

Glenohumeral osteoarthritis (OA) causes progressive joint damage with extensive bone remodelling and osteophyte formation. As a result, it has been observed that OA humeral heads are morphologically different from normal humeral heads. However, little research has examined and compared the size and morphology of arthritic humeral heads to normal humeral heads.[7] Conversely, the arthritic glenoid has been well investigated.[6] Characteristic erosion patterns of the arthritic glenoid have been classified,[5] and regional variations in density, shape, orientation, and porosity have been reported.[1–4]

Although morphological changes to the humeral head are known to occur,[7] an anatomic characterization of the unique morphology of the osteoarthritic humeral head is lacking. As such, the purpose of this study was to evaluate and compare the size and morphology of normal and osteoarthritic humeral heads. Additionally, we sub-classified our osteoarthritic cohort as having symmetric or asymmetric (type B2)[5] glenoid erosion, in order to assess whether humeral head morphology varied by the type of glenoid erosion. We hypothesized that due to erosion the arthritic humeral head has a larger spherical diameter and is thinner, relative to the osteotomy plane, than normal humeral heads. This information may improve our understanding of glenohumeral pathoanatomy, posterior glenoid erosion patterns, and assist with implant design.

METHODS

One hundred fifty computed tomography scans of the shoulder were studied. Three-dimensional models were constructed for each shoulder using medical imaging software validated for anatomical measurements. The subjects were separated into three groups, (1) normal glenohumeral joint, (2) osteoarthritic joint with symmetric glenoid erosion, and (3) osteoarthritic with asymmetric (type B2) glenoid erosion. Each group comprised 50 non-paired shoulders (30 male and 20 female). The humeral head was virtually excised by one of two experienced shoulder surgeons. Three-dimensional point coordinates were collected on the articular surface of all humeral heads and a sphere fit algorithm was used to determine the diameter of each humeral head. To account for the curvature of non-spherical humeral heads, circle fits were performed along planes in the anteroposterior (A-P) and superoinferior (S-I) directions (Figure 1). The thickness of each humeral head was also determined as the perpendicular distance from the osteotomy plane to the intersection of the A-P and S-I planes on the articular surface.

RESULTS

The sphere fit diameter of the excised humeral head for the entire OA cohort (100 patients, mean diameter 59.3±8.7 mm) was significantly greater ($p<0.001$) than the normal cohort (50 patients, mean diameter 48.8±5.0 mm). This statistical trend persisted when examining males ($p<0.001$) and females ($p<0.001$) independently. However, when comparing symmetric to asymmetric glenoid erosion OA cohorts, no significant differences were observed for the sphere fit diameter.

Similarly, the humeral head circle fit diameters in the S-I and A-P planes were significantly greater ($p<0.001$) in the combined OA cohorts (59.4±8.7 mm and 56.4±9.8 mm, respectively) as compared to the normal cohort (51.0±5.1 mm and 47.1±5.0 mm, respectively). However, there were no significant differences ($p\geq0.099$) between the symmetric and asymmetric OA cohorts in S-I or A-P circle fit diameters. The mean

Copyright 2016 The Organizing Committee for the 2016 Summer Biomechanics, Bioengineering and Biotransport Conference

values of humeral head heights were 18.7 mm, 18.2 mm, and 18.2 mm for the normal, symmetric OA, and asymmetric OA cohorts, respectively. These values were not significantly different (p=0.382).

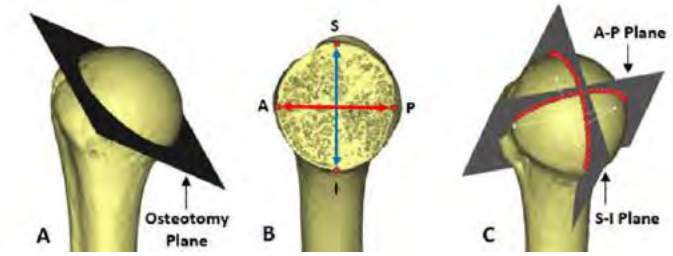

Figure 1: The osteotomy plane (A). Superior (S), inferior (I), anterior (A), and posterior (P) points on the humeral head-neck osteotomy plane. The blue arrow represents the S-I chord distance, and the red arrow represents the A-P chord distance (B). Points on the humeral head used for circle fitting in the S-I and A-P planes (C).

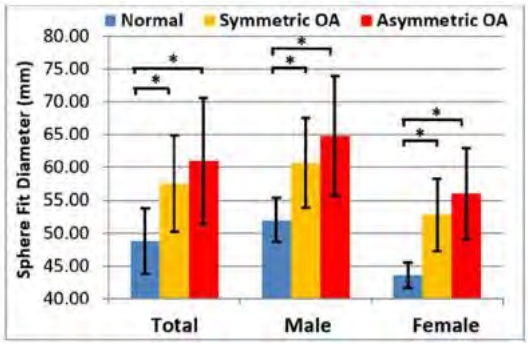

Figure 2: Mean sphere fit diameter of the humeral head articular surface for three cohorts. Significance is indicated by *, p<0.05.

DISCUSSION

Significant differences were observed between normal humeral head diameters and osteoarthritic humeral head diameters in two common glenoid erosion morphologies. The results of this study indicate that the size of the arthritic humeral head varies from the normal humeral head, but not as a function of the Walch classification between symmetric and asymmetric (B2) glenoids. The increased diameter associated with the osteoarthritic humeral head has unknown consequences for soft tissue stretching and associated soft-tissue balancing following total shoulder arthroplasty procedures. This information may have implications in our understanding of posterior erosion patterns and their treatments, as well as the design of humeral head replacement components.

ACKNOWLEDGEMENTS

The authors would like to thank Subin Choi for her assistance with data collection. Nikolas K Knowles is supported in part by the Natural Sciences and Engineering Research Council (NSERC) of Canada.

REFERENCES

1. Churchill R, Spencer E, Fehringer E. Quantification of B2 glenoid morphology in total shoulder arthroplasty. J Shoulder Elbow Surg 2015; 24(8):1212-1217.
2. Knowles NK, Keener J, Ferreira LF, Athwal GS. Quantification of the position, orientation, and surface area of bone loss in type B2 glenoids. J Shoulder Elbow Surg 2015;24(4):503-510
3. Knowles NK, Athwal GS, Keener JD, Ferreira LM. Regional bone density variations in osteoarthritic glenoids : a comparison of symmetric to asymmetric (type B2) erosion patterns. J Shoulder Elbow Surg 2015;24(3):425-432.
4. Simon P, Gupta A, Pappou I, Hussey MM, Santoni BG, Inoue N, et al. Glenoid subchondral bone density distribution in male total shoulder arthroplasty subjects with eccentric and concentric wear. J Shoulder Elbow Surg 2015;24(3):416-424
5. Walch G, Badet R, Boulahia A, Khoury A. Morphologic study of the glenoid in primary glenohumeral osteoarthritis. J Arthroplasty 1999;14(6):756-760.
6. Walch G, Mesiha M, Boileau P, Edwards TB, Lévigne C, Moineau G, et al. Three-dimensional assessment of the dimensions of the osteoarthritic glenoid. Bone Joint J 2013;95-B(10):1377–1382.
7. Youderian A, Ricchetti E. Determination of humeral head size in anatomic shoulder replacement for glenohumeral osteoarthritis. J Shoulder Elbow Surg 2014;23(7):955-963.

Copyright 2016 The Organizing Committee for the 2016 Summer Biomechanics, Bioengineering and Biotransport Conference

Proceedings of the ASME 2016 Summer Bioengineering Conference
SBC2016
June 29 – July 2, 2016, National Harbor, Maryland, USA
SB³C2016-19

PREVENTING UPPER AIRWAY COLLAPSE USING CPAP WITH AND WITHOUT PRESSURE OSCILLATIONS

Al-Jumaily[1], A.M., Ashaat[1], S., Huang[2], L.

[1]Institute of Biomedical Technologies,
Auckland University of Technology,
Auckland, New Zealand

[2]Department of Mechanical and
Production Engineering,
Auckland University of Technology,
Auckland, New Zealand.

ABSTRACT

Upper airway (UA) collapse occurs when the forces of the airway wall muscles become less than the forces generated from the airway negative pressures during the respiration process. Continuous Positive Airway Pressure (CPAP) treatment is considered the most effective treatment for patients diagnosed with moderate to severe obstructive sleep apnea (OSA). It provides a continuous flow of pressurized and humidified air to prevent airway collapse; however, there is a high rejection rate due to its high operating pressure. Using MRI scans, this paper investigates the effects of using the pressure oscillations (PO) superimposed on the CPAP to keep the airway open at lower pressure distributions inside the UA and consequently increase patients' comfort and reduce device rejection.

INTRODUCTION

As sleep onsets, the UA muscles relax causing the airway lumen to narrow which increases the resistance to airflow [1]. Further when an OSA patient sleeps in the supine position, the uvula and the tongue move towards the airway wall due to gravitational forces, reducing the air gap which increases the chance for airway obstruction and collapse [2]. These events occur hundreds of times every night resulting in restless sleep and many health implications such as diabetes, arrhythmia, stroke, hypertension, memory loss and cardiovascular disease [3]. The CPAP is considered the first line of treatment for patients diagnosed with moderate to severe OSA [4], however, there is a high patients' rejection rate due to its high operating pressure [5]. PO have been reported to increase the activity of the UA muscles [6], however, their effect on the performance of the UA when superimposed on the CPAP have never been previously investigated. Therefore this paper investigates the conditions of UA collapse in a group of apneic patients and presents the resulting pressure distributions inside their UA when the CPAP is used alone or with superimposed PO.

METHOD

While awake and in supine position, MRI data of the UA were collected for 10 non-smoking OSA patients (7 males and 3 females) with 42–66 years of age. Ethical approval was granted by The Auckland University of Technology Ethics Committee and consents were obtained prior to initiation of the study procedures. UA models from the nasopharynx to the hypopharynx were accurately constructed using 3D-DOCTOR software, then were imported to the ANSYS Workbench to conduct the simulations, Figure 1.

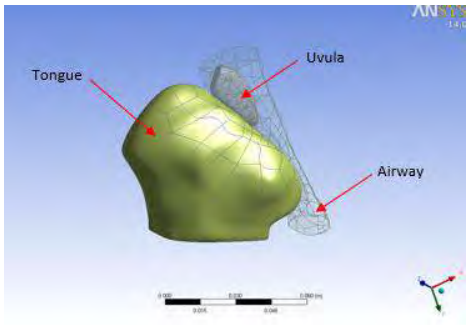

Figure 1: Entire UA model

The airway models were solved by the CFD methods using the Fluid-Flow (CFX) Modeller on the ANSYS Workbench. The interaction between the airflow and the deformations of the uvula and tongue was investigated by the Fluid-Structure Interaction (FSI)

Copyright © 2016 by ASME
Copyright 2016 The Organizing Committee for the 2016 Summer Biomechanics, Bioengineering and Biotransport Conference

methods using the Static-Structural Modeller on the ANSYS Workbench. The soft tissues were replaced by a hyper-elastic rubber enclosure, Figure 2, of 1 mm thickness, density of 1000 kg/m^3 and the temperature was set to 38^{o}C as that of the air coming from the lungs.

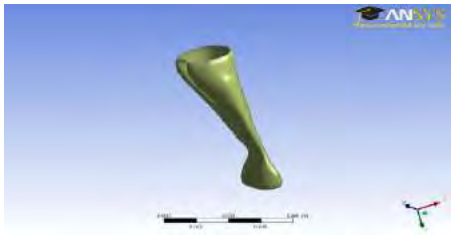

Figure 2: 1 mm thickness rubber enclosure

To investigate the effect of PO on the UA of an apnoeic subject, simulations were repeated until collapse was detected. CPAP was applied to keep the airway open and then PO were superimposed in such a way that the static pressure at the level of the nasopharynx is the same before and after using the PO.

RESULTS AND DISCUSSION

Standards RANS k-ε and RANS SST turbulence models were used; however the results of the latter model were more reasonable and therefore are presented in this paper. The boundary conditions were chosen to fulfil a pharyngeal pressure range of -1.4:1.5 kPa [7]. Collapse was detected during inspiration at the rear of the tongue when P_{in} = 1 kPa and P_{out} = -1.1 kPa, Figure 3. PO were applied at the inlet, with P_{in} = 0.9+0.1 Sin (2πf t) kPa, f=40 Hz.

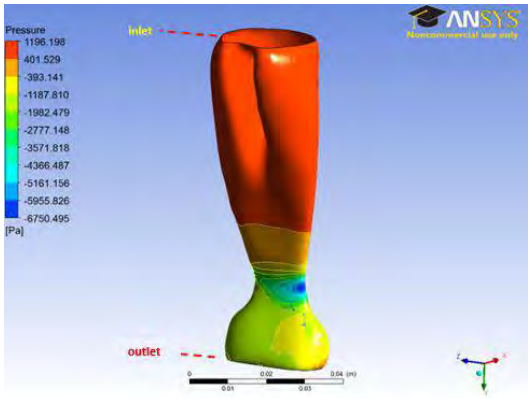

(a)

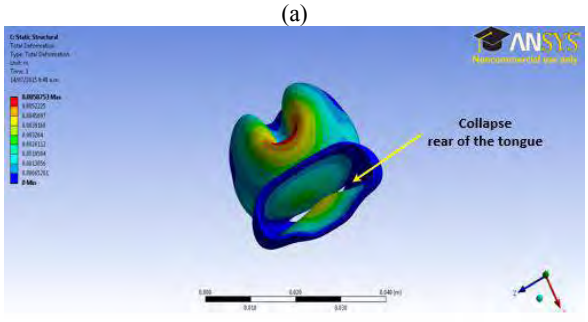

(b)

Figure 3: (a) pressure distribution and (b) bottom view of the airway during inspiration

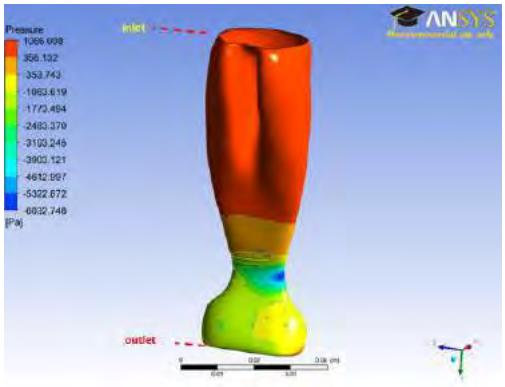

(a)

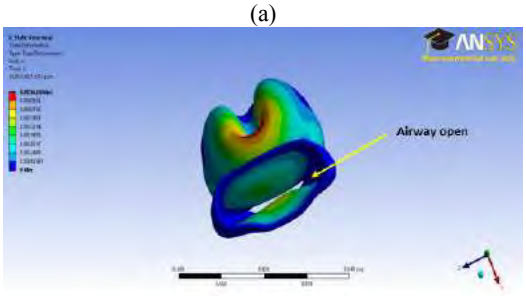

(b)

Figure 4: (a) pressure distribution and (b) bottom view of the airway during inspiration showing open airway

These results show that the use of the PO has successfully kept the airway open at much lower pressure distribution compared to the use of the CPAP alone. Also, the use of the RANS SST turbulence model has resulted in more reasonable values compared to the RANS k-ε, and therefore it is recommended to be used in similar future studies.

AKNOWLDGEMENT

We acknowledge Fisher &Paykel Healthcare Ltd for their support and the New Zealand Ministry of Science and Innovations (MSI) for financially supporting the project via grant number FAPX1109.

REFERENCES

[1] Horner, R.L., Motor control of the pharyngeal musculature and implications for the pathogenesis of obstructive sleep apnea. Sleep, 1996. 19(10): p. 827-853.
[2] Fouke, J.M.et al. "Effect of position and lung volume on upper airway geometry". J. of Appl. Physiology, 1987. 63(1): p. 375-380.
[3] Emsellem, H.A. and K.E. Murtagh, Sleep apnea and sports performance. Clinics in Sports Medicine, 2005. 24(2): p. 329-341.
[4] Bassiri, A.G. and C. Guilleminault, Clinical features and evaluation of obstructive sleep apnea-hypopnea syndrome. Principles and Practice of Sleep Medicine, 2000. 3: p. 869-878.
[5] Zozula, R., R. Rosen, and B. Phillips, Compliance with continuous positive airway pressure therapy: Assessing and improving treatment outcomes. Current Opinion in Pulmonary Medicine, 2001. 7(6): p. 391-398.
[6] Henke, K.G. and C.E. Sullivan, Effects of high-frequency oscillating pressures on upper airway muscles in humans. Journal of Applied Physiology, 1993. 75(2): p. 856-862.
[7] Bijaoui, E.L., et al., Mechanical properties of the lung and upper airways in patients with sleep-disordered breathing. American journal of respiratory and critical care medicine, 2002. 165(8): p. 1055-1061.

Copyright © 2016 by ASME
Copyright 2016 The Organizing Committee for the 2016 Summer Biomechanics, Bioengineering and Biotransport Conference

SB³C2016
Summer Biomechanics, Bioengineering and Biotransport Conference
June 29 –July 2, National Harbor, MD, USA
SB³C2016-20

FASCICLES AND THE INTERFASCICULAR MATRIX SHOW SUPERIOR FATIGUE RESISTANCE IN ENERGY STORING TENDONS

Chavaunne T. Thorpe (1), Graham P. Riley (2), Helen L. Birch (3), Peter D. Clegg (4), Hazel R. C. Screen (1)

(1) School of Engineering and Materials Science
Queen Mary University of London
London, UK

(2) School of Biological Sciences
University of East Anglia
Norwich, UK

(3) Institute of Orthopaedics and Musculoskeletal Science
UCL
Stanmore, UK

(4) Institute of Ageing and Chronic Disease
University of Liverpool
Neston, UK

INTRODUCTION

Tendon is composed of rope-like fascicles bound together by interfascicular matrix (IFM). Our previous work shows that the IFM is critical for tendon function, facilitating sliding between fascicles to allow tendons to stretch [1]. We have shown that this is particularly important in energy storing tendons such as the human Achilles tendon and equine superficial digital flexor tendon (SDFT), which can experience strains as high as 16% during intense exercise [2], and therefore require the capacity for considerable inter-fascicular sliding and recoil. This capacity is not required in positional tendons (e.g. equine common digital extensor tendon (CDET)). While the quasi-static properties of the IFM have been elucidated [1], the fatigue resistance of the IFM in functionally distinct tendons has not been established. The aim of this study was therefore to compare the fatigue properties of fascicles and IFM in two functionally distinct tendons. We tested the hypothesis that fascicles and IFM in the energy storing equine SDFT are more fatigue resistant than those in the positional CDET.

METHODS

The SDFT and CDET were harvested from the forelimbs of horses aged 3 to 7 years (n=5). For fascicle tests, individual fascicles were dissected from each tendon (n=8). For IFM tests, groups of 2 fascicles (bound together by IFM) were dissected from each tendon (n=12). Using a polarised light microscope and a dissection rig, the opposing end of each fascicle was cut transversely, leaving a 10 mm length of intact IFM (Fig.1).

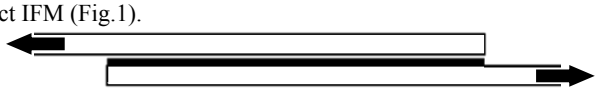

Fig.1 Schematic of IFM test. 2 fascicles (white) bound together by 10mm of IFM (black) were pulled apart, testing the IFM in shear.

Samples were gripped in individual loading chambers and secured in a mechanical test frame (Electroforce, TA instruments). A pre-load was applied to remove slack from the samples (0.1N for fascicles and 0.02N for IFM tests). One loading cycle of 1mm displacement was then applied (equivalent to 50% failure extension). The peak load measured at this displacement was recorded, and this load was subsequently applied to the fascicles in a cyclic manner at a frequency of 1 Hz until sample failure. Load and displacement data were recorded continuously throughout the test at a frequency of 100 Hz. In addition, the maximum and minimum load and displacement were recorded for each cycle.

For each test, the number of cycles to failure was recorded. The maximum and minimum displacement data were used to plot creep curves to failure (Fig. 2) and the gradients of the maximum and minimum displacement curves during secondary creep were calculated.

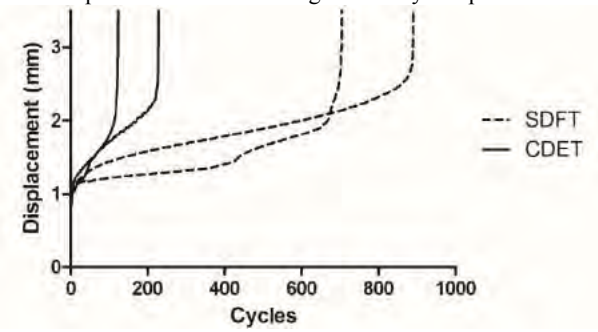

Fig.2. Typical creep curves for IFM samples in the SDFT and CDET.

For each sample, force extension curves were plotted and hysteresis calculated at various cycles throughout testing. Fascicle

Copyright 2016 The Organizing Committee for the 2016 Summer Biomechanics, Bioengineering and Biotransport Conference

elongation was calculated at cycle 10 and at the cycle prior to failure by subtracting the maximum extension at cycle 1 from the maximum extension in these cycles. It was not possible to calculate IFM elongation in the same manner, relative to the first cycle, as the low forces involved in this load controlled experiment required several cycles to fully stabilise.

Statistical significance was determined using Analysis of Variance (Minitab 17). A general linear model was fitted to the data, with donor and tendon type as factors. Data were tested for normality (Anderson–Darling test). Data that were not normally distributed were transformed (Box-Cox). Data are displayed as mean ± SD.

RESULTS

Fascicles and IFM from the SDFT resisted significantly more cycles before failure than those from the CDET (Table 1).

Table 1. Number of cycles to failure * indicates significant difference between tendon types (p<0.01).

	SDFT	CDET
Fascicles	2709 ± 4819	139 ± 157*
IFM	921 ± 1947	215 ± 145*

The gradients of the maximum and minimum creep curves for fascicle tests were significantly greater in the CDET than in the SDFT (p<0.001). For IFM tests, the gradient of the maximum creep curve was also significantly greater in the CDET than in the SDFT (p<0.01).

Initial fascicle elongation was greater in the CDET than in the SDFT (Fig. 3). However, in the last cycle prior to failure, fascicle elongation was greater in the SDFT than in the CDET (Fig. 3).

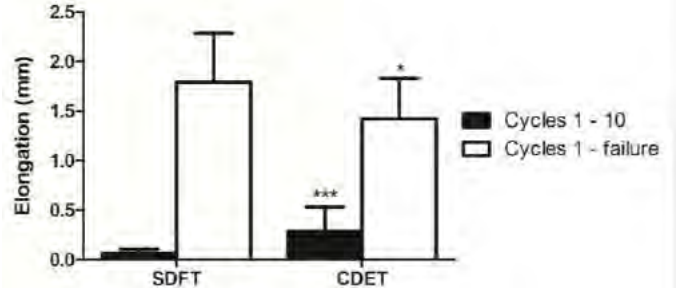

Fig.3. Fascicle elongation during fatigue testing. . * indicates significant difference between tendon types: *p<0.05; *** p<0.001.

Hysteresis was significantly greater in CDET fascicles than in SDFT fascicles at all time points assessed. In both tendon types, hysteresis decreased over the course of fatigue testing but increased in the cycles prior to failure (Fig.4a). A similar pattern was observed in the IFM, with a trend towards greater hysteresis in the CDET, which reached significance at the mid-point of fatigue testing (Fig.4b).

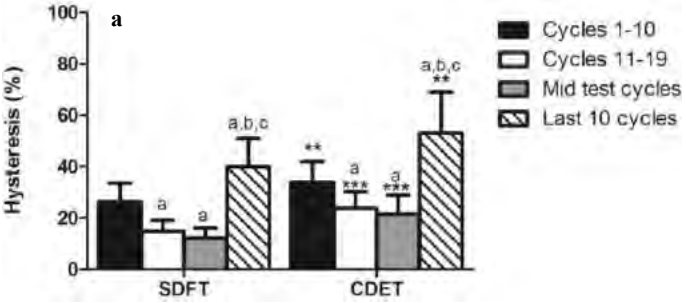

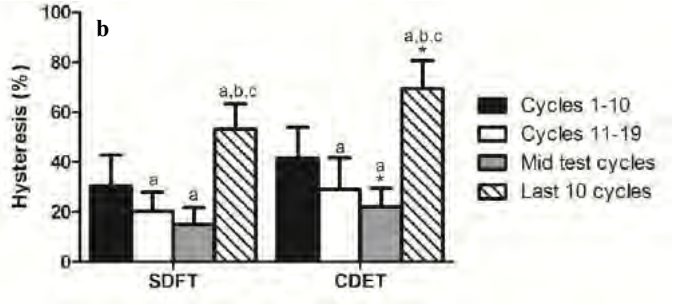

Fig.4. Hysteresis during fascicle (a) and IFM (b) fatigue testing. * indicates significant difference between tendon types: *p<0.05; ** p<0.01; *** p<0.001. [a] indicates significant difference relative to cycles 1-10 (p<0.05); [b] indicates significant difference relative to cycles 11-20 (p<0.001); [c] indicates significant difference relative to mid test cycles (p<0.001).

DISCUSSION

The data support our hypothesis, demonstrating that both fascicles and IFM in the energy storing SDFT are more fatigue resistant than those in the positional CDET. This is in agreement with previous studies which have shown lower levels of hysteresis and stress relaxation in fascicles and IFM in the SDFT compared to the CDET during cyclic loading [3].

When considering the fascicle response to fatigue loading, fascicles from the SDFT were able to resist almost 20 times more cycles to failure than those from the CDET, and exhibited lower hysteresis throughout fatigue testing. Interestingly, fascicles from the SDFT exhibited less elongation initially, but were able to elongate further before failure than those from the CDET.

The IFM exhibited surprisingly high fatigue resistance, which was greater in the SDFT than in the CDET. It is not possible to directly compare the fatigue resistance of fascicles and IFM due to differences in the testing methods used, but the results indicate that the IFM has a functional role within tendon and contributes significantly to tendon mechanical properties.

Previous studies indicate that fascicles from the SDFT have a helical substructure, allowing them to act as springs, which likely results in their superior fatigue resistance [4]. Specialisation of the IFM has also been observed in the SDFT, with localization of lubricin and elastin to this region [5]. Lubricin likely acts to aid sliding between fascicles, while elastin may provide the ability to recoil efficiently and contribute to improved fatigue resistance.

Taken together, these data indicate that both fascicles and IFM in the energy storing SDFT exhibit compositional and structural specialisations that likely contribute to superior fatigue resistance in the tendon as a whole. These data provide important advances into fully characterising structure-function relationships within tendon.

ACKNOWLEDGEMENTS

Funded by the BBSRC, UK (BB/K008412/1).

REFERENCES

[1] Thorpe, CT et al., *J R Soc Interface;* 9:3108-17, 2012.
[2] Stephens, PR et al., *Am J Vet Res*; 50:1089-95, 1989.
[3] Thorpe, CT et al., *J Mech Behav Biomed Mater; 52:85-94*, 2015.
[4] Thorpe, CT et al., *Acta Biomater;* 9:7948-56, 2013.
[5] Thorpe, CT et al., *Bone Joint J;* 97-B (Supp 11), 20, 2015.

Copyright 2016 The Organizing Committee for the 2016 Summer Biomechanics, Bioengineering and Biotransport Conference

SB³C2016
Summer Biomechanics, Bioengineering and Biotransport Conference
June 29 –July 2, National Harbor, MD, USA
SB³C2016-21

AN EXPERIMENTAL CANINE PATENT DUCTUS ARTERIOSUS OCCLUDER BASED ON SHAPE MEMORY POLYMER FOAM IN A NITINOL CAGE

Mark A. Wierzbicki[1], Bradley H. Due[1], Landon D. Nash[1], Brandis Keller[1], Sonya G. Gordon[2], Matthew W. Miller[3], Duncan J. Maitland[1]

(1) Department of Biomedical Engineering
Texas A&M University
College Station, TX, USA

(2) Department of Small Animal Clinical Sciences
Texas A&M University
College Station, TX, USA

(3) Texas Institute for Preclinical Studies
Texas A&M University
College Station, TX, USA

INTRODUCTION

Patent ductus arteriosus (PDA) occurs when a normal fetal connection between the aorta and main pulmonary artery (MPA) does not close following birth, leading to continuous left to right shunting of blood from the descending aorta to the MPA. This can lead to significant cardiac remodeling and complications [1, 2].

Surgical ligation, the traditional method of closure, is highly invasive and carries non-trivial risks [2]. In an effort to mitigate these risks, minimally invasive treatment methods were developed, such as the Amplatz® Canine Ductal Occluder (ACDO) (Infiniti Medical, LLC, Menlo Park, CA) (Figure 1A), a device composed of a dense nitinol mesh forming multiple disks used for positioning and stability. While effective, this device has limitations, including its large sized (≥4Fr sheath) delivery system, which limits the treatment of smaller canines with larger PDAs [3, 4] and high cost, indicating a clinical need for a device to address these issues.

The nitinol foam cage (NFC) prototype utilizes a low profile nitinol frame to aid in positioning and stability, and a shape memory polymer foam (SMP) foam to provide a tissue scaffold for occlusion and healing. SMPs are a class of materials, which through an entropy driven process, are capable of being programmed into a secondary shape and actuated to their primary shape when heated above their characteristic glass transition temperature [5]. These materials have been proposed for use in medical devices and embolic agents [6]. The NFC prototype (Figure 1 B&C) was constructed, and evaluated in mechanical, fatigue, and *in vitro* studies and compared to the mechanical properties and characteristics of the ACDO.

METHODS

NFC prototypes were fabricated and evaluated in multiple verification tests including: Axial fatigue, radial pressure, and benchtop *in vitro* tests evaluating device stability in simplified PDA models.

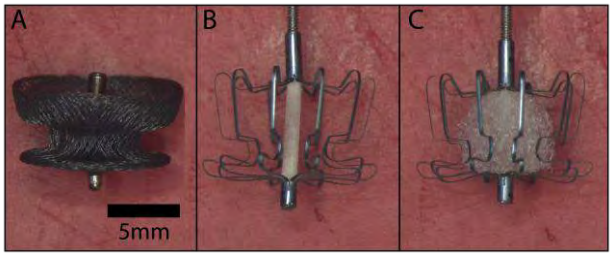

Figure 1: Device comparison. A: ACDO. B: NFC with foam compressed. C: NFC with foam expanded. Scale is the same across frames.

The NFC prototype, previously developed by Wierzbicki et. al [7], has been redesigned to address device stability issues of the original prototype. Briefly, devices were constructed by laser cutting slots into nitinol tubing (NDC, Fremont, CA) using an excimer laser (Resonetics, Nashua, NH). Following deburring and cleaning the laser cut tube, the NFC was attached to a custom fixture, compressed into the desired shape and set through heat treating at 550°C for twenty five minutes followed by a quench in water. A threaded release mechanism was laser welded to the proximal end to allow for repositioning and detachment from the delivery cable. A compressed 8mm diameter SMP foam was epoxied into the proximal portion of the tube.

A preliminary assessment of the fatigue characteristics was carried out by axially cycling the nitinol frame on a dynamic mechanical analysis unit (DMA Q800, TA instruments, New Castle, DE). Three NFC frames were cyclically extended by 1mm at a rate of 2Hz for one

Copyright 2016 The Organizing Committee for the 2016 Summer Biomechanics, Bioengineering and Biotransport Conference

million cycles, corresponding to approximately 6 days once implanted.

Radial force measurements were recorded using a J-Crimp™ RJA62 Radial Compression Station (Blockwise Engineering LLC, Tempe, AZ) attached to an Instron 5965 Test Frame (Instron, Norwood, MA). The radial force of the NFC was measured in 4, 6, 8, 10, and 11mm ampulla diameters and compared to that of the ACDO in all cases to assess the force that would be imparted to the ampulla wall, located on the aortic side of the PDA vessel.

Thin walled silicone models mimicking simplified PDA geometries including IIA, IIB, and wide ampulla (WA) models were created to evaluate delivery characteristics, and device migration. The devices, sized to occlude a 3mm MDD PDA, were tested in a gravity fed flow system (maximum head pressure of 240mmHg) with an adjustable pressure control valve. Seven different models were evaluated: 3mm and 5mm minimal ductal diameter (MDD) IIA, IIB, and WA, and a 3x4mm ovular MDD IIA model. The NFC was designed to occlude 3mm MDDs but the 5mm MDDs were tested to determine efficacy during undersized device deployment conditions. The devices were delivered into the system using a 4Fr sheath and tested at two pressures, physiological (100mmHg)[8], and elevated pressure (171±11 mmHg for 3mm MDD; 115±3 mmHg for 5mm MDD) developed by fully opening the pressure control valve. The devices were subjected to the physiological and elevated pressures for five minutes each to ensure that they would not migrate, or move from their desired deployed position. Images were recorded at one minute intervals and were analyzed for device motion following the experiment using ImageJ image analysis software (NIH, Bethesda, MD).

RESULTS

All three devices withstood one million cycles under a load of 0.019± 0.0012N throughout the test with no visible cracks or damage observed on the struts.

The radial force exerted by the NFC was lower than the ACDO for all diameters tested (Figure 2). The maximum and minimum force generated by the devices occurred in the 4mm and 11mm ampulla respectively.

The NFC and ACDO both exhibited negligible migration in the simplified models at both physiological and elevated pressures (Figure 3). The largest motion seen (0.3mm) was in the 3mm WA model.

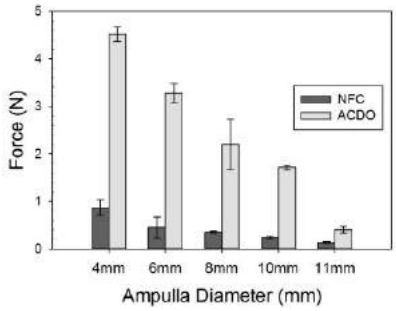

Figure 2: Radial Force of the NFC and ACDO in different ampulla diameters.

DISCUSSION

The fatigue results show that the prototype should not fracture or fail shortly after implantation. These promising results were achieved with minimal post-processing following laser cutting. While the device passed this metric, the final implant would be electropolished, a method to used improve surface finish, biocompatibility, and reduce stress concentrations, to further improve fatigue life, warranting further investigation.

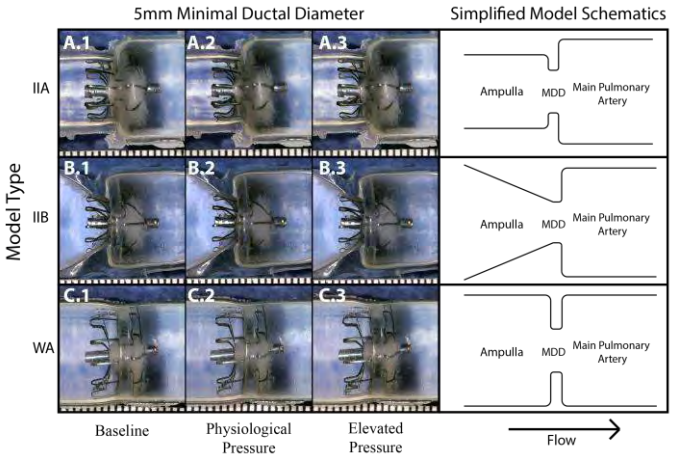

Figure 3: NFC *in vitro* device stability tests display negligible motion in all model types and MDD configurations. (A) IIA 5mm; (B) IIB 5mm; (C) WA 5mm. Images are taken (*.1) immediately after deployment; (*.2) after five minutes at physiological pressure gradient (100mmHg); and (*.3) after five minutes at an elevated pressure gradient (115±3 mmHg). Flow is left to right. Simplified model schematics are shown on the right illustrating the anatomy. Scale in mm.

The lower radial pressure exerted by the NFC compared to the ACDO shows that the device should not impart significant vessel trauma or rupture the ampulla wall. Despite the lower radial pressure, the NFC did not exhibit device migration, even in the WA models in which the struts did not contact the ampulla wall. Therefore, radial pressure alone is not a sufficient indicator of device stability. The oversized nitinol waist and ability for the device to catch on the taper prevented migration of both the NFC and ACDO. Additionally, the NFC withstood an elevated pressure gradient, similar to those that can develop acutely after closure. Finally, the softer nature may allow the NFC to better conform to irregular or ovular PDA geometries.

In addition to the positive *in vitro* tests, the low profile of the NFC could allow for a smaller delivery system (4Fr catheter, 0.038”ID) in comparison to the ACDO (4Fr sheath, 0.052” ID), based on compression limitation of the SMP foam and diameter of the nitinol tube, instead of a dense nitinol mesh.

The presented results and promising clinician feedback indicate that with minimal design refinement the NFC device could be used to treat canine PDA.

ACKNOWLEDGMENTS

We extend thanks to our colleagues in the Biomedical Device Laboratory for helpful discussion and support throughout this project.

REFERENCES

[1] Achen, S. E., et al., J. Vet. Intern. Med., 22, 6, pp. 1348-1352, 2008.
[2] Nguyenba, T. P., et al., J. Vet. Intern. Med., 22, 1, pp. 129-134, 2008.
[3] Tobias, A. H., et al., Vet. Clin. N. Am-Small, 40, 4, pp. 581-603, 2010.
[4] Miller, M. W., et al., J. Vet. Cardiol., 8, 2, pp. 109-114, 2006.
[5] Lendlein, A., et al., Angew. Chem. Int. Edit., 41, 12, pp. 2034-2057, 2002.
[6] Maitland, D. J., et al., J. Biomed. Opt., 12, 3, pp. 2007.
[7] Wierzbicki, M. A., et al., J. Mech. Behav. Biomed., 59, -, pp. 156 - 167, 2016.
[8] Singh, M. K., et al., J. Vet. Intern. Med., 26, 1, pp. 85-92, 2012.

Copyright 2016 The Organizing Committee for the 2016 Summer Biomechanics, Bioengineering and Biotransport Conference

SB^{3}C2016
Summer Biomechanics, Bioengineering and Biotransport Conference
June 29 –July 2, National Harbor, MD, USA
SB^{3}C2016-22

COMPUTER SIMULATION OF LUMBAR FLEXION SHOWS IN-PLANE AND THROUGH-PLANE SHEAR OF THE FACET CAPSULAR LIGAMENT

Amy A. Claeson and Victor H. Barocas

Department of Biomedical Engineering
University of Minnesota – Twin Cities
Minneapolis, MN, USA

INTRODUCTION

Structurally and kinematically, the FCL is a complex tissue whose structure and functional responsibilities change with location along the spinal column. All FCLs contain two distinct materials that transition through the ligament thickness. Specifically to the lumbar FCL, the dorsal surface (i.e., the surface viewed from the posterior aspect and facing out from the joint space) consists of highly aligned collagen fiber bundles that preferentially align between the rigid articular facets. The ventral surface (anterior aspect), which interacts with the synovial fluid within the joint space, is rich with unorganized elastin fibers. The FCL has a convex curvature because it follows the geometry of the articular facets, and, because it is a capsule, it has multiple insertion sites across the facet joint. Articular facet kinematics drive FCL deformations that occur during all spinal motions (flexion/extension, lateral bending, and axial rotation), and which may be quite complex. Additionally, the contained synovial fluid constantly pressurizes the FCL. Therefore, the elaborate structure compounded with the kinematic response gives rise to complicated 3D deformations *in vivo*.

Previous studies have aimed to quantify three-dimensional (3D) deformations of the lumbar spine during flexion, but have fallen short of tracking the complex deformation of the FCL. Kozanek et al.[1] elucidated the kinematics of the articular facets, but did not characterize FCL deformation. A study by Ianuzzi et al.[2] extracted the 3D soft tissue deformations of the lumbar FCL in isolated spines, but calculated one tissue averaged principal strain to define the whole capsule deformation. A study from our group[3] quantified lumbar FCL deformations by optically tracking structural characteristics inherent to the FCL over a course of static bending. This work, however, only captured a portion of the capsule, and the deformations across the FCL emulated flexion, but were not indicative of true flexion. Thus, there exists a gap in our knowledge involving quantification of the full 3D deformations of the lumbar FCL during physiologic spine motions.

Realistic finite element (FE) models of the joint can provide complementary analysis when properly informed by experimental data. To construct a FE model of the lumbar FCL, three pieces of information are necessary: geometry, boundary conditions, and material properties. Figure 1 shows schematically how these inputs were obtained. Previously, our group published continuous *in vivo* vertebral kinematics during flexion/extension to quantify intervertebral margin strains[4]. Facet joint motion was extrapolated from vertebral kinematics in the sagittal plane. Also, we previously characterized the instantaneous material properties of healthy cadaveric L4-L5 FCLs using a hyperelastic model with two fiber distributions[5]. Thus, except for FCL geometry, the necessary information is available to undertake a computational analysis of lumbar FCL motion.

The goal of the current study was to quantify the continuous deformation of the lumbar FCL during flexion and extension by means of a realistic FE model.

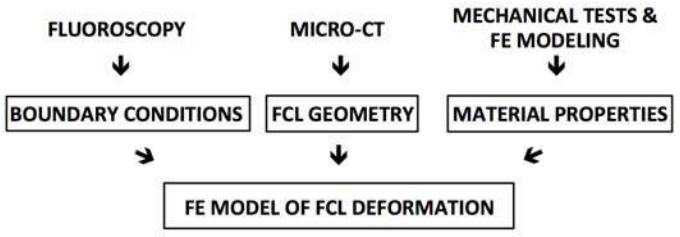

Figure 1. Finite element (FE) model construction

METHODS

Geometry Acquisition through micro-CT: A visually healthy cadaveric L3-L4 facet joint capsule was resected from the motion

Copyright 2016 The Organizing Committee for the 2016 Summer Biomechanics, Bioengineering and Biotransport Conference

segment and cleared of all posterior musculature. Radiopaque paint coated the dorsal surface to define the boundary of the radiolucent ligament. The coated facet capsule was imaged with a voxel resolution of 21.5μm, and the resulting image stack was segmented manually, smoothed, meshed and imported into the FEBio[6] software suite.

Material Model Specifications: Three material definitions were used in the model: two rigid bodies, one for each articular facet, and the material defining the ligament. The FCL material was defined with an eight-parameter hyperelastic strain-energy density function; a neo-Hookean ground matrix with two embedded fiber families described by an exponential strain-energy density function and a 2D von Mises distribution of fiber orientation. The parameters of this function were optimized[5] to minimize the error between the model output and experimental data of L4-L5 FCLs (n=6) under planar equibiaxial tension. The material was warped to the curved geometry of the current model (Figure 2) based on the direction (increasing, planar, decreasing) of the normal vectors of the surface elements.

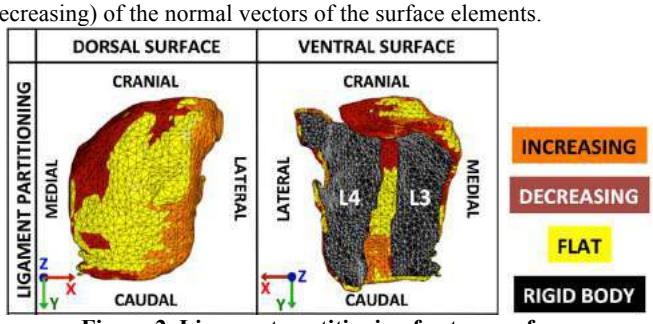

Figure 2. Ligament partitioning for two surfaces

Joint Kinematics in Spinal Motion: Kinematics of L3-L4 motion segments were extracted from left sagittal fluoroscopic data of ten healthy individuals during voluntary flexion. Further information regarding the fluoroscopic data sets and extraction of vertebral motion is given in Nagel et al.[5] The left lateral kinematics obtained were mirrored to mimic the kinematics of a right facet joint. The analysis of the sagittal plane fluoroscopy data yielded subject-specific kinematics (n=10) to be used as inputs to the FE model of a right FCL. Each of the ten sets of kinematics was used to simulate vertebral motion. Vertebral motion was prescribed to the rigid materials that define the L3 and L4 articular facets. Global coordinates are defined in Figure 2 with right lateral as +X, caudal as +Y, and ventral as +Z. In general, flexion induced ventral displacement ($+u_Z$), cranial displacement ($-u_Y$), and sagittal plane rotation ($-R_X$) for both vertebrae, which L3 rotating and displacing farther than L4 as the joint flexed. The ligament surface remained free, and during the simulation it deformed in response to displacements applied to the rigid articular facets.

RESULTS

Surface Strains during Simulated Flexion: Surface strains of the ventral and dorsal FCL (Figure 3) were generated by the relative rotation and displacement of the articular facets. The net effect of prescribed motion created compression in the Y direction, and the Z direction thickened because motion in this direction was unconstrained. In-plane shear (XY) strains were pronounced, and resulted from the caudal displacement of the L3 articular facet (black arrow) and fixed motion in the X direction. Dorsal surface strains were more diffuse than ventral surface strains because of a larger ligamentous area and greater deformability.

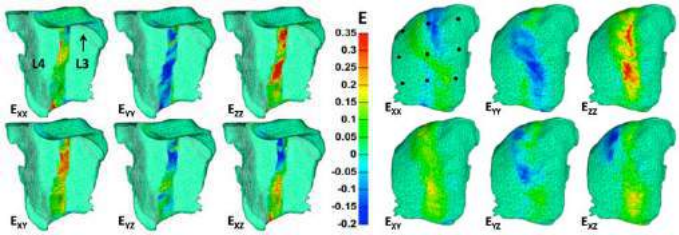

Figure 3. Ventral and dorsal surface strains

Surface Stresses during Simulated Flexion: Surface Cauchy stresses on the ventral and dorsal FCL (Figure 4) are generated by the structure and in-plane orientation of the embedded fiber families. Stresses are lower on the dorsal aspect compared to the ventral aspect because the fibers had more area to reorganize before acquiring tension. The two fiber families of the model were prescribed in the XY plane, and accordingly, σ_{XX}, σ_{YY}, and σ_{XY} exhibited the largest tensile stresses. Furthermore, through-thickness stresses, perpendicular to the fiber alignment, were smaller in value, but not negligible.

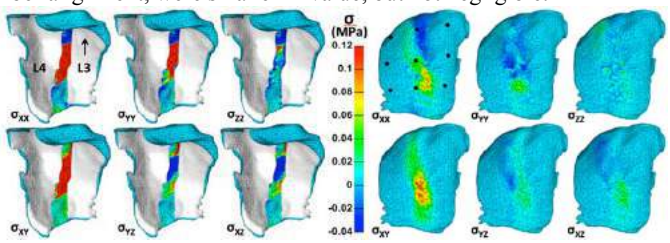

Figure 4. Ventral and dorsal surface Cauchy stresses (MPa)

DISCUSSION

A realistic finite element model of the lumbar facet joint during flexion elucidated the importance-of in-plane (XY) and through-plane (YZ, XZ) shear deformations on the ventral and dorsal surfaces of the FCL. The largest tensile strains were a function of unconstrained motion and the largest tensile stresses were a function of fiber direction. Human cervical, thoracic, and lumbar FCLs are densely innervated with proprioceptive, nociceptive, and mechanoreceptive nerve endings[7]. Based on our findings, the middle-body of the FCL would be a logical location for position- and pain-sensing nerve endings because of the large and readily occurring stress and strain values, at least in the case of lumbar flexion. Also, based on innervation and large deformations involved, the FCL may be sensitive to degenerative changes (osteophyte and enthesophyte formation[8]) and may play a role in low back pain. These ideas must be investigated further, both experimentally and theoretically, but our results suggest possible avenues for further exploration of lumbar FCL mechanobiology. Clearly, any such study should consider shear as well as tensile deformation.

This study considered only flexural motion, only one FCL of one (L3-L4) motion segment, and there was no accounting for individual variations in vertebral anatomy or ligament properties, except for our use of spine kinematic data from 10 different subjects.

In summary, we found large in-plane and through-plane shear deformations are in finite element simulations of a lumbar facet capsular ligament during flexion. Simulation results could inform future studies of lumbar FCL mechanobiology during realistic spinal flexion.

ACKNOWLEDGMENTS

This work was supported by NIH/NIAMS T32 AR050938 Musculoskeletal Training Grant and NIH grant U01-EB016638. We also thank the Minnesota Supercomputing Institute, the University of Minnesota Anatomy Bequest Program, and Dr. Alex Fok.

REFERENCES

[1] Kozanek, M et al., *Spine*, 2009. [2] Ianuzzi, A et al., *Spine J*, 2004. [3] Claeson, AA et al., *Ann Biomed Eng*., 2015. [4] Nagel, TM et al., *Eur Spine J*, 2014. [5] Claeson, AA et al., *submitted*. [6] Maas, SA et al., *J Biomech Eng*., 2012. [7] McLain, RF. *Spine*, 1998. [8] Boszczyk, BM. *J Neurosurg*, 2003.

Copyright 2016 The Organizing Committee for the 2016 Summer Biomechanics, Bioengineering and Biotransport Conference

SB^{3}C2016
Summer Biomechanics, Bioengineering and Biotransport Conference
June 29 –July 2, National Harbor, MD, USA
SB^{3}C2016-23

RECRUITING AND SUPPORTING TRANSFER STUDENTS TO MECHANICAL ENGINEERING PROGRAM AT UMBC

L Zhu (1), D. Arola (2), A Spence, (1), C Romero-Talamas (1), C Eggleton (1)

(1) Department of Mechanical Engineering
University of Maryland Baltimore County
Baltimore, Maryland, USA

(2) Department of Materials Science & Engineering
University of Washington
Seattle, Washington, USA

INTRODUCTION

Community colleges serve more than 46% of all professional engineers.[1] The recent economic recession has forced many students to start their college life in community colleges due to its affordability. Among the roughly 300,000 undergraduate students in Maryland in 2013, 49% of them enrolled in community colleges.[2] And of the community college students enrolled in Fall 2012, 37% were underrepresented minorities (6% Hispanics and 31% African American). In the six targeted community colleges in Maryland, 5.3% of the 9006 graduates were Hispanics and 22.8% are African American.[2] Therefore, regional community colleges serve a larger pool of underrepresented minorities to draw upon as transfer students to 4 year universities.

Despite substantial progress in the past several years, the percentage of Hispanic students in Mechanical Engineering (ME) at the University of Maryland Baltimore County (UMBC) is currently 3.7%, As indicated, regional community colleges have the essential student pool to diversify the ME Program at UMBC. Drawing from this pool could help produce engineers that are more reflective of the state's demographics. Offering scholarships to those students is a significant incentive to continue pursuit of a 4-year college degree. Therefore, having continuous improvement in the collaboration between UMBC and local community colleges will be essential. Identifying the most effective means to communicate educational opportunities at UMBC to local community college students is necessary to further bolster the transfer process.

Attracting talented students is only the first step. Keeping them engaged will be the next. Although UMBC has an existing student support structure and program elements currently in place, active mentoring of minority students is needed to address the diverse issues facing them in engineering fields. At the national level, among 20 engineering disciplines, ME ranks 16th in the enrollment of female students. That is unfortunate as ME currently has the largest undergraduate enrollment overall.[3] Numerous studies have demonstrated the success of interdisciplinary fields such as biomedical engineering in attracting talented female/minority students. One of the reasons may be related to the social relevancy of those curricula and how engineering can help humanity.

UMBC was awarded an NSF S-STEM grant in 2010 and a renewal in 2014. This paper is intended to report our approaches and educational outcomes of the Mechanical Engineering S-STEM Scholarship Program in the past six years at UMBC, with emphasis on recruiting and supporting transfer students that were attracted from local community colleges in the State of Maryland.

METHODS

We have decided not to rely on traditional recruitment methods to increase the rate of transfer students to UMBC. Our goal is to enhance collaborations with community colleges via the following approaches. We found that there was little interaction between the faculty at UMBC and the faculty and staff members in the local community colleges. Hence, over the past six years we visited community colleges on a regular basis, and also invited community college faculty members and their students to visit our campus. It was found that the major obstacle that students encountered is a lack of information on the transfer process and the responsible contact person on both campuses. Our department has re-designed the departmental website clearly describing the transfer process and requirements. There is at least one faculty member at each community college designated as our contact, and the faculty member can connect the students on their campus with faculty at UMBC. We also send our current S-STEM

Copyright 2016 The Organizing Committee for the 2016 Summer Biomechanics, Bioengineering and Biotransport Conference

scholars back to their community colleges to describe the ME program at UMBC, the S-STEM program, and to share their experiences.

Once the students are awarded an S-STEM scholarship, they are assigned a faculty member as their mentor so that they can have regular meetings with them to discuss their concerns. Since most of our students do not live on campus, we have established program activities for community building, including retreats, holiday parties, a room designated for S-STEM scholars, etc.

The Mechanical Engineering faculty members at UMBC have a strong research emphasis on bioengineering. However, there is a lack of interest in our undergraduate students to engage in research-related activities available in the department. To address this disconnect, we have developed a seminar series consisting of entry-level topics in bioengineering, with support from the S-STEM program. Faculty in the department actively invite outside speakers to give research seminars. Typically, three research seminars are scheduled each year and integrated into the regular Departmental series. We also help our students to locate internship opportunities and internal and external research experiences in research laboratories. In addition, the ME S-STEM Program provides funds to reimburse research expenses to faculty laboratories hosting our scholars, and to support our scholars to attend research conferences to disseminate their results.

RESULTS

In the past six years, we have supported 49 ME undergraduate students with diverse backgrounds, including 17% African Americans, 18% Hispanics, and 18% women, as shown in Figure 1. The connection with local community colleges and proactive recruitment strategy are particularly strong components of the program. Overall, 45% of the scholars are transfers from local community colleges. Among the 49 ME STEM scholars, 0 dropped out of college and only 5 scholars transferred to another major. None of the students who did not get a scholarship renewal are community students. The overall retention rate of our program is 89%, which is substantially higher than that of the control student group (ME department: 40%).

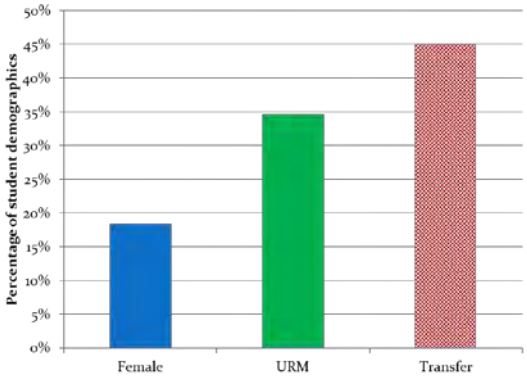

Figure 1: Percentage of underrepresented minority, female, and transfer students in the ME S-STEM program.

The scholars' attendance at all the activities (retreat, seminar, and mentor meeting) ranges from 87% to 95%. We implement regular email notices to students to remind them of various activities sponsored by the program. We have allowed students to make up their missed seminar by attending other research seminars. More than 90% of the students stated that they are satisfied or very satisfied with the research seminars and meetings with their assigned mentors.

Providing research seminars and facilitating internships are also effective. Despite the technical depth in the seminars and that half the scholars are freshmen or sophomores, the undergraduate students have found that the topics are easy to understand. They appreciate the opportunity and have suggested that we invite more researchers from industry/government agencies, and/or researchers who graduated from UMBC. Both suggestions have been implemented by our program. We have hosted 18 seminars in the past six years, among them 7 speakers are female or underrepresented minorities, 6 are UMBC graduates or affiliates, and 4 are from industry or a government agency. One encouraging result is the catalytic effort of the seminar on the undergraduate students. We have found some scholars have attended other research seminars even if it is not required. It is great to see that our scholars have invited their friends to attend the seminars. The scholars had an average of 1.2 internships and/or research experiences over their S-STEM experience; 61% had at least one internship and/or research opportunity.

35 scholars (average GPA at graduation: 3.5/4.0) had completed the BS degree in ME, 25% are pursuing graduate study in an STEM major and 69% are now working in an STEM industry, as shown in Figure 2. The 25% is much higher than the typical 10-15% of regular ME students who pursue graduate schools. We believe that this is partially due to our effort of incorporating research into education. No significant difference in the average GPA is found between scholars who transferred from community colleges and scholars who entered UMBC after they graduated from high school.

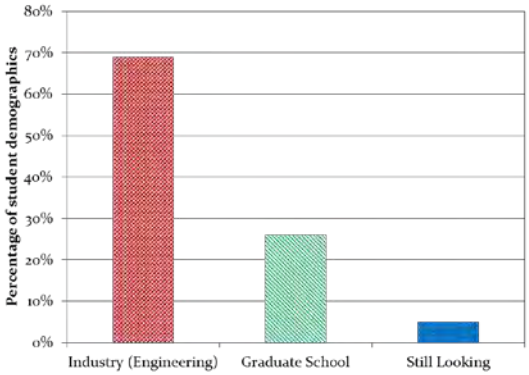

Figure 2. Placements of the 32 scholars who graduated from our program.

In summary, with the support of two NSF S-STEM grants, the UMBC Mechanical Engineering Department has established an S-STEM scholarship program that has supported 49 undergraduate students with diverse backgrounds. It has shown the success of recruiting community college students via implementing our approaches. The program outcomes of more than 80% retention rate and satisfaction rate have been achieved. 94% of the scholars who graduated from our program are either working in industry (69%) or in graduate school (25%). The high graduate school placement may reflect our efforts of incorporating research into education.

ACKNOWLEDGEMENTS

This research was supported by an NSF S-STEM grant DUE-1356440.

REFERENCES

[1] Levine, M., Shartle-Galotto, M. K., and Linhart, C., Report to the Montgomery Community College President. 2006, http://www.montgomerycollege.edu/planning/AMP/MCAPM.pdf
[2] MACC. March 2013, http://www.mdacc.org/publications/fiscal2013.html
[3]. US Department of Education, 2006, http://www.ed.gov/about/inits/ed/competitiveness/strengthening/strengthening.pdf

Copyright 2016 The Organizing Committee for the 2016 Summer Biomechanics, Bioengineering and Biotransport Conference

SB³C2016
Summer Biomechanics, Bioengineering and Biotransport Conference
June 29 –July 2, National Harbor, MD, USA
SB³C2016-24

VALIDATION OF IMAGE-ASSISTED MODELING APPROACH TO DESIGN HEATING PROTOCOLS IN MAGNETIC NANOPARTICLE HYPERTHERMIA

A M LeBrun (1), T Joglekar (2) C Bieberich (2), R Ma(1), L Zhu (1)

(1) Department of Mechanical Engineering
University of Maryland Baltimore County
Baltimore, Maryland, USA

(2) Department of Biology
University of Maryland Baltimore County
Baltimore, Maryland, USA

INTRODUCTION

Hyperthermia treatment using physical modalities has attracted a lot of attention in the past decades in cancer treatment. The amount of thermal damage to tumor cells is usually affected by the extent of temperature elevations in the tissue and its exposure time [1, 2]. Among all the thermal ablation techniques, magnetic nanoparticles have gained prominence in the last two decades for use in hyperthermia. Designing an optimal heating protocol to cause irreversible thermal damage to tumors while preserving the surrounding healthy tissue, relies on a wide range of heating parameters such as magnetic field strength, frequency, local concentration of nanoparticles and heating duration. The designed heating protocol also depends on the specific cell line, growth stage, and their surrounding tissue environment. Evaluating a designed heating protocol via using magnetic nanoparticles in animal models is the first step to test its efficacy in a biological environment, leading to validation of the theoretical modeling approach for future optimal designs in clinical settings.

In a previous study by our group [3], a heating protocol is designed to determine the heating time to induce complete thermal damage to PC3 tumors implanted on mice, with minimal collateral damage. The objectives of this study are to evaluate thermal damage by measuring tumor shrinkage over eight weeks and performing histological analyses after magnetic nanoparticle hyperthermia, and to evaluate whether the designed treatment protocol induces adequate thermal damage to tumors.

METHODS

22 Balb/c Nu/Nu female mice were used (25 ± 2.6 g) to test the efficacy of the designed heating protocol. Once the tumors reached a minimum diameter of 1 cm, the mouse was weighed and anesthetized using sodium pentobarbital (40 mg/kg, i.p.). The mouse was then placed on a water-jacketed heating pad to maintain the normal core body temperature. Some tumors were injected with 0.1 cc of the commercially available ferrofluid used previously at a rate of 3 μL/min, while other tumors were used as the control. After the injection, the needle was removed and the mouse was placed inside a two-turn water-cooled coil with the water-jacketed heating pad. The alternating magnetic field induced by the coil has a magnetic strength of approximately 5 kA/m and a frequency of 190 kHz [3]. The heating duration is based on our designed protocol.

Three groups (five tumors in each group) were tested for the tumor shrinkage: 25 minutes of heating (the Arrhenius integral $\Omega \geq 4$), 12 minutes of heating ($\Omega \geq 1$), and the control group with no ferrofluid injection but subjected to the alternating magnetic field for 25 minutes. After the heating experiment, the mouse was allowed to fully recover before it was then returned to the animal facility at UMBC, The tumor growth/shrinkage was measured daily over the next eight weeks using a Vernier caliper. Histological studies were performed via H&E staining following the heating experiment, and observation of thermal damage under light microscope. The protocol has been approved by the IACUC at UMBC.

RESULTS

The shrinkages/growths of the tumors in all three groups are list in Table 1. The tumors in the control group without heating almost doubts their size within 10 days, and at the end of the observation period of eight weeks, the volume increases more than 700%. In the undertreated group (with the Arrhenius integral $\Omega = 1$) the tumors shrink 85% within ten days, suggesting some positive outcomes in damaging tumor cells. Unfortunately, later the previously

Copyright 2016 The Organizing Committee for the 2016 Summer Biomechanics, Bioengineering and Biotransport Conference

disappearing tumors start to grow back. In the $\Omega = 4$ heating group (25 minute heating, fully treated), all tumors disappeared completely after the 3rd day, and the treatment site maintained the disappearance for the eight week observation period.

Table 1: Average tumor volumes in the three groups over the eight-week observation period.

	Day 0	Day 3	Day 10	Day 56
Control	307 mm^3	379 mm^3	532 mm^3	2618 mm^3
Undertreated	690 mm^3	384 mm^3	115 mm^3	1080 mm^3
Fully treated	655 mm^3	0	0	0

We further evaluate whether heating inhibits tumor growth, illustrated in Figure 1. The tumor growth rate in the control group is slower at the very beginning, then accelerating later with an average growth rate of approximately 67 mm^3/day. The growth rates in the undertreated group in weeks 3 – 8, when the tumors grow back, are noticed as approximately 35 mm^3/day. The results suggest that heating inhibits tumor growth, although that the thermal dosage in the undertreated group is not sufficient to obliterate the entire tumors. When one compares the shrinkage rates between the undertreated group and the fully treated group, it is evident that high thermal dosage in the $\Omega = 4$ group increases the shrinkage rate by 200%, therefore, accelerating the tumor shrinkage after heating.

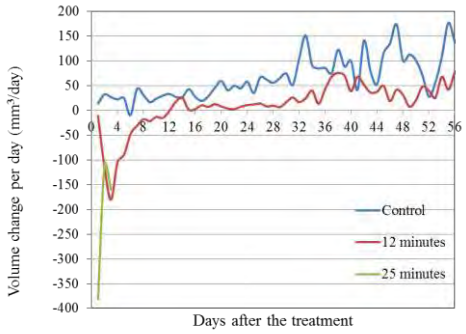

Figure 1. Tumor growth rates (mm^3/day) in the three groups over the observation duration of 56 days.

The top panel in Figure 2 provides the typical H&E staining of PC3 tumors with neither nanoparticle injection nor heating at the 25× magnification. The lower right hand side shows the tumor periphery noted by the light pink region of muscle. It is evident that there are necrotic regions in the untreated tumor. Under normal conditions, the presence of necrotic region in PC3 tumors is not uncommon, and it is most likely due to poor blood supply to those regions and/or the aggressive growing nature of the particular tumor. The typical H&E staining of PC3 tumor tissue in the sham group injected with ferrofluid, however, without heating is shown in the bottom panel in Figure 2. The PC3 tissue in the sham group still resembles normal PC3 cells. The reddish black area in the stain is a small deposition of the ferrofluid. It is shown that the presence of nanoparticles from the direct intratumoral injection does not seem to result in any additional cell necrosis to the tumor region. The tumor periphery still resembles normal PC3 cells with healthy fat and muscle layers.

Figure 3 shows the stained images of a tumor slice under 25× and 100× magnification after the tumor was heated for 25 minutes. It can be clearly seen that there are several areas of tumor cells containing no discernable nuclei and areas of cells detaching from their surrounding cells. The nuclei are significantly darker suggesting that the cells are pyknotic, a condensing of the nuclei that is pre-apoptotic or necrotic [4]. Cells in the immediate vicinity of the ferrofluid deposition region (dark red in the center of the image) are indiscernible as the cell structures have been completely destroyed and they appear "liquefied," much different than the region surrounding the ferrofluid in Figure 2. The muscle surrounding the periphery of the tumor also shows severe thermal damage due to heating, suggesting that heat penetration to the periphery regions is prevalent.

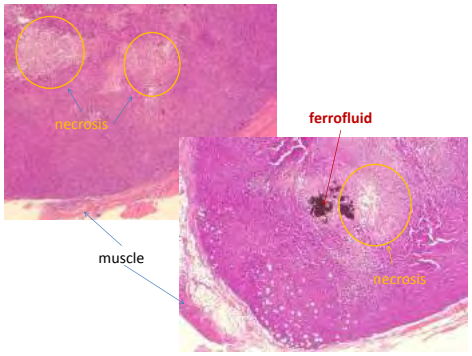

Figure 2. H&E staining images of tumors at 25× magnification for the control group without heating (top panel) and the sham group (bottom panel). The yellow circle shows the necrotic region.

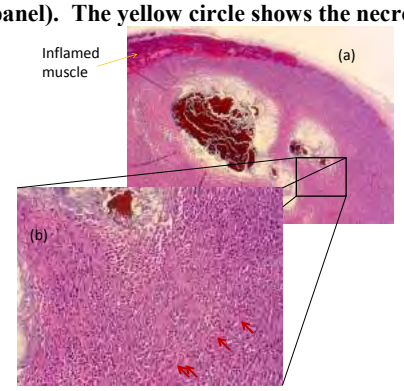

Figure 3. Histologic images of immediately resected PC3 tumors after 25 minutes of heating (a) 25× and (b) 100× magnification.

In summary, *in vivo* experiments have been performed to induce temperature elevations in implanted PC3 tumors in mice using magnetic nanoparticles following the same heating protocol designed in our theoretical study. It has been shown that the 25 minutes heating on tumor tissue is effective to cause irreversible thermal damage to PC3 tumors, while lowering the heating time results in an initial shrinkage, however, later tumor recurrence. On the other hand, the tumors in the control group without heating show approximately an increase of more than 700% in volume over the eight week observation period. In addition, results of the histological analysis suggest vast regions of apoptotic and necrotic cells, consistent with the regions of significant temperature elevations.

ACKNOWLEDGEMENTS

This research was supported by an NSF research grant CBET-1335958.

REFERENCES

1. Dewhirst MW, Viglianti BL, Lora-Michiels M, Hanson M, Hoopes PJ. *International Journal of Hyperthermia* 2003; **19**(3): 267-294.
2. Bai JF, Liu P, Xu LX. *IEEE Transactions on Biomedical Engineering* 2014; **61**(5); 1497-1505.
3. Lee, A. S., LeBrun, A., Ma, R., and Zhu, L. Summer Biomechanics, Bioengineering, & Biotransport Conference, Snowbird, Utah, June 2015, paper number #15-A-300-SB3C.
4. Kumar V, Abbas AK, Fausto N, Mitchell R. *Robbins basic pathology* 8th ed. Philadelphia, PA: Elsevier/Saunders; 2007.

Copyright 2016 The Organizing Committee for the 2016 Summer Biomechanics, Bioengineering and Biotransport Conference

SB³C2016
Summer Biomechanics, Bioengineering and Biotransport Conference
June 29 –July 2, National Harbor, MD, USA
SB³C2016-25

QUANTIFICATION OF BIVENTRICULAR MYOCARDIAL STRAINS FROM CINE MAGNETIC RESONANCE IMAGES OF PULMONARY HYPERTENSIVE PATIENTS USING HYPERELASTIC WARPING

Ce Xi
Michigan State University
Lansing, MI, USA

Xiaodan Zhao
National Heart Center
Singapore

Liang Zhong
National Heart Center
Singapore

Martin Genet
École Polytechnique
Paris, France

Lik Chuan Lee
Michigan State University
Lansing, MI, USA

INTRODUCTION

Pulmonary hypertension (PH) is a disease resulting from a restricted flow in the pulmonary arterial circulatory system that is reflected by an increase in pulmonary vascular resistance. Without treatment, the disease can quickly lead to decompensated right heart failure and death. The quantification of RV function is essential for effective clinical management of PH patients. Recent studies have demonstrated that RV strains are associated with the right ventricular (RV) function, and is a potentially useful prognostic marker for the progression of disease in PH patients. Compared to the left ventricle (LV) that can be approximated by a truncated ellipsoid, *in vivo* quantitative assessment of strains in the RV is challenging because of its complex geometry and thin wall. Here, we overcome these challenges by the application of a hyperelastic warping technique [1] for quantifying biventricular regional strains in PH patients using regular cine magnetic resonance (MR) images.

METHODS

Cine MR images were obtained for the entire cardiac cycle in 5 PH patients (1 male and 4 females) and 5 age- and gender-matched healthy adults. Ventricular pressure was also measured in each PH patient by right heart catheterization.

Hyperelastic warping, an image registration technique, was applied to these images to compute the myocardial strains throughout the cardiac cycle. Briefly, a finite element (FE) representation of the biventricular unit in the template image (T) was constructed and then deformed into alignment with the corresponding object target image (S) during the registration process (**Fig. 1a**). The forces responsible for the registration deformation were derived from the differences in image intensity between the template image and the target images at different time points in a cardiac cycle. The deformation map is denoted by $\varphi(\mathbf{X}) = \mathbf{x} = \mathbf{X} + \mathbf{u}(\mathbf{X})$, where $\mathbf{x}$ are the current (deformed) coordinates corresponding to $\mathbf{X}$, and $\mathbf{u}(\mathbf{X})$ is the displacement field. The deformation gradient is given as:

$$\mathbf{F}(\mathbf{X}) = \frac{\partial \varphi(\mathbf{X})}{\partial \mathbf{X}} \ . \tag{1}$$

The local change in volume is directly related to $\mathbf{F}$ through the Jacobian ($J = \det \mathbf{F}$), and the right Cauchy-Green deformation tensor is defined as $\mathbf{C} = \mathbf{F}^{\mathbf{T}}\mathbf{F}$.

The registration of MR images can be posed as the minimization of an energy functional E that consists of two terms. This can be defined with respect to the current configuration as:

$$E = \int_{\beta} W(\mathbf{X}, \mathbf{C}) \frac{dv}{J} - \int_{\beta} U(T(\mathbf{X}), S(\varphi)) \frac{dv}{J}, \tag{2}$$

Here, W is a prescribed hyperelastic strain energy density function that provides regularization and/or some type of constraint on the deformation map, while U is an image energy density functional that depends on the image data in the template and target images and takes the form:

$$U(\mathbf{X}, \varphi) = \frac{\lambda}{2}(T(\mathbf{X}) - S(\varphi))^2, \tag{3}$$

where λ is a penalty parameter that enforces the alignment of the template model to the target image.

In Eq. (2), the first variation of W yields the standard weak form of the momentum equations for nonlinear solid mechanics, whereas the first variation of the functional U with respect to $\varphi(\mathbf{X})$ in direction η produces the image-based force term:

$$DU(\mathbf{X}, \varphi) \cdot \eta = -\lambda[(T(\mathbf{X}) - S(\varphi)) \frac{\partial S(\varphi)}{\partial \varphi} \cdot \eta]. \tag{4}$$

This term drives the deformation of the template based on the pointwise difference in the image intensities and the gradient of the target intensity evaluated at material points associated with the template. A Neo-Hookean potential with unit stiffness was used for W and the penalty parameter λ was adjusted until the deformation field converges.

The local circumferential direction was assigned using Laplace-Dirichlet Rule-Based (LDRB) algorithm (**Fig. 1b**), which ensures that the circumferential orientation varies smoothly and continuously throughout the entire myocardium [2]. The biventricular unit was divided into 3 material regions, namely, the left ventricular free wall (LVFW), the right ventricular free wall (RVFW) and the septum (**Fig. 1c**). The average circumferential strain was computed in each region.

Copyright 2016 The Organizing Committee for the 2016 Summer Biomechanics, Bioengineering and Biotransport Conference

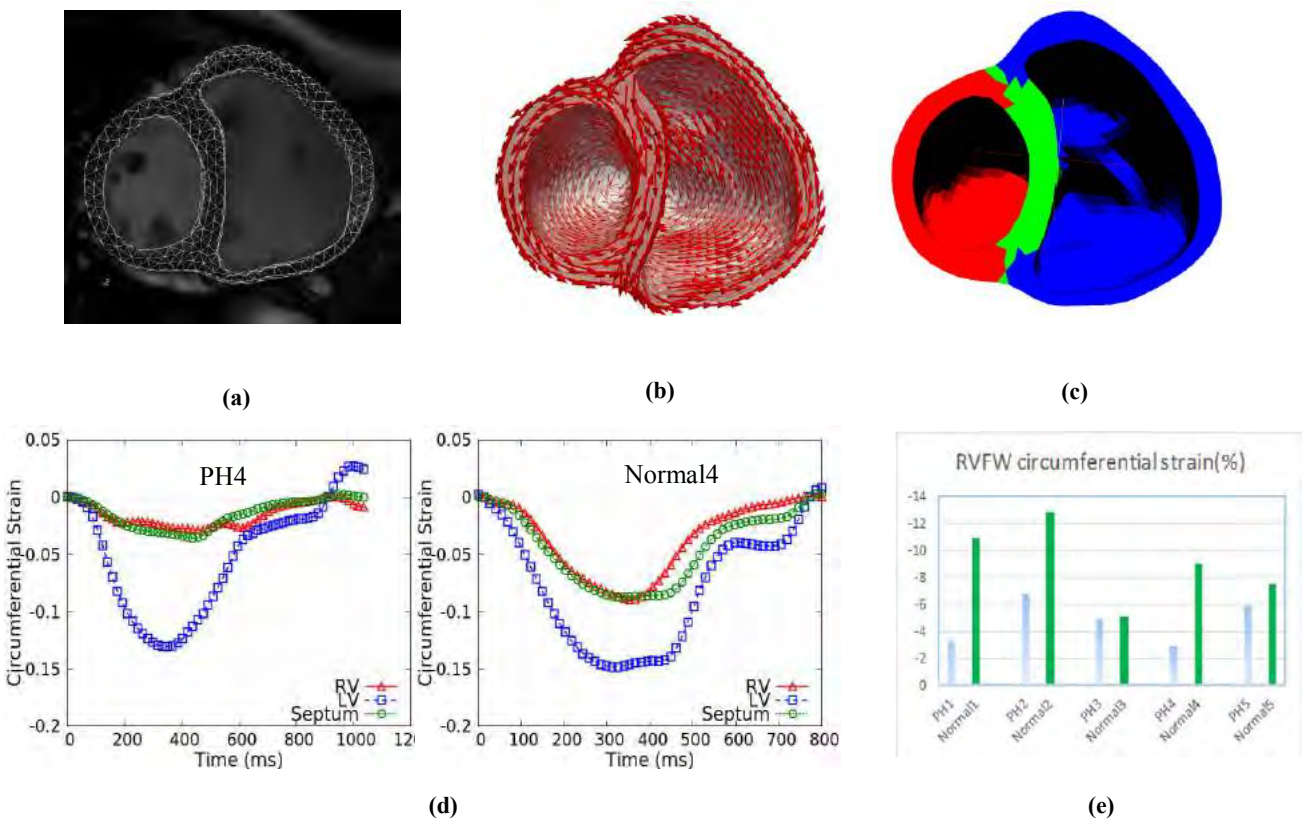

Figure 1. **(a)**: Segmentation of the biventricular unit in the template MR images. **(b)**: circumferential orientation in the biventricular unit. **(c)**: material regions (red: LVFW, green: Septum and blue: RVFW). **(d)**: regional circumferential strain vs. time over a cardiac cycle in a PH patient and a normal subject. **(e)**: comparison of RVFW circumferential strains between PH patients and healthy controls.

RESULTS

The average age of the PH patients was 50 ± 13 years. Peak RV systolic pressure was significantly higher in the PH patients (62.4 ± 9.0 mmHg) than normal range values (around 28 mmHg), and the RV end-systolic volumes were substantially higher in the PH patients than those in normal controls (128 ± 59 mL vs. 53 ± 16 mL). Global systolic circumferential strains of RVFW, LVFW and septum were quantified for the patients and controls (**Fig. 1d** and **Fig. 1e**). The results showed that all patients had a significantly depressed peak RVFW circumferential strain as compared to controls (-3.9 ± 1.8% (PH) vs -9.0 ± 3.0% (Normal), P=0.012), However, the LVFW and septum peak systolic circumferential strain predictions of PH patients were not statistically different from those of healthy controls (LVFW:-13.4 ± 5.0% (PH) vs -14.2 ± 2.4% (Normal), P=0.753; septum:-5.0 ± 3.0% (PH) vs -7.2 ± 2.0% (Normal), P =0.107).

DISCUSSION

In this study, we have used a deformable image registration technique known as hyperelastic warping to quantify the global circumferential strain of the biventricular unit constructed from MR images in patients with PH. Our findings show that the PH patients have significantly reduced RV peak systolic circumferential strains as compared with healthy controls. This result is consistent with a previous study, in which strain-encoded MR imaging is adopted to analyze RV peak regional strains in PH patients [3]. In their study, there are also significant reductions of the RV peak circumferential strain at the basal level in PH patients (-13.0 ± 4.8% vs. -20.4 ± 4.6%), which is qualitatively consistent with our findings. This may indicate that reduced RV circumferential strain could serve as a potentially useful indicator for the evaluation of global RV dysfunction in PH patients.

Besides RV strain, our study also shows that the LV and septum circumferential strains are reduced in PH patients. This finding is consistent with a previous study [4], which shows that patients with PH have significantly reduced septum circumferential strains (-17.6 ± 5.8% vs. -23.1 ± 4.87%; P<0.001) and LV circumferential strains (-11.9 ± 5.0% vs. -14.5 ± 6.1%; P<0.002). However, our finding shows that the differences of septum and LV circumferential strains between PH patients and normal controls are not statistically significant.

We are currently calculating the RV longitudinal strain in these patients so as to obtain a more comprehensive evaluation of the RV contractile dysfunction associated with PH.

REFERENCES

[1] Veress, A. I., et al. "A comparison of hyperelastic warping of PET images with tagged MRI for the analysis of cardiac deformation." *Journal of Biomedical Imaging* 2013 (2013): 9.

[2] Bayer, J. D., et al. "A novel rule-based algorithm for assigning myocardial fiber orientation to computational heart models." *Annals of biomedical engineering* 40.10 (2012): 2243-2254.

[3] Oyama-Manabe, N., et al. "The strain-encoded (SENC) MR imaging for detection of global right ventricular dysfunction in pulmonary hypertension." *The international journal of cardiovascular imaging* 29.2 (2013): 371-378.

[4] Puwanant, S., et al. "Ventricular geometry, strain, and rotational mechanics in pulmonary hypertension." *Circulation* 121.2 (2010): 259-266.

Copyright 2016 The Organizing Committee for the 2016 Summer Biomechanics, Bioengineering and Biotransport Conference

SB³C2016
Summer Biomechanics, Bioengineering and Biotransport Conference
June 29 –July 2, National Harbor, MD, USA
SB³C2016-27

IMAGE-BASED COMPUTATIONAL MODELING OF THE VENTRICULAR MECHANICS IN PATIENTS WITH PULMONARY HYPERTENSION

Ce Xi
Michigan State University
Lansing, MI, USA

Xiaodan Zhao
National Heart Center
Singapore

Liang Zhong
National Heart Center
Singapore

Martin Genet
École Polytechnique
Paris, France

Lik Chuan Lee
Michigan State University
Lansing, MI, USA

INTRODUCTION

Pulmonary hypertension (PH) is associated with an elevated pressure in the pulmonary arterial system that can be due to idiopathic reasons or caused by other conditions (e.g., presence of ventricular septal defect). Prolonged PH produces functional, structural and geometrical changes in the right ventricle (RV). Without treatment, PH can quickly lead to decompensated RV failure and death. Currently, the prognosis of PH remains poor with about 15% mortality within 1 year on modern therapy. To the best of our knowledge, there are currently no in vivo studies that determine the impact of PH on the regional ventricular mechanics and mechanical properties in the human heart. To resolve the gap in our current understanding of PH, the overall goal here is to use image-based patient-specific computational modeling to quantify *in vivo* changes in the regional ventricular mechanics and mechanical properties in PH patients.

METHODS

Magnetic resonance (MR) images were obtained from PH patients as well as gender- and age-matched normal human subjects. Ventricular, atrial and artery pressure were measured in PH patients by right heart catheterization. On the other hand, ventricular pressure was estimated for the normal human subjects based on previous studies. Left and right ventricular (LV and RV) volumes were measured at different time frames in a cardiac cycle from the MR images based on the segmentation of the biventricular geometry. These measurements (as well as the pressure estimation for normal human subjects) were used to construct pressure-volume loops of the RV and LV for PH patients and normal controls.

A cardiac electromechanics model [2] was used to quantify the regional ventricular mechanics in a PH patient and a normal subject. Briefly, mechanics in a cardiac cycle was described by a Fung-type passive constitutive model and a cellular-based active stress constitutive model. In this model, the Cauchy stress tensor is given as follows:

$$\boldsymbol{\sigma} = -p\boldsymbol{I} + \frac{1}{det\boldsymbol{F}}\boldsymbol{F}\cdot\frac{dW(\boldsymbol{E};C)}{d\boldsymbol{E}}\cdot\boldsymbol{F^T} + \boldsymbol{\sigma}^a\left(\boldsymbol{s},\lambda_e,\dot{\lambda}_e;T_{ref}\right) \qquad (1)$$

In Eq. (1), W is the Fung-type strain energy function, $\boldsymbol{F}$ is the deformation gradient tensor, $\boldsymbol{E} = \frac{1}{2}(\boldsymbol{F^T F} - \boldsymbol{I})$ is the Green strain tensor, $\boldsymbol{\sigma}^a$ is an active stress tensor that is a function of (i): state variables $\boldsymbol{s}$ describing membrane channels and intracellular ionic concentration, and (ii): elastic myofiber stretch λ_e and rate of stretch $\dot{\lambda}_e$. In this model, the parameters C and T_{ref} are directly associated with the diastolic passive stiffness and ventricular contractility.

The unloaded biventricular finite element (FE) geometries for the PH patient and normal subject were reconstructed from the corresponding MR images at early diastole when the pressures were at the lowest. Pressure measurements in the LV and RV were used to prescribe the boundary conditions in the computational models. These models were divided into 2 distinct material regions, namely, LV (including the septum) and the RV free wall (RVFW) (**Fig. 1a**). Myofiber orientation was prescribed using a Laplace-Dirichlet Rule-Based algorithm [3]. Fiber helix angle with a transmural variation from 60° (endocardium) to -60° (epicardium) was assigned to the biventricular unit (**Fig. 1b**). Ejection phase was simulated by connecting the LV and RV volumes to a 3-parameter Windkessel model.

The parameters C and T_{ref}, as well as the peripheral resistance in the Windkessel model, were adjusted in the LV and RVFW to match the experimentally measured PV loops. Regional ventricular wall stresses and strains were computed for the PH patient and the normal subject. The differences of all quantified variables and parameters (e.g., regional ventricular strain and passive stiffness determined from FE modeling) were compared between the PH patient and normal subject. Regional differences between quantities obtained from LV and RV were also compared in each individual model.

RESULTS

We were able to match the measured PV loops in the RV and LV for the PH patient and normal subject (**Fig. 1c**). In the PH patient, the peak RV pressure was substantially higher than that found in the normal subject (65 mm Hg vs. 20 mmHg). End-diastolic volumes in the PH patient were also comparatively larger (LV: 160 ml vs.105 ml; RV: 275 ml vs. 100 ml). Ejection fractions were lower in the PH patient (LV: 38% vs. 69%; RV: 19% vs. 67%).

Copyright 2016 The Organizing Committee for the 2016 Summer Biomechanics, Bioengineering and Biotransport Conference

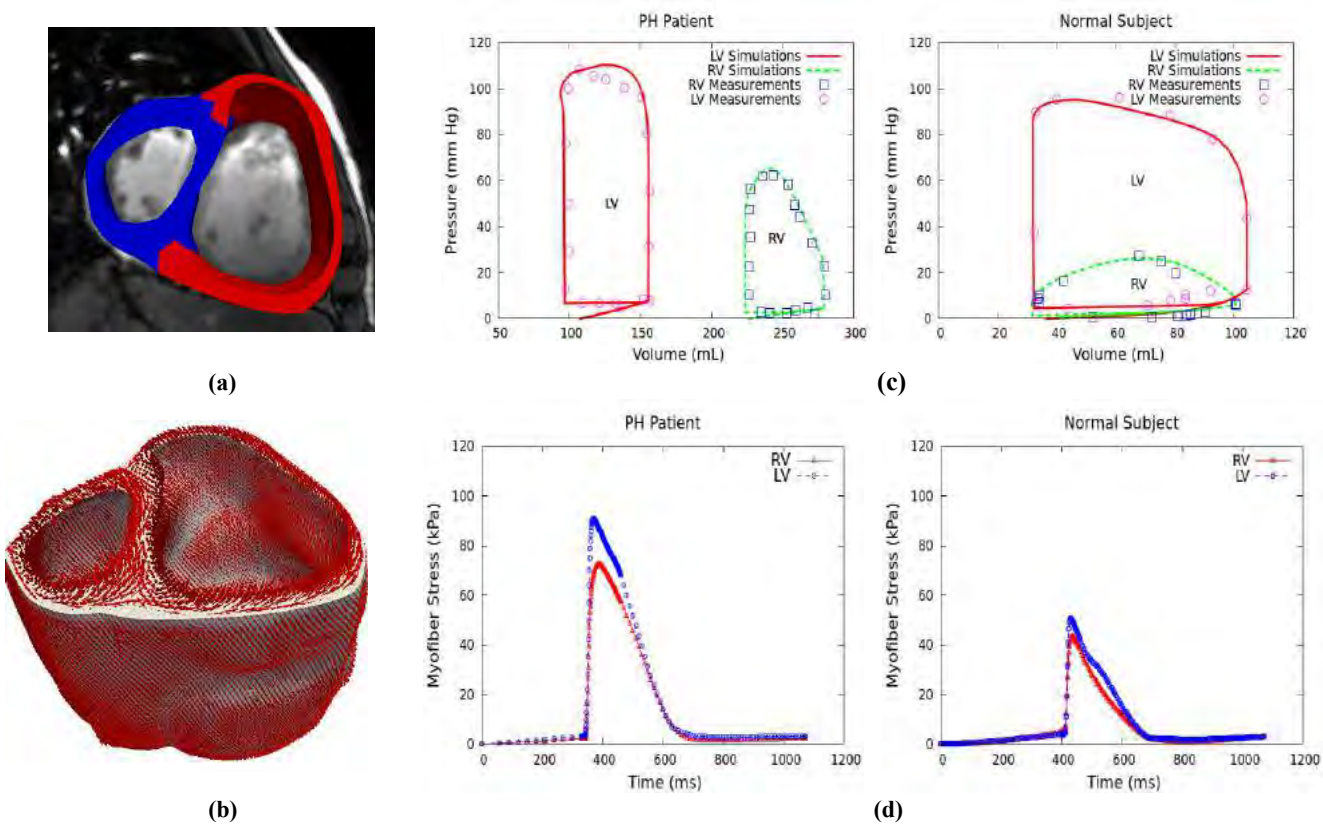

Figure 1. **(a)**: Two material regions in the biventricular unit: LV (blue) and RVFW (red). **(b)**: Myofiber orientation. **(c)**: Pressure-volume loops from experimental measurements and simulation results of a PH patient (left) and a normal subject (right). **(d)**: LV and RV myofiber stress vs. time over a cardiac cycle in the PH patient (left) and the normal subject (right).

To match the PV loops, the diastolic passive stiffness in the PH patient was found to be larger than that in the normal subject. Specifically, compared to the normal subject, the parameter C was found to be ~20 and ~60 times larger at the RVFW and LV in the PH patient, respectively. The RVFW to LV ratio of the parameter C was 1:1 in the PH patient and 3:1 in the normal subject.

On the other hand, the ventricular contractility was higher in the PH patient than in the normal subject. Compared to the normal subject, the value of T_{ref} was about twice as large. The RVFW to LV ratio of T_{ref} was slightly lower in the PH patient (0.43) compared to the normal (0.5). Peripheral resistance (afterload) in the RV was about 4 times higher in the PH patient. By contrast, we found no changes in the peripheral resistance in the LV between the PH patient and the normal subject.

Myofiber stress in the PH patient was significantly higher than that of the normal subject in the entire biventricular region (**Fig. 1d**). Peak myofiber stress in the RVFW and LV of the PH patient was almost 2 times of that in the normal subject (73kPa vs. 43kPa in the RVFW and 91kPa vs. 50kPa in the LV).

DISCUSSION

We have used an image-based cardiac electromechanics model to quantify the regional ventricular mechanics in a PH patient and a normal human subject in this study. Our findings indicate that the diastolic passive stiffness and the ventricular contractility of the PH patient are larger than those in the normal subject in both the LV and RVFW. The RVFW/LV contractility ratio (~ 0.5) is the same in the PH patient and the normal subject.

The increase in RVFW diastolic stiffness is consistent with a previous study [3], which shows that both collagen content and the passive tension of isolated cardiomyocytes from the explanted RV tissue samples of PH patients are increased when compared to those taken from normal controls. In that study, RV diastolic stiffness is also found to be significantly increased in PH patients and closely associated with the disease severity.

Although our finding that the contractility in the RV is increased runs somewhat contrary to the fact that PH is usually associated with severe RV systolic dysfunction, this finding is supported in that same study [3], which shows that the RV end-systolic elastance (a global measure) and the force-generating capacity of isolated RV cardiomyocytes (a local measure) are increased in PH patients compared to normal subjects. This finding is also observed in previous studies on rats. The increase in RVFW contractility is most likely a compensatory mechanism to the increase in afterload (peripheral resistance) in PH patients.

Last, our finding that the LV diastolic passive stiffness and ventricular contractility is also increased in the PH patient, suggests that the disease can affect the left heart as well. We are currently performing the same analysis on more PH patient data.

REFERENCES

[1] Sundnes, J., et al. "Improved discretisation and linearisation of active tension in strongly coupled cardiac electro-mechanics simulations." *Computer methods in biomechanics and biomedical engineering* 17.6 (2014): 604-615.

[2] Bayer, J. D., et al. "A novel rule-based algorithm for assigning myocardial fiber orientation to computational heart models." *Annals of biomedical engineering* 40.10 (2012): 2243-2254.

[3] Rain, S., et al. "Right ventricular diastolic impairment in patients with pulmonary arterial hypertension." *Circulation* 128.18 (2013): 2016-2025.

Copyright 2016 The Organizing Committee for the 2016 Summer Biomechanics, Bioengineering and Biotransport Conference

SB³C2016
Summer Biomechanics, Bioengineering and Biotransport Conference
June 29 –July 2, National Harbor, MD, USA
SB³C2016-28

CAP INFLAMMATION LEADS TO LARGE PLAQUE CAP STRESS DECREASE AND STRAIN INCREASE: MRI-PET/CT-BASED FSI MODELING

Dalin Tang (1,2*), Chun Yang (1,3), Sarayu Huang (4), Venkatesh Mani (4), Zahi A. Fayad (4)

(1) Mathematical Sciences Department
Worcester Polytechnic Institute
Worcester MA 01609, USA

(2) School of Biological Science
and Medical Engineering
Southeast University
Nanjing, China, 210096USA

(3) China Information Tech. Designing
& Consulting Institute Co., Ltd.,
Beijing, 100048, China

(4) Department of Radiology
Translational and molecular imaging institute
New York, USA

INTRODUCTION

Recent studies indicated that plaque rupture may be associated with: a) extreme mechanical stress/strain conditions; b) large lipid-rich necrotic cores; c) thin and weakening fibrous cap; d) cap inflammation; e) intraplaque hemorrhage; f) activities at molecular and cellular level which may be related to plaque rupture; and g) factors from genetic, diet, disease, behavior, chemical, mental stress, work conditions and others people think that may have linkage to plaque progression and rupture [1-5]. Extreme mechanical stress and strain conditions have been identified as a potential risk factor for plaque rupture [3]. However, accuracy of computational in vivo stress/strain calculations is affected by available in vivo image data. While it is believed that inflammation weakens plaque cap and may have considerable impact on cap stress and strain conditions, no single image modality is able to provide vessel geometry, plaque components and inflammation at the same time. Fayad et al and others have been developing multi-modality imaging technology using PET/CT (Positron Emission Tomography/ Computed Tomography) and MRI (magnetic resonance imaging) to identify inflammation in arteries [6,7]. Combining PET/CT with MRI, we are able to obtain plaque morphology with inflammation information on cap surface. This gives us the base for better modeling stress/strain predictions. The goal of this paper is to investigate possible impact of cap inflammation on plaque stress/strain and flow shear stress conditions, with plaque and inflammation data provided by PET/CT combined with MRI.

MRI AND PET/CT DATA ACQUISITION AND FSI MODELS

The data under consideration was acquired as part of a clinical trial imaging patients to assess arterial inflammation within the bilateral carotid arteries and ascending aorta. The 74 year old, male patient with coronary heart disease was imaged with Magnetic Resonance Imaging (MRI) and 18F-fluorodeoxyglucose (18F-FDG) PET/CT (Positron Emission Tomography/Computed Tomography) in separate imaging sessions approximately 12 days apart. For the MRI examination the patient was imaged in a head-first supine position. 2-D multi-contrast (T2-weighted, T1-weighted and proton-density weighted) dark-blood turbo spin-echo images of the bilateral carotids were acquired as part of a longer imaging study. The PET/CT was performed after the patient had fasted overnight, and 120 min after injection of 15mCi of 18F-FDG. A low-dose, non-contrast-enhanced CT scan was used for attenuation correction and anatomical information for the PET scan. The carotid arteries were imaged with a 15 min PET scan of one bed position in 3D mode. The MRI and PET/CT data were segmented and registered for modeling use (see Fig 1 for the registration of MRI with PET/CT) [6,7].

An MRI-PET/CT-based modeling approach is proposed to develop fluid-structure interaction (FSI) models for human carotid plaque assessment and quantify the effect of inflammation on plaque stress/strain conditions. For the 15-slice MRI/PET/CT data set acquired from the above procedures, inflammation was identified for S4-S10. The 3D FSI model was built following established procedures [Tang]. The artery wall was assumed to be hyperelastic, isotropic, incompressible and homogeneous. The nonlinear modified Mooney-Rivlin (M-R) model was used to describe the material properties of the vessel wall [BE38P 19, Tang2004]. Blood flow was assumed to be laminar, Newtonian, viscous and incompressible. Details of the FSI model were given in Tang, et al. [3]. Material stiffness for the fibrous cap was adjusted lower to reflect the cap weakening caused by cap inflammation. Setting stiffness ratio (SR) to be 1.0 for the baseline model, coefficients c_1 and D_1 in the M-R model were multiplied by SR=0.5, 0.25, and 0.1 to make the cap softer. The 3D FSI models were solved by a commercial finite element package ADINA (ADINA R & D, Watertown, MA, USA) using unstructured finite element methods

Copyright 2016 The Organizing Committee for the 2016 Summer Biomechanics, Bioengineering and Biotransport Conference

for both fluid and solid domains. Plaque cap stress, strain and flow shear stress data from all 4 cap stiffness variations corresponding to peak systolic pressure were recorded for analysis.

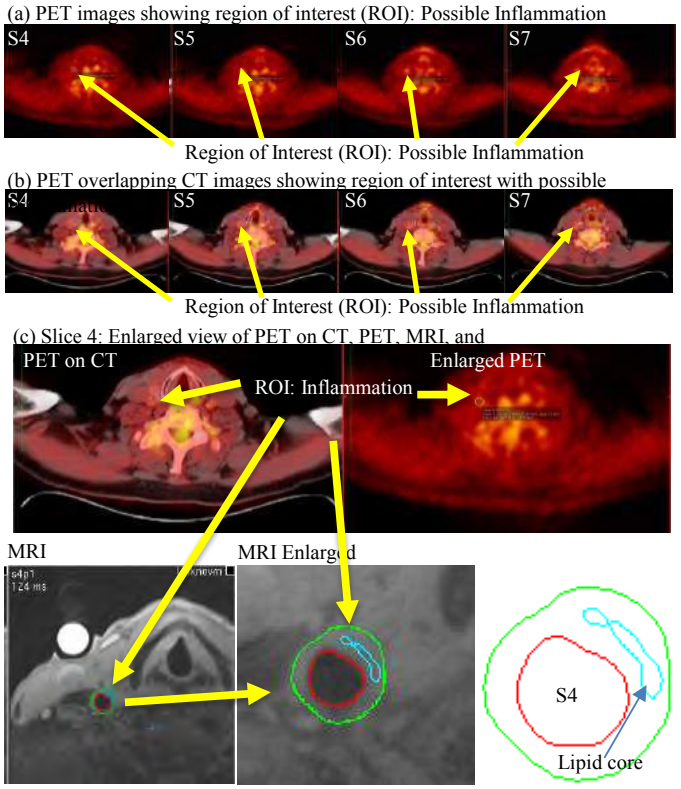

Figure 1. PET and CT images from S4-S7 with lipid-rich necrotic core and enlarged view S4 with MRI showing Region of Interest (ROI) with possible inflammation.

RESULTS

Figure 2 shows selected stress, strain and FSS plots from models with SR=1.0 and 0.1 respectively. Local maximum cap stress value without inflammation (SR=1.0) was 47.19 kPa. Corresponding to SR=0.5, 0.25, and 0.1, the local maximum cap stress values were 34.04, 27.69, and 18.95 kPa, respectively. The local maximum cap stress value reduced 60% from SR=1.0 to SR=0.1. Checking each slice, for example, looking at a S6, the local maximum cap stress value reduced from 62.79 kPa (SR=1.0 case) to 17.22 kPa (SR=0.1), a 72% decrease. On the other hand, local maximum stress values on S4 and S8 were much limited (<20%).

Our results also indicated that cap inflammation led to higher cap strain values. Cap strain variations caused by inflammation were much greater. Figure 2 (b) shows that the local maximum cap strain value without inflammation (SR=1.0) was 0.1065. Corresponding to SR=0.5, 0.25, and 0.1, the local maximum cap strain values were 0.1730, 0.2388 and 0.3178, which was 62.4%, 124%, and 195% higher than that of SR=1.0, respectively. The local maximum cap stress value reduced 60% from SR=1.0 to SR=0.1. Checking slice by slice, from S6, the local maximum cap strain value increased from 0.1392 with SR=1.0 to 0.4372, a 214% increase. Strain values on S4 and S8 increased less from SR=1.0 to SR=0.1. But the increases were still around 100%.

Cap inflammation has small impact on flow shear stress changes. Figure 4 (c) shows that flow shear stress (FSS) on a sagittal cut had an 8% increase from SR=1.0 model to SR=0.1 model. FSS mean values on the cap nodes changed from slice to slice, indication flow pattern changes. All FSS values stayed in a narrow range within their SR=1.0 values.

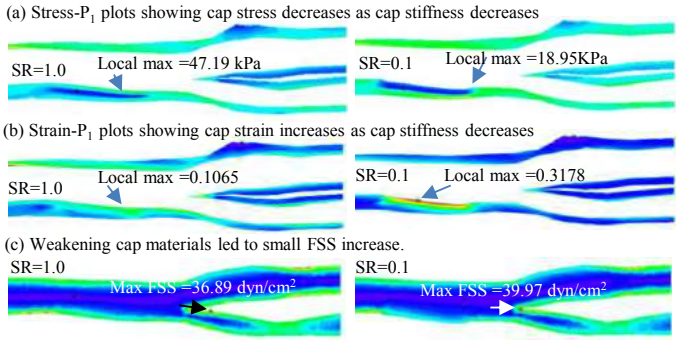

Figure 2. Stress, strain and flow shear stress plots from SR=1.0 and SR=0.1 models showing weakening cap materials led to decreased cap stress, increased cap strain, and small FSS changes.

DISCUSSION AND CONCLUSION

Significance of cap inflammation: huge impact on cap strain, reduced cap stress. Most investigations for atherosclerosis plaque rupture and vulnerability have been focused on flow shear stress and extreme cap stress conditions. Our findings in this paper indicated that inflammation may lead to lower cap stress and higher strain. That suggests our future effort should be focused more on cap strain conditions. Indeed, while stress is determined by both material stiffness and strain, strain is more an intrinsic condition of the plaque. Weakened plaque cap becomes softer and its lower stiffness reduces cap stress level. On the other hand, the increased strain may serve as a critical vulnerability indication. Needless to say, mechanical testing of plaque cap materials to find out its material strength would be a task for researchers in this field to provide threshold values to serve as base for model predictions.

Impact of plaque morphology and components. It is clear from this sample that the impact of inflammation on stress/strain is heavily dependent on the location and size of the plaque component, tissue type, and vessel material properties. This paper serves as a motivation to demonstrate the impact of inflammation on plaque mechanical conditions and the importance of further investigations.

Acknowledgement: This work was supported in part by NIH grants NIH/NIBIB R01 EB004759, NIH/NHLBI R01 HL071021, and National Sciences Foundation of China grant 81571691.

REFERENCES

1. Fuster V et al., The Vulnerable Atherosclerotic Plaque: Understanding, Identification, and Modification, AHA Monograph series, Futura Publishing, Armonk NY. 1998.
2. Fuster V et al., Circulation 82, SII-47-59. 1990.
3. Tang D. Kam RD et al., J Biomech. 47(4):834-46, 2014.
4. Friedman MH et al., Ann. Biomed Eng 38(3), 1178-1187. 2010.
5. Fleg et al., 2012. JACC Cardio Imaging. 5(9):941-55. 2012.
6. Fayad ZA et al., Am Heart J. 2011 Aug;162(2):214-221.e2.
7. Calcagno et al., Eur J Nucl Med Mol Imaging. 2013 Dec;40(12):1884-93. doi: 10.1007/s00259-013-2518-4.

Copyright 2016 The Organizing Committee for the 2016 Summer Biomechanics, Bioengineering and Biotransport Conference

SB³C2016
Summer Biomechanics, Bioengineering and Biotransport Conference
June 29 –July 2, National Harbor, MD, USA
SB³C2016-29

USING PATIENT-SPECIFIC MRI-BASED RIGHT VENTRICLE MODELS WITH DIFFERENT ZERO-LOAD DIASTOLE AND SYSTOLE GEOMETRIES FOR BETTER STRESS AND STRAIN CALCULATIONS AND POST-SURGERY OUTCOME PREDICTION

Dalin Tang (1,2*), Pedro J. del Nido (3), Chun Yang (1,4), Heng Zuo (1), Xueying Huang (1,5), Rahul H. Rathod (6), Alexander Tang (6), Zheyang Wu (1), Kristen L. Billiar (7), Tal Geva (5)

(1) Math Sciences Department
Worcester Polytechnic Institute
Worcester MA 01609, USA

(2) School of Biological Science and Medical Engineering
Southeast University
Nanjing, China, 210096USA

(3) Dept. of Cardiac Surgery,
Children's Hospital Boston,
Harvard Medical School,
Boston, MA 02115 USA

(4) China Information Tech. Designing & Consulting Institute Co., Ltd., Beijing, 100048, China

(5) School of Mathematical Sciences
Xiamen University
Xiamen, 361005, China

(6) Dept of Cardiology,
Children's Hospital
Harvard Medical School
Boston, MA 02115 USA

(7) Department of Biomedical Engineering,
Worcester Polytechnic Institute
Worcester, MA 01609, USA

INTRODUCTION

Accurate ventricle stress and strain calculations are of fundamental importance for cardiovascular research and investigations. From mechanical point of view, zero-stress ventricle geometry information is required for its stress/strain calculations. Ventricle modeling, especially ventricle active contraction modeling based on in vivo data, is extremely challenging because of complex ventricle geometry, dynamic heart motion and active contraction and relaxation where the reference geometry (zero-stress geometry) changes constantly in a cardiac cycle. Peskin pioneered heart modeling effort and simulated blood flow in a pumping heart with his immersed boundary method [1]. McCulloch et al. and Hunter et al. conducted comprehensive investigations for cardiac mechanics, and their papers and the Continuity package provide excellent review of the field [2,3]. In our previous papers, patient-specific MRI-based computational right ventricle/left ventricle (RV/LV) models (called 1G model thereafter) with fluid-structure interactions were introduced to assess outcomes of various RV reconstruction techniques with different scar tissue trimming and patch sizes [4-6].

Active contraction is caused by sarcomere shortening which leads to increased strain and stress. Due to sarcomere shortening, zero-load ventricle systole geometry is smaller than its zero-load diastole geometry. A new modeling approach using two different zero-load geometries (diastole and systole) was introduced in this paper (called 2G model thereafter) to properly model active contraction and relaxation and provide ventricle diastole and systole stress and strain calculations based on their respective zero-load geometries. The new morphological and stress/strain results from the new 2G models were used to identify potential predictors for post pulmonary valve replacement (PVR) outcome for Tetralogy of Fallot (TOF) patients.

MRI DATA ACQUISITION, MODELS AND METHODS

Cardiac MRI (CMR) data were acquired from 16 TOF patients before and after PVR surgery with patients' consent obtained. Data acquisition procedures were described in [7]. The patients were divided into Group 1 (n=8) with better outcome and Group 2 (n=8) with worst outcome based on their change in RV EF from pre- to post-PVR. RV EF was chosen due to its strong association with adverse clinical outcomes in patients with repaired TOF. Three-dimensional RV/LV geometry and computational mesh were constructed following the procedures described in [3]. An iterative pre-shrink process was applied to the in vivo minimum volume ventricular geometry to obtain the two zero-load geometries so that when in vivo pressure was applied, the ventricle would regain its in vivo geometry. As patient-specific fiber orientation data was not available, our 2-layer RV/LV models were constructed using fiber orientation angles given in [3,8].

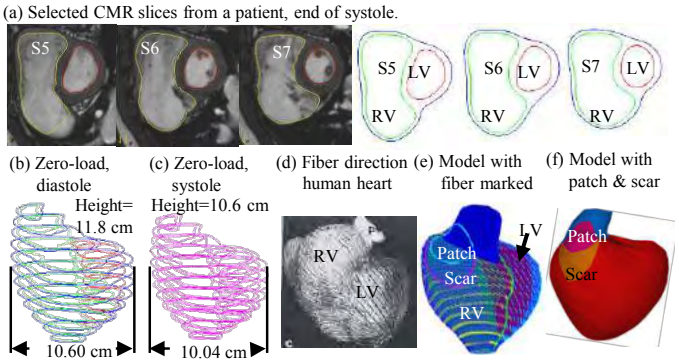

Figure 1: Selected CMR images of a TOF patient, 2-zero-load geometries, and the reconstructed 3D geometry with patch.

Copyright 2016 The Organizing Committee for the 2016 Summer Biomechanics, Bioengineering and Biotransport Conference

The anisotropic RV/LV computational models were constructed for the 16 patients and the models were solved by ADINA (ADINA R&D, Watertown, MA, USA) using unstructured finite elements and the Newton-Raphson iteration method. For each 3D CMR data set (9-14 slices), ventricular wall thickness (WT), circumferential curvature (C-cur), longitudinal curvature (L-cur), and stress/strain were calculated at all nodal points (100 points/slice). The "slice" values of those parameters were obtained by taking averages of those quantities over the 100 points for each slice and saved for analysis. Pairwise T-test and Linear Mixed Effect (LME) model were used to determine if the differences from the new and old models were statistically significant with the dependence of the pair-wise observations the clustering effects taking into consideration [6]. For group comparisons, continuous variables (RV volumes, WT, C-cur, L-cur, and stress and strain values) were summarized as mean ± SD and compared between the outcome groups using an unpaired Student t-test. Associations between pre-PVR RV parameters and the outcome (change in RV EF) were explored using Pearson correlation analysis. Logistic regression analysis was used to identify pre-PVR parameters that best predicted the primary outcome—RV EF response to PVR. The sensitivity and specificity of these parameters and their area under the receiver operating characteristic curve (AUC) were determined.

RESULTS

Our results included the following: a) differences between the 1G and 2G models; b) differences in morphological and mechanical risk parameters between the two patient groups using 2G models; c) post PVR outcome prediction results using the 2G models.

The overall results from the 16 patients indicated that peak-systolic (begin-systole from our model) stress from the 2G model was 28% higher than that from the 1G model (108.4 kPa vs. 84.7 kPa). The begin-diastole stress values from the two models were about the same (7.17 kPa vs. 7.32 kPa, 2% difference). Peak-systolic (begin-systole from our model) strain from the 2G model was 39.6% higher than that from the 1G model (0.606 vs. 0.434). The begin-diastole strain value from the 2G model was 23% lower than that from 1G model (0.048 vs. 0.062).

Comparisons of RV WT, C-curvature, L-curvature, and stress and strain values between Group 1 and Group 2 at begin-filling, end-filling, begin-systole, and end-systole indicated that RV stress is the only parameter with significant difference between the two groups. At begin-systole (maximal volume and pressure), mean RV stress of Group 2 was 57.4% higher than that of Group 1 (130.1 ±60.7 vs. 82.7±38.8 kPa; P=0.0042). Differences at other three time points were similar.

The logistic regression method was applied to all 255 possible combinations of the 8 candidate predictors to calculate their prediction accuracy for patient's group category. The 8 predictors are WT, C-cur, L-cur, RV volume, and stress at begin-systole, plus three stress variations from one time point to another: StressE-D is the difference between begin-systole and end-diastole stresses; StressE-F is the difference between begin-systole and end-systole stresses; and StressE-C is the difference between begin-systole and begin-diastole stresses. Strain was not taken as a predictor because it had no statistically significant difference between the two groups. Table 1 shows the 6 best combinations (out of 255) of RV parameters that correctly assigned patients to their ultimate outcome group and the prediction accuracy and ranking of the single predictors. Pre-PVR RV stress at begin-systole was the best single predictor among the 8 individual parameters with an area under the ROC curve of 0.782. The best combination of parameters was C-cur + RV volume + StressE-F with an area under the ROC curve of 0.855.

DISCUSSION AND CONCLUSION

Accurate stress/strain calculation is of fundamental importance for many cardiovascular research where mechanical forces play a role. The 2G modeling approach is setting up the right stage for diastole and systole stress/strain calculations using proper zero-load geometries. It should be noted that direct measurements of stress, strain, and sarcomere length are either extremely difficult or even impossible. Data from the literature or from ex vivo experiments (such as fiber orientation, sarcomere length contraction rate) have to be used to complete the computational models.

The current surgical approach to address chronic pulmonary regurgitation includes pulmonary valve replacement/insertion (PVR) with or without RV remodeling. However, while most patients demonstrate a variable degree of decrease in RV size, many do not experience an improvement in RV function and some show a decline after PVR [7]. It has remained unclear why some patients had experienced an improvement in RV EF whereas in others RV function had deteriorated. Our modeling and identified predictors provided a potential approach to identify patients and factors for possible surgical outcome improvements.

Table 1. Prediction AUC values of parameters for outcome group prediction by the logistic regression method.

Parameter	Prob. CutOff	AUC	AUC Ave	95% Conf. Interval		Rank
C-Cur+V+ StressE-F	0.996	0.854	0.855	0.843	0.861	1
C-Cur+V+ StressE-D	0.999	0.830	0.853	0.847	0.861	2
C-Cur+L-Cur+ V+ StressE-F	0.032	0.857	0.841	0.835	0.859	3
C-Cur+V+ StressE-C	0.949	0.864	0.841	0.836	0.845	4
C-Cur+V+ StressE	0.998	0.854	0.837	0.832	0.844	5
C-Cur+StressE-F +V+StressE-D	0.023	0.865	0.816	0.811	0.841	6
Stress E	0.446	0.782	0.769	0.762	0.771	25
Stress E-D	0.445	0.765	0.756	0.749	0.759	32
Stress E-F	0.504	0.721	0.747	0.742	0.757	37
Stress E-C	0.378	0.749	0.747	0.732	0.753	38
WT	0.552	0.571	0.526	0.522	0.532	243
L-Cur	0.352	0.534	0.525	0.520	0.528	244
V	0.379	0.502	0.504	0.497	0.510	247
C-Cur	0.859	0.410	0.399	0.394	0.413	255

Acknowledgement: This research was supported in part by NIH-1R01-HL 089269 (del Nido, Tang, Geva), NIH–HL63095 (del Nido) and NIH 5P50HL074734 (Geva, del Nido), and in part by National Sciences Foundation of China 81571691 and 11171030.

REFERENCES

1. Peskin CS. J Com Phys. 25:220-252, 1977.
2. McCulloch AD et al., Critical Rev. in Biomed Eng, 1992; 20(5,6): 427-449.
3. Hunter PJ et al., Annu Rev Biomed Eng., 2003; 5:147-77.
4. Tang D et al., J. of Biomech. Engineering, 2008;130(4) 041010.
5. Tang D et al., Computers & Structures, 89, 1059-1068, 2011.
6. Tang D et al., J Thorac Cardiovasc Surg. 2014 147(1):537-8.
7. Geva T et al., Circulation. 2010 Sep 14;122(11 Suppl):S201-8.
8. Sanchez-Quintana D et al., Heart, 1996;76:280-286.

Copyright 2016 The Organizing Committee for the 2016 Summer Biomechanics, Bioengineering and Biotransport Conference

SB^{3}C2016
Summer Biomechanics, Bioengineering and Biotransport Conference
June 29 –July 2, National Harbor, MD, USA
SB^{3}C2016-30

MULTISCALE REGRESSION MODELING IN MOUSE SUPRASPINATUS TENDONS REVEALS REGIONAL CONTRIBUTION OF DYNAMIC PROCESSES TO STRUCTURE-FUNCTION RELATIONSHIPS

Brianne K. Connizzo (1), Sheila M. Adams (2), Thomas H. Adams (2), Abbas F. Jawad (3), David E. Birk (2), Louis J. Soslowsky (1)

(1) McKay Orthopaedic Research Laboratory
University of Pennsylvania
Philadelphia, PA, USA

(2) Department of Molecular Pharmacology & Physiology
University of South Florida
Tampa, FL, USA

(3) Department of Pediatrics, Perelman School of Medicine
University of Pennsylvania and the Children's Hospital of Philadelphia
Philadelphia, PA, USA

INTRODUCTION

To enable transmission of force from muscle to bone, tendon exhibits nonlinear, anisotropic, viscoelastic and dynamic properties. This mechanical function is modulated by *dynamic processes* that occur at the micro- and nanoscale during loading, specifically fiber uncrimping, fiber re-alignment, fibril deformation and fibril sliding. These mechanisms are thought to reduce strain on individual fibrils during the initial response to load and to prevent irreversible damage. The contribution of these dynamic processes to the mechanical response to load is thought to be dependent on region (insertion site versus midsubstance), alluding to the significance of extracellular matrix composition and structure in these processes. This matrix, comprised predominantly of collagen type I, is organized in a hierarchical manner spanning from the single collagen fibril to full tendon [1]. In addition to collagen I, the extracellular matrix contains quantitatively minor collagens and proteoglycans with glycosaminoglycans (GAGs). These elements all play a role in tendon mechanical function.

Despite previous studies [2-5], current explanations of load sharing are insufficient, suggesting that the mechanical behavior of tendons cannot be explained solely by composition and structure. Recent advances have allowed for the measurement of dynamic parameters, but only a limited number of studies have investigated the role of dynamic processes in structure-function relationships. Therefore, the purpose of this study was to investigate the role of composition, structure, and the dynamic response to load in predicting tendon mechanical properties using a multi-level statistical regression analysis mimicking native hierarchical collagen structure.

METHODS

Data analyzed in this study was gathered in a recent series of experiments [6, 7] measuring the multi-scale composition, structure, and mechanical response of mature supraspinatus tendons from wild type, collagen V heterozygous and tendon/ligament-specific collagen V null mice. The statistical analysis was "blind" to mouse genotype, allowing for the hypotheses to be tested by determining how variances in predictors affect mechanical properties, regardless of how those variances were achieved. Due to the destructive nature of many of the assays performed, it was not possible to obtain values for every parameter from a single specimen. Therefore, imputation was performed on the data set using the fully conditional specification method with 10 iterations for five imputations [8].

Summary statistics of all variables were examined to ensure that assumptions for linear regression were met. This study consisted of three sets of defined variables: (1) mechanical properties, (2) dynamic processes (fiber re-alignment & crimp, fibril deformation & sliding), and (3) composition/structure (cell morphology, fibril morphology, initial d-period and variance, extracellular matrix composition). Pearson correlation coefficients were first used to determine univariate relationships between predictor variables with significance at $p<0.05$. Multiple linear regression models were then used to quantify the relationships: (Regression A) between mechanical properties and dynamic processes, and (Regression B) between composition/structure and dynamic processes. A series of stepwise regression models using least-square estimation with forward elimination were used to predict these relationships, where variables were included in the model if they improved the model via an F test with significance set at $p<0.05$.

RESULTS

At the insertion site, glycosaminoglycan (GAG) content was positively correlated with total collagen (COL) content and negatively correlated with pyridinoline crosslinks (PYD) (not shown). COL was negatively correlated with PYD and positively correlated with fibril

Copyright 2016 The Organizing Committee for the 2016 Summer Biomechanics, Bioengineering and Biotransport Conference

density. Fibril density was also negatively correlated with PYD. At the midsubstance, fibril diameter and fibril density were negatively correlated.

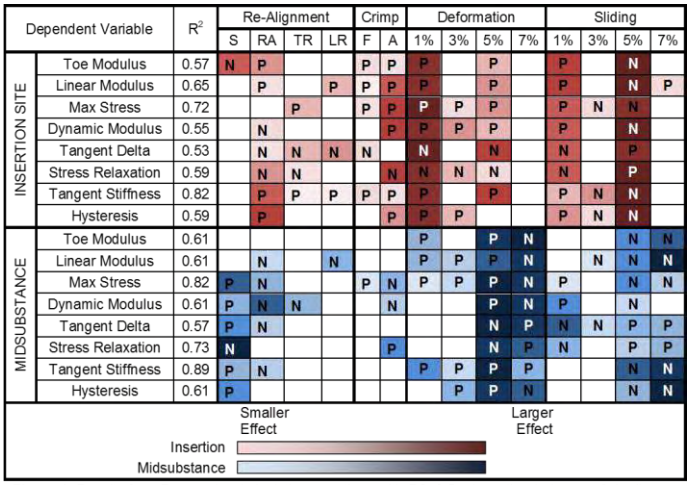

Figure 1. Results from Regression A depicting equations with R2>0.5, where the darkness of shading represents the importance of the contribution of each predictor. Note: S = strain required to re-align, RA = amount of re-alignment, TR = toe region re-alignment, LR = linear region re-alignment, F = crimp frequency, A = crimp amplitude; P = positive predictor, N = negative predictor.

Dynamic parameters were strong predictors of mechanical properties, with R^2 values reaching as high as 0.89 (Fig. 1). Tangent stiffness was the strongest predicted mechanical parameter in both regions. At the insertion site, mechanical parameters were well predicted by linear combinations of all four dynamic parameters, with fibril sliding and deformation making the largest contributions to the models. Fibril deformation at 1% and 5% applied strain were strong positive predictors of mechanics while deformation at 7% applied strain was not predictive. In contrast, the midsubstance mechanical parameters were best predicted by fibril deformation, with sliding and re-alignment playing more minor roles. Fibril deformation from 1-5% applied strain was a positive predictor of mechanics while deformation at 7% applied strain was a negative predictor. Finally, fibril sliding was a positive predictor at 1% applied strain and a negative predictor at higher strain levels in both regions.

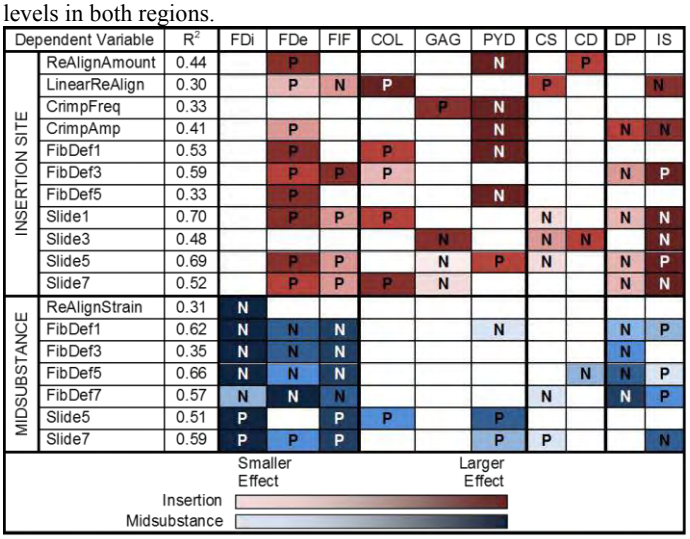

Figure 2. Results from Regression B depicting equations with $R^2 > 0.3$, where the darkness of shading represents the importance of the contribution of each predictor. *Note:* FDi = fibril diameter, FDe = fibril density, FIF = fibril irregularity, CS = cell shape, CD = cell density, DP = intial d-period, IS = initial variance of d-period; P = positive predictor, N = negative predictor.

Dynamic properties were moderately predicted by parameters of composition and structure, with R^2 values reaching 0.70 (Fig. 2). Deformation and sliding were the best predicted parameters, while re-alignment and crimp were only moderately predicted. Many parameters at the insertion site were strongly predicted by pyridinoline crosslinks content, fibril density, and initial d-period variance. Pyridinoline content was a negative predictor of re-alignment, crimp and deformation, but a positive predictor of sliding. Fibril density was a positive predictor of all dynamic processes. Initial d-period variance was a negative predictor of re-alignment and sliding. At the midsubstance, the strongest predictors of dynamic properties were fibril morphology (diameter, density, irregularity) and initial d-period length and variance. Fibril diameter and density were negative predictors of deformation and positive predictors of sliding. Initial d-period variance was a positive predictor of re-alignment, crimp, and deformation and a negative predictor of sliding. Initial d-period was a positive predictor of sliding and a negative predictor of deformation.

DISCUSSION

Mechanical properties were strongly predicted by dynamic processes, and the contribution of each process was location-dependent. The mechanical properties of the insertion site were predicted by all dynamic processes. Given that the insertion site experiences the highest strains [9], it likely utilizes re-alignment, uncrimping, and sliding in order to delay the onset of direct deformation to the fibrils/fibers. Due to the increased organization and structure at the midsubstance, this region of the tissue likely responds primarily through deformation of the fibrils and fibers themselves.

Dynamic processes were only moderately predicted by structure and composition. While increased crosslink density is thought to increase mechanical properties [10, 11], our models suggest that such an increase would reduce the dynamic responses. Since increased crosslink density may also increase the brittleness of collagen fibrils [12], this could result in early damage. Fibril diameter and density were strong predictors of dynamic function at the midsubstance, often both in the same direction, which is in contrast to results in univariate correlations. However, deformation was predicted negatively and sliding was predicted positively by both parameters, suggesting that they are negatively correlated to balance these two dynamic responses.

In conclusion, the mechanical properties at the midsubstance of the tendon are controlled primarily by fibril structure via fibril deformation and sliding. Conversely, mechanical function at the insertion site is more complicated, as it is controlled by many other important parameters via all four dynamic mechanisms. Overall, this study presents a strong foundation on which to design future experimental and modeling efforts in order to fully understand the complex structure-function relationships present in tendon.

ACKNOWLEDGEMENTS

This study was supported by NIH/NIAMS (T32-AR007132, AR044745, AR065995) and the Penn Center for Musculoskeletal Disorders (NIH, P30 AR050950).

REFERENCES

[1]Birk DE, et al. Dev Dyn. 202:229-43, 1995. [2]Ansorge HL, et al. J Biomech. 45:1288-92, 2012. [3]Freedman BR, et al. J Orthop Res. 2015. [4]Chan BP, et al. J Orthop Res. 16:597-603, 1998. [5]Haut RC, et al. J Biomech. 25:163-73, 1992. [6]Connizzo BK, et al. Royal Society Interface Focus. 2015. [7]Connizzo BK, et al. In Review at Journal of Orthopaedic Research. 2015. [8]White IR, et al. Stat Med. 30:377-99, 2011. [9]Shaw HM, et al. Scand J Med Sci Sports. 17:303-15, 2007. [10]Ng KW, et al. Cell Tissue Bank. 14:21-32, 2013. [11]Alfredo Uquillas J, et al. J Mech Behav Biomed Mater. 15:176-89, 2012. [12]Buehler MJ. J Mech Behav Biomed Mater. 1:59-67, 2008.

Copyright 2016 The Organizing Committee for the 2016 Summer Biomechanics, Bioengineering and Biotransport Conference

SB³C2016
Summer Biomechanics, Bioengineering and Biotransport Conference
June 29 –July 2, National Harbor, MD, USA
SB³C2016-31

CHEMICALLY CONJUGATED GROWTH FACTORS ON ELECTOSPUN BIOMIMETIC SCAFFOLDS ENHANCE CELL ADHESION AND PROLIFERATION

Hannah M. Pauly (1), Ketul C. Popat (1,2), Nicholas J. Dunne (3,4), Daniel J. Kelly (5) Tammy L. Haut Donahue (1,2)

(1) School of Biomedical Engineering
Colorado State University
Fort Collins, CO, USA

(2) Department of Mechanical Engineering
Colorado State University
Fort Collins, CO, USA

(3) School of Mechanical and Aerospace Engineering
Queen's University of Belfast
Belfast, United Kingdom

(4) School of Mechanical and Manufacturing Engineering
Dublin City University
Dublin, Ireland

(5) Trinity Centre for Bioengineering
Trinity College, Dublin
Dublin, Ireland

INTRODUCTION

The field of tissue engineering aims to combine scaffolds, cells, and biological cues to create viable replacements for damaged biological tissue. Tendons and ligaments are an area of focus for tissue engineering research due the high incidence of injury and limited capacity for healing [1]. Surgical techniques to repair damaged tendons and ligaments are often inadequate at restoring function which further motivates the development a tissue engineered replacement [2].

Electrospinning is a technique that creates a non-woven mat of polymer nanofibers [3]. Modification of the electrospinning process can result in fibers that are aligned in a single direction, thus mimicking the anisotropy of collagen fibers found in tendons and ligaments [4]. A major drawback of conventional flat electrospun scaffolds is their failure to recapitulate the complex hierarchical structure of native tendons and ligaments.

Growth factors are often integrated into polymer scaffolds to encourage cell proliferation and differentiation. Connective tissue growth factor (CTGF) and basic fibroblastic growth factor (bFGF) have been shown to encourage fibroblastic differentiation of stem cells, as evidenced by cell proliferation, gene expression changes and increased matrix deposition [5,6]. Growth factors present some practical challenges including rapid inactivation and a short half-life in plasma [7]. Chemical conjugation of growth factors to polymer surfaces creates functionalized nanofiber scaffolds with attenuated growth factor release and a prolonged influence on cell behavior [8].

Our research group has developed a technique to create cylindrical bundles of aligned nanofibers that mimic the hierarchical structure of tendons and ligaments. Aligned nanofiber bundles have a modulus of ~50 MPa and a yield stress of ~20 MPa at 50% strain [9]. The goal of this work was to assess the influence of two chemically conjugated growth factors on the adhesion, proliferation and morphology of adipose derived stem cells grown on novel biomimetic aligned electrospun nanofiber scaffolds.

METHODS

Flat sheets of aligned nanofibers were fabricated using a 10% w/v solution of polycaprolactone that was prepared in a 3:1 v/v mixture of chloroform and methanol. The collector surface was a rotating aluminum drum located 10 cm from the needle tip and rotating with a linear velocity of approximately 12 m/s. Nanofibers were collected for 15 minutes resulting in a sheet approximately 20 µm thick. Sheets were then rolled to create cylindrical bundles of nanofibers approximately 0.5 mm in diameter and 175 mm length, with nanofibers aligned along the longitudinal axis (Figure 1). For further experiments nanofiber bundles were cut to 20 mm in length.

Either CTGF or bFGF were covalently conjugated to the nanofibers via a multi-step technique. First scaffolds were incubated in a 5% v/v aqueous solution of polyallylamine with simultaneous ultraviolet radiation for 25 minutes. Next scaffolds were incubated on a shaker plate in a solution of N-succinimidyl-3-maleimidoproprionate and N,N-dimethylformamide for 1 hour. Finally, the scaffolds were incubated in a 50 ng/mL solution of the designated growth factor for two hours. Between subsequent steps the scaffolds were rinsed to ensure no residual chemicals remained within the scaffold structure. Growth factor conjugation efficiency was assessed using X-ray photoelectron spectroscopy (XPS) conducted after each subsequent modification step to assess the accumulation of nitrogen.

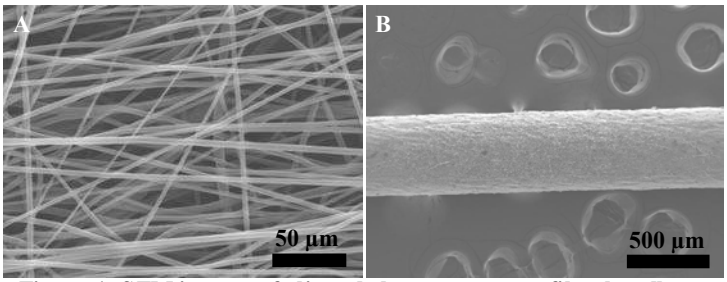

Figure 1: SEM images of aligned electrospun nanofiber bundles at (A) 20x and (B) 1000x magnification.

Copyright 2016 The Organizing Committee for the 2016 Summer Biomechanics, Bioengineering and Biotransport Conference

After growth factor conjugation, scaffolds were sterilized using 70% ethanol and 30 minutes of exposure to ultraviolet light. Human adipose derived stem cells at passage 4 were seeded on scaffolds at a density of 10,000 cells/cm^2. Morphology and spatial organization of cells on seeded scaffolds were assed using scanning electron microscopy (SEM) after 1, 4, and 7 days of culture. Cell viability was measured at the same time points using a commercially available CellTiter Blue assay. Additionally cells were stained with 5-Chloromethylfluourescein Diacetate (CMFDA – live cells), rhodamine-phalloidin (actin – cytoskeleton), and 4'6-diamidino-2-phenylindole (DAPI – nucleus) to assess cell adhesion and proliferation.

RESULTS

After each conjugation step the relative percentage of nitrogen in the scaffold increased, indicating successful conjugation (Table 1). High resolution N1S scans were also taken and the results indicated an increase in the percentage level of nitrogen on the surface.

Table 1: Relative percentage of elemental nitrogen after subsequent modification steps.

	Nitrogen Composition
Unmodified	0%
After amine modification	1.5%
After maleimide modification	2.3%
After CTGF modification	3.5%
After bFGF modification	3.7%

Live cell counts based on fluorescence imaging showed the number of cells significantly increased over time in culture (Figure 2A) for all scaffolds. A culture period of 7 days for the presence of conjugated growth factors was required to significantly increase the number of cells on scaffolds compared to controls ($p<0.05$). The CellTiter Blue assay indicated that there were no cytotoxic effects for any scaffolds (Figure 2B). At days 4 and 7 the metabolic activity of cells on CTGF or bFGF scaffolds was significantly greater than the metabolic activity of cells on control scaffolds. At day 4 the metabolic activity of cells on CTGF scaffolds was significantly greater than that of cells on bFGF scaffolds; however no differences were seen between the two growth factor groups at days 1 and 7. SEM images showed that cells adhered, spread, and colonized on all scaffolds (Figure 3A). Additionally cells appeared to elongate along the direction of the nanofibers (along the longitudinal axis of the scaffolds) for all groups. Similarly by day 7 immunofluorescence images showed elongated cells covering the surfaces of all nanofiber bundle scaffolds (Figure 3B).

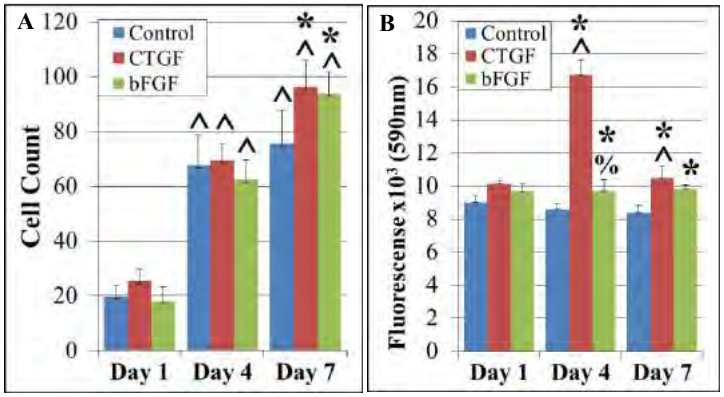

Figure 2: (A) Counts of cell nuclei. (B) Metabolic activity. * indicates significantly different from control. % indicates significantly different from CTGF. ^ indicates significantly different from previous time point ($p<0.05$).

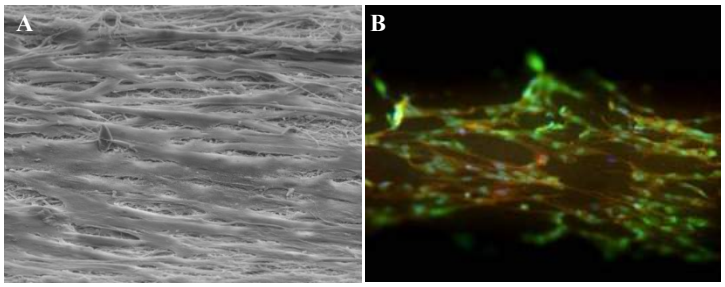

Figure 3: (A) SEM and (B) immunofluorescence images of cells on nanofiber bundles conjugated with CTGF after 7 days of growth.

DISCUSSION

Chemical modification of polycaprolactone can be reliably assessed using XPS. During the conjugation procedure the polymer nanofibers are first modified with amines, and correspondingly an increase in nitrogen is evident on the XPS spectra. Next maleimide linkers are conjugated to the surfaces, resulting in a further increase in amount of nitrogen. Finally, when either bFGF or CTGF are conjugated to the maleimide linkers the nitrogen percentage continues to increase. Since XPS is a depth sensitive technique the observed relative changes in composition indicates successful conjugation of bFGF and CTGF to the surfaces.

After 7 days in culture, counts of DAPI stained nuclei showed significantly higher numbers of cells on scaffolds conjugated with either CTGF or bFGF compared to control scaffolds. This indicates that although all scaffolds provided a favorable surface for cell growth, the scaffolds with conjugated growth factors encouraged additional cell proliferation.

Interestingly, results of the CellTiter Blue metabolic assay indicate higher rates of metabolic activity for cells on scaffolds with conjugated CTGF or bFGF compared to control scaffolds at both days 4 and 7. Additionally at day 4 cells on scaffolds conjugated with CTGF showed a significant spike in metabolic activity. The cause of the spike in metabolic activity is not completely know, however it could be indicative of other cellular processes [10]. The SEM images indicated that cells in all groups similarly aligned along the direction of the nanofibers. Although this could indicate that the presence of the growth factors have no influence on cell morphology, additional time in culture could result in further elongation of cells.

Overall these results indicate that the conjugation of either CTGF or bFGF to the polymer nanofibers that compose aligned electrospun nanofiber bundles significantly increased the proliferation of adipose derived stem cells. Future work will investigate the effects of the conjugated growth factors over longer time points to assess the deposition of collagen types I and III and sulfated glycosaminoglycans, indicative of fibroblastic differentiation.

ACKNOWLEDGEMENTS

This material is based upon work supported by the National Science Foundation under Grant No. DMR 1306741.

REFERENCES

[1] Arnoczky S et al., *Clin. Orthop. Relat. Res*, 19-25, 1983.
[2] Guccione A et al, *Am. J. Public Health*, 84:351-8.
[3] Pharm, Q et al., *Tissue Eng*, 12:1197-211, 2009.
[4] Baker, B et al. *Biomaterials*, 28:1967-77, 2007.
[5] Lee, C et al. *J Clin Invest*, 120:3340-3349, 2010.
[6] Hankemeier, *H et al. Tissue Eng*, 11:41-49, 2005.
[7] Chan, B et al. *Acta Orthop Scand*, 71:513-518, 2000.
[8] Choi, J et al. *Biomaterials*, 29:587-596, 2008.
[9] Pauly, H et al. *SB3C 2005*, Abstract #141, 2015.
[10] Rao, et al. *Neuroscience*, 113:547-553, 2002.

Copyright 2016 The Organizing Committee for the 2016 Summer Biomechanics, Bioengineering and Biotransport Conference

SB³C2016
Summer Biomechanics, Bioengineering and Biotransport Conference
June 29 –July 2, National Harbor, MD, USA
SB³C2016-32

THE RhoA/ROCK PATHWAY MEDIATES NOCICEPTIVE SIGNALING AFTER PAINFUL LIGAMENT LOADING

Sijia Zhang (1), Beth A. Winkelstein (1,2)

(1) Department of Bioengineering
University of Pennsylvania
Philadelphia, PA, USA

(2) Department of Neurosurgery
University of Pennsylvania
Philadelphia, PA, USA

INTRODUCTION

The cervical facet capsular ligament (FCL) encapsulates the bilateral spinal facet joints and is a common source of pain due to its innervation by pain fibers [1,2]. Excessive FCL stretch can induce morphological changes in its embedded nociceptors, altered expression of neurotransmitters in the dorsal root ganglion (DRG), and neuronal hyperexcitability in the spinal cord, all of which lead to pain [2-4]. In addition to trauma, inflammatory mediators, like nerve growth factor (NGF), in the facet joint can also initiate nociception [5]. Despite both mechanical and chemical stimuli to the FCL leading to pain, the molecular pathways are poorly understood, hampering effective treatments for facet and joint pain.

There is growing evidence that RhoA-mediated pathways are important in neuronal injury. Mechanical stress can up-regulate RhoA activity via adhesive interactions between cells and the extracellular matrix [6]. Active RhoA binds and activates Rho associated protein kinase (ROCK), triggering a host of downstream signaling cascades, including those involved in the pathogenesis of neural injury [7,8]. ROCK inhibition enhances axonal regeneration, attenuates morphological abnormality, reduces synaptic strength, and alleviates pain in inflammation and spinal nerve transection models [8-11]. Unlike mechanical loading, NGF is suggested to down-regulate RhoA activity [12]. As such, the RhoA/ROCK pathway is hypothesized to contribute to the onset of pain from FCL trauma, but not from NGF.

To test this hypothesis, RhoA activity was first measured in the DRGs from rats that underwent either a painful FCL distraction or painful NGF joint injection. Based on findings that RhoA activity is elevated *only* after the mechanical trauma to the facet joint, we used an in vitro neuron-collagen construct (NCC) system to further probe the role of the RhoA/ROCK pathway in nociceptive signaling due to loading. NCCs underwent biaxial loading to simulate FCL strains that induce pain in vivo. Expression of the pain-related neurotransmitter, substance P (SP), which is produced by afferents in the FCL [1], was measured after loading, in the presence or absence of a ROCK inhibitor to test if the RhoA/ROCK pathway mediates substance P.

METHODS

All animal procedures were IACUC-approved. Briefly, FCL distraction was imposed using bilateral tensile stretch across the C6/C7 facets (n=4) [13]. In a separate group of rats (n=6), 3μg of rat NGF was injected into the bilateral C6/C7 facet joints [5]. Sham rats with no FCL stretch (n=2) and rats with vehicle injection (n=3) were included as controls. Pain was assessed in the forepaw before (baseline) and 1 day after distraction or injection using von Frey filaments, and quantified as fold-change over baseline. DRG tissue at C6 was harvested at day 1 and RhoA activity was measured using an ELISA-based assay. The ratio of active to total RhoA was calculated relative to appropriate control group [14]. Differences in pain responses and RhoA activity between the groups were tested by separate t-tests.

NCCs were made using a solution of rat tail collagen I (2mg/ml) cast in a 12-well plate and punched into a cruciform shape with each arm being 6.25mm by 8mm. Embryonic (day 18) Sprague Dawley rat DRG explants were plated on the collagen gels and additional collagen was added 2 days later to encapsulate the DRGs. On day 5, NCCs underwent equibiaxial stretch to 1.5mm (~20% strain) [4] at 0.3mm/s using a 574LE2 planar biaxial testing machine (TestResources) (Fig. 1a). During loading, force-displacement data were recorded and a grid of markers on the NCC surface was tracked to measure the maximum principal strain (MPS) (Fig. 1). Unloaded gels were included as controls for RhoA activity and SP expression. RhoA activity relative to controls was measured at 30 minutes (n=3/group) or 6 hours (n=5/group) after loading to assess changes that could not be measured

Copyright 2016 The Organizing Committee for the 2016 Summer Biomechanics, Bioengineering and Biotransport Conference

in vivo due to the confounding effects of anesthesia. T-tests were used to detect differences in RhoA activity in loaded and unloaded NCCs.

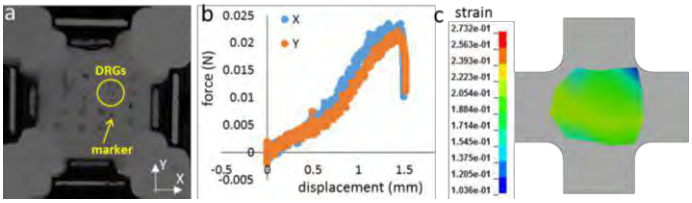

Fig. 1. (a) The biaxial test set-up with a loaded NCC, (b) force-displacement responses, and (c) a strain map.

To determine if the RhoA/ROCK pathway affects nociceptive signaling after loading, ROCK activity was inhibited (n=6) immediately after painful loading for 24 hours using 10μM of Y27632 (Selleckchem) [15]. SP expression was measured 1 day after loading. SP was also evaluated in NCCs that were loaded but not treated (n=6) and those not loaded either with (n=6) or without (n=5) Y27632 treatment. NCCs were immunolabeled for SP (1:500; Neuromics), and the average intensity per unit area of 5-10 axons from each DRG was measured by ImageJ and normalized to controls. Differences in SP expression between groups were detected by a two-way ANOVA with Tukey's test. To ensure consistent loading, the maximum force and MPS of treated and untreated NCCs were compared by t-tests.

RESULTS

Both FCL distraction and NGF injection induce pain at day 1, as evident in the lowered paw withdrawal thresholds relative to baseline ($p<0.05$); yet, there is no difference between the two groups (Fig. 2a). In contrast, only painful distraction, but not painful NGF injection, up-regulates RhoA activity at day 1 (Fig. 2b). RhoA activity in the DRG after FCL loading is 1.63±0.38 times ($p=0.046$) the level in the corresponding unloaded shams, which is also significantly greater than ($p=0.003$) normalized levels after the painful NGF injection (Fig. 2b).

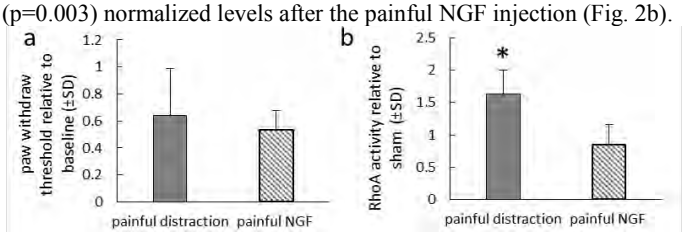

Fig. 2. FCL distraction & NGF joint injection induce (a) similar pain but (b) different DRG RhoA activity (*p=0.003) at day 1.

Similar to in vivo results (Fig. 2), stretch of the NCCs in vitro also up-regulates RhoA activity in the associated DRGs. RhoA activity after loading increases by 2.1±0.78 times at 30 minutes ($p=0.045$) and 1.8±0.84 times at 6 hours ($p=0.037$) over levels in unloaded controls. RhoA activity is not different between the two time points, indicating early and sustained activation of the RhoA pathway.

The increase in SP in the DRGs that is induced after painful NCC loading is prevented by inhibiting ROCK. The untreated and treated NCCs underwent comparable loading. The average MPS is 18.9±2.9% and 18.8±3.4% for the treated and untreated groups, respectively; the maximum force is not different between those NCC groups (Fig. 3). SP expression increases after loading ($p<0.01$) (Fig. 4). Y27632 treatment inhibiting ROCK in loaded NCCs significantly decreases SP expression ($p<0.01$) compared to the untreated group after the same loading, to levels lower even than in unloaded control NCCs (Fig. 4).

DISCUSSION

Mechanical loading of the FCL initiates a host of nociceptive responses in the DRG [3,4], which are associated with pain. Yet, the local mechano-transductive mechanisms that translate mechanical cues

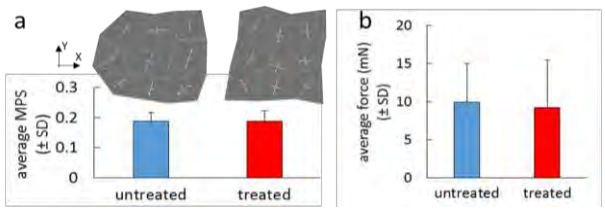

Fig. 3. Neither the (a) MPS direction & magnitude nor (b) maximum force differ between Y27632 treated & untreated NCCs.

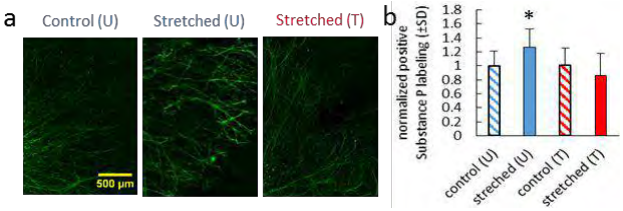

Fig. 4. (a) Images & (b) quantification of SP in Y27632 treated (T) & untreated (U) NCCs. SP in untreated stretched NCCs exceeds that in untreated controls & in treated stretched NCCs (*p<0.001).

into nociceptive signaling in the afferents remain unknown. This study shows that the RhoA pathway, which contributes to cellular force balance and underlies neuropathology [6-12], can be rapidly activated in DRG neurons by excessive sub-failure local strains (Figs. 2-4). The persistent early RhoA activation in vivo and in vitro suggests its potential role in initiating loading-induced facet pain. Despite the RhoA/ROCK pathway being associated with inflammatory pain induced by formalin injection in mice [8], excess intra-articular NGF in the facet joint that causes pain does not alter RhoA activity in the rat DRG (Fig. 2). As such, RhoA-dependent pathways are likely specifically involved in neuronal mechanotransduction of pain.

ROCK inhibition in vitro prevented the loading-induced increase in the expression of SP (Fig. 4), which has been directly related to facet pain [3]. ROCK is a promising target for neurological disorders [7] and this study further supports its potential for treating pain from neuronal trauma (Fig. 4). Yet, this in vitro model injures *both* the soma and axons of neurons; studies are needed to evaluate the effectiveness of ROCK inhibitors on alleviating facet pain from FCL trauma in vivo – a case where only axons undergo injury. Also, we did not probe the biomechanical mechanisms by which tissue deformation alters RhoA signaling in neurons. Since excessive FCL strains can induce collagen matrix reorganization [16], it is possible that integrin-mediated force transmission leading to RhoA signaling may cause FCL pain. Nevertheless, this study, for the first time, identified RhoA and ROCK as mediators of nociception after mechanical trauma to the FCL.

ACKNOWLEDGEMENTS

Funding support provided by the NIH (U01EB016638).

REFERENCES

[1] Kallakuri, S et al. *Wold J Orthop*, 3:10-4, 2012. [2] Kallakuri, S et al. *Eur Spine J*, 17:556-63, 2008. [3] Lee, K & Winkelstein, B. *J Pain*, 10:436-45, 2009. [4] Dong, L et al. *Brain Res*, 1461:51-63, 2012. [5] Kras, J et al. *Osteoarthritis Cartilage*, 23:1999-2008, 2015. [6] Marjoram, R et al. *Curr Mol Med*, 14:199-208, 2014. [7] Mueller, B et al. *Rev Drug Discov*, 4:387-98, 2005. [8] Tatsumi, S et al. *Neuroscience*, 131:491-8, 2005. [9] Hiraga, A et al. *J Peripher Nerv Syst*, 11:217-24, 2006. [10] Hemphill, M et al. *PLoS One*, 6:e22899 2011. [11] González-Forero, D et al. *J Neurosci*, 32:68-84, 2012. [12] Jeon, C-Y et al. *Exp Mol Med*, 42:335-44, 2010. [13] Crosby, N et al. *Neurosci Lett*, 542:102-6, 2013. [14] Keely, P et al. *Methods Enzymol*, 426:27-45, 2007. [15] Joshi, A et al. *Exp Neurol*, 263:28-38, 2015. [16] Quinn & Winkelstein, *J Biomed Opt*, 14:054010, 2009.

Copyright 2016 The Organizing Committee for the 2016 Summer Biomechanics, Bioengineering and Biotransport Conference

SB^{3}C2016
Summer Biomechanics, Bioengineering and Biotransport Conference
June 29 –July 2, National Harbor, MD, USA
SB^{3}C2016-33

DETECTION OF SK CHANNELS ON NEURONAL AXONS

Krithika Abiraman (1), Anastasios V. Tzingounis (2), George Lykotrafitis (1, 3)

(1) Department of Biomedical Engineering
University of Connecticut
Storrs, CT, USA

(2) Department of Physiology and Neurobiology
University of Connecticut
Storrs, CT, USA

(3) Department of Mechanical Engineering
University of Connecticut
Storrs, CT, USA

INTRODUCTION

Small-conductance calcium-activated potassium (SK) channels are a family of potassium channels that are voltage independent and are activated solely by intracellular calcium (Ca^{2+}) through constitutively bound calmodulin. SK channels exist within microdomains of Ca^{2+} sources that provides Ca^{2+} for its activation [1]. SK channels mediate afterhyperpolarization and thereby regulate neuronal excitability. The location and density of ion channels on neurons are important determinants of their functional and physiological impact. SK channels are expressed widely in the mammalian central nervous system. The three subtypes of SK channels, SK1, SK2 and SK3, have partially overlapping yet distinct distributions in the brain. Although all three subtypes are present in hippocampal CA1 pyramidal neurons, SK2 is the most abundant (Stocker 2000, Sailer 2004). SK2 channels reside primarily in dendrites and regulate dendritic integration, control the kinetics of excitatory post-synaptic potentials and are involved in long-term potentiation, and learning and memory [2-4]. In contrast, the expression of SK2 channels on the soma is much lower. However, it remains unclear if SK channels are present on axonal membranes. A recent study suggests that the neuronal excitability observed due to N and P/Q Ca^{2+} channel block could be due to the loss of SK channels in axons [5]. Other immunohistochemical studies indicate that SK3 channels are the subtype present in neuronal axons [6, 7].

To test whether SK channels are localized on axons, we used single molecule atomic force microscopy (AFM) combined with natural toxins. We exploited the selective block of SK channels by bee venom toxin, apamin, to detect SK channels on the axonal membrane. We primarily focused on detecting SK channels on the axon initial segment, which is ~20μm-40μm from the soma. The results presented here demonstrate that apamin-sensitive SK channels are distributed along the axon initial segment

METHODS

Primary culture of rat hippocampal neurons

E18 rat hippocampal tissue obtained from Brainbits (Brainbits LLC, Springfield, IL), was dissociated onto 30 mm diameter poly-D-lysine (Sigma) coated coverslips and grown in neurobasal media supplemented with B27, pencillin streptomycin and glutamax (Invitrogen).

Transfection

Neurons at 8-10 DIV were transfected with tau-gfp plasmid using Lipofectamine 2000 (Invitrogen) according to manufacturer instructions.

Atomic force microscopy measurements

Force-distance curves were obtained from Asylum MFP 3D-BIO (Asylum Research, Santa Barbara, CA). HEK293T cell measurements were performed in a solution containing (mM): 2.5 KCl, 144 NaCl, 10 HEPES, 22 D-Glucose and 2.2 $CaCl_2$, pH 7.2. Neuronal experiments were carried out in neurobasal media supplemented with 2% B27, 1% penicillin-streptomycin, 0.25% glutamax, and HEPES to maintain constant pH. All measurements and drug incubations were carried out at 37°C. Cells were identified using differential interference contrast microscopy, and a scan area of 1μm^2 with a lateral resolution of 31 nm was chosen. All force measurements were carried out at a nominal loading rate of 24,000 pN/s, calculated by multiplying the tip retraction velocity by the cantilever spring constant (pN/nm). The cantilevers used had a nominal spring constant of 30 pN/nm as

Copyright 2016 The Organizing Committee for the 2016 Summer Biomechanics, Bioengineering and Biotransport Conference

provided by the manufacturer, the exact values of which are obtained via a thermal noise based method implemented by the manufacturer. The approach and retraction velocities are held constant at 800 nm/s. Probes had nominal tip radii of 20 nm and nominal angle of 20°, as provided by the manufacturer.

Data processing and analysis

The distribution of SK2 channels on the cell surface was detected by recording spatially resolved unbinding force maps over 1 μm^2 areas using an apamin functionalized probe. Unbinding forces were extracted from each of the 1024 force curves generated from each test (Figure 1B). A MATLAB (Mathworks) program developed in our lab was then used to create unbinding force maps where each pixel represents an independent rupture force obtained from the retraction portion of the force-distance curve.

RESULTS

Atomic force microscopy cantilever functionalized with apamin was used to detect SK channels on the axonal membrane. The axon was identified by transfecting the rat hippocampal neurons with tau-gfp. Although both dendrites and axons are fluorescent, axons are clearly distinguishable by their distinct morphology. 1μm^2 scan areas were probed along the axon initial segment (~20µm-40µm from the soma) and we observed mean unbinding forces of 20±8.0pN in about 5.6% of the sampled sites (Figure 1B, red, n=6). In order to test the specificity of the unbinding force we repeated the experiments on cells pretreated with apamin. We observed a significant decrease in the frequency of the unbinding forces (0.58%, Figure 1B, blue, n=3). This data clearly demonstrates the specificity of single molecule AFM-based assay to identify SK channels on the axon. Next, we tested if the axonal SK channel expression was under the control of cAMP-PKA SK2 channel properties and cell-surface expression is regulated by cAMP dependent protein kinase A (PKA) activity [8-10]. To this end, we pretreated the cells with Rp-cAMP, a cAMP analog that prevents activation of PKA by cAMP. We found mean unbinding forces similar to that obtained at baseline but with higher frequency (µ=20±9pN, surface density = 10.1%, n= 5, Figure 1B, purple). This suggests that indeed axonal SK channels are under the control of cAMP-PKA.

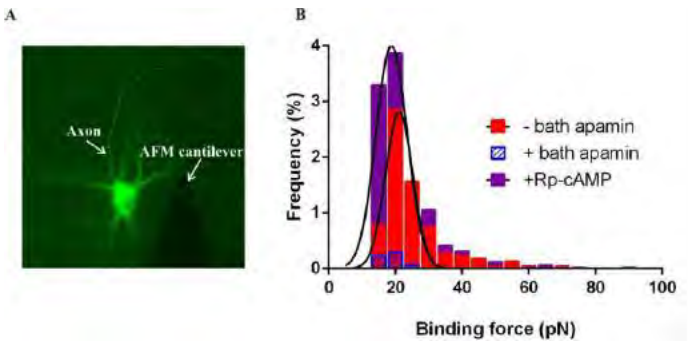

Figure 1: SK channels are present on neuronal axons and are regulated by cAMP

DISCUSSION

In this study, we show that SK channels are present in neuronal axons, particularly in the axon initial segment. Our study also provides insight into the role of cAMP in regulating the distribution of SK channels in neuronal axons.

ACKNOWLEDGEMENTS

This work is supported by the National Science Foundation (CMMI-1354363, CAREER Award; G.L.), NIH/NINDS (NS073981; AVT) and by the University of Connecticut Research Foundation (AVT, GL, KA).

REFERENCES

1. Fakler, B. and J.P. Adelman, *Control of KCa Channels by Calcium Nano/Microdomains.* Neuron, 2008. **59**(6): p. 873-881.
2. Ngo-Anh, T.J., et al., *SK channels and NMDA receptors form a Ca2+-mediated feedback loop in dendritic spines.* Nat Neurosci., 2005. **8**(5): p. 642 - 649.
3. Adelman, J.P., J. Maylie, and P. Sah, *Small-Conductance Ca2+-Activated K+ Channels: Form and Function.* Annu Rev Physiol, 2012. **74**(1): p. 245-269.
4. Faber, E.S.L., A.J. Delaney, and P. Sah, *SK channels regulate excitatory synaptic transmission and plasticity in the lateral amygdala.* Nat Neurosci., 2005 **8**(5): p. 635-41.
5. Yu, Y., et al., *P/Q and N Channels Control Baseline and Spike-Triggered Calcium Levels in Neocortical Axons and Synaptic Boutons.* The Journal of Neuroscience, 2010. **30**(35): p. 11858-11869.
6. Obermair, G.J., et al., *The small conductance Ca2+-activated K+ channel SK3 is localized in nerve terminals of excitatory synapses of cultured mouse hippocampal neurons.* European Journal of Neuroscience, 2003. **17**(4): p. 721-731.
7. Ballesteros-Merino, C., et al., *Differential subcellular localization of SK3-containing channels in the hippocampus.* European Journal of Neuroscience, 2014. **39**(6): p. 883-892.
8. Ren, Y., et al., *Regulation of Surface Localization of the Small Conductance Ca2+-activated Potassium Channel, Sk2, through Direct Phosphorylation by cAMP-dependent Protein Kinase.* J Biol Chem, 2006. **281**(17): p. 11769-11779.
9. Lin, M.T., et al., *SK2 channel plasticity contributes to LTP at Schaffer collateral-CA1 synapses.* Nat Neurosci., 2008. **11**(2): p. 170-7.
10. Faber, E.S.L., et al., *Modulation of SK Channel Trafficking by Beta Adrenoceptors Enhances Excitatory Synaptic Transmission and Plasticity in the Amygdala.* J Neurosci, 2008. **28**(43): p. 10803-10813.

Copyright 2016 The Organizing Committee for the 2016 Summer Biomechanics, Bioengineering and Biotransport Conference

SB³C2016
Summer Biomechanics, Bioengineering and Biotransport Conference
June 29 –July 2, National Harbor, MD, USA
SB³C2016-34

IN VIVO MEASUREMENTS OF WALL SHEAR STRESS ENVIRONMENT IN FETUS UMBILICAL ARTERIES AND VEINS

Shier Nee SN. Saw (1), Dawn D. Chia (2), Citra Nurfarah Zaini CNZ. Mattar (2), Arijit A. Biswas (2), Choon Hwai CH. Yap (1)

(1) Department of Biomedical Engineering, National University of Singapore, Singapore.

(2) Department of Obstetrics and Gynecology, National University of Singapore, National University Health Systems, Singapore.

INTRODUCTION

Endothelial cells (ECs) of the umbilical vessels are known to respond to wall shear stress (WSS) of blood flow and WSS is an important factor in controlling vascular growth and remodeling [1]. Umbilical vascular ECs are popular cell sources in mechanobiology studies, but detailed measurements of their native WSS environment is not comprehensively done. In diseases such as intrauterine growth restriction, where flow resistance in the placenta is high, understanding the WSS environment may provide clues for treatment / diagnosis.

In this study, we characterize WSS environment in human umbilical arteries (UAs) and umbilical vein (UV) using patient-specific 3D clinical ultrasound scans and computational simulations and found that umbilical arteries and veins have essential differences. Further, we investigated the effects of umbilical cord bending and found that the spiral shape of umbilical arteries played a role in maintaining constancy of flow resistance and WSS despite bending.

METHODS

28 pregnant women who underwent routine growth scan from 32nd to 33rd week of gestational age in the National University Hospital, Singapore were recruited with IRB approvals. Vascular cross-sectional areas were quantified through 3D reconstruction of the vascular geometry from 3D B-mode ultrasound images and flow velocities were quantified through pulse wave Doppler.

WSS in UA (τ_v) was obtained via Poiseuille's equation:

$$\tau_v = \frac{2\mu V_v^{US}}{R_v} \qquad (1)$$

where μ is the viscosity of fetal blood (0.005Pa.s), V_v^{US} is maximum flow velocity at the center of the parabolic profile measured from ultrasound and *Rv* is the radius of UV.

WSS in the UAs, due to its spiral geometry, could not be computed with Poiseuille's equation, and were computed based on an iterative scheme of CFD simulation. Each UA was modelled as a rigid helical pipe with physiological lumen diameter measured from ultrasound, helical pitch of 5cm and helical diameter of 17.4mm (Fig. 1a, b). Steady state simulation was performed. WSS results were obtained from the cross-sectional plane at the mid-length of UA. Bending of the umbilical cord was simulated by generating helical geometry spiraling around a bent centerline of the cord (Fig 1c).

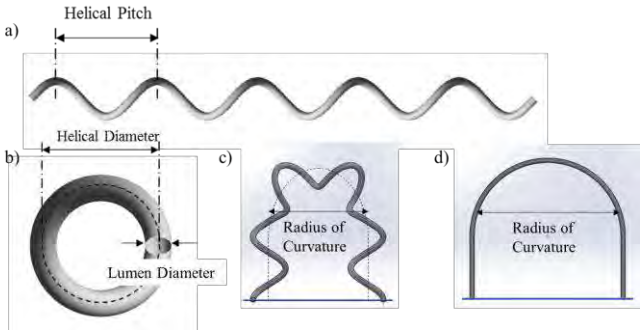

Figure 1(a) Geometry of helical geometry of UA used in CFD. (b) Transverse view of helical UA. (c) Helical UA after cord bending. (d) Straight UA after cord bending.

RESULTS

Ultrasound measurements showed that blood flow velocities in both umbilical arteries and veins were found to be relatively constant over different vascular sizes (Fig. 2a, 2b). CFD studies showed that UA's WSS remained relatively constant across vessel diameter (Fig. 2c) but UV's WSS showed a strong negative correlation with the vessel diameter (Fig. 2d).

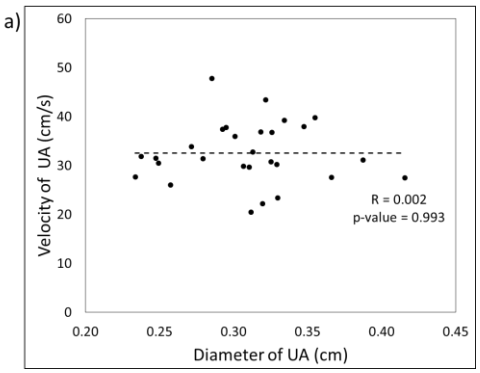

Copyright 2016 The Organizing Committee for the 2016 Summer Biomechanics, Bioengineering and Biotransport Conference

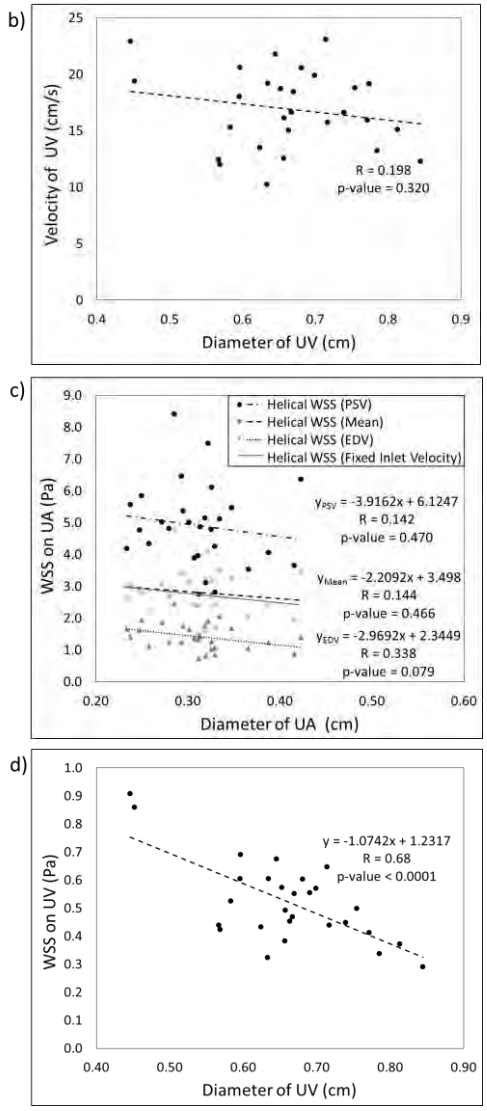

Figure 2. (a,b) Ultrasound measurements showed that blood velocities in the (a)UA and (b) UV are relatively constant over different vascular sizes. (c,d) Results of WSS computations for (c) UA and (d) UV. Since flow in UA was pulsatile, WSS for UA is plotted for peak systolic velocity (PSV), end diastolic velocity (EDV) and at the mean flow rate (Mean). Results showed relatively constant WSS over different sizes for UA, but not for UV. R is correlation coefficient. P-value determines the significance of coefficient of the regression line.

Typical secondary flow patterns and WSS spatial distributions are shown in Figure 3. Generally, velocities were skewed towards the outer wall of the helix (distal from the helical center), dean's vortices secondary flows were observed, and WSS were elevated on the outer wall of the helix but reduced in the inner wall.

Figure 4 shows the results of CFD of bent umbilical cords. Results are plotted as percentage change in resistance or WSS from the case of no umbilical cord bending to the case of umbilical cord bending. Cord bending was tested to various radii of curvatures. If the UA was straight and non-helical, both WSS and vascular resistance increased linearly with the inverse of radius of curvature of the bend. If the umbilical UA artery was spiral as it naturally is, however, bending of the umbilical cord did not significantly affect WSS or vascular resistance.

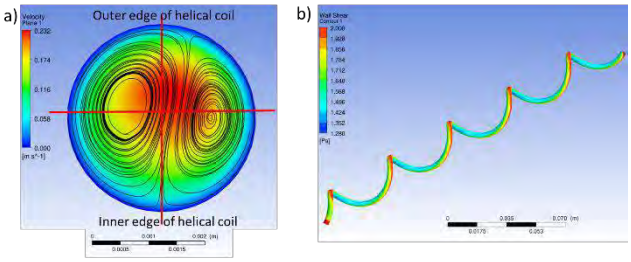

Figure 3 (a) In-plane streamlines and axial-velocity contour on the cross-sectional plane at mid-length of the UA model. (b) Wall shear stress contour on the UA.

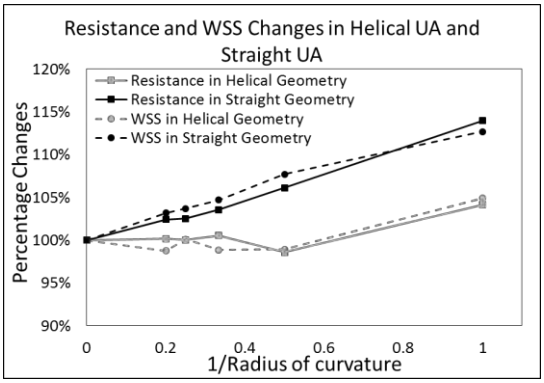

Figure 4 Comparison of resistance and WSS between helical UA and straight UA.

DISCUSSION

UA diameter's independence of WSS supports the hypothesis the vessel grows or regresses to maintain constancy in the shear stress environment. Nonetheless, this was not observed for UV. This might due to UV utilizes different cues for vascular remodeling. The constancy in flow velocity across vascular diameters suggests growth and remodeling according to rate of mass transport.

Umbilical cord coiling and bending occurs all the time in the womb, our study investigates the effect of coiling/bending of UA. Our results showed that bending of UA did not affect the WSS much, suggesting that helical geometry provides a more stable hemodynamic condition compared to straight bend geometry. Such a feature be the basis for the UA to sense hemodynamic flow rates without being interfered by cord bending.

ACKNOWLEDGEMENTS

This study was supported by the NMRC-CRBG-NIG grant by the Ministry of Health (Grant number: NMRC/BNIG/2020/2014, PI: Yap Choon Hwai). We thank Nyien Chan Ko Ko for his assistance in the data processing. All authors have no conflict of interest to declare.

REFERENCES

[1] Nakatsu, M.N., et al., *Lab Invest*, 83: 1873-85, 2003.
[2] Barbieri, C., etl.al., *J Obstet Gynaecol,* 32: 230-236, 2012.
[3] Tchirikov, M., et al., *Ultrasound in Obstetrics and Gynecology,* 20: 580-585, 2002.

Copyright 2016 The Organizing Committee for the 2016 Summer Biomechanics, Bioengineering and Biotransport Conference

SB³C2016
Summer Biomechanics, Bioengineering and Biotransport Conference
June 29 –July 2, National Harbor, MD, USA
SB³C2016-35

FLUID-STRUCTURE INTERACTION OF A RUPTURED INTRACRANIAL ANEURYSM: DOES PATIENT-SPECIFIC WALL THICKNESS MATTER?

Philipp Berg (1,2), Samuel Voß (1,2), Sylvia Glaßer (1,3), Thomas Hoffmann (1,4), Simon Weigand (4), Gábor Janiga (1,2)

(1) STIMULATE Research Campus
University of Magdeburg
Magdeburg, SA, Germany

(2) Department of Fluid Dynamics and Technical Flows
University of Magdeburg
Magdeburg, SA, Germany

(3) Department of Simulation and Graphics
University of Magdeburg
Magdeburg, SA, Germany

(4) Department of Neuroradiology
University Hospital Magdeburg
Magdeburg, SA, Germany

INTRODUCTION

Although many numerical studies were carried out to improve the understanding of remodeling processes in intracranial aneurysms, almost all of them consider rigid vasculature. Only some groups take the interaction between blood flow and the surrounding vessels into account, but in most cases constant extrusions of the luminal surface are present [1,2]. Due to the lack of possibilities to precisely measure local wall thicknesses, corresponding studies are extremely rare. Cebral et al. [3] used the local wall shear stress (WSS) distribution of a rigid-wall simulation to estimate the local wall thickness, since it induces several pathophysiological processes in the vessel wall. A correlation between the wall thickness as well as its stiffness and the rupture site is presented. However, the real local wall thicknesses were still absent to validate the proposed approach.

The recent study focusses on a patient-specific intracranial aneurysm that was prepared ex vivo. Afterwards, microCT was used to acquire the inner and outer vessel surface. Computational Fluid Dynamics (CFD) in combination with fluid-structure interaction allows the examination of hemodynamic as well as structural parameters that influence the aneurysm wall. To compare the results with previous approaches, the luminal surface was extruded in normal direction and the simulation was repeated under identical conditions. Hence, this numerical study demonstrates a consequent step towards a better understanding of the thickness to stress relation and provides further insights regarding the rupture risk assessment of intracranial aneurysms.

METHODS

Image acquisition and vascular reconstruction

A complete Circle of Willis and adjacent vessels were harvested from a 33-year-old male person post mortem as part of a forensic examination and further investigated with the approval of the local ethics committee. The aneurysm, which was located at the anterior communicating (Acom) artery, was separated from the surrounding tissue and flushed with saline to remove intraluminal blood clots (see Figure 1). Since the aneurysm previously ruptured, the corresponding site was identified by a neuroradiologist.

To acquire the anatomy of the investigated aneurysm, a microCT scan was performed and the 3D model was manually reconstructed using MeVisLab 2.6.2 (MeVis Medical Solutions AG, Bremen, Germany). The results are displayed in Figure 1 and were revised by experienced neuroradiologists. To allow a comparison with the patient-specific vessel wall model the inner surface was extruded in normal direction by 300 μm.

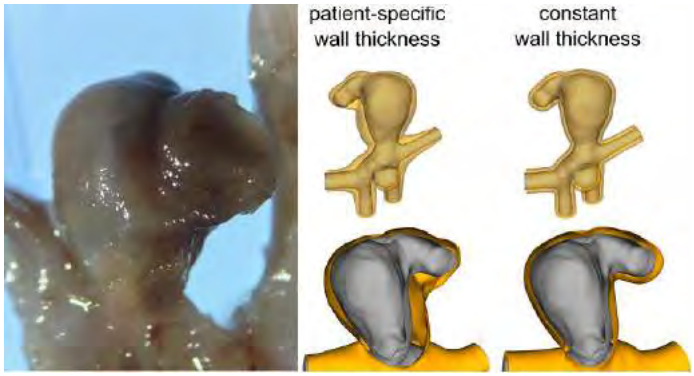

Figure 1: Ex vivo preparation of the Acom Aneurysm (left), patient-specific and constant vessel wall thickness from different perspectives (right).

Copyright 2016 The Organizing Committee for the 2016 Summer Biomechanics, Bioengineering and Biotransport Conference

Spatial discretization and hemodynamic simulation

The fluid and solid domains are represented by polyhedral as well as prism cells that possessed an adequate size to resolve the existing velocity gradients appropriately. This resulted in a total number of cells of approx.1.2 and 1.1 million for the patient-specific and the constant wall thickness, respectively.

Steady-state simulations were carried out using the finite-volume solver STAR-CCM+ V9.04 (CD-adapco, Melville, New York, USA). At the inflow cross-sections a mean velocity was applied that was previously measured in a healthy volunteer using 7T PC-MRI [4]. At both outlets a zero-pressure condition was applied. Blood was treated as a laminar, Newtonian fluid (ρ=1055 kg/m^3, η=4 mPa·s).

For the fluid-structure interaction a two-way coupling was chosen that considers the impact of pressure on the deformation and vice versa. The arterial wall was assumed to be homogenous with isotropic material properties and a commonly used linear elastic material behavior is considered. For the Young's modulus a value of 1 MPa was chosen and a Poisson ratio of 0.45 and a density of 1050 kg/ m^3 for the solid were defined, respectively.

RESULTS

Due to the page limit within this abstract only comparisons between displacement as well the stress distributions on the outer vessel wall surface are presented. As illustrated in Figure 2, the highest displacement is predicted in equivalent areas for the patient-specific and the constant wall thickness, respectively. However, the absolute values for the maximum displacement strongly deviate resulting in an over-estimation by the constant wall thickness approach.

Regarding the stress on the outer surface it can be noticed that due to the homogenous wall thickness in the artificial model almost no elevated values occur. In contrast, the patient-specific configuration shows spots of high stresses that are close to the identified rupture site.

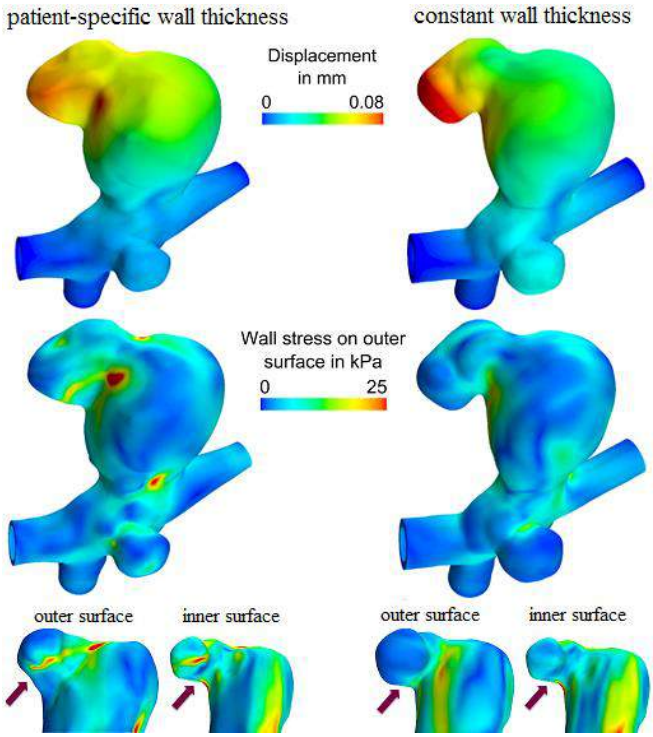

Figure 2: Comparison of displacement and wall stress for the patient-specific (left) and constant vessel wall (right) from different views. The rupture site is indicated with the arrow.

Further hemodynamic and structural parameters were analyzed in detail. Those as well as a quantitative comparison will be presented at the conference.

DISCUSSION

The consideration of a constant wall thickness to model fluid-structure interactions of intracranial aneurysms is a common approach since state-of-the-art imaging modalities are unable to capture cerebral vessel wall properties in vivo. In order to evaluate this method, locally varying wall thicknesses were acquired for an Acom aneurysm ex vivo. The comparison of both configuration reveals drastic differences regarding the analyzed parameters. Hence, assuming a constant vessel wall thickness might lead to wrong conclusions regarding the rupture probability of a certain aneurysm. Furthermore, using patient-specific data with locally varying wall thicknesses appears to be out of alternative to capture a realistic scenario.

Nevertheless, the presented approach still contains several limitations that need to be critically reflected. Firstly, the preparation might have led to some distortions of the geometry and hence a deviation to the in vivo configuration occurred. Secondly, since the aneurysm was harvested ex vivo, no patient-specific flow conditions were available and 7T PC-MRI data needed to be used. Thirdly, isotropic, homogenous, linear-elastic vessel walls were assumed due to the lack of material measurements. To overcome this issue, histologic analyses of the investigated aneurysm are carried out as presented in Figure 3 for two exemplary slices.

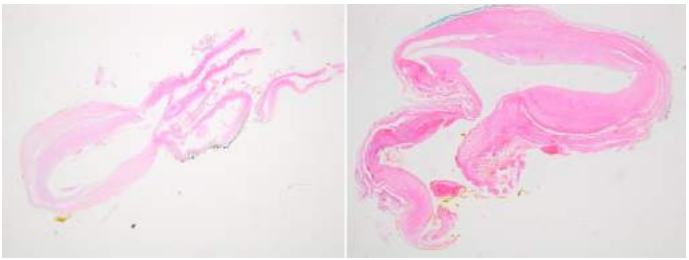

Figure 3: Two exemplary histologic slices to examine local wall thicknesses as well as the corresponding wall compositions.

Besides the mentioned limitations the presented study demonstrates the importance of acquiring patient-specific wall properties to understand the aneurysmal pathology. Further advances regarding the wall composition will be incorporated into the numerical studies and might lead to the assessment of reliable rupture risk criteria.

ACKNOWLEDGEMENTS

This work was partly funded by the Federal Ministry of Education and Research in Germany within the Research Campus STIMULATE under grant number 03FO16102A.

The authors acknowledge Dr. Oliver Beuing (Department of Neuroradiology, University Hospital Magdeburg) for his assistance regarding the rupture site identification.

REFERENCES

[1] Torii, R et al., *Int J Numer Methods Eng*, 26:336-347, 2010.
[2] Valencia, A et al., *Comput Math Methods Med*, 2013:1-18, 2013.
[3] Cebral, J et al., *J Neurointerv Surg*, 7:530-536, 2015.
[4] Berg, P et al., *J Biomech Eng*, 136:1-9, 2014.

Copyright 2016 The Organizing Committee for the 2016 Summer Biomechanics, Bioengineering and Biotransport Conference

SB³C2016
Summer Biomechanics, Bioengineering and Biotransport Conference
June 29 –July 2, National Harbor, MD, USA
SB³C2016-36

BLOCK CO-POLYMER BASED HYDROGELS FOR MENISCAL REPLACEMENT

Kristine M. Fischenich[1], Jackson T. Lewis[1], Travis S. Bailey[1,2], Tammy L. Haut Donahue[1,3]

(1) School of Biomedical Engineering
Colorado State University
Fort Collins, CO, USA

(2) Chemical and Biological Engineering
Colorado State University
Fort Collins, CO, USA

(3) Mechanical Engineering
Colorado State University
Fort Collins, CO, USA

INTRODUCTION

Meniscal damage can be caused by age related degradation, obesity, overuse from athletic activities, and trauma[1]. Once damaged, the meniscus has limited healing ability due to its primarily avascular nature[2]. Meniscal allograft research has been investigated, but has been met with mixed results[3] and no long term data, leaving it a procedure with limited utility. Cell seeded scaffolds have been shown to allow the growth of meniscus like fibrocartilaginous tissue, but these scaffolds are limited mechanically[4]. There is a need for a permanent meniscal replacement with mechanical integrity similar to the native tissue. The objective of this study was to evaluate the time dependent compressive properties of a polystyrene (PS) - polyethylene oxide (PEO) diblock and PS-PEO-PS (SOS) triblock copolymer compared to the native meniscus. Specifically, it is hypothesized that this hydrogel can be tuned to have similar compressive modulus and cyclical relaxation profiles of the native tissue.

METHODS

The PS-PEO-PS triblock copolymer has been previously described[5]. The amount of triblock (SOS) was varied to determine the effects on mechanical behavior. Dry polymer was compressed at 500 psi for 5 minutes, cooled, and swollen in DI water. All mechanical tests were performed on a servo hydraulic test system (Bionic Model 370.02 MTS Corp, Eden Prairie, MN) using a 8.9 N load cell (Futek LSB200, Irvine, California) and were tested in a water bath to maintain hydration. Prior to indentation or cyclic compression tests, samples were preloaded to 12% strain over 1 second. Indentation relaxation tests were carried out for 300 seconds to allow for equilibrium and a spherical indenter tip (1.59 mm diameter) was used. Cyclical compression tests were performed on cylindrical disks 8mm in diameter mounted between two aluminum plates to assess the relaxation of the copolymer over 1,000 cycles at a frequency of 1Hz. Hertzian contact was used to assess both the instantaneous and equilibrium moduli of the indentation tests. Peak compressive force and displacements for each cycle were used to determine the compressive modulus for the cyclical results. Data from both the indentation relaxation and cyclical compression were compared to human meniscal values. Values for human menisci indentation (n=11) were taken from previous indentation relaxation work done by this group[6] and a preliminary cyclical compression test. Approval from Colorado State University Institutional Review Board was obtained for the human samples as well as consent forms from patients (age= 58 ± 4, BMI= 33 ± 6). Finally, to test the fatigue resistance of the hydrogel (6 mm) diameter plugs were swollen 1xPBS and subjected to 500,000 cycles at room temperature in a custom built bioreactor. Samples were compressed to 12% strain at a frequency of 1Hz. Data was recorded for 1,000 cycles every 24 hours for the duration of the test. Following the 500,000 cycles, samples were allowed to rest and were later subjected to an additional 1,000 cycles to evaluate recovery. Peak stress and strain were used to assess modulus, and values from the recorded 1000 cycles were averaged.

RESULTS

Increases in triblock percentage resulted in higher compressive modulus value, both instantaneously and at equilibrium (Figure 1). Instantaneous compressive modulus values were also within the range of healthy human menisci. There was a visible decrease from instantaneous to equilibrium modulus in all samples, with higher triblock SOS samples having a greater decrease. These decreases were at higher SOS content similar to those seen in the human samples

Copyright 2016 The Organizing Committee for the 2016 Summer Biomechanics, Bioengineering and Biotransport Conference

tested with the greatest decrease in SOS 93 around a 70% drop compared to the average meniscus decreasing around 83%. It is evident that these SOS triblock copolymers have similar compressive properties to that of the native meniscus.

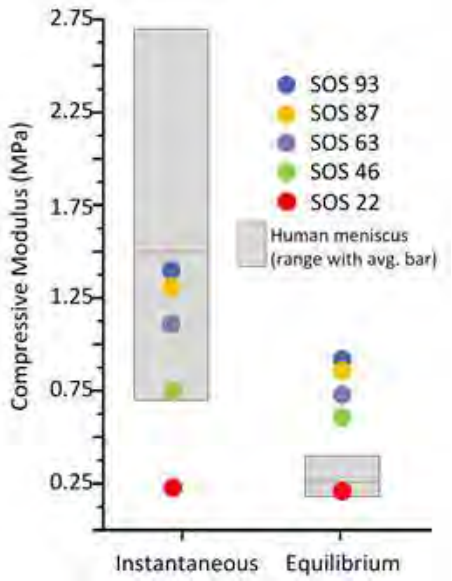

Figure 1: Indentation relaxation results

Two of the SOS triblock concentrations were used for cyclical testing (Figure 2). Similar to the differences seen in the static indentation testing, the human meniscus tended to relax more than the SOS triblock samples. Over the course of 1,000 cycles there was a total decrease of 40% in the human sample while the SOS 22 and SOS 46 relaxed 21% and 17%, respectively.

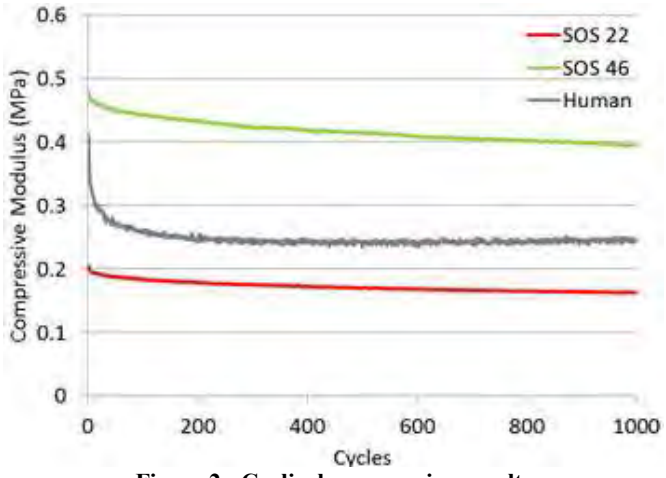

Figure 2: Cyclical compression results

A SOS triblock concentration of 61% was selected for the 500,000 cycle test. Initial modulus was similar to previous testing and there was minimal to no degradation over time. Over a half million cycles, the modulus varied between 0.4-0.5 MPa and recovered to within 1% of original modulus following a 12 hours rest period (Figure 3).

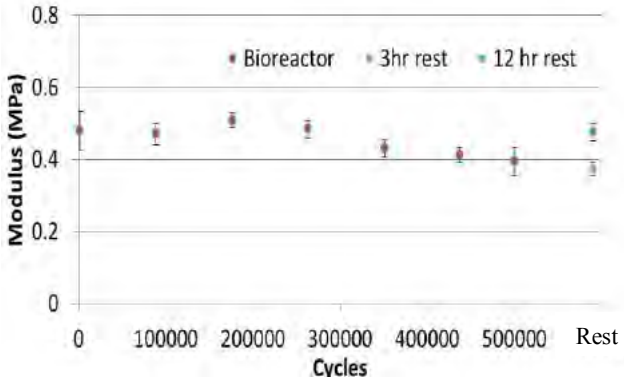

Figure 3: Cyclical fatigue results

DISCUSSION

This study proved that the compressive properties of the human meniscus can be mimicked with a SOS triblock copolymer. By increasing the triblock content, we are able to increase the compressive modulus while still maintaining a relaxation profile. The hydrogel is also able to maintain its mechanical integrity over the course of half a million cycles, which is further supported by the recovery of the gel after 12 hours of rest. This marks one of the first hydrogels of its kind to show mechanical integrity after repeated cycling.

Our group has been successful in creating a simple crescent shape with the same general dimensions of a sheep medial meniscus (Figure 4). Future work is underway to incorporated nylon fibers into the hydrogel to achieve anisotropy and similar tensile properties to the native human meniscus. Since load is distributed circumferentially in the native tissue, obtaining higher tensile strength will be necessary for this replacement to be viable. Additional testing will also be performed to determine more thoroughly investigate they hydrogels properties the long term wear of the 3D construct.

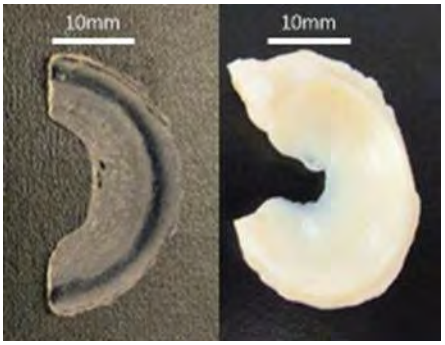

Figure 4: 3D hydrogel vs. sheep meniscus

ACKNOWLEDGEMENTS

The authors would like to acknowledge Colorado State University for their financial support.

REFERENCES

[1] Neogi T, Zhang Y., *Rheum Dis Clin North Am*., 39(1):1-19., 2013
[2] Mow VC, et al., *Knee Meniscus: Basic and Clinical Foundations*, Raven Press; 1992.
[3] Goble EM, et al., *Scand. J. Med. Sci. Sports,* 9(3):146–57,1999.
[4] Guo W, et al., *Stem Cells Int.* 517520, 2015.
[5] Guo C, Bailey TS., *Soft Matter* 6(19):4807, 2010.
[6] Fischenich KM, et al., *J. Biomech,* 48:1407–11, 2015.

Copyright 2016 The Organizing Committee for the 2016 Summer Biomechanics, Bioengineering and Biotransport Conference

SB^{3}C2016
Summer Biomechanics, Bioengineering and Biotransport Conference
June 29 –July 2, National Harbor, MD, USA
SB^{3}C2016-37

A METHODOLOGY FOR THE QUANTIFICATION OF UPPER LIMB PROSTHETIC SOCKET INTERFACE MECHANICS

Jonathon S. Schofield (1), Jason P. Carey (1), Paul D. Marasco (2), Jacqueline S. Hebert (3)

(1) Mechanical Engineering
University of Alberta
Edmonton, Alberta, Canada

(2) Biomedical Engineering
Cleveland Clinic
Cleveland, Ohio, United States

(3) Faculty of Medicine and Dentistry
University of Alberta
Edmonton, Alberta, Canada

INTRODUCTION

One of the most influential factors for the use of upper limb (UL) prostheses is the socket design(1). The socket functions as the point of attachment between the prosthesis and the user's residual limb (RL). At this crucial junction, the soft tissue of the limb must interface with the rigid materials of the prosthesis. Sockets are designed to strategically compress areas of the user's limb to achieve suspension of the prosthesis and aid in movement control. Consequently, a prosthetic socket must be custom designed to accommodate the individual's morphology as to avoid discomfort and potential damage to the tissue. Achieving this task requires a high degree of expertise to manufacture a socket of suitable geometry that appropriately distributes interfacial pressures over the RL.

In clinical practice, the implications of proper design are well acknowledged and much of a prosthetist's effort will be specifically dedicated to socket fabrication(2). Yet surprisingly, UL socket fabrication relies heavily on heuristic practice as interfacial pressure distributions have yet to be comprehensively defined in literature. To date, Daly et al. present one of the only UL pressure measurement studies and report mean and maximum interface pressure(3). However, their work does not report the locations at which these pressures occur, limiting the translation of results into a design context.

At present 20-39% of UL prosthetic users abandon their device with socket discomfort highlighted as a major contributing factor(4). Development of novel prosthetic sockets specifically designed to optimize patient comfort may greatly increase device satisfaction. Yet, the absence of quantitative documentation impedes the ability of clinicians to innovate designs and fully appreciate the biomechanical implications on user comfort and potential tissue damage.

In lower limb prostheses, interfacial pressures have been well defined(2) facilitating quantitative design practices. Therefore, this work aims to evaluate and develop a methodology to adapt lower limb pressure measurement technologies for UL prostheses. Specifically, force sensing resistor (FSR) technology was evaluated under simulated biomechanical conditions of an UL prosthetic environment. The ability of this technology to define UL socket pressure distributions was then demonstrated in 2 participants with transhumeral (above elbow) amputation.

METHODS

FSRs are commercially available thin film polymer sensors commonly employed in lower limb prosthetic pressure measurement. Their versatility and thin profile make them attractive sensors for prosthetic applications. Yet FSRs have well known limitations such as sensitivity to temperature, curvature and substrate compliance(5,6). Prior to implementing these sensors in an UL prosthetic application, the effect of these unavoidable variables was first quantified and the results used to develop compensatory calibration practices. Varying levels of temperature (room: 21°C and body: 37°C), sensor curvature (5th percentile female wrist: 44mm diameter, 95th percentile male thigh: 215mm diameter, and flat) and surface compliance (human tissue analog and a rigid surface) were systematically assessed using a full factorial design-of-experiments approach. Two FSRs of 3 different models were evaluated (400, 402 and 406, Interlink Electronics). Calibration equations under 12 unique combinations of temperature, curvature and compliance were determined for each sensor. Root mean squared error was calculated and Main Effects ANOVAs used to determine statistical significance ($p<0.05$) of variables. Results were used to inform the design of calibration practices and a calibration

Copyright 2016 The Organizing Committee for the 2016 Summer Biomechanics, Bioengineering and Biotransport Conference

apparatus for the implementation of FSRs in an UL prosthetic environment.

The calibration practices and apparatus were used with 2 transhumeral amputee participants. A commercially available FSR-based prosthetic measurement system (9811E sensors and VersaTek System, Tekscan Inc) was employed to capture interfacial pressure on the RL. First, sensor location relative to each participant's anatomy was defined in 3-dimensional space using a FARO Edge Coordinate Measurement Machine. Participants then donned their prosthesis, positioned the prosthetic elbow at 90° flexion and statically held this position for 3 seconds. The corresponding interfacial pressures were captured. This pressure measurement data was then paired with the sensor location data in ParaView 5.0 software to reconstruct 3-dimensional pressure contour maps.

RESULTS

ANOVA results indicated that the calibration of all three FSR models was significantly affected by temperature, curvature and compliance (Table 1). The sensitivity to each variable differed for each sensor model. It was concluded that FSRs implemented in such biomechanical environments must therefore be calibrated as close to their intended use to minimize error.

Table 1: ANOVA Results- Temp, Curve, and Comp denote temperature, curvature and compliance respectively. Hyphenated variables denote interaction effects.

Model	Significant Variable	p-value
400	Temp-Comp	0.02
	Curve-Comp	<0.01
402	Comp	<0.01
	Curve-Comp	<0.01
406	Curve	<0.01
	Curve-Comp	<0.01

Correspondingly, the participant testing required a calibration apparatus capable of calibrating the Tekscan FSR sensors at the same temperatures, curvatures and tissue compliances as the UL prosthetic environment that they were to be used. An inflatable bladder system was developed that allowed for sensors to be positioned on the participant's RL at the time of calibration. The participant then placed their RL into a chamber where a bladder is inflated to a series of known calibration pressures around the RL (Figure 1). These pressures were input into the Tekscan Versatek system to facilitate its calibration algorithms.

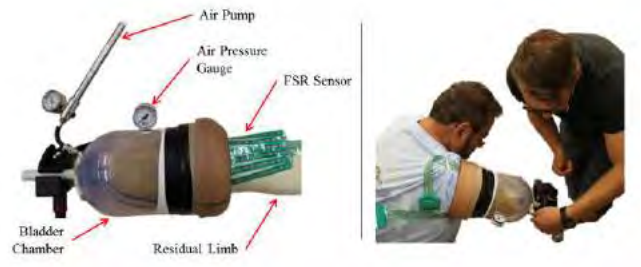

Figure 1: Calibration Apparatus- Shown both schematically and in use with a participant

Once calibrated and the pressure of donning the prosthesis was captured, FSR data was paired with the sensor location data. The resulting pressure contour maps are shown in Figure 2. In both participants, local regions of high pressure were found at the distal regions corresponding to the end of the residual humerus, and in the medial soft tissue close to the axilla.

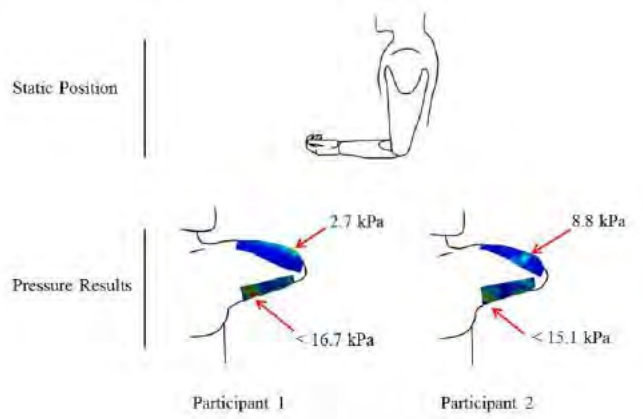

Figure 2: Resulting 3-Dimensional Pressure Contour Maps

DISCUSSION

UL prosthetic socket fit is a pivotally important factor in user acceptance and device satisfaction. Development of a well-fitting UL socket is a challenge that is fundamentally biomechanical in nature. Yet little quantitative work has been performed to define the interface mechanics of the socket and limb.

This work highlights a methodology that uses commercially available technology to quantify UL socket interface mechanics. This methodology takes compensatory steps to minimize error during calibration. Additionally, it is able to map pressure distribution patterns to the anatomy of the participant. This can provide crucial data to inform quantitative design and fabrication practices.

Follow-up work with an amputee population is warranted to comprehensively evaluate efficacy of the presented techniques. This methodology is directly translatable to research and clinical settings and has the potential to help guide analytically informed fabrication methods. More broadly, our work presents the first steps toward a departure from strictly experience-based practices, and holds the potential to improve the quality of patient care and UL prosthetic satisfaction.

ACKNOWLEDGEMENTS

Thanks to Katherine Evans and Michael Dawson. This work was funded by the US taxpayers through a National Institutes of Health, Office of the Director, Common Fund, Transformative R01 Research Award grant # 1R01NS081710 – 01.

REFERENCES

(1) Lake, C et al., *Phys Med Rehabil Clin N Am* 17:49-72, 2006.
(2) Sanders, JE., *Med Biol Eng Comput*, 33:509-516, 1995
(3) Daly, W et al., *JPO*, 26:99-106, 2014.
(4) Biddiss E, et al., *Prosthet Orthot Int* 31:236-257, 2007.
(5) Polliack, AA et al., *Prosthet Orthot Int* 24:63-73, 2000.
(6) Herbert-Copley, AG et al., *IEEE MeMeA*:265-267, 2013.

Copyright 2016 The Organizing Committee for the 2016 Summer Biomechanics, Bioengineering and Biotransport Conference

SB³C2016
Summer Biomechanics, Bioengineering and Biotransport Conference
June 29 –July 2, National Harbor, MD, USA
SB³C2016-39

THE RELATION BETWEEN SHEAR STRESS METRICS AND ATHEROSCLEROSIS: A FOLLOW-UP STUDY IN THE CAROTID ARTERIES OF ATHEROSCLEROTIC MICE

David De Wilde (1), Bram Trachet (1,2), Guido R. Y. De Meyer (3), Patrick Segers (1)

(1) Department of Electronics and Information Systems
Ghent University-iMinds-IBiTech
Gent, Belgium

(2) Institute for Bioengineering
Ecole Polytechnique Fédérale de Lausanne
Lausanne, Switzerland

(3) Division of Physiopharmacology
University of Antwerp
Antwerp, Belgium

INTRODUCTION

Atherosclerosis is a cardiovascular disease characterized by the formation of plaque in large- to middle-sized arteries. It is generally accepted that low and oscillatory wall shear stress (WSS) favors the initiation and development of atherosclerosis. However, the slow progression time of atherosclerosis in humans makes it difficult to perform a quantitative analysis of the association between shear stress metrics in vivo on a within-subject basis. Therefore, in studies involving humans, shear stress patterns in a group of healthy subjects (providing baseline WSS metrics) are typically compared with plaque locations from a second group of subjects (suffering from atherosclerosis). To assess the correlation between WSS metrics and plaque location in such a cross-sectional between-group design, aggregation (averaging) of the datasets is needed. This aggregation possibly leads to an overestimation of the correlation between the baseline WSS metrics and the plaque location.

This study is the first to elucidate the relationship between shear stress and plaque location on a within-subject basis. To this end we performed a point-by-point quantitative comparison (based on surrogate sample data analysis) of baseline shear stress patterns (based on mouse-specific fluid-structure interaction simulations) and intermediate/end-stage plaque locations (based on a tracer for macrophage infiltration) in dedicated mouse models. We subsequently analyzed which WSS metric had the best correlation with plaque location, and compared the resulting correlations of the within-subject data to those based on aggregated datasets.

METHODS

At the age of 6 weeks four female ApoE$^{-/-}$ mice were put on a western type of diet to induce atherosclerotic plaque formation. The animals underwent an imaging protocol after 10, 15 and 20 weeks on the diet.

At the first imaging time point, the geometry of both carotid bifurcations was obtained by a gold-nanoparticle contrast- enhanced μCT scan (contrast agent: Aurovist 15nm). Ultrasound measurements were performed to generate mouse-specific boundary conditions for FSI simulations of the blood flow in the carotid arteries. Furthermore, the FSI model also included the in vivo prestress state of the arterial wall and the external tissue was modeled with springs. From these simulations several WSS metrics were calculated: time-averaged wall shear stress (TAWSS), oscillatory shear index (OSI), relative residence time (RRT), transverse wall shear stress (transWSS), the dominant harmonic (DH) and the harmonic index (HI). A more detailed description of the FSI setup can be found in [1].

In the same mice, follow-up μCT scans were performed at weeks 15 and 20 (5 and 10 weeks after the baseline scan). As we have previously demonstrated that Aurovist particles from previous injections accumulate in the atherosclerotic plaques (or more precise in macrophages), a surface map of the presence of macrophages and thus plaque development was constructed [2].

We subsequently mapped both the WSS metrics and the macrophage infiltration (μCT) data to a common rectangular grid per branch for every bifurcation (see figure 1) using VMTK (www.vmtk.org) [3]. Afterwards statistical testing was performed on an individual branch level, an individual bifurcation level and a population bifurcation level. Spearman's correlation coefficient (ρ) and Pearson's correlation coefficient (r) were calculated. For the individual branch and bifurcation level statistical test, the surrogate sample data analysis was applied [4]. For this test two conditions have to be met for significance: (i) $p<0.05$ and (ii) the confidence bound (1-tailed equivalent of confidence interval) cannot include a zero

Copyright 2016 The Organizing Committee for the 2016 Summer Biomechanics, Bioengineering and Biotransport Conference

correlation value. At the population level, a t-test approach was followed after applying a Fisher r to z transformation. For a detailed description of the methodology the reader is referred to [5].

RESULTS AND DISCUSSION

In Figure 1, panel A displays the mapped values of RRT along the left carotid artery of a representative animal, calculated from FSI simulations using data measured at week 10. The highest values are found in the external carotid artery (ECA) and in the immediate vicinity of the bifurcation in the common (CCA) and internal (ICA) carotid artery. Panel B quantifies the presence of contrast agent (~macrophage infiltration) at week 20 within the arterial wall of the same animal. Visually, regions with a high RRT value and macrophage infiltration overlap in the ECA and close to the bifurcation.

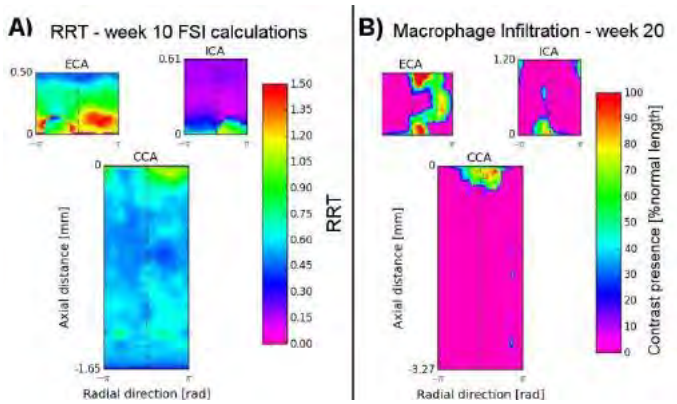

Figure 1: Representative case of a left carotid bifurcation splitted in its three main branches: CCA, ECA and ICA. (A) The relative residence time (RRT) calculated from mouse specific FSI simulations. At this time point no atherosclerotic plaques were discernable. (B) 10 weeks later the macrophage infiltration, as a marker of atherosclerotic plaque, was assessed using gold-particle enhanced μCT.

Maps as displayed in Figure 1 could be derived for 7 carotid bifurcations. When analyzing data at an individual branch level, no correlation was found between any of the hemodynamic wall parameters and the localization of contrast in the ECA and ICA. Only for the CCA, a significant correlation could be detected between RRT and presence of contrast in 4 out of 7 datasets (with similar results for OSI and TAWSS).

For the complete data set, the quantitative spatial correlation between the distribution of different wall shear stress metrics and the presence of contrast agents at week 20 is summarized in Figure 2. For each metric, the upper two symbols display the Spearman (ρ;diamond) and Pearson (r; triangle) correlation coefficients at bifurcation level taking into account the data from the 7 bifurcations. The highest correlations are found with RRT (positive correlation) and TAWSS (negative correlation). When analyzing aggregated datasets (lower two symbols; aggregate ρ: square; aggregate r: circle), the magnitude of the correlation tended to increase, with the highest value found for the Pearson correlation coefficient between aggregated maps of RRT and presence of contrast (r=0.575, P<0.001)

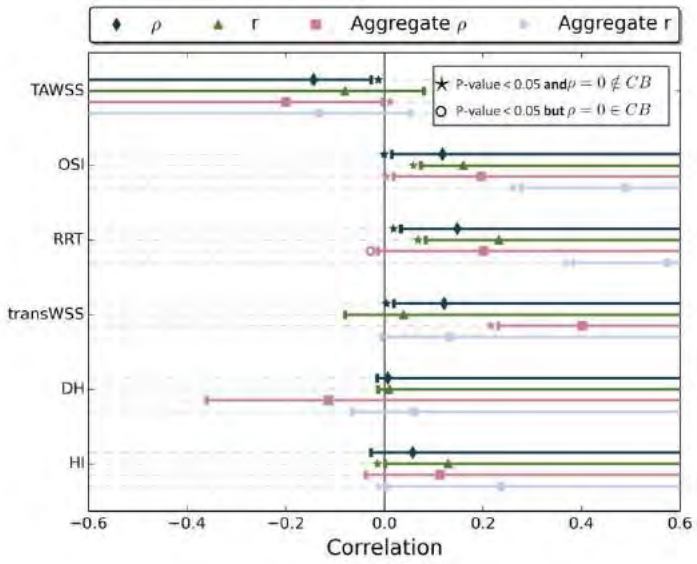

Figure 2: For the different shear stress metrics, the Spearman's (ρ) and the Pearson's (r) correlation coefficients are plotted together with the corresponding confidence bounds (CB). For the aggregated datasets, the correlation is overestimated.

CONCLUSION

We conclude that in the carotid bifurcation of the ApoE$^{-/-}$ mouse: (i) hemodynamic wall parameters are associated significantly with macrophage infiltration; (ii) the strongest spatial correlation between hemodynamics and atherosclerosis development was found for the relative residence time (RRT) and time averaged wall shear stress (TAWSS); (iii) data aggregating tends to overestimate the correlation.

ACKNOWLEDGEMENTS

DDW is recipient of a PhD grant by IWT-Flanders; BT is a post-doctoral fellow of FWO-Vlaanderen (Fund for Scientific Research Flanders).

REFERENCES

[1] De Wilde, D et al., *J Biomech,* in press, http://doi.org/10.1016/j.jbiomech.2015.11.048.

[2] De Wilde, D et al., *Mol Imaging*, 14:1-10, 2015, http://doi.org/10.2310/7290.2015.00009.

[3] Antiga, L et al., *IEEE Trans Med Imaging*, 23:704–13,2004, http://doi.org/10.1109/TMI.2004.826946.

[4] Peiffer, V et al., *J Biomech Eng*, 135:021023, 2013, http://doi.org/10.1115/1.4023381.

[5] De Wilde, D et al., *Ann Biomed Eng,* in press, http://doi.org/10.1007/s10439-015-1540-z.

Copyright 2016 The Organizing Committee for the 2016 Summer Biomechanics, Bioengineering and Biotransport Conference

SB^{3}C2016
Summer Biomechanics, Bioengineering and Biotransport Conference
June 29 –July 2, National Harbor, MD, USA
SB^{3}C2016-42

A CELLULAR AUTOMATA MODEL VERIFYING OSTEOBLASTIC BONE FORMATION *IN VITRO*

Estee L. George (1), Flora F. Opoku Asantewaa (2), Gabrielle K. Van Scoy (2), Alicia Prieto-Langarica (2), Marnie M. Saunders (1)
(1,2)

(1) Department of Biomedical Engineering
The University of Akron
Akron, OH, USA

(2) Department of Mathematics and Statistics
Youngstown State University
Youngstown, OH, USA

INTRODUCTION

Bone remodeling is a tightly regulated multicellular process by which osteocytes, osteoblasts and osteoclasts function to maintain or modify bone; this is done by creating, destroying and monitoring the bone matrix [1]. Regulation by bone-forming osteoblasts and bone-resorbing osteoclasts is influenced by a variety of factors including genetic and metabolic diseases, metastases, medications and altered loading environments. Understanding the interactions among cells in the presence of these factors is critical to manipulate bone's inherent remodeling ability to cure osteoporosis, halt metastatic bone progression, improve implant longevity and develop functional tissue-engineered substitutes. While *in vitro* cellular systems have been used to study bone cell interactions, the results of the studies cannot be extended beyond the specific model, environment and conditions established in the experiment. As such, there is tremendous variation in experimental results across laboratories, and extrapolating findings back to the *in vivo* system is challenging. To advance research in the bone field will require the development of novel model systems that incorporate the multicellular interactions of the osteocytes, osteoclasts and osteoblasts and enable the systematic investigation of soluble signals, cell contact and cellular communication. The development of cellular automata (CA) and agent-based models (ABMs) of bone dynamics offers the potential to provide an approach that can reflect biologic complexity and parallel biologic discovery without relying on a governing state equation. The objective of this study, to develop a CA to model bone formation, or mineralization, of osteoblasts *in vitro*, is a first step in this resolve.

METHODS

Preosteoblastic MC3T3-E1 cells were chosen for their ability to form bone in culture under induction conditions. Cells were seeded onto polystyrene tissue culture wells and maintained. Upon reaching 100% confluence, the cells were induced to differentiate into osteoblastic (bone-forming) cells by the addition of L-ascorbic acid (vitamin C) and beta-glycerophosphate to the culture medium. For quantification of bone formation, assays that indicate the presence of bone were performed. These assays were von Kossa stains, which reveal the presence of phosphate, and alizarin red stains, which show calcium. The percent area of culture well covered by each stain was quantified at differing time points using measurement features in the ImageJ software. In this study, the time point of interest was 26 days; this is the time at which cells have reached their maximum bone-forming potential.

In a CA model, the state of each element within an n-dimensional matrix is updated randomly by use of rules or transition probabilities that depend on the current state of the element and the current state of elements in its neighborhood [2]. To develop the model, an initial matrix containing all zeros was formed to represent the cell culture well. By use of experimental data and a count of the initial number of mineral sites, a random number of elements n within an MxNx1 sub-matrix was chosen. To begin the simulation, each element was changed to a positive number generated from a normal distribution. At each time step (here time is measured in days), the value of each element in the matrix changed stochastically depending on the total amount of mineral formed by the cells in the neighborhood. Larger quantities of mineralization, then, represented by large values in the simulation matrix, increase the chance that the value of a nearby cell will become “bone-forming” in the next time step.

For the CA model, Monte Carlo simulations were run to determine the average area covered by bone at 26 days. To validate the model, permutation tests were performed by use of the computer software R [3], and experimental and simulated data were compared.

Copyright 2016 The Organizing Committee for the 2016 Summer Biomechanics, Bioengineering and Biotransport Conference

RESULTS

Alizarin red stains of cell culture wells after 26 days are illustrated in Figure 1; von Kossa stains, not shown, were similar. Results of the mathematical simulations are depicted in Figure 2. For the CA model, 10,000 Monte Carlo simulations were performed; nine are shown. Figure 3 represents a comparison of the average percent areas covered by mineral for each analysis (alizarin red, von Kossa, CA simulation). The CA simulation presents a 35.10% increase in the average area covered by mineral from the alizarin red analysis; the simulation presents a 35.76% increase in the average area covered by mineral from the von Kossa analysis.

Permutation testing gave a test statistic of 2.61% and a *P*-value of 0.6389. Thus, it was sufficiently evident that the two data sets, experimental and simulated, were not statistically different from one another. In other words, the mathematical model was proven to produce results in keeping with experimental results.

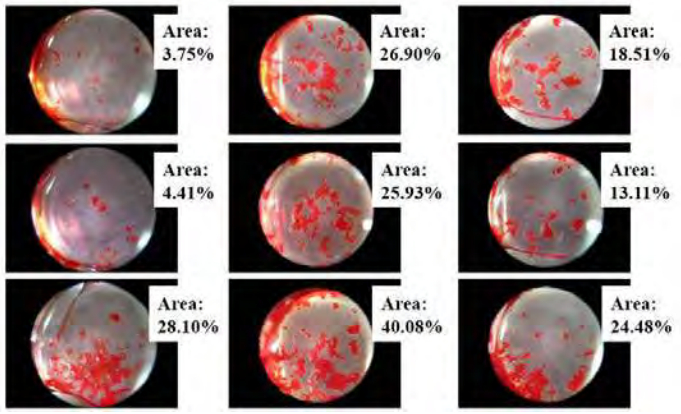

Figure 1: Experimental results of alizarin red analysis. Whole cell culture wells measure 1.9cm^2.

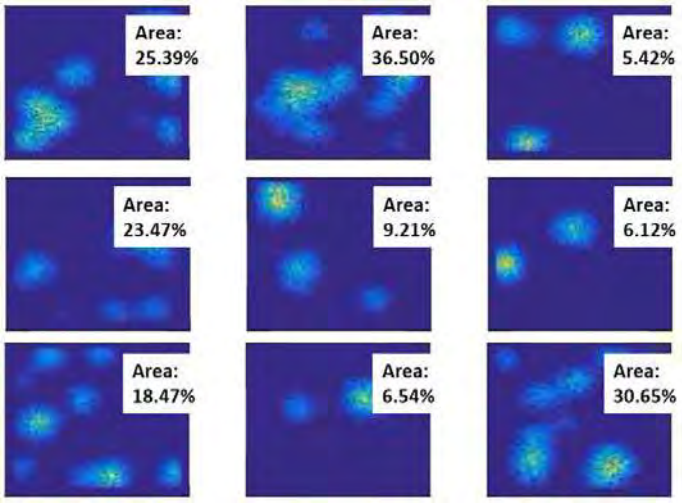

Figure 2: Simulation results. The scale for each image is 100*100 units. One unit is the mean length of one bone cell.

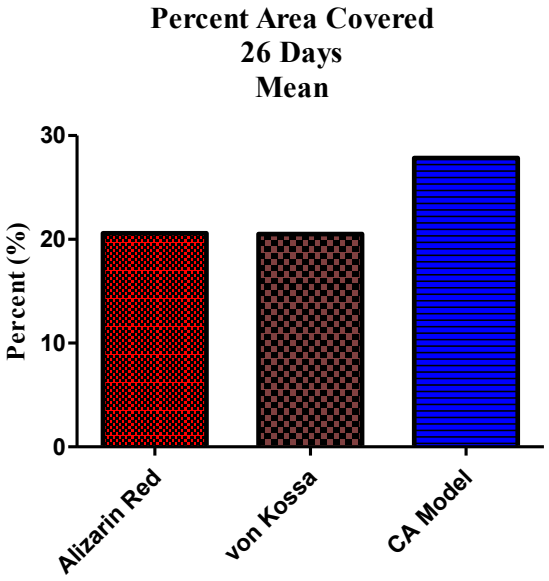

Figure 3: Average percent areas covered by mineral for each analysis. Results indicate the average percent area covered by alizarin red within experimental culture wells at 26 days was 20.6% (red); the average percent area covered by von Kossa was 20.5% (brown) and the average percent area covered for the CA model was 27.83% (blue).

DISCUSSION

This work is the first of a series of CA models which are being developed in order to better understand the mechanisms of bone formation and bone metabolism. This CA models with considerable accuracy the area covered by osteoblastic bone formation. In the future, the model will be expanded to incorporate elemental composition of mineral formed, concentration of alizarin red dye present within stained cultures, osteoblastic alkaline phosphatase activity (expressed during the formation of hard mineral) and the roles of biological markers/cytokines in bone formation/remodeling. As more data from *in vitro* studies are collected, the CA model will be further calibrated. Continued efforts will enable the development of an ABM that can incorporate multicellular interactions and reflect the contribution of the biologic milieu and the mechanical environment. Ultimately the goal is to develop an ABM capable of predicting bone remodeling as a function of environmental conditions.

ACKNOWLEDGEMENTS

This work is supported by The National Science Foundation through a CAREER grant (1060990) and by The National Institutes of Health NIDCR through an R15 grant (DE022664).

REFERENCES

[1] Burr, D et al., editors, *Elsevier*, 2013.
[2] Corne, D et al., *Biosystems*, 91(3):531-544, 2008.
[3] R Core Team, *R Foundation for Statistical Computing*, 2015.

Copyright 2016 The Organizing Committee for the 2016 Summer Biomechanics, Bioengineering and Biotransport Conference

SB3C2016
Summer Biomechanics, Bioengineering and Biotransport Conference
June 29 –July 2, National Harbor, MD, USA
SB³C2016-43

PROLIFERATION OF HUMAN ADIPOSE DERIVED STEM CELLS CULTURED ON POROUS POLY (L-LACTIC ACID) SCAFFOLDS PREPARED BY THERMALLY CONTROLLED METHOD

Harish Chinnasami and Ram Devireddy

Department of Mechanical Engineering,
Louisiana State University,
Baton rouge, Louisiana 70803, USA

INTRODUCTION

A tissue-engineered scaffold structurally mimics the intended tissue to be developed with adequate pore sizes for the stem cells to proliferate and differentiate. The initial scaffolds developed were primarily composed of ceramic compounds like hydroxyapatite, akermanite and tricalcium phosphate that are structurally rigid and resemble the mineral composition in bones. In recent years, many research works stressed on the advantages of using bio-compatible polymers such as poly (l-lactic acid) (PLLA), Polycaprolactone (PCL), poly (l-glycolic acid) (PLGA) as a scaffold material. Some of the prominent methods used to make polymer scaffolds are solvent casting, fiber bonding, membrane lamination and particulate leaching [1]. Absolute control over the 3D micro-structure of the scaffolds has been achieved by advanced methods such as computational topology design (CTD) and solid free-form fabrication (SFF) [2]. But these methods are very expensive when compared to TIPS, which could be easier to implement in large scale production.

The objective of this study was to (i) select suitable PLLA scaffolds for cell culture, (ii) to observe the viability of human adipose stem cells (hASCs) when cultured on these scaffold and (iii) to quantify the cellular growth inside the PLLA scaffolds selected. The future scope of this project is to make cryo-preservable bone-grafts for *in vivo* implantation into patients when needed.

MATERIALS AND METHODS

In thermally induced phase separation (TIPS) method, crystalline PLLA was dissolved in 1,4 Dioxane at 3, 7 and 10 (wt/vol)% to form a homogenous clear solution. These solutions were each frozen to a low temperature (-60°C), at 1, 10 and 40°C/min cooling rates (C.R.). The frozen solutions were lyophilized (freeze-dried) to remove the frozen solvent resulting in the final scaffold, which was 3D porous PLLA structure. The porous morphology of the scaffold was partly determined by the crystal formation of dioxane in the solution which was influenced by the applied freezing profile.

Porosity (%) of a scaffold was calculated at two positions (0-5 mm and 5-10 mm from bottom) by weighing a known volume of the scaffold and from the following formula:

$$Porosity\ (\%) = \left(1 - \frac{Scaffold\ Density}{Polymer\ Density}\right) \times 100 \quad (1)$$

Table 1: Porosities of the scaffolds made using the specified PLLA:Dioxane (wt/v) composition and the C.R.

PLLA: Dioxane	-1°C/min		-10°C/min		-40°C/min	
	(0-5) mm	(5-10) mm	(0-5) mm	(5-10) mm	(0-5) mm	(5-10) mm
3% (wt/v)	96.96%	96.89%	96.34%	96.75%	95.56%	95.50%
7% (wt/v)	94.16%	93.98%	93.92%	93.96%	91.81%	93.28%
10% (wt/v)	90.47%	89.46%	89.25%	89.69%	88.82%	88.39%

Figure 1: Cross-sectional SEM images of the micro-pore structures of the 7% (wt/vol) scaffolds cooled at (a) 1°C/min, (b) 10°C/min and (c) 40°C/min

Scaffold sections of 12mm diameter and 5mm height were coated with Platinum (15nm thick) using EMXS550X Sputter Coater. JEOL JSM-6610LV Scanning Electron Microscope was used to scan the samples and capture SEM images to qualitatively observe the pore structure and measure the pore sizes.

Copyright 2016 The Organizing Committee for the 2016 Summer Biomechanics, Bioengineering and Biotransport Conference

INSTRON 5900 Series – Advanced Mechanical Testing Systems Compression tester was used to compress scaffolds of 12mm in diameter and 10mm in height to 20% of its initial height, while simultaneously recording the applied load and strain. Compressive modulus was calculated as follows:

$$Compressive\ Modulus = \frac{\left(\frac{Applied\ Load}{Cross\ sectional\ area\ of\ scaffold}\right)}{Compressive\ strain} \quad (2)$$

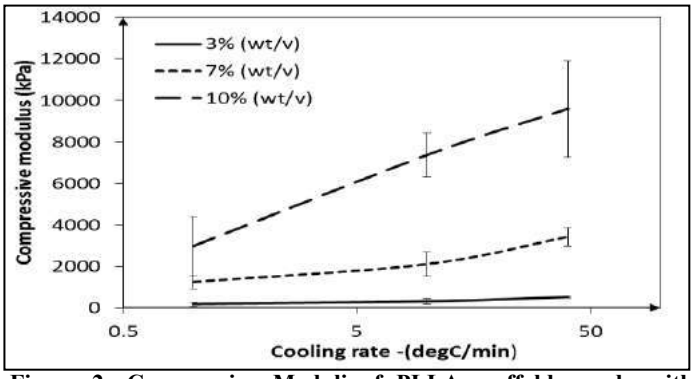

Figure 2: Compressive Moduli of PLLA scaffolds made with PLLA in Dioxane in 3, 7 and 10% (wt/vol) initially and also their variation with increasing cooling rate.

From the compression test results shows that 3% (wt/vol) scaffolds have very low modulus resulting in a weak scaffold that is difficult to manipulate during cell culture. Scaffolds cooled at 1°C/min showed irregular microporous structure. Therefore 7 & 10% (wt/vol) frozen at 10°C/min was selected for cell culture.

Cell Culture: Cryo-preserved hASCs were thawed and cultured in traditional Stromal Medium (SM) containing 90%(v/v) DMEM/F-12 (Gibco), 10%(v/v) Fetal Bovine Serum (Gibco), Penicillin - 90 IU/mL , Streptomycin – 90 µg/mL and Amphotericin B – 225 ng/mL. The PLLA Scaffolds were attached to the bottom of the 6-well plates using 1% Agarose (Sigma) as an adhesive. Equal number of hASCs was cultured simultaneously on both 3D porous scaffolds and 2D wells without scaffold as a control.

DNA Quantification: Number of cells on each sample at time point 0: ~10^5. The PLLA Scaffolds, homogenized with Dounce tissue grinder pestle (7 mL) (Sigma) as well as the control samples were incubated at 37°C with Lysis buffer (0.2 mg/mL Sodium Dodecyl Sulfate and 0.2 mg/mL Proteinase K) for 20 mins. The DNA present in the Lysis buffer was quantified using Quant-iT™ PicoGreen® dsDNA Assay Kit (Invitrogen) according to the manufacturer's protocol. The total DNA in each sample was normalized with the surface area exposed to SM in 1mm (150.80 mm^2), 5mm (263.89 mm^2) thick scaffolds and compared to 2D cell growth on control (962 mm^2).

Live/Dead Viability Assay: Number of cells on each sample at time point 0: ~10^4. Samples were incubated in staining solution of 2 µM Calcein AM and 4 µM Ethidium homodimer-1 (EthD-1) was prepared using LIVE/DEAD® Viability/Cytotoxicity Kit (Molecular Probes) stock solutions in DPBS for 20 mins at 37°C and were taken for fluorescence imaging using SteREO Lumar.V12 (Zeiss).

RESULTS

The proliferation of hASCs in scaffolds was measured by quantifying the amount of DNA in scaffolds and the viability was checked by fluorescence imaging after staining with live/dead dyes.

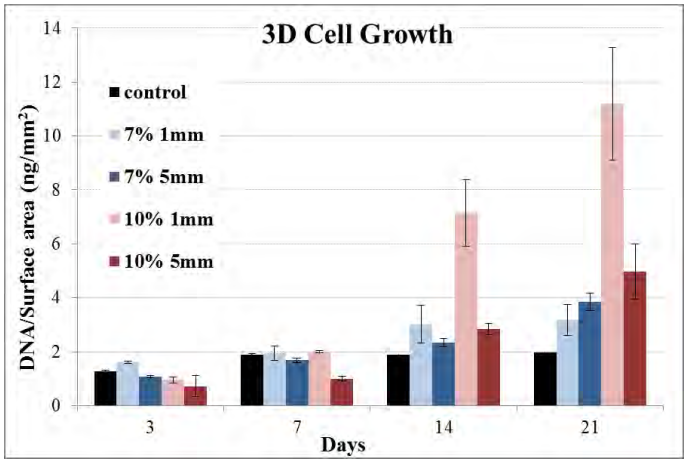

Figure 3: 3D cell growth measured by relative increase of DNA surface density (ng/mm^2) of scaffolds over control with time progression.

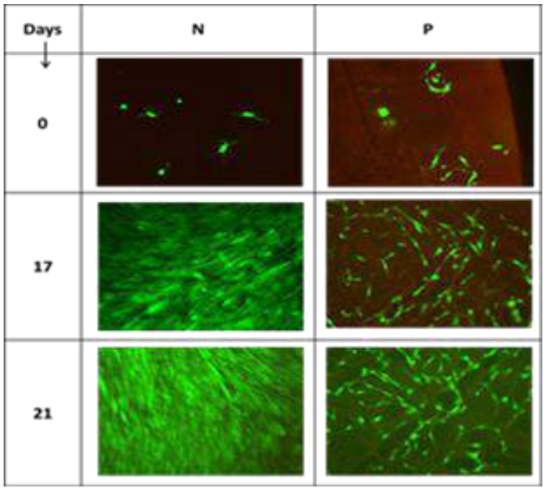

Figure 4: Live Cells (green) and dead cells (red) in Control samples (N) and PLLA Scaffolds (P) during time points 0, 17 and 21 days

DISCUSSION

Fig.3 shows DNA surface density increases with time in 3D scaffolds compared to 2D control where the cell growth stops at ~1.95 ng/mm^2 at day 7. This implies that cells are permeating through the scaffolds' micro-porous structure. 10% scaffolds show better cell growth than 7% even though the pore-sizes were comparatively low. This maybe because PLLA indeed promotes cell growth as seen in live/dead stain showing very little dead cell (similar to control). Therefore PLLA is also bio-friendly and shows no cytotoxicity to hASCs. The abundant growth in 10% 1mm scaffolds maybe because of better exposure to SM. Hence, either regular microstructure in scaffolds or simple increase in PLLA quantity could be favorable for cell growth, which will be investigated in future.

REFERENCES

1. Qingpu Hou et al., *J.Biomed Mater Res. Part B: Applied biomaterials*, 67(2):732-740, 2005
2. Scott J. Hollister, *Nature Materials*, 4:518-524, 2005.

Copyright 2016 The Organizing Committee for the 2016 Summer Biomechanics, Bioengineering and Biotransport Conference

SB^{3}C2016
Summer Biomechanics, Bioengineering and Biotransport Conference
June 29 –July 2, National Harbor, MD, USA
SB^{3}C2016-45

SCHWANN CELLS PROMOTE PENETRATION AND MYELINATION OF REGENERATED AXONS INTO PATTERNED CHANNELS

Chun Liu (1) and Christina Chan (1,2)

(1) Chemical Engineering and Materials Science Department
Michigan State University
East Lansing, MI, USA

(2) Biochemistry and Molecular Biology Department
Michigan State University
East Lansing, MI, USA

INTRODUCTION

Bioengineered scaffolds have the potential to enhance the organization of axon growth and guidance through the injury site after spinal cord injury [1-3]. Considerable progress has been made in enhancing the growth potential of injured adult axons, including aligning, lengthening, thickening, and myelinating the axons. Previously, we developed a pre-stretched anisotropic surface that successfully induced axon alignment and thickness of dorsal root ganglion (DRG) neurons and myelination [4].

Despite promising demonstrations in animal models, repair of long distance nerve injury with functional recovery is still challenging due to multiple factors, including axonal disruption, growth inhibitory molecules in the scar, lack of growth-promoting molecules, and incomplete remyelination [5-7]. Therefore, treatments to overcome these multiple deficits will require a multifaceted strategy, i.e. a multifunctional scaffold that can not only enhance axon growth and alignment but also deliver growth factors and promote myelination.

Schwann cells (SCs) are essential to the survival and function of neurons and play a vital role in the peripheral nervous system (PNS) by maintaining and aiding in the regeneration of axons [8]. It is known that SCs provide trophic support to promote the growth of axons from developing neurons [9]. SCs are also known to migrate into the central nervous system (CNS) and remyelinate the demyelinated axons after spinal cord injury (SCI). Due to their ability to secrete multiple growth factors, transplanting SCs hold promise as a therapeutic strategy for nerve regeneration.

We showed previously that the size of the channels of transplantable scaffolds strongly affects SC migration speed [10]. Here we explore axon growth in channels coupled with the migration of SCs, which offer trophic support to the regenerating axons. We designed a micropatterned channel platform using polydimethylsiloxane (PDMS) and co-cultured DRG neurons with SCs for 21 days to investigate the presence of migrating SC on the penetration and myelination of the axons into the channels. The effect of SCs on the axons were compared with nerve growth factor (NGF) released from a collagen gel and in different size channels.

METHODS

Patterned channel cell co-culture system fabrication

The micropatterned PDMS channels are prepared as [11], with two squares cut closely along with both ends of channels as an open area to seed cells. In order to create a sealed channel environment, the side of channel pattern is facing down and tightly attached to the PLL coated polystyrene substrate. Crosslinked collagen gel (375µl type I collagen + 27µl NaHCO3 + 50µl DMEM) was used as a glue to seal the edges, which helps to prevent the cells to be flushed outside the channel system.

Fluorescent imaging

The penetration of axons into channels was visualized through fluorescent live cell imaging, by adding 1µl of Fluo-4 into each well and incubate the cells at 37 °C for 30 mins. Fluorescent images were taken by a Leica DM IL inverted microscope (Bannockburn, IL) equipped with SPOT RT color camera (Diagnostics Instruments, MI) using a 10X objective.

Quantification of axon penetration depth

The axon penetration depth is defined as the furthest position the axons reach in each condition on each size channel. To quantify the axon penetration depth, a stage micrometer was first placed on objective to measure the diameter of the field viewed in eye pieces. The axon

Copyright 2016 The Organizing Committee for the 2016 Summer Biomechanics, Bioengineering and Biotransport Conference

penetration depth was quantified under the microscope according to the diameter and the size of channels. All the numbers are estimated values down to tens. 5 batches of biological replicates were quantified with each batch containing at least 4 identical replicates for each condition and each channel size.

RESULTS

Design of the patterned channel cell co-culture system

We co-cultured DRGs and SCs at opposite ends of the micropatterned channels (Figure 1a) and evaluated different size channels (50μm, 100μm, 150μm, and 200μm) as shown in Figure 1c. Freshly isolated DRGs were seeded at one end of the channels so that the cell bodies attached to the open area. As the axons grew and reached the start of the channels, they begin to penetrate into the channels, whereupon SCs were seeded at the other end of the channels to provide growth factors and migrate to the axons. As a positive control, in lieu of SCs, collagen gel pre-loaded with nerve growth factor (NGF) was added at one end of the channels as shown in Figure 1d, which provided growth factors to the axons extending from the other side. As a negative control, the one end of the channels, previously seeded with SCs or coated with NGF-containing collagen gel, was left blank (Figure 1b).

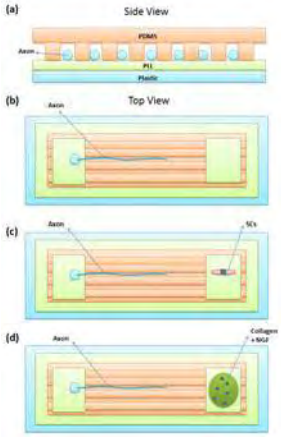

Figure 1: Schematic of micropatterned co-culture platform.
(a) Side view of the sealed channels. Polystyrene substrate is coated with a thin layer of PLL prior to overlaying the micropatterned PDMS. The sides of the channels are flush with the substrate to ensure a sealed channel environment for the axons to penetrate. (b) Top view of the platform. Freshly isolated DRG neurons are seeded in the open area at one end of the channels, with the regenerated axons penetrating into the channels. The open area on the opposite end of (Figure 1) the channels is left empty in the negative control group. (c) As the regenerated axons reach the end of the channels, SCs are seeded at the other end of the open area to promote axon penetration. (d) Collagen gel pre-loaded with NGF is alternatively added to the other end of the channels as a positive control.

Axon penetration depth and myelination under different conditions

We quantified the penetration depth after 21 days of culture of each group in each channel size as shown in Figure 2.

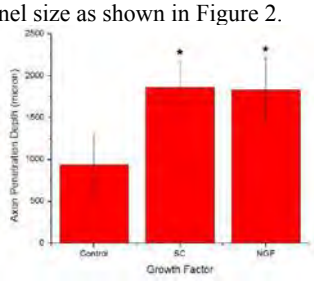

Figure 2. Quantification of axon penetration depth.
Comparison of penetration depth with all conditions and all channel sizes.

Both the SC and the positive control (NGF) group show much longer axons than the negative control group for all four channel sizes (Figure 2). However the difference between the SC and positive control group is not significant, but nevertheless differs with the channel size (data not shown). The addition of SCs minimized the effect of channel size. The results indicate that the addition of SCs or the NGF encapsulated gel effectively promote the penetration of the axons into the microchannels as compared to the negative control. However, the SCs group has the added benefit of enabling myelination of the axons (Figure 3). Findings from this study could inform the future transplantable scaffold design for nerve repair.

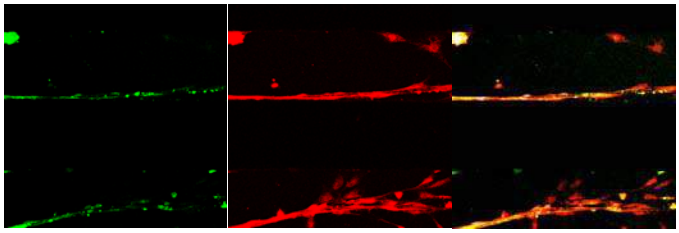

Figure 3. Quantification of myelination in the SC group.
Green is staining Tuj1 (indicator of axons), red is staining P0 (indicator of myelination) and yellow/orange is overlay of axons with SCs/myelination.

DISCUSSION

The addition of SCs offers two main advantages. First SCs are known to secrete growth factors that are beneficial to axon growth, and second migrating SCs decreases the diffusion distance to the axons thereby accelerating the delivery of the secreted growth factors. However, it is important to regulate the timing of SC addition since SCs could hamper the growth of the axons due to competition for nutrition as well as secretion of factors inhibitory to axon growth. Therefore, an ideal transplantable scaffold should be able to inhibit SCs from migrating towards the axons until after the axon growth period is completed. However, the scaffold should attract SCs towards the axons after their growth period to thereby myelinate the axon. To enable better control of SC migration, LbL self-assembled multilayers could be used in future to provide sandwich layers of compounds to repel and attract the SCs.

ACKNOWLEDGEMENTS

This study was supported in part by the National Science Foundation (CBET 0941055 & CBET 1510895), the National Institutes of Health (R21CA176854, R01GM089866, & R01EB014986).

REFERENCES

[1] Reffay, M et al., *Biophys J*, 100(11):2566-2575, 2011.
[2] Hamilton, DW et al., *Cell Motil Cytoskel*, 66(5):260-271, 2009.
[3] Walboomers, XF et al., *Biomaterials*, 19(20):1861-1868, 1998.
[4] Gupta, D et al., *Acta Biomaterialia*, 5(7):2560-2569, 2009.
[5] Gerecht, S et al., *Biomaterials*, 28(28):4068-4077, 2007.
[6] Teixeira, AI et al., *J Cell Sci*, 116(10):1881-1892, 2003.
[7] Mai, JY et al., *Biomed Microdevices*, 9(4):523-531, 2007.
[8] Silver, J et al., *Nat Rev Neurosci*, 5(2):146-156, 2004.
[9] Schwab, ME, *Curr Opin Neurobiol*, 14(1):118-124.153, 2004.
[10] Chen, BK et al., *J Neurotraum*, 26(10):1759-1771, 2009.
[11] Liu, C et al., *Tissue Eng Part C Methods*, In review, 2015.

Copyright 2016 The Organizing Committee for the 2016 Summer Biomechanics, Bioengineering and Biotransport Conference

SB^{3}C2016
Summer Biomechanics, Bioengineering and Biotransport Conference
June 29 –July 2, National Harbor, MD, USA
SB³C2016-46

EVALUATION OF A DISPLACEMENT-DRIVEN MODEL FOR ASSESSING PATELLOFEMORAL JOINT CONTACT MECHANICS

Jonathan A. Gustafson (1), Kyle A. Berkow (1), Richard E. Debski (1), Shawn Farrokhi (1)

(1) Department of Bioengineering
University of Pittsburgh
Pittsburgh, PA, USA

INTRODUCTION

The use of computational models is a highly attractive solution for studying the effect of joint injuries and diseases on joint mechanics. Specifically, the knee is one of the most at-risk joints for developing osteoarthritis (OA), a debilitating joint disease that is a 50% lifetime risk at the tibiofemoral joint and afflicts 25% of the population at the patellofemoral joint [1]. A recent review on the use of computational models for assessing knee joint contact mechanics describes the potential clinical utility of these models while stressing the importance of understanding the assumptions and limitations of different modeling techniques [2].

Models employing both finite element analysis (FEA) and discrete element analysis (DEA) methods typically require estimations of muscle and soft-tissue forces along with load-based optimization techniques to drive the models. Displacement control of models can bypass several of these passive and active force assumptions utilized with current force-control methods; however, highly accurate kinematics are essential for implementing displacement-driven models, as described by Fregly and co-workers [3]. Theoretically, these displacement-driven models could be incorporated with highly accurate in vivo kinematic data collection techniques, such as biplane fluoroscopy, to estimate knee joint contact mechanics in patients with knee OA during functional tasks with the hopes of providing better rehabilitative and treatment options for this patient population.

The objective of this work was to develop a computational framework for employing DEA methods driven by knee joint kinematics of different degrees of tibiofemoral flexion using experimental data. We assessed the models knee joint contact mechanics at several joint positions and compared contact mechanics values to prior literature employing force-control methods.

METHODS

One fresh-frozen cadaveric knee was initially prepared by: 1) isolation of the quadriceps tendons, 2) affixing rigid registration blocks to the femur, patella and tibia for digitization, and 3) acquiring high resolution MRI scans of the extended, unloaded knee. Experimentally, a six degree of freedom knee jig was used to apply physiologic compressive loading to the tibiofemoral joint and tensile loading to the quadriceps tendons at tibiofemoral flexion angles of 0° - 60° with 5° of varying internal/external femoral rotation at 0° and 15° to simulate gait kinematics during loading response. Kinematic data was collected at each position using a mechanical digitizer (Faro Arm®, Lake Mary, FL; Single-point precision = 0.025 mm).

Inputs to the computational model included specimen-specific knee geometry, cartilage material properties, and experimental kinematics. Model geometry of the knee was developed from manual segmentation (Mimics®, Materialise, Leuven, Belgium) of bone, cartilage, and registration blocks from the MRI scans. Surface geometry was created from the segmentation process and imported into meshing software (Hypermesh, Altair Engineering Inc., Troy, MI). Tetrahedral, shell elements with an average element size of 1 mm were used to model the bones and cartilage.

DEA was utilized for computational analysis at each position by creating compression-only springs (E=4MPa, ν=0.42 [4]) at the centroid of each element of the segmented femoral and patellar cartilage surfaces [5]. Local coordinate systems built on the surface of the registration blocks were used to relate the position of the knee model from the MRI scans to each of the experimental positions in order to load the joint [6]. Contact pressure distributions were estimated using the following linear elastic modeling equation:

Copyright 2016 The Organizing Committee for the 2016 Summer Biomechanics, Bioengineering and Biotransport Conference

$$P = \frac{(1-\nu)E}{(1+\nu)(1-2\nu)h}d, \quad (1)$$

where h is the undeformed surface to surface cartilage thickness and d is the spring deformation upon positioning the joint to its final, loaded state. Spring deformation was determined through a penetration analysis, where overlapping femoral and patellar cartilage elements were identified by computing the sign of the dot product of each element's outward normal and the vector connecting closest elements on each surface [4, 5]. Contact pressure was then calculated for each element (equation 1) and divided into medial and lateral patellar facet regions, defined by drawing a line through the inferior apex to the superior-most point on the base of the patella. The DEA algorithm was implemented using MATLAB (2015a, The Mathworks, Natick, MA).

RESULTS

Qualitatively, the contact pressure patterns between the varying femoral rotation angles were as expected, demonstrating increasing lateral facet pressure with increasing internal femoral rotation (**Figure 1**). Quantitatively, there was an increase of 5% contact area, 10% average contact pressure, and 5% peak contact pressure on the lateral patellar facet when going from an externally rotated femur to an internally rotated femur at 0° of flexion (**Table 1**). Additionally, there was a total increase of 276% contact area, 320% average contact pressure, 13% peak contact pressure when going from 0° to 60° of tibiofemoral knee flexion (**Table 2**).

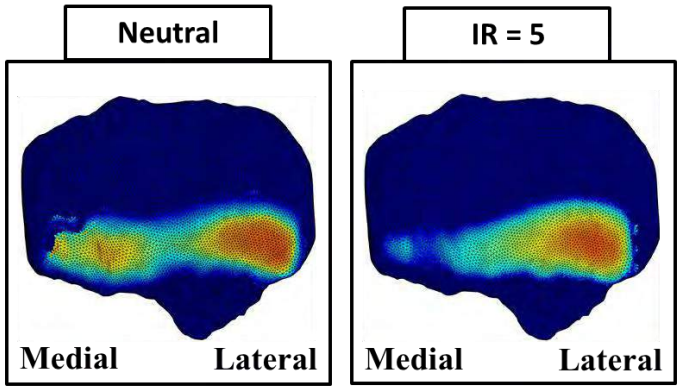

Figure 1: Patellofemoral pressure plots at 15° of flexion with 5° of femoral rotation (IR = Internal Rotation).

Table 1: Patellofemoral contact variables at 0° and 15° of flexion with 5° of femoral rotation (ER/N/IR = External/Neutral/Internal).

Position	Contact Area (mm^2) ER vs N vs IR	Avg. Pressure (MPa) ER vs N vs IR	Peak Pressure (MPa) ER vs N vs IR
Flexion = 0°			
Lateral Facet	144/149/151	0.50/0.45/0.55	5.09/4.22/5.34
Medial Facet	125/134/113	0.25/0.19/0.17	5.21/3.10/3.50
Flexion = 15°			
Lateral Facet	282/306/271	0.70/0.71/0.80	4.72/4.70/5.09
Medial Facet	301/304/230	0.57/0.55/0.30	4.13/3.90/3.27

Table 2: Patellofemoral contact variables from 30° - 60° of flexion

Position	Contact Area (mm^2)	Avg. Pressure (MPa)	Peak Pressure (MPa)
Flexion = 30°			
Lateral Facet	420	0.87	3.97
Medial Facet	415	0.80	3.82
Flexion = 45°			
Lateral Facet	509	1.03	3.92
Medial Facet	489	1.00	3.84
Flexion = 60°			
Lateral Facet	537	1.16	4.18
Medial Facet	526	1.09	3.92

DISCUSSION

This study assessed the utility of employing displacement-driven computational models in estimating patellofemoral joint contact mechanics. An important finding from this study is the models ability to differentiate between the different loaded positions. Specifically, the increase in contact area and contact pressure on the lateral patellar facet with increasing internal femoral rotation was expected and is significant. Patients with patellofemoral OA have demonstrated increased femoral rotation during walking [7]; thus, the model must be able to discriminate contact mechanics between small changes in femoral rotation to be used with kinematics collected in vivo.

The magnitude of our computational results is similar to prior studies [6, 8, 9]. Specifically, Fitzpatrick and co-workers report values for contact area, average and peak contact pressure between the range of 100 – 500 mm^2, 0.5 – 1.25 MPa, and 1.5 – 5 MPa, respectively [9]. Our model results for peak pressure are marginally higher, especially at the lower flexion angles (i.e. 0° and 15°), potentially due to the definition of cartilage to cartilage overlap, where in these lower flexion angles contact may be happening between cartilage and bone.

A number of limitations with the current study should be noted. First, results are indirectly compared with prior studies, which implemented different modeling techniques. However, these prior studies provide a benchmark for results from the current model. Additionally, cartilage is modelled as a linear, elastic material, though this assumption can be suitable under small durations of loading.

Future studies will perform direct validation of several knees in vitro as well as incorporate the use of these validated computational models with accurate 3D knee joint kinematics to estimate knee joint contact mechanics in patients with knee OA during dynamic activities in vivo. This study presents ground work for the potential use of displacement-driven models in assessing the effect of clinical intervention strategies for patients with knee OA.

ACKNOWLEDGEMENTS

The project described was supported by the National Institutes of Health (K12 HD055931) and the Pittsburgh Claude D. Pepper Older Americans Independence Center (P30 AG024827).

REFERENCES

[1] Arden, N et al., *Best Pract Res Cl RH*, 20:3-25, 2006.
[2] Henak, CR et al., *J Biomech Eng*, 135:021003, 2013.
[3] Fregly, BJ et al., *J Orthop Res*, 26:1173-1179, 2008.
[4] Blankevoort, L et al., *J Biomech*, 24:1019-1031, 1991.
[5] Elias, JJ et al., *J Biomech Eng*, 135:081011, 2013.
[6] Fischer, KJ et al., *J Biomech*, 34:377-383, 2001.
[7] Farrokhi, S et al., *J Biomech*, 48:1707-1712, 2015.
[8] Besier, TF et al., *J Orthop Res*, 23:345-350, 2005.
[9] Fitzpatrick, CK et al., *J Biomech Eng*, 132:121013, 2010.

Copyright 2016 The Organizing Committee for the 2016 Summer Biomechanics, Bioengineering and Biotransport Conference

SB³C2016
Summer Biomechanics, Bioengineering and Biotransport Conference
June 29 –July 2, National Harbor, MD, USA
SB³C2016-47

STUDY VASCULAR PERMEABILITY IN A MICROFLUIDIC DEVICE

Yaling Liu[1*], Chris Uhl[2], Antony Thomas[2], Salman Sohrabi[1]

[1]Department of Mechanical Engineering and Mechanics
[2]Bioengineering Program
Lehigh University, Bethlehem, PA

INTRODUCTION

Inflammatory response in endothelial cells leads to increased vascular permeability by formation of intercellular gaps. In this work we use an engineeredbiomimetic blood vessel microfluidic model to characterize the dynamic nature of increase in vascular permeability and compare these results to traditional transwell insert permeability assays. The biomimetic blood vessel model has a monolayer of endothelial cells cultured under *in vivo* levels of flow. This endothelial monolayer was treated with thrombin, a serine protease that induce a rapid and reversible increase of endothelial cell monolayer permeability. Tracer molecule samples were collected in real time and analysed via spectroscopy to reveal the dynamic nature of inflammation induced permeability change.

METHODS

Fabrication and EC culture on bio-mimetic blood vessel model

Channels made of polydimethylsiloxane (PDMS) were photolithographically patterned and fabricated, and a monolayer culture of BAOECs was attained as explained in our prior work [28].The upper and lower channels are casted out of Sylgard 184 PDMS(Dow Corning Corp.).The upper and lower channels are casted out of PDMS. The upper channel is 20 mm long, 350 μm wide and 100 μm tall, and the lower channel is 5 mm long, 1000 μm wide and 100 μm tall. A polycarbonate (PC), track-etched thin clear membrane (Whatman, GE Healthcare) with 1 μm diameter pores is embedded between two PDMS channels. The bottom channel PDMS layer is bonded on to a thin glass slide by exposing the sides in contact to oxygen plasma. Upper PDMS channels is bonded to the membrane by using a thin PDMS mortar film. The upper channel bonded to the membrane is then bonded to lower channel after making sure the channels are aligned. After each step the components were placed in an oven at 60oC for an appropriate time to enhance bonding. Inlet and outlet ports were punched to provide access to upper and lower channels.

Cell seeded devices were placed in an incubator under standard culture conditions (37^{o}C and 5% CO^2) overnight to allow cell attachment and spreading on the membrane. On reaching confluence, the BAOECs were subjected to a physiologically relevant FSS of 12 dyne/cm^2. The flow was brought using a high precision and extremely low pulsation peristaltic pump (ISMATIPC-N series) and the entire setup was placed in standard culture conditions. Recirculation of media was not permitted while thrombin and tracer molecules were passed through the channels.

Thrombin treatment and cell permeability assay

BAOECs were treated with thrombin at 1 Unit (U)/ml concentration after being subjected to 6 hrs or more of flow in the microfluidic model. Thrombin induces an acute inflammatory response on endothelial cells and leads to profound increase in cell monolayer permeability. Thrombin was added to flow media along with the tracer molecule and the treatment was performed under flow on the apical side of the cells. For this the BAOECs were seeded at a density of 2×10^4 cells in the luminal chamber of ThinCert transparent insert for 12-well plates having a membrane with 1 μm pore diameter. Cells were cultured in DMEM with 10% of heat inactivated fetal bovine serum and, upon confluence the cells were treated with thrombin by replacing the medium in the luminal side with fresh DMEM (1% heat inactivated serum) supplemented with thrombin and tracer molecule.

Vascular permeability occurs through intercellular gap formation. We quantified the dynamics and kinetics of cell permeability caused by thrombin on BAOECs using the biomimetic blood vessel model. Fluorescent FITC sodium salt (376 Da), FITC-Dextran 4k Da and FITC-Dextran 70k Da molecular weight were used as tracer molecules. FITC sodium salt was flowed at 0.625 mg/ml and the FITC-Dextran molecules at 5 mg/ml. The desired tracer molecule was included in flow media along with thrombin in the luminal upper channel and the extent of tracer molecule permeation to the abluminal lower channel is a direct indication of the level of vessel permeability. This was monitored in real time by withdrawing 6 μl samples from the outlet of the lower channel every 10 minutes. These samples were analyzed photometrically using Infinite 200 PRO NanoQuant microplate readers at 490 nm excitation and 521 nm emission. The volume of buffer solution in the lower channel was maintained constant by adding 6 μl of PBS to the inlet before withdrawing the data sample. The abluminal media sample collected every 10 min for the transwell insert static cell case was also analyzed as described above.

RESULTS

On-chip cell culture

Characterization of endothelial cell culture on the biomimetic blood vessel microfluidic device has been detailed in our prior work The device has the upper channel arranged perpendicularly to the lower channel. The media, thrombin and tracer molecule are flowed in through the inlet of the upper channel (**Error! Reference source not found.**A).The porous PC membrane is cell culture friendly and provides the base for cell growth and proliferation as demonstrated before[28, 37-40]. Transport between the upper and lower channels is limited through the membrane pores present at an average density of $1.5*10^7/cm^2$. This high pore density and the 1 μm pore diameter (**Error! Reference source not found.**B) allow diffusion of tracer molecules through the membrane to the lower channel once it passes through the EC layer. As explained in **Error! Reference source not found.**C, thrombin and tracer molecule flow along

Copyright 2016 The Organizing Committee for the 2016 Summer Biomechanics, Bioengineering and Biotransport Conference

with media and thus thrombin would act on the endothelial cell from the apical side. With the onset of cell-cell gap formation the tracer molecule would permeate through these gaps toward the lower channel. Thus the extent of vessel permeability can be quantified from the amount of tracer molecule in the lower channel.

An intact blood vessel endothelium is constantly exposed to FSS at its apical side due to blood flow. Therefore integrating in vivo levels of flow to the endothelial cell culture is important in limiting the chances of the cell monolayer undergoing phenotype drift and thus no longer reflecting in situ characteristics. Figure 1 D is a micrograph of F-actin stained flow aligned (12 dyne/cm2 FSS for 6 hrs) confluent BAOEC monolayer completely covering the base of the upper channel in our blood vessel model. The integrity and confluence of the cell layer was ensured to be optimal (at least 90% and comparable to Figure 1 D) through phase contrast microscopy before tests were performed.

Characterization of vascular permeability on biomimetic blood vessel model

Our platform is utilized to understand the increase in vessel permeability during an inflammatory state under physiologically relevant conditions. We used fluorescent tracer molecules of three different molecular weights and analyzed their diffusive permeability from the upper to the lower channel of the device, separated by the endothelial cell monolayer. The amount of tracer molecule transported to the lower channel will be a measure of vascular permeability based on its inflammatory response to thrombin treatment.

Endothelial barrier integrity was determined by real-time measurement of tracer molecule transport to the lower abluminal channel from the upper luminal channel, where the endothelial cells were grown to confluence on the semi-permeable membrane separating the two channels. FITC sodium salt, FITC-dextran 4kDa and FITC-dextran 70kDa were used as tracer molecules of different molecular weights and they were analyzed photometrically. Figure 2 A, B and C show the permeability curve for FITC sodium salt, FITC-dextran 4kDaand FITC-dextran 70 kDa respectively, along with the control case where the cells were not treated with thrombin. The data sample was collected from the lower abluminal channel every 10 min and the tracer molecule concentration was quantified by comparing the fluorescence intensity of collected data samples to a concentration calibration curve. It is observed that for all the tracer molecules the concentration in lower channel starts to increase acutely within 10 min of thrombin treatment and reaches the max value (0.09 mg/ml for FITC sodium salt, 0.34 mg/ml for FITC-Dextran 4kDa and 0.18 mg/ml for FITC-Dextran 70kDa) within 20-30 min. This means the permeability or gap formation of the endothelial cell monolayer initializes rapidly and reaches its maximum within 20-30 minutes. There is an increase of around 3.5 times in permeability for all the tracer molecules and this is a direct measurement of the change in endothelial cell-cell gap formation. Then a fall in abluminal concentration of tracer molecule is observed which plateaus to a minimum value at about 60-70 min. This signifies the decrease in endothelial cell permeability due to the reduction in intercellular gaps as a result of barrier recovery by the endothelial cells after the acute increase in permeability. FITC sodium salt and FITC-dextran (4 and 70 kDa) were included in flow media at different concentrations in the luminal channel for ease of photometrical detection and analysis.

Figure 2 C compares the concentration of the tracer molecules in the abluminal channel to their luminal concentration. For this, the concentration of tracer molecule in the abluminal channel is divided by the corresponding luminal concentration and compared with the thrombin treatment time. This normalizes the effect of doing the tests at different luminal concentrations to an extent and provides insights on how the size of the tracer molecule affects permeability. It is found that the permeability of tracer molecule across the endothelial cells decreased with increasing molecular weight. The lower molecular weight FITC sodium salt diffused faster and in larger quantity through the intercellular gaps than the higher molecular weight FITC-dextran 4kDa and 70 kDa. A reduction in diffusivity was observed with an increase in molecular weight of the tracer molecule.

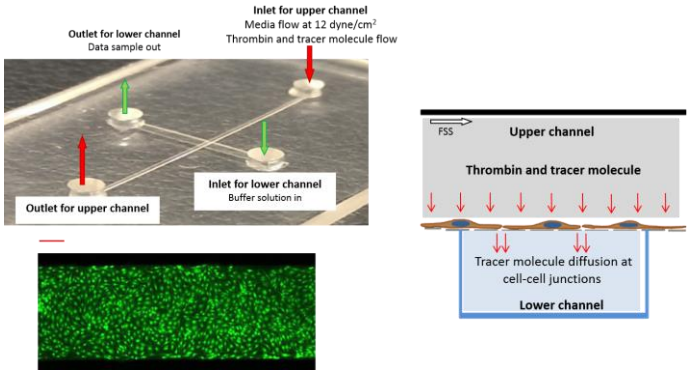

Figure 1: (A) Photograph of the bi-layer device showing the upper and lower channel separated by the semi-permeable membrane along with their inlets and outlets. The apical side of the EC layer face the upper channel and are exposed to media flow. Thrombin and tracer molecule are added to media to study blood vessel permeability under acute inflammation. Tracer molecule diffusion to lower channel is controlled by the extend of EC permeability under inflammation. The diffused data sample is collected from the lower channel. (B) Bright field image of the membrane with 1 µm diameter pores at an average density of 1.5*107/cm2. (C) Schematic depict EC growth on semi-permeable membrane, thrombin treatment from upper channel and tracer molecule diffusion through intercellular gaps. (D) Fluorescence labeled actin cytoskeleton (FITC-phalloidin) images of confluent BAOEC layer aligned to flow (12 dyne/cm2 FSS for 6 hrs) in the upper channel. Arrow shows flow direction (Scale bar: 100 µm)

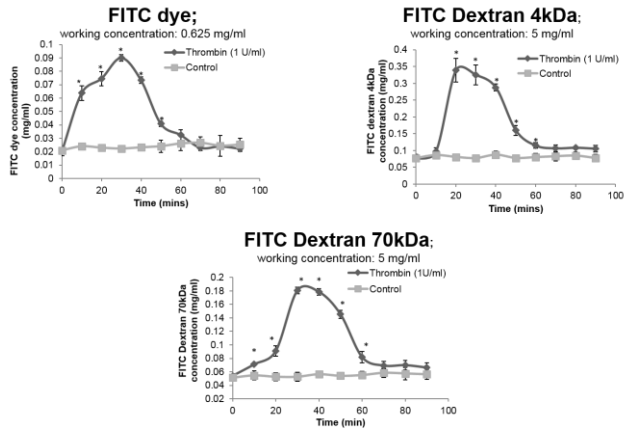

Figure 2: Permeability of the tracer molecule through the EC layer in the biomimetic device. (A) Permeability of FITC dye through the EC layer when treated with thrombin at 1 U/ml compared to control case. (B) Permeability of FITC dextran 4kDa through the EC layer when treated with thrombin at 1 U/ml compared to control case. (C) Permeability of FITC dextran 70kDa through the EC layer when treated with thrombin at 1 U/ml compared to control case. (D) Normalized comparison of FITC dye and FITC dextran 4 kDa permeability on the EC monolayer when treated with thrombin at 1 U/ml. FITC dye with a lower molecular weight has higher permeability compared to FITC dextran 4 kDa. Asterisks indicate values significantly different from control values ($p < 0.05$).

ACKNOWLEDGEMENTS

The authors acknowledge the supports of this work from National Science Foundation (NSF) CAREER grant CBET-1113040, NSF CBET-1067502, and National Institute of Health (NIH) grant EB015105.

REFERENCES

1. A. Thomas, D. Ou-Yang, L. Lorentz, V. Muzkantov, Y. Liu, "Biomimetic Channel Modeling Local Vascular Dynamics of Pro-inflammatory Endothelial Changes", *Biomicrofluidics*, 10, 014101, 2016

2. A. Thomas, J. Tan, Y. Liu, "Characterization of Nanoparticle Delivery in Microcirculation through a Microfluidic Device", Microvascular Research, 94: p. 17-27, 2014

Copyright 2016 The Organizing Committee for the 2016 Summer Biomechanics, Bioengineering and Biotransport Conference

SB^{3}C2016
Summer Biomechanics, Bioengineering and Biotransport Conference
June 29 –July 2, National Harbor, MD, USA
SB^{3}C2016-48

A MODEL FOR BIOLOGICAL FIBERS DERIVED FROM IMPLICIT ELASTICITY

Alan D. Freed

Department of Mechanical Engineering
Texas A&M University
College Station, TX 77845

INTRODUCTION

Collagen fibers are aggregate assemblages of collagen fibrils. Fibrils have a linear elastic response [1]. As a fiber becomes extended, individual fibrils get recruited and begin to bare traction [2]. The integral sum over this stochastic Poisson process [3] produces a stress-strain curve that starts out with a soft compliant response—nonlinear in stress—and finishes up with a stiff response—linear in stress. Applications of this strategy are computationally intensive [4]. In this paper an alternative approach is presented for describing an elastic biological fiber. The model was derived from thermodynamics and has been recently published by the author and his colleague [5].

FIBER MODEL

Consider two neighboring particles along the backbone of a fiber separated by a distance dX in some reference state that is free from traction. Under a state of traction, these particles become separated by a distance dx of which some fraction $d\xi$ represents a contribution caused solely by an unraveling of molecular configuration, e.g., a straightening of the crimp in collagen fibers. From these measures of length one can establish an overall stretch of $\lambda = dx/dX$, a stretch $\lambda^C = dx/d\xi$ where collagen carries the bulk of the traction, and a stretch $\lambda^E = d\xi/dX$ where an elastin network entangling the collagen carries the bulk of the traction. From the product rule, $\lambda = \lambda^C\lambda^E$ and $d\lambda = d\lambda^C\,\lambda^E + \lambda^C\,d\lambda^E$, the latter of which is coupled. This sum uncouples by dividing the equation through by the stretch λ, after which one gets $d\lambda/\lambda = d\lambda^C/\lambda^C + d\lambda^E/\lambda^E$ or $d\varepsilon = d\varepsilon^C + d\varepsilon^E$ which are logarithmic strain rates. Consequently, these strains add in the sense that $\varepsilon = \varepsilon^E + \varepsilon^C$ wherein $\varepsilon = \ln\lambda$, $\varepsilon^C = \ln\lambda^C$ and $\varepsilon^E = \ln\lambda^E$ are all true strain measures.

This additive decomposition in strain allows the work that is being done on a fiber, viz. $dW = \tau\,d\lambda$ wherein τ denotes the traction, to take on an equivalent form of $dW = \sigma\,d\varepsilon = \sigma\,d\varepsilon^C + \sigma\,d\varepsilon^E$ wherein $\sigma = \lambda\tau$ is the true stress of Cauchy. This stress acts on both strain increments. Consequently, the work being done becomes a sum of two separate work terms: $dW = dW^C + dW^E$ wherein $dW^C = \sigma\,d\varepsilon^C$ and $dW^E = \sigma\,d\varepsilon^E$.

Freed & Rajagopal [5] built their model for biological fibers in accordance with the graphic of Fig. 1. Like Carton et al. [6] and Maksym & Bates [7], we modeled elastin with a strain limiting material model. The difference being, their models were phenomenological in origin, whereas ours was derived rigorously from thermodynamics. To the strain attributed to elastin, in accordance with the above additive decomposition of strain, we add a linear strain accumulation attributed to collagen.

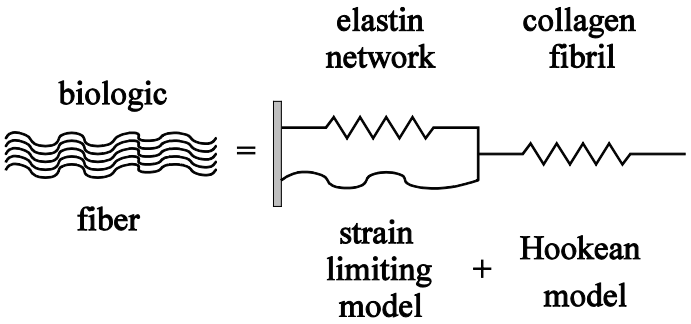

Figure 1: Schematic for modeling the elastic response of biological fibers. The elastin network is described by a strain limited spring, while the collagen is described by a Hookean spring.

Copyright 2016 The Organizing Committee for the 2016 Summer Biomechanics, Bioengineering and Biotransport Conference

From an energetic perspective, and in accordance with the above decomposition of work, Freed & Rajagopal [5] modeled the strain contribution arising from a stressing of the collagen with a classic Gibbs potential, and we modeled the strain contribution arising from a stressing of the elastin with a novel, implicit, energy potential—an idea proposed by Rajagopal [8] in 2003—where here the energy potential depends upon both stress and strain. The stored energy potentials that we selected led to strain relationships of

$$\varepsilon^C = \frac{\sigma}{E^C} \quad and \quad \varepsilon^E = \frac{1}{\beta}\left(1 - \frac{1}{\left(1+(\beta-1)\sigma/E^E\right)^{\beta/(\beta-1)}}\right) \tag{1}$$

where strain $\varepsilon = \varepsilon^E + \varepsilon^C$ is described in terms of three material constants: E^C ($> E^E$) is the elastic modulus of the collagen fiber, i.e., the terminal stiffness, E^E (> 0) is the elastic modulus of the elastin network, i.e., the initial modulus, and $\beta = 1/\varepsilon^E_{max}$ (> 1) is a reciprocal to the limiting state of the molecular reconfiguration strain ε^E. These material constants can be acquired through a graphical procedure, as illustrated in Fig. 2.

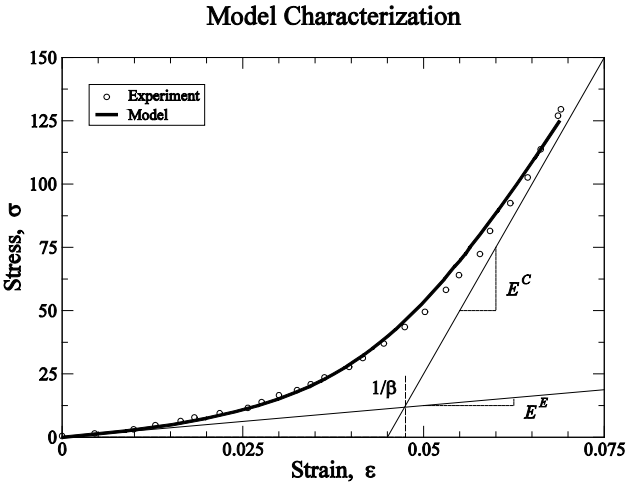

Figure 2: Illustration of graphical parameterization of model (1). E^C and E^E are the asymptotes for the tangent moduli at large and small strains, respectively, while 1/β is approximated well as the strain at the intersection of these two asymptotic lines.

RESULTS

The data presented in Fig. 2 are for a porcine chordae tendineae excised from a mitral valve [9]. The material constants for model (1), as drawn in Fig. 2, are: $E^C = 5000$ N/m, $E^E = 250$ N/m and $\beta = 21$. These parameters were obtained graphically. No computer optimization algorithm was employed, nor required. The model does an excellent job of describing these data.

DISCUSSION

Babu et al. [10] used the four-parameter, transversely isotropic model of Holzapfel et al. [11] where an exponential is employed to describe the strain response of the fiber. They used this model to describe the loading response of human aortas excised from sixteen individuals who suffered an aortic dissection, ages 7 to 71. They were unable to assign, with statistical significance, any dependence upon age to the parameters from the parametric fits of this model to their data. This led them to propose a phenomenological description of their data, which they described in terms of three parameters: E^C, E^E and σ^T. These are the same material parameters that the author derived from theory, as presented in Eq. (1), in that their transition stress σ^T equals our E^E/β.

The parameters of our material model (1) are unique, physical and intuitive. They are true material constants whose values will permit inferences to be drawn between different biologic materials, e.g., natural vs. engineered tissues. Furthermore, these material constants can be extracted from a tensile curve using simple graphical techniques.

In work that is underway, the elastic fiber model presented here has been extended into the viscoelastic domain. Also, multidimensional formulations based on this one-dimensional theory are being developed.

ACKNOWLEDGEMENT

The author would like to thank Prof. Jun Liao for making available the raw data from his thesis, as presented in Fig. 2.

REFERENCES

[1] Sasaki, N., Odajima, S., *J. Biomech.*, **29**:655-658, 1996.
[2] Lanir, Y., *J. Biomech.*, **12**:423-436, 1979.
[3] Soong, T.T., Huang, W.N., *Biomech.*, **6**:451-458, 1973.
[4] Fan, R., Sacks, M.S., *J. Biomech.*, **47**:2043-2054, 2014.
[5] Freed, A.D., Rajagopal, K.R., *ACTA Mech*., in press.
[6] Carton, R.W., et al., *J. Appl. Physiology*, **17**:547-551, 1962.
[7] Maksym, G.N., Bates, J.H.T., *J. Appl. Physiology*, **82**:32-41, 1997.
[8] Rajagopal, K.R., *Applic. Math.*, **48**:297-319, 2003.
[9] Liao, J., PhD thesis, Cleveland State Univ., Cleveland, OH, 2003.
[10] Babu, A.R. et al., *J. Biomech. Engr*., **137**:081013, 2015.
[11] Holzapfel, G.A. et al., *J. Elasticity*, **68**:1-48, 2000.

Copyright 2016 The Organizing Committee for the 2016 Summer Biomechanics, Bioengineering and Biotransport Conference

SB^{3}C2016
Summer Biomechanics, Bioengineering and Biotransport Conference
June 29 –July 2, National Harbor, MD, USA
SB^{3}C2016-49

USING AN ELECTROACTIVE POLYMER, DIELECTRIC ELASTOMER, FOR MAKING IMPLANTABLE BLOOD PUMPS

Sheldon Ho (1), Yoke Yin Foo (1), Hareesh Godaba(2), Phan Thien Nhan (2), Zhu Jian(2), Choon Hwai Yap (1)

(1) Department of Biomedical Engineering.
National University of Singapore, Singapore

(2) Department of Mechanical Engineering.
National University of Singapore, Singapore

INTRODUCTION

Current Ventricular Assist Device and Total Artificial Hearts are actuated based on continuous rotary pumps or hydraulic/pneumatic pumps. We propose to use an electroactive polymer, Dielectric Elastomer (DE), to fabricate these implantable blood pumps. DE is an advanced robotics material that sustains large deformations when given voltages, and has been recently hailed as "artificial muscles", as it is closest to natural muscles than alternatives, in terms of energy density and actuation magnitude. Due to its flexibility, high deformation capability[1], high energy density[2] and inexpensive nature[2], DE is explored for multiple applications such as linear actuators[3], generators[4] and microfluidic pump[2]. Much exploration is needed for application in macro-scale pump.

Using DE to make blood pumps allow reduction of device foot print, via removal of hydraulic/pneumatic systems, and allow a more organic shaped blood pump which can preserve natural fluid dynamics of the heart to reduce blood damage.

Traditional DE, fabricated with an acrylic polymer, VHB™ (3M Inc.)[3,4] suffers from high viscoelasticity[5], resulting in energy loss and damping of motion, compromising pumping performance at higher frequencies. In the current study, we investigate the use of a composite material in DE and show that it can generate higher flow rates and power outputs at frequencies close to the heart rate.

METHODS

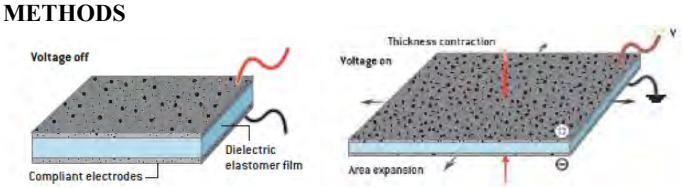

Fig 1. Dielectric Elastomer is actuation based on electrostatic attraction of soft electrodes

The non-composite DE was fabricated using one layer of 10mm thick VHB polymer (VHB4910, 3M Inc.), while the composite DE was fabricated using 2 layers of 5mm thick VHB polymer sandwiching a thin layer (0.16mm) of Latex membrane (Oppo 8001). Carbon grease was used as electrodes and was applied on both side on the DE. DE works on the principles of hydrostatic attraction between the soft electrodes for actuation (Figure 1).

A simplified DE fluid pump was fabricated by attaching a DE membrane to a PVC cylinder (56mm diameter). The DE membrane was subjected to 200% prestretch before attachment to the cylinder. The DE fluid pump was attached to a water reservoir via soft tubing of 2cm diameter and the water column is raised to about 80-120mmHg (figure 2). AC voltage was supplied to bring about cyclic expansion and then contraction of the DE membrane to cause pulsatile pumping (figure 2b). The pump was tested at various frequencies with increasing voltages until breakdown occur.

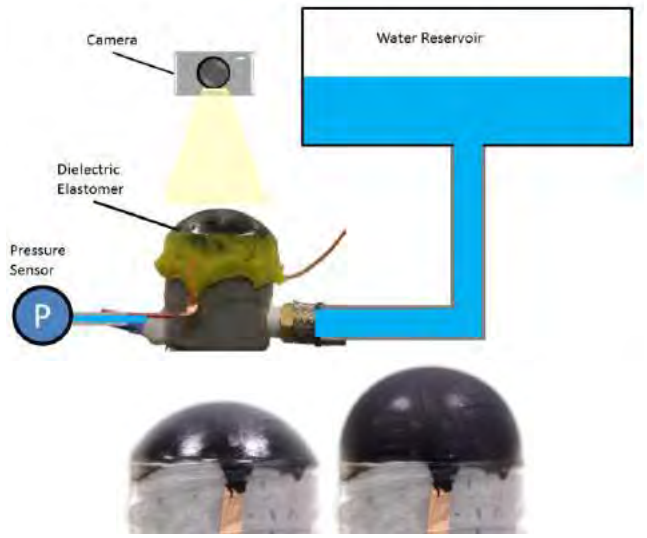

Figure 2: (a) Schematic of in-vitro flow setup to test the DE fluid pump. A large water reservoir was used to maintain a constant hydrostatic pressure. A pressure sensor measured localized transient pressure within the pump. (b) left: unactuated pump, right: actuated pump with voltage supplied.

Copyright 2016 The Organizing Committee for the 2016 Summer Biomechanics, Bioengineering and Biotransport Conference

RESULTS

In the fluid pump, the breakdown voltage increased from 6kV in the non-composite DE to 10kV in the composite DE due to the change in dielectric strength and the increase in thickness.

Representative plots of volume of the non-composite DE pump over time are shown in figure 3, which demonstrates the role of viscoelasticity in reducing pump performance. With increasing pumping frequency, viscoelasticity limits the deformation motion of the DE membrane to cause reduction in the actuation volume (difference between maximum and minimum volumes). There is thus a need for a new material for better performance at higher frequencies.

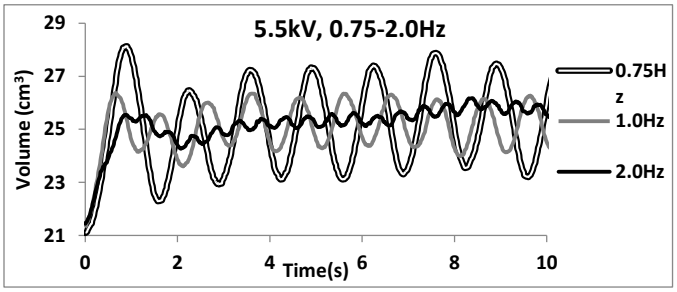

Figure 3: Plot of volume of non-composite (VHB) DE pump versus time between frequencies of 0.75Hz to 2Hz.

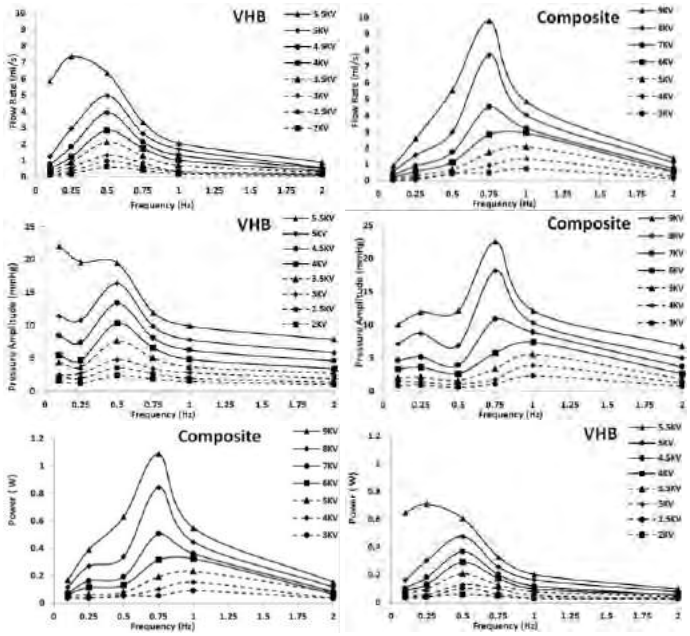

Figure 4: Comparison of DE fluid pump's net volumetric flow rate and pressure at frequencies and voltages before breakdown.

Figure 4 shows the comparison in the pumping performance between the traditional, non-composite DE fluid pump, versus the composite DE fluid pump. The resonance frequencies were found to be around 0.5 Hz for non-composite DE, but at around 0.75 Hz for composite DE. At the same time, the maximum flow rate achievable with the composite DE pump was 9.79 ml/s, which was higher than that in the non-composite DE pump (7.37 ml/s). At the higher frequencies of 0.75 Hz and above, the composite DE pump brought twice as much flow rate as the non-composite DE pump. For example, at 1 Hz, maximum achievable flow rate increased by 135% from 2.08 ml/s to 4.87 ml/s.

It is thus observed that through modifying the composition of the polymeric body of the DE, we could engineer its natural frequency to control resonance and yield much higher flow rate at higher frequencies. It is observed that pumping at the resonance frequency yields much higher performance than at non-resonance frequency indicating the importance of usage at the appropriate frequency and optimizing the composition to meet required frequency.

In terms of actuation pressure amplitudes generated by the DE fluid pump, as shown in figure 3b, both composite and non-composite DE pump generated similar pressure amplitudes, demonstrating maximum achievable pressure amplitudes of 22.1 mmHg and 22.6 mmHg respectively.

Finally, we observed that pump flow rates are greatly enhanced close to the resonance frequency, and were significantly higher than if the pump was operated not near to resonance frequency, underlying the importance of designing the natural frequency of the pump to specific applications.

DISCUSSION

To understand the role of viscoelasticity in causing this difference, we first note that actuation cycle of the DE membrane was such that the membrane expanded when the voltage was non-zero, and relaxed when the voltage was zero. Viscoelasticity, as a damping force on deformation, caused the DE membrane to relax towards its initial configuration gradually instead of immediately. At higher frequency, there is insufficient time during the relaxation phase for the membrane to relax completely before the next cycle started. Thus, the membrane could only oscillate between two very similar volume states, reducing the actuation amplitude and eventually leading to drastic drop in pumping performance for the non-composite DE pump.

The motivation for our selection of a composite of both VHB and latex was because of desirable qualities of both materials. On one hand, latex had very low viscous properties, and could down-moderate the high viscous properties of VHB in the composite. On the other hand, VHB was more elastic, and could sustain large deformations, but latex could not. DE pump made completely from latex yielded very poor results with negligible volume changes, due to the high stiffness of the latex and poor expansion capabilities under Maxwell stresses. A composite consisting of both materials was thus a good way to get the best of the two materials.

Heart failure is accountable for 2.8% of all deaths, and cost an estimated $32 billion per year in the US alone. There is much incentive and urgency to develop improved prosthetic hearts and cardiac assist devices to treat patients. With its properties that mimics natural muscles, DE is a promising material to use to fabricate the next generation implantable blood pumps and warrants investigations. DE also holds the promise of eventually developing into a more organically-shaped heart retaining the geometry and actuation motions of the natural heart.

ACKNOWLEDGEMENTS

The authors acknowledge funding support from The Singapore Millennium Foundation, grant number R397-000-200-592 (PI: Yap).

REFERENCES

[1] Gobada, H et al., *Applied Physics Letters*, 2014, 105, 112901.
[2] S. Ashley, *Scientific American*, 2003, 289, 52-59.
[3] Huang, J et al., *Applied Physics Letters*, 2012, 100, 211901.
[4] Shian, S et al., *Adv Mater*, 2014, 26, 6617-6621.
[5] Fan, F et al, *Macromolecular Mat and Eng*, 2015, 300, 99-106.

Copyright 2016 The Organizing Committee for the 2016 Summer Biomechanics, Bioengineering and Biotransport Conference

Proceedings of the ASME 2016 Summer Bioengineering Conference
SBC2016
June 29 – July 2, 2016, National Harbor, Maryland, USA
SB³C2016-50

UPPER AIRWAY DYNAMIC CHARACTERISTICS IN HEALTHY SUBJECTS AND OSA PATIENTS

Ashaat[1], S., Al-Jumaily[1], A.M., Huang[2], L.

[1]Institute of Biomedical Technologies,
Auckland University of Technology,
Auckland, New Zealand

[2]Department of Mechanical and
Production Engineering,
Auckland University of Technology,
Auckland, New Zealand.

ABSTRACT

The dynamic characteristics of human upper airway (UA) differ from healthy subjects to obstructive sleep apnea (OSA) patients. It is very difficult to find a common term of reference for comparison as many anatomical parameters are involved, such as air gaps at the rear of the mouth, volume of airway, uvula and tongue. This study investigates these characteristics in healthy subjects and OSA patients and introduces new common ground parameters for comparison. The objective of this study is to identify the causes of collapse by comparing between these characteristics in the two groups. MRI data of the UA were collected on 18 volunteers (8 healthy subjects and 10 OSA patients), and 3D models were constructed and simulated. Also, measurements of the UA were determined and compared in the two groups. The outcomes suggest that the apneic events are primarily caused by the large size of the tongue and uvula, and the air volume is not the main contributor to UA collapse. Finally for each subject's specifics, the natural frequencies of the uvula and tongue models are very close to one another, which suggests that they can be stimulated at the same time with approximately the same frequencies.

INTRODUCTION

OSA is the most prominent UA respiratory system disease [1]. It occurs due to obstruction in the UA region [2] and is characterized by repeated episodes of obstruction and collapse of the pharyngeal airway during sleep [3]. UA collapse occurs when the forces of the airway wall muscles become less than the forces generated from the airway negative pressures during the respiration process [4].

The tendency for UA obstruction increases when the patient sleeps in supine position, as gravitational forces pull the uvula and tongue towards the airway walls reducing the air gap between these tissues and the airway walls, which increases the chance for airway obstruction and collapse [5]. OSA can lead to many health implications such as hypertension, stroke and cardiovascular disease [6].

The dynamic characteristics of human upper airways differ from healthy subjects to OSA patients. Also, having a common term of reference for comparison is very difficult as many anatomical parameters are involved such as: volume of airway, uvula and tongue, and air gaps at the rear of the mouth. This study investigates these characteristics for healthy subjects and OSA patients and proposes new common ground parameters for comparison. The objective of this study is to identify the causes of collapse by comparing those characteristics between healthy subjects and OSA patients.

METHOD

While awake and in supine position, MRI data of the UA were collected for 18 non-smoking volunteers, consisting of 8 healthy subjects (4 males and 4 females) and 10 OSA patients (7 males and 3 females) with age of 31.12±10.10 and 55.00±8.22 years; respectively. BMI was 25.42±1.46 kg/m^2 for the healthy subjects; and 36.58±9.37 kg/m^2 for OSA patients. Ethical approval was granted by The Auckland University of Technology Ethics Committee and consents were obtained prior to initiation of the study procedures.

Three dimensional models for the UA including air, uvula and tongue were constructed from the MRI data using 3D-DOCTOR software and their sizes and the air gaps at the rear of the uvula and tongue and at the mid-sagital plane (MSP) were determined. Uvula and tongue models were simulated on the ABAQUS software to determine their natural frequencies. Figure 1 shows the region of interest and samples of the constructed models for air, uvula and tongue.

Copyright © 2016 by ASME
Copyright 2016 The Organizing Committee for the 2016 Summer Biomechanics, Bioengineering and Biotransport Conference

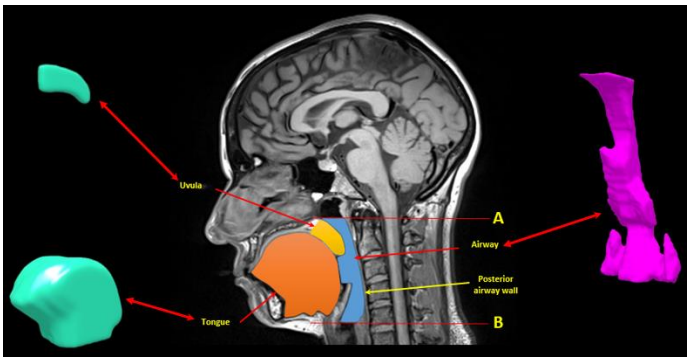

Figure 1: Region of interest expanding from the nasopharynx (A) to the hypopharynx (B); and samples of the constructed models

RESULTS AND DISCUSSION

Air gap at the rear of mouth: The values for the minimum air gaps at the rear of the uvula and tongue at MSP were 5.18±2.75 mm and 7.74±4.15 mm, respectively for healthy subjects; 6.43±1.19 mm and 8.22±2.10 mm, respectively for OSA patients. These results show that OSA participants have relatively larger air gaps at the rear of the mouth than the healthy participants.

Air Volume: For healthy subjects, the air volume was 12272.40±4161.57 mm^3 occupying 13.47±3.39% of the entire UA volume; while for OSA patients the air volume was 18830.10±8172.50 mm^3 occupying 12.76±4.31% of the entire UA volume. These results show that the participating OSA patients seem to have larger air volume than healthy subjects but with a slightly smaller percentage of the total UA volume.

Uvula Volume: For healthy subjects, the uvula volume was 1250.38±247.95 mm^3 occupying 1.57±0.23% of the total UA volume; while for OSA patients the uvula volume was 1942.90±234.03 mm^3 occupying 1.34±0.18% of the total UA volume. These results show that OSA patients have extremely larger uvulas than their healthy counterparts but with a slightly less percentage of the total UA volume.

Tongue Volume: For healthy subjects, the tongue volume was 66536.22±10097.45 mm^3 occupying 84.98±3.36% of the total UA volume; while for OSA patients the tongue volume was 124539.96±11917.40 mm^3 occupying 85.90±4.20% of the total UA volume. These results show that OSA patients have extremely larger tongues than their healthy counterparts (almost double the tongue volume of the healthy subjects), however the percentages are very close to each other.

VBMI: The above results may be misleading as the two participating groups have many differences such as body size, age range, ethnicities and weight categories. Therefore the changes in the volume and BMI were combined into a new parameter, namely VBMI which represents the ratio of an element volume (mm^3) to the BMI (kg/m^2). Values for VBMI of air, uvula and tongue for the healthy subjects and OSA patients are summarized in Table 1.

TABLE 1: VBMI for healthy and OSA subjects

VBMI	Healthy Subjects	OSA Patients
Air	486.25±175.32	527.65 ±226.61
Uvula	48.97±7.80	55.19±10.90
Tongue	2627.45±383.30	3716.00±479.50

Data in Table 1 shows that OSA patients compared with healthy subjects have: (i) slightly larger $(VBMI)_{air}$; (ii) larger $(VBMI)_{uvula}$ and (iii) much larger $(VBMI)_{tongue}$.

Natural Frequencies: For each subject specifics, the values for the first and second natural frequencies of the uvula and tongue models were very close to one another as shown in Figure 2, which indicates that both of these tissues can be stimulated at the same time with approximately the same frequencies. However, there were no significant differences in the obtained natural frequencies for the uvula and tongue models between the two participating groups.

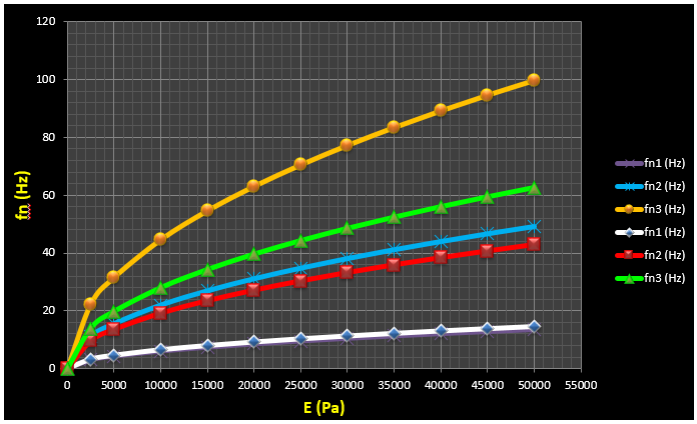

Figure 2: First natural frequencies of the uvula and tongue

These results suggest that the airway volume is not the main contributor to UA collapse, as OSA patients had significantly larger airways compared to the healthy subjects. However, the significantly large size of the uvula and tongue in the apneic group may be the main contributor to UA collapse.

AKNOWLDGEMENT

We acknowledge Fisher &Paykel Healthcare Ltd for their support and the New Zealand Ministry of Science and Innovations (MSI) for financially supporting the project via grant number FAPX1109.

REFERENCES

[1] Fan, Y., Cheung, L.K., Chong, M.M., et al, Computational fluid dynamics analysis on the upper airways of obstructive sleep apnea using patient-specific models, IAENG International Journal of Computer Science, 2011. 38(4): p. 401-408.
[2] Meoli, A.L., Casey, K.R., Clark, R.W., et al, Hypopnea in sleep-disordered breathing in adults, Sleep, 2001. 24(4): p. 469-470.
[3] Guilleminault, C., Tilkian, A., and Dement, W.C., The sleep apnea syndromes, Annual Review of Medicine, 1976. 27: p. 465-489.
[4] Wellman, A., Eckert, D.J., Jordan, A.S., et al, A method for measuring and modeling the physiological traits causing obstructive sleep apnea, Journal of Applied Physiology, 2011. 110(6): p. 1627-1637.
[5] Fouke, J.M., and Strohl, K.P., Effect of position and lung volume on upper airway geometry, Journal of Applied Physiology, 1987. 63(1): p. 375-380.
[6] Bassiri, A.G., and Guilleminault, C., Clinical features and evaluation of obstructive sleep apnea-hypopnea syndrome, Principles and Practice of Sleep Medicine, 2000. 3: p. 869-878.

Copyright © 2016 by ASME
Copyright 2016 The Organizing Committee for the 2016 Summer Biomechanics, Bioengineering and Biotransport Conference

SB^{3}C2016
Summer Biomechanics, Bioengineering and Biotransport Conference
June 29 –July 2, National Harbor, MD, USA
SB^{3}C2016-51

QUANTIFYING CEREBROSPINAL FLUID DYNAMICS USING REAL-TIME PHASE CONTRAST MRI

S. Yildiz (1), J. Oshinski (2), K. Sabra (1)

(1) Woodruff School of Mechanical Engineering, Georgia Institute of Technology, Atlanta, GA, USA, 30332-0405

(2) Department of Radiology & Imaging Sciences and Biomedical Engineering, Emory University, Atlanta, GA, USA, 30322

INTRODUCTION

Cerebrospinal fluid (CSF) undergoes periodic pulsations in the skull and the spinal canal primarily driven by the cardiac force [1-3] and respiratory force [2-5]. Earlier studies investigating CSF flow dynamics have demonstrated the impact of these forces invasively through spinal taps [2,6] and non-invasively through phase contrast (PCMRI). For instance spinals taps showed the impact of cardiac and respiratory forces as well as transient events such as coughing and sneezing on CSF dynamics. Phase contrast (PC) MRI studies [7,8] have primarily showed the influence of only the cardiac forces on CSF flow dynamics as most PCMRI studies used a conventional cine-phase cardiac-gated sampling technique which cannot quantify CSF dynamics that are not synchronized with the cardiac cycle, such as respiration or other short transient events like coughing or Valsalva maneuver. Understanding and quantifying respiratory mechanisms and such transient fluctuations of CSF flow dynamics requires the ability to perform *real-time* measurements of CSF flow along the spine and cranial cavity. Indeed, a very recent *real-time* MRI study [9] demonstrated the CSF flow velocity and directionality due to cardiac and respiration effects. However this previous study did not assess the accuracy of real-time measurements and the measurements were not made in the spinal subarachnoid space (SSS).

To address these limitations we aimed to continuously quantify CSF flow dynamics using a novel *real-time* phase contrast magnetic resonance imaging (RT-PCMRI) [10, 11] in order to explore the effects of respiration and transient events such as coughing and sneezing on CSF flow at the level of Foramen Magnum (FM). To date, this RT-PCMRI technique has only been used to perform real-time blood flow velocities across the heart chambers [11] but has not been used for *real-time* quantification of CSF velocities across the spinal canal.

METHODS

The study was approved by the institutional review board, and was performed after informed consent was obtained from each subject. Eight health subjects (four men and four women, mean age: 41 ± 13 years; age range: 27-60 years) with no neurological disorder or spinal trauma, allergic or respiratory disorders, pregnancy, and any contraindications for MRI, were enrolled in the study. MR images were acquired on a Siemens 3T scanner (Tim Trio, Siemens Healthcare, Erlangen, Germany) using multi-channel head and neck coils for subjects lying in supine. First, high-resolution sagittal T2-weighted fast spin echo MR images were collected to determine the location of FM. Transverse images were acquired at the FM using the conventional PCMRI and the RT-PCMRI sequence (e.g., see Fig. 1a). During the approximately 1-min RT-PCMRI acquisitions, subjects were instructed to perform deep diaphragmatic breathing, 20s breath-holding preceded and followed by deep diaphragmatic breathing, and forced contractions of perineum and abdomen during 20s breath-holding (for mimicking coughing and sneezing). Electrocardiogram (ECG), blood finger pulse and chest motion were also measured and synchronized with MRI acquisition.

In order to quantify the inter-subject variability for deep diaphragmatic breathing, the mean and standard deviation (N=8) of the following five set of dependent variables were calculated (see Table 1): maximum and minimum values of CSF velocity waveform (1) and the respiration component of this CSF velocity waveform (2); peak frequency of the respiration component (3) and cardiac component (4) of the CSF velocity waveform; and peak-to-peak amplitude ratio [r/c] of the respiration versus cardiac components (5).

Copyright 2016 The Organizing Committee for the 2016 Summer Biomechanics, Bioengineering and Biotransport Conference

RESULTS

During deep diaphragmatic breathing (Fig. 1d), the slow oscillations (period ~10s) with large amplitude variations (up to 3cm/s) correspond to the continuous respiration forcing of the CSF flow during successive inhale and exhale cycles, while the superimposed rapid oscillations (period ~1s) with smaller amplitude variations (~1cm/s) are due to cardiac forces during successive systole-diastole cycles. This is confirmed in Fig. 1e showing that during the 20s long breath-hold (between t=10-30s), only the small cardiac fluctuations are visible as respiratory effects are suppressed (in agreement with previous findings from [15]) and that the respiratory forcing is enhanced between t=37-47s after the subject was instructed to take a few deep recovery breaths (causing CSF velocity up to 4cm/s). Finally, we found that large and abrupt changes in peak CSF velocity values can occur while the subject performs continuous perineum and abdominal contractions during breath-hold (see t=15-35s on Fig. 1e); this effect is likely due to the resulting abrupt intrathoracic pressures changes being communicated to the CSF via the venous system [12].

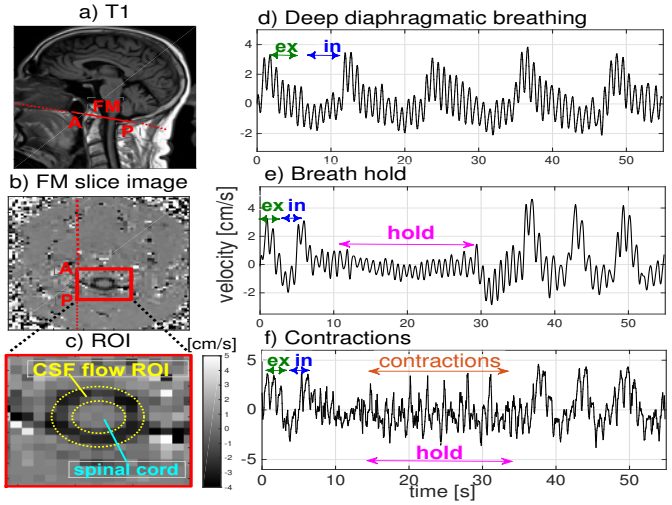

Figure 1: Sagital anatomical MRI image showing measurement slice at Foramen magnum (FM) (red line). b) Velocity distribution measured along this whole FM slice with RT-PCMRI at the time of peak exhalation. c) Zoom-in of (b) showing the annular region of interest (ROI) (yellow line) containing the CSF flow. d) Deep diaphragmatic breathing; cephalad (upward) direction with inhale (blue) and caudad (downward) with exhale (green). e) Breath hold. f) Contractions mimicking coughing/sneezing.

The inter-subject variability of CSF velocity measurements at the FM among eight subjects is shown in Table 1 in terms of (1) maximum and minimum measured velocities (2.09 ± 0.85 cm/s and -2.15 ± 0.82 cm/s), (2) maximum and minimum measured velocities for the respiration components (f<0.5Hz) (0.90 ± 0.62 cm/s and -1.06 ± 0.49 cm/s), (3) peak frequency for the respiration component of the CSF velocity waveforms (0.10 ± 0.04 Hz), (4) peak frequency for the cardiac component of the CSF velocity waveforms (1.19 ± 0.14 Hz), and (5) the peak spectral amplitude of the respiration vs. cardiac component [r/c] = 0.8 ± 0.33.

Table 1. Inter-subject variability (N=8) of CSF velocity measurements obtained with RT-PCMRI during deep diaphragmatic breathing.

In-vivo measurements		All (N=8)
Peak CSF Velocity	*max*	2.09 ± 0.85 cm/s
	min	-2.15 ± 0.82 cm/s
Peak CSF Velocity (respiration component only)	*max*	0.90 ± 0.62 cm/s
	min	-1.06 ± 0.49 cm/s
Estimated frequencies	*respiration*	0.10 ± 0.04 Hz
	cardiac	1.19 ± 0.14 Hz
Peak-to-peak spectral ratio [r/c]		0.8 ± 0.33.

DISCUSSION

RT-PCMRI measurements of CSF flow at the FM revealed a comparable contribution of cardiac pulsations and respiration on CSF velocity magnitude during deep breathing, breath-holding, and forced contractions. The observed modulations of the CSF velocity waveforms during deep breathing were consistent with measurements obtained in the brain and basal cisterns from a recent study using another RT-PCMRI technique [10].

Current routine clinical phase contrast MRI (PCMRI) measurements conducted for patients with Chiari Malformation (CM) are commonly done at level of the FM where their herniated cerebellar tonsils can hamper the normal CSF flow. Therefore, our RT-PCMRI technique measuring CSF flow velocity at FM can be applied to better understand the influence of respiratory mechanisms and transient events such as coughing and sneezing in populations with CM. Furthermore, on-going research suggests that the "glymphatic system", a functional waste clearance pathway between the CSF and the interstitial fluid (ISF) of the brain, is critical for maintaining CNS homeostasis and changes in the normal CSF circulation have been associated with the CNS diseases. Therefore, better understanding the mechanisms of CSF circulation is essential to support and improve the normal physiologic functions of the CNS.

In conclusion, we have demonstrated that RT-PCMRI technique provides a means to measure CSF flow modulations that are not repeatable cycle-to-cycle for each heartbeat, which are not-measurable with conventional cardiac-gated PCMRI.

ACKNOWLEDGEMENTS

The authors thank Xiaodong Zhong and Ning Jin for their assistance with the RT-PCMRI sequence, and Frank Loth and Suraj Thyagaraj for useful discussions on CSF dynamics and CM.

REFERENCES

[1] Enzmann DR, Pelc NJ, *Radiology,* 178:467– 474, 1991.
[2] Nitz WR et al., *Radiology*, 183: 395–405, 1992.
[3] Williams B, *Acta Neurochir (Wien),* 58:167–185, 1981.
[4] Schroth G, Klose U, *Neuroradiology*, 35:10-15, 1992.
[5] Kao YH, et al, *Magn. Reson. Imaging*, 26, 198–205, 2008.
[6] Williams, B. *Acta Neurochir (Wien)*, 59 (1-2), 123–142, 1981.
[7] Kalata W et al., *IEEE Trans Biomed Eng*. 56:1765–1768, 2009.
[8] Pahlavian SH et al., *J Biomech Eng*. 137(5), 2015.
[9] Chen L et al., *NeuroImage*, 122:281-287, 2015.
[10] Lin H et al., *Magn. Reson. Med,* 68, 703–10, 2012.
[11] Thavendiranathan P et al., *JACC Cardiovasc Imaging*, 5(1):15-24, 2012.
[12] Van der Bergh R, *J Neurol.* 239:263-266, 1992.

Copyright 2016 The Organizing Committee for the 2016 Summer Biomechanics, Bioengineering and Biotransport Conference

SB³C2016
Summer Biomechanics, Bioengineering and Biotransport Conference
June 29 –July 2, National Harbor, MD, USA
SB³C2016-52

MICRO-STRUCTURALLY MOTIVATED CONSTITUTIVE MODEL FOR HUMAN SKIN

S. Chen (1), A. Ni Annaidh (2), S. Roccabianca (1)

(1) Mechanical Engineering Department
Michigan State University
East Lansing, Michigan

(2) Mechanical and Materials Engineering
University College Dublin
Dublin, Ireland

INTRODUCTION

Skin is the largest organ of the human body and it serves multiple purposes including providing protection from mechanical, biological and viral insults, and allowing regulation of heat and water exchange with the surroundings. As with most soft biological tissues, skin biochemical behavior is affected by the evolving mechanical behavior. For this reason, a model that describes the biomechanical characteristics of the tissue can be helpful in areas like plastic surgery, wound healing, and radiotherapy side effects.

The purpose of this work is to describe skin from the mechanical perspective by employing a constrained mixture theory approach, which has shown predictive capability in the cardiovascular field [1]. Specifically, in this model each distinct constituent (collagen fibers and elastin) was endowed independently with a constitutive descriptor and allowed to have a different natural (stress-free) configuration. This endows us to identify the independent contribution of each constituent to the overall mechanical behavior of this complex system.

METHODS

Skin can be described as a nonlinear, anisotropic, nearly incompressible elastic material. These characteristics can be explained by looking at the components of the tissue: families of collagen fibers aligned along preferential directions endow skin with its nonlinear, anisotropic behavior, while elastin give skin its elastic response [2]. Moreover, the presence of the Langer's lines shows that the constituents are experiencing a certain level of deformation in the in vivo, homeostatic state. For these reasons, we describe the mechanical behavior of skin employing a constrained mixture theory, inspired by the work done by Humphrey and colleagues in the field of cardiovascular mechanics [3-4].

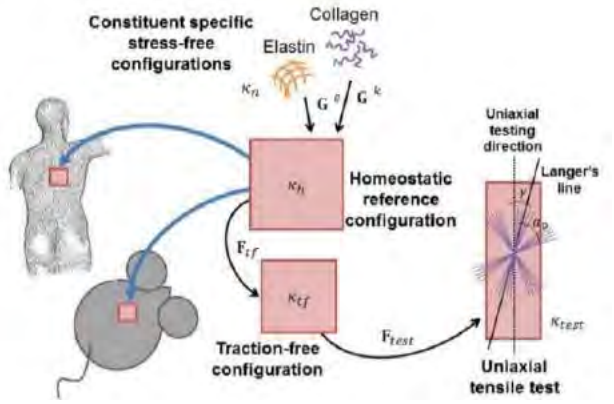

Figure 1. Schematic representation of the configurations of interest in the model.

Kinematics. We modeled the skin as a planar, three dimensional layer. Let the in vivo homeostatic configuration κ_h serve as a computationally convenient and biologically relevant reference configuration (Fig. 1). Moreover, let each constituent within the tissue possess a separate natural, stress-free configuration κ_n^α, where $\alpha = k, e$ for elastic fibers and $k = 1,2,3$ families of collagen fibers, respectively. Deformations between each natural configuration κ_n^α and the homeostatic configuration κ_h are defined by a constituent-specific deposition stretch tensor $\boldsymbol{G}^\alpha$.

Constitutive description. To describe the nonlinear, orthotropic behavior of skin we employ a mass averaged strain energy function (SEF) of the form

Copyright 2016 The Organizing Committee for the 2016 Summer Biomechanics, Bioengineering and Biotransport Conference

$$W = \phi^e W^e(\mathbf{F}^e) + \sum_{k=1}^{3} \phi^k W^k(\lambda^k). \quad (1)$$

where ϕ^α and W^α represent the mass fraction and the SEF for each constituent, respectively, with $\alpha = e, k$ for elastic fibers and families of collagen fiber ($k = 1,2,3$), respectively. We considered 3 collagen fibers families in this work, namely $k = 1$ for fibers in the direction of the Langer's line and $k = 2,3$ for symmetric diagonal fibers with respect to the Langer's line, see Figure 1. Elastin has been described by using a neo-Hookean constitutive model,

$$W^e(\mathbf{F}^e) = \frac{c^e}{2}(tr\mathbf{C}^e - 3), \quad (2)$$

where c^e represent a material parameter with the dimensions of stress and $\mathbf{C}^e$ represents the right Cauchy-Green tensor describing the deformation that affects the elastic network, i.e., $\mathbf{C}^e = (\mathbf{F}^e)^T\mathbf{F}^e$ with $\mathbf{F}^e = \mathbf{F}\mathbf{G}^e$. Collagen fibers mechanical behavior has been described by using a Fung-type exponential SEF

$$W^k(\lambda^k) = \frac{c_1^k}{4c_2^k}\left\{\exp\left[c_2^k((\lambda^k)^2 - 1)^2\right] - 1\right\}, \text{ for } \lambda^k > 1, \quad (3)$$

where c_1^k and c_2^k are material parameters, with the dimension of stress and dimensionless respectively, λ^kdescribes the stretch in the direction of k^{th} collagen fiber family defined as $\lambda^k = G^k\sqrt{\mathbf{M}^k \cdot \mathbf{C}\mathbf{M}^k}$, where $\mathbf{M}^k = \left(0, \sin\alpha_0^k, \cos\alpha_0^k\right)$ with angles $\alpha_0^1 = \gamma$, $\alpha_0^2 = \alpha_0 + \gamma$ and $\alpha_0^3 = -\alpha_0 + \gamma$. Material parameters for collagen fibers in compression are considered to be 20% of the tensile parameters.

Experimental data. Details on how the experiments were conducted can be found in [2-5]. Briefly, 43 samples from 6 human subjects were collected and mechanically tested by means of a quasi-static uniaxial tensile test. In this study, samples were grouped based on subject and inclination with respect to the Langer's line (i.e., $0°, 45°, 90°$) then averaged. The averaged datasets were used to estimate best-fit material parameters as a cohesive protocol.

Parameter estimation. We used a nonlinear least-squares regression to determine best-fit values of the material parameters by minimizing the error between theoretically predicted (subscript "th") and experimentally measured (subscript "exp") stresses.

RESULTS

Experimental data and model predictions are shown in Fig.2. Table1 shows best-fit values of the six material parameters for the constitutive model. Goodness of fit is showed in Table 1 in terms of the root mean sum-of-the-squares of the error (RMSE). Table 1 shows that the mechanical behavior of skin is dominated by the presence of collagen fiber, represented by the mechanical parameters of collagen being several orders of magnitude bigger than the one for elastin.

Due to the lack of histological quantitative information found in literature on the variation of content of constituents with age in skin as a first approximation we considered the mass fractions of both collagen and elastin equal to one. To refine this value, will be the subject of future studies. Deposition stretches for elastin and collagen, $\mathbf{G}^e$ and G^k respectively, cannot be measure or estimated easily experimentally. For this reason, we conducted a parametric study to assess the sensibility of the model to the deposition stretches values. Variation of $\mathbf{G}^e$ from 1.00 to 2.00 (i.e., in the direction of the Langer's line) has little effect on the accuracy of the prediction, measured as variation of RMSE. This could be due to the material parameter associated with elastin being small, however $\mathbf{G}^e$ will have an important effect on the estimation of pre-stress along the Langer's line. Due to lack of information on the pre-stress (i.e., deformation of the tissue upon excision) we set $\mathbf{G}^e = \boldsymbol{I}$, where is $\boldsymbol{I}$ the identity matrix. Following the work done by Humphrey and colleagues [3-4] we used a compressive deposition stretch, $G^k < 1$, to describe the fact that collagen fibers are coiled in the in vivo, homeostatic configuration. A parametric study showed that $G^k = 0.95$ gives the overall the lower value of RMSE for all the samples. Moreover, following [4], we model the compressive behavior of collagen fibers using the same SEF used to describe the tensile behavior, imposing the compressive parameters to be 20% of the tensile ones (i.e., average of values in Table 3 in [4]).

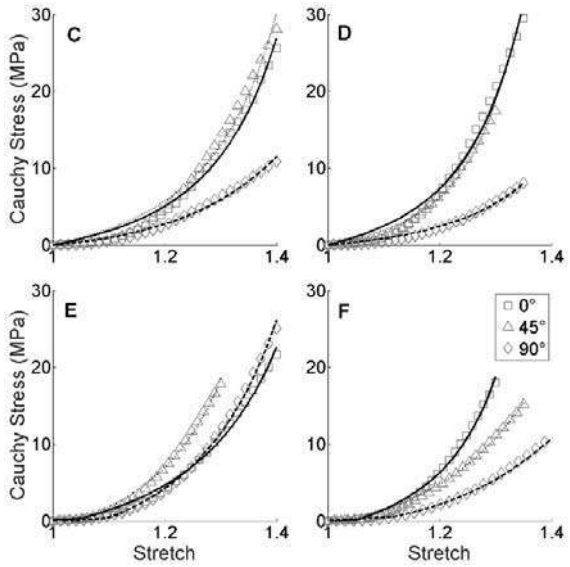

Figure 2: Experimental data as showed in [4], and model prediction.

DISCUSSION

To the authors' knowledge, we are the first to apply a constrained mixture theory approach to human skin. While further experimental data is required to verify the value of $\mathbf{G}^e$ and G^k determined numerically here, as well as the mass fractions ϕ^e and ϕ^k, a framework has been developed which can accurately represent the mechanical contributions of both elastin and collagen to the behavior of skin.

Table 1: Best-fit material parameters of the constitutive model

Subject	c_e [MPa]	c_1^1 [MPa]	c_2^1	$c_1^{2,3}$ [MPa]	$c_2^{2,3}$	α_0 [deg]	RMSE
A	1.4E-07	34.8	0.1	28.0	0.9	63.5	0.06
B	2.8E-11	25.4	0.4	27.3	0.7	64.0	0.05
C	1.0E-06	11.9	0.8	13.9	0.9	55.5	0.09
D	8.7E-07	17.1	1.3	14.0	2.1	54.3	0.09
E	3.2E-06	10.7	0.8	18.4	1.8	59.2	0.07
F	2.7E-06	13.4	2.0	12.3	0.6	55.8	0.07

REFERENCES

[1] S. Roccabianca et al., *J. R. Soc. Interface*, vol. 11, no. 97, p. 20140397, Aug. 2014.

[2] A. Ní Annaidh et al., *J. Mech. Behav. Biomed. Mater.*, vol. 5, no. 1, pp. 139–148, Jan. 2012.

[3] Humprey J. D. et al. *Biomechanics and Modeling in Mechanobiology*, 2:109-126, 2003.

[4] Bellini et al. *Annals of biomedical engineering* 42.3 (2014): 488-502.

[5] A. N. Annaidh et al., *Ann. Biomed. Eng.*, vol. 40, no. 8, pp. 1666–1678, Mar. 2012.

Copyright 2016 The Organizing Committee for the 2016 Summer Biomechanics, Bioengineering and Biotransport Conference

SB³C2016
Summer Biomechanics, Bioengineering and Biotransport Conference
June 29 –July 2, National Harbor, MD, USA
SB³C2016-53

CHARACTERIZATION OF WHITE MATTER USING ASYMMETRIC INDENTATION AND INVERSE MODELING IN LARGE STRAIN

Y. Feng (1, 3), C.-H. Lee (2), L. Sun (1, 3), S. Fu (1)

(1) School of Mechanical and Electronic Engineering
Soochow University
Suzhou, Jiangsu, China

(2) Center for Cardiovascular Simulation
Institute for Computational Engineering & Sciences
Department of Biomedical Engineering
The University of Texas at Austin, Austin, TX, USA

(3) Robotics and Microsystems Center
Soochow University
Suzhou, Jiangsu, China

INTRODUCTION

Characterizing brain tissue is important to understand the mechanics of brain development, injury, and repair. Structurally, white matter tissue contains distinct myelin-sheathed axonal fiber bundles. This fiber-reinforced structure indicates that white matter is both structurally and mechanically anisotropic. A recent study using a combination of shear and indentation tests has demonstrated that a transversely isotropic model can be used to characterize the anisotropic behavior of white matter in small strain regime [1]. However, large deformation (>5% strain) commonly exists in many behaviors of soft biological tissues, especially in development and injury. Thus, the focus of this study is to further investigate the anisotropic behavior of white matter under large deformation.

Multiple testing methods have been proposed to characterize transversely isotropic materials, for example, shear-indentation tests [1] and extension-torsion tests [2], among others. However, the combination of two testing methods involves complicated tissue handling, transporting and testing processes. Therefore, a single experimental technique that allows for characterizing axonal fiber reinforced white matter is desired. Among typical mechanical testing methods, indentation has been widely adopted in studying many soft tissues, e.g. brain tissue [3] and corneal stroma [4]. Nevertheless, isotropic material models were typically adopted for parameter estimation in most of those studies, whereas studies using anisotropic material models are still lacking or restricted to certain tissue preparation and testing setup [5].

In this present work, we used asymmetric indentation to characterize white matter under large deformation. A minimal form of incompressible transversely isotropic (MITI) material model of both anisotropic invariants (I_4 and I_5) was employed. Three parameters of the model were estimated by an inverse finite element (FE) method.

METHODS

Tissue preparation: porcine brains (3-5 month old) were obtained from a local slaughterhouse 2 to 4 hours post-mortem. White matter tissues were dissected from the corpus callosum region similar to the method presented in a previous study [1]. Briefly, the flat corpus callosum region was exposed by cutting the tentorium. Using a circular punch, cylinder-shaped samples were produced from the central corpus callosum region where axonal fibers can be seen connecting the left and right hemisphere. A total of 12 samples were acquired. The average sample thickness was 3.3 mm with a diameter of 14 mm. During the experiment, samples were moisturized with phosphate-buffered saline solutions.

Asymmetric indentation testing: we used a custom-built asymmetric indentation device (Fig. 1) to measure the indentation force and displacement. A rectangular indenter, 2mm wide and 20 mm long, was used. To characterize white mater under large deformation, each sample was indented by 10% of its thickness parallel (0-deg) and perpendicular (90-deg) to the dominating fiber direction, with an average strain rate of ~0.2 s^{-1}. A custom-written MATLAB program was used for indenter control and data acquisition. Linear fitting was applied to the force-displacement curve in which portion the indenter velocity was constant.

Inverse modeling based material parameter characterization: to estimate the model parameters, the asymmetric indentation was simulated using commercial FE software (ABAQUS 6.12, Providence, RI, USA). The following MITI material model [1] was implemented in a user-material subroutine UMAT:

$$\psi = \frac{\mu}{2}[(I_1 - 3) + \zeta(I_4 - 1)^2 + \phi I_5^*], \quad (1)$$

Copyright 2016 The Organizing Committee for the 2016 Summer Biomechanics, Bioengineering and Biotransport Conference

where μ is the shear modulus and ζ and ϕ are the anisotropic parameters related with invariant I_4 and I_5, $I_5^* = I_5 - I_4^2$. A quarter model was used due to symmetry of the sample and the indenter head. The metallic indenter head was treated as a rigid body, and a clamped boundary condition was prescribed at the bottom of the sample. The rigid indenter head was meshed with 23,600 R3D4 elements, while the quarter sample was meshed with 39,312 C3D4H elements. The friction coefficient between the indenter head and the sample was set to 0.5.

Parameter estimation was performed based on an inverse FE modeling approach by minimizing the objective function below:

$$f_{obj}(\mu,\zeta,\phi) = \left[\frac{1}{2}\sqrt{\frac{1}{n}\sum_{i=1}^{n}\left(F_{FE}^{i} - F_{exp}^{i}\right)^2}\right]_{0-deg} + \left[\frac{1}{2}\sqrt{\frac{1}{n}\sum_{i=1}^{n}\left(F_{FE}^{i} - F_{exp}^{i}\right)^2}\right]_{90-deg}, \quad (2)$$

where n=25 is the total number of indentation incremental steps, F_{FE}^{i} and F_{exp}^{i} are the predicted and experimentally measured indentation forces at increment i, respectively.

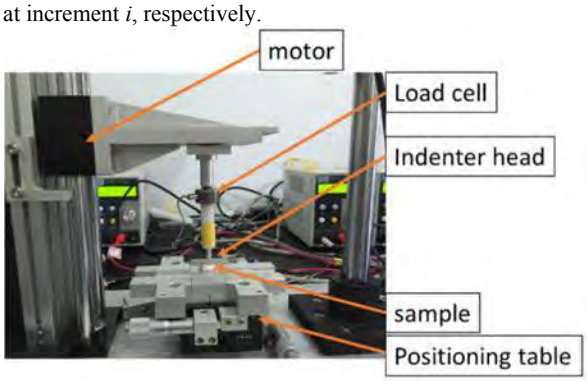

Figure 1. The custom-built asymmetric indentation device used to characterize white matter in large strain.

RESULTS

A representative force-displacement curve from the experiments is shown in Fig. 2. The average indentation stiffness for 0-deg testing configuration was 72.9 mN/mm, whereas the average indentation stiffness of 170.5 mN/mm was obtained for 90-deg testing configuration. A student *t*-test indicates a significant difference of indentation stiffness between the two testing configurations (p<0.001).

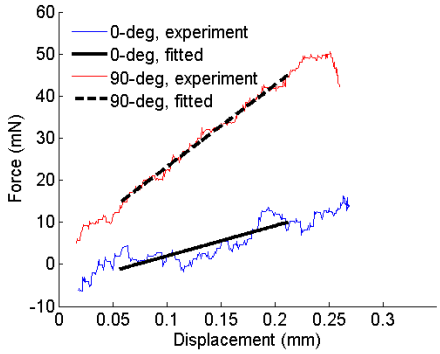

Figure 2. Measured and fitted force-displacement relationships of asymmetric indentation of the white matter.

Estimated parameters based on the inverse FE modeling are μ=0.15 kPa, ζ=3.84, ϕ=0.6 with f_{obj}=0.104. Numerical simulations of the indentation processes showed that the stress and deformation concentrated at the indenter-sample interaction region (Fig. 3).

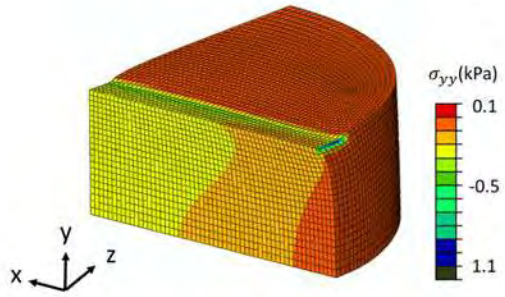

Figure 3 Predicted Cauchy stress component σ_{yy} from the FE simulation of 90-deg indentation.

DISCUSSION

The quantified indentation stiffness and the difference between the two testing configurations indicated a strong anisotropy of white matter tissue. This anisotropic property of porcine white matter in large strain regime agrees with the findings from indentation of lamb white matter in small strain regime [1].

This study characterized white matter tissue under large deformation, which is different from the previous study [1] and other indentation-based brain tissue characterization [3]. Under 10% indentation, we noticed that the indentation relationships were similar to those of 5% indentation strain. Moreover, a linear behavior during the indentation process was still observed. This linear behavior of white matter during the indentation process provides useful indications for brain tissue modeling in transit state.

We have demonstrated that with asymmetric indentation as a single experimental technique, the hyperelatic model parameters of the white matter can be estimated using an inverse FE modeling approach. Although, the characterization procedure in this work was limited to the elastic domain, where viscoelastic effect was not considered, the proposed techniques and acquired data will serve as a logical first step towards a complete characterization of white matter tissue and other transversely isotropic soft tissues.

ACKNOWLEDGEMENTS

This work is supported by grant BK20140356 (YF) from Jiangsu Province, grant 61503267 (YF) from National Natural Science Foundation, and by grant K511701515 (YF) from Scientific Research Foundation for the Returned Overseas Chinese Scholars, State Education Ministry.

REFERENCES

[1] Feng, Y., et al., J Mech Behav Biomed Mat, 23: 117-132, 2013.
[2] Horgan, C. and J. Murphy, J Elast, 108(2): 179-191, 2012.
[3] Budday, S., et al., J Mech Behav Biomed Mat, 46: 318-330, 2015.
[4] Hatami-Marbini, H. and E. Etebu, J Biomech, 46(10): 1752-1758, 2013.
[5] Hortin, M., et al., J Mech Behav Biomed Mat, 45(0): 75-82, 2015.

Copyright 2016 The Organizing Committee for the 2016 Summer Biomechanics, Bioengineering and Biotransport Conference

SB^{3}C2016
Summer Biomechanics, Bioengineering and Biotransport Conference
June 29 –July 2, National Harbor, MD, USA
SB^{3}C2016-54

MODELING ACTIVE CONTRACTION OF LEFT VENTRICLE USING DIFFERENT ZERO-LOAD DIASTOLE AND SYSTOLE GEOMETRIES

Longling Fan (1), Jing Yao (2), Chun Yang (3), Di Xu (2), Dalin Tang (1,4*)

(1) Department of Mathematics
Southeast University
Nanjing, 210096, China

(2) Department of Cardiology
First Affiliated Hospital of Nanjing Medical University, Nanjing 210029, China

(3) China Information Tech. Designing & Consulting Institute Co., Ltd.
Beijing, 100048, China

(4) Math Sciences Department
Worcester Polytechnic Institute
Worcester MA 01609, USA

INTRODUCTION

Modeling ventricle active contraction based on in vivo data is extremely challenging because of complex ventricle geometry, dynamic heart motion and active contraction and relaxation where the reference geometry (zero-stress geometry) changes constantly in a cardiac cycle. From mechanical point of view, zero-stress ventricle geometry information is required for its stress/strain calculations. Considerable progress in ventricle modeling has been made in recent years and excellent reviews are given by [1, 2]. Pezzuto and Ambrosi focus on the contraction of the left ventricle in a finite elasticity framework, adopting the "prolate ellipsoid" geometry and the invariants-based strain energy proposed by Holzapfel and Ogden [3]. In our previous papers, patient-specific Echo-based left ventricle (LV) models were introduced to quantify differences in morphology, mechanics and biology between patients with myocardial infarction and healthy volunteers [4, 5].

Active contraction is caused by sarcomere shortening which leads to increased strain and stress (called active strain and stress). At the beginning of active contraction, the zero-stress sarcomere length is shortened in a very short time duration while ventricle volume has no change, so in vivo sarcomere length does not change, which leads to ventricle strain and stress increases, equivalent to the active tension in models in [1, 2] for the stress part. Due to sarcomere shortening, zero-load ventricle systole geometry is smaller than its zero-load diastole geometry. A new modeling approach using two different zero-load geometries (diastole and systole) was introduced in this paper (called 2G model thereafter) to properly model active contraction and relaxation and provide ventricle diastole and systole material parameter values, stress and strain calculations based on their respective zero-load geometries.

3D ECHO DATA ACQUISITION, MODELS AND METHODS

Echo image data were acquired from 5 healthy volunteers. Details of the data acquisition procedures were described in [4]. The ventricle material was assumed to be hyperelastic, anisotropic, nearly-incompressible and homogeneous. As patient-specific fiber orientation data was not available from these patients, we chose to construct a two-layer LV model and set fiber orientation angles using fiber angles given in [2]. Modeling active LV contraction and relaxation is very difficult, Material stiffening and softening were achieved by adjusting parameter values at each Echo-time step (28 Echo frames per cycle) to simulate active contraction and expansion and match LV volume data. The least-squares method was used to find the equivalent Young's moduli (YM) for the material curves for easy comparison.

In our model construction process, an iterative pre-shrink process was applied to the in vivo minimum volume ventricular geometry to obtain the two zero-load geometries so that when in vivo pressure was applied, the ventricle would regain its in vivo geometry. To get the zero-load diastole geometry, we start with a 4% shrinkage, construct the model, and apply the minimum pressure to see if the pressurized LV volume matches the Echo data. If not, we adjust the shrinkage, re-made the model, pressurize it and check again. The process is repeated until LV volume matches Echo volume with error < 0.5%. For the zero-load systole geometry, assuming a 10-15% sarcomere shortening, we start with a 14% shrinkage. Different shrinkage rates were used for LV inner and outer surfaces so that mass conservation law was enforced. The same process was repeated until the pressurized LV volume under end-systole pressure matched the Echo-measured end-systole volume data. The anisotropic LV computational models were constructed for the 5 patients and the models were solved by ADINA (ADINA R&D, Watertown, MA, USA) using unstructured finite elements and the Newton-Raphson iteration method.

Copyright 2016 The Organizing Committee for the 2016 Summer Biomechanics, Bioengineering and Biotransport Conference

Maximum principal stress (Stress-P_1) and strain (Strain-P_1) were used for analysis and referred to as stress and strain. For each 3D Echo data set (11 slices), ventricular wall thickness (WT), circumferential curvature (C-cur), longitudinal curvature (L-cur), and stress/strain were calculated at all nodal points (100 points/slice). The "slice" values of those parameters were obtained by taking averages of those quantities over the 100 points for each slice and saved for analysis. Pairwise T-test and Linear Mixed Effect (LME) model were used to determine if the differences from the new and old models were statistically significant with the dependence of the pair-wise observations the clustering effects taking into consideration [6].

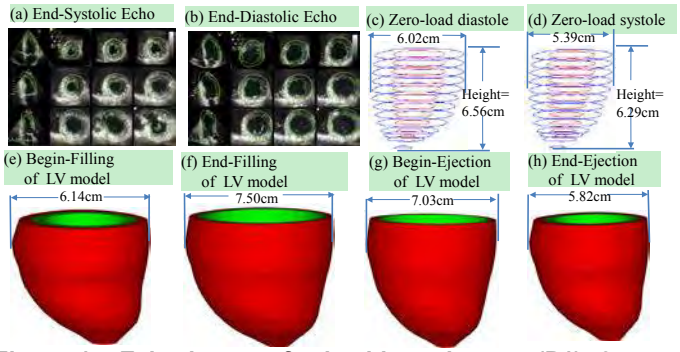

Figure 1: Echo image of a healthy volunteer (P1), 2-zero-load geometries, and the reconstructed 3D geometry.

RESULTS

Our results showed significant differences between the 1G and 2G models. For the 1G model, results at begin-filling (BF) and begin-ejection (BE) corresponding to minimum and maximum pressure and RV volume were obtained for comparison. For the 2G model, results at begin-filling (BF), end-filling (EF), begin-ejection (BE), and end-ejection (EE) were obtained for comparison. The traditional peak-systole, end-systole, end-diastole, and begin-diastole conditions correspond to our begin-ejection, end-ejection, end-filling, and begin-filling, respectively. They may be used interchangeably as needed.

Using the mean values of 1G models as the baseline values, at begin-filling, the mean YM value for the fiber direction (YM_f) from 2G model was 82% stiffer than that from the 1G model (342.33 kPa vs. 621.39 kPa). At begin-ejection, YM_f from 2G model was 54% softer than that from the 1G model (193.47 kPa vs. 86.10 kPa). Further analysis, begin-ejection YM_f was higher 6.8% that its end-filling value (86.10 kPa vs. 75.00 kPa), end-ejection YM_f was higher 70% that its begin-filling value (1056.05 kPa vs. 621.39 kPa). This indicated that the sarcomere length will shorten in isovolumic contraction and the sarcomere length will expand in isovolumic relaxation.

When comparing other parameters, the overall results indicated that peak-systolic (begin-systole from our model) stress from the 2G model was 39% higher than that from the 1G model (349.79 kPa vs. 251.23 kPa). The begin-diastole stress values from the two models were about the same (2.2748 kPa vs. 2.8165 kPa, 5% difference). Peak-systolic strain from the 2G model was 17% higher than that from the 1G model (1.0268 vs. 0.8812). The begin-diastole strain value from the 2G model was 117% lower than that from 1G model (0.0530 vs. 0.1149). Begin-diastole WT from the 2G model was 12% higher than that from the 1G model (1.1145 cm vs. 1.2059 cm). The Peak-systolic WT value from the 2G model was 11% lower than that from 1G model (0.7175 cm vs. 0.7952 cm). Peak-systolic C-cur and L-cur from the two models were about the same (0.6245 1/cm and 0.2794 1/cm vs. 0.6178 1/cm and 0.2931 1/cm, 1% and 4.9% difference respectively). The begin-diastole C-cur and L-cur from the two models were about the same (0.8971 1/cm and 0.3445 1/cm vs. 0.9042 1/cm and 0.3337 1/cm, 0.8% and 3% difference respectively).

DISCUSSION AND CONCLUSION

Ventricle remodeling, disease development, tissue regeneration, patient recovery after surgery and many other cell activities are closely associated with ventricle mechanical conditions. The 2-geometry modeling approach is setting up the right stage for diastole and systole stress/strain calculations using proper zero-load geometries. It should be noted that direct measurements of stress, strain, and sarcomere length are either extremely difficult or even impossible. Data from the literature or from ex vivo experiments (such as fiber orientation, sarcomere length contraction rate) have to be used to complete the computational models. In our previous study [5], we put forward a modeling approach to estimate in vivo ventricles material properties. At this point, the modeling approach was used investigate material property changes in a cardiac cycle, including diastole, isovolumic contraction, systole and isovolumic relaxation four phases.

Table 1. Material parameter values from the new (2G) and old (1G) models. BF: Begin-Filling; BE: Begin-Ejection; EF: End-Filling; EE: End-Ejection.

	1G-BF		2G-BF		2G-EF	
	C(kPa)	YM_f (kPa)	C(kPa)	YM_f (kPa)	C(kPa)	YM_f (kPa)
P1	11.9064	342.33	19.1224	549.81	2.4174	69.50
P2	12.0868	347.52	26.8796	772.84	2.3813	68.47
P3	12.2672	352.71	22.0088	632.80	3.1750	91.29
P4	11.0044	316.40	19.6636	565.37	2.8864	82.99
P5	12.2672	352.71	20.3852	586.12	2.1828	62.76
Mean	**11.9064**	**342.33**	**21.6119**	**621.39**	**2.6086**	**75.00**
	1G-BE		**2G-BE**		**2G-EE**	
	C(kPa)	YM_f (kPa)	C(kPa)	YM_f (kPa)	C(kPa)	YM_f (kPa)
P1	5.9532	171.17	2.5256	72.62	33.5544	964.76
P2	5.412	155.61	2.7060	77.80	42.7548	1229.29
P3	8.2082	236.00	3.5539	102.18	35.7192	1027.00
P4	7.9376	228.22	3.8425	110.48	34.4564	990.69
P5	6.1336	176.35	2.3452	67.43	37.1624	1068.50
Mean	**6.7289**	**193.47**	**2.9946**	**86.10**	**36.7294**	**1056.05**

Acknowledgement: This research was supported in part by NIH-1R01-HL 089269 and National Sciences Foundation of China grant 81571691.

REFERENCES

1. McCulloch AD et al., Critical Rev. in Biomed Eng, 1992; 20(5,6): 427-449.
2. Hunter PJ et al., Annu Rev Biomed Eng., 2003; 5:147-77.
3. Pezzutoi S et al., Int J Numer Method Biomed Eng. 2014; 30:1578-96.
4. Fan R et al., Computer Modeling in Engineering & Sciences, 2014; 99:491-508.
5. Fan L et al., J. Biomech. Eng., 2015; 137: 081005.
6. Tang D et al., J Thorac Cardiovasc Surg. 2014 147(1):537-8.

Copyright 2016 The Organizing Committee for the 2016 Summer Biomechanics, Bioengineering and Biotransport Conference

SB³C2016
Summer Biomechanics, Bioengineering and Biotransport Conference
June 29 –July 2, National Harbor, MD, USA
SB³C2016-55

COMPUTATIONAL MODELING OF EMBOLUS MIGRATION IN THE HUMAN INFERIOR VENA CAVA

Kenneth I. Aycock (1,2), Robert L. Campbell (2,3), Brent A. Craven (4), Keefe B. Manning (1,5)

(1) Department of Biomedical Engineering
The Pennsylvania State University
University Park, PA, USA

(2) Applied Research Laboratory
The Pennsylvania State University
University Park, PA, USA

(3) Department of Mechanical and Nuclear Engineering
The Pennsylvania State University
University Park, PA, USA

(4) Division of Applied Mechanics
Office of Science and Engineering Laboratories
Center for Devices and Radiological Health
U.S. Food and Drug Administration
Silver Spring, MD, USA

(5) Department of Surgery
Penn State Hershey Medical Center
Hershey, PA, USA

INTRODUCTION

Pulmonary embolism is a common disease (annual incidence rate of approximately 1 per 1,000 [1]) that occurs when an embolus travels from the legs into the pulmonary arteries and occludes blood flow to the lungs. The disease is traditionally treated using anticoagulation therapy. When anticoagulants are ineffective or contraindicated, an inferior vena cava (IVC) filter may instead be placed to serve as a mechanical barrier to embolus passage. However, despite years of innovation, IVC filters still fail to capture all hazardous emboli [2].

Computational fluid dynamics (CFD) has been used previously to model the migration of arterial (e.g., [3-7]) and venous (e.g., [8]) emboli. Most computational models use empirical drag laws to calculate the forces on the emboli and are thus only valid for modeling small emboli (i.e., emboli smaller in volume than the volume of the computational cells in the discretized fluid domain). More advanced models have also been developed that resolve the fluid-structure interactions between the blood and rigid [8] or even deforming [7] emboli using the arbitrary Lagrangian-Eulerian method. However, these models, particularly those considering embolus deformation, are computationally expensive and are currently impractical for evaluating large numbers of emboli trajectories.

We have developed a novel model of embolus migration that uses a coupled fictitious domain/discrete element method (FD/DEM) [9, 10] to balance computational cost with computational accuracy. The model uses a single Eulerian mesh to simulate fluid-structure interactions between blood and the emboli, thus reducing the computational cost in comparison with other methods that require either dynamic mesh motion or remeshing of the fluid domain at each time step. Using this model, we simulate the migration and capture of rigid, spherical emboli in the IVC, and predict the embolus trapping efficiency of an IVC filter for emboli of various sizes and densities.

METHODS

The human IVC was modeled as a straight, cylindrical tube with rigid walls and a diameter of one inch (Fig. 1). Virtual placement of an IVC filter (G2 Express, Bard Peripheral Vascular, Tempe AZ) was simulated in the idealized IVC using our previously developed computational workflow [11]. Emboli were modeled as rigid spheres with diameters ranging from 3 to 7 mm in increments of 1 mm and embolus-to-blood density ratios of $\rho_p/\rho_f = 0.98$ (buoyant), $\rho_p/\rho_f = 1$ (neutrally-buoyant), and $\rho_p/\rho_f = 1.02$ (physiological; [12]).

A series of 128 simulations was performed for each combination of embolus diameter and embolus-to-blood density ratio, yielding a total of 1,920 simulations (5 x 3 x 128). For each of the independent simulations performed, the embolus starting position was randomized in a 30° slice of the IVC lumen to take advantage of symmetry (Fig. 1a). The initial velocity of each embolus was set to the corresponding velocity of the flow at the embolus starting position (Fig. 1b). For each set of 128 simulations, the trapping efficiency was calculated as the number of emboli trapped in the IVC filter divided by the total number of emboli simulated. An embolus was considered trapped if the embolus velocity decreased to below one micron per second.

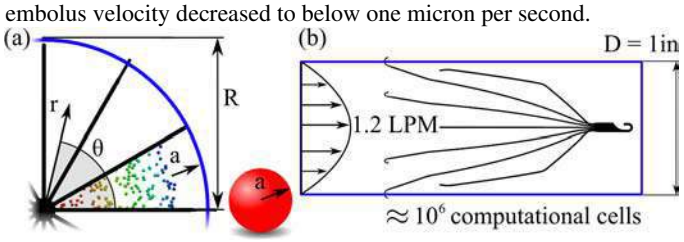

Figure 1: (a) Cross-sectional view of the IVC and placed IVC filter showing the starting positions for the virtual emboli. (b) Computational domain for the embolus migration simulations.

Copyright 2016 The Organizing Committee for the 2016 Summer Biomechanics, Bioengineering and Biotransport Conference

Steady, fully developed flow was specified at the inlet of the IVC at a flow rate of 1.2 LPM (Fig. 2b), corresponding to an average resting flow in the IVC [13]. Blood was modeled as a Newtonian fluid with a density of 1060 kg/m^3 and a viscosity of 3.5 cP. Gravitational effects were considered, with the gravity vector oriented opposite to the direction of the flow (i.e., representative of a patient standing upright). The presence of the IVC filter was modeled in the DEM to account for collisions between the emboli and the IVC filter. However, because preliminary CFD simulations showed that the IVC filter only had a negligible effect on the upstream flow, the presence of the IVC filter was not included in the flow solution for simplicity.

Embolus migration simulations were performed by solving the Navier–Stokes and Newton–Euler equations in a coupled fashion using a modified version of the resolved FD/DEM solver developed by Hager et al. [10]. This solver has been extensively validated against benchmark experimental data [10]. However, the original solver [10] considered only the translational motion of the spheres, neglecting rotational effects. Previous literature (e.g., [14]) has shown that rotational effects contribute to the migration of spheres across streamlines in shear flow, which may be important for accurately predicting embolus trajectories. Therefore, we modified the solver to include rotational effects (i.e., six degrees of freedom) by calculating the fluid-induced moments on the spheres and solving the equations for the conservation of angular momentum in the DEM solver.

RESULTS

Emboli are transported downstream with the flow and either pass through gaps in the IVC filter struts or are brought to rest and captured by the IVC filter. When an embolus is captured, a wake develops downstream of the trapped embolus (e.g., Fig. 2a). The volume of the wake increases with increasing embolus diameter.

Cross-streamline migration of the emboli occurs for all embolus sizes and all embolus-to-blood density ratios (e.g., Fig. 2b). Dense emboli ($\rho_p/\rho_f = 1.02$) migrate towards the centerline of the vessel, buoyant emboli ($\rho_p/\rho_f = 0.98$) migrate towards the vein wall, and neutrally buoyant emboli ($\rho_p/\rho_f = 1$) migrate towards an equilibrium position between the vessel centerline and the vein wall (≈0.6R).

Multiple embolus trapping locations are observed in the IVC filter (Fig. 2c). Emboli travelling near the vessel centerline are trapped in the center of the vessel lumen near the apex of the IVC filter. Other emboli are trapped either between two of the inner filter struts (i.e., the struts with hooks) or between two of the outer filter struts and one of the inner filter struts (Fig. 2c). Trapping locations shift upstream with increasing embolus diameter (Fig. 2c).

The embolus trapping efficiency of the IVC filter increases with increasing embolus diameter and density ratio (Fig. 2d). The embolus trapping efficiency reaches 100% for all embolus diameters when considering emboli with a density greater than that of blood due to the cross-streamline migration of the emboli towards the vessel centerline and the subsequent capture of the emboli at the filter apex (Fig. 2d).

DISCUSSION

Our simulations predict that the embolus-to-blood density ratio has a strong influence on embolus trajectories and the IVC filter trapping efficiency (Fig. 2d). Emboli that are denser than blood migrate towards the center of the vessel lumen, where capture is more likely to occur, while emboli that are buoyant migrate away from the center of the vessel lumen, where the gaps between the filter struts are larger and, thus, capture is less likely to occur. Previous studies of arterial blood flow (e.g., [6, 7]) have also predicted that embolus trajectories are sensitive to embolus density.

The simulations also predict multiple embolus trapping locations

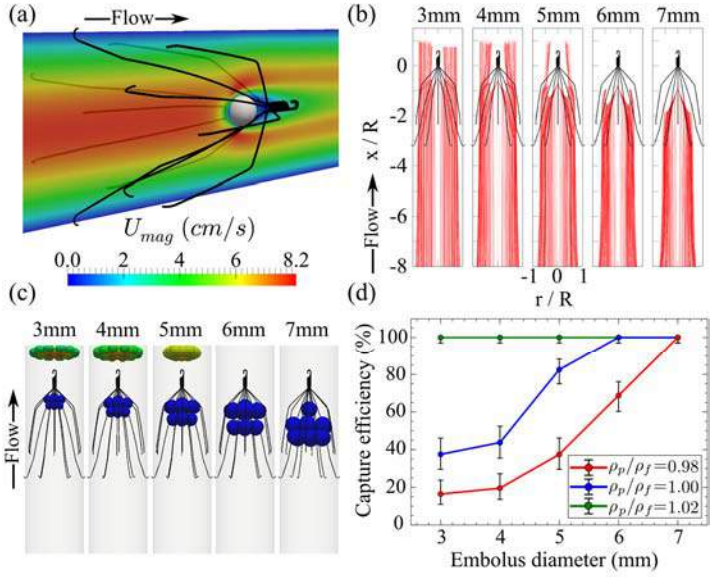

Figure 2: (a) Velocity magnitude contours for an example case with a 5mm embolus. (b) Trajectories for neutrally buoyant emboli. (c) Predicted trapping positions for neutrally buoyant emboli. (d) Predicted embolus trapping efficiencies for the filter.

for the IVC filter (Fig. 2c). Some studies have speculated that near-wall embolus trapping locations may increase the risk for intimal hyperplasia (e.g., [15]). Our model is the first that can predict embolus trapping locations and the subsequent IVC hemodynamics.

Some limitations should be noted. Emboli were modeled as rigid and spherical, while real emboli are compliant and usually cylindrical in shape. Thus, the IVC filter trapping efficiencies predicted in these simulations should be interpreted with care. However, spherical emboli likely represent the worst-case scenario for embolus capture, and therefore, merit study.

Furthermore, the simulations predict that 100% of the dense emboli are trapped in the IVC filter (Fig. 2d) due to their cross-streamline migration. We believe this result is due to the use of an idealized IVC geometry and a nominally placed IVC filter. Future simulations will consider patient-specific IVC morphology and tilted filter configurations for increased clinical relevance.

ACKNOWLEDGEMENTS

This research was supported by the Walker Assistantship program at the Penn State Applied Research Laboratory.

REFERENCES

[1] Silverstein, M D et al., *Arch Intern Med.*, 158:585–593, 1998.
[2] Cipolla, J et al., *OPUS 12 Scientist*, 2:11–24, 2008.
[3] Clark, W D et al., *Cardiovasc Eng Tech.*, 6:242–255, 2015.
[4] Argueta-Morales, R I, et al., *J Biomech Eng.*, 136:071008, 2014.
[5] Carr, I A et al., *Heart Circ Physiol.*, 305:H732–9, 2013.
[6] Fabbri, D et al., *Biomech Model Mechanobiol.*, 13:289–302, 2014.
[7] Abolfazli, E et al., *Fluid Dyn Res.*, 46:055505, 2014.
[8] Swaminathan, T N et al., *J Biomech Eng.*, 128:360–70, 2006.
[9] Glowinski, R et al., *J Comput Phys.*, 169:363–426, 2001.
[10] Hager, A, et al., *J Comput Multiph Flows*, 6:13-28, 2014.
[11] Aycock, K I et al., *J Biomech Eng.*, 136: 1–13, 2014.
[12] Nahirnyak, V, *J Acoust Soc Am.*, 119:3766–3772, 2006.
[13] Cheng, C P, et al., *Heart Circ Physiol.*, 284:H1161–7, 2003.
[14] Segré G and Silberberg A, *Nature*, 189:209–210, 1961.
[15] Stewart, S F C et al., *Ann Biomed Eng.*, 36:1764–81, 2008.

Copyright 2016 The Organizing Committee for the 2016 Summer Biomechanics, Bioengineering and Biotransport Conference

SB^{3}C2016
Summer Biomechanics, Bioengineering and Biotransport Conference
June 29 –July 2, National Harbor, MD, USA
SB³C2016-56

PREDICTION OF ABDOMINAL AORTIC ANEURYSM SHAPE EVOLUTION USING GAUSSIAN PROCESS IMPLICIT SURFACES

Huan N. Do [(1)], Jongeun Choi [(1,2)], Seungik Baek [(1)]

(1) Department of Mechanical Engineering
Michigan State University
East Lansing, MI, U.S.A.

(2) Department of Electrical and Computer Engineering
Michigan State University
East Lansing, MI, U.S.A.

INTRODUCTION

An abdominal aortic aneurysm (AAA) is a form of vascular disease causing focal enlargement with about a 5% expansion rate of mean diameters per year [1]. Although the measurement of the maximum diameter provides an important factor for deciding the time of surgical treatment, recent studies suggest that the physician should consider other factors such as morphological changes and the patient with a small aneurysm should be examined with the interval of 6-36 months depending on the size. While advances in biomechanics provide state-of-the-art spatial estimates of mechanical stress distributions of AAAs, there are still limitations in modeling its shape evolution in time and the confidence regions. To date, there is no framework combining of biomechanics and the shape evolution to utilize a series of medical images that would aid physicians in detecting small aneurysms with high risk of rupture. Therefore, we define a problem as follows. Given a series of computer tomography scans (CT scans) of AAAs taken at different times, the model will predict the spatio-temporal evolution of AAAs at arbitrary time.

DATA AND METHODS

We used longitudinal data of 37 CT scan images from 7 different patients and the intervals of scan imaging were recorded. The resolutions of these CT scans are approximately 0.7 mm per pixel. This study was subject to internal review board (IRB) approvals at both Michigan State University and Seoul National University Hospital. Three dimensional (3D) models are reconstructed from CT scans using Mimics (Materialise, Leuven, Belgium) to get the longitudinal models using semi-automatic segmentation. Finally, we sample from the longitudinal models to create point cloud data sets, which are used as the observation to our proposed model.

For this study, we develop to model the spatio-temporal patient-specific geometrical evolution using a purely statistical framework. We adapt the Gaussian process implicit surfaces (GPIS) technique [2] that was originally applied for grasping and robot manipulation. The posterior mean of the GP represents our estimated object, and the posterior variance provides the uncertainty in the estimation.
An implicit surface potential (ISP) field is a continuous function:

$$f_t(\boldsymbol{x}) \begin{cases} = 0 \text{ if } \boldsymbol{x} \text{ is on the surface,} \\ > 0 \text{ if } \boldsymbol{x} \text{ is outside,} \\ < 0 \text{ if } \boldsymbol{x} \text{ is inside,} \end{cases} \quad (1)$$

where $\boldsymbol{x} \in \mathbb{R}^3$ is a coordinates vector in 3D space and t is a time index, i.e., $t \in [0, \infty)$ for a continuous stochastic process. Thus, $f_t(\boldsymbol{x}) = 0$ for all $\boldsymbol{x}$ belongs to the point cloud. The time-varying ISP field can be considered as a Gaussian process. A stochastic process is a Gaussian process if for all the choices $\{t_1, \dots, t_k\}$, the random variables $\{f_{t_1}, \dots, f_{t_k}\}$ are jointly Gaussian. Therefore, given a number of observations, the ISP field at arbitrary time has a predictive conditional Gaussian distribution. The development of the AAA surface can be inferred through the ISP field.

We investigate the implicit surface on a grid that is defined by the discretization of the space. We discretized the 3-D continuous space into n spatial sites $S := \{s^{[1]}, \dots, s^{[n]}\} \in \mathbb{R}^{n \times 3}$, where $n = h(x_{\max} - x_{\min}) \times h(y_{\max} - y_{\min}) \times h(z_{\max} - z_{\min})$. h is chosen such that n is a positive integer. The spatial limitations are determined from the training data set. The collection of the realized values of the ISP on the lattice is denoted as $z := (z^{[1]}, \dots, z^{[n]})^T$, where $z^{[i]} := z(s^{[i]})$. We make inference on the ISP field as a Gaussian process, i.e., $z \sim GP(\mu(\boldsymbol{x}, t), K(\boldsymbol{x}, t, \boldsymbol{x}', t'))$, where $\mu(.)$ and $K(.,.)$ are the mean and covariance functions. An example of an ISP field in 2-D space is shown in Figure 1. The boundary of the 2-D object will be a

Copyright 2016 The Organizing Committee for the 2016 Summer Biomechanics, Bioengineering and Biotransport Conference

closed contour in a plane. In particular, let the object be a disk with the radius of 2 and centers at (0, 0). Figure 1 shows the observations z from the locations that belong to the object's surface (black circles), inside the object (black crosses), and outside the object (black diamonds). Locations at which the ISP field values set zero are considered to be on-surface.

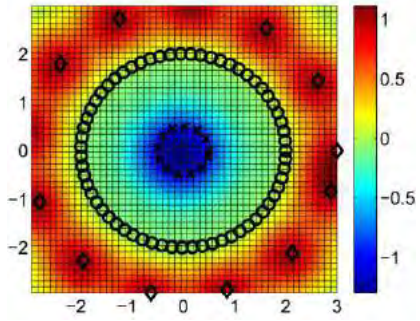

Figure 1. Example of an implicit surface for a 2-D object.

RESULTS

We use all the available scans from a patient *except* the most recent one as the training data, and run our prediction model on the date of the last scan to evaluate our method. Then, we compare the predicted results with the real scan. Figure 2 shows a 3D reconstruction using the PCL package [3] based on the real and the estimated point cloud from our proposed method. Figure 2 (b) shows the lattice with all the off-surface points are filtered out.

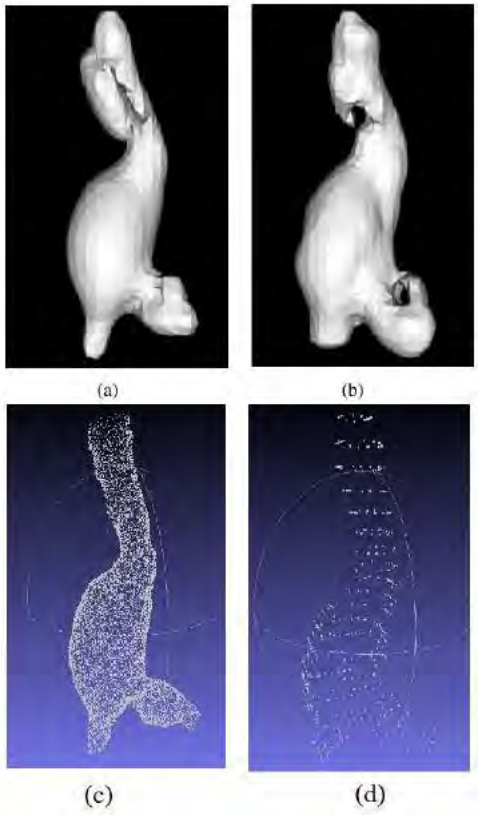

Figure 2. 3D reconstruction of (a) true and (b) estimated AAA surface using (c) true and (d) estimated point clouds.

One of the merits of our approach is that it provides the uncertainty in its prediction. In order to compute the confidence region, we generate the ISP fields on the grid by sampling from the multivariate Gaussian distribution with the posterior mean vector and covariance matrix in a Monte Carlo (MC) simulation with 100 runs. Then, we estimate 100 AAA surfaces that are corresponding to the realized ISP fields. With a sufficient number of MC runs, the set of surfaces forms the confidence region of the prediction. Each realization of the AAA surface from the posterior distribution is plotted with 2% occupancy in Figure 3. Therefore, spatial regions that appear brighter imply higher reliability of the prediction. The true point clouds are plotted in red dots. As shown in Figure 3, the confidence region covers the majority of the real AAA.

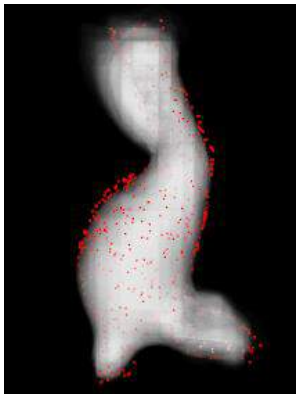

Figure 3. Confidence region: the real point cloud is plotted in red dots.

DISCUSSION

The goal of this paper is to provide a data-driven, nonparametric statistical framework using patient-specific data for improving the prediction results for aneurysm growth, hence assisting clinical management planning. The results of the case study showed excellent performance of our algorithms when they are compared to the true CT scan images.

To the best of our knowledge, this is the first study that predicts the AAA growth using available (patient-specific) CT scan data in a statistical perspective allowing uncertainty quantification in the prediction.

ACKNOWLEDGEMENTS

This work has been supported in part by the National Heart, Lung, and Blood Institute of the National Institutes of Health (R01HL115185 and R21HL113857), National Science Foundation CAREER Award (CMMI-1150376), and the Vietnam Education Foundation (first author).

REFERENCES

[1] H. Gharahi, B. Zambrano, C. Lim, J. Choi, W. Lee, and S. Baek, ”On growth measurements of abdominal aortic aneurysms using maximally inscribed spheres”, *Medical Engineering & Physics, 37:683-691,* 2015.

[2] S. Dragiev, M. Toussaint, and M. Gienger, “Gaussian process implicit surfaces for shape estimation and grasping”, *2011 IEEE International Conference on Robotics and Automation (ICRA).* 2845-2850, 2011.

[3] R. B. Rusu and S. Cousins, “3D is here: Point Cloud Library (PCL)”, *IEEE International Conference on Robotics and Automation (ICRA),* 9-13, 2011.

Copyright 2016 The Organizing Committee for the 2016 Summer Biomechanics, Bioengineering and Biotransport Conference

SB^{3}C2016
Summer Biomechanics, Bioengineering and Biotransport Conference
June 29 –July 2, National Harbor, MD, USA
SB^{3}C2016-57

COMPUTATIONAL ASSESSMENT OF HEMODYNAMIC PARAMETERS OF BICUSPID AORTIC VALVE AORTOPATHY

K. Cao (1), P. Sucosky (2)

(1) Department of Aerospace and Mechanical Engineering
University of Notre Dame
Notre Dame, IN, USA

(2) Department of Mechanical and Materials Engineering
Wright State University
Dayton, OH, USA

INTRODUCTION

The bicuspid aortic valve (BAV) is a valvular defect present in 1-2% of the general population. As compared to the normal tricuspid aortic valve (TAV) which consists of three leaflets, the most prevalent type-I BAV is characterized by one regularly sized leaflet and one larger leaflet. While 71% of type-I BAVs result from the fusion between the left- and right-coronary leaflets (LR subtype), 15% feature right- and non-coronary cusp fusion (RN subtype) and 3% present with non- and left-coronary cusp fusion (NL subtype). As compared to TAV patients, BAV patients have a much higher risk of developing secondary aortopathies such as aortic dilation. In addition, the particular leaflet fusion type affects the expression of dilation and thinning of the ascending aorta (AA) downstream of a BAV. While BAV aortopathy has been historically linked to a genetic predisposition, the abnormal BAV hemodynamics has emerged as a potential coincident etiology. Recent studies have revealed the existence of correlations between the locations of abnormalities in flow skewness, asymmetry, helicity and wall shear stress (WSS) in dilated BAV aortas and the sites of aortopathy development. However, the use of those metrics as predictors of disease initiation prior to dilation has not been thoroughly evaluated. Therefore, the objective of this study is to assess computationally the prognostic value of these hemodynamic parameters for BAV aortopathy, prior to dilation.

METHODS

Unified valve-aorta geometry: A realistic three-dimensional unified valve-aorta geometry was designed in SolidWorks 2014 (Dassault Systemes, Inc) and consisted of the aortic root and the aorta (**Fig. 1**). The non-dilated aorta geometry was created based on a series of computed tomography images of a human aorta. The aorta geometry included the ascending aorta and the aortic arch along with brachiocephalic (BCA), left common carotid (LCCA) and left subclavian (LSCA) arteries. Consistent with our previous valve models[1], the TAV geometry consisted of three identical leaflets attached to the root of the aortic sinus. Dimensional parameters for the aortic sinus and leaflets were obtained from published human aortic valve data. The LR-BAV was characterized by the presence of a normal non-coronary leaflet and a larger leaflet mimicking the two fused coronary leaflets. Consistent with previous morphologic studies, the non-coronary leaflet and the corresponding sinus occupied a circumferential span of 150°. The left- and right-coronary leaflets were assumed to be identical and the raphe was placed along the free edge of these two leaflets. The RN-BAV and NL-BAV anatomies were obtained by rotating the LR-BAV by 120° and 240°, respectively, with respect to the aortic root.

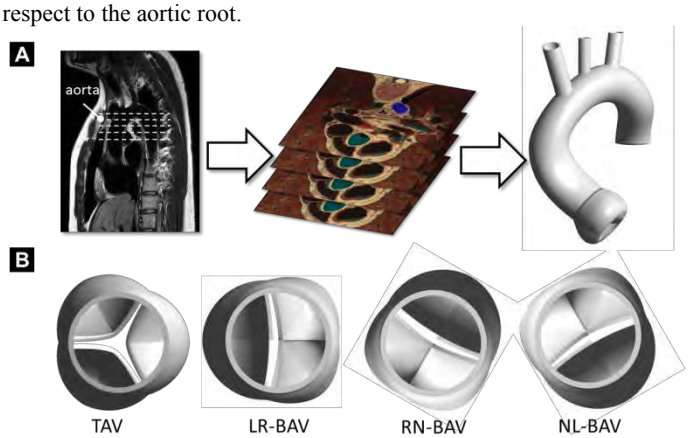

Figure 1: (A) aorta reconstruction methodology; (B) TAV and type-1 BAV geometries

Copyright 2016 The Organizing Committee for the 2016 Summer Biomechanics, Bioengineering and Biotransport Conference

Material: The leaflet material was modeled as hyperelastic using a three-parameter incompressible Mooney-Rivlin model. This material model has been used successfully in a previous study to simulate physiologic hemodynamics through the aortic valve[1]. The aortic wall was approximated as a linear, elastic and isotropic material (elastic modulus: 2 MPa; Poisson's ratio: 0.45)[2]. Blood was modeled as an incompressible, homogeneous and Newtonian fluid (density: 1050 kg/m^3; dynamic viscosity: 0.0035 Pa·s).

Boundary conditions: Flow boundary conditions consisted of a physiologic ventricular pressure waveform varying between 0 and 130 mmHg at the inlet of the fluid domain and physiologic pressure waveforms at the four outlets of the aorta (BCA, LCCA, LSCA and descending aorta). The aortic wall was constrained in the axial direction at the inlet and outlet sections but was allowed to move in the radial and circumferential directions.

Hemodynamic characterization: Flow eccentricity was quantified in terms of the flow displacement (d) at the proximal and middle AA, which represents the radial distance between the center of the slice and the centroid of the region containing the top 15% of velocities at peak systole (**Fig. 2A**). Flow skewness was assessed in terms of the systolic flow angle (θ) between the net systolic flow velocity vector and the normal vector to the slice (**Fig. 2B**). Flow helicity was characterized in terms of the peak-systolic in-plane vorticity and positive helix fraction (PHF) defined as the ratio between right-handed helix and the totality of the rotating flux (**Fig. 2C**). The local magnitude and temporal characteristics of the longitudinal WSS (**Fig. 2D**) were assessed in terms of the temporal shear magnitude (TSM),

$$\mathrm{TSM} = \frac{1}{T}\int_0^T |\tau| dt \,,$$

and the oscillatory shear index (OSI),

$$\mathrm{OSI} = \frac{1}{2}\left[1 - \left(\left|\int_0^T \tau dt\right| \Big/ \int_0^T |\tau| dt\right)\right].$$

The TSM represents the time-averaged magnitude of WSS along the circumference of a slice over one cardiac cycle. The OSI characterizes the oscillatory nature or the directionality of WSS (OSI=0: purely unidirectional/pulsatile WSS; OSI=0.5: purely bidirectional/oscillatory WSS).

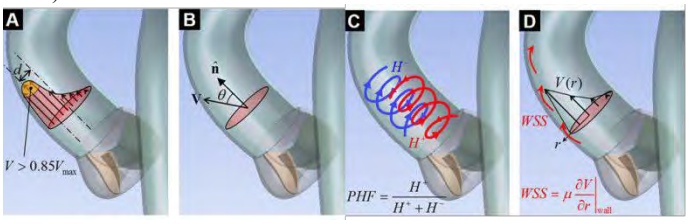

Figure 2: flow parameters: (A) flow displacement; (B) flow angle; (C) PHF; (D) WSS

RESULTS

Flow helicity: Flow in the TAV AA was shown to include both right-handed and left-handed helicity without a dominant helical flow pattern (PHF=0.51) (**Figure 3**). In contrast, flow in BAV AAs is mainly characterized by strong righted-handed helicity. Despite limited left-handed vortex near the periphery of the aortic wall, the LR-BAV is dominated by strong right-handed vortex at the anterior region (PHF=0.68). While the RN-BAV (PHF=0.71) and NL-BAV (PHF=0.72) generate vortex distributions qualitatively similar to the LR-BAV, they generate high vorticity over larger regions than those generated by the LR-BAV.

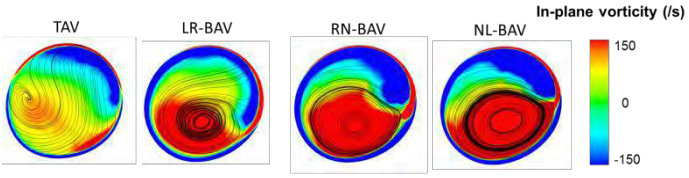

Figure 3: In-plane vorticity and streamlines

Flow eccentricity and skewness: The TAV generates essentially axisymmetric velocity fields in the proximal AA (θ=4.6°; d=1.3 mm). The flow velocity fields in all BAV AAs exhibit a higher degree of eccentricity towards the aortic wall (θ>11.2°; d>4.9 mm). While the flow captured in the middle segment of the TAV AA deviates slightly towards the periphery of the aortic wall due to the wall curvature (θ=5.5°; d=3.3 mm), the velocity fields predicted in all BAV AAs exhibit more skewness (θ>12.1°; d>6.8 mm).

TSM: The RN-BAV generates WSS levels (TSM=15.3 dyn/cm^2) similar to those predicted downstream of the TAV (TSM=15.4 dyn/cm^2) in the proximal AA, but the LR-BAV (TSM=19.9 dyn/cm^2) and RN-BAV (TSM=19.3 dyn/cm^2) AAs are subjected to WSS overloads. In the middle AA, the RN-BAV generates a WSS overload (TSM=19.5 dyn/cm^2) while the LR-BAV and NL-BAV generate sub-physiologic WSS levels (TSM=16.8 and 17.4 dyn/cm^2, respectively) relative to the TAV AA (TSM=18.9 dyn/cm^2).

OSI: While the TAV subjects the proximal AA to a bidirectional WSS distribution (OSI=0.37), the BAVs generate more pulsatile WSS environments (OSI<0.19). In the middle AA, while the TAV AA (OSI=0.17), RN-BAV AA (OSI=0.13) and NL-BAV AA (OSI=0.13) remain exposed to a relatively unidirectional WSS, the LR-BAV AA experiences a more oscillatory WSS (OSI=0.24).

DISCUSSION

This study reveals that the BAV generates abnormal aorta hemodynamics characterized by increased flow helicity, flow angle, flow displacement and disturbed regional WSS. These hemodynamic abnormalities are dependent on the valve cusp fusion and correlate with the sites on the aortic wall reported as vulnerable to dilation. Our results show that global flow metrics (i.e., PHF, flow angle and flow displacement) considered in past clinical measurements may not be sensitive enough to identify BAV patients and predict disease progression prior to dilation. Instead, WSS metrics (i.e., TSM and OSI) which are more challenging to measure by MRI, seem to exhibit superior predictive capabilities and to be better risk assessment markers for BAV aortopathy, prior to dilation and regardless of the BAV morphotype. These WSS metrics may be important in the development of new treatment strategies for monitoring and normalizing BAV flow in young patients prior to aortic dilation.

Acknowledgement

This work was supported by the National Science Foundation under Grants CMMI-1148558 and CMMI-1550144; and the American Heart Association under Grant 14PRE18940010.

REFERENCES

[1] Cao K, Bukač M, Sucosky P. Three-Dimensional Macro-Scale Assessment of Regional and Temporal Wall Shear Stress Characteristics on Aortic Valve Leaflets. *Comput Methods Biomech Biomed Engin*. 2015;

[2] Atkins SK, Cao K, Rajamannan NM, Sucosky P. Bicuspid aortic valve hemodynamics induces abnormal medial remodeling in the convexity of porcine ascending aortas. *Biomech. Model. Mechanobiol*. 2014;13:1–17.

Copyright 2016 The Organizing Committee for the 2016 Summer Biomechanics, Bioengineering and Biotransport Conference

SB^{3}C2016
Summer Biomechanics, Bioengineering and Biotransport Conference
June 29 –July 2, National Harbor, MD, USA
SB^{3}C2016-58

COMPUTATIONAL MODELING OF THE ARTERIAL WALL BASED ON LAYER-SPECIFIC HISTOLOGICAL DATA

T. Jin, I. Stanciulescu

Civil and Environmental Engineering
Rice University
Houston, TX 77005, USA

INTRODUCTION

Understanding the structure-function relationship of individual arterial wall layers provides insight into the pathophysiology of arterial wall diseases such as arteriosclerosis, allows for better predictions for the outcome of interventional treatments such as balloon angioplasty (Holzapfel et al., 2002), and advances various biomedical applications such as artificial heart valve (Durst et al., 2011; Hasan et al., 2014).

Uniaxial (in vitro) tension tests are widely used to study the mechanical behavior of different arterial wall layers. However, these tests are not sufficient for the construction of multi-dimensional models to predict the material behavior in physiological loading states. Conducting experiments that closely mimic the in vivo loading state would provide more valuable information, but such experiments often put higher demands on the equipment and human skills. On the other hand, developing numerical strategies involving layer-specific histological information may provide an effective and inexpensive choice to study the material behavior of different arterial wall layers under complex loading conditions.

In this work, we present two different constitutive modeling approaches for arterial walls, the embedded fiber (EF) approach belonging to the detailed modeling strategy and the angular integration (AI) approach belonging to the homogenized modeling strategy, to simulate the anisotropic behavior of individual arterial wall layers using layer-specific histological data. Both approaches take into consideration the influence of fiber dispersion introduced by fiber angular distribution (departure of individual fibers from the mean orientation) and fiber waviness. Through a comprehensive parametric study, we establish relationships between the phenomenological parameters used in the AI approach and those used in the EF approach that have straightforward physical meanings. These relationships are helpful to form a better understanding of the connection between the microscopic structure and the macro-mechanical functions of different arterial wall layers.

METHODS

Arterial walls are typically composed of three different layers in the thickness direction: intima, media and adventitia. Although each layer has different histological structure, they all can be modeled as fiber-reinforced materials with two families of collagenous fiber bundles symmetrically arranged in an isotropic soft ground matrix (Holzapfel et al., 2000; Holzapfel, 2006).

In the embedded fiber (EF) approach, a random walk algorithm (Spanos and Esteva, 2009; Jin and Stanciulescu, 2015) is implemented to generate the fiber microscopic arrangement. The fiber dispersion has two different causes, departure of individual fibers from the mean orientation measured by the initial angle and the fiber waviness represented by the relative angle. In order to directly incorporate the generated fiber microscopic structure into the numerical simulation, the embedded fiber approach is adopted. This approach assumes that fibers are embedded in the ground matrix and the two material components deform together, thus is essentially equivalent to the affine fiber kinematics (Lanir, 1983; MacKintosh et al., 1995; Agoram and Barocas, 2001; Storm et al., 2005). Figure 1 shows a rectangular arterial wall layer sample with two families of fibers synthetically generated by the random walk algorithm.

The angular integration (AI) approach follows a homogenization methodology that smears the two families of fibers into the ground matrix and treats the material as homogeneous. In the finite element formulation, the anisotropy introduced by fibers is considered at the constitutive level. The total strain energy is decoupled into two parts, the isotropic part representing the contribution from the ground matrix enhanced by the anisotropic terms representing the contributions from

Copyright 2016 The Organizing Committee for the 2016 Summer Biomechanics, Bioengineering and Biotransport Conference

the two families of fibers. The fiber dispersion caused by departure of individual fibers from the mean orientation is considered by the Von Mises parameter, and the dispersion caused by fiber waviness is considered in this approach by introducing a correction term. The finite element formulation captures the anisotropy at the constitutive level with several phenomenological material parameters.

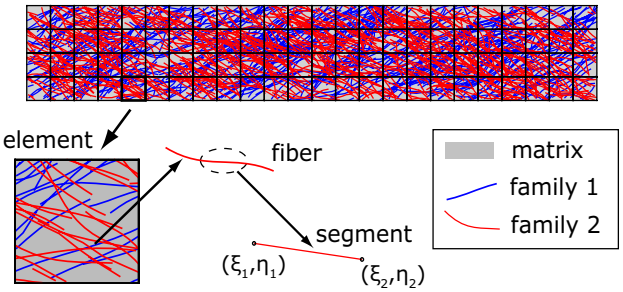

Figure 1: Synthetically generated arterial wall layer sample meshed with four-node quad element

RESULTS

Figure 2 shows the distribution of the generated initial angle of fibers in the intima layer and the resulted geometry of the two families of fibers generated by the random walk algorithm. Figures 3 and 4 show the comparison between the experimental data and the simulation results based on the AI and EF approaches. For both methods, the simulation results match the experimental data very well. Figure 5 shows the relationship between the parameters reflecting the fiber waviness in the EF and AI approaches.

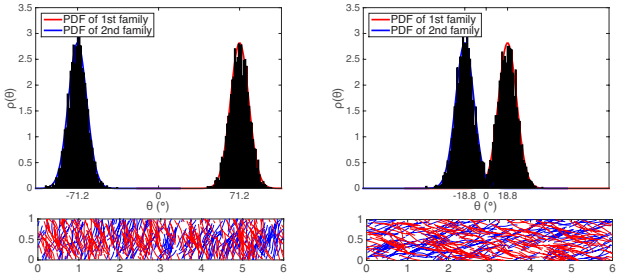

(a). Circumferential sample (b). Axial sample

Figure 2: Distribution of the initial angle of fibers in the intima layer and the generated geometry of the two families of fibers

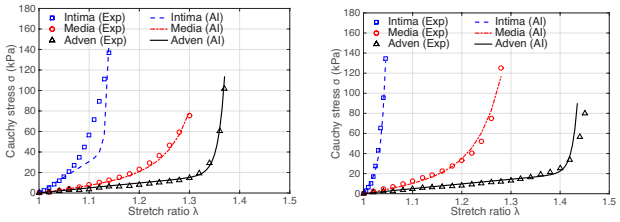

(a). Circumferential direction (b). Axial direction

Figure 3: Comparison of the numerical results via the angular integration (AI) approach with the experimental data (Exp)

DISCUSSION

In this paper we present two different modeling approaches, the embedded fiber (EF) approach and the angular integration (AI) approach, to simulate the anisotropic behavior of individual arterial wall layers using layer-specific histological data. Both approaches include the influence of fiber dispersion caused by fiber angular distribution (departure of individual fibers from the mean orientation), and take into consideration the dispersion caused by fiber waviness, which has not been previously considered. By comparing the numerical results with published experimental data of different layers of a human abdominal aorta, we show that both approaches can successfully capture the material nonlinearity and anisotropy. Furthermore, we establish the relationships between the AI phenomenological parameters and the EF parameters having straightforward geometrical or mechanical interpretations. Through a comprehensive parametric study, we demonstrate the validity and accuracy of these relationships. This study provides valuable insight for the calibration of phenomenological parameters used in the homogenized modeling taking into account the material microscopic arrangement. Moreover, it can facilitate a better understanding of individual arterial wall layers, which will eventually advance the study of the structure-function relationship of the whole arterial wall.

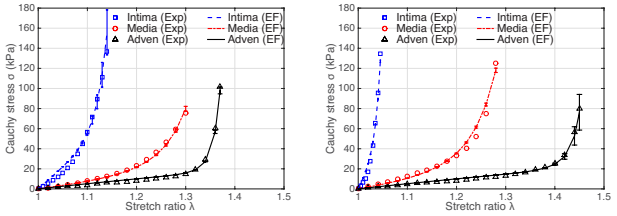

(a). Circumferential direction (b). Axial direction

Figure 4: Comparison of the numerical results via the embedded fiber (EF) approach with the experimental data (Exp)

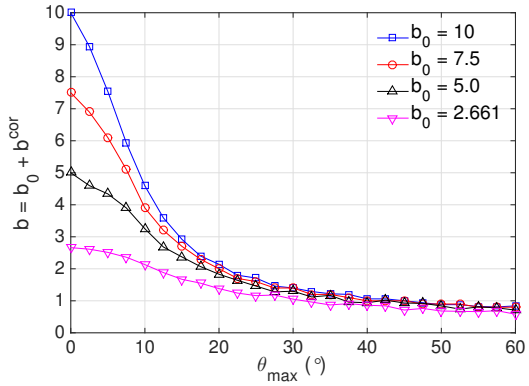

Figure 5: Relationship between the parameters reflecting fiber waviness in the EF and AI approaches

ACKNOWLEDGEMENTS

The authors thank Prof. Jane Grande-Allen for useful discussions and suggestions. This work was partially funded by NSF (grant No. 1463432).

REFERENCES

Selected References:

[1] Fung, Y.C., *American Journal of Physiology*, Vol. 23, No. 6, 1967.
[2] Holzapfel, G.A. and Gasser,T.C., *J Elasticity*, 61:1-48, 2000.
[3] Balzani, D., *Int J Solid and Structure*, 43:6052-6070, 2006.
[4] Nemir, S. et al., *Biotech Bioeng*, Vol. 105, No. 3, 2009.
[5] Carleton, J.B. et al., *Acta Biomaterialia*, 2015;12:93 – 101.
[6] Jin, T. and Stanciulescu, I., *Biomech Model Mechanobiol*, 2015.

Copyright 2016 The Organizing Committee for the 2016 Summer Biomechanics, Bioengineering and Biotransport Conference

SB^{3}C2016
Summer Biomechanics, Bioengineering and Biotransport Conference
June 29 –July 2, National Harbor, MD, USA
SB^{3}C2016-59

MESO-SCALE REORGANIZATION OF METABOLIC BRAIN NETWORKS IS ASSOCIATED WITH PERSISTENT TMJ PAIN

Megan M. Sperry (1), Sonia Kartha (1), Eric J. Granquist (1,2), Beth A. Winkelstein (1,3)

(1) Bioengineering
University of Pennsylvania
Philadelphia, PA, USA

(2) Oral & Maxillofacial Surgery
University of Pennsylvania
Philadelphia, PA, USA

(3) Neurosurgery
University of Pennsylvania
Philadelphia, PA, USA

INTRODUCTION

Chronic pain affects over 100 million adults in the US with annual costs of $560-635 [1]. Temporomandibular joint (TMJ) disease is a common musculoskeletal disorder, second only to low back pain [2]. Osteoarthritis (OA) is the most common TMJ pathology; this low-grade inflammatory condition in the TMJ synovium has a complex and multifactorial etiology including pain [3]. In most patients TMJ pain resolves without needing further clinical action. Yet, for a subset of patients, chronic TMJ disorder develops, with physical, psychological, and pain symptoms [4]. The transition to chronic pain is due to sustained hyperexcitability in the central nervous system (CNS) that amplifies nociceptive signals from peripheral sources, increases spontaneous activity, and reduces activation thresholds, which can lead to changes in the spinal cord and brain circuitry [5].

Since the neuroplastic changes in the CNS vary in magnitude and regionally, complex network analysis is useful to begin to understand how such changes may relate to pain [6]. In fact, functional brain networks exhibit modified circuit connectivity during the transition to chronic neuropathic pain [7]. Limbic system circuitry changes have been noted with chronic pain after spared nerve injury in the rat, with increased connectivity *within* the limbic system, as well as between the limbic and sensorimotor regions [7]. Yet, little is known about the extent and time course of brain remodeling in *osteoarthritic* pain.

This study investigated the relationship between TMJ pain and the neuron-specific brain networks using acute/resolving and persistent pain models of TMJ pain [8]. Positron emission tomography (PET) imaging was used to investigate the global topological features of metabolic brain networks when pain is present. The structure of brain networks was also examined using community detection to investigate brain networks in the context of the different pain outcomes – persistent or acute/resolving pain.

METHODS

All procedures were IACUC-approved and used female Holtzman rats. TMJ OA was induced by separate magnitudes of mouth-opening load to induce pain that resolves within 7 days after loading (2N; n=7) or persistent pain after loading (3.5N; n=7) [8]. Steady mouth-opening was imposed daily for 60mins on 7 consecutive days under inhalation isoflurane anesthesia. Orofacial pain was measured during and after loading using von Frey filaments to quantify a withdrawal threshold as a measure of mechanical hyperalgesia [8]. Differences in pain were detected by a two-way repeated measures ANOVA with Tukey's test.

^{18}F-fludeoxyglucose (FDG)-PET images were acquired at day 0 (baseline) and day 7, which was 1 day after loading cessation for each rat. Prior to each imaging session, rats were anesthetized with isoflurane and ^{18}F-FDG given by a tail vein catheter. Then rats were transitioned to dexmedetomidine (0.075mg/kg) and allowed to rest for 1hr before imaging, providing time for radionuclide distribution. PET images were acquired using a small animal PET scanner, functionally similar to the Philips Mosaic; images were reconstructed and registered to Schwarz's FDG PET-specific stereotaxic rat brain template by Advanced Normalization Tools [9,10]. Image volumes were normalized to the visual cortex, which is an unaffected region.

To evaluate metabolic brain networks, registered PET images were parcellated into anatomic regions using the Schwarz rat brain atlas. Each brain region was represented as a node; edges connecting two nodes were defined by the Pearson correlation coefficient between the average FDG uptake in two brain regions for all rats [11]. All rats were combined to construct baseline and day 7 brain networks since the pain responses are similar in both groups at those days [8].

A variety of topological properties of each network was assessed: the *clustering coefficient* evaluated segregated information transfer, *efficiency* assessed integrative information transfer, *node strength*

Copyright 2016 The Organizing Committee for the 2016 Summer Biomechanics, Bioengineering and Biotransport Conference

computed the strength of network interconnectivity, and *modularity* quantified the degree to which the network can be subdivided into distinct groups. Modules were defined as those sets of nodes that are highly inter-connected [12]. Topological features were assessed by the Brain Connectivity Toolbox (BCT) in Matlab [13]. Differences in topological properties were measured with a pairwise t-test between corresponding nodes in each network. Also, changes in the community structure of the networks was estimated using the Louvain algorithm, also with the BCT. Because later pain patterns differ between the 2N and 3.5N groups [8], separate brain networks were also constructed for those groups at day 7; community detection identified changes in the *number* and *composition* of communities between the networks.

RESULTS

The withdrawal threshold significantly decreases ($p<0.001$) from baseline at day 7 for both groups (Fig. 1). Yet, after the rest-period with no loading (at day 14), sensitivity only remains in the 3.5N group ($p<0.001$), but returns to baseline in the 2N group (Fig. 1).

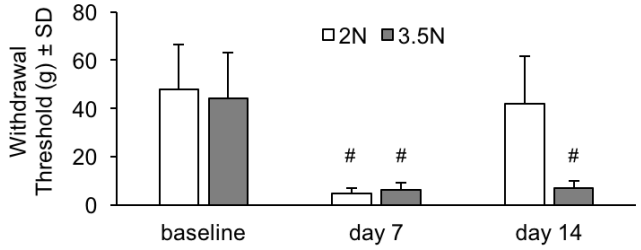

Fig 1. Orofacial sensitivity increases at day 7 (#p<0.001). But it only remains at day 14 in the 3.5N group (#p<0.001).

Evaluating the global topological properties reveals significant increases in the post-loading metabolic network at day 7 compared to baseline ($p<0.001$) for the mean clustering coefficient (0.61±0.05 baseline; 0.71±0.04 day 7), node strength (30.37±3.30 baseline; 34.31±2.82 day 7), and efficiency (0.60±0.05 baseline; 0.69±0.04 day 7). Network modularity significantly decreases ($p<0.0001$) at day 7 (0.050±0.001) from baseline (0.085±0.001). Despite differences in modularity, the networks consistently exhibit 3-modules at both baseline and day 7 (Fig. 2). Although there is consistency between those networks before and after loading, the composition of the subdivisions changes over time (Fig. 2). The sensory regions (somatosensory cortex, medulla, cerebellum) cluster more strongly at day 7 and the affective regions form two smaller subdivisions (Fig. 2).

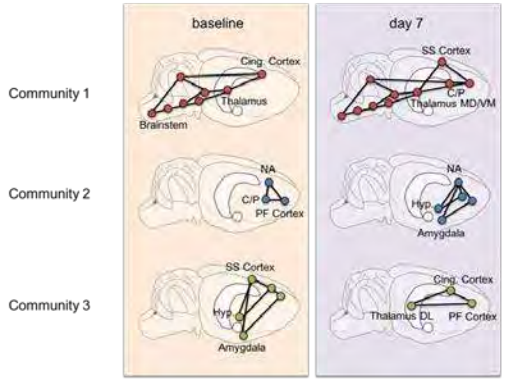

Fig 2. Metabolic network components in the brain reorganize following induction of TMJ OA (SS=somatosensory, NA=nucleus accumbens, Hyp=hypothalamus, C/P=caudate/putamen, PF=pre-frontal, DL=dorsolateral, MD=mediodorsal, VM= ventromedial).

The three-community structure is evident in the correlation network matrices for all rats at both days (Fig. 3). Considering the groups separately at day 7, a change in community structure emerges in the 3.5N group that is not evident in the 2N group (Figs. 1 & 3). The brain network in the 3.5N group shifts to two larger equally-sized communities (Fig. 3), but the 2N group maintains the three-modules.

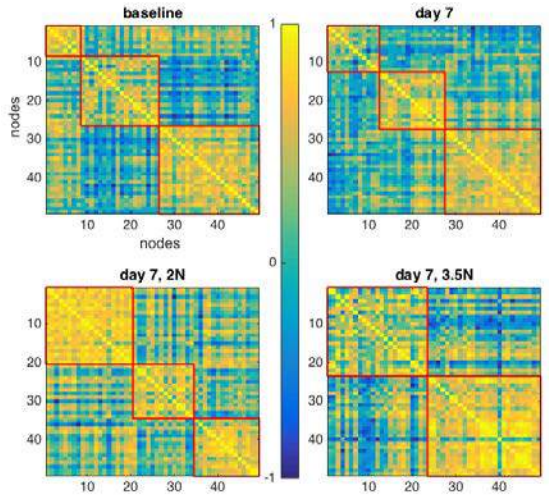

Fig 3. Correlation network matrices at baseline and day 7 show 3 communities (in red). At day 7, only 3.5N has a two-community structure. Color bar shows strength of connectivity (R).

DISCUSSION

This work shows metabolic brain networks are altered in TMJ OA pain and may predict the likelihood of pain becoming chronic (Figs. 1-3). The marked increases in the clustering coefficient, efficiency, and node strength between baseline (no pain) and day 7 (pain in both groups) suggests that select brain regions are becoming more tightly correlated with each other. Although the *global* topological properties used here strongly support brain networks being altered in this pain state, the *local* topological properties that may provide insight into sub-circuit modifications [7], were not evaluated.

Since the community structure is stable for acute pain (2N) but is altered when it persists (3.5N) (Figs. 1 & 3) these metrics may provide a diagnostic for pain prediction. Further, the transition to a two-module community structure in the chronic pain case [8] highlights the increasing correlation across local and remote brain areas, possibly indicating remodeling. This phenomenon is also seen in functional connectivity analyses of a host of clinical pain states [14]. Since we did not use fMRI or dynamic PET, our findings are restricted to correlation networks and did not evaluate functional connectivity. Nonetheless, findings highlight the possibility for networks from metabolic brain imaging to *predict* which cases will develop into persistent pain, which has tremendous clinical utility.

ACKNOWLEDGEMENTS

Support from OMSF, Penn Dental's Schoenleber Fund, and NIH (T32-AR007132). We also thank E. Blankemeyer and Y-H Yu.

REFERENCES

[1] Gaskin & Richard, *J Pain* 13:715-24,2012. [2] NIDCR, *TMJD & Orofacial Pain Prog* 2010. [3] Wang et al, *J Dent Res* 94:666-73,2015. [4] Scrivani et al, *N Engl J Med* 359:2693-705,2008. [5] Woolf, *Pain* 152:S2-15,2011. [6] Bullmore & Sporns, *Nat Rev Neurosci* 10:186-98,2009. [7] Baliki et al, *Sci Rep* 4,2014. [8] Kartha et al, *J Oral Maxillofac Surg* 74:54.e1-10,2016. [9] Schwarz et al, *Neuroimage* 32:538-50,2006. [10] Avants et al, *Neuroimage* 54:2033-44,2011. [11] Zhang et al, *PLoS One* e28817,2011. [12] Blondel et al, *J Stat Mech* P10008,2008. [13] Rubinov & Sporns, *NeuroImage* 52:1059-69,2010. [14] Farmer et al, *Neurosci Lett* 520:197-203,2012.

Copyright 2016 The Organizing Committee for the 2016 Summer Biomechanics, Bioengineering and Biotransport Conference

SB^{3}C2016
Summer Biomechanics, Bioengineering and Biotransport Conference
June 29 –July 2, National Harbor, MD, USA
SB^{3}C2016-60

MEASUREMENT OF AORTIC STENT GRAFT COEFFICIENTS OF FRICTION

Matthew G. Doyle (1,2), Michael Lancaster (1), Leonard W. Tse (2), Thomas L. Forbes (2), Cristina H. Amon (1,3)

(1) Department of Mechanical and Industrial Engineering
University of Toronto
Toronto, Ontario, Canada

(2) Division of Vascular Surgery
University of Toronto
Toronto, Ontario, Canada

(3) Institute of Biomaterials and Biomedical Engineering
University of Toronto
Toronto, Ontario, Canada

INTRODUCTION

An abdominal aortic aneurysm (AAA) is a pathological dilation of the abdominal aorta, which, if left untreated, will continue to grow and eventually rupture with a mortality rate of up to 90%, making AAAs the 13th leading cause of death in the United States [1]. Endovascular aneurysm repair is a minimally invasive procedure used to treat AAAs in which a stent graft (SG) is packaged in a sheath, delivered through the iliac artery, and unsheathed in the abdominal aorta. During the unsheathing process, SGs can unexpectedly rotate such that their deployed position differs from what was intended. For standard SGs, this rotation is generally a minor issue, which can result in kinking of the limbs or limb deployment on the opposite side to the surgical plan. However, for fenestrated SGs, which have fenestrations (holes) that are to be aligned with the branch vessels (renal arteries, superior mesenteric artery, and/or celiac artery), SG rotation can be a major problem, which can result in branch artery occlusion and potentially renal failure or bowel ischemia if not corrected.

We hypothesize that SG rotation during unsheathing is caused by an accumulation of rotational energy in the SG during delivery through iliac arteries that are tortuous, calcified, and/or stenotic, that is released during the unsheathing. To better understand this phenomenon, the overall goal of our research project is to develop finite element models of the delivery and deployment of standard and fenestrated SGs that take into account these rotational effects. Results from these simulations will be compared to ongoing experimental studies in our lab, in which SGs are delivered and deployed in arterial phantoms, as well as to clinical findings obtained as part of an ongoing prospective clinical study.

To develop models of SG delivery, we need to properly account for the friction between the packaged SG, its sheath, and the iliac artery to ensure accurate calculations of rotational energy accumulation. While a previous study [2] determined coefficients of friction for deployed SGs, there have been no studies that have measured these quantities in undeployed SGs. The objectives of this study were therefore to develop an apparatus to measure frictional forces and use these force measurements to determine the coefficients of friction between i) stents and the inner surface of the sheath (S-Sh$_i$), ii) graft fabric and the inner surface of the sheath (G-Sh$_i$), and iii) the outer surface of the sheath and a mock artery material (Sh$_o$-MA).

METHODS

An experimental apparatus (Fig. 1) was designed and built to measure the friction force between two materials. One material was fixed in position, and the other material was affixed to a moveable sled. A precision mass was affixed to the sled as well to ensure the contact of the two materials and to increase the normal force to a measurable level. The surfaces of both materials were wetted with saline solution to mimic *in vivo* conditions. A load cell was attached to the sled and to a motor via a nylon monofilament. The motor pulled the sled at 1 mm/s and the load cell recorded the frictional force between the two materials.

The SG used for the experiments was a standard Cook Zenith Flex SG (Cook Medical, Bloomington, IN, USA) which was separated into its polyester graft fabric and stainless steel stents by removing the sutures used to attach the stents to the graft fabric. The mock arterial material was chosen to be polyurethane, which was selected as a potential material for arterial phantoms to be used in ongoing SG delivery and deployment experiments. For each material pair (S-Sh$_i$, G-Sh$_i$, and Sh$_o$-MA), 20 trials were performed. To account for anisotropy of the graft fabric and the inner and outer surfaces of the sheath, experiments were conducted in both axial and circumferential directions for the G-Sh$_i$ and Sh$_o$-MA material pairs.

Copyright 2016 The Organizing Committee for the 2016 Summer Biomechanics, Bioengineering and Biotransport Conference

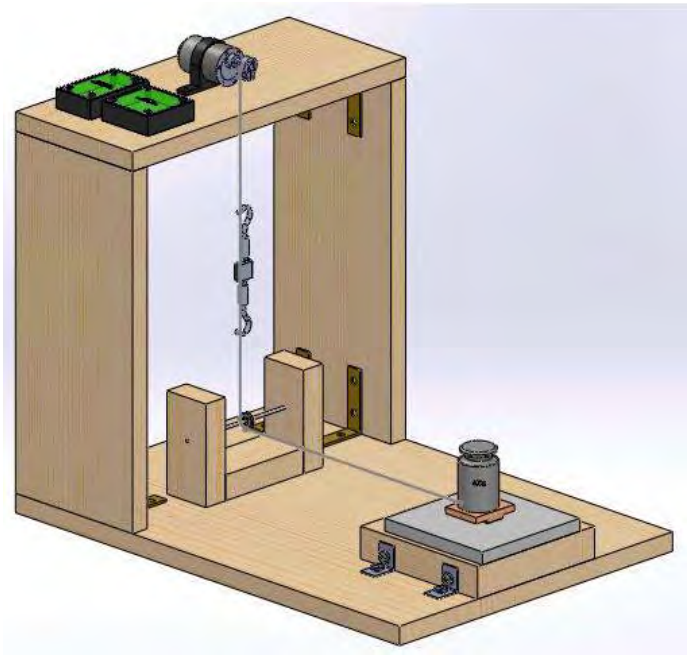

Figure 1: Schematic of experimental apparatus for measurement of friction forces between two materials.

For each material pair, static and kinetic coefficients of friction, μ_s and μ_k respectively, were calculated as

$$\mu_j = \frac{F_j - L}{N}, \quad (1)$$

where F_j ($j = s$ or k) is the average frictional force measured by the load cell, L is the weight of the load cell, and N is the normal force, measured as the weight of the sled assembly. The average static frictional force F_s for each material pair was calculated as the average of the maximum of the first 30-40 sample points for each of the 20 trials. The average kinetic frictional force F_k for each material pair was calculated by firstly averaging each of 120-160 sample points across the 20 trials and then fitting an average horizontal line through the resulting average data in the region following the peak.

RESULTS

Static and kinetic coefficients of frictions for the S-Sh_i, G-Sh_i, and Sh_o-MA material pairs are summarized in Table 1 for both axial and circumferential directions, where applicable. As expected, for all cases μ_s was found to be greater than μ_k. For both the G-Sh_i and Sh_o-MA pairs, the coefficients of friction in the circumferential direction were found to be greater than the corresponding values in the axial direction and in all cases, the differences were found to be statistically significant (p <0.05). The G-Sh_i material pair was found to have the largest coefficients of friction followed by the Sh_o-MA pair and the S-Sh_i pair. However, it should be noted that the values for the Sh_o-MA pair are dependent on the mock artery material used and could vary substantially with different materials.

The apparatus that we built for these experiments yielded consistent results across the 20 trials for each case with standard deviations of less than 14% over all tests. The apparatus is also easily reconfigurable to test different material pairs with different base piece configurations, allowing quick switches between a fixed material with a large surface, such as the mock artery material, to a fixed material with a small surface area, such as the inner surface of the sheath.

Table 1: Coefficients of friction for Cook Zenith Flex stent grafts

	stent-sheath (S-Sh_i)	**graft-sheath (G-Sh_i)**	**sheath-mock artery (Sh_o-MA)**
$\mu_{s,axial}$	0.058±0.0080	0.144±0.069	0.109±0.012
$\mu_{k,axial}$	0.044±0.0038	0.135±0.050	0.091±0.012
$\mu_{s,circumferential}$	--	0.157±0.004*	0.161±0.020*
$\mu_{k,circumferential}$	--	0.145±0.005*	0.131±0.008*

* Indicates statistically significant (p < 0.05) difference between directions.

DISCUSSION

The apparatus and protocols developed for the experiments needed to obtain coefficients of friction can and will be applied to other material pairs. Firstly, we will perform experiments with a material pair consisting of the outer surface of the sheath and porcine aortic tissue, as a surrogate for human iliac and aortic tissue. It is important to determine the coefficients of friction between the sheath and actual arterial tissue to estimate the coefficients of friction in the *in vivo* environment. Ideally, this would be done with human iliac artery tissue; however, the more readily available porcine aortic tissue will act as a reasonable surrogate.

Once we determine estimates of *in vivo* coefficients of friction, we will test a variety of mock artery materials in contact with the outer surface of the sheath to attempt to find one with comparable frictional properties. In parallel with this, we will be testing the mechanical properties of these mock artery materials to find a material that has comparable mechanical properties to those found in aged human iliac arteries as defined in Ref. [3]. We will use the results from these tests to select the optimal material that best matches iliac artery mechanical and frictional properties. By approximating both the mechanical and frictional behavior of human iliac arteries in our mock artery material, our experimental and computational studies will best reflect the *in vivo* environment enabling direct comparisons between experimental, computational, and clinical measurements of SG rotation following delivery through the iliac artery.

In conclusion, an experimental apparatus was designed and constructed to allow for the measurement of the frictional forces between two materials, and these measurements were then used to determine the static and kinetic coefficients of friction between these two materials. We presented coefficients of friction for three material pairs, stainless steel stents and the inner surface of a sheath, polyester stent graft fabric and the inner surface of a sheath, and the outer surface of a sheath and a mock artery material. These coefficients of friction are required for finite element simulations of stent graft delivery and deployment and have not been previously reported.

ACKNOWLEDGEMENTS

Funding provided by a Natural Sciences and Engineering Research Council of Canada (NSERC) Undergraduate Summer Research Award (ML).

REFERENCES

[1] Kuivaniemi, H *et al*., *Circulation*, 117:242-252, 2008.
[2] Vad, S *et al*., *J Biomech Eng*, 132:121007-1-121007-10, 2010.
[3] Schulze-Bauer, CAJ *et al*., *J Biomech Eng*, 125:395-306, 2003.

Copyright 2016 The Organizing Committee for the 2016 Summer Biomechanics, Bioengineering and Biotransport Conference

SB^{3}C2016
Summer Biomechanics, Bioengineering and Biotransport Conference
June 29 –July 2, National Harbor, MD, USA
SB^{3}C2016-61

AUDIO RESPONSE SYSTEM FOR ACTIVE LEARNING IN A LARGE LECTURE CLASS

Craig J. Goergen (1)

(1) Biomedical Engineering
Purdue University
West Lafayette, IN, 47906

INTRODUCTION

Audience response systems allow teachers and students to dynamically interact by posing questions and collecting answers in real-time. This is especially important in large biomedical engineering lecture classes where encouraging active learning and class participation is important but difficult. The purpose of this report was to evaluate the effectiveness of a clicker system designed to improve learning outcomes in a cell biology course specifically designed for engineers with 282 enrolled students.

METHODS

Students enrolled in a Cell Biology course during the fall of 2013 (BIOL 230, Purdue University) were required to have and use an "i>clicker" or clicker as 3% of their overall class grade (Figure 1; [1]). This system requries a 900 MHz base with a 300 foot range for recording responses, customiziable software for displaying anwers (version 6.3), and each student to have their own clicker to answer questions. While short answer questions are possible with this system, only multiple choice questions with five possible answers were used during this class. A total of 282 students were enrolled in the course, the majority of whom were students majoring in biological, biomedical, chemical, and industrial engineering. Responses are reported for 8 lectures, with anywhere between 2 and 12 questions given per class for a total of 36 questions and an average of 4.5±3.4 questions per lecture. Attendance was determined as the maximum number or responses recorded for each lecture.

Figure 1: Both student (left) and instructor (right) versions of the iClicker 2 remotes [1].

Copyright 2016 The Organizing Committee for the 2016 Summer Biomechanics, Bioengineering and Biotransport Conference

Figure 2: Base needed to collect responses. The system operates at 900 MHz base, has a 300 foot range, and is USB compatible.

RESULTS AND DISCUSSION

The number of students enrolled in the course and average attendance, total responses, and correct responses are displayed in Figure 1 below. Average attendance was 80.8% of total enrollment, a substantial improvement over previous years when clickers were not used. Most students who attended lecture used their clickers consistently to respond to the questions (98.2%). Of these responses, only 62.9% were correct, a rate that we believe challenges the students to think without making answers obvious.

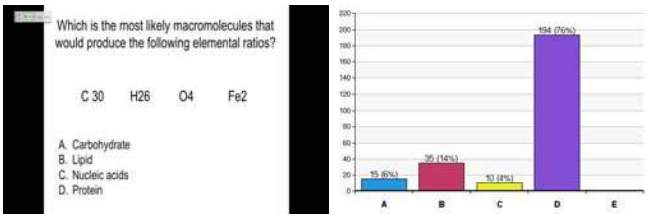

Figure 3: Example question (left) shown to the class and real-time student responses (right).

Indeed, much work has been done to determine the principles of good clicker questions that stimulate active engagement and engender fundamental understanding [2]. Development of questions focused on higher levels of learning is especially important for courses taken by engineering students that tend to be more focused on understanding of concepts versus rote memorization. Incorrect answers allowed us to slow the pace of the class and cover topics in more detail. Still, we are likely to change the grading of clicker questions in future years to provide incentives for answering questions correctly. It appeared most students made an honest effort to give correct answers, but we observed a small portion of the class that chose answers at random as points were awarded only for participation, thus negating any learning effect. In summary, an audience response or clicker system, if used effectively, can improve attendance, encourage active learning, and provide real-time feedback to instructors regarding the covered material. This type of clicker system can be effective in engineering courses if clicker questions are developed that encourage higher level thinking.

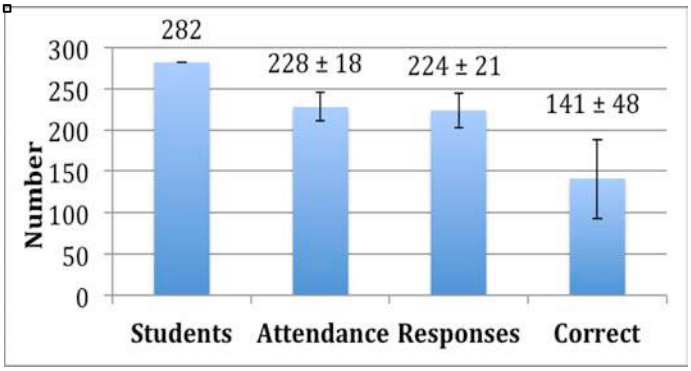

Figure 4: Student enrollment and average attendance, number of responses, and correct answers for each class session. With a course of 282 students, an average of 228±18 students attended each lecture, representing 80.8% of the total class. Responses were collected from 224±21 students, or 98.2%, of those who attended. Only 141±48, or 62.9%, of the responses were correct.

REFERENCES

[1] http://www1.iclicker.com/.
[2] Sullivan, R. (2009). Principles for Constructing Good Clicker Questions: Going beyond Rote Learning and Stimulating Active Engagement with Course Content. *Journal Of Educational Technology Systems*, *37*(3), 335-347.

Copyright 2016 The Organizing Committee for the 2016 Summer Biomechanics, Bioengineering and Biotransport Conference

SB^{3}C2016
Summer Biomechanics, Bioengineering and Biotransport Conference
June 29-July 2, National Harbor, MD, USA
SB^{3}C2016-62

A FINITE ELEMENT ANALYSIS OF THE OCCIPITOATLANTAL CAPSULAR LIGAMENTS AS THE PRIMARY STABILIZERS OF THE ADULT AND PEDIATRIC CRANIOCERVICAL JUNCTION

Rinchen Phuntsok (1, 2),
Douglas L. Brockmeyer (3), Benjamin J. Ellis (1, 2)

(1) Department of Bioengineering
University of Utah
Salt Lake City, Utah, USA

(2) Scientific Computing and Imaging Institute
University of Utah
Salt Lake City, Utah, USA

(3) Department of Neurosurgery
University of Utah
Salt Lake City, Utah, USA

INTRODUCTION

Traditional cadaveric biomechanical testing of the craniocervical junction (CCJ) demonstrates that the occipitoatlantal (OA) joint relies primarily on three ligamentous structures for stability: the tectorial membrane (TM), the transverse ligament (TL) and occipitoatlantal capsular ligaments (OACL). Most studies demonstrate that the TM plays the dominant role in stability, with the role of the TL and OACLs being less clearly defined. However, cadaveric biomechanical testing suffers from the inherent methodological flaw of sequential tissue disruption while trying to isolate a structure of interest. Stability studies involving isolated transection of OA structures have been performed, but are far less common, and do not adequately mimic the injury patterns seen in craniocervical trauma. The results from previous studies have held conflicting views on the role played by the TM in OA stability, with Werne et al. concluding it restricts CCJ extension and Oda et al. reporting it limits flexion [1, 2]. Tubbs et al. concluded the TM prevents impingement of the cervical canal by the odontoid [3]. Similarly, a finite element (FE) parametric study on ligament properties by Brolin et al. concluded that capsular ligaments had the most impact on joint motions [4]. Clearly, knowledge gaps exist in our understanding of OA stability. Furthermore, since all previous testing has been performed on adult cadavers, little is known about the inherent biomechanical properties of the developing CCJ.

To address these issues, we created a validated finite element model (FEM) of the normal pediatric CCJ, as well as adapted a previously published adult CCJ FEM [5, 6]. In this study, our goal is to examine the individual and combined contributions of the TM, TL and OACL on OA joint stability in both the pediatric and adult CCJ. Injury scenarios of the TM, TL and OACLs are examined in isolated and combined fashion. Specifically, we sought to explore the poorly understood role played by the OACL complex on adult and pediatric CCJ stability.

METHODS

Pediatric FE Model

The pediatric FE model was generated from CT scans of a 13 month old female (IRB# 00066287). We have reported on the surface generation, meshing, material properties, boundary conditions and the validation of the normal model in a previous study [4].

Adult FE Model

A previously validated adult FEM was used for adult injury simulations. The geometry for the model was generated from the CT scan of a single, fresh frozen female cadaveric spine (age: 64 year, height: 170 cm, weight: 74kg) [5]. The meshes from this model were imported into FEBio's preprocessor, PreView (http://febio.org/). Linear material properties were used for ligamentous structures (e.g. OACL, TM, and TL) as described in the pediatric model [4]. This normal model was reevaluated by comparing the flexion-extension ROM data obtained under physiological loads to Panjabi et al. flexion-extension experimental data, as well as the FE data reported previously by the model source (Fig. 1 Left) [5][7].

Sensitivity Studies (Ligamentous injury models)

Stability of the OA joint was evaluated for both the pediatric and adult FEMs. The intact normal FEMs were modified to evaluate the sensitivity of the models when damage to TM, TL and OACL were simulated.

Seven sets of scenarios were simulated for flexion-extension. These include 1) removal of TM, 2) TL, 3) removal of both TM and TL, 4) OACL injury model (i.e. reducing the stiffness of the OACL by orders of magnitude from 2.94 N/mm for pediatric and 29.4 N/mm for adult to 0.1 N/mm) 5) OACL injury model with TM, 6) TL, 7) and

Copyright 2016 The Organizing Committee for the 2016 Summer Biomechanics, Bioengineering and Biotransport Conference

both TM and TL removed. Boundary conditions used for the models are the same as reported previously [4, 5]. A moment of 0.1 Nm was applied to all pediatric FE models. A moment of 1.5 Nm was applied to the adult FE model for validation, but only 0.5 Nm was applied to the injury models because the injury models behaved non-physiologically beyond this level of torque. FEBio was used for all analysis and post processing was completed using FEBio's post-processor, PostView. C0-C2 rotations were predicted for flexion-extension. Rotations are reported for normal models and percent increases from normal are reported for the injury models.

RESULTS

The flexion-extension ROMs predicted by the normal pediatric and adult models were within one standard deviation of previously reported data (Table 1 & Fig. 1, left) [5-7]. An isolated injury to the OACL caused the largest increase in flexion ROM (Table 2). Adult FEMs with isolated OACL injury showed a 30.5% increase in flexion (Fig.2 Top) and pediatric FEMs showed an 80.2% increase in flexion (Fig. 2 Bottom). Isolated TM, TL and TM-TL removal cases increased flexion ROM a maximum of 6%. For both pediatric and adult FEMs, an OACL injury combined with removal of TL, TM or both further increased flexion ROM from the isolated OACL injury by <5%. There was less than 1% increase in extension ROM for all pediatric injury models while adult FEMS showed over 30% increase in ROM.

Table 1. C0-C2 ROM data for normal adult and pediatric FEMs.

FEM	Load (Nm)	Flexion (degree)	Extension (degree)
Adult	1.5	28	29.8
Pediatric	0.1	23.5	16.4

Table 2. C0-C2 ROM % increase from normal (Table 1) FEMs for OACL, TM, TL, TM-TL injuries and OACL combined (+) injury cases.

Injury Simulations	FEM	Flexion (%)	Extension (%)
OACL Injury	Adult	30.5	30.7
	Pediatric	80.2	<1
TL removed	Adult	5.8	< 1
	Pediatric	4.9	< 1
TM removed	Adult	2.9	< 1
	Pediatric	4.4	< 1
TM-TL removed	Adult	5.8	< 1
	Pediatric	5	< 1
OACL + TL removed	Adult	31.4	35.4
	Pediatric	84.7	<1
OACL + TM removed	Adult	31.3	32.6
	Pediatric	83.6	<1
OACL + TM-TL removed	Adult	31.6	41.6
	Pediatric	84.8	<1

DISCUSSION

The results of this study show that the OACL plays a major role in contributing to the ROM and stability of both the adult and pediatric CCJ. In contrast to other studies, we found the TM and TL to be relatively small contributors to the stability [8, 9]. In extension, the adult model was far more sensitive to the OACL injury than the pediatric model. This could be due to the flatter facets in the pediatric C0-C1 condyle (Fig 1. Right) compared to the relatively more round and congruent adult facets [10, 11]. The FEMs in this study used linear material properties to save computational time and obtain converged results. These materials provide realistic predictions for normal adult and pediatric flexion-extension ROMs and previous studies of the lumbar spine have used a similar approach [12].

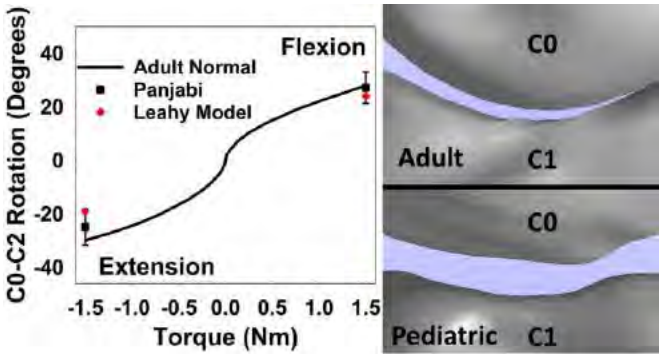

Figure 1: Left: ROM of current adult FEM compared to previous experimental (Panjabi) and FE studies (Leahy). Right: Comparison between adult and pediatric C0-C1 condyle shape.

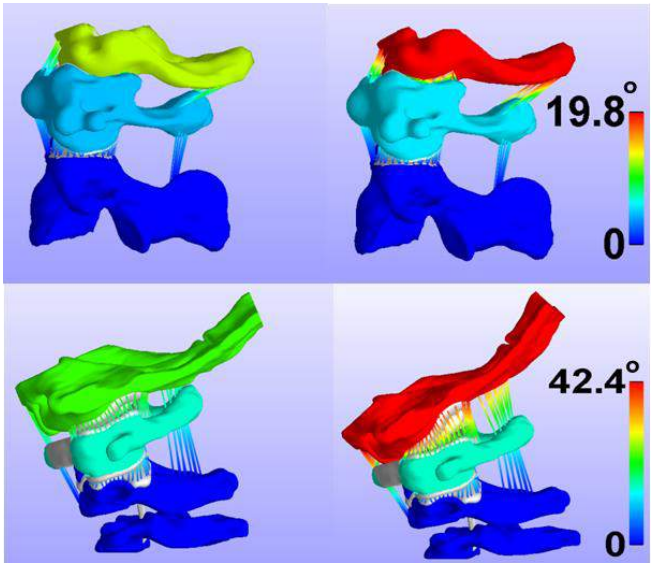

Figure 2: Top: FE model of Flexion (degrees) in adult normal (Left) and injury (Right). Bottom: FE model of Flexion in pediatric normal (Left) and injury (Right).

ACKNOWLEDGEMENTS

The Marion L. Walker, M.D. Endowment is gratefully acknowledged for funding this research. We also thank Christian Puttlitz, PhD, Colorado State University for sharing the adult model surfaces and meshes.

REFERENCES

[1] Werne, S., *Acta Orthop Scand,*23: 1-150, 1957. [2] Oda, T. et al.,*Clin Biomech,*7: 201-207, 1992. [3] Tubbs, R. S. et al.,*Clin Anat,*20: 382-386, 2007. [4] Brolin, K. et al.,*Spine (Phila Pa 1976),*29: 376-385, 2004. [5] Phuntsok, R. et al.,*J Neurosurg Pediatr*: 1-7, 2015. [6] Leahy, PD. PhD Thesis, Colorado State University, 2012. [7] Panjabi, M. et al.,*J Spinal Disord,*4: 157-167, 1991. [8] Tubbs, R. S. et al.,*J Neurosurg. Spine,*14: 697-709, 2011. [9] Fielding, J. W. et al., *J Bone Joint Surg Am,*56: 1683-1691, 1974. [10] Browd, S. et al.,*J Neurosurg,*105: 50-54, 2006. [11] Smith, P. et al.,*AJNR*, 2015. [12] Kuo, C. S. et al.,*BMC Musculoskelet Disord,*11: 151, 2010.

Copyright 2016 The Organizing Committee for the 2016 Summer Biomechanics, Bioengineering and Biotransport Conference

SB^{3}C2016
Summer Biomechanics, Bioengineering and Biotransport Conference
June 29 –July 2, National Harbor, MD, USA
SB^{3}C2016-63

MODELING BONE FORMATION WITH A LAB-ON-A-CHIP PLATFORM

Marnie M. Saunders, Spencer L. York, Estee L. George, Erica L. Grutkowski, Jennifer L. Smith

Department of Biomedical Engineering
The University of Akron
Akron, OH, USA

INTRODUCTION

A lab-on-a-chip (LOC) is a miniaturized platform that has the ability to integrate multiple functional elements to construct a complete analytic microsystem. A LOC removes spatial and temporal limitations lending to its applicability in the biological sciences, such as in genomics, proteomics, clinical diagnostics, and drug discovery. LOCs are equipped to culture small numbers of cells under precisely regulated conditions with the consumption of minimal amounts of reagents. This benefit has led to a substantial degree of work being aimed at developing these systems to mimic tissues, organs, and organ systems.

While many areas of research have adopted this technology to great benefit, the bone field has been slow to appreciate the opportunities that these systems provide. Presently, much of what is known about the response of bone cells to mechanical stimulation has been gathered from *in vitro* mechanotransduction studies. These systems are not able to adequately mimic the physiologic environment of the bone or integrate many of the fundamental elements known to be crucial in mechanotransduction. The incorporation of the three cell types (osteocytes, osteoclasts and osteoblasts) on the same platform removes spatial and temporal limitations. That is, bone cells possess vastly dissimilar lifecycle timescales, with osteocytes and osteoclasts differing by years. With respect to spatial limitations, physiologically each cell type is rarely observed in the same location simultaneously. And, the LOC platform can be designed to enable quantification of functional outcomes. As such, we believe the LOC technology offers opportunities to bridge the gap between *in vitro* experiments and animal models.

Here, we laid the groundwork for a LOC bone remodeling platform. We fabricated the platform and subjected osteocytes to short-term mechanical stimulation quantifying the soluble effects of conditioned medium on osteoblast bone formation.

METHODS

The platform was designed from a mask devised in AutoCad and fabricated using Prototherm 12120 high-resolution stereolithography in a 0.05mm build. A platform configuration of three separate wells was utilized to isolate the cell types and investigate soluble activity. The well size of the configurations was approximately 7mm. PDMS was poured on the surface of the mask of the LOC contained within a leveled, Plexiglas chamber machined in-house. After curing for 24 hours, the PDMS was removed and covered to prevent accumulation of dust and other particles. Before use with cell culture, the product was sterilized. The streamlined equipment and process for the manufacture of the LOC ensured accurate reproducibility between batches. It was critical to maintain the appropriate thickness given the mechanical characterization was completed as a function of well thickness.

Osteocytes Osteocytic, MLO-Y4 cells were seeded at an initial density of $3*10^4/cm^2$ and grown to 85-90% confluence cultured in minimum essential alpha medium (α-MEM, Gibco) supplemented with 5% fetal calf serum (Hyclone), 5% fetal bovine serum (Hyclone), and 1% penicillin/streptomycin (Invitrogen). Cells were maintained in culture (5% CO_2 and 37°C) in $25cm^2$ flasks coated with rat tail collagen type I (CTI) (BD Bioscience). Flasks were coated using a $5\mu g/cm^2$ CT1 solution in 0.2M acetic acid (Sigma) for 1hr, prior to rinsing in Dulbecco's phosphate buffered saline solution with calcium and magnesium (Hyclone). Osteocytes were maintained in culture on the CTI-coated PDMS (10:1 mixture ratio) for a minimum of

Copyright 2016 The Organizing Committee for the 2016 Summer Biomechanics, Bioengineering and Biotransport Conference

72hr to establish typical morphology and phenotype prior to loading.

Osteocyte loading was applied for 15min using a platform developed in-house. Physiologic loading (≤10% strain) was generated using a platen distention of 3804μm; physiologic/supraphysiologic loading (15-19% strain) was generated using a platen distention of 5720μm [1]. CM was collected following a 90 min post-load incubation.

Osteoblasts MC3T3-E1 cells were seeded on polystyrene at an initial density $2.5*10^3/cm^2$ and grown to 100% confluence cultured in minimal essential alpha medium (MEMα, Gibco) supplemented with 10% fetal bovine serum (Hyclone) and 1% penicillin/streptomycin (Invitrogen). Cells were induced to differentiate at 100% confluence with a cocktail containing 50μg/ml ascorbic acid (AA) and 10mM β-glycerophosphate (BGP) in culture medium. Cells were fed with 90% switch medium (medium with BGP and L-ascorbic acid (AA)) and 10% CM every 3rd day for 26 days. Bone formation was quantified using standard alizarin red (calcium) and von Kossa (phosphate) staining.

RESULTS

The fabricated platform is shown in Figure 1. While a picopump (Harvard Apparatus) may be hooked up to the LOC to circulate fluid within and between the wells, initial work was completed with static cultures.

Shown in Figure 2, is a typical SEM image of polystyrene-seeded osteoblasts prior to CM addition. A typical outcome is shown in Figure 2b for the physiologic and physiologic/supraphysiologic CM results. The CM from physiologic loading resulted in a 36% increase in bone formation. Typical quantitative results are plotted in Figure 2c and 2d for alizarin red extraction at physiologic loading levels and the percent area covered for physiologic/supraphysiologic loading levels. In both experiments, CM experiments are compared to controls (Neg 1 – cells cultured in medium containing osteocytes/ no mechanical stimulation, Neg 2 – cells cultured in osteocyte medium (no cells) and Pos 1 – cells cultured in osteoblast medium). For alizarin red extraction, calcium concentration was 23%, 25% and 20% higher from cells treated with CM from physiologic levels of stimulation in comparison to Neg 1, Neg 2 and Pos controls, respectively. In contrast, physiologic/supraphysiologic levels of stimulation resulted in a reduced area of calcium positive nodules with Neg 1, Neg 2 and Pos controls exhibiting a 116%, 46% and 2% increase in area coverage over the osteoblasts treated with the CM. In comparing the physiologic to the physiologic/supraphysiologic experiments, alizarin red extraction was decreased 17%, percent area coverage of alizarin red was decreased 15% and percent area coverage of von Kossa was decreased 17% in the physiologic/supraphysiologic samples. Given a limited volume of medium available from the initial stimulatory trials, rigorous statistics were not completed. A minimum n of 3 is represented.

DISCUSSION

We advocate for the development of LOC bone remodeling platforms. These systems have the potential to accurately represent complex multicellular interactions in a highly controlled and reproducible environment. As a proof-of-concept, we developed a platform and subjected osteocytes to a brief bout of stimulation (15min) at normal and elevated mechanical levels. Soluble factors from that brief loading bout were then assessed

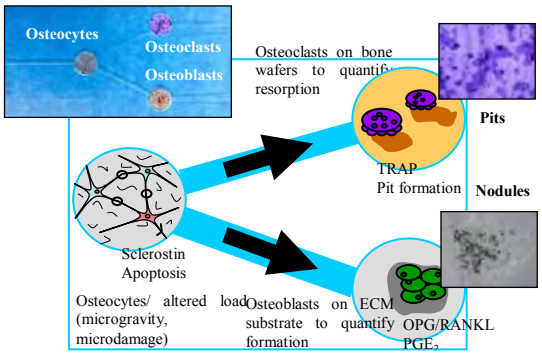

Figure 1: LOC fabrication and development. Cartoon rendering of the LOC platform to study soluble interactions in bone remodeling. The actual platform is shown in the inset with osteocytes stained for viability, osteoclasts stained with toluidine blue on wafers (only osteoblasts discussed here) and osteoblasts stained with alizarin red to identify calcium deposits.

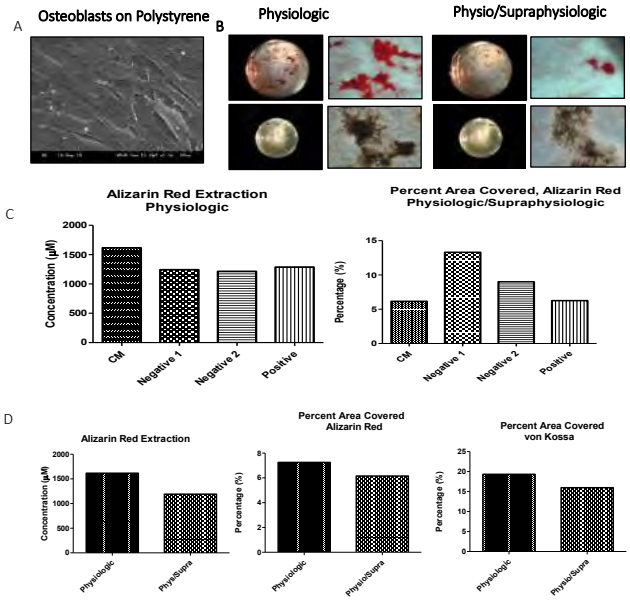

Figure 2: Physiologic levels of short-term osteocyte mechanical stimulation resulted in increased bone formation in comparison to physiologic/supraphysiologic levels.

for their effects on bone formation. Physiologic levels increased formation over physiologic/supraphysiologic levels. Given the brief bout of loading the 36% increase in formation is sufficient to demonstrate proof-of-concept. Additional testing is needed to further assess the soluble factors, cell contact and cell communication. The synthesis of data from these studies will begin to allow us to understand the elegant and intricate process of bone remodeling.

ACKNOWLEDGEMENTS

This work was supported by a Career Award from the NSF (CBET 1060990) and an AREA Award from the NIH (NIDCR DE022664).

REFERENCES

[1] York, S et al., *Ann Biomed Eng*, 10.1007/s10439-015-1376-6, 2016

Copyright 2016 The Organizing Committee for the 2016 Summer Biomechanics, Bioengineering and Biotransport Conference

SB^{3}C2016
Summer Biomechanics, Bioengineering and Biotransport Conference
June 29 –July 2, National Harbor, MD, USA
SB^{3}C2016-64

THE CONTRIBUTION OF ARTICULAR CARTILAGE FOCAL DEFECT SIZE AND LOCATION ON WHOLE KNEE COMPUTATIONAL MODELS

Benjamin C. Marchi (1), Rhima Coleman (1,2), Ellen M. Arruda (1,2,3)

(1) Mechanical Engineering
University of Michigan
Ann Arbor, MI, USA

(2) Biomedical Engineering
University of Michigan
Ann Arbor, MI, USA

(3) Macromolecular Science and Engineering
University of Michigan
Ann Arbor, MI, USA

INTRODUCTION

Articular cartilage focal defects are a common knee pathology that has been linked to the progression of degenerative soft tissue diseases, like osteoarthritis (OA). OA affects approximately 15% of the adult American population [1] and typically presents initially as a decline in cartilage integrity, eventually developing into through-thickness lesions. Focal defects occur most frequently on the femoral cartilage, about 60% based on previous arthroscopy studies, with an average area of 2.1 cm^2 and corresponding range of 0.5 – 4 cm^2 [2]. While focal defects predominately appear in weight bearing and high wear regions, with prolonged joint use focal defects without intervention tend to expand [3] and show signs of cartilage degeneration in the neighborhood around the original focal defect [4]. It has been shown that the presence of focal defects influences both near and fear field strains during sliding contact typical of normal gait using bovine cartilage explants [5]. However, the general and coupled contribution of focal defects within whole joints has not been fully explored.

This work attempts to fundamentally quantify the role of articular cartilage focal defect size and location in joint mechanics by illustrating the impact of defects on both local tissue deformation and global joint kinematics. Tibial and femoral cartilage strain distributions were determined first for native, healthy anatomies during a simulated gait cycle and compared to models containing various femoral cartilage focal defects within a whole knee model built using geometrically and physiologically accurate representations of important tissue structures. Cartilage strains located on and adjacent to the perimeter of focal defects were calculated. We show the tremendous influence of focal defects on tissue deformation, manifesting in alterations in deformation of cartilage with and without focal defects, and joint motion.

METHODS

A three dimensional finite element (FE) model was developed using a combination of computerized tomography and magnetic resonance digital images from a healthy adult female with no history of knee injury or tissue disease. The joint motion and deformation of individual tissue structures were examined during a simulated stance phase of normal gait in an explicit FE framework using a general purpose FE code, Abaqus v6.13 (SIMULA, Providence, Rhode Island, United States). The stance phase was approximated by a linear time varying load, equal to roughly one body weight (F_{max} = 800 N) applied at the distal tibia; the anterior/posterior (A-P) and medial/lateral (M-L) translations of the tibia were constrained numerically at the ankle, while rotations of the tibia about the ankle remained free. The proximal femur was translationally fixed and rotationally free at the hip. Friction was modeled generally among structures in the joint, where the relationship between the coefficient of friction and the relative shear slip rate was derived from relevant experimental studies of cartilage to cartilage contact [6].

The whole joint model included key soft and hard tissue structures, including bones (femur, patella, tibia, and fibula), ligaments, muscles, tendons, articular cartilage, and menisci. Constitutive descriptions for each tissue type were developed from appropriate experimental evidence available in the literature. Bones were modeled supposing rigid behavior due to the negligible contribution of deformable bones on total deformation [7]. The menisci were assumed to be transversely isotropic, linear elastic [8]. The trans-knee muscles, muscle tendons, auxiliary ligaments, and meniscal horn attachments were constructed using uniaxial elements, each with independent, potentially nonlinear constitutive descriptions [9]. The constitutive responses of the major ligaments—the anterior cruciate ligament, posterior cruciate ligament, medial collateral

Copyright 2016 The Organizing Committee for the 2016 Summer Biomechanics, Bioengineering and Biotransport Conference

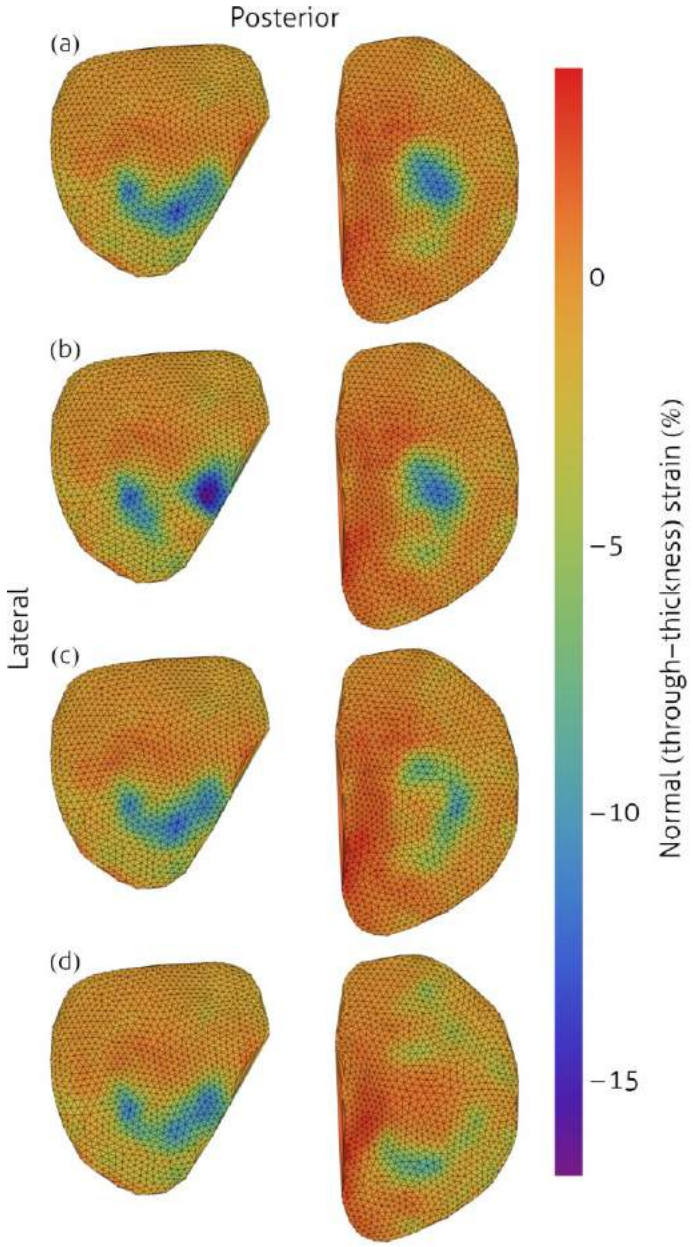

Figure 1: Surface normal strains of tibial articular cartilage that is (a) anatomically native, contains a small femoral focal defect located (b) laterally or (c) medially, or (d) an averaged sized femoral medial defect.

ligament, and lateral collateral ligament—were modeled using a transversely isotropic form of an isotropic eight-chain model of rubber elasticity [9-11]. Tibial and femoral cartilages were assumed to have spatially heterogeneous mechanical property fields that were constructed using the transversely isotropic eight-chain model [12,13]; sparse experimental moduli distributions were completed by a smooth and continuous interpolation scheme. Focal defects were included on the femoral condyles assuming a cylindrical defect shape (defect sizes and locations: 0.5 cm^2 (medial and lateral) and 2.1 cm^2 (medial)).

Table 1: Effect of focal defect size and location on joint motion.

	Relative anterior tibial translation (mm)	Relative interior tibial rotation (°)	Knee flexion (°)
Native	0.742	3.26	1.42
Lateral – Small	0.899	2.59	2.05
Medial – Small	-0.455	2.51	1.09
Medial – Average	2.88	-5.36	-0.494

RESULTS

Figure 1 illustrates normal (through-thickness) strain distributions located on the tibial cartilage corresponding to femoral cartilage with (Fig. 1b-d) and without (Fig. 1a) focal defects at the time of maximum loading. From Fig. 1 it is clear that the presence of focal defects, Fig. 1b-d, fundamentally alters, with respect to Fig. 1a, the evolution of strain within the joint capsule. A small lateral defect increases the maximum thought-thickness compressive strain (from 13.5% to 16.8%), shifting the maximum strains on the lateral plateau medially toward the center of the tibia. Small and averaged sized medial defects decreased the maximum observed compressive strains to 12.7% and 11.4%, respectively. There was also a noticeable decrease in the dispersion of compressive strain on the medial tibial plateau, Fig. 1c-d, as compared to the intact joint.

Altering cartilage integrity not only affects local tissue deformation, but also global joint kinematics—presented in detail in Table 1. As the size of the defect increased on the medial condyle, the directions of relative internal tibial rotation and knee flexion flipped with respect to both the native knee and small sized defect models. A decrease in the amount of relative internal tibial rotation was observed corresponding to each of the small sized defect models. The presence of a small medial defect resulted in relative tibial motion opposite to the anticipated anterior tibial translation (ATT), while increasing the defect size drastically increased the observed ATT.

DISCUSSION

Whole joint computational biomechanics models have the potential to generate clinically meaningful insights and inform optimal, patient-specific treatments by illustrating the highly coupled and nonlinear behavior of joints with complex anatomies and pathologies. The size and location of cartilage focal defects leads to alternations in local deformations in tissues with and without defects, as well as changes in the measured joint kinematics. These deviations motivate the clinically observed, widespread effects of focal defects on surrounding tissues [3-5] and offer to further the understanding of potentially dangerous articular cartilage focal defects that may require surgical intervention.

REFERENCES

[1] Lawrence, R et al., *Arthritis & Rheumatism*, 58:26-35, 2008.
[2] Hjelle, K et al., *Arthroscopy*, 18:730-734, 2002.
[3] Wang, Y et al., *Rheumatology*, 45:79-84, 2006.
[4] Lefkoe, T et al., *J Orthop Trauma*, 7:458-467, 1993.
[5] Wong, B et al., *J Ortho Res*, 28:1554-1561, 2010.
[6] Qian, S et al., *J. Bionic Engineering*, 3:79-85, 2005.
[7] Donahue, T et al., *J Biomech*, 36:19-34, 2003.
[8] Tissakht, M et al., *J Biomech*, 28:411-422, 1995.
[9] Kiapour, M et al., *J. Biomech Eng*, 136:011002, 2014.
[10] McLean, S et al., *J Biomech Eng*, 137:020906, 2015.
[11] Bischoff, J et al., *J App Mech*, 69:570-579, 2009.
[12] Deneweth, J et al., *J Biomech*, 46:1064-1610, 2013.
[13] Deneweth, J et al., *Int J Non-Lin Mech*, 68:146-156, 2015.

Copyright 2016 The Organizing Committee for the 2016 Summer Biomechanics, Bioengineering and Biotransport Conference

SB^{3}C2016
Summer Biomechanics, Bioengineering and Biotransport Conference
June 29 –July 2, National Harbor, MD, USA
SB^{3}C2016-65

MECHANICS OF HEART TUBE FORMATION IN THE CHICK EMBRYO

Hadi S. Hosseini (1, 2), Larry A. Taber (1)

(1) Department of Biomedical Engineering
Washington University
St. Louis, MO, USA

(2) Department of Physics
Washington University
St. Louis, MO, USA

INTRODUCTION

In the embryo, the heart is initially a simple tubular structure that undergoes complex morphological changes as it transforms into a four-chambered pump. This work focuses on the mechanisms that create the heart tube (HT). The early embryo is composed of three relatively flat primary germ layers called endoderm, mesoderm, and ectoderm. Precardiac cells located within bilateral regions of the mesoderm called heart fields (HFs) fold and fuse along the embryonic midline to create the HT. This folding is part of a more global folding of the endoderm and mesoderm, which essentially comprise a bilayered epithelial plate. The right and left halves of this plate fold symmetrically to bring their upper edges into contact along the midline, where they fuse (see Figure 2F-H). In a region near the fusion line, these layers then separate to generate the primitive HT and foregut, which then extend vertically. The anterior intestinal portal (AIP) is the opening at the caudal end of the foregut, which descends as the HT lengthens (Figure 2B-D) [1-3].

The biomechanical mechanisms that drive this folding are poorly understood. Here, we consider folding and extension of the endo-mesodermal plate, excluding separation of the layers. Our central hypothesis is that folding is caused by differences in growth between the endoderm and mesoderm, while subsequent extension is driven by contraction along the AIP. The feasibility of this hypothesis is examined using experiments with chick embryos and finite-element modeling.

METHODS

Experimental Method

Fertilized white Leghorn chicken eggs were incubated at 38°C rof approximately 22-33 hours until the appropriate Hamburger and Hamilton stage (HH5 to HH9) was reached [4]. Whole embryos using a filter paper carrier method [5]. To inhibit contraction, embryos were cultured in media containing blebbistatin (myosin II inhibitor; 100μM) for 18h (from HH5 to HH10).

Finite-Element Models

Three-dimensional models were created using ABAQUS (D. S. Simulia). The initial geometry consists of a flat plate including two layers representing the mesoderm and endoderm (Figure 1).

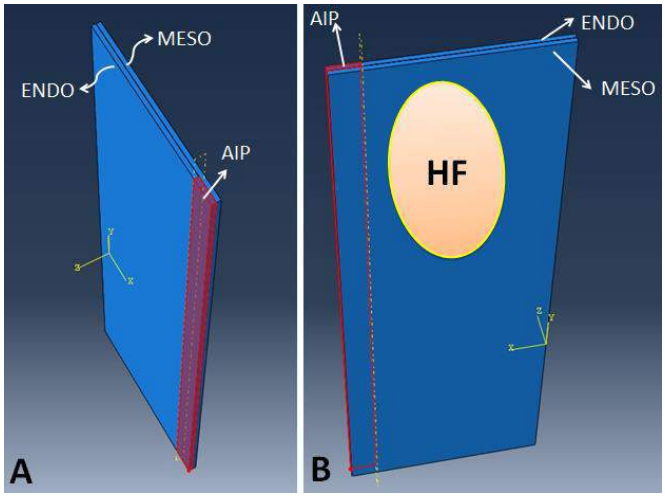

Figure 1: Initial model geometry for embryo at stage HH5. (A, B) Ventral /Dorsal view. ENDO = endoderm; MESO = mesoderm; HF = heart field; AIP = presumptive anterior intestinal portal.

Copyright 2016 The Organizing Committee for the 2016 Summer Biomechanics, Bioengineering and Biotransport Conference

Only half of the embryo is modeled with symmetry conditions specified along the plate edge at the embryonic midline. Rollers are specified along the lower edge, and the other edges are initially free. After folding brings the upper edge to the midline, fusion is simulated by converting the free boundary condition into a symmetry condition. After fusion occurs, the AIP contracts tangent to the plate edge.

Nonlinear material properties were taken from previous studies [3, 6]. Growth and contraction (negative growth) were simulated using the theory of Rodriguez et al [7], where the total deformation gradient is given by

$$\mathbf{F} = \mathbf{F}^{*}.\mathbf{G} \qquad (1)$$

In which **G** is the growth tensor and **F*** is the elastic deformation gradient tensor. The growth tensor defines the stress-free configuration for each material element after it grows. Here we take

$$\mathbf{G} = G_x e_x e_x + G_y e_y e_y + G_z e_z e_z \qquad (2)$$

With $\dot{G}_z = 0$, $\dot{G}_x < \dot{G}_y$ for both layers, $\dot{G}_{ENDO} < \dot{G}_{MESO}$, and $\dot{G}_y < 0$ for AIP contraction.

RESULTS

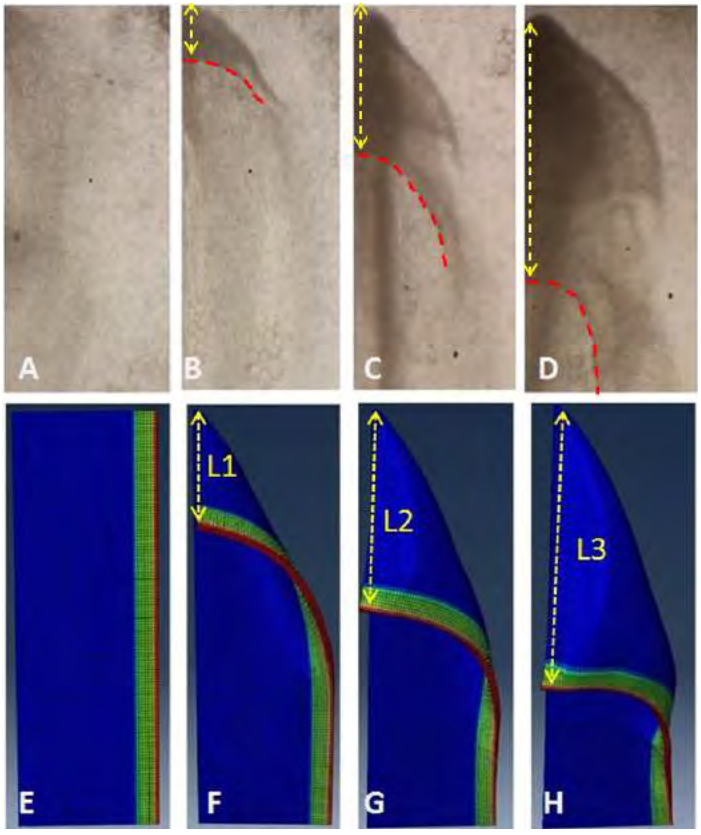

Figure 2: (A-D) Heart development in early chick embryo at stages HH5, HH7, HH8, and HH9. Red dashed lines outline AIP. (E, F) Computational model for initial folding of mesoderm-endoderm plate. (G, H) AIP contraction stretches the combination HT and foregut.

In embryos exposed to blebbistatin, initial folding and AIP descension occurred normally. However, after HFs partially fused to create the upper part of the HT, fusion and AIP descension stopped, and the HT failed to grow longer. These results suggest that cytoskeletal contraction is required only for the later stages of HT formation.

In the model, a larger biaxial growth rate in the mesoderm compared to the endoderm causes the bilayered plate to bending ventrally, as the upper edge moves toward the midline, where it 'fuses' with the other half (Figure 2E,F). This folding creates the upper section of the HT, as well as the foregut pocket bordered by the AIP [8, 9]. After this phase completes by stage HH7, contraction along the arch-shaped AIP pulls the lower edge of the plate downward, stretching the two layers. All of these results are consistent with experimental data for control embryos (Figure 2), as well as embryos treated with blebbistatin.

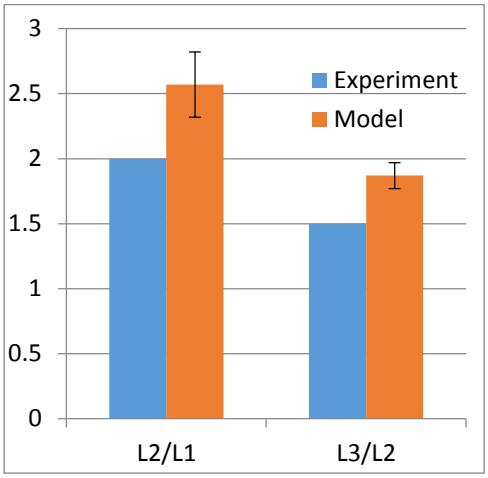

Figure 3: Comparison of experimental measurements (n= 4) and model results for length ratio of fused midline at different stages. L_1, L_2 and L_3 are shown in Figure 2.

DISCUSSION

As one test of the model, we measured the change in length of the midline of the folding epithelial plate above the AIP in both cultured embryos and the model. Figure 3 shows reasonable agreement between model and experiment at different stages of development. In conclusion, the results of our experimental and theoretical study support our hypothesis for folding and extension of the endo-mesodermal plate. Future work is warranted to further test this idea.

ACKNOWLEDGEMENTS

This work was funded by NIH grant R01 NS070918 (LAT).

REFERENCES

[1] Abu-Issa, R. et al., *Annu. Rev. Cell Dev. Biol.* 23 45–68, 2007.
[2] Cui, C. et al. *Dev. Biol.* 332, 212-222, 2009.
[3] Varner, V. et al., *Development*, 139 1680–90, 2012.
[4] Hamburger, V. and Hamilton, H, *J Morphology,* 88:49-91, 1951.
[5] Voronov, DA., Taber, LA, *Dev. Dyn*. 224(4), pp. 413–421, 2002.
[6] Xu, G. et al., *J Biomech.*, 132(1):011005, 2010.
[7] Rodriguez, E. K.et al., *Journal of Biomechanics*, 27:455-467, 1994.
[8] Bellairs, R. et al., *J. Embryol. Exp. Morphol.,* 1, 369-385, 1953.
[9] Stalsberg, H. et al., *Dev. Biol.* 18, 198-215, 1968.

Copyright 2016 The Organizing Committee for the 2016 Summer Biomechanics, Bioengineering and Biotransport Conference

SB³C2016
Summer Biomechanics, Bioengineering and Biotransport Conference
June 29 –July 2, National Harbor, MD, USA
SB³C2016-66

COMPUTATIONAL FLUID FLOW MODELING OF A PULMONARY VASCULAR PHANTOM WITH EXPERIMENTAL VALIDATION

Alifer D. Bordones (1,2), Matthew Leroux (1,2), Vitaly O. Kheyfets (3), Ender A. Finol (1)

(1) Department of Biomedical Engineering
University of Texas at San Antonio
San Antonio, TX, USA

(2) Graduate Program in Biomedical Eng.
University of Texas Health Science
Center at San Antonio
San Antonio, TX, USA

(3) Department of Bioengineering
University of Colorado Denver
Denver, CO, USA

INTRODUCTION

Pulmonary hypertension (PH) is a chronic progressive disease characterized by a higher than normal pressure in the main pulmonary artery, caused by an increase in resistance in the distal vasculature. Computational fluid dynamics (CFD) can be used to identify metrics representative of the stage of PH disease. Nevertheless, experimental validation of CFD models is often not pursued due to the geometric complexity of the model or shortcomings in the reproduction of the required flow conditions. The goal of this research was to validate experimentally a CFD model of a pulmonary artery phantom using a stereo particle image velocimetry (PIV) technique.

METHODS

The patient-specific pulmonary artery geometry was reconstructed from chest computed tomography angiography (CTA) images, which were segmented using the application Mimics (Materialise, Belgium). The lumen of the phantom was built up to the first bifurcation of the left pulmonary artery by means of a MakerBot Replicator Z18 3D printer (Makerbot, Brooklyn, NY) using a polylactide resin filament (Makerbot, Brooklyn, NY). Following a lost-core technique, liquid silicone (Applied Silicones, Inc., Santa Ana, CA) was poured on the rapid prototype, cured for 24 hours and dissolved using dichloromethane [1].

The ensuing silicone phantom was connected to a flow loop with in-line electromagnetic flow meters and pressure transducers at the inlet and each outlet. Fully developed flow was achieved by extending the inlet cross-section ten hydraulic diameters using a matching diameter connector constructed with stereolithographic techniques. Similar connectors were used for the phantom outlets. The blood-mimicking fluid (BMF) used in the experiments consisted of water, glycerol, sodium iodine, sodium thiosulphate, and aluminum thiosulphate. The measured density of the BMF was 1.245 g/cm^3 (at 22.4 ºC) and viscosity of 4.17 cP. The bench-top experiment was operated at constant flow rate conditions with a Reynolds number of 877, which is typical of time-averaged flow conditions in the human main pulmonary artery. A stereo PIV system (LaVision, Germany) was used for flow visualization and velocity quantification at select planes of interest within the phantom [1].

The phantom geometry was modified for the computational simulations using CAD editing software at the inlet and outlets to ensure fully developed flow. This can prevent potential numerical errors to be transferred to the vessels and it can reduce inconsistencies between the experimental and computational flows [2-4]. To ensure the results obtained are independent of the mesh size, a wall shear stress (WSS) based grid convergence analysis was performed [5]. The CFD modeling was carried with the solver Ansys Fluent (Ansys Inc., Canonsburg, PA) using an unsteady algorithm. The boundary conditions involved a constant flow rate at the inlet, a no-slip condition at the walls and a pure resistance structured-tree outflow boundary condition at the three outlets. Velocity contours, WSS and flow rates obtained with the CFD simulations were compared to the counterparts from the PIV flow visualization experiments.

RESULTS

CFD simulations were performed on the patient-specific pulmonary model with a Reynolds number, viscosity and density of the fluid matching those used with the PIV experiments. The BMF was considered incompressible and Newtonian, with an inlet velocity of 9.16 cm/s and a flow rate of 95 mL/s, obtained after a Reynolds number similarity analysis was performed. The vascular resistance was

Copyright 2016 The Organizing Committee for the 2016 Summer Biomechanics, Bioengineering and Biotransport Conference

calculated for each outlet and adjusted following an iterative process until the flow measured at the right pulmonary artery (RPA) and left pulmonary artery (LPA) matched those measured in the PIV experiment. Table 1 describes the volume flow rates calculated from the CFD simulations and measured in the experimental setup.

Table 1: Volume flow rates predicted by CFD simulation of the pulmonary model and measured in the PIV experiment.

Pulmonary model branch	Q_{CFD} (cm^3/s)	Q_{PIV} (cm^3/s)	Relative difference with respect to Q_{PIV} (%)
MPA	95.00	94.97	0.03
RPA	36.08	36.28	0.55
LPA	39.32	39.22	0.25
TA	19.59	22.28	12.07

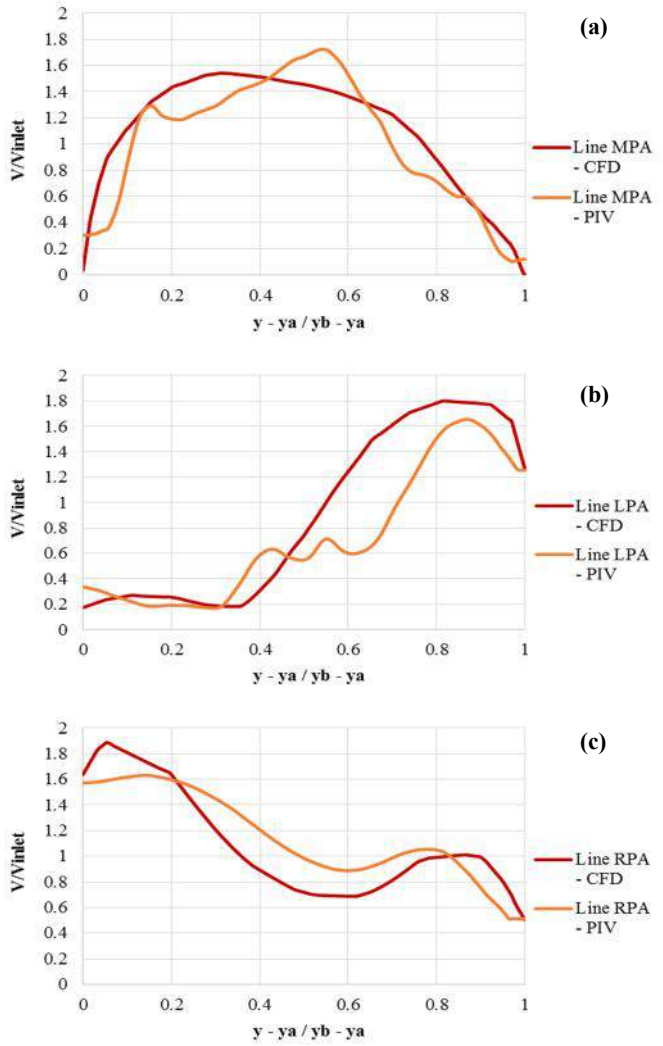

Figure 1: Non-dimensional velocity profiles obtained through a CFD simulation and PIV experiment along the cross-sections shown in Fig. 2(a) at each major pulmonary artery branch – (a) MPA, (b) LPA, and (c) RPA.

Hemodynamic parameters such as wall shear stress (WSS) and flow field velocity vectors were also computed. Figure 1 presents a comparison between velocity profiles obtained in the CFD simulations and the PIV experiments. There is good agreement in all velocity profiles based on relative RMS errors for cross-sections at the MPA, RPA, and LPA of 0.2133, 0.3396, and 0.2047, respectively. Four planes of visualization, shown in Fig. 2(b), were chosen to compare the average velocity at each plane, as described in Table 2.

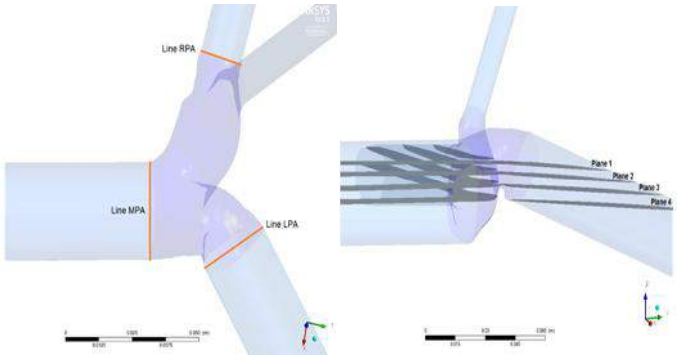

(a) **(b)**

Figure 2: (a) Location of the cross sections at each major branch used to compare the velocity profiles; (b) planes of visualization for the comparison of the average velocity predicted by CFD simulations and the PIV experiments.

Table 2: Average velocities at the visualization planes predicted by the CFD simulation and PIV experiment.

Plane	Average V_{CFD} (cm/s)	Average V_{PIV} (cm/s)	Relative difference with respect to V_{PIV} (%)
1	10.08	11.25	10.40
2	9.47	10.90	13.11
3	9.13	9.70	5.87
4	7.95	8.81	9.76

DISCUSSION

There are small differences between the CFD and PIV predicted average velocities, which could be the result of discrepancies in the geometry of the computational domain relative to the physical dimensions of the flow phantom. An exact agreement between the computational and experimental results should not be expected considering the impossibility of constructing a perfect pulmonary phantom. These differences can be attributed to the simplifications and assumptions made in the numerical simulations, surface roughness of the phantom's lumen, mismatch in the precise location of the planes of interest between the computational and experimental models, and the use of structured tree outflow boundary conditions in the CFD model, which lacked the precise intraluminal pressure measurements at each outlet. In addition, the silicone phantom, which was assumed to have a rigid wall in the CFD simulations, was observed to have a finite compliance in the PIV experiments.

REFERENCES

[1] Leroux, M. MS Thesis, University of Texas at San Antonio, Biomedical Engineering Graduate Program, San Antonio, TX, 2014.
[2] Tu, J., Yeoh, G. and Liu, C. Computational Fluid Dynamics—a Practical Approach Burlington, MA: Elsevier Inc, 2008.
[3] Ponzini, R. at al. Med Eng Phys, 30(7), 809–816, 2008.
[4] Boutsianis, E. et al. Ann Biomed Eng, 36(12), 2068–2084, 2008.
[5] Prakash, S. and Ethier, C. J Biomech Eng, 123(2), 134-144, 2001.

Copyright 2016 The Organizing Committee for the 2016 Summer Biomechanics, Bioengineering and Biotransport Conference

SB^{3}C2016
Summer Biomechanics, Bioengineering and Biotransport Conference
June 29 –July 2, National Harbor, MD, USA
SB³C2016-67

MONITORING TUMOR RESPONSE TO THERAPEUTIC TR4 FUSION PROTEIN VIA *IN VIVO* IMAGING

Marianna Prokopi[1], Costas Pitsillides[2], Mahendra Deonarain[3], Konstantinos Kapnisis[2], Spyros Stylianou[4], George Kousparos[5], Christina Kousparou[1], Andreas Anayiotos[2], Agamemnon Epenetos[1]

(1) Trojantec Ltd, Nicosia, Cyprus

(2) Department of Mechanical and Materials Science and Engineering, Cyprus University of Technology, Limassol, Cyprus

(3) ShyDen Biotechnology Ltd, Stevenage, Herts, UK

(4) Translational Genetics Team, The Cyprus Institute of Neurology & Genetics, Nicosia, Cyprus

(5) Frimley Park Hospital, NHS Foundation Trust, Surrey, UK

INTRODUCTION

The Notch signaling pathway has been associated with breast, cervical and lung cancer, neuroblastomas and acute T-cell lymphoblastic leukemia and is strongly implicated in tumorigenesis. [1] Notch genes encode large single pass transmembrane proteins that regulate cell fate. Upon activation, Notch undergoes cleavage, releasing its intracellular domain NICD and translocates into the nucleus for transcriptional activation of its downstream target genes. [2] Discovery of this pathway has prompted many pharmaceutical companies to develop novel anti-Notch therapeutics. We (Trojantec Ltd) have generated a novel fusion protein TR4 that inhibits the Notch pathway at the transcriptional level and can potentially reduce tumor growth *in vivo*. TR4 consists of the truncated version Mastermind-like (MAML) that behaves in a dominant negative fashion and inhibits Notch activation and the cell penetrating peptide Antennapedia (Antp). The fusion protein is able to translocate into the cell nucleus and suppress Notch activation thus reverting the transformed phenotype, inhibiting the anchorage dependent growth and inducing apoptosis in highly metastatic epithelial human breast cancer cells.

Utilizing a state-of-the-art *in vitro* pharmacokinetics and toxicology program, in combination with innovative imaging techniques such as *in vivo* flow cytometry and whole body fluorescence reflectance imaging, we have investigated the pharmacokinetic and pharmacodynamic behavior of the TR4 protein in order to define its mode of action and establish safety and efficacy in treating tumors in animal models of breast adenocarcinoma.

METHODS

A comprehensive *in vitro* and *in vivo* pharmacokinetics study that included apoptotic, toxicology and immunogenicity assays was undertaken through administration of various concentrations of TR4 in 10 immuno-competent mice in order to determine the effects of TR4 and define the mechanism(s) of action. Blood samples were collected for toxicological assays and to monitor the immune response by ELISA whereas major organs were excised for immunohistochemistry to determine tissue toxicity and induction of apoptosis.

The dynamics of the TR4 fusion protein were investigated in animal cancer models, through the successful conjugation of the TR4 to proprietary fluorescent markers (Cy5.5). Molecular modeling studies were performed to identify appropriate conjugation sites on the TR4 molecule to ensure no loss of the membrane transfer capabilities of the fusion protein. A group of fluorescent dyes was prepared, with maleide groups appropriate for bioconjugation to thiols on the TR4 molecule. TR4-Cy5.5 conjugates were chosen based on their optical properties (absorption 600-650 nm, emission 650-700 nm) and suitability for the *in vivo* imaging study. Conjugated TR4 was purified using proprietary methods to ensure protein solubility and avoid excessive aggregation and was further tested to ensure that the protein retained the ability to translocate in breast cancer cells.

The *in vivo* pharmacodynamic behavior of the fluorescent TR4-Cy5.5 was investigated using fluorescence-based *in vivo* flow cytometry and whole body imaging. These molecular imaging techniques have the ability to monitor and quantify fluorescently labeled vehicles in circulation, to detect and image the biodistribution and incorporation of therapeutic agents in cells and organs of both healthy and tumor-bearing mice, as well as to provide a quantifiable assessment of tumor growth over time. Following intravenous administration of the TR4-Cy5.5 in non-tumor bearing mice (n=5) the non-specific uptake of the protein by circulating blood cells was assessed via *in vivo* flow cytometry, while the biodistribution of the protein accumulating in different organs/tissues was imaged using whole body reflectance imaging. The accumulation of TR4 in various

Copyright 2016 The Organizing Committee for the 2016 Summer Biomechanics, Bioengineering and Biotransport Conference

major organs (liver, kidney, lung and brain) was further verified by Western blot analysis.

An orthotopic mouse model for breast cancer disease was developed via injection of $7x10^6$ MDA-MB-231 GFP labeled cells in SCID mice, in order to enable the imaging and assessment of tumor growth *in vivo*. Animals that expressed a detectable fluorescent signal from established orthotopic tumors were selected and divided into two (n=5) groups: untreated (control) and treated with TR4 (day 0). Mice were monitored for 2 weeks via *in vivo* imaging and were then euthanized at the end of the experiment (day 14).

RESULTS

The pharmacokinetics studies indicated that TR4 did not induce any overt toxicity, notable death of cells, organ dysfunction, or any toxic manifestations that were predicted materially to reduce the life span of the animals. The immunogenicity tests indicated that animals do not raise an antibody response against the injected TR4 protein. Finally, no murine antibodies against full-length TR4 were detected by ELISA in mice serum.

TR4-Cy5.5 conjugates prepared via molecular modeling studies (Fig. 1A) and selected based on their optical characteristics (Fig. 1B) were first validated *in vitro* for their membrane translocation ability (Fig. 1C) prior to their use for the *in vivo* part of the study.

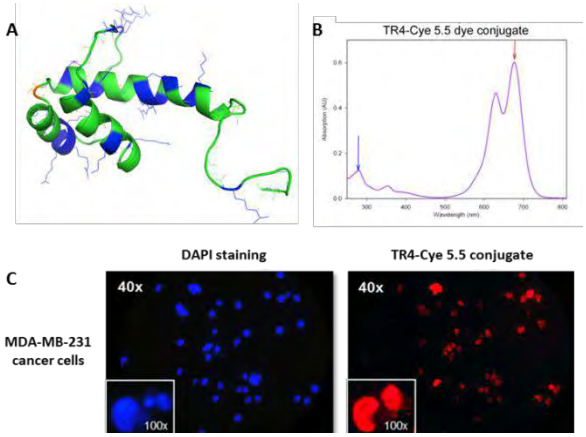

Figure 1: (A) The TR4 model containing 24 arginine residues (green), 9 lysine residues (blue) and 4 cysteine thiol residues (orange). (B) UV-vis spectra showing the quality of the conjugation and the peak absorbance shifts. (C) Cell penetration of TR4-Cy5.5 in MDA-MB-231 cancer cells.

In vivo flow cytometry in mice, injected i.v. with the TR4-Cy5.5 conjugates, showed that free, non-internalized protein was rapidly cleared from circulation, as the background (noise) signal collected from the blood vessels did not substantially increase. Furthermore, fluorescently labeled circulating cells that may have internalized the TR4 protein were not detected at any time point. Whole body imaging showed that TR4-Cy5.5 accumulated in some of the major organs/tissues imaged and was cleared within 24 hrs via the gastrointestinal tract (Fig. 2A-B). This is in agreement with the Western blotting analysis of excised liver and kidney (Fig. 2C).

Assessment of tumor burden via *in vivo* imaging demonstrated a reduction in tumor growth over time in mice treated with TR4-Cy5.5 compared to untreated mice (Fig. 3). The figure shows an overall increase of less than 50% in the relative intensity of fluorescence signal in the treated mice (right panel) compared to a 3-fold increase in signal and thus tumor size in untreated mice by day 14 (left panel).

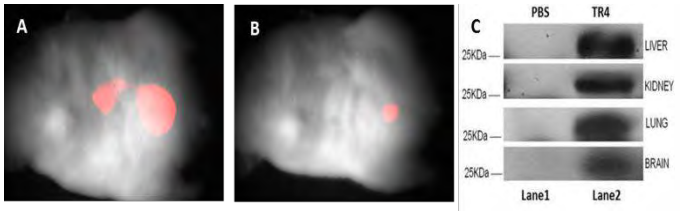

Figure 2: The TR4 protein biodistribution at (A) 2h and (B) 24h post injection. (B) Western blot analysis of excised mouse liver, kidney, lung and brain.

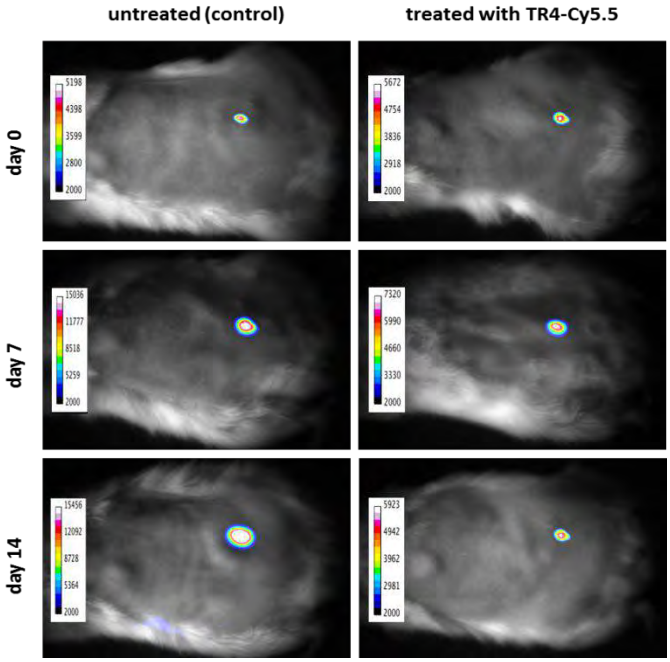

Figure 3: Tumor response in untreated (control) and treated with TR4-Cy5.5 mice at day 0, 7 and 14 post injection (representative images of the n number of mice tested).

DISCUSSION

In this report we have performed preclinical studies to validate TR4 as a promising therapeutic strategy for breast adenocarcinoma. The dynamics of the drug molecule have been investigated in an *in vivo* setting in order characterize its therapeutic efficacy in an animal tumor model. Mechanisms of action have been investigated via the application of innovative imaging modalities with the aim of guiding the technology closer to the market by completing the necessary preclinical studies in order to optimize the TR4 fusion protein as a novel therapy for invasive cancer disease.

ACKNOWLEDGEMENTS

This work was co-funded by Eureka Eurostars Program and the Cyprus Research Promotion Foundation (E!8520 - TROJANDRUG).

REFERENCES

[1] Prokopi M, Kousparou CA, Epenetos AA. The Secret Role of microRNAs in Cancer Stem Cell Development and Potential Therapy: A Notch-Pathway Approach. Front Oncol. 2014; 4: 389.

[2] Kopan R, Ilagan MX. The canonical Notch signaling pathway: unfolding the activation mechanism. Cell (2009) 137:216–33.

Copyright 2016 The Organizing Committee for the 2016 Summer Biomechanics, Bioengineering and Biotransport Conference

SB³C2016
Summer Biomechanics, Bioengineering and Biotransport Conference
June 29 –July 2, National Harbor, MD, USA
SB³C2016-68

UNCERTAINTY AND SIMILARITY IN BRAIN STRAINS RESULTING FROM SHAPE VARIATION IN HEAD ROTATIONAL VELOCITY PROFILE

Wei Zhao (1), Songbai Ji (1,2)

(1) Thayer School of Engineering
Dartmouth College
Hanover, NH, USA

(2) Department of Surgery and of
Orthopaedic Surgery
Dartmouth College
Hanover, NH, USA

INTRODUCTION

Traumatic brain injury (TBI) remains a major socioeconomic public health problem. The importance of head rotation for inducing brain strains and the resulting diffuse axonal injury is well-recognized [1,2]. Because rotational velocity ($\boldsymbol{v}_{rot}$), as opposed to rotational acceleration ($\boldsymbol{a}_{rot}$), is more strain-relevant [3–6], recent brain injury criteria have explicitly incorporated peak magnitude of $\boldsymbol{v}_{rot}$ to assess the risk and severity of TBI (e.g. RIC, PRIC, [7] and BrIC [6]).

Still, these kinematics-based injury criteria do not inform regional brain strains. To better understand the rotation-strain causal relationship, Yoganandan et al. employed a 2D finite element (FE) head model to study the significance of idealized $\boldsymbol{a}_{rot}$ profile shapes and acceleration-deceleration separation time on regional brain strains [8]. With more realistic $\boldsymbol{a}_{rot}$ profiles and a 3D head FE model, Post et al. observed a substantial influence of $\boldsymbol{a}_{rot}$ shape on brain strains [9].

In contrast, Ji and Zhao [3] found that brain strains were insensitive to $\boldsymbol{a}_{rot}$ peak magnitude ($\boldsymbol{a}_{rot}^{p}$) or shape in monophasic, acceleration-only rotation. Virtually identical peak strains were obtained when simulating head rotations of the same $\boldsymbol{v}_{rot}$ peak magnitude (v_{rot}^{p}) and impulse duration (Δt), regardless of their differences in $\boldsymbol{a}_{rot}$ shape (triangular, sine, or haversine, with $\boldsymbol{a}_{rot}^{p}$ difference by up to 21.5%). Longer Δt but identical v_{rot}^{p} in an acceleration-only rotation led to a decrease in strains [3,5,10], likely due to the increase in strain energy dissipation resulting from the brain's viscoelastic properties. These findings confirm that both v_{rot}^{p} and Δt are important to brain strains.

However, despite the general notion that $\boldsymbol{v}_{rot}$ is more strain-relevant, no study appears to exist that investigates how its shape, beyond v_{rot}^{p} and Δt, affects brain strains. To this end, we conducted this study to evaluate the uncertainty and similarity in $\boldsymbol{v}_{rot}$-induced strain responses as a result of shape variation in $\boldsymbol{v}_{rot}$ temporal profile.

METHODS

We used the 58 reconstructed NFL cases [11] to extract $\boldsymbol{v}_{rot}$ profile shapes. First, all $\boldsymbol{a}_{rot}$ profiles were filtered using an SAE 180 low-pass filter [4]. The x-components of these $\boldsymbol{a}_{rot}$ profiles were then numerically integrated (zero initial velocity or integration constant) to allow simulating uniaxial coronal head rotations (from left to right). The complete largest $\boldsymbol{v}_{rot}$ peak capturing rotation from onset to full stop was identified for each case (**Figure 1a**). Profiles with negative $\boldsymbol{v}_{rot}^{p}$ were negated to maintain a left-to-right rotation (**Figure 1b**). Profiles that did not record a full stop were discarded (**Figure 1c**). This led to a total of 44 $\boldsymbol{v}_{rot}$ profiles. They were further scaled to maintain an identical $\boldsymbol{v}_{rot}^{p}$ and Δt, corresponding to the average values from all the retained $\boldsymbol{v}_{rot}$ profiles (23.4 rad/s and 46.3 ms, respectively; **Figure 1d**). The scaling allowed isolating the shape of $\boldsymbol{v}_{rot}$ profiles for investigation.

All brain strain responses were simulated using the Dartmouth Head Injury Model (DHIM). Element-wise peak maximum principal strain regardless of the time of occurrence (ε^{p}) was determined. To facilitate comparison, the group average ε^{p} from the 44 simulated responses ($\overline{\varepsilon^{p}}$) was computed for each element to serve as a reference. For each ε^{p}, a volume-weighted average percentage error (err%) was defined to measure the magnitude difference relative to $\overline{\varepsilon^{p}}$:

$$err = \sum_{i=1}^{n} \left\| \left(\varepsilon_i^{p} - \overline{\varepsilon_i^{p}} \right) / \varepsilon_i^{p} \right\| \times V_i \Big/ \sum_{i=1}^{n} V_i \qquad (1)$$

Copyright 2016 The Organizing Committee for the 2016 Summer Biomechanics, Bioengineering and Biotransport Conference

where ε_i^p and $\overline{\varepsilon_i^p}$ are the ε^p and $\overline{\varepsilon^p}$ values of the i^{th} element (n elements in total), and V_i is its volume. To evaluate the similarity in ε^p distribution or "pattern", Pearson correlation coefficients between each ε^p and $\overline{\varepsilon^p}$ were calculated. All responses were spatially resampled on a regular grid at a resolution of 2 mm to generate strain-encoded coronal images for illustration and comparison.

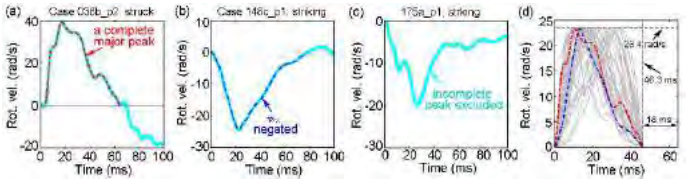

Figure 1: Illustration of $\boldsymbol{v}_{rot}$ profile selection and scaling for impact simulation. The largest $\boldsymbol{v}_{rot}$ peak capturing head rotation from onset to full stop was first identified (a) and (b). Those not capturing a full stop were discarded (c). The selected $\boldsymbol{v}_{rot}$ profiles were then scaled to maintain an identical v_{rot}^p and Δt (d; those from (a) and (b) highlighted).

RESULTS AND DISCUSSION

The average err% between ε^p and $\overline{\varepsilon^p}$ was 10.14±0.04% (range 4.29–17.89%). **Figure 2** shows the element-wise minimum, average, and maximum ε^p along with the standard deviations. They were not necessarily from a specific head impact, but represented element-wise "ranges" and "typical" responses. The four head impacts that led to the most similar and most different ε^p relative to $\overline{\varepsilon^p}$ were identified according to err% and correlation coefficient, respectively (**Figure 3**).

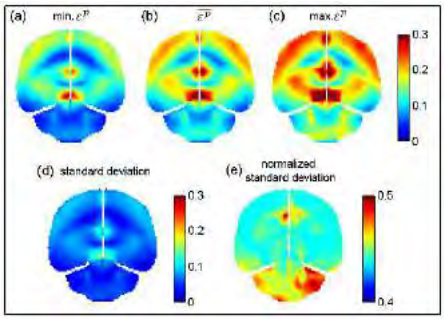

Figure 2 The minimum (a), average (b), and maximum (c) ε^p along with the standard deviation (d) (further normalized by the corresponding $\overline{\varepsilon^p}$ (e)) on a representative resampled coronal plane. Note that these responses are not necessarily from a given specific head impact.

The average element-wise differences between the maximum and minimum ε^p relative to $\overline{\varepsilon^p}$ was 47.9±17.0% (range 17.0–150.3%; **Figure 2**). In terms of CSDM, a variation of up to 23.9% was observed at a strain threshold of 0.1. These disparities suggest the shape of $\boldsymbol{v}_{rot}$ profiles is an important contributor to brain strain magnitude. Because only a limited number of uniaxial coronal head rotations were simulated, the observed uncertainty represented a lower bound of that expected in arbitrary, real-world head impacts. These findings are important to assess the effectiveness of kinematics-based injury metrics that indirectly rely on brain strains.

Despite the uncertainty in strain magnitude, the pattern of high/low strain exposures remained largely unchanged, regardless of the $\boldsymbol{v}_{rot}$ profile shapes (**Figure 3**; average correlation coefficient of 0.98±0.01, range 0.95–0.99). Such consistency in strain pattern may allow using targeted brain regions (vs. whole-brain) as the basis to develop a potentially more effective injury metric in the future. The targeted or more vulnerable regions can be determined via pre-computation [3,10].

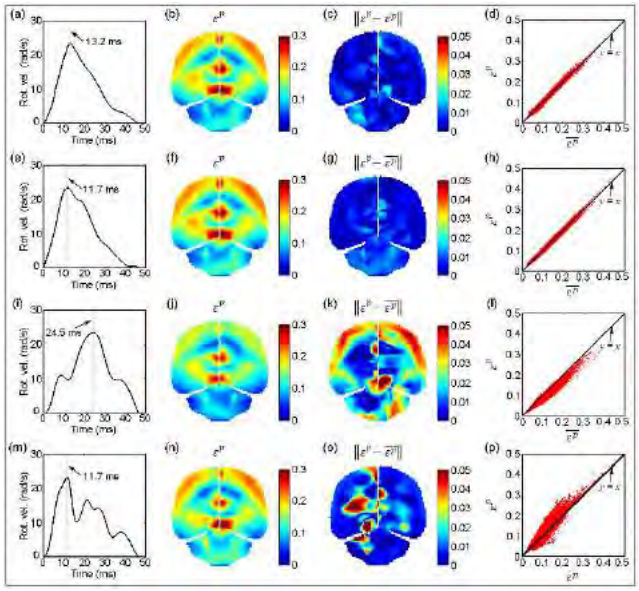

Figure 3 Comparison between ε^p and $\overline{\varepsilon^p}$. Left to right: $\boldsymbol{v}_{rot}$ profiles, ε^p, absolute difference between ε^p and $\overline{\varepsilon^p}$, and element-wise comparison between ε^p and $\overline{\varepsilon^p}$. Top to bottom: impacts leading to the smallest err%, the largest correlation coefficient, the largest err%, and the smallest correlation coefficient, respectively.

The two $\boldsymbol{v}_{rot}$ profiles that led to the most similar strain responses relative to $\overline{\varepsilon^p}$ in terms of err% and correlation coefficient (4.16% and 1.00 (p=0), respectively) also had similar shapes in $\boldsymbol{v}_{rot}$ profile (**Figure 3**). This observation suggests that a response-guided approach using group averaged brain strains may offer a useful, alternative method to "inversely" identify and characterize "typical" head impacts (vs. to operate directly on acceleration profiles [12,13]).

CONCLUSIONS

The shape of $\boldsymbol{v}_{rot}$ profile significantly affects brain strain magnitude, but not the pattern under uniaxial head rotations with identical peak $\boldsymbol{v}_{rot}$ magnitude and impulse duration. These findings offer important insight into the uncertainty or confidence in kinematics-based brain injury metrics. Further, they suggest the potential of using strains in targeted, more vulnerable regions (vs. whole-brain) to improve injury prediction performance in the future.

ACKNOWLEDGEMENTS

Funding is provided by the NIH grants R01 NS092853, R21 NS088781 and R21 NS078607.

REFERENCES

[1] Holhourn, *Br. Med. Bullitin.*, 3(6): 147–149, 1943.
[2] King, et al., *IRCOBI Conference*, Lisbon, Portugal, 2003.
[3] Ji and Zhao, *Ann. Biomed. Eng.*, 43(8): 1877–1895, 2015.
[4] Kleiven, *Stapp Car Crash J.*, 51: 81–114, 2007.
[5] Kleiven, *Int. J. Crashworthiness*, 11(1): 65–79, 2006.
[6] Takhounts et al., *Stapp Car Crash J.*, 57: 243–66, 2013.
[7] Kimpara and Iwamoto, *Ann. Biomed. Eng.*, 40(1): 114–26, 2012.
[8] Yoganandan et al., *J. Biomech.*, 41(10): 2253–2262, 2008.
[9] Post et al., *J. Biomech.*, 42(1): 11–24, 2014.
[10] Zhao and Ji, *IRCOBI Conf.*, Lyon, France, 2015.
[11] Newman et al., *Stapp Car Crash J.*, 44: 215–247, 2000.
[12] Ji et al., *Ann. Biomed. Eng.*, 42(1): 11–24, 2014.
[13] Rowson et al., *J. Biomech. Eng.*, 131(6): No. 061016, 2009

Copyright 2016 The Organizing Committee for the 2016 Summer Biomechanics, Bioengineering and Biotransport Conference

SB³C2016
Summer Biomechanics, Bioengineering and Biotransport Conference
June 29 –July 2, National Harbor, MD, USA
SB³C2016-69

WHITE MATTER INJURY SUSCEPTIBILITY USING WHOLE-BRAIN TRACTOGRAPHY: CONCEPT ILLUSTRATION

Wei Zhao (1), James C. Ford (2), Laura A. Flashman (2), Thomas W. McAllister (3), Songbai Ji (1, 4)

(1) Thayer School of Engineering,
Dartmouth College
Hanover, NH, USA

(2) Department of Psychiatry,
Geisel School of Medicine
Dartmouth College
Hanover, NH, USA

(3) Department of Psychiatry,
Indiana University School of Medicine
Indianapolis, IN, USA

(4) Department of Surgery and of
Orthopaedic Surgery
Dartmouth College
Hanover, NH, USA

INTRODUCTION

Finite element models of the human head estimate impact-induced regional brain mechanical responses (e.g. strain and stress) that are believed to initiate injury [1] but are not feasible to measure *in vivo*. Therefore, they are important in the study of the biomechanical mechanisms of traumatic brain injury (TBI).

Most model-based TBI studies employ isotropic variables such as maximum principal strain (ε_{ep}), despite the fact that white matter (WM) structural anisotropy is well-known. These isotropic measures are unable to fully characterize WM axonal shearing or elongation along fibers; however efforts to incorporate WM structural anisotropy into injury analysis are now emerging [2]. Initial evidence has shown that elongation along WM fiber directions (termed as "fiber" or "axonal" strain, ε_n) improves injury prediction performance compared to ε_{ep} [3,4]. To-date, however, these studies have been limited to averaged fiber directions at coarse elements [4,5] or image voxels [3].

Evaluating WM fiber strains at a finer spatial resolution has the potential to further improve injury prediction performance. This is because a single, averaged fiber direction is unable to accurately describe the structural anisotropy in regions of crossing fibers or complex fiber configurations (occurring in as much as 63–90% of human brain WM [6]).

WM tractography from diffusion MRI identifies brain anatomical connections that form the substrate for information transfer between functionally eloquent cortical areas. High-resolution sampling points along the tractography fibers (or "streamlines" representing them) enable a more accurate estimation of WM fiber orientations than those using less accurate or precise averaging.

This study is aimed at developing a technique to evaluate ε_n using anatomically constrained whole-brain tractography [8]. A novel injury susceptibility index was also proposed to quantify injury vulnerabilities of discrete WM voxels and individual neural tracts. As an initial step, this study focuses on comparing a new tractography-based technique with our previous voxel-based approach for ε_n evaluations.

METHODS

Brain strain responses corresponding to axial, coronal and sagittal (anterior-posterior direction) rotations were selected from an existing pre-computed brain response atlas (pcBRA; [7]). The pcBRA employs triangulated rotational acceleration (a_{rot}) impulses as inputs. The selected brain responses corresponded to peak a_{rot} of 4.5 krad/s^2 and impulse duration of 10 ms (identical to those used in our most recent study [8]). Whole-brain tractography was generated via ExploreDTI using pre-season DTI scans corresponding to the same individual used to create the Dartmouth Head Injury Model (DHIM). The accumulated peak tractography-based ε_n (ε_n^p), regardless of time of occurrence, was then calculated at all sampling points based on a Lagrangian strain tensor [3]. A fiber sampling point was considered "injured" when its ε_n^p exceeded a given threshold, and a voxel-wise injury susceptibility index (φ_{voxel}) was defined as the fraction of "injured" sampling points within the voxel as shown in equation (1),

$$\varphi_{voxel}(\varepsilon_{thresh}) = \frac{\#\ of\ injured\ sampling\ points\ within\ the\ voxel}{total\ \#\ of\ sampling\ points\ within\ the\ voxel}. \quad (1)$$

To calculate a tract-wise injury susceptibility index (φ_{tract}), identifying an anatomically constrained neural tract is necessary. For illustration, three sub-regions of the corpus callosum (CC) were localized by registering the JHU-ICBM-81 WM atlas [9] with the T1-weighted MRI corresponding to the DHIM. Fibers traversing each CC sub-region were identified by testing if fiber sampling points fell inside the anatomical boundary. We then defined, φ_{tract} analogously to φ_{voxel} as the fraction of "injured" WM fibers:

Copyright 2016 The Organizing Committee for the 2016 Summer Biomechanics, Bioengineering and Biotransport Conference

$$\varphi_{tract}(\varepsilon_{thresh}) = \frac{\#\ of\ injured\ fibers\ for\ the\ given\ neural\ tract}{total\ \#\ of\ fibers\ for\ the\ given\ neural\ tract}. \quad (2)$$

The values of φ_{voxel} and φ_{tract} are percentages ranging from 0% (no injury) to 100% (fully damaged).

RESULTS

The voxel- and tractography-based ε_n^p distributions were largely similar but the latter appeared smoother (**Figure 1)**. This was because the tractography-based approach used much finer resolution sampling points to compute an average ε_n^p at each WM voxel.

Binary injury maps were also compared (**Figure 2**). For the voxel-based method, a voxel was considered "injured" if the corresponding ε_n^p exceeded a given threshold. For the tractography-based approach, voxels with φ_{voxel} >50% were considered as "injured". The two techniques produced discordant voxel-wise injury distributions, especially when ε_{thresh} was high (the average dice coefficient of the three rotations dropped from 0.81 to 0.66 when ε_{thresh} increased from 0.09 to 0.18).

Figure 3 shows φ_{tract} as a function of ε_{thresh} for each CC sub-region. Consistent with φ_{voxel} (**Figure 1g-i**), axial and sagittal rotations were the most and least damaging, respectively. The directional dependency of φ_{tract} was evident. At the "optimal" ε_{thresh} of 0.18, the largest φ_{tract} of 96.8% was observed in the genu for an axial rotation. The largest values for coronal and sagittal rotations were 25.3% and 8.3%, respectively, in the CC main body (**Figure 3**).

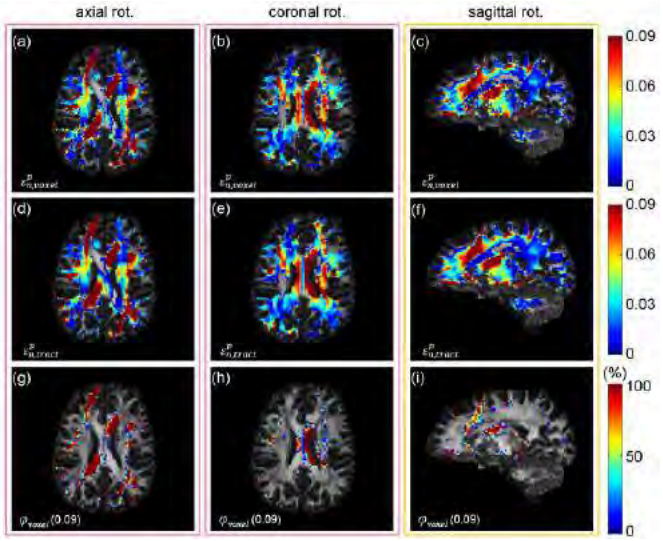

Figure 1 Maps of ε_n^p using the voxel- (top) and tractography-based (middle row) approaches, along with φ_{tract} maps (bottom) on a selected MRI in axial, coronal, and sagittal rotations (from left to right).

DISCUSSION AND CONCLUSION

We have developed a tractography-based technique to evaluate WM fiber strain [8]. The technique was compared with a previously developed voxel-based method, as illustrated using rotations in three directions and three CC sub-regions. Maps of ε_n^p were largely similar across methods, suggesting a certain fundamental concordance between the two methods. However, their binary injury maps based on voxel-wise ε_n^p or φ_{voxel} differed significantly. Because of the much finer spatial resolution used in the tractography-based method, "graded" injury susceptibility may provide a confidence measure for local structural integrity (larger φ_{voxel} indicates higher likelihood of injury).

A unique capability of the tractography-based method was to enable injury assessment for functionally important neural tracts, which was not possible with the voxel-based analogue. As neural tracts connect cell bodies and transmit information between them [10], it is reasonable to assume any damage along axons, regardless of location, would lead to functional impairment [11]. This logic led to the tract-based φ_{tract} to quantify the vulnerabilities of WM neural pathways.

The current study focused on introducing the use of whole-brain tractography to better evaluate WM fiber strain. Future studies using real-world brain injury cases will reveal whether the new injury predictors can improve injury predictive power in a practically useful way. In addition, they may allow assessment of relative vulnerabilities of neural pathways and identification of the most vulnerable ones in real-world head impacts.

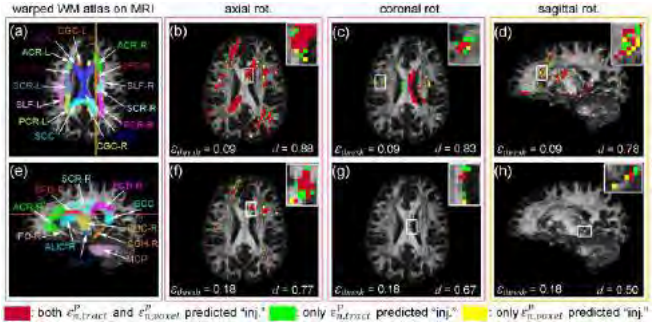

Figure 2 Binary injury maps for the voxel- and tractography-based approaches overlaid on an axial (axial (b and f) and coronal (c and g) rotations) and a sagittal (sagittal rotation (d and h)) MRI along with the ICBM-81 WM atlas warped onto the individual's anatomical MRI (a and b). Dice coefficient (*d*) was reported for each MRI.

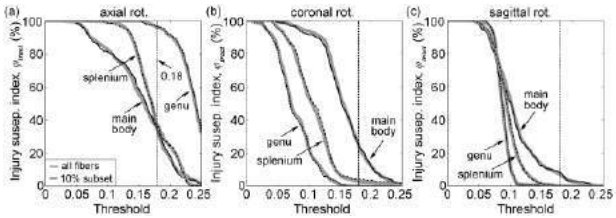

Figure 3 Tract-wise φ_{tract} as a function of ε_{thresh} for each CC sub-region in (a) axial, (b) coronal, and (c) sagittal rotations. The results from the 10% randomly selected fiber sample were virtually identical to those from the full set.

ACKNOWLEDGEMENTS

Funding is provided by the NIH grants R01 NS092853, R21 NS088781 and R21 NS078607.

REFERENCES

[1] King, et al., *IRCOBI Conference*, Lisbon, Portugal, 2003.
[2] Carlsen and Daphalapurkar, *Front. Neurol*, 6, 28, 2015.
[3] Ji et al. *J. Neurotrauma*, 32(7): 441–454, 2015.
[4] Giordano and Kleiven, *Stapp Car Crash J.*, 58: 29–61, 2014.
[5] Chatelin et al., *J. Mech. Behav. Biomed. Mater.*, 4: 1905–1919, 2011.
[6] Jeurissen et al., *Hum. Brain Mapp.*, 34(11), 2747–2766, 2013.
[7] Ji and Zhao, *Ann. Biomed. Eng.*, 43(8): 1877–1895, 2015.
[8] Zhao et al., *J. Neurotrauma*, 2016 (acceped and in press).
[9] Mori et al., *Neuroimage*, 40(2): 570–582, 2008.
[10] Debanne et al., *Physiol. Rev.*, 91(2): 555–602, 2011.
[11] Kraft et al., *PLoS Comput. Biol.*, 8(8): No. e1002619, 2012.

Copyright 2016 The Organizing Committee for the 2016 Summer Biomechanics, Bioengineering and Biotransport Conference

SB³C2016
Summer Biomechanics, Bioengineering and Biotransport Conference
June 29 –July 2, National Harbor, MD, USA
SB³C2016-70

BISPHOSPHONATE CAN RESCUE THE DAMAGED ARTICULAR CARTILAGE IN VITRO

Yilu Zhou, Mengxi Lv, Marisa Bisram, Joshua A. Blotnick, Liyun Wang, X. Lucas Lu (1)

(1) Department of Mechanical Engineering, University of Delaware,
Newark, DE

INTRODUCTION

Osteoarthritis (OA) could result from the traumatic damage to the diarthrodial joint, such as the meniscus rupture, anterior cruciate ligament tear, and trauma induced joint bleeding. Few therapeutic techniques are now available to prevent post-traumatic OA (PTOA). Using PTOA animal model, a few studies found that systematic administration of bisphosphonates (BPs) can significantly slow down the development of OA after traumatic damages, including dislocation of meniscus, ACL transaction, and carrageenan-induced inflammation [1]. BPs are a class of commercial drugs widely used for the treatment of bone loss by the dysfunction of osteoclasts [2]. Little knowledge is available about the promising rescue effects of BPs on PTOA. A few studies conjectured that BPs protect the cartilage through the prevention of bone loss after joint trauma [3-4].

In this study, we tested a bold hypothesis that the chondro-protective function of BPs could be related to their direct regulation of the metabolic activities of chondrocytes, which further preserve the integrity of the cartilage solid matrix. Using a long-term *in vitro* culture model, the effect of bisphosphonates on cartilage explants with no subchondral bone attached was investigated.

METHODS

Cartilage explants were harvested from the femoral condyle head of 3-month old calf knee joints using a biopsy punch (diameter: 3mm), as illustrated in Fig. 1. The superficial-middle zones of cartilage (height: 2 mm) were obtained using a custom-designed cutting tool. All cartilage samples were cultured in serum supplemented medium (DMEM, 10% FBS, 1% P/S) for 1 week to simulate the traumatic damage on cartilage caused by joint bleeding. Previous studies from ours and other groups showed that the mechanical integrity of cartilage explants was significantly impaired after long-term exposure to serum medium [5-6]. Damaged samples were then separated into two groups (N=10) and cultured in chemically defined serum-free medium (DMEM, 1% ITS, 50 μg/mL L-proline, 0.9 mM sodium pyruvate, and 50 μg/mL ascorbate 2-phosphate [7]) with or without the supplement of 1 μM zolendronic acid (ZA, Zometa® from Novartis Pharmaceuticals Corporation, an FDA approved BP). The samples were cultured in rescue medium for 4 weeks. Mechanical and dimensional properties of cartilage explants were measured longitudinally on days 2, 8, 15, and 29. The equilibrium Young's modulus and dynamic compressive modulus of samples were determined using unconfined compression tests. GAG content of samples was measured at the end of the 4-week culture using dimethylmethylene blue dye-binding assay. The Mann-Kendall test was performed to analyze the trend of parameters with culture time.

RESULTS

Mechanical Properties: During the 4-week culture, mechanical properties of cartilage explants decreased in the control group (Fig. 2A-2B), while samples in the ZA supplemented medium maintained the mechanical modulus at a relatively constant level (Young's modulus: 0.21~0.25 MPa, dynamic modulus: 4.70~5.53 MPa), and significantly higher than those of corresponding controls. The Mann-Kendall test showed that the difference gap between the two groups increased with culture time (confidence factor > 95%). Young's modulus of the samples in the ZA group became significantly higher than the control after a 15-day culture (Fig. 2A). The dynamic modulus started to show a difference between the two groups after merely 8 days (Fig. 2B).

Biochemical Analysis: After the 4-week culture, GAG content of cartilage in the control group (Fig. 2C) was significantly lower than that in the ZA treated group (3.59% vs. 4.06%).

Copyright 2016 The Organizing Committee for the 2016 Summer Biomechanics, Bioengineering and Biotransport Conference

Dimensional Analysis: The 1-week culture in serum supplemented medium increased the height of cartilage explants by 60% (from the initial 2 mm to 3.2 mm). Increase of height slowed down after switching into serum-free medium (40.6% after 4 weeks). No significant difference was detected in thickness between the control and ZA-treated groups (Fig. 2D). Diameter of the explants (Fig. 2E) increased in both groups, but samples in the ZA group swelled significantly less after 29 days. Thus the volume of explants in the ZA group is significantly smaller than that of control (Fig. 2F). The Mann-Kendall test showed that the difference gap between the two groups increased with culture time (confidence factor > 95%).

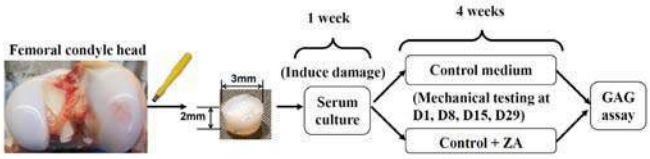

Figure 1: Cartilage explants were harvested from the femoral condyle head, followed by a 1 week culture in serum medium (DMEM+10% FBS). Samples were then separated into 2 groups, control and ZA supplemented group, for another 4-week culture. Mechanical properties were measured longitudinally on days 1, 8, 15, and 29.

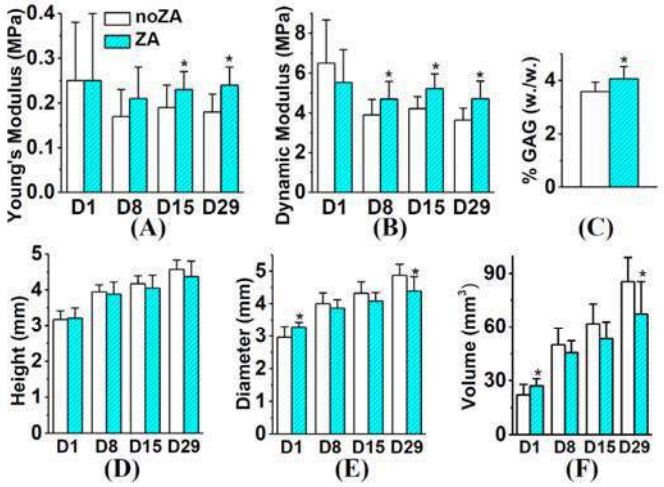

Figure 2: (A) The equilibrium Young's modulus and (B) dynamic modulus of cartilage explants were determined longitudinally by unconfined compression tests on days 1, 8, 15, and 29 (n = 10). Samples were cultured in chemical defined medium with no dexamethasone. (C) GAG content of cartilage explants was determined at the end of the 4-week culture. Geometric dimensions of the cylindrical explants were measured longitudinally including the (D) height, (E) diameter, and (F) volume of cartilage explants. (* $p<0.05$)

DISCUSSION

As an FDA approved drug for two decades, bisphosphonates could represent a new therapeutic medicine for the prevention of PTOA. This concept-proof study showed that BPs can directly regulate the metabolic activities of chondrocytes in a beneficial direction. Besides revealing the chondro-protective mechanisms of BPs, the results also provided us extra confidence for studying BPs for PTOA. This new evidence, however, does not necessarily conflict with the conjecture that the chondro-protective effect of bisphosphonate is related to its inhibition of bone loss. BPs might protect the cartilage after joint trauma through both mechanisms, i.e., preventing bone loss and regulating chondrocytes activities.

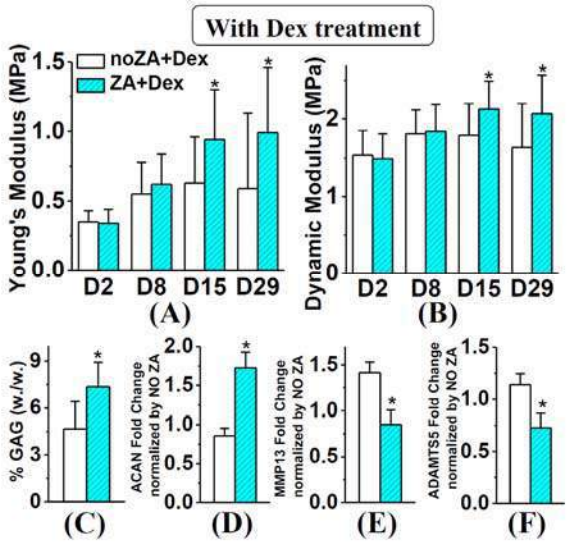

Figure 3: (A) Equilibrium Young's modulus and (B) dynamic modulus of cartilage explants were determined longitudinally on days 2, 8, 15, and 29 in serum-free culture supplemented with dexamethasone. (C) GAG content after 4-weeks culture. Gene expression of chondrocytes after 2-week culture: (D) Aggrecan, (E) MMP-13, and (F) ADAMTS5.

In our previous study [7], we investigated the effect of ZA on cartilage explant with the addition of dexamethasone in the culture medium, in which ZA showed similar chondro-protective effects in terms of the mechanical modulus (Fig. 3A-B), GAG content (Fig. 3C) and the gene expression of chondrocytes (Fig. 3D-F). Dexamethasone has a strong chondro-protective effect by upregulating the anabolic genes and suppressing the catabolic genes in chondrocytes. In the present study, dexamethasone was removed from the culture medium, and the beneficial effects of bisphosphonate were retained. Therefore, it is clear that BPs can directly regulate the metabolic activities of chondrocytes.

ZA treatment increased the GAG content in cartilage explants. As the GAG chains are negatively charged, more GAG generates higher osmotic swelling pressure in the solid matrix [8]. However, explants in the ZA group swelled less than the control group. This implies that the collagen networks in ZA treated samples should be much stronger than those in control medium, which is reflected by the mechanical testing results (Fig. 2A-2B) and MMP gene expression (Fig 3E). Therefore, ZA protects the mechanical integrity of the solid matrix in cartilage.

ACKNOWLEDGEMENTS

This work is supported by DOD W81XWH-13-1-0148 and NIH P30GM103333-01.

REFERENCES

[1] Saag, KG, Ann Rheum Dis, 67.10: 1358-1359, 2008.
[2] Rogers, MJ et al., *Cancer,* 88.S12: 2961-2978, 2000.
[3] Herrak, P et al., Arthritis Rheum, 50.7: 2327-2337, 2004.
[4] Muehleman, C et al. *Osteoarthr. Cartil*, 10.3: 226-233, 2002.
[5] Zhou, Y et al., *J Biomech,* 48.6: 990-996, 2015.
[6] Bian, L et al., *J Biomech*, 41.6: 1153-1159, 2008.
[7] Zhou, Y et al. ORS proceedings, 2015.
[8] Mow, VC et al., *Annu. Rev. Biomed. Eng.*, 4.1: 175-209, 2002.

Copyright 2016 The Organizing Committee for the 2016 Summer Biomechanics, Bioengineering and Biotransport Conference

SB^{3}C2016
Summer Biomechanics, Bioengineering and Biotransport Conference
June 29 –July 2, National Harbor, MD, USA
SB^{3}C2016-71

MODELING SOFT TISSUE DAMAGE AND FAILURE USING A HYBRID PARTICLE/CONTINUUM APPROACH

Manuel K. Rausch (1), George E. Karniadakis (2), Jay D. Humphrey (1)

(1) Department of Biomedical Engineering
Yale University
New Haven, CT

(2) Department of Applied Mathematics
Brown University
Providence, RI

INTRODUCTION

Biological soft tissues resist loads under physiological conditions remarkably well. Nonetheless, they can fail due to disease or simply age; examples range from torn ligaments [1] to arterial dissections [2]. Because soft tissues have complex geometries and complex, non-linear material properties, computational methods are essential to the study of soft tissue damage and failure. However, traditional approaches, such as the Finite Element Method, are limited.

Here, we test the utility of a novel mixed particle/continuum approach to the study of soft tissue damage and failure. Specifically, we combine traditional continuum damage mechanics with Total Lagrangian SPH (Smoothed Particle Hydrodynamics) to model soft tissue damage and discontinuous failure, respectively. While SPH was originally conceived for applications other than solid mechanics, recent improvements have made the method a promising alternative to the Finite Element Method in a number of applications [3].

The purpose of this work is to demonstrate SPH's potential advantage for damage and failure modeling with an example of a generic, anisotropic soft tissue sample subject to finite deformations.

METHODS

SPH for Solid Mechanics. In SPH, physical quantities at point $\boldsymbol{X}_i$ are smoothed over the "particle's" immediate neighborhood within the domain of interest:

$$\hat{g}(\boldsymbol{X}_i) = \int f(\boldsymbol{X})\widehat{W}(\boldsymbol{X}-\boldsymbol{X}_i,h)\mathrm{d}\boldsymbol{X}, \tag{1}$$

where $\widehat{W}$ is referred to as the smoothing kernel. Spatial discretization is further performed by approximating the above integral expression by a finite sum over discrete neighboring points $\boldsymbol{X}_j$ within the smoothing length *h*. Thus,

$$g(\boldsymbol{X}_i) = \sum_{j\in S} f_j\, V_j W(\boldsymbol{R}_j,h), \tag{2}$$

where $f_j = f(\boldsymbol{X}_j)$, V_j is the volume associated with each neighboring particle, and $W(\boldsymbol{R}_j,h)$ is the kernel weight as a function of particle distances, with $\boldsymbol{R}_j = \boldsymbol{X}_j - \boldsymbol{X}_i$. The gradient of $g(\boldsymbol{X})$ follows from,

$$\nabla_{\boldsymbol{X}} g(\boldsymbol{X}_i) = \sum_{j\in S} f_j\, V_j \nabla_{\boldsymbol{X}} W(\boldsymbol{R}_j,h). \tag{3}$$

Because the standard SPH method lacks 0th order and 1st order completeness, two ad-hoc corrections are performed, viz.,

$$\tilde{\nabla}_{\boldsymbol{X}} g(\boldsymbol{X}_i) = \sum_{j\in S} (f_j - f_i)\, V_j \mathbf{A}^{-1}\nabla_{\boldsymbol{X}} W(\boldsymbol{R}_j,h), \tag{4}$$

where,

$$\mathbf{A} = \sum_{j\in S} V_j\, \nabla_{\boldsymbol{X}} W(\boldsymbol{R}_j,h)\otimes\boldsymbol{R}_j. \tag{5}$$

Given this basic framework, we explicitly solve the local strong form of the equilibrium equations in referential form,

$$m_i\ddot{\boldsymbol{x}}_i = \boldsymbol{f}_i^{\,int} + \boldsymbol{f}_i^{\,ext}, \tag{6}$$

by first approximating the deformation gradient,

$$\boldsymbol{F}(\boldsymbol{X}_i) = \sum_{j\in S} \boldsymbol{r}_j \otimes V_j \mathbf{A}^{-1}\nabla_{\boldsymbol{X}} W(\boldsymbol{R}_j,h), \tag{7}$$

where $\boldsymbol{r}_j = \boldsymbol{x}_j - \boldsymbol{x}_i$. Next, assuming the existence of a strain energy density function ψ, we derive the first Piola-Kirchhoff stress tensor according to,

Copyright 2016 The Organizing Committee for the 2016 Summer Biomechanics, Bioengineering and Biotransport Conference

$$\boldsymbol{P}(\boldsymbol{X}_i) = 2\boldsymbol{F}(\boldsymbol{X}_i)\frac{\partial \psi(\boldsymbol{X}_i)}{\partial \boldsymbol{C}(\boldsymbol{X}_i)}. \quad (8)$$

Finally, we calculate the particle forces $\boldsymbol{f}_i^{int}$ from the divergence of $\boldsymbol{P}(\boldsymbol{X}_i)$ using above expressions and ad-hoc corrections,

$$\boldsymbol{f}_i^{int} = \sum_{j \in S} V_i V_j \left(\boldsymbol{P}_i \mathbf{A}^{-1} \nabla_{\boldsymbol{X}} W(\boldsymbol{R}_j, h) - \boldsymbol{P}_j \mathbf{A}^{-1} \nabla_{\boldsymbol{X}} W(\boldsymbol{R}_i, h) \right). \quad (9)$$

Thus, once the internal and external forces are known, the acceleration can be updated for each particle according to equation (6) and integrated twice via the Leap-Frog scheme to obtain the current nodal positions.

Damage and Failure Modeling. We assume that our test material behaves according to following strain energy density function [4],

$$\psi(\boldsymbol{C}, \boldsymbol{M}) = \frac{\mu}{2}(I_1 - 3) + \mu \ln J + \frac{\lambda}{2}(\ln J)^2 + \frac{k_1}{4k_2}[\exp(k_2(I_4 - 1)^2) - 1], \quad (10)$$

where $I_1 = \boldsymbol{C}:\boldsymbol{I}$, $I_4 = \boldsymbol{C}:\boldsymbol{M}\otimes\boldsymbol{M}$, $J = \det\boldsymbol{F}$, and $\boldsymbol{M}$ is the direction vector of structural fibers embedded in a neo-Hookean ground substance. Isotropic continuum damage is further modeled by employing an approach first proposed by Simo in which the original strain energy function ψ is modified by a reduction factor $(1 - D)$, where D is the damage variable [5,6]. Therefore,

$$\psi(\boldsymbol{C}, \boldsymbol{M}, D) = (1 - D)\psi_0(\boldsymbol{C}, \boldsymbol{M}) \text{ and } \boldsymbol{S} = 2(1 - D)\frac{\partial \psi_0}{\partial \boldsymbol{C}}. \quad (11)$$

In our examples, the damage evolution is prescribed through following exponential law,

$$D = \begin{cases} \exp\left(\left((\lambda_m - \lambda_{crit})/\tau\right)^2\right) - 1 & \lambda_m \geq \lambda_{crit} \\ 0 & \lambda_m < \lambda_{crit} \end{cases}. \quad (12)$$

Here τ and λ_{crit} are material specific damage parameters and λ_m is the largest previously experienced maximum principal stretch, $\lambda_m(t) = \max_{s\in(-\infty,t]} \lambda(s)$.

Once, the damage variable D reaches a value of one, the material is considered fully damaged. Continuum methods have no capacity to model material behavior beyond this point. However, knowing the behavior of soft tissue following damage and failure may be important as new surfaces, for example, could be subject to applied tractions and loads. Because in SPH particle connectivity is determined based on a list of neighboring particles, we model strong discontinuities following irreversible tissue damage, such as crazing or rupture, by a simple modification to this list.

RESULTS

To verify the implementation of equations (1) - (12), we simulated simple uniaxial and biaxial tensile tests of an anisotropic soft tissue strip and, compared to the analytical solution, found a maximum error of less than 1%.

Further, to demonstrate the ability of our novel hybrid approach to model strong material discontinuities that occur during damage and failure of soft tissue, we also modeled the response of a cylindrical, anisotropic soft tissue sample to clamped uniaxial extension, see Figure 1. Because rupture initializes at focal material points, we assigned the critical damage parameter λ_{crit} for each particle according to a normal distribution. The figure illustrates the damaged soft tissue sample with fibers oriented in horizontal direction at six time points between the reference configuration and catastrophic failure.

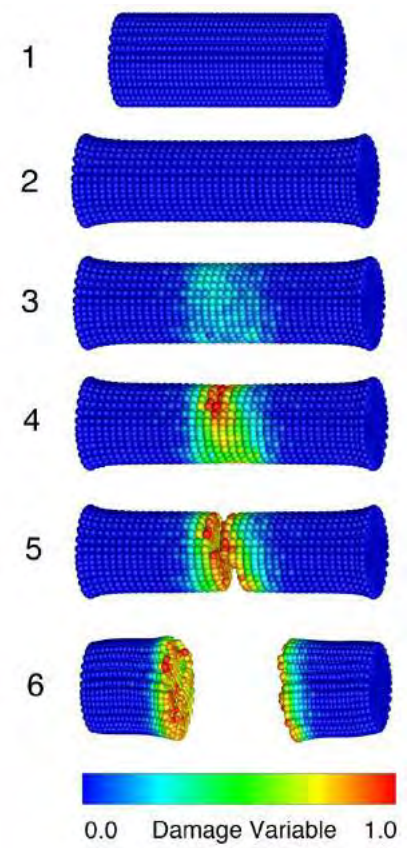

Figure 1: Example of a cylindrical tissue sample under clamped uniaxial extension to failure. Shown is the evolution of the damage variable at six time points: 1) reference configuration, 2) before damage, 3) initial damage in areas of highest stress, 4) first particles reach damage values of one, 5) particles disconnect to form a rupture surface, 6) full rupture.

DISCUSSION

SPH suffered from a number of short-comings which have limited its use in solid mechanics and specifically soft tissue mechanics. However, recently introduced correction steps have improved the accuracy of SPH as shown in our verification problems. Furthermore, as we demonstrated, SPH may provide advantages over more established methods, especially where catastrophic failure such as crazing, dissection, and rupture is modeled. Of course, this is only a first step toward establishing SPH as a reliable numerical method for soft tissue mechanics and specifically damage and failure, however, we believe further research is warranted.

ACKNOWLEDGEMENTS

This research was supported, in parts, by NIH grants R01 HL086418, U01 HL116323, and T32 HL007974. The authors declare that they have no conflict of interest.

REFERENCES

[1] Weiss, JA et al., *Crit Rev Biomed Eng*, 29:303-371, 2001. [2] Roccabianca, S et al., *Biomech Model Mechanobiol*, 13:13-25, 2014. [3] Ganzenmueller, GC, *Comput Struct*, 150:71-78, 2015. [4] Holzapfel, GA et al., *J Elasticity*, 61:1-48, 2000. [5] Simo, J, *Comput Method Appl M*, 60:153-173, 1987. [6] Rausch, MK et al., *J Mech Behav Biomed Mater,* 55:12-20, 2015.

Copyright 2016 The Organizing Committee for the 2016 Summer Biomechanics, Bioengineering and Biotransport Conference

SB^{3}C2016
Summer Biomechanics, Bioengineering and Biotransport Conference
June 29 –July 2, National Harbor, MD, USA
SB^{3}C2016-72

MULTISCALE MECHANICS OF HUMAN SUPRASPINATUS TENDON IN SHEAR AFTER PROTEOGLYCAN DEPLETION

Fei Fang (1), Spencer P. Lake (1-3)

(1) Department of Mechanical Engineering & Materials Science
(2) Department of Biomedical Engineering
(3) Department of Orthopaedic Surgery
Washington University in St. Louis
St. Louis

INTRODUCTION

The evaluation of tendon composition and structure could facilitate an understanding of how tendon behavior changes as tissue properties are modified in injury and aging. Unfortunately, studies evaluating the contribution of tissue constituents with small quantities (e.g., proteoglycans (PGs)) have yielded inconsistent results. PGs, composed of a core protein attached to glycosaminoglycan (GAG) chains, have been observed in high-resolution micrographs; some studies have utilized computational modeling to suggest that these PGs maintain tendon mechanical integrity by bridging adjacent collagen fibrils [1-3]. Experimental studies report conflicting results: tensile mechanics were unchanged after partially enzymatic depletion of GAGs, while tendons from PG-null mice showed inferior failure loads and dynamic mechanics in an age-dependent manner [1,4-6]. While these studies have focused on tensile loading, the contribution of PGs to the mechanical response of tendons under other loading scenarios has not been as well addressed [1-6]. In particular, understanding the role of PGs under shear loading would be beneficial since shear is likely to cause more sliding between collagen fibers and could better explore the possibility of force transfer assisted by PGs side-chains. Damage to the oft-injured supraspinatus tendon (SST) may be partially due to shearing through the tendon thickness [7,8], so tissue constituents that govern the shear response may play a critical role in SST mechanics. In this study, we examined if PGs influence the multiscale mechanics of human SST, using micromechanical shear testing with two-photon microscopy before and after enzymatic digestion.

METHODS

Biomechanical testing. SSTs (n=10) were obtained from fresh frozen human cadaver shoulders (age: 70.8±21.4 years), with torn tendons excluded. 10×8 mm (LxW) full-thickness samples were cut from three distinct SST regions (Fig. 1A, A: anterior, M: medial, P: posterior), corresponding to previous studies [8,9]. After leveling surfaces on a microtome, samples were incubated for 30 min in a 100 μg/ml 5-DTAF solution to stain collagen [10]. Following PBS washes, samples were mounted in a micromechanical test device secured to the stage of a Zeiss two-photon confocal microscope system. Four adjacent squares (100×100μm) were photobleached at three locations (bursal to joint) at a depth of ~50μm after applying a 0.005N pre-load. Incremental stress-relaxation shear testing was applied (Fig. 2B), and multi-channel z-stacks were collected as described previously [10,11]. Then, clamps were locked and one set of samples (n=5/region) was randomly selected for treatment with Chondroitinase ABC (ChABC) solution (described below), while the other set (n=5/region) was incubated in PBS. Following incubation, all samples were retested with the same shear loading protocol and two-photon images acquired.

ChABC treatment and GAG quantification. The efficiency of ChABC on SST was examined in concentration- and time-dependent testing. Results (not shown) indicated an optimal treatment of 0.2 units/ml ChABC buffer for 8 hours. Due to the relatively large size of samples and the method used for mounting samples within the test device, the depth to which ChABC could penetrate into the tissue and digest PGs was also evaluated. For these preliminary tests, bovine deep digital flexor tendons (DDFTs) were used for their easy accessibility. Samples (n=8) of similar size were cut from the proximal region of four bovine DDFTs [10,11]. Samples were glued to shear clamps and the clamp-sample assemblies were incubated in either ChABC solution (n=4) or PBS (n=4) for 8 hours. Five small tissue pieces weighing 40-50 mg each were evenly taken from locations along the thickness of each sample using a freezing stage sledge microtome. Total GAG amount in digested samples was quantified using a 1,9-Dimethylmethylene Blue Assay and normalized by GAG quantity in a corresponding control sample [12].

Data analysis. Peak/equilibrium stresses, and local matrix-based strains were calculated as in previous studies [10,11]. Rotation was

Copyright 2016 The Organizing Committee for the 2016 Summer Biomechanics, Bioengineering and Biotransport Conference

defined as the angle change between the deformed horizontal photobleached lines and the image x-axis (Fig. 1E). Normalized stresses were computed as shear stresses after ChABC treatment/PBS incubation normalized by the last step peak stress of the corresponding samples before treatment/incubation (control). Mechanical differences between control and treated samples were evaluated by paired *t*-tests, while unpaired *t*-tests were used to evaluate local matrix-based strains and rotations. One-way ANOVAs with Bonferroni post-hoc tests were used to find differences across the three SST regions. Significance was set at $p < 0.05$. Data are shown as mean ± SD.

RESULTS

ChABC treatment caused a gradient distribution of GAGs in tendon, with 20.0±13.0% left on the surface of samples and 69.0±5.9% in the middle (Fig.2A). Shear stress values were similar for all regions,

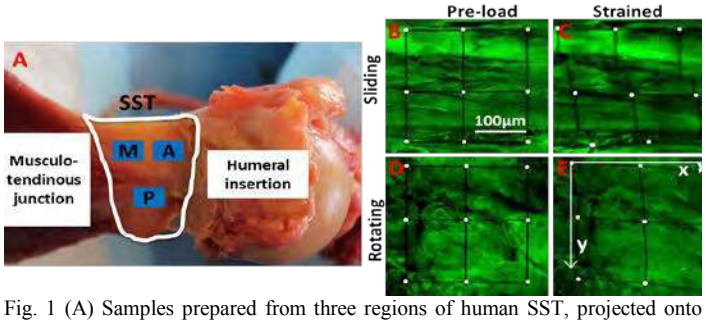

Fig. 1 (A) Samples prepared from three regions of human SST, projected onto the joint side of the tendon. Compared to pre-load images (B,D), sliding between fibers (C) and rotation of fibers (E) are shown in two-photon microscopy images.

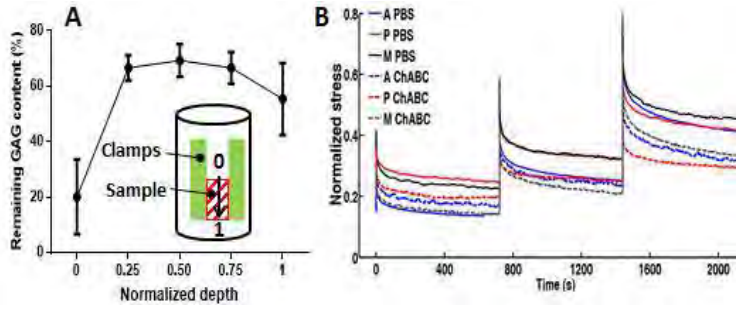

Fig. 2 (A) Remaining GAG content along the depth; inset shows a sample (red block) attached to clamps (green blocks) incubated in ChABC solution. The normalized depth is defined as 0 (top) to 1 (bottom). Averaged stress-time curves (B) of PBS incubated and ChABC treated groups, normalized by corresponding control stresses.

and stress profiles decreased more for ChABC-treated samples than PBS-incubated samples (Fig. 2B). Control samples (i.e., before digestion) exhibited larger peak and equilibrium stresses than treated samples in all three SST regions; digestion decreased peak and equilibrium stresses by an average of 30.7 and 27.2%, respectively (Fig. 3A&B), although these differences were not significantly different. On the microscale, areas of both organized and disorganized collagen were found in most SST samples, showing microstructural heterogeneity. For loaded samples, breaking and rotation of photobleached lines were found in all regions (Fig. 1C&E), demonstrating fiber sliding and reorganization. Local matrix-based strains were similar before and after treatment, and were generally smaller than clamp strains (Fig. 3C), demonstrating strain attenuation. Rotation increased with increasing applied strains (Fig. 3D).

DISCUSSION

Although not attaining statistical significance, digested SSTs exhibited decreased stresses, and even smaller normalized stresses

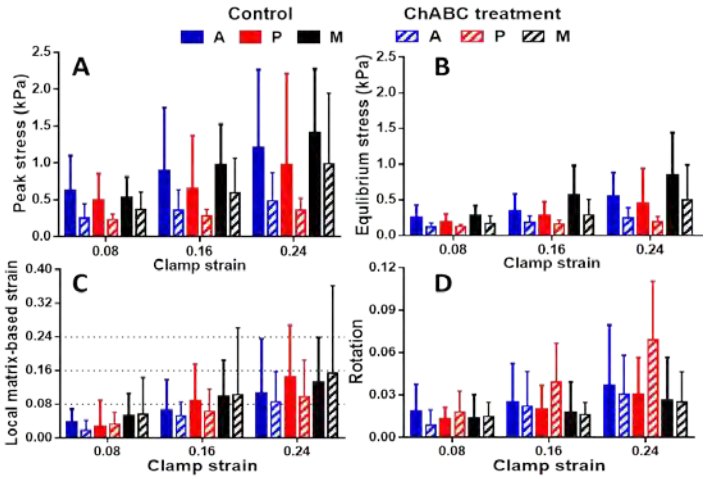

Fig. 3 Peak (A) and equilibrium (B) stresses of SST samples before (control) and after (ChABC) treatment. Similar local matrix-based strains (C) and rotations (D) across different regions, and even between control and treated samples.

than PBS incubated SSTs under shear loading. These results suggest that PGs provide force support under shear loading. The high variability of tendon stress values may be due to the wide age range and (assumed) varied loading history of cadaveric human tissue tested in this study; evaluation of additional samples could raise differences observed herein to the level of statistical significance. Our study also illustrates the limited penetration of ChABC inside SST to digest GAGs, indicating the limitation of the enzyme-treated approach to examine the role of tissue constituents [1,6]. Mechanical results of digested samples were compared to data from PBS-incubated samples to account for effects due to tendon swelling. Similar microscale strain across all three regions and even between control and treated tendons may be due to SST high microstructural heterogeneity (i.e., disorganized collagen fibers). Sliding between collagen fibers and fiber reorganization appear to be the physical mechanisms on the microscale-level that regulate tendon behavior under shear. Previous studies reported fiber elongation and sliding in tendon as deformation mechanisms under tensile loading [13,14]. One limitation of this study was that PGs were only partially digested, particularly in the middle of samples, which limits the magnitude of the effect by ChABC treatment. By analyzing multiscale mechanical behavior of SST under shear loading before and after PG digestion, this study provides insight into the role of tissue constituents of relatively small amounts in tendon, which may help predict how non-tensile mechanics are altered with degeneration/injury-related changes to compositional properties of tendons.

ACKNOWLEDGEMENTS

This work was supported by a pilot grant from Washington University Musculoskeletal Research Center (NIH P30 AR057235).

REFERENCES

[1] Fessel, G+, *Matrix Biol*, 28:503-510, 2009. [2] Ahmadzadeh, H+, *J Biomech*, 46:2497-2503, 2013. [3] Szczesny, SE+, *JBMMB*, 40:325-338, 2014. [4] Gordon, JA+, *J Biomech*, 2015. [5] Dunkma, AA+, *Matrix Biol*, 35:232-238. [6] Svensson RB+, *Connect Tissue Res*, 52:415-421, 2011. [7]Soslowsky LJ+, *Ann Biomed Eng*, 30:1057-1063, 2002. [8] Lake, SP+, *J Orthop Res*, 27:1596-1602, 2009. [9] Lake, SP+, *J Biomech,* 43:727-732, 2010. [10] Fang, F+, *J Orthop Res*, 33:1704-1712, 2015. [11] Fang, F+, *J Biomech*, 47:2869-2877, 2014. [12] Zheng, C+, *Eur Cell Mater*, 29:224-236, 2015. [13] Cheng VW+, *J Mater Sci*, 42:8957-8965, 2007. [14] Shepherd, JH+, *JBMMB*, 38:163-172, 2014.

Copyright 2016 The Organizing Committee for the 2016 Summer Biomechanics, Bioengineering and Biotransport Conference

SB^{3}C2016
Summer Biomechanics, Bioengineering and Biotransport Conference
June 29 –July 2, National Harbor, MD, USA
SB^{3}C2016-73

MODULATION OF ICAM-4 ADHESION RECEPTORS ON SS-RBCS REVEALED BY ATOMIC FORCE MICROSCOPY

J. Zhang (1), B. Andemariam (2), G. Lykotrafitis (1,3)

(1) Department of Mechanical Engineering
University of Connecticut
Storrs, CT, USA

(2) Adult Sickle Cell Center
University of Connecticut Health Center
Farmington, CT, USA

(3) Department of Biomedical Engineering
University of Connecticut
Storrs, CT, USA

INTRODUCTION

Painful vaso-occlusive episodes in sickle cell disease (SCD) are largely due to abnormal adherence among red blood cells (RBCs), leukocytes, platelets, and the endothelium [1]. Adhesion receptors expressed on RBCs regulate RBC adherence to the endothelium and to blood cells. ICAM-4 is an adhesion receptor interacting with αvβ3, an integrin expressed on endothelial cells and platelets [2].

Here, we employ atomic force microscopy (AFM) to detect the distribution of active ICAM-4 molecules on the RBC membrane and measure the unbinding force between ICAM-4 and αvβ3.

METHODS

Human subjects and blood preparation

Homozygous SCD (SS) patients were eligible to participate if they were at least 18 years old and at steady state. Additionally, they were not on treated with hydroxyurea and had no blood transfusion in the past three months. Blood samples were obtained from fresh-drawn, heparin-anticoagulated venous blood of qualified volunteers. The whole blood was centrifuged at 145×g for 5 min at 4 ℃ to separate the RBCs. The plasma and buffy coat were extracted and discarded. Then the RBCs were washed three times with Alsever's solution and stored at 4 ℃.

Ligand and reagents

Human integrin αvβ3 protein was obtained from Millipore (Billerica, MA). Alsever's solution, epinephrine (Epi), forskolin (FSK), KT 5720, Rp-Adenosine 3′,5′-cyclic monophosphorothioate triethylammonium salt (Rp-cAMPS), bovine serum albumin (BSA), valsartan were purchased from Sigma-Aldrich (St. Louis, MO). St-Ht 31 inhibitor peptide and St-Ht 31P control peptide were purchased from Promega (Madison, WI).

Probe functionalization

Silicon nitride probes (Bruker AFM Probes, Camarillo, CA) were first aminated with 2% v/v 3-aminopropyltriethoxysilane (APTES) in acetone for 10 min, then rinsed with deionized (DI) water. Probes were soaked in 0.5% glutaraldehyde (solution in DI water) for 30 min to attach the flexible glutaraldehyde molecule linker, then rinsed again with DI water and incubated in 100 μg/mL αvβ3 solution. After 30 min, the probes were rinsed again with DI water and immersed in BSA for 1 min to block remaining aldehyde groups. Probes were stored in PBS at 4℃ and used in three days.

AFM setup and data recording

Experiments were performed using the MFP-3D-BIO AFM (Asylum Research, Santa Barbara, CA), which was mounted on an inverted microscope (Zeiss Axiovert A1). Through the microscope we were able to position the AFM cantilever on a chosen RBC (Fig. 1a). The nominal spring constant of the applied cantilever was 30 mN/m. RBCs were pretreated with biomedical reagents and incubated at 37℃ (30 min: epinephrine, FSK, KT 5720, Rp-cAMPS, valsartan; 2h: St-Ht 31, St-Ht 31P).

Adhesive interactions were quantified by recording force-distance curves between a αvβ3-functionalized cantilever and ICAM-4 receptors at 32×32 points homogeneously distributed in 1μm^2 area of the RBC membrane. Each curve comprised a complete approach and retraction cycle. An unbinding force was measured as the abrupt drop to zero in the retraction path. The approach and retraction speeds were controlled at 800 nm/s, which gave an effective loading rate of 24 000 pN/s. Furthermore the unbinding forces were plotted as a force map

Copyright 2016 The Organizing Committee for the 2016 Summer Biomechanics, Bioengineering and Biotransport Conference

displaying the spatial distribution of the active ICAM-4 receptors on the RBC surface (Fig. 1b). Therefore, we were able to measure changes in the expression of force maps due to modulation of the density of activated ICAM-4 molecules in the presence of biochemical reagents that interfere with the cAMP-dependent PKA pathway.

Statistical analysis

The unbinding forces between αvβ3 ligands and ICAM-4 receptors were measured using frequency (%) distribution and box-and-whisker plots. In the frequency distribution plots (not shown here), each bin represented the number of unbinding forces within the bin width. We found that the mean value of the unbinding forces did not depend on the employed reagents. Collective frequency (CF, %), denoting the surface density of active ICAM-4 receptors, was defined as the number of curves with nonzero forces divided by the number of all curves in each experimental condition, accumulating all tested cells. The collective frequencies from different groups were reported as mean ± SE and illustrated by box-and-whisker plots then compared using non-parametric statistical test. The results were considered significant if $p<0.05$.

RESULTS

Here we show at the single molecule level that in SS-RBCs the interaction between ICAM-4 and αvβ3 is strongly mediated by cAMP-dependent PKA-signaling pathway (Fig 1c). Stimulation of β2-adrenergic receptors (β2-ARs) activates the Gas proteins, which are associated to G protein-coupled receptor (GPCRs), and stimulate adenylyl cyclase (AC). AC catalyzes the conversion of ATP to cAMP which then activates PKA that binds to A-kinase anchoring proteins (AKAPs) causing activation of ICAM-4 [3]. First, we performed experiments on SS-RBCs without reagents to measure the baseline unbinding frequency (BF) of ICAM-4. Then we used epinephrine, a catecholamine that stimulates the β2-ARs resulted in a significant increase in the average BF from 10.08±0.85% to 21.41±2.27%. Next, we used forskolin (FSK), a strong AC activator, which raised the average BF to 26.55±2.68%. In order to confirm that the modulation was acting via PKA, we used known PKA inhibitors KT 5720 and Rp-cAMPS which respectively decreased the average BFs to 8.94±0.83% and 6.49±0.96%. Furthermore, following treatment of the SS-RBCs with St-Ht31 (a peptide which inhibits binding of PKA to AKAPs), the average BF decreased to 5.33±0.88%. As a negative control, we used St-Ht31P which did not alter the frequency. To investigate whether AKAP inhibition would block ICAM-4 activation, we treated SS-RBCs with St-Ht31 and FSK subsequently. Indeed, we observed that AKAP inhibition prevented forskolin-mediated ICAM-4 and αvβ3 adhesion.

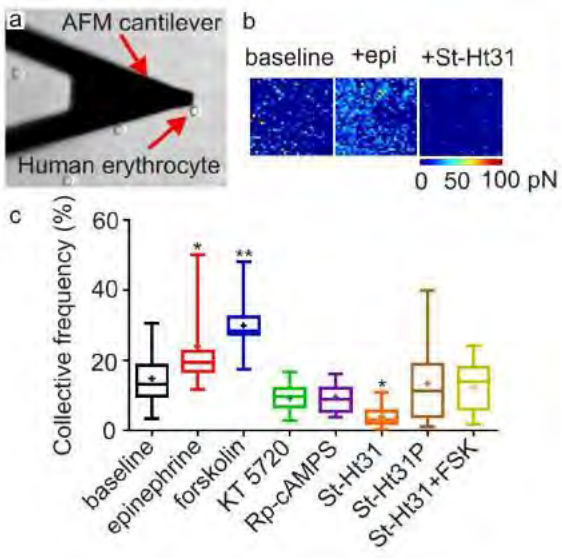

Figure 1: (a) Representative optical microscopy image showing human RBCs and an AFM cantilever. (b) Adhesion force maps. (c) Box-and-whisker plot of the collective frequency of detected ICAM-4 receptors on SS-RBCs after treatment with biochemical reagents modulating the cAMP-dependent PKA pathway. Significance relative to baseline is denoted as * such that $p < 0.05$ and ** such that $p < 0.005$.

DISCUSSION

In this study, we have demonstrated at the single molecule level that the activation of ICAM-4 receptors on SS-RBC membrane is critically dependent on the cAMP-dependent PKA pathway.

ACKNOWLEDGEMENTS

This work is supported by NSF (CMMI-1235025, PHY-1205910), CICATS at UCHC, and AHA (12SDG12050688).

REFERENCES

[1] Hines, P et al, *Blood*, 101: 3281-3287, 2003.
[2] Zennadi, R et al., *Blood*, 119:1217-1227, 2012.
[3] Benovic, J et al., *J Allergy Clin Immunol*, 110: S229-235, 2002.

Copyright 2016 The Organizing Committee for the 2016 Summer Biomechanics, Bioengineering and Biotransport Conference

SB^{3}C2016
Summer Biomechanics, Bioengineering and BIotransport Conference
June 29 –July 2, National Harbor, MD, USA
SB^{3}C2016-74

TRIBOLOGICAL REHYDRATION I: A NEW MECHANISM OF INTERSTITIAL FLUID RECOVERY

Axel C. Moore (1) and David L. Burris (1,2)

(1) Department of Biomedical Engineering
University of Delaware
Newark, DE, USA

(2) Department of Mechanical Engineering
University of Delaware
Newark, DE, USA

INTRODUCTION

It is now generally accepted that the primary lubrication mechanism of articular cartilage is derived from the deformation induced pressurization of interstitial fluid [1]. The pressurized fluid stiffens the matrix, supports load, shields the solid matrix, and reduces friction by ~2 orders of magnitude [2]. However, interstitial pressure also drives fluid from the tissue resulting in the loss of interstitial fluid, pressure, and lubrication over time.

The apparent fact that interstitial pressure is self-defeating has raised concerns that interstitial lubrication cannot possibly contribute to joint lubrication in the long-term. However, *in-vivo* joint-space and contact stress measurements prove that interstitial fluid, pressure, and lubrication are retained indefinitely in healthy joints [3]. Caligaris and Ateshian offered the first direct insight into why joints retain interstitial fluid [4]. They showed that interstitial lubrication can be retained indefinitely if the contact migrates across the cartilage as is the case in natural joints. They proposed that migration helped retain interstitial fluid, pressure, and lubrication by moving before the fluid could respond.

However, this migration theory fails to explain how cartilage recovers fluid following inactive periods of sitting and standing. *In-vivo* studies have shown that interstitial fluid is recovered during activity [5], thus enabling long-term sustainability. It is proposed that cartilage recovers fluid because articulation intermittently exposes the contact to the synovial bath where it can freely imbibe fluid; to our knowledge, this remains the only explanation for cartilage recovery. Here we present the first direct evidence of an alternate mechanism of fluid recovery. Cartilage lost, retained, and recovered interstitial fluid in a rapid, predictable, and controllable manner without ever exposing the contact area to the bath. This study demonstrates a fundamentally new mechanism, which we call tribological rehydration.

METHODS

Cartilage samples, Ø 19 mm osteochondral cores, were taken from the femoral condyles of mature bovine stifles. Immediately after removal, samples were rinsed, soaked in phosphate buffered saline (PBS), and refrigerated for less than 5 days, a time frame that produces no statistically significant changes in properties [6]. The cartilage was placed in stationary contact (SCA [4]) against an optically smooth/flat glass slide in a PBS flooded contact. All friction experiments used a reciprocation track length of 20 mm, speeds of 0, 10, and 60 mm/s, a normal force of 5 N, and a measured contact diameter of 5 ± 0.4 mm. Normal force, friction force, and compression were measured *in-situ*.

RESULTS

The friction coefficient (μ) and compression are plotted versus time in Figure 1. The original 19 mm diameter sample started below μ = 0.01 and equilibrated near μ = 0.02, an observation that appears at odds with interstitial lubrication theory [4]. Due to the sample diameter (19 mm) being much larger than the contact diameter (5 mm), the contact produced a convergent wedge, *i.e.* a means for fluid entrainment and hydrodynamic pressurization. To test this effect, the sample was cut to Ø 12 mm then to Ø 6 mm; the test was repeated on the same sample at each size condition.

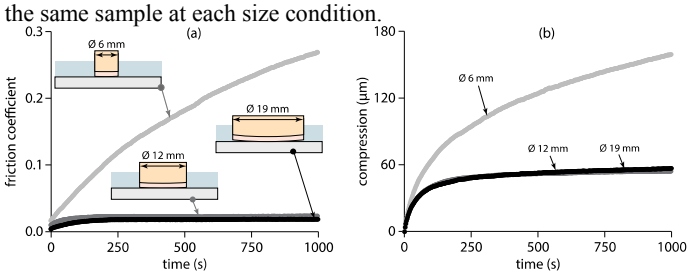

Figure 1. (a) Friction coefficient and (b) compression of a single representative cartilage sample cut to varying size (19, 12, 6 mm diameter) and reciprocated at 60 mm/s. The sample surface was convex with a curvature radius of 21.5 mm in the direction of sliding.

The friction response to SCA sliding only transitioned to high friction when the sample size approached the contact diameter, which eliminated the hydrodynamic convergence zone; this observation appears to suggest that low sustained friction coefficients of larger

Copyright 2016 The Organizing Committee for the 2016 Summer Biomechanics, Bioengineering and Biotransport Conference

sizes can be attributed to hydrodynamic fluid films [7]. However, the compression measurements in Figure 1b are inconsistent with this hypothesis.

When the sample was significantly larger than the contact, cartilage maintained a strain of ~5%, which is consistent with that found in healthy active joints [3]. When the sample size approached the contact size, fluid exudation (compression) persisted and friction increased as expected for the SCA testing configuration [4]. The fact that the effect dissipates when the convergence zone is compromised suggests that hydrodynamic effects arrest or compete with the exudation process.

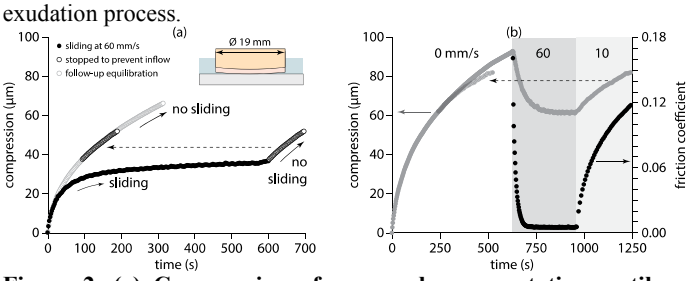

Figure 2. (a) Compression of a second representative cartilage sample versus time in a start-stop SCA test configuration. The sample was loaded to 5 N and slid at 60 mm/s. Reciprocation was stopped at 600 s to provide a period of static equilibration. The sample was then unloaded and soaked for 1 hour to restore interstitial fluid and equilibrated again under static loading at 5 N. (b) Compression and friction versus time for a third representative sample of 19 mm diameter in a stop-start test configuration. Following a period of static equilibration, the sample began sliding at 60 mm/s until reaching a dynamic equilibrium; at which point the sliding speed was reduced to 10 mm/s.

Follow-up experiments were conducted to elucidate the dynamics of the exudation and recovery processes. A second representative 19 mm diameter sample was slid at 60 mm/s for 600 seconds and then stopped; the compression of this sample is shown as a function of time in Figure 2a. In this case, exudation ceased at a compression asymptote of ~40 μm (~5% strain) during sliding, but resumed once sliding stopped. Following re-equilibration by soaking in PBS, the sample was compressed statically at 5 N to obtain the static equilibration response. Comparisons to the original test results produced two noteworthy observations. Firstly, the initial compressive response during sliding was identical to the initial response under static loading, which suggests that the competing effects of hydrodynamic pressurization were negligible initially. Only after ~15 μm of compression did the curves diverge, suggesting that significant deformations are required to produce competitive hydrodynamic pressures (the integration of deformation and hydrodynamics is the defining feature of elastohydrodynamics or EHD). Secondly, the static exudation response following sliding overlays nearly perfectly onto the control equilibration response, suggesting that the exudation response is strain dependent and history independent. Since sliding speed has no theoretical connection to interstitial exudation in the SCA configuration, these results suggest that, at dynamic equilibrium, EHD pressurization during sliding drove fluid into the surface at a rate equal to that of exudation.

Figure 2b illustrates the recovery of interstitial fluid following static loading and gross exudation. In this case, a representative sample was compressed by 90 μm over 600 seconds of static loading. On the first sliding cycle at 60 mm/s the friction coefficient was $\mu = 0.16$. Thereafter the friction coefficient and compression decreased monotonically with continued sliding and eventually reached asymptotes of $\mu \sim 0.005$ and $\delta \sim 65$ μm (~5% strain), respectively.

Following equilibration at 60 mm/s, the sliding speed was reduced to 10 mm/s to test the hypothesis that inflow becomes less competitive with exudation when hydrodynamic pressures decrease at lower speeds. The reduced sliding speed caused an immediate increase in friction (from 0.005 to 0.02) and compression rate; as the overlay in Figure 2b illustrates, the compression rate at 10 mm/s was less than that under static conditions, which indicates that EHD pressurization at lower speeds remains finite but is less competitive with exudation. In general, increased speeds caused thickening and decreased friction, while decreased speeds caused compression and increased friction; this observation is consistent with the hypothesis that exudation from interstitial lubrication is offset by inflow from external EHD pressurization, which is strongly speed dependent [8]. We call the EHD-driven inflow mechanism 'tribological rehydration' and we define the 'convergent-SCA', as a SCA in which there is a clear convergence zone for hydrodynamic pressurization.

DISCUSSION

The results of this study demonstrate that cartilage can recover interstitial fluid and lubrication in a convergent-SCA. This fact cannot be explained by the existing hypothesis, which is that cartilage recovers fluid when joint articulation exposes the compressed area to the bath. This study suggests a new mechanism, tribological rehydration, in which fluid drawn into the contact by sliding is pressurized elastohydrodynamically and subsequently forced into the porous articular surfaces to restore hydration.

Because joints and other migrating contacts possess entrainment zones for hydrodynamic pressurization, it is difficult to determine if migration, bath exposure, or tribological rehydration is primarily responsible for observations of recovery and retention of interstitial fluid during activity. To our knowledge this paper is the first to demonstrate these important physiological phenomena under conditions that isolate a single mechanism, tribological rehydration.

ACKNOWLEDGEMENTS

The authors acknowledge financial support from the NIH (grant P20-RR016458) for the development of the experimental methods described in the paper.

REFERENCES

[1] Ateshian, G. A., 2009, Journal of Biomechanics, 42(9), pp. 1163-1176.
[2] McCutchen, C. W., 1962, Wear, 5, pp. 1-17.
[3] Eckstein, F., et al., 2006, Journal of Anatomy, 208(4), pp. 491-512.
[4] Caligaris, M., et al., 2008, Osteoarthritis and Cartilage, 16(10), pp. 1220-1227.
[5] Ekholm, R., et al., 1951, Acta Societatis Medicorum Upsaliensis, 57(1-2), pp. 39-59.
[6] Moore, A. C., et al., 2015, Osteoarthritis and Cartilage, 23(1), pp. 161-169.
[7] Dowson, D., 1967, Proc. IMechE, 181, pp. 45-54.
[8] Hamrock, B. J., et al., 1978, Journal of Lubrication Technology-Transactions of the Asme, 100(2), pp. 236-245.

Copyright 2016 The Organizing Committee for the 2016 Summer Biomechanics, Bioengineering and Biotransport Conference

SB^{3}C2016
Summer Biomechanics, Bioengineering and Biotransport Conference
June 29 –July 2, National Harbor, MD, USA
SB^{3}C2016-75

EFFECTS OF PROXIMAL TIBIA ANTERIOR CLOSING WEDGE OSTEOTOMY ON ACL FORCE AND KNEE KINEMATICS

Kent T. Yamaguchi (1), Daniel V. Boguszewski(1), Edward C. Cheung (1), Justin Mathew (1), Keith L. Markolf (1), David R. McAllister (1), Frank A. Petrigliano (1)

(1) Department of Orthopaedic Surgery
University of California Los Angeles
Los Angeles, CA, USA

INTRODUCTION

Rupture of the anterior cruciate ligament (ACL) is one of the most common ligamentous injuries of the knee. Although many patients have a good outcome after ACL reconstruction, there are a number of individuals that experience continued instability secondary to a failed or stretched-out graft. Some individuals go on to have multiple failed ACL revision reconstructions. While effect of tunnel placement, graft selection, and fixation technique have been evaluated relating to a successful ACL reconstruction, there is a lack of basic science research evaluating the effect of changing the anatomy of the knee on ACL reconstruction surgery. There is increasing evidence that the posterior tibial slope (PTS) of the tibial plateau, and in particular PTS differences between the medial and lateral compartments, may play a role in ACL injury [1-3]. In theory, contact force on a steeper PTS would translate the tibia anteriorly, and an increased slope of the lateral plateau would cause additional anterior subluxation of the lateral plateau, producing an internal tibial rotation. Thus, some clinicians have begun treating select ACL revision reconstruction cases with a PTS-reducing osteotomy with the hope of reducing force acting on the ACL graft [4-6]. While it is known that anterior tibial translation and internal tibial rotation increase ACL force [7], there remain questions as to the biomechanical role of the PTS on knee kinematics and the resulting force generated in the ACL. To date there have been no biomechanical studies evaluating the effect of such a procedure on the human knee. Our hypothesis was that a proximal tibia closing wedge osteotomy to reduce the PTS will alter tibiofemoral kinematics and reduce ACL force.

METHODS

Seven fresh-frozen knee specimens with a mean age of 23 years (range: 18-34 years) were used for this study. For all knees, the distal tibia and proximal femur were potted in PMMA. Using an established technique [7], the femoral attachment of the ACL was mechanically isolated and attached to a calibrated load cell in order to directly measure resultant ACL force. Using a 6-DOF robot, each knee was flexed from 0°-50° while maintaining 200N of tibiofemoral compression force (TFC) in combination with the following forces and/or torques: 1) 45N anterior tibial force (AF); 2) 5Nm valgus moment (VM); 3) 2Nm internal torque (IT); and 4) 45N AF + 2 Nm IT + 5Nm VM. After testing each normal knee, a proximal tibia anterior closing wedge osteotomy was performed to decrease the PTS by 10° (Figure 1). The wedge of bone was removed 20mm distal to the tibial plateau. With the posterior cortical bone acting as a hinge, the plateau was lowered (reducing the PTS) and secured with a rigid external fixator. The osteotomized knee was then re-tested for each loading condition. Resultant ACL force and knee kinematics were recorded for each test. Statistical analysis was performed between normal and osteotomized knees with paired t-tests at every 5° of flexion. Significance level was set at $p < 0.05$.

Figure 1. Closing wedge osteotomy procedure: A) remove the wedge of bone, B) closed the tibial plateau, C) secure with an external fixator, and D) add PMMA for additional support.

RESULTS

The osteotomy produced 10° of tibiofemoral hyperextension and

Copyright 2016 The Organizing Committee for the 2016 Summer Biomechanics, Bioengineering and Biotransport Conference

shifted the tibia 6.7mm posteriorly, 2.3° internally, and 3.3° valgus. Compared to the normal knee, in the absence of IT, the osteotomy significantly reduced resultant ACL force ($p<0.04$; Figure 2a-b). However, with the application of IT, ACL force was not reduced (Figure 2c-d). After osteotomy, relative anterior translation was significantly reduced with only an applied VM ($p<0.02$; Figure 3b), while anterior translation increased beyond 35° flexion under the combined loading condition ($p<0.04$; Figure 3d). After osteotomy, relative internal rotation was only significantly reduced with an applied VM ($p<0.02$; Figure 4b), while all other loading conditions showed significant increases in internal rotation ($p<0.05$; Figure 4a,c,d). After osteotomy, relative valgus rotation was not altered with an applied AF (Figure 5a), but showed significant decreases for all other loading conditions ($p<0.03$; Figure 5b-d).

DISCUSSION

Our results show that a PTS-reducing osteotomy significantly reduced ACL force under TFC when combined with AF or VM. However, we found no significant differences in ACL force under all conditions when IT was applied. We postulate that these effects are due to the resulting altered kinematics, most notably, the observed increase in internal tibial rotation and decrease in valgus rotation. Though we found that the PTS-reducing osteotomy is effective reducing force in the ACL in the absence of internal torque, the osteotomy shows little benefit under combined loading conditions simulating forces known to increase ACL injury risk. In summary, while a PTS-reducing osteotomy may reduce force across an ACL graft during non-strenuous knee motion, its protective effect may be lost during rigorous activity such as athletic knee "cutting" motions.

ACKNOWLEDGEMENTS

The authors thank Lindsey McAllister for her help during the study. This study was supported in part by the H H Lee Surgical Research Program. Specimens for this study were obtained from the Musculoskeletal Transplant Foundation.

REFERENCES

[1] Brandon, ML et al., *Arthroscopy*, 22(8):894-9, 2006; [2] Giffin, JR et al., *Am J Sports Med*, 32(2):376-82, 2004; [3] McLean, SG et al., *Clin Biomech*, 25(8):781-8, 2010; [4] Dejour, D et al., *Rev Chir Orthop*, 84:28-9, 1998; [5] Sonnery-Cottet, B et al., *Am J Sports Med*, 42(8):1873-80, 2014; [6] Dejour, D et al., *Knee Surg Sports Traumatol Arthrosc*, 23(10):2846-52, 2015; [7] Markolf, KL et al., *J Bone Joint Surg Am*, 72(4):557-67, 1990.

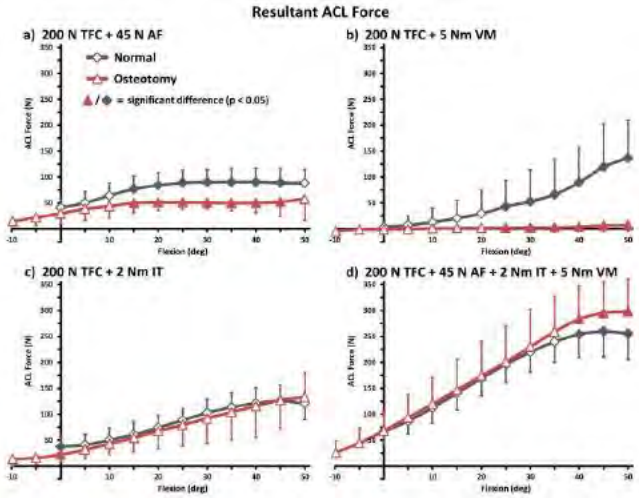

Figure 2: Resultant ACL force (mean ± SD) before and after PTS-reducing osteotomy.

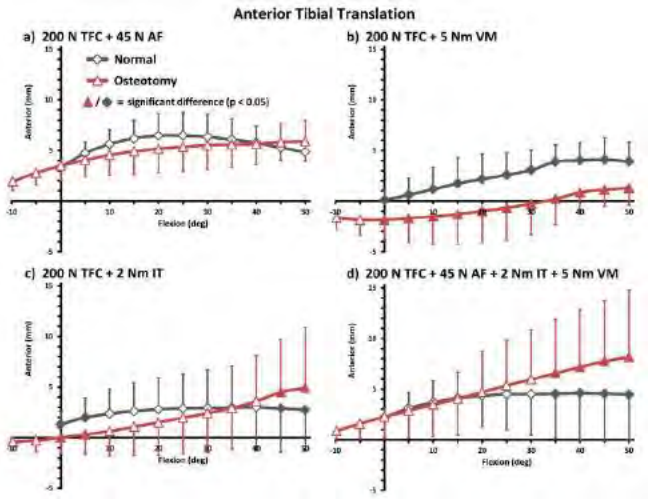

Figure 3: Anterior tibial translation (mean ± SD) before and after PTS-reducing osteotomy.

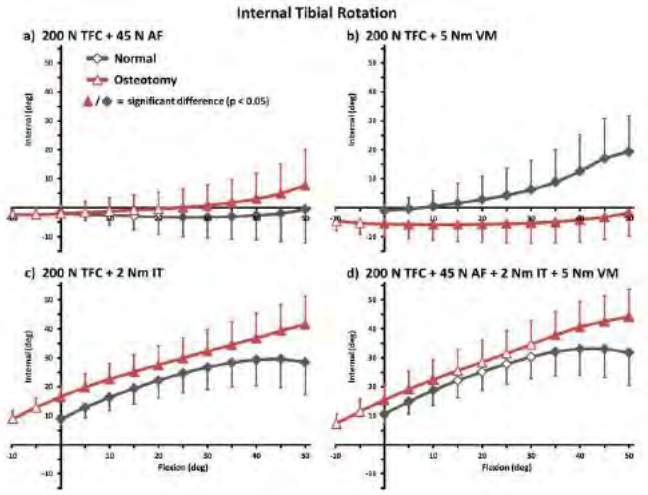

Figure 4: Internal tibial rotation (mean ± SD) before and after PTS-reducing osteotomy.

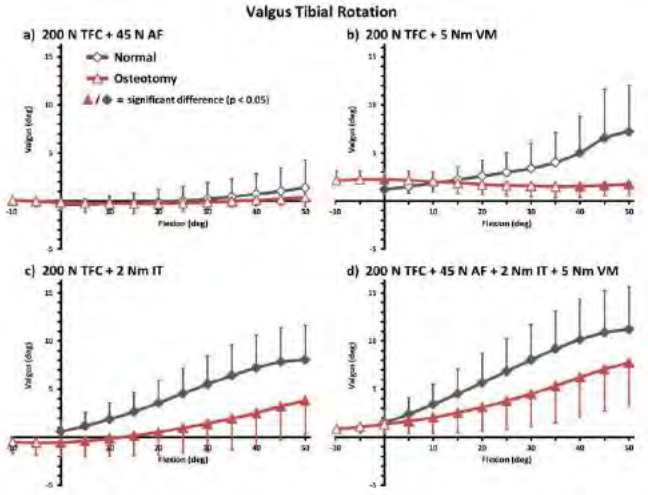

Figure 5: Valgus tibial rotation (mean ± SD) before and after PTS-reducing osteotomy.

Copyright 2016 The Organizing Committee for the 2016 Summer Biomechanics, Bioengineering and Biotransport Conference

SB^{3}C2016
Summer Biomechanics, Bioengineering and Biotransport Conference
June 29 –July 2, National Harbor, MD, USA
SB^{3}C2016-76

A TESTING PROTOCOL FOR EVALUATING AND CLASSIFYING SPINAL ORTHOSES

Denis J. DiAngelo (1), John C. Simmons (1), Daniel M. Wido (1)

(1) Department of Orthopaedic Surgery and Biomedical Engineering
University of Tennessee Health Science Center
Memphis, TN, USA

INTRODUCTION

Back braces are used to treat a variety of spine-related problems (e.g., disc degeneration, spinal stenosis, weakness with aging, injury and scoliosis). Due to the substantial differences between these conditions and the individual needs of each patient, numerous spinal orthoses have emerged to provide varying degrees of mobility, rigidity, and positional control. However no scientific data or testing methodology exists to determine the structural properties of an orthosis or how well back orthoses work for treating specific disease or injury modalities. The selection process is often random and empirical [1,2]. A mechanical analog of the upper torso and lower spine was developed and integrated into a robotic testing platform to determine the structural properties and load carrying capacities of a commercially available lumbar spine orthosis. The spinal loading mechanics of typical daily living activities were simulated.

METHODS

Human Analog and Spinal Orthosis. A life size upper torso, lumbar spine and pelvic girdle assembly (the human analog) was designed that emulated the mechanical properties of the human spine. The biomimetic lumbar spine consisted of individual components having shape, size and material properties comparable to human lumbar spine motion segments. The biomimetic spine was partially concealed by the pelvic girdle assembly during testing. However, the hip/girdle assembly did not make contact with the spine or base load cell (Fig. 1A). A commercially available dynamic stabilizing orthosis (DSO) (Orthotrac Pneumatic Vest^{TM}, Kinesis Medical, Minneapolis MN) was "worn" by the human analog during orthosis testing (Fig. 1B). The orthosis used pneumatic air cylinders to apply a distractive force across the spine and was conceptually designed to provide flexion/extension and lateral stability.

Testing Platform. The human analog was mounted in a multi-axis robotic testing platform (Fig. 1) that included two six-axis load cells mounted to the upper gimbal assembly and lower base plate. The upper load cell (ULC) measured applied forces and moments while the base load cell (BLC), attached to the base of the spine, simultaneously captured forces and moments transferred through the lower spine. The resultant mechanics of the spine (Fx', Fz', BM') in Fig. 2 were analyzed at the L5-Sacrum disc plane (SDP). Differences in the two load cell readings transformed to the SDP represented the portion of the torso forces and bending moments carried by the orthosis.

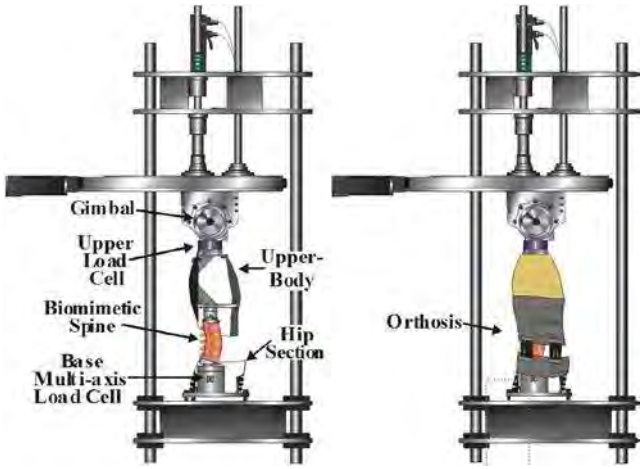

A) **B)**

Figure 1. BioRobotic Testing Platform and Human Analog.

Copyright 2016 The Organizing Committee for the 2016 Summer Biomechanics, Bioengineering and Biotransport Conference

Testing Protocol. The robot was programmed to actuate the human analog through ranges of physiologic flexion and extension under upper torso loading conditions. The following postural conditions were simulated: vertical orientation, initiation of motion (up to 5deg) and extended ranges of motion (10deg extension through 28deg flexion). The applied loading conditions simulated upper torso weight, i.e., up to 400N vertical compression, 20Nm flexion, and 10Nm extension. Measurements of the loads acting at the lower lumbar spine (compression, shear, and rotational moments) were used to determine the biomechanical function of the orthoses including its load-sharing and structural stiffness properties. The pneumatic pressure settings of the orthosis were increased to accommodate increased torso loads (i.e., 10, 20, 20 and 30 PSI for torso loads of 100, 200, 300, and 400N respectively).

RESULTS

The compressive loads acting at the SDP for the different torso weights are shown in Table 1. For the applied load conditions of 100 and 200 N (with orthosis pressures of 10 and 20 PSI), the majority of the applied load was carried by the orthosis and transferred to the pelvic girdle assembly. However, for the 300 N torso load with the orthosis pressure held to 20 PSI, 224N of the torso load was carried by the brace (i.e., 75% of the applied load). When the orthosis pressures were increased an additional 10 PSI to 30 PSI and the applied torso load increased to 400 N, the brace loads were 294N or 74% of the applied load.

The bending moment mechanics of the DSO during the initiation of flexion and extension movement is shown in Fig. 3. Throughout extension the majority of the applied bending moment was transferred to the spine. During flexion, the brace moment support progressively increased. The percentage of the applied bending moment carried by the brace at end limits of extension and flexion is provided in Table 2. At 5 degrees of flexion and applied load condition of 300N and 18Nm flexion moment approximately 63% of the flexion moment was supported by the brace. At 3 degrees of extension and applied loads of 300N and 7.1Nm extension moment, 18% of the applied bending moment was support by the brace. The slope of the curve represents the rotational stiffness properties. The flexion stiffness was 1.25Nm/deg and the extensional stiffness was 0.09Nm/deg.

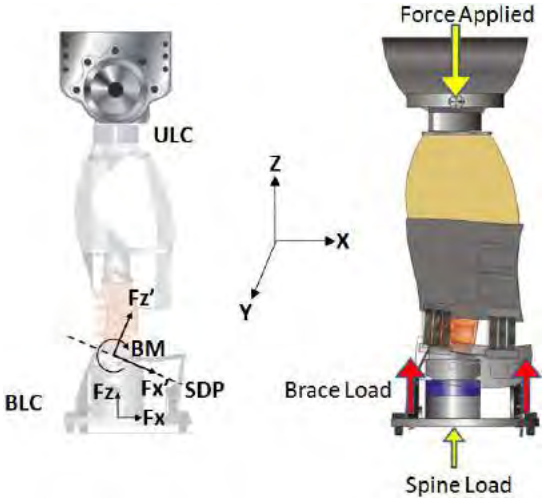

Figure 2. Force Analysis. Applied loads were controlled at ULC. Loads transferred through the lower spine were measured at the BLC. The ULC and BLC forces were transformed to the sacral disc plane and compared.

Table 1: Compressive Load Response of DSO

Applied Load (N)	Brace Load (N)	Brace Effect as Percent of Applied Load (Brace/Applied*100)
100	86	86%
200	206	103%
300	224	75%
400	294	74%

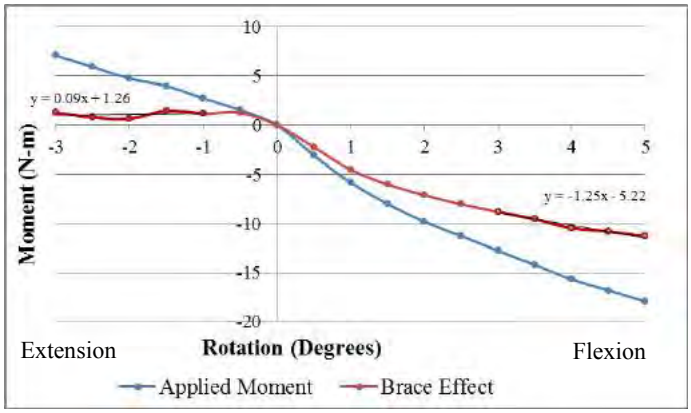

Figure 3. Bending Moment Mechanics During Extension and Flexion Testing for 300N Applied Load.

Table 2: The Brace Effect on Applied Moment for 300N Applied Load

Degrees of Rotation	Applied Moment (Nm)	Brace Effect (Nm)	Brace Effect as Percent of Moment (Brace/Applied*100)
At 3deg Extension	7.1	1.3	18%
At 5deg Flexion	18	11.3	63%

DISCUSSION

For all tests, motion was confined to the sagittal plane and the spinal loading mechanics were analyzed at the L5-S disc plane. The mechanical analog lumbar spine was validated under flexion and compression loading only. During the rotational tests (i.e., 3deg extension and 5deg flexion) only the force components of the gravitational torso mechanics were simulated but not the in vivo spinal bending moment. The applied moment was a function of the biomimetic spine's structural stiffness properties as well as the DSO. In summary, the unique biofidelic testing platform and biomimetic human analogue were able to assess the beneficial and/or adverse clinical function and biomechanical capacity of a spinal orthosis. Outcomes from this study provide the basis for developing a technical standard for evaluating, ranking and classifying lumbar spine orthoses.

ACKNOWLEDGEMENTS

Research supported by the BioRobotics Laboratory in Department of Orthopaedic Surgery and Biomedical Engineering at The University of Tennessee Health Science Center (UTHSC).

REFERENCES

[1] T. M. Gavin, "Preliminary Results of Orthotic Treatment for Chronic Low Back Pain," *Journal of Prosthetics and Orthotics, 1993. Bol. 5 Num 1. Pp. 5-9.*

[2] Orthoses for Osteoporosis. AAOS Atlas of Orthoses and Assistive Devices, 4th Edition. Chapter 11 page 1. Copyright © 2008 Mosby, An Imprint of Elsevier.

Copyright 2016 The Organizing Committee for the 2016 Summer Biomechanics, Bioengineering and Biotransport Conference

SB^{3}C2016
Summer Biomechanics, Bioengineering and Biotransport Conference
June 29 –July 2, National Harbor, MD, USA
SB^{3}C2016-77

ELECTRIC PROPERTIES OF CORTICAL BONE ARE STRONG PREDICTORS OF BONE MECHANICAL PROPERTIES

Mustafa Unal (1), Fatih Cingoz (2), Cevat Bagcioglu (3), Yilmaz Sozer (2), Ozan Akkus (1,4)

(1) Department of Mechanical and Aerospace Engineering
Case Western Reserve University
Cleveland, OH, USA

(2) Department of Electrical and Computer Engineering,
The University of Akron,
Akron, OH, USA

(3) Department of Biomedical Engineering
The University of Akron
Akron, OH, USA

(4) Department of Orthopaedics and Biomedical Engineering
Case Western Reserve University
Cleveland, OH, USA

INTRODUCTION

Skeletal fragility is a major social-health problem affecting the lives of millions of people. Accurate assessment of fracture risk would help timely inception of therapy or help avoid unnecessary treatments. Bone mineral density-based diagnosis cannot assess bone fragility with high accuracy, calling for information on other measures that affect bone strength. During the past two decades, the electrical properties of bone have gained an increasing attention since their measurements may hold potential for the diagnosis of bone quality. Although many earlier studies focused on the electrical properties of cortical bone as a function of moisture level and/or measurement direction of bone [1] to the best of our knowledge, the interrelationship between electrical and mechanical properties of cortical bone was not investigated. Furthermore, the contributions of individual bone composition including unbound water, bound water, organic matrix and mineral to electrical properties of cortical bone are still unclear. In this perspective, it would be valuable to perform a systematic investigation about the interrelationship between electrical and mechanical properties of cortical bone, and the role of bone composition in this interrelationship as a first step toward developing a potential diagnostic method for assessing bone quality. Therefore, this study was intended to investigate associations of electrical properties of cortical bone with mechanical properties and bone composition of cortical bone.

METHODS

This study was planned in three experimental phases. In the first phase, the correlations between electrical (i.e., impedance, conductivity and dielectric constant) and mechanical properties (i.e., toughness, elastic modulus and ultimate strength) of cortical bone (35x3x1.1 mm, N=24) were assessed. In the second phase, the contributions of unbound water, bound water, organic matrix and mineral to electrical properties of bone was investigated. In the third phase, the associations of different bound water compartments (mineral vs. collagen bound) with the electrical properties of cortical bone were assessed. In this way, we sought to assess the interrelationships between electrical and mechanical properties of cortical bone, and the potential role of different water compartments in this interrelationship. Briefly, following biomechanical testing, bone samples were probed by sequential heat treatment process: 1) dehydration at 40 °C for 48 h to remove unbound water, 2) dehydration at 200 ^{o} C for 30 min to evaporate bound water in bone samples, 3) heat treatment at 1000 ^{o} C for 30 min to remove the organic phase. Electrical impedance (at the frequency range of 5 kHz-2 MHz) of bone (7x3x1.1 mm) was immediately measured in wet state and after each step of heat treatment episode to record the change in electrical impedance by a LCR meter and associated text fixture. From the known impedance magnitude (|Z|) and phase angle (θ), the parameter values of the circuit model can be extracted as follows:

$$R = |Z|/\cos\theta \quad (1)$$

$$C = -\sin\theta/(2\pi f|Z|) \quad (2)$$

By using these calculated values, the electrical and dielectric properties of a bone sample can be obtained as follows:

$$\sigma = \frac{1}{R}(l/A) \quad (3)$$

$$\varepsilon' = \frac{C}{\epsilon_o}(A/l) \quad (4)$$

where σ and ϵ' are the electrical conductivity and dielectric constant, respectively, and the ϵ_o is the vacuum permittivity. The l and A are the length and the measured surface area of samples. In parallel with thermal analysis and electrical measurement, the Raman spectra were also collected immediately after each heat treatment episode to

Copyright 2016 The Organizing Committee for the 2016 Summer Biomechanics, Bioengineering and Biotransport Conference

confirm completion of elimination of corresponding bone composition. The contributions of collagen- and mineral-bound water to electrical properties were further investigated by our novel Raman spectroscopy-based method [2]. Electrical parameters obtained after each heat treatment episode were compared using one-way ANOVA followed by Tukey's post-hoc test. Linear regression analyses were performed between electrical properties and mechanical properties of bone and between electrical properties and bound water amount. Statistical significance was set at $p< 0.05$.

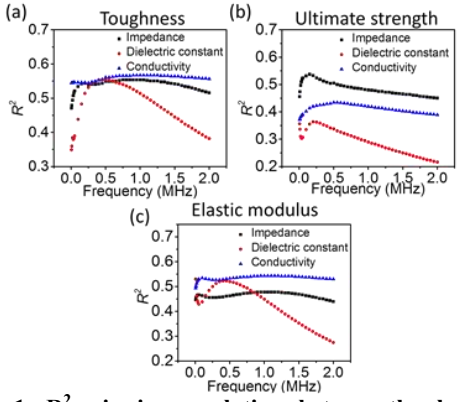

Figure 1: R^2 pairwise correlations between the electrical properties and (a) toughness, (b) ultimate strength and (c) elastic modulus of bone as a function of frequency.

RESULTS

The linear correlations between impedance, conductivity and mechanical properties are less susceptible over the wide range of the frequency while the correlations between dielectric constant and mechanical properties were strongly dependent on the frequency (Fig. 1). Dielectric constant at 0.5 MHz displayed the highest correlation with toughness and elastic modulus (R^2=0.56 and R^2=0.52, respectively) (Fig. 1a and 1c) while the correlation peaked at 0.2 MHz (R^2=0.36) for ultimate strength (Fig. 1b). Bone impedance and conductivity at around 1 MHz displayed the highest correlation with both toughness (R^2=0.56 and R^2=0.57, respectively) (Fig. 1a) and elastic modulus (R^2=0.48 and R^2=0.54, respectively) (Fig.1c) while the correlations of the impedance and conductivity with ultimate strength peaked at 0.2 MHz (R^2=0.54) and at 0.5 MHz (R^2=0. 43), respectively (Fig. 1b). Fig. 2 shows that the average changes in electrical properties were predominantly associated with unbound and bound water in bone. The elimination of organic matrix in bone only affected the conductivity at all frequency ranges (Fig. 2c) and affected the impedance at only low and middle frequency ranges (Fig. 2a). The correlations of specific impedance with collagen- and mineral bound water peaked at 0.75 MHz (R^2=0.45) and at 1.25 MHz (R^2=0.45), respectively (Fig.3a). For dielectric constant, the highest correlation was observed at 0.5 MHz (R^2=0.58), and 0.75 MHz (R^2=0.56) for collagen- and mineral-bound water, respectively (Fig. 3b). For conductivity, the highest correlation was observed at 1 MHz (R^2=0.55), and 2 MHz (R^2=0.62) for collagen- and mineral-bound water (Fig. 3c).

DISCUSSION

For the first time in the literature, our results show that electrical properties of cortical bone have strong correlations with the mechanical properties. The highest correlations between electrical and mechanical properties of cortical bone are typically found at the frequencies of 0.2, 0.5 and 1 MHz. At these specific frequencies, our results also indicate that unbound and bound water compartments are the major determinant of the electrical properties. Our findings provide first evidence that collagen- and mineral-bound water may contribute differentially to the electrical properties of bone (Fig.3). For example, mineral-bound water predominantly determines conductivity behavior of cortical bone at high frequencies.

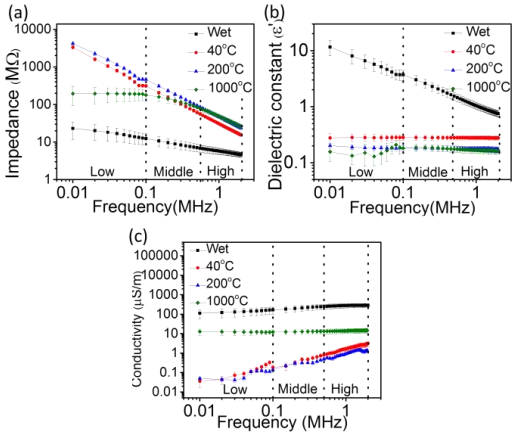

Figure 2: Average changes in (a) impedance, (b) dielectric constant and (c) conductivity of cortical bone samples during sequential heat treatment as a function of frequency at low (≤100 kHz), middle (100-500 kHz) and high (≥500 kHz) frequencies.

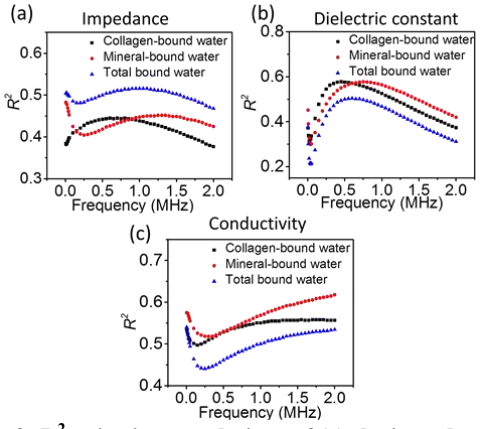

Figure 3: R^2 pairwise correlations of (a) the impedance, (b) dielectric constant and (c) conductivity with the corresponding amount of total bound, collagen- and mineral-bound water in the bone estimated by Raman spectroscopic analysis.

Since water amount of bone is associated with multiple factors, including porosity, mineralization, collagen crosslinks, collagen quality and non-collagenous proteins which are all interrelated [3], this may be elucidation why the associations between electrical and mechanical properties are mainly determined by the amount of unbound and bound water compartments. In conclusion, the significant correlations among electrical and mechanical properties and water compartments suggest that measurement of electrical properties as a tool to assess bone strength. The findings also underline the necessity for developing techniques to measure these electrical properties *in vivo* to improve the current diagnosis of those who may be at risk of bone fracture due to aging and diseases.

ACKNOWLEDGEMENTS

This research is partially supported by think [box] Student Research Fund at CWRU.

REFERENCES

[1] Saha et al., *J Bioelectricity*, 3:347-356, 1984.
[2] Unal et al., *Bone*, 81:315-326, 2015.
[3] Granke et al.,*Calcified Tissue Int*., 97: 292–307, 2015.

Copyright 2016 The Organizing Committee for the 2016 Summer Biomechanics, Bioengineering and Biotransport Conference

SB^{3}C2016
Summer Biomechanics, Bioengineering and Biotransport Conference
June 29 –July 2, National Harbor, MD, USA
SB^{3}C2016-78

MOLECULAR SPECTROSCOPIC IDENTIFICATION OF THE WATER COMPARTMENTS IN CARTILAGE

Mustafa Unal (1), Ozan Akkus (1,2,3)

(1) Department of Mechanical and Aerospace Engineering
Case Western Reserve University
Cleveland, OH, USA

(2) Department of Biomedical Engineering
Case Western Reserve University
Cleveland, OH, USA

(3) Department of Orthopaedics
Case Western Reserve University
Cleveland, OH, USA

INTRODUCTION

Osteoarthritis (OA) is a debilitating musculoskeletal disease characterized by degeneration of articular cartilage and affects the lives of millions of people. Since cartilage has a limited ability for self-repair, it is crucial to detect early stage OA to increase the success of treatment. Therefore, a great amount of effort has been focused on developing non-destructive methods for early detection of OA. The cartilage matrix mainly contains water (70-80 wt. %), type II collagen (15-25 wt. %), and proteoglycan (PG) (5-10 wt. %) [1]. The majority of water in cartilage exists in a mobile-like state (also referred as unbound) as a result of electrostatic equilibrium between water molecules and glycosaminoglycan (GAG) chain(s). The rest of the water is bound to collagen and PG phases of cartilage with various degrees of affinity. Early stage of OA is characterized by a damaged collagen network, loss of PG and an increase in water content by up to 10% [2]. Although measurement of water content in the cartilage holds a great potential for early detection of OA, there is a dearth of nondestructive methods for studying the hydration status of cartilage. MRI-based methods are among the few available non-destructive methods for analyzing water content in cartilage; however, the sensitivity of MRI analyses to detect small changes in water content and cartilage matrix in early stages of OA is limited due to the partial-volume averaging effects [2]. Thus, a broader range of methods is needed to infer the hydration status of cartilage. Raman spectroscopy is one of the few nondestructive methods to assess hydration status of cartilage with the unique advantages on determination of type of water with various energy levels and the moiety to which water molecules are bound to [3]. However, to date, OH-related Raman bands of cartilage have not been studied by Raman spectroscopy since the most commercial Raman spectroscopy systems lack sensitivity into the OH-stretch range (3100-3800 cm^{-1}). Recently, we developed a custom designed short-wave infrared (SWIR) Raman spectroscopy system and successfully identified the water fractions of bone with the moiety to which water molecules are attached to [3]. In the present work, for the first time in the literature, Raman OH-stretch band of cartilage was investigated to identify water fractions in cartilage as a first step developing new non-destructive method for early diagnosis of OA.

METHODS

A refined analysis of the water content in biological tissues is challenging with standard Raman systems because of protein related background fluorescence. Furthermore, the CCDs of most commercial Raman systems lack sensitivity in the OH-stretch range since the Raman scattered photons of the OH range shift deeper into the infrared region. Therefore, we built a custom short-wave infrared (SWIR) Raman system to survey the OH-stretch range while accommodating the background fluorescence. Our custom SWIR system involved excitation at 847 nm (Axcel Photonics) at ~40 mW on the sample and signal collection using a shortwave InGaAs IR spectrometer (BaySpec, Inc., CA, USA) optimized for 1000-1400 nm wavenumber range that is suited for OH-stretch vibrations [3]. Bovine articular cartilage plugs (diameter: 4 mm, N=6) were excised from knee joints of freshly slaughtered animals. Since Raman OH stretch band originates from the hydroxyl groups of proteins, water molecules (bound, loosely bound and unbound) and contribution from the NH-stretch of proteins, a sample treatment protocol was developed so as to probe the contributions of different sources to the bands of interest. Water compartments were interrogated by a sequential dehydration process: 1) drying in ambient conditions for 60 min, 2) oven drying at 40° C for 48 h, 3) hydrogen-deuterium (H/D) exchange up to 7 days [3]. Raman spectra were recorded immediately after each treatment. The low energy air- and oven-drying employed in this study is expected to

Copyright 2016 The Organizing Committee for the 2016 Summer Biomechanics, Bioengineering and Biotransport Conference

remove the mobile-like water and have minimal effect on tightly bound water compartments. The long term H/D exchange beyond oven drying provides information on the rate of dissociation of different moieties of bound water through observation of the disappearance of OH-related Raman peaks. The remaining part after H/D exchange is expected to be associated with organic matrix [3]. Bulk water spectra were recorded as another reference. The collected spectra were fitted through second derivative method to identify each peak locations.

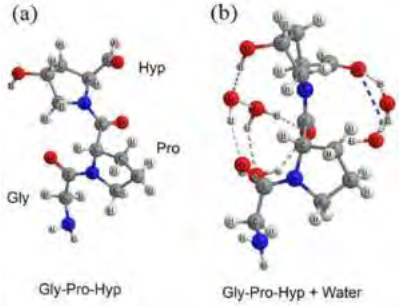

Figure 1: The optimized equilibrium structure of molecular models of (a) Gly-Pro-Hyp amino acid sequence and (b Gly-Pro - Hyp amino acid sequence of collagen with five water molecules.

Raman bands of glycine-proline-hydroxyproline (Gly-Pro-Hyp) amino acid sequence of collagen were generated computationally (Fig. 1) via ChemBio 3D Ultra software. Simulations were run with and without the surrounding water molecules to further verify the assignment of the experimentally observed Raman bands. Overall, the sequential water removal protocol and computational analysis allowed the interpretation of the locations of Raman bands associated with mobile-like, loosely and tightly bound water as well as organic matrix.

RESULTS

The presented spectral data result from the average of three Raman spectra taken at different locations. The spectral range of 2700-3100 cm^{-1} manifests CH-stretch that is predominantly associated with the matrix phase of cartilage whereas the OH-stretch extends across 3100-3800 cm^{-1}. The cartilage spectra were scaled to obtain the same intensity at the CH-stretch peak (Fig. 2a). Therefore, changes in the Raman intensities were normalized by the amount of matrix. Direct comparison of Raman spectra of bulk water with wet and oven-dried cartilage samples indicated the prominence of mobile water related intensity in cartilage which accounted for ~90% of the Raman intensities (Fig. 2a). The results of H/D exchange demonstrated that remaining Raman signal was associated with tightly bound water compartments and organic matrix (~10%) (Fig.3a). Using secondary derivative method and computational analysis together, six peaks in OH-stretch bands of wet cartilage were revealed (Table 1). Among these peaks, ~3630 and 3655 cm^{-1} are solely associated with unbound (mobile-like) water compartments since these peaks were no longer visible in the spectra even after air-drying for 1h (Fig. 2b and Table 1). The peaks centered at ~3200 (the range of 3180-3260 cm^{-1}), 3435 and 3520 cm^{-1} in wet cartilage seem to be the combination of mobile-like, bound water compartments and the OH of matrix proteins (Fig. 2b and 3b-c). More specifically, the peaks at ~3254, 3315, 3330, 3430, 3455, 3470 and 3490 cm^{-1} are associated with different bound water compartments with various energy levels (ranging from loosely to tightly) (Table 1). The peak centered at ~3345 cm^{-1} is associated with NH-stretch band of collagen and ~3450 cm^{-1} is associated with OH group of hydroxyproline, also confirmed by molecular dynamics. The remaining peaks at ~3190 and ~3515 cm^{-1} may be associated with PG matrix since it is the only candidate for these peaks.

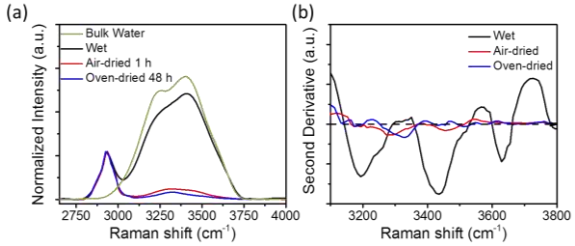

Figure 2: (a) Raman bands of wet and dehydrated samples, (b) second derivative spectra during sequential dehydration.

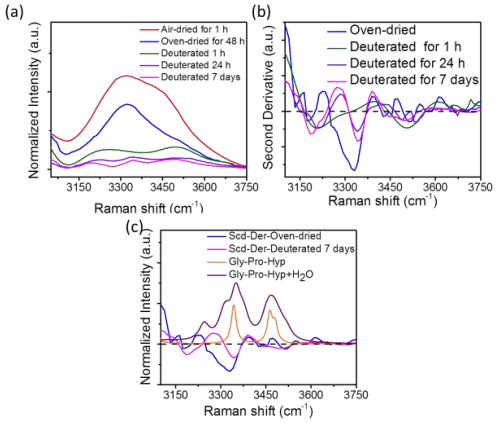

Figure 3: (a) Raman bands of deuterated samples, (b) second derivative spectra as water exchanges with deuterium oxide over time, (c) comparison of computationally obtained Raman spectra with second derivative spectra of oven and deuterated samples.

DISCUSSION

For the first time in the literature, OH-stretch band in cartilage was investigated to identify the water compartments which are mobile-like (removable by prolonged drying at low temperature), and semi-bound and tightly bound (removable by deuterium following prolonged drying) to the matrix of cartilage. It was found that the OH-stretch band in wet cartilage represents mainly mobile-like water molecules (~90%). Identified water compartments in cartilage by Raman spectroscopy in this study collectively indicate that assessment of water content by Raman spectroscopy can be used as a potential diagnostic approach in early OA. Immediate next step in this project will be identifying the associations of these peaks with mechanical behavior of cartilage as well as assessing the variations of these peaks between arthritic and healthy human cartilage.

Table 1: Raman peaks in cartilage

	Wavenumbers (cm^{-1})					
Wet	~3200	~3260	~3435	~3520	~3630	~3655
Air dried	~3180	~3215	~3285	~3345	~3460	
Oven dried	~3180	~3254	~3330	~3430	~3455	~3520
Deuterated 1 h	~3210	~3315	~3470	~3510		
Deuterated 24 h	~3205	~3340	~3490	~3530		
Deuterated 7 days	~3190	~3345	~3450	~3515		

ACKNOWLEDGEMENTS

This research is partially supported by think[box] Research Fund at CWRU.

REFERENCES

[1] Cohen, N.P et al., *J. Orthop. Sports Phys. Ther*. 28:203–215, 1998

[2] Padalkar, M.V et al., *Annals of Biomedical Engineering*, 41, 2426-2436, 2013.

[3] Unal, M et al., *Bone*, 67:228-236, 2014.

Copyright 2016 The Organizing Committee for the 2016 Summer Biomechanics, Bioengineering and Biotransport Conference

SB³C2016
Summer Biomechanics, Bioengineering and Biotransport Conference
June 29 –July 2, National Harbor, MD, USA
SB³C2016-80

BIOMECHANICAL COMPARISON OF YOUTH AND ADULT FOOTBALL HELMETS: STANDARDS TESTING

David W. Sproule and Steven Rowson

Biomedical Engineering and Mechanics
Virginia Tech
Blacksburg, Virginia, USA

INTRODUCTION

Of the estimated 5 million people that participate in organized football each year, approximately 70% are youth players between the ages of 6 and 13 [1]. Currently, youth helmets, which are intended for players younger than 14 years old, undergo an identical impact testing protocol and are held to the same performance criteria as adult helmets in the NOCSAE safety standard. Although NOCSAE is in the process of developing a test standard specific to youth helmets [2], there are many challenges in determining how a youth helmet standard should differ from the adult standard.

Several studies investigating head impact exposure in youth football players of various age groups have demonstrated that the number of head impacts and severity of impact increases with age. Although high severity impacts occur less frequently in younger players, impact magnitudes greater than 80 g were recorded in all age groups [3]. While the front of the helmet is the most commonly impacted location in adult and youth players, youth players experience a greater proportion of impacts to the side of the head, which is likely attributed to weaker necks and relatively heavier helmets [3].

Head mass and size are about 95% of adult size at 3.5 years old and stay relatively constant until around age 10, when the head size gradually increases to 100% around age 16 or 17 [4]. However, children have a larger head-to-body ratio than adults, which is accompanied by reduced neck and shoulder musculature [5]. Other concerns specific to the susceptibility of concussion in youth are an immature CNS, thinner cranial bones, a larger subarachnoid space in which the brain can move, and differences in cerebral blood flow [6].

Developing youth-specific helmets has proven challenging given the differences in head impact exposure, anthropometry, and physiology. Furthermore, no data are currently available on the relative impact performance of youth and adult helmets. This study aims to evaluate the relative impact performance of youth and adult helmets during standards testing, which will provide insight towards the development of a youth-specific standard.

METHODS

A total of 256 tests were conducted to evaluate differences between youth and adult helmets. Helmets were selected on the condition that a specific model was available in both adult and youth versions. This criterion included 8 helmets on the market: Riddell 360, Schutt Air XP Pro, Schutt DNA Pro+, Rawlings NRG Impulse, Riddell Speed, Riddell Speedflex, Schutt Vengeance DCT, and Xenith X2E.

Matched tests were conducted using a NOCSAE style drop test for the youth and adult helmets. This series of drop tests consisted of 4 impact locations (front, side, rear, and top) and 4 drop heights (24, 36, 48, and 60 inches) [7], resulting in 16 tests for each helmet. For each test, a triaxial accelerometer at the center of gravity of the NOCSAE headform was sampled at 20,000 Hz and filtered to SAEJ211 specification (CFC 1000). Peak linear acceleration and Severity Index (SI) were calculated for each impact. Differences between youth and adult models were compared for each impact configuration and evaluated using a paired t-test. Significance was set as $p<0.05$.

RESULTS

Of the 8 helmets tested, 3 were found to have significant differences in peak linear acceleration. These were the Schutt Air XP Pro ($p=0.028$), Schutt DNA Pro+ ($p=0.004$), and the Riddell Speed ($p=0.006$) (Table 1). A negative difference indicates that the youth helmet had a lower peak acceleration than the matched adult helmet. In each of the significant cases, the youth helmets performed better.

Copyright 2016 The Organizing Committee for the 2016 Summer Biomechanics, Bioengineering and Biotransport Conference

Table 1: Average difference ± standard deviation for linear acceleration and Severity Index. Peak linear acceleration and Severity Index were significantly lower for the Schutt DNA Pro+. Peak linear acceleration was also significantly lower for the Riddell Speed and Schutt Air XP Pro.

Model	Linear Acceleration Difference (g)	P-value	Severity Index Difference	P-value
360	0 ± 6	0.901	0 ± 21	0.932
Speed	-4 ± 5	0.006*	-8 ± 18	0.077
Speedflex	-1 ± 5	0.625	-2 ± 13	0.499
Air XP	-4 ± 6	0.028*	-12 ± 28	0.119
DNA	-7 ± 8	0.004*	24 ± 18	<0.001*
Vengeance	-1 ± 13	0.769	11 ± 45	0.329
Impulse	-2 ± 6	0.262	-11 ± 41	0.317
X2E	0 ± 3	0.781	4 ± 10	0.116

In terms of Severity Index, youth and adult versions were only significantly different for the Schutt DNA Pro+ (p=<.001) (Table 1). The maximum observed Severity Index values were 518 for the youth helmet and 618 for the adult helmet. Both peak values occurred at the top location in the Rawlings NRG Impulse from the 60 in. drop height.

Adult helmets generally performed better in rear impacts, and youth helmets better in the top, side, and front locations. Higher drop heights were associated with larger differences (Figure 1).

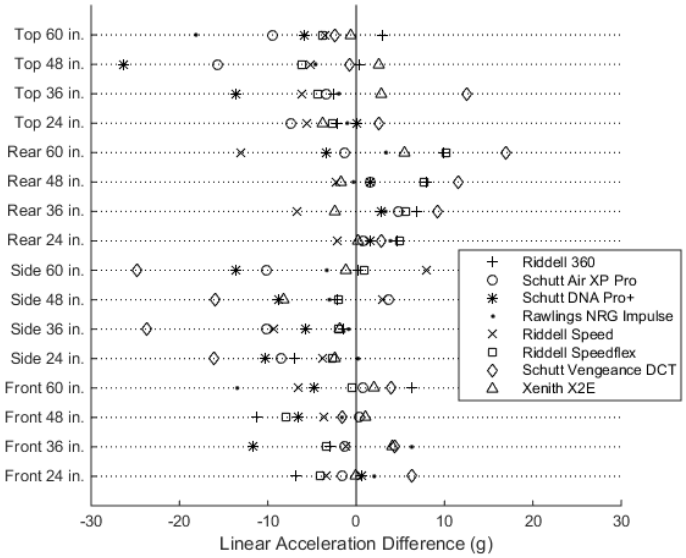

Figure 1: Differences for each test scenario for each helmet model. Points to the left of zero indicate better performance by the youth helmet and points to the right indicate better performance by the adult helmet. Individual differences between youth and adult helmet varied by impact location and drop height.

DISCUSSION

Although 3 helmet models produced significant differences, it is important to put these differences in context of injury risk. For example, the average difference seen in the Schutt DNA Pro+ would relate to less than a 5% reduction in concussion risk in adults [7]. Overall, helmet performance for youth and adult helmets were very similar. While individual differences varied by impact location and drop height, average differences were low, with standard deviations overlapping no difference.

All adult helmets tested had a polycarbonate plastic shell and all youth helmets had an acrylonitrile butadiene styrene (ABS) plastic shell, with the exception of the Rawlings NRG Impulse, which utilizes polycarbonate for both youth and adult models. Generally, the youth helmets performed slightly better in all tests, which is likely attributed to the alternate shell material. The ABS plastic used in youth helmets is a cheaper and lighter material, however it has decreased durability. This is recognized by helmet companies as the warranties offered for youth helmets are typically shorter than warranties for adult helmets. Since both youth and adult helmets performed similarly, the benefit of an adult helmet is a more durable shell, and the advantage of the youth helmet is that it is about 5% lighter (excluding facemask) due to the shell material.

In NOCSAE's draft of proposed youth standards, more tests are suggested at each location. Additionally, the 4.88 m/s (48 in.) impact has a lower threshold of 600 SI along with the 1200 SI threshold for all tests. A mass limit of 1.3 kg, including all accessories, is also proposed for this standard [2]. Currently, all of the youth football helmets that were tested would meet the impact criteria. However, all would fail the 1.3 kg mass limit. For the youth helmets in this study the average mass was 1.3 kg without a facemask, and 1.7 kg including a facemask.

This study has several limitations. The first of which is that only one sample was used for each helmet. Secondly, rotational acceleration, known to contribute to concussion risk, was not evaluated [1]. Third, it is still unknown which impacts are the most important. Future studies should use both on-field head impact data and laboratory tests to better inform standards testing.

This study quantified the relative performance of matched youth and adult football helmets using methods similar to the NOCSAE certification process. These data have direct applications to future youth specific football helmet standards.

ACKNOWLEDGEMENTS

The authors gratefully acknowledge the National Institutes of Health (National Institute of Neurological Disorders and Stroke) R01NS094410-02 for sponsoring this work.

REFERENCES

[1] Daniel, R.W., J Biomech Eng, 2014. 136(9):094501, 2014.
[2] NOCSAE, *DRAFT-Standard Perfomance Specification for Newly Manufactured Youth Football Helmets.* 2011.
[3] Young, T.J., et al.,. *Clin J Sport Med*, 24:416-421 ,2014
[4] Olvey, S.E.,. SAE Technical Paper Series, 2006.
[5] Karlin, A.M., American Academy of Physical Medicine and Rehabilitation, 3:S369-S379, 2011.
[6] Graham, R. et al., Sports-Related Concussions in Youth, 2014.
[7] Rowson, S., Ann Biomed Eng, 39(8): 2130-40, 2011.

Copyright 2016 The Organizing Committee for the 2016 Summer Biomechanics, Bioengineering and Biotransport Conference

SB³C2016
Summer Biomechanics, Bioengineering and Biotransport Conference
June 29 –July 2, National Harbor, MD, USA
SB³C2016-81

ENERGY STORING AND POSITIONAL HUMAN TENDONS: MECHANICS AND CHANGES WITH AGEING

Dharmesh Patel (1), Ewa M. Spiesz (1), Chavaunne T. Thorpe (1), Helen L. Birch (2), Graham P. Riley (3), Peter D. Clegg (4), Hazel R.C. Screen (1)

(1) School of Engineering and Materials Science,
Queen Mary University of London,
London, United Kingdom

(2) Institute of Orthopaedics and Musculoskeletal Science,
University College London,
London, United Kingdom,

(3) School of Biological Sciences,
University of East Anglia,
Norwich, United Kingdom

(4) Department of Musculoskeletal Biology,
University of Liverpool,
Liverpool, United Kingdom

INTRODUCTION

The primary function of tendon is to transmit forces from muscle to bone. However, some tendons, such as the human Achilles tendon and equine superficial digital flexor tendon (SDFT) also store and release energy during locomotion, and are consequently known as energy storing tendons. These energy storing tendons have specialised properties but are prone to injury (1,2,3).

Specialised properties of tendons have been most studied in equine tendons. Mechanical properties of equine tendons have shown higher failure strains in the SDFT than in the common digital extensor tendon (CDET; a positional tendon) during *in vitro* testing, indicating specialisation of the tendon to meet its secondary function (4). Subsequent microstructural studies have found that the inter-fascicular matrix (IFM) exhibits lower stiffness in the SDFT than the CDET, and is also better able to withstand cyclic loading, potentially facilitating the additional extension and energy storing capacity of the SDFT, through fascicle sliding and recoil (4,5). In the equine SDFT, ageing leads to stiffening of the IFM, and reduced functionality of the IFM is linked to compromised tendon function (5).

Knowledge of tendon microstructure and the related micro-mechanics is currently limited in human tissues. Human tendons are generally smaller than those in the equine model, but also have different functional roles, potentially leading to differences in the properties and significance of the IFM. This study investigates the mechanical properties of the IFM and fascicular matrix (FM) of three functionally distinct human tendons (Achilles, anterior tibialis, and posterior tibialis), and additionally, explores the effect of ageing on IFM and FM mechanics, and how this influences bulk tendon mechanical behaviour. It is hypothesised that the IFM of the Achilles tendon is more elastic to facilitate energy storage, but this specialisation is lost with ageing.

METHODS

The mechanical properties of three lower leg tendons were compared; the Achilles tendon (an energy storing tendon), the anterior tibialis tendon (a positional tendon), and the posterior tibialis tendon (a positional tendon with a minor energy storing function). All tendons were obtained with ethical approval. Matched samples from each tendon type were compared, and samples categorised into two age groups: middle-aged tendons (46-57 years old; 3 donors) and old-aged tendons (87-94 years old; 4 donors).

FM and IFM samples were prepared from each tendon for mechanical testing. Fascicles of approximately 40mm length were dissected for FM testing and the diameter of each specimen measured using a laser micrometer. The FM specimens were then pre-loaded to 0.02N, pre-conditioned with 10 loading cycles between 0 and 2.5% strain at 1Hz, and then pulled to failure at a strain rate of 5%/second. For IFM testing, fascicle pairs (i.e. two adjoining parallel fascicles) were isolated from the same region of each tendon as used to isolate FM specimens. The opposing ends of the fascicle pairs were dissected such that 10mm of IFM was left intact between the two fascicles, enabling the IFM to be tested in shear by pulling the opposing fascicle ends in a uniaxial manner (4). The IFM specimens were pre-loaded to 0.02N, pre-conditioned with 10 loading cycles between 0 and 0.25mm at 1Hz, and then pulled to failure at a rate of 1mm/second.

RESULTS

FM test data were used to calculate the ultimate tensile strength (UTS), failure strain and max modulus (Table 1), whilst IFM test data

Copyright 2016 The Organizing Committee for the 2016 Summer Biomechanics, Bioengineering and Biotransport Conference

Table 1: Mechanical properties of the FM in three human tendons (data shown as mean ± standard error). The properties of the FM remain similar between tendon types, however ageing significantly affects the Achilles tendon and the posterior tibialis tendon.

FM

	Achilles Tendon		Posterior Tibialis Tendon		Anterior Tibialis Tendon	
Property	Middle-Aged	Old-Aged	Middle-Aged	Old-Aged	Middle-Aged	Old-Aged
UTS (MPa)	27.2 ± 2.8	43.3 ± 3.2 #	26.3 ± 7.2	60.1 ± 6.5 * #	35.2 ± 3.9	38.3 ± 2.5
Failure Strain (%)	14.9 ± 0.6	12.6 ± 0.3 * #	13.5 ± 1.5	15.3 ± 0.7	14.1 ± 0.7	14.4 ± 0.3
Max Modulus (MPa)	332.1 ± 31.4	645.6 ± 48.3 #	402.9 ± 92.3	736.3 ± 62.5 c #	444.2 ± 42.5	511.5 ± 48.1 b
Hysteresis (%)	55.2 ± 2.3	45.7 ± 1.1 * #	58.0 ± 2.3	52.7 ± 1.7	58.2 ± 1.7	55.3 ± 1.1 #
Stress Relaxation (%)	17.8 ± 2.0	15.6 ± 1.9	18.1 ± 2.7	17.9 ± 1.7	19.7 ± 3.5	19.9 ± 1.1

*Key for significant difference (P<0.05): # = between age groups, * = between tendon types, a = compared to Achilles tendon, b = compared to posterior tibialis tendon, and c = compared to anterior tibialis tendon.*

were used to calculate the ultimate tensile force (UTF), extension at failure and max stiffness. Hysteresis and stress or force relaxation were also calculated from the initial 10 cycles for both FM and IFM samples.

The mechanical properties of the FM from middle-aged tendons showed no significant difference between tendon types. Comparing middle-aged and old-aged tendons, the mean UTS significantly increased with ageing in both the Achilles tendon and posterior tibialis tendon, which resulted in a significantly greater mean UTS in the old-aged posterior tibialis compared to both the Achilles and anterior tibialis tendons (Table 1). Ageing also showed a significant increase in the mean max. modulus of the Achilles tendon and posterior tibialis tendon, and a significant reduction in the mean hysteresis of the Achilles tendon and anterior tibialis tendon (Table 1).

Concerning the IFM from middle-aged tendons, no significant differences were observed in the mean failure extension or max. stiffness between tendon types. However, the mean UTF of the Achilles tendon IFM (1.6N) was significantly higher than the posterior tibialis tendon (0.4N) and anterior tibialis tendon (0.8N), while the mean force relaxation of the Achilles tendon IFM (17.0%) was significantly lower than the posterior tibialis tendon (37.4%) and notably lower than the anterior tibialis tendon (28.0%). Ageing was also seen to affect the IFM of the Achilles tendon only, significantly decreasing the mean UTF (figure 1a) and increasing the percentage of force relaxation (figure 1b).

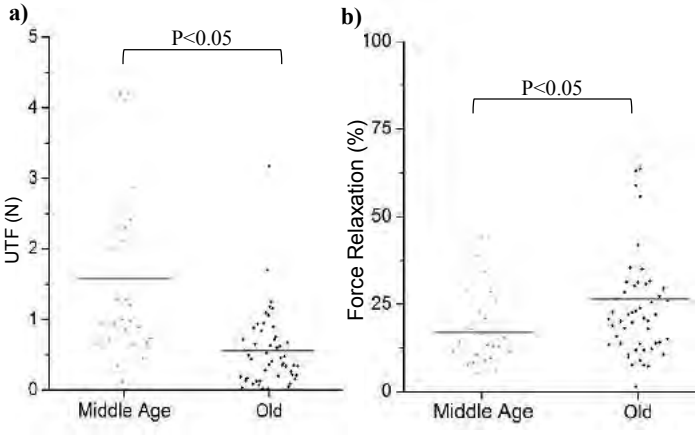

Figure 1: a) Mean UTF and b) mean force relaxation of the Achilles tendon IFM. Dots indicate data points and horizontal lines indicate the mean. Old-aged tendons show significantly decreased UTF (P<0.05), while percentage force relaxation increased (P<0.05).

DISCUSSION

This is the first study to look at microstructure and mechanics across a range of functionally distinct human tendons. The mechanical properties of the FM of all three tendon types were similar, suggesting that the structures which contribute to the energy storing function, and consequently tendon specialisation, are positioned outside the FM. However, it is interesting to note that ageing significantly affected the properties of the FM in the Achilles and posterior tibialis tendon only. Both of these tendons have a degree of energy storage, indicating structural or compositional changes with age in energy storing tendons only, which could lead to the increased injury risks in the elderly.

It has been previously demonstrated that the IFM in equine tendons possesses the ability to recover from cyclic loading, particularly in the energy storing SDFT, where the IFM has a greater capacity for recovery than the positional CDET. Furthermore, ageing reduced elasticity of the IFM in the equine SDFT (4,5). The current data provides further evidence that the IFM has considerable mechanical strength, being able to withstand loads in excess of 1N in the Achilles tendon. The IFM of the Achilles tendon was also found to exhibit higher failure forces and behave more elastically than that of the other tendons; properties which are beneficial for energy storage. Ageing was found to only effect the IFM of the Achilles tendon and not the other tendon types, reducing failure force and increasing viscoelasticity, bringing values closer to those of the posterior and anterior tibialis tendons, suggesting a potential loss of energy storing capabilities.

The SDFT and Achilles tendon are structurally different as, unlike the SDFT, the fascicles in the Achilles tendon are further grouped into higher order bundles. A bundle describes a group of fascicles originating from a distinct triceps surae muscle belly, demarcated by a surrounding matrix known as the inter-bundle matrix (IBM). As the Achilles tendon is shorter than the equine SDFT, it is likely the majority of sliding in the Achilles tendon occurs between the bundles, in the IBM. Further mechanical tests will therefore be performed to ascertain the properties of the IBM and its contribution to the extensibility mechanisms in the Achilles tendon and the effect of ageing. Mechanical tests on quarter tendons will also provide a reference to compare the contribution of FM, IFM and IBM to the overall mechanical properties.

ACKNOWLEDGEMENTS

Funded by Arthritis Research UK (Grant No. 20262).

REFERENCES

[1] Knobloch, K et al., *Foot Ankle Int*, 29:671-6, 2008.
[2] Hess, GW et al., *Foot Ankle Spec*, 3:29-32, 2010.
[3] Kasashima, Y et al., *Equine Vet J*, 36:346-50, 1999.
[4] Thorpe, C et al., *J R Soc Interface*, 9:3108-17, 2012.
[5] Thorpe, C et al., *J Mech Behav Biomed Mater*, 52:85-94, 2015.

Copyright 2016 The Organizing Committee for the 2016 Summer Biomechanics, Bioengineering and Biotransport Conference

SB^{3}C2016
Summer Biomechanics, Bioengineering and Biotransport Conference
June 29 –July 2, National Harbor, MD, USA
SB^{3}C2016-82

THE RESONANCE OF THE THORACIC SPINE UNDER WHOLE BODY VIBRATION IS NON-LINEAR & DEPENDS ON ACCELERATION: AN IN VIVO STUDY USING A RAT MODEL

Timothy P Holsgrove (1), Martha E Zeeman (1), William C Welch (2), Beth A Winkelstein (1,2)

(1) Department of Bioengineering
University of Pennsylvania
Philadelphia, PA, United States

(2) Department of Neurosurgery
University of Pennsylvania
Philadelphia, PA, United States

INTRODUCTION

Low back and neck pain is common in the general population [1], is a leading cause of disability [2], and accounts for 70% of all years lived with disability due to a musculoskeletal disorder [3]. Whole body vibration (WBV) at the resonance of the spine has been suggested to damage the underlying structures of the spine [4]; even a single WBV exposure is sufficient to induce sustained pain and neuroinflammation in a rat model [5]. However, the effect of WBV on pain, injury, degeneration, or its therapeutic effects are not well-defined.

Helicopter pilots are subject to vibrations along the spine's long-axis, and there is evidence suggesting that such vibrations can occur at resonance during routine flights [6]. In fact, the resonant frequency for seated subjects has been defined at 4-5Hz [7-9], with the resonance along the long-axis of the spine in other species being estimated at 4.5Hz in rabbits [10] and 8-9Hz in rats [5]. Those studies exposed subjects to vibrations of either a single root mean squared (RMS) acceleration or a single peak-to-peak (PTP) displacement, and the human spine exhibits a 'softening' non-linear effect with the resonant frequency decreasing as the RMS acceleration increases [8]. Yet, the resonance has not been investigated for sinusoidal vibration, which is commonly used to replicate occupational vibration exposure [5,9,11], nor has it been characterized over the wide range of frequencies that may be encountered during occupational WBV exposures [7].

A rat model of WBV has been established to study the biomechanical, behavioral, and biological effects of vibration [5,11,12]. WBV exposures with a PTP displacement of 5.0mm and frequency of 8Hz were found to produce greater behavioral sensitivity (i.e. pain) than exposures with a PTP displacement of 1.5mm and frequency of 15Hz, despite both exposures having approximately the same RMS acceleration [5]. Accordingly, this study aimed to define the resonant frequency of the rat spine at different PTP displacements in order to understand the mechanical effects of displacement and acceleration on the resonance of the spine.

METHODS

All procedures were IACUC-approved. Two groups of male Holtzman rats (Envigo) were exposed to sinusoidal WBV under isoflurane inhalation anesthesia. Rats were positioned prone on a platform using straps placed behind the shoulders and above the pelvis [5], enabling application of WBV along the long-axis of the spine. The platform was attached to a shaker (K2007E01; The Modal Shop); uniaxial accelerometers (7521A2; 120 Hz; Dytran) were affixed to the platform and also strapped to the thoracic spine [5].

One group of rats (n=8; 353±11g mass) was exposed to vibrations of 1.5mm and 5.0mm PTP displacements to match those used in previous studies [5,11,12], and a second group (n=8; 426±12g mass) was exposed to vibrations of 0.435mm, 0.735mm, and 2.5mm PTP displacements in order to define the resonant frequency over a wider range of exposures. Vibration at each displacement was performed from 3-15Hz, at 1Hz intervals. Due to the power capacity of the shaker, for the 2.5mm and 5.0mm amplitudes, the maximum frequency was limited to 12Hz and 9Hz, respectively. For each displacement, the WBV was performed in increasing frequency. Each frequency was applied for 1min, with a period of approximately 2mins between each exposure to minimize any residual effects of the previous test(s).

Accelerometer data were filtered with a 5th-order Butterworth filter (Matlab2010; Mathworks). The transmissibility was calculated at each frequency for each PTP displacement by dividing the RMS rat acceleration by the RMS platform acceleration [5]. The resonant frequency for each PTP displacement was defined as the frequency with the greatest transmissibility. To assess the effect of resonance on transmissibility, the transmissibility at the resonant frequency was

Copyright 2016 The Organizing Committee for the 2016 Summer Biomechanics, Bioengineering and Biotransport Conference

compared to the transmissibility at all other frequencies using repeated-measures ANOVAs and Bonferroni post-hoc test. A power regression using the RMS acceleration at each resonant frequency was used to determine the relationship between those two parameters.

RESULTS

For all PTP displacements, the transmissibility at 3Hz is consistently below 1.0, which is likely to be due to those accelerations being close to the level of noise detected by the accelerometers. As the frequency increases, the calculated transmissibility is consistent with theoretical transmissibility curves. Increasing the PTP displacement of WBV reduces the resonant frequency (Fig. 1). This reduction in resonant frequency also corresponds to an increase in RMS acceleration (Fig. 2).

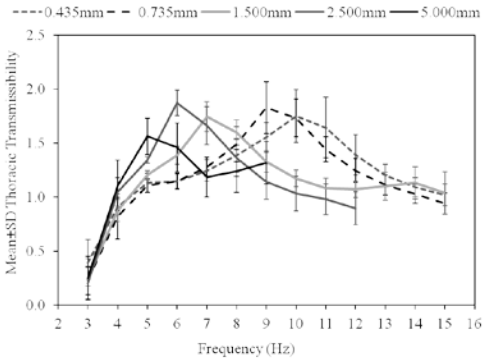

Fig. 1. Thoracic transmissibility, showing that the resonant frequency decreases as the PTP displacement increases.

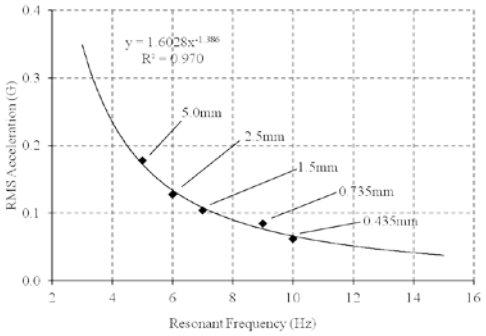

Fig. 2. Power regression of the RMS acceleration at the resonant frequency for each of the PTP displacements.

For PTP displacements of 2.5mm, the transmissibility at resonance is 6Hz (Fig. 1) and is significantly greater than all other frequencies ($p<0.03$). At PTP displacements of 1.5mm and 0.735mm, the transmissibility at resonant frequencies of 7Hz and 9Hz, respectively are significantly greater than at all other frequencies ($p<0.01$) with the exception of one frequency (8Hz for 1.5mm; 10Hz for 0.735mm) adjacent to the resonant frequency ($p>0.85$). This suggests that the resonance is likely between those values. For 5.0mm PTP displacements, the transmissibility at 5Hz is significantly greater ($p<0.031$) than all but 6Hz and 9Hz, suggesting the true resonance is between 5Hz and 6Hz, and that a secondary resonance may exist at approximately 9Hz. The transmissibility curve is more rounded for 0.435mm PTP displacements, and the peak transmissibility at 10Hz is not different from transmissibilities at 8Hz, 9Hz, or 11Hz ($p>0.2$), despite being greater than at all other frequencies ($p<0.013$).

An analysis using power regression of the RMS acceleration in relation to the resonant frequency closely fits the data (Fig. 2), with an R^2 value of 0.970 fit by the equation $y=1.6028x^{-1.386}$.

DISCUSSION

This study demonstrates that resonance can occur over a wide range of frequencies commonly encountered during occupational WBV [9], and that the resonant frequency of the rat spine is non-linear (Figs. 1 & 2). These findings are consistent with the non-linear 'softening' of the human spine that has been reported with random vibrations with increasing RMS acceleration [8]. By using sinusoidal WBVs and determining the resonance over a range of PTP displacements, the current study also provides a means of predicting the resonance for specific vibration signals. Although these findings are specific to the rat, the approach can be extended for other species.

The statistical analysis of transmissibility suggests that at some of the PTP displacements, the true resonance actually exists *between* the discrete frequency exposures used here. Investigating those exposures may further improve the fit of the power curve. Nevertheless, the curve already closely fits the current data (Fig. 2), so the added benefit may be limited. The PTP displacement of 5.0mm led to a secondary maximum transmissibility at 9Hz (Fig. 1); which may be a secondary resonant frequency, as has been previously reported in human subjects in-vivo [8]. However, since this was only evident at one PTP displacement (5.0mm), it also may be due to confounding effects of using the strap to fix the accelerometer to the rat at the highest accelerations used in our study (RMS 0.576G). Also, the different shape of the transmissibility curve for the PTP displacement of 0.435mm may mean that resonance is increasingly difficult to determine as the RMS acceleration decreases; this challenge is consistent with the shape of the power regression (Fig. 2). Together, these findings suggest that for low accelerations, resonance may occur over a wide range of frequencies with very little change in RMS acceleration.

The complex interactions of the parameters of a vibration signal with the tissues of the spine not only complicates the experimental use of WBV, but also may explain the lack of consensus around which conditions may be harmful and which may be beneficial [4]. Low-amplitude, high-frequency vibrations are generally used therapeutically [4,13], but have also been shown to lead to osteoarthritis and disc degeneration in a murine model [13]. Our results provide a link between the RMS acceleration and resonance, which can be used to predict the most detrimental vibrations in terms of acceleration and PTP displacement. In addition, these data may be used to inform further studies of occupational WBV in the rat and other species, as well as in the translation of such work to the human. Those studies will ultimately improve the effectiveness of systems designed to prevent pain and injury, and may also improve the safety of therapeutic vibration devices.

ACKNOWLEDGEMENTS

This work was supported by grants from the Department of Defense (W81XWH-10-2-0140) and the Catherine Sharpe Foundation.

REFERENCES

1. Manchikanti L et al. *Pain Physician,* 12(4):E35-70, 2009. 2. Global Burden of Disease Study. *Lancet,* 386(9995):743-800, 2015. 3. Vos T et al. *Lancet,* 380(9859):2163-96, 2012. 4. Hill TE et al. *J Biomech,* 42(16):2631-5, 2009. 5. Zeeman ME et al. *Clin Orthop Relat Res,* 473(9):2936-47, 2015. 6. De Oliveira CG & Nadal J. *Aviat Space Environ Med*, 76(6):576-80, 2005. 7. Baig HA et al. *J Biomech Eng,* 136(10):101002, 2014. 8. Mansfield NJ & Griffin MJ. *J Biomech,* 33(8):933-41, 2000. 9. Panjabi MM et al. *J Bone Joint Sur Am,* 68(5):695-702, 1986. 10. Weinstein J et al. *Spine,* 13(5):521-5, 1988. 11. Kartha S et al. *Spine,* 39(19):1542-8, 2014. 12. Baig HA et al. *J Orthop Res,* 31(11):1739-44, 2013. 13. McCann MR et al. *Arthritis Rheumatol,* 67(8):2164-75, 2015.

Copyright 2016 The Organizing Committee for the 2016 Summer Biomechanics, Bioengineering and Biotransport Conference

SB³C2016
Summer Biomechanics, Bioengineering and Biotransport Conference
June 29 –July 2, National Harbor, MD, USA
SB³C2016-83

PATIENT-SPECIFIC COMPUTATIONAL FLUID DYNAMICS SIMULATIONS OF THE HUMAN FETAL LEFT VENTRICLE BASED ON 4D CLINICAL ULTRASOUND IMAGING

Changquan Lai (1), Guat Ling Lim (2), Muhammad Jamil (3), Citra Nurfarah Zaini Mattar (2) Arijit Biswas (2), Choon Hwai Yap (3)

(1) Singapore MIT Alliance for Research and Technology, Singapore

(2) Department of Obstetrics and Gynecology, National University Health Systems, Singapore

(3) Department of Biomedical Engineering, National University of Singapore, Singapore

INTRODUCTION

Congenital cardiovascular malformations occurs in 0.6-1.9% of the population, some with devastating consequences [1]. Studies in small animal embryos have shown that abnormal blood flow mechanics may play a role in causing these defects [2]. It is thus important to understand how mechanical forces influence prenatal cardiovascular development, so as to develop suitable treatments. Such an understanding may also enable novel fetal surgeries to be performed to rectify congenital cardiovascular defects.

Currently, although congenital malformations are detectable prenatal, intervention can only be given after birth, at which time, the regenerative ability of the fetus would have been lost, and the defect is complete in its formation. Fetal surgery intervenes at an earlier time point to restore normal blood flow mechanics and coax the fetal body to remodel away from the defect. Fetal heart surgery had already been performed for the Hypoplastic Left Heart Syndrome using minimally invasive techniques [3], and this technique had been rapidly adopted since.

To improve our understanding of human fetal cardiovascular fluid mechanical environment, we developed a technique to perform patient-specific computational fluid dynamics (CFD) simulations of human fetuses, based on 4D clinical ultrasound scans. We applied the technique on 3 human fetuses at 20 weeks of gestation to study the fluid dynamics of their left ventricles.

METHODS

4D ultrasound scans of human fetuses at 20 weeks of gestation was performed at the National University Hospital Systems, Singapore, with appropriate IRB approvals and consent. Ultrasound scans were performed in the Spatio-Temporal Image Correlation (STIC) mode to ensure sufficient temporal resolution. The 4D images over one cardiac cycle were exported as 29 image stacks corresponding to 29 time points and the left ventricle blood space was segmented using an open-source software VMTK.

Ventricular wall motion was quantified using a polar coordinate system (θ,ϕ,r) from the centroid of the left ventricle, by specifying the radial distance from the centroid to the wall:

$$r(\theta,\phi,t) = \alpha(\theta,\phi)\Omega(t) + r_0(\theta,\phi) \qquad (1)$$

where Ω is the characteristic waveform of wall motion over time, α is the amplitude of wall motion, and r_0 is the initial condition. Ω is specified using pulsed-Doppler ultrasound measurements of the inflow at the mitral valve and outflow at the aortic valve, from the literature, while α and r_0 were obtained through the segmentation from our ultrasound images. A 2D polynomial fitting was applied to α for smoothing as well as to obtain a continuous mathematical description of wall position.

	I	II	III
Heart Rate (bpm)	147	147	156
End Diastolic Volume (mm^3)	584	713	886
End Systolic Volume (mm^3)	146	188	150
Ejection Fraction (%)	75.0	73.6	83.1
Diameter of Mitral Inlet (mm)	5.0	3.9	4.6
Diameter of Aortic Outlet (mm)	3.0	4.6	3.1
Mesh Elements ($x10^6$)	1.19	1.33	1.39

Table 1. Characteristics of the 3 fetal hearts and their CFD model.

Dynamic mesh CFD was performed with ANSYS Workbench® (Ansys Inc.), using a user-defined-function for programming wall motion. Boundary conditions were such that the mitral inlet was a zero-pressure inlet during diastole and a wall during systole, while the aortic

Copyright 2016 The Organizing Committee for the 2016 Summer Biomechanics, Bioengineering and Biotransport Conference

outlet was a zero-pressure outlet during systole and a wall during diastole. Non-newtonian fluid following the Carreau viscosity model was specified (η_0=0.0056Pa.s, η_∞=0.0035Pa.s). Simulations were performed for 4 cardiac cycles to remove initial condition artifacts.

RESULTS

Table 1 shows the characteristics of the 3 fetal hearts studied. Figure 1 shows cross-sections of the raw images, their 3D segmentations, and the CFD mesh at various time points. Figure 2 shows the results of the simulations, with vorticity visualized in 3D using the Lambda-2 criteria, and with wall shear stress plotted using surface color contours.

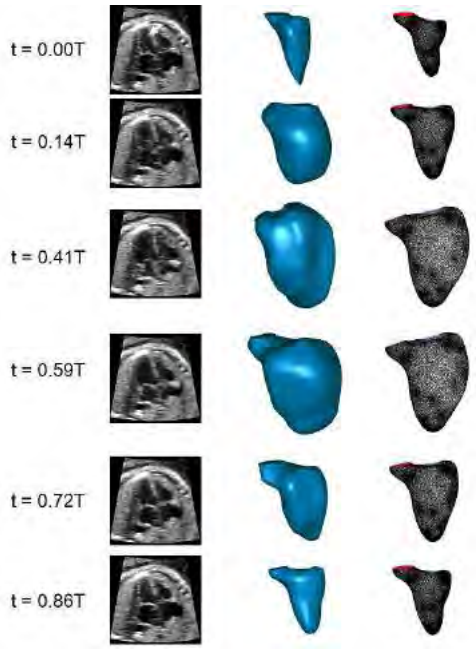

Figure 1. Ultrasonic 4-chamber view (first column), 3D surface reconstruction (second column) and simulated mesh (third column) of a fetal left ventricle over time. The left ventricle is indicated by a white arrow in the ultrasound image at t = 0.00T. T refers to the period of 1 cardiac cycle.

The dominant feature of the fluid dynamics of the 20 weeks human fetal left ventricle is the formation of 2 vortex rings during diastole, corresponding to the E- and A- wave. In the fetus, the A-wave is much stronger than the E-wave, thus resulting in a larger vortex ring during late diastole. The vortex rings were observed to move towards the apex while interacting with the ventricular wall, bringing about complex secondary hairpin vortices around the primary ring, as well as higher shear stresses, in the range of 0.5-5Pa, where the vortex ring approached the vicinity of the wall. At the same time, vorticity is being dissipated away via diffusion and stretching phenomenon. However, since the fetal heart rate is about 2.5 times higher than adult human heart rate, there was insufficient time for the vortex rings to completely dissipate, resulting in remnant vorticity structures being ejected from the heart into the aorta, providing the aortic outflow with some helicity.

DISCUSSION

Our results showed that just like in adult hearts, the human fetal left ventricle also featured dual vortex rings corresponding to the E- and A-wave. A worthy future work would be to experimentally confirm the presence of these vortex rings via clinical measurements. In adult hearts, vortex rings characteristics were hypothesized to contain information on the health of the heart. We hypothesize that the same apply to the fetal hearts as well, where vortex ring features may inform clinicians of abnormalities.

In the human fetal heart, it has been hypothesized that fluid wall shear stresses are important stimuli for proper growth of the cardiac ventricles, and the lack of flow in the left heart has been thought to be the factor causing the Hypoplastic Left Heart Syndrome. Here, our results showed the vortex ring to be the driving force for elevated wall shear stresses on the left ventricular wall, suggesting these ventricular vortex rings are important to developmental health.

There are some limitations to our study, including the absence of mitral valve and papillary muscles in the simulations, and the lack of wall twisting in our ventricular wall motion. Our future work include resolving these limitations, as well as studying diseased fetal hearts.

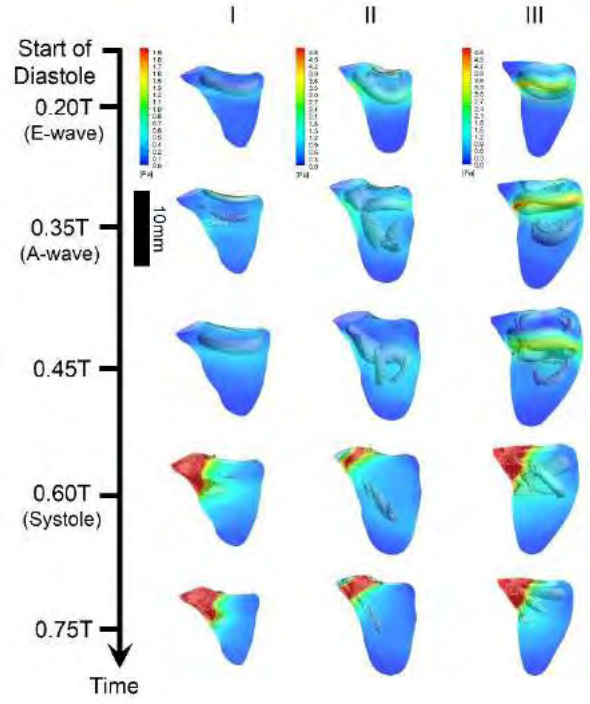

Figure 2. Wall shear stress distribution in the left fetal ventricular wall and the isosurfaces of vortex rings plotted with the lambda-2 criterion. T = duration of 1 cardiac cycle.

CONCLUSION

We developed a technique for patient-specific CFD simulations of the human heart chambers, and for the first time, performed patient-specific CFD of three 20-weeks human fetal left ventricles.

ACKNOWLEDGEMENT

We thank the Singapore Ministry of Health, National Medical Research Council Grant Number NMRC/BNIG/2020/2014 (PI: Yap) for funding.

REFERENCES

[1] Hoffman, JI et al., *J Am Coll Cardiol*, 39(12):1890-900, 2002.
[2] Tobita K et al., *Am J Physiol Heart Circ Physiol*, 279(3):H959-69,2000
[3]Tworetzky W et al., *Am J Cardiol*, 85(10):1230-3, 2000.

Copyright 2016 The Organizing Committee for the 2016 Summer Biomechanics, Bioengineering and Biotransport Conference

SB^{3}C2016
Summer Biomechanics, Bioengineering and Biotransport Conference
June 29 –July 2, National Harbor, MD, USA
SB^{3}C2016-84

TEMPORAL HEALING RESPONSE OF ACHILLES TENDONS IN RODENTS FOLLOWING INJURY DEPENDS ON SURGICAL TREATMENT AND RETURN TO ACTIVITY TIME

Benjamin R. Freedman, Tyler R. Morris, Nabeel S. Salka, Joshua A. Gordon, Adam M. Pardes, Corinne N. Riggin, Courtney A. Nuss, Jennica J. Tucker, Pankti R. Bhatt, George W. Fryhofer, Daniel C. Farber, Louis J. Soslowsky

McKay Orthopaedic Research Laboratory
University of Pennsylvania
Philadelphia, PA, USA

INTRODUCTION

Achilles tendon ruptures affect over 8 in 100,000 people each year in North America [1]. Unfortunately, optimized treatment and rehabilitation protocols throughout the healing process for Achilles tendon ruptures remain unknown [2]. Despite the higher costs and risks for complication, operative treatment has been believed to result in superior function and lower re-rupture rates compared to non-operative treatment [3]. However, recent reviews have suggested that outcomes for Achilles tendon ruptures are not necessarily improved with surgical treatment [3].

The effect of loading environment on Achilles tendon healing has been evaluated only for relatively short time points of healing (~14-21 days [4, 5]). Although early weight bearing has been suggested to be equally effective as immobilization [6] – and, in some cases, beneficial for Achilles tendon healing in humans [7] – the benefit of return to activity (RTA) following various periods of immobilization is unknown.

The objective of this study was to investigate the effects of surgical repair and RTA on joint function and Achilles tendon mechanical, structural, and histological properties after 1, 3, and 6 weeks of injury. We hypothesized that non-repaired tendons and early RTA would result in a superior healing response.

METHODS

Sprague Dawley rats (n=216) received 2 weeks of treadmill exercise training (up to 60 minutes at 10m/min) (IACUC approved) prior to blunt mid-substance transection of the right Achilles tendon and surgical removal of the right central plantaris longus tendon. Animals were then randomized into repaired (Modified Kessler approach) (n=108) or non-repaired (n=108) groups, and all hind limbs were immobilized in plantarflexion. These groups were further divided into animals with RTA after 1- (RTA1), 3- (RTA3), or 6- (RTA6) week cast immobilization (**Figure 1**). Functional evaluation (n=18/group) of passive ankle joint range of motion (ROM) and stiffness for dorsiflexion and plantarflexion was completed using a custom torque cell and accelerometer-based device on anesthetized animals. Quantitative gait assessment was performed prior to surgery and 3, 4, and 6 weeks after surgery.

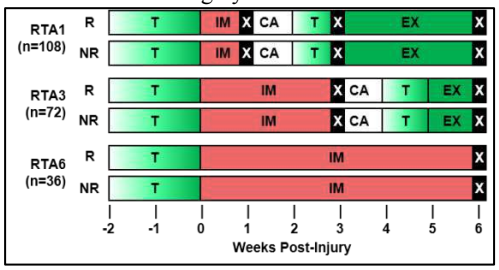

Figure 1: Study Design. Animals were treadmill trained (T) for two weeks. Following injury, animals were divided into repaired (R) and non-repaired (NR) groups, and were returned to activity (RTA) after 1- (RTA1), 3- (RTA3), or 6- (RTA6) weeks of cast immobilization (IM). *CA- cage activity; EX- exercise; X-sacrifice.*

All *ex vivo* assays were performed following sacrifice at 6-weeks post injury. After sacrifice, the Achilles tendon-foot complex was carefully removed *en bloc*, fine dissected, measured for cross sectional area (CSA), and secured in fixtures. Tendons were loaded at 1N in a PBS bath while a series of sagittal B-mode high frequency ultrasound images (HFUS) were acquired using a 40MHz scanner (Vevo 2100, MS550D; VisualSonics) (n=9-11/group). Echogenicity and collagen fiber alignment were evaluated from the HFUS images for the injury

Copyright 2016 The Organizing Committee for the 2016 Summer Biomechanics, Bioengineering and Biotransport Conference

region. Tendons were then mechanically tested and imaged (n=9-11/group) with a protocol consisting of stress relaxation (6% strain), a low-load dynamic frequency sweep (0.1 to 10 Hz), and fatigue testing (~10-75% of ultimate failure load) at 2Hz using a sinusoidal waveform until failure (Instron Electropuls 3000). Percent relaxation, |E*|, tanδ, toe and linear modulus, hysteresis, cycles to failure, and laxity were computed from mechanical and optical data. Cellularity and cell shape were evaluated using hematoxylin- and eosin-stained paraffin sections.

To evaluate the role of RTA on tissue healing 6-weeks post injury for RTA1 and RTA3 groups, 6-week post-injury data were normalized to either 1-week or 3-week post-injury data. Data were analyzed with parametric or non-parametric two-way ANOVAs (treatment and RTA), with post hoc Fisher's tests or Mann Whitney U-tests.

RESULTS

RTA3 groups had decreased dorsiflexion (**Figure 2A**) and plantarflexion ROM compared to RTA1 groups at 6-weeks post injury. These decreases in ROM occurred in concert with increased toe stiffness (not shown). No changes in quantitative ambulatory measures (vertical force (**Figure 2B**), braking force, propulsion force, lateral force, step width, stride length, or velocity) were found.

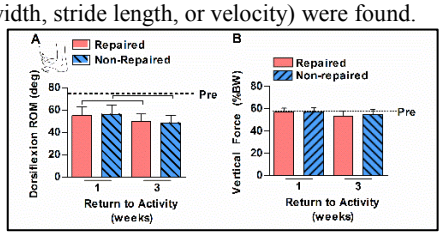

Figure 2: Ankle ROM and Gait. RTA was a significant factor (p<0.05) on dorsiflexion ROM (A), but not vertical force (B) after 6-weeks of healing. Data shown as mean ± SD. *Lines- significant differences (p<0.05). "Pre"- pre-surgery values.*

At 6-weeks post injury, longer periods of immobilization resulted in decreased CSA for all groups, and non-repaired tendons had decreased CSA for all RTA periods (**Figure 3A**). Delayed RTA decreased the number of cycles to failure in non-repaired tendons only (**Figure 3B**). For RTA1 and RTA3 groups, non-repaired tendons withstood a greater number of cycles to failure than repaired tendons. In addition, the linear modulus was elevated in non-repaired RTA1 and RTA3 tendons (**Figure 3C**). Treatment (but not RTA) was a significant factor for toe-modulus, dynamic modulus, hysteresis, and laxity (not shown). On HFUS imaging, delayed RTA was associated with increased fiber organization in repaired tendons. Increased echogenicity (a surrogate measure of matrix density) was observed with delayed RTA for both repaired and non-repaired tendons. Treatment was a significant factor on cell shape, but not cellularity.

Rates of property change following RTA were dependent on RTA time. RTA1 groups affected the rate of change of tissue CSA, toe modulus, fiber alignment, and echogenicity. Compared to RTA6 tendons, RTA1 groups had increased rate of CSA increase (**Figure 4A**), decreased rate of toe-modulus increase for repaired tendons, increased rate of disorganization in repaired tendons, and decreased rate of echogenicity increase (**Figure 4B**). RTA1 groups had no effect on the rates of change for percent relaxation, transition strain, or the linear modulus; however, rates for these properties did differ between treatments. In contrast, RTA3 groups affected the rates of change of only two properties; rates of CSA increase and echogenicity increase were both increased (**Figure 4C,D**). RTA3 groups did not affect the rate of change for percent relaxation, toe modulus, transition strain, fiber alignment, or linear modulus; however, these rates did differ in some cases between treatment groups.

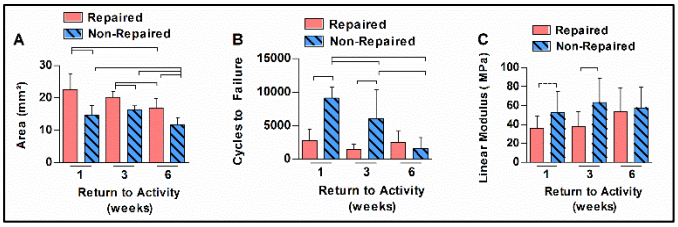

Figure 3: Mechanical Testing. Repair was a significant factor on tendon CSA (A), linear modulus (B), and cycles to failure (C) (p<0.05). RTA was a significant factor on tendon CSA and cycles to failure (A,C) (p<0.05). Data shown as mean ± SD. *Lines- significant differences (p<0.05); Dashed lines- trends (p<0.1).*

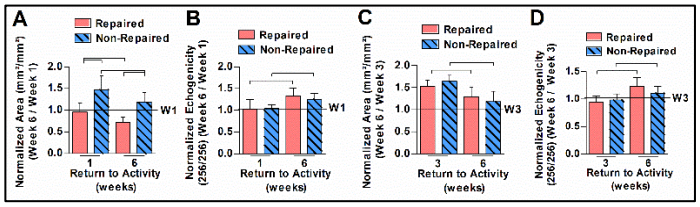

Figure 4: Effect of RTA. RTA1 and RTA3 groups had a significant effect on the rate of change of tendon CSA (A,C), but not the linear modulus (B,D). Data shown as mean ± SD. *Lines- significant differences (p<0.05); Dashed lines- trends (p<0.1).*

DISCUSSION

Achilles tendon healing following a variety of common clinical treatment methods was evaluated 6-weeks post injury in a rat model. Functional benefits of RTA1 groups identified on Achilles tendon healing include elevated range of motion and decreased ankle toe stiffness closer to pre-injury values. Although tendons with delayed RTA had higher echogenicity and alignment compared to other groups, they also had lower CSA, which likely limited the capacity of the more aligned tendon to withstand fatigue loading. Ultrasound evaluation detected changes in healing capacity between groups with different RTA strategies. Surgical treatment was a significant factor for mechanical properties, particularly the number of cycles to failure for RTA1 and RTA3 groups.

This study provides insight into how RTA affects healing. RTA1 groups maximize the effect of RTA with CSA, toe modulus, alignment, and echogenicity all affected. RTA3 also affected the rate of CSA and echogenicity increase, but did not affect tissue alignment or toe modulus. Taken together, these data highlight the capacity to tailor specific mechanical and structural property changes with RTA alone. Future work will evaluate the biological changes that may also be affected by RTA and the long-term effects of these treatment and return to activity protocols.

ACKNOWLEDGEMENTS

We acknowledge financial support from NIH/NIAMS (R01AR064216, P30AR050950, T32AR007132, and TL1TR000138) and the NSF GRFP. We thank Bob Zanes, James Cirone, Kerrie Tiedemann, and Joanna Fried.

REFERENCES

[1] Suchak, A.A. et al., *Foot & Ankle Int*, 11:932-936, 2005.
[2] AAOS, Guideline on Diagnosis of Achilles, 2009.
[3] Soroceanu, A. et al., *JBJS*, 94:2136-2143, 2012.
[4] Andersson, T. et al., *J Appl Physiol*, 113:1398-1402.
[5] Eliasson, P. et al., *J Appl Physiol*, 107:399-407.
[6] McCormack, R. et al., *Br J Sports Med*, 49:1329-1335, 2015.
[7] Schepull, T. et al., *AJSM*, 41:2550-2557, 2013.

Copyright 2016 The Organizing Committee for the 2016 Summer Biomechanics, Bioengineering and Biotransport Conference

SB³C2016
Summer Biomechanics, Bioengineering and Biotransport Conference
June 29 –July 2, National Harbor, MD, USA
SB³C2016-85

COMPUTATIONAL FLUID DYNAMICS OF FETAL RIGHT VENTRICLE BASED ON PATIENT-SPECIFIC ULTRASOUND IMAGES

Hadi Wiputra(1), Changquan Lai(1), R Nivetha(1), Khong Chun Chua(1), Joel Heng(1), Guo Lan(1), Guat Ling Lim (2), Citra Nurfarah Zaini Mattar(2), Arijit Biswas(2), Hwa Liang Leo(1), Choon Hwai Yap(1)

(1) Department of Biomedical Engineering
National University of Singapore
Singapore

(2) Department of Obstetrics and Gynecology
National University Hospital Systems, Singapore
Singapore

INTRODUCTION

Congenital Cardiovascular Malformation (CCM) affects 0.6-1.9% of the population [1] and is the leading cause of birth-defect related death. Many have shown that abnormal hemodynamics condition can affect the development of animal embryonic hearts to cause CCM [2]. It is thus important to understand how blood flow mechanics affects embryonic cardiovascular development. Such an understanding may be used for predicting CCM, and for planning fetal cardiovascular surgery. Fetal heart surgery is fast becoming the norm [3].

We recently developed a new technique to elucidate human fetal heart fluid dynamics, using 4D clinical ultrasound scans, and performing patient-specific Computational Fluid Dynamics (CFD) simulations of these human fetal hearts [4]. In the current study, we applied this technique to 2 human fetal hearts at 20-week gestation to elucidate the fluid mechanics within the right ventricle, and we have also performed energy balance analysis to understand whether the diastolic vortex rings play a role in conserving kinetic energy of flow from one cycle to the next.

In adult hearts, it is known that the right ventricle wall exhibits peristaltic-like contractile wave which moves from near the tricuspid inlet to the pulmonary outlet [5]. We analyzed wall motion from our images and found that such a peristaltic motion also exists in the 20-week human fetal hearts.

METHODS

4D ultrasound images of two 20 weeks old human fetal hearts were obtained using the Voluson 730 ultrasound machine (GE Healthcare Inc.) under STIC (Spatio-Temporal Image Correlation) mode. Images were exported as a 3D stack of images over 29 time points.

The images were first re-sampled along multiple slices from the tricuspid inlet to the pulmonary outlet. The luminal cross-sectional area of the right ventricle was segmented using custom written lazy snapping algorithm over all time points, over all slices. The results were examined for any contraction delay from the ventricular wall near the inlet to that near the outlet to quantify the right ventricular peristalsis.

The right ventricle chambers were segmented in 3D using the open-source program, VMTK, for 3D segmentation, for CFD analysis. The motion of the ventricle wall was first defined in polar coordinates, as the radial distance (r_{model}) between the centroid of the right ventricle to the wall endothelial surface:

$$r_{model}(\theta, \phi, t) = \alpha(\theta, \phi)\Omega(t) + r_0(\theta, \phi) \quad (1)$$

where Ω is the characteristic waveform over time, r_0 is the initial condition of the radius parameter, α is the amplitude of changes in radius over one cycle, θ and ϕ are angle coordinates and t is time.

Ω was formulated using Pulsed-Wave Doppler ultrasound velocity reading at the tricuspid inlet and the pulmonary outlet, from the literature, and was described mathematically via a 1D Fourier transformation of the data points. A mathematical description of α was obtained through a 2D Fourier Transformation of the radius amplitudes measured from the 3D segmentation. These equations were utilized to control dynamic mesh wall motion in the CFD simulations.

CFD simulation is done with FLUENT 16.0 (ANSYS Inc.). The boundary conditions were such that during diastole, the outlet was a zero velocity wall and the inlet was a zero pressure inlet, and that during systole, the outlet was a zero pressure outlet and the inlet was a zero velocity wall. Non-Newtonian fluid following the Carreau model was utilized, and the simulations were performed for 4 complete cardiac cycles to remove initial condition artefacts.

RESULTS

From the quantification of the luminal cross-sectional areas, we found that the maximum cross-sectional area occurred earlier in the cross-sections nearer to the tricuspid inflow, and later in the cross-sections nearer to the pulmonary outflow. The total delay from the inflow region to the outflow region was approximately 73ms and 49ms (17.5% and 12.9% of cardiac cycle) for the 2 hearts (Figure 1). These indicated that the initiation of contraction occurred first in the myocardium nearer to the tricuspid inflow and spread linearly towards myocardium near to the pulmonary outflow, suggesting that the right ventricular peristalsis occurred in fetal hearts just like in adult hearts.

Figure 2 shows the results of wall motion modeling for use in CFD. Results showed a good match with the 3D reconstruction from the

Copyright 2016 The Organizing Committee for the 2016 Summer Biomechanics, Bioengineering and Biotransport Conference

ultrasound images.

Figure 3 shows the results of the simulations, in terms of the spatial pressure variations and wall shear stresses on the walls of the fetal right ventricle, and the vortex dynamics within the ventricle.

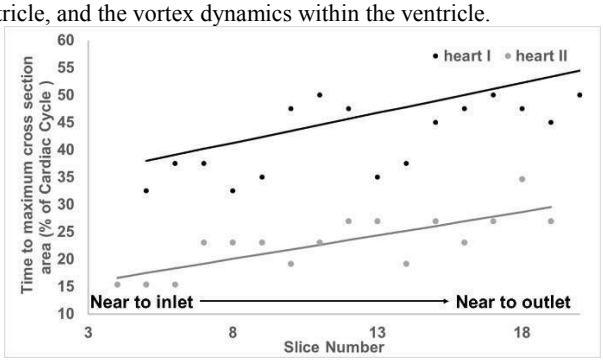

Figure 1: Time maximum luminal cross-sectional area at different cross-section slices from the tricuspid inlet to the pulmonary outlet shows a linear trend, showing that contraction occurred in a "peristaltic" wave.

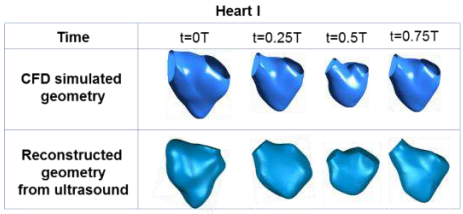

Figure 2: Ventricle wall motion programmed in CFD matches segmentations from ultrasound images well.

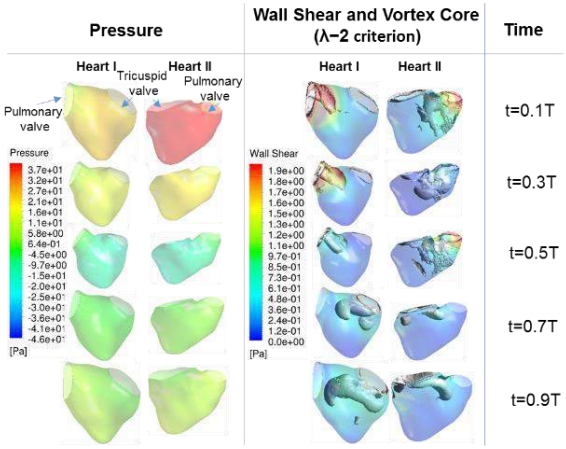

Figure 3: Results of the CFD simulation in the 20 weeks fetal right ventricle. The wall pressures, wall and the vortex dynamics in the ventricle are illustrated at various time points in the cardiac cycle.

The human fetal ventricular fluid dynamics appeared to be dominated by the formation of two vortex rings during diastole, corresponding to the E- and the A-wave. These vortex rings carried a downward momentum towards to the apex. In the fetus, the A-wave is much stronger than the E-wave, unlike in adults. As a result, the A-wave vortex was larger and had higher momentum than the E-wave vortex. Consequently, the second vortex caught up with first vortex and combined into a single vortex. Furthermore, the vortices do not dissipate fully at the end of diastole, and appeared to conserve kinetic energy of flow into the following systole. The vortex structures persist and were ejected through the pulmonary valve during systole, giving the pulmonary outflow a helical flow pattern.

It was also observed that the location of high wall shear stress coincides with the location of high vorticity, as the vortices generated velocity tangential to the heart wall, which led to elevated wall shear stresses (0.7-1.2 Pa). During systole, fast moving outflow through the pulmonary valve also created high wall shear stresses (1.5-2.9 Pa) in the outflow tract.

Figure 4 shows our quantification of kinetic energy (KE) of right ventricular flow. Elevations of KE was observed during systolic outflow and during both the E- and A-wave of diastolic inflow. The results showed that an average of 24% of the peak kinetic energy from diastole is transferred to the subsequent systole.

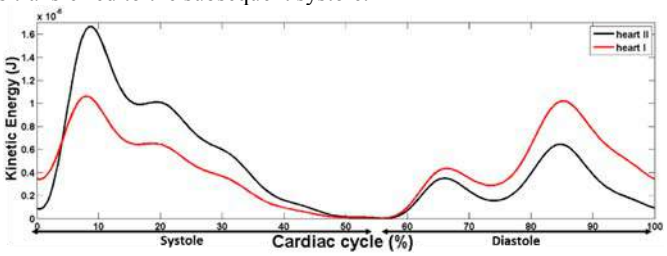

Figure 4: Kinetic energy within the right ventricle chamber at different time points.

DISCUSSION

Our studies have revealed that right ventricular peristalsis occurs in the human fetal heart, just like in adult hearts. We hypothesize that this peristaltic motion, which squeezes on the blood at the inlet first and outlet later, provides higher efficiency in draining blood from the ventricle during systole. We are currently investigating this notion via CFD simulations.

For the first time, we performed patient-specific CFD simulations of the human fetal right ventricle based on 4D clinical ultrasound imaging. Our simulations revealed interesting fluid dynamics in the human fetal right ventricle, where two independent vortex rings were observed to merge over the course of diastole. We hypothesize that the characteristics of these vortices can be used as markers for heart diseases, like that proposed for adult hearts.

Many studies have demonstrated that fluid forces can affect the development of embryo in both animals [2] and human [3]. Understanding the fluid forces, such as pressures and wall shear stresses, imposed onto the human ventricular walls may be important to understanding the pathway at which fluid forces influences development. Interestingly, our results showed that the ventricular vortices were driving forces behind the elevation of shear stresses during diastole. It is thus important to further study their features.

Additionally, it has been hypothesized that ventricular vortices have the function of preserving energy from diastolic inflow for the subsequent systolic outflow, as an evolutionary trait to reduce energy expenditure of the heart function. In our study we observe that a significant part (24%) of the kinetic energy after diastole is carried over to systole, corroborating with this energy conservation hypothesis.

ACKNOWLEDGEMENTS

We thank the Singapore Ministry of Health, National Medical Research Council Grant Number NMRC/BNIG/2020/2014 (PI: Yap) for funding.

REFERENCES

[1] Hoffman, J.I et al., *J. Am Coll Cardiol*, 39(12):1890-900, 2002.
[2] Yang, Q., et al., *Birth Defects Res A Clin Mol Tetratol,* 76(10):706-713, 2006.
[3] Tworetzky, W., et al., *Circ*, 110(15):2125-31, 2004.
[4] Lai, C.Q. et al., *Biomech Model Mechanobiol*, pp.1-14, 2015.
[5]Geva, Tal, et al., *Circ*, 98(4):339-345, 1998.

Copyright 2016 The Organizing Committee for the 2016 Summer Biomechanics, Bioengineering and Biotransport Conference

SB³C2016
Summer Biomechanics, Bioengineering and Biotransport Conference
June 29 –July 2, National Harbor, MD, USA
SB³C2016-86

IMPORTANCE OF INCLUDING PAPILLARY MUSCLES AND TRABECULAE IN CARDIAC FLOW SIMULATIONS

Jonas Lantz (1,2), Lilian Henriksson (2), Anders Persson (1,2), Matts Karlsson (2,3), Tino Ebbers (1,2)

(1) Department of Medical and Health Sciences
Linköping University
Linköping, Sweden

(2) Center for Medical Image Science and Visualization (CMIV)
Linköping University
Linköping, Sweden

(3) Department of Management and Engineering
Linköping University
Linköping, Sweden

INTRODUCTION

The blood flow in the left ventricle (LV) is normally very complex, with intricate flow patterns on both small and large scales. The flow in the LV is driven by the myocardial motion and strongly interacts with valves, papillary muscles and also the protruding surfaces, trabeculae, which constitute parts of the innermost surface in the LV. Computed tomography (CT) is able to provide information about the heart and coronary arteries with geometrical details on sub-millimeter levels. While CT is unable to measure flow, the high-resolution geometry can instead be used in numerical models to compute the flow. Such models often simplify the endocardial surface, and papillary muscles and trabeculae have often been neglected.

The overall goal of this study was to develop a novel and efficient computational model for computing hemodynamics of physiologically realistic hearts. The flow was computed in the left atrium, ventricle, and parts of the ascending aorta, and the model included patient-specific wall motion, valves, trabeculae, and papillary muscles. To investigate the importance of computing the flow in a realistic heart geometry, a comparison with a smoothed geometry, resembling models often found in literature, was performed.

METHODS

Coronary CT angiography was performed on a 76 year old male with a dilated left ventricle. No significant stenoses were present in the coronary arteries and left ventricular function was considered to be normal. Image acquisition was performed using a third generation dual source CT (Siemens SOMATOM Force, Siemens Medical Solutions, Forcheim, Germany). In-plane image resolution was 512x512 pixels and the reconstructed resolution was 0.35x0.35x0.25 mm^3 and 20 time frames per cardiac cycle. From the 4D CT data, a map of the patient-specific wall motion was obtained through a non-parametric diffeomorphic image registration algorithm [1]. Approximately 500 000 vertices were located on the model wall and a one-to-one vertex correspondence between the time frames described the wall motion over the entire cardiac cycle. Besides a baseline model where the trabeculae and papillary muscles were included, a smoothed model was also included where the ventricular surface was smoothed and the papillary muscles were removed, see Figure 1. The dynamics of the valves could not be resolved with sufficient detail by the CT measurement, but the open and closed positions could be extracted. In order to resolve the geometrical details of the ventricle, the total number of mesh cells was on the order of 12 million anisotropic cells. Automatic remeshing was triggered during the simulation when the mesh quality became too poor

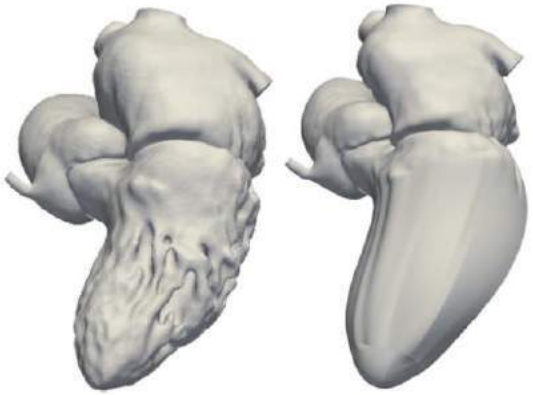

Figure 1. Left: reference geometry with trabeculations and papillary muscles, right: smoothed model.

Copyright 2016 The Organizing Committee for the 2016 Summer Biomechanics, Bioengineering and Biotransport Conference

or when the topology changed. The meshing strategy was fully automated and capable of handling the folding and unfolding of the complex trabeculated structures. The flow simulation was performed using ANSYS CFX 16.0, and the wall motion was specified from the image registration process. Pressure boundary conditions were applied at the pulmonary veins and ascending aorta. The time step was 1e-4 s and intermediate meshes at each time step were computed during run time using a fast cubic interpolation FORTRAN-subroutine [2] to ensure that both velocity and acceleration of the wall were continuous and smooth.

RESULTS

A cross-sectional plane through the atrium, LV and aortic sinuses was used to display velocity magnitude and vectors at three different phases during the cardiac cycle, see Figure 2. During systole (time = 0.1T) the flow field is similar between the models, with a high velocity region in the left ventricular outflow tract and through the aortic valve. This could be expected since both geometries were similar in that region and the LV stroke volume and ejection fraction was almost the same. The velocity in the apical region is lower in the baseline model than the smoothed model. During diastole the flow patterns appeared different between the baseline and smoothed models; the smoothed model had a high velocity flow in the mid region while the flow was more stagnant in baseline model. Instead the papillary muscles seem to divert the flow and created a large vortex in the middle of the LV, which was not as prominent in the smoothed model. The LV filling pattern in this patient was asymmetrical, with a mitral jet directed towards the lateral side of the ventricle. Thus, a large vortex formed behind the anterior mitral leaflet, and was allowed to expand in the ventricle, while the flow on the posterior side strongly interacted with the wall.

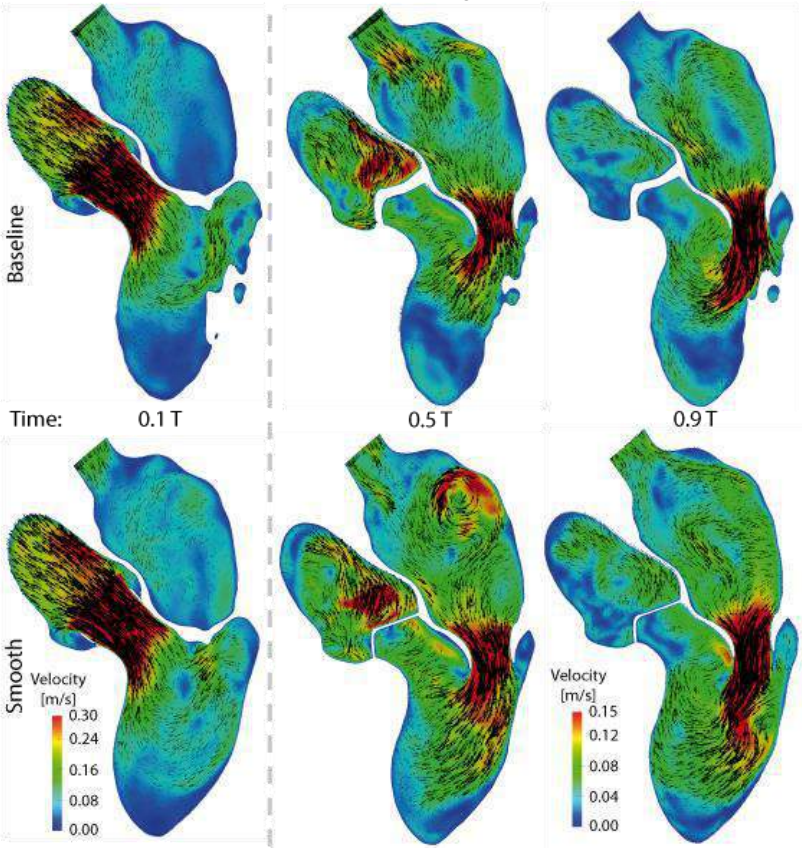

Figure 2. Flow field in the baseline model with trabeculations and papillary muscles (top) and in the smoothed model (bottom). Timing is indicated as fraction of cardiac cycle (T).

DISCUSSION

In the present study, a framework for computing patient-specific hemodynamics in physiologically realistic hearts was developed and applied to a patient with a dilated left ventricle. The framework only required time-resolved CT images of the heart. The model included papillary muscle motion and the folding and unfolding of left ventricular trabeculae, and the results indicated that these are important aspects to consider when computing cardiac blood flow. In addition, the model also included the atrium, ventricle, valves, aortic root and part of the coronary arteries and ascending aorta, which has, to the authors' knowledge, never been achieved before in a computational flow model. The simulation time was the same for both models, even though the baseline model included more geometrical details. Thus, the framework was able to handle complex geometrical LV features without any additional computational cost.

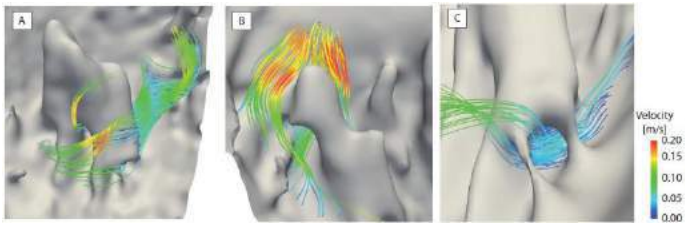

Figure 3. Visualization of particle traces near the papillary muscles and trabeculated structures. A: anterior papillary muscle, B: posterior papillary muscle, C: geometrical structure below the anterior papillary muscle.

Compared to simplified models commonly found in literature, the blood in the physiological model interacted strongly with papillary muscles and trabeculae which in turn affected the computed flow field. Specifically, the simulations showed that the complex flow patterns in the LV were affected by the blockage effect posed by the papillary muscles, which effectively reduced the amount of energetic flow that reached the apical part of the heart. The interstitial spaces in the trabeculated surface could promote stagnant blood flow, as regions of high residence time could be found in such structures. As such, the presented results suggest that over-simplified models are unable to capture details that could have important physical implications. From a clinical perspective, the framework developed here opens up for the possibility to artificially add pathologies such as myocardial infarction or hypertrophy to the model. The wall motion can be turned off or tuned, the size of LV can be changed, and the valves can allow for regurgitant flow.

In conclusion, the novel framework developed in this study enables the inclusion of geometrical features on a scale that has never been achieved before. In addition, the feasibility, as well as importance, of including the motion of papillary muscles and trabeculae in computational models of cardiac hemodynamics was demonstrated.

ACKNOWLEDGEMENTS

The authors acknowledge funding from Knut and Alice Wallenberg Foundation through the project *Seeing organ function*. The Swedish National Infrastructure for Computing (SNIC) is acknowledged for computational resources provided by the National Supercomputer Centre (SNIC2014-11-22).

REFERENCES

[1] Thirion, J-P, *Medical image analysis,* 2(3), p. 243-260, 1998
[2] Lantz, J et al., *CVET*, 5(3) p. 261-269, 2014

Copyright 2016 The Organizing Committee for the 2016 Summer Biomechanics, Bioengineering and Biotransport Conference

SB^{3}C2016
Summer Biomechanics, Bioengineering and Biotransport Conference
June 29 –July 2, National Harbor, MD, USA
SB^{3}C2016-87

Impact of Bi-Axial Shear on Atherogenic Gene Expression by Endothelial Cells

Amlan Chakraborty (1), Sutirtha Chakraborty (4), Venkatakrishna R. Jala (3), Jonathan M. Thomas (1), M. Keith Sharp (2), R. Eric Berson (1), Haribabu Bodduluri (3)

(1) Department of Chemical Engineering
University of Louisville
Louisville, KY, USA

(2) Department of Mechanical Engineering
University of Louisville
Louisville, KY, USA

(3) Department of Microbiology & Immunology
James Brown Cancer Center
University of Louisville
Louisville, KY, USA

(4) Department of Bioinformatics & Biostatistics
University of Louisville
Louisville, KY, USA

INTRODUCTION

Hemodynamic forces, especially wall shear stress (WSS), are well documented to affect atherosclerotic plaque formation[1,2]. This study explores the effects of the directionality of pulsatile WSS on the gene expression of endothelial cell grown on the bottom of a Petri dish subjected to orbital flow on a shaker platform. A 3D computational fluid dynamics (CFD) model[3] quantified the oscillating WSS. WSS magnitude was relatively uniform temporally and spatially at low orbital speed. At higher orbital speeds, it remained fairly uniform near the center of the dish and fluctuated significantly near the side walls. An extension to Stokes' second problem was used to validated the CFD model. Atherogenic gene expression was measured under the same flow conditions in the presence of leukotrienes (LTB_4) and lipopolysaccharide (LPS), since the role of LTB_4 and LPS are implicated in several inflammatory diseases[4]. Statistical analysis showed that expression of I-CAM and E-Selectin was significantly influenced by directional oscillatory shear index (DOSI), but not by WSS magnitude.

METHODS

1. Multiphase CFD model

ANSYS Fluent was used to model the flow. The unsteady laminar fluid motion in the orbiting dish was simulated with a multiphase volume of fluid (VOF) model in which the two fluids across the interface share the same stress and velocity boundary conditions.

2. Determination of velocity and WSS – Analytical approach

Stokes' second problem was extended to orbital motion of the plate, which gives the velocity of the fluid relative to the plate as

$$\mathbf{V}(z,t) = U\exp\left(-\sqrt{\frac{\omega}{2\upsilon}}z\right)\left[-\sin\left(\omega t-\sqrt{\frac{\omega}{2\upsilon}}z\right),\cos\left(\omega t-\sqrt{\frac{\omega}{2\upsilon}}z\right)\right]+U(\sin\omega t,-\cos\omega t) \quad (1)$$

where $U = R\omega$ is the dish velocity magnitude, R is orbital radius, ω is orbital speed, $\nu = \mu/\rho$ is kinematic viscosity, μ is absolute viscosity, ρ is density, z is the vertical coordinate and t is time. Using the dish velocity magnitude, wall shear stress is

$$\vec{\tau}_w = R\sqrt{\frac{\rho\mu\omega^3}{2}}(\cos\omega t+\sin\omega t,\sin\omega t-\cos\omega t) \quad (2)$$

3. Directional Oscillatory Shear Index

Directional Oscillatory Shear Index (*DOSI*) was used as a measure of bi-axiality [3]. *DOSI* is given by

$$DOSI = 1 - (OSI_2/OSI_1) \quad (3)$$

where OSI (Oscillatory Shear Index) components are given by[5]

$$OSI_1 = 1-\left|\int_0^T\tau_1 dt\right|\Big/\int_0^T|\vec{\tau}_w|dt \quad , \quad OSI_2 = 1-\left|\int_0^T\tau_2 dt\right|\Big/\int_0^T|\vec{\tau}_w|dt$$

where principal direction 1 is that of the larger of the two oscillations, and $\overrightarrow{\tau_w}$ is the two-dimensional WSS vector.

4. Cell culture and shear stress applications

Human umbilical vein endothelial cells (HUVECs) were grown at controlled radial locations. The dishes were placed on an orbital shaker platform to generate pulsatile flow. Two sets of plates contained HUVECs in the presence of media containing either LTB_4 (100 nM) or LPS (100 ng/ml) or both. One set of dishes was exposed to shear stress and another was grown under stationary conditions. Changes in gene concentration were calculated using Real Time PCR method. The effects of DOSI and shear magnitude on the atherogenic genes were analyzed at 20% and 85% radial locations of the dish.

Copyright 2016 The Organizing Committee for the 2016 Summer Biomechanics, Bioengineering and Biotransport Conference

5. *Statistical Analysis*

ANOVA was used to identify the effects on gene expression of DOSI and shear magnitude with the model given by

$$Y_{ijk} = \mu_{mean} + G_i + T_j + I_i + (GT)_{ij} + (GI)_{ij} + D_{ijk} + M_{ijk} + (DG)_{ijk} + (DT)_{ijk} + \varepsilon_{ijk} \quad (4)$$

where μ_{mean} is the general mean effect, G_i, T_j and I_k, are the additional effects due to the *i*th gene, *j*th treatment and *k*th individual (replicate) respectively. $(GT)_{ij}$ is the interaction effect between gene and treatment, $(GI)_{ik}$ is the interaction effect between gene and individual. D_{ijk} and M_{ijk} are the values of *DOSI* and shear magnitude. $(DG)_{ijk}$ and $(DT)_{ijk}$ are the interaction effects of *DOSI* with gene and treatment respectively. ε_{ijk} is the random error component for the *i*th *DOSI*, *j*th treatment and *k*th replicate.

RESULTS

1. *Validation of 3D CFD model with analytical solution*

Agreement between CFD and the analytical solution for simplified inertial flow was within 1% for velocity components (Figure 1), which establishes the accuracy of the model.

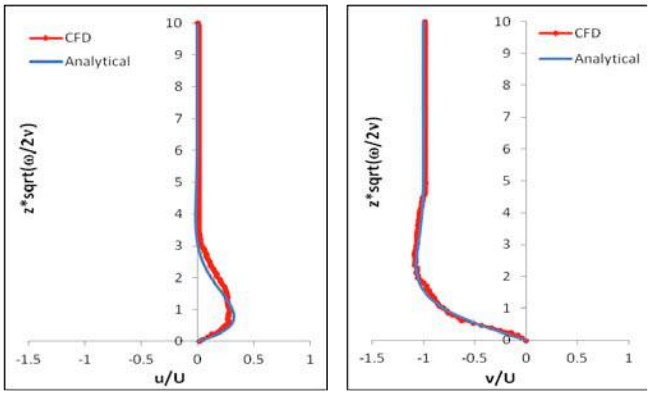

Figure 1. Normalized velocity components for analytical and CFD models.

2. *Oscillatory WSS for experimental conditions: DOSI*

Highest WSS was observed near the vertical wall and lower shear was observed near the center of the dish (Figure 2). WSS ranged from 0-9 dyne/cm^2 at 85% of the radius, and 0-1 dyne/cm^2 at 20% radial location, respectively. *DOSI* was calculated (Table 1) on the basis of principal axes. The first principal direction was the direction of the resultant of the two (radial and tangential) shear components. The second principal direction is perpendicular to the first.

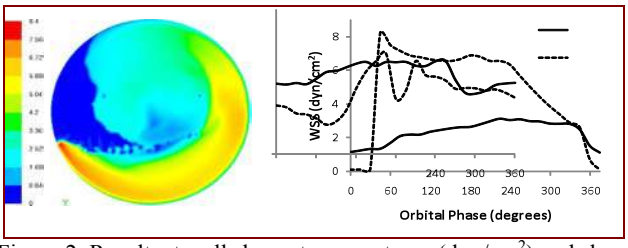

Figure 2. Resultant wall shear stress contours (dyn/cm^2) and shear waveforms at different radial locations.

Table 1. *DOSI* at different radial locations

Radial location (%)	OSI_{tan}	OSI_{rad}	DOSI
20	0.892	0.620	0.305
85	0.986	0.06	0.994

3. *Impacts of shear stress on atherogenic gene expressions in the presence of LTB_4 and LPS*

I-CAM expression was significantly lower at high *DOSI* in the presence of LPS only, while E-Selectin was significantly lower at high *DOSI* regardless of treatment (Figure 3). ANOVA (Table 2) further reinforced the significance of *DOSI* on those gene expressions by the strength of its interactions with other atherogenic factors.

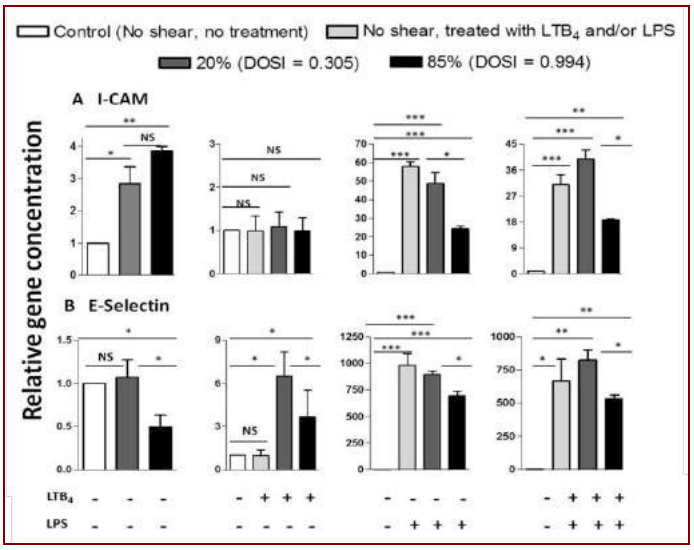

Figure 3. Effects of *DOSI* and shear magnitudes on gene expressions (I-CAM, E-Selectin) at different radial locations. Statistical significance : $*p < 0.05$, $**p < 0.01$, and $***p < 0.001$, respectively.

Table 2. ANOVA of gene expression – Statistical significance (p) of *DOSI*, shear magnitude, and treatment by Eqn. 4.

Gene (G)	Treatment (T)	DOSI (D)	Magnitude (M)	GT	DG	DT
<0.001	<0.001	<0.01	NS	<0.001	<0.001	<0.001

DISCUSSION

This study demonstrated the validation of computational and analytical models of oscillating shear and velocity components in an orbiting Petri dish. Further, the model was used to quantify pulsatile WSS to understand the effects of WSS directionality on cell function, in particular, expression of genes involved in atherosclerosis. The ANOVA model characterizes the main and interaction effects of the genes (ICAM, E-selectin, IL-6), treatment (LTB_4, LPS), *DOSI* and shear magnitude. The significance of *DOSI* and its interactions within the fitted model reveal the significant individual impact of bi-axiality and its interactive effects with the other factors in altering the cellular gene expression. So *DOSI*, as an index of bi-axial oscillatory shear, characterizes its impact either singly or in consort with a variety of other cofactors on different types of responses. This study suggests that the directionality of shear modulates gene expression and, thus, may influence the formation of atherosclerotic plaque.

REFERENCES

[1]Libby, P. *Nature* 420(6917):868-874, 2002.
[2]Cunningham, K. S., *et al. Lab. Invest.* 85(1):9-23, 2005.
[3]Chakraborty, A., *et al. Biotech & Bioengg* 109(3):695-707, 2012.
[4]Mehrabian, M., *et al. Circ. Res.* 91(2):120-126, 2002.
[5]Ku, D. N., *et al. Arteriosclerosis* 5(3):293-302, 1985.

Copyright 2016 The Organizing Committee for the 2016 Summer Biomechanics, Bioengineering and Biotransport Conference

SB^{3}C2016
Summer Biomechanics, Bioengineering and BIotransport Conference
June 29 – July 2, 2016, National Harbor, MD, USA
SB^{3}C2016-88

COMPARISON OF PEDIATRIC AND ADULT BLOOD VISCOELASTICITY

M. Keith Sharp, Sc.D.[1], Mary Gregg[2], Guy Brock, Ph.D.[3], George M. Pantalos, Ph.D.[4],

(1) Department of Mechanical Engineering
University of Louisville
Louisville, KY, USA

(2) School of Public Health
University of Louisville
Louisville, KY, USA

(3) Department of Pharmacology and Toxicology
The Ohio State University
Columbus, OH, USA

(4) Department of Cardiovascular and Thoracic Surgery
University of Louisville
Louisville, KY, USA

INTRODUCTION

Driven by the increasing number of surgical cardiac procedures performed and by the advancement in surgical techniques, mechanical circulatory support has become progressively more viable and more frequently utilized as a treatment option for pediatric patients [1,2]. While methods of providing circulatory support have improved significantly over the years, complications with hemolysis and thrombus formation still persist as serious concerns. Numerous investigations have demonstrated that shear-induced hemolysis, mechanical stress, and device surface contact associated with mechanical circulatory support can lead to thromboembolism, bleeding, and infection [3-5]. In order to better understand and more effectively study these complications, Bachmann *et al.* established the importance of using a fluid that simulates the properties of blood during *in vitro* testing of pediatric ventricular assist devices [6]. Viscoelasticity of whole blood, even in normal subjects, varies over a wide range due to the strong influence of hematocrit, plasma viscosity, and protein concentrations. These physiological factors influence the viscoelasticity of blood, and thus the flow dynamics through assist devices, and should also be taken into consideration during blood pump design and performance testing [7-8]. This study compares blood rheology between adult and pediatric cardiac surgery patients to improve the understanding of design criteria for pediatric devices.

METHODS

Informed consent was obtained from parents of pediatric patients scheduled for cardiac surgical procedures at the Kosair Children's Hospital, Louisville, KY, and from adult patients scheduled for cardiac procedures at Jewish Hospital, Louisville, KY. The research protocol and consent forms were approved by the Institutional Review Board at the University of Louisville and the Norton Healthcare Research Office. The focus of the pediatric study was to be on patients weighing less than 25 kg based on the specifications of the NHLBI Pediatric Assist Device Program [9]. The age, weight, most recent hospital hematological data, and surgical procedure to be performed were recorded at the time of blood sample collection. Each sample was obtained from an indwelling catheter at the time of surgery and was immediately placed into a 3 mL EDTA blood collection tube and iced until analyzed by a Vilastic-3 viscoelasticity rheometer (Vilastic Scientific, Inc., Austin, TX) within two hours of collection. Viscous and elastic components of complex viscoelasticity were measured in a capillary tube of 0.504 mm radius and 6.33 cm length at temperature of 37^{o}C and frequency of 2Hz over a range of shear strain from 0.15 to 25 (shear rate 1.8 to 251 s^{-1}). Spun hematocrit was also determined.

Samples were collected from 35 adult and 35 pediatric patients. Viscosity and elasticity measurements were reviewed to insure physiological validity. Patient data sets were removed when elasticity was higher than viscosity (5 adult and 4 pediatric samples). Samples that were more than 3 standard deviations were removed as outliers (2 adult and 2 pediatric samples). Viscosity and elasticity were interpolated to get values at strain rates of 0.2, 1, and 5, corresponding to the rheology of erythrocyte aggregates, individually suspended cells, and oriented, layered cells, respectively.

Analysis used the natural logarithms of viscosity, elasticity, and strain values, as the natural log transformation of these variables produced an approximately linear relationship. The model takes the form:

$$y_{ij} = \beta_0+u_{0i}+(\beta_1+u_{1i})x_{1ij}+\beta_2x_{2ij}+\beta_3x_{3ij}+\beta_4x_{1ij}x_{2ij}+\beta_5x_{1ij}x_{3ij}+\beta_6x_{2ij}x_{3ij}+\varepsilon_{ij}$$

where y_{ij} represents the logarithm of (centered) viscosity or elasticity measurement from subject i on observation j, x_1 is log strain, x_2 is hematocrit, x_3 is subject age, and ε_{ij} are independent and identically distributed N(0, σ) error terms.

RESULTS AND DISCUSSION

Only the viscosity results are presented here. A preliminary model was fit that included fixed effects of age, hematocrit, strain, age-by-strain, hematocrit-by-strain, and hematocrit-by-age interactions. A likelihood ratio test for the significance of the random coefficient for log strain was highly significant ($p < 0.0001$),

Copyright 2016 The Organizing Committee for the 2016 Summer Biomechanics, Bioengineering and Biotransport Conference

indicating substantial variation in slopes among subjects. A significant age-by-strain interaction indicates that increasing age decreases the average slope of the log strain effect on log viscosity. Negative log strain and log strain-by-age coefficients suggest that age increases the effect of strain on viscosity. A similar relationship exists between hematocrit and strain. The hematocrit-by-age interaction was not significant (p-value 0.4439), indicating the effect of hematocrit on viscosity is independent of age, and was subsequently removed from further models.

To determine whether the effect of age was linear, a model was built with categorical age quartiles and strain as fixed effects. The large difference observed between the second and third quartiles in the estimated coefficients for the age main effect and age-by-strain interaction, along with the similarity in the third and fourth quartile estimates suggested a difference in age effect and its interaction with strain occurring in the third quartile. To pinpoint where the distinction occurred, fitted strain coefficient values, representative of the slope of subjects' log strain versus log viscosity curves, from a model including only strain as a predictor variable were plotted against subject age (Figure 1, top). The regression line and loess curve in Figure 1 illustrate the the age-by-strain interaction. A similar plot of the fitted intercepts against age was produced to detail any trend in the strain main effect as age increased (Figure 1, bottom). The inflection points of the loess curves in these graphs occur in the 14-36 age range. As puberty is a biologically plausible phase, fourteen was selected as the cut point and further analysis focused on differences between juveniles (defined as subjects aged fourteen and under) and adults.

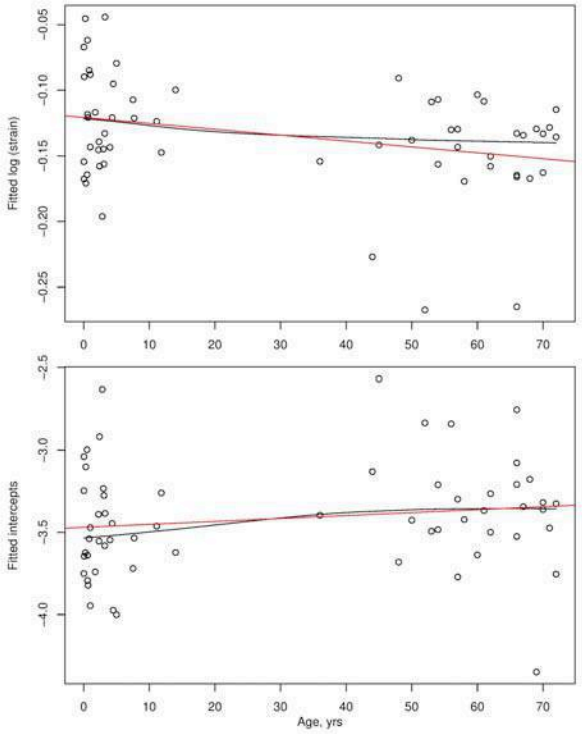

Figure 1. Top: Fitted log strain and intercept values plotted against age from modeling outcome of viscosity as a function of log strain. Top: The points represent fitted log strain values from a linear mixed model of log viscosity as a function of log strain, including a random intercept and random coefficient for log strain. The red line represents the linear model and the black line the smoothed loess curve.

Bottom: The points represent fitted intercept values from a linear mixed model of log viscosity as a function of log strain, including a random intercept and random coefficient for log strain. The red line represents the linear model of the fitted intercepts as a function of age. The black line is the smoothed loess curve of the age-intercept function.

To reflect this difference between juveniles and adults, the age-by-strain interaction was replaced by separate adult-by-strain and juvenile-by-strain interaction terms, with adult status being an indicator variable (taking value 1 for subjects > 14 and 0 otherwise) and the juvenile term simply the juvenile age. The inclusion of two strain-by-age interaction terms allows the slope of log strain to vary depending on juvenile or adult status. The juvenile-by-strain interaction is a linear term that modifies the log-strain slope per year increase in age up to age 14, while the adult-by-strain interaction is a constant modifier of the log-strain slope for all subjects over age 14. While the juvenile-by-strain interaction was not significant, it is included in the model as it is biologically implausible that the observed difference in slope of log strain between juveniles and adults begins suddenly at a certain age.

An important outcome of this analysis is that the likelihood ratio test for the combined effects of both age-by-strain interaction terms was significant (p-value 0.0177). The new model incorporating these interactions, therefore, facilitates improved design of cardiovascular devices across diverse patient groups.

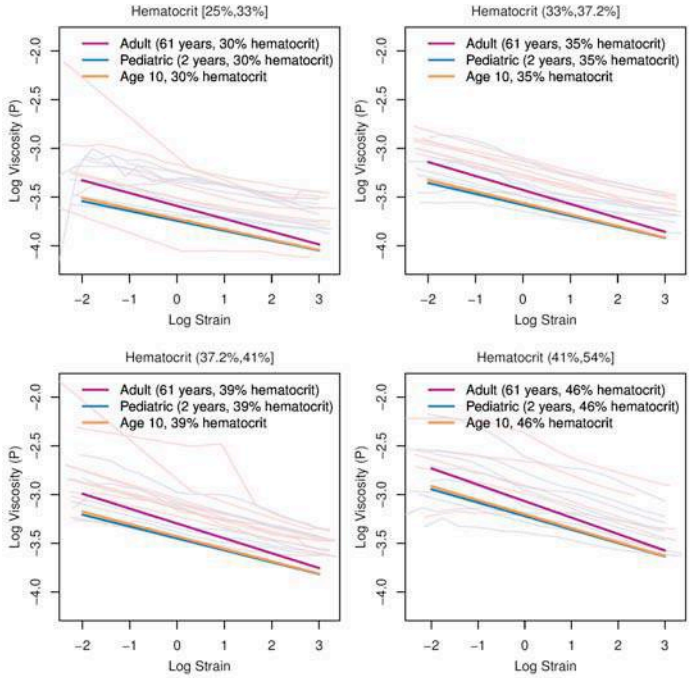

Figure 2. Comparable log viscosity response for pediatric and adult subjects at given hematocrit values. The solid lines represent log viscosity values for adult and pediatric subjects at the respective hematocrit percentiles as predicted by our final model. Each panel represents the midpoint of its respective hematocrit quartile. Pediatric lines were modeled at age 2, while adult lines were modeled at age 61.

ACKNOWLEDGEMENTS

Funding for this project was provided by the National Institutes of Health Heart, Lung and Blood Institute (Grant 2 R44 HL059810 and Contract No. HHSN268200449189C), the Jewish Hospital & St. Mary's Foundation (Louisville, KY), and Kosair Charities, Louisville, KY. Thanks to Dr. Mark Slaughter and Dr. Erle Austin III for their cooperation in arranging for patients to participate in this investigation.

REFERENCES

[1] VanderPluym. *Circulation* 129: 1530-1537, 2014
[2] Stiller. *Heart* 97: 596-602, 2011.
[3] Leverett. *Biophys J* 12: 257-273, 1972.
[4] Thompson. *ASAIO J* 49: 518-526, 2003.
[5] Walters. *Ann Thorac Surg* 60:329 –337, 1995.
[6] Bachmann. *Artif Organs* 24: 362-372, 2000.
[7] Long. *ASAIO J* 51:563-566, 2005.
[8] Burton. Physiology and Biophysics of the Circulation. Year Book Medical Publishers Incorporated. pp. 39-48, 1972.
[9] Baldwin. *Circulation* 113:147-155, 2006.

Copyright 2016 The Organizing Committee for the 2016 Summer Biomechanics, Bioengineering and Biotransport Conference

SB^{3}C2016
Summer Biomechanics, Bioengineering and Biotransport Conference
June 29 –July 2, National Harbor,MD, USA
SB³C2016-89

COMPARISON OF *IN VITRO* ENDOTHELIAL WOUND HEALING IN BARE METAL VS. DRUG-ELUTING STENTS

Elizabeth E. Antoine, Abdul I. Barakat

Hydrodynamics Laboratory (LadHyX)
Department of Mechanics
Ecole Polytechnique
Palaiseau, France

INTRODUCTION

The pathological complications of atherosclerosis, namely heart attacks and strokes, are the leading cause of mortality in the world. While the use of endovascular stents to open blocked arteries is broadly successful, stent deployment triggers a complex set of biological responses leading in some cases to in-stent restenosis (ISR) or late stent thrombosis (LST). Understanding the biological pathways involved in these and other stent pathologies under physiological conditions remains a major challenge. Although *in vivo* studies and computational models provide invaluable information about the biology of atherosclerosis and inform stent design strategies, the availability of *in vitro* devices for controlled studies of atherosclerosis and validation of numerical work remains critically limited [1,2].

Implantation of a stent in an artery leads to endothelial cell (EC) denudation which disrupts communication between ECs and smooth muscle cells (SMCs) necessary for homeostasis. EC-SMC interactions in response to wounding have been studied in classical monolayer cultures; however, the similarity of such experiments to *in vivo* conditions is limited. Furthermore, in most cases stent deployment is not possible in *in vitro* devices and therefore effects specific to stenting such as localized sustained drug release cannot be reproduced.

At SB^{3}C 2015 we presented the design and development of an *in vitro* artery within which a stent can be deployed and cellular response studied. Here we revisit this system, presenting a robust methodology for quantification of endothelial wound healing and investigating differences in wound healing after deployment of a drug-eluting stent (DES) compared with a bare metal stent (BMS).

METHODS

The *in vitro* artery was assembled as described previously [3]. Briefly, collagen I from rat tail tendon was combined with 200,000 cells/mL bovine aortic SMCs (Tebu-Bio) labeled with a red fluorescent marker (Vybrant CM-DiI, Fisher) and polymerized in an annular shape in a polymer tube (Figure 1**a**). Bovine aortic ECs (Georges Pompidou Hospital, Paris) labeled with a green fluorescent marker (Vybrant DiO, Fisher) were seeded on the lumenal surface of the collagen. The device was perfused (Figure 1**b**) over 72 hours with stepwise-increasing flow of culture medium (DMEM supplemented with 10% fetal bovine serum and 1% penicillin/streptomycin, Invitrogen) to condition the endothelial monolayer and finally obtain pulsatile flow conditions hydrodynamically similar to human coronary artery flow (Reynolds number = 360, Womersley number = 16) (Figure 1**c**).

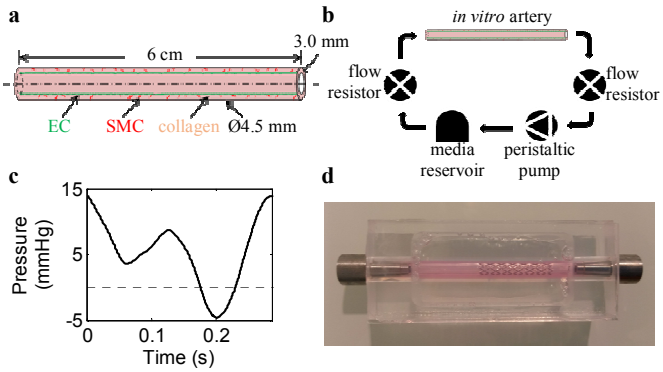

Figure 1: The *in vitro* artery. (a) Schematic. (b) Flow components used to generate pulsatile coronary flow. (c) Pressure trace under coronary flow conditions. (d) Photograph of stented *in vitro* artery.

Copyright 2016 The Organizing Committee for the 2016 Summer Biomechanics, Bioengineering and Biotransport Conference

After preconditioning and perfusion at the final flow condition for 18 hours, either a BMS (Tsunami Gold, Terumo) or a biolimus-eluting stent with biodegradable polymer coating (Nobori, Terumo) was inserted in the *in vitro* artery (Figure 1**d**). Each stent, nominally designed for a 3.0 mm artery, was overexpanded 10% to 3.1 mm to ensure retention in the *in vitro* artery during and after catheter removal.

Cell migration was recorded after stent deployment using time-lapse imaging on an epifluorescent microscope (Ti-E, Nikon) and 4X magnification (1.66 µm/pix). Phase contrast and fluorescence images were acquired every 30 minutes using a motorized stage to acquire a grid covering the entire *in vitro* artery (Figure 2). The camera was focused at the nearest plane tangent to the lumen in order to best record endothelial motion. Image acquisition and stitching were performed using either ImageJ plugins (NIH) or NIS Elements (Nikon).

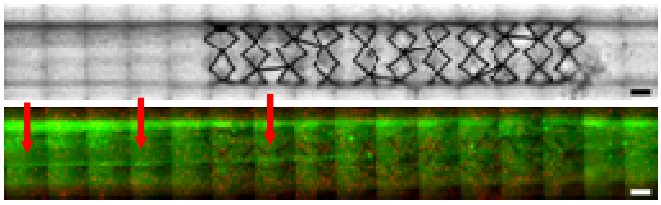

Figure 2: *In vitro* artery immediately after deployment of the BMS. (top) phase contrast. (bottom) overlay of endothelium (green) and smooth muscle (red). Arrows indicate denuded region. Scale bar: 1 mm. Flow: left to right.

Endothelial wound healing analysis was performed in MATLAB. First, two regions of interest (ROIs) of similar size were selected, each containing a well-defined section of wound: one ROI upstream of the stent and one ROI within the stent (Figure 3, images). Whole-image shifts in the time-lapse sequence were corrected using a PIV-based image registration scheme. Because the wound boundary is poorly defined due to variation in individual cell position as well as heterogeneous cell fluorescence, bulk analysis was performed on profiles obtained by averaging the fluorescence intensity in the FITC (endothelial) channel along the length of the wound (Figure 3, profiles). Subsequently, each profile was normalized to reduce the influence of lighting variations. The speed of wound healing was computed robustly using parametric variation in the intensity threshold used to estimate boundary position as well as the number of frames (time points) used in linear regression for slope estimation. This parametric variation provided 54 "replicates" for each wound boundary within each ROI (upstream and in-stent). Comparisons were performed using ANOVA and Tukey's post-hoc test.

RESULTS

Catheter insertion and stent deployment resulted in large patches of denuded lumen (Figure 2**,** arrows) for both stented arteries. Although endothelial cells migrated to fill the wounds in both cases, qualitatively their behavior differed significantly between the BMS and the DES artery. In the BMS artery, endothelial front advancement was organized, appearing to be group motion with a well-defined trajectory into the wound (Figure 3). In contrast, endothelial cells in the DES artery appeared to migrate independently of one another and with less directionality. Furthermore, endothelial cells appeared less healthy and were more apt to detach from the lumen in the DES case, resulting in a sparser endothelium 24 hours after stent deployment.

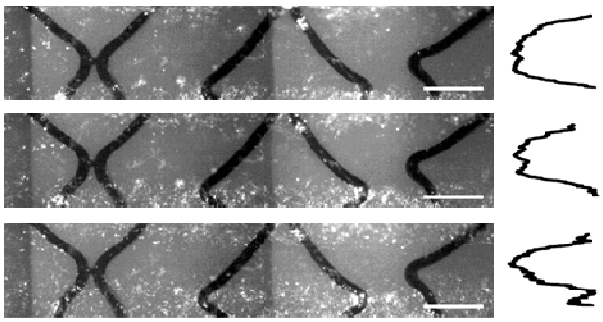

Figure 3: Wound healing in an in-stent ROI of the BMS-implanted *in vitro* artery. Top to bottom: 0, 5, and 10 hours post-stent. The mean intensity profile is used to estimate the rate of endothelial wound healing. Scale bar: 500 µm.

Quantification of the speed of wound healing (Figure 4) revealed that the endothelium repaired itself considerably faster ($p<0.0001$) in the BMS *in vitro* artery (15.0 ± 0.5 µm/h) than in the DES *in vitro* artery (0.63 ± 0.02 µm/h) (mean ± SEM, $p<0.0001$). While the wound healing speed was not significantly different between the BMS upstream and in-stent regions ($p\sim0.8$), a small yet significant ($p<0.0001$) decrease was found within the DES (0.43 ± 0.02 µm/h) compared with the artery section upstream (0.84 ± 0.02 µm/h). All results reported are mean ± SEM.

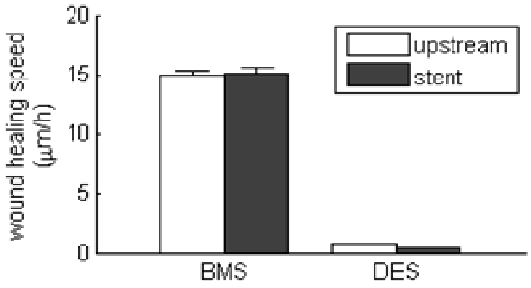

Figure 4: Comparison of endothelial wound healing in BMS- vs. DES-implanted *in vitro* arteries. Error bars indicate the standard error of the mean.

DISCUSSION

We successfully deployed a BMS and a DES in a novel *in vitro* artery platform and quantified the rate of endothelial wound healing in each. We identified significant inhibition to wound healing in the DES-implanted *in vitro* artery, a result which is consistent with *in vivo* data. The endothelial response quantified here will be combined with the accompanying analysis of SMC migration to better understand EC/SMC interaction in response to stent deployment.

ACKNOWLEDGEMENTS

E. Antoine is funded by a Whitaker Postdoctoral Fellowship. The research is partially supported by a permanent endowment in Cardiovascular Cellular Engineering from the AXA Research Fund.

REFERENCES

[1] Morlacchi, S and F Migliavacca, *Ann Biomed Eng,* 41:1428-1444, 2013.

[2] Kolandaivelu, B et al., *J Biomech,* 47:908-921, 2014.

[3] Antoine, E and A Barakat, *Proceedings of the 2015 Summer Biomechanics, Bioengineering, and Biotransport Conference*, SB^{3}C2015-368.

Copyright 2016 The Organizing Committee for the 2016 Summer Biomechanics, Bioengineering and Biotransport Conference

SB^{3}C2016
Summer Biomechanics, Bioengineering and Biotransport Conference
June 29 –July 2, National Harbor, MD, USA
SB^{3}C2016-90

KEY INPUTS FOR THE GENERATION OF PATIENT-SPECIFIC FINITE ELEMENT MODELS OF THE KNEE JOINT

Hongqiang Guo (1), Thomas J. Santner (2), Amy L. Lerner (3), Suzanne A. Maher (1)

(1) Department of Biomechanics
Hospital for Special Surgery
New York, NY, USA

(2) Department of Statistics
The Ohio State University
Columbus, OH, USA

(3) Department of Biomedical Engineering
University of Rochester
Rochester, NY, USA

INTRODUCTION

In vivo animal models and *in vitro* tissue explant studies have indicated that increased joint translation, contact stress, and impact force are associated with increased likelihood of cartilage degeneration [1, 2]. The holy grail of orthopedics is to translate this emerging body of knowledge to clinical care: in theory, a deeper understanding of a patient's joint mechanics could be used to assess the risk of joint tissue degeneration after injury. Finite element (FE) models of cadaveric specimens are created from inputs that include joint geometry, tissue properties, and joint kinematics [3], and comparisons between the outputs from FE and the corresponding cadaveric models can be made [4]. However, for patient-based models it is impossible to measure joint tissue properties and thus to compare FE model outputs with physical model outputs. To realize the vision of creating patient-specific FE models requires researchers to determine if realistic models can be created based only on clinically derived inputs.

The goal of this study was to establish key inputs for the development of patient-specific FE models of the knee joint. To satisfy this goal, we applied a statistically-augmented FE approach to three human cadaveric knees for which full geometric and kinematic data was available. Two sets of conditions were simulated: (I) FE Inputs were varied to represent all possible combinations of a 'normal' patient population (II) clinically measurable FE Inputs were fixed at specific values while other inputs were varied over `normal` values (called *patient derived inputs,* or PDIs). By assessing the *range* of contact mechanics outputs for conditions I vs. II, we quantified the decrease in model output uncertainty due to fixing specific PDIs.

METHODS

Three knee-specific FE models were created from MR scans of cadaveric knees. Articular cartilage and menisci were modeled as elastic materials, and menisci were assumed to be transversely isotropic. Kinematic inputs derived from physical simulations of gait on each knee were input: anterior-posterior translation, medial-lateral translation, varus-valgus angle, internal-external angle, flexion-extension angle, and axial force, applied to the mid-point of the femoral epicondylar axis [4].

Condition I: A set of 21 FE runs was made for each knee in which the values of meniscus and cartilage tissue properties, meniscal insertion position, length, and stiffness, and body mass index were varied to represent all possible combinations of the 'normal' patient population (Table 1). The combinations of input values for each FE run were determined using a space-filling algorithm [5]. An additional 180 FE runs was added using a grid pattern approach to ensure adequate coverage of the design space [4]. Condition II: *Patient derived inputs,* PDIs: Subsequent to the above analysis, inputs to the FE model that could be readily quantified in a clinical setting were identified: BMI (which can be quantified in an office setting) and position of meniscal-bony insertion points (which can be extracted from MR scans). For each knee, all other inputs (Table 1) were allowed to vary across the range for normal knees, but the PDIs were fixed at five combinations: (1) BMI, IP_a, IP_p: 22, -2.4, -2.4, respectively (2) BMI, IP_a, IP_p: 22, -2.4, 2.4 (3) BMI, IP_a, IP_p as 27, 0, 0, (4) BMI, IP_a, IP_p as 32, 2.4, -2.4 (5) BMI, IP_a, IP_p as 32, 2.4, 2.4.

The output from each FE run was the percent of load acting through the cartilage-cartilage (C-C) contact region on the tibial plateau, which was predicted at additional input combinations based on a MATLAB driven Gaussian Process interpolator [6, 7]. Percent load in the C-C zone was computed at three points in the gait cycle where the axial force magnitude peaked: 4, 14 and 45% (peaks 1, 2 and 3, respectively) of the gait cycle. Main effect sensitivity indices (SIs) [8] were computed for the nine variables for condition I. Results

Copyright 2016 The Organizing Committee for the 2016 Summer Biomechanics, Bioengineering and Biotransport Conference

for peak 2 of the gait cycle are presented herein.

Table 1. FE model input variables and their ranges. For IP_a and IP_p +ve value indicates more anterior, -ve value indicates more posterior.

Input Variable	*Lower Bound*	*Upper Bound*
Body Mass Index (**BMI**) [9]	22	32
Anterior-Posterior position of the bony insertion point of the anterior meniscal attachments, $\mathbf{IP_a}$ (mm) [10]	-2.4	2.4
Anterior-Posterior position of the bony insertion point of the posterior meniscal attachments, $\mathbf{IP_p}$ (mm) [10]	-2.4	2.4
Circumferential modulus of the meniscus, $\mathbf{E_{cm}}$ (MPa) [11]	80	220
Radial/axial modulus of the meniscus, $\mathbf{E_{rm}}$ (MPa) [11]	11.5	35
Elastic modulus of the articular cartilage, $\mathbf{E_c}$ (MPa) [12]	11.5	35
Stiffness of the meniscal attachments, $\mathbf{S_{ma}}$ (N/mm) [13]	140	220
Length of the anterior meniscal attachments, $\mathbf{L_a}$ (mm) [13]	10	17
Length of the posterior meniscal attachments, $\mathbf{L_p}$ (mm) [13]	6	11

RESULTS

When the mean values of all 9 input parameters were used, the three knee-specific FE models had very different contact stress distributions (**Fig. 1**), which were similar to that recorded from the experimental testing of each knee [4].

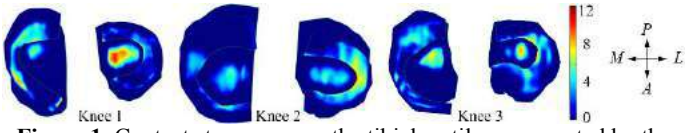

Figure 1. Contact stress map on the tibial cartilage computed by the knee-specific FE models at peak 2 of the gait cycle for 3 knees.

Condition I: When all possible ranges of meniscal and cartilage tissue properties, meniscal fixation characteristics, and BMI inputs were considered, the range of percent load in the C-C zone was wide and variable across knees (see group 0 in **Fig. 2**). Condition II: Fixing the three PDIs at specific values decreased the range of percent load in the C-C zone for each knee. The amount by which it was reduced was variable across knees.

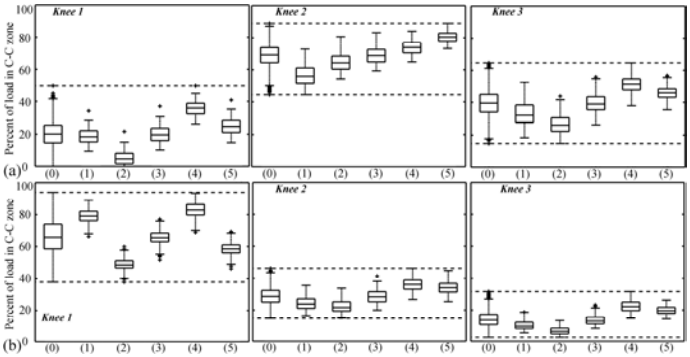

Figure 2. Range of percent of load in C-C zone of the medial (a) and lateral (b) compartments at peak 2 of the gait cycle. On the y-axis, group (0) represents the output from condition I, where all nine variables span the range of normal patient population, groups (1-5) represent the outputs where PDIs were fixed.

To understand which of the nine input variables were responsible for changes in the range of the percent load in the C-C zone for each knee, the main effect sensitivity indices were estimated (**Fig. 3**). Of the nine inputs studied, five (BMI, IP_a, IP_p, E_{cm}, and E_{rm}) had the most profound and consistent effects, while the other four variables (i.e. E_c, S_{ma}, L_a, and L_p) had minimal effect. The effect of each input was highly variable between knees and compartments. For both medial and lateral compartments of knee 1, the three PDIs accounted for ~60% of variation of the percent of load in the C-C zone; while for knees 2 and 3, the three PDIs accounted for ~40% of the variation. Of note, for all knees for all conditions, increasing BMI and moving IP_a in an anterior direction increased the percent of load in the C-C zone. While increasing E_{cm} and E_{rm}, and moving IP_p in the anterior direction decreased the percent of load in the C-C zone.

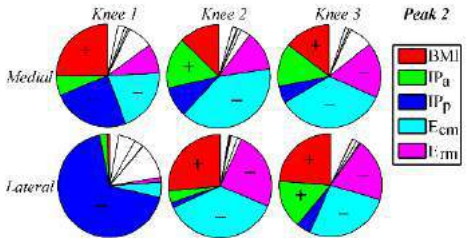

Figure 3. Pie charts representing the main effect sensitivity indices of the input variables for the percent load in the C-C zone of medial compartment at peak 2 of the gait cycle. The '+' sign indicates that increasing the input increases the percent of load in the C-C zone. Simultaneously moving IP_a in an anterior direction and IP_p in the posterior direction both increased the percent of load in the C-C zone.

DISCUSSION

Our goal was to establish key inputs for the development of patient-specific FE models. We computed the range of possible outputs for two conditions: condition I where inputs were allowed to represent variability in a normal patient population, and condition II where three inputs that could be clinically quantified, PDIs, were fixed, but all other inputs could vary. The output (percent of load in the C-C zone) was highly variable between knees *and* compartments, illustrating the importance of patient-specific geometry and kinematics in dictating the response of the model. But, for a particular compartment of each knee, the range of outputs was significantly reduced (between a third and a half), when PDIs were included. Our analysis indicates in the best case scenario, where geometry, kinematics, BMI, and meniscal insertion points are known, an FE model can be used to calculate the percent load in the C-C zone with an uncertainty range of 10-30%. In future studies, we aim to apply this approach to the study of patients undergoing meniscal surgeries.

ACKNOWLEDGEMENTS

This study was supported by NIH R01 AR057343 and Russell Warren Chair in Tissue Engineering.

REFERENCES

[1] Friel and Chu, 2013, Clin. Spts Med, **32**(1), 1-12. [2] Guilak, F., 2011, Best Prac Clin Rheum, **25**(6), 815-823. [3] Mononen et al., 2015, Comp. Mthds. in Biomech & Biomed Eng, **18**(2), 141-152. [4] Guo, et al. 2015, J. Biomech, **48**(8), 1444-1453. [5] Draguljić et al., 2012, Technometrics, **54**(2), pp. 169-178. [6] Svenson, et al., 2014, J. Statistical Planning and Inference, **144**(pp. 160-172. [7] Santner, et al., 2003, The design and analysis of computer experiments, Springer. [8] Svenson 2011, "Computer experiments: multiobjective optimization and sensitivity analysis," The Ohio State University. [9] Flegal, et al., 2012, 1999-2010," JAMA, **307**(5), 491-497. [10] Johannsen et al., 2012, AJSM, **40**(10), 2342-2347. [11] Tissakht and Ahmed,, 1995, J. Biomechanics, **28**(4), 411-422. [12] Li, L., Buschmann, M., and Shirazi-Adl, A., 2003, J. Biomechn Eng **125**(2), 161-168. [13] Hauch Villegas and Haut Donahue 2010, J. Biomech **43**(3), 463-468.

Copyright 2016 The Organizing Committee for the 2016 Summer Biomechanics, Bioengineering and Biotransport Conference

SB^{3}C2016
Summer Biomechanics, Bioengineering and Biotransport Conference
June 29 –July 2, National Harbor, MD, USA
SB^{3}C2016-91

CORONARY CIRCULATION IN AN *IN VITRO* MULTI-SCALE MODEL OF NORWOOD CIRCULATION

Lauren E. Carter[1], Tim Conover[1], Tian-qi Hang[1], Richard Figliola[1]

(1) Department of Mechanical Engineering
Clemson University
Clemson, SC, USA

INTRODUCTION

Hypoplastic Left Heart Syndrome (HLHS), a congenital heart disease where the left ventricle and ascending aorta are underdeveloped, is commonly treated by a set of 3 surgeries. The first of these surgeries is the Norwood. In this surgery, the reconstructed aorta is anastomosed to the right ventricle, thus allowing systemic blood flow. To oxygenate the blood, options such as the modified Blalock-Taussig (mBT) are chosen to divert some of the systemic blood flow to the pulmonary circulation and create a balance between the two. In the case of the mBT, a shunt is connected from the brachiocephalic trunk to the pulmonary artery (PA).[1]

The coronary circulation is the means by which the heart receives oxygenated blood. The coronary artery descends from the ascending aorta into the myocardium to supply oxygen, and deoxygenated blood returns to the right atrium via the coronary sinus. In the case of HLHS patients with an mBT shunt, retrograde flow from the coronary circulation to the pulmonary circulation via mBT shunt is a common problem during diastole.[1] This shunt steal of coronary blood can lead to detrimental issues such as myocardial ischemia leading to right ventricular dysfunction.[2] Hence, it is essential to understand the relationship between mBT shunts and coronary blood flow so that these damaging circumstances can be avoided.

Multi-scale computational models of the Norwood circulation have modeled the coronary circulation and the effects of varying mBT shunts on coronary[2,3,4] and cerebral perfusion[3]. To our knowledge, limited work has been done in developing an *in vitro* multi-scale model of the same kind. This may be due to the intricate nature of the heart and its effect on the coronary flow. The contraction during systole and relaxation during diastole of the myocardium around coronary vessels provides a varying resistance to blood flow through the coronary circulation. Although the computational models have presented evidence of the effects the mBT shunt has on Norwood circulation, *in vitro* multi-scale models are commonly used for validation studies of such computational models. Therefore, the objective of this study is to implement the coronary circulation into a pre-existing *in vitro* model of the Norwood circulation so that phenomena such as shunt steal can be studied.

METHODS

An *in vitro* mock circulatory system (MCS) coupling a three-dimensional (3D) test section of the aorta with a lumped parameter network (LPN) describing the global hemodynamics of the Norwood patient's circulation was previously validated.[5] The coronary circulation and circulation values are based on a previous multi-scale model.[4]

As shown in Fig. 1, the expanded MCS's LPN is separated into four sub-circulations: upper body, lower body, pulmonary, and coronary. Each is composed of physical elements modeling the resistance, compliance, and inertance of that particular area. The system's driving mechanism is a ventricular assist device (Berlin Heart), which provides the patient-specific input to the 3D aortic test section. The system can be tuned to patient-specific values.

In particular to this system, the coronary circulation features the single ventricle pressure (SVP) signal in conjunction with the compliance, C_{ACE}, that dictates how the pressure, P_{ACE}, responds. The physical *in vitro* representation of this is an active compliance element (ACE) made up of a hydraulic and pneumatic chamber, and a connecting compliant diaphragm. The SVP signal is applied pneumatically to the air-filled chamber. The high systolic and low diastolic pressures of this signal act through the diaphragm into the hydraulic chamber connected to the LPN. P_{ACE} is accordingly raised

Copyright 2016 The Organizing Committee for the 2016 Summer Biomechanics, Bioengineering and Biotransport Conference

or lowered due to this signal, such as when the myocardium tightens and relaxes around the coronary vessels.

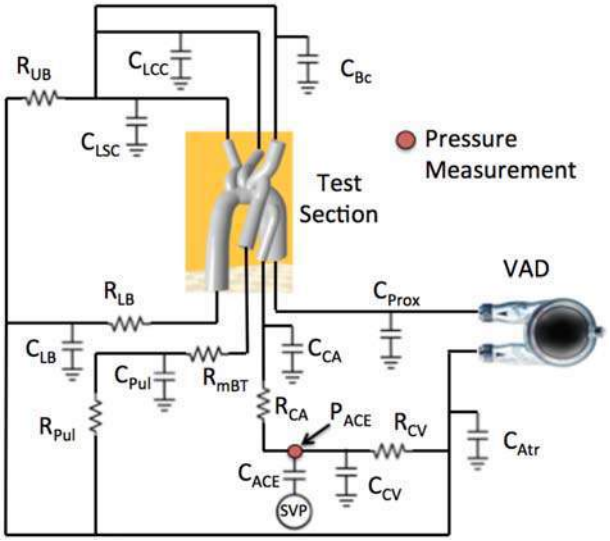

Figure 1: MCS of the coupled LPN and 3D test section that is pneumatically powered by a ventricular assist device (VAD). R, resistance; C, compliance; Prox, proximal; Bc, brachiocephalic artery; LCC, left common carotid; LSC, left subclavian; UB, upper body; LB, lower body; mBT, modified Blalock-Taussig shunt; Pul, pulmonary; CA, coronary artery; ACE, active compliance element; SVP, single ventricle pressure; CV, coronary vein; Atr, atrium.

Initial testing of the *in vitro* system was done in which a 3D test section[3] was introduced into the system under parameters described by Lagana et al.[4] The results were compared to those from a newly developed complete LPN model of the system in Fig. 1. Flow and pressure measurements from the experimental model closely matched those from the LPN model, thus verifying the *in vitro* setup represented the LPN. Further tests were completed with patient specific 3D test sections and hemodynamic parameters. The MCS was validated by recapitulating physiological flow and pressure measurements.

RESULTS

Preliminary testing of the coronary circulation's ACE was completed to ensure a proper SVP signal could be generated to create the appropriate response at P_{ACE}. In these tests, pneumatic pressure signals of the ACE were compared to SVP signals from the LPN and clinically obtained ventricle pressure waveforms. As shown in Fig. 2, a physiological SVP was achieved. Further, the response of the P_{ACE} is in accordance to previous studies that found decreased coronary flow during systolic ventricular contraction.[3] The increase in SVP (Fig. 2) corresponds with the onset of systole. Concurrently, P_{ACE} increases, which opposes flow through the coronary circulation. At the onset of diastole when SVP decreases, P_{ACE} also decreases, allowing flow to continue through the coronary circulation. These signals were achieved at a mean coronary flow rate of 0.08 ± 0.02 L/min, which corresponds to the mean flow found in previous studies.[4]

Further testing of the entire MCS was then conducted and results closely matched those of the LPN model and clinical data.

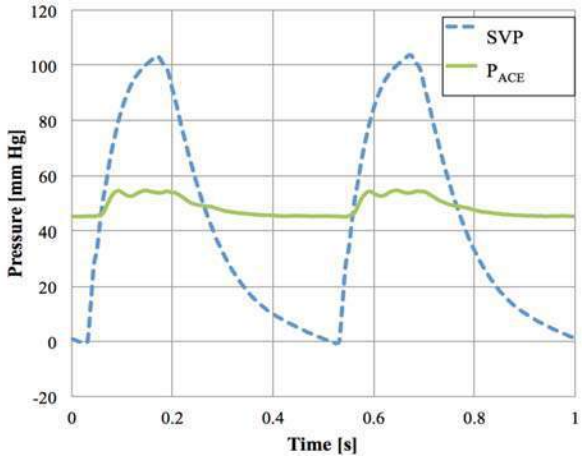

Figure 2: The SVP signal made in the ACE and the corresponding pressure measured at the connection of the ACE and *in vitro* LPN, P_{ACE}. Mean coronary flow of 0.088 ± 0.018 L/min.

DISCUSSION

The previous standard of testing coronary circulation of Norwood patients relied on multi-scale computational models.[3,4] Most *in vitro* systems did not include coronary circulation due to its complexity. However, it is believed that *in silico* models cannot be validated by clinical data; that there must be an *in vitro* MCS to bridge that connection.

Preliminary results show that an *in vitro* MCS including the coronary circulation is feasible for studying Norwood hemodynamics. Additionally, the ACE coupled with the SVP is instrumental in modeling the myocardium's interaction with coronary vessels to accurately dictate coronary flow and pressure. In the future, this expanded *in vitro* system can be used to study the effects of varying patient physiologies, such as coarctation and the effects of shunt size.

The combination of aortic coarctation and the mBT shunt in Norwood patients has been shown to result in shunt steal.[3] Shunt steal can be harmful because it corresponds to decreased coronary flow, and thus decreased oxygen delivery to the heart. In Norwood circulation, the right ventricle is already having to support both systemic and pulmonary blood flow. Decreased coronary oxygen supply can change the elastance of the heart, resulting in less cardiac output and less oxygenated blood to the body. This would result in a damaging cyclic reaction where the heart continues to not receive enough blood and becomes more and more weak.[2] Shunt steal has also been linked with decreased cerebral perfusion.[3] And so, expanding on this new *in vitro* MCS will be pertinent in developing an even greater understanding of how the various Norwood surgical options can present positive or negative hemodynamics.

The results show that an *in vitro* multi-scale model of Norwood circulation, including the coronary, is possible and can be used to study the coronary steal phenomenon.

ACKNOWLEDGEMENTS

This study is supported by the Leducq Foundation, Paris.

REFERENCES

[1] Migliavacca, F. et al. *J Biomech*, 39:1010-1020, 2006.
[2] Mahdi, E. et al. *J Biomech,* 134:051002, 2012.
[3] Corsini, C. et al. *Ann. Thorac Surg*, 98:648-654, 2014.
[4] Lagana, K. et al. *J Biomech*, 38:1129-1141, 2005.
[5] Hang, T. et al., *ASAIO J*, 62(3), 2016 in press.

Copyright 2016 The Organizing Committee for the 2016 Summer Biomechanics, Bioengineering and Biotransport Conference

SB³C2016
Summer Biomechanics, Bioengineering and Biotransport Conference
June 29 –July 2, National Harbor, MD, USA
SB³C2016-92

COLLAGEN DEGRADATION ALTERS FAILURE PROPERTIES & MATRIX REORGANIZATION DURING TENSILE LOADING

Meagan E. Ita (1), Beth A. Winkelstein (1,2)

(1) Department of Bioengineering
University of Pennsylvania
Philadelphia, PA, United States

(2) Department of Neurosurgery
University of Pennsylvania
Philadelphia, PA, United States

INTRODUCTION

The spinal facet joints are a common source of pain, which can be induced by degeneration due to either aging or injury [1,2]. Degeneration of spinal tissues is associated with changes in tissue composition [3], including enzymatic tissue degradation via increases in collagenase protein and mRNA [2]. Collagenase activity in degenerative states can degrade collagen, which is the main component of the facet capsular ligament (FCL) [3,4]. Although enzymatic digestions simulating tissue degradation alter the mechanical properties of tissue [5], the effect of collagen degradation on ligament mechanics is not well defined. Also, it is unclear how collagen degradation affects failure responses and if, and how, a loss of collagen alters how a collagen matrix reorganizes under load.

FCL loading that induces microstructural damage and pain coincides with anomalous collagen matrix reorganization [6-8]. That microstructural damage occurs before any tissue rupture and is associated with decreased tissue stiffness and ligament laxity [6,8,9]. Further, the regional strains at microstructural damage correspond to those that induce pain in vivo and activate neurons embedded in collagen networks in vitro [7,8]. Although collagen degradation occurs in degeneration-induced pain [2,3], the effects of that degradation on ligament mechanics and/or the potential for injury is not known.

Accordingly, collagen degradation is hypothesized to lower the macroscopic failure properties and also to alter matrix reorganization during tensile loading. To test this hypothesis, an in vitro collagen gel model was modified using bacterial collagenase to enzymatically degrade collagen. First, the effect of digestion time on collagen loss was assessed. From that work, a digestion time that appreciably decreases collagen density while leaving the collagen gel intact was identified and used in a second study that quantified failure mechanics, local strain, and matrix reorganization under tensile distraction.

METHODS

To assess the effect of collagenase digestion time on collagen gel degradation, compositional experiments analyzed collagen loss after 10mins or 35mins. Gels were formed in 24-well plates with 800µl rat tail collagen I solution at 2mg/ml (Corning) and allowed to gel overnight at 37ºC (n=4). Bacterial collagenase (Sigma C0130) was dissolved in DMEM (2mg/ml) and heated for 30mins at 37ºC [10]. After digestion in 2.5ml of collagenase solution for the designated time, gels were washed in PBS; separate groups were lyophilized or post-fixed for immunolabeling of collagen (n=4). Matched gels were digested in DMEM for 10mins or 35mins to serve as controls (n=4).

To quantify collagen loss, dry weights (DW) were measured after lyophilization for 24hrs at <0.12mBar and -43ºC. To measure collagen changes by immunolabeling, gels were blocked, incubated overnight at 4°C with collagen antibody (anti-mouse, Abcam, 1:400), and then incubated for 2hrs with Alexa Fluor 488 (1:1000). Images (n=5) were taken throughout each gel at 40X using a Zeiss LSM510 confocal microscope. Collagen labeling was quantified using densitometry and t-tests compared the digest and control groups at each time point.

Based on that work, the effect of collagen degradation on tensile failure, local strain, and matrix reorganization was evaluated with gels digested for 35mins. Gels were formed in dog-bone molds with 5ml collagen I (2mg/ml) [7,11] and digested in collagenase or bathed in DMEM as controls (n=4/group). Gels were washed before mounting in an Instron5865 [7]. A grid of markers was tracked by a Phantom v9.1 camera (Vision Research) at 500fps to quantify strains. Polarized light imaging was acquired during loading at 500fps to generate alignment maps of collagen fibers that were used to calculate the circular variance (CV) which measures the spread of fiber angles [6,7,12].

Gels were distracted to failure at 0.5mm/sec. Force and displacement data were collected at 1kHz and synchronized with video

Copyright 2016 The Organizing Committee for the 2016 Summer Biomechanics, Bioengineering and Biotransport Conference

data for strain and CV calculations. Force data were digitally filtered [9] and force-displacement curves used to define failure, which was the maximum force during loading (Fig. 1). Stiffness was defined as the slope of the loading curve at 20-80% of maximum force (Fig. 1) [13]. The maximum principal strain (MPS) at failure was computed using the marker displacements and LS-DYNA, with the peak MPS recorded at failure [7]. CV values were calculated both before loading (reference) and at failure to compare collagen matrix reorganization after digestion but before loading, and at failure. Lower CV values indicate a more random fiber orientation and higher values indicate preferential fiber alignment [7,12]. T-tests compared all measures separately between the digest and control gels.

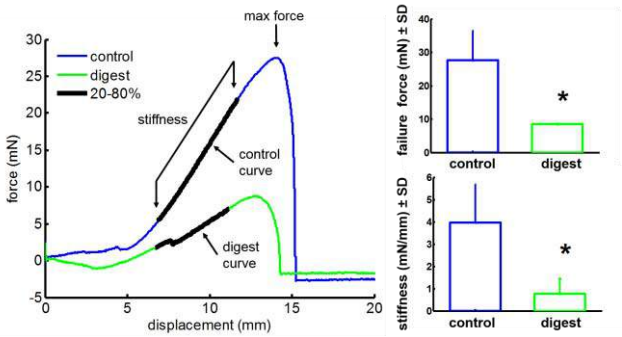

Fig. 1. Representative force-displacement curves. Failure force and stiffness are lower for digest than control gels (*p<0.03).

RESULTS

Collagen loss was detectable after 35mins, but not 10mins, of digestion with significantly less (p=0.03) collagen immunolabeling only in 35mins digest gels (Fig. 2). The decreased collagen labeling corresponds to lower DW of 28.6% and 40.0% after 10mins and 35mins, respectively. Before loading, macroscopic defects like small tears and thinning of the gel were evident only after digestion and not in control gels (Fig. 2). Despite those defects, no differences in the collagen fiber orientation was detected between digest (0.0007±0.0010) and control (0.0012±0.0010) gels before loading.

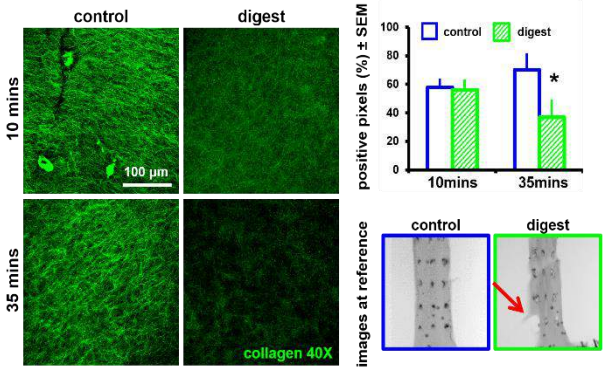

Fig. 2. Representative confocal images of immunolabeled gels prior to distraction show decreased collagen (*p=0.03) & macroscopic structural defects (red arrow).

The failure force was significantly lower (p=0.022) in digest gels (8.48±0.29mN) than controls (27.70±8.74mN) (Fig. 1). Tensile stiffness was similarly decreased (p=0.025) by 75.6±44.8% after digestion (Fig. 1). However, the displacement at failure was not altered (control: 8.60±4.06mm; digest: 6.72±5.3mm), nor was peak MPS. But, the dramatic increase in fiber alignment at failure that was observed in controls was not evident in digested gels (Fig. 3). In fact, the difference in CV at failure between groups was significant (p=0.045).

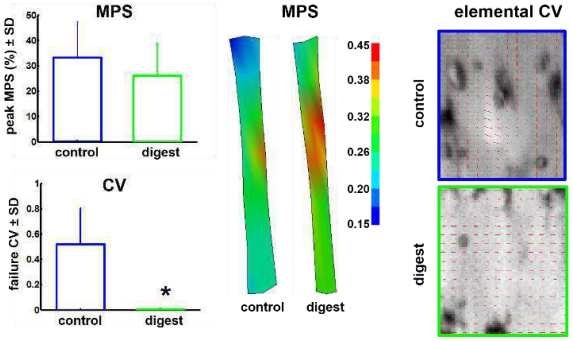

Fig. 3. Collagenase digestion does not alter the peak MPS at failure but does prevent the increase in CV that is evident in control gels, which is significant (*p=0.045).

DISCUSSION

Collagen degradation decreases failure force and stiffness but does not change failure strains (Figs. 1 & 3). Although the peak MPS is not altered by digestion, collagen matrix kinematics are different, with less reorganization at failure (Fig. 3). Both groups fail at displacements (~7-9mm) that initiate neuronal activation and at strains exceeding a transition for collagen fiber kinematics in this same collagen gel system [7]. Those same strains also correspond to pain in vivo [8,13]. Taken with the literature, our results suggest that a substantial loss in collagen may not alter the regional strains in a degraded ligament and that similar mechanotransductive signaling may be initiated under the same biomechanical conditions regardless of the extent of tissue degradation. However, because pain is evident with degeneration in the absence of excessive tissue loading [2,3], biochemical mediators or other non-mechanical factors may contribute to degeneration-associated pathology.

Transient FCL tension that causes pain also decreases ligament stiffness and fiber realignment in vivo [8]. Yet, in our study, collagen degradation does *not* cause fiber realignment (Fig. 3), suggesting that collagen degradation alters how the matrix responds to loading. Since collagenase preferentially degrades *unstrained* collagen fibers [10] and unloaded gels were digested, a greater degree of collagen degradation is expected here than for a degenerated ligament in vivo. Yet, since FCL injury induces both degeneration and laxity [2,3,8], degeneration may alter the loading state of a ligament in vivo and cause some fibers to be strained more than others, which would also cause unstrained collagen fibers to degrade more quickly than strained fibers [10]. Such an inhomogeneous biomechanical environment has implications for neurons in unloaded regions of a ligament. As such, imposing tension after digestion of pre-loaded gels would reveal any changes in the global and/or regional mechanics [10]. Nonetheless, this work begins to define how collagen degradation affects global and local mechanics, and highlights potential pathomechanisms by which degenerative processes may mediate biomechanical and physiological responses.

ACKNOWLEDGEMENTS

This project was funded by the NIH (U01EB016638).

REFERENCES

1. Institute of Medicine *National Academies*, 2011; 2. Kim J et al *Osteoarthr Cartilage* 23:2242-51, 2015; 3. Jaumard N et al *J Biomech Eng* 133:071010, 2011; 4. Yamashita T et al *Spine* 21:538-43, 1996; 5. Barbir A et al *J Biomech* 43:1067-73, 2010; 6. Quinn K & Winkelstein B *J Biomed Opt* 14:054010, 2009; 7. Zhang S et al *J Biomech Eng* in press 2016; 8. Quinn K et al *Stapp J* 51:169-87, 2007; 9. Quinn K et al *J Biomech* 43:1870-5, 2010; 10. Bhole A et al *Philos T Roy Soc A* 367:3339-62, 2009; 11. Lake S & Barocas V *Ann Biomed Eng* 39:1891-903, 2011; 12. Miller K et al *Ann Biomed Eng* 40:1102-10, 2012; 13. Lee K et al *J Biomech* 39:1256-64, 2006.

Copyright 2016 The Organizing Committee for the 2016 Summer Biomechanics, Bioengineering and Biotransport Conference

SB³C2016
Summer Biomechanics, Bioengineering and Biotransport Conference
June 29 –July 2, National Harbor, MD, USA
SB³C2016-93

ASSESSING HEMODYNAMIC RESPONSE TO EXERCISE FOR PATIENT WITH LEFT VENTRICULAR HYPERTROPHY BY INTEGRATING CARDIOVASCULAR AND AUTONOMIC NERVOUS SYSTEMS

Weiwei Jin (1), Fuyou Liang (2), Hao Liu (1,2)

(1) Graduate School of Engineering
Chiba University
Chiba-shi, Chiba, Japan

(2) Department of Naval Architecture and Ocean Engineering
Shanghai Jiao Tong University and Chiba University International Cooperative Research Center (SJTU-CU ICRC), Shanghai Jiao Tong University, Shanghai, China

INTRODUCTION

Dynamic exercise influences the cardiovascular system in various ways, especially for patients with cardiovascular diseases (CVD). As a usual tool to quantify the dynamic exercise, exercise test is often utilized in clinical field to evaluate the severity of CVD. In reality, both myocardial infraction and death have been reported to occur at an incident rate of 1/2500 during the test [1], and a simulation-based exercise test for patients with CVD can be affective to avoid such risk. Pervious numerical studies have been carried out to investigate how the patients with CVD respond to exercises, whereas, the exercise data were either obtained based on the experiment, or simply by adjusting the resistance in arterial system [2–4]. Here we have designed a virtual exercise test by developing an integrated computational model, which coupled the cardiovascular system (CVS) and the autonomic nervous system (ANS). As a case study for CVD, we performed the simulation-based exercise test on patients with left ventricular hypertrophy (LVH), one of the chronic cardiac diseases with an annual mortality rate of 2.1% [5]. In this study, we compared the hemodynamic features between healthy subjects and patients with LVH during cycling exercise to assess hemodynamic response to exercise with and/or without LVH as well as to discuss their functional discrepancy.

METHODS

A double-closed-loop model for hemodynamic prediction and cardiovascular regulation that involves a CVS model, an ANS model, and an exercise model has been established. The CVS model is a time-domain closed-loop lumped model, which consists of 4 cardiac chambers and 266 arteries. The CVS model and the ANS model are coupled in terms of blood pressure, heart rate, cardiac contractility, arteriolar resistance, and compliance and unstressed volume of veins. Descriptions of the governing equations associated with the CVS and ANS models in detail can be found in our previous study [6].

In the exercise mode, the input is set to be the intensity of exercise which is determined by oxygen intake, and also relates to workload. The outputs of the exercise model influence both the CVS model and the ANS model. The blood pressure in the CVS model is influenced dynamically by muscle pump, mechanovasodilation, and metabovasodilation; the ANS model is affected by a combination of resetting of operating pressure threshold of the arterial baroreflex, central command model, and summary of mechanoreflex, metaboreflex and baroreflex. To provide a peek of the exercise model, modeling equations for the muscle pump are illustrated below.

$0 \le t_{im} \le T_{con}$:

$$p_{im} = p_{imp} \cdot sin\left(\frac{\pi}{2} \cdot \frac{t_{im}}{T_{con}}\right) \quad (1)$$

$T_{con} < t_{im} \le T_{rel}$:

$$p_{im} = p_{im}|_{T_{con}} \cdot sin\left(\frac{3\pi}{2} \cdot \frac{t_{im} - T_{con}}{T_{rel} - T_{con}}\right) \cdot \left(1 - \frac{t_{im} - T_{con}}{T_{rel} - T_{con}}\right) \quad (2)$$

$without\ muscle\ pump$:

$$p_{im} = 0 \quad (3)$$

where t_{im} [s] is a moment during muscle contraction-relation cycle; T_{con} [s] is the duration of muscle contraction; T_{rel} [s] is a specified moment before the end of a contraction-relaxation cycle; p_{im} [mmHg] is the extravascular pressure; p_{imp} [mmHg] is the peak value of p_{im}, which is dependent on the oxygen intake [7].

The LVH model is based on the previous study [8]. Peak systolic and diastolic wall stress σ_s [kPa] and σ_d [kPa] are related to the wall thickness in left ventricle, therefore the maximum and minimum values of the elastance in left ventricle can be presented as follow:

Copyright 2016 The Organizing Committee for the 2016 Summer Biomechanics, Bioengineering and Biotransport Conference

$$e_{lv,max} = \frac{\frac{\sigma_s h(2r+h)}{r^2}}{LVESV - V_d} \quad (4)$$

$$e_{lv,min} = \frac{\frac{\sigma_d h(2r+h)}{r^2}}{LVEDV - V_d} \quad (5)$$

where $e_{lv,max}$ [mmHg · ml^{-1}] and $e_{lv,min}$ [mmHg · ml^{-1}] are the maximum and minimum values of the elastance in left ventricle, respectively; h [cm] is the wall thickness in left ventricle; r [cm] is the cavity radius in left ventricle; $LVESV$ [ml] and $LVEDV$ [ml] are the end systolic and end diastolic volume in left ventricle, respectively; V_d [ml] is a volume axis related to the end-systolic *P-V* relation in left ventricle.

RESULTS

Mean blood pressure (MBP), heart rate, and cardiac output in healthy subjects and patients with LVH during the rest and the exercise are illustrated in Figure 1, 2, and 3, respectively. During the exercise, MBP increased in healthy subjects, while barely changed in patients with LVH. The difference of heart rate between healthy subjects and patients with LVH is relatively small during the exercise (rest: 10%, exercise: 4%). Meanwhile, the increase of heart rate form the rest to the exercise is extensive, and the increased amount is relatively small in patients with LVH (healthy subjects: 36%, patients: 27%). The increase of cardiac output from the rest to the exercise is relatively low in patients with LVH (healthy subjects: 35%, patients: 14%). Therefore, cardiac output for healthy subjects and patients with LVH is close during the rest, while decreased in patients with LVH during the exercise. In addition, the simulated data for both healthy subjects and patients with LVH during the rest are consistent with the experimental results in the previous study [9].

DISCUSSION

The simulated results of MBP and heart rate obviously show a trend in the increased stiffness of blood vessel and workload of the heart, along with the decreased cardiac function in the patients with LVH. We further observed that the insufficient blood supply in the patients with LVH during the exercise, indicating that the dynamic exercise may endanger the patients. This points to the importance of a virtual exercise test as a useful tool to reduce the burden of the patients during clinical testing. On the other hand, the major limitation in this study is the lack of clinical data for constructing a patient specific model, which will be our future work. Despite of this, the current study demonstrates the potential of utilizing the detailed mathematical exercise model to quantify and assess the severity of CVD in concert with including LVH.

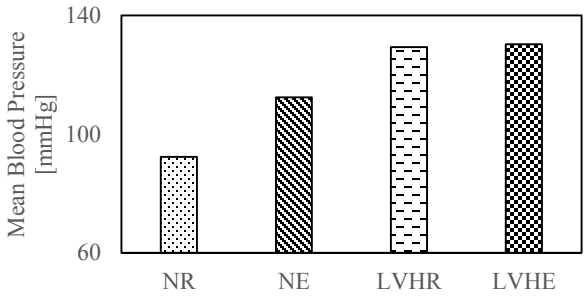

Figure 1: Mean blood pressure for healthy subjects during the rest (NR) and the exercise (NE), patients with LVH during the rest (LVHR) and the exercise (LVHE).

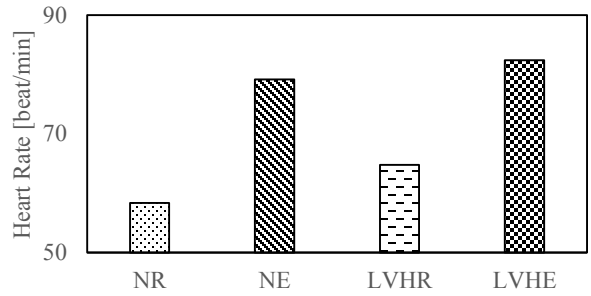

Figure 2: Heart rate for healthy subjects in the rest (NR) and during the exercise (NE), patients with LVH in the rest (LVHR) and during the exercise (LVHE).

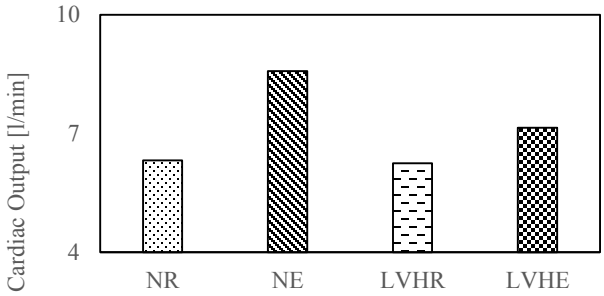

Figure 3: Cardiac output for healthy subjects during the rest (NR) and the exercise (NE), patients with LVH during the rest (LVHR) and the exercise (LVHE).

ACKNOWLEDGEMENTS

Financial support provided by Japanese Government (Monbukagakusho: MEXT) scholarship to WJ is acknowledged.

REFERENCES

[1] Akinpelu, D., *Medscape*, 2015.
[2] Kung, E., et al., 2014, *J. Biomech. Eng.*, 136:1–13, 2014.
[3] Jiang, J., and Strother, C., *J. Biomech. Eng.*, 131:091001, 2009
[4] Kim, H. J., et al., 2010, *Ann. Biomed. Eng.*, 38:2314–30, 2010.
[5] Kokkinos, P., et al., *Annual Scientific Meeting*, 2012.
[6] Liang, F., and Liu, H., 2006, *J. Physiol. Sci.*, 56:45–65, 2006.
[7] Laughlin, M. H., *Am. J. Physiol.*, 253:993–1004, 1987.
[8] Segers, P., et al., *Am. J. Physiol. Heart Circ. Physiol.*, 279:1120-1127, 2000.
[9] Ishii, K., et al., 2012, J. Appl. Physiol., 112:1961–1974, 2012.

Copyright 2016 The Organizing Committee for the 2016 Summer Biomechanics, Bioengineering and Biotransport Conference

SB^{3}C2016
Summer Biomechanics, Bioengineering and Biotransport Conference
June 29 –July 2, National Harbor, MD, USA
SB^{3}C2016-94

COMPUTATIONAL INVESTIGATION OF HYDROGEL INJECTION CHARACTERISTICS FOR MYOCARDIAL SUPPORT

Hua Wang (1), Christopher B. Rodell (2), Mandonna E. Lee (3), Neville N. Dusaj (4), Jason A. Burdick (2), Robert C. Gorman (3), Jonathan F. Wenk (1, 5)

(1) Department of Mechanical Engineering
University of Kentucky
Lexington, Kentucky, USA

(2) Department of Bioengineering
University of Pennsylvania
Philadelphia, Pennsylvania, USA

(3) Gorman Cardiovascular Research Group,
University of Pennsylvania
Philadelphia, Pennsylvania, USA

(4) Department of Chemistry and Physics
University of Pennsylvania
Philadelphia, Pennsylvania, USA

(5) Department of Surgery
University of Kentucky
Lexington, Kentucky, USA

INTRODUCTION

The material properties of myocardium are an important determinant of global left ventricular (LV) function in both health and disease. In vivo studies have demonstrated that hydrogel injections can mitigate the adverse effects of myocardial infarction. More importantly, the stiffness of these injections can be tuned to minimize wall thinning and ventricular dilation. The current investigation combines experimental data and finite element (FE) modeling to correlate how injection stiffness and volume influence myocardial wall stress and wall thickness. The results indicate that increased injection stiffness reduced LV myofiber stress. Also, stiffer hydrogel injections maintained an increased level of LV wall thickness. Overall, this study may predict that stiffer and bigger hydrogel injection can reduce MI bulging during LV remodeling.

METHODS

In order to evaluate the effects of hydrogel injections on myocardial wall stress, FE models of the LV with two different injection volumes were generated (150μL and 300μL). The size and shape of the hydrogel injections were based on MRI of injected explant tissue (Table 1). The geometry of the LV wall was based on experimental measurements from the ovine hearts. Since the model was meant to mimic the initial time frame after infarction, it was assumed that 30 minutes post-MI the myocardial properties around the injections would be roughly unchanged [2]. The myofiber orientation was assigned to vary linearly from epicardium to endocardium using the angles of -37 degrees to 83 degrees, respectively. For the control case, the undeformed wall thickness was approximately 1.3cm. For the models with hydrogel injections, the control model was modified to include a 4 x 4 pattern of 16 injections around the free wall (Figure 1).

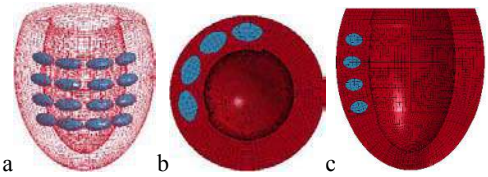

Figure 1: (a) FE model of ovine LV with 16 300μL hydrogel injections in the free wall. (b) Short axis view of LV wall. (c) Long axis view of LV wall.

150μL	
a	5.50mm
b	3.15mm
c	2.4mm

300μL	
a	6.60mm
b	3.94mm
c	2.73mm

Table 1: Ellipsoidal dimensions of the 150μL hydrogel injection and 300 μL hydrogel injection, based on MRI data.

The material response of the myocardium was represented using a nearly incompressible, transversely isotopic, hyperelastic constitutive law, which was defined using the following strain energy function:

$$-(e \quad 1) + -(J \quad 1) \qquad (1)$$
$$(E \qquad) + \quad (E \qquad)$$

where E_{ij} are the deviatoric components of the Green-Lagrange strain tensor relative to the myofiber coordinate system (f=fiber direction, s=cross-fiber in-plane direction, n= transverse-fiber

Copyright 2016 The Organizing Committee for the 2016 Summer Biomechanics, Bioengineering and Biotransport Conference

direction) and J is the determinant of the deformation gradient. The diastolic material parameters were assigned to be C = 0.51 kPa, b_f = 22.84, b_t = 3.45, and b_{fs} = 12 [1], while the bulk modulus was κ = 1e10^3 kPa. The material response of the hydrogel injections was represented using a nearly incompressible, isotopic, hyperelastic constitutive law, which was defined using the following strain energy function:

$$W_{injection} = \frac{E}{2(1+\nu)}\,\mathrm{tr}(\mathbf{E}^2) + \frac{E}{6(1-2\nu)}\,\ln(J)^2 \qquad (2)$$

where $\mathbf{E}$ is the deviatoric Green-Lagrange strain tensor. The material parameters for Young's modulus (E) were assigned in a range between 0.1kPa to 100kPa, while the Poison ratio (ν) was assigned a value of 0.499. A pressure of 10 mmHg was assigned as a boundary condition on the endocardial wall in each of the FE models.

RESULTS

Figure 2a shows that when the injection stiffness is 0.1kPa the transmural distribution of stress is nearly unchanged compared to the control. For hydrogel stiffness of 25kPa, the 150µL injection reduced the myofiber stress by roughly 18.9% at the epicardium, 0% at mid-myocardium, and 21.6% at endocardium compared to the control (Figure 2b). While, the 300µL injection reduced the myofiber stress by roughly 31% at the epicardium, 10.6% at the mid-myocardium, and 34.7% at endocardium compared to the control (Figure 2b). For hydrogel stiffness of 100kPa, the 150µL injection reduced the myofiber stress by roughly 39.2% at the epicardium, 18.3% at mid-myocardium, and 38.7% at endocardium compared to the control (Figure 2c). While, the 300µL injection reduced the myofiber stress by roughly 56.8% at the epicardium, 36.5% at the mid-myocardium, and 55.2% at endocardium compared to the control (Figure 2c).

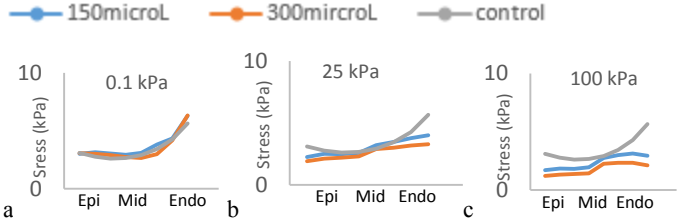

Figure 2: (a-c) End-diastolic transmural distribution of myofiber stress using stiffness 0.1kPa, 25kPa and 100kPa hydrogel injection between 150µL injection and 300µL injection.

Additionally, the results of average myofiber stress in the myocardium surrounding the 150µL and 300µL injection, using different hydrogel stiffness, is shown in Figure 3. When the injection stiffness is increased, the myofiber stress was decrease. It should be noted that the slope of the trend lines decreased after 50kPa, indicating that the influence of stiffness begins to level off. Figure 4 shows the average wall thickness as a function of injection stiffness. When the injection stiffness increased, the wall thickness was increased. The average wall thickness at end-diastole for the control was approximately 1cm, while the thickness for the 150µL injection with 25kPa stiffness was 1.1cm and 300µL was 1.2cm. For the case of 150µL injection with 100kPa stiffness, the thickness was 1.2cm while 300µL was 1.3cm. This is primarily driven by the fact that the stiffer injections maintained their original shape during deformation, which allowed the LV wall to remain thick (Figure 5c and 5f). However, it can be seen that the 0.1kPa injection effectively collapse as the LV wall is loaded by the pressure on the endocardium (Figure 5a and 5d).

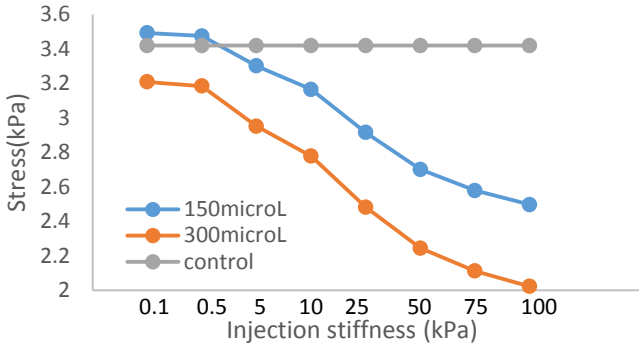

Figure 3: Average end-diastolic myofiber stress surrounding the injection as a function of injection stiffness and volume.

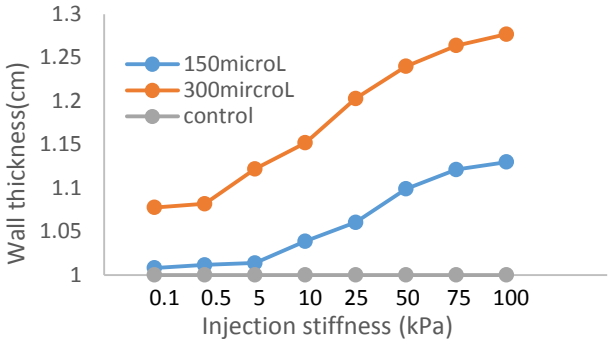

Figure 4: End-diastolic myocardial wall thickness in the injection region as a function of injection stiffness and volume.

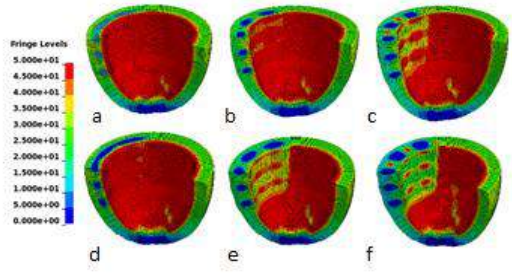

Figure 5: (a-c) The LV myofiber stress distribution around 150 µL injections and (d-f) 300 µL injections with stiffness values of 0.1kPa, 25kPa and 100kPa.

DISCUSSION

FE models were generated using experimentally measured LV and injection geometry. The modeling results show a clear reduction of myofiber stress based on the hydrogel injection volume. Additionally, by turning the stiffness of the hydrogel, greater reductions in stress can be achieved. The current results indicated that stiffer, bigger hydrogel injections could reduce myofiber stress further. These improvements taper after a stiffness of 50kPa.

ACKNOWLEDGEMENTS

This study was supported by NIH grants R01 HL063954 (R. Gorman), R01 HL111090 (J. Burdick), R01 HL73021 (J. Gorman), and by a grant from the AHA 14BGIA18850020 (J. Wenk).

REFERENCES

[1] Tous et al. Ann Biomed Eng. 42:1546-1556, 2014.
[2] Holmes et al. Annu. Rev. Biomed. Eng. 7:223–253, 2005.

Copyright 2016 The Organizing Committee for the 2016 Summer Biomechanics, Bioengineering and Biotransport Conference

SB^{3}C2016
Summer Biomechanics, Bioengineering and Biotransport Conference
June 29 –July 2, National Harbor, MD, USA
SB³C2016-95

A MULTIPHYSICS MODEL OF THE PACINIAN CORPUSCLE

Julia C. Quindlen (1), Henryk K. Stolarski (2), Martha Flanders (3), Victor H. Barocas (1)

(1) Department of Biomedical Engineering
University of Minnesota – Twin Cities
Minneapolis, MN, USA

(2) Department of Civil Engineering
University of Minnesota – Twin Cities
Minneapolis, MN, USA

(3) Department of Neuroscience
University of Minnesota – Twin Cities
Minneapolis, MN, USA

INTRODUCTION

Mechanoreceptors located throughout the body transduce mechanical stimuli into neural signals that produce sensations such as touch and pain [1]. The Pacinian corpuscle (PC), located within the skin, responds to 50-1000 Hz vibrations [2]. The PC structure allows transmission of vibrations through its layers (lamellae), ultimately resulting in deformation of the centrally-located nerve fiber (neurite) and neuronal action potentials. The mechanisms by which mechanical stimuli pass through the PC lamellae to the nerve fiber, and by which neurite deformation induces neural response, remains unknown. This work combines a mechanical model of the PC with an electrochemical model of nerves to simulate the entire tactile response of the system.

The PC shows two distinct neural responses to mechanical stimulation: high-pass filtration of oscillating stimuli [3,4] and rapid adaptation to sustained stimuli [5]. Attempts have been made to address these observations separately [6,7] and to determine the relationship between PC structure and its unique mechanical response. No study has been able to unify these observations to answer the fundamental question of how the PC responds to mechanical stimulation, which requires a multiphysics and multiscale analysis. In this work, we examined the filtering and adaptation properties of the PC via a single mechanically and electrochemically unified model.

METHODS

A three-stage model was developed, consisting of three separate models applied in series. The input to Stage 1 was a mechanical stimulus applied to the PC outer surface, which supplied inner core deformation to Stage 2. The output of Stage 2 was the neurite membrane strains, which were input into Stage 3 to control stretch-gated channel dynamics. The output of Stage 3 was the neural response to the specific stimulus applied in Stage 1. A schematic of the three-stage model is shown in **Figure 1**.

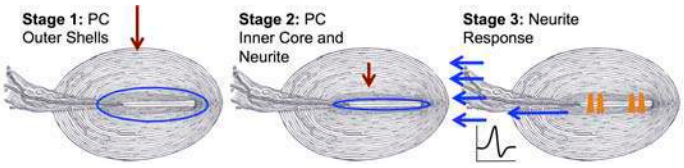

Figure 1: Three-stage dynamic model used in study.

Stage 1: Outer core spherical shell mechanical MATLAB model: A detailed model was developed of the alternating fluid and lamellar layers in the outer core, whose structure is hypothesized to control the PC's high-pass filtering [2,6]. The mechanics of the lamellae were modeled with the equations of equilibrium for spherical shells, and the fluid was modeled as a thin lubricating layer. Alternating layers of fluid and solid were coupled in a finite-element model. A 30-layer model was assigned parameters obtained from a previous study [7]. The elastic modulus of each lamella was 500 kPa, with layer thicknesses of 0.1-0.4 μm, and the fluid viscosity was 7 mPa-s. Oscillating pressure was applied to the outer shell at 1-10^8 Hz. Sustained pressure was applied with square wave displacements generated via a Fourier series and applied to the outer shell. The displacements of each shell were obtained in the simulations.

Stage 2: Inner core and neurite mechanical COMSOL model: A second mechanical model was created to account for the complex morphology of the PC neurite. Simulations of the inner core and neurite were performed in COMSOL's frequency domain mode to compute neurite mechanics in response to vibrations of the inner core.

The inner core was modeled as a sphere, and the neurite was modeled as a cylinder with five filopodia (2 central, 3 distal). The domain was modeled as an isotropic linearly elastic material with a Young's modulus of 7kPa [8], a Poisson's ratio of 0.49, and density of 1000 kg/m^3. Damping was modeled by an isotropic loss factor of 0.2.

Copyright 2016 The Organizing Committee for the 2016 Summer Biomechanics, Bioengineering and Biotransport Conference

The outer boundary of the inner core received a prescribed displacement equal to that of the innermost shell in Stage 1. Simulations were run at 30-1000 Hz.

Stage 3: Electrochemical neurite model: A model was created in NEURON to convert strain on the neurite membrane into opening of stretch-gated cation channels at the base of the filopodia [9]. Stretch-gated channel opening was approximated by an increase in injected current at each location on the membrane. Current proportional to the strain measured at the base of each filopodia in the COMSOL model was inserted at the base of the corresponding dendrite in the NEURON model. Simulations were run for 1000 ms. Membrane potential and action potential firing rate were calculated.

RESULTS

Stage 1: Simulations were run for spheres of different sizes to observe the effect of shell number on the frequency response. The number of layers was increased from 2 to 30 shells. The displacement amplification is shown for different frequencies and PC sizes in **Figure 2**. The model showed characteristic high-pass behavior in models with more than 10 shells.

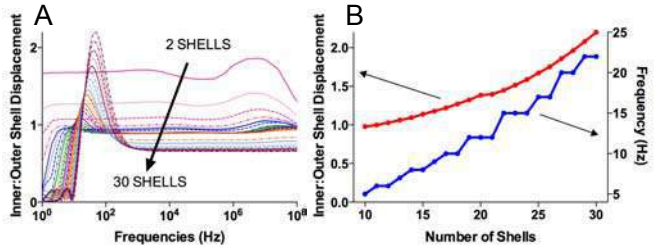

Figure 2: (A) Ratio of inner to outer maximum displacements vs. frequency for spheres of 2-30 shells. (B) Peak displacement and frequency at peak displacement for spheres of 10-30 shells.

The inner and outer shell displacements during the square wave simulations are shown in **Figure 3**. The PC mechanically adapts in response to the sustained pressure, as the inner core displaces only during the onset and offset of the stimulus, as seen experimentally [5].

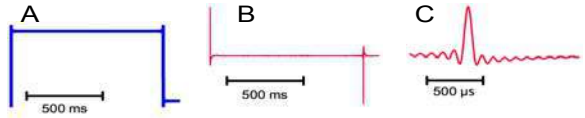

Figure 3: (A) Outer and (B) inner shell displacements in square wave simulations from summation of 0.5-1000.5 Hz simulations. (C) Inner displacement zoomed-in on stimulus onset response.

Stage 2: **Figure 4** shows the first principal strain of the neurite alone at the peak displacement during a 150 Hz simulation. High strain occurred near the filopodia at the distal end of the neurite (Location I).

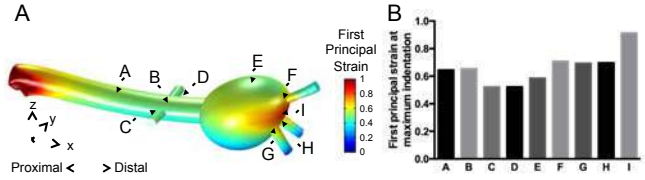

Figure 4: First principal strain on neurite surface at maximum displacement. The graph in (B) plots value at the locations in (A).

Stage 3: The firing rate in response to current injection proportional to the Stage 2 neurite strains was calculated. **Figure 5A** shows experimental [3] firing rates recorded from PCs stimulated with sinusoidal indentations at increasing displacement. The plots in **Figure 5** have been color-coded to show similarities between experiments and simulated neurite firing rates obtained from the NEURON model (**Figure 5B**). In both cases, the intermediate frequencies show the highest sensitivity (i.e., respond to the smallest amplitude stimuli).

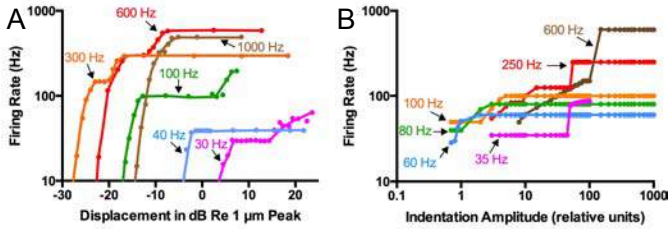

Figure 5: (A) Experimental [3] and (B) simulated data of neurite firing rates resulting from displacements at various frequencies.

DISCUSSION

The Stage 1 results show that incorporating the layered PC structure introduces the high-pass filtering response into the model, as suggested previously [2,6]. The results of Stage 2 complement previous studies [9] that suggest that mechanogated cation channels at the base of the neurite's filopodia would be well positioned to transduce temporal, and possibly spatial, information. This study presents new information that the distal, rather than the central, filopodia are better positioned for mechanosensation.

The Stage 1 sustained indentation simulations show that the outer core adapts mechanically to a square wave displacement. Previous studies showed that the intact PC fires action potentials only at stimulus onset and offset [5], an effect that disappears upon removal of the PC capsule [10]. Those studies proposed that the PC adaptation rate is dependent on the mechanical properties of the lamellae. This work supports that hypothesis and concludes that adaptation can arise entirely from the PC mechanics without neuron adaptivity.

A strength of this work is that it is the first model (1) to include the entire mechano-to-neural transduction process of the PC by combining three stages that deal with specific mechanisms of this transduction, (2) to simulate PC response to both vibratory and sustained indentation, and (3) to account for both the structure of the PC core and the morphology of its neurite.

A limitation of this work is that the neural model in Stage 3 must be tuned to match experimental observation better. The simulated and experimental results in **Figure 5** showed similar trends at high frequencies, but the simulated PC did not follow the experimental trend at lower frequencies. Second, the mechanics of the inner core are unknown, so neurite properties were used in Stage 2. Also, the spherical shape of the Stage 1 model could be transformed to an ellipsoid, which would allow the study of directional tuning of the PC.

The detailed mechanical and neural models created in this study allow for characterization of the mechano-to-neural transduction of the PC. By understanding this process in the PC, we can also begin to characterize the mechanosensation of other receptors and nerve endings to eventually understand how hundreds of receptors in a single hand interact to send detailed sensory feedback to our somatosensory cortex and create our sensation of touch.

ACKNOWLEDGEMENTS

This research was supported by an NSF IGERT fellowship (Systems Neuroengineering, DGE-1069104). Computational resources were provided by the Minnesota Supercomputing Institute. COMSOL guidance was provided by Dennis Tweten.

REFERENCES

[1] Abraira, V et al., *Neuron*, 79:618-639, 2013. [2] Bell, J et al., *Prog Neurobiol,* 42:79-128, 1994. [3] Bolanowski, S et al., *J Neurophys*, 51:793-811, 1984. [4] Bolanowski, S et al., *J Neurophys*, 51:812-830, 1984. [5] Gray, J et al., *J Physiol*, 114:454-464, 1951. [6] Loewenstein, W et al., *J Physiol*, 182:346-378, 1966. [7] Biswas, A et al., *IEEE Trans Haptics*, 8:31-42, 2015. [8] Grevesse, T et al., *Sci Rep*, 5:9475, 2015. [9] Pawson, L et al., *J Neurosci*, 29:2695-2705, 2009. [10] Loewenstein, W et al., *J Physiol*, 177:377-397, 1965.

Copyright 2016 The Organizing Committee for the 2016 Summer Biomechanics, Bioengineering and Biotransport Conference

SB^{3}C2016
Summer Biomechanics, Bioengineering and Biotransport Conference
June 29 –July 2, National Harbor, MD, USA
SB^{3}C2016-96

ANTEROLATERAL CAPSULE OF THE KNEE FUNCTIONS AS A SHEET OF TISSUE BASED ON TISSUE STRAIN

Stephanie L. Sexton (1), Daniel Guenther (1,2), Kevin M. Bell (1), Sebastian Irarrazaval (1), Ata A. Rahnemai-Azar (1), Freddie H. Fu (1), Volker Musahl (1), Richard E. Debski (1)

(1) Orthopedic Robotics Laboratory,
Departments of Orthopedic Surgery and Bioengineering
University of Pittsburgh
Pittsburgh, Pennsylvania, USA

(2) Trauma Department
Hannover Medical School
Hannover, Germany

INTRODUCTION

Knee injuries are one of the most common reasons for physician appointments. The most commonly injured ligament in the knee requiring surgery is the anterior cruciate ligament (ACL) [1]. ACL reconstruction is the sixth most common orthopedic surgical procedure in the US, with an estimated 150,000 ACL reconstructions performed annually [2]. Normal structure and function of the knee was restored in only 37% of the patients undergoing ACL reconstruction [3]. However, injuries of the anterolateral capsule are often under diagnosed in conjunction with ACL injuries, which can lead to decreased rotational stability of the knee and early arthritis.

Significant clinical interest exists in the structure and function of the anterolateral capsule. A ligamentous structure inserting midway between Gerdy's Tubercle and the tip of the fibular head was recently described [4] and it has been found to serve as a secondary stabilizer in the ACL-deficient knee [5]. However, this structure is integrated into the anterolateral capsule. Traditionally, ligaments transmit tensile loads along their length and are stretched along their longitudinal axis, resulting in a relatively uniform strain pattern in their midsubstance. The purpose of this study was to determine the magnitude and direction of the strain in the anterolateral capsule in response to external loads applied to the ACL deficient knee throughout a range of flexion angles. Our hypothesis was that the direction of the strain in the anterolateral capsule does not align with the proposed ligamentous structure. Knowledge of the function of the anterolateral capsule can lead to development of an injury model and more informed choices of repair.

METHODS

Seven fresh frozen cadaveric knees (mean age 53.7 years, range 46-59 years) were dissected until the anterolateral capsule was clearly visible. Twenty-four black markers were placed on the mid-substance of the anterolateral capsule in a 4 x 6 grid, approximately 1 cm superior to Gerdy's tubercle and the LCL insertion and 5 mm anterior to the LCL origin and insertions. The specimens were then mounted into a robotic testing system (MJT Model FRS2010, Chino, Japan). The femur was rigidly fixed relative to the lower plate of the robotic testing system and the tibia was attached to the upper end plate of the robotic manipulator through a 6-degree-of-freedom universal force/moment sensor (UFS, ATI Delta IP60 (SI-660-60), Apex, NC). The robotic testing system was used to apply loads to the knee at 3 flexion angles and a motion capture system (Spica Technology Corporation, Haiku, HI) was utilized to track motion of the strain markers attached to the surface of the capsule. The externally applied loads were: anterior tibial load (134N), external rotation torque (7 Nm), internal rotation torque (7Nm), and posterior tibial load (134N). The loading conditions were applied at 30°, 60°, and 90° of knee flexion for the ACL deficient knee.

The magnitude and direction of the maximum principal strain in the midsubstance of the anterolateral capsule were computed by comparing the positions of the strain markers in a non-strained reference configuration to the loaded configurations using ABAQUS (Dassault Systems, Velizy-Villacoublay, France) (Figure 1). The direction of the maximum principal strain of each element was quantified using Image J software (National Institute of Health, Bethesda, MD). The angle between the direction vectors representing each element in the anterolateral capsule and the anterolateral ligament proposed by Claes et al. was determined in a counterclockwise manner from the ligament [4]. The angles of each element were averaged per

Copyright 2016 The Organizing Committee for the 2016 Summer Biomechanics, Bioengineering and Biotransport Conference

loading condition and flexion angle for the seven specimens and then the mean of the angles of the seven specimens was calculated. Angles were in the range of 0-180° [6]. One tailed paired t-tests with significance set at $p < 0.05$ were used to compare the angles with 0°.

To compare the magnitude of the strain distribution within the anterolateral capsule at each flexion angle and loading condition, histograms were generated for the magnitude of the maximum principal strain at the centroid of each element for each specimen, flexion angle, and loading condition. The magnitudes of the maximum principle strain were compared between flexion angles and loading conditions as histograms normalized with bins from 0 to 90% strain at increments of 5%. The histograms could then be compared to the uniform strain distribution expected for a typical ligament based on the variance and kurtosis.

RESULTS

The average angles calculated between the direction vectors of the maximum principal strain and the proposed ligament's direction vary depending on loading condition (Figure 2). The mean angles ranged between 38° and 129.9°. All angles were significantly different than 0°.

The histograms for strain magnitude did not represent normal distributions and varied and between specimen, loading condition, and flexion angle. Overall, the mean kurtosis was 1.296±0.955 and the mean variance was 0.015±0.008 (Figure 3). The variance is linked to the spread of the strain magnitudes between bins and the kurtosis indicates the prevalence of strain magnitudes over the range of bins.

DISCUSSION

The direction of the strain does not align with the proposed ligament, supporting our hypothesis. The average direction vectors over all specimens and loading conditions were significantly different from 0°. The direction vectors were varied throughout the entire capsular mid-substance. (Figure 1). For a typical ligament, the distribution of the direction vectors would have been consistently close to the longitudinal direction of the proposed ligament [4] and had little variation.

The magnitudes of the maximum principal strain also did not act in a ligamentous fashion. A histogram of the magnitude of the maximum principle strain of a traditional ligament would have a high kurtosis and the variance would be low. However, compared to expected values for a typical ligament, the anterolateral capsule kurtosis was lower than expected and the variance was higher. The magnitudes of the maximum principle strain were not uniformly distributed (Figure 3).

Mapping the three-dimensional direction vectors into two dimensional space in order to calculate the angles with the proposed ligament introduced some variability. Thus, in the future, a statistical comparison between multiple observers orienting the direction vectors will be compared to determine repeatability.

In conclusion, the angle and the magnitude of the maximum principal strain in the anterolateral capsule during four loading conditions suggest that the anterolateral capsule functions more like a sheet of tissue than a traditional ligament. Knowledge of the behavior of the capsule can help to improve injury prevention models and repair procedures for the anterolateral capsule.

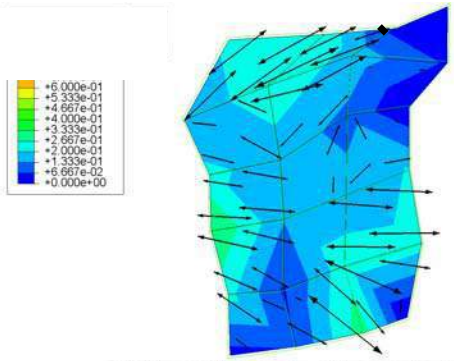

Figure 1: Sample fringe plot with direction vectors and magnitude gradient in response to external rotation torque at 90° of flexion for one specimen. Thick black line = proposed ligament

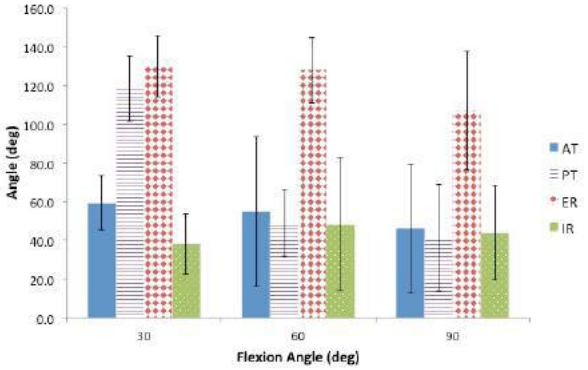

Figure 2: Mean angle between the angle vectors and the proposed ligament. AT =anterior tibial load, PT= posterior tibial load, ER= external rotation torque, IR=internal rotation torque.

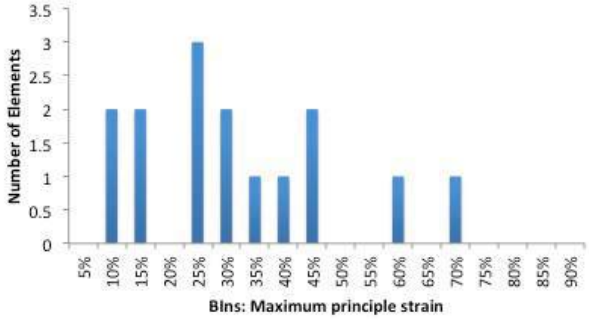

Figure 3: Example histogram of magnitudes of maximum principle strain in response to internal rotation torque at 90° of flexion for one specimen.

ACKNOWLEDGEMENTS

Support from Department of Orthopedic Surgery and Bioengineering is gratefully acknowledged.

REFERENCES

[1] Miyasaka et al. *Am J Knee Surg.,* **4**, 43–48, 1991. [2] Spindler KP, Wright RW. *N Engl J Med.,***359**(20):2135-2142, 2008. [3] Biau et al. *Clin Orthop Relat Res.,* **458**:180-187, 2007. [4] Claes, S et al., *J of Anatomy*, **223**(4):321-8, 2013. [5] Parsons EM et al. *Am J of Sports Med*. **43**(3), 669-674, 2015. [6] Moore et al. *Ann Biomed Eng* **38**(1):66-76, 2010.

Copyright 2016 The Organizing Committee for the 2016 Summer Biomechanics, Bioengineering and Biotransport Conference

SB^{3}C2016
Summer Biomechanics, Bioengineering and Biotransport Conference
June 29 –July 2, National Harbor, MD, USA
SB³C2016-97

BIOMECHANICAL REGULATION OF ANGIOGENESIS BY CANCER-ASSOCIATED FIBROBLASTS

M.K. Sewell-Loftin (1), Elizabeth L. Crist (1), B. Taylor Hughes (1), Samantha van Hove (2), Gregory Longmore (2,3), Steven C. George (1)

(1) Department of Biomedical Engineering
Washington University in St. Louis
St. Louis, MO, USA

(2) Department of Cell Biology and Physiology
Washington University in St. Louis
St. Louis, MO, USA

(3) Department of Medicine, Oncology Division
Washington University in St. Louis
St. Louis, MO, USA

INTRODUCTION

During tumor progression, angiogenesis occurs to develop enhanced vascular networks to deliver nutrients to the ever expanding tumor tissue. As a hallmark of tumor progression, angiogenesis has long been targeted in anti-cancer therapeutic strategies with varying amounts of effectiveness (1). This is due, in part, to a limited understanding of biomechanical regulation of blood vessel growth in the tumor microenvironment. Much research has been dedicated to soluble signaling factors, including vascular endothelial growth factor (VEGF), but it is only recently that biomechanical factors have been appreciated as regulators of angiogenesis. Cancer-associated fibroblasts (CAFs) have been described as important stromal regulators of tumor progression, playing a role in ECM remodeling, blood vessel growth, and tumor metastasis (2). CAFs differ from normal fibroblasts by demonstrating a myofibroblast-like phenotype. Recent work has shown that CAFs demonstrate higher tensile forces when plated on 2D polyacrylamide gels when compared to normal fibroblasts (3). CAFs have also demonstrated mechanosensitive behavior, specifically responding to stiffness cues from the ECM via YAP signaling (4). Additionally, mechanical forces have been shown to initiate epithelial-to-mesenchymal transformations (EMT), which is remarkably similar to the process used to form tip cells in angiogenesis (5). While much is known about the soluble signaling factors regulated by CAFs, less is understood regarding the complex biomechanical behaviors of these cells and how that may alter angiogenesis in the tumor microenvironment. Together, this prompted our global hypothesis that CAF-mediated strain may play a previously underestimated role in the development of tumor associated vascular networks specifically by increasing the activation of tip cells to enhance and direct angiogenesis in the tumor microenvironment.

METHODS

Our lab has developed a 3D *in vitro* tissue engineered model of the vascularized tumor microenvironment (6-7). Using this model, we embedded a 1:1 ratio of umbilical cord blood derived endothelial cells and either normal breast fibroblasts (NBFs) or CAFs in a fibrin gel and cultured for 7 days. Gels were then fixed and stained for CD31 to identify blood vessel growth. Images were taken corresponding to the center of each gel using an inverted microscope. Vessel length was measured with AngioTool, with four replicates per condition. Fibrin concentration was altered to vary gel stiffness. For inhibition studies, the VEGF pathway was inhibited using a small molecule VEGF-receptor inhibitor (SU-5402, Abcam) supplemented in the media after 3 days of culture. Mechanical strain induced by NBFs and CAFs was determined using a custom designed bead tracking algorithm in MATLAB. Fibroblasts only were seeded at $2.5x10^6$ cells/mL in 10mg/mL fibrin gels containing fluorescent beads (FluoSpheres, 1μm diameter). Cells were allowed to grow overnight before analysis. Bead movement was tracked over the course of 1h in an environmental chamber maintained at 37^{o}C on an Olympus IX83 inverted microscope. Images were collected over 100μm z-stack, with a slice at every 0.5μm. A minimum of 50 beads per sample were analyzed. Bead displacement was interpreted as ECM deformation or strain induced by either NBFs or CAFs.

RESULTS

CAFs support the development of blood vessel networks in 3D fibrin gels, while NBFs do not (Figure 1). This is consistent for all concentrations of fibrin tested. Increasing the fibrin concentration above 2.5mg/mL enhances vessel growth supported by CAFs,

Copyright 2016 The Organizing Committee for the 2016 Summer Biomechanics, Bioengineering and Biotransport Conference

although no affect is seen upon further increase. NBFs do not support vessel formation regardless of fibrin gel concentration. A VEGFR inhibitor fails to completely suppress blood vessel growth supported by CAFs (Figure 2). CAFs exhibit significantly higher gel deformations, as measured by fluorescent bead displacement, compared to NBFs (Figure 3A). The distribution of deformations is heterogeneous for both cell types (Figure 3B).

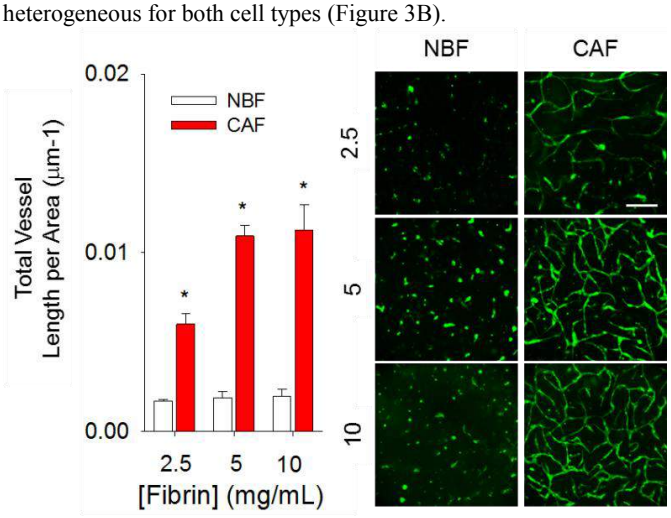

Figure 1: Blood vessel growth in fibrin gels is supported by CAFs but not NBFs. Increased stiffness of fibrin gels above 5mg/mL did not significantly affect blood vessel formation. . * p < 0.001 vs. NBF at same concentration; scale bar = 250μm.

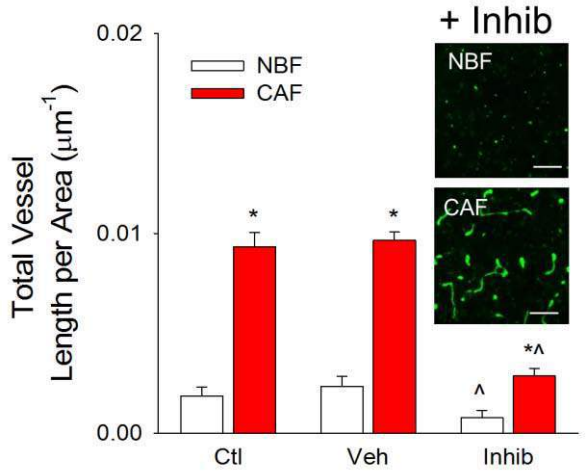

Figure 2: Inhibiting VEGF receptors suppresses, but does not eliminate, blood vessel formation supported by CAFs. Insets show treated samples. * p < 0.001 vs. NBF at same treatment; ^ p < 0.001 vs. NBF-Ctl scale bar = 250μm.

DISCUSSION

The role of CAFs in tumor progression and angiogenesis is complex and needs to be further studied. These studies show CAFs but not NBFs support vascularization in our 3D tissue model. Our results also indicate that fibrin concentration, which correlates with gel stiffness, demonstrates little effect on blood vessel formation. While increasing fibrin concentration also increases integrin signaling, this can be viewed as "effective gel stiffness" interpreted by the cell (8). This enhanced integrin signaling may play a role in the increase in blood vessel growth seen between 2.5 and 5mg/mL fibrin gels. Increased vessel formation in CAF samples in the 5 and 10mg/mL fibrin gels supports the idea that CAF biomechanics are an important factor in tumor associated angiogenesis. Furthermore, the VEGFR inhibitor studies indicate that CAF supported vascularization may not occur solely through the VEGF pathway. Additionally, we have developed an algorithm capable of tracking bead displacements generated by cells growing in 3D fibrin gels. Our studies show that CAFs have a significantly higher average magnitude of ECM deformation compared to NBFs.

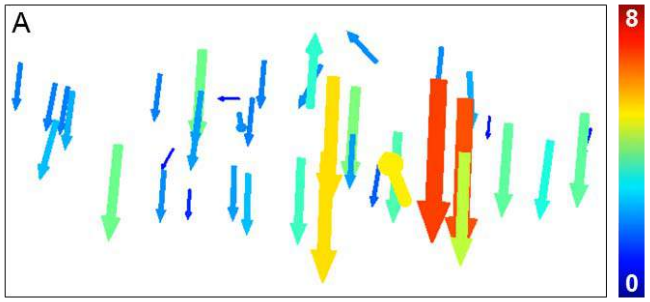

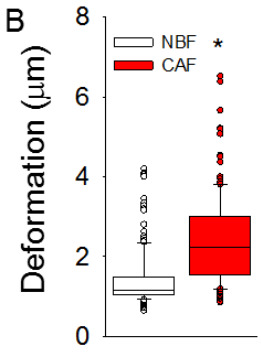

Figure 3: A) Representative image of bead displacement vectors shows CAF induced deformations in 3D fibrin gels. Color and size of arrow correspond to magnitude. Displacements induced by NBFs are much smaller and difficult to visualize so are not shown here. B) Distribution of bead displacement magnitudes for NBFs and CAFs. * p < 0.001.

Future studies will examine the mechanistic pathways important in CAF biomechanical regulation of blood vessel growth in the tumor microenvironment. Additionally, we will investigate the ECM deformations generated by CAFs and NBFs during blood vessel growth using our optimized bead tracking algorithm. Results from these studies will elucidate biomechanical factors associated with CAFs that are important for angiogenesis during tumor progression. Ultimately, we believe this work will provide information to develop novel anti-cancer treatment strategies by inhibiting angiogenesis.

ACKNOWLEDGEMENTS

The authors wish to acknowledge the following funding from the NIH: UH3-TR00048 and R01-CA170879.

REFERENCES

1) Hanahan, D et al. *Cell*, 144(5): 646-674, 2011.
2) Orimo, A et al. *Cell*, 121(3): 335-348, 2005.
3) Alcoser, T et al., *Cell Mol Bioeng*, 8(1): 476-86, 2015.
4) Calon, A et al. *Semin Cancer Biol*, 25:15-22, 2014
5) Gjorevski, N et al. *Cancer microenvironment*, 5(1): 29-38, 2012.
6) Moya, M et al. *Tiss Eng Part C Methods*, 19(9): 730-737, 2013.
7) Moya, M et al. *Methods Mol Biol*, 1202: 21-27, 2014.
8) Ghajar, C et al. *Biophys J*, 94: 1930-1941, 2008.

Copyright 2016 The Organizing Committee for the 2016 Summer Biomechanics, Bioengineering and Biotransport Conference

SB^{3}C2016
Summer Biomechanics, Bioengineering and Biotransport Conference
June 29 –July 2, National Harbor, MD, USA
SB^{3}C2016-98

A THEORETICAL EXAMINATION OF POTENTIAL STRATEGIES FOR ENHANCING CELLULAR ANABOLISM IN THE EXTRACELLULAR MATRIX OF THE INTERVERTEBRAL DISC

S. Asfour (1), J.P. de Rivero Vaccari (2), F. Travascio (1)

(1) Department of Industrial Engineering
University of Miami
Coral Gables, FL, USA

(2) Department of Neurosurgery
University of Miami
Coral Gables, FL, USA

INTRODUCTION

Intervertebral disc (IVD) homeostasis results form a balance between anabolic and catabolic activity of cells in the extracellular matrix (ECM) of the tissue. When catabolism overcomes anabolism, the IVD degenerates [1]. A possible strategy for restoring degenerated IVDs may consist in enhancing the cellular anabolism in the ECM of the disc. However, anabolic processes in IVD are complex and not entirely understood. This prevents the development of successful anabolic therapies for degenerated IVD.

Insulin-like growth factor-1 (IGF-1) plays a central role in IVD homeostasis, stimulating cell proliferation and biosynthesis of the ECM in a dose-dependent fashion [2, 3]. IGF-1 is either endogenously produced by disc cells, or exogenously delivered *via* plasma from the liver. Once in the IVD, this molecule binds to IGF-1 cell surface receptors (IGF-1R), initiating the signaling cascade that leads to the production of new ECM [4]. Hence, in order to enhance ECM anabolism in IVD, increased binding of IGF-1 to its receptor is highly desirable.

The interaction between IGF-1 and its receptor is only one of the many competing reversible chemical reactions occurring in the disc. For instance, IGF-2, delivered *via* plasma to the IVD can also bind to IGF-1R. However, such interaction has no downstream consequences in terms of ECM biosynthesis. Similarly, no downstream effects occur when either IGF-1 or IGF-2 bind to IGF-2R. Moreover, IGF molecules can be 'sequestered' by IGF-binding proteins (IGFBP). Particularly, IGF-1 and IGF-2 can reversibly bind to five IGFBPs (i.e., IGFBP-(1-5)). In addition, IGF-2 has a high affinity for IGFBP-6 [4]. The results of these reversible reactions are bound complexes that prevent IGF-1 and IGF-2 from interacting with their cell receptors. It has been proposed that the presence of IGFBP extends the half-life of IGF in the IVD [5, 6, 8].

The objective of this study is to theoretically examine possible strategies to enhance binding of IGF-1 to its receptor, with the ultimate goal of providing guidelines for the development of drug delivery approaches to cure IVD degeneration.

This is done *via* a novel pharmacokinetic model of IVD homeostasis that is capable of describing the role of IGF-1 in disc anabolism. More specifically, the model is deployed to test several approaches to increase IGF-1 binding to the IGF-1R. This is based on the use of inhibitors of competing signals or on the delivery of stimulants. The amount of complex obtained by IGF-1 binding to IGF-1R (i.e., IGF-1/IGF-1R) is used as a biological marker to quantify the level of anabolic activity in the IVD.

METHODS

The model is based on previous diffusive-reactive theoretical frameworks describing the role of IGF-1 in the homeostasis of cartilaginous tissues [5-10]. The IVD is schematized as composed of 3 regions: the nucleus pulposus (NP) in the center, surrounded by the annulus fibrosus (AF), and enclosed within the cartilage endplates (CEP). Molecular solutes (i.e., IGF-1, IGF-2, IGFBP-(1-6), and bound complexes) are delivered to the IVD via the vascular network surrounding the AF and in contact with the CEP, and diffuse through the ECM of the disc [8-10]. Disc cells in the ECM express surface receptors (i.e., IGF-1R and IGF-2R) to which growth factors bind, and can also endogenously produce IGF-1 [8]. The interactions of IGF-1 with its cell receptor and the other competitors are schematically reported below (Figure 1). Model parameters are taken from previous studies [5-10].

A straightforward mechanism to stimulate IGF-1/IGF-1R formation is to increase IGF-1 concentration in the plasma. However,

Copyright 2016 The Organizing Committee for the 2016 Summer Biomechanics, Bioengineering and Biotransport Conference

high levels of IGF-1 in plasma have been associated to cancer. Hence, it would be desirable to seek for alternative strategies.

In this study, four strategies are simulated. For each one of them, the values of IGF-1/IGF-1R formed in each compartment of the disc (i.e., NP, AF, and CEP) are normalized with respect to baseline values attained when no treatment is performed on the disc.

In the first strategic approach, stimulants for increasing the expression of IGF-1R in disc cells may be delivered. This is supposed to increase the availability of binding sites for both growth factors, thus increasing the amount of IGF-1/IGF-1R formed. This is simulated in the model by parametrically increasing the concentration of IGF-1 receptors in disc cells. In the second approach, binding proteins IGFBP-(1-5) are exogenously delivered, since they increase the half-life, and consequently the bioavailability, of IGF-1 in the ECM. This is simulated by parametrically increasing the concentrations of such proteins at disc boundaries. A third method would be the delivery of an inhibitor of IGFBP-6 in order to prevent the formation of an IGF-2/IGFBP-6 bound complex and reduce the half-life (bioavailability) of IGF-2, which competes with IGF-1 in binding to IGF-1R. This is implemented by parametrically reducing the boundary-concentration of IGFBP-6. The last approach would consist of delivering an inhibitor of IGF-2, thus preventing this growth factor to compete with IGF-1 in binding to IGF-1R. This is implemented by parametrically reducing IGF-2 boundary-concentrations.

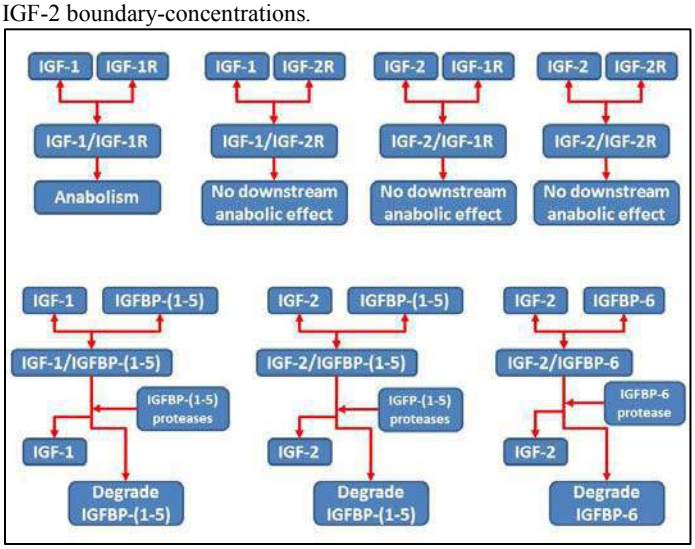

Figure 1: Schematic of competing binding reactions among growth factors IGF-1 and IGF2, binding proteins IGFBP-(1-6) and cell receptors IGF-1R and IGF-2R.

RESULTS

For the four therapeutic approaches simulated, steady-state average concentrations of IGF-1/IGF-1R complex have been reported and normalized to the scenario when no treatment is added to the disc (Figure 2).

The highest increases in the IGF-1/IGF-1R complex-formation are found when IGF-2 is inhibited (Figure 2d). Such type of approach is especially effective for promoting bound complex-formation at the CEP. In contrast, stimulation of IGF-1R expression has similar effects across all disc regions (Figure 2a). The low increases are observed when modulating the concentration of IGFBPs. Doubling plasma concentration of IGFBP-(1-5) only increases the formation of IGF-1/IGF-1R in the NP by about 20% (Figure 2b). Even smaller effects are observed when IGFBP-6 is inhibited. Accordingly, changes in IGF-1/IGF-1R are less than 10% in all disc regions (Figure 2c).

DISCUSSION

A new pharmacokinetic model for IVD homeostasis was deployed for investigating potential therapies for disc degeneration based on increasing anabolism in the ECM of the disc.

Anabolism in IVD was modeled as the result of IGF-1 binding to its cell surface receptor IGF-1R. However, several other competing interactions among proteins and receptors in the ECM of the disc simultaneously occur, which limit the formation of the IGF-1/IGF-1R complex. The therapeutic approaches herby investigated aimed at modulating the bioavailability of proteins and receptors in the disc to favor the interaction of IGF-1 with IGF-1R.

It was found that increased anabolism can be obtained by inhibiting IGF-2, since this growth factor competes with IGF-1 in biding to IGF-1R. However, a significant increase in IGF-1/IGF-1R mainly occurs at the CEP, and it requires a reduction of up to 25% of IGF-2 when compared to the normal physiological concentration. Stimulation of IGF-1R expression also increases anabolism, but major changes occurs only if IGF-1R concentration is increased 1.5- to 2-fold. Modulation of IGFBPs bioavailability produced minor changes in IGF-1/IGF-1R formation. Similar results have been reported in a theoretical analysis on cartilage homeostasis [5].

In conclusion, this study suggests that drug delivery protocols for IVD regeneration should be combinatorial by tackling simultaneously as many factors involved in disc anabolism as possible.

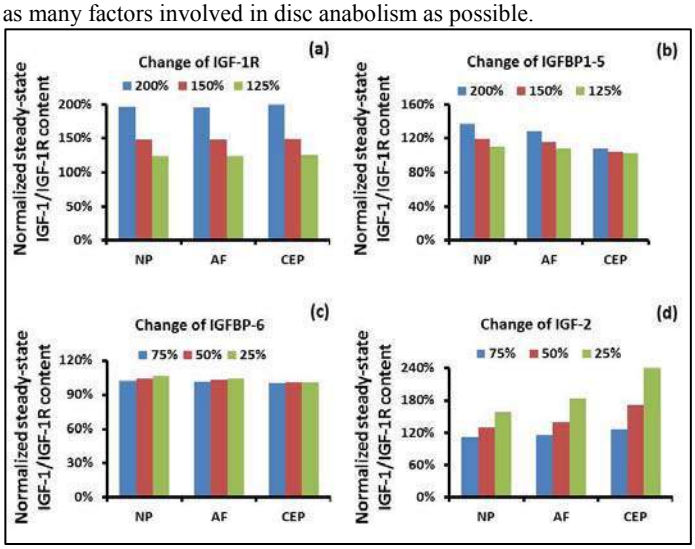

Figure 2: Effect of therapeutic approaches on the availability of IGF-1/IGF-1R: (a) stimulation of IGF-1R; (b) delivery of IGFBP-(1-5); (c) inhibition of IGFBP-6; (d) inhibition of IGF-2.

ACKNOWLEDGEMENTS

Study supported by funds donated to Biomechanics Research Group at University of Miami.

REFERENCES

[1] Masuda, K et al., *Spine* 29:2757-69, 2004.
[2] Pratsinis, H et al., *Eur J Spine* 16: 1858-66, 2007.
[3] Osada, R et al., *J Orthop Res* 14:690-99, 1996.
[4] Foulstone, E et al., *J Pathology* 205:145-53, 2005.
[5] Zhang, L et al., *PloS one* 8:6, 2013.
[6] Zhang L, et al., *J Theor Biol* 263:20–29, 2010.
[7] Travascio, et al., *Biomech. Model Mechanobiol* 13:945-959, 2013.
[8] Asfour, S et al., *J Biomech* 48: 332-39, 2014.
[9] Travascio, F et al., *J Biomech* 47:2269-76, 2014.
[10] Elmasry, S et al., *PloS one* 10:8, 2015.

Copyright 2016 The Organizing Committee for the 2016 Summer Biomechanics, Bioengineering and Biotransport Conference

SB³C2016
Summer Biomechanics, Bioengineering and Biotransport Conference
June 29 –July 2, National Harbor, MD, USA
SB³C2016-99

EFFECTS OF HEMODYNAMIC CHANGES ON THE DEVELOPING DORSAL AORTA OF THE CHICK EMBRYO

Gabriela Espinosa (1), Larry Taber (1,2), Jessica Wagenseil (2)

(1) Biomedical Engineering
Washington University
St. Louis, MO, United States

(2) Mechanical Engineering and Materials Science
Washington University
St. Louis, MO, United States

INTRODUCTION

Congenital heart defects (CHD) account for almost a quarter of birth defect related infant deaths and are diagnosed in 8 out of every 1000 live births, often leading to further development of cardiovascular disease in adulthood [1]. Since it is well established that hemodynamic forces influence cardiovascular development, several groups have used surgical interventions to alter blood flow and induce cardiovascular defects in chicken embryos. The chick embryo is particularly well suited for direct physical manipulations, therefore eliminating unintended effects common to biochemical treatments. Two common interventions, outflow tract banding (OTB) and vitelline vein ligation (VVL), are frequently used to increase and decrease blood flow velocity, respectively [2]. Previous studies have shown that these alterations result in remodeling of the heart, aortic arches, and capillary plexus, but have not investigated their impact on large, elastic artery development.

The chick embryo's dorsal aorta (DA) is the first intraembryonic vessel to form, later developing into the adult descending aorta. Its passive mechanical properties are determined by the deposition of elastin and collagen, beginning at about Hamburger-Hamilton stage (HH) 29 or embryonic day (E) 6 [3-4]. We hypothesize that hemodynamic changes will affect the structure and development of the DA. We used Doppler velocimetry to measure blood velocity and immunofluorescence to examine the DA's wall structure and components in embryos under control and VVL conditions. These data will further our understanding of the relationship between hemodynamics and vessel maturation, supplementing current knowledge of vascular CHDs and directing efforts in the field of arterial tissue engineering.

METHODS

Fertilized White Leghorn chicken eggs were incubated blunt side up for approximately 70 hours at 37°C yielding embryos at HH 18-19. The embryo was exposed by creating a small window in the shell above the air cell and removing the membranes above the areas of interest. Control embryos were sealed with tape, while experimental embryos had the right vitelline vein ligated using a 10-0 monofilament suture prior to sealing.

A 20-MHz pulsed Doppler flowmeter probe (Iowa Doppler Products) was placed on the DA at the level of the sinus venosus to measure blood velocity along the DA centerline of control and VVL embryos at HH 18-19, 22-23, 25-26, and 28-29. A custom Matlab program was used to calculate the heart rate and peak velocities. Additionally, a Vevo 2100 ultrasound system (VisualSonics) was used to measure DA blood velocity for control embryos at HH 30-31 and 33-34. Corresponding VVL embryo measurements are forthcoming.

Immunofluorescence was used to characterize DA lumen area, wall area, and fiber alignment in whole embryo cryosections for controls. These sections were taken transversely at levels corresponding to the heart, liver, and mesonephros. Dimensional measurements were performed using ImageJ (NIH) and alignment was determined using its Directionality plugin. Circular statistics were employed to assign an R-value to the fibers, where R=1 indicates perfect alignment. Isolated control and VVL DAs at HH 36-37 were also stained to determine the percent quantities of elastin, collagen, and cells in the arterial wall. A Matlab script was developed to quantify these measurements. Statistical significance in comparisons between controls and VVLs was determined using unpaired, two-tailed t-tests with unequal distributions.

Copyright 2016 The Organizing Committee for the 2016 Summer Biomechanics, Bioengineering and Biotransport Conference

RESULTS

These results are the first to include blood velocity measurements in the chick embryo DA using ultrasound, a more reliable technique for late developmental stages (Figure 1). They confirm that VVL immediately reduces blood velocity, but is quickly normalized. Additional ultrasound data will show whether or not this normalization persists though day 8. Heart rate is unaffected by the ligation.

We determined that the lumen area, wall area, and elastic fiber orientation all increase over time in control embryos, but also observed substantial thinning along the length of the DA (Figure 2). At HH 36, we found that VVL DAs show a significant decrease in elastin content, while maintaining the same collagen and cell volume fractions (Figure 3).

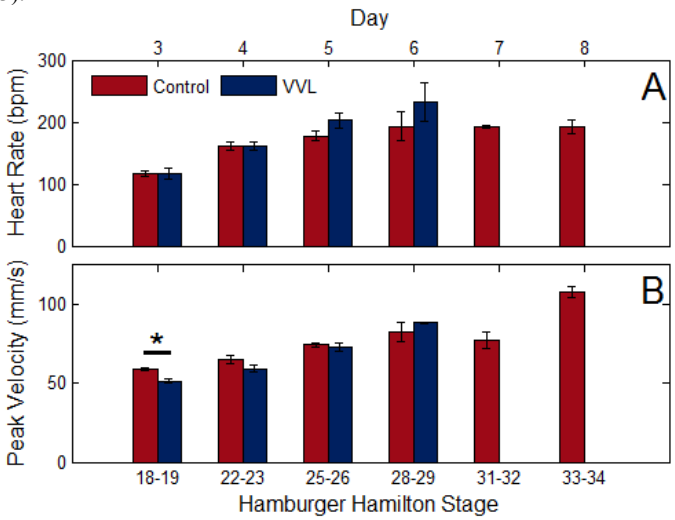

Figure 1: Heart rate (A) and peak velocity (B) of control and ligated embryo DAs. *=P<0.05 compared to control.

DISCUSSION

Doppler measurements along with analysis of immunofluorescence micrographs show that ligation causes a modest, but significant, 13% reduction in DA blood velocity. Despite this small and short-lived change, elastin content in the DA wall of ligated embryos is dramatically decreased by almost 65%. These results suggest that decreased blood flow hinders elastin lamellar development and support our hypothesis.

Dimensional measurements of control DAs provide a standard to which VVL DAs can be compared in future work. Corresponding measurements in VVL DAs are forthcoming. This data will be used to ascertain whether or not the compositional changes due to ligation are also accompanied by structural changes.

Given the uncertainty associated with immunofluorescence, further quantification will be performed using RT-PCR. This will not only measure the expression of matrix genes, but also genes associated with smooth muscle cell phenotype and endothelial cell shear stress response. Future work will also include mechanical testing, which will provide valuable information showing how hemodynamics can affect the mechanical properties of the maturing DA.

ACKNOWLEDGEMENTS

Washington University's Chancellor's Graduate Fellowship for their support. Funding provided, in part, by NIH grant R01 NS 070918.

REFERENCES

[1] Kowalski, W.J., et al. *Front Physiol* 5 (2014).
[2] Midgett, M., et al. *Front Physiol* 5 (2014).
[3] Rosenquist, T.H., et al. *Anat Rec* 221.4 (1988): 860-871.
[4] Hamburger, V., et al. *J Morphol* 88.1 (1951): 49-92.

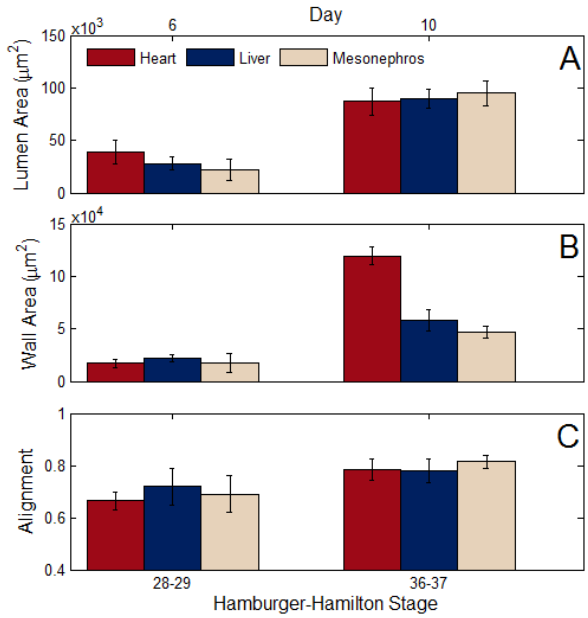

Figure 2: Lumen area (A), wall area (B), and fiber alignment (C) of control embryo DAs.

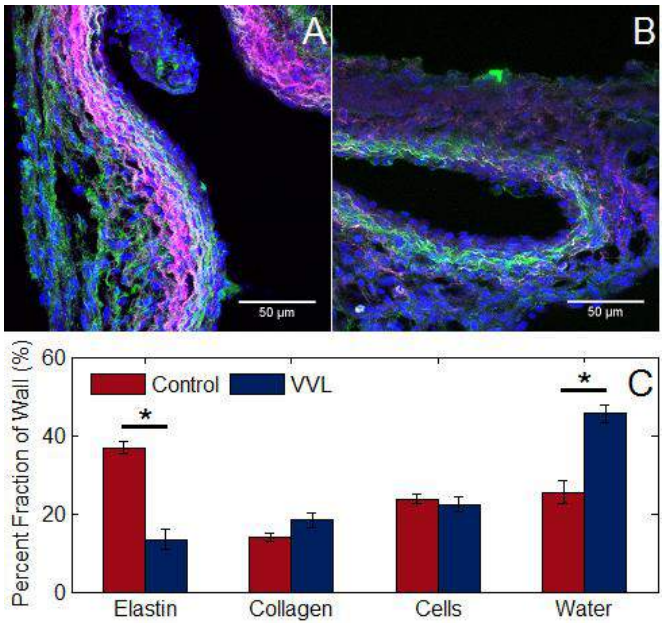

Figure 3: Elastin (magenta), collagen (green), and cells (blue) in control (A) and VVL (B) embryos. Ligation decreases elastin content in VVL DAs. *=P<0.05 compared to control.

Copyright 2016 The Organizing Committee for the 2016 Summer Biomechanics, Bioengineering and Biotransport Conference

SB³C2016
Summer Biomechanics, Bioengineering and Biotransport Conference
June 29 –July 2, National Harbor, MD, USA
SB³C2016-101

COMPREHENSIVE HEMDODYNAMICS OF LIVING DONOR LIVER TRANSPLANT

David R. Rutkowski (1,2), Scott B. Reeder (2,3,4,5), Luis A. Fernandez (6), Alejandro Roldán-Alzate (1,2)

(1) Mechanical Engineering
University of Wisconsin-Madison
Madison, WI, United States

(2) Radiology
University of Wisconsin-Madison
Madison, WI, United States

(3) Medical Physics
University of Wisconsin-Madison
Madison, WI, United States

(4) Biomedical Engineering
University of Wisconsin-Madison
Madison, WI, United States

(5) Medicine & Emergency Medicine
University of Wisconsin-Madison
Madison, WI, United States

(6) Surgery
UW Hospital and Clinics
Madison, WI, United States

INTRODUCTION

Liver transplantation is a successful and definitive treatment for patients with liver failure. Yet, over the last two decades, there has been a short supply of organs from deceased donors. This has motivated the implementation of living donor liver transplantation (LDLT), a therapy that has produced results comparable to traditional liver transplants.[1,2] However, little is known about the effects that LDLT has on the liver hemodynamics of the donor. To investigate these effects, studies have been conducted to examine alterations due to surgery in the underlying fluid dynamics of blood flow using in vitro experiments, numerical simulation, and clinical studies[3]. In order to implement a methodology that provides further insight into the hemodynamic alterations, this study employs patient specific 4D Flow MRI, in vitro physical model experiments, and computational fluid dynamics simulation in living donor portal venous models before and after the LDLT procedure. Additionally, the validity of the in vitro and simulation analysis methods is examined through a comparison of each method at the same operating conditions.

METHODS

In this IRB-approved and HIPAA-compliant study, a LDLT donor (33 year-old female, 68 kg) was imaged after written informed consent before and within one month after surgery. The subject was scanned after at least 5 hours of fasting to avoid variability in splanchnic flow[4]. The study was conducted on a clinical 3T scanner (Discovery MR 750, GE Healthcare, Waukesha, WI) with a 32-chanel body coil (NeoCoil, Pewaukee, WI). 4D velocity mapping was achieved using a cardiac-gated time-resolved 3D radially undersampled phase contrast acquisition (5-point PC-VIPR)[5] with increased velocity sensitivity performance[5,6]. Radial 4D flow MRI image parameters included: imaging volume: 32x32x24cm spherical, 1.25mm acquired isotropic spatial resolution, TR/TE=6.4/2.2ms. The subject received 0.05 mmol/kg of gadoxetic acid (Eovist, Bayer Healthcare, Wayne, NJ). Pre- and post-surgery 4D flow MRI imaging protocols were identical.

The vessels of the patient liver were segmented using MIMICS (Materialise, Leuven, Belgium) from PC angiograms (Figures 1a. and 2a.). Using Ensight (CEI, Apex, NC), cut-planes were manually placed in the Splenic Vein (SV), Superior Mesenteric Vein (SMV), and the Left (LPV), Right (RPV), and Main portal Veins (PV), where flow measurements were taken.

The segmented pre- and post-surgery liver models were prepared for in vitro flow experiments using 3-matic (Materialise, Leuven, Belgium). The models were then fabricated using selective laser sintering (DTM Sinterstation 2500CI ATC with 30 Watt coherent laser and 3 axis M3ST scanning system). The printed models (Figures 1b. and 2b.) were connected to a perfusion pump (Stockert SIII Heart-Lung Machine) using surgical tubing. Fluid was pumped through the models at rates of 1 and 2 liters per minute, and flow measurements were recorded at each inlet and outlet vessel using a flow probe (Transonic PXL Flowsensor). The in vitro set-up was then taken to a magnetic resonance scanner, where the same flow experiments were conducted. The 4D Flow MR data were then analyzed using cut planes in Ensight (CEI, Apex, NC), as done in the in vivo case analysis.

The same segmented pre- and post- surgery liver models that were used for the in vivo analysis and in vitro model fabrication were also prepared for numerical simulation using the mesh generation software ICEM (ANSYS). The computer models were then imported to Fluent (ANSYS) and computational fluid dynamics simulations were conducted at the same conditions present in the in vitro model experiments. Results from the simulations were analyzed in Ensight in the same manner as the in vitro experimental results.

Copyright 2016 The Organizing Committee for the 2016 Summer Biomechanics, Bioengineering and Biotransport Conference

RESULTS

Comparison of the in vivo 4D Flow MRI results showed an increase in the average and maximum fluid velocity throughout the portal venous system in the post-surgery case compared to the pre-surgery case. This relationship held true in the in vitro experiment and CFD simulation results as well. A visual representation of this phenomenon can be seen though a comparison of the pre- and post-surgery in vitro experiment streamlines (Figure 1c. and figure 2c.) and the CFD simulation velocity vectors (Figure 1d. and Figure 2d.). The CFD simulation results also displayed an increase in the pressure gradient across the portal venous system in the post-surgery models.

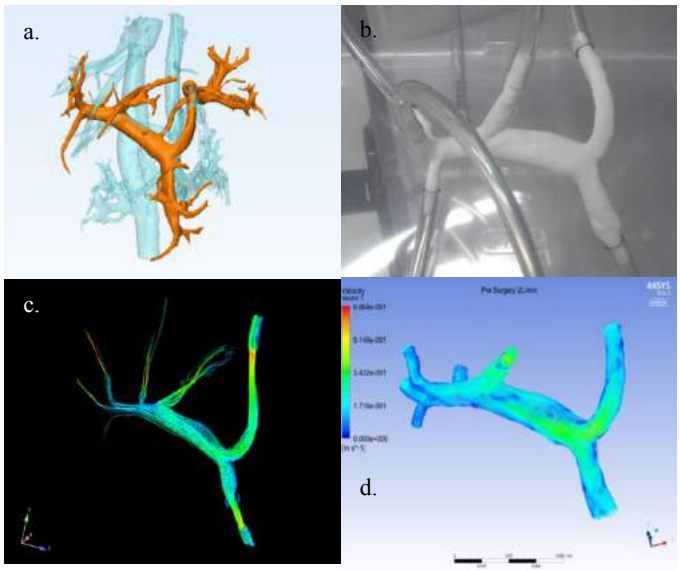

Figure 1: Pre-Surgery portal vein described as follows: a) In vivo segmented model, b) In vitro 3D printed experimental model, c) In vitro experiment velocity streamlines, d) CFD simulation velocity vectors.

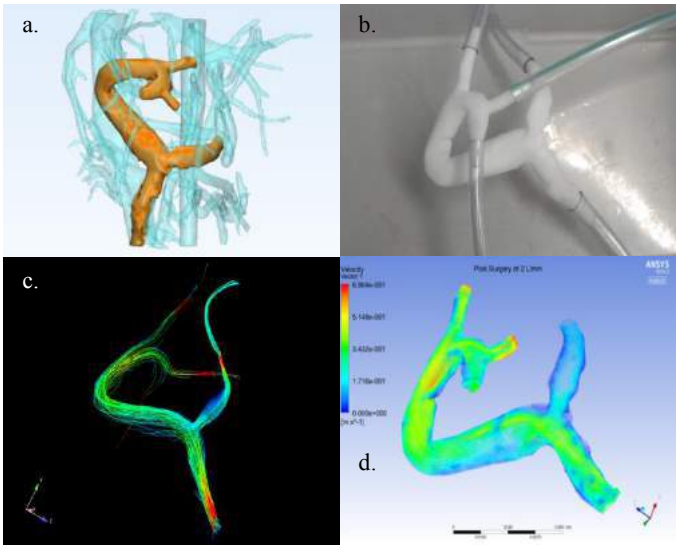

Figure 2: Post-Surgery portal vein described as follows: a) In vivo segmented model, b) In vitro 3D printed experimental model, c) In vitro experiment velocity streamlines, d) CFD simulation velocity vectors.

In addition to the post-surgery increase in velocity and pressure gradient, an increase of fluid flow in both the Left Portal Vein (LPV) and Superior Mesenteric Vein (SMV) was observed in the post-surgery models compared to pre-surgery conditions. Again, these results held true for each analysis method.

Lastly, when comparing the results of the in vitro experiments and CFD simulations from the same case, the difference between the flow values remained within 5% on all vessels, except for the SMV and SV in the pre-surgery models, which produced a 8% difference. The in vitro and CFD simulation flow values displayed a 10 to 15 percent difference from the flow probe measurements.

DISCUSSION

Living donor liver transplant has been a successful treatment for liver failure. However, the health and safety of the donor post-transplant is of paramount importance, and there remains insufficient data. Given the difficulty of assessing in vivo liver function and the inability to predict how a specific procedure will alter liver hemodynamics, further work is needed. To develop a methodology to better predict this outcome, this study employed MRI in vivo flow analysis, in vitro experiments, and computational fluid dynamics simulations.

In the transplant case examined in this study, the right lobe of the liver was resected, eliminating the RPV. Thus, the results that displayed an increase in fluid velocity throughout the portal vein were expected due to the decrease in total portal vein volume. The increase in LPV flow was also expected, as after surgery the LPV provided the only path for blood flow. However, what could not be predicted through physical examination was the magnitude of the change in blood flow through each of the PV branches and the change in pressure that these alterations would induce.

The methods used in this study successfully measured the hemodynamic changes that could not otherwise be predicted. The pressure gradients were quantified and visual representations of the fluid flow paths were provided so that a comparison could be made between pre- and post- surgery anatomical configurations. In addition, the use of multiple methods of analysis provided a process to validate the flow quantification data of each method against the others.

The capability to predict the hemodynamic changes induced by a surgery before it occurs may be of great value in the surgical planning process. In future studies, the methods described here will be expanded to multiple cases so that more insight may be gained on their validity and utility.

ACKNOWLEDGEMENTS

The authors wish to acknowledge support from the NIH (R01 DK096169), as well GE Healthcare who provides research support to the University of Wisconsin.

REFERENCES

[1] Yagi J, *Transplantation* 2005
[2] Kim PT, Testa G.. *HepatoBiliary Surg Nutr,* 2015.
[3] Hwang, Shin et al., *Liver Transplanation,* 18:858-866, 2012.
[4] Roldán-Alzate, *JMRI,* 2015
[5] Johnson, *MRM,* 2010
[6] Gu, *AJNR,* 2007

Copyright 2016 The Organizing Committee for the 2016 Summer Biomechanics, Bioengineering and Biotransport Conference

SB^{3}C2016
Summer Biomechanics, Bioengineering and Biotransport Conference
June 29 –July 2, National Harbor, MD, USA
SB^{3}C2016-102

INJURY-BASED ADVANCED AUTOMATIC CRASH NOTIFICATION ALGORITHM IMPROVES MOTOR VEHICLE CRASH OCCUPANT TRIAGE

Samantha L. Schoell (1,2), Ashley A. Weaver (1,2), Jennifer W. Talton (3), Ryan T. Barnard (3), R.Shayn Martin (1), J. Wayne Meredith (1), Joel D. Stitzel (1,2)

(1) Wake Forest University School of Medicine, Winston-Salem, NC, USA

(2) Virginia Tech - Wake Forest Center for Injury Biomechanics, Winston-Salem, NC, USA

(3) Wake Forest University School of Medicine, Division of Public Health Sciences, Winston-Salem, NC, USA

INTRODUCTION

Advanced Automatic Crash Notification (AACN) algorithms have shown promise in improving the trauma triage process by predicting occupant injury severity using vehicle telemetry data to recommend a transportation decision (trauma center versus non-trauma center). Current AACN algorithms such as OnStar and URGENCY incorporate model variables such as crash direction, delta-v, multiple impacts, belt use, vehicle type, age, and sex [1-2]. Both algorithms use Abbreviated Injury Scale (AIS) metrics to define severely injured patients. Although AIS-based metrics are most commonly used, other methods of injury scoring have been developed to better discriminate severely injured patients.

The objective of this study was to develop an AACN algorithm and evaluate its performance in making optimal occupant triage decisions using an injury-based approach. In addition, a benefits analysis was conducted to estimate the reduction in undertriage (UT) and overtriage (OT) if the algorithm was implemented nationwide.

METHODS

The developed AACN algorithm uses measurements obtainable from vehicle telemetry to predict risk of overall occupant injury and recommend a transportation decision for the occupant, particularly whether transport to a Level I/II trauma center is recommended. A list of injuries associated with a patient's need for treatment at a Level I/II trauma center was determined using an injury-based approach based on three facets (severity, time sensitivity, and predictability). Severity was scored based on mortality risk ratios (MRRs) obtained from the National Trauma Data Bank (NTDB) [3]. Time sensitivity was scored using expert physician survey data which incorporated the recommended treatment location and a rank of urgency for treatment [4]. Predictability was scored using two components: an occult score and a transfer score. The occult score is a measure of the likelihood that an injury is missed using expert survey data from physicians and emergency medical services (EMS) professionals. The transfer score is a measure of the likelihood that an injury is present in patients that require transfer from a non-trauma center to a Level I/II trauma center using the National Inpatient Sample (NIS) database [5].

Scores of each of these facets (severity, time sensitivity, and predictability) were computed for each of the 240 frequent motor vehicle crash AIS 2+ injuries and normalized on a zero to one scale in which scores closer to one were more severe, more time sensitive, and less predictable. The AACN algorithm inputs include a Target Injury List and 38,970 National Automotive Sampling System-Crashworthiness Data System (NASS-CDS) 2000-2011 occupants used to train and evaluate the algorithm (Figure 1). The Target Injury List is determined by multiplying the severity, time sensitivity, and predictability scores by a weighting coefficient and then summing these values to produce an injury score. Injuries meeting or exceeding a variable injury score threshold are included on the Target Injury List (Figure 1). The Target Injury List is not a static list and is capable of being varied in order to optimize the algorithm.

The AACN algorithm uses multivariate logistic regression to predict an occupant's risk of sustaining an injury on the Target Injury List from the following model variables: longitudinal delta-v (in frontal and rear crash modes), lateral delta-v (in near side and far side crash modes), number of quarter turns (in rollover crash mode), belt status, multiple impacts, and airbag deployment. The algorithm features five tunable variable parameters allowing for extensive optimization. These include severity, time sensitivity, and

Copyright 2016 The Organizing Committee for the 2016 Summer Biomechanics, Bioengineering and Biotransport Conference

predictability multipliers, an injury score and risk threshold. The severity, time sensitivity, and predictability multipliers are coefficients used to weight each injury's contribution to the injury score. Above the injury score threshold, an injury is included on the Target Injury List. The risk threshold is the tolerable risk for any target injury. At or above this threshold, the algorithm recommends triage to a Level I/II trauma center (Figure 1). The AACN algorithm transportation decision for each NASS-CDS occupant is compared to a dichotomous representation of their Injury Severity Score (ISS). Occupants with ISS 16+ should be transported to a Level I/II trauma center. AACN algorithm optimization minimized UT and OT with the goal of producing UT < 5% and OT < 50% as recommended by the ACS [6].

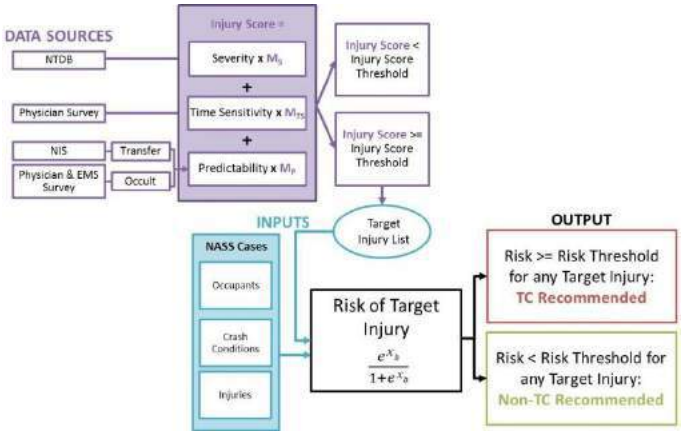

Figure 1: Overview of AACN algorithm.

RESULTS

The resulting OT and UT metrics for the optimal variable parameters are listed in Table 1. UT rates for far side and near side met the 5% ACS recommendation. OT rates for frontal, rear, far side, near side, and rollover all met the 50% ACS recommendation.

Table 1: Over/under triage rates (OT/UT) and true positives (TP), false positives (FP), true negatives (TN), and false negatives (FN) for the AACN algorithm by crash mode.

Crash Mode	OT	UT	TP	FP	TN	FN
Frontal	49.7%	5.9%	903	10451	10312	57
Rear	44.0%	7.0%	40	1470	1154	3
Far side	48.7%	2.9%	232	1727	1642	7
Near side	47.9%	4.6%	559	1723	1581	27
Rollover	49.7%	16.0%	871	3040	3005	166

DISCUSSION

The AACN algorithm was developed with an injury-based approach that examined three injury facets to identify injuries necessitating treatment at a Level I/II trauma center. Large hospital and survey datasets containing information on injuries, mortality risk, treatment urgency, and hospital transfers were used in conjunction with large crash datasets with crash, vehicle, occupant, and injury data. The algorithm has been rigorously optimized and has demonstrated improved UT rates compared to other AACN algorithms in the literature and OT rates meeting ACS recommendations. These results are encouraging as the algorithm uses only crash characteristics that are obtainable from vehicle sensors, whereas the majority of published algorithms use variables such as age or gender that are not obtainable directly from the vehicle. The AACN algorithm appears to be doing "more with less" than several algorithms to which it has been compared and shows great promise as an improved approach for triaging patients. Since the AACN algorithm uses only data elements specified in Part 563 regulation, it could be readily incorporated into new vehicles to inform emergency personnel of recommended occupant triage decisions [7].

Benefits of an existing AACN algorithm were estimated using the differential between the number of MVC occupants correctly triaged using the AACN algorithm compared to actual triage decisions for real-world occupants. Actual triage decisions were extracted from NASS-CDS 2000-2011 to compare each occupant's ISS (≥ 16 vs < 16) versus the occupant's actual triage destination (trauma center or non-trauma center). Analyses included 47,361 unweighted occupants representing 9,763,984 weighted occupants with complete information on the crash mode (frontal, far side, near side, rear, rollover), hospital destination (trauma center or non-trauma center), and a valid ISS.

The weighted analysis of 12 years of NASS-CDS data revealed an UT rate of 20% and an OT rate of 54% among real-world MVC occupants across all crash modes. If the triage rates from the AACN algorithm were applied to these occupants by crash mode, the UT and OT rates would be reduced to 11% and 34%, respectively. Across a 12 year period, this would result in an UT improvement for 32,959 (44%) occupants and OT improvement for 1,947,620 (38%) occupants for an estimated total of 1,980,579 occupants who would now be triaged correctly with the AACN algorithm. Thus, with nationwide implementation of the AACN algorithm, we estimate a potential benefit of improved triage decision-making for 165,048 occupants annually (one-twelfth of the 1.98 million occupants). Annually, this translates to more appropriate care for 2,747 seriously injured occupants and reduces unnecessary utilization of trauma center resources for 162,302 minimally injured occupants.

The projected reduction in UT for the U.S. population attributable to AACN has important implications for decreasing MVC mortality and morbidity, while reduction of OT will lead to better hospital resource utilization and decreased healthcare costs. The AACN algorithm developed in this study will aid emergency personnel in making the correct triage decision for an occupant after a MVC, and once incorporated into the trauma triage network it can reduce response times, increase triage efficiency, and improve overall patient outcome.

ACKNOWLEDGEMENTS

Funding has been provided by Toyota Motor Corporation and Toyota's Collaborative Safety Research Center. Views expressed are those of the authors and do not represent the views of any of the sponsors. The authors acknowledge Clay Gabler, Eddie Ip, Patrick Kilgo, Kathryn Loftis, and Katrina Swett for their contributions to the study design and data analyses.

REFERENCES

[1] Bahouth, G et al., *Ann Adv Automot Med*. 56:223-230, 2012.
[2] Kononen, DW et al., *Accid Anal Prev*. 43(1):112-122, 2011.
[3] Weaver, AA et al., *Ann Adv Automot Med*. 57:235-245, 2013.
[4] Schoell, SL et al., *J Am Coll Surg*. 220(3):305-312, 2015.
[5] Schoell, SL et al., *Injury*. 46(4):558-563, 2015.
[6] ACS Committee on Trauma, *Resources for Optimal Care of the Injured Patient*, 2006.
[7] NHTSA. *Event Data Recorders; Final Rule*, Vol 49 CFR Part 563. 2006.

Copyright 2016 The Organizing Committee for the 2016 Summer Biomechanics, Bioengineering and Biotransport Conference

SB^{3}C2016
Summer Biomechanics, Bioengineering and Biotransport Conference
June 29 –July 2, National Harbor, MD, USA
SB^{3}C2016-103

SKELETAL MUSCLE PERMEABILITY: DIRECT EXPERIMENTAL EVALUATION AND MODELING IMPLICATIONS

Benjamin B. Wheatley (1), Gregory M. Odegard (2), Kenton R. Kaufman (3), Tammy L. Haut Donahue (1, 4)

(1) Department of Mechanical Engineering
Colorado State University
Fort Collins, CO, USA

(2) Department of Mechanical Engineering – Engineering Mechanics
Michigan Technological University
Houghton, MI, USA

(3) Department of Orthopedic Surgery
Mayo Clinic
Rochester, MN, USA

(4) School of Biomedical Engineering
Colorado State University
Fort Collins, CO, USA

INTRODUCTION

Skeletal muscle consists of approximately 75% fluid [1] in addition to muscle fibers and extracellular matrix and can thus be characterized as a biphasic material. Other biphasic biological tissues such as cartilage utilize fluid content to lubricate joints and distribute loads under compression [2]. Yet the biphasic properties of muscle, specifically permeability, are often overlooked in experimental and modeling studies. The role that permeability plays in skeletal muscle mechanics is unclear. Permeability is often neglected in computational models of skeletal muscle, or simply approximated using viscoelastic modeling. The goals of this work were to 1) characterize skeletal muscle permeability by direct experimental measurement, and 2) identify how various permeability implementations affect finite element analyses of skeletal muscle.

METHODS

Four New Zealand White Rabbits ~2.5 kg in weight, either male or female, were euthanized with Colorado State University Institutional Animal Care and Use Committee approval. The biceps femoris muscles were harvested from the left or right hind limb and all experimental work was completed within 6 hours post mortem to reduce the effects of rigor mortis [3]. Cylindrical samples for permeability testing were removed from the muscle mid-belly using a custom fabricated drop cutter with high profile histology blades spaced 4 mm apart and a biopsy punch 8 mm in diameter. Since skeletal muscle exhibits transverse isotropy [3, 4], samples were obtained in the longitudinal and the transverse directions.

Each sample was directly evaluated in a permeation test device similar to previously published work [5]. In short, this device applied a known flow rate (0.5 mL/min) with a syringe pump to phosphate buffered saline across a tissue sample while measuring the pressure difference across the sample. Additionally, since permeability is typically a function of tissue strain [5], samples were compressed axially (12.5% and 25%) to replicate transverse or longitudinal compression or compressed laterally (25% and 50%) to simulate longitudinal stretch. Pressure (ΔP), flow rate (Q), specimen dimensions (L_0 and A), and strain (ε) were utilized to calculate the permeability of the tissue [5] (Equation 1). A paired t-test was utilized to compare permeability values between longitudinal and transverse samples and a general linear model was utilized to determine if permeability varied with strain level ($p<0.05$ for both analyses).

$$k = \frac{QL_0(1-\varepsilon)}{A\Delta P} \quad (1)$$

To identify the effect of permeability on muscle behavior, a 3D finite element (FE) model representing muscle tissue was developed using FEBio (febio.org) to simulate passive stretch and transverse compression. This model consisted of a cuboid with a cross section of 4 mm x 4 mm and a length of 20 mm, with muscle fibers running parallel to the length of the cuboid. To represent the transversely isotropic behavior of skeletal muscle [3, 4] as well as biphasic behavior, a poroelastic fiber reinforced coupled Mooney-Rivlin constitutive model was implemented. For finite element implementation strain-dependent permeability is a function of the volume ratio J, the undeformed void ratio φ_0 (0.19 for skeletal muscle [1]), and material properties k_0, M, and α (Equation 2, [5]).

$$k(J) = k_0\left(\frac{J-\varphi_0}{1-\varphi_0}\right)^{\alpha}\exp\left[\frac{M}{2}(J^2-1)\right] \quad (2)$$

To study how a biphasic approach affects model behavior, four permeability conditions were utilized in separate simulations. First, a solid analysis (no permeability) was used as the simplest approach ("Solid"). Next, a constant, isotropic permeability was calculated from experimental data for a baseline biphasic model ("Constant"). Finally,

Copyright 2016 The Organizing Committee for the 2016 Summer Biomechanics, Bioengineering and Biotransport Conference

two separate fits of Equation 2 to the experimental data to were utilized to generate anisotropic and strain dependent responses ("Fit I" and "Fit II"). Fit I is a conservative strain dependent formulation while Fit II is a case of extreme strain dependence (Table 1 and Figure 1).

The model was subject to two different loading conditions in separate analyses, longitudinal strain and transverse compression. Each condition consisted of a quick ramp phase from 0-10% strain over 1 second and 300 seconds of relaxation followed by a constant rate load to 50% strain at 1% second^{-1}. This evaluated how various permeability implementations affect transient muscle behavior under tensile and compressive conditions. The mean Cauchy stress over the whole model was calculated for comparison between simulations.

RESULTS

The mean permeability value for all samples was 7.41×10^{-11} m^4/N-s with a standard error of 2.22×10^{-11} m^4/N-s. There was no statistical effect of either strain level (p=0.398) or orientation (p=0.158) on skeletal muscle permeability.

Table 1: Permeability implementations for the FE simulations. The Solid analysis had no biphasic parameters, the Constant analysis had a single permeability value, and finally the Fit analyses had fully anisotropic strain dependence with different parameter values.

	k_0 (m^4/N-s)		M (-)		α (-)	
	Long	Trans	Long	Trans	Long	Trans
Solid	N/A	N/A	N/A	N/A	N/A	N/A
Constant	7.41 E-11		N/A	N/A	N/A	N/A
Fit I	1.1 E-10	4.2 E-11	0.63	0.16	0.097	0.97
Fit II	5.0 E-10	4.0 E-11	10	1	2	0.5

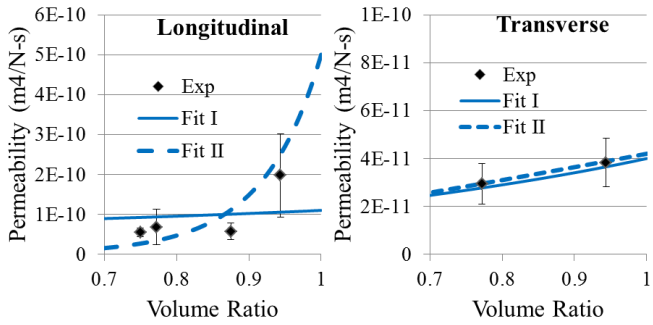

Figure 1: Permeability experimental data (diamonds with standard error bars), Fit I (solid line) for conservative strain dependence, and Fit II (dashed line) for extreme strain dependence.

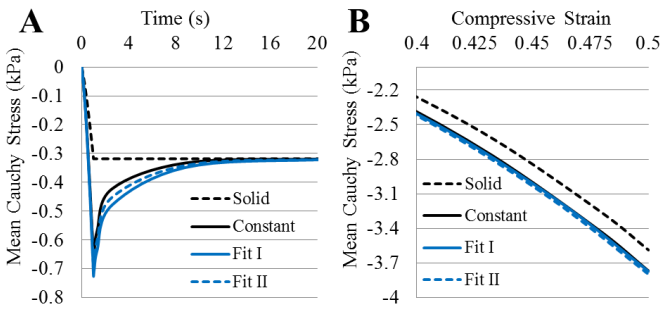

Figure 2: Model outputs for each of the four simulations under compression for ramp and relaxation (A) and constant rate (B).

Utilizing a biphasic approach affected tissue behavior (Figure 2 and Table 2). While variations in strain dependence and anisotropy affect results, they played less of a role than simply defining a constant, isotropic permeability. More specifically, inclusion of a biphasic analysis versus a solid analysis greatly affects the transient response of the tissue under compressive conditions, as evident by the increases in peak stresses in the biphasic analyses (Figure 2A and Table 2). Additionally, under tensile transient conditions, inclusion of a biphasic approach affected model output to a greater extent than anisotropic strain dependent permeability (Table 2).

Table 2: Percent differences between mean Cauchy stress of model outputs when compared to the Constant analysis at two different model instants: after a fast ramp strain of 10% and at 50% strain. Bold represents the highest percent error between analyses. The Solid analysis experienced the highest percent difference (up to 52%) for three of the four measurements.

	Solid		Fit 1		Fit 2	
	Tension	Comp	Tension	Comp	Tension	Comp
10% strain peak	**2.1%**	**52%**	0.62%	8.6%	0.035%	4.3%
50% strain	0.067%	**4.8%**	0.19%	0.11%	**0.24%**	0.82%

DISCUSSION

This work provided, to the authors' best knowledge, the first direct measurement of skeletal muscle permeability. The observed permeability values from this work reflect a difference of roughly 4-5 orders of magnitude over other biological tissues such as cartilage or ligament [2, 5]. This is not surprising since low muscle permeability would resist muscle deformation, thus significantly reducing contractile capabilities.

Additionally, this work provides insight into how various assumptions about muscle permeability affect tissue behavior from a computational standpoint. Statistical results showed no dependence of permeability on strain level or orientation, while modeling results agreed that utilizing an anisotropic, strain dependent permeability formulation typically had a minor effect on behavior. Model calculated stresses had good agreement with previously published experimental work under both compression [3] and tension [4], which gives greater confidence in these results.

However, the differences between a biphasic analysis and a solid only analysis should not be ignored, especially in an instance where compression occurs (Table 2). Thus a simple biphasic analysis (isotropic, constant permeability) should be utilized for skeletal muscle models involving compression, particularly under highly transient conditions. Future work should be conducted to identify how skeletal muscle models with complex geometries or contact are affected by a biphasic approach.

ACKNOWLEDGEMENTS

This work was funded by the National Instituties of Health: National Institute of Child Health & Human Development [R01HD31476-12].

REFERENCES

[1] Sjøgaard, G and Saltin, B, *Am J Physiol*, 243:271-80, 1982.
[2] Mansour, J and Mow, V, *J Bone Joint Surg Am*, 58:509-516, 1976.
[3] Van Loocke, M, et al., *J Biomech*, 39:2999-3009, 2006.
[4] Takaza, M et al., *J Mech Behav Biomed*, 17:209-220, 2012.
[5] Weiss, J, and Maakestad, B, *J Biomech*, 39:276-283, 2006.

Copyright 2016 The Organizing Committee for the 2016 Summer Biomechanics, Bioengineering and Biotransport Conference

SB³C2016
Summer Biomechanics, Bioengineering and Biotransport Conference
June 29 –July 2, National Harbor, MD, USA
SB³C2016-104

CONTRIBUTION OF GLYCOSAMINOGLYCANS TO EXTRACELLULAR MATRIX FIBER RECRUITMENT AND ARTERIAL WALL MECHANICS

Jeffrey M. Mattson (1), Raphaël Turcotte (2,3), Yanhang Zhang (1,2)

(1) Department of Mechanical Engineering
Boston University
Boston, MA, USA

(2) Department of Biomedical Engineering
Boston University
Boston, MA, USA

(3) Center for Systems Biology, Advanced Microscopy Program, Wellman Center for Photomedicine
Massachusetts General Hospital, Harvard Medical School
Boston, MA, USA

INTRODUCTION

Elastic and collagen fibers are well-known to be the major load-bearing extracellular matrix (ECM) components of the arterial wall. Despite the important mechanical role of glycosaminoglycans (GAGs) in other tissues such as cartilage, GAGs are only recently gaining attention in mechanical studies of arterial tissue. The goal of this study was to study the mechanical and structural contributions of GAGs to the arterial wall. Biaxial tensile testing was paired with multiphoton microscopic imaging of elastic and collagen fibers in order to establish the structure-function relationships of porcine thoracic aorta before and after enzymatic GAG removal.

METHODS

Sample Preparation: Descending porcine thoracic aortas were obtained from a local abattoir and cleaned of loose connective/fatty tissue. Approximately 20 mm sized square samples (n=6) were cut so that one edge is parallel to the longitudinal direction and the other edge is parallel to the circumferential direction of the artery.

Enzymatic GAG Removal Treatment: To enzymatically remove GAGs in arterial tissue, a protocol adapted from Lovekamp et al. [1] was used by adding heparinase to the treatment. Briefly, samples were treated in 100 mM ammonium acetate buffer, pH 7.0, 2-5 U/mL hyaluronidase, 0.025 U/mL chondroitinase ABC, 0.25 U/mL heparinase and gently agitated for 24 hours at 37°C to remove GAGs. Samples were then rinsed and mechanically tested in 150 mM phosphate buffered saline (PBS).

Mechanical Testing: A custom designed biaxial tensile testing device was used to mechanically test the tissue samples before and after GAG removal. Tissue deformation, was measured by tracking four carbon marker dots on the tissue during a tension control protocol using a custom LabVIEW program. Samples were hooked on each edge and connected to the linear positioners with sutures. A preload of 5 ± 0.050 N/m was applied in order to straighten the sutures connecting the tissue to the device. Samples were loaded with 10s half-cycles at 50 N/m until a consistent preconditioning response was achieved. Then the samples were subjected to an equibiaxial loading condition of 400 N/m to characterize the anisotropic mechanical behavior. To examine the viscoelastic behavior of arteries and the effect of GAG removal, a 400 N/m equibiaxial loading was reapplied with a 2s rise time and held at a constant stretch for 900s for the stress relaxation test. To quantify the effect of GAG removal on stress relaxation, normalized stress relaxation curves are obtained by normalizing to the peak stress. Percent stress relaxation is taken as the decrease in normalized value for the end of the test at 900s.

Multiphoton Microscopy and Image Analysis: To understand the contribution of GAGs to the structure and function of the arterial wall, and the interaction of GAGs with other ECM constituents, mechanical loading was paired with multiphoton imaging of tissue with GAGs removed following methods detailed by Chow et al. [2] to allow for comparison with untreated tissue. The adventitial side was imaged to a depth of 60 μm, whereas the medial side was imaged to a depth of 40 μm and maximum intensity projections of the Z-stacks were made. Images were cropped from 360x360 μm^2 to 110x110 μm^2 regions with optimal fiber coverage, which were used for analysis. Samples were imaged from 0 to 40% equibiaxial strain in 5% increments. These images were then used in the analysis of fiber straightening and recruitment in response to mechanical loading. Adventitial collagen fiber waviness was quantified with NeuronJ by measuring the end-to-end distance (L_o) and total fiber length (L_f), to define a straightness parameter, $P_s = L_o / L$, which is equal to 1 for a straight line. This manual

Copyright 2016 The Organizing Committee for the 2016 Summer Biomechanics, Bioengineering and Biotransport Conference

tracing method cannot be applied to the more intricate elastic and collagen fiber network in the media. Therefore, fractal analysis was also used as a broad measure of fiber recruitment following the protocol described by Chow et al. [2].

RESULTS AND DISCUSSION

Equibiaxial testing results show that the treated samples stiffening at lower strains than untreated samples (Figure 1).To quantify the changes in mechanical properties due to GAG removal, initial and stiff slopes were determined by linear fit to the regions of stress-strain curves from 0-20 kPa and 180-200 kPa, respectively. Transition stress/strain was then calculated as the intersection of the bilinear curve fit to the initial and stiff regions of the stress-strain curves (Fig. 1) [3]. For treated samples, the transition points of the circumferential (p=0.04) and longitudinal (p=0.002) directions are at significantly lower strain measurements, indicating earlier stiffening behavior of the arterial wall. However, the initial and stiff slopes for each direction are not significantly different after treatment (all p>0.1), suggesting GAG removal results in earlier stiffening, but not absolute stiffening.

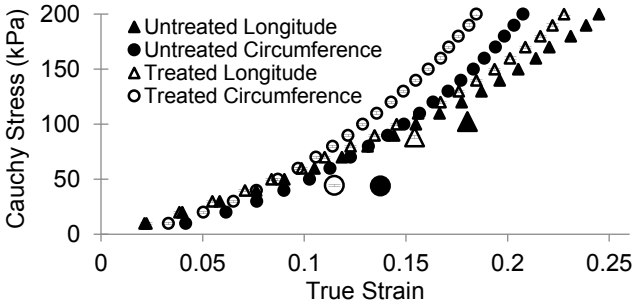

Figure 1: Averaged stress-strain curves of untreated and treated aorta. Treated samples have transition points (larger symbols) at significantly lower strain (p<0.05).

Results of multiphoton imaging (Fig. 2) show that after removing GAGs, adventitial collagen fibers are straighter and recruited at lower levels of strain, supporting the finding of lower transition point from straighter fibers that are recruited at lower levels of strain. Waviness of adventitial collagen fibers was quantified with the straightness parameter (Fig. 3). At 0% strain, the straightness parameter for adventitial collagen fibers of tissue with GAGs removed was significantly higher than for untreated tissue from Chow et al. [2]. While delayed collagen fiber engagement behavior, i.e., fibers do not show significant straightening until around 20% strain, was observed in the adventitial collagen from untreated tissue, this behavior is absent from the treated tissue. In fact, removing GAGs (P_s=0.92) has a similar effect on the waviness of adventitial collagen fibers to applying between 20% (P_s=0.90) and 25% (P_s=0.94) strain to untreated tissue [2]. A possible explanation is that GAGs inflated from the repulsive charges and swelling pressure may contribute to collagen fiber waviness, so removing GAGs would allow the collagen fibers to be straighter.

Fractal analysis further revealed that in addition to adventitial collagen fibers, medial collagen and elastin fibers in the treated samples are also recruited at low levels of strain and show small changes after being fully recruited (Fig. 3). These results are consistent with the finding that the ECM fibers appear to be straighter and are engaged earlier than the untreated tissue. Previous histology studies suggest that GAGs fit within wavy collagen fibers perpendicular to the local fiber direction, similar to a laterally supported Euler column [4]. Such interactions may contribute to the entanglement of fibers, and provide support to fibers. Moreover GAGs can delay fiber engagement in the direction of mechanical loading. As a result of GAG removal, these fibers can engage earlier in response to mechanical loading.

Figure 2: Representative multiphoton images of adventitial collagen at 0 (left), 20 (middle) and 40% strain (right). The circumferential direction is horizontal. Images are 110×110 μm.

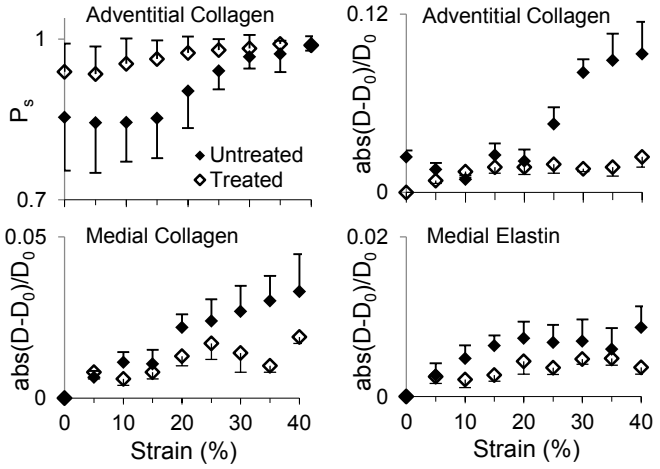

Figure 3: Straightness parameter (P_s) and fractal analysis (abs(D-D_0)/D_0) shows that GAG removal results in straighter fibers that are recruited at lower levels of strain, where D and D_0 are the average fractal number for the deformed and undeformed state, respectively.

Stress relaxation tests were performed to examine the contribution of GAGs to the viscoelastic behavior of arteries. Removing GAGs significantly reduce the percent stress relaxation from 8.77% to 7.14% (p=0.01) and 9.90% to 7.83% (p=0.03) in the longitudinal and circumferential directions, respectively. The finding of decreased stress relaxation after removing GAGs suggests that GAGs contribute to the viscoelastic behavior of arteries.

GAGs serve many functions in development, maintenance, and repair of a variety of tissues. An increase in GAG depleting enzymes such as those used in this study are noted in conditions such as hyperglycemia and hyperlipidemia that are prevalent in diabetes and atherosclerosis. Overall, our study suggests that despite the relatively low mass fraction of GAGs in arterial tissue, GAGs play an important role in contributing to the structural and mechanical properties of the arterial wall, and GAGs should be considered in addition to elastic and collagen fibers when studying arterial function.

ACKNOWLEDGEMENTS

This work was supported, in part, by a grant from National Science Foundation (CMMI 1463390) and a pre-doctoral training grant (2T32HL007969) from National Institutes of Health.

REFERENCES

[1] Lovekamp JJ, et al. *Biomaterials*, 27:1507–18, 2006.
[2] Chow M-J, et al. *Biophys J*, 106:2684–92, 2014.
[3] Chow M-J, et al. *J Biomech Eng*, 133:111009–111019, 2011.
[4] Bellini C, et al. *Ann Biomed Eng*, 42, 488-502, 2014.

Copyright 2016 The Organizing Committee for the 2016 Summer Biomechanics, Bioengineering and Biotransport Conference

SB³C2016
Summer Biomechanics, Bioengineering and Biotransport Conference
June 29 –July 2, National Harbor, MD, USA
SB³C2016-105

OVERLAP BETWEEN ANTERIOR CRUCIATE LIGGAMENT AND THE ANTEROLATERAL MENISCAL ROOT INSERTIONS: A SCANNING ELECTRON MICROSCOPY STUDY

Brett D. Steineman (1), Samuel G. Moulton (2), Tammy L. Haut Donahue (1, 3), Chase S. Dean (2), Robert F. LaPrade (2, 4)

(1) School of Biomedical Engineering
Colorado State University
Fort Collins, Colorado, USA

(2) Steadman Philippon Research Institute
Vail, Colorado, USA

(3) Department of Mechanical Engineering
Colorado State University
Fort Collins, Colorado, USA

(4) The Steadman Clinic
Vail, Colorado, USA

INTRODUCTION

Reconstructions of the anterior cruciate ligament (ACL) attempt to restore knee function after ACL injuries and studies have demonstrated the efficacy of ACL reconstructions to significantly improve knee integrity [1]. However, recent investigations have highlighted concern over iatrogenic injury of anterior meniscal root insertions caused by reaming of replacement ACL tibial bone tunnels, specifically the anterolateral meniscal root (ALMR) insertion.

Recently, the ALMR has been described to insert underneath the lateral portion of the ACL with 41% of the ACL insertion area overlapping an average of 63% of the ALMR insertion [2]. Investigations of ACL reconstruction tunnel reaming demonstrated an average injury area of at least 25% of the original ALMR insertion and significantly decreased ultimate tensile strength of the attachment [3, 4]. While these studies begin to describe the risk of ALMR injury during ACL reconstruction and the complex relationship between the insertions, further investigation of how the insertions interact is necessary to understand and define the three-dimensional relationship of these two structures.

The purpose of this study was to investigate the microstructural relationship between the tibial ACL and ALMR insertions using scanning electron microscopy (SEM) of coronal and sagittal sections and quantify the overlap of the two insertions. It was hypothesized that the maximum percentage of tibial ACL insertion overlapping with the ALMR insertion would be the same in both the coronal and sagittal planes.

METHODS

Institutional review board approval was not necessary for this study because de-identified cadaveric specimens are exempt from review at our institution. Ten cadaveric knees, five males and five females, mean age 52.7 (range, 33-63), mean BMI 22.4 (range, 15-34), and no history of knee injury were used. Care was taken to isolate and preserve the entire ACL and ALMR throughout the dissection before a rectangular bone block was cut to include the tibial ACL and ALMR insertions.

Samples were prepared for SEM using standard methods [5]. Briefly, the samples were placed in fixative (2.5% glutaraldehyde) for 48 hours at room temperature. The samples were then submerged in 10% formic acid to decalcify at room temperature. Following decalcification, the samples were immersed in a 1% tannic acid solution buffered with 0.05 M cacodylate (pH 7.2) for 4 hours and then rinsed in distilled water for 24 hours. Samples were then dehydrated in ascending concentrations of ethanol and cut into 2 mm sections. Five specimens were cut into coronal sections with the ALMR insertion fibers running approximately parallel to the section plane and the remaining five specimens were cut into sagittal sections with the ACL fibers running parallel to the section plane. Once sectioned, the samples were placed into ascending concentrations of hexamtheyldisilazane (HMDS) and dried in a vacuum desiccator. Samples were mounted with conductive tape, coated with a 10 nm layer of gold, and scanned using a JSM-6400 scanning electron microscope (JEOL, Peabody, MA) in the secondary electron emission mode (SEI) with an accelerating voltage of 15 kV.

To evaluate the relationship between the tibial ACL insertion and the ALMR insertion in the coronal plane, sections taken from the middle of the ALMR insertion were imaged. In the sagittal plane, imaged sections were taken closer to the lateral side of the ACL insertion to incorporate the ALMR insertion. Each section was imaged at high magnification (up to 1,500X) to view fiber direction and to identify the entirety of the ACL and ALMR insertions. Lower magnification (15X) images were taken across the entirety of each sample and stitched

Copyright 2016 The Organizing Committee for the 2016 Summer Biomechanics, Bioengineering and Biotransport Conference

together for quantitative analysis of the insertion relationship using ImageJ software (NIH, Bethesda, MD).

To further understand the relationship between the two insertions, the percentage of the tibial ACL that interacts with the ALMR insertion instead of inserting into subchondral bone was determined (Figure 1). For each sample, the length of the ACL visibly inserting into subchondral bone was initially determined by measuring the boundary between the ligament-bone interface for indirect fibers and insertion tidemark of the direct fibers described in previous literature [5]. The length of the ACL insertion visibly overlapping with the ALMR insertion was also measured. The two length measurements were then used to calculate the percentage of overlap between the two insertions. Measurements were taken from the stitched SEM images using ImageJ software.

A two-sample, equal variance Student's t-test was performed on the coronal and sagittal percentages of overlap with significance determined as $p < 0.05$.

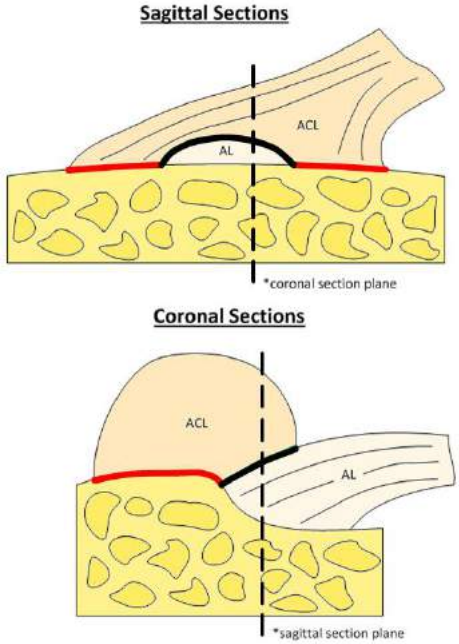

Figure 1: Schematic of method used to analyze the percentage of tibial ACL insertion interacting with the ALMR insertion fibers instead of inserting into subchondral bone. Solid red = ACL into subchondral bone; solid black = interaction between ACL and ALMR; dashed black = sections taken of other plane.

RESULTS

Macroscopically, the ALMR inserted underneath the lateral side of the ACL in all ten specimens. The relationship between the tibial ACL and the ALMR insertions was also clearly visible upon forming the coronal and sagittal sections. Microscopically, the tibial ACL insertion displayed an intimate relationship with the ALMR insertion as they transitioned into bone in all specimens. Direct four-phase fibers of the tibial ACL insertion were also identified directly adjacent to the ALMR insertion as they attached onto the tibial plateau in the coronal plane (Figure 2).

After identifying the insertion fibers of the tibial ACL and ALMR, the percentages of the ACL insertion overlapping with the ALMR insertion were calculated for each section in both planes. The tibial ACL insertion overlapped the ALMR insertion in the coronal and sagittal sections with a mean percentage of 40 ± 8% and 43 ± 9%, respectively. There was no significant difference in the percentage of insertion interaction between the coronal and sagittal sections ($p = 0.32$).

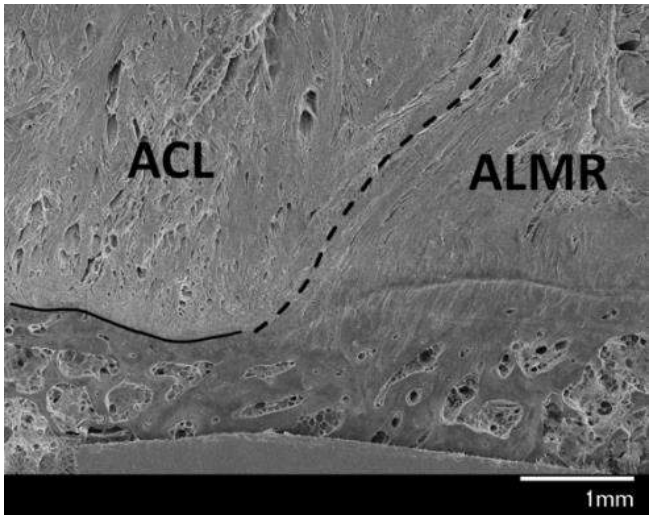

Figure 2: SEM image of insertion relationship in coronal plane. Note the direct fibers of the ACL insertion with the tidemark (solid line) separating the uncalcified fibrocartilage layer from the calcified fibrocartilage layer directly adjacent to the ALMR insertion. The dashed line represents the interaction between the ACL and ALMR. 15X; Working distance = 25 mm.

DISCUSSION

This study investigated the relationship between the tibial ACL and ALMR insertions using SEM and quantified percentages of interaction in the coronal and sagittal planes. The results of this study suggest that a significant portion of the tibial ACL insertion in the coronal and sagittal planes overlaps with the ALMR insertion instead of inserting directly into subchondral bone. There was no significant difference between the targeted maximum percentage of insertion interaction in the coronal and sagittal planes, which suggests the ALMR equally interacts with the tibial ACL insertion in both planes.

The clinical implications of this finding are currently unknown; however, acceptance of a guide pin placed laterally in the tibial ACL insertion may have even more significance than previously thought. During ACL reconstruction, reaming over a laterally misplaced guide pin could lead to complete or functional detachment of the anterior horn of the lateral meniscus after tunnel reaming, potentially leading to iatrogenic injury and development of osteoarthritis over time.

The goal of an ACL reconstruction should be to place a tibial tunnel within the center of the direct fibers of the insertion, described as the most structurally important attachment fibers [6]. The direct fibers of the tibial ACL were found medially adjacent to the ALMR insertion in the central coronal plane. This intricate relationship and overlap complicates the placement of a tibial tunnel for an ACL reconstruction. Therefore, thorough investigation of the tibial ACL direct fibers with respect to the location of the ALMR insertion fibers is warranted.

REFERENCES

[1] Tsai AG et al., *Am J Sports Med*, 38(2):263-272, 2010.
[2] LaPrade CM et al., *Am J Sports Med*, 42(10):2386-2392, 2014.
[3] Watson JN et al., *Am J Sports Med*, 23(8):2360-2366, 2014.
[4] LaPrade CM et al., *Am J Sports Med*, 43(1):200-206, 2015.
[5] Zhao L et al., *J Anat*, 224(6):624-633, 2014.
[6] Gao J et al., *J Anat*, 188:367-373, 1996.

Copyright 2016 The Organizing Committee for the 2016 Summer Biomechanics, Bioengineering and Biotransport Conference

SB³C2016
Summer Biomechanics, Bioengineering and Biotransport Conference
June 29 –July 2, National Harbor, MD, USA
SB³C2016-106

CHARACTERIZATION OF PARTICULATE AND VAPOR PHASE NICOTINE IN ELECTRONIC CIGARETTES

Mark C. Daley (1), James W. Baish (1), Dabrina D. Dutcher (2), Timothy M. Raymond (2)

(1) Biomedical Engineering
Bucknell University
Lewisburg, PA, USA

(2) Chemical Engineering
Bucknell University
Lewisburg, PA, USA

INTRODUCTION

Electronic cigarettes, colloquially known as e-cigs, are rapidly increasing in popularity among both users and non-users of traditional cigarettes[1,2,3]. Unfortunately, knowledge of their relative health hazards is sparse despite this popularity.

Unlike conventional cigarettes, which deliver nicotine along with known carcinogens via smoke from the combustion of tobacco, electronic cigarettes operate by vaporizing an e-liquid, consisting of propylene glycol, vegetable glycerin, flavoring agents, and nicotine[1]. Heating the e-liquid generates an inhalable aerosol that delivers these ingredients into the user's respiratory system, simulating the experience and nicotine delivery of traditional cigarettes. While the basic components of e-liquids, excluding nicotine, are generally considered safe for human consumption, findings show significant presence of heavy metals and carcinogens in electronic cigarette vapor[4,5]. For these reasons, many nations including the United States are proposing regulations to control health risks[1].

However, there are relatively few studies on electronic cigarettes, resulting in gaps in necessary knowledge. Given their intended use to deliver nicotine to the bloodstream, the dosage amount and rate are of interest to regulators. Previous studies show that users' nicotine levels increase more slowly as compared to conventional cigarettes[6]. One possible explanation for this is a difference in the manner in which nicotine is delivered. Nicotine in the vapor phase, large particles, and small particles will be delivered to different areas of the respiratory system[7,8]. The disparity in absorption rate is thought to be because nicotine is rapidly delivered to the body via the pulmonary route while it is considerably slower when administered orally or dermally[9,10].

This study was designed to determine the mass and distribution of nicotine available to users from electronic cigarettes between particulate and vapor phases to account for observed differences in absorption.

METHODS

The first task of the investigation was to effectively capture both the vapor and particulate phase nicotine separately while precisely controlling puff parameters. An Arduino-controlled device regulated the puff duration, puff intervals, number of puffs, and electronic cigarette voltage. For this investigation, each sample consisted of 30 puffs separated by 30 seconds each. Puffs lasted for 3 seconds with a flow rate of 35 ml/s with the heater coil in the electronic cigarette being turned on 1 second prior to air flow. A KangerTech™ T3'D Dual Coil Clearomizer with ZigZag™ Dragonberry flavor 18 mg nicotine/mL e-juice was utilized for all sampling.

Puffs were sampled through a 4.7 cm diameter quartz filter and then 3 inch and ½ inch long open-cell polyurethane foam (PUF) filters each with a 2 inch diameter (Figure 1). Prior to use, the quartz filters were rinsed three times with deionized water via vacuum filtration and dried in a high temperature oven overnight. The PUF filters were rinsed three times in excess methanol and allowed to air dry. Additionally, the mass of the clearomizer was taken before and after each trial. This process was repeated a total of three times for each voltage: standard (3.7 V), high (4.8 V), extreme (5.5 V).

Once the electronic cigarette emission samples were collected, the quartz and ½ inch PUF filters were placed in 25 mL of methanol and the 3 inch PUF filters were placed in 150 mL of methanol and sonicated for 60 seconds. A small aliquot of each solution was taken to be analyzed by Gas Chromatography Mass Spectrometry (GC-MS).

Copyright 2016 The Organizing Committee for the 2016 Summer Biomechanics, Bioengineering and Biotransport Conference

An Agilent 7890A GC with an Agilent HP-5MS capillary column and an Agilent 5975C VL MS were utilized. A 1 µL volume was injected and run using a method previously used for detecting urinary nicotine[11]. The peak attributed to nicotine appeared at 8.42 minutes.

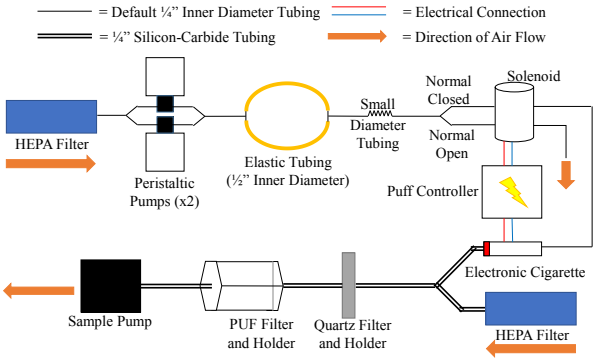

Figure 1: Flow diagram of emission sample collection.

A standard curve was created using solutions prepared from ≥99% pure nicotine in methanol in order to associate chromatographic peak area to nicotine concentration. The total mass captured by the filter was calculated by multiplying concentration by solution volume. If nicotine vapor breakthrough was detected, as indicated by detected nicotine on the ½ inch PUF filter, the trial was excluded due to sample loss.

Nicotine from the quartz filters was considered particulate and nicotine from PUF filters was considered to be vapor phase. A theoretical amount of total nicotine available was also calculated by assuming that the e-liquid had a density equal to an average of propylene glycol and glycerin, and a nicotine content of 18 mg/mL as labeled. The theoretical mass of nicotine available, m_{theor}, is found from:

$$m_{theor} = \frac{\Delta m \cdot C}{\rho} \quad (1)$$

where Δm is the change in clearomizer mass, C is the concentration of nicotine, and ρ is the density.

RESULTS

The theoretical and experimental amounts of nicotine were determined for each voltage setting with the power calculated from the measured resistance of the coil (Figure 2).

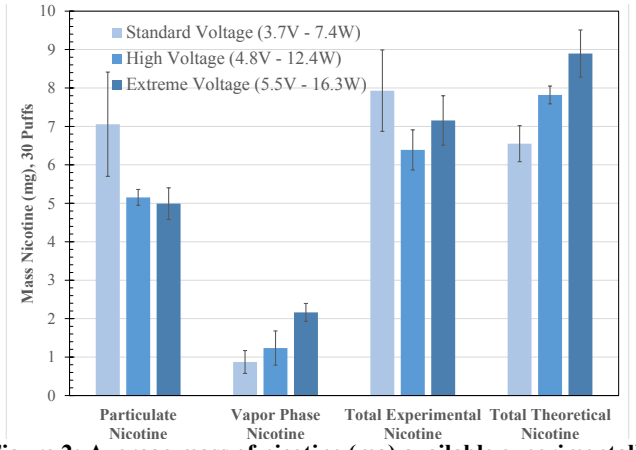

Figure 2: Average mass of nicotine (mg) available experimentally from the particulate and vapor phases as well as the total nicotine available theoretically and experimentally, with average deviation.

The total mass of theoretical nicotine as well as the experimental vapor phase nicotine available increased with power. The amount of experimental particulate phase nicotine available was larger at the standard power and approximately the same at both the high and extreme powers. Since the total experimental nicotine was simply the sum of the vapor and particulate phases, it was the highest at the standard voltage and lower at both the high and extreme voltage, increasing approximately with vapor phase nicotine. With the exception of the standard voltage, experimentally available nicotine was less than the theoretically available nicotine. This lack of mass balance may be due to the portion of e-liquid observed in the tubing near the electronic cigarette's mouthpiece, which was unaccounted for in either the vapor or particulate phases.

DISCUSSION

As predicted, nicotine from electronic cigarettes is distributed between the particulate and vapor phases (Figure 1). A majority, regardless of power, is found in the particulate phase. The associated particle size would determine where in the respiratory tract this nicotine would be available[7,8]. It is unclear why particulate phase nicotine is more abundant at standard power, but the overlap in average deviation between total experimental and theoretical mass at standard power suggests a mass balance is achieved at this lower power. This same mass balance was not achieved at the high or extreme powers due to the lower mass of particulate phase nicotine.

As vapor phase nicotine increases with power, a larger portion of the nicotine is available for rapid absorption in the lungs. This means, that at higher powers, electronic cigarettes can better simulate rapid rise in plasma nicotine levels produced by traditional cigarettes[10]. The increase in total available nicotine also means that a higher level of blood nicotine levels can be achieved. This combination supports previous findings that later generation electronic cigarettes, which operate at higher powers, cause more rapid nicotine absorption[6].

For the high and extreme voltages, the total theoretical nicotine was larger than the total experimental nicotine, indicating a portion would not be distributed throughout the respiratory system. Instead, it is possible that a portion is simply mechanically splattered into the mouth and absorbed orally. The e-liquid observed in the tubing directly following the mouthpiece seems to account for this possibility. A portion of the nicotine may have also been chemically converted.

The proposed distribution of bioavailable nicotine between the mouth, upper airways, and lungs explains the nicotine absorption pattern of electronic cigarettes as compared to traditional cigarettes.

ACKNOWLEDGEMENTS

This research was supported by the Bucknell Program for Undergraduate Research under the Helen E. Royer Undergraduate Research Fund. Funding for materials was provided by the Biomedical and Chemical Engineering Departments at Bucknell University.

REFERENCES

[1] Grana, R et al., *Circulation*, 129:1972-1986, 2014.
[2] Porter, L et al. *Plos One*, 10:e0124385, 2015.
[3] McMillen, R et al. *Nicotine Tob Res*, 17:1195-1202, 2015.
[4] Williams, M et al., *Plos One*, 8:e57987, 2013.
[5] Jensen, R et al., *New Engl J Med*, 374:392-394, 2015.
[6] Farsalinos K et al., *Sci Rep*, 4:4133-4140, 2014.
[7] Heyder, J et al., *J Aerosol Sci*, 17:811-825, 1986.
[8] Darquenne, C. *J Aerosol Med Pulm D*, 25:140-147, 2012.
[9] Schroeder, M and Hoffman, A. *Tob Control*, 23:ii30-ii35, 2014.
[10] Berridge, M et al., *Psychopharmacology*, 209:282-394, 2010.
[11] Iwai, M et al., *Nagoya J Med Sci*, 75:255-261, 2013.

Copyright 2016 The Organizing Committee for the 2016 Summer Biomechanics, Bioengineering and Biotransport Conference

SB^{3}C2016
Summer Biomechanics, Bioengineering and Biotransport Conference
June 29 –July 2, National Harbor, MD, USA
SB^{3}C2016-107

INDIVIDUAL-SPECIFIC FINITE ELEMENT MODEL OF THE RAT OPTIC NERVE HEAD UNDER ELEVATED INTRAOCULAR PRESSURE CONDITIONS

Stephen A. Schwaner (1), Marta Pazos (2,3), Hongli Yang (3), Elaine C. Johnson (4), John C. Morrison (4), Claude F. Burgoyne (3), C. Ross Ethier (1,5)

(1) George W. Woodruff School of Mechanical Engineering, Georgia Institute of Technology, Atlanta, GA, USA

(2) Ophthalmology Department, Hospital de l'Esperanca-Parc de Salut Mar., Institut Mar d'Investigacions Mèdiques, Barcelona, Spain

(3) Devers Eye Institute, Optic Nerve Head Research Laboratory, Portland, OR, USA

(4) Casey Eye Institute, Oregon Health and Science University, Portland, OR, USA

(5) Coulter Department of Biomedical Engineering, Georgia Institute of Technology/Emory, Atlanta, GA, USA

INTRODUCTION

Glaucoma is the second most common cause of blindness worldwide, and is characterized by the death of retinal ganglion cells (RGC) which carry vision information to the brain [1]. A key risk factor in glaucoma is elevated intraocular pressure (IOP). IOP induces stress and strain in the tissues of the optic nerve head (ONH), which is thought to contribute to retinal ganglion cell axon insult. The ONH is a region in the posterior eye with complex tissue morphology, including a passage in the sclera (connective tissue shell of the eye) known as the scleral canal. RGC axons pass through a web of connective tissue (lamina cribrosa) that spans this canal as they exit the eye and converge to form the optic nerve (Fig 1). Data suggest that the ONH is the main site of axonal damage in glaucoma and that ONH biomechanics is important in glaucoma [2], motivating previous modeling studies of the human ONH [3]. However, there is a need to better understand ONH biomechanics of animal models used in glaucoma research.

The rat is a well-accepted animal model for glaucoma. Such studies using the rat are based on elevation of IOP and observation of resulting biological and structural changes in the ONH. However, rat ONH biomechanics have not been characterized, and there are significant structural differences between the rat and human ONH, including the lack of a connective tissue lamina cribrosa spanning the rat neurovascular scleral canal (Figs 2 and 3), the presence of a vascular plexus between the optic nerve and the sclera of the neurovascular canal, and the presence of a separate, inferior arterial canal. Digital 3D histomorphometric reconstructions of the rat ONH (Fig 2) are now available, making eye-specific finite element (FE) modeling of the rat ONH possible [5]. We present herein the first eye-specific FE models of the normal rat ONH under elevated IOP conditions, with the goal of understanding rat ONH mechanobiology.

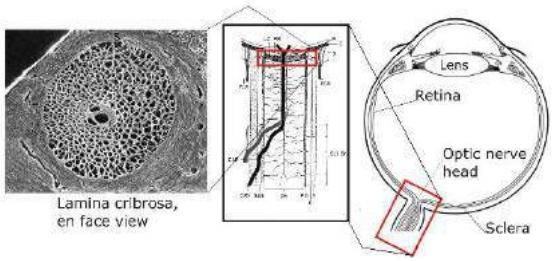

Figure 1: From left to right: electron microscopic image of the lamina cribrosa, schematic of the ONH, and schematic of the eye anatomy [4]. All three represent human anatomy.

METHODS

A finite element model was constructed from manual delineation of a normal rat ONH within a digital 3D histomorphometric reconstruction, created as follows. Following perfusion fixation, the ONH from a normotensive rat eye was embedded in paraffin and serial sectioned. After each cut, the block face was stained and photographed. All images were aligned and stacked into a digital 3D reconstruction [5]. Digital radial and transverse cross sections of the reconstruction were viewed in order to delineate key ONH tissues (Fig 2). Points were manually placed on the borders of the sclera, nerve, central retinal artery (CRA), central retinal vein (CRV), perineural vascular plexus (PNVP), and inferior arterial canal (IAC). CAD software (Rhino) was used to fit NURBS surfaces to 3D point clouds, creating an ONH geometry for FE modeling using Abaqus. Tissues were treated as isotropic, nearly-incompressible, neo-Hookean materials and assigned properties (Table 1) from previous modeling studies of the human ONH [3] since little information about rat-specific tissue properties is currently available.

Copyright 2016 The Organizing Committee for the 2016 Summer Biomechanics, Bioengineering and Biotransport Conference

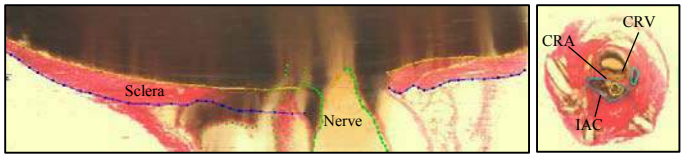

Figure 2: Radial (left) and transverse (right) digital sections of a rat ONH with manual delineations of tissues (colored dots).

The model was meshed using 10-node, hybrid tetrahedral elements (C3D10H in Abaqus). Approximately 350,000 elements were used. Pressure was applied to the anterior surface of the model (interior ocular surface) to simulate IOP. Because the eyes were perfusion fixed while experiencing an IOP of approximately 10 mmHg, pressures applied to the model represent a change in IOP from a reference state at 10 mmHg. Arterial and venous pressures were applied to the CRA and CRV lumens. Boundary conditions were applied using a submodeling approach as follows. A generic posterior eye (GPE) model was created by embedding simplified ONH tissue geometries in a semi sphere of 6.41 mm diameter and 0.2 mm thickness and applying IOP up to 30 mmHg. The geometric best fit match between the GPE and the ONH models was found, and displacements from matching locations of the GPE model were applied to the edges of the local ONH model as boundary conditions.

	Young's Modulus (MPa)	Poisson's Ratio
Sclera	3.0	0.49
Nerve	0.03	0.49
CRA	0.3	0.49
CRV	0.3	0.49
PNVP	0.1	0.49
IAC	0.1	0.49

Table 1: Material properties of model components

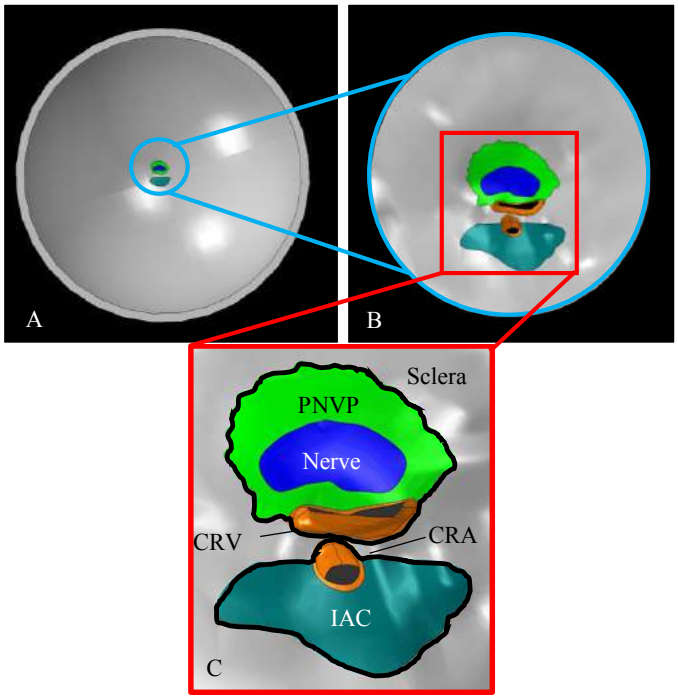

Figure 3: Generic posterior eye model (A), and local ONH model (B, C). Central retinal artery (CRA), central retinal vein (CRV), perineural vascular plexus (PNVP), inferior arterial canal (IAC).

RESULTS

As a proof of principal, we modeled an applied pressure of 20 mmHg (simulating an IOP of 30 mmHg), and CRA and CRV blood pressures of 70 and 20 mmHg (Figure 4). Within the optic nerve, the site of axonal damage, the model predicted 95th percentile first principal strain (logarithmic) and stress of 19.1% and 8.5 kPa, respectively. This strain value exceeds that predicted in the human: 95th percentile first principal strain of ~7.5% in the prelaminar nerve at an even higher IOP of 50 mmHg [3]. Higher strains in the rat nerve are expected due to the absence of structural support from a lamina cribrosa which is present in the human.

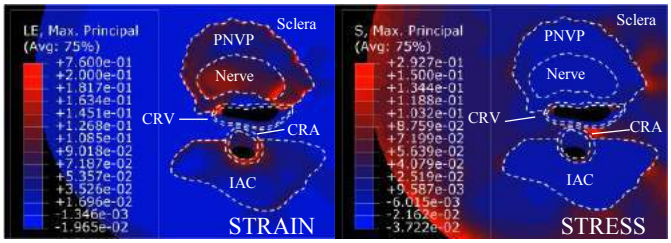

Figure 4: First principal strain (logarithmic) and stress (MPa) in the ONH. Central retinal artery (CRA), central retinal vein (CRV), perineural vascular plexus (PNVP), inferior arterial canal (IAC).

DISCUSSION

We present an initial FE model of the biomechanics of the rat ONH. The results of this study are promising, as an FE model utilizing complex, individual-specific ONH geometry was successfully solved under elevated IOP loading conditions. Future work is underway and includes the following. 1) Although we expect that rat tissue material properties are relatively similar to values in the human, values specific to the rat will be obtained and used. 2) Although we have included a significant portion of the rat ONH morphology, additional tissues are being added to the model in order to capture even more of the complex rat ONH geometry. 3) We will model additional individual-specific ONH geometries (including from contralateral experimental glaucoma eyes [6]) to evaluate biomechanical effects of rat-to-rat ONH morphology variation and of glaucomatous structural changes. These models will allow us to relate regionally specific stress and strain levels to biological outcomes in rat glaucoma models, which will in turn provide better context for interpreting outcomes of past and future rat studies, thus improving our understanding of glaucoma pathogenesis.

ACKNOWLEDGEMENTS

NIH T32 EY007092 (SAS), Georgia Research Alliance (CRE), NIH RO1 EY010145 (JCM) and P30 EY010572 (JCM), Research to Prevent Blindness (JCM), EY011610 (CFB), Legacy Good Samaritan Foundation (CFB), AGS Mid-Career Award (CFB), Sears Medical Trust (CFB), Alcon Research Institute (CFB).

REFERENCES

[1] Varma, R et al., *Am J Opthalmol*, 152(4): 515-22, 2011.
[2] Burgoyne, CF, *Exp Eye Res*, 93(2): 120-132, 2011.
[3] Sigal, I et al., *Biomech Model Mechanobiol*, 8(2): 85-98, 2009.
[4] Ethier, CR and Simmons, CA, *Introductory Biomechanics: From Cells to Organisms*, Cambridge University Press, 2007.
[5] Pazos, M and Yang, H et al., *Exp Eye Res*, 139: 1-12, 2015.
[6] Pazos, M and Yang, H et al., *Exp Eye Res*, 145: 173-186, 2016.

Copyright 2016 The Organizing Committee for the 2016 Summer Biomechanics, Bioengineering and Biotransport Conference

SB^{3}C2016
Summer Biomechanics, Bioengineering and Biotransport Conference
June 29 –July 2, National Harbor, MD, USA
SB^{3}C2016-108

MACROSCOPIC PREDICTIONS OF THROMBUS GROWTH IN A THREE-DIMENSIONAL BACKWARD-FACING STEP

Joshua O. Taylor (1,2), Steven Deutsch (2), Keefe B. Manning (1,3)

(1) Department of Biomedical Engineering
The Pennsylvania State University
University Park, PA, USA

(2) Applied Research Laboratory
The Pennsylvania State University
State College, PA, USA

(3) Department of Surgery
The Penn State College of Medicine
Hershey, PA, USA

INTRODUCTION

The efficacy of blood-contacting devices has improved significantly over the years; yet, thrombosis still remains a co ncern with current device technology. To help better understand and predict thrombus deposition and growth, many thrombosis models have been developed for use in computational fluid dynamics (CFD) simulations. However, due to the convoluted and multi-scale nature of the thrombotic process, the most thorough models need to track tens of species and consider dozens of coupled reactions, making them too computationally expensive to use in the complex, three-dimensional flows associated with blood-contacting devices. Additionally, they often rely on *a priori* knowledge to dictate locations of initial thrombus deposition and/or are not rigorously validated due to a lack of *in vitro* or *in vivo* thrombus growth data.

One of the primary causes of device-induced thrombosis is disrupted blood flow through the device [1]. Specifically, regions of high shear stress can activate platelets, while regions of low wall shear stress (WSS) promote thrombus deposition. A thrombosis model for use in blood-contacting devices must be able to simulate the entire thrombotic process; platelet activation, platelet adhesion, and thrombus growth; at both high and low shear conditions, relying purely on the fluid dynamics of the system to dictate locations of thrombus deposition.

METHODS

A single-scale thrombosis model, initially developed by Fogelson [2], is modified to predict macroscopic device-induce thrombosis. The model considers bulk concentrations of platelets, non-activated (ϕ_n) and activated (ϕ_a), and adenosine diphosphate (ADP – a platelet agonist), and terms for mechanical platelet activation and WSS-dependent thrombus deposition and growth are added. The concentrations of activated platelets and ADP are calculated with Eqns (1) and (2), respectively.

$$\frac{\partial \phi_a}{\partial t} + (\boldsymbol{u}\cdot\nabla)\phi_a = D_a\nabla^2\phi_a + \{[A_C(ADP)]\phi_n + [A_M(\phi_f,\tau)](\phi_a+\phi_n)\} \quad (1)$$

$$\frac{\partial ADP}{\partial t} + (\boldsymbol{u}\cdot\nabla)ADP = D_{ADP}\nabla^2 ADP + R_{ADP}\{[A_C(ADP)]\phi_n + [A_M(\phi_f,\tau)](\phi_a+\phi_n)\} \quad (2)$$

Mechanical platelet activation (A_M) is quantified through an Eulerian power law model – Eqn (3) – adapted from Soares *et al*. [3].

$$A_M(\phi_f,\tau) = (1-\phi_f)C^{\frac{1}{\beta}}\beta\phi_f^{\frac{\beta-1}{\beta}}\tau^{\frac{\alpha}{\beta}} \quad (3)$$

Thrombus deposition and growth is quantified through the use of a scalar aggregation intensity (ε), quantified using Eqn (4), which relies on a novel WSS-dependent weighting function, P_{TSP} in Eqn (5), to determine locations of deposition and the subsequent rate of thrombus growth. P_{TSP} is based on a thrombus susceptibility potential (TSP) metric developed to quantify the risk of thrombosis in pulsatile blood pumps [4].

$$\frac{\partial \varepsilon}{\partial t} = \alpha_\varepsilon P_{TSP}(\tau_w)\phi_a^2 - \beta_\varepsilon(\tau_w)\varepsilon \quad (4)$$

$$P_{TSP}(\tau_w) = \begin{cases} 1 \; for \; |\tau_w| \le \tau_{low} \\ 1 - \frac{|\tau_w|}{\tau_{high}} \cdot \frac{e^{\frac{|\tau_w|-\tau_{low}}{\tau_{high}-\tau_{low}}}-1}{e^1-1} \; for \; \tau_{low} < |\tau_w| < \tau_{high} \\ 0 \; for \; |\tau_w| \ge \tau_{high} \end{cases} \quad (5)$$

Lastly, a growing thrombus is coupled to the velocity field through the use of a modified Brinkman term, *F*, in the Navier-Stokes equations, Eqn (6).

$$\frac{\partial \boldsymbol{u}}{\partial t} + (\boldsymbol{u}\cdot\nabla)\boldsymbol{u} = -\frac{1}{\rho}\nabla p + \nu\nabla^2\boldsymbol{u} - \nu F(\varepsilon)\boldsymbol{u} \quad (6)$$

Copyright 2016 The Organizing Committee for the 2016 Summer Biomechanics, Bioengineering and Biotransport Conference

Many model parameters are taken from literature, but some are estimated from an *in vitro* study of thrombus growth in a BFS using magnetic resonance imaging (MRI) [5]. The governing equations are solved using the open-source CFD toolbox OpenFOAM in a 3D BFS domain (Fig. 1). Steady flow, resulting in a laminar upstream Reynolds number of 490, is imposed at the inlet to match the experimental conditions [5], and 10 ms time steps are used to simulate thrombus growth for 30 min. The computational domain matches the dimensions of the *in vitro* model and consists of 2.15 million cells.

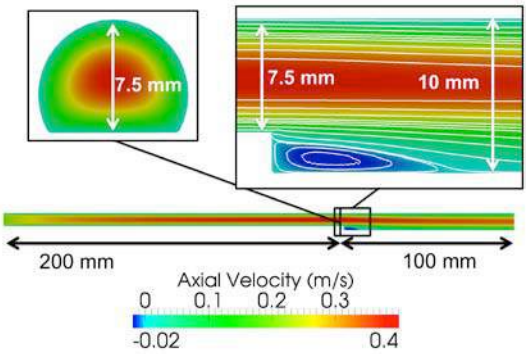

Figure 1: Axial velocity distribution in the BFS domain. An axial slice through the centerline is displayed in the bottom of the image, with two regions selected for enlargement. In the upper left, a transverse cross section just upstream of the step is displayed. In the upper right, a portion of the axial centerline near the step is displayed, with contour lines used to illustrate flow recirculation. Additionally, the velocity scale is non-linear to accentuate regions of flow reversal (dark blue).

RESULTS

Simulated thrombus growth begins near the step, in the region of separated flow, and thus low WSS, produced by the sudden expansion and at the reattachment point (see Fig. 2). The two distinct thrombi merge between 5 and 10 min into the simulation and continue to grow into the lumen. Thrombus growth reaches the step height after approximately 20 min (Fig. 2D), and by 30 min, nearly the entire initial region of flow separation is filled with thrombus.

Fig. 3 provides a quantitative look at simulated thrombus growth, and direct comparisons between the CFD and *in vitro* [5] results. Both thrombus height and length are normalized by the step height, 2.5 mm, and the trend for thrombus height shows excellent agreement with the MRI data, as quick initial growth approaches a normalized asymptotic height near one (Fig. 3A). However, the thrombus appears to initially lengthen much too quickly, but this is due to the fact that some deposition occurs near the reattachment point within the first few minutes of the simulation. There is nice agreement between the predicted and *in vitro* length at 25 minutes, but the predicted length is much longer at 30 minutes than that determined with MRI: 7.5S and 4.7S, respectively (Figure 3B). Nevertheless, if simulated thrombus length is extrapolated toward 60 minutes, it appears the simulation and MRI results will again agree.

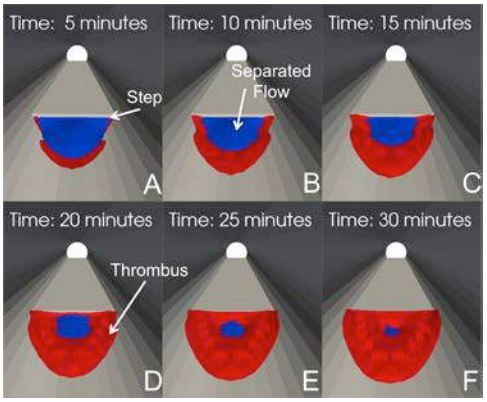

Figure 2: Simulated thrombus growth for (A) 5 minutes, (B) 10 minutes, (C) 15 minutes, (D) 20 minutes, (E) 25 minutes, and (F) 30 minutes of blood flow.

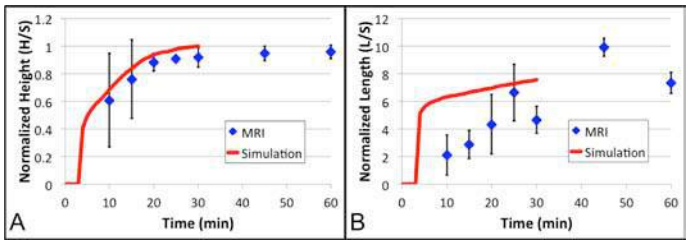

Figure 3: Simulated thrombus (A) height and (B) length compared to the MRI results of Taylor *et al.* [5], and both thrombus height (H) and length (L) are normalized using the step height (S). Error bars denote the 95% confidence intervals of the MRI data.

DISCUSSION

A thrombosis model is used in a three-dimensional BFS domain, and the present simulations represent the first three-dimensional growth simulations of a thrombus on spatial and time scales relevant to medical devices. The simulations show great promise toward the eventual application to medical device development, as thrombus deposition location, general shape, and height trends all agree well with the *in vitro* thrombus data [5]. However, additional work is still needed to ensure thrombosis model accuracy under more clinically relevant flow conditions, such as pulsatile or turbulent flow. Importantly, the three-dimensional simulation results provide evidence that the reduction of the thrombotic process to the present governing equations is appropriate in situations relevant to device-induced thrombosis, as simulated thrombus growth agrees, at least macroscopically, with the *in vitro* whole blood experiments [5], and thus the full thrombotic network.

ACKNOWLEDGEMENTS

A Walker Graduate Assistantship from the Applied Research Laboratory at the Pennsylvania State University and a Penn State Grace Woodward Foundation grant supported this work.

REFERENCES

[1] Deutsch S, *et al.*, *Annu Rev Fluid Mech*, 38:65-86, 2006.
[2] Fogelson AL, *SIAM J Appl Math*, 52(4):1089-1110, 1992.
[3] Soares JS, *et al.*, *Biomech Model Mechanobiol*, 12:1127-41, 2013.
[4] Topper SR, *et al.*, *Cardiovasc Eng Technol*, 5(1):54-69, 2014.
[5] Taylor JO, *et al.*, *J Biomech Engr*, 136:071012, 2014.

Copyright 2016 The Organizing Committee for the 2016 Summer Biomechanics, Bioengineering and Biotransport Conference

SB^{3}C2016
Summer Biomechanics, Bioengineering and BIotransport Conference
June 29-July 2, 2016, National Harbor, MD, USA
SB^{3}C2016-109

EFFECT OF COLLAGEN FIBRIL ALIGNMENT ON VISCOELASTIC MECHANICAL PROPERTIES OF LIGAMENT

Erica E. Morrill (1), Christina J. Stender (1), Raquel J. Brown (2), Trevor J. Lujan (1)

(1) Department of Mechanical and Biomedical Engineering
Boise State University
Boise, ID, USA

(2) Biomolecular Research Center
Boise State University
Boise, ID, USA

INTRODUCTION

The mechanical behavior of ligament is governed by the organization and composition of its fibrous protein network. To stabilize joints, ligaments resist deformation by storing energy (elastic properties) and dissipating energy (viscoelastic properties). The structural origin of these mechanical properties is either the fibrillar network or the ground substance of the extracellular matrix. Type I collagen is the primary load bearing constituent of ligament, however it is unknown what features of the collagen fibrillar network are required to successfully describe the viscoelastic mechanical behavior. A focus has been placed on measuring collagen material features such as fiber orientation, fiber dispersion (or alignment index), fiber diameter, and number of intersections [1,2]. Typically, healthy ligament contains very aligned (low dispersion) collagen networks, however, it can also exhibit disordered or multiaxial fiber networks [3,4]. Disorganized collagen networks are also prevalent throughout granulation tissue and scar tissue and may be connected to inferior mechanical properties observed in repaired ligament [5,6]. Multi-scale analysis of tendon has shown that fiber sliding was the largest contributor to stress relaxation [7], however the connection between viscoelastic properties and fibril organization in ligament tissue remains unclear.

Understanding the relationship between structure and function of collagen networks can give insight into pathologies associated with damaged ligament and assist in treatment development. The objective of this study is to determine if correlations exist between collagen fibril orientation distribution and the viscoelastic behavior of ligament.

METHODS

Overview. Forty ligament specimens from ten adult bovine hooves were mechanically tested in uniaxial tension under cyclic loads. Collagen fibril microstructure was imaged using confocal microscopy and analyzed using the fast Fourier transform (FFT) to quantify the fibril orientation distribution. Regression analysis was performed to determine relationships between the fibril orientation distribution and mechanical properties of the specimens.

Test Protocol. The lateral collateral sesamoid ligament (LCSL) and palmar annular ligament (PAL) were harvested from ten bovine hooves. Fascicle orientation in the LCSL tissue was visibly aligned, whereas the PAL tissue contained more disorder. Dog-bone shaped specimens were prepared in both the transverse (trv) and longitudinal (lng) directions of primary loading. Mechanical testing was performed using an Instron E10000. After preconditioning and a 2-minute rest period, the specimen was pulled to 5% or 8% clamp strain for transverse and longitudinal samples, respectively. Stress relaxation was measured for a 2-minute interval; viscoelastic testing proceeded with ten 1 Hz sinusoidal cycles oscillating from 4 to 6% clamp strain for transverse samples and 7 to 9% clamp strain for longitudinal samples. Data from the last four cycles was used for mechanical analysis [8].

Confocal Imaging and Image Processing. At the conclusion of testing, the samples were sliced to 50 μm using a cryostat at -20°C. The 405 nm laser of a confocal microscope, in coordination with ZEN software, was used to capture the autofluorescence of collagen fibrils by utilizing the 63x objective lens [9]. Three z-stack projections were obtained for all LCSL longitudinal specimens (Figure 1A) and all PAL specimens (Figure 1B), for a total of 90 z-stacks.

Image analysis was performed to determine the fibril orientation distribution for each specimen. Each z-stack projection was first filtered using ImageJ and saved as an 8-bit grayscale image. FiberFit, an FFT software program developed internally, was used to quantify the fibril orientation distribution. The preferred fibril orientation, θ_p and fibril dispersion, k were used to define the semi-circular von Mises distribution (P) for each collagen network. In addition, we defined a third term called

Copyright 2016 The Organizing Committee for the 2016 Summer Biomechanics, Bioengineering and Biotransport Conference

the fiber contribution factor (*FCF*). In Figure 1C, the fibril stretch λ and von Mises distribution P are plotted with respect to the spatial orientation θ. The light gray shaded region represents the fibrils in tension ($\lambda \geq 1$). The dark-gray area, where the fibrils are in tension represents the *FCF*. The remaining fibrils are in compression and, therefore are assumed to not resist tensile deformation.

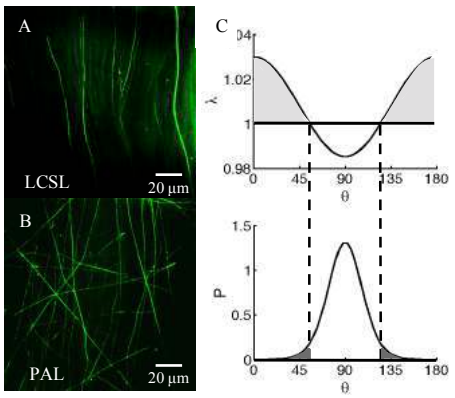

Figure 1. Collagen fibril networks captured with confocal microscopy: (A) LCSL and (B) PAL tissue. (C) Graphical representation of FCF calculation.

Statistical Correlations. A MANOVA was used to test for differences in microstructural properties (θ_p, k, and *FCF*) and mechanical properties (dynamic modulus, stress relaxation, and phase shift) across groups; the four groups were defined by the loading direction (longitudinal or transverse) and ligament (LCSL or PAL) ($p_{critical} = 0.05$). Microstructural properties that showed significance between groups were used as predictors for regression models.

RESULTS

Microstructural Properties. The PAL and LCSL tissues had significant differences in preferred orientation and *FCF* (Table 1). For the transverse specimens, the average preferred orientation was further from the loading axis in the LCSL specimens when compared to the PAL specimens ($p = 0.048$). In addition, the aligned LCSL tissue had a lower *FCF* than the disordered PAL tissue ($p = 0.001$). There were no differences observed between PAL and LCSL specimens for the longitudinal loading direction.

Table 1. Microstructural parameters from confocal images

Specimen Type	Fibril Dispersion Mean $k \pm$ SD	Preferred Fibril Orientation Mean $\theta_p \pm$ SD (°)	Fiber Contribution Factor (*FCF*)
LCSL Lng.	5.58 ± 5.04	4.8 ± 14.1	0.95 ± 0.05**
LCSL Trv.		94.8 ± 14.1*	0.15 ± 0.12*
PAL Lng.	3.21 ± 3.03	4.8 ± 18.6	0.92 ± 0.06**
PAL Trv.	1.24 ± 0.79	2.6 ± 56.3	0.58 ± 0.25*

Note: 0° is along the loading axis. * = significant difference from all other groups, ** = significant difference from both transverse groups

Mechanical Properties. The dynamic modulus and stress relaxation results reflected the microstructural results. In the transverse loading direction, the disordered PAL tissue had a higher dynamic modulus and stress relaxation than the more aligned LCSL tissue ($p = 0.002$ and $p < 0.0005$), however the phase shift did not show any differences (Figure 2A-C). In the longitudinal loading direction, there were no differences between the PAL and LCSL tissues.

Regression Analysis. Using *FCF* as a predictor gave moderate correlations for the transverse loading direction. The *FCF* describes 20% of the variation in dynamic modulus, 22% of the variation in stress relaxation, but only 7% of the variation in phase shift (Figure 2D-F).

DISCUSSION

This study investigated the correlations between microstructural collagen organization and ligament mechanical behavior. Using confocal imaging and FFT analysis, fibril orientation distribution parameters were quantified and regression analysis revealed several important correlations. There were only moderate correlations between the *FCF* and viscoelastic properties, except for the phase shift, which did not show a correlation. The dynamic modulus and stress relaxation both followed the same trends as the elastic modulus, suggesting a relationship between elastic and viscoelastic mechanical properties.

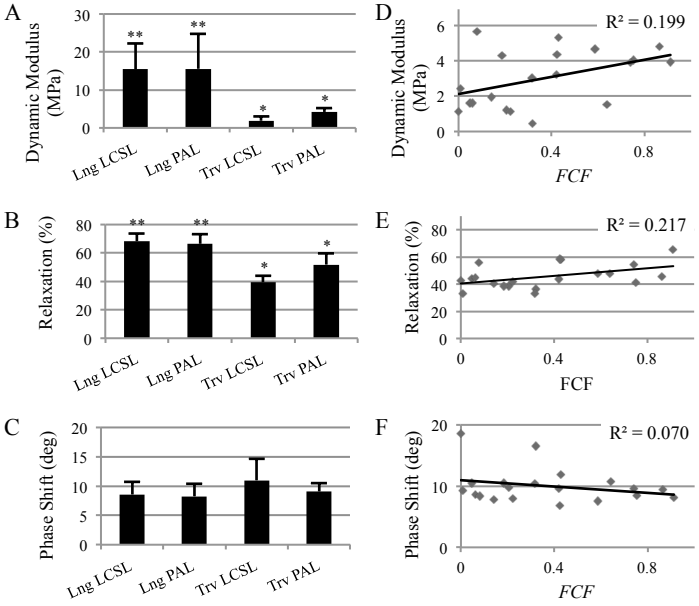

Figure 2. Viscoelastic properties of LCSL and PAL specimens: (A) dynamic modulus, (B) stress relaxation, and (C) phase shift with corresponding correlations (D-F).

Note: * = Significant difference from all other groups, ** = significant difference from both transverse groups

It is important to note that for the bovine ligament specimens used in this study, the fibril dispersion was not significantly different among testing groups and required the novel *FCF* term to see differences in microstructure. The results from this study indicate that both the fibril dispersion and orientation are important when describing mechanical properties of ligament tissue. While moderate correlations were present, this study also suggests that other microstructural properties may be required in order to accurately predict ligament mechanical behavior. This may include specimen specific fiber density or average fiber diameter.

This study had limitations. Bovine ligament was used instead of human ligament. However, published mechanical properties are similar [10,11]. In the described imaging methodology, both collagen and elastin were captured under autofluoresence. While elastin only makes up about 5% of ligament dry weight, it still likely influences the calculated microstructural parameters [12]. Additionally, only one strain rate was used for viscoelastic analysis.

In summary, this study suggests that viscoelastic mechanical behavior of ligament cannot be described solely using the orientation distribution of its collagen fibril network. However, it is clear that both the orientation and dispersion of fibrils are important parameters to include in constitutive models describing energy dissipation mechanics of collagenous soft tissues.

ACKNOWLEDGEMENTS

This project was supported by the Biomolecular Research Center at Boise State University and funded by NIH NIGMS P20GM109095.

REFERENCES

[1] D'Amore, A. et al., *Biomaterials*, 31:5345-5354, 2010. [2] Sun, M et al., *PLos ONE*, 10(7), 2015. [3] Provenzano, P and Vanderby, R, *Matrix Biol*, 25:71-84, 2006. [4] Gohlke, F et al., *J Shoulder Elbow Surg*, 3:111-128, 1994. [5] Frank, C et al., *J Musculoskel Neuron Interact*, 7:130-140, 1999. [6] Abramowitch, S et al., *Ann of Biomed Eng*, 32:329-335, 2004. [7] Gupta, H et al., *J Struct Biol*, 169(2):183-91, 2010. [8] Lujan, T et al., *J Appl Physiol*, 106:423-431, 2009. [9] Pini, M et al., *J Periodontal Res*, 37:237-44, 2002. [10] Eleswarapu, S et al., *PLoS ONE*, 6, 2011. [11] Gentleman, et al., *Biomaterials*, 24:3805-3813, 2003.

SB³C2016
Summer Biomechanics, Bioengineering and Biotransport Conference
June 29 –July 2, National Harbor, MD, USA
SB³C2016-110

COMPARISON OF FLOW CONDITIONS IN ANEURYSMS AT THE BASILAR TIP AND INTERNAL CAROTID ARTERY TERMINUS

Ravi Doddasomayajula (1), BongJae Chung (1), Farid Hamzei-Sichani (2), Christopher M. Putman (3), Juan R. Cebral (1)

(1) Bioengineering Department
George Mason University
Fairfax, Virginia, USA

(2) Interventional Neuroradiology
Mount Sinai Hospital
New York, New York, USA

(3) Interventional Neuroradiology
Inova Fairfax Hospital
Falls Church, Virginia, USA

INTRODUCTION

Cerebral aneurysms is a common disease affecting a significant portion of the population (estimated at 2-5%) [1]. Rupture of an intracranial aneurysms have devastating consequences with high mortality and disability rates. Consequently, many physicians often preventively treat incidentally discovered aneurysms. However, the treatment risk can exceed the low natural risk of rupture of incidental aneurysms [2]. Therefore, it is important to precisely distinguish high risk aneurysms for immediate treatment from low risk aneurysms which could be conservatively followed.

Several patient, demographic and behavioral characteristics have been investigated as possible risk factors, including gender, age, family history, smoking and hypertension, population, etc. According to past studies, the most important aneurysm-specific rupture risk factors are size and location [3]. In particular, aneurysms in the posterior circulation have been shown to have in general higher rupture risk than aneurysms in the anterior circulation. The cause of this difference in rupture risk is largely unknown [4]. Since aneurysm evolution is thought to be governed by a progressive degradation and weakening of the wall in response to abnormal hemodynamics [5], it is reasonable to ask whether differences in the aneurysm hemodynamics, induced by different configurations and geometries of vessels of the anterior and posterior circulations, could help explain the different rupture rates.

The purpose of this study was to test this hypothesis by comparing the hemodynamic environments of aneurysms at the tip of the basilar artery (posterior circulation) and aneurysms at the internal carotid artery bifurcation (anterior circulation). These two locations were selected because they are anatomically similar, i.e. the terminal bifurcation of a major feeding artery, but one in the anterior circulation and the other in the posterior circulation.

METHODS

We have developed a database of intracranial aneurysms imaged with 3D rotational angiography (3DRA). This database contains 3DRA images and anonymized clinical information including rupture status, size and location, gender and age, etc. of approximately 1800 intracranial aneurysms. All aneurysms from our database located at either the tip of the basilar artery (BAtip) or the terminus or bifurcation of the internal carotid artery (ICAbif) were included in the study.

A total of 117 aneurysms were studied, 63 at the BAtip (27 ruptured, 36 unruptured, rupture rate=43%), and 54 at the ICAbif (11 ruptured, 43 unruptured, rupture rate=20%).

Computational fluid dynamics (CFD) models of all 117 aneurysms were constructed from the corresponding 3DRA images. Pulsatile simulations were carried out by numerically solving the 3D unsteady Navier Stokes equations assuming Newtonian viscosity and rigid walls. The simulations had a minimum mesh resolution of 200 μm and a time resolution of 0.01 sec and were run for two cardiac cycles. A number of flow variables were then computed from the results of the second cycle to characterize the aneurysm flow conditions [6, 7].

To test whether aneurysms at the BAtip have different hemodynamic environments than those at the ICAbif, and if ruptured and unruptured aneurysms have different flow conditions at each of these two location, the set of flow variables used to characterize the intracaccular flow environment were compared between these groups using the Mann-Whitney U test. Differences were considered statistically significant if $p<0.05$ (95% confidence).

RESULTS

The distribution of ruptured and unruptured aneurysms at the BAtip and ICAbif are presented in Fig.1(a). A 2x2 contingency table

Copyright 2016 The Organizing Committee for the 2016 Summer Biomechanics, Bioengineering and Biotransport Conference

analysis based on the Fisher exact test confirmed that there is a statistically significant association between the location at the BAtip or the ICAbif with aneurysm rupture (p=0.0107).

Comparisons of flow variables between all aneurysms at the BAtip and at the ICAbif are presented in Fig.1(b). Similarly, comparisons of flow variables between ruptured and unruptured aneurysms at the BAtip and ICAbif are shown in Fig.1 (c) and (d), respectively. The bars in these graphs represent the ratio of mean values of variables of the BAtip group over mean values of the ICAbif groups. Variables that are significantly different between these groups are marked with a *.

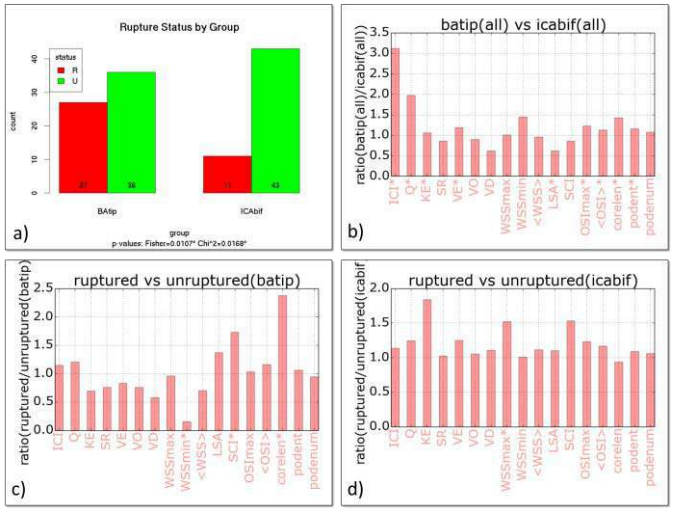

Fig. 1: Distribution of ruptured and unruptured aneurysms at the BAtip and ICAbif (a). Comparison of flow variables between BAtip and ICAbif aneurysms (b) and between ruptured and unruptured aneurysms at the BAtip (c) and the ICAbif (d).

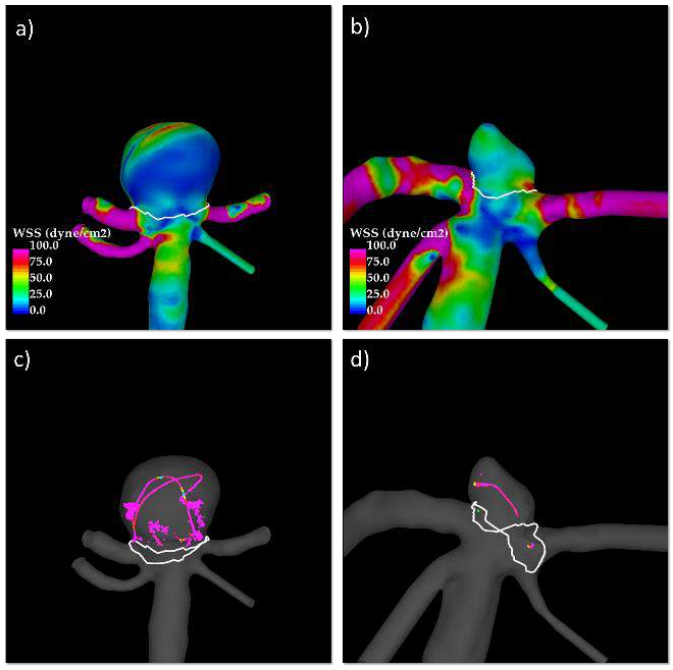

Fig. 2: BAtip: concentrated WSS (a) and complex flow (c) in ruptured aneurysm; diffuse WSS (b) and simple flow (d) in unruptured aneurysm.

On average, aneurysms at the BAtip had more concentrated inflow jets (ICI, p<0.001), larger inflow rates (Q, p<0.001), larger maximum oscillatory shear index (OSI, p=0.003), more complex flows (corelen, p=0.033) and smaller areas under low WSS (LSA, p<0.001) than aneurysms at the ICAbif (Fig.1 b).

Ruptured aneurysms at the BAtip had more concentrated wall shear stress distributions (SCI, p=0.011), more complex flows (corelen, p<0.001) and smaller minimum WSS (p=0.012) than unruptured aneurysms at this location. On the other hand, ruptured aneurysms at the ICAbif had larger maximum WSS (WSSmax, p=0.017) than unruptured aneurysms at this location.

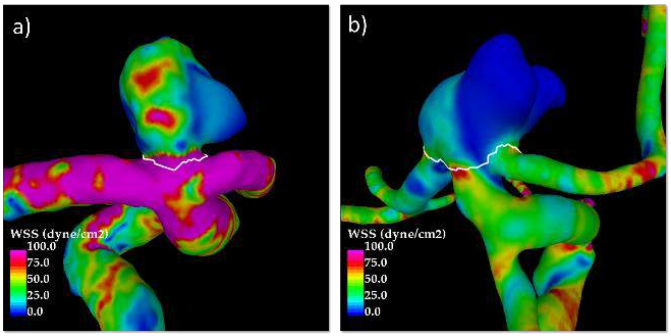

Fig. 3: ICAbif: high maximum WSS in ruptured aneurysm (a); low maximum WSS in unruptured aneurysm (b).

Examples of ruptured and unruptured aneurysms illustrating the statistically significant differences between ruptured and unruptured aneurysms at the BAtip and ICAbif are presented in Fig. 2 and 3, respectively.

DISCUSSION

According to our series, aneurysms at the basilar tip have a rupture rate larger by a factor of 2.15 than aneurysms at the internal carotid bifurcation.

Compared to aneurysms at the ICA bifurcation, aneurysms at the basilar tip have different hemodynamic environments, characterized by higher flow conditions (higher inflow rate into the aneurysm, more concentrated inflow jets, more unstable and oscillatory flow patterns, and smaller areas under low wall shear stress). These differences are likely due to the different configuration (bifurcation asymmetry, bifurcation angles, etc.) and geometry (curvature, tortuosity, tapering, etc.) of the internal carotid and basilar arteries.

At each of these two locations, a different set of flow variables associated with rupture. This observation suggests that at both locations hemodynamics may play an important role in the evolution and rupture of aneurysms, but the underlying mechanisms may be different.

REFERENCES

[1] Rinkel, GJ et al. *Stroke,* 29: 251-9, 1998.
[2] Investigators T.I.S.U.I.A, *N Engl J Med,* 339:1725-33, 1998.
[3] Clarke, M *Neuroradiol,* 50(8):653-64, 2008.
[4] van der Kolk et al. *Cerebrovasc Diseases,* 30(1): 29-35, 2010.
[5] Sforza, D et al. *Ann Rev Fluid Mechanics,* 41:91-107, 2009.
[6] Mut, F et al. *Int J Num Meth Biomed Eng,* 27: 822-839, 2011.
[7] Byrne, G et al. *Am J Neuroradiol,* 35(2): 333-8, 2014.

Copyright 2016 The Organizing Committee for the 2016 Summer Biomechanics, Bioengineering and Biotransport Conference

SB^{3}C2016
Summer Biomechanics, Bioengineering and Biotransport Conference
June 29 –July 2, National Harbor, MD, USA
SB^{3}C2016-111

MECHANICAL EFFECTS OF DYNAMIC BINDING BETWEEN TAU PROTEINS ON MICROTUBULES DURING AXONAL INJURY

Hossein Ahmadzadeh (1), Douglas H. Smith (2), Vivek B. Shenoy (1)

(1) Department of Materials Science and Engineering
University of Pennsylvania
Philadelphia, Pennsylvania, USA
(2) Penn Center for Brain Injury and Repair and Department of Neurosurgery
University of Pennsylvania
Philadelphia, Pennsylvania, USA

INTRODUCTION

The unique viscoelastic nature of axons is thought to underlie selective vulnerability to damage during axonal injury. In particular, dynamic loading of axons has been shown to mechanically break microtubules and create axonal swellings at the time of injury. Alternatively, under slow pulling rates, axon has been shown to resist large tensile strain without any evidence of microtubule rupture or cytoskeletal damage. In our previous work[1] we presented a computational model for uniaxial tension of axon where a bundle of microtubules were interconnected by tau proteins and the applied load was transferred through the sliding and stretching of the microtubules, regulated by the tau proteins. There we showed that the viscoelastic behavior of the tau proteins could increase the chance of the microtubule rupture at the time of the injury[1]. Although the mentioned model was successful to predict the rate dependent behavior of the axons observed in experimental studies, here in the next step we present a more comprehensive model where by including the rupture of the connections between the linking tau proteins, the pathway of the load transfer within the axon can be obstructed and correspondingly the axon response can be altered. In this model$_2$, under different pulling rates, we monitor the rupture of the connections between the attached tau proteins and the tensile force exerted on the microtubules and at the end, present conditions leading to the rupture of the microtubules or the complete disassembly of the microtubule bundle. By including the rupture of the interconnecting elements within the axon, our current model can provide a picture of the damaged axon following traumatic brain injury where distinct regions including ruptured microtubules and disassembled microtubule bundles can be distinguished explicitly.

METHODS

Our axon model consists of staggered array of MTs with length L, outer and inner radii 12.5 nm, 7 nm enclosed by the axon lipid membrane. Tau proteins are bonded to the outer surface of the MTs at their MT binding domains while the distance between the adjacent tau proteins on a single MT is 30nm. Also the zipper bond dimer configuration is adopted for the connection between the tau proteins belonging to neighboring MTs. To include the viscoelastic response of the tau proteins, we modeled the tau proteins with two parallel springs, representing the backbone stiffness and the rate-dependent stiffness that arises from the intramolecular bonds within the tau protein.

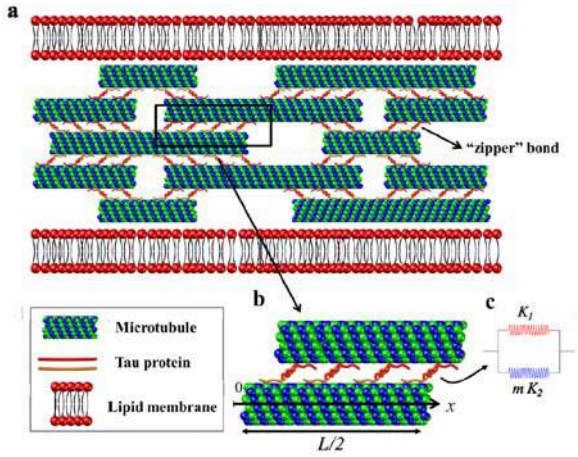

Fig. 1. (a,b) Axon model consists of MTs and tau proteins enclosed by axon lipid membrane. (c) A mechanical element for the tau proteins.

Copyright 2016 The Organizing Committee for the 2016 Summer Biomechanics, Bioengineering and Biotransport Conference

While the connection between the two tau proteins can rupture at a critical force, floating end of a free tau protein can still reattach to the tail of the next available tau protein and reengage in the load transfer mechanism if the applied loading rate is sufficiently slow (quasi-static loading). As illustrated in Fig. 2, this recruitment process of the free tau proteins can be repeated until the ends of the adjacent MTs pass each other.

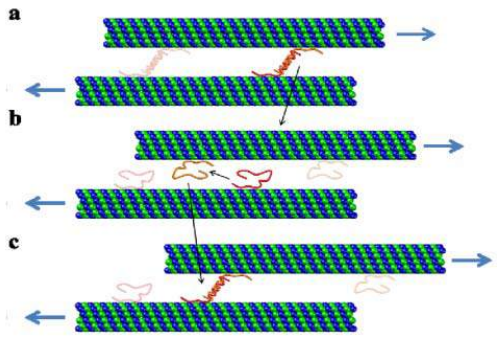

Fig. 2. (ac) Recruitment of the free tau proteins after rupture incorporated in our model when the loading rate is sufficiently slow (quasi-static loading).

RESULTS

MT rupture is sensitive to strain rate compared to strain

As shown in Fig. 3, under dynamic loading rates (1–50 sec-1), MTs are under a significantly larger force (almost 3–4 times) than the quasistatic rate. In this case, the large force can lead to the rupture of the MTs and the subsequent interruption of the cargo transport similar to the observations for the axons injured by TBI. For the unruptured MTs, due to the large extension of the tau proteins, the zipper bond connecting tau proteins start to break. Eventually by the rupture of the majority of the interconnections, the unruptured MT bundle disassembles and the force-strain curve displays a rapid drop as the axon loses its load bearing capacity completely.

For the quasi-static loading the axon behavior is considerably different. While the force exerted on the MTs is significantly small compared to the dynamic loading, with the help of the reformation process (explained in Fig. 2), the free tau proteins can still reengage in the load transfer mechanism and avert the drop of the force. As a result, we observe a slow decline in the force as well as the concentration of the connected tau proteins with strain.

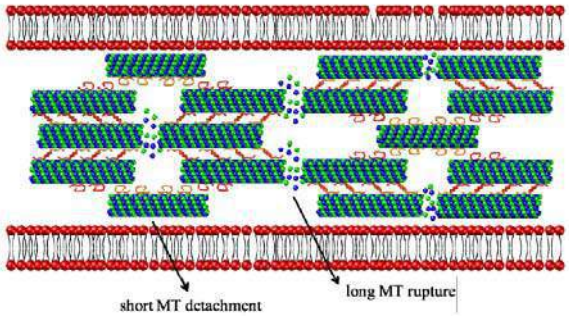

Fig. 3. (left) The force exerted on the MTs at different strain rates. The MT length is 200μm in both figures.

The pattern of the MT bundle disassembly depends on the strain rate

By increasing the applied tensile strain, the connections between the attached tau proteins start to rupture. As shown in Fig 4 the model predicts that under the fast loading rate, the rupture of the tau-tau bonds starts from the ends of the MTs and progresses sequentially toward the interior points. In the contrary under slow loading rate, these bonds rupture simultaneously and cause a rapid drop in the stiffness of the axon at a threshold strain.

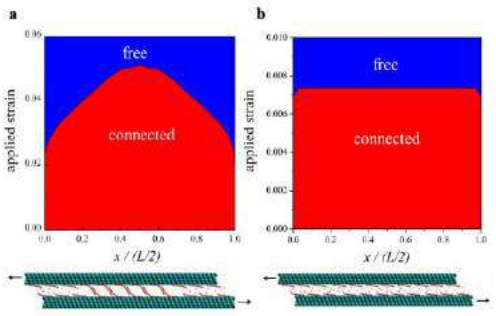

Fig.4. Breaking of the tau-tau connection by (a): fast (50 sec-1) and (b): slow (quasi-static) loading rates. MT length is 50μm.

Following TBI, the long MTs inside the axon break while the short MTs detach from the MT bundle.

For varying lengths of for the microtubules under a fast pulling rate, we obtained the force exerted on the microtubules with strain. Our model predicts that the long MTs inside the axon experience large tensile forces while the short MTs undergo relative sliding with respect to the neighboring MTs without any significant force. On the other hand, the tau proteins attached to long MTs undergo different degrees of elongation depending on their position relative to the MT ends while, the tau proteins connecting the short MTs are extended equally to accommodate the relative sliding. As a result, while the large force on the long MTs would eventually break the MT, the large sliding of the short MTs would result in the MT disassembly from the rest of the MTs by an instantaneous rupture of the interconnection bonds between the tau proteins. Based on this prediction, our model presents a picture of the damaged axonal cytoskeleton by injury. In this picture (Fig 4) the long microtubules are broken while the short microtubules are detached from the microtubule bundle and remain unaffected.

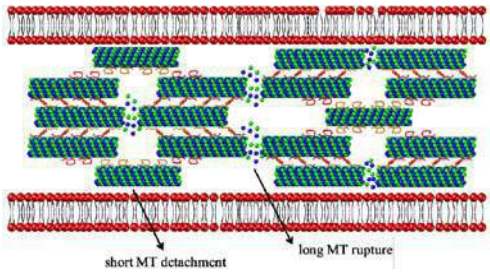

Fig. 5. Predicted damaged picture of the axon following TBI.

Discussion

In this study we presented a computational model to explain the axonal pathology observed in traumatic brain injury. While the fast loading rates rupture the long microtubules inside the axon, the slow loading rates cause disassembly of the unruptured microtubules.

REFERENCES

[1] Ahmadzadeh, et al., Bio Phys J., 106:1123–1133,2014.
[2] Ahmadzadeh, et al., Bio Phys J., 109: 2328–2337,2015.

Copyright 2016 The Organizing Committee for the 2016 Summer Biomechanics, Bioengineering and Biotransport Conference

SB^{3}C2016
Summer Biomechanics, Bioengineering and Biotransport Conference
June 29 –July 2, National Harbor, MD, USA
SB^{3}C2016-112

RECOVERY OF FUNCTIONAL PROPERTIES DURING NEONATAL TENDON REGENERATION

Kristen Howell (1), Rebecca Bell (2), Sara F. Tufa (3), Douglas R. Keene (3), Nelly Andarawis-Puri (2), Alice H. Huang (1)

(1) Department of Orthopaedics
Icahn School of Medicine at Mount Sinai
New York, NY, USA

(2) Department of Mechanical and Aerospace Engineering
Cornell University
Ithaca, NY, USA

(3) Micro-Imaging Center
Shriners Hospital for Children
Portland, OR, USA

INTRODUCTION

Tendon injury is a common clinical problem characterized by slow recovery and high recurrence after treatment. Adult tendon heals via fibrosis (scarring), and this failure to re-establish native tendon structure is likely the leading cause of injury recurrence. Improving tendon healing to a regenerative, tenogenic state is therefore a crucial research priority. In a previous study, we showed that neonatal mice may harbor a unique regenerative capacity [1]. Lineage tracing further revealed that neonatal and adult tendons heal via distinct cellular mechanisms; while the cells driving neonatal regeneration are recruited from intrinsic tenocytes, the cells driving adult fibrosis are completely derived from extrinsic cells [2]. To date, considerable evidence in the literature suggests that adult tendon healing results in impaired ultrastructure and mechanical properties, however the functional outcomes of neonatal tendon healing have not been fully investigated. The objective of the current study was therefore to determine long-term structural and functional properties of tendon after neonatal and adult injury.

METHODS

Achilles tendons of postnatal day P5 (neonate) or P112 (adult) ScxGFP mice [3] were transected at the mid-substance and left unrepaired, in accordance with IACUC, while contralateral tendons were used as non-injured controls. For consistency, all surgeries were carried out on the right hindlimb. To determine matrix ultrastructure, transmission electron microscopy (TEM) was carried out for d56 transverse sections (n=3), and collagen fibril diameters measured using Image J. To determine mechanical properties, tensile testing was carried out on d56 samples (n=12). Briefly, tendons were preloaded to 0.05N for ~1 min, followed by ramp to failure at 1%/sec in PBS at room temperature. Gait analysis was performed on injured and non-injured mice at d3 and 14 after injury using the Digigait Imaging System with treadmill speed of 5 cm/s (n=5). Parameters were normalized to Stride length to minimize variations due to mouse size. Neonatal tendons were also harvested at d3, 7, 14, and 28 after injury for RNA isolation (Trizol-chloroform), cDNA synthesis and qPCR amplification with SYBR Green (n=5-7). Expression data was quantified relative to standards generated from E14.5 embryonic limbs, and normalized to GAPDH. In situ hybridization (ISH) and immunostaining was carried out on d 14 cryosections. For statistics, qPCR data were analyzed using two way ANOVA with Tukey's posthoc with timepoint and injury as independent variables (Systat). Mechanical and gait data were analyzed using paired t-tests. Significance was set at $p<0.05$.

RESULTS

We previously showed that neonatal tendons regenerate a *ScxGFP*+ 'neo-tendon' structure following complete transection, in contrast to adult tendons, which heal via formation of *ScxGFP*-negative tissue (**Fig 1**). Immunostaining for laminin and αSMA (two myofibroblast markers) showed strong positive staining throughout the newly formed tissue in adults and weak punctate staining in the 'neo-tendon' in neonates at d14 after injury (not shown). Real time qPCR analysis showed enhanced expression of tendon markers after neonatal injury, with detectable differences in *Scx* and *Tnmd* by d14 ($p<0.05$) while *Mkx* expression was not significantly increased until d28 ($p<0.05$) (**Fig 1**). ISH using a probe against *Scx, Col1a1,* and *Tnmd* detected expression in both control tendon and injured 'neo-tendon' by d14 (not shown). **Collectively, these results suggest that neonatal tendons heal via tenogenesis while adult tendons heal via fibrosis.**

To determine structural properties, we used TEM imaging to assess collagen fibril diameter. Overall, collagen fibril diameter was

Copyright 2016 The Organizing Committee for the 2016 Summer Biomechanics, Bioengineering and Biotransport Conference

highly reduced in injured tendon from both neonatal and adult groups compared to respective controls. While control tendons showed a heterogeneous distribution of fibril diameters across a wide range of sizes, fibril diameters in injured tendon were far more homogeneous. However, the fibril population of the neonatal injury group showed a shift toward fibrils of larger sizes (~3x the number of >60 nm fibrils) compared to adult injury tendons which had a higher population of lower sized fibrils (2x the number of <60 nm fibrils) (**Fig 2**).

Interestingly, while the matrix of injured tendons appeared immature, tensile properties of neonatal injured tendons were fully restored by d56, with no difference in maximum load or stiffness ($p>0.1$) (**Fig 3A**). In contrast, adult tendon stiffness remained lower after injury. Using gait analysis as an additional assay for function, we identified parameters associated with injury using d3 adult injured mice. These parameters include %Swing, %Brake, and %Propel, all of which were significantly different between the left and right hindlimbs of injured mice (**Fig 3B, C**). Notably, no difference was ever detected between hindlimbs of non-injured age-matched mice. While %Swing was recovered in both injury groups by d14, %Brake and %Propel remained significantly abnormal. However, the difference between left and right hindlimbs was much reduced in the neonatal group compared to adult for both parameters, suggestive of rapid recovery (%Brake: 25% vs 50% diff; %Propel: 17% vs 25% diff). **Taken together, our functional data suggests that neonatal tendons heal more rapidly compared to adult tendons with restoration of tendon properties.**

DISCUSSION

In this study, we test the regenerative capacity of neonatal tendon and show that mechanical properties are restored following complete transection in neonates, in contrast to adult tendon, in which mechanical properties are permanently impaired [4, 5]. We further demonstrate that neo-tendon differentiation after injury begins at d14, coincident with upregulation of tenogenic markers *Scx* and *Tnmd*. Delayed expression of *Mkx* is consistent with its role in collagen maturation during development [6]; however, the overall small size of fibrils after injury suggests that additional factors that regulate matrix maturation may not be present. This is supported by recent data in which ectopic Mkx expression in MSCs resulted in only a modest increase in fibril diameter [7]. This dichotomy suggests that Mkx may be necessary but not sufficient for matrix maturation. Finally, although gait parameters are not fully recovered at d14, we already observed more rapid recovery compared to adult at this early timepoint; evaluating later timepoints is the focus of ongoing work.

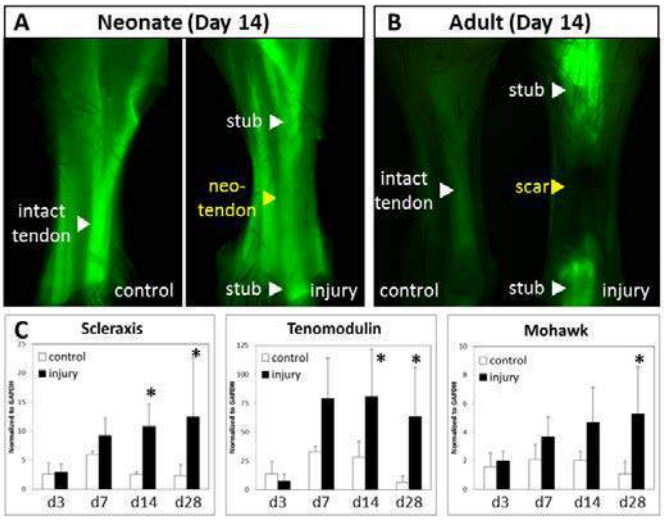

Figure 1: Neonatal tendon heals via tendon differentiation. (A, B) Whole mount ScxGFP limbs at d14. (C) RT-PCR of tendon markers. * indicates significance vs control within timepoint ($p<0.05$). n=5-7.

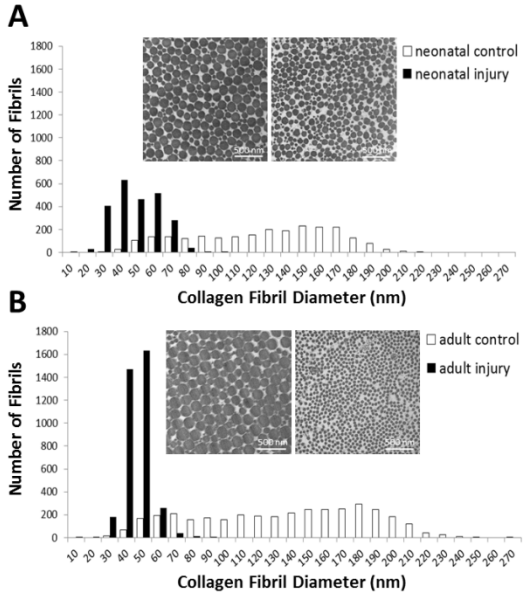

Figure 2: Shift toward larger collagen fibrils in neonatal injured tendons compared to adult. (A, B) Quantification of fibril diameter and TEM micrographs. N=3 mice (1200 fibrils/tendon). Scale: 500nm.

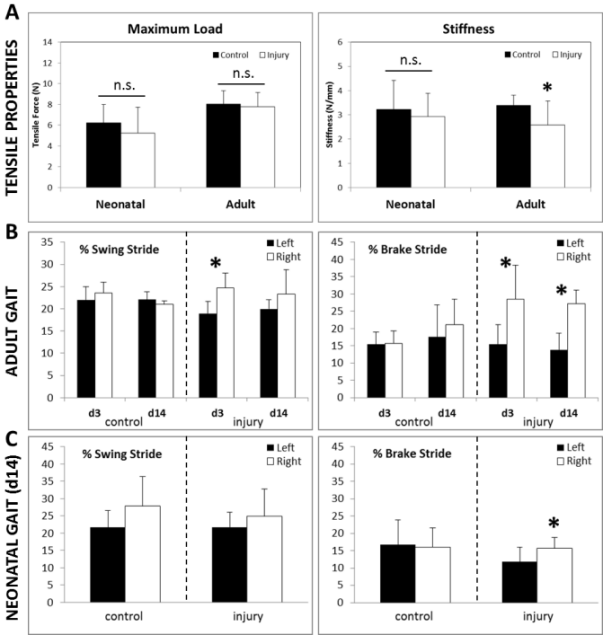

Figure 3: Functional properties are largely restored after neonatal tendon injury. (A) Maximum load and stiffness at d56, n=12. (B, C) Gait parameters predictive of tendon injury and healing, n=5. * indicates significance vs control within timepoint ($p<0.05$).

ACKNOWLEDGEMENTS

This work was supported by Mount Sinai and the Orthopaedics Dept. We also thank Dr. Ronen Schweitzer for the ScxGFP mice.

REFERENCES

[1] Howell+, *Trans ORS*, 2015. [2] Howell+, *Trans ORS*, 2016. [3] Pryce+, *Dev Dyn*, 2007 [4] Ansorge+, *JOR*, 2011 [5] Lalley+, *JOR*, 2015 [6] Li+, [7] Liu+, *Stem Cells*, 2014.

Copyright 2016 The Organizing Committee for the 2016 Summer Biomechanics, Bioengineering and Biotransport Conference

SB^{3}C2016
Summer Biomechanics, Bioengineering and Biotransport Conference
June 29–July 2, 2016, National Harbor, Maryland, USA
SB³C2016-113

COAGULATION CASCADE MODEL REDUCTION USING A GENETIC ALGORITHM

Kirk B. Hansen and Shawn C. Shadden

Department of Mechanical Engineering
University of California, Berkeley
Berkeley, CA, US

INTRODUCTION

The coagulation cascade is a complex system of biochemical reactions involving dozens of reactive species. It is mathematically modeled by a system of ordinary differential equations (ODEs) for the well-mixed case, or by advection-diffusion-reaction partial differential equations (PDEs) for the flow-mediated case. Due to the many species that must be tracked, numerical problems introduced by the high Schmidt and Peclet numbers inherent to intra-arterial mass transport problems, and a wide range of temporal scales, computational modeling of these types of problems is often prohibitively expensive, especially for three-dimensional, unsteady, patient-specific cases [1]. These models also require the knowledge of a large number of parameters (e.g. 42 reaction rates and 34 initial conditions in the well-known Hockin-Mann model [2]), many of which are impossible to ascertain on a patient-specific basis.

Previous researchers have shown that thrombin generation curves can be reproduced by significantly simplified models [3, 4]. These models, however, ignored intermediate species that may be important in incorporating additional aspects of clot formation, e.g. activated and non-activated platelets. The parameter fitting methods were also not reported. In this work, we develop a framework for coagulation cascade model reduction using genetic algorithm optimization techniques.

METHODS

The reduced-order model chosen for this work describes the tissue-factor-initiated extrinsic pathway to thrombin generation, and is based on the model suggested by Wagenvoord et al. [3]. A schematic of the model is shown in Fig. 1. The model includes eight biochemical species, although only seven are solved for as the tissue factor concentration is considered known. The reactions between the species are controlled by seven rate constants. Although Wagenvoord et al. suggested the use of Michaelis-Menten kinetics, linear reactions were found to be sufficient and are used in this work for simplicity. For example, the ODE for thrombin generation is

$$\frac{d[\mathrm{IIa}]}{dt} = k_0[\mathrm{Xa}][\mathrm{II}] + k_1[\mathrm{Va{:}Xa}][\mathrm{II}] - k_2[\mathrm{IIa}]. \qquad (1)$$

By employing a reduced-order model, the reactions actually represent systems of reactions, and thus the kinetic rate constants are unknown. These rate constants are found by fitting the reduced-order ODE system results to those obtained with the Hockin-Mann model [2].

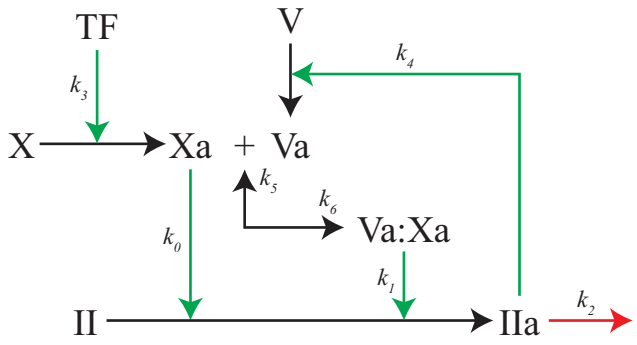

FIGURE 1: REDUCED-ORDER EIGHT-SPECIES MODEL OF THE TISSUE FACTOR (TF) INITITIATED EXTRINSIC COAGULATION CASCADE TO THROMBIN (IIa) PRODUCTION.

To fit the reduced-order model results to those from the full model, a cost function was defined as

$$\Phi = \sum_{i=1}^{n_{\text{species}}} \sum_{j=1}^{n_{\text{tsteps}}} w_i \left[\tilde{c}_i(t_j) - c_i(t_j)\right]^2, \qquad (2)$$

where w_i is a weight for species i, t_j is the time at timestep j, and $\tilde{c}_i$ and c_i are the concentrations of species i obtained using the Hockin-Mann and reduced-order models, respectively. The weighting function is used to normalize the influence of each species by its maximum concentration. It can also be used to assign a greater weight to species that are deemed more important; in this work a five-times greater importance was assigned to thrombin concentration.

The cost function defined in Eq. (2) was minimized using a continuous, unbounded genetic algorithm. All operations were performed on the logarithms of the rate constants both to ensure positiveness and to allow them to evolve by orders of magnitude. Initial guesses for the rate constants were taken from the Hockin-Mann model. A population of 300 was initially seeded with Gaussian

Copyright 2016 The Organizing Committee for the 2016 Summer Biomechanics, Bioengineering and Biotransport Conference

distributions around the guesses. Tournament selection, uniform crossover, and Gaussian mutation were performed for each of 500 generations to evolve the population. The crossover and mutation steps utilized an adaptive algorithm to facilitate convergence to the best-fit solution [5]. Genetic algorithms do not guarantee convergence to a minimum value, so the algorithm was run ten times.

RESULTS AND DISCUSSION

Time evolution curves for each species are shown in Fig. 2. The reduced-order results for all species show a good fit to those obtained with the Hockin-Mann model. The thrombin (factor IIa) generation curve, which was weighted five times more than the others, shows excellent agreement.

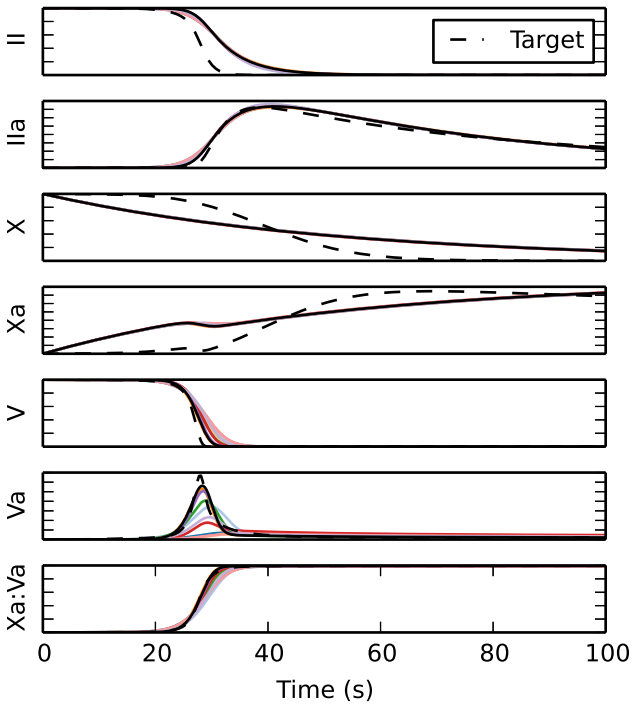

FIGURE 2: RESULTS FROM TEN RUNS OF THE GENETIC ALGORITHM. THE DASHED LINE IS THE OUTPUT OF THE HOCKIN-MANN MODEL, AND THE BLACK SOLID LINE IS THE BEST FIT.

These results indicate that such a reduced-order model is capable of describing the coagulation cascade. While other researchers have found that thrombin generation curves can be accurately reproduced by reduced-order models, this is the first work that has shown that an optimized model can replicate the other key species as well. This is significant, as it allows for the incorporation of additional biophysics with the coagulation model. For example, some reaction rates are dependent on the local availability of binding sites on activated platelets. Properly modeling the evolution of species involved in these reactions allows for the coupling of platelet activation and coagulation cascade submodels, whereas a coagulation cascade model optimized only to reproduce a thrombin generation curve would produce erroneous results.

The reduced-order model provides an improvement over more comprehensive models such as Hockin-Mann for two key reasons. First, by reducing the number of species equations from 34 to 7, the required computational cost is reduced by nearly a factor of five. This cost reduction could be significant when incorporated into thrombosis models that are already computationally expensive. Second, the number of rate constant parameters is significantly reduced, in this case from 42 to 7. This reduces the severely underconstrained nature of trying to fit such a model to limited patient-specific data.

ACKNOWLEDGMENTS

This work was supported by the NSF GRFP and NSF Career Award #1150947.

REFERENCES

[1] Hansen, KB and SC Shadden, *Biomech Model Mechan*, doi:10.1007/s10237-015-0719-4, 2015.
[2] Hockin, MF et al., *J Biol Chem*, 277(21):18322–18333, 2002.
[3] Wagenvoord, R et al., *J Thromb Haemost*, 4(6):1331–1338, 2006.
[4] Papadopoulos, K et al., *Med Eng Phys*, 36(2):196–204, 2014.
[5] Srinivas, M and LM Patnaik, *IEEE T Syst Man Cyb*, 24(4):656–667, 1994.

Copyright 2016 The Organizing Committee for the 2016 Summer Biomechanics, Bioengineering and Biotransport Conference

SB³C2016
Summer Biomechanics, Bioengineering and Biotransport Conference
June 29 –July 2, National Harbor, MD, USA
SB³C2016-114

INVERSE MODELING BASED ESTIMATION OF IN-VIVO STRESSES AND THEIR RELATION TO SIMULATED LAYER-SPECIFIC INTERSTITIAL CELL DEFORMATIONS IN THE MITRAL VALVE

Chung-Hao Lee (1), Kristen Feaver (1), Will Zhang (1), Robert C. Gorman (2), Joseph H. Gorman (2), Michael S. Sacks (1)

(1) Center for Cardiovascular Simulation
Institute for Computational Engineering & Sciences
Department of Biomedical Engineering
The University of Texas at Austin
Austin, TX, USA

(2) Department of Surgery
Gorman Cardiovascular Research Group
University of Pennsylvania
Philadelphia, PA, USA

INTRODUCTION

Recent studies have showed unsatisfying recurrence of severe mitral regurgitation 3-5 years after initial surgical repair, suggesting that surgery-induced excessive tissue stresses and the resulting tissue failure are related to the success of surgical repair for treating mitral valve (MV) diseases [1-3]. Moreover, the underlying biomechanical behaviors of soft tissues and cellular mechanobiological responses are critical in design of individual-optimized surgical repair strategies with improved long-term durability. Therefore, quantification of the regional tissue stresses, characterization of the MV leaflet mechanical behaviors, and quantification of the mitral valve interstitial cell (MVIC) deformations at normal and surgically repaired conditions are the main focus of this work. In this study, we used an enhanced finite element (FE) based inverse modeling method combined with the in-vivo kinematics for estimating the valvular stresses. This work sheds light on proper linking of in-vitro mechanical testing data with clinical in-vivo modeling and will ultimately help in gaining insight into the primary drivers for MV remodeling in response to surgical repair.

METHODS

Sonocrystal data acquisition, key kinematic states, and in-vivo deformation analysis: Previously, we have used 3D echocardiography for acquiring the in-vivo sonocrystal data of the ovine mitral valve anterior leaflet (MVAL) in large animal studies using six 35-40kg male adult Dorset sheep [4]. Sonomicrometry positional data were taken at an acquisition interval of 5 ms (Fig. 1a) and transvalvular pressure was monitored over cardiac cycles (Fig. 1b). The 3D positional data were then used for the subsequent analysis of MVAL deformations and strains as well as the inverse modeling based estimation of the in-vivo valvular stresses. Here, we adopted the notations for each kinematic state (Fig. 1c): in-vitro reference state (β_0) for biaxial mechanical testing, in-situ unloaded state (β_1), in-vivo reference state (β_2) associated with onset ventricular contraction, and pressure-loaded state (β_t). Based on the population-averaged positions (n=6) of the four corner fiducial markers at various states, in-surface deformation gradient tensors ${}^1_0\mathbf{F}$, ${}^2_1\mathbf{F}$, and ${}^2_0\mathbf{F}$ were quantified using one single 4-node bilinear finite element.

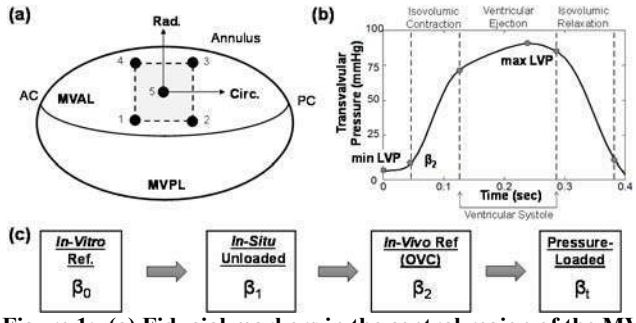

Figure 1: (a) Fiducial markers in the central region of the MV anterior leaflet, (b) typical pressure profile over the cardiac cycle, and (c) key states for analyzing the deformation and strain.

Estimation of the in-vivo functional valvular stresses: The inverse modeling technique developed previously [5] was modified into a two-stage FE simulation to account for the measured deformation gradient ${}^2_0\mathbf{F}$ between states β_2 and β_0 in the in-vivo parameter quantification. Briefly, the MVAL FE model with discretized 1,600 (40x40) shell elements was allowed to deform freely with the inversion of ${}^2_0\mathbf{F}$ employed throughout the tissue to simulate the shrinking process from the in-vivo reference state to the in-vivo

Copyright 2016 The Organizing Committee for the 2016 Summer Biomechanics, Bioengineering and Biotransport Conference

reference state. The inverse modeling was performed to quantify the in-vivo mechanical properties of the MVAL by accounting for the pre-strains (from β_0 to β_2) and simulating MV deformations over the cardiac cycle (from β_2 to β_t) with prescribed transvalvuar surface pressure (Fig. 1b) and time-varying boundary displacements. The in-vivo valvular stresses were then estimated using the optimal parameters obtained from the genetic algorithm based global optimization. Note that a simplified structural constitutive model, linking the 2nd Piola-Kirchhoff stress tensor **S** and the Green strain tensor **E**=(**C**-**I**)/2 with fiber unit vector **N**=[cos(θ), sin(θ)]^T, was used in the inverse modeling pipeline, which consists of five parameters (matrix neo-Hookean parameter η_m, two collagen fiber parameters c_0 and c_1, and the preferred fiber direction μ_Γ and fiber splay σ_Γ):

$$\mathbf{S}(\mathbf{E}) = \eta_m(\mathbf{I} - C_{33}^{-1}\mathbf{C}^{-1}) + \int_{-\pi/2}^{+\pi/2} \Gamma(\theta;\mu_\Gamma,\sigma_\Gamma)\, c_0(e^{c_1\mathbf{N}\cdot\mathbf{E}\mathbf{N}} - 1)\mathbf{N}\otimes\mathbf{N}d\theta \quad (1)$$

Liking with cellular deformations: Following the previously developed down-scale modeling approach [6], one representative volume element (RVE) model of the MVIC microenvironment was constructed for each of the four tissue layers, *atrialis*, *spongiosa*, *fibrosa* and *ventricularis* layers, by accounting for layer respective compositions and microstructural information. In brief, the measured deformation gradients ${}^1_0\mathbf{F}$ and ${}^1_2\mathbf{F}$ were incorporated as boundary displacements on the RVE model to quantify the layer-specific MVIC deformations at both in-vitro and in-vivo reference states. Here, a dimensionless indicator—nucleus aspect ratio (NAR), which is the ratio of the circumferential dimension to the transmural dimension, was used for quantifying the layer-specific MVIC deformations.

RESULTS

Averaged positions with their variations of the fiducial markers at various states were obtained from the sonocrystal data (Fig. 2a) with their respective quantified deformation gradients between any two states (Fig. 2b), demonstrating fairly isotropic pre-stretches (λ_C=1.323 and λ_R=1.346) exhibited in the MVAL tissues from the in-vitro reference state (β_0) to the in-vivo reference state (β_2).

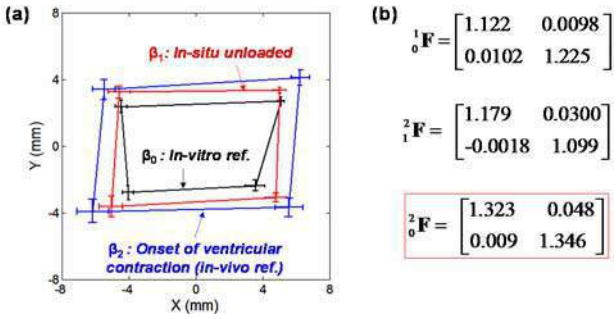

Figure 2: (a) Averaged positions of the fiducial markers at various kinematic states, and (b) quantified deformation gradient tensors.

Using the quantified in-vivo mechanical properties based on the inverse modeling approached and incorporating the analyzed deformation gradient ${}^2_0\mathbf{F}$, the functional valvular stresses along the circumferential and radial directions at the in-vivo and in-vitro reference states were estimated (Fig. 3a-b). The amount of the pre-stresses for the MVAL tissues was also determined from the FE-based numerical calculations (σ_C=30.4 kPa, σ_R=20.4 kPa).

By applying the tissue-level deformations as boundary displacements on the MVIC microenvironment model, the layer-specific NARs were for the first time quantified from the FE simulations of each RVE model for the four MVAL tissue layers. Interestingly, we found substantial discrepancy between the predicted extracellular (ECM) deformation and cellular deformation (Fig. 4a) and larger values of NAR and d(NAR)/dt in the fibrosa layer (Fig. 4b-c), which is the primary load-bearing layer consisting of dense collagen fiber networks along the circumferential direction.

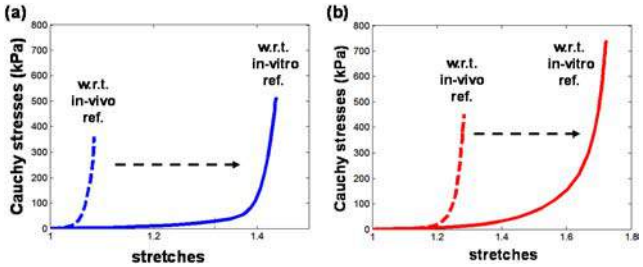

Figure 3: Predicted functional stresses of the MVAL tissues at β_2 and β_0 in the (a) circumferential and (b) radial directions.

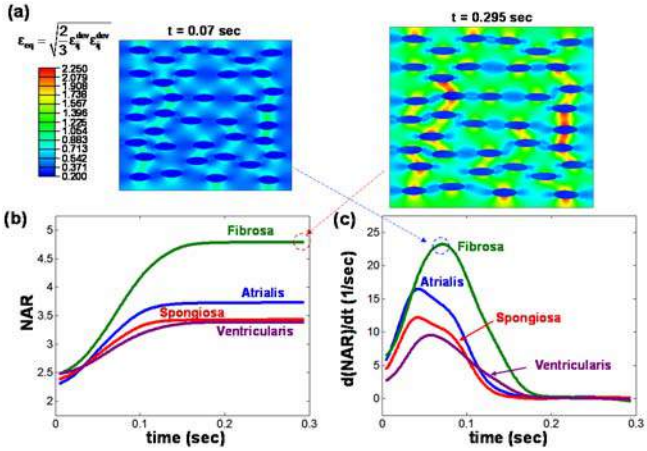

Figure 4: (a) Predicted von Mises equivalent strain (ε_{eq}) profiles of the fibrosa RVE model at the highest deformation rate (0.07 sec) and at the largest deformation (0.295 sec). (b-c) Predicted layer-specific MVIC deformations and rates with respect to state β_0.

DISCUSSION

The estimated pre-stresses were relatively small compared to the estimated in-vivo functional stresses. The results also indicated that the long toe-region of the MV stress-strain relation, typically observed in in-vitro mechanical testing data, is completely taken up by the pre-strain in the in-vivo functional state. Moreover, the novel predicted in-vivo MVIC deformations demonstrated substantial layer-specific variations in the deformation level and rate during isovolumetric contraction. Finally, the proposed modeling approaches are currently applied for estimating repair-induced changes of the MV stresses and MVIC deformations with various annuloplasty ring designs, and the acquired information will be integrated with the computational framework for organ-level simulations of the MV closing behavior [7], which will ultimately help in developing optimal therapeutic strategies with best restoration of MV functionality and improved durability.

ACKNOWLEDGEMENTS

This work is supported by the NIH R01 grants HL119297, (MSS), HL103723 and HL73021 (RCG and JHG).

REFERENCES

[1] Flameng, W. et al., *Circulation*, 107: 1609-1613, 2003.
[2] Gillinov, AM et al., *J Thorac Cardiovas Surg*, 135: 885-593, 2008.
[3] Bouma, W et al. *Ann Thorac Surg*, available online first (In press), doi: 10.1016/j.athoracsur.2015.09.076, 2015.
[4] Amini, R et al., *Ann Biomed Eng*, 40: 1455-1467, 2012.
[5] Lee, CH et al., *J Biomech*, 47: 2055-2063, 2013.
[6] Lee, CH et al., *J Theor Biol*, 373: 26-39, 2015.
[7] Lee, CH et al., *Biomech Model Mechanobiol*, 14: 1281-1302, 2015.

Copyright 2016 The Organizing Committee for the 2016 Summer Biomechanics, Bioengineering and Biotransport Conference

SB^{3}C2016
Summer Biomechanics, Bioengineering and Biotransport Conference
June 29 –July 2, National Harbor, MD, USA
SB^{3}C2016-115

UPPER CERVICAL SPINE LOADING SIMULATING LOW-SPEED COLLISIONS SIGNIFICANTLY INCREASES FACET STRAINS COMPARED TO EQUIVALENT QUASISTATIC LOADING

Timothy P Holsgrove (1), Nicolas V Jaumard (1,2), Nina Zhu (1), Nicholas S Stiansen (1), William C Welch (2), Beth A Winkelstein (1,2)

(1) Department of Bioengineering
University of Pennsylvania
Philadelphia, PA, United States

(2) Department of Neurosurgery
University of Pennsylvania
Philadelphia, PA, United States

INTRODUCTION

Between one-quarter and one-third of people exposed to low-speed rear-end collisions experience neck injury [1], and 15-40% of those injuries will develop into chronic neck pain, which can extend to the head, shoulders, and arms [2]. In 35-60% of people with chronic neck pain, the cervical facet joint is its source [3-5], with the C2/C3 and C5/C6 levels most common for trauma and idiopathic origin [3-5].

The facet capsule has both low- and high-strain threshold units, which discharge at 10% and 47% strain, respectively [6]. Some low-threshold units are likely to play a role in proprioception, but capsular strains as low as 19% have been shown to induce behavioral sensitivity in the absence of any facet capsule ligament failure [7]. Although facet strain has been related to injury from dynamic loading exposures, the regional strain magnitudes, and their relationships to facet kinematics during such loading is not known.

Despite a high prevalence of injuries from dynamic neck loading and the large proportion of injuries being attributed to the upper cervical spine [3-5], the full-field strain responses of the C2/C3 facet capsule are not known. Further, the facet's behavior during potentially injurious exposures has not been contextualized relative to vertebral kinematics. This study investigated the response of the C2/C3 facet joint to dynamic flexion-extension loading using a human cadaveric model, and compared the vertebral rotations and full-field capsular strains at C2/C3 with those responses during quasistatic loading to determine if, and how, dynamic loading increases the risk of C2/C3 facet capsule injury and whether the vertebral rotations in the upper cervical spine are alerted compared to normal physiological loading

METHODS

Fresh frozen, ligamentous specimens from the occiput (Occ) to the C3 vertebra (n=6), were acquired by appropriate methods and procedures for our institution. Specimens were potted in a two-part fast curing polymer (Smooth Cast 300; Smooth-On, Inc.) combined with self-tapping screws and Kirschner wires to aid fixation. A surrogate replicating the mass and moment of inertia of the human head [8] was affixed to the occiput, and the C3 vertebra was rigidly fixed to an actuation cradle coupled to a servo-hydraulic MTS test machine (Fig. 1a). The cranial end allowed movement only in the sagittal and axial planes. Tracking markers were placed on the head, C1 and C2, the cradle, and to the surface of the C2/C3 facet capsule.

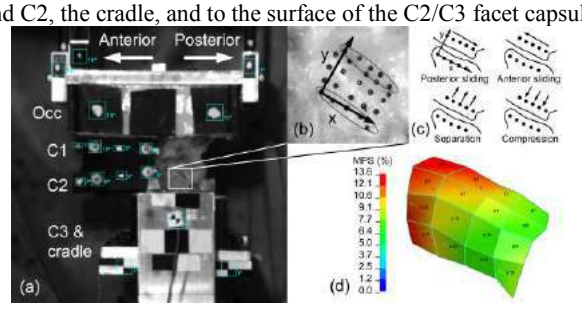

Fig. 1. Sagittal view (a) of an occiput-C3 specimen, with tracking markers. The C2/C3 facet capsule was imaged (b) to measure facet kinematics (c); 3D reconstructions were used for MPS (d) and SS.

Quasistatic flexion/extension loading was applied over physiological ranges of motion (ROMs) before and after dynamic loading to provide comparison data and to assess the effect of dynamic loading on neck kinematics. The vertebral motions and C2/C3 three-dimensional (3D) deformations of the facet capsule surface were acquired during all tests. Quasistatic testing was performed by manually guiding the head through flexion/extension with the C3 vertebra held stationary. For dynamic loading, the head was held in the neutral position using an electromagnet and was released upon actuation of C3 via the cradle. To simulate the rotation of the C3

Copyright 2016 The Organizing Committee for the 2016 Summer Biomechanics, Bioengineering and Biotransport Conference

vertebra during low-speed rear-end and frontal collisions [9], dynamic tests were imposed at 100°/s to 6.1° in each of flexion and extension. A high-speed camera (V4; Vision Research) tracked the vertebral kinematics in the sagittal plane. Two additional cameras (Miro eX1; Vision Research) tracked the capsule markers (Fig. 1b) to measure the C2/C3 kinematics (Fig. 1c) and linear strain across the facet [10]; and enabled the 3D reconstruction of the capsule. Using that reconstruction, the maximum principal strain (MPS) and shear strain (SS) on the surface of the C2/C3 facet capsule was estimated (Fig. 1d), using images at 20ms prior to actuation as the reference (0% strain) condition. All image data were synchronized and captured at 1kHz.

The quasistatic tests for each specimen were compared at 1° increments of global ROM from 16° of flexion to 13° of extension. Comparisons of the rotation at each cervical level (Occ/C1, C1/C2, C2/C3) relative to the global ROM were made using two-way repeated measures ANOVAs. Wilcoxon signed-rank tests compared the MPS and SS of the C2/C3 level at 10ms intervals over 150ms during dynamic loading with those strains at equivalent rotations during quasistatic loading.

RESULTS

The intervertebral rotations during quasistatic loading were not altered at any level by the dynamic loading (Occ/C1 p=0.997; C1/C2 p=0.999; C2/C3 p=0.714). The average respective acceleration and deceleration of the MTS actuator during dynamic tests was 2.8±0.8g and 2.8±0.8g in flexion, and 1.8±0.2g and 2.8±0.3g in extension. Dynamic flexion initially produced extension at C2/C3 (maximum 2.2±0.7°), which was reversed when actuation stopped, forcing the C2/C3 joint into flexion (maximum 2.4±2.1°). The opposite response was produced in dynamic extension, with C2/C3 rotation first peaking in flexion (1.4±1.1°) and then moving into extension (maximum 1.5±1.0°). The maximum and minimum rotation in dynamic tests was generally less than rotation during quasistatic tests.

Both the MPS and SS were inhomogenous in both dynamic and quasistatic loading (Fig. 2). The location of the peak MPS was in the center and towards the anterior aspect of the facet capsule in dynamic flexion (Fig. 2), and in the center and towards the posterior aspect of the capsule in dynamic extension. The direction of the peak MPS was orientated approximately along the facet joint, particularly in the region of the capsule where the peak MPS was sustained (Fig. 2a).

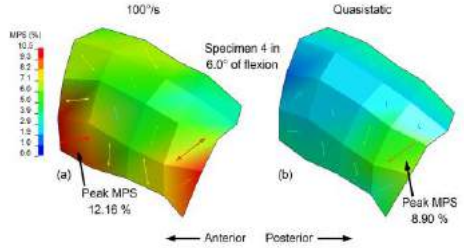

Fig. 2. Inhomogeneous MPS at its peak during dynamic flexion and for quasistatic loading at equivalent C2/C3 vertebral rotation.

Strain during dynamic flexion continued to increase after C3 rotation stopped, peaking at 12.5±4.6%. Quasistatic loading produced significantly lower (p=0.028) MPS (7.6±4.4%) at equivalent C2/C3 rotations (Fig. 3a). In contrast, dynamic extension produced peak strains during the actuation of C3, and did not alter the MPS at equivalent quasistatic C2/C3 rotations (Fig. 3a). The maximum SS was significantly greater in both dynamic flexion (p=0.028) and extension (p=0.028) compared to quasistatic loading at equivalent C2/C3 rotations (Fig. 3b); yet, minimum shear strains were not different.

Posterior-anterior facet sliding exhibited similar behavior, with the facet undergoing posterior sliding during actuation in dynamic flexion, changing to anterior sliding at approximately the time that actuation stopped; the reverse occurred in dynamic extension. Peak posterior-anterior sliding of -1.1±0.5mm in dynamic flexion and 1.2±0.5mm in dynamic extension were significantly greater than during equivalent quasistatic C2/C3 rotations (p≤0.043). There was more facet compression in dynamic flexion than equivalent quasistatic loading (p=0.027); yet, the magnitudes were small and all within 0.5mm of separation and 0.6mm of compression. The maximum linear strain across the facet joint of 3.9±1.5% in dynamic flexion and 2.8±1.2% in dynamic extension was lower than the peak MPS from the full-field analysis. No differences were detected between the linear facet strain in dynamic and quasistatic loading (p>0.35).

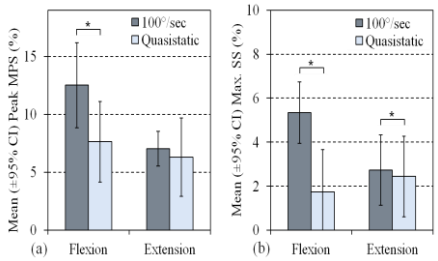

Fig. 3. Peak MPS & maximum SS in dynamic (100°/sec) flexion is greater (*p=0.028) than in quasistatic loading.

DISCUSSION

Dynamic flexion simulating a low-speed, rear-end collision increases the C2/C3 facet capsule strains compared to quasistatic loading at equivalent joint rotations (Fig. 3). Since vertebral rotations during dynamic loading remain within physiological ROMs [11], the increased strains may be due to abnormal local joint motions. The inertia of the head when C3 stops moving altered the flexion/extension behavior of C2/C3. In dynamic flexion this inertial effect produced increased peak MPS, maximum SS, and maximum anterior facet sliding compared to equivalent quasistatic loading.

Full-field capsular strain analysis shows that both MPS and SS were inhomogeneous (Fig. 2). Peak MPS during dynamic flexion approached the magnitude that has been reported to lead to pain (19.4±11.4%) from facet capsule stretch in the rat [7], suggesting the potential for tissue injury. Assessing linear facet strain [10] did not reveal differences between dynamic flexion and quasistatic loading, suggesting that full-field strain measurements of the capsule more accurately identify local responses within the facet capsule, and may, be better for predicting the risk of injury, pain and/or other pathophysiological dysfunctional responses due to traumatic exposure.

Combining these data with microstructural analyses of the tissues could help fully define how such loading exposures occur, and what conditions pose the greatest risk of injury. The results also indicate that the deceleration following a rear-end collision is critical for altering facet mechanics and generating the peak strains, which provides a potential for injury mitigating designs and approaches.

ACKNOWLEDGEMENTS

This work was supported by the Catherine Sharpe Foundation.

REFERENCES

1. Zuby DS et al. *J Occup Environ Med*, 52(4):428-33, 2010. 2. Schofferman J et al. *J Am Acad Orthop Surg*, 15(10):596-606, 2007. 3. Barnsley L et al. *Spine*, 20(1):20-5; 1995. 4. Lord SM et al. *Spine*, 21(15):1737-44, 1996. 5. Bogduk N et al. *Spine*, 13(6):610-7, 1988. 6. Lu Y et al. *Stapp Car Crash J*, 49:49-65, 2005. 7. Dong L et al. *Brain Res*, 1461:51-63, 2012. 8. Yoganandan N et al. *J Biomech*, 42(9):1177-92, 2009. 9. Deng B et al. *Stapp Car Crash J*, 44:171-88, 2000. 10. Pearson AM et al. *Spine*, 29(4):390-7, 2004. 11. Anderst WJ. *J Biomech*, 48(7):1270-6, 2015.

Copyright 2016 The Organizing Committee for the 2016 Summer Biomechanics, Bioengineering and Biotransport Conference

SB^{3}C2016
Summer Biomechanics, Bioengineering and Biotransport Conference
June 29 –July 2, National Harbor, MD, USA
SB^{3}C2016-117

MUSCLE VOLUME PREDICTION USING ANTHROPOMETRIC MEASUREMENTS AND POPULATION DERIVED STATISTICAL MODELS

Shasha Yeung (1), Justin Fernandez (1,2), Geoffrey Handsfield (1), Cameron Walker (2) Thor Besier (1,2), Ju Zhang (1)

(1) Auckland Bioengineering Institute
University of Auckland
Auckland, New Zealand

(2) Department of Engineering Science
University of Auckland
Auckland, New Zealand

INTRODUCTION

Knowledge of subject-specific muscle volumes can be used to estimate muscle forces and joint loads, patient strength, and to properly scale computational muscle models. Historically in biomechanics, cadaver data were used to make these estimates, but muscle volumes vary significantly between cadavers and *in vivo* imaging [1]. Cadaver data are limited due to dehydrated muscle in fixed static poses and are usually not of healthy populations. In vivo imaging studies to date have been limited in population size, thus calling into question the ability to generalize these data to large, diverse clinical populations. Hence, there has been a drive towards population based modeling from large image datasets.

Current methods for predicting muscle volumes use either manual or semi-automated segmentation, both of which require manual user intervention and are not practical for large populations. Previous studies using model-based muscle volume predictions used only a few anatomical inputs, such as muscle lengths, shapes and belly cross sections; have been based on manually segmented datasets from Magnetic Resonance Imaging (MRI), which is less abundant clinically than Computed Tomography (CT) data; and have used only athletic humans which may not be applicable to sedentary populations [1-4].

The aim of this study was to develop a population-based statistical tool to rapidly predict lower limb muscle volume from sedentary and non-sedentary population data. This model was designed to be fast, utilize simple anthropometric inputs and be validated against manually segmented MRI data. Statistical models allow for quick muscle volume prediction, which can be used to compute subject-specific muscle forces, and can be used to compare biomechanics between populations.

METHODS

CT image data was obtained with ethical approval (applications EC9/2007 and EC10/2007) from the Victorian Institute of Forensic Medicine (VIFM), the University of Melbourne. Data were from thirty healthy individuals with no pathologies. Half of the subjects were male with an average age of 56 ± 26 years, weight of 65 ± 13 kg and height of 167 ± 6 cm, while the female subjects had an average age of 50 ± 25 years, weight of 66 ± 17 kg and height of 160 ± 6 cm.

Total muscle volumes were acquired by semi-automatically segmenting the CT images to extract total lower limb muscle volume from the top of the iliac crest to the malleoli. The algorithm used image filtering (adjusted to the population set) to define bulk muscle boundaries, and voxel clustering to segment the bulk muscle volume. Once the total muscle volume was extracted, individual muscle volumes were calculated using known leg muscles proportions [1,3].

Partial Least Squares Regression (PLSR) [5] was used to model the relationships between total muscle volume and anthropometric measurements, thereby creating a total muscle volume predictor. Measurements used were height, weight, sex, age, leg length, thigh length, shank length, thigh girth, shank girth, and Anterior Superior Iliac Spine (ASIS) distance, which is the distance from the left pelvic ASIS point to the right pelvic ASIS point. The PLSR predictor was validated firstly using a 'leave-one-out' analysis, and secondly using manually segmented muscle volumes from an independent MRI study [1]. The 'leave-one out' analysis predicted each subject's muscle volume using a predictor trained on all other subjects' data, and compared the prediction to the subject's segmented volume. The second validation used a predictor trained on all 30 subjects to predict

Copyright 2016 The Organizing Committee for the 2016 Summer Biomechanics, Bioengineering and Biotransport Conference

the muscle volumes of a separate dataset of MRI subjects with known anthropometry and muscle volume [2]. In a further analysis, step-wise regression (using the Akaike Information Criteria (AIC) fitness criterion [6]) was used to determine the optimal subset of anthropometric parameters needed to predict muscle volume using linear regression [6]. Figure 1 highlights the general methodology for this study.

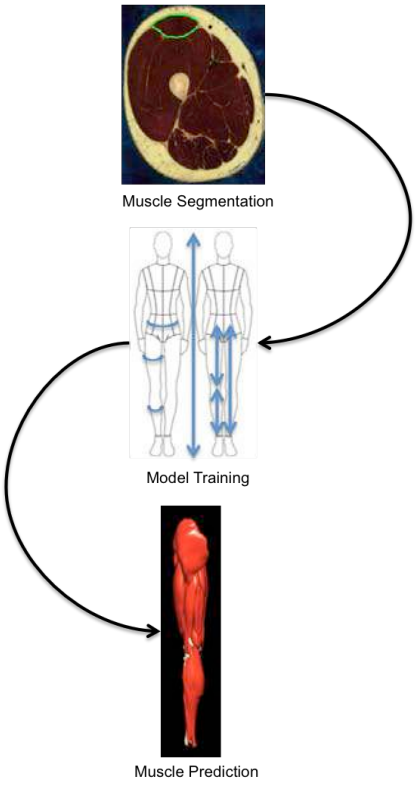

Figure 1: Muscle volume prediction framework

RESULTS

The R^2 prediction error from the 'leave-one-out' analysis was 0.96 using all anthropometric measurements, 0.84 when only given height, and 0.90 when given height and weight. For the MRI dataset, the PLSR-predicted and segmented muscle volumes yielded an average R^2 of 0.91 using all anthropometric measurements.

The optimal step-wise regression model yielded an adjusted R^2 of 0.93 using seven anthropometric measurements (Table 1). The most significant anthropometric measurements were shank girth, sex, leg length, age, and shank length, in that order. Height and thigh girth were insignificant components in the optimal model, while ASIS distance, weight, and thigh length were discarded by the stepwise regression.

Table 1: Results of anthropometric parameters significance.

Parameters	Estimate	Std. Error	t value	Pr(>|t|)	Signif. Code
Sex	3190209	786464	4.056	0.00365	**
Height	-12653	11678	-1.083	0.31019	
Age	-56171	20985	-2.677	0.02807	*
Leg Length	33566	8722	3.849	0.00489	**
Thigh Girth	-17864	16039	-1.114	0.2977	
Shank Length	12567	5076	2.476	0.03837	*
Shank Girth	101960	21048	4.844	0.00128	**
Signif. Codes:	0 '***'	0.001 '**'	0.01 '*'	0.05 '.'	0.1 ' '

DISCUSSION

The PLSR model was able to explain 91% of the variation in muscle volume when all parameters were included through evaluation against a second MRI study. This offers confidence in the PLSR model, which can only improve with larger population training sets.

The results of this study show that sex, leg length and shank girth are the most important variables for predicting muscle volume. This suggests there is a significant difference between the muscle volumes of the lower limb in females and males. It also suggests that shank girth is important, which could be due to lower fat-to-muscle ratio in the shank area (as opposed to thigh areas).

An interesting result was the 2 non-significant covariates in Table 1, thigh girth and height. This suggests that, since height is highly related to leg length, with either contribution the other is made redundant. The fact that thigh girth was not significant in the step-wise regression suggests that in the general population, thigh girth is more dependent on body fat percentage than muscle volume.

These findings offer a better understanding of muscle volume anthropometric dependencies. It presents ability to quickly generate lower limb muscle volumes for population analysis and muscle force predictions scaled by muscle volume. This in turn will help clinical analysis of musculoskeletal joint loadings.

ACKNOWLEDGEMENTS

The authors of this study would like to thank the MedTech Core seed project for funding this study, the VIFM and Dr Jacqui Hislop-Jambrich for providing the CT images.

REFERENCES

[1] Handsfield, G. G., Meyer, C. H., Hart, J. M., Abel, M. F., & Blemker, S. S. (2014). Relationships of 35 lower limb muscles to height and body mass quantified using MRI. *Journal of biomechanics*, *47*(3), 631-638.

[2] Holzbaur, K. R., Murray, W. M., Gold, G. E., & Delp, S. L. (2007). Upper limb muscle volumes in adult subjects. *Journal of biomechanics*, *40*(4), 742-749.

[3] Mersmann, F., Bohm, S., Schroll, A., Boeth, H., Duda, G., & Arampatzis, A. (2015). Muscle shape consistency and muscle volume prediction of thigh muscles. *Scandinavian journal of medicine & science in sports*, *25*(2), e208-e213.

[4] Zheng, L., Siegmund, G., Ozyigit, G., & Vasavada, A. (2013). Sex-specific prediction of neck muscle volumes. *Journal of biomechanics*, *46*(5), 899-904.

[5] Wold, S., Ruhe, A., Wold, H., & Dunn, III, W. J. (1984). The collinearity problem in linear regression. The partial least squares (PLS) approach to generalized inverses. *SIAM Journal on Scientific and Statistical Computing*,*5*(3), 735-743.

[6] James, G., Witten, D., & Hastie, T. (2014). An Introduction to Statistical Learning: With Applications in R.

Copyright 2016 The Organizing Committee for the 2016 Summer Biomechanics, Bioengineering and Biotransport Conference

SB³C2016
Summer Biomechanics, Bioengineering and Biotransport Conference
June 29 –July 2, National Harbor, MD, USA
SB³C2016-118

PATIENT-SPECIFIC CFD OF CLINICAL MITRAL REGURGITATION AS A NOVEL METHOD TO QUANTIFY REGURGITATION SEVERITY

Muhammad Jamil (1), Kian Keong Poh (2), C.H. Yap (1)

(1) Department of Biomedical Engineering
National University of Singapore,
Singapore.

(2) Department of Medicine, Yong Loo Lin
School of Medicine, National University of
Singapore.

INTRODUCTION

Mitral regurgitation (MR) is a highly prevalent cardiovascular disease which is estimated to affect significant number of people[1, 2]. MR results from incomplete closing of the mitral leaflets. Correct assessment of MR severity is crucial in utilizing the protocols needed for prognosis, disease management and patient outcome.

Doppler echocardiography is routinely used to quantify the MR severity. It can potentially provide the information about type and mechanism of regurgitation, anatomical features, extent of regurgitation and reparability assessment. Current gold standard is the 2D proximal isovelocity surface area (PISA) method which is based on the conservation of mass principle. As the fluid is squeezed through the orifice, it forms a series of concentric hemispherical shells of decreasing surface area and increasing velocities. Known limitations of the 2D-PISA method include heavy user dependency, poor repeatability, sensitivity to orifice shape and the need for the angle correction[3].

In this study, we propose a novel method of MR assessment, which relies on the curve fitting between 3D clinical color Doppler data of the regurgitation and data from patient-specific CFD of the same valve. We first demonstrate the feasibility of performing patient-specific CFD of mitral regurgitation based on clinical ultrasound scans. Subsequently we performed experimental assessment of our new technique and found it to be more precise, and in some cases, more accurate, than 2D PISA.

METHODS

Patient-specific CFD of mitral regurgitation was performed as follows: 3D B-mode ultrasound scans of the mitral valve and 3D color Doppler images of regurgitant jet were obtained from the National University Hospital, Singapore. Images were exported as a stack of images and was segmented with VMTK, an open-source software. (www.vmtk.org). The regurgitation jet segmentation was subtracted from the mitral valve segmentation to create the regurgitation orifice (Figure 1). CFD simulation of the regurgitation was then performed for this patient-specific geometry using an assumed physiological pressure gradient of 120 mm of Hg.

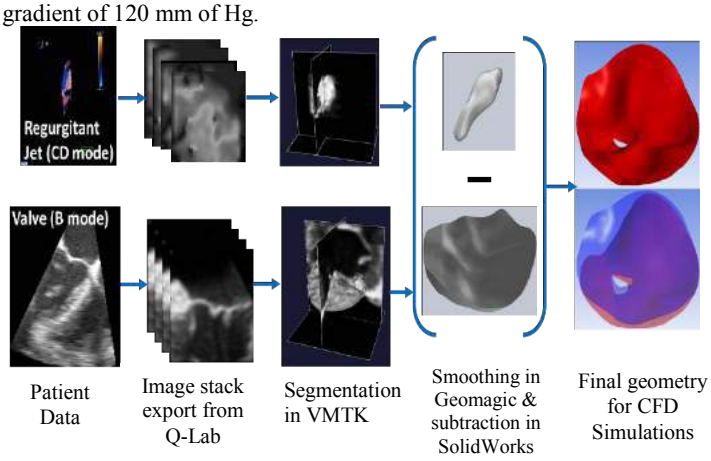

Figure 1: Schematic of methods used to perform patient-specific CFD of mitral regurgitation based on ultrasound scans.

The above CFD technique was then applied to quantify mitral regurgitation by curve fitting of the resulting CFD velocities in the flow convergence zone to the 3D clinically imaged Color Doppler data of the same valve. Our technique is summarized as follows:

Step 1: Obtain 3D color Doppler velocities (V_{us}) and 3D B-mode data of the valve from clinical ultrasound scan.

Copyright 2016 The Organizing Committee for the 2016 Summer Biomechanics, Bioengineering and Biotransport Conference

Step 2: Run CFD of regurgitation at an assumed flow rate (Q_{CFD}) to obtain velocities (V_{CFD}) at the same points as ultrasound data.

Step3: Finding the mean ratio between numerical and Ultrasound velocities: $Mean\ Ratio = \frac{1}{N}\sum_{all\ points}(V_{CFD}/V_{US})$

Step 4: Rescaling Q_{CFD} to obtain the predicted regurgitation flow rate:

$$Q_p = \frac{Q_{CFD}}{Mean\ Ratio} \qquad (1)$$

To validate our proposed method, we set up a steady flow loop to simulate the mitral regurgitation in vitro (Figure 2). Detachable plate with orifice allowed for incorporation of different orifice shapes. For this study, a circular and a slit orifice were experimented with. Experiments were performed at 5-7 different flow rates and a research 3D ultrasound machine (SonixTablet, Ultrasonix Inc) was used to obtain the ultrasound Color Doppler data. Simulations were ran with Ansys Workbench (Ansys Inc.), and the above 4 step technique was used to compute regurgitation flow rate. The results were compared to the truth flow rates obtained via physical measurements.

Figure 2: The experimental flow loop setup. White arrows show the flow direction.

RESULTS

Figure 3 shows the CFD results of patient specific real valve geometry under physiological pressure gradient. Results from our proposed method were compared with 2D-PISA method.

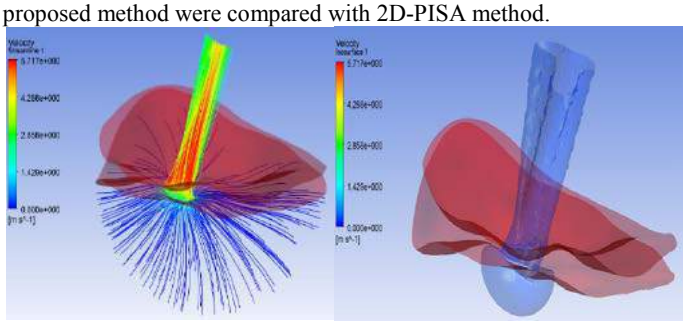

Figure 3: Streamlines (left) and iso-velocity surface (right) of the flow convergence zone CFD results based on ultrasound scans of a mitral regurgitation patient

Fig. 4 compares the results of proposed method with 2D-PISA method for circular orifice. As can be seen that our method accurately predicts the regurgitant flow rate (<5% error) while 2D-PISA incurs large inaccuracies especially at higher flow rates. For slit orifice our method had comparable accuracy with that of 2D-PISA method. However, in both orifices, our method had better precision, as can be observed by the smaller standard deviations.

REFERENCES

1. Iung B. et. al., *Nat Rev Cardiol* 8: 162-172, 2011.
2. Jones E. C. et. al., *The American Journal of Cardiology* 87: 298-304, 2001.
3. Sonntag S. J. et. al., *Annals of Biomedical Engineering* 42: 971-985, 2014.

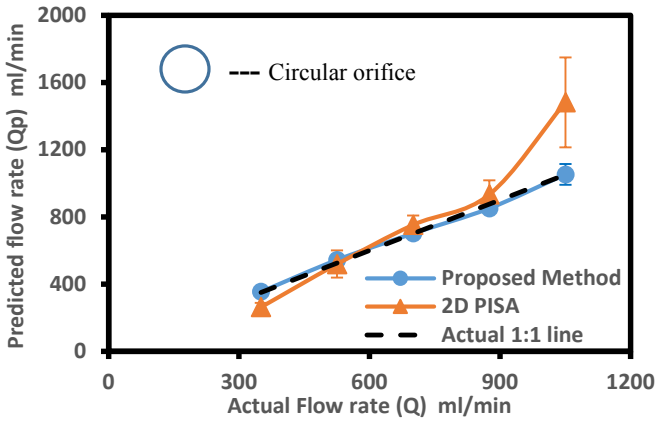

(a)

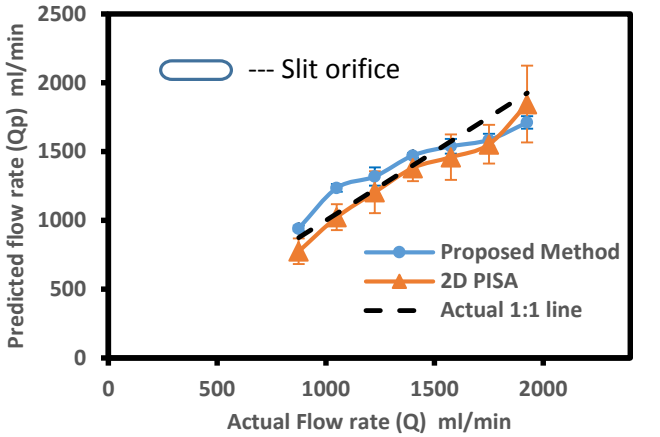

(b)

Figure 4: Comparison of predicted flow rate for circular (a) and slit orifice (b) between 2D-PISA method and proposed method

DISCUSSION

Our work can show that ultrasound-based CFD is a r ealistic technique that can be used to aid patient diagnosis. In the current study, we show that such simulations can be used for improved quantification of the mitral valve regurgitation flow rates, but other applications such as understanding the energy losses of blood flow, turbulent stresses imposed on bl ood to cause blood damage, and the shear stresses imposed by blood on the mitral valve, can be realized as well.

Our new method for quantification of mitral regurgitation showed promise, in the two simplified orifices tested, our technique showed excellent accuracy for circular orifice (<5 %, better than 2D PISA) and comparable accuracy 2D PISA for the straight slit orifice (mean error of <9 %), and our technique showed consistently higher precision. These could be explained by considering that our technique uses the curve fitting of an entire velocity field instead of a single PISA radius measure for flow rate quantification, rendering it less sensitive to localized noise and imaging errors.

Our future work includes in vitro testing of the new technique with more orifice shapes, such as a realistic 3D printed valve geometry, and in vivo testing of the efficacy of our technique in diagnosis and prognosis of mitral regurgitation patients.

ACKNOWLEDGEMENTS

We thank the Singapore Ministry of Education, Academic Research Fund Grant number R397-000-182-112 for funding.

Copyright 2016 The Organizing Committee for the 2016 Summer Biomechanics, Bioengineering and Biotransport Conference

SB^{3}C2016
Summer Biomechanics, Bioengineering and Biotransport Conference
June 29 –July 2, National Harbor, MD, USA
SB^{3}C2016-119

ENDOTHELIAL CELL GLYCOCALYX MODULATES SHEAR-INDUCED TUBULE FORMATION

P. Zhao, X. Liu, X.Y. Deng

Key Laboratory for Biomechanics and Mechanobiology of the Ministry of Education, School of Biological Science and Medical Engineering, Beihang University, Beijing, China.

INTRODUCTION

Angiogenesis, the process of blood vessels form from existing ones, is the most common form of vessel formation during development and in adulthood. Abnormal or immature angiogenesis has been implicated in more than 70 disorders such as obesity, asthma, diabetes, cirrhosis, multiple sclerosis, endometriosis, AIDS, bacterial infections and autoimmune disease so far, and the list is ever growing [1]. Sprouting angiogenesis, known as the major form, involves a series of cellular events including basal membrane degradation, endothelial cell proliferation and migration, tube formation and pericyte recruitment.

Although the detailed mechanism leading to pathological angiogenesis remains unknown, flow-induced stress has shown significant impact on vessel growth. Early studies by Clark et al. [2] demonstrated that small blood vessels exposed to high shear stress sprouting while vessels tend to regress after a decrease or a halt in the flow. Recent investigations indicate shear stress on endothelium regulate endothelial cell (ECs) morphology and function, hence affect angiogenesis. Kang et al. [3] found that the distance of endothelial cell invasion into three-dimensional collagen matrices was proportional to the magnitude of shear stress. An in vitro study by Tressel et al. [4] reported that laminar shear stress inhibits endothelial cell migration and tubule formation, two important functions in blood vessel formation..

The responses of ECs to shear stress have been investigated extensively. However, how shear stress is sensed and transmitted into chemical signals and thereby regulates neovascularization is still uncertain. Previously, various membrane molecules and cellular microdomains were proposed as mechanosensors of endothelial cells, including integrins, G proteins, growth factor receptors, caveolae, ion channels, adhesion proteins and the cytoskeleton [5]. Recent researches on the glycocalyx have verified its pivotal role in the shear stress–sensing mechanism.

Endothelial glycocalyx layer (EGL), coating at the luminal surfaces of vascular endothelium, is a bush-like structure composed of heparan sulfate (HS), chondroitin sulfate (CS), and hyaluronic acid (HA) [6]. Theoretical study indicates that flow-induced shear stress can hardly act on ECs directly but is transmitted to the cells largely by the EGL [7]. Experimental studies demonstrated that glycocalyx modulates cell proliferation, migration and shear-induced nitric oxide release of vascular endothelium in response to fluid shear stress [8]. All of these functions are essential in sprouting angiogenesis.

Therefore, we hypothesizes that as a mechanotransducer, the endothelial glycocalyx may sense the change of shear stress, hence affect the sprouting angiogenesis. To test the hypothesis, we investigate the tubule formation of endothelium exposed to shear stress in a parallel-plate flow chamber.

METHODS

A parallel plate flow chamber was employed to expose human umbilical vascular endothelial cells (HUVECs) monolayers to a physiological level of shear stress (15 dyn/cm^2) for 24 hours. Heparinase II (Hep.II) was applied to selectively degrade heparan sulfate on the ECs surface. Then, cells were used in Matrigel tubule formation assay and total tubule length was compared among the following four groups of cells: 1) untreated with no flow, 2) Hep.II treatment with no flow, 3) untreated with flow of 15 dyn/cm^2 exposure, and 4) Hep.II treatment with flow of 15 dyn/cm^2 exposure.

RESULTS

Tubule formation was observed using a phase contrast microscope at 5x magnification (Fig. 1) and total tubule length was

Copyright 2016 The Organizing Committee for the 2016 Summer Biomechanics, Bioengineering and Biotransport Conference

quantified using AngioTool. Results show that flow-induced shear stress significantly suppressed endothelial tubule formation in cells without Hep.II treatment, whereas the suppression was reduced in sheared, enzyme treated cells. No difference of total tubule length was found between enzyme treated and untreated cells in static state (Fig. 2).

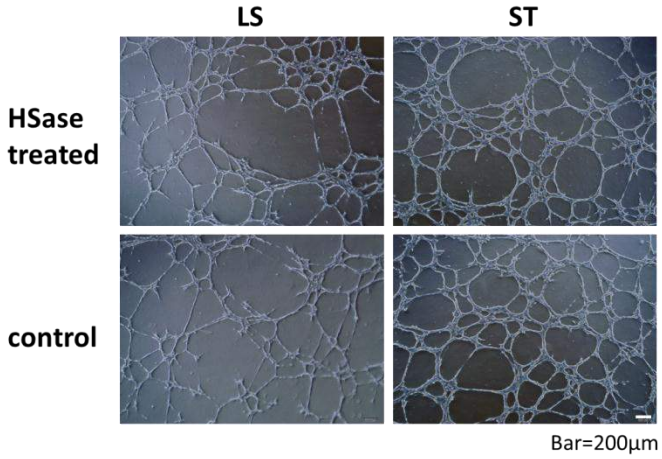

Figure 1: Endothelial cells tubule formation on Matrigel. Enzyme treated and untreated cells showed different capacity of tubule formation in laminar shear (LS) and static state (ST).

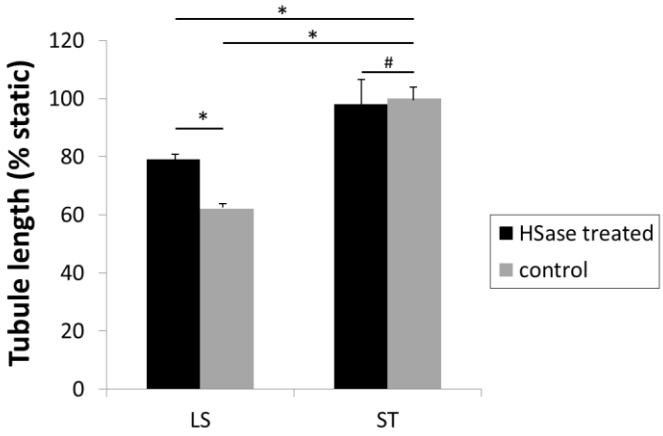

Figure 2: Shear stress inhibits endothelial cell tubule formation. (mean±SD, *P<0.05, #P>0.05)

DISCUSSION

Since angiogenesis involved in so many diseases, controlling angiogenesis has become an important therapeutic target nowadays. Among the numerous factors, shear stress is considered as a strong stimulus to angiogenesis, but the specific mechanism is unclear. Recent studies have shown that the endothelial glycocalyx acting as a mechanotransducer, play important role in fluid shear stress transmission and transduction. In the present work, we try to detect the relationship between glycocalyx and angiogenesis. To this end, one of the classic assays for angiogenesis study, endothelial cell tubule formation which focuses on the ECs differentiation was observed.

We found that laminar shear stress could suppress ECs tubule formation, indicating flow-induced shear stress may inhibit angiogenesis, which is consistent with the observation by Tressel et al [4]. Meanwhile, our results showed that without flow imposing on the cells, Hep.II treatment alone could not decrease tubule formation, implying the integrity of glycocalyx does not affect angiogenesis directly. However, compared to cells in static control, enzyme treatment can significantly reduce the suppression caused by shear stress. Therefore, the suppression of tubule formation induced by shear stress may partially be mediated by glycocalyx.

ACKNOWLEDGEMENTS

This work is supported by Grants-in-Aid from the National Natural Science Research Foundation of China (No. 31200703, 11332003, 31570947, 11572028, 11421202), Specialized Research Fund for the Doctoral Program of Higher Education (20121102120038) and the 111 Project (B13003).

REFERENCES

[1] Carmeliet, P, *Nature*, 438: 932-936, 2005.
[2] Clark, ER, *Am J Anat*, 23:37-88, 1918.
[3] Kang, H et al., *Am J Physiol Heart Circ Physiol*, 295: H2087-2097, 2008.
[4] Tressel, SL et al., *Arterioscler Thromb Vasc Biol*, 27: 2150-2156, 2007.
[5] Fisher, AB et al., *Am J Physiol Lung Cell Mol Physiol*, 281: L529-L533, 2001.
[6] Weinbaum, S et al., *Annu Rev Biomed Eng*, 9:121-167, 2007.
[7] Liu, X et al., *ASAIO J*, 57:487-494, 2011.
[8] Kang, HY et al., *Am J Physiol Heart Circ Physiol*, 300: H76–H83, 2011.

Copyright 2016 The Organizing Committee for the 2016 Summer Biomechanics, Bioengineering and Biotransport Conference

SB^{3}C2016
Summer Biomechanics, Bioengineering and Biotransport Conference
June 29 –July 2, National Harbor, MD, USA
SB^{3}C2016-120

THE EFFECT OF CELL DENSITY ON PRESTRESS DEVELOPMENT IN ENGINEERED MICROTISSUES

Mathieu A.J. van Kelle (1,2), Sandra Loerakker (1,2), Carlijn V.C. Bouten (1,2)

(1) Department of Biomedical Engineering
Eindhoven University of Technology
Eindhoven, The Netherlands

(2) Institute for Complex Molecular Systems
Eindhoven University of Technology
Eindhoven, The Netherlands

INTRODUCTION

Many cells used in soft tissue engineering exhibit a contractile phenotype. These cell-generated contractile forces lead to the development of tissue prestress. In heart valve tissue engineering in particular, prestress can lead to leaflet retraction, which in many cases results in failure of the valve. In addition, tissue prestress changes the apparent stiffness of the biological material. To successfully mimic the properties of native tissues in engineered tissues, it is therefore important to understand what biological factors determine the level of tissue prestress. In the current study, the effect of cell density on cell-generated forces and resulting tissue prestress was investigated using a high-throughput microfabricated tissue gauge (µTUG) setup, allowing for the culture of contractile microtissues.

METHODS

Microtissue Culturing

First, the µTUG setup was fabricated from polydimethylsiloxane (PDMS). Each setup consist of 80 microwells, each embedding 4 compliant microposts (Figure 1a). Next, cells with a contractile phenotype were suspended in a collagen-based gel and centrifuged into the µTUG setup. Within a few hours, the cells compacted the surrounding matrix around the microposts and formed a microtissue (Figure 1b)[1]. Initial seeding densities of 0.5, 1 and 2 million cells per 80 microwells were used. The microtissues were cultured up to 24 hours after seeding.

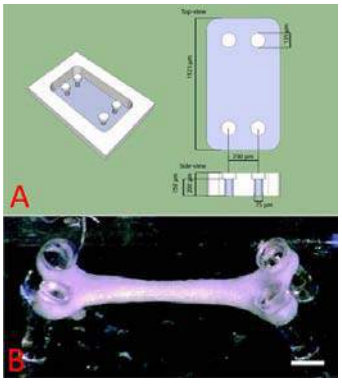

Figure 1: A) µTUG design B) Microtissue compacting microposts[1]

Microscopy

Both brightfield and confocal microscopy was used in order to:

1. Count the number of cells per microtissue:

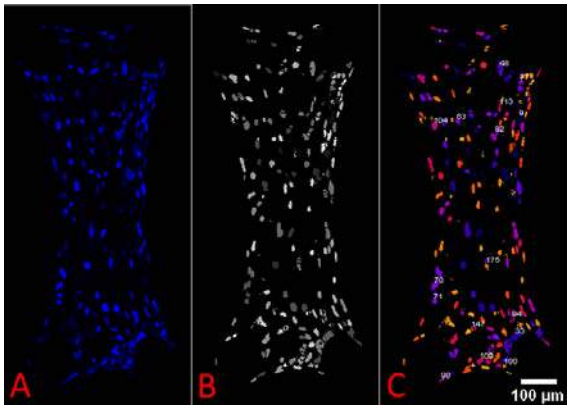

Figure 2: Process of obtaining the number of cells per microtissue

Microtissues were DAPI stained and Z-stack images were made using confocal microscopy (A). After preprocessing, these images were segmented using a 3D-watershed algorithm (B). Finally, the amount of cells per microtissue was determined by counting the number of separate components in the entire 3D segmented images (C).

2. Quantify microtissue forces:

Copyright 2016 The Organizing Committee for the 2016 Summer Biomechanics, Bioengineering and Biotransport Conference

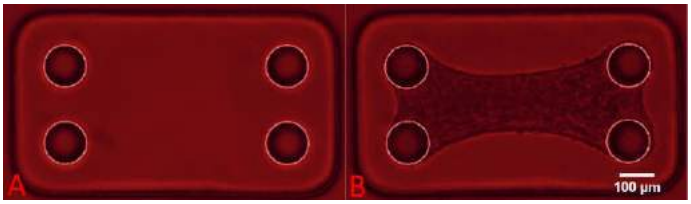

Figure 3: Force quantification using brightfield images

Brightfield images were taken of the empty microwells before seeding (A), and after a microtissue had formed in the well (B). Next, the displacement of the top of the microposts was determined by finding the center of the 4 strongest circles (red) in the reference image, and the image containing the microtissue. A spring constant for the microposts was determined using finite element analysis [N/m] which was then used to determine the total microtissue force.

3. Determine the tissue's cross-sectional area (CSA):

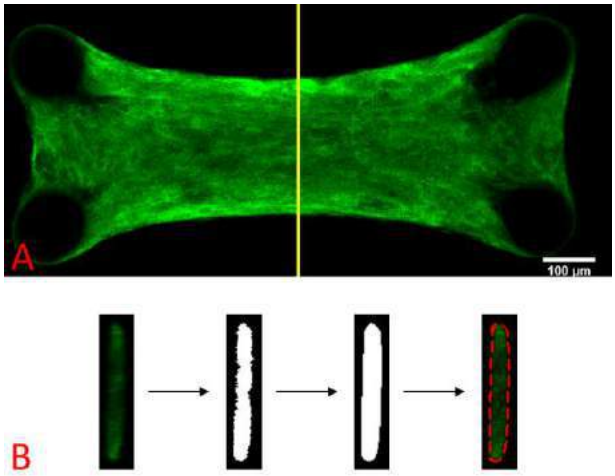

Figure 4: CSA of a collagen-stained microtissue

The collagen of each microtissue was stained with CNA[2], after which it was subjected to confocal life imaging (A). The obtained Z-stack images were rotated such that their main orientation coincides with the long axis of the image. Next, the amount of pixels of each later slice were obtained. Finally, using a convexhull of the smallest lateral slice, the microtissue CSA was determined (B).

RESULTS

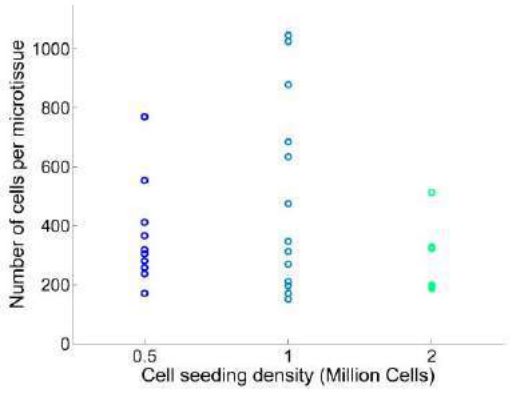

Figure 5: Cell seeding density against the number of cells per microtissue

First, figure 5 shows that the initial seeding density (per 80 µTUGs) was not the major determinant of the final amount of cells in each microtissue. Second, there appeared to be a large discrepancy between the number of cells per microtissue (±150 – 1050 cells).

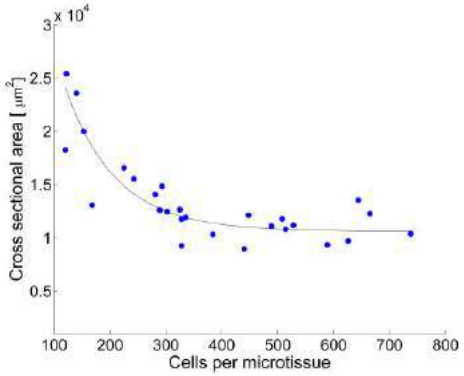

Figure 6: Microtissue cell number against cross sectional area [µm^2]

Furthermore, the tissue CSA decreased with the number of cells up to ±300 cells per microtissue. However, for higher cell numbers, the microtissue CSA does not depend on the number of cells (figure 6).

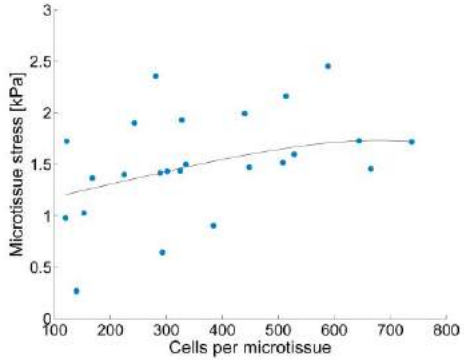

Figure 7: Microtissue cell number against microtissue stress (kPa)

Finally, microtissue stress was determined using the microtissue force and CSA. An increase in cell number results in a higher microtissue stress (figure 7).

DISCUSSION

Surprisingly, the number of cells seeded in 80 microwells, turned out to have no effect on the number of cells ending up in each individual microtissue. There appeared to exist a biphasic relation between the number of cells and the CSA of the microtissues. A similar inverted relationship existed between microtissue cell density and stress. A potential explanation for this result is that there exists a preferred tissue prestress which can only be achieved with a certain minimal amount of cells. This study shows the importance of considering tissue prestress and actual cell density in tissue engineering applications.

ACKNOWLEDGMENTS

We acknowledge the support from the Netherlands Cardiovascular Research Initiative (CVON 2012-01): The Dutch Heart Foundation, Dutch Federation of University Medical Centers, the Netherlands Organization for Health Research and Development and the Royal Netherlands Academy of Sciences.

REFERENCES

[1] Van Spreeuwel, A.C.C. et al., *Intergr. Biol*, 6:422-429, 2014
[2] Boerboom RA et al., *J. Struct. Biol.* 159(3):392–399, 2007

Copyright 2016 The Organizing Committee for the 2016 Summer Biomechanics, Bioengineering and Biotransport Conference

SB^{3}C2016
Summer Biomechanics, Bioengineering and Biotransport Conference
June 29 –July 2, National Harbor, MD, USA
SB³C2016-121

PATIENT-SPECIFIC CFD SIMULATIONS OF INTRAVENTRICULAR HAEMODYNAMICS BASED ON 3D ULTRASOUND IMAGING

Alessandra M. Bavo (1), Alison M. Pouch (2), Joris Degroote (3), Jan Vierendeels (3), Joseph H. Gorman (2), Robert C. Gorman (2) and Patrick Segers (1)

(1) IbiTech-bioMMeda, ELIS department, iMinds Medical IT, Ghent University, Ghent, Belgium
(2) Gorman Cardiovascular Research Group, University of Pennsylvania, PA.
(3) Department of Flow, Heat and Combustion Mechanics, Ghent University, Belgium.

INTRODUCTION

The combined use of computational simulations and clinical images can provide interesting insights and advance the analysis and interpretation of intraventricular haemodynamics. In previous studies, the cardiac fluid-dynamics have been simulated with a prescribed geometry approach, imposing the patient-specific motion of the ventricle as a boundary condition [1-6]. Different approaches can be adopted to include the mitral valve (MV) in the model. The first technique is the use of an on/off procedure, with the MV open upon ventricular filling and closed during systole [1,2]. A more advanced choice includes the projection of the valvular orifice open area on the valvular plane, to model the gradual opening of the leaflets [3,4]. Nevertheless, the 3D valve leaflets have a great impact on the haemodynamics of the region and on the clinical interpretation of the results of the model [4,5]. In only a few studies, the moving MV was introduced in the model as a shell structure in an immersed boundary framework [5, 6]. However, in [5] the motion of the LV is not directly derived from clinical data.

The goal of this paper is to present a CFD-based model to study the intraventricular flows in a patient-specific framework, overcoming some of the limitations listed above. From a geometrical point of view, the fully three-dimensional moving mitral valve and left ventricle were included in the simulation. Their kinematics were retrieved from high resolution segmented clinical preoperative real-time transesophageal ultrasound (rt-TEE US) images. From a methodological point of view, the described model had been especially designed for a CFD simulation with an Arbitrary Lagrangian-Eulerian (ALE) description of the fluid domain.

METHODS

The *a priori* knowledge of the position of the LV and MV structures was available from preoperative rt-TEE images. The MV and LV were segmented in all the available frames using a previously described method that combines multi-atlas label fusion and deformable medial modeling to obtain volumetric geometrical models [7], resulting in a set of triangulated surfaces (of the LV and MV) throughout the cardiac cycle, which were used as reference surfaces to prescribe the motion. The 3D, time-dependent position of the MV and LV was transferred to the fluid solver with adequate interpolation schemes. In particular, third-order natural splines were used for the time interpolation and an adaptive scheme based on the three nearest neighbor points was used for the space interpolation, to decouple the reference meshes from the computational mesh. A constant zero pressure was imposed at the inlet (atrium) and a pressure of 100 mmHg was imposed at the aortic outlet during systole. The aortic surface outlet was converted into a wall during diastole to account for the presence of the closed aortic valve, with an on/off procedure. The calculation was performed in Fluent 15.0 (Ansys), solving the Navier-Stokes equations using the arbitrary Lagrange-Eulerian approach. The dataset used for this study was obtained from a female patient undergoing surgery for treatment of aortic valve stenosis. Written informed consent was obtained from the patient and the study was approved by the local ethical committee.

RESULTS

In figure 1a the flows at the mitral and the aortic surface are shown, while in figure 1b the flow field is reported, during systole and diastole. During systole (panels i-iii), the flow was accelerated by the ventricular contraction and was almost immediately aligned with the major direction of the blood (i). After the peak of systole (ii) the

Copyright 2016 The Organizing Committee for the 2016 Summer Biomechanics, Bioengineering and Biotransport Conference

ventricle shrunk to its lowest volume configuration while the blood decelerated until complete standstill (iii). No significant vortex structure was detected in this phase. During diastole, the typical two-peak-shaped transmitral flow was recorded (fig. 1a, solid line). The flow streamlines were mainly aligned with the valvular leaflets during the entire phase (panels iv-vi). The presence of the valve provided the orientation to the blood flow into the LV. In fig. 1b, panels iv-vi, the vortex structure is also visualized. The vortex arose from the free edge of the valve (iv), travelled lower into the ventricular cavity (v) and dissipated when impacting the lateral wall (vi).

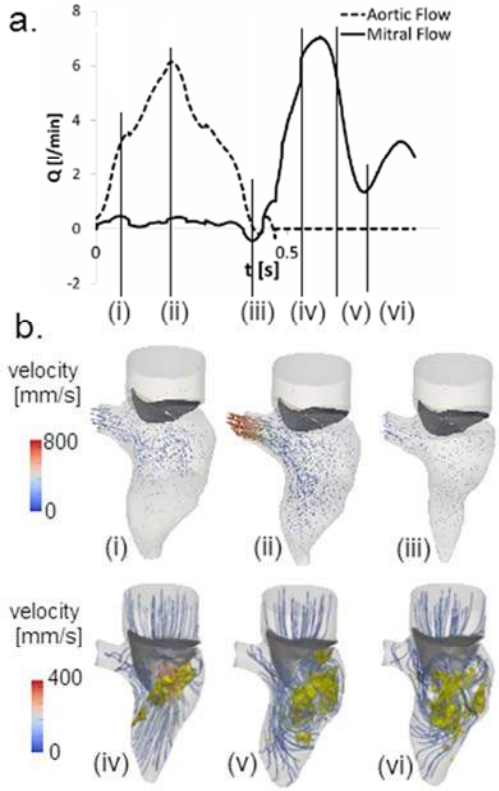

Figure 1: (a) flow curves at the mitral and aortic surfaces. (b) Systolic flow field: velocity vectors. (c) Diastolic flow field: velocity streamlines and vortex structure.

The model allowed to verify the complexity of the intraventricular flow, in particular during diastole. In fig. 2 (a-b) two views of the LV at the same time point (t=0.6s) are displayed. Together with the formation of a larger primary vortex structure (V1), a secondary vortex structure V2 was generated in the proximity of the septal wall. Additional tests could also be performed with the model, as a proof of concept. In fig. 2 (a and c), the flow field at t=0.6s is reported in the model including the MV (a) and in the model where the MV has been previously removed (b), to highlight the effect of the presence of the valvular leaflets. In the latter case, the presence of the MV was included with the on/off procedure, as done for the aortic valve.

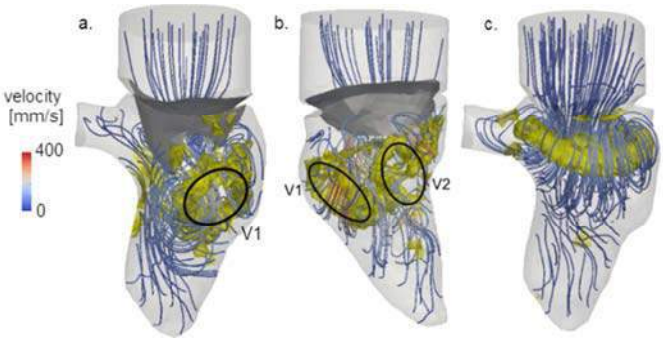

Figure 2: (a) diastolic flow field at t=0.6s, (b) back view at t=0.6s, (c) diastolic flow field at t=0.6s without the mitral valve.

DISCUSSION

Thanks to the use of rt-TEE images as a reference, the described model resulted in a patient-specific CFD model of the left ventricle, which included the presence of the moving ventricular wall and the fully three-dimensional moving mitral valve. The results obtained were in good agreement with the expected haemodynamics of the region (fig.1). The chosen algorithms for the interpolation resulted in a valid kinematics of the LV and MV, leading to realistic flow patterns. As indicator of potential pathologies, the vortex structure was identified during the cardiac cycle. Of paramount importance was the presence of the 3D valve [5]. In fact, during diastole, the flow was oriented according to the valvular leaflets into the ventricular cavity, impacting the lateral wall of the LV. The absence of the valve, on the contrary, resulted in a central blood jet during diastole, which generated a much broader vortex, located in a higher position in the LV (fig. 2a, 2c).

In conclusion, in this work we described a CFD model with imposed moving boundaries of a patient-specific left ventricle, including the three-dimensional mitral valve. The model was based on segmented rt-TEE ultrasound images, which allowed for a patient-specific model and provided the *a priori* knowledge of the position of the structures of interest. The described modeling choices for the interpolation provided a realistic kinematics of the LV and MV, leading to a high quality flow field analysis. The model allowed to analyze the intraventricular haemodynamics throughout the entire cardiac cycle, of particular importance were the results obtained in the diastolic phase, where it was possible to monitor the vortex formation and development.

ACKNOWLEDGEMENTS

This work has been developed as a result of a mobility stay funded by the Erasmus Mundus Program of the European Commission under the Transatlantic Partnership for Excellence in Engineering – TEE Project.

REFERENCES

[1] Long Q. et al., Engineering in Medicine 222: 475-485, 2008.

[2] Saber N.R. et al., Ann Biomed Eng, 31: 42-52, 2003.

[3] Krittian S. et al., Ann Biomed Eng. 38 (8): 2676-2689, 2010.

[4] Schenkel T. et al., Ann Biomed Eng. 37(3): 503-515, 2008.

[5] Seo J.H. et al., Phys. Fluids. 26(12), 121901: 1-14, 2014 .

[6] Mihalef V. et al., Interface Focus. 1: 286-296, 2011.

[7] Pouch A.M. et al., Medical Image Analysis 18(1): 118-129, 2014.

Copyright 2016 The Organizing Committee for the 2016 Summer Biomechanics, Bioengineering and Biotransport Conference

SB^{3}C2016
Summer Biomechanics, Bioengineering and Biotransport Conference
June 29 –July 2, National Harbor, MD, USA
SB^{3}C2016-122

INVESTIGATING PRESSURE INDUCED DEEP TISSUE INJURY USING MRI AND 3D FINITE ELEMENT ANALYSIS

Willeke A. Traa (1), Mark C. van Turnhout (1), Jules L. Nelissen (1), Gustav J. Strijkers (2), Klaas Nicolay (1), Dan L. Bader (1)(3), Cees W.J. Oomens (1)

(1) Department of Biomedical Engineering
Eindhoven University of Technology
Eindhoven, The Netherlands

(2) Department of Biomedical Engineering and Physics
Amsterdam Medical Centre
Amsterdam, The Netherlands

(3) Department of Health Sciences
University of Southampton
Southampton, United Kingdom

INTRODUCTION

Pressure ulcers occur as a result of (prolonged) mechanical loading. They represent a common complication in the management of a range of patients and can be considered as an indicator of quality of healthcare. In many cases, pressure ulcers are avoidable [1]. Currently the proposed mechanisms for pressure ulcer formation are: 1) ischemia, 2) direct deformation, 3) ischemia-reperfusion injury, and 4) lymphatic blockage [2]. To understand how these processes induce pressure ulcer formation controlled experiments can unravel the specific temporal and spatial effects of each of these mechanisms. In the past a combined experimental-numerical approach has been used. A load was applied via an indenter to the tibialis anterior muscle (TA) of the hind leg of Brown-Norway rats. The experiment was monitored with magnetic resonance imaging (MRI), providing data on changes in tissue geometry and physiology. By correlating finite element analysis (FEA) and T_2-weighted MRI a threshold level of applied deformation energy was identified above which damage occurred [3]. However, this study was limited to a local 2D analysis directly under the indenter. The aim of the current study was to determine the global effects of loading muscle tissue by extending the analysis to 3D. The experimental protocol was adapted accordingly and 3D FEA was performed.

METHODS

Experimental: The TA of Sprague- Dawley rats (♀, n=7) was loaded for 2 hours using an indenter with a spherical head (diameter: 3 mm, Fig 1). Before, during and after loading MRI was performed using a 7T Bruker small animal scanner with a 86mm excitation coil and 20mm diameter receiver coil. Anatomy and geometry was determined by T_1 weighted MRI and physiological changes with T_2 mapping MRI (FOV 25x25x20 mm, MTX 256x256x20, T_1: TE/TR 11.50/800.0 ms, T_2: TE 6.95-180.7 ms, 26 echos).

Damage/T_2-analysis: T_2-maps ware obtained by fitting the MR signal (S) voxelwise to equation (1). The TA was manually drawn on the T_2-scans ro represent the region of interest (ROI). Voxels were accepted for analysis if the $R^2 > 0.8$ and SNR > 4. Slices were accepted for further analysis if >90% of the voxels in the ROI fulfilled the previous criteria. The mean and standard deviation of the mean (SD_μ) were determined for the ROI in the T_2-map prior to loading. Voxels were considered elevated (damaged) if they exceeded a threshold (Th) (2). Regions > 3 adjacent voxels were used for analysis. The leg was divided into 3 regions of 4 slices: distal to, underneath and proximal to indentation. The results per region were averaged over the analyzed slices

$$S = S_0 e^{\frac{-TE}{T_2}} \quad (1)$$

$$Th = \mu_{T_2} + 3 \times SD_{\mu_{T_2}} \quad (2)$$

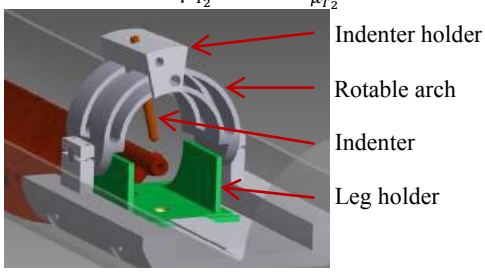

Fig. 1: The experimental set-up. The hind limb of the rat is fixated with a cast in the holder. The optimal indenter position is obtained by rotating the arch and the indenter holder. The indenter is applied manually.

Copyright 2016 The Organizing Committee for the 2016 Summer Biomechanics, Bioengineering and Biotransport Conference

FEA: Animal specific FEA was performed (n=5). Skin and bone contours were determined from the T_1 scans before and during loading using the GIBBON toolbox [4] (Fig 2A-B). The orientation and endpoint of the indenter were obtained from the T_1 scans during loading. The start point of the indenter was obtained by giving an offset to the indenter in its direction to make sure the start point was outside the contours of the model. Essential boundary conditions were the movement of the indenter and the bone. To match the experiment a rigid cast was simulated (Fig 2C). The model was solved in Abaqus 6.14 using the Ogden material law. To determine the elements of the TA, the ROI before indentation was interpolated on the original model using a natural neighbor algorithm.

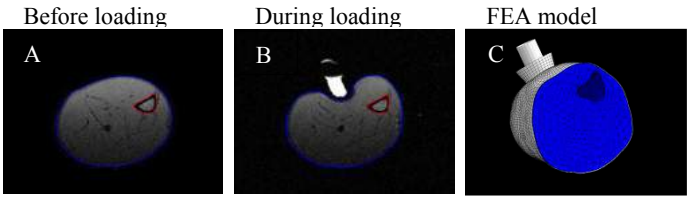

Fig. 2: T_1 images before (A) and during (B) loading. The skin contour is shown in blue and the bone contour in red. C) The front view of a reference state of one finite element model. Soft tissue in blue, the cast and indenter in white.

RESULTS

A structured increase in T_2-value was found after indentation (Fig 3). The region of indentation consistently has the highest volume of elevated T_2-values (Fig 4). High strain energies were found in the regions with the most T_2-elevation (Fig. 3 K,N). However, in regions with low strain energy values, namely the proximal and distal regions, T_2-elevation was also evident (Fig 3,J,L,M,O).

DISCUSSION

This study shows that the effects of mechanical loading extends outside the region of indentation. The loading threshold for deformation damage found previously [3] was clearly exceeded in all experiments in the current study. However, these experiments show that the linear relationship previously found does not extend to regions outside indentation. This may be explained as follows. An increase in T_2-value represent an increase in free water, which occurs due to oedema formation and/or intracellular fluid leakage [5], both considered early signs of tissue damage by the authors. In the destruction phase of muscle injury, transection of muscle fibers creates a release of intracellular fluid [6]. The buildup of fluid within the muscle can potentially diffuse between the muscle fibers, explaining the propagation of T_2-elevation. A previous study has shown that 24 hours after loading T_2-elevation highly correlated with a loss of cross striation and infiltration of inflammatory cells [7]. This indicates the applicability of T_2-values as an early sign of muscle damage. To further map the physiological changes occurring in regions outside of indentation histology needs to be performed.

ACKNOWLEDGEMENTS

This research was supported by the Dutch Technology Foundation (STW), which is part of the Netherlands Organisation for Scientific Research (NWO) and which is partly funded by the Ministry of Economic Affairs. The authors gratefully acknowledge David Veraart, Leonie Niessen and Carlijn Tijsen-van Helvert for their assistance with the animal experiments.

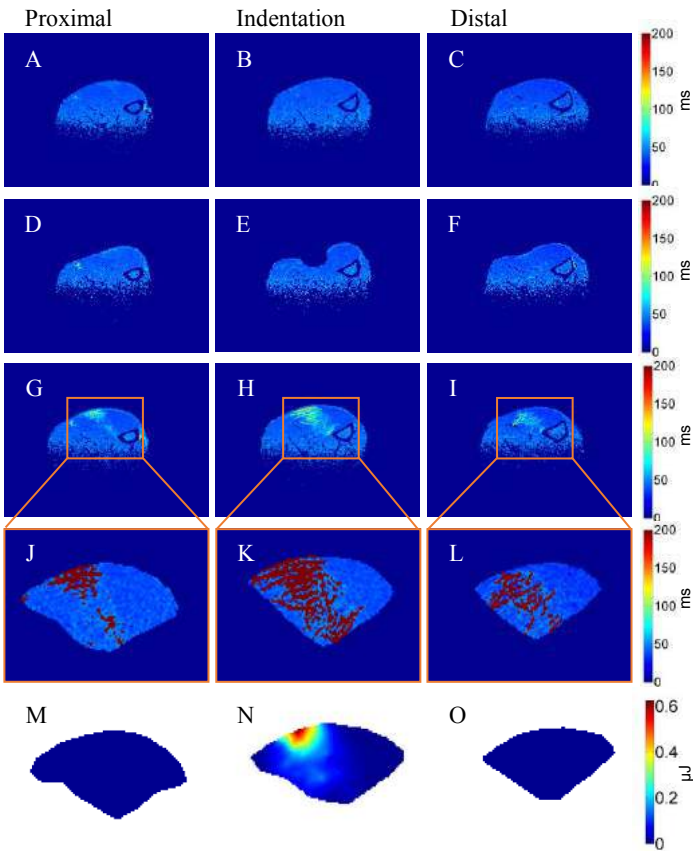

Fig. 3: T_2 an FEA results of the proximal (column 1), indentation (column 2) and distal regions (column 3). T_2 –map (A-L) with voxels accepted for analysis: (A-C) before (D-I) during and (G-I) 90 minutes after indentation. The regions of elevated T_2-values are depicted with red in the ROI (J-L). The corresponding strain energy in the ROI of the TA is shown (M-O).

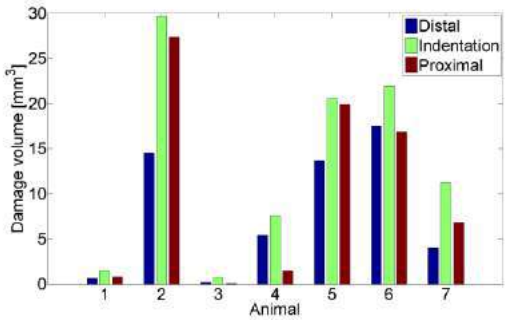

Fig. 4: The averaged elevated T_2-volume per region per animal (n=7).

REFERENCES

[1] Black, J et al., *Ostomy Wound Manag*, 56:28-44, 2010
[2] Mak, A et al., *Annu. Rev. Biomed. Eng*, 12:29-53, 2010
[3] Loerakker, S et al., *Ann Biomed Eng*, 38:2577-2587, 2010
[4] Moerman, K et al., *Proc. 11th Int Symp. CMBBE,* 2013
[5] Berquist, T et al., *MRI of the Musculoskeletal System*, 6th ed., 2012
[6] Jarvinen, T et al., *Am J Sports Med*, 33:745-764, 2005
[7] Bosboom, M et al., *J Appl Physiol*, 95:2235-2240, 2003

Copyright 2016 The Organizing Committee for the 2016 Summer Biomechanics, Bioengineering and Biotransport Conference

SB^{3}C2016
Summer Biomechanics, Bioengineering and Biotransport Conference
June 29 –July 2, National Harbor, MD, USA
SB^{3}C2016-123

CHANGES IN CERVICAL SPINE INTERVETEBRAL DISC PROPERTIES WITH REPETITIVE AXIAL LOADING

Brian D. Stemper, PhD (1,2), Alok S. Shah, MS (1,2), Narayan Yoganandan, PhD (1,2), Mingxin Zheng, MS (3,4) Brian Snyder, MD, PhD (3,4)

(1) Department of Neurosurgery
Medical College of Wisconsin
Milwaukee, Wisconsin, USA

(2) Research Service
Zablocki Veterans Affairs Medical Center
Milwaukee, Wisconsin, USA

(3) Beth Israel Deaconess Medical Center
Boston, Massachusetts, USA

(4) Harvard Medical School
Harvard University
Cambridge, Massachusetts, USA

INTRODUCTION

High rates of neck pain in military personnel may be attributable to vibrational environments that can subject the cervical spine to repetitive axial loading. Those types of environments can be experienced in military helicopters, fixed-wing aircraft, and fast boats. For example, the rate of recurrent neck pain in military helicopter pilots was reported to be approximately 30% [1], compared to 14% in the general population [2]. Additionally, the effect of axial vibration can be exaggerated with the use of helmets and helmet-mounted instrumentation that can increase the inertial load on the cervical spine. Non-specific neck pain could be attributed to progressive subfailure changes in cervical spine biomechanics associated with fatigue of the spinal soft tissues. Characterizing these changes is important for the development of environment-specific exposure limits. However, previous efforts to determine the fatigue response of spinal tissues have focused on the onset of tissue failure [3] or characterizing the effect of spinal implants [4]. Therefore, the objective of the current study was to characterize the effect of repetitive compressive loading on cervical spine biomechanics in an experimental study incorporating Post-Mortem Human Subjects (PMHS), focusing on the influence of spinal level and loading rate.

METHODS

Cervical spine intervertebral disc segments were used to quantify the progressive change in compressive stiffness during repetitive loading. Cervical spines were obtained from fresh/frozen PMHS with mean age of 55±11 years and sectioned into C2/3, C4/5, and C6/7 motion segments. The posterior elements were then removed at the pedicle, resulting in intervertebral disc segments that consisted of adjacent vertebral bodies, the intervertebral disc, and the anterior and posterior longitudinal ligaments. The cranial and caudal aspects of the specimens were potted in polymethylmethacrylate (PMMA) to facilitate fixation to the loading apparatus.

Each specimen was subjected to five sets of 10,000 compression cycles (total 50,000 cycles) between 0 and 150 N using a sine wave function. All testing was conducted in a physiologic saline bath at 37 deg C to simulate in vivo conditions. Cyclic compressive loading was applied to the specimen using an electrohydraulic testing device (MTS Systems Corporation, Eden Prairie, MN). The protocol consisted of five consecutive sets of 10,000 cycles separated by an approximately 60-minute rest period between sets. Cyclic compression testing was conducted at either 2 or 4 Hz.

Axial force was measured at 100 Hz using a uniaxial load cell mounted to the piston of the electrohydraulic testing device. Piston displacement was measured at 100 Hz using a linear variable differential transducer (LVDT). Displacement of the piston was quantified for each 150-N cycle and slope of the force versus displacement trace was used to compute compressive stiffness. Stiffness magnitudes were then compared between spinal levels, cycles, and loading rates using multiple factor repeated measures Analysis of Variance (ANOVA). Pairwise comparisons were conducted for significant main effects using Bonferroni adjustment to account for multiple comparisons.

RESULTS

Twenty-one cervical spine intervertebral disc segments (8 C2/3, 6 C4/5, 7 C6/7) obtained from 12 PMHS were subjected to 50,000 cycles of compressive loading. Eleven specimens were tested at 2 Hz and 10 specimens were tested at 4 Hz. Stiffness progressively increased throughout the testing period, with consistent set-to-set behavior characterized by a sharp increase in stiffness during the first 1,000 cycles followed by a more gradual increase for the remaining

Copyright 2016 The Organizing Committee for the 2016 Summer Biomechanics, Bioengineering and Biotransport Conference

9,000 cycles of each set (Figures 1, 2). Multi-factor ANOVA revealed that compressive stiffness was significantly dependent upon loading rate ($p<0.0001$), cycle ($p<0.0001$), and spinal level ($p<0.0001$). Post hoc analysis revealed that each spinal level demonstrated significantly different stiffness profiles compared to every other spinal level ($p<0.001$). The C6/7 spinal level demonstrated the greatest stiffness and the C2/3 level generally demonstrated the lowest stiffness. Post hoc analysis of cycle-by-cycle stiffness demonstrated that stiffness magnitudes during the first 10,000 cycles were significantly different from all other sets ($p<0.01$) and that stiffness during the last 10,000 cycles was significantly different than the first 30,000 cycles ($p<0.05$). In general, stiffness values during the first set were lower than the subsequent sets.

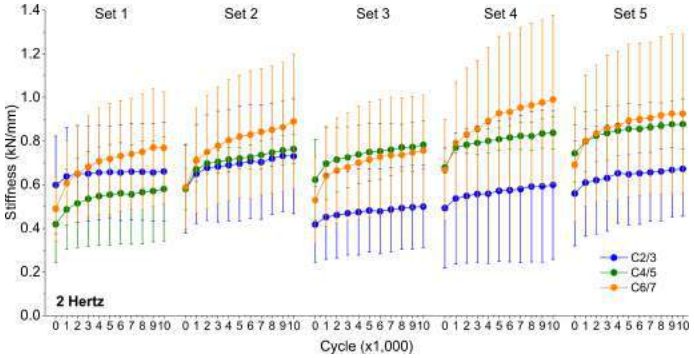

Figure 1: Compressive stiffness of intervertebral disc segments during 2 Hz repetitive loading.

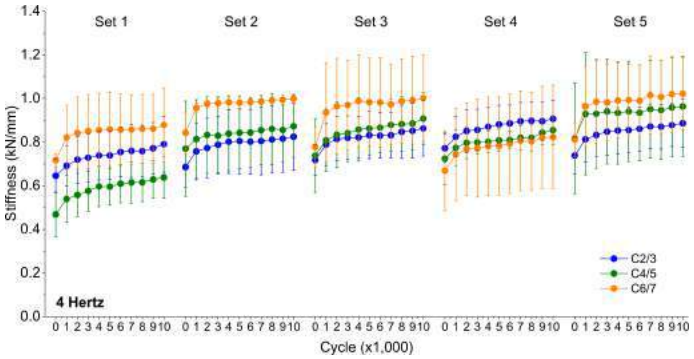

Figure 2: Compressive stiffness of intervertebral disc segments during 4 Hz repetitive loading.

The change in stiffness (N/mm/cycle) for each 10,000-cycle set was mathematically modeled using a bilinear approximation, with the first regression characterizing the slope of increasing stiffness for cycles 1 to 1,000 and the second regression characterizing the slope of increasing stiffness for cycles 1,001 to 10,000. ANOVA analysis demonstrated that the slope of stiffness change during the first 1,000 cycles was significantly dependent on spinal level ($p<0.05$) but not cyclic testing rate, with a greater increase in compressive stiffness occurring at the C6/7 spinal level than the other tested levels (Figure 3). However, the slope of stiffness change during the last 9,000 cycles was significantly dependent on both spinal level and cyclic testing rate (Figure 4). Statistically significant increases in stiffness for both spinal level and cyclic loading rate were driven primarily by the large increase in C6/7 stiffness during the last 9,000 cycles for the 2-Hz cyclic loading rate.

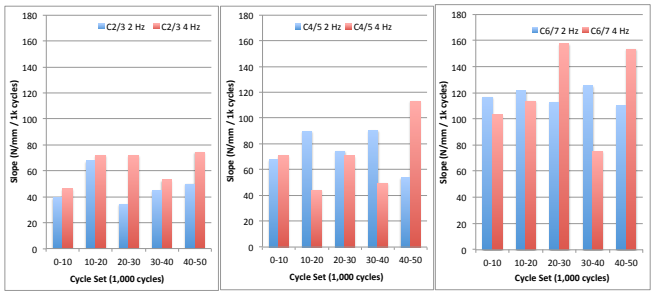

Figure 3: Slope of increasing stiffness during the first 1,000 cycles of each set of cyclic compressive loading.

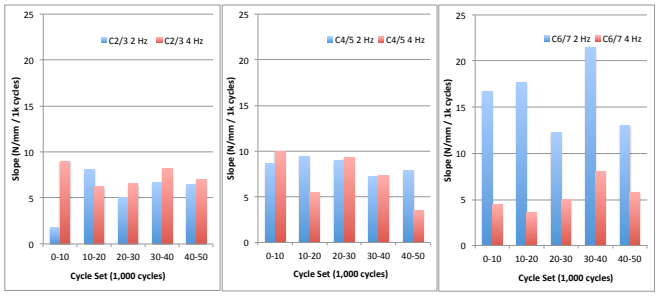

Figure 4: Slope of increasing stiffness during the last 9,000 cycles of each set of cyclic compressive loading.

DISCUSSION

Results of this study characterized the change in compressive stiffness of the cervical intervertebral disc during cyclic loading designed to mimic the types of inertial loading experienced in vibrational environments. Although testing was conducted below the threshold for injury, level-based differences may imply a greater likelihood for injury at the C6/7 level compared to other tested levels due to greater initial stiffness and a greater effect of cyclic loading evident by the increased slope of the regression fit over the last 9,000 cycles of each set. Increased propensity for lower cervical spine injury is consistent with studies quantifying injury in automotive environments [5] and may focus future analyses of exposure limits to vibrational environments. Another important factor not accounted for in this analysis may be an effect of gender, wherein prior studies have indicated significantly different mechanical response of spinal disc segments between men and women [6]. Given an increased combat role for females in the military, delineation of possible gender effects in fatigue response of the spine remains of focus of this ongoing research. Future research in this area will also focus on characterizing the effect of loading rate/duration and increased helmet mass on the fatigue response of the cervical spine intervertebral disc.

ACKNOWLEDGEMENTS

This work was supported by the U.S. Army Medical Research and Materiel Command Fort Detrick, Maryland (01026018, Contract No. W81XWH-13-1-0050), and the Department of Veterans Affairs Medical Research.

REFERENCES

[1] Ang, B et al., *Aviat Space Environ Med* 77(7): 713-19, 2006.
[2] Bovim, G et al. *Spine* 19(12): 1307-09, 1994.
[3] Hansson, TH et al., J Orthop Res 5: 479-87, 1987.
[4] Ordway, NR et al., J Orthop Res 30(4): 587-92, 2012.
[5] Yoganandan, N et al., J Clin Eng 15(6), 505-12.
[6] Stemper, BD et al., J Craniovert Jun Spine 1(1): 18-22.

SB^{3}C2016
Summer Biomechanics, Bioengineering and Biotransport Conference
June 29 –July 2, National Harbor, MD, USA
SB^{3}C2016-124

EFFECTIVE STIFFNESSES FOR THE HUMAN BUTTOCKS AND THIGH REGIONS OBTAINED THROUGH *IN VIVO* METHODS: APPLICATIONS TO MEDICAL SEATING

W. Pan (1), Z. Sadler (1), L. Nault (1) TR. Bush (1)

(1) Mechanical Engineering
Michigan State University
East Lansing, MI, USA

INTRODUCTION

Soft tissue mechanical properties are necessary for both human body modeling and devices that interact with people. In particular, the human gluteus and thigh regions are of great interest for the study sitting biomechanics which has applications in medical seating (wheelchair design), automotive safety, office chairs, and pressure ulcer studies [1], [2]. Many studies have evaluated tissue properties of the skin; muscle and bone separately through *in-vitro* methods [3], [4]. However, data that defines the tissue properties of the entire tissue system *in vivo* are not currently available. The goal of this study was to determine the soft tissue stiffness in the human gluteus and thigh regions. To accomplish this goal, we also developed a method that enables data collection and measurement of stiffnesses for these sensitive and difficult to test regions.

METHODS

A hand-held indenter was developed by attaching a 5 x 5 cm block system to a six-axis load cell (MC3A, AMTI, USA) (Fig 1 a). The indenter also had reflective markers attached so that the movement could be captured by a 3D motion capture system (Qualisys, USA) and deflection computed. Additional markers were attached to the participants' hips and knees so the body location in space could be obtained.

Since a focus of this work was for seating applications, it was necessary for the data to be gathered in a seated position. Other positions that may have been easier to test, such as lying in a prone position, would not obtain the same tissue tensions; in seating the pelvis and knees are rotated causing a tension that is not present in the prone position. Therefore, a custom chair was built to allow indentation tests to be performed while participants were seated (Fig 1 b,c,d). The seat pan included two removable boards allowing the indenter to reach different regions on the thigh from underneath. The chair was also elevated so that the motion cameras could capture data from the indenter while positioned under the chair.

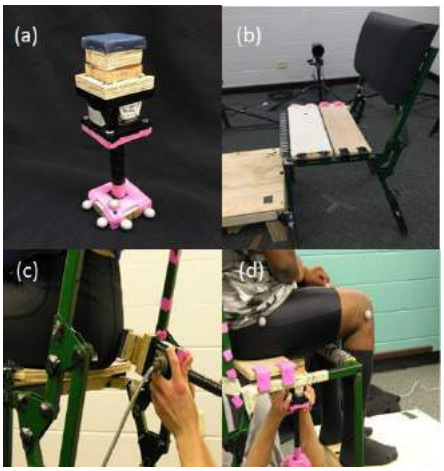

Figure 1: Tissue stiffness test set up: (a) indenter with load cell and motion capture markers (b) customized test chair with removable seat pan sections (c) testing on the lower gluteus (d) testing on the proximal thigh

Six different body regions on the right side were tested including: the top region of gluteus, lower gluteus, under the Ischial Tuberosity (IT), as well as proximal, middle and distal thigh (Fig. 2). The force was applied manually at a constant rate through the use of a metronome until a physiological barrier was felt and then it was

Copyright 2016 The Organizing Committee for the 2016 Summer Biomechanics, Bioengineering and Biotransport Conference

released. Each location was tested three times and a minimum of 5 mins between each trial was provided for tissue recovery.

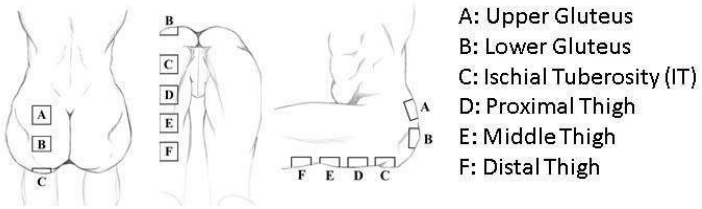

Figure 2 Six test regions on gluteus and thigh

Using the forces from the load cell, initial contact and maximum forces were identified; these corresponded to the initiation of deflection and maximum deflection. Since the motion and force data were synchronized, the indenter movement could be matched with the force data. Displacement for the thigh regions was calculated with respect to the vector between the hip and knee joints and gluteus displacement was with respect to the marker on the greater trochanter. These data were analyzed with a custom written MATLAB code.

RESULTS

Ten men and ten women were tested, however only the male data are presented and discussed here. The ten male participants had an average age of 20.9 yr (SD 1.7 yr), their average height was 170.5cm (SD 2.7 cm), and the average weight was 76.5kg (SD 3.6 kg).

The force-displacement relationships for all test participants for all three trials were then plotted together. Figure 2 shows an example of the stiffness plot for upper gluteus and middle thigh region. It can be seen that upper gluteus region is stiffer than the tissue in the middle thigh. This trend held true with the highest stiffness occurring along the back of the buttocks and the stiffness decreasing from the IT region to the distal thigh region.

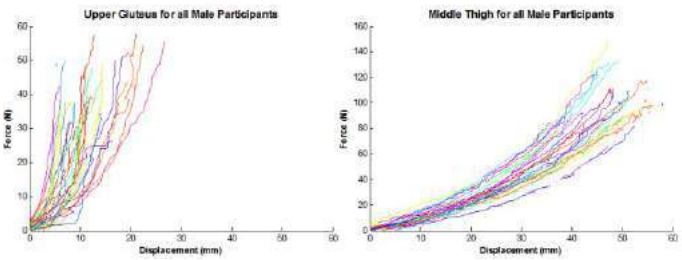

Figure 2: Tissue force-displacement data for the upper gluteus region (left) and the middle thigh region (right).

For seating, we are most concerned with the final deflections, as the tissues are fully loaded in this position. As a preliminary estimation of stiffness for the seated condition, we applied linear regression analysis to the last 1/3 of the stiffness data for all 6 regions for each of the test trials. These average stiffness results are listed in Table 1. Current work is being conducted to use strain energy and inverse Finite Element Methods to classify the entire curve for other applications.

Results indicate a clear trend that the tissues in the gluteus are stiffer than the tissue in the thigh region. The stiffness of the tissue in region D was slightly deviated from the trend, which was due to the testing region being in between a supporting bar of the chair and the front seat pan, causing the tissue to be in higher tension and present an increased stiffness.

Table 1: Average *in-vivo* tissue stiffness for human gluteus and thigh regions for the last one third of each force-deflection curve.

Region*	A	B	C	D	E	F
Average (N/mm)	7.45	7.145	6.65	7.37	4.16	3.09
SD (N/mm)	3.35	4.38	3.63	4.18	1.56	0.71

Note: region A—upper gluteus; B—lower gluteus; C—ischial tuberosity; D—proximal thigh; E—middle thigh; F—distal thigh

DISCUSSION

Human skin and muscle are a multi-layer material and exhibit complex material behavior. However, it is usually difficult to differentiate each layer's mechanical properties during *in vivo* testing. Thus, we have taken a systems approach by determining an effective stiffness that can represent the entire set of tissue.

The *in vivo* stiffness data collected for the human gluteus and thigh are extremely valuable for developing human body model and advancing the study of seating mechanics. These data will be used to develop a better understanding of how the tissue interacts with the seat cushion, and in turn lead to improved human body models and medical seating. In addition, these data will be beneficial for designing prosthetic limbs and sockets that have interface regions with material properties that are closer to actual human tissue material properties. Furthermore, these data could be used for establishing more accurate human tissue models for pressure ulcers research.

One potential limitation of this work is that the population of the test participants was generally young and active, so the obtained data represents this group. To better understand the tissue stiffness in across the general population, a more diverse participant group will be needed with variations in age and BMI.

Future reports will include results from the female participants and a population with higher BMI. Furthermore, inverse Finite Element Methods and strain energy approaches will be used to fully classify the entire force-deflection curve.

ACKNOWLEDGEMENTS

The authors would also like to thank Josh Drost, Racheal Geary, Kelly Patterson, Connor LaPres for their assistance in data collecting and processing.

REFERENCES

[1] A. Gefen, M. Megido-Ravid, M. Azariah, Y. Itzchak, and M. Arcan, "Integration of plantar soft tissue stiffness measurements in routine MRI of the diabetic foot," *Clin. Biomech.*, vol. 16, no. 10, pp. 921–925, 2001.

[2] H. V Tran, F. Charleux, M. Rachik, A. Ehrlacher, and M. C. Ho Ba Tho, "In vivo characterization of the mechanical properties of human skin derived from MRI and indentation techniques.," *Comput. Methods Biomech. Biomed. Engin.*, vol. 10, no. 6, pp. 401–407, 2007.

[3] J. W. Y. Jor, M. P. Nash, P. M. F. Nielsen, and P. J. Hunter, "Estimating material parameters of a structurally based constitutive relation for skin mechanics.," *Biomech. Model. Mechanobiol.*, vol. 10, no. 5, pp. 767–78, 2011.

[4] M. Geerligs, L. van Breemen, G. Peters, P. Ackermans, F. Baaijens, and C. Oomens, "In vitro indentation to determine the mechanical properties of epidermis.," *J. Biomech.*, vol. 44, no. 6, pp. 1176–1181, Apr. 2011.

Copyright 2016 The Organizing Committee for the 2016 Summer Biomechanics, Bioengineering and Biotransport Conference

SB³C2016
Summer Biomechanics, Bioengineering and Biotransport Conference
June 29 –July 2, National Harbor, MD, USA
SB³C2016-126

COMPARISON OF CEREBRAL ANEURYSM FLOW FIELDS OBTAINED FROM CFD AND DSA

Juan R. Cebral (1), BongJae Chung (1), Fernando Mut (1), Fred van Nijnatten (2), Danny Ruijters (2)

(1) Bioengineering Department
George Mason University
Fairfax, Virginia, USA

(2) IGT Innovation
Philips Healthcare
Best, Netherlands

INTRODUCTION

Quantifying the flow dynamics in cerebral aneurysms is important to understand the mechanisms responsible for aneurysm progression and rupture and develop improved aneurysm risk assessment procedures (diagnosis) as well as for understanding and evaluating endovascular interventions such as flow diversion (treatment).

Many studies have used computational fluid dynamics (CFD) to model the flow in cerebral aneurysms to study rupture as well as flow diversion treatments. On the other hand, attempts at measuring the *in vivo* flow fields have been made with phase-contrast magnetic resonance as well as dynamic angiographic velocimetry [1]. The latter technique is attractive because it can be used during the angiographic evaluation of the aneurysm or during its endovascular treatment.

Previous studies have shown the potential clinical value of the angiography-based flow quantification and have compared the results to Doppler ultrasound and synthetic angiograms generated from CFD simulations [2, 3]. The purpose of our study was to further evaluate the angiography-based flow field quantification by comparing against patient-specific CFD models with angiographic aneurysm patient data.

METHODS

A total of 15 cerebral aneurysms imaged with 3D rotational angiography (3DRA) and 2D digital subtraction angiography (DSA) at 60 frames per second were studied. The DSA images were acquired from two different viewpoints trying to minimize the overlap between the aneurysm and the surrounding vessels. In two patients only a single view was acquired (total 28 views for all 15 patients).

Two dimensional flow fields in the aneurysm and connected vessels were reconstructed from the corresponding DSA images using a previously developed optical flow technique [1]. The mean aneurysm flow amplitude (MAFA) was calculated from the DSA images in the aneurysm region as in previous studies [4].

Patient-specific CFD models were constructed from the 3DRA images and ran with pulsatile flow conditions derived from DSA-based flow measurements in the parent artery. The mean aneurysm flow velocity (VEL) was computed as the spatial average of the CFD velocity magnitude over the aneurysm region and over time.

Since the DSA and 3DRA images were acquired relative to the same reference frame, the CFD flow fields were projected to the same views used in the DSA acquisitions. Both the DSA and CFD flow fields were averaged over the cardiac cycle, and the CFD flow fields were further averaged along the line of sight. The DSA and CFD flow fields were then compared visually by plotting streamlines in the projected 2D images, and quantitatively using a similarity measure defined as:

$$s = \frac{1}{N} \sum_{i \in ROI} \boldsymbol{a}_i \cdot \boldsymbol{b}_i / (|\boldsymbol{a}_i||\boldsymbol{b}_i|) \qquad (1)$$

where $\boldsymbol{a}_i$ and $\boldsymbol{b}_i$ are the velocity vectors in the two flow fields, ROI the region of interest, N the number of pixels in ROI, and the . operator denotes the dot product. This quantity measures the similarity of the directions of the two vector fields. A similarity of 1 means a perfect match, random input would yield 0, and opposing fields would give -1.

RESULTS

The average similarity of all DSA and CFD flow fields was s=0.66. Restricting the comparison to the vessel (i.e. excluding the aneurysm region) resulted in an average similarity of s=0.78. Considering only the aneurysm regions, the average similarity was s=0.37.

In 8/15 patients (53%) there was at least one view in which the CFD and DSA flow fields agreed with a similarity s>0.5. Four examples

Copyright 2016 The Organizing Committee for the 2016 Summer Biomechanics, Bioengineering and Biotransport Conference

are shown in Fig. 1. In these cases, the main intra-aneurysmal vortex structures are seen in both fields.

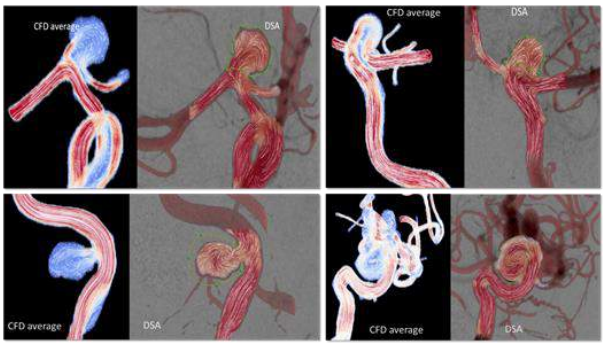

Fig. 1: Average CFD and DSA flow fields in good agreement.

An important issue affecting the results of the DSA flow quantification is overlap between the aneurysm and surrounding vessels. Two examples are shown in Fig.2. In the first case (top), the overlap is emphasized by computing the maximum intensity projection (MIP) along the line of sight (left most picture), and can be seen to affect both the projected CFD and the DSA flow fields. In the second case (bottom), the aneurysm wraps around the parent vessel making it impossible to find a view without vessel overlap. Nevertheless, the main vortex structure inside this aneurysm is well captured by the DSA flow.

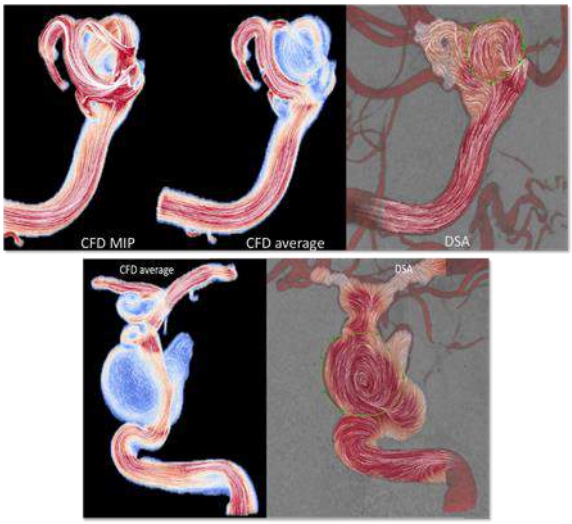

Fig. 2: CFD and DSA flow fields in cases with overlapping vessels.

In 7/15 patients (47%) the DSA and CFD flows did not agree (s<0.5). Some of these disagreements were due to vessel overlaps as explained before, but in other cases a "sink" effect was observed in the DSA field where the flow is directed towards the center of the vortex instead of around it. Two examples of are presented in Fig.3. In the first case (top), it can be seen that within the aneurysm the DSA flow points radially towards the center of the vortex seen in the CFD flow. In the second case (bottom), the DSA flow seems to go over the vortex center seen in the CFD field. This effect could be due to under sampling in the DSA quantification. This may happen when the time interval between DSA images is comparable to the time it takes for a particle to travel around the vortex core. For example a particle that is initially seen at the aneurysm inflow would be seen in the next frame close to the exit, and thus the trajectory would look like those of the bottom case of Fig. 3. It may also occur when the cardiac wave length is large compared to the aneurysm perimeter.

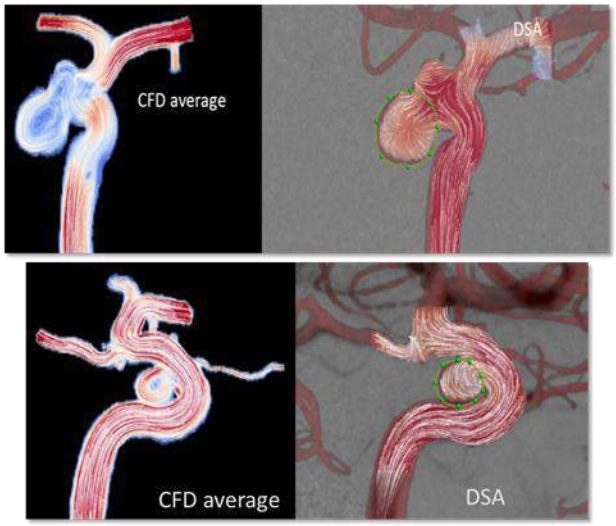

Fig. 3: Cases where a "sink" effect can be seen in the DSA flow.

The mean aneurysm velocity (VEL) and MAFA values are compared in Fig. 4 (left). After discarding views with significant vessel overlaps (red dots) regression analysis shows a linear correlation between VEL and MAFA (R=0.80, p<0.0001). However, the relative difference between VEL and MAFA increases with VEL (fig. 4, right) which is consistent with the notion of under sampling for a fixed frame rate when the aneurysm velocity increases.

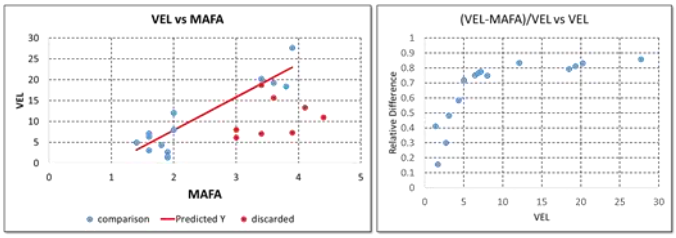

Fig. 4: Relation between MAFA and mean aneurysm velocity (left), and relative difference (right).

DISCUSSION

In general there was good agreement between DSA and CFD flow fields. In the aneurysm, where the flow can be quite complex the agreement was not as good as in the vessel. In some cases a "sink" effect was observed that could be due to under sampling. Further study is necessary to understand this effect. Vessel overlap has a strong influence on DSA flow results and should be avoided, however sometimes it is not possible to find views without overlapping vessels.

The MAFA value previously defined seems to be linearly correlated with the mean aneurysm velocity, which suggests that it could be a good parameter to evaluate aneurysms or treatments. However, the difference between the MAFA and the mean aneurysm velocity increases with the velocity. Increasing the framerate of the DSA measurements could improve both the agreement of the MAFA with the mean aneurysm velocity and resolve the "sink" effect.

ACKNOLEDGEMENTS

We thank Philips Health care for financial support.

REFERENCES

[1] Bonnefous, O et al. *Med Phys,* 39(10): 6264-75, 2012.
[2] Brina, O et al. *Am J Neuroradiol,* 35(12): 2348-53, 2014.
[3] Pereira, VM et al., *Am J Neuroradiol,* 35(1): 156-63, 2014.
[4] Pereira, VM et al. *Am J Neuroradiol,* 34(4): 808-15, 2013.

Copyright 2016 The Organizing Committee for the 2016 Summer Biomechanics, Bioengineering and Biotransport Conference

SB^{3}C2016
Summer Biomechanics, Bioengineering and Biotransport Conference
June 29 –July 2, National Harbor,MD, USA
SB^{3}C2016-127

A PROBABILISTIC FINITE ELEMENT ANALYSIS OF THE ANNULUS FIBROSUS ELASTIC PROPERTIES INFLUENCE ON THE BEHAVIOR OF THE HUMAN L4-L5 AND L5-S1 SEGMENTS

H. E. Jaramillo (1), J. J. García (2)

(1) Departamento de Energética y Mecánica
Universidad Autónoma de Occidente
Cali, Valle, Colombia

(2) Escuela de Ingeniería Civil y Geomática
Universidad del Valle
Cali, Valle, Colombia

INTRODUCTION

The uncertainty in loads, geometry and material properties is present in the biomechanics of the spine. However, few probabilistic analysis [1–5] have been performed to obtain a more accurate estimate of the influence of such uncertainties in the mechanical response of the spine [6,7]. Considering that there may be substantial variations of the mechanical properties of biological tissues among individuals, this paper presents probabilistic finite element (FE) analyses intended to assess the effects of the variations of the elastic constants of the annulus fibrosus (AF) on the biomechanics of the lumbar spine. In particular, the range of motion (ROM) of the L4-L5 and L5-S1 segments loaded under flexion, extension, lateral bending and axial rotation was analyzed for different combinations of the elastic properties of the AF.

METHODS

We extracted the geometries of the L4-L5 and L5-S1 AFs from a realistic FE model [8]. To take into account the high stiffness of the vertebrae with respect to that of the AF, the endplates were considered to be rigid. The AF was represented as a homogeneous hyperelastic matrix reinforced with two families of fibers [9,10] oriented at ±30° [11–13] with respect to the transverse plane. Consistent with previous studies, a Yeoh energy function W_m was used for the matrix while a the hyperelastic function W_f was used for the fibers, as follows,

$$W_m = c_1(I_1 - 3) + c_2(I_1 - 3)^2 + c_3(I_1 - 3)^3 \quad (1)$$

$$\mathrm{W_f} = \frac{\mathrm{a_1}}{\mathrm{a_2}}\left[\mathrm{e}^{\mathrm{a_2}(\mathrm{I_4}-1)^2} + \mathrm{e}^{\mathrm{a_2}(\mathrm{I_6}-1)^2}\right], \quad (2)$$

where c_1, c_2, c_3, a_1 and a_2 are material constants; I_1 is the first invariant of the deviatoric Green deformation tensor, and I_4 and I_6 are the deviatoric invariants associated with the two families of fibers. A subroutine Uanisohyper of the program Abaqus 6.14.2 (Dassault Systemes SA, USA) was developed to implement the Equations (1) and (2). A set of 100 combinations of constants a_1 (mean=0.23 MPa, DS=0.15) and a_2 (mean=7.44 MPa, DS=7.5) was determined randomly using Excel (Microsoft, USA) according to a normal distribution and experimental measurements accomplished by Cortes et al. [14]. The constants c_1, c_2, and c_3 were equal to 0.035 MPa, 0.00065 MPa and 0.00045 MPa, respectively [8].

For each AF, the caudal endplate was fully restricted while a pure moment ramped from 0 to 8 N-m was applied to the cranial endplate in each of flexion, extension, lateral bending, and axial rotation movements. A convergence analysis was performed to develop a final mesh of 9472 eight-node hybrid hexahedral elements (C3D8H).

The ROM was selected as the output variable and compared with experimental data. The ROM was plotted as a function of a_1 and a_2 and various surface equations were fit to the response using a nonlinear least squares algorithm. The cumulative probability and the probability density functions were obtained using Origin 8.5 software (Northampton, UK). The ROM sensitivity to each of the input random variables (a_1, a_2) was calculated according to the equation proposed by Thacker et al. [5]. The coefficient of variation (CV) for the ROM was calculated in order to obtain a measure of data dispersion.

RESULTS

The ROM dispersion (Fig. 1) for the segment L4-L5 was greater in axial rotation (CV=14.6%) and extension (CV=12.6%) followed by lateral flexion (CV=8.7%) and flexion (CV=6.3%). For the L5-S1 segment (Fig. 2) the greater dispersion was observed in axial rotation (CV=14.0%), followed by lateral flexion (CV=11.5%), extension (CV=10.6%) and flexion (CV=5.6%). The percentages of points within the experimental range for the L4-L5 disc were 100%, 50%, 48.3%, and 25.7% in flexion, lateral flexion, extension, and axial rotation, respectively. For the L5-S1 disc, these percentages were

Copyright 2016 The Organizing Committee for the 2016 Summer Biomechanics, Bioengineering and Biotransport Conference

95.9%, 94.2%, 38.0%, and 15.8% in flexion, axial rotation, lateral flexion, and extension.

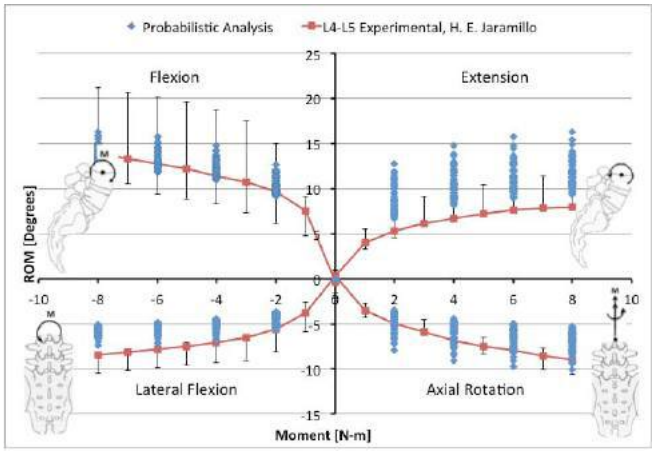

Figure 1: Results of parametric analyses for the L4-L5 disc compared with experimental ROM

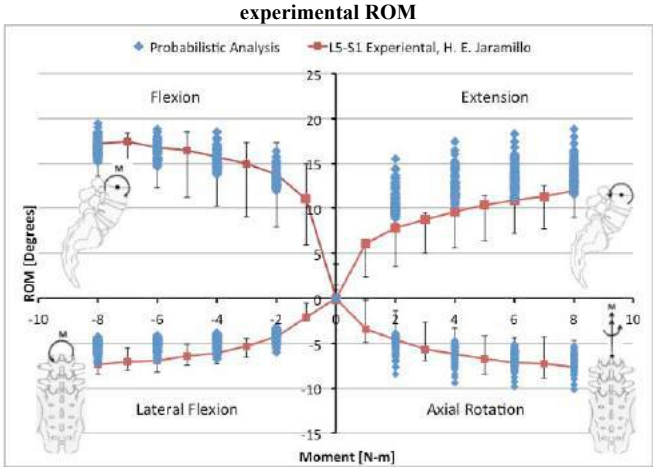

Figure 2: Results of parametric analyses for the L5-S1 disc compared with experimental ROM

The ROM response surfaces for the two segments were similar. The Equation (3) provided the best fit to the computational points:

$$\mathrm{ROM} = \mathrm{Zo} + \mathrm{Be}^{\left[-\frac{a_1}{C}-\frac{a_2}{D}\right]}, \quad (3)$$

where Zo, B and C are constants obtained during the fitting procedure. These constants were between 5% and 31% higher for the L5-S1 segment than the L4-L5 segment, while D showed an opposite trend in extension, lateral flexion and axial rotation (Table 1). From this fitting process, the averages of coefficients of determination (R^2) were 0.974 for the L4-L5 disc and 0.966 for the L5-S1 disc.

Table 1: Constants of Equation (3) that fit the computational response (M=8 N-m)

	Movement	Z_0 [Deg.]	B [Deg.]	C [MPa]	D	Chi-Square	R^2
L4-L5 Disc	Flexion	11.6	7.2	0.45	17.5	0.015	0.980
	Extension	8.4	12.6	0.42	16.0	0.043	0.980
	Lateral Flexion	4.7	4.5	0.43	15.4	0.005	0.979
	Axial Rotation	4.5	8.7	0.48	16.1	0.045	0.955
L5-S1 Disc	Flexion	13.9	8.6	0.59	19.6	0.023	0.975
	Extension	10.2	13.6	0.54	15.5	0.050	0.977
	Lateral flexion	3.6	5.3	0.58	17.1	0.024	0.935
	Axial Rotation	4.6	9.1	0.53	14.4	0.021	0.978

The ROM was about 26 and 38 times more sensitive to a_1 than to a_2. In their order, the ROM was more sensitive to the input variables in extension, flexion, axial rotation and lateral bending. The ROM probability density function analyzed at 8 N-m showed that the L5-S1 ROM has a higher probability to be lower in lateral flexion and higher in flexion, extension and axial rotation, with respect to the L4-L5 ROM.

DISCUSSION

The high level of uncertainty of the mechanical properties of the AF produced a significant dispersion in the biomechanical response, which cannot be fully described with a deterministic model [4].The proposed analytical surface showed an excellent fit (R^2=0.98) to the probabilistic ROM points. Hence, the equations of these surfaces may be used to expedite the calibration process of the AF of FE lumbar models.

A relatively high percentage of the theoretical ROM points (97.9% in flexion, 32.0% in extension, 44.0% in lateral flexion and 59.9% in axial rotation) were within the experimental ranges. This suggests that the values of a_1 and a_2 reported by Cortes et al. [14], which were used as a point of departure to select the set of input data, are reliable to be used in probabilistic analysis and in the calibration of the AF properties. Higher differences in some movements with respect to the experimental data may have been due to the adopted homogeneous properties, as other studies have documented [14–18] that elastic constants variations in the circumferential and radial directions may have more effect in some movements than others. Further analyses should be accomplished to address this issue.

Some FE models [12, 19, 20] include the AF properties without performing a calibration using experimental data. As the AF is one of the main elements to support spine loads, the calibration of its properties should be the first step during the validation of a spine segment model. A bad calibration of the AF can generate overload in other elements of the segment such as the ligaments and facet joints. The sensitivity analysis suggests that a_1, which is the constant that defines the initial slope of the stress-strain curve for the fibers, should be calibrated before a_2. With respect to the movements, it is indicated to calibrate flexion first, followed by extension, lateral bending and axial rotation.

ACKNOWLEDGEMENTS

The authors appreciate the support of the Universidad del Valle and Universidad Autónoma de Occidente (Cali-Colombia).

REFERENCES

[1] Spilker, R. L. et al., *J. Biomech. Eng.,* 108:1–11, 1986.
[2] Fagan, M. J. et al., *Proc. Inst. Mech. Eng*., 216: 299–314, 2002.
[3] Malandrino, A. *J., Biomech.,* 42: 2780–2788, 2009.
[4] Niemeyer, F. et al., *J. Biomech.,* 45: 1414–1423, 2012.
[5] Thacker, B. et al., *Abaqus*., 1: 1–12, 2013.
[6] Madsen, H. O., et al., USA. Dover Publications Inc., 1986.
[7] Laz P. J. et al., *Proc. Inst. Mech. Eng. [H]*., 224: 927–943, 2010.
[8] Jaramillo, H. E. et al., *ACTA Bioeng. Biomech.,* 17, 2, 2015.
[9] Ayturk, U. M. et al., *J. Biomech. Eng.,* 132: 61007–61007, 2010.
[10] O'Connell, G. D. et al., *J. Biomech. Eng.,* 131:111007, 2009.
[11] Lodygowski, T. et al., *Acta Bioeng. Biomech.,* 7: 29–37, 2005.
[12] Dreischarf, M. et al., *J. Biomech.,* 47: 1757–1766, 2014.
[13] Shin, D. S. et al., *Comput.-Aided Des.,* 39: 559–567, 2007.
[14] Cortes, D. H. et al., *J. Orthop. Res.*, p. n/a–n/a, 2013.
[15] Green, T. P. et al., *Eur. Spine J.,* 2: 209–214, 1993.
[16] Malgorzata, Z. et al., *Acta Bioeng. Biomech.,* 15: 51–59, 2013.
[17] Fujita, Y. et al., *J. Orthop. Res.,* 15: 814–819, 1997.
[18] Cortes, D. H. et al., *Bi. Model. Mechanobiol.,* 11: 781–790, 2012.
[19] Prendergast, P., *Clin. Biomech.,* 12:343–366, 1997.
[20] Guan, Y. et al., *Med. Biol. Eng. Comput.,* 44: 633–641, 2006.

Copyright 2016 The Organizing Committee for the 2016 Summer Biomechanics, Bioengineering and Biotransport Conference

SB^{3}C2016
Summer Biomechanics, Bioengineering and Biotransport Conference
June 29 –July 2, National Harbor, MD, USA
SB^{3}C2016-128

ALTERED MECHANICS OF SUPRASPINATUS TENDONS FROM ELASTIN-DEFICIENT GENETICALLY-MODIFIED MICE

Fei Fang (1), Gabriela Espinosa (2), Lindsey Kahan (2), Robert P. Mecham (3), Spencer P. Lake (1, 2, 4)

(1) Department of Mechanical Engineering & Materials Science
(2) Department of Biomedical Engineering
(3) Department of Cell Biology & Physiology
(4) Department of Orthopaedic Surgery
Washington University in St. Louis
St. Louis

INTRODUCTION

Elastic fibers, composed primarily of elastin and fibrillin-rich microfibrils, impart important mechanical properties (i.e., elastic recoiling, energy storing) to skin, vasculature, and lung tissue [1]. With high elastin content (58-75% of dry weight) in arteries and skin, decreased mechanical integrity results from degeneration and disease that disrupt elastic fibers in these tissues [2]. Although connective tissues such as intervertebral disc and ligament have much fewer elastic fibers, reduced mechanical strength has been attributed to depletion of elastic fibers [3, 4]. Tendons also contain small amounts of elastic fibers, but an understanding of their contribution to tendon mechanical behavior is lacking. The aim of this study was to measure the uniaxial tensile mechanics of supraspinatus tendons (SSTs) from unaffected (*Eln*+/+, WT), elastin haploinsufficient (*Eln*+/-, HET), and elastin knockout mice with a bacterial artificial chromosome (BAC) encoded human elastin gene (*Eln*-/-, hBAC-KO) [5, 6]. SSTs function in a complex loading environment, are often torn, and are difficult to repair, thus motivating efforts to understand how tissue properties relate to mechanical function. Histological, biochemical, immunostaining, and ultrastructural analysis of SSTs were also performed to provide structural and compositional data to further investigate structure-function relationships and the role of elastin in tendon mechanics.

METHODS

Biomechanical testing. Humerus-SST complexes were dissected from 3-month-old WT (n=6), HET (n=8), and hBAC-KO (n=10) C57BL6 male mice. A non-contact laser scanning system was used to measure cross-sectional area (CSA). Samples were placed in custom clamps, submerged in a PBS bath, and mounted onto a tensile testing machine [7]. After applying a 0.1 N pre-load, samples were loaded in uniaxial tension at 0.5-0.75%/sec until failure. Camera images were collected for strain calculation.

Biochemical analysis. After mechanical testing, tendons were separated from the humerus and pooled into groups of three by genotype for biochemical analysis. Similar to previous studies [8], a ninhydrin-based assay and nonequilibrium competitive enzyme-linked immunosorbent assay were used to determine quantities of total protein and desmosine, a marker of elastin. Elastin amounts were converted from desmosine and normalized by total protein.

Histology, immunostaining, and transmission electron microscopy (TEM). For histological analysis, each humerus-SST complex was fixed in 10% neutral buffered formalin and decalcified in 14% EDTA. Samples were then dehydrated with 70% ethanol, embedded in paraffin, sectioned at 5 μm, and stained with hematoxylin and eosin (H&E), Verhoeff-Van Gieson (VVG), and picrosirius red. Elastin distribution was also visualized by immunostaining. Fresh-frozen sections of SST from each genotype were cut at 5 μm on a cryostat. Sections were fixed with cold methanol and treated with hyaluronidase to improve immunodetection of elastin. Sections were blocked with 1% fish gelatin, then incubated with primary [9] and secondary antibodies. After washing, sections were mounted with DAPI aqueous medium. TEM analysis was also conducted to examine the distribution of elastic and collagen fibers on the nanoscale. The tendon midsubstance was cut from the humerus, fixed in 0.1M sodium cacodylate, post-fixed in 1.25% osmium tetroxide, dehydrated in alcohol, and embedded in Poly/Bed® 812 resin. Samples were cut in transverse and longitudinal orientations at 90 nm and stained with uranyl acetate and lead citrate.

Data Analysis. The minimum CSA along the tendon length was selected for computing stress and modulus. Linear modulus was computed from the linear region of stress-strain curve. Maximum force and stress were calculated as the loading point at failure. Engineering strains were calculated by tracking marks on tendon surface with a custom MATLAB program. All data are presented as mean±standard deviation. Comparisons across genotypes of different parameters (i.e.,

Copyright 2016 The Organizing Committee for the 2016 Summer Biomechanics, Bioengineering and Biotransport Conference

CSA, maximum stress, linear modulus, elastin content) were performed with one-way ANOVA and Bonferroni post-hoc tests. Significance was defined as $p<0.05$.

RESULTS

Maximum stresses (Fig. 1A), linear modulus (Fig. 1B), stiffness (Fig. 2A), and CSA (not shown) of SSTs were statistically different by genotype, with decreased values from WT to HET to hBAC-KO. While collagen content was similar among different genotypes (not shown), elastin content in HET was 42.7% less than WT, and, surprisingly, hBAC-KO had 200% of elastin in WT (Fig. 2B).

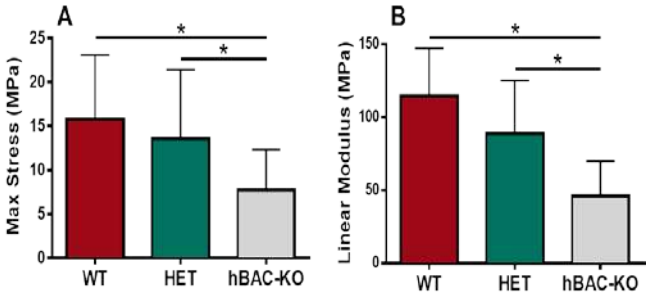

Fig. 1. Maximum stress (A) and linear modulus (B) were statistically different across genotype, with significantly smaller values in hBAC-KO mice. *$p<0.05$.

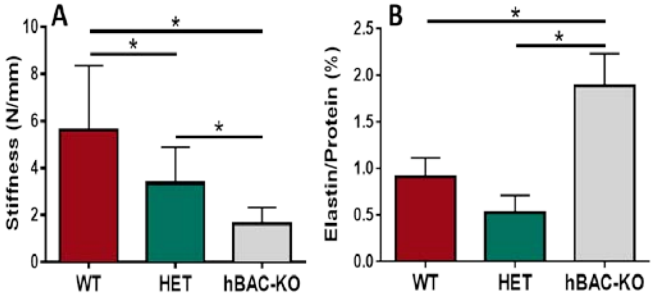

Fig. 2. Stiffness (A) and elastin content (B) for tendons from each genotype (mean ± standard deviation). *$p<0.05$.

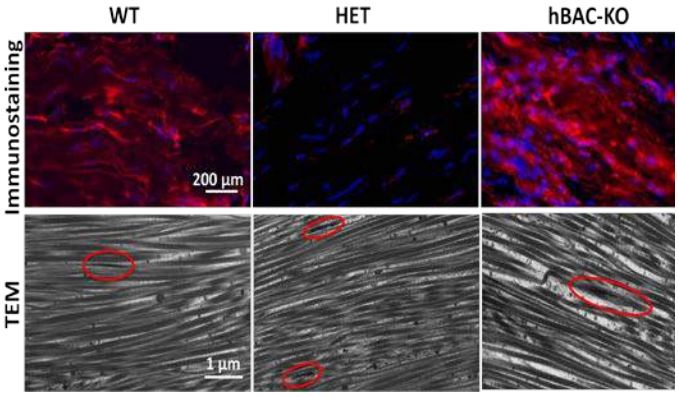

Fig. 3. Immunostaining images (top) show elastin (red) and nuclei (blue) in tendon sections. TEM micrographs (bottom) show elastin (denoted by red ellipses) in longitudinal sections of each genotype.

Consistent with the biochemical data, immunostaining images showed moderate levels of elastin in WT tendons, much less staining in HET, and dramatically increased elastin in hBAC-KO (Fig. 3). VVG staining provided additional evidence of increased elastin in hBAC-KO tendons (not shown). Elastic fibers were aligned along collagen fibrils in TEM micrographs, and no obvious structural differences were observed in different genotypes (Fig. 3). H&E staining showed fairly consistent collagen structure and cellularity between genotypes (not shown). Collagen crimp pattern shown by picrosirius red staining varied across the entire tendon and even among different tendons of the same genotype.

DISCUSSION

This study demonstrates that elastin, even in relatively small quantities, contributes to the mechanical properties of tendon, which is consistent with previous studies that showed decreased stress under both transverse tensile and shear loading for elastase-treated ligaments [3,4,11]. Elastin, and corresponding elastic fibers, may help to support load, facilitate stress/strain transfer among collagen fibers, and/or maintain the mechanical integrity of tendon [10] Compared to WT, HET tendons followed the pattern that inferior mechanics correspond to less elastin in a dose-dependent manner. However, hBAC-KO tendons exhibited larger elastin quantities yet smallest maximum stress and linear modulus values, which conflicts with this concept. Results for hBAC-KO may be due to improper assembly of elastic fibers encoded by the human elastin gene, such that these elastic fibers are not involved in supporting force during loading; this hypothesis needs further evaluation by differentiating human and mouse elastin-gene encoded elastic fibers. Contrary to results of the current study, arterial walls from both HET and hBAC-KO mice were stiffer than those of WT mice in a previous study [6]. These differences may be due to very different relative amounts and distributions of elastin and collagen in vessels compared to tendon. The mechanics of elastin-deficient vessels are defined by the stiffer collagen network, while elastin depletion in tendon may limit force transfer along collagen, thereby weakening the mechanical response. Compared to elastin depletion via elastase [3,4,11], gene-modified animal models with protein reductions could be a better approach to examine the role of elastin, since elastase has been reported to change tissue structure and other components [11]. The animal models used in this study can isolate the effect of elastin-deficiency on tendon mechanics separate from that of other tissue constituents, however compensatory mechanisms in genetically manipulated models are always a possibility. These results suggest that elastin, as part of properly-formed elastic fibers, provides mechanical strength in a disproportionate degree relative to its small quantity in tendon, further improving the understanding of tendon composition-function relationships.

ACKNOWLEDGEMENTS

We thank Qi Wu and Ivan Stoilov for their contribution to biomechanical testing and biochemical analysis, respectively. We also thank Dr. Jessica Wagenseil for providing mice.

REFERENCES

1. Wagenseil, JE et al., *Birth Defects Res C Embryo Today*, 81:229-240, 2007. **2**. Kielty, CM et al., *Expert Rev Mol Med*, 8:1-23, 2006. **3**. Henninger, HB et al., *J Orthop Res*, 31:1226-1233, 2013. **4**. Smith, LJ et al., *Ann Biomed Eng*, 36:214-223. **5**. Li, DY et al., *J Clin Invest*, 102:1883-1787, 1998. **6**. Hirano, E et al., *Circ Res*, 101:523-531, 2007. **7**. Skelley, NW et al., *Am J Sports Med*, 2015. **8**. Watanabe, T et al., *Tokai J Exp Clin Med*, 14:347-356, 1989. **9**. Kozel, BA et al., *J Biol Chem*, 278:18491-18498, 2003. **10**. Henninger, HB et al., *Acta Biomater*, 25:304-312, 2015. **11**. Grant, TM et al., *Ann Biomed Eng*, 1-10, 2015.

Copyright 2016 The Organizing Committee for the 2016 Summer Biomechanics, Bioengineering and Biotransport Conference

SB^{3}C2016
Summer Biomechanics, Bioengineering and Biotransport Conference
June 29 –July 2, National Harbor, MD, USA
SB^{3}C2016-129

AQUEOUS HUMOR FLOW IN THE POSTERIOR CHAMBER OF THE EYE WITH IRIDOTOMY

Mariia Dvoriashyna (1), Rodolfo Repetto (1), Jennifer H. Tweedy (2)

(1) Department of Civil, Environmental and Chemical Engineering
University of Genoa
Genoa, Italy

(2) Department of Bioengineering
Imperial College London
London, UK
(this author formerly published under the surname Siggers)

INTRODUCTION

Iridotomy is a procedure in which a hole is surgically created in the iris to allow aqueous humour to flow from the posterior to the anterior chamber. It is done in cases in which there is a concern that this flow might otherwise not occur freely (e.g. pupillary block). The problem of the choice of the optimal size and location of an iridotomy is still poorly understood. In the biomechanical literature there are a number of works about aqueous flow, however very few consider the effect of iridotomy. Fleck [1] proposed a basic mathematical model of aqueous flow through an iridotomy in the case pupillary block, using Poiseuille formula to calculate the pressure drop across the iridotomy hole. Silver and Quigley [2] studied aqueous flow in the iris-lens channel driven by aqueous production in the ciliary body and they also considered the presence of an iridotomy.

We extend these works and study aqueous flow in the posterior chamber of the eye due to aqueous production and miosis (e.g. pupil contraction). We also consider the cases of partial and complete pupillary block. We develop and solve a mathematical model of the fluid dynamics of an iridotomy, and use it to comment on the effect of the location and size of the hole and investigate the pressure and stress on the surrounding tissues, which we show are usually within safe levels. We propose a mathematical theory, which allows us to solve the problem semi-analytically. This gives us insight into the pressure difference between anterior and posterior chambers and allows us to predict conditions that can lead to angle closure glaucoma. During miosis our results indicate there could be a strong jet through the hole, which could, in turn, damage the cornea.

METHODS

Since the posterior chamber is long and thin, we use lubrication theory to simplify the Navier-Stokes equations and assume miosis can be modeled as quasi-steady. This implies that we keep the domain fixed and impose a given velocity distribution $\boldsymbol{v}$ on the iris.

We work in spherical coordinates (r, θ, φ) and denote by R the radius of the lens and $h(\theta)$ height of the posterior chamber. Then, the simplified equation for the pressure is

$$\frac{1}{12\mu}\nabla_h \cdot (h^3 \nabla_h p) = v_r + \\ + \frac{h}{2(R+h)}\nabla_h \cdot \left((R+h)\mathbf{v_h}\right) - \frac{1}{2}\nabla_h h \cdot \mathbf{v_h}, \qquad (1)$$

where μ is dynamic viscosity, v_r is r component of the velocity of the iris, p is independent of r and 'h' is a subscript indicating that only the (θ, φ) components are considered with $r = R + h$ fixed.

We assume that the volumetric flux through the iridotomy hole is proportional to the pressure drop across the hole and compute it using Dagan's formula [3]. The iridotomy is modeled as a point sink, thus, in order to avoid singularity of the pressure there, we work in terms of a suitably regularised pressure, which is defined as follows

$$p_{\text{reg}} = p - \frac{6\mu Q}{\pi h_i^3} ln \frac{\tan\left(\frac{\theta'}{2}\right)}{\tan\left(\frac{\theta_d}{2}\right)}, \qquad (2)$$

where Q is volumetric flux through the iridotomy, h_i is a height of the posterior chamber at the point of the iridotomy, θ' is a distance in θ component from the point of the hole, θ_d is radius of the iridotomy divided by R.

Therefore, equation (1) has to be solved for the unknown regularized pressure (2) and for the flux through the iridotomy Q. The solution is obtained using a second order finite difference scheme and realistic shapes of the posterior chamber, which are inferred from

Copyright 2016 The Organizing Committee for the 2016 Summer Biomechanics, Bioengineering and Biotransport Conference

ultrasound scan images. The resulting linear system is solved with modified reduction method.

RESULTS

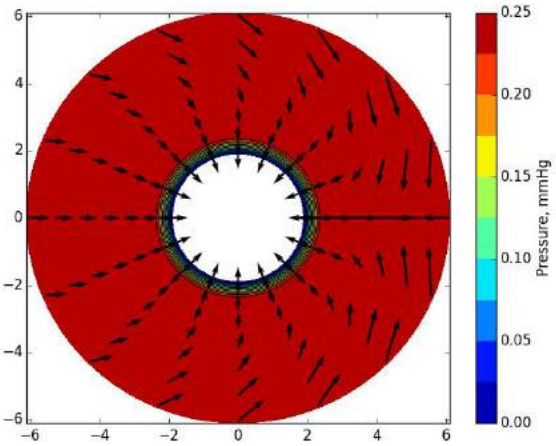

Figure 1: Predicted flow in posterior chamber from ciliary body (outer boundary) to pupil (central hole) showing calculated pressure (colorbar) and depth-averaged velocity vectors (arrows). The iridotomy has diameter 50 μm and is located at a distance of 5 mm to the right of the pupil. 29% of the total volumetric flux passes through the iridotomy.

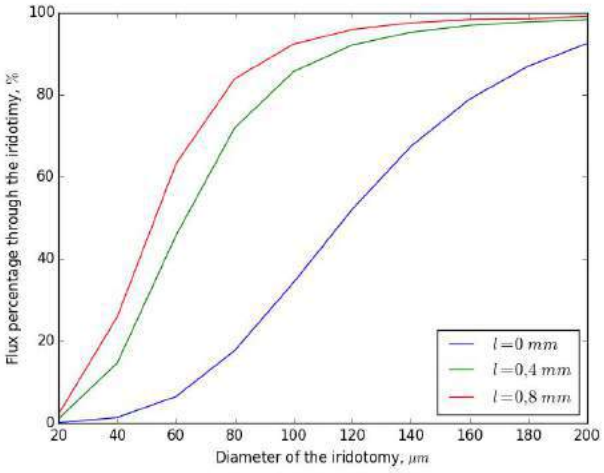

Figure 2: Percentage of the total volumetric flux that passes through the iridotomy for different lengths of iris-lens channel *l*. The height of the iris-lens channel is fixed at 7 μm. The red curve is for a channel of length 0.8 mm, the green one 0.4 mm and the blue one has the height 7 μm only at the pupil (channel length 0). The iridotomy is located at a distance 4.5 mm from the center of the pupil.

In this section by the term "pressure" we mean the pressure difference between the anterior and the posterior chamber. We calculated the pressure distribution and the velocity field in the posterior chamber of the eye for different pupil diameters, iridotomy diameters, length of the iris-lens channel and with and without miosis; an example is shown in figure 1. We note that the pressure along the domain remains almost constant, except for the iris-lens channel, where it rapidly drops from about 0.25 mmHg to 0 mmHg at the pupil.

Figure 2 shows the percentage of flux through the iridotomy with respect to the total flux, as a function of the diameter of the iridotomy. Each curve corresponds to a different value of the iris-lens channel (a region with a height from 3 to 7 μm [2]). The results show that geometry of the posterior chamber (in particular the height and length of the iris-lens channel) and the diameter of the iridotomy significantly influence the pressure distribution and flow. On the other hand, the location of the iridotomy on the iris does not have a significant effect. The pressure drop from the posterior to the anterior chamber is below 1 mmHg during aqueous production, if the iridotomy is bigger than 20 μm in diameter.

During miosis different velocity distributions on the iris give different volumetric fluxes through the iridotomy. However, the overall percentage of the flux that passes through the iridotomy remains almost unchanged. For a given geometry there is a value of the iridotomy for which the velocity of the aqueous jet passing through the iridotomy is maximal. This velocity is much higher during miosis than when the iris is stationary.

In the case of pupillary block an iridotomy with a diameter of at least 20 μm is needed to avoid dangerously high pressures. Partial pupillary block (the case when some region of the pupil is blocked for the outflow) causes the dangerously high pressures only with if the blocked region is more than 90%. However, with the presence of a small iridotomy with diameter 15 μm the pressure drops to less than 1 mmHg.

DISCUSSION

The ideal size and location of an iridotomy is influenced by various geometrical and fluid mechanical factors. We find the most significant ones are the size of the hole, the width and height of the narrow iris-lens channel and the possible presence of complete or partial pupillary. For certain iridotomy diameters, we cannot rule out the possibility that the jet velocity through the iridotomy during miosis might become large enough so as to cause corneal damage.

ACKNOWLEDGEMENTS

Supported financially by Ophtec BV, Groningen, The Netherlands. Disclosure: M. Dvoriashyna, None; R. Repetto, Ophtec BV (C); J.H. Tweedy, Ophtec BV (C);

REFERENCES

[1] Fleck, B.W., *British Journal of Ophtalmology*, 74:583-588, 1990;
[2] Silver, D.M. and Quigley, H.A., *J Glaucoma*, 13:100-107, 2004;
[3] Dagan, Z. et al., *J Fluid Mechanics*, 115:505-523, 1982.

Copyright 2016 The Organizing Committee for the 2016 Summer Biomechanics, Bioengineering and Biotransport Conference

SB^{3}C2016
Summer Biomechanics, Bioengineering and Biotransport Conference
June 29-July 2, National Harbor, Maryland, USA
SB^{3}C2016-130

SUBSTITUTE VOICE PRODUCTION VIA A MECHANICALLY-DRIVEN ARTIFICIAL LARYNX

Michael R. Baldwin
Clarkson University
Potsdam, New York, United States

Kateri A. Kaminski
Clarkson University
Potsdam, New York, United States

Janet A. Hrdina
Clarkson University
Potsdam, New York, United States

Evan T. Cody
Clarkson University
Potsdam, New York, United States

Erik A. Gillespie
Clarkson University
Potsdam, New York, United States

Tyler G. Tuttle
Clarkson University
Potsdam, New York, United States

Faculty Advisors

Byron D. Erath, Ph.D.
Clarkson University
Potsdam, New York, United States

INTRODUCTION

The human larynx contains two vocal folds that, when driven by air expelled from the lungs, undergo self-sustained oscillations, thereby producing sound. [1] Laryngeal cancer and other diseases can necessitate the removal of the larynx (laryngectomy), rendering conventional voiced speech production impossible. On a global scale, there are approximately 160,000 cases of laryngeal cancer each year. Of those cases, roughly 80,000 receive laryngectomies. The United States comprises ~3,000 annual procedures. While the past 15 years have shown a decrease in laryngectomies in the United States, there is increasing occurrence in Latin America, Asia, Southern Europe, and Eastern Europe. [2]

Following laryngectomy, a handheld artificial larynx (AL) is employed to restore voice. An AL produces sound from a driven striker that impacts a diaphragm, causing the diaphragm to vibrate. When the diaphragm makes contact with the neck, sound is transmitted through the tissue and into the oral cavity, producing sound that is then modulated by the lips and tongue to form intelligible speech. [3] Unfortunately, ALs produce harsh and monotonic sound with significant background noise, resulting in suboptimal voice production. These drawbacks are further compounded by the fact that AL's are electrically powered and as such, prohibitively expensive (O($1,000), which limits deployment to developed countries.

Prior research regarding AL development has explored neural control for hands-free and on-demand sound production yielding ALs that are activated electromyographically; that is, the user is able to activate the AL and modify pitch using signals arising from muscle activation. [4] Other efforts have improved AL output sound quality by utilizing inverse filtering of the frequency response functions (FRF) of the throat, which allows the AL output to be optimized for the FRF of a human throat through modification of the AL input signal. [5] While these advances serve to greatly improve AL performance they do not address the issue of high cost, which prohibits their widespread deployment to developing countries.

The objective of this study is to develop a mechanically-driven artificial larynx (i.e. mechanolarynx (ML)) at a price that will facilitate access to patients in developing countries. Device design is driven by end-user feedback to determine features of greatest importance. A system dynamics model was employed in order to determine the key design variables that impact oscillation frequency (pitch), and loudness.

PRODUCT DESIGN

The conceptual design of the ML follows basic wind-up mechanics. Figure 1 provides a schematic and Table 1 lists the relevant parts. A constant torque spring, wound by use of an external knob (Part No. 5 and 18, respectively), acts as the energy storage device. A constant torque spring ensures constant amplitude and frequency, thereby providing constant voice pitch for the user until the spring winds down. A gear and pawl system holds the wound spring until a button is pressed, releasing it. Releasing the button causes the mechanism to stop the spring from unwinding. As the compressed spring begins to unwind, it transmits energy to a gear train (Part No. 10-12, 14), causing a knocker (No. 13) to periodically impact a rigid membrane (No. 2), which is mounted into the AL head with a circumferential rubber O-ring (No. 3), to provide compliance and allow it to vibrate.

Initially, the design comprised of two flexible membranes in series, similar to that of current ALs; however, it was found that the device could be simplified to the knocker, and one membrane. This concept was validated by attaching a knocker with 2 heads to an electric motor running at 83Hz. The flexible

Copyright 2016 The Organizing Committee for the 2016 Summer Biomechanics, Bioengineering and Biotransport Conference

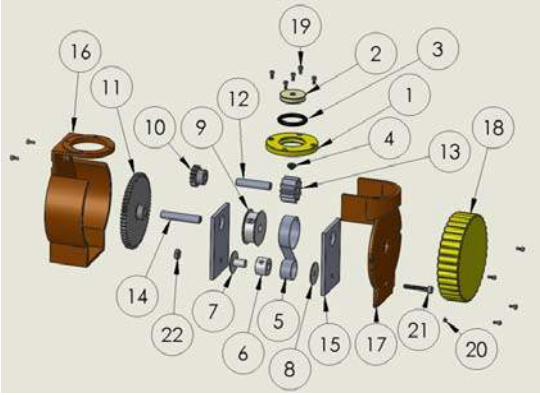

Figure 1: Exploded schematic of the mechanolarynx.

membrane was impacted at 166 Hz, successfully producing voice when pressed to the user's throat.

User feedback established that the device should operate at approximately 120Hz with 10s of phonation time. In order to determine parameters needed to achieve these characteristics, the vibration of the membrane was modeled as a spring-mass damper system with a constant force input (from the knocker), with the time history of the vertical motion given as:

$$y = Ae^{-\beta t}\cos(\omega_d t + \phi) + \left(\frac{F}{\omega Z_m}\right)\sin(\omega t - \theta)$$

where ω_d is the driving frequency, Z_m is the mechanical impedance, F is the amplitude of a sinusoidal-varying constant force input, and ω is the resonance frequency ($\omega = \sqrt{k/m}$) – m is equal to the mass and k is equal to the spring constant. Beta, β, is the temporal absorption coefficient, phi, ϕ, and A, are the phase angle and the amplitude respectively and are determined by initial conditions, and theta, θ, is the phase angle of the forcing function.

The model predicts that a rubber O-ring spring constant of ~ 21.6 N/m and a fixed 1.5 g membrane mass will yield a fundamental frequency of 120 Hz. Along with a 4-headed knocker, and a gear ratio of 10:1, a carbon steel constant torque spring with diameter of approximately 5cm and an arbor diameter of 2.54 mm will be implemented. The spring will have a spring constant of 3.6 g/mm, a width of 1.3cm and thickness of 0.08mm. It is estimated that the spring will provide 3.4 N-m of torque with an unwind speed of 3 rev/sec. This will yield a phonation time of > 10 seconds, with the knocker frequency impacting the membrane at its fundamental frequency.

BUDGET & MARKET ANALYSIS

Table 1 includes a parts list for the proposed AL design and the anticipated prototyping costs. Costs are based on commercial pricing. While the raw material prototype cost for the ML is ~$15.00, additional costs for the prototype development include material for the 3D printer, machining labor, an electrical motor for benchtop validation, prefabricated gear trains, and anticipated overruns of fasteners, springs, etc. As such, the prototype budge is estimated to be ~$250.00

Final production costs are estimated at $5.40/device allowing a for a reasonable target price point of $20.00. Based on the aforementioned global statistics it is estimated that there

Table 1: ML part list with prototype and production costs.

Part Name	Prototype Cost	Production Cost
(1) Outer head	$0.76	$0.10
(2) Inner head	$0.35	$0.05
(3) O-ring	$0.03	$0.02
(4) Impact cone	$0.15	$0.03
(5) Constant torque spring	$7.60	$3.15
(6, 9) Rotating spring cylinders	$0.74	$0.09
(7, 8) Static spring shaft and cap	$0.45	$0.07
(10, 11) Gears	$0.46	$0.30
(12, 14) Gear shafts	$0.34	$0.23
(13) Knocker	$0.50	$0.08
(15) Spring mounting plate	$0.81	$0.11
(16, 17) Casing	$1.38	$0.19
(18) Winding dial	$0.97	$0.13
(19, 20, 21, 22) Fasteners	$0.84	$0.45
Subtotal	**$15.38**	**$5.40**

are approximately 1.2 million potential customers. An initial target of 10,000 units in the first year would capture a conservative market share of ~1.0%. Assuming a compounding market share of ~1.40 annually will enable capturing ~25% of the market over the next 10 years. A production schedule of 10,000 units in the first year would generate revenue of $146,000. A 25% market share within 10 years would result in selling 20,000 units on an annual basis, producing $292,000 in gross profit annually.

This profit is not sufficient, however, to reasonably finance staff salaries, infrastructure, utility and manufacturing start-up costs. Therefore, the strategy that will be employed is to license the design to an existing biomedical firm (e.g. InHealth). Consequently, a provisional patent will be filed to protect intellectual property, and a Limited Liability Corporation (LLC) is being established through collaborations with the Clarkson University Shipley Center for Entrepreneurship.

Nevertheless, the ML design is novel in that it provides speech through a simple mechanical system that does not require the use of batteries or electricity, thereby satisfying a demonstrated market need. This simple design results in a device that is able to produce outcomes similar to those of an EL but at a fraction of the cost of currently available devices.

ACKNOWLEDGEMENTS

This work was supported by the National Science Foundation under Grant No. (NSF-CBET 1510367).

REFERENCES

[1] Berke, G.S. et al., 1993, J Voice., 7:123-128**.**
[2] Ge, X. et al.., 2014, JBI Database Reports., 12:424-438.
[3] Liu, H. et al., 2007, Auris Nasus Larynx., 34:327-332.
[4] Kubert, H.L. et al., 2009, J Commun Disord., 42:211-225.
[5] Norton, R.L. et al., 1993, Ann Biomed Eng., 21:163-174.

Copyright 2016 The Organizing Committee for the 2016 Summer Biomechanics, Bioengineering and Biotransport Conference

SB^{3}C2016
Summer Biomechanics, Bioengineering and Biotransport Conference
June 29 –July 2, National Harbor, MD, USA
SB^{3}C2016-131

IMAGE-BASED SIMULATIONS SHOW SIGNIFICANT FLOW FLUCTUATIONS IN A NORMAL LEFT VENTRICLE

Christophe Chnafa (1,2), Simon Mendez (2), Franck Nicoud (2)

(1) Biomedical Simulation Laboratory, Department of Mechanical & Industrial Engineering, University of Toronto, Toronto, Ontario, Canada.

(2) Institute of Montpellier Alexander Grothendieck, University of Montpellier Montpellier, France.

INTRODUCTION

The hemodynamics of the left ventricle (LV) conveys information regarding the heart function. Observation of LV flow may thus reflect the presence of an existing pathology. In addition, there is substantial evidence that the LV hemodynamics can be responsible for the initiation of ventricular remodeling through mechanosensitive feedbacks modulating cardiomyocytes architecture and thus cardiac function [1]. Therefore, accurate assessment of the intraventricular flow is of paramount importance to get further comprehension of the role played by the hemodynamics in normal and abnormal LV.

Previous in vivo studies have been heavily based on velocity data obtained thanks to phase-contrast cardiovascular magnetic resonance (CMR) imaging. However, cycle-to-cycle variations and instabilities in the flow cannot be observed with CMR velocity mapping as the spatio-temporal resolution is relatively low and the measurements are not real-time but rather provide a mean cycle.

Used with caution, image-based computational fluid dynamics (CFD) can retrieve all the scales of the instantaneous flow, hence being able to capture disturbed flows. However, pioneering CFD studies focused only on the large-scale features of the flow i.e. the jets and the large recirculating cell. Apart from a few studies that mentioned the potential presence of flow instabilities, little focus has been given to the disturbed nature of the LV flow, despite its potential importance. However, using a new CMR method to evaluate the intensity and the localization of velocity fluctuations, Zajac et al.[2] recently confirmed the presence of non-negligible in vivo levels of "turbulent" kinetic energy in abnormal and normal LVs.

We emphasize that in addition to be controversial, the nature of the flow in normal heart does not comply with the canonical definition of developed turbulence, which makes even the definition of intracardiac "turbulence" problematic. Nevertheless, non-periodic, 3D fluctuations may appear, given the Reynolds number of order 5000, the flow domain complexity and the pulsatile nature of the flow.

The purpose of this study is to elucidate if a normal LV could harbor flow instabilities, to analyze them and to describe the potential consequences of their presence.

METHODS

Large-eddy simulations were preformed to compute 35 cardiac cycles using the in-house YALES2BIO solver developed at IMAG (www.math.univ-montp2.fr/~yales2bio) in a patient-specific left heart model obtained from CMR images. The 4D image set consists in 20 3D images of spatial resolution $5.0\times1.1\times1.1$ mm^3, which correspond to $21\times256\times256$ voxels. The subject was 26 years old and his cardiac cycles lasted on average T = 750 ms. The model includes the valves, atrium, ventricle, papillary muscles and ascending aorta. The deformations of the heart all along the heart cycle match the CMR exam thanks to an image registration technique [3].

The heart geometry is discretized using ten million tetrahedral elements. The average edge length is close to 0.55 mm during diastole. The time step, based on a Courant-Friedrichs-Lewy stability number of 0.9, varies from 0.2 ms during the beginning of diastole to 0.5 ms during diastasis.

RESULTS

The LV large-scale flow features i.e., the blood ejection, the two vortex rings for the E and A waves and the recirculating cell, are well retrieved (Fig. 1, only diastole is shown here) in accordance with the numerous observations performed in vivo, in silico, and in vitro. However, the present results reveal also large velocity fluctuations during diastole (Fig. 2).

Copyright 2016 The Organizing Committee for the 2016 Summer Biomechanics, Bioengineering and Biotransport Conference

The largest fluctuations are predominantly located in the first third of the LV and their frequency content reaches 200 Hz (Fig. 3).

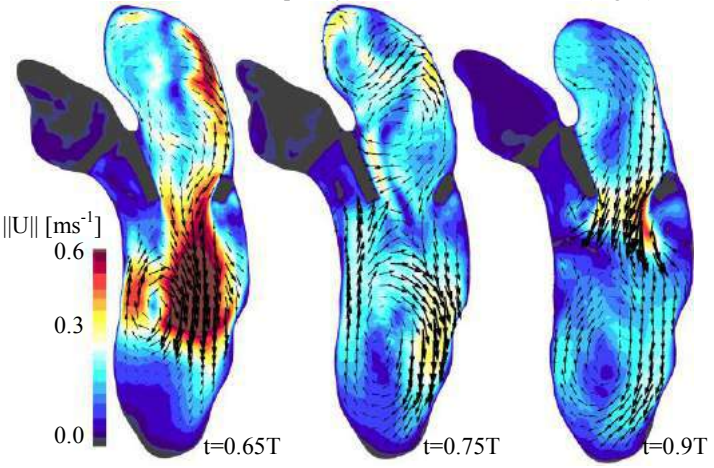

Figure 1: Phase-averaged diastolic velocity field and magnitude over a plane through the left heart. Valves are depicted in black

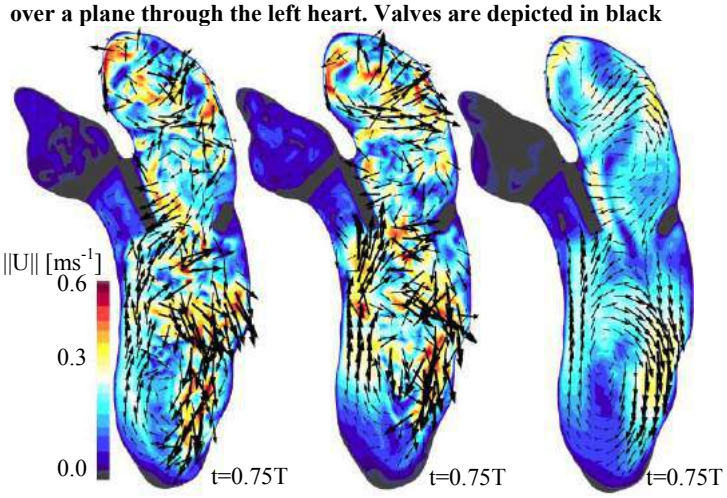

Figure 2: Left and middle plots: typical instantaneous velocity fields at 0.75 T for two consecutive heart cycles. Right plot: phase-averaged velocity field over thirty heart cycles at 0.75 T.

DISCUSSION

Our results question the common idea of laminar flow in the normal LV. Imposing the flow to be laminar (as often done in CFD for the LV) may be sufficient to retrieve main large-scale hemodynamic features, namely jets, recirculating cell, and ejection. However, a transitional or turbulent state features small-scale phenomena that cannot be retrieved under the laminar hypothesis. Therefore, our results suggest that the laminar assumption often made implicitly should be reconsidered in LV CFD if one wants to simulate all the flow features.

It is worth noting that any CFD study where flow instabilities are not properly represented cannot address the prevalence of LV bruits. Among the sounds usually reported, the S3 bruit (detected in one third of asymptomatic individuals younger than 40 [4]) is a brief sound harboring a main frequency content in the range of 10-100 Hz and occurring at the end of the E wave, 120-200 ms after the start of diastole. It is widely reported that "vibrations" occurring during the deceleration of the E wave generate this sound. These "vibrations" may be generated by the interaction of the flow instabilities with the LV tissue. While we do not directly prove that the reported fluctuations are responsible for the S3 bruit, we show here that flow fluctuations obtained in the present calculations are in the same frequency range as the S3 bruit.

As shown in vivo by Zajac et al.[2] a certain level of fluctuations intensity can be a sign of cardiac dysfunction. Nevertheless, in light of their results and ours, it seems that velocity fluctuations in LV flows are actually not a synonym of pathological flows: they should not be considered as an absolute proof of a pathological state.

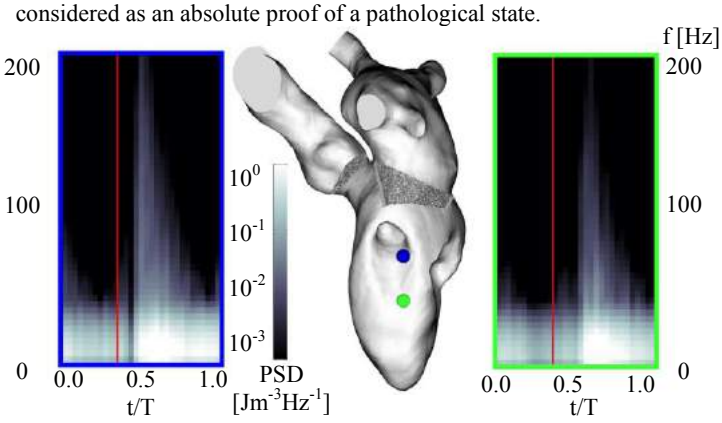

Figure 3: Time-frequency representation of the Power Spectral Density (PSD) of the velocity fluctuations at two locations. Each vertical slice of a spectrogram exhibits the frequency spectrum of the flow at a specific time. Red lines on spectra delimit systole (0 to 0.34 T) from diastole (0.34 to 1.0 T).

As CMR is widely used to explore the LV flow, the prevalence of fluctuations in normal LV serves as a reminder that time-resolved velocity fields measured with CMR are not instantaneous. Blood flow patterns and derived quantities correspond to mean flow fields, not the actual flow seen by the cells. While the same mean flow as CMR is retrieved, Fig. 2 shows how different the instantaneous flow may be.

These fluctuations amplify the forces exerted by the blood on the LV wall cells and can potentially trigger mechanosensitive feedbacks [1]. It has been shown in vitro that even weak flow stimuli can induce modifications of gene expression, which may result in its functional modification. Although the remodeling mechanisms of the LV are not completely understood and that the relevance of these fluctuating velocities compared with the mean flow field remains to be defined, fluctuations can be expected to play an important role in myocardial function and adaptations.

In conclusion, as the nature of the flow directly affects the characteristic time scales and local levels of flow stresses, it can be speculated that our findings point toward new directions for future clinical research, complementing conventional studies focusing on the mean flow field for the assessment of the cardiovascular flow and the heart mechanosensitive feedbacks.

ACKNOWLEDGEMENTS

Dr. R. Moreno from the Rangueil University Hospital, Toulouse (France) is acknowledged for the CMR exams. Dr. V. Moureau and Dr. G. Lartigue from the CORIA lab, and the SUCCESS scientific group are acknowledged for providing the YALES2 code, which served as a basis for the development of YALES2BIO.

REFERENCES

[1] Pasipoularides et al, *Cardiovasc. Transl. Res.,* 8:76–87, 2015.
[2] Zajac et al., *J. Magn. Reson. Imaging,* 41:1021–9, 2015.
[3] Chnafa et al., *Comput. Fluids,* 94:173–187, 2014.
[4] Collins et al., *Congest. Hear. Fail*., 11:242–247, 2005.

Copyright 2016 The Organizing Committee for the 2016 Summer Biomechanics, Bioengineering and Biotransport Conference

SB³C2016
Summer Biomechanics, Bioengineering and Biotransport Conference
June 29 –July 2, National Harbor, MD, USA
SB³C2016-132

INTRASACCULAR HEMODYNAMICS, WALL INFLAMMATION AND DEGENERATIVE CHANGES OF CEREBRAL ANEURYSM WALL

Juan R. Cebral (1), Eliisa Ollikainen (2), BongJae Chung (1), Fernando Mut (1), Visa Sippola (2), Behnam R. Jahromi (2), Riikka Tulamo (2), Juha Hernesniemi (2), Mika Niemela (2), Anne Robertson (3), Juhana Frosen (2,4)

(1) Bioengineering Department
George Mason University
Fairfax, Virginia, USA

(2) Neurosurgery Research Group
Biomedicum & Helsinki Unniversity Hospital
Helsinki, Finland

(3) Mechanical and Material Science & Bioengineering Departments
University of Pittsburgh
Pittsburgh, Pennsylvania, USA

(4) Hemorrhagic Brain Pathology Research Group, Neurocenter
Kuopio University Hospital
Kuopio, Finland

INTRODUCTION

Intracranial aneurysms are common, they affect 2-3% of the population, and have devastating consequences if they rupture [1]. Fortunately, aneurysm rupture is quite rare and many aneurysms never rupture. Because the risk of interventions can outweigh the natural risk of rupture, it is important to discriminate between rupture prone aneurysms and those that are very unlikely to rupture.

Aneurysm enlargement is thought to be governed by a progressive degradation and weakening of the wall induced by abnormal hemodynamics [2]. The strength of the wall depends on its structure (cellular content and collagen fiber architecture). Histological changes of the wall, mainly inflammation and decelullarization, have been previously observed in ruptured and rupture prone aneurysms [3]. However, the causes of this degenerative remodeling of the wall are largely unknown.

Previous studies have identified hemodynamic differences between ruptured and unruptured aneurysms that suggest that hemodynamics may affect the structure of the wall and its strength [4,5].

Thus, the purpose of this article is to present recent results regarding associations between intrasaccular flow characteristics of cerebral aneurysms and wall inflammation and other degenerative changes of the aneurysm wall [6].

METHODS

A total of 20 patients with intracranial aneurysms undergoing surgical clipping were studied. Pre-operative 3D computed tomography angiography (CTA) images were used to build patient-specific computational fluid dynamics (CFD) models. Pulsatile simulations were carried out by numerically solving the 3D unsteady Navier Stokes equations assuming Newtonian viscosity and rigid walls. The numerical simulations had a minimum mesh resolution of 200 μm and a time resolution of 0.01 sec and were run for two cardiac cycles. A number of hemodynamic variables were then computed from the results of the second cycle to characterize the aneurysm flow conditions, as in previous studies [7].

During surgery, tissue samples were resected from the aneurysm domes and analyzed with histology and immunohistochemistry. Specifically, the 20 samples were analyzed for the presence of inflammatory cells (CD45 staining), lipid accumulation (ORO staining), and the presence of organized thrombus (HE staining), as in previous studies [6, 8].

To test the hypothesis that abnormal wall shear stress (WSS) is associated with inflamed walls, the number of CD45+ cells was compared between aneurysms with low WSS (<4.5 dyne/cm^2), high WSS (>18 dyne/cm^2), and medium WSS (between 4.5 and 18 dyne/cm^2). Similarly, flow variables were compared between aneurysms with high wall inflammation (CD45+ counts > 100), low wall inflammation (CD45+ counts < 10) and mild wall inflammation (CD45+ counts between 10 and 100). The statistical comparisons between these aneurysm groups were carried out using the one-sided Wilcoxon test due to the small sample size. Differences were considered statistically significant if $p<0.05$ (95% confidence).

RESULTS

Comparisons of mean flow variables (averaged over the aneurysm region and over time) between aneurysms with different levels of wall inflammation are presented in Fig.1 (top). For simultaneous display and comparison, the flow variables in this graph have been scaled to the maximum, corresponding to the high CD45 group.

Copyright 2016 The Organizing Committee for the 2016 Summer Biomechanics, Bioengineering and Biotransport Conference

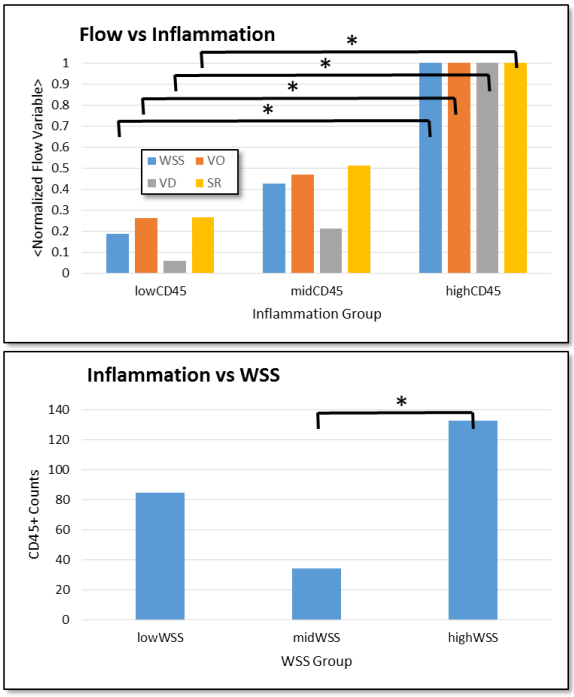

Figure 1: Hemodynamics and Wall Inflammation. Top: mean wall shear stress (WSS), vorticity (VO), viscous dissipation (VD) and shear rate (SR) in walls with low, middle and high inflammation. Bottom: Number of inflammatory cells (CD45+) in aneurysms with low, middle and high WSS.

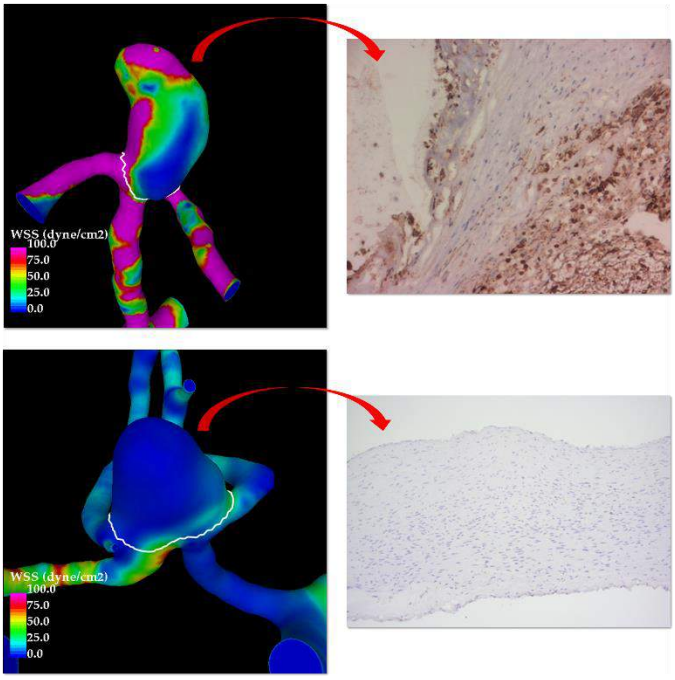

Figure 2: Example aneurysm with high WSS (top-left) and high wall inflammation (top-right), and aneurysm with low WSS (bottom left) and low wall inflammation (bottom right). Visualizations show peak systole WSS.

In our study, no association between flow variables and aneurysm rupture reached statistical significance. On the other hand, increased wall inflammation was associated with rupture (CD45+, p=0.031).

Aneurysms with high inflammation (high CD45+ group) had significantly larger wall shear stress (WSS, p=0.032), vorticity (VO, p=0.046), viscous dissipation (VD, p=0.046) and shear rate (SR, p=0.046) than aneurysms with low inflammation (low CD45 group).

Similarly, aneurysms in the high WSS group had significantly larger numbers of inflammatory cells than aneurysms with WSS in the middle range (Fig.1 – bottom). Aneurysms in the low WSS group also had larger number of inflammatory cells than aneurysms in the mid WSS group but this trend did not reach statistical significance.

Additionally, high vorticity (p=0.034), viscous dissipation (p=0.020), and shear rate (p=0.034) were also associated with endothelium damage, which in turn associated with wall inflammation (p=0.034). Although organized luminal thrombosis associated with inflammation (p=0.018), organized thrombosis was associated with low minimum WSS (p=0.034) but not with the flow conditions that associated with inflammation.

DISCUSSION

In our series, inflammation associated with aneurysm rupture. As such, inflammation could be considered a potential biomarker for rupture, which could potentially be imaged clinically.

Our results indicate that there is a connection between intrasaccular flow characteristics with inflammation and other histological changes of the aneurysm wall. Inflammation associated with increased wall shear stress, vorticity, viscous dissipation and shear rate, i.e. a high flow environment. Interestingly, high levels of wall inflammation were also observed in a few samples with low wall shear stress, suggesting that both abnormally high and low WSS may induce degenerative changes to the wall. However, in general high and low wall shear stress levels associated with different histological changes of the aneurysm wall, possibly suggesting different pathways or mechanisms of wall degeneration.

The current study supports the idea that image-based CFD models could be used to identify unruptured intracranial aneurysms at higher risk of developing wall inflammation, and since inflammation is associated to rupture, these aneurysms would require more careful observation or preventive treatment.

ACKNOWLEDGEMENTS

This work was partially supported by the National Institutes of Health (NIH-NINDS) grant #R21NS080031.

REFERENCES

[1] Vlak, MH et al. *The Lancet. Neurology,*10:626-636, 2011.
[2] Sforza, D et al. *Ann Rev Fluid Mechanics,* 41:91-107, 2009.
[3] Frosen, J et al. *Acta Neuropathologica,* 123: 773-786, 2012.
[4] Cebral, JR et al. *Am J Neuroradiol,* 32: 145-151, 2011.
[5] Xiang, J et al. *Stroke,* 42: 144-152, 2011.
[6] Cebral, JR et al. *Stroke,* 2016 - in review.
[7] Mut, F et al. *Int J Num Meth Biomed Eng,* 27: 822-839, 2011.
[8] Ollikainen, E et al. *J Nouropathol Exp Neurol,* 73: 855-864, 2014.

Copyright 2016 The Organizing Committee for the 2016 Summer Biomechanics, Bioengineering and Biotransport Conference

SB³C2016
Summer Biomechanics, Bioengineering and Biotransport Conference
June 29 –July 2, National Harbor, MD, USA
SB³C2016-133

A NEAR INFRARED LASER-ACTIVATED "NANOBOMB" FOR BREAKING THE BARRIERS TO MICRORNA DELIVERY

H. Wang (1,2,3), X. He (1,2,3)

(1) Department of Biomedical Engineering
The Ohio State University
Columbus, Ohio, USA

(2) Davis Heart and Lung Research Institute
The Ohio State University
Columbus, Ohio, USA

(3) Comprehensive Cancer Center
The Ohio State University
Columbus, Ohio, USA

INTRODUCTION

Cancer stem-like cells (CSCs) have attracted a great deal of attention as the target of cancer therapy due to their high resistance to chemotherapy and capability of initiating and/or reinitiating tumor growth. The miR-34a, originally studied as a p53 target, has been identified as a key negative regulator of the variant CD44 receptors overexpressed on the prostate CSCs.[1] However, as with many other genetic materials, the use of free miR-34a as a medicine is limited by extracellular barriers including its unstable molecular structure in the environment including air, rapid clearance in blood, and poor intracellular uptake. Recent advances in nanotechnology make it possible to overcome the extracellular barrier by encapsulating the genetic materials in nanoparticles to shield them from the enzymatic environment outside the cells and increase their half-life in circulation.[2] However, nanoparticles are usually taken up by cells via endocytosis, which results in the intracellular barrier that can easily degrade the genetic materials released from the nanoparticles. Therefore, the major challenge to nanoparticle-mediated delivery of miRs is to achieve endosomal/lysosomal escape and ensure effective release of the miRs into the cytosol where they perform their biological functions. To overcome this challenge, we present a novel strategy by using a near-infrared (NIR) laser to activate "bomb-like" nanoparticles for endosomal/lysosomal escape and cytosolic gene delivery.

METHODS

To prepare HLPP or HLPP-IAR nanoparticles, various amounts of PLGA, DPPC (lipid), and PF127 were dissolved in 2 ml of methylene chloride. After adding 0.4 ml of DI water either with or without ICG (0.25 mg/ml), ammonium bicarbonate (10 mg/ml), miR-34a (0.25 mg/ml), and chitosan (1 mg/ml), the immiscible solutions were emulsified by sonication for 1 min. Then, this first emulsion and 4 ml of chitosan-PF127 and HA solution (in DI water) were emulsified by sonication for 2 min. After rotary evaporation to remove the organic solvent, the nanoparticles were collected by centrifugation at 1620g for 10 min at room temperature and washed twice with DI water.

In vivo antitumor efficacy and systemic toxicity. After tumors reached ~5 mm in diameter, mice were treated intravenously via the tail vein with 100 μl saline or blank HLPP nanoparticles, free miR-34a (1.5 mg/kg body weight), HLPP-IA nanoparticles (ICG: 1.5 mg/kg body weight), HLPP-AR nanoparticles (miR-34a: 1.5 mg/kg body weight), and HLPP-IAR nanoparticles (miR-34a: 1.5 mg/kg, ICG: 1.5 mg/kg body weight) at day 1, 7, 14, and 21. At 12 h after each the intravenous injection, NIR irradiation at 0.7 W/cm^2 for 2 min was applied on the tumors. Tumor growth was monitored every two days. The tumor volume (V) was calculated as: $V = (L \times W^2)/2$, where L is long diameter and W is short diameter determined using a caliper. The mice were euthanized at day 30 after the first injection. Tumors, livers, lungs, hearts, spleens, and kidneys were collected, formalin fixed, paraffin embedded, and haematoxylin&eosin (H&E) stained for further histological analysis.

RESULTS

Ammonium bicarbonate (NH_4HCO_3) could be thermally triggered to generate carbon dioxide (CO_2) and ammonia (NH_3) gases. Therefore, we hypothesized that the endosomes/lysosomes could be broken open if the ammonium bicarbonate encapsulated inside the nanoparticles turns into gases when heated up. We synthesized the nanoparticles using five different materials approved by the U.S. Food and Drug Administration (FDA) for medical use: poly (D,L-lactide-co-glycolide) (PLGA), Pluronic F127 (PF127), chitosan, hyaluronic acid (HA), and

Copyright 2016 The Organizing Committee for the 2016 Summer Biomechanics, Bioengineering and Biotransport Conference

dipalmitoyl phosphatidylcholine (DPPC).[3] Three agents are encapsulated inside the nanoparticles including miR-34a for gene therapy of prostate CSCs, indocyanine green (ICG) for NIR laser activated photothermal effect, and ammonium bicarbonate for gas generation under heating. We prepared the nanoparticles using a modified/improved double-emulsion method (**Figure 1A**). First, aqueous solution containing ICG, ammonium bicarbonate, miR-34a, and chitosan was emulsified with organic solvent containing PF127, PLGA, and DPPC to form a water-in-oil structure where ICG, ammonium bicarbonate, and miR-34a were encapsulated in the hydrophilic core dispersed in organic solvent. Unlike conventional double-emulsion approach that uses PVA as the stabilizer during the second emulsion, a mixture of chitosan-PF127 and HA was used instead in this study for surface modification with HA for targeting CSCs.[4]

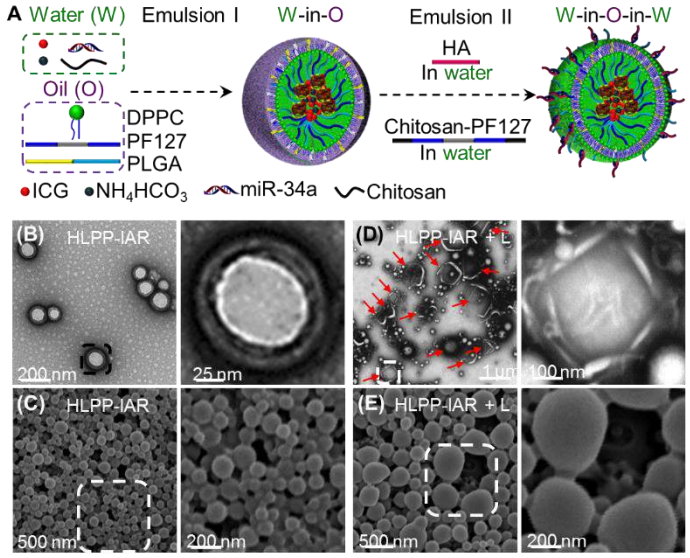

Figure 1: A schematic illustration and characterizations of the "bomb-like" effect of the nanoparticles.

Typical transmission (TEM) and scanning (SEM) electron microscopy images of the miR-34a, chitosan, ammonium bicarbonate, and ICG-laden HLPP (HLPP-IAR) nanoparticles are shown in **Figure 1B** and **1C**, respectively. The HLPP-IAR nanoparticles have a uniform size, spherical morphology, and core-shell structure. Chitosan was mixed with miR-34a before encapsulation, which significantly increases the encapsulation efficiency to more than 85% from ~45% without chitosan. Interestingly, for the HLPP-IAR nanoparticles: their size decreased to <100 nm when heated from 22 °C to 37 °C and mostly increased to >300 nm with further heating to 43 °C (**Figure 1D**). Some of the large particles might break up into small nanoparticles as shown in **Figure 1E**. The former is desired for tumor targeting at the body temperature while the latter can be used to break open the endosome/lysosome (~150-200 nm in diameter) and release the encapsulated miR-34a into the cytosol.

As shown in **Figure 2A**, overlap between the HLPP-IAR nanoparticles (red) and endosomes/lysosomes (green) is evident in the 2D cultured cancer cells, which gives the bright yellowish appearance when merged. In contrast, with NIR laser irradiation, the overlap was minimal and the miR-34a (red) distributed throughout the cytosol (bottom, w/ laser), indicating the NIR laser triggered escape of the nanoparticles from the endosomes/lysosomes. We next investigated the biodistribution in mice of the HLPP-IAR nanoparticles to understand the enhanced in vivo antitumor capacity. As shown in **Figure 2B**, highly enhanced fluorescence of ICG was observable in tumor at 6 h after intravenous injection of the HLPP-IAR nanoparticles, compared to free ICG. Lastly, we tested the safety and efficacy of the HLPP-IAR nanoparticles for gene therapy of prostate cancer using human prostate tumor grown in nude mice. Except for the saline and HLPP groups, all the other groups were with NIR laser irradiation at 12 h after intravenous injection of the gene formulations. As shown in **Figure 2C**, the HLPP-IAR nanoparticles with laser irradiation (HLPP-IAR+L) exhibited outstanding antitumor capacity and significantly reduced the tumor volume during the entire observation period. It is the "nanobomb" effect due to the combination of both ICG and ammonium bicarbonate with NIR that breaks the intracellular barrier to deliver the miR-34a specifically into the cytosol where the miR-34a performs its function to destroy tumor. The size and weight of the tumors harvested from the HLPP-IAR+L group on day 30 were significantly less than that from the other groups.

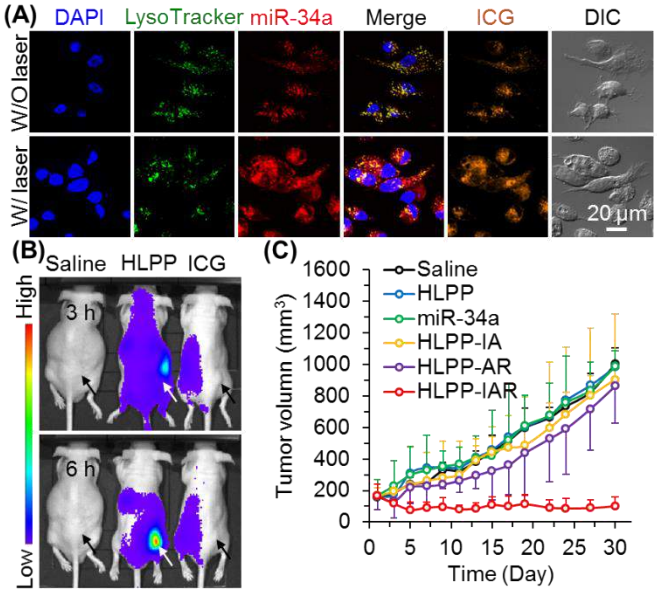

Figure 2: NIR Laser controlled endosomal and lysosomal escape and cytosolic release of miR-34a and its impact on excellent antitumor efficacy and safety *in vivo*.

DISCUSSION

Although the tissue penetration of the NIR is limited to less than ~1 cm and multiple polymers are needed for preparing the nanosystem, NIR could be delivered into deep tissue using minimally invasive approaches and the preparation of the nanosystem using the double-emulsion method is straightforward. Therefore, the present study demonstrates the great potential of the NIR laser-activatable "nanobomb" for microRNA delivery to augment cancer therapy.

ACKNOWLEDGEMENTS

This work was supported by an American Cancer Society (ACS) Research Scholar Grant (# 120936-RSG-11-109-01-CDD) to XH and a Pelotonia Postdoctoral Fellowship to HW.

REFERENCES

[1] Liu, C et al., *Nat. Med*, 17:211-215, 2011.
[2] Sanders, N et al., *Adv Drug Deliv Rev*, 61:115-127, 2009.
[3] Wang, H et al., *Adv Mater*, 28:347-355, 2016.
[4] Wei, R et al., *ACS Nano*, 9:5725-5740, 2015.

Copyright 2016 The Organizing Committee for the 2016 Summer Biomechanics, Bioengineering and Biotransport Conference

SB^{3}C2016
Summer Biomechanics, Bioengineering and Biotransport Conference
June 29 –July 2, National Harbor, MD, USA
SB^{3}C2016-134

PROGRAMMNG 'ON-DEMAND' DELIVERY FROM MECHANICALLY ACTIVATED MICROCAPSULES

Bhavana Mohanraj (1), Miju Kim (3), Daeyeon Lee (3), George R. Dodge (3,4), Robert L. Mauck (1,3,4)

(1) Department of Bioengineering
University of Pennsylvania
Philadelphia, PA, USA

(2) Department of Chemical and Biomolecular Engineering
University of Pennsylvania
Philadelphia, PA, USA

(3) Department of Orthopaedic Surgery
University of Pennsylvania
Philadelphia, PA, USA

(4) Translational Musculoskeletal Research Center
Department of Veterans Affairs
Philadelphia, PA, USA

INTRODUCTION

Stimuli-responsive drug delivery systems have several advantages, including local delivery, maintenance of drug concentrations within a therapeutic range, and preservation of activity. One desirable feature for these systems is self-regulation, wherein physiology controls release via stimuli-sensitive triggers (e.g. temperature, pH, or enzyme activity [1]). However, to date, few systems exist that take advantage of the mechanical environment to tune release [2]. Tissues within the body experience mechanical perturbation across multiple force magnitudes and length scales, from mechanotransduction at the cellular level [3] to the dynamics of whole joints. These forces provide feedback to regulate cell biology and maintain tissue integrity, but can also, at supra-physiologic levels, initiate degeneration [4]. Current strategies to repair degenerated tissues include combinations of cells, scaffolds, and growth factors; however, maturation of such engineered tissues in a demanding mechanical environment may require additional factors, and most delivery systems for such factors are operative over time scales based on material degradation rather than based on the physical environment. To address this, we developed and characterized a novel mechano-activated microcapsule (MAMC) technology for "on-demand" drug delivery based on mechanical inputs as a new approach to regenerative medicine.

METHODS

MAMCs were fabricated using a glass capillary microfluidic device [5] to form a monodisperse Water/Oil/Water (W/O/W) double emulsion. For proof-of-concept, the inner aqueous phase contained FITC-dextran (2 MDa) and was sheathed by an oil phase consisting of poly(lactic-co-glycolic) acid (PLGA 50:50 + Nile Red 0.001% w/v) to form the microcapsule shell. Shell thickness and outer diameter were tuned by controlling the sheath flow rates and polymer concentration **(Fig 1)**. To demonstrate mechano-activation, a layer of MAMCs was subjected to increasing load (~500 MAMCs, parallel plate compression test, n=3/load). Intact microcapsules served as negative controls, and microcapsules compressed to 5N served as positive controls. Following compression, MAMCs were imaged by confocal microscopy to determine the empty fraction. The slope of the % empty vs. load curve was determined for each formulation. To determine the impact of degradation on release, MAMCs were incubated at 37^{o}C in PBS, and mechano-activation was evaluated after 1 (1hr), 3, 7, and 14 days. Confocal 3D volume reconstructions and scanning electron micrographs were also obtained. Mechano-activation was further

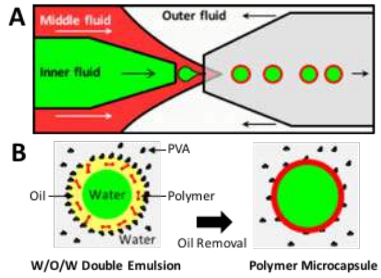

PLGA Conc. (w/v %)	Inner (mL/hr)	Middle (mL/hr)	Thickness (t, μm)	Outer Diameter (D, μm)	t/D
(C) 0.9	1	5	0.5	76	0.006
(D) 1.8	2	6	0.65	105	0.006
(E) 2.7	2	6	1.01	105	0.009

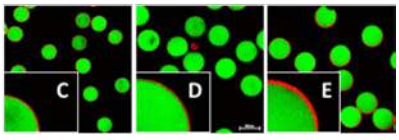

Figure 1. (A-B) Schematic of double emulsion microcapsule generation using a glass capillary microfluidic device. (C-E) Fabrication parameters (polymer concentration and flow rates) determine MAMC dimensions.

Copyright 2016 The Organizing Committee for the 2016 Summer Biomechanics, Bioengineering and Biotransport Conference

assessed in 3D constructs by embedding MAMCs in a 30% w/v photo-crosslinked poly(ethylene glycol) diacrylate (PEGDA) hydrogel whose stiffness was comparable to native articular cartilage. Using a custom confocal-mounted compression device [6], MAMC-laden hydrogels were compressed in unconfined compression and their deformation and rupture were tracked (0-20% strain, steps of 4%, followed by compression until hydrogel failure).

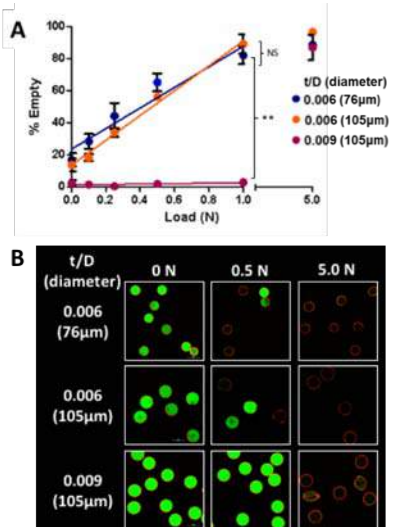

Figure 2. Mechanical release profiles of MAMCs containing dextran (green) with labeled shells (red). (A-B) MAMCs deform and fracture with increasing load, dependent on the t/D ratio (slopes differ: **p<0.01).

RESULTS

Mechanical testing of MAMCs demonstrated that microcapsule rupture and release depended on the shell thickness to diameter ratio (t/D), with a decreasing ratio resulting in MAMCs with increased sensitivity to load (**Fig 2**). MAMCs with matched t/D ratios, but different shell thicknesses and diameters, showed similar mechano-activation profiles. In these model microcapsules, PLGA was chosen due to its biocompatibility; however, polymer degradation might impact MAMC response. Indeed, PLGA MAMCs showed increased sensitivity to load after seven days of incubation at 37°C (**Fig 3**), and by day 14 had lost structural integrity. Confocal reconstructions and SEM confirmed the spherical, intact shape of naïve MAMCs, with failure in compressed MAMCs illustrated by ruptured morphology of the shell wall (**Fig 3C**). In 3D constructs, MAMCs deformed with increasing gel compression, becoming ellipsoid at 20% and rupturing at 60% strain (hydrogel failure, **Fig 4**).

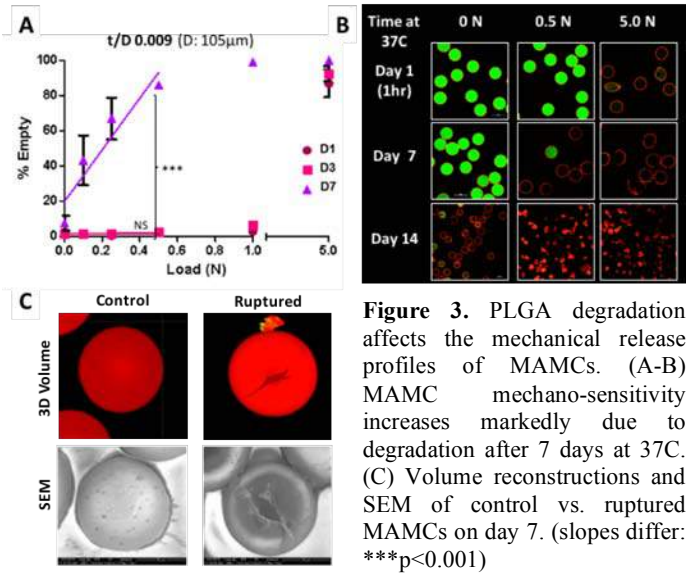

Figure 3. PLGA degradation affects the mechanical release profiles of MAMCs. (A-B) MAMC mechano-sensitivity increases markedly due to degradation after 7 days at 37C. (C) Volume reconstructions and SEM of control vs. ruptured MAMCs on day 7. (slopes differ: ***p<0.001)

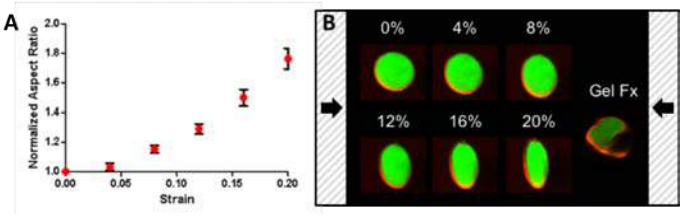

Figure 4. Micro-compression of MAMCs embedded within hydrogels show MAMC deformation (aspect ratio) with hydrogel compression (A-B). MAMCs ruptured only upon hydrogel fracture (n = 11 MAMCs/ 3 hydrogels).

DISCUSSION

This study demonstrated the production of tunable mechano-activatable microcapsules (MAMCs) whose failure characteristics depend on the physical properties of the microcapsule. As shown here, both the shell thickness to diameter ratio and polymer degradation process affect MAMC sensitivity to mechano-activation. We also observed MAMC deformation and release within 3D constructs (i.e. mimicking MAMCs in engineered tissues for repair of a cartilage defect). Controlling the MAMC and surrounding matrix properties within this model will enable tuning of release in response to physiologic loading scenarios. Ongoing studies are exploring the effects of long-term dynamic loading on MAMC release profiles in concert with efficacy studies to demonstrate the chondrogenic effects of bioactive molecules (e.g. TGF-β) released from MAMCs in an engineered cartilage system.

As we continue to characterize this novel technology, we envision the creation of a suite of MAMCs with different physical and compositional properties that are programmed to release within particular physiologic or supra-physiologic loading scenarios. By combining cohorts of microcapsules with different rupture thresholds, release events can be programmed sequentially to stimulate tissue repair in an autonomic manner. Applications for this technology include direct injection for release during passive loading with rehabilitation, prophylactic injection prior to the start of high impact activities, as well as MAMCs embedded within engineered tissues to stimulate growth and repair in a manner that is dictated by the evolving mechanical properties of the newly formed tissue. Importantly, these applications are not limited to one tissue or loading scenario, due to the tunable nature of the MAMCs, and as such this technology is a valuable platform for self-regulated drug delivery across the musculoskeletal system.

ACKNOWLEDGEMENTS

This work was supported by an NSF Graduate Research Fellowship and an NIH/NIAMS Training Grant (T32 AR007132).

REFERENCES

[1] Kost, J., et al., *Adv Drug Deliv Rev*, 46:125-148, 2001.
[2] Korin, N., et al., *Science*, 337: 738-742, 2012.
[3] Engler, A.J., et al., *Cell*, 126: 677-689, 2006.
[4] Sun, H.B., *Ann NY Acad Sci*, 1211: 37-50, 2010.
[5] Tu, F., et al., *Langmuir*, 28: 9944-9952, 2012.
[6] Farrell, M.J., et al., *Eur Cells Mat*, 23: 425-440, 2012.

Copyright 2016 The Organizing Committee for the 2016 Summer Biomechanics, Bioengineering and Biotransport Conference

SB³C2016
Summer Biomechanics, Bioengineering and Biotransport Conference
June 29 –July 2, National Harbor, MD, USA
SB³C2016-136

PCOM ANEURYSMS: ANGIO-ARCHITECTURE, HEMODYNAMICS AND GEOMETRY

BongJae Chung (1), Ravi Doddasomayajula (1), Fernando Mut (1), Farid Hamzei-Sichani (2), Christopher M. Putman (3), Michael Pritz (1), Carlos M. Jimenez (4), Juan R. Cebral (1)

(1) Bioengineering Department and
Krasnow Institute for Advanced Studies
George Mason University
Fairfax, Virginia, USA

(2) Interventional Neuroradiology
Mt. Sinani Hospital
New York, New York, USA

(3) Interventional Neuroradiology
Inova Fairfax Hospital
Falls Church, Virginia, USA

(4) Neurosurgery Department
University of Antioquia
Medellin, Colombia

INTRODUCTION

Because of the devastating consequences of cerebral aneurysm rupture, physicians often perform prophylactic interventions. However, interventions still carry significant risks that can exceed the natural risk of rupture [1]. Thus, it is important to improve aneurysm evaluation to treat only high risk aneurysms avoiding unnecessary interventions.

Numerous patient and behavioral characteristics have been investigated as possible risk factors, including gender, age, family history, smoking and hypertension. According to past studies, the most important aneurysm-specific rupture risk factors are size and location [2]. However, it is well known that small aneurysms do rupture [3]. On the other hand, the posterior communicating artery (PCOM) is a common site for aneurysm development and aneurysms at this location have larger risks than those at other locations such as the middle cerebral artery or other segments of the internal carotid artery [4]. Therefore, often clinicians need to decide whether to treat or not PCOM aneurysms, but do not have reliable parameters to guide or support their decisions.

The purpose of this study was to propose a new angio-architecture classification of PCOM aneurysms and to test if the proposed classes have different rupture rates as well as hemodynamic and geometric characteristics that could be used to improve aneurysm evaluation.

METHODS

We have constructed a database of over 1800 aneurysms imaged with 3D rotational angiography (3DRA). This database contains 3D images and anonymized clinical information such as rupture status, aneurysm location and size, patient gender and age, etc.

All PCOM aneurysms in our database (n=275, 127 ruptured, 148 unruptured) were included in the current study. Computational fluid dynamics (CFD) models of all PCOM aneurysms were constructed from the 3DRA images. Pulsatile simulations were carried out by numerically solving the 3D unsteady Navier Stokes equations assuming Newtonian viscosity and rigid walls. The simulations had a minimum mesh resolution of 200 μm and a time resolution of 0.01 sec and were run for two cardiac cycles. A number of flow variables were then computed from the results of the second cycle to characterize the aneurysm flow conditions [5,6].

All PCOM aneurysms were classified into different angio-architecture types depending on the location of the aneurysm orifice with respect to the ICA-PCOM bifurcation, as shown in Fig. 1. Rupture rates as well as geometric and hemodynamic variables were statistically compared between the different angio-architectures.

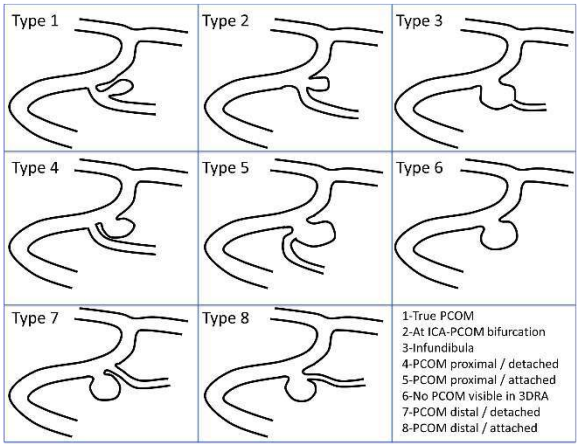

Fig. 2: Angio-architectures of PCOM aneurysms.

Copyright 2016 The Organizing Committee for the 2016 Summer Biomechanics, Bioengineering and Biotransport Conference

RESULTS

The distribution of all ruptured and unruptured aneurysms of our database, subdivided by location, is presented in Fig.2a) (ACA= anterior cerebral artery, ACOM= anterior communicating artery, ICA= internal carotid artery, MCA= middle cerebral artery, PCOM= posterior communicating artery, BA= basilar artery, VA= vertebral artery, PCA=posterior cerebral artery). This graph shows that PCOM location has the second largest proportion of ruptured aneurysms after ACOM. Fig. 2b) shows the distribution of ruptured and unruptured PCOM aneurysms by size, showing that the majority of ruptured PCOM aneurysms are between 3-10mm, i.e. are relatively small.

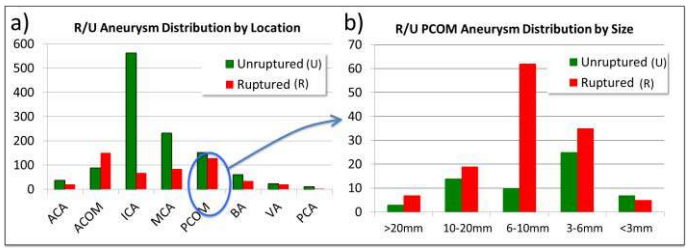

Fig. 2: Distribution of ruptured and unruptured aneurysms of our database by location (a), and PCOM aneurysms by size (b).

In our series, no PCOM aneurysms were found in types 7 or 8. The distribution of ruptured and unruptured PCOM aneurysms by angio-architecture is presented in Fig.3a), showing that type 2 (G2= aneurysms with orifices involving both the ICA and the PCOM) have the largest rupture rate. Grouping types 1-2 (G12=aneurysms with orifices involving the PCOM artery) and types 3-6 (G36=aneurysms with orifices involving only the ICA) yields the ruptured/unruptured distribution presented in Fig.3b), showing that group G12 has a larger rupture rate (62%) than group G36 (38%). Contingency table analyses using the Chi-Square test (and Fisher test for 2x2 tables of Fig.3b) indicate that the associations between angio-architecture and aneurysm rupture are statistically significant ($p<0.0001$).

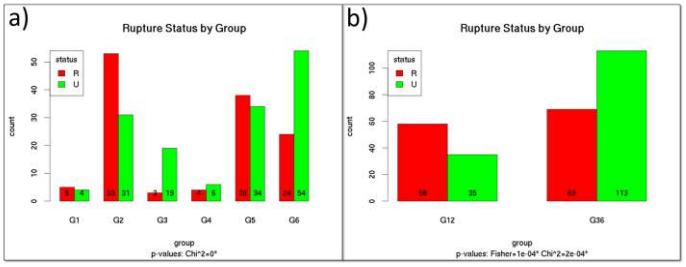

Fig. 3: Number of ruptured and unruptured aneurysms in each angio-architecture class (a), and by merging types 1-2 (G12) and types 3-6 (G36) (b).

Comparisons of geometric and flow variables between aneurysms of groups G36 and G12 are presented in Fig.4 a) and b), respectively. These graphs shows the ratio of mean variables of the G12 group over the mean values of the G36 group. Statistically significant differences ($p<0.05$, 95% confidence) according to the unpaired Wilcoxon test are indicated with an * next to the variable names. Aneurysms in G12 (larger rupture rate) had significantly larger aspect ratio (AR, p=0.0236), larger maximum wall shear stress (WSSmax, p=0.0077), more concentrated WSS distributions (SCI, p=0.0048), larger oscillatory shear index (OSImean, p=0.0164), and more unstable flow patterns (podent, p=0.025).

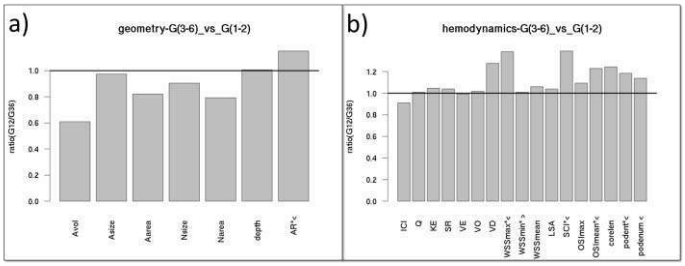

Fig. 4: Comparison of geometric (a) and hemodynamic (b) variables between aneurysms of groups 1-2 and 3-6.

DISCUSSION

In this study we proposed a new PCOM aneurysm classification strategy based on different angio-architecture classes that take into account the location of the aneurysm orifice and the origin of the PCOM artery with respect to the aneurysm sac. Aneurysms in the different angio-architecture classes have different rupture rates. The association between angio-architecture and aneurysm rupture suggest that angio-architecture could be considered a potential PCOM aneurysm risk factor that could help improve evaluation of aneurysms at this location.

Our study identifies type 2 (at the ICA-PCOM bifurcation apex) as the angio-architecture with the largest rupture rates, and type 6 (lateral aneurysms with no visible PCOM) with the lowest rupture rate. Grouping types 1-2 and 3-6 reveals that aneurysms with orifices involving the PCOM (G12) have higher rupture rate and that these aneurysms have different hemodynamic environments than aneurysms with orifices on the ICA (G36). The hemodynamic environments associated with the higher rupture rate angio-architecture are characterized by increased maximum wall shear stress, more concentrated WSS distributions and more unstable and oscillatory flow patterns.

The current study suggests that the proposed angio-architecture classification could be used to identify PCOM aneurysms at higher risk of rupture, and that the observed differences in hemodynamic environments could help explain the different rupture rates associated with the various angio-architectures.

ACKNOWLEDGEMENTS

This work was supported by the National Institutes of Health (NIH-NINDS) grant #R21NS094780.

REFERENCES

[1] Investigators T.I.S.U.I.A, *N Engl J Med,* 339:1725-33, 1998.
[2] Clarke, M *Neuroradiol,* 50(8):653-64, 2008.
[3] Joo, SW et al. *J Korean Neurosurg Soc,* 45(2): 85-9, 2009.
[4] Cebral, JR et al. *Ann Biomed Eng,* 41(7): 1366-83, 2013.
[5] Mut, F et al. *Int J Num Meth Biomed Eng,* 27: 822-839, 2011.
[6] Byrne, G et al. *Am J Neuroradiol,* 35(2): 333-8, 2014.

Copyright 2016 The Organizing Committee for the 2016 Summer Biomechanics, Bioengineering and Biotransport Conference

SB^{3}C2016
Summer Biomechanics, Bioengineering and Biotransport Conference
June 29 –July 2, National Harbor, MD, USA
SB³C2016-137

A NOVEL STRUCTURAL CONSTITUTIVE MODEL FOR PASSIVE RIGHT VENTRICULAR MYOCARDIUM: TOWARDS AN UNDERSTANDING OF REMODELING DURING PULMONARY HYPERTENSION

Reza Avazmohammadi, Michael S. Sacks

Center for Cardiovascular Simulation,
Institute for Computational Engineering and Sciences
Department of Biomedical Engineering
The University of Texas at Austin, Austin, USA

INTRODUCTION

The right ventricular (RV) is recognized to play a key role in development of cardiopulmonary disorders such as pulmonary arterial hypertension (PAH) [1]. From mechanistic point of view, PAH imposes a pressure overload on the RV free wall (RVFW), leading to elevated wall stress. This leads to progressive hypertrophy and remodeling, and ultimately in mechanical failure of the right heart [2]. Our recent studies [3, 4] have demonstrated substantial remodeling occurs in the RVFW under PAH. These observations highlight the need for a constitutive model for RV myocardium under remodeling conditions.

Our objective in the present work is to develop a structural constitutive model of the viable, passive RV myocardium that extends previous approaches by accounting realistic 3D distribution of the myocardium constituents. The model incorporates the novel transmural distribution of myo- and collagen fiber orientation as separate architecture of each fiber type, and accounts for the collagen fiber recruitment. We utilized extant tissue structural information and comprehensive mechanical data, available from recent works on the murine experimental studies [3, 4], to estimate parameters. A novel aspect of the present approach is the incorporation of the effects of fiber-fiber interactions.

METHODS

Mechanical testing and structural quantification data. Details of the experimental methods have been previously presented [3]. Briefly, viable RV myocardium specimens (n=5) were isolated from the rats and attached to the biaxial mechanical testing device [3]. Myofiber and collagen fiber orientation distributions were determined (n=3) by analyzing transmural histological sections.

Biomechanical Modeling. The RVFW is primarily composed of two major fiber types: the myo- and collagen fibers. For the collagen fibers, we make a distinction between two sub-groups: the "thick" perimysial fibers observed to be approximately aligned with the myofibers [3], and "fine" endomysial collagen fibers that surround individual myofibers and connect to the thicker collagen fibers. Assuming that the constitutive behavior of each constituent can be described by a pseudo-hyperelastic strain energy function, the total energy function of the myocardium can be written as

$$\Psi(\mathbf{E}) = \phi^{mat}\,\Psi^{mat}(\mathbf{E}) + \phi^{myo}\,\Psi^{myo}(\mathbf{E}) + \phi^{col}\left[\Psi^{col}(\mathbf{E}) + \Psi^{m\text{-}c}(\mathbf{E})\right] \quad (1),$$

where $\mathbf{E}$ is the Green-Lagrange strain tensor, Ψ^{mat}, Ψ^{myo} and Ψ^{col} are the strain energy functions associated with the matrix phase, myofibers and (thick) collagen fibers, respectively, and $\Psi^{m\text{-}c}$ refers to the energy contribution of interaction between the myo- and (thick) collagen fibers which is intended to (at least partially) capture the mechanical contribution of the "fine" collagen fibers. Also, ϕ denotes the volume fraction of respective phases. The final expression for 2nd Piola-Kirchhoff stress tensor $\mathbf{S}$ derived from proposed energy terms in (1) reads as

$$\mathbf{S} = \partial\Psi / \partial\mathbf{E} - p(2\mathbf{E}+\mathbf{I})^{-1} = \phi^{mat} k^{mat}\,\mathbf{I} - p(2\mathbf{E}+\mathbf{I})^{-1} + 1/H \times$$

$$+\left[\phi^{myo} k_1^{myo} \int_0^H \int_{-\pi/2}^{\pi/2} \Gamma^{myo}\,(1 - 1/\sqrt{I_4})\; e^{\left[k_2^{myo}(\sqrt{I_4}-1)^2\right]}\;(\mathbf{N}\otimes\mathbf{N})\; d\Theta\, dZ\right.$$

$$\left.+\,\phi^{col} k^{col} \int_0^H \int_{-\pi/2}^{\pi/2} \Gamma^{col} \int_{\lambda_{lb}}^{\lambda_{ub}} (D(\lambda_s)/\lambda_s^2)(1-\lambda_s/\sqrt{I_6})\, d\lambda_s\;(\mathbf{M}\otimes\mathbf{M})\, d\Phi\, dZ\right.$$

Copyright 2016 The Organizing Committee for the 2016 Summer Biomechanics, Bioengineering and Biotransport Conference

$$+\phi^{col} k_1^{m-c} \int_0^H \int_{-\pi/2}^{\pi/2} \int_{-\pi/2}^{\pi/2} \int_{\lambda_{lb}}^{\lambda_{ub}} \Gamma^{myo} \Gamma^{col} D(\lambda_s) \left\{ (\varphi_1 - \varphi_2) / \lambda_s^2 (\mathbf{M} \otimes \mathbf{M}) \right.$$

$$\left. + \left\{ \varphi_1 - \left[k_2^{m-c} (I_6 / \lambda_s^2 - 1) + 1 \right] \varphi_2 \right\} (\mathbf{N} \otimes \mathbf{N}) \right\} d\lambda_s \, d\Phi \, d\Theta \, dZ], \quad (2)$$

where k's are material constants associated with each phase, $D(\lambda_s)$ is the recruitment function for (thick) collagen fibers with lower and upper bounds λ_{lb} and λ_{ub}, $\mathbf{M}$ and $\mathbf{N}$ denote myo- and collagen fiber directions (see Figure 1), respectively, H is the normalized thickness of the RVFW, Z denotes the transmural direction, Γ's are transmural distribution functions for fiber orientation, p is unknown hydrostatic pressure, and $\mathbf{I}$ is the identity tensor. Also, $\varphi_1 = \exp[k_2^{mc}(I_4 + I_6 - 2)]$ and $\varphi_2 = \exp[k_2^{mc}(I_4 - 1)]$ with kinematical invariants $I_4 = 2\mathbf{N}\cdot(\mathbf{EN}) + 1$ and $I_6 = 2\mathbf{M}\cdot(\mathbf{EM}) + 1$.

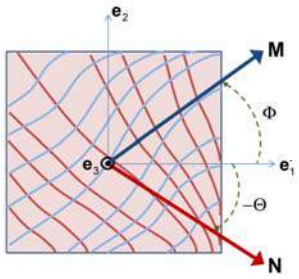

Figure 1: Ensembles of myo- and collagen fibers with uniform orientations, characterized by unit vectors $\mathbf{N}$ and $\mathbf{M}$.

A novel feature of the constitutive model (2) is that it accounts for the interaction between all ensembles of myo- and undulated collagen fibers (represented by the expression following k_1^{m-c}). Finally, the measurement data of (3-D) orientation distribution of myo- and collagen fibers (Γ^{myo} and Γ^{col}) were used directly in our model to fit the multi-protocol stress-strain data available from biaxial tests.

RESULTS

The model fit the mechanical data very well, with the lowest $r^2 \approx 0.92$. The average (n=3) transmural distribution functions for myo- and collagen fiber orientation exhibit strong 3-D dispersion throughout the RVFW (see Figure 2) . Figure 3 shows representative

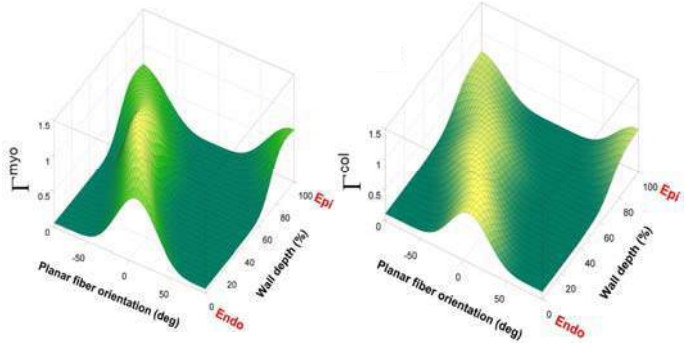

Figure 2: 3-D transmural distribution of myo- and collagen fiber orientation in RVFW.

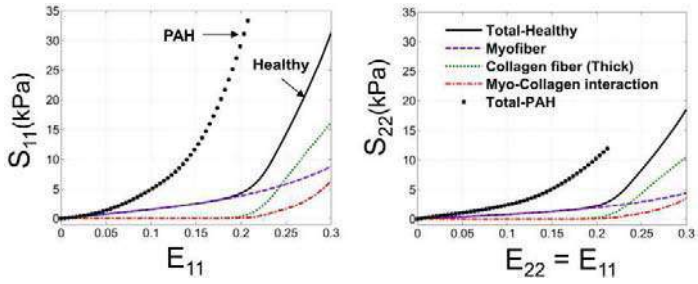

Figure 3: Contributions of fibers and interaction among them in the in-plane stress components under equibiaxial loading path. The results for the case of PAH [3] are included for comparison.

results for mechanical contribution of myo- and collagen fibers and the interaction among them in the in-plane stress components in healthy murine RVFW under equibiaxial loading condition. In this figure, we also included corresponding experimental results (for the total stress) for the case of PAH-induced (hypertensive) RVFW [3].

DISCUSSION

In this work, we took an essential step towards the modeling the biomechanical behavior of RV myocardium by formulating a structurally-consistent constitutive model for the passive RVFW that incorporates the full 3-D orientation distribution of myo- and collagen fibers and accounts for interactions among fiber types.

RVFW tissue exhibited pronounced stress stiffening along the mean fiber direction. Histological study revealed that local material axes of the RVFW are not generally orthogonal, and therefore, the behavior of the RVFW is not locally orthotropic. This is in contrast to the assumption of locally orthotropic behavior in constitutive modeling of the left ventricular myocardium often used in the literature [5]. The results of our model supported the hypothesis that, in the low strain regime, the behavior of the RVFW is governed by myofiber response alone, beyond which undulated collagen fibers and their interactions with myofiber begin to gradually contribute to the behavior as their recruitment proceeds. Once fully straightened, the collagen fibers become a major contributor to the RVFW behavior. Moreover, our results suggest that there is a substantial mechanical coupling between myofibers and thick collagen fibers. We inferred that this coupling could be in part due to the existence of a rather dense network of fine collagen struts running across myofibers and thicker collagen fibers. Finally, the comparison between results for healthy and hypertensive murine RVFW showed a substantial increase in the tissue stiffness and a decrease in the strain range within which the collagen fibers are recruited. To fully understand and characterize these changes, our next step is to implement the constitutive model for PAH data which will provide insights into the relationships between micro-scale hypertrophy and remodeling events and macro-scale biomechanics of RV myocardium during PAH.

ACKNOWLEDGEMENTS

We would like to thank Drs. Michael Hill, Marc Simon and Will Zhang for assisting in experimental data analysis.

REFERENCES

[1] Stone, AC et al, *Pulmonary Hypertension*. 93-125, 2008.
[2] Bogaard, HG et al., *Chest*, 135:794-804, 2009.
[3] Hill, MR et al, *Ann Biomed Eng*, 42:2451-65, 2014.
[4] Valdez-Jasso, D et al, *J Physiol*, 590:4581-65, 2012.
[5] Costa, KD et al, *Phil Trans R Soc Lond*, 359:1233-50, 2001.

Copyright 2016 The Organizing Committee for the 2016 Summer Biomechanics, Bioengineering and Biotransport Conference

SB^{3}C2016
Summer Biomechanics, Bioengineering and Biotransport Conference
June 29 –July 2, National Harbor, MD, USA
SB^{3}C2016-138

REPRODUCTION INDUCES ADAPTATION OF THE MATERNAL SKELETON AND ALTERS PATTERNS OF POSTMENOPAUSAL BONE LOSS

Chantal M.J. de Bakker, Allison R. Altman-Singles, Wei-Ju Tseng, Laurel Leavitt, Connie Li, X. Sherry Liu

Department of Orthopaedic Surgery
University of Pennsylvania
Philadelphia, PA, USA

INTRODUCTION

Reproduction and lactation cause substantial changes in the maternal skeleton. During lactation, a woman's bone mineral density (BMD) has been found to decline by up to 1-1.5% per month [1], while in rodents around 30% of bone volume fraction (BV/TV) is lost over the course of 3 weeks of lactation [2,3]. Although reproductive bone loss has been well characterized, the extent of recovery post-weaning and the long-term effects of these dramatic skeletal changes are less clear. Pregnancy- and lactation-induced bone loss has been shown to undergo a partial but incomplete recovery after weaning [2,3]. However, clinical studies have found that reproductive and lactation history have no detrimental effect on post-menopausal risk of fracture [4,5]. This suggests that the changes in skeletal architecture induced by reproduction may constitute a structural adaptation rather than deterioration. Additionally, the altered bone architecture and biology following reproduction may confer protective effects post-menopause. This study aims to define the adaptations undergone by maternal trabecular bone as a result of reproduction on two timescales: (1) immediately after pregnancy, lactation, and weaning, and (2) over the long-term, including postmenopausal effects. We hypothesized that reproduction and lactation lead to a modified maternal bone phenotype, where the skeleton undergoes a partial recovery post-weaning, resulting in adaptation to physiological loading, and increasing its resistance to postmenopausal, estrogen-deficiency-induced bone loss.

METHODS

All animal experiments were approved by IACUC. *Short-term effects at multiple skeletal sites:* Rats (aged 6-7 mo at sacrifice) were divided into 4 groups: Virgin (n=6), Pregnancy (n=6, euthanized at parturition), Lactation (n=5, euthanized after 2 wks of lactation), and Weaning (n=5, euthanized 2 wks post-weaning). The proximal tibiae, L4 vertebrae, and femoral midshafts were μCT scanned *ex vivo* at 10.5 μm resolution (vivaCT 40, Scanco Medical) for analysis of bone structure. Femurs were loaded to failure in 3-point bending to assess stiffness and peak load. *Long-term and postmenopausal effects:* Rats were assigned to 4 groups: Virgin OVX (n=4), Reproductive OVX (n=4), Virgin Control (n=10), and Reproductive Control (n=7). Reproductive rats underwent 3 cycles of pregnancy, lactation, and weaning starting at age 3 mo. At age 12 mo, OVX groups underwent ovariectomy (OVX) surgery to induce estrogen deficiency, and their proximal tibiae were scanned by *in vivo* μCT [6] at 0, 4, 8, and 12 wks post-OVX (10.5μm, vivaCT 40). Rats were sacrificed at age 14-19 mo, and L4 vertebrae and femurs were harvested and scanned by μCT. Femoral stiffness and peak load were measured via 3-point bending.

RESULTS

Short-term effects at multiple skeletal sites: The two trabecular sites examined, L4 and tibia, showed 67% and 84% reduced trabecular bone volume fraction (BV/TV), respectively, in post-lactation rats, relative to controls (Fig 1B). This recovered partially after weaning, and in post-weaning rats, the BV/TV of L4 and the proximal tibia were 27% and 40% lower than virgin controls. Additionally, the tibia underwent significant and irreversible deterioration in trabecular number (Tb.N; Fig 1C) and connectivity density (Conn.D; data not shown), while there were minimal changes in these parameters at L4. Reproduction resulted in an irreversible 10-12% reduction in cortical area (Ct.Area; Fig 1D) at the femur midshaft. However, whole-bone stiffness and peak load were not different between reproductive and virgin rats (Fig 1E,F). *Long-term and postmenopausal effects:* Prior to OVX surgery, reproductive rats had 36% and 31% lower BV/TV, 46% and 24% lower Tb.N, and 67% and 34% lower Conn.D than virgins at the proximal tibia and L4 vertebra, respectively, indicating long-lasting effects of reproduction on trabecular bone. Bone-loss patterns

Copyright 2016 The Organizing Committee for the 2016 Summer Biomechanics, Bioengineering and Biotransport Conference

post-OVX were dramatically different between reproductive and virgin rats. At the tibia, reproductive rats underwent a 51% decrease in BV/TV, but underwent no changes in Tb.N or Conn.D (Fig 2). In contrast, tibial BV/TV of virgin rats decreased by 76%, and virgins also showed 50% and 86% reductions in Tb.N and Conn.D, respectively ($p<0.05$). Even more striking, there was no difference between Reproductive OVX and Reproductive Controls in BV/TV, Tb.N, and Tb.Th at L4 (Fig 3), indicating no OVX bone loss in reproductive rats at this site. In contrast, Virgin OVX rats had 36% lower BV/TV and 23% lower Tb.Th at L4 relative to Virgin Controls. Comparisons between Reproductive and Virgin OVX rats at 12 weeks post-OVX indicate no remaining differences between groups in BV/TV at both the tibia and L4. Structural and mechanical testing of the femur midshaft indicated no significant differences among groups in Ct.Area, stiffness, and peak load.

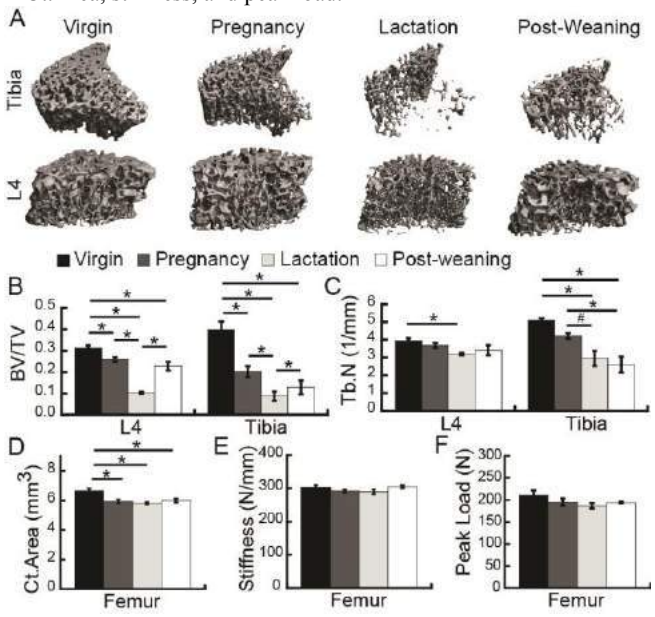

Figure 1: Reproductive effects at multiple skeletal sites. (A) 3D renderings, (B) BV/TV and (C) Tb.N indicate variable effects of reproduction on trabecular bone at the tibia and L4. (D) Cortical area, (E) stiffness, and (F) peak load at the femur midshaft indicate structural deterioration of reproductive bone, but no impact on mechanical competence (*: $p<0.05$, #: $p<0.1$).

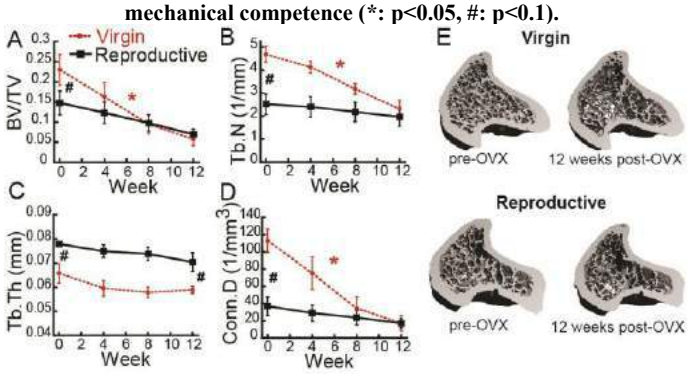

Figure 2: Effects of OVX on (A) BV/TV, (B) Tb.N, (C) Tb.Th, and (D) Conn.D in rats with and without a reproductive history. (E) 3D renderings of virgin and reproductive rats before and after OVX. * in red: significant difference between 0 and 12 wks post-OVX in virgin rats ($p<0.05$). #: significant difference between virgin and reproductive rats at wk 0 or wk 12 ($p<0.05$).

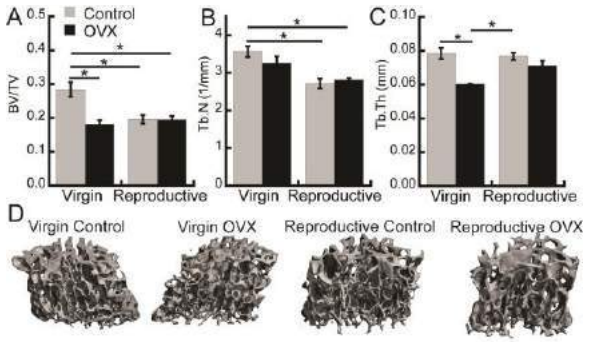

Figure 3: Effects of OVX on (A) BV/TV, (B) Tb.N, (C) Tb.Th, and (D) 3-D renderings of L4 in reproductive and virgin rats. *: $p<0.05$.

DISCUSSION

Similar to previous studies [3], reproduction had differential effects depending on the skeletal site, indicating that pregnancy, lactation, and weaning induced a redistribution of bone mass, which resulted in an altered cortical and trabecular phenotype in post-reproductive animals. This redistribution may be due to variations in the balance between the metabolic and structural functions of the bone. The mechanical integrity of the highly load-bearing regions, such as the vertebral trabeculae and the femoral cortex, were largely preserved. On the other hand, trabecular bone at the proximal tibia (which is surrounded by a dense cortex) plays a less crucial role in the bone's load-bearing function, which may help to explain its dramatic deterioration. Effects of reproduction on trabecular bone were long-lasting, as evaluation of the tibia and L4 after 3 reproductive cycles, but prior to OVX, indicated a reduced trabecular bone quality at both sites in reproductive rats relative to virgins. However, reproductive rats appeared to compensate for structural deficiencies through an adapted response to OVX: Although both groups lost bone at the tibia post-OVX, virgin rats underwent substantial deterioration of trabecular structural integrity while reproductive rats underwent minimal changes in trabecular architecture, indicating that post-reproductive bone was more resistant to estrogen deficiency-induced bone loss. Even more striking, reproductive rats underwent no changes in trabecular bone quality at L4, while virgin rats underwent dramatic structural deterioration at this site after OVX. At both the tibia and L4, there were no differences between reproductive and virgin rats in BV/TV, Tb.N, and Conn.D at 12 weeks post-OVX, which may help to explain the paradox that reproductive history does not negatively impact postmenopausal fracture risk [4,5], despite its long-lasting skeletal effects. Additionally, the lack of deterioration in bone quality post-OVX in reproductive rats at the load-bearing vertebral trabecular bone suggests that reproductive history may enhance the bone's mechano-sensitivity, resulting in reduced bone loss at load-bearing sites. Taken together, short-term and long-term results indicate, that although reproduction significantly changes bone structure, these alterations may constitute adaptations rather than deteriorations, and the post-reproductive skeleton appears to be mechanically equivalent, but better able to withstand postmenopausal bone loss than that of virgins.

ACKNOWLEDGEMENTS

NIH/NIAMS P30AR050950, NIH/NIAMS R03-AR065145, NSF Graduate Student Research Fellowship. Thanks to Tiao Lin, Wei Tong, Haoruo Jia, & Xiaoyuan Ma for assistance with OVX surgeries.

REFERENCES

[1] Sowers M et al., *JAMA*, 269:3130-5, 1993; [2] Bowman BM et al., *Bone,* 25:553-9, 1999; [3] Liu XS et al., *J Bone Miner Res*, 27:865-75, 2012; [4] Alderman BW et al., *Am J Epidemiol*, 124:262-7, 1986; [5] Kauppi M et al., *Osteoporos Int*, 22:1765-71, 2011; [6] Lan S et al., *Bone*, 56:83-90, 2013.

Copyright 2016 The Organizing Committee for the 2016 Summer Biomechanics, Bioengineering and Biotransport Conference

SB^{3}C2016
Summer Biomechanics, Bioengineering and Biotransport Conference
June 29 –July 2, National Harbor, MD, USA
SB³C2016-140

Co-localizations and Correlations of Established and Emerging Indicators of Disturbed Wall Shear Stress at the Normal Carotid Bifurcation

Diego Gallo (1), David A. Steinman (2), Umberto Morbiducci (1)

(1) Department of Mechanical and Aerospace Engineering
Politecnico di Torino
Turin, Italy

(2) Department of Mechanical & Industrial Engineering
University of Toronto
Toronto, ON, Canada

INTRODUCTION

In arterial bifurcations the preferential development of atherosclerosis has been attributed to the atherogenic role played by low and oscillatory wall shear stress (WSS) on endothelial cells (ECs). This theory is challenged by evidences underlining how the ECs are exposed to a complex hemodynamic milieu that can be only partially described by the low/oscillatory WSS [1]. In fact, the established descriptors quantifying low and oscillatory WSS, proposed over the years as potential indicators and localization factors of vascular wall dysfunction, are significant but moderately weak predictors of vascular wall dysfunction. Discrepancies can be observed when comparing low/oscillatory WSS distribution with location of regions with lesion prevalence [1]. The endeavor to explain these discrepancies led to findings on ECs sensing of flow direction. In particular, there is evidence for a relation between flow directionality and ECs mechanotransduction pathway [2]. In this context, two different quantitative approaches for the characterization of WSS multidirectionality have been recently proposed, quantifying the WSS component orthogonal to the temporal mean WSS vector [1], or the WSS vector component aligned along the main flow direction [3]. However, an in depth, quantitative analysis of the extent of the co-localization of regions of low/oscillatory and multidirectional WSS at the luminal surface of the carotid bifurcation is still lacking.

Here we explore the relationship between the recently-proposed descriptors quantifying WSS multidirectionality and "established" WSS-based hemodynamic descriptors in a representative sample of subject-specific computational models of ostensibly normal carotid bifurcations. To do so, we quantitatively assess the co-localization of those descriptors at the luminal surface, aiming at providing connections (if any) among the peculiar hemodynamic features captured by the different descriptors.

METHODS

Data from this study are a subset (N=46) of the Vascular Aging – The Link That Bridges Age to Atherosclerosis (VALIDATE) study. The carotid geometry of each participant was acquired from contrast-enhanced angiography. Inlet/outlet velocities of each participant were acquired from phase contrast MRI to ensure patient-specific boundary conditions. As detailed elsewhere [4], lumen geometries were reconstructed from the thoracic segment of the common carotid artery (CCA) to above the bifurcation. The distributions at the luminal surface of five WSS-based descriptors were computed in the 46 cases. Three descriptors are "established" WSS-based descriptors, namely time-averaged wall shear stress (TAWSS), oscillatory shear index (OSI) and relative residence time (RRT). Two additional descriptors quantifying WSS multidirectionality are considered. The first is transWSS, defined as the time-averaged WSS component in the direction normal to the mean WSS vector direction along the cardiac cycle [1]. The second is the time-averaged value of the projection of the WSS vector along the main flow direction (WSS_{ax}), locally identified as the direction of the tangent to the vessel's centerline [3].

For OSI, RRT and transWSS threshold values were calculated corresponding to the 80th percentile value of the descriptor distribution of the combined surface of all models. For TAWSS, threshold values related to the 20th percentile were considered. Negative values were considered for WSS_{ax}, thus highlighting regions where WSS_{ax} direction is opposed to the main flow direction. For a given model, disturbed flow was quantified as its relative surface area (SA) exposed to OSI, RRT, or transWSS above (TAWSS and WSS_{ax} below) respective thresholds, normalized by the SA to the total surface area of the model clipped at CCA3, ICA5 and ECA2 (as in Figure 1). In this way, it was possible to characterize disturbed shear in each

Copyright 2016 The Organizing Committee for the 2016 Summer Biomechanics, Bioengineering and Biotransport Conference

carotid bifurcation by means of scalar values, hereafter denoted as TAWSS20, OSI80, RRT80, transWSS80, and WSS_{ax}^{-}, representing the fraction of the luminal surface exposed to "disturbed" shear.

The analysis of the co-localization of the considered indicators of disturbed shear can be thought of as consisting of two components. One component is correlation, evaluated through the Spearman rank correlation coefficient r for each of the 10 unique pairings of wall descriptors. The second component of co-localization analysis is co-occurrence, and consists in the evaluation of the spatial overlap of the SAs exposed to OSI, RRT, or transWSS above (TAWSS, WSSax below) respective thresholds. Co-occurrence of the two generic descriptors i and j was evaluated for each case by the similarity index (SI):

$$SI_{ij} = \frac{2 \times (SA_i \cap SA_j)}{SA_i + SA_j} \quad (1)$$

SI_{ij} ranges from 0 (SAs by the two descriptors have no spatial overlap) to 1 (SAs are equivalent and perfectly spatially overlapped). The distribution of the SI for two generic WSS-based descriptors was characterized in terms of median (Me) and median absolute deviation (MAD), to measure the dispersion.

RESULTS

An explanatory visualization of the identified SAs in a representative carotid bifurcation is shown in Figure 1. The correlations among the SA exposed to descriptors above or below the respective threshold show that the ranking of cases is similar for TAWSS20 and OSI80 (positive correlation, r=0.54). Strong positive correlations are observed also between RRT80 and both TAWSS20 and OSI80, as expected from RRT definition. WSS_{ax}^{-} is moderately positively correlated with OSI80 and transWSS80 (r=0.46 and r=0.53, respectively). A significant albeit weak negative correlation is found between transWSS80 and TAWSS20 (r=-0.43).

From the quantitative analysis of co-occurrence, evaluated in terms of SI distribution for the 10 pairings of WSS-based descriptors (Table 1), it emerges that the SA exposed to low WSS values co-localizes with the area exposed to high OSI (even though with a marked dispersion, MAD=0.13) and strongly with the area characterized by high RRT. The SI values between high transWSS and low TAWSS are very low, suggesting that the average WSS component orthogonal to the mean WSS direction is not characterized by low WSS values. It also emerges that regions of flow reversal are moderately co-localized with low WSS regions (Me=0.46). Considering OSI, it emerges that OSI co-localization with RRT is slightly weaker than TAWSS versus RRT, indicating that RRT is mainly biased by low WSS values rather than high OSI values. In addition, OSI co-localizes weakly with transWSS (Me=0.13), implying that OSI captures mainly oscillations along the mean WSS direction, rather than along the direction orthogonal to it. In this sense, OSI and WSS_{ax}^{-} are moderately co-localized (Me=0.56), suggesting that a relevant part of the WSS oscillation accounted for by OSI is aligned with the main flow direction, in regions where flow reversal is predominant. The two descriptors of WSS multidirectionality, transWSS and WSS_{ax}^{-}, are weakly co-localized (Me=0.14), implying that in areas of flow reversal the WSS component orthogonal to the mean WSS direction is low.

DISCUSSION

It is worth noting that OSI per se does not distinguish between uniaxial pulsatile flow and multidirectional flow, but insights into OSI nature at the carotid bifurcation are given here. High OSI at the carotid bifurcation is likely due to pulsatile flow with flow reversal in the axial direction, since high OSI co-localizes with negative WSS_{ax} and not with transWSS. The very weak or null co-localization observed between transWSS *vs*. the other descriptors likely reflects the fact that transWSS is highest at the bifurcation apex (Figure 1), while the other descriptors concentrate at the carotid bulb and around the bifurcation expansion. Interestingly, the use of transWSS in the study of onset of atherosclerosis at the carotid bifurcation seems to be questionable from our results, as the bifurcation apex, where transWSS concentrates, is not a common location where atherosclerosis is observed. It is likely that the different WSS features captured by the considered descriptors might have to be concurrent, in light of atherosclerosis initiation. Alternatively, the considered descriptors are just an "echo" of the complex mechanism that encompasses the vascular response.

In conclusion, the results of the present study suggest that, for the carotid bifurcation, the hemodynamic disturbances captured by the recently-proposed descriptors based on WSS multidirectionality are different from those given by low TAWSS and high OSI. Regions of low TAWSS and high OSI are not co-localized with high transWSS regions, and weakly with negative WSS_{ax} regions. In general, for practical purposes we suggest that the two categories of WSS descriptors ("established" descriptors, based on low and oscillatory WSS, and multidirectional WSS descriptors) represent different hemodynamic disturbances with different impact on ECs homeostasis, depending on the specific arterial district. However, the role of multidirectional WSS on carotid bifurcation pathophysiology needs to be clarified and further research is encouraged. Potentially, the considered descriptors could be part of WSS phenotypes more effective in localizing the map of vascular atherosclerotic lesions.

ACKNOWLEDGEMENTS

This work was supported by the Project for the Internationalization of Research 2014 from Compagnia di San Paolo Foundation and Politecnico di Torino.

REFERENCES

[1] Peiffer, V et al., *J Biomech*, 46:2651-2658, 2013.
[2] Martorell, J et al., *Cardiovasc Res*, 103(1):37-46, 2014.
[3] Morbiducci, U et al., *J Biomech*, 48:899-906, 2015.
[4] Gallo, D et al., *Ann Biomed Eng*, 43:68-81, 2015.

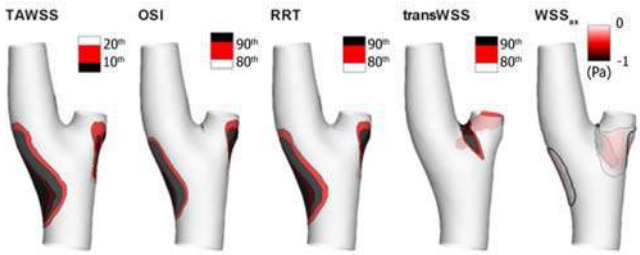

Fig. 1. WSS-based descriptors distributions for a representative case.

SI Me, MAD	OSI	RRT	transWSS	WSS_{ax}
TAWSS	0.69, 0.13	0.87, 0.05	0.00, 0.00	0.46, 0.12
OSI		0.80, 0.08	0.13, 0.08	0.56, 0.09
RRT			0.039, 0.03	0.50, 0.13
transWSS				0.14, 0.07

Table 1. Median (Me) and median absolute deviation (MAD) values for the 10 pairings of WSS-based descriptors. Pairings are determined by the intersection of row and column.

SB³C2016
Summer Biomechanics, Bioengineering and Biotransport Conference
June 29 –July 2, National Harbor, MD, USA
SB³C2016-142

IN VITRO CHARACTERIZATION OF TRACHEAL PRESSURES FOR INFANT NASAL AIRWAY REPLICAS RECEIVING HIGH-FLOW NASAL CANNULA THERAPY

D. Rebstock[1], I. M. Katz[2,3], M. L. Noga[4], G. Caillibotte[2], W. H. Finlay[1], A. R. Martin[1]

(1) Mechanical Engineering
University of Alberta
Edmonton, AB, Canada

(2) Medical R&D, Air Liquide Santé International,
Paris-Saclay Research Center
Les Loges-en-Josas, France

(3) Mechanical Engineering
Lafayette College
Easton, PA, USA

(4) Radiology and Diagnostic Imaging
University of Alberta
Edmonton, AB, Canada

INTRODUCTION

High-flow nasal cannula (HFNC) therapy has become ubiquitous in hospital settings as a form of respiratory support. During HFNC therapy, an oxygen/air blend is administered through nasal cannula at a high constant flow, intended to meet or exceed patient inspiratory flow rates. The exact mechanics of the therapy are not fully defined [1]. In particular, the airway pressures developed during HFNC therapy are of great interest, with an increase in positive end-expiratory pressure (PEEP) seen as a potential benefit in airway support and alveolar recruitment [1,2]. The present research focused on evaluating airway pressures in the application of HFNC therapy to infants.

Due to the invasive nature of acquiring the desired airway pressure and breathing pattern data, in vivo experiments in a clinical setting are challenging to perform [3]. Our work explored in vitro bench testing on realistic airway models as a promising method to investigate the physical phenomena involved in determining tracheal pressures during HFNC therapy.

METHODS

Ten realistic nasal airway replicas were previously built using rapid prototyping based on CT scans of infants ranging in age from 3 to 18 months [4]. The airways were deemed to be normal and healthy. For this study, each airway replica was supplied typical HFNC flow rates equivalent to 1 L/kg/min and 2 L/kg/min [1], with the weight of each subject calculated based on recorded age and sex [5,6].

Breathing was simulated using an ASL-5000 lung simulator (Ingmar Medical, PA). The lung was modeled as a single compartment, with the resistance being set individually for the inspiration (21 cm H20/L/s) and expiration (25 cm H2O/L/s) portions of the breath. The compliance of the lung model was set to 12 ml/cm H2O. The uncompensated residual capacity (URC) was set to 0.2 L. These URC, compliance, and resistance settings were predefined in the lung simulator's Infant Bronchiolitis breathing script and were held constant through all measurements. Experiments were performed in all ten replicas at breathing frequencies of 29 and 40 breaths per minute. A control measurement was taken for each airway replica at either breathing frequency, in which high flow was not supplied, and the cannula was not inserted. In these control measurements, simulated patient effort was adjusted individually for each replica in order to achieve tidal volume of 7 ml/kg, based on average tidal volume measured in infants with bronchiolitis [7].

The HFNC therapy was provided using a Precision Flow (Vapotherm Inc, MD). Temperature was regulated by the device to 37 degrees Celsius, and the fraction of inspired oxygen was set to 0.21. The same cannula (Pediatric Small; Vapotherm Inc, MD) was used for all 10 subjects. Subsequent data were obtained for dry air delivered using a mass flow controller (M-100; Alicat, AZ), where the outer diameter of the cannula prongs was slightly enlarged by wrapping with Parafilm (Bemis NA, WI). This procedure increased the outer diameter at the midpoint of the cannula prongs from 3.75 mm to 4.5 mm and 5.25 mm.

For data analysis, an annular area was defined as the difference between the cannula obstruction area and the total nostril area. A non-dimensionalized PEEP, K, was defined as

Copyright 2016 The Organizing Committee for the 2016 Summer Biomechanics, Bioengineering and Biotransport Conference

$$K = P/((\rho U^2)/2)(\quad (1)$$

where K is an Euler number, P is PEEP, ρ is the density of the gas, and U is the average velocity of the air through the annular area.

Reynolds numbers were calculated using the hydraulic diameter of the annular area as the characteristic length.

RESULTS

The peak expiratory pressures, positive end-expiratory pressures, and average inspiratory pressures were determined for all trials using the non-modified cannula (Table 1).

TABLE 1. AVERAGE PRESSURES VALUES

	Control	1 L/kg/min	2 L/kg/min
Peak Expiratory Pressure @ f=29 min^{-1} (cm H_2O)	1.4 ± 0.8	3.4 ± 0.9	8.0 ± 2.8
Peak Expiratory Pressure @ f=40 min^{-1} (cm H_2O)	1.6 ± 0.9	3.7 ± 0.8	8.2 ± 2.5
PEEP @ f=29 min^{-1} (cm H_2O)	-0.02 ± 0.01	1.7 ± 0.7	6.1 ± 2.5
PEEP @ f=40 min^{-1} (cm H_2O)	-0.03 ± 0.01	1.7 ± 0.6	6.3 ± 2.4
Average Inspiratory Pressure @ f=29 min^{-1} (cm H_2O)	-0.5 ± 0.4	0.7 ± 0.8	4.9 ± 2.5
Average Inspiratory Pressure @ f=40 min^{-1} (cm H_2O)	-0.9 ± 0.7	0.4 ± 0.9	4.5 ± 2.4

f = breath frequency
PEEP = positive end-expiratory pressure
Values expressed as mean ± standard deviation (n=10).

The non-dimensional pressure was calculated using the PEEP values for all the experimental trials as well as the additional occlusion trials (Figure 1). The data indicates that the non-dimensionalized PEEP increases with the annular area. A least square regression provides a linear relationship of with an R^2 value of 0.68.

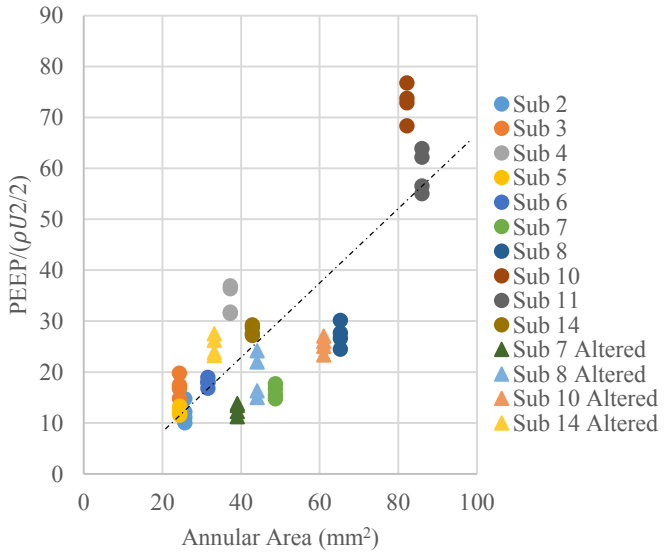

Figure 1: Non-Dimensionalized PEEP vs Annular Area

The Reynolds number was also calculated at PEEP for all the trials. The data indicates a downwards trend in non-dimensionalized pressure drop as the Reynolds number increases for each subject (not shown).

DISCUSSION

There is a significant increase in pressures from the 1 L/kg/min data to the 2 L/kg/min data. At the 2 L/kg/min level, the PEEP values are elevated to potentially clinically significant values for the majority of the subjects. For the 1 L/kg/min trials, no subjects achieve a clinically significant PEEP. Potential clinical significance was defined as being greater than 4 cm H_2O, the lower threshold in continuous positive airway pressure (CPAP) therapy (2).

There is a clear correlation between the annular area and the non-dimensionalized PEEP. Such a correlation allows delivered PEEP to be estimated based on a subject's nostril area, the outer diameter of the nasal prongs, the gas flow rate delivered through the nasal cannula, and the gas density.

ACKNOWLEDGEMENTS

The support of Alex Sagatov and Air Liquide Healthcare Canada in supplying the Precision Flow device and all associated consumables is gratefully acknowledged. This work was funded by Air Liquide.

REFERENCES

[1] Dysart K, Miller TL, Wolfson MR, Shaffer TH. Research in high flow therapy: mechanisms of action. Respiratory Medicine 2009;103(10):1400–5.

[2] Sinha IP, McBride AS, Smith R, Fernandes RM. CPAP and High-Flow Nasal Cannula Oxygen In Bronchiolitis. Chest. 2015;148(3):810-823

[3] Beggs S, Wong ZH, Kaul S, Ogden KJ, Walters JAE. High-flow nasal cannula therapy for infants with bronchiolitis (Review). The Cochrane Library 2014, Issue 1

[4] Storey-Bishoff J, Noga M, Finlay W.H.. Deposition of micrometer-sized aerosol particles in infant nasal airway replicas. Aerosol Science 39 (2008) 1055 – 1065

[5] CDC. Birth to 36 months: Boys Length-for-age and Weight-for-age percentiles. May 30, 2000

[6] CDC. Birth to 36 months: Girls Length-for-age and Weight-for-age percentiles. May 30, 2000

[7] Totapally BR , Demerci C, Zureikat G, Nolan B. Tidal breathing flow-volume loops in bronchiolitis in infancy: the effect of albuterol. *Critical Care* 2002, **6**:160-165

Copyright 2016 The Organizing Committee for the 2016 Summer Biomechanics, Bioengineering and Biotransport Conference

SB³C2016
Summer Biomechanics, Bioengineering and Biotransport Conference
June 29 –July 2, National Harbor, MD, USA
SB³C2016-143

FLOW DIVERTING CHARACTERISTICS OF ENDOLUMINAL AND INTRASACCULAR DEVICES: A COMPARISON

Fernando Mut (1), Pedro Lylyk (2), Davis F. Kallmes (3), Juan R. Cebral (1)

(1) Center for Computational Fluid Dynamics
George Mason University
Fairfax, VA, USA

(2) Interventional Neuroradiology
Instituto Clinico ENERI
Buenos Aires, Argentina

(3) Department of Radiology
Mayo Clinic
Rochester, MN, USA

INTRODUCTION

Cerebral aneurysms is a devastating disease with high mortality and morbidity rates [1]. Endoluminal flow diverters have been used successfully to treat large aneurysms with wide necks that cannot be treated with traditional techniques such as coils [2]. However, they may fail in preventing the blood flow from entering the aneurysm in the event, for example, of mal apposition against the vessel wall [3]. Intrasaccular flow diverters, although developed for the treatment of bifurcation aneurysms, may overcome this difficulty since they are released inside the aneurysm sack.

The purpose of this study was to compare the flow diversion effects of endoluminal and intrasaccular flow diverters in a saccular aneurysm.

METHODS

A cavernous aneurysm that was treated with an endoluminal flow diverter, and that remained open at a 6 month follow up was selected for this study (see Figure 1). A patient-specific model of the aneurysm and surrounding vessels was created from a 3D angiography taken prior to treatment [4].

Detailed models of the pipeline embolization device (PED) used for the treatment, and of an intrasaccular device (WEB) were created and virtually deployed. The virtual deployment process starts by computing a centerline at the location where the device will be released. Using this centerline, a cylindrical support surface is created and expanded until it completely touches the wall or the maximum allowed diameter has been reached. The "inflated" support surface is then used to obtain the device in its final "deployed" state, by means of a mapping process which takes into account foreshortening effects [5].

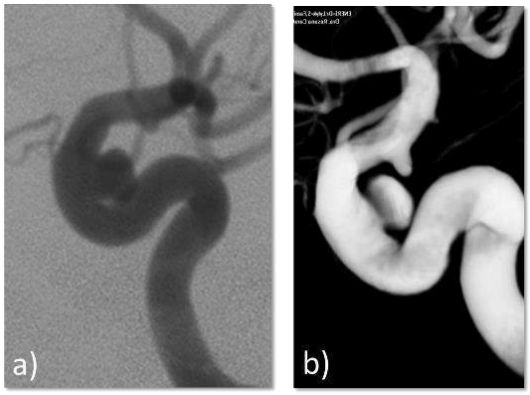

Figure 1: a) DSA before treatment, b) DSA at 6 months after treatment with PED

For this study, a set of three centerlines were computed: one following the parent vessel across the aneurysm neck (endoluminal), and two entering the aneurysm (intrasaccular) with slightly different angles in order to study two possible WEB deployment "scenarios". Since the intrasaccular devices are closed at the ends (as opposed to the endoluminal devices which are open ended), the support surface corresponding to such devices need to be closed before doing the mapping. For that purpose, each of the end sections of the cylinders was extruded toward its centroid following a user-given profile. Figure (2) shows an example of the deployment technique applied to the intrasaccular device in the reference configuration.

Copyright 2016 The Organizing Committee for the 2016 Summer Biomechanics, Bioengineering and Biotransport Conference

Four pulsatile computational fluid dynamics (CFD) simulations were performed using immersed unstructured grids [4]: 1) pre-treatment (PRE), 2) post-treatment with PED, 3) post-treatment with WEB (scenario 1) and 4) post-treatment with WEB (scenario 2).

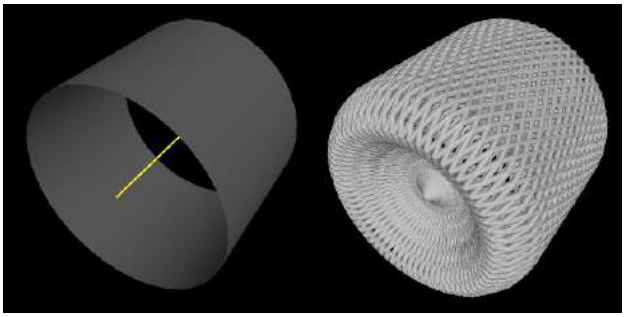

Figure 2: Virtual deployment: centerline and support surface (left), and device mapped on the support surface (right).

RESULTS

A comparison of the inflow streams at the peak systole before and after device implantation is presented in Figure 3. As it can be seen from the plots, the endoluminal device failed to substantially reduce the flow into the aneurysm because of mal apposition against the wall. On the other hand, both implantations of the intrasaccular device achieved a significant inflow reduction.

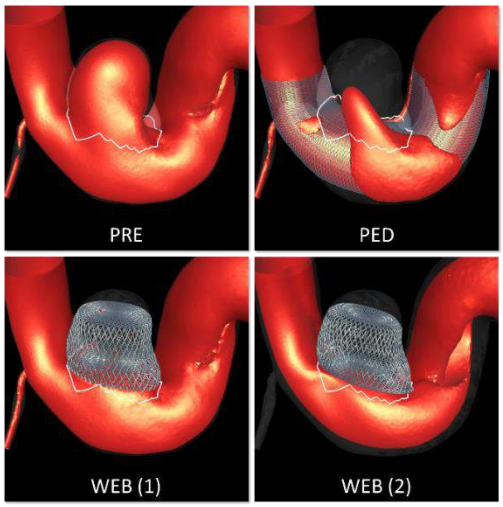

Figure 3: Inflow stream before and after device implantations.

The distribution of wall shear stresses (WSS) at the peak systole are shown in Figure 4. In this case, the endoluminal device performed better in protecting the wall at the neck of the aneurysm by means of flow redirection. In contrast, the intrasaccular device failed in preventing the blood flow from hitting the aneurysm neck, thus leaving this region unprotected, as in the pre-treatment case (see arrows).

A summary of the aneurysmal flow changes obtained for each of the device implantations is presented in Figure 5. The main hemodynamic variables that were considered for the comparison are: Mean Inflow Rate (Q), Mean Velocity (VEL), Mean Vorticity (VOR), Mean Viscous Dissipation (DISSIP), Mean Shear Rate (SR) and Mean Wall Shear Stress (WSS). As it can be seen, the intrasaccular device outperformed the endoluminal device in both scenarios. However, the WSS was better controlled by the endoluminal device due to its flow redirection effect.

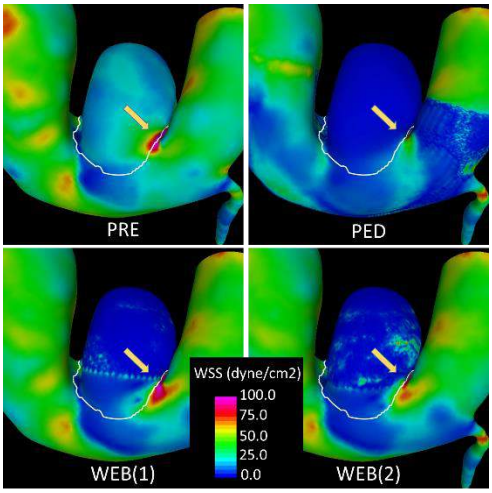

Figure 4: Wall Shear Stresses (WSS) before and after device implantations.

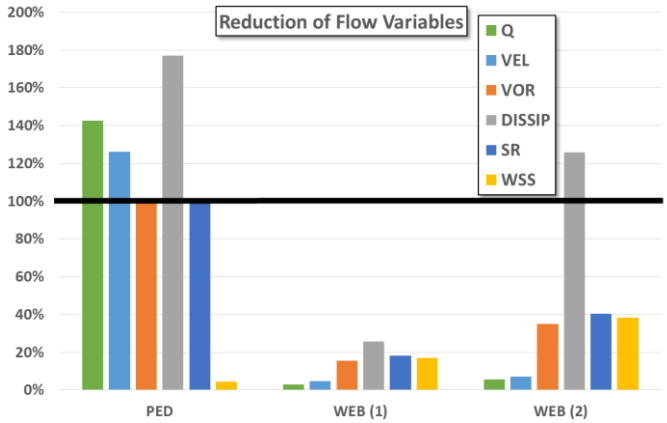

Figure 5: Changes in aneurysmal flow variables after implantation of PED or WEB devices.

DISCUSSION

Endoluminal flow diverting devices may result in poor hemodynamics performance due to mal apposition against the wall when deployed on irregularly shaped parent arteries. Intrasaccular flow diverters, although originally developed for bifurcation aneurysms, may solve this problem if the ostium is completely covered. However, while these devices may be more efficient in preventing the blood flow from entering the aneurysm sack, they may leave parts of the aneurysm neck exposed to the parent artery main flow.

In the case studied, the intrasaccular device had substantially larger flow diversion effects than the endoluminal device, suggesting that in this case a faster and complete occlusion of the aneurysm could have been achieved.

ACKNOWLEDGEMENTS

This work has been supported by the National Institutes of Health (NIH-NINDS) grant #R01 NS076491.

REFERENCES

[1] Rinkel, GJ et al. *Stroke,* 29: 251-9, 1998.
[2] Nelson, PK et al. *Am J Neuroradiol*, 32: 34-40, 2011.
[3] Mut, F et al. *J Neuro Interv Surg,* 7: 286-90, 2015.
[4] Cebral,JR et al. *IEEE Trans Med Imag,* 24: 468-77, 2005.
[5] Mut, F et al. *Am J Neuroradiol,* 33: 2010-16, 2012.

Copyright 2016 The Organizing Committee for the 2016 Summer Biomechanics, Bioengineering and Biotransport Conference

SB^{3}C2016
Summer Biomechanics, Bioengineering and Biotransport Conference
June 29 –July 2, National Harbor, MD, USA
SB^{3}C2016-144

SEX DIFFERENCES IN ACHILLES TENDON PROPERTIES THREE WEEKS AFTER INJURY IN RATS

G.W. Fryhofer, B.R. Freedman, A.M. Pardes, C.D. Hillin, L.J. Soslowsky

McKay Orthopaedic Laboratory
University of Pennsylvania
Philadelphia, PA, USA

INTRODUCTION

Achilles tendon ruptures are common injuries that result in significant pain and disability. Clinical studies demonstrate the risk of Achilles tendon rupture to be much lower in women compared to men, with as many as 84% of ruptures occurring in men [1]. It is not known if sex-related differences in injury may be extended to include differences in Achilles tendon healing, as well. Therefore, the objective of this study was to determine if sex or hormone-related differences are present in Achilles tendon healing following acute tendon rupture, in order to better inform sex-specific treatment recommendations. We hypothesized that healing female Achilles tendons would exhibit superior mechanical properties compared to healing male tendons; however, there would be no difference in the functional performance of male and female ankle and hindlimb. This study also includes a group of females that have undergone ovariectomy (OVX) to mimic ovarian hormone deficiency, and we hypothesized that tendons from OVX females would exhibit inferior mechanical properties and contribute to inferior ankle functional performance compared to non-OVX female Achilles tendon.

METHODS

Study Design: Male (400-450g), female (250-300g), and ovariectomized (OVX) female (250-300g) Sprague Dawley rats were used in this study. One group of animals was sacrificed as uninjured animals at ~19wks of age (n=12 each per M/F/OVX). The other group received 2 weeks of treadmill exercise training (up to 60 min/day at 10m/min) to ensure that animals could complete our rehabilitation protocol to be used following injury. Following exercise training, animals underwent surgical removal of the right central plantaris longus tendon and blunt transection of the right Achilles tendon mid-substance (n=16 per M/F/OVX, IACUC-approved). For OVX animals, ovariectomy was performed 4 weeks before Achilles tendon surgery (previous studies in female rats have demonstrated significant alterations in bone morphology and muscle mass as early as two and four weeks after ovariectomy [2, 3]). Following surgery, the right hindlimb of each animal was immobilized in full plantarflexion for 1 week, followed sequentially by 1 week of cage activity and 1 week of gradually increasing treadmill time (up to 60 min/day at 10m/min). All animals in the surgical group were euthanized at 3 weeks post-injury. *In vivo* Functional Evaluation: Passive ankle joint range of motion (ROM) and stiffness were measured using a custom torque cell and accelerometer-based device on anesthetized animals [4]. Ground reaction forces of the right hindlimb were also measured using an instrumented walkway equipped with a load cell [5]. *Ex vivo* Mechanical Testing: After euthanasia, the Achilles tendon-foot complex was carefully removed *en bloc*, fine dissected, measured for cross sectional area, and secured in fixtures. Tendons were imaged and mechanically tested (n=10/group) with a protocol that included stress relaxation (6% strain), low-load dynamic frequency sweep (0.1 to 10 Hz), and fatigue testing (~10-75% of ultimate failure load) at 2 Hz using a sinusoidal waveform until failure (Instron Electropuls 3000). Data Analysis: Functional ankle ROM and rotational stiffness (bilinear fit of torque-angle data for dorsiflexion and plantarflexion) were calculated. For mechanical testing data, Achilles tendon percent relaxation, dynamic modulus, dynamic stiffness, tanδ, hysteresis, laxity, and linear modulus were also computed [6]. To account for sex- and hormone-related differences in baseline properties, properties obtained for injured animals were normalized by group using values obtained from uninjured animals. One-way ANOVAs were performed for each *normalized* variable of interest at 3 weeks post-injury and, if found to be significant ($p < 0.05$), were followed by post-hoc t-tests (M vs. F, F vs. OVX) with Bonferroni corrections ($p < 0.025$).

Copyright 2016 The Organizing Committee for the 2016 Summer Biomechanics, Bioengineering and Biotransport Conference

RESULTS

At 3 weeks post-injury, relative dorsiflexion and plantarflexion ROM were superior in females compared to males; relative plantarflexion ROM was also superior in females compared to OVX (**Fig 1**). Females had relative plantarflexion toe-stiffness values closer to pre-injury values compared to both males and OVX; relative plantarflexion linear-stiffness was increased from pre-injury values in females compared to males, but similar to OVX. OVX had relative dorsiflexion toe-stiffness values closer to pre-injury values compared to females; there were no other differences in relative dorsiflexion stiffness between groups.

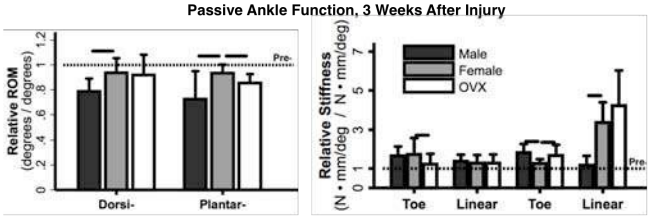

Figure 1: Ankle joint passive range of motion (ROM) and stiffness at 3 weeks post-injury in male (black), female (grey), and OVX (white) animals. Sex was a significant factor for relative ROM, toe-stiffness, and linear-stiffness at 3 weeks post-injury. Solid lines denote significance (p<0.025). Dashed line indicates "Pre"-injury baseline.

Active ankle function was also assessed at 3 weeks post-injury by measurement of relative ground reaction forces. Males exerted maximum relative braking force closer to pre-injury values compared to females (**Fig 2**). Females exerted relative lateral, braking, and vertical forces closer to pre-injury values compared to OVX.

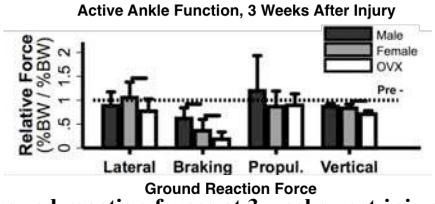

Figure 2: Ground reaction forces at 3 weeks post-injury. Sex was a significant factor determining active ankle functional performance. Solid lines denote significance (p<0.025).

Mechanical testing was performed on uninjured tendons and on tendons 3 weeks post-injury. In injured tendons, relative CSA, percent relaxation, strain (1Hz), hysteresis (50% fatigue life), and linear modulus were closer to pre-injury values in males compared to females (**Fig 3**). Females were closer to pre-injury values for relative tanδ (0.1Hz, 10Hz) and dynamic stiffness vs. males. Compared to females, OVX were closer to pre-injury values for relative hysteresis (50% fatigue life) and laxity (95% fatigue life). No other differences were present for relative stress, strain, tanδ, laxity, or cycles to failure.

DISCUSSION

Achilles tendon functional and mechanical properties were evaluated in males, females, and OVX three weeks after tendon injury.

With respect to active ankle functional measures, males performed "better" (i.e. closer to uninjured levels) than females, and females performed better than OVX. OVX has been associated with behavioral changes, including decreased cage locomotor activity [7]. Therefore, it is possible that the decreased relative ground reaction forces observed in the OVX group at 3 weeks post-injury may be the result of continued behavioral adaptation in the setting of recent ovariectomy. The functional data also suggest that the effect of male sex yields better functional outcomes 3 weeks post-injury compared to females, which mirrors clinical observations [8]. Such an interpretation of male functional advantage is challenged, however, by the results of passive functional testing, in which females had better relative ROM and better relative plantarflexion toe-stiffness than male and OVX, despite their "worse" relative plantarflexion linear-stiffness.

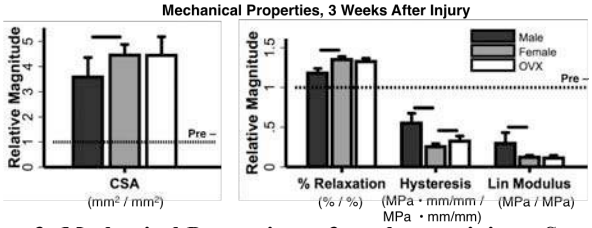

Figure 3: Mechanical Properties at 3 weeks post-injury. Sex was a significant factor determining relative cross-sectional area (CSA), % relaxation, hysteresis (at 50% fatigue life), and linear modulus. Solid lines denote significance (p<0.025).

Mechanical testing data reveal the post-injury properties of male tendons to be superior to those of female tendons. Relative percent relaxation and hysteresis in male tendons closer to baseline indicate that male tendons are able to return stored elastic energy in a manner more similar to uninjured tendon. Similarly, the increased relative linear modulus of injured male tendons compared to female tendons indicates that male tendons may more effectively transmit stress from muscle to bone. OVX does not appear to be a significant factor in determining tendon mechanical properties 3 weeks after injury, which is consistent with observations from a similar study of tendon healing at later time points [9]. Finally, the increased relative CSA in females compared to males may reflect a sex-related difference in scar formation and inflammatory response; increased testosterone levels associated with male sex could allow for a decreased inflammatory response in males compared to females [10].

This study does have some limitations. Despite steps to maximize human relevance through the use of clinically translatable immobilization and rehabilitation protocols, some elements of the study may not reflect a human environment. In addition, the data for injured tendons in this study were obtained at a relatively early phase of the recovery process, and it is likely that the functional and mechanical properties measured here will continue to evolve over time. And finally, without additional biological data, we are currently unable to provide a mechanism to explain why, compared to males, females exhibit inferior Achilles tendon healing at 3 weeks post-injury despite their relative protection against tendon injury at baseline. We are particularly interested in potential differences in the inflammatory response between sexes. Further work is needed to study tendon properties at later time points and to identify biological mechanisms to explain these sex-related differences in Achilles tendon healing.

ACKNOWLEDGEMENTS

This study was supported by NIH/NIAMS (R01AR064216S1), the NIH/NIAMS supported Penn Center for Musculoskeletal Disorders (P30AR050950), the NIH/NCATS (TL1TR000138), and NSF GRFP. The authors thank N. Salka and S. Weiss for their contributions.

REFERENCES

[1] Vosseller JT et al. *Foot Ankle Int*, 34:49-53, 2013. [2] Fisher JS et al. *J Appl Physiol*, 88:265-271, 2000. [3] Lambers FM et al. *Calcif Tissue Int*, 90:108-119, 2012. [4] Peltz CD et al. *J Orthop Res*, 28:841-845, 2010. [5] Sarver JJ et al. *J Biomech*, 43:778-782, 2010. [6] Freedman BR et al. *J Biomech*, 47:2028-2034, 2014. [7] Witte MM et al. *Gen Comp Endocrinol*, 166:520-528, 2010. [8] Silbernagel KG et al. *Orth J Sports Med*, 3:2325967115586768, 2015. [9] Circi E et al. *Int Orthop*, 33:1461-1466, 2009. [10] Malkin CJ et al. *J Clin Endocrinol Metab*, 89:3313-3318, 2004.

Copyright 2016 The Organizing Committee for the 2016 Summer Biomechanics, Bioengineering and Biotransport Conference

SB^{3}C2016
Summer Biomechanics, Bioengineering and Biotransport Conference
June 29 –July 2, National Harbor, MD, USA
SB^{3}C2016-145

EVALUATION OF SENSITIVITY AND ACCURACY OF INFRARED THERMOGRAPHY FOR MELANOMA SCREENING

L Li (1), A M LeBrun (2), L D T Topoleski (2), L Zhu (2)

(1) Department of Mechanical Engineering
Beijing University of Aeronautics & Astronautics
Beijing, China

(2) Department of Mechanical Engineering
University of Maryland Baltimore County
Baltimore, Maryland, USA

INTRODUCTION

It is well known that blood perfusion rate in tissue has a profound influence on its temperature. Based on the Pennes bioheat equation[1], local blood perfusion rate can act as either a sink or a source, depending on whether the local tissue temperature is higher or lower than the arterial temperature of 37°C. The thermal effect of local blood perfusion rate has been investigated in the past to extract its value based on transient temperature measurements[2-5]. All of the previous research has demonstrated that dynamic responses of skin temperature after heating or cooling may be sensitive to local blood perfusion rate in the targeted tissue region.

This study focused on evaluating approaches to increase sensitivity for screening melanoma using the temperature profile of the skin surface. It has been suggested that melanomas may have higher blood perfusion demands, due to their more aggressive nature and higher metabolism, than the surrounding skin. A 2-D heat transfer model consisting of a melanoma lesion embedded in a cylinder of tissue was developed. The model was used to investigate potential temperature differences between the melanoma lesion and its surrounding tissue, when the skin was initially subjected to a convection boundary and later subjected to a constant heat flux. Experiments were also performed using an infrared camera to record the skin surface temperature profile. The effect of the unknown emissivity of the skin and the influence of the surrounding environment on the recorded temperature reading were investigated.

METHODS

The computational thermal model consisted a melanoma (10 mm in diameter and 5 mm in thickness) embedded in a tissue cylinder (100 mm diameter and 60 mm height) (Figure 1). The geometries were selected because a large mole is one of the risk factors leading to melanoma, and the tissue cylinder was sufficiently large that the boundary conditions at the bottom and side surfaces did not affect the temperature field of the melanoma significantly. The top surface was initially subjected to a convection boundary condition (convection coefficient h =6 W/m^2 ^{o}C and air temperature T_{air}=20°C) under thermal neutral conditions. The boundary condition was changed to a combination of free convection and a constant heat flux impacting on the surface q_o''. The side surface of the tissue cylinder was adiabatic and the bottom surface had a prescribed constant temperature of 37°C.

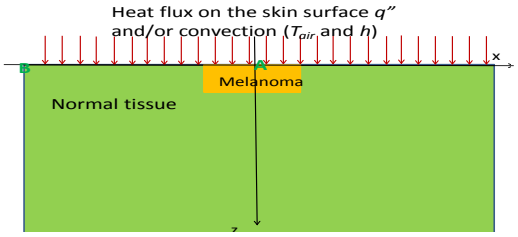

Fig. 1. Schematic diagram of the 2-D axisymmetric geometry of a melanoma embedded in a tissue cylinder.

The Pennes bioheat equation[1] was used to simulate the steady state or transient temperature field inside both the melanoma and the normal tissue, and is written as:

$$\rho c \frac{\partial T}{\partial t} = k\nabla^2 T + q_m + \omega\rho c(37 - T) \qquad (1)$$

where k is thermal conductivity, ω is the local blood perfusion rate, ρ is density, c is specific heat, and q_m is metabolic heat generation rate. Simulation of the transient temperature field was carried out by COMSOL 4.3 software. Sensitivity to meshing and time steps was examined to ensure that the maximum temperature changed by less

Copyright 2016 The Organizing Committee for the 2016 Summer Biomechanics, Bioengineering and Biotransport Conference

than 1% when the size of the elements and/or time step were decreased by 50%.

An infrared camera (Fluke Ti100, Everest, WA) was used to evaluate temperature uncertainty associated with an unknown skin surface emissivity. A temperature image of a skin surface requires inputs of both the emissivity and the environmental temperature. In this study, a thermal image of a skin surface was recorded both indoors and outdoors. The images were analyzed to assess the effects of the value of the emissivity on the temperature reading at a skin location.

RESULTS

All the properties used in the model are given in Table 1. Note that the blood perfusion rate of the melanoma was an order of magnitude larger than that of the normal tissue.

Table 1 Thermal and physiological properties of normal skin tissue, melanoma, and blood.

	ρ (kg/m^3)	c (J/kg°C)	k (W/m°C)	q_m (W/m^3)	ω (1/s)
Tissue	1000	3800	0.5	342	0.0003
Melanoma	1000	3800	0.5	2280-9120	0.002-0.008
Blood	1000	3800	0.5	n/a	n/a

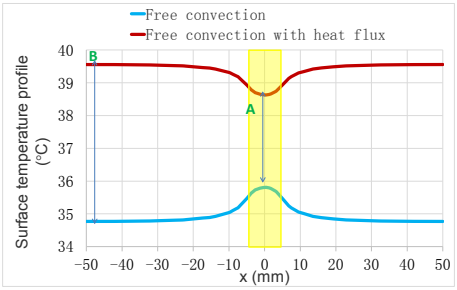

Fig. 2. Steady state surface temperature profiles under thermal neutral conditions (blue) and when the surface is subject to heating (red).

The steady state surface temperature profiles predicted by the model (Figure 2) shows the elevated temperature in the melanoma surface (blue line) due to its large blood perfusion rate (0.008 (1/s)), compared to that in the normal tissue (0.003 (1/s)). Under thermal neutral conditions, the temperature difference between them was approximately 1.03°C. Once the surface was subject to a constant heat flux of 140 W/m^2, the normal tissue temperature (location B) increased from 34.8 to 39.4°C (4.6°C), however, the temperature increase at the melanoma center was limited to only 2.8°C (from 35.8°C to 38.6°C). Therefore, the temperature elevation due to surface heat flux may be less profound to the larger blood perfusion in the melanoma lesion.

Figure 3 compares the transient temperature rises at a normal tissue location (location B in Figure 2) and at the center of the melanoma (location A in Figure 2) to evaluate how fast the temperature rises in the melanoma. It took several hours to establish a steady state. Examining the rise curves, 50% of the temperature rise occurred after heating for only 500 seconds. The temperature rise rate of the first 500 seconds at location B is 10%-47% higher than that at location A when the melanoma blood perfusion rate varied from 0.002-0.008 (1/s). Clinically, the skin surface with the melanoma lesion could be exposed to a heater to induce local temperature rises. However, it would not be feasible to wait several hours to establish the 2nd steady state (the red line in Figure 2).

The major challenge of implementing the approach is the unknown emissivity values of melanoma and normal skin. It has been shown that normal skin emissivity varies from 0.95 to 0.99, depending on skin tone. Many infrared cameras on the market use an equation to predict temperature that requires the emissivity value, as that given below, modified from Bernard *et al.*[6]:

$$T = \sqrt[4]{\frac{q_{ck}}{\sigma\varepsilon} - \frac{1-\varepsilon}{\varepsilon} T_{amb}^{\ 4}} \qquad (2)$$

where q_{ck} is the heat flux received by the camera and ε is the emissivity of the surface. The ambient temperature T_{amb} affects the reading only when the surface is not a blackbody surface. Figure 4 gives the deviation of the temperature reading from that when ε is selected as 1, based on inputs of ε and T_{amb} to the recorded infrared image of human skin using the infrared camera. In a room temperature environment (T_{amb} = 22.5°C), changing ε from 1 to 0.96 resulted in an uncertainty of 0.5°C. The potential error is more profound when T_{amb}=8.6°C, with a deviation of 0.83°C. The results from the camera reading are consistent with those predicted by Equation 2.

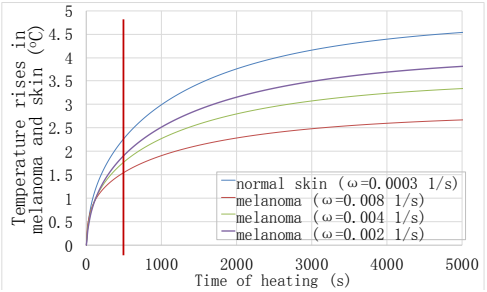

Fig. 3. Temperature rise curves after the skin is exposed to a constant of heat flux of 140 W/m^2.

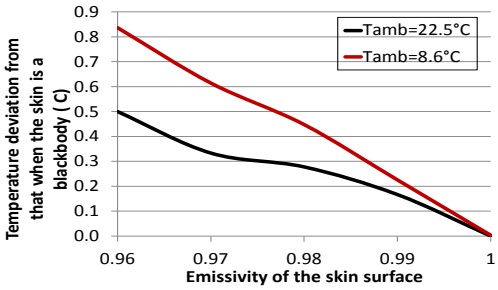

Fig. 4. Effect of skin emissivity and ambient temperature on the temperature reading of a skin location given by the Fluke camera.

In summary, the developed 2-D heat transfer model suggests that a normal temperature profile can be used to screen melanomas that have a large blood perfusion rate. A temperature rise rate after a surface heating is more sensitive and therefore better able to distinguish melanoma from normal tissue. However, caution is needed to interpret experimental results because the emissivity may not be known. The temperature reading error can be as large as 0.5°C in a normal room temperature environment, and the error is bigger (0.8°C) when the image is taken in a cooler environment.

ACKNOWLEDGEMENTS

This research was supported by UMBC and the Chinese Scholarship Council.

REFERENCES

[1] Pennes, H. H., 1948, *J. Applied Physiology*, 1, 93-122.

[2] Mudaliar, A. V., Ellis, B., Ricketts, P. L., Lanz, O. I., Lee, C. Y., Diller, T. E., and Scott, E. P., 2008, ASME *Journal of Biomechanical Engineering*, 130(6), pp. 061013(1-8).

[3] Liu, J., Zhou, Y. X., and Deng, Z. S., 2002, IEEE *Transaction in Biomedical Engineering*, 49, pp. 867-877.

[4] Centingul, M. P., and Herman, C., 2011, ASME *Journal of Thermal Science and Engineering Applications*, 3, pp. 031006(1-9).

[5] LeBrun, A and Zhu, L., 2015, SB^{3}C proceedings, paper #15-A-126-SB3C.

[6] Bernard, V., Staffa, E., Mornstein, V., and Bourek, A., 2013, *Physica Medica*, 29, pp. 583-591.

Copyright 2016 The Organizing Committee for the 2016 Summer Biomechanics, Bioengineering and Biotransport Conference

SB³C2016
Summer Biomechanics, Bioengineering and Biotransport Conference
June 29 –July 2, National Harbor, MD, USA
SB³C2016-147

INVESTIGATING THE *IN VITRO* AND *IN VIVO* BIOCOMPATIBILITY OF A NOVEL BIODEGRADABLE FE-316L STENT

Jennifer Frattolin (1,2), Richard Leask (3), Stephen Yue (4), Olivier F. Bertrand (1,5), Rosaire Mongrain (1,2)

(1) Department of Mechanical Engineering, McGill University, Montreal, QC, Canada

(2) Montreal Heart Institute Montreal, QC, Canada

(3) Department of Chemical Engineering, McGill University, Montreal, QC, Canada

(4) Department of Mining and Materials Engineering McGill University, Montreal, QC, Canada

(5) Interventional Cardiology Laboratories, Quebec Heart and Lung Institute, Laval University, Quebec City, Quebec, Canada

INTRODUCTION

Coronary artery disease (CAD) is the leading cause of death worldwide. The current trend in disease treatment has witnessed an innovative shift from permanent metallic stents to the implementation of biodegradable scaffolds. Clinicians and scientists agree that there are three general requirements for biodegradable stent feasibility: (1) its mechanical properties are similar to those of stainless steel 316L, the industry's gold standard for stent design; (2) the stent material is biocompatible, and its degradation products are non-cytotoxic and; (3) it has a controlled corrosion rate, with little degradation occurring during vessel remodeling (approximately 3–6 months), but completely degraded within 12–24 months [1]. The combination of these properties has yet to be realized in a single stent, however.

Therefore, a novel biodegradable metallic amalgamate for stent application has been proposed [2]. Cold-gas dynamic spraying (CGDS), with iron and stainless steel 316L powders, is utilized to fabricate a nanostructured biomaterial. This reduction in grain size leads to an improvement of the material's strength, fatigue and wear properties. In this study, the biocompatibility of the proposed Fe-316L stent is investigated through *in vitro* and *in vivo* tests. Cell viability was assessed by MTT assay on flat specimens [3], while stent deliverability and biocompatibility were evaluated through an *in vivo* animal stent implantation.

METHODS

Commercially available iron and stainless steel 316L powders (SandVik Osprey, United Kingdom) were mixed in a 4:1 weight ratio. Coatings were sprayed on 5 mm diameter cylindrical rods using cold spray, as shown in Figure 1(a-b). The rods were then heat treated at 1150°C in a tube furnace with oxidation control. To reduce coating thickness to approximately 0.25 mm, the specimens were ground utilizing centreless grinding (Figure 1(c)). Electrical discharge machining was utilized to separate the coating from the substrate, as shown in Figure 1(d). Lastly, femto laser cutting produced the desired stent cell design, followed by electropolishing (Figure 1(e)). The finalized stent was 0.8 cm in length, with a strut thickness of 145 μm.

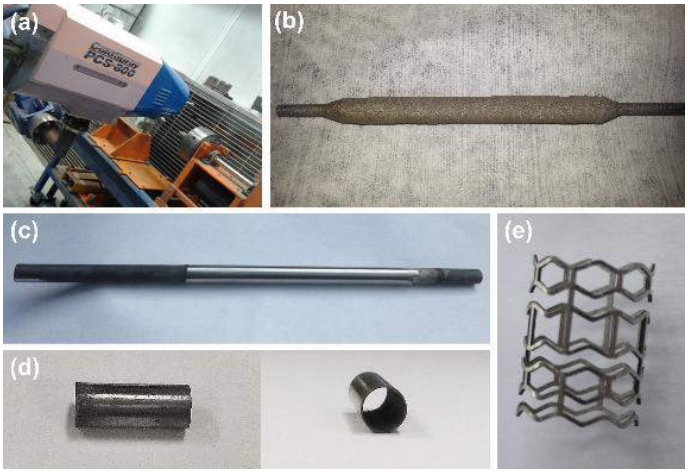

Figure 1: Stent manufacturing process: (a) cold-gas dynamic spraying, (b) coated specimens, (c) centreless grinding, (d) EDM, (e) femto laser cutting and electropolishing.

The biocompatibility of the proposed Fe-316L biodegradable was assessed through two investigations. First, a cell viability test was conducted, where endothelial cells from the human abdominal aortic artery, with added MTT (Sigma-Aldrich, M5655), were grown on the surface of 80Fe-20SS and SS316L flat specimens. A media only control

Copyright 2016 The Organizing Committee for the 2016 Summer Biomechanics, Bioengineering and Biotransport Conference

was also analyzed. After 24 hours, images were taken using a stereo microscope at 225x magnification. Cell viability was then determined by MTT assay, which measures the metabolic activity of cells. The specimens were incubated in a MTT solution (0.5 mg mL^{-1}) for 4 hours at 37°C. After incubation, the change in the absorbance was measured by spectrophotometer at 540 nm. The tests were conducted in triplicate.

A preliminary animal study was also conducted at AccelLAB (AccelLAB Inc., Canada) to assess stent deliverability and biocompatibility *in vivo*. Two Fe-316L stents were crimped on 5 mm diameter balloon catheters, and subsequently expanded in the left and right femoral arteries of an adult swine specimen. Four weeks post-insertion, the specimen was euthanized and the stented arteries were removed for histological examination and testing.

RESULTS

The biocompatibility of the Fe-316L stent was assessed by means of two different investigations; first, a cell viability test, and second, a preliminary *in vivo* study. The efficacy of endothelial cells to grow and proliferate on the 80Fe-20SS surface was evaluated by MTT assay. Stereo images of the specimen surface were taken after 24 hours. Oxidoreductase enzymes found in living cells will reduce MTT, a yellow tetrazole, to purple formazan. As evident by the purple pigmentation in Figure 3(a), cell growth was observed along the amalgamate's surface. When analyzing the results of the MTT assay (Figure 3(b)), it was found that the average mitochondrial activity of the 80Fe-20SS specimen was similar to that of 316L. Statistical analysis was performed utilizing Bonferroni's Multiple Comparison Test, where it was determined that the mitochondrial activity of the 80Fe-20SS was not significantly different from 316L.

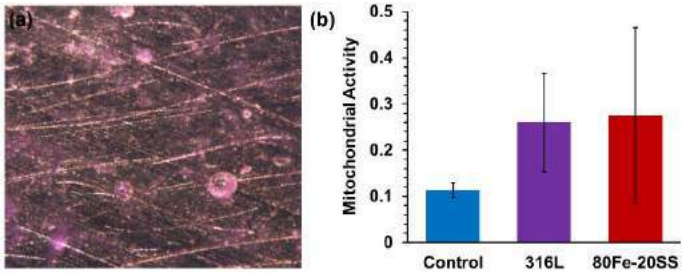

Figure 2: (a) Stereo image of 80Fe-20SS, and (b) mitochondrial activity of the tested specimens with cells (mean ± SD, n = 3).

A preliminary *in vivo* study was also conducted to further assess the biocompatibility of the proposed stent. The crimped stents were successfully expanded within the swine femoral arteries, and were visible under angiography and x-ray (Figure 3).

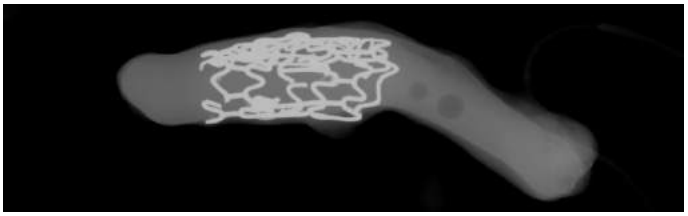

Figure 3: X-ray of expanded stent

The stented femoral arteries were removed from the swine specimen after four weeks for histological examination. When analyzing the cross-section of the stented artery, it was observed that no significant thrombus formation had developed after implantation (Figure 4(a)). In addition, degradation of the stent was also evident, where Fe^{2+} ions appear to diffuse into the surrounding arterial tissue (Figure 4(b)).

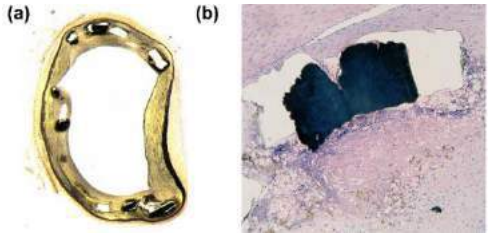

Figure 4: (a) Cross-section of the stented artery four weeks post-insertion, and (b) the degradation of a strut after four weeks.

DISCUSSION

In order for biodegradable stents to become a viable clinical alternative to permanent metallic stents, a critical requirement is that the material is biocompatible, and its degradation products are non-cytotoxic. Therefore, *in vitro* and *in vivo* tests were conducted to assess the biocompatibility of the proposed 80Fe-20SS biodegradable stent.

In order to facilitate vessel healing and remodeling post-insertion, it is critical that cells are able to grow, proliferate, and remain viable on the stent surface [4]. This was established through the cell viability test, where it was found that endothelial cells grew and proliferated on the 80Fe-20SS surface. In addition, the average mitochondrial activity of the amalgamate was similar to the gold standard of stent design, 316L.

For the MTT assay investigation, the test was conducted in triplicate, and the standard deviation showed a large variability in the mitochondrial activity of both 316L and 80Fe-20SS specimens. In particular for the 80Fe-20SS specimens, this variability may be a result of interference caused by specimen degradation during testing. The degradation products may cause interference with spectroscopy, which is employed to quantify the formazan colour shift induced by mitochondrial activity. If a significant degree of degradation occurred, this may introduce some error within the results, which is a limitation of the work. In future studies, more conclusive cell viability tests should be conducted, which avoid degradation product interference.

While this limitation may have an effect on the conclusive nature of the cell viability results, the biocompatibility of the proposed Fe-316L stent was evident during *in vivo* testing. Histological examination demonstrated that the 80Fe-20SS amalgamate did not induce a thrombogenic response *in vivo*. There was no significant evidence of thrombotic tissues, inflammation or neointimal proliferation. This animal study also established the ability of the stent to degrade *in vivo*. As shown in Figure 4(b), degradation products (Fe^{2+} ions) were found in the surrounding arterial tissue. This is critical to clinical implementation, as *in vitro* corrosion tests are often conducted in an environment that strays from a true physiological representation, which leads to an overestimate of the stent's degradation ability.

In the presented work, the biocompatibility of the proposed 80Fe-20SS biodegradable stent was assessed. The preliminary *in vitro* and *in vivo* results support the use of cold-gas dynamic spraying to fabricate a biocompatible metallic amalgamate for biodegradable stent application.

ACKNOWLEDGEMENTS

This research was supported by the Natural Sciences and Engineering Research Council of Canada (NSERC), and the McGill Engineering Doctoral Award (MEDA).

REFERENCES

[1] Serruys, PW et al. *N Engl J Med*, 354:483-495, 2006.
[2] Frattolin, J et al., *Ann Biomed Eng,* 2015. DOI:10.1007/s10439-015-1458-5.
[3] Sgarioto, M et al., *Front Bioeng Biotechnol,* 3:52, 2015
[4] Simsekyilmaz, S et al., *Thromb Haemost*, 113:464-472, 2015.

Copyright 2016 The Organizing Committee for the 2016 Summer Biomechanics, Bioengineering and Biotransport Conference

SB³C2016
Summer Biomechanics, Bioengineering and Biotransport Conference
June 29 –July 2, National Harbor, MD, USA
SB³C2016-148

BIFURCATION ANGLE AND FRACTIONAL FLOW RESERVE: A MULTISCALE NUMERICAL STUDY OF CORONARY BIFURCATION LESIONS

Catherine Pagiatakis (1,2), Jean-Claude Tardif (2,3), Philippe L'Allier (2,3), Rosaire Mongrain (1,2)

(1) Department of Mechanical Engineering
McGill University
Montreal, Quebec, Canada

(2) Montreal Heart Institute
Montreal, Quebec, Canada

(3) Faculty of Medicine
Université de Montréal
Montreal, Quebec, Canada

INTRODUCTION

Despite the designation of fractional flow reserve (FFR) as the gold-standard clinical diagnostic index for the functional evaluation of coronary lesions, it is used in less than 10% of all catheterization labs prior to percutaneous coronary intervention (PCI) [1]. The computation of FFR using numerical methods [2] is increasing in popularity, however there is much reservation in its clinical use. Interventional cardiologists thus still rely heavily on angiography to evaluate coronary lesion severity, despite its poor correlation with ischemic considerations [3]. Consequently, in order to improve the accuracy of the current diagnostic procedures, an understanding of the relative influence of geometric characteristics (of the stenoses and the arteries) on the induction of ischemia is required.

A notable proportion of all PCIs involves the treatment of coronary bifurcation lesions (CBLs). The study of CBLs is important because procedures are high risk and accurate angiographic evaluations are difficult to obtain due to complex bifurcation geometry [4]. Furthermore, CBLs are subject to haemodynamic interactions that complicate their dynamics and thus their clinical manifestation. To date, a systematic evaluation of the factors affecting CBL functionality (quantified by FFR), has not been executed.

Clinically, bifurcation angle is an important parameter because it influences the outcome of PCI [5]. Whereas in healthy bifurcations, the angle has been shown to affect the flow patterns in the daughter vessels [6], its effect on the clinical manifestation of CBLs remains unknown. Therefore, the objective was to compute and compare the FFR of different CBL configurations with varying angulations.

METHODS

A geometric multiscale (MS) computational fluid dynamics (CFD) model of an idealized left main coronary artery (LMCA) bifurcation was developed [7] and used to compute the flow-based FFR (ratio of the diseased to healthy flow), in each daughter vessel (Figure 1).

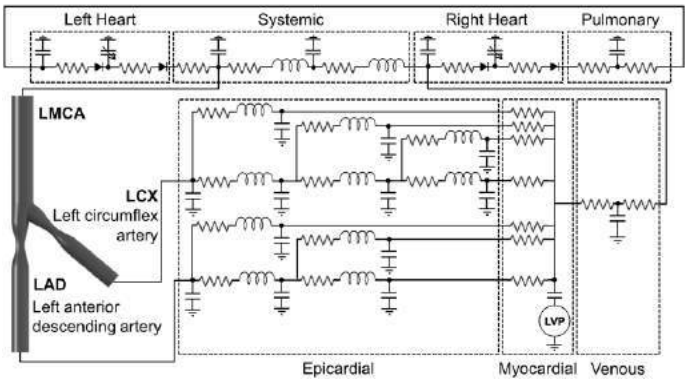

Figure 1: MS model of the LMCA bifurcation.

Four multilesional CBL configurations based on the Medina classification [7], four stenosis severities and five bifurcation angles were considered (total of 80 simulations, examples provided in Figure 2). The transient, incompressible and Newtonian Navier Stokes equations modelling the 3D fluid domain were solved using ANSYS Fluent (Canonsburg, PA, USA). Average uniform pressure boundary conditions were applied at the inlet and outlets and were calculated at each timestep from the nonlinear system of ordinary differential equations describing the dynamics of the 0D model. The heterogeneous coupling between the two models, achieved using a partitioned approach [8], was implemented directly within ANSYS by a fully-automated, in-house user-defined function written in C.

Copyright 2016 The Organizing Committee for the 2016 Summer Biomechanics, Bioengineering and Biotransport Conference

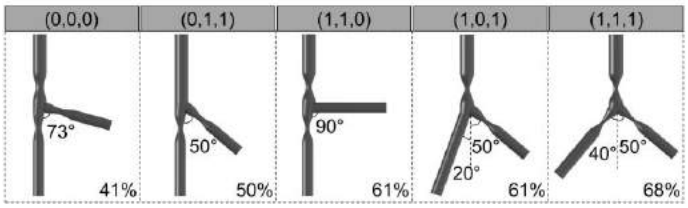

Figure 2: Examples of the CBL configurations, stenosis severities and bifurcation angles employed in the study.

RESULTS

For all configurations, when the angle of the LCX was varied between 50° and 90° relative to the centerline of the LMCA, differences in FFR were not observed in either of the daughter vessels, over the entire range of stenosis severities (Figure 3); the maximum relative difference in FFR between the angles was 1.0% and was recorded within the LAD of the (1,1,1) configuration with a 68% diameter reduction.

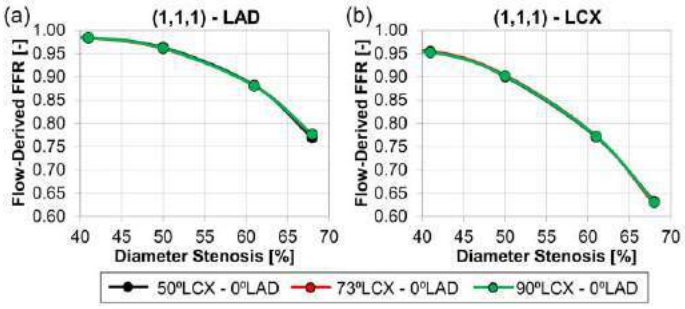

Figure 3: Effect of varying LCX angle on FFR within the (a) LAD and (b) LCX for the (1,1,1) configuration.

When the angle of the LAD was varied between 0° and 20°, for all configurations and diameter reductions, a negligible difference in FFR was observed (up to 1.7%) in both the LAD and the LCX (Figure 4). Interestingly, when further increasing the angle to 40°, configurations with a stenosis in the supplying vessel, namely the (1,1,0), (1,0,1) and (1,1,1) cases, resulted in an observable decrease in the LAD FFR and an increase in the LCX FFR, relative to the 0° geometry (Figure 4).

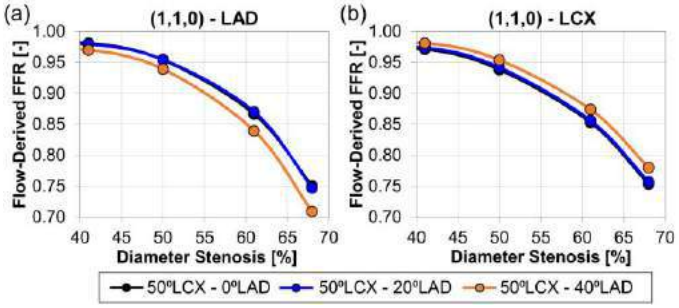

Figure 4: Effect of varying LAD angle on FFR within the (a) LAD and (b) LCX for the (1,1,0) configuration.

More specifically, the maximum relative difference in FFR, computed to be 5.7%, occurred in the LAD of the (1,1,0) configuration at a 68% diameter reduction. The corresponding increase in LCX FFR was on the order of 3.4%. The relative differences in FFR corresponded to absolute differences in FFR of 0.04 and 0.02 in the LAD and LCX respectively. The relative and absolute differences in FFR for the (1,0,1) and (1,1,1) configurations were of similar magnitude to that of the (1,1,0) configuration. Finally, in the (0,1,1) case, the relative difference in FFR with varying LAD angle remained below 1.0%.

DISCUSSION

Bifurcation angle displays significant interpatient variability, correlates with localized flow patterns in healthy daughter vessels [6] and influences the outcome of PCI. Although it is a key geometric parameter with important clinical implications, the presented work was the first, to the best of the authors' knowledge, to study its effect on CBL functionality.

In clinic, absolute differences of 0±0.04 have been recorded between successive FFR measurements [9]; as such the differences computed in the current study with varying angle were within the reported clinical variance, even for an LAD angle of 40° which displayed the most notable discrepancy compared to the remaining cases. The observed differences in the 40° LAD case are interestingly attributed to a shift in the carina towards the centerline of the LMCA, rather than to the change in bifurcation angle. In the configurations where the supplying vessel was diseased, there was a high momentum jet emerging from the neck of the LMCA stenosis which, due to the shift of the carina, resulted in an increase in flow to the LCX. This observation is supported by the fact that the decrease in LAD FFR was coupled with an increase in the LCX FFR. In addition, within the (0,1,1) configuration, negligible differences in FFR relative to the other angles were observed for the 40° LAD geometry.

Interventional cardiologists still rely on angiography to diagnose coronary lesions [1] despite its inability to identify the presence of ischemia. An understanding of the influence of geometric parameters on FFR could improve diagnostic accuracy of imaging techniques and thus better substantiate the decision to perform PCI. This idea is especially important in the case of CBLs, where PCI is high risk. In this study, by implementing a geometric MS CFD model, the functionality (FFR) was computed and systematically compared between different bifurcation angles in multilesional CBL configurations with varying stenosis severity. Although *in vivo,* coronary morphology is curved and tortuous, idealized geometries were employed in the simulations. The use of simplified geometries lends well to studies of parametric nature; in this study, it allowed to isolate the effect of a single geometric parameter on CBL functionality. This idea will also prove to be beneficial in future works where other geometric parameters (ex. lesion length) will be investigated so as to obtain a comprehensive view on CBL dynamics, although patient-specific geometry should eventually be utilized for corroboration purposes.

In summary, in the context of the current model, the results of the study indicate that bifurcation angle has a negligible effect on the functionality of CBLs.

ACKNOWLEDGEMENTS

The financial support of the Natural Sciences and Engineering Research Council of Canada Collaborative Health Research Projects grant (NSERC-CHRP grant no. 385833-10), the Canadian Institutes of Health Research grant (CIHR grant no. CPG-104292) and the McGill Engineering Doctoral Award is acknowledged.

REFERENCES

[1] Morris, PD et al., *J Am Coll Cardiol: Cardiovasc Interv*, 8:1009-1017, 2015.
[2] Norgaard, BL et al., *J Am Coll Cardiol*, 63:1145-1155, 2014.
[3] Pijls, NH, *Circ J*, 77:561-569, 2013.
[4] Louvard, Y et al., *Catheter Cardiovasc Interv*, 71:175-183, 2008.
[5] Amemiya, K et al., *Am J Cardiovasc Dis*, 4:168-176, 2014.
[6] Chaichana, T et al., *J Biomech*, 44:1869-1878, 2011.
[7] Pagiatakis, C et al., *J Biomech*, 48:3103-3111, 2015.
[8] Quarteroni, A et al., *Comput Vis Sci*, 4:111-124, 2001.
[9] Berry, C et al., *J Am Coll Cardiol*, 61:1421-1427, 2013.

Copyright 2016 The Organizing Committee for the 2016 Summer Biomechanics, Bioengineering and Biotransport Conference

SB³C2016
Summer Biomechanics, Bioengineering and Biotransport Conference
June 29 –July 2, National Harbor, MD, USA
SB³C2016-149

DEVELOPMENT OF A 3-D WHOLE BODY HEAT TRANSFER MODEL FOR ACCURATELY PREDICTING TIME OF DEATH IN FORENSIC SCIENCE

C Bartgis (1), A M LeBrun (1), A Saharkhiz (1), R Ma (1), L Zhu (1)

(1) Department of Mechanical Engineering
University of Maryland Baltimore County
Baltimore, Maryland, USA

INTRODUCTION

Determining postmortem interval is vital to the study of forensic science. Knowing the time of a murder can be used to exonerate or incriminate a person of interest. In the past two centuries, multiple approaches have been developed to determine postmortem interval using biochemical markers as well as physical measurements.[1] In additional to using biochemical markers appearing after death, body temperatures are normally measured to determine the time of death. The Algor Mortis approach provides a simple two-segment linearly declining temperature curve and uses a fixed temperature decay rate for the 1st 12 hours (~0.78°C/hr) and another decay rate for the 2nd 12 hours (~0.39°C/hr). Other approaches state that the temperature delay follows an exponential function with a time constant. A more accurate method was proposed to implement a correction factor into a body weight dependent formula to take into consideration of the number of layers of clothing, whether the air is still or moving, whether the clothing is dry or wet, etc.[1] Unfortunately, none of the methods have considered all the factors that may influence the cooling processes of the body.

This study is focused on developing a whole body heat transfer model to simulate not only the time decay after death, but also the temperature distribution of the body before the death. The steady state temperature field is also used to quantify the lumped thermal resistance between the skin and the environment based on an assumed thermal equilibrium before the death. From this initial temperature distribution, temperature decay curves at various body locations will be simulated postmortem and a curve fitting formula describing the cooling process will be tested for practical use.

METHODS

The whole body model shown in Figure 1 is based on a female having a height of 1.68 meters and a weight of 68 kilograms. The body is composed of five main sections: legs, arms, neck, torso, and head. For each section, a layer of skin, a layer of fat, and a region of muscle are the major components. In the torso, the internal organs are modeled as an embedded rectangular region that also has higher metabolism and blood perfusion rate than that of muscle. The Pennes bioheat equation, modified from the traditional heat conduction equation with extra source/sink terms describing the thermal effect of local blood perfusion rate ω and metabolism q_m, is used to simulate the temperature fields before and after death:

$$\rho_t c_t \frac{\partial T_t}{\partial t} = k_t \nabla^2 T + \omega \rho_a c_a (T_a - T_t) + q_m \qquad (1)$$

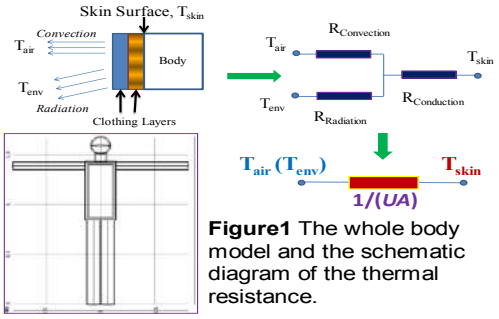

Figure1 The whole body model and the schematic diagram of the thermal resistance.

How easy to cool a body relies on thermal resistance between the skin surface and the environment (air). Combining the three resistances shown in Figure 1 and assuming that $T_{env}=T_{air}$, one can lump them into a single resistance $1/(UA)$, where U is the overall heat transfer coefficient describing thermal barrier between the skin and the air, and A is surface area of the body. We assume that the person would have proper clothing, move under the sun or in shade, etc., so that he/she feels thermally comfortable. The value of U is adjusted so

Copyright 2016 The Organizing Committee for the 2016 Summer Biomechanics, Bioengineering and Biotransport Conference

that a weighted average temperature of the body equals the arterial temperature at 37°C, when the body establishes a thermal equilibrium with the environment. The weighted average temperature is derived from the Pennes bioheat equation, and is defined as

$$\overline{T}_t = \iiint_V \omega T_t dV \Big/ \iiint_V \omega dV \qquad (2)$$

Eq. 1 without the last two source terms and the same overall coefficient U will then be used again in the postmortem simulation of temperature decays at various body locations.

RESULTS

Properties such as the density ρ, thermal conductivity k, and specific heat c, are listed in Table 1.[2] Table 2 shows how the air temperature affects the overall heat transfer coefficient. A smaller U associated with cold air temperature situations implies that the person wearing more clothing. When the air temperature decreases from 30°C to 10°C, the overall heat transfer coefficient decreases almost 80% from 5.5 to 1.2 W/m^{2}C, suggesting that the thermal resistance increases more than 350%. The last row of Table 2 gives the weighted average body temperature, which is very close to the arterial temperature of 37°C.

Table 1. Material properties of different tissue regions

Material	Skin	Fat	Muscle	Brain	Internal Organs
k (W/mK)	0.47	0.21	0.642	0.49	0.592
ρ (kg/m^3)	1085	900	1000	1080	1000
c (J/kg)	3680	3500	3500	3850	3500

Table 2. Overall heat transfer coefficient U and the calculated weighted average body temperature $\overline{T}_t$

T_{air} (°C)	10	15	20	25	30
U (W/m^2°C)	1.2	1.5	2	3	5.5
$\overline{T}_t$ (°C)	37.00	37.00	37.00	36.99	37.00

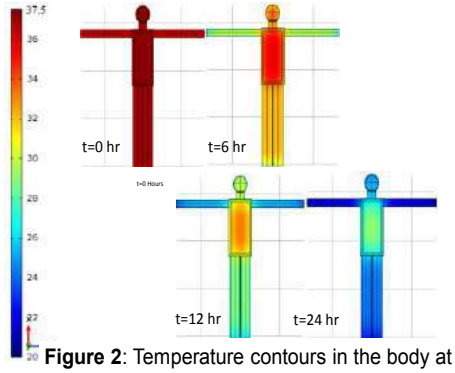

Figure 2: Temperature contours in the body at various time instants after death.

The upper left image in Figure 2 shows a cross sectional temperature field before death, with the hottest temperature in the body located in the internal organs and the brain, approximately 37.3°C, 0.3°C higher than the arterial blood of 37°C. The steady state temperature is slightly lower in the muscle regions and is the lowest in the skin region. The steady state temperature field agrees very well with previous simulations and literatures.[3] The other three images in Figure 2 illustrate how the body is cooled when subject to an air temperature of 20°C after death. One can see that the extremities cool at the most rapid rate, followed by the head, and the internal organs cool the slowest among all the body regions. After 24 hours the only noticeable temperature difference above the air temperature is located in the internal organs. The deep brain region has a temperature very similar to that in the internal organ before death; however, due to the small size of the head, its temperature decays faster than that of the internal organs.

In this study we propose a formula for practical use to fit the temperature decay curves, the formula is given below:

$$\Theta(t) = \frac{T(t) - T_{air}}{T_{initial} - T_{air}} = \begin{Bmatrix} 1 & t < t_{delay} \\ \exp\left[-\frac{t - t_{delay}}{\tau}\right] + & t \geq t_{delay} \end{Bmatrix} \qquad (3)$$

where t is the time, $\Theta(t)$ is the normalized temperature at a location, T_{air} is the environmental temperature, $T_{initial}$ is the initial temperature at the same specific location. The temperature is normalized so that Θ only varies between 1, when time is zero, and 0, when time is infinite. Based on our preliminary study, one finds that there is an initial period of t_{delay}, when the temperature at the tissue location is almost unchanged from its the initial temperature $T_{initial}$. After t_{delay}, the temperature decay is proposed to follow an exponential function. The R^2 values of all curve fittings are larger than 0.998.

At the head center, the fitted t_{delay} varies slightly around 1.6 hours for all the air temperatures, while t_{delay} is longer at the center of the internal organs, varying from 2.4 to 2.9 hours. The time constants for both locations are shown in Figure 3. The time constant τ provides the measurement window after death to be between 8 hours to 31 hours if the brain site is used, while τ increases 60%-95% at the internal organ site. The time constant is larger when the body is exposed to colder air, since a person usually wears more clothing when it is cold outside to keep the body warm and comfortable. Assuming that after death, the body has the same clothing as that before the death, the larger thermal resistance due to clothing in colder air would slow down heat conduction from the body core to the skin, leading to a slower cooling rate of the body.

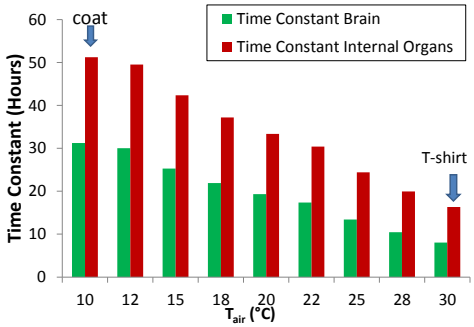

Figure 3:Effects of the air temperature and body location on the time constant.

In summary, we have articulated the limitations of current practices of determining post mortem time in practice, and elaborated the rationales of simulating temperature cooling curves based on development of rigorous 3-D whole body heat transfer models. The results given in this study has demonstrated the accuracy of determining the overall heat transfer coefficient or the thermal resistance between the skin and air via an indirect approach assuming thermal equilibrium. The curve fitting techniques used in this study have been tested to understand how the air temperature affects the overall heat transfer coefficient, the initial time delay, and the time constant associated with the body cooling.

ACKNOWLEDGEMENTS

This research was supported by UMBC.

REFERENCES

[1] Payne-James, J., Jones, R., Karch, S. and, Manlove, J. (2011). Simpson's Forensic Medicine London, England: Hodder and Stoughton Ltd.

[2] Erdmann, B., Lang, J. and, Seebass, M. (2006). *Annals of the New York Academy of Sciences*, 858:36-46.

[3] Zhu, L., Schappeler, T., Cordero-Tumangday, C., and Rosengart, A. J. (2009) *Advances in Numerical Heat Transfer*, 3, 197-219.

Copyright 2016 The Organizing Committee for the 2016 Summer Biomechanics, Bioengineering and Biotransport Conference

SB³C2016
Summer Biomechanics, Bioengineering and Biotransport Conference
June 29 –July 2, National Harbor, MD, USA
SB³C2016-150

MODELING AND OPTIMIZATION OF SILICA GEL ENCAPSULATED SYNERGISTIC BACTERIA

Baris R. Mutlu (1), Jonathan K. Sakkos (1), Sujin Yeom (2), Lawrence P. Wackett (2,3), Alptekin Aksan (1,3)

(1) Department of Mechanical Engineering, University of Minnesota, Minneapolis, MN 55455, USA

(2) Department of Biochemistry, Molecular Biology and Biophysics, University of Minnesota, Minneapolis, MN 55455, USA

(3) BioTechnology Institute, University of Minnesota, St Paul, MN 55108, USA

INTRODUCTION

Synergistical bacterial species can perform more varied and complex transformations of chemical substances than either species alone, but this is rarely used commercially because of technical difficulties in maintaining mixed cultures. Typical problems with mixed cultures on scale are unrestrained growth of one bacterium, which leads to suboptimal population ratios, and lack of control over bacterial spatial distribution, which leads to inefficient substrate transport. To address these issues, we designed and produced a synthetic ecosystem by co-encapsulation in a silica gel matrix, which enabled precise control of the microbial populations and their microenvironment. As a case study, two greatly different microorganisms: *Pseudomonas sp.* NCIB 9816 and *Synechococcus elongatus* PCC 7942 were encapsulated. NCIB 9816 can aerobically biotransform over 100 aromatic hydrocarbons, a feat useful for synthesis of higher value commodity chemicals or environmental remediation. In our system, NCIB 9816 was used for biotransformation of naphthalene (a model substrate) into CO2 and the cyanobacterium PCC 7942 was used to provide the necessary oxygen for the biotransformation reactions via photosynthesis (Figure 1). A mathematical model was constructed to determine the critical cell density parameter to maximize oxygen production, and was then used to maximize the biotransformation rate of the system. Experimental results showed that the system was able to support the oxygen demand of the biotransformation reactions, and performed better than oxygenation by external supplementation. It is proposed that this was due to micron-scale proximity of the co-encapsulated bacteria, which was verified by confocal microscopy.

METHODS

Silica gel synthesis and encapsulation of bacteria

Tetraethyl orthosilicate (TEOS) was hydrolyzed by stirring 2 h at a 1:5.3:0.0013 molar ratio of TEOS:water:HCl. The pH of the SNPs was adjusted to 7.4 by adding 1M hydrochloric acid. After pH adjustment, PBS was added to further stabilize the pH of the SNPs and improve overall cytocompatibility of the solution. Bacteria suspension was added to SNP/PBS solution, and hydrolyzed TEOS was added to the SNP/PBS/bacteria solution by pipetting a few times to obtain a homogeneous sample. Final volume of the gels consisted of 40% of silica precursors (TEOS + SNP) and 60% of (PBS + Bacteria suspension).

Oxygen generation/consumption and naphthalene biotransformation rate measurement

Oxygen generation and consumption rates of the silica gel encapsulated bacteria were measured by using an Oxygraph Oxytherm System (Hansatech Instruments Ltd., United Kingdom). Silica gels were made into cylindrical 200 µL test pieces by mixing the reagents and bacteria suspension in a 96-well plate. After gelation, a thin copper wire was used to extract the test pieces (radius = 0.32 cm and height = 0.62 cm) and suspend them in the reaction chamber during measurement. For oxygen production measurements with cyanobacteria containing gels, 3 mL of PBS was added to the chamber and the LED was turned on to provide light to the cyanobacteria. For oxygen consumption measurements with NCIB 9816 containing gels, 3 mL solution of PBS saturated with naphthalene was added to the chamber.

For biotransformation rate measurements, NCIB 9816 and PCC 7942 were mixed gently via vortexing prior to encapsulation. Silica gels with co-encapsulated cells were synthesized (500 µL volume, height = 0.15 cm) in septa sealed, glass vials. After gelation, 9 mL of saturated naphthalene + BG11 solution was added on top of the gel, ensuring that the vial was completely filled before sealing (except for the samples with additional 4 mL of headspace). Then, the samples were placed on a shaker setup and naphthalene concentrations in the solution were measured intermittently, as described in [1].

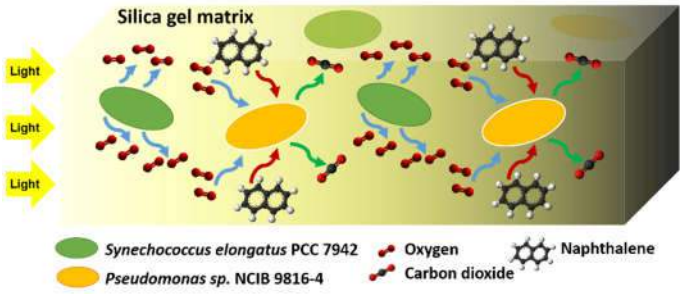

Figure 1 – Silica gel encapsulated synergistic bacteria

RESULTS

Modeling of oxygen generation by silica gel encapsulated PCC 7942

Light intensity varies through the gel as both the silica gel and the encapsulated bacteria within contribute to light attenuation (At) via absorption and scattering, and can be modeled by a modified Beer-Lambert law as follows:

$$At(\rho, x) = \frac{-(C_1\,\rho + C_0(1-\rho))}{C_S}x \quad (1)$$

where attenuation coefficient C_1 represents the contribution of cells to light attenuation, C_0 represents the contribution of the gel to light attenuation, C_S represents the contribution of the back-scattering effects,

Copyright 2016 The Organizing Committee for the 2016 Summer Biomechanics, Bioengineering and Biotransport Conference

ρ is the cell density (of the photosynthetic bacteria), and x is the pathlength of light in the gel.

Coefficients of Eq. 1 were determined experimentally by measuring light transmittance through silica gel with encapsulated PCC 7942 at different cell densities, as well as with free PCC 7942 in suspension (C_1 = 116.42 mL/(mL cells-cm) and C_0 = 0.089 1/cm). Using Eq. 1, transmittance (T) at a distance x from the gel surface for encapsulated PCC 7942 was determined as:

$$T(\rho, x) = exp(-At) = exp(-(C_1\,\rho + C_0(1-\rho))x) \quad (\mathbf{2})$$

Based on Eq. 2, two volume elements (Figure 2a) for cells encapsulated in a silica gel of uniform cross-section (UCS) and non-uniform (cylindrical) cross-section (NUCS) were defined. For UCS, a differential volume can be defined as:

$$dV = A\,dx$$

where A is the uniform cross-sectional area (the differential volume definition and the derivation of the following equations for NUCS is not discussed here). Oxygen generation rate of cyanobacteria is known to be linearly correlated with light intensity up to a saturation limit where photo-inhibition effects start damaging the oxygen evolution complex [2]. The system was designed to operate below the saturation limit, so the net oxygen generation rate ($d\dot{q}$) in the differential volume was defined as:

$$d\dot{q} = (k_{gen}\rho_C T(\rho_T, x) - k_{con}\rho_C - k_{deg}\rho_N)dV \quad (\mathbf{3})$$

where $\boldsymbol{k_{gen}}$ is O_2 generation rate constant per unit volume of PCC 7942, $\boldsymbol{k_{con}}$ is O_2 consumption rate constant per unit volume of PCC 7942, $\boldsymbol{k_{deg}}$ is O_2 consumption rate constant during naphthalene transformation per unit volume of NCIB 9816. The net oxygen generation rate in the volume was then obtained by integrating Eq. 3 over the whole volume, and incorporating the consumption by the NCIB 9816, as shown in Eq. 4:

$$\dot{Q} = \int_{x=0}^{x=L} (k_{gen}\rho_C T(\rho_T, x) - k_{con}\rho_C - k_{deg}\rho_N)A\,dx \ \text{(UCS)} \quad (\mathbf{4})$$

The results obtained from the mathematical model were verified experimentally. Cell density (ρ_C) was varied from 1% to 30% [v/v] in the silica gel with PCC 7942 to determine how ρ_C affected oxygen generation rate. The net oxygen generation rate of the whole gel increased with increasing ρ_C up to a certain point, then slightly decreased (Figure 2b). The maximum oxygen generation rate of 3.7 ± 0.7 nmoles/min was achieved at ρ_C = 20% [v/v]. Base oxygen consumption rate constant of PCC 7942 (k_{con}) was measured in the absence of light as 22.1 ± 1.7 nmoles/(min.mL-cells). Incorporating k_{con} and other known experimental parameters for encapsulated cells into Eq. 4, k_{gen} was determined as 721.74 nmoles/(min.mL-cells), and C_s was determined as 1.88 with a fit as shown in Figure 2b (red line). For comparison, a model that did not incorporate the back-scattering effects is also shown in Figure 2b (blue line). The model with the back-scattering effects was then used to optimize the relative densities of the co-encapsulated cells for naphthalene biotransformation.

Optimization of the co-encapsulation matrix and synergistic biotransformation study

The goal of the optimization study was to maximize the biotransformation rate of naphthalene to CO_2 while minimizing the required amount of cells. We proposed that under optimal operating conditions, the system is to have neither an oxygen surplus (*i.e.* excess PCC 7942) nor an oxygen deficit (*i.e.* excess NCIB 9816). This design requirement was satisfied by solving Eq. 4 for $\dot{Q} = 0$, which yielded a non-linear ρ_C vs. ρ_N curve (Figure 2c). It can be seen that ρ_C increased with increasing ρ_N, up to ρ_N = 0.4% [v/v] where a ρ_{cr} value of 40% [v/v] was reached. If ρ_N is increased beyond this critical point, additional PCC 7942 cannot provide more oxygen for the biotransformation reactions, yielding an oxygen deficit ($\dot{Q} < 0$).

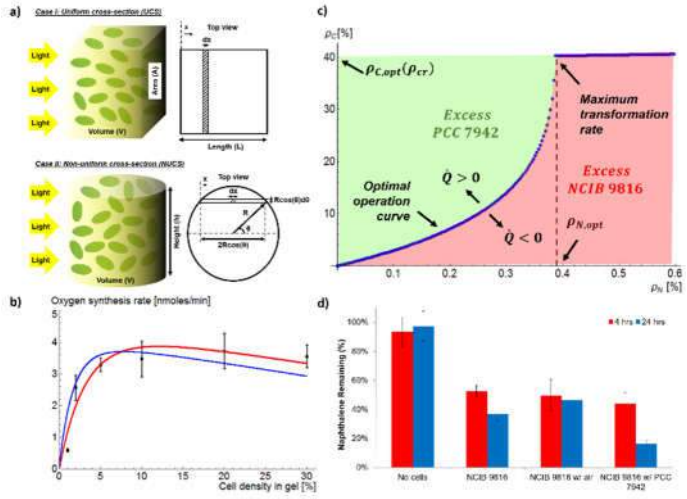

Figure 2 – Oxygen generation modeling and naphthalene biotransformation optimization results

Naphthalene biotransformation experiments with silica gel co-encapsulated cells were tested with four cases: (I) No cells: Silica gel without cells, (II) NCIB 9816: Silica gel encapsulated NCIB 9816, (III) NCIB 9816 with air: Silica gel encapsulated NCIB 9816 with additional headspace which provides additional oxygen for biotransformation reactions and (IV) NCIB 9816 with PCC 7942: Silica gel co-encapsulated NCIB 9816 and PCC 7942. In Case I, naphthalene concentration decreased only slightly over 24 hours (Figure 2d), verifying that the disappearance of naphthalene due to effects other than biotransformation was minimal. For cases II, III and IV, naphthalene concentrations were comparable after 4 hours at 52.3 ± 4.1%, 49.8 ± 10.9% and 43.9 ± 7.6% respectively. These values indicated that when a sufficient amount of dissolved oxygen was present in the solution, oxygen generation by encapsulated cyanobacteria did not make a difference. At 24 hours, the naphthalene concentrations in cases II and III were still comparable, whereas the naphthalene concentration for case IV was measured as 16.3 ± 2.3%, which was significantly lower than cases II and III. This indicated that dissolved oxygen was depleted in solution sometime between 4 and 24 hours, and after the depletion of dissolved oxygen, PCC 7942 provided oxygen to further drive the biotransformation reactions. Experimental results also verified that oxygenation via co-encapsulated PCC 7942 (Case IV) was more efficient than providing oxygen externally (Case III).

REFERENCES

[1] Sakkos JK, Kieffer DP, Mutlu BR, Wackett LP, Aksan A. Engineering of a silica encapsulation platform for hydrocarbon degradation using Pseudomonas sp. NCIB 9816-4. Biotechnology and bioengineering 2015.

[2] Bechet Q, Shilton A, Guieysse B. Modeling the effects of light and temperature on algae growth: State of the art and critical assessment for productivity prediction during outdoor cultivation. Biotechnology Advances 2013;31(8):1648-63.

Copyright 2016 The Organizing Committee for the 2016 Summer Biomechanics, Bioengineering and Biotransport Conference

SB^{3}C2016
Summer Biomechanics, Bioengineering and Biotransport Conference
June 29 –July 2, National Harbor, MD, USA
SB^{3}C2016-151

MECHANICAL CONTROL OF ENDOCHONDRAL BONE REGENERATION BY ENGINEERED CHONDROGENIC MESENCHYMAL CONDENSATES

Anna M. McDermott (1,*), Samuel Herberg (2,*), Hope B. Pearson (1), Devon E. Mason (1), Eben Alsberg(2,†), Joel D. Boerckel (1,†)

(1) Aerospace and Mechanical Engineering
University of Notre Dame
Notre Dame, Indiana, USA

(2) Biomedical Engineering
Case Western Reserve University
Cleveland, OH, USA

INTRODUCTION

Long bone morphogenesis is initiated by condensation of mesenchymal cells in the early limb bud and progresses through chondrogenic differentiation and subsequent hypertrophy, forming the cartilaginous anlage that serves as a template for endochondral bone formation [1]. This process is remarkably efficient, forming a vascularized, hierarchical architecture capable of longitudinal growth. This endochondral ossification process is also recapitulated in fracture healing through callus formation and has inspired biomimetic tissue engineering paradigms that aim to replicate development for postnatal tissue regeneration [2,3].

Strikingly, the process of endochondral ossification in both development and fracture healing is controlled by extrinsic mechanical stimuli. *In utero*, chemical or surgical induction of muscular paralysis inhibits longitudinal and volumetric bone growth through reduced chondrocyte proliferation and delayed ossification [4]. Similarly, in fracture healing, compressive interfragmentary motion is necessary for cartilaginous callus formation and endochondral healing [1]. However, the role of mechanical loading in endochondral bone defect regeneration has not been investigated.

Here we report the necessity of *in vivo* mechanical loading for functional bone regeneration through endochondral ossification of human mesenchymal stem cells, self-assembled in high-density sheets with growth factor-releasing gelatin microspheres to replicate the chondrogenically primed mesenchymal condensate found in early endochondral bone development [1]. This approach eliminates the typical need for lengthy chondrogenic pre-differentiation *in vitro*, and enables direct investigation into the temporal interactions between endochondral lineage specification and mechanical stimulation *in vivo*.

We hypothesized that the timing and magnitude of mechanical loading *in vivo* would control cell differentiation and endochondral ossification for functional regeneration of large bone defects.

METHODS

Chondrogenically-primed engineered mesenchymal condensates were created by seeding hMSCs mixed with recombinant human transforming growth factor-β1 (TGF-β1)-bound gelatin microspheres (GM) on 12 mm transwell plates (3μm pore size) at a density of 2 x 10^6 cells/well [5]. High density cell sheets were self-assembled for 2 days *in vitro* prior to histology and message-level gene expression analysis or implantation. Each sheet received 600 ng TGF-β1.

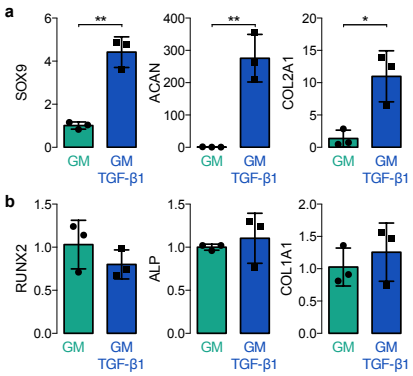

Figure 1: Engineered mesenchymal condensates at day 2 *in vitro*. (a) mRNA expression of chondrogenic markers SOX9, Aggrecan (ACAN), and Collagen 2A1 (COL2A1). (b) mRNA expression of osteogenic markers RUNX2, Alkaline phosphatase (ALP), and Collagen 1A1 (COL1A1). For each, expression is normalized to GAPDH and growth factor-free gelatin microsphere-containing controls (GM). * p < 0.05, ** p < 0.01; Student's t-test.

Critical sized 8 mm segmental bone defects were created in 14 week-old male RNU nude rat femora and stabilized with custom fixation plates that allow controlled transfer of ambulatory loads *in vivo* [6]. The experimental design featured three groups: control limbs (stiff) were stabilized with fixation plates that limited load transfer (k_{axial} = 214 N/mm). Early loading limbs were stabilized by axially compliant fixation plates (k_{axial} = 8.4 N/mm) that allowed load transfer immediately upon implantation (early). Delayed loading limbs were stabilized by the same compliant plates initially implanted in a locked configuration to prevent loading, but after four weeks the plates were surgically unlocked to enable load transfer (n = 9-10 per group).

In all three groups, each defect received three high-density cell sheets, contained within perforated electrospun polycaprolactone nanofiber mesh tubes [6] for a total of 6 x 10^6 cells and 1.8 μg TGF-β1

Copyright 2016 The Organizing Committee for the 2016 Summer Biomechanics, Bioengineering and Biotransport Conference

per defect. Bone regeneration was longitudinally evaluated *in vivo* by radiographs and microCT, with post-mortem analysis at week 12 by high-resolution (20 μm voxel size) microCT, torsional testing to failure, and histology. Mechanical properties were compared to age-matched un-operated limbs (n = 7). To distinguish between cell-mediated and growth factor-mediated bone regeneration, an additional stiff fixation plate group was included featuring the same cell sheets, except the cells were devitalized by three freeze-thaw cycles immediately prior to implantation (n = 6).

Bridging rate was evaluated by chi-square test for trend, and differences between groups were assessed by Student's t-test or ANOVA with Tukey's post-hoc tests ($\alpha = 0.05$). Error bars are shown as SD (Figs. 1-3) or interquartile box with min/max whiskers (Fig 4).

RESULTS

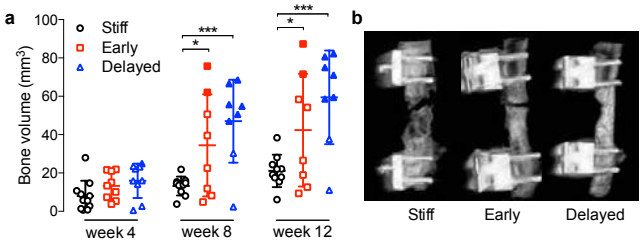

Figure 2: Longitudinal evaluation of bone formation *in vivo*. (a) Bone volume quantification. Shaded data points indicate radiographic bridging of the defect at that time point. (b) Representative 3D reconstructions of bone formation at week 12. * p < 0.05, *** p < 0.001; ANOVA with Tukey's post-hoc test.

Histological (data not shown) and gene expression analysis (Fig. 1) of hMSC sheets at day 2 *in vitro* demonstrated chondrogenic, but not osteogenic, priming of engineered mesenchymal condensates at the time of implantation.

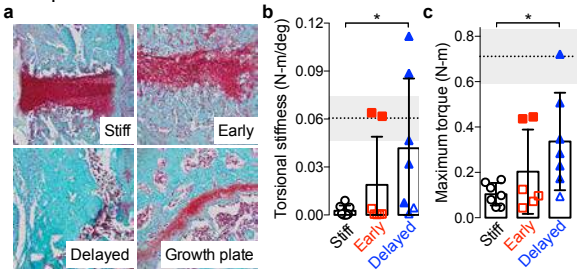

Figure 3: Post-mortem analysis. (a) Safranin-O/fast green histological staining of glycosaminoglycans (red; images at 10x). (b) Torsional stiffness. (c) Maximum torque at failure. Dotted lines and shaded regions indicate mean ± SD of age-matched intact bone properties. Shaded data points indicate radiographically bridged samples. * p < 0.05; ANOVA with Tukey's test.

In vivo, the delayed loading group was the only to exhibit a significantly increasing trend in radiographic bridging over 12 weeks ($p < 0.001$, data not shown). There was no difference in bone volume between loading groups at week 4, but by week 8, 4 weeks after loading was initiated in the delayed group, both early and delayed loading groups were significantly greater than the stiff group, and these differences persisted over 12 weeks (Fig. 2).

Post mortem microCT analysis and histology revealed a cortex-like shell with internal trabeculae (data not shown) in all three groups, but also gaps of unmineralized cartilage tissue in stiff and early loading samples, with characteristics similar to growth plate cartilage (Fig. 3a). Mechanical testing (Fig. 3b,c) revealed significantly higher torsional stiffness and maximum torque in the delayed loading group compared to the stiff plate controls. Only the delayed group had mechanical properties not significantly different from intact femora ($p > 0.05$, $\beta = 0.71$). In both bone volume and mechanical testing, a bimodal response was observed in the early loading group, consistent with persistence of cartilage tissue in non-mineralized gaps.

Comparison of regeneration in constructs containing TGF-β1 with MSCs either alive or devitalized prior to implantation showed significantly lower regeneration in constructs with devitalized cells at week 12 (Fig. 4).

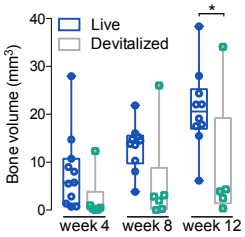

Figure 4: Bone formation *in vivo* induced by constructs containing live cells, or cells devitalized prior to implantation. Both groups feature stiff fixation plates. *p < 0.05; ANOVA with Tukey's test.

DISCUSSION

We present a tissue engineering approach that recapitulates the early mesenchymal condensation necessary for endochondral bone morphogenesis through spatiotemporal control of growth factor-mediated MSC self-assembly and demonstrate the necessity of *in vivo* mechanical stimulation for functional regeneration through the endochondral pathway. Bone regeneration progressed by endochondral ossification as demonstrated by histological and morphological analysis in all three groups, but mechanical loading enhanced bone formation and functional regeneration, in a manner dependent on magnitude and timing. Both load initiation during chondrogenic differentiation at the time point of implantation and loading delayed until after the onset of ossification significantly enhanced bone formation, but only delayed loading restored functional mechanical properties to the regenerated limbs. The early-loaded group exhibited a bimodal distribution with both responders and non-responders compared to the more uniform distribution seen with delayed loading. Despite a significant increase in bone volume, few samples in the early loading group achieved radiographic defect bridging over 12 weeks, with regions of persistent non-mineralized cartilage tissue. In the early group, the large strains applied during the differentiation process may have induced pseudarthrosis, resulting in a cartilaginous nonunion with morphological similarity to the native growth plate. Importantly, the endochondral regeneration response was not dependent only on the delivered growth factor, but required delivery of live cells.

Taken together, these data demonstrate that the timing and magnitude of *in vivo* mechanical loading on engineered mesenchymal condensates directed tissue formation and enhanced functional bone regeneration through endochondral ossification in a manner mimetic of bone morphogenesis.

ACKNOWLEDGEMENTS

This work was supported in part by grants from the Naughton Fnd. (to JDB, AMM), the Indiana CTSI (NIH/NCRR UL1TR001108 to JDB), and the NIH (1F32DE024712 to SH, R01AR063194 to EA). Equal author contributions indicated by * and †.

REFERENCES

[1] Shapiro F. *European Cells and Materials*. 15:53-76, 2008.
[2] Ingber D et al. *Tissue Engineering*. 12(12):3265-83, 2006.
[3] Alsberg E et al. *Proc. Natl. Acad. Sci*. 99(19):12025-30, 2002.
[4] Drachman D & Sokoloff L. *Dev Biol* 14:401-420, 1966.
[5] Solorio L et al. *J Control Release*.158(2):224-32, 2012.
[6] Boerckel J et al. *Proc. Natl. Acad. Sci*. 108(37):E674-80, 2011.

Copyright 2016 The Organizing Committee for the 2016 Summer Biomechanics, Bioengineering and Biotransport Conference

SB^{3}C2016
Summer Biomechanics, Bioengineering and BIotransport Conference
June 29-July 2, 2016, National Harbor, Maryland, USA
SB^{3}C2016-152

EFFECT OF AGE ON THE MECHANICAL PROPERTIES OF THE PORCINE TEMPOROMANDIBULAR JOINT DISC

J. Lowe (1), A. Almarza (1,2,3)

(1) Department of Bioengineering
University of Pittsburgh
Pittsburgh, PA, USA

(2) McGowan Institute of Regenerative Medicine
Pittsburgh, PA, USA

(3) Department of Oral Biology
University of Pittsburgh
Pittsburgh, PA, USA

INTRODUCTION

It is currently estimated that roughly 10 million Americans have temporomandibular joint disorders (TMDs). These TMDs encompass a variety of conditions, such as structural abnormalities of the TMJ, which can be accompanied by severe pain. The causes for TMDs are varied, and can include trauma, parafunction, unstable occlusion, functional overloading, and increased joint friction. Patients with TMD can show symptoms of persistent pain affecting normal life activities, such as malocclusion, facial asymmetry, locked jaw, and the deterioration of tissues around the joint space.

Roughly 80% of TMD patients are women between the ages of 20-40, which necessitates an effective, long term clinical treatment for TMDs. The current clinical treatment for patients with irreparable TMJ disc damage is the use of autogenous tissue sources, which resorb over time, making them ineffective for long term treatment required. In an effort to create site appropriate therapies, tissue engineering has been used to create implants that can remodel into tissues that possess near-native properties. [1]

Before the efficacy of such treatments can be assessed, however, the native mechanical properties of a healthy TMJ disc must be understood. To this end, several studies have been performed investigating the tensile and compressive properties of skeletally mature pigs, but no study has looked into age-dependent mechanical properties of growing pigs.[2-3] Since in-vivo tissue engineering studies involve implanting devices into pigs that are skeletally immature and growing, it is necessary to determine what effects age would have on native discs. Therefore, the objective of this study is to determine the tensile and compressive mechanical properties of the native porcine TMJ disc at 3, 6, and 9 months of age. We hypothesize that there will be an age dependent effect, with mechanical properties increasing with age.

METHODS

Female porcine heads (n=9) from 3, 6, and 9 month animals were procured from a local abattoir and both TMJ discs were excised immediately. For tensile testing, anterior-posterior samples were collected from the intermediate zone of the TMJ disc, and a dogbone shape was created in the tissue by punching two holes about 2 mm apart with a 8 mm dermal biopsy punch. Each anterior-posterior sample was cut using a cryotome to produce multiple 300-400 micrometer sections per disc, which were kept in sequential order. Samples were then allowed to equilibrate in phosphate buffered saline in individual wells of a 6 well plate for at least one hour.

The samples were tested for tensile properties using an Instron 5565 mechanical testing apparatus. The ends of each sample were gripped using 400 grit sandpaper in a pneumatic clamp. Samples were preloaded to 0.2 N. After the preload was applied, 20 cycles of 5% strain were applied at 10 mm/min for preconditioning. The samples were then pulled to failure at a strain rate of 10 mm/min. Samples were analyzed for the peak stress (stress at first rupture in the tissue), strain (clamp to clamp strain at first rupture in the tissue), and modulus (slope of stress-strain behavior from 5-10% strain). These parameters were collected for all the inferior-superior sections of each individual disc, and averages from each disc were used to collect an aggregate value for each parameter.

For compression testing, 4 mm dermal punches were taken from the punched tissue collected to create a dogbone shape in each disc. The discs were allowed to equilibrate in phosphate buffered saline for at least one hour. Each sample was then tested in unconfined stress relaxation compression in a water bath at 37 ^{o}C. Samples were preloaded to 0.05 N. 10 cycles of 10% strain were applied at a strain rate of 9%/min for preconditioning. The samples then had a stress relaxation compressive load applied at a strain rate 9%/min from 0-

Copyright 2016 The Organizing Committee for the 2016 Summer Biomechanics, Bioengineering and Biotransport Conference

30% strain, in 10% increments. The tissue was allowed to relax for 30 min between each step. Samples were analyzed for peak stress (stress at ending of ramping phase), and modulus (last 20% of the stress/strain curve of the ramping phase).

RESULTS

For tensile stress (Figure 1), no significant differences ($p<0.05$) were seen between the 3 month (3.91 ± 1.81 MPa), 6 month (5.24 ± 1.69 MPa), and 9 month (4.57 ± 1.60 MPa) age groups. For tensile modulus (Figure 2), no significant differences ($p<0.05$) were seen between the 3 month (28.62 ± 9,16 MPa), 6 month (38.25 ± 10.09 MPa), and 9 month (29.84 ± 8.27 MPa) age groups.

For compressive stress (Figure 3), significant differences ($p<0.05$) were seen between the 3 month (65.1 ± 49.6 MPa), and 9 month (80.4 ± 34.5 MPa) age groups. For compressive modulus (Figure 4), significant differences ($p<0.05$) were seen between the 3 month (710 ± 456 MPa) age group and both the 6 month (1108 ± 512 MPa), and 9 month (893 ± 294 MPa) age groups.

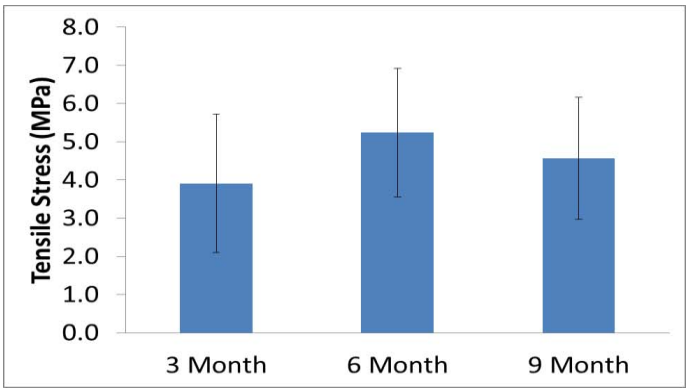

Figure 1; Tensile stress at tissue failure for 3, 6, and 9 month old pigs (n=9).

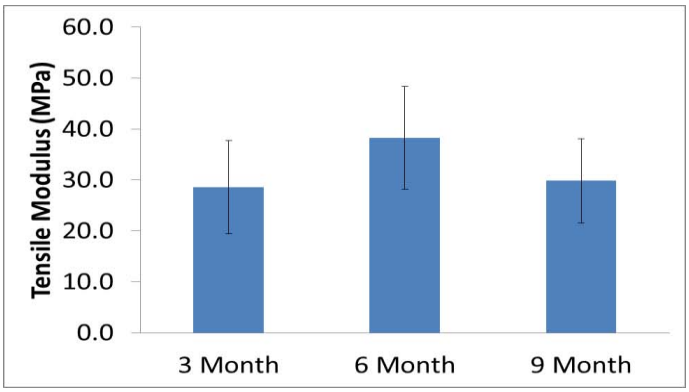

Figure 2; Tensile modulus for 4-8% of stress-strain curve for 3, 6, and 9 month old pigs. (n=9).

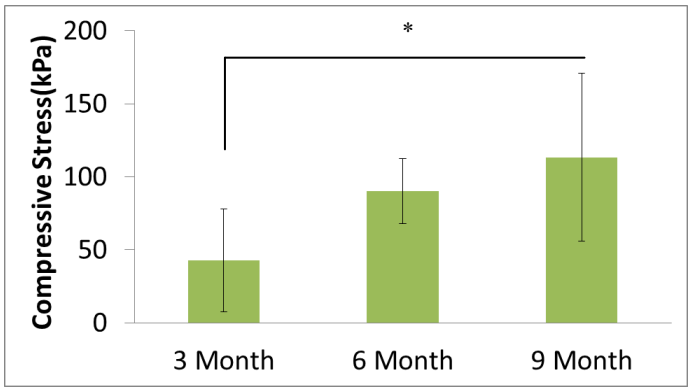

Figure 3; Compressive stress at 30% strain for 3, 6, and 9 month old pigs (n=9).

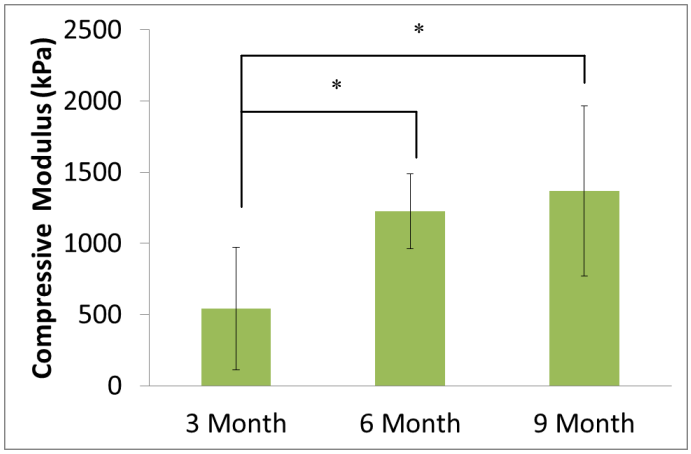

Figure 4; Compressive modulus of the last 20% of the loading curve at 30% strain for 3, 6, and 9 month old pigs (n=9).

DISCUSSION

As shown in these results, the compressive properties of the porcine TMJ disc do change over time, whereas the tensile properties do not. The variation in these trends show that depending on the type of mechanical testing being performed for an in vivo test, it is important to include age-matched controls. Otherwise, differences observed between end stage experimental groups and early native pigs may be confounded by age-induced mechanical property differences.

ACKNOWLEDGEMENTS

This research was completed with funding from the Biomechanics in Regenerative Medicine training grant from the National Institute of Health (NIH), grant #NIH T32 EB003392.

REFERENCES

[1] Brown, B et al., Inductive, Scaffold-Based, Regenerative Medicine Approach to Reconstruction of the Temporomandibular Joint Disc, *J Oral Maxillofac Surg*, 70:2656-2668, 2012

[2] Kalpacki, KN et al., An Interspecies Comparison of the Temporomandibular Joint Disc, *J Dent Res*, 90:193-198, 2010

[3] Detamore, MS, Athanasiou, KA, Tensile Properties of the Temporomandibular Joint Disc, *J Biomech*, 125:558-565, 2003.

Copyright 2016 The Organizing Committee for the 2016 Summer Biomechanics, Bioengineering and Biotransport Conference

SB^{3}C2016
Summer Biomechanics, Bioengineering and Biotransport Conference
June 29 –July 2, National Harbor, MD, USA
SB^{3}C2016-154

SCALING BETWEEN HUMAN AND PORCINE MODELS FOR TRAUMATIC BRAIN INJURY

Siddiq M. Qidwai (1), Robert N. Saunders (2)

(1) Multifunctional Materials Branch
US Naval Research Laboratory
Washington, DC, USA

(2) MCET Department
Leidos Corporation
Arlington, VA, USA

INTRODUCTION

The motivation to study the causes and mechanisms of traumatic brain injury (TBI) is quite evident from the news, events, and investigative reports and studies being published in mass media and scientific journals over the last decade. The issue has attained such gravity and momentum that all manners of *in vitro*, *in vivo*, *ex vivo*, *in silico*, and surrogate methods and techniques have been incorporated to study it [1]. Indeed, the complexity of a stress wave propagating through a highly heterogeneous biomaterial system such as the head and neck complex with its intricate interfaces and diverse materials, multi-phase components, and multi-scale and multi-physics mechanisms, demands a multi-prong approach. Thus, live animal models, e.g., pigs are also now being used as surrogates based on certain physiological and morphological reasons to study TBI in humans [2, 3]. However, ethical considerations, cost, and insufficient granularity of data are concerns that reduce the viability of this approach. This is where computational modeling may both complement and supplement experimentation.

There are two challenges associated with the use of computational models of animals, or pigs as is the case in this study. The first is validation, which is the universal bane of most models, especially in biomechanics because of the difficulties in accruing consistent and accurate granular data. The second is the applicability of data from porcine modeling, or even porcine testing, on humans. In this study, we investigate the later challenge based on the notion that we already have a validated model (being reported in a companion paper). Thus, development of scaling or correspondence rules that link the pig and human together is considered in this study, with specific focus on blast induced TBI.

The procedure followed for the overall study is straightforward: 1) create the human and porcine computational models of the head, 2) validate the models, 3) simulate the two models under the same impact scenarios, and 4) compare and analyze injury prediction to formulate scaling or correspondence rules.

METHOD

The development and validation of the porcine head and upper torso model are described in relatively greater details in the companion paper. That same approach has also been used for the human head and neck model. Thus, we only describe the first two steps of the aforementioned procedure briefly here. Gray-scale magnetic resonance imaging (MRI) scans with a resolution of 1 mm were procured for both species. For the pig, CT scans with a resolution of 0.6 mm were also obtained. The human subject was a 50th percentile Caucasian male of 26 years age, whereas the porcine subject was a 36.5 kg mini-Yucatan pig. Then, through careful image-to-voxel transformation, all major components of the head have been included in the geometric models, as well as heart and lung for the porcine upper torso. Material models for each component have been chosen and calibrated based on the latest available data over the loading regime of interest (quasi-static to 1000/s). The hybrid finite element mesh, created from the voxel data, is composed of linear and quadratic tetrahedral elements, which are placed according to the compressibility of the associated material regions. The two finite element models are shown in Figure 1. For validation, the human head model has been tested against four well-known experimental studies related to the automotive sector (e.g., [4, 5]). Similarly, the porcine head and upper torso model has been validated against blast tube injury response data obtained elsewhere (e.g., [3]).

For the next step in the development of scaling rules, the finite element models are simulated under the same frontal blast loading conditions. A planar Friedlander pressure wave profile based on the

Copyright 2016 The Organizing Committee for the 2016 Summer Biomechanics, Bioengineering and Biotransport Conference

peak magnitude and pulse duration of an in house open-field test is used as the template (see Figure 2). A parametric study based on peak pulse magnitudes of 37, 50, and 62 psi with the same duration is carried out. The boundary conditions are set to least disrupt the similarity in loading conditions although some discrepancy is inevitable at later times in the loading when reflections from the boundaries reach the brain. Pressure, maximum shear stress (or Tresca stress) and principal strain are used as predictors of injury, with threshold values of 235 kPa, 7.8 kPa, and 5%, respectively [6].

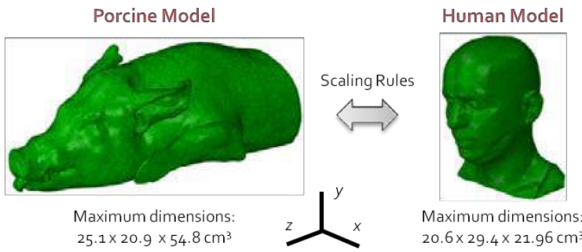

Figure 1: Finite element models of the porcine and human subjects.

RESULTS

Even at the minimum applied peak pulse of 37 psi, the human brain exhibits the onset of TBI. In Figure 2, the predicted injured volume as a function of blast time is shown for the three injury measures, with an additional threshold for pressure at 173 kPa added for educational purposes (as it is suggested as a measure of mild TBI in the literature). It is noted that only pressure-induced TBI is observed for the humans, whereas the porcine brain shows no severe injury.

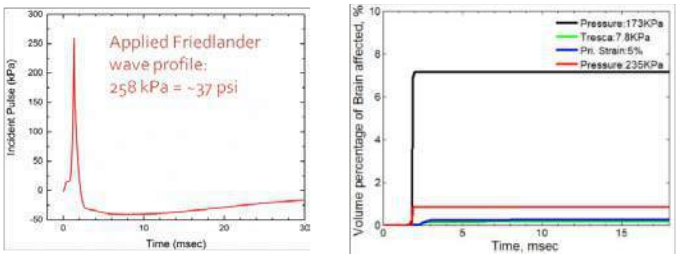

Figure 2: (Left) Friedlander pulse profile for a peak magnitude of 37 psi; (Right) Predicted TBI by percent volume of the human brain as a function of time based on pressure, shear and strain.

This particular trend continues for the peak magnitudes of 50 psi and 62 psi. In the top row in Figure 3, the spatial extent of TBI based on the pressure threshold of 235 kPa is shown in red color for the human brain. The porcine brain again exhibits no severe injury; mild TBI is probable though based on the threshold of 173 kPa. This is demonstrated by the comparative evolution of the injured volumes of the human and pig as a function of blast time in the bottom row of Figure 3. All other injury measures predicted no injury.

DISCUSSION

It is obvious from these results that frontal blast insult predominantly induces only pressure-based TBI up to significantly large insults (at least 62 psi) in humans. The mini-Yucatan pig remains unaffected, however. It appears from the closer inspection of the simulation data that the pig skull acts as a pathway for the frontal blast transmission away from the brain. This implies that blast impacts from oblique or transverse orientations may be better to yield TBI in pigs. Work is already underway with initial results for the porcine model showing the onset of pressure-based PSI at only 40-50 psi range under side-on blast impact. Also, the frontal blast parametric study has been extended to include 80, 100 and 120 psi peak magnitude pulses. Already, at 80 psi, the onset of pressure based TBI has been observed in pigs. Thus, one can note the scaling pattern that is developing for frontal impact, i.e., higher insults are needed to cause TBI in pigs than in humans.

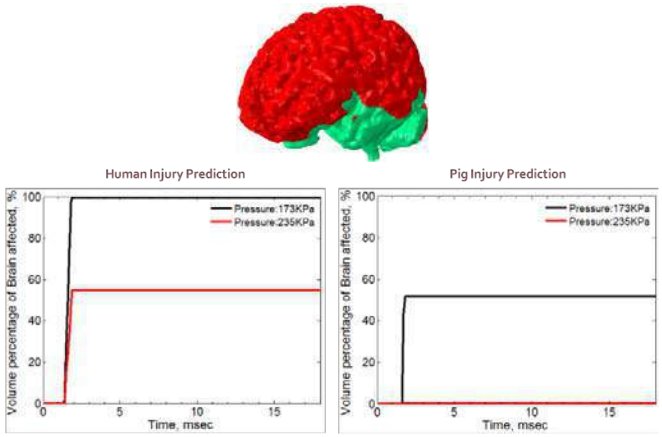

Figure 3: (Top) Spatial extent of pressure-induced TBI (235 kPa threshold, in red color) in human brain under 62 psi peak pressure frontal blast insult; (Bottom) Comparison of pressure-induced TBI as a function of time for both human and pig models.

The absence of injury as predicted by shear and strain is quite interesting. Does it mean that blast insults cannot really cause these modes of injury or is it that their appearance in significant manner may only happen at higher insults or insults from orientations other than the front? It will also be interesting to see if similar injury patterns, both in terms of location and volume, appear at different applied insults in human and pigs because that would be pertinent to developing meaningful scaling rules for various classes of injury. All these issues are under consideration as this study is continuing and we hope to answer a majority of them in the near future.

An important note of caution is necessary here. The success of developing scaling rules is predicated on the notion that the threshold values and the predicting variables are indeed accurate and reliable. This is an area of research that needs to be paid more attention by the community.

ACKNOWLEDGEMENTS

This work was supported by the Office of Naval Research (ONR) under contract number N001415WX00531 and the Department of Defense (DoD) High Performance Computing Modernization Program (HPCMP) using the Air Force Research Laboratory (AFRL) Major Shared Resource Center (MSRC) under project 416, subproject 231.

REFERENCES

[1] Gulf War and Health, Volume 9: Long-Term Effects of Blast Exposures, National Academies Press, 2014.

[2] Bass, C et al., *Ann Biomed Eng*, 40:185-202, 2012.

[3] Shridharani J et al, *Front Neurol*, 3, Art. 70, 2012.

[4] Nahum, AM et al., *Proc 21st Stapp Car Crash Conference*, 339-366, 1977.

[5] Trosseille X et al., *Proc 30th Stapp Car Crash Conference*, 235-253, 1992.

[6] Wright, RM, and Ramesh, KT, *Biomech Model Mechanobiol*, 11:245–260, 2011.

Copyright 2016 The Organizing Committee for the 2016 Summer Biomechanics, Bioengineering and Biotransport Conference

SB^{3}C2016
Summer Biomechanics, Bioengineering and Biotransport Conference
June 29 –July 2, National Harbor,MD, USA
SB³C2016-155

MULTIDOMAIN PARTICLE DYNAMICS SIMULATOR ENGINE

Vl Q. Ha (1), George Lykotrafitis (1)

(1) Department of Mechanical Engineering
University of Connecticut
Storrs, CT, USA

INTRODUCTION

In this work, we introduce a lightweight, fast-paced, and easily customizable C++ particle dynamics simulator engine that is designed to run on large-scale parallel distributed-memory computing clusters. The simulator uses message passing interface (MPI) for parallel computing operations. It is easily customizable and provides a highly intuitive user interface by using contemporary pragmatic object-oriented pointer systems that allows easily access to suitable components of the molecular dynamics (MD) engine. Modern MD simulator programs are limited to primary employing spatial distribution. Here we introduce a simulator engine that offers three interacting domain that can be modularly programmed: spatial domain, network domain and continuum domain.

METHODS

Spatial distribution allocates particles to processors according to their positions to attain high efficient short-range MD computations. The simulator utilizes the linked list method to construct a robust cell list algorithm. The spatial decomposition algorithm and cell list method allow extremely fast paced and efficient computations of large-scale short-range MD simulations of particles interacting within a cut off radius. In addition, specific long-range interactions are realized via the introduction of a second interaction domain, the global network domain. The global network registers particles as nodes and connects them via edges. This allows efficient interaction between particles regardless of their spatial position or the processors they reside within the cluster. The third interaction domain that we introduce is the continuum space domain. In the current version of the code, the simulator employs an explicit finite difference algorithm to solve the diffusion equation. The continuum domain allows communication between particles or between particles and the environment via diffusion. Particles from the network domain, spatial domain, and the continuum domain are able to interact with one another. For example, calculations of the chemotaxic response of particles moving in the spatial domain and subjected to a chemical concentration gradient in the continuum domain are perfectly feasible. The introduction of particles, nodes and their interactions are easily programmable. The simulator provides tools to program each particle or a defined group of particles individually.

RESULTS

The simulator can be employed in numerous biological cases. The spatial domain allows users to simulate short-range MD simulations. Users can also easily simulate more complex scenarios such as diffusion of cell membrane proteins. The network domain allows user to simulate long distance protein-protein interactions while the continuum space allows simulation of chemical diffusing in the environment.

Users have the option to create any combinations of provided domains in the simulation. Users can easily assign multiple domains of the same type or completely turn a domain off to avoid unnecessary memory consumption. For example, particles from a spatial domain interact in two continuum domains with two independent diffusing chemical. An example is provided below. Another example is simulating mixture of molecules of different sizes and properties by creating several spatial domains with different cut off radius in other to avoid impairment of computational efficiency.

Copyright 2016 The Organizing Committee for the 2016 Summer Biomechanics, Bioengineering and Biotransport Conference

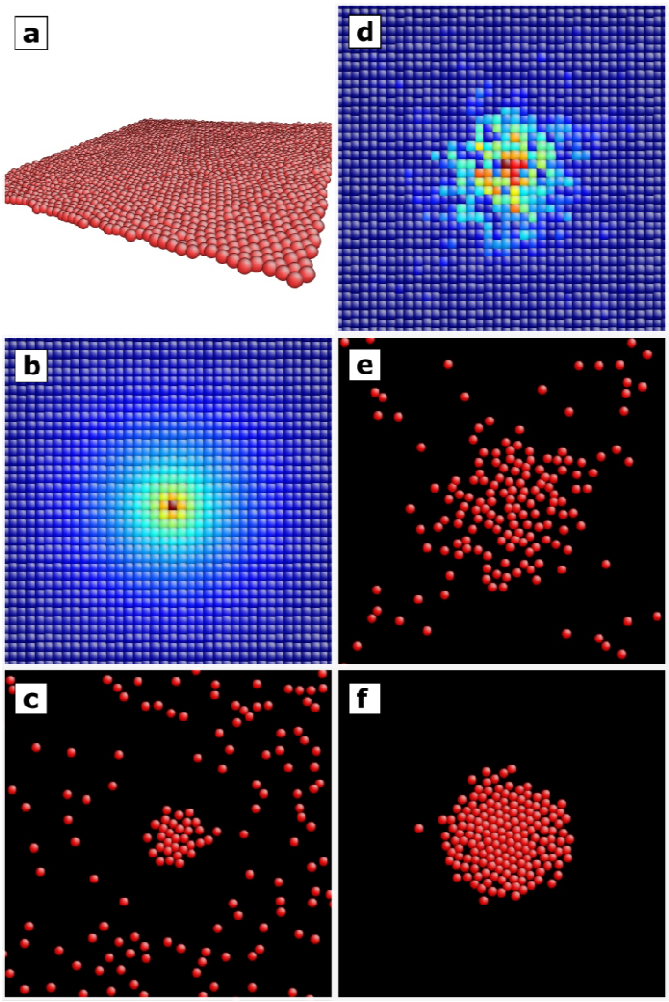

Figure 1. A simulation of the cytoskeleton and membrane of the red blood cell (RBC) is presented (a). Two simulation cases are performed to demonstrate the significance of LTB_4 as a relay signal that amplifies neutrophil chemotaxis to wound sites. Case 1: Neutrophils interacting with 1 continuum domain (b) which has a constant source of fMLP, shown at equilibrium. Local Neutrophil reacts to this by migrating towards the wound site (c), however, distanced Neutrophil are unable to acknowledge the wound, since they cannot detect the weakened signals of fMLP. Case 2 : Neutrophils interacting with 2 continuum domains (b) a constant source of fMLP and (d) an LTB_4 domain emitted by Neutrophils. When a Neutrophil Cell detects fMLP, it will locally produce LTB_4 of proportioned concentration. (e) shows the early stage of Neutrophil migration and produced LTB_4 signals (d) as it detects fMLP. By being chemotaxically attracted to LTB_4 produced by neighboring Neutrophils, the system emerges a collective migration behavior (f), where distanced Neutrophils also migrate to the wound site via chemotaxis.

DISCUSSION

Two examples are provided in this paper to demonstrate the function of the simulation engine (Figure 1).

1) The membrane of the red blood cell (RBC) is being modeled (Fig. 1a). The membrane comprises a phospholipid bilayer represented as a single layer of particles and a spectrin network. Each phospholipid bilayer particle represents a patch of a phospholipid bilayer of 5nm diameter. The particles interact with each other via a potential that depends on the relative distance and the orientation of the particles [1-3]. The potential is not spherically symmetric but it forces the particles to form a thermally oscillating 2D membrane sheet. The cytoskeleton of the RBC membrane comprises spectrin filaments that are connected at actin junctions forming a canonical hexagonal. In this simulation, the spectrin filaments are replaced by the worm-like chain potential (WLC) applied between two actin junctions. The model is discussed in detail in [1, 4]. Each actin junction is modeled as a network node. Two nodes that are connected by a spectrin filament may belong to different processors. Each actin junction also dynamically interacts with the phospholipid bilayer. Each spectrin filament of the cytoskeleton is represented as a network connection (edge) between the nodes.

2) A simulation of Neutrophil aggregation during wound healing is presented (Fig. 1b-f). Neutrophil recruitment to inflammation sites often shows extremely coordinated chemotaxis and cluster formation. Upon injury, chemoattractants such as formyl peptides (fMLP) are emitted from bacteria. Neutrolphil near the wound site are able to detect the secreted fMLP signals and subsequently release a secondary chemoattractant leukotriene B_4 (LTB_4) to stimulate neighboring neutrophils. Our simulation demonstrates that LTB_4 plays a very powerful role in neutrophil activation and migration to fMLP by serving as a signal-relaying molecule that regulates and amplifies neutrophil chemotaxis to fMLP [5-7]. In the simulation Neutrophil are modeled as particles in a spatial domain interacting with two continuum domains: fMLP chemical domain and LTB_4 chemical domain. Neutrophils migrate along both the gradient of concentration of fMLP and LTB_4 simultaneously. In addition, Neutrophils emit LTB_4 concentration proportional to the fMLP it detects (Fig. 1d-f). It is shown by the simulation that the lack of LTB_4 emission will severely hinder neutrophil chemotaxis to the wound site (Fig. 1b,c).

ACKNOWLEDGEMENTS

Funding: This work was supported by the National Science Foundation (Grants NSF, No. CMMI-1235025, CMMI-1354363, CAREER Award; and No. PHY-1205910) and the American Heart Association (Grant No. 12SDG12050688).

REFERENCES

1. Li, H. and G. Lykotrafitis, *Two-Component Coarse-Grained Molecular-Dynamics Model for the Human Erythrocyte Membrane.* Biophysical Journal, 2012. **102**(1): p. 75-84.
2. Li, H. and G. Lykotrafitis, *Erythrocyte Membrane Model with Explicit Description of the Lipid Bilayer and the Spectrin Network.* Biophysical Journal, 2014. **107**(3): p. 642-653.
3. Yuan, H., et al., *One-particle-thick, solvent-free, coarse-grained model for biological and biomimetic fluid membranes.* Phys Rev E Stat Nonlin Soft Matter Phys, 2010. **82**(1 Pt 1): p. 011905.
4. Boal, D.H., *Mechanics of the cell*. 2nd ed. 2012, Cambridge ; New York: Cambridge University Press. xiv, 608 p.
5. Afonso, Philippe V., et al., *LTB4 Is a Signal-Relay Molecule during Neutrophil Chemotaxis.* Developmental Cell, 2012. **22**(5): p. 1079-1091.
6. Cai, D. and D.J. Montell, *Diverse and dynamic sources and sinks in gradient formation and directed migration.* Current Opinion in Cell Biology, 2014. **30**: p. 91-98.
7. Lammermann, T., et al., *Neutrophil swarms require LTB4 and integrins at sites of cell death in vivo.* Nature, 2013. **498**(7454): p. 371-375.

Copyright 2016 The Organizing Committee for the 2016 Summer Biomechanics, Bioengineering and Biotransport Conference

SB^{3}C2016
Summer Biomechanics, Bioengineering and Biotransport Conference
June 29 –July 2, National Harbor, MD, USA
SB^{3}C2016-156

VALIDATION OF A PORCINE HEAD AND UPPER TORSO MODEL

Robert Saunders (1), Siddiq M. Qidwai (2)

(1) MCET Department
Leidos Corporation
Arlington, VA, USA

(2) Multifunctional Materials Branch
US Naval Research Laboratory
Washington, DC, USA

INTRODUCTION

A RAND report estimates that nearly 20% of deployed service members experience some level of traumatic brain injury (TBI) [1]. Blast events account for as much as 70% of these injuries and is the primary cause of mild TBI (mTBI) [1]. The exact injury mechanisms in mTBI are not well understood and for obvious reasons, the blast events cannot be replicated on *in vivo* human subjects. Thus, in order to better understand mTBI, researchers rely upon computational simulations of human and animal testing combined with physical and physiological scaling procedures. One such animal that has been studied due to its similarities to the human size and physiology is the pig [2]. To bridge the gap between simulations of human subjects and animal testing, computational models of animal subjects have also been created to make comparison. Using computational models of animals is significantly less expensive than conducting a large number of tests on animals as the computational models can be validated against a smaller number of experiments and then applied to an extensive set of problems. A number of complications arise when creating, verifying, and validating these computational models. The models must first have a high level of detail in the geometry, and second, the constitutive description of the materials must be accurate when compared to experiments. Lastly, the validation process has to be performed against a limited amount of data that is available in the literature, which potentially impedes the iterative corrective development such complex models need.

METHODS

The high level of geometric detail can be obtained by using high-resolution magnetic resonance imaging (MRI) and computed tomography (CT) scans of the subject and converting the 3-D voxels into a finite element mesh. This process has been implemented to obtain the geometry of a porcine head and upper torso as shown in Figure 1. The 0.6-mm resolution CT scans and 1-mm resolution MRI scans allowed for a high fidelity model geometry to be constructed, which includes all major organs and features. These are the: skin, eyes, cranium (inner and outer table and diplöe), facial bones and muscles, falx cerebri, tentorium cerebelli, air sinuses, cerebro-spinal fluid (CSF), ventricles, meninges (dura mater and pia-arachonoid), cerebrum and cerebellum (gray and white matter), brain stem, muscles, and spinal column (cervical vertebrae, intervertebral disks, and spinal cord).

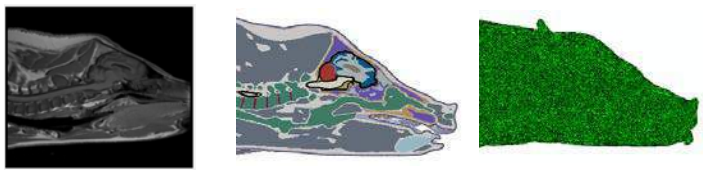

Figure 1. Transformation of porcine CT and MRI scans into a 3-D geometric model and then conversion to a finite element mesh.

Constitutive behavior of the organs is determined by collecting the latest available data in literature over the loading regime of interest (quasi-static to 2000/s strain rates). Material parameters are obtained using a global optimization scheme that compares the experimental curves to a hyper-viscoelastic functional form, e.g., in the case of the brain component, which is able to capture both large strain hyperelastic and rate-dependent viscoelastic behavior. The process of data collection through calibration is briefly illustrated in the top row in Figure 2 where the data for grey matter is obtained, extracted, and then conditioned. The first two images in the bottom row of Figure 2 show the respective efficacy of two optimization schemes at both low

Copyright 2016 The Organizing Committee for the 2016 Summer Biomechanics, Bioengineering and Biotransport Conference

and high strain rates while the third image demonstrates the predicted behavior at a variety of strain rates of interest.

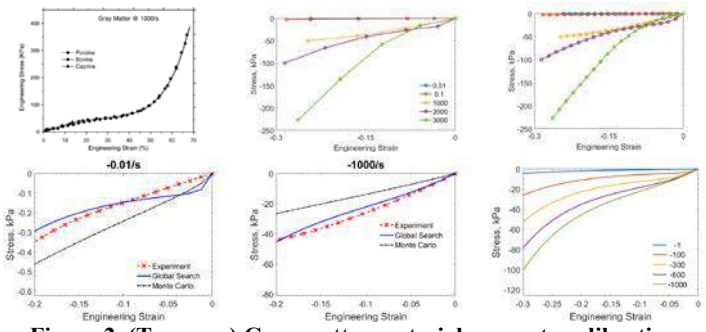

Figure 2. (Top row) Grey matter material property calibration process moving from published data [3] to (Bottom row) a model that closely approximates the behavior under both high and low rates.

There are several ongoing challenges in validating the computational pig model against a limited amount of data. In this study, the porcine model is being validated against two types of data sets: 1) high-rate blast tube data and 2) low-rate magnetic resonance elastography (MRE) data. The former has already been utilized in the validation process, whereas the later data is currently being generated by collaborators. The high-rate blast data involving porcine subjects is obtained from [3, 4]. In both tests, a pig is subjected to a side-on blast wave with its torso protected from the blast.

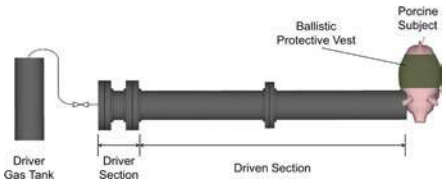

Figure 3. Test setup of [3] using shock tube to apply a side-on pulse to a porcine subject.

In the first case [3], the blast wave is applied using a shock tube as shown in Figure 3. For the simulations, the applied load is assumed to be an ideal Friedlander wave with peak overpressure and positive phase durations specified in the study. Both kinematic and kinetic responses are measured inside and outside of the cranium as shown in Figure 4. In the second case [4], the blast is produced by an explosive charge in a blast tube. The wave generated by this charge is provided by the original authors and applied to the computational porcine model. Unlike [3], the data measured in [4] is purely kinetic, which only allows for a partial validation.

Figure 4. Kinetic and kinematic sensor location on the pig from the test setup in [3].

MRE tests on porcine subjects are currently underway and will be able to provide small strain measurements over the entire brain. Incorporating the MRE strain data into the validation process allows the model to be compared against both low and high-rate kinematic data as well as blast-level kinetic data, for a comprehensive validation process.

RESULTS AND DISCUSSION

The results of the initial validation attempt against the kinetic data of [3] are shown in Figure 5. The external pressure response measured compared to what was simulated shows good agreement after the initial peak pulse in the comparison on the top. The absence of the peak pressure in the simulation is found to be due to volumetric locking of the linear tetrahedral elements used in the skin. We also notice a delay in the intracranial pressure in the bottom plots, which is likely due to contact conditions around the brain. In light of these results, a second iteration of the model composed entirely of quadratic elements for the removal of volumetric locking and modified contact conditions has already been performed and simulations are being run. Regardless, the preliminary results indicate that the model is effectively capturing the prominent features of both internal and external pressure responses well.

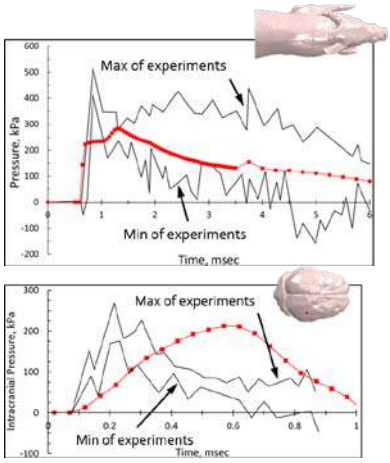

Figure 5. Preliminary side-on blast results compared to the test of [3].

The process detailed above does highlight the challenges associated with the validation of complex models when the experimental data is scarce; however, as shown here, a car eful progressive use of it may nonetheless lead to the objective. As the model is being improved based on data from [3], true validation will be attempted against the larger set of unused data from [4] and the MRE test results in the near future.

ACKNOWLEDGEMENTS

This work was supported by the Office of Naval Research (ONR) under contract number N001415WX00531 and through the US Naval Research Laboratory's Basic Research Program; and the Department of Defense (DoD) High Performance Computing Modernization Program (HPCMP) using the Air Force Research Laboratory (AFRL) Major Shared Resource Center (MSRC) under project 416, subproject 231.

REFERENCES

[1] Gupta, R. & Przekwas, A., *Front Neurol 4*, Art. 59, 2013.
[2] Bass, C. et al., *Ann Biomed Eng*, 40:185-202, 2012.
[3] Shridharani J. et al, *Front Neurol*, 3, Art. 70, 2012.
[4] Zhu F. et al, *Int J Numer Meth Biomed Eng*, 29:392-407, 2012.

Copyright 2016 The Organizing Committee for the 2016 Summer Biomechanics, Bioengineering and Biotransport Conference

SB^{3}C2016
Summer Biomechanics, Bioengineering and Biotransport Conference
June 29 –July 2, National Harbor, MD, USA
SB^{3}C2016-157

THE EFFECT OF LIMITED FRACTIONAL ANISOTROPY REPRESENTATION ON BRAIN INJURY PREDICTIONS

Shankarjee Krishnamoorthi (1), Siddiq M. Qidwai(2)

(1) NRL/ASEE Postdoctoral Fellowship
US Naval Research Laboratory
Washington, DC, USA

(2) Multifunctional Materials Branch
US Naval Research Laboratory
Washington, DC, USA

INTRODUCTION

Traumatic brain injury (TBI) is currently one of the leading causes of disability in the warfighters returning from the battlefield. Amongst various types of impacts that may lead to TBI, the interaction of an explosive blast wave with the head is arguably the most complex event due to its global effect on the brain. Modeling has already been used to investigate blast wave propagation in the human head to varying degrees of success. One of the most critical drawbacks in these efforts, however, relates to the incomplete material description of the brain, or more specifically the description of its spatially varying anisotropy.

Magnetic resonance imaging (MRI)-based diffusion tensor imaging (DTI) and magnetic resonance elastography (MRE) techniques have demonstrated in the last several years that the human brain cannot be construed as a simple, homogeneous isotropic material. It is in fact composed of the highly heterogeneous white matter, which in turn is made of fiber tracts of different morphologies surrounded by an isotropic matrix, and the tightly bound, hierarchical cortical columns or gray matter in the outer regions. The gray matter is also present in the internal brain regions intermixed with the white matter to various levels of geometric complexity. Thus, this material anisotropy has to be taken into account if an accurate description of wave propagation from any impact and its effect on the brain needs to be described.

DTI essentially describes the anisotropic diffusion behavior of water in the brain represented by the so-called fractional anisotropy (FA) data, which is then used to construct fiber tractography (morphology and size of fiber bundles). The range of FA values chosen to be included determines the completeness of anisotropic representation; for example, typically $FA < 0.2 = FA_{cri}$ is assumed to be isotropic and anything greater anisotropic. MRE, in contrast, is a relatively recent and rapidly developing technology that is being used to assess the mechanical properties of biological soft tissues. MRE obtains stiffness information of the tissue by evaluating the propagation of mechanical waves.

The present work aims to understand the effect of the partial inclusion of fractional anisotropy in the models as described by the DTI and MRE data, i.e., fiber tractograghy and associated material anisotropy, respectively, on the accuracy of brain injury predictions. This is achieved by accommodating partial to complete description of the fiber tractography and degree of material anisotropy in a series of simulations of the same human head model under blast loading, and comparing predicted locations and levels of TBI.

METHODS

The first part of this work is focused on developing the procedures for transferring the relevant DTI data (fiber orientation tensor) and utilizing the MRE data (derived small strain elasticity stiffness tensor), obtained in house, from unrelated subjects to a previously validated high fidelity finite element (FE) model of the human head, also developed using MRI. (Details of registration of the structured MRI data to an unstructured finite element mesh are discussed in a companion paper.)

Once the MRI data is matched with the FE head model, the DTI data describing material principal orientations are transferred for each finite element using a linear invariant based tensor interpolation scheme [1]. The degree to which fiber tractography is accounted for in the model is controlled by the range of FA values chosen to be included. For an assumed value of FA_{cri} say 0.5 the scheme would eliminate fiber bundle orientation and thus material anisotropy from larger regions of white matter than for the traditional choice of $FA_{cri} = 0.2$. The implication is that all material having less than FA_{cri} value is isotropic.

Having defined the brain material orientation this way, the Hookean stiffness data from the MRE scans is transferred to the FE model using the nearest neighbor interpolation. The FE model uses anisotropic hyper-viscoelastic material description to capture large rate-

Copyright 2016 The Organizing Committee for the 2016 Summer Biomechanics, Bioengineering and Biotransport Conference

dependent deformation of the brain tissue under blast insult. To relate the Hookean stiffness data with anisotropic data, initially viscous effects are ignored and the relevant hyperelastic parameters are determined by minimizing the differences in the internal energy of the brain using both the Hookean stiffness tensor and the hyperelastic strain energy function. A schematic of the procedure is shown in Fig 1.

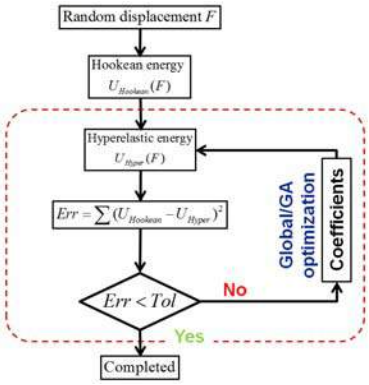

Figure 1: Optimization routine used to compute parameters in hyperelastic material model using small strain MRE data.

The viscous part of the material model is then computed by fitting the full hyper-viscoelastic model to the available experimental rate-dependent data [2] using the parameters obtained in the previous step. Various heuristic and non-heuristic optimization algorithm schemes were explored to achieve this. Lastly, the isotropic regions of the brain, i.e., those regions with FA < FA_{cri}, are modeled with an isotropic two-term Ogden hyper-viscoelastic description based on the data from [2] directly. Currently, a parametric study is being performed where FA_{cri} value is varied from 0.2 to 1 in increments of 0.1. The minimum value represents a fully anisotropic representation of the brain, whereas the maximum one describes a fully isotropic one.

RESULTS AND DISCUSSION

Fig. 2 describes the ability of the developed procedure in transferring the DTI data from an unrelated subject to the existing human head FE model. It shows the volumetric histogram of FA values from the original MRI data and the interpolated FE data. For lower values of FA, the volumetric differences are significant. One potential explanation for this is the fact that there is a substantial difference in the brain volumes of the MRI subject and the FE mesh subject and the isotropic volume (typically FA < 0.2) being large in both cases, it shows the most effect at lower values. Despite this discrepancy, the quality of results is not compromised severely because it is the higher values of FA that define white matter anisotropy, which are captured sufficiently both from volume and tractography standpoints.

Fig. 3 shows the comparison of anisotropy in terms of fiber tractography (orientations) included in the FE model of the brain when different values FA_{cri} are chosen as thresholds for anisotropy. Similarly, Table 1 shows the anisotropic brain volume percentage as a function of ranges of FA that are being included in the parametric study. It can be inferred from the spatial differences in Fig. 3 and volume magnitudes in Table 1 that the mechanical response of the brain to blast loading will be affected by the choice of FA_{cri}.

The parametric FE study based on ranges of FA values is under progress now. The blast loading is being applied from the front of the head and is defined by a planar Friedlander pressure wave based on data obtained from an in-house field test. Injury predictors based on invariants of stresses, strains and translational/rotational accelerations will be computed for all these models. The injured brain volume percentage will be calculated based on thresholds available in the literature, and compared. The results from these simulations will be used to provide a rational basis for choosing the FA range(s) prudentially, and they will be applicable to studies related to all impact types, especially blunt impacts incurred in recreational and vehicular incidents.

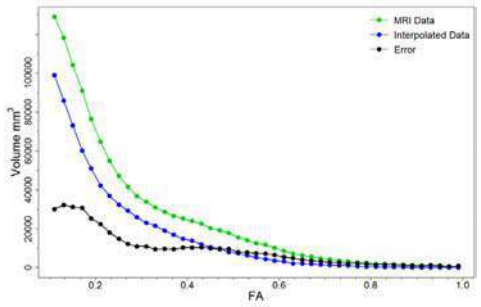

Figure 2: Comparison of volume histogram for FA values between the original MRI data and the interpolated data in the FE mesh. The error is simply computed as the difference.

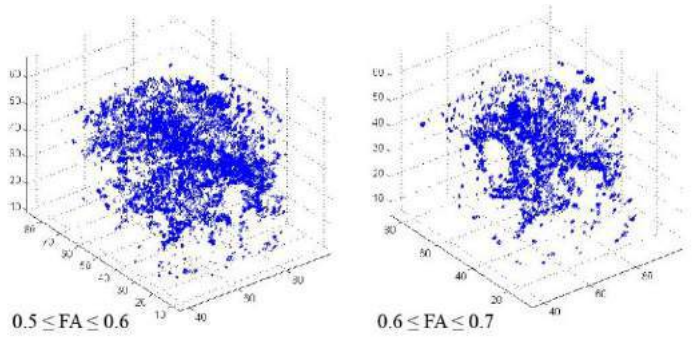

Figure 3: Comparison of interpolated orientation data in the FE model of the brain for different FA ranges

Table 1: Comparison of anisotropic brain volume as function of FA ranges

FA Range	Anisotropic brain volume	FA range	Anisostropic brain volume
≥ 0.2	31.2%	≥ 0.6	1.61%
≥ 0.4	8.8%	≥ 0.8	0.19%

ACKNOWLEDGEMENTS

The authors gratefully acknowledge the support from the American Society for Engineer Education postdoctoral fellowship to Shankarjee Krishnamoorthi. This work was supported by the Office of Naval Research (ONR) under contract number N001415WX00531 and through the US Naval Research Laboratory's Basic Research Program, and the Department of Defense (DoD) High Performance Computing Modernization Program (HPCMP) using the Air Force Research Laboratory (AFRL) Major Shared Resource Center (MSRC) under project 416, subproject 231.

REFERENCES

[1] Gahm, J.K et al. *Medical Image Computing and Computer-Assisted Intervention–MICCAI,* 494-501, 2012.

[2] Pervin F and Chen W.W, *Journal of biomechanics*, **42**(6):731-736, 2009.

Copyright 2016 The Organizing Committee for the 2016 Summer Biomechanics, Bioengineering and Biotransport Conference

SB^{3}C2016
Summer Biomechanics, Bioengineering and Biotransport Conference
June 29 –July 2, National Harbor, MD, USA
SB^{3}C2016-158

DISORDER AS A BIOMECHANICAL PATTERN FORMING MECHANISM THAT GUIDES SYMMETRIC VERTEBRATE BODY ELONGATION

Dipjyoti Das (1), Thierry Emonet (1,2), Scott A. Holley (1)

(1) Department of Molecular, Cellular and Developmental Biology
Yale University
New Haven, CT, USA

(2) Department of Physics
Yale University
New Haven, CT, USA

INTRODUCTION

Throughout vertebrate trunk elongation, prospective mesodermal cells arrive at the posterior tailbud in an epithelium. These cells undergo an epithelial-to-mesenchymal transition (EMT), which represents a transition from ordered to disordered motion and disperse symmetrically into the left and right paraxial mesoderm (*1-3*). This symmetric dispersion is necessary to prevent scoliosis, i.e. an abnormal lateral curvature of the spine.

The tailbud is the posterior leading edge of the growing vertebrate embryo consisting of motile progenitors of the axial skeleton, musculature and spinal cord as well as bipotential neural/mesodermal stem cells (Fig. 1A and B) (*4-9*). Prior studies in zebrafish established that cell migration, not cell proliferation, is the primary driver of body elongation (*10-13*). Here, we devise a simple theoretical model of collective cell migration within a finite tailbud-like geometry to assess the importance of the disordered cell motion for development.

METHODS

Using 4-D confocal imaging, cell segmentation and cell tracking, we mapped the cell flow of the paraxial mesoderm and its progenitors during trunk elongation. The dataset from each embryo averages ~2500 tracks per time-point and 55 time-points. We divided the tracks into four tailbud regions based on morphology and patterns of gene expression to facilitate statistical comparison of different regions of the tailbud (Fig. 1A-D)(*14, 15*).

Here, we quantitatively examine the possible mechanisms of symmetric trunk elongation. We develop a theoretical model of cell migration in the tailbud. Following a coarse-grain methodology commonly used in physics and biology to study bird flocks (*16, 17*), bacterial swarms (*18, 19*), and cell migration (*20, 21*), we represent cells as self-driven particles that interact via an adhesion-repulsion potential and tend to align their motion with that of their neighbors (*16, 17, 20, 22-25*). Using this framework we then systematically study how the dynamics and symmetry of the trunk elongation process depend on the dynamical behavior of the individual cells within the tissue and the interaction among them. Finally, we examine the in vivo data to test whether the theory aligns with the biology.

RESULTS

A key theoretical prediction that emerges from our model is that the variability in the alignment of the individual cell motion with the average direction of its neighbors is a critical cellular parameter that must be regulated at the EMT in order to avoid trunk elongation defects. We call this parameter *angular noise*. If there is not enough angular noise, the overall motion becomes highly ordered and cells start swirling on either side of the axis, breaking trunk symmetry. If there is too much angular noise, the motion becomes overly disordered, and the rate of trunk elongation is reduced. We qualitatively confirm these theoretical predictions by examining experimental data using the same quantitative metrics used to analyze the numerical simulations. As in our model, wild-type embryos exhibit fluctuations between sinstral and dextral biases in the cell flow. Disordered cell motion in the PZ destabilizes these biases in the flow such that they even out over time and lead to bilaterally symmetric trunk elongation. Analysis of Cadherin 2 mutants and embryos with reduced Wnt signaling further support our model. We conclude that the dynamical regulation of cell motion from an ordered regime (epithelium) to a disordered regime (mesenchyme) in the posterior tailbud is critical for the embryo to achieve both rapid and bilaterally symmetric trunk elongation.

Copyright 2016 The Organizing Committee for the 2016 Summer Biomechanics, Bioengineering and Biotransport Conference

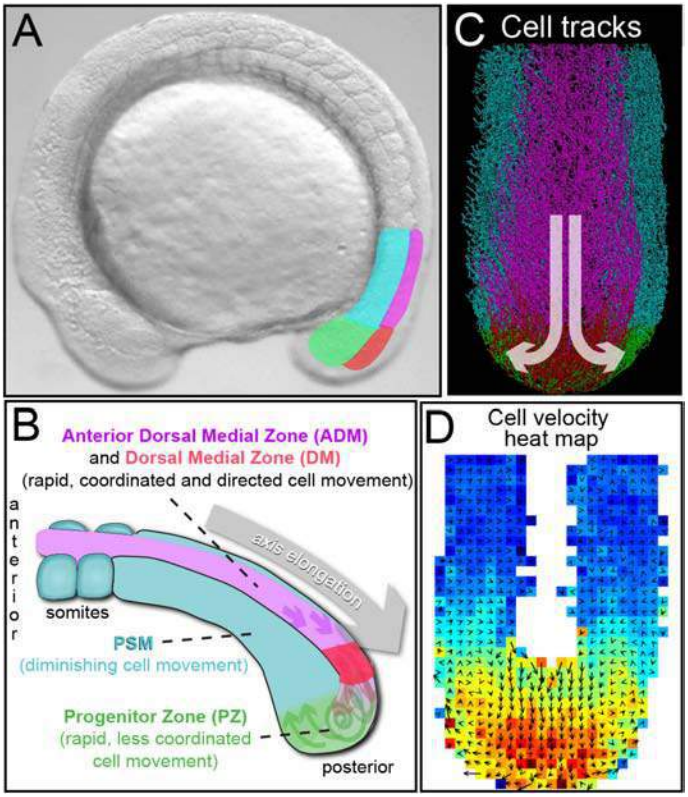

Figure 1: Cell flow in the zebrafish tailbud. (A) A 16-somite stage embryo with the tailbud domains colored as in B and C. **(B)** A schematic summary of tailbud cell motion. EMT occurs as cells migrate from the DM (red domain) to the PZ (green domain). **(C)** A dorsal view of the cell tracks in the tailbud. Arrows indicate the general bilaterally symmetric direction of cell flow. **(D)** Cell motion visualized by projecting the 3D cell velocities into 2D and averaging over 10 mm^2 sectors. Warmer colors indicate higher average velocities. Note that the ADM has been removed.

DISCUSSION

We find that localized disorder in cell motion ensures organism level order. The localized disorder is created by an epithelial to mesenchymal transition in the posterior of the elongating vertebrate embryo. The transition continues post-gastrulation as the vertebrate trunk is being formed and has been observed in zebrafish, mouse and chick. Mesodermal progenitors undergo EMT, enter a zone of disordered cell motion and then segregate bilaterally into the left and right paraxial mesoderm. These cells will then undergo an MET during somite formation and ultimately contribute to the vertebral column and musculature. Why do these cells undergo a transient transition to a mesenchyme in all vertebrate embryos and why is there a zone of disordered cell motion at the posterior tip of these embryos? We find that the answer arises from the fundamental fact that EMT represents a transition from an ordered to disordered tissue morphology. The ordered epithelium allows cells to efficiently migrate to the growing posterior tip of the embryo. If the tissue is prematurely disordered, we find that the rate of elongation is stunted. However, the transition to a disordered state is necessary for these cells to evenly disperse along the left and right sides of the paraxial mesoderm. We find that if the cells remained too ordered, a vortex forms in the cell flow and trunk elongation loses bilateral symmetry leading to scoliosis.

Over the past few decades, we have learned that embryos expend much effort in pattern formation to guide normal development. Pattern formation is fundamentally an ordering process. What we find here that regulated localized intercellular *disorder* is an integral part of a pattern forming mechanism. Moreover, this mechanism crosses scales from local cellular disorder to organism level symmetry. Thus, our study answers a vexing problem in vertebrate development and conceptually introduces a counter intuitive relationship between disorder and pattern formation.

ACKNOWLEDGEMENTS

Support provided by the NIH Common Fund Single Cell Analysis Program (1R33GM114257-01).

REFERENCES

1. S. Ohta, K. Suzuki, K. Tachibana, H. Tanaka, G. Yamada, *Development* **134**, 4315-4324 (2007).
2. V. Wilson, R. S. Beddington, *Mech Dev* **55**, 79-89 (1996).
3. A. J. Manning, D. Kimelman, *Dev Biol*, (2015).
4. C. M. Griffith, M. J. Wiley, E. J. Sanders, *Anatomy and embryology* **185**, 101-113 (1992).
5. D. E. Holmdahl, *Anat Anz* **59**, 393-396 (1925).
6. V. Wilson, I. Olivera-Martinez, K. G. Storey, *Development* **136**, 1591-1604 (2009).
7. B. L. Martin, D. Kimelman, *Dev Cell* **22**, 223-232 (2012).
8. T. Takemoto *et al.*, *Nature* **470**, 394-398 (2011).
9. E. Tzouanacou, A. Wegener, F. J. Wymeersch, V. Wilson, J. F. Nicolas, *Dev Cell* **17**, 365-376 (2009).
10. J. P. Kanki, R. K. Ho, *Development* **124**, 881-893 (1997).
11. M. J. Harrington, K. Chalasani, R. Brewster, *Dev Dyn* **239**, 747-762 (2010).
12. E. Quesada-Hernandez *et al.*, *Curr Biol* **20**, 1966-1972 (2010).
13. L. Zhang, C. Kendrick, D. Jülich, S. A. Holley, *Development* **135**, 2065-2070 (2008).
14. N. Dray *et al.*, *Curr Biol* **23**, 1335-1341 (2013).
15. A. K. Lawton *et al.*, *Development* **140**, 573-582 (2013).
16. M. Ballerini *et al.*, *Proc Natl Acad Sci U S A* **105**, 1232-1237 (2008).
17. W. Bialek *et al.*, *Proc Natl Acad Sci U S A* **109**, 4786-4791 (2012).
18. A. Baskaran, M. C. Marchetti, *Proc Natl Acad Sci U S A* **106**, 15567-15572 (2009).
19. A. Czirok, E. Ben-Jacob, I. I. Cohen, T. Vicsek, *Physical review. E, Statistical physics, plasmas, fluids, and related interdisciplinary topics* **54**, 1791-1801 (1996).
20. B. Szabó *et al.*, *Physical Review E* **74**, 061908 (2006).
21. M. Basan, J. Elgeti, E. Hannezo, W. J. Rappel, H. Levine, *Proc Natl Acad Sci U S A* **110**, 2452-2459 (2013).
22. I. D. Couzin, J. Krause, R. James, G. D. Ruxton, N. R. Franks, *Journal of theoretical biology* **218**, 1-11 (2002).
23. G. Grégoire, H. Chaté, Y. Tu, *Physica D: Nonlinear Phenomena* **181**, 157-170 (2003).
24. T. Vicsek, A. Zafeiris, *Physics Reports* **517**, 71-140 (2012).
25. H. Levine, W. J. Rappel, I. Cohen, *Physical review. E, Statistical, nonlinear, and soft matter physics* **63**, 017101 (2001).

Copyright 2016 The Organizing Committee for the 2016 Summer Biomechanics, Bioengineering and Biotransport Conference

SB^{3}C2016
Summer Biomechanics, Bioengineering and Biotransport Conference
June 29 –July 2, National Harbor, MD, USA
SB^{3}C2016-159

VASCULAR SMOOTH MUSCLE CELL MECHANO-ADAPTATION LAWS

Kerianne E. Steucke(1), Zaw Win (1), Emily E. Walsh (1), Taylor R. Stemler (1), and Patrick W. Alford (1)

(1) Biomedical Engineering
University of Minnesota
Minneapolis, MN, USA

INTRODUCTION

Vascular diseases, such as hypertension, can alter the forces on vascular cells, leading to growth and remodeling of the vessel wall [1]. It has been suggested that vascular smooth muscle cells (VSMCs) adapt themselves and their environment in response to mechanical perturbation to maintain a 'target stress' [2,3]. While extracellular matrix remodeling is important long term, early vessel adaptation is the result of changes in contractility [4]. VSMCs are the active mechanical component of the vessel wall and are known to respond to mechanical perturbations by altering phenotype, active contraction, proliferation, and hypertrophy [1, 5-6].

Tissue-scale vascular growth and remodeling can be described using the linearized form of Fung's growth law:

$$\dot{G} = A(\sigma - \sigma_o). \quad (1)$$

Where $\dot{G}$ is the growth rate with respect to time, σ is the current stress state, σ_o is the target stress, and A is a constant [2,3], though other forms have been suggested [7]. However, mechano-adaptation of individual vascular cells has not been directly measured or characterized. **Here, we have measured and determined VSMC mechano-adaptation laws with biologically meaningful parameters using traction force microscopy methods. The result will provide increased insight to vascular pathologies and improve current multi-scale vascular models.**

METHODS

Cell Culture. Passage 5-7 human umbilical artery VSMCs purchased from Lonza were used for all experiments. VSMCs were cultured in Medium 199 in 5% CO_2 at 37^{o}C. Constructs were seeded at 15cells/mm^2 and in serum free media 24h prior to applying strain.

Construct Fabrication. Fibronectin (FN) was micropatterned on polyacrylamide gels doped with fluorescent microspheres and constructed on clean elastomer membranes secured in steel clamps as depicted in figure 1A. Briefly, FN was incubated on micro-raised rectangular features (26μmx184μm) on polydimethylsiloxane stamps for 1h. Then, the stamp feature-side was placed in conformal contact with coverslips for 30m. Clean and secured elastomer membranes were treated with 10% benzophenone [8]. A pre-polymer solution of 10% acrylamide, 0.13% bis-acrylamide, and 1% red 0.2μm fluorescent beads was degassed and then 0.2% tetramethylethylenediamine, 1M hydrochloric acid to a pH of 7.0-7.4, 10ug/ml N-hydroxysuccinimide-acrylic ester, and 0.05% aminopropylsilane was added [9]. Quickly, 10μl of this solution was placed on the elastomer membrane and the FN patterned coverslip was placed face-down on the droplet. The polyacrylamide gels were cured and rehydrated allowing the coverslip to be removed. The polyacrylamide gels were passivated in 4% bovine serum albumin.

Traction Force Microscopy Experiments. A linear motor was used to apply either 10% or 20% strain at 2% strain/s along the patterned VSMCs' longitudinal axis. Images of the fluorescent beads immediately below the VSMCs and bright field images of the cells were taken on an Olympus IX81ZDC confocal microscope (fig. 1B) at 0h, 4h, 8h, 24h, and 48h post-stretch. Images were acquired pre-treatment (reference state) and 5m post-treatment with 0.1% sodium dodecyl sulfate (SDS). All experiments were conducted in serum free Medium 199.

Cell Force Analysis. Substrate displacements were determined by comparing SDS post-treatment fluorescent bead images to the pre-treatment image reference state using published particle image

Copyright 2016 The Organizing Committee for the 2016 Summer Biomechanics, Bioengineering and Biotransport Conference

velocimetry software in ImageJ (fig. 1B) (fig. 2A) [10]. Bead displacements and known polyacrylamide gel properties were used to calculate traction forces using an unconstrained FTTC algorithm in ImageJ [10]. Cell Cauchy stress was calculated using a force balance and the cross-sectional area of the cell.

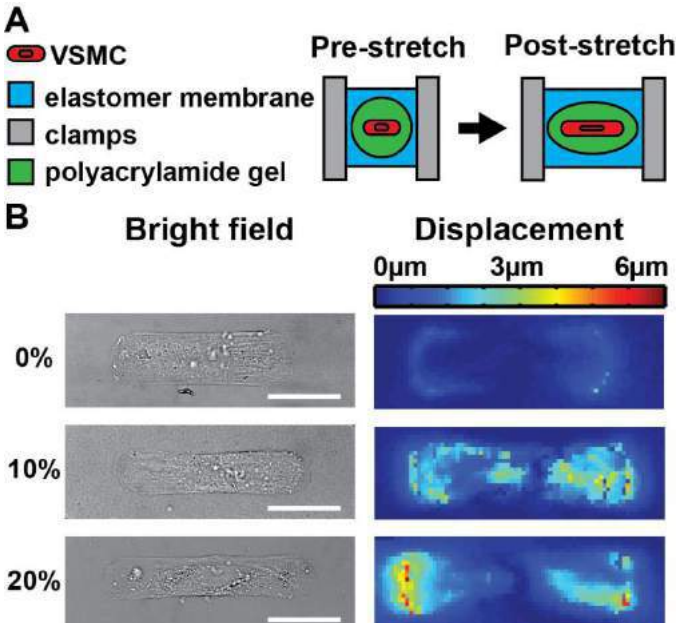

Figure 1: Chronic strain traction force microcopy method. A. Top-down schematic of FN patterned VSMC on chronic strain construct. **B. Left:** Bright field images of VSMC at 0h stretched to 0%, 10%, or 20% applied strain. Scale bar: 50μm **Right:** Displacement field of respective VSMC bright field images at 0h as determined from comparing pre-treatment reference state to SDS post-treatment state.

Mechano-adaptation Law Determination. Experimental Cauchy stress data (fig. 2B) was used to fit both the standard growth law (fig. 2C) and a growth law incorporating hyper-restoration (fig. 2D) using a custom MATLAB script. Briefly, the data was fit to equation 1 for the standard growth law and the hyper-restoration model fit equation 1 and the following equation:

$$\dot{\sigma_o} = -\beta(\sigma - \sigma_o). \quad (2)$$

Where $\dot{\sigma_o}$ is the rate of change of target stress and β is a constant. The strain energy density was assumed to be Neo-Hookian.

RESULTS

We applied a step-change in strain of 0%, 10%, or 20% to micropatterned VSMCs and tracked the evolution of their traction stresses. Immediately post-stretch, cell strained 10% and 20% exhibited greater than a 2-fold increase in stress compared to controls (0%). By 48h, the 10% and 20% constructs approach the control values as predicted by equation 1 (fig. 2B). We fit a standard growth law (Eq. 1) and hyper-restoration growth law (Eq. 1 and Eq. 2) to the data and found that neither optimally fit the data, but that the more dynamically adaptive hyper-restoration law fit the data better than the standard law.

DISCUSSION

Here, we developed a system to measure the temporal stress behavior of VSMCs in response to an applied chronic strain to experimentally determine a VSMC mechano-adaptation law. Our data contains features of the standard targeted growth law, such that initially stress increases with applied strain and approaches the homeostatic stress. However, the resulting fit (fig. 2C) fails to capture the temporal changes in stress. We applied hyper-restoration theory [7], which was better able to capture the experimental results (fig. 2D). To improve the fit, we will examine the role of VSMC biological pathways in mechano-adaptation to generate a robust VSMC mechano-adaptation law with additional biologically meaningful parameters. Ultimately, this will further our understanding of vascular disease initiation and progression and improve multi-scale vascular disease models.

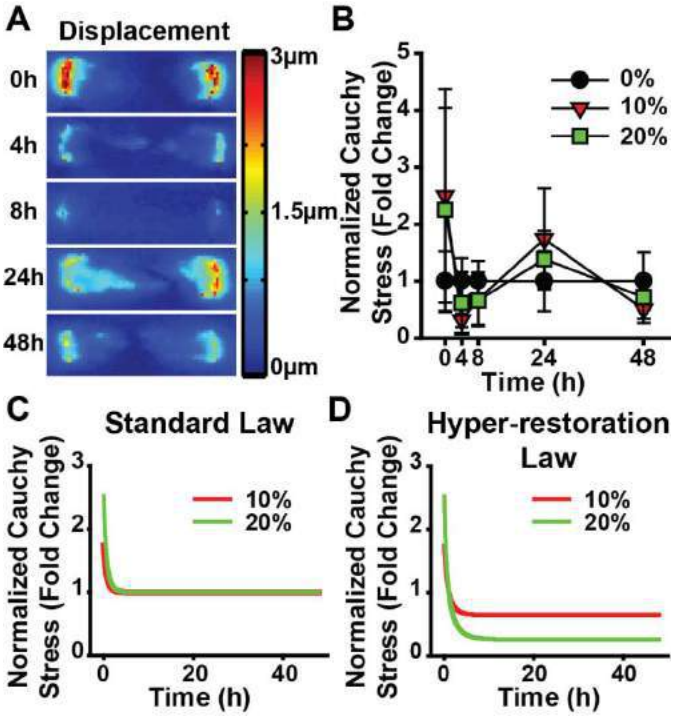

Figure 2: VSMCs Mechano-adaptation in response to chronic strain. A. Displacement field for 20% strain VSMC at different time points. **B.** Normalized Cauchy stress as compared to the 0% construct for each respective time point. Mean±Std. **C.** Standard growth fit VSMC mechano-adaptation law. **D.** Hyper-restoration fit VSMC mechano-adaptation law.

ACKNOWLEDGEMENTS

We wish to thank our funding by American Heart Association (15PRE21790000 (KES)) and National Institute of Health (1R03EB016969 (PWA)). Device fabrication was performed at the Minnesota NanoCenter at the University of Minnesota (a member of the National Nanotechnology Infastructure Network), which is supported by the National Science Foundation.

REFERENCES

[1] Fung, YC and Liu, SQ, *Circulation Research*, 65:1340-1349, 1989.
[2] Fung, YC, Biomech: Mech Prop of Living Tissues, *Springer*, 2004.
[3] Taber, LA, *J Biomech Eng,* 120:348-354, 1998.
[4] Fridez, P et al. *Ann Biomed Eng*, 30:905-916, 2002.
[5] Alford, PW et al., *PNAS*, 108:12705-12710, 2011.
[6] Alexander, RW, *Hypertension*, 25:155-161, 1995.
[7] Taber, LA, *Biomech and Model in Mechanobio*, 7:427-441, 2008.
[8] Simmons, CS et al., *Lab Chip,* 13:646-649, 2013.
[9] Polio, SR et al., *Methods in Cell Bio*, 17-31, 2014.
[10]Tseng, Q et al., *PNAS*, 109:1506-1511, 2012.

Copyright 2016 The Organizing Committee for the 2016 Summer Biomechanics, Bioengineering and Biotransport Conference

SB^{3}C2016
Summer Biomechanics, Bioengineering and Biotransport Conference
June 29 –July 2, National Harbor, MD, USA
SB^{3}C2016-160

ANTERIOR CRUCIATE LIGAMENT FEMORAL ENTHESEAL SHAPE AND INSERTION ANGLE ARE RISK FACTORS FOR INJURY

Callan M. Luetkemeyer, Ellen M. Arruda

Mechanical Engineering Department
University of Michigan
Ann Arbor, Michigan, USA

INTRODUCTION

Anterior cruciate ligament (ACL) tears are the most common knee ligament injury, occurring more than 200,000 times per year in the United States [1]. These injuries are especially common in female athletes, who are two to five times more likely to sustain an ACL tear than their male counterparts [2]. Complete tears of the ACL often require surgical reconstruction and increase the susceptibility to knee osteoarthritis within 10 years of the injurious event [3]. Clinically, the most common location for an ACL tear is at or near the femoral insertion [4], but the reasons for this region's susceptibility are not yet well understood. In recent histological studies, Beaulieu and colleagues identified six human ACL femoral enthesis shapes based on the order and concavity of tidemark profiles in addition to measuring the angle of attachment of the ACL [5,6]. We hypothesized that the differences observed in profile and attachment angle would have important implications on the strain field in the ACL. Therefore, the objective of this study was to identify which of these aspects of geometry of the femoral attachment may increase ACL injury risk.

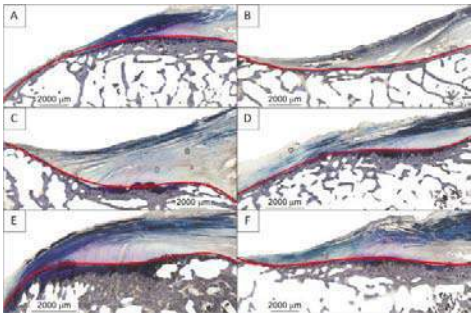

Figure 1: Entheseal shape categories identified by Beaulieu et al.

METHODS

The ACL femoral enthesis was modeled as a body of width (2D) or diameter (3D) w rigidly attached to a fixed boundary, $y=A(x)$, representing the enthesis. This boundary characterized the entheseal shape at the junction of the calcified and uncalcified fibrocartilage, and it had an overall slope of a/w, such that the insertion angle of the enthesis (ϕ) was 13 degrees or 7 degrees, representing the average angle of attachment for men and women, respectively [6]. The opposite edge of the body ($y=L$) represented the ligament proper, and it was assumed to undergo a uniform displacement δ.

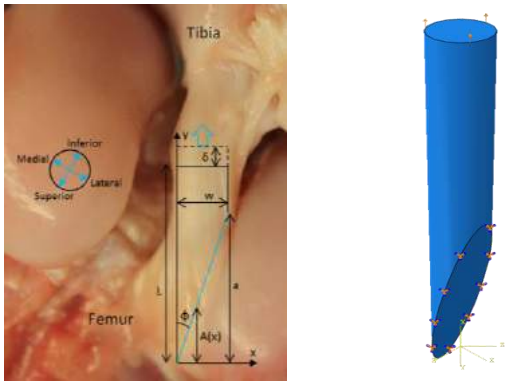

Figure 2: (Left) Schematic showing the geometry and variables used to create the models. (Right) Finite element model with boundary conditions.

The Lagrangian and von Mises strain fields were calculated using a simplified 2D model, and these were compared to the logarithmic

Copyright 2016 The Organizing Committee for the 2016 Summer Biomechanics, Bioengineering and Biotransport Conference

and von Mises strain fields computed using a 3D finite element model rendered in ABAQUS 6.13 (Abaqus, Inc.), utilizing a Holzapfel constitutive relation [7] fit to experimental data.

RESULTS

Shear strain was dramatically affected by both the shape of attachment and angle of insertion, which consequently influenced the von Mises strain. For the male insertion angle of 13 degrees, the convex shape (A) reduced the maximum von Mises strain by more than 23% compared to a linear (no curvature) shape, while the concave shape (B) increased the maximum von Mises strain by nearly 25%.

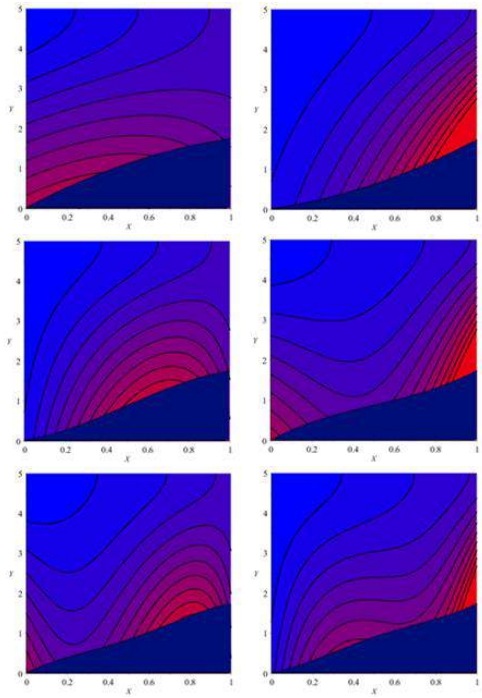

Figure 3: Example von Mises strain fields computed with the 2D model for shapes A-F. Red represents high strain and blue, low. Navy blue represents bone.

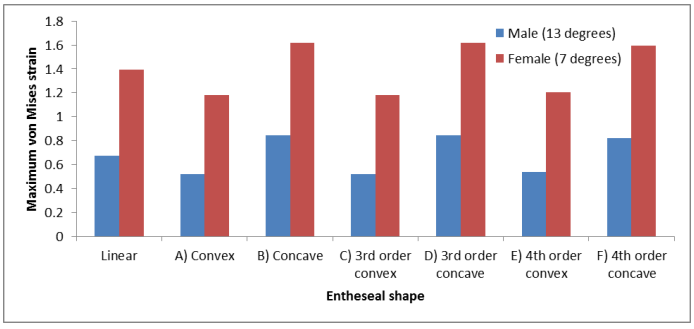

Figure 4: The maximum von Mises strain for male and female attachment angles, calculated with the 2D model for shapes A-F and linear.

Entheseal shapes A, C and E reduced the maximum von Mises strain compared to a linear shape, while shapes B, D and F increased maximum strains. Not surprisingly, a smaller attachment angle increased shear strain, thus increasing the maximum von Mises strain for all shapes. The 3D finite element model produced similar results.

DISCUSSION

Shapes with convexity of the bone near the inferior corner of attachment (A, C and E) are the most advantageous tidemark profiles, while shapes with concavity in that region (B, D and F) may put an athlete at greater risk for ACL injury. This is because the convex shapes effectively reduce the local shear strain near the most vulnerable point of attachment by locally increasing the attachment angle there. These results lend insight into why most ACL failures occur at the femoral enthesis, and suggest that failure may initiate at the inferior aspect. The acute attachment angle produces a considerable amount of shear strain in the ligament near the attachment. The more acute the attachment angle, the greater the von Mises strain, and thus, the more likely it is to fail. While shear strain clearly plays a critical role in ligament mechanics, most studies have focused on the tensile properties of ligaments. More research is needed to characterize their shear properties and to determine the role of shear in ligament failure.

Most importantly, these results may help explain why women are more susceptible to ACL injury. Not only do women, on average, have a more acute angle of attachment, but they are also more likely to have one of the less advantageous entheseal shapes. Grouping the shape data by gender, we found that nearly half of all female sections in the Beaulieu et al. study (43%) had shapes B, D or E, while less than 20% of the male sections possessed one of these less advantageous shapes. Injury risk related to smaller attachment angle may also provide a mechanistic understanding of the correlation observed between injury risk and smaller notch width [8], as a smaller intercondylar notch width would necessarily require a smaller insertion angle.

Both models used in the study have limitations. Neither model took into account the fact that the enthesis is functionally graded. However, while the gradient in stiffness of the enthesis does mitigate the stress/strain concentration, it does not eliminate it. Both models also assumed a regular geometry and single bundle, which is a physiologic simplification. Additionally, both models assumed a simple uniform displacement. The strengths of this study lie in using realistic attachment angles and amplitudes of concavity/convexity. In addition, the finite element model incorporated three-dimensional effects, anisotropy, and a realistic Poisson's ratio of nearly one half. Thus, the results of this study still provide realistic conclusions; concavity of entheseal shape and smaller insertion angle of the femoral ACL enthesis are risk factors for ACL injury. These results provide a mechanistic explanation for why women are more susceptible to these injuries.

ACKNOWLEDGEMENTS

This material is based upon work supported by the National Science Foundation Graduate Research Fellowship under Grant No. 2014191332.

REFERENCES

[1] Mather, RC et al., *J Bone Joint Surg*, 95: 1751-1759, 2013.
[2] Swenson, DM et al., *Med Sci Sports Exerc*, 45: 462-9, 2013.
[3] Lohmander, LS et al., *Am J Sports Med*, 35: 1756-69, 2007.
[4] Zantop, T et al., *Clin Orthop Relat Res*, 454: 48-53, 2007.
[5] Beaulieu, ML, PhD Thesis, University of Michigan, 2015.
[6] Beaulieu, ML et al., *J Orthop Res*, 33:1811-1817, 2015.
[7] Holzapfel, GA et al., *Elasticity*, 61:1-48, 2000.
[8] Simon, RA et al., *J Biomech*, 43: 1702-1707, 2010.

Copyright 2016 The Organizing Committee for the 2016 Summer Biomechanics, Bioengineering and Biotransport Conference

SB^{3}C2016
Summer Biomechanics, Bioengineering and Biotransport Conference
June 29 –July 2, National Harbor, MD, USA
SB^{3}C2016-161

A COMPARISON OF PHENOMENOLOGIC GROWTH LAWS FOR MYOCARDIAL HYPERTROPHY

Colleen M. Witzenburg (1), Jeffrey W. Holmes (1,2,3)

(1) Department of Biomedical Engineering
University of Virginia
Charlottesville, VA, USA

(2) Department of Medicine
University of Virginia
Charlottesville, VA, USA

(3) Robert M. Berne Cardiovascular Research Center
University of Virginia
Charlottesville, VA, USA

INTRODUCTION

The heart grows in response to both normal developmental and pathologic changes in hemodynamic loading. In general, a left ventricle (LV) subjected to chronic pressure overload (PO) exhibits concentric growth (thickening of individual myocytes and the heart wall), and one experiencing chronic volume overload (VO) exhibits eccentric growth (lengthening of myocytes and dilation of the cavity).

In the past 20 years there has been considerable effort to simulate growth within the heart; predictive models of growth could be important tools in planning treatment and designing novel therapies for a range of diseases. However, no direct comparisons of the various published models have been performed. In this work, we compare seven growth laws in order to determine if they are capable of predicting both eccentric and concentric growth following perturbations in mechanics characteristic of VO and PO.

METHODS

During the cardiac cycle, peak stretches occur in the circumferential and longitudinal directions at end-diastole, associated with significant radial thinning. Thus, to provide a simple test-bed for comparing different growth laws, we simulated cyclic equibiaxial stretch of a thin slab of myocardium between prescribed end-diastolic (ED) and end-systolic (ES) stretches, and observed the predicted growth responses when ED and ES stretches were altered to match reported values from *in vivo* PO and VO studies.

We established normal values for ED and ES stretch relative to the unloaded state by comparing reconstructed sarcomere lengths in beating hearts to their values in unloaded arrested hearts [1, 2]. Thus, the baseline ES and ED stretches were 1.05 and 1.30, respectively for both the fiber and cross-fiber directions. For the radial direction, baseline ES and ED stretches were 0.90 and 0.59. For growth laws in which stress was an input (i.e. L&T and GCG) the constitutive equation provided was used to calculate stress. The input set-points (Table 1) for each growth law were modified such that repeated cycling between normal ED and ES stretches induced zero growth.

Table 1: Growth Laws Compared and Modified Input Set-Points

Law	Original Input Set-Point	Modified Input Set-Point
L&T [3]	$\sigma_{set,f} = \sigma_{set,c} = \sigma_{set,r} = 0$ mmHg	$\sigma_{set,f} = \sigma_{set,c} = 1.07$ mmHg $\sigma_{set,r} = -1.02$ mmHg
KFR [4]	$s_{hom} = 0.13$	$s_{hom} = 0.30$
KUR [4]	$s_{hom} = 0.13$	$s_{hom} = 0.30$
GEG [5]	$F_{g,f,max} = 1.50$ $\lambda^{crit} = 1.01$	$F_{g,f,max} = 1.50$ $\lambda^{crit} = 1.30$
GCG [5]	$F_{g,c,max} = 3.0$ $p^{crit} = 0.0120$ MPa	$F_{g,c,max} = 3.0$ $p^{crit} = 0.0124$ MPa
ART [6]	${L_{s,0}}^1 = 1.44\ \mu m$ $L_{s,max,adapt} = 2.30\ \mu m$ $L_{s,min,adapt} = 1.75\ \mu m$	${L_{s,0}}^1 = 1.85\ \mu m$ $L_{s,max,adapt} = 2.40\ \mu m$ $L_{s,min,adapt} = 1.95\ \mu m$
KOM [7]	$E_{f,set} = \mathrm{N/A}$ $E_{cross,set} = \mathrm{N/A}$	$E_{f,set} = 0.341$ $E_{cross,set} = 0.0555$

Next, experiments in which PO or VO were induced were considered [8-14]. To avoid potentially confounding effects of growth normalizing the inciting stimulus, only studies that recorded ED and ES dimensions *prior to appreciable change in LV mass* were considered. ED dimension increased significantly with VO ($p=0.02$), but was unchanged with PO ($p=0.23$). ES dimension increased significantly following PO ($p=0.01$) and was slightly depressed following VO ($p=0.05$). Accordingly, both fiber and cross-fiber ES and ED stretches were set to 1.19 and 1.31 for PO and 1.01 and 1.40 for VO simulations, respectively. Radial ES and ED stretches were 0.71 and 0.58 for PO and 0.98 and 0.51 for VO, respectively.

All growth laws considered (Table 1) utilize the framework of

Copyright 2016 The Organizing Committee for the 2016 Summer Biomechanics, Bioengineering and Biotransport Conference

[15], in which material is added or removed through a growth deformation, F_g, changing the local stress-free configuration. The overall deformation is given by $F_{eg} = F_e F_g$; only the elastic deformation, F_e, contributes to stress. For each law, after ES and ED stretches were set, the growth inputs were computed and F_g was calculated. Since F_{eg} was constant, a new F_e could be computed. Alternating periods of stretch and growth were simulated until a steady-state was achieved or growth diverged ($F_g > 20$ or $F_g < 0.05$).

RESULTS

Since VO is known to provoke LV dilation, fiber growth was expected. L&T, KFR, GEG, and KOM all predicted the same level of steady-state fiber growth in response to simulated VO (Fig. 1A). Interestingly, these laws predicted very different patterns of growth in the cross-fiber and radial directions. ART predicted fiber growth and radial and cross-fiber atrophy but did not achieve a steady-state. GCG predicted no growth.

Since PO triggers wall thickening *in vivo*, radial growth was expected. KOM predicted a large degree of steady-state radial growth ($F_{g,r} = 1.13$) in response to simulated PO (Fig. 1B). ART predicted radial and cross-fiber growth and fiber atrophy, but again did not achieve a steady-state. GCG predicted maximal radial growth (limited to 3.0 by law). Steady-state radial growth levels were very low for L&T, KFR, and KUR and were unlikely to produce the degree of thickening typically observed during PO. Finally, GEG exhibits no radial growth, but instead grew in the fiber direction.

Next, we computed the ratio of fiber to radial growth from each simulation, and compared them to the range of reported values for changes in myocyte length-to-width ratio following *in vivo* PO and VO [16-19]. The steady-state growth ratios predicted by KOM for both PO and VO simulations closely resemble experimental values. Since ART did not reach a steady-state, we halted the PO simulation at the point when the predicted growth ratio best matched the reported mean. When the VO simulation was stopped at the same point, ART yielded a growth ratio close to the reported mean. Similarly, for GCG we halted the PO simulation when the growth ratio matched the reported mean. When the VO simulation was stopped at the same point, GCG fell outside the experimental range. The steady-state growth ratio predicted by GEG matches reported values well following VO and poorly following PO. L&T overestimates the steady-state growth ratio during PO and greatly underestimates it during VO. Finally, by definition, KUR and KFR yield isotropic growth.

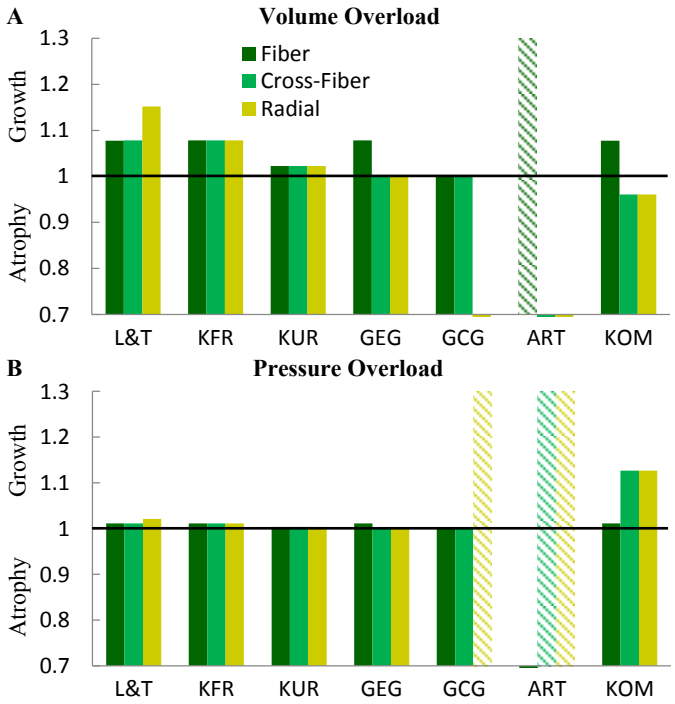

Fig. 1: Growth stretches induced by VO (A) and PO (B).

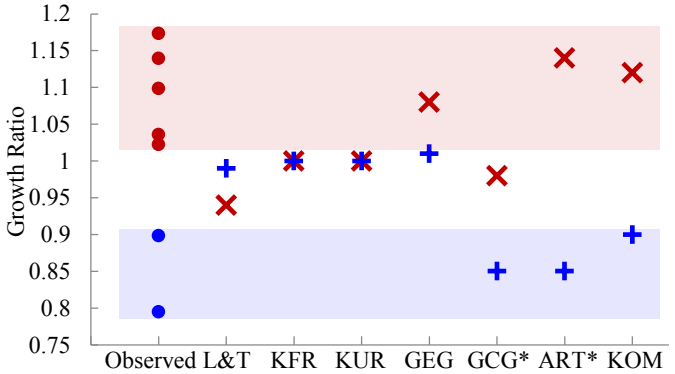

Fig. 2: Growth ratios for experiments where PO and VO were induced are column one [16-19]; red and blue boxes emphasize their range. Growth ratios for PO and VO simulations are indicated by (+) and (×), respectively. (*) indicates simulations stopped prior to divergent growth ($F_g > 20$ or $F_g < 0.05$).

DISCUSSION

The published laws that were most successful in capturing growth following PO and VO in our study employed two different inputs: KOM employed strain components in two different directions, while ART used stretches computed at different time points during the cardiac cycle. In theory, laws based on a single input could still predict different patterns of growth for VO and PO if that input increased for VO and decreased for PO (or vice versa). However, many of the single-input laws considered here (L&T, KFR, KUR, and GEG) employed end-diastolic stretch or stress, which increase in VO and are unchanged in PO. Thus, most of these laws were able to capture the VO response to some extent, but not the PO response.

In our simulations, some laws did not reach steady-state. In some cases this was partly due to the simplified nature of our simulation; we fixed the overall ED and ES stretches at literature-derived values rather than letting them evolve with growth (as was done in [5]). In order to ensure a steady-state, some laws explicitly limit growth to a maximum value (e.g. GEG), while others impose a diminishing growth rate (e.g. KOM). However, the broader question of whether growth always resolves the inciting stimulus *in vivo* remains open.

ACKNOWLEDGEMENTS

This study was supported by the Hartwell Foundation (CMW) and the National Institutes of Health (HL-120862, JWH).

REFERENCES

[1] Rodriguez, EK, *Am J Physiol*, 264:H1048–56, 1993 [2] Guccione, JM, *Am J Physiol*, 272:H469–77, [3] Lin, IE, *J Biomech Eng*, 117:343–9, 1995 [4] Kroon, W, *Biomech Model Mechanobiol*, 8:301–9, 2009 [5] Göktepe, S, *J Theor Biol*, 265:433–42, 2010 [6] Arts, T, *Am J Physiol Heart Circ Physiol*, 288:H1943–54, 2005 [7] Kerckhoffs, RCP, *Mech Res Commun*, 42:40–50, 2012 1997 [8] Holmes, JW, *J Appl Physiol*, 97:1453–60, 2004 [9] Chen, Y, *J Mol Cell Cardiol*, 49:70–8, 2010 [10] Nakano, K, *J Clin Invest*, 87:2077–86, 1991 [11] Alyono, D, *Surgery*, 96:360–7, 1984 [12] Nakamura, A, *Am J Physiol Hear Circ Physiol*, 281:H1104–12, 2001 [13] Sasayama, S, *Circ Res*, 38:172–8, 1976 [14] Tachibana, H, *Biochem Biophys Res Commun*, 343:1060-6, 2006 [15] Rodriguez, EK, *J Biomech*, 27:455-67, 1994 [16] Liu, Z, *Circ Res*, 69:52–8, 1991 [17] Liu, Z, *Circ Res*, 69:59–65, 1991 [18] Campbell, SE, *Circ Res*, 68:984–96, 1991 [19] Gerdes, AM, *Lab Invest*, 59:857–61, 1988.

Copyright 2016 The Organizing Committee for the 2016 Summer Biomechanics, Bioengineering and Biotransport Conference

SB³C2016
Summer Biomechanics, Bioengineering and Biotransport Conference
June 29 –July 2, National Harbor, MD, USA
SB³C2016-162

SURFACE MODIFICATION OF ELECTROSPUN GELATIN/FIBRINOGEN SCAFFOLDS TO ENCOURAGE ENDOTHELIAL CELL FUNCTION

Catalina Ardila (1), David Maestas (2), Victoria Lundine (2), Marvin Slepian (3,4), Jonathan Vande Geest (5)

(1) Graduate Interdisciplinary Program of Biomedical Engineering, The University of Arizona, Tucson, AZ, USA, 85721

(2) Department of Biomedical Engineering, The University of Arizona, Tucson, AZ, USA, 85721

(3) Sarver Heart Center, The University of Arizona, Tucson, AZ, USA, 85724

(4) Interventional Cardiology, The University of Arizona, Tucson, AZ, USA, 85724

(5) Department of Bioengineering, University of Pittsburgh, Pittsburgh, PA, USA, 15260

INTRODUCTION

Surface modification of biomaterials is a popular method in tissue engineering for increasing the biocompatibility of a polymer. It is known that the chemical and physical structure of the scaffold surface is the principal characteristic responsible for the attachment, viability, and biological response of cells in the biomaterial [1]. Endothelial cells (EC) are present in the most inner layer of the vasculature and are responsible for vasoregulation and the control of blood coagulation, making them important for vascular tissue engineering applications [2]. In order to mimic the antithrombogenic endothelium, it is important that the biomaterial surface promotes viability and proper function of endothelial cells. A healthy endothelium is able to produce protective molecules such nitric oxide (NO) whose principal role is the modulation of vascular dilator tone [3]. Also, functional EC are able to respond to elevated doses of interleukin-β (IL-1 β) by increasing the production of the intercellular adhesion molecule 1 (ICAM-1) and vascular cell adhesion molecule 1 (VCAM-1), both implicated in leukocyte/EC interactions in inflammation [4]. Importantly, a healthy endothelium limits platelet adhesion and aggregation in the vascular surface and inhibits the expression of plasminogen activator inhibitor-1 (PAI-1), a prothrombotic protein [5].

In this work gelatin/fibrinogen electrospun flat scaffolds were surface modified by thermoforming, coating with ECM proteins, and including polycaprolactone (PCL) in the electrospun solution. Human cord blood derived endothelial cells (hCB-ECs) were seeded in the surface modified scaffolds and a growth, inflammatory response, eNOS production, and platelet activity were evaluated.

METHODS

Gelatin extracted from porcine skin and fraction I bovine fibrinogen were mixed at 80:20 ratio w/w respectively (80:20 G-F). Electrospun sheets with this composition have been previously shown to promote porcine vascular smooth muscle (SMC) cell adherence and proliferation [6]. This blend was dissolved in HFP to create a 10% (w/v) solution. The polymeric solution was electrospun onto glass cover slips attached to a metallic target to create fine fibers. The resultant flat sheets were crosslinked in 25% glutaraldehyde vapor, which was then removed in a ventilated oven. A second polymeric blend consisting in 50% 80:20 G-F and 50% PLC in HFP was electrospun as described above. All the resultant flat scaffolds were sterilized and surface modified by either coating with a mixture of 2.5 ug/ml Collagen IV and d 2.5ug/ml Fibronectin, or by thermoforming in a water bath at 45°C for 5 min and then applying pressure in between 2 glass slides to smooth the surface. A third experimental group consisted of a combination of both coating and thermoforming. hCB-ECs were seeded at a density of $1x10^5$ cells/scaffold and cultured for 7 days. To assess cell viability, cell nuclei were stained with DAPI, and Alexa Fluor® 568 phalloidin was used to visualize f-actin. Scaffolds and cells were imaged with a laser scanning multiphoton microscope. By this qualitative assessment of viability, a surface treatment was selected and the following experiments were performed to evaluate cell function. eNOS production was evaluated by in-cell ELISA using mouse to human eNOS primary antibodies and rabbit anti mouse secondary antibodies HRP conjugated. Absorbance was measured at 450 nm. For inflammatory response, cultures were stimulated with 0.5 ng/ml of IL-1β for 3 days and the production of ICAM-1 and VCAM-1 was measured by in-cell ELISA using mouse to human ICAM-1 and VCAM-1 primary antibodies and HRP secondary antibodies as described above. Platelet activation was studied by a platelet activity state (PAS) assay, a prothrombinase based experiment; calculating the platelet activation rate (PAR) obtained from the slope of the PAS values after 2h [7]. The PAS values were normalized against fully activated platelets (obtained by sonication). The normalized value represents the fraction of thrombin

Copyright 2016 The Organizing Committee for the 2016 Summer Biomechanics, Bioengineering and Biotransport Conference

that is produced by the sonicated platelets. All the assays were performed under static conditions. Significant difference was found using one way ANOVA.

RESULTS

Multiphoton images qualitatively show variation in growth of hCB-ECs in the different surface modified constructs. 50% PCL-50% 80:20 G-F electrospun scaffolds thermoformed and coated demonstrated the best results in cell growth, having an almost complete coverage of the scaffold surface in 7 days (**Figure 1**). hCB-ECs seeded in the chosen surface modified scaffold increased the production of ICAM-1 and VCAM-1 when stimulated with IL-1β (**Figure 2**). Intracellular eNOS was detected after 7 days in culture. Also, platelets had lower activation when hCB-ECs were growing in these selected constructs (**Figure 3**).

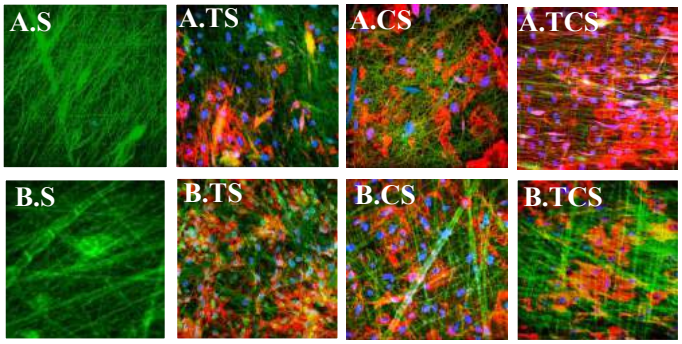

Figure 1: Multiphoton imaging of seeded scaffolds in an xy plane. Blue: Cell nuclei, Green: electrospun fibers, Red: f-actin. A) 50%PCL-50% □0:20 G-F. B) □0:20 G-F.- S. Scaffold non-treated, TS=Thermoformed, CS=Coated, TCS=Thermoformed and coated.

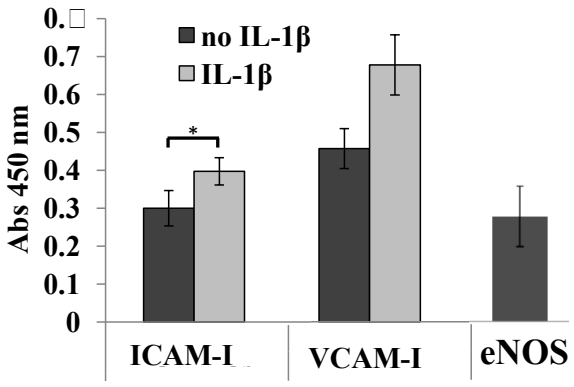

Figure 2: Inflammatory response and intracellular eNOS production of hCB-ECs growing in 50%PCL-50% □0:20 G-F thermoformed and coated. To stimulate inflammatory response IL-1β was added to the culture media. Error bars are standard deviation, n=4, □p□0.05.

DISCUSSION

The results indicated that surface topology and chemistry of the scaffolds have an effect on EC viability. Specifically, hCB-ECs show a better growth when the electrospun constructs were thermoformed to smooth the surface and also coated with ECM proteins present in the

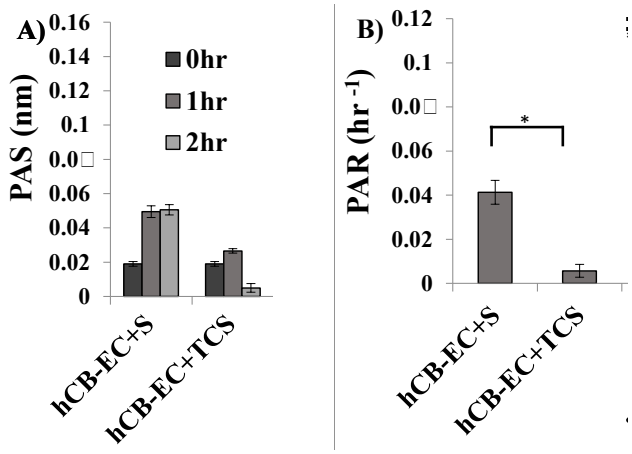

Figure 3: (A) Platelet activity state (PAS) and (B) platelet activation rate (PAR) of platelets on hCB-EC growing on nontreated 50%PCL-50% □0:20 G-F (S), and thermoformed and coated scaffolds (TCS). Error bars are standard deviation, n=4, □p□0.05.

vessel lamina such as collagen IV and fibronectin. The presence of PCL made the thermoforming process easier, which is the presumed reason why 50%PCL-50% 80:20 G-F electrospun scaffolds that were thermoformed and coated had a better cell coverage. Although the experiments were performed in static conditions, comparable levels of intracellular eNOS were detected in the hCB-ECs which can be an indication that the EC phenotype is conserved. hCB-EC function was also evaluated by the assessment of inflammatory response. Cells growing in the selected scaffold upregulated the production of ICAM-1 and VCAM-1 as occurs in a healthy endothelium when proinflammatory cytokines, such as IL-1β, are present. Antithrombogenic function was also evaluated using a platelet activation assay. It was shown that platelet activation state and rate decreased in both hCB-ECs when the constructs were surface modified. As a conclusion, 50%PCL-50% 80:20 G-F electrospun scaffolds thermoformed and coated encourage hCB-ECs growth, and the vasoregulatory, inflammatory, and antithrombogenic functions are well maintained.

ACKNOWLEDGEMENTS

This research was funded by the NIH, grant NHLBI-1R21HL111990-01A1 to J. Vande Geest, Co-I M. Slepian. C. Ardila is funded by the Cardiovascular Training Grant NIH 232HL007995.

REFERENCES

[1] H.-I. Chang and Y. Wang, *Regenerative Medicine and Tissue Engineering - Cells and Biomaterials*, INTECH, 2011.
[2] K. K. Sankaran et al., *Biotechnology journal,* vol. 10, pp. 96-108, 2015.
[3] R. K. Kharbanda et al., *Coronary artery disease,* vol. 12, pp. 485-491, 2001.
[4] S. J. O'Carroll et al., *Journal of neuroinflammation,* vol. 12, p. 131, 2015.
[5] U. Landmesser, B. Hornig, and H. Drexler, "Endothelial function a critical determinant in atherosclerosis□," *Circulation,* vol. 109, pp. II-27-II-33, 2004.
[6] D. C. Ardila, et al., *Biomaterials,* vol. 37, pp. 164-173, 2015.
[7] V.M. Merkle, et al, *ACS applied materials and interphases*, vol. 7, pp. 8302-8312, 2015.

Copyright 2016 The Organizing Committee for the 2016 Summer Biomechanics, Bioengineering and Biotransport Conference

SB^{3}C2015
Summer Biomechanics, Bioengineering and BIotransport Conference
June 29 –July 2, National Harbor, MD, USA
SB^{3}C2016-163

TRIBOLOGICAL REHYDRATION II: INSIGHTS INTO THE MECHANICS OF CARTILAGE RECOVERY

David L. Burris (1,2) and Axel C. Moore (1)

(1) Department of Biomedical Engineering
University of Delaware
Newark, DE, USA

(2) Department of Mechanical Engineering
University of Delaware
Newark, DE, USA

INTRODUCTION

Cartilage is a porous hydrated tissue and this fact has vital implications for joint function. During contact, interstitial fluid pressurizes to support load and provide hydrostatic lubrication; this 'interstitial lubrication' effect simultaneously explains the high stiffness and low friction of joint surfaces [1]. Like a punctured tire, loaded cartilage inherently leaks pressurized fluid and eventually 'deflates', resulting in the loss of load-carrying and lubrication capabilities. Remarkably, however, healthy joints do not 'deflate' as expected for reasons that remain uncertain.

Caligaris and Ateshian [2] showed that lubrication could be maintained indefinitely when a glass sphere migrated against cartilage and proposed that the contact moved before interstitial fluid could flow. Similarly, Eckstein *et al.* showed that joints maintained thickness during exercise but thinned during inactivity [3]. Ekholm and Ingelmark showed thickening when activity resumed and concluded that 10 minutes of activity was sufficient to recover the fluid lost during 30 minutes of non-weight-bearing rest [4]. To our knowledge, the accepted and only existing theory to explain this recovery phenomenon involves the passive imbibition of cartilage when exposed to the bath during articulation.

Here, we review recent experimental results that require an alternate explanation of interstitial fluid recovery by cartilage. Cartilage lost, retained, and recovered interstitial fluid in response to sliding in stationary contact areas (SCAs) that eliminated migration and bath exposure as potential contributors. The goals of this paper are to 1) elucidate the mechanism responsible for this 'tribological rehydration' phenomenon, 2) evaluate the extent to which tribological rehydration likely contributes to the recovery of whole joints, and 3) highlight important health-care implications of the results.

METHODS

Three 19 mm diameter osteochondral cores were taken from three mature bovine femoral condyles; more than 20 samples have been tested to confirm generality of these results. The samples were lubricated by saline (PBS), loaded to 5 N, and slid (0, 10, or 60 mm/s over a 20 mm long track) against a large glass flat to eliminate migration and intermittent bath exposure as potential contributors to the retention and recovery mechanics. The contact area was limited to 5 mm in an effort to ensure a convergence zone for hydrodynamic pressurization as illustrated in Figure 1a; we sub-classify this as the convergent SCA or cSCA. Normal force, friction force, and compression were measured *in-situ*.

RESULTS

Figure 1a illustrates the effect of sample size on the compression response of cartilage during sliding. The smallest sample size produced the time-dependent creep response expected of the SCA sliding configuration. Larger samples limited compression to ~60 μm. These results suggest that the presence of a convergence zone for hydrodynamic pressurization helped arrest the anticipated exudation response.

Figure 1b illustrates the recovery response to sliding following 600 seconds of static loading. Sliding at 60 mm/s led to an initial friction coefficient of $\mu \sim 0.16$ and thickening of the cartilage. With continued sliding, friction and compression decreased in concert until reaching steady states at $\mu \sim 0.005$ and $\delta \sim 65$ μm, respectively.

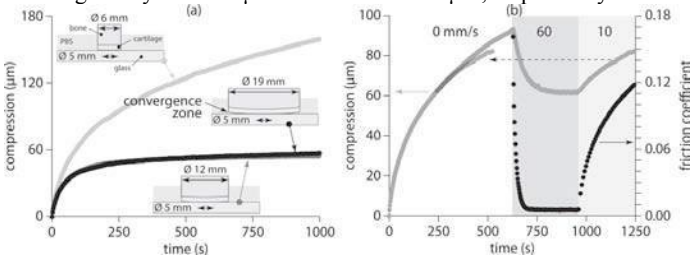

Figure 1. (a) compression of a single representative cartilage sample cut to varying size (19, 12, 6 mm diameter) and reciprocated at 60 mm/s as a function of time. (b) Compression and friction versus time for a second representative sample of 19 mm diameter in a stop-start test configuration. Following a period of static equilibration, the sample began sliding at 60 mm/s until

Copyright 2016 The Organizing Committee for the 2016 Summer Biomechanics, Bioengineering and Biotransport Conference

reaching a dynamic equilibrium; at which point the sliding speed was reduced to 10 mm/s.

DISCUSSION

The results of this study demonstrate that cartilage can retain and recover interstitial fluid and lubrication. Previous observations of similar phenomena in migrating contacts were attributed to the facts that: 1) migration provides insufficient time for flow [2] and 2) migration enables passive imbibition during intermittent bath exposure [4–6]. The cSCA used in this study excludes both. Therefore, the retention and recovery phenomena observed here require a new mechanism, which we call 'tribological rehydration'.

In light of this alternate hypothesis of cartilage recovery, it is appropriate to revisit conclusions regarding the recovery mechanisms in joints. Linn's measurements (Figure 2a) best-illustrate the loss and recovery mechanics of a typical joint (canine ankle) [6]. As shown in Figure 2b, removing potential contributions from migration and bath exposure using the cSCA had no obvious detrimental effect on recovery efficacy, which suggests that the recovery of Linn's ankle, and joints in general, are more likely attributable to tribological rehydration than migration or free swelling.

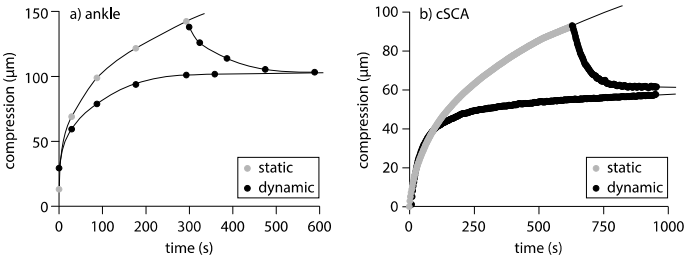

Figure 2. Comparison between Linn's results [6] and those from comparable experiments with the cSCA. The figures demonstrate striking resemblance despite grossly different loads, contact areas, reciprocation lengths, material properties, and testing configuration (whole joint (a) versus cSCA (b)).

The comparison in Figure 2 suggests that tribological rehydration is an important physiological process and the results from this study provide important clues into the underlying mechanics. First, the effect was eliminated when reduced sample size eliminated the convergence zone for hydrodynamic pressurization. Secondly, the effect was reduced when sliding speed was reduced. These facts strongly suggest that the recovery response was driven by hydrodynamics.

Joints are widely believed to be lubricated by hydrodynamic fluid films [7], which implies a broader belief that the hydrodynamic pressures developed during joint articulation must reach physiological contact pressures (1-10 MPa) [8]. This study supports the importance of hydrodynamics while simultaneously raising doubt about the importance of fluid films. The high initial friction in Figure 1b is the best evidence that hydrodynamic pressurization does not necessarily lead to the formation of fluid films. Instead, friction decreased with decreased compression, which suggests that pressurized fluid flowed into the surface to restore interstitial lubrication rather than between surfaces to create a lubricating fluid film.

The main disadvantage of hydrodynamic fluid film lubrication, particularly when applied to the diarthrodial joint, is film collapse during inactivity. Hydrostatic lubrication requires no relative motion and is associated with even lower friction coefficients. The main disadvantage of hydrostatic lubrication is the complexity of the fluid pressurization and supply system [9].

By integrating these seemingly disparate lubrication systems, Nature appears to have eliminated the disadvantages of each. When cartilage is hydrated, interstitial fluid is automatically pressurized by contact thereby providing hydrostatic lubrication [1]. Cartilage also effectively acts as a fluid reservoir, maintaining reasonable pressures over normal periods of inactivity (*e.g.* 10-60 minutes) [1]. However, because pressurized fluid escapes the cartilage as it does any hydrostatic bearing, the lack of a fluid supply is an obvious problem. This study shows that cartilage is resupplied with fluid during activity and suggests that external hydrodynamic pressurization pushes fluid back into articular surfaces to restore hydration and to prepare surfaces for subsequent inactivity.

This concept supports previous assertions that porous surfaces are not well-suited for the generation of fluid films [1]. If surfaces are in direct frictional contact, as we believe they are under most circumstances, then boundary films must be critical for wear prevention at locations of contact. Thus, we propose that 1) boundary films primarily prevent wear, 2) interstitial lubrication primarily reduces friction and protects boundary films by substantially reducing their load-carrying burden, and 3) hydrodynamics are primarily responsible for maintaining and restoring interstitial lubrication.

This cooperative joint lubrication system has important health-care implications. First, it suggests a completely different approach to joint replacement. Currently, designers either acknowledge direct unmitigated contact between surfaces and use polymers for tolerance to contact [10], or they use smooth, hard and well-defined surfaces in an effort to separate surfaces with hydrodynamic fluid films [11]. This study suggests that Nature uses neither approach. Secondly, it implies that activity is the engine by which the joint prevents the otherwise inevitable collapse of cartilage as a functional load-bearing tissue. This fact may help explain recent and counterintuitive findings that runners have reduced risk of joint disease [12]. It also helps reinforce the U.S. Surgeon General's call for increased physical activity to reduce risk of major health problems, including joint disease [13].

ACKNOWLEDGEMENTS

The authors acknowledge financial support from the NIH (grant P20-RR016458) for the development of the experimental methods described in the paper.

REFERENCES

[1] Ateshian, G.A. J. Biomech. 42, 1163–76 (2009).
[2] Caligaris, M. Osteoarthr. Cartil. 16, 1220–1227 (2008).
[3] Eckstein, F. J. Anat. 208, 491–512 (2006).
[4] Ekholm, R. Acta Soc. Med. Ups. 57, 39–59 (1951).
[5] McCutchen, C.W. Wear. 5, 1–17 (1962).
[6] Linn, F.C. J. bone Jt. Surg. 49, 1079–1098 (1967).
[7] Mansour, J.M. Kinesiol. Mech. pathomechanics Hum. Mov. 66–79 (2009).
[8] Brand, R. Iowa Orthop. J. 25, 82–94 (2005).
[9] Hamrock, B. McGraw-Hill (1994).
[10] Charnley, J. Ann. Rheum. Dis. 19, 10–19 (1960).
[11] Smith, S.L. Proc. Inst. Mech. Eng. H. 215, 161–70 (2001).
[12] Williams, P.T. 45, 1292–1297 (2013).
[13] Physical activity and health: a report of the Surgeon General. (1996).

Copyright 2016 The Organizing Committee for the 2016 Summer Biomechanics, Bioengineering and Biotransport Conference

SB³C2016
Summer Biomechanics, Bioengineering and Biotransport Conference
June 29 –July 2, National Harbor, MD, USA
SB³C2016-164

A MECHANOSTATISTICAL MODEL FOR THE RAPID ASSESSMENT OF FEMORAL NECK CORTICAL FRACTURE RISK

X. Wang (1), R. Das (2), P. Hunter (1), J. Fernandez (1,3)

(1) Auckland Bioengineering Institute
The University of Auckland
Auckland, New Zealand

(2) Department of Mechanical Engineering
Faculty of Engineering
The University of Auckland
Auckland, New Zealand

(3) Department of Engineering Science
Faculty of Engineering
The University of Auckland
Auckland, New Zealand

INTRODUCTION

Femoral neck fractures associated with ageing and disease are a leading cause of morbidity. As the cortex of the bone bears most of the load in daily activities, fracture usually initiates in cortical bone and thus is the focus of this study.

By informing an accurate hip and femur geometry derived from the Visible Human [1] with Haversian-level models of cortical bone, experimentally determined muscle forces from gait analyses, and spatially-varying porosity data in the femoral neck, it is possible to construct a database of femoral neck strains after strain adaptation through finite element (FE) simulations for different known load intensities. A statistical method can then be used to call upon this database to rapidly estimate strains from new load scenarios.

The objective of this study was to develop a multiscale mechanostatistical FE cortical bone model, combined with Frost's remodelling rules and cutting cone behaviour. The model estimates physiologically adapted regional femoral neck strains as a result of walking and running gaits to build a database of load-strain scenarios. Partial least squares regression (PLSR) [2] is trained on a set of mechanics simulations to rapidly estimate strains for new load scenarios, avoiding additional expensive simulations.

METHODS

The framework for the multiscale model is shown in Figure 1, indicating the flow of information across the scales.

Macroscale: Gait-relevant skeletal muscle and bones were segmented from the Visible Human Male data and meshed with hexahedral 5 mm elements with walking- and running- level muscle loads [3], extracted at toe-off stance, under the assumption that the model is adapted to walking loads. Loads were transferred from the acetabulum to the mesoscale proximal femur model (the region of interest), and were recorded for subsequent simulations.

Mesoscale: Load was transferred from the macroscale to the proximal femur, resulting in strains in the femoral neck cortex. Eigenvectors associated with the maximum principal strains in the cortical elements were used as estimates for the fibre directions for the definition of a transversely isotropic cortical bone material. Spatially varying porosities were assigned to the cortical bone elements according to a periodic B-spline function with parameters determined from experimental data [4] for subjects who had, and had not experienced an intracapsular (femoral neck) fracture. These were then converted into bone densities via an empirical relation [5].

Microscale: Porosities assigned to the cortical bone mesoscale elements were used to section cuboid blocks, containing representative Haversian structures, off a healthy region of cortical bone obtained through voxel meshing of μCT images. Each mesoscale cortical element was assigned microscale cortical bone blocks with matching porosities. The microscale models have local coordinates globally aligned with fibre directions determined in the mesoscale. Elements in the microscale models were assigned densities calculated from the corresponding mesoscale cortical element density, and a porosity value was determined from this density. These porosities were converted to to element-wise transversely isotropic material properties [6] in the microscale. Strains passed down to the elements were used to evolve density via Frost's mechanostat and cutting cone behaviour directed by high-strain regions, driving material property adaptations. Load cycles were applied for 3 simulated months. These properties were then passed back up the mesoscale for the reapplication of loads.

PLSR: The simulation of various loads on microscale models and the resultant homogenised material property adaptations were stored in a database, and PLSR was used to call upon this database to quickly

Copyright 2016 The Organizing Committee for the 2016 Summer Biomechanics, Bioengineering and Biotransport Conference

estimate homogenised material properties for unsimulated loads passed down from the mesoscale. Element-wise material properties in the mesoscale cortical elements were rapidly estimated. From the different macroscale loads applied, high strain regions were rapidly identified and noted for fracture risk.

RESULTS

The cortical bone remodelling and cutting cone algorithms changed the material properties of the cortical bone and new Haversian canals tunnelled in the estimated fibre directions in the microscale models. PLSR from the various different loads rapidly predicted homogenised material properties with low errors.

Spatially varying porosities in the cortical bone informed significant differences in strain magnitudes across the geometry of the femoral neck cortical bone. For the model emulating the case of subjects who did not suffer intracapsular fracture, walking loads showed no significant change in material properties in the cortical layer, while adaptation from running loads increased bone strength for a short while. The strength increase quickly plateaued. For the case of subjects who have suffered intracapsular fracture, walking loads also showed no significant change in material properties; however, strain magnitudes are much higher for many more regions of the femoral neck cortex. These two load cases are highlighted in Figure 2.

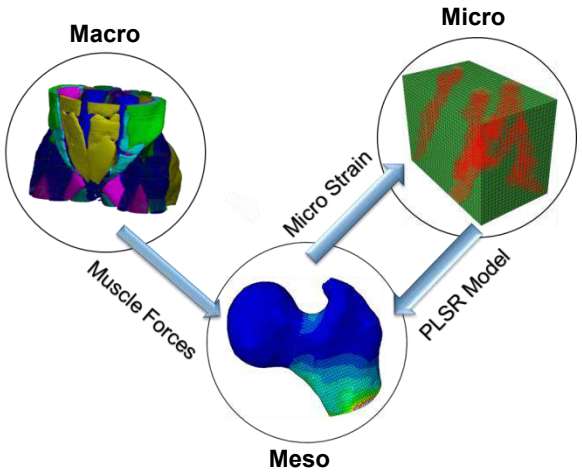

Figure 1: Framework for multiscale model.

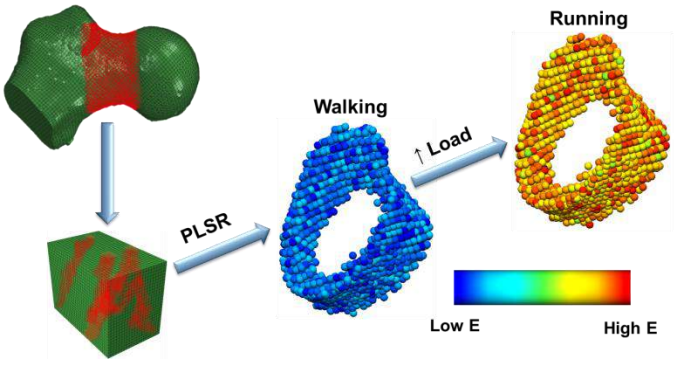

Figure 2: Remodelling adaptation to increased loads (*E*: Young's Modulus)

DISCUSSION

Microscale: For the non-fracture case, material property changes in the microscale model showed no change for walking-level loads and an increase in general bone strength in the fibre direction for running-level loads as an appropriate physiological adaptive response to increased strains in the non-fracture case. These strength changes plateaued fairly quickly due to the 'fading memory' effect proposed in [7]. For the intracapsular fracture case, many microscale models showed strains breaching the damage zone of the mechanostat, present in running-level loads; stronger bone maintained or increased their strength, while more porous bone received damaging strains causing a decrease in bone strength. For both cases, Haversian canal tunnelling occurred towards the direction of highest applied strain, maintaining the fibre directions estimated in the mesoscale. PLSR was shown to be a good rapid estimator of homogenised material properties in the microscale models.

Mesoscale: Microscale changes were reflected in the mesoscale femoral neck model. Walking and running level loads showed no noticeable fracture risk indicated by high strain regions in the femoral neck cortex for the case without intracapsular fracture. Walking level loads also did not show an increase in high strain regions in the post-fracture case. However, running-level loads resulted in high strains in some femoral neck areas, notably in some regions with high porosities which bear high loads. This indicates that the porosity variation implemented and the resultant strain patterns were in agreement with the stress distributions of mid femoral neck during normal and traumatic loading [8], and was a good estimator for fracture risk.

ACKNOWLEDGEMENTS

We acknowledge the New Zealand Ministry of Business, Innovation and Employment (MBIE) for the funding of this work.

REFERENCES

[1] Ackerman M.J., *J Biocommun*, 18(2):14, 1991.
[2] Wold S., Sjostrom M., Eriksson L., *Chemometr Intell Lab*, 58(2):109-130, 2001.
[3] Fernandez J. et al., *Int J Numer Method Biomed Eng*, 30(1):28-41, 2014.
[4] Bell K.L. et al., *Bone*, 24(1):57-64, 1999.
[5] Bousson V. et al., *Radiology*, 217(1):179-87, 2000.
[6] Dong X.N., Guo X.E., *J Biomech*, 37(8):1281-7, 2004.
[7] Wang X. et al., *Biomech Model Mechanobiol*, [Published online ahead of print] DOI: 10.1007/s10237-015-0669-x
[8] Lotz J.C., Cheal E.J., Hayes W.C., *Osteoporosis Int*, 5:252-261, 1995.

Copyright 2016 The Organizing Committee for the 2016 Summer Biomechanics, Bioengineering and Biotransport Conference

SB^{3}C2016
Summer Biomechanics, Bioengineering and Biotransport Conference
June 29 –July 2, National Harbor, MD, USA
SB^{3}C2016-165

EFFECT OF THREE DIMENSIONAL SPHEROID CULTURE ON BIPOTENT MURINE LIVER PROGENITOR CELLS

Kenichiro Nishii (1), Erik Brodin (1), Taylor Renshaw (1), Rachael Weesner (1), Jessica L. Sparks (1)

(1) Chemical, Paper and Biomedical Engineering Department
Miami University
Oxford, OH, United States

INTRODUCTION

Adult livers harbor bipotent hepatic progenitor cells (HPCs) that can become either biliary cells or hepatocytes [1]. In diseased livers, HPCs can mount a proliferative response followed by a remodeling phase. During this HPC-mediated regenerative process, the HPCs recapitulate aspects of liver development and morphogenesis. This regenerative response, termed the ductular reaction, can repair the injured liver and restore healthy tissue [2]. However, in many cases the regenerative response is misregulated, resulting in scarring and increased risk of primary liver cancer [3]. The mechanisms that dictate whether the regenerative response will lead to repair or misrepair are still unknown. There is a need to better understand the mechanisms controlling the liver regenerative response.

In order to address this issue, physiologically realistic cell culture environments are essential. The objective of this study was to develop and test a three-dimensional culture system for bipotent hepatic progenitor cells. To better mimic in vivo conditions, we sought to create a 3D culture system capable of applying interstitial flow to cultured cells and spheroids, with estimated target shear stresses in the range of 1-15 dynes/cm^2 [4]. In addition, the system incorporates an extracellular matrix (ECM) gel formed from hyaluronic acid, collagen III, and laminin, components of the hepatic progenitor cell niche.

METHODS

Study Design. Bipotent murine oval liver (BMOL) cells, a well-established hepatic progenitor cell line [5], were used for the experiments. Cells were studied under four conditions: traditional 2D culture on tissue culture plastic (2D); 3D spheroid culture using hanging drop culture conditions (3D); 2D cultured cells suspended in ECM (ECM2D); and 3D spheroids suspended in ECM (ECM3D). For each culture condition, two types of media were compared: Williams' E medium (WE) (Fisher, Waltham, MA) prepared with 2% fetal bovine serum and supplemented as described previously for routine BMOL cell culture [5]; and serum-free InSight Liver Maintenance medium (IS) (InSphero, Brunswick, ME) developed for 3D spheroid culture applications. Quantitative reverse-transcriptase PCR (qRT-PCR) was used to evaluate the effect of culture condition (2D, 3D, ECM2D, ECM3D) and media type (WE, IS) on BMOL gene expression. GAPDH and PPIA were reference genes, and target genes were ALB, CK19, HNF4α, HNF6, and SOX9. Each experiment was done in triplicate, and all technical replicates were done in triplicate.

Cell Culture. Cells from the BMOL cell line were obtained from Dr. Janina Tirnitz-Parker [5]. BMOL cells were cultured in 25 cm^2 culture flasks (Fisher) for at least 2 weeks for cell stabilization after they were thawed from Lq N_2. Culture medium was changed every other day, and cells were passaged every 4 days through trypsinization. For 2D culture, BMOL cells were cultured in a flat bottom 6 well cell culture plate for 48 hours before the gene analysis. For 3D culture, an InSphero GravityPLUS hanging drop culture plate (InSphero, Brunswick, ME) was used to make spheroids. BMOL cells were cultured in the GravityPlus plate for 4 days and transferred into a GravityTRAP plate (InSphero, Brunswick, ME). The spheroids were cultured in the GravityTRAP for 48 hours before the analysis. ECM was prepared from Hystem hydrogel (ESI Bio, Alameda, CA) at a concentration of 5 mg/mL (corresponds to 0.5%), collagen III (Sigma, St. Louis, MO) at 1 mg/mL (0.1%), laminin (Sigma, St. Louis, MO) at 1mg/mL (0.1%). The ECM components were dissolved in Tris buffered NaCl (pH≈7.3), followed by PEGDA (ESI Bio, Alameda, CA) cross linker addition at 5 mg/mL (0.5%) concentration. The ratio between the ECM solution and cross linker was 4:1. 2D cultured cells and 3D spheroids were suspended in the ECM and cultured for 48 hours before the analysis.

Copyright 2016 The Organizing Committee for the 2016 Summer Biomechanics, Bioengineering and Biotransport Conference

Analysis. Microscopy images were taken after each culture condition with a Zeiss AXIO Vert A1 light microscope (Zeiss, Atlanta, GA). RNA was extracted with a Maxwell 16 instrument and Maxwell 16 LEV simplyRNA tissue kit (Promega, Madison, WI), and RNA integrity was assessed with an Agilent 2100 Bioanalyzer and Agilent RNA 6000 Pico kit (Agilent Technologies, Santa Clara, CA). Quantitative RT-PCR gene expression analysis was conducted using a CFX Connect Real Time PCR Detection system (Bio Rad, Hercules, CA) and qBasePlus (Biogazelle, Zwijnaarde, Belgium) was used for statistical analysis of the results (ANOVA, significance level 0.05). Expression was normalized to the two reference genes (GAPDH, PPIA) using the delta delta Ct method.

Chamber Design. The flow chamber design was adapted from Ng and Swartz [6] with modifications in dimensions and ECM components (Figure 1). Cover glass on the top and bottom was cleaned with 0.1M NaOH followed by functionalization with (3-Aminopropyl) trimethoxysilane and glutaraldehyde (Sigma, St. Louis, MO). Pressure applied to the hydrogel was monitored by measuring the height of the fluid column. Permeability (K) and shear stress (τ) applied to the encapsulated cells were estimated from equations (1) and (2) from [6]:

$$K = \frac{Q\mu ln(r_o/r_i)}{2\pi h \Delta P(t)} \ [m^2] \qquad (1)$$

$$\tau = \frac{Q\mu}{2\pi r h}(K)^{-\frac{1}{2}} \ [Pa] \qquad (2)$$

where Q is fluid flow rate in [m/s], μ is viscosity of perfusion media [Pa·s], r_i and r_o and are inner and outer radius of the ECM hydrogel ring [m], h is height of the ECM hydrogel [m], $\Delta P(t)$ is pressure difference at time t [Pa]. For this experiment, 0.0012 Pa·s (=1.2 cP) was used for the media viscosity for both perfusion media. 3.4 mm and 9.15 mm were used for r_i and r_o, and 1.6 mm for h. Each experiment was done in triplicate.

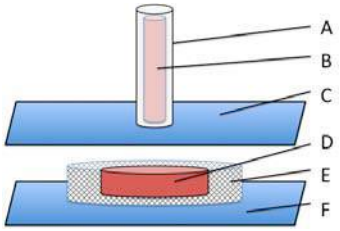

Figure 1: Flow chamber. A: Fluid column pipe, B: Fluid column, C: Top cover glass, D: Hydrogel, E: Porous mesh, F: Bottom cover glass.

RESULTS

Cells spheroids showed increased intercellular attachment and more uniform spheroid geometry in IS media compared with WE media (Figure 2). RNA integrity results are listed in Table 1. In some trials, the amount of RNA obtained was too low to perform the integrity evaluation (shown as N/A in Table 1). Accordingly, results for the ECM2D WE and ECM2D IS conditions were excluded from further analysis due to insufficient RNA quality. qRT-PCR results are shown in Table 2, with the 2DWE condition as the control. The average pressure drop across the ECM gel was 1428 Pa. Mean permeability was K_{ave}=1.48x10^{-11}±1.34x10^{-11} m^2, and mean shear stresses were $\tau_{i,ave}$=1.16±0.68 Pa, $\tau_{o,ave}$=0.43 ±0.25 Pa.

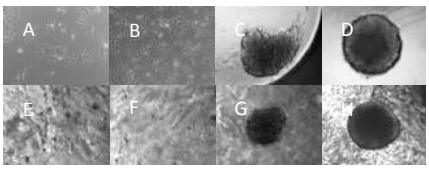

Figure 2: Microscopy at 40x. A: 2DWE, B: 2DIS, C: 3DWE, D: 3DIS, E: ECM2DWE, F: ECM2DIS, G: ECM3DWE, H: ECM3DIS.

Table 1: RNA Integrity Results.

	Medium	Trial 1	Trial 2	Trial 3	Average	St Dev
2D Cultured Cells (2D)	WE	8.5	9.2	7.7	8.47	0.75
	IS	8.4	9	7.4	8.27	0.81
3D Spheroids (3D)	WE	8.2	8.2	6.8	7.73	0.81
	IS	8.5	7.8	N/A	8.15	0.49
2D Cultured Cells in ECM (ECM2D)	WE	N/A	N/A	5.8	N/A	N/A
	IS	N/A	N/A	6.5	N/A	N/A
3D Spheroids in ECM (ECM3D)	WE	5.9	N/A	4.2	5.05	1.20
	IS	5.6	6.3	7.2	6.37	0.80

Table 2: qRT-PCR Results.

	GAPDH	PPIA	CK19	ALB	HNF4a	HNF6	SOX9
2DWE (control)	1 ±0.08	1 ±0.06	1.01 ±0.08	1.10 ±0.47	1.07 ±0.08	1.02 ±0.15	1.11 ±0.09
2DIS	1.19 ±0.07	1.19 ±0.08	1.17 ±0.07	1.81 ±0.28	0.95 ±0.1	4.72 ±0.96*	0.64 ±0.08
3DWE	0.85 ±0.1	0.85 ±0.05	1.31 ±0.1	4.09 ±0.88	0.45 ±0.04	45.99 ±7.1*	2.17 ±0.2
3DIS	0.78 ±0.14	0.78 ±0.06	1.78 ±0.14	5.05 ±0.59	0.36 ±0.04*	29.06 ±5.4*	1.57 ±0.18
ECM3DWE	1.07 ±0.1	1.07 ±0.07	0.31 ±0.1*	N/A	0.31 ±0.04*	14.51 ±4.68*	1.15 ±0.13
ECM3DIS	1.2 ±0.07	1.2 ±0.14	0.59 ±0.07	1.55 ±0.21	0.44 ±0.05	12.69 ±4.88*	1.99 ±0.28

*Statistically significant difference ($p<.05$) compared to control

DISCUSSION

Hepatic progenitor (BMOL) cells were successfully grown in spheroid culture, and expression levels of six target genes were characterized to determine the effects of spheroid culture on gene expression. HNF6, a biliary marker, was significantly elevated in BMOL cells in 3D culture, for both media types and with and without the presence of ECM (Table 2). HNF6 was also slightly elevated in the 2DIS condition compared with the 2DWE control; this represented the only statistically significant difference attributed to media type alone. HNF4a, expressed in hepatocytes, was slightly decreased in two of the four 3D culture conditions (3DIS, ECM3DWE). Importantly, Table 2 results suggest that the BMOL cells maintained bipotent progenitor cell status in 3D culture. This is supported by the observed co-expression of ALB, a hepatocyte marker, and CK19, a marker of biliary and progenitor cells, and by the consistent expression of SOX9, an indicator of stem/progenitor status. Chamber results demonstrate that the ECM gel, which mimics hepatic progenitor niche components, has a permeability consistent with other collagen I-based interstitial flow systems [6] and can produce approximate shear stresses within the targeted range of 0.1-1.5 Pa (1-15 dynes/cm^2). Future work will use this system to investigate BMOL cell response to interstitial flow.

ACKNOWLEDGEMENTS

The authors acknowledge Dr. Andor Kiss (Center for Bioinformatics and Functional Genomics) for assistance with qRT-PCR, and Dr. Jason Berberich for assistance with glass functionalization. Funding provided by the Chemical, Paper and Biomedical Engineering Department of Miami University.

REFERENCES

[1] Duncan AW, et al. Gastroenterology 2009;137:466-481
[2] Boulter L, et al. Nature Medicine 2012;18(4):572-579
[3] Diehl AM. Nature Medicine 2012;18(4):497-499
[4] Debbaut C, et al. J Biomech Eng 2012;134:011003-1
[5] Tirnitz-Parker J, et al. Int J Biochem Cell Biol 2007;39:2226-2239
[6] Ng C et al. Am J Phys Heart Circ Phys 2003;284(5): H1771-H1777

Copyright 2016 The Organizing Committee for the 2016 Summer Biomechanics, Bioengineering and Biotransport Conference

SB^{3}C2016
Summer Biomechanics, Bioengineering and Biotransport Conference
June 29 –July 2, National Harbor, MD, USA
SB^{3}C2016-166

DEVELOPMENT AND EVALUATION OF AN IMAGE ANALYSIS APPROACH FOR THE STUDY OF RECURRENCE IN COIL EMBOLIZED CEREBRAL ANEURYSMS

Anna L. Schumacher (1), Luca Antiga (2), Tatiana Correa (1), David M. Hasan (3), Madhavan L. Raghavan (1)

(1) Department of Biomedical Engineering
University of Iowa
Iowa City, IA, USA

(2) Orobix Srl
Bergamo, Italy

(3) Department of Neurosurgery
University of Iowa
Iowa City, IA, USA

INTRODUCTION

In cerebral aneurysms treated by coil embolization, incidences of and complications from recurrence – or the reentry of blood into the coiled aneurysm sac – are not insignificant. Identifying the mechanism underlying cerebral aneurysm recurrence will improve patient selection for coil embolization treatment, as well as impact coil device design. Coil mass compaction inside a cerebral aneurysm is a plausible mechanism, but quantitative evidence to support it as the presumptive mechanism is lacking, since the supporting evidence usually collected are visual inspections of 2D angiograms. Growth of the aneurysm sac is an alternative recurrence mechanism; in an earlier study we reported sac growth may be equally as or more important than coil compaction as a recurrence mechanism. [1] In a similar study with four patients, De Craene et al. [2] reported that all showed longitudinal sac growth while only one patient showed coil compaction. Caution is warranted in drawing conclusions from both studies because, in addition to having small study populations, neither demonstrated the fidelity of the image-processing methods by using non-recurrence controls. The aims of this study were three-fold: 1) to develop an objective image analysis approach to assess the incidences of cerebral aneurysm growth and coil compaction, 2) to evaluate the user sensitivity in the developed approach and 3) to independently assess the association of sac growth and coil compaction with recurrence in human subjects.

METHODS

To independently assess aneurysm growth and coil compaction in patients who underwent coil embolization treatment of their aneurysm and later presented with recurrence, three-dimensional rotational angiography (3DRA) scans were retrieved from four time points: pre-first treatment (1-), post-first treatment (1+), pre-second treatment (2-), and post-second treatment (2+). Note that patients with recurrence are routinely coiled a second time. In contrast, the 3DRA scans obtained for the control patients (also coil embolization patients, but those that did not present with recurrence during follow-up) were from three time points: 1-, 1+, and 2- (since these patients do not undergo a second coiling treatment). The collected 3DRA scans were then used to create 3D models of the aneurysm sac, contiguous vessels, and aneurysm coil mass for each study time point using a dedicated image analysis pipeline. This pipeline was built using Vascular Modeling Toolkit (VMTK) 1.0.0 libraries (D.Steinman-L.Antiga © 2004-2012); additionally, some new VMTK libraries were also developed such that automated image segmentation and automated aneurysm isolation could be implemented. These new libraries have since been incorporated into VMTK 1.2. Afterward, the volumes of the following structures were computed from the representative aneurysm and coil mass models: the aneurysm sac volume at the 1- time point (V_{S1-}), the aneurysm sac volume at the 1+ time point (V_{S1+}), the aneurysm sac volume at the 2- time point (V_{S2-}), the aneurysm sac volume at the 2+ time point (V_{S2+}), the coil mass volume at the 1+ time point (V_{C1+}), and the coil mass volume at the 2- time point (V_{C2-}), as illustrated in Figure 1. Volumetric sac growth, V_{SG}, was computed as the difference in sac volume between follow-up and initial presentations. Given the four study time points, there can be two sac volumes at initial presentation (V_{S1-}, V_{S1+}); similarly there can be two sac volumes at follow-up (V_{S2-}, V_{S2+}). In theory these volume pairs should be equal but in practice small differences exist due to factors like differences in image artifacts and in aneurysm isolations relative to the parent vessel. An independent investigation showed that such differences did not impact our findings. [3] As a result, aneurysm sac growth can be defined as the difference in the sac volume between the 2+ and 1- presentation:

$$V_{SG} = V_{S2+} - V_{S1-} \quad (1)$$

Copyright 2016 The Organizing Committee for the 2016 Summer Biomechanics, Bioengineering and Biotransport Conference

Therefore, $V_{SG} > 0$ indicates growth of the aneurysm sac. Next volumetric coil mass growth, V_{CG}, was computed as the difference in the coil mass volume between the 2- and the 1+ presentation:

$$V_{CG} = V_{C2-} - V_{C1+} \quad (2)$$

Therefore, $V_{CG} < 0$ indicates compaction of the coil mass. To document the sensitivity of the image analysis pipeline to the investigator a second user, blinded from the first, used it to calculate aneurysm and coil volumes for a subgroup of eight recurrence patients. The volumes computed by each investigator were compared. To assess the association of sac growth and coil compaction with recurrence, paired Wilcoxon tests (statistical significance at $p<0.05$, one-tailed) were conducted to test the hypotheses that $V_{SG} > 0$ and $V_{CG} < 0$ for the recurrence and control cohorts.

RESULTS

Three-dimensional rotational angiography (3DRA) scans were retrospectively collected for 15 recurrence aneurysms and 12 non-recurrence control aneurysms (consecutively chosen) that were initially completely coiled by a single neuroradiologist between July 2009 and September 2012 at The University of Iowa Hospitals and Clinics (UIHC). The study was approved by Institutional review board (No. 201210828). The developed image analysis pipeline was used to compute the aneurysm sac and coil volumes for all aneurysms. A second blinded investigator used the pipeline to compute aneurysm sac and coil volumes for a subgroup of eight recurrence patients. The aneurysm and coil volumes estimated by the two blinded investigators were found to agree quite strongly, with coefficients of determination for the aneurysm sac and coil mass volumes of 0.998 and 0.999 respectively, see Figure 2. Note that imaging data was available to calculate V_{SG} in all 15 subjects within the recurrence cohort and all 12 subjects in the control cohort; however, imaging data was only available to calculate V_{CG} in 9 of 15 aneurysms in the recurrence cohort and 9 of 12 aneurysms in the control cohort. Therefore aneurysm sac growth was found to exist with statistical significance in the recurrence cohort (min, median, max V_{SG} = -0.044, +0.083, +0.580 cc; $p<0.05$). In contrast, sac growth was not found to exist with statistical significance in the control cohort (min, median, max V_{SG} = -0.009, +0.001, +0.024 cc; $p>0.05$). Coil compaction was not found to occur with statistical significance in either the recurrence (min, median, max V_{CG} = -0.265, +0.004, +0.359 cc; $p>0.05$) or control cohorts (min, median, max V_{CG} = -0.013, 0.000, +0.008 cc; $p>0.05$). It is noteworthy that the control cohort had smaller aneurysms at initial presentation compared to the recurrence cohort (sac size median = 10 versus 6.5 mm; $2p<0.05$ by Mann-Whitney U-test).

DISCUSSION

We have developed a new and objective image analysis pipeline to estimate aneurysm and coil mass volume growth. Unlike previous studies the aneurysm population in this study was free of any selection bias as it included all aneurysms that presented with recurrence at the UIHC between July 2009 and September 2012 for which 3DRA scans were available. This is the first study to include control aneurysms. The automated image analysis pipeline was shown to be objective and insensitive to the investigator. Details of our developed pipeline and analyses may be found in our recent report [3].

Aneurysm sac growth was found to be associated with recurrence in this study with sensitivity and specificity. Coil compaction was not found to be associated with recurrence. These findings are consistent with De Crane et al.'s earlier report [2] and also with a recent report by Abdihalim et al. [4]. Nevertheless this study has limitations. For instance, it is a single-center, single-practitioner experience. The sample size, though largest to date, is limited; aneurysms in the control cohort are smaller than those in the recurrence cohort (which was inevitable because size is independently associated with recurrence risk).

Contrary to conventional wisdom, this study found little association between recurrence in coil embolized cerebral aneurysms and coil compaction; particularly, aneurysm sac growth was found to be the predominant etiology of recurrence. This suggests that a growing aneurysm may also be at a high risk for recurrence and hence better treated by other modalities; this also suggests that it would not be prudent to presume the existence of coil compaction in embolized aneurysms that present with recurrence. Coil designs targeted toward minimizing compaction may only have modest impact in reducing incidences of recurrence.

ACKNOWLEDGEMENTS

This study was supported by grants from NIH/NINDS R03NS079227-01A1, NIH/NHLBI R01HL083475, and K08NS082363-01A1.

REFERENCES

[1] Hasan, D et al., *Stroke,* 43:866-8, 2012.
[2] De Craene, M et al., *SPIE Med Imag,* 2008.
[3] Hoppe, A et al., *PLOS One,* 10:e0123017, 2015.
[4] Abdihalim, M et al., *J Neuroimag,* 24:171-5, 2014.

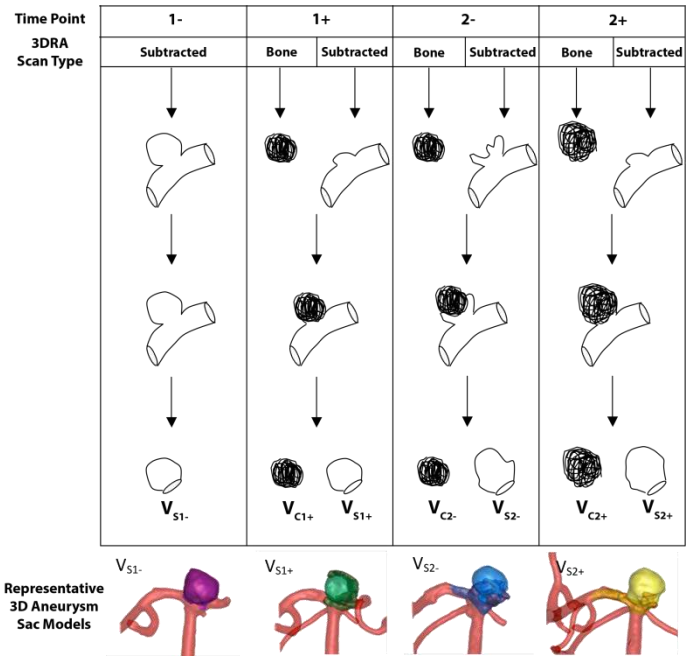

Figure 1: Schematic illustration of the image analysis approach.

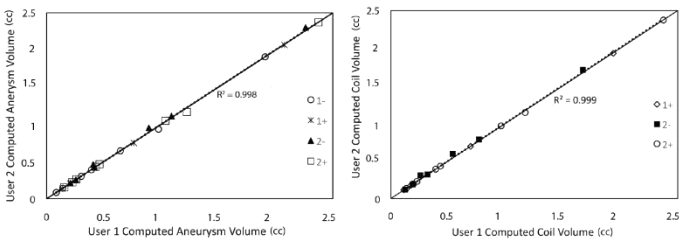

Figure 2: User sensitivity in computed aneurysm and coil volumes for various time points, suggesting a highly objective methodology.

Copyright 2016 The Organizing Committee for the 2016 Summer Biomechanics, Bioengineering and Biotransport Conference

SB³C2016
Summer Biomechanics, Bioengineering and Biotransport Conference
June 29 –July 2, National Harbor, MD, USA
SB³C2016-167

LOSS OF ELASTIC FIBER INTEGRITY DUE TO FIBULIN-5 DEFICIENCY ALTERS AORTIC ELASTICITY, CENTRAL HEMODYNAMICS, AND CARDIAC FUNCTION

Jacopo Ferruzzi (1,2), Paolo Di Achille (2), Pradyumn Agarwal (3), Federica Cuomo (3), C. Alberto Figueroa (3), Jay D. Humphrey (2,4)

(1) Department of Biomedical Engineering
Boston University
Boston, MA, USA

(2) Department of Biomedical Engineering
Yale University
New Haven, CT, USA

(3) Department of Biomedical Engineering
University of Michigan
Ann Arbor, MI, USA

(4) Vascular Biology & Therapeutics Program
Yale School of Medicine
New Haven, CT, USA

INTRODUCTION

Central artery stiffness has emerged over the past decade as a clinically significant indicator of cardiovascular function and initiator of disease. Loss of elastic fiber integrity is one of the primary contributors to increased arterial stiffening in normal aging and in pathologic conditions such as hypertension and aortic aneurysms. The current clinical gold standard metric of central artery stiffness is the carotid-to-femoral pulse wave velocity (*cf*-PWV). Despite showing a steady increase with age [1] and being associated with increased risk of cardiovascular events [2], *cf*-PWV represents a global measure of arterial stiffness that integrates individual contributions of the heterogeneous arterial segments separating the carotid and the femoral arteries. Detectable changes in local mechanical properties of the aorta have been shown to precede measurable changes in *cf*-PWV and blood pressure, hence suggesting that altered hemodynamics could be a consequence, not a cause, of irreversible degenerative processes [3]. Therefore, local measures of arterial stiffness could delineate regional variations in central artery function, perhaps enabling earlier diagnosis and thus preemptive treatment.

Motivated by the need to associate local changes in aortic geometry and properties with global changes in cardiovascular function, we characterized aortic wall mechanics, central hemodynamics, and left ventricular function in wild-type ($Fbln5^{+/+}$) and fibulin-5 deficient ($Fbln5^{-/-}$) mice. Arteries from $Fbln5^{-/-}$ mice are characterized by a severe fragmentation of medial elastic lamellae [4], which renders them more tortuous [5]. Based on a novel combination of *in vitro* and *in vivo* data on regional aortic mechanics, we suggest that fibulin-5 deficiency results in a preferential lengthening and loss of elasticity of the ascending thoracic aorta, which in turn underlies increased pulse wave velocity and compromised left ventricular function.

METHODS

Adult $Fbln5^{+/+}$ (n = 13) and $Fbln5^{-/-}$ (n = 13) mice of both sexes were subjected to ultrasound imaging using the Visualsonic Vevo 2100 system. Echocardiographic examination of the left ventricle (LV) was followed by assessment of arterial diameters (via M-Mode imaging) and blood velocities (via pulsed-wave Doppler). These measurements were performed at four locations of interest within the central vasculature: ascending thoracic aorta (ATA), suprarenal abdominal aorta (SAA), infrarenal abdominal aorta (IAA), and common carotid artery (CCA). B-Mode scans of the ATA from a long axis view allowed monitoring the cyclic changes in both luminal diameter and axial length. A 1F Millar pressure catheter was then inserted via the right carotid artery and used in combination with ultrasound imaging to measure invasively blood pressure in the ATA and pressure-volume relationships in the LV. Finally, micro-CT scans were collected to measure the tortuosity of the $Fbln5^{-/-}$ central vasculature.

Echocardiographic data from the LV were analyzed by a trained cardiac sonographer, whereas vascular ultrasound data were analyzed automatically using both commercial and custom software. Briefly, the biaxial motion of the ATA was quantified from B-Mode cine loops using the VevoStrain and custom MATLAB software to reconstruct waveforms of luminal diameter and axial length. In addition, a graphical user interface (GUI) was developed to extract regional waveforms of luminal diameter and blood velocity via image analysis. Luminal edges were detected from M-Mode stacks by means of the Canny methods [6] and Doppler velocities were extracted using automatic tracing in the Visualsonic software. Aortic pulse transit time (PTT) was calculated as the time delay between proximal and distal velocity waveforms and used, in combination with the aortic path lengths (L) from micro-CT scans, to approximate aortic pulse wave velocity as PWV = L / PTT.

Copyright 2016 The Organizing Committee for the 2016 Summer Biomechanics, Bioengineering and Biotransport Conference

The *in vivo* mechanical behaviors of the most proximal (ATA) and most distal (IAA) aortic segments were estimated by combining knowledge of intrinsic material properties [7] with noninvasively measured deformations. The complex mechanical properties of each aortic segment are described by a single scalar quantity – the elastic stored energy W – from which one can compute biaxial stress and stiffness. We adopted the following functional form

$$W = \frac{c}{2}\left(I_C - 3\right) + \sum_{i=1}^{4} \frac{c_1^i}{4c_2^i}\left(\exp\left[c_2^i\left(IV_C^i - 1\right)^2\right] - 1\right), \quad (1)$$

where $I_C = \text{tr}\,\mathbf{C}$, $IV_C^i = \mathbf{C} : \mathbf{M}^i \otimes \mathbf{M}^i$, and $\mathbf{C} = \text{diag}[\lambda_\vartheta^2, \lambda_z^2, \lambda_r^2]$. It should be noted that the principal stretches λ_ϑ and λ_z were calculated from the average waveforms extracted from ultrasound, whereas [c, c_1^i, c_2^i] and $\mathbf{M}^i$ represent, respectively, values of the material parameters and collagen fiber orientations reported in [7].

RESULTS

Micro-CT images confirmed the elevated arterial tortuosity of fibulin-5 null aortas reported previously [5] whereas mean aortic PTTs were found to be similar across genotypes and sexes, thus suggesting that PWV is higher in *Fbln5*$^{-/-}$ mice primarily due to longer aortas. Central blood pressure was characterized by normal systolic pressures but increased pulse pressures, primarily due to lower diastolic values. On the cardiac side, systolic LV function measured both non-invasively and invasively was essentially preserved, despite lower cardiac outputs in male *Fbln5*$^{-/-}$ mice. Diastolic LV function, measured via transmitral Doppler, was instead significantly impaired in *Fbln5*$^{-/-}$ mice of both sexes. These results suggest that the fibulin-5 mutation results in a cardiovascular phenotype consistent with accelerated aging.

Regional measurements of local distensibility from M-Mode images showed differences in luminal diameters of ATA and SAA (with *Fbln5*$^{-/-}$ aortas being smaller than normal) while IAA and CCA were undistinguishable from wild-types. Regardless of size, circumferential deformations during the cardiac cycle were maintained nearly normal, despite a trend towards lower cyclic strains in the ATA. These findings were confirmed by the speckle-tracking analysis of ATA biaxial motion from B-Mode scans (Figure 1-a). *Fbln5*$^{-/-}$ ATAs were found to have significantly smaller diameters and to be significantly longer than controls, independent of sex (Figure 1-b,c). In addition, they preserved a normal range of axial strains induced by cardiac contractions, possibly thanks to an adaptive axial lengthening.

Mechanical properties calculated under *in vivo* deformations showed that *Fbln5*$^{-/-}$ aortas – both ATA and IAA – experience significantly reduced stresses (particularly in the axial direction) despite maintaining nearly normal values of biaxial stiffness. Instead, calculations of W over a single cardiac cycle showed that *in vivo* elastic energy storage was compromised in the ATA (Figure 1-d) but not in the IAA. Thus, loss of elasticity due to mutation in the fibulin-5 gene seems to alter biaxial mechanical properties preferentially in the ATA.

DISCUSSION

Loss of elastic fiber integrity is a degenerative process that occurs gradually with aging and that is accelerated by hypertension. Herein, we employed the *Fbln5*$^{-/-}$ mouse model to evaluate the effects of a severe elastopathy on local arterial mechanics and its relationship with central hemodynamics and cardiac function. Our approach relies on a unique combination of *in vitro* biaxial data on regional mechanics with *in vivo* ultrasound data on cyclic deformations, which also accounted for the effects of perivascular support. We focused our estimations of *in vivo* arterial mechanics solely based on passive elasticity, despite the need to consider also the effects of contractility and viscoelasticity in the future. Our results showed higher central pulse pressure and signs of diastolic dysfunction in *Fbln5*$^{-/-}$ mice, consistent with other studies [4,8]. In addition, we found that increased PWV in the *Fbln5*$^{-/-}$ model is a result of a preferential lengthening of the thoracic aorta and not a product of early wave reflection, as proved by normal PTTs. *Fbln5*$^{-/-}$ arteries seem to preserve normal cyclic strains during the cardiac cycle, thus loss of cyclic energy storage (i.e., loss of cushioning function) in *Fbln5*$^{-/-}$ ATAs is a result of intrinsic differences in material properties. The present study demonstrates that by impairing storage of elastic energy in the ascending aorta, arterial stiffening impairs global cardiovascular function and can potentially contribute to diastolic heart failure.

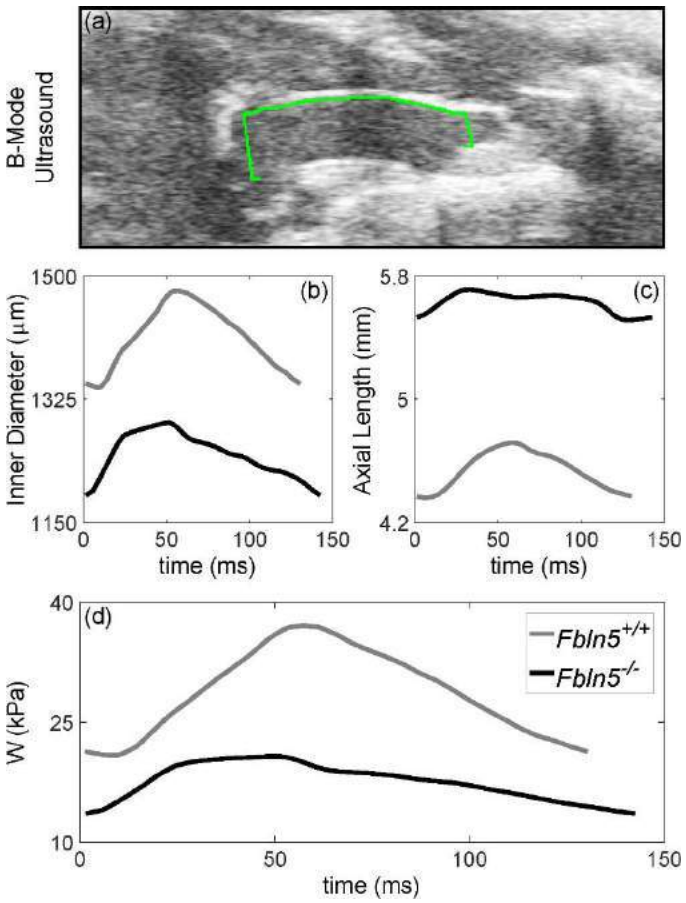

Figure 1: Long axis view of the ATA and overlaid speckle-tracking contour (a). Representative waveforms of diameter (b), length (c), and energy (d) comparing *Fbln5*$^{+/+}$ (gray) with *Fbln5*$^{-/-}$ (black).

ACKNOWLEDGEMENTS

This work was funded by NIH grants HL-105297 and EB-016810. We acknowledge Nicole Mikush who performed the echocardiographic studies, and Dr ZhenW. Zhuang who executed the micro-CT scans.

REFERENCES

[1] AlGhatrif, M. et al., *Hypertension*, 62: 934-941, 2013.
[2] Mitchell, G.F. et al., *Circulation*, 121:505-511, 2010.
[3] Redheuil, A. et al., *Hypertension*, 55: 319-326, 2010.
[4] Yanagisawa, H. et al., *Nature*, 415: 167-171, 2002.
[5] Nakamura, T. et al., *Nature*, 415: 171-175, 2002.
[6] Canny, J., *IEEE Trans Pattern Anal Mach Intell*, 8: 679-698, 1986.
[7] Ferruzzi, J. et al., *ASME J Biomech Eng*, 137: 031007, 2015.
[8] Le, V.P. et al., *Physiol Rep*, 2: e00257.

Copyright 2016 The Organizing Committee for the 2016 Summer Biomechanics, Bioengineering and Biotransport Conference

SB^{3}C2016
Summer Biomechanics, Bioengineering and Biotransport Conference
June 29 –July 2, National Harbor, MD, USA
SB^{3}C2016-168

DYNAMIC VAPOR SORPTION IN TREHALOSE/SALT MIXTURES: EFFECT OF COMPOSITION ON RETENTION OF THE AMORPHOUS STATE

Babak Bagheri, Lindong Weng, Matthew Van Vorst, Gloria D. Elliott

Department of Mechanical Engineering and Engineering Science, University of North Carolina at Charlotte, Charlotte, NC, USA

INTRODUCTION

Trehalose has been widely used in the pharmaceutical and food industries to stabilize dried products because of its high viscosity and low molecular mobility in the glassy state[1]. The glassy state is a metastable state that will eventually convert to a crystal, at a rate dependent on the environmental temperature and humidity level. Sugar crystallization, however, can have a detrimental effect on preserved materials, so additives are sometimes used to stabilize the glassy state either by increasing the glass transition temperature (T_g) or by interfering with the crystallization process[2,3].

In previous molecular modelling work we observed that trehalose and sodium phosphate (Na_2HPO_4) mixtures yielded a higher T_g than pure trehalose because marginally self-aggregated HPO_4^{2-} ions established a strengthened hydrogen-bonding network with trehalose molecules[4]. In contrast dihydrogen phosphate ($H_2PO_4^-$) ions served only as plasticizers, resulting in a lower T_g of the mixtures than trehalose alone, creating large-sized ionic pockets, weakening interactions, and disruption of the original hydrogen-bonding network amongst trehalose molecules. This work inspired us to also look at the effect of sugar-salt molecular interactions on water uptake and the persistence of the amorphous state at high humidity levels. Because we had observed in previous work that choline (Ch^+) $H_2PO_4^-$ was a good stabilizer for proteins[5] we investigated mixtures of trehalose with NaH_2PO_4 and Na_2HPO_4, as well as ChH_2PO_4 and $ChHPO_4$, in order to understand their effectiveness at suppressing crystallization and retaining the desired glassy form.

METHODS

A stock solution of 30.8 wt% trehalose (1.3 M), made in 1X TE buffer (1X Tris-EDTA buffer, pH 8.0, consisting of 10 mM Tris-HCl and 1 mM EDTA), was used to prepare solutions with varying amounts of phosphate salts (salt to trehalose molar ratio (R) of 1:4.8, 1:2 and 1:0.7). Compositions of salts with trehalose in buffer solution were made by combining aliquots of the trehalose stock solution together with the appropriate mass of salt in order to achieve the desired molar ratios of salt to trehalose in the final volume of 1X TE buffer.

To investigate moisture sorption in different trehalose/salt compositions, a closed environment that maintained a stable relative humidity over the test duration was prepared. Supersaturated salt solutions of sodium bromide (prepared by following ASTM Protocol E 104-02) are capable of producing an environment with constant relative humidity of 61%.[6] This composition was prepared and placed in Kilner glass jars with rubber seals and clamps or Mason glass jars with screw caps to create controlled humidity vessels (1 L, total height of 159 mm, mouth diameter of 89 mm).

To create the glassy samples, a 100 μL droplet of the solution studied was pipetted on the treated side of Thermanox coverslips (Nunc, Thermo Fisher Scientific, Rochester, NY, Dia. 22mm) inside a custom-made 11% RH environmental chamber, which was then placed on a custom turntable for microwave assisted drying at 11% RH and 23.5±1.5 °C (SAM 255, CEM Corp., Matthews, NC). The end moisture content was determined to be below 0.105 gH_2O/gdw, which is known to produce a T_g higher than room temperature in the case of aqueous trehalose solutions.[2] The dried samples were then transferred from the 11% RH environment into the fixed relative humidity jar of 61% RH. Other studies have shown that amorphous trehalose crystallizes in environments with 44% RH and higher.[2] The dynamic vapor sorption (DVS) method was then used to monitor moisture sorption in the microwave-processed trehalose samples before and after crystallization (crystals detected visually in samples).

Copyright 2016 The Organizing Committee for the 2016 Summer Biomechanics, Bioengineering and Biotransport Conference

The gravimetric method was used to determine the dry weight of samples with different compositions (expressed in terms of mass of water per mass of dry solids). The dry weight of different compositions was determined by pipetting small volumes of solution onto a glass fiber absorbent pad (CEM Corp., Matthews, NC) and then baking in a convection oven (VWR International, West Chester, PA) for 48 hours at 95 °C.[7,8] The sample was then cooled in a desiccator containing phosphorus pentoxide (P_2O_5) which maintained the humidity near 0% RH. By recording the initial wet mass and the bake-out dry mass, the percent dry weight of each composition was obtained, and used for subsequent determination of water contents in processed samples.

RESULTS

Figure 1 shows the moisture absorption kinetics in amorphous trehalose with or without ChH_2PO_4. The absorption profile of pure trehalose illustrates that the amorphous sample took up water until an adequate amount was absorbed to enable the formation of trehalose dihydrate (~0.105 gH_2O/g trehalose), which is consistent with previous findings.[2] For pure trehalose samples, the formation of trehalose dihydrate crystals was observed at day 1. When ChH_2PO_4 was added to trehalose, the onset of sugar crystallization was delayed in proportion to the amount of salt in solution (Ex. 7 days for the salt:sugar ratio of 1:0.7). Initially the compositions absorbed more than the needed amount to crystallize, but upon crystallization, the moisture content in the sample gradually decreased to ~0.105 gH_2O/gdw during the following 18 days. The initial moisture uptake increased as the ChH_2PO_4 concentration increased. Pure ChH_2PO_4 was observed to be very hygroscopic. Interestingly, given that trehalose/ChH_2PO_4 samples picked up more moisture at 61% RH than pure trehalose, the higher volume of moisture and therefore the plasticizing effect of water did not promote the formation of trehalose dihydrate crystals.

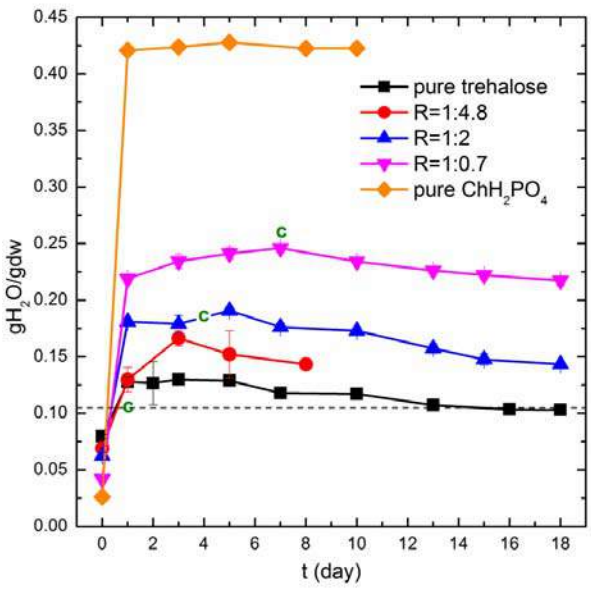

Figure 1. Moisture absorption kinetics in amorphous trehalose/ChH_2PO_4 systems of different ratios of ChH_2PO_4 to trehalose. The onset of crystallization as observed visually is indicated with the letter c.

Of all the salts tested, Ch_2HPO_4 was most effective at suppressing crystallization. No crystals were observed in trehalose/Ch_2HPO_4 samples after 15 days (1:0.7 molar ratio) at 61% RH. We observed that the crystallization suppression efficacy increased with increasing concentration of salt in the mixture for all salts tested, with the exception of compositions containing NaH_2PO_4 in which samples at all molar ratios crystallized within the same time period as pure trehalose (1 day).

DISCUSSION

The present study demonstrated that Ch_2HPO_4 is a promising agent for crystallization suppression in trehalose glasses. In relatively high salt mass fractions of choline hydrogen phosphate the crystallization of trehalose was delayed for a considerable period of time (>2 weeks). The samples absorbed a considerable amount of water compared to pure trehalose, suggesting that the mechanism of crystallization suppression was associated with hindered nucleation and not increased glass transition temperature.

ACKNOWLEDGEMENTS

This study was supported by grant #5RO1GM101796 from the National Institutes of Health.

REFERENCES

1. Hancock BC and Zografi G, Characteristics and significance of the amorphous state in pharmaceutical systems. *J Pharm Sci* 86:1-12,1997.

2. Iglesias HA, Chirife J and Buera MP, Adsorption isotherm of amorphous trehalose. *J Sci Food Agric* 75:183-186, 1997.

3. Zhang J and Zografi G, Water vapor absorption into amorphous sucrose-poly (vinyl pyrrolidone) and trehalose-poly (vinyl pyrrolidone) mixtures. *J Pharm Sci* 90:1375-1385, 2001.

4. Weng L, and Elliott GD. Distinctly Different Glass Transition Behaviors of Trehalose Mixed with Na_2HPO_4 or NaH_2PO_4: Evidence for its Molecular Origin. *Pharm Res* 32(7):2217-28, 2015.

5. Weaver KD, Vrikkis RM, Van Vorst MP, Trullinger J, Vijayaraghavan R, Foureau DM, McKillop IH, MacFarlane DR, Krueger JK and Elliott GD, Structure and function of proteins in hydrated choline dihydrogen phosphate ionic liquid. *Phys Chem Chem Phys* 14:790-80, 2012.

6. Greenspan L, Humidity fixed points of binary saturated aqueous solutions. *Journal of Research of the National Bureau of Standards* 81:89-96, 1977.

7. Mazzobre M, Longinotti M, Corti H and Buera M, Effect of salts on the properties of aqueous sugar systems, in relation to biomaterial stabilization. 1. Water sorption behavior and ice crystallization/melting. *Cryobiology* 43:199-210, 2001.

8. Labrousse S, Roos Y and Karel M, Collapse and crystallization in amorphous matrices with encapsulated compounds. *Sci Aliments* 12:757-769, 1992.

9. Cardona S, Schebor C, Buera MP, Karel M and Chirife J, Thermal Stability of Invertase in Reduced-Moisture Amorphous Matrices in Relation to Glassy State and Trehalose Crystallization. *J Food Sci* 62:105-112, 1997.

Copyright 2016 The Organizing Committee for the 2016 Summer Biomechanics, Bioengineering and Biotransport Conference

SB³C2016
Summer Biomechanics, Bioengineering and Biotransport Conference
June 29 –July 2, National Harbor, MD, USA
SB³C2016-169

INFLUENCE OF STANDARDIZATION OF AIRWAY GEOMETRY ON AIRFLOW AND PARTICLE TRANSPORT

Toshihiro Sera (1), Hiroaki Kuninaga (2), Kazuaki Fukasaku (3), Hideo Yokota (3), Masao Tanaka (2)

(1) Department of Mechanical Engineering
Kyushu University
Fukuoka, Fukuoka, Japan

(2) Graduate School of Engineering Science
Osaka University
Toyonaka, Osaka, Japan

(3) Image Processing Research Team
RIKEN
Wako, Saitama, Japan

INTRODUCTION

Pulmonary airways consist of tapered, curved, branching tubes of a range of length and diameter, which become narrower, shorter, and more numerous as they penetrate deeper into the lung. The trachea divides into right and left main bronchi, which in turn bifurcate into lobe, then segmental bronchi. This complex geometry can affect respiratory function.

Airway geometry has been studied using measurements of mammalian-lung cast models [1, 2]. Recently, 3D anatomical data of the human conducting airways were measured using high-resolutions computed tomography (CT) images [3]. Furthremore, 3D airway tree models were generated into the lung lobes by the specific algorithms [4 ,5], and have been used widely for pulmonary biomechanics [6, 7]. However, there are some differences in the airway geometry even among healthy subjects,

In this study, we focused on central airways and investigated the influence of standardization of airway geometry on pulmonary function, in particular, airflow and particle transport.

METHODS

In this study, thorax CT images of the four healthy male subjects (A1, A2, A3, and A4) were obtained. The voxel size was approximately 0.5mm or 1.0 mm. The study protocol was approved by RIKEN Ethics Committee.

The airway regions were segmented the 3D region-growing method using Amira software (Visage Imaging, Germany). The generation of the segmented airway was 6 as a function of Weibel generation [1]. After segmentation, the airway skeleton and branching points were calculated without the topology using a 3D thinning algorithm (Amira software, Visage Imaging, Germany). As the results, the Euclidian distance to the nearest boundary was stored at every skeleton voxel as local diameter, that is, the diameter of a sphere superimposed on the duct.

Based on the airway skeleton of four subjects, the averaged skeleton was calculated. All airway models consisted of 45 airway segments. The origin was defined as the branching point of trachea and main right and left bronchi, and each segments were averaged from the origin. Each segment was moved based on the averaged starting branching point of the segment, thereafter the coordinates and the Euclidian distance of all segment voxels were averaged. Finally, the averaged airway model was obtained from the averaged skeletons and Euclidian distances using an inverse 3D thinning algorithm (Amira software, Visage Imaging, Germany).

In this study, we evaluated the steady inspiratory flow and particle transport in each airway model and the averaged model. Assuming laminar and incompressible airflow, the governing equations are expressed as:

$$\nabla \cdot u = 0 \tag{1}$$

$$\rho\left(\frac{\partial u}{\partial t} + u \cdot \nabla u\right) = -\nabla p + \mu \nabla^2 u \tag{2}$$

where u represents the velocity, p is the pressure, μ is the dynamic viscosity (1.81×10^{-5} g/mm/s), and ρ is the density (1.2×10^{-6} g/mm^3).

In particle deposition in the alveolar region, the governing equations are expressed as:

$$\frac{\pi}{6}{D_p}^3\rho_p\frac{dU_p}{dt} = \left(\frac{\pi}{8}C_D\rho{D_p}^3\left|U - U_p\right|\left(U - U_p\right) + \frac{\pi}{6}{D_p}^3\left(\rho_p - \rho\right)g\right. \tag{3}$$

$$C_D = \left(\frac{24}{Re_p}\left(1 + 0.15{Re_p}^{0.678}\right)\right. \tag{4}$$

where U is the air velocity, Up is the particle velocity, ρ_p is the particle density, D_p is the particle diameter, C_D is the drag coefficient, and Re_p is the particle Reynolds number [8]. In this simulation, we assumed that acting forces on particles were convection and gravity, not Brownian

Copyright 2016 The Organizing Committee for the 2016 Summer Biomechanics, Bioengineering and Biotransport Conference

forces. For particle diameters of D_p = 1.0 ~ 10.0 μm, ρ_p was set equal to the density of water (1.0 g/cm^3). In this study, we evaluated the escape particles through the airway model. The fraction of escape particles was calculated as the ratio of the number of escape particles to the initial number of particles.

To define the boundary condition, we focused on the heterogeneous ventilation and obtained the CT images at functional residual capacity and after tidal volume. The flow rate was determined from volume change of each lobe and applied at each distal bronchus as boundary condition.

An unstructured mesh with tetrahedral volume elements were generated in each airway models, for a total of approximately ~ 6 M cells. These equations (1 - 4) were solved using OpenFOAM (OpenCFD Ltd.).

RESULTS

Qualitative comparison of the individual and averaged models is presented in Fig. 1, and the averaged airway model exhibits macroscopic geometrical characteristics of the individual model. Table 1 shows the airway characteristics, and also shows the direct averaged values calculated from the individual models. The averages do not completely match the direct average, and particularly the volume was smaller slightly.

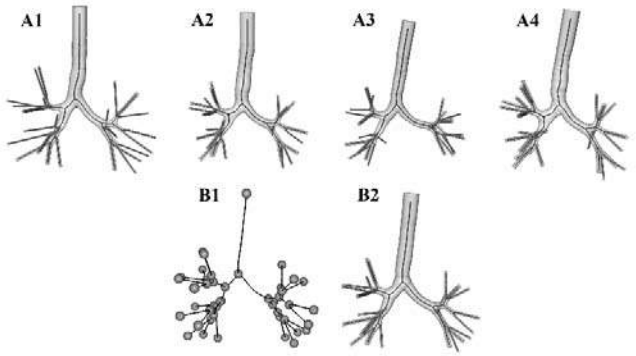

Figure 1: The surfaces of the individual airway models (A1, A2, A3, and A4), and averaged airway skeleton (B1) and model (B2). Black lines indicate airway skeleton. Spheres (B1) are branching points.

Table 1: The geometric characteristics of the individual airway models (A1, A2, A3, and A4) and averaged airway model

	A1	A2	A3	A4	Averaged model	Direct average
Volume [cm^3]	98.1	79.5	63.4	86.6	76.3	80.8
Height [cm]	24.5	22.3	20.3	22.6	20.6	22.1
Width [cm]	21.6	17.3	17.6	17.3	18.0	18.4
Length [cm]	14.2	10.7	11.4	10.2	10.5	11.4

Figure 2 shows the qualitative comparison in streamline of the individual and averaged models. Although there are small differences at the distal bronchi and the bifurcation among individual models as well as between average and individual models, the macroscopic flow patterns in the averaged model are good agreement with individual models.

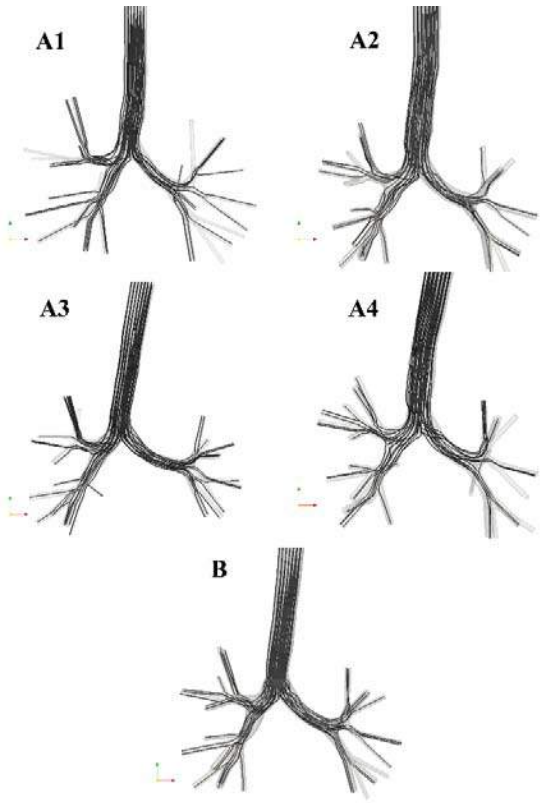

Figure 2: The streamlines in the individual airway models (A1, A2, A3, and A4) and averaged airway model (B).

Regarding the particle transport, in individual models, the fractions of escape particles were ranged 14.4 ~ 24.8 % in right lung and 42.7 ~ 50.6 % in left lung, respectively. In averaged model, the values were 29.5 % and 42.9 %, respectively.

DISCUSSION

In this study, the averaged model of the central airways was developed from four healthy airways using 3D skeleton, and preserved the geometrical characteristics of individual airways. The reduction in volume of the averaged model may be caused by the exclusion of the fake segments in average processes. The irregularity of the surface can induce the fake segments, in particular around branching points.

We investigated numerically whether the averaged model can predict pulmonary function, in particular, airflow and particle transport. Regarding the fraction of escape particles, the averaged model did not anticipate the individual models, because the particle transports may be influenced strongly by the bifurcation geometry. However, our results indicate that the airflow and particle transports in averaged model can estimate the individual phenomena macroscopically.

REFERENCES

[1] Weibel ER. Morphometry of the Human lung. 1963.
[2] Horsfield, K et al., *J Appl Physiol*, 31; 207-217, 1971.
[3] Sauret, V et al., *J Anat*, 200; 123-134, 2002.
[4] Kitaoka, H et al., *J Appl Physiol*, 87; 2207-2217, 1999.
[5] Tawhai, MH et al., *J Appl Physiol*, 110; 1466-1472, 2010.
[6] Politi, AZ et al., *J Theor Biol*, 166; 614-24, 2010
[7] Swan, AJ et al., *J Theor Biol*, 300; 222-31, 2012
[8] Schiller, L et al., *Verein Deutscher Ingenieure*. 77; 318, 1933

Copyright 2016 The Organizing Committee for the 2016 Summer Biomechanics, Bioengineering and Biotransport Conference

SB^{3}C2016
Summer Biomechanics, Bioengineering and Biotransport Conference
June 29 –July 2, National Harbor, MD, USA
SB^{3}C2016-171

SUBJECT SPECIFIC SIMULATION OF ENTIRE CEREBRAL ARTERIAL TREE: IMPLEMENTATION OF AUTOMATIC PARAMETRIC MESH GENERATION.

Mahsa Ghaffari (1), Ben C. Schneller(1), Ali Alaraj (2), Andreas A. Linninger (1,2)

(1) Department of Bioengineering
University of Illinois at Chicago
Chicago, Illinois, US

(2) Department of Neurosurgery
University of Illinois at Chicago
Chicago, Illinois, US

INTRODUCTION

Current computational fluid dynamic (CFD) have played an important role in simulating cerebral hemodynamics in various cerebrovascular diseases. This include future aneurysm hemorrhage assessment, understanding hemodynamics changes post intervention and understanding flow and wall shear stress changes in parent vessels and inside cerebral aneurysms post flow diverting stents. Yet such CFD simulations have limitations related to basic assumptions that affect results of such simulations. These include assumptions related to inflow and outflow boundary conditions and simulation on a short segment of the arterial tree. In this paper, we will introduce a pipeline for subject-specific hemodynamic simulation of entire intracranial arterial tree using a fully automatic parametric mesh generation and subject-specific boundary conditions assignment.

METHODS

Magnetic resonance angiograms (MRA) were acquired on volunteer subjects, and Hessian-based vessel filter and image processing techniques are carried out for cerebral angioarchitecture reconstruction [1]. After image filtration, we extract the vessel centerline and radius to reconstruct the vascular skeleton, Figure (1).

Current mesh generation methods require user interaction and cannot be used for very large vascular tree with hundreds bifurcation. We used a fully automatic hexahedral parametric mesh generation techniques to represent complex cerebral tress with smooth virtual surface and low mesh density. An in-house meshing algorithm is developed to automatically decompose the skeleton, generate and index parametric mesh from image-based data [2].

Regional volumetric cerebral blood flow is measured at selective large vessels using phase contrast MR angiography (PC-MRA) using commercially available NOVA software (VasSol Inc). Flow rate were measured for Inflow arteries including left and the right internal carotid arteries (LICA and RICA) and basilar artery (BA); and outflow arteries including the anterior cerebral arteries (LACA and RACA); middle cerebral arteries (LMCA and RMCA) and posterior cerebral arteries (LPCA and RPCA). Inflow measurements were directly used as inlet boundary conditions. The unsteady hemodynamic simulations were carried out using computational fluid dynamic solver ANSYS Fluent 15.0 (ANSYS Inc., Canonsburg, PA). Rigid wall assumption is used for the hemodynamic simulation.

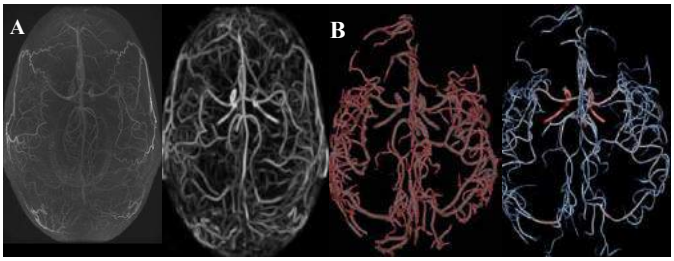

Figure 1: Image filtration and geometrical descriptor extraction of cerebrovascular tree. A) Hessian-based filters were implemented for suppressing signals from non-vascular tissues. B) Vascular skeleton, centerline and radius are extracted using VMTK software.

Copyright 2016 The Organizing Committee for the 2016 Summer Biomechanics, Bioengineering and Biotransport Conference

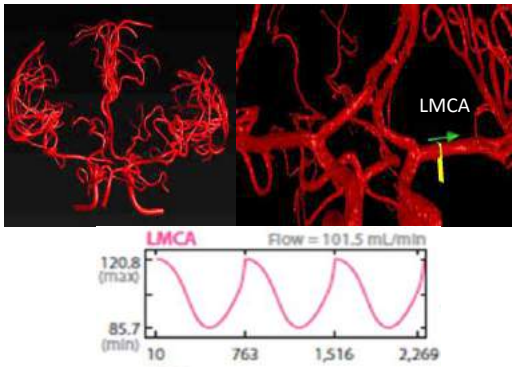

Figure 2: Regional blood flow measurement using PCMRI and Nova software. The flow direction and the slice plane perpendicular to the longitudinal axis of a vessel segment showing where the measurement was made in LMCA.

RESULTS

Figure (2) shows an example volumetric flow measurement using NOVA. The perpendicular plane to the longitudinal axis of LMCA segment is generated to measure time-dependence flow rate. Inflow measurements were converted to velocity profile to be used as inlet boundary conditions in our simulations. Then outlets are labeled based on their anatomical region in the six groups of LMCA, RMCA, RPCA, LPCA and LACA, RACA Figure (3B). For validation purpose, pressure boundary conditions in these six anatomical regions are adjusted to match results with NOVA measurement.

Figure (3A) illustrates a schematic view of Circle of Willis anatomy with hypoplastic Left Pcom. Subject specific arterial map is generated and color coded in eight anatomical regions, Figure (3B). Vascular skeleton was decomposed into Bifurcation (Bif), Bifurcation to Bifurcation (Bif-Bif) and Bifurcation to Terminal (Bif-Term). Then, Bezier curve approximation is used for smooth centerline generation and parameterization. Figure (3D-F) show the distribution of pressure and wall shear stress and vorticity along cerebral arterial tree, respectively.

DISCUSSION

In this study, we developed the largest subject specific intracranial modeling with automated mesh generation techniques and physiological boundary conditions. Using a large cerebral tree model, we can assess local and global effect of any endovascular intervention in upstream and downstream vessels. There are a multitude of quantifiable flow effects that can be studied within the hemodynamics of an aneurysm, including velocity, pressure, vorticity, helicity, wall shear stress, oscillatory shear index, and various flow structures and characteristics. Furthermore, vascular skeleton can be used for morphological feature analysis such as anastomosis and subject specific vascular map can be used for both surgical and educational purpose.

In conclusion, we introduce a pipeline for development the largest cerebrovascular model for hemodynamic analysis. Patient specific blood flow measurement and modeling will broaden the application of CFD analysis among neurosurgeons. Subject specific hemodynamic analysis is a promising procedure for assessment of different endovascular treatments such as stenting, angioplasty or bypass surgery.

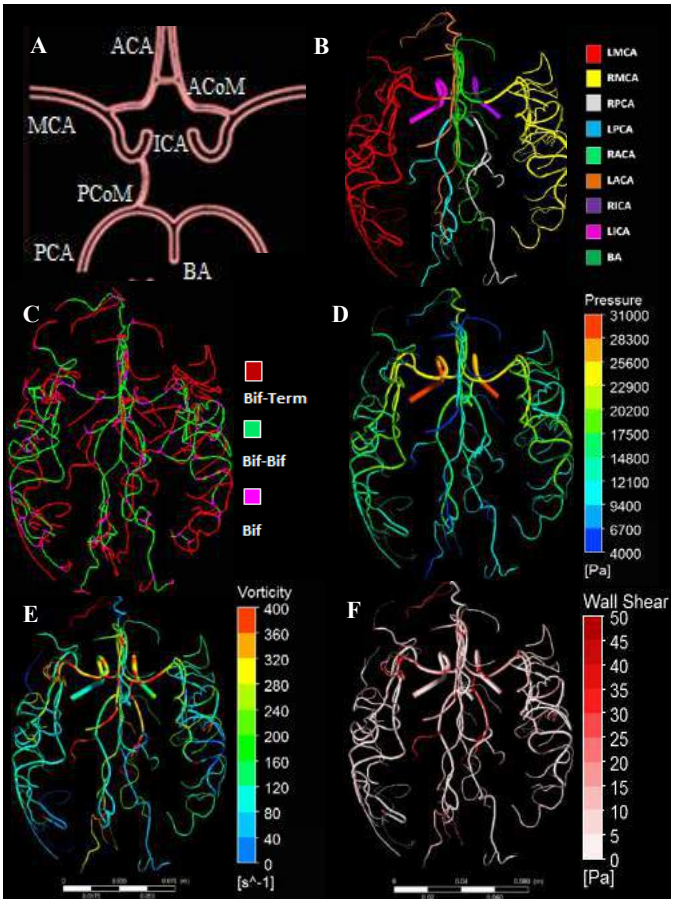

Figure 3: Patient specific hemodynamic simulation of arterial cerebral trees A) Schematic frontier view of CoW anatomical variation. B) Atlas of cerebral arteries is labeled based on their anatomical regions. C) Vascular skeleton decomposition for automatic mesh generation. D) Pressure distribution results. E) Visualization of blood flow vorticity in arterial trees to show the presence of secondary flow patterns. F) Wall shear stress on arterial wall at the systole peak.

ACKNOWLEDGEMENTS

The authors would like to gratefully acknowledge the partial support of this project by NSF grants CBET-0756154 and CBET-1301198.

REFERENCES

[1] Hsu CY, Schneller B, Ghaffari M, Alaraj A, Linninger A. Medical Image Processing for Fully Integrated Subject Specific Whole Brain Mesh Generation. *Technologies*. 2015 May 21;3(2):126–41.

[2] Ghaffari M, Hsu CY, Linninger AA. Automatic Reconstruction and Generation of Structured Hexahedral Mesh for Non-planar Bifurcations in Vascular Networks. *12th Int. Symp. Process Syst. Eng., 25th Eur. Symp. Comput. Aided Process Eng*, (37):635:639.

Copyright 2016 The Organizing Committee for the 2016 Summer Biomechanics, Bioengineering and Biotransport Conference

SB^{3}C2016
Summer Biomechanics, Bioengineering and Biotransport Conference
June 29 –July 2, National Harbor, MD, USA
SB^{3}C2016-172

PLA / PLGA-COATED CHITOSAN MICRO-IMPLANTS FOR SUSTAINED RELEASE OF METHOTREXATE TO TREAT VITREO-RETINAL DISEASES

Soumyarwit Manna[1], Marwan F. Al-Rjoub[1], Anna Donnell[2], Necati Kaval[2], James J. Augsburger[3], Zelia M. Correa[3], Rupak K. Banerjee[1]

(1) Dept. of Mechanical and Materials Engineering
University of Cincinnati
Cincinnati, Ohio, USA

(2) Dept. of Chemistry
University of Cincinnati
Cincinnati, Ohio, USA

(3) Dept. of Ophthalmology
University of Cincinnati
Cincinnati, Ohio, USA

INTRODUCTION

At present, Methotrexate (MTX), a *hydrophilic* antimetabolite chemotherapeutic drug is being used for the management for vitreo-retinal (VR) diseases, such as intraocular lymphoma, uveitis, retinal detachment and proliferative vitreoretinopathy. Serial intravitreal injections containing ~ 400 µg of MTX is being administered in clinical practice, which results in rapid clearance of the hydrophilic MTX with a short half-life of 14.3 hours (1). In order to maintain therapeutic efficacy, repetitive intravitreal injections of MTX are administered, which often results in collateral trauma, complications and ocular toxicity. It is expected that a sustained release drug delivery device (micro-implant), which maintains a therapeutic release rate of *0.2-2.0 µg/day* of MTX for a period of a month or more would avoid the possible complications associated with an injection (2).

Currently, no sustained release devices for hydrophilic drugs, such as MTX, in the VR domain have been reported. The *challenge* to fabricate a sustained release device for hydrophilic drugs is that they do not blend well with existing FDA approved lipophilic materials, such as poly-lactic acid (PLA) and poly-(lactic-co-glycolic) acid (PLGA), which is a copolymer of PLA and poly-glycolic acid (PGA). Due to the similar hydrophilic nature, chitosan (CS), a biocompatible and biodegradable polymer, is used as a matrix to blend MTX. Since both CS and MTX are hydrophilic in nature, MTX is expected to be released rapidly out of the CS-MTX micro-implant. Therefore, a lipophilic surface modification of the CS-MTX micro-implant is required to cause sustained release of MTX.

In a prior study, a PLA-coated CS-MTX micro-implant was fabricated which was able to administer therapeutic release rate of MTX for 50-70 days (3). In this study, PLGA copolymer and PLA has been used for improved control of MTX release rate. The *objective* of this study is to characterize the influence of a) PLA:PGA copolymer ratio in PLGA and b) the molecular weight of PLA on the MTX release rate, swelling and structural stability of the micro-implants.

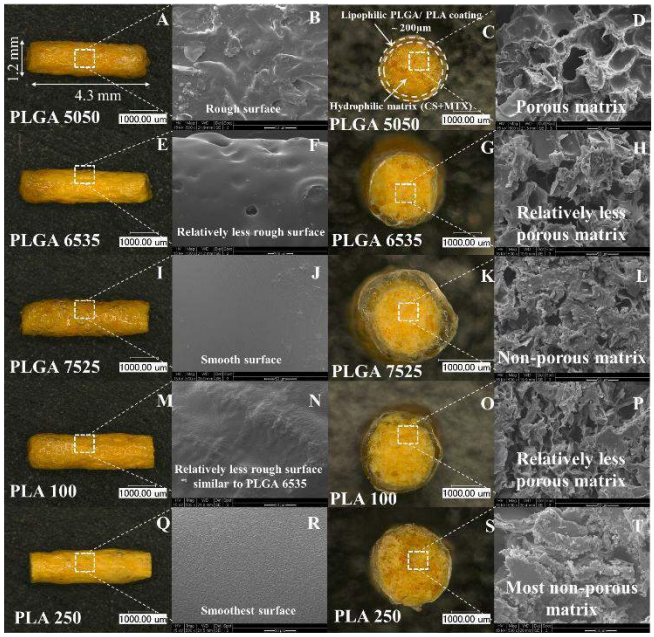

Figure 1: Optical microscopy and SEM images of the top view And the cross-sectional view of the CS-MTX micro-implants coated by PLGA 5050 (A.,B.,C.,D, respectively); PLGA 6535 (E.,F.,G.,H, respectively); PLGA 7525 (I.,J.,K.,L., respectively); PLA 100 (M.,N.,O.,P, respectively); and PLA 250 (Q.,R.,S.,T, respectively)

Copyright 2016 The Organizing Committee for the 2016 Summer Biomechanics, Bioengineering and Biotransport Conference

METHODS

MTX is blended with CS (M.W: 50,000-190,000) in dilute HCl to obtain a mixture containing 40% w/w MTX. The CS-MTX mixture is injected into Tygon tubing (1/16 in I.D) and *freeze-dried* to obtain CS-MTX fibers, which are cut into desired length (~ 4 mm) (3). For lipophilic surface modification, the CS-MTX micro-implants containing ~ 400 µg of MTX, are *dip coated* with fixed concentrations of different PLGA combinations (PLGA 5050, PLGA 6535 and PLGA 7525, where PLA: PGA – 50:50, 65:35, 75:25, respectively; M.W: 54,400 – 103,000) and PLA combinations (PLA 100 and PLA 250 of MW: 102,000 and 257,000, respectively). Fourier transform infrared spectroscopy (FTIR) are employed to characterize chemical bonding of the coating with the CS-MTX matrix. The comparative assessment of a) the MTX release rate and b) the swelling of the different PLA / PLGA coated CS-MTX micro-implants is conducted to investigate the effect of the lipophilic surface modification on the sustained release of MTX. The MTX release rate study and the swelling analysis are conducted by placing the PLA / PLGA-coated CS-MTX micro-implants (n = 3, for each type of coating) in a vial containing 5 ml of phosphate buffered saline (pH 7.4) in a water bath at 38°C. Samples are assayed at predetermined time intervals for a) MTX release rate using UV-Visible Spectrophotometer (MTX characteristic peak-258 nm) and b) swelling (% weight difference) of the micro-implant.

RESULTS

Morphology and Structure. The length and cross-sectional diameter of the micro-implants are 4.3 mm and 1.2 mm, respectively. The *porosity* of the micro-implant surface and matrix is reduced with an increase in a) PLA content in PLGA and b) molecular weight of PLA (Fig. 1). FTIR results show the characteristic peaks of CS and MTX (3355 cm^{-1} and 3284 cm^{-1} for O-H and N-H stretching) and that of PLA / PLGA (2996 cm^{-1} and 2943 cm^{-1} for stretching of alkyl groups; 1747 cm^{-1} for carbonyl stretching and 1180 cm^{-1} for C-O stretching) are restored in the PLA / PLGA coated CS-MTX micro-implant (Fig. 2). This confirms that there is *no chemical bonding* between the PLA / PLGA coating and the CS-MTX matrix.

MTX Release. The mean release rate of the coated CS-MTX micro-implants is 5.4 ± 0.1 µg/day (PLGA 5050), 5.7 ± 0.5 µg/day (PLGA 6535), 3.4 ± 0.6 µg/day (PLGA 7525), 3.3 ± 0.3 µg/day (PLA 100) and 1.8 ± 0.1 µg/day (PLA 250) (Fig. 3). The total release duration of MTX from the coated CS-MTX micro-implants is 82 days (PLGA 5050), 82 days (PLGA 6535), 138 days (PLGA 7525), 138 days (PLA 100) and 150 days (PLA 250). The half-life ($t_{1/2}$) of MTX release from the coated micro-implants is 11.3 days (PLGA 5050), 11.8 days (PLGA 6535), 24.9 days (PLGA 7525), 18.6 days (PLA 100) and 100.3 days (PLA 250), when the release data is fitted to the *first-order* equation.

Swelling Analysis. The peak swelling of the CS-MTX micro-implants coated with PLGA 5050, PLGA 6535, PLGA 7525, PLA 100 and PLA 250 is observed to be 6.2 times (30th day), 7.4 times (82nd day), 6.2 times (114th day), 2.2 times (22nd day) and 2.1 times (22nd day), respectively (Fig. 4).

CONCLUSIONS

It is observed that with an increase in a) PLA content in PLGA and b) molecular weight of PLA, the mean release rate of MTX and swelling of the micro-implant reduces, stability improves and the overall release duration of MTX increases. Therefore, the lipophilic surface modification of the CS-MTX micro-implant surface is important for improving and optimizing the release duration of MTX.

REFERENCES

1. *Velez et al.* Archives of Ophthalmology. 2001;119(10):1518-24.
2. *Palakurthi et al.* Curr Eye Res. 2010;35(12):1105-15
3. *Manna et al.* ASME J Biomech Eng. 2014; 136(2): 021018,1-15

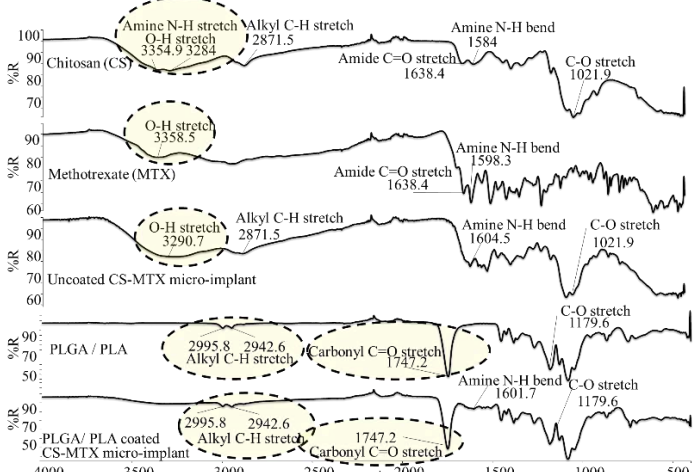

Figure 2: FTIR spectra of CS, MTX, uncoated CS-MTX micro-implant, PLGA/PLA, and PLGA/PLA- coated micro-implant

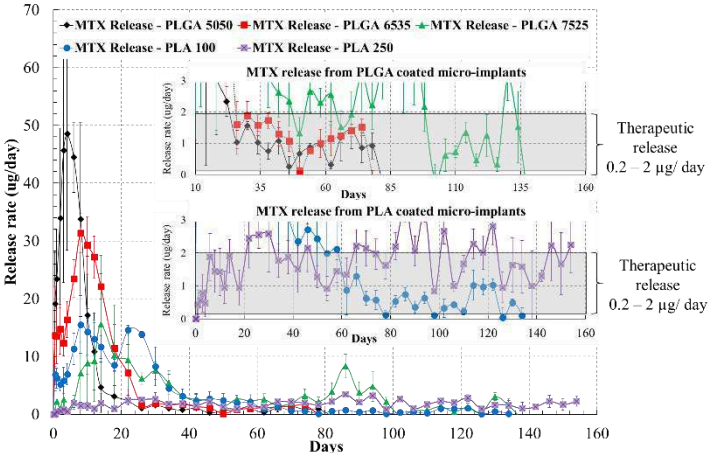

Figure 3: Release rate profiles of MTX from the PLGA-coated micro-implants and PLA-coated micro-implants

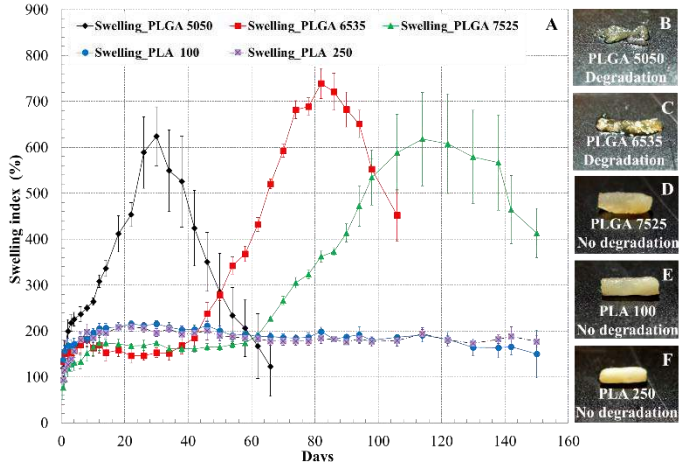

Figure 4: Swelling profile of the PLGA-coated micro-implants and PLA-coated micro-implants

Copyright 2016 The Organizing Committee for the 2016 Summer Biomechanics, Bioengineering and Biotransport Conference

SB^{3}C2016
Summer Biomechanics, Bioengineering and Biotransport Conference
June 29 –July 2, National Harbor, MD, USA
SB^{3}C2016-568

WEAR TESTING OF AN INNOVATIVE DESIGN FOR HIP RESURFACING

John B. Everingham (1), Jillian L. Helms (1), Kevin J. Warburton (1), Jeff Brourman, DVM, MS (2), Steven Fox, DVM, Ph.D. (3), Trevor J. Lujan, Ph.D. (1)

(1) Department of Mechanical & Biomedical Engineering
Boise State University
Boise, ID, USA

(2) WestVet Animal Emergency & Specialty Center
Garden City, ID, USA

(3) MWI Veterinary Supply Co.
Boise, ID, USA

INTRODUCTION

Hip osteoarthritis is a debilitating and irreversible disease that gradually degenerates the articular cartilage in the hip joint. In the United States, the lifetime risk to develop hip osteoarthritis is 25% in humans, and this disease also affects 50% of some canine breeds. The standard treatment for humans and animals with hip osteoarthritis is a total hip replacement (THR). Although THR has been successful at reducing pain and returning patients to a moderate activity level, THR is not ideal for younger patients, as implant life is relatively short (10-15 years) and there is a limited number of revision surgeries due to invasive bone removal during surgery. Another option for patients with hip osteoarthritis is Hip Resurfacing, where surgeons "resurface" the hip joint by fitting it with a cup and ball. Hip Resurfacing, introduced in 2006, better mimics the natural hip anatomy and has three functional benefits: lower cost, optimized bearing dimensions that improve mobility, and bone preservation that extends implant lifespan [1]. Despite these advantages, Hip Resurfacing has not been widely adopted due to complications related to metal wear debris generated by friction between the metal ball and metal cup [2]. Metal wear debris could be eliminated by using an ultrahigh-molecular-weight polyethylene (UHMWPE) plastic liner in the cup, but this solution has not been viable due to the high wear rates of UHMWPE combined with inherent size constraints of the cup and ball geometry. However, new material processing techniques have been developed to increase cross-linking in the UHMWPE microstructure, which greatly increases wear resistance. These advances in material engineering could potentially enable polymer liners to be used in Hip Resurfacing.

The objective of this research is to determine the wear behavior of a hip resurfacing implant for canines that uses a highly cross-linked UHMWPE liner. This implant is the first of its kind, and is composed of a thin titanium acetabular shell with a press fit highly cross-linked UHMWPE liner that articulates on a cobalt chromium (CoCr) femoral head (Fig. 1A). The wear behavior of this implant will be measured during the simulation of over one million cycles of canine hip motion. These wear tests will give veterinarian surgeons confidence to implant this new hip resurfacing device in canines, and results from this work will support translation of this technology to human application.

METHODS

Materials. Six acetabular liners (three control, three wear) of 24mm diameter highly cross-linked UHMWPE were tested. The acetabular liners were irradiated with 75kGy in vacuum with annealing. (Securos Surgical, Fiskdale, MA). Titanium shells were cemented into the holding fixtures of the wear simulator with the liners press fit into the shells (Fig. 1B). Femoral heads were press fit and cemented onto a separate holding fixture (Fig. 1C). The 24 mm CoCr femoral heads were coated with titanium niobium nitride (Ti-Nb-N) and had a surface roughness of ~0.77 microns (Fig. 1A-B).

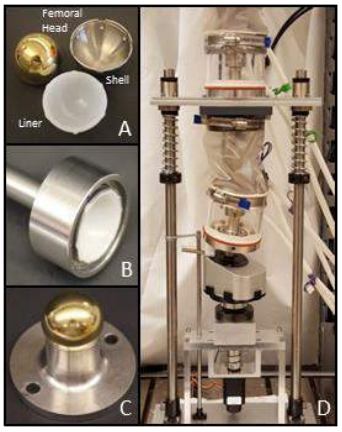

Figure 1: Implants and Hip Simulator (A) Implant components, (B) Shell in fixture, (C) femoral head in fixture, (D) hip simulator.

Hip Simulator Details. Wear tests were performed using a custom hip wear simulator (Fig. 1D). The simulator is a single axis orbital bearing machine (OBM) designed to produce canine hip

Copyright 2016 The Organizing Committee for the 2016 Summer Biomechanics, Bioengineering and Biotransport Conference

kinematics for an average sized German Shepard [3]. The simulator consists of two chambers each housing one implant. The top chamber serves as a load soak control, while the bottom chamber is loaded and rotated for wear testing. Vertical load was applied through the top implant fixture and transferred onto the bottom implant with a mechanical actuator (Instron, Norwood, MA; E10000). The implants were loaded at 10 N during the swing phase and at a peak of 211 N during the stance phase. The total range of flexion and axial rotation in the wear tested implant was +/-10° C with the max load reached at roughly 45% of the canine gait cycle. These two waveforms have been shown to closely match canine gait patterns [3]. The range of abduction does not correlate well with canine gait due to limitations inherent in the OBM simulator design, but this is shown to not greatly affect the resulting wear patterns [3].The implants in each chamber were lubricated with HyClone bovine calf serum, diluted with deionized water to a protein concentration of 2.0–2.5 g/100ml. Additional deionized water was added to replenish fluid lost from evaporation and small leaks in accordance with international standards for wear testing of total hip replacements (ISO 14242-3). The bovine serum was heated in external tanks and circulated through each chamber using a peristaltic pump. The bovine serum was changed every 550,000 cycles.

Testing Procedure. The implants were tested for a total of 1,100,000 cycles, broken into four stages of 275,000 cycles. Tests were conducted at 2 HZ. The peak load and tank temperature was sampled every 550 cycles to ensure that the implants were loaded consistently (± 5N) and that the circulating lubricant remained within the proper range (38.3 ± 1.67 °C). The motor position, load, and actuator displacement were sampled at the beginning, middle, and end of each testing phase to ensure the motor and load remained in phase.

Gravimetric wear analysis was performed every 275,000 cycles (ISO 14242-2). Prior to testing, liners were initially weighed after presoaking in diluted bovine serum for 48 hours. During testing, implants were removed from their test chamber and were immersed in an ultrasonic cleaner for 4 cycles: 10 minutes with deionized water, 10 minutes with detergent, 10 minutes with deionized water, 3 minutes in deionized water. Liners were then dried with a nitrogen gas jet, soaked in isopropyl alcohol for 5 minutes, then dried again with the nitrogen gas jet, and finally dried for 30 minutes in a vacuum desiccator. Each liner was weighed 3 times with a microbalance (Metter, Toledo OH; AT201, resolution = 0.1 mg). The net weight loss was calculated by adding the weight gain of the load-soak control liners to the weight loss of the wear tested liners (ISO 14242-2). An ANOVA test was performed to determine statistical difference in net mass loss between testing stages.

RESULTS

The average total wear rate and average total mass loss for the liners was 1.3 mg/10^6 cycles and 1.4 mg, respectively (Table 1). There was no significant difference seen in the net mass loss between testing stages ($p<0.52$; Fig. 2). No liners, shells, or femoral heads had any catastrophic failure due to cracking or any significant visual damage from wear.

TABLE 1. Average Wear Rate and Total Wear for each Testing Trial

Trial	Average Wear Rate a_G (mg/10^6 Cycles)	Corrected Net Mass Loss W_T (mg)
1	0.9	1.5
2	2.0	1.7
3	1.0	1.2
Average	1.3+/-0.6	1.4+/-0.3

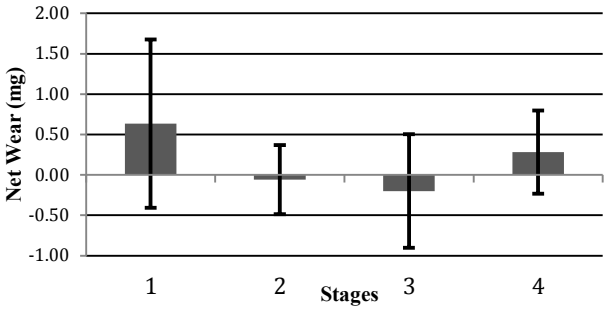

Figure 2: Net Mass Loss per Stage (each stage = 275,000 cycles)

DISCUSSION

This study introduced a novel hip resurfacing device and found that this device withstood wear testing with minimal amounts of weight loss and no visible signs of failure. This device is innovative since it is the first to incorporate a polymer liner into a hip resurfacing design. The liner is very thin, with a thickness of 1.5 mm, compared to an average thickness of 8 mm in UHMWPE liners used in human THR implants [4]. The thin liner is necessary due to geometric constraints inherent in hip resurfacing, where there is a large femoral head and a limited amount of acetabulum bone for implant fixation. Because of the thin liner, it was important to determine if the liner would crack or wear through during long-term testing. Our results indicate a successful design that may be ready for canine implantation and eventual translation to human patients.

The wear rate per million cycles for the highly cross-linked UHMWPE liner used in this study was similar to wear rates for similar liners used in human THR studies [5][6]. For example, Saikko et al. found wear rates of 2.4 mg per million cycles, which was 54% greater than our wear rate. Although canine implants experience 5x less load than human implants, the similar amount of wear can likely be attributed to the high surface roughness of the femoral heads used in this study (0.77 μm) compared to the "worst-case" surface roughness used by Saikko et al. (0.14-0.184 μm) [7]. Therefore, the roughness of the femoral heads used for testing the canine liners can be considered extreme, and the actual wear in canines would likely be less. Weight gain was seen in stage three (Fig. 2). While not expected, other studies have observed weight gain in cross-linked polymer liners [5][6].

This study had limitations. First, implants were tested for only 1.1 million cycles; comparable human studies tested for upwards of 3 million cycles [5][6]. However, the life expectancy of a canine is only 9-13 years so the required implant life is much shorter. Second, no analysis was done on the size or shape of the wear debris. Wear debris that are too small (< 10 μm diameter) can provoke an adverse inflammatory response that can lead to osteolysis and subsequent implant loosening [8]. The bovine serum used as lubricant in this study has been stored for future wear debris analysis.

This is the first study to report wear testing of a canine hip implant. The canine hip replacement market has an annual growth of 5%, and it is hoped that the technology introduced in this study can reduce the high out-of-pocket cost incurred to canine owners. This technology may also benefit human healthcare, since the development of a hip resurfacing device that eliminates metal wear debris would be an appealing procedure for younger patients.

ACKNOWLEDGEMENTS

This research was supported by the Idaho Global Entrepreneurial Mission. Kind support was received from MWI and Misumi.

REFERENCES

[1] Amstutz, H. C. et al., *Hip International,* 25(4), 330-338, 2015.**[2]** Junnila, M et al., *Acta Orthopaedica,* 86.3: 345-350, 2015. **[3]** Warburton, K et al. SB^3C2015-1174 **[4]** Ebrahimpour, M et al., *ORTHOPEDICS*, 1:34:e133-e137 **[5]** D'lima, D et al., *J Orthopaedic Research,* 21(5), 761-6, 2003 **[6]** Saikko, V et al., *J. Biomed. Mater. Res.*, 63: 848-853, 2002. **[7]** Sychterz, CJ et al., *Clin Orthop*, 358:223-234, 1999. **[8]** Endo, M.M. et al. *Bio-Medical Materials& Engineering*, 11(1), 23, 2001

Copyright 2016 The Organizing Committee for the 2016 Summer Biomechanics, Bioengineering and Biotransport Conference

SB^{3}C2016
Summer Biomechanics, Bioengineering and Biotransport Conference
June 29 –July 2, National Harbor, MD, USA
SB^{3}C2016-569

A STUDY FOR THE EFFECTS OF THE MECHANICAL TRAPPING OF THE NUCLEUS ON CELLULAR EVENTS USING A MICROPILLAR SUBSTRATE

Kazuaki NAGAYAMA

Micro-Nano Biomechanics Laboratory,
Department of Intelligent Systems Engineering, Ibaraki University
4-12-1 Nakanarusawa-cho, Hitachi-shi, Ibaraki 316-8511, Japan

INTRODUCTION

The nucleus is the largest and stiffest organelle in eukaryotic cells [1] and is exposed to the mechanical forces transmitted through the cytoskeleton from outside the cell and the intracellular tension generated by the actin-myosin contractile cytoskeleton via nuclear membrane proteins [2]. The nucleus itself has been proposed to act as a cellular mechanosensor, and the changes in nuclear shape or its deformation possibly affect the regulation of cell functions. Recently, we demonstrated the mechanical deformation and trapping of the intracellular nucleus using polydimethylsiloxane (PDMS)-based microfabricated substrates with an array of micropillars, and found that the cell proliferation was dramatically inhibited by cultivation on the micropillar substrates, even though remarkable deformation of nuclei was observed [3]. In the present study, we further investigated the effects of nuclear deformation on the physiological function, such as cell migration, DNA synthesis, and contractile differentiation of vascular smooth muscle cells (SMCs).

METHODS

Porcine aortic SMCs were used as the test model. Micropillar array substrates were fabricated by replica-molding [4]. In this study, we designed the PDMS micropillar array substrates with a hexagonal arrangement and with a pillar diameter, length, and center-to-center spacing of 3, 9, and 9 μm, respectively. The Young's modulus of the PDMS substrate was ~1.6 MPa [3], which was of the same order of magnitude as extracellular matrices such as elastin (~0.6 MPa [5]) surrounding SMCs *in vivo*.

Both micropillar array substrates and the flat substrates made of the same lot of PDMS were placed in the glass-bottom culture dishes. The surfaces of both substrates were exposed to oxygen plasma (5 mA, 10 Pa) for 2 min using a plasma generator (SEDE-P, Meiwafosis, Tokyo, Japan). All surfaces of both the pillar and flat substrates were coated with fibronectin (50 μg/ml) to allow cell adhesion. SMCs were cultured on these two substrates in DMEM supplemented with 10% FBS at 37ºC.

To investigate the effects of the mechanical trapping of the nucleus on cell migration, we obtained time course images of the cells cultured on the flat and micropillar substrates for 24 h at 5-min intervals using a microscope imaging system with a compact CO_2 incubator. Then, we measured and compared the cell proliferation and DNA synthesis on the both substrates using BrdU assay. To investigate the effects of the nuclear deformation on smooth muscle contractile differentiation, changes in the expression level of α-smooth muscle actin following the cultivation on the micropillar substrates was measured. We also investigated the distribution of intranuclear DNA and lamin A/C which is the main component of nuclear lamina by using confocal microscopy.

RESULTS AND DISCUSSION

Typical fluorescent images of SMCs cultured on the PDMS pillars and flat substrates are shown in Figure 1. SMCs elongated well on the flat substrates, and their nuclei had elliptical shapes with smooth surfaces (Fig. 1A). The cells also spread completely between the fibronectin-coated pillars, leading to strong deformations of their nuclei (Fig. 1B). The nuclei in SMCs were entirely inserted into the grooves between the pillars and they appeared to be "trapped" mechanically on the array of pillars, although they remained in an elongated shape (Fig. 1B). Such nuclear deformation did not affect cell viability; the viabilities of SMCs on the pillar substrate were greater than 98%. These results demonstrated that the SMC nuclei had the ability to deform in response to the micropillared surface.

Copyright 2016 The Organizing Committee for the 2016 Summer Biomechanics, Bioengineering and Biotransport Conference

Such mechanical trapping of the SMC nuclei with the micropillars significantly inhibited cell migration (Fig. 2), and they also prominently inhibited DNA synthesis (Fig. 3). It has generally been suggested that contact inhibition of cell proliferation occurs when a cell culture reaches confluence [6]. However, the proliferation of SMCs was significantly inhibited in the micropillar substrates even though the cells did not reach the confluent state. We also found that not only the migration and cell proliferation of SMCs but also their contractile protein expression was dramatically inhibited by cultivation on the micropillar substrates (Fig. 4). A detailed image analysis with confocal microscopy revealed that expression of lamin A/C was significantly decreased in the region deforming along the pillar surfaces (Fig. 5C), and underlying DNA distribution became more heterogeneous (Fig. 5D). These results may indicate that lamin A/C has a role of mechanosensor to detect an excessive deformation of nucleus, and they switch the cell state from an "active phase" to a "resting phase".

ACKNOWLEDGEMENTS

This work was supported in part by a Grant-in-Aid from the Ministry of Education, Culture, Sports, Science and Technology, Japan (nos. 24680051, 25111711, and 26560207) and AMED-CREST, Japan (No. 15gm0810005h0001).

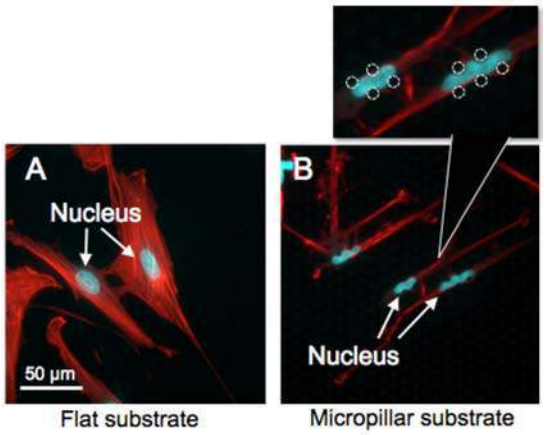

Figure 1: Typical examples of fluorescence images of actin filaments (red) and nuclei (cyan) in vascular smooth muscle cells. The cells were cultured on the PDMS substrates, which have flat surfaces (A) or the array of micropillars (B).

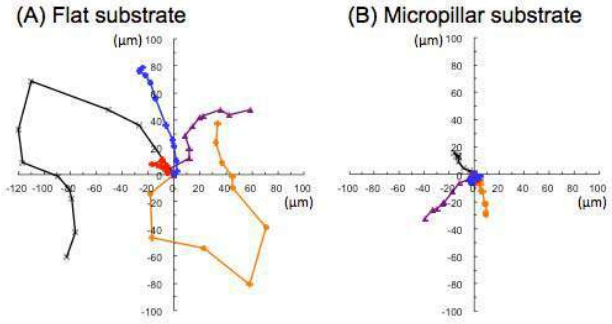

Figure 2: The examples of the movement trajectories of the vascular smooth muscle cells on the flat (A) and the micropillar (B) substrates.

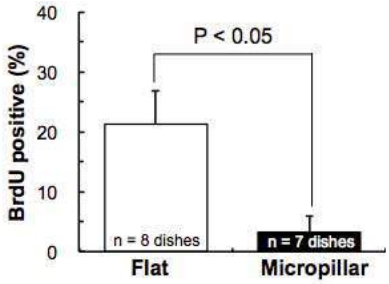

Figure 3: Detection of BrdU-labeled vascular smooth muscle cells on the flat and the micropillar substrates.

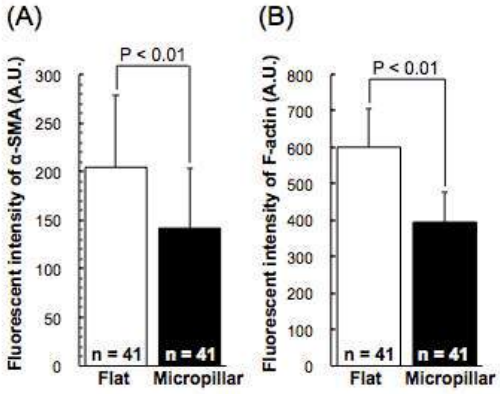

Figure 4: Changes in the fluorescent intensity of α-SMA (A) and F-actin (B) in vascular smooth muscle cells cultured on the flat and micropillar substrates.

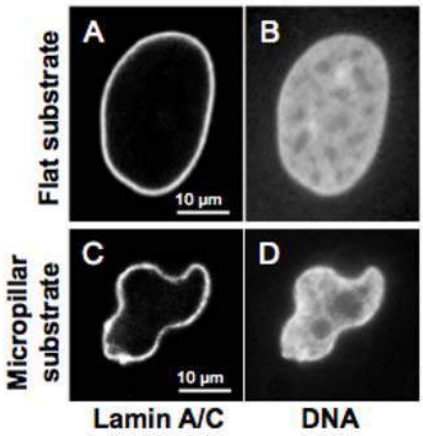

Figure 5: Typical examples of confocal fluorescence images of lamin A/C (A, C) and intranuclear DNA (B, D) in the vascular smooth muscle cells cultured on on the flat (A, B) and micropillar (C, D) substrates.

REFERENCES

[1] Dahl KN et al., *Circ. Res.* 102:1307–1318, 2008.
[2] Nagayama K, et al., *FEBS Lett,* 585:3992–3997, 2011.
[3] Nagayama K, et al., *J Biomech*, 48:1796-1803, 2015.
[4] Tan JL, et al., *PNAS*, 100(4):1484-1489, 2003.
[5] Fung YC, *Biomechanics*, Springer, New York:196–214, 1981.
[6] Hneino M, et al., *J Vasc Res,* 46:85–97, 2009.

Copyright 2016 The Organizing Committee for the 2016 Summer Biomechanics, Bioengineering and Biotransport Conference

SB^{3}C2016
Summer Biomechanics, Bioengineering and Biotransport Conference
June 29 –July 2, National Harbor, MD, USA
SB^{3}C2016-570

A chemo-mechanical free-energy-based approach to model durotaxis and extracellular stiffness dependent contraction and polarization of cells

Vivek B. Shenoy (1), Hailong Wang (1), Xiao Wang (1)

(1) Department of Materials Science and Engineering,
University of Pennsylvania

INTRODUCTION

Cytoskeletal tension is fundamental to many cellular processes such as cell motility, cytokinesis, tissue morphogenesis, and remodeling, as well as pathologic processes such as tumor growth, metastasis, and fibrosis. Cells modulate their contractility and adapt to different tissue-specific and extra cellular environments in both normal and pathological settings. Stiffness of the extra cellular environment plays a crucial role in determining the contractility of cells. Because of the coupled nature of the mechanical and biochemical signaling processes, progress in understanding how they interact to control cell contractility and more importantly, cell shape has proved challenging. Predictive quantitative models that link biochemical signaling pathways that control recruitment of molecular motors leading to changes in contractility with the mechanics of the extracellular environment can provide a means to interpret and predict cell functions in normal and pathological conditions.

However, most of the current models do not treat these chemo-mechanical processes in a consistent and unified manner [1-3]. A key drawback of these models reviewed do not consider the chemical, mechanical and interfacial contributions to the free energy of a given shape and polarization of a cell, and thus are not able to predict which configuration (for example, spindle shaped or spherical) is favored from an energetic perspective. It is also well known that cells migrate towards regions of larger mechanical stiffness, a process referred to as durotaxis. However, the energetic driving forces for this process have not been quantitatively studied to date. Given the key role that cytoskeletal tension plays in physiological processes, it is important to develop a mathematical description that treats the mechanics of the cell and the ECM and the biochemistry of stress fiber formation on an equal footing.

METHODS

We develop a unified framework to study contractility and polarization of cells as a function of the stiffness of their surroundings by considering the chemical free energy available from the assembly of stress fibers and the mechanical energy due to the deformation of cells and the extracellular matrix [4]. The key kinematic variables that describe the cell are the strain and the contractility tensors and the free energy of the cell-matrix system is expressed in terms of these variables. We explicitly include a term that couples the stress and contractility tensors, thus are able to capture how the contractility of the cell can change in response of mechanosensitive signaling pathways (Fig. 1).

$$U(\rho,\epsilon) = \frac{K}{2}\epsilon^2 - \int_0^{\varepsilon} \sigma d\varepsilon + \frac{\beta}{2}(\rho-\rho_0)^2 - \alpha \int_0^{\rho} \sigma d\rho + \rho\varepsilon. \qquad (1)$$

By using the principles of non-equilibrium thermodynamics, we relate the rate of myosin recruitment and cross-bridge sliding to variations of the free energy with respect to contractility and the active strain. We show that the rate of change of contractile strain is linearly related to stress, providing derivation of the Hill law based on considerations of free energy, rather than phenomenology. We then show that the overall free energy of cells is lowered in stiffer environments due to recruitment of myosin motors, providing a means to evaluate the thermodynamic driving force for durotaxis. By comparing the predictions of our simulations with experiments on cells deformed using the atomic force microscope we obtain estimates of the chemo-mechanical coupling parameters. We also study how the free energy and polarization of cells depend on their shape in 3D matrices, on 2D substrates and on micropost arrays. The chemo-mechanical parameters we have derived can be used to quantitatively model cell sorting, motility and morphogenesis in complex 3D environments.

Copyright 2016 The Organizing Committee for the 2016 Summer Biomechanics, Bioengineering and Biotransport Conference

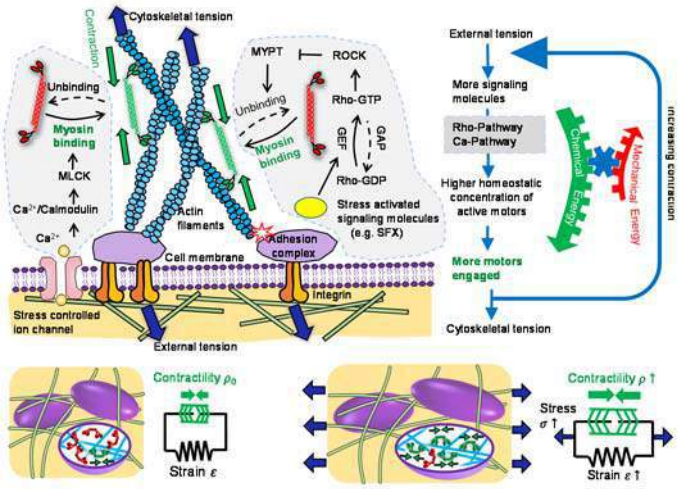

Figure 1: Schematic depiction of the chemo-mechanical coupling and stress-dependent feedback mechanisms in our model.

RESULTS

We consider three examples to validate our 3D chemo-mechanical model, namely, cells on a bed of microposts [2] (Fig. 2), cells on 2D substrates [5] (Fig. 3) and cells in 3D matrices (Fig. 4). In all of these examples, our focus is on the elucidation of the variations of the chemical and mechanical free energies as a function of the stiffness of the posts, substrates and matrices.

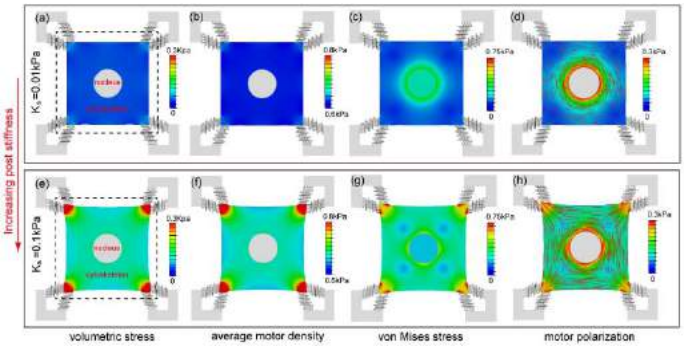

Figure 2: The steady-state distributions of the volumetric stress, average motor density, von Mises stress, and motor polarization with various post stiffnesses.

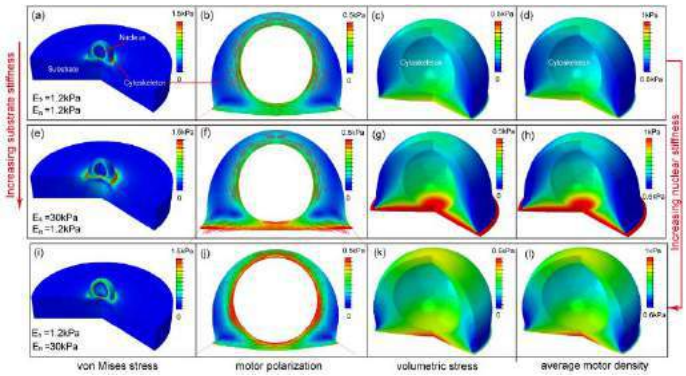

Figure 3: The steady-state distributions of the von Mises, motor polarization, volumetric stress, and average motor density of cytoskeleton for varying substrate and nuclear stiffnesses.

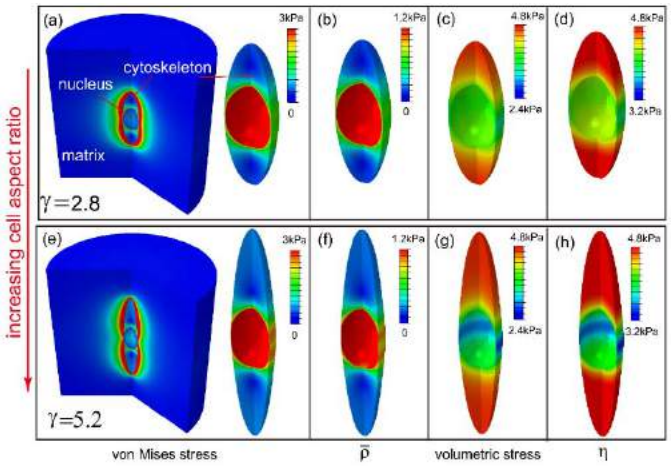

Figure 4: The steady-state distributions of the von Mises stress, motor polarization, volumetric stress, and average motor density of cytoskeleton for various cell aspect ratio.

These observations provide the basis for durotaxis, where cells preferentially migrate towards stiffer regions of the extracellular environment. Our models also explain, from an energetic perspective, why the shape of cells changes in response to the stiffness of the surroundings. The effect of cell shape on the shape of the nucleus has also been studied.

DISCUSSION

We have developed a model that explicitly includes stress dependent recruitment of molecular motors to develop a chemo-mechanical description of polarization and strain in contractile cells. The basic variables that describe the model are the strain tensor and the contractility tensor that depends on the spatial distribution of the molecular motors. In contrast to previous models, we do not keep track of individual fibers, but capture the effect in a coarse-grained sense; the principal direction of the contractility tensor with the largest principal value gives the orientation of the stress-fibers and the difference between the largest and smallest principal values of contractility gives the polarization of the cells. We have derived the free energy of the cell in terms of these variables. The free energy includes the elastic strain energy of the cytoskeleton, the mechanical work done by the molecular motors and the chemical free energy of motor recruitment. The dynamic laws for the evolution of the active strain and the contractility tensor are derived based on the second law of thermodynamics. In this manner, we are able to recover the well-known Hill relation for active stresses in tissues, based on fundamental principles of irreversible thermodynamics rather than phenomenology.

ACKNOWLEDGEMENTS

This work is supported by grants NIH-R01EB017753, NIH-U54CA193417 and NSF-CMMI131239

REFERE

[1] Barocas, VH, et al. *J. Biomech. Eng*. 119: 137–145, 1997

[2] Deshpande, VS, et al. *Proc. Natl. Acad. Sci. U. S. A*. 103: 14015–14020, 2006

[3] Wang H et al., *Proc. Natl. Acad. Sci. U. S. A.* , 110, 20923–20928, 2013

[4] Shenoy, VB et al., *Interface Focus*, 6:20150067, 2016

[5] Dowling, EP et al. *J. R. Soc. Interface* **9**, 3469–3479, 2012

Copyright 2016 The Organizing Committee for the 2016 Summer Biomechanics, Bioengineering and Biotransport Conference

SB^{3}C2016
Summer Biomechanics, Bioengineering and Biotransport Conference
June 29 –July 2, National Harbor, MD, USA
SB^{3}C2016-572

FINITE ELEMENT MODEL OF OCULAR ACCOMMODATION MECHANISM BASED ON LENS PRE-TENSIONING AND CILIARY MUSCLE CONTRACTION

K. Knaus (1), A. Hipsley (2), S. Blemker (1)

(1) Department of Biomedical Engineering
University of Virginia
Charlottesville, VA, USA

(2) Ace Vision Group Inc.
Akron, OH, USA

INTRODUCTION

Accommodation of the human eye transitions from distant to near focus through deformation of the lens. This lens change is caused by contraction of the intraocular ciliary muscle, relieving tension on the lens through the suspensory zonule fibers, allowing the thickness and surface curvature of the lens to increase [1]. The ring-shaped ciliary muscle is composed of three uniquely oriented fiber groups (longitudinal, radial, and circular) that contract toward the center and anterior of the eye [2]. The deformation of the ciliary due to the contraction of the different muscle fibers translates a change in tension to the surface of the lens through the zonule fibers, whose complex patterns of attachment to the lens and ciliary dictate the resultant changes in the lens during accommodation [3]. Ciliary muscle contraction also applies strain at its connections to the sclera, the white outer coat of the eye, and the choroid, the inner connective tissue layer between the sclera and retina.

As people age, they develop presbyopia and lose accommodative ability, leaving people over the age of 50 with an almost complete lack of focusing ability for near vision [1]. Although scientists have studied accommodation for centuries the functional mechanism is not well understood. Most presbyopia research has focused on property changes of the aging lens without examining the accommodative mechanism as a whole, basically ignoring the complicated role of the ciliary muscle. Without understanding the interactions of the muscle, lens, and other structures that alter the eye's optic power, treatments for presbyopia that effectively restore this ability cannot be successfully developed. This lack of understanding is also in part due to the limited data, especially *in vivo* or dynamic, of healthy human eyes; most current measurement techniques require isolating or disturbing some portion of the accommodative system and are limited to cadavers or monkey models [3,4]. These data provide a disjointed comprehension of the accommodative mechanism and the implications of age-related changes to eye structure.

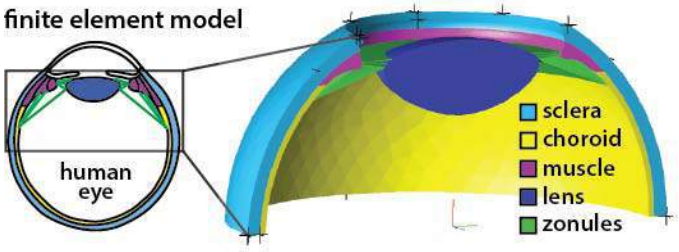

Figure 1: FEM of ocular structures involved in accommodation

A computational model is critical to understanding how the complex movements of the ciliary muscle drive the lens changes necessary for accommodation, and to understand how age-related changes lead to presbyopia. Most previous models focused solely on the actions of lens and zonules, simplifying ciliary movement to a single displacement, and simulating the transition from the accommodated state where the lens is un-stretched but the muscle is contracted, to the unaccommodated state where the muscle is at rest and the lens is stretched. This method depends on a simplified arrangement of the zonule attachments and also ignores the complex behaviors of the ciliary muscle, whose movements are constrained by its attachments to the sclera and choroid. The goal of this study was to develop a multi-component finite element (FE) model of the accommodative mechanism that includes the ciliary muscle, lens, zonules, sclera, and choroid [Fig. 1], to characterize the role of complex ciliary muscle action in producing the lens changes required for accommodative function.

Copyright 2016 The Organizing Committee for the 2016 Summer Biomechanics, Bioengineering and Biotransport Conference

METHODS

Representative 3D geometry of the resting ocular structures was defined computationally based on extensive review of literature measurements and medical images of the anatomy of the young adult eye. AMPS software (AMPS Technologies, Pittsburgh, PA) was used for geometric meshing, defining material properties and boundary conditions, and to perform finite element analysis. The ciliary muscle and zonules were represented as a transverse isotropic material with orientations specified to represent the complex fiber directions [5]; computational fluid dynamic simulations were used to produce fiber trajectories, which were then mapped to the geometry. The lens began in the relaxed configuration and was stretched through pre-tensioning of the zonule fibers to the unaccommodated position and shape. Unaccommodated lens position was reached when zonules were shortened to 77% of their starting length [Fig. 2]. Then accommodative motion was simulated by active contraction of the fibers of the ciliary muscle, using a previous model of skeletal muscle that was modified to represent the specific dynamics of the ciliary muscle [5]. Model results of lens and ciliary anterior movement and deformed thickness at the midline and apex, respectively, were validated through comparison to literature measurements of accommodation [4]. To investigate contributions of the different fiber groups to the action of the ciliary muscle, the simulation was repeated with each fiber group activated in isolation while the other groups remained passive.

RESULTS

Model results of displacement and deformation of the lens and ciliary muscle fell within the range of literature values for accommodation of a young adult human [Fig. 3]. Pre-tensioning of the zonules prior to muscle contraction was necessary for the model to produce appropriate lens deformation. The contraction of specific fiber groups contributed disproportionately to different aspects of lens change in accommodation [Fig. 3]. Contraction of the radial fibers contributed most to anterior movement of the lens (fiber contraction responsible for anterior lens movement was 44% longitudinal, 73% radial, and -18% circular), and circular fibers contributed most to thickening of the ciliary at the apex lens (fiber contraction responsible for ciliary apex thickening was 27% longitudinal, 21% radial, and 52% circular), which leads to lens thickening and increased curvature.

DISCUSSION

This model provides novel insight into the interactions of the components of the accommodative mechanism through incorporation of decades of previous research. The model results were effectively validated with existing data; these comparisons are bounded by the limitations of current measurements, they suggest new experiments for future study of accommodation. New appreciation of ciliary muscle function gained through simulations of its specific actions motivates hypotheses for targeted therapies for presbyopia. Moving forward, we plan to use this model to systematical investigate the effect of age-related changes to the eye of the action of the ciliary muscle to determine major influences of presbyopia the accommodative mechanism. We will also test hypothesized therapies effectiveness at restoring normal function to the presbyopic eye.

ACKNOWLEDGEMENTS

Funding for this study was provided by Ace Vision Group Inc.

REFERENCES

[1] Croft, M et al., *Internat. Ophthalmology Clinics*, 41:33-46, 2001.
[2] Hogan, M et al., *Histology of the human eye*, Philadelphia, 1971.
[3] Lütjen-Drecoll, E et al., *IOVS* 51no3:1554-64, 2010
[4] Croft, M et al., *IOVS* 54no7:5035-58, 2013
[5] Blemker, S et al., *J Biomechanics*, 38:657-665, 2005

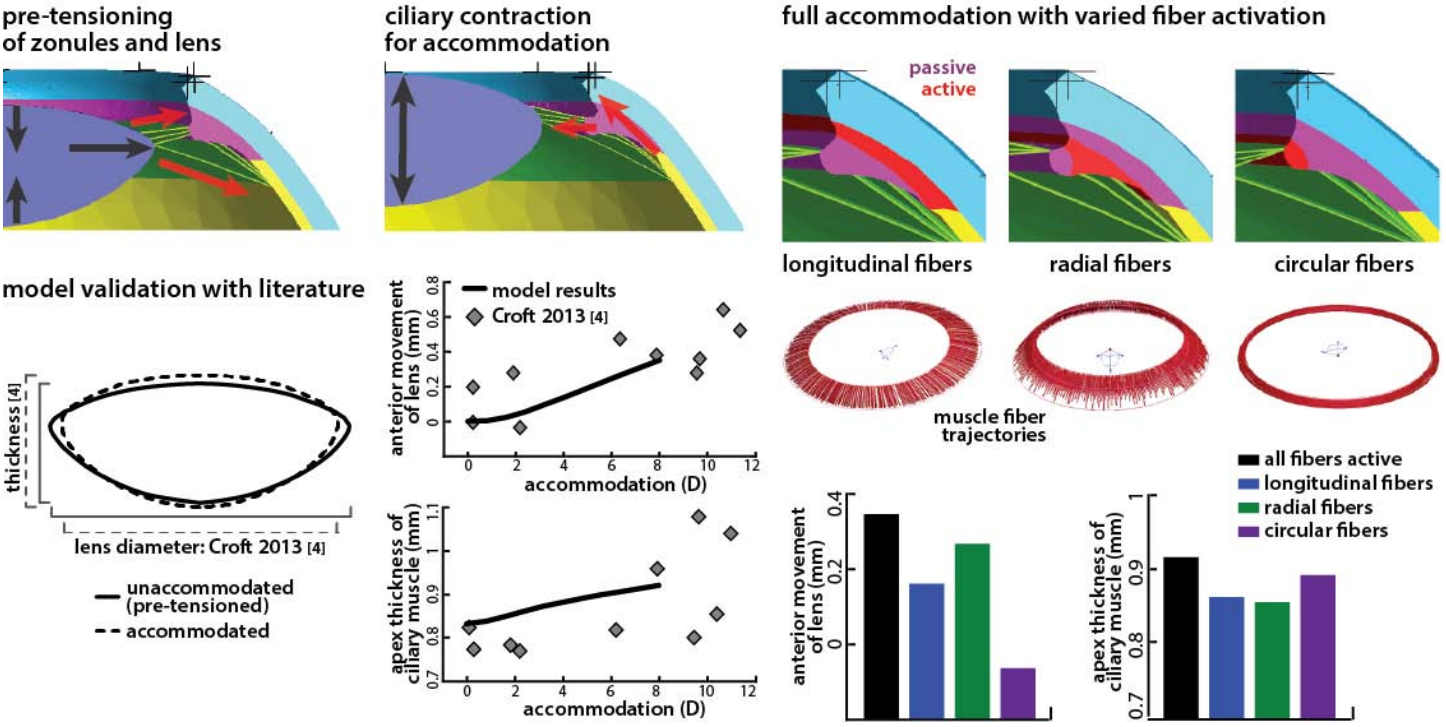

Figure 2: Zonules were pre-tensioned to stretch the lens from anatomic measurements [4] of resting shape to unaccommodated. Accommodation was simulated through ciliary muscle contraction, and validated through comparison to literature measurements of lens and ciliary displacement and deformation [4]. Simulations of accommodation were repeated with muscle fiber groups activated in isolation.

Copyright 2016 The Organizing Committee for the 2016 Summer Biomechanics, Bioengineering and Biotransport Conference

SB^{3}C2016
Summer Biomechanics, Bioengineering and Biotransport Conference
June 29 –July 2, National Harbor, MD, USA
SB^{3}C2016-573

MECHANOSTATISTICAL CARTILAGE PELLET MODEL TO EVALUATE CARTILAGE GROWTH IN SCAFFOLDS

Christopher Miller (1), Ben Schon (2), Tim Woodfield (2), Thor Besier (1), Justin Fernandez (1)

(1) Auckland Bioengineering Institute
University of Auckland
Auckland, New Zealand

(2) Department of Orthopedic Surgery and
Musculoskeletal Medicine
University of Otago
Christchurch, New Zealand

INTRODUCTION

Articular cartilage is a specialized tissue that operates within a hostile biomechanical environment. As with the majority of musculoskeletal tissues, cartilage is able to sense its mechanical environment and adapt accordingly to the physical requirements of the body. It is well evidenced from in vivo and in vitro experimental models that it requires regular mechanical stimulation within a window of "reasonable" physiological loading to stimulate growth and maintain its functional integrity, with loading outside of this range deleterious to its general structure and composition [1]. This is an indication that there is a quantified correlation between loading circumstances and tissue remodeling, comparable to the mechanostat growth/loss model for bone.

The inherent complexity in assessing the remodeling response to physical stimuli and the broad range of spatial scales involved, make it highly challenging to assess cartilage mechanobiology experimentally. As such, the precise events, their sequence and the mechanisms associated with the contribution of joint loading history to cartilage remodeling have yet to be fully eluded too and properly quantified. The computational modeling of cartilage remodeling presents a means of separating the myriad of internal and external mechanisms influencing the development of functional engineered cartilage and seeking out dominant underlying factors [2].

However research in this area is sparse and traditionally models have been deterministic in nature. They therefore do not readily account for random variation in experimental parameters and initial circumstances. Statistical methods are widely used in the musculoskeletal modeling discipline and their use in simulating mechanically mediated cartilage remodeling presents a means of overcoming current shortcomings. Presented here is a novel experimentally informed population based statistical model to predict cartilage pellet growth in scaffolds. Its function is to determine cell and protein spatio-temporal distributions based upon the system input conditions and localized mechanical environment.

The potential uses of such a model are extensive; the intention is that it be used as the building block for an overall multi-scale mechanobiological framework, whose aim is to simulate mechanically mediated tissue remodeling within patella-femoral joint implanted tissue engineered constructs, see Figure 1.

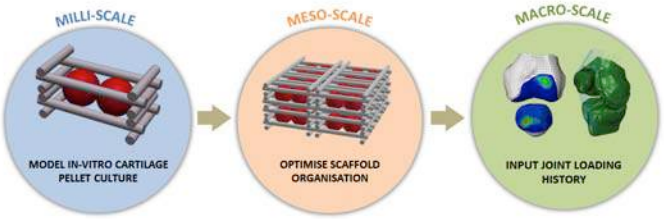

Figure 1: Schematic Diagram of Multi-scale Cartilage model.

METHODS

Data concerning the fusion of cartilage pellets within 3D scaffold architectures was used to construct the model (see Figure 1, far left). Inverted scope microscopy, histology, and biochemical analysis were performed to investigate the contribution of cell co-culture on chondrogenic differentiation, the formation of functional cartilaginous tissue and pellet interaction within the scaffold.

Four experimental groups were considered; the AC (Articular Chondrocyte) and the MSC (Mesenchymal Stem Cell) groups used pellets containing those cell types exclusively. The MSC-AC group used a pellet populated with either; whilst the pellets of the mix group were populated with a combination of both cell types.

Copyright 2016 The Organizing Committee for the 2016 Summer Biomechanics, Bioengineering and Biotransport Conference

Histological images were used to gather information concerning the 2D distribution of cells and glycosaminoglycan (gag) within cultured pellet configurations. A semi-automated GUI was used to extract cell location, whilst gag distribution was gathered by assuming a linear relationship between image intensity and gag concentration, see Figure 2. The positioning of both fields are described based on the normalized distance from the pellet periphery and the angle made with the horizontal axis, this was to take into account pellet geometrical changes. Pellet shape progression was determined by fitting a pair of ellipses to the inverted scope images.

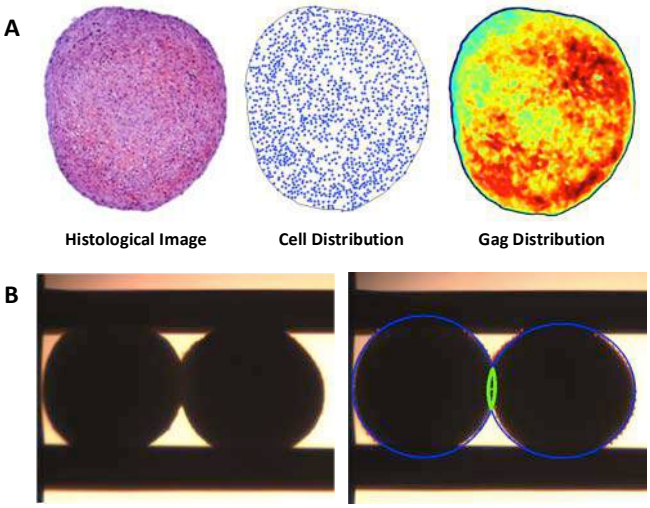

Figure 2: Examples of (A) Extracted Cell & Gag Distributions and (B) Pellet Geometry Determination.

A combination of univariate and multivariate inverse transform sampling methods were used to generate sets of pseudorandom initial pellet configurations. These were then translated to Abaqus FE software. Mass diffusion analyses were performed, where the governing equations are an extension of Ficks-law (1), to determine spatio-temporal alterations in distribution. Gag and cell movement were modeled individually with spatially varying diffusion coefficients directing movements between adjacent elements, cell proliferation and gag synthesis were accounted for via positive or negative body concentration fluxes for relevant elements. The diffusion coefficient distributions were also generated randomly based on those estimated directly from experimental data.

$$J = -D \cdot \left(\frac{\partial c}{\partial x} + sk_p \frac{\partial p}{\partial x}\right) \quad (1)$$

The generated datasets were used as the predicted and observable variables to train a partial least squares regression (PLSR) machine-learning model [3]. An iterative optimization scheme was used to attain a statistical model best able to approximate the diffusion coefficient profile that resulted in the culture outcome for the extracted experimental data. The impact of hydrostatic pressures on the diffusion of cell and gag fields throughout the pellet system was also analyzed through the inclusion of the pressure gradient term in the governing equations for a number of external loading circumstances.

In addition to the methodology discussed, an eigenvector morphological analysis was performed to reveal different cell phenotypes and alternate cell states.

RESULTS

The statistical model was able to estimate diffusion coefficient profiles for the experimental circumstances that when inputted into the Abaqus mass diffusion model, predicted the culture outcome for the experimental case reasonably well. The model predicted temporal alteration to a high degree of accuracy, however the spatial variation was predicted poorly when proliferation was excluded and only diffusive migration was accounted for. Figure 3 is an example of the evolution of the gag distributions over the seven-day culture period, with blue and red parts of the image corresponding to low and high concentrations respectively.

The addition of the hydrostatic pressure term to the FE model had a significant impact on culture outcomes. Even at small loads, the pattern of applied loading was observed to heavily determine the spatial evolution of the cell and gag distributions, with both fields preferentially migrating to areas of small relative pressures.

The cell morphology analysis allowed for cell phenotype and those undergoing apoptosis to be readily determined based on the roundness and size of cells respectively. Thus permitting a better quantification of cell type and state than existing image classifications.

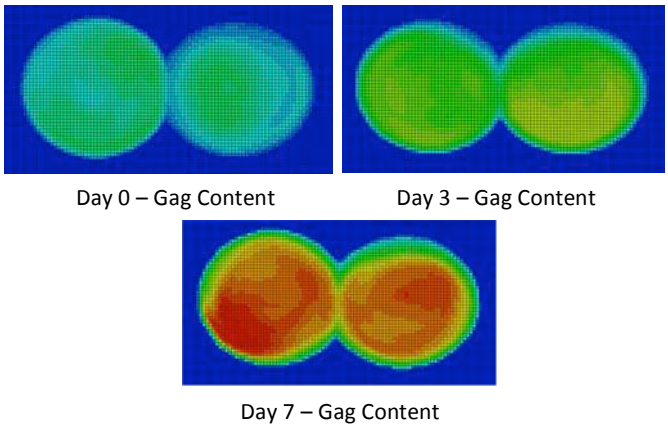

Figure 3: Example of Gag Diffusion Over Seven Days of Culture.

DISCUSSION

The observation that the model predicted better temporal than spatial distribution of cell and gag concentration when proliferation was omitted from the governing equation, suggests that cell genesis and gag synthesis play a strong role in the evolution of the cartilage pellet experiment. The model demonstrated a complimentary role in cartilage experimental evaluation by highlighting the significant effect of hydrostatic pressure on culture outcomes that are difficult to perform experimentally.

Furthermore, the model lends itself naturally to inclusion within a multi-scale framework; acting as a building block for subsequent investigation. Cell and Gag distribution can be related to material properties and hydrostatic pressure accounted for in the statistical procedure to evaluate loading independent of normal culture behavior. Coupling the model with larger scale FE models will permit material optimization to be carried out and the effect of joint loading history on remodeling to be analysed.

REFERENCES

[1] Grodzinsky, AJ et al., *Annu Rev Biomed Eng*, 2:691-713, 2000.
[2] Sengers, B et al., *Biomaterials*, 28:1926-1940, 2007.
[3] Mateos-Aparicio,G, *Commun Stat-Theor M*, 40:2305-2317, 2011.

Copyright 2016 The Organizing Committee for the 2016 Summer Biomechanics, Bioengineering and Biotransport Conference

SB^{3}C2016
Summer Biomechanics, Bioengineering and Biotransport Conference
June 29-July 2, National Harbor, Maryland, USA
SB^{3}C2016-574

IMPROVED ANKLE FOOT ORTHOSIS FOR CLUBFOOT TREATMENT

Alissa L. Adams
University of Alberta
Edmonton, Alberta, Canada

Brianna M. Bruni-Bossio
University of Alberta
Edmonton, Alberta, Canada

Angela P. Guardia
University of Alberta
Edmonton, Alberta, Canada

Faculty Advisor:

Alberto Palomino
University of Alberta
Edmonton, Alberta, Canada

Rex Wu
University of Alberta
Edmonton, Alberta, Canada

Dr. Kajsa Duke
University of Alberta
Edmonton, Alberta, Canada

INTRODUCTION

Clubfoot, the most common congenital deformity of the feet in newborns, affects about 1 in 1000 children [1]. Children born with clubfoot have misaligned bones in their lower extremities due to short muscles causing their feet curl in adduction and plantar flexion. Clubfoot is corrected through a treatment consisting of manipulation, casting, minor surgery, and bracing [2]. The first three parts of the treatment aim to bring the feet to a correct anatomical position and last approximately 3 months. The corrected feet require bracing for a period of approximately 4 years to prevent the feet from returning to their deformed position.

Ankle foot orthoses (AFOs) are the braces commonly used for clubfoot treatment. The purpose of a clubfoot AFO is to maintain the feet at specific, physician-prescribed angles of abduction (rotation of the foot outwards) and dorsiflexion (flexion of the foot upwards).

Existing clubfoot AFOs consist of a pair of boots connected by a rigid bar. Limitations of these systems are: comfort, as the straps often cause rubbing or abrasion; difficulty in donning and properly securing the child's feet; expensive retail prices of around $600 (CAD); and bars that are typically rigid, therefore restricting independent motion of the feet and inhibiting natural crawling motion of the child.

Our design team was approached by a client requiring the development of a new orthosis to correct the deficiencies in current devices while providing a more affordable brace option. Upon examination of the flaws in current designs, three main design objectives were identified: i) the bar must allow mobility to facilitate the child's crawling, and its length must be adjustable to match the child's growth throughout the entire treatment; ii) the boots must be able to be put on and secured more efficiently while proper abduction and dorsiflexion angles of the foot are maintained, for which the client favored alternatives to the existing belt straps; iii) the design must have a more affordable retail cost than existing designs, consequently a predefined criteria from the client was that 3D printing techniques be used where possible.

PRODUCT DESIGN

The design was divided into three main areas: the bar, the boot, and the mechanism that attaches the bar to the boot (Figure 1).

The bar design consists of two aluminum 6061 T6 pieces. Each piece has two bolt holes on the inside end and 4 bolt holes on the outside end. The inside holes are used to connect the two bars together in either a pinned or locked configuration. The pinned configuration allows movement to facilitate a more natural crawling motion. The outside holes on the bar permit incremental length adjustments to match the shoulder width of the child for comfort. The bar is designed to span the average change in shoulder width undergone by a child from ages 0 to 4 so it can be used for the entire duration of the treatment.

The attachment mechanism was designed to serve two main purposes. First, to attach the boot and bar assemblies. Second, to set the abduction angle. It consists of a top and a bottom clip. Seventy degrees of abduction, in 10 degree increments, can be achieved by changing the positions of the top and bottom clips relative to one another. Typically, the prescribed angle of abduction does not change throughout the course of treatment. The range from 0-70 degrees allows flexibility to achieve the spectrum of angles a doctor may prescribe. The top clip connects to the bottom of the boot with a quick release mechanism which facilitates the process of inserting and removing the boots from the bar. Both the top and the bottom attachment mechanism clips are 3D printed as single Acrylonitrile-Butadiene-Styrene (ABS) pieces.

The boot is also printed as one ABS piece. It features three Nylon webbing straps, which are used to maintain foot position. These are secured using Velcro and a quick release buckle. These straps are easier to secure and more comfortable than belt straps typically used in clubfoot AFOs. The underside of the boot has a compartment compatible with the top attachment mechanism to quickly secure it to the bar.

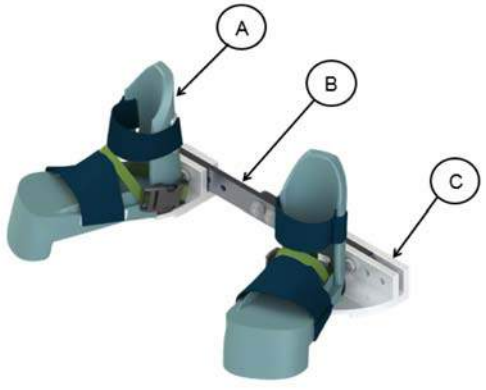

Figure 1: Final design with labeled major components; A: boots, B: bar and C: attachment mechanism.

Copyright 2016 The Organizing Committee for the 2016 Summer Biomechanics, Bioengineering and Biotransport Conference

INNOVATION

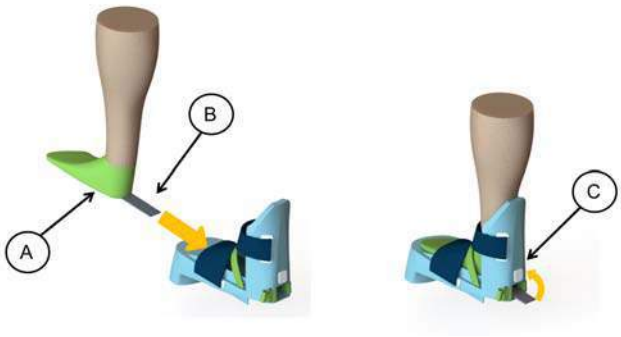

Figure 2: Sock-tab function; A: sock, B: Velcro tab and C: Velcro connection

Conventional clubfoot braces are difficult to properly put on and secure. Upon careful review of existing designs, two main difficulties were identified: proper insertion of the foot within the boot and maintaining correct foot placement while securing the boot.

These difficulties require attention because placement of the feet within the boots is needed for effective treatment. To ensure proper dorsiflexion and abduction, the child's heel needs to be in complete contact with the back of the boot. A sock-tab accessory was designed to address this issue. The sock-tab is simply a sock with a Velcro tab sewn at the heel (Figure 2). This tab can be pulled through an opening at the heel of the boot to easily align the heel at the back of the boot. The Velcro strip on the tab attaches to a corresponding Velcro piece on the back of the boot, keeping the foot in place while the boot straps are secured. This accessory eases the process of inserting the foot, allowing inexperienced people such as family members or babysitters to put on the boots.

FEASIBILITY ANALYSIS

Anthropometric data of the strength of children was used to define worst case loading scenarios for the device. The analysis varied depending on the material of the part being analyzed. The microstructure of 3D printed materials is anisotropic because of the linear printing pattern of the polymer jet; therefore, the mechanical properties of the 3D printed part will be orthotropic. Parts manufactured using commercial 3D printers are printed as a shell and are filled with infill. The latter does not bear a significant portion of the load; therefore, the structures must be interpreted as shells. To account for the shell-like structure, the maximum stresses were scaled using correction factors that accounted for the effect of the change in the geometry on the particular loading scenario. The values of the maximum stresses were determined using hand calculations and FEM simulations. The nominal stresses were then scaled using the correction factors to obtain the corrected stresses, and then compared to the material's failure stress.

The distortion energy failure criterion for ductile materials was used for the analysis of the aluminum bar. The maximum stresses for the different loading scenarios were determined to ensure that the bar will not be loaded more than at an acceptable stress level, much less than the yield strength.

All loading scenario stresses for the bar and 3D printed pieces were below the failure stress. Therefore, the device should not fail under anticipated loading conditions.

BUDGET & MARKET ANALYSIS

The budget for the prototype was required to be under $100. All components were donated from various departments of the University of Alberta and our client so no funds were spent making the prototype. However, a detailed breakdown of the expected part costs can be seen in Table 1.

Table 1: Breakdown of Part Costs for Clubfoot Orthosis

Parts	Quantity.	Total Price (CAD$)
Attachment components (screws, nuts, washers etc.)	22	1.07
Buckle	2	3.80
Velcro	6	0.92
Straps	6	1.68
Adhesive Foam	2	0.44
Bar	2	22.05
Top Attachment	2	2.11
Bottom Attachment	2	7.35
Boot	2	29.08
Total	-	**68.50**

The client plans to deal with customers directly in the Edmonton and Calgary area using a website to place orders. The product is currently being tested by the client and user feedback is being collected. Our client intends to use crowd funding through an organization such as Kickstarter to source funds and potentially start making early sales. This would also enable the start of early production. The client has connections with patient populations diagnosed with clubfoot, a clubfoot clinic, and some orthotists to whom he can pitch the product. The initial scale of manufacture for the product is of 1000 units. At this scale, the material and manufacturing costs of the orthosis amount to $69.00. The average retail cost of the current products on the market is $580.00; this allows for substantial flexibility in our products' final retail cost which is to be determined by the client. The largest investment cost will be the accrual of a 3D printer. The 3D printer that was selected by the client costs $55,000. The large price is a consequence of the quality desired in the product.

ACKNOWLEDGEMENTS

Mr. Ryan Skinner (client); Professor Zengtao; Ms. Kimberley Giesbrecht; Mr. Rob Bouma; Mr. Jonathon Schofield; University of Alberta department of physics machine shop.

REFERENCES

[1] Su, Yuxi, and Guoxin Nan. "Manipulation and Brace Fixing for the Treatment of Congenital Clubfoot in Newborns and Infants." BMC Musculoskeletal Disorders (2014) Web.
[2] Zhao et al. "Relapse of Clubfoot after Treatment with Ponseti Method and Brace" Clinics in Orthopedic Surgery. Vol. 6, No. 3, (2014) Web.

Copyright 2016 The Organizing Committee for the 2016 Summer Biomechanics, Bioengineering and Biotransport Conference

SB³C2016
Summer Biomechanics, Bioengineering and Biotransport Conference
June 29 –July 2, National Harbor, MD, USA
SB³C2016-575

BEST PRACTICES IN TEACHING BIOMECHANICS: CONNECTING BIOMECHANICS BEYOND THE CLASSROOM

Laurel Kuxhaus

Mechanical & Aeronautical Engineering
Department
Clarkson University
Potsdam, NY, USA

INTRODUCTION

Engineering students must attain technical proficiency in their chosen discipline. Developing this proficiency often relies on analysis of 'textbook problems' which are typically simplified versions of real-life scenarios. As such, students perceive this disconnect between their classroom studies and real-world problems. Making the connections between classroom content and life outside the classroom is both challenging and essential. Furthermore, instances of academic dishonesty are reduced when students can identify the importance of classroom topics to their lives, as these types of activities increase students' intrinsic motivation for learning. [1]

Topics covered in biomechanics classes have clear application to life outside the classroom, from injury prevention and healing to the mechanics of pulmonary circulation. However, transferring the skills learned in the classroom to real-life applications can pose a barrier for students. For example, students will likely not perform a full finite element model to analyze their grandmother's pending hip replacement (though they may be interested in reading about the results of such models.) This abstract presents some ready-to-implement activities to connect biomechanics content directly to students' experiences outside of the classroom.

METHODS

The activities described here were employed to foster connection between content learned in the classroom to students' lives outside the classroom. All can be integrated into a typical classroom setting without radical disruption of an existing course syllabus and schedule. The author has implemented these in her undergraduate biomechanics class, which typically attracts 30-35 students, primarily from Mechanical and Chemical Engineering. These activities are intended to be customized to individual classrooms as needed. Each activity is described, and followed by observations from implementation and some suggested variations.

Popular Press Assignment

Description: The goal of the popular press assignment is for students to connect popular media reporting of biomechanical studies to the source of the findings. Ultimately, students compare the peer-reviewed scientific article to the media report.

Students start with a news article that reports a finding from a biomechanical study that has been published recently (that is, within the current semester.) The story can be from any media source; popular sources include the NY Times, IFL Science, and cnn.com. The article must contain sufficient information about the authors and/or the peer-reviewed publication to find the source article. Students must then find the peer-reviewed article (or articles) referenced in the news story.

After reading both, students must write a short (one-page) essay summarizing the scientific findings and comparing/contrasting the peer-reviewed article with the news report thereof. Students are asked to consider the accuracy and completeness of the news story.

Following this analysis, students share their observations in small group discussions (3-4 students per group.) The class discussion concludes with one person from each group summarizing their story for the class, and a tally of how many of the group's stories "got it right", "sort of got it right", and "were pretty much wrong." Students were assessed based on their written essay (including documentation of their news story and journal article), and participation during the in-class discussion.

Observations and Variations: Students are generally able to complete this assignment; common pitfalls include procrastination (which may

Copyright 2016 The Organizing Committee for the 2016 Summer Biomechanics, Bioengineering and Biotransport Conference

not allow sufficient time for an Interlibrary Loan article to arrive) or difficulty in finding an article (searching for "knee replacements" may yield better news results than "biomechanics"). The general conclusion is that popular media reporting of biomechanics studies gets most of the facts right, though is often incomplete. Possible variations on this activity include having the students format their essay as a letter to the editor, with a concluding statement about the media's responsibility to ensure accuracy when reporting about biomechanics. [1]

TED-style Talks

Description: With the widespread popularity of TED (Technology, Entertainment, and Design) Talks, [2] this format is nearly ubiquitous in the consciousness of today's college students. Hallmarks of TED talks include engaging presenters with minimal visual aids and clear take-home messages. The topics of TED talks vary widely. Asking students to give a TED-style talk encourages connection to the world outside of the classroom. This activity is particularly well-suited to an end of semester time (such as: during a scheduled Final Exam period.)

In the author's class, students gave TED-style talks subject to the following constraints: 1) the length had to be 4:00-4:30 minutes (so that all students could present within the allotted time); 2) the topic could be anything, so long as there was at least one reference to a specific biomechanics example somewhere; 3) students were permitted one static (animation-free) PowerPoint slide, from a template that included a countdown timer. Logistically, slides were assembled in a random order (with the next speaker's name appearing on the slide) and set to auto-advance at the end of the maximum allotted time. Students were encouraged to be creative in both their topic selection and delivery.

Students were assessed on both their preparation and delivery. An in-class worksheet guided students through a brainstorming activity to explore possible topics and get feedback from their peers. Additional aspects of student assessment included preparing their PowerPoint slide by the specified deadline, and documenting two instances of practicing their talk (at least once with a video recording, and at least once in front of another person). The presentation delivery was evaluated on its timeliness, the effectiveness of the visual aid, elocution and eye contact, and creativity. A panel of judges from the community without expertise in biomechanics was invited to select awardees for Best Overall Presentation and one Honorable Mention. Students also voted for an Audience Choice award.

Observations and Variations: From the instructor's perspective, this activity was worthwhile; students were highly engaged and motivated to give a strong presentation, and the topics of the talks were extremely diverse. Some students built their talks around biomechanics (such as: the history of high heels and gait); others had a more motivational appeal (such as: what one's legacy should be), or high relevance to college student life (such as: binge drinking). The most common, though rare, pitfalls were a short presentation or a nervous presenter. Most students reported that the required practice helped them stay within the time limits. Anecdotally, students reported that they found this activity worthwhile and more enjoyable than preparation for a standard exam. Most had not previously recorded themselves giving a presentation, and were surprised at their own mannerisms and stage presence. Possible variations of this assignment might include narrowing the topic further (e.g., requiring it to be relevant to sports performance), or modifying the format. For example, Ignite talks [3] place more emphasis on the display of visual aids.

Short Writing Exercises (can be used in class, on exams, or other)

Description: As previously-described [4], and inspired by "Emergency Assessments" [5], this technique encourages students to connect their course-related experiences to their present and future lives outside the classroom. Students write in response to a prompt, such as:

> *You've applied for a job as a technical consultant for the next Batman movie. They liked your application and have called you in for an interview. The person doing the hiring says "I see that you have taken a course in Biomechanics. How will a background in that make you a better member of our crew?" What will you reply?* (modified from [5])

Observations and Variations: Students seem to find these exercises enjoyable; some have commented that questions like this are helpful to think about in anticipation of job interviews. Pitfalls in this activity are rare, though some students are unfamiliar with Batman. The writing prompt can vary; possible ideas include asking students to design a web page for a summer biomechanics camp for middle-school students (see [1, 4]), or name particular search tools (e.g., PubMed) and search terms that they might use to help an elderly relative learn what to expect from an anticipated hip replacement.

DISCUSSION

All of these activities foster intrinsic motivation for learning, and therefore are challenging for students to plagiarize. [1] In addition to fostering intrinsic motivation [1], these activities develop lifelong learning skills. In the Popular Press Assignment, students observe firsthand the inaccuracies inherent with news reporting of scientific results and the importance of critically reviewing such stories. Students may continue to seek source material throughout their lifelong learning. The TED-style talk assignment fosters good presentation preparation by requiring students to view a practice of their own talk, and then practice again. Students may continue to use this technique to prepare presentations in the workforce. Short writing exercises encourage both reflective thinking and connection to extracurricular activities. Additional activities, such as Journal Clubs can also help students connect classroom knowledge to other aspects of their lives; most students in a biomechanics journal club have discussed their journal club articles outside of the classroom. [6] These activities are also beneficial to the instructor; reading student responses can inform future classroom discussions.

In conclusion, these activities encourage students to connect their classroom experiences to their extracurricular lives. All can be implemented into existing courses with little disruption of the structure.

ACKNOWLEDGEMENTS

The author thanks her students for their willingness to try these activities in class.

REFERENCES

[1] Lang, J. Cheating Lessons. Harvard U. Press. 272pp. (2013)
[2] TED talks, https://www.ted.com/talks
[3] Ignite talks, http://www.ignitetalks.io/
[4] Kuxhaus, L. et al, SB3C (2015).
[5] Huston, T. Teaching what you don't know. Harvard U. Press. 320pp. (2012).
[6] Kuxhaus, L. et al, World Congress of Biomechanics. (2014)

Copyright 2016 The Organizing Committee for the 2016 Summer Biomechanics, Bioengineering and Biotransport Conference

SB^{3}C2016
Summer Biomechanics, Bioengineering and Biotransport Conference
June 29 –July 2, National Harbor, MD, USA
SB^{3}C2016-576

GENERATING A SUBJECT-SPECIFIC MUSCULOSKELETAL MODEL OF THE KNEE USING MOTION CAPTURE DATA AND MEDICAL IMAGING

M. Kazemi (1), H. Sorby (1), T. Besier (1, 2), J. Zhang (1)

(1) Auckland Bioengineering Institute
University of Auckland
Auckland, New Zealand

(2) Department of Engineering Science
University of Auckland
Auckland, New Zealand

INTRODUCTION

Kinematics and load sharing of the knee joint are essential to understanding the mechanical etiology of knee disorders such as osteoarthritis. Tibiofemoral kinematics are controlled by a complex combination of soft tissue constraints and articular contact [1]. Kinematics and load sharing at the tibiofemoral joint can be predicted using computational models generated from medical imaging data [2]. Accounting for subject-specific geometry alters the lengths and moment arms of soft tissues crossing the joint, improving the prediction of *in vivo* joint contact forces compared to 'scaled' generic geometry [3]. However, creating musculoskeletal models from medical imaging data is time consuming and costly, thus limiting their uptake in a clinical setting. Furthermore, there is typically a 'disconnect' in model geometry between musculoskeletal models used to estimate muscle forces and finite element models used to estimate cartilage deformation.

Rigid-body musculoskeletal models typically ignore cartilage deformation due to its small strain compared to the large transformation of the joint segments. It is also common for rigid body models to treat the joint as a mechanical hinge, ignoring cartilage contact. Understanding the influence of body motion on cartilage stress and potential pathology requires deformable, finite element contact models [4]. However, finite element models developed from medical imaging data often rely on rigid-body models for estimates of loads and boundary conditions and only include anatomical information from the imaging field of view.

For computational models to have a clinical impact they must have a consistent representation of patient geometry. Therefore, we need to bridge the gap between rigid-body and finite element models. In addition, the models need to be rapidly generated from routine clinical data.

We present an integrated workflow to rapidly generate subject specific knee models from motion capture and small field-of-view imaging data, implemented in an open source software framework, the Musculoskeletal Atlas Project (MAP)[1] [5]. The workflow can generate models for rigid-body modelling, finite element simulations, and statistical modeling.

METHODS

Our workflow used statistical shape models to combine motion-capture data with MR images of the knee to generate subject specific bone and cartilage meshes 3D magnetic resonance images of the knee (slice thickness: 1.5 mm, pixel size: 0.55 × 0.55 mm, field of view: 12 × 12 cm) from 23 subjects in the supine position with the knee at full extension were segmented using a custom Matlab script. The boundaries of the bony segments (femur, tibia-fibula, and patella) and the articular cartilage surfaces were digitized. Reflective markers were placed on anatomical landmarks and recorded using a motion capture (mocap) system. Using a lower limb statistical shape model [6], marker data and segmented surfaces were fused using a custom MAP Client workflow. Whole-bone surface meshes were predicted from mocap marker locations, while parts of the meshes within the field of view of the MR image were fit to the segmented bone surfaces. Tendon and ligament attachment regions were digitized from a reference subject and embedded on the bone meshes as material points. Thus attachment regions were customized for each subject during mesh fitting. Articular cartilage thickness 'fields' were

[1] https://map-client.readthedocs.org/en/latest/

Copyright 2016 The Organizing Committee for the 2016 Summer Biomechanics, Bioengineering and Biotransport Conference

calculated from the distance between segmented bone surface and corresponding articular cartilage surfaces. Each field was sampled from a dense distribution of material points in the cartilage region on the bone mesh. For each material point, the distance between the closest segmented articular surface and bone surface points along the material point normal vector were considered as cartilage thickness. Segmented and ligamentous attachment zones were embedded on each bone mesh by projection and calculation of their mesh material coordinates. We performed principal component analysis (PCA) to assess variations [7] on the shape and cartilage thickness for all bone and cartilage layers of the knee. We assessed the accuracy of our predicted bone surface geometry by calculating the distance between the closest points on the fitted mesh and the segmented point clouds.

RESULTS

Twenty-three knee models were generated using the MAP-Client workflow, each taking ~22 minutes using a single CPU PC. Each model was composed of femur, tibia-fibula, and patella surface meshes (mean errors of 1.45±0.37, 1.82±0.32 and 1.54±0.78 mm, respectively; distribution in figure 1), tibiofemoral and patellofemoral cartilage thickness fields, and ligament insertion zones (Figure 2).

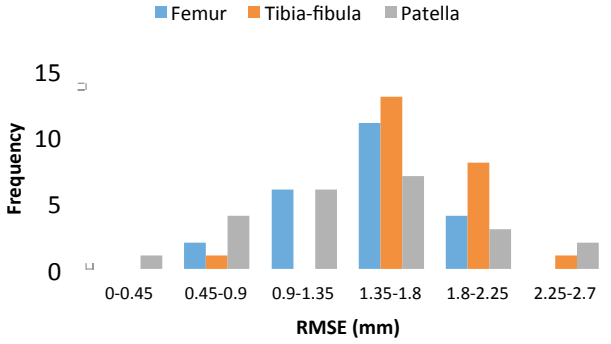

Figure 1: Local fitting error (RMSE) for all subjects.

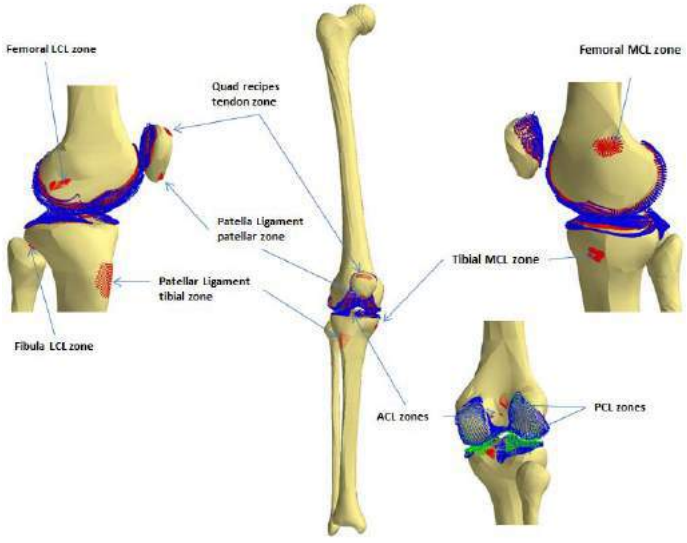

Figure 2: 3D knee model of subject # 1 developed from MRIs and motion capture data. Each model is composed of whole bone surface meshes, cartilage thickness fields (blue), attachment zones (red) and segmented point clouds (green).

DISCUSSION

The presented workflow generated subject-specific knee joint models with embedded muscle and ligament attachments as well as articular cartilage thickness. The models were used to train a statistical shape model of the knee joint for further predictive application. The bone meshes were generated with accuracy close to voxel size of the image. However, it remains to be seen whether these models can adequately predict kinematics and contact pressure in loaded and unloaded joints at various degrees of knee flexion. To achieve this, a deformable knee joint contact model has been developed, using our generated knee models. In addition, the generated models have been used to train a statistical shape model of the knee. This shape model will be used to efficiently generate complete knee model geometries from sparse data.

Our population-based models also have application to use in motion retraining procedures or evaluate of the implant designs and surgical procedures.

ACKNOWLEDGEMENTS

This research was proudly supported by the Royal Society of NZ Marsden Fund.

REFERENCES

1. Morrison, J., *The mechanics of the knee joint in relation to normal walking.* Journal of biomechanics, 1970. **3**(1): p. 51-61.
2. Baldwin, M.A., et al., *Efficient probabilistic representation of tibiofemoral soft tissue constraint.* Computer Methods in Biomechanics and Biomedical Engineering, 2009. **12**(6): p. 651-659.
3. Gerus, P., et al., *Subject-specific knee joint geometry improves predictions of medial tibiofemoral contact forces.* Journal of biomechanics, 2013. **46**(16): p. 2778-2786.
4. Baldwin, M.A., et al., *Development of subject-specific and statistical shape models of the knee using an efficient segmentation and mesh-morphing approach.* computer methods and programs in biomedicine, 2010. **97**(3): p. 232-240.
5. Zhang, J., et al., *The MAP Client: User-Friendly Musculoskeletal Modelling Workflows*, in *Biomedical Simulation*. 2014, Springer. p. 182-192.
6. Zhang, J., et al., *Lower Limb Estimation from Sparse Landmarks Using an Articulated Shape Model.* Computational Methods in Biomechanics and Bioengineering, 2015.
7. Heimann, T. and H.-P. Meinzer, *Statistical shape models for 3D medical image segmentation: a review.* Medical image analysis, 2009. **13**(4): p. 543-563.

Copyright 2016 The Organizing Committee for the 2016 Summer Biomechanics, Bioengineering and Biotransport Conference

SB³C2016
Summer Biomechanics, Bioengineering and Biotransport Conference
June 29 –July 2, National Harbor, MD, USA
SB³C2016-577

Implications of Desiccation Induced Microheterogeneity on Protein Stability

Sampreeti Jena (1), Raj Suryanarayanan (2), Alptekin Aksan (1)

(1) Mechanical Engineering Department
University of Minnesota
Minneapolis, Minnesota, USA

(2) Department of Pharmaceutics
University of Minnesota
Minneapolis, Minnesota, USA

INTRODUCTION

Freeze-drying and desiccation are widely-applied processes to increase the shelf life of food products, enzymes, vaccines and cells. Lyoprotectants are chemicals in the presence of which proteins have been known to retain their stability and native conformation in the face of freezing and drying induced stresses. Disaccharides such as trehalose and sucrose are used as lyoprotectants. The sugar matrix formed by disaccharides, upon vitrification, surrounds the protein and slows down its degradation kinetics. Trehalose especially is favored due to its non-reducing nature, resistance to hydrolysis and high glass transition temperature.

It is very important for the lyoprotectant to be retained amorphous during freeze-drying or air drying. Crystallization or phase separation would render it completely ineffective [1]. Trehalose by itself crystallizes only after prolonged annealing. But recent studies have reported trehalose crystallization while freezing and drying in the presence of readily crystallizing solutes such as mannitol [2].

In the present study, we have explored the effects of desiccation on the physical form of trehalose and its ability to stabilize bovine serum albumin (BSA) during desiccation.

METHODS

Solutions were prepared gravimetrically with ultrapure water. Bovine serum albumin (MW 66.5 kDa, ≥99% Purity, Sigma-Aldrich, St. Louis, MO) and D-(+)- trehalose dihydrate (MW 378.33 kDa, 99.9% pure, Sigma-Aldrich, St. Louis, MO) were used as received.

Fourier Transform Infrared (FTIR) Spectroscopy was used to study the composition of the dried samples at different spatial locations. For analysis, solutions containing 20% (w/w) trehalose in water with an albumin to trehalose ratio of 1:3 (6.67% w/w albumin) were used. This resulted in an albumin mass concentration of 66.6 mg per ml of water.

100 nL of the experimental solution was sandwiched between two CaF2 windows. The windows were propped apart with shims and transferred to the infrared microscope attached to the FTIR spectrometer (Thermo-Nicolet Continuum equipped with a Mercury Cadmium Telluride detector, Thermo Electron, Waltham, MA) equipped with an FDCS 196 (Linkam Scientific Instruments Ltd., UK) freeze-drying cryostage. A constant vacuum of 40 Torr was applied inside the cryostage. During acquisition of spectra we chose a resolution of 4 cm^{-1}, and a total of 128 IR scans were averaged per spectrum in the 4000−930 cm^{-1} wavenumber range. The IR spectra were analyzed using OMNIC (Thermo-Nicolet) software.

RESULTS

Gradual removal of water by application of vacuum resulted in sample vitrification. This was reflected in the shifts in the peak locations of the amide II at 1550 cm^{-1} and the ν-(C-O) peak at 1150 cm^{-1} for BSA and trehalose, respectively. Light microscopy images of the sample clearly showed an interface that gradually advanced from the outer periphery to the center of the sample (Figure 1). It separated the sample into an inner vitrified zone and an outer zone, which was completely dry. IR spectra of the dry regions showed a significantly reduced signal intensity (low signal to noise ratio) due to the absence of water. Spectra obtained carefully from the interface clearly indicated crystallization of trehalose (Figure 2). This was evident from the bifurcation of the ν-(C-H) peak (2970-2910 cm^{-1}), and the ν-(C-O-C) peak (1010-975 cm^{-1}) [3].

Second derivative analysis of amide II peak revealed two peaks. The peak at 1526−1504 cm^{-1} was assigned to intermolecular and antiparallel β-sheet structures, while the band at 1560−1530 cm^{-1} was assigned to a combination of α-helix and β -sheet structures [4]. The % beta sheets defined as (Beta Sheet)/(Alpha Helix + Beta Sheet) was calculated by taking the ratio of the integrated areas of the two peaks obtained from Amide II, as mentioned above. It was observed that spectra obtained from the interface yielded considerably higher percent of beta sheets than the spectra taken from the vitrified interior (Figure 3).

Copyright 2016 The Organizing Committee for the 2016 Summer Biomechanics, Bioengineering and Biotransport Conference

The position of the amide II band can be used to determine the extent of association (hydrogen bonding) and the hydration level of BSA [5]. Amide II in the spectra taken from the vitrified interior was located at (1547-1548 cm^{-1}), which was comparable to the amide II location in spectra taken of the wet sample before desiccation. On the other hand, amide II in spectra obtained from the interface was located at much lower wavenumbers (1544-1545 cm^{-1}).

On fixing the aperture at a given location in the sample with continuous spectra acquisition, distinctive changes in the spectra were observed. The ν-(C-O) peak at 1150 cm^{-1} originates from vibrational stretching of the glycosidic linkage connecting the two glucose pyranose rings in trehalose. Therefore, this peak position was used to determine the flexibility of the glycosidic linkage of trehalose [6]. With the gradual approach of the interface and removal of water, the glycosidic peak shifted to lower wavenumbers until trehalose completely crystallized (Figure 4).

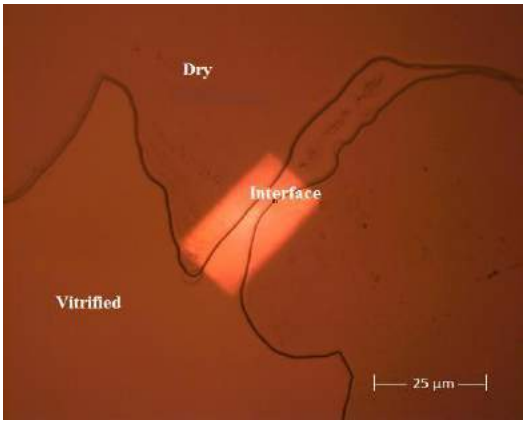

Figure 1: Transmitted Light Microscopy image of the partially dried sample. The bright rectangle is the aperture from which infrared spectra is collected.

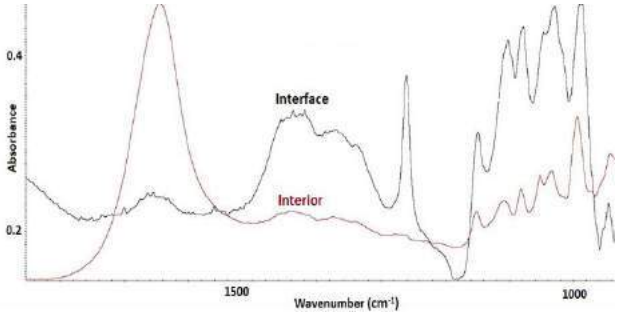

Figure 2: Fingerprint region of overlaid IR spectra obtained from the interface and the vitrified interior.

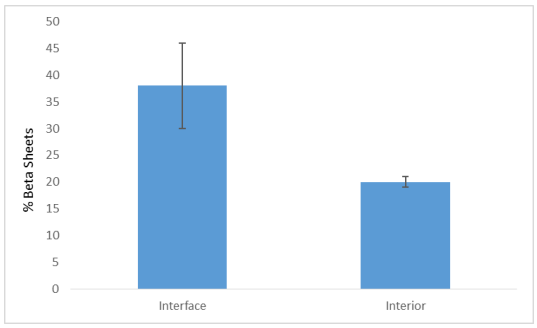

Figure 3: % intermolecular and antiparallel beta sheets calculated using second derivative of Amide II (n = 6).

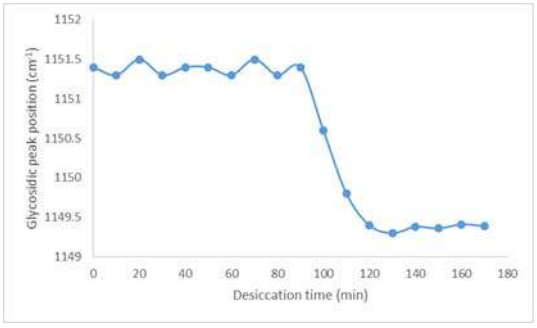

Figure 4: Trehalose glycosidic peak position at a fixed location in the sample as a function of drying time.

DISCUSSION

Desiccation of a solution containing trehalose and BSA resulted in a heterogeneous end product with portions of the sample being completely dry (crystallized trehalose) and others being vitrified (viscous matrix). Upon vitrification, there was a pronounced strengthening in inter-molecular association and local hydrogen bonding. On complete dehydration, these vitrified regions underwent trehalose crystallization. Removal of water resulted in "stiffening" of the trehalose molecule about its glycosidic linkage, followed by trehalose crystallization at the interface. BSA distributed near the interface where trehalose crystallization occurred, showed significantly lower levels of hydration and higher percentage of intermolecular and anti-parallel beta sheets than the BSA in the vitrified interior, clearly indicating unfolding of secondary structure and a possibility of aggregation.

ACKNOWLEDGEMENTS

This research was funded by an NSF grant (CBET-1335936) to A.A.

REFERENCES

[1] Izutsu, K et al., *PharmRres*, 10:1232-1237, 1993.
[2] Sundaramurthi, P et al., *PharmRres*, 27:2384-2393, 2010.
[3] Lin, SY et al., *PharmRres*, 20:1926-1931, 2003.
[4] Van Stokkum, IHM et al., *Biochem,* 34:10508-10518, 1995.
[5] Malsam, J et al., *J Phys Chem B*, 113: 6792-6799, 2009.
[6] Ragoonanan, V et al.,. *Biophys J*, 94:2212-2227, 2008.

Copyright 2016 The Organizing Committee for the 2016 Summer Biomechanics, Bioengineering and Biotransport Conference

SB^{3}C2016
Summer Biomechanics, Bioengineering and Biotransport Conference
June 29 –July 2, National Harbor, MD, USA
SB^{3}C2016-578

REAL-TIME MONITORING OF THE MECHANICAL PROPERTIES OF ENGINEERED TISSUES DURING GROWTH AND REMODELING

Pim J.A. Oomen (1,2), Cees W.J. Oomens (1), Carlijn V.C. Bouten (1,2) & Sandra Loerakker (1,2)

(1) Department of Biomedical Engineering, Eindhoven University of Technology, Eindhoven, Netherlands

(2) Institute for Complex Molecular Systems, Eindhoven University of Technology, Eindhoven, Netherlands

INTRODUCTION

One of the hallmarks of biological tissues is their capability to grow and remodel in response to changes in their environment. It has been hypothesized that this occurs to maintain a certain mechanical homeostasis, yet there is no consensus as to which mechanical quantity is the driving factor behind tissue growth and remodeling [1]. A deeper knowledge of this mechanical homeostasis will greatly benefit the field of tissue engineering as well as our understanding of healthy and pathological tissue development.

Currently, we aim to study the mechanical tissue homeostasis in growing tissues by quantifying the evolution of stress and stretch is to be quantified. To this end, multiple tests on a single sample are required over time and, therefore, most of the common biomechanical tests such as biaxial tensile tests are not applicable. The presence of cell traction-induced prestretch further complicates testing [2,3].

In order to real-time estimate the mechanical properties of growing tissues, we developed a nondestructive mechanical test and inverse analysis method, which aims to overcome issues that are typically encountered when mechanically characterizing biological tissues, such as tissue thickness and prestretch.

METHODS

Circularly constrained tissue-engineered samples were exposed to a dynamic hydrostatic pressure to induce tissue growth and remodeling. Ultrasound (Esaote MyLab 70 with a 7.5 MHz linear transducer) is used to noninvasively visualize the samples during deformation (Figure 1). A custom image processing script was developed in Matlab to automatically obtain the tissue thickness, profile displacement, in-plane stretches and curvatures (Figure 1).

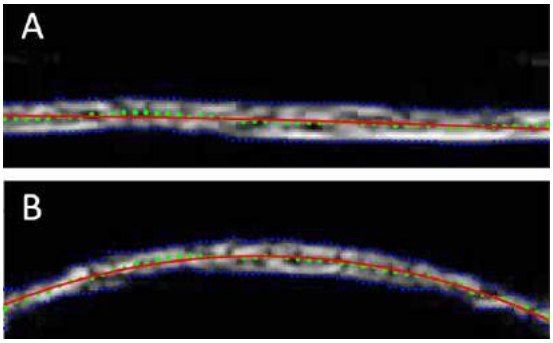

Figure 1: Ultrasound images and profile tracking of an engineered tissue at 0.0 kPa (A) and at 4.5 kPa (B).

The inverse analysis to estimate the material parameters comprises two steps. The first step is computationally cheap yet its accuracy is limited by the assumptions made in shell theory (i.e. limited thickness) and does not account for prestretch. Therefore, the parameter estimation of this step is used as an initial estimate in step 2, which is computationally costly yet provides a more accurate solution.

In the first step, classical shell theory is used to compute the in-plane principal tensions T_1 and T_2 (Figure 2A) directly from the experiment, as only pressure (p) and principal curvatures (κ_1 and κ_1) are required:

$$T_1 = \frac{p}{2\kappa_2}$$
$$T_2 = \frac{p}{\kappa_2}\left(1 - \frac{\kappa_1}{2\kappa_2}\right) \quad (1)$$

Copyright 2016 The Organizing Committee for the 2016 Summer Biomechanics, Bioengineering and Biotransport Conference

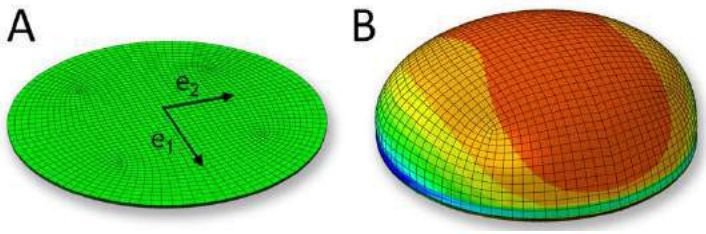

Figure 1 Finite element model of the bulge test before (A) and after (B) pressure application.

The in-plane tensions can also be obtained by calculating the integral of the in-plane Cauchy stress (σ_1 and σ_2) through the sample thickness t:

$$T_1^{\text{est}} = \int_{-t/2}^{t/2} \sigma_1(\lambda_1, \xi)\, dz$$
$$T_2^{\text{est}} = \int_{-t/2}^{t/2} \sigma_2(\lambda_2, \xi)\, dz \quad (2)$$

where $\lambda_{1,2}$ are the in-plane stretches as function of tissue depth [4] and ξ is a set of material parameters. A trust-region algorithm was used to minimize the difference between $T_{1,2}$ and $T_{1,2}^{est}$ and hence obtain an initial estimate of the material parameters.

In the second step, a full inverse finite element (FE) method is employed, where the estimate from the first step is used as initial estimate to dramatically decrease computational time. The experimental setup was mimicked with a FE model in Abaqus (Figure 2) using quadratic brick elements. The material parameters are estimated by minimizing the difference between the measured and simulated profile displacement. A fiber-reinforced material model was used, where the matrix contribution is modeled by a Neo-Hookean material and the fiber component by a Holzapfel model with either an isotropic or anisotropic fiber distribution [5,6].

In order to validate the proposed method, virtual experiments were generated by performing FE simulations (Figure 2) with different sample thicknesses (0.1, 0.2, 0.3, 0.4 and 0.5 mm) and prestretch magnitudes (1.0, 1.1, 1.2 and 1.3 at a thickness of 0.1 mm). The sample diameter was set at 10.0 mm and a pressure of 8.0 kPa was gradually applied while displacement at the outer nodes was suppressed.

RESULTS

The first step of the parameter estimation of the virtual experiments yielded parameter sets that were close to, yet did not match the input parameters exactly (Figure 3). For both the isotropic (not shown) and anisotropic samples, the analytical method over-estimated the stiffness of the material, which became more severe when a prestretch was introduced in the samples (Figure 3B).

By using these parameter sets as initial estimates in the full inverse FE method, the estimated parameters matched the input parameters exactly for all sample thicknesses and prestretches (Figure 3). When performing the full inverse FE method with a random initial estimate rather than with the outcomes from the analytical estimation, the number of increments until convergence increased two-fold, while in two cases convergence was not even reached.

DISCUSSION

Previous studies have commonly employed either analytical or inverse FE approaches to estimate the material parameters from a mechanical test. In the current method, we combined these two approaches to retain the advantages of both while eliminating their disadvantages. The analytical approach significantly reduces the computational cost and instability of the full inverse FE method by

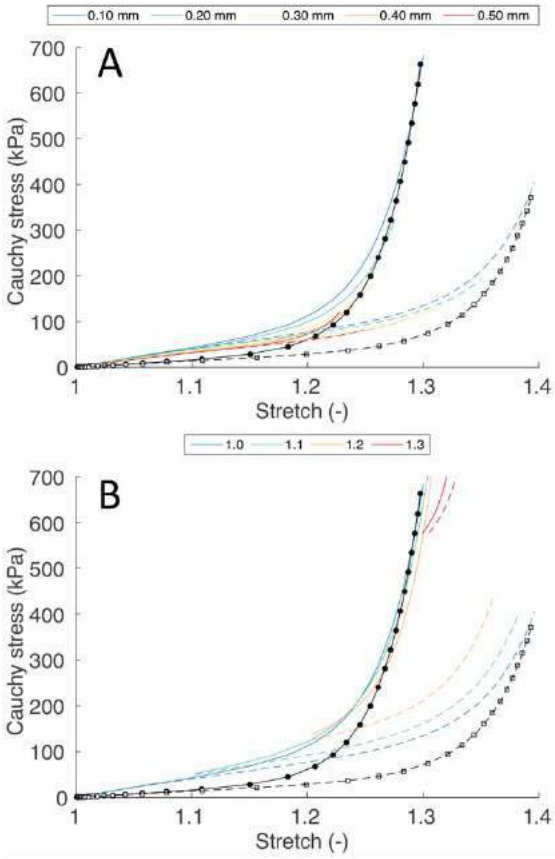

Figure 3: Estimated stress-stretch curves for anisotropic virtual simulations with various thicknesses (A) and prestretches (B). The circular and square markers indicate the true behavior in the fiber and cross-fiber direction, respectively; and the lines indicate the estimated behavior of the shell analysis (colored) and all finite element fits (in black, overlapping each other).

providing a rapid initial estimate; while the full inverse FE method is capable of a more accurate parameter estimation than the shell analysis on its own.

Currently, experiments are being performed to validate this method with rubber and tissue-engineered samples and compare the results with biaxial tensile tests. The tissue prestretch in tissue-engineered samples is still to be measured, yet is known to be stable over time [2].

In conclusion, we presented a method to characterize the mechanical behavior of isotropic and anisotropic planar tissues, which can be used to track the mechanical properties of growing tissues over time. A combination of experimental and inverse methods was employed that is nondestructive and is not limited by prestretch or excessive tissue thickness.

ACKNOWLEDGMENTS

The research leading to these results has received funding from the European Union's Seventh Framework Programme under Grant agreement n° 604514 (ImaValve).

REFERENCES

[1] Humphrey, JD et al., *Nat Rev Mol Cell Biol*, 15:802-812, 2014.
[2] Van Vlimmeren, AA et al., *BMMB*, 11(7):1015, 1027.
[3] Rausch, MK and Kuhl, E, *J Mech Phys Sol*, 61:1955-1969, 2013.
[4] Tonge, TK et al., *Acta Biomater*, 9:5926-5942, 2013.
[5] Driessen, NJB et al., *J Biomech Eng*, 127:494-503, 2005.
[6] Loerakker, S et al., *J Biomech*, 46(11):1792-1800, 2013.

Copyright 2016 The Organizing Committee for the 2016 Summer Biomechanics, Bioengineering and Biotransport Conference

SB^{3}C2016
Summer Biomechanics, Bioengineering and Biotransport Conference
June 29 –July 2, National Harbor, MD, USA
SB^{3}C2016-579

NON-NEWTONIAN VS. NUMERICAL RHEOLOGY: PRACTICAL IMPACT OF SHEAR-THINNING ON THE PREDICTION OF STABLE AND UNSTABLE FLOWS IN INTRACRANIAL ANEURYSMS

M. Owais Khan (1,2), David A. Steinman (1), Kristian Valen-Sendstad (2)

(1) Mechanical & Industrial Engineering
University of Toronto
Toronto, Ontario, Canada

(2) Simula Research Laboratory
Lysaker, Norway

INTRODUCTION

Risk associated with treatment options of incidentally detected, asymptomatic, unruptured intracranial aneurysms can often exceed the natural risk of aneurysm rupture[1]. Image-based computational fluid dynamics (CFD) is arguably a robust tool to estimate hemodynamic forces, particularly variants of wall shear stress (WSS), and to investigate their role in initiation, growth, and rupture of intracranial aneurysms[2]. Although plausible correlations between various hemodynamic metrics and aneurysm rupture status have been derived from retrospective image-based CFD studies, criticism has been raised regarding the use of CFD in aneurysm rupture risk assessment[3], partially aimed towards CFD-modeling assumptions and uncertainties.

The effect of non-Newtonian vs. Newtonian rheology models on aneurysm CFD has been investigated in previous studies[4,5], but there exists no consensus regarding its impact. One challenge in interpreting these findings is that there is usually little context of what constitutes a 'significant' impact of rheology model on hemodynamic predictors of rupture status. Further, a key deficiency in the majority of these and other non-Newtonian aneurysm CFD studies is that they typically rely on low-order stabilized numerical schemes, previously termed normal-resolution (NR)[6], that introduce artificial numerical viscosity to avoid numerical instabilities. Therefore, it is difficult to distinguish between the effects of numerical viscosity versus non-Newtonian viscosity, and which of the two has a dominant effect on the hemodynamic indices.

The effects of added numerical viscosity have shown to inevitably predict laminar and stable flow patterns at the reported temporal and spatial resolutions[6]. This latter point is important, as recent CFD studies using a high-resolution (HR) solution strategy have highlighted the presence of "turbulent-like" flows that alter the hemodynamic stimuli. Since these HR simulations used Newtonian rheology for blood, it is not completely understood how the shear-thinning non-Newtonian rheological models would alter the "turbulent-like" flow instabilities. The aim of the present study was two-fold: 1) To investigate the effect of non-Newtonian rheology in intracranial aneurysms using an HR strategy with models previously shown to exhibit flow instabilities; and 2) To contextualize the practical impact of non-Newtonian rheology against artificial numerical viscosity introduced by common-place NR solution strategies.

METHODS

We focused on three previously published middle cerebral artery (MCA) aneurysm cases that exhibited flow patterns that were stable (case8), mildly unstable (case9), or highly unstable (case16)[7]. These models were meshed to have ~800,000 elements with 4 boundary layers. Pulsatile simulations were run with 5600 time-steps per cardiac cycle. We applied a cross-sectional average velocity of 0.37 m/s resulting in cycle-averaged flow rates of 1.11, 1.93, and 2.12 mL/s. A fully developed Womersley velocity profile was applied at the inlet, and zero pressure was specified at the outlets. A second-order accurate, minimally dissipative energy-preserving CFD solver was used with linear tetrahedral elements[7]. Newtonian blood viscosity and density were assumed to be 3.690 mPa-s and 1.056 g/cm^3, respectively. We then ran the exact same simulations using a modified-Cross viscosity model to simulate the shear-thinning properties that dominate blood's non-Newtonian behavior, using published parameters. To contextualize the effects of non-Newtonian rheology against solver strategy, we performed the same Newtonian simulations using the exact same meshes and a typical NR solver. To be consistent with the literature and our previous refinement study, for the NR simulations, we reduced the temporal resolution to 1400

Copyright 2016 The Organizing Committee for the 2016 Summer Biomechanics, Bioengineering and Biotransport Conference

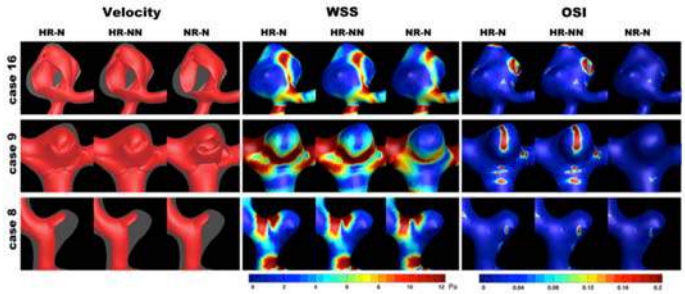

Figure 1: Qualitative impact of Newtonian (N) vs. non-Newtonian (NN) rheology and solution strategy on isosurfaces of time-averaged velocity, and surface distributions of WSS and OSI. HR refers to "high-resolution" and NR refers to "normal-resolution" CFD strategy.

time-steps/cycle (i.e $dt = 0.7ms$). We used a first-order accurate discretization in time to mimic the default and recommended settings in most widely used commercial CFD solvers. This solution strategy involves adding artificial numerical viscosity to stabilize the solution to account for numerical stability criteria not being met at this temporal resolution[8]. The impact of non-Newtonian rheology and solution strategy was qualitatively evaluated via volumetric maps of cycle-averaged velocity and shear rates, and surface maps of WSS magnitude, and oscillatory shear index (OSI). For quantitative evaluations we computed the following: dome-averaged WSS and dome-maximum WSS (MWSS), both normalized to parent artery WSS, and dome-averaged OSI.

RESULTS

Qualitative results of time-integrated quantities are shown in **Figure 1**. First focusing on velocity isosurfaces from Newtonian vs. non-Newtonian HR simulations (HR-N vs. HR-NN), we observe negligible visual differences for velocity for all cases. However, when comparing Newtonian HR vs. NR solutions (i.e., HR-N vs. NR-N) differences are evident, particularly for case 16 and 9, models that have previously been shown to exhibit high frequency fluctuations. Now looking at the qualitative WSS maps, it is evident that there are negligible differences between HR-N and HR-NN. However, differences are evident between HR-N and NR-N for cases 9 and 16, due to the different velocity pattern and shifted impingement region, respectively. Finally, for OSI, there again are negligible differences between HR-N and HR-NN. In contrast, OSI has been completely suppressed by the NR-N simulations. These qualitative results indicate that, for time-integrated quantities and frequency content, non-Newtonian rheology has *relatively* negligible impact on the hemodynamic environment when compared to solution strategy.

More practically, the quantitative impact of rheology vs. solution strategy on proposed scalar metrics of rupture status is shown in Figure 2. As seen from the plot, non-Newtonian rheology has relatively negligible impact on WSS, MWSS and OSI metrics when compared to solution strategy. WSS and MWSS scalars are noticeably reduced due to NR-N scheme, particularly for cases 9 and 8. Similar trends are observed for OSI; however, in this case the rank ordering of cases is altered by the NR-N approach, owing to the steep reductions in OSI for cases 9 and 16. These results indicate that quantitative scalar metrics are sensitive to solution strategy but not non-Newtonian rheology.

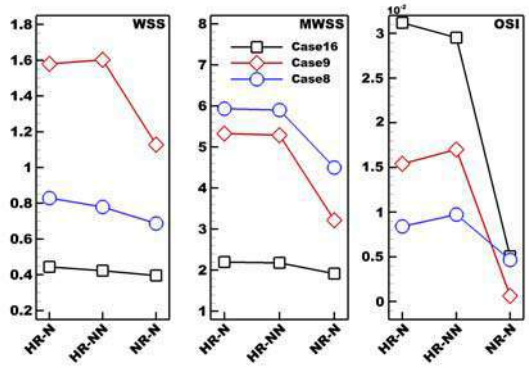

Figure 2: The quantitative impact of rheology and solution strategy on selected reduced hemodynamic indices, as indicated at the top right corner of each plot.

DISCUSSION

Based on our results, it seems evident that CFD solution strategy has greater impact on hemodynamic parameters compared to non-Newtonian rheology. To better understand why our conclusions differ from those of Xiang et al.[5], we note that those authors based their conclusions on normalizing WSS and viscosity values from the non-Newtonian simulations by the respective point-wise values from the Newtonian simulations, which they denoted WSS* and viscosity*, respectively. Indeed, as shown in Figure 3, results viewed in this way seem to suggest non-negligible overestimation of WSS (i.e., WSS* < 1) and similar overestimation of viscosity (i.e., viscosity* > 1), coinciding, as expected, with regions of low shear rate also highlighted in Figure 3. For example, focusing on the bleb-like region of case 16, marked in red circle, the Newtonian and non-Newtonian WSS values in this region were 0.45 Pa and 0.32 Pa, respectively, giving WSS* ~ 0.7 and suggesting a ~40% overestimation of WSS by the Newtonian simulation. However, one could argue that such differences in already-low WSS regions have questionable physiological or mechanobiological relevance.

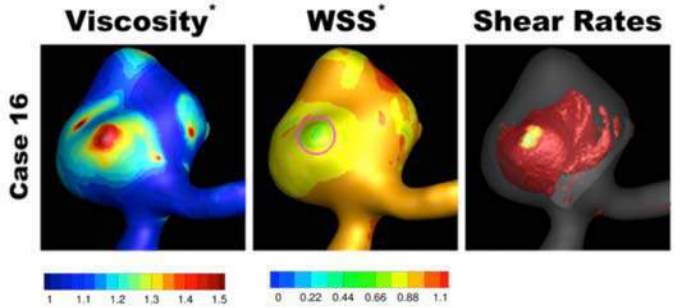

Figure 3: Normalized quantities and shear rates.

REFERENCES

[1] Wiebers D., *Lancet.* 2003;362(6):103-110.
[2] Cebral, J. R., et al., *AJNR* 26.10 (2005): 2550-2559.
[3] Kallmes, D. F., *AJNR* 33.3 (2012): 395-396.
[4] Xiang, J., et al., *JNeurointerventionalSurgery* (2011):
[5] Evju, Ø. Et al., *JBioMech*46.16 (2013): 2802-2808.
[6] Valen-Sendstad, K. et al., *AJNR* 35.3 (2014): 536-543.
[7] Mortensen, M., et al. CompPhysComm 188 (2015): 177-188.
[8] Khan, M. O., et al., *AJNR* (2015).

Copyright 2016 The Organizing Committee for the 2016 Summer Biomechanics, Bioengineering and Biotransport Conference

SB^{3}C2016
Summer Biomechanics, Bioengineering and Biotransport Conference
June 29 –July 2, National Harbor, MD, USA
SB^{3}C2016-580

THE FDA'S NOZZLE BENCHMARK: IN THEORY, THERE IS NO DIFFERENCE BETWEEN THEORY AND PRACTICE. BUT, IN PRACTICE, THERE IS.

Aslak W. Bergersen (1), Mikael Mortensen (1,2), Kristian Valen-Sendstad (1)

(1) Simula Research Laboratory
Lysaker, Norway

(2) Department of Mathematics
University of Oslo
Oslo, Norway

INTRODUCTION

Cardiovascular diseases are burdening the healthcare systems and the costs are expected to rise in the years to come[1]. Although systemic risk factors have been associated with higher prevalence of cardiovascular diseases, it has been shown that blood flow induced abnormal wall shear stress is correlated with disease development at specific locations. However, in contrast to traditional engineering disciplines, geometries, boundary conditions, flow conditions, and fluid properties are not necessarily well defined in biomedical engineering because many studies are retrospective. Additionally, one often has to rely on medical image segmentation[2] that can involve a significant amount of manual labor that may introduce noise and variability. Verification and validation is therefore especially important and the U.S. Food and Drug Administration (FDA) therefore devised a benchmark of a *standard model of a generic medical device, consisting of a nozzle with a conical change in diameter at one end of the throat, and a sudden change at the other end*.

The first round of experiments and computational fluid dynamic (CFD) simulations showed an acceptable agreement for low and high Reynolds number flows; however, large discrepancies were found for the weakly transitional flows with a Reynolds number of 3500[3]. The aim of this study is therefore twofold: 1) To validate our open-source CFD solver *Oasis*[4] against experimental data, 2) Investigate the Reynolds number flows that showed the largest variability (Re = 3500).

METHODS

The computational domain was chosen to be -0.12 to 0.20 m, relative to the sudden expansion. Meshes were created using ICEM-CFD (Ansys Inc., Canonsburg, PA, USA) with 4 boundary layers. In total 4 meshes where produced consisting of 5, 10, 17 and 28 million tetrahedron cells, refereed to as 5M, 10M, 17M, and 28M, respectively. We chose to specify a constant node spacing to ensure that the meshes can be reproduced. The time step was kept fixed at $\Delta t = 10^{-5}$ s for all simulations which was based on setting the Courant number to ½ for the 28M mesh. The initial conditions were set to zero and we specified a parabolic inlet velocity profile, no-slip at the wall, and zero pressure at the outlet. CFD simulations were performed using our open-source finite element method-based solver, *Oasis*[4], where special care has been taken to ensure a second-order accurate temporal and spatial discretization so that the numerical solution of the Navier-Stokes equation is energy kinetic preserving and minimally dissipative[5].

We recorded the velocity as a function of time along the centerline in multiple points. We then decomposed the instantaneous velocity u_i in to the time averaged velocity $\bar{u}$ and the fluctuating velocity u', i.e., $u_i = \bar{u} + u'$. The power spectral density was computed based on $|u'|$ using Welch's method, Hann windowing function, and 8 segments with 50% overlap. The kinetic turbulence is defined as $k(t) = \frac{1}{2}(u'^2 + v'^2 + w'^2)$.

RESULTS

Figure 1 (top) shows the instantaneous velocity magnitude in a plane at time 1.0 s. Figure 1 (bottom) shows velocity traces, turbulent kinetic energy, and power spectral density from 1.0 - 1.1s in rows a, b, and c, respectively. Focusing now on sub-plot 1a and 1b, there are high frequent but low amplitude fluctuations in the 5M simulation, which are confirmed by 1c. Looking at plot 2a and 2b, just

Copyright 2016 The Organizing Committee for the 2016 Summer Biomechanics, Bioengineering and Biotransport Conference

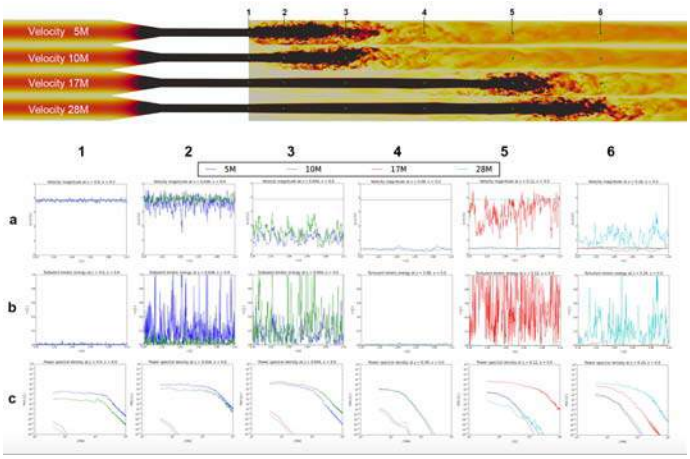

Figure 1: Top of the figure are instantaneous velocity fields at t = 1.0 s. The first row (a) is velocity traces, second (b) is the turbulent kinetic energy, and the last row (c) is the power spectral density of $|u'|$, all from 1.0 to 1.1 s.

downstream of the sudden expansion, the 5M and 10M simulations are clearly unstable, and the velocity at the centerline is high. In plot 2c, the 5M and 10M simulations show that there is a large amount of turbulent energy at a wide spectra as opposed to 17M and 28M. Further downstream in plot 3a we can see that the centerline velocity magnitude is reduced for 5M and that the fluctuations are less high frequent in 3b. This is reflected by 3c where the high frequency components contain slightly less energy, while 10M contains slightly more. On the other hand, 17 and 28M are almost unchanged. Further downstream in plots 4a and 4b both 5 and 10M develop equally; the centerline velocity is stable and contains only small and low frequent fluctuations. In plot 4c, the 17M and 28M simulations show that the instabilities are growing whereas the energy of the 5M and 10M flows are decreasing due to dissipation. Now, 10 diameters downstream of the sudden expansion, the 17M jet breaks down and can be viewed in plot 5a and 5b. The energy spectra plot 5c shows that the 28M simulation also have increased instabilities. In the last column of Figure 1 we can se that the centerline velocity of 5M, 10M, and 17M now have close to the same magnitude, although 17M have larger fluctuations. The jet in the 28M simulations has at this point started to break down, as shown in plot 6a, 6b, and 6c, and the power spectral density of the 17M simulations has also lost width.

DISCUSSION

One of the objectives of the study was to validate our solver against experimental data. However, our results would seem to suggest that we have falsified it instead. Before concluding firmly that our solver is erroneous, let's consider a few aspects of the benchmark case and our approach.

First of all, it is evident from Figure 1 (sub-plot 1c) that the two coarsest simulations predict an unstable flow developing in the inner pipe, whereas the fine simulations predict stable flow. This fundamental difference has a profound impact on the flow as the jet enters the large pipe. The coarse, already unstable, simulations break up immediately, whereas the fine simulations remain laminar for 10-15 diameters downstream before transition occurs. The coarse simulations are in acceptable agreement with the experiments, but what is correct?

To shed some light on our results we turn to linear stability theory. A linear stability analysis amounts to computing the leading eigenvalues of the linearized Navier-Stokes operator, as well as the corresponding eigenmodes, representing the perturbations to the laminar base flow. The growth rate (i.e., the eigenvalues) of the perturbations reveal whether or not the flow is linearly stable. A leading positive eigenvalue represents an unstable mode and a negative eigenvalue represents a stable mode. To perform the analysis on the FDA case we used the open source spectral element code Semtex (http://users.monash.edu.au/~bburn/semtex.html). Since we were mainly interested in whether or not the flow in the inner pipe should be unstable, we split the domain at position 1 in Figure 1, and performed two analyses, one for the inlet section and one for the outlet. The analyses reveal that all eigenvalues in the first pipe, diverging inlet section, and inner pipe are all negative, which indicates a stable and laminar region, whereas the outlet section contains positive eigenvalues and thus unstable eigenmodes. Having said that, linear stability theory doesn't provide definite proof and is often very conservative compared to experiments.

Now looking at the results from a numerical point of view, the first thing to notice is the presence of noise in the 5 and 10M simulations shown in plot 1c, which is absent at higher mesh resolutions. This noise represents deviation from the stable and symmetric 2D laminar solution, caused by an asymmetry in the tetrahedral mesh. A tetrahedral mesh will always introduce skewed elements and a completely symmetric mesh in a pipe is only possible to achieve using cylinder coordinates. Furthermore, a coarse mesh will lead to more asymmetry and noise than a fine mesh, which is what we observe. What is interesting, though, is that noise (and any other instability) will either grow or decay, depending on the Reynolds number. Reynolds actually addressed this himself for pipe flow and reported that transition varied between Re 1800 and 13,000 depending on how carefully the noise was controlled[6]. Conceptually, we can of course do the same by putting some physics back in CFD by breaking symmetry at the inlet. We therefore added white noise with magnitude 0.001m/s at the inlet velocity in the angular direction at the inlet of the 17M simulation. The noise grew in the inner pipe and gave phenotypically similar results that match those from the experiments and our coarse simulations. The amount of noise[7] that is needed to get an unstable flow typically scales with 1/Re. We therefore added the same noise also to the Re 500 and 6500 simulations using the 17M mesh. As expected, at these Reynolds numbers, the flows were completely unaffected by noise; the Re 500 case was still stable and breakdown of the Re 6500 jet was unchanged.

The impact of our study is debatable but can potentially explain the *discrepancies in transition*[8] between 'sterile' CFD and experiments that are inherently 'noisy', and offer a plausible explanation for the reported discrepancies in the original challenge for Re 3500.

REFERENCES

[1] Murray, C et al. The Lancet 349.9064 (1997): 1498-1504.
[2] Steinman, D. A., et al. AJNR 24.4 (2003): 559-566.
[3] Hariharan, P., et al. J BiomechEng 133.4 (2011): 041002.
[4] Mortensen, M., et al. CompPhysComm 188 (2015): 177-188.
[5] Simo, J.C., et al. CompMethApplMechEng 111.1(1994):111-154.
[6] Reynolds, O. *ProcRoyalSocLondon* 35.224-226 (1883): 84-99.
[7] Hof, B. PhysRevLetr 91.24 (2003): 244502.
[8] Griffith, M. D., et al. PhysFluids (2012).

Copyright 2016 The Organizing Committee for the 2016 Summer Biomechanics, Bioengineering and Biotransport Conference

SB^{3}C2016
Summer Biomechanics, Bioengineering and Biotransport Conference
June 29 –July 2, National Harbor, MD, USA
SB^{3}C2016-581

EFFECTS OF OPENING ANGLE, AXIAL STRETCH AND CIRCUMFERENTIAL SHRINKAGE ON BLOOD VESSEL STRESS AND STRAIN CALCULATIONS

Liang Wang (1), Jian Zhu (2), Akiko Maehara (3), Jie Zheng (4), Chun Yang (1,5), David Muccigrosso (4), Gary S. Mintz (3), Dalin Tang (1,6)

(1) Mathematical Sciences Dept, Worcester Polytechnic Institute Worcester, MA 01609 USA

(2) Department of Cardiology, Zhongda Hospital, Southeast University Nanjing, 210009, China

(3) The Cardiovascular Research Foundation, Columbia University, New York, NY 10022

(4) Mallinckrodt Inst of Radiology, Washington University St. Louis, MO USA 63110

(5) Network Technology Research Inst. China United Network Comm. Co., Ltd. Beijing, China 100048

(6) Department of Mathematics, Southeast University Nanjing, 210096, China

INTRODUCTION

Mechanical forces play an important role in atherosclerotic plaque progression and rupture. Image-based computational models have been introduced to obtain plaque stress, strain and flow shear stress conditions to identify risk factors and mechanisms associated with plaque progression and rupture. For models constructed from in vivo data, residual stress defined as the stress in the blood vessel under no-load state remains to be an issue. Model construction normally starts from no-load state geometry, but in vivo blood vessels are under pressure, axially stretched, not in no-load state. Furthermore, blood vessel under no-load state is still not stress-free [1].

Researchers have proposed several modeling techniques to deal with the residual stress issue and have demonstrated that residual stress has a significant influence on stress/strain distribution under in vivo conditions. Using an opening angle method in human carotid model to quantifying residual stress, Delfino et al. claimed that the circumferential stress throughout the wall is much more uniform with residual stress was included [2]. Ohayon et al. showed that peak strain in the thin fibrous cap was overestimates by a factor of as much as four if residual stress was not considered [3]. In an in vivo MRI data study, Huang et al. indicated that stress-P_1 and strain-P_1 at the plaque cap increased 23.7% and 25.9%, respectively, under 10% axial stretch and patient-specific circumferential shrinkage [4]. Speelman et al. adopted a backward incremental method to account for the initial stress under in vivo state, and found abdominal aortic aneurysms (AAA) wall stresses as computed with initial stress considered were higher than without initial stress [5].

It should be noted that stress distribution in vivo concerns not only the classically-known opening angle, but also axial shrinkage and circumferential (radial) shrinkage. In this paper, a 3D computational model was constructed using a three-step procedure: a) wrap a stress-free circular sector to form a cylinder to obtain residual stress; b) pressurize the cylinder to in vivo pressure; c) stretch the cylinder axially to its "in vivo" state. Eight models were constructed to investigate the effects of opening angle, axial stretch and circumferential shrinkage on stress distribution under physiological conditions.

METHODS

Blood vessel geometry: the cross-section of the blood vessel under zero-stress state is induced from the ideal geometry in vivo state based on incompressibility of the material and the assumption that the circumference of the middle line of the vessel wall remains un-changed. The cross section of the blood vessel in vivo was assumed to be circular with inner diameter 3.343 mm and wall thickness 0.436 mm which were taken from human coronary IVUS data. The vessel in vivo length was 20 mm (pre-stretch length 18.18 mm, with 10% axial stretch gave 20 mm). The zero-stress state of the blood vessel is a circular sector with an opening angle 120 degree based on the real human coronary data in previous work of Kural et al. [6]. Figure 1 shows the geometries of the blood vessel at zero-stress state and no-load state.

Structure model and boundary conditions: 8 3D computational structure models were constructed with various combinations of wrapping, axial shrink/stretch and circumferential shrinkage/ pressurization (see Table 1). The blood pressure applied on the lumen is 70-130mmHg. The Mooney-Rivlin material model was used to describe the material properties of the blood vessel tissue. The strain energy density function is:

$$W = c_1(I_1 - 3) + c_2(I_2 - 3) + D_1 e^{\{D_2(I_1-3)-1\}} + \frac{K_1}{2K_2} e^{\{K_2(I_4-1)-1\}} \quad (1)$$

where I_1, I_2 are the first and second invariants of right Cauchy-Green

Copyright 2016 The Organizing Committee for the 2016 Summer Biomechanics, Bioengineering and Biotransport Conference

deformation tensor **C.** Parameter values in the Mooney-Rivlin model was selected to fit our b iaxial testing data using a human coronary sample. The parameter values were: c_1= -1312.9 kPa, c_2=114.7 kPa, D_1=629.7 kPa, D_2=2.0, K_1=35.9 kPa, K_2=23.5 in this work.

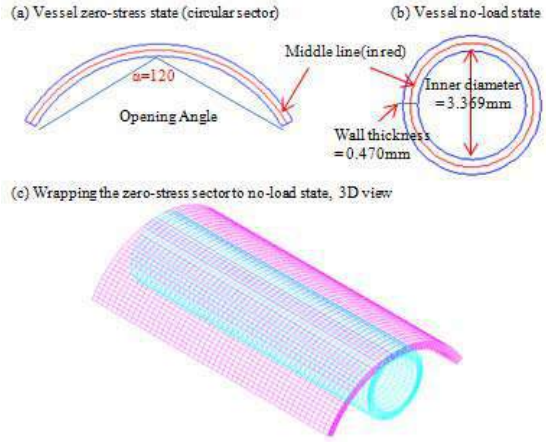

Figure 1: the geometries of th e cross-section of th e blood vessel under no-load state and in vivo state, and 3D geometry.

Table 1: 8 model cases and their descriptions.

Models	Description
M1(base)	With wrapping, 10% axial stretch, with radial shrinking
M2	With wrapping, 10% axial stretch, no radial shrinking
M3	With wrapping, no axial stretch, with radial shrinking
M4	With wrapping, no axial stretch, no radial shrinking
M5	Without wrapping, 10% axial stretch, with radial shrinking
M6	Without wrapping, 10% axial stretch, no radial shrinking
M7	Without wrapping, no axial stretch, with radial shrinking
M8	Without wrapping, no axial stretch, no radial shrinking

RESULTS

Circumferential shrinkage determination: Using trial-and-error method to find out when lumen and wall shrinkage are set to -0.78% and -2.3%, respectively, blood vessel will fully recovered into in vivo state after pressurized and 10% axial stretch.

Models comparison: Figure 2 and Figure 3 give the stress-P_1/strain-P_1 distribution of all 8 models on a given plane-cut at pressure=130mmHg. Table 2 lists the average values of stress-P_1 and strain-P_1 on the lumen at the same pressure condition for each model. According to table 2, the circumferential shrinkage does not have much influence on s tress/strain distributions, given the lumen/wall shrinkage is small in this study. The wrapping process will decrease the average stress on lumen because the lumen will be compressed and out-boundary will be stretched during the wrapping process. And if the axial stretch is not considered, stress-P_1 will decrease about 120% when wrapping process is involved and 28% when wrapping process is not involved.

Table 2: Average value of s tress-P_1/strain-P_1 on lumen at mi n pressure=70 mmHg of all 8 models are listed.

Model cases	Average Stress-P_1	Average Strain-P_1
M1(baseline)	66.87kPa	0.1051
M2	69.85kPa	0.1051
M3	-13.95kPa	0.0010
M4	-10.54kPa	0.0069
M5	148.6kPa	0.1051
M6	143.8kPa	0.1051
M7	108.0kPa	0.1094
M8	102.4kPa	0.1071

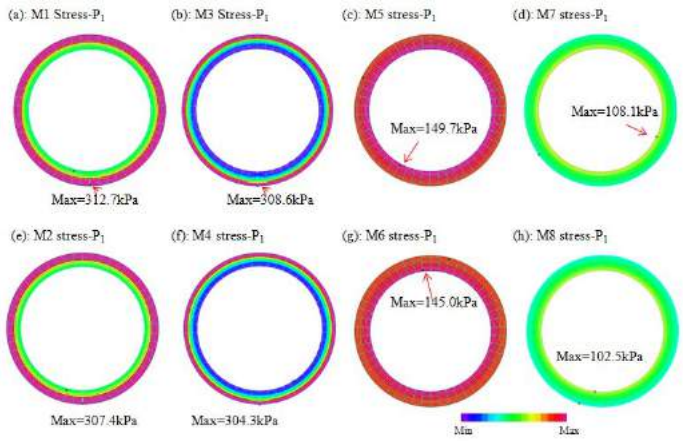

Figure 2: the plots of unsmoothed stress distribution of all models on a plane-cut at pressure=130 mmHg.

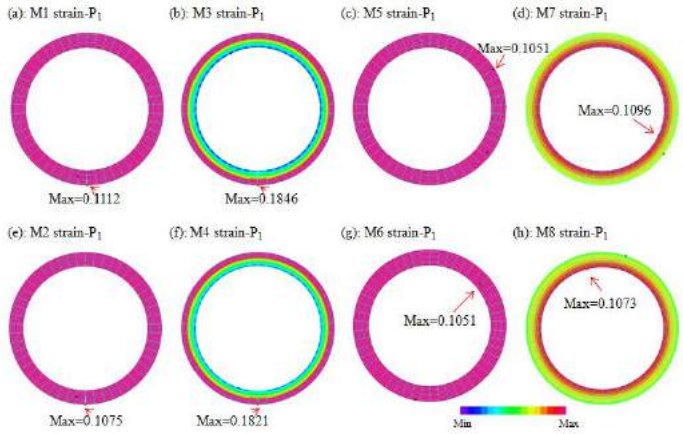

Figure 3: the plots of unsmoothed strain distribution of all models on a plane-cut at pressure=130mmHg

DISCUSSION

The stress distribution on l umen will be reduced when residual stress in blood vessel is taken into consideration while axial stretch will increase the stress distribution on the lumen. Circumferential shrinkage have little influence on stress/strain distribution given the lumen/wall shrinkage in this study is so small.

ACKNOWLEDGEMENTS

This research was supported by NIH grant NIH/NIBIB R01 EB004759. Chun Yang's research is supported in part by National Sciences Foundation of China 11171030.

REFERENCES

[1] Fung YC et al. Am J Physiol. 262(2) : H544-52, 1992.
[2] Delfino A et al. J Biomech. 30(8):777-86, 1997.
[3] Ohayon J et al. Am J Physiol. 293(3):H1987-96, 2007.
[4] Huang X et al. Mol Cell Biomech. 6(2):121-34, 2009.
[5] Speelman L et al. J Biomech. 42(11):1713-9, 2009.
[6] Kural MH et al. J Biomech. 45(5):790-8, 2012.

Copyright 2016 The Organizing Committee for the 2016 Summer Biomechanics, Bioengineering and Biotransport Conference

SB^{3}C2016
Summer Biomechanics, Bioengineering and Biotransport Conference
June 29 –July 2, National Harbor, MD, USA
SB^{3}C2016-582

ALGINATE HYDROGEL MICROENCAPSULATION INHIBITS DEVITRIFI CATION AND ENABLES LARGE-VOLUME LOW-CPA CELL VITRIFI CATION

H. Huang (1,2), J. K. Choi (1), X.He (1,2)

(1) Department of Biomedical Engineering
The Ohio State University
Columbus , OH, USA

(2) Department of Mechanical Engineering
The Ohio State University
Columbus , OH, USA

INTRODUCTION

Cryopreservation of stem cells is important to meet their ever-increasing demand by the burgeoning cell-based medicine. The conventional slow freezing for stem cell cryopreservation suffers from inevitable cell injury associated with ice formation and the vitrifi cation (i.e., no visible ice formation) approach is emerging as a new strategy for cell cryopreservation. A major challenge to cell vitrifi cation is intracellular ice formation (IIF, a lethal event to cells) induced by devitrifi cation (i.e., formation of visible ice in previously vitrified solution) during warming the vitrified cells at cryogenic temperature back to super-zero temperatures. Consequently, high and toxic concentrations of penetrating cryoprotectants (i.e., high CPAs, up to ≈8 M) and/or limited sample volumes (up to ≈2.5 μL) have been used to minimize IIF during vitrification. It is revealed that alginate hydrogel microencapsulation can effectively inhibit devitrifi cation during warming. The data show that if ice formation were minimized during cooling, IIF is negligible in alginate hydrogel microencapsulated cells during the entire cooling and warming procedure of vitrifi cation. This enables vitrifi cation of pluripotent and multipotent stem cells with up to ≈4 times lower concentration of penetrating CPAs (up to 2 M , low CPA) in up to ≈100 times larger sample volume (up to ≈250 μL, large volume).

METHODS

Cell encapsulation by microfluidics: To produce alginate hydrogel microcapsules, the core fluid consisting of 2% (w/v) purified sodium alginate and 0.5 M trehalose either with or without stem cells (cell density 2.5 × 106 cells ml^{-1}) was introduced into the non-planar microfluidic device. The presence of trehalose in the core fluid can pre-dehydrate the cells, which may help to suppress intracellular ice formation during cryopreservation. The shell fluid was prepared by dissolving purified sodium alginate (2%, w/v) in 0.25 M aqueous D-mannitol solution to achieve an osmolality of 280 mOsm determined by a micro osmometer (Advanced Instruments). The carrier oil emulsion was made using a method reported by us previously. All these solutions were introduced into the microfluidic device using syringe pumps (Harvard Apparatus). The flow rates of core, shell and carrier fluids were 75 μl, 75 μl, and 7 ml per hour, respectively.

Vitrification by plastic straw (PS): To minimize the contact time to the hypertonic vitrification solution of PS (VSP) and enhance the diffusion of 1,2-propanediol (PROH) into cells, the encapsulated or non-encapsulated cells were incubated in their medium with 2 M PROH for 30 min at 4 °C, and then transferred into VSP within 1 minute before vitrification. For vitrification, the sample-laden PS was plunged into liquid nitrogen and held for 3 min that is long enough to cool the sample to the temperature of liquid nitrogen. The samples were then warmed back to room temperature by taking the PS out of liquid nitrogen and plunging them into 1x PBS with 0.2 M trehalose at room temperature. The cell suspension post vitrification was one-step unloaded from the PS into cell culture medium with 5 μM of calcein AM and 5 μM of ethidium homodimer (Invitrogen) to stain live and dead cells, respectively. After incubation at 37 °C for 10 min, the live and dead cells stained green and red, respectively, were checked and counted under fluorescence microscopy to determine cell viability.

Cryomicroscopy study of inhibiting devitrification by alginate hydrogel microencapsulation: A total of 4 μl cell culture medium (either with or without 1.5 M PROH and 0.5 M trehalose) containing alginate hydrogel microcapsules was loaded into the sample crucible of the Linkam cryomicroscopy system and sandwiched with a coverslip (9 mm in diameter) to obtain a thin solution film for taking clear images during both cooling and warming. The samples were first cooled to -60 °C rapidly at 60 °C min-1, held for 2 min, warmed back at 60 °C min-1 to either -7 °C (without CPA) or -15 °C (with CPA), and held at the respective temperature for 20 min for annealing to observe ice formation/growth inside and outside the microcapsule under both polarized and phase contrast light microscopy.

RESULTS

The quantitative and qualitative data of cell viability of mouse embryonic stem cells (mESCs) and human adipose-derived stem cells

Copyright 2016 The Organizing Committee for the 2016 Summer Biomechanics, Bioengineering and Biotransport Conference

(hADSCs) post vitrification using the PS together with VSP are shown in Figures 1. These data show that most of the microencapsulated cells could survive while almost all non-encapsulated cells are killed during the vitrification procedure. They demonstrate that IIF induced by devitrification during warming kills most non-encapsulated cells and alginate hydrogel microencapsulation can effectively protects the encapsulated cells by inhibiting devitrification to minimize IIF. We have performed this experiment for many times (>10) and the results are consistent. However, the survived cells must be capable of functioning normally in order to ascertain the effectiveness of our low-CPA (2 M penetrating CPA) vitrification approach with the PS developed in this study. Therefore, further studies were performed to examine the functional properties including stemness and capability of guided (or directed or coaxed) differentiation of the mESCs and hADSCs before and after the low-CPA vitrification with PS.

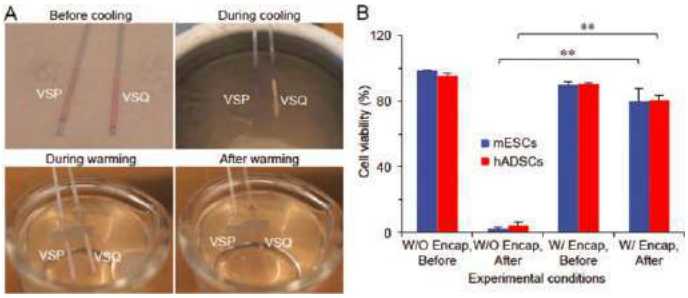

Figure 1: Low-CPA vitrification of stem cells with conventional plastic straw (PS). (A) Typical images showing the vitrification of VSP during cooling with PS and devitrification of the vitrified VSP during warming with the PS. VSP: Vitrification solution for PS which is the culture medium of mESCs or hADSCs with 2 M PROH (penetrating) and 1.3 M trehalose (non-penetrating). (B) Viability of mESCs and hADSCs either with (w/) or without (W/O) alginate hydrogel encapsulation (Encap) before and after vitrification in VSP. **: $p < 0.01$.

We further investigated the capacity of inhibiting devitrification by alginate hydrogel microencapsulation using cryomicroscopy. Figure 2 shows the size and morphology of visible ice crystals outside the alginate hydrogel microcapsule in the bulk solution, at -60 °C (at the end of cooling) and at -7 or -15 °C (during warming) of mESC medium either without (Figure 2A) or with (Figure 2B) CPA (1.5 M PROH and 0.5 M trehalose) under phase (grayscale) and polarized (color) light microscopy. The blue and pink regions in the polarized microscopy images indicate ice crystals of different crystallographic orientations. For medium without CPA, fine ice crystals (FICs, single asterisk) suddenly form around -20 °C during cooling and do not change much with further cooling to -60 °C. During warming, however, the FICs outside the microcapsules grow and merge into large ice crystals (LICs, double asterisks) at -7 °C (after 20 min annealing) with their boundaries being clearly visible as whitish curves in the phase image (Figure 2A). More importantly, the aforementioned growth of FICs into LICs during warming outside the microcapsules does not occur inside the alginate hydrogel microcapsule at all according to Figure 2B: no visible ice formation is observable inside the microcapsule throughout the entire cooling and warming procedure. This confirms the exceptional capability of alginate hydrogel microcapsules in inhibiting devitrification during warming, which should contribute to the high viability and intact functionality of the microencapsulated stem cells post vitrification using PS.

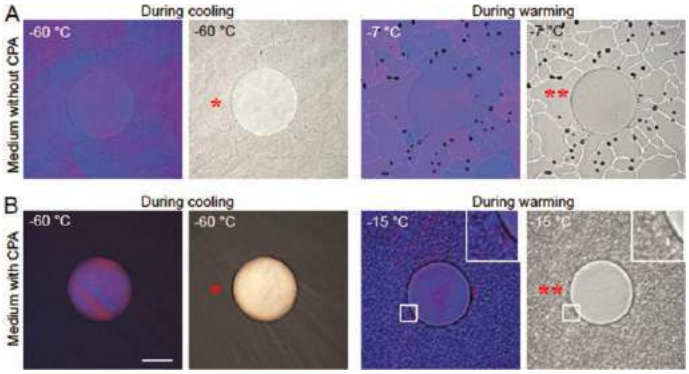

Figure 2: Alginate hydrogel microencapsulation inhibits devitrification during warming. Polarized (color) and phase contrast (grayscale) images at -60 °C at the end of cooling and at -7 and -15 °C during warming with annealing for 20 min for an alginate hydrogel microcapsule in mESC medium without (A) and with (B) CPA (1.5 M PROH and 0.5 M trehalose), respectively. No visible ice formation inside the microcapsule is observable during both cooling and warming while the fine ice crystals (FIC, *) outside the microcapsules in the bulk solution merge into large ice crystals (LIC, **) during warming. Scale bar: 100 µm.

DISCUSSION

In the alginate hydrogel microcapsule, by contrast, devitrification during warming is effectively inhibited. As a result, IIF in the microencapsulated cells is minimized during warming and a high cell viability post vitrification ensues. Of note, although the capability of alginate hydrogel microencapsulation in inhibiting devitrification may depend on the thermal profile of the device used for vitrification, it was verified over a wide range of warming rate between 100,000 °C/min and 2000 °C/min in this study. This is probably because the hydrogel network of the polymer can effectively dampen the movement of water molecules to prevent devitrification from occurring, due to its immense viscosity at subzero temperature and/or the polymer can bind to the surface of invisible nascent ice crystals to inhibit their growth. Further investigations are certainly needed to identify the exact mechanisms that are responsible for the exceptional capability of inhibiting devitrification by the alginate hydrogel microencapsulation.

ACKNOWLEDGEMENTS

This work was partially supported by grants from NSF (CBET-1154965) and NIH (R01EB012108).

REFERENCES

Huang, H et al., *Adv. Funct. Mater.*, 25: 6839–6850, 2015.

Copyright 2016 The Organizing Committee for the 2016 Summer Biomechanics, Bioengineering and Biotransport Conference

SB³C2016
Summer Biomechanics, Bioengineering and Biotransport Conference
June 29 –July 2, National Harbor, MD, USA
SB³C2016-583

A NOVEL IMAGING TECHNIQUE TO QUANTIFY SURFACE WEAR IN JOINT REPLACEMENT DEVICES

Katherine A. Hollar (1), Daniel Ferguson (2), John B. Everingham (1), Jillian L. Helms (1), Trevor J. Lujan, Ph.D. (1)

(1) Department of Mechanical and Biomedical Engineering
Boise State University
Boise, ID, USA

(2) Global Inspection Solutions, LLC
Portland, OR, USA

INTRODUCTION

The prevention of premature failure in joint replacement devices has been an ongoing challenge for engineers and physicians. Joint replacement devices are now being designed with highly cross-linked polymers that improve wear resistance of the bearing surfaces to increase implant longevity [1]. In order to assess the wear performance of advanced materials, the amount and location of bearing wear must be accurately measured and analyzed. The conventional methods used to locate wear on the bearing surface include micro computed tomography (μCT) and coordinate measuring machines (CMMs) [2,3]. Imaging with μCT offers good spatial volume resolution, but is limited by cost, operator subjectivity and complexity [4]. Accuracy can be improved using CMMs, which provide highly-accurate three dimensional (3D) renderings of implant surfaces by using a stylus to probe thousands of points on the bearing surface. CMMs are limited by inter-operator error and manual operation [4, 5]. Therefore, a need exists to develop a novel imaging technique that accurately and automatically quantifies the topology of the bearing surface. This technology would help detect regions of abnormal wear and could shorten the time required for clinical studies of new implants.

A novel approach to measuring wear in joint replacement devices is to use a 3D structured-light scanner. A 3D structured-light scanner uses projected light patterns and cameras to quickly and accurately model the 3D geometry of physical objects. These imaging devices are typically used for quality control in manufacturing and reverse engineering of complex components. The objective of this research is to verify that wear on joint replacement devices can be detected using a 3D structured-light scanner. This study will first validate the accuracy of the 3D scanner and will then use the 3D scanner to detect wear in a hip resurfacing implant made with a highly cross-linked wear resistant polymer for the bearing surface.

METHODS

Setup and Calibration. The 3D structured-light scanning system consisted of two cameras, a projector, and a rotary table (LMI Technologies, Delta, Canada) (Fig. 1). The system was setup with two low-profile camera lenses angled at 45 degrees. A 4.5 x 3.5 x 3 cm space was calibrated using a 2 mm calibration card positioned at various angles relative to the two cameras. The card was imaged when it was tilted left, right, close, and far to the cameras. A total of 30-50 calibration grid positions were required for a successful calibration space. A rotary table was used to make scanning objects more efficient, since it was able to align meshes as it captured 360 degrees of scans at user-defined increments. The rotary table was calibrated by placing the 2 mm calibration card on the rotary table at an angle that approximated the object of interest (e.g. hip implant). For a successful alignment of the rotary table, the calibration card was visible through five pre-set rotations.

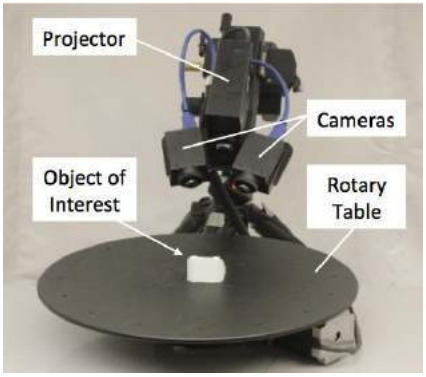

Figure 1: 3D Scanner Components

Verification. To verify the accuracy of the 3D scanner, a brass and opaque plastic reference block were machined with known recesses of 0.05, 0.04, 0.03, 0.02, and 0.01 mm (Fig. 2). Brass and plastic were chosen as materials because brass could be machined to

Copyright 2016 The Organizing Committee for the 2016 Summer Biomechanics, Bioengineering and Biotransport Conference

excellent tolerances and the plastic was chosen to mimic the natural low-light reflectance of the opaque polymers used in total joint replacements. Prior to scanning, each reference block was sprayed with a light coating of white foot powder. This further reduced the light reflectance and enhanced the quality of the scan. Each block was then scanned in 8 increments of 45 degrees. The software associated with the 3D scanner, FlexScan 3D, was then used to measure the recess depth. Three points were selected on the non-machined surface to create a plane. Points were then selected on the recessed surfaces and the shortest distance between these points and the plane was calculated. This procedure was repeated 8 times for each recessed surface, for a total of 40 measurements on each block. Error was measured as the difference between the predicted and known recess depth, divided by the known depth. Significant differences were determined with an ANOVA.

Figure 2: Reference Blocks

Application. After verifying accuracy, the 3D scanner was then used to measure wear in a highly-crosslinked ultra-high-molecular-weight polyethylene liner that was used as a bearing surface in a hip resurfacing implant for canines (Figure 3A). These liners had a thickness of 1.5mm ± 0.05mm. For this project, two plastic liners were

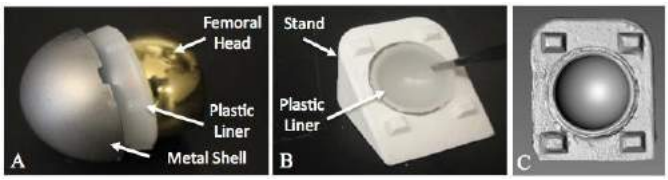

Figure 3: Hip Implant. A) Implant components. B) Alignment stand for plastic liner. C) 3D scan of stand and liner.

subjected to 1,100,000 cycles of loading in a canine hip simulator. The hip simulator is a single axis orbital bearing machine designed to reproduce canine hip kinematics (peak load = 211 N, 2 Hz). The plastic liners received 3D scans before and after cyclic loading. These scans included filling and smoothing algorithms, and took approximately 25 minutes.

In order to have a repeatable frame of reference to measure wear between the two time points, the plastic liner was inserted on a custom stand fabricated with a 3D printer (Fig. 3B). The stand and liner were sprayed with white powder-based spray and scanned at 18 increments of 20 degrees. Using FlexScan 3D, the post-wear image was first aligned to the pre-wear image and then the stand's 3D geometry was selected to refine image registration. The software merged the two images, with the average deviation of the stand surface between scans being 0.038 mm (Figure 3C). It's important to note that the stand was aligned independently of the plastic liner. Therefore, any deviation in the implant liner surface between scans was due to wear. Average differences in wear for the liner surface was measured, as well as average differences in wear for the central region of the liner.

RESULTS

The scanner was able to detect 40 μm changes in the surface topology of the brass and plastic reference blocks with an error less than 13% and 10%, respectively (Fig 4A). Error increased for smaller recesses ($p=0.004$), and this error exceeded 40% when measuring indents of 20 μm or below. The scanner was more accurate when scanning brass than plastic ($p<0.01$).

The central region of the canine hip liner had 30% more wear than the average wear rate of the liner (Fig. 4B, Fig. 5). The greatest liner wear depth was 0.3 mm, which was ~20% of the liner thickness.

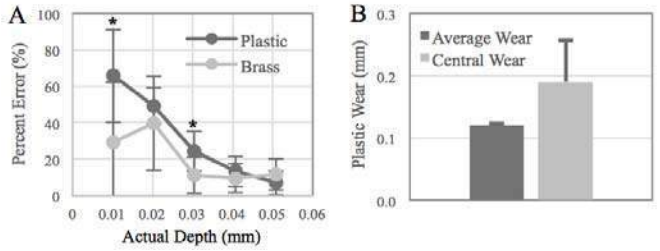

Figure 4: 3D scanner results. A) Accuracy (*= significant difference between brass and plastic). B) Wear of hip implants.

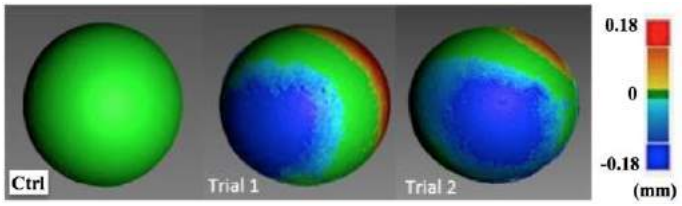

Figure 5: Wear observed in a non-tested implant (Ctrl) compared to implants that receive one-million loading cycles (Trial 1-2)

DISCUSSION

Wear in canine hip liners was successfully imaged and measured using a 3D structured-light scanner. Wear was localized near the central region of the plastic liner, and had a depth of penetration less than 20% of the implant thickness. To our knowledge, this is the first time a 3D structured-light scanner has been used to measure wear in a joint replacement device.

A structured-light scanner has advantages as an imaging technique for wear measurement. First, the structured light scanner can detect changes of 30 μm or more with reasonable error. The accuracy reported for μCT and CMM is 300 μm and 190 μm, respectively [4]. Second, the 3D scanner is relatively fast and automated, taking under 30 minutes to create a 3D representation of a liner. CMMs take roughly the same amount of time [5], but the process requires operator intervention, which is less efficient and reduces measurement objectivity. Third, the 3D scanner is cost-effective relative to microCT and high-end CMM instruments.

A limitation of 3D structured-light scanners is the need to apply powder-based spray during scanning, as this powder can potentially interfere with weight measurements and wear testing. Therefore, it is recommended that powder be applied only after gravimetric testing is completed. The accuracy of the method is also dependent on a repeatable protocol to remove and insert the liner into the stand (Fig. 3B). For this study, a metal shell component (Fig 3A) was cemented into the stand to improve the repeatability of this process.

This study found that structured-light scanners can be used to assess wear in joint replacement devices. These imaging systems can be used to identify abnormal wear patterns and assist the design of durable devices that enhance implant longevity.

ACKNOWLEDGEMENTS

Funding kindly provided by the Idaho Grant Entrepreneurial Mission.

REFERENCES

[1] Muratoglu O et al, *J Arthroplasty*, 16:149-160, 2001. [2] Affatato, S et al., *Biomaterials*, 26:3259-3267, 2005. [3] Bills, P et al., *Wear*, 274-275:212-219, 2012. [4] Goldvasser D et al, *Acta Ortho*, 85 (3):271-275, 2014. [5] Tuke, M et al., *Precis Eng,* 34:777-783, 2010.

Copyright 2016 The Organizing Committee for the 2016 Summer Biomechanics, Bioengineering and Biotransport Conference

SB³C2016
Summer Biomechanics, Bioengineering and Biotransport Conference
June 29 –July 2, National Harbor, MD, USA
SB³C2016-584

DEVELOPMENT OF A NOVEL FISTULA OCCLUSION DEVICE

Alyssa K. Rollando (1), Sara E. Wilson (2), Stephen C. Waller (3), Richard Gilroy (4), James M. Stiles (5)

(1) BioEngineering Graduate Program
University of Kansas
Lawrence, KS, USA

(2) Department of Mechanical Engineering
University of Kansas
Lawrence, KS, USA

(3) Department of Internal Medicine
University of Kansas Medical Center
Kansas City, KS, USA

(4) Department of Gastroenterology, Hepatology and Motility
University of Kansas Medical Center
Kansas City, KS, USA

(5) Department of Electrical Engineering and Computer Science
University of Kansas
Lawrence, KS, USA

INTRODUCTION

Fistulas are a pathological tunnel between two organs within the body [1]. Fistulas most commonly occur between the gastrointestinal tract or biliary system and the skin or between two abdominal cavities, for instance the bowel and bladder [2]. The exact prevalence of fistulas in the US populations is unknown due to its under-reporting, however, enterocutaneous fistulas effect approximately 2% of all bowel surgeries [2]. Unrepaired fistulas lead to significant morbidity and are associated with prolonged hospitalization and costs. Sepsis may accompany gastrocutaneous fistulas with a mortality rate as high as 85% [3]. As a function of the challenges, morbidity, potential mortality and costs associated with fistulas the medical field continues to search for better solutions to this challenging clinical dilemma.

Fistulas are difficult to repair and the only current method is invasive surgery that removes some of the surrounding and potentially otherwise healthy tissue [4]. Some patients are not surgical candidates because of other health complications [5].

Mechanical closure methods include clips and plugs. Comprehensive studies on the application of clips are extremely limited and a vast majority of the available literature is reliant on individual case studies [6]. Approximately 50% of all clips fail due to poor clip position, early detachment and densely epithelialized tissue [6]. Plugs are the newest advancement in fistula repair. They can be made of synthetic silicones or bioabsorbable xenografts. They are currently being used exclusively for anal fistulas. Despite the recent innovation, plug extrusion occurs in between 10-41% of cases and only heals 49% of fistulas in twelve months [7, 8].

Various forms of glues have been explored as a non-surgical closure method with limited success to date; typically because of the inability to maintain a precise location once injected [9]. Before curing, one glue, cyanoacrylate with a low viscosity, easily flows through the catheter for placement of an occlusive plug, but unfortunately continues to flow once within the fistula of interest potentially causing occlusion downstream. Decreasing the cure time is possible with additives; however, additives often clog the injection catheter causing it to stick to the delivery device or cause premature obstruction of the fistulous tract leaving an enteric hole inadequately treated to prevent recurrence of the fistula. In summary, closure precision remains especially important in the eradication of fistulas.

Considering the poor treatment options available for fistulas, it is imperative to create a device that is minimally invasive and offers better quality of life for these patients. The preliminary design work presented here hopes to form the foundation for a more effective fistula occlusion technology. The aims of this project are to create a method to control placement of ferromagnetic glue deployed from a catheter.

METHODS

The goal of this specific portion of the fistula occlusion device was to develop a prototype that could move magnetically responsive material. In future studies, the steel balls, used here for simplicity, will be replaced with ferromagnetic glue.

Prototypes were built on 20 cm of the distal end of Angiodynamics Soft-Vu Berenstein 5F catheters. This would allow for the eventual deployment of the electromagnetic glue through the 0.97 mm lumen. The solenoid was built on the last 2 cm of the catheter. To create the core of the solenoid alternating layers of iron paint (Modern Metals Metalic Oxidizing Iron Paint, 49.97% wt) and iron wire (0.35mm) were applied. Three types of each experimental group were built according to the specifications shown in Table 1. These materials were chosen from previous prototype iterations utilizing the Taguchi method.

Copyright 2016 The Organizing Committee for the 2016 Summer Biomechanics, Bioengineering and Biotransport Conference

Table 1: Specifications of core materials and weight for each prototype.

	Relative Weight (g)								
Prototype	2A	2B	2C	3A	3B	3C	4A	4B	4C
Catheter weight	0.33	0.35	0.37	0.28	0.36	0.35	0.34	0.35	0.45
1 wire	0.25	0.24	0.25	0.30	0.26	0.22	0.22	0.23	0.23
1 paint	0.02	0.02	0.02	0.02	0.03	0.04	0.04	0.02	0.03
2 wire	0.30	0.29	0.30	0.31	0.29	0.31	0.30	0.29	0.31
2 paint	0.08	0.09	0.06	0.09	0.01	0.08	0.08	0.05	0.06
3 wire				0.30	0.38	0.35	0.39	0.35	0.37
3 paint				0.13	0.10	0.17	0.13	0.05	0.11
4 wire				0.43	0.42	0.09	0.46	0.40	0.47
4 paint				0.18	0.17	0.54	0.27	0.18	0.21
5 wire							0.63	0.48	0.59
5 paint							0.41	0.36	0.38
6 wire							0.76	0.77	0.90
6 paint							0.37	0.72	0.40
Iron Core Weight	0.60	0.59	0.59	1.55	1.51	1.39	3.40	3.20	3.46
Avg	0.59			1.48			3.35		
Stdev	0.00			0.08			0.14		

After drying, an external coil was constructed using coated copper wire with a diameter of 0.33 mm wrapped tightly approximately 50 times around the iron core. This coil was connected to the power supply in order to create the magnetic field.

To verify the presence of a magnetic field, each prototype was set in a slim track and secured. A 1.5 mm steel ball was placed 3 mm away from the distal end of the solenoid and the power supply was turned on. The current through the external coil was increased until the magnetic field pulled the steel ball towards the solenoid.

RESULTS

Nine prototypes (three of each construction) were built using the described method. Each prototype moved the ball within the limits of the power supply, no more than 10A of current. Preliminary results indicate that solenoids on this scale can be used to move magnetically reactive materials. Initial results indicate that this design may provide a viable control mechanism for the deployment of electromagnetic glue. It was expected that there would be a relationship between the iron core weight and the required current to move the ball. However, the results were inconsistent between trials and prototype groups indicating an issue with either alignment, resolution of the power supply or variability in the construction. Reliability needs to be addressed in the experimental set up before making sweeping conclusions. This demonstrates that magnetic force can be achieved at this scale. However, it is yet to be determined if that magnetic force is sufficient for the application.

DISCUSSION

This work represents the beginning of a body of work to develop a device to repair fistulas. This study was limited by the resolution of the available power supply and the ability to control the alignment of each prototype into the track. Researchers could also not control for friction within the track, although all attempts were made to reduce friction as much as possible. Further steps in the development of this device include quantifying the magnetic force supplied by each prototype to determine the most appropriate for the application. This will likely be done in an inverted scenario so friction can be neglected and the force opposing the magnetic field will be gravity.

Additionally, the electromagnetic glue will need to be characterized. This is important so that the flow patterns are understood when being deployed. Although previous research indicates the applicability of fibrin glue to this scenario, it is unknown if the addition of ferrous particles will alter its composition too much. Evaluating different glue ratios in combination with solenoid catheters will help to fine-tune the design parameters of both components.

The method of creating a solenoid-catheter described here provides a promising foundation for future iterations of the device. Further verification is needed before conclusions can be drawn regarding the usefulness of the design.

ACKNOWLEDGEMENTS

We would like to acknowledge the Madison and Lila Self Graduate Fellowship for their support of this research as well as the Graduate Student Research Fund at the University of Kansas for financial assistance.

REFERENCES

[1] Crespo Vallejo E, Martinez-Galdamez M, Del Olmo Martínez L, Crespo Brunet E, Santos Martin E. Percutaneous treatment of a duodenocutaneous high-flow fistula using a new biological plug. Diagn Interv Radiol Ank Turk. 2015;21:247–51.

[2] Gastrointestinal fistula: MedlinePlus Medical Encyclopedia [Internet]. [cited 2015 May 4]. Available from: http://www.nlm.nih.gov/medlineplus/ency/article/001129.htm

[3] Papavramidis, "Endoscopic management of gastrocutaneous fistula after bariatric surgery by using fibrin sealant" (2004).

[4] Dubose JJ, Lundy JB. Enterocutaneous Fistulas in the Setting of Trauma and Critical Illness. Clin Colon Rectal Surg. 2010;23:182–9.

[5] Owen RM, Love TP, Perez SD, Srinivasan JK, Sharma J, Pollock JD, Haack CI, Sweeney JF, Galloway JR. Definitive surgical treatment of enterocutaneous fistula: outcomes of a 23-year experience. JAMA Surg. 2013;148:118–26.

[6] Teitelbaum, "Combined endoscopic cautery and clip closure of chronic gastrocutaneous fistulas" (2005).

[7] Amrani, "The Surgisis anal fistula plug: a new and reasonable alternative for the treatment of anal fistula" (2008).

[8] Stamos, "Prospective Multicenter study of a synthetic bioabsorbable anal fistula plug to treat cryptoglandular transshincteric anal fistulas" (2015).

[9] Draus, "Enterocutaneous fistula: Are treatments improving?" (2006).

Copyright 2016 The Organizing Committee for the 2016 Summer Biomechanics, Bioengineering and Biotransport Conference

SB³C2016
Summer Biomechanics, Bioengineering and Biotransport Conference
June 29 –July 2, National Harbor, MD, USA
SB³C2016-585

CHARACTERIZING A NOVEL EX-VIVO ANIMAL KNEE MODEL: ACL RUPTURE AND MENISCUS COMPRESSIVE STRENGTH

Nicole L. Zaino, Mark J. Hedgeland, Laurel Kuxhaus, Arthur J. Michalek

Mechanical and Aeronautical Engineering
Department
Clarkson University
Potsdam, NY, USA

INTRODUCTION

The knee is a complex part of the body, function of which is critical to quality of life, but is prone to injury, with 200,000 anterior cruciate ligament (ACL) injuries annually [1]. Accurate knee models assist surgeons in practicing new reconstruction techniques, and are crucial to the advancement of technology and rehabilitation. Animal knee models are often suboptimally sized or have differently-shaped menisci. Many models excel in one aspect compared to the human knee, but not all, thus an improved ex-vivo animal model is needed that better mimics the human knee in all aspects. We evaluated the cervine (white-tailed deer) knee with the expectation that it would be a closer model to the human knee compared to current animal models, due to similar body weight. To evaluate the cervine knee, we measured its range of motion, cross-sectional area and rupture strength of the ACL, bony morphometry, and compressive properties of the meniscus.

METHODS

Twelve fresh frozen left hind legs (5 male, 7 female, 2.7±0.5 years old) from white tailed deer were obtained (Nolt's Custom Meat Cutting, Lowville, NY, and Twiss' Custom Meat Cutting, Potsdam, NY). Passive range of motion was measured before transecting the joint capsule, medial and lateral collateral ligaments, and posterior cruciate ligament after meniscus removal. The femur and tibia were then potted in Bondo (Auto Body Filler, 3M, St. Paul, MN). Throughout testing specimens were kept moist with 0.159 M saline.

The cross-sectional area of the ACL was measured using a dental impression material (Jeltrate Plus, Dentsply, York, PA). The knee was held at 140° (included joint angle) under approximately 8 N of tension during the measurement (Figure 1A). A positive cast was transected at mid-length and photographed twice next to a ruler with a microscope camera (AmScope Inc., Irvine, CA). Images were analyzed using ImageJ (Figure 1B). Our validation showed that this technique was accurate with a random error of ±4%, and a +3% bias.

The rupture strength of the ACL was measured in a hydraulic axial load frame using a custom fixture (MTS 809 Axial/Torsion Test System, MTS Systems Corp., Eden Prairie, MN). Force and displacement data were collected at 100Hz. The knees were secured at an included joint angle of 140°, then distracted in displacement control at a constant rate of 3.33mm/s until failure following pre-conditioning (10 cycles, 5-7mm amplitude, at 20mm/minutes).

Peak stress was computed for the midsubstance failure specimens. Differences between male and female specimens were compared using two-tailed t-tests. Median ACL rupture strength was assessed using a Kaplan-Meier survival estimator in order to account for specimens which did not fail in midsubstance. Following ACL rupture the articulating surfaces were photographed next to a ruler. Morphometry was measured using ImageJ: femoral bicondylar width, intercondylar notch width, intercondylar notch height, (Figure 1C) and tibial plateau slope angles (medial and lateral).

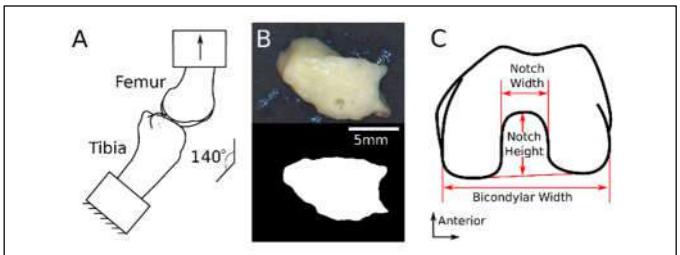

Figure 1: (A) ACL rupture test (B) cross-sectional area and imaging (C) tibial morphometry

Copyright 2016 The Organizing Committee for the 2016 Summer Biomechanics, Bioengineering and Biotransport Conference

To further validate the deer as an ex-vivo knee model, the structure and function of the menisci were analyzed. Cryosections (40µm thick, Microm HM560, ThermoScientific, Kalamazoo, MI)) from the central portion of the axial-radial plane, mounted on coated glass slides, (MAS-GP, Matasunami Glass, Osaka, Japan) were counterstained with Sararanin O (Sigma-Aldrich, St. Louis, MO) to visualize proteoglycans and Methyl Blue (Sigma-Aldrich, St. Louis, MO) to visualize collagen. Brightfield imaging was performed using an inverted microscope (Olympus IMT2, Olympus Scientific, Waltham, MA) using a 2x objective and digital camera.

Unconfined compression tests were performed on ten specimens in a custom-built axial testing machine. 5mm cylindrical plugs of tissue were prepared (2.5mm thick) and compressed between 100 grit sandpaper and a smooth glass plate. Stress-relaxation tests (3-28% strain) were performed at 2%/s and held for 180 seconds. Reaction forces were measured at 100 Hz.

RESULTS

The cervine knee appears similar to the human knee (Figure 2A,B). The femur and tibia are principally connected with anterior and posterior cruciate ligaments, and both medial and lateral collateral ligaments. The joint capsule contains two menisci (Figure 2C) and a patella. Visually, the ACL shows clear evidence of a double-bundle structure. The range of motion was 147°±10° without a significant difference between male and female specimens ($p=0.26$). Mean measured ACL cross-sectional area was 44.75±18.3mm^2, slightly smaller than reported human ACL measurements. Most measured morphometry parameters were greatly similar between deer and humans. The medial and lateral tibial slope measurements were closer to human values than other quadrupeds. There were no significant differences found in the measured bony parameters between our male and female specimens ($p>0.19$ for all parameters).

The cross-section of the cervine meniscus appears similar to the human meniscus. (Figure 2D) There are large collagen fiber bundles in the axial, radial, and circumferential directions, with high density in the peripheral "red zone". Proteoglycan density is greatest in the "white zone". Equilibrium compressive modulus was 70 ±25kPa.

All specimens failed during the rupture test at a stress of 50±18MPa (Table 1). ACL rupture occurred in 5 specimens through tearing at mid-substance, which was evident mechanically as a linear increase in reaction force with increasing joint extraction followed by a pair of sudden force drops indicating failure of the two ACL bundles (Figure 2E). The remainder experienced avulsion fractures, including 1 tibial avulsion and 6 Salter-Harris type fractures across the distal femoral epiphyseal plate [2]. All but one of these specimens also had visible evidence of partial tearing of the posterior bundle of the ACL.

DISCUSSION

The goal of this study was to identify an optimal ex-vivo animal model for ACL rupture and repair research. An improved ex-vivo model will offer a testing platform for orthopaedic implants, a training analogue for surgeons, and will accelerate translation of results from the laboratory to the clinic.

The deer knees had a high degree of morphological similarity to those of humans. In cervine (as with other quadrupeds) the patellar trochlea is deeper and extends further proximally up the femur than in humans. White-tailed deer do not have a fibula, so the lateral collateral ligament is attached directly to the tibia. Among the currently-used ex-vivo knee models some have a full fibula, some have no fibula, and some have a vestigial proximal fibula element. Tibial plateau slope and notch are commonly associated with ACL rupture risk in humans which is important when finding a valid animal model [10].

Table 1: Deer, human[3,4,5], sheep[6,7], & pig[8,9] comparison

	Bicondylar Width (mm)	Notch Width (mm)	Notch Height (mm)	Lateral tibial slope (deg)	Medial tibial slope (deg)	Rupture Force (N)
Deer	53.5 ±3	14.7 ±2.5	16 ±2.5	17.6 ±4.7	16.7 ±2.1	2150 ±397
Human	66 ±5	19.2 ±3.4	31.4 ±3.6	7.8 ±3.9	6.2 ±3.7	2160 ±157
Sheep	47.2 ±1.8	10.8 ±1.2	13.9 ±3.4	--	--	605 ±256
Pig	42.9 ±2.4	8.5 ±1.2	--	34.9 ±4.4	29.5 ±4.5	1720 ±196

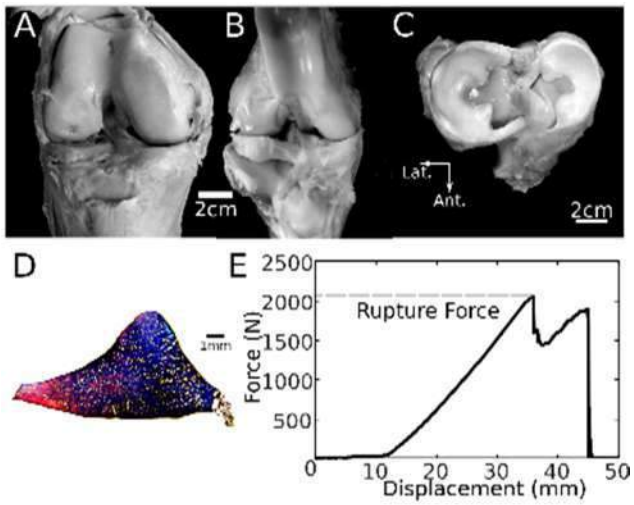

Figure 2: Comparison of anterior aspects of intact (A) human and (B) deer knees. (C) Superior view of cervine tibial plateau with menisci. (D) Meniscus cross-section counterstained with Safranin O. and Methyl Blue. (E) Typical force displacement trace for ACL rupture test showing two rupturing events

Similarities in morphology extend to the soft tissues. ACL structure, cross section, and rupture strength are comparable to those in humans, as are meniscus geometry, composition, and compressive stiffness. The specimens in this study were wild so exact ages could not be determined with high certainty. The use of these skeletally immature specimens accounts for the Salter-Harris fractures during the ACL rupture testing [2]. Overall, our results suggest the white-tailed deer to be an optimal ex-vivo animal model of the human knee.

ACKNOWLEDGEMENTS

The authors thank Mario Ciani and Alexander Martin Clark.

REFERENCES

[1] Baer GS et al., *Clinics in Sports Medince*, 26:661-81, 2007
[2] Salter et al., *JBJS,* 45:587-622, 1963
[3] Celarek A et al., *J Mech Behav Biomed Mater,* 36 29:286-94, 2014
[4] Dargel J et al., *J Arthroplasty*, 26:346-53, 2011.
[5] Hashemi J et al.,*AISM* , 38:54-62, 2010
[6] Osterhoff G et al., *The Knee*, 18:98-103, 2011
[7] Strickland SM et al., *AISM*, 31:210-5, 2003
[8] Proffen BL et al., *The Knee*, 19:493-499, 2012
[9] Kiapour AM et al., *Clin Orthop Relat Res*, 473:639-50, 2015
[10] Brophy RH et al., *JBJS [Am],* 96:801-5, 2014

Copyright 2016 The Organizing Committee for the 2016 Summer Biomechanics, Bioengineering and Biotransport Conference

SB^{3}C2016
Summer Biomechanics, Bioengineering and Biotransport Conference
June 29 –July 2, National Harbor, MD, USA
SB^{3}C2016-586

COMPARISON OF COMPUTED TOMOGRAPHY IMAGING MEASUREMENTS TO CREATED INJURIES UNDER UBB LOADING CONDITIONS

Nathanael P. Kuo, Christopher J. Dooley, Constantine K. Demetropoulos, Kyle A. Ott, Andrew C. Merkle

Research and Exploratory Development Department
Johns Hopkins University Applied Physics Laboratory
Laurel, Maryland, USA

INTRODUCTION

Improvised explosive devices have accounted for a significant number of injuries over the last decade. Military vehicles have evolved to become more resistant to these types of attacks, but the massive amount of energy imparted during under-body blast (UBB) events still results in debilitating injuries to vehicle occupants. These events are characterized by short duration, high amplitude accelerative loading delivered through the vehicle structure, both directly to the occupants and through the seat system [1]. This type of loading may generate a range of injuries, including spinal injuries concentrated in the thoracolumbar junction and the lumbar spine [2-5]. Spinal injuries are of particular concern due to their debilitating nature and long term effects.

Prior biomechanics research on spinal injury has primarily focused on component level testing. Classically, bone quality measurements, such as quantitative computed tomography (qCT) and dual-energy x-ray absorptiometry (DEXA), have been used as specimen selection criteria to ensure that a tested postmortem human surrogate (PMHS) specimen falls within a representative range based on medical data. Studies have investigated individual vertebral bodies [6], three vertebra segments [7], and larger functional units [8]. These studies highlight mechanical parameters and mechanisms that are predictive of vertebral body failure. Yet, it is unclear if the current bone quality measurements sufficiently predict localized fracture risk.

This study leverages a unique data set to investigate if pre-test computed tomography (CT) imaging identifies individual vertebral bodies or functional segments that are at an increased risk for compression fracture under high rate vertical loading.

METHODS

For this study, specimen variability was minimized through tight restrictions on anthropometry and bone quality. The targeted specimen was between 18 and 80 years of age with anthropometry within one standard deviation of the 50th percentile military male and a DEXA Lumbar T-score between -1.0 and 2.5. The average specimen was 72 ± 3 years of age, weighed 82.5 ± 10.6 kg, and had a total stature of 177.6 ± 6.4 cm. Average specimen body mass index was 26.2 ± 3.1 and Lumbar T-Score was 1.2 ± 0.1. Specimens with prior traumatic injuries to the spine, skull, or long bones were excluded from the study, as were specimens with spinal degeneration such as bridging osteophytes and degenerative disc disease.

Twelve whole body PMHS specimens were tested on the Vertically Accelerated Load Transfer System (VALTS) at the Johns Hopkins University Applied Physics Laboratory. The VALTS is a custom designed, pneumatically driven system constructed to recreate UBB conditions, which are characterized by their short duration and high velocity. Tests included in this data set were conducted at different input conditions using a rigid floor and seat (**Table 1**). Specimens 6, 8, 9 and 12 had personal protective equipment, including a vest and helmet. Specimens 11-12 were tested with a pad system installed on the rigid seat.

Whole body CT scans were taken prior to testing with a slice thickness of 0.625 mm. Individual vertebrae in the pre-test CT were analyzed to determine average Hounsfield unit (HU) intensities at three levels using an analysis technique adopted from Schrieber et al. [9]. The three elliptical regions of interests (ROI) per vertebral body were manually delineated on axial slices of the CT scan: one immediately inferior to the superior endplate, one in the middle of the vertebral body, and one immediately superior to the inferior endplate (**Figure 1**). Each ROI was drawn as large as possible while avoiding

Copyright 2016 The Organizing Committee for the 2016 Summer Biomechanics, Bioengineering and Biotransport Conference

cortical bone, and the mean intensities were calculated for each ROI. All three mean intensities were then averaged to compute a final mean HU intensity for each vertebral body. We conducted the above analysis using FIJI [10], which is a distribution of the freeware image analysis software known as ImageJ [11].

RESULTS

Vertebrae L5 to T5 were analyzed to compute mean body HU intensities from the CT scans of the twelve specimens (**Table 2**). After each specimen was tested, a licensed medical examiner evaluated each PMHS specimen for vertebral body fractures (bolded and boxed values) by both CT and anatomical dissection.

A one-tailed t-test was also conducted between the mean HU intensities of the six fractured vertebral bodies and those of the remaining bodies to test the hypothesis that the mean of the population of all fractured bodies is less than that of the unfractured bodies. The resulting p-value was 0.048. Significance was set at $p < 0.05$.

Additionally, a two-tailed t-test was conducted between the mean HU intensities of the fractured vertebral bodies from T5 to T10 and the intensities of those fractured from T11 to L5. A significant p-value of 0.0184 resulted from the test, suggesting that fractured vertebral bodies attached to the sternum via the ribcage (T5 to T10) have a different mean HU intensity compared to the other levels evaluated (T11 to L5).

DISCUSSION

It is important to note that there are limitations in our data analysis. First, our dataset is small with only twelve specimens and six total vertebral body fractures. While these numbers are sufficient to make some statistical conclusions, more data is needed to build a stronger case. The testing conditions for the specimens in our dataset also vary, and may prove to be confounding variables in our experiments. Finally, we did not calibrate bone density against a radiographic phantom in this work, as Schrieber et al. [10] also did not incorporate a phantom in their methods. We hope to investigate the effects of incorporating a phantom in the future. Despite these limitations, the low resulting p-values provide reasonable confidence for our statistical conclusions. Moreover, this data set represents a large number of specimens when compared to similar studies.

In this study, we have demonstrated that vertebral bodies that are prone to fracture generally have lower mean HU intensities than non-fractured vertebral bodies. This fact may prove valuable in the prediction of vertebral body fracture risk, both in experimental specimens, and potentially, in patient populations.

ACKNOWLEDGEMENTS

This effort was funded by contract #N00024-13-D-6400, U.S. Army Research, Development and Engineering Command. The content included in this work does not necessarily reflect the position or policy of the U.S. government.

REFERENCES

[1] Arepally, S et al., No. TARDEC-19214RC, 2008.
[2] Blair, J et al., *The Spine Journal,* 12:762-768, 2012.
[3] Ragel, B et al., *Spine*, 34:2400-2405, 2009.
[4] Stemper, B et al., *J Biomech Eng*, 133:081002, 2011.
[5] Possley, D et al., *The Spine Journal*, 12:843-848, 2012.
[6] Dooley, C et al., *Biomed Sci Instrum,* 49:172-179, 2013.
[7] Baker, A, *Classic Papers in Orthopaedics*, 289-292, 2014.
[8] Yoganandan, N et al., *Stapp Car Crash Journal,* 58:123, 2014.
[9] Schreiber, J et al., *J Bone Joint Surg Am*, 93:1057-1063, 2011.
[10] Schindelin, J et al. *Nature Methods*, 9:676-682, 2012.
[11] Schneider, C et al. *Nature Methods,* 9:671-675, 2012.

Table 1: Velocity and time-to-peak (TTP) input conditions for VALTS testing

Specimens	Seat		Floor	
	Velocity (m/s)	TTP (ms)	Velocity (m/s)	TTP (ms)
1 - 4	4	5	4	5
5 - 9	4	10	6	5
10 - 12	6	10	8	5

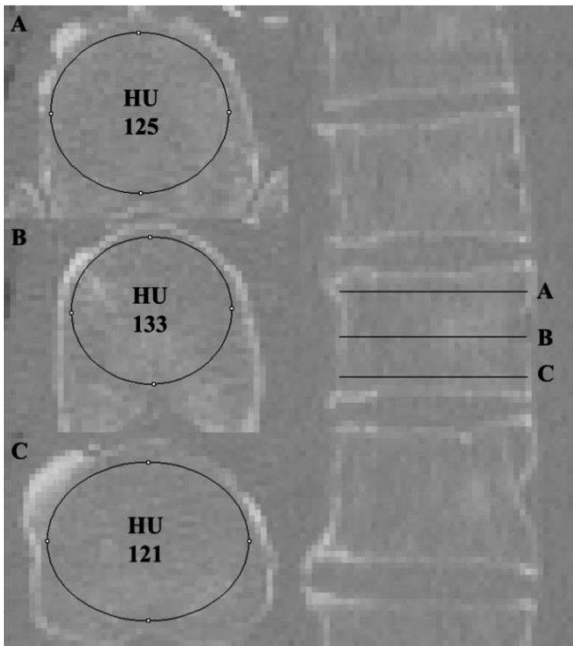

Figure 1: CT depiction of the elliptical regions utilized to characterize the bone density for each vertebral body

Table 2: Summary of mean HU values of each vertebral body from L5 to T5 (span of sustained injuries) for the twelve tested specimens

Vertebral Body \ Specimen #	1	2	3	4	5	6	7	8	9	10	11	12
L5	185	114	142	149	107	153	126	175	123	157	86	**118**
L4	173	146	99	136	**91**	142	119	164	115	144	97	109
L3	175	120	89	152	85	125	117	154	107	149	**94**	96
L2	145	106	90	143	85	130	118	144	102	133	84	111
L1	130	91	78	118	85	113	122	145	112	87	89	105
T12	118	172	112	123	104	109	131	163	116	**96**	106	102
T11	121	140	126	142	136	115	132	165	132	91	128	115
T10	168	123	107	147	162	116	133	161	137	133	123	127
T9	167	200	110	138	109	128	116	149	133	118	122	131
T8	122	191	96	139	89	123	131	181	130	144	147	114
T7	136	189	100	164	142	112	131	190	133	157	143	122
T6	128	133	129	157	184	117	**133**	198	135	192	150	119
T5	167	144	105	178	239	118	116	217	137	200	**139**	123

Copyright 2016 The Organizing Committee for the 2016 Summer Biomechanics, Bioengineering and Biotransport Conference

SB³C2016
Summer Biomechanics, Bioengineering and Biotransport Conference
June 29 –July 2, National Harbor, MD, USA
SB³C2016-587

OFF-AXIS BIAXIAL ANALYSIS OF SYNTHETIC SCAFFOLDS FOR HERNIA REPAIR

Savannah E. Est (1,2), Maddie E. Roen (2), Vivian T. Chi (1), Adrian A. Simien (1), Ryan M. Castile (3), Dominic M. Thompson, Jr. (1), Corey R. Deeken (4), Spencer P. Lake (2,3)

(1) Department of Surgery, Section Minimally Invasive Surgery

(2) Department of Biomedical Engineering

(3) Department of Mechanical Engineering & Materials Science
Washington University in St. Louis
St. Louis, MO

(4) Covalent Bio, LLC
St. Louis, MO

INTRODUCTION

Hernias remain one of the most common ailments to affect men and women. In the late 1950s, surgical mesh materials were first used to reinforce a defect during surgery [1]. Today, there are over 50 prosthetic meshes available for hernia repair [1]. With the multitude of available options, surgeons are faced with the problem of how to pick which mesh is best for each patient. During surgery, meshes are typically placed in the most convenient orientation for the surgeon, which may not provide the best match of the mesh to the properties of the implantation site. If the mechanics of the mesh are not compatible with the surrounding tissue, mismatch can occur, which could lead to complications (e.g., mesh failure and/or hernia recurrence).

To better describe properties of synthetic meshes, we developed a set of standard characterization techniques and a classification system [2,3,4]. We found that meshes exhibit dramatically different mechanical properties (e.g., stiffness, nonlinearity, hysteresis). In addition, many meshes exhibit considerable mechanical anisotropy, which has important implications for dictating how these materials will be loaded once implanted within the abdominal wall. As the forces within the body are multidirectional, it is essential to classify prosthetic hernia reinforcements in a variety of orientations. Therefore, the purpose of this study was to provide a more complete mechanical analysis of a variety of commercially available prosthetic meshes for hernia repair. Twenty different meshes were subjected to equibiaxial tensile tests at both 90° and 45° orientations, and results were analyzed for relative strength, strain behavior, anisotropy, and nonlinearity.

METHODS

Twenty different commercially available meshes were evaluated in this study, which were grouped according to whether or not they included a barrier coating. Samples (n = 5/mesh type) were prepared by cutting 45mm x 45mm square pieces of each mesh at 90° and 45° orientations. 90° was denoted as orthogonal alignment of the warp and weft direction of the mesh, and is the orientation when removed from packaging. To obtain 45° samples, meshes was rotated 45° from the warp/weft alignment, and cut into 45mm x 45mm squares.

Samples were marked with 4 equidistant dots for strain tracking, then soaked in 0.9% saline for 15 minutes to hydrate adhesion barriers. For testing, meshes were subjected to three different loading protocols for both the 90° and 45° orientations: a 1-3 direction strip biaxial test, a 2-4 direction strip biaxial test, and an equibiaxial test. For 90° samples, the warp of the mesh was oriented along the 1-3 axis, while the 45° samples had the mesh's stiffest direction along the 1-3 axis. Each mesh was pre-loaded to 0.1 N, then stretched to a 2.5mm displacement (~12.5% strain) over 5 seconds for 10 cycles, with data collected for the 10th cycle. Digital images were acquired for strain calculations.

Force values were divided by the width of the channels within each grip to convert to membrane tension values. Tension-displacement data from each test type (equibiaxial, 1-3 strip, 2-4 strip) were averaged across samples from each mesh to characterize the mechanical anisotropy, nonlinearity, and relative strength of each type of mesh at each orientation (90° and 45°). Peak tensions along each axis (i.e., T_{13} and T_{24}) were evaluated to compare relative mesh strength. For the ratio T_{13}/T_{24}, values close to 1 indicate isotropy, whereas values >1.5 indicate significant anisotropy. Data for the 1-3 and 2-4 strip tests were analyzed similarly. Images were analyzed to compute orthogonal strains of both the 90° and 45° orientations along the 1-3 and 2-4 axes of each mesh during biaxial and strip tests (E_{11} and E_{22} strains, respectively).

RESULTS

Peak tension values varied dramatically across all mesh types for all directions for both the 90° and 45° orientations (not shown). Meshes

Copyright 2016 The Organizing Committee for the 2016 Summer Biomechanics, Bioengineering and Biotransport Conference

oriented in either direction with a barrier coating tended to have higher peak equibiaxial tensions than those without a coating. Likewise, peak equibiaxial tensions in the 90° direction were higher than peak tensions in the 45° orientation for almost every mesh, indicating the mechanical impact of the warp/weft direction. Ratios of the 1-3 and 2-4 actuator peak tensions exhibit a large variation in the degree of anisotropy across samples (Figure 1). For the majority of the samples, the 90° orientation was observably more anisotropic when compared to the ratio of the same mesh in the 45° orientation.

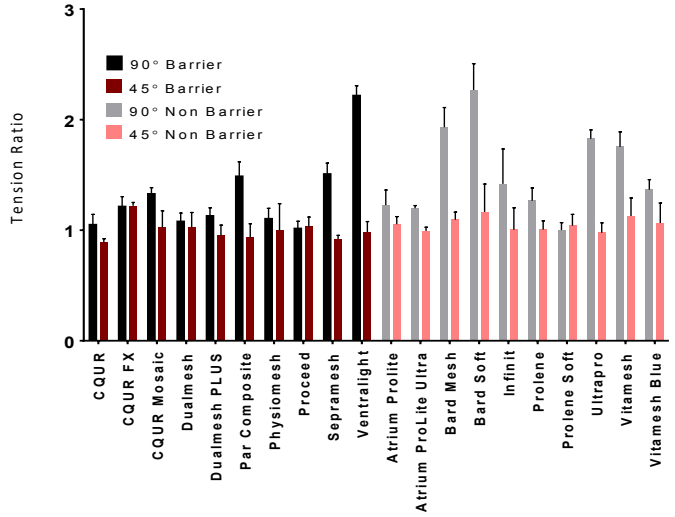

Figure 1: Ratio of peak tensions (F_{13}/F_{24}) in equibiaxial tests. Tension ratios provide a measure of mechanical anisotropy: several samples are isotropic (ratios of ~1) while others were highly anisotropic (ratios >1.5). Meshes oriented in the 45° were significantly more isotropic than those in the 90° orientation.

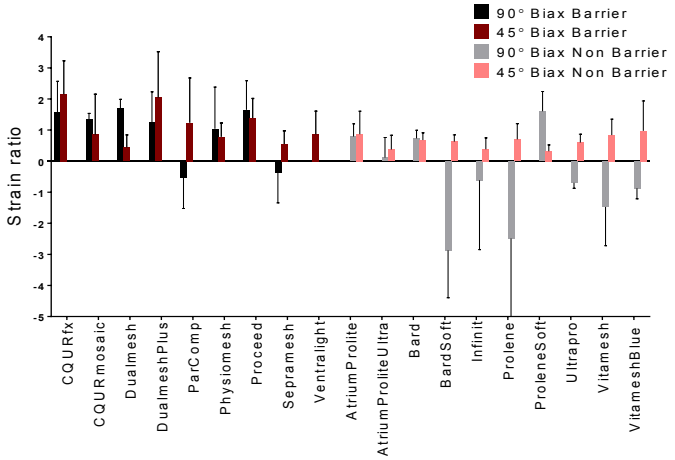

Figure 2: Ratio of peak strains (E_{11}/E_{22}) in equibiaxial tests. These ratios provide an approximation of the Poisson effect, and in turn, deformation anisotropy: some samples had ratios close to 1 and are considered isotropic while others were highly anisotropic. Meshes oriented in the 45° direction had ratios closer to 1 and were more isotropic than those in the orthogonal orientation.

Likewise, peak equibiaxial strain varied greatly across samples, with strain values ranging from almost -5% to 10% strain (not shown). There was no clear difference between peak equibiaxial strains of barrier and non-barrier groups. The ratio of peak equibiaxial strains (Figure 2) supports these observations, with very few samples having ratios close to 1, meaning there is a high prevalence of anisotropy in mesh deformation behavior across samples in both orientations. Similar to the tension ratios, the 90° orientation exhibited higher values for each mesh than the 45° orientation, indicating a higher degree of anisotropy in the orthogonal orientation. Likewise, it can be observed that the non-barrier meshes show several negative strain ratios with large magnitudes, which are not present in the barrier group. These high negative ratios are caused by a significant Poisson effect for meshes tested at angles not aligned to the warp/weft direction. The strip biaxial tests further confirmed the high variability among mesh samples as well as the wide ranges of strength and anisotropy of mechanics and deformation when the 1-3 strip peak values were compared to the 2-4 strip peak values (not shown).

DISCUSSION

The directions and magnitudes of forces present on a hernia defect within the body and the corresponding requirements for a successful prosthetic mesh are not well understood. As observed in this study, there is great mechanical variability amongst commercially available meshes. Likewise, there is a significant degree of anisotropy across the range of meshes, and even further, an observable difference between the anisotropy of barrier and non-barrier meshes.

While the magnitudes of the forces on biological abdominal wall are unknown, it is known that the forces on a hernia defect are present from all directions. If a mesh is highly anisotropic, there may be a greater risk of surgical failure. However, some meshes when tested at a 45° orientation displayed more isotropic behavior, meaning it may be advantageous for a surgeon to place meshes strategically depending on the patient's defect rather than what is most convenient.

A barrier coating is meant to prevent adhesion to the abdominal wall. However, results of this study suggest that a coating may also have the added effect of contributing to a more isotropic mesh, which may promote mechanical success in addition to preventing adhesion.

In order to provide the most successful hernia repair to a patient, a surgeon should consider not only the size and placement of the mesh, but the mechanical characterization of the mesh as well. As shown by the variability in the data, certain meshes may be more appropriate depending on the forces they will encounter within the body than others. In some cases, an isotropic mesh will be more successful, while other conditions for a specific patient may dictate a more anisotropy mesh. While further study of prosthetic meshes, in addition to better characterization of properties of the human abdominal wall, are needed, the results of this study provide valuable data that may aid clinicians in optimizing mesh selection for specific patients and repair conditions.

ACKNOWLEDGEMENTS

The authors thank Peggy Frisella, Jeffrey Blatnik, MD, and Michael Brunt, MD. Mesh samples donated by Bard, Inc., Atrium Medical Corp.,, and Ethicon, Inc.

REFERENCES

[1] Read, R., *Hernia,* 8(1):8-14, 2004.
[2] Deeken, C. et al., *Surgical Endoscopy,* 25(5):1541-1552, 2011.
[3] Deeken, C. et al., *Surgical Endoscopy,* 26(2):566-567, 2012.
[4] Deeken, C. et al., *JMBBM,* 38:6-16, 2014.

Copyright 2016 The Organizing Committee for the 2016 Summer Biomechanics, Bioengineering and Biotransport Conference

SB^{3}C2016
Summer Biomechanics, Bioengineering and Biotransport Conference
June 29 –July 2, National Harbor, MD, USA
SB^{3}C2016-588

THE EFFECT OF VARIABILITY IN WARFIGHTER POPULATION ON INJURY: A MODELING STUDY

Shankarjee Krishnamoorthi (1), Amit Bagchi (2), Siddiq M. Qidwai(2)

(1) NRL/ASEE Postdoctoral Fellowship
US Naval Research Laboratory
Washington, DC, USA

(2) Multifunctional Materials Branch
US Naval Research Laboratory
Washington, DC, USA

INTRODUCTION

Traumatic brain injury (TBI) is currently one of the leading causes of disability in the warfighters returning from the battlefield. While the exact mechanism of TBI is yet to be determined, it is often sustained during the interaction of blast with the head. Accurate modeling of this interaction can improve the understanding of TBI and aid in developing mitigating strategies by providing insights on the biomechanical measures like stress, strain, and pressure experienced by the tissue during such loading. Computational modeling has been used to understand the interaction between the human head and blast wave (e.g., [1]-[3]), however such modeling efforts do not account for the inherent variations in blast magnitude, human head size, shape and associated biological material properties. Hence such deterministic head models are not equipped to take into account the effect of variations on the occurrence and extent of TBI. The present work aims to compare blast-induced traumatic brain injury (TBI) response variation in warfighters by accounting for uncertainty or variations in insults, and warfighter characteristics (material and geometry). Blast simulations incorporating variations in four major inputs (blast magnitude, head volume, skull stiffness and brain shear stiffness) are performed. For each instance the injury response is evaluated by calculating the injured brain volume based on various injury thresholds for TBI. The comparison of injury responses allows development of effective mitigation strategies for actual representative population groups. The findings are also useful in understanding the effect of inherent variability among population groups in various other scenarios including blunt impact, vehicular collision and falls.

METHODS

A previously validated high fidelity geometric model [1] of the human head developed at Naval Research Laboratory is used for generating each instance of simulation. These individual instances are generated by applying affine transformations (generated by matching FE model to available human templates), changing the material property, or changing the blast magnitude (or a combination of these). The original geometry was developed using magnetic resonance imaging (MRI) scans of a human head (average 50th percentile Caucasian male of 26 years age). The 1-mm resolution scans provided a high fidelity head geometry, and captured all the important components (see Fig. 1(a)). Experimentally observed behavior of constituents, such as the hyper-viscoelasticity of the brain, rate-dependence of skull response, and incompressibility of CSF, dictated the choices of material models. This original validated head model is referred to as the 50th Percentile case.

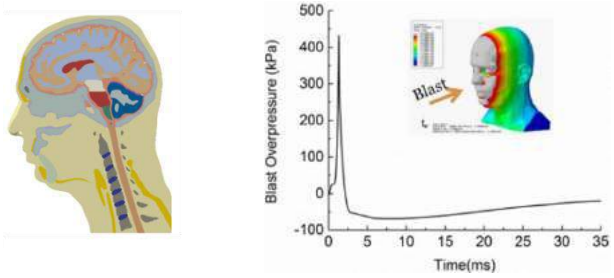

Figure 1: a) Interior structure of the model, b) Applied Friedlander wave profile and loading direction.

The blast loading on the 50th percentile case is simulated by applying a planar Friedlander pressure wave on the exposed surfaces of the head (see Fig. 1(b)). The individual model instances are created by accommodating variations in four major inputs. The magnitude of

Copyright 2016 The Organizing Committee for the 2016 Summer Biomechanics, Bioengineering and Biotransport Conference

variation of each input is based on the available data in literature (e.g., [[4, 5]), and is presented in Table 1. As a first step three distinct levels for each input variation are considered, requiring 81 separate blast simulations to be analyzed. Design of experiment techniques are therefore used to reduce the simulations set size. Specifically, a preliminary Taguchi L9 orthogonal design array is used to reduce the requirement to 12 distinct cases. For comparison, the injured brain volume percentage is calculated based on five different injury measures (stress and strain invariant) with thresholds obtained from the literature (see Table 2).

Table 1: Input variation used for various instances.

Input	Variation (%)
Blast magnitude	± 20
Head volume	± 25
Skull stiffness	± 20
Brain shear stiffness	± 20

Table 2: Injury measures and associated thresholds. Measure	Value	Injury
Pressure (kPa)	> 235	Severe TBI
	> -100	50% probability of DDM
Effective stress (kPa)	33	50% probability of severe DAI
Shear stress (kPa)	7.8	50% probability of mild TBI
Principal strain (%)	15	50% probability of mild TBI CSDM
Effective strain (%)	35	50% probability of severe DAI

RESULTS

From the predicted injury volume the main effect plot which compares the change in injured volume with variation in individual parameters is shown in Fig 2. The main effect plot was generated as follows. For a given value of blast magnitude, say nominal value, the other three parameters (head volume, skull and shear stiffness) were varied and the injured volumes were calculated and its mean was also calculated. The same is repeated for low and high values of blast magnitude. This results in 9 different values which are plotted. The mean values are connected by dotted lines and this is used to draw inferences on the influence of blast magnitude on injury volume. The same procedure is repeated for all the other variables and different injury measures.

Looking at the main effect plot for stress based criterion (Fig 2. (a)-(d)) the following are inferred:

1. Increasing the shear modulus leads to increase in injury volume as predicted by Tresca and Mises measures; however, it has minimal effect on pressure based criterion.
2. Change in volume has minimal effect on all injury measures.
3. Increase in blast magnitude and decrease in skull stiffness leads to increase in all injury measures.

In the case of principal strain based criterion (Fig 2. (e)) the inferences are similar to those observed with stress invariants except that a decrease in shear modulus leads to increase in injury measure. With an effective strain based criterion (Fig 2. (f)), the inferences are similar to those of principal strain except that now head volume affects injury measure.

DISCUSSION

The results indicate that the response of injury measure with variation in input is not always intuitive. A single factor can be either positively correlated or negatively correlated, or not correlated to the injured volume. The addition of variability in input shows different outcomes for injury measures when changing certain parameters. The effect plots showcase the challenge of using currently suggested injury measures in the literature. The deterministic simulations so far have been focused on comparing and evaluating injury measures. These results highlight the shortcomings of a single simulation performed on an average human head, and strongly motivate the case for accounting for variability and reevaluation of injury measures suggested in literature in the same context.

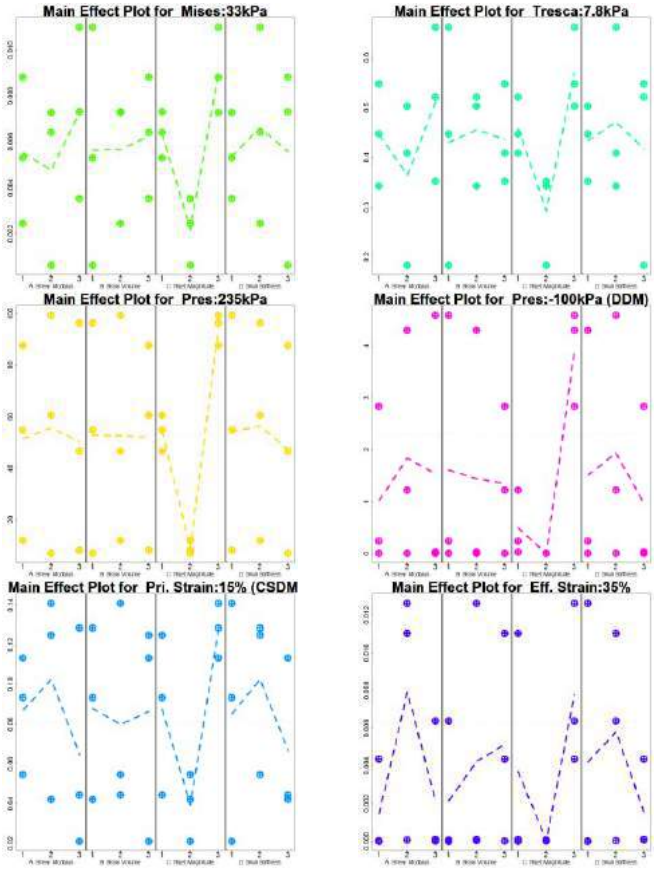

Figure 2: Main effect plot of different injury measures (a) – (d) stress invariant based measures, (e) principal strain and (f) effective strain.

ACKNOWLEDGEMENTS

The authors gratefully acknowledge the support from the American Society for Engineer Education postdoctoral fellowship to Shankarjee Krishnamoorthi. This work was supported by the Office of Naval Research (ONR) under contract number N001415WX00531 and through the US Naval Research Laboratory's Basic Research Program.

REFERENCES

[1] Cotton, RT et al., *Comput Method Biomec*, **19**(1):101-113.

[2] Zhang, L et al., *SAE Technical Paper,* SAE. No. 2001-22-0017. 2001.

[3] Takhounts, EF et al., *SAE Technical Paper,* SAE. No. 2003-22-0007, 2003.

[4] Gordon, CC et al. 2010 Anthropometric Survey of US Marine Corps Personnel: Methods and Summary Statistics. No. NATICK/TR-13/018, 2013.

[5] Rashid, B et al., *J Mech Behav Biomed*, 10:23-38, 2012.

Copyright 2016 The Organizing Committee for the 2016 Summer Biomechanics, Bioengineering and Biotransport Conference

SB^{3}C2016
Summer Biomechanics, Bioengineering and Biotransport Conference
June 29 –July 2, National Harbor,MD, USA
SB³C2016-589

POLYDOPAMINE BASED INSULATING COATING FOR SHAPE MEMORY ALLOY BIOMEDICAL DEVICES

Mohammad Sahlabadi, Yao Zhao, Fei Ren, Parsaoran Hutapea*

Department of Mechanical Engineering
Temple University
1947 N 12th Street
Philadelphia, PA, USA
* hutapea@temple.edu

INTRODUCTION

Shape memory alloy (SMA) materials, such as Nickel Titanium (NiTi), can generate stress and strain during phase transformation induced by thermomechanical stimulation. Therefore, they may be used to construct active actuating devices for various biomedical applications such as smart needles [1,2]. Since temperature rise during the operation of SMA devices may damage the surrounding tissue, it is important to thermally shield such devices.

We propose to use polydopamine (PDA) [3, 4] as an insulating coating for NiTi-based smart needles. PDA is a biomolecule (dopamine) derived polymer, that can form conformal coating on various materials including NiTi. It is hypothesized that the surface temperature of the PDA coated needle can be reduced by the low thermal conductivity of PDA and the thermal resistance of the PDA/NiTi interface.

Our preliminary experiments conducted in ambient air at room temperature showed that the coating reduced the surface temperature by 45%. In this paper, we will present the thermal insulating performance of the PDA coating on NiTi wires. An experimental setup where the wire is embedded inside a gel phantom [5] has been developed to simulate needle-tissue interaction. Effects of the coating thickness (material thermal resistance) and the number of layers (interfacial thermal resistance) will be discussed. Experimental data will also be compared with finite element analysis (FEA) results.

METHODS

In this study, PDA films were applied onto NiTi wires using a dip coating method. Coating was conducted in mild base solutions at room temperature. Samples with different PDA layer thickness and total number of layers were fabricated. The thickness of the PDA coating was controlled by varying the coating time.

Thermal properties of the PDA were studied using differential scanning calorimetry and thermogravity analysis. Coating morphology and thickness were examined by scanning electron microscopy (SEM) and atomic force microscopy (AFM).

To study the thermal insulation performance, NiTi wires with and without PDA films were inserted into a gel phantom [5]. Electrical current was applied through the wires, and the temperature distribution in the gel surrounding the wires was measured using thermalcouples and infrared imaging.

On the other hand, finite element analysis (FEA) was performed to study the temperature distribution, where the thermal properties of the materials were obtained from experimental measurements (i.e. differential scanning calorimetry).

RESULTS

The NiTi wires can be coated with PDA, and the thickness varies from tens to hundreds of nanometers. The thickness of the coating on the wire can be observed using SEM (Fig 1). Fig. 1(a) shows a bare NiTi wire surface without PDA coating. The grain boundaries can be clearly identified. Fig. 1(b) shows a PDA-coated NiTi wire surface, where a continuous film was observed and the grain boundaries became blurry to distinguish .Fig. 1(c) is a backscattered electron image of the cross-section of a coated NiTi wire. Fig. 1(d) shows a combined secondary/backscattered electron microscopy image of the cross-section of a PDA-coated NiTi wire, where the PDA coating can be idenfitied.

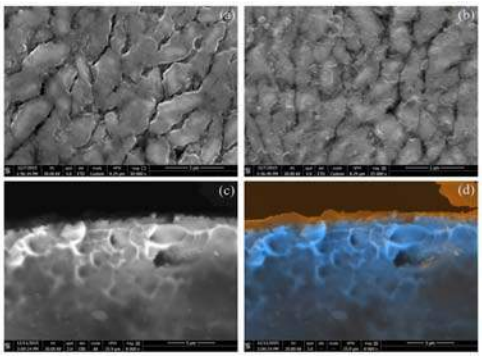

Figure 1: SEM images of NiTi wire with and without PDA coating. (a) NiTi wire without PDA coating. (b) NiTi wire with PDA coating. (c) The cross-section of NiTi wire (brighter) with PDA coating (darker film). (d) The overlay image of secondary/backscattered electrons of PDA coating (orange) on the surface of NiTi alloy (blue).

Copyright 2016 The Organizing Committee for the 2016 Summer Biomechanics, Bioengineering and Biotransport Conference

A preliminary study using NiTi wires with diameter of 0.25 mm was performed. The uncoated and coated wires were tested using the test setup as shown in Fig. 2. The NiTi wire was dipped inside of the PDA solution which was made by adding dopamine hydrochloride into Tris buffer. The NiTi wires were activated using Joule heating by applying current as a ramp function and wire temperature was measured using k-type thermocouples. Note in this experiment, the wire was exposed to the ambient air.

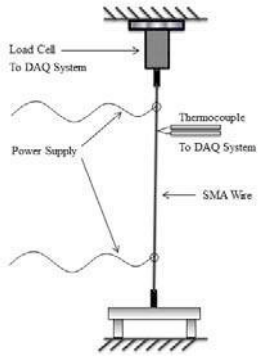

Figure 2: Schematic of test setup to measure the surface temperature on the coated and uncoated wires by using thermocouples.

In this preliminary study, a series of experiments on coated and uncoated wires were performed. As shown in Fig. 3, the average surface temperature is about 80-82 ºC on the uncoated wires and 47-48 ºC on the coated wires. This represents a 45% reduction of temperature when the wires were coated by PDA.

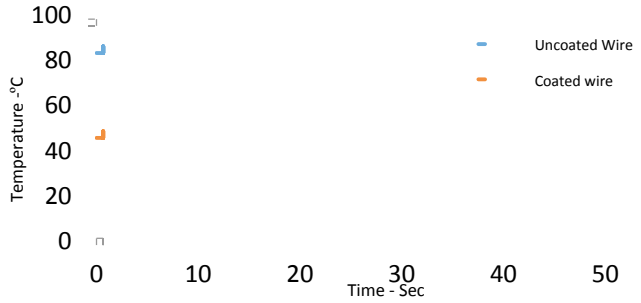

Fig. 3. The surface temperature as a function of time on coated and uncoated NiTi wires tested in ambient air.

In order to simulate the influence of the temperature change of the wire on tissues, an experimental setup was developed such that the wires are embedded in a gel phantom. Fig. 4(a) shows the experimental setup, which is used in this study. The gels is made of PVC in combination with a softener, and wire placed inside the gels in a way which all its part is in full contact with the gel. As a result of the good connection, conduction is believed to be the major mechanism of heat transfer. Fig. 4(b, c, d)) represent the temperature distributions around the uncoated NiTi wire inside the gels. As it shows in Fig. 4, the temperature decreases when moving away from the NiTi wire.

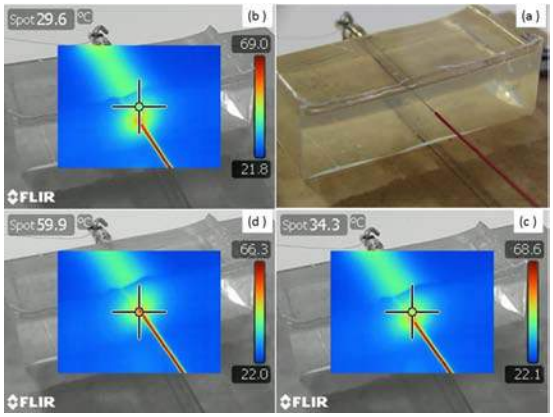

Figure 4: Temperature distribution near an uncoated Ni-Ti wire measured using an IR camera. (a) Experimental setup. (b), (c), (d) temperature distribution around the wire at different distances .

DISCUSSION

Our preliminary results (Figure 3) indicate the PDA coating can effectively reduce the surface temperature of an activated NiTi wire. Two mechanisms may be responsible for this effect: low thermal conductivity of the PDA film, and the NiTi/PDA interface. Detailed study will be carried out to evaluate the contribution of the two factors to determine which is the major contributor to the enhanced thermal resistance.

On the other hand, finite element analyses (FEA) will be used to study the thermal distribution on the interface of the wires and tissues. The FEA results will be used to optimize the coating parameters including the thickness and number of NiTi/PDA interfaces.

ACKNOWLEDGEMENTS

The authors thank the Department of Defense (DoD) CDMRP Prostate Cancer Research Program (Grants# W81XWH-11-1-0397/98/99) for the funding support and Temple University Seed and Bridge Grant Funds.

REFERENCES

1. N. V. Datla, P. Hutapea, “Flexure-based active needle for steering within soft tissue,”*ASME Journal of Medical Devices*, Vol. 9, No. 4, 041005-041005-6, August 2015, doi:10.1115/1.4030654.
2. B. Konh, N. V. Datla, P. Hutapea, “Feasibility of SMA Wire Actuation for an Active Steerable Cannula,” *Journal of Medical Devices*, Vol. 9, No. 3, 021002-021002-11, June 2015.
3. Q. Wei, F. Zhang, J. Li, B. Li, and C. Zhao, “Oxidant-induced Dopamine Polymerization for Multifunctional Coatings,” *Polymer Chemistry*, The Royal Society of Chemistry, 1430-1433, 2010.
4. Zhou P, Deng Y, Lyu B, Zhang R, Zhang H, Ma H, et al, “Rapidly-Deposited Polydopamine Coating via High Temperature and Vigorous Stirring: Formation, Characterization and Biofunctional Evaluation,” *PLoS ONE* 9(11): e113087. doi: 10.1371/journal.pone.0113087.
5. N. V. Datla, J. Koo, D. Choi, B. Konh, T. M. Nguyen, T. K. Podder, K. Darvish, A. P. Dicker, Y. Yu, P. Hutapea, “Polyacrylamide Phantom for Needle-Tissue Interaction Studies with Active Needles,” *Medical Engineering and Physics*, 36, pp. 140 – 145, 2014.

Copyright 2016 The Organizing Committee for the 2016 Summer Biomechanics, Bioengineering and Biotransport Conference

SB^{3}C2016
Summer Biomechanics, Bioengineering and Biotransport Conference
June 29 –July 2, National Harbor, MD, USA
SB^{3}C2016-590

REGISTRATION, REGIONAL IDENTIFICATION, AND TRANSFER OF DATA FROM MRI SCANS TO FINITE ELEMENT MODELS

Shankarjee Krishnamoorthi (1), Siddiq M. Qidwai (2)

(1) NRL/ASEE Postdoctoral Fellowship
US Naval Research Laboratory
Washington, DC, USA

(2) Multifunctional Materials Branch
US Naval Research Laboratory
Washington, DC, USA

INTRODUCTION

With advances in imaging technology, magnetic resonance imaging (MRI) and diffusion tensor magnetic resonance imaging (DT-MRI) data have proven to be very useful in multiple ways. The generated images chiefly provide detailed anatomical information for prognostic purposes, but computational modelers have found them to be as advantageous. Computational analysts typically face two-pronged challenges in handling MRI-based scans: (i) registration, i.e., alignment of data, and (ii) transfer of data to the numerical model using consistent interpolation techniques. The finite element (FE) models used for modeling the brain are typically deterministic in nature, whereas the human head is subject to variability. Hence, the main issue of registration is the need to transform the MRI data into the FE model coordinate system and match (through translation, shear and scaling) the topologies. The DT-MRI data representing the white matter fiber tractography essentially requires the same treatment with more robust considerations for the mapping due to the tensorial complexity of fiber orientations.

Manual registration of regions in the brain is error prone and also prohibitive in terms of time spent. In a very effective study on automatic registration with head and brain as the focus, Klein et al [1] evaluated 14 different nonlinear algorithms (FLIRT, AIR, ANIMAL, ART, Diffeomorphic Demons, FNIRT, IRTK, JRD-fluid, ROMEO, SICLE, SN and 4 different SPM5 based methods), and identified three schemes as the most effective ones. However, the transformation methods analyzed in their study are applicable to transferring data from one MRI structured dataset to another structured dataset and not from an MRI dataset to an unstructured dataset as in an FE mesh. To address this gap we layout one method here, which can be used to transfer data between structured datasets as well as between non structured data sets. We cast the problem into a point cloud matching problem and compute an affine transform which maps given source and target point clouds. We demonstrate the scheme by registering and transferring data between MRI's and also from MRI to an FE mesh. Then using the transformed dataset we interpolate diffusion tensor data from MRI to the same FE mesh.

METHODS

In the proposed scheme, we do not match MRI's to each other or the FE model described by the mesh, based on topology or topological features. For each voxel, a point is generated at its center and, in turn, the point cloud this generates represents the brain captured by the MRI. In the case of an FE mesh a similar point cloud can be generated from the nodal locations or integration points within each element, or elemental centroids. In our work we use the elemental centroid. Now the problem is matching up point clouds, which is routinely performed in disparate tasks such as surface reconstruction and optimal path planning.

Iterative Closest Point (ICP) [2] is a computational scheme for registration of 3D shapes including free form curves and surfaces. A typical ICP algorithm only involves rotation and translation. A finite version of the same called as FICP involves scaling, rotation and translation. The scaling part is crucial when trying to match up point clouds where the bounding box sizes are not close enough. The basic steps involved in point cloud matching are

1. For each point in the source point cloud the closest point in target point cloud is computed.
2. An affine transformation is applied to the entire source point cloud and the distance between each affine transformed source point and closest target found in step 1 is accumulated.
3. The accumulated distance function is minimized to get the next set of affine transformation coefficients.

Copyright 2016 The Organizing Committee for the 2016 Summer Biomechanics, Bioengineering and Biotransport Conference

4. The procedure is repeated till the accumulated distance error is minimized as defined.

The FICP routine library implemented in Matlab [3] was used in the following work.

DT-MRI measurements were conducted on a healthy 29 year old male; the accumulated data is used as the structured target data. The brain atlas developed by Oishi et al [4] is used as the structured source data. This particular atlas is chosen because 189 unique brain regions are identified in it, which is useful for injury analysis purposes in later studies. Lastly, the unstructured target data is obtained from an in-house FE model of a human male of 26 year age.

RESULTS

Fig 1(a) shows the initial exterior point cloud of the target and source scans, and 1(b) shows the final point cloud generated after applying the affine transformation by FICP.

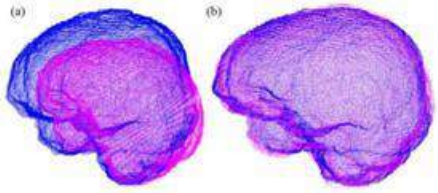

Figure 1: The exterior point cloud of the source and target scans: a) brain atlas, i.e. the source, is blue and target in magenta, b) Superposed transformed source point cloud over the target cloud.

The goodness of the fit was evaluated using error metrics used in [1] and the values obtained are tabulated in Table 1. A value of 1 means perfect total overlap, mean and union overlap, whereas 0 implies the same for volume similarity, false positive and false negative. In another post-processing step, for each target voxel the nearest source point within a cube of 3 units centered at the target voxel was identified and given the same region as the target voxel. The resultant target data with regions assigned is shown in Fig 2.

Table 1: Values of error metrics.

Volume Similarity	Total Overlap	Mean Overlap	Union Overlap	False Positive	False Negative
0.105	0.885	0.932	0.872	0.017	0.127

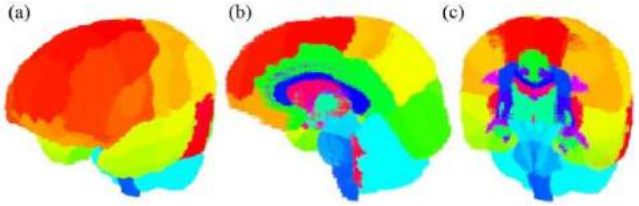

Figure 2: Target scans with 189 regions color coded displayed similar to color coded brain atlas scans.

For the process to match structured dataset to unstructured dataset, the exterior of the FE model of the human brain was extracted. However, the detailed mesh includes folded features in the brain namely the sulci, which are not present in the exterior of the source MRI scan. To circumvent this issue only the convex hull of the mesh was chosen as the target cloud. As the convex hull was sparse, for every point on the hull a closest neighbor was also generated on the hull. Fig 3 shows these point clouds and the final transformed point clouds.

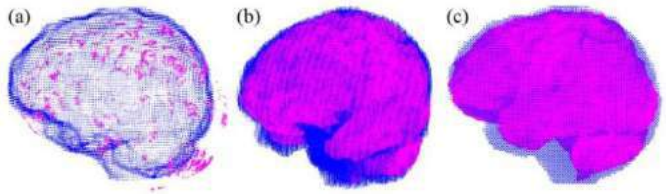

Figure 3: (a) Blue denotes the MRI exterior point cloud and magenta the convex hull + neighbors of the FE mesh. Two views of the transformation are shown in (b) and (c).

To evaluate the fit for the second transformation, diffusion tensor data from the DT-MRI scans was interpolated to the FE model using the Log Euclidean interpolation method (details withheld for brevity). The primary diffusion tensor directions are plotted for both the MRI scan and the interpolated data in the FE scan in Fig. 3. For the sake of visual comprehension, only vectors for a partial range of fractional anisotropy (FA) values are displayed here.

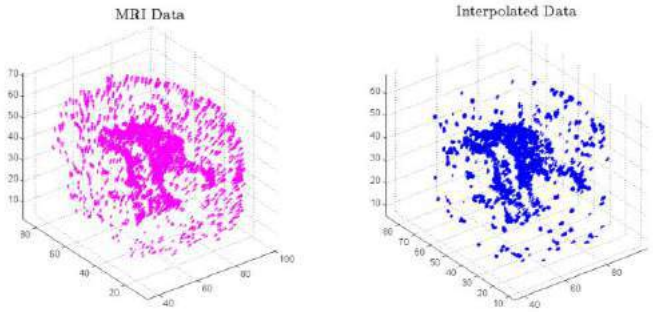

Figure 4: The primary fiber vector plot for the original MRI dataset and the interpolated data in the FE model, for a limited range of fractional anisotropy (FA) values: $0.7 \leq FA \leq 0.8$.

DISCUSSION

In this work we have implemented an affine transformation based image mapping scheme which can be used both for structured and unstructured grid image data. We used it to transfer data between structured MRI datasets, and also between MRI and an unstructured FE mesh. The errors computed using popular error metric values are shown to be within reasonable limits. The proposed scheme is also successfully used to transfer diffusion tensor data to the FE model. This accomplishment now allows for full anisotropic representation of the brain in computational modeling as well as fitting of data from variable subjects to one FE model. The later point is important because it is exceedingly difficult usually to get all the pertinent data (MRI, DTI, computed tomography (CT), magnetic resonance elastography (MRE), etc.) from one subject for computational modeling needs.

ACKNOWLEDGEMENTS

The authors gratefully acknowledge the support from American Society for Engineer Education postdoctoral fellowship to Shankarjee Krishnamoorthi. This work was supported by the Office of Naval Research (ONR) under contract number N001415WX00531 and through the US Naval Research Laboratory's Basic Research Program.

REFERENCES

[1] Klein, A et al., *Neuroimage*, **46**(3):786-802, 2009.

[2] Besl, PJ and McKay ND, *International Society for Optics and Photonics*, **14**(2):239-256,1992.

[3] Kroon, D. J, *University of Twente*, 2011.

[4] Oishi, K et al., *Neuroimage*, **46**(2):486-499, 2009.

Copyright 2016 The Organizing Committee for the 2016 Summer Biomechanics, Bioengineering and Biotransport Conference

SB^{3}C2016
Summer Biomechanics, Bioengineering and Biotransport Conference
June 29 –July 2, National Harbor, MD, USA
SB^{3}C2016-591

STOCHASTIC HEAD MORPHOLOGY DESCRIPTION FOR UNCERTAINTY QUANTIFICATION OF TBI PREDICTION

Kirubel Teferra (1), Siddiq M. Qidwai (2), Shankarjee Krishnamoorthi (3)

(1) Multifunctional Materials Branch
US Naval Research Laboratory
Washington, DC, USA

(2) Multifunctional Materials Branch
US Naval Research Laboratory
Washington, DC, USA

(3) NRL/ASEE Postdoctoral Fellowship
US Naval Research Laboratory
Washington, DC, USA

INTRODUCTION

Detailed finite element (FE) modeling of the human head subjected to blast loading scenarios currently provides the only viable means to quantifying mechanical response within the brain for traumatic brain injury (TBI) prediction. Although the exact relation between tissue mechanical response and injury is still quite unknown, the exceedance of threshold values based on direct and derived measures of stress, strain and acceleration within the brain are commonly used as criteria for injury. Similarly, while preliminary parametric studies varying head morphology and material properties of head components have shown significant variation in predicted injury response, an established relationship is yet undetermined. Furthermore, there is a lack of prediction consistency for the given criteria due to parametric variation. To illustrate this point, Figure 1 shows the results of a parametric study exposing the dependence of predicted injury criteria on head morphology and properties. The head volume, skull stiffness, brain shear stiffness, and blast magnitude are varied by $\pm 25\%$, $\pm 20\%$, $\pm 20\%$, and $\pm 10\%$, respectively, with respect to a model representing the 50th percentile Caucasian male. Injury for contusion and laceration are considered when pressure magnitude exceeds 173kPa and -100kPa, respectively, while shear injury is considered where principal strain magnitude exceeds 5%. These results show strong sensitivity of injury criteria (i.e., mechanical response) to reasonable parametric variation, and that the different criteria have different behaviors with respect to this variability. Due to the large input parameter dimension needed to describe human and loading scenario variations, it is not apparent upfront how to construct transfer functions relating input variation and injury criteria, which is necessary to determine, for example, the probability of exceeding the given threshold responses.

This work lies within an overall effort to improve the confidence as well as quantify the uncertainty of TBI prediction, whereas its focus is on developing an accurate and parsimonious representation of the variation of human head morphology. An improved understanding of inter-subject morphological variation is essential to obtaining accurate mechanical response variation. Since this input uncertainty must be propagated through large FE models, the goal is to identify a stochastic reduced order model that has the least number of parameters while retaining accuracy with respect to an error measure.

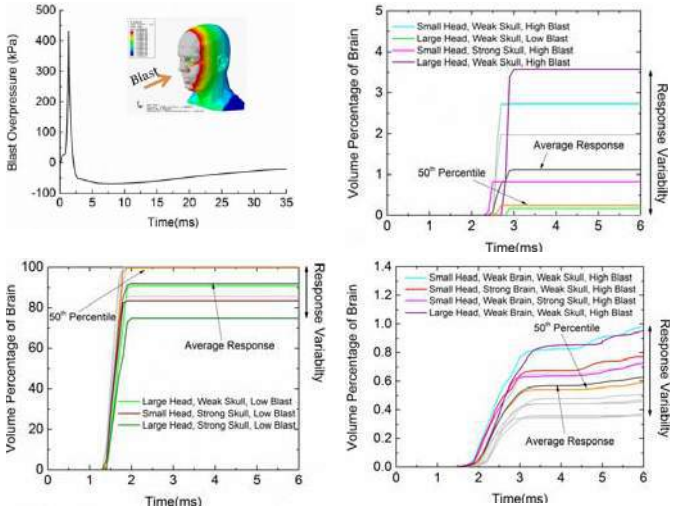

Figure 1: (a) Head subjected to blast loading modeled as a planar Friedlander pressure wave (top left) along with percent

Copyright 2016 The Organizing Committee for the 2016 Summer Biomechanics, Bioengineering and Biotransport Conference

volume of brain exceeding injury criteria for: laceration (top right), contusion (bottom left), and shear injury (bottom right).

METHODS

The procedure introduced herein to develop a stochastic model of the human head is to: (1) warp a template model to individual subjects; (2) apply dimensionality techniques to reduce the number of parameters describing the mappings; and (3) employ stochastic simulation algorithms to generate optimally selected samples to undergo detailed FE analysis for uncertainty propagation.

The data of head morphology is obtained from the International Consortium for Brain Mapping (ICBM) database, which is a collection of serial section grayscale images (e.g. magnetic resonance images (MRIs)) of human heads from varying sources. Out of the 1342 subjects, 185 that were identified to have full head and brain scans are selected for the study. These 3D images are segmented using BrainSuite(R) to extract masks for the brain and the whole head. The template used as the source of the warping algorithms is a high-resolution whole head T1-weighted MRI dataset of a healthy 26 year old male, representing the 50th percentile Caucasian male, which has been manually segmented using Simpleware(R) software to identify 33 unique regions [1]. The effectiveness of two warping algorithms among many suggested in [2] to map a template head to each one of the subjects is first studied for tradeoff between accuracy and model size. The first choice is the use of affine transformations, which contain only 9 parameters (without considering translation). The second choice of diffeomorphism mappings, such as Statistical Parametric Mapping (SPM) [3], do not have a restrictive model form but requires costly optimization routines to obtain a stationary point for its large parameter set (e..g $O(10^6\text{-}10^7)$). In order to propagate this large parameter set through expensive computational models, linear (principal component analysis) and nonlinear dimension reduction techniques, such as local linear embedding and related methods, need to be applied to the mappings to extract a set of intrinsic parameters of low order dimension.

The next step is then to derive the statistical distributions of the mapping parameters obtained from either scheme and use them with the stochastic simulation techniques (e.g., Nataf transform or Markov Chain Monte Carlo) to generate instances of accurate virtual head models. These instances are judged against the template MRI dataset to ensure that they fall within accepted variations and an attempt then can be made to identify the characteristic geometric features of the human head common across all instances.

RESULTS

Masks for the head and head-brain were created for all the subjects and the template, and Figure 2 shows these images for the template. Initial studies mapping these template masks to each subject via global affine maps resulted in significant errors. An error metric is defined as the total mismatch volume normalized by the volume of the subject, given as

$$E = \frac{|\, t(\boldsymbol{x}) \setminus (t(\boldsymbol{x}) \cap s(\boldsymbol{x}))| + |\, s(\boldsymbol{x}) \setminus (t(\boldsymbol{x}) \cap s(\boldsymbol{x}))|}{|t(\boldsymbol{x})|}, \quad (1)$$

for $t(\boldsymbol{x}), s(\boldsymbol{x})$ being the target and the warped template masks, respectively, and $|\cdot|, \setminus, \cap$ denoting volume, set difference, and set intersection, respectively. The histograms of this error for the head and head-brain masks are shown in Figures 2a and 2b, respectively. The errors for the affine transformation are too large to be acceptable. Since the injury criteria are rather sensitive to morphology and properties, as illustrated in Figure 1, mapping errors will have significant unwanted contributions to the variance of predicted injury response. For this reason, the affine transformation model is deemed an insufficient stochastic model for head morphology. The SPM model has also been implemented and the results of an optimization from the template to one subject is shown in Table 1. The exceptional improvement in accuracy is accompanied by the expensive optimization problem and large dimension of the mapping. Currently, the mappings to all 185 subjects are being executed by the SPM algorithm upon which statistical dependence among the parameters will be evaluated to extract an accurate, low dimensional representation. This representation will then be described statistically and stochastic simulation techniques will be used to generate virtual head models.

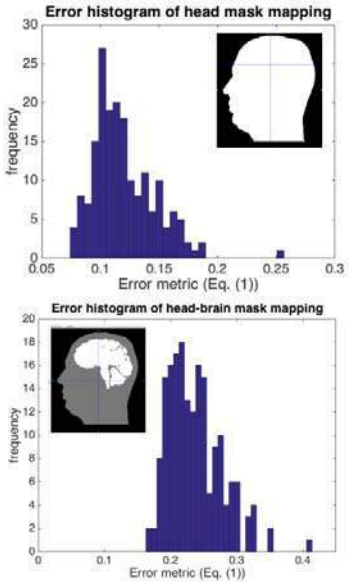

Figure 2: Error metric (Eq. (1)) histogram for affine transformation for head and head-brain mask.

Table 1: Error metric (Eq. (1)) to compare affine transformation with SPM for an arbitrarily selected subject.

	Affine	SPM
Head mask	11.2%	1.6%
Head-brain mask	19.6%	3.8%

DISCUSSION

Due to the sensitivity of the injury criteria to head morphology and properties, the affine transformation based stochastic model contains too much error to provide the probability distribution of injury criteria with high confidence. The initial accuracy of SPM algorithm suggests that its mapping results will provide an accurate stochastic model. It is likely that the extremely large parameter space can be reduced to a low dimensional set of parameters, such that it is feasible to propagate this uncertainty through expensive computational models. The results of this ongoing study will soon be completed and presented.

ACKNOWLEDGEMENTS

This work was supported by the Office of Naval Research (ONR) through the US Naval Research Laboratory's Basic Research Program.

REFERENCES

[1] R.T. Cotton, C.W. Pearce, P.G. Young, N. Kota, A.C. Leung, A. Bagchi, and S. Qidwai, *Comput. Methods Biomech. Biomed. Engin.* 19 (2015) p. 1.

[2] A. Klein, et al., *Neuroimage.* 46 (2009) p. 786.

[3] J. Ashburner, *Neuroimage.* 38.1 (2007) p. 95.

Copyright 2016 The Organizing Committee for the 2016 Summer Biomechanics, Bioengineering and Biotransport Conference

SB³C2016
Summer Biomechanics, Bioengineering and Biotransport Conference
June 29 –July 2, National Harbor, MD, USA
SB³C2016-592

EFFECT OF ABLATION PATTERN ON MECHANICAL FUNCTION IN THE ATRIUM: A FINITE-ELEMENT STUDY

Thien-Khoi N. Phung (1), Patrick T. Norton (3), John D. Ferguson (2), Jeffrey W. Holmes (1, 2, 4)

(1) Department of Biomedical Engineering
University of Virginia
Charlottesville, VA, USA

(2) Department of Medicine
University of Virginia
Charlottesville, VA, USA

(3) Department of Radiology
University of Virginia
Charlottesville, VA, USA

(4) Robert M. Berne Cardiovascular Center
University of Virginia
Charlottesville, VA, USA

INTRODUCTION

Catheter ablation is a common treatment for atrial fibrillation (AF). Ablation is used to electrically isolate specific regions by cauterizing regions of atrial muscle, which are then replaced by non-conducting scar. Successful ablation frequently restores sinus rhythm; however, it does so at the cost of decreasing the amount of viable myocardium. Ablation patterns have been designed to isolate regions of the atrium including the step-wise pulmonary vein isolation (PVI) and wide area circumferential ablation (WACA), with many studies comparing the efficacy of these two techniques [1-5]. The WACA pattern has been shown to be moderately more successful when coupled with additional ablation lines determined by electrical mapping to target areas with complicated electrical signals [6-8]. The progression of ablation techniques has seen the development of patterns targeting the different atrial walls, as well as more aggressive catheters that increase scar volume and transmurality [9-13].

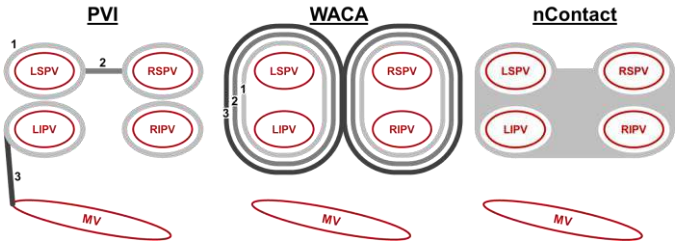

Figure 1: Left atrial ablation scar patterns in relation to mitral valve (MV), left superior (LSPV), left inferior (LIPV), right superior (RSPV), and right inferior (RIPV) pulmonary veins for the step-wise PVI (left, 3 steps shown), three variants of the WACA (center), and nContact's posterior ablation (right).

The general trend in ablation for atrial fibrillation has been to induce larger amounts of scar in the hopes of preventing AF recurrence and the need for repeat procedures; however, relatively little attention has been paid to the consequences of more aggressive ablation for mechanical function. Studies of ablation efficacy have been limited to global volume-based analyses, indicating a need for regional analysis to determine the functional impact of scar on different atrial areas [14]. Our group has previously published a coupled finite-element and circulation model of the left atrium, which was used to explore the mechanics of AF [15]. We used the baseline AF model to simulate various ablation patterns and determine their effect on atrial function. In particular, we included a recently introduced ablation pattern that targeted the entire posterior wall. With the different ablation patterns varying in scar volume and location, we hypothesized that placing ablation scar in areas with the highest baseline regional function will decrease atrial mechanical function.

METHODS

The coupled finite-element and circulation model of the left atrium used a transversely-isotropic Mooney-Rivlin material for the myocardium [15]. The baseline AF model features a dilated atrial geometry, diffuse fibrosis, increased loading pressure, delayed conduction velocity, and impaired left ventricular relaxation. This model was used as a platform to simulate atrial function after introducing various amounts and patterns of ablation scar. Material properties for the scar were created by isotropically stiffening the myocardial material, eliminating all anisotropic properties, and removing active contraction.

Ablation scar was introduced to the model by transmurally modifying local material properties prior to simulation. 13 ablation patterns were modeled including the step-wise PVI, WACA with circles of three different radii, and a posterior ablation developed by nContact,

Copyright 2016 The Organizing Committee for the 2016 Summer Biomechanics, Bioengineering and Biotransport Conference

Inc (Fig. 1). The PVI and WACA lines were simulated with two widths (4 and 8 mm) to represent RF and cryo-ablation lines.

Ablation scar was quantified as wall volume percentage of the left atrium. We analyzed global pressure-volume loops and regional function for each ablation model. Both global and regional volume changes were quantified separately for the passive and active phases of atrial emptying. Regional analysis of wall motion was performed using a floating origin coordinate system and regions defined by the pulmonary veins [15, 16]. Wall motion was calculated as the change in radius from maximum volume to minimum volume throughout the cardiac cycle.

RESULTS

The ablation patterns simulated spanned a range of 5% to 31% scar volume. In the presence of ablation, the passive atrium was stiffer, which hindered passive filling (Fig. 2). Active work by the atrium also decreased with increasing ablation scar. Total emptying volumes decreased by 0.3 to 10.9 mL in comparison to baseline. The passive emptying portion did not change much, -0.5 to 0.4 mL; however, active emptying decreased by 0.1 to 11.3 mL with increasing scar volumes.

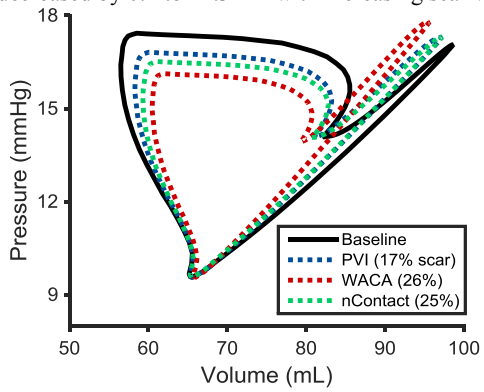

Figure 2: Pressure-volume loops comparing cryo-PVI, cryo-WACA, and nContact ablation patterns.

To compare active function among the different ablation patterns, we used wall motion in the inferior, lateral, and superior regions. Fig. 3 compares the cryo-PVI, cryo-WACA, and nContact ablation pattern. Cryo-WACA impaired global function primarily through a decrease in lateral wall motion. With similar scar volumes, nContact changed wall motion less in most regions, with regional and global effects more similar to the lower scar volume cryo-PVI.

DISCUSSION

Our simulated ablation scar volumes covered a comprehensive range consistent with imaging-based quantification of scar in clinical studies [14, 17]. Globally, adding ablation scar increased passive stiffness of the atrium, which is intuitive from the stiffer material properties of the scar. With similar scar volumes of 26% and 25% for cryo-WACA and nContact respectively, the cryo-WACA model had a higher passive stiffness, seen during passive filling and emptying (Fig. 2). This indicates that in addition to scar volume, scar location is an important determinant of passive atrial mechanics. Active function – reflected in the area inside the PV loop – followed similar trends, with cryo-WACA resulting in the greatest impairment, again suggesting that scar location is an important determinant of functional impact in addition to scar volume.

The nContact scar is similar to a PVI with the addition of ablation to the entire posterior wall extending into the inferior wall (Fig. 1). As a result, the inferior wall motion for nContact is similar to that of the cryo-WACA pattern (Fig. 3). However, the nContact lesion set avoids regions of the atrium that normally move the most, particularly the lateral wall. The cryo-WACA pattern extended into the lateral wall, creating a stiff belt of scar that inhibited motion. Because the nContact and cryo-PVI patterns did not extend into the lateral wall, they had a smaller impact on regional wall motion. These regional differences in wall motion are important metrics for evaluating mechanical function with regards to scar location.

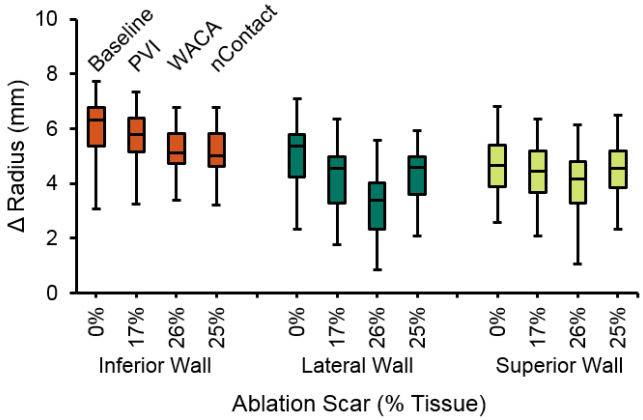

Figure 3: Inferior, lateral, and superior wall motion analysis comparing cryo-PVI, cryo-WACA, and nContact ablation patterns.

Given the different varieties of ablation techniques, we were able to directly compare how the different scar volumes and locations affected atrial mechanical function. In particular, we identified the effect of three different scar patterns on function of the free walls of the atrium (inferior, lateral, and superior). Our results suggest that different ablation patterns have different effects on post-ablation mechanical function. Specifically, ablations that involve regions with the highest baseline regional function (the atrial free walls) reduce function more than ablations in regions with low baseline function such as the posterior wall. The nContact pattern creates a large scar volume; however, the scar location is primarily on the posterior wall, an area that normally moves little because it is anchored by the four pulmonary veins. In clinical practice, the risks of recurrence must be weighed against the risks of damaging mechanical function when planning ablation; moving forward, there is a need for models that can simulate not only mechanical but also electrical effects of specific ablations.

ACKNOWLEDGEMENTS

This work was partially supported by a grant from nContact, Inc. The authors wish to thank Christian Moyer for technical assistance with the modeling and Jim Whayne (nContact) for valuable discussions.

REFERENCES

[1] Oral, H et al., *Circulation*, 108(19):2355-2360, 2003. [2] Hocini, M et al., *Circulation*, 112(24):3688-3696, 2005. [3] Karch, M et al., *Circulation*, 111(22):2875-2880, 2005. [4] Lemola, K et al., *J Am Coll Cardiol*, 46(6):1060-1066, 2005b. [5] Arentz, N et al., *Circulation*, 115(24):3057-3063, 2007. [6] Schmitt, C et al., *J Cardiovasc Electrophysiol*, 18(10):1039-1046, 2007. [7] Oral, H et al., *J Am Coll Cardiol*, 53(9):782-789, 2009. [8] Terasawa, T et al., *Ann Intern Med*, 151(3):191-202, 2009. [9] Elayi, C et al., *Heart Rhythm*, 5(12):1658-1664, 2008. [10]Segerson, N. et al., *J Cardiovasc Electrophysiol*, 21(2): 126-132, 2010. [11] Akoum, N et al., *J Cardiovasc Electrophysiol*, 22(1):16-33, 2011. [12] Gillinov, A and P McCarthy, *Ann Thorac Surg*, 74(6):2165-2168, 2002. [13] Pajitnev, D et al., *Thorac Cardiovasc Surg*, 61(S 01), 2013. [14] Cochet, H et al., *J Cardiovasc Electrophysiol*, 25(7):671-679, 2014. [15] Moyer, C et al., *Ann Biomed Eng*, 43(7):1600-1613, 2015. [16] Moyer, C et al., *IEEE Trans Med Imag*, 32(10): 1765-1776, 2013. [17] Badger, T et al., *Circ Arrhythm Electrophysiol*, 3(3):249-259, 2010.

Copyright 2016 The Organizing Committee for the 2016 Summer Biomechanics, Bioengineering and Biotransport Conference

SB^{3}C2016
Summer Biomechanics, Bioengineering and Biotransport Conference
June 29 –July 2, National Harbor, MD, USA
SB^{3}C2016-593

IMPACT OF IDEALIZED VERSUS MEASURED VELOCITY PROFILES IN COMPUTATIONAL MODELS OF MASS TRANSPORT IN THE HUMAN AORTA

G. De Nisco (1), P. Zhang (2), G. Usala (1), D. Gallo (1), X. Liu (2), X. Deng (2), G. Rizzo (3), U. Morbiducci (1)

(1) Department of Mechanical and Aerospace Engineering
Politecnico di Torino
Turin, Italy

(2) School of Biological Science and Medical Engineering
Beihang University
Beijing, China

(3) IBFM
Research National Council
Milan, Italy

INTRODUCTION

The complex hemodynamics observed in the human aorta make this district a site of election for an in depth investigation of the relationship between fluid structures, transport and patho-physiology.

Hemodynamics plays an important role in the mass transport in blood flow, and in turn, in the localization of vascular disease in areas of complex arterial flow. The accumulation of lipoproteins in the arterial intima is a hallmark of atherosclerosis. Low density lipoproteins (LDL) are the most abundant atherogenic lipoproteins in plasma and high plasma levels of LDL are causally related to the development of atherosclerosis [1]. In detail, it is found that the occurrence of LDL concentration polarization in the arterial system can affect the residence time and the deposition of atherogenic particles at the luminal surface. The LDL accumulation within the arterial wall then increases the risk of the atherogenesis [2].

In the last decade the coupling of medical imaging and computational fluid dynamics (CFD) has demonstrated its potency, contributing to enhance the comprehension of the aortic hemodynamics, with the possibility to obtain highly resolved blood flow patterns in anatomically realistic arterial models. In particular, in the context of a subject-specific oriented approach, PC-MRI has emerged as able to provide the anatomical and hemodynamic inputs to even more realistic, fully personalized flow simulations [3]. Moreover, personalized computational modeling of mass transfer has been proposed as a powerful way of addressing abnormalities in mass transfer patterns, which could be in themselves atherogenic [4]. In this regard, a recent study investigated the effects of geometric features of human aorta on the flow pattern and the luminal surface LDL concentration. It was detailed the role played by aortic torsion, branching, taper, and curvature on LDL transport and luminal surface distribution in four aortic models with different geometry [5].

In this study we analyze the influence of different possible strategies of applying PC-MRI measured data as boundary conditions (BCs) to confidently model LDL transport and transfer in image-based hemodynamic models of human aorta. In detail, the influence on LDL transport of assumptions regarding the velocity profile at the inlet section of the ascending aorta. We impose PC-MRI measured 3D velocity profiles (i.e. locations-dependent direction and magnitude of velocity vectors at the inlet section) at the inlet of the computational model and compare the obtained results, in terms of low-density lipoproteins transport, to the results of two equivalent computational models with the same instantaneous flow rate prescribed as measured 1D velocity profiles (i.e. magnitude of velocity vectors normal to the inlet surface) and flat velocity profile inlet BCs. Technically, steady-state flow simulations were carried out at three representative phases of the cardiac cycle for the three inlet velocity profiles considered. The LDL distribution at the aortic luminal surface was computed and the results were compared. The study here presented would contribute to clarify which is the impact of the conditions applied at inflow boundaries on aortic LDL transport. In particular, the comparison of LDL transport at the aortic luminal surface as obtained prescribing idealized *vs* measured velocity profiles as inflow BCs, will contribute to clarify which is the level of detail obtained from measured phase velocity, sufficient to satisfactorily simulate mass transport/transfer in personalized computational hemodynamics models of human aorta.

METHODS

In this study the geometry of an ostensibly healthy human aorta was reconstructed from 4D PC-MRI images. PC-MRI slices were used to generate the model of aorta into the Vascular Modeling Toolkit environment (http://www.vmtk.org/) by applying a multiple step procedure for the extraction of the surface mesh of the thoracic aorta

Copyright 2016 The Organizing Committee for the 2016 Summer Biomechanics, Bioengineering and Biotransport Conference

from PC-MRI data [6]. The finite volume method was applied to perform numerical simulations under steady flow conditions. The general purpose CFD code Fluent (ANSYS Inc., USA) was used on computational mesh-grids with high quality hexahedral cells near the wall at the inlet surface and structured tetrahedral elsewhere, semi-automatically generated using ICEM (ANSYS Inc., USA). The domain was equipped with straight flow extensions at the outlet faces and divided into about $4 \cdot 10^6$ cells. Blood was modeled as an isotropic, incompressible, homogeneous, Newtonian viscous fluid (density equal to 1060 kg/m^3; dynamic viscosity equal to 3.5 cP). The LDL diffusion coefficient in blood was set to $6.3 \cdot 10^{-9}$ kg/m s. Arterial walls were assumed to be rigid with no-slip condition at the wall. At the outlet sections of the model measured flow rate ratios were imposed as outflow BCs, as detailed in [6].

Steady state LDL transport in flowing blood can be described by the convective-diffusion equation for the LDL concentration C:

$$u \cdot \nabla C - D_L \nabla^2 C = 0 \qquad (1)$$

where u is the velocity vector and D_L is the diffusivity of LDL in flowing blood, set to $4.8 \cdot 10^{-12}$ m^2/s [2]. Steady-state flow simulations were carried by applying conditions at boundaries as measured at three different phases of the cardiac cycle (i.e. acceleration phase, systolic peak and deceleration phase, Figure 1), for a total number of nine simulations. The following BC strategies were applied at the inlet section of the ascending aorta. The first strategy consists in the application of the measured PC MRI velocity profiles at the inlet section. Technically, at the inlet section the measured three components of the velocity were extracted from the phase images. Using phase-contrast flow data, two different inflow conditions were generated, by imposing at the inlet of the ascending aorta: (1) PC-MRI measured 3D velocity profile at systolic peak, and at two phases of the cardiac cycle, one along the acceleration phase and the other along the deceleration phase; (2) PC-MRI measured 1D velocity profile at the same phases as described above, obtained considering the measured velocity component orthogonal to the inlet section of the anatomic model (i.e., the axial velocity component). The second strategy is a widely applied approach and consists in the application of the measured velocity waveform at the inlet surface in terms of idealized flat velocity profile. Velocity magnitude of flat profile was computed by averaging 1D velocity profile for each considered instant of cardiac cycle. LDL transport in the aortic arch was computed for the three inflow conditions cases and the impact of the choice of idealized rather than measured velocity profiles as inflow BCs was investigated focusing on LDL transfer to the aortic luminal surface.

RESULTS

As result we report the LDL wall concentration in aorta, normalized with respect to the initial LDL concentration C_0 at the aortic inlet section. Figure 1 presents the LDL accumulation profiles at the luminal surface obtained by imposing in silico (FLAT panel) and in vivo (1D and 3D panels) velocity profiles as inflow BCs for the three simulated phases of the cardiac cycle. Notably, differences in LDL patterns at the luminal surface are obtained, depending on the applied velocity profile at the inflow. In detail, the surface area subjected to elevated LDL accumulation is markedly wider than the 3D and 1D cases, when flat velocity profile is prescribed at the aortic inflow section. The FLAT case presents three luminal regions at the aortic arch subjected to severe polarization of LDL, more evident during the acceleration phase of the cardiac cycle (inner lateral edge of the brachiocephalic artery, intrados of the ascending aorta and inner wall of the descending aorta). The same regions were identified in [5], as interested by elevated LDL accumulation. LDL polarization at these luminal regions sensibly decreases in 1D and 3D simulation cases. Results obtained for 3D and 1D cases show a more uniform LDL distributions at the wall along the aortic arch, with a weak increase of LDL polarization at the inner wall of the descending aorta. In general, Figure 1 confirms that light or negligible differences can be appreciated in LDL transport between 1D and 3D cases at the three cardiac phases here investigated.

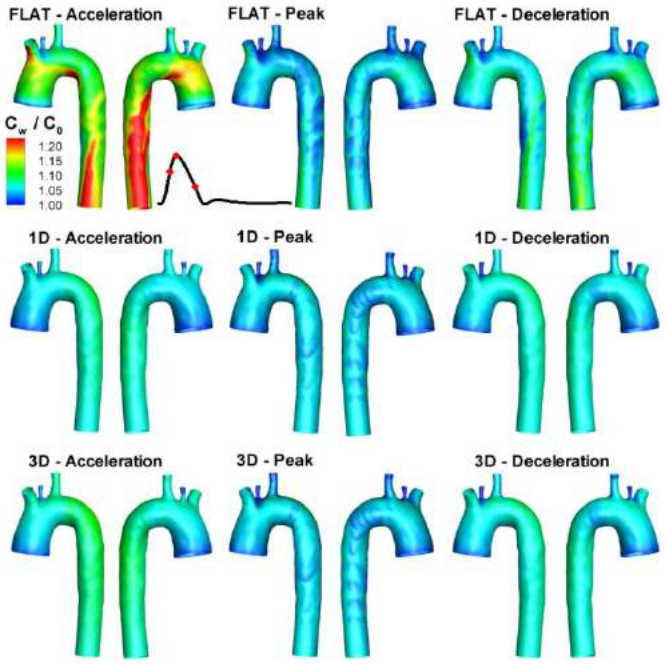

Figure 1. Comparison of the normalized LDLs concentrations at the luminal surface for the simulated inflow boundary conditions.

DISCUSSION

The findings of this study show that the imposition of idealized velocity profile as inlet BCs in subject-specific computational hemodynamics models of mass transport in the human aorta could largely affect the location and extension of regions of LDL polarization at the luminal surface. We conclude that the plausibility of the assumption of idealized velocity profiles as inlet BCs in personalized model of the aortic hemodynamics could not, or could loosely, hold true. This finding needs further investigation, because of the fact that it is derived from steady-state flow analysis. The same analysis will be extended to unsteady-state simulations, applying the same scheme as proposed in previous works [3]. In general, the approach here proposed could be helpful to elucidate the role played by the aortic helical flow in mass transport, in particular in testing the hypothesis that the promoted-by-helicity mixing of blood could be beneficial in suppressing severe LDL polarization at peculiar aortic regions, thus being part of the physiologic atheroprotective mechanism.

REFERENCES

[1] Tarbell, JM, *Annual Rev Biomed Eng*, 5: 79–118, 2003.
[2] Chen, J et al., *J Biomech*, 47: 544–552, 2014.
[3] Morbiducci, U et al., *J Biomech*, 46(1): 102–109, 2013.
[4] Ethier, CR., *Annals of Biomed Eng*, 30:461–471, 2002.
[5] Liu, X et al., *Am J Phys Heart Circ Phys*, 297: H163–H170, 2009.
[6] Gallo, D et al., *Annals of Biomed Eng*, 40(3):729–741, 2012.

Copyright 2016 The Organizing Committee for the 2016 Summer Biomechanics, Bioengineering and Biotransport Conference

SB³C2016
Summer Biomechanics, Bioengineering and Biotransport Conference
June 29 –July 2, National Harbor, MD, USA
SB³C2016-595

THE EFFECT OF LOADING FREQUENCY ON TENOCYTE METABOLISM

Chineye P. Udeze (1), Eleanor R. Jones (2), Graham P. Riley (2), Dylan Morrissey (3,4), Hazel R. C. Screen (1)

(1) School of Engineering and Material Science, Queen Mary University of London, Mile End Road, London, UK

(2) University of East Anglia, Norwich Research Park, Norwich, Norfolk, UK

(3) Sport and Exercise Medicine, Queen Mary University of London, UK

(4) Physiotherapy Department, Bart's Health NHS Trust, London, UK

INTRODUCTION

Achilles tendinopathy is a prevalent highly debilitating and painful condition. It is believed to result from repetitive overuse of the tendon, which can create micro-damage that accumulates over time, and initiates a catabolic cell response [1; 2].

The aetiology of tendinopathy remains poorly understood, therefore the ideal treatment remains unclear. A wide range of treatments are available, however, current data support the use of shock wave therapy or eccentric exercise as some of the more effective treatment options [3; 4]. Previous studies have demonstrated that both eccentric loading and shockwave therapy result in perturbations within tendon at a frequency of approximately 10Hz [5; 6]. Consequently, we hypothesis that 10Hz loading initiates an increased metabolic response in tenocytes that can promote tendon repair. Our primary aim is to investigate the effects of perturbations at 10Hz on tenocytes metabolism comparing tenocyte gene expression in response to10Hz and 1Hz.

METHODS

Human tenocytes from healthy hamstring tendons (3 donors aged 21±1 years) and tendinopathic Achilles tendons (3 donors aged 48±3 years) were derived by collagenase digest and explant outgrowth respectively. Cells were expanded and seeded into 3D collagen gels. In preparing the gel, 0.5ml of 10x concentration Dulbecco's Modified Eagle's medium (DMEM) (Gibco) was added to rat-tail type I collagen solution (First Link), the mix was neutralised with NaOH and carefully stirred to avoid creating air bubbles. A cell suspension (0.5ml of $1x10^6$ cells/ml solution) was immediately added to the mix, and then transferred to a mould (22 x 33 x 10 mm^3) and allowed to incubate at room temperature for 30 minutes to polymerise. The collagen gel was then compressed using the plastic compression technique, where the collagen matrix was placed between nylon meshes, and onto a stainless-steel mesh on double layer absorbent Whatman filter paper. A 120g metal block was placed onto the matrix to squeeze out the water and to make a flat collagen sheet (100-200μm thick) which could then be rolled to make a tube easily gripped for mechanical loading [7].

The gels were fixed in custom-made chambers, housed in an Electro-force loading frame within an incubator (fig. 1) and left for 24hrs whilst gene expression stabilized before mechanical loading. Cell viability over this time-frame was confirmed by monitoring constructs secured within the chambers for 48 hours, with and without the inclusion of mechanical stimulation (n=2). The gels were removed from the chamber, placed in a solution of 2ml of DMEM, containing Calcein AM (0.01mg/ml) and Ethidium homodimer (3.75μM/ml), and incubated at 37ºC for 30minutes. Stained samples were rinsed and placed on the stage of a confocal microscope, and the number of live and dead cells counted to provide a percentage viability.

For mechanical stimulation, cyclic uniaxial strain at 1% ± 1% was applied to the gels, at either 1Hz (n=4) or 10Hz (n=4) for 15 minutes. Samples were then maintained in the chambers under 1% static strain for 24hrs.

Gene expression was determined using qRT-PCR on several genes of interest (MMP1, MMP2, MMP13**,** COL1A1, COL3A1, COL5A1, ADAMTS5, IL6, IL8, TIMP3 and 18S).

The data are displayed as Geometric mean ± standard error of the mean and statistical analyses were performed using the student's t test (two tailed distribution, equal variance).

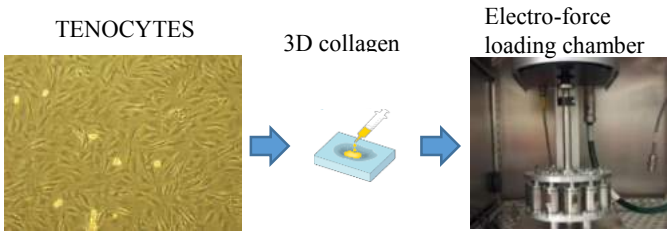

Fig 1. Schematic depicting the methodology: seeding cells onto gels and mechanically loading them, prior to assessment of cell viability and gene expression.

Copyright 2016 The Organizing Committee for the 2016 Summer Biomechanics, Bioengineering and Biotransport Conference

RESULTS

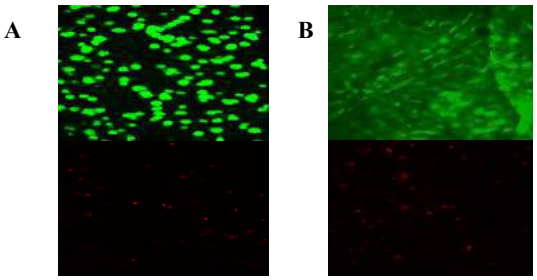

Fig 2: Cells were stained using Calcein AM (live cells – green) and Ethidium Homodimer (dead cells – red). (A) Non-strained, (B) strained. These images are representative of a large number of images taken at different positions of the 3D gels (n=7). Cell viability was 78-97 %, established by counting cells in the field of view looking at 3 viewpoints per sample.

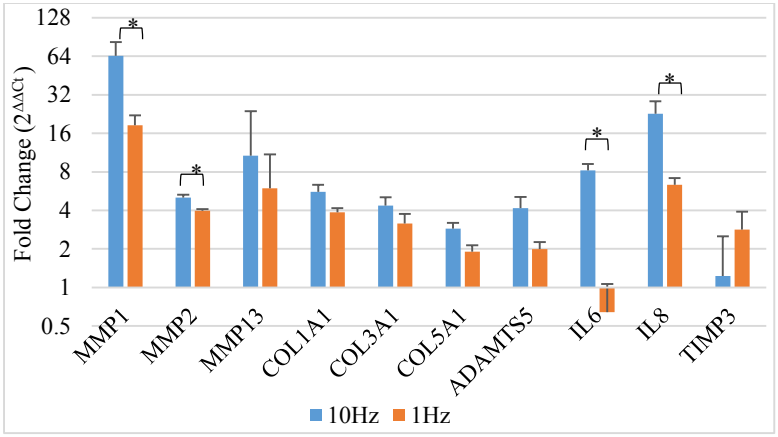

Fig 3. Expression of mRNA in healthy human hamstring tenocytes normalised to 18S (n=3). There was an upregulation of the majority of genes with loading, and four genes increased significantly in response to 10Hz loading compared to 1Hz loading. *= significant difference between 10Hz & 1Hz loading ($p<0.05$)

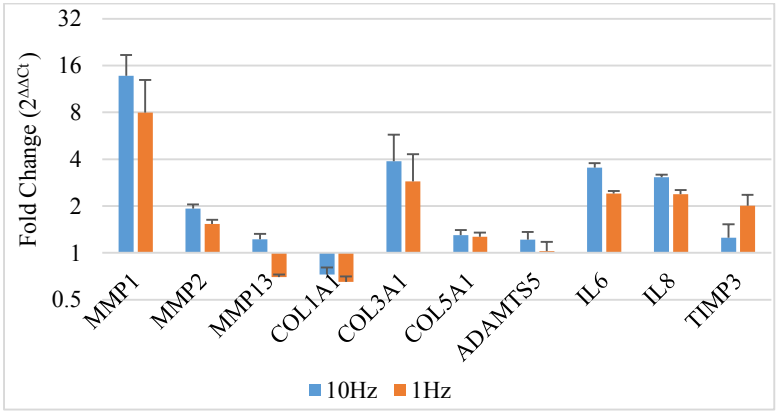

Fig 4. Expression of mRNA in tendinopathic Achilles tenocytes normalised to 18S (n=3). There was upregulation of a number of genes with loading, but fold changes were less than seen with healthy cells. Some genes showed less than a two-fold change in expression. No significant differences were seen in the response to 10Hz & 1Hz loading.

Fig. 2 showed that cells within the collagen gels remained viable throughout the test period, with and without loading. However, data suggests less cell death in non-strained groups compared to the strained groups. Fig. 2B also showed that in the strained matrices, the cells were aligned in the direction of loading, whereas in non-strained samples (fig. 2A), there is no clear orientation indicating an adaptation in morphology in response to mechanical load.

In healthy cells (fig. 3), there was an increased expression of the majority of genes after loading. Furthermore, although the majority of genes showed no significant difference in their response to 10Hz and 1Hz loading, the increase in gene expression was generally larger in the higher frequency (10Hz) loading group, across all genes, with the exception of TIMP3. Tendinopathic cells (fig. 4) showed a more varied response, with upregulation of MMP1, MMP2, COL3A1, IL6, and IL8. However, some genes (MMP13, COL1A1, COL5A1, and ADAMTS5) were unresponsive when all three donor groups were merged. This could reflect the difference in tissue source of the cells (hamstring and Achilles for healthy and tedinopathic cells respectively), or might also be a consequence of the different cell derivation methods (collagenase digest and explant outgrowth for healthy and tedinopathic cells respectively).

DISCUSSION

Generally, the viability data showed good cell viability in the system, while the gene expression preliminary data suggest increased matrix turnover as a result of loading, and a more extensive increase with 10Hz loading, particularly in healthy tenocytes. As such, the data tentatively support our hypothesis that 10Hz loading initiates a greater metabolic cell response. However, the data showed wide variations in response across the three donors thus, further research is required to clarify this.

Fig. 3 shows a significant difference in cell response to 10Hz and 1Hz loading in healthy cells for MMP1, MMP2, IL6 and IL8 which may indicate early matrix breakdown and a slow remodeling process. The mechanism by which 10Hz loading results in increased expression of MMPs and interleukins in healthy tendon are yet to be determined, however, previous studies have shown that cyclic loading induces the expression of IL1 [8]. Further, stimulation with IL1 increases expression of MMPs and IL6 [8; 9], suggesting that the IL1 signaling pathway may be involved in the greater tenocyte response to loading at a frequency of 10Hz.

By contrast, the profile of tendinopathic cells may indicate an early healing response, where collagen type III is preferentially upregulated relative to types I&V. Overall, tendinopathic cells appeared less responsive to strain with greater fold changes in gene expression observed in healthy cells, and no significant differences between the 10Hz and 1Hz loading groups.

This study has demonstrated for the first time that loading at a frequency of 10Hz may enhance metabolic response in healthy tenocytes. However, this response appears to be lost in tendinopathic cells. As such, further studies are needed to establish the mechanisms by which 10Hz loading stimulates increased gene expression.

ACKNOWLEDGEMENTS

This work was funded by Orthopaedic Research UK

REFERENCES

[1] Kountouris, A. and Cook, J., *Best Prac. & Res Clinical Rhe*, 21(2):295-316, 2007.
[2] Birch, H.L et al., *Equine Vet J*, .30(6): 534-539, 1998.
[3] Alfredson, H. and Cook, J., *Br J Sports Med*, 41: 211-216, 2007.
[4] Lorenz, D. and Reiman, M. *The Int J Sports Phy Therapy*, 6(1): 27-44, 2011.
[5] Mani-Babu, S et al., *The American J Sports Med*, 1-9, 2014.
[6] Chaudhry, S et al., *J App Biomechanics,* 31: 69-78, 2015.
[7] Cheema, U. and Brown, R. A., *In Vitro. Advances in wound Care*, 2(4): 176-184, 2003
[8] Tsuzaki, M. et al., *j Cellular Bio*, 89:556-562, 2003.
[9] Archambault, J. et al., *J Orth Res,* 20: 36-39, 2002.

Copyright 2016 The Organizing Committee for the 2016 Summer Biomechanics, Bioengineering and Biotransport Conference

SB^{3}C2016
Summer Biomechanics, Bioengineering and Biotransport Conference
June 29 –July 2, National Harbor, MD, USA
SB^{3}C2016-596

THE SYNERGISTIC USE OF HAPTIC FEEDBACK WITH AN EMG CONTROLLED TRANSFEMORAL POWERED-KNEE PROSTHESIS

J. Miles Canino (1), Kevin B. Fite (1)

(1) Mechanical and Aeronautical Engineering
Clarkson University
Potsdam, NY, USA

INTRODUCTION

Lower limb-loss rehabilitation is an arduous task that does not always result in favorable outcomes, particularly in patients with dysvascular etiologies. The causative agents behind this lack of effective rehabilitation are many and greatly varied, but a steep learning curve and improper implementation of prosthetic control techniques greatly contribute to poor rehabilitative outcomes. Communicating proper gait mechanics via kinesthetic haptic feedback rhythms to the amputee during the rehabilitation process may help to flatten this learning curve, encourage proper prosthetic usage, and lead to an increase in successful outcomes [1, 2].

Researchers have demonstrated that the usage of haptic feedback in electromyography (EMG)-controlled prosthetic systems can offer greater acuity in user-mediated controls, particularly in more dexterous tasks. This has been shown in the object manipulation of an upper limb prosthetic [3, 4]. With upper limb object manipulation, a user often has the benefit of concurrent visual feedback. With lower limb amputees however, adequate visual feedback is not available during locomotion. Communicating state information about the prosthetic limb could ameliorate any deficits caused by this deficit. Other researchers have worked towards a similar goal with successful outcomes in transtibial applications [5]. The goal of this research is to further investigate one's ability to effectively understand and respond to varying haptic modalities, with and without the presence of visual feedback, while trying to volitionally control a dynamic system through EMG inputs. It is suspected that haptic feedback will be effective in communicating relevant limb information in the absence of visual feedback.

METHODS

Two prototype haptic feedback systems were designed and fabricated for experimentation. The vibrotactile array consisted of three linearly arranged vibrating motors suspended in silicone sockets that could be affixed to the subject via Velcro straps (Figure 1). The second feedback system pneumatically actuated and composed of a linear array of machined aluminum pressure vessels with expanding silicone membranes sealing the expanding skin-interface orifice (Figure 1). When these pressure vessels are pressurized through the actuation of a micro-solenoid valve, the chamber fills to ~5psi, thus expanding the silicone membrane and imparting the pressure sensation to the skin interface. Both systems' actuations were mediated by a digital output prompted via a course-corrective, error-feedback control schema embedded in the Simulink control code developed for this testing.

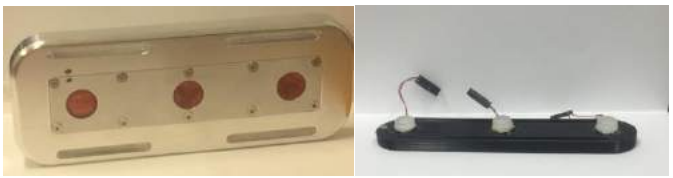

Figure 1: Pneumatic tactile array (left) and vibrotactile array (right).

For this experimental protocol, 4 sets of 7 possible tests were conducted wherein each of the tests were repeated 6 times (N = 42 for each set). Testing sought to investigate the efficacy of these haptic feedback systems in visual and non-visual environments. These tests were performed by two able-bodied, informed and consenting subjects, a 27 year old female and 24 year old male, who were asked to control a virtual limb and a powered transfemoral prosthetic. This was conducted under Clarkson University IRB approval # 14-34.

Copyright 2016 The Organizing Committee for the 2016 Summer Biomechanics, Bioengineering and Biotransport Conference

The virtual limb was modeled as a simple pendulum with a controlled torque about its pivot. The control architecture for the prosthetic and the virtual limb is as described by the works of Dawley et al. [6]. The control torque of both systems was volitionally controlled by the user through EMG interfacing. The prototypical transfemoral powered knee prosthetic used in this study is described in detail by Hoover et al. [7].

For both systems, testing was conducted in the following manner. The subject was first required to go through an initialization and calibration routine [6]. The EMG electrodes used to control the limbs were then attached to the subject's dominant quadriceps and biceps femoris. Data was then sequentially recorded with the subject relaxed and with the subject performing sustained isometric flexion and extension contractions from 0 to 100% of max voluntary contraction. This data was then used to complete the principal component analysis (PCA) required for calibration. This PCA establishes all pertinent constants necessary to map between normalized EMG and limb impedance, like equilibrium point and effective stiffness [6]. After this initialization routine, the subject trained with the virtual and prototype limb for approximately 2 hours, getting accustomed to how the EMG input would visually affect the graphically represented limb angle or physically affect the prosthetic limb.

On subsequent testing days, the initialization routine was repeated, and the subject was then presented with randomized tests which incorporated or restricted visual feedback and haptic feedback modalities. In these tests, the subject attempted to follow a randomly generated trajectory presented on a monitor with the graphical representation of the limb's current state overlaying the desired limb state. Subjects were instructed to first stabilize about a random band-limited (25-65 degrees), limb angle which would then, at some random time (10-20 seconds), change up or down in a pseudo-random band-limited step response limited to a minimum of ±5 and maximum of ±20 degrees. The subject would then have to stabilize about this new desired limb angle. To provide or restrict visual feedback, the subject was either shown their current trajectory overlaying the desired trajectory, or they were just shown the desired trajectory and had to guess where they thought the limb was. Each of these randomized tests was performed 6 times per subject, per limb type, including the control. During the control tests, the subject had a goniometer affixed to their sound limb and they would attempt this test with visual feedback.

The efficacy of haptic feedback to communicate in visually devoid environments was explored using one-way ANOVA. The null-hypothesis was that the concurrent usage of haptic feedback modalities has no effect on the accuracy of an EMG controlled virtual limb (N=42 for each of the 4 sets). The independent variables investigated were each of the possible test configurations. The dependent variable investigated was the root mean square (RMS) deviation of desired versus actual limb angle for each test. The normality of the data sets was analyzed using a one-sample Kolmogorov-Smirnov test, and the data was found to be normally distributed.

Both the Welch and Brown-Forsythe tests confirmed that these data sets were robust enough to continue ANOVA. Because the data was robust but not homogeneous in its variance, the Games-Howell approach was used to perform multiple comparisons.

RESULTS

Figure 2 shows a sample performance of a test subject attempting the trajectory-following task with (left) and without (right) pneumatic haptic feedback in the absence of visual feedback. Figure 3 shows the plot of mean data and the marked performance improvement in visually deprived environments with haptic feedback intervention.

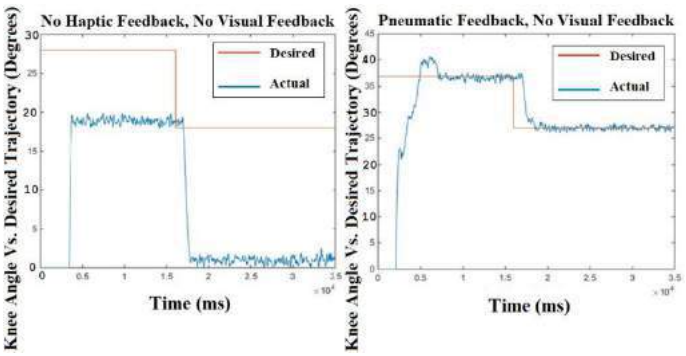

Figue 2: Sample trajectory of non-visual testing with and without haptic feedback.

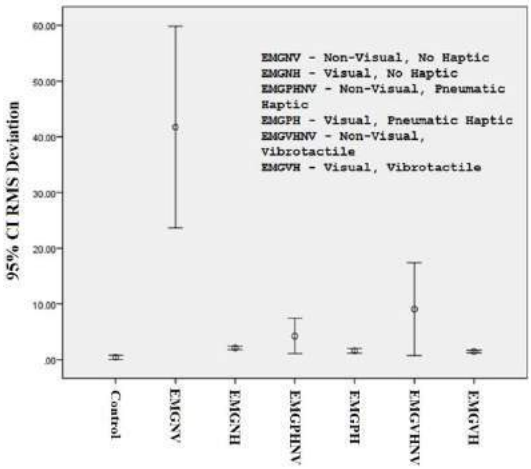

Figure 3: Plot of mean comparison data for all test sets.

DISCUSSION

The concurrent usage of pneumatic haptic feedback with volitional EMG control was found to be significantly synergistic in both test subjects , particularly when used in an environment where visual feedback is limited or completely absent ($p = 0.007$). The usefulness of haptic feedback in conveying limb-state information is consistent with that of other research endeavors [3-5], but it should be noted that vibrotactile haptic feedback was not found to be significantly useful for one of the test subjects ($p = 0.045$), who experienced desensitization phenomenon with the vibrotactile arrays.

This raises an interesting question on how to dissuade desensitization, or to better establish the localizability of the vibrotactors in individuals who have a physiological difficulty in perceiving their location. Future studies will investigate using rhythmic patterns to stave off mechanoreceptor adaptation, or possibly the usage of a unique pulse pattern for each tactor. This future research will work to inform the design and development of a kinesthetic haptic feedback rehabilitative aid.

REFERENCES

[1] Dillingham, T, et al, Phys. Med. and Rehab, 89:1038-1045, 2008
[2] Fu, M, et al., Orthopedics, 37: E993-E998, 2014
[3] Brown, J.D., et al., World Haptics Conference: 271-276, 2013
[4] Pistohl,T., et al, IEEE Trans. Neural Syst. Rehabil. Eng, 23: 498-507, 2015
[5] Fan, R., et al., IEEE Trans. Neural Syst. Rehabil. Eng, 16:270-277, 2008
[6] Dawley, J., et al.," Proceedings of ICORR:1-6, 2013
[7] Hoover, C., et al., J. of Med Dev, 6: 011005-1-011005-12, 2012

Copyright 2016 The Organizing Committee for the 2016 Summer Biomechanics, Bioengineering and Biotransport Conference

SB³C2016
Summer Biomechanics, Bioengineering and BIotransport Conference
June 29 –July 2, National Harbor, MD, USA
SB³C2016-597

COMPUTATIONAL ASSESSMENT OF THE EFFECT OF ARTERIOVENOUS GRAFT FLOW RATE ON VASCULAR ACCESS HEMODYNAMICS IN A NOVEL MODULAR ANASTOMOTIC VALVE DEVICE

Andrew McNally (1), A. George Akingba (2), Philippe Sucosky (3)

(1) Department of Aerospace & Mechanical Engineering
University of Notre Dame
Notre Dame, IN, USA

(2) Department of Surgery
Indiana University School of Medicine
Indianapolis, IN, USA

(3) Department of Materials and Mechanical Engineering
Wright State University
Dayton, OH, USA

INTRODUCTION

End-stage renal disease (ESRD) results from conditions that chronically decrease renal function and is most commonly treated with hemodialysis (HD) while patients await kidney transplant. Current methods for maintenance of HD vascular access are fraught with problems that compromise patency of these surgically created shunts. The major cause of shunt failure is thrombosis caused by occlusion of the outflow venous anastomosis and draining vein. Intimal hyperplasia (IH), a thickening of the vessel wall, initiates the pathogenesis of venous stenosis. While the pathogenesis of IH is not completely understood, the perturbed hemodynamics generated by the vascular access is increasingly pointed to as a potential contributor as venous wall regions experiencing low and oscillatory wall shear stress (WSS) have been shown to be particularly vulnerable to IH development[1].

In this context, improvement of vascular access patency could be sought through strategies aimed at preserving normal venous hemodynamics in HD patients. In pursuit of this effort, we previously proposed a novel modular anastomotic valve device (MAVD)[2]. This device features a shuttle valve system which can block or allow arteriovenous graft (AVG) flow (Fig. 1). Preliminary computational testing suggested the ability of this device to maintain physiologic venous flow in the closed position (i.e., between HD sessions) and the benefits of smaller anastomotic angles to maintain WSS levels above their pathologic threshold[2]. While AVG flow rates are only clinically effective between 600 and 2000 mL/min, the impact of the AVG flow rate on the MAVD hemodynamics is unknown. The goal of this study was to quantify computationally the hemodynamics of the open MAVD (i.e., during hemodialysis) over the range of flow rates enabling effective HD.

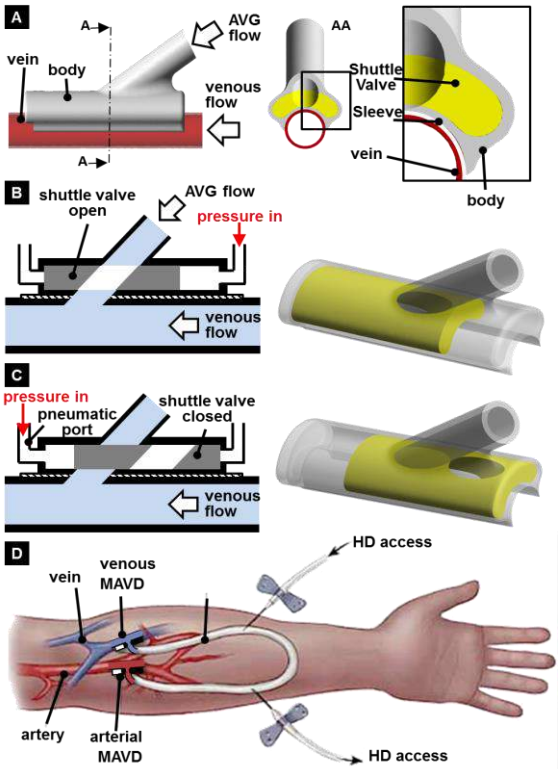

Fig. 1: MAVD design. (A) Prototype MAVD, (B) schematic of operation in open and (C) closed positions, and (D) clinical implementation.

Copyright 2016 The Organizing Committee for the 2016 Summer Biomechanics, Bioengineering and Biotransport Conference

METHODS

The impact of the AVG flow rate on the vascular access WSS environment was quantified computationally. The three-dimensional (3D) geometry of the open MAVD mounted onto the brachiocephalic vein was designed in SolidEdge. Fully-coupled, transient fluid-structure interaction (FSI) simulations were run in ANSYS. The vein was modeled as an incompressible, isotropic and hyperelastic material using a previously published Mooney-Rivlin model[3]. Blood was modeled as a non-Newtonian fluid using a modified power-law model[2]. Pulsatile boundary conditions at the MAVD model inlet were obtained experimentally in a bench-top vascular access flow loop using an in-line ultrasonic flow sensor. The setup consisted of a programmable pulsatile pump, a reservoir, a compliance chamber and a 3D-printed MAVD prototype. Average graft flow rates of 800, 1000, and 1500 mL/min were generated while maintaining a physiologic heart rate of 70 bpm and an aortic blood pressure of 120/80 mmHg. For each flow rate, the pulsatile graft flow rate waveform was measured at 160 time points over the cardiac cycle and input to the model. The model was validated by comparing the FSI velocity predictions to Doppler ultrasound velocimetry measurements performed at the venous anastomosis. Global flow metrics were assessed in terms of streamlines and WSS fields. The FSI model was used to identify regions of low WSS (WSS < 0.5 Pa) on the vein wall and to further characterize them in terms of temporal shear magnitude (TSM) and oscillatory shear index (OSI). The impact of the incoming graft flow on the vein wall was also assessed in terms of maximum wall displacement.

RESULTS

The comparison between the predicted and measured maximum velocity in the mid-anastomosis region of the vein revealed less than 8% difference over the range of tested flow rates. Regardless of the AVG flow rate, the model isolated only one low WSS region present along the anastomotic side of the vein, 7.5 mm distal to the anastomosis. The comparison of the TSMs (800 mL/min: 0.57 Pa, 1000 mL/min: 0.04 Pa, and 1500 mL/min: 0.11 Pa) and OSIs (800 mL/min: 0.00, 1000 mL/min: 0.06 Pa, and 1500 mL/min: 0.15) captured on this segment of the vein revealed an increasingly pathogenic WSS environment under increasing AVG flow rate.

The open MAVD streamline patterns (Fig. 2a) indicate that the high-velocity AVG flow generates a low-flow region near the anastomotic side of the vein distal to the anastomosis generating low and oscillatory WSS. A less significant reduction in WSS (WSS < 1 Pa) is observable on the anastomotic side of the vein wall immediately proximal to the anastomosis. The incoming flow also generates a high-flow, high WSS region on the non-anastomotic side of the vein. The predicted WSS distribution (Fig. 2b) confirms this observation, as demonstrated by the existence of high WSS levels in the vein distal to the anastomosis, and regions of lowered wall shear stress on the anastomotic side of the vein wall proximal and distal to the anastomosis.

The maximum displacement of the vein wall predicted at peak systole (800 mL/min: 0.004 mm, 1000 mL/min: 0.006 mm, and 1500 mL/min: 0.011 mm) was shown to remain negligible relative to the vein diameter, over the range of AVG flow rates tested.

DISCUSSION

This study demonstrates the significant impact of AVG flow rate on vascular access flow and the higher potential of elevated AVG flow rate to generate near-wall hemodynamics promoting IH pathogenesis. The vascular access flow loop also constitutes a new bench-top tool for the in vitro evaluation of vascular access hemodynamics. Ongoing work includes animal trials of implanted MAVDs which may shed new light on the capability of the MAVD to reduce IH development.

ACKNOWLEDGEMENTS

This project was funded with support from the Indiana Clinical and Translational Sciences Institute funded, in part, by Grant Number UL1TR001108 from the National Institutes of Health, National Center for Advancing Translational Sciences, Clinical and Translational Sciences Award.

REFERENCES

[1] Akoh, J. A. Prosthetic arteriovenous grafts for hemodialysis. *J. Vasc. Access* **10,** 137–47 (2009).

[2] McNally, A. *et al.* Novel modular anastomotic valve device for hemodialysis vascular access: preliminary computational hemodynamic assessment. *J. Vasc. Access* (2014).

[3] Rezakhaniha, R. *et al*. A structural model of the venous wall considering elastin anisotropy. *J. Biomech. Eng.* **130,** 31017 (2008).

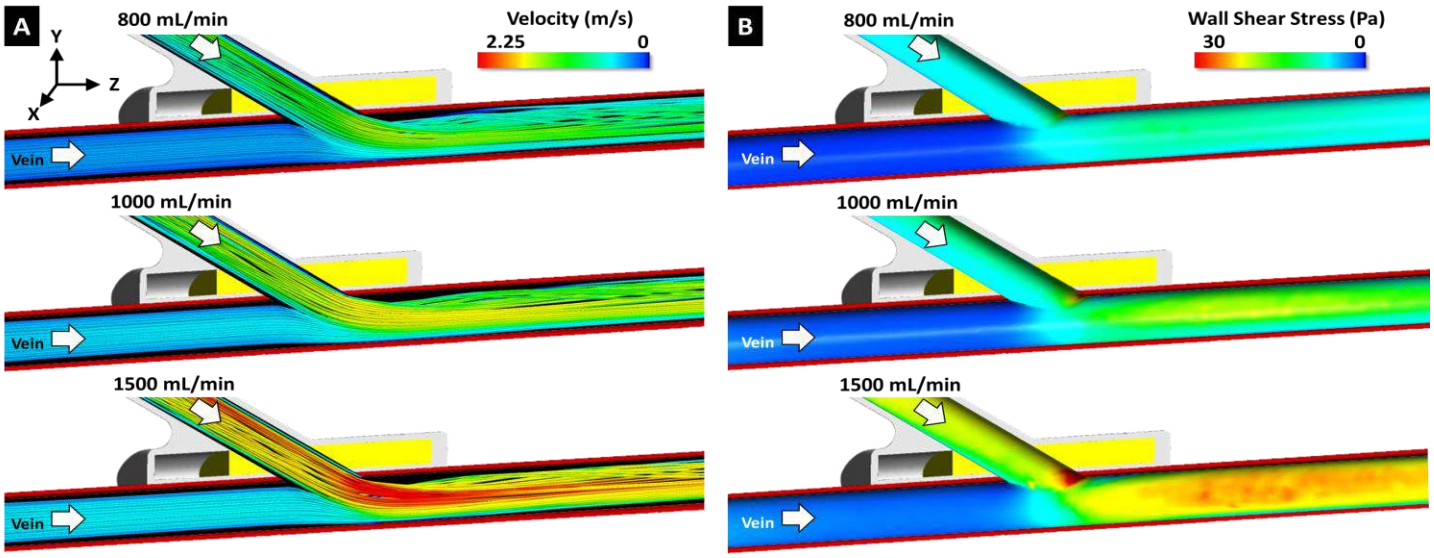

Fig. 2: Hemodynamics in the 750 (top), 1000 (middle), and 1500 mL/min (bottom) Open MAVDs (A) Streamlines, (B) velocity fields.

Copyright 2016 The Organizing Committee for the 2016 Summer Biomechanics, Bioengineering and Biotransport Conference

SB³C2016
Summer Biomechanics, Bioengineering and Biotransport Conference
June 29 –July 2, National Harbor, MD, USA
SB³C2016-599

INVESTIGATING FORCE TRANSFER DURING PARTURITION USING EXPERIMENTAL AND COMPUTATIONAL METHODS

Alexa Baumer (1), Roseanna Pealatere (2), Lisa J. Fauci (2), Megan C. Leftwich (1)

(1) Mechanical and Aerospace Engineering
The George Washington University
Washintgon, D.C., U.S.A.

(2) Department of Mathematics
Tulane University
New Orleans, LA, U.S.A.

INTRODUCTION

The Cesarean section is a traumatic and costly operation. The surgery, originally designed to preserve the lives of mother and infant in severe cases has gained widespread use in less dire circumstances. Hospital stays post-surgery are much greater than that of a natural delivery [1]. In addition to the economic considerations, natural delivery has been shown to give neonates distinct advantages, including: a bacterial biome transfer from mother to child and an easier time breathing after birth since the fluid is squeezed out of the lungs in the birth canal [1]. Investigating the role of fluid in the mechanics of labor and delivery may lead to methods to reduce the rate of Cesarean section and to increase the rate of natural delivery.

The laboring uterus is a complex and dynamic fluids system. The two primary fluids of interest, amniotic fluid and vernix caseosa, play integral roles in the force transferred to the fetus during the final stages of parturition. Amniotic fluid, comprising between 12 – 30 % of the uterus's total volume at delivery, possesses somewhat different bulk properties for each individual woman. Vernix caseosa, consisting of skin cells and secreted oil, covers the fetus and acts as a lubricant during delivery [2]. Relatively little it known about the fluid properties of the laboring system. This investigation probes the role of fluid in the force transfer during delivery by considering computational and physical models that determine the role of various components of the full system. The results of these methods are given and compared below.

METHODS

In the experimental investigation, the birth canal and the fetus are modeled as two concentric cylinders. The experiment is contained in a 15.25 x 75 cm tank. In the center of the tank, a thin, latex membrane is supported on its ends by collars and secured to the base of the tank. The latex is 68.5 μm thick. The test section is 14 cm long. A track of aluminum runs the length of the tank, passing through the latex membrane. The track is supported on both sides of the test section, in order to prevent deformation.

The inner cylinder is an acrylic, rigid rod with a 0.3175 cm hole drilled through its center. Two hooks are secure to the front end of the rigid rod, spaced equidistant from the center hole. The rigid cylinder moves through the flexible, outer membrane with a prescribed velocity, u. The diameter of the outer membrane is 3.8 cm, leaving a 0.31 cm gap between the cylinders. The experimental design is summarized in Figure 1.

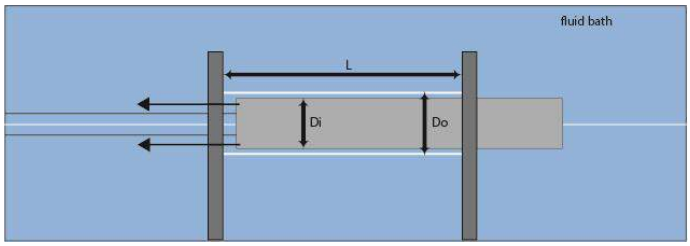

Figure 1: Experimental schematic for concentric cylinders setup

Copyright 2016 The Organizing Committee for the 2016 Summer Biomechanics, Bioengineering and Biotransport Conference

As the cylinder moves through the testing section, a high-speed camera records its motions at 60 frames/second. For each of the testing fluids, 30 trials are performed. Each of these trials is put through DLFdv5 Matlab software [3]. These digitized values are converted to find the force at each position.

Though the mechanical properties of amniotic fluid are unknown, it has been described as water-like [4]. Therefore, to study the role of fluid, the tank is filled with fluids of varying viscosities. The first fluid is water at $\mu = 1.00$ cp, followed by two methyl cellulose solutions at $\mu = 10$ cp and $\mu = 100$ cp, respectively.

In the numerical investigation, the system is modeled as a rigid cylinder moving at a constant velocity (u = 3 cm/s) through the center of a passive elastic tube. The entire model is immersed in a highly viscous fluid. Due to a low Reynolds; number, the Stokes equation is used to describe the relationship between velocity and forces in the system. The mathematical model uses the method of regularized Stokeslets to estimate the pulling force necessary to move the rigid inner cylinder at a constant velocity. The elastic tube is constructed using a discrete network of Hookean springs, with macroscopic elasticity matched to the tube used in the physical experiments.

RESULTS

The average removal force, defined as the average force exerted on the inner cylinder to pull it through the outer cylinder, is normalized by $\mu UA/h$ and plotted against the Reynolds number, where μ is the fluid viscosity, ρ is the fluid density, A is the surface area of the rod (0.028 m^2), and h is the fluid filled gap (0.0031 m). This is summarized in Figure 2.

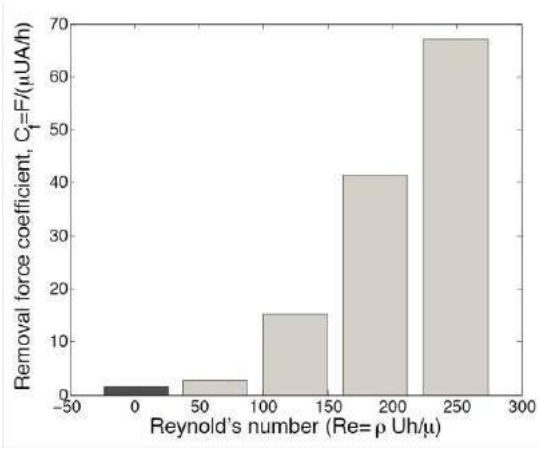

Figure 2: Average force plotted against Reynolds number; the dark grey bar represents the methylcellulose trials

In the numerical investigation, the tube behavior as the rod travels through its center, and at the fluid pressure and velocity in the system over time was observed. As the rod moves through the tube, the tube bulges outward as expected. When it reaches the end of the tube, there is some folding of the elastic tube, similar to what occurs in the physical experiment.

As the rod leaves the tube, the tube buckles in a six-petaled flower pattern due to the pressure drop inside the tube behind the rod. The buckling begins to relax as the rod moves further away from the tube. When the rod moves through the tube, and vacates the region directly behind it, the pressure drops and fluid rushes to fill the empty space. This drives the buckling of the tube. It appears that the lubrication between the tube and the rod causes the rod to move more easily through the fluid than it would without the tube's presence.

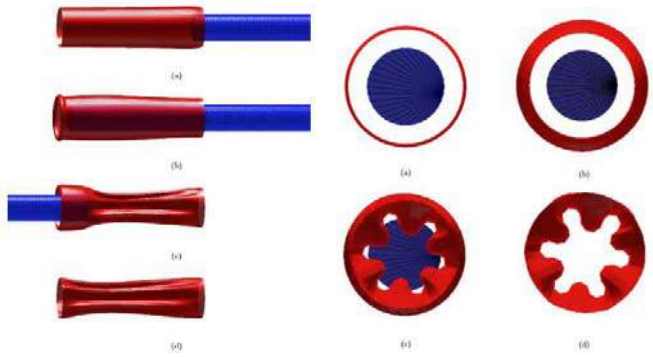

Figure 3: The rod (blue) and the tube (red) are viewed at various times throughout the simulation. The initial outward bulging of the tube can be seen, followed by the six-petaled flower buckling of the tube as the rod begins to exit

DISCUSSION

The physical experiment results demonstrate a positive trend between increasing Reynold's number and increasing force to pull the cylinder.

Buckling has been seen in the physical experiment trials; however, more runs are necessary in the physical experiment to determine if the buckling follows a similar six-petal flower pattern as seen in the computational results.

In the future, using more complex, anatomically accurate geometries as well as including peristaltic activation of the elastic tube may provide further insights into the relationship between viscosity and force during human birth.

ACKNOWLEDGEMENTS

The authors would like to thank the George Washington University Institute of Biomedical Engineering interdisciplinary research fund and the National Science Foundation Grant number CBET-1437611 for financial support of this project.

REFERENCES

[1] Buhimschi, C.S. and Buhimschi, I. A. (2006). "Advantages of vaginal delivery". *Clinical Obstetrics & Gynecology* **49(I):** 167-183.

[2] Hoath S.B., Pickens W.L., and Visscher M.O. (2006). The biology of vernix caseosa. *International Journal of Cosmetic Science* **28:** 319-333

[3] Hedrick, T.L. (2008). "Software techniques for two and three-dimensional measurements of biological and biomimetric systems." *Bioinspiration and Biomimetrics*. **3(3):**1748-3182.

[4] Uyeno, Doko et al. (1917). "The physical properties and chemical composition of amniotic fluid." Journal of Biological Chemistry. 37: 77-103.

Copyright 2016 The Organizing Committee for the 2016 Summer Biomechanics, Bioengineering and Biotransport Conference

SB^{3}C2016
Summer Biomechanics, Bioengineering and Biotransport Conference
June 29 –July 2, National Harbor, MD, USA
SB^{3}C2016-602

BANDWIDTH REQUIREMENTS FOR WEARABLE HEAD IMPACT SENSORS

Lyndia C. Wu (1), Kaveh Laksari (1), Calvin Kuo (2), David B. Camarillo (1,2)

(1) Bioengineering Department
Stanford University
Stanford, CA, USA

(2) Mechanical Engineering Department
Stanford University
Stanford, CA, USA

INTRODUCTION

Wearable head impact sensors use MEMS accelerometers and gyroscopes to obtain head impact measurements for traumatic brain injury research. These sensors are being deployed to human subjects to study promising injury criteria, but the choice of sensor specifications has not been scientifically justified. When selecting inertial sensors for head impact sensing, it is important to consider sensing requirements of the target head impact response. One important consideration that is often overlooked is the frequency content of head impacts, which will determine key sensor specifications including bandwidth and sampling rate. Although voluntary human motion is often low frequency, blunt impacts to the head are expected to have higher frequency content and only last up to tens of milliseconds. It is unknown whether existing MEMS sensors are sufficient for fully capturing the desired head impact response.

Despite this uncertainty, a variety of head impact sensors have been developed and piloted in various helmeted and unhelmeted sports. These sensors typically have a sampling rate of 1000Hz, with accelerometer bandwidths within 500Hz and gyroscope bandwidths within 200Hz. With more and more researchers using these sensors, we need to scientifically investigate whether such sensor bandwidths and sampling rates are sufficient. The answer will depend on the injury risk criteria being studied and the study population, since the frequency response of different types of contact will differ, and each injury criterion will have varying sensitivities to different frequency components of kinematic measures. For example, barehead impacts may have different frequency response and different requirements from helmeted impacts. However, similar sensors are currently deployed to both types of sports.

The objective of this study is to determine bandwidth requirements in different model systems for studying different injury criteria. We investigated three model systems: helmeted cadaver head drop (no neck), unhelmeted cadaver head drop (no neck), and a dummy linear impact model (hybrid III neck). We evaluated the effect of varying sensor bandwidth on kinematics-based and finite element (FE) based injury criteria. The results of this study will help inform sensor design and selection. It will also give insight into the components of head frequency response that are important for each injury criterion.

METHODS

Our dataset contains high bandwidth accelerometer and gyroscope measurements from helmeted cadaver head drops, unhelmeted cadaver head drops, and helmeted dummy horizontal spring-driven impact tests (Table 1). The high bandwidth data are treated as ground truth measurements of skull kinematics. We computed injury criteria from such ground truth measurements and filtered measurements (representing lower bandwidth) to determine the resulting attenuation in injury risk predictions.

For the ground truth data set, we used drop test data from a male cadaver head specimen, in either a helmeted or unhelmeted configuration at 6 impact locations each. A 6-degree-of-freedom block was rigidly attached to the occiput. Bandwidth of the accelerometer was 25kHz, and that of the gyroscope was 2kHz. The dummy head data set was collected using a 6aω sensor set up [1]. The accelerometer has a bandwidth of 10kHz, and the gyroscope has 2kHz bandwidth. For both scenarios, we collected sensor data at 100kHz for 600ms, with 100ms pre-impact and 500ms post-impact. Ground truth signals were obtained by filtering raw data at sensor bandwidths with a 4th order butterworth filter. To obtain lower-bandwidth signals, we filtered raw data at the following cut-off values: 50Hz, 100Hz, 300Hz, 500Hz, 1000Hz, and 1650Hz.

Copyright 2016 The Organizing Committee for the 2016 Summer Biomechanics, Bioengineering and Biotransport Conference

Table 1: Model Systems and Impact Conditions

Model System	Method	Conditions
Cadaver unhelmeted 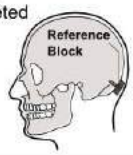	Drop test on aluminum plate	Frontal Oblique Frontal Occipital Parietal Vertex Occipital Oblique
Cadaver helmeted 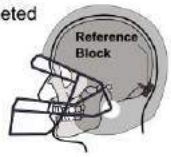	Drop test on aluminum plate	Frontal Oblique Facemask Frontal Occipital Parietal Vertex
Dummy helmeted with neck 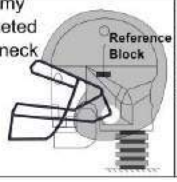	Horizontal spring-driven impact with stiff elastomer impactor head	Frontal Oblique Facemask Frontal Occipital Parietal

To calculate kinematics-based criteria, we used ground-truth sensor signals projected to the center of gravity of the head transformed to anatomical axes. We calculated linear criteria (peak linear acceleration magnitude, HIC15, SI), rotational criteria (peak rotational acceleration magnitude, peak change in rotational velocity, BrIC, PRHIC), and 6-degree-of-freedom criteria (HIP, GAMBIT, GAMBIT HITS, PCS). To calculate finite element model-based injury criteria, we ran simulations using the KTH head model [2]. From simulation outputs, we extracted peak principal strain in the whole brain, peak principal strain rate in the whole brain, and POP90 peak principal strain and strain rate.

We calculated injury criteria for each impact location in each model system for ground truth measurements and lower-bandwidth (i.e. filtered) measurements. The percent attenuation of each case from the ground truth was calculated and we determined the minimum bandwidth required to achieve less than 10% attenuation.

RESULTS

The unhelmeted cadaver head drops generally required the highest sensor bandwidths, followed by helmeted cadaver head drops, and helmeted dummy head impacts (Figure 1). For most kinematics-based criteria in the unhelmeted cadaver model, accelerometer bandwidth needs to be more than 500Hz, which is more than what is available in most current sensors. Rotational velocity bandwidth has a more significant effect on FE-based injury criteria than linear acceleration bandwidth, and strain rate criteria have higher bandwidth requirements than strain criteria. Although strain criteria do not require more than 50Hz accelerometer bandwidth, they need at least 100Hz gyroscope bandwidth. To calculate strain rate criteria in the unhelmeted model system, a bandwidth of 500Hz is required for the gyroscope, while 300Hz is sufficient for the helmeted model system – both much higher than the bandwidth of existing sensors. Kinematics-based criteria generally require higher sensor bandwidth than FE-based criteria. In addition, although peak kinematic measures (e.g. peak linear acceleration magnitude) are often used to validate sensors, their bandwidth requirements are often lower than many other injury criteria, including both compound kinematic injury criteria (e.g. HIC) and FE criteria (e.g. strain rate).

DISCUSSION

In this study, we determined minimum bandwidth requirements for studying various injury criteria in different model systems. We found that for both kinematics-based criteria and FE-based criteria, higher bandwidths are required for the unhelmeted cadaver drop test model. This implies that barehead sports will likely require higher bandwidth sensors than helmeted sports. Since many women's and children's sports (e.g. soccer) are unhelmeted, having higher sensor bandwidths is essential to study such populations. In fact, bandwidths of current sensors are insufficient in many of the cases evaluated. Another key finding is that peak kinematics-based validation of sensors may not be sufficient to ensure that injury criteria calculations also have acceptable error. This is based on the observation that many injury criteria have higher sensor bandwidth requirements than peak kinematic criteria. Thus, future efforts to validate head impact sensors may need to consider setting error thresholds on injury criteria computation.

Since much current research effort is directed towards collection of human data to study injury thresholds, it is important that head impact data are properly captured to include information essential for injury risk estimation. Our findings provide guidelines for researchers to design/select sensors for traumatic brain injury research.

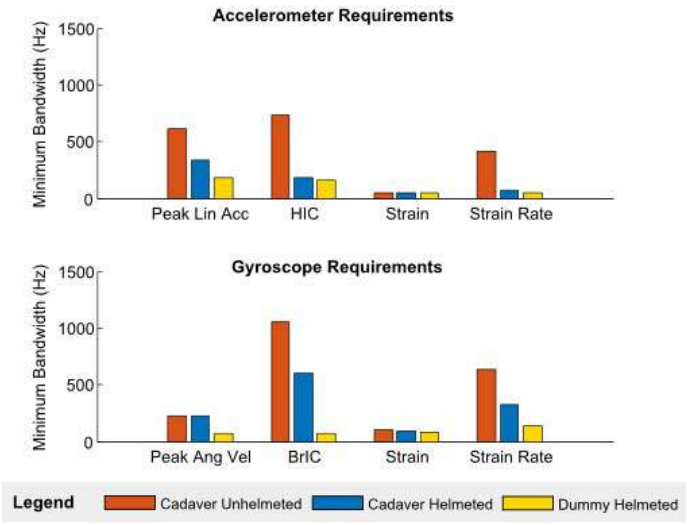

Figure 1: Sensor Bandwidth Requirements. This figure illustrates the minimum bandwidths required to achieve within 10% error in calculating common injury criteria.

ACKNOWLEDGEMENTS

We would like to acknowledge Dr. Svein Kleiven for providing the KTH head model, Dr. Dale Bass and Dr. Jason Mihalik for our partnership in post-mortem human subject experiments. We would also like to acknowledge funding sources including National Institutes of Health, David and Lucile Packard Foundation, Stanford Child Health Research Institute, Stanford BioX, and Natural Sciences and Engineering Research Council of Canada.

REFERENCES

[1] Camarillo, David B., et al. *ABME,* 41.9: 1939-1949, 2013

[2] Kleiven, Svein. *Stapp Car Crash J,* 51: 81-114, 2007.

Copyright 2016 The Organizing Committee for the 2016 Summer Biomechanics, Bioengineering and Biotransport Conference

SB³C2016
Summer Biomechanics, Bioengineering and Biotransport Conference
June 29 –July 2, National Harbor, MD, USA
SB³C2016-603

MICROCHIP ELECTROPHORESIS PLATFORM FOR POINT-OF-CARE DIAGNOSIS OF SICKLE CELL DISEASE

R. Ung (1), Y. Alapan (2), M. N. Hasan (2), M. Romelfanger (1), T. Rosanwo (3), A. Akkus (1), M. A. Cakar (4), K. Icoz (4), C. Piccone (3), J. A. Little (3), U. Gurkan (1,2)

(1) Department of Biomedical Engineering
Case Western Reserve University
Cleveland, OH, USA

(2) Department of Mechanical and Aerospace Engineering
Case Western Reserve University
Cleveland, OH, USA

(3) Department of Medicine
Case Western Reserve University
Cleveland, OH, USA

(4) Department of Electrical and Electronics Engineering
Abdullah Gul University
Kayseri, Turkey

INTRODUCTION

In developing countries, diagnostic tests for homozygous (HbSS) or compound heterozygous (HbSC or HbS-Beta thalassemia) sickle cell disease (SCD) are not readily available at the point-of-care (POC). Very few infants are screened in Africa for SCD because of the high cost, time for sample transfer to/from a central laboratory (2-6 weeks), and level of skill needed to run traditional tests, which are high performance liquid chromatography (HPLC) and bench-top hemoglobin electrophoresis. The World Health Organization recognizes a crucial need for early detection of SCD in newborns, and it is estimated that 70% SCD-related deaths in Africa are preventable with early cost-effective interventions [1]. The diagnostic barrier can be broken with affordable, POC tools that facilitate early detection immediately after birth or at the time of immunization [2]. To address this unmet clinical need, we have developed a microchip electrophoresis platform (HemeChip) for reliable, affordable, and rapid diagnosis of SCD.

METHODS

The HemeChip uses a microfabricated platform, with a material cost less than $1 per device, housing a cellulose acetate electrophoresis substrate to rapidly separate hemoglobin (Hb) types (Fig. 1A-E). Less than 5 microliters of blood, which can be obtained through a finger stick or heel stick, is processed on a piece of cellulose acetate paper via an applied electric field (250 V and 5 mA) in alkaline buffer within 10 minutes. Hb types are identified and relative percentages are quantified using image processing (Fig. 2). A mobile user interface was developed in Matlab and was established to be compatible with cloud computing resources. We clinically tested and benchmarked HemeChip against standard clinical methods using 51 blood samples.

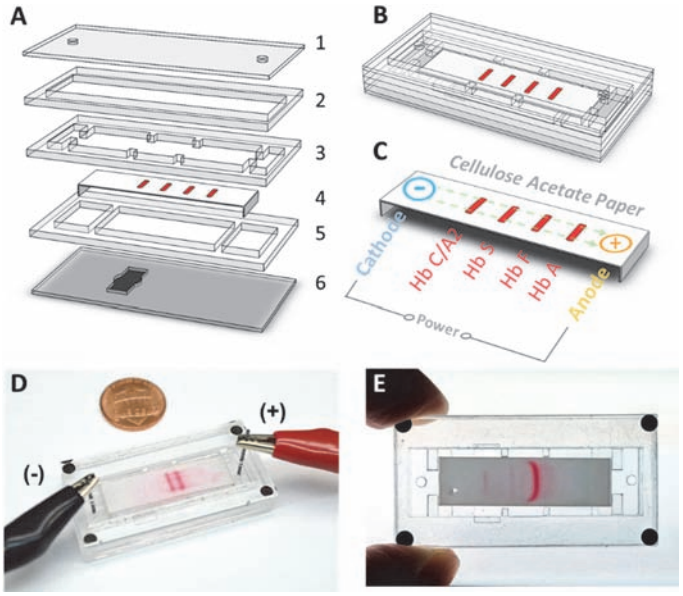

Figure 1. HemeChip for diagnosis of sickle cell disease. (A) HemeChip is fabricated with multiple layer lamination of PMMA (1-3, 5-6) encompassing a single strip of cellulose acetate paper (4). **(B)** HemeChip has a compact design and can be carried in a pocket. **(C)** Separation of hemoglobin types: Normal hemoglobin (Hb A0), Fetal hemoglobin (Hb F), Sickle hemoglobin (Hb S), and Hemoglobin C (Hb C) or A2. **(D)** Hemoglobin separation occurs via an applied electrical field between anode (+) and cathode (-). **(E)** A HemeChip prototype is shown with a miniscule amount of blood sample that has been separated into hemoglobin bands.

Copyright 2016 The Organizing Committee for the 2016 Summer Biomechanics, Bioengineering and Biotransport Conference

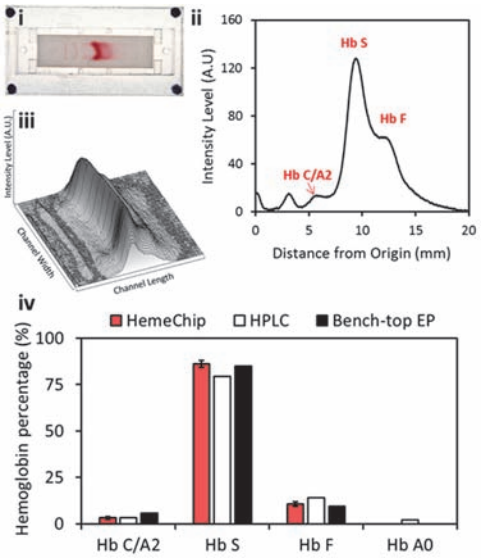

Figure 2. Identification and quantification of hemoglobin types. An HbSS sample is shown. (i) Hemoglobin bands formed in HemeChip allows identification of hemoglobin types. (ii) Measured and averaged pixel intensities reveal intensity peaks identifying hemoglobin types. (iii) 3D surface profile of pixel intensities. (iv) Hemoglobin percentages measured using HemeChip, HPLC, and bench-top electrophoresis are compared.

RESULTS

The HemeChip reliably identifies and discriminates amongst Hb C/A2, S, F and A0. The ROC curves showed more than 0.89 sensitivity and 0.86 specificity for identification of hemoglobin types. The HemeChip Hb% results correlated with HPLC results. HemeChip and HPLC results showed a strong agreement in quantified hemoglobin percentages, analyzed using Bland–Altman plot. The majority (95.5%) of the differences were within the limits of agreement (Fig. 3A-D).

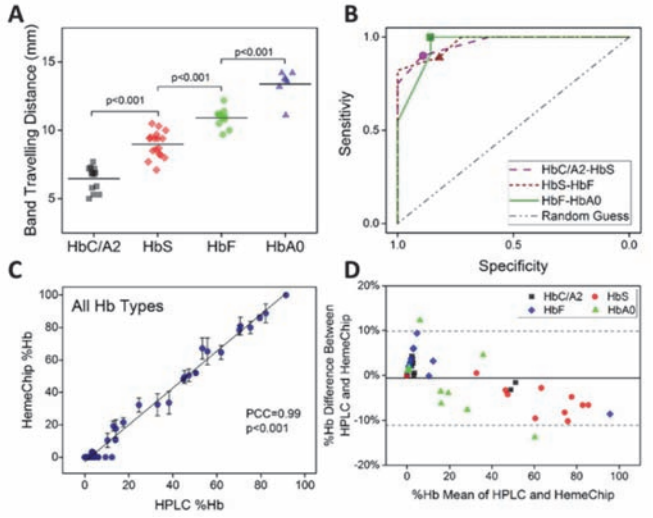

Figure 3. Clinical assessment of HemeChip. (A) The distance traveled from the application point for each hemoglobin band is used to identify the separation and presence of each hemoglobin type. **(B)** ROC curves show sensitivity and specificity for differentiating between adjacent hemoglobin bands based on the travelling distance. **(C)** Correlation plot for comparison of HPLC and HemeChip. **(D)** Bland-Altman plot showed strong agreement for the measurement of Hb% between HemeChip and HPLC.

We developed a web-based image processing application for automated and objective quantification of HemeChip results at the POC using cloud computing resources. This intensity-based mobile phone image quantitation method showed high correlation with HPLC results for tested patient blood samples (Fig. 4A-C). Moreover, the Bland-Altman analysis showed strong agreement between the HemeChip results analyzed with the mobile user interface and HPLC. The majority (91%) of the differences were within limits of agreement.

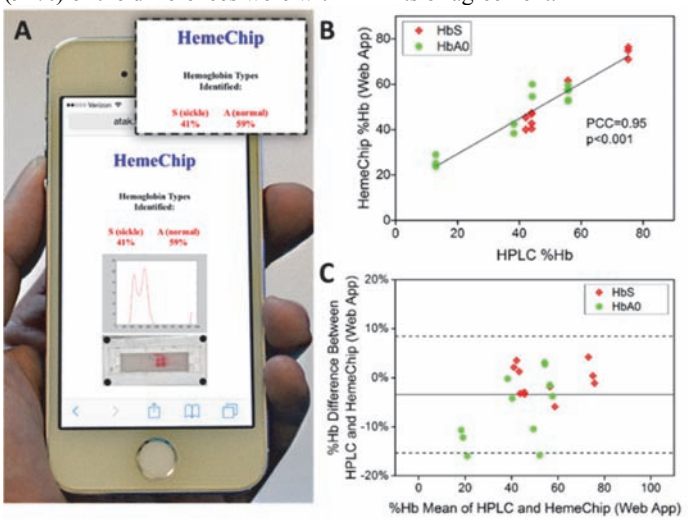

Figure 4. Web based mobile imaging and quantification of HemeChip results. (A) Mobile phone image depicting an analyzed HemeChip result and corresponding hemoglobin types along with their percentages. **(B)** Transfused SCD patient blood samples tested with HemeChip and quantified using the web service are plotted with HPLC results. **(C)** Bland-Altman plot showed strong agreement between HemeChip results analyzed with the mobile imaging modality and HPLC.

DISCUSSION

HemeChip technology offers a low-cost, easy to use, rapid approach and an innovative solution to POC diagnosis of SCD and other hemoglobin disorders. HemeChip can distinguish between different patient phenotypes, including HbSS (HbS only), transfused HbSS (HbS and HbA), and Hemoglobin SC disease (HbS and HbC). In summary, the HemeChip identification and quantification of hemoglobin phenotypes, as a POC technique, were comparable to standard clinical methods. This platform has clinical potential in under-served populations worldwide, in which SCD is endemic.

ACKNOWLEDGEMENTS

This work was made possible by an award from the Case-Coulter Translational Research Partnership (CCTRP) and an award from the Clinical and Translational Science Collaborative (CTSC) of Cleveland: UL1TR000439 from the National Center for Advancing Translational Sciences (NCATS) component of the National Institutes of Health (NIH) and NIH roadmap for Medical Research. Its contents are solely the responsibility of the authors and do not necessarily represent the official views of the NIH. Authors acknowledge the Center for Integration of Medicine & Innovative Technology (CIMIT) Student Technology Prize for Primary Healthcare for supporting this study.

REFERENCES

[1] Makani, J et al., *PloS one*, 6:e14699, 2011.
[2] Odame I., *Nature*, 515, 10, 2014.

Copyright 2016 The Organizing Committee for the 2016 Summer Biomechanics, Bioengineering and Biotransport Conference

SB^{3}C2016
Summer Biomechanics, Bioengineering and Biotransport Conference
June 29 –July 2, National Harbor, MD, USA
SB^{3}C2016-604

METHODOLOGY TO REDUCE DIMENSIONAL VARIABILITY IN TENSILE TESTING OF SOFT FIBROUS TISSUE

Madison E. Krentz, Jaremy J. Creechley, Trevor J. Lujan, Ph.D.

Department of Mechanical and Biomedical Engineering
Boise State University
Boise, ID, USA

INTRODUCTION

Tensile testing is frequently used to quantify the mechanical properties of many soft fibrous tissues, including ligament, tendon, and meniscus. The measurement of accurate mechanical properties from tensile testing requires the preparation of a large number of specimens with consistent dimensions from a finite number of donors. While maintaining good dimensional tolerances within and between specimens is critical to reduce uncertainty of the measured properties, the heterogeneous, amorphous and flexible nature of soft fibrous tissue has made consistent dimensioning a challenging task. As a result, studies that conduct tensile tests on connective tissue have reported high dimensional variability, which range from 10-38% between specimens [1,2] and range from 7-26% within specimens [3]. Therefore, standardized experimental techniques need to be developed and validated that reduce the dimensional variability of soft tissue specimens used for tensile testing.

The objective of this study is to develop and validate a fast, precise, and affordable methodology to acquire tensile specimens of soft fibrous tissue with low dimensional variability. The preparation of specimens for tensile testing requires tissue to be separated, or layered, to a specified thickness and cut, or stamped, into dog-bone shapes with a specified aspect ratio (ASTM 23479). Established methods to layer tissue include the use of a vibratome, microtome or deli slicer [3,4,5,6,7]. However, a deli slicer has only been used to layer soft organs, and not fibrous connective tissue. Established methods to stamp tissue include the use of custom metal punches or manual dissection tools, such as a scalpel [1,5,6,7,8,9]. Custom metal punches are precise, but expensive; while manual dissection tools are imprecise, but affordable. This study will determine if the dimensional variability of meniscus tensile specimens can be reduced by using a deli slicer and an inexpensive punch, made using a 3D printing device.

METHODS

Materials: All meniscus used in this study were extracted from five medial and lateral bovine knees between the ages of 18-22 months. After harvest (Fig. 1A), all meniscus were wrapped in saline solution-coated gauze, and were frozen for a minimum of 24 hours at -4 ℃. Menisci were then separated into three wedges (Fig. 1), where the central third was used in this study. A total of 30 tensile specimens were acquired from the meniscus wedges for this experiment.

Specimen Layering: The effect of layering techniques on dimensional variability was analyzed for three different approaches. In the first approach, a "bare" meniscus wedge was layered using a commercial vibratome (Fig. 1B-C). A 1x1 inch square of hot glue was mounted on the vibratome plate and the meniscus was fixed on top of the stage using cyanoacrylate glue. Glue was applied with caution, and the layer closest to the area where the glue was applied was discarded to ensure that no contaminated specimens were included in analysis. The vibratome plate was placed inside the bath which was then filled with saline solution that had been refrigerated for 24 hours prior to testing. The speed of the cut was 0.25 mm/s, at a 1 mm amplitude and

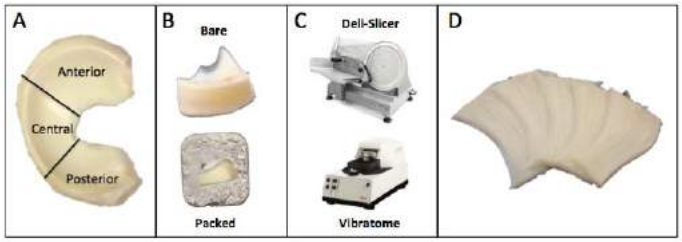

Figure 1: Specimen Layering. A) Meniscus either sectioned B) bare or packed in cellulose matrix for layering in a C) deli-slicer or vibratome. D) layered specimens from deli-slicer.

Copyright 2016 The Organizing Committee for the 2016 Summer Biomechanics, Bioengineering and Biotransport Conference

80 Hz frequency [10]. The cutting angle was 15 degrees. Ten cuts were collected from two separate central wedges and prepared for measurement analysis.

For the second approach, the "bare" meniscus wedge was layered using a commercial deli slicer (Fig 1C). The meniscus wedge was placed with the outer rim against the deli slicer fence. The control knob was set to a cutting thickness of 1 mm. A custom fixation device was applied to the bare meniscus to prevent meniscus slipping, and the deli slicer blade was sprayed on both sides with saline solution to reduce friction. Cutting speed was estimated at 0.25 mm/s.

The third approach also used the deli slicer, but first packaged the meniscus in a cellulose matrix. The cellulose solution was created using a mixture of 500 mL of cellulose clay, paper, and 250 mL of water. The cellulose matrix and meniscus was packed into a 2x2 inch square plastic container, with roughly ¼" of cellulose separating the meniscus from the container walls. The "packed" meniscus was frozen (Fig. 1C) and was then layered using the same approach described above. The reason for embedding the meniscus is that the cellulose media freezes into a solid cube and thereby provides planar surfaces that improve the slicing of the meniscus tissue into uniform layers (Fig. 1D).

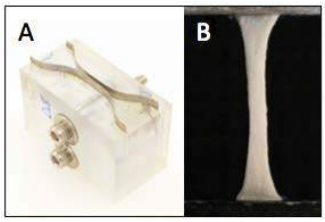

Figure 2: Specimen stamping. A) 3D printed punch. B) Dog-bone-shaped sample.

Specimen Stamping: After the layers were prepared, they were stamped using a custom punch fabricated from a 3D printer and flexible disposable razors (Fig. 2A). These punches had two curved channels to insert the blades and two machine screws to secure the blades to the plastic block. The length to width aspect ratio for this punch was set to 8:1 (Fig. 2B).

Imaging and Measurement: Layers were imaged post-punch in a custom device where the camera was fixed approximately 100 mm away from the specimen (Fig. 3A). Each prepared layer was placed inside mechanical testing clamps 13 mm apart and pulled in tension prior to imaging. In order to measure layers as precisely as possible, each picture was run through a program in which it was binarized and the thickness across the layer was recorded in pixel length (Fig. 3C), along with the standard deviation of the values with respect to the intra-specimen mean (Fig. 3D). In order to keep consistency in collecting data, the middle 11 mm values were analyzed. The average value of the pixel length across the specimens was then converted to millimeters using a conversion factor found by taking an image of a 10 mm square in position of a layer on the camera setup, which returned a value of 172.6 pixels/mm.

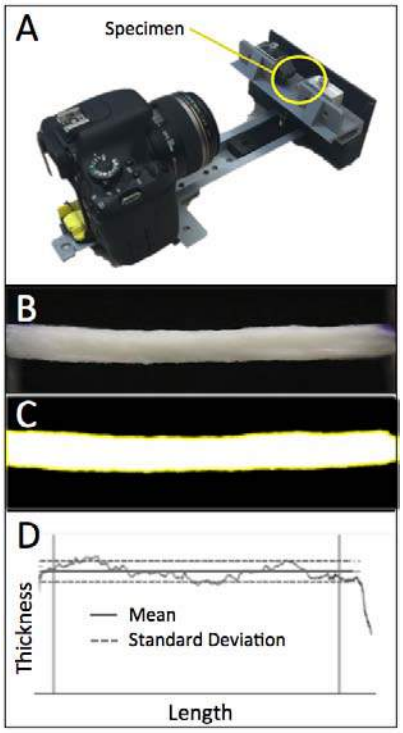

Figure 3: Measuring thickness. A) Fixture to capture images of B) specimen profile. C) Edge detection to D) measure intra-specimen variability.

A one-way ANOVA test was performed on the intra-sample standard deviation values that were normalized by the average thickness for each specimen (N=30). As a final verification step, specimens that were acquired using the "packed" deli-slicer method were strained to failure in a mechanical test system. The location of failure was recorded to determine if these specimens facilitated ideal mid-substance failures, or if they resulted in imperfect clamp failures.

RESULTS

The lowest inter- and intra-variability in specimen dimensions was produced when using the frozen-packed deli slicer method (Table 1). There was a significant difference in standard deviation values when comparing the frozen packed deli slicer method to the bare deli slicer and vibratome methods (p=0.028 and p=0.007, respectively). Out of nine uniaxial failure tests that used specimens from the frozen packed deli-slicer, seven resulted in mid-substance failures, and only one resulted in a clamp site failure.

Table 1: Specimen thickness and variability

Layering Device	Prep Method	Thickness (mm)	Inter-sample variability (%)	Intra-sample variability (%)
Vibratome	Bare	1.31 ±0.11	18.17	16.07 ± 7.36
Deli Slicer	Bare	1.16 ±0.07	6.39	13.00 ± 6.10
	Packed	1.18 ±0.04	5.89	6.55 ±3.40

DISCUSSION

This study found that the dimensional variability of meniscus specimens was most reduced when using a deli-slicer to layer frozen meniscus that was embedded in a cellulose matrix. This experimental approach reduced the intra-specimen variability by over 2 fold compared to other techniques. Compared to the vibratome, the deli-slicer reduced the inter-specimen variability nearly 3 fold.

This study introduced several novel techniques in tensile testing of fibrous soft tissue. Although a deli-slicer had been used to cut soft organs, such as liver and kidneys, we had not seen it used for fibrous connective tissue. The use of a cellulose matrix was a novel concept that was developed to provide a planar surface for more repeatable cutting. In addition, this study used 3D printed punches to reduce the cost and improve the precision of stamping tissue to specified aspect ratios. This advance could allow the fast and inexpensive identification of specimen geometries that reduce the occurrence of clamp failure. Collectively, these new techniques were able to improve the dimensional tolerancing of specimens, and can be applied toward the tensile testing of other fibrous connective tissue.

ACKNOWLEDGEMENTS

This project was supported by the Biomolecular Research Center at Boise State University and funded by NIH NIGMS P20GM109095.

REFERENCES

[1] Abdelgaied, A et al., *J Biomech*, 48:1389-1396, 2015.[2] O'Leary, S.A et al., *J Biomech,* 47:1430-1473, 2014.[3] Danso, E.K et al., *J Biomech*, 47: 200-206, 2014.[4]Freutel, M et al., *J Biomech*, 48: 1350-1355, 2015.[5]Lakes, E.H et al., *J Biomech*, 2015.[6] Brunon, A et al., *J Biomech*, 43:2221-2227, 2010.[7] Manoogian S.J et al., *J Biomech,* 41:3436-3440, 2008. [8] Fischenich, K.M et al., *J Biomech*, 48: 1407-12411, 2015. [9] Untaroiu, C.D et al., *JMBBM*, 41:280-291, 2015.[10]Leica VT10000S Vibratome Manual

Copyright 2016 The Organizing Committee for the 2016 Summer Biomechanics, Bioengineering and Biotransport Conference

SB^{3}C2016
Summer Biomechanics, Bioengineering and Biotransport Conference
June 29 –July 2, National Harbor, MD, USA
SB^{3}C2016-605

RELATIONSHIP BETWEEN MECHANICAL STIFFNESS AND MULTIPLE CANCER CELL LINE PROLIFERATION AND MORPHOLOGY IN 3D ENCAPSULATED GELATIN METHACRYLATE HYDROGELS

Sean Hennigan (1), Susan A. Pomilla (2), Melissa A. DePrato (1), John R. Beliveau (1) and Jason W. Nichol (1,2)

(1) Department of Biology and Biotechnology
Endicott College
Beverly, MA USA

(2) Department of Bioengineering
Endicott College
Beverly, MA USA

INTRODUCTION

Cancer is the uncontrollable growth of cells, which can lead to tumors and devastating results if allowed to persist [1]. The extracellular matrix (ECM) plays a key role in cancer cell phenotype in that stiffer matrices have been shown to increase cell proliferation, leading to more ECM secretion, resulting in a positive feedback loop [2]. Key aspects of this relationship are poorly understood, which limits the ability of clinicians and researchers to battle these different types of tumors effectively. Broad based treatments such as chemotherapy have a myriad of side effects and are potentially less effective than treatments aimed at specific types of cancer, or even particular genetic strains. It is presumed that cancer cells originating from stiffer, or softer, tissues will sense their environment differently, as has been proven for normal cells [3] and stem cells [4] which could yield important information in understanding the ability of different malignant cancers to effectively extravasate and repopulate in different areas of the body.

Gelatin methacrylate (GelMA) is a UV-crosslinkable hydrogel that has been shown to be effective in culturing cells in both 2D and 3D in a wide variety of applications [5]. Cells can easily bind to GelMA surfaces, or native binding sites (RGD) within 3D structures, and can proliferate, elongate, migrate and remodel their surroundings. A highly elastic material capable of full recovery from >90% compression, mechanical stiffness can be varied from < 1 to >30 kPa through variation of the gel concentration, and the degree of methacrylation. Within this system we have demonstrated the ability to micropattern cells in 3D to investigate behaviors such as elongation and proliferation in response to mechanical stiffness and 3D geometry [6]. Recently this system has been used to investigate cancer cell migration [7], demonstrating its enormous potential in investigating the relationships between cancer cell physiology and the mechanical stiffness of the surrounding extracellular matrix.

In this study, breast cancer (MDA), cervical cancer (SiHa) and osteosarcoma cell lines (U2OS) were embedded within 3D GelMA hydrogels of low, medium and high stiffness. To achieve this range, the same formulation of GelMA was employed at three different concentrations 7.5% (low), 10% (medium) , and 12.5% (high). The embedded cells were counted over the course of four days, while proliferation and elongation were determined from histological images. Results demonstrated many significant differences in the rate of both proliferation and elongation vs time in culture and mechanical stiffness of the matrix which varied with cell type. Preliminary results with the MDA and SiHa cells demonstrate a cell specific effect, suggesting that there is evidence that different cancer cell types react differently to levels of mechanical stiffness. Further experiments will aim to further elucidate these effects and the factors driving these phenomena.

METHODS

Briefly, GelMA was created as described previously by dissolving 10% gelatin into 100ml of stirred PBS at 50^{o}C, while methacrylic anhydride was added dropwise until 4 ml was added [5]. This mixture was reacted for roughly 3 hours at 50^{o}C in a fume hood, then dialyzed in distilled water within 12,000 kDa cutoff tubing at 50^{o}C for up to 1 week to remove methacrylic acid and other byproducts, and dried in a SpeedVac for at least 24 hours. To create GelMA hydrogels, 7.5%, 10% or 12.5% of GelMA precursor was dissolved in an appropriate volume of PBS at 50^{o}C containing 0.5% Irgacure 2959 (photoinitiator, PI), with 250 ml of the mixture (precursor) then pipeted into wells of a standard 24 well plate, then

Copyright 2016 The Organizing Committee for the 2016 Summer Biomechanics, Bioengineering and Biotransport Conference

polymerized with UV light exposure for 80s (high), 100s (medium), or 120s (low). The variation is due to the increased presence of methacrylate groups leading to increased speed of polymerization with increased concentration.

All 3 cell types were cultured using standard techniques and media containing 10% FBS and 1% antibiotic/antimycotic. For experiments, cells were trypsinized, centrifuged to remove trypsin, then were counted and 150,000 cells were added to 250 ml of GelMA precursor/PBS/PI mixture, mixed well and added to a well of a 24 well plate. Plates were then quickly polymerized with the appropriate UV exposure with all gels in 1 plate having the same concentration of GelMA to make UV exposure time constant for all cells.

Immediately following encapsulation, and at 2 and 4 days post encapsulation, images were randomly taken of 5 locations in each gel to analyze cell number and elongation. Cell proliferation was determined by comparing the average cell number on days 2 and 4 as compared to day 0, while elongation was measured relatively as the percentage of cells in the images with an elongated phenotype. Statistical difference within groups were determined with student t tests, while comparisons between groups will be determined by ANOVA with post-hoc testing between individual groups with $p < 0.05$ considered significant.

RESULTS

Experimental results were obtained for the MDA and SiHA cells, and are still ongoing for the U2OS cells due to their more difficult nature to culture in our hands. Cell proliferation in both cases increased significantly ($p < 0.05$) by day 4, though variation was such that clear trends with low n's were inconsistent. In addition, there was an apparent trend with both cell types of increased proliferation with increased matrix stiffness however, insufficient n size and large variation made statistical evaluation difficult. Experiments are ongoing to address these issues and to include analysis of the U2OS cells as well.

For the cervical cancer (SiHa) cells, there was an increase in cell number from day 0 to 4 in all 3 matrix stiffnesses that was significant when comparing day 0 to day 4 in the medium and high stiffness gels, and when comparing day 2 to day 4 in the low stiffness gels (Figure 1). When comparing cell count on day 4 between the different stiffnesses, there was no difference between the medium and high groups, however there was a nearly significant difference between both the medium and high groups as compared to the low group ($p < 0.06$).

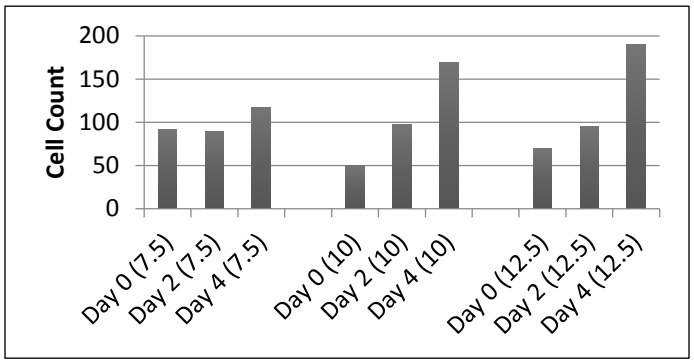

Figure 1: Cell count (per image area) vs time in 3D culture for SiHa cells in 7.5% (low), 10% (medium) and 12.5% (high) stiffness GelMA hydrogels.

For the breast cancer (MDA) cells, there was again an increase in cell number from day 0 to 4 in all 3 matrix stiffnesses, and again this difference was significant when comparing day 0 to day 4 in the medium and high stiffness gels, however this was only true when comparing day 0 to day 2 in the low stiffness gels (Figure 2). When comparing cell count on day 4 between the different stiffnesses, there was again no difference between the medium and high groups, however there was a highly significant difference between both the medium and high groups as compared to the low group ($p < 0.01$ for each).

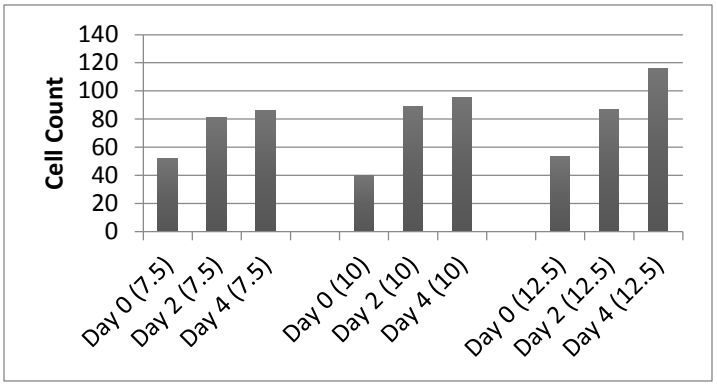

Figure 2: Cell count (per image area) vs time in 3D culture for MDA cells in 7.5% (low), 10% (medium) and 12.5% (high) stiffness GelMA hydrogels.

DISCUSSION

The results presented are ongoing, however preliminary data highly suggest an increase in proliferation in response to increased stiffness in both the breast and cervical cancers, with minor unique differences in each. When subsequent experiments to increase n size and experiments with the osteosarcoma cells are complete, it is expected that there will be substantive differences between the cells presented here and the osteosarcoma cells who are accustomed to a much stiffer native environment. The results presented also suggest that future studies focus on increasing hydrogel stiffness above 12.5%, or otherwise increasing stiffness to further differentiate the responses of the different cell types. While the mechanical properties of GelMA are well characterized, the mechanical properties of this specific batch of GelMA are still ongoing and will inform future studies of the precise range of mechanical stiffness that each case is undergoing.

Future studies will focus on decoupling the mechanical properties from the hydrogel concentration, by varying just the methacrylation degree to avoid also drastically changing the porosity and concentration of native binding and degradation sites.

ACKNOWLEDGEMENTS

We could like to thank Endicott College for travel funding as well as course releases and laboratory supplies for JW Nichol to make this research possible.

REFERENCES

[1] Hanahan, D. & Weinberg, R. *Cell*. 100: 57-70, 2011.
[2] Mylona, E. *et al.*, *ESBME Proceedings*. 2008.
[3] Levental, I. *et al. Soft Matter*.3: 299-306, 2008.
[4] Engler, A. *et al. Cell.* 126(4): 677-689, 2006.
[5] Nichol, J.W., S. Koshy *et al. Biomaterials.* 31(21): 5536-44, 2010.
[6] Aubin, H., J.W. Nichol *et al. Biomaterials.* 31(27); 6941-51, 2010.
[7] Peela, N. *et al. Biomaterials.* 81: 72-83 (Epub), 2016.

Copyright 2016 The Organizing Committee for the 2016 Summer Biomechanics, Bioengineering and Biotransport Conference

SB^{3}C2016
Summer Biomechanics, Bioengineering and Biotransport Conference
June 29 –July 2, National Harbor, MD, USA
SB^{3}C2016-606

VISCOELASTIC PROPERTIES OF HUMAN PATELLAR TENDONS MEASURED USING CONTINUOUS SHEAR WAVE ELASTOGRAPHY

Courtney T. Cox (1) Jennifer A. Zellers (2) Karin G. Silbernagel (3) Daniel H. Cortes (4)

(1) Department of Biomedical Engineering
University of Delaware
Newark, DE, USA

(2) Program in Biomechanics and Movement Science
University of Delaware
Newark, DE, USA

(3) Department of Physical Therapy
University of Delaware
Newark, DE, USA

(4) Department of Mechanical Engineering
Penn State University
University Park, PA, USA

INTRODUCTION

Patellar tendinopathy is a musculoskeletal disorder resulting from overuse of the knee that is common in athletes participating in sports that involve repetitive jumping, such as basketball and volleyball[1].

Tendon injuries such as this often alter viscoelastic mechanical properties[1]. We recently developed a non-invasive ultrasound elastography technique called continuous shear wave elastography (cSWE) to measure viscoelastic properties of the Achilles tendon[2]. Prior studies, using similar elastography techniques, performs the measurement on the patellar tendon with the knee at 20-30 degrees of flexion to minimize the tension on the tendon[3]. However, our method is designed to evaluate properties of tissues with stiffness higher than maximum values that can be measured with commercial systems. Consequently, cSWE can potentially allow measuring viscoelastic properties of the patellar tendon at higher angles of knee flexion.

The purpose of this study is to determine if cSWE can be used to evaluate healthy patellar tendons at higher values of knee flexion, and if the technique can distinguish between healthy and injured patellar tendons.

METHODS

The patellar tendon was imaged using B-mode ultrasound for tendon length and width and cSWE for viscoelastic properties with the following vibration frequencies: 323, 340, 358, 379, 403, 430, 461, 496, 538, 586, and 645 Hz. The effect of placing actuator on patella versus distal quadriceps muscle belly and the influence of different knee angles (30, 60 and 90 degrees) were tested on 4 healthy subjects.

Based on this pilot study, a final procedure was developed. Subjects (15 healthy and 2 tendinopathic patients) were positioned supine with the actuator placed on the quadriceps muscle. Furthermore, data was collected at 30 and 90 degrees of knee flexion using a knee brace (Figure 1). Data is reported as mean (SD). A paired t-test was used to compare the viscoelastic properties of the tendon at different knee angles. The level of significance was set at $p<0.05$.

Figure 1: Subject positioning for elastography measurements.

RESULTS

There were no significant differences in patellar tendon shear modulus and viscosity between 30 and 60 degrees of knee flexion; however, there were significant differences between the 30 and 90 degrees. When evaluating actuator placement, placement on the quadriceps muscle was more comfortable than the patella for subjects, and it was easier to maintain consistent position during testing. In addition to this, placing the actuator on quadriceps muscle versus patella did not negatively affect quality of data.

When evaluating the effect of the vibration frequency, it was observed that higher frequencies produced waves with a wavelength shorter than the field of view. Having wavelengths shorter than the field of view increases the accuracy of the calculated viscoelastic

Copyright 2016 The Organizing Committee for the 2016 Summer Biomechanics, Bioengineering and Biotransport Conference

properties. Therefore, the highest 6 frequencies were used for data analysis.

The shear modulus and viscosity in healthy patellar tendons were significantly higher at 90 degrees when compared to 30 degrees (Figure 2).

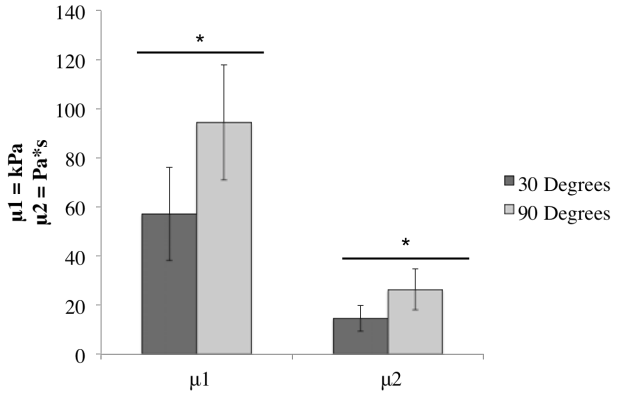

Figure 2: Shear modulus (μ1) and viscosity (μ2) at 30 and 90 degrees for healthy tendons. *p<0.001

Data collected from the two tendinopathic tendons also revealed that values for shear modulus and viscosity were higher at 90 degrees compared to 30 degrees (Table 1).

Table 1: Shear modulus and viscosity of two tendinopathic patellar tendons.

Subject	Angle	μ1 (kPa)	μ2 (Pa*s)
1	30 Degrees	61.7	17.6
	90 Degrees	80.7	22.1
2	30 Degrees	66.4	11.3
	90 Degrees	90.5	26.5

When comparing data collected from the healthy tendons to the two tendinopathic tendons, it is seen that the mean value for shear modulus and viscosity in healthy tendons is lower than both tendinopathic cases at 30 degrees, and higher than both cases at 90 degrees. In addition to this, Figures 3-5 show that proximal patellar tendon thickness in tendinopathic tendons (0.97 cm and 0.89 cm) is greater than that of healthy tendons (0.61 cm (0.10 cm)). Furthermore, the tendinopathic tendons showed increased values for shear modulus and viscosity in the deep half of tendon (Figure 6-7).

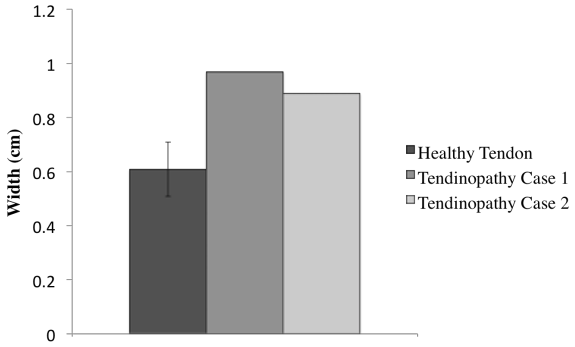

Figure 3: Width at 30 degrees for healthy vs. unhealthy tendons.

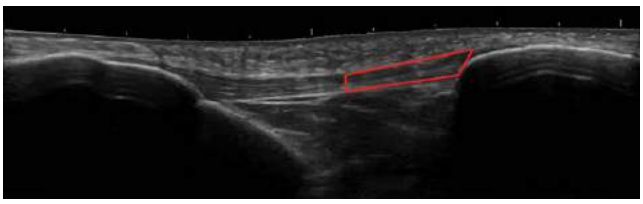

Figure 4: Healthy tendon at 30 degrees.

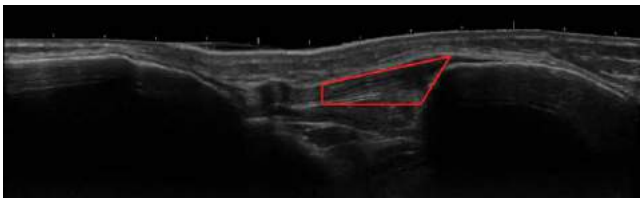

Figure 5: Tendinopathic tendon at 30 degrees.

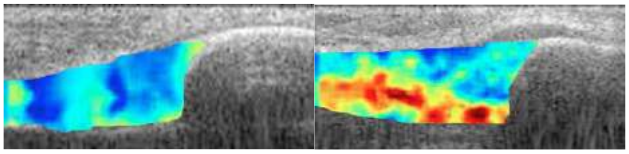

Figure 6: Shear modulus of healthy vs. tendinopathic tendon at 30 degrees.

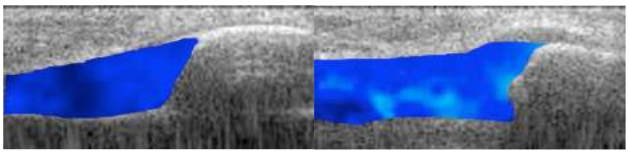

Figure 7: Viscosity of healthy vs. tendinopathic tendon at 30 degrees.

DISCUSSION

This study showed that it is feasible to measure viscoelastic properties at different knee angles using cSWE. Furthermore, our results suggest that cSWE can potentially identify regions in the tendon with altered mechanical properties caused by pathological conditions such as tendinopathy. The results of this study are consistent with prior studies, which have showed that elasticity is dependent on knee position and increased proximal patellar tendon thickness is indicative of patellar tendinopathy[3,4]. A limitation of the current study is the low number of tendinopathic patients. Future studies will involve recruiting more patellar tendinopathy subjects to further investigate the differences between healthy and unhealthy patellar tendons.

ACKNOWLEDGEMENTS

Austin Barth, Patrick Corrigan, Samantha Dargis, Jake Fish, Tiana McKim, Angela Smith, Tyler Tice, and Rachel White for assistance with data collections.

REFERENCES

[1] Pearson, S and Hussain S, *Sports Medicine,* 44:1101-1112, 2014.
[2] Cortes, D et al., *Ultrasound I Med. & Biol.,* 41:1518-1529, 2015.
[3] Berko, N. et al., *Clinical Radiology,* 70:1083-1086, 2015.
[4] Visnes, H et at., *Scand J Med Sci Sports,* 25:205-215, 2015.

Copyright 2016 The Organizing Committee for the 2016 Summer Biomechanics, Bioengineering and Biotransport Conference

SB³C2016
Summer Biomechanics, Bioengineering and Biotransport Conference
June 29 –July 2, National Harbor, MD, USA
SB³C2016-607

IN VITRO RUPTURE PATTERNS OF ASCENDING THORACIC AORTIC ANEURYSMS

Yuanming Luo (1), Ambroise Duprey(2), Stéphane Avril (2), Jia Lu (1)

(1) Department of Mechanical & Industrial Engineering
The University of Iowa
Iowa City, IA, USA

(2) Ecole Nationale Suprieure des Mines de Saint-Étienne, CIS-EMSE,
INSERM U1059
St. Étienne, France

INTRODUCTION

Ascending thoracic aortic aneurysms (ATAAs) are focal dilatations of the aortic wall. ATAAs are a serious life-threatening pathology and their incidence is estimated at 10.4 per 100,000 people, suggesting that approximately 45,000 cases are diagnosed each year in Europe and the United States [1]. If an ATAA spontaneously ruptures, the result is almost invariably death [2]. While in principle ATAA rupture can be attributed to a mechanical failure, which occurs when the acting wall stresses exceed the tensile strength of the wall tissue, the exact mechanism remains poorly understood. Since ATAAs undergo continuous pathological remodeling resulting in a highly heterogeneous structure, it is difficult to delineate the local mechanical condition in traditional experiments. In this study, we used a pointwise approach to identify the full field stress, strain and mechanical properties of harvested ATAA samples. This method allowed us to resolve the mechanical conditions to a sub-millimeter resolution. At this resolution, the ATAAs appear to exhibit some distinct rupture patterns. One of these patterns is reported in this presentation.

METHODS

ATAA sections were collected from patients undergoing elective surgery in accordance with a protocol approved by the Institutional Review Board of the University Hospital Center of St. Etienne. Samples of ~4 cm in diameter were pressurized incrementally until rupture. The experimental method was documented in [3]. Briefly, stereoscopic digital image correction (DIC) was used to obtain full-field displacement measurements, and consequently to compute the surface strain distribution. To obtain the stress distribution, we employed an inverse elastostatic method [4] which capitalizes on the property of *static determinacy* to identify the stress field without prior knowledge of the tissue properties. Upon obtaining the distributions of stress and strain at multiple loaded states, the elastic property of the tissue is characterized locally using pointwise stress-strain data. All stress-strain curves we obtained exhibited a profound exponential hardening and moderate anisotropy. To model the stress function we employed a structurally motivated strain energy function:

$$w = \frac{\mu_1}{2}(I_1 - \ln(I_2) - 2) + \frac{\mu_2}{2\gamma}(e^{\gamma(I_k-1)^2} - 1)$$

Here $I_1 = tr\mathbf{C}$, $I_2 = det\mathbf{C}$ are the principal invariants of the Cauchy-Green deformation tensor, and I_k is a compound invariant that takes into account of both the orientation and distribution of the collagen fibers. This invariant boils down to two parameters, a preferred direction **M** and a dispersity parameter, κ. The vector **M** represents the direction at along which collagen fibers are preferentially oriented, giving the highest stiffness among all directions.

Later, the direction of **M** is correlated locally to the orientation of the orifice. The initial orifice was identified from the images immediate before rupture. The red ellipses in Figure 1(a) indicate rupture sits. The arrows point to the transverse direction of the orifice. The 'fiber direction' (the stiffest direction) at the rupture sites was obtained by averaging the identified **M** angle within a designed set of Gauss points inside the ellipses. For the example in Fig.1, the averaged stiffest directions are marked in Fig. 1(b).

RESULTS

In all cases, the orifices are found to be perpendicular to the stiffest direction. The angles of the stiffest direction and the orifice transverse direction (the orifice angle) are plotted in Fig. 2. A linear relation ($y = x$) is revealed.

Copyright 2016 The Organizing Committee for the 2016 Summer Biomechanics, Bioengineering and Biotransport Conference

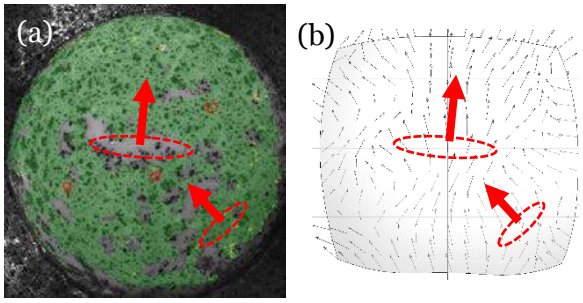

Fig.1 (a) Initial orifice and orientation; (b) Stiffest direction

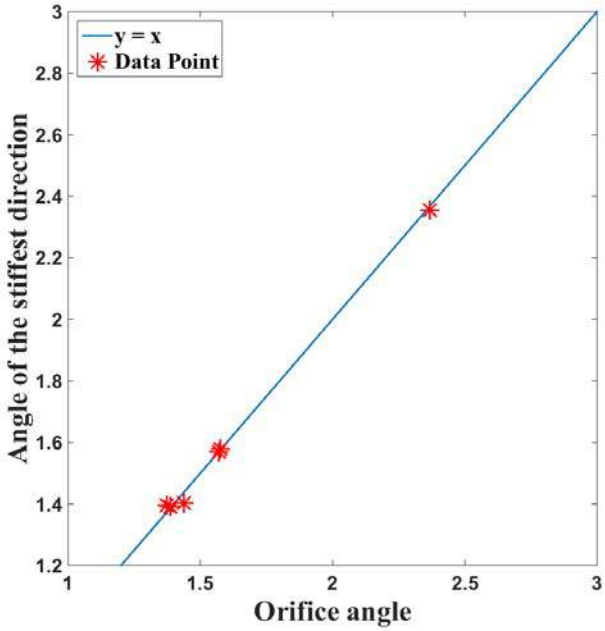

Fig. 2. Local stiffest direction versus orifice orientation

In addition, the cracks appear to *propagate* perpendicular to the stiffest direction. Two representative cases are shown in Fig. (3). The orifices are identified from the last image of each test. They are outlined in the left panel of Fig.3. The local **M**-vectors in the rupture region can be seen from the maps in the right panel.

DISCUSSION

In most biomechanical studies reported thus far, ATAAs sample of centimeter size have been invariably treated as a homogeneous. Uniaxial or biaxial tensile tests were typically used to identify the mechanical properties including the rupture strength. Sometimes conflicting results were reported with regard to the directional strength of ATAA tissues. A fundamental limitation of these tests is the assumed homogeneity. Studies including our own indicated that ATAAs are highly heterogeneous; the stress and strain vary significantly, even at the millimeter scale. Consequently, homogenized test results can hardly reflect the local condition at the rupture site. We suggest that identifying the local condition is critical for understanding ATAA rupture.

Perhaps the most unexpected result of the present study is that the cracks initiate and propagate perpendicular to the local stiffest direction, in other words, cutting through the fibers. This result is counter-intuitive, as one would expect the cracks cleave normal to the direction of the least stiffness. This finding, if independently verified, can have a profound implication in understanding ATAA rupture and strength. If we recall that the **M** vector indicates the direction of predominate collagen distribution, the finding suggests that the amount of collagen content is not, at least not the *only*, determinant of rupture strength. Other factors reflecting the quality of collagen network, such as fragmentation and the density of crosslinks, could be important. This speculation is in line with the report of Pichamuthu et al [5] which showed that differences in mechanical properties are not attributable to absolute collagen content but may be accounted for by microstructural changes in the collagen framework. It also resonates with the work of Borge et al [6] which found that collagen is reduced and disrupted in aneurysms and dissections of ascending aorta. Carmo et al [7] suggested that in aneurysmal aortic walls old collagen accumulates cross-links while new collagen biosynthesis is somehow defective, again pointing to the role of crosslinks. Much needs to be done for understanding ATAA rupture. In future, we plan to carry out imaging studies to investigate the microstructural difference, if any, in collagen network near and away from a rupture site.

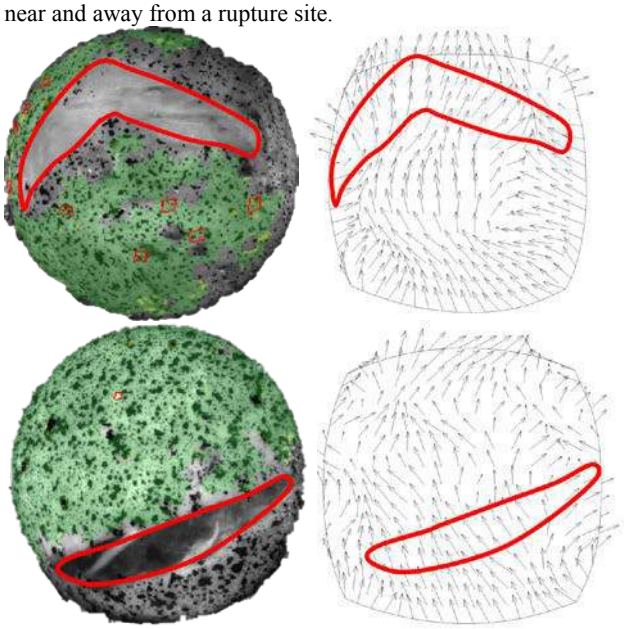

Fig 3. Left panel: images after rupture, with orifices outlined; Right panel: **M**-vector map.

ACKNOWLEDGEMENTS

The authors would like to thank Dr. Frances M. Davis for her early involvement in this study.

REFERENCES

[1] Elefteriades, J.A. et al, Journal of the American College of Cardiology, 55: 841-857, 2010
[2] Juvonen, T. et al, Annals of Thoracic Surgery, 64: 594-594, 1997
[3] Davis, F. et al, Biomechanics and Modeling in Mechanobiology, 14:967-978, 2015
[4] Lu, J. et al. Biomechanics and Modeling in Mechanobiology, 7:477-86, 2008
[5] Pichamuthu, J.E. et al, The Annals of thoracic surgery, 96.6:2147-2154, 2013
[6] Figueiredo Borges, L. et al, Human Pathology, 39:437-443, 2008
[7] Carmo, M. et al, Eur J Vasc Endovasc Surg, 23: 543-549, 2002

Copyright 2016 The Organizing Committee for the 2016 Summer Biomechanics, Bioengineering and Biotransport Conference

SB³C2016
Summer Biomechanics, Bioengineering and Biotransport Conference
June 29 –July 2, National Harbor, MD, USA
SB³C2016-608

MICROBIAL REGENERATION OF ADSORBENT SILICA GEL FOR SUSTAINABLE TREATMENT OF ENVIRONMENTAL POLLUTANTS

Jonathan K. Sakkos (1), Lawrence P. Wackett (2,3), Alptekin Aksan (1,3)

(1) Department of Mechanical Engineering
University of Minnesota
Minneapolis, MN, USA

(2) Department of Biochemistry, Molecular Biology, and Biophysics
University of Minnesota
Minneapolis, MN, USA

(3) BioTechnology Institute
University of Minnesota
St Paul, MN, USA

INTRODUCTION

Environmental pollution with aromatic hydrocarbons is a ubiquitous and deleterious consequence of extensive fossil fuel use that poses significant human health concerns. Conventional water treatment methods (physical, chemical, and thermal) cannot readily remove low concentrations of aromatic hydrocarbons in water in an economical and efficient manner. However, certain naturally-occurring bacteria can readily metabolize aromatic hydrocarbons[1]. The issue then becomes one of developing ways to integrate these bacteria into existing industrial treatment processes in a well-engineered and robust delivery system to address control, stability, cost, and longevity issues.

Adsorbents, such as granulated activated carbon (GAC), are commonly used for removing hydrocarbons from water, due to their high removal capacity and low cost. However, this treatment method does not provide a permanent solution, and merely concentrates the chemicals for disposal in a landfill. By utilizing biodegrading bacteria in combination with an adsorbent material, a hybrid approach can be taken, which combines the strengths of adsorbents and biodegradation.

Through the use of bioencapsulation (physical confinement of cells in a 3D matrix), we can synthesize an adsorbent material surrounding the bacterial cells. Silica gel encapsulation is an ideal candidate for this purpose, because silica is inert, cytocompatible, and inexpensive. Silica encapsulation of biodegrading bacteria has been shown to be an effective method for destruction of hazardous chemicals from water[2]. Organically-modified silica (ORMOSIL) has the additional benefit of strongly adsorbing aromatic hydrocarbons.

In this study, we report a combined adsorption/biodegradation approach to enable rapid removal and subsequent biodegradation of aromatic hydrocarbons. By incorporating a very small amount of Pseudomonas sp. NCIB 9816-4 into an ORMOSIL gel, we are working to develop a low-cost, yet effective biohybrid material to remove hydrocarbons repeatedly and regenerate the adsorbent capacity of the material, without significant loss in effectiveness over time. The focus of this preliminary study was to combine a mass transport model with experimental data to inform the final design of the material and determine how the distribution coefficient (K_d) will affect biodegradation.

METHODS

Cell growth and harvesting

Pseudomonas sp. NCIB 9816-11 was inoculated from a Luria Broth (LB) plate culture into 5 mL of LB and incubated at 28C for 8 hours. 1 mL of the culture was then placed into 300 mL Mineral Salts Broth (MSB) with 0.8g succinate and incubated overnight with shaking at 200 rpm. To induce naphthalene dioxygenase, 0.7g salicylic acid was added 2 hrs prior to harvest. Cells were harvested by centrifugation at 6000 x g for 15 minutes.

Initial Rate Measurement

Pseudomonas sp. NCIB 9816 is a naturally occurring bacterium which can degrade over 100 aromatic hydrocarbons[3]. Here, we used naphthalene as a substrate in combination with a knockout mutant strain, NCIB 9816-11, which lacks a dihydrogenase enzyme and accumulates *cis*-naphthalene dihydrodiol. The rate of naphthalene biocatalysis was determined by measuring the oxygen consumption within a sealed chamber. Oxygen consumption was measured using an Oxygraph Oxytherm System (Hansatech Instruments Ltd., United Kingdom).The chamber was filled with 3 mL of naphthalene in Phosphate buffered saline (PBS) and 10 mg cells were added. The system was allowed to equilibrate for 1 minute before measurement was started to ensure that the rates were linear within the range tested.

Copyright 2016 The Organizing Committee for the 2016 Summer Biomechanics, Bioengineering and Biotransport Conference

Oxygen consumption was measured for 5 minutes for each sample. Samples were performed in triplicate.

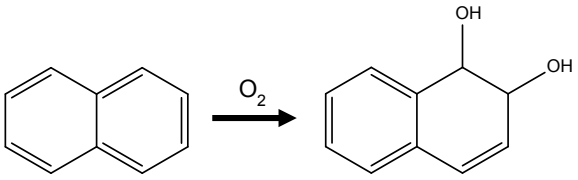

Figure 1: Naphthalene dihydroxylation by NCIB 9816-11

Mass Transport Modelling

The diffusion, reaction, and adsorption processes were modelled using a partial differential equation of the form:

$$\frac{\partial C}{\partial t} = \frac{\left[D_e \nabla^2 C - \frac{V'_{max} \rho_c C}{K_m + C}\right]}{\varepsilon + K_d \rho} \quad (1a)$$

with initial condition:

$$C(x,t) = 0, t \leq 0 \quad (1b)$$

and boundary conditions:

$$\frac{\partial C}{\partial t} = 0, x = 0, t \geq 0 \quad (1c)$$

$$C(x,t) = 250\ \mu M, x = L, t \geq 0 \quad (1d)$$

A semi-infinite slab was simulated using Matlab (Mathworks, Inc., Natick, MA, USA), in order to resemble future experimental setups. The model was solved numerically for a period of 10^5 seconds, with a range of K_d values.

RESULTS

The initial rate experiments revealed that the reaction with whole cells obeyed Michaelis-Menten kinetics (Figure 2). V'_{max} amd K_m can be seen in Table 1. The modelling results showed a reduction in naphthalene degradation with increasing K_d (Figure 3). At short time-scales, this difference was negligible, likely due to the low concentration of naphthalene in the gel. As the naphthalene diffused into the gel, the disparity increased. At long time-scales, the rate of degradation appeared to decrease, possibly due to a large amount of adsorbed naphthalene.

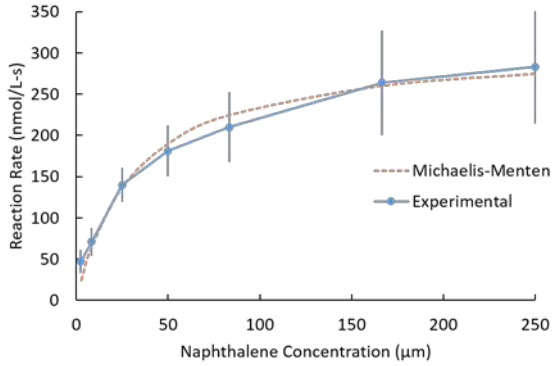

Figure 2: Free cell kinetics of *Pseudomonas sp* NCIB 9816-11 biodegrading naphthalene, measured by oxygen consumption, with 10 mg cells in a 3 mL volume.

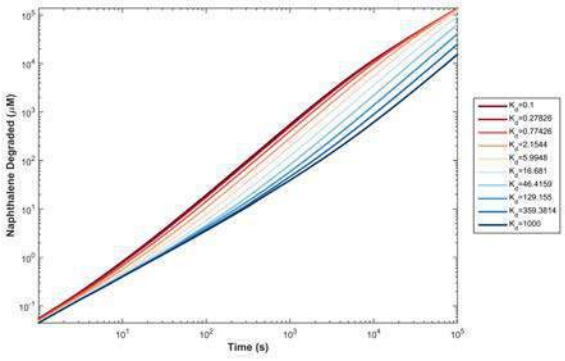

Figure 3: Model results for naphthalene biodegradation over time with an infinite bath of 250 µM naphthalene on a semi-infinite slab containing a cell loading of ρc=10-4 g-cells/mL gel.

DISCUSSION

In order for the system to be both highly adsorptive and regenerative, the cell loading (reaction rate) and adsorptivity (K_d) of the gel must be tuned. Based on the model, we see that having a gel which is excessively adsorptive may hinder the overall biodegradation and thus take longer to regenerate. Furthermore, a high K_d acts to reduce the diffusion through the porous media. Experimental measurement of K_d will be required to determine the optimal cell loading.

Future work will focus on synthesis and characterization of the adsorbent silica gel to determine what values of K_d can be achieved and optimization of the cell loading to minimize cost.

Table 1: Model parameters

Symbol	*Definition*	*Value*	*Units*
C	Naphthalene concentration		µM
D_e	Effective Diffusion Coefficient for Naphthalene	1 x 10^{-4}	mm^2/s
V'_{max}	Maximum specific reaction velocity	3.09x10^{-5}	mol/(L-s-g-cell)
K_m	Michealis-Menten Constant	3.14x10^{-5}	mol/L
ρ_c	Cell loading		g-cells/mL
ρ	Gel Density	0.35	g/mL
ε	Gel Porosity	0.8	mL/g
K_d	Distribution Coefficient	10^{-1}-10^{3}	L/mol
L	Thickness	3	mm

ACKNOWLEDGEMENTS

We thank Mr. Baris Mutlu for his helpful discussion. This research was funded by a grant to AA from the University of Minnesota Institute on the Environment and a University of Minnesota Office of the Vice President for Research grant to AA and LPW.

REFERENCES

(1) Wammer, K. H.; Peters, C. a. *Environ. Sci. Technol.* **2005**, *39*, 2571.

(2) Sakkos, J. K.; Kieffer, D. P.; Mutlu, B. R.; Wackett, L. P.; Aksan, A. *Biotechnol. Bioeng.* **2015**, *9999*, n/a.

(3) Aukema, K. G.; Kasinkas, L.; Aksan, A.; Wackett, L. P. *Appl. Environ. Microbiol.* **2014**, *80*, 4968.

Copyright 2016 The Organizing Committee for the 2016 Summer Biomechanics, Bioengineering and Biotransport Conference

SB³C2016
Summer Biomechanics, Bioengineering and Biotransport Conference
June 29 –July 2, National Harbor, MD, USA
SB³C2016-609

NUMERICAL MODELING OF POST-SURGICAL FLOW IN BASILAR ARTERY ANEURYSMS

Alireza Vali (1), Michael T. Lawton (2), David Saloner (3) and Vitaliy L. Rayz (1,4)

(1) Neurosurgery
Biotechnology and Bioengineering Center
Medical College of Wisconsin
Milwaukee, WI, USA

(2) Neurological Surgery
University of California San Francisco
San Francisco, CA, USA

(3) Radiology and Biomedical Imaging
University of California San Francisco
San Francisco, CA, USA

(4) Mechanical Engineering
University of Wisconsin - Milwaukee
Milwaukee, WI, USA

INTRODUCTION

Approximately 10% of all strokes are related to cerebral aneurysms. Untreated cerebral aneurysms may rupture, leading to hemorrhage with a high mortality rate of 50% [1,2]. Saccular aneurysms can usually be removed from the circulation by either surgical clipping or endovascular coiling. In contrast, fusiform aneurysms cannot be treated by these methods, since the vessel wall in this case is bulged circumferentially. The alternative methods involve reduction of the blood flow to the lesion by proximal or distal occlusion, in order to induce thrombotic occlusion of aneurysm. This indirect aneurysm occlusion usually requires sacrificing flow to the distal vasculature as it alters the flow dynamics [3]. Such treatment is particularly challenging for the fusiform aneurysms of the basilar artery as it can result in occlusion of the basilar side branches (brainstem perforators), thus causing stroke. Therefore, the indirect occlusion methods require careful modeling studies prior to procedure and understanding of the advantages and disadvantages of different interventional options for the flow alteration is crucial.

Recently, image-based computational fluid dynamics (CFD) in patient-specific geometries combined with *in vivo* velocimetry (*e.g.*, 4D MRV) has been shown to be a viable method to examine the flow fields resulting from different interventions [3,4]. Useful information from flow simulation such as shear stress, flow patterns and flow residence time can assist in making clinical decisions [5]. However, more progress is required to develop an ultimate computational tool which can reliably predict postoperative thrombus deposition. For example, due to the complexity of the geometry and the flow in patient-specific models, our understanding of flow alteration is mostly qualitative, which may result in ambiguity when treatment outcomes are compared. In the case of fusiform cerebral aneurysms, a good evaluation of surgical options is impossible without understanding of flow in small vessels and perforators. In this work, a method is presented for quantification of post-surgical flow through different parts of aneurysmal geometries.

METHODS

The computational analysis was conducted on basilar artery aneurysm patients recruited using institutionally approved IRB consent. The patient-specific preoperative vascular models were constructed from high-resolution, contrast-enhanced MRA data. The computational domain included the aneurysms with its proximal and distal vessels. Since the aneurysms in this study were located in a region of the basilar artery with small side branches, idealized geometries of several brainstem perforators and anterior inferior cerebellar arteries (AICAs) were added to the models. One representative case will be described here due to space limitations. The computational model is shown in Figure 1 (a), and a Digital subtraction angiography (DSA) image, showing the filling of the basilar artery with contrast is shown in panel (b).

Alternative postoperative geometries were created by modifying the preoperative model. Treatment options considered in this study included clipping of specific vessels to reduce the blood flow to the basilar aneurysm. The interventions were virtually modeled by removing vessel segments that would be surgically clipped.

The flow fields were determined by solving the transient Navier-Stokes equations using a finite-volume solver, ANSYS FLUENT 16. The advection-diffusion equation was coupled with the flow simulation in order to model transport of a passive scalar variable, representing flow of a virtual contrast agent, through the flow domain [5]. The virtual contrast following the blood flow is used as a method for the flow

Copyright 2016 The Organizing Committee for the 2016 Summer Biomechanics, Bioengineering and Biotransport Conference

visualization, and indicates flow residence time in different parts of the model. A computational mesh of tetrahedral elements was generated over the domain. Patient-specific flow waveforms obtained from PC-MRI were used at the inlet boundaries and the outlet pressure was set to zero for all of the outlets. For transport of the contrast, the inlet boundary condition was a constant value and the entire domain was initialized with a zero contrast concentration. For postoperative simulations, the inlet flow rates were adjusted assuming that the same amount of blood flow was required by distal vessels before and after the procedure. After solving the flow field and the contrast transport, an in-house post-processing program was used to find the ratio of the volume filled with virtual contrast to the total volume of various distal vessels and regions of interest.

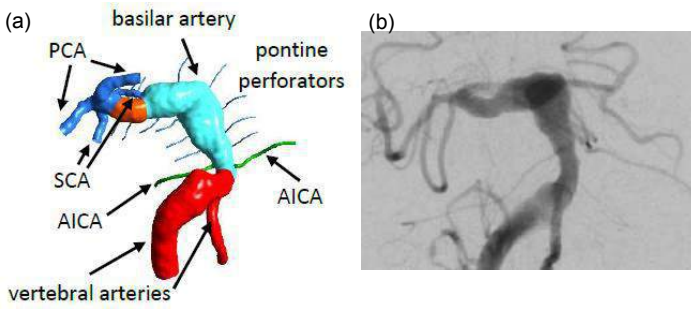

Figure 1: (a) Image-based model showing different components, (b) DSA showing filling of the basilar aneurysm with contrast.

RESULTS

Three interventional options that would reduce the flow through the basilar artery were considered in this study. Those are the occlusion of the left posterior cerebral artery (PCA), clipping of both PCAs, or clipping of the basilar artery proximal to the superior cerebral arteries (SCAs). In the rest of this report, the methods will be referred to as option 1, 2, and 3, respectively. The flow simulations were conducted for the duration of 10 cardiac cycles (total time of 5.2 s) for the preoperative and postoperative cases.

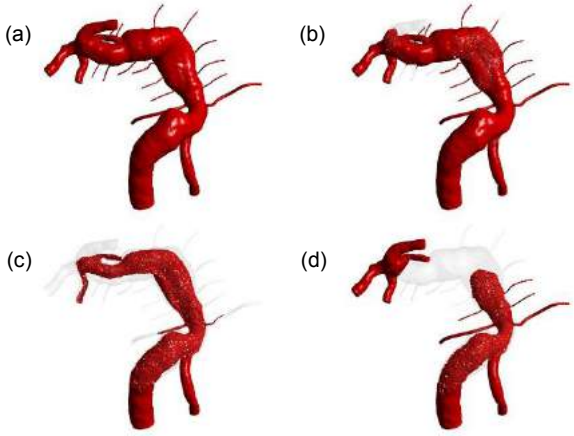

Figure 2: Comparison of virtual contrast transport for (a) postoperative, (b) option 1, (c) option 2, and (d) option 3

Figure 2 shows the transport of virtual contrast within the computational domain at the end of tenth cardiac cycle. The areas filled with red color indicate the regions where the concentration of virtual contrast is above a threshold (in this case 0.5). This method can be used to decide which segments of the vasculature receive sufficient blood flow following the treatment. For example, it is clear that while option 2 (panel c) was better than option 1 (panel b) in reducing blood flow through the aneurysm, it was less effective in feeding the brainstem perforators. It should be noted that in panel (d) the blood to the basilar apex (upper region of the model) was supplied through the right PCA from a bypass connecting it to the anterior circulation.

A quantitative comparison among various options is shown in Figure 3. For each option, the ratio of the volume filled with contrast to the total volume is presented for the basilar aneurysm and the left AICA. As shown, if option 1 is applied, after approximately eight cardiac cycles (4 second), the basilar aneurysm is almost completely filled with virtual contrast, which makes this option inefficient in reducing the basilar flow. Options 2 and 3 reduce the virtual contrast volume in the aneurysm by 50% and 75%, respectively. Also, it can be seen from Figure 3 (b) that option 3 is a better flow scenario as compared to option 2 since the left AICA is filled with contrast after seven cycles.

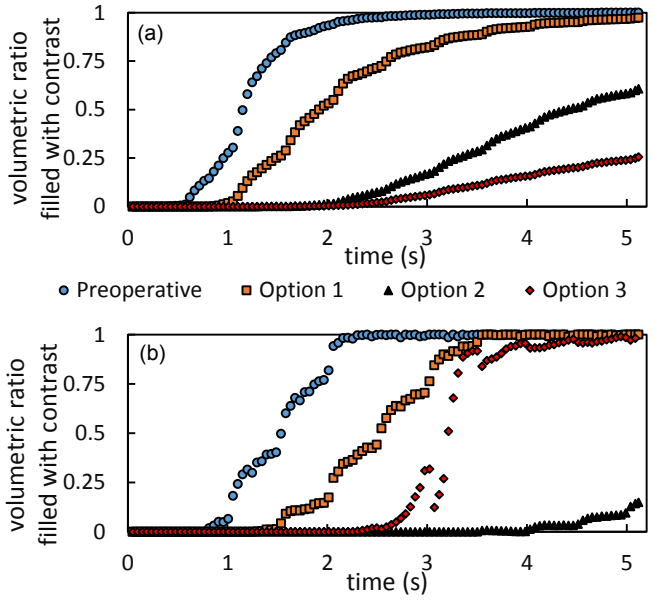

Figure 3: Volumetric ratio of (a) basilar aneurysm and (b) left AICA filled with virtual contrast

DISCUSSION

Three flow altering surgeries were considered in this study and compared against each other. The best interventional option would be the one that reduces the blood flow to the aneurysm in order to induce thrombotic occlusion while preserving the flow the AICAs and perforators. A quantitative method for the evaluation of the postoperative flow was proposed by coupling the transport of a virtual contrast with velocity field. These results show that image-based CFD models can provide guidance in evaluation of alternative treatment options for cerebral aneurysms.

ACKNOWLEDGEMENTS

We acknowledge Grant support from the NIH HL115267 (VLR).

REFERENCES

[1] Bederson, J.B. et al., *Stroke*, 31(11):2742-2750, 2000.
[2] Ma, B. et al., *Ann Biomed Eng*, 32:264-273, 2004.
[3] Rayz, V.L. et al., *Ann Biomed Eng*, 43:1210-1222, 2015.
[4] Cebral, J.R. et al. *AJNR Am. J. Neuroradiol,* 30:95–98, 2009.
[5] Rayz, V.L. et al. *Ann Biomed Eng*, 38(10):3058-3069, 2010.

Copyright 2016 The Organizing Committee for the 2016 Summer Biomechanics, Bioengineering and Biotransport Conference

SB³C2016
Summer Biomechanics, Bioengineering and Biotransport Conference
June 29 –July 2, National Harbor, MD, USA
SB³C2016-610

CHARACTERIZATION OF FRACTURE BEHAVIOR OF HUMAN ATHEROSCLEROTIC FIBROUS CAPS USING A MINIATURE SINGLE EDGE NOTCHED TENSILE TEST

Lindsey A. Davis (1,4), Samantha E. Stewart (1,4), Christopher G. Carsten III (2), Bruce A. Snyder (2), Michael A. Sutton (3,4), and Susan M. Lessner (1,4)

(1) Department of Cell Biology and Anatomy
University of South Carolina, School of Medicine
Columbia, SC, USA

(2) Department of Vascular Surgery
Greenville Health System
Greenville, SC, USA

(3) Department of Mechanical Engineering
University of South Carolina
Columbia, SC, USA

(4) Biomedical Engineering Program
University of South Carolina
Columbia, SC, USA

INTRODUCTION

There are multiple mechanisms that can lead to ischemic stroke. One well-established cause is plaque rupture, which accounts for approximately 15% of all ischemic strokes [1], during which a tear in the fibrous cap of an atherosclerotic plaque exposes the highly thrombogenic necrotic core material. This mechanism generally occurs in lesions called thin-cap fibroatheromas (TCFAs), characterized by a thin fibrous cap covering a large necrotic core [2]–[4]. Though these morphological characteristics provide a good framework for identifying vulnerable plaques, the true test of plaque vulnerability is whether or not the mechanical strength of the tissue can withstand the physiological loading conditions to which it is subjected.

Characterizing the material response of the fibrous cap at failure may provide insight into the mechanism and likelihood of plaque rupture. This study undertakes a qualitative and quantitative approach to analyze the mechanical failure behavior of atherosclerotic plaque tissue. We aim to quantitatively characterize the fracture behavior of fibrous caps using the CTOD metric to assess fracture toughness. To the authors' knowledge, this is the first application of CTOD in vascular tissue.

METHODS

The current study was approved by the IRB at Greenville Health System and all patients gave written informed consent. Human carotid endarterectomy specimens were obtained from 8 patients at the time of surgery at Greenville Memorial Hospital. Two plaque specimens generated multiple samples from the same patients (Samples III and IV; Samples VII and VIII). The excised specimens were immediately immersed in Belzer UW Cold Storage Solution (Bridge to Life Ltd., Columbia, SC) and were kept cool until testing. All mechanical testing was completed within 48 hours of tissue harvest.

The fibrous cap was isolated for mechanical testing by dissection from the remaining plaque. The tissue was oriented in the circumferential direction and mounted into a set of metal grips with 100 grit sandpaper on the inner surface. The grips were connected to a Bose 3200 Test Instrument, and a miniature single edge notch tension (MSENT) test was performed on each sample. An initial notch between 45% - 70% of the overall width of the tissue was made with a scalpel perpendicular to the direction of the applied load. Cyclical controlled displacement was applied such that the tissue tore in several cycles of small tears, each approximately 0.4 mm in length. The crack tip opening displacement (CTOD) was calculated at several points during tearing by measuring the distance between the intersections of a 90 degree vertex centered at the crack tip with the crack edges, as first suggested by Rice [5]. Additionally, the circumferential Cauchy stress in the uncracked segment was calculated at the initiation of tearing in each cycle.

After mechanical testing, the samples were fixed in a solution of 4% paraformaldehyde in 0.1 M phosphate buffer, pH 7.4, embedded in paraffin, and sectioned at a thickness of 5 μm. Picrosirius Red staining was conducted to determine the collagen content in each sample.

Significant relationships between measured parameters were assessed using linear regression to test the null hypothesis that the slope is equal to zero. The null hypothesis was rejected, with statistical significance, if $P < 0.05$.

RESULTS

In each specimen, the CTOD increased with increasing crack growth (Figure 1). Nearly all the initial CTOD values are clustered

Copyright 2016 The Organizing Committee for the 2016 Summer Biomechanics, Bioengineering and Biotransport Conference

around 0.5 mm, with the exception of samples IV and X, which have higher initial CTOD values (0.96 mm and 1.01 mm, respectively).

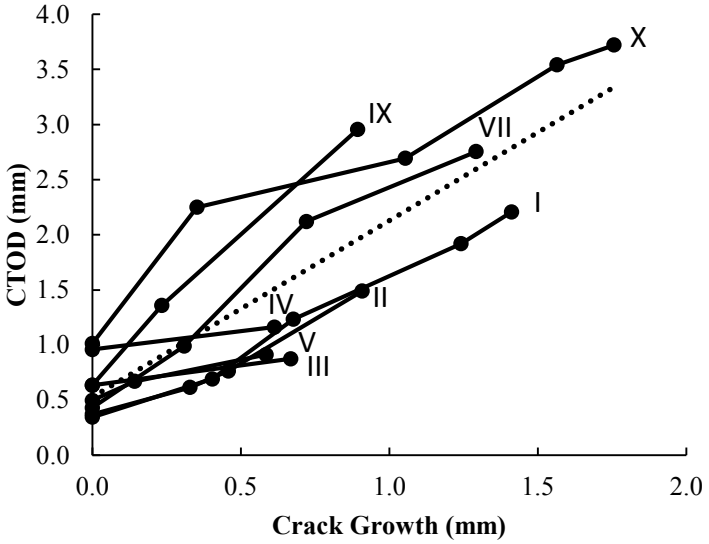

Figure 1: CTOD increases with crack growth. The median [IQR 1, IQR 3] initial CTOD is 0.54 [0.42, 0.71] mm, and the median [IQR 1, IQR 3] slope of the CTOD curve is 1.30 [0.59, 1.51].

Two samples (VI and VIII) exhibited a high degree of blunting such that a 90 degree vertex never intersected the edges of the crack and CTOD could not be determined. However, the radius of curvature of the crack tip at the initiation of tearing was measured in all samples to assess the degree of crack tip blunting. The median [IQR 1, IQR 3] radius of curvature of the crack tip at initial tearing was 0.24 [0.13, 0.27] mm.

The stress in the uncracked segment was calculated at the initiation of tearing for each cycle (Figure 2). Several samples exhibited very consistent stress values over multiple tearing cycles (VI, IX, and X), while other samples exhibited variation in stress values between consecutive cycles (I, II, V, VII), as shown in Figure 2. Because atherosclerotic tissue can be heterogeneous [6], this variation is not surprising.

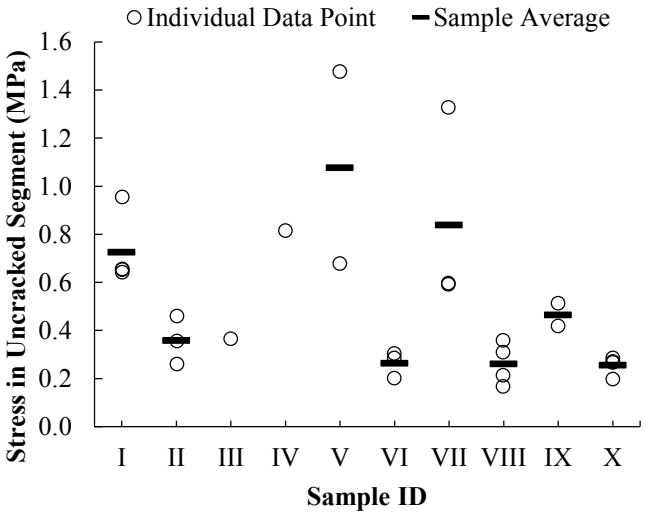

Figure 2: Stress in the uncracked segment. The median [IQR 1, IQR 3] values of stress are 0.366 [0.279 0.648] MPa.

Collagen content was measured in each specimen after mechanical testing and compared to calculated stress in the uncracked segment, initial CTOD, and initial radius of curvature at the crack tip. The median [IQR 1, IQR 3] values of collagen content are 32.8 [30.0, 42.0] percent. There is a statistically significant proportional relationship between collagen content and the stress in the uncracked segment ($p < 0.05$ that slope is zero). The radius of curvature at the crack tip is a measure of the degree of blunting at the crack tip and is shown to have a statistically significant inverse relationship with collagen content ($p < 0.05$). There is also a statistically significant relationship between collagen content and initial CTOD ($p < 0.05$). The results suggest that samples with higher collagen content begin tearing with a sharper crack tip and exhibit higher stresses at the initiation of tearing.

DISCUSSION

To the authors' knowledge, this is the first study that has investigated the fracture behavior of fibrous cap tissue and the first to use CTOD as a fracture parameter in vascular tissue. Materials that fracture at a higher stress are considered to be stronger than materials that fracture at a lower stress. A material with a higher CTOD is considered more resistant to fracture than a material with a lower CTOD. The results from this study show that tissues with a greater collagen content fail at a higher stress, but a smaller CTOD, than those with a lower collagen content. These divergent fracture parameters suggest a conflicting ranking of mechanical strength of fibrous caps. Generally, fibrous cap stability has been assessed by the stress at which failure occurs, rather than the CTOD or the strain, but our results suggest that stress may not always be the most appropriate metric to use.

This study shows, for the first time, that CTOD can be used as a comparative metric for fracture toughness in atherosclerotic fibrous cap samples from individual patients. Collagen content is important in determining the mechanical behavior and response of fibrous caps in atherosclerosis. High collagen content is associated with a sharper crack tip, suggesting that collagen fibers may impede blunting of the crack tip. These results show that analyzing the stress in fibrous caps only provides part of the picture when considering the problem of plaque rupture. The strain, or deformation, which a fibrous cap is able to withstand is also an important aspect of plaque stability which is often ignored in the analysis of plaque rupture.

ACKNOWLEDGEMENTS

The authors would like to acknowledge financial support from the National Science Foundation through grant number CMMI-1200358. The authors would also like to acknowledge funding through the Aspire II program from the Office of the Vice President of Research at the University of South Carolina.

REFERENCES

[1] G. W. Petty et al., *Stroke*, vol. 30, no. 12, pp. 2513–2516, 1999.
[2] J. F. Bentzon et al., *Circ. Res.*, vol. 114, no. 12, pp. 1852–1866, Jun. 2014.
[3] A. V. Finn et al., *Arterioscler. Thromb. Vasc. Biol.*, vol. 30, no. 7, pp. 1282–92, Jul. 2010.
[4] R. Virmani et al., *Arterioscler. Thromb. Vasc. Biol.*, vol. 20, no. 5, pp. 1262–1275, May 2000.
[5] J. R. Rice, *J. Appl. Mech.*, vol. 35, no. 2, pp. 379–386, 1968.
[6] P. Tracqui et al., *J. Struct. Biol.*, vol. 174, no. 1, pp. 115–123, Apr. 2011.

Copyright 2016 The Organizing Committee for the 2016 Summer Biomechanics, Bioengineering and Biotransport Conference

SB³C2016
Summer Biomechanics, Bioengineering and Biotransport Conference
June 29 –July 2, National Harbor, MD, USA
SB³C2016-611

POSITIVE AND NEGATIVE CUES FOR MODULATING NEURITE DYNAMICS AND RECEPTOR EXPRESSION TO IMPROVE PERIPHERAL NERVE REGENERATION

Melissa R. Wrobel (1), Harini G. Sundararaghavan (1)

(1) Biomedical Engineering
Wayne State University
Detroit, MI, USA

INTRODUCTION

Following injury, axons have the capacity to regenerate at rates of 2-5 mm/day [1]. Yet, each year more than 200,000 peripheral nerve injury (PNI) patients require surgical intervention, contributing $150 billion to annual US healthcare costs [2]. Furthermore, as the injury exceeds a critical defect size of ~3cm, current treatments such as coaptation, autografts, and allografts are insufficient to achieve full functional recovery. Tissue engineered nerve guide conduits have emerged as a promising alternative to current treatments. However, most research groups focus only on delivery of growth promoting factors to encourage neurite regeneration, when combined positive *and negative* cues more faithfully recapitulate the *in vivo* environment during PNI repair.

Chondroitin sulfate proteoglycans (CSPGs) are extracellular matrix (ECM) molecules traditionally studied as barriers to regeneration in the central nervous system. However, CSPGs are also released by endothelial, inflammatory, and Schwann cells following injury in the peripheral nervous system. Few groups have explored the effect of CSPGs on retraction of peripheral neurons. Therefore, the objectives in this study were to quantify the effects of a characteristic CSPG, Chondroitin Sulfate A (CSA), on axon extension and retraction in real-time, to measure the ability of CSA to induce cell-substrate receptor expression in peripheral neurons using flow cytometry, and to investigate the ability of a novel biomaterial, derived from porcine spinal cord matrix (SCM), to improve neurite outgrowth in the presence of the inhibitory CSA. We hypothesized that CSPGs prime neurons for growth by inducing the upregulation of receptors, especially of the Syndecan family, and we are interested in exploiting this property as part of a PNI repair strategy.

METHODS

Spinal Cord Matrix Isolation: Our novel adhesive substrate was derived by isolating proteins from frozen, closed herd porcine spinal cords. Cords were disinfected, washed, digested in 0.2M acetic acid, then salt precipitated and lyophilized for the final product. Dried matrix was dissolved in acetic acid for the following cell experiments.

Cell Culture: Dissociated chick embryo dorsal root ganglion (DRG) neurons were plated (6000 cells/cm^2) in a 24-well tissue culture plastic plate coated with either 5 μg/cm^2 spinal cord matrix (SCM, experimental condition) or laminin (LAM, positive control) via adsorption or left uncoated (denoted TCP, negative control). Neurons were cultured for 2 days in serum free media (SFM) supplemented with 50 ng/mL nerve growth factor (NGF) and either with (+) or without (-) 10 μg/mL Chondroitin Sulfate A (CSA).

Time Lapse and Fluorescence Microscopy: Neurite dynamics were recorded using a Nikon inverted microscope with a micro-incubation chamber (37C, 5% CO_2). At 48 hours, cells were fixed (4% paraformaldehyde) and stained with anti-neurofilament and 4',6-diamidino-2-phenylindole (DAPI) to visual neurites and nuclei, respectively.

Video and Image Analysis: Final neurite lengths were measured from fluorescent micrographs and average neurite extension and retraction rates (μm/min) and retraction frequency (%) were measured from the time lapse videos. Neurite length was measured as a straight line from the center of the neuron cell body to the neurite tip. The change in neurite length between each video frame was used to determine if the neurite was actively extending, retracting, or remaining unchanged/ stalled ($< \pm 5$μm). To analyze frequency of retraction, the three types of neurite movement were then reported as percentages of a given neurite's total movements. All measurements were analyzed with ImageJ.

Flow Cytometry: Flow cytometry was used to determine the effect of CSA on Syndecan-3 (SYN-3) receptor expression in the DRG neurons (protocol adapted from [3]). Briefly, cells were cultured on TCP in SFM with NGF and 10 μg/mL CSA, as above. After 48 hours, neurons were detached from the plate using Accutase. The cell suspension was washed, fixed, and incubated in an anti-receptor antibody against

Copyright 2016 The Organizing Committee for the 2016 Summer Biomechanics, Bioengineering and Biotransport Conference

SYN-3 followed by a fluorescent secondary antibody. Samples were analyzed using an Attune Acoustic Focusing Cytometer. Neurons cultured without CSA were used to determined basal expression levels of SYN-3. Syndecan receptor expression levels are reported using fluorescence intensity histograms and the median fluorescence intensity (MFI) normalized to cells that were not exposed to CSA using the equation:

$$(MFI^{+CSA} - MFI^{-CSA})/MFI^{-CSA} \times 100\% \quad (1)$$

where MFI^{+CSA} is the median fluorescence intensity of the treated cells and MFI^{-CSA} is the median fluorescence intensity of the untreated cells.

Statistical Analysis: Sample means were compared using ANOVA and Fisher's LSD post hoc analysis. Data is reported as mean ± standard error with statistical significance $p<0.05$, unless noted.

RESULTS

Final neurite lengths were significantly reduced in the presence of the CSA for neurons grown on all substrates (*). However, neurons grown on SCM with CSA were significantly longer then all conditions except LAM-CSA and SCM-CSA (#), including those cells on TCP *without* CSA treatment, suggesting that our matrix promotes neurite growth even in the presence of a soluble inhibitor. Summarized results and example fluorescent micrographs shown in Figure 1A and 1B.

Neurites spent an average of 17.7 ± 2.8% of their "time" (meaning of the video frames) retracting for all culture conditions tested ($p = 0.22$). However, neurons cultured on the SCM spent significantly more time actively extending, complemented by a significant decrease in the time the neurites spent stalled/unmoving, compared to both control substrates. This trend was maintained for conditions with and without the CSA. A complete summary of neurite movements for cells grown in each of the six culture conditions is presented in Figure 1C and 1D.

Average neurite extension and retraction rates were also measured from the time lapse videos. Extension rates (range: 0.87-1.00 μm/min) were statistically similar between all six experimental conditions ($p = 0.19$) Surprisingly, however, neurites grown on the SCM had significantly increased retraction rates compared to the two control substrates even though these cells had the longest final neurite lengths overall. These results suggest that significantly increased outgrowth on the SCM over both controls (fluorescence microscopy result) can be attributed to the neurites' increased extension frequency over time spent stalled (video microscopy result) rather than changes in neurite growth rates.

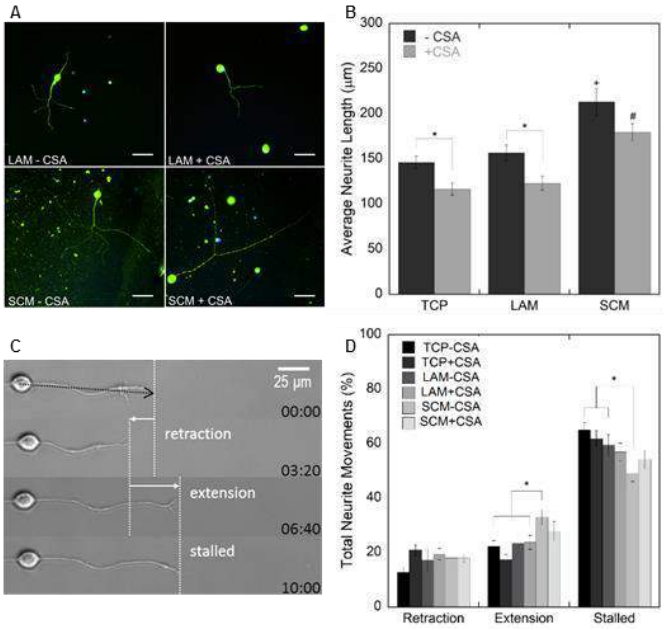

Figure 1. (A) DRG neurons stained with anti-NF (green) and DAPI (blue). Scale bars = 50 μm. (B) Quantified neurite outgrowth after 48 hours. $p<0.05$; $n>95$ neurites per condition. (C) Time lapse video stills illustrate the three types of neurite movements analyzed. Time in hh:mm. (D) Quantification of neurites' time spent extending, retracting, or stalled as a percentage of the neurites' total movements. * $p<0.05$; $n>18$ neurites per condition.

Next we investigated the influence of CSA on SYN-3 receptor expression using flow cytometry. The results revealed a 21.5 ± 7.6% increase in SYN-3 expression for the neurons treated with CSA compared to the untreated controls ($p=0.037$; unpaired t-test) indicating that SYN-3 receptors were significantly influenced by the presence of the CSA. Figure 2 contains a representative fluorescence intensity histogram showing increased SYN-3 expression for CSA-treated cells as evidenced by the peak shift.

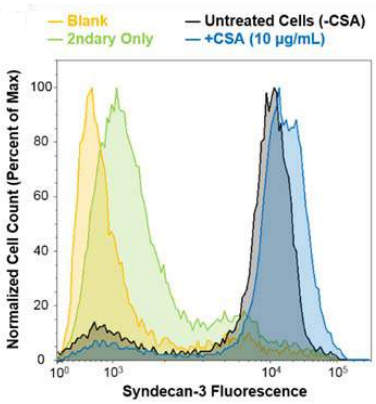

Figure 2. Increased expression of SYN-3 receptors on CSA-treated DRG neurons at 2 days (n=6).

DISCUSSION

In this study, we have demonstrated the effectiveness of porcine spinal cord matrix as an adhesive substrate for peripheral nerve outgrowth particularly for overcoming inhibition by chondroitin sulfate using time resolved and quantified retraction data. Additionally, this was the first look at the influence of a CSPG on syndecan receptor expression in one of very few flow cytometry studies with chick embryo DRG neurons. Furthermore, the CSA-induced upregulation of SYN-3 receptors elucidates at least one positive role for Schwann cell deposited CSPGs following PNI. We have hypothesized several mechanisms by which the upregulated receptors could mediate the improved outgrowth observed on the SCM. First, we speculate that the upregulated syndecans bind to sulfated glycosaminoglycans present in the SCM, allowing extending neurites to maintain strong adhesion to the substrate without saturating other key binding receptors. Secondly, the CSA-induced syndecans could act as co-receptors for the binding of integrins mediating improved focal adhesion formation. Finally, the increased syndecan receptors could stimulate neurite outgrowth by sequestering NGF in the media at the cells' surface.

Other studies have used CSA specifically as an inhibitory molecule in the study of axon behavior. Unfortunately, those studies typically look at blocking the CSPG's effects pharmacologically through enzymatic degradation or downstream signaling inhibitors. We propose that these methods may be counteractive for treating PNI because they would alter the CSA-syndecan response measured here and ultimately may alter the cells ability to bind to ECM well during regeneration. In the future, we propose to exploit CSPGs, coupled with the growth-permissive SCM, as part of tissue engineered scaffold that could potentially direct and accelerate neurite outgrowth better in large nerve gaps than current popular strategies.

ACKNOWLEDGEMENTS The authors thank Dr. Olivia Merkel and Steve Jones for assistance with flow cytometry. This research was supported by the Thomas C Rumble Graduate Fellowship.

REFERENCES [1] Brushart TM, *Nerve Repair,* Oxford University Press, New York. 9:250-352, 2011. [2] Apel PJ et al., *J Hand Surg,* 33:1541-7, 2008. [3] Walwyn W et al., *J Neurosci*, 27:5092-5104, 2007.

Copyright 2016 The Organizing Committee for the 2016 Summer Biomechanics, Bioengineering and Biotransport Conference

SB^{3}C2016
Summer Biomechanics, Bioengineering and Biotransport Conference
June 29 –July 2, National Harbor, MD, USA
SB^{3}C2016-612

TISSUE ENGINEERING PLATFORM FOR MOLECULAR MANIPULATION OF TENOGENESIS

Chun Chien (1), Brian Pryce (2), Sara F. Tufa (2), Douglas R. Keene (2), Alice H. Huang (1)

(1) Department of Orthopaedics
Icahn School of Medicine at Mount Sinai
New York, NY, USA

(2) Shriners Hospital for Children
Portland, OR, USA

INTRODUCTION

Although tendons are important in mediating movement, the cellular and molecular processes governing tendon formation remain largely unknown. Studies of gene function in tendon have been severely limited by the absence of a standard *in vitro* system to facilitate experiments that combine multiple mutations, physical manipulations and nimble gene mis-expression strategies. To address these limitations, we adapted a method from the Kadler lab [1] for generating 3D tendon-like structures for use with mouse embryonic cells, thereby harnessing the strength of mouse genetics for *in vitro* studies. Using this model, we induced tenogenic differentiation of mouse embryonic fibroblasts (MEFs) by TGFβ supplementation, and optimized parameters to direct *in vitro* recombination of conditional mutant cells using an adenovirus encoding Cre recombinase (AdCre). Using Smad4 flox/flox MEFs as a proof of concept study, we demonstrated efficacy of our optimized platform for testing gene function and showed that while TGFβ-induced proliferation depends on downstream Smad signaling, the tenogenic effects of TGFβ appear independent of Smads.

METHODS

For all studies, the ScxGFP tendon reporter [2] was used in all mouse lines to enable cell sorting and visualization of tenogenesis. Mouse embryonic fibroblasts (MEFs) are a heterogeneous population and encompass cells from multiple lineages. In preliminary studies, we were unable to generate constructs using all the cells as isolated. Therefore, to obtain cells with high tenogenic relevance, MEFs were generated from ScxGFP embryos and sorted by FACS following a single 20hr pulse of 20ng/mL TGFβ2 (to re-induce GFP expression in responsive cells, ~45%). Sorted MEFs were further expanded (2-3 passages) before use. To fabricate constructs, custom plates were prepared as in [1] (**Fig 1**). Briefly, Sylgard was cured in 6-well plates and two suture segments pinned ~10mm apart. In each well, sorted MEFs were seeded into fibrin gel at 750K per construct as a continuous layer and maintained in DMEM with 10% FBS, 1% PS and 200 μM ascorbic acid. Gels were allowed to contract for 7-14 days until a linear construct had formed (T0) and subsequently cultured for an additional 10-14 days (T10-14). In Study 1, we characterized wild type (WT) constructs in the presence or absence of 10 ng/mL TGFβ2. Preliminary studies showed optimal tenogenesis with minimal chondrogenesis when TGFβ2 was introduced after T0. In Study 2, MEFs from Rosa TdTomato (RosaT) Cre reporter embryos and Scx f/f; RosaT embryos were used for dosage and timing studies to optimize recombination using an adenovirus for Cre recombinase (AdCre, 2 day incubation). In Study 3, recombination of Smad4 f/f; RosaT MEFs was subsequently carried out using MOI 100 AdCre added prior to construct formation (T-14) and 10 ng/mL TGFβ2 added after construct formation (T0 to T14) (**Fig 1**).

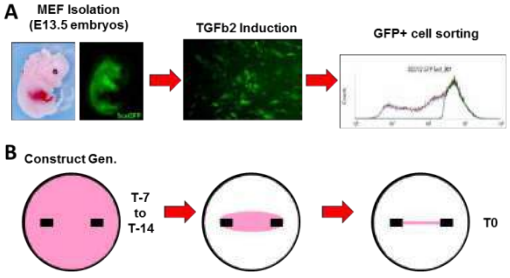

Figure 1: Schematic of MEF cell isolation and construct formation. (A) MEF isolation and cell sorting by ScxGFP. (B) Stages of gel contraction into a 3D linear construct under static tension.

Copyright 2016 The Organizing Committee for the 2016 Summer Biomechanics, Bioengineering and Biotransport Conference

RESULTS

Study 1: In the absence of TGFβ2, control MEFs spontaneously re-expressed ScxGFP, which had been lost with expansion after sorting. MEFs cultured in TGFβ2 exhibited a more elongated, fibroblastic morphology compared with controls, aligning in the direction of tension. TGFβ treatment also increased construct size. Interestingly, while ScxGFP+ cells were uniformly distributed in controls, ScxGFP+ cells were localized in the outer regions of TGFβ constructs. Because DAPI staining showed fewer cells in the central regions, we evaluated apoptosis by TUNEL, which surprisingly revealed the presence of apoptotic cells in control but not TGFβ2 constructs. Cell counts of DAPI stained nuclei further confirmed a dramatic loss of cells from T0 to T14 in control constructs, while TGFβ2 treatment improved cell number (**Fig 2**).

Study 2: Increasing concentrations of AdCre resulted in increasing numbers of Tomato+, recombined cells. Functional recombination was supported by PCR showing increasing amounts of Scx-/- DNA, indicating generation of null cells. Using MOI 10, we found that AdCre added at T-14 resulted in uniform distribution of Tomato+ cells; however, AdCre added at T0 resulted in recombination only at the periphery (**Fig 3**). Using optimized parameters of MOI 100 dose and T-14 timing, we found that constructs can be generated with high numbers of recombined, labeled cells with minimal toxicity (not shown).

Study 3: Since all canonical TGFβ signaling is mediated by the Smad4, we deleted Smad signaling using AdCre as a proof of concept study to test the efficacy of our system for interrogating gene function. Both WT and Smad4 Mut groups formed viable constructs within 14 days and transverse sections at T0 showed that WT and Mut constructs were indistinguishable (not shown). Interestingly, Smad4 Mut constructs failed to grow in response to TGFβ2 stimulation, indicating that the proliferative activity of TGFβ2 in this context is likely mediated by Smad signaling. However, ScxGFP expression was enhanced in Mut-TGFβ2 compared to Mut controls, and the peripheral cells were organized circumferentially around the construct, a pattern which was also observed in WT TGFβ2 constructs. TEM imaging of T14 constructs showed that collagen fibrils were relatively homogeneous within each group, indicative of an immature matrix phenotype, however fibril density appeared higher in TGFβ2 treated groups (not shown). Quantification of fibril diameter revealed increased diameter with TGFβ2 for both WT and Mut groups relative to controls. Interestingly, while control Mut fibrils were smaller in size compared to control WT, Mut-TGFβ2 fibrils were significantly larger compared to WT TGFβ2 fibrils (**Fig 4**). **Collectively, this data suggests that while the proliferative effect of TGFβ depends on Smad signaling, the tenogenic effects of TGFβ treatment may be independent of Smad.**

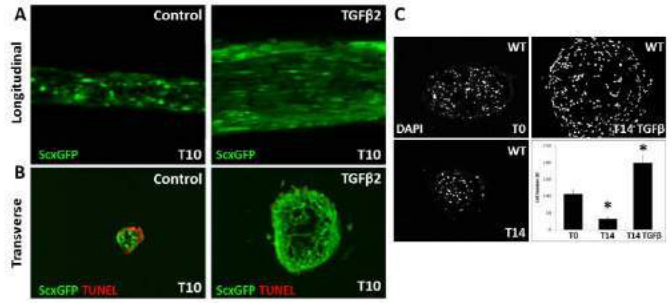

Figure 2: TGFβ2 induction of tendon differentiation in 3D linear constructs. (A) ScxGFP expression in whole mount constructs. (B) TUNEL staining of transverse sections. (C) Cell counts of T0 and T14 constructs. * indicates significance vs T0 control ($p<0.05$). n=3.

DISCUSSION

In this work, we developed a system using existing technologies to study gene function in an *in vitro* model of tendon formation, with Smad4 as a proof of concept case study. The use of conditional cells allows control over the timing and extent of recombination through AdCre. While AdCe activity is transient, genetic deletion by Cre is specific and permanent, enabling long-term studies that would not be possible using siRNA silencing. The presence of the RosaT reporter allele to label cells also facilitates studies of interactions between WT and mutant cells. Our results suggest that the tenogenic activity of TGFβ (which has been widely reported [3-5]) may be independent of Smads; however additional data such as tendon/cartilage marker expression, biochemical content, and mechanical properties will be required to confirm this hypothesis and is the focus of ongoing studies.

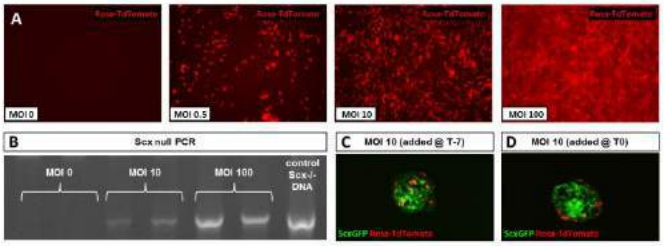

Figure 3: AdCre optimization for functional cell recombination. (A) AdCre dosage study MOI 0-100. (B) Effective recombination of floxed Scx gene in MEFs using AdCre. (C, D) AdCre timing study (before or after construct formation) using MOI 10.

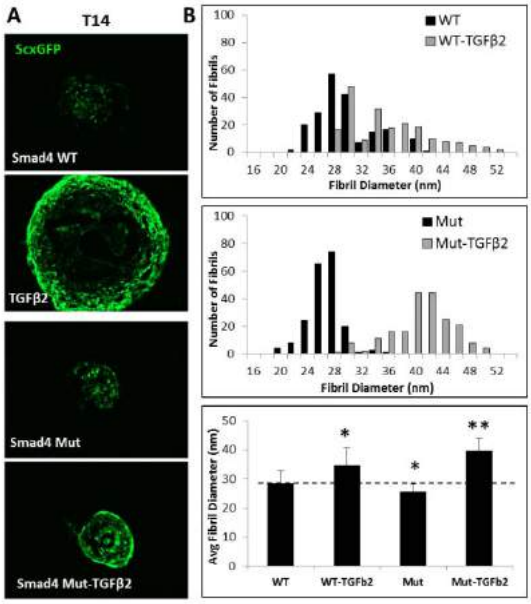

Figure 4: Smad4 deletion . (A) ScxGFP expression in transverse sections (Scale: 10x). (B) Collagen fibril diameters of WT and Mut constructs, with and without TGFβ2 supplementation. * indicates significance vs WT, ** indicates significance vs all groups ($p<0.001$).

ACKNOWLEDGEMENTS

This work was supported by Mount Sinai and the Orthopaedics Dept. We also thank Dr. Ronen Schweitzer for all mouse lines.

REFERENCES

[1] Kapacee+, *Matrix Bio,* 2008. [2] Pryce+, *Dev Dyn*, 2007 [3] Pryce+, *Development,* 2009 [4] Breidenbach+, Tissue Eng Part A, 2015 [5] Brown+, *J Biomech*, 2014.

Copyright 2016 The Organizing Committee for the 2016 Summer Biomechanics, Bioengineering and Biotransport Conference

SB^{3}C2016
Summer Biomechanics, Bioengineering and Biotransport Conference
June 29-July 2, National Harbor, Maryland, USA
SB^{3}C2016-615

AN ADAPTABLE, AFFORDABLE, AND REUSABLE INTERIM PROSTHETIC LEG

Andrew M. Milhoan
University of Mount Union
Alliance, OH, USA

Nathan L. Levengood
University of Mount Union
Alliance, OH, USA

Jason A. Shar
University of Mount Union
Alliance, OH, USA

Faculty Advisor(s)

Dr. Joshua Gargac
Department of Engineering
University of Mount Union
Alliance, OH, USA

Dr. Matthew Volansky
Department of Physical Therapy
University of Mount Union
Alliance, OH, USA

INTRODUCTION

Interim lower leg prosthetics are important since they allow amputees to begin rehabilitation before receiving a definitive prosthetic. This allows patients to return to a normal walking gait in a relatively short amount of time. Changes proposed by the Durable Medical Equipment Medicare Administrative Contractor (DME MAC) for Jurisdiction A, NHIC Corp, to Medicare's Lower Limb Prosthesis Plan (LCD DL 33787), would eliminate coverage for the interim prosthetic.[1]

Physical therapists (PTs) have identified the high cost of prosthetic legs as barrier to their access, and expect delays to a patient's rehabilitation. Contemporary prosthetics are expensive because each is created individually to match its intended patient, and often outfitted with microprocessors and hydraulics to enable ankle actuation. In order to prevent the cost of these necessary prosthetics from being transferred to the patient, PTs require a new prosthetic that could be owned by the clinic and used for many patients. For this reason, the engineering and PT departments at the University of Mount Union are collaborating to design a new lower leg interim prosthetic.

The clients for this project (Century Oak Care Center, Cleveland, OH) would like a prosthetic leg that could be adjusted to fit below-the-knee amputees ranging in height from 147 cm (4'-10") to 183 cm (~6') and in weight from 68 kg (150 lbs.) to 160 kg (~350 lbs.). Multiple prosthetic legs will be used in a therapy gym where walking will be the most rigorous activity. Afterward, the device with be sanitized, and fit onto the next patient for immediate use. As additional constraints, this device must be lightweight, withstand the loading and wear from use, and the prototype must cost less than $1000.

PRODUCT DESIGN

The design of the prosthetic was simplified to three main components: the socket interface, pylon, and articulating ankle (Fig. 1a). A scoring matrix was used to select the best design concepts measured by the complexity, durability, marketability, adaptability to different patients, and the ease of sanitation between patients use. Since the prosthetic will be adjustable, its height will vary from 42 cm to 53 cm. For an average person (5'-10") with an amputation 15 cm below the knee, the device would have a height of approx. 52 cm and weight of 1.9 kg (~4.3 lbs.). This compares reasonably to the weight of an average limb, which is 5.8% of a person's overall body weight, and to other prosthetics, which weigh between 4-6 lbs.[2]

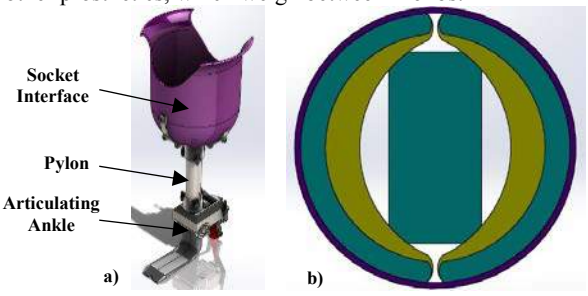

Figure 1: The interim prosthetic (a) consists of three components. The top view (b) shows the arrangement of the air bladders both empty (blue) and inflated (yellow).

Socket Interface: The socket will be formed by molding thermoplastic around the cast of a generic residual limb, and lined with a series of three 9"x5" neoprene air bladders along the inner wall (Fig. 1b). These bladders will be sewn together in a vinyl lining, and attached to the thermoplastic with Velcro strips. This simple attachment will allow the socket lining to be removed for sanitation between patients. The

Copyright 2016 The Organizing Committee for the 2016 Summer Biomechanics, Bioengineering and Biotransport Conference

bladders will be inflated to different volumes by connecting a small hand pump to tubes extending through the cast, allowing the prosthetic to fit residual limbs of different sizes, and accommodate swelling during healing.

The maximum pressure experienced by the air bladders was estimated by simplifying the limb-bladder interface to two spheres in contact. For this analysis, elastic moduli of 60 kPa and 15 MPa were assigned to the residual limb and the air bladder, respectively, and a compressive force of 1280 N was applied[3]. This analysis yielded a maximum pressure of 165 kPa at the interface, which is 53% lower than the average pain threshold for a residual limb of 350 kPa[4]. Using a tensile strength of 3.45 MPa for the neoprene air bladders, the factor of safety was calculated to 1.3.

A stainless steel socket crown was designed to disperse the patient's weight across the socket. Using finite element analysis (ANSYS, Canonsburg, PA), a force of 778 N was applied to the bottom of the crown, with the bolt holes of the crown fixed in all directions. This analysis resulted in a factor of safety of 1.5 for the socket crown, and 15 for the thermoplastic.

Pylon: Since the pylon will act as the primary transmitter of force to the ankle, a prefabricated titanium pylon (Streifeneder USA, Tampa, FL) was selected to support 160 kg.

Changing the pylon will provide the means for adjusting the height of the prosthetic. Pylons will range from 6.5 cm – 17 cm, to accommodate a wide-range of users of different height and amputation location. As an example, a 9.5 cm pylon would be used for a 1.8 m patient, whereas an 8.0 cm pylon would be used for a 1.5 m patient.

Articulating Ankle: The ankle was designed with purely mechanical components to mimic a normal walking gait. Striking of the silicone heel column will release the foot from its locked position. Two springs (2.0" length, 0.375" OD, and 0.048" wire) will force the foot into contact with the ground. The combination of three-pin aluminum gears (~2.5 cm in diameter and 2.5 cm thick) in conjunction with a locking-ratchet mechanism (Fig. 2) allows the ankle to rotate in one direction. When the foot returns to its initial joint angle, the rotation of foot becomes locked for the remainder of the cycle (Fig 3).

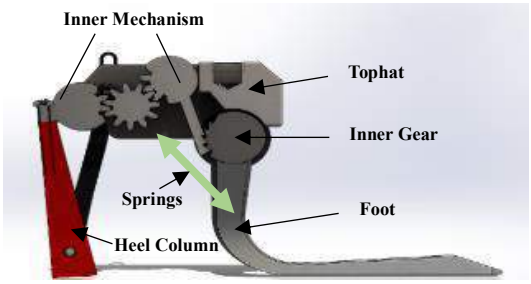

Figure 3: The gear-based ratchet system allows the joint to rotate during gait.

The ankle was designed to handle a maximum force of 778 N. Using a finite element analysis, a load of 778 N was applied to the top section of the ankle housing, and the gear insertions were fixed. Within the assembly, the minimum factor of safety was calculated to 2.5.

BUDGET & MARKET ANALYSIS

It is estimated that by 2030, there will be nearly 58,000 amputations per year in the United States stemming from the geriatric population alone[5]. Most of these patients will not receive a definitive prosthetic until 4 to 12 months after their amputation[6]. This delay is caused by the individual patient's activity level, weight-bearing tolerance, and limb shrinkage[5]. If the proposed changes to the Medicare benefit by the DME MAC are approved, PT clinics will need an interim prosthetic device to facilitate rehabilitation.

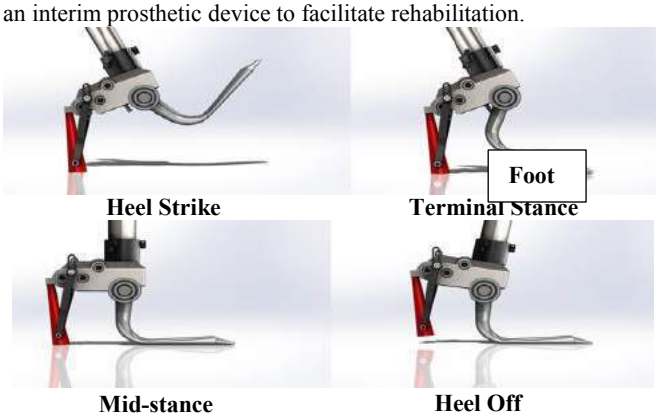

Figure 3: During the normal gait of the prosthetic, the force from the heal strike will unlock the ratchet mechanism. The ankle will articulate until locking at mid-stance.

One of the primary goals of this project was to offset increases in cost to both the amputees and rehabilitation clinics. To this end, this device was designed to be purchased by and housed at rehabilitation centers. In this scenario, the device would be used by many patients, eliminating the need for insurance to cover individual interim prosthetics. The adjustable socket interface also eliminates the need for new socket casts over time.

From communication with PTs, it was determined that rehabilitation centers would be willing to spend between $1500 and $2500 for this prosthetic device. The materials to create a working prototype cost $905, with the articulating ankle accounting for 56%, the socket interface 25%, and the pylon subassembly 19% of this cost. Once the prototype is completed and tested, a more in depth market analysis will be performed. The cost of manufacturing and machining expenditures will be explored to determine an acceptable retail price that is both profitable and affordable. As a preliminary estimate, these devices would be priced at approximately $2200.

CONCLUSION

As designed, this new interim prosthetic leg satisfies all of the original criteria specified from the client. The socket interface lined with air bladders and interchangeable pylons, allows the device to be used by multiple patients, and the articulating ankle will allow for a functional walking gait for patients up to 160 kg (~350 lb). Given the potential changes to Medicare coverage and the growing rates of amputations in the geriatric population, this device could be a marketable product once completed.

ACKNOWLEDGEMENTS

We would like to thank the Century Oak Care Center for identifying the need for this project, and Barry Minor of the Hanger Clinic in Alliance, Ohio for providing insight into how prosthetics interact with patients.

REFERENCES

1. Dunn, S et al., *Lower Limb Prostheses Draft*: 1-6, 2015.
2. Osterkamp, L. K et al., *J.A.D.A,* 95(2): 215-218, 1995.
3. Mak, F.T et al., *J.R.R.D,* 31(3): 188-198 1994.
4. Mak, F.T et al., *LLP Biomech Res*, 38(2): 161–174, 2001.
5. Fletcher, D.D et al., *A.P.M.R*, 83(10):1389-1393 2002.
6. Kapp, S et al., *Transtibial Amputation*: 18B 1992.

Copyright 2016 The Organizing Committee for the 2016 Summer Biomechanics, Bioengineering and Biotransport Conference

SB³C2016
Summer Biomechanics, Bioengineering and Biotransport Conference
June 29-July 2, National Harbor, Maryland, USA
SB³C2016-616

CABLE ACTUATED 3D PRINTED EXOSKELETON: FOR RESTORATION OF HAND MOTOR FUNCTION IN STROKE AFFECTED PATIENTS

Aaron Brice
Mechanical Engineering
University of Alberta
Edmonton, AB, Canada

Muxi Li
Mechanical Engineering
University of Alberta
Edmonton, AB, Canada

Stéphane Magnan
Mechanical Biomedical Engineering
University of Alberta
Edmonton, AB, Canada

Jin Wang
Mechanical Engineering
University of Alberta
Edmonton, AB, Canada

Tyler Friesen
Mechanical Engineering
University of Alberta
Edmonton, AB, Canada

Faculty Advisor(s)

Dr. Yongsheng Ma
Course Coordinator
University of Alberta
Edmonton, AB, Canada

Dr. Ahmed Qureshi
Advisor
University of Alberta
Edmonton, AB, Canada

Jonathon S. Schofield
Sponsor
University of Alberta
Edmonton, AB, Canada

INTRODUCTION

Stroke is the second leading cause of disability affecting 5 million people globally per year [1]. The primary cause of adult disability is cerebral vascular stroke, from which more than 80% of survivors suffer hemiparesis in their upper limb. This form of partial paralysis often results in hand function impairments impacting the patient's ability to perform tasks of daily living such as grasping items, writing and indicating objects [2]. A common clinical approach for successful rehabilitation and recovery of motor function, after a brain injury, such as a stroke, is through performing highly repetitive tasks [3]. However, even after extensive rehabilitation, compromised hand function is likely a reality the patient must face. Nearly 66% of hemiplegic stroke patients fail to fully regain motor function in the paretic arm when evaluated 6 months post stroke [3].

The conventional repetitive rehabilitation training for stroke patients is performed with physiotherapists directly moving the affected hand. This large amount of physical interaction with physiotherapists results in a long and costly recovery process [3]. This method also does not provide accurate gauging of a patients progress as the manual therapy is highly subjective to the therapist's judgment of progress. Recently the introduction of robotic training systems, such as hand exoskeletons, may alleviate some of the difficulties associated with the manual physiotherapy methods. Robotic systems are capable of performing the necessary repetitive motions for successful rehabilitation without a large amount of therapist intervention.

Currently, literature hosts a number of exoskeleton systems for hand rehabilitation [3]. However these systems are largely experimental, high cost and inaccessible to clinicians and stroke patients. Our client identified the limitations of existing exoskeletal technologies. They requested our assistance in the development of a mechanical exoskeletal system capable of being 3D printed, and released open-source. The design must be able to be coupled with their existing electromyography control system for use in hand rehabilitation with clinical and potential take-home applications.

PRODUCT DESIGN

The exoskeletal system is comprised of two main systems; the first is the mechanical system, which was the primary focus of our design scope, and the electrical system which was developed by the client outside the scope of our work. Although beyond the scope of our design, it is important to note that the electrical system utilizes commercially available components including an Arduino microcontroller and electromyography sensors (EMGs) along with a LCD display and a push-button interface that allows the wearer to select and perform various grasping patterns.

The client required the mechanical system to be adjustable in size between the 5th and 95th percentile male hand, provide a minimum 90° of total flexion for each finger, have a built in safety mechanism to prevent possible injury, be compatible with their existing electronics system and provide minimal obstruction to the underside of the wearer's hand.

A Cable Actuated Rigid Body System (CARBS) was designed, using Solidworks CAD software, for direct export and ease of fabrication on a 3D deposition printer. It utilizes a 3D printable rigid body over-structure, worn on top of the patient's hand, which actuates each finger through the use of a two cable system (Figure 1). Its design allowed the removal of obstruction to the underside of the hand allowing the user's finger tips and palm access to cutaneous feedback when performing the repetitive tasks. The two cable system along with the rigid linkages create a biomimetic concept with the two cables simulating the flexor and extensor tendons of the finger while the linkages simulate the phalanges of the finger. Utilizing the client specified servomotor (HS-55, Hitec RCD) and a dual-groove pulley the linkage of each finger is able to be flexed by retracting the lower-flexor, cable and extending the upper-extensor, cable causing flexion of the device.

Copyright 2016 The Organizing Committee for the 2016 Summer Biomechanics, Bioengineering and Biotransport Conference

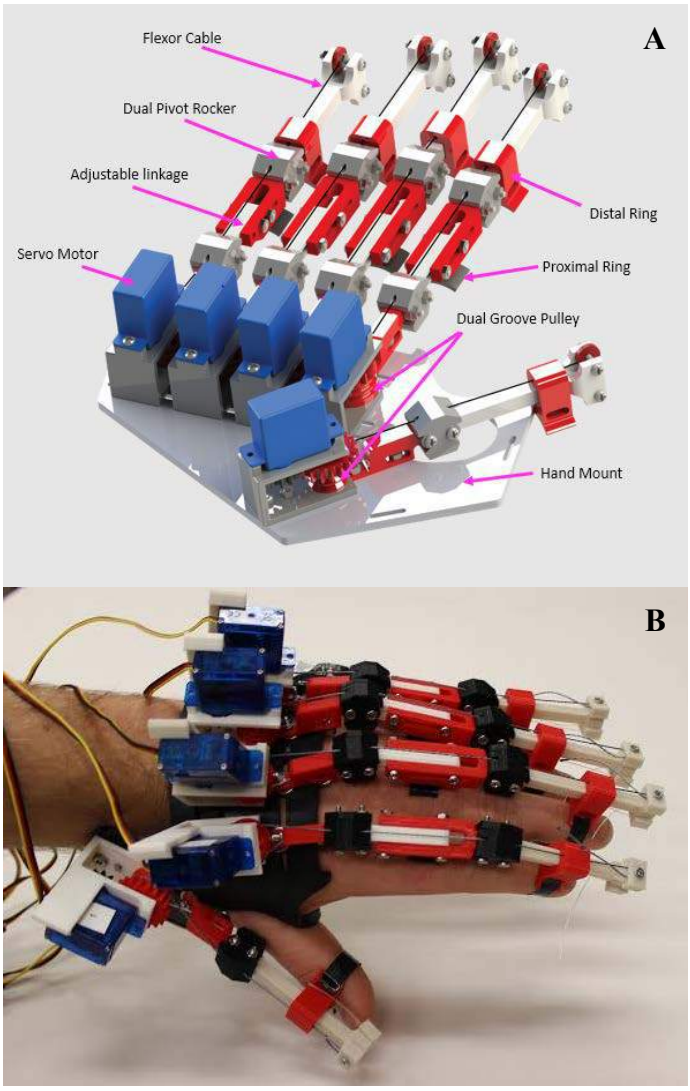

Figure 1: A) Cad Render of the Cable Actuated Rigid Body System (CARBS) with critical components identified. B) Prototyped system mounted to a user's hand.

To extend the linkages of the hand the extensor cable is retracted while the flexor cable is extended causing the device to open. The rotation of the device occurs at a dual pivoting rocker link which simulates the knuckles of the wearer's hand. The rocker links were designed with physical stops which limit total flexion of each joint in the finger to 60° flexion and 5° hyperextension. This results in a maximum total range of motion of 120° flexion and 10° hyperextension for each finger (2 rockers are used per finger, and 60° flexion/5° hyperextension for the thumb, 1 rocker is used for the thumb). To achieve movement of the user's digits distal and proximal rings were designed to mount into the finger linkages of the CARBS and attach to the wearers fingers via hook and loop straps. The distal and proximal rings provide two primary functions in the devices operation; the first is to transmit the movement of the CARBS into movement of the patient's digits and the second is to provide an arc length compensation for the device. Due to the separation of the CARBS' neutral axis and the neutral axis of the patient's digits, the distal and proximal rings were designed to translate longitudinally along the linkages to compensate for the difference in arc length changes during flexion of the CARBS and the hand.

To create adjustability in the device both the finger linkages and the hand mount were designed with sliding adjustment points. The finger linkages use a two pin and slot link which allows the distal rocker to be positioned on the wearer's finger such that when flexed it is located directly above the second joint of the finger. The hand mount grooves allow each of the finger linkages to be translated such that they can be centered along each of the fingers to ensure proper fitment. Using these two methods of adjustment the system is able to be fitted to 97% of the total population including and surpassing the original goal of the 5th to 95th percentile male hand.

BUDGET & MARKET ANALYSIS

Typically the costs of a rehabilitative device, like an exoskeleton, are not covered by a patient's benefits or insurance and the purchase is often times an out of pocket expense. The implications of high cost were addressed by our client prior to the development of the device and the intent is to release the product as a low cost, open source alternative in order to alleviate the financial burden of purchasing a r ehabilitative exoskeleton. As such, the desired cost of mechanical components was set to $500 CA. The complete budget when coupled with the client's electronics package was set to a maximum allowable cost of $1000 CA.

As an open-sourced technology the project was built with the intent of being accessible for free to any patient, and/or clinician. Consequently, the focus of the project was to minimize manufacturing cost as much as possible in order to ensure complete accessibility. The resulting manufacturing cost for the mechanical system was $91 CA. The client's completed electronics package was determined to have a cost of $291 resulting in a total cost of $382 for the complete exoskeletal device.

Through a study of existing exoskeletal devices it was determined that the only commercially available device offering similar functionality as our design has a cost in the range of $48,000 CA.[4] which makes our 3D printed open-source concept an accessible and highly cost effective alternative to existing technologies.

ACKNOWLEDGEMENTS

Funding provided through Dr. Jacqueline Hebert and Bionic Limbs for Improved Normal Control (the BLINC Lab).

Thank you to Gwen Dziwenko, Occupational Therapist II, for her help and contributions.

REFERENCES

[1] World Heart Federation: The Global Burden of Stroke http://www.world-heart-federation.org/cardiovascular-health/stroke

[2] Conti et al., *Diversity of approaches in assessment of executive functions in stroke: Limited evidence?,* 2015

[3] Heo et al., *Current Hand Exoskeleton Technologies for Rehabilitation and Assistive Engineering,* 2012

[4] Hand of Hope http://www.rehab-robotics.com/

Copyright 2016 The Organizing Committee for the 2016 Summer Biomechanics, Bioengineering and Biotransport Conference

SB^{3}C2016
Summer Biomechanics, Bioengineering and Biotransport Conference
June 29 –July 2, National Harbor, MD, USA
SB^{3}C2016-617

BIOMECHANICAL ANALYSIS OF KICKS IN SOCCER AND KICKS IN FOOTBALL

**Allison M. Gerren, Tori L. Breitenbach, Jacob M. Forstat,
Jonathan T. Fox, and Mohamed S. Hefzy**

Biomechanics and Assistive Technology Laboratory
Departments of Bioengineering and Mechanical, Industrial & Manufacturing Eng.
The University of Toledo, Toledo, Ohio, 43606

INTRODUCTION

Two of the most popular sports in the world are football and soccer. Both sports are similar in the fact that kicking is a main part of the sport. The two kicks are similar with a few differences. For the purpose of this study, the typical soccer kick starts with a curved approach toward the ball; this corresponds to a "free kick" during play. One can identify three steps during this approach: a long stride with the plant foot (non-kicking foot), a long stride with the kicking foot, and a long stride with the plant foot. After the ball is kicked, the kicking leg crosses the sagittal plane of the body instead of going straight. The kicking foot can make contact with the ball at different parts of the foot (top of the foot, near the medial arch, or the medial aspect of the heel) [1]. The football kick is used for either kickoffs or for field goals during the game. The most common football kick involves taking 3 steps back from the ball and then 2 steps to the left. The kicker then approaches the ball in a manner similar to that for the soccer kick following three steps but in a straight path; these three steps are identified by a short stride with the plant foot as a jab type step, a long stride with the kicking foot, and a long stride with the plant foot. After the ball is kicked the kicking leg continues its swing without crossing the sagittal plane of the body and following a curved path [2]. The kicking right foot can make contact with the ball only with the middle of the top of the foot.

The purpose of this study is to determine the differences in the two kicking styles and how they affect the kinematics of the kicking leg and trunk along with the effects of ground reaction forces on the plant foot.

METHODS

Three team members performed the kicks in a lab environment. A 10-camera Raptor-E motion analysis system and a synchronized force plate were used to collect kinematic and force plate data. Seventeen reflective markers were placed on each individual according to the Helen Hayes arrangement for the lower body [3]. In addition, two markers were placed on the most lateral point of the left and right acromia, respectively. A line joining the midpoint between these two points and the midpoint between the greater trochanters was used to define the trunk segment. The foot, shank, and thigh segments were defined according to [3]. Ankle, knee, and hip angles were then calculated. Also, trunk flexion-extension and left-right bending angles were calculated.

Each team member used their right foot to kick and their left foot as the plant foot. During each kick style the ground reaction forces (GRF) of the plant (non-kicking) foot were simultaneously collected and normalized with respect to body weight. Because the ball was simply used as a focus point rather than as part of the kicking motion, a foam block was used in place of a ball to prevent damage to the lab's camera system. For both kicking styles, the team member began by standing on the force plate next to the ball. The participant then took three steps backwards and two steps to the left to find their starting position. As discussed in the introduction, the team member moved directly towards the ball for the football kick and in a curved, sweeping path for the soccer kick. In both instances, the plant foot landed on the force plate next to the designated location of the ball.

Five phases can be identified in each kick: approach, pre-swing, connect, post-swing and recovery phases as portrayed in figure 1. The approach phase starts with the first step of the plant foot moving towards the ball and ends at the point where the plant foot lands on the force plate. As mentioned earlier, the approach phase entails the three steps as the kicker moves toward the ball and ends at the instant the kicking leg starts its' wind up. The preswing phase encompasses the wind up of the kick and ends just before contact with the ball. The connect phase ends at the point where the kicking foot comes in contact with the ball; at this instant the kicking leg passes the plant leg.

Copyright 2016 The Organizing Committee for the 2016 Summer Biomechanics, Bioengineering and Biotransport Conference

The post-swing phase ends at the instant where the kicking leg finishes its ascent and the recovery phase ends at the instant where the kicking foot comes in contact with the ground.

RESULTS

Figure 1 depicts the five phases of both kicks. The results reported in tables 1 and 2 represent averages among the three team members. Table 1 lists the maximum average values for trunk flexion-extension and left-right bending. It also includes the maximum average values for hip flexion-extension and ab- adduction, and ankle plantar and dorsi-flexion for the kicking leg for both soccer and football kicks. It also includes the maximum and minimum knee flexion angles. Table 2 lists the maximum average values of the normalized (w.r.t. body weight) vertical, anterior-posterior, and medial-lateral components of the ground reaction forces of the non-kicking leg

DISCUSSION

Results show noticeable differences in the ground reaction forces (GRF) on the planted left leg with larger vertical and medial components during the football kick. A larger posterior component of the GRF was observed during the soccer kick. The larger GRF vertical component observed during the football kick suggests that this kick is more forceful overall when compared to the soccer kick. Also, the larger posterior GRF component on the planted leg observed during the soccer kick suggests that a more neutral-to-posteriorly-canted stance is required in the soccer kick than in the football kick. This further suggests that this posture when kicking the ball helps in improving the possibility of scoring a goal since a relatively smaller maximum reach height is required by the ball to score the goal.

The trunk was flexed more during the football kick than during the soccer kick with maximum flexion occurring during the post swing phase of the kick. On the other hand, the trunk was extended more during the soccer kick with maximum extension occurring during the connect phase of the kick.

The right hip (hip of kicking leg) was abducted and adducted more during the soccer kick with the maximum abduction and maximum adduction occurring during the connect phase and the post-swing phase, respectively. On the other hand, the ankle of the kicking foot was plantar flexed and dorsi flexed more during the football kick with maximum plantar flexion and maximum dorsi flexion occurring during the connect phase and the pre-swing phases, respectively.

The large plantar flexion angles observed during the football kick during the connect and post swing phases confirms the need for a more pointed toe during the kick; doing so would help to increase proper contact with the 1st metatarsal for maximum energy transfer as detailed in [2]. Also the large hip abduction and adduction angles observed during the soccer kick confirms that an increased amount of leg cross-over is used during a soccer kick, which is utilized more in the "sweeping" style of soccer kick and when trying to curve the ball [1]

Future work includes involving college players in this study to determine how their performances can be improved.

ACKNOWLEDGEMENTS

This work was supported by the College of Engineering at the University of Toledo.

REFERENCES

[1] "Kicking A Soccer Ball: Pro Tips and Techniques." Soccer Training Methods. Web. 17 December 2015. http://www.soccer-training-methods.com/kicking-a-soccer-ball.html.

[2] "Lean How To Kick a Field Goal in Football: Soccer Style." American Kicker. Web. 17 Decem ber 2015. http://www.americankicker.com/how-to-kick-a-field-goal/

[3] M. Kadaba, H. Ramakrishnan and M. Wootten, "Measurement of Lower Extremity Kinematics During Level Walking," *Journal of Orthopaedic Research,* pp. 383-92, 1990.

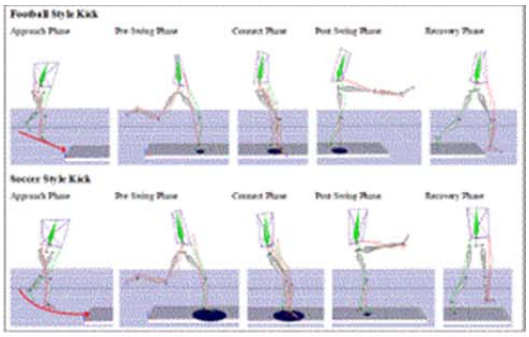

Figure 1. Five Phases of Kick Cycle

Table 1: Peak angles of the 4 analyzed motion segments

MOTION SEGMENT	FOOTBALL KICK PEAK ANGLE	SOCCER KICK PEAK ANGLE
TRUNK		
FLEXION	24.7°	15.77°
EXTENSION	5.41°	8.41°
LEFT BENDING	15.76°	18.95°
RIGHT BENDING	10.44°	10.55°
RIGHT HIP		
FLEXION	13.65°	9.43°
EXTENSION	75.45°	75.44°
ADDUCTION	5.35°	18.86°
ABDUCTION	14.71°	17.02°
RIGHT KNEE		
FLEXION MAX	67.73°	62.65°
FLEXION MIN	6.07°	9.94°
RIGHT ANKLE		
PLANTAR FLEXION	44.36°	36.14°
DORSIFLEXION	6.27°	2.42°

Table 2: Normalized Ground Reaction Forces

DIRECTION	FOOTBALL KICK	SOCCER KICK
VERTICAL	2.177	1.682
ANTERIOR	0.395	0.366
POSTERIOR	0.189	0.281
MEDIAL	0.411	0.33
LATERAL	0.014	0.038

Copyright 2016 The Organizing Committee for the 2016 Summer Biomechanics, Bioengineering and Biotransport Conference

SB³C2016
Summer Biomechanics, Bioengineering and Biotransport Conference
June 29 –July 2, National Harbor, MD, USA
SB³C2016-618

ALTERATIONS IN THE ANTERIOR CAPSULE CORRELATE WITH IMPAIRED JOINT MECHANICS IN A RAT ELBOW MODEL OF POST-TRAUMATIC JOINT STIFFNESS

Chelsey L. Dunham (1), Ryan M. Castile (2), Leesa M. Galatz (3), Spencer P. Lake (1,2,4)

(1) Department of Biomedical Engineering
Washington University in St. Louis
St. Louis, MO, USA

(2) Department of Mechanical Engineering & Materials Science
Washington University in St. Louis
St. Louis, MO, USA

(3) Department of Orthopaedic Surgery
Mount Sinai Hospital
New York, NY, USA

(4) Department of Orthopaedic Surgery
Washington University in St. Louis
St. Louis, MO, USA

INTRODUCTION

Post-traumatic joint stiffness (PTJS) due to elbow injury is a challenging clinical problem due to the anatomical and biomechanical complexity of the elbow [1,2]. Injury to the elbow disturbs joint congruity and often leads to functional impairment due to tissue contracture and stiffness. While it remains unclear how each of the peri-articular joint structures (e.g. ligaments, tendons, muscles) are affected in PTJS, changes to the capsule have been consistently implicated as a contributing factor [3,4,5]. Biologically, elbow capsule tissue in human PTJS showed increased cellularity, thickness and disorganized collagen [3,4,6,7]. Increased production and abnormal organization of collagen was also observed in posterior knee capsules in a rabbit model of PTJS [8].

Recently, our group developed an animal model of PTJS in the rat elbow, that established a model system to enable investigation of clinical injuries specific to the elbow [9]. Biomechanical results in our model mimicked symptoms common to human PTJS flexion-extension and pronation-supination (i.e. decreased range of motion and neutral zone length), which persisted long-term following joint remobilization, demonstrating a permanent contracture within the elbow. However, we have not examined biological changes in our model to determine if they match what is observed in human patients. The purpose of this study was to evaluate the histological properties of the anterior capsule and determine if these changes correlate with the altered mechanics in elbow PTJS.

METHODS

In this IACUC approved study, male Long-Evans rats (300-343g) underwent surgery to replicate soft tissue injuries seen in subluxation/dislocation, namely an anterior capsulotomy and lateral collateral ligament transection [9]. Injured limbs were immobilized for six weeks, after which half of the animals were sacrificed (immobilization only or IM), while the other half were remobilized with unrestricted cage activity for six weeks (immobilization-remobilization or IM-RM) [8]. Control animals were allowed unrestricted cage activity.

Elbow joints were subjected to mechanical testing using protocols described previously for flexion-extension (F-E) [9] and pronation-supination (P-S) [10] (F-E: n=10-18/group; P-S: n=6-13/group). Force and displacement were converted to torque and angular position and loading curves were analyzed for total ROM and NZ length (angular span of functional range). After mechanical testing, elbow joints (n=3/group) were prepared for histological assessment as described previously [9]. Sagittal sections were cut and stained with hematoxylin and eosin (H&E), toluidine blue (TB) and picrosirius red (PR).

A blind analysis of the anterior capsule was performed for the H&E slides by a musculoskeletal pathologist and semi-quantitative scores were assigned for biological characteristics of interest [9]. Capsule thickness was measured and reported semi-qualitatively since these values can vary for sections cut at different depths: thickness values were averaged across each group, normalized by the control capsule thickness and converted to a symbolic grading scheme for comparison between groups. Anterior capsules of the TB and PR sections were analyzed qualitatively for cellularity, collagen density and debris (particles) within the synovial fluid.

RESULTS

In flexion-extension, injured limbs demonstrated significantly decreased total range of motion and neutral zone length compared to control and contralateral (CL) limbs for both IM and IM-RM (Figure 1). In pronation-supination, injured limbs showed significantly decreased total range of motion and neutral zone length compared to CL for both IM and IM-RM (Figure 1).

H&E staining revealed an increase in the amount of adhesions, cellularity and thickness of the IM capsule compared to control and CL

Copyright 2016 The Organizing Committee for the 2016 Summer Biomechanics, Bioengineering and Biotransport Conference

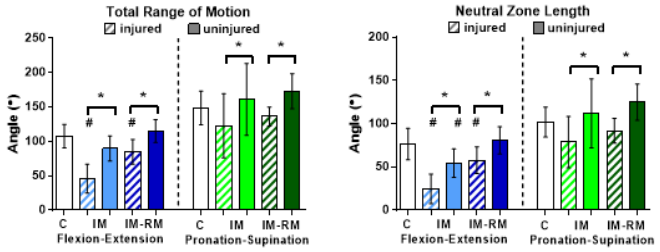

Figure 1: Persistent significant decrease in joint mechanics from immobilization (IM) to immobilization-remobilization (IM-RM) for both flexion-extension and pronation-supination. (average ± standard deviation, C = control, # = different from control, * = different from contralateral limb, $p < 0.05$)

Table 1: Histological evaluation of H&E stained anterior

	Adhesion	Cellularity	Inflammation	Thickness	Vascularity
Control	-	+	-	-	+
IM	+	++	-	++	+
IM CL	-	+	-	-	+
IM-RM	+	+	-	+++	+
IM-RM CL	-	+	-	-	+

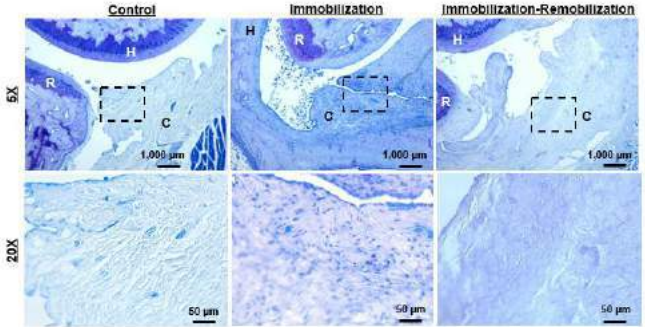

Figure 2: Representative sagittal histology sections for toluidine blue at 5X and 20X. (H = humerus, R = radius, C = capsule)

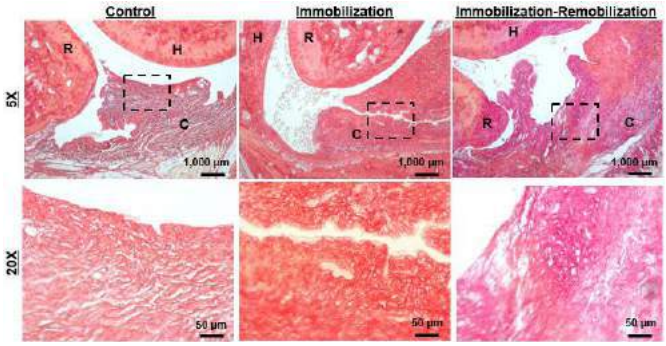

Figure 3: Representative sagittal histology sections for picrosirius red at 5X and 20X. (H = humerus, R = radius, C = capsule)

(Table 1). IM-RM capsule also exhibited increased adhesions and thickness compared to control and CL; however, cellularity decreased while the thickness increased from IM to IM-RM. Signs of inflammation were not present in any group; however, this is likely because of the relatively late time points evaluated.

TB staining demonstrated IM anterior capsule had a large increase in cellularity and debris within the synovial fluid cavity compared to control (Figure 2). IM-RM anterior capsule not only showed decreased cellularity compared to IM but also had a lower number of cells than the control.

PR staining showed an increase in collagen density for both IM and IM-RM anterior capsule (Figure 3). While the collagen density was increased continuously throughout the entire IM capsule, the IM-RM capsule had regions of higher and moderate density. Both TB and PR staining demonstrated an increase in debris in the synovial fluid cavity for IM, followed by a decreased in debris for IM-RM.

DISCUSSION

This study shows that our rat elbow model of PTJS exhibits biological changes similar to the human condition, including an increase in collagen density, capsular thickness and a temporary increase in cellularity as the total range of motion and neutral zone length remains significantly decreased from IM to IM-RM.

Human capsule tissue exhibits hypercellularity with the development of PTJS [3,5], which was evident in capsule of IM animals in this study. The IM-RM capsule demonstrated a return to normal levels of cells following remobilization, similar to reports by Doornberg et al. in contracted human elbows [11] and by Abdel et al. in a rabbit knee contracture model [12], where the number of myofibroblasts initially increased then decreased at longer times. While Hildebrand et al. found that myofibroblasts and mast cells remained elevated from the acute to chronic stage in their rabbit knee contracture model, the cellularity did not increase past four weeks [5].

Since mechanical parameters (i.e. total and functional range of motion) remain significantly impaired long-term, yet cellularity returns to normal levels, these results indicate that cells are not responsible for the permanently altered joint mechanics. Instead persistent contracture appears to be caused by the increased and disorganized collagen. The initial increase in cellularity may lead to increased collagen and capsular thickness, but a lack of increasing vascularity (Table 1) may then contribute to the decreased cell number. Both IM and IM-RM capsules exhibited disorganized collagen and larger capsular thickness, consistent with previous work in human elbow capsule and rabbit knee models of PTJS [4,7,8], which may contribute directly to altered joint mechanics. While this work focused on the capsule, we are currently investigating how the other peri-articular tissues are contributing to joint dysfunction.

In conclusion, this study shows that our animal model of PTJS mimics biomechanical and biological features of the human condition, validating its use in evaluating the pathogenesis of the PTJS. The increased disorganized collagen and thickness likely contribute to persistent decrease in total range of motion and neutral zone length in both F-E and P-S. Future work evaluating genetic expression and collagen content will help identify the specific biological change in the elbow responsible for contracture, so better prevention and treatment strategies can be developed.

ACKNOWLEDGEMENTS

The authors thank the Washington University Musculoskeletal Research Center (NIH P30 AR057235) for histology processing and the American Shoulder and Elbow Surgeons for funding and Dr. Necat Havlioglu for the blind analysis of the H&E stained samples.

REFERENCES

[1] King, G+, *JSES*, 2:165-174, 1993. [2] Safran, M+, *JSES* 14:S179-S189, 2005. [3] Germscheid, +, *CORR*, 450:219-224, 2006. [4] Cohen, +, *JSES*, 16:484-490, 2007. [5] Hildebrand, K+, *JOR*, 26:1313-1319, 2008. [6] Monument, M+, *J Orthop Sci*, 18:869-877, 2013. [7] Charalambous, C+, *JBJS*, 94:1428-1437, 2012. [8] Steplewski, A+, *JOR*, 2016. [9] Lake, S+, *JOR*, 2016. [10] Dunham, C+, *Trans ORS*, 2016. [11] Doornberg, J+, *JBJS*, 96:e36, 2014. [12] Abdel, M+, *JOR*, 30:713-719, 2012.

Copyright 2016 The Organizing Committee for the 2016 Summer Biomechanics, Bioengineering and Biotransport Conference

SB³C2016
Summer Biomechanics, Bioengineering and Biotransport Conference
June 29 –July 2, National Harbor, MD, USA
SB³C2016-619

MODELLING CORNEAL MECHANICAL BEHAVIOR WITH A BIPHASIC TRANSVERSELY ISOTROPIC POROVISCOELASTIC CONSTITUTIVE MODEL

H. Hatami-Marbini (1)

(1) Department of Mechanical & Industrial Engineering, University of Illinois at Chicago, Chicago, Illinois 60607

INTRODUCTION

The cornea is a hydrated soft tissue which transmits the incident light while acting as a resilient barrier to the mechanical forces. We have recently investigated the mechanical behavior of the cornea using unconfined compression experiments [1]. In this experimental technique, a circular specimen is immersed in a bathing solution and is compressed between two rigid platens. Over the past few decades, different types of mixture theories have been proposed to curve-fit the experimental measurements and subsequently determine the material properties [2]. The simplest model, the linear isotropic biphasic theory, was proposed in 1980 [3]. In this model, the tissue is assumed to be made up of a solid phase with linear elastic behavior and an incompressible viscous fluid phase. While the linear isotropic biphasic theory has been successfully used to describe the creep and stress-relaxation behaviors of various soft tissues, there is a substantial difference between the model predictions and unconfined compression experimental measurements of the corneal tissue [3,4].

The stromal layer, which is made up of thin parallel-to-the-surface collagen lamellae embedded in a proteoglycan matrix, is primarily responsible for the mechanical strength of the cornea. It has been well-developed that the stromal microstructure is transversely isotropic [1]. Because of this particular microstructure, it is expected that the parallel-to-the-surface properties (in plane of material isotropy) to be different that those in the normal direction. Based on this observation, a linear transversely isotropic biphasic model was employed to analyze the unconfined compression experimental measurements. It was observed that this experimental and computational technique resulted in a relatively accurate estimate of the corneal out-of-plane modulus, in-plane modulus, and permeability coefficient as a function of thickness [1,4]. Nevertheless, it was also seen that the linear transversely isotropic biphasic theory could not fully curve-fit the experimental stress relaxation history in unconfined compression. Since the primary ingredients of the stromal layer are viscoelastic, the objective of the present work was to develop an analytical model which is able to account for the intrinsic viscoelasticity of the tissue constituents. For this purpose, a linear transversely isotropic poroviscoelastic theory was created by combining a viscoelastic material law with the transversely isotropic biphasic model. The predictions of the proposed model were compared against those of the linear transversely isotropic, viscoelastic, and cone-wise viscoelastic theory.

METHODS

In biphasic mixture theory, the tissue is considered as a binary mixture of an incompressible solid phase and an incompressible fluid phase. Therefore, the total stress can be written as [5]

$$\boldsymbol{\sigma} = -p\mathbf{I} + \boldsymbol{\sigma}^{vs} \tag{1}$$

where I is identity vector, p is the fluid pressure, and $\boldsymbol{\sigma}^{vs}$ is the stress vector of the solid phase. The intrinsic viscoelastic properties of the solid phase is described with an integral type viscoelastic model, i.e.

$$\boldsymbol{\sigma}^{vs} = \int_{-\infty}^{t} g(t-\tau)\mathbf{S}^{eq^{-1}} : d\boldsymbol{\varepsilon}(\tau) \tag{2}$$

where $\mathbf{S}_{eq}$ is the compliance matrix and g(t) is given by

$$g(t) = 1 + c\left(E(-t/\tau_1) - E(-t/\tau_2)\right) \tag{3}$$

where $E(x) = -\int_{-x}^{\infty} e^{-t}/t \, dt$.

Copyright 2016 The Organizing Committee for the 2016 Summer Biomechanics, Bioengineering and Biotransport Conference

It can be shown that the governing equations of the biphasic model simplify to

$$\frac{\partial^2 \bar{u}_r}{\partial r^2} + \frac{\partial \bar{u}_r}{r\partial r} - \left(\frac{1}{r^2} + f\right)\bar{u}_r = \frac{f}{2} r \bar{\varepsilon}_{zz}$$
$$\frac{\partial \bar{p}}{\partial r} = \frac{s}{\kappa}\left(\bar{u}_r + \frac{\bar{r}}{2}\bar{\varepsilon}_{zz}\right) \quad (4)$$

where κ is the permeability coefficient, overbar denotes Laplace transformed quantities, s is the Laplace transform variable, f is expressed in terms of material coefficients [5]. The above equation can be solved for a circular button tested in an unconfined compression and obtain the closed-form solution for the radial displacement u_r and p in Laplace domain. The total compressive stress is given by

$$\bar{\sigma} = \frac{1}{\pi r_0^2}\int_0^{r_0} (-\bar{p} + \bar{\sigma}_{zz}) 2\pi r dr \quad (5)$$

which can be inverted back to the time domain using a numerical Laplace inversion algorithm.

In order to assess the model, unconfined compression experiments were conducted on porcine samples. Briefly, porcine eyes were obtained from a local slaughter house and corneal discs from the central corneal region were punched. An RSA-G2 machine (TA instruments, Delaware) was used to perform unconfined compression experiments. For this purpose, a compressive tare stress was used to determine the initial thickness of the samples and stress-relaxation tests were conducted by bringing the head down. A compressive strain of 5% with a strain rate equal to 0.1/s was used. In order to find the material constants and curve-fit the experimental data, a multidimensional curve-fitting was carried out.

RESULTS

It is first noted that the model proposed here reduces to the linear transversely isotropic biphasic theory by adjusting the material parameters [5]. Figure 1 shows a typical behavior of the porcine corneal stroma under unconfined compression. In this plot, the symbols show the total experimental reaction stress and the lines show the numerical model predictions. The theoretic fits were obtained using different constitutive models, i.e. linear isotropic, transversely isotropic, isotropic viscoelastic and transversely isotropic viscoelastic models. It is seen that the present model resulted a significant improvement in curve-fitting the unconfined compression experiments ($R^2 = 0.99$).

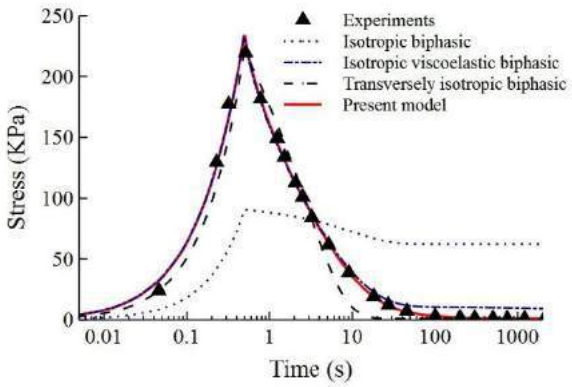

Figure 1: The unconfined compression response of the cornea and the theoretical curve-fits obtained from the linear isotropic biphasic, isotropic viscoelastic biphasic, transversely isotropic biphasic, and transversely isotropic viscoelastic (present model) theories. The horizontal axis is plotted in logarithmic scale to depict a better comparison between different models.

DISCUSSION

The primary objective of the present work was to create a linear transversely isotropic biphasic poroviscoelastic model for the mechanical behavior of the corneal tissue in unconfined compression and investigate whether this model would be able to give a better representation of the experimental data. We have previously shown that the linear isotropic biphasic model cannot represent the unconfined compression response of the cornea [4]. Because of the transversely isotropic microstructure of the corneal stroma, a linear transversely isotropic biphasic model was used in a recent study to model the stress-relaxation of cornea in unconfined compression experiments [4]. Nevertheless, despite the significant improvement, it was observed that even this model was not able to fully capture the experimental stress relaxation behavior. Since collagen fibrils and the proteoglycan matrix are both viscoelastic, we hypothesized that a linear transversely isotropic poroviscoelastic model should give a better theoretical representation of the constitutive behavior of the corneal tissue and subsequently a more accurate assessment of the material properties. This model includes the contributions from both the fluid flow and the intrinsic viscoelasticity to the overall stress-relaxation under unconfined compression. It is noted that although the poroviscoelastic model formulation presented here has nine material constants: five elastic parameters, one permeability coefficient, and three viscoelastic parameters, the shear modulus does not enter the formulation in modelling the unconfined compression experiments and needs to be determined separately [6]. In Figure 1, the behavior of the cornea under unconfined compression is shown. It is clear that the proposed model resulted in a significant improvement over other models. It also needs to be mentioned that the model predictions are comparable with those obtained using a biphasic-CLE-QLV model [7] (Results not shown).

ACKNOWLEDGEMENTS

This study was supported in part by National Science Foundation (1351461).

REFERENCES

[1] Hatami-Marbini, H, et al. *Exp Eye Res*, 116:47-54, 2013
[2] Hatami-Marbini, H, Handbook on Micromechanics and Nanomechanics 273–302, 2013.
[3] Mow V et al., *J Biomech Eng*. 102:73-84, 1980.
[4] Hatami-Marbini, H, et al., *Biorheology*, 50:133–147, 2012.
[5] Hatami-Marbini, H, et al., *J Biomech Eng*. in press.
[6] Hatami-Marbini, H, et al., *J. Biomech*, 47:723–728, 2014.
[7] Huang C et al, *J Biomech Eng*. 123:410-417, 2001.

Copyright 2016 The Organizing Committee for the 2016 Summer Biomechanics, Bioengineering and Biotransport Conference

SB^{3}C2016
Summer Biomechanics, Bioengineering and Biotransport Conference
June 29 –July 2, National Harbor, MD, USA
SB^{3}C2016-620

EFFECTS OF SAGGING VERSUS STRETCHED LEAFLETS ON BIOPROSTHETIC HEART VALVE DURABILITY

Nandini Duraiswamy (1), Parinaz Fathi (1, 2), Stephen M. Retta (1), and Jason D. Weaver (1)

(1) Food and Drug Administration
Center for Devices and Radiological Health
Office of Science and Engineering Labs
Division of Applied Mechanics
Silver Spring, MD

(2) Oak Ridge Institute for Science and Education (ORISE)
Oak Ridge, TN

INTRODUCTION

Surgical bioprosthetic valve experience has demonstrated the importance of proper leaflet coaptation, the absence of which could change the leaflet kinematics and lead to early structural deterioration of the leaflets [1, 2, 3]. The leaflets are known to coapt nominally in a circular configuration. Finite element analyses (FEA) of elliptical configurations of heart valve frames have shown an increase in leaflet stresses and strains compared to circular configuration [4, 5, 6]. We also observed leaflet coaptation differences with the elliptical configurations, in particular the existence of sagging versus stretched leaflets in the same valve configuration [5, 6]. Leaflet coaptation patterns have also been shown computationally to influence fatigue damage [7]. To better evaluate the relative performance of nominal, sagging, and stretched leaflets, we conducted accelerated wear testing (AWT) using circular and elliptical valve configurations.

METHODS

Accelerated Wear Testing: AWT was conducted on six 25 mm bovine pericardial surgical aortic valves (Model 2800 from Edwards Lifesciences) using Dynatek Dalta's M6 Durability Tester. Two samples were tested in a circular configuration as controls and four were tested in annularly distorted elliptical configurations that are well beyond the design requirements for a surgical valve. Two of the four elliptical valves had a commissure on the major axis (EMaj), and the remaining two had a commissure on the minor axis (Emin, see Figure 1). Average aspect ratios (AR: major to minor axis ratio) of two valves were 1.04±0.02 for Circ, 1.35±0.01 for EMaj, and 1.27±0.05 for Emin configurations. These aspect ratios were chosen because of potential differences between elliptical configurations in deformable valves, but neither has been shown to be applicable to a non-deformable surgical valve such as the test valve in the clinical setting. AWT was conducted in 0.9 % saline solution with 0.02% sodium azide bacteriostat at 37^{o}C for 123 million (M) cycles at rates ranging from 980 to 1066 rpm. Differential pressures were taken using Endevco pressure transducers. Although the minimum target differential pressure required was 100 m mHg per ISO 5840-3 standard, the mean differential pressure in the six chambers ranged from 129 to 194 mmHg, with a mean percent cycle time above target ranging from 5.25 to 9.86 percent. The valves were removed from the tester and visually examined at 0, 41, 80, and 123 million cycles.

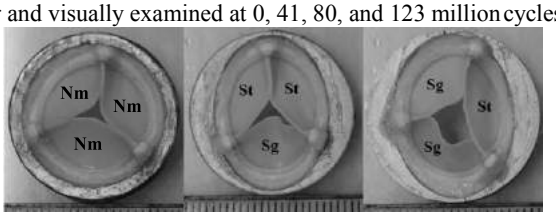

Figure 1: Left: Circular configuration (Circ); **Center:** Elliptical Major configuration (EMaj); **Right:** Elliptical Minor configuration (Emin); nominal, sagging, and stretched leaflets are denoted as "Nm", "Sg" and "St" respectively.

Ultimate Tensile Strength (UTS) Testing: After 123M cycles, a rectangular sample (~18 x 6 mm) with rounded edges was cut from the center of each leaflet of all valves. The sample thickness was measured using an optical microscope and each sample was pulled to failure at 120 mm/min. The working length of the samples between the chucks was typically 8-9 mm, and samples underwent ten cycles of preconditioning up to 5% strain prior to being pulled to failure. UTS testing was performed on three circular nominal leaflets (not fatigued, control), six circular nominal fatigued leaflets, six sagging leaflets, and six stretched leaflets.

Copyright 2016 The Organizing Committee for the 2016 Summer Biomechanics, Bioengineering and Biotransport Conference

RESULTS

Two main modes of leaflet damage were observed in AWT as indicated in Figure 2: (1) Leaflet tear at the commissure posts (CMT), and (2) leaflet tears at the free edge (FET). Fabric tear exposing the underlying commissure metal post (CMPE) was also observed, but did not affect leaflet integrity in most cases. CMTs occurred in all leaflet types irrespective of valve configuration. Leaflet thinning at the free edge and FETs occurred in all six sagging leaflets and only one stretched leaflet of EMaj and Emin shaped valves but it did not occur in the nominal leaflets of circular valves. CMPEs were observed in the commissure posts of all leaflet types irrespective of valve configuration. All six valves achieved complete opening and closing of the leaflets throughout testing, as shown with one EMaj valve in Figure 3 below.

Figure 2: Left: commissure tear (CMT); **Center:** free edge tear (FET) in a sagging leaflet; **Right:** commissure post exposed (CMPE);

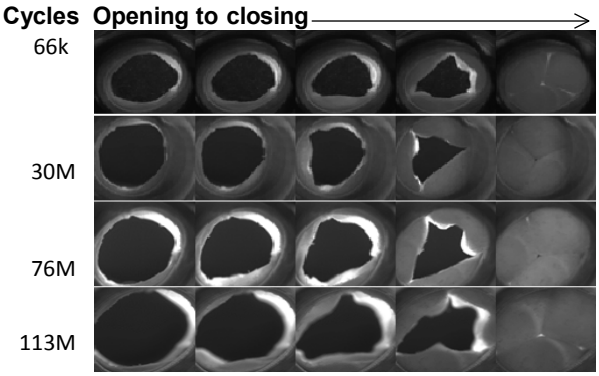

Figure 3: Images showing complete opening and closing of one EMaj valve in the AWT with cycling (top to bottom rows). Note orientations of St and Sg leaflets are not the same in all rows.

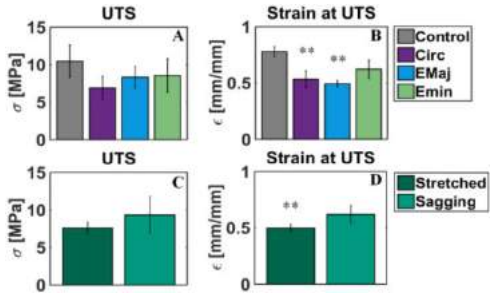

Figure 4: A) UTS by valve configuration; **B)** Strain at UTS by valve configuration; **C)** UTS for all stretched and sagging leaflets; **D)** Strain at UTS for all stretched and sagging leaflets; Error bars represent standard error; Asterisks (**) indicate statistically significant difference from the not fatigued control, P ≤0.1

The average UTS was not significantly different in the fatigued nominal, sagging, and stretched leaflets compared to the not fatigued control as shown in Figure 4. Although not significant, the average UTS and average strain at UTS was lower in the stretched leaflets than the sagging leaflets of elliptical configurations.

DISCUSSION

Conditions in our AWT system (mounting of the valves, high differential pressures, and extreme elliptical configurations for a surgical valve) produced a high damage rate as demonstrated by a single CMPE initiated failure (with the commissure pulling out) with one circular configuration valve with nominal, well-coapted leaflets. These conditions were not typical of those used in determination of long-term durability of a bioprosthetic valve, and the present results cannot be used to assess the longevity or failure modes of the surgical valves. Instead, these results are limited to understanding the nature of damage caused by stretched and sagging leaflets, and underscoring the importance of designing for complete coaptation.

CMTs in all leaflet types appeared to initiate at the bend of the commissure metal post closer to the leaflet belly and propagate towards the commissure closer to the free edge. The CMTs and CMPEs existed in all leaflet types and the severity of these failures was independent of valve configuration.

FETs occurred only in the sagging and stretched leaflets of elliptical configurations and not in the nominal leaflets of circular configurations. Leaflet thinning appeared to begin in the outermost fibrous layers of the pericardial tissue and progresses inwards towards the serous layer of the tissue, which finally resulted in a complete leaflet FET. Leaflet thinning at the free edge was noted in all sagging (Sg) leaflets; in some cases leaflet thinning was also noted in the belly region of the stretched (St) leaflets. Sagging (Sg) leaflets tore first near the unsupported free edge in each elliptical configuration.

The average UTS was lower for the fatigued leaflets of circular and elliptical configurations compared to the not fatigued leaflets of circular configuration (not statistically significant) showing fatigue inducing damage in all leaflet types (Figure 4). The average UTS and strain at break for the St leaflets were lower than the Sg leaflets showing possible leaflet damage at the belly with fatigue in St leaflets. This observation was unexpected but it is to be noted that the samples for UTS testing constituted most of the tissue from the leaflet belly (slightly away from the free edge) while the tears for the Sg leaflets occurred after leaflet thinning was initiated at the free edge.

In conclusion, our AWT results show that the sagging leaflets tore at the unsupported free edge before the stretched leaflets in both elliptical configurations, while the nominal leaflets did not see this type of failure. This is initiated by leaflet thinning that appears to be propagating from the ventricular to the aortic side of the leaflets. This study once again highlights the importance of proper leaflet coaptation in the design of a bioprosthetic heart valve. The extent of support between leaflets needs to be considered to improve long-term performance.

ACKNOWLEDGEMENTS

The authors would like to express our gratitude to: FDA Office of Women's Health (funding), the CDRH Research Participation Program administered by ORISE, Edwards LifeSciences, Dynatek Dalta, and Terry Woods, Ph.D.

REFERENCES

[1] Schoen, F. J. et al., *J Biomed Mater Res*, 47:439-465, 1999.
[2] Vesely, I., *Cardiov Pathol*, 12:277-286, 2003.
[3] Thubrikar, M. et al, *Am J Physiol*, 241:H795-H801, 1981.
[4] Sun, W. et al., *J Biomech*, 43(16):3085-3090, 2010.
[5] Gunning, P.S. et al., *Annl of Biomed Engg*, 42(9):1989-2001, 2014.
[6] Duraiswamy, N. et al., *ASME Fron in Med Dev Proceedings*, 2013.
[7] Martin, C. et al., *J Biomech*, 48(12):3026-3034, 2015.

Copyright 2016 The Organizing Committee for the 2016 Summer Biomechanics, Bioengineering and Biotransport Conference

SB^{3}C2016
Summer Biomechanics, Bioengineering and Biotransport Conference
June 29 –July 2, National Harbor, MD, USA
SB^{3}C2016-621

EVALUATION OF POLYMERIC SCAFFOLDS USING A VERTICAL LAYERED CO-EXTRUSION FOR TOPICAL DRUG DELIVERY APPLICATIONS AND COMPARISON WITH ELECTROSTATIC SPINNING

Mohammad Mofidfar, Eric Baer, Gary E. Wnek*

Department of Macromolecular Science and Engineering, CWRU
Cleveland, OH, USA
****Contact e-mail address: gew5@case.edu***

INTRODUCTION

Targeting the skin for drug delivery offers several advantages over the oral route, including obviating the need for constant self-administration, easy termination of therapy at any point of time, and potential reduction of side effects. Drug delivery for topical applications using polymeric scaffolds has several advantages over monolithic patches as well as ointments and creams, including better control of delivery kinetics via mass transport from the fibers, the ability to construct multiple layers with different drugs and/or doses, and improved patient comfort and hence better compliance [1]. Here we report on the use of a new,melt co-extrusion process to prepare polymer fibers containing the anti-fungal compound clotrimazole. An advantage over electrospinning, for which we have considerable experience, is that the new process is a continuous one, alleviating problems of rather low throughput for electrospinning.

One of the major disadvantages associated with clotrimazole is its poor aqueous solubility, requiring a hydrophobic carrier such as a non-polar oil for topical administration. Thus, a relatively non-polar polymer, poly(caprolactone) or PCL, was selected as the matrix for the drug since PCL is readily processed by the continuous new co-extrusion approach which has been described in considerable detail elsewhere [2] and thus it is only briefly outlined in Figure 1.

METHODS

Two grades of PEO (Dow POLYOX N80 (Mw = 200 kg/mol) and POLYOX N10 (Mw = 100 kg/mol) was pre-blend using Haake Rheodrive 5000 twin-screw extruder with a weight ratio of 30:70 (N80:N10). PCL and clotrimazole were prepared in the same screw extruder with two different ratios of 96:4 and 92:8 (PCL:Clotrimazole).

The melt flow indexing of blends was prepared to determine the correct correct viscosity match and temperature of co-extrusion of PCL:Clotrimazole and PEO blend.

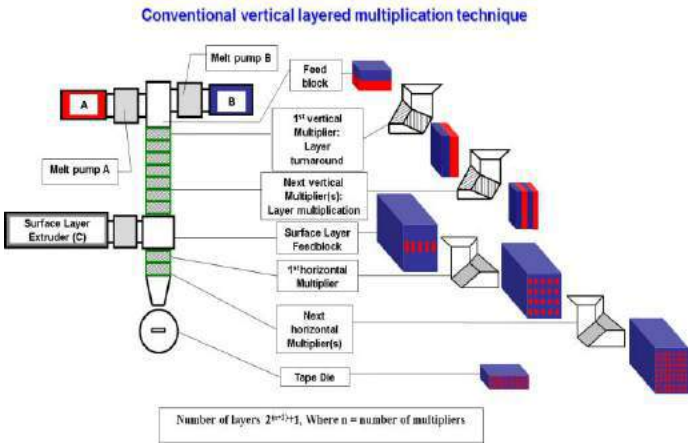

Figure 1. Schematic representation of producing rectangular mats using co-extrusion and two-dimensional multiplication processes.

Briefly, a key feature of the co-extrusion process is a set of multipliers used to drive the controlled stacking of the melts. The overall process can be characterized by four regions: (a) co-extrusion, a region where a molten layer of one polymer is stacked onto a layer of a second polymer; (b) vertical layer multiplication, involving cutting the flow horizontally to double number of vertical layers; (c) the surface-layering region where vertical layers are covered with two surface

Copyright 2016 The Organizing Committee for the 2016 Summer Biomechanics, Bioengineering and Biotransport Conference

layers of one of the polymers (or a third, different polymer); and (d) the horizontal layering region, where surface-layered composites stack on the side and on the top of one other by horizontal-layer multipliers. The extrusion was performed at 180°C, at which the viscosities of PCL and PEO match with each other [2].

We have demonstrated that PEO can be removed form co-extruded composites of PCL/Clotrimazole and PEO tape through immersion in distilled water for 7 days followed by drip-drying for 24 h. 95-98% of total PEO can be removed from as-coextruded mats in this manner.

RESULTS

Co-extruded fibers were sputter coated with 10 nm of gold and imaged for shape and size distribution using a scanning electron microscope (SEM, JEOL-JSM-6510LV) to determine the fiber sizes under an emission voltage of 10 kV. We note that the fibers from this process are rectangular (T=(T=2.89±1.23µm, W=0.98±0.65µm) rather than cylindrical due to cutting and layering steps (Figure 2).

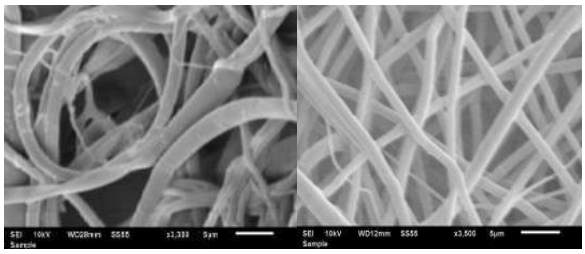

Figure 2. SEM images of co-extruded and electrospun PCL:Clotrimazole fibers with 4% drug loading.

Thermogravimetric analyses were performed using a Q500 TA instruments TGA analyzer. TGA experiments proved that clotrimazole, PCL, and PCL:Clotrimazole blends were stable at the thermal processing temperature as degradation occurs above 200°C. Using the nonisothermal mode of TGA, it was observed that clotrimazole alone begins to decompose above 190°C. This experiments shows that co-extrusion process at 180°C could be suitable for high thermal stability of the clotrimazole at PCL/PEO composite fiber system.

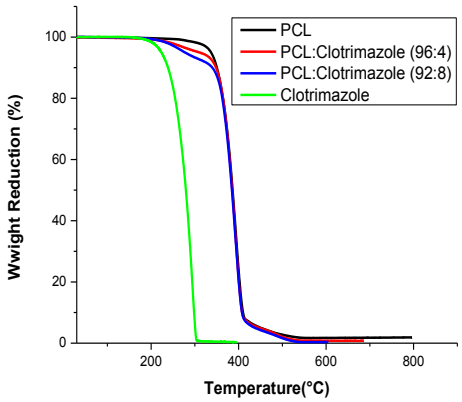

Figure 3: TGA of PCL, Clotrimazole and PCL:Clotrimazole blend in TGA as a function of temperature.

The in-vitro antifungal activity of clotrimazole in electrospun and co-extruded nanofibers was determined against A. fumigatus. A. fumigatus strains used in this study were cultured on plates of Vogel's Minimal Media (VMM). All media preparations were autoclaved for 30 min. In these instances, the A. fumigatus cultures were filled with PCL fiber mats prepared and then incubated for up to 24 h at 37°C, and the zone of inhibitions was measured (Figure 4).

Figure 4: Zones of inhibition from co-extruded fibers of clotrimazole:PCL.

DISCUSSION

The continuous extrusion process has been applied successfully to pharmaceutical formulations, specifically demonstrating incorporation of clotrimazole in PCL scaffolds as a carrier. Drug-releasing scaffold patches represent a potentially attractive opportunity for translation of the co-extrusion scaffolds to clinical applications. The present study demonstrates that clotrimazole has chemical stability with polymers, PEO and PCL, in co-extrusion processing and post-processing. Our findings indicate that the co-extrusion PCL with clotrimazole is capable of providing more sustained release. Clinical translation of this and related polymer/drug systems is in progress. Nanofiber patches could now be used in clinical applications.

ACKNOWLEDGEMENTS

Financial support from the NSF Science and Technology Center for Layered Polymeric Systems (Grant 0423914) is gratefully acknowledged, as is the use of fungal culture facilities in the laboratory of Prof. Mahmoud Ghannoum at CWRU.

REFERENCES

[1] E. R. Kenawy, G. L. Bowlin, K. Mansfield, J. Layman, D. G. Simpson, E. Sanders and G. E. Wnek, *J. Contr. Release*, **81**, 57 (2002)

[2] J. Wang, D. Langhe, M. Ponting, G.E. Wnek, L. T. J. Korley, and E. Baer, *Polymer*, **55**, 673 (2014)

Copyright 2016 The Organizing Committee for the 2016 Summer Biomechanics, Bioengineering and Biotransport Conference

SB^{3}C2016
Summer Biomechanics, Bioengineering and Biotransport Conference
June 29 –July 2, National Harbor, MD, USA
SB^{3}C2016-622

EFFECT OF SODIUM HYPOCHLORITE ON THE FATIGUE PERFORMANCE AND CORROSION RESISTANCE OF NITINOL WIRES

Erick J. Gutierrez (1,2), Srinidhi Nagaraja (1), Shiril Sivan (1,2), Jason D. Weaver (1), Matthew Di Prima (1)

(1) Division of Applied Mechanics
Office of Science and Engineering Laboratories
Center for Devices and Radiological Health
U.S. Food and Drug Administration
Silver Spring, Maryland, USA

(2) Oak Ridge Institute for Science and Education
Oak Ridge, Tennessee, USA

INTRODUCTION

Nitinol (NiTi) is a metal alloy commonly known for its unique properties such as super elasticity, shape memory, and fatigue resistance [1]. Because of the wide range of features, Nitinol has become a material of choice for medical devices like endovascular stents. During the manufacturing process however, inclusions can develop on the surface of Nitinol. These inclusions can be present in the form of carbides, oxides, and intermetallic precipitates [2]. The presence of inclusions on a metal surface is undesirable since they act as stress concentrators by virtue of their geometry and are also more susceptible to corrosion in the presence of chlorine ions.

Recent studies have shown that when a nitinol surface is immersed in 6% sodium hypochlorite (NaClO), commonly known as bleach, corrosion of inclusions will occur, resulting in a visible black flocculent [2]. Hence, this method could be used to identify or eliminate inclusions on the surface of Nitinol devices. However, there are concerns that treatment of Nitinol surfaces with NaClO could lead to surface damage. Given that research done on NaClO and its impact on Nitinol is limited, and that Nitinol performance continues to be of significant interest for the medical field, this project is aimed to investigate in a broad context the effect of NaClO on the corrosion and fatigue performance of Nitinol and evaluate the use of NaClO to detect inclusions.

METHODS

In order to evaluate the corrosion and fatigue performance of Nitinol post exposure to NaClO, two different surface finishes of Nitinol wire were used, black oxide (BO) and electropolished (EP), to assess the impact on each surface finish. Nitinol used complied with specifications set per ASTM F2063. Prior to conducting fatigue and corrosion testing, samples were split into two groups and subjected to one of the following: a) Nothing, i.e. As Received, b) NaClO Soaked for 15 minutes followed by a DI water rinse. Rotary bend fatigue testing was used to determine the fatigue life of Nitinol wires at alternating strains of 0.8, 1.0, and 1.2%. Six wire samples from each surface finish were used for each strain level and condition assessed. This test was conducted in a phosphate buffered saline bath at 37^{o}C using Valley Instruments wire fatigue testers (Positool Technologies, OH) until fracture or runout to one million cycles. In order to evaluate the effect of NaClO on the corrosion susceptibility of Nitinol, cyclic potentiodynamic polarization testing was conducted. Six samples from each surface finish and test condition were evaluated per ASTM F2129 using an Interface 1000 potentiostat (Gamry, PA). Scanning electron microscopy (SEM) imaging was performed prior to conducting fatigue and corrosion tests to inspect the surface of as received and NaClO soaked wires using a JSM-6390LV (JEOL, MA).

RESULTS

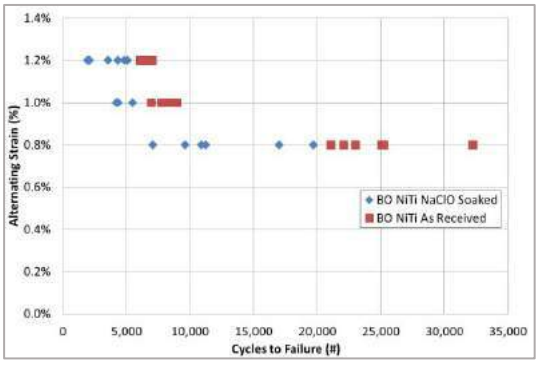

Figure 1: Strain-life diagram for black oxide Nitinol (BO NiTi) showing fatigue performance for As Received and NaClO Soaked conditions.

Copyright 2016 The Organizing Committee for the 2016 Summer Biomechanics, Bioengineering and Biotransport Conference

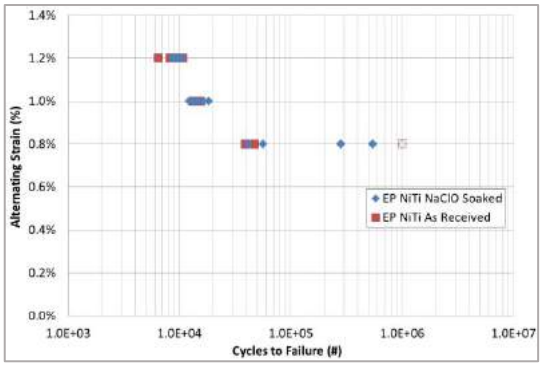

Figure 2: Strain-life diagram for electropolished Nitinol (EP NiTi) showing fatigue performance for As Received and NaClO Soaked conditions. Note that unfilled shapes indicate runouts.

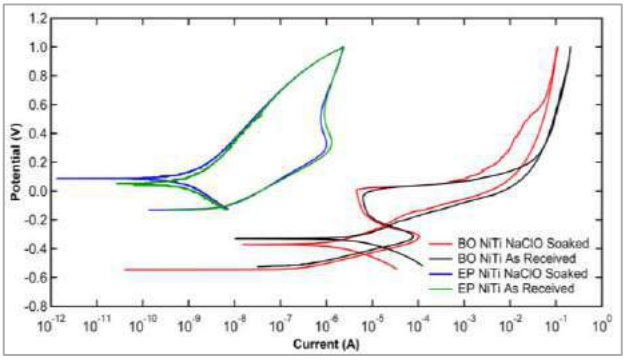

Figure 3: Cyclic potentiodynamic curves for black oxide and electropolished Nitinol (BO NiTi, EP NiTi respectively) for As Received and NaClO Soaked conditions.

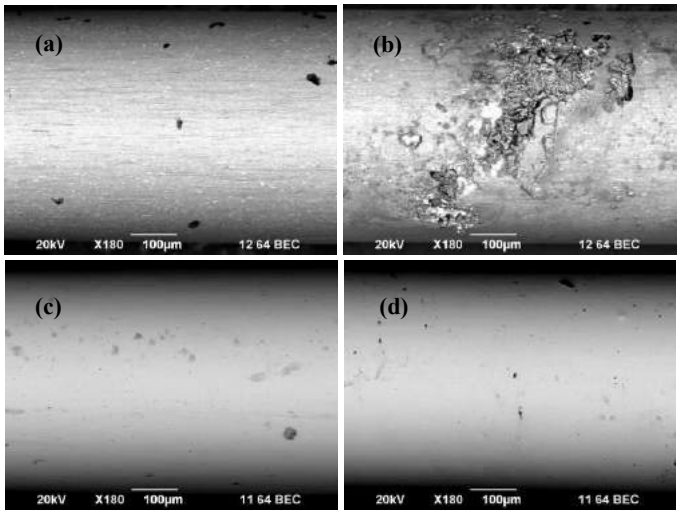

Figure 4: SEM micrographs of Nitinol wires prior to testing per ASTM F2129: (a) BO NiTi As Received, (b) BO NiTi NaClO Soaked, (c) EP NiTi As Received, (d) EP NiTi NaClO Soaked.

Fatigue results for the black oxide Nitinol (BO NiTi) and electropolished Nitinol (EP NiTi) can be seen in Figure 1 and Figure 2, respectively. The number of cycles to fracture between the NaClO soak group and the as received group were compared with an analysis of covariance using strain as a covariate. The NaClO soak was found to have a statistically significant reduction on the fatigue life of the black oxide Nitinol ($p<0.001$), but not on the electropolished Nitinol ($p=0.518$). The as received group had a higher number of runouts (4 of 6) to one million cycles than the NaClO soak group (2 of 6) in the 0.8% strain tests on electropolished Nitinol.

Corrosion test results showed that NaClO soaked and as received black oxide Nitinol samples broke down at similar potentials. As received and NaClO soaked electropolished and black oxide Nitinol samples followed a similar current vs. potential profile (Fig. 3).

Visible black flocculent was not observed in the solution after soaking any of the wire specimens in NaClO. SEM imaging performed on black oxide Nitinol showed that exposure to 6% NaClO triggered corrosion damage in some segments of the wires (Fig. 4b). The 6% NaClO solution did not appear to cause corrosion in the segments of the electropolished Nitinol wires that were observed under SEM (Fig. 4d).

DISCUSSION

Corrosion damage due to NaClO was confirmed with SEM to have occurred on black oxide Nitinol wires after the NaClO soak. However, black flocculent was not observed on any of the Nitinol samples after NaClO soak in contrast with results reported by Rokicki et al. [2]. Corrosive damage to the black oxide Nitinol wires during exposure to 6% NaClO prior to fatigue testing may explain the reduced fatigue performance seen as compared to as received samples. Crack initiation may have occurred where corrosion pits formed and resulted in a decreased fatigue life. There was no significant effect of the NaClO soak on fatigue performance of the electropolished Nitinol wires, although more of the as received wires reached runout than the NaClO soaked wires at the lowest alternating strain tested (0.8%). Since inclusions are known to play an important role in high cycle Nitinol fatigue in particular [3], lower alternating strain values should be examined in future work to obtain larger number of cycles to failure. Such data would be more representative of implanted cardiovascular devices which are expected to survive hundreds of millions of cycles.

The results gathered from ASTM F2129 testing indicate that soaking samples in 6% NaClO did not greatly impact the pitting corrosion behavior.

Overall, exposure of Nitinol to 6% NaClO did not identify surface inclusions and had some detrimental effects to material performance in our testing. Further investigation into this topic, including immersion testing and more fatigue testing, is warranted to provide a better understanding of how NaClO affects other aspects of Nitinol performance.

ACKNOWLEDGEMENTS

This project was funded by the Division of Applied Mechanics and an appointment to the Research Participation Program at the Center for Devices and Radiological Health administered by the Oak Ridge Institute for Science and Education through an interagency agreement between the U.S. Department of Energy and the U.S. Food and Drug Administration.

REFERENCES

[1] Duerig, T. et al, *MSE*, A273-275: 149-160, 1999.
[2] Rokicki, R et al, *JMEP*, 24:1634-1640, 2015.
[3] Robertson, S et al, *JMBBM*, 51: 119-131, 2015.

Copyright 2016 The Organizing Committee for the 2016 Summer Biomechanics, Bioengineering and Biotransport Conference

SB^{3}C2016
Summer Biomechanics, Bioengineering and Biotransport Conference
June 29 –July 2, National Harbor, MD, USA
SB^{3}C2016-623

KINEMATIC EVIDENCE OF RING APOPHYSIS FRACTURE DURING CYCLIC LOADING TYPICAL OF ADLS

Nicole C. Corbiere (1), Stacey L. Zeigler (2), Kathleen A. Issen (1), Arthur J. Michalek (1), and Laurel Kuxhaus (1)

(1) Mechanical and Aeronautical Engineering Department
Clarkson University
Potsdam, NY, USA

(2) Physical Therapy Department
Clarkson University
Potsdam, NY, USA

INTRODUCTION

Ring apophysis fractures (RAFs) are avulsion type fractures to the posterior aspect of the lumbar vertebral body. They initiate at the ring apophysis, propagate either anteriorly or through the vertebral endplate, and occur most frequently in healthy young athletes [1,2]. These fractures present with symptoms such as: low back pain, limited mobility, and often along with intervertebral disc herniation. Patients often cannot recall an extreme event that caused the RAF. This suggests that activities of daily living (ADLs) contribute to these RAFs. The effects of repetitive small movements during ADLs on vertebral fractures is unknown. It is presumed that these fractures may be initiated by normal ADLs, during which the most common movement for the lumbar spine is flexion of less than 15° [3].

To test this hypothesis, white tailed deer (*O.virginianus*) vertebrae, with a similar degree of skeletal maturity and range of motion [4] to adolescent humans, were loaded in cyclic flexion. The immediate goal was to mechanically simulate RAFs under low-load low-angle cyclic loading, in these cervine lumbar 5-vertebra motion segments.

METHODS

Nine 5-vertebra motion segments (L1-L5, 8 male, 1 female, 2.56 ± 0.46 years) were harvested from cervine [5-6] donors (Nolt's Custom Meat Cutting, Lowville, NY) and potted as previously described [5]. X-rays (Multix X-Ray System, Siemens, Berlin, Germany), dual-energy x-ray absorptiometry (DXA) scans (Lunar Prodigy Advance DXA System, GE Healthcare, Little Chalfont, Buckinghamshire, United Kingdom) and micro-computed tomography (μCT) scans (Phoenix Nanotom, General Electric, Wunstorf, Germany) were collected to verify the absence of pre-existing pathologies such as osteophyte formation. The bone mineral density (BMD) was 1.17 ± 0.15 g/cm^2 which is comparable to healthy human bone. Retroreflective markers (4mm hemispheres) were secured to each vertebral body with cyanoacrylate adhesive to enable motion capture. A paint speckle pattern was applied to the cortical shell to enable observation of surface deformation.

Motion segments were cyclically loaded at 2.0Hz past failure; one specimen was loaded at 0.5Hz. Each motion segment was cycled in displacement control between displacement values that corresponded to a neutral position and 15° of flexion (Figure 1). A pinned end condition fixture (Figure 1) was used to allow flexion of the specimen.

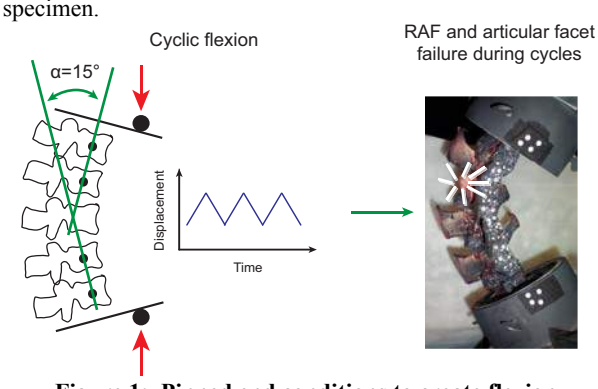

Figure 1: Pinned end conditions to create flexion.

3-D digital image correlation (3D-DIC) and motion capture data were collected during periods of slower (0.1Hz) cycling as appropriate (after cycles 1, 1,000, 3,000, 6,000, 10,000, 12,000, 20,000, and 40,000 if applicable), including one imaging set after failure was aurally and/or visually observed. This slower loading rate during

Copyright 2016 The Organizing Committee for the 2016 Summer Biomechanics, Bioengineering and Biotransport Conference

imaging ensured accurate image recording. The area of the load-displacement hysteresis loops was used to quantify damage accumulation. A 4-camera Qualisys motion capture system (Oqus 500 cameras, Qualisys Inc., Sweden), with an accuracy of 0.1mm, was used to measure the regional centroid angle (α) [7] as well as intervertebral angles throughout the test following the ISB standards [8]. 3D-DIC images of the cortical shell were also taken during the slow loading cycles. Clinically relevant fractures were confirmed by x-ray and μCT.

RESULTS

All specimens fractured; at least six had RAFs as confirmed by μCT. Articular facet failure was observed during cyclic loading as early as 1,400 cycles (and as late as 40,000 cycles). RAFs were created in all specimens and it is important to note that the level of the RAF corresponded to the articular facet level failure during cyclic loading. In a representative specimen (Figure 2), the articular facet failure was at the L2/L3 level and the μCT scan confirmed a Type I RAF [1] in the caudal end of the L2 vertebra.

The images from the slow imaging cycles provide evidence of fracture during the cyclic loading. For this specimen, aural and visual observations note that at approximately cycle 25,000 the articular facet joint started to fail at the L2/L3 level. Figure 2 shows a crack in the cortical bone opening during the 30,000th cycle (the next imaging cycle after initial failure).

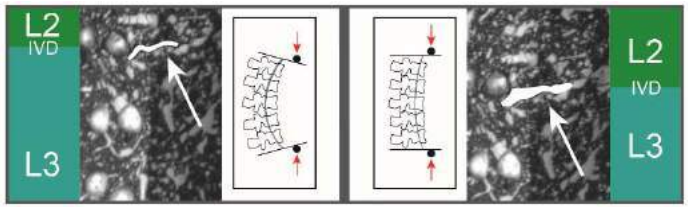

Figure 2: Cortical shell damage on the anterior aspect. The arrow shows an open crack in right image.

The L2/L3 intervertebral angle (from a different specimen) over the cyclic loading confirms a noticeable change in the kinematics of the motion segment (Figure 3a). While the total flexion angle does not change markedly, the slope of the angle curve within a cycle develops an inflection point at about 5° of flexion as the number of cycles increases (Figure 3a, green trace compared to red trace), indicating a change in intervertebral kinematics after fracture.

The hysteresis loop area gradually decreased with increasing cycle number, indicating the accumulation of damage to the 5-vertebra motion segment (Figure 3b and 3c). No observable differences in load-displacement hysteresis loops were observed between the specimens cycled at 2.0Hz and the one at 0.5Hz.

DISCUSSION

RAFs can occur during low-load low-angle cyclic loading as confirmed by kinematic changes, physical evidence observed during loading and images of the cortical shell. The change in kinematics during the experiment, although small, occurred after fracture was observed. This could lead to *in-vivo* kinematics-based methods to predict vertebral fracture location.

Different cycling rates (2.0 and 0.5Hz) were used due to equipment limitations. The similarity of our results at different cycling frequencies does not suggest any cycling rate dependent fracture mode behavior; future testing of additional specimens will confirm this.

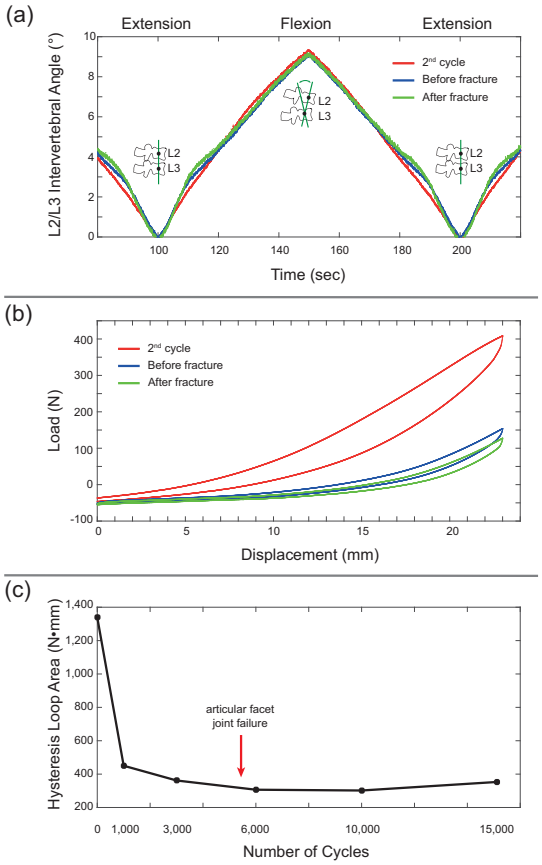

Figure 3: (a) L2/L3 intervertebral angle, (b) Hysteresis loops at the start of the cycling, and before and after fracture, (c) Hysteresis loop area. (Specimen failed at the L2/L3 level.)

To date, this research shows that cycling of small movement ADLs can contribute to RAF. Limitations include a small sample size and the use of cervine specimens (not commonly used as an *in-vivo* model). Future work will include quantifying common parameters used to describe the trabecular geometry prior to failure, and testing more cervine and cadaver specimens, which could include several different postures. Health care providers may need to consider small movement ADLs in fracture prevention education. Patient-specific exercise regimes could be developed to prevent RAFs. This work will ultimately provide the appropriate medical evidence for advanced fracture risk guidance and will improve rehabilitation techniques.

ACKNOWLEDGEMENTS

The authors thank Mark Hedgeland at Clarkson University; Sandra Thitten, Arlene Roach, and Ashley Fish at Canton-Potsdam Hospital; as well as Jeffrey Urbanski and Whitney Yetter at GE Inspection Technologies. The authors have no conflicts of interest.

REFERENCES

[1] Takata, K et al., *JBJS [AM],* 70A: 589-594, 1988.
[2] Singhal, A et al., *Pediatric Neurosurgery*, 49: 16-20, 2013.
[3] Cobian, D et al., *J of ASTM Int*, 9, 2011.
[4] Lingle S, *Can. J. Zool*, 71, 1993.
[5] Corbiere, N et al., *J Biomech Eng*, 126, 2014.
[6] Kumar, N et al., *Anat Rec*, 260: 189-203, 2000.
[7] Briggs A et al., *Physical Therapy*, 87: 595-607, 2007.
[8] Wu, G et al., *J Biomech*, 35: 543-548, 2002.

Copyright 2016 The Organizing Committee for the 2016 Summer Biomechanics, Bioengineering and Biotransport Conference

SB^{3}C2016
Summer Biomechanics, Bioengineering and Biotransport Conference
June 29 –July 2, National Harbor, MD, USA
SB^{3}C2016-624

KNEE AND ANKLE BIOMECHANICS DURING SQUATTING WITH HEELS ON AND OFF OF THE GROUND, WITH AND WITHOUT BODY WEIGHT SHIFTING

Jonathan T. Fox[1], Mohamed S. Hefzy[1] and Charles W. Armstrong[2]

[1]Biomechanics and Assistive Technology Laboratory
Departments of Bioengineering and Mechanical, Industrial & Manufacturing Engineering

[2]Department of Kinesiology

The University of Toledo, Toledo, Ohio, 43606

INTRODUCTION

Squatting is a common daily activity in many cultures. In western cultures squatting is used in sports, work, and in leisure, and in Asian cultures squatting is also used for daily activities such as using the restroom and waiting.[1] During periods of long squatting activities it is common for people to shift their weight to maintain comfort. Additionally, various postures are often employed when squatting; the two most common being the Asian Squat, which involves the heels remaining on the ground throughout the squat, and the Catcher's Squat in which the heels are raised from the ground throughout the movement. However, neither the biomechanics of body weight shifting nor the specific effects of posture on squatting has been well studied. Furthermore, the muscle activity used to maintain these postures is not well known.

The purpose of this study was thus to examine the biomechanics of the knee and ankle joints with and without body weight shifting during a deep squatting activity while the heels were both on and off the ground positions. This study also looked at the muscle activities associated with each squatting activity.

METHODS

Ten Raptor-E cameras (Motion Analysis, Inc.) were used to collect motion data during squatting while two AMTI force platforms were used to collect ground reaction force data. Additionally, ten Trigno® wireless EMG sensors (Delsys, Inc.) were used to record data from muscle activities. Eight subjects, four males and four females, were each instrumented with twenty-one reflective markers that were placed on the 3rd metatarsal, the medial and lateral malleolus, the calcaneus, the anterior of the shank, the medial and lateral epicondyle, the anterior of the thigh, the grater trochanter, and the anterior-superior iliac spine (ASIS) on both the left and right side of the body, as well as placing one marker on the sacrum. The ten EMG sensors were placed on the bicep femoris, rectus femoris, tibialis anterior, and the medial and lateral head of the gastrocnemius on both the right and left side of the body. The EMG sensors were placed on the skin over the belly of the muscles with the electrodes in the direction of the fibers.

The testing protocol was approved by the IRB of the University of Toledo. Maximum voluntary contraction tests were performed as the subjects sat with their legs restrained while they contracted each muscle one at a time as hard as they could. Once these tasks were completed each of the subjects performed four separate squatting tests. The first test was a stand then squat test keeping the heels on the ground (Asian squat). Subjects squatted down at a self-selected pace and then immediately returned to a standing position. Then the test was repeated while lifting the heels off of the ground (Catcher's squat). The third task was an Asian squat with weight shifting. Subjects squatted down at a self-selected pace and were then verbally instructed to shift their weight to the right, then to the left, back to center, and then finally returned to a standing position. The final task was to repeat the weight shifting squat activity for the Catcher's squat. Each activity was repeated until 5 successful trials were recorded.

The data were collected and processed using the software Cortex (Motion Analysis, Inc.). Cortex simultaneously collected and synchronized the motion, GRF, and EMG data. The KinTools RT kit and Excel were used to calculate the kinetics data, while the EMGworks Analysis software (Delsys, Inc.) and Excel were used to analyze the EMG data. The individual trials from each volunteer were averaged over time to get four sets of data. The data from the four activities were then averaged together to get average male and female

Copyright 2016 The Organizing Committee for the 2016 Summer Biomechanics, Bioengineering and Biotransport Conference

volunteer data sets. Finally the trials from all volunteers were averaged together to get one average data set for each squatting activity.

RESULTS

The average results for all subjects are shown in Table 1. Forces and moments are normalized to body mass and given in N/kg and Nm/kg, respectively. Flexion angles are given in degrees, and muscle activities are given as a % of the maximum voluntary contractions.

Table 1: Ground reaction forces, joint moments, joint angles, and average muscle activities as an average for all subjects during all four squatting activities.

		Asian Squat		Catcher's Squat	
		No Shifting	Shifting	No Shifting	Shifting
	Max Right Vertical GRF	0.566	0.808	0.556	0.814
	Max Left Vertical GRF	0.451	0.791	0.537	0.795
Right Knee	Max Flexion	121.21	118.32	131.20	131.93
	Max Moment	0.73	1.04	0.82	1.36
Left Knee	Max Flexion	116.71	113.52	127.62	128.23
	Max Moment	0.63	0.99	0.74	1.33
Right Ankle	Max Plantarflexion	15.15	14.09	13.28	13.41
	Max Dorsiflexion	9.66	15.79	7.55	9.86
	Max Moment	0.23	0.57	0.56	0.71
Left Ankle	Max Plantarflexion	15.84	15.02	13.78	13.63
	Max Dorsiflexion	9.59	17.17	8.26	12.21
	Max Moment	0.26	0.64	0.56	0.79
Right Leg	Mean Hamstring	13.1%	12.0%	13.7%	11.2%
	Mean Quadricep	60.5%	67.7%	51.5%	57.7%
	Mean TA	52.7%	56.1%	19.0%	20.8%
	Mean M Gastroc	97.9%	97.0%	110.1%	104.7%
	Mean L Gastroc	50.5%	50.2%	65.5%	51.5%
Left Leg	Mean Hamstring	16.4%	16.2%	16.5%	16.2%
	Mean Quadricep	56.2%	69.9%	49.7%	60.4%
	Mean TA	69.5%	70.8%	41.4%	40.8%
	Mean M Gastroc	23.6%	28.8%	53.8%	42.3%
	Mean L Gastroc	64.8%	62.8%	73.3%	62.0%

DISCUSSION

On average lifting the heels off the ground caused the knee extension moments to increase. The maximum knee flexion angle experienced also increased with lifting the heels off the ground. This implies that performing a Catcher's squat requires both a greater range of motion and a greater knee joint moment. The right leg also experienced a knee extension moment greater than the left leg during the Asian and Catcher's squats. This implies that the volunteers favored their right leg for support during the squatting motion. The right leg also had knee flexion angles that were greater than the left leg during the Asian and Catcher's squats. This could be due either to placing more weight on the right leg, the differences in foot placement, or a combination of both. The data also imply that performing a Catcher's squat requires a greater ankle joint moment, but does not require as great of a range of motion. During the Catcher's squats the volunteers held a more rigid ankle angle in order to hold the position and maintain balance due to lifting their heels off of the ground.

On average shifting weight caused the knee flexion moments to increase during both the Asian and Catcher's squats. As weight was shifting to one side of the body the knee extension moment increased on the same side while decreasing on the contralateral side. This implies that shifting weight from side to side does not greatly change the flexion angle of the knee, but it increases the moment experienced by the knee. The Catcher's squat caused a greater increase in the knee extension moment when weight shifting occurred. This could be due to volunteers being able to shift their weight more easily during the Catcher's squat than during the Asian squat or due to the difference in moment arm between the two positions. The data also imply that shifting weight from side to side decreases the plantarflexion angle of the ankle, but it increases the dorsiflexion angle and the plantarflexion moment experienced by the ankle.

The activity of the quadriceps muscles generally increased as the knee flexion angle increased. On average the quadriceps muscles experienced more activity during the Asian squat than during the Catcher's squat. Weight shifting also increased the activity during both squats. The tibialis anterior muscles activity also generally increased as the knee flexion angle increased, and had decreased activities during weight shifting. Hamstring and both gastrocnemius muscle activities were relatively steady throughout all squatting activities. The gastrocnemius muscles showed a large degree of activity, but they did not change much throughout the squatting motion from the values when the volunteer was standing.

To summarize, it was found that the Catcher's squat caused greater knee extension and plantarflexion moments. The Catcher's squat also had greater knee flexion angles and ankle plantarflexion angles, but had smaller ankle dorsiflexion angles. Additionally, the Catcher's squat caused the muscle activity in the quadriceps and tibialis anterior muscles to decrease, and the muscle activity in the hamstrings and gastrocnemius muscles to increase. Weight shifting caused knee extension moments and ankle plantarflexion moments to increase over the non-weight shifting cases as weight was placed onto one leg. The weight shifting also caused an increase in the ankle dorsiflexion angle and a decrease in the ankle plantarflexion as more weight was placed onto one leg and caused the ankle to shift to support more weight. The quadriceps and hamstring muscle activities increased during weight shifting, but the tibialis anterior and gastrocnemius activity decreased. It was also found, but not shown in the table, that on average the male volunteers also had greater knee flexion angles, and smaller knee extension and ankle plantarflexion moments than the female volunteers. The significance of this work cannot be overlooked, since squatting is a daily activity performed by people throughout the world, and may have implications for the development and response of a variety of orthopedic conditions.

ACKNOWLEDGEMENTS

This work was supported by the Department of Bioengineering at the University of Toledo.

REFERENCES

1. *Mulholland and Wyss, Int J Rehabil Res, 2001.* ***24****(3): p. 191-8.*

Copyright 2016 The Organizing Committee for the 2016 Summer Biomechanics, Bioengineering and Biotransport Conference

SB^{3}C2016
Summer Biomechanics, Bioengineering and Biotransport Conference
June 29 –July 2, National Harbor, MD, USA
SB^{3}C2016-625

FOUL TIP IMPACT ATTENUATION OF BASEBALL CATCHER MASKS USING HEAD IMPACT METRICS

Christopher P. Eckersley (1), Terrance R. White (1), Hattie C. Cutcliffe (1), Jay K. Shridharani (1), Cameron 'Dale' R. Bass (1)

(1) Biomedical Engineering
Duke University
Durham, North Carolina, USA

INTRODUCTION

Major League Baseball foul tips have been shown to cause career altering injury to catchers like the case of Joe Mauer [1]. Catcher's first line of defense against foul tips is their mask – traditionally made of steel. Recently a lighter more comfortable titanium mask was introduced. Following their introduction reported concussions due to foul tips spiked, leading many to speculate titanium masks were the cause. In response, many catchers reverted to steel masks [2]. We hypothesize that since the titanium mask is lighter and has a higher yield strength, wearing it will result in higher head injury metrics upon impact with a simulated foul tip. However, the mask material, steel or titanium, is not the only unsettled question with potential relevance to the spike in reported concussions. Even though some studies have looked at the attenuation of both traditional and hockey style masks, none have examined the titanium variant, and there still remains the debate of how all of these mask types compare [3,4,5,6]. Because of this, our study investigates the impact response of four styles of masks (traditional steel, traditional titanium, hockey style, and hockey style with shock adsorption) to assess impact attenuation and compare them based on peak resultant acceleration, Head Injury Criterion (HIC), and Head Impact Power (HIP).

METHODS

To provide a catcher surrogate, a Hybrid III 50th percentile male head form was equipped with a six degree of freedom sensor package at the head's center of gravity as well as a load cell positioned at the joint between the head and neck. The six degree of freedom sensor package measured linear accelerations and angular rates of the head upon impact while the load cell measures the force interactions between the head and neck. The four masks selected for testing were the Wilson Dyna-Lite Titanium Mask, the Wilson Dyna-Lite Steel Mask, the Easton Rival Hockey Style Mask, and the Wilson Shock FX 2.0. A pneumatic cannon was constructed using three inch PVC pipe and used to propel Rawlings Official Major League Baseballs at 50 and 60 PSI, resulting in ball velocities of approximately 70 and 80 MPH. Data collection was conducted using a MeDAQ data acquisition system (Hi-Techniques, USA) sampling at 200 kHz and filtered at 1650 Hz using an eighth order Butterworth filter. A Phantom High Speed Camera (Vision Research, USA) captured video of the impact. The test series consisted of six trials at each speed, impacting the head at the nasion. Twelve trials were completed for each mask, although ultimately some trials were excluded from analysis because the masks were too deformed to provide proper protection. At each speed, three bare head trials were conducted for control analysis. Using MATLAB (MathWorks, USA), a custom analysis suite was constructed for extracting peak resultant acceleration, HIC, and HIP values for each trial, while JMP Pro 11 Statistical Package (SAS, USA) was used to conduct an ANCOVA comparing peak resultant linear acceleration, HIC values, and HIP values between masks. Equations 1 and 2 provide how the HIC and HIP values were calculated respectively.

$$HIC = \left[\frac{1}{t_2 - t_1}\int_{t_1}^{t_2} a(t)dt\right]^{2.5} * (t_2 - t_1) \quad (1)$$

$$HIP = 4.5 * \left(a_x \int a_x(t)dt + a_y \int a_y(t)dt + a_z \int a_z(t)dt\right) + 0.016(\alpha_x \int \alpha_x(t)dt) + 0.024\left(\alpha_y \int \alpha_y(t)dt\right) + 0.022(\alpha_z \int \alpha_z(t)dt) \quad (2)$$

RESULTS

Figures 1 and 2 show resultant linear acceleration and HIP values respectively. These were chosen to represent an injury metrics that use linear acceleration and one that includes angular acceleration.

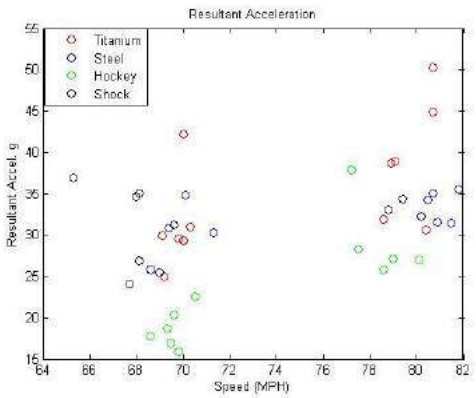

Figure 1: Resultant Acceleration vs. Speed

Copyright 2016 The Organizing Committee for the 2016 Summer Biomechanics, Bioengineering and Biotransport Conference

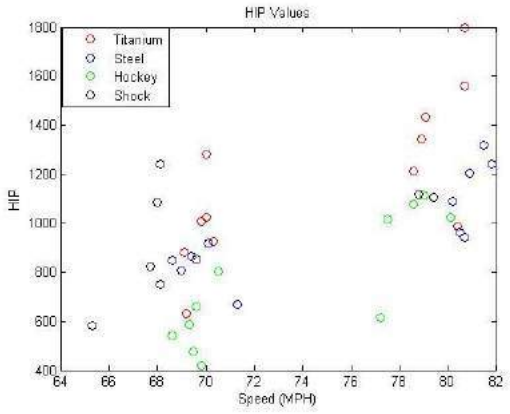

Figure 2: HIP vs. Speed

Results of the ANCOVA tests summarized in Table 1 grouped the masks based on statistical difference. Masks are grouped by numbers and lower numbers indicate better performance.

Table 1: Summary of ANCOVA Statistical Tests Ranked By Performance

		Head Impact Metric		
		Res. Accel.	HIC	HIP
Mask Type	Trad. Steel	2	2	2, 1
	Trad. Titanium	2	3	3
	Hockey Style	1	1	1
	Hockey Shock	2	2	3, 2

The ANCOVA results show that the hockey style mask performed better than each of the other styles for every metric and for each metric the Titanium mask was associated with the groups with the worst performance. Furthermore, the shock absorbing mask had the second worst performance, even though it was a hockey style mask.

DISCUSSION

There are two ideas behind why the hockey style mask performed the best out of the four styles. First, it is one of the heaviest masks which results in lower accelerations. Second, preliminary analysis shows that the material used in the helmet liner plays a large role in how energy from a ball impact is transferred into the head. The foam found within the hockey style mask is more viscoelastic than that found in the other masks. This means it has the potential to absorb more energy upon impact resulting in lower head accelerations. These results provide evidence that contradict the belief that the traditional steel mask is better for frontal foul tips than the hockey style mask.

It was expected that the shock absorbing mask would perform just as well if not better than the hockey style mask. However, the mask deteriorated quickly upon multiple impacts to a point where it would no longer protect the player. This reducing the number of trials conducted with the mask making the statistical analysis more susceptible to variation. The deterioration along with the limited number of trials may have led to the masks poorer performance.

The results support the hypothesis that based on its material properties, the titanium mask results in higher impact metrics compared to three other common mask types. This shows that catchers fear of titanium masks may be warranted. The data however does not provide evidence that wearing titanium masks results in more concussions because of the limitations of this study. Even though these head impact metrics could be compared to injury risk curves found in literature, values found in this test are not representative of an actual catcher wearing a mask. First the only similarities between the Hybrid III head and a human head are the geometry and mass. The various tissues found in the head and their interactions may have significant effects on impact transfer through the mask and into the head that cannot be modeled by the Hybrid III. Furthermore, the load cell depicts interactions between the Hybrid III head and neck during peak acceleration, and since the Hybrid III neck is not perfectly biofidelic, these may be different in human subjects. Finally, while these metrics are currently the best tools we have to correlate head impact and concussion, it is still not fully known how these head metrics relate to concussive impacts.

To ameliorate some of these limitations, future tests will be conducted with cadaveric specimen and detailed helmet design analysis to determine how aspects of each helmet positively and negatively impact performance to provide suggestions to make future helmets safer.

While this study is limited in its ability to correlate helmet design and concussion rate it is a step towards creating a safer playing experience for catchers at all levels. With concussions becoming a growing concern, it is important that helmets are designed not just to meet standards, but to be as safe as practically given by the constraints of game play. From the data collected in this study it is seen that different helmet materials and helmet styles vary in their level of protection from head accelerations after being impacted by a simulated foul tip. It is seen that design changes from the standard traditional steel mask have been both positive and negative with the introduction of the Hockey Style mask and Titanium mask respectively.

AKNOWLEDGEMENTS

I would like to thank the Duke University Department of Biomedical Engineering, the Pratt Fellows Research Program, and the Duke University Undergraduate Research Support Office for their support of this study.

REFERENCES

1. Gleeman, Aaron. "What Happened to Joe Mauer?" *AaronGleemancom*. Web. 15 Jan. 2016. <http://aarongleeman.com/2015/06/12/what-happened-to-joe-mauer/>.
2. "A's Catcher John Jaso Swaps Titanium Mask for Steel after Concussion." Major League Baseball. Web. 5 Aug. 2015. <http://m.mlb.com/news/article/68017354/as-catcher-john-jaso-swaps-titanium-mask-for-steel-after-concussion>.
3. Laudner, K. G., et al. "Comparison of Impact Characteristics of Traditional Style Headgear and Hockey Style Headgear for Baseball Catchers. J Athl Enhancement 3: 1." *of* 4 (2014): 2.
4. Shain, Kellen S., et al. "Analysis of the ability of catcher's masks to attenuate head accelerations on impact with a baseball." *Clinical Journal of Sport Medicine* 20.6 (2010): 422-427.
5. Berra, Liny. "Old-School Catcher's Masks Help Protect from Concussions." *Major League Baseball*. Web. 15 Jan. 2016. <http://m.mlb.com/news/article/62938052/>.
6. Rosenthal, Ken. "Baseball Looks to Protect Catchers." *Fox Sports*. 26 Aug. 2013. Web. 13 Jan. 2016. <http://www.foxsports.com/mlb/story/concussions-growing-problem-six-catchers-on-seven>.

Copyright 2016 The Organizing Committee for the 2016 Summer Biomechanics, Bioengineering and Biotransport Conference

SB^{3}C2016
Summer Biomechanics, Bioengineering and Biotransport Conference
June 29 –July 2, National Harbor, MD, USA
SB^{3}C2016-626

THE EFFECT OF ELECTROPOTENTIAL ON NITINOL FATIGUE LIFE

Shiril Sivan (1, 2), Matthew A. Di Prima (1), Jason D. Weaver (1)

(1) Division of Applied Mechanics, Center for Devices and Radiological Health, Office of Science and Engineering Laboratories, United States Food and Drug Administration, Silver Spring, MD, USA

(2) Oak Ridge Institute of Science and Education, Oak Ridge, TN, USA

INTRODUCTION

Nitinol is one of the most common metals used for cardiovascular devices primarily because of its excellent shape memory and superelastic properties [1]. The *in vivo* clinical performance of these devices depends of a number of factors which include Nitinol's mechanical properties, fatigue and corrosion resistance, and its ability to withstand the local biological response once the device is implanted. It is well established that the rest potential of a metal surface depends on its local environment [2]. For example, on implantation, a foreign body reaction is initiated during which a cascade of immune and inflammatory cells can alter the local environment by reducing the pH [3]. This will lead to a rise in the metal's rest potential to a more anodic potential. Whereas, in a configuration where there are overlapping stents, the overall electropotential can undergo a cathodic shift if fretting occurs [4]. Hence, the electropotential of a metal surface can vary in response to its surrounding environment. At present, very little is known regarding the effect of voltage on the fatigue life of metal wires. Therefore there is a need to evaluate the effect of electropotential on the fatigue life of Nitinol in-order to determine if fatigue life of Nitinol wires depends on the overpotential enforced.

METHODS

Electropolished Nitinol wires having a diameter of 0.5 mm were used for all experiments. The breakdown potential of the wires was evaluated per ASTM F2129. Potentiodynamic scans were performed from rest potential to at least 800 mV (vs. SCE) and then back to rest potential for the reverse scans. Fatigue life was evaluated at 1.2, 1.0, 0.8 and 0.6 % alternating strain (ε_a) using a rotary bend wire fatigue tester (Blockwise, Tempe, AZ). Wire fatigue tests were conducted at 3600 rpm with the wires submerged partially in phosphate buffered saline (PBS) maintained at 37 ºC. The cut ends of the wire in the wire fatigue tester chucks were insulated using MICCROStop lacquer (Tobler Chemical Division, Hope, AR) to prevent the transfer of any transient electrochemical noise from the wire fatigue testers to the test specimens. All electrochemical measurements were achieved using a three electrode system with graphitic carbon rod as a counter electrode and standard calomel electrode (SCE) as a reference electrode. To test the effect of overpotential on the fatigue life of samples, the rest or open circuit potential (OCP) was first measured for 10 minutes after which the wire was potentiostatically held at the overpotential being investigated. The cycles to failure for ε_a of 1% was evaluated for wires at -500 to +600 mV (vs. SCE) (in steps of 100 mV). To understand the effect of ε_a and overpotential on fatigue performance, SN curves for ε_a of 1.2, 1.0, 0.8, 0.6 were generated for -400, 0, OCP and 400 mV (vs. SCE). Current density was monitored during the potentiostatic tests using either a Princeton Applied Research Model 263 potentiostat or a Gamry Interface 1000 System. For experiments where no voltage was applied, the open circuit potential (OCP) was monitored for 10 minutes after which the fatigue test was initiated and OCP was monitored until the wire failed. To account for variability, 6 samples were used for each test condition.

RESULTS

Of the six samples subjected to ASTM F2129 testing, four had a breakdown potential of approximately 250 mV (vs. SCE) while the other two did not exhibit breakdown. Figure 1(A) shows the rest potential of a Nitinol wire when subjected to alternating strain of 1% with no applied voltage. There is a steep cathodic shift in electropotential of the wire when the fatigue test is initiated. The electropotential of the wire remains stable and then gradually decreases as the fatigue test progresses. This results in a drop in

Copyright 2016 The Organizing Committee for the 2016 Summer Biomechanics, Bioengineering and Biotransport Conference

electropotential of the wire from -150 mV (vs. SCE) to -650 mV (vs. SCE). At approximately 140 seconds wire fracture occurs, at which point the fatigue test is terminated. The subsequent recovery of electropotential of the wire is typical recovery of the open circuit potential.

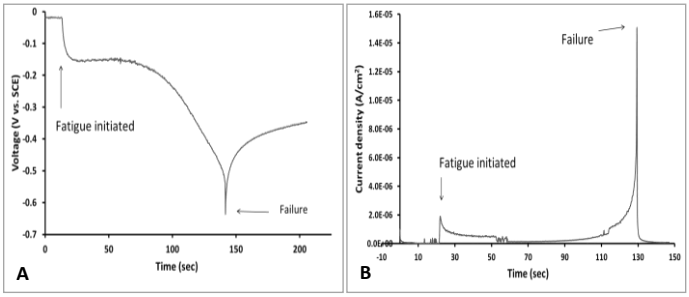

Figure 1: (A) shows a typical voltage transient observed when a Nitinol wire is subjected to alternating strain of 1 % using a rotary bend wire fatigue tester. (B) Shows the current density monitored while a wire was potentiostatically held at 100 mV (vs. SCE) and subjected to alternating strain of 1%.

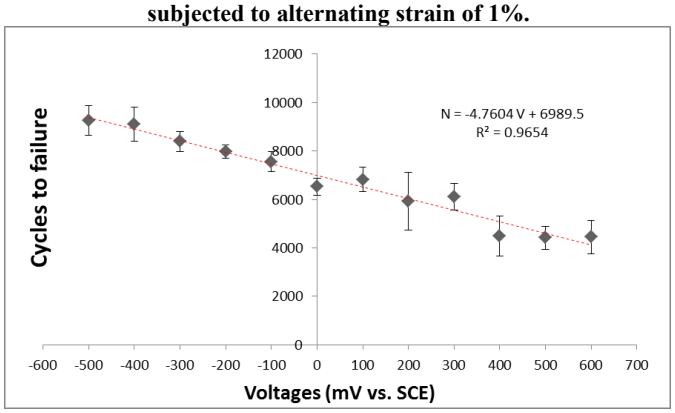

Figure 2: Number of cycles to failure for a Nitinol wire undergoing 1% alternating strain while being potentiostatically held at voltages between -500 mV and +600 mV (vs. SCE).

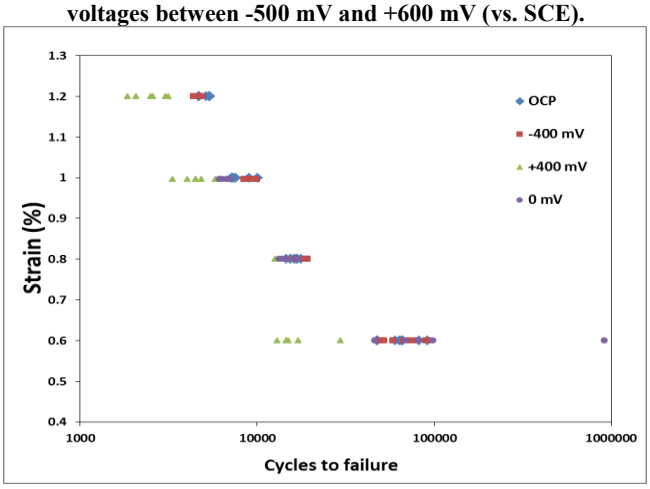

Figure 3: Number of cycles to failure at different alternating strains when no voltage was enforced (OCP), -400, 0 and 400 mV.

The current response of a wire potentiostatically held at 100 mV (vs. SCE) is shown in Figure 1B. The current plateaus after 10 seconds after which the wire fatigue test was initiated. The current density instantaneously rises when fatigue is initiated and decays to reach a steady state. The current density again rises rapidly and ultimately peaks to its highest value as the wire fractures at which point the fatigue test is stopped. This is followed by an immediate drop in current density as the fractured surfaces repassivate. The graph in Fig. 2 shows a linear relationship between number of cycles to failure and electropotential of the wire (R^2 =0.96) ($p < 0.001$) for wires tested at 1.0% alternating strain. The number of cycles to failure for a range of alternating strains, overpotentials and OCP is shown in Figure 3.

DISCUSSION

The results presented in this study show that the overpotential of the wire can have an effect on its fatigue life. More anodic shifts in potential from OCP led to fewer numbers of cycles to failure. Whereas, the more cathodic the shifts from OCP, the greater the number of cycles to failure.

At cathodic potentials, oxidation reactions are suppressed. This results in a larger number of cycles to failure perhaps because fracture initiation and propagation in this regime are predominantly due to surface defects already present on the wire surface. Whereas, at potentials anodic to the OCP, oxidation reactions are enhanced causing the formation of new surface defects from corrosion occurring on the metal surface. This may lead to stress risers which ultimately result in the formation of a crack.

Thus, during the OCP fatigue test shown in Fig. 1A, after the test was initiated the surface oxide on the wire cracked and exposed the underlying metal to the test solution. The surface repassivated instantly resulting in a cathodic shift in the wire's electropotential. Similar behavior was seen on the potentiostatic test where a sudden rise in current density was observed when fatigue was initiated (Fig 1B).

The cathodic potentials and current densities attained here can cause oxidative stress in cells in the local environment [5]. This could initiate an inflammatory reaction during which cells can secrete reactive oxygen species, which is known to not only alter the rest potential of the metal surface but also aggravate corrosion.

The SN curve (Fig. 3) shows clustering of data points for OCP, 0 and -400 mV; whereas cycles for failure for the 400 mV condition are typically lower (except for 0.8 % strain). This may be because the OCP of the Nitinol wire is approximately -150 mV which is closer to 0 and -400 mV; whereas, the breakdown potential for these wires was around 250 mV (closer to 400 mV).

The results of this study have shown that the voltage of the metal wire can influence its fatigue life and should be considered when evaluating medical device durability. This is important because most of the testing currently done assumes that there is no inflammatory reaction or fretting occurring on the implant surface. Voltage excursions away from OCP to more anodic potentials under inflammatory conditions could have a negative impact on the fatigue life and ultimately affect the clinical performance of these devices.

ACKNOWLEDGEMENTS

This project was supported by the Division of Applied Mechanics and an appointment to the Research Participation Program at the Center for Devices and Radiological Health administered by the Oak Ridge Institute for Science and Education through an interagency agreement between the U.S. Department of Energy and the U.S. Food and Drug Administration.

REFERENCES

[1] Duerig, T. W et al *Mat Sci and Eng: A* 273 (1999): 149-160
[2] Ehrensberger, M. T. et al (2010), JBMR, 93B: 106–112
[3] Babior, B. M. (2000). *AmerJour of Med*, *109*(1), 33-44
[4] Swaminathan, V, *Biomat* 33.22 (2012): 5487-5503
[5] Sivan S et al. *JBMR B* (2013) 101.8: 1489-1497

Copyright 2016 The Organizing Committee for the 2016 Summer Biomechanics, Bioengineering and Biotransport Conference

SB^{3}C2016
Summer Biomechanics, Bioengineering and Biotransport Conference
June 29 –July 2, National Harbor, MD, USA
SB^{3}C2016-627

PERFORMANCE OF THREE VARIABLE-LENGTH INTRAMEDULLARY NAILS: THE EFFECT OF THE LENGTH-ADJUSTMENT MECHANISM

Mark J. Hedgeland (1), Alexander Martin Clark (2,3), Laurel Kuxhaus (1)

(1) Mechanical and Aeronautical Engineering Department
Clarkson University
Potsdam, NY, USA

(2) Canton-Potsdam Hospital
Potsdam, NY, USA

(3) Sharon Hospital
Sharon, CT, USA

INTRODUCTION

As many as 87% of orthopaedic surgeons choose intramedullary (IM) nailing for closed tibial diaphyseal fractures [1]. While current methods and devices used for this procedure are successful, there is still a need for improvement. Typically nails are only offered in discrete lengths, so hospitals must stock many sizes to accommodate their potential trauma patients. Discretely-sized nails are not only expensive to stock, they often do not fit a patient's IM canal perfectly, leading to non-union of the fractures, mechanical failure of the nail, and delayed rehabilitation [2,3]. An adjustable-length intramedullary nail, specifically for tibial fractures, has been developed to address these issues [2]. In this work, three unique adjustable-length prototypes were tested in both simple quasi-static loading, and have been evaluated further by testing their fatigue properties. Prototype A is distally adjustable, prototype B is proximally adjustable, and prototype C is discretely-distally adjustable via a pin mechanism (Figure 1). This study aims to quantify the differences in expected performance of each prototype. We expect all three to survive fatigue testing and to find a minimal difference in dynamic bending stiffness from the first cycle to the last, indicating complete fatigue survival.

METHODS

Three adjustable-length IM nails were manufactured from surgical stainless steel (316L). The prototypes were tested in 4-point bending, axial, and torsional quasi-static loading. The prototypes were loaded at rates of 0.1 mm/sec (bending and axial) at increments of 1-2 mm up to 5mm, and 0.1 degrees/sec (torsional) at 1 degree increments up to 10 degrees, according to the ASTM standard (ASTM F1264) [4]. All mechanical testing was done on a hydraulic load frame (MTS 809 Axial/Torsional Test System, Eden Prairie, MN). Prior to testing for

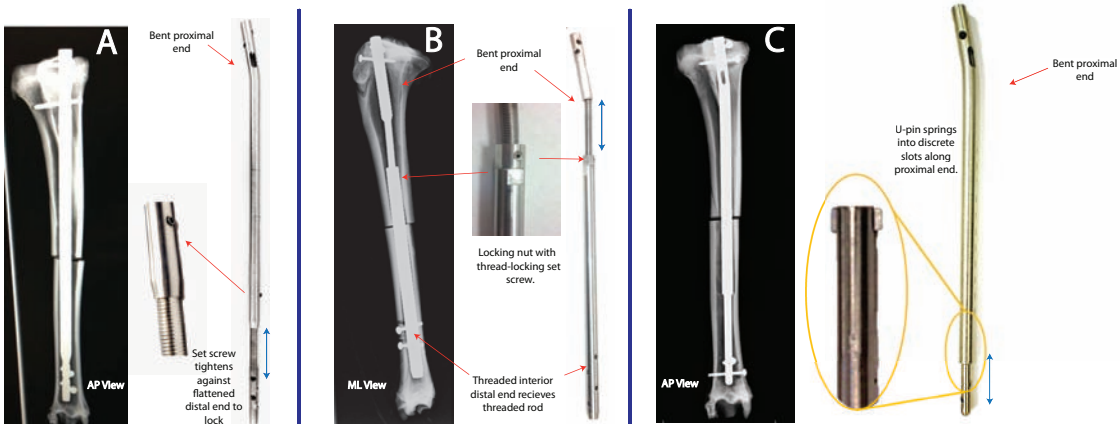

Figure 1 From left to right: Prototypes A (distally-adjustable), B (proximally-adjustable), and C (pin-mechanism). X-rays, models, and adjustment methods shown.

Copyright 2016 The Organizing Committee for the 2016 Summer Biomechanics, Bioengineering and Biotransport Conference

axial and torsional modes, the prototypes were surgically inserted into cervine tibiae specimens (9 specimens, (5 male, 4 female) 2.1 ± 0.6 yrs). All insertions were made under the direction of a board-certified orthopaedic surgeon (AMC). After insertion, the tibiae were potted in Bondo™ (Auto Body Filler, 3M, St. Paul, MN) and then tested either in torsion or axial compression. The load-displacement data from each trial was used along with a custom MATLAB (R2012b, The Mathworks, Natick, MA) code to calculate stiffness (see Equations 1, 2, and 3).

Each prototype was also tested in fatigue loading in a custom-built 4-point bending fixture (Figure 2) and according to ASTM standards [4]. Roller diameter of the fixture was 2.54 cm. Each of the nails were loaded cyclically between 50 N and 500 N (R=0.1) at a frequency of 5 Hz for 1 million cycles performed over multiple days. The test lengths were determined by selecting a section of prototype with no geometric anomalies within three diameter lengths (of the IM Nail) of either outside roller, as outlined in ASTM F1264. Force and displacement data were analyzed via a custom MATLAB code. Bending fatigue limit was determined empirically and hysteresis loops from the first and last cycles were plotted and compared for each prototype. Dynamic bending stiffness was calculated at the beginning and end of each prototype's testing using these loops (both loading and unloading phases), Equation 3, and the RMS method of determining a line of best fit. In addition, peak displacement over time was observed.

$$K_A = {}^{\Delta F}/_{\Delta \delta} \qquad (1)$$

Where F is force in N and δ is displacement in mm.

$$K_T = \Delta M/\Delta\theta \qquad (2)$$

Where M is Torque in Nm and θ is angle in degrees

$$K_{Bending} = \frac{(L+2c)(\Delta F/\Delta\delta)s^2}{12} \qquad (3)$$

Where L is total span, s and c are sub-span (all in mm), F is force in N, and δ is displacement in mm

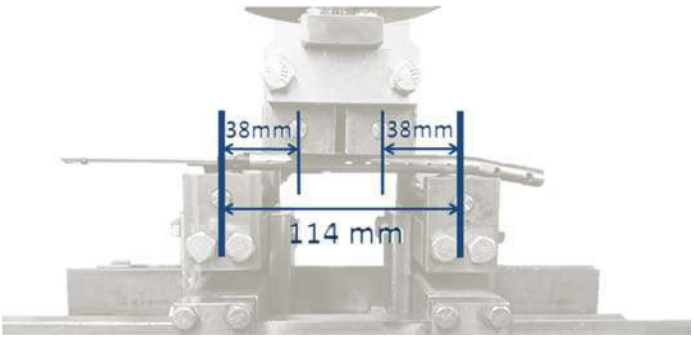

Figure 2: Prototype 2 shown as tested in, with appropriate dimensions labeled.

RESULTS

In quasi-static loading, prototype A's stiffnesses (2.66 N/m axial, 0.46 Nm/degree torsional, and 36.82 Nm^2 bending) were considerably lower than those of prototypes B (1.05 Nm/degree torsional and 80.10 Nm^2 bending) and C (1.49 N/m axial, 2.59 Nm/degree torsional, and 59.02 Nm^2 bending). All three prototypes survived fatigue bending without visual or auditory signs of failure. This indicates that the 4-point bending fatigue limit when cycling at 5 Hz with an applied load of 500 N and R=0.1 is higher than 1 million cycles in all three prototypes. In addition, the dynamic bending stiffness changed by only 1.63 % on average from the first cycle to last cycle for all three types of adjustability. Figure 3 shows a summary of the dynamic bending stiffness at each end of fatigue testing. Peak displacement over all cycles was nearly constant for all prototypes, which supports the result that the dynamic bending stiffness changed minimally.

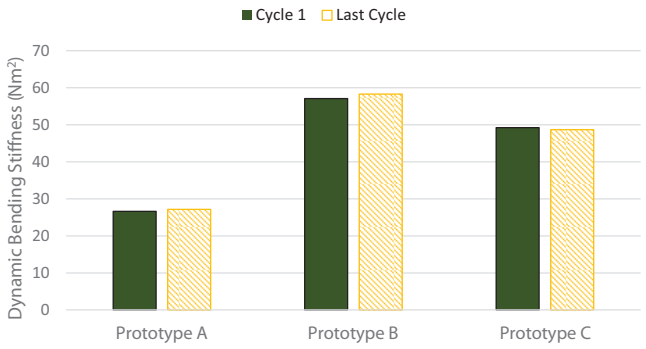

Figure 3: Dynamic bending stiffness of the first (solid green) and last cycle (hatched yellow).

DISCUSSION

All three adjustable length IM nail prototypes survived fatigue testing despite their variance in cross-section, which could create a stress concentrator within the test length. This is well above the expected number of cycles an IM nail would experience before complete bone healing occurs [4]. The minimal change in the hysteresis loops (slope) from cycle 1 to cycle 1 million shows that the structural integrity of the prototypes was not compromised and no plastic deformation or damage occurred. The prototypes' survival through all cycles should serve to supplement proof of safety and effectiveness for eventual FDA 510(k) approval. A successful adjustable-length IM nail that is deemed safe and effective would allow surgeons to repair a patients' long bone fractures more rapidly and accurately. The change to adjustable-length would allow for a better fit in the IM canal which would lead to increased implant performance and therefore a faster rehabilitation process. Regardless of its survival in fatigue testing, prototype A's lower stiffnesses in quasi-static loading suggest it would not perform as well in an *in vivo* setting as the two other methods of adjustability embodied in prototypes B and C. This study is limited by its small sample size and lack of published comparative data. However, even on its own these results indicate that the expected *in vivo* performance of an adjustable-length IM nail is promising and merits further testing.

ACKNOWLEDGEMENTS

The authors thank Dan Valyou and Mathew Ingraham for load frame help, and Nicole Corbiere for specimen supervision.

REFERENCES

[1] Cowie, J. et al. *Bone Joint J*. 2012.
[2] Throop, A. D. et al., *J. Med. Dev.* 2015.
[3] Bone, LB et al. *J Bone Joint S.* 1997. 79:1336-
[4] 1341ASTM International, 2007. F 1264.

Copyright 2016 The Organizing Committee for the 2016 Summer Biomechanics, Bioengineering and Biotransport Conference

SB^{3}C2016
Summer Biomechanics, Bioengineering and Biotransport Conference
June 29 –July 2, National Harbor, MD, USA
SB^{3}C2016-628

DIFFERENCES BETWEEN THE MECHANICAL AND MICROSTRUCTURAL PROPERTIES OF THE HUMAN ACL AND PCL

Ryan M. Castile (1), Nathan W. Skelley (2), Jon O. Wright (3), Robert H. Brophy (2), Spencer P. Lake (1,2,4)

(1) Department of Mechanical Engineering & Materials Science
Washington University in St. Louis
St. Louis, MO, USA

(2) Department of Orthopaedic Surgery
Washington University in St. Louis
St. Louis, MO, USA

(3) Department of Orthopaedic Surgery
Beaumont Health
Royal Oak, MI, USA

(4) Department of Biomedical Engineering
Washington University in St. Louis
St. Louis, MO, USA

INTRODUCTION

The anatomy of the anterior cruciate ligament (ACL) and of the posterior cruciate ligament (PCL) has been commonly described as being composed of two bundles [1,2]. The ACL is composed of the anteromedial (AM) and posterolateral (PL) bundles while the PCL is composed of the anterolateral (AL) and posteromedial (PM) bundles. Together the ACL and PCL provide translational and rotational stability to the knee, and the structure and interaction of these ligaments is critical for joint function. Previous work characterizing the mechanical properties of the ACL and PCL has focused predominantly on whole ligament or bundle analyses, and very little work has examined the microstructural organization of these ligaments [3-6]. New sample preparation techniques and imaging technologies developed by our group have enabled more detailed evaluation of material properties of ligament samples. Our recent work quantified the bundle-specific mechanical and microstructural properties of the ACL and PCL [7-9]. For reconstructive surgery of the ACL and PCL, surgeons currently use the same graft materials when repairing the torn ligaments. It is vital to have a better understanding of the material properties of both the ACL and PCL so informed graft choices could be made. Therefore, the purpose of this study was to compare the mechanical and microstructural properties of the ACL and PCL to determine the relative magnitude and heterogeneity of properties in these anatomically proximate ligaments in the knee.

METHODS

Thirty-seven human cadaver knees (avg. age = 42.5 ± 6.2) with no history of trauma or surgery were collected and dissected as previously described [6]. Peripheral soft tissues were removed to expose and isolate the intact ACL and PCL. The division between the two bundles of each ligament was identified, and each bundle was gently isolated and divided into three sections via two incisions in the coronal plane. Each section was then sharply detached from its femoral and tibial attachments, yielding a total of six samples per ligament. Each sample was thinned on a freezing stage microtome to a uniform ~600 micrometer thickness and loaded in a tensile test machine. Using a division-of-focal-plane polarization camera [10], the average direction of collagen orientation (AoP = Angle of Polarization) and the degree to which the fibers are aligned in that direction (DoLP = Degree of Linear Polarization) were quantified on a pixel-wise basis throughout testing (Fig.1). The testing protocol consisted of preconditioning, a stress-relaxation test, and a quasi-static ramp to failure [7]. Microstructural analysis focused on the average (AVG) DoLP and standard deviation (STD) AoP within the central portion of each sample, which was the same region that was tracked optically to compute 2D Lagrangian strains. The ramp to failure data was fit with a bi-linear curve (Fig. 2A), and polarization data were analyzed at specific strain points: zero, transition point, and linear region (i.e., 2X transition strain). Elastic modulus values were computed for the toe- and linear-region of the ramp. Statistical analysis was performed using a linear

Copyright 2016 The Organizing Committee for the 2016 Summer Biomechanics, Bioengineering and Biotransport Conference

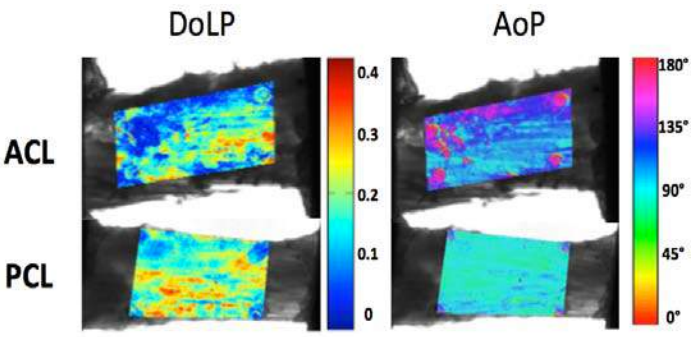

Fig. 1: Representative ACL and PCL samples stretched to 5% strain. DoLP indicates the degree of alignment (averaged through the tissue thickness) and AoP indicates the average angle of collagen alignment.

mixed model for bundle-to-bundle comparisons within each ligament. Unpaired *t*-tests were used to statistically evaluate comparisons between the ACL and PCL. Significance was defined as $p<0.05$.

RESULTS

In the toe-region, modulus values were relatively similar in magnitude between the ACL and PCL and not statistically different (Fig. 2B). In contrast, linear-region moduli were

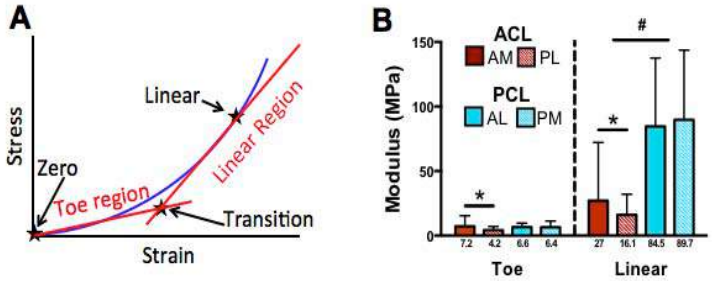

Figure 2: (A) Schematic of a typical stress/strain curve with a bilinear curve fit highlighting the toe- and linear-region moduli, and the zero, transition and linear strain points. (B) Toe-region modulus was similar magnitude in the ACL and PCL, while linear-region modulus was significantly larger in the PCL. The ACL exhibited bundle-bundle differences in both parameters while the PCL were homogeneous (* = statistically significant bundle-bundle differences within ligament; # = significant ACL-PCL differences)

significantly larger for the PCL. Within the ACL, bundle-bundle comparisons were statistically significant for both toe- and linear-region modulus (AM>PL), while there were no bundle-bundle differences in the PCL (AL=PM). Thus, the PCL demonstrates more mechanical homogeneity than the ACL, which exhibits location-specific variation in mechanics. For microstructural properties, STD AoP values were significantly larger for the ACL than the PCL at all three strain points, demonstrating more spread in the angular orientation of collagen (Fig. 3A). The ACL showed significant bundle-bundle differences at transition and linear strains (PL>AM), while there were no interbundle differences for the PCL (AL=PM). STD AoP values decreased for both ligaments from zero to

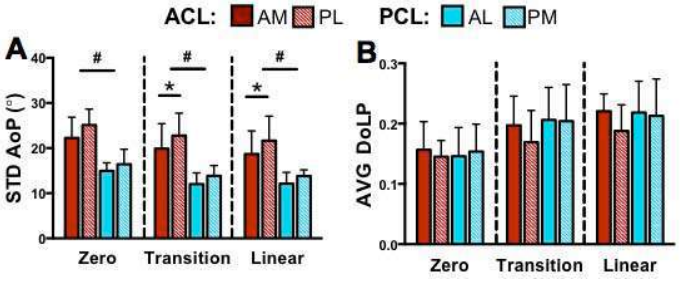

Figure 3: (A) STD AoP was consistently higher for the ACL compared to the PCL, indicating more uniform collagen alignment for the PCL. The ACL exhibited significant bundle-bundle differences at transition and linear points, while the PCL was more homogeneous (B) AVG DoLP was similar for the ACL and PCL with no bundle-bundle differences (* = statistically significant bundle-bundle differences within ligament; # = significant ACL-PCL differences)

transition to linear, indicating collagen realignment during the ramp to failure (Fig. 3A). AVG DoLP values exhibited no differences between the ACL and PCL, and neither ligament showed statistically significant differences between its two bundles (Fig. 3B). AVG DoLP values increased consistently from zero to transition to linear, demonstrating a higher degree of collagen alignment at increasing strain.

DISCUSSION

The microstructural and material properties of the ACL and PCL in the human knee have subtle but potentially important differences. First, there are some differences between the ligaments themselves. The PCL exhibits larger modulus values in the linear region of the stress-strain curve and smaller STD AoP values compared to the ACL. Thus, the PCL exhibits a more uniform distribution of collagen orientation, and a corresponding stiffer mechanical response than the ACL. Second, the ACL demonstrates bundle-bundle differences in mechanical and microstructural parameters while the PCL does not. Thus, the PCL is more homogeneous than the ACL, which demonstrates region-specific variation. The ACL-PCL differences observed in this study may be important for guiding surgical technique and graft choice when reconstructing these ligaments. Further research is necessary to assess how these findings can evaluate current and future graft options for ACL and PCL reconstruction and help optimize surgical techniques and repair strategies.

ACKNOWLEDGEMENTS

Aided by a grant from the Orthopaedic Research and Education Foundation (OREF) with funding provided by the Musculoskeletal Transplant Foundation (MTF).

REFERENCES

[1] Steckel H+ Sc and J Med Sci Sports 2007. [2] Amis+ Knee Surg. Sports 2006 [3] Race A+ J Biomech 1994. [4] Prietto MP+ Trans ORS 1988. [5] Butler DL+ J Biomech 1986. [6] Kennedy JC+ JBJS 1976. [7] Skelley NW+ AM J Sports Med. 2015. [8] Castile+ J. Biomech 2015. [9] Wright+ ORS 2016. [10] York T+ J Biomed Opt 2014.

Copyright 2016 The Organizing Committee for the 2016 Summer Biomechanics, Bioengineering and Biotransport Conference

SB^{3}C2016
Summer Biomechanics, Bioengineering and Biotransport Conference
June 29-July 2, National Harbor, MD, USA
SB^{3}C2016-629

CELLULAR ARCHITECTURE DICTATES ANISOTROPIC MECHANICAL PROPERTIES OF VASCULAR SMOOTH MUSCLE CELLS

Z. Win (1), J. M. Buksa (1), P. W. Alford (1)

(1) Department of Biomedical Engineering
University of Minnesota - Twin Cities
Minneapolis, MN, USA

INTRODUCTION

Cutting edge biomechanical models, such as constrained mixture and multiscale models[1,2], treat individual components of tissues independently, necessitating a firm understanding of the properties of each component. Cell elastic properties are normally reported as Young's modulus[3] but Young's modulus is only valid for isotropic materials undergoing small strains. Vascular smooth muscle cells (VSMCs) are highly anisotropic and undergo large strains *in vivo*. The gold standard for determining tissue-scale anisotropic material properties is biaxial testing. Here, we have developed a method to perform biaxial testing on a single cell, which we used to measure anisotropic mechanical properties of isolated VSMCs and demonstrate that cellular architecture affects the mechanical properties of VSMCs.

METHODS

Substrate fabrication. Micropatterned polyacrylamide-elastomer composites (Fig. 1A inset) were fabricated as described in Simmons et al. and Polio et al. Human umbilical artery vascular smooth muscle cells were obtained from Lonza and cultured at 37 ºC and 5% CO_2. Passages 4-7 were used for experiments. Cells were seeded and cultured overnight in growth medium[6]. Cells were serum starved for >24 hrs prior to stretching.

Cell stretching. Stretching experiments were conducted in Tyrode's buffer at 37 °C as outlined in Fig. 1B (Steps 1-5). Specifically, elastomer membranes were stretched uniaxially (axially and transversely) to 25% (0.5%/s) strain or biaxially to 20% (0.5%/s) strain. Brightfield images of cells and fluorescent images of beads in the top layer of the polyacrylamide gel were obtained during stretch. Cells were then treated with HA-1077 (100 μM) to inhibit contraction. Passive cells were stretched and images were obtained. Cells were then lysed with 0.1% SDS and the substrate was stretched again to obtain cell-free deformation images of the substrate.

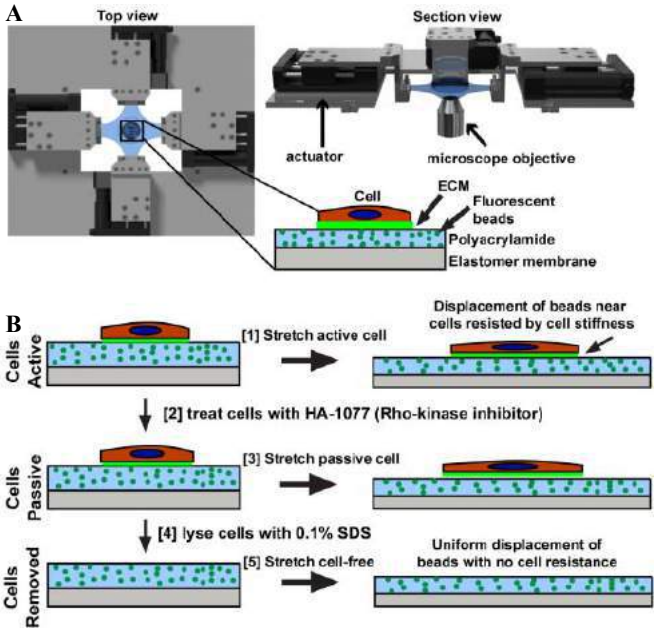

Figure 1. Cell-scale biaxial stretcher. (A) Computer render of microscope-mounted cell-scale stretcher. Inset: Cells are micropatterned onto a bead-doped polyacrylamide-elastomer composite. (B) Cell stretching and image acquisition protocol.

Copyright 2016 The Organizing Committee for the 2016 Summer Biomechanics, Bioengineering and Biotransport Conference

Calculation of traction forces and Cauchy stress. A PIV algorithm[7] implemented in ImageJ was used to calculate bead displacements in the top surface of the gel by comparing cell and cell-free images for active and passive stretches. Traction stresses were calculated using an unconstrained Fourier transform traction cytometry algorithm[8]. Traction stress vectors were discretized to 5 x 5 μm^2 grids. Total traction force applied by the cell to the substrate, T_i, in the i-direction was calculated as:

$$T_i = \sum_n A_n |\vec{T}_{i,n}| \quad [1]$$

where A is the discretized unit surface area of the cell and $\vec{T}_i$ are the traction stress vectors. Cell architecture was measured using confocal microscopy and mean Cauchy stress in the central plane of the cell was calculated using measured cross-sections.

RESULTS

We have developed a novel cell-scale biaxial stretcher to determine the mechanical properties of isolated VSMCs (Fig. 1A). The stretcher consists of four grips with independent actuators that can apply any uniaxial or biaxial stretching protocol to a polyacrylamide-elastomer composite. Polyacrylamide gel micropatterning is used to control cellular architecture and fluorescent beads embedded in the gel are used for quantification of cellular traction forces on the substrate.

VSMCs (aspect ratio 1:4) were stretched either uniaxial axially (Fig. 2A), uniaxial transversely (Fig. 2B), or biaxially (Fig. 2C). Bead displacements generated by the cells on the substrate and traction stresses were determined as outlined in Methods. Total traction force applied by the cells, T_i, were calculated using Eqn. [1] for both active and passive stretch. When cells are stretched uniaxial axially, there is a ~2-3 fold increase in traction force in the direction of stretch (T_x) for both active and passive stretch (Fig. 2A iii-iv). However, when cells are stretched transversely there is little change in traction force (T_y) for both active and passive stretch (Fig. 2B iii-iv). These data show that patterned VSMCs exhibit mechanical anisotropy.

To determine the effect of cellular architecture on cell mechanical properties, VSMCs were micropatterned into aspect ratios: 1:1, 1:2, 1:4, 1:8 (Fig. 3A) and stretched uniaxially in either the axial (x) or transverse (y) direction. As the aspect ratio of the cell increases,

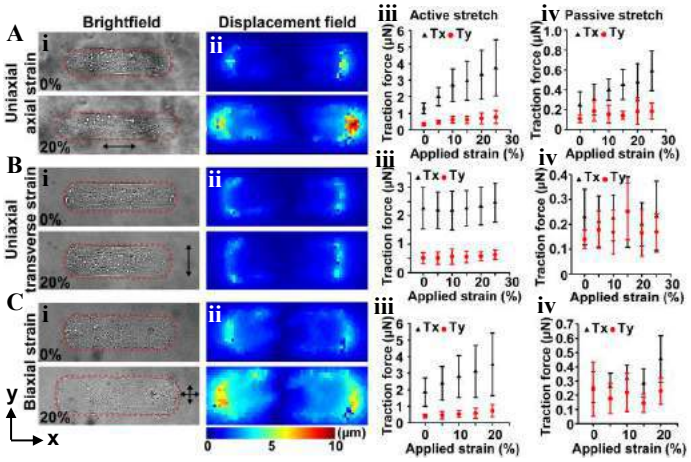

Figure 2. Uniaxial and biaxial stretching of 1:4 aspect ratio VSMCs. (A) Uniaxial axial stretch. (B) Uniaxial transverse stretch. (C) Biaxial stretch. (A-C) (*i*) Brightfield images at 0% and 20% strain. Cells outlined in red. (*ii*) Bead displacement fields at 0% and 20% strain. (*iii*) Traction forces during active stretch. (*iv*) Traction forces during passive stretch. Error bars: standard deviation.

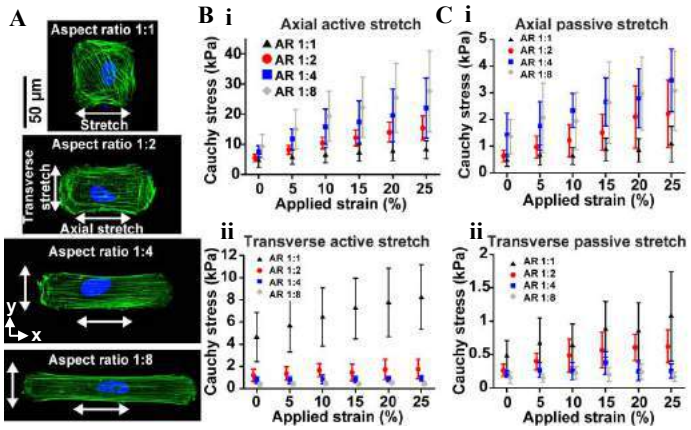

Figure 3. Uniaxial testing of VSMCs. (A) Micropatterned VSMCs. Green: f-actin. Blue: nuclei. (B) Uniaxial active stretch. (C) Uniaxial passive stretch. (B-C) (*i*) Cauchy stress (σ_x) during axial stretch. (*ii*) Cauchy stress (σ_y) during transverse stretch. Error bars: standard deviation.

there is a larger increase in Cauchy stress (σ_x) as the cell is stretched axially and a smaller increase in Cauchy stress (σ_y) when the cell is stretched transversely (Fig. 3B-C). These data show that as aspect ratio increases, the cells become stiffer in the axial direction, along the direction of actin fiber alignment.

DISCUSSION

Patient-specific models (PSMs) of blood vessel mechanics can provide physicians with an additional tool to track aneurysm growth and rupture likelihood[9]. In models utilizing rule-of-mixtures theory, the material properties of each component of blood vessels must be known. Due to a lack of appropriate tools to study and develop constitutive models for VSMCs, current PSMs do not fully incorporate complex cellular mechanical properties, which may limit their capabilities.

Our previous work has shown that cellular architecture affects contractile stress generation in VSMCs[6]. However, the effect of cellular architecture on anisotropic mechanical properties of VSMCs is not fully understood. Here, we show that cell stiffness in the direction of actin fiber alignment increases with cell aspect ratio. Our results suggest that Young's modulus is insufficient to describe the intricate mechanical properties of VSMCs and more complex constitutive models are needed. Future work will include developing a constitutive model that can describe the full 3D mechanical properties of VSMCs.

ACKNOWLEDGEMENTS

We acknowledge financial support from the American Heart Association Scientist Development Grant 13SDG14670062 (PWA), American Heart Association Pre-doctoral Fellowship 16PRE2770112 (ZW) and the University of Minnesota Doctoral Dissertation Fellowship (ZW).

REFERENCES

[1] Lai, VK et al., *J Biomech Eng*, 135(7):071007-071009-9, 2013.
[2] Alford, PW et al, *Biomech Model Mechanobiol*, 7(4):245-62, 2008.
[3] Janmey, PA et al., *Annu Rev Biomed Eng*, 9:1-34 2007.
[4] Simmons, CS et al., *Lab Chip*, 4:646-649, 2013.
[5] Polio, SR et al., *Methods Cell Biol*, 121:17-31, 2014.
[6] Win, Z et al., *Integr Biol*, 6:1201-1210, 2014.
[7] Tseng, Q et al., *PNAS*, 109:1506-1511, 2011.
[8] Butler, JP et al., *Am J Phys*, 232:C595-605, 2002.
[9] Neal, ML et al., *Brief Bioinform*, 11(1): 111-126, 2010.

Copyright 2016 The Organizing Committee for the 2016 Summer Biomechanics, Bioengineering and Biotransport Conference

SB^{3}C2016
Summer Biomechanics, Bioengineering and Biotransport Conference
June 29 –July 2, National Harbor, MD, USA
SB^{3}C2016-630

EFFECTS OF TIBIOFEMORAL COMPRESSION ON ACL FORCES AND KNEE KINEMATICS UNDER COMBINED KNEE LOADS

Kent T. Yamaguchi (1), Daniel V. Boguszewski (1), Justin Mathew (1), Keith L. Markolf (1), David R. McAllister (1)

(1) Department of Orthopaedic Surgery
University of California Los Angeles
Los Angeles, CA, USA

INTRODUCTION

Injury to the anterior cruciate ligament (ACL) is one of the most serious knee injuries for athletes of all levels, with reported incidence rates between 80,000 and 125,000 per year in the US [1,2]. While over 70% of ACL injuries occur in noncontact situations [3], the exact mechanism is still unknown. However, it is generally believed that some combination of anterior tibial force (AF) [4], valgus knee moment (VM) [3], and internal tibial torque (IT) [5] is present in most non-contact ACL injury scenarios. A second, less understood factor in ACL injury is the role tibiofemoral compression (TFC). While it is believed that TFC plays an important role in ACL injuries, few would argue that these injuries occur without the presence of other forces and moments acting on the knee in conjunction with TFC.

Previous biomechanical studies have examined strain in the ACL with applied AF, VM, and IT at fixed flexion angles [6], but direct measurement of resultant ACL force has not previously been reported during continuous knee flexion under TFC combined application of AF, VM, and IT. Such data are needed to better simulate in vivo sports injury conditions and provide a more complete understanding of ACL injury mechanisms.

The objective of this study was to examine the effects of increasing TFC in combination with AF, VM, and IT (alone and combined) on resultant ACL force and knee kinematics. We hypothesized that TFC would increase ACL force and alter knee kinematics under these simulated ACL injury loading mechanisms.

METHODS

Eight fresh-frozen human cadaveric knee specimens were used, average age of 24.3 years (range 18-34 years). The tibia and femur of each specimen had all soft tissue removed to within 10 cm of the joint line, and both bones were potted in cylindrical molds of PMMA. Using an established technique, the femoral attachment of the ACL was mechanically isolated and attached to a calibrated load cell in order to directly measure resultant ACL force. Using a six degree-of-freedom (DOF) robot, each knee was flexed from 0°-50° while simultaneously seeking target levels of force or moment in the remaining DOFs. Knees were tested with 25N, 200N, and 500N TFC (in that order) combined with application of 1) 45N AF, 2) 5Nm VM, 3) 2Nm IT, and 4) 45N AF + 5Nm VM + 2 Nm IT for each level of TFC. To maintain the mechanical integrity of the ACL/load cell attachment, 350N was the maximum allowable resultant ACL force. Due to the magnitude of ACL force during the combined loading condition at deeper flexion angles, all 500N TFC tests were limited to 0°-30° flexion.

A paired T-test was used to compare 25N TFC to 200N TFC and 200N TFC to 500N TFC at every flexion angle in 5° increments. The level of significance was $p<0.05$.

RESULTS

Resultant ACL force significantly increased with increasing levels of TFC (Figure 1). For each level of TFC, ACL force tended to increase with knee flexion for all loading modes. The combined load of 45N AF + 2Nm IT + 5Nm VM produced the largest amount of resultant ACL force.

Anterior tibial translation significantly increased with increasing levels of TFC (Figure 2), but remained relatively constant with increasing knee flexion for all loading modes. TFC combined with 45N AF alone produced the largest amount of anterior translation.

Both internal tibial rotation (Figure 3) and valgus rotation (Figure 4) showed no significant differences between each level of TFC. Likewise, both internal and valgus tended to increase with increasing flexion for all loading modes. The combined load of 45N AF + 2Nm

Copyright 2016 The Organizing Committee for the 2016 Summer Biomechanics, Bioengineering and Biotransport Conference

IT + 5Nm VM produced the largest amounts of both internal and valgus rotation.

DISCUSSION

This study examined the role of TFC on forces generated in the ACL during isolated and combined modes of knee loading relevant to knee injury. To our knowledge, this study represents the first direct measurement of resultant ACL force and knee kinematics using a robotic testing system during continuous knee flexion while maintaining TFC.

We found that during knee flexion, application of valgus moment produced a coupled internal tibial rotation and application of internal torque produced a coupled valgus rotation at all levels of applied TFC.

Our results also show that for all knee loadings, increasing the level of TFC acted to translate the tibia anteriorly with an associated increase in ACL force; internal and valgus rotations associated with these loading modes did not change significantly when the TFC level was increased. It is well recognized that anterior tibial translation is an important mechanism for generating ACL force. Our results demonstrated that TFC activated this mechanism of ACL force generation, even when the ACL had been pre-loaded under the combined AF + IT + VM condition. Since all of our specimens had posteriorly sloping medial and lateral tibial plateaus, the presumed mechanism for ACL force generation during all tests with TFC was anterior tibial displacement produced by tibiofemoral contact force acting on the articular cartilage interfaces.

In summary, the primary effect of TFC for all isolated and combined loading modes was to increase anterior tibial translation, which in turn increased ACL force but did not affect internal or valgus rotations.

ACKNOWLEDGEMENTS

The authors thank Lindsey McAllister for her help during the study. This study was supported in part by the H H Lee Surgical Research Program. Specimens for this study were obtained from the Musculoskeletal Transplant Foundation

REFERENCES

[1] Griffin, LY et al., *J Am Acad Orthop Surg*, 8(3):141-50, 2000; [2] Kim, S et al., *J Bone Joint Surg Am*, 93(11):994-1000, 2011; [3] Boden, BP et al., *Orthopedics*, 23(6):573-8, 2000; [4] Fleming, BC et al., *J Biomech,* 26(1):51-58, 1993; [5] Meyer, EG et al., *Am J Sports Med,* 36(10):1966-77, 2008; [6] Fukuda, Y et al., *J Orthop Res,* 21(6):1107–12, 2003.

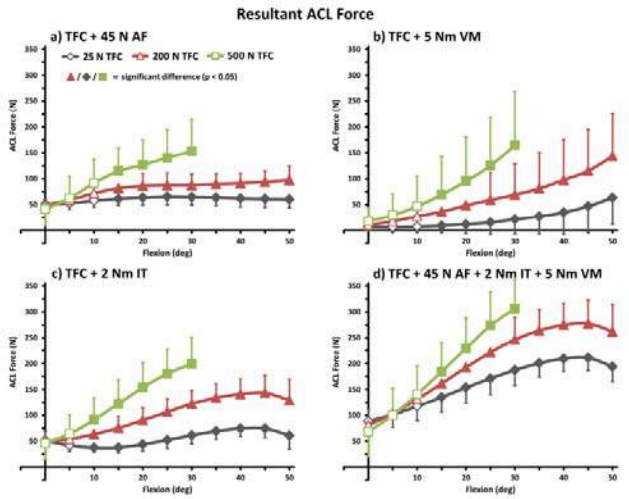

Figure 1: Resultant ACL force comparing different levels of TFC for each knee loading condition.

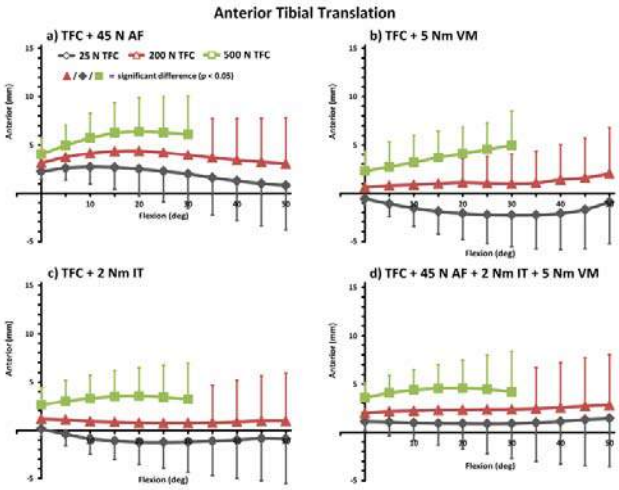

Figure 2: Anterior tibial translation comparing different levels of TFC for each knee loading condition.

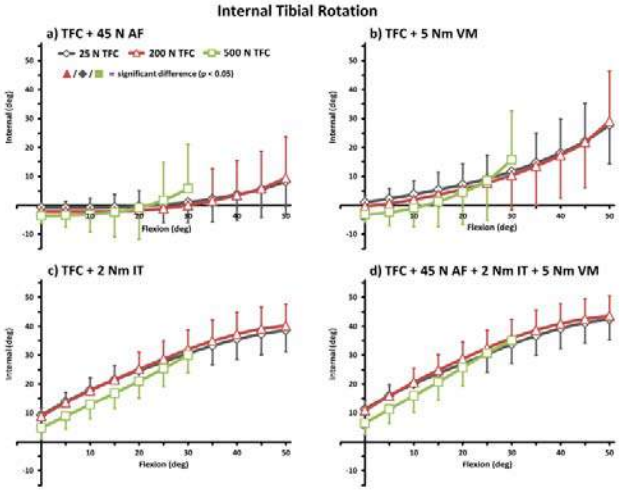

Figure 3. Internal tibial rotation comparing different levels of TFC for each knee loading condition.

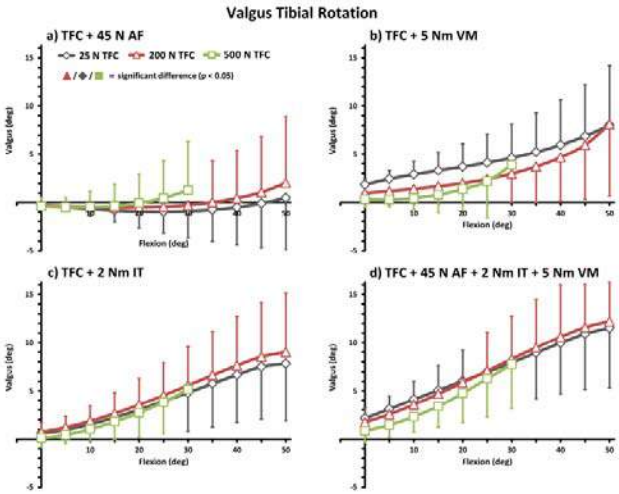

Figure 4. Valgus tibial rotation comparing different levels of TFC for each knee loading condition.

Copyright 2016 The Organizing Committee for the 2016 Summer Biomechanics, Bioengineering and Biotransport Conference

SB^{3}C2016
Summer Biomechanics, Bioengineering and Biotransport Conference
June 29 –July 2, National Harbor, MD, USA
SB^{3}C2016-631

TUNABLE AND SELECTIVE NANOFIBER DEGRADATION REGULATES 3D CELL MIGRATION

Feini Qu (1,2,3), Julianne L. Holloway (2,3), Jason A. Burdick (2,3), Robert L. Mauck (1,2,3)

(1) McKay Orthopaedic Research Laboratory
Department of Orthopaedic Surgery
University of Pennsylvania
Philadelphia, PA, USA

(2) Department of Bioengineering
University of Pennsylvania
Philadelphia, PA, USA

(3) Translational Musculoskeletal Research Center
Philadelphia VA Medical Center
Philadelphia, PA, USA

INTRODUCTION

Repair of dense connective tissues is limited, given the density of the matrix and the low cellularity of adult tissues [1]. Efforts to augment repair often involve delivering cells and/or growth factors to the wound site via a biomaterial. Electrospinning, a technique that draws polymers into nanofibrous networks, is a versatile platform that offers tunable control over the combinatorial delivery of therapeutics, including their temporal release profile via material degradation and fiber modification. Previously, we fabricated dual-component scaffolds that delivered a matrix-degrading enzyme in a burst-like fashion via the dissolution of water-soluble poly(ethylene oxide) (PEO) nanofibers to expedite integration of the injured knee meniscus [2]. Here, we hypothesized that the addition of slower-degrading fibers composed of hyaluronic acid (HA) [3], a natural polysaccharide, would allow further control of scaffold degradation but that these fibers impede cell infiltration by increasing scaffold density. This study evaluated the time- and enzyme-dependent characteristics of tri-component scaffolds containing poly(ε-caprolactone) (PCL), PEO, and HA, and the migration of adult meniscal cells through these scaffolds. Our results show that the dynamic nature of this microenvironment permits cell migration in the long term, making it a promising material for tissue engineering and drug delivery.

METHODS

Nanofibrous scaffold fabrication and characterization: Composite scaffolds were fabricated through tri-jet electrospinning onto a common rotating mandrel [4] with the following components: poly(ε-caprolactone) (PCL), poly(ethylene oxide) (PEO), and 25% hydroxyethyl methacrylate (HeMA)-modified hyaluronic acid (HA) [3]. Afterwards, scaffolds were crosslinked via UV light and imaged using SEM, where fiber diameter was measured using ImageJ (NIH) (n=4 samples, 50 fibers/sample). To visualize distinct fiber fractions, the PCL, PEO, and HA solutions were doped with rhodamine, fluorescein, and 4',6-diamidino-2-phenylindole (DAPI), respectively, and imaged by fluorescence microscopy. Fiber degradation was evaluated by immersing scaffolds in PBS (~10 mg, 0.5 mm thick) and collecting the eluant at set times (n=3–5 samples). Bulk scaffold mass loss was determined through the dry scaffold weight before and after immersion over 96 hours. The amount of uronic acid, a component of HA, in the supernatant was quantified over 45 days using a modified uronic acid assay [5].

Analysis of cell migration: Cell invasion into nanofibrous composites was evaluated using rhodamine-doped nanofibers spun on glass slides (~20 μm thick). Three randomly aligned substrates were tested: PCL/PEO/PEO (high porosity), PCL/PEO/HA (low porosity), or PCL/PEO/HA treated with 1 mg/mL hyaluronidase (HASE) for 72 hours. Prior to tissue culture, all substrates were washed in PBS to remove the PEO fiber fraction. Adult bovine meniscal explants (5 mm diameter, 3 mm height) were incubated in CellTracker Green for 1 hour and then placed atop substrates to allow for cell egress. After 72 hours in basal media, explants were removed and the egressed cells were stained with DAPI to visualize nuclei. Confocal z-stacks were obtained in the FITC, DAPI, and TRITC channels to visualize cells, corresponding nuclei, and nanofibers. To assess scaffold porosity, the pore area fraction was quantified in Fiji using a central z-slice (n=3 stacks/group). Cell infiltration depth was calculated as the distance between the apical surface of the scaffold and z-centroid location of the nucleus (n=20 cells/group). The average width of nuclei projected in 2D was determined using the Local Thickness plugin in Fiji.

Statistical analysis: Significance was assessed by one-way ANOVA with Tukey's HSD post hoc for pore area fraction, infiltration depth, and average nuclear width ($p \leq 0.05$). Data are

Copyright 2016 The Organizing Committee for the 2016 Summer Biomechanics, Bioengineering and Biotransport Conference

presented as mean ± standard deviation unless specified otherwise.

RESULTS

Composite nanofibrous scaffolds containing poly(ε-caprolactone) (PCL), poly(ethylene oxide) (PEO), and hyaluronic acid (HA) with HeMA functionalization were electrospun (PCL/PEO/HA). SEM micrographs revealed smooth and uniform fibers, with an average fiber diameter of 308 ± 143 nm. Images of fluorescently labeled fibers validated the presence of three discrete populations (Fig. 1C).

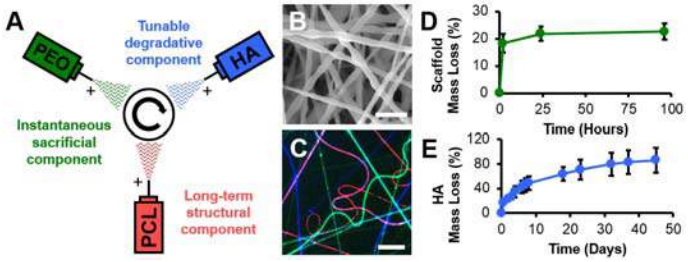

Fig. 1: Controlled fiber degradation from tri-component scaffolds. (A) Electrospinning schematic. (B) SEM micrograph of PCL/PEO/HA scaffold. Scale = 5 µm. (C) Fluorescent image of PCL (red), PEO (green), and HA (blue) fibers. Scale = 20 µm. (D) Bulk scaffold and (E) HA mass loss in PBS (n=3–5 samples).

Degradation of each fiber fraction was time-dependent and occurred independently of one another. After 2 hours in PBS, 18% of the total scaffold mass was lost, likely representing the loss of the PEO via dissolution and diffusion of uncrosslinked HA from the network (Fig. 1D). After 24 hours, mass loss reached 22% and remained constant thereafter, indicating that the majority of PEO had been removed from the scaffold. In contrast, HA degradation showed a more linear profile, with 35% and 60% mass loss after 4 and 16 days (Fig. 1E). After 45 days, only 14% of the HA remained, resulting in a scaffold that was comprised primarily of PCL.

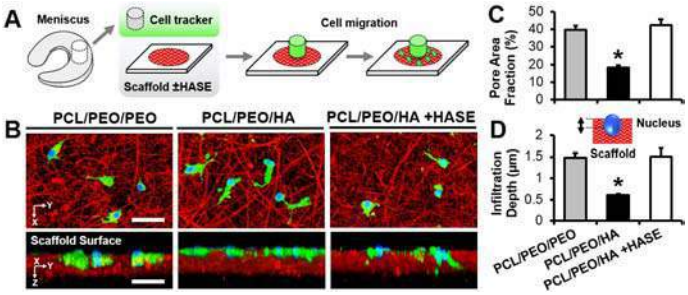

Fig. 2: High porosity scaffolds expedite cell infiltration. (A) Experimental schematic. (B) Images of cells within scaffolds. Scales = 50 µm. (C) Pore area fraction (n=3 samples/group). (D) Cell infiltration depth with schematic inset (mean ± standard error; n=20 cells/group). * = p≤0.05 vs. all other groups.

Adult meniscal cells from explants adhered, spread, and infiltrated into nanofibrous substrates within 72 hours (Fig. 2B). Analysis of cell infiltration into high (PCL/PEO/PEO) and low (PCL/PEO/HA) porosity scaffolds revealed that infiltration depth was affected by nanofiber density. The inclusion of HA fibers reduced the pore area fraction to less than half of the PCL/PEO/PEO substrate, which contained an additional sacrificial PEO fraction (Fig. 2C, p≤0.05). Consequently, infiltration depth was lower for cells on PCL/PEO/HA compared to cells on PCL/PEO/PEO (Fig. 2D, p≤0.05). When HA fibers were selectively removed by hyaluronidase digestion (+HASE), the pore area fraction was restored and cells migrated to a similar extent as on PCL/PEO/PEO (Figs. 2C and 2D, p≤0.05). In addition, cells migrating through PCL/PEO/HA had larger and rounder nuclei than those within PCL/PEO/PEO and PCL/PEO/HA +HASE (Fig. 3A), and contained the greatest average nuclear width among groups (Fig. 3B, p≤0.05). Combining data from all groups revealed a negative linear correlation between average nuclear width and infiltration depth (y = -0.32x + 4; R^2 = 0.35) (Fig. 3C).

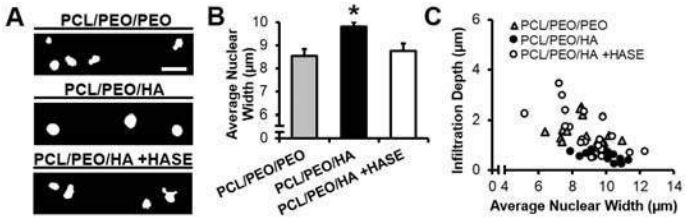

Fig. 3: Nuclear deformation during cell migration. (A) Binarized 2D projections of cell nuclei (top down view). Scale = 20 µm. (B) Average nuclear width (mean ± standard error; n=20 cells/group). * = p≤0.05 vs. all other groups. (C) Infiltration depth as a function of average nuclear width (n=20 cells/group).

DISCUSSION

Cellular colonization is essential for acellular scaffolds that rely on endogenous matrix deposition to bolster mechanical properties and ensure survival in a dynamically loaded environment. However, rapid cell attachment and proliferation on the scaffold surface may prevent cell penetration into the scaffold depth, resulting in a cell-rich outer edge but a necrotic center. As such, achieving sufficient cell density and homogenous distribution within the scaffold are vital steps towards generating functional tissue replacements. Our findings indicate that nuclear deformation and scaffold porosity are necessary for cell migration through nanofibrous microenvironments. In order to pass through confined space, cells must overcome the steric constraints that are imposed on its nucleus, which is 2–4 times stiffer than the surrounding cytoplasm and considered the rate-limiting organelle in migration [6, 7]. Indeed, the majority of mobile cells are characterized by small and deformed nuclei, suggesting that nuclear plasticity plays an essential role in navigating tight interstitia. In this study, modification of HA with HeMA groups promoted fiber degradation in aqueous environments via a hydrolyzable ester group, resulting in a HA mass loss of approximately 80% after 4 weeks. While the addition of HA fibers may be an impediment to migration early on, selective removal of HA with hyaluronidase increased the scaffold porosity and cell infiltration, suggesting that this material will permit cell colonization in the long term. Fibers may be further functionalized to include biofactors, which can be released as the material degrades over time to influence cells in a temporally targeted manner. By designing smart, dynamic scaffolds that reflect the optimal microenvironmental niche for cell and tissue ingrowth over time, ultimately we hope to recapitulate the natural biological cues that direct repair and regeneration of dense connective tissues.

ACKNOWLEDGEMENTS: This work was supported by the NIH (R01 AR056624, T32 AR007132) and the VA (I01 RX000174).

REFERENCES: [1] Ionescu LC et al., *Tissue Eng Part A*, 17(1-2):193-204, 2011. [2] Qu F et al., *Biomaterials*, 39:85-94, 2015. [3] Purcell BP et al., *Biomaterials*, 33(31): 7849-57, 2012. [4] Baker BM et al., *J Biomech Eng*, 131(10): 101012, 2009. [5] Khetan S et al., *Soft Matter*, 5(8): 1601-6, 2009. [6] Guilak F et al., *Biochem Biophys Res Commun*, 269(3): 781-6, 2001. [7] Wolf K et al., *J Cell Bio*, 201(7):1069-84, 2013.

Copyright 2016 The Organizing Committee for the 2016 Summer Biomechanics, Bioengineering and Biotransport Conference

SB^{3}C2016
Summer Biomechanics, Bioengineering and Biotransport Conference
June 29 –July 2, National Harbor, MD, USA
SB^{3}C2016-633

SIMULATION OF STRAIN INDUCED DAMAGE DURING DELIVERY

Olivier Mayeur (1,2), Estelle Jeanditgautier (3), Pauline Lecomte (1,2), Jean-François Witz (2), Chrystelle Rubod (2,3), Michel Cosson (2,3) and Mathias Brieu (1,2)

(1) Centrale Lille,
Cité scientifique CS 20048,
F-59000 Lille, France

(2) Laboratoire de Mécanique de Lille - LML,
CNRS FRE 3723, Univ. Lille,
F-59000 Lille, France

(3) Hôpital Jeanne de Flandres,
CHRU de Lille,
Lille, France

INTRODUCTION

The study of the physiology and pathology of the pelvic organs is a research activity whose aims have increased gradually in recent years. The pelvic floor presents a complex equilibrium related to the mechanical properties of tissues involved and their geometries [1]. Disturbance of such an equilibrium may induce pathophysiology mobility such as genital prolapse, which is a major health problem concerning 30% of the women population [2]. Different anatomical structures seem to play a key role in that balance and the authors have remained on the role of the pelvic muscles. Recently it has been demonstrated that the uterosacral ligaments also play an important role in supporting organs [3, 4]. This complex equilibrium might be impacted by the life events such as aging, pregnancy or delivery.

During pregnancy, a modification of the pelvic floor appears [5]. The main hypothesis of these changes demonstrated previously is the modification of biomechanical properties of the pelvic tissues [6]. Modifications that occur in the parturient lead us to study the sustainable structures to increase our understandings. Computer simulation using Finite Element (FE) method is one tool helping to achieve this through the study of strains and stresses during pregnancy and vaginal delivery. However, it is necessary to have a complete biofidelic model described by all ligaments and muscles to undertake this type of analysis.

The objective of our work falls within this approach using numerical models of a pregnant woman, at different terms of pregnancy, during delivery and during the post-partum period. Firstly, all of these models will be used to observe the geometrical changes during pregnancy. Secondly we can simulate childbirth to analyze the deformations that occur on the pelvic floor during delivery. The analysis of all these results will bring a better understanding of the phenomena involved on those different configurations.

METHODS

Different MRI (Magnetic Resonance Imaging) sequences in T1 and T2 and proton density were performed on a pregnant primiparous woman, without notable medical history. MRI are performed at different terms of pregnancy eg 16, 32, and 38, weeks of gestation (WG) and two months after delivery. These sequences allow us to get a slice imaging of the pelvic cavity used to generate four 3D models representing the pelvis during pregnancy and after delivery. A manual segmentation of the images is achieved on the software AVIZO Standard Edition 7® (VSG Visualization Sciences Group, SAS). It is performed by surgeons and anatomists whose skills can identify with confidence each anatomical structure. All sections are analyzed to select organs, muscles and ligaments useful in the study and the bone structure.

Visually, the MRI slices do not permit easy observations of a possible change in the muscles and ligaments. To distinguish some geometric differences, for each term, a digital model is generated on the basis of our 3D reconstructions. To exploit these representations, it is necessary to transform them into surfaced model to quantify efficiently the possible differences on sustainable structures. It consists in creating B-Splines on each anatomical structure to have a wireframe model on which surfaced patches are applied, defining each organ, muscle and ligament. Eighteen representative structures are identified individually for each term in order to establish with precision the geometrical changes during pregnancy.

The advantage of this model is to make it compatible to perform simulations with FE method (Abaqus/CAE 6.12-2 software). For the numerical simulations, we assign mechanical properties from preliminary works referenced in the literature [7, 8]. Boundary conditions follow also the same protocol as the one established on the study of physiological [1] or pathological mobility [9]. We use an FE

Copyright 2016 The Organizing Committee for the 2016 Summer Biomechanics, Bioengineering and Biotransport Conference

model corresponding to the 16WG representation and we perform different changes of the loading conditions to match with the growing weight at 32WG and 38WG. From the FE simulation results, the anatomical structures are analyzed on the deformed mesh to quantify geometrical modifications such as the ligament lengthening and compare it with the geometrical analysis of each MRI.

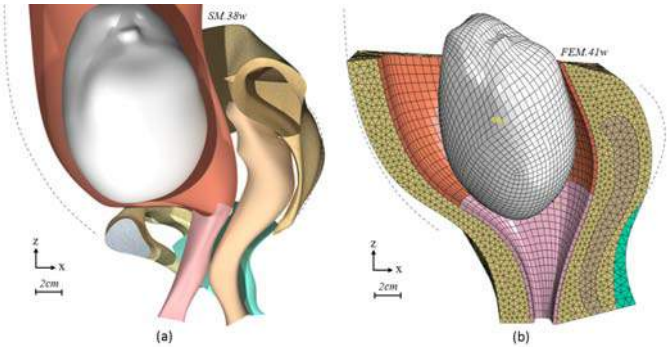

Figure 1: (a) 3D model of the pelvic at 38WG, (b) FE model of delivery with full cervical dilatation and LOA presentation.

The last study uses the geometric model at 38WG that corresponds to the representation of the pelvic floor 3 weeks before delivery. We perform some modifications on the surfaced model to represent a full cervical dilatation (expulsion stage) and model the fetal head in the descent position (figure 1). The imposed trajectory of the head was defined thanks to the geometrical representation at 38WG; displacement and rotational equations are established to match with a left occipito-anterior scenario (LOA) that corresponds to the most common form of cephalic presentation. The trajectory of the fetal head is an input parameter on the FE model and can be modified to correspond to other cephalic configurations to be compared to each other and to investigate their impact on the pelvic system.

Our study can be summarized by the analysis of geometrical modifications, stresses and strains applied on the pelvic floor during pregnancy and after several delivery scenarios. This protocol employed 3 types of analysis:

- Geometrical analysis on the four 3D models from MRI.
- FE analysis during pregnancy with evolution of weight.
- FE analysis during delivery with different configurations.

RESULTS

For the analysis of anatomical sustainable structures from the four MRI models, we initially studied the evolution of the ligamentous system. The first result shows an increase in the length of the uterosacral ligaments (USL) according to the term, followed by a decrease in postpartum. For 16, 32, 38 weeks of gestation, the lengths of the USL are respectively 40mm, 46mm, 51mm. Two months after delivery, there is a decrease in USL size, without return of values observed at the beginning of pregnancy. Regarding the muscular structures of the pelvic floor, our analysis is mainly focused on puborectal levator ani muscle (PLAM). During this analysis, the same type of evolution is observed on the puborectalis muscle which is a part of PLAM. We find an increase in the thickness depending on the pregnancy term, followed by a decrease on postpartum. The decrease observed 2 months after delivery is not so complete because we do not find the values of early pregnancy. Variations on the USL and the puborectalis muscle do not seem to be equivalent to other anatomical structures of suspension where geometrical changes are insignificant compared to them.

The FE analysis performed on our model during pregnancy by changing the weight of uterus also allows us to observe an increase in the USL length. However we do not reach the lengthening levels observed on the previous geometrical analysis based on the 4 MRI models. FE simulations during pregnancy help us to highlight that hyperelasticity of material properties does not return to these strain levels, reflecting that other factors influence the change of anatomical structures during pregnancy. The geometrical modifications do not depend only on weight gain. This finding leads to the contribution of hormonal factors in pelvic changes.

The last FE simulation is focused on the fetal expulsion stage thanks to the passage of fetal head in the parturient canal (Figure 1b). To ensure the computational convergence, a structured mesh is employed in accordance with each delimitation of anatomical structures. During the engagement of the head in the transverse position, the numerical simulation enables us to identify areas with high strain level near the cervix. These stressed areas move near the vagina during the descent and flexion phases. The pelvic floor muscles are highly stressed when the head reaches the vulva. Such simulation will help to a better understanding of the strain mapping within the pelvic system and lead to a better understanding on the consequences of delivery on the mechanical properties of soft tissues since their behavior and damage are strain depending.

DISCUSSION

Through this summarized study, we can notice different changes in the ligamentous and muscular geometries during pregnancy. These preliminary results observed thanks to MRI at different terms have been compared to FE simulations of gestation to highlight that these geometric changes are not only due to loading conditions (pregnancy weight gain). The level of impairment from FE simulations is lower than that observed on MRI, which induces that hormonal factors could be involved. Secondly, this protocol allows us to perform FE simulations of the delivery on a biofidelic model of the entire pelvic cavity, with a refined mesh of the muscles and ligaments. Such a tool is useful to identify the highly stressed areas following the cephalic presentations and the kinematics of the head. This research performed on the whole sustainable structure will help us to take into account the high stress induced damages and identify potential failure areas. Investigating soft tissue injury is the next step leading to better understanding of involved phenomena during delivery and adapted obstetric gesture and surgery.

Current limitations of this study are the imposed trajectory of the head descent. However, the imposed trajectory allows us to analyze the influence of several scenarios to identify strain and stress during labor and delivery complications. The next steps are to use uncontrolled trajectory and estimate the consequences of delivery on the strain induced damageable behavior of all the pelvic structures and finally to reach the patient-specific simulations.

ACKNOWLEDGEMENTS

This research is a part of the project « MAMAN » financially supported by the University of Lille 2.

REFERENCES

[1] Mayeur, O et al., *Annals of Biomed Eng*, 44(1):202-212, 2016.
[2] Samuelsson, E et al., *Am J Obstet Gynecol,* 180:299-305, 1999.
[3] Wei, JT et al., *Clin Obstet Gynecol*, 47(1):3-17, 2004.
[4] Cosson, M et al., *Int Urogynecol J*, 24(1):105-12, 2013.
[5] O'Boyle, AL et al., *Int Urogynecol J*, 14(1):46-9, 2003.
[6] Rahn, DD et al., *Am J Obstet Gynecol*, 198(5):590.e1-6, 2008.
[7] Chantereau, P et al., *Int urogynecol. J,* 25(11):1547-1553, 2014
[8] Rubod, C et al., *J Uro*. 79(4):1346-1354, 2012.
[9] Mayeur, O et al., *Biomedical Simulation*, 8789:220-227, 2014.

Copyright 2016 The Organizing Committee for the 2016 Summer Biomechanics, Bioengineering and Biotransport Conference

SB^{3}C2016
Summer Biomechanics, Bioengineering and Biotransport Conference
June 29 –July 2, National Harbor, MD, USA
SB^{3}C2016-634

SHAPE OPTIMIZATION OF LUMBAR INTERVERTEBRAL CAGES FEATURING DIFFERENT CROSS-SECTION SHAPES

Chaochao Zhou (1), Khalid Sethi (2), Ryan Willing (1)

(1) Department of Mechanical Engineering
Binghamton University
Binghamton, New York, USA

(2) Senecka Spine
Binghamton, New York, USA

INTRODUCTION

Intervertebral lumbar fusion using an implanted cage is the gold standard surgical treatment for disc diseases such as disc collapse and spinal cord compression, when more conservative medical therapy fails [1]. Titanium (Ti) alloys are widely used implant materials due to their superior biocompatibility and corrosion resistance [2]. A new Ti cage concept featuring I or H shaped cross-sections was recently proposed, with the intent to allow bone graft paste injection and perfusion secondary to cage implantation. However, subsidence or loosening of high stiffness Ti implants due to stress shielding is a concern [3]. Design optimization is a systematic and iterative technique for designing components which perform optimally with respect to one or more performance metrics. In these cages, we desire a clear pathway for bone graft to be injected into the implants, and perfused into the surrounding intradiscal space as much as possible. Therefore, in this study, we have employed shape optimization to maximize the sizes of cage windows (and simultaneously increase cage compliance to relieve stress shielding), subject to maintaining stresses below a threshold where fatigue failure is a concern.

METHODS

Fig. 1 shows the general shapes of three interbody cage conceptual designs, which consist of an I-shaped cage with a 45° wedge, a hollow cage with a 45° wedge, and a double-configuration (DC) cage with 45° and 60° wedges, which were modelled parametrically in ANSYS Mechanical APDL 15.0. The DC cage (Fig. 1(c)) can be inserted into the intradiscal space in both an I-configuration (principal configuration) and an H-configuration (secondary configuration), thus allowing a single component to provide two height options by manufacturing the implant with unequal width and height. Here, in order to make comparison among these cage designs, the same overall dimensions of 30 mm in length, 11 mm in width, and 11 mm in height were chosen for all the cages, based on the dimensions of existing commercially available lumbar cage designs. As illustrated by Fig. 2, the location (x_1), length (x_2), and width (x_3) of each window on the flanges and webs have a considerable impact on stress concentrations and bone diffusion/fusion, thus they are considered as design variables for shape optimization. Our design objective is to maximize the window sizes by adjusting these design variables to enhance bone graft perfusion and encourage larger mechanical stimuli for bone growth within these cages.

Any candidate cage design must also be able to pass pre-clinical testing, which is often assessed using ASTM standard protocols. Dynamic testing of each candidate implant design was simulated using the configuration described in ASTM F2077. A force-distributed multi-point constraint technique was employed in ANSYS to simulate the connections between the interbody cage and two polyurethane testing blocks. As shown in Fig. 3, two pilot nodes were respectively attached at the geometric centers of the upper and lower testing blocks. A compressive load (F) of 500 N and a fully reversing bending moment (M) with the amplitude of 2750 Nmm was applied on the pilot node of the upper testing block. The pilot node of the lower testing block was fully constrained. The bending moment simulated the effect of the primarily compressive load acting at a distance of half the cage width from the cage center.

All cages were modeled using pure Ti (grade 4) material properties, with a Young's modulus of 104 MPa, Poisson's ratio of 0.3, endurance limit (S_e) of 260 MPa, and yield strength (S_y) of 462 MPa. The Sorderberg's equation considering both effects of stress intensity amplitude (σ_a) and mean stress intensity (σ_m) was slightly

Copyright 2016 The Organizing Committee for the 2016 Summer Biomechanics, Bioengineering and Biotransport Conference

modified to establish an infinite-life fatigue criterion (Eq. 1), such that any fatigue factor (k) less than or equal to one was defined as safe,

$$k = \frac{\sigma_a}{S_e} + \frac{\sigma_m}{S_y} \leq 1 \quad (1)$$

The fatigue factors at all nodes of each cage model were calculated based on the stress intensity results solved using ANSYS, but only the maximum nodal fatigue factor was used to evaluate the safety of a candidate cage design. Shape optimization of each cage was performed using the Optimization Toolbox in MATLAB R2015a, and the nonlinear constraints were represented by the proposed infinite-life fatigue criterion (Eq. 1).

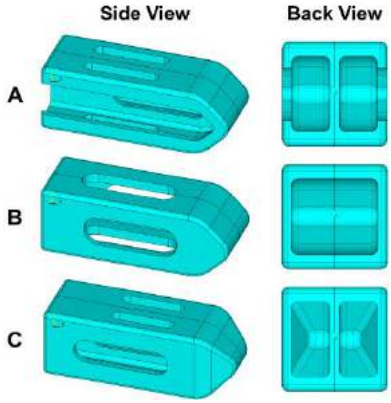

Figure 1: The initial designs of three interbody cages featuring different cross-section shapes. (a) I-shaped cage; (b) Hollow cage; (c) DC cage.

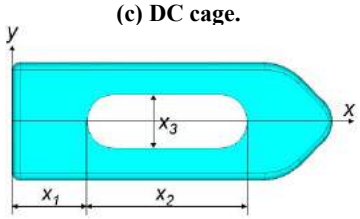

Figure 2: The design variables adopted in the shape optimization, including the location (x_1), length (x_2), and width (x_3) of each window in all cage designs.

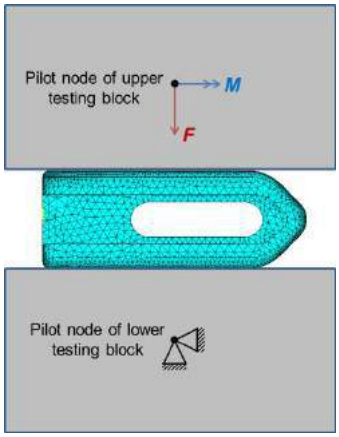

Figure 3: The finite element model of the interbody cage and the dynamic loads applied in the fatigue analysis.

RESULTS

According to the stress analysis results shown in Fig. 4, each of the general cage designs were more stressed after shape optimization than they were initially (Fig. 1), indicating that increasing mechanical stimuli existed within the bone graft space. Although fatigue failure typically occurs at the locations of maximum stress intensity (Fig. 4), the fatigue analysis demonstrated that all cage structures are sufficiently reliable for long term loading, since they satisfy our proposed infinite-life criterion (Eq. 1).

The material volumes of all cages were reduced to accommodate more bone graft with respect to their initial designs. Among these cages, however, the minimum material volume (798 mm^3) and optimal window layouts were obtained for the hollow cage (Fig. 4(b)), where the enlarged windows will promote bone fusion with vertebral endplates and bone graft diffusion through side windows. For the I-shaped cage design (Fig. 4(a)), the web window size was reduced significantly and the flange windows were shifted away from the center of the cage in order to alleviate stress concentrations. Although the window layouts of the DC cage design (Fig. 4(c)) were improved, the shifted windows on the flanges may also cause poor bone fusion with vertebral endplates when using the I-configuration.

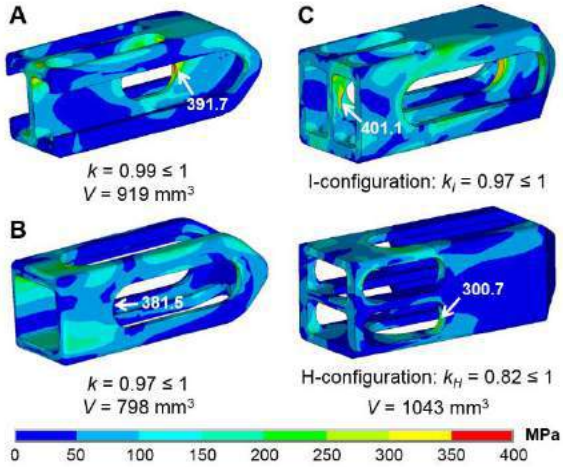

Figure 4: Comparison of the resulting implant shapes and stress distributions of three cage designs after shape optimization. (a) I-shaped cage; (b) Hollow cage; (c) DC cage in both configurations. The fatigue factor (k) of each cage was evaluated using the stress intensity results. The maximum stress locations were marked using white arrows.

DISCUSSION

The larger windows and allowable deformation within these cage designs are expected to promote bone fusion after discectomy surgery. In particular, shape optimization of the hollow cage design (Fig. 4(b)) led to the ideal window layouts for bone fusion and diffusion, as well as meeting the infinite-life fatigue criterion. However, designs developed using optimization techniques are necessarily a product of assumptions relating to what design variables can be modified and what loads are expected. Future work should further validate whether or not each resulting cage design has reached the true global optimum in the feasible design space, and include a greater number of design variables (thus, a larger design space) and a wider variety of loading scenarios to test the performance of candidate implant designs. Experimental validation will also be a focus of future work. In conclusion, we have demonstrated that the bone graft perfusion windows of these cage concepts can be maximized using design optimization, while considering fatigue stresses as a constraint.

REFERENCES

[1] Espinha et al. 2013. Journal of Biomechanics; [2] Niinomi. 1998. Materials Science and Engineering; [3] Cabraja et al. 2012. BMC Musculoskeletal Disorders.

Copyright 2016 The Organizing Committee for the 2016 Summer Biomechanics, Bioengineering and Biotransport Conference

SB³C2016
Summer Biomechanics, Bioengineering and Biotransport Conference
June 29 –July 2, National Harbor, MD, USA
SB³C2016-635

STUDY OF TWO ARTERIAL WALL DELAMINATION EXPERIMENTS

Xiaochang Leng (1), Boran Zhou (2), Xiaomin Deng (1), Lindsey Davis (2,3), Susan M. Lessner (2,3), Michael A. Sutton (1,2), Tarek Shazly (1,2),

(1) Department of Mechanical Engineering
University of South Carolina
Columbia, SC, U.S.A

(2) Biomedical Engineering Program
University of South Carolina
Columbia, SC, U.S.A

(3) Department of Cell Biology & Anatomy
University of South Carolina
Columbia, SC, U.S.A

INTRODUCTION

Abdominal aortic dissection, manifested as delamination and separation of the media layer from the arterial wall, may direct blood flow into the newly created false lumen, and the blood flow in turn aggravates the delamination in the form of Mode I or mixed-mode failure [1, 2]. Moreover, with the inherent inhomogeneity of the arterial wall along the delamination path, the delaminated media layer may be peeled from the arterial wall in a mixed-mode failure process [3]. Existing studies in the literature have investigated the dissection of the arterial wall, but experimental investigations of arterial wall delamination events and the analyses and numerical simulations of such events have been limited. To this end, two types of delamination experiments on porcine abdominal aorta specimens have been carried out, and these experiments have been simulated numerically using the finite element method and the cohesive zone model approach. A comparison of these two types of experiments and their analyses is presented here.

METHODS

Mechanical Testing

An abdominal aorta sample was isolated from freshly harvested adult porcine kidneys and rinsed with phosphate buffered saline. An approximately 30 mm long segment was cut, following a radial cut imposed onto the sample along the vessel axis, yielding a strip. Two groups of specimens oriented at an angle of 0° and 90° with respect to the circumferential vessel axis were cut from the sample.

Two types of delamination experiments were performed, as shown in Fig. 1. In each case, to initiate a delamination process in the media layer of the arterial wall, a small initial delamination flaw with a straight delamination front was carefully introduced at one end of the specimen inside the media layer. In the "mixed-mode" experiment (see Figs. 1a and 1c), the bottom surface of the lower portion of the specimen was glued to a glass plate in order to restrict its motion during loading, and the proximal end of the upper delaminated portion was peeled away by a micro-clamp. During the delamination process, the delaminated upper portion became almost parallel to the lower portion and to the not-yet delaminated interface (Fig. 1c). In the "Mode I" experiment (see Figs. 1b and 1d), the proximal end of one of the two initially separated portions of the specimen was fixed by tissue glue to a glass plate and the proximal end of the other separated portion was pulled away by a micro-clamp. During the delamination process, the two delaminated portions stay parallel to each other but are approximately perpendicular to the not-yet delaminated interface (Fig. 1d).

During each experiment, the prescribed displacement and reaction load were recorded via the system actuator and load cell (Bose ELF 3200, Biodynamic Co, MN). The delamination process was recorded by a computer vision system in which two cameras were perpendicularly positioned to get both front and side views of the specimen.

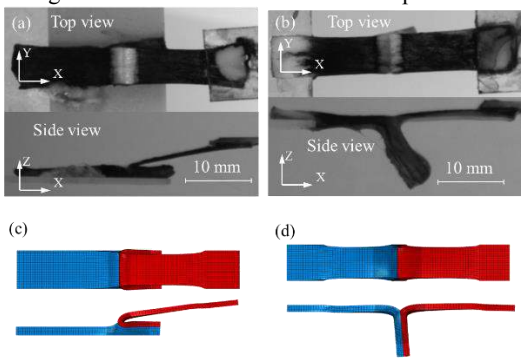

Figure 1: Images of (a) mixed-mode and (b) mode-I delamination experiments on porcine abdominal aorta specimens, and deformed shapes of (c) the mixed-mode and (d) mode-I specimens from finite element simulations.

Copyright 2016 The Organizing Committee for the 2016 Summer Biomechanics, Bioengineering and Biotransport Conference

Theoretical Framework

The mechanical properties of abdominal aorta depend on the properties and spatial arrangement of elastin and collagen, which are major load bearing structural constituents. We adopt the analytical form of the strain energy density function $\bar{\Psi}$ motivated by the structure of the arterial wall, as stated in the HGO model in [4].

$$\bar{\Psi} = \frac{\mu}{2}(\bar{I}_1 - 3) + \sum_{i=1,2} \frac{k_1}{2k_2}\left[e^{k_2[\kappa \bar{I}_1 + (1-3\kappa)\bar{I}_{4i} - 1]^2} - 1\right] \quad (1)$$

where μ is a stress-like parameter, representing the shear modulus of the amorphous matrix; $\bar{I}_1 = tr(\bar{\boldsymbol{C}})$ is the first invariant of $\bar{\boldsymbol{C}}$ which is the right Cauchy-Green strain tensor; k_1 denotes the relative stiffness of fibers; k_2 is a dimensionless parameter; $\bar{I}_{41}$ and $\bar{I}_{42}$ are tensor invariants equal to the square of the stretch in the direction of two families of fibers, respectively; and κ is the dispersion parameter, describing the dispersion of the two families of fibers in the arterial wall. $\kappa = 0$ when the two families of collagen fibers are parallel to each other and $\kappa = 1/3$ when collagen fibers distribute isotropically.

The cohesive zone model (CZM) is used to characterize the interfacial damage behavior of the arterial tissue, with the form as follows:

$$d = \frac{e\sigma_c\delta_0\left[1-\left(1+\frac{\delta_{max}}{\delta_0}\right)exp\left(-\frac{\delta_{max}}{\delta_0}\right)\right]}{G_c} \quad (2)$$

where $e = \exp(1) \approx 2.71828$ and σ_c denotes the strength of the material; $\delta_0 = \frac{G_c}{e\sigma_c}$ is the maximum effective separation at $t = \sigma_c$; where δ_{max} denotes the maximum effective separation during one delamination cycle (Fig. 2),

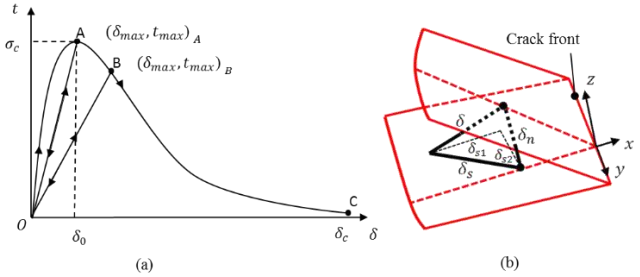

Figure 2. (a) Irreversible exponential cohesive zone model labeled with normalized effective traction and effective separation; (b) a schematic of sliding (δ_s), opening (δ_n) and effective (δ) separations.

RESULTS

The material parameter values associated with the HGO model for the aortic layer and CZM for the delamination interface were identified by matching simulation predictions of the overall load-displacement curve of cycle 1 from the loading phase and the delamination phase with experimental measurements from the mixed-mode and mode I delamination experiments, respectively [3]. Simulation predictions of the load-displacement curves for cycle 2 and cycle 3 of the delamination experiments are shown in Fig.3a, b and Fig.3c, d, respectively.

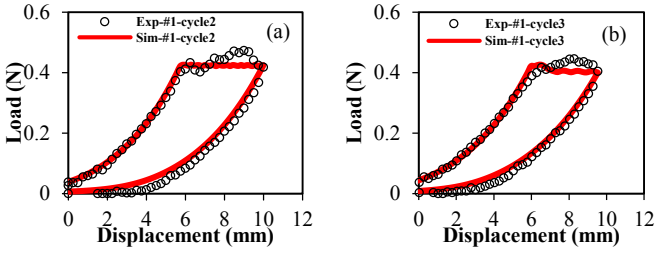

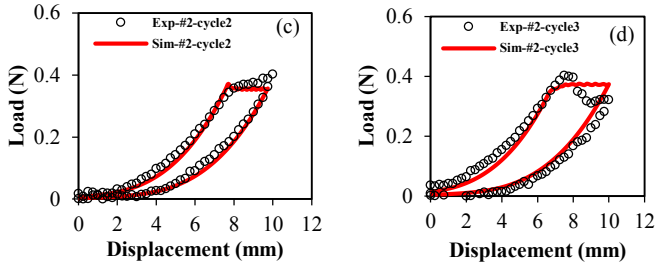

Figure 3. Comparison of predicted load-displacement curves of one loading-unloading cycle with the measured curves. (a) (b) mixed-mode experiment; (c) (d) mode I experiment.

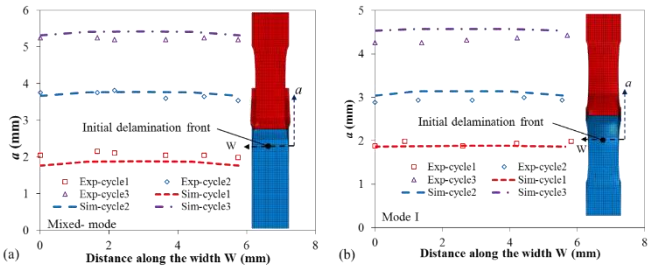

Figure 4. Comparison of predicted and measured delamination front profiles: (a) mixed-mode experiment; (b) mode I experiment.

When the delamination process is in a steady state, the delamination fronts move forward with the separation of two aortic layers. Figure 4 compares the total delamination distances from cycle 1 to cycle 3 with respect to the initial crack front for mixed-mode (Fig. 4a) and mode I (Fig. 4b) experiments, respectively.

DISCUSSION

For both basic science and clinical studies, including disease diagnosis and risk evaluation, it is advantageous to understand the arterial mechanical response during delamination under various loading conditions. The major goals of vascular biomechanics are to determine the appropriate mathematical formulations that describe tissue mechanical properties and interface damage strength, allowing the solution of boundary value problems with predictive power. In this study, the use of an arterial wall structure-motivated constitutive law and a cohesive zone model have enabled the simulation of aortic media delamination behavior based on the critical energy release rate from mechanical testing. This integrated theoretical-experimental approach was demonstrated by comparing the loading-delamination-unloading curves and the crack fronts between numerical simulation predictions and experimental measurements for two types of experiments. The delamination simulation facilitates quantification of the delaminated mechanical response of arterial walls and the understanding of the pathophysiological mechanical performance, and may shed light on the genesis and progression of certain forms of arterial aneurysms and dissections.

REFERENCES

[1] Gasser TC, Holzapfel GA. Modeling the propagation of arterial dissection. European Journal of Mechanics - A/Solids 2006;25:617.

[2] Ferrara A, Pandolfi A. A numerical study of arterial media dissection processes. Int J Fract 2010;166:21.

[3] Leng X, Chen X, Deng X, Sutton M, Lessner S. Modeling of Experimental Atherosclerotic Plaque Delamination. Ann Biomed Eng 2015;43:2838-51.

[4] Gasser TC, Holzapfel GA. Modeling the propagation of arterial dissection. European Journal of Mechanics - A/Solids 2006;25:617-33.

Copyright 2016 The Organizing Committee for the 2016 Summer Biomechanics, Bioengineering and Biotransport Conference

SB^{3}C2016
Summer Biomechanics, Bioengineering and Biotransport Conference
June 29 –July 2, National Harbor, MD, USA
SB^{3}C2016-636

PREDICTING FALSE LUMEN THROMBOSIS IN 3D PATIENT-SPECIFIC MODELS OF TYPE B AORTIC DISSECTION

Claudia Menichini (1), Zhuo Cheng (1), Richard G.J. Gibbs (2), Xiao Yun Xu (1)

(1) Department of Chemical Engineering
Imperial College London
London, UK

(2) Department of Surgery and Cancer
St. Mary's Hospital, Imperial College NHS Trust
London, UK

INTRODUCTION

Aortic dissection is a major aortic disease with high morbidity and mortality, which compromises blood perfusion in the entire body. Dissection is caused by a tear on the inner layer of the aortic wall, which allows flow diversion and causes splitting of the wall layers, leading to the formation of a "false lumen" (FL). Type B (distal) dissections are treated either medically or through endovascular stenting (TEVAR). For Type B patients, there is a large variability in post-discharge prognosis, with mortality rates ranging between 48 and 82% [1]. The status of FL (patent, partially or completely thrombosed) was identified as a significant predictor for late outcomes [1, 2]. Partial FL thrombosis is associated with higher mortality rates, due to a possible increase in pressure and a higher risk for expansion and rupture. Yet, complete FL thrombosis is associated with improved prognosis and effective endovascular treatments.

The use of computational methods holds much promise in understanding what conditions favour FL thrombosis in order to optimize treatment strategies. Here we present the application of a hemodynamics-based model to the study of FL thrombosis in patient-specific dissections. Model predictions are based on the distribution of time-averaged hemodynamic parameters and a limited number of transport equations. The model is applied to patient-specific cases following either medical treatment or TEVAR, and FL thrombosis and its effects on flow are simulated under physiological flow conditions. Predicted thrombus growth patterns are compared with follow-up CT scans in order to validate predictions and assess the capability of the model to predict FL thrombosis for different treatment strategies.

METHODS

Patient-specific geometries were reconstructed from CT scans by using the image processing software Mimics (Materialize HQ). Patients were classified into four groups: (i) medically treated, with no thrombosis (NT1); (ii) medically treated with partial FL thrombosis (S1 and S4, obtained from the same patient six months apart); (iii) TEVAR with partial FL thrombosis (I1); and (iv) TEVAR with complete FL thrombosis (C1). All patients were kept under CT surveillance for a period of at least three years, and follow-up CT scans were available for validation.

A hemodynamics-based model was used to predict thrombus formation and growth. The model is based on transport equations for a limited number of variables (e.g. residence time, different forms of platelets, and a coagulant), and predictions are driven by the distribution of time-averaged hemodynamic parameters. Regions of thrombus formation are identified through a low shear threshold. The momentum equation was modified to account for the porosity ϵ of clots, and a source term S_M was added to account for the resistance caused by a growing thrombus to the flow:

$$\rho\frac{\partial\epsilon\mathbf{u}}{\partial t}+\nabla\cdot(\rho\epsilon\mathbf{u}\times\mathbf{u})=-\epsilon\nabla p+\nabla\cdot(\mu\epsilon(\nabla\mathbf{u}+\nabla\mathbf{u}^T))-\epsilon S_M \quad (1)$$

Copyright 2016 The Organizing Committee for the 2016 Summer Biomechanics, Bioengineering and Biotransport Conference

Each geometric model was discretized into an unstructured mesh, comprising a tetrahedral core and 10 prismatic layers near the walls with a total of approximately 3,000,000 elements. A pulsatile flow waveform was applied at the inlet, and the walls were assumed to be rigid. Zero pressure and/or three-element Windkessel model were imposed at the outlets. A physiological resting platelet concentration of $2.5 \cdot 10^8$ platelets/cm^3 was prescribed at the inlet, with zero concentration for all other species.

RESULTS

Predicted thrombus growth patterns were compared with follow-up CT scans (Figs 1 and 2) and a good agreement was found in all cases. In patient S1 (not shown here), thrombus growth was initiated at the top of FL. The formation of a middle tear in model S4 altered the flow pattern and gave rise to a recirculation zone in-between the proximal and middle tears, resulting in thrombosis on the lateral side of FL. Fast and complete FL thrombosis was observed in patient C1 (Fig 2b), while in patient I1 thrombus was formed much slowly with its FL remaining partially patent (Fig 2a). No thrombus growth was observed in patient NT1.

DISCUSSION

For Type B dissections, FL thrombosis has been recognized as an indicator of patient prognosis [1, 2]. However, no methods are currently available to predict the chances for FL thrombosis and the extent of thrombosis for an individual patient. This study presents the application of a newly developed hemodynamics-based model to the formation and growth of thrombus in patient-specific dissections. Predicted thrombus growth patterns agreed well with in vivo observations from follow-up CT scans, demonstrating that the model is able to capture how different morphologies and flow features may lead to different thrombus growth patterns, and how the expansion of thrombus may affect the flow. While previous computational studies were mostly focused on modeling the complex chain of biochemical processes involved in the coagulation cascade and were more likely to be limited to simple geometries and/or steady flows [3,4], our model can identify regions of potential growth from flow features, allowing us to study physiological flows and geometries of clinical interest. To minimize computational costs, predictions are based on time-averaged parameters and accelerated kinetics. Although this approach is unable to capture real-time growth rates, it is effective in reproducing thrombus growth patterns over time and has been shown to be applicable to both medically and TEVAR treated patients.

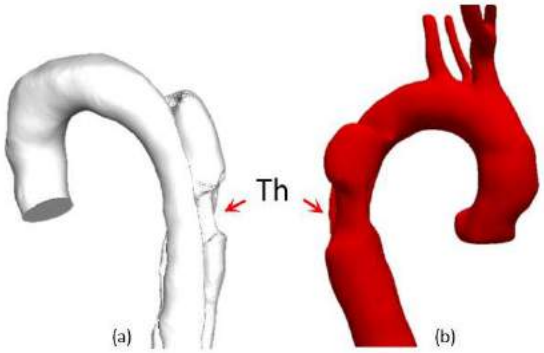

Figure 1: (a) Lumen surface predicted in patient #S4 after FL thrombosis (Th). (b) Follow-up patient geometry reconstructed from CT scans from the same patient.

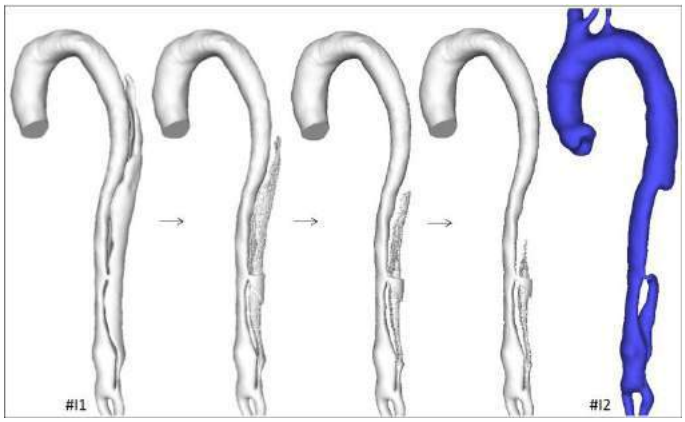

(a)

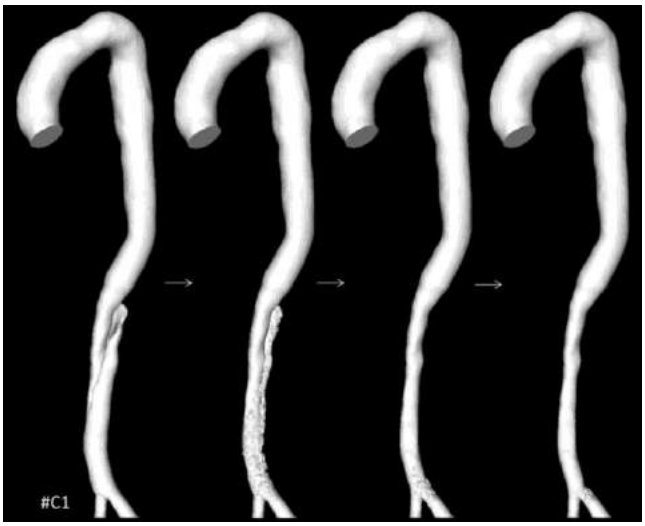

(b)

Figure 2: Time-evolution of the lumen surface following FL thrombosis in (a) #I1, compared to geometry #I2 extracted from follow-up CT scans from the same patient; and (b) #C1.

This is an on-going research aimed at identifying key parameters inducing FL thrombosis in order to optimize treatment strategies. Further studies will be carried out on more clinical cases.

ACKNOWLEDGEMENTS

This study was funded by a PhD scholarship awarded by the Department of Chemical Engineering at Imperial College.

REFERENCES

[1] Tsai, T.T. et al., *New Eng J Med*, 357(4):349–359, 2007.
[2] Trimarchi, S. et al., *J Thorac Cardiov Sur*, 145(3):S208-212, 2013.
[3] Cito, S. et al. *Thromb Res,* 131.2: 116-124, 2013.
[4] Leiderman, K. et al., *Math Med Biol*, 28(1):47-84, 2011.

Copyright 2016 The Organizing Committee for the 2016 Summer Biomechanics, Bioengineering and Biotransport Conference

SB^{3}C2016
Summer Biomechanics, Bioengineering and Biotransport Conference
June 29 –July 2, National Harbor, MD, USA
SB^{3}C2016-637

THE IMPACT OF OCULAR PRESSURES, MATERIAL PROPERTIES AND GEOMETRY ON OPTIC NERVE HEAD DEFORMATION

A. Feola (1), J.G. Myers (2), J. Raykin (1), E.S. Nelson (2), B. Samuels (3), C.R. Ethier (1)

(1) Department of Biomedical Engineering, Georgia Institute of Technology/Emory University, Atlanta GA

(2) NASA Glenn Research Center, Cleveland, OH

(3) Department of Ophthalmology, U. Alabama at Birmingham, Birmingham, AL

INTRODUCTION

Alteration in intracranial pressure (ICP) has been associated with various ocular pathologies that cause visual impairment, including glaucoma, idiopathic intracranial hypertension and Visual Impairment and Intracranial Pressure (VIIP) syndrome. While much research has focused on how elevated intraocular pressure (IOP) alters the deformation of optic nerve head (ONH) tissues, it is unclear how ICP alters deformation of ocular tissues and eventually leads to vision loss.

Recently, understanding the effect of elevated ICP on ocular tissues has become a major concern for NASA, where 42% of astronauts that partake in long duration space missions suffer from VIIP syndrome. Astronauts with VIIP syndrome suffer from visual impairment and changes in ocular anatomy that persist after returning to earth (1). It is hypothesized that the cephalad fluid shift that occurs upon entering microgravity increases ICP, which leads to an altered biomechanical environment in the posterior globe and optic nerve sheath, and subsequently VIIP syndrome.

Our goal was to develop a finite element (FE) model to simulate the acute effects of elevated ICP on the posterior eye. Here, we simulated how inter-individual differences in pressures, tissue material properties and ocular geometry affect the deformation of ONH tissues.

METHODS

Our geometric model was an extension of an established model of the posterior eye (2), including the annular scleral ring, pia mater, dura mater, and optic nerve. The pia mater, dura mater and optic nerve were extended posteriorly 10 mm from the ONH. We also included a single central retinal vessel to include the effects of blood pressure (Figure 1). The open-source program Gmsh was used for geometric model creation and mesh generation (3). For all simulations we used the finite element solver FEBio (4). The geometry of the eye for FE analysis was treated as axisymmetric – represented as a 3° wedge about an axis of symmetry passing though the central retinal vessel due to constraints of the FEBio solver.

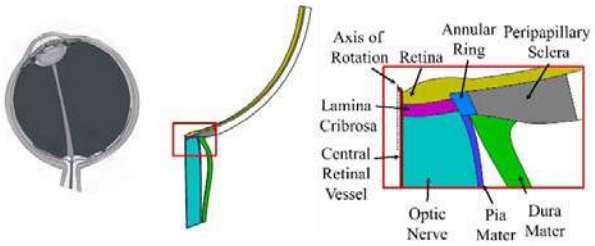

Figure 1: Left: Overview of eye (Acharya et al., 2008.) Center: Axisymmetric geometric model of the posterior eye and optic nerve sheath. Right: zoomed image of the ONH.

The lamina cribrosa, optic nerve, central retinal vessel and retina were modeled as isotropic, linear-elastic and homogenous. The baseline Young's modulus and Poisson ratio for each tissue component were based on previously reported values (2). All other tissues were modeled as a Mooney-Rivlin solid with embedded collagen fibers, distributed according to a von Mises distribution (5).

We adapted a Latin hypercube sampling (LHS) approach to simulate inter-individual variations in the pressures and material parameters. First, using a baseline ocular geometry we considered three ICP conditions: the upright and supine position on earth and an elevated ICP assumed to occur in chronic microgravity or intracranial hypertension. Intraocular pressure (IOP) and mean arterial pressure (MAP) values were provided by Lifetime Surveillance of Astronaut Health (LSAH) Program, NASA Johnson Space Center, from

Copyright 2016 The Organizing Committee for the 2016 Summer Biomechanics, Bioengineering and Biotransport Conference

measurements on astronauts in-flight. For each ICP condition (upright, supine and elevated), the IOP, ICP, MAP and twenty material properties were varied independently. Our outcome measures were the peak strains (95th percentile) in the lamina cribrosa, optic nerve and retina, since these peak strains can alter cell phenotype and induce tissue remodeling.

To assess the impact of ocular geometry, we independently varied scleral radius and thickness, two quantities previously reported as being the most influential geometric attributes affecting ONH strains (2). These previous studies focused on the impact of IOP and not ICP; therefore, we also varied the thickness of the pia mater, which is directly affected by changes in ICP. For these additional 6 geometries (Table 1) we specified IOP, ICP, MAP and material properties from the elevated ICP condition of our baseline model.

	Baseline	Low	High
Sclera Radius (mm)	12	9.6	14.4
Sclera Thickness (mm)	0.8	0.64	0.96
Pia Thickness (mm)	0.06	0.048	0.072

Table 1: Baseline, low and high values considered for geometric attributes in sensitivity analysis. Each attribute was varied independently, resulting in 6 additional models.

RESULTS

While investigating how ICP altered the strains within the ONH we found that strains in the lamina cribrosa and retina generally decreased as ICP increased; however, within the optic nerve, the incidence of extreme strains – strains above those experienced in the upright and supine conditions – increased in the elevated ICP condition. Specifically, ~47% of simulations in the elevated ICP condition showed peak strains in the optic nerve that exceeded the most extreme strains expected under terrestrial conditions (Figure 2).

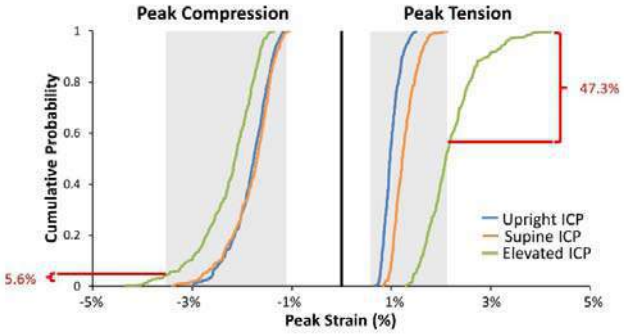

Figure 2: Cumulative probability distributions for predicted peak tensile and compressive strains in the optic nerve across a simulated population of individuals, generated by LHS. Each curve corresponds to one ICP condition, as indicated. The shaded regions show strain ranges expected under terrestrial conditions. The red lines identify the percentage of simulations experiencing "extreme strains" when exposed to elevated ICP in space.

Examining how ocular geometric attributes altered the distributions of peak strains in the elevated ICP condition, we found that the scleral radius had a minor effect on peak strains in the ONH. However, the scleral thickness had a large impact on the strains in the lamina cribrosa. Further, we found that pia mater thickness influenced the peak strains experienced in the optic nerve (Figure 3).

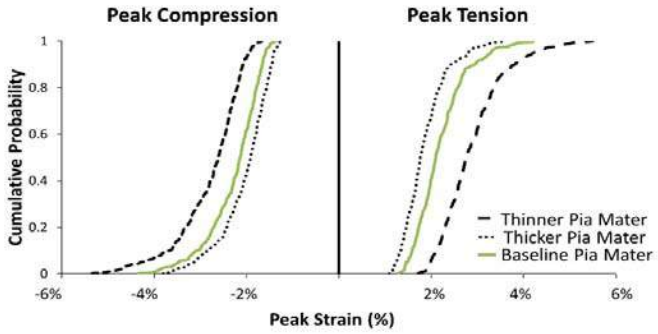

Figure 3: Cumulative probability distributions for the predicted peak tensile and compressive strains in the optic nerve for different pia mater thicknesses. A thinner pia mater resulted in increased peak strain magnitudes in the optic nerve, while a thicker pia mater led to decreased strains. All simulations were performed in the elevated ICP condition (solid green curve).

DISCUSSION

ICP is thought to be involved in VIIP syndrome and several other visual disorders. These results suggest a significant effect of elevated ICP on the optic nerve, resulting in extreme strains which may trigger a mechanobiologic response. The use of a LHS approach with FE modeling is a powerful technique to identify individual-specific risk factors for biomechanical insult to ocular tissues.

In addition, we examined how several geometric attributes influenced the strains experienced under elevated ICP, and found that the radius of the sclera did not have a significant effect on ONH strains as ICP is changed, opposite to what has been previously reported when IOP is elevated (2). However, we found that thickness of the sclera and pia mater altered the peak strains experienced in the lamina cribrosa and optic nerve, respectively. While these geometric changes primarily affected strains experienced in a single region of the ONH, these simulations highlight the importance of different geometric factors (ONH anatomy).

This study had several limitations. First, we assumed an axisymmetric geometry for the posterior eye, which is a simplification and may affect the strains in the optic nerve head tissues. A second limitation was the use of linear-elastic and isotropic tissue models for the complex geometric and biomechanical response of the lamina cribrosa; future work will aim to incorporate more advanced material models. Lastly, we looked at a limited number of geometric attributes that were varied independently. Additional simulations examining other ocular attributes (e.g. dura mater thickness) and varying these attributes simultaneously will improve our understanding of ICP on ONH deformation.

ACKNOWLEDGEMENTS

Financial support from the Georgia Research Alliance and NASA (grant NNX13AP91G) is gratefully acknowledged. We thank Wafa Taiym for providing in-flight measurements of the astronauts' intraocular and blood pressures. We also thank DeVon Griffin and Beth Lewandowski for administrative support.

REFERENCES

[1] Alexander, DJ, et al., Evidence Report: Risk of spaceflight-induced intracranial hypertension and vision alterations. NASA, 2012.
[2] Sigal, I et al., IOVS, 45(12):4378-87, 2004.
[3] Geuzaine, CR, et al., Int J Num Meth Eng, 79(11):1309-31, 2009.
[4] Maas, SA, et al., J Biomech Eng. 134(1):011005, 2012.
[5] Zhang et al.IOVS 56:2031-2042, 2015

Copyright 2016 The Organizing Committee for the 2016 Summer Biomechanics, Bioengineering and Biotransport Conference

SB^{3}C2016
Summer Biomechanics, Bioengineering and Biotransport Conference
June 29 –July 2, National Harbor, MD, USA
SB^{3}C2016-638

BLOOD COOLING USING CRYOGENIC NITROGEN

Brian K. Dixon (1), Joseph R. Licwinko (1)

(1) Mechanical Engineering
Rowan University
Glassboro, New Jersey, United States

INTRODUCTION

Therapeutic hypothermia involves controlled cooling the patient's body temperature or part of the patient's body. It is used to prevent further organ damage after a traumatic brain injury, stroke, or cardiac arrest. Cooling to between 30 C and 32 C is commonly desired and it is beneficial reach this temperature as quick as possible to prevent further injury. The purpose of cooling the patient is to reduce the metabolic rate of cells, reduce intracranial pressure, and prevent reperfusion injury. [1]

The two types of cooling methods that are used to cool the patient are external and invasive. The CoolGuide Catheter is an invasive method involving a tri-lumen catheter, the design of the catheter is pictured below in figure 1. The two outside lumens are connected at the end of the catheter to allow for a coolant loop and the third center lumen allows for chilled blood to enter the body.

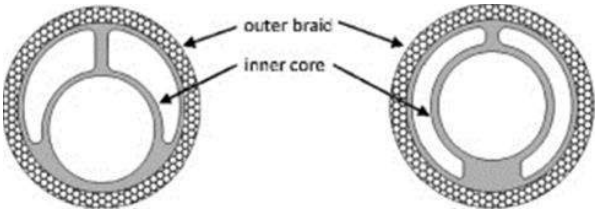

Figure 1: Two designs for the CoolGuide Catheter. The design on the right was modeled due to its partially axisymmetric shape. [2]

The purpose of this study was to explore an avenue to improve on existing blood and tissue cooling technologies, namely the current CoolGuide catheter, by replacing the cooling medium of saline with Cryogenic nitrogen. The main purpose of this change is to try and gain cooling efficiency per length of catheter, and to eliminate the need for a pump, while reducing pressure in the catheter.

METHODS

To compare the cooling power and the pressure drop of the coolant, a 115mm section of the catheter was modeled in COMSOL Multiphysics 5.1. The model was evaluated as steady state to reduce the computational time required to compare the two coolants. To simplify the model the geometry was approximated as 2-D axisymmetric with coolant flow in one direction. This represents a section of the catheter with 160 degrees of axial symmetry. Although the rest of the catheter is important for finding the total cooling power and coolant pressure drop, this approximated model was compared to known experimental results and was used to compare the nitrogen coolant to the traditional saline coolant used in the experiments.

The materials that were used in the model included the COMSOL built-in properties for nitrogen and water. The saline was approximated to have the same properties as water so that it can be modeled simply. The built-in properties for both of these materials have functions that correct of differences in temperature and pressure. This is especially important for the nitrogen as the large temperature changes cause large differences in the density and other material properties. For the purposes of this simulation, blood was modeled as a newtonian fluid with a dynamic viscosity of 3.5 cP [3], a specific heat capacity of 3490 J/(Kg*K) [4], a density of 1042 kg/m^3 [4], [5] (original text), and a thermal conductivity of 0.492 W/(m*K) [6]. Although blood is a non-newtonian fluid, it can be approximated as newtonian as long as the conduit is in is larger than 40–50 mm [7].

Copyright 2016 The Organizing Committee for the 2016 Summer Biomechanics, Bioengineering and Biotransport Conference

The properties of Teflon were found on the website of the company which developed it, DuPoint. The thermal conductivity for Teflon was 0.25 W/(m*K), the specific heat capacity was 1400 J/(Kg*K), and the density was 2160 kg/m^3[8].

RESULTS

The model with 6.667E-4 kg/s of saline, which was created to be compared to the experimental data [2], predicted 15 watts of cooling. The predicted pressure drop through the catheter with saline coolant was 3.37 Kpa. Although these results do not match the experimental results, the discrepancy can be attributed to the simplification of the geometry and the relative values of the results for nitrogen and saline are expected to be similar in more complex simulations and in experimental work.

With a mass flow rate of 2.22E-4 kg/s of nitrogen, which entered the catheter at 95 K, 35 watts of cooling was predicted. The cooling that was predicted for this flow rate was well above the predicted cooling of 15 watts for the saline model, however, the pressure drop of 57 Kpa was also much higher for this flow rate so it would be inaccurate to determine that the nitrogen is a better coolant from this result. To find a nitrogen flow rate which more closely compares to the saline model, as well as to determine the effect of different nitrogen flow rates, the flow rate of nitrogen was varied from 4.44E-05 kg/s to 2.67E-04 kg/s. The results for each flow rate are shown in table 1.

Table 1: Data from Parametric study of Nitrogen Mass Flow rate. This table shows how the key results are affected by changes in the nitrogen flow rate, and that dropping to flow rate to reduce pressure has a significant effect on the cooling power of the device. For this study the aorta blood flow rate was 0.0575 kg/s, the catheter blood flow rate was 8.33E-04 kg/s, the nitrogen inlet temperature was 95 K, and the body temperature was 310.15 K.

Nitrogen Mass Flow Rate [kg/s]	Pressure Drop [Pa]	Cooling Power [W]	Catheter Outflow Temperature [K]	Aorta Outflow Temperature [K]
4.44E-05	6815	9.88	305.41	309.40
6.67E-05	11424	14.08	303.88	309.22
8.89E-05	16665	17.90	302.51	309.05
1.11E-04	22490	21.41	301.26	308.90
1.33E-04	28801	24.67	300.12	308.75
1.56E-04	35501	27.68	299.05	308.62
1.78E-04	42514	30.49	298.07	308.49
2.00E-04	49830	33.11	297.15	308.38
2.22E-04	57415	35.58	296.27	308.27
2.44E-04	65196	38.05	295.34	308.13
2.67E-04	73075	40.26	294.57	308.02

At a nitrogen mass flow rate of 8.89E-5 kg/s, which resulted in comparable cooling a saline at the same flow rate of 6.667E-4 kg/s used in previous work [2], the pressure drop through the modeled section was 16 KPa. This compares to a pressure drop of 3.37 KPa predicted for the saline. The large pressure drop compared to the saline may be an issue for the nitrogen, as reducing the pressure in the device was one of the primary goals for exploring nitrogen. The results for the pressure drop are not necessarily an accurate representation due to the limited size of the model; further work would be necessary to know how the pressures on the catheter would compare for the nitrogen and the saline. The lowest flow rate of nitrogen tested, 4.44E-5 kg/s, still created a pressure drop over twice that of the saline, and yet resulted in under 10 watts of cooling.

DISCUSSION

Due to the much higher predicted pressure of the coolant for the same cooling power, cryogenic nitrogen was not predicted to be a better coolant then saline. The elimination of the pump using the expansion of evaporating liquid nitrogen can be useful if it is worth the decrease in cooling power of the device. Other cryogenic gases, such as hydrogen, can also be explored to attempt to get better cooling at lower pressures than saline. Another avenue of testing that could be undertaken would be designing a different catheter optimized for use with expanding gas, with either asymmetric lumens for the gas to expand to minimize pressure drop, or utilizing a two piece catheter design, with a short stronger portion to address the increase in pressure that comes from the expanding gas.

It is worth discussing the strengths and limitations of the model used in this study, due to the fact that some of the limitations have the potential for large swings in results. The largest is that this model does not account for the transient behavior of the cooling, and instead relies on comparing the steady state results to the same model run using the current method. This was done to lower the computational burden of the model. Another simplification done to ease computation was the setup of the model as a 2d axisymmetric model, neglecting the return flow of the coolant. Also, by only modeling a section of the catheter, the density of the gas would change considerably more than it does in the model. Future work with more complete models can reduce the error in the results.

ACKNOWLEDGEMENTS

We would like to acknowledge Dr. Merrill for his guidance and previous work in this field.

REFERENCES

[1] M. Luscombe and J. Andrzejowski, "Clinical applications of induced hypothermia", Contin Educ Anaesth Crit Care Pain, vol. 6, no. 1, pp. 23-27, 2006.

[2] T. Merrill, D. Merrill, T. Nilsen and J. Akers, "Design of a Cooling Guide Catheter for Rapid Heart Cooling", J. Med. Devices, vol. 4, no. 3, p. 035001, 2010.

[3]P. Paulev, Textbook in medical physiology and pathophysiology. Copenhagen: Copenhagen Medical Publishers, 1999.

[4]G. Elert, 'Density of Blood', Hypertextbook.com, 2015. [Online]. Available: http://hypertextbook.com/facts/2004/MichaelShmukler.shtml. [Accessed: 30- Nov- 2015].

[5]Thermal Properties, 1st ed. p.2.<http://users.ece.utexas.edu/~valvano/research/Thermal.pdf>

[6]J. Cutnell and K. Johnson, Physics. New York: Wiley, 1998.

[7] Q. Liu, D. Mirc and B. Fu, "Mechanical mechanisms of thrombosis in intact bent microvessels of rat mesentery", Journal of Biomechanics, vol. 41, no. 12, pp. 2726-2734, 2008.

[8]Teflon PTFE Properties Handbook[Online], DuPoint, <http://www.rjchase.com/ptfe_handbook.pdf>

Copyright 2016 The Organizing Committee for the 2016 Summer Biomechanics, Bioengineering and Biotransport Conference

SB^{3}C2016
Summer Biomechanics, Bioengineering and Biotransport Conference
June 29 –July 2, National Harbor, MD, USA
SB^{3}C2016-639

A CELL MIGRATION MODEL INTEGRATING THE MECHANICAL STRESS GENERATION AND SENSING WITH BIOCHEMICAL SIGNALS

Hongyan Yuan (1), Kevin K. Parker (2)

(1) Department of Mechanical, Industrial and Systems Engineering
University of Rhode Island
Kingston, RI, USA

(2) School of Engineering and Applied Sciences
Harvard University
Cambridge, MA, USA

INTRODUCTION

Cell migration plays an essential role in many biological processes such as tissue morphogenesis, tumor metastasis, angiogenesis, and wound healing. In recent experiments, mechanical stresses generated by cytoskeleton contraction have been shown to not only move the cell body forward but also play an active role in regulating other components of cell migration such as protrusion, cell-matrix and cell-cell adhesions, and cytoskeletal organization [1-3]. Our understanding of the biochemical aspects of cell migration has advanced greatly over the past decades. However, we know little about how mechanical and biochemical signals are integrated spatially and temporarily across the cell.

In the present work, a mathematical model for cell migration has been developed to study how the mechanical stresses experienced by a cell are integrated with biochemical activities for cell migration.

METHODS

We have formulated mathematical equations to describe various cell activities including cell contraction, cell protrusion and retraction, cell-matrix and cell-cell interactions. Continuum mechanics theory and finite element method are used for calculating cellular stress and traction stress (see Figure 1). Numerical algorithm similar to cellular automaton is used to simulate cell protrusion and retraction. Reaction-diffusion equations are used to describe spatiotemporal evolution of protrusion and retraction signals, and rate equations are used to describe the dynamic remodeling of mechanical properties of cytoskeleton and cell-matrix and cell-cell adhesions. Mechanobiochemical integration will be implemented by coupling the parameters in these equations (see Figure 2).

RESULTS

The finite element simulation results show that the mechanical stresses alone are sufficient to initiate the spatial pattern formation for actomyosin stress fiber organizations, focal adhesion distributions, and lamellipodia extension from an isotropic and homogeneous initial condition. The simulation results suggest that mechanobiochemical couplings at the whole-cell level enable cells to sense their shape. It has been demonstrated that this model can simulate durotaxis in which cell migration direction is guided by the rigidity of the substrate. Furthermore, by adding a cell-cell adhesion component to the single-cell migration model, cell-pair morphogenesis when the shape of the microtissue is constrained was simulated and compared with previous experiments involving cardiac microtissues.

Copyright 2016 The Organizing Committee for the 2016 Summer Biomechanics, Bioengineering and Biotransport Conference

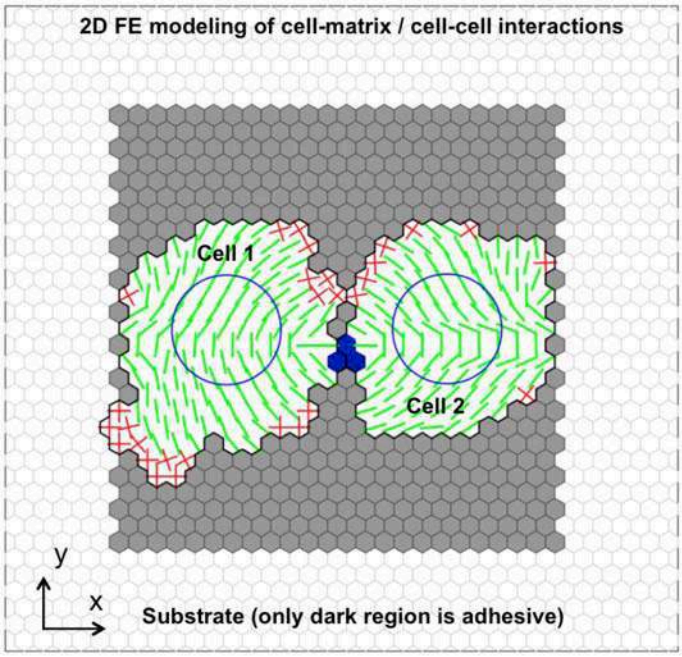

Figure 1: Finite element model of 2D cell migration in a multicellular environment.

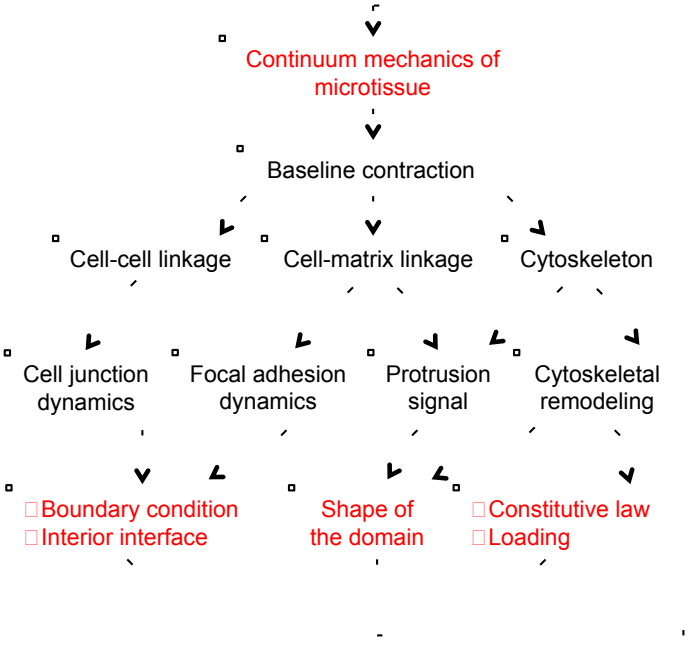

Figure 2: A flow diagram showing the assumptions of mechanobiochemical coupling and integration in cell migration.

DISCUSSION

This whole-cell level model for cell migration can help understand how the interior activities of a cell are merged with active sensing of mechanical cues of the external microenvironment. It can be used to study the effect of mechanical microenvironments in many biological problems such as tissue formation, cancer metastasis, would healing.

ACKNOWLEDGEMENTS

This work was funded by National Institutes of Health Grants R01 HL079126 and UH2 TR000522-01 (PI: Kevin K. Parker) and the 2014 Haythornthwaite Research Initiation Grant Award of ASME (to H.Y.)

REFERENCES

[1] Parker, K. K. et al. Directional control of lamellipodia extension by constraining cell shape and orienting cell tractional forces. Faseb J 16, 1195–1204 (2002).

[2] Parker, K. K., Tan, J., Chen, C. S. & Tung, L. Myofibrillar architecture in engineered cardiac myocytes. Circ Res 103, 340–342 (2008).

[3] Grosberg, A. et al. Self-Organization of Muscle Cell Structure and Function. PLoS Comput Biol 7, e1001088 (2011).

Copyright 2016 The Organizing Committee for the 2016 Summer Biomechanics, Bioengineering and Biotransport Conference

SB^{3}C2016
Summer Biomechanics, Bioengineering and Biotransport Conference
June 29 –July 2, National Harbor, MD, USA
SB^{3}C2016-640

N-CADHERIN ADHESIVE INTERACTIONS MODULATE ECM MECHANOSENSING AND FATE COMMITMENT IN MESENCHYMAL STEM CELLS

Brian D. Cosgrove (1,2,3), Keeley L. Mui (4), Tristan P. Driscoll (1,2), Steven R. Caliari (1,3), Richard K. Assoian (4), Jason A. Burdick (1,3), Robert L. Mauck (1,2,3)

(1) Department of Bioengineering
University of Pennsylvania
Philadelphia, PA, 19104

(2) McKay Orthopaedic Research Labs
University of Pennsylvania
Philadelphia, PA, 19104

(3) Translational Musculoskeletal Research Center
Philadelphia VA Medical Center
Philadelphia, PA, 19104

(4) Department of Pharmacology
University of Pennsylvania
Philadelphia, PA, 19104

INTRODUCTION. Over the past decade, it has been well established that, in addition to soluble factors and extracellular matrix (ECM) ligands, the mechanical cues from the microenvironment can direct stem cell behaviors such as proliferation, migration, and differentiation[1-2]. During connective tissue development, the microenvironment gradually changes from one that is rich in cell-cell interactions to one that is increasingly typified by cell-ECM interactions. In mesenchymal cells, this cell-cell contact is largely mediated through the homotypic interaction of N-Cadherin on adjacent cells. Studies have shown that N-Cadherin can play a large role in stem cell differentiation, as blockade of N-Cadherin expression inhibits limb bud development[3]. Additionally, there is a degree of mechanical crosstalk that exists between integrins (cell-ECM) and cadherins (cell-cell) as they are both coupled to the actin cytoskeleton and can mediate signaling events. However, determining how these signaling modalities converge to regulate cell mechanosensing is currently difficult, as presentation of these cues cannot readily be decoupled *in vivo* or *in vitro*. Culture systems for inducing cell-cell contact are not able to fully decouple cell-cell and cell-ECM inputs, and cannot control for non-cadherin cell-cell interactions that also occur with dense culture (eg. nectins, Notch/Delta, paracrine signaling), making interpretation of downstream signaling convoluted. Here, we developed an engineered hyaluronic acid (HA) hydrogel system that enables independent co-presentation of N-Cadherin and fibronectin adhesive domains (HAVDI and RGD, respectively), while additionally tuning matrix stiffness to study adhesive interactions.

METHODS. Hyaluronic Acid Hydrogels: Methacrylate-modified hyaluronic acid was synthesized and polymerized[5]. Fibronectin adhesive domain ("**RGD**", GCGYG**RGD**SSPG-), N-Cadherin adhesive domain ("**HAVDI**", **HAVDI**GGGC-), and non-functional scrambled HAVDI ("scram", AGVGDHIGC-) peptide sequences were conjugated to methacrylate groups (**Fig. 1**). Traction Force Microscopy (TFM): TFM was performed[6] on 10 kPa MeHA gels modified with 1 mM HAVDI (or scram) and 1 mM RGD. Cell Culture and Immunofluorescence: Juvenile bovine MSCs were isolated from bone marrow and cultured for one passage before being plated on gels for 18 hours prior to fixation and staining. Antibodies used included anti-YAP/TAZ (#sc-101199), anti-RUNX2 (Abcam#76956), anti-Myosin-IIA (Abcam#24762), and an N-Cadherin neutralizing Ab (Sigma# GC4). YAP/TAZ and RUNX2 nuclear-to- cytoplasmic ratios were determined by measuring the average fluorescent intensity in each domain using ImageJ. ROCK was inhibited with 10 μM Y-27632, while Rac1 activity was inhibited with 50 μM NSC-23766, both for 1hr. To introduce constitutively active (CA) Rac1, MSCs were cultured for 1 day prior to adenoviral transduction (LacZ control/CA Rac1 V12) at 750 MOI for 24hrs, followed by transfer to gels. Myosin-IIA content in focal adhesions was visualized by immunostaining and quantification[7]. Osteogenic differentiation was carried out by culturing bMSCs in growth media for one day prior to culture in an osteoinductive media for two days (growth media w/ 0.1 uM dexamethasone, 50 μg/mL A2P, 10 mM β-GP). Statistics: Analysis performed using GraphPad as noted in the legends.

RESULTS. Culture of MSCs on HAVDI/RGD substrates did not significantly alter the cell spread area or induce cadherin clustering or change expression compared to MSCs on scram/RGD gels (data not shown). The YAP/TAZ complex has recently been implicated as a mechanical 'rheostat' in the cell and translocates to the nucleus upon mechanical stimulation[8]. Quantification of the YAP/TAZ nuclear to cytoplasmic ratio revealed that N-Cadherin presentation significantly lowered YAP/TAZ ratios in MSCs on intermediate stiffness substrates

Copyright 2016 The Organizing Committee for the 2016 Summer Biomechanics, Bioengineering and Biotransport Conference

(10/15 kPa). but had no effect on YAP/TAZ localization on lower/upper boundaries of substrate stiffness (**Fig. 2A**). Examining the dose-dependence of this response showed that increasing amounts of HAVDI resulted in lower YAP/TAZ ratios (**Fig. 2B**). Blocking extracellular N-Cadherin with a neutralizing antibody prior to seeding completely abrogated these differences in YAP/TAZ nuclear localization on intermediate stiffness gels (**Fig. 2C**). This HAVDI interaction also markedly decreased downstream cell functions, including proliferation (in basal media) and osteogenesis (in osteogenic medium) (**Fig. 2D-E**).

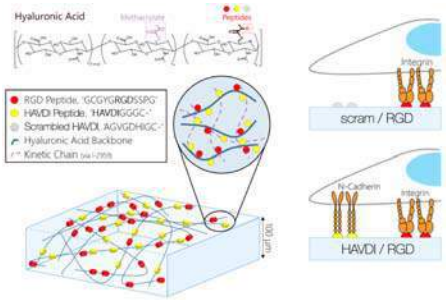

Figure 1- Schematic of MeHA gel platform.

To assess the degree to which N-Cadherin presentation perturbed the mechanical state of the cell, we next examined how the actin cytoskeleton changed in response to HAVDI presentation on 10 kPa gels. TFM showed that cells on HAVDI/RGD substrates exerted ~50% less traction stress on the substrate compared to scrambled controls (**Fig. 3A**). Treatment with NSC-23766 (a pharmacological inhibitor of Rac1 activation) abrogated any differences in YAP/TAZ signal between scram/RGD and HAVDI/RGD conditions (**Fig. 3B**). Conversely, treatment with Y-27632, a ROCK inhibitor that decreases contractility, resulted in less nuclear YAP/TAZ for both groups, without reducing the effect of HAVDI. Combination of both inhibitors further decreased nuclear YAP/TAZ, and abrogated the differences seen with HAVDI presentation. To confirm the hypothesis that HAVDI was inhibiting Rac1 activation, we transduced MSCs with adenoviral constructs containing a constitutively active (CA) version of Rac1. Compared to untreated and LacZ transduced controls, CA Rac1 "rescued" YAP/TAZ signaling in MSCs on 10 kPa HAVDI/RGD gels (**Fig. 3C**). Recently, Pasapera and colleagues showed that Rac1 activity promotes Myosin-IIA incorporation into focal adhesions, leading to maturation of these adhesions and generation of increased contractile forces[7]. Interestingly, this Rac1-dependent incorporation of Myosin-IIA occurred maximally on intermediate stiffness substrates (8.6 kPa), but had minimal effect at upper and lower bounds of substrate stiffness (0.7 and 55 kPa). To determine if HAVDI-induced differences in YAP/TAZ signaling on intermediate stiffness substrates were a result of this mechanism, we determined if there was increased Myosin-IIA incorporation into focal adhesions in our system. Analysis of confocal images of paxillin and Myosin-IIA revealed that, consistent with this mechanism, there was significantly reduced Myosin-IIA in FAs of MSCs with HAVDI presentation (**Fig. 3D**) and blockade of this incorporation with the a PKCβII-inhibitor that acts downstream of Rac1 blocked any differences in YAP/TAZ ratios (data not shown).

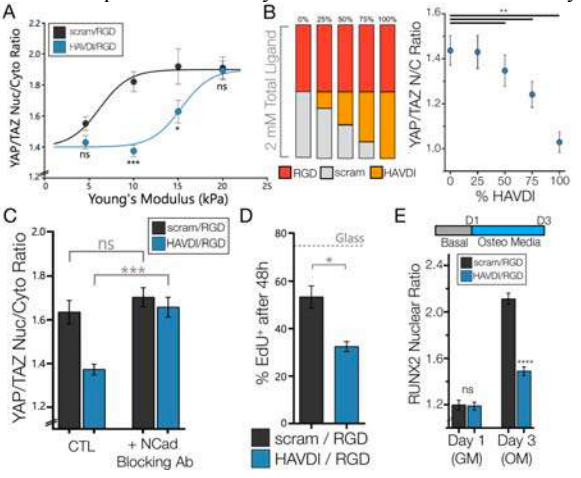

Figure 2- (**A**) YAP/TAZ ratios on scram/RGD and HAVDI/RGD gels (**B**) Dose-dependence of HAVDI presentation on YAP/TAZ ratios. (**C**) YAP/TAZ ratios of MSCs following N-Cadherin blockade. (**D**) Proliferation (EdU) and (**E**) osteogenic differentiation (RUNX2) of MSCs. Parts **B-E** performed on 10 kPa hydrogels. Graphs show mean ± SE, with *=p<0.05, **=p<0.01, ***=p<0.001, by 2-way or 1-way ANOVA w/Bonferroni post-hoc).

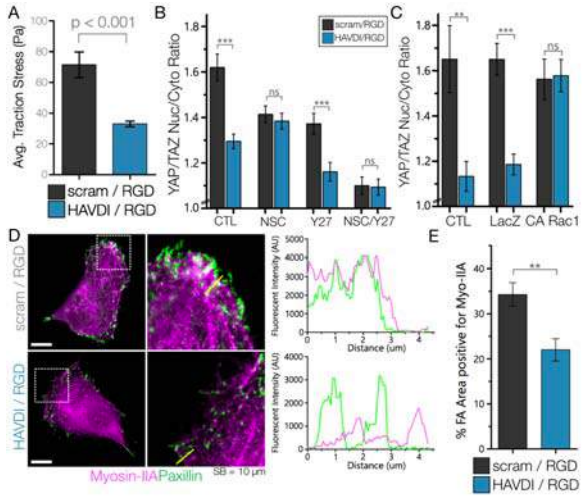

Figure 3- Mechanism experiments all performed on 10 kPa hydrogels. (**A**) Traction stress generation in MSCs. (**B**) YAP/TAZ for MSCs treated with 50μM NSC-23766, 10μM Y-27632, or both. (**C**) YAP/TAZ ratios following adenoviral transduction with CA Rac1. (**D**) Confocal imaging of Myosin-IIA and Paxillin and (**E**) quantification of Myosin-IIA content. Graphs show mean ± SE, with *=p<0.05, **=p<0.01, ***=p<0.001 by 1 or 2-way ANOVA w/Bonferroni post-hoc).

DISCUSSION. Our findings show that, on hydrogels of intermediate stiffness, HAVDI presentation (in the context of constant RGD) decreases the contractile state and YAP/TAZ nuclear localization of mesenchymal progenitors in a Rac1-depdendent fashion, resulting in altered interpretations of ECM stiffness. This change in interpretation of ECM stiffness is concurrent with alterations in downstream stem cell behavior such as proliferation and differentiation. Currently, it is thought that matrix elasticity functions to establish a contractile state in the cell that then drives mechanosensitive pathways towards a particular phenotype (eg. YAP/TAZ promoting lineage commitment). Therefore, any perturbation of the mechanical state of the cell on a given stiffness ECM (HAVDI ligation from N-Cadherin in the case of this work), can offset the mechanosensitive signaling, shifting the response curves. This ECM stiffness "shielding" through N-Cadherin is likely an important component of the development of mesenchymal tissues, and may be relevant in pathologies that disrupt the balance of cell-ECM and cell-cell signaling. These findings may be leveraged towards biomaterials design in order to better direct stem cell behavior.

ACKNOWLEDGEMENTS. This work was supported by the NIH (R01 EB008722, HL 15553) and the Penn Center for Musculoskeletal Disorders. **REFERENCES.** [1] McBeath+, *DevCell*, 2004. [2] Engler+, *Cell*, 2006. [3] Oberlender+, *Development*, 1994. [4] Borghi+, *PNAS*, 2002. [5] Burdick+, *BioMacroMol*, 2005. [6] Tseng+, *PNAS*, 2012. [7] Pasapera+, *Current Biology*, 2015. [8] Dupont+, *Nature*, 2011.

Copyright 2016 The Organizing Committee for the 2016 Summer Biomechanics, Bioengineering and Biotransport Conference

SB^{3}C2016
Summer Biomechanics, Bioengineering and Biotransport Conference
June 29 –July 2, National Harbor, MD, USA
SB^{3}C2016-641

EARLY PRODUCTION OF PHOSPHOLIPASE A_2 ACCOMPANIES SPINAL NEUROINFLAMMATION AND PAIN FOLLOWING NERVE ROOT COMPRESSION

Sonia Kartha (1), Jenell R. Smith (1), Beth A. Winkelstein (1,2)

(1) Department of Bioengineering
University of Pennsylvania
Philadelphia, PA, USA

(2) Department of Neurosurgery
University of Pennsylvania
Philadelphia, PA, USA

INTRODUCTION

Chronic neck pain is a debilitating disorder affecting two-thirds of the general population in their lifetime [1]. The spinal nerve root is a common source of pain and can be directly injured via compression by disc herniation, spondylosis, or other spinal traumas [2]. Even transient root compression can lead to chronic pain, in part due to the robust immune response at the injury site and more remotely in the spinal cord [3-5]. Changes in the spinal neuronal and neuroinflammatory responses contribute to the onset *and* maintenance of pain [6,7]. Activation of resident glial cells in the spinal cord, specifically microglia, release many chemical mediators, including inflammatory cytokines and prostaglandins [8], which further facilitate inflammation in the spinal cord and induce and/or sustain pain.

In addition to immune cells, a sub-family of the phospholipase A_2 enzymes, secretory phospholipase A_2 ($sPLA_2$), has an important role in inflammation [9]. PLA_2 enzymes catalyze the hydrolysis of the sn-2 positions of glycerophospholipids in cellular membranes to produce free fatty acids. Inflammatory cytokines induce $sPLA_2$ activity, which generates more free fatty acids that are used in the cyclooxygenase pathway to produce prostaglandins and other inflammatory molecules [10]. Increases in $sPLA_2$ have been reported in painful spinal discs and after disc herniation [11]. Spinal $sPLA_2$ is also upregulated early after spinal cord injury and is hypothesized to exacerbate inflammation and contribute to cell death [12]. Despite evidence suggesting a role for $sPLA_2$ and inflammation at neural injury sites, the role of spinal $sPLA_2$ in pain from trauma to the peripheral nerves is not known.

This study investigated the early neuroinflammatory responses and $sPLA_2$ expression in the spinal cord in the context of pain using a rat model of nerve root compression, with different loading profiles that separately do and do not induce pain. Immunohistochemistry was used to determine both overall $sPLA_2$ expression and to probe its expression in neurons and glia in the spinal cord.

METHODS

All procedures were IACUC-approved. Male Holtzman rats underwent a unilateral C7 dorsal root compression by a 10gf clip for 15 (painful), 3 (non-painful) or 0 (sham) minutes, as described [3,4,13,15]. Behavioral sensitivity to mechanical stimuli was measured in the ipsilateral and contralateral forepaws at baseline (BL) before injury and at 1 day after injury, using von Frey filaments [3,5,13-15]. The difference in sensitivity between the paw ipsilateral to the injury and the one on the contralateral side was determined for BL and day 1; the fold-change difference relative to BL was measured. Sensitivity at day 1 was compared between groups by an ANOVA and Tukey's test.

After behavioral testing on day 1, the C7 spinal cord was harvested (painful n=6; non-painful n=5; sham n=5) and fixed in 4% paraformaldehyde. Tissue from naïve rats (n=2) was also included for normalization. The spinal cord was axially cryosectioned at 14μm and mounted onto slides. Sections were blocked using 10% normal donkey serum (Vector) with 0.3% Triton-X 100 and incubated in antibodies to goat anti-$sPLA_2$ (1:500; Santa-Cruz), rabbit anti-Iba1 (1:500; Wako) and mouse anti-MAP2 (1:250; Covance). Sections were incubated in the corresponding species-matched secondary antibodies. For each rat, 4-6 sections of the ipsilateral and contralateral superficial dorsal horns (DH) were imaged at 20X using an Olympus 5X51 microscope.

To fully characterize $sPLA_2$ expression in the spinal cord, the amount of $sPLA_2$ and that co-labeled with each of Iba1 (microglia) and MAP2 (neurons) was quantified. Using the images of the bilateral dorsal horn, expression of each of $sPLA_2$ and the cellular markers in the superficial laminae of the DH was analyzed as previously detailed [13,15]. Images were cropped to include only the superficial laminae

Copyright 2016 The Organizing Committee for the 2016 Summer Biomechanics, Bioengineering and Biotransport Conference

and a custom MATLAB script performed quantitative densitometry to separately count the total percent of pixels positive for each of $sPLA_2$, Iba1 and MAP2; those levels were compared separately between groups and sides, using a two-way ANOVA with Tukey's test. To evaluate the distribution of $sPLA_2$ in neurons and microglia, the total co-localized pixels of $sPLA_2$ and MAP2 and also $sPLA_2$ and Iba1 were quantified. Neuronal and microglial $sPLA_2$ was quantified by dividing the total number of co-localized pixels for each by the total area positive for $sPLA_2$. Differences were detected between groups and sides by separate two-way ANOVA's with Tukey's test.

RESULTS

A 15 minute compression induces sensitivity in the ipsilateral forepaw at day 1, with increases over both a 3 minute compression ($p=0.018$) and a sham procedure ($p=0.026$) (Fig 1). Paralleling pain responses, spinal $sPLA_2$ expression is more robust in the ipsilateral DH of the painful group than in both of the non-painful groups (Fig. 2). Expression of $sPLA_2$ in the ipsilateral DH is significantly increased after painful compression, with greater levels than after non-painful compression and sham ($p<0.001$). After painful injury, that increase in $sPLA_2$ is also elevated ($p<0.001$) over the contralateral DH (Fig. 3). Ipsilateral DH expression of Iba1 is also significantly elevated over the expression in the sham ($p<0.001$) and normal rats ($p=0.007$). Yet, the MAP2 expression is not different between DH sides or across groups.

In addition, DH $sPLA_2$ co-labeling increases after a p ainful injury. Neuronal $sPLA_2$ expression more than triples, which is a significant ($p<0.001$) increase (Fig 3). The extent of neuronal $sPLA_2$ in the ipsilateral DH is 28±0.27% greater than levels in the contralateral DH ($p=0.041$) (Fig. 3). The same expression pattern is evident for microglial $sPLA_2$ ($p<0.001$), with ipsilateral expression greater than other groups and its contralateral expression ($p<0.045$) (Fig 3).

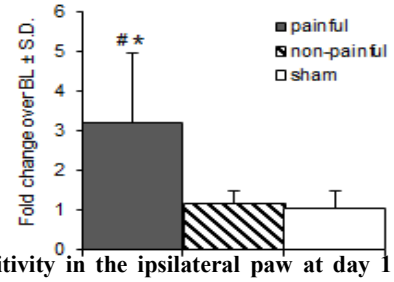

Fig 1. Sensitivity in the ipsilateral paw at day 1 is significantly greater after a painful injury than after a non-painful injury (*p=0.018) and sham (#p=0.026), which are both similar.

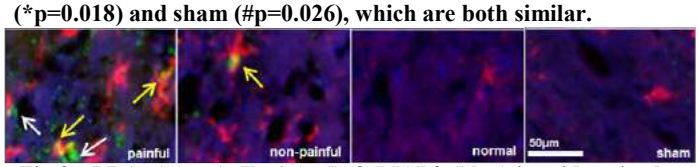

Fig 2. $sPLA_2$ (green), Iba1 (red) & MAP2 (blue) is evident in the ipsilateral DH. Painful injury induces greatest overall, microglial (yellow arrow) & neuronal (white arrow) $sPLA_2$.

DISCUSSION

This study shows that $sPLA_2$ in the spinal cord increases early after a mechanical root injury, in parallel with pain onset (Figs 1-3). The increase in $sPLA_2$ at day 1 occurs in both neurons and microglia (Figs 2 & 3). Together, these results suggest that early production of spinal $sPLA_2$ may contribute to pain from a peripheral neural injury, which is consistent with a report that inhibiting spinal $sPLA_2$ attenuates pain after an inflammatory injection in the rat's paw [10].

Despite a peripheral injury to the nerve root, both $sPLA_2$ and Iba1 expression increase in the spinal cord, while MAP2 expression is unchanged. The increase in Iba1 expression in the ipsilateral DH with pain (Figs 1 & 3) is consistent with a prior study in this same injury model in which infiltration of activated microglia into the spinal cord was also observed at this same time, along with pain [3]. Moreover, MAP2 is not expected to increase since the number of spinal neurons after root injury would not change at this time point and would only *decrease* due to their degeneration [5,15]. Taking these findings together with the overall and cell-specific increases in $sPLA_2$ after painful injury (Fig 3), it can be inferred that both neurons and microglia actively produce *more* $sPLA_2$ in response to a painful injury. It is also possible that the increased $sPLA_2$ may also be due to increased production in microglia that may also be trafficking in to the spinal cord after injury [16]. Regardless of the cell source, the increased spinal $sPLA_2$ may be due to inflammatory cytokines which can activate glial cells and induce different biochemical pain mediators, and are upregulated early in conjunction with pain after root compression [17]. Since it is unknown how soon $sPLA_2$ production begins after injury and how long it persists, additional studies are needed to understand whether it promotes, or is in response to, spinal inflammation and pain onset and/or maintenance. Nonetheless, this work shows that $sPLA_2$ plays an active role in inflammation after painful nerve root injury and may be a potential target to treat chronic pain.

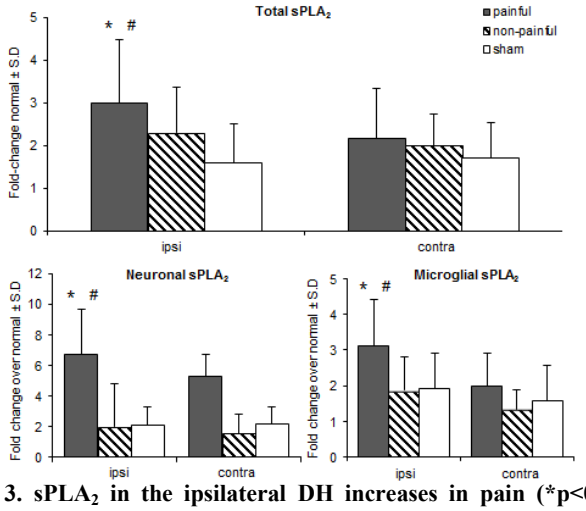

Fig 3. $sPLA_2$ in the ipsilateral DH increases in pain (*p<0.001), with more expression than in the contralateral DH (#p<0.001). Neuronal and microglial $sPLA_2$ also increase (*p<0.001), with greater expression in the ipsilateral DH (#p=0.041).

ACKNOWLEDGEMENTS

Grant support was provided by the Catherine Sharpe Foundation and the Cervical Spine Research Society. We also thank Dr. Kristen Nicholson for tissue and Dr. Zhileng Cheng for the $sPLA_2$ antibody.

REFERENCES

1. Hogg-Johnson S et al *J Manip Physiol Ther* 32:S46-60, 2009; 2. Abbed K et al *Neurosurgery* 60:S28-34, 2007; 3. Rothman S et al *J Neuro Res* 87:2709-17, 2009; 4. Rothman S et al *Brain Res*,1181:30-43, 2007; 5. Hubbard R et al *Exp Neurol* 212:482-9, 2008; 6. DeLeo J et al *Pain* 90:1-6, 2001; 7. Winkelstein B et al *Brain Res* 956:294-301, 2002; 8. Ren K et al *Curr Opin Anaesthesiol* 21:570-9, 2008; 9. Titsworth W et al *CNS Neurol Disord Drug Target* 7:254-69, 2008; 10. Svensson C et al *Neuroscience* 133:543-5, 2005; 11. Ren D et al *J Orthop Res* 10:38, 2015; 12. Titsworth W et al *Glia* 57:1521-37, 2009; 13. Nicholson K et al *J Neuro Res* 92:116-29, 2014; 14. Kras J et al *Spine* 39:207-12, 2014; 15. Nicholson K et al *Neuroscience* 209:187-95, 2012; 16. Sheng W et al *J Neuroinflamm* 8:121, 2011; 17. Rothman S et al *Spine* 36:197-202, 2011.

Copyright 2016 The Organizing Committee for the 2016 Summer Biomechanics, Bioengineering and Biotransport Conference

SB^{3}C2016
Summer Biomechanics, Bioengineering and Biotransport Conference
June 29 –July 2, National Harbor, MD, USA
SB^{3}C2016-642

CONNEXIN 43 STABILITY AND GAP JUNCTION CHANNEL FUNCTIONALITY: THE ROLE OF HEPARAN SULPHATE

S. Mensah (1), H. Homayoni (2), M. Cheng (2), B. Plouffe (1), E. Ebong (1, 2,)

(1)Department of Bioengineering
Northeastern University
Boston, MA, USA

(2) Department of Chemical Engineering
Northeastern University
Boston, MA, USA

INTRODUCTION

In recent times, endothelial glycocalyx (GCX) has been a target for the detection and prevention of some pathological conditions including global ischemia and atherosclerosis. GCX location in the vascular system ensures that endothelial cells (EC) are well protected and stimulated. GCX is composed of core proteins (CPs) which form the backbone structure and extensions that connect to CPs called glycosaminoglycans (GAGs) [1]. GAGs are repeating disaccharide units that form GCX components, such as heparan sulphate (HS), chondroitin sulphate (CS), and hyaluronic acid (HA), commonly associated with EC. The function of GCX is very much dependent on the arrangement of the GAGs [2]. All the various GAGs mentioned above play an important role in the function of GCX, but for the scope of this project, we considered HS. HS is the dominant constituent of GCX; it is sulphated, consists of 40-300 sugar residues approximately 20-150 nm in length, and it is attached to the apical CPs syndecans and glypicans [3] and contributes to the overall stability of GCX.

In addition to GCX that helps stabilizes endothelial cells, there exist also inter-endothelial cell gap junction which consists of a group of protein channels that connect neighboring cells. This connection enables the transport of ions and other small molecules across EC. For the purpose of this study, a gap junction protein (GJP) called connexin will be considered. To date over 20 different types of mammalian connexin have been identified, with three of them - connexin37, connexin40 and connexin43 (Cx43) - directly related to EC. There are ongoing studies trying to better understand the relationship between GCX and connexin channels. Some studies have reported the effect of shear stress induces GCX remodeling that has an impact on GJP distribution[4]. A study by Thi *et al* has linked GCX to the organizational changes that occur to EC GJPs due to shear stress applied from blood flow [5]. Here, we extend the study of Thi et al.

Our goal is to investigate the relationship between GCX, namely the HS component, and both organization and function of Cx43. We hypothesize that the degradation of HS from GXC will disrupt CX43 and gap junction function; while subsequent restoration of HS in GCX will restore Cx43 and gap junction channels function.

METHODS

We tested our hypothesis by [I] degradation of HS from rat fat pad endothelial cell (RFPEC) GCX using 15mU/ml of the enzyme Heparanase lll; [II] replacement of HS after enzyme degradation with 59mg/ml of exogenous heparan sulphate; [III]

Copyright 2016 The Organizing Committee for the 2016 Summer Biomechanics, Bioengineering and Biotransport Conference

determination of the effect of degradation and replacement of HS on Cx43 distribution at borders between neighboring RFPEC and [IV] quantification of the role of GCX on the opening and closing of gap junction channels, using the well-established Lucifer Yellow dye transfer technique.

RESULTS

The results indicate that the removal of HS from RFPEC GCX causes a statistically significant decrease in membrane localized Cx43 expression from 59.61 ± 3.20% to 30.40 ± 4.65%. Samples in which HS was replaced after degradation showed an increase in membrane Cx43 expression from 30.40 ± 4.65% to 46.45 ± 4.20%, a statistically significant improvement in comparison with enzyme treated samples and control samples. Cell to cell communication as assessed by Lucifer yellow dye showed a 2.6 ± 0.16 cells spread of the dye in control conditions but was reduced to 1.6 ± 0.16 cells in enzyme treated samples, showing a statistical significant decrease in dye spread in comparison with control conditions. However, there was no significant difference between enzymes treated samples and those in which HS was replaced (1.6 ± 0.16 cells and 1.5 ± 0.16 cells respectively).

DISCUSSION

Recent studies have shown the ability to degrade several components of GCX in order to better understand the way its components contribute to its entire integrity [6,7]. There are few studies of GCX regulation of intercellular gap junctional communication. Thi et al [5] performed a well controlled study demonstrating that removal of HS, results in GJPs becoming insensitive to shear stress from the flow of blood which then causes the protein to be displaced. We continued this work by establishing the fact that the removal of HS has the ability to disorganize gap junction protein, namely Cx43, and also the removal of HS greatly reduced the ability of GJP channels to transport ions and molecules between EC. Furthermore, GCX repair with exogenous HS restores gap junction protein placement which is promising for reactivating gap junction channel activity. The inability of Cx43 channels to re-open after HS restoration is not clear. It is known that there exists some connection between GCX and cortical actin web and, downstream, some connection between the actin cortical web and the cell-to-cell junctions. So, it is possible that disruption of GCX from enzymatic degradation or certain disease conditions causes the delocalization of actin cortical web from the cell periphery, which in turn causes the misalignment of junctional proteins like Cx43. Cx43 misalignment would hinder the movement of Lucifer yellow dye, and ions and signaling molecules, across Cx43-containing gap junction channels. In conclusion, we have shown that the structural integrity of EC GJP is also dependent on the state of GCX Heparan Sulphate. The inability to restore GJP communication after HS replacement may involve non-Cx43 GJP (Cx40 and Cx37) and other GAGs (CS and HA), which are outside the scope of this present investigation.

ACKNOWLEDGEMENTS

We acknowledge the financial support of the National Institutes of Health (K01 HL125499 awarded to Ebong). We also thank Northeastern University for start up funds, a Tier 1 Provost Grant, and use of the confocal microscope available in the Department of Pharmaceutical Sciences.

REFERENCES

[1] Ebong, E.E., et al., *Imaging the endothelial glycocalyx in vitro by rapid freezing/freeze substitution transmission electron microscopy.* Arterioscler Thromb Vasc Biol, 2011. 31(8): p. 1908-15.

[2] Tarbell, J.M., et al, *Mechanosensing at the vascular interface.* Annu Rev Biomed Eng, 2014. 16: p. 505-32.

[3] Giantsos-Adams, K.M., et al., *Heparan Sulfate Regrowth Profiles Under Laminar Shear Flow Following Enzymatic Degradation.* Cell Mol Bioeng, 2013. 6(2): p. 160-174.

[4] Tarbell, J.M., et al, *Cellular fluid mechanics and mechanotransduction.* Ann Biomed Eng, 2005. 33(12): p. 1719-23.

[5] Thi, M.M., et al., *The role of the glycocalyx in reorganization of the actin cytoskeleton under fluid shear stress: A "bumper-car" model*: Proc Natl Acad Sci U S A. 2004 Nov 23.

[6] Zeng, Y., et al., *The structural stability of the endothelial glycocalyx after enzymatic removal of glycosaminoglycans*. PLoS One, 2012. 7(8): p. 14.

[7] Grondahl, F., et al., *Easy HPLC-based separation and quantitation of chondroitin sulphate and hyaluronan disaccharides after chondroitinase ABC treatment*. Carbohydr Res, 2011. 346(1): p. 50-7.

Copyright 2016 The Organizing Committee for the 2016 Summer Biomechanics, Bioengineering and Biotransport Conference

SB³C2016
Summer Biomechanics, Bioengineering and Biotransport Conference
June 29 –July 2, National Harbor, MD, USA
SB³C2016-643

AORTIC REGURGITATION ON LEFT VENTRICULAR DIASTOLIC FLOW

Ikechukwu (Ikay) Okafor (1), Vrishank Raghav (2), Gautam Kumar (3), Ajit Yoganathan (1,2)

(1) School of Chemical and Biomolecular Engineering
Georgia Institute of Technology
Atlanta, GA, USA

(2) Wallace H. Coulter Department of Biomedical Engineering
Georgia Institute of Technology
Atlanta, GA, USA

(3) Department of Cardiology
Emory University and Atlanta VA Medical Center
Atlanta, GA, USA

INTRODUCTION

Aortic regurgitation (AR) is a valvular disease in which the aortic valve (AV) leaflets fail to coapt properly, thereby allowing backflow of blood from the aorta to the left ventricle (LV). This backward flow manifests itself as a high velocity jet through the AV into the LV during the ventricular filling phase of the cardiac cycle.

It has been observed that during diastole, a single vortical ring structure is formed as a result of the interaction between the blood and the mitral annulus and leaflets [1], [2]. The part of the vortical ring structure proximal to the inferolateral wall of the LV breaks down as a result of its constant shearing along the myocardium. The remainder of the vortical structure then grows in size until it engulfs the entire LV. This observed flow pattern during diastole has been shown to minimize energy dissipation and maximize the momentum of the inflow jet from the left atrium, while redirecting itself toward the LV outflow tract as it prepares for ejection during the systolic portion of the cardiac cycle [3].

In the presence of AR, the regurgitant jet from the aorta is expected to collide with the trans-mitral filling jet from the left atrium, leading to energy losses. In a simplified form, this phenomenon is expected to resemble the collision of jets of different spatial magnitudes and strengths.

Fluid flow in the LV in the presence of AR has not yet been investigated in a finely controlled setting. In order to the bridge this gap in knowledge, we analyze and quantify the fluid dynamic changes within the LV resulting from the alteration of AR severity.

METHODS

Left Heart Simulator (LHS): The *in vitro* LV model (Figure 1a) used in this work was made from silicone rubber. The model [4] was enclosed in an acrylic chamber (refractive index of 1.49), which was filled with a 36v/v% mixture of glycerin-water solution. This fluid was used to mimic the kinematic viscosity of blood at 37°C (3.5 cSt). The motion of the LV wall was induced via a programmable piston pump connected to the outer chamber housing the LV. Systemic resistance and compliance elements were included in the flow circuit to obtain physiological flow rates and pressures. The same fluid as the blood analogue was used in the outer chamber surrounding the LV.

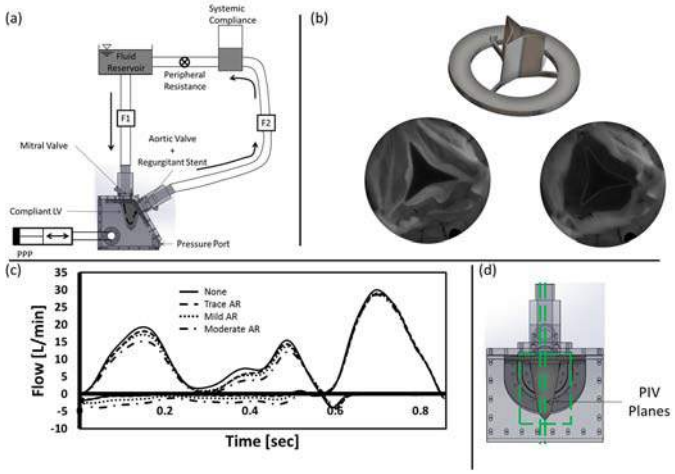

Figure 1: (a) Left heart simulator. (b) AR stent. (c) Flow profiles for control and AR conditions. (d) Schematic of PIV planes.

Aortic Valve: A 23 mm aortic valve excised from a porcine heart was used. The valve was sutured to a 3-pillared stent. To induce AR, a second stent (AR stent) was inserted in to the coaptation zone of the AV preventing full leaflet closure and resulting in central AR (Figure

Copyright 2016 The Organizing Committee for the 2016 Summer Biomechanics, Bioengineering and Biotransport Conference

1b). These stents induced AR with regurgitant fractions (RF) ranging from ~5 to ~40% (mild to mild/moderate according to AHA guidelines).

Hemodynamics: The LHS was initially tuned with a competent valve to physiological flow rates and pressures. A cardiac output of 5.0 L/min and aortic pressures of 120/80 mmHg at a heart rate of 70 beats/min were set. Once the LHS was tuned to these conditions, the AR stents were sequentially introduced to the system (Figure 1c). 200 cycles of hemodynamic data (pressures and flow rates) were acquired at 2 kHz using LabView.

Particle Image Velocimetry: Two-component, planar PIV was performed on the central long-axis plane of the LV, which cuts through the center of the mitral and aortic valves (Figure 1d). The fluid inside the LV was seeded with neutrally buoyant fluorescent particles. These particles were illuminated using a laser sheet of 1mm thickness generated from a double-cavity Nd:YAG laser. The particles were imaged with a PIV CCD camera (LaVision, Germany, Imager ProX, 1600 × 1200 pixels). 200 phase-locked PIV data were acquired at 35 time points, spaced 25 ms apart over the cardiac cycle. Metrics calculated include out of plane vorticity and energy dissipation rate (EDR).

RESULTS

Control/NoAR: Figure 2 illustrates the streamlines of intra-ventricular diastolic flow field overlaid on iso-vorticity contours for the control case. It was observed that the trans-mitral pressure gradient during the beginning of the E-wave gave rise to the passive filling of the LV. The trans-mitral jet resulted in a clockwise rotating vortical structure which engulfed the entire LV (Figure 2).

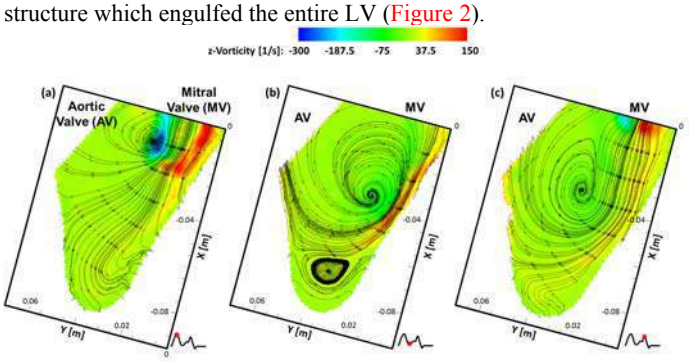

Figure 2: Out-of-plane iso-vorticity contour map overlaid with streamlines of the flow field for the central plane of control case at T = (a) 0.15 s, peak E-wave, (b) 0.275 s, end E-wave, and (c) 0.5 s, peak A-wave

AR: As the pressure inside the LV decreased during the beginning of diastole (the E-wave), the AR jet developed immediately, before the development of the trans-mitral filling jet. The AR jet impinged on the inferolateral wall of the LV (Figure 3). Due to the presence of the strong AR jet, the trans-mitral filling vortex was hindered from developing and growing in strength. Comparing the control and AR cases, it can be clearly observed how the presence of AR would contribute towards destroying the coherent trans-mitral filling vortex. Following the completion of the E-wave, the AR jet completely annihilated the remnant trans-mitral filling vortex generated by the E-wave. The filling of the LV due to the A-wave does not result in a vortical structure, unlike the control case with no regurgitation.

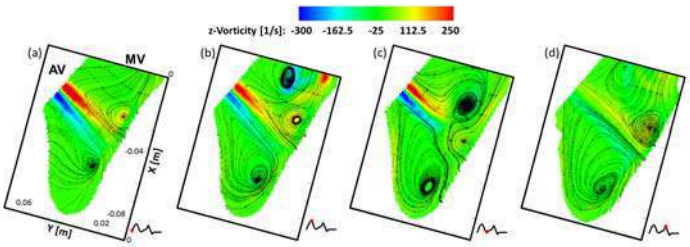

Figure 3: Out-of-plane iso-vorticity contour map overlaid with streamlines of the flow field for the central LVOT plane of AR 2 case at T = (a) 0.05 s, start E-wave, (b) 0.15 s, peak E-wave, (c) 0.275 s, end E-wave, and (d) 0.5 s, peak A-wave.

Energy Losses Due to AR: High EDR values were primarily located close to the AR jet region, the collision region of the AR and trans-mitral jet, and at the location where the AR jet strikes the posterior wall. The spatially averaged EDR at each measured time point in the cardiac cycle showed that EDR increases with increasing AR severity. We speculate that these observations would have an adverse effect on the filling efficiency of the LV. The efficiency of LV filling has been hypothesized to be directly dependent on the dynamics of the trans-mitral E-wave filling vortex [5].

DISCUSSION

The mechanism through which AR hinders the efficient filling of the LV appears to be through the formation of a 'kinematic wall'; a barrier that evidently blocks the flow from the mitral valve into the LV. It was observed that in all the AR cases tested in this work, the regurgitant jet impinged on the inferolateral wall. Similar observations were also noted in canine subjects with induced aortic insufficiency resulting in aortic regurgitation and in human subjects with AR [6]. Viscous energy losses were quantified using EDR, which was sufficient to characterize the energy losses arising due to AR. The temporal variations of EDR suggest that the energy losses are directly correlated to the AR jet's interaction with the trans-mitral E and A-waves. EDR exhibited a bi-phasic behavior coinciding with the E- and A-waves during diastole. Similar results were observed by Stugaard et al. [6].

This study has successfully replicated AR in a bench top *in vitro* setup and performed a parametric characterization of LV diastolic flow in the presence of AR. The flow structures observed in the left ventricle during the diastolic phase of the cardiac cycle drastically change during aortic regurgitation, primarily due to the collision of the regurgitant jet and trans-mitral filling vortex. This collision leads to a marked increase in viscous energy dissipation rates as the aortic regurgitation fraction increases, demonstrating that energy dissipation rate can be used to evaluate severity of aortic regurgitation.

ACKNOWLEDGEMENTS

We thank Ven Air (Terrassa-Barcelona, Spain) for casting the silicone LV.

REFERENCES

[1] Okafor, I et al., *J Biomech*, 137:121007, 2015.
[2] Domenichini, F et al., *J. Biomech*, 40:1988-94, 2007.
[3] Eriksson, J et al., *J. Heart Circ. Physiol.*, 300:H2135-41, 2011
[4] Okafor, I et al., *J. Cardiovasc. Magn. Reson.*, 17:51, 2015
[5] Pierrakos, O et al., *J. Biomech. Eng.*, 128:527-39, 2006
[6] Stugaard, M et al., *Eur. Hear. J.–Cardio. Imag.*, 16:723-30, 2015

Copyright 2016 The Organizing Committee for the 2016 Summer Biomechanics, Bioengineering and Biotransport Conference

SB^{3}C2016
Summer Biomechanics, Bioengineering and Biotransport Conference
June 29 –July 2, National Harbor, MD, USA
SB^{3}C2016-644

QUANTIFY PATIENT-SPECIFIC CORONARY VESSEL MATERIAL PROPERTY AND ITS IMPACT ON PLAQUE STRESS/STRAIN CALCULATIONS USING CINE IVUS AND 3D FSI MODELS

Xiaoya Guo (1), Jian Zhu (2), Liang Wang (3), Akiko Maehara (4), Jie Zheng (5), Chun Yang (6), David Muccigrosso (5), Gary S. Mintz (4), Dalin Tang (3)

(1) Department of Mathematics, Southeast University Nanjing, 210096, China

(2) Department of Cardiology, Zhongda Hospital, Southeast University Nanjing, 210009, China

(3) Mathematical Sciences Dept, Worcester Polytechnic Institute Worcester, MA 01609 USA

(4) The Cardiovascular Research Foundation, Columbia University, New York, NY 10022

(5) Mallinckrodt Inst of Radiology, Washington University St. Louis, MO USA 63110

(6) Network Technology Research Inst. China United Network Comm. Co., Ltd. Beijing, China 100048

INTRODUCTION

Computational models have been used as a powerful tool to perform mechanical analysis and identify risk factors and mechanisms which may be associated with plaque progression and rupture [1]. Modeling results and stress/strain predictions are influenced by many complex factors including plaque morphology, components, material properties, and modeling assumptions [2,3]. Since patient-specific vessel material properties are in general not available, most current models used material properties from existing literature [4,5]. It is desirable to have patient-specific material properties in computational models for more accurate stress/strain predictions. In this paper, in-vivo Cine intravascular ultrasound (IVUS) data and 3D IVUS-VH data were acquired from the same patient to construct 3D plaque models with patient-specific vessel material properties determined from Cine IVUS. Results from models with different material parameters were compared.

METHODS

IVUS and IVUS-VH data. IVUS and IVUS-VH data were acquired during cardiac catheterization from one patient (M, age: 58) with informed consent obtained. 3D IVUS-VH data (41 slices) were acquired to construct the 3D model following established procedures [4]. Cine IVUS data were acquired at two different locations to determine vessel material properties (Fig. 1). Cine data were matched with their corresponding IVUS-VH slices. Segmented Cine data contained only lumen contour and wall contour (Fig. 1).

Thin-slice model and 3D vessel model. The IVUS-VH slices (slice 6, 18) registered with Cine IVUS were used to make thin-slice models (3D model using 1 slice data) while the in vivo lumen circumference variations from Cine IVUS were used to determine material parameter values. The thin-slice models were made by adding a thin slice thickness to the 2D data so that the model became 3D and axial stretch could be applied for better parameter estimation. The 3D model for the vessel were used to compare stress/strain differences caused by different material parameter values. A modified Mooney-Rivlin (M-R) model was used to describe the anisotropic material properties of blood vessel:

$$W=c_1(I_1-3)+ c_2(I_2-3)+ D_1\{\exp(D_2(I_1-3))-1\}+K_1/2K_2\ \{\exp(K_2(I_4-1)^2-1)\}.$$

Vessels with plaque were stiffer than healthy vessels, axial shrinkage was set at 5% in this paper for simplicity. Pressure boundary condition was imposed on the lumen surface using patient's arm pressures. The external pressure was set to zero. The thin-slice 3D models and 3D vessel models were solved by ADINA (ADINA R & D, Watertown, MA, USA). Solution procedures and model details can be found in [6,7].

The iterative scheme to determine lumen shrinkage and parameter values. For each thin-slice model, an iterative procedure was used to adjust the parameter values in the M-R model and the circumferential shrinkage rate to match both maximum and minimum Cine lumen circumferences corresponding to systolic and diastolic pressures, respectively. Material parameters c_1=-1312.9 kPa, c_2=114.7 kPa, D_1=629.7 kPa, D_2=2.0, K_1=35.9 kPa, K_2 =23.5 kPa from our previous paper [4] were set as initial estimates of parameter values. The initial lumen shrinkage rate S1 was set to be 10%. At each iteration step, the lumen contour would be shrunk by S1. The slice outer-boundary shrinkage rate was determined using conservation of the vessel volume. Material parameter values would be adjusted so that the lumen circumference matched minimum Cine lumen circumference. The lumen circumference under maximum pressure was obtained and compared with the maximum Cine lumen circumference. If not matched (i.e., error > tolerance), then S1 would be adjusted and the iteration continued. The iterative procedure was set to stop if the

Copyright 2016 The Organizing Committee for the 2016 Summer Biomechanics, Bioengineering and Biotransport Conference

relative changes of the shrinkage and parameter values were less than 0.01 (1%).

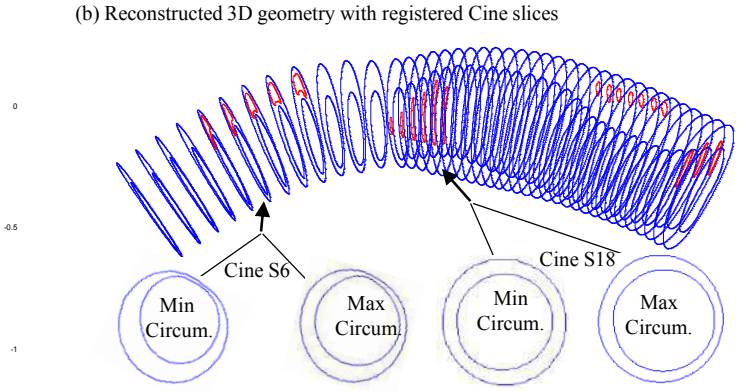

Figure 1: Plots of two sample IVUS images, contours, 3D reconstructed plaque, vessel curvature, Cine data at min and max pressures in two location.

RESULTS

Patient-specific and location-specific material parameter values. Table 1 shows the material parameter values and lumen shrinkage under 5% axial stretch. Cine data indicated that S6 and S18 circumference variations were 3.6% and 4.2%, which means that S18 was soft than S6. Material parameter values for S6 were about twice as high as those of S18.

Figure 2 gives stress and strain plots from 4 models for comparisons. Model 1: using material parameter values given in the Method section [4]; Model 2: using material parameter values from S6; Model 3: using material parameter values from S18; Model 4: Vessel part made of S1-S13 used S6 material values, vessel part made of S14-S41 used S18 material values. Maximum stress values from M1, M2 and M4 were close, while maximum stress from M3 was about 26 %, 41.6%, and 27.4% higher than those from M1, M2 and M4, respectively. Results from strain comparisons were similar.

DISCUSSION AND CONCLUSION

A Cine IVUS-based thin-slice modeling approach was introduced to obtain patient-specific in-vivo vessel material parameter values and shrinkages which are needed for models based on in vivo data. This fills a gap the current literature. Our 3D model results indicate that material parameters have impact on stress and strain calculations. Our results about the material parameter values from Slice 6 and Slice 18 indicated that different locations may have different material parameter values and shrinkages. Axial shrinkage is also an important factor for determining material parameter values.

Table 1. Material parameters, axial shrinkage and lumen shrinkage acquired from two different location by thin 3D model.

Slice 6	Min circumference	Max circumference	Min pressure	Max pressure
Cine lumen	0.9600cm	0.9949cm	70mmHg	130mmHg
Material parameters	C1=-525.16kPa, C2=45.88kPa,	D1=251.88kPa, D2=2.0,	K1=14.36kPa, K2=23.5	
Axial shrinkage	5%	Lumen shrinkage	5.7%	
Slice 18	Min circumference	Max circumference	Min pressure	Max pressure
Cine lumen	1.1969cm	1.2472cm	70mmHg	130mmHg
Material parameters	C1=-262.58kPa, C2=22.94kPa,	D1=125.94kPa, D2=2.0,	K1=7.18kPa, K2=23.5	
Axial shrinkage	5%	Lumen shrinkage	9%	

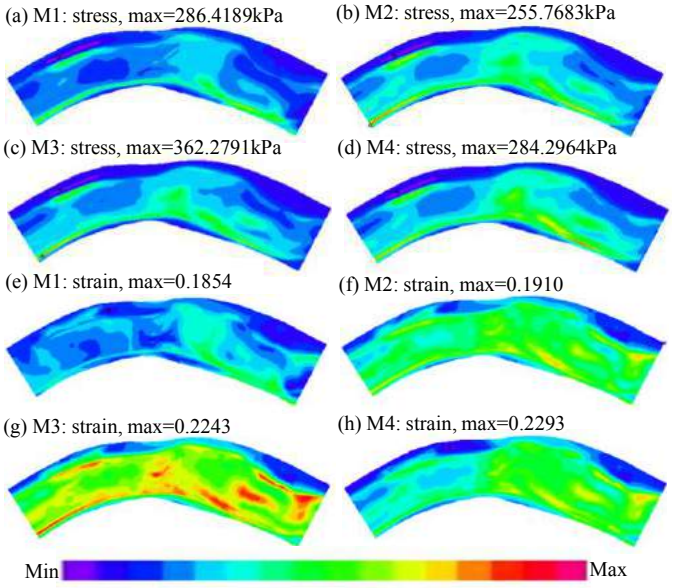

Figure 2: Stress and strain plots from M1-M2 showing modeling differences.

Acknowledgement: This research was supported by NIH grant NIH/NIBIB R01 EB004759. Discussions with and guidance from Professor Roger Kamm and Professor Don Giddens are happily acknowledged.

REFERENCES

1. Friedman MH et al., Ann. Biomed Eng., 2010:38(3), 1178-1187.
2. Tang D et al., J. Biomech. 47(4):834–846, 2014.
3. Tang D et al., Journal of biomechanical engineering, 2009, 131(6): 061010.
4. Humphrey JD, Cardiovascular Solid Mechanics, Springer-Verlag, New York, 2002.
5. Holzapfel GA et al., J Biomech Eng. 2004:126(5):657-665.
6. Liu H et al., Journal of biomechanical engineering, 2012, 134(1): 011008.
7. Yang C et al., IEEE Transactions on Biomedical Engineering 56(10):2420-2428, 2009.

Copyright 2016 The Organizing Committee for the 2016 Summer Biomechanics, Bioengineering and Biotransport Conference

SB³C2016
Summer Biomechanics, Bioengineering and Biotransport Conference
June 29 –July 2, National Harbor, MD, USA
SB³C2016-645

DESIGN OF AN AFFORDABLE OUTDOOR ADD-ON TO A MANUAL WHEELCHAIR FOR DEVELOPING COUNTRIES

S. Dash, V. Sarda, A. Sharma, S. Sujatha

Department of Mechanical Engineering
Indian Institute of Technology Madras
Chennai, India

INTRODUCTION

A wheelchair is one of the most commonly used devices for mobility. Of the estimated 65 million in the world who need a wheelchair, very few, especially in low-resource settings such as developing countries, have access to an appropriate one [1,2]. In many developing countries like India, the terrain can be uneven. The terrain makes it difficult to use a typical manual wheelchair that has two rear wheels for propulsion and two front castors (hereon referred to as 4W wheelchair). 4W wheelchair users complain about the strenuous effort required in bad terrains and there is also the danger of falling out of the wheelchair. Generally, a tricycle is the preferred device for moving in these terrains. A tricycle is more stable than a wheelchair due to its longer base and three-point contact, and propelling it is more efficient than manual wheelchair propulsion [3]. However, a tricycle cannot be used as an indoor device due to its large size. Moreover, transferring from a wheelchair to a tricycle for outdoor mobility becomes cumbersome for the user. The objective of this work is to develop a solution which provides the wheelchair user complete mobility i.e., both indoors and outdoors. We have developed a quick and easy add-on to a manual wheelchair to convert it into a manual hand cycle (tricycle) or a powered scooter. This solution provides the advantages of wheelchair for indoor use and tricycle for outdoor use.

METHODS

Interaction with numerous wheel chair users and a survey of different rural areas with the most uneven terrains in India led to the following requirements that must be met – (1) the solution should be affordable, (2) modular to fit wheelchairs of different designs and sizes, (3) accommodate Indian attire, viz., sarees worn by women, dhotis, lungis, etc., worn by men. and (4) the add-on must ensure a minimum ground clearance of 3-4 inches to ensure that the castor wheels do not come in contact with the ground.

The proposed add-on device is designed such that it can be made using cycle parts to ensure affordability and easy maintenance and/or replacement of parts. The design includes a V-block attachment (called the adapter, Fig. 1) which needs to be attached to the 4W wheelchair intended to be used with the add-on. The adapter allows for various pipe diameters of different conventionally available wheelchairs.

Figure 1: The adapter attached to the wheelchair to enable use of the add-on.

The add-on is designed to be attached from the sides to accommodate Indian attire. The spacing between the side bars is adjustable to accommodate wheelchairs of different widths. Spring-loaded pins on the sides engage with the adapter attached to the wheelchair. The height of the pin self-adjusts such that when the user

Copyright 2016 The Organizing Committee for the 2016 Summer Biomechanics, Bioengineering and Biotransport Conference

pulls the device closer, the pin engages with the adapter making it easier for the user to attach the add-on. After engaging the pins, the user needs to push the add-on forward creating a moment on the add-on that is transmitted to the wheelchair to lift the wheelchair and engage the add-on.

Figure 2: Add-on attached to the 4W wheelchair. A pin mechanism engages into the adapter. The white wheels on the add-on enable it to stay upright and move easily for attachment/detachment. The castors of the 4W wheelchair and the wheels of the add-on are lifted off the ground effecting the change to a tricycle.

To disengage the add-on from the wheelchair a lever-cable mechanism similar to brake actuation in bicycles is used to pull up the pins and disengage the add-on. A stand with the small white wheels (Fig. 2) is provided to keep the add-on upright and moveable for attachment and detachment. An improvement planned is to replace the small wheels with castors giving the user more control while engaging the device.

RESULTS

The prototype shown in Fig. 2 has been tested with 5 wheelchair users with Spinal Cord Injury at the Association of People with Disability (APD), Bangalore. We have received positive feedback on the effectiveness of the device. The users found the add-on easy to engage/disengage and the tricycle was easy to use. Improvements were suggested to the ergonomics of the handle. We are improving this and other ergonomic and cosmetic aspects with the second prototype.

DISCUSSION

The 4W wheelchair is the most commonly distributed wheelchair to economically disadvantaged users in India through charitable organizations, government schemes, etc. However, these wheelchairs are put to limited use since the users find it difficult to use them in the uneven terrain around their homes. In many cases, their homes may even be too small for them to use the wheelchair inside, so the devices provided become static chairs, instead of mobility devices. The inability to move around restricts livelihood opportunities, social interactions, and presents secondary health problems.

The proposed add-on provides an affordable, easy and quick solution to give a wheelchair user both indoor and outdoor mobility. The add-on is cost-effective since it uses local, easily available parts and simple manufacturing techniques, stable and can be attached to/detached from a conventional wheel chair in less than 5 seconds. The design is versatile since with the right adapter, any existing 4W wheelchair can benefit from the add-on, unlike other add-ons that are designed for use with a specific wheelchair [4]. It is also more portable than a conventional tricycle.

Limitations include the fact that an existing 4W wheelchair to which the add-on is attached may not be robust enough to traverse long distances on uneven terrain. For instance, the 4W wheelchairs are generally provided with solid tires. These tires are unsuitable for outdoor terrain, where they provide a very rough ride and wear quickly. Therefore, for better utility, we plan to provide the add-on with a set of pneumatic tires to replace the existing solid tires. However, this addition would increase the cost of the device. 4W wheelchairs with more robust frames would also be more durable and we are planning to design one specifically for use with this add-on.

The current design for the add-on meets the requirements of functionality and affordability for rural users and extends the use of a 4W wheelchair they may already have. We are also working on developing a motorized version of the add-on device so that a 4W wheelchair can be used in manual or motorized mode, a need articulated by urban users in India. A provisional patent is pending on the manual and motorized add-on designs.

ACKNOWLEDGEMENTS

We would like to thank the TTK Center for Rehabilitation Research and Device Development (R2D2) and the Central Workshop at IIT Madras, and the Enable Makeathon organized by the International Committee of the Red Cross (ICRC) for providing the resources for the development of this device. We also thank APD, Bangalore for help with the user-testing. We gratefully acknowledge the inputs and contacts enabled by the Spinal Foundation, a self-help group for users with Spinal Cord Injury. We also acknowledge the Wellcome Trust, UK for the funding provided to the Affordable Standing Wheelchair Project, which enabled many of the learnings on this project.

REFERENCES

[1] WHO Guidelines on the provision of manual wheelchairs in less-resourced settings. WHO Press. Geneva 2008.
[2] Sheldon S, Jacobs NA, eds. Report of a Consensus Conference on Wheelchairs for Developing Countries, Bangalore, India, 6–11 November 2006.
[3] Van der Woude LHV, Dallmeijer AJ, Janssen TWJ, et al:
Alternative modes of manual wheelchair ambulation: An overview.
Am J Phys Med Rehabil 2001 (80), 765–777.
[4] http://www.motivation.org.uk/our-products/tricycles/

Copyright 2016 The Organizing Committee for the 2016 Summer Biomechanics, Bioengineering and Biotransport Conference

SB³C2016
Summer Biomechanics, Bioengineering and Biotransport Conference
June 29 –July 2, National Harbor, MD, USA
SB³C2016-646

THE EFFECT OF DEGENERATION ON THE SIX DEGREE OF FREEDOM MECHANICAL PROPERTIES OF HUMAN SPINE SEGMENTS

John J. Costi (1), Dhara B. Amin (1), Dana Sommerfeld (2), Isaac M. Lawless (1), Richard M. Stanley (1), Boyin Ding (3)

(1) Medical Device Research Institute
Flinders University
Adelaide, South Australia, Australia

(2) Institute of Biomechanics
TUHH Hamburg University
Hamburg, Hamburg, Germany

(3) School of Mechanical Engineering
The University of Adelaide
Adelaide, South Australia, Australia

INTRODUCTION

Disc degeneration leads to biochemical and mechanical changes resulting from structural alterations in the nucleus, annulus and endplate. These changes place higher stresses on the annulus fibrosus, theoretically contributing to a more viscoelastic mechanical response. Zirbel et al. found significant differences in spine segment stiffness between degenerative grades during axial rotation, bending, and compression where the difference in stiffness between grades 3 and 5 discs were as high as a factor of 5x [1].

While the effects of degeneration on compression and rotation motions have been studied, to our knowledge there is no data for shear loading, nor across the full suite of six degree of freedom (6DOF) motions on the same spine segments. Clinical research has shown that people with low back pain (a potential consequence of degeneration) experience a 75% greater lateral shear force than those without it [2], indicating the importance of shear loading and its mechanical response [3,4]. A better understanding of this response can lead to improvements in the design of spinal implants and more rigorous finite element models. Furthermore, while stiffness has been reported in most studies, there is limited data on the energy absorption (phase angle) behavior of the segment in 6DOF.

The aim of this study was to determine and compare the 6DOF changes in spine segment stiffness and phase angle between degenerative groups.

METHODS

Fourteen intact functional spinal units (FSUs) were dissected from human lumbar spines (L1-2 x 5, L2-3 x 3, L3-4 x 4, L4-5 x 2, mean (SD) age 76.2 (11) years). Each FSU was tested in ±6DOFs at 0.1 Hz while exposed to physiologic preload (0.5 MPa), hydration (protease-inhibited, phosphate-buffered saline bath) and temperature (37°C) conditions in a hexapod robot [5]. The primary testing axis was driven in position control while the off-axis coupling was minimized in load control. Non-destructive cycle amplitudes were 1.1 MPa compression, 0.6 mm shear, 3° lateral bending, 5° flexion, 2° extension and 2° axial rotation.

Degenerative grade was determined macroscopically, based on the Thompson scale [6]. Data from the final cycle of each test were processed. Stiffness for each DOF was calculated using linear regression to determine the slope over a specific range of the loading portion of the load-displacement curve. Phase angles for each DOF were calculated between the input displacements and measured forces for all cycles using a cross spectral density estimate function.

Separate ANOVAs were performed on the dependent outcome measures of stiffness and phase angle having an independent factor of degenerative grade (mild, moderate, and severe) for each DOF. Post-hoc multiple comparisons using a Bonferroni correction on alpha were performed when significant

Copyright 2016 The Organizing Committee for the 2016 Summer Biomechanics, Bioengineering and Biotransport Conference

main effects were present. Paired t-tests between left and right lateral shear, lateral bending, and axial rotation were performed to assess symmetry of DOFs. Significant differences were accepted when $p<0.05$ (2-tailed).

RESULTS

Specimens were classified into grades 3 (N=5), 4 (N=6), and 5 (N=3) and categorized as mild, moderate, and severe degeneration respectively. Paired t-tests to analyse symmetry found no significant differences between left and right lateral shear, lateral bending, and axial rotation ($p>0.05$). The means for left and right were therefore averaged for each of those three DOFs and used in the analysis of the data.

Significant overall effects in stiffness were found between mild and moderately degenerated groups in lateral shear, flexion, and axial rotation ($p<0.020$, Figure 1). Post-hoc tests for lateral shear and axial rotation revealed that moderately degenerated groups had decreased stiffness compared to mild ($p=0.001$). For flexion, the severely degenerated group had a significantly larger stiffness than mild ($p=0.022$). For phase angle, significant overall effects were seen in anterior shear, and axial rotation ($p<0.027$, Figure 2), where phase angles for mild degeneration were less than moderate for both DOFs ($p<0.028$).

DISCUSSION

Degeneration significantly affected lateral shear, axial rotation and flexion for stiffness, and anterior shear and axial rotation for phase angle. The initial decrease in stiffness for shear and axial rotation DOFs could be attributed to an increase in delamination and annular clefts. The stiffness trends for mild and severely degenerated groups were larger than moderate in antero/postero shear, and all bending DOFs, which is consistent with previous research [1] and corresponds to the Kirkaldy-Willis and Farfan instability theory [7]. Trends of stiffness under compression and bending were relatively similar between mild to moderately degenerated groups, and increased from moderate to severe. In these directions, the major stress components are compressive and tensile, where solidification of the nucleus for severe degeneration could theoretically lead to an increased stiffness.

Generally, phase angle increased from mild to moderate degeneration, with a decrease between moderate and severe FSUs for most DOFs. There was little difference in phase angle between moderate and severe degeneration in compression and anterior shear, and this may be caused by increased contact pressure in the posterior elements once the disc becomes moderately degenerated.

Clinically, the identification of the DOFs that are most affected by degeneration could be used in rehabilitation to improve supplemental stabilization of core muscle groups.

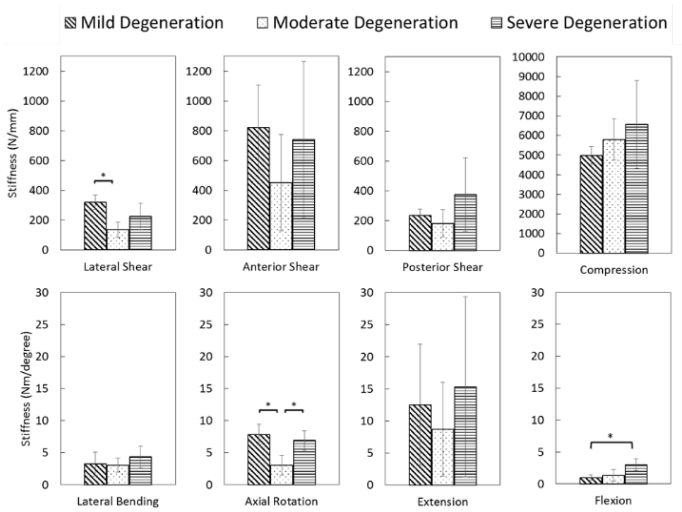

Figure 1: Mean (95% CI) stiffness for all three degenerative grades. *significant differences between groups ($p<0.05$).

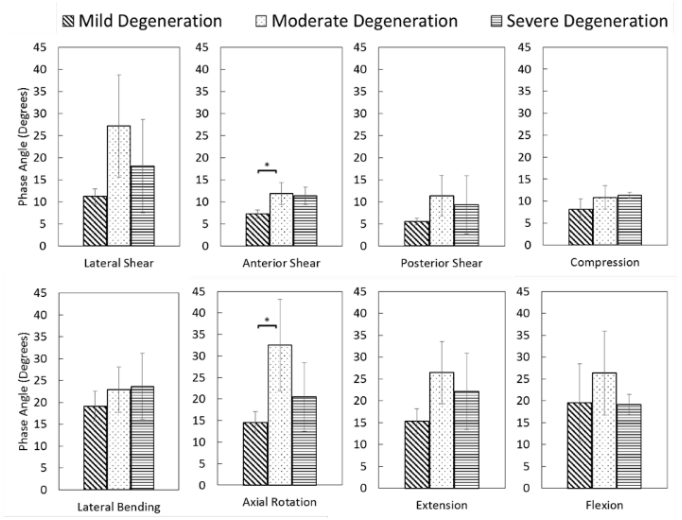

Figure 2: Mean (95% CI) phase angle for all three degenerative grades. *significant differences between groups ($p<0.05$).

ACKNOWLEDGEMENTS

This project was supported by a scholarship from Whitaker International Program administered by the Institute of International Education (IIE).

REFERENCES

[1] Zirbel, SA et al., *Spine,* 13(9):1134-47, 2013.
[2] Marras, WS et al., *Spine,* 26:2566-2574, 2001.
[3] Kim, J et al., *Ann Biomed Eng*, 40:1996-2004, 2012.
[4] McGill, SM et al., *Clin Biomech,* 15:777-780, 2000.
[5] Ding, B et al, *J Dyn Sys-T ASME,* 136(6):1-12, 2014
[6] Thompson, JP et al, *Spine,* 15:411-415, 1990.
[7] Kirkaldy-Willis, WH and Farfan, HF, *Clin Orthop Rel Res*,110-123. 1982.

Copyright 2016 The Organizing Committee for the 2016 Summer Biomechanics, Bioengineering and Biotransport Conference

SB³C2016
Summer Biomechanics, Bioengineering and Biotransport Conference
June 29 –July 2, National Harbor, MD, USA
SB³C2016-647

SHEAR DEPENDENT SICKLE RED BLOOD CELL ADHESION IN SHEAR GRADIENT HELE SHAW FLOW

E. Kucukal (1), U. Gurkan (1, 2, 3)

(1) Mechanical and Aerospace Engineering Department
Case Western Reserve University
Cleveland, OH, USA

(2) Biomedical Engineering Department
Case Western Reserve University
Cleveland, OH, USA

(3) Orthopaedics Department
Case Western Reserve University
Cleveland, OH, USA

INTRODUCTION

The adhesive and biomechanical characteristics of red blood cells play a critical role in vascular occlusions that lead to life-threatening crises in sickle cell disease (SCD). The altered properties of sickle erythrocytes due to the presence of homozygous sickle hemoglobin reduces cellular deformability and increases cell adhesion onto (sub)-endothelium matrix proteins such as Laminin (LN) and Fibronectin (FN) [1]. This sophisticated dynamic process takes place within a wide range of shear rates specific to different types of microvasculature (Fig. 1a). In literature, there have been several approaches to simulate shear rate variance based mostly on discrete shear alterations rather than a continuous gradient. Here, we present a physiologically relevant microfluidic device which creates a shear gradient along the flow direction to investigate the adhesion of sickle Red Blood Cells (sRBC) under continuously transitioning shear rates. We report a new parameter, namely Shear Dependent Adhesion Rate (SDAR), which is significantly greater in RBC-LN interaction particularly for deformable sRBCs suggesting a potential association between cell deformability and shear dependent adhesion. We further report normalized SDAR numbers for each cell type (i.e., deformable cells, non-deformable cells), which indicated that the non-deformable sRBC adhesion to FN is the least shear-dependent. Moreover, those cells required significantly higher shear rates than physiological conditions to be entirely removed from the channels.

METHODS

Hele-Shaw microfluidic device was manufactured using a lamination technique as we described earlier [1]. Briefly, a top plastic cover was assembled onto a functionalized glass slide through a 50 μm thick double sided adhesive film. The adhesive part forms a diverging flow field through which the shear rate constantly reduces to simulate the physics of flow in terms of shear distribution inside branching blood vessels (Fig. 1a&b), especially in post-capillary venules.

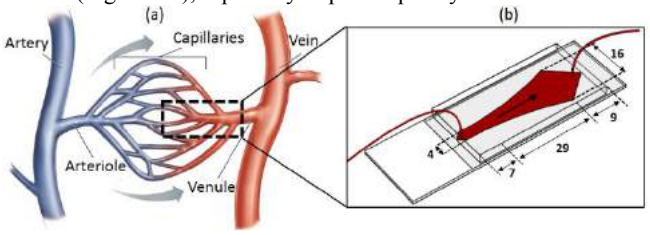

Figure 1: The variable shear-gradient microdevice to probe the shear-dependent adhesion of sRBCs. (a) A schematic view of the human microvasculature system is shown. Every branch has characteristic shear rates determined by the vessel diameter. (b) The shear gradient channel enables shear transition in a continuous manner at a single flow rate. The dimensions are in millimeters.

Numerical simulations were performed (COMSOL 4.3) to characterize the velocity and shear rate profiles in microchannel. Prior to experimental investigations, we chose a rectangular region of interest (ROI) based on computational simulations, in which the average shear rate showed more than a 3-fold reduction along the X axis (Fig. 2a).

RESULTS

We observed greater adhesion of sRBCs at lower shear sites (Fig. 2b), as expected. To assess the extent to which individual sRBC subpopulations respond to shear rate gradient, we plotted the number of adhered cells against the shear rate and fitted a linear curve in FN and

Copyright 2016 The Organizing Committee for the 2016 Summer Biomechanics, Bioengineering and Biotransport Conference

LN coated channels for both deformable and non-deformable sRBCs. Then, we defined SDAR as the slope of the fitted curve in degrees (Fig. 3). However, the shear effect was suppressed in the case of too few adherent cells, which was observed for some patients. Therefore, we normalized the SDAR based on adhesion in the first sub-region of channels ($nSDAR=\frac{\text{Number of adhered RBCs in a subregion}}{\text{Number of adhered RBCs in first subregion}}x100$).

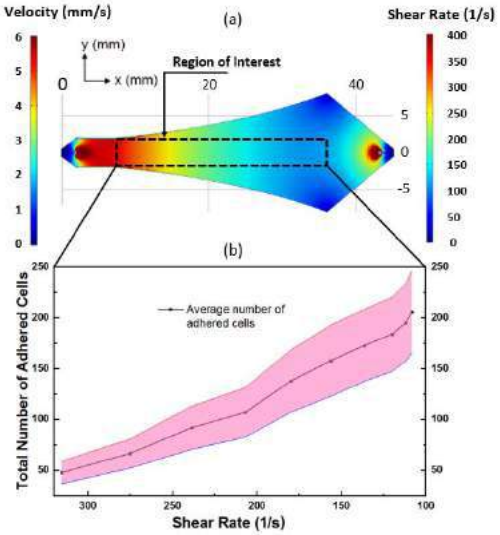

Figure 2: Computational flow simulations and quantified cell numbers in shear gradient channel. (a) The contours of velocity and shear rate were calculated on a plane 10 μm above the bottom surface, and rectangular region of interest (ROI) was chosen in which the experimental data analyses were performed. (b) The total number of adhered cells increases with decreasing shear rate downstream the flow. The shaded region represents standard error of average (n=18).

Deformable cells displayed the highest rate of shear dependent adhesion to LN (Fig. 4a). nSDAR also suggested that those cells are sensitive to changes in shear rate and can be removed significantly more with increasing shear (Fig. 4b). We also observed that non-deformable cells adhered to FN are the least shear-influenced subgroup that often require greater shear rates over the physiological range (~1000 s^{-1}) for complete detachment. Moreover, the relative nSDARs between deformable and non-deformable sRBCs were more pronounced in FN channels, where more deformable cells detached with increasing shear rate than non-deformable cells.

In addition to SDAR and nSDAR parameters, we further calculated the X-axis intercept of the fitted curves obtained for each patient sample, which we defined as Zero-Adhesion Shear Rate (ZASR) (Fig. 5). The intercept point represents the estimated shear rate required to remove all of the adhered RBCs to the specific endothelium protein. We have shown that adhered sRBCs to FN may necessitate ZASR values greater than the typical physiological shear rate of 1000 s^{-1}.

DISCUSSION

We present a new microfluidic platform that allows convenient, one-step analysis of sRBC adhesion at dynamically transitioning continuous shear rates. We have shown that red cell adhesion is influenced by shear rate at different levels depending on cell type and endothelium proteins coated on the channel surface. Based on shear-dependent adhesion analyses, we report patient specific SDAR and nSDAR values, which may help in understanding the dynamic pathophysiology of SCD and importance of shear rate in a sequence of events that eventually lead to vaso-occlusion crises. The flow and shear characteristics in different tissues and organs exhibit a wide range of variations. Therefore, this continuous shear gradient microdevice can be utilized to simulate cell to endothelium protein interactions at shear conditions observed in various organs.

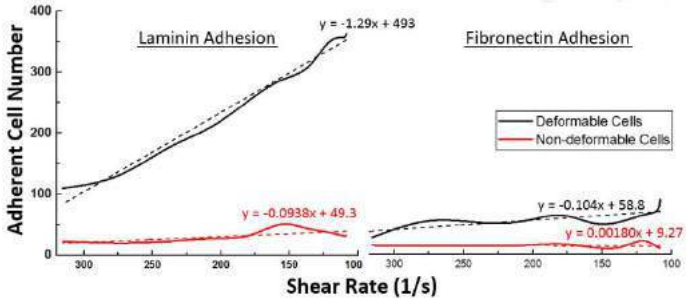

Figure 3: Typical distribution of adhered deformable and non-deformable cell numbers in LN and FN coated microchannels with varying shear rates. Dashed lines represent the linear fitted curves and their equations were used to quantify shear-related adhesion data.

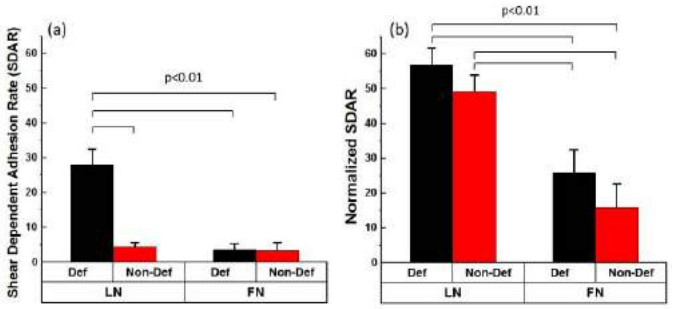

Figure 4: SCD patient based quantification of SDAR and normalized-SDAR values in LN and FN channels. (a) High levels of adhesion amplifies the SDAR for deformable cells. (b) An enhanced shear dependent adhesion was observed in LN channels based on the normalized SDARs. Error bars represent standard error (n=7-18). The statistical significance is based on one-way ANOVA.

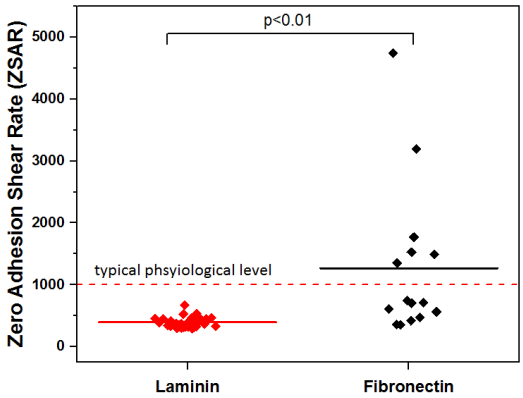

Figure 5: Estimated zero-adhesion shear rates for sRBC adhesion to LN and FN in patients with SCD. In some patients, ZASR is greater than the physiological shear rates in FN channels, which suggests a greater chance of cellular adhesive related clinical events in these patients.

REFERENCES

[1] Y. Alapan, J. Little and U. Gurkan, "Heterogeneous Red Blood Cell Adhesion and Deformability in Sickle Cell Disease," *Scientific Reports,* vol. 4, p. 7173, 2014.

Copyright 2016 The Organizing Committee for the 2016 Summer Biomechanics, Bioengineering and Biotransport Conference

SB³C2016
Summer Biomechanics, Bioengineering and Biotransport Conference
June 29 –July 2, National Harbor, MD, USA
SB³C2016-649

CHARACTERIZATION OF THE FAILURE RESPONSES OF SKIN: COMPARISON OF UNIAXIAL AND EQUIBIAXIAL PLANAR MECHANICS

Samantha N. Schumm (1), Meagan E. Ita (1), Beth A. Winkelstein (1,2)

(1) Department of Bioengineering
University of Pennsylvania
Philadelphia, PA, USA

(2) Department of Neurosurgery
University of Pennsylvania
Philadelphia, PA, USA

INTRODUCTION

Skin undergoes variable, multi-dimensional loading through physiological movement, surgery, and injury [1]. Skin is multi-layered with an outer epidermal layer and inner dermis, both of which are innervated and contain mechanoreceptors for touch and sensation [2,3]. Cutaneous mechanoreceptors in the skin respond to motions and deformations differently depending on t heir size and morphology, depth in the skin, and whether they are slow- or rapid-adapting nerve fibers [3,4]. For example, the Pacinian corpuscle (PC) is an unmyelinated nerve ending surrounded by membranous lamellae and detects high frequency vibrations with high sensitivity [3,4]. The Ruffini's corpuscles are also mechanoreceptors, but they respond to stretch and little else is known about them [3]. Epidermal innervation is also implicated in pain through altered nerve fiber density [2,5]. Recent simulation of skin using a finite element model of the PC within a fiber network demonstrated the low spatial resolution characteristic of the PC in response to indentation pressure [6]. As such, understanding the mechanical response of skin to different loading conditions is important to defining the local mechanical environment of nerves and mechanoreceptors.

In addition to defining the local mechanics for sensation, macroscopic skin responses have direct implication in wound healing and skin grafting [7,8]. Skin has been reported to exhibit non-linearity in its viscoelastic response [7], which further advocates for its multi-dimensional mechanical characterization, but which is currently lacking for skin tissue. Although parameters like tensile strength, failure strain, and elastic modulus have been defined for skin under uniaxial tension [1,9], there are few studies investigating planar biaxial loading of skin [8]. Accordingly, this study assessed the mechanical response of rat skin subjected to uniaxial and equibiaxial planar loading to evaluate and define any differences in the mechanical behavior of skin due to different loading paradigms. The macroscopic failure mechanics, as well as strain responses at failure, were compared to begin to characterize the mechanical response of skin and also to provide insight into its regional mechanical environments.

METHODS

All procedures were IACUC-approved and used male Holtzman rats (410-446g; n=3). The skin along the dorsal aspect of the rat was shaved and excised by surgical scissors and a scalpel. Square samples (1.5cmX1.5cm) were taken from the area over the shoulder blades. Connective tissue was removed; the thickness was measured with digital calipers in 3 locations and averaged for each sample. Samples were loaded into a custom 574LE2 planar biaxial test system (Test Resources) equipped with 4 linear actuators and 4 load cells oriented orthogonally. Specimens were affixed to each actuator by customized grips and needles to prevent slip (Fig. 1). All samples were oriented with the rostral-caudal direction along the y-axis and the lateral-medial

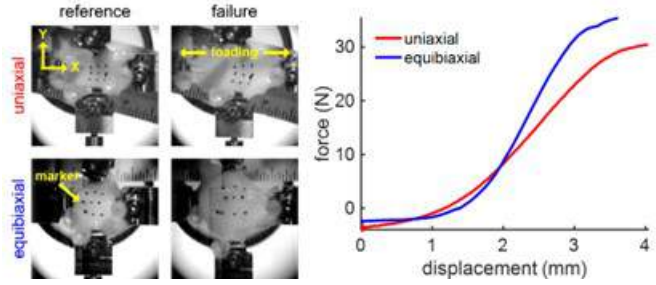

Fig. 1. In uniaxial tests, specimens were clamped on all axes but were loaded along the x-axis; equibiaxial tests were simultaneously distracted in x and y. Failure loads are similar for both test types.

Copyright 2016 The Organizing Committee for the 2016 Summer Biomechanics, Bioengineering and Biotransport Conference

direction along the x-axis (Fig. 1). A 3x3 grid of markers was applied to the dermal surface to track displacements during loading.

A 5N preload (10% of failure from pilot studies) was applied to both the x- and y-axis. All samples were pre-conditioned using a 2mm peak-to-peak equibiaxial distraction for 30 cycles at 0.5Hz. After pre-conditioning and a rest-period of 5 minutes, samples were randomized to undergo either uniaxial (n=4) or equibiaxial (n=4) tension. Uniaxial testing applied distraction along the primary loading axis at 2mm/s until failure. A 2mm distraction was also applied to the off-loading axis at 2mm/s and maintained for the entire test. Although not typical for uniaxial tensile testing [1,9], constraining the off-loading axis isolated deformation along a primary in-plane axis to both inform constitutive modeling and differentiate axis-dependent mechanical properties. In the equibiaxial tests, both axes were simultaneously distracted to failure at 2mm/s. Force and displacement data were recorded at 100Hz; video data were simultaneously collected at 500Hz using a high-speed camera (Phantom v9.1; Vision Research).

Tissue failure was defined as the first occurrence of any load cell reaching its maximum, regardless of the axis. For each specimen, the force at that time was averaged across all load cells of the loading axes and taken as the force at failure. Failure displacement was similarly calculated. Strains at failure were calculated using the markers, with the reference frame taken at 3sec prior to the start of the test. Marker centroids were digitized in ImageJ, and LS-DYNA calculated the maximum principal strain (MPS) fields at failure [10,11]. The force, displacement, and peak MPS at failure were compared between the uniaxial and equibiaxial tests, using separate t-tests for each outcome.

RESULTS

Sample thickness was 2.87±0.32mm and not different between the two groups (p=0.2). The failure force was not different between uniaxial (39.2±11.2N) and equibiaxial (36.6±5.3N) loading (Figs. 1 & 2). However, the displacement at failure was significantly (p=0.025) lower for equibiaxial loading than for uniaxial loading (Fig. 2). Although the macroscale displacement at failure was lower in equi-biaxial tension, the MPS was higher (Figs. 2 & 3). The peak MPS at failure was significantly different (p=0.039) between the groups, with the mean peak MPS in equibiaxial loading nearly 1/3 greater than the mean peak MPS in uniaxial loading (Fig. 3). Tissue rupture occurred at the grips for all specimens and the location of the first visible rupture did not always coincide with the location of the peak MPS at failure.

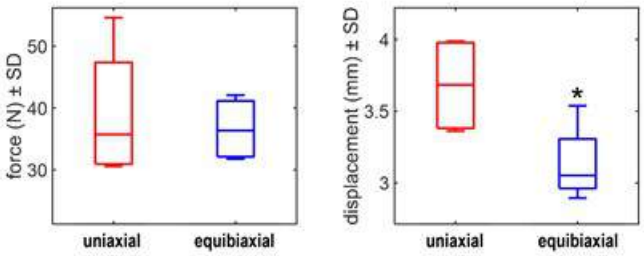

Fig. 2. Force at failure does not differ between load conditions. Displacement at failure is lower (*p=0.025) for equibiaxial testing.

DISCUSSION

This work is the first to characterize the macroscale failure mechanics of rat skin in response to biaxial loading and to define differences in failure responses between two planar loading paradigms. No difference in the failure force of skin was detected between uniaxial and biaxial tension (Fig. 2); but, the mean failure load (37.5±7.9N) for all specimens is less than half of that estimated from a prior study of skin under uniaxial tensile failure (~100N) [1]. Although the two studies used samples from the same region of the rat, our analysis was biased by the selection of the failure point. Defining failure at the *first* occurrence of peak load by any transducer imposes the most conservative definition since it discounts the possibility that other transducers might subsequently reach a higher peak. This same limitation may also underestimate the failure threshold, which could be beneficial for injury applications, but have negative effects in the context of defining the requisite stiffness of skin tissue grafts. As such, continued investigation of this, and alternate methods of failure analysis, is needed to better understand and define the macroscale and regional biomechanical responses of skin under planar loading. Moreover, since failure displacement and strains are different between uniaxial and biaxial conditions (Figs. 2 & 3) and because skin undergoes multi-axial loading *in vivo* in both physiological and injury conditions, continued characterization of its failure, and sub-failure, responses under complex planar loading is needed to define those biomechanical relationships with the most physiological meaning.

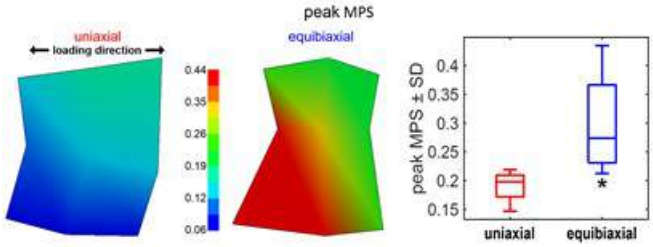

Fig. 3. MPS at failure is more variable and has a greater peak (*p=0.039) for equibiaxial than for uniaxial loading.

Although tissue displacement at failure is greater in uniaxial tension along the loading axis, the corresponding strains at failure are lower in that condition than for equibiaxial tension (Figs. 2 & 3). This counterintuitive result may be attributed to the effect of clamping the off-loading axis which effectively applies a controlled displacement boundary condition that restricts tissue deformation along that axis. Regardless of the biomechanical metrics, applying displacement along both planar axes in equibiaxial tension is a more physiologically relevant test condition for a tissue like skin. Further, cellular responses to macro-mechanical stimuli depend on t he *local* mechanical environment [3,4], which can be described in some cases by strain. For skin in particular, relating the local and regional strains and loads to activation of cutaneous mechanoreceptors, either experimentally or computationally [6,12,13], will provide important insight into this understudied biomechanical system. Certainly, continued work with skin that integrates a variety of mechanical profiles with physiological assessment of the mechanoreceptors embedded within it would begin to define the pathways through which local mechanical stimuli are translated in sensation and/or touch.

ACKNOWLEDGEMENTS

This project was funded by a grant from NIH (U01EB016638).

REFERENCES

1. Haut R *J Biomech Eng* 111:136-40, 1989; 2. Duraku L et al *Exp Neurol* 241:13-24, 2013; 3. Purves D et al *Neuroscience* pp189-228, 2001; 4. Johnson K *Curr Opin Neurobiol* 11:455-61, 2001; 5. Kambiz S et al *J Neurosurg* 123:254-69, 2015; 6. Quindlen J et al *PLoS Comput Biol* 11:e1004370, 2015; 7. Lanir Y & Fung Y *J Biomech* 7:171-82, 1974; 8. Schneider D et al *Arch Otolaryngol* 110:329-33, 1984; 9. Ni Annaidh A et al *J Mech Behav Biomed* 5:139-48, 2012; 10. Quinn K & Winkelstein B *J Biomech* 43:2637-40, 2010; 11. Zhang S et al *J Biomech Eng* in press, 2016; 12. Dong Y et al *J Neurophysiol* 109:1350-9, 2013; 13. Lesniak D et al *Elife* 3:e01488, 2014.

Copyright 2016 The Organizing Committee for the 2016 Summer Biomechanics, Bioengineering and Biotransport Conference

SB³C2016
Summer Biomechanics, Bioengineering and Biotransport Conference
June 29 –July 2, National Harbor, MD, USA
SB³C2016-650

UNDERSTANDING THE FLUID MECHANICS OF AORTIC REGURGITATION

Samantha Houser (1), Ikechukwu Okafor (2), Vrishank Raghav (1), Ajit Yoganathan (1,2)

(1) Department of Biomedical Engineering
Georgia Institute of Technology
Atlanta, GA, USA

(2) School of Chemical and Biomolecular Engineering
Georgia Institute of Technology
Atlanta, GA, USA

INTRODUCTION

Several cardiovascular diseases result in the impairment of the aortic valve function resulting in incomplete leaflet closure and retrograde flow of blood during the diastolic phase of the cardiac cycle. This back flow of blood from the aorta into the left ventricle, clinically referred to as aortic regurgitation (AR), is usually characterized by a high velocity jet which permeates into the left ventricle (LV). AR imposes severe hemodynamic and structural penalties on the normal functioning of the heart leading to diminished effective cardiac output [1] and LV remodeling [2]. In the presence of AR, the retrograde flow of blood from the aorta is expected to collide with the blood flowing into the left ventricle from the left atrium during diastole. Complex intra-ventricular flow patterns are expected due to this collision of a jet with a vortical structure in the LV, resulting in increased viscous energy losses. A recent clinical study by Stugaard et al. [3] concluded that the viscous energy loss in the LV increases with the severity of AR in both human and canine models. Furthermore, this altered flow could result in abnormal shear stress distributions that may be sensed by cardiac tissue [4] to initiate the process of first regional and then global cardiac remodeling.

The high variability in the temporal progression of the disease as well as the multiple confounders that exist with the disease present a significant challenge in gaining an in-depth insight into AR in a clinical or *in vivo* setting. On the contrary, a bench-top *in vitro* study could help parametrically evaluate the effect of AR on the intra-ventricular fluid mechanics and on the functioning of the LV. Such a study could lead to an in-depth understanding of AR and eventually help develop better clinical interventional timing strategies for patients. The fluid mechanics problem of AR is essentially that of the oblique collision between a jet and a vortical structure within a flexible walled constrained environment. However, to understand the fundamental fluid mechanics of AR, it is useful to decouple the fluid-structure interaction in a flexible walled cavity. This allows for a fundamental study while minimizing the complexities of the native LV, such as the motion of the ventricle walls, the asymmetrical shape, and the complex network of chordae tendineae. This work aims to understand the fundamental fluid mechanics of the AR by studying the interaction of a jet with a vortical structure in an unconstrained quiescent medium.

METHODS

The flow loop used in this work is a simplified model of the left heart. It consists of a large tank with the regurgitant jet flow and the MV inflow as shown in Figure 1. Water was used as the working fluid in this study. The flow loop (Figure 1) was fabricated with two separate pumps, a pulsatile pump that is responsible for the mitral inflow vortex, and a steady flow pump that generates the steady regurgitant flow. Two bileaflet mechanical valves are used in the pulsatile part of the flow loop to ensure unidirectional flow. The pulsatile pump was actuated at a frequency of 0.5 Hz, with pauses of 2 seconds and 4 seconds before systole and diastole, respectively. The authors clearly acknowledge that this frequency is not physiological, however, this study attempts to isolate any interactions between cardiac cycles and hence focusing on one cycle at a time. The pulsatile pump was controlled via a LabVIEW program.

These pauses are utilized to ensure a quiescent medium before the ejection of the fluid, as well as to minimize any interactions due to backflow. This creates a max flow rate of 107.17 cc/s (6.43 L/min) through the mitral orifice. Two ultrasonic flow probes were placed

Copyright 2016 The Organizing Committee for the 2016 Summer Biomechanics, Bioengineering and Biotransport Conference

before both the entrance length tube and the regurgitation jet tube to measure the flow rates for each case. The AR jet pipe, with an inner diameter of 5.6 mm, was fixed in the LV chamber at a set distance and orthogonal angle from the pulsatile mitral flow.

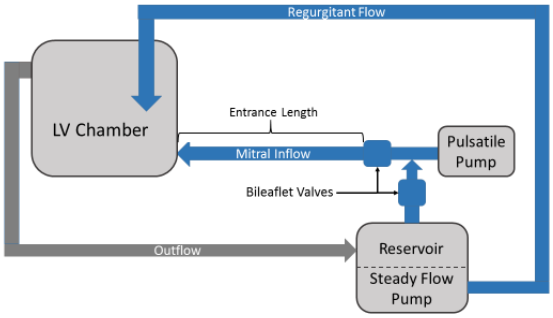

Figure 1: Schematic of the flow loop used in this study

Flow visualization was conducted with a mitral inflow of 107.17 cc/s for all cases, and a variable AR jet ranging from 25.67 to 102.67 cc/s. The ratio of regurgitant jet flow to mitral vortex flow (J/V ratio) for each condition are displayed in the Table below. Blue color dye was used for the AR jet while a pink color dye was used for the mitral inflow (vortex). A high-speed camera was used to capture the interaction between the jet and the vortex.

Regurgitant jet (cc/s)	Max mitral flow (cc/s)	J/V Ratio
25.67	107.17	0.24
51.33	107.17	0.48
77.00	107.17	0.72
102.67	107.17	0.96

RESULTS

The primary result of this study provides a qualitative understanding of the interaction between the jet and the vortex. Figure 2 illustrates flow visualization of the interaction between the jet and vortex at different J/V ratios. The variation in the interaction as the J/V ratio changes is clearly captured in the flow visualization photographs. At the lowest J/V ratio of 0.24, the jet is strongly affected by the vortical structure and it can be observed that the jet deflects towards the mitral inflow orifice. Furthermore, at this J/V ratio the jet is completely entrained into the coherent vortical structure. At a higher J/V ratio of 0.48, the jet structure away from the vortical structure is not affected. However, some entrainment of the jet into the vortical structure can be observed. At a J/V ratio of 0.72, the jet structure is not affected by the presence of the vortex and the entrainment of the jet into the vortex is not observed. Furthermore, the vortical structure appears to be disintegrating due to the interaction. At the highest J/V ratio of 0.96, the jet structure appears to be unaffected by the vortex and the coherent vortical structure disintegrates after the collision with the jet.

DISCUSSION

The results clearly demonstrate the mechanism of interaction of the jet and the vortical structure at different ratios of the jet to vortex flow rates (J/V ratio). As the J/V ratio increases two main changes were observed: a) the entrainment of the jet into the vortex reduces and b) the vortex begins to disintegrate upon interaction with the jet. Here, the J/V ratio can be thought of as the ratio of the strength of the flows; hence, as the J/V ratio increases the jet contributes towards the disintegration of the vortex after the collision.

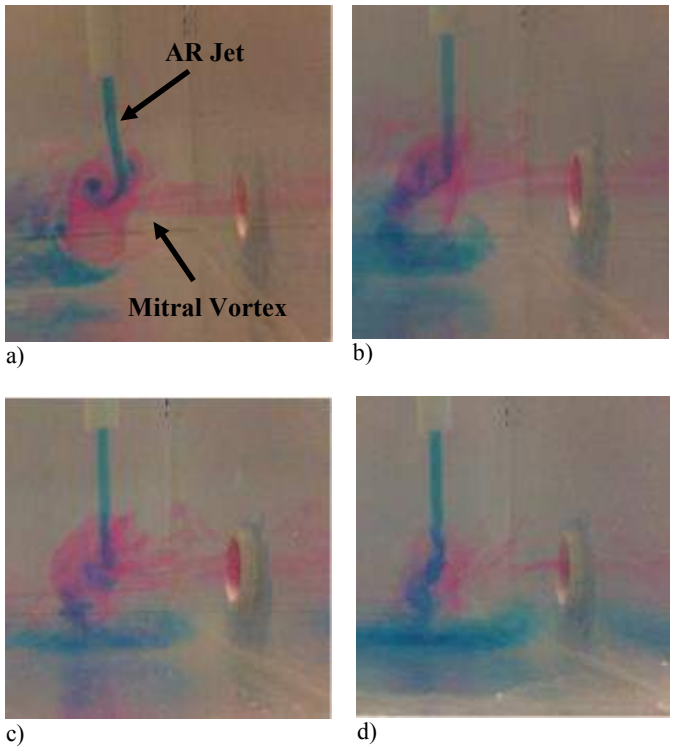

Figure 2: Flow visualization demonstrating the interaction of the jet and a vortical structure at different Jet/Vortex ratios a) J/V = 0.24, b) J/V = 0.48, c) J/V = 0.72, and d) J/V = 0.96. The blue dye indicates jet flow and the pink dye indicates vortex flow.

At the lower J/V ratio, the vortex strength is much greater than the jet strength; hence the induced velocity field of the vortex strongly influences the upstream part of the jet, causing the observed deflection in Figure 1a. Physiologically, the increase in J/V ratio simulates the increasing severity of AR in the LV. These results indicate that as the AR severity increases the physiological flow in the LV in the form of a vortical structure could disintegrate up on collision with the AR jet. This disintegration has a two-fold impact: a) it impairs the capability of the vortical structure to conserve the momentum of the fluid during diastole in preparation for systolic ejection and b) it leads to higher viscous energy loss resulting in a lowering of the efficiency of the LV filling. Furthermore, the increased viscous energy losses manifests itself in the form of increased cardiac loading during systolic ejection. These results will lead to a fundamental understanding of AR which is necessary to develop better metrics to grade AR severity.

ACKNOWLEDGEMENTS

The authors would like to thank the members of the CFM lab and the funding support from discretionary funds available to the PI.

REFERENCES

[1] Bekeredjian and Grayburn, *Circulation,* 112:125-134, 2005
[2] Uretsky et al., *J. Cardiov. Magn. Reson.,* 12, 2010
[3] Stugaard et al., *Eur. Heart. J. Cardiov. Imag.,* 2015
[4] Pedrizzetti and Sengupta, *Eur. Heart. J. Cardiov. Imag*, 2015

Copyright 2016 The Organizing Committee for the 2016 Summer Biomechanics, Bioengineering and Biotransport Conference

SB3C2016
Summer Biomechanics, Bioengineering and Biotransport Conference
June 29 –July 2, National Harbor, MD, USA
SB³C2016-651

ENHANCEMENT OF CRYOPRESERVATION OUTCOME OF ADIPOSE TISSUE DERIVED STEM CELLS BY THERMAL STRESS

M. Shaik[1], J. Gimble[2], R. Devireddy[1]

[1]Department of Mechanical Engineering
Louisiana State University
Baton Rouge, Louisiana, USA

[2]LaCell Incorporation
New Orleans, Louisiana, USA

INTRODUCTION

Human adipose-derived stromal/stem cells (huASCs) can differentiate along multiple lineage pathways, including adipocytes, chondrocytes, myocytes, neurons and osteoblasts [1]. As new stem-cell-based therapies become the standard of care for a wide variety of diseases, appropriate cryopreservation protocols will be necessary to increase patient access, reduce cost, and enhance the safety and effectiveness of huASCs. Recent studies from our laboratories have described the in vitro cryopreservation of huASCs frozen in a media consisting of minimal amounts of dimethyl sulfoxide (DMSO) and serum (animal or human) [2]. However, the infusion of cells cryopreserved in DMSO has been associated in nearly all patients with nausea, chills, hypotension, dyspnea and cardiac arrhythmia [3]. Therefore, the practical goals of this study are the development and optimization of a serum-free and DMSO-free cryoprotective medium.

Numerous reports in literature suggest that the up regulation of Heat Shock Proteins (HSPs) can provide cytoprotection in various diseases [4, 5]. Instigating the cell's natural cytoprotective mechanisms such as heat shock response could help in alleviating the damages associated with cryopreservation on cells thus reducing the amount of cryoprotectants used. Therefore, this study is aimed to evaluate the effect of heat shock response on cryopreservation of huASCs by determining the optimal expression of heat shock proteins.

METHODS

Cell culture: The huASCs were obtained from Lacell incorporation, New Orleans and cultured till passage 2 using the medium containing DMEM, 10% FBS, and 1% antibiotic in a cell culture incubator at 37 ºC.

Heat shock: The cells were given heat shock by exposing to 43ºC for 1 hour in a cell culture incubator. After the heat shock the cells were allowed to recover in 37ºC incubator for 1, 3, 9, 18 and 48 hours respectively before further analysis.

Western blot: RIPA buffer is used to lyse the cells and the total protein content is estimated using BCA assay kit. For the western blot, 25 ug of protein is loaded per lane in polyacrylamide gel and SDS PAGE is carried out followed by the transferring of proteins on to nitrocellulose membrane. The antibodies (Santa Cruz Biotechnology) for HSP90, HSP70, HSP27, and β-actin in the dilutions of 1: 200, 1: 200, 1: 5000, and 1: 200 were used for blotting.

QPCR: The RNA was isolated using pure link RNA mini kit and the purity is measured using nanodrop instrument. cDNA was synthesized using High Capacity cDNA reverse transcription kit. The synthesized cDNA was used to do QPCR with primers for HSP90, HSP70, HSP27 and cyclophilin B (normalizer).

Cryopreservation/Thawing: The huASCs are cryopreserved at 3, 9, and 18 hour time point post heat shock at a cooling rate of -1°C /min using control rate freezer till -80ºC in different groups with CPAs either DMSO or polyvinylpyrrolidone (PVP) followed by plunging in liquid nitrogen. Thawing was performed using 37ºC water bath incubator by shaking gently for 1-2 minutes.

Cell viability assay: After thawing the cells were cultured for 24 hours. The live cells attached to surface of culture flask were harvested using 0.05% trypsin and the dead floating cells in the medium were

Copyright 2016 The Organizing Committee for the 2016 Summer Biomechanics, Bioengineering and Biotransport Conference

collected. The post thaw cell viability was assessed using the apoptosis kit (BD Biosciences) that uses annexin V/ propidium iodide.

RESULTS

QPCR:

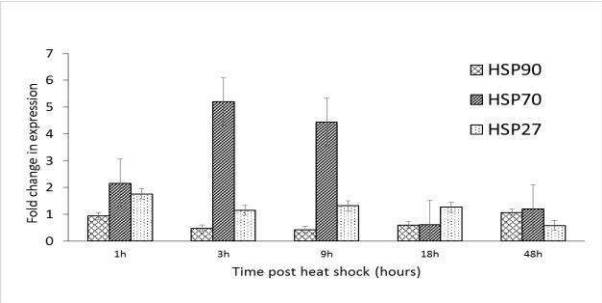

Figure 1: HSPs expression in huASCs after heat shock at 43°c for 1 hour.

Western Blotting

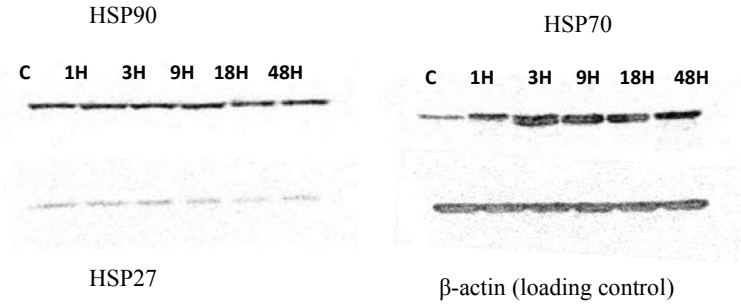

Figure 2: The expression of HSPs at various times (1, 3, 9, 18, and 48 hours) following the heat shock (43°C for 1 hour).

Post thaw cell viability: The bar graphs below represents the post thaw cell viability of heat shocked huASCs cryopreserved at different time points after heat shock either with 1% DMSO or PVP.

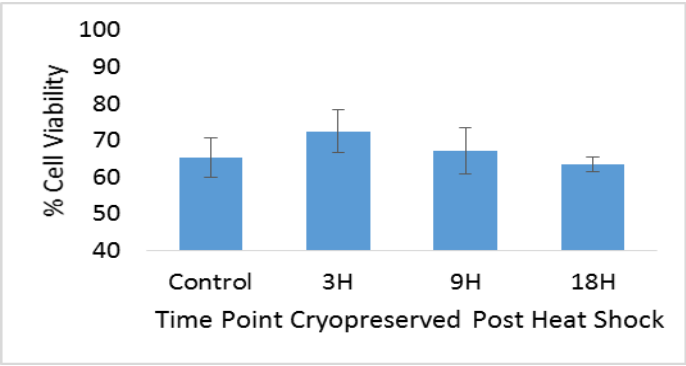

Figure 3: Post Thaw Viability of Heat Shocked huASCs Cryopreserved in 1% DMSO

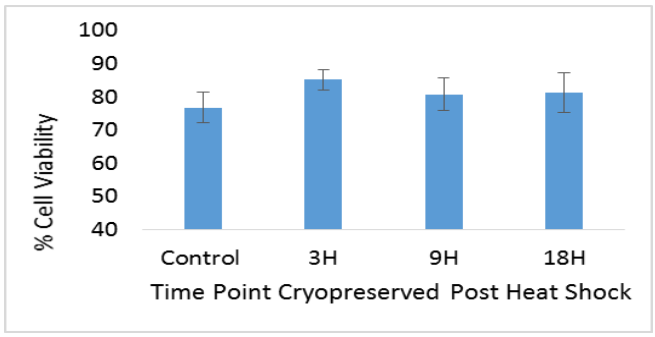

Figure 4: Post Thaw Viability of Heat Shocked ASCs Cryopreserved in 1% DMSO.

DISCUSSION

It is well known that HSPs can be overexpressed by mild thermal stress and act as molecular chaperones which assist in proper folding of misfolded proteins. Several reports suggest that preconditioning the cells to induce the HSPs expression offers the protection against apoptosis, ischemic/reperfusion injuries of heart and brain tissues, and oxidative stress [4].

The QPCR and western blotting results indicate the increase in expression of HSP70 after heat shock. The expression profile of HSP70 post heat shock gradually tends to increase, peaks at 3 hour time point and reaches base level at 48 hours. The huASCs cryopreserved at 3 hour time point resulted in maximal post thaw viability than other time points suggesting that cryopreservation at maximal HSP70 expression improves cryopreservation outcome. The improvement in post thaw viability is found to be function of HSP expression and consistent with different CPAs either intracellular or extracellular (DMSO or PVP). However, the expression of HSP90 and HSP27 showed very little change. Therefore, it can be possible that the increase post thaw viability is a result of HSP70 upregulation, however, it is also possible that there may be other HSPs which are being upregulated as result of heat shock. Our next step would be to determine the expression of other HSPs and also to overexpress HSPs individually or in combinations by genetic engineering tools so that a better cryopreservation protocol to replace CPAs or to minimize their usage could be developed.

ACKNOWLEDGEMENTS

Research reported in this was supported by institute of Diabetes and Digestive and Kidney Diseases of the National Institutes of Health under award number R21DK91852. The content is solely the responsibility of the authors and does not necessarily represent the official views of the National Institutes of Health.

REFERENCES

[1] Zuk, PA et al., *Tissue Eng,*7 (2):211-28, 2001
[2] Thirumula, S et al., *J Tissue Eng Regen Med.* 4(3):224-32, 2010
[3] David, B et al., *Am J Hematol.* 82(6): 463–472, 2007
[4] Kalmar, B et al., *Adv Drug Deliv Rev.* 28;61(4):310-8, 2009
[5] Sharp, FR et al., *Transl Stroke Res.* 4(6):685-92, 2013

Copyright 2016 The Organizing Committee for the 2016 Summer Biomechanics, Bioengineering and Biotransport Conference

SB^{3}C2016
Summer Biomechanics, Bioengineering and Biotransport Conference
June 29 –July 2, National Harbor, MD, USA
SB^{3}C2016-652

RIGHT VENTRICULAR ADAPTATION TO PRESSURE OVERLOAD CONDITIONS IN MICE

Tik Chee Cheng (1), Diana Tabima (1), Zhijie Wang (1), Tim Hacker (2), Naomi Chesler (1,2)

(1) Department of Biomedical Engineering
University of Wisconsin-Madison
Madison, WI, USA

(2) Department of Medicine
University of Wisconsin-Madison
Madison, WI, USA

INTRODUCTION

Pulmonary arterial hypertension (PAH) is a debilitating disease that lowers the medial survival years of untreated individuals to 2.8 years [1]. It is characterized by the progressive narrowing of pulmonary arteries (PA) throughout the vasculature, which results in the persistently elevated ventricular afterload. The typical cause of death is right ventricular (RV) failure. To better understand the pathogenesis of PAH, including the transition from RV adaptation to RV failure, animal models of PAH are widely used. An early study of pulmonary artery banding (PAB) in mice reported RV chamber dilatation with decreased RV ejection fraction and increased end-diastolic volume resembling RV dysfunction in humans with PAH [2]. However, RV function was not measured comprehensively, such as can be done with the ventricular-vascular coupling (VVC) efficiency, which measures RV mechanical performance in the context of altered RV afterload [3,4]. We hypothesize that 21 days of PAB in mice results in RV hypertrophy and right ventricular-pulmonary vascular uncoupling and tested this hypothesis using invasive measurements of RV structure and function as previously established by our group [5].

METHODS

Adult male C57BL6/J mice (n=10), 10 weeks of age, were subjected to PAB to create severe RV pressure overload. Under anesthesia, a left lateral thoracotomy was performed and a suture was knotted around the main PA. The thorax and skin were then sutured together to close the wound. During surgery, 5 mice died due to bleeding or excessive banding. With the remaining 5 mice, serial ultrasound measurements, such as RV wall thickness (WT), LV percentage of fractional shortening (FS), and LV ejection fraction (EF), and transthoracic echocardiograms on M-mode were collected before surgery (baseline) and after PAB weekly for up to three weeks (21-PAB). Two mice were sacrificed at 14 days and are not included in the analysis below. At 21 days, in a terminal procedure, *in vivo* RV pressure and volume (PV) measurements were obtained in the remaining 3 mice.

The terminal collection of hemodynamic measurements involved an invasive open chest surgery. Before the operation, the mouse was weighed, anesthetized with urethane (to maintain a physiological heart rate), intubated, and ventilated with room air at a set tidal volume and respiratory rate. Following exposure of the RV, a 1.2 F catheter-tipped pressure transducer was introduced into the right carotid artery and into the ascending aorta to monitor systemic blood pressure. A 20-gauge needle was used to puncture the apex of the heart where a 1.2 F admittance PV catheter was then inserted into the RV. Baseline readings of RV PV loops were acquired. Brief inferior vena cava occlusions to alter venous return were then performed to derive RV end-diastolic and end-systolic pressure relations.

Standard hemodynamic variables, such as heart rate (HR), end-diastolic pressure (EDP), end-systolic pressure (ESP), end-diastolic volume (EDV), and end-systolic volume (ESV), and RV function parameters, such as cardiac output (CO), EF, relaxation factor (τ), RV chamber compliance, and stroke volume (SV), were calculated using the baseline PV loops. To assess RV contractility, end-systolic elastance (Ees) derived from the slope of PV loops and preload recruitable stroke work (PRSW) acquired during vena cava occlusion were computed. Ventricular-vascular coupling (VVC) was also evaluated as the ratio between Ees and effective arterial elastance (Ees/Ea). Following hemodynamic data collection, the animals were euthanized and their hearts were excised to determine the mass of RV, LV, and septum (S) needed to calculate Fulton index as the weight ratio of RV and (LV+S).

Copyright 2016 The Organizing Committee for the 2016 Summer Biomechanics, Bioengineering and Biotransport Conference

Comparable RV structure and function data on adult male C57BL6 mice from a prior study [6] are used as control (n=9). For statistical analysis of the ultrasound measurements, a one-way ANOVA ($P<0.05$) was first performed to screen for statistical significance followed by Tukey's HSD multiple comparison test for post hoc analysis in R software. A two-tailed t-test of unequal variance was performed on the invasive hemodynamic measurements using Microsoft Excel.

RESULTS

Over the 3 weeks following PAB, ultrasound measurements showed a trend of increase in RV WT and decrease in LV EF and LV FS, suggesting cardiac remodeling affecting LV contractility in response to PAB (Table 1). Between Day 7 and 21, LV FS was significantly decreased by 43%.

Table 1. RV morphology and LV function of PAB mice

	Baseline	Day 7	Day 13	Day 21
N	3	3	2	3
RV WT, mm	0.50 ± 0.06	0.56 ± 0.08	0.54 ± 0.03	0.63 ± 0.08
LV EF, %	53.23 ± 7.58	79.35 ± 3.15	69.61 ± 8.28	53.04 ± 5.76
LV FS, %	27.59 ± 4.93	47.22 ± 3.07	38.76 ± 6.64	26.97 ± 3.70*

Values are presented as mean ± standard error. N=2 for RV WT measurement at Day 21. *P<0.05 compares values between Day 7 and Day 21.

At the terminal study (Table 2), body weight and heart rate of 21-PAB mice did not differ signficiantly from the control. Fulton index was increased in 21-PAB mice ($P<0.05$) indicating RV hypertrophy. The success of PAB in generating PAH is demonstrated by the dramatically elevated RV ESP ($P<0.05$). Furthermore, RV ESV and EDV increased significantly ($P<0.05$ and $P<0.01$).

CO, EF ($P<0.01$), SV ($P<0.05$), and RV chamber compliance ($P<0.01$) decreased in PAB mice compared to the control. The preload independent index for RV diastolic function τ remained unchanged. No signficant changes in load-independent measures of contractility, Ees and PRSW, were found. VVC efficiency tended to decrease but the change was not significant.

Table 2. Hemodynamic, RV function, and VVC among the study groups

Group	CTL	21-PAB
BW, g	25.3 ± 0.6	26.3 ± 0.2
HR, beats/min	547 ± 19	565 ± 26
Fulton Index, -	0.26 ± 0.01	0.60 ± 0.04**
Hemodynamic parameters		
ESP, mmHg	26 ± 1	74 ± 10**
EDP, mmHg	0.8 ± 0.1	1.0 ± 0.3
ESV, µL	9.8 ± 0.6	45.7 ± 5.3**
EDV, µL	23.8 ± 1.0	53.0 ± 4.2*
RV function		
CO, mL/min	8.2 ± 0.6	4.2 ± 1.2
RV compliance, µL /mmHg	0.53 ± 0.03	0.11 ± 0.03*
EF, %	56.27 ± 2.7	14.14 ± 3.78*
τ, ms	5.7 ± 0.5	6.0 ± 0.1
SV, µL	14.7 ± 1.0	7.3 ± 1.8**
Contractility		
Ees, mmHg/µL	1.34 ± 0.09	3.95 ± 1.06
PRSW, mmHg	18.7 ± 0.9	45.5 ± 7.7
Coupling efficiency		
VVC, -	0.76 ± 0.06	0.34 ± 0.17

Values are presented as mean ± standard error. *p<0.01 and **p<0.05 compare against control group.

DISCUSSION

This pilot study supports our hypothesis that 21 days of PAB in mice results in RV hypertrophy; while VVC efficiency tended to decrease, the change was not significant, likely due to the small sample size. This study also confirms that 21 days of PAB decreases EF and increases EDV as shown previously after 14 days [2]. The significant increase in RV EDV and decrease in SV coupled with the decrease in EF, as found in 21-PAB here, are associated with poor prognosis in human patients with PAH [7,8]. Taken together, the RV structural and functional changes suggest maladaptive RV remodeling, which will require a larger sample size to validate.

A comparison can be made with identical hemodynamic measurements obtained in a well-established model of severe PAH generated with chronic hypoxia (10% O2) and VEGF receptor inhibitor SU5416 for 28 days (28-HySu) [6]. Despite the shorter exposure time, RV ESP, ESV, and EDV are dramatically higher in 21-PAB compared to 28-HySu. Also, EF, and SV were not significantly diminished in 28-HySu, which confirm that 21-PAB more severely impairs RV structure and function compared to 28-HySu.

Future molecular assays for pathological RV hypertrophy and apoptosis markers, such as Modulatory Calcineurin Interacting Protein-1, natriuretic peptide A, phospholamban, Bax, and caspase-3, can better verify this physiological to pathological transition in mice exposed to 21-PAB [2,9,10]. Additionally, sham thoracotomy will need to be used as control.

In conclusion, this study demonstrates the feasibility of using PAB to cause maladaptive RV remodeling in mice and our ability to comprehensively quantify the changes in RV structure and function with invasive hemodynamic measurements.

ACKNOWLEDGEMENTS

The authors wish to thank Mark Golob, David Schreier, and Aiping Liu for their guidance and input in the data analysis. We would also like to thank Gaoussou Diarra for his surgical service. This investigation was supported by the National Institutes of Health, under Ruth L. Kirschstein National Research Service Award T32 HL 07936 from the National Heart Lung and Blood Institute to the University of Wisconsin-Madison Cardiovascular Research Center. In part, the study was supported by the U.S.-Israel Binational Science Foundation.

REFERENCES

[1] Humbert, M. et al., *Circulation,* 122:156–163, 2010.
[2] Rockman, H. A. et al., *Proceedings of the National Academy of Sciences*, 91: 2694-2698, 1994.
[3] Suga, H, *Japanese heart journal*, 10: 509-515, 1969.
[4] Sunagawa, K, et al., *Am J Physiol Heart Circ Physiol*, 245: H773-H780, 1983.
[5] Tabima, D. M. et al., *Am J Physiol Heart Circ Physiol*, 299: H2069-H2075, 2010.
[6] Wang, Z. et al. *Physiological reports*, 1.7, 2013.
[7] van Wolferen, S. A. et al, *Eur. Heart J*, 28:1250–1257, 2007.
[8] van de Veerdonk, M. C., Kind, T., Marcus, J. T., Mauritz, G. J., Heymans, M. W. et al., *J Am Coll Cardiol*, 58: 2511-2519, 2011.
[9] Bartelds, B et al., *Eur J Heart Fail*, 13: 1275-1282, 2011.
[10] Ravassa S et al., *Hypertension*, 36:1065 – 1071, 2000.

Copyright 2016 The Organizing Committee for the 2016 Summer Biomechanics, Bioengineering and Biotransport Conference

SB^{3}C2016
Summer Biomechanics, Bioengineering and Biotransport Conference
June 29 –July 2, National Harbor, MD, USA
SB^{3}C2016-653

PRODUCTION OF MONODISPERE SILICA GEL MICROSPHERES FOR BIOENCAPSULATION BY EXTRUSION INTO AN OIL CROSSFLOW

Joey J. Benson (1), Lawrence P. Wackett (2,3), Alptekin Aksan (1,3)*

(1) Department of Mechanical Engineering
University of Minnesota
Minneapolis, MN, USA

(2) Department of Biochemistry, Molecular Biology and Biophysics
University of Minnesota
Minneapolis, MN, USA

(3) BioTechnology Institute
University of Minnesota
St Paul, MN, USA

INTRODUCTION

Since 1954 synthetic hydrogels have extensively been used in drug delivery, tissue engineering, separation and adsorption processes, biosensensing, biocatalysis, and bioremediation.[1] Spherical hydrogel microcapsules are particularly attractive due to their transport characteristics and surface properties.

Silica is an ideal material for the synthesis of microspherical hydrogels to encapsulate biological materials as silica gels have favorable mechanical properties, are chemically stable, biocompatible, do not swell, and resist leakage of the encapsulated cells. Silica gels can be formed by sol-gel transformation of a silicon alkoxide.[2] Furthermore, hydrolyzed alkoxide can be combined with silica nanoparticles (SNPs) to produce a silicon alkoxide cross-linked silica nanoparticle gel network with significantly higher porosity.

Hydrogel microspheres are usually produced by creating an emulsion of gel precursors in an immiscible phase and then allowing the precursors to separate out and aggregate followed by gelation. An emulsion consisting of monodisperse silica precursor microspheres can be produced using variety of techniques including turbulent drop breakup, microfluidic devices, membrane emulsification, microchannel emulsification, and extrusion.

Extrusion methods are appealing because they do not require any special microengineering techniques or tools, no large power input, often consist of parts that are cheap and commercially available, and can often be assembled quickly and easily. These systems form an emulsion by extruding microspheres of gel precursor (sol) through a needle or a nozzle into an immiscible phase. After extrusion from the needle precursor microspheres must remain separated until they are gelled to avoid coalescence. In system described here, quasi-steady state microsphere separation was achieved by extruding the microspheres into cross-flowing oil that carried the microspheres downstream maintaining their separation until they gelled.

In order for the extrusion system to produce monodisperse microspheres the flow rate of the gel precursor injected into the cross-flow stream and the flowrate of the cross-flow stream were optimized. At low capillary and Webber numbers drops detach from the needle via dripping while at high capillary and Webber numbers jetting occurs. Monodisperse microspheres are almost always produced in the dripping regime because dripping results from an absolute instability, while jet breakup is governed by a convective instability.

The extrusion system described here was designed for the production of silica gel microspheres by extruding the gel precursor (the sol) continuously from a needle into a cross-flowing stream of mineral oil. After detachment from the needle, the spherical sol travels in the oil stream, maintaining its separation from the other sol spheres until gelation is completed. The system was designed to produce silicon alkoxide cross-linked silica nanoparticle microspheres encapsulating bacteria at a throughput of 12-13 ml per hour.

METHODS

The pH of NexSil 125-40 silica nanoparticle sol was adjusted to 7 by adding 1M HCl.. *E. coli* cells were suspended in isotonic phosphate buffered saline solution (PBS) at a concentration of 1 g /ml. This suspension was then added to the pH neutralized SNP sol. In the meantime, tetraethoxysilane (TEOS) was hydrolyzed by adding 1M hydrochloric acid and water at a 1 : 5.3 : 0.0013 molar ratio of TEOS : water : HCl. At this ratio TEOS hydrolyzes rapidly and condensation reactions occur slowly. Mixing of the silicon alkoxide solution and the SNP cell mixture induced a rapid condensation reaction, which spanned the sol and transitioned it into a gel.

Copyright 2016 The Organizing Committee for the 2016 Summer Biomechanics, Bioengineering and Biotransport Conference

The silicon alkoxide solution and the SNP + cell mixture were filled into 12 ml syringes. The syringes were placed in syringe pumps connected via a Y connection. The outlet of the Y connector was joined to an 18-gauge 1.5" blunt end needle via the residence tube. The extent of polymerization that the gel precursor undergoes before it enters the oil stream can be controlled by adjusting the length of the residence tube. Sol was injected through the needle into the oil crossflow, where it assumed a spherical shape due to the hydrophobic nature of the oil, and the sol microspheres were carried in the oil stream until they gelled.

The emulsion system was tested at oil flow rates: of 10, 6.2, and 4.2 ml/min and gel flow rates of 36, 24, and 12 ml/hr. A gel formula with a 1:1 volumetric ratio of silicon alkoxide solution : SNP sol was used and no PBS or cells were added. The system was then used to encapsulate *E. coli* in a silica gel that has previously been reported to be biocompatible and mechanically strong [3-5]. *E. coli* were suspended in PBS at a concentration of 1g/ml. A 1:7:1 ratio of silicon alkoxide solution : SNPs : cells in PBS was used.

RESULTS

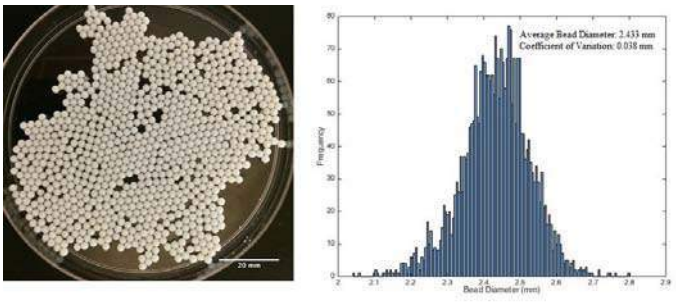

Figure 1: *E. coli* containing microsphere size distribution

Table 1: Silica microsphere sizes produced at three different oil flowrates and three different precursor flowrates

Gel Precursor Flowrate (ml/hr)	Average Microsphere Diameter (mm)	Coefficient of Variation
Slow oil flowrate (4.2 ml/min)		
12	2.50	0.024
24	2.71	0.027
36	2.86	0.048
Medium oil flowrate (6.2 ml/min)		
12	1.89	0.036
24	2.07	0.030
36	2.155	0.029
Fast oil flowrate (10 ml/min)		
12	1.256	0.059
24	1.403	0.064

Microsphere sizes produced using three different oil flowrates and three different precursor flowrates are given in ***Table 1***. Increasing the oil flowrate caused the microsphere diameter to decrease while increasing the coefficient of variation. Increasing the precursor flow rate also increases the microsphere diameter, but not as strongly as the oil flowrate.

The emulsion system was also used to produce silica microspheres that contained encapsulated *E. coli*. The medium oil and medium gel precursor flowrate combination was used and the microspheres are shown in ***Figure 1***. The emulsion system was continuously operated for 100 minutes and produced approximately 65 ml of microspheres.

DISCUSSION

An emulsion system was designed and manufactured to produce silica gel microspheres that contain encapsulated biocatalysts in a diameter range from approximately 1.3 to 2.9 mm. Microsphere size was mainly controlled by the oil flowrate, and the microsphere throughput was determined by the gel precursor flowrate. The emulsion system produced monodisperse microspheres with a coefficient of variation of less than 3% when operated at the optimum oil and precursor flowrate values. This is on par with the coefficient of variation values achieved using microfluidic devices, but much higher in terms of yield. Under all other conditions, the microspheres had a coefficient of variation less than 6.5%, which is a much more narrow size distribution than the microspheres produced using microchannel arrays (considering microspheres in a similar size range), turbulent microsphere breakup, or membrane emulsification.

The throughput of the extrusion system ranges from 12-36 gel ml/hour, which translates to 20-60 ml of microspheres per hour assuming a 60% microsphere packing density. This throughput is much greater than that achieved using single junction microfluidic devices, it is similar to that achieved in typical microchannel devices, and it is much less than that achieved using turbulent microsphere breakup and membrane emulsification.

Microspheres produced containing encapsulated *E. coli* were larger and had a greater CV than microspheres produced with similar flowrates during characterization. The microsphere size and size distribution changed when cells were added because adding cells to the gel precursor changes the formation of the gel network, the precursor density, and the precursor viscosity. Each of these factors affects the microsphere detachment process and the microsphere size.

ACKNOWLEDGEMENTS

The authors thank Ms. Sujin Yeom for growing the bacteria used in this research. This research has been funded through a University of Minnesota IonE Discovery grant and a MnDRIVE Transdisciplinary Initiative of the University of Minnesota.

REFERENCES

1. Gill, I.; Ballesteros, A., Bioencapsulation within synthetic polymers (Part 1): sol-gel encapsulated biologicals. *Trends in Biotechnology* **2000,** *18* (7), 282-296. DOI: 10.1016/s0167-7799(00)01457-8.
2. Brinker, C. J.; Scherer, G. W., *Sol-gel science: the physics and chemistry of sol-gel processing*. Academic press: 2013.
3. Mutlu, B. R.; Yeom, S.; Tong, H.-W.; Wackett, L. P.; Aksan, A., Silicon alkoxide cross-linked silica nanoparticle gels for encapsulation of bacterial biocatalysts. *Abstracts of Papers of the American Chemical Society* **2014,** *247*.
4. Mutlu, B. R.; Yeom, S.; Wackett, L. P.; Aksan, A., Modelling and optimization of a bioremediation system utilizing silica gel encapsulated whole-cell biocatalyst. *Chemical Engineering Journal* **2015,** *259*, 574-580. DOI: 10.1016/j.cej.2014.07.130.
5. Sakkos, J. K.; Kieffer, D. P.; Mutlu, B. R.; Wackett, L. P.; Aksan, A., Engineering of a silica encapsulation platform for hydrocarbon degradation using Pseudomonas sp. NCIB 9816-4. *Biotechnology and bioengineering* **2015**.

Copyright 2016 The Organizing Committee for the 2016 Summer Biomechanics, Bioengineering and Biotransport Conference

SB³C2016
Summer Biomechanics, Bioengineering and Biotransport Conference
June 29 –July 2, National Harbor, MD, USA
SB³C2016-654

A POPULATION DERIVED MECHANOSTATISTICAL MODEL OF THE HUMAN AND SHEEP SPINE TO EVALUATE SPINAL FUSION IMPLANTS

Alex Swee (1), Vickie Shim (1), Justin Fernandez (1,2)

(1) Auckland Bioengineering Institute
University of Auckland
Auckland, New Zealand

(2) Department of Engineering Science
University of Auckland
Auckland, New Zealand

INTRODUCTION

Computational models provide *in silico* solutions to orthopaedic device testing without ethical concerns to inform clinical decisions. The lumbar spine is a complex multi-facet joint, bears most of the body weight, and exhibits numerous degenerative bone and disc problems that are highly suited to computational testing. One solution to degenerative spine complications is a spinal fusion implant that reduces pain by minimising motion between two intervertebrae [1]. Spinal surgeons orient spinal fusion device location and wedge angle in order to minimise bone stress shielding (which leads to bone resorption) and maximise osseointegration of bone into the porous trabecular metal structure of the spinal fusion implant.

In addition to computational models of the human spine, animal models (especially sheep) are often used to evaluate implant devices [2]. Sheep models are popular test subjects as they have similar anatomical characteristics to human spines and hence studies often assume you may translate findings directly to the human condition. However, the loading pattern is often substantially different and performance of implant devices in sheep models may not reflect performance in the implanted human.

The objective of this study is to present a population based mechanostatistical model of the spine in order to evaluate spinal fusion devices on bone remodelling and osseointegration outcomes. The model evaluates disc stress and bone stress shielding for standard spinal fusion devices in both the human and sheep. Bone osseointegration in the spinal fusion device is also predicted using bone diffusion analysis and knowledge of implant stress and strain. Using an optimisation tool the most ideal human spine posture is identified that produces the closest stress and loading conditions to that observed in the implanted sheep. This allows implant outcomes predicted in the sheep to be translated to the human.

METHODS

Figure 1 shows the complete workflow diagram for this study. Three-dimensional finite element (FE) models of the human lumbar spine (L3-L5) were developed using 40 patient CT data sets. The proximal femoral head, sacrum, coccyx and pelvis were included in the simulation, with axial ground reaction loads applied to the distal femur ends to provide physiologically realistic boundary conditions. The Von Mises stresses were then predicted using commercial FE software (Abaqus CAE). The spine model setup was evaluated by predicting and comparing surface bone strains against a cadaver sheep that was strain gauged.

The original lumbar spines were only available in a neutral posture so a range of synthetic postures was generated using an automated procedure. A spine-specific joint coordinate system (JCS) was first computed based on detected geometric features and used for bone transformation. The intervertebral disc was modelled using a Cartesian stiffness matrix to allow for coupled motion. Using a Gilbert-Johnson-Keerthi distance algorithm [3], each vertebrae was then moved to its maximum possible position (e.g. maximum flexion when placing the spine under flexion) until collision was detected in the bone facets. The spine was placed in maximum flexion, extension, medial and lateral tilt.

A Partial Least Squares Regression (PLSR) statistical model was then trained to relate spinal position with computed Von Mises stress in the human. Optimisation was used to iterate through multiple spinal positions to find the best match in Von Mises stress to a sheep lumbar spine model that represents typical experimental conditions.

The optimal human FE model was then modified by inserting a titanium Anterior Lumbar Interbody Fusion (ALIF) device between the L3 and L4 intervertebral disc space. Isotropic elastic formulation was used to simulate the material properties of titanium (Young's

Copyright 2016 The Organizing Committee for the 2016 Summer Biomechanics, Bioengineering and Biotransport Conference

modulus: 115 GPa, Poisson's ratio: 0.3). Tissue stress along with potential bone remodelling around the implant was predicted using pressure stress induced mesenchymal cell migration into the implant. The same implant design was integrated into the sheep model for bone stress evaluation. The sheep and human implant models are evaluated to predict implant outcome differences that may be expected when translating the sheep spine to the human condition.

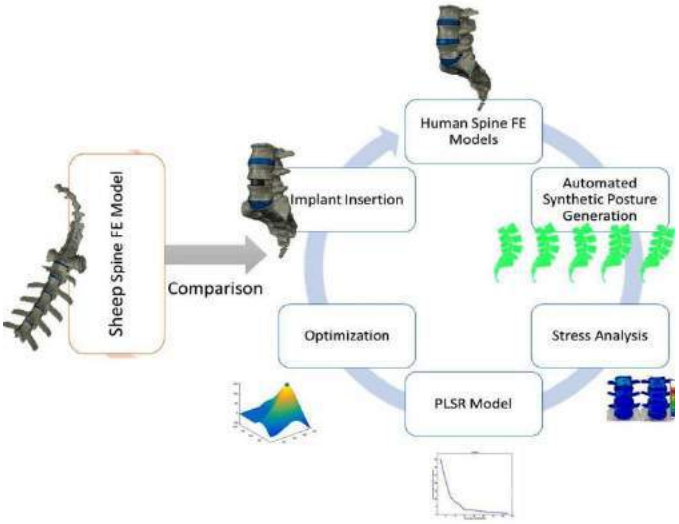

Figure 1: Modelling framework

RESULTS

The automated JCS and posture placement of the spine for each lumbar vertebrae was consistent and robust. Our method conforms to the ISB standard of determining JCS for the lumbar vertebrae [4] An example of the automatically detected JCS of L4 of a random human subject can be seen in Figure 2.

The PLSR model predicted human spinal tissue stress with an average accuracy of 70% after training on the population data set. The spatial pattern of stress was a good match but errors were observed primarily in the peak magnitude values.

All human FE spine models predicted stress levels within the range of those found in literature [5, 6]. Bone remodelling predictions of tissue differentiation and migration levels in the ALIF implant (Figure 3) were consistent with what was observed in clinical studies [7].

Comparing normal stress distributions in the average human and sheep spines, it is evident that the overall Von Mises stress values are higher for sheep. The primary difference observed between the patterns of stress in both models is that the stress distributions are primarily towards the medial vertebrae with higher stress at the vertebral foramen for the human spine. In contrast, stress distributions in the sheep spine were exhibited primarily in the anterior region of the vertebrae.

DISCUSSION

The current study examines the translational relationship of human and sheep spine orthopaedic outcomes and provides a clinically relevant framework for spinal fusion device evaluation. Critical parameters to consider when translating findings between sheep and human models include the size of the vertebrae and the thickness of the intervertebral disc.

The main assumption in this study is the generation of synthetic poses from a population of neutral spine positions. This is due to difficulty in obtaining actual MRI of a population of spinal postures. However, we assume that the spinal postures generated are realistic based on the limited range of motion of the human spine from the literature and the use of the ISB standard JCS. Although spinal discs and vertebrae ligaments were included in the model there were no muscles. Inclusion of muscles may alter the stress pattern and influence bone remodelling prediction.

This study also demonstrates a novel, yet accurate method in automated detection of the JCS for lumbar vertebrae. With the methods presented in this study, clinical evaluations of orthopedic implants can be performed with greater speed and compared with a population of spines.

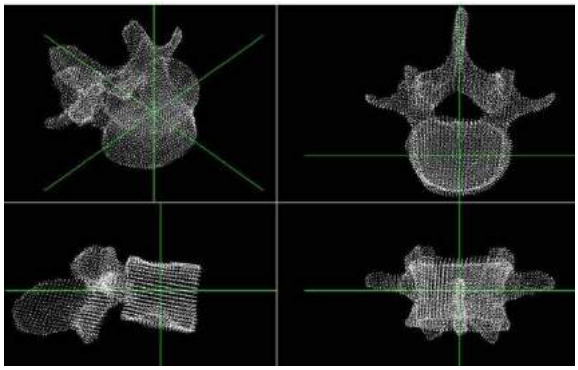

Figure 2: Lumbar vertebrae Joint Coordinate System

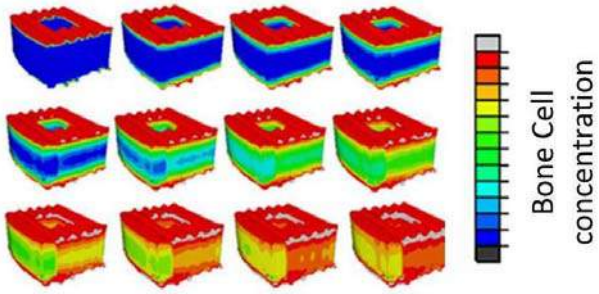

Figure 3: Predictions of bone remodelling within the ALIF implant for the duration of 300 days that is required for full fusion to occur (red is high bone ingrowth)

ACKNOWLEDGEMENTS

This project was funded by a Faculty Research Development Fund.

REFERENCES

[1] Bergmann, G et al., *J Biomech*, 34:859-871, 2001.
[1] Serhan, H et al., *SAS J*, 5(3):75-89, 2011.
[2] Martz, EO et al., *J Biomed Mater Res*, 38(3):267-288, 1997.
[3] Gilbert, EG et al., *Robotics and Automation, IEEE*, 6(1):53-61, 1990.
[4] Wu, G et al., *J Biomech*, 35(4):543-548, 2002.
[5] Wang, J et al., *ICSC 2012, Part I*, 390-398, 2012.
[6] Divya, V et al., *ICECT*, 3:350-354, 2011.
[7] Paganias, CG et al., *Indian J Orthop*, 46(5):505-513, 2012.

Copyright 2016 The Organizing Committee for the 2016 Summer Biomechanics, Bioengineering and Biotransport Conference

SB^{3}C2016
Summer Biomechanics, Bioengineering and Biotransport Conference
June 29 –July 2, National Harbor,MD, USA
SB^{3}C2016-655

REPRODUCIBILITY OF MOUSE TRABECULAR BONE MICROSTRUCTURE AT MULTIPLE SKELETAL SITES BY IN VIVO MICRO COMPUTED TOMOGRAPHY IMAGING

Chih-Chiang Chang, Hongbo Zhao, Youwen Yang, Chantal M. de Bakker, Wei-Ju Tseng, X. Sherry Liu

McKay Orthopaedic Research Laboratory
University of Pennsylvania
Philadelphia, PA, USA

INTRODUCTION

Micro computed tomography (μCT) has been widely used to study 3-dimensional (3D) microstructure of bone specimens. In the recent decade, *in vivo* μCT scanners have also become available to monitor longitudinal bone changes in different rodent species [1]. The current *in vivo* μCT scan can obtain images with an isotropic voxel size up to 10.5 μm, which is high enough for direct 3D bone microstructural analyses. For accurate detections of bone microstructure over time, it is critical to understand the reproducibility of these measurements in different scan protocols. Although the reproducibility of the *in vivo* μCT measurements have been reported in rats and mice, the scanning site of these *in vivo* studies have been limited to the proximal tibia [2,3]. The influence of animal reposition and motion artifact associated with *in vivo* scans at other important skeletal sites, such as the lumbar vertebrae and femur, have not been studied. Thus, the goal of this study is to establish a feasible μCT scanning protocol and measurement regime that yield the highest precision in monitoring mouse femoral and vertebral bone in response to diseases and treatments. The first objective of the current study was to investigate the short-term reproducibility of trabecular bone microstructure measurements by utilizing customized scan holders. The second objective was to test whether a 3D image registration can reduce the precision error caused by animal repositioning.

METHODS

Animals: Eight thirteen-week-old female C57BL/6J mice were used in this study. All mice were scanned 4 times at both the 4th lumbar vertebra (L4) and right distal femur within 12 hours (for a total of 32 scans for each site). Each mouse was removed from the holder and allowed to recover from anesthesia between scans. All experiments were approved by IACUC of University of Pennsylvania.

μCT scans: All mice were anesthetized (4.0/2.25% isoflurane) and scanned at the L4 and right femur by an *in vivo* μCT system (vivaCT 40, Scanco Medical AG, Switzerland). An animal fixture was custom-designed by SolidWorks software and manufactured by a 3D printer to minimize motion artifact and ensure that scan sites were positioned in a similar 3D orientation between scans (Fig.1). Before each scan, a 2D scout view was employed to determine the region of interest. For the distal femur, 212 slices below growth plate were scanned at 10.5 μm voxel size. For the L4, 212 slices at the center of L4 were scanned at 15μm resolution. The scanner was operated at 55 kVp energy, 145 μA intensity, and 200 ms integration time and the average time for each scan was about 10 minutes.

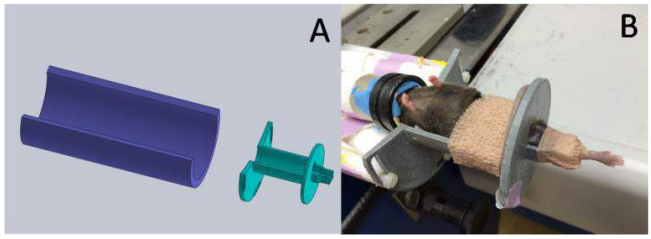

Figure 1: (A) The custom-designed holder for stabilizing the mouse to ensure minimal motion artifacts. (B) Positioning of a mouse for *in vivo* μCT scanning.

Image registration: A two-step image registration method was employed using a landmark-initialized, mutual information based registration kit (National Library of Medicine Insight Segmentation and Registration Toolkit, USA). Based on grayscale images of the baseline and follow-up scans, this registration scheme minimizes the joint entropy and marginal probabilities of the fixed and moving images to derive a transformation matrix **T,** which represents the

Copyright 2016 The Organizing Committee for the 2016 Summer Biomechanics, Bioengineering and Biotransport Conference

rigid-body transformation, including a 3D rotation and translation, between image coordinates of the baseline and follow-up scans (Fig. 2A). To evaluate the trabecular bone microstructure of the registered baseline and follow-up scans, the trabecular bone compartment of each follow-up scan was semi-automatically contoured and saved as a volume of interest (VOI) mask. Then, the transformation matrix **T** was applied to rotate and translate the VOI mask of the follow-up scan (Fig. 2C). The transformed VOI mask from the follow-up scan corresponded to the same VOI of the baseline scan (Fig. 2D).

Microstructure Analysis: A total of 60 slices of the reconstructed images, corresponding to a 0.63 mm region at the metaphysis region of the distal femur and 60 slices (0.9 mm) of the center of L4 were identified as the VOI at the baseline scan. The corresponding VOI of follow-up scans were identified through image registrations (Fig. 2D). These VOIs were smoothed by a Gaussian filter (sigma=0.6, support=1) and then thresholded with a segmentation threshold corresponding to 387 mgHA/cm^3. Bone volume fraction (BV/TV), trabecular thickness (Tb.Th), trabecular spacing (Tb.Sp), trabecular number (Tb.N), structure model index (SMI), connectivity density (Conn.D), and trabecular volumetric bone mineral density (Tb.vBMD) were evaluated by manufacturer-provided software (Scanco Medical AG, Switzerland).

Statistics: Reproducibility of each measure was evaluated by the root mean square average of the percent of coefficient of variance (RMSCV), and intra-class correlation coefficients (ICC). Paired Student's t-tests were performed to compare the CV of repeat scans before and after image registration.

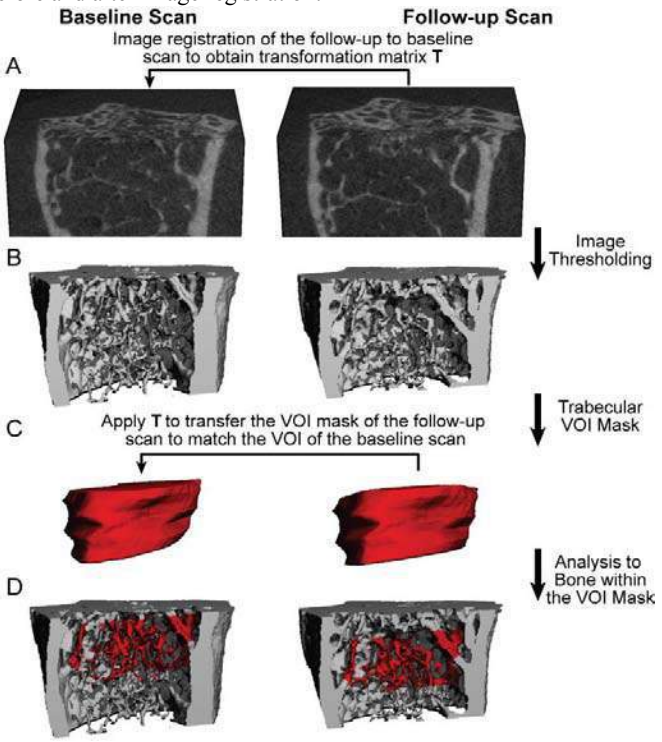

Figure 2: Schematics of the image registration and microstructural analysis of trabecular bone.

RESULTS

Prior to image registration, reasonable reproducibility was found for most parameters. For the femur, the precision errors associated with BV/TV, Tb.N, Tb.Th, Tb.Sp, SMI, and Tb.BMD ranged between 4.0% and 12.4% with an exception for Conn.D (33.5%). Similar results were found for the L4. Moderate to good reproducibility were found for most parameters prior to registration (precision error 6.5-17.6%) with an exception for Conn.D (30.7%).

After image registration, precision errors of most of the measurements for the femur went down (Table 1). Particularly, improvement in precisions of BV/TV, Tb.Th, Tb.BMD for the femur reached statistical significance. There were pronounced improvements in measurement precisions by image registration at the L4. All precision errors except for SMI ($p=0.1$) were significantly reduced after image registration ($p<0.05$). Moreover, ICC for femur represented excellent reliability for most of the parameters, with exceptions for SMI and Conn.D, which were in good to excellent range (0.587-0.958). Similarly, ICCs of all parameters indicated excellent reliability (0.838-0.973) for the L4.

Table 1: Reproducibility for morphological parameters after registration was demonstrated as precision error and ICC.

	BV/TV	Conn.D	SMI	Tb.N	Tb.Th	Tb.Sp	Tb.BMD
Femur							
Mean±SD	0.06±0.01	29±14	3.5±0.1	4.0±0.3	0.04±0.00	0.25±0.02	99±15
PE$_{\%CV}$	5.01	26.9	2.90	4.18	3.05	3.78	4.33
ICC	0.958	0.587	0.676	0.800	0.924	0.834	0.920
Vertebrae							
Mean±SD	0.14±0.06	95±51	2.7±0.6	4.6±0.7	0.05±0.00	0.23±0.03	181±34
PE$_{\%CV}$	5.23	18.9	8.55	6.33	3.11	5.51	3.11
ICC	0.973	0.851	0.875	0.838	0.939	0.861	0.97

DISCUSSION

In this study, we developed an *in vivo* μCT scan protocol which can be applied to scan multiple skeletal sites (Femur, Tibia, Vertebrae) for mice and offers an excellent reproducibility by utilizing custom-designed holder and image registration techniques. Previous studies have demonstrated reproducibility for mouse limb and spine *ex vivo* [5]. Reproducibility of *in vivo* μCT measurements has only been evaluated for the mouse tibia [3]. The current protocol overcomes this limitation and provides capability for scanning multiple skeletal sites for mice. According to our results, reasonable precision can be achieved by the standard scan and analysis procedure for most microstructure and density measurements. In addition, 3D image registration helped to reduce precision errors in BV/TV, Tb.Th, and Tb.BMD for the femur and in almost all parameters for the L4. However, reproducibility of Conn.D measurements was moderate for both the femur and vertebra, even after image registration. The elevated precision error in Conn.D has also been reported in previous studies of rat and mouse tibia [2, 3]. This might be because Conn.D measurements are more sensitive to image quality and motion artifacts than other microstructure measurements [5]. Furthermore, the mouse strain used in the current study has a particularly low Conn.D, which also contributed to higher variance in its measurement.

In conclusion, we established an *in vivo* μCT scan and analysis protocol for assessment of longitudinal bone changes at multiple skeletal sites for mice with excellent reproducibility. The current study utilized a mouse strain of low bone mass. We expect to achieve similar or better reproducibility for other mouse strains with similar or higher bone mass.

ACKNOWLEDGEMENTS

This study is supported by the fund NIH/NIAMS P30AR050950, and NIH/NIAMS K01-AR066743.

REFERENCES

[1] Schulte FA et al., Bone 2011;48:433–42. [2] Lan S et al., Bone 2013; 56(1), 83-90. [3] Nishiyama KK et al., Bone 2010; 46(1), 155-161. [4] Shrout PE et al., Psychological Bulletin 1979, 86(2), 420-428. [5] Kohler T et al., Calcif Tissue Int 2005;77:281–90.

Copyright 2016 The Organizing Committee for the 2016 Summer Biomechanics, Bioengineering and Biotransport Conference

SB³C2016
Summer Biomechanics, Bioengineering and Biotransport Conference
June 29 –July 2, National Harbor, MD, USA
SB³C2016-657

EFFECT OF INFLOW BOUNDARY CONDITION ON NASAL TRANSITIONAL FLOW

SHUN SHIMIZU (1), TAKASHI SAKAMOTO (1), SHINYA KIMURA (1), GAKU TANAKA (1), TOSIHIRO SERA (2), HIDEO YOKOTA (3), KENJI ONO (4)

(1) Graduate School of Engineering
Chiba University
Chiba, Chiba, Japan

(2) Graduate School of Engineering
Kyushu University
Fukuoka, Fukuoka, Japan

(3) Image Processing Research Team
RIKEN
Kobe, Hyogo, Japan

(4) Advanced Visualization Research Team
RIKEN
Kobe, Hyogo, Japan

INTRODUCTION

The nose plays an important role by filtering, warming, and humidifying inspired air. Thus, modeling of airflow in the nasal cavities is important for evaluating nasal functions. Recently, experimental studies showed that airflow in nasal cavity has unsteadiness such as laminar to turbulent transitional flow[1, 2]. Computational fluid dynamics (CFD) has enabled detailed simulation of airflow throughout the nasal cavity based on CT scans of individual subjects. Laminar or steady Reynolds-Averaged Navier-Stokes (RANS) models, large eddy simulation (LES) were conducted in most of previous studies[3]. Because of advances in computing performance, direct numerical simulation (DNS) was performed to predict transitional airflow in the nasal cavity without turbulence models[4, 5]. Several studies prescribed simplified flat inflow profile, whereas Taylor et al.[6] showed that the use of truncated inflow in models of nasal inspiration affects the flow within the nasal cavity.

The present study investigates the effect of inflow velocity profile on transitional flow during steady nasal inspiration.

METHODS

The nasal cavities of a healthy male aged 51 years were reconstructed using CT slices. Firstly, virtual boundaries definitions of the nasal airway and external face boundaries were generated applied to the CT image datasets. Then, these segmented images were placed into a 3D polygon model. Finally, a uniform cartesian grids were obtained from the 3D polygon model. The mesh size was defined to 0.05 mm (approx. 4 billion grids) according to Kolmogorov microscale. Non-dimensional wall distance y+-value is estimated at 0.21 in the nasal valve, using the Blasius' correlation instead of wall shear stress to calculate a friction velocity.

The governing equations for the conservation of mass, momentum for the 3D incompressible unsteady flow were solved using FFV-C ver. 2.1.5 (RIKEN), performed on K computer. The third-order MUSCL method was selected for the spatial discretization of the advection term and the first-order forward Euler method was used for the time integration. Figure 1 shows boundary condition. In this study, two patterns boundary conditions were given. (i) A traction-free condition was applied at the entrance to the bounding box upstream of the model, and constant inspiratory flow rate of 230 ml/s was applied at the throat. (ii) A flat velocity profile was applied at nostril, and pressure gradient of zero was applied at throat. The direction of the flat velocity profile and velocity magnitude were defined according to the result of natural velocity profile.

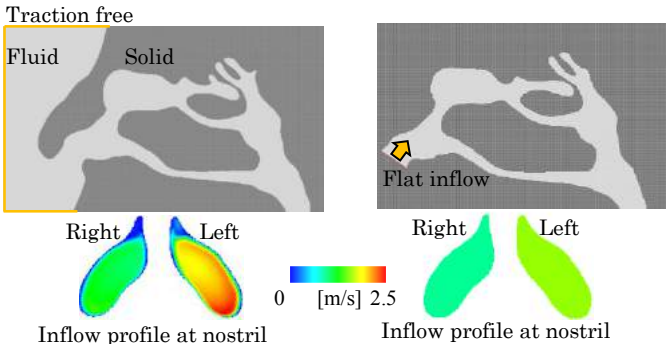

(i) Natural velocity profile **(ii) Flat velocity profile**

Figure 1: Inflow boundary condition

Copyright 2016 The Organizing Committee for the 2016 Summer Biomechanics, Bioengineering and Biotransport Conference

RESULTS

Figure 2 shows the contours of instant vorticity magnitude on sagittal plane in the left nasal cavity. The vorticity magnitude distribution of the natural developed velocity profile indicates the structure of flow converging through the nasal vestibule, which forms a high-speed jet at nasal valve and a recirculation region at the top front of nasal cavity. These flow features is confirmed in the case of simplified flat velocity profile. A breakdown of free shear layer between the jet and the recirculation region is confirmed in the natural velocity profile, whereas, in the flat velocity profile, that is not confirmed. The fluctuation of vorticity at the rear of middle nasal meatus (dotted round, figure 2) is confirmed in the both cases. Figure 3 shows contours of turbulence kinematic energy (TKE) on sagittal plane in the left nasal cavity. The high level TKE is confirmed in front of nasal cavity and middle nasal meatus in the natural velocity profile. The maximum value of TKE in front of nasal cavity is 58.4×10^{-3} m^2/s^2 (natural), 2.11×10^{-3} m^2/s^2 (flat).

DISCUSSION

The difference of flow patterns is confirmed to compare the natural developed velocity profile with the simplified flat velocity profile. The remarkable difference is shear layer between the jet and the recirculation region. Though the magnitude of velocity gradient is same degree, the thickness of free shear layer in the natural velocity profile is thinner than that in the flat velocity profile. TKE on the shear layer in the natural velocity profile is one order bigger than that in the flat velocity profile.

The inflow boundary profile is found to affect the stability of a free shear layer behind the nasal valve. Therefore it is important to consider actual inflow velocity profile surrounding the external face to predict transitional flow in the nasal cavity.

ACKNOWLEDGEMENTS

This research was supported by JSPS KAKENHI Grant Number 26630059 and MEXT SPIRE Super computational Life Science.

REFERENCES

[1] Im, S. et al, "Tomographic PIV measurements of flow patterns in a nasal cavity with geometry acquisition", *Experiments in Fluids*, Vol. 55, 1644 (2014).

[2] Doorly, D.J. et al, "Experimental investigation of nasal airflow", *Journal of Engineering in Medicine*, Vol. 222, pp. 439-453, (2008).

[3] Mylavarapu, G. et al, "Variation of computational fluid dynamics methodology used for human upper airway flow simulations", *Journal of Biomechanics*, Vol. 42, pp. 1553-1559, (2009).

[4] Wang, Y. et al, "On locating the obstruction in the upper airway via numerical simulation", *Respiratory Physiology & Neurobiology*, Vol. 193, pp. 1-10, (2014).

[5] Bates, A.J. et al, "Dynamics of airflow in a short inhalation", *the Royal Society Interface*, Vol. 12, (2014).

[6] Taylor, D.J. et al, "Inflow boundary profile prescription foe numerical simulation of nasal airflow", *the Royal Society Interface*, Vol. 7, pp. 515-527, (2010).

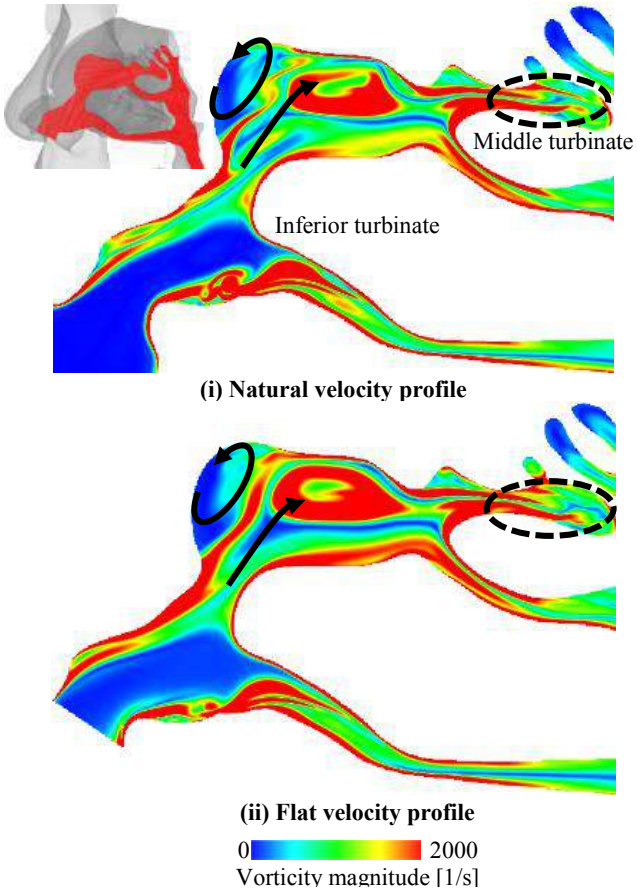

Figure 2: Contours of instant vorticity magnitude on sagittal plane in left nasal cavity

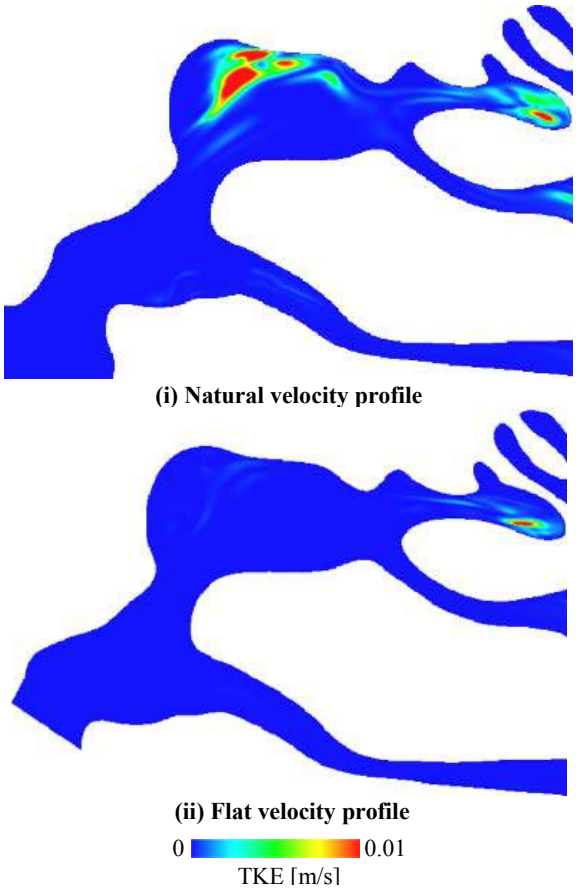

Figure 3: Contours of TKE on sagittal plane in left nasal cavity

Copyright 2016 The Organizing Committee for the 2016 Summer Biomechanics, Bioengineering and Biotransport Conference

SB^{3}C2016
Summer Biomechanics, Bioengineering and Biotransport Conference
June 29 –July 2, National Harbor, MD, USA
SB^{3}C2016-658

INFLUENCE OF PLAQUE STIFFFNESS ON DEFORMATION AND FLOW OF ARTERIAL STENOSIS MODEL FOR PERCUTANEOUS TRANSLUMINAL CORONARY ANGIOPLASTY

Shunichi Kobayashi (1), Daiki Miyamoto (2), Hajime Kitami (1)

(1) Faculty of Textile Science and Technology
Shinshu University
Ueda, Nagano, Japan

(2) Graduate School of Science and Technology
Shinshu University
Ueda, Nagano, Japan

INTRODUCTION

Percutaneous Transluminal Coronary Angioplasty (PTCA) is one of the minimally-invasive procedure for coronary disease. Detailed assessment of the deformation of plaque in a coronary disease during the dilation by PTCA balloon catheter, and recovery of blood flow is important for the development of the balloon catheter and improvement of the procedure. Firstly, we developed the arterial stenosis model as a diseased blood vessel model made of polyvinyl alcohol (PVA) hydrogel (tube portion) and vinyl acetate (plaque portion) [1]. The sticky vinyl acetate was coated by thin PVA layer to avoid adhesion of balloon catheter, but the coating was insufficient. In this study, we changed the material of plaque portion to the oil-based cray, and discussed the influence of plaque stiffness on deformation and flow of the arterial stenosis model.

METHODS

Figure 1 shows the stenosis model. The inner diameter D and the thickness h of straight tube, and the length of stenosis Ls are, 3.5 mm, 1 mm, and 8 mm, respectively. Nominal stenosis severity St and eccentricity Ec is at zero luminal pressure are

$$St_{nominal} = (1 - Ds/D) \times 100 \ [\%], \quad Ec = e/((D - Ds)/2) \times 100 \ [\%]. \quad (1)$$

We used the stenosis models of $St_{nominal}$ = 60 - 80%, and Ec = 100%. Polyvinyl alcohol (PVA) hydrogel was used for healthy straight sections (tube portion). Dimethyl sulfoxide was added to PVA solution before the gelation. The mechanical property of this PVA hydrogel was closer to that of coronary artery [1]. Oil-based cray (Leon cray) was used for the plaque portion to represent the plastic deformation during the dilation by the balloon catheter. There different stiffness of crays were prepared for the plaque portion. Young's modulus E (the average value when 0 to 0.4 of strain) of the crays are 0.3, 0.6, and 1.2 MPa for soft, normal, and hard plaque, respectively. These values are the almost same to that of stenosis model used for stent placement [2]. Figure 2 (A) shows the experimental setup. The working fluid used was water at 24 ˚C. The computer-controlled gear pump was used for the pulsatile flow. The average upstream and downstream pressures were set at 90 mmHg and 70mmHg, respectively. Flow rates and pressures upstream and downstream of the stenosis model were measured. The stenosis model was attached on the sliding surface of rotating eccentric cam to change the curvature of stenosis model (Figure 2 (B)). The rotation of the eccentric cam is in synchronization with pulsatile flow. Luminal area / average curvature, change of curvature radius of the stenosis model were set at 0.08, 10mm, respectively [3]. Firstly, a guide wire was inserted into the stenosis model. Then, the balloon catheter was inserted

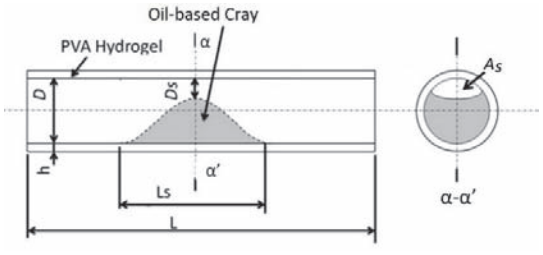

(A) Schematic diagram

(B) Photograph

Figure 1: Stenosis model.

Copyright 2016 The Organizing Committee for the 2016 Summer Biomechanics, Bioengineering and Biotransport Conference

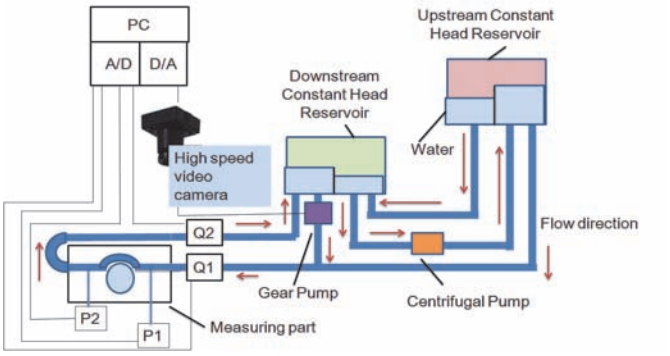

(A) Flow loop

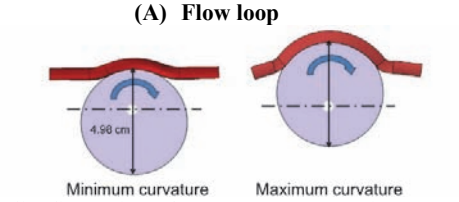

(B) Configuration of the cam and stenosis model

Figure 2: Experimental setup.

along the guide wire and pressurized and expanded by the indeflator. Tomographic images of the stenosis model were taken by micro CT before and after the flow experiment.

RESULTS AND DISCUSSION

Figure 3 shows the micro CT images of the stenosis. Plaque part was deformed concavely. We measured luminal area from the images and evaluated true stenosis severity St_{true} :

$$St_{true} = (A_S / A) \times 100\ [\%], \qquad (2)$$

where $A(= \pi D^2/4)$ and A_S are luminal areas of straight portion and apex of stenosis, respectively. Figure 4 shows the reduction of true stenosis severity (St_{true_bi} - St_{true_ad}) after the dilation by the balloon catheter. The reduction was decreased when the true stenosis severity before dilation St_{true_bi} was increased. This is caused that the greater volume of plaque portion becomes difficult to deform to increase the minimum area of stenosis. The reduction for soft plaque is greater than that for normal plaque, because softer cray deforms greater to reduce the stenosis severity. For the measured flow rates, we evaluated the ratios of increase and recovery of flow by dilation of stenosis:

$$R_{QI} = Q_{ave_ad} / Q_{ave_bi}, \quad R_{QR} = Q_{ave_ad} / Q_{ave_st0}, \qquad (3)$$

where Q_{ave_ad} is the average flow rate after the dilation and removal of the catheter, Q_{ave_bi} is average flow rate before the catheter intersection, Q_{ave_st0} is average flow rate when $St_{true} = 0$ % as the no stenosis healthy arterial model. R_{QI} represents the ratio of increase of flow, and R_{QR} represents the ratio of recovery of flow to the healthy condition, by the dilation of plaque in the stenosis model. Figure 5 shows the relationship between stenosis severity St_{true_bi} and the ratios of increase and recovery of flow. R_{QI} increased with an increase in St_{true_bi}. This is explained that the initial flow rate (before insertion and pressurization of balloon) becomes smaller as greater stenosis severity, not influenced by the greater reduction of stenosis severity. There was no greater difference of R_{QI} by changing stiffness of plaque. For the normal and soft plaque, R_{QR} was almost constant and there was no greater difference between two plaques. But R_{QR} was decreased with an increase in $St_{true\ bi}$ of hard plaque. This is considered that the initial flow rate and the reduction of

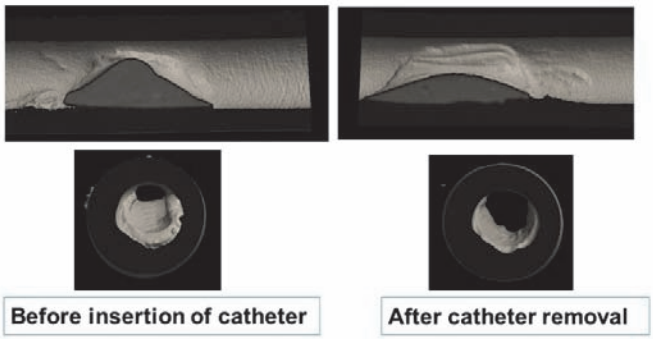

Figure 3: Micro CT imaging of stenosis ($St_{nominal}$ =70%).

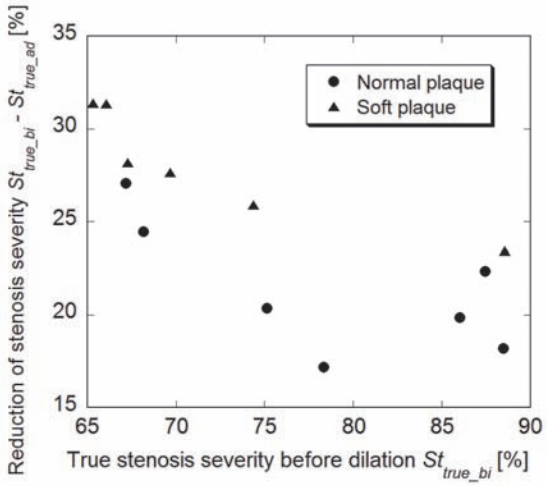

Figure 4: Reduction of true stenosis severity by dilation of balloon.

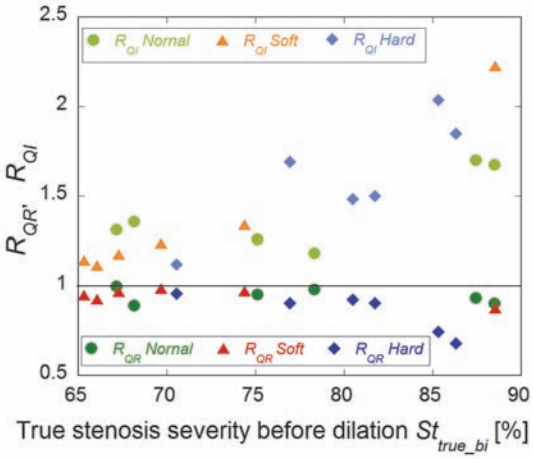

Figure 5: Relationship between true stenosis severity St_{true_bi} and ratios of increase and recovery of flow R_{QI}, R_{QR}.

stenosis severity by the dilation were smaller for greater St_{true_bi} of hard plaque.

REFERENCES

[1] Kobayashi, S et al., *Proc. SB³C2015,* 1141, 2015.
[2] Okamoto,Y et al., *Proc. IFMBE* 31, 398–401, 2010.
[3] Weydahl, E. S et al., *J. Biomech*, 34 (9) , 1189-1196, 2001.

Copyright 2016 The Organizing Committee for the 2016 Summer Biomechanics, Bioengineering and Biotransport Conference

SB³C2016
Summer Biomechanics, Bioengineering and Biotransport Conference
June 29 –July 2, National Harbor, MD, USA
SB³C2016-659

ABNORMAL CHARACTERISTICS OF BLOOD FLOW IN HUMAN LEFT ATRIUM WITH PRIOR HISTORY OF EMBOLIC STROKE : COMPUTATIONAL FLUID DYNAMCS STUDY

Tomohiro Otani (1), Shigeo Wada (1), Hiroshi Ashikaga (2)

(1) Department of mechanical Science & Bioengineering
Graduate School of Engineering Science, Osaka University
Toyonaka, Osaka, Japan

(2) Division of Cardiology and Department of Biomedical Engineering
Johns Hopkins University School of Medicine
Baltimore, Maryland, USA

INTRODUCTION

The left atrium (LA) is one of the upper chambers of the heart and transports the oxygenated blood from the pulmonary veins (PVs) to the left ventricle (LV) through the mitral valve (MV). Atrial fibrillation is the most common arrhythmia in human beings, which is associated with an increased risk of embolic stroke [1]. However, recent epidemiologic studies suggest that AF may not be responsible for the thromboembolic events [2], but pathologic alterations in the LA structure and function may be causally related to thromboembolism. In fact, many indices of LA structural remodeling are associated with stroke, such as larger LA size [3], larger extent of LA fibrosis [4], lower LA function [5] and lower LA appendage (LAA) function [6] in sinus rhythm. These findings suggest that LA structural remodeling may promote blood flow stasis which leads to thrombus formation embolic stroke. Thus, detailed understanding of the effects of the LA structural remodeling on the blood flow characteristics within the LA is potentially useful for predicting the stroke risk in individual patients.

Computational fluid dynamics (CFD) is a powerful tool to analyze the blood flow characteristics in the heart. However, it is challenging to solve complex fluid-structure interactions using CFD in the LA due to the lack of knowledge of the material and mechanical properties of the LA wall. To overcome this issue, we propose an alternative approach to perform personalized blood flow analysis in the human LA by providing the 3-D LA endocardial surface motion derived from patient-specific cardiac CT images [7]. This approach allows personalized LA blood flow analysis which incorporates important patient-specific indices of LA structural remodeling that are associated with stroke. In this contribution, we applied this approach to patients with and without a prior history of stroke to evaluate the blood flow characteristics within the LA.

METHODS

The overall methodology of blood flow analysis in the human LA is described elsewhere [7]. Cardiac CT images of the 18 AF patients (Case=10, Control=8) were acquired during normal sinus rhythm using a 64-slice multi-detector CT scanner (Aquilion 64, Toshiba America Medical Systems, Inc. Tustin, CA) for a total of 20 phases during a cardiac cycle (0%RR, 5%RR, ..., 95%RR). The reconstructed image size was 512×512 with a pixel size of 0.5×0.5 mm^2. Slice number of images were 351 ± 55 (Case) and 320 ± 45 (Control) with the slice thickness of 0.5-1.0 mm. LA was segmented in the CT images at all the 20 phases using the cardiovascular segmentation tool of Mimics Medical 18.0 (Materialise, Inc. Plymouth, MI). Using the segmented CT images, LA endocardial surface mesh reconstruction and LV inner volume measurements were performed at all the phases. Representative geometry of LA in a patient with a prior history of stroke is shown in Fig. 1(a). The cycle length of the cardiac cycle was 0.80 ± 0.24 sec (Case) and 0.81 ± 0.15 sec (Control).

The patient-specific LA motion was obtained by using a non-rigid registration technique. The template surface mesh was constructed from the LA surface geometry at electrocardiographic ventricular end diastole using Pointwise V17.3R1 (Pointwise, Inc. Fort Worth, TX) and the motion estimation of the LA endocardial surface was performed in each phase. From the matched surface meshes in all phases, three-dimensional displacement vectors of all nodes constituting the LA endocardial surface mesh were calculated. These discrete displacement vectors given in 20 phases were interpolated to the trigonometric function given in arbitrary time t with using the discrete Fourier transform.

Tetrahedral meshes were constructed in the LA including the PVs using Pointwise for the blood flow analysis. Blood flow analysis in the

Copyright 2016 The Organizing Committee for the 2016 Summer Biomechanics, Bioengineering and Biotransport Conference

LA was implemented in OpenFOAM 2.3.1. We assumed the blood as an incompressible fluid with density ρ of 1.05×10^3 kg/m^3 and the blood viscosity μ was assumed to be non-Newtonian fluid obeying the Carreau-Yasuda model with the same parameters of [8]. The flow in the LA was modelled with the incompressible Navier-Stokes equation and the equation of continuity given by

$$\rho\left(\frac{\partial \mathbf{v}}{\partial t}+\mathbf{v}\cdot\nabla\mathbf{v}\right)=-\nabla p+\mu\nabla^2\mathbf{v}\,, \quad (1)$$

$$\nabla\cdot\mathbf{v}=0\,, \quad (2)$$

where the **v** is the velocity vector and p is the pressure. These equations were solved with coupling using the Pressure Implicit with Splitting of Operations (PISO) algorism. The blood flow analysis in each case was performed with the time increment of 1×10^{-4} sec.

The boundary conditions of the CFD studies were as follows. The velocity vector at the wall boundary was determined by the wall motion in each time step and the zero gradient pressure was adopted. At the distal end of each PV, the velocity boundary condition was chosen to permit both inflow and outflow in the PVs that are observed during the cardiac cycle in human heart [9] and total pressure was constantly set to be zero. The boundary condition of the MV annulus during ventricular systole was treated as a wall boundary. During the ventricular diastole, patient-specific volume of blood ejected through the MV from LA to LV were assigned, in which the time cause of the blood volume was measured from the LV volume changes obtained by the CT images. The MV was considered to be closed during ventricular systole and open during ventricular diastole, and the time required for MV opening and closure was considered to be negligible. Ventricular systole and diastole were defined by the time course of LV volume.

For the evaluation of the flow characteristics in LA, a change of the shear flow field was investigated by introducing the shear rate defined by the $2\sqrt{II_{\mathbf{D}}}$, where $II_{\mathbf{D}}$ is the second invariant of the shear strain tensor **D** [8].

RESULTS

Figure 1(b)-(f) show representative snapshots of the iso-surface of the shear rate (=15 s^{-1}) during a cardiac cycle in patients with a prior history of stroke, whose LA had larger size and lower function. The shear rate was consistently low in LAA during a cardiac cycle. The shear rate was lower than 15 s^{-1} in LAA and some regions of LA during the ventricular systole (Fig. 1(b) and (c)). The regions with low shear rate (<15 s^{-1}) in the LA and LAA became smaller at the end of ventricular systole (Fig. 1(d)) and disappeared in LA during the ventricular diastole, whereas those in LAA persisted throughout the cardiac cycle (Fig. 1(e) and (f)). This pattern of time course of the shear flow was observed in all patients and spatiotemporal averaged shear rate in LAA was almost same in both case and control patients (30 s^{-1}). However, several case patients, whose LA had larger size or lower functions, had consistently low spatiotemporal averaged shear rate and larger volume of low shear rate (15 s^{-1}) in the LAA.

DISCUSSION

We find that the shear rate was consistently low (<15 s^{-1}) in LAA in patients with a prior history of stroke and LA structural remodeling. This finding is consistent with the fact that thrombus formation in the LAA is one of the main culprits of embolic stroke [10], and that the thrombus tends to form in the region with shear rate lower than 15 s^{-1} [11]. Our CFD results account for the hemodynamic effects of abnormal structural remodeling within LA associated with embolic stroke. Furthermore, our results also highlight the strength of our approach to understanding the risk of intracardiac thrombogenesis and embolic stroke.

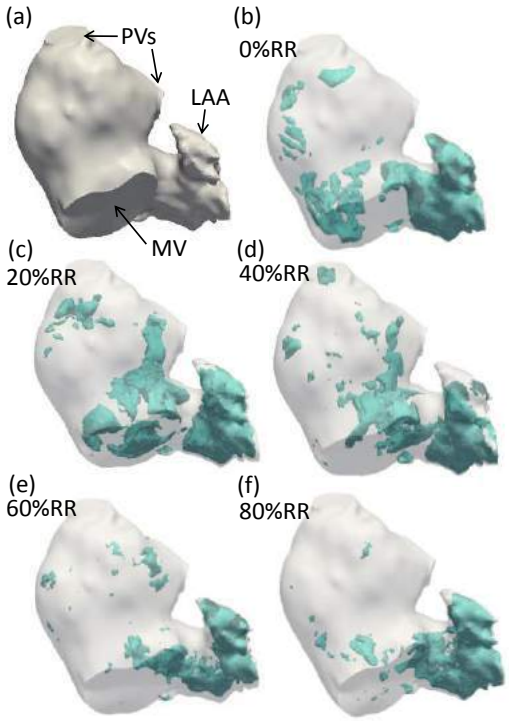

Figure 1: Representative LA geometry with prior history of stroke (a) and snapshots of the iso-surface of shear rate (=15 s^{-1}) during a representative cardiac cycle (b)-(f). RR indicates the interval between two consecutive electrocardiographic R waves and 0%RR indicates ventricular endo-diastole.

ACKNOWLEDGEMENTS

This work was supported by research grants from the Japan Society for the Promotion of Science (Research Fellowship for Young Scientist A2616220, to Otani), Magic That Matters Fund for Cardiovascular Research (to Ashikaga) and Zegar Family Foundation (to Ashikaga).

REFERENCES

[1] Wolf, PA et al., *Stroke*, 22(8):983–988, 1991.
[2] Piccini, JP and Daubert, JP, *Hear. Rhythm*, 8(9):1424–1425, 2011.
[3] Benjamin, EJ et al., *Circulation*, 92(4):835–841, 1995.
[4] Daccarett, M et al., *J. Am. Coll. Cardiol*., 57(7):831–838, 2011.
[5] Inoue, YY et al., *J. Am. Heart Assoc*., 4(4):e001844–e001844, 2015.
[6] Al-Issa, A et al., *Eur. Hear. J.–Cardiovasc. Imaging*, p. jev207, 2015.
[7] Otani, T et al., *Ann. Biomed. Eng*., *In Review*.
[8] Leuprecht, A and Perktold, K, *Comput. Methods Biomech. Biomed. Engin*., 4(2):149–63, 2001.
[9] Smiseth, A et al. *J. Am. Coll. Cardiol*., 34(3):802–809, 1999.
[10] Blackshear, JL and Odell, JA, *Ann. Thorac. Surg.* 61:755–759, 1996.
[11] Cabel, M et al., *Am. J. Physiol*., 272(2):H1020–32, 1997.

Copyright 2016 The Organizing Committee for the 2016 Summer Biomechanics, Bioengineering and Biotransport Conference

SB^{3}C2016
Summer Biomechanics, Bioengineering and Biotransport Conference
June 29 –July 2, National Harbor, MD, USA
SB^{3}C2016-660

QUANTITATIVE ASSESSMENT OF INTRACELLULAR DELIVERY OF MEMBRANE-IMPERMEABLE MACROMOLECULES USING CELL DEFORMATION

K. Kurata (1), A. Kurogawa (2), T. Fukunaga (1), H. D. Wang (1), H. Takamatsu (1)

(1) Department of Mechanical Engineering
Kyushu University
Fukuoka, Fukuoka, Japan

(2) Graduate School of Engineering
Kyushu University
Fukuoka, Fukuoka, Japan

INTRODUCTION

Intracellular delivery of genes and macromolecules is an essential technique in biological research and clinical applications. Several methods including electroporation, sonoporation, microinjection, lipofection, and transfection mediated by a viral vector have been used to deliver impermeable molecules into cells. However, achieving high delivery efficiency and cell viability is difficult.

Under these circumstances, a unique method of intracellular delivery using the rapid squeezing of cells has been recently established [1][2]. Here, a cell suspension with delivery materials is passed into a narrow microchannel. Fluid shear stress and rapid compressive deformation of the cell membrane temporarily increases the permeability of the membrane and makes it possible to introduce various macromolecules into the cells. This method has the advantage of a high throughput and applicability to various cell types, while realizing both high delivery efficiency and viability. However, the mechanism behind membrane perforation is not well elucidated because the previous device was unsuitable for the observation of membrane deformation and repair process.

Therefore, this study aimed to reveal the contribution of compressive deformation to the intracellular delivery of macromolecules and the repair process of the cell membrane. We developed a new perfusion chamber system for microscopic observations of cells under compressive deformation. The kinetics of intracellular delivery and membrane repair were examined by circulating medium with four macromolecules at different time points after the application of compressive deformation.

METHODS

The setup of the perfusion chamber system is described in Fig. 1. The chamber was constructed between two glass plates, the top of which was connected to syringe pumps and a drain for perfusion and the bottom of which was placed on a clamp plate. A 5-μm thick double-coated adhesive film with a cutout measuring 40 mm long and 4 mm wide was sandwiched between the glass plates, thus producing a chamber.

Human prostate cancer cell line PC-3 was used for experiments. The cells were suspended at a density of 10^6 cells/ml in phenol-red free α-minimum essential medium (α-MEM) containing 20 mM HEPES. After dropping 0.76 μl of the cell suspension on the chamber, the upper slide glass and clamp plate were covered and screwed in firmly, causing the cells to be subjected to compressive deformation.

Immediately after the application of compressive deformation, phenol-red free α-MEM containing 20 mM HEPES was supplied from syringe pump 2 at a flow rate of 200 μl/min. By aspirating the medium using syringe pumps 3 and 4 at flow rates of 188 and 12 μl/min, respectively, the medium ran in the perfusion chamber at a flow rate of 12 μl/min. Syringe pump 1 was filled with the medium and delivery macromolecules: 2 mg/ml propidium iodide (PI, molecular weight (MW): 668), 1.25 mg/ml Cascade Blue dextran (MW: 3,000), Texas Red dextran (MW: 40,000), or FITC dextran (MW: 70,000). By

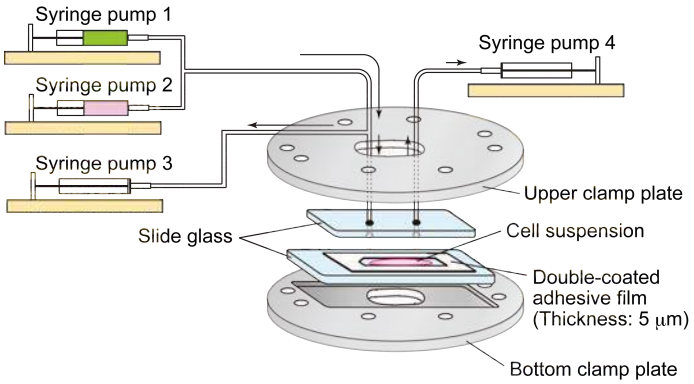

Figure 1: Schematic showing the structure of the perfusion chamber mounted on a microscope stage.

Copyright 2016 The Organizing Committee for the 2016 Summer Biomechanics, Bioengineering and Biotransport Conference

switching the operation of syringe pump 2 to syringe pump 1, the medium with macromolecules was supplied to the perfusion chamber for only 1 min at 0.5, 5, 10, 12, 15, or 20 min after the application of compressive deformation.

Following the 1-min perfusion of macromolecules, the plain medium was supplied again until the medium with macromolecules was completely washed out from the chamber. Then, phase-contrast and fluorescent images observed using a fluorescent microscope (Eclipse E600FN, Nikon, Tokyo, Japan) with a 20× objective were captured using a digital microscope (VHX-1000, Keyence, Osaka, Japan).

RESULTS

Prior to the perfusion experiments, the diameters of PC-3 cells were microscopically measured before and after the application of compressive deformation. The average diameter of the cell contour in the top view increased from 18.4 ± 1.7 μm (mean ± standard deviation) to 22.7 ± 3.1 μm.

Figure 2 shows an example of phase-contrast and fluorescent images of cells exposed to the medium with PI at 0.5 and 15 min after the application of compressive deformation. At 0.5 min, most of the cells were stained by PI, emitting red fluorescence. The outlines of these cells were ruffled in the phase-contrast images. At 15 min, the cells almost completely excluded the intracellular delivery of PI. The ruffled outlines of the cells were recovered as sharp boundaries.

Figure 3 shows the percentage of dye-permeable cells as a function of the time spent under compression. The smallest molecular size PI permeated through the cell membrane for 10 min after the application of compressive deformation. The delivery efficiency reached 60%–80%. It suddenly decreased 12.5 min after compression, and dropped to approximately 10% at 15 min. Dextran with molecular weights of 3,000 and 40,000 were also diffused into cytoplasm for 10 min after the application of compressive deformation. The delivery efficiency decreased depending on the increased molecular weight. At 15 min after the application of compressive deformation, the delivery efficiency decreased below 10%. However, almost no cells received dextran with molecular weights of 70,000, which is comparable with the control without the application of compressive deformation.

DISCUSSION

In this study, the effects of the compressive deformation of the cell membrane on the intracellular delivery of macromolecules and repair process were examined using a perfusion chamber system. The exogenous macromolecules were introduced into the cells via the deformed cell membranes in a molecular weight-dependent manner. The state of high permeability of the cell membranes was maintained for 10 min after the application of compressive deformation. The damaged membranes were gradually repaired and finally recovered their integrity 15 min after compression. This finding shows that a resting period of at least 15 min after the application of compressive deformation is required for the identification of dead cells using PI staining since PI is permeable for 10 min regardless of whether the cells are alive or dead.

The cell strain was estimated with the assumption that a spherical cell is compressed by two parallel plates, as shown in Fig. 4. The area expansion ratio γ is calculated using the following equation by assuming that the cell volume is constant [3];

$$\gamma = \left(\frac{2}{3} - \frac{\pi^2}{16}\right)\left(\frac{h}{d_0}\right)^2 + \frac{1}{3}\left(\frac{d_0}{h}\right) + \frac{\pi}{4}\left(\frac{h}{d_0}\right)^2 \sqrt{\frac{\pi^2}{16} + \frac{2}{3}\left\{\left(\frac{d_0}{h}\right)^3 - 1\right\}} \qquad (1)$$

where d_0 is the diameter of a cell before deformation and h is the gap between the parallel plates. Considering that d_0 = 18.4 ± 1.7 μm and h = 5.9 μm based on microscopic measurements, γ is calculated to be 1.33–1.49. A biological cell membrane stretched to γ =1.51 forms small pores with diameters of approximately 4 nm [4]. The estimated pore size is sufficiently large to introduce Texas Red dextran (MW: 40,000), which has a diameter of approximately 3 nm, but not FITC dextran (MW: 70,000), which has a diameter of approximately 5 nm. This may be the reason for undelivered FITC dextran to the deformed cells.

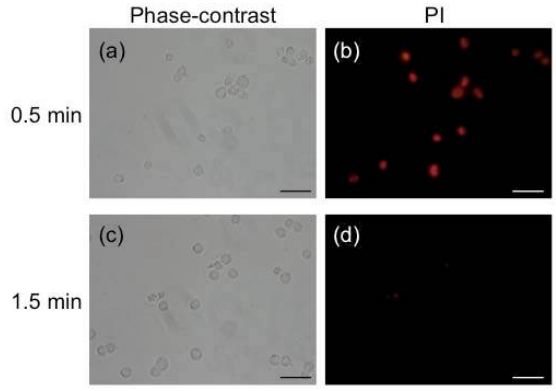

Figure 2: Phase-contrast and fluorescent micrographs of cells exposed to the medium with PI at 0.5 min (a)(b) and 15 min (c)(d) after the application of compressive deformation. Bar: 50 μm.

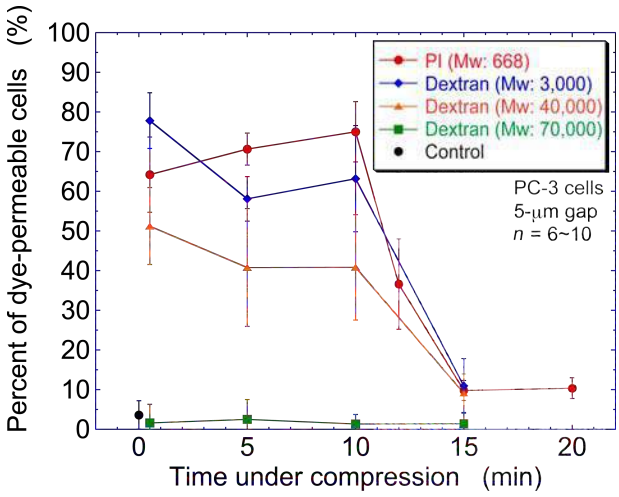

Figure 3: Percent of dye-permeable cells as a function of the time spent under compression.

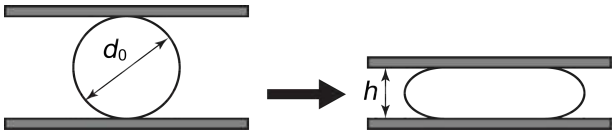

Figure 4: Model for estimating cell strain by deformation.

REFERENCES

[1] Sharei, A et al., *Proc Natl Acad Sci USA*, 110:2082-2087, 2013.
[2] Sharei, A et al., *Integr Biol*, 6:470-475, 2014.
[3] Takamatsu, H et al., *J Biomech*, 38:117-124, 2005.
[4] Shigematsu, T et al., *Sci Rep*, 5:15369, 2015

Copyright 2016 The Organizing Committee for the 2016 Summer Biomechanics, Bioengineering and Biotransport Conference

SB³C2016
Summer Biomechanics, Bioengineering and Biotransport Conference
June 29 –July 2, National Harbor, MD, USA
SB³C2016-661

VIRTUAL DESIGN OF MODULAR 3D PRINTED ANKLE FOOT ORTHOSES

A. Ielapi (1), B. Verhegghe (1), M. Vermandel (2), J. P. Deckers (2), M. Forward (3), E. Vasiliauskaite (3), M. De Beule (1)

(1) Institute Biomedical Technology (IBiTech)
Ghent University
9000 Gent, Belgium

(2) V!GO N.V. / S.A.
9230 Wetteren, Belgium

(3) Gait & Movement Analysis Laboratory
University Hospital Ghent
9000 Gent, Belgium

INTRODUCTION

Ankle foot orthoses (AFOs) are external mechanical devices which are applied across the ankle joint encompassing the foot and calf so as to assist and improve the gait of patients with muscular and/or neurological problems affecting the leg. Their production is a time-consuming and manual process: the techniques involved are common and used for many years without significant innovation. Their performance are determined by the specific technical knowledge of the CPO (Certified Prosthetic Orthotist) and the manual skills of the technicians during production. However this way of manufacturing does not allow control of such AFO properties as thickness or stiffness. Perhaps using 3D printing, as process of production, would allow standardization and better control on the mechanical properties of these devices.

Different research projects have been reported on this topic, but few of them were focusing on the construction of finite element models of 3D printed ankle foot orthoses [1-2]. Probably this is due to the difficulty in finding materials, with the suitable flexibility and stiffness, that can be used in the application. Therefore this study is based on the creation of several finite element models of 3D printed ankle foot orthoses of different subjects and on the evaluation of their mechanical properties. The validation of these models will be made through the utilization of a dedicated experimental set-up.

METHODS

The starting point for this study was the utilization of stl files of AFOs, which are widely used for 3D printing. They only describe the surface geometry of a three-dimensional object, represented by a set of raw unstructured triangles. If directly used for finite element simulations, they may lead to inaccurate results because of the irregular shape of the triangles and also, the thickness of the device would not be taken into account. For solving these problems, an efficient approach was developed. By means of the open-source software pyFormex [3], an algorithm was created to allow the creation of a new regular mesh of the device with quadrilateral elements. The algorithm enables separate consideration of the internal and the external surfaces of the selected AFO and then slicing to obtain several polylines: a polyline is a set of points, where line segments are drawn between consecutive points. The next step was to reconnect all the polylines and obtain a regular representation of quadrilateral elements. This mesh is obtained by the average of the meshes of the new internal and the external surfaces. For the calculation of the thickness, which is not uniform along the device, the distance between the new mesh and the initial stl was considered. The effect of the algorithm is visible in Figure 1.

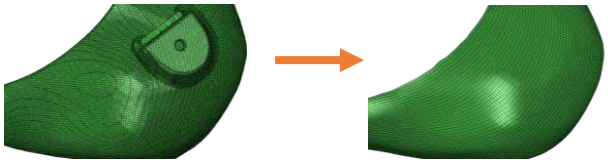

Figure 1: Effect of the algorithm on the mesh of the AFO.

The AFOs used for the study are mainly composed of two parts: the foot and the calf, which have been subjected to the procedure just described. The quadrilateral elements used for the new representation are S4R: shell elements with four nodes and reduced integration. This choice allows more flexible elements and less computational costs. The two parts are connected by beam elements, which represents the two rods of the device, and solid blocks, which are the connection parts between the rods and the foot/calf. In total 4 finite element models have been created,

Copyright 2016 The Organizing Committee for the 2016 Summer Biomechanics, Bioengineering and Biotransport Conference

each of them for different AFO/people. The finite element analyses were performed using Abaqus/Standard 6.14 and consisted of two bending tests called dorsiflexion and plantarflexion. Dorsiflexion is defined as the movement of the AFO calf towards the foot section in the sagittal plane and plantarflexion by the reverse movement. In both cases an angle of 30 degrees is applied as maximal rotation. This rotation is applied through a point identified as the center of the ankle and allows the calculation of the moments acting on the device during the movement. In this way it is possible to define the AFO stiffness, which is the moment around the ankle joint exerted by the AFO per degree of joint rotation [4]. The effect of dorsiflexion and plantarflexion on the device at the maximal rotation of 30 degrees is visible in Figure 2.

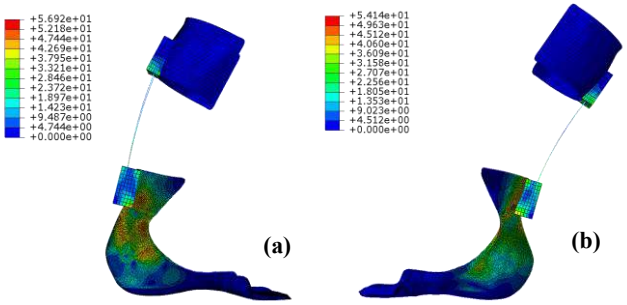

Figure 2: Dorsiflexion (a) and plantarflexion (b) on the device at the maximal rotation of 30 degrees.

The simulation strategy is based on applying the same boundary conditions that are going to be imposed in an experimental set-up, which is still under development. This has to facilitate the comparison between the results and predictions thus provide a means for model validation. The heel part and the zone in correspondence of the metatarsal-phalangeal (MTP) joint are kept fixed in all the directions. The internal surface of the calf part, instead, is constrained to move together with a point that represents the center of the leg. The rods are made of carbon and considered orthotropic. The foot, the calf and the solid blocks are realized in Polyamide 12 which has elasto-plastic properties: a Young's modulus of 1827 MPa and a Poisson's ratio of 0.41 are combined with experimental data provided by the Department of Materials Science and Engineering of Gent University. Moreover, the simulations aim to predict not only how the stiffness changes with the different shapes of the devices but also in relation to the diameter of the carbon rods: hence, tests were conducted with rod diameter of 8 mm and 6 mm.

RESULTS & DISCUSSION

The resulting stiffness values for the four AFOs models during plantarflexion and dorsiflexion are shown in Figure 3, 4, 5 and 6.

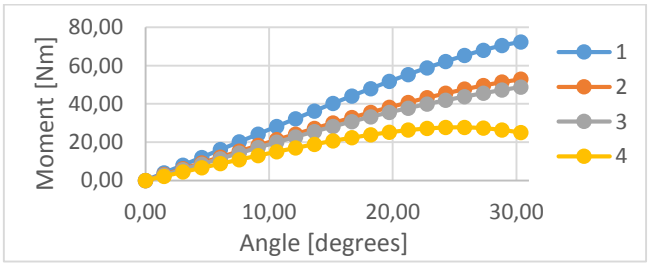

Figure 3: Stiffness during plantarflexion and 8 mm rod diameter

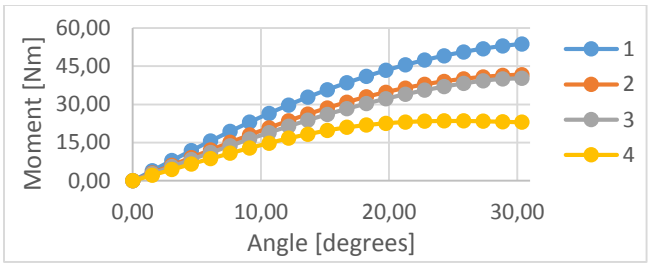

Figure 4: Stiffness during dorsiflexion and 8 mm rod diameter

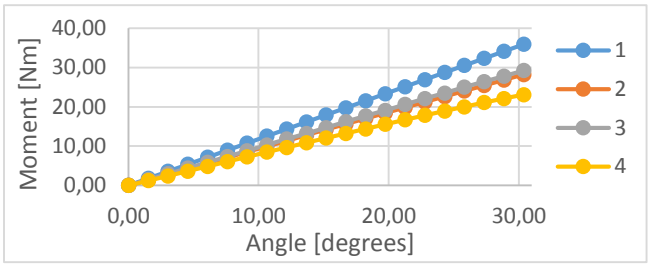

Figure 5: Stiffness during plantarflexion and 6 mm rod diameter

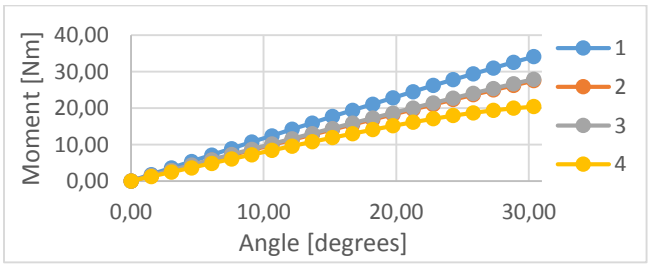

Figure 6: Stiffness during dorsiflexion and 6 mm rod diameter

The results show that the different shape of the devices has an impact on the stiffness, especially on subjects 1 and 4. The data related to subject 2 and 3, instead, have similar values. In general higher stiffness values are reached during the tests with carbon rods of 8 mm, but at the same time all these AFOs reach the plastic region. Further research is needed to investigate whether the AFOs with a rod diameter of 8 mm are also plastically deformed in real life.

CONCLUSION

Using pyFormex, a powerful tool was developed to convert stl files of 3D printed AFOs to high quality finite element models. From the finite element analysis it can be concluded that the different shape and the diameter of the carbon rods influence the stiffness of the devices. Therefore the use of advanced computer modelling algorithms with 3D printing techniques is a strong combination that is acting to revolutionize the manufacturing process of AFOs and to offer several benefits such as the decrease of the production costs, time and errors.

ACKNOWLEDGEMENTS

This research was funded by the IWT STREAM-A_STREAM_AFO project. The authors would like to thank prof. W. Van Paepegem and dr. N. Lammens for providing the materials data.

REFERENCES

[1] Faustini, M. et al., *IEEE*, 55:784-790, 2008.
[2] Schrank, E. et al., *J Biomech*, 135:101011(1)-101011(7), 2013.
[3] Internet address pyFormex: http://www.nongnu.org/pyformex
[4] Bregman, D.J.J. et al., *Gait & Posture* , 30:144-149, 2009.

Copyright 2016 The Organizing Committee for the 2016 Summer Biomechanics, Bioengineering and Biotransport Conference

SB³C2016
Summer Biomechanics, Bioengineering and Biotransport Conference
June 29 –July 2, National Harbor, MD, USA
SB³C2016-662

A NOVEL TECHNIQUE FOR ASSESSMENT OF MECHANICAL PROPERTIES OF VASCULAR TISSUE

Stefan N. Sanders, Frans N. van de Vosse, Marcel C.M. Rutten

Biomedical Engineering
Eindhoven University of Technology
Eindhoven, The Netherlands

INTRODUCTION

Rupture of atherosclerotic plaques in the carotid artery is a major cause for stroke. Rupture is a dangerous event, since it causes total vessel obstruction through thrombosis, and as such may be a lethal condition. Currently, the level of lumen occlusion caused by the stenosis is used to estimate the risk of plaque rupture. However, plaque rupture occurs when the mechanical stresses in the cap of the plaque exceed the local tissue strength, not necessarily when the luminal occlusion exceeds a certain level. Therefore, a biomechanical model of the plaque and its mechanical properties may help to better assess rupture risk.

To determine the risk of rupture, mechanical properties of plaque components and cap strength are measured in 2D inflation experiments and inverse numerical modelling. Since plaque material is highly inhomogeneous, tests on complete, intact vessels only elucidate global properties of the vessel. To make a distinction between individual constituents of a diseased vessel, tests on small samples in which each of the material components can be visualized, are required.

METHODS

In this study, we develop a method to assess material properties of (diseased) vascular tissue in a quasi-2D setting. Thin slices of material were cut and slightly compressed between two glass plates. Fluid was injected into the lumen, through a hole in the bottom plate, to inflate the sample (figures 1, 2). A pressure sensor monitored the intraluminal pressure, while a high speed camera recorded the displacement of the sample. The lumen diameter was calculated from these images. The experiments were modelled in the FEBio finite element package (v2.3.1) to assess material properties during pressure increase [1].

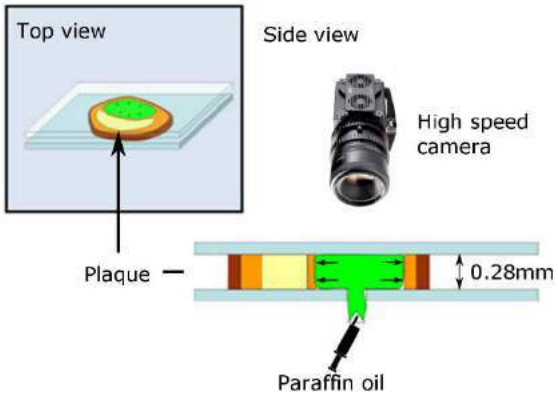

Figure 1: Schematic overview of the experiment.

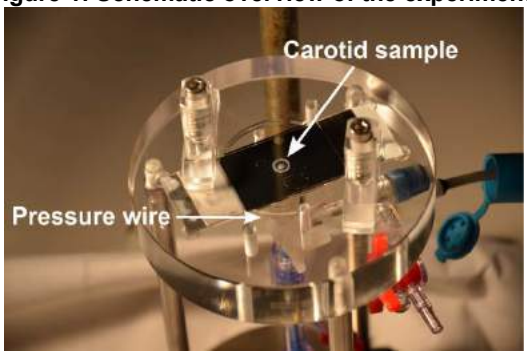

Figure 2: Experimental setup.

Copyright 2016 The Organizing Committee for the 2016 Summer Biomechanics, Bioengineering and Biotransport Conference

For validation purposes, thin rings of silicone rubber (Wacker elastosil M 4601 A/B), with known material properties, were inflated in the experiments (n = 7). The obtained material properties, using a Neo-Hookean model, were compared to the properties calculated from tensile tests on rectangular samples (n = 12) of the same material.

Next, for validation with fresh carotid tissue, ultrasound measurements have been performed on 3 healthy porcine carotid arteries [2]. Thin slices (0.3mm of thickness) were cut from these arteries and measured in the inflation experiment. The Gasser-Ogden-Holzapfel material model [3] was used in both the ultrasound as inflation experiment to obtain matrix stiffness, collagen fiber stiffness and the fiber stiffening parameter, c, k_1 and k_2, respectively. The collagen fiber angle, γ, was set at 31° in the stress-free state [4], fiber dispersion was not taken into account.

RESULTS

The inflation experiment using silicone rubber rings, showed typical Neo-Hookean behaviour (figure 3).

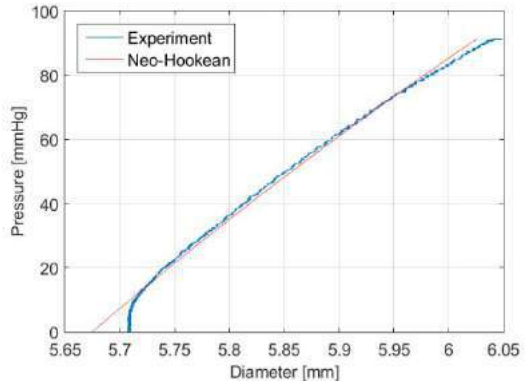

Figure 3: Comparison between inflation experiment and model for silicone rubber rings.

Similar E-moduli are calculated in the inflation experiment and tensile test (figure 4). The mean of both groups are not significantly different (Student's t-test, $p = 0.2 > 0.05$).

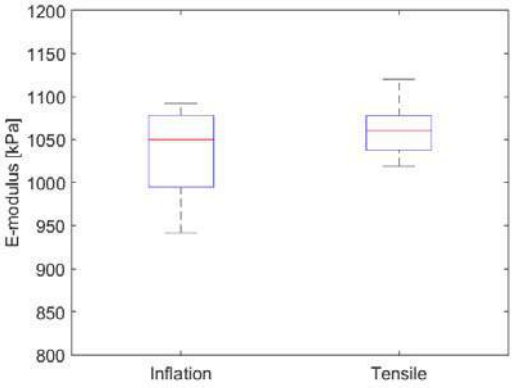

Figure 4: Figure 4: Boxplot of the E-moduli obtained from the inflation experiment and tensile tests.

Strain stiffening was observed at higher pressures in the carotid inflation experiments (figure 5).

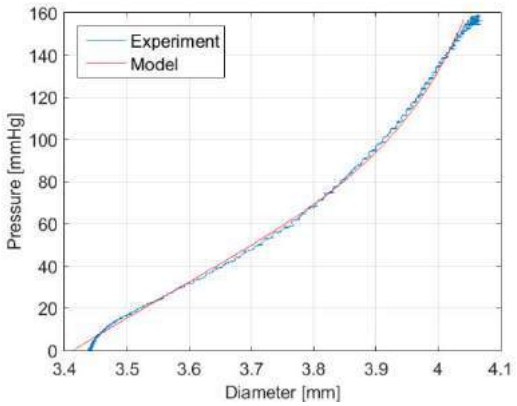

Figure 5: Comparison between inflation experiment and model for carotid tissue

A similar matrix stiffness is found in the inflation and ultrasound experiment (Table 1). The collagen fiber parameters show more variation between the two methods.

	Inflation experiment			Ultrasound experiment		
Sample	c [kPa]	k_1 [kPa]	k_2 [-]	c [kPa]	k_1 [kPa]	k_2 [-]
1	56	10	23	55	5	34
2	68	5	39	65	5	48
3	40	7	27	38	11	11

Table 1: Gasser-Ogden-Holzapfel model parameters obtained from the inflation and ultrasound experiments.

DISCUSSION

The results reveal a good agreement between properties found by classic tensile tests and our new method, for the silicone rubber rings. Increasing the number of inflation measurements could possibly further increase the p-value. A good agreement was found between whole-vessel inflation tests and our method. The fiber stiffness parameters are sensitive to small errors in the measurements, leading to a larger variation when comparing both experiments. Matrix stiffness, however, was similar in the inflation and ultrasound measurements.

The results so far hint towards a method that may successfully be applied for assessment of vascular properties, in a quasi 2D experiment. In future applications, heterogeneous properties, like in atherosclerotic plaque material, may be assessed as well, using vital staining techniques to distinguish different tissue components without affecting their mechanical behaviour.

ACKNOWLEDGEMENTS

This project is funded by the STW open technology program (STW #12548).

REFERENCES

[1] Maas, SA et al., *J. Biomech. Eng.*, 2012 Jan;134(1).
[2] Boekhoven, RW et al., *Ultr. Med. & Biol.,* 39:1875-1886, 2013.
[3] Gasser, TC et al., *J. R. Soc. Int.,* 3:15-35, 2006.
[4] van der Horst, A et al., *Biomech. Mod. Mech..,* 11:533-542, 2012.

Copyright 2016 The Organizing Committee for the 2016 Summer Biomechanics, Bioengineering and Biotransport Conference

SB³C2016
Summer Biomechanics, Bioengineering and Biotransport Conference
June 29 –July 2, National Harbor, MD, USA
SB³C2016-663

A MATHEMATICAL MODEL OF POSTERIOR VITREOUS DETACHMENT AND GENERATION OF VITREORETINAL TRACTIONS

Federica Di Michele (1), Rodolfo Repetto (2), Amabile Tatone (1)

(1) Department of Information Engineering, Computer Science and Mathematics
University of L'Aquila, Italy

(2) Department of Civil, Chemical and Environmental Engineering
University of Genoa, Italy

INTRODUCTION

Retinal detachment (RD) is a serious condition and one of the most frequent causes of blindness in Western countries, affecting approximately 10 out of 100,000 people [1]. The most common type of RD is the rhegmatogenous retinal detachment (RRD), which occurs when liquefied vitreous enters the subretinal space through a retinal tear. Retinal tears are most often generated as a consequence of vitreoretinal tractions. With ageing the vitreous humor undergoes degeneration processes such that the vitreous gel liquefies in certain regions and progressively shrinks (vitreous syneresis). This typically leads to a posterior vitreous detachment (PVD), i.e. a detachment of the jelly vitreous from the retinal in the posterior region of the eye, where vitreoretinal adhesions are normally weaker than in the front. PVD is normally harmful but can lead to strong tractions on the retina if there are regions of vitreous tightly attached to the retina. Such tractions are the most common cause of non-traumatic tearing of the retina [2].

Vitreoretinal tractions generated in the presence of PVD can have both a static or dynamic nature. Dynamic mechanical stimuli on the retina are due to eye rotations that produce oscillations of the detached vitreous and, consequently, tractions on the retina, particularly at the attachment points of the gel-like vitreous to the retina [3]. Static forces on the retina are induced by the quasi-static shrinking of the vitreous humor produced by vitreous syneresis. Both types of forces are thought to have the potential to lead to retinal breaks. In the present work we propose a mathematical model of the quasi-static generation of tractions on the retina produced by syneresis of the vitreous humor.

METHODS

We consider a solid that initially has a spherical shape and represents the healthy vitreous humor within the vitreous chamber.

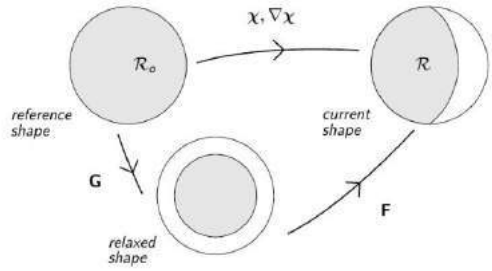

Figure 1: Schematic sketch of the modeling of the contraction and deformation processes.

We model the process of vitreous contraction (syneresis) assuming that the vitreous body progressively shrinks in time. Mathematically, we consider the following decomposition of the deformation gradient

$$\nabla\chi = FG, \tag{1}$$

where G denotes the distortion due to the contraction of the vitreous and F the elastic distortion. We model the contraction process as homogeneous and isotropic and thus we write $G = \gamma I$, with I the identity tensor and γ a positive scalar quantity decreasing in time from an initial value $\gamma(0) = 1$. This implies that, starting from an initially spherical shape and in the absence of any external forces or constraints, the body would shrink maintaining a spherical shape and without generating stresses. The meaning of equation (1) is pictured in Figure 1. In the figure the configuration R_0 represents the reference shape of the body. By looking at the decomposition (1), the deformation χ, which maps this configuration into the current

Copyright 2016 The Organizing Committee for the 2016 Summer Biomechanics, Bioengineering and Biotransport Conference

configuration ($\chi: R_0 \to R$) can be seen as made up, at least locally, of two steps: first G applies the contraction, then F applies an additional elastic distortion, which the body needs to reach the current shape while fulfilling the boundary conditions and preserving the material continuity.

The evolution of the system is governed by the following principle, written as a power balance on the reference configuration

$$\int_{\partial R_0} t_0 \cdot u dA - \int_{R_0} S_0 \cdot \nabla u dV - \int_{\partial R_0} \tilde{S}_0 \cdot \tilde{\nabla} u dA = 0 \quad \forall u. \quad (2)$$

In the above equation t_0 represents the external traction acting on the bounding surface of the body R_0, S_0 is the Piola stress and u a test velocity field. The last term in the balance principle accounts for the presence of a skin wrapping the body, so that $\tilde{S}_0$ represents a surface stress and $\tilde{\nabla} u$ denotes the restriction of ∇u to the boundary R_0. This is consistent with our basic kinematic assumption: the skin deformation is the restriction to the boundary of the bulk deformation, $\tilde{\chi} = \chi|_{\partial R_0}$, which implies that the skin deformation gradient is the restriction of the bulk deformation gradient $\tilde{\nabla} \chi = \nabla \chi|_{\partial R_0}$. The skin models the presence of the vitreous cortex, which is the outermost layer of the vitreous and is stiffer than the bulk vitreous. The vitreous cortex is also assumed to progressively contract in time, so that after introducing the skin deformation gradient decomposition, $\tilde{\nabla} \chi = \tilde{F} \tilde{G}$, we get

$$\tilde{F} \tilde{G} = (FG)|_{\partial R_0}, \quad (3)$$

with $\tilde{G} = \tilde{\gamma} I$ and $G = \gamma I$. If the skin contracts in the same way as the bulk body ($\tilde{G} = G|_{\partial R_0}$) then $\tilde{F} = F|_{\partial R_0}$. If the skin and the bulk body are subject to different contraction laws, the elastic distortions will be related to one another by the compatibility condition (3).

The material characterization of the vitreous body and the vitreous cortex is modeled through the response functions, $S_0 = \gamma^2 \Gamma(F)$ and $\tilde{S}_0 = \tilde{\gamma} \tilde{\Gamma}(\tilde{F})$. It is worth noting that we can set different elastic properties for the bulk material and the skin. We model both the bulk vitreous and the vitreous cortex as incompressible Neo-Hookean materials. This means that the strain energy function depends linearly on the first invariant of the right Cauchy-Green tensor, through the shear modulus, which we denote by k_b for the bulk solid and k_s for the skin.

At the boundary ∂R_0 we assume that the contact between the vitreous and the retina is described by a traction field made up of two contributions: an adhesive attractive force per unit area and a repulsive force per unit area. Both are assumed to be zero on the reference shape. The magnitude of the adhesive force depends locally on the distance between the current position of a material point on the boundary and its reference position. It is characterized by a limit value K_{ad}, corresponding to the onset of vitreous detachment. The magnitude of the repulsive force depends on the distance d from the inner wall of the vitreous chamber, which we can therefore think of as a rigid container. It grows very rapidly as d approaches zero and effectively keeps the vitreous body confined. Together with these two contributions we consider a viscous adhesive traction that avoids a sudden detachment of the body from the wall that would lead to numerical issues.

In the simulations we impose a limit value K_{ad} for the adhesion force per unit area that varies spatially along the surface of the wall. A very high value for K_{ad} in a small region will denote a focal adhesion, while a very low value will trigger the initial detachment. We also assume that K_{ad} grows from the back to the front of the vitreous chamber, consistently with clinical observations.

RESULTS

All simulations started with the vitreous body completely filling the vitreous chamber. We then observed the evolution of the shape of the detached vitreous during the contraction process and the consequent generation of stresses on the boundary and within the vitreous.

In Figure 2a,b we show two examples of three-dimensional configurations of the vitreous attained during the progression of the PVD process. In the first case (Figure 2a) we show a "complete vitreous detachment". In this case we assume that K_{ad} grows from the back (right in the plot) to the front (left in the plot) of the vitreous chamber. Thus the vitreous detaches first on the back of the vitreous chamber and then the detachment proceeds evenly towards the front.

In this Figure 2b we show the case of a PVD in the presence of a focal vitreoretinal adhesion at the back of the vitreous chamber. This case is known to be potentially dangerous in terms of tractions on the retina. In this case the model predicts that the vitreous deforms substantially during the contraction process, thus also generating large stresses. Both configurations reported in Figure 2 are very similar to configurations of PVDs that can be observed in reality. This suggests that the model retains the most important ingredients of the contraction process of the vitreous body.

In can be shown that, for a given spatial variation of the adhesive traction on the boundary, the shape of the detaching vitreous is completely determined once two dimensionless parameters are fixed: the ratio between the elastic moduli of the bulk solid and the skin (k_b/k_s) and the ratio between the elastic modulus of the solid and the limiting adhesive traction (k_b/K_{ad}).

The model can be used to identify shapes of the detaching vitreous that are likely to be associated with large tractions on the retina and to the existence of particularly strong focal adhesions on the retina, which are risk factors for the generation of retinal tears.

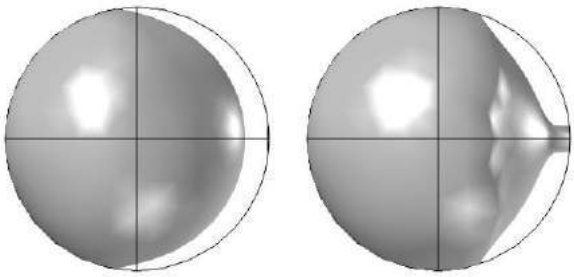

Figure 2: Twos examples of the shape taken by the contracting vitreous during PVD, as predicted by the model. (a) Complete PVD, (b) case in which there is a focal adhesion region at the back of the vitreous chamber.

REFERENCES

[1] Mitry, D. et al., *Retina*, 30(10):1561-1572, 2010.

[2] Foulds, W. S., in Sebag J., ed., *Vitreous in Health and Disease*, Springer-Verlag, 375-393, 2014.

[3] Repetto, R. et al., Biomech. Model. Mechanobiol., 10:191-202, 2012.

Copyright 2016 The Organizing Committee for the 2016 Summer Biomechanics, Bioengineering and Biotransport Conference

SB^{3}C2016
Summer Biomechanics, Bioengineering and Biotransport Conference
June 29 –July 2, National Harbor, MD, USA
SB^{3}C2016-664

THE RESPONSE TO STRESS DEPRIVATION DIFFERS BETWEEN THE INTERFASCICULAR AND FASCICULAR MATRIX OF TENDON

Daniel T. Rowson (1), Martin M. Knight (1), Hazel R.C. Screen (1)

(1) School of Engineering and Materials Science,
Institute of Bioengineering,
Queen Mary University of London
London, UK

INTRODUCTION

Stress deprivation in tendon leads to reduced tendon strength as well as gene expression regulation similar to that seen in tendinopathy. It has been suggested that localized stress deprivation may be a mechanism involved in tendinopathy [1]. Tenocytes express primary cilia, which elongate when tendon is stress deprived [1]. With cilia length previously shown to regulate cell signalling, alterations to cilia length could have implications in tendon healing and tendinopathy [2].

Tendon is made up of strong elastic collagen fascicles bound together with a highly hydrated matrix called the inter-fascicular matrix (IFM). Previous work indicates differences in the morphology and metabolism of the tenocytes resident in the tendon fascicular matrix (FM) and the IFM, as well as differing cellular responses to mechanical overload [3]. This study tests the hypothesis that primary cilia of the cells in these two regions also respond differently to stress deprivation, and that this is associated with differences in the biomechanical degradation of tendon FM and IFM.

METHODS

Dissected rat tail tendons were either tested immediately (fresh), or maintained in media for 1 week, either stress deprived or at 4% static strain. Samples from each group were prepared for cilia imaging and mechanical testing.

In order to determine cilia length, fascicles and their surrounding IFM were fixed, stained and imaged (n = 80-120 cilia per group from 18 fascicles from 3 rats). An additional 30 fascicles from 1 rat were also dissected for a stress deprivation time course, fixing samples for imaging after 4, 6, 16, 24 and 168 hours of stress deprivation.

For mechanical testing, both fascicle and IFM samples were prepared from each test group (n = 6-8 per group per test). For FM testing, 20mm length fascicles were dissected, their diameter measured, and 10 cycles of 0-4% cyclic loading were applied followed by a quasi static pull to failure test. Testing was performed with an Instron (ElectroPuls1000, Canton, MA) mechanical testing machine. For IFM testing, two fascicles were dissected as a unit, and the opposing ends cut from the fascicles at a 20mm separation distance, to leave an isolated region of IFM for shear testing by pulling the fascicles apart along their long axis. The IFM was subjected to a quasi static pull to failure test.

RESULTS

Cilia length in the IFM & FM of fresh samples was not significantly different (fig1). However, cilia were significantly more aligned in FM than in IFM (fig1).

After 1 week of stress deprivation, the cilia significantly increased in length in both the IFM & FM, but the increase was significantly greater in the IFM (fig1). By contrast, when the tissue was maintained at 4% static strain, the cilia in both the IFM and FM regions were significantly shorter than those in stress deprived tissue, however they remained longer than those in fresh tissue (fig1). The time course clarified that while some of the lengthening occurred within the first four hours of stress deprivation, the majority of lengthening and the differential cilia response between the FM and IFM cells all occurred after 24 hours of stress deprivation.

Copyright 2016 The Organizing Committee for the 2016 Summer Biomechanics, Bioengineering and Biotransport Conference

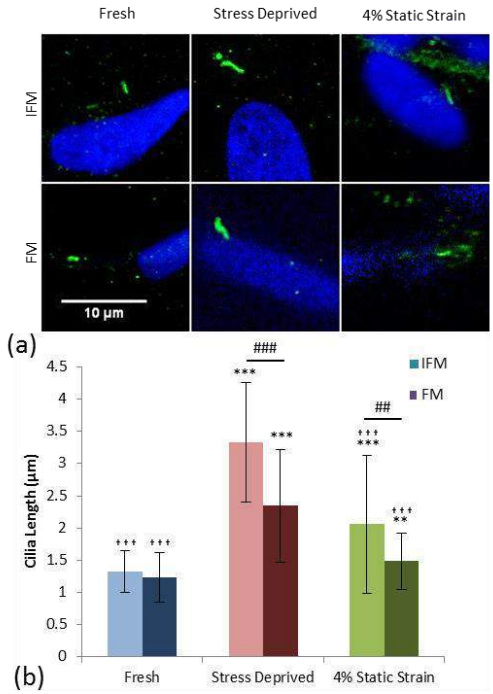

Figure 1: a) images of representative cilia for each condition. b) Mean cilia length in each condition. Stars (*) show significance from the same region in fresh tissue. Crosses (ˈ) show significance from the same region in stress deprived tissue. Hashes (#) show significance between the two tendon regions for a given condition. */ˈ/#=p<0.05, **/ˈˈ/##=p<0.01, */ˈˈˈ/###=p<0.001. Error bars show ±1 standard deviation.**

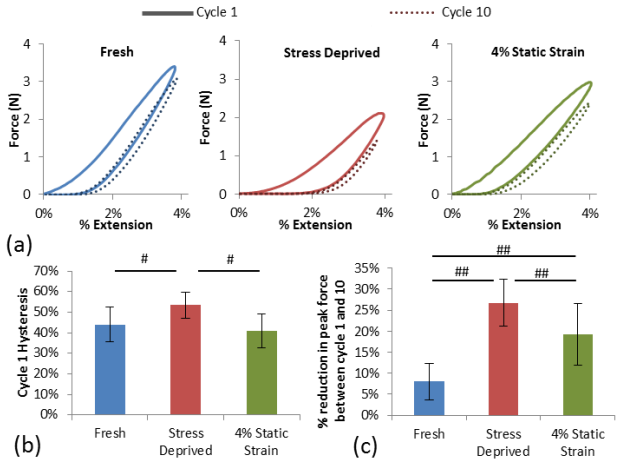

Figure 2: a) representative 4% preconditioning loops for each test group, comparing cycle 1 and 10. b) Average percentage hysteresis in the first preconditioning cycle. c) Percentage reduction in peak force over the 10 cycles. #=p<0.05, ##=p<0.01, ###=p<0.001. Error bars show ±1 standard deviation.

The tensile strength of fascicles was not significantly affected by either the stress deprivation or static strain conditions. However, the viscoelastic properties of the stress deprived fascicles were significantly reduced (fig2). Fascicles under static loading had some loss of viscoelastic properties but it was significantly less than the loss seen in the stress deprived fascicles (fig2). IFM shear force tests showed a dramatic and significant reduction in the quasi static mechanical properties of the IFM after stress deprivation, indicating large amounts of cell mediated degradation in this region (fig3).

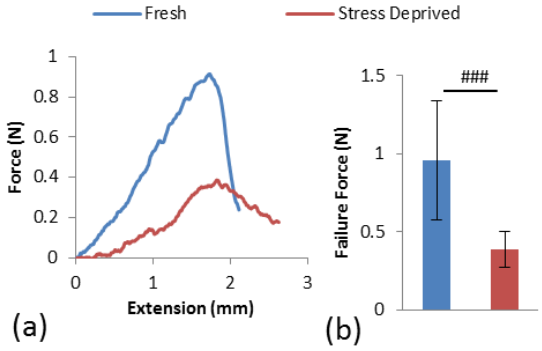

Figure 3: a) Representative force-extension curves to failure for the IFM in stress deprived and fresh samples, alongside b) mean IFM failure force data. ###=p<0.001. Error bars show ±1 standard deviation.

DISCUSSION

The different responses to stress deprivation in the two tendon regions imply a more pronounced cellular response in the IFM. The IFM has also been shown to have an increased response to overload [3], suggesting that cells in this region of the tendon may play a role in the aetiology of tendinopathy.

These data suggest that primary cilia elongation in tendon may be mediated by matrix degradation rather than the absence of strain, since elongation took in excess of 24 hours, and it has been previously established that cilia can respond to changes in strain within 3 hours [4]. The likely response of cilia specifically to matrix degradation may have important consequences for cilia signaling in tendon and in other connective tissues. The differential response of cilia to stress deprivation in the IFM and FM provides further indications that there are differences in the cell populations of these regions. Cilia are key regulators of cell signaling and differences in cell signaling between tendon regions will likely have multiple downstream effects.

ACKNOWLEDGEMENTS

This work was funded by the EPSRC and the Institute of Bioengineering at QMUL.

Rat tails supplied by Professor A. T. Michael-Titus at the Centre for Neuroscience and Trauma, Blizzard Institute, Barts and The London School of Medicine and Dentistry.

REFERENCES

[1] K. Gardner, et al., *J. Orthop. Res.* 29:4 (582–7) 2011

[2] C. L. Thompson, et al., *Osteoarthr. Cartil.*, 22:3 (490–8) 2014.

[3] E. M. Spiesz, et al., *J. Orthop. Res.*, 33:6 (889-97), 2015.

[4] T. Y. Besschetnova, et al., *Curr. Biol.*, 20:2 (182–7) 2010.

Copyright 2016 The Organizing Committee for the 2016 Summer Biomechanics, Bioengineering and Biotransport Conference

SB^{3}C2016
Summer Biomechanics, Bioengineering and Biotransport Conference
June 29 –July 2, National Harbor, MD, USA
SB^{3}C2016-665

CELL ORGANIZATION DICTATES STRESS GENERATION IN TISSUE ENGINEERED CELL SHEETS

Inge A.E.W. van Loosdregt (1,2), Patrick W. Alford (3), Cees W.J. Oomens (1,2), Sandra Loerakker (1,2), Carlijn V.C. Bouten (1,2)

(1) Department of Biomedical Engineering
Eindhoven University of Technology
Eindhoven, The Netherlands

(2) Institute for Complex Molecular Systems
Eindhoven University of Technology
Eindhoven, The Netherlands

(3) Department of Biomedical Engineering
University of Minnesota
Minneapolis, Minnesota, USA

INTRODUCTION

Many cell types exert contractile stresses onto their surroundings via actin stress fibers [1]. In order to obtain mechanically functioning engineered cardiovascular tissues it is important to understand and control the cell contractility, because it affects the tissue organization as well as the (apparent) mechanical properties. One technique to gain more insight into the cellular stress generation is the thin film method [2]. With this technique, the stress generated by a monolayer of cells attached to a thin silicon film can be determined via the deformation of this film by the cells. Current thin film studies have mainly focused on determining the contractile properties of perfectly aligned cells with the same orientation, such as in smooth, skeletal, and cardiac muscle tissue [3-5]. However, the cells in engineered cardiovascular tissues (e.g. heart valves) are in most cases not perfectly aligned in the same direction. It may be questioned whether the stress exerted by perfectly aligned monolayers represents the stress distribution inside these tissues. The aim of the present study is to determine the influence of the degree of cell alignment on the stress generation.

METHODS

To determine the influence of cell alignment on stress generation, fibronectin was micro-contact printed on thin film constructs [2,3] (figure 1). The fibronectin was either patterned as 10 µm wide lines parallel to the long axis of the film (0°) or as a fishnet pattern with 5 µm wide lines with an angle of ± 45° with respect to the long axis.

Subsequently, 80,000 human myofibroblasts were seeded onto each construct and cultured for two days at 37°C and 5% CO_2. After culture, the samples were fixed and stained with DAPI (nuclei) and phalloidin (actin fibers) for 1 hour and visualized with a fluorescent microscope to quantify the alignment of the cells and their actin cytoskeleton using Mathematica and Matlab.

In a separate experiment, after culture, the constructs were transferred to a Petri dish with preheated culture medium. Rectangular films were cut from the constructs (figure 2) and the medium was allowed to cool down below 32°C to dissolve the pIPAAm (poly-N-isopropylacrylamide). This enabled the myofibroblasts to deform the PDMS (polydimethylsiloxane) layer. A picture of the initial curvature (0 h) was taken using a stereomicroscope and the thin films were placed back at 37°C. After 1 hour, the contractile equilibrium was reached and another picture was taken. The curvature of the films was determined from the images using Matlab after which the cellular stress was estimated via finite element modeling in Abaqus. The model consisted of a layer with Neo-Hookean material properties (E=1.58 MPa, ν=0.49) representing PDMS, and a fiber-reinforced layer with an active stress component ($\boldsymbol{\sigma}_{ca}$) representing the cell sheet:

$$\boldsymbol{\sigma}_{ca} = \sum_{i=1}^{N} \varphi_{sf}\sigma_{max}\vec{e}_{sf}\vec{e}_{sf} \qquad (1)$$

where σ_{max} represents the maximum cell stress and φ_{sf} the (Gaussian)

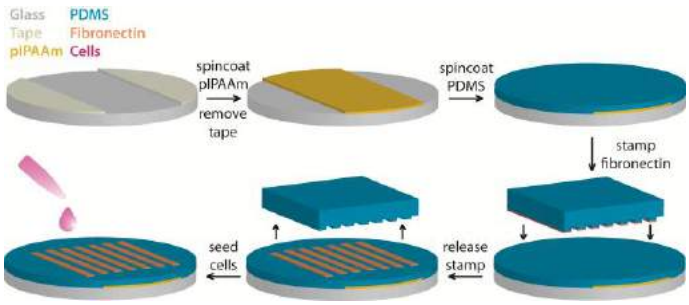

Figure 1: Creation of thin film constructs followed by micro-contact printing and seeding of cells.

Copyright 2016 The Organizing Committee for the 2016 Summer Biomechanics, Bioengineering and Biotransport Conference

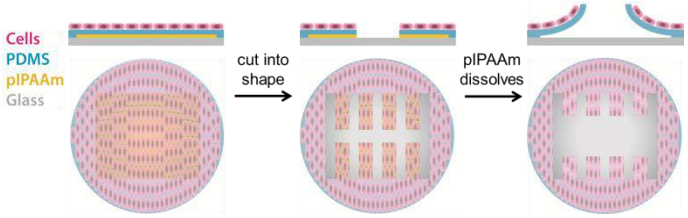

Figure 2: Cutting and release of the individual thin films.

actin stress fiber distribution:

$$\varphi_{sf}^{i} = Aexp\left(\frac{-(\gamma-\mu)^2}{2\sigma^2}\right) \quad (2)$$

with the main fiber direction (μ) in the long axis direction. The standard deviation (σ) was determined from the fiber distribution obtained from the fluorescent images.

Statistical differences ($p<0.05$) in curvature between groups were analyzed with SPSS using a Mann-Whitney U test. Differences over time were analyzed using a related samples Wilcoxon signed rank test.

RESULTS

In both groups the nuclear and actin fiber orientation coincide strongly. In the 0° samples the nuclei and actin fibers mainly align in the length direction of the film (σ=11°; figure 3a, c). In the 45° samples the cells adopt a random orientation (σ=360°; figure 3b, d).

Figure 4c shows that the median curvature increases over time from 0.28 mm^{-1} to 0.54 mm^{-1} in the 0° group while it stays the same in the 45° group (0.12 mm^{-1} and 0.13 mm^{-1}). The curvature of the films in the long axis direction of the 45° group is approximately two times lower than the initial curvature of the 0° group and approximately four times lower at equilibrium. The σ_{max} developed by the cells in the 45° group (1.24 kPa) is more than two times lower in the 0° group (2.91 kPa) at equilibrium while there is no difference initially (figure 4d).

DISCUSSION

In this study we investigated the influence of the degree of cell alignment on stress generation. When all cells are aligned in the same direction, σ_{max} at equilibrium is more than two times as high as when the cells are randomly distributed. These results therefore suggest that

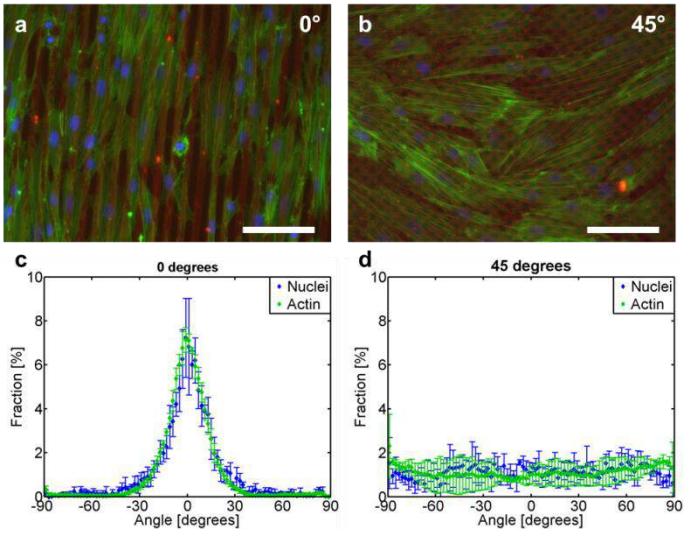

Figure 3: (a, b) Nuclei (blue) and actin fibers (green) of myofibroblasts on fibronectin (red) patterns; scale bar: 100 µm. (c,d) Histograms of the nuclear (blue) and actin fiber (green) orientation where the long axis of the construct is at 0° (n=5).

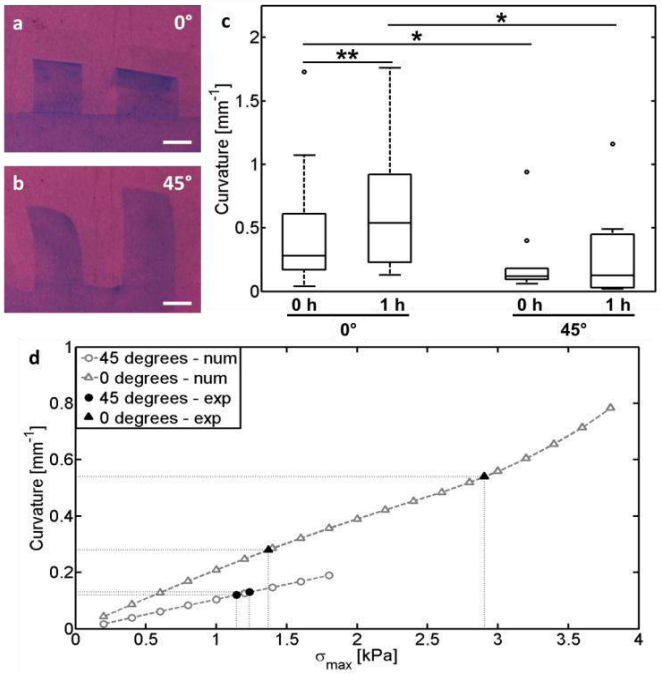

Figure 4: (a,b) Representative top view images of bend films at equilibrium; scale bar: 1 mm. (c) Boxplots of curvature (n=9-22), * p<0.05: Mann-Whitney U test; ** p=0.000: Wilcoxon signed rank test. (d) Numerically obtained relationship between σ_{max} and curvature and corresponding experimental median curvature.

the total active stress distribution cannot only be derived from the stress fiber organization, as the stress that each cell can exert (σ_{max}) apparently depends on the overall cellular organization. This study showed that the cellular orientation affects the stress distribution. In engineered cardiovascular tissues this will in turn influence the mechanical properties and thus the functionality of these tissues. [6,7].

It is hypothesized that the high variation in curvature is caused by the difference in cell density of each individual thin film. In previous experiments a large spread in cell density between individual thin films was observed, with differences up to two-fold (data not shown). In future studies, we aim to decrease this variation by correcting for the cell density of each thin film, which can be achieved by using a Hoechst staining of the cell nuclei. In addition, not only the extremes of alignment (perfect alignment and completely random) but also some in-between degrees of alignment will be investigated by printing fibronectin lines with different angles. This will give more insight into the stress development of e.g. tissue engineered heart valves as these degrees of alignment will be more representative for these tissues.

ACKNOWLEDGMENTS

This work was supported by a grant from the Dutch government to the Netherlands Institute for Regenerative Medicine (NIRM, grant No. FES0908)

REFERENCES

[1] Chen, C.S., *J. Cell Sci*, 121:3285-3292, 2008.
[2] Grosberg, A. et al., *Lab. Chip.*, 11:4165-4173, 2011.
[3] Alford, P.W. et al., *Integr. Biol.*, 3:1063-1070, 2011.
[4] Sun Y. et al., *Acta Biomat.,* 9:7885-7894, 2013.
[5] McCain, M.L. et al., *Biomaterials,* 35:5462-5471, 2014.
[6] Argento, G. et al., *J. Biomech*., 45(16):2893-2898, 2012.
[7] Loerakker, S. et al., *J. Biomech.,* 46(11):1792-1800, 2013.

Copyright 2016 The Organizing Committee for the 2016 Summer Biomechanics, Bioengineering and Biotransport Conference

SB^{3}C2016
Summer Biomechanics, Bioengineering and Biotransport Conference
June 29 –July 2, National Harbor, MD, USA
SB^{3}C2016-667

THE DYNAMICS OF PROTEOGLYCAN LOSS IN ARTICULAR CARTILAGE FOLLOWING MECHANICAL PERTURBATION.

Lorenza Henao Murillo, Keita Ito, Corrinus C. van Donkelaar

Orthopaedic Biomechanics, Department of Biomedical Engineering
Eindhoven University of Technology, Eindhoven, The Netherlands.

INTRODUCTION

It is commonly accepted that excessive mechanical loading may induce damage in articular cartilage. Given the poor repair capacity of the tissue, damage may accumulate, progressing to severe osteoarthritis when adverse mechanical conditions persist [1]. Unfortunately, the success of clinical treatment is also limited. This makes osteoarthritis one of the most frequent, painful and disabling diseases among people over 60 years of age.

The first signs of cartilage deterioration include surface roughening and proteoglycan (PG) loss [2]. This induces cartilage softening, which makes the tissue vulnerable to further damage. Both collagen damage and PG loss may occur following few excessive loading events, or they may develop after sustained or repetitive loading. Collagen damage has been hypothesized to occur as a result of excessive straining of the collagen fibrils [3]. This occurs during overloading, but not after the traumatic load has been released. In contrast, PG loss has been reported to occur in a delayed manner, extending up to 56 hours after excessive loading was applied and released [4]. We hypothesize that the mechanical conditions during this period, even when these conditions themselves would not be excessive, may have an effect on the PGs loss. This would then imply that PG loss may be modulated by changing the conditions during this post-loading period, which may be of clinical relevance.

The present study addresses the above hypothesis. More specific, the aim is to determine whether a period of moderate cyclic loading after excessive loading of articular cartilage, changes the loss of PGs from an osteochondral explant during the first 56-hours after the excessive loading was applied.

METHODS

Osteochondral explants were harvested from the metacarpal joint of 1-year old calves (obtained through a local abattoir). While keeping the tissue moist, 7.5 mm diameter plugs were drilled perpendicular to the surface using a diamond core drill. Plugs were shortened to 5-7 mm and stored at -20˚ C until further use.

For mechanical testing, samples were thawed in PBS during 24 hours and remain submerged in PBS while they were fixed into a custom-made chamber in a tensile tester (Zwick/Roell). Samples were subjected to loading with a 2 mm diameter stainless steel indenter. Six loading protocols were designed (n=4 per group), as explained in Figure 1. These included either a fast (F_x^{fast}), slow (F_x^{slow}), or no (F_x^{none}) excessive loading, with (F_{cycles}^{x}) or without (F_{rest}^{x}) subsequent cyclic compression during which 5 minutes of 0.1 N and 5 minutes of 5 N at 1 Hz is repeatedly applied with the same indenter.

Displacement and force were monitored over time throughout the experiment, and stored for later analysis of changes in tissue thickness and tissue properties (data not shown).

PBS was collected and refreshed at the end of the 24 hours equilibration period (t=0), after the cyclic loading (t=8 hours), and at the end of the experiment (t=56 hours; see Figure 1). Collected PBS was stored frozen (-20˚ C) until quantification of the released PG using a standard DMMB assay with shark chondroitin sulfate as standard.

At the end of the experiment, tissue was frozen for histology, including staining for PG content and immunohistochemical staining of collagen damage (data not shown).

Copyright 2016 The Organizing Committee for the 2016 Summer Biomechanics, Bioengineering and Biotransport Conference

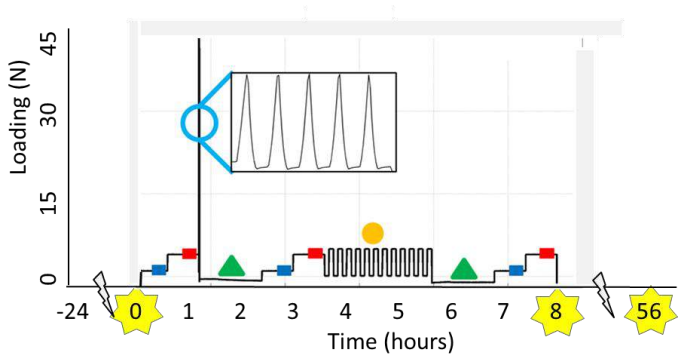

Figure 1: Total duration of the loading protocol was 8 hours (starting at t=0h). It was preceded by 24 hours equilibration time and followed by 56 hours of free swelling.
Colored areas in the figure represent: Green triangle: 70 min unloading; Blue and red bars: 35 min of 1N and 35 min of 4N constant load; Orange dot: 2 hours of cyclic loading (0.1-5N, 5 min on/off). Blue circle: five times 45N, applied at 5 mm/min (slow) or 120 mm/min (fast). Yellow stars: PBS was collected and refreshed. Flash-signs indicate jumps in time on the horizontal axis.

RESULTS

Total PG release into the PBS was measured at three time points, and presented as a release per hour in Figure 2 for the various loading cases.

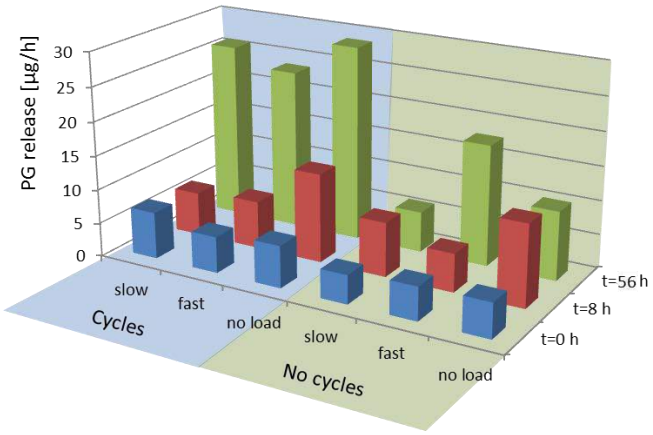

Figure 2: PG (PG) release into the PBS, calculated as the average release per hour over the relevant time period (Fig 1), plotted as a function of loading case and moment in time.
Blue: Release prior to loading. Red: Release between t=0h and t=8h. Green: Release between t=8 and t=45h.

Three things are important to observe. First, the blue bars are equal, demonstrating that there is no difference between groups prior to the experiment. Second, PG release after the cycles (t=8h) equals the release prior to loading for the groups that were loaded at t=0h, but is higher for the groups that did not receive the excessive loading. Third, after 56 hours, PG release in all groups which received cyclic loading is higher than in the groups that didn't.

DISCUSSION

This study shows that PG release into the bathing solution is dependent on the mechanical loading conditions. In agreement with our hypothesis, this release is delayed with increased release until 56 hours after loading, and it can significantly be modulated by a modest mechanical loading regime after an excessive loading event. Interestingly, the effect of the modest cyclic loading is more significant than the effect of the preceding five loads that had 9-fold larger magnitude.

The PG release after the 8 hours loading protocol was delayed. Within the 8 hours of loading, no enhanced PG release was observed, whereas release was elevated in most groups 56 hours after the first excessive loading. Such delayed response concurs with other studies, where enhanced PG loss was observed 56 hours after loading.

At 8 hours, surprisingly, the groups that did not receive the early five peaks of higher load, regardless of whether they received cyclic loading or not, showed more PG loss than the ones that were mechanically challenged. Assuming that the non-loaded samples represent the natural PG loss, apparently the ones that did receive the higher loads were protected against PG loss. An explanation of this phenomenon may be that the loaded samples were compacted by the loading, and that the denser matrix contained PG more than the non-compacted matrix in the other groups. This was confirmed by the measurements of tissue height (blue bars in Fig 1; data not shown).

At 56 hours, PG loss from all cyclically loaded groups was significantly enhanced compared to the groups without cycles and compared to the measurements after 0 and 8 hours. We hypothesize that the fluid flow that is induced in and out the matrix during the 5 minute loading cycles may drag PGs along. Thus, convective transport is added to the natural diffusion-driven PG release. Although this is a plausible hypothesis, it remains unclear why such convection would result in a delayed PG release, rather than an immediate PG loss.

In conclusion, the present study confirms the hypothesis that PG release from cartilage can be modulated by a mechanical loading regime, and that the consequent PG release is delayed. It is enhanced 56 hours after the mechanical perturbations stopped, but it was not yet enhanced within the 8 hour loading protocol, which contained the PG-release stimulating, cyclic loading protocol. Loading- and time-dependent PG kinetics such as those shown in the present study further our insight in the complexity of post-traumatic cartilage degradation. Ultimately, these insights may result in improved clinical treatment of cartilage defects or for guiding post-traumatic recovery.

ACKNOWLEDGEMENTS

The authors acknowledge financial support from the program for doctoral studies "Francisco José de Caldas Generación del Bicentenario año 2010" awarded by the Administrative Department of Science, Technology and Innovation of the Republic of Colombia, Colciencias.

REFERENCES

[1] Mansour, JM, *Biomechanics of cartilage*, Ch 5: 68-67, 2003
[2] Ewers, BJ et al, *J Orthopaedic Research,* 19:779-784, 2001
[3] Wilson, W et al, *J Orthopaedic Research,* 24(2):220-228, 2006
[4] Patwari, P et al, *Arthritis & Rheumatism,* 48(5):1292-1301, 2003

Copyright 2016 The Organizing Committee for the 2016 Summer Biomechanics, Bioengineering and Biotransport Conference

SB³C2016
Summer Biomechanics, Bioengineering and Biotransport Conference
June 29 –July 2, National Harbor, MD, USA
SB³C2016-668

AN EXPLORATIVE CFD STUDY ON STENOSIS-INDUCED FLOW INSTABILITIES IN THE CAROTID ARTERY

Viviana Mancini (1), Jan Vierendeels (2), Daniela Tommasin (1), Simon Shaw (3), Abigail Swillens (1), Awais Yousaf (4), Stephen E. Greenwald (4), Patrick Segers (1)

(1) IBiTech-bioMMeda
Ghent University
Ghent, Belgium

(2) Department of Flow, heat and combustion mechanics
Ghent University
Ghent, Belgium

(3) BICOM (Brunel Institute of Computational Mathematics) and Mathematics
Brunel University
London, UK

(4) Blizard Institute, Barts and The London School of Medicine and Dentistry
Queen Mary University of London
London, UK

INTRODUCTION

Atherosclerosis is the leading cause of death in the westernized societies and the primary cause of stroke. Atherosclerotic plaques can grow into the arterial lumen sufficiently to obstruct the blood flow. The local narrowing of the lumen, known as stenosis, leads to the occurrence of flow phenomena such as separation, recirculation and instabilities in the downstream region, in addition to larger velocity values as the flow accelerates through the throat of the stenosis. Flow bench studies on stenosed tubes embedded in tissue mimicking gels demonstrate that flow instabilities and pressure fluctuations induce mechanical waves that can be detected by means of accelerometers or laser Doppler vibrometry (LDV). As part of the H2020 project CARDIS, we are exploring the use of LDV as a non-invasive diagnostic tool for carotid stenosis via detection of stenosis induced vibrations at the level of the skin.

In addition to and complementing in-vivo and experimental studies, computational fluid dynamics may provide a better understanding of flow related phenomena leading to the generation of mechanical waves and their propagation through soft tissues. In this study, we present initial computational results obtained in two different settings: (i) flow in a simple tubular model with a 75% area stenosis (mainly for assessment of numerical parameter evaluation), (ii) a patient specific case, with a maximum area stenosis of 82%. The later stages of the study will involve the evaluation of the arterial wall movement generated by flow instabilities and the study of the propagation of the pressure waves from the arterial wall to the skin as compressional and shear waves.

METHODS

The geometry of the first model consists of an axisymmetric 75% area stenosis with length (L) equal to twice the tube diameter (D=6mm). The total length of the model corresponds to 5D and 10D for the upstream and the downstream side, respectively. Previous studies have shown that an upstream length of 2D is sufficient to obtain results independent of the position of the inflow boundary [1]. A Cooper-type meshing was performed in order to obtain a grid of 3251688 hexahedral elements with uniform spacing in the axial direction. Simulations were performed using Fluent (Ansys) with time-dependent 3D Large Eddy Simulations (LES) carried out with the Smagorinsky–Lilly constant C_s equal to zero in order to nullify the viscosity added by the model. Bounded schemes were used for the momentum and for the transient formulation. The time step was set to 1 millisecond. The constant inlet velocity value U corresponded to a volumetric flow rate (Q) of 1000 ml/min, leading to a Reynolds number (Re) based on the tube diameter of 1240. A zero pressure condition was set at the outflow boundary. For the patient-specific case, the geometry consists of a carotid bifurcation with a non-axisymmetric 82% area stenosis of the internal carotid artery (ICA). Initial simulations were carried out on a relatively coarse hexahedral grid (439680 elements) with the same settings as in the simplified model except for Q=250 and 500 ml/min, leading to Re=230 and 460, respectively. The outflow boundary was set as flow ratio of 32% for the ICA as defined by Harald et al.[2]. In both cases, simulations were performed for a total duration of 2 seconds with the last 500 milliseconds used for spectral analysis (FFT) to assess the frequency content of the signal. As this is an early stage of the study, in both models the arterial walls are supposed to be rigid.

RESULTS AND DISCUSSION

Although flow in a straight tube would not be transitional (since Re < 2300), in the 75% stenosis model pressure instabilities such as those depicted in Figure 1 are observed: the flow is not able to stay attached and vortices form downstream of the stenosis, as the flow

Copyright 2016 The Organizing Committee for the 2016 Summer Biomechanics, Bioengineering and Biotransport Conference

diverges and decelerates. The area-weighted average of velocity at the throat of the stenosis reached a value of 4*U*. The maximum amplitude of the observed pressure oscillations was 0.854 Pa. Frequency analysis of the pressure field showed the highest frequency peaks between 2D and 4D away from the stenosis throat and always in the frequency range of 10-450 Hz, consistent with experimental observations.

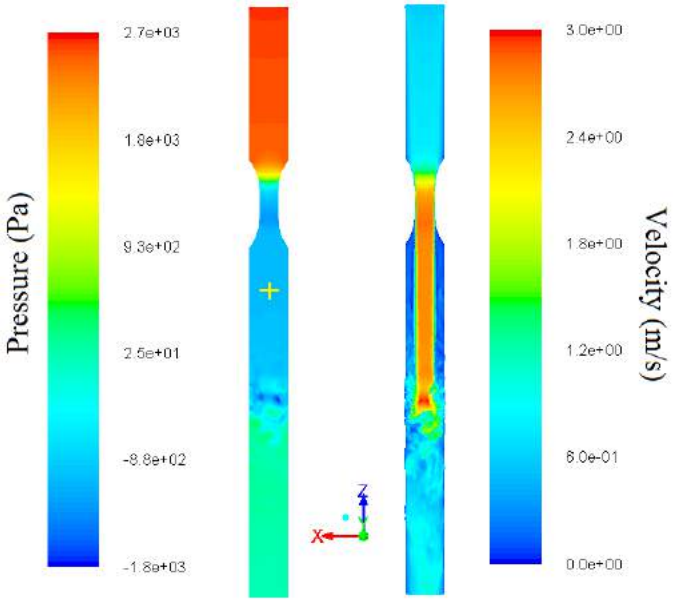

Figure 1: pressure and velocity instabilities at t=0.06s of the 75% simplified model. The yellow crosshair indicates the point where the frequency spectrum was calculated.

For the patient-specific case, only results for Re=460 will be shown. Instabilities are manifested by the swirling motion of the fluid in the post-stenotic region (Figure 2).

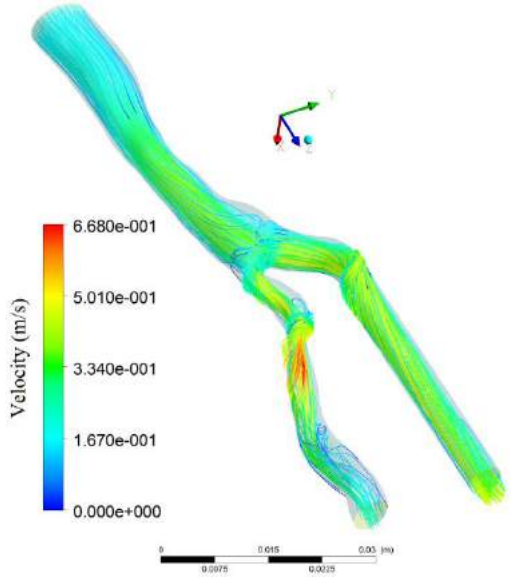

Figure 2: pressure for the patient specific case at t=2s for Re=460

The pressure and its frequency spectrum depicted in Figure 3 were calculated for a point located on the centerline of the ICA at a distance of 2.6 D from the stenosis center. The amplitude of pressure oscillations is in the order of 1.547 Pa. The FFT indicates peaks in the 10-450 Hz frequency band, with an intense low frequency peak. For Re=230 results are entirely different: the pressure does not show any peak at any location in the model. This is likely to be due to the low flow rate, which is insufficient to cause flow instabilities. Further analysis will be performed at different flow rates. The sensitivity of the results to the mesh density and to the time step will be further explored. We believe that the regularity of fluctuations in the patient-specific case, compared to the simple tube model, are likely to be induced by a relatively coarser mesh or low flow. Furthermore, the dependency of the pressure oscillations (and their frequency spectrum) on the shape and degree of stenosis will be assessed.

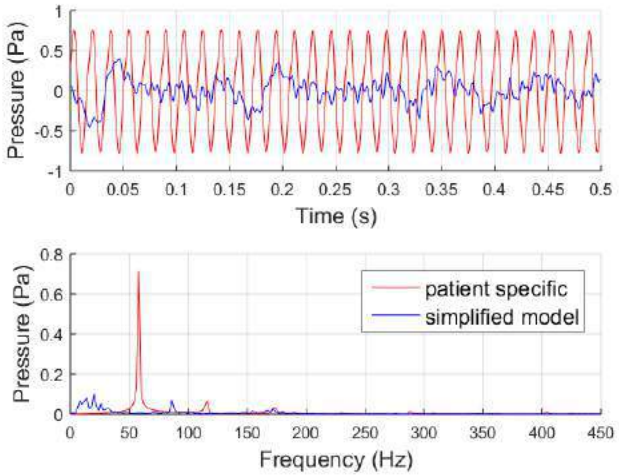

Figure 3: pressure and its frequency spectrum: comparison between the patient-specific model for Re=460 (red) and the simplified model (blue).

CONCLUSIONS

These initial CFD results are in line with previous studies with similar models [3] and our own experimental observations, and indicate that the stenosis-induced flow instabilities for the tested settings give rise to pressure fluctuations in the frequency range of 10-450 Hz.

The 3D printed phantom of the patient-specific model studied in this abstract will be the subject of future experimental studies. The integrated experimental-computational approach will provide further details on fluid dynamics and mechanical phenomena, and give more insights into the sensitivity and specificity of the use of LDV to detect carotid stenosis, providing subsequently guidance for studies on patients.

ACKNOWLEDGEMENTS

Funded by the H2020 funding programme (CARDIS; ICT-26-2014)

REFERENCES

[1] Mallinger F. et al., *Int Jou Heat and Fluid Flow* 23:657-663 2002.
[2] Harald C.G. et al., *J Biomech*, 43:2332-2338, 2010.
[3] Sherwin A.J. et al., *J Fluid Mech,* 533:297-327, 2005.

Copyright 2016 The Organizing Committee for the 2016 Summer Biomechanics, Bioengineering and Biotransport Conference

SB^{3}C2016
Summer Biomechanics, Bioengineering and Biotransport Conference
June 29 –July 2, National Harbor, MD, USA
SB^{3}C2016-669

FATIGUE TESTING OF A COMPOSITE MENISCUS IMPLANT – WHAT ARE THE LIMITS?

Jonathan J. Elsner (2), Maoz Shemesh (1), Eyal Zylberberg (1), Adaya Shefy-Peleg (1), (3)
Zahava Barkay, Eran Linder-Ganz (1),

(1) Research and Development, Active Implants, Netanya, Israel
(2) Active Implants LLC, Memphis, TN, 38120
(3) Wolfson Applied Materials Research Center, Tel-Aviv University, Tel Aviv 6997801, Israel

INTRODUCTION

Long-term fatigue remains the main obstacle in the introduction of a synthetic total meniscus implant. Different materials have been proposed for this application, but none remained undamaged when tested in pre-clinical studies. For example, Kelly et al. (2007) chose to use a hydrogel material to create a meniscal implant, which was tested in an ovine model. Significant cartilage degeneration and implant failures occurred after 1 year. In another canine study by Hannink et al., (2011) a porous poly-caprolactone polyurethane meniscus implant experienced rapid degradation and subsequent loss of mechanical properties occurred after 2 years.

In recent years, the concept of composite design has emerged as a means to improve function and long-term stability of orthopedic devices. The first meniscus implant concept to have reached the clinical study phase (Figure 1) was developed by our group. It is constructed from a polycarbonate-urethane matrix that is reinforced with ultrahigh molecular weight polyethylene (UHMWPE) fibers. While preliminary results of this concept in an ovine model seem promising (Zur et al. 2010), its expected service-life has not yet been established. Furthermore, there is also need to characterize potential failure modes of such device. Controlled long-term fatigue experiments are a useful tool that can be used to evaluate the potential life-span of any orthopedic implant, yet no such study has been reported for the meniscus. In this study, fatigue testing was conducted up to 25 million loading cycles, to evaluate the polycarbonate-urethane meniscus implant.

METHODS

The fatigue resistance of the meniscus implant was characterized by means of S-N curve. The pattern of the cyclic load applied in the study was based on the vertical loading component of ISO-14243-3 (Wear of total knee-joint prostheses), which was scaled as follows: The minimum in the series of 5 loading conditions was that of normal gait (2500N peak load, ~ 3 times body weight, Figure. 1). Four additional loading conditions were created by rescaling the force curve so that the maximum peak load increased to 3000N, 3500N, 4000N and 4500N. The last three loads, 3500-4500N, represent approximately 5 to 6-times body weight – the typical load in the knee during higher impact activities such as running. Each test was performed on n=5 sterile implants. Each new meniscus specimen was placed between rigid UHMWPE surfaces that simulate the geometry of the articulating surfaces of the tibial plateau and femoral condyle in the medial compartment.

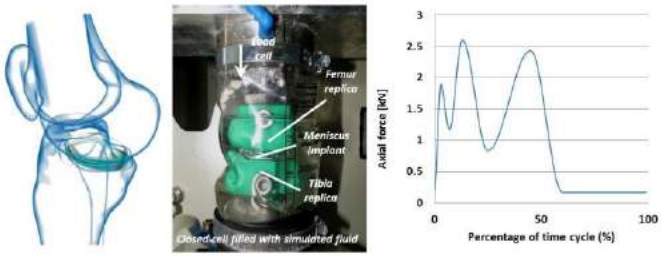

Figure 1. Illustration of the knee joint with the meniscus implant, the corresponding testing apparatus replicating the femur and tibia surfaces, and loading cycle of the medial compartment.

The testing cell was then sealed and filled with heated distilled water (37°C) and loaded axially at an accelerated rate (2 Hz) until failure was detected. Failure was defined as tear of either one of the composite material's components (PCU or UHMWPE fibers), which

Copyright 2016 The Organizing Committee for the 2016 Summer Biomechanics, Bioengineering and Biotransport Conference

could potentially lead to device failure and require an additional surgical intervention. If failure did not occur up to 25 Mc, the test was discontinued. The implants were evaluated macroscopically after 0.2, 0.5, 1 Mc and at 1 Mc intervals until reaching 25 Mc or failure.
Upon completion of the fatigue testing, the implants were imaged with FEI Quanta 200 FEG ESEM (environmental scanning electron microscope) under low vacuum conditions. The analysis of implants after failure was focused on the area of failure, and the damaged areas of the articulating surfaces, if not.

RESULTS

For the minimum in the series of loads (that of ISO-14243-3), all five implants reached 25 Mc without failing. The UHMWPE fibers remained intact, embedded within their designated tunnels in the PCU matrix. Mild deformation of the PCU material was noted mainly in the central region of the implant. When the peak load was increased to 3000N, the implants did not reach the ultimate goal (25 Mc), but still had a very long service-life of 15±3.1 Mc. The predominant mode of failure in the majority of specimens (4/5) was thinning of the PCU material in the central region of the implant due to creep, which then developed into a localized tear. The results under higher loading conditions (3500N, 4000N and 4500N) demonstrated a similar mode of failure, but shorter failure times, as shown in Figure 2. Specifically, under maximal loads of 3500N, 4000N and 4500N the average time to failure obtained was 5.2±1.3 Mc, 3.0±0.8 Mc and 2.1±0.9 Mc, respectively.

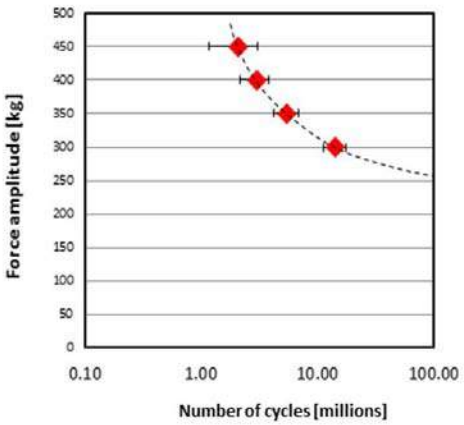

Figure 2. S-N curve of the NUsurface(R) Meniscus Implant.

Microscopic evaluation of the samples by ESEM showed that the surface prior to simulation was relatively smooth. Following the simulation, it became dominated by depressions and protrusions that occurred mainly in the middle portion of the superior articulating surface of the implant (Figure 3). The depressions varied in size and shape from small and round to broad and diffused. The inferior surface showed a much lower damage level compared to the superior surface, consisting of shallow pits that appeared infrequently on the surface. The deformation was not found to be homogenous over the surface. Specifically, the deformation inside the main axial load center tended to show no specific orientation while outside the main axial load center, a radial orientation of deformation was observed as well as tear generation. The tear damage that developed during the simulation demonstrated features distinctive of fatigue damage. Typically, the edges of the tear were uneven, likely because of gradual propagation of the tear. Characterization of the surface morphology (in the tear's inner walls) showed a rough and non-homogenous texture.

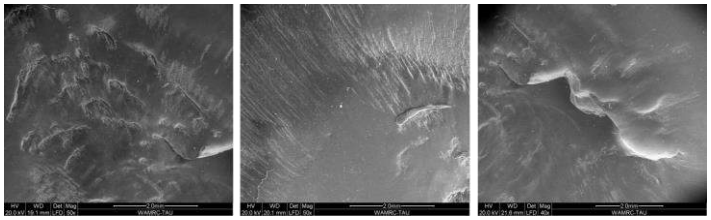

Figure 3. Surface characterization of the superior articulating surface showing the deformation at the main axial load center (Left), outside the center (Center) and the development of the tear damage (Right)

DISCUSSION

Uniaxial fatigue testing of a novel composite PCU/UHMWPE medial meniscus implant was performed. The S-N curve results show that under forces representing the expected activities of implanted patients (3 to 4 times body weight), the resistance of the device is at least 15 Mc.

The ISO-14243-3 standard is currently the most widely used standard for long-term fatigue of total knee replacement devices, and with the absence of any standard for meniscus implants, it serves as the best reference for their testing. Employing this standard also adds robustness by the introduction of an additional safety factor: the knee loads that fall on the medial knee compartment comprise roughly only 60-70% of the total knee load.

While in theory, this endurance limit represents a stress level below which the material does not fail and can be cycled infinitely, additional factors such as wear, weren't simulated in this study, and can contribute to earlier failure of the implant. Notwithstanding this, the meniscus implant has proven to be particularly resilient to fatigue, even at loads higher than those dictated by ISO-14243-3, which is a significant improvement compared to other materials that have been tested as meniscus replacement materials.

ACKNOWLEDGEMENTS

This Study was funded by Active Implants.

REFERENCES

[1] Kelly et al., 2007. The American journal of sports medicine, 35(1): 43-52.
[2] Hannink et al. 2011. Knee surgery, sports traumatology, arthroscopy, 19(3): 441-451.
[3] Zur et al., 2011. Knee Surgery, Sports Traumatology, Arthroscopy, 19(2): 255-63

Copyright 2016 The Organizing Committee for the 2016 Summer Biomechanics, Bioengineering and Biotransport Conference

SB³C2016
Summer Biomechanics, Bioengineering and Biotransport Conference
June 29 –July 2, National Harbor, MD, USA
SB³C2016-670

MILD TRAUMATIC BRAIN INJURY RESULTED IN INCREASED AQUAPORIN-4 EXPRESSION – RELEVANCE TO POST INJURY EDEMA

Nasya M. Sturdivant (1), Sean Smith (1), Syed F. Ali (2), Jeff Wolchok (1), and Kartik Balachandran (1)

(1) Department of Biomedical Engineering
University of Arkansas
Fayetteville, AR, USA

(2) Division of Neurotoxocology
National Center for Toxicological Research/ FDA
Jefferson, AR, USA

INTRODUCTION

Traumatic brain injury (TBI) is characterized by damage to the brain caused by an external force such as a blow or jolt to the head. Mild TBI (mTBI), as opposed to moderate or severe TBI, is the most common type seen in both civilian and military settings [1]. Most studies on mTBI are focused on how initial cell and tissue-level deformation alters overall neuronal and glial function [2].

Cerebral edema is one of the major factors that leads to high mortality and morbidity in TBI patients. Unfortunately, the mechanisms for immediate cell swelling and potential preventative treatments are not well studied. The discovery of aquaporins provides a basis for the understanding of water transport in the brain and could lead to the development of new treatment methods for injury-induced edema.

Aquaporin-4 (AQP4) is a highly permeable water channel largely expressed in astrocytes of mammalian brains [3,4]. These water channels play a critical role in the water uptake of astrocytes following injury. Since its initial detection in the brain, various studies have shown an upregulation of AQP4 following brain injury, however, the mechanistic link between the regulation of AQP4 and cytotoxic edema has been poorly researched. [5,6]. To better understand this link we have engineered a three-dimensional astrocyte-construct that can be subjected to a high-speed mechanical stretch. This construct provided a platform to investigate the effect of a mTBI on astrocyte vitality and swelling. We hypothesized that TBI-mediated cerebral edema occurs via an aquaporin-4 (AQP4)-mediated mechanism leading to increased intracellular volume and subsequent cell death.

Acetazolamide (AZA) is an antiepileptic drug that has been proven to inhibit AQP4 [7] as well as reduce injury-induced brain edema and neuronal death in vivo [8]. The most significant increase in cell vitality was seen when AZA was added 15 minutes before stretch of the construct. Following the vitality assay, we investigated the effect stretch and AQP4 inhibition had on cell swelling. To our knowledge, our study is the first time AZA has been used to mitigate the effects of TBI injury in vitro.

METHODS

Fabrication of a 3D strain model. A cell stretching device was designed and machined to have control over the stretch and stretch rate. There were two main components to this setup: the cell chamber and the cell stretching device/control system (Fig. 1A). A stretchable cell chamber was made by mounting a 10 mm tall piece of silicon tubing on top of an 8cm x 7cm, 0.010" polydimethylsiloxane (PDMS)-membrane.).

Cell Culture and mTBI Stretch. Preliminary culture of C8D1A mouse-derived astrocyte cells (ATCC® CRL2541™) was done in

Figure 1. (a) Top and (b) side view of an elastic chamber mounted on top of the high speed stretcher device (c) Representative SEM image of tissue-engineered astrocyte construct.

standard feed media (Dulbecco's Modified Eagle Medium (DMEM) and 10% fetal bovine serum (FBS)) at 37°C and 5% CO_2. To prepare samples for mTBI stretch, a layer of Corning Matrigel Basement Membrane Matrix was evenly spread within the stretchable chamber and set in the 37°C incubator for 20 minutes to polymerize. 350,000 – 500,000 cells were then removed from preliminary culture, resuspended in feed media/2.5% Matrigel and seeded on top of the polymerized layer of Matrigel to create a three-dimensional culture. The tissue-engineered astrocyte construct was incubate at 37°C for 24 hours to allow proper time for cell attachment to the Matrigel before being subjected to 10% stretch. After stretch, the astrocytes were isolated from the Matrigel using Corning Cell Recovery Solution before performing proteomic analysis.

AQP4 Inhibition. AQP4 expression was inhibited with 20 μM Acetazolamide (AZA) (Sigma-Aldrich, St. Louis, MO). AZA was put into contact with the cells (via feed media) at the time of seeding, 15 minutes before stretch, or immediately after stretch.

Cell Vitality. Astrocyte vitality following a mTBI was assessed using a commercially available cytotoxicity assay (LIVE/DEAD Cell Vitality Assay Kit, C12-Resazurin/SYTOX Green; Molecular Probes, Eugene OR) and flow cytometry. Twenty-four hours following deformation the tissue-engineered construct was rinsed 3 times with cold PBS. The cells were then isolated from the Matrigel with the use of Corning Cell Recovery Solution. After isolation from the Matrigel, astrocytes were resuspended in PBS and incubated with 50 μM C12-resazurin 1 μM SYTOX Green for 30 minutes at 37°C. Stained samples were then analyzed via flow cytometry. The percentage of live, injured, and dead cells present following a mTBI were normalized to the control (0% stretch, No AZA) and presented.

S100B and AQP4 Immunostaining. Astrocyte/Matrigel samples were immunostained with antibodies against DAPI, AQP4 and GAPDH. Briefly, twenty-four hours after injury, the samples were rinsed with 1X PBS and fixed in 4% paraformaldehyde. 20% goat serum was then pipetted onto the cells, for blocking, and incubated at 37°C for 1 hour. Next, anti-AQP4 antibody and anti-S100B antibody (abcam, ab52642) supplemented with 2% goat serum, were pipetted

Copyright 2016 The Organizing Committee for the 2016 Summer Biomechanics, Bioengineering and Biotransport Conference

onto the gels and allowed to sit overnight in 4°C. Secondary antibody solution comprised of DAPI, donkey anti-rabbit 594 and donkey anti-mouse 488. Secondary stain was left on and protected from light for 1-2 hours. The cells were imaged using a Nikon Eclipse epifluorescent microscopy at a 20X magnification. Fluorescent images were analyzed semi-quantitatively with the use of ImageJ. Results were presented as a ratio of the number of nuclei to the antibodies coverage area.

Western Blotting of AQP4. After isolation from Matrigel, the cells were lysed, centrifuged at max speed 4°C and cell debris was withdrawn. A BCA protein assay was done on the supernatant. 40 µg/lane of protein was loaded onto a TGX gel and subsequently transferred onto PVDF (polyvinyl difluoride) membrane. The membrane was probed with Rabbit anti-AQP4 antibody (abcam, ab46182) and Mouse anti-GAPDH (abcam, ab8245) and visualized with a Li-Cor scanner. GAPDH was used as the gel loading control.

Calcein Imaging. While still attached to the Matrigel, the cells were washed with PBS and stained with Calcein for 45 minutes. The cells were then incubated with Tyrode's buffer and stretched. Immediately after stretch, the cells were analyzed under a multi-photon microscope. A 40x (0.80 NA) water immersion lens with a 2x additional zoom was used to image the astrocytes. Excitation wavelength was 980 nm and emission was collected at 525/50 nm. Z-stack images with 1 µm z-height were acquired every 10 minutes for 1 hour for volumetric analysis. Cell volumes were assessed by importing a z-stack into a custom MATLAB script.

Statistical Analysis. Data was first tested for normality using the Shapiro-Wilk test. Statistical analysis was carried out by two-way analysis of variance (ANOVA) for normal data. Non-parametric analysis was used for data that was not normally distributed. SigmaPlot software was used for the statistical analysis. Values were expressed as mean ± standard error (SEM). A p value less than 0.05 was considered significant

RESULTS

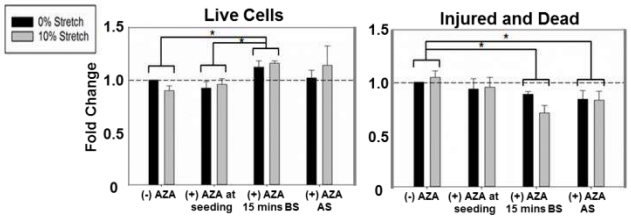

Figure 2. Cell Viability. Fold change in percentage of (a) live cells and (b) injured/dead

The tissue-engineered astrocyte construct was subjected to a mild TBI as described in the experimental section of this paper. The cell viability assay was aimed at finding the most effective time to add AZA to the tissue-engineered construct to best mitigate the effects of a mTBI. The key findings were that: (1) the 10% stretch did not have a significant effect on cell viability, (2) the addition of AZA increased the number of live cells and decreased the number of injured and dead cells in all conditions except the control, and (3) adding AZA 15 minutes before stretch resulted in the highest average number of live cells and lowest number of injured and dead cells.

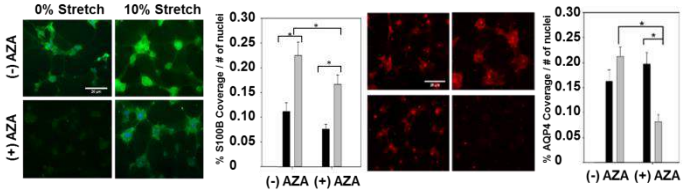

Figure 3. (a) S100B and (b) AQP4 immunofluorescent images and semi-quantification

Immunocytochemistry (ICC) was done on the tissue-engineered constructs to detect the presence of S100B, a marker for cell injury and AQP4 (Fig. 3). Semi-quantitative analysis of the ICC images showed that subjecting the cells to a mTBI significantly increased the expression of S100B and AQP4 following a 10 percent stretch, and a reduction of this expression when AZA was added. AQP4 western blots also showed that TBI resulted in a significant increase of expression.

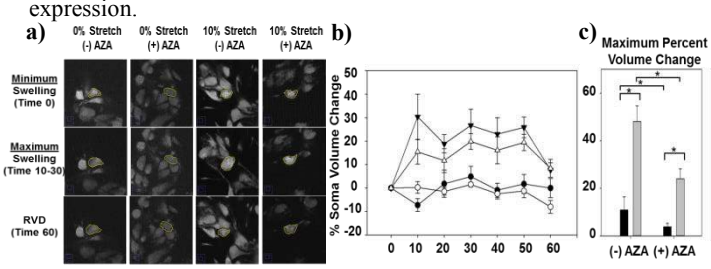

Figure 4. (a) Multi-photon images (b) Percent Soma Volume Change in the 60 minutes following stretch, and (c) Maximum Percent Volume Increase achieved by the cell.

A z stack of the cells were taken once every ten minutes for one hour to calculate the cells volume. Figure 4b shows the percent the soma volume changed from time 0. Key findings include: The percent volume change remained higher for cells that were injured, compared to cells that were not injured, for the entire hour following the stretch; adding AZA to the cells 15 minutes before they were stretched decreased the average volume increase from time 0 at every time point except at the 60 minute mark; and 60 minutes after stretch, the cells showed a drastic decrease in cell volume from the previous time point, this shrinkage reflects the cells regulatory volume decrease. Because the time point at which maximum swelling was observed could have been altered due to the amount of time it took to load the sample onto the microscope stage, we also reported the maximum cell volume increase for each condition, regardless of the time it was observed, to clearly see how stretch and the addition of AZA effected cell swelling.

Figure 4c shows the average maximum percent volume increase among cells in each condition. Cells that were stretched had a significantly higher maximum volume increase than cells that were not stretched (about 5 times higher) and the addition of AZA to the construct significantly decreased the percentage cells increased in size approximately in half.

DISCUSSION

The goal of this study was to better understand the link between the regulation of AQP4 and TBI-induced cytotoxic edema. Several studies have concluded that AQP4 expression increases following a TBI and/or observed decreased cellular edema and reduced mortality in AQP4-deficient mice. Our study presents an in vitro brain tissue model in which we (a) observed an increased expression in AQP4 following a mTBI, (b) observed an increase in astrocyte soma volume following the mTBI, and (c) administered the AQP4 inhibitory drug, AZA, prior to a mTBI and observed a less significant cell volume increase following the injury. Because this drug proved to be effective in pre-TBI administration, there is a possibility we can administer it to military personnel prior to combat and immediately attack the secondary injuries caused by the TBI. To our knowledge, our study is the first to observe astrocyte swelling in vitro following a mechanically induced TBI via imaging.

ACKNOWLEDGEMENTS

NSF grant no. CMMI-1404716 and the NSF DGE-1450079.

REFERENCES

[1] Rosenfeld, J.V., et al., Lancet Neurol. **12**(9):882-893, 2013.
[2] Yung Chia Chen, et al., J Neurotrauma. **26**:861-876, 2009.
[3] Nagelhus, E.A. et al., Physiol Rev. **93**(4):1542-1562 2013.
[4] Zador, Z., et al., Handb Exp Pharmacol. **190**:159-170, 2009.
[5] Manley, G.T., et al., Neuroscience. **129**(4):983-91, 2004.
[6] Xiao, M. and G. Hu, CNS Neurosci Ther. **20**(5):385-90, 2014.
[7] Huber, V.J., et al., Bioorg Med Chem. **17**(1): 418-424, 2009.
[8] Guo, F., et al., Transl Stroke Res. **3**(1):130-137, 2011.

Copyright 2016 The Organizing Committee for the 2016 Summer Biomechanics, Bioengineering and Biotransport Conference

SB³C2016
Summer Biomechanics, Bioengineering and Biotransport Conference
June 29 –July 2, National Harbor, MD, USA
SB³C2016-671

PROBING THE TRANSITION FROM COMPACTION TO FATIGUE IN HUMAN ARTICULAR CARTILAGE UNDER CYCLIC LOADING

Jonathan T. Kaplan (1,2), M. Hicham Drissi (3), Corey P. Neu (4), David M. Pierce (1)

(1) Biomedical Engineering & Mechanical Engineering
University of Connecticut
Storrs, CT, USA

(2) Biomechanics Research and Engineering
Natick Soldier RD&E Center
Natick, MA, USA

(3) Orthopaedic Surgery
University of Connecticut Health Center
Farmington, CT, USA

(4) Mechanical Engineering
University of Colorado
Boulder, CO, USA

INTRODUCTION

Osteoarthritis (OA) is one of the most common musculoskeletal diseases, characterized by joint pain and swelling, lack of mobility and resultant loss of life quality. Strong motivations to study the mechanics of human articular cartilage include the lack of understanding of the early stages of OA and the limited viable treatment options for those affected by the disease. OA appears to be a mechanically driven process that occurs over a relatively long period of time. Understanding the transition from normal function to mechanical fatigue may provide insight into when cartilage is no longer functionally stable, what activities may result in higher incidences of damage and if mechanical fatigue serves as a precursor for OA.

In daily living articular cartilage sustains a variety of loading magnitudes and frequencies depending on the activity performed and joints involved. Healthy joints during light activities typically undergo loadings resulting in stresses ranging from 1 to 6 MPa [1]. Light activities are typically more frequent than high impact activities, but some common tasks can generate significant loads on cartilage. For example, non-uniform contact stresses reached up to 18 MPa in an instrumented hip while an individual simply rose to stand from a seated position in a standard chair [2].

In this study, we seek to probe the transition from normal mechanical compaction to functional deterioration (fatigue) during a range of physiologically motivated loadings. We hypothesize that with both increased loading magnitude and number of loading cycles, cartilage will mechanically soften during loading and will reach hydrostatic equilibrium faster (during creep displacement under constant load) due to fatigue.

METHODS

We prepared cartilage samples (3 mm Ø, full thickness) from the knees of six male donors from 22 to 34 years of age (M=27.7) from the Musculoskeletal Transplant Foundation. We tested location-matched samples in unconfined compression (Bose LM1, Eden Prairie, MN with a Futek load cell, Irvine, CA) under a range of loading conditions motivated by those seen *in vivo* and beyond (Table 1). Load magnitudes approximated walking, extreme weightlifting, and injury, while frequencies approximated walking and running (six total combinations, C1-C6). We tested samples from each donor and each combination of magnitude and frequency (36 total tests) with the following protocol, repeated three times after preconditioning: recovery for 2k sec, force ramp to peak force, creep displacement for 3.6k sec, recovery for 2k sec, and force controlled cyclic loading for 12k cycles. We measured sample thickness prior to loading and after every 12k cycles of loading. Throughout testing samples were bathed in PBS (0.01 M, pH 7.4) with protease inhibitors at 37°C.

Table 1: Test conditions C1-C6.

		1.44 Hz	2.88 Hz
Walking	**20 N (2.83 MPa)**	C1	C2
Weightlifting	**120 N (17.0 MPa)**	C3	C4
Injury	**200 N (28.3 MPa)**	C5	C6

Copyright 2016 The Organizing Committee for the 2016 Summer Biomechanics, Bioengineering and Biotransport Conference

We plotted first Piola-Kirchhoff vs. stretch (during load ramp to creep test) and creep displacement vs. time, both as a function of cyclic loading, for each test condition using MATLAB (The MathWorks, Natick, MA). Additionally we calculated effective stiffness (force/displacement near peak load), time to equilibrium during creep and sample thickness, all as a function of cyclic loading. To determine the significance of test conditions on mechanical responses, we conducted a repeated measures ANOVA (IBM SPSS Statistics 23). To probe the mechanisms underlying changes in the mechanical response, we studied images from histology and confocal microscopy via Second Harmonic Generation (SHG).

RESULTS

Under low load magnitudes the tissues generally stiffened with increasing cycles while at relatively high loads the tissues softened. Figure 1 shows representative creep and stress-stretch responses for Donor 1 under C1 loading conditions.

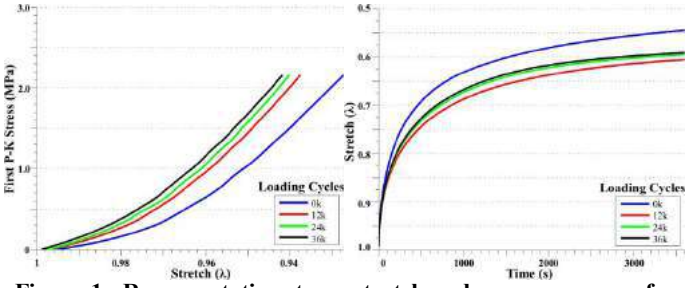

Figure 1: Representative stress-stretch and creep responses for Donor 1 under C1 loading (20 N force at 1.44 Hz).

Table 2, results from the repeated measures ANOVA, shows significant changes in effective stiffness and sample thicknesses among loading magnitudes but not frequencies.

Table 2: *p*-values (* $p<0.05$) from repeated measures ANOVA.

	Cycles	Force (N)	Freq. (Hz)
Change in Effective Stiffness	**0 – 12k**	0.000*	0.464
	0 – 24k	0.000*	0.707
	0 – 36k	0.000*	0.459
Change in Time to Equilibrium	**0 – 12k**	0.360	0.084
	0 – 24k	0.236	0.130
	0 – 36k	0.818	0.535
Change in Sample Thickness	**0 – 12k**	0.000*	0.951
	0 – 24k	0.000*	0.606
	0 – 36k	0.000*	0.894

There were statistically significant correlations between the magnitude of loading and all changes in effective stiffness and additionally the changes in sample thicknesses. Additionally there was a significant difference between loading with the low force magnitude (walking) and both of the larger applied forces (weightlifting and injury) for all changes in stiffness. There was no statistically significant correlation between the loading frequencies and changes to any of our mechanical metrics. Time to equilibrium is longest with the lowest force magnitude and decreases with larger forces. All samples' thicknesses decreased with increased number of loading cycles and a greater percentage of the initial height is recovered under loading with the lowest force. SHG images showed that the collagen network of cartilage cracks and rearranges under loading approximating weightlifting and injury. Frequency of loading has no visible effect on the collagen network.

DISCUSSION

Compressive stiffness has been correlated with the concentration of chemical constituents of cartilage, particularly glycosaminoglycans (GAGs) [3]. When cartilage is compressed, negatively charged proteoglycans (PG), held in place by a network of collagen, are pushed together, thus increasing repulsive forces resulting in greater stiffness. Stiffness generally increased with increasing cycles of loading, significantly after the first stage and more slowly with each increasing stage, cf. Fig. 1. Softening did occur in some test conditions. We attribute loss of mechanical function under cyclic loading to disruption in the collagen network as a result of mechanical fatigue. This softening of cartilage could be the first detectable sign of cartilage degradation [4].

Time to equilibrium during creep testing can be used to understand the mechanical integrity of the tissue. The tissue will reach thermomechanical equilibrium once all the unbound water is pressed out. The time to equilibrium is not affected by the loading conditions but the total stretch at equilibrium generally reduces after each sequence of 12k loading cycles, cf. Fig. 1, due either to compaction (less initial fluid retained) or fatigue (disruption of extra cellular matrix).

To investigate the mechanisms of (recoverable) mechanical compaction versus detrimental fatigue, we measured the changes in tissue thickness during testing and once again after 24 hrs of recovery in the PBS solution at 37°C. We attributed changes in sample thickness after 24 hrs of recovery to fatigue effects and not compaction. In every loading condition, some fatigue appeared to have been present.

We propose that cyclic loading up to 36k cycles disrupts the collagen network but does not allow sufficient time for the PG content to be diminished. In this scenario the permeability of the tissue is relatively unchanged (same total PG content) while the compressibility is altered (disrupted interaction between PG and collagen). These effects may not be as dramatic *in vivo* in light of the supporting subchondral bone and attached cartilage. In the future we aim to apply such results to better understand the mechanisms of cartilage degeneration and to inform computational models of tissue remodeling or damage, eg. [5].

ACKNOWLEDGEMENTS

We thank the Musculoskeletal Transplant Foundation (MTF).

REFERENCES

[1] Park, S., et al., *Osteoarthritis Cartilage*, 12:65-73, 2004.
[2] Hodge, W.A., et al., *Proc Natl Acad Sci U S A*, 83:2879-83, 1986.
[3] Kempson, G.E., et al., *Biochim Biophys Acta*, 215:70-7, 1973.
[4] Lyyra, T., et al., *Med Eng Phys*, 17:395-9, 1995.
[5] Stender, M.E., et al., *J Biomech Eng*, 137:081010, 2015.

Copyright 2016 The Organizing Committee for the 2016 Summer Biomechanics, Bioengineering and Biotransport Conference

SB^{3}C2016
Summer Biomechanics, Bioengineering and Biotransport Conference
June 29 –July 2, National Harbor, MD, USA
SB^{3}C2016-672

EVALUATION OF PULSATILE AND CONTINUOUS FLOW VENTRICULAR ASSIST DEVICE IMPLEMENTATION IN THE SINGLE-VENTRICLE CIRCULATION: A LUMPED-PARAMETER MODELING STUDY

Tyler M. Schmidt (1), David N. Rosenthal (2), Olaf Reinhartz (2), Alison L. Marsden (3, 4), Ethan O. Kung (1, 4), The Modeling of Congenital Hearts Alliance (MOCHA) Investigators (4)

(1) Department of Mechanical Engineering
Clemson University
Clemson, SC, USA

(2) School of Medicine
(3) Department of Pediatrics
Stanford University
Stanford, CA, USA

(4) Institute of Cardiovascular Sciences
University College London
London W1T 7HA, UK

INTRODUCTION

Approximately 1 in 2000 children born in the United States has only one functioning ventricle. Surgical intervention is needed within several days of birth for survival. The Fontan procedure is a multi-step surgical operation that reconnects the systemic and pulmonary circulations to restore a series circulation using the patient's single working ventricle. However, due to increased load on the single ventricle, some patients require bridge-to-recovery or bridge-to-transplant ventricular support. Therefore, ventricular assist devices (VAD) have been used as a means of artificial, mechanical support for single ventricle patients.

Nonetheless, survival rates of VAD patients with congenital heart defects has been observed to be significantly lower than patients without. Major physiological differences can also exist between pulsatile and continuous flow VAD support for single ventricle patients. This research aims to understand the physiological response of pulmonary shunted single ventricle patients to VAD treatment and identify major resulting physiological differences between the use of pulsatile and continuous flow VADs.

METHODS

A lumped-parameter model (LPM) based on previous work [1] was used to computationally model the cardiovascular system. To simulate a ventricular assist scenario, the VAD inflow and outflow cannulas were connected to the ventricle and aorta respectively. A pulmonary shunt was represented by a connection between the aorta and pulmonary arteries. The pressure drop across the shunt was calculated using a model by Migliavacca et al. [2]. To accurately simulate ventricular pressures during suction, a passive pressure-volume relationship for the negative pressure region was created using results from Nikolić et al. [3].

Clinical data from six pulmonary shunted single ventricle patients ($BSA \sim 0.3$) was obtained from the Great Ormond Street Hospital, Medical University of South Carolina, and University of Michigan. For the LPM simulations to accurately replicate each patient's physiology uniquely, the LPM element values were tuned for each patient separately with the goal of achieving pre-VAD simulation results within ±10% of the patient's clinical measurements. Once tuning was complete, ventricular contractility was set to zero to simulate heart failure.

Mathematical models were created to represent VADs being used in the simulations. These models were created from either experimental data or manufacturer specifications. The pulsatile flow VAD model describes the Berlin Heart, which is pneumatically driven by an external air compressor to create a pressure waveform. Berlin Heart sizes of 10, 25, and 50 mL were considered in this study. The continuous flow VADs used quadratic and linear trendlines to relate pressure and volumetric flowrate data for the HeartWare (centrifugal) and HeartMate II (axial) VADs respectively.

Since a VAD may induce suction on the ventricle, a model was needed to simulate the effective resistance, R_{SUC} (mmHg•s/mL), resulting from ventricular suction effects. Several existing models were tested but the accuracy of each was insufficient. We developed a new model using experimental ventricular suction data extracted from several prior studies. The new model is linearly related to ventricular pressure, P_{SV}, and uses 0 mmHg as the threshold pressure, P_{TH}. This new model is:

$$R_{SUC} = \begin{cases} 0 & if\ P_{SV} \geq P_{TH} \\ -0.01885(P_{SV} - P_{TH}) & if\ P_{SV} < P_{TH} \end{cases} \quad (1)$$

All simulations were run with a fourth order Runge-Kutta algorithm using FORTRAN, and data were analyzed using MATLAB.

Copyright 2016 The Organizing Committee for the 2016 Summer Biomechanics, Bioengineering and Biotransport Conference

Data from the last cardiac cycle (where the simulation has reached periodicity) were used in the analyses.

Two sets of simulations were done. One set used 6 mm inner diameter (ID) cannulas, and the second used 12 mm ID. The 6 mm ID is considered age appropriate for small children. For the Berlin Heart, variable inputs were the device's "heart rate" and size. For continuous flow VADs, the only variable input was motor RPM. The simulations were intended to emulate clinical use of VADs in pulmonary shunted single ventricle patients. Therefore, the simulation settings used for the VADs reflect this as much as possible. This included the peak VAD ejection pressure (desired mean aortic pressure + 100 mmHg), filling pressure (-40 mmHg), and diastolic filling ratio (60%).

RESULTS & DISCUSSION

The pre-VAD LPM results matched all clinical data to within 10% in all six patients except for atrial pressure (up to ±30%) in three patients and pulmonary flow (up to ±20%) in two patients.

For a pulsatile flow VAD, the ideal theoretical cardiac output (CO) is VAD stroke volume (SV) times VAD heart rate (HR). The ideal CO was achieved for the 10 mL Berlin Heart in all simulations. However, a reduction in CO occurred at higher heart rates for the 25 mL and 50 mL Berlin Heart (Figure 1).

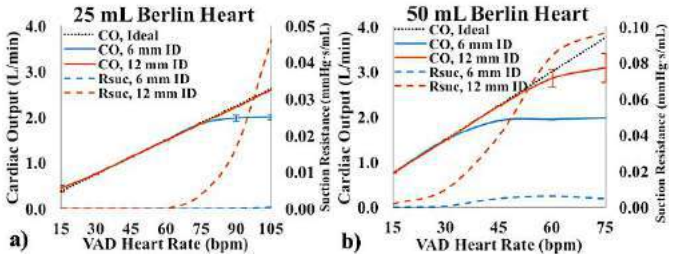

Figure 1: Cohort mean cardiac output and suction resistance vs heart rate for the a) 25 mL and b) 50 mL Berlin Heart.

For both the 25 and 50 mL Berlin Heart, the 12 mm ID cannula resulted in greater CO than the 6 mm ID at higher heart rates. The 12 mm ID resulted in the ideal CO at all heart rates for the 25 mL size. Since doubling the diameter decreased the resistance by approximately a factor of 32 as $R \propto ID^{-4}$, the higher CO for the 12 mm ID cannula may be attributed to its lower resistance, which allows more flow.

The departure in CO from ideal levels in the 25 and 50 mL size Berlin Heart can be examined more closely by looking at the filling and ejection of blood. To attain ideal CO, the Berlin Heart must both fill and eject blood completely in each cardiac cycle. In other words, ideal CO for a 50 mL size would occur only when minimum and maximum volumes are 0 and 50 mL respectively. The minimum and maximum volumes of blood in the 50 mL size for both cannula IDs is shown in Figure 2.

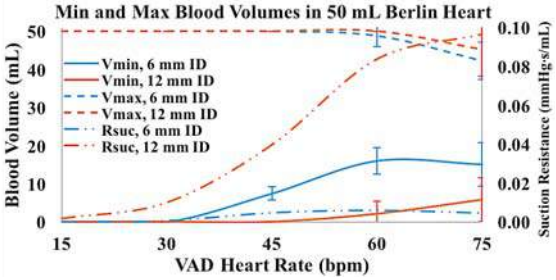

Figure 2: Cohort mean minimum and maximum volumes and suction resistance for the 50 mL Berlin Heart.

A minimum blood volume greater than 0 mL represents incomplete ejection of blood. This reduces stroke volume of the VAD and consequently CO. Figure 2 shows that incomplete ejection increased with heart rate for both cannulas. However, since incomplete ejection occurred with the 6 mm ID cannula earlier than with the 12 mm ID, this explains why the 6 mm ID produced a drop in CO at a lower heart rate (Figure 1). Note that incomplete ejection occurred before incomplete filling for both cannulas. Interestingly, ventricular suction did not have a major impact on filling. The maximum volume decreased from 50 mL to only 42.2 and 45.2 mL for the 6 and 12 mm ID cannulas respectively at the highest heart rate. The cause of incomplete filling may be a combination of ventricular suction effects and reduced VAD diastolic time. This may justify clinical use of the 50 mL size only up to 60 bpm.

For a continuous flow VAD, CO is a function of motor RPM only. The CO for both VADs increases steadily as motor RPM increases (Figure 3).

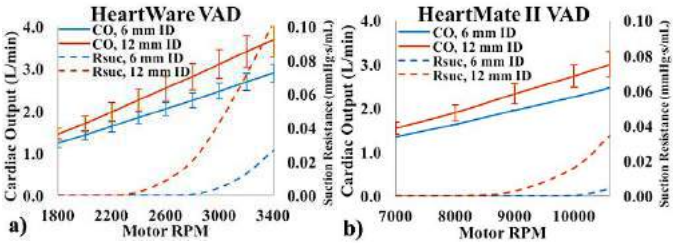

Figure 3: Cohort mean cardiac outputs vs motor RPM for a) HeartWare and b) HeartMate II VADs.

Since current clinical practice desires to avoid ventricular suction lest heart tissue be damaged, the actual "clinical" CO that could be practically achieved (scenarios with zero R_{SUC}, Figures 1 & 3) is lower than the maximum CO possible. With this constraint, the "clinical" mean CO for the 6 mm ID cannula were 1.85, 2.05, and 1.95 L/min for the Berlin Heart, HeartWare, and HeartMate II VADs respectively. For the 12 mm ID, the mean CO were 1.49, 1.97, and 1.90 L/min for the Berlin Heart, HeartWare, and HeartMate II VADs respectively. For both cannula IDs, the continuous flow VADs enabled greater CO than the pulsatile flow VAD, which is consistent with clinical observations. Ventricular suction began at lower heart rates or motor RPMs with the larger 12 mm ID (Figures 1 & 3). The larger ID cannula with the lower cannula resistance allows the VAD to more quickly draw blood from the ventricle to the point of creating suction.

There remains a need for future work on models for ventricular suction resistance and the negative pressure-volume passive curve. The majority of existing work focuses on animal experiments, from which it is unknown how well these translate to humans. In summary, our results reveal several underlying mechanisms affecting VAD output in a mechanically assisted, pulmonary shunted single ventricle circulation and that continuous flow VADs produce higher CO (both with and without a suction constraint) than pulsatile flow VADs, which corroborates clinical observations.

ACKNOWLEDGEMENTS

This work was supported by the Leducq Foundation as part of the Transatlantic Network of Excellence for Cardiovascular Research. We would like to thank the Department of Mechanical Engineering at Clemson University for funding support and Fei He for preliminary work on the ventricular suction model.

REFERENCES

[1] Kung E, et al., *J Biomech Eng,* 46:2, 423-429, 2013.
[2] Migliavacca F, et al., *J Biomech*, 33:5, 549-557, 2000.
[3] Nikolić S, et al., *Circulation Research,* 62:6, 1210-1222, 1988.

Copyright 2016 The Organizing Committee for the 2016 Summer Biomechanics, Bioengineering and Biotransport Conference

SB³C2016
Summer Biomechanics, Bioengineering and Biotransport Conference
June 29 –July 2, National Harbor, MD, USA
SB³C2016-673

A MASTER OF ENGINEERING IN DESIGN AND COMMERCIALIZATION

Alan W. Eberhardt (1), William B. Kirkland (2), Ophelia Johnson (3),
Joel H. Dobbs (4), Lee G. Moradi (2)

(1) Department of Biomedical Engineering
University of Alabama at Birmingham
Birmingham, Alabama, USA

(2) Department of Mechanical Engineering
University of Alabama at Birmingham
Birmingham, Alabama, USA

(3) School of Engineering
University of Alabama at Birmingham
Birmingham, Alabama, USA

(4) Collat School of Business
University of Alabama at Birmingham
Birmingham, Alabama, USA

INTRODUCTION

Today's biomedical engineers are at the forefront of innovative technological solutions to global health problems. The National Institute for Biomedical Imaging and Bioengineering supports the adoption of interdisciplinary, team-based approaches to STEM education that are attentive to the practical value of new knowledge and focus on innovative technologies [1]. To maintain America's position as a world leader in the education of emerging engineers, universities must promote multi-disciplinary teamwork among students in order to produce higher quality results and added value through collaboration and new opportunities [2].

Since 1998, the lead author has received support through the NSF Research to Aid Persons with Disabilities (RAPD) program (now GARDE) to fund undergraduate senior design projects in the area of assistive technologies. Teams of students work with clinicians, therapists, and disabled individuals from special care facilities such as the United Cerebral Palsy of Greater Birmingham and the Bell Center of Homewood. Over the years, students have designed, constructed and delivered various prototype devices that meet the special needs of children and adults with disabilities. While none of these projects led to commercialized products, the efforts have benefited both the students and the disabled community, as observed by others [3].

With the receipt of an NIH R25 award in 2013, a working partnership was formed with the UAB Collat School of Business to bring engineering and business undergraduates together to foster commercialization strategies around new medical device designs. Project scopes were also expanded to include other medical device needs from pediatric neurosurgery, medical simulation, and orthopedic surgery, among others. These capstone projects produced numerous intellectual property (IP) disclosures, four provisional patents and one Patent Cooperation Treaty (PCT) filing. Unfortunately, lack of a viable environment to continue research and development of these projects beyond the end of the capstone activities has hindered commercialization.

The UAB Master of Engineering (MEng) in Design and Commercialization, launched in Fall 2015, provides an opportunity to address these needs. Multi-disciplinary teams of engineering and business graduate students and faculty engage in Innovation-Commercialization (IC) projects and course work that take promising innovative ideas through the R&D process to create marketable devices and start new businesses. The current manuscript describes the curriculum, which includes engineering and business courses, along with overviews of some new courses specifically developed for the MEng program. The purpose of this curriculum is to empower our students to work well in multi-disciplinary teams while shaping them to be successful innovators.

METHODS

In the MEng, engineering students engage in Innovation-Commercialization (IC) projects and take structured coursework designed to take innovative ideas through the research and development (R&D) process to create marketable devices. The curriculum (Fig. 1) contains 24 credit hours in engineering and 12 credit hours in the Master of Business Administration (MBA) program, which earn students the MEng degree as well as a Graduate Certificate in Technology Commercialization and Entrepreneurship from the UAB Collat School of Business.

New courses developed specifically for the MEng program include BME 630, Engineering Design and Commercialization, and EGR 693/694/695, Innovation-Commercialization Project I/II/III. In BME

Copyright 2016 The Organizing Committee for the 2016 Summer Biomechanics, Bioengineering and Biotransport Conference

630, engineering students select their IC projects and begin the R&D processes with client meetings to review the problem and need statement. They perform "deep dives" into the project background, market research, and explore the intellectual property/patent landscape in their design space. The students are incorporated together as "engineers" in a "virtual company" and deliver weekly memos and prototypes reflecting progress. The students receive prompt feedback from the course instructor, or "CEO", for rapid implementation. IC projects adopted this year include a recumbent patient weighing device and a hemostasis tool, two past capstone projects, as well as two projects from external sources. Formal presentations are held periodically for faculty in engineering and business, as well as patent attorneys in UAB's Institute for Innovation and Entrepreneurship (IIE), to offer feedback throughout the development and commercialization processes.

EGR 693 focuses on hands-on "maker activities" that allow students to build competency in prototyping. Students review Computer Aided Drawing (CAD) and are tasked to model a beam with a through-hole in the shape of any card suit (heart, spade, diamond, or club). Students first make their "beam with a hole" by hand machining. As the card suits contain sharp internal corners, students experience the limitations of manual approaches. Next, they create their beam designs using 3D printers as well as Computer Numerical Control (CNC) machining, where they are introduced to G-code and CNC mills. Students gain experience with contemporary electronics by integrating breadboards Arduino (Arduino, LLC, Cambridge, MA) and Raspberry Pi (Adafruit, New York, NY), as well as soldering printed circuit boards (PCBs). Students are provided with equipment to encourage further investigations outside of class. By course end, the student engineers know how to prototype and recognize which advanced methods are required during the process.

ME 677, Systems Engineering (taken in the fall), covers project life cycles, system hierarchy, risk and cost analyses, engineering alternatives and systems processes. Through the spring and summer project courses, EGR 694/695, the MEng students will implement the tools gained from EGR 693 to develop a series of improved prototypes. EE 605, Embedded Systems (spring), focuses on embedded electrical systems design and rapid prototyping. MSE 610, Advanced Materials and Manufacturing (summer), introduces students to modern manufacturing with application to their projects. MEng students are also required to take two graduate level engineering electives, which may include internships with partner organizations.

In the fall semester, the MEng students join with MBA students in MBA 681, Idea to IPO, which addresses how to take a device from the benchtop to the marketplace. MBA 690, Leading Innovation (fall), introduces Lean Startup principles, building mission and vision, and understanding business pivot points. MBA 673, Technology-based Venture Planning (spring), educates students on business plans, capital raising, and competitive analysis. In MBA 691, i2i Entrepreneur Accelerator, teams will be coached through SPARK, a mentoring program organized by the Birmingham Business Alliance to help start-ups succeed at pitching their companies at the Alabama Launchpad business plan competition. Winners gain financial support to launch a start-up company at Innovation Depot, the largest and most successful business technology incubator in the Southeast. As such, we have created an ecosystem that may allow student teams to successfully take their technologies to commercial viability (Fig. 2).

RESULTS AND DISCUSSION

The MEng is new and the first cohort of students is currently enrolled; therefore, no assessment data yet exists regarding student or program success. Targeted program outcomes include the number and quality of products completed, as well as the progress made towards commercialization, such as IP disclosures and patents filed. An important expected outcome is that upon program completion, students will gain competitive positions in industry, launch new start-ups, or be accepted into other graduate programs focusing on innovation and entrepreneurship. One promising early outcome: co-author Ophelia Johnson won a Marshall Scholarship to pursue a graduate

Figure 1: MEng curriculum

Figure 2. Flowchart of MEng activities towards commercialization

degree in medical device design and entrepreneurship at Imperial College London, which suggests our MEng graduates will be competitive at an international level.

As recommended by the National Research Council [4], the MEng program helps students learn through cohesive and engaging clinical and industrial experiences. These experiential/case-centered learning activities teach critical thinking and integrate new knowledge with prior learning. These activities also facilitate development of metacognitive skills, including planning the approach, monitoring comprehension, and evaluating progress towards completion [5].

In the MEng, students engage with professional engineers led by the senior author. The goal is to inspire and encourage the students, so they will gain confidence and develop skills necessary to provide innovative solutions to engineering problems. Our goals are consistent with Ramirez [6], who reports that successful mentoring ensures that students are content with their majors and reach their academic potential, leading them to pursue career paths and advanced study that they may not have otherwise contemplated pursuing.

ACKNOWLEDGEMENTS

The authors gratefully acknowledge support from NSF CBET-1263941, NIH 5 R25HD078327-02, the UAB School of Engineering, Collat School of Business, and Engineering Innovation & Technology Development.

REFERENCES

[1] http://www.nibib.nih.gov/about-nibib/strategic-plan.5
[2] Terpenny, J et al., Internat. J. Eng. Educ., 22(3): 609-616, 2006.
[3] Miyares, U et al., ASEE Conf & Expo, Honolulu, Hawaii, 2007.
[4NRC, How People Learn: Bridging Research and Practice, 2003.
[5] Brown, A, Metacognition, Motivation, & Understanding, 1987.
[6] Ramirez, J Undergrad Neurosci Educ, 11(1): A55-A63, 2012.

Copyright 2016 The Organizing Committee for the 2016 Summer Biomechanics, Bioengineering and Biotransport Conference

SB³C2016
Summer Biomechanics, Bioengineering and Biotransport Conference
June 29 –July 2, National Harbor, MD, USA
SB³C2016-674

UNINJURED SUPRASPINATUS TENDONS IN RODENTS DO NOT EXHIBIT DIFFERENT MATERIAL PROPERTIES ACROSS SEX

Kelsey A. Robinson, Adam M. Pardes, Benjamin R. Freedman, Louis J. Soslowsky

McKay Orthopaedic Research Laboratory
University of Pennsylvania
Philadelphia, PA, USA

INTRODUCTION

Injuries to the rotator cuff are common causes of disability among otherwise healthy individuals, especially in an aging population [1]. Although the exact prevalence of rotator cuff tears has not been established, known risk factors include increasing age [2], hypercholesterolemia [3], smoking [4], and family history [5]. While the relationship between sex and rotator cuff tears is debated [6, 7, 8, 9], gender is known to be a risk factor for other soft tissue injuries. For example, 84% of Achilles ruptures occur in men [10], while ACL injuries are more common in women [11]. Previously, we demonstrated that uninjured male and female Achilles tendons in rodents have different mechanical properties, which may partially explain the disproportionate clinical incidence of spontaneous Achilles ruptures in men [12]. Unfortunately, this mechanical property information has yet to be established for the supraspinatus tendon. Therefore, the objective of this study was to determine the mechanical properties of uninjured supraspinatus tendons in male, female, and ovariectomized (OVX) rats. OVX rats were used to mimic females with attenuated sex hormone levels. We hypothesized that the supraspinatus tendon of female and OVX rats would exhibit decreased cross-sectional area but equal mechanical properties to male supraspinatus tendons.

METHODS

Shoulders were randomized and harvested from 36 age-matched adult male (n=12), female (n=12), and OVX (6-weeks after OVX) (n=12) Sprague-Dawley rats. The supraspinatus tendon and humerus were fine dissected and Verhoeff's stain lines were placed at the bony insertion site and 8 mm proximally. Tendon cross-sectional area was measured with a custom laser device [13]. Humeri were then potted in PMMA, and cyanoacrylate was used to secure the tendon between two pieces of sandpaper leaving an 8mm gage length. A custom fixture was used to secure the potted samples in an Instron ElectroPuls E3000 affixed with a 250 N load cell. Tendons were submerged in a 1x 37°C PBS bath and underwent ramp to failure testing at 0.1% strain/sec. Using the captured load-displacement data, quasi-static mechanical properties were computed. A bilinear fit was applied to the force-displacement curve to delineate between toe and linear regions of the loading response. Researchers were blinded to animal groups during mechanical testing and data analysis. Comparisons between groups were made with one-way ANOVAs and significant relationships were evaluated with post-hoc t-tests with Bonferroni corrections (α=0.05/3).

RESULTS

The cross-sectional area of male supraspinatus tendons was significantly larger (30%) than female and OVX tendons (Figure 1). The maximum loads of male tendons were significantly larger (50%) than female and OVX tendons (Figure 2A). Stiffness in the linear region of the load-displacement curve was significantly larger (40%) in male tendons compared to female and OVX tendons (Figure 2C). The modulus of the toe region of the stress-strain curve was significantly smaller (30%) in male tendons compared to female and OVX tendons (Figure 2D). While changes in cross-sectional area and maximum loads were dramatic and expected, there were no significant differences in maximum stress, linear modulus, toe stiffness or transitional strain among groups (Figures 2B-E).

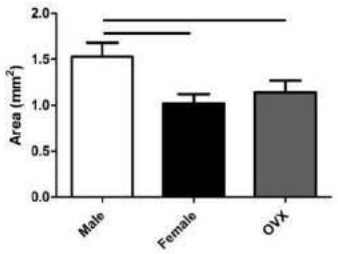

Figure 1: Cross-sectional area of male supraspinatus tendons is greater than that of female or OVX tendons. Data represented as mean and standard deviation. Significance bars indicate p<0.017.

Copyright 2016 The Organizing Committee for the 2016 Summer Biomechanics, Bioengineering and Biotransport Conference

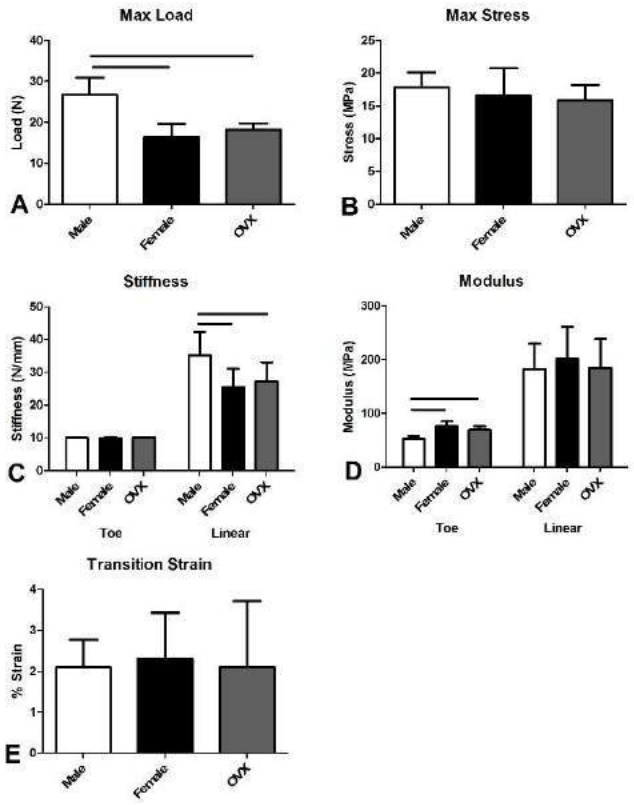

Figure 2: Mechanical properties of supraspinatus tendons. A. maximum load, B. maximum stress, C. stiffness, D. modulus, E. transition strain (between toe and linear regions of the force-displacement curve). Maximum load and stiffness in the linear region of the force displacement curve were significantly greater in male tendons, while toe modulus was significantly smaller than female and OVX tendons. Data represented as mean and standard deviation. Significance bars indicate p<0.017.

DISCUSSION

The objective of this study was to evaluate differences in the mechanical properties of supraspinatus tendons in male, female, and ovariectomized rats. In accordance with our first hypothesis, male tendons had increased cross-sectional area compared to female and OVX tendons. This increased cross-sectional area likely contributed to the greater maximum load in the male supraspinatus tendons. The increased linear stiffness in male tendons was also expected given the increased size of these tendons and maximum load. These results are in contrast to findings in the Achilles tendon, where there was no difference in linear stiffness across sex (Figure 3). The greater modulus of the toe region, but not the linear region, of female supraspinatus tendons suggests that sex may impact collagen fibril uncrimping [14]. Interestingly, this data is also in contrast to our previous results in the Achilles tendon, where the modulus of both the toe and linear regions of female tendons were greater than in male tendons (Figure 3). This Achilles tendon finding suggests that the protection from injury may, in part, be due to differences in the quality of this tendon tissue. The similar maximum stress, transitional strain, and linear modulus of the supraspinatus tendon among groups suggests that the mechanical properties of male tendons are generally similar to that of female and OVX tendons.

Unlike the Achilles tendon, which ruptures spontaneously clinically, supraspinatus injuries are typically degenerative [14, 15]. Therefore, it is possible that the similar supraspinatus tendon mechanical properties observed between sexes may result in degeneration occurring at a similar rate regardless of sex. This would support the lack of a clear relationship between gender and incidence of tears reported in the literature. One potential limitation of this study is the age of the animals, as differences in mechanical properties may be more prominent in aged animals, given that rotator cuff tears are most common in older adults.

Future work will investigate dynamic properties and histologic features of the supraspinatus tendon and muscle in order to further compare and contrast the mechanisms underlying tissue-specific sex differences.

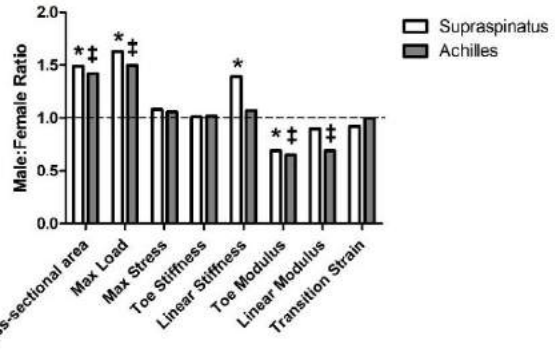

Figure 3: Tendon-specific sex differences in mechanical properties for supraspinatus and Achilles. Ratio of male to female means were taken for each parameter. Data that is significantly different between male and female supraspinatus or Achilles tendons are indicated by * and ‡, respectively. There were significant sex differences in cross-sectional area, maximum load, and toe modulus in both supraspinatus and Achilles tendons. Male supraspinatus tendons had increased linear stiffness and male Achilles tendons had decreased linear modulus compared to female tendons. No direct comparisons were made between supraspinatus and Achilles tendon property male:female ratio. Dotted line represents a ratio of 1.0.

ACKNOWLEDGEMENTS

This study was supported by NIH/NIAMS (R01AR064216S1), the NIH/NIAMS supported Penn Center for Musculoskeletal Disorders (P30AR050950), the NIH/NCATS (TL1TR000138), and the authors thank M. Hast for his contributions.

REFERENCES

[1] Chakravarty, K. & Webley, M., *J Rheumatology*, 20:1359-1361, 1993. [2] Yamaguchi, K. et al., *J Bone Joint Surg*, 88-A: 1699-1704, 2006. [3] Abboud, J. & Kim, J. *Clin Orthop Relat Res*, 468:1493-1497, 2010. [4] Baumgarten, K. et al., *Clin Orthop Relat Res*, 468: 1534-1541, 2010. [5] Tashjian, R. et al., *J Bone Joint Surg Am*. 91: 1136-1142, 2009. [6] Keener, et al. *J Shoulder Elbow Surg*, 19:1191-1198, 2010. [7] Milgrom, C, et al., *J Bone Joint Surg Br*, 77:296-298, 1995. [8] da Rocha Motta, G. et al., *J Shoulder Elbow Surg* 23:227-235, 2014. [9] Yamamoto, A. et al., *J Shoulder Elbow Surg*, 19:116-120, 2010. [10] Vosseller, J. et al. *Foot Ankle Int*, 34:49-53, 2013. [11] Wojtys, E. et al., *Am J Sports Med*, 30: 182-188, 2002. [12] Pardes, A. et al., Sex differences are present in uninjured Achilles tendon and muscle [Abstract]. *ORS*, 2016. [13] Favata, M, Dissertations available from ProQuest, Paper AAI3246156, 2001. [14] Miller, K. et al, *J Biomech*, 45: 2061-2065, 2012. [15] Tashjian, R., *Clin Sports Med*, 31:589-604, 2012. [16] Clayton, R., *Injury*, 39:1338-1344, 2008.

Copyright 2016 The Organizing Committee for the 2016 Summer Biomechanics, Bioengineering and Biotransport Conference

SB^{3}C2016
Summer Biomechanics, Bioengineering and Biotransport Conference
June 29 –July 2, National Harbor, MD, USA
SB^{3}C2016-676

A STRUCTURAL FINITE ELEMENT MODEL FOR LAMELLAR UNIT OF AORTIC MEDIA INDICATES HETEROGENEOUS STRESS FIELD AFTER COLLAGEN RECRUITMENT

James R. Thunes (1), Joseph Pichamuthu (1), Julie A. Phillippi (1,2,3,4), Thomas G. Gleason (1,2,3,4), David A. Vorp (1,2,3,4), Spandan Maiti (1)

(1) Department of Bioengineering
University of Pittsburgh
Pittsburgh, PA, USA

(2) Department of Cardiothoracic Surgery
University of Pittsburgh
Pittsburgh, PA, USA

(3) Department of Surgery
University of Pittsburgh
Pittsburgh, PA, USA

(4) Center for Vascular Remodeling and Regeneration
University of Pittsburgh
Pittsburgh, PA, USA

INTRODUCTION

Important factors in the pathophysiology of the ascending thoracic aorta (ATA) are the biomechanical properties of the wall. Current literature has modeled the tissue with structurally motivated constitutive models that include fiber orientation and tortuosity. While an improvement over purely phenomenological material models, they are unable to consider the local effect of the collagen network on the non-collagenous matrix. Local variations in the collagen network can give rise to heterogeneity in the stress-state in the surrounding tissue which may influence structural and functional remodeling of the extracellular matrix through mechanosensitive pathways in the vascular smooth muscle cells (VSMCs). With this purpose, we have developed a micro-structural finite element model of ATA wall tissue including an experimentally derived collagen network embedded within the non-collagenous matrix. The fidelity of the model is shown by comparison to experimental uniaxial stress-strain data. Additionally, it is shown that the tissue stress, initially homogeneous, become heterogeneous due to collagen fiber recruitment. Finally, we show that the realignment of the network during loading creates "stress paths" which our model revealed to be the primary load bearing mechanism at high applied stretch.

METHODS

The ATA media is composed of repeating lamellar units (LU). Each LU is composed of an interlaminar space containing VSMCs and collagen networks surrounded by elastin lamellae (Fig. 1a). We modeled a single LU for the simulation of biomechanical response of the media to stretch. The symmetry in the radial (RAD) direction was utilized to create a representative volume element (RVE) modeling half of the LU. A custom nonlinear finite element code was utilized to simulate the mechanical response of the model. The collagen fibers were modeled with 1D bar elements embedded within the solid 3D elements representing the interlaminar space and elastic lamellae. For finite element mesh convergence, the RVE required 22,500 8-noded hexahedral elements (Fig. 1b). The collagen network was constructed with an isotropic voronoi tessellation. The initial network was then modified through a combination of affine transformation, fiber addition, and fiber deletion to yield a final network that was statistically matched with the experimentally measured network parameters[1] (two-sample chi-squared test $p \leq 0.05$ for fiber orientation distribution (OD)). Network parameters were areal density, fiber length, intersection density, and OD. The final network matches the experimental OD (Fig. 1c) and was composed of 860 fiber segments (Fig. 1d)

Collagen fibers were modeled using a bilinear constitutive response

$$\sigma = \begin{cases} 0 & \text{if } \lambda < \lambda_r \\ E_f(\lambda - \lambda_r) & \text{if } \lambda \geq \lambda_r \end{cases} \quad (1)$$

where λ is the fiber stretch, λ_r is the recruitment stretch of the fiber, and E_f the elastic modulus of the fiber. All fibers were modeled with the diameter of 3μm. The non-collagenous component of the model was composed of two constituents: the elastin lamellae and the interlaminar space. Both were modeled as one parameter isotropic incompressible neo-Hookean materials with the strain energy function

$$\Psi = \frac{\mu}{2}(I_1 - 3) \quad (2)$$

with μ the shear modulus and I_1 the first invariant of the right Cauchy-Green deformation tensor. The shear modulus of the EL was taken as 1000 kPa. The shear modulus of the IL (μ_{IL}), E_f, and λ_r were determined through regression against the experimental data.

Copyright 2016 The Organizing Committee for the 2016 Summer Biomechanics, Bioengineering and Biotransport Conference

The RVE was loaded to $\lambda = 1.5$ in the circumferential (CIRC) direction to simulate uniaxial test. The LONG faces and symmetry plane were on rollers. Stretch was applied over 400 load steps. Convergence studies were performed to ensure convergence in both mesh and loading. The CIRC component of the stress in the IL near the collagen network was gathered at each loadstep.

RESULTS

Regression against prior experimental data[2] provided the material parameters $\mu_{IL} = 170$ kPa, $E_f = 80$ MPa, and $\lambda_r = 1.25$. These parameters fall within experimentally reported ranges in the literature[2, 3]. The fit between the experimental and simulated stress-strain response was $R^2 = 0.996$ (Fig 1e).

The stress-state in the IL was homogenous under low stretches (less than λ_r) and heterogeneous at strains above the fiber recruitment stretch (Fig 2a,b). The coefficient of variance in the IL element stresses at $\lambda = 1.1$ was 0.1 while at $\lambda = 1.5$ was 1.25. Levene's test showed no difference in the standard deviation of the stress below $\lambda = 1.25$ but a significant difference above $\lambda = 1.25$ ($p < 0.01$). Fibers gradually began to bear load starting at $\lambda = 1.25$, with 90% of the total fibers bearing load at the end of the simulation.

The fibers in the networks reoriented under the applied stretch (Fig 2c,d) with most of the reorientation occurring in fibers initially oriented within 30° of the CIRC direction. Fibers orthogonal to the loading direction (±15° to the LONG direction) changed orientation by less than 1% over the course of the simulation. Low stretches (less than λ_r) yielded no fiber stress while high stresses revealed significant fiber stress. The fiber stress was not homogenous. Fibers aligned in the CIRC direction experienced the maximum stress while fibers orthogonal to the loading direction were unloaded over the course of the simulation. Continuous "stress paths" spanned the domain and were a result of the initial network architecture and gradual reorientation of the network over the course of the analysis. Disruptions in the fiber network such as loss of connectivity and areas of decreased fiber density were found to be colocalized with stress concentrations in the IL stress (white arrows in Fig 2).

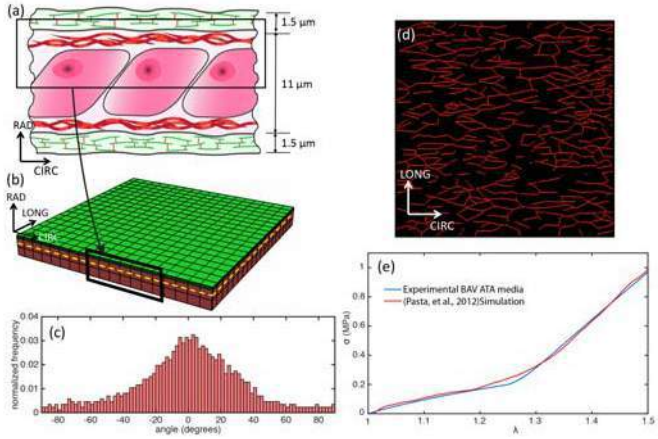

Figure 1: (a) The lamellar unit is composed of an interlaminar space surrounded by elastin lamellae. VSMCs and collagen networks reside within the IL. Half of the LU is taken as the RVE. (b) The RVE ($250\ \mu m \times 250\ \mu m \times 6.25\ \mu m$) was modeled hexahedral elements. The EL is shown in green and the IL in red. The fiber network (yellow) is situated directly below the elastin. A $75\ \mu m \times 75\ \mu m \times 6.25\ \mu m$ section of the mesh is shown. (c) the OD of the fiber network matches the experimental[1]. (d) The final network is composed of 860 fiber segments. (e) Fit between the simulated (blue) and experimental (red)[2] stress-stretch data.

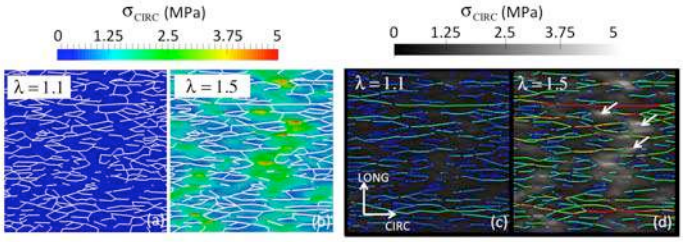

Figure 2: Local variation in the CIRC component of the IL stress in the deformed configuration at (a) $\lambda = 1.1$ and (b) $\lambda = 1.5$. The fibers are represented by white lines. Fiber stresses are shown in the same locations at (c) $\lambda = 1.1$ and (d) $\lambda = 1.5$. IL stress is shown in greyscale for comparison. The white arrows show regions of network disruption. These disruptions cause stress concentrations in the IL stress.

DISCUSSION

With a combination of a one parameter incompressible neo-Hookean solid and linear elastic fiber material model, the complex stiffening behavior of aortic tissue was captured. This was possible due to the novel fiber embedded finite element method utilized in this work. In contrast to previous work with embedded fibers, this method allows for arbitrary placement of fibers within the volumetric domain instead of along the edges of the volumetric elements. This capability drastically simplifies both volumetric element and fiber network design.

Fiber recruitment not only gave rise to the stiffening response of the stress-stretch curve, but yielded the heterogeneous stress-state in the IL tissue. Below the recruitment stretch of the fibers, the stress was homogenous, with the standard deviation in the stress increasing rapidly at high stretches.

The collagen fibers effectively shielded the surrounding matrix from stress. Thus, matrix stress along the "stress paths" was relatively low. In regions where there was disruption in the fiber network however, there was focal stress in the matrix. As VSMCs are mechanosensitive, this degradation could therefore induce local ECM remodeling.

This work has some limitations. An isotropic solid was assumed for the IL whereas VSMCs reside in this tissue in vivo. An additional source of material heterogeneity as well as the contractile nature of VSMCs are thus neglected. Failure is not included in this model. High stress regions of the domain could experience failure which would alter the stress state. Finally, we have modeled only a uniaxial tensile loading case. Future work will explore more physiological loading conditions.

ACKNOWLEDGEMENTS

J.Thunes was supported by the University of Pittsburgh Department of Bioengineering.

REFERENCES

1 J. A. Phillippi, B. R. Green, M. A. Eskay, M. P. Kotlarczyk, M. R. Hill, A. M. Robertson, S. C. Watkins, D. A. Vorp, and T. G. Gleason, J Thorac Cardiovasc Surg **147**, 1056 (2014).

2 S. Pasta, J. A. Phillippi, T. G. Gleason, and D. A. Vorp, J Thorac Cardiovasc Surg **143**, 460 (2012).

3 M. A. Zulliger and N. Stergiopulos, J Biomech **40**, 3061 (2007).

Copyright 2016 The Organizing Committee for the 2016 Summer Biomechanics, Bioengineering and Biotransport Conference

SB^{3}C2016
Summer Biomechanics, Bioengineering and Biotransport Conference
June 29 –July 2, National Harbor, MD, USA
SB^{3}C2016-677

ATHEROGENIC STRETCH PROMOTES NUCLEAR EXPRESSION OF NF-κB IN ENDOTHELIAL CELLS

Ryan M. Pedrigi, Konstantinos I. Papadimitriou, Avinash Kondiboyina, Sukhjinder Sidhu, James Chau, Emmanuel M. Drakakis, Rob Krams

Department of Bioengineering
Imperial College London
London SW7 2AZ, United Kingdom

INTRODUCTION

Coronary heart disease (CHD) is a chronic inflammatory process that manifests as atherosclerotic plaques composed of lipids and immune cells within the intima of coronary arteries. CHD is associated with a dysfunctional endothelium that is characterized by a pro-inflammatory phenotype [1]. Although numerous systemic factors contribute to this phenotypic modulation of the endothelial cell, the local mechanical environment plays a central role. Towards this end, most studies have focused on hemodynamics and atherosclerotic plaques have been shown to localize to regions of specific flow profiles typically described as disturbed or atherogenic [2]. However, few studies have examined altered vessel wall mechanics in the development of atherosclerosis and no study has examined an atherogenic stretch regimen that is analogous to atherogenic flow.

Herein, we built a custom cell stretching device with four independently controlled motors to mimic the stretch environment of the vascular endothelial cell *in vivo*, including: normal cyclical stretch, a reduced magnitude of cyclical stretch, which occurs with aging and development of arteriosclerosis, and a varied stretch condition that represents an idealized pro-inflammatory endothelial cell stretch stimulus. Cellular response to these different stretch conditions was gauged by the degree of nuclear expression of NF-κB, a known pro-inflammatory and atherogenic transcription factor [3].

METHODS

Cell Culture. The EA.hy926 endothelial cell line was used for all experiments. Cells were maintained in culture medium within a humidified incubator at 37ºC and 5% CO_2. Prior to stretching experiments, an elastic silicon membrane was covalently coated with 0.1% gelatin from bovine skin to facilitate cell adherence [4] and attached to four polycarbonate legs of the stretching device. Cells were seeded on each membrane in up to four separate quadrants using cloning rings and incubated for 2 days before starting the experiment.

Cell Stretching Device. We built a custom cell stretching device that allowed independent control over four high torque stepper motors in terms of displacement magnitude, direction, frequency, and variations in these parameters over time. Each motor of the device was attached via a stainless steel rod to one polycarbonate leg, to which the cell seeded membrane was attached. Membranes were calibrated to determine membrane stretch versus rod displacement and verify homogeneity of the imposed stretch across the cell-seeded portion of the membrane. The motors were controlled by a high speed microcontroller and motor drivers, all located on a separate custom-made printed circuit board. Three experimental conditions were considered: normal cyclical stretch in one direction (representing the circumferential direction of the vessel) of 1.08 [5] with an additional pre-stretch of 1.06 in the circumferential direction and 1.12 in the orthogonal (representative axial) direction [5], reduced uniaxial cyclical stretch of 1.02 with the same biaxial pre-stretch, and varied cyclical stretch magnitude (either normal or reduced) and direction (either circumferential or axial) every 30 minutes with no pre-stretch. For all conditions, the frequency of stretch was 1 Hz and the duration of each experiment was 6 hours.

NF-κB Staining, Imaging, and Analysis. At the end of each stretching experiment, media was drawn out of the stretching device chamber and replaced with 4% paraformaldehyde in PBS while continuing to stretch for another 5 min. The membrane was then removed from the device and the four quadrants (given by the four cloning rings used during seeding), each representing a separate cell monolayer, were immunostained with an antibody targeting the p65 domain of NF-κB, cell nuclei were counter-stained with DAPI, and both stains were imaged with a Zeiss PALM laser capture fluorescent

Copyright 2016 The Organizing Committee for the 2016 Summer Biomechanics, Bioengineering and Biotransport Conference

microscope at 20X magnification. A custom Matlab program was used to segment the cells within each image and compute the nuclear to cytoplasmic ratio of NF-κB, which accounted for possible variations in stain intensity between different staining sessions and was the primary readout of the study. The mean of this metric over all cells segmented from a monolayer was then computed, giving one value per monolayer. The mean of this ratio over all monolayers of a given experimental condition is reported, scaled by the mean of the cell monolayers exposed to normal stretch.

Statistical Analysis. Data are reported as mean±SD. A one-way ANOVA was used to evaluate statistical differences in nuclear to cytoplasmic expression of NF-κB between stretch conditions and a posthoc multiple comparisons test was employed with a Bonferonni correction to explore the significance of individual comparisons. P<0.05 was used as the threshold for statistical significance.

RESULTS

To test whether stretch could induce an atheroprone endothelial cell phenotype, we examined cell nuclear expression of NF-κB in three different stretch conditions: normal (physiological) cyclical stretch, reduced (pathological) cyclical stretch, and an idealized varied (pathological) cyclical stretch condition with changes in stretch magnitude and direction over time (Figure 1).

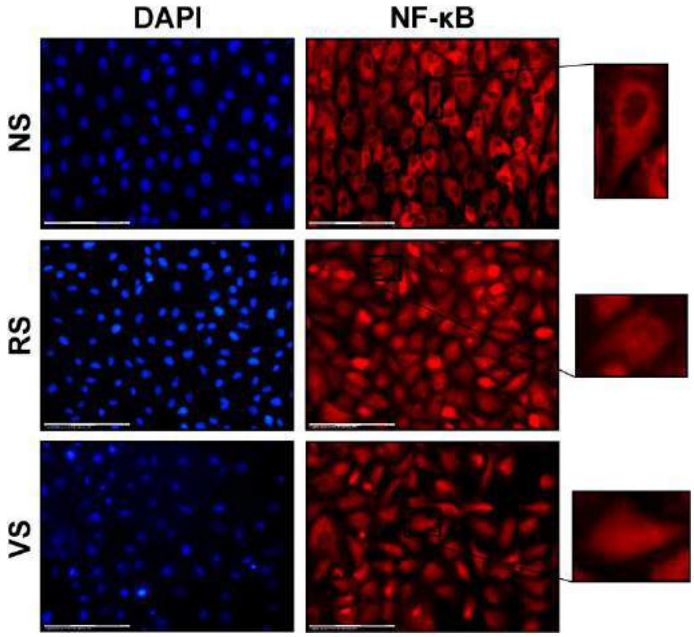

Figure 1: DAPI and NF-κB stains in cells exposed to normal (NS), reduced (RS), or varied (VS) stretch. Inset shows NF-κB in a representative cell for each stretch condition, demonstrating increased nuclear expression in those cells exposed to pathological stretch.

Cells experiencing the normal stretch condition exhibited the lowest expression of nuclear NF-κB of 1.0±0.1 (n=8 monolayers). Nuclear NF-κB levels were increased to 1.3±0.3 in the reduced stretch condition (n=10) compared to the normal condition (p=0.068). More strikingly, cells exposed to the varied stretch condition exhibited a much larger increase in nuclear NF-κB expression of 1.7±0.1 (n=7), which was statistically higher than both the normal (p<0.001) and reduced stretch conditions (p<0.01; Figure 2).

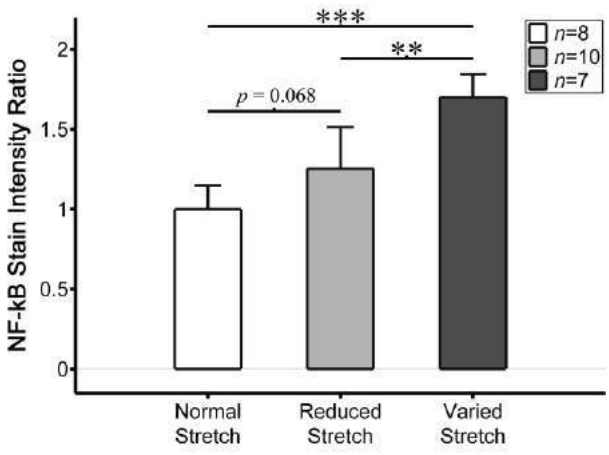

Figure 2: Nuclear to cytoplasmic NF-κB stain intensity ratio in cells exposed to normal, reduced, or varied stretch. Number of cell monolayers per condition is given by *n*. Asterisks indicate **p<0.01 and ***p<0.001. Bars are mean±SD.

DISCUSSION

Numerous studies have demonstrated that specific atherogenic flow profiles promote expression of pro-inflammatory signaling molecules in endothelial cells and localize to regions of the vasculature containing atherosclerotic plaques [2, 6]. Given that vessel wall mechanics is also an important part of the tissue mechanical environment of the endothelial cell and solid wall stress is several orders of magnitude larger than shear stress, it is likely that solid wall mechanics also influences endothelial cell behaviors and deviations from normal may promote a pro-atherogenic phenotype. Although previous studies have partially addressed this postulate by examining endothelial cell function under physiological levels of stretch [7], very little has been done to examine atherogenic stretch conditions. Herein, we developed a custom stretching device that allowed control over stretch magnitude and direction to examine the effects of two pathological stretch conditions on endothelial cell function. Each of these stretch conditions was motivated by an analogous atherogenic flow profile, reduced stretch comparable to reduced flow and varied stretch comparable to multidirectional or oscillatory flow. Both of these pathological stretch conditions were shown to up-regulate the pro-atherogenic transcription factor NF-κB compared to the normal stretch condition, which suggests that stretch can be atherogenic similar to flow. These findings motivate inclusion of vessel wall mechanics, in addition to hemodynamics, in mechanobiological studies of atherosclerosis.

ACKNOWLEDGEMENTS

We would like to thank the British Heart Foundation (grants RG/11/13/29055 and PG/15/49/31595) for financial support.

REFERENCES

1. Libby, P. et al., *Nature*, 473, 317-325, 2011.
2. Pedrigi, R.M. et al., *Circulation*, 132, 1003-1012, 2015.
3. Frueh, J. et al., *Cardiovasc Res*, 99, 334-341, 2013.
4. Braakman, S.T. et al., *Exp Eye Res*, 127, 224-235, 2014.
5. Masson, I. et al., *J Biomech*, 41, 2618-2627, 2008.
6. Samady, H. et al., *Circulation*, 124, 779-788, 2011.
7. Zhao, S. et al., *Arterioscl Throm Vasc Biol*, 15, 1781-1786, 1995.

Copyright 2016 The Organizing Committee for the 2016 Summer Biomechanics, Bioengineering and Biotransport Conference

SB^{3}C2016
Summer Biomechanics, Bioengineering and Biotransport Conference
June 29 –July 2, National Harbor, MD, USA
SB^{3}C2016-678

RHEOLOGICAL CHARACTERIZATION OF AN EMBRYO CULTURE LIQUID AND IMPLICATIONS FOR CULTURE IN MICROFUIDIC DEVICES

Irene Nepita (1), Alberto Lagazzo (1), Stefano Barone (2), Giovanni Besio (1), Alessandro Stocchino (1) and Rodolfo Repetto (1)

(1) Department of Civil, Environmental and Chemical Engineering, University of Genoa, Genoa, Italy

(2) Ospedale della Versilia, Centro Procreazione Assistita, USL Nordovest, Lido di Camaiore, Italy

INTRODUCTION

Infertility affects a large number of people worldwide; in [1] it was reported that approximately 10% of the world's population suffers from infertility. A progressively increasing number of people resort to in vitro fertilization techniques (IVF) to treat infertility. In IVF units embryos are normally cultured in micro droplets in static conditions and at 37 °C. Dynamic culture in microfluidic systems has been proposed in recent years as a viable approach to improve the rate of embryo implantation after IVF, which is still relatively low.

One of the key parameters to be accounted for in the design of a microfluidic device is the wall shear stress (WSS) experienced by the embryo during its development and this, obviously, depends on the rheological properties of the culture liquid.

In this work we characterize the rheology of a liquid used as medium for embryo culture (G-1 PLUS, Vitrolife) and find that it has non-Newtonian properties. We show with three-dimensional numerical simulations that fluid properties significantly affect the stress acting on the embryo.

RHEOLOGICAL TESTS

Rheological measurements have been performed using a rotational viscometer (Physica Anton Paar MCR 301) with a torque resolution of 0.1 nN·m, in the range between 0.05 μN·m and 200 mN·m. The measurement chamber was kept at a controlled temperature of 37°C. In order to obtain a constant shear rate throughout the sample a cone-plate configuration was adopted, with a conical rotor of 50 mm in diameter and an angle of 2°. The sample is placed in a 0.21 mm gap between the two plates.

We performed both tests at a constant rotational velocity, which allowed us to determine the stress-shear rate curve, and also oscillatory tests, from which we estimated the complex modulus of the liquid.

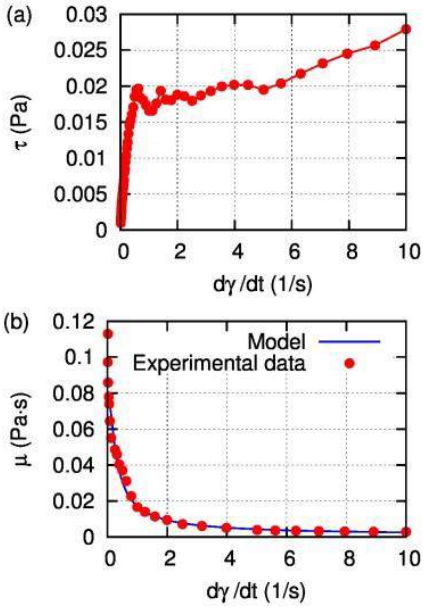

Figure 1: (a) Stress (τ) versus shear rate ($d\gamma/dt$). (b) Effective viscosity, defined as $\mu_e = \tau/(d\gamma/dt)$.

The results show that the behaviour of the fluid is highly non-Newtonian at low values of the shear rate, which are typical in microfluidic devices. This is shown in Figure 1a, where we report the stress (τ)-shear rate ($d\gamma/dt$) curve. In particular, the fluid

Copyright 2016 The Organizing Committee for the 2016 Summer Biomechanics, Bioengineering and Biotransport Conference

approximately behaves according to the Bingham model: for small values of shear rate the effective viscosity grows to very large values and it becomes constant for large enough values of the shear rate. In Figure 1b we show the effective viscosity μ_e, defined as the ratio between the stress and the shear rate at each point of the curve in Figure 1a.

The oscillatory tests provided the elastic and viscous responses of the fluid, quantified by its storage G' and loss modulus G''. At very low values of the stress ($\tau \lesssim 10^{-3}$ Pa), we find that G' becomes comparable to G'' ($G'' > G'$ for larger values of the stress), which implies that the sample presents characteristics analogous to those of a solid in this region.

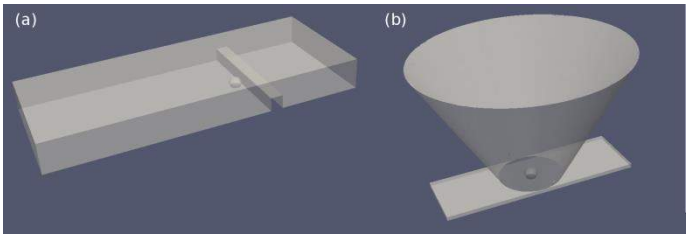

Figure 2: Sketch of the geometries considered in the numerical simulations. (a) microchannel, (b) microfunnel.

NUMERICAL SIMULATIONS

Various authors have studied the characteristics of microfluidic devices by performing numerical simulations of fluid flow [2, 3]. In all works we are aware of the mechanical properties of water have been adopted for the culture liquid. In order to assess the importance of the real rheological properties of the fluid on flow characteristics and, in particular, on the wall shear stress experienced by the embryo we performed numerical simulations adopting the two different geometries shown in Figure 2 and also considered by previous authors [2]. For each geometry we run two series of simulations: i) in the first we considered the rheological properties of the fluid as measured in the present work, in the second series we run the same simulations adopting the viscosity of water for comparison. In order to model the non-Newtonian properties of the fluid and avoid the numerical complications arising from the use of a constitutive law with a yield stress, we modelled the liquid adopting the Carreau-Bird law [4]. This implies that effective viscosity of the fluid is assumed to decrease with the rate of strain from a maximum value μ_0 to a minimum asymptotic value μ_∞. The curve resulting from fitting the four parameters of model with the experimental results is shown in Figure 1b in blue. We verified that changes in the value of μ_0 do not affect significantly the numerical results, which indicates that the use of the Carreau-Bird constitutive equation is appropriate for the present purposes. The numerical simulations are carried out using the open source software OpenFOAM [5], which is based on the finite volume method.

In Figure 3 we show the velocity magnitude on a longitudinal cross-section of the microchannel as predicted by the numerical simulations. In Figure 4 we report the ratio between the maximum wall shear stress on the embryo in the case of the Carreau-Bird model and in the case of a Newtonian fluid with the same properties as water as a function of the inlet velocity. The results suggest that the WSS predicted in the case of a non-Newtonian fluid is much higher than that obtained in the case of water, especially at low values of the velocity and consequently of the shear rate. For the smallest value of the velocity (which is consistent with real microfluidic devices) the stress is predicted to be almost 40 times higher when the real properties of the culture liquid are accounted for. Similar results are obtained in the case of the microfunnel geometry.

DISCUSSION

In this paper we have characterized the rheology of an embryo culture liquid (G-1 PLUS, Vitrolife). Various different culture fluids are available on the market, however most of them have similar constituents. Thus, we expect that tests performed on other brand fluids would lead to qualitatively similar results.

We showed that the fluid has non-Newtonian properties and this is particularly relevant at low values of the rate of strain $d\gamma/dt$. We note that in real microfluidic devices the values of the shear rate reached on the embryos are expected to be small enough for variation of the effective viscosity to be very significant.

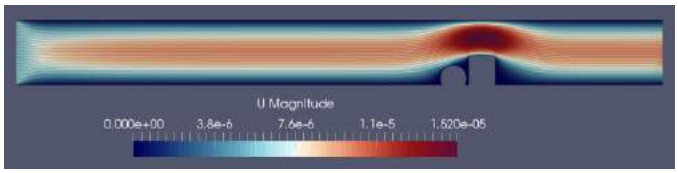

Figure 3: Velocity magnitude on a longitudinal cross-section of the microchannel.

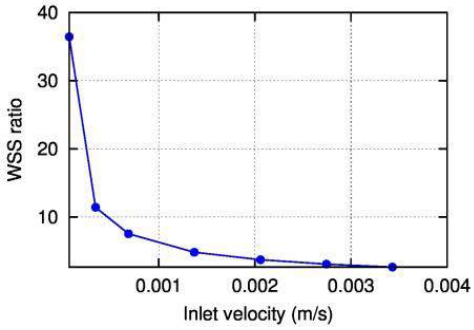

Figure 4: Ratio between the maximum wall shear stress on the embryo in the case of the Carreau-Bird model and in the case of a Newtonian fluid with the same properties as water. The geometry considered is the microchannel (Figure 2a).

The only feasible way of assessing the amount of stress that a laminar flow exerts on an embryo in a microfluidic device is to resort to numerical simulations of fluid flow, owing to the difficulty of performing direct measurements. The present work stresses the importance of measuring the rheological properties of culture liquid, the knowledge of which is a prerequisite for running feasible numerical simulations of fluid flow.

REFERENCES

[1] Direkvand-Moghadam, A., *Int. J. Epidem. Res.*, 1(1),35-43, 2014.
[2] Heo, Y. et al. Human reproduction, 25(3): 613-622, 2010.
[3] Lee, P. J. et al., *Biotechno. Bioeng.,* 94(1):5-14, 2005
[4] Carreau, P. J. University of Wisconsin–Madison, 1968.
[5] http://openfoam.com.

Copyright 2016 The Organizing Committee for the 2016 Summer Biomechanics, Bioengineering and Biotransport Conference

SB^{3}C2016
Summer Biomechanics, Bioengineering and Biotransport Conference
June 29 –July 2, National Harbor, MD, USA
SB^{3}C2016-679

A CHEMO-MECHANICAL MODEL FOR EXTRACELLULAR MATRIX AND NUCLEAR RIGIDITY REGULATED SIZE OF FOCAL ADHESION PLAQUES

Xuan Cao (1), Yuan Lin (2), Tristan P. Driscoll (3), Janusz Franco-Barraza (4), Edna Cukierman (4), Robert L. Mauck (3), Vivek B. Shenoy (1,3)

(1) Department of Materials Science and Engineering,
University of Pennsylvania
Philadelphia, PA 19104, USA

(2) Department of Mechanical Engineering,
The University of Hong Kong
Hong Kong SAR, China

(3) Department of Bioengineering,
University of Pennsylvania
Philadelphia, PA 19104, USA

(4) Cancer Biology Program,
Fox Chase Cancer Center, Temple Health
Philadelphia, PA 19111, USA

INTRODUCTION

To perform functions such as proliferation (1), differentiation (2) and locomotion (3), living cells establish stable attachments to the extracellular matrix (ECM) via the formation of specialized receptor mediated contact foci, referred to as focal adhesions (FAs). Accumulating evidence has demonstrated that, besides biochemical factors, the formation and function of FAs is tightly regulated by mechanical cues (4, 5). Theoretically, various FA models have been proposed (6–8) to test theories regarding the physics of FA formation. Despite these aforementioned efforts, several important issues remain unsettled: in most existing models, the size of the adhesion plaque has often been taken as a constant (6) or did not enter the formulation at all (7, 8); additionally, the impact of extracellular matrix structure and stiffness on FA assembly has also been reported (9); finally, recent observations also suggest that the physical properties of cell nucleus (10) can influence the size of FAs, however, to the best of our knowledge, no theoretical explanation has been provided. Aiming to address these problems, we developed a chemo-mechanical model to describe the growth dynamics of adhesion plaques as a function of substrate and nuclear stiffness. In particular, we will demonstrate the existence of a critical nucleation size for nascent patches to evolve into mature ones, and the extent to which stable plaque size is influenced by both the substrate and the nuclear rigidity.

METHODS

As described in the literature, a focal adhesion (FA) consists of a cluster of proteins (including individual integrin molecules that bind to ECM), that is then connected to the cell nucleus via the actomyosin stress fibers (Fig. 1a). A schematic of our proposed structural model describing the full mechanical feedback loop regulating FAs, the cytoskeleton and the nucleus is shown in Fig. 1b. The FA and ECM complex are treated as a spring (green box in Fig. 1b) whose stiffness is dependent on the FA structure and ECM mechanical properties. The actomyosin responsible for contractile force generation is illustrated in the blue box, and the nucleus is modeled as an elastic component to capture nuclear deformability (yellow box, Fig. 1b). The structure of the FA-ECM complex allows for sensing of ECM mechanical properties through force dependent assembly or disassembly of adhesions. Since cells have been shown to sense the ECM as fibers or non-fibers depending on ECM structure, we considered both fibrous and non-fibrous ECM types. If the ECM protein tethering spacing were larger than the FA size, a cell would sense the material as fibrous (Fig. 1c). However, if the ECM protein tethering spacing were smaller than the FA size, a cell would sense the ECM as a continuous elastic material (Fig. 1d). The model was combined with energy criteria for FA plaque recruitment to study the FA size dependence on the model parameters.

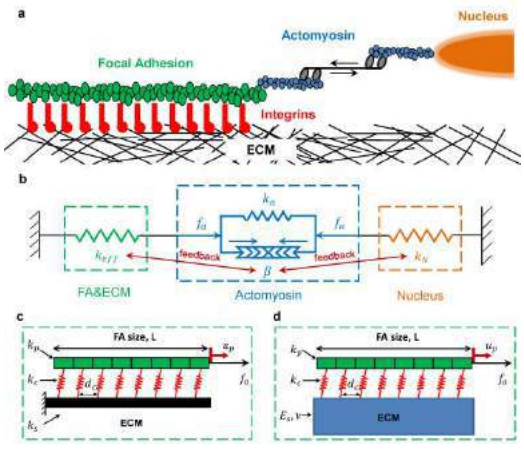

Figure 1: Illustration of cell-ECM adhesion (a). Schematic of model (b) and structures of FA-ECM complex on different kinds of ECM, fibrous (c) and continuous elastic (d).

Copyright 2016 The Organizing Committee for the 2016 Summer Biomechanics, Bioengineering and Biotransport Conference

RESULTS

The stiffness a cell senses increases first and then decreases as FA becomes larger

As discussed above, the FA effective stiffness (k_{eff}) can be determined by solving the mechanical governing equations. This physical parameter indicates the actual mechanical stiffness of the extracellular environment that the cell senses. This k_{eff} is plotted as a function of both the FA size and ECM rigidity in Fig. 2a and 2b for ECMs treated as fibrous or continuous elastic materials respectively. Interestingly, as FA size (L) increases, k_{eff} first climbs to a maximum before undergoing a monotonic decrease for both ECM types. The difference between the two models is that for gels there is a saturated effective stiffness, which is related to gel modulus: the stiffer the gel, the higher the effective stiffness. In conclusion, the effective stiffness of the extracellular environment that cells sense, first increases and then decreases as FAs becomes larger for both fibrous and non-fibrous ECMs.

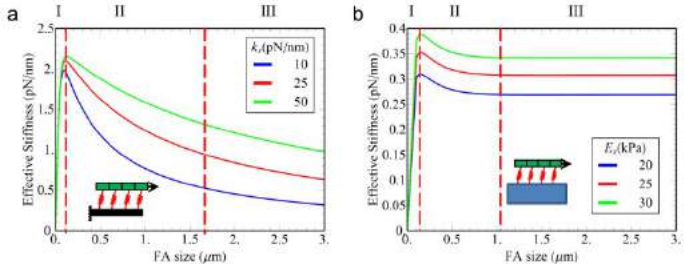

Figure 2: Effective stiffness of FA (k_{eff}) with respect to FA size (L) on different fibers with stiffness k_s (a) or on non-fibrous elastic materials with modulus E_s (b).

FA plaque recruitment is divided into three regimes by two important sizes: nucleation size and stable size.

Both models show the generic shape of the plaque recruitment flux J, as a function of FA size as shown in Fig. 3a. An immediate observation is that the value of J is positive only when $L_{nu} < L < L_{st}$ where L_{st} stands for the stable size of the plaque while L_{nu} can be considered the critical size a nascent plaque must overcome in order to grow and become fully developed. As such, the plaque dynamics can be divided into three regimes as depicted in Fig. 3a. Newly nucleated FAs with sizes smaller than L_{nu} will dissemble and eventually disappear. In comparison, a nascent FA will develop into a stable one once its size stochastically reaches this critical value. Larger FAs ($L > L_{st}$) are expected to shrink until reaching the predicted stable size. Fig. 3b shows the extent to which ECM rigidity influences the growth rate of FAs. Our results suggest that the stable size increases monotonically as the substrate becomes more rigid.

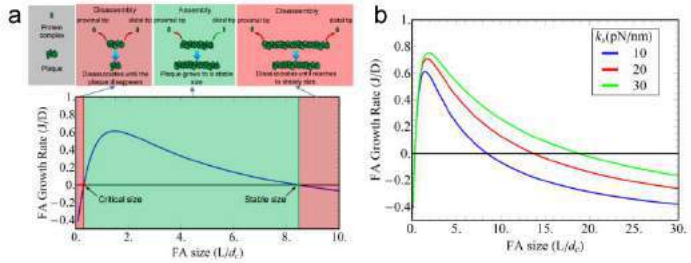

Figure 3: Two essential sizes for a FA plaque: critical size and stable size are predicted by the model (a). FA growth rate for different substrate stiffnesses (b) indicates stable FA size is larger on stiffer substrate.

Cells with stiffer nuclei have a lower barrier to form FAs and would assemble larger FAs, while higher contractility leads to a small drop in the FA nucleation barrier and a significant increase in stable FA size.

Our model predicts the dependence of FA size on nuclear stiffness. As shown in Fig. 4a, cells with stiffer nucleus would have a smaller critical FA recruitment size, which means the FA recruitment barrier is lower for these cells. Meanwhile, the model predicts that stiffer nuclei would also lead to a larger FA stable size, allowing for more and larger FAs to form.

Cell contractility is essential for FA formation and regulates FA size. Our model predicts the extent to which contractility regulates FA growth. For lower levels of cell contractility (20% lower actin pulling force) our model predicts that the FA nucleation barrier is larger and the stable size is smaller (Fig. 4b).

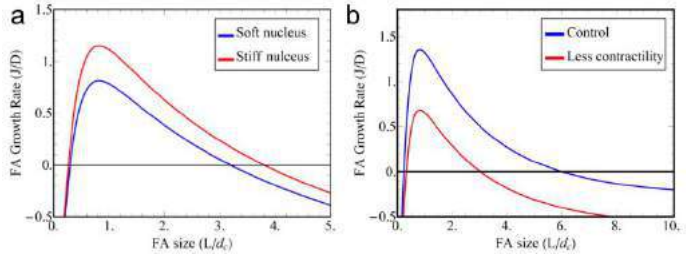

Figure 4: Effect of nuclear stiffness on FA recruitment (a). Stronger feedback effects with increased contractility result in larger stable FA and smaller FA nucleation barrier (b).

DISCUSSION

In this study, a chemo-mechanical model was developed to predict the growth of focal adhesion plaques, a process heavily influenced by the assembly of adhesion proteins as well as the stress build-up in the plaque itself (induced by actomyosin contractility). Main findings obtained here are summarized as follows:

- Two quantities of key interest, i.e. the stable size of adhesion plaques and the critical size for newly nucleated plaques to grow into mature ones, have been identified.
- A stiffer substrate/nucleus will lead to larger plaques. The prediction is consistent with experimental findings that large focal adhesions are formed on rigid surface (5).
- Interestingly, it was also found that the mechanosensitivity of the plaque is significantly influenced by contractility. Specifically, high levels of contractility will lead to bigger plaques.

We believe that the present model can also be used in studying phenomena such as cell locomotion and stretch-induced cell reorientation where contractile forces are generated inside the cell and the turnover of FAs play pivotal roles, indeed efforts along these lines are currently underway.

ACKNOWLEDGEMENTS

This work was supported by the University Research Foundation of the University of Pennsylvania and the NIH (R01 AR056624).

REFERENCES

[1] Nelson, C.M, et al., *PNAS*. 102: 11594–9, 2005.
[2] Engler, A.J, et al., *Cell*. 126: 677–89, 2006
[3] Janmey, P. A, et al., *Cell Motil. Cytoskeleton*. 66: 597–605, 2009.
[4] Oakes, P.W., et al., *J. Cell Biol*. 196: 363–74, 2012
[5]Plotnikov, S. V, et al., *Cell*. 151: 1513–1527, 2012
[6] Nicolas, A., et al., *PNAS*. 102: 12520–12525, 2004
[7] Shemesh, T., et al., *PNAS*. 102: 12383–8, 2005
[8] Chan, C., et al., *Science*. 322: 1687–1691, 2008
[9] Trappmann, B., et al., *Nat. Mater*. 11: 642–9, 2012
[10] Chancellor, T.J., et al., *Biophys. J*. 99: 115–23, 2010

Copyright 2016 The Organizing Committee for the 2016 Summer Biomechanics, Bioengineering and Biotransport Conference

SB^{3}C2016
Summer Biomechanics, Bioengineering and Biotransport Conference
June 29 –July 2, National Harbor, MD, USA
SB^{3}C2016-680

TOWARDS THE CHARACTERIZATION OF CAROTID PLAQUE TISSUE TOUGHNESS: LINKING MECHANICAL PROPERTIES TO BIOLOGICAL CONTENT

Hilary E. Barrett (1,2), Eoghan M. Cunnane (1,2), Eamon G. Kavanagh (3) and Michael T. Walsh (1,2)

(1) Centre for Applied Biomedical Engineering Research (CABER), Health Research Institute (HRI), Material Surface Science Institute (MSSI), University of Limerick, Ireland.

(2) Department of Mechanical, Aeronautical and Biomedical Engineering University of Limerick, Ireland.

(3) Department of Vascular Surgery, University Hospital Limerick, Ireland.

INTRODUCTION

Atherosclerotic plaque localized at the carotid artery bifurcation remains one of the most difficult regions of the human vasculature to treat using endovascular device based intervention. The treatment has been associated with a high rate of peri-procedural complications and the lesion has a higher predisposition to develop restenosis. Several studies have indicated that cutting balloon angioplasty (CBA) can achieve a large acute lumen gain through the use of force focused fractures controlled by longitudinal incisions in a plaque. The blade incisions created by CBA dilatation relieve the hoop stress of the plaque by disrupting and fragmenting the calcific deposits embedded in the stenosis [1] facilitating lumen expansion. However, vascular calcification is diverse in both its origin and manifestation and has material moduli ranging from 10-25GPa [2]. The ubiquitous use of CBA to treat calcified carotid plaques is partially impeded by the paucity of biomechanical data indicating the material properties of the plaque and its resistance to blade penetration.

In this regard the characterization of toughness, a mechanical parameter which determines the plaques resistance to crack propagation, can assist in quantifying the necessary cutting forces to propagate a crack in the mineralized structures. This study characterizes the toughness properties of carotid bifurcation plaque stenosis that is compounded with a number of pathological components using a custom designed guillotine-cutting tester in order to develop a longitudinal profile of the toughness properties across the length of the bifurcated vessel incorporating the three anatomical regions namely the internal, bifurcation and common carotid artery. Additionally, the fractured surfaces were structurally examined in order to better understand the unique mechanisms of plaque dissection.

METHODS

Sample Acquisition: Human carotid plaque samples were obtained from twenty-one endarterectomy patients in the University Hospital Limerick in a manner that conformed to the declaration of Helsinki and was approved by the hospital's Ethical Research Committee. Toughness values of the internal, bifurcation and common carotid artery plaque were measured. Each carotid plaque sample was segmented in 7mm intervals isolating a total of 62 rectangular sections of carotid plaque (common; CCA=17, bifurcation; BIF=21 and internal; ICA=24).

Mechanical Testing: The toughness of the carotid plaques was tested using a custom designed guillotine-cutting tester [3, 4] which characterized the mechanical work done to pass a surgical blade through the longitudinal axis of plaque measuring the resistance of the plaque to blade penetration across a unit length [4]. The applied work done (W, Joules) by the blade in cutting two new surfaces in the carotid plaque segment was calculated as follows;

$$W = \int F\, dx \tag{1}$$

The toughness (R, J/m^2) a measure of the energy provided by the system to grow the crack in the plaque segment was calculated by;

$$R = \frac{\mathrm{W_{cutting}} - \mathrm{W_{friction}}}{\mathrm{Area}} \tag{2}$$

The area was calculated using the sample thickness (t) and cutting length (L) and accounting for two new surface areas created.

Biological and Structural Characterization: The biochemical composition of each segment was acquired from Fourier transform infrared (FTIR) spectroscopy using an attenuated total reflectance probe across the fractured luminal surface at 4 separate points (total spectra 248). The analysis identified the biochemical composition of the plaques lipid, calcification and collagen which were related to toughness defining a toughness-composition relationship. Scanning electron microscopy (Hitachi SU-70) was coupled with an energy

Copyright 2016 The Organizing Committee for the 2016 Summer Biomechanics, Bioengineering and Biotransport Conference

dispersive x-ray spectroscope (EDX) and used to examine the fractured surfaces. Calcification was confirmed by identifying the presence of Ca and P.

RESULTS

Location specific toughness: The mechanical tests identified a significant difference in plaque toughness at each of the three anatomical locations examined. The bifurcation and internal regions of the carotid artery are both significantly tougher than the common carotid region ($p=0.004$ and $p=0.0005$) respectively as illustrated in figure 1A. Boxplots also indicated a considerable overlap with the toughness of common segments. All segments were subsequently divided into two toughness groups classified as low (0-364J/m^2) and high (>365J/m^2) based on reference toughness ranges of aortic tissue (250±110J/m^2) [4] and bone (365-7960J/m^2) [5] respectively. Of the internal carotid segments examined, 62.5% fell into the low toughness group while 50% of the bifurcation segments fell into the high toughness group displaying the toughest properties overall.

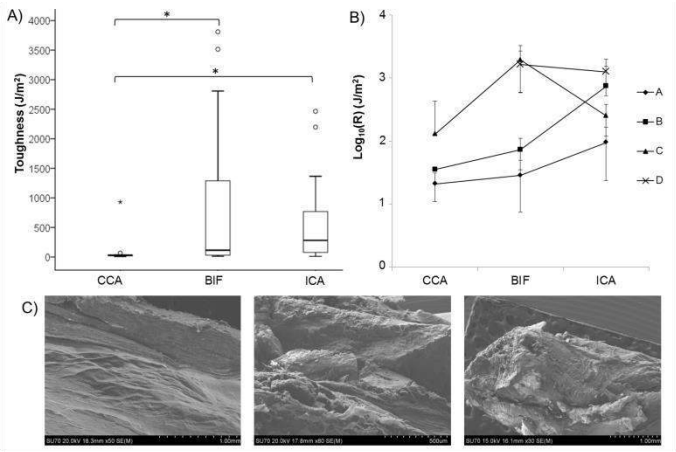

Figure 1: A) Box-plot of toughness properties for each location B) Log-linear plot of longitudinal toughness profile of each plaque type and C) corresponding electron micrographs of fractured surfaces.

Plaque specific toughness: Figure 1B illustrates the four unique longitudinal profile types of the toughness properties distributed across the length of the bifurcated vessel. Type A (38%) demonstrated low toughness properties in all three regions. Type B and C (47%) demonstrated high toughness properties in the internal or bifurcation and type D (14%) demonstrated high toughness properties in both. A non-significant difference was found at the transition between bifurcation and internal for type B ($p=0.383$) as a result of the high degree of heterogeneity contained within the stenosis. A significant toughness difference was identified at the transition between the common and bifurcation and bifurcation and internal for type C ($p<0.05$).

Structural characterization: Electron microscopy further rationalized the range of toughness values identified within the plaque segments. The failure analysis exposed the internal morphology of carotid calcification deposits and the array of different fractured calcified surfaces within the plaques cross sectional thickness indicating a number of distinct fracture mechanisms (Figure 1C). The material composition varied considerably across the length of the plaque. A clear distinction between the layers of fibrous tissue in the common segments (low toughness) was observed by the thickened fatty layer and thin outer plaque medial layer in comparison with the large calcification deposits located in the bifurcation and internal segments (high toughness).

DISCUSSION

This study identified the toughness of carotid artery plaques and distinguished the severely heterogeneous composition through determining the toughness properties at each anatomical location defining both the upper and lower scale toughness limits of necrotic plaque tissue. The mechanical tests determined the necessary cutting forces required for successful fragmentation and disruption of severely toughened plaque segments containing high calcific portions while additionally, characterizing fracture mechanisms of calcification.

A significant difference in toughness properties exists at each anatomical location of the carotid vasculature. The proximal end of the carotid artery contained distinct longitudinal sections of mismatching material properties demonstrating dissimilar toughness properties. The bifurcation segments demonstrated the toughest properties suggesting the calcification in this region to be far more advanced than the calcification development in the internal core region. Examination of the fracture sites indicates the crystallographic imperfections and the distorted crystal structure in the mineral deposits. High forces were required for propagating a crack in the calcified material. A force focused crack was propagated in the calcific deposit and complete fracture was achieved denoted by a reduction of force. A possible explanation for the variation in toughness properties of the calcified deposits could be related to the varying degree of maturity and crystallinity which evolve separately and have been shown to affect the calcification's characteristics and also have different implications on the biomechanical properties [6].

This study identifies four unique toughness profiles that incorporate the three anatomical regions of the carotid artery and are characteristic of localized calcifications. The clinical implications of the variation in toughness properties distributed along the length of the lesion are a possible explanation for the high restenotic response endured from the procedure. This advocates the need for a device that targets the specific high tough regions while conserves the lower scale soft tissue to prevent vessel perforation. It is important to distinguish the material properties between the different regions in the plaque, as stress is not uniformly distributed across the lesion during stenting and the internal region is more stressed than the common branch [7].

The experimental toughness values reported in this study are to serve as a fundamental basis for future studies to numerically simulate the concentration of the stresses observed around the cutting blade penetrating the severely toughened plaque segments and also to determine the mechanism of dilating the calcification component.

ACKNOWLEDGEMENTS

The authors would like to acknowledge that the source of funding for this work was from the Irish Research Council Grant no. (GOIPG/2013/1309) and the framework of the Irish Government's Programme for Research in Third Level Institutions Cycle 5, with the assistance of the European Regional Development Fund.

REFERENCES

[1] Karvouni, E et al., Catheter & Cardiovas Interv 54:473–481, 2001.
[2] Buffington, C et al., Cardiovasc Eng & Tech, 2014.
[3] Cunnane, E et al., Acta Biomaterialia, 2015.
[4] Chu, B et al., JMBBM, 17:126–136, 2013.
[5] Melvin, J et al., J of Bio-mech Eng, 115, 549-554, 1993.
[6] Farlay, D et al., J Bone Miner Metab, 28:433–45, 2010.
[7] Aurrichio, F et al., Med Eng & Phys, 33: 281–289, 2011.

Copyright 2016 The Organizing Committee for the 2016 Summer Biomechanics, Bioengineering and Biotransport Conference

SB^{3}C2016
Summer Biomechanics, Bioengineering and Biotransport Conference
June 29 –July 2, National Harbor, MD, USA
SB³C2016-682

DEVELOPMENT AND CHARACTERIZATION OF PROTEIN NANOPARTICLES DERIVED FROM LUNG EXTRACELLULAR MATRIX

Patrick A. Link (1), Sirish K Desai (2), Robert A. Pouliot (1), Nan Zhou (3), Da-Ren Chen (3) Rebecca L. Heise (1,4)

(1) Biomedical Engineering
Virginia Commonwealth University
Richmond, VA, USA

(2) J.R. Tucker High School
Richmond, VA, USA

(3) Mechanical and Nuclear Engineering
Virginia Commonwealth University
Richmond, VA, USA

(4) Physiology and Biophysics
Virginia Commonwealth University
Richmond, VA, USA

INTRODUCTION

Chronic Obstructive Pulmonary Disease (COPD) is the leading cause of chronic respiratory disease mortality. Morbidity rates due to COPD are rising faster than any other of the major causes of death. Pathological challenges associated with COPD increase the barriers for treatment efficacy. Major physiological changes include increased mucus production, alveolar deterioration, and airway lumen narrowing. The lungs are difficult to target via intravascular (IV) or ingestion routes due to first pass metabolism, proteolytic activity, and translocation into other organs. Inhaled nanoparticles can achieve 50% alveolar deposition, over twice the deposition compared to other inhaled therapeutics. Engineered nanoparticles designed for therapeutic drug delivery offer many enhancements. Engineering nanoparticles can achieve specific attributes such as size, surface charge, density, solubility, and hydrophobicity. Increased drug localization enables improved therapeutic effects and reduced side effects.

Numerous materials have been used to form nanoparticles each with adverse attributes. Long-term safety of polymers inhaled into the lungs is questionable [1]. Inhaled liposomes are considered safe, but undergo reduction or hydrolysis reactions causing cellular toxicity [2]. Tissue derived proteins have predictable degradation products making them the best suited for the treatment of chronic lung diseases. The objective of this study was to establish a novel drug delivery system and evaluate the cytotoxicity in vitro. This carrier is comprised of nanoparticles formed from natural lung-derived, extracellular matrix components.

METHODS

ECM Powder: Extracellular matrix powder was produced by decellurizing porcine lung tissue using aorta and tracheal perfusion of Triton-x and SDS for 3 days. After decellularization, the remaining tissue was lyophilized and cryomilled to form powder.

Electrospray deposition: The ECM powder was digested in various commonly used solvents at 5mg/ml for 4 hours with 0.5% $CaCl_2$. Solvents used include distilled water, Acetone with DMSO, ethanol with water and acetic acid. All of which are commonly used solvents for electrospray [3]. The solution was drawn into a syringe pump. Aluminum foil was placed 10cm away, perpendicular to the target. A voltage difference of 25 kV was applied between the nozzle (22 gauge, 0.403mm inner diameter) and the aluminum foil. At a flow rate of 0.2ml/hr the solvent evaporated before reaching the foil, leaving only the solid particles attached to foil. Nanoparticles were sterilized in ethanol after electrospray deposition. Lyophilization to remove the ethanol was performed.

Nanoparticle determination: Dynamic light scattering (DLS) and image analysis of SEM images were used to determine particle sizes after electrospraying. 1 mg/ml of lyophilized particulate was placed in 1 ml of filtered ultrapure water and added to a disposable cuvette (Malvern). The cuvette was placed in the Zetasizer and DLS was performed.

Hitachi SU-70 SEM images were taken and quantified using ImageJ to determine the average particle diameter [4], and to ensure the resulting ESD products met nanoparticle criteria of at least 1% of diameter sizes between the range of 1 nm to 100 nm.

Zeta Potential: Zeta potential is a measure of the surface charge of nanoparticles. Zeta potential was measured before and after electrospraying using a Zetasizer ZS90 (Malvern). 900 µl of solution was placed in a quartz cuvette (Malvern) and measured on a Zetasizer.

Cell proliferation and Cytotoxicity: The human alveolar epithelial-like cell line, A549s (ATCC) were cultured in tissue culture dishes (25,000 cells/cm^2) to achieve 80% confluence after 24 hours

Copyright 2016 The Organizing Committee for the 2016 Summer Biomechanics, Bioengineering and Biotransport Conference

with RPMI media supplemented with 10% FBS (Gibco). After 24 hours, the media was removed and replaced with nanoparticles in media. Various concentrations of sterile nanoparticles were added to media to determine cytotoxic effects of nanoparticle. Live/Dead staining (Invitrogen) and MTT metabolic assays (Roche) were used to quantify cytotoxicity and proliferation of nanoparticles.

RESULTS

Solvent selection: Acetic acid was chosen because the protein remained in the suspension for over 24 hours imaging showed the most consistent spheroid particles.

Electrospray deposition: Before acid digestion the majority of particles are about 0.3 µm, followed by 1.7 µm. After acid digestion the particle size peaks were found at 1.1 µm, 200 nm and 30 nm with the Zetasizer (Malvern).

Zeta potential: The most neutral zeta potential was found to be 2 mV in the 50% acetic acid solution with 0.5% $CaCl_2$ (Table 1). Of the solvents tested Acetic Acid retained protein in solution and had the lowest zeta potential magnitude ($p<0.05$). The addition of calcium chloride salt significantly decreased the zeta potential of the resulting nanoparticles ($p<0.05$).

Table 1. Characterization of nanoparticles after sterilization.

Electrospray solvent	DLS Measured radius of nanoparticles (nm)	Z eta Potential (mV)	St. Dev.
50% Acetic Acid (AA)	492	3.6	1.963
50% AA w/ 0.5% CaCl	124	-13.2	1.436

Nanoparticle determination: Scanning Electron Microscopy images were taken of the electrosprayed nanoparticles (Figure 1). Then using ImageJ 50 random particles from 3 different batches were measured. Average size was determined to be 277 nm (range 50-1500 nm) with 34% of measured particles smaller than 100 nm. The Zetasizer size determination was 492 nm average. Both of these ranges are sizes produced without filtering the nanoparticles after sterilization.

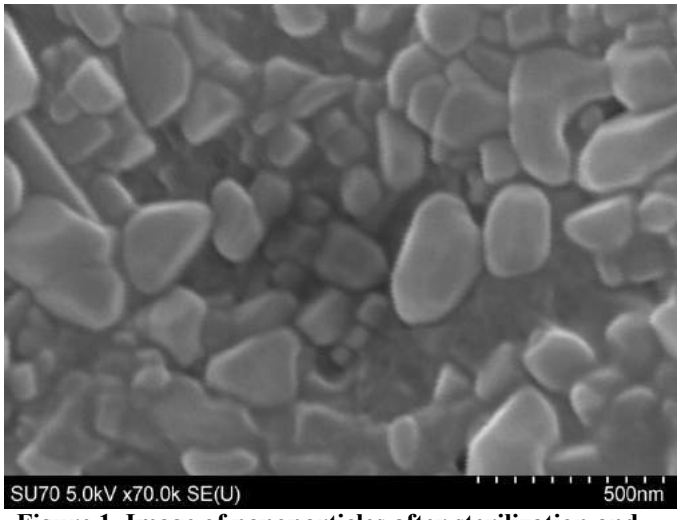

Figure 1. Image of nanoparticles after sterilization and lyophilization.

Cytotoxicity: Preliminary cytotoxicity results demonstrate increased cell proliferation with protein nanoparticle addition. A dose of 2 mg of nanoparticles added to 1 ml of growth media increases cell proliferation by almost 25% over controls according to MTT results. Live/Dead Staining shows increases in number of live cells but similar quantities of dead cells when 2 mg/ml nanoparticles are compared to control group (Figure 2).

DISCUSSION

Nanoparticles were formed through electrospray deposition of ECM components. Acid digestion resulted in a separation of components. Salt addition reduced the zeta potential, and decreased the success of electrospray deposition. Increased magnitude of zeta potential reduces particle agglomeration but increases cytotoxicity [5]. The formed particles demonstrated increased cell proliferation and metabolism compared to control groups. Hyperbranched PAMAM of equivalent size decreases proliferation by 15% in HEK293 and COS7 cells [6]. Equivalently sized chitosan particles at similar concentrations decreased A549 proliferation by 80% [7].

Future work will continue assessing solvents as well as minor protocol changes such as speed, use of antisolvents. examine stabilizer addition to improve long-term storage stability of nanoparticles. Macrophage activation and endocytosis will be investigated. Additionally, mucus penetration and and drug encapsulation will be determined.

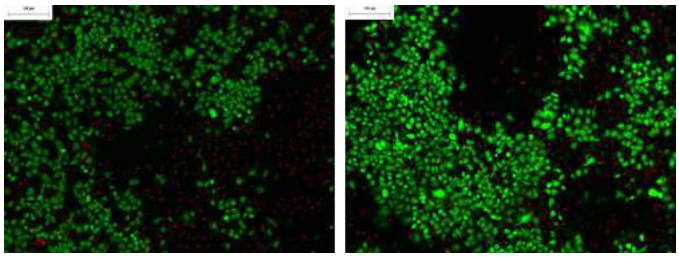

Figure 2. Image of Live (Green)/Dead(Red) staining of A549 cells after incubation. A) control cells wit no nanoparticles added. B) Cells plated with 2 mg of nanoparticle per ml of media for 48 hours. Scale bar 200 µm

ACKNOWLEDGEMENTS

Special thanks to the VCU Nanotechnology Core Characterization Facility (NCC) for SEM imaging. These investigations would not have been possible without the use of the electrosprayer and Zetasizer performed in Dr. Hu Yang's lab. Lastly, we thank Smithfield Farms for providing the porcine lung. Funding for this study was provided by the Commonwealth Health Research Board and NSF CAREER Award CMMI 1351162

REFERENCES

1. Liechty W et al., *Annu Rev Chem Biomol Eng,* 1:149-73 2010.
2. Shah, R, Lipid Nanoparticles Production, Characterization and Stability, pp. 86, 2014.
3. Whittal R, http://www.chem.ualberta.ca/~massspec/ESIsol.htm, 2009.
4. Schindelin J et al., Fiji: an open-source platform for biological-image analysis. *Nat Methods,* 9:676–82, 2012.
5. Fröhlich E et al., *Int J Mol Sci*, 15:4795–822, 2014.
6. Zhu K et al., *Int J Pharm*, 423(2):378–83, 2012.
7. Huang M et al., *Pharm Res*, 21:344–53, 2004

Copyright 2016 The Organizing Committee for the 2016 Summer Biomechanics, Bioengineering and Biotransport Conference

SB^{3}C2016
Summer Biomechanics, Bioengineering and Biotransport Conference
June 29 –July 2, National Harbor, MD, USA
SB^{3}C2016-683

FLAP MOTION AND FLOW REVERSAL VARY WITH NUMBER OF TEARS IN AN *IN VITRO* MODEL OF DESCENDING THORACIC AORTIC DISSECTION

Joav Birjiniuk (1), Lucas H. Timmins (1,2), Mark Young (3), John N. Oshinski (1,2), Ravi K. Veeraswamy (4), David N. Ku (4,5)

(1) Department of Biomedical Engineering
Georgia Institute of Technology and
Emory University School of Medicine
Atlanta, GA, USA

(2) Department of Radiology
Emory University School of Medicine
Atlanta, GA, USA

(3) Cardiac and Vascular Group
Medtronic, Inc.
Santa Rosa, CA, USA

(4) Division of Vascular Surgery,
Department of Surgery
Emory University School of Medicine
Atlanta, GA, USA

(5) George W. Woodruff School of
Mechanical Engineering
Georgia Institute of Technology
Atlanta, GA, USA

INTRODUCTION

Dissection of the descending aorta, a potentially fatal condition of the aortic wall, occurs as a tear in the intimal leads to blood flow in between medial layers. This leads to diversion of blood flow from the original, true lumen into the intra-medial space, known as the false lumen. As a result, aortic branch vessels may be compromised, leading to visceral ischemia. Patients with such complications are treated with endovascular intervention in addition to the standard medical therapy initiated in all patients presenting with aortic dissection. However, in the absence of overt complications, the evidence is less clear [1]. Endovascular intervention has not been shown to be superior to optimal medical therapy in this sizable patient population [2].

Outcomes in these patients have been linked to the presence of false lumen thrombosis [3] as well as the diameter of the descending aorta [4]. The latter is a measure of aneurysmal degeneration of the aorta, a later stage complication that prompts endovascular intervention. Previous work has demonstrated a relationship between these pathologic processes and aortic hemodynamics that can arise from flow separation, reversal, and recirculation. In particular, altered wall shear stress and shear rate may lead to thrombosis [5] and correspond to locations atherogenesis [6] and aneurysm [7]. Additionally, outcomes have been correlated with different tear configurations in the aorta [8].

Previous investigation into the fluid dynamics of aortic dissection has relied on both computational [9] and experimental [10,11] models. These studies, however assumed either rigid geometries or non-anatomic aortae, respectively. The reported experimental model possesses anatomic geometry as well as compliant vessel walls and dissection flap, which are critical to modeling the fluid mechanics of the dissected aorta [11]. We hypothesize that flap motion will decrease with increased number of reentry tears. Thus, more tears are expected to decrease flow reversal observed in both the true and false dissection lumina.

METHODS

Silicone models of aortic dissection were fabricated as previously described [12]. Model flaps were incised at the level of the flexure of the lesser curvature and at dissection exit, in order to create entry and exit tears, respectively. In addition to these primary entry and exit tears at the extents of the dissection (Figure 1A), secondary tears were introduced at 50% (Figure 1B) and 75% (Figure 1C) along the length of the dissection distal to the entry tear. These tears extended along the circumferential extent of the false lumen.

The models were connected to a flow loop consisting of medical-grade PVC tubing, which was subsequently filled with water and purged of air. Physiologic flow was developed via a custom-built positive displacement pump. Pressure was measured using a pressure transducer (Harvard Apparatus, Holliston, MA) connected to a multipurpose access (MPA) catheter advanced to the proximal ascending aorta in an antegrade fashion. A flow probe (Transonic, Ithaca, NY) was connected inline with the flow loop. Flow rates of 4 L/min were maintained at physiologic (Figure 2) and pathologic pressures. A 33 mm aortic balloon catheter (B. Braun, Bethlehem, PA) was introduced into the model and inflated to distend the false lumen.

Models were imaged in a 3 Tesla Prisma magnetic resonance imaging (MRI) scanner (Siemens, Erlangen, Germany). Anatomic images were acquired using 2D ciné sequences, whereas flow images were acquired using both 2D and 4D phase contrast magnetic resonance (PCMR) protocols. Electrocardiogram (EKG) gating was triggered using the pulsatile pump output.

Image and data analysis were performed in custom software written in Matlab (The Mathworks, Natick, MA). Qualitative analysis

Copyright 2016 The Organizing Committee for the 2016 Summer Biomechanics, Bioengineering and Biotransport Conference

of velocity profiles was performed with vector plots and color Doppler overlays of through-plane 2D PCMR images. Bulk flow rates were calculated via integration of through-plane velocity profiles over cross-sections obtained normal to the aortic wall. Luminal areas were calculated over the course of the cardiac cycle. In addition, flap displacement was measured over time. Four-dimensional PCMR data were used to visualize flows across the whole aorta.

RESULTS

PCMR-derived bulk flow rate across the luminal flow divider was conserved and matched flow rates measured inline with the flow meter. However, flow division was modulated in time as a result of dissection flap motion.

In the absence of secondary tears, the whole of the dissection flap was observed to oscillate in conjunction with the cardiac cycle. While the false lumen was distended, its cross-section varied in shape and area along the dissection. Thus, in certain locations, the false lumen was the larger of the two lumina ("false-dominant"), compressing the true lumen, whereas in other locations the contrary was true ("true-dominant"). Relative true lumen area was calculated as 55% +/- 3 at the level of the entry tear, 36% +/- 7 at the middle of the dissection, and 91% +/- 3 at the exit tear, each being significantly different from the other in pairwise comparisons ($p<0.0001$). Flow reversal was observed in certain planes within the dominant lumen (Figure 1D). This phenomenon was initiated during the systolic deceleration phase, continuing through diastole.

Dissections with secondary tears exhibited similar oscillatory behavior. However, in these models, each segment of the dissection flap was observed to move independently of the others. Each inter-flap segment was able to assume an independent conformation, such as a widely-distended (Figure 1B, middle segment), tapered (Figure 1B, lower segment), or closed false lumen (Figure 1C, lower segments).

Flow reversal was still seen in the false lumen at mid-dissection level in the case of a single secondary tear (Figure 1E). This effect was however attenuated relative to the reversal seen without secondary tears (% forward flow in diastole: 2 tears – 40%, 3 tears – 93%, 4 tears – 100%). Furthermore, flow reversal was also present in the true lumen in this situation. Alternatively, in the case of multiple secondary tears, more distal segments remained collapsed, allowing for the mid-dissection tear to act as an exit tear. In this case, all false lumen flow was forward, with flow reversal occurring in the true lumen (Figure 1F). Flow separation and reversal in all cases is observed during systolic deceleration and diastole, as the dominant lumen expands in size.

DISCUSSION

We demonstrate that the number of reentry tears has an effect on the mobility of the dissection flap, which in turn influences aortic hemodynamics in an *in vitro* model of aortic dissection. As hypothesized, dissections with increased numbers of reentry tears exhibit less flap motion, and less flow reversal, than those containing only primary entry and exit tears. These phenomena have not been reported previously in controlled investigation.

Additionally, the presence of flow reversal, as well as a possible mechanism for its cause is demonstrated. As blood flow decelerates in late systole, the dominant false lumen at a given location is observed to expand. This may be a result of increased pressure as flow velocity decreases. With deceleration and expansion, an adverse pressure gradient may be created, leading to reversal of flow in the false, expanded lumen.

These results may provide insight into the natural history of clinical disease. Sustained flap motion and flow reversal may lead to aneurysmal degeneration of the aorta, which would require endovascular intervention. Thus, patients that possess these hemodynamic effects may be selected for earlier intervention to prevent formation of aneurysm. Alternately, areas of recirculating, low shear flow may be subjected to some level of thrombosis. In this case, close followup in these patients may be necessary to determine the extent of thrombosis and the need for intervention. Future work aims to relate these phenomena to patient anatomies and hemodynamics for improved patient selection.

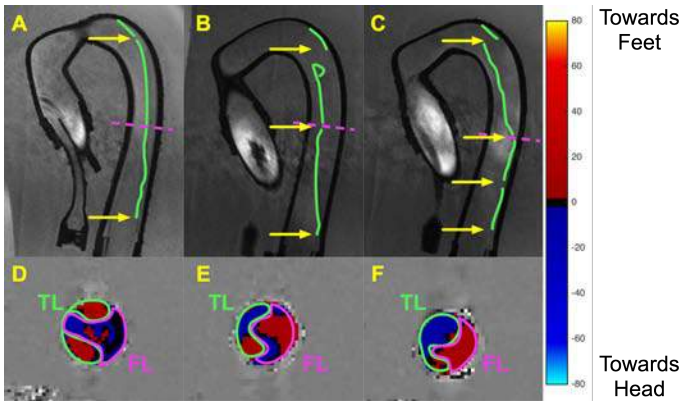

FIGURE 1. Dissection model tear locations (A,B,C) with corresponding mid-dissection color Doppler flows (D,E,F) in late diastole. Scale on right shows flow velocity and direction.

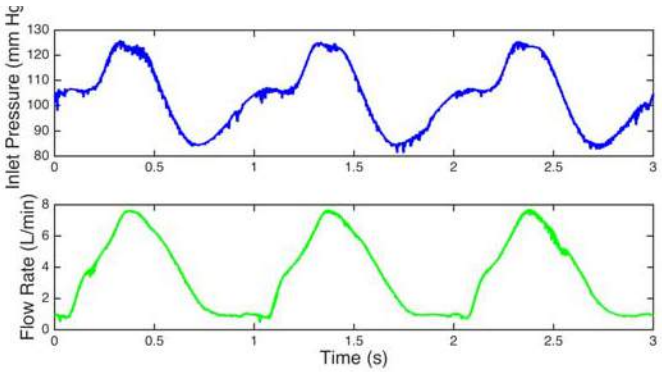

FIGURE 2. Physiologic pressure and flow meter waveforms produced by positive displacement pump.

ACKNOWLEDGEMENTS

This research was supported by a grant from Medtronic, Inc.

REFERENCES

[1] Fattori, R et al., *J Am Coll Card*, 61:1661-1678, 2013.
[2] Nienaber, CA et al., *Circulation*, 120:2519-2528, 2009.
[3] Tsai, TT et al., *New England J Med*, 357:349-359, 2007.
[4] Onitsuka, S et al., *Ann Thor Surg*, 78:1268-1273, 2004.
[5] Jackson S, *Blood*, 209:5087-5095, 2007.
[6] Moore, JE et al., *Atherosclerosis*, 110:225-240, 1995.
[7] Cecchi, E et al., *Atherosclerosis*, 214:249-256, 2011.
[8] Tolenaar, JL et al., *Ann Thor Surg*, 96: 39-42, 2013.
[9] Cheng, Z et al., *Ann Biomed Eng*, 43:177-189, 2014.
[10] Tsai, TT et al., *J Vasc Surg*, 47:844-851, 2008.
[11] Rudenick, PA, *PLOS One*, 10:e0124011.
[12] Birjiniuk, J et al., *J Surg Res*, 198:502-507, 2015.

Copyright 2016 The Organizing Committee for the 2016 Summer Biomechanics, Bioengineering and Biotransport Conference

SB^{3}C2016
Summer Biomechanics, Bioengineering and Biotransport Conference
June 29 –July 2, National Harbor, MD, USA
SB^{3}C2016-684

UTILIZING PROBLEM-BASED LEARNING TO TEACH BIOMEDICAL ENGINEERING AS A CHEMICAL ENGINEERING ELECTIVE

Victor K. Lai (1)

(1) Department of Chemical Engineering
University of Minnesota – Duluth
Duluth, MN, USA

INTRODUCTION

The chemical engineering program at the University of Minnesota – Duluth is primarily a teaching-focused program, with a total undergraduate enrollment of about 250 students. In Fall 2014, I was asked to create a new graduate-level elective class in Biomedical Engineering for the program. In that first year, with 6 students in the class, I employed largely a traditional classroom approach: lectures on anatomy and physiology, biomechanics, biomaterials and tissue engineering, and biotransport were coupled with two teaching assignments on special topics (bioinstrumentation, bioelectricity, bioimaging), where students were expected to conduct independent research on their assigned topic and teach the material to the class. Based on end-of-semester evaluations, this approach to teach this class yielded mixed results: some students found the material too difficult, and others did not enjoy the special topics assigned to them.

After attending the education workshop on problem-based learning at SB3C2015, I decided to replace the teaching assignments with two research projects, the first related to biomechanics, and the second related to tissue engineering and biotransport. With only 4 students in Fall 2015, these projects were attempted in two groups of 2 students each. These projects started after the necessary content has been covered in lectures.

METHODS

Each project was divided into three sections, and every group was required to make an oral presentation for each section. The two projects are detailed below.

(1) Biomechanics: The first project involved the study of prosthetics used by two different celebrities (Amy Purdy, Noah Galloway) in "Dancing With the Stars":

Section 1: Students researched on their assigned celebrity – why were they famous, how they lost a part of their limbs and require prosthetics, and pick a (quasi)static pose/move during one of their dances on the show.

Section 2: Based on their selected pose/move, students performed a statics analysis to determine the forces and moments exerted on the prosthetic. Student were also required to evaluate qualitatively the effects of the prosthetic on joint reaction forces, compared to a person with a normal limb.

Section 3: Students applied their knowledge of material properties and deformable body mechanics to analyze the amount of deformation (compression/elongation, deflection) on the prosthetic due to the forces and moments exerted during the pose, and accessed critically the material used to design the prosthetic.

(2) Tissue Engineering and Biotransport: This project involved the study of a bioengineered tissue from a research paper of the students' choice, and setting up a mass transfer problem to analyze the culture conditions described in the paper:

Section 1: Students picked a research paper on a bioengineered tissue of their choice and summarized the paper, emphasizing concepts taught in class (e.g., describing and characterizing the biomaterials used, identifying components of the tissue engineering triad, etc.).

Section 2: Based on the geometry of the tissue, as well as the culture media and conditions, students were required to set up a mass transfer problem analyzing the concentration profile of a certain nutrient (e.g., oxygen, glucose) through the tissue.

Section 3: Students looked up another article by a different research group on the same bioengineered tissue, and compared and contrasted the methods used to engineer and test the tissue (materials used, culture conditions, testing methods, etc.).

Copyright 2016 The Organizing Committee for the 2016 Summer Biomechanics, Bioengineering and Biotransport Conference

RESULTS

While the official end-of-year evaluations have not been made available, anecdotal information from conversations with the students suggests they enjoyed and appreciated this format of teaching. Specifically, students demonstrated the ability to apply lecture concepts to more open-ended problems:

(1) With the biomechanics problem, students applied successfully concepts from the statics and deformable body mechanics lectures to simplify their dance pose into a free-body diagram, identify correctly the forces and moments on the limb or prosthetic, and estimate the amount of deformation placed on the prosthetic during the pose. Figure 1 shows an example of the pose chosen by the students (A), and the free-body diagram (B). More importantly, they gained an appreciation of the assumptions that were made in their analysis, ranging from the use of general anthropometric data, to the geometry and homogeneity of the limb or prosthetic.

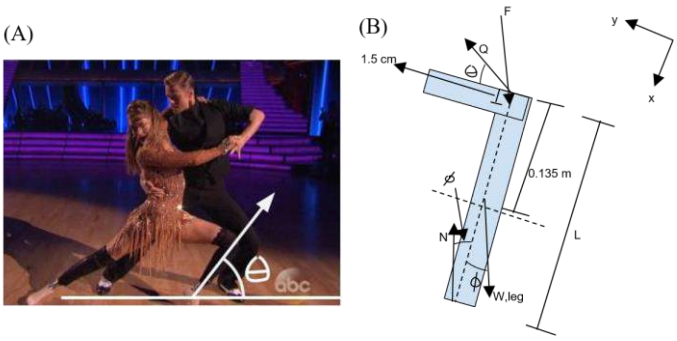

Figure 1: (A) One of the dance poses chosen by the students assigned Amy Purdy as their celebrity. (B) Free-body diagram generated by the students to analyze the forces and moments exerted on the prosthetic leg.

(2) The tissue engineering / biotransport problem was a more abstract exercise. Specific learning outcomes of this project include (a) students would be able to read and summarize a journal article related to tissue engineering, and (b) apply concepts of biotransport to set up fully (but not solve) a mass transfer problem related to the culture conditions listed in the article. This project yielded mixed results. One group was able to dig deep into their problem to set up complex differential equations with appropriate boundary conditions to govern the nutrient concentration in their bioengineered tissue, using histological images in the article to estimate dimensions of different layers. The second group, however, came up with an over-simplified solution to their problem, neglecting many assumptions regarding the geometry of their tissue, as well as the different layers present.

DISCUSSION

The primary goal of adopting problem-based learning in this class last Fall is to try out a different active-learning approach in teaching Biomedical Engineering. Previously, in using the teaching assignments to cultivate independent learning in students, I found that (a) the topics were too broad, such that students lacked direction in how much they should learn and cover in their presentations, and (b) expecting undergraduate students to read, understand, and teach on a topic that was had not been covered in class was not realistic, even though this was a graduate level class taken by juniors or seniors. This problem-based approach still achieved my desired goal of encouraging independent learning (and teaching, through presentations), but also provided a more structured framework for students to apply prior knowledge from lecture material.

One of the main difficulties of teaching an elective class in a broad field such as Biomedical Engineering is juggling breadth with depth. In my first year, I opted to go for both, going in depth in topics such as Biomechanics, Biomaterials, and Biotransport, but still "covering" other topics by making students learn the material independently and teach them to the other students. In my opinion, sacrificing breadth for depth last Fall was more ideal. While the students were made aware of these other topics that are also important to Biomedical Engineering, the above-mentioned topics covered in-depth were more in-line with the interests of my Chemical Engineering students, and were related to several other core chemical engineering classes (Properties of Engineering Materials, Heat and Mass Transfer, Fluid Dynamics, etc.). In addition, problem-based learning to apply lecture concepts enhanced significantly their understanding of the lecture material, and gave them a greater appreciation of the assumptions associated with the analysis.

ACKNOWLEDGEMENTS

Anecdotal feedback was provided by the students in this elective class in Fall 2015 (Jordan Remme, Andrew Commers, Jason Burns-Gausman, Erik Keeler). Material taken from students' work were reproduced with permission from the respective students.

REFERENCES

None.

Copyright 2016 The Organizing Committee for the 2016 Summer Biomechanics, Bioengineering and Biotransport Conference

SB^{3}C2016
Summer Biomechanics, Bioengineering and Biotransport Conference
June 29 –July 2, National Harbor, MD, USA
SB^{3}C2016-685

FOOTWEAR AFFECTS MUSCLE ACTIVITY DURING RAMP WALKING

Feng Wei (1,2,3), Andrew J. Crechiolo (1,3), Roger C. Haut (1,2,3)

(1) Orthopaedic Biomechanics Laboratories
Michigan State University
East Lansing, MI, USA

(2) Department of Radiology
Michigan State University
East Lansing, MI, USA

(3) Department of Mechanical Engineering
Michigan State University
East Lansing, MI, USA

INTRODUCTION

Habitual footwear use has been reported to influence foot structure with an acute exposure being shown to alter foot position and mechanics [1]. The foot is highly specialized thus these changes in structure and position could influence functionality [2,3]. Numerous studies have been conducted to investigate the effects of footwear on gait, specifically focusing on assessment of kinematics, kinetics, and muscle activity between walking barefoot and in common footwear. Few studies, however, have yet investigated how footwear affects gait and foot/leg functionality while walking on a ramp.

The random nature of outdoor terrain makes controlled studies of outdoor footwear biomechanics extremely challenging. As a result, a solid, general understanding of such involvement in foot biomechanics does not exist. The purpose of the current study, which was our first step in an attempt to simulate various outdoor terrains in a laboratory setting, was to build an instrumented ramp with adjustable incline/decline angles and utilize it to investigate leg muscle activity during ramp walking in various footwear designs and barefoot condition. The hypothesis was that differences in muscle activity due to various footwear and barefoot conditions, even subtle changes that would not normally be measured during level walking, could be detected while walking on a ramp.

METHODS

Three male subjects were tested with ages ranging from 21 to 36, mean height of 173.5 ± 5.0 cm, and mean weight of 70.5 ± 6.8 kg. Prior to the tests written, informed consent was received from each subject, and approval of the study was obtained from the Michigan State University Institutional Review Board. Subjects were interviewed to ensure they were healthy with no known pathology or major lower body injuries within the past ten years.

A 16 feet long, 0-20 degree adjustable ramp was developed and used for level and angled walking trials. An AMTI force plate (Advanced Mechanical Technology Inc., Watertown, MA, USA) was embedded in the center of the ramp walkway, flush with the walking surface. The force plate data were not shown in the current abstract. A textured paint was applied to the surface of the ramp and force plate to increase traction and create a non-slip condition that was required at augmented angles. A platform which remained level at each angle was attached to the top of the ramp, and railings were added to the platform and sides of the walkway for safety purposes.

Figure 1: From left to right: Chameleon Low, Chameleon Medium, and Mattertal High.

Three pairs of Merrell footwear were used in the study (Figure 1). Surface electromyography (EMG) data were collected at a sampling rate of 2000 Hz from each subject performing three walking trials while wearing these footwear designs and in the barefoot condition at five different ramp angles, i.e. 0, ±10, and ±20 degrees (zero represents level, and plus and minus represent incline and decline, respectively). EMG sensors were attached to four leg muscles on the

Copyright 2016 The Organizing Committee for the 2016 Summer Biomechanics, Bioengineering and Biotransport Conference

right limb, i.e. the tibialis anterior (TA), the medial gastrocnemius (MG), the rectus femoris (RF), and the biceps femoris (BF).

After a short practice walking on the ramp and prior to data collection, maximal voluntary contraction (MVC) was performed for each of the four leg muscles, according to Preston et al. [4], while the corresponding EMG data were collected to normalize EMG data collected while walking. During a single trial of ramp walking five or six steps were recorded from each subject and data from the third, fourth, and fifth steps were used in the post analyses. Raw EMG data were bandpass-filtered (20-500 Hz), rectified, and then low-pass-filtered with a cut-off frequency of 6 Hz to obtain a linear envelope for each muscle. Mean peak amplitude, averaged across three steps and three trials for each subject and reported in % of MVC, was used as a measure of muscle activity. Data from the three subjects were then averaged and compared between the barefoot condition and while wearing the three footwear designs between level and angled walking.

Two-way ANOVA and Student-Newman-Keuls post hoc tests were used to determine differences in EMG measures between the barefoot and various footwear conditions (factor one) for different ramp angles (factor two). Significance was indicated for $p < 0.05$.

RESULTS

In the MG, RF, and BF muscles significant differences were observed between level walking (0 degree) and angled walking ($p < 0.001$), with greater muscle activity being generated during angled walking (Figure 2). For the TA muscle there were significant differences between level walking and 10 and 20 degrees of incline walking ($p < 0.001$), but not between level and decline walking.

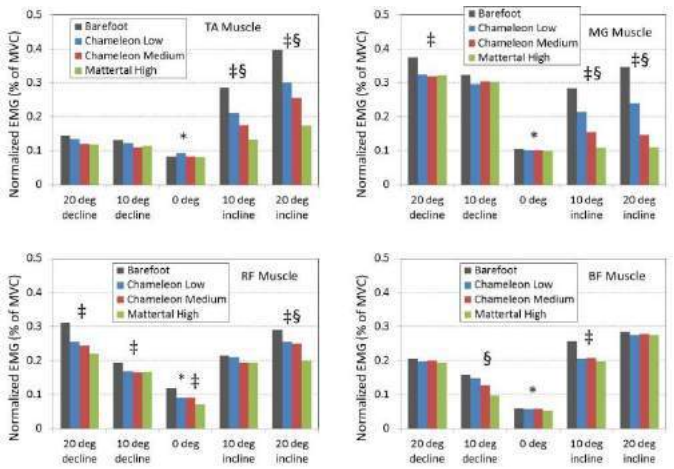

Figure 2: Normalized muscle activity (mean peak amplitude) in different leg muscles during ramp walking with barefoot and in various footwear designs. * indicates significant differences between level and angled walking. ‡ indicates significant differences between barefoot and footwear conditions. § indicates significant differences between footwear designs. For clarity, standard deviations across subjects were not shown in these plots.

In general, walking barefoot generated greater leg muscle activity than walking in footwear (Figure 2). This fact was especially true during incline walking versus decline walking. Specifically, during 10 and 20 degrees of incline walking significantly greater muscle activity was observed walking barefoot than in footwear for the TA and MG muscles ($p < 0.001$). The MG muscle also showed greater activity during 20 degree of decline walking ($p < 0.001$). For the RF muscle statistically significant difference between barefoot and footwear walking was found during 20 degree of incline walking ($p = 0.021$), level walking ($p = 0.001$), 10 degree of decline walking ($p = 0.030$), and 20 degree of decline walking ($p < 0.001$). For the BF muscle, however, significant difference between barefoot and footwear walking was only observed during 10 degree of incline walking ($p < 0.001$).

In addition, walking in different footwear designs generated significantly different muscle activity, with a trend for the Mattertal High to be the lowest, especially during incline walking and in lower leg muscles (Figure 2). Walking in the Chameleon Low generated the highest muscle activity while walking in the Mattertal High generated the lowest activity in the TA muscle for 10 ($p = 0.037$) and 20 ($p = 0.018$) degrees of incline walking and in the MG muscle for 10 ($p = 0.025$) and 20 ($p = 0.020$) degrees of incline walking. For the RF muscle different footwear designs generated statistically different muscle activity during 20 degree of incline walking ($p = 0.041$), while for the BF muscle footwear differences led to variations in muscle activity during 10 degree of decline walking ($p = 0.045$).

DISCUSSION

The current study, even with a limited number of subjects, was able to show significant differences in leg muscle activity between barefoot and footwear walking, and between walking in various footwear designs. As a result it was able to support the hypothesis that footwear effects on muscles, even subtle influences that would not normally be measured during level walking, can be detected while walking on a ramp.

Several studies in the literature use EMG measures to determine differences in muscle activity patterns while walking shod and barefoot, partially supporting the results of the current study. Scott et al. [5] demonstrate that the TA displays significantly reduced mean peak amplitudes from barefoot to shoes ($p < 0.001$), but the MG shows no difference. In addition to findings of differences between barefoot and shoes, our study may serve as a significant contribution to the literature by exposing the important role that ramp walking may play in amplifying the effects of footwear on leg muscle activity during walking.

The results of the current study may also suggest that footwear with higher and potentially stiffer uppers, such as the Mattertal High boots used in the current study, may have provided more ankle/lower leg support so as to require less muscle activity during angled walking. With more subjects being recruited into this ongoing study, more and greater effects of footwear are expected. The current study represents our first step in an attempt to simulate outdoor environments in a lab setting, potentially contributing to a scientific base on which new footwear can be designed for various terrains that might help limit muscle overuse-caused conditions, such as fatigue.

ACKNOWLEDGEMENTS

The authors would like to thank Mr. Clifford Beckett and Mr. Jerrod Braman for their technical support in this study. The authors would also like to thank Wolverine WorldWide, Inc. for a financial gift to help support our laboratories.

REFERENCES

[1] Franklin, S et al., *Gait & Posture*, 42:230-239, 2015.
[2] Ramanathan, AK et al., *Foot Ankle Surg*, 17:218-223, 2011.
[3] Robbins, S et al., *Age Ageing*, 24:67-72, 1995.
[4] Preston, D et al., *EMG & Neuromuscular Disord*, 3rd Ed., Elsevier, p169-198, 2012.
[5] Scott, L et al., *J Electromyogr Kinesiol*, 22:1010-1016, 2012.

Copyright 2016 The Organizing Committee for the 2016 Summer Biomechanics, Bioengineering and Biotransport Conference

SB³C2016
Summer Biomechanics, Bioengineering and Biotransport Conference
June 29 –July 2, National Harbor, MD, USA
SB³C2016-686

VALVE INTERSTITIAL CELL CONTRACTILE STRENGTH AND METABOLIC STATE ARE DEPENDENT ON ITS SHAPE

Ngoc T. Lam (1), Timothy J. Muldoon (2)
Narasimhan Rajaram (2) and Kartik Balachandran (2)

(1) Cell and Molecular Biology Program,
University of Arkansas, Fayetteville AR, USA

(2) Department of Biomedical Engineering,
University of Arkansas, Fayetteville AR, USA

INTRODUCTION

Abnormal hemodynamics experienced by the heart valve cells are associated with valvulopathy. This altered mechanical environment also leads to modulation in valve cellular shape and architecture. Significant prior work has focused on t he role of the mechanical environment in potentiating cellular alterations and subsequent progression toward disease.[1-3] However, the role of cellular shape and architecture in regulating or predicting the overall balance between health and disease in the context of the valve is not well understood.

We hypothesized that by engineering the shape of single VICs to acquire the AR of cells seen in normal and pathological conditions, we could induce changes in cell architecture, subsequently potentiating acute alterations in cell function, specifically cell contractility and metabolism. Our objectives include 1) quantify and correlate the cell cytoskeletal and nuclear architecture with contractility measured via traction force microscopy 2) assess cell metabolism by us ing endogenous FAD/NADH metabolic redox ratio imaging.

METHODS

1. Microcontact printing and cell culture

50μg/mL Fibronectin was put onto the PDMS stamps with 3 different aspect ratios (AR) features and incubated for 1 hour at room temperature. 3 ARs were 1:3, 1:5 and 1:7 corresponded to 3 different cellular states: non stretched, normal stretched and elevated stretched.[4] The stamp was then placed in contact with PDMS-coated coverslips for 5 minutes, thereby transferring the pattern. VICs were seeded at 1000 cells/cm^2 and cultured at 37°C, 5% CO_2.

2. Fluorescent staining of actin and cell nucleus

After 48 hour s of culture, cells were fixed with 4% paraformaldehyde (PFA) and stained for F-actin using Alexa Fluor 488 phalloidin and for nuclei using 25μg/mL 4',6-diamidino-2-phenylindole (DAPI) for 1 h our at room temperature. Samples were then mounted onto a glass slide, allowed to dry overnight and imaged using a custom-built resonant-scanning multiphoton microscopy. Actin alignment was quantified using a custom-written MATLAB script. Nuclear shape was analyzed by fitting an ellipse to each nucleus using ImageJ. Nuclear chromatin density was calculated using images of the nucleus at the mid-point of each cell.

3. Traction force microscopy

VICs were seeded on 9kPa polyacrylamide gels for traction force microscopy (TFM) using methods published by others.[5] Fluorescent images of the beads immediately beneath the patterned cells were recorded using our two-photon microscope with a 960nm excitation wavelength and a 525nm/45nm emission filter. The change in the position of the fluorescent beads was quantified using a MATLAB script. Cell contractility was quantified by VIC response to 50nM ET-1 (Sigma) after 5 minutes. VIC basal tone was quantified by VIC response to a 100μM saturating dose of the rho-activated kinase inhibitor and vasodilator HA-1077 after 5 minutes.

4. Two-photon redox imaging

VIC samples were placed in heated imaging chambers and imaged using the same two-photon microscopy system described earlier. The laser excitation source was tuned to 755nm (NADH fluorescence) or 860nm (FAD fluorescence) and images were acquired via a 466nm/40nm (NADH) or 525nm/45nm (FAD) bandpass filters, respectively. Images were analyzed using a cu stom MATLAB script and redox ratio was calculated using the following equation on a per pixel basis.

RESULTS

1. Actin and nuclear architecture and orientation varied as a function of cellular shape

Phalloidin staining of F-actin, showed that the filaments became more prominent and aligned along the longitudinal direction of the cell as AR increased (Fig. 1A). Nuclear staining using DAPI revealed increased nuclear elongation as cell AR increased (Fig. 1B). Quantification of actin alignment using a previously developed technique revealed actin alignment to be statistically higher ($p<0.05$) at a stretch ratio of 1:7 compared to 1:5 and 1:3 (Fig. 1C) Quantification of the nuclear eccentricity from the DAPI stains indeed did indicate significantly increasing eccentricity increased with increasing cellular AR (Fig. 1D). The nucleus did not elongate to the same extent as the cell, probably due its higher mechanical rigidity. Analysis of chromatin density from the DAPI stains revealed significantly higher intensity in the 1:5 AR sample compared to 1:3 or 1:7 AR samples (Fig. 1E). There was no statistical difference in nuclear area at different ARs (Fig. 1F).

Copyright 2016 The Organizing Committee for the 2016 Summer Biomechanics, Bioengineering and Biotransport Conference

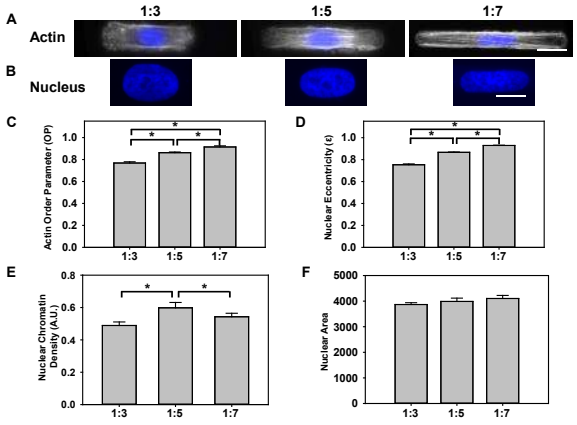

Figure 1: Actin orientation and nuclear morphology analysis of single cells

2. Elongated VICs generated greater contractile traction

VIC contractile strength, as computed by the traction stress applied by the cell on i ts substrate due to ET-1, significantly increased with increasing cellular elongation (Fig. 2A, C). Basal tone, as quantified from the response to HA-1077, was low at 1:3 AR and significantly higher at 1:5 AR (Fig. 2B, D). However there was no s ignificant difference in basal tone between 1:5 and 1:7 ARs.'

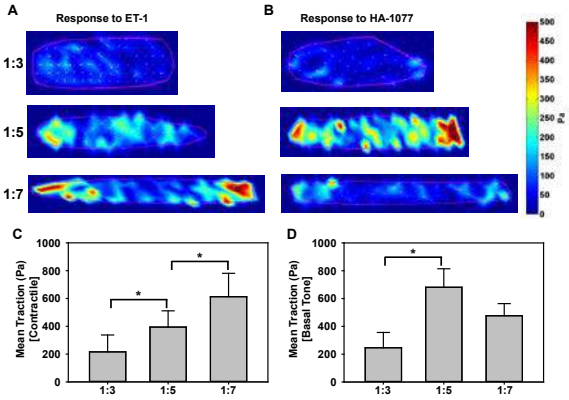

Figure 2: Traction force microscopy data

3. Elongated VICs exhibited reduced FAD/NADH redox ratio

We asked if the ratio of FAD to NADH fluorescence, termed the metabolic redox ratio, was altered as a function of cellular AR elongation. Our results show that as cellular AR increased, there was a significant increase in NADH intensity (Fig. 3A,B). FAD intensity also increased with increasing cellular AR, but there were only significant differences between the 1:3 and 1:7 AR (Fig. 3B). The above resulted in overall decrease in redox ratio (Fig. 3C). A previous study reported that a decrease in redox ratio was inversely proportional to cellular metabolic activity.[6]

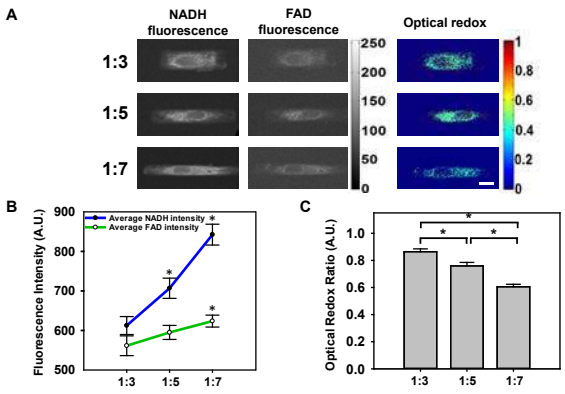

Figure 3: Redox imaging of single cells

DISCUSSION

We demonstrate the strong correlation between VIC shape and its contractile and metabolic function using single cell VIC model. VIC shape change could be thus seen as an indication of potential changes in the cell activity and vice versa. We also proposed the possibility of using redox ratio as one of the tools for early detection pathological state of VICs.

ACKNOWLEDGEMENTS

We acknowledge financial support from the Arkansas Biosciences Institute Grant 000943, and American Heart Association Predoctoral Fellowship 15PRE25710370 (NTL).

REFERENCES

[1] K. Balachandran, *et al.*, "Elevated cyclic stretch induces aortic valve calcification in a b one morphogenic protein-dependent manner," *Am J Pathol,* vol. 177, pp. 49-57, Jul 2010.

[2] W. D. Merryman, *et al.*, "Correlation between heart valve interstitial cell stiffness and transvalvular pressure: implications for collagen biosynthesis," *American journal of physiology Heart and circulatory physiology,* vol. 290, pp. H224-31, 2006.

[3] C. Y. Yip, *et al.*, "Calcification by valve interstitial cells is regulated by the stiffness of the extracellular matrix."

[4] M. S. Sacks, *et al.*, "On the biomechanics of heart valve function," *Journal of biomechanics,* vol. 42, pp. 1804-24, 2009.

[5] M. Versaevel, *et al.*, "Spatial coordination between cell and nuclear shape within micropatterned endothelial cells," *Nature communications,* vol. 3, p. 671, 2012.

[6] M. Skala and N. Ramanujam, "Multiphoton redox ratio imaging for metabolic monitoring in vivo," *Methods in molecular biology (Clifton, N J),* vol. 594, pp. 155-62, 2010.

Copyright 2016 The Organizing Committee for the 2016 Summer Biomechanics, Bioengineering and Biotransport Conference

SB^{3}C2016
Summer Biomechanics, Bioengineering and Biotransport Conference
June 29 –July 2, National Harbor, MD, USA
SB^{3}C2016-687

MAGNETIC RESONANCE ELASTOGRAPHY OF WHITE MATTER BRAIN TISSUE *EX-VIVO*

John L. Schmidt (1), Dennis J. Tweten (1), Andrew A. Badachhape (2), Ruth J. Okamoto (1), Joel R. Garbow (3), Philip V. Bayly (1,2)

(1) Mechanical Engineering and Materials Science
Washington University
St. Louis, MO, USA

(2) Biomedical Engineering
Washington University
St. Louis, MO, USA

(3) Biomedical Magnetic Resonance Laboratory, Department of Radiology
Washington University
St. Louis, MO, USA

INTRODUCTION

Understanding mechanical properties of brain tissue is essential to the understanding of traumatic brain injury (TBI). Researchers have studied the mechanical properties of soft tissues, both *in vivo* and *ex vivo*, using magnetic resonance elastography (MRE) [1], ultrasound elastography [2] and direct tests [3,4]. Brain tissue has been studied *ex vivo* using ultrasound elastography [5], MRE and dynamic shear testing (DST) [6], and *in vivo* using MRE [7,8,9]. However, estimates of brain shear modulus *in vivo* by MRE are higher than estimates from DST *ex vivo*. It is not clear how much of these differences are due to methodology (MRE vs DST), the frequencies studied in each test, or to true differences between the properties of live and dead tissue. MRE studies of brain tissue *ex vivo* are needed for direct comparison to *ex vivo* DST and *in vivo* MRE. Directional differences in stiffness are also important and may be detected by MRE [1]. The aim of this study is to improve the understanding of brain material properties as well as the relationship between MRE and direct tests of brain tissue.

METHODS

Brains were obtained from two pigs (13 weeks; 38.5kg, 44.5 kg). In each brain, a disk-shaped sample (48 mm dia; ~8 mm thick) of mainly white matter (WM) was dissected from the corpus callosum and surrounding areas (Fig. 1(a)). Samples were embedded in food grade gelatin (Knox, 4% wgt/vol in 50% pre-buffered saline / 50% glycerol solution) within a 48mm ID cylinder. A 3-mm diameter Delrin rod provided axial (z) excitation at 200 and 300 Hz, leading to shear waves with radial propagation direction ($\boldsymbol{n} \approx \boldsymbol{e_R}$, Figure 1b). To confirm axon orientation in white matter, diffusion tensor imaging (DTI) was performed (30 directions, b=2000 s/mm^2). Time from animal sacrifice to DTI/MRE experiment was ~5.5 and 7.5 hours for samples #1 and #2.

To estimate material properties, shear wave images were analyzed using 3D local frequency estimation (LFE) [10]. In uniform media, shear modulus may be estimated directly from wavelength. Since the sample is heterogeneous, MRE results were compared to finite element simulations of the experiment to estimate shear modulus. A finite element (COMSOL^{TM} Multiphysics 5.1) model [11] was created of an 8 mm layer of brain tissue (shear modulus μ, loss factor η, density ρ) between two 20 mm gelatin layers (μ=1000 Pa, η=0.1, ρ=1000 kg/m^3). The boundary conditions (BCs) are: 20 μm axial harmonic excitation at 200 Hz on the inner radius (1.5 mm); 2.5 μm axial excitation at 200 Hz on the outer radius (24 mm); and free top and bottom faces (Fig. 2). A quarter wedge was simulated with symmetrical BCs on the *xz* and *yz* planes; the full field size of 50x50x48 mm^3 was created by interpolation.

RESULTS

Figure 1 panels (c-e, d-f) highlight the difference in both wavelength and dissipation between *ex vivo* brain tissue and gelatin. Average wavelengths were longer in brain tissue than in gelatin (Figure 3(a,c,d)). Shear waves were found to dissipate at a much greater rate within brain tissue when compared to gelatin. Shear wave fronts emanating from the center of the sample were found to be slightly elliptical in Sample #1 but similar elliptical behavior was not found in Sample #2. Figure 3c shows the wavelengths found, by slice, for Sample #1. Slices with predominantly *ex vivo* brain tissue and gelatin are highlighted. Figure 3d shows wavelengths found, by slice, for the simulation shown in Fig. 2. Radially propagating wave fronts were fit to ellipses, and the ratio of the major semi-axes and minor semi-axes were found for the different materials (Fig. 3b).

Copyright 2016 The Organizing Committee for the 2016 Summer Biomechanics, Bioengineering and Biotransport Conference

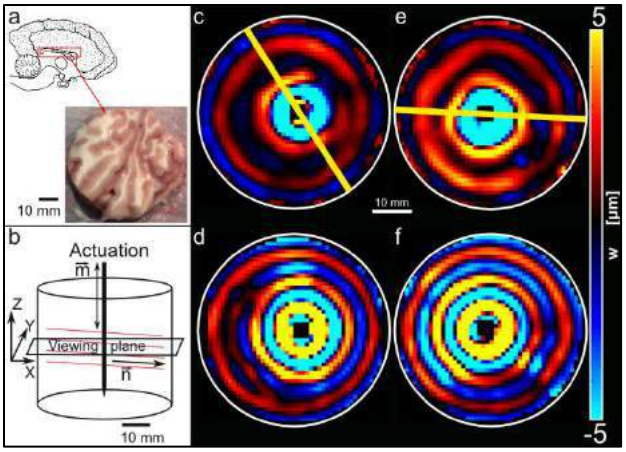

Figure 1: (a) Representative section of porcine brain including corpus callosum. (b) Schematic of MRE experiment with axial excitation. (c-f) Wave propagation in axially-excited specimens. Yellow line represents anterior/posterior orientation. (c) Sample #1 (200 Hz actuation), showing a slice containing brain tissue. (d) Sample #1 (200 Hz actuation), in a slice containing gelatin. (e) Sample #2 (200 Hz actuation), in a slice containing brain tissue. (f) Sample #2 (200 Hz actuation), in a slice containing gelatin.

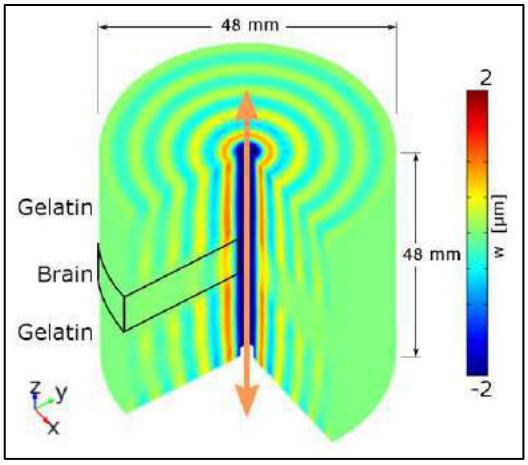

Figure 2: Finite element simulation model of an 8mm stiff layer ("brain", shear modulus μ = 2.5 kPa, loss factor η=0.5, and density ρ=1000 kg/m^3) sandwiched between two large (20 mm) soft layers ("gelatin", μ = 1.0 kPa). The center of the cylinder is excited in the z-direction producing shear waves in the xy plane.

DISCUSSION

Preliminary MRE results are consistent with white matter in the brain being stiffer (μ ~ 2.5 kPa) and more dissipative (η~0.5) at 200 Hz than surrounding gelatin. Slightly elliptical wavefronts suggest mild anisotropy. For comparison, a semi-axis ratio significantly greater than 1 was previously found in other transversely isotropic tissues [1].

Limitations of this study currently include the time from sacrifice to experiment and the composition of the surrounding gelatin. Current inversion and analysis methods must be adapted for thin tissue samples of non-uniform thickness and composition. The current comparison method with FE models serves to obtain rough estimates; however, automated methods are needed. The current FE model does not account for anisotropy due to axonal fibers, the difference between gray and white matter, or slip between tissue and gelatin. Reducing the shear stiffness of the surrounding gelatin may reduce its influence on shear waves in the brain tissue. While axonal orientation within the white matter may affect wave propagation, as in studies of other fibrous soft biological tissue [1], the fiber orientation within these brain tissue samples was not as consistent as the orientation of samples used in prior studies (aligned fibrin gel or ex vivo turkey breast). This heterogeneity complicates the interpretation of these wavefronts.

This present study provides new data on MRE of *ex vivo* white matter/brain tissue. Clear differences in shear wave wavelength and dissipative properties were found between slices containing predominantly brain tissue and gelatin. Future work will focus on developing automated analysis methods for thin, heterogeneous embedded samples and interpreting shear wave data with respect to the geometry and fiber directions in the sample. This study should advance the understanding of brain material properties *in vivo* and *ex vivo* as well as the relationship between MRE and direct tests of brain tissue *ex vivo*.

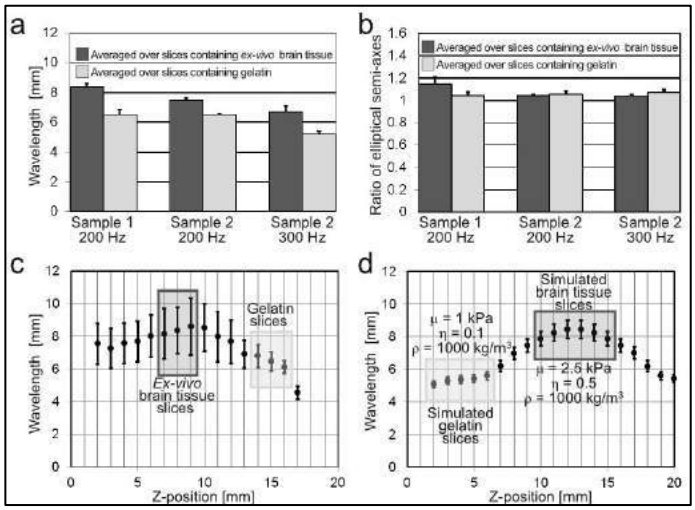

Figure 3: (a) Wavelength of shear waves within slices containing ex vivo brain tissue (dark bars) compared with slices containing gelatin (light bars). (b) Ratio of elliptical fit axes for slices containing ex vivo brain tissue (dark bars) compared to slices containing gelatin (light bars). (c-d) Wavelength found within experimental (c) and simulated (d, "thin" tissue shear modulus, μ = 2.5 kPa; "gelatin" shear modulus, μ = 1.0 kPa) setups. Error bars represent standard deviation of wavelength estimation within the z-position/slice.

ACKNOWLEDGEMENTS

Support from NIH grant NS055951 (PVB) and NSF grant CMMI-1332433 (PVB) is gratefully acknowledged.

REFERENCES

[1] Schmidt, JL et al., *Proc. SB3C*, 244-245, 2015.
[2] Wang, M et al., *IEEE Trans. Med. Imaging*, 32:1671-1684, 2013
[3] Feng, Y et al., *JMBBM*, 23:117-132, 2013.
[4] Kaster, T et al., *J. Biomech*, 44:1158-1163, 2011
[5] Jiang, Y et al., *Biomech Model Mechanobiol*, 14:1119-1128, 2015
[6] Vappou, J et al., *Magn. Reson. Mater. Phy*, 20:273-278, 2007
[7] Clayton, EH et al., *J. R. Soc. Interface*, 9:2899-2910, 2012
[8] Green, MA et al., *NMR Biomed*, 21:755-764, 2008
[9] Johnson, CJ et al., *Magn. Reson. Med*, 70:404-412, 2013
[10] Knutsson, H et al., *Proc. Intl. Conf. Imag. Proces*, 1:36-40, 1994
[11] Tweten, DJ et al., *J. Biomech*, 48:4002-4009, 2015

Copyright 2016 The Organizing Committee for the 2016 Summer Biomechanics, Bioengineering and Biotransport Conference

SB³C2016
Summer Biomechanics, Bioengineering and Biotransport Conference
June 29 –July 2, National Harbor, MD, USA
SB³C2016-688

A COURSE IN "MAKER ACTIVITIES" FOR A MASTER OF ENGINEERING IN DESIGN AND COMMERCIALIZATION

William B. Kirkland (1), Ophelia Johnson (2), Alan W. Eberhardt (2)

(1) Department of Mechanical Engineering
University of Alabama at Birmingham
Birmingham, Alabama, USA

(2) Department of Biomedical Engineering
University of Alabama at Birmingham
Birmingham, Alabama, USA

INTRODUCTION

According to the Strategic Plan of 2012-2016 [1], the National Institute for Biomedical Imaging and Bioengineering (NIBIB) supports a global shift to adopt an interdisciplinary approach to STEM education that is attentive to the practical value of new knowledge with a focus on innovative technologies. To ensure America's position as a world leader in the education of engineering talent, curricula are needed that teach students how to apply their knowledge using hands-on approaches. There is growing recognition of the potential for the "maker movement" to transform how and what people learn in STEM disciplines. According to President Obama and the Educate to Innovate campaign, makers "see the promise of being the makers of things, and not just the consumers of things" [2].

The Master of Engineering (MEng) in Design and Commercialization program at the University of Alabama at Birmingham (UAB) was designed to support the principles of hands-on learning in interdisciplinary teams and innovative environments. Teams comprised of engineering and business graduate students engage in hands-on design and prototyping of Innovation-Commercialization (IC) projects that take promising new ideas through the R&D process to create marketable products. This year's team has adopted projects with clients and faculty mentors from UAB Hospital and Children's Hospital of Alabama, among others. These partners, as well as participating local companies, share clinical, technological and business know-how with the students as the projects develop, and provide for experiential learning opportunities such as internships.

The curriculum for engineering students in the MEng consists of 24 credit hours in engineering and 12 credit hours in the MBA program, which earn students the MEng degree as well as a Graduate Certificate in Technology Commercialization and Entrepreneurship from the UAB Collat School of Business. The course sequence was coordinated to parallel the IC project development. The MEng students join with MBA students to form teams in the fall business course, MBA 681 Idea to IPO. Concurrent enrollment in the year-long MBA 691 course, i2i Entrepreneur Accelerator Independent Study, provides mentoring for commercialization that will culminate with students pitching their start-up companies at the Alabama Launchpad business plan competition, with the opportunity of gaining financial support to incubate a new business in the Innovation Depot.

The present manuscript documents the development of a new course, EGR 693 Innovation-Commercialization Project I, which focuses on hands-on training of "maker activities," including computer aided drawing (CAD), machining, and electronics, which allow students to build their competency in prototyping. The goal of the course is to provide students with the hands-on skills necessary for the development of innovative solutions to real-world problems, with the potential for commercialization.

METHODS

In EGR 693, students first review Computer Aided Drawing (CAD), a natural precursor to fabrication, using Creo software (PTC, Needham, MA). Students are tasked to model a beam with a through-hole in the shape of any suit from a deck of cards (heart, spade, diamond, or club). Students are then required to make their "beam with a hole" by hand-machining. The beam example extends to Computer Numeric Control (CNC) machining, where they are introduced to G-code and CNC mills. Next, they learn to 3D print their beams, with lectures on printing materials and hobbyist machines versus professional industrial printers. At the conclusion of the beam example, students are able to

Copyright 2016 The Organizing Committee for the 2016 Summer Biomechanics, Bioengineering and Biotransport Conference

compare each machining method and determine which method(s) would best suit their needs when prototyping.

In addition, the students explore contemporary electronics through hands-on activities using breadboards in conjunction with Arduino (Arduino, LLC, Cambridge, MA) and Raspberry Pi (Adafruit, New York, NY). Students are provided with kits to work on coding examples during class and to encourage further investigations outside of class. Finally, students receive instruction and lab experience on soldering printed circuit boards (PCBs). The end result of this course are students who have gained an invaluable set of engineering skills and capabilities for prototyping and applying advanced methods when developing complex projects.

The primary learning outcome for the EGR 693 course is that students will demonstrate proficiency in the maker skills to which they were introduced. To examine the levels of student proficiency, an assessment survey was given to each student to score their perceived levels of competency in each maker activity reviewed.

RESULTS

All students in the program (n = 11) successfully completed each module related to the "beam with a hole" exercise, which included CAD drawings, hand-machining, 3D printing and CNC machining (Fig. 1). Approximately 80% of students in the MEng program had previous experience with using the Creo CAD software; thus, they were able to quickly demonstrate proficiency in this activity. During the hand-machining activity, students experienced the limitations of hand-machining through difficulties creating profiles of card suits, which contain several sharp internal corners. Students found that CNC and 3D printing yielded higher levels of precision in comparison to the hand-machined parts. Students also noted the increased efficiency in the time, cost and labor required to machine parts using CNC machines and 3D printers.

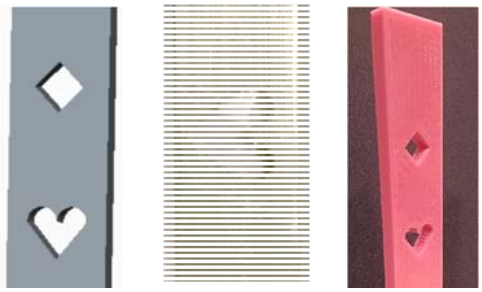

Figure 1: Example CAD drawings, hand machined, and 3D printed versions of the "beam with a hole."

Using a Sparkfun RedBoard and the Arduino IDE software, students programmed a variety of codes with circuits they built to apply integration techniques. Figure 2 illustrates an example completed by a student in which she integrated breadboards, programming and the microcontroller in order to control a multi-LED circuit.

The results of the student surveys indicate substantial increases in the perceived levels of competency among the various maker activities upon completion of the course (Fig. 3). In addition, the students' knowledge, retention, and personal investment have been seen to improve based on increased interest outside the classroom. For example, some students have invested in 3D printing for personal work outside of the course requirements. Similarly the same involvement beyond the classroom can be seen in their use of Raspberry Pi and embedded Linux systems. These investments by the students point to the intrinsic motivation inspired by the class. Student comments indicated that they feel more employable as a direct result of this course. Through the pursuit of commercialization and product development, each student has built up a work portfolio. Such example work greatly improves the resume of each student, which supports one of the desired program outcomes of aiding students in gaining competitive career placements.

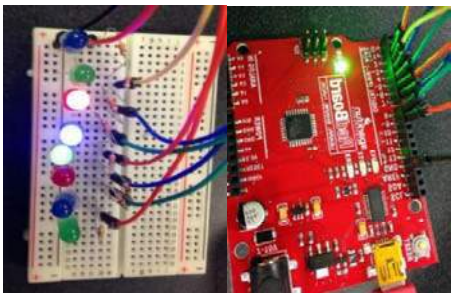

Figure 2: The assembled Multi-LED circuit and Arduino

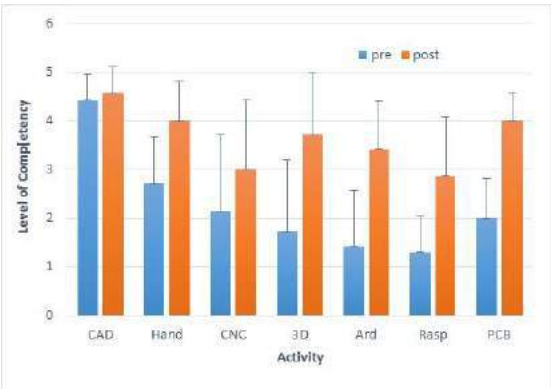

Figure 3: Perceived competency levels (mean + st. dev.) as reported by the students

DISCUSSION

The new EGR 693 course was successfully developed and led to increasing student competency in methods used in prototyping innovative technologies. Students now have firsthand experience in many manufacturing methods with "maker activities" serving as the vehicle for education. As the program has not yet graduated its first engineers, expected outcomes include improved employment opportunities for graduates; e.g., students will gain competitive positions in industry, launch new start-ups, or be accepted into PhD programs. Other desired outcomes include intellectual property gained by the university, and increased program funding with reviews and completed projects serving as evidence of the quality of the MEng in Design and Commercialization at UAB.

ACKNOWLEDGEMENTS

The authors gratefully acknowledge the support of the School of Engineering (SoE) and Department of Biomedical Engineering at UAB. Special thanks to Mr. Justin Koch for his patience and expertise on the CNC machines and 3D printers in the SoE Design Lab.

REFERENCES

[1] Today's Vision, Tomorrow's Healthcare, The 2012- 2016 Strategic Plan of the National Institute for Biomedical Imaging and Bioengineering, http://www.nibib.nih.gov/about-nibib/strategic-plan.

[2] Obama, B. (2009). Remarks by the President on the "Education to Innovate" campaign. [Press release]. Washington, DC: White House Office of the Press Secretary. www.whitehouse.gov/the-press-office/remarks-president-education-innovate-campaign.

Copyright 2016 The Organizing Committee for the 2016 Summer Biomechanics, Bioengineering and Biotransport Conference

SB^{3}C2016
Summer Biomechanics, Bioengineering and Biotransport Conference
June 29 –July 2, National Harbor, MD, USA
SB^{3}C2016-689

TSAI-HILL MAXIMUM-WORK THEORY AS A FAILURE CRITERION FOR FIBROUS BIOLOGICAL TISSUES

Christopher E. Korenczuk (1), Victor H. Barocas (1)

(1) Department of Biomedical Engineering
University of Minnesota – Twin Cities
Minneapolis, MN, USA

INTRODUCTION

Showing the von Mises stress in computer simulations of a tissue at risk of failure has become a routine practice (e.g., [1, 2, 3]). While its ease of calculation and its availability as a standard output in most finite-element software make the von Mises stress attractive, its use is accompanied by the implicit assumption that the von Mises failure criterion is applicable to the tissue in question. The von Mises criterion, however, is inherently isotropic and thus may make poor predictions in anisotropic tissues. In order to predict failure of such tissues accurately, one must use a failure criterion that can account for the anisotropy.

Extensive work has been done to analyze the failure behavior of non-biological fiber composites [4]. The Tsai-Hill theory [5,6] has been derived as a maximum-work theory to characterize the failure of anisotropic materials. The theory provides a single scalar failure criterion based on the principal material direction strengths and the shear strength. Thus, it provides a potential platform to analyze how off-axis loading affects an anisotropic fibrous material.

Arteries are anisotropic tissues that contain an underlying fiber laminate structure comprised mainly of collagen and elastin. The collagen fibers exhibit a strong preferential alignment in the circumferential direction, along with a weaker, but still significant preference for the axial direction, making these two fiber alignments the assumed principal material directions. Thus, the arterial wall provides an excellent representative system on which to study the efficacy of the von Mises and Tsai-Hill failure criteria. In this work, we studied porcine aortic tissue.

METHODS

Cadaveric porcine abdominal aortas were cut into uniaxial dog-bone-shaped samples with fiber angles ranging from 0° to 90° in increments of 15° (Fig. 1). Fiber angle was randomized along the length of the vessel to account for any regional heterogeneity (samples were not cut sequentially as shown). Samples were imaged before testing, and morphological measurements were computed with ImageJ. Samples were subjected to uniaxial tensile loading tests (Instron 8800 Microtester) at 10 mm/min until failure. Each sample was speckled with Verhoeff's stain in order to produce a distinct surface texture for full field strain tracking analysis via digital image correlation.

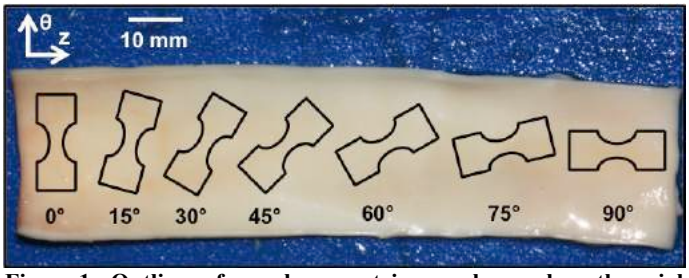

Figure 1: Outlines of sample geometries are shown along the axial length of the vessel. Angles were taken to be relative to the circumferential orientation (0°). Scale bar shown in white at top.

Failure stresses and stretches of each sample were analyzed in MATLAB. 1st Piola-Kirchhoff stresses were computed based on initial sample geometry and were converted to Cauchy stresses assuming tissue incompressibility. Statistical analysis was performed using GraphPad Prism 6.

The Tsai-Hill model for a uniaxial test takes the form [4]

$$\frac{\cos^4\theta}{\sigma_{LU}^2} - \frac{\cos^2\theta\sin^2\theta}{\sigma_{LU}^2} + \frac{\sin^4\theta}{\sigma_{TU}^2} + \frac{\sin^2\theta\cos^2\theta}{\tau_{LTU}^2} < \frac{1}{\sigma_x^2} \qquad (1)$$

Copyright 2016 The Organizing Committee for the 2016 Summer Biomechanics, Bioengineering and Biotransport Conference

where σ_{LU}, σ_{TU}, and τ_{LTU} are constants representing the material behavior. For our system, the preferred principal material direction is assumed to be the circumferential alignment, and the transverse direction would then follow as the axial alignment. Therefore, θ is the counterclockwise fiber angle relative to the circumferential direction, σ_{LU} is the circumferential (0°) failure stress, σ_{TU} is the longitudinal (90°) failure stress, τ_{LTU} is the shear stress, and σ_x is the failure stress in uniaxial extension at a given fiber angle. The three constants σ_{LU}, σ_{TU}, and τ_{LTU} were fit to the experimental data. Curve fitting was performed in MATLAB.

RESULTS

Experimental testing (n>5 for each angle) showed that the largest failure stress occurred in the circumferentially aligned tests (0°) at 2.97 ± 0.66 MPa (mean ± 95% CI). A decrease in failure stress was seen with an increase in fiber angle to the fully axially aligned case (90°) at 1.15 ± 0.64 MPa (Fig. 2). The smallest failure stress was seen in the 75° case at 0.96 ± 0.30 MPa. A one-way ANOVA showed that the effect of fiber angle change on the failure stress was highly significant ($p < 0.0001$), and a Tukey-HSD comparison showed a significant difference between the 0° and 90° alignment cases ($p = 0.0001$). These results indicate that an isotropic failure criterion, such as the von Mises criterion, is not acceptable.

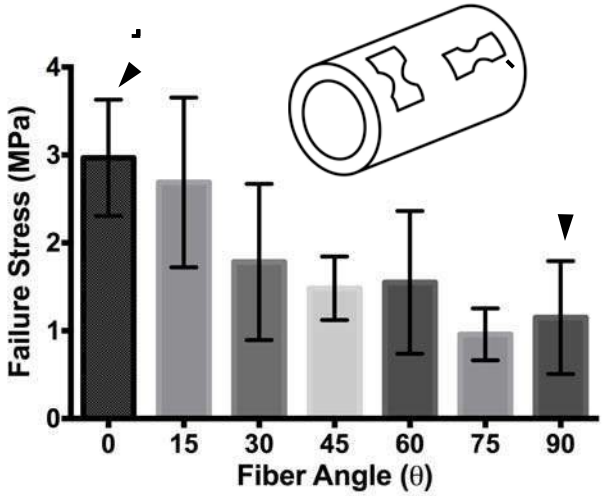

Figure 2: Failure stresses at each fiber angle. ANOVA showed that change in fiber angle is statistically significant ($p < 0.0001$). Error bars show 95% CI's. Note: the 60° case had two outliers removed due to high residual stresses affecting failure stress.

The Tsai-Hill maximum-work theory model (Eq. 1) showed a very good fit to the experimental data ($R^2 = 0.96$) (Fig. 3). Fitting the model provided a σ_{LU} value of 3.01 ± 0.51 MPa, a σ_{TU} value of 1.12 ± 0.34 MPa, and a τ_{LTU} value of 1.02 ± 0.35 MPa.

DISCUSSION

Uniaxial testing of porcine aorta confirmed previous work showing a higher circumferential failure stress compared to the axial alignment [7]. An increase in fiber angle to produce off-axis stresses resulted in decreased failure stress. These results show that failure stress is dependent upon fiber angle, a consideration not accounted for by the von Mises failure criterion. For a uniaxial test, the von Mises failure criterion reduces to a single, direction-independent tensile stress at failure, not accounting for the anisotropy of the tissue.

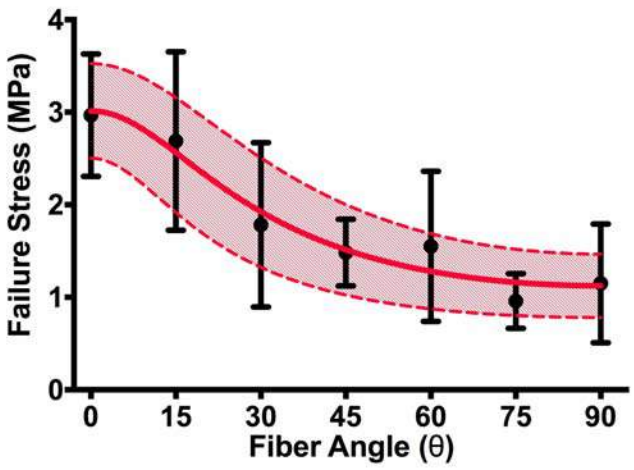

Figure 3: Experiment (points) and Tsai-Hill maximum-work theory model (solid line). Black error bars show 95% CI's on experimental points. The shaded region indicates the 95% CI on the fitted model.

The Tsai-Hill maximum-work theory provides a single scalar function incorporating both the fiber orientation and the directional strength interaction (longitudinal, transverse, and shear strengths). It is a more robust and physiologically relevant failure criterion, considering many tissues, such as arteries, contain anisotropic fibrous networks. Our results show its potential as a tool to predict failure in anisotropic tissues, including the porcine abdominal aorta studied here.

In our experiments, the minimum failure stress occurred at an angle of 75° from the preferred direction, but that failure stress was not significantly different from the failure stress at 90° ($p = 0.9987$). The Tsai-Hill criterion can support a non-monotonic failure-angle relation, as is often seen in synthetic fiber composites [4]. Whether the minimum at 75° was real or noise, and whether other tissues do or do not observe a local minimum in failure stress, are questions that merit further exploration.

Though the Tsai-Hill maximum-work theory model accounts for fiber anisotropy, it is possible that a different criterion may work better. Different tissues, for example, may exhibit regional heterogeneity and fiber anisotropy, in which case a modified approach must be used. Also note that the Tsai-Hill maximum-work theory only accounts for two fiber families, but arteries and other fibrous tissues have been characterized by four or more fiber families [8], so a more extensive model can also be explored.

ACKNOWLEDGEMENTS

This work was supported by the National Institutes of Health (R01EB005813). Tissue was provided by the Visible Heart Laboratory at the University of Minnesota. We gratefully acknowledge the technical assistance of Lauren Votava and Jacob Solinksy.

REFERENCES

[1] Volokh, K.Y., *J Mech Behavior Biomed Mat,* 4.8:1582, 2011. [2] Karimi, A. et al., *J App Physics*, 116.6: 064701, 2014. [3] Wood, S.A. et al., *J Biomech,* 44.10: 1831, 2011. [4] Agarwal, B.D., et al., *Analysis and performance of fiber composites.* Wiley, 2006. [5] Tsai, S.W., *Fundamental Aspects of Fiber reinforced Plastic Composites*, Interscience, N.Y., 1968. [6] Hills, R., *The Mathematical Theory of Plasticity*, Oxford University Press, 1950. [7] Teng, Z., et al., *Ann BME,* 1, 2015 [8] Humphrey, J.D., et al., *J Biomech Eng,* 109.4:298, 1987.

Copyright 2016 The Organizing Committee for the 2016 Summer Biomechanics, Bioengineering and Biotransport Conference

SB³C2016
Summer Biomechanics, Bioengineering and Biotransport Conference
June 29 –July 2, National Harbor, MD, USA
SB³C2016-690

A PREDICTIVE MULTISCALE MODEL FOR SIMULATING FLOW-INDUCED PLATELET ACTIVATION: CORRELATING WITN IN-VITRO RESULTS

Peng Zhang (1), Chao Gao (1), Jawaad Sheriff (1), Marvin J. Slepian (1,2), Yuefan Deng (3), Danny Bluestein (1)

(1) Biomedical Engineering Department
Stony Brook University
Stony Brook, NY, United States

(2) Departments of Medicine and Biomedical Engineering
Sarver Heart Center, University of Arizona
Tucson, AZ, United States

(3) Applied Mathematics Department
Stony Brook University
Stony Brook, NY, United States

INTRODUCTION

The coagulation cascade of blood may be initiated by shear-induced platelet activation, which prompts clot formation in prosthetic cardiovascular devices. Upon activation, platelets undergo complex morphological changes. Activated platelets polymerize fibrinogen into a fibrin network that enmeshes red blood cells. Continuum methods fail to capture the molecular mechanisms such as filopodia formation during platelet activation, while utilizing molecular dynamics is computationally prohibitive. A multiscale approach offers a means to bridge the gap between macroscopic flow and the cellular scales

We are developing a predictive multiscale numerical method that combines a Dissipative Particle Dynamics (DPD) model of viscous blood flow interfaced with a Coarse Grained Molecular Dynamics (CGMD) model of mechanobiology-based platelets, to simulate their activation via mechanotransduction pathways. This model bridges the gap between macroscopic transport flow-induced platelet activation scales and the ensuing molecular events. Platelets dynamically change their shapes in viscous shear flows and synergistically activate by a biomechanical transductive linkage chain. The CGMD platelet model is embedded in the DPD blood flow model, with macroscopic dynamic stresses interactively transferred to the platelet model. Hemodynamic stresses that lead to platelet activation and filopodial formation are mapped on membrane and simultaneously transmitted to cytoskeleton. Upon activation, platelets with intracellular constituents evolve as they lose their quiescent discoid shape and form filopodia. Actin filaments that are exposed to the highest stresses undergo filopodial formation. Model predictions are correlated with in vitro results.

METHODS

Our multiple spatial-temporal methods employ DPD to describe viscous blood flow and CGMD to model the intra-platelet constituents. Spatially, the DPD-CGMD interface was established by imposing a hybrid force field [1]. A 4-level multiple time-stepping (MTS) scheme was used [2] as an efficient numeric solver.

In the microscale, we improved the DPD formula by adding a Morse-based repulsive term for favorably producing Poiseuille flow of an incompressible fluid through a stenosis where the compressibility becomes a problem for DPD. We conducted a comparative study to investigate the fluid flow properties of DPD-Morse and DPD fluids through a 67% stenotic microchannel. Our DPD-Morse can extend the conventional DPD to sustain large compression caused by a stenosis.

In nanoscale, we built a mechanobiology-based platelet model by describing key constituents and biophysical properties. We modeled a bilayer membrane, ellipsoid shape, rigid filamentous core, gel-like cytoplasm using Morse potential [3], and filamentous actin. An α-helix structure was used to mimic a protrusible actin filament.

We validated our numerical method by correlating numerical simulations and model predictions with in vitro platelet activation experiments. Purified platelets [4] were prepared from whole blood obtained from consenting healthy donors of both genders. Platelets were exposed in a Hemodynamic Shearing Device to different shear stress-exposure time combinations up to 50 dyne/cm^2 and 4 min, respectively. Platelet samples were fixed with 2% glutaraldehyde, mounted on glass slides, and dehydrated through an ethanol series prior to imaging with scanning electron microscopy. We particularly examined the average number of visible filopods per platelet, circularity of activated platelets, and the position of filopods.

RESULTS

Our multiscale model describes the biophysical properties for platelets down to the nanoscales (Fig. 1). Membrane Young's modulus is 31.2 μN/m and shear elastic modulus is 33.0±9.0 μN/m. Cytoplasm viscosity is 4.1 mPa·s. Actin filament stiffness is 56.3±1.0 pN/nm.

Copyright 2016 The Organizing Committee for the 2016 Summer Biomechanics, Bioengineering and Biotransport Conference

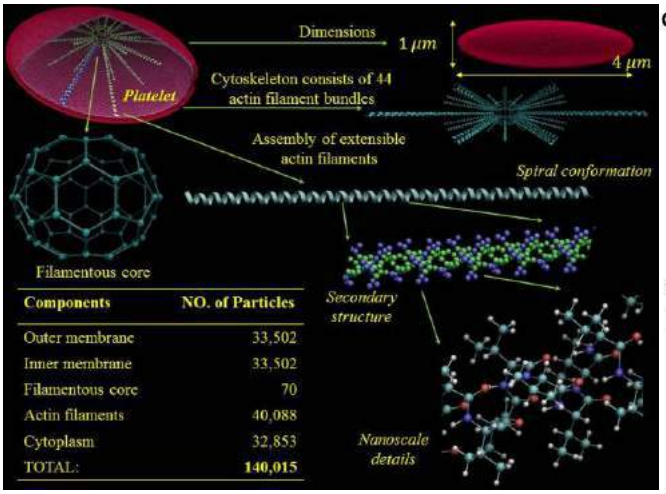

Figure 1: The nanoscale platelet model and its constituents

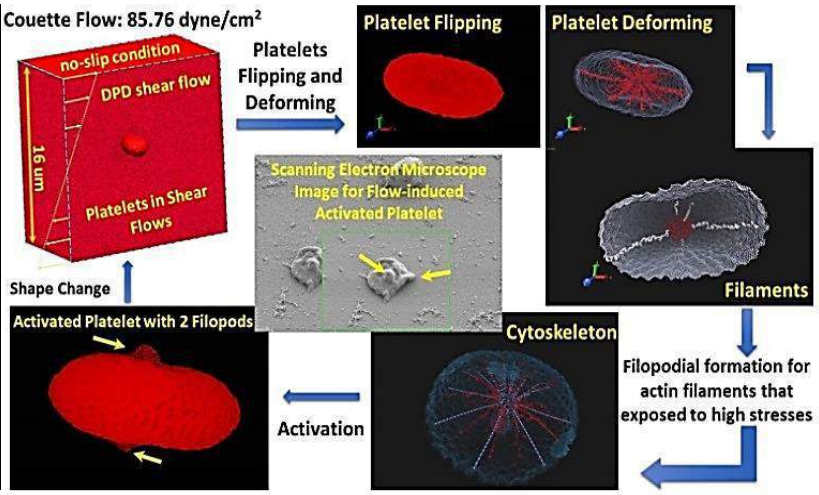

Figure 2: Mechanotransduction of the hemodynamic stresses and filopodial formation (two filopodia for activated platelet)

Using this model, we simulated the flow-induced platelet activation (Fig. 2). We assessed shear stress accumulation for flowing platelets in a flipping period. When platelets were flipping in the viscous flow, dynamic stresses were mapped on the cytoskeleton, with simultaneous accumulation of the mapped stresses over the period. This emulated the effect of mechanotransduction process of dynamics stresses in platelets. Filopodial formation is applied to actin filaments that are exposed to the highest stresses.

We correlated the morphological changes for activated platelets between numerical simulations (*A*) and in vitro results (*B-D*) (Fig. 3). (*A*) is morphological detail of our platelet model. (*B*) is a SEM image for cytoskeleton reorganization. (*C*) is the surface of activated platelets; (*D*) is the rendered view of a tomographic volume for a filopodium.

We correlated our numerical results for flow-induced platelet shape change with in vitro results. We counted the average number of visible filopods per platelet, the circularity of activated platelets, and the position of filopods of varying lengths. The in vitro results show that the average number of visible filopods is 2-3 per platelet, and their lengths ranged between 0.5~1.0 μm. The long filopods grew mostly on the edge of a platelet, while the filopods on the center were short. The majority of activated platelets preserved their ellipsoid shape and their circularity had no significant change. Our model assembled 44 actin filaments so it was capable of imitating enough visible filopods. In addition, our model also agreed with the preservation of the ellipsoid shape and reflected the position of the short and long filopods.

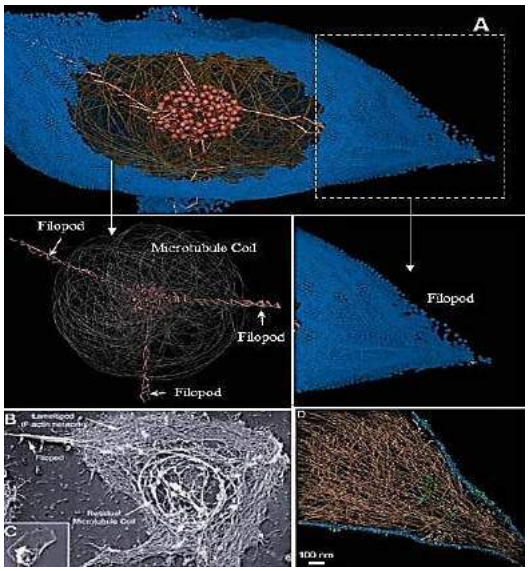

Figure 3: Morphological comparison between numerical model (A) and in vitro results (*B-D*). Credits: (*B*) and (*C*) are from J. H. Hartwig's book chapter [5]. (*D*) is from S. Sorrentino's work [6].

DISCUSSION

Our simulations do not only agree with the in vitro results but also suggest new testable predictions. Our results reveal that (1) decreasing membrane stiffness plays an essential role in promoting the formation of long filopods. In addition, (2) increasing numbers of longer filopods, for highly activated platelets, strongly correlates with microstructural rearrangement and mechanical properties. We show that a platelet needs to sustainably increase its protrusive force to grow a longer filopod and requires a stronger cytoskeleton to support more filopods growing radially outward. In this regard, a stronger structural arrangement and a stiffer mechanical property are supportive.

Our approach is the first computationally affordable numerical method for simulating the platelet activation by highly resolved mapping of mechanical stresses on the cytoskeleton in dynamic flow. Biophysical properties of a platelet are accurately described down to nm-length and ps-time scales. The viscous flows are described at μm-length and ns-time scales. Phenomena of filopodia formation are mimicked and correlate well with in vitro results. This model can be further employed to model the initiation of thrombosis in blood flow and study the effects of modulating platelet properties to enhance their shear resistance via mechanotransduction pathways.

ACKNOWLEDGEMENTS

This project funded by NIH (NHLBI R21 HL096930-01, NIBIB Quantum U01EB012487, DB) and used the XSEDE awards on TACC Stampede (DMS140019, PZ) and SDSC COMET (DMS150011, PZ).

REFERENCES

[1] Zhang, P et al., *Cell Mol Bioeng*, 7:552-574, 2014.
[2] Zhang, P et al., *J Comput Phys*, 284:668-686, 2015.
[3] Zhang, N et al., *J Comput Phys*, 257:726-736, 2014.
[4] Pothapragada, S et al., *Int J Numer Method Biomed Eng,* 31: e02702, 2015.
[5] Hartwig, J., Chapter 8 in *Platelets* (3rd Edition), 145-168, 2013.
[6] Sorrentino, S et al., *Eur J Cell Biol*, 94:129-138, 2015.

Copyright 2016 The Organizing Committee for the 2016 Summer Biomechanics, Bioengineering and Biotransport Conference

SB^{3}C2016
Summer Biomechanics, Bioengineering and Biotransport Conference
June 29 –July 2, National Harbor, MD, USA
SB^{3}C2016-691

LOCAL CHANGES TO THE GROWTH PLATE IN RESONSE TO INJURY

Lauren M. Mangano (1), Meghan E. Kupratis (1), Katie Li (1), Eric Rapp (2), Louis C. Gerstenfeld (3), Elise F. Morgan (1,2,3)

(1) Biomedical Engineering
Boston University
Boston, MA, USA

(2) Mechanical Engineering
Boston University
Boston, MA, USA

(3) Orthopaedic Surgery
Boston University
Boston, MA, USA

INTRODUCTION

Injury to the growth plate is associated with growth disturbances, including premature cessation of growth and angular deformities (*1, 2*). Developing successful, less invasive treatments for growth plate injury has been impeded by incomplete understanding of the features of the injury response that cause these growth problems. Radiographic evidence indicates that the growth disturbances are associated with formation of bony bridges at the injury site (*3*); however, conflicting reports exists as to whether these bridges form via intramembranous or endochondral ossification (*4,5*). Histological evidence has revealed disorganized chondrocyte columns and increased growth plate thickness in the region of the growth plate adjacent to the injury site, suggesting that local changes in cellular activity may contribute to angular deformities (*6-8*). Using contrast-enhanced micro-computed tomography (CECT) for cartilage imaging (*9*), local changes in the cartilaginous and osseous tissues in the healing growth plate can be robustly examined with quantitative, three-dimensional measurement.

The goal of this study was to quantify spatial changes in the morphology and composition of the growth plate following injury. The specific objectives were: 1) to quantify local and global changes in growth plate thickness and CECT attenuation (indicative of glycosaminonglycan (GAG) content); 2) to quantify the amount of bone formed within the growth plate following injury.

METHODS

Animal model: All animal experiments were conducted according to a protocol approved by an Institutional Animal Care and Use Committee (IACUC). A 0.51mm-diameter pin was used to make a hole defect in the distal femoral growth plates of 39 four-week-old, male, C57BL/6 mice. Mice were sacrificed one, three, or six weeks following injury. Injured and contralateral femora were collected and stored at -80°C.

Micro-computed tomography (μCT): Femora were imaged using μCT (μCT40, Scanco Medical, Brüttisellen, Switzerland) at a nominal resolution of 6 μm/voxel, before and after incubation CA4+, a cationic contrast agent, for 14 hours (Figure 1A). Pre- and post-incubation images were aligned using rigid-body registration and then subtracted from one another (Amira 5.2.2, Visage Imaging, Andover, MA). Cartilage was identified in the subtracted image by applying a threshold based on a four-part Gaussian fit of the intensity of the subtracted image (*10*). Thickness of the growth plate was calculated using distance-transformation methods (Scanco Medical). The average thickness and CECT attenuation of the growth plate were measured within a 1mm-diameter volume of interest (VOI) centered at the injury site ("near"; Figure 2B inset) and within the rest of the growth plate ("far"). For comparison purposes, near and far VOIs were defined at matched sites in the growth plate of the contralateral bone. For assessing bony bridges, the bone volume fraction (BV/TV) and tissue mineral density (TMD) of bone within the entire growth plate were measured in the pre-incubation scan (Figure 1B). For injured growth plates, BV/TV and TMD were also calculated near (within 0.75mm of the injury site) and far from the injury site.

Histology: Decalcified, paraffin-embedded sections of the distal femur were stained with hematoxylin and eosin, safranin O, and fast green.

Statistical Analysis: Growth plate thickness, growth plate CECT attenuation, BV/TV, and TMD were each compared between injured and contralateral sides, between near and far VOIs, and among time points using a repeated-measures ANOVA (JMP 11, SAS Institute Inc., Cary, NC). When indicated by the ANOVA result, pairwise *post hoc* tests using the Bonferroni correction were carried out.

RESULTS

Growth plate thickness and CECT attenuation varied spatially

Copyright 2016 The Organizing Committee for the 2016 Summer Biomechanics, Bioengineering and Biotransport Conference

within the growth plate and over time, and were affected by injury (Figure 2A). Although thickness decreased over time ($p<0.0001$), this decrease was least pronounced at the injury site: thickness in the near VOI of the injured growth plate was higher than those in the far VOI ($p<0.0001$) and in the near VOI of the contralateral growth plate ($p<0.0001$; Figure 2B). Similarly, injury slowed the temporal decrease in CECT attenuation: whereas attenuation progressively decreased from day 7 to 21 and 42 in the contralateral VOIs ($p<0.0001$), no temporal changes were seen in the injured near VOI ($p=0.12$). In the injured far VOI, attenuation did not differ between days 7 and 21 ($p=0.65$), but was lower at day 42 vs. days 7 and 21 ($p<0.0001$).

Bony bridges were evident by histological analysis in most samples by day 7 and in all samples at later time-points (Figure 3A,B). While BV/TV and TMD increased over time within both injured and contralateral growth plates ($p<0.0001$), these changes were most pronounced at the injury site (Figure 3C). At day 21, BV/TV and TMD were higher near the injury site compared to far from the injury site and to the entire contralateral growth plate ($p<0.01$). At all three time points, BV/TV was higher in the contralateral growth plate than in the injured growth plate far from the injury site ($p<0.01$).

In day-7 samples with no evident bony bridging, CECT indicated a lack of cartilage at the injury site. Histological analysis confirmed the presence of loose connective tissue at this site. At later time points, some samples showed safranin O staining at the injury site, and CECT showed the presence of mineralized tissue. Disorganized chondrocyte columns were observed adjacent to the injury site at all time points, and the presence of large, round, hypertrophic chondrocytes was seen at days 7 and 21 (Figure 3B).

DISCUSSION

These results demonstrate that growth plate injury leads to localized changes in cartilage and bone. Injury resulted in reduced age-related thinning of the growth plate near the injury and slower loss of CECT attenuation, a measure of GAG, across the entire growth plate. These results, together with the disruption of the typical columnar organization of proliferating chondrocytes and the advent of many hypertrophic chondrocytes adjacent to the injury site, suggest that the healing response following injury involves local dysregulation of the normal endochondral process responsible for longitudinal growth.

Consistent with previous studies, injury resulted in the formation of bony bridges at the injury site (*3*). Use of CECT allowed identification of a defect in the cartilage preceding formation of bony bridges. Safranin O staining seen subsequently at the injury site, paired with CECT evidence of mineralized tissue at this site, supports the hypothesis that endochondral ossification contributes to bony bridge formation (*4,11*). However, increased TMD at the injury site compared to in the contralateral growth plate suggests that the bony bridges induced by injury are compositionally different from those formed during the normal aging process in mice. Surprisingly, while BV/TV was highest at the injury site, BV/TV was higher in the contralateral growth plate than in the injured far VOI. This relative paucity of bone away from the injury site combined with the high BV/TV at the injury site is further indicative of endochondral dysregulation and may contribute to angular deformities. Ongoing immunohistochemistry analyses are focused on identifying cellular and molecular mechanisms underlying this dysregulation.

ACKNOWLEDGEMENTS

National Science foundation Graduate Research Fellowship Program, Jon Freeman, Mark Grinstaff.

REFERENCES

1. R. Salter and W. Harris, *J Bone Joint Surg* 45:587-622, 1963. **2.** A. Czitrom, et al., *Int Orthop* 4:269-277, 1981. **3.** J. Ogden, *J Bone Joint Surg* 69:1297-1302, 1987. **4.** C. Xian, et al., *J Orthop Res* 22:417-426, 2004. **5.** R. Chung and C. J. Xian, *J of Mol Endocrinol* 53:T45-T61, 2014. **6.** C. Macsai et al., *Bone* 49:904-912, 2011. **7.** R. Coleman *et al.*, *Bone* 46:155-1563, 2010. **8.** R. Seil, et al., *Arthroscopy:* 24:824-833, 2008. **9.** N. Joshi, et al, *J Amer Chem Soc* 131:13234-13235, 2009. **10.** L. N. M. Hayward, et al, *J Orthop Res* 31:567-573, 2013. **11.** R. Chung, et al, *J Leukocyte Biol* 80:1272-1280, 2006.

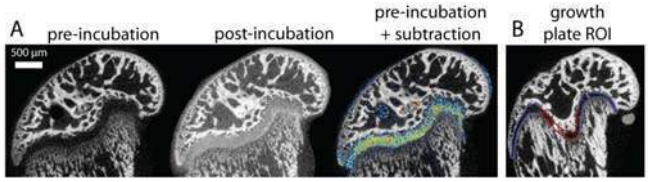

FIGURE 1. A) From left to right: pre- and post-incubation µCT scans; subtraction image overlaid on the pre-incubation scan. B) BV/TV and TMD were measured in the entire growth plate and, for the injured bone, within the regions near (red) and far (blue) from the injury site

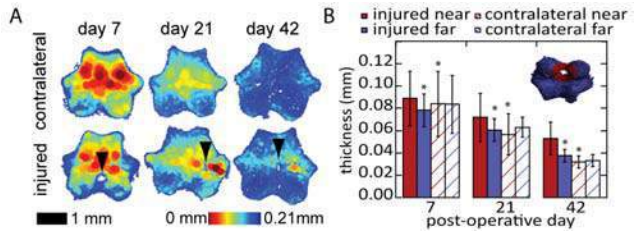

FIGURE 2. A) Local thickness of the growth plate in a representative sample from each group. B. Average thickness of the growth plate in near and far VOIs. *p<0.0001 vs. injured near (over all time points)

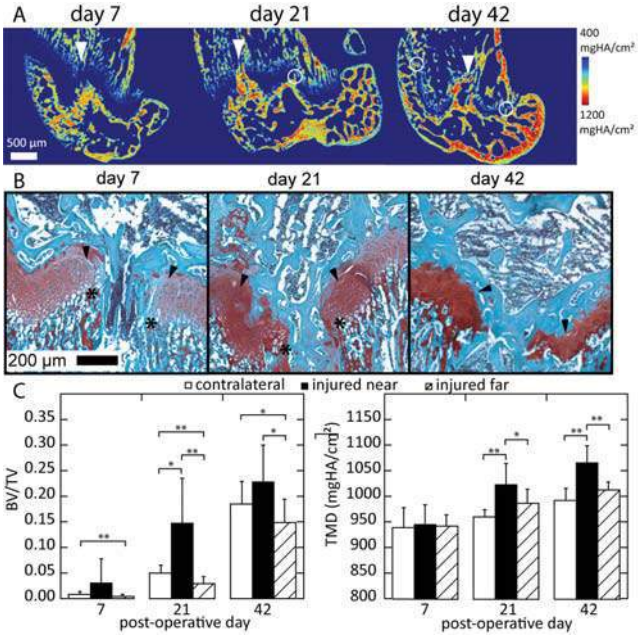

FIGURE 3. A) Density maps of the distal femur: arrowheads indicate the injury site; circles indicate bone bridges outside the injury site. B) Histology of injury site: arrowheads denote disorganized chondrocyte columns; asterisks denote hypertrophic chondrocytes. C) BV/TV (left) and TMD (right) of the entire contralateral growth plate, the growth plate at the injury site (near), and the growth plate outside the injury site (far). *p<0.01 **p<0.001, **p<0.0001

Copyright 2016 The Organizing Committee for the 2016 Summer Biomechanics, Bioengineering and Biotransport Conference

SB^{3}C2016
Summer Biomechanics, Bioengineering and Biotransport Conference
June 29 –July 2, National Harbor, MD, USA
SB^{3}C2016-692

A MATHEMATICAL MODEL OF VITREOSCHISIS

Krystyna Isakova (1), Jan O. Pralits (2), Outi-Leena Tammisola (1), Rodolfo Repetto (2)

(1) Faculty of Engineering
University of Nottingham
Nottingham, UK

(2) Department of Civil, Chemical and Environmental Engineering
University of Genoa
Genoa, Italy

INTRODUCTION

The vitreous humor is a substance that consists mainly of water, hyaluronan, collagen and additional molecular components. In youth, the vitreous is tightly adherent to the retina. With advancing age, changes in vitreous macromolecular interactions result in the formation of a liquefied vitreous that consists primarily of hyaluronan and water. Moreover, with aging the vitreous cortex (the outermost layer of the vitreous body) gets thinner, leading to the formation of small pockets of liquefied vitreous humor. These pockets slowly move through the thin cortex layer and settle between the cortex and the retina. These two processes, vitreous liquefaction and cortex thinning, normally occur simultaneously and result, in the majority of cases, in a posterior vitreous detachment (PVD) [1]. The effect of PVD may vary from negligible to significant, depending on the conditions of the vitreoretinal interface [2].

A split in the vitreous cortex, known as vitreoschisis, is a consequence of anomalous PVD (see Figure 1). It may result in different pathologies, including macular holes, macular puckers and retinal detachment. It is believed that the point where the two layers of the vitreous cortex re-join into a full-thickness layer is often site of significant tractions upon the retina [3]. In this work we study how the stresses exerted on the retina are spatially distributed in the presence of vitreoschisis and seek a mathematical explanation of the possible generation of strong retinal tractions.

METHODS

We study the generation of tractions on the retina during eye movements. In particular, we consider small-amplitude harmonic torsional oscillations of the eye. We model the vitreous chamber as a sphere and the vitreous body as a homogeneous viscoelastic fluid, with properties taken from [4]. The assumption of small-amplitude eye rotations allows us to linearize the governing equations. It is known from clinical observations [1, 2, 3] that the split in the vitreous is very thin with respect to the size of the domain. Based on this observation, we neglect the thickness of the split and model the vitreoschisis as a region of the eye wall on which the no-slip condition is partially relaxed. In particular, we assume that the velocity of the vitreous humor over the split is slightly smaller with respect to the velocity of the fluid attached to the normal vitreous cortex, where the usual no-slip boundary condition is imposed. Thus, we write that the normalized azimuthal velocity at the wall U reads

$$U = \left(1 - \varepsilon f(\theta, \phi)\right) \sin(\theta) \sin(t), \qquad (1)$$

where θ and ϕ are the zenithal and azimuthal angles and t is time. Moreover, $f(\theta, \phi)$ is the function describing the spatial variation of the slip: this is zero everywhere apart from in correspondence of the vitreoschisis where it attains positive values. Finally ε is a constant. In order to face the problem analytically we assume that $\varepsilon \ll 1$ and adopt a perturbation approach. This means that we consider a basic flow (the flow of a viscoelastic fluid in a harmonically rotating sphere [4]) and a perturbation, which accounts for the presence of the vitreoschisis. We find the solution using an expansion in vector spherical harmonics of the unknowns.

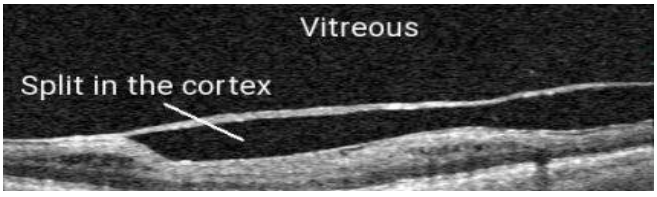

Figure 1: Clinical image of a vitreoschisis (modified from [1]).

Copyright 2016 The Organizing Committee for the 2016 Summer Biomechanics, Bioengineering and Biotransport Conference

RESULTS

In Figure 2 we show the boundary condition at the wall, described by equation (1). The vitreoschisis is located on the equatorial plane and has a round shape. Note that in Figure 2 we have assumed ε large enough for the spatial variation of the velocity imposed at the wall to be visible in the plot. In Figure 3 we plot the total wall shear stress (WSS) maximized over the time. The figure shows that in correspondence of the vitreoschisis the WSS decreases with respect to the normal case. However, in the region where the split closes, the model predicts the generation of peaks of the WSS (dark red regions along the equatorial plane in Figure 3). The total stress is normalized with the maximum value of the WSS for the basic flow.

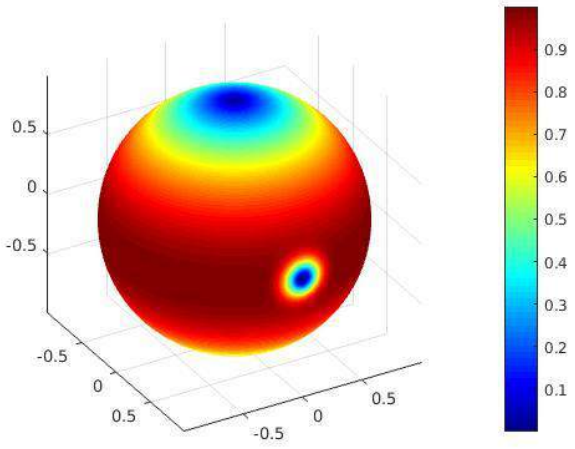

Figure 2: Normalized velocity imposed at the wall at time t = π/2. The blue spot on the equatorial plane is where the no slip condition is relaxed (vitreoschisis).

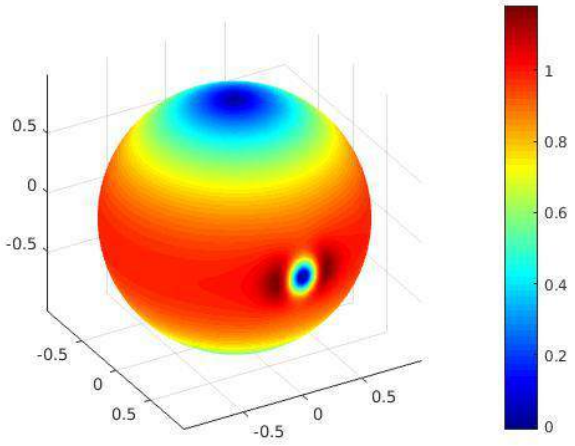

Figure 3: Map of the dimensionless WSS for the perturbation at the time instant t=π/2. The stress is normalized with $A\rho\omega^2R^2$, where A is the small amplitude of oscillations, ρ fluid density, ω the frequency of oscillations and R the radius of the sphere. ω=10 rad/s and ε=0.02.

In Figure 4 we plot the maximum total WSS (in time) along the equatorial plane. The WSS is normalized with the corresponding values in the absence of vitreoschisis (blue line). The red lines indicate the re-joining points of the split. Again, it appears that in these regions the WSS peaks, whereas it has a minimum in the middle of the vitreoschisis.

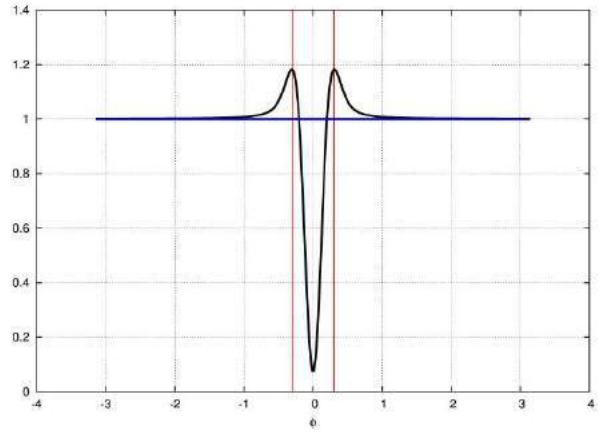

Figure 4: Maximum (in time) wall shear stress along the equatorial plane (θ = π/2). The stress is normalized with the maximum value of the wall shear stress of the basic flow (solid blue line). The red lines mark the points where the split re-joins. The frequency of oscillations is equal to $\omega = 10$ rad/s and $\varepsilon = 0.02$.

We also have studied how the effect of the vitreoschisis on the WSS depends on the mechanical properties of the fluid, finding that this grows both with the viscosity and the elasticity of the fluid.

DISCUSSION

In this work we have presented a mathematical model of vitreoschisis, i.e. a split in vitreous cortex, which is found in approximately half patients with macular holes and macular puckers. It is believed that the WSS in the region where the vitreous cortex split closes is larger than normal. The results of the model confirm that, during eye rotations, the WSS on the retina in presence of vitreoschisis experiences large peaks in the region where the vitreoschisis split re-joins. This provides a sound mechanical basis for the clinical observation that these regions are site of significant retinal tractions.

REFERENCES

[1] Sebag, J. and Balazs, E.A. *Invest. Ophthal. Vis. Sci*, 30(8):1867-1871, 1989.
[2] Green, W.R. and Sebag, J. *Retina*, 3:1882-1960, 2006.
[3] Sebag, *J. Graefes Arch. Clin. Exp. Ophthalmol.*, 246(3):329-332, 2008.
[4] Nickerson, C. S. et al., J. *Biomech.*, 41(9): 1840-6, 2008.
[5] Meskauskas, J. et al.. *J. Fluid Mech.*, 685, 1-22, 2011.

Copyright 2016 The Organizing Committee for the 2016 Summer Biomechanics, Bioengineering and Biotransport Conference

SB^{3}C2016
Summer Biomechanics, Bioengineering and Biotransport Conference
June 29 –July 2, National Harbor, MD, USA
SB^{3}C2016-694

VARIATIONS IN THE RELATIVE SIZE OF THE CRUCIATE LIGAMENTS AND MENISCI IN THE PORCINE STIFLE JOINT THROUGHOUT SKELETAL GROWTH

Stephanie G. Cone (1), Hope E. Piercy (1), Lynn A. Fordham (2), Jorge A. Piedrahita (3), Jeffrey T. Spang (4), Matthew B. Fisher (1,4)

(1) Department of Biomedical Engineering
University of North Carolina – Chapel Hill
and North Carolina State University
Raleigh, North Carolina, USA

(2) Department of Radiology
University of North Carolina – Chapel Hill
Chapel Hill, North Carolina, USA

(3) College of Veterinary Medicine
North Carolina State University
Raleigh, North Carolina, USA

(4) Department of Orthopaedics
University of North Carolina – Chapel Hill
Chapel Hill, North Carolina, USA

INTRODUCTION

With recent increases in youth sports involvement, the incidence rates of many musculoskeletal injuries in pediatric patients have been rapidly rising. For example, the incidence of anterior cruciate ligament (ACL) injuries of the knee joint have grown by as much as 11% per year in pediatric populations [1]. These injuries can lead to meniscal tears, chondral damage, and an increased risk for early-onset osteoarthritis [2].

In order to develop diagnostic tools and treatment algorithms and approaches specific to this growing patient population, it is important to understand the changes, and mechanisms of change, occurring in the knee joint during skeletal growth. Specifically, the nature and timing of tissue growth within and between tissues is not well understood, which in turn may have an impact on their relative function. As such, the objective of the current research was to characterize and compare volumetric size changes in the ACL, posterior cruciate ligament (PCL), medial meniscus, and lateral meniscus at several stages throughout skeletal growth in a large animal model. We hypothesized that the sizes of the tissues would scale similarly at all ages.

METHODS

For this study, hind limbs were collected from female Yorkshire pigs at ages of 1.5 months (n=6), 3 months (n=6), 6 months (n=6) and 18 months (n=5). These age groups are equivalent to juvenile (1.5 and 3 months), early adolescent (6 months), and late adolescent (18 months) age groups in humans. The stifle (knee) joints were isolated and stored at -20°C between experimental procedures.

The joints were imaged near full extension (approximately 30° flexion in the pig) using a 7.0 Tesla Magnetic Resonance Imaging (MRI) system (Siemens Magnetom) at the Biomedical Research Imaging Center at the University of North Carolina – Chapel Hill. Imaging scans were performed with a double echo steady state scan sequence (DESS, flip angle: 25°, TR: 17 ms, TE: 6 ms) with a voxel size of 0.42x0.42x0.4 mm and no gap between slices. Image series were analyzed using a commercial software package (Simpleware). Image segmentation and analysis was performed to collect the cross sectional area for each tissue in individual slices. Tools within Simpleware were then utilized to create and smooth 3D models for all knees (Fig. 1) and collect the volume of each tissue. Tissue dimensions were normalized as a percentage of their average late adolescent values in order to facilitate comparative analysis. Statistical tests included two-way analysis of variance with age and tissue type as factors followed by Bonferroni post hoc tests. Significance was set as $p<0.05$.

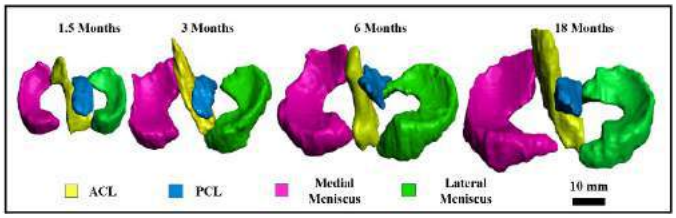

Figure 1: Models of porcine soft tissues at 1.5, 3, 6 and 18 months resulting from MR imaging and 3D reconstruction.

RESULTS

Two-way ANOVA testing of the normalized tissue volumes revealed age as a significant factor ($p=0.000$) and a significant interaction factor between age and tissue type ($p=0.032$), indicating a need to investigate individual groups using post-hoc tests.

Figure 2 shows the normalized volume of each tissue at 1.5, 3, 6, and 18 months of age. Statistical testing revealed that the PCL, medial meniscus, and lateral meniscus experienced similar and significant increases in normalized volume between 1.5 and 3 months ($p<0.05$) and

Copyright 2016 The Organizing Committee for the 2016 Summer Biomechanics, Bioengineering and Biotransport Conference

3 to 6 months ($p<0.05$), with little change afterwards ($p>0.05$). Dissimilarly, the ACL experienced statistically significant growth between 1.5 and 3 months ($p<0.05$), but there was no significant change between either 3 and 6 or 6 and 18 months ($p>0.05$).

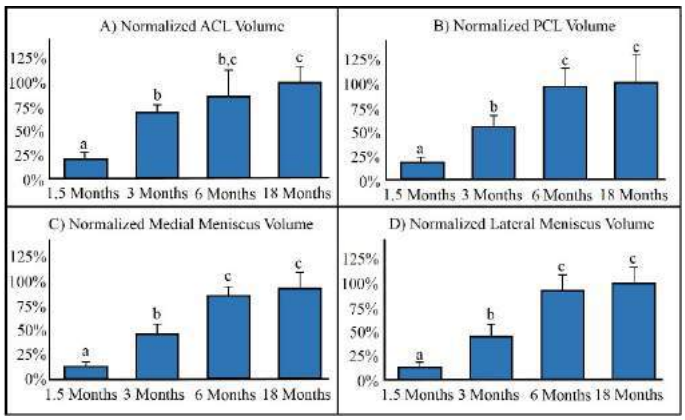

Figure 2: Normalized tissue volume (relative to the 18 month group) with respect to age in the A) ACL, B) PCL, C) medial meniscus, and D) lateral meniscus. Different letters represent statistically significant differences ($p<0.05$).

Figure 3 shows the normalized volume of all tissues at each age group. At 1.5 months of age, the ACL and PCL are approximately a fifth of their final size (20% and 18%) while the medial and lateral menisci are an average of 13% and 12% of their final size. Significant differences were found between the lateral meniscus and both the ACL and the PCL ($p<0.05$). By three months of age, the volume of the ACL increases to an average of 69% final size, while normalized volume of the PCL, medial meniscus, and lateral meniscus are 55%, 49%, and 46%, respectively. At this age, values for the ACL are significantly different than those for both the lateral and medial menisci ($p<0.05$). In both the 6 and 18 month age groups, normalized volumes were not significantly different between any of the tissue types ($p>0.05$).

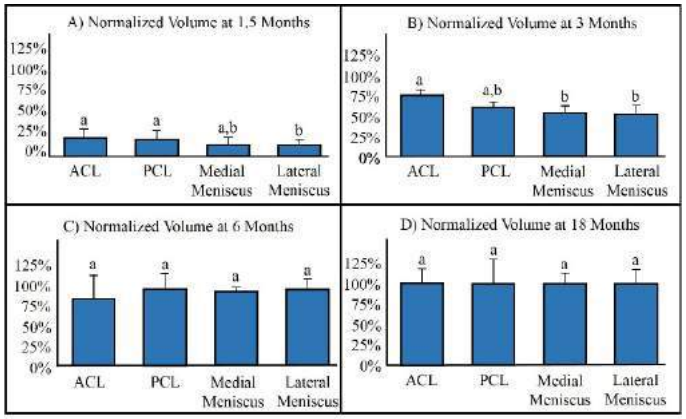

Figure 3: Normalized tissue volumes (relative to the 18 month age group) at A) 1.5 months, B) 3 months, C) 6 months, and D) 18 months of age. Different letters represent statistically significant differences ($p<0.05$).

Figure 4 illustrates the mean change in normalized volume between each age group (as a percentage of total per month, or "growth rate") for all four soft tissues. Between 1.5 and 3 months, the volume of the PCL, medial meniscus, and lateral meniscus grew at average rates of 24%, 23%, and 25% per month, while the volumes for the ACL increased at a higher rate of 32% final volume per month. Conversely, from 3 to 6 months, the average volumes of the PCL, medial meniscus, and lateral meniscus grew at rates of 14%, 16%, and 15% of the final volume each month while the values for the ACL increased more slowly, increasing by only 5% of its final volume per month. Growth slowed to under 2% per month in all groups from 6 to 18 months.

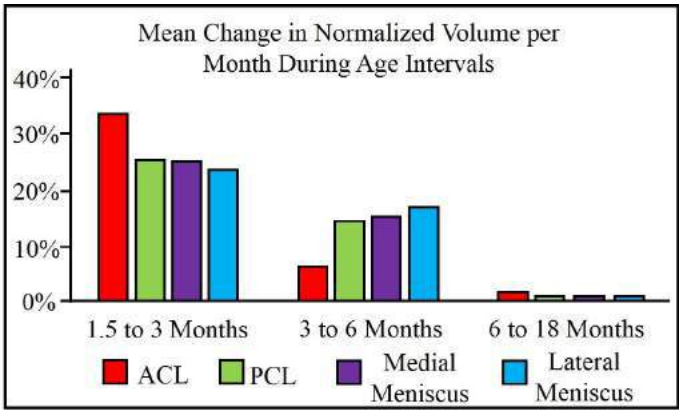

Figure 4: Volumetric changes for each tissue represented as the percentage increase in total volume per month.

DISCUSSION

This study provides a comparison of the volumetric changes in four soft tissues of the porcine stifle joint during skeletal growth. Contrary to our hypothesis, the ACL, PCL, medial meniscus, and lateral meniscus do not maintain a consistent scale during growth. Similar trends were found in the PCL, medial meniscus, and lateral meniscus, with steady increase in volume on average occurring up to 6 months of age (early adolescence) and more limited changes thereafter. However, the ACL experienced rapid increases in volume (49% of the final volume) between 1.5 and 3 months, with less drastic increases occurring during each age interval afterwards. Future studies examining the impact of these varying relative sizes with respect to relative tissue function throughout skeletal growth are warranted. A limitation of this study is the use of a porcine model. Although this model is commonly accepted as an analog for the human knee, key anatomical differences do exist [4], and further study of the human knee joint throughout skeletal growth is needed. Nevertheless, this model provides a valuable tool to compare a large number of samples at well-defined ages. An additional limitation is that only four tissues were studied. Inclusion of other tissues, such as the medial collateral ligament, lateral collateral ligament, cartilage, and epiphyseal bone, may reveal further insight into musculoskeletal growth. Nevertheless, these initial findings provide insight into the nature of tissue growth in the knee, and reveal a need for further investigation into the function of musculoskeletal soft tissues in skeletally immature joints.

ACKNOWLEDGEMENTS

We would like to acknowledge the Biomedical Research Imaging Center at the University of North Carolina – Chapel Hill for their contributions to this study. Funding provided by the National Institutes of Health (R03 AR068112).

REFERENCES

[1] Collins, SL et al., Pediat Therapeut, 4(2): 2014. [2] Rothermich, MA et al., Journal of Pediatric Orthopaedics, 2015. [3] Kim, HK et al., Radiology, 247(3):826-835, 2008. [4] Proffen, BK et al., The Knee, 19: 493-499, 2012.

Copyright 2016 The Organizing Committee for the 2016 Summer Biomechanics, Bioengineering and Biotransport Conference

SB³C2016
Summer Biomechanics, Bioengineering and Biotransport Conference
June 29 –July 2, National Harbor, MD, USA
SB³C2016-695

DETERMINING THE EFFECT OF ELASTIN DIGESTION ON THE REGIONAL BIAXIAL MECHANICAL PROPERTIES OF THE MURINE CERVIX

Victoria L. Morris (1), Cassandra K. Conway (1), Kristin S. Miller (1)

(1) Biomedical Engineering
Tulane University
New Orleans, LA, USA

INTRODUCTION

Preterm birth affects 12.7% of all pregnancies and is a significant cause of infant morbidity and mortality [1]. During pregnancy, microstructural and compositional alterations lead to drastic changes in mechanical properties and structural integrity [2]. The cervix must remain closed to maintain the growing fetus and then open sufficiently to allow passage at term. Incompetence of the cervix is a highly misdiagnosed form of preterm birth and leads to the rapid expulsion and often death of the fetus [3]. While the etiology of incompetence remains unknown, it has been suggested that decreased elastin content may contribute to cervical dilation and loss of mechanical integrity [3]. The role of elastin in normal cervical mechanical function, however, remains unknown. Further, while the cervix has been mechanically characterized in uniaxial tensile or compression [c.f., 4], the biaxial mechanical behavior of the cervix has not been evaluated. The cervix experiences multiaxial loading within the body, hence biaxial tests may provide additional insight into the physiologic mechanical state of the cervix and the contribution of each load-bearing constituent. Therefore, the objectives of this study are to: 1) Determine the regional passive biaxial mechanical properties of the murine cervix at estrus and to 2) Delineate the contribution of elastin to cervical mechanical properties. We hypothesize that: 1) The external os of the cervix will demonstrate a larger linear modulus compared to the internal os; and 2) Regardless of the region, the cervix will demonstrate a larger linear modulus following elastase digestion.

METHODS

Cervical complexes from female C57/BL/6 mice at 4-6 months of age (IACUC approved, n=8 at estrus) were dissected out and mounted within a custom biaxial testing system and the contralateral uterine horn was ligated with 6-0 silk suture. **MECHANICAL TESTING.** All specimens were subjected to pressure-diameter tests ($P = 0$ to 200 mmHg) at three different axial extensions around the estimated *in vivo* axial stretch and to axial force-length tests at three different pressures (67, 133, 200 mmHg) [5]. The outer diameter was tracked optically at both the internal and external os. For three samples, following mechanical testing, the specimens were intraluminally exposed to 1mL of pancreatic elastase at a concentration of 3.75 U/mL for 15 minutes while the cervix was subject to 0 mmHg pressure at the estimated *in vivo* axial extension. Following treatment, the cervix was rinsed with Hank's solution and allowed to equilibrate before the mechanical tests were repeated. Following mechanical testing, opening angle experiments were performed via isolating 0.5mm rings from the internal and external os. **DATA ANALYSIS.** A bilinear curve fit was applied to the local stress-strain data to quantify the moduli in the toe- and linear-regions for each mechanical test [6]. Opening angles were measured from the midpoint of the inner wall to the tips of the outer wall of the opened sections [7]. **STATISTICAL ANALYSIS.** 2-way ANOVAs (elastase treatment, region) with Bonferroni corrections were used if the interaction was significant. Following the ANOVAs, paired post-hoc t-tests were performed when appropriate. Data is presented as mean + SEM.

RESULTS

The 2-way ANOVA (regional location and elastase at estrus) identified that both location and elastase digestion had a significant effect on the toe- and linear-region moduli as well as the transition stress. Regional location had a significant effect on the transition strain. Additionally, elastase digestion was identified to have a significant effect on the *in vivo* axial stretch, unloaded length, thickness, and opening angle. No significant interactions between regional location and elastase treatment were identified.

Copyright 2016 The Organizing Committee for the 2016 Summer Biomechanics, Bioengineering and Biotransport Conference

The external os demonstrated a higher toe- and linear-region modulus, compared to the internal os for both the control and elastase test. Additionally, the external os demonstrated a higher transition strain and stress compared to the internal os for both tests.

Following elastase digestions, the linear modulus increased following elastase digestion at both the internal and external os, while the toe-region moduli increased at the external os. Transition stress was significantly increased following elastase digestion at the external os. A significant increase in the *in vivo* axial stretch and a corresponding decrease in the unloaded length were identified following elastase digestion. Additionally, the wall thickness decreased and the opening angle increased at both locations.

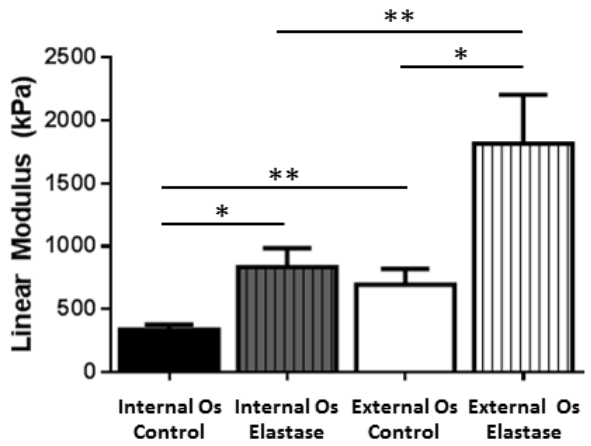

Figure 1: Linear-region moduli were significant higher at the external os compared to the internal os before and following elastase digestion (; p<0.05). Additionally, moduli values increased following elastase digestion at both locations (*; p<0.05).**

DISCUSSION

The current study demonstrates that the mechanical properties of the murine cervix vary with regional location, where the external os demonstrated larger toe- and linear-region moduli compared to the internal os (Figure 1). Previous studies have reported an increase in collagen content and a corresponding decrease in smooth muscle near the external os of the cervix in comparison to the internal os [8]. Hence, the higher collagen content at the external os may contribute to the larger moduli identified in this study. A higher transition strain and stress was also identified at the external os, which may suggest that the undulation of collagen fibers vary with regional location [9]. Further, it suggests that additional structural and compositional features (such as collagen cross-links and proteoglycan composition) may vary by location and influence local mechanical properties [10,11]. Future work, however, is needed to locally quantify local microstructural parameters and to elucidate their correlation to murine local cervical mechanical behavior.

In this study, cyclic pressure-diameter tests and associated Cauchy stress-strain curves confirm a large increase in stiffness and loss of distensibility at both the internal (Figure 2A) and external os (Figure 2B) of the murine cervix following exposure to elastase. These results, in addition to the increased linear modulus identified at both locations (Figure 1), suggest that elastic fibers contribute to the mechanical properties of the murine cervix and may interact with collagen fibers to prescribe cervical mechanical function. A prior study in carotid arteries noted a similar loss of distensibility following elastase digestion [12]. Future work, however, is necessary to quantify the microstructural orientation of elastic fibers in the cervix and their potential role in collagen fiber recruitment.

Further, this study reports a decrease in the unloaded length and increase in the *in vivo* axial stretch following elastase digestion in cervical tissue. Ferruzzi et al. demonstrated an increased unloaded length and decreased *in vivo* axial stretch for carotid arteries subsequent to elastase digestion in a preceding study. Herein, the cervical tissue displayed opposite behavior to what was observed in the carotid artery, despite a similar circumferential mechanical response [12]. Hence, the mechanical contribution of elastin in the tissue may be anisotropic. Consequently, there is a pressing need for additional information on the underlying microstructure, deposition, and turnover of elastin within the murine cervix.

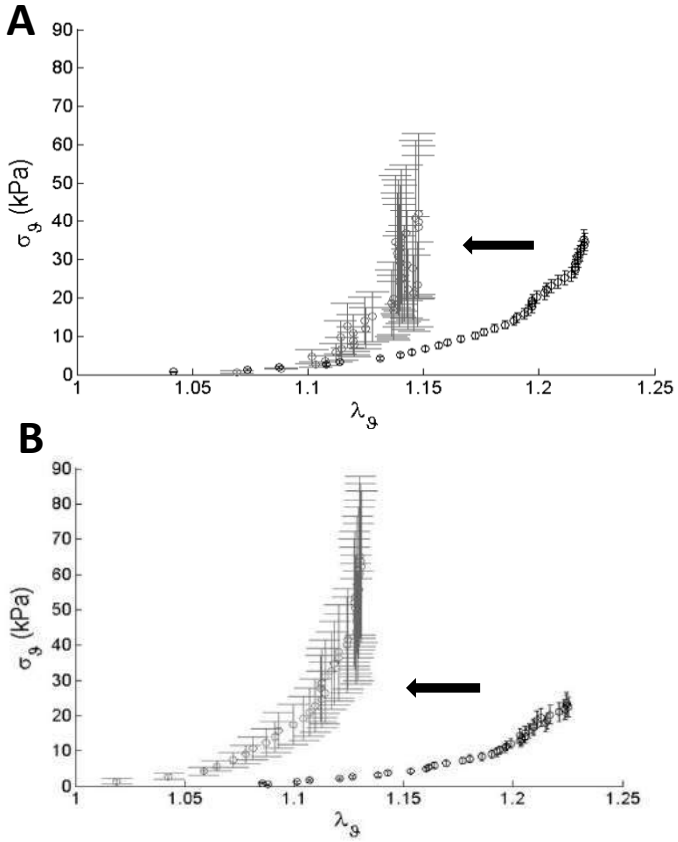

Figure 2: Circumferential Cauchy stress-strain curves for the internal (A) and external (B) os of the murine uterine cervix before (black) and following elastase digestion (grey) at the *in vivo* axial extension. Dark arrow denotes shift following digestion.

ACKNOWLEDGEMENTS

The authors would like to acknowledge Derek Bivona for assistance and the LA EPSCoR SURE program for financial assistance.

REFERENCES

[1] Anum, E et al., *Placenta*, 30, 207–215, 2009. [2] Mahendroo, M et al., *Reproduction*,143(4): 429-438, 2012. [3] Leppert, P et al., *Am J Ob Gyn*, 157(5):1134-9, 1987. [4] Myers, K et al., *J Biomech Eng*, 132(2):021003, 2010. [5] Ferruzzi, J et al., *Ann Biomed Eng*, 41(7): 1311-1330, 2013. [6] Lake et al., *JOR*, 27(12):1596-602, 2009. [7] Humphrey, J, *Card Sol Mech*, Springer, 2002. [8] Harkness, M et al., *J Physiol*, 148:524-47, 1959. [9] Miller, K et al., *J Biomech Eng*, 134(4):041004, 2012. [10] Yoshida, K et al., *PloS One*, 9(11):e112391, 2014. [11] Zork, N et al., *Am J Ob Gyn*, 212(3):321.e1-8, 2015. [12] Ferruzzi, J et al., *Card Res*, 92:287-295, 2011.

Copyright 2016 The Organizing Committee for the 2016 Summer Biomechanics, Bioengineering and Biotransport Conference

SB^{3}C2016
Summer Biomechanics, Bioengineering and Biotransport Conference
June 29 –July 2, National Harbor, MD, USA
SB^{3}C2016-696

NOVEL INSTRUMENTED MOUTHGUARD DESIGNS TO ACCURATELY MEASURE HEAD KINEMATICS FOR TRAUMATIC BRAIN INJURY

Calvin Kuo (1), Lyndia C. Wu (2), David B. Camarillo (1,2)

(1) Mechanical Engineering Department
Stanford University
Stanford, CA, USA

(2) Bioengineering Department
Stanford University
Stanford, CA, USA

INTRODUCTION

Wearable head motion sensors are designed to provide quantitative measurements of rapid head kinematics for traumatic brain injury (TBI) research and diagnosis [1]. However, most sensors used either commercially or in research suffer from a lack of sufficient coupling to the skull. Clothing/equipment sensors can move with respect to the skull during impact and skin-mounted sensors are prone to errors resulting from soft tissue motion [2]. Errors in kinematic measurements have led to inconclusive findings on the mechanisms underlying TBI and could result in improper diagnosis on the field. Thus, there is a pressing need to develop accurate sensors to advance our understanding of TBI and properly diagnose its occurrence.

The instrumented mouthguard was thought to provide accurate head kinematic measurements because it has superior coupling to the skull through the upper dentition – an exposed hard surface attached to the skull via stiff ligaments. However, three previous laboratory validations of mouthguard accuracy yielded varying results [3,4,5]. In linear impact tests on anthropomorphic test dummies (ATD), Bartsch et al and Camarillo et al both showed the mouthguard had excellent kinematic accuracy [3,4] while Siegmund et al showed the mouthguard overestimated head kinematics in certain impact conditions [5].

In a series of free drop ATD and post mortem human subject (PMHS) tests, we found that perturbations from the mandible were the likely cause for the discrepancy in previous validation results and a major source of kinematic measurement error in the mouthguard [6]. We identified a mechanism underlying the mandible and mouthguard interaction responsible for kinematic measurement errors. We modeled the mandible and mouthguard as a mass-spring system with the mandible representing the mass and the mouthguard ethylene vinyl acetate (EVA) material representing the spring. The modeled characteristic frequency closely matched observed error frequencies in ATD and PMHS testing.

Because current mouthguard designs may suffer from kinematic measurement errors as a result of our identified mandible-mouthguard interaction, new mouthguard designs must be developed and evaluated before they can be used to collect reliable head impact kinematics for TBI research and diagnosis. Thus, the goal of this work is to evaluate three novel mouthguard designs that mitigate mandible perturbances.

METHODS

In our previous work to identify the mandible-mouthguard interaction, we used a mouthguard with a kinematic sensor located at the rear molars encased between two layers of 3mm thick EVA (original design) [6]. The actual thickness of the mouthguard was near 2mm because the mouthguard formation process melts and stretches the EVA material around subject specific dentitions. The kinematic sensor included a tri-axial accelerometer and a tri-axial gyroscope measuring kinematics at 1000Hz over 100ms (Figure 1).

We designed three mouthguards to mitigate potential mandible perturbances. We used the same kinematic sensor as the original design to ensure it was not a confounding factor. Our first design encased the kinematic sensor at the rear molars between two layers of 1mm EVA, resulting in a mouthguard thickness of less than 1mm (thin design). The second design encased the kinematic sensor at the rear molars between three layers of 3mm EVA (one layer between the teeth and sensor and two layers over the sensor), resulting in a thickness of approximately 3.5mm (thick design). These varying thickness designs were chosen to explore the effect of adjusting the EVA spring stiffness in our representative mass-spring mandible-mouthguard model.

Copyright 2016 The Organizing Committee for the 2016 Summer Biomechanics, Bioengineering and Biotransport Conference

The final design placed the kinematic sensor in front of the incisors and encased them between two layers of 3mm EVA (incisor design). In addition, material was removed from the bite plane at the incisors (Figure 1).

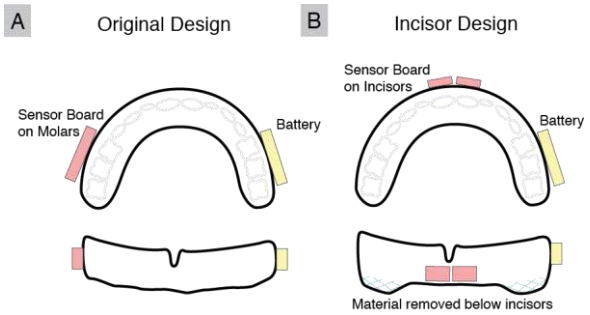

Figure 1: Mouthguard Designs. (A) Original design with the kinematic sensor at the rear molars. (B) Incisor design with the kinematic sensor at the incisors and additional material removed.

For each design, we evaluated its kinematic measurement accuracy performance using free drop impacts on a football helmeted ATD. We performed free drops at three drop heights: 10cm, 60cm, and 100cm, over 6 impact locations: vertex, frontal, facemask, frontal oblique, parietal, and occipital. These drops explored the range of impact conditions commonly observed in football [1]. The ATD mandible was left free to articulate to exercise the new designs in the scenario with the highest errors identified in our previous work (Figure 2).

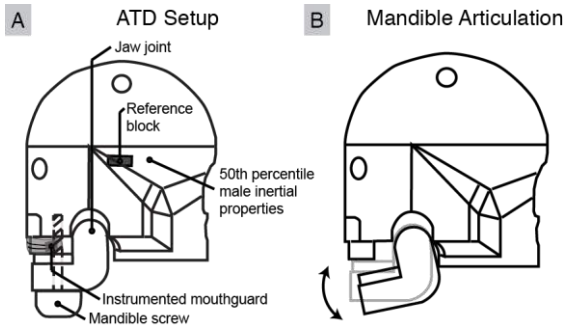

Figure 2: ATD Testing. (A) ATD test setup with mouthguard and reference sensors. (B) Mandible dynamics during an impact.

To assess mouthguard accuracy, we compared mouthguard kinematics against kinematics from a high rate reference sensor affixed to the center of mass of the ATD (Figure 2). This reference sensor consisted of a tri-axial accelerometer and a tri-axial gyroscope measuring kinematics at 10kHz over one second.

Linear acceleration and angular velocity data was collected from both the mouthguard and reference sensors. Angular acceleration was computed by performing a 5-point stencil differentiation on the angular velocity signal. We then performed a linear regression with forced zero intercept on the aggregated peak angular acceleration magnitudes and peak linear acceleration magnitudes from all free drops. A perfectly accurate sensor would have a linear regression m=1.0 and R^2=1.0.

RESULTS

Our results show that the thin and thick designs still had significant overestimation in kinematic measurements, while the incisor design showed improved accuracy (Figure 3). In both peak angular acceleration magnitude and peak linear acceleration magnitude regressions, the thin design had the highest overestimation error (angular m=2.4, R^2=0.4 and linear m=2.0, R^2=0.2), while the incisor design had the best accuracy (angular m=0.8 and R^2=0.9, linear m=1.0, R^2=0.9). The incisor design did underestimate peak angular acceleration magnitudes; however this was consistent with previous findings [4].

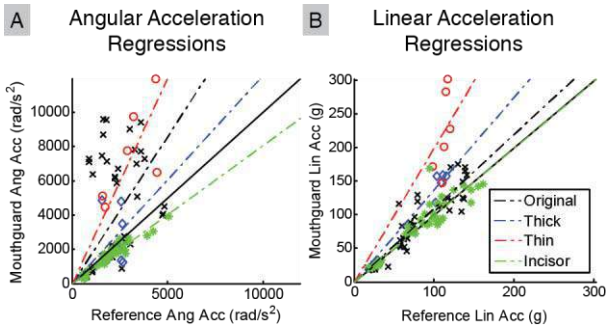

Figure 3: Regression Results: (A) Angular acceleration magnitude regressions for the original and three novel mouthguard designs. (B) Linear acceleration magnitude regressions.

DISCUSSION

In this study, we evaluated the kinematic measurement accuracy of three novel mouthguards that were designed to mitigate errors from mandible dynamics. We found that the incisor design effectively mitigated errors from mandible dynamics, while the remainder had overestimations in both angular and linear acceleration. Overestimation in angular acceleration magnitude correlated with thinner mouthguards. This indicates that thicker EVA material may dampen the magnitude of mandible perturbations. However, at 3.5mm, the mouthguard still overestimated kinematic values and even thicker mouthguards may be impractical for field deployment. Future work will refine and evaluate the performance of these new designs in more bio-fidelic PMHS tests.

The incisor design had the best accuracy because it isolated mandible perturbations at the rear molars from the kinematic measurement sensor at the incisors. This design demonstrates that while mandible perturbations can affect mouthguard accuracy, they can be mitigated with proper design of the mouthguard and placement of instrumentation. Our novel incisor design represents a new trend in head kinematic measurement device development that accounts for known sources of error and provides superior measurement accuracy. This design may fill the pressing need for an accurate head kinematic sensor in TBI research and, as we learn more about the mechanism of TBI, has the potential to translate towards real-time injury screening of athletes, military personnel, and other high-risk populations.

ACKNOWLEDGEMENTS

We would like to acknowledge funding sources, including the National Institute of Health, the Stanford Child Health Research Institute, and Stanford Bio-X. In addition, we would like to acknowledge Dr. Dale Bass at Duke University and Dr. Jason Mihalik at the University of North Carolina Chapel Hill for our partnership in evaluating head impact sensors.

REFERENCES

[1] Duma, Stefan M., et al. *Clin J of Sport Med*, 15.1: 3-8, 2005
[2] Wu, Lyndia C., et al. *ABME*, 2015.
[3] Bartsch, Adam, et al. *Stapp Car Crash J*, 58: 1-27, 2014.
[4] Camarillo, David B., et al. *ABME,* 41.9: 1939-1949, 2013
[5] Siegmund, Gunter P., et al. *ABME*, 42.9: 1834-1845, 2014
[6] Kuo, Calvin, et al. *J Biomech*, *submitted*

Copyright 2016 The Organizing Committee for the 2016 Summer Biomechanics, Bioengineering and Biotransport Conference

SB³C2016
Summer Biomechanics, Bioengineering and Biotransport Conference
June 29 –July 2, National Harbor, MD, USA
SB³C2016-698

CERVICAL SPINAL CORD STRESS: A COMPREHENSIVE FINITE ELEMENT MODEL OF CERVICAL SPINAL CORD

Kirsten E. Stoner (1), Kingsley O. Abode-Iyamah (2), Douglas C. Fredericks (3), Matthew A. Howard (2), Nicole M. Grosland (1,3)

(1) Biomedical Engineering
University of Iowa
Iowa City, IA, USA

(2) Department of Neurosurgery
University of Iowa Hospitals and Clinics
Iowa City, IA, USA

(3) Department of Orthopaedics
University of Iowa Hospitals and Clinics
Iowa City, IA, USA

INTRODUCTION

Cervical spondolytic myelopathy (CSM) is the most common form of spinal cord injury with approximately 19,000 surgical cases annually in the USA[1]. It is caused by chronic, dynamic compression of the spinal cord by either osteophytes, herniated intervertebral discs, or ossified ligaments. The symptoms are often debilitating, presenting as loss of upper extremity function, gait disturbances, and most severe, quadriplegia. Treatment usually entails surgical intervention with the aim being to reduce the impingement of the spinal cord and stabilize the spine.

While treatment of CSM is based on intuition of the spinal cord mechanics little is actually understood regarding the changes in spinal cord stress and strain during motion. Since measuring *in vivo* cord mechanics on human subjects is infeasible, finite element (FE) modeling can be used to investigate cord stress distributions[2,3]. Currently published models have provided insight into cord dynamics but are primitive in anatomic and material property assumptions. It was therefore the goal of our study to create an FE model incorporating all major musculoskeletal and neurologic anatomy of the normal C2-T1 spine to predict cord mechanics during flexion and extension.

METHODS

A 3D FE model of the cervical spine (C2-T1) was previously developed and validated[4]. A CAD model of the cervical spinal cord was created based on histologic sections from levels C3, C5, C8 and scaled to fit the geometry of the aforementioned C2-T1 model. IA-FEMesh was used to create a hexahedral mesh of the cord, from which quadrilateral elements were extracted to define the pia. In a similar manner, a quadrilateral mesh of the dura was generated. A convergence study was performed to ensure solution stability. The resulting cord, including the pia and dura, is defined by 42,239 elements. Once introduced into the C2-T1, the entire model consisted of 229,649 elements. Dentate and mengiovertebral ligaments were modeled as compression free truss elements. Placement of the dentate and mengiovertebral ligaments was based on anatomical reports[5]. The dura, pia, and cord were modeled as hyperplastic Mooney-Rivlin and material constants were calculated based on published in vitro tissue testing[6]. The dentate and mengiovertebral ligaments were modeled as linear elastic. The cerebral spinal fluid (CSF) was modeled as a fluid cavity enclosed by the dura and pia, while the pressure in the extradural and intradual space was based on published data[7]. General contact was used to define contact between all surfaces.

The inferior endplate of the T1 vertebra was fixed in all directions as were the inferior most nodes of the spinal cord, pia, and dura. Using Abaqus 6.13-1/Standard a quasi-static rotation of 28° in flexion and 25° in extension was applied to the most superior portion of C2. This rotation corresponded to the average flexion and extension achieved by healthy controls during flexion and extension MRIs. To model the attachment of the spinal cord to the brain, a follower load was applied to the superior end of the spinal cord, dura and pia. During flexion 7.70N of tension and during extension 1.61N of compression was applied. These loads correspond to the force needed to achieve physiologic axial cord root displacement. Axial stretch between cord root entries (cord stretch) were obtained as were the von Mises stresses and logarithmic strains throughout the cord.

RESULTS

In extension, cord stretch between the root entries in the axial direction ranged from -6.34 mm at C2-C3 to 0.00 mm at C6-C7, average -2.15 ± 2.74 mm. At full extension von Mises stress on the anterior cord ranged from 0.008-0.081 MPa and 0.008-0.034 MPa on the posterior

Copyright 2016 The Organizing Committee for the 2016 Summer Biomechanics, Bioengineering and Biotransport Conference

cord. Interestingly, even with normal anatomy, anterior bony impingement occurred during extension causing a maximum stress of 0.081 MPa at the C56 level (Fig1). Locations of max principle logarithmic strain mirrored those of stress ranging from 0.80-14.8% with the maximum occurring at the C56 level of impingement (Fig2)

In flexion, cord stretch between the root entries in the axial direction ranged from 1.84 mm at C2-C3 to -0.71 mm at C4-C5, average 0.14 ± 1.02 mm. At full flexion von Mises stress on the anterior cord ranged from 0.001-0.009 MPa and 0.0017-0.033 MPa on the posterior cord (Fig1). Compressive stress was present anteriorly and tensile stress posteriorly. No bony impingement occurred. Max principle logarithmic strain ranged from 1.00-6.50% with highest strains occurring posteriorly.

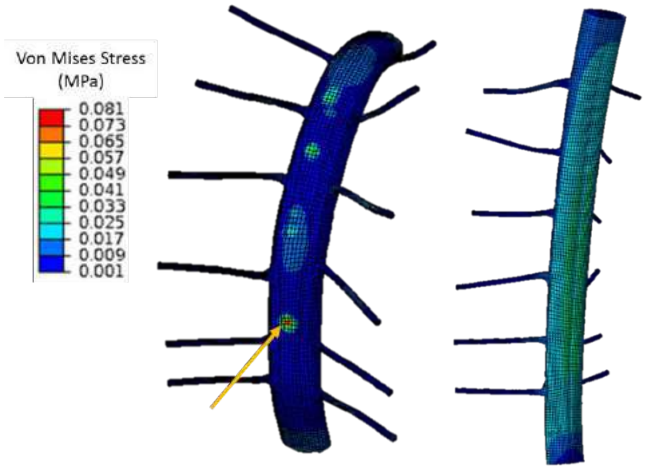

Figure 1: Spinal cord in extension (left) and flexion (right). Arrow highlights bony impingement on anterior surface. Tension stresses can be seen on the posterior surface of flexed cord.

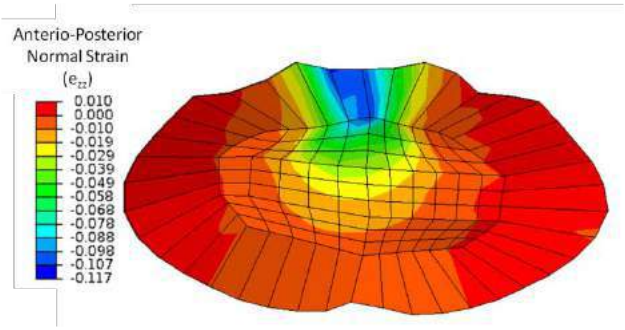

Figure 2: Axial cross section of C56 bony impingement during extension. Compressive strains (blue) can be seen below area of impingement where tensile strains (red) occur at the surface.

DISCUSSION

In this study we developed a model of the C2-T1 cervical spinal cord including the pia, dura, CSF, dentate and mengiovertebral ligaments and incorporated it into our pre-existing cervical spine model. We utilized this model to determine cord stretch, stress, and strain of the cord during physiologic motion. As with all FE models, our model has certain intrinsic limitations such as using a single anatomic model as a global representation and simplified material properties for biologic tissues. However we have aimed to minimize these limitations by incorporating all major spinal anatomy and using hyper-elastic material properties for the spinal cord.

Extension and flexion axial cord stretch between the root entries of our FE model were comparable, but on average are slightly larger, than those we obtained from control patient MR images which range from -0.57 to 8.83 mm in extension and -4.11 to 7.86 mm in flexion. This discrepancy is most likely due to differences in bony anatomy between patients as parametrically changing the force applied to the spinal cord in the FE model did not significantly alter cord stretch. This finding is particularly interesting when considering CSM is caused by altered musculoskeletal anatomy, suggesting that differences in the anatomy of cord compression may significantly affect cord mechanics.

The range of von Mises stress occurring in our model is comparable to previously published CSM FE models. Kim *et al* reported stresses ranging from 0.005 to 2.70 MPa depending on amount of cord compression and Ichihara *et al* reported 0.03 MPa.[3,8] Our model, with maximum von Mises Stress of 0.081 MPa in extension, overlaps the lower end of this spectrum which is to be expected as it is a model of normal anatomy and not CSM.

Unexpectedly, mild cord compression due to bony impingement occurred even in this normal disease free model. This unintended bony impingement shows the propensity of this model to accurately model CSM in the future. Firstly, the location of greatest compression occurred at the C56 level which is the most common level for occurrence of CSM[9]. Secondly the patterns of logarithmic strain caused by this compression closely match those reported by Bhatnagar *et al* in their *in vitro* MRI strain analysis of contused rat spinal cords[10]. Our magnitude of strains is much less than that of Bhatnagar et al as our model does not include such severe contusion. However, the fact that the FE spinal cord is behaving similarly to *in vitro* data is promising. Obviously, human and rat cord mechanics are not identical. In order to ensure that our model truly behaves as the human spinal cord, our goal is to validate our model with patient strain data calculated from mapping flexion and extension MR images to their respective neutral MR image.

Overall we have developed a model of the cervical spine and spinal cord which allows us to predict cord stresses and strain during dynamic motion of the neck. This will, in the future, help us to better understand the progression of cervical myelopathy specifically by incorporating anatomic abnormalities such as osteophytes which lead to stenosis. Finally we aim to model surgical treatments of stenosis to investigate which surgical interventions most effectively relieve spinal cord stress and strain.

ACKNOWLEDGEMENTS

This research was funded in part by grant #1U49CE002108-03 of the National Center for Injury Prevention and Control / CDC and the University of Iowa Deans Graduate Research Fellowship.

REFERENCES

[1] Nouri, A et al., *Spine*, 15;40(12):E675-93, 2015.
[2] Kato, Y et al., *J Neurosurg Spine*. 8(5):436-41, 2008.
[3] Ichihara, K et al., *J. Neurosurg. Spine*, 99(3), pp. 278–285, 2003.
[4] Kode, S et al., *Iowa Orthop J.* 34:150-7, 2014.
[5] Shi, B et al., *Spine J. Off. J. North Am. Spine Soc*., 14(11):2733–2739, 2014.
[6] Tunturi, AR et al., J. Neurosurg., 48(6), pp. 975–979, 1978.
[7] Abel AS, et al., *J Neuroophthalmol*. 34(3):218-22, 2014.
[8] Kim YH, et al., *Med. Eng. Phys*., 35(9), pp. 1266–1271, 2013.
[9] Matsumoto M, et al., *J. Bone Joint Surg. Br*., 80-B(1):19–24, 1998.
[10] Bhatnagar, T et al., *Comput Methods Biomech Biomed Engin*. 19(4):386-95, 2015.

Copyright 2016 The Organizing Committee for the 2016 Summer Biomechanics, Bioengineering and Biotransport Conference

SB³C2016
Summer Biomechanics, Bioengineering and Biotransport Conference
June 29 –July 2, National Harbor, MD, USA
SB³C2016-699

SURFACE PROTRUSION OF HUMAN ENDOTHELIAL CELLS: EXPERIMENT AND MODEL

Jin-Yu Shao, Jin Hao, Yong Chen

Department of Biomedical Engineering
Washington University in Saint Louis
Saint Louis, MO, USA

INTRODUCTION

At sites of infection, injury, or atherosclerotic lesions, human leukocytes first roll on the endothelium, then become activated and firmly-adherent, and finally migrate out of blood vessels. One the one hand, unstable rolling impairs effective neutrophil and lymphocyte recruitment to infected tissues and renders human beings defenseless against invading microorganisms, resulting in immunological diseases such as leukocyte adhesion deficiency syndrome. On the other hand, stable rolling is essential for monocyte infiltration into the aortic intima that initiates and exacerbates cardiovascular diseases like atherosclerosis [1, 2]. Elucidating the mechanisms that underlie leukocyte rolling can pave the way toward therapeutic amelioration of such pathologies.

The rolling of leukocytes is a complex dynamic process that is mediated concertedly by adhesive receptor-ligand bonds between leukocytes and endothelial cells (ECs), shear stress due to blood flow, and cellular mechanical properties such as membrane surface protrusion and tether extraction. Surface protrusion is a solid-like behavior of cell membrane when it is subjected to a point force, whereas tether extraction is a fluid-like behavior of cell membrane that follows surface protrusion when the pulling force is large enough. Due to its important role in stabilizing leukocyte rolling, tether extraction of leukocytes and ECs has been extensively characterized [3, 4] and its features, including shear thinning, non-zero threshold force, and possible negative velocity, can be described by the following equation [5],

$$F = \alpha(U_t - U_0)^{\beta}, \quad (1)$$

where F is the pulling force, U_t is the tether velocity, U_0 is the tether velocity when $F = 0$, and α and β are constants. Although surface protrusion of leukocytes has been well-studied [6-8] and it is known that it can be simulated by the three-parameter solid model (a spring element connected in series with a Kevin element), surface protrusion of ECs remains poorly-understood. Recently, using the micropipette aspiration technique (MAT), Chen et al. found that both the protrusional stiffness and the crossover force (at which cellular deformation will make the transition from surface protrusion to tether extraction) increased when human umbilical vein endothelial cells (HUVECs) were pulled with forces at increasing loading rates from ~10 to 3000 pN/s [9]. However, reliable model parameters are still lacking even if we assume EC surface protrusion can be simulated by the three-parameter solid model. In this work, we report our measurement of the protrusional stiffness of HUVECs at near zero force loading rates and our simulation of HUVEC surface protrusion with the three-parameter solid model. This model is the last piece of the puzzle in regard to incorporating cellular mechanical behaviors into modeling leukocyte rolling systematically.

METHODS

Experiment

HUVEC culture and preparation, bead and micropipette preparation and diameter measurement, the micropipette manipulation system and its data analysis procedures can be found in the literature [10-12]. Figure 1 shows how a HUVEC can be pulled with the MAT. A latex bead that was coated with antibodies against CD31 was placed inside a micropipette. The bead fitted snugly inside the micropipette with only a very small gap between them so that the bead could move freely inside the micropipette. The pressure in the micropipette can be precisely controlled by a manometer. The bead was first driven by a positive pressure to contact the cell on the left. Then a negative suction pressure was applied so that the cell would be pulled if molecular bonds had formed during the contact. The antibody concentration on the bead was reduced until infrequent adhesion (frequency < 25%) occurred between the bead and cell. With this low adhesion frequency, the adhesion

Copyright 2016 The Organizing Committee for the 2016 Summer Biomechanics, Bioengineering and Biotransport Conference

between the bead and cell was very likely mediated by a single bond [13, 14]. Thus, the cell would be pulled through a single receptor, equivalent to being pulled by a point force. Four different suction pressures were used in our experiments: 0.25, 0.375, 0.5, 0.625 pN/μm^2.

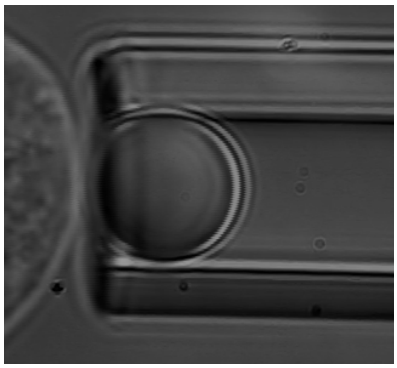

Figure 1. A video micrograph showing how a HUVEC was pulled by a point force with the MAT. The cell on the left was held by another micropipette, which was invisible on the left.

Model

Our viscoelastic model for HUVEC surface protrusion studied with the MAT consists of the three-parameter solid model connected in parallel with a dashpot. The additional dashpot here represents the damping of the surrounding medium imposed on the bead and its drag coefficient (η_{drag}) can be calculated from the bead free motion velocity under a suction pressure. In the three-parameter solid model, k_i (spring element) represents the initial elastic response, and k_d and η_d (Kelvin element) represent the slow elongation response. Under a pulling force with constant loading rate (τ_0), the force imposed on the cell (f) and the length of surface protrusion (ΔL) can be calculated from

$$f = \tau_0 t + \frac{\eta_{drag}\tau_0}{Q_2}[A_1 + A_2], \tag{2}$$

$$\Delta L = \frac{\tau_0 A_1}{\lambda_1 Q_2}\left[\frac{t\lambda_1}{1 - e^{\lambda_1 t}} - 1\right] + \frac{\tau_0 A_2}{\lambda_2 Q_2}\left[\frac{t\lambda_2}{1 - e^{\lambda_2 t}} - 1\right], \tag{3}$$

where

$$A_1 = \frac{k_i + k_d + \eta_d\lambda_1}{\lambda_1(\lambda_1 - \lambda_2)(k_i + k_d)}\left(1 - e^{\lambda_1 t}\right), \tag{4}$$

$$A_2 = \frac{k_i + k_d + \eta_d\lambda_2}{\lambda_2(\lambda_2 - \lambda_1)(k_i + k_d)}\left(1 - e^{\lambda_2 t}\right). \tag{5}$$

$$\lambda_1 = \frac{-Q_1 + \sqrt{Q_1^2 - 4Q_0Q_2}}{2Q_2}, \tag{6}$$

$$\lambda_2 = \frac{-Q_1 - \sqrt{Q_1^2 - 4Q_0Q_2}}{2Q_2}, \tag{7}$$

$$Q_0 = \frac{k_i k_d}{k_i + k_d}, \tag{8}$$

$$Q_1 = \frac{k_i\eta_d + k_i\eta_{drag} + k_d\eta_{drag}}{k_i + k_d}, \tag{9}$$

$$Q_2 = \frac{\eta_d\eta_{drag}}{k_i + k_d}, \tag{10}$$

RESULTS

Figure 2 shows a typical case of a HUVEC pulled under a constant suction pressure of 0.5 pN/μm^2. The cellular deformation (L) was fitted to the following equation

$$L = L_\infty\left(1 - e^{-t/t_c}\right), \tag{11}$$

where L_∞ is the asymptotic value when time t approaches infinity and t_c is the characteristic time. Converting the pressure to the corresponding pulling force and dividing the force by L_∞ yields the protrusional stiffness at near zero force loading rates, which can be inferred from Fig. 2. With all the suction pressures used, we obtained an average protrusional stiffness value of 55.0 ± 0.7 pN/μm. With this stiffness as the constraint for k_i and k_d , we fitted Eqs. 2 and 3 to all the protrusional stiffness data by Chen et al. [9] and obtained the following parameters for HUVEC surface protrusion: $k_i = 592$ pN/μm, $k_d = 60$ pN/μm, and $\eta_d = 108$ pN·s/μm.

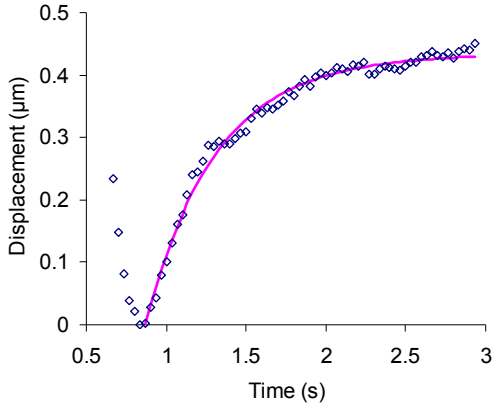

Figure 2. The displacement of an anti-CD31-coated bead before and after it adhered to an attached HUVEC under a constant suction pressure of 0.5 pN/μm^2. The solid line represents the fitting of Eq. 11 to the data.

DISCUSSION

EC surface protrusion has been largely overlooked in modeling and understanding leukocyte rolling. However, it is a critical precursor for tether extraction. Here, we have identified all the parameters that are needed for simulating EC surface protrusion during leukocyte rolling. Combining them with our previous findings on tether extraction, we can illustrate a complete picture of how ECs deform during leukocyte rolling. More importantly, we can now study how ECs influence leukocyte rolling stability with systematic simulation of leukocyte rolling. We can now also reliably predict how ECs will respond to point forces in other situations like creep, relaxation, and hysteresis.

ACKNOWLEDGEMENTS

This work was supported by AHA and NIH.

REFERENCES

[1] Ross, R., *N. Engl. J. Med.*, 340:115-126, 1999.
[2] Ross, R., *Nature*, 362:801-809, 1993.
[3] Shao, J. Y., *Current Topics in Membranes: Leukocyte Rolling and Adhesion*, K. Ley, ed. Academic Press, San Diego, CA, 25-45, 2009.
[4] Shao, J. Y., et al., *PNAS*, 95:6797-6802, 1998.
[5] Chen, Y., et al., *Ann. Biomed. Eng.*, 38:3756-3765, 2010.
[6] Springer, T. A., *Annu. Rev. Physiol.*, 57:827-872, 1995.
[7] Xu, G., et al., *AJP Cell Physiology*, 295:C1434-C1444, 2008.
[8] Evans, E., et al., *Biophys. J.*, 88:2288-2298, 2005.
[9] Chen, Y., et al., *Biophys. J.*, In press, 2016.
[10] Shao, J. Y., et al., *J. Biomech. Eng.*, 124:388-396, 2002.
[11] Chen, Y., et al., *AJP Cell Physiol*, 292:C1272-C1279, 2007.
[12] Girdhar, G., et al., *Biophys. J.*, 87:3561-3568, 2004.
[13] Chesla, S. E., et al., *Biophys. J.*, 75:1553-1572, 1998.
[14] Shao, J. Y., et al., *Ann. Biomed. Eng.*, 35:397-407, 2007.

Copyright 2016 The Organizing Committee for the 2016 Summer Biomechanics, Bioengineering and Biotransport Conference

SB^{3}C2016
Summer Biomechanics, Bioengineering and Biotransport Conference
June 29 –July 2, National Harbor, MD, USA
SB^{3}C2016-701

MEASURING IN-VIVO THE INTERPLAY BETWEEN INTRAOCULAR AND INTRACRANIAL PRESSURE EFFECTS ON THE OPTIC NERVE HEAD

Ian A. Sigal (1,2), Huong Tran (1,2), Alexandra Judisch (1,2), Bo Wang (1,2), Matthew A. Smith (1,2), Andrew Voorhees (1), Joel Schuman (1-3) and Gadi Wollstein (1,2)

(1) Ophthalmology
University of Pittsburgh
Pittsburgh, PA, USA

(2) Bioengineering
University of Pittsburgh
Pittsburgh, PA, USA

(3) Ophthalmology
New York University
New York, NY, USA

INTRODUCTION

Glaucoma a leading cause of blindness worldwide, and elevated intraocular pressure (IOP) is the main risk factor for the development and progression of vision loss.[1] While much attention has been given to the mechanical insult and risk of vision loss associated with elevated IOP,[2] the role of intracranial pressure (ICP) is rarely considered. Recent epidemiological evidence suggests that ICP may have an important influence on the susceptibility to glaucoma. [3] This is thought to involve pressure-related insult of the lamina cribrosa, a structure in the posterior pole where retinal ganglion cell axons exit the eye, and where neural tissue damage initiates. [1,3]

Our goal was to measure and map with high detail in a primate model the in-vivo biomechanical insult to the lamina cribrosa caused by acute changes in intraocular and/or intracranial pressures Specifically, we determined the lamina cribrosa anterior-posterior displacements, stretch and compression under controlled levels of IOP and ICP.

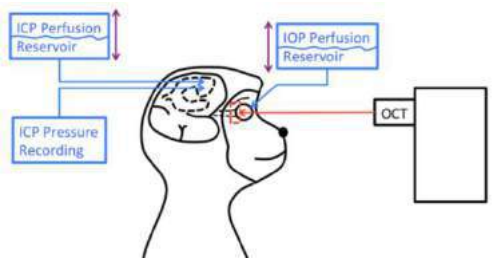

Figure 1: We imaged in-vivo the posterior pole of the monkey eye using optical coherence tomography while controlling intraocular and intracranial pressures (IOP and ICP).

METHODS

Four eyes of 3 macaque monkeys were imaged in-vivo with spectral domain optical coherence tomography (Bioptigen, Durham, NC), while IOP and ICP were controlled through cannulas in the anterior chamber and lateral ventricle, respectively (Figure 1). Pressures were set to all combinations of the following levels (mmHg): for IOP 15 (baseline), 5, 30 and 50, and for ICP 10 (baseline), 5, 25 and 40. To allow viscoelastic effects to dissipate, images used were acquired 10 minutes after a pressure change..

The anterior lamina cribrosa (ALC) and scleral canal opening at Bruch membrane (BMO) were manually marked in 18 radial virtual B-scans per scan. Custom code was used to reconstruct 3D ALC surfaces and register BMOs. ALC depths were computed relative to the BMO best-fit plane within regions visible in all scans of an eye, and normalized to baseline in each monkey.

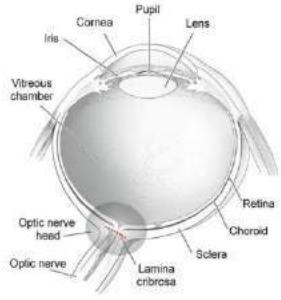

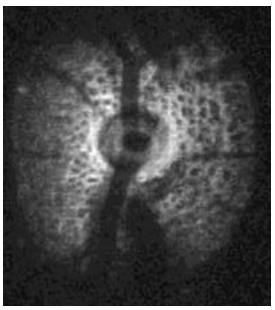

Figure 2: (Left) Eye diagram [4] and (right) example coronal view of the lamina cribrosa of Monkey 2 (red dotted line on left) at the baseline pressures: IOP=15 mmHg and ICP=10 mmHg. Note that this is a single 2D view through a 3D scan.

Copyright 2016 The Organizing Committee for the 2016 Summer Biomechanics, Bioengineering and Biotransport Conference

A recently developed tracking algorithm based on image registration [4] was adapted to OCT and used to extract the pressure-induced tissue displacements, and from these to compute the stretch and compression.

RESULTS

IOP and ICP had nonlinear effects on the median ALC depth (Figure 3). There were strong interactions between the pressure effects, meaning that the effects of one pressure depended strongly on the other pressure. Pressure effects were non-monotonic. For example, in eye 3R at 20mmHg ICP, the ALC displaced anteriorly when IOP increased from 8 to 15 mmHg, and posteriorly for IOP from 15 to 30mmHg. In all 4 eyes, the most anteriorly ALCs occurred with IOPs below baseline (15mmHg) and very high ICP (20-45mmHg).

Pressure variations from the baseline caused substantial lamina cribrosa stretch and compression, sometimes exceeding 30% (Figure 4). Effects differed between lamina regions and animals, and depended on whether the pressures were increased or decreased.

DISCUSSION

The in-vivo effects of IOP and ICP on the lamina cribrosa are substantial, highly nonlinear and interact strongly. Deformations were larger than predictions with generic homogenized numerical models [2,4], but consistent with ex-vivo experiments [5], and recent micro-structure aware models [6]. The complex nonlinear effects indicate that the translaminar pressure difference (IOP – ICP) is too simplistic a parameter to describe lamina cribrosa mechanics. Our methods open a new way to investigate the interplay between IOP and ICP. The longer term effects of variations in IOP and ICP remain to be determined.

ACKNOWLEDGEMENTS

Funding: NIH R01-EY023966, R01-EY25011, P30-EY008098 and T32-EY017271, the Eye & Ear Foundation (Pittsburgh, PA). CIHR MOP123448.

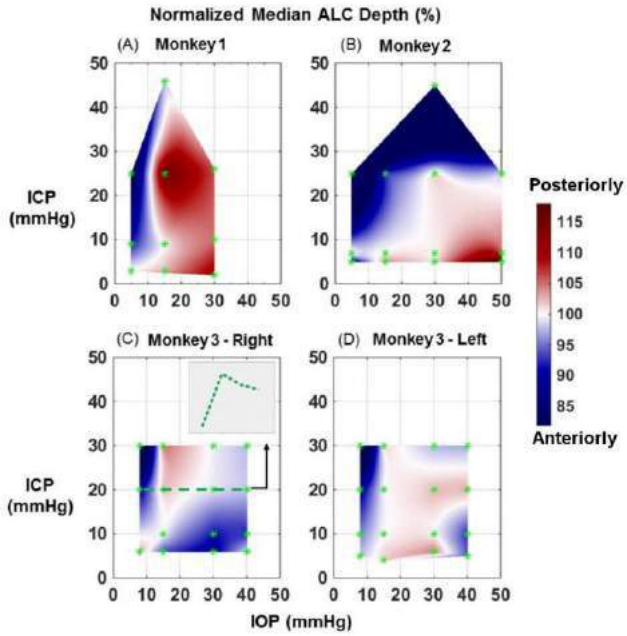

Figure 3: Effects of IOP and ICP on the LC in-vivo. Shown are median values in %, normalized to baseline values, with green asterisks corresponding to the actual pressure conditions. Dashed green line shows an example of a non-monotonic effect in 3R.

REFERENCES

[1] Quigley, HA et al., *Br J Ophthalmol,* 90(3):262-267, 2006. **[2]** Sigal, IA et al., *Exp Eye Res*, 88:799-807, 2009. **[3]** Berdahl, JP et al., IOVS, 49(12):5412-5418, 2008. **[4]** Adapted from Sigal et al. *BMMB* 8(2): 85-98, 2009. **[5]** Sigal, IA et al. *IOVS*, 55(1):1-15, 2014. **[6]** Voorhees, A et al. SB3C, June 29 – July2, 2016

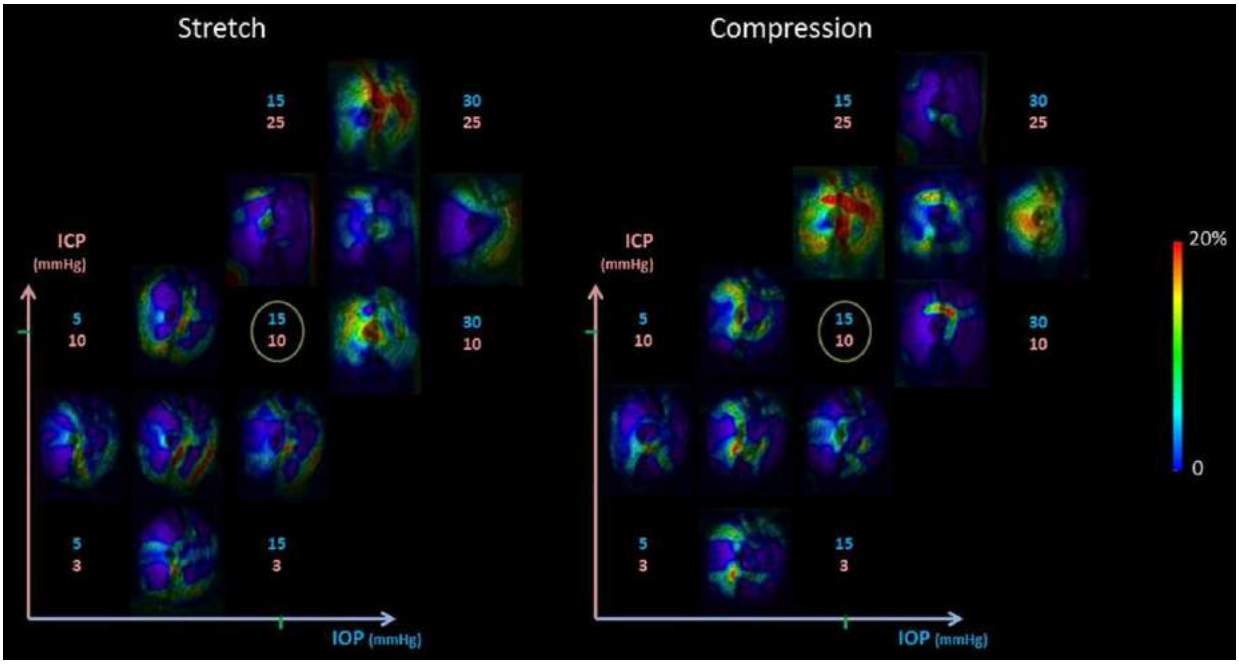

Figure 4: Coronal views through the lamina cribrosa of Monkey 2 color-coded by stretch and compression (1st and 3rd principal strains) resulting from acute pressure changes from the baseline (green circle). In this eye, increases in IOP caused lamina stretch, larger at elevated ICP. Increases in ICP caused lamina compression, larger at baseline IOP. Decreases in IOP or ICP caused less lamina stretch and compression. Simultaneous changes in IOP and ICP produced smaller, but still significant deformations, even if translaminar pressure was maintained at the baseline level.

Copyright 2016 The Organizing Committee for the 2016 Summer Biomechanics, Bioengineering and Biotransport Conference

SB³C2016
Summer Biomechanics, Bioengineering and Biotransport Conference
June 29 –July 2, National Harbor, MD, USA
SB³C2016-702

DESIGN OF A NOVEL IN VITRO SIMULATION OF A DYNAMICALLY CONTRACTING MITRAL VALVE ANNULUS

Thomas F. Easley (1,2), Charles H. Bloodworth IV (1), and Ajit P. Yoganathan (1,3)

(1) Parker H. Petit Institute for Bioengineering and Bioscience
Georgia Institute of Technology
Atlanta, GA, USA

(2) George W. Woodruff School of Mechanical Engineering
Georgia Institute of Technology
Atlanta, GA, USA

(3) Wallace H. Coulter Department of Biomedical Engineering
Georgia Institute of Technology
Atlanta, GA, USA

INTRODUCTION

Moderate to severe mitral valve regurgitation (MR) has an occurrence rate of 1.7% among the adult US population [1]. In MR, the mitral valve (MV) leaflets do not completely coapt, leading to backward flow of blood from the ventricle to the atrium. In categorizing MR there are two classifications: (1) degenerative and (2) functional [2]. Although the MV is structurally normal in functional MR, the complexity of the valvular anatomy and the multitude of repair and replacement techniques makes using *in vivo* models difficult. In using *in vitro* models for functional MR, where a healthy MV can be used, the structural and fluid mechanics of the MV as well as surgical techniques are able to be studied in a more controlled environment.

In current *in vitro* models, the structural complexity of the excised MV is preserved and can be studied [3]. However, these models rely on certain simplifications, one being that the MV is mounted to a static, rigid annulus (leaflet attachment to the myocardium). This simplification of the annulus is justified when looking to control factors that are separate from a study's interest, e.g. investigating chordal forces. However, in order to study, for example, how current *in vivo* MR quantification techniques account for a moving leak in the valve (MR jet orifice), a more physiological model with dynamic contraction to move the jet orifice is needed. Motivated by this need, the work of this study provides the novel design and development of a dynamically contracting MV annulus within an *in vitro* left heart simulator.

METHODS

Mitral Valve Annulus Plate Design and Development

Designed to fit within the existing modular Georgia Tech Left Heart Simulator, it was critical to maintain the imaging capabilities of the previous version of the simulator [4]. First, a spring was embedded within a Dacron cuff which makes up the MV annulus. Then a wire was fed through the center of the spring. Finally, the wire was attached to the piston heads of two linear actuators (HAD2-2, RobotZone, Winfield, KS) (Figure 1).

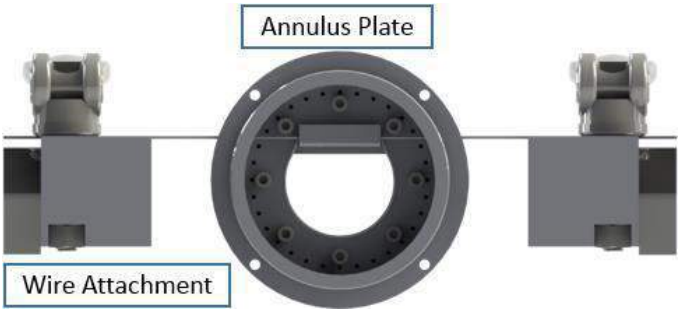

Figure 1. Simplified diagram of the dynamically contracting annulus setup with the annulus plate centered between the wire attachments at the ends of the linear actuators.

The linear actuators were displacement driven and controlled individually using PID and H-bridge controllers (DeviceCraft, Fitchburg, MA). The input displacement array consisted of healthy, ovine MV annular perimeter derived from prior *in vivo* work [5].

Experimental Setup

A healthy mitral valve was excised from a fresh ovine heart (Superior Farms, Denver, CO). During excision, the annulus and subvalvular structures (i.e. chordae tendineae and papillary muscles) were preserved. The valve was then mounted into the left heart chamber

Copyright 2016 The Organizing Committee for the 2016 Summer Biomechanics, Bioengineering and Biotransport Conference

with the MV annulus sutured to the annulus cuff and the papillary muscles (PM) attached to the PM rods for proper positioning (Figure 2).

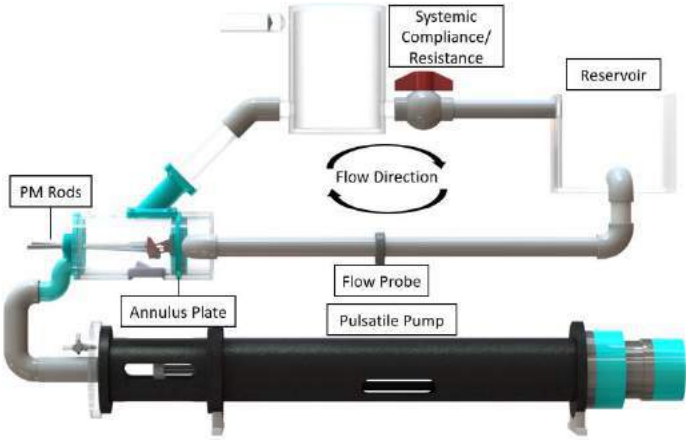

Figure 2. Overview of left heart simulator flow loop with the pulsatile pump.

A ratio of 35% systole and 65% diastole was utilized at 70 beats/min, and systemic resistance and compliance were tuned to reach a cardiac output of 5 L/min and a peak systolic pressure of 120 mmHg. In order to control the pulsatile pump (Vivitro Labs, Victoria, BC, CA) and the linear actuators, and record flow loop hemodynamics, custom codes were written in LabVIEW (2015, National Instruments, Austin, TX).

For MV visualization, 3D echocardiography via ie33 xMatrix ultrasound system and x7-2 probe (Philips Healthcare, Andover, MA) was performed. The motor position was measured using the built-in potentiometers of the linear actuators and compared to the desired displacement using LabVIEW.

RESULTS

Using the newly designed annulus plate, the hemodynamic criteria of the methods were all met. From the resultant images (Figure 3), the annular area was measured to be 4.84 cm^2 at peak diastole and 4.03 cm^2 at peak systole (-16.73% change). This result is similar to prior *in vivo* work (-19.02±4.94%) [5].

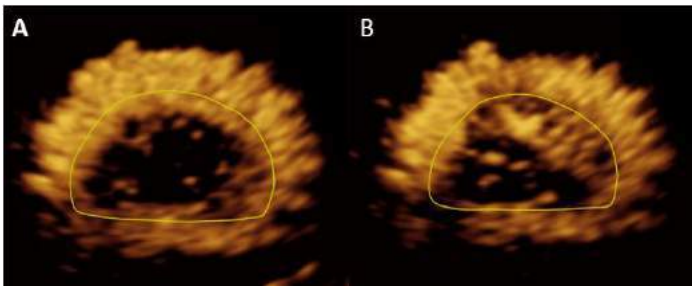

Figure 3. Acquired echocardiography of the mitral valve using the dynamically contracting annulus at peak (A) diastole and (B) systole. Annular area: A = 4.84 cm^2 and B = 4.03 cm^2.

In addition, annular perimeter, as measured by actuator piston position (Figure 4), showed strong agreement with the target waveform (RMSE = 8.69 µm, R^2 = 0.99).

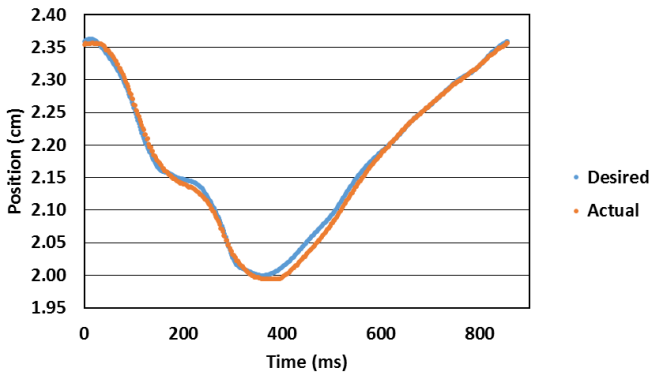

Figure 4. Comparison of desired and actual displacements of the linear actuators. RMSE = 8.69 µm and R^2 = 0.99.

DISCUSSION

This work provides the first *in vitro* MV simulator with a dynamically contracting annulus. The *in vitro* setup was tested at physiological conditions (i.e. flow rates and pressures) and maintained the size and shape of previous setups. In addition, the linear actuators were able to provide MV annular contraction, and reproduce the annulus perimeter motion and area change of previous *in vivo* studies.

The main limitation of this new annular design is that the annulus is flat and its contraction is limited to 2-D, planar motion. Physiologically, the MV annulus has a 3-D contractile motion over the cardiac cycle, changing between a saddle-shape and a more flat-shape. This out-of-plane shape change could play additional roles in leaflet billowing and tissue stresses [6].

The dynamically contracting annulus addition to the MV *in vitro* model enables another level of detail needed to advance mechanical understanding of the MV through experimental work, as well as computational modeling and quantification. Future work will focus on, but will not be limited to the following: (1) further validation of healthy and diseased annular motion, (2) comparison of physiological and pathophysiological MV mechanics of static vs dynamic annulus, (3) removing static assumptions from MR quantification, e.g. a nonmoving regurgitant orifice for proximal isovelocity surface area of MR, and (4) enhancing MV computational simulations using *in vitro* validation.

ACKNOWLEDGEMENTS

This work was supported by the National Heart Lung and Blood Institute under Grant R01HL119297. The authors would also like to thank Eric Pierce for his assistance in reviewing work.

REFERENCES

[1] Mozaffarian, D, et al., *Circulation*, 131.4:e29, 2015.
[2] Schmitto, J et al., *Cardiology in Review*, 18.6:285-291, 2010.
[3] Siefert, A et al., *CVET*, 6.2: 193-207, 2014.
[4] Rabbah, J et al., *ABME*, 41.2:305-315, 2013.
[5] Levack, M et al., *Circulation*, 126.11 suppl 1:S183-S188, 2012.
[6] Lee, A et al., *Circulation*, 127:832-841, 2013.

Copyright 2016 The Organizing Committee for the 2016 Summer Biomechanics, Bioengineering and Biotransport Conference

SB^{3}C2016
Summer Biomechanics, Bioengineering and Biotransport Conference
June 29 –July 2, National Harbor, MD, USA
SB^{3}C2016-703

EFFECT OF ELASTIN DIGESTION ON THE BIAXIAL MECHANICAL RESPONSE OF THE MURINE VAGINA

Katy M. Robison (1), Derek J. Bivona (1), Kristin S. Miller (1)

(1) Biomedical Engineering
Tulane University
New Orleans, LA, US

INTRODUCTION

Pelvic Organ Prolapse (POP) is a global health concern, affecting over 41% of women [1]. POP is characterized by the atrophy of the vaginal wall and the prolapse of the pelvic organs which leads to both physical and emotional health consequences. Little is known about the underlying pathology of POP; however, dysfunction of the elastin metabolism within the vaginal extracellular matrix has been implicated [2-4]. Compromised elastin integrity may lead to an increase in matrix-metalloprotease activity within the vaginal extracellular matrix, which may increase the degradation of collagen fibers and compromise vaginal mechanical integrity [3]. In addition to the aforementioned biochemical role, elastin may also contribute to vaginal mechanical integrity by providing tissue resilience. Hence, the combined effect of elastin alteration and collagen turnover may affect the biomechanical properties of the vagina and contribute to the development of POP [3]. The role of elastin in normal vaginal mechanical function, however, is not fully understood [2-4]. Therefore, the objective of this study is to quantify the biaxial mechanical properties of the murine vagina before and after elastase digestion to determine the contribution of elastin to vaginal mechanical function. We hypothesize that the depletion of elastin will result in higher transition stress and strain (right-ward shift in the stress-strain curve) and an increased linear modulus.

METHODS

Five female C57/BL/6 mice (IACUC approved) were euthanized at 4-6 months of age while in estrus. After one freeze/thaw cycle, the reproductive tract was excised, and the vagina was isolated from the surrounding tissue. **MECHANICAL TESTING.** Samples were mounted onto metal cannulas within a pressure-myograph. Following preconditioning and equilibration, specimens underwent pressure-diameter tests ($P = 0$ to 25 mmHg) at three different axial extensions around the estimated *in vivo* axial stretch λ_z^{iv}, followed by axial force-length tests at four different pressures (2, 8, 17, 25 mmHg) [5]. After mechanical testing, specimens were intraluminally exposed to 1 mL of porcine pancreatic elastase at 15 U/mL for 45 minutes at the *in vivo* configuration [6]. The vagina was re-equilibrated in Hank's solution and the mechanical tests repeated. Following testing, a ring (~0.5 mm thick) was cut transversely in the center of the vagina, at the location at which the tissue diameter was tracked during the mechanical testing. The ring then was placed in Hank's solution, and following a 30-minute equilibration period, rings were imaged. The anterior section of the ring was cut radially, and the near zero-stress state was imaged 30 minutes later. **DATA ANALYSIS.** A bilinear curve fit was applied to the local stress-strain data to quantify the moduli in the toe- and linear-regions [7]. The opening angle was measured from the midpoint of the inner wall to the tips of the outer wall of the opening sections [8]. **STATISTICAL ANALYSIS.** Differences between the unloaded geometry, opening angle, toe- and linear-region moduli, and transition stress and deformation at the intersection of the toe- and linear-regions between the pre- and post-elastase digestion groups were analyzed using a paired two-tailed student's t-test, with $p < 0.05$ considered significant. Data is presented as mean ± SEM.

RESULTS

Intraluminal exposure to elastase for 45 minutes induced marked changes in the vaginal biaxial mechanical response (Figure 1). Both cyclic pressure-diameter (not shown) and corresponding circumferential Cauchy stress-strain curves (Figure 1) demonstrated the marked shift of the mechanical response following digestion. Bilinear curve fits demonstrated that the stress at the transition point between the toe- and linear-regions of the stress-strain curve

Copyright 2016 The Organizing Committee for the 2016 Summer Biomechanics, Bioengineering and Biotransport Conference

significantly increased following elastase digestion and that the linear modulus increased (Figure 1). Further, a decrease in the unloaded thickness and a significant increase in the opening angle were determined following elastase digestion.

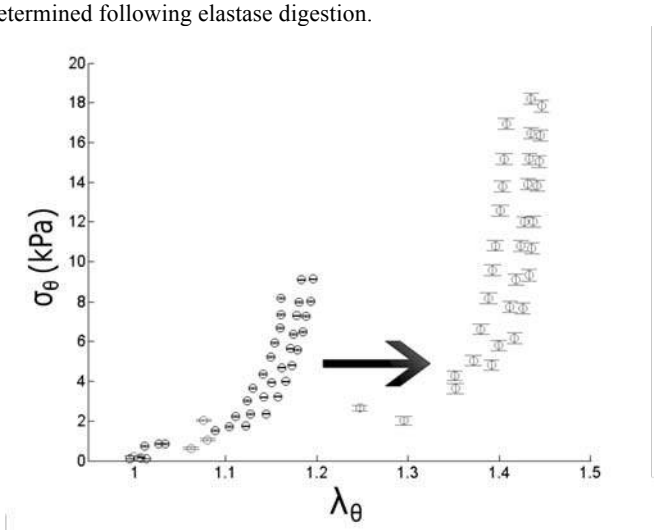

Figure 1: Circumferential Cauchy stress-strain curves for the vagina before (black) and after elastase digestion (grey) at 3 different axial extensions around the estimated *in vivo* axial stretch λ_z^{iv}. The dark arrow demonstrates the extended toe-region of the stress-strain curve following elastase digestion.

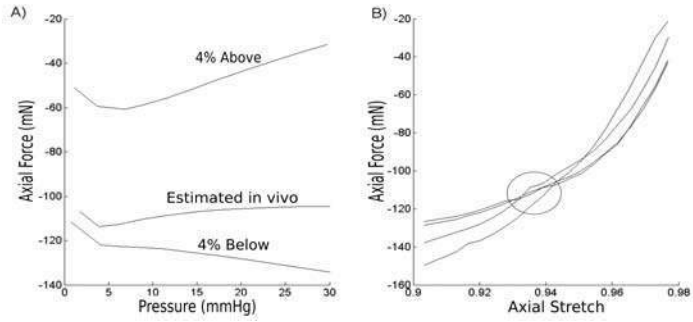

Figure 2: The estimation of the *in vivo* axial stretch ratio based on the near constancy of the transducer-measured force-pressure response during the cyclic pressure-diameter testing (Panel A), and typical force-length responses for which the intersection in the force-λ_z data, denoted by the circle, reveals the *in vivo* axial stretch (Panel B).

The values of *in vivo* axial stretch λ_z^{iv} (0.96±0.008 vs. 0.96±0.002) were not statistically different following elastase digestion. The vagina, however, demonstrated a similar behavior to that of arteries, wherein the measured axial force remained nearly constant in response to changes in luminal pressure at the estimated *in vivo* axial stretch (Figure 2A) [5]. The values of λ_z^{iv} were confirmed as the value of axial stretch where the $f - \lambda_z$ responses overlapped for multiple luminal pressures (Figure 2B). The transition strain, unloaded outer diameter, unloaded length, and toe-region modulus were not shown to be statistically different.

DISCUSSION

In this study, intraluminal exposure to elastase for 45 minutes induced significant changes in the nonlinear mechanical behavior of the murine vagina. The cyclic pressure-diameter tests (not shown) and associated Cauchy stress-strain plots (Figure 1) suggest that elastin may contribute to the mechanical response of the vagina in the low-strain regime. A reduction of tissue stress in the toe-region of the stress-strain curve following elastase digestion has also been observed in ligaments [9]. In this study, digestion of elastin resulted in a higher value of stress at the toe- to linear-region transition and a rightward shift of the associated stress-strain curve (Figure 1). The opposite trend, however, has been observed in the external os of the cervix (unpublished pilot study) and in carotid arteries wherein tissues demonstrated a marked loss of distensibility following digestion in the low-strain regime [6, 10]. Further, Ferruzzi et al. identified a significant loss of collagen fiber undulation following the removal of elastin, consistent with the marked increase in stiffness [6]. Hence, the rightward shift of the stress-strain curve observed in this study may indicate that the collagen undulation has increased following elastase digestion, resulting in a rightward shift of the stress-strain curve. These results may also be explained, in part, by the compressive λ_z^{iv} identified in the vagina in contrast to the axial prestretch observed in vasculature and the murine cervix (Figure 2B). These findings suggest, however, that both the mechanical contribution of elastin and the potential microstructural interactions of elastin and collagen within vaginal tissue may differ from cervical tissue and vasculature. Hence, future work is needed to rigorously quantify the microstructure of the vagina, including potential elastin-collagen interactions.

Further, in this study an increase in the opening angle was observed following elastase digestion, and as expected from the previous results, studies in vasculature report the opposite: a dramatic decrease in the residual-stress related opening angle [6,10]. Opening angles are thought to arise, in part, from the deposition of stable elastin during development and the continual turnover of collagen and smooth muscle at consistent preferred stretches within the ground matrix [11]. The stability and turnover of elastin within the vagina is currently unknown. Hence, there is a pressing need to determine the prestretch of elastin and the deposition timecourse within the vagina, as well as to ascertain how its deposition characteristics may affect collagen undulation and organization.

Our results presented herein differ from the findings of Rahn et al.; however, this may be due to differences in testing methods as well as elastin isolation. Rahn et al. conducted uniaxial tests consisting of rings of vaginal tissue mounted between stainless steel wires, whereas we performed biaxial tests with simultaneous axial extension [3]. Additionally, the use of a genetically-compromised mouse model of elastin compared to an elastase digestion in healthy tissues may contribute to variations in mechanical response. As demonstrated in both studies, however, a loss of elastin integrity clearly changes the mechanical response of the vagina, which may thus alter the environment for the cells residing in the extant matrix and subsequently disrupt vaginal homeostasis (e.g., lead to alteration in smooth muscle phenotype from contractile to synthetic). Hence, we submit there is a pressing need to further delineate the contribution of elastin to vaginal homeostasis and the potential development and progression of vaginal prolapse.

ACKNOWLEDGEMENTS

We would like to acknowledge Victoria Morris for assistance.

REFERENCES [1] Hendrix, S et al., *Am J Obst Gyn*, *186*(6), 1160–1166, 2002. [2] Drewes P et al., *Am J Path*, 170(2):578-589, 2007. [3] Rahn D et al., *Am J Ob Gyn*, 198(5):590.e1-6, 2008. [4] Downing, K et al., *J Mech Beh Biomed Mat*, 29:190-8, 2014. [5] Ferruzzi, J et al., *Ann Biomed Eng,* 41(7):1311-1330, 2013. [6] Ferruzzi, J et al., *Card Res*, 92:287-295, 2011. [7] Lake, S et al., *J Ortho Res*, 27(1):1596-602, 2009. [8] Humphrey, J. *Card Sol Mech*, Springer, 2002. [9] Henninger, H. *J Ortho Res*, 31(8):1226-33, 2013. [10] Fonck, E et al., *Am J Phy*, 292:H2754-63, 2007. [11] Cardamone, L., et al., *Biomech Model Mechano*, 8(6):431-46, 2009.

Copyright 2016 The Organizing Committee for the 2016 Summer Biomechanics, Bioengineering and Biotransport Conference

SB^{3}C2016
Summer Biomechanics, Bioengineering and Biotransport Conference
June 29 –July 2, National Harbor, MD, USA
SB^{3}C2016-704

MRI QUANTIFICATION OF HUMAN SPINE CARTILAGE ENDPLATE GEOMETRY

John F. DeLucca (1), John M. Peloquin (1, 2), Lachlan J. Smith (3), Nichol Reisher (1), Alexander C. Wright (4), Edward J. Vresilovic (5), Dawn M. Elliott (1)

(1) Department of Biomedical Engineering
University of Delaware
Newark, DE, USA

(2) Department of Bioengineering
University of Pennsylvania
Philadelphia, PA, USA

(3) Department of Neurosurgery
University of Pennsylvania
Philadelphia, PA, USA

(4) Department of Radiology
University of Pennsylvania
Philadelphia, PA, USA

(5) Department of Orthopedic Surgery
Pennsylvania State University
Hershey, PA, USA

INTRODUCTION

The cartilage endplate (CEP) is a thin layer that separates the intervertebral disc from the adjacent vertebral endplate and vertebral body. The geometry of the CEP is critical to its functions of load bearing and transport. The CEP must be thick enough to transmit loads across the disc-bone interface, and thin enough to minimize the distance solutes must travel to reach disc cells. These functions may be affected by degeneration. With degeneration, CEP permeability decreases [1], its tensile modulus decreases [2], and it may become calcified or damaged [3]. While these biochemical and mechanical changes are known, the effect of disc degeneration on CEP geometry remains unknown.

Magnetic resonance imaging (MRI) is a non-invasive technique to assess tissue structure, but unfortunately, current clinical MRI sequences cannot distinguish the CEP from surrounding tissues. Recent advances in MRI have utilized two sequences, ultrashort time-to-echo (UTE) [4] and fast low-angle shot (FLASH) [5], that have enhanced the contrast between the CEP and the surrounding tissues. In the present study, we apply the FLASH sequence because it is readily available on clinical scanners and usually requires shorter scan times for the same field of view and resolution [5].

The objective of this study was to quantify 3D CEP geometry using a FLASH MRI sequence to evaluate relationships between CEP geometry and age, degeneration, spine level, and disc geometry. Additionally, we assessed the accuracy and repeatability of the MR-based measurements compared to morphological images.

METHODS

Human male lumbar motion segments (n = 22) from 9 cadavers (age 60.9 ± 10.2 yrs; range 42-75 yrs) were imaged using a Siemens 7T magnet. Disc degeneration was assessed by the Pfirrmann grading system and by T2 mapping and average T2* in the central nucleus pulposus [1]. Enhancement of CEP contrast was achieved using a 3D MRI FLASH sequence [5]. Imaging parameters were TR = 9 ms, TE = 3.7 ms, flip angle = 20°, 0.2 mm isotropic resolution [5].

Mid-sagittal and Axial Geometry

CEP thickness, anterior-posterior (A-P) width, lateral width, and axial area were measured. Thickness was measured in mid-sagittal plane images (Fig. 1A). Thickness was calculated for 5 evenly spaced regions across the CEP. Within a given region, the CEP was outlined using the polygon selection tool in ImageJ and converted to a binary mask. Thickness was calculated as the mask area divided by the mask width. A-P width, lateral width, and axial area were measure in the axial plane using OsiriX. Due to the curvature of the disc-bone interface, MR images were post-processed into thick mean intensity slabs of 1.5 mm.

Statistics

Many factors may affect CEP geometry including age, T2* value, Pfirrmann grade, spine level, disc height, and disc axial geometry. Therefore, multiple regression was performed using R software to identify the effect of each factor on each CEP geometry parameter.

Assessment of Accuracy and Repeatability

Two discs imaged with MRI were also processed for morphology analysis. Each disc was fixed in 10% formalin for 1 week and decalcified for 2 weeks with Formical-2000, refreshing the solution every 2-3 days. Discs were bisected along their mid-sagittal plane and

Figure 1: MR (A) and morphology (B) images were overlaid (C)

Copyright 2016 The Organizing Committee for the 2016 Summer Biomechanics, Bioengineering and Biotransport Conference

imaged.

The mid-sagittal morphology image (Fig. 1B) was paired with the corresponding mid-sagittal plane MRI image and overlaid using OsiriX software (Fig. 1C). Each image pair was evaluated for CEP thickness by 2 raters, who each independently measured CEP thickness on the MR image and the morphology image on 4 separate days. Accuracy was evaluated by correlating the MRI measurements with the paired morphology measurements. Residuals were calculated as the vertical distance between the MRI-morphology pairing and a 1:1 line. Repeatability was evaluated by calculating the coefficient of variation (CV) for each location and each rater. CV is defined as the ratio of the standard deviation to the mean. The average CV for each user was then compared.

RESULTS

Accuracy and Repeatability

MRI measurements were accurate compared to the paired morphology measurements (slope = 1.005) with an average residual of 0.02 ± 0.14 mm. The standard deviation of the residual (0.14) was less than the MRI resolution 0.2 mm. The method was also repeatable as the coefficients of variation were 13.6% and 14.5% for rater 1 and 2, respectively. For a CEP thickness of 0.5 mm these repeatability measures equate to 0.068 mm and 0.073 mm, respectively, both of which are below the MRI resolution.

CEP Geometry

CEP thickness was greater in anterior and posterior locations than in the center of the disc (Fig. 2A). Therefore, three thickness parameters were used in the multiple regression analysis: center thickness, anterior and posterior (A/P) average thickness, and average thickness for all 5 regions.

Several CEP geometry parameters correlated with age. Average thickness (r=-0.44, $p<0.01$, Fig. 2B), A-P thickness (r=-0.40, $p<0.01$), axial area (r=-0.37, $p<0.01$, Fig. 2C), and lateral width (r=-0.42, $p<0.01$) all decreased with age. Surprisingly, no CEP geometry parameter correlated with degeneration measured by T2* or Pfirrmann grade (Fig. 2D).

While no thickness parameter changed with disc level, some axial geometries did: CEP axial area was 35% greater in L3-L4 than in L5-S1 ($p<0.05$) and CEP A-P width was 20% greater in L3-L4 than L5-S1 ($p<0.05$).

No CEP geometry parameters correlated with disc height (Fig. 2E). However, some axial CEP geometry parameters correlated with disc axial geometry. CEP axial area correlated with disc axial area (r=0.47, $p<0.01$, Fig. 2F) and covers 31 ± 7% of the disc axial area. CEP A-P width correlated with disc A-P width (r=0.31, $p<0.05$) and covers 56 ± 8% of the disc A-P width. CEP lateral width correlated with disc lateral width (r=0.32, $p<0.05$) and covers 57 ± 8% of the lateral disc width.

DISCUSSION

This study quantified CEP geometry using MRI and evaluated potential relationships between CEP geometry and age, degeneration, spine level, and disc geometry.

We found that CEP thickness was greater at the anterior and posterior margins than in the center. This may be due to the anchoring of the inner annulus fibrosus through the CEP at those margins, which could require more material for mechanical support. CEP axial geometry correlated with disc axial geometry, and the CEP spans a larger area of the disc (30%) than just the NP (~25%). CEP thickness did not correlate with disc height, which may be valuable for the transport functions of the CEP. Larger disc heights are already burdened with a long diffusion distance from the solute supply to the cells in the center of the disc. If CEP thickness increased with disc height, this burden would only increase.

This study also assessed potential changes of CEP geometry with age and degeneration. Surprisingly, no g eometric parameters correlated with degeneration measured by either T2* or Pfirrmann grade. However, several properties (CEP axial area, lateral width, anterior and posterior thickness, average thickness) significantly decreased with age. The fact that CEP geometry changes with age and not with degeneration reinforces the notion that CEP degeneration may proceed differently than disc degeneration [1]. It is unclear what processes lead to a smaller CEP with aging. The CEP is prone to damage [2], herniation [6], and calcification [4] which may manifest in changes in CEP geometry.

We previously presented FLASH MRI as a tool to measure CEP geometry and demonstrated the potential clinical feasibility of the technique [5]. In the current study, we demonstrated outstanding accuracy and repeatability of the technique through paired MRI and morphology comparisons. Importantly the repeatability and inter-user error were both below the resolution of the MRI (< 0.2 mm). Moreover, the measurements of CEP thickness obtained from the MRI technique (0.3–1mm) were comparable to previous measurements using histology (0.4–0.8 mm) [3]. Thus the MRI technique, if modified for clinical feasibility, could be valuable for assessing CEP geometry in low back pain patients.

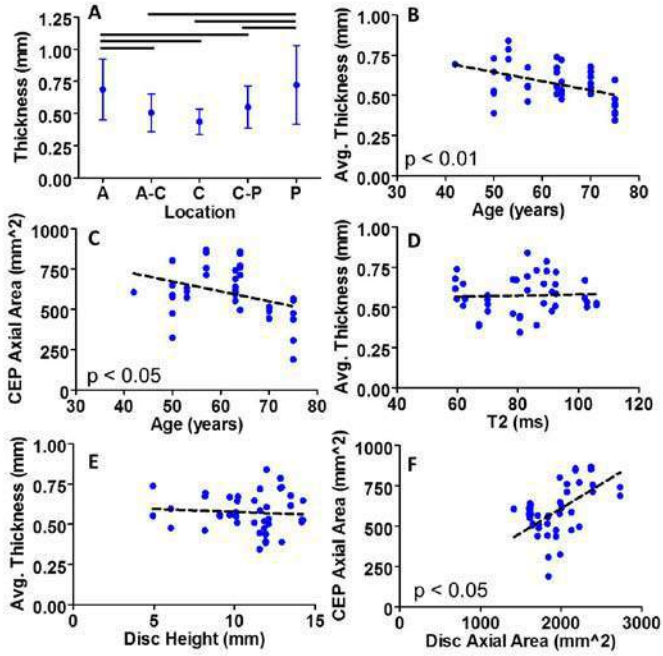

Figure 2: CEP was thickest at the periphery and thinnest in the center (A, p<0.01). Average thickness (B, p<0.01) and axial area (C, p<0.05) correlated with age. Average thickness did not correlate with T2* (D) or disc height (E). CEP axial area correlated with disc axial area (F, p<0.01).

ACKNOWLEDGEMENTS

This study was funded by NIH R01AR050052.

REFERENCES

[1] DeLucca et al., *J Biomech*, 2016. [2] Fields et al., *J Ortho Res*, 32(2):245-52, 2014. [3] Roberts et al., *Spine*, 14:166-74, 1989. [4] Fields et al., *Radiol*, 2014. [5] Moon et al., *Eur Spine J*, 2013. [6] Lama et al., *Eur Spine J*, 23(9):1869-77, 2014.

Copyright 2016 The Organizing Committee for the 2016 Summer Biomechanics, Bioengineering and Biotransport Conference

SB³C2016
Summer Biomechanics, Bioengineering and Biotransport Conference
June 29 – July 2, National Harbor, MD, USA
SB³C2016-707

MODELING THE GAS FOAMING PROCESS FOR EXPANDING ELECTROSPUN NANOFIBER MEMBRANES IN THE THIRD DIMENSION

Zhuoran Li (1), Jingwei Xie (2), Linxia Gu (1,3)*

(1) Department of Mechanical and Materials Engineering
University of Nebraska-Lincoln
Lincoln, Nebraska, United States

(2) Department of Surgery-Transplant and
Holland Regenerative Medicine Program,
University of Nebraska Medical Center
Omaha, Nebraska, United States

(3) Nebraska Center for Materials and Nanoscience
Lincoln, Nebraska, United States

INTRODUCTION

Three dimensional (3D) cell culture systems gain popularity due to its biomimicry in the anatomical architecture of a tissue [1]. A number of techniques have been developed for creating a range of 3D tissues where the spatial organization of scaffolds was constructed. Jiang et al. reported a modified gas foaming technique for expanding electrospun poly(ε-caprolactone) (PCL) nanofiber mats to a 3D scaffold with layered structure. However the detailed expanding process of nanofiber scaffolds, i.e., the gas bubble nucleation, growth, and coalescence is not well understood.

The goal of this work is to develop a numerical framework for capturing the expanding process of electrospun nanofiber membranes. A computational fluid dynamics (CFD) model was developed considering a gas-liquid two-phase flow to increase the gap distance between the adjacent layers of nanofiber scaffolds. A volume of fluid (VOF) method [2] was adopted to move the gas-liquid interface and thus track the fluid movement. The flow dynamics of the expanding process were systematically studied in order to optimize and control the spatial structure of 3D electrospun nanofiber scaffolds.

METHODS

The expanding process between two layers was considered using a VOF model in this work (Figure 1). Five inlets were constructed at the bottom layer to initiate the gas flow and mimic the gas bubble nucleation. The inlet velocity of gas was assumed as 2 m/s to simulate the bubble growth. The standard atmospheric pressure (1.013e5 Pa) was assigned at the outlet. The liquid with a density of 1000 kg/m³ and a dynamic viscosity 0.001 Pa·s was considered. The gas was taken as incompressible air with a density of 1.225 kg/m³ and a dynamic viscosity of 1.7894e-5 Pa·s. The surface tension is assumed as 0.07 N/m.

Flow dynamics of the gas and liquid was governed by the momentum and mass conservation equations:

$$\rho_f \Delta \cdot v = 0 \tag{1}$$

$$\rho_f \frac{\partial \boldsymbol{v}}{\partial t} + \rho_f ((\boldsymbol{v} - \boldsymbol{d}_f^{'}) \cdot \nabla)\mathbf{v} = \nabla \cdot \boldsymbol{\tau}_f + \boldsymbol{f}_f^B \tag{2}$$

where ρ_f is the fluid density, τ_f is the fluid stress tensor, f^B_f is the body forces per unit volume, υ is the fluid velocity vector, d'_f is the moving coordinate velocity and υ-d'_f is the relative velocity of the fluid with respect to the moving coordinate velocity.

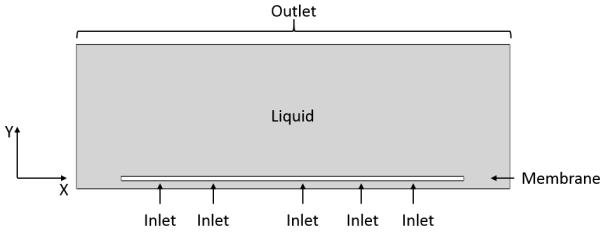

Figure 1: The CFD model of the electrospun nanofiber scaffold.

RESULTS

The volume fractions of the gas during the expanding process were described in the Figure 2. The VOF model tracked the volumes of gas in each numerical grid. Specifically, the blue region corresponds to near zero volume fraction of gas, indicating a liquid phase. The red region with a unity volume fraction indicated a gas phase. Here we tracked the gas-liquid interface based on a given volume fraction of 0.5, i.e., each grid that is half full with gas. It is clear that gas started to merge at t=0.0003s depending on the distance

Copyright 2016 The Organizing Committee for the 2016 Summer Biomechanics, Bioengineering and Biotransport Conference

between two nucleation sites. A short distance led to earlier gas bubble coalescence. The gas bubbles almost fully formed into one single large bubble after t=0.0011s. This process was also speculated in the work by Jiang et al. [1].

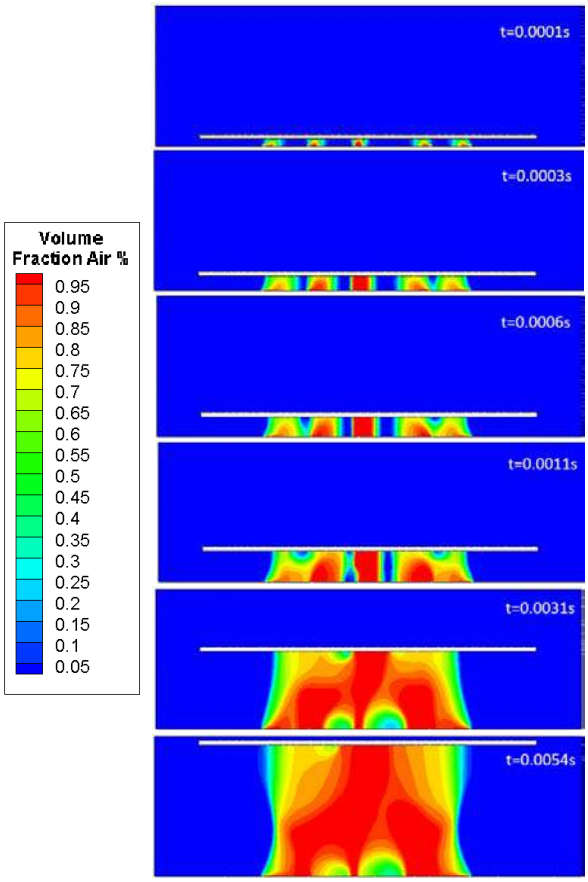

Figure 2: The expanding process of electrospun nanofiber membrane.

The streamline plots of the two phase flow during the expanding process of membranes were depicted in the Figure 3. The flow of gas phase was clearly observed between two membranes. The expansion process drove the growth of turbulence at both ends of membranes.

DISCUSSION

In this study, the gas foaming process for expanding electrospun nanofiber membranes in the third dimension was captured through a gas-liquid two-phase flow CFD model. The variations in the gas and liquid volume fraction shown in Fig. 2 illustrated the expanding process of scaffold, including the gas bubble nucleation, growth, and coalescence.

Theoretical models were proposed to address gas bubble issues during micro or nanoimprint lithography. Liang et. al. developed an analytical model to understand a single air bubble expansion and dissolution [3]. However the interaction between gas bubbles. i.e., bubble coalescence were not considered in their work. Reddy et al. also proposed a theoretical VOF model to study the bubble merging [4]. In this work, we combined these discrete theoretical bases and developed a VOF numerical model to capture the complete expanding process of gas bubbles in a liquid environment. The expansion speed of membranes was calculated based on the volume of incompressible liquid. Our results demonstrated that gas bubbles bridging two layers are noncircular, different with classical free-floating bubbles. This could be explained by the surface tension of bubble as well as the pressure gradient at both ends of the membrane. The observed turbulence intensity at both ends of membranes is related to the speed of gas growth. In the current model, the nanofibers between membranes was ignored which might alter the bubble expansion speed and disturb the bubble growth and merge. In summary, our preliminary model could capture the nanofiber membrane expanding process.

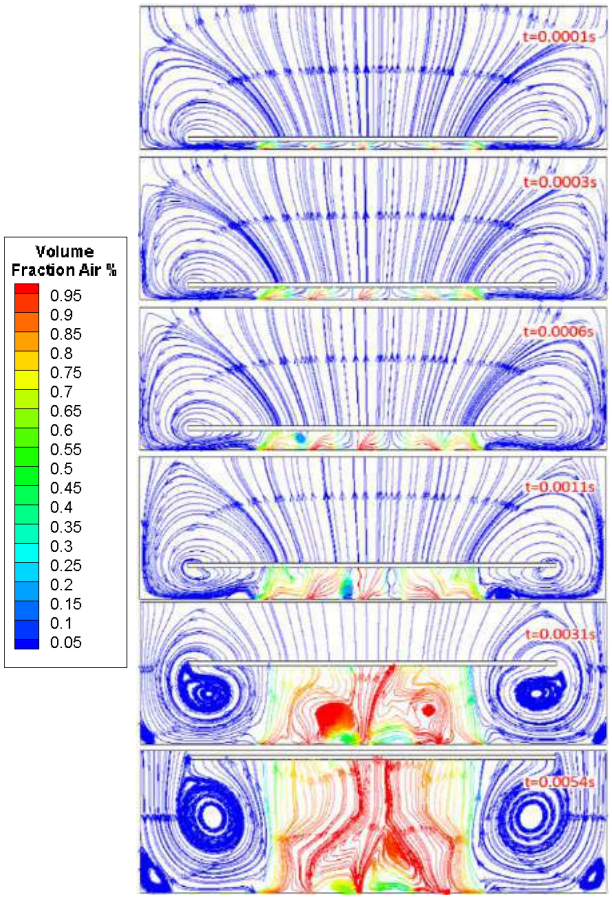

Figure 3: The streamline plots of the gas foaming process.

REFERENCES

[1] Jiang, Jiang, et al. "Expanding Two-dimensional Electrospun Nanofiber Membranes in the Third Dimension By a Modified Gas-foaming Technique." *ACS Biomaterials Science & Engineering* 1.10 (2015): 991-1001.

[2] Hirt, Cyril W., and Billy D. Nichols. "Volume of fluid (VOF) method for the dynamics of free boundaries." *Journal of Computational Physics* 39.1 (1981): 201-225.

[3] Liang, Xiaogan, et al. "Air bubble formation and dissolution in dispensing nanoimprint lithography." *Nanotechnology* 18.2 (2007): 025303.

[4] Reddy, Shravanthi, and Roger T. Bonnecaze. "Simulation of fluid flow in the step and flash imprint lithography process." *Microelectronic Engineering* 82.1 (2005): 60-70.

Copyright 2016 The Organizing Committee for the 2016 Summer Biomechanics, Bioengineering and Biotransport Conference

SB^{3}C2016
Summer Biomechanics, Bioengineering and Biotransport Conference
June 29 –July 2, National Harbor, MD, USA
SB^{3}C2016-708

SUBCONCUSSIVE HEAD IMPACT EXPOSURE FOR CONCUSSED AND NON-CONCUSSED DIVISION III COLLEGE FOOTBALL ATHLETES

Alok S. Shah (1,2), Brian D. Stemper (1,2), James K. Murtha (1), Rachel A. Chiariello (1,2), John R. Humm (1,2), Ashley LaRoche (1), Michael McCrea (1,2)

(1) Department of Neurosurgery
Medical College of Wisconsin
Milwaukee, WI, USA

(2) Neuroscience Research
Veterans Affairs Medical Center
Milwaukee, WI, USA

INTRODUCTION

An estimated 300,000 sports-related concussions occur in the United States annually [1]. A recent report from the Institute of Medicine and National Research Council of National Academies showed that male high school and collegiate football players reported higher rates of concussion compared to other contact sports [2]. Even though there has been a rise in the rate of sports-related concussion, the relationship between subconcussive head impacts and the onset of concussion remains unclear. Subconcussive impacts through routine participation in sports have been associated with structural and functional MRI changes, along with decreased cognitive abilities [3][4], even in the absence of concussive onset. Accordingly, it can be theorized that subconcussive impacts contribute to increased concussion susceptibility [5]. Therefore, it is important to characterize head impact history and determine whether that history differs between players that sustain concussion and those that do not. This study quantified head impact history during one athletic season using head impact sensors in college football athletes and compared subconcussive exposure between athletes that did or did not sustain concussion.

METHODS

The procedures described in this abstract were approved by the Institutional Review Board (IRB) at our Institution. Informed consent was obtained from all participants prior to data collection. One hundred and ninety-one athletes from four NCAA Division III football teams participated during the 2015 football season. Athletes were issued helmets containing the Head Impact Telemetry System (HITS) (Simbex, Lebanon, NH). Athletes wore the sensor during all uniformed activities (games, practices and scrimmages) throughout the season. Data collection and system maintenance were performed by study coordinators at each site.

The helmet-based HITS is an impact measurement sensor developed for use in football helmets. The sensor consists of 6 single-axis accelerometers mounted inside the helmet. The sensor starts data collection when a single accelerometer exceeds a pre-defined threshold. Once triggered, the sensor collects 40ms (8ms pre and 32ms post) of data at a sampling rate of 1,000Hz. The data are wirelessly transmitted to the sideline controller and downloaded to the computer for storage and processing. An algorithm is used to calculate head impact magnitude and location about the head center of gravity [6].

The sensors were mounted inside Riddell Speed Helmets (Des Plaines, IL). At the end of each activity, the data were downloaded from the sensor to the sideline controller for storage and processing. The system uses a proprietary algorithm to filter non-head impacts such as walking or running. HITS has been used in several studies for head impact measurement with extensive laboratory validation data available in the literature [7].

Head impact exposure data were compared between concussed and non-concussed players. Head impact history was compared between the groups by evaluating the magnitude and number of head impacts sustained by participants throughout the season. Resultant Peak Linear Acceleration (PLA) and Resultant Peak Rotational Acceleration (PRA) were compared between the groups. Data were also compared between concussed and non-concussed players based on player position.

RESULTS

Present results include data from 191 participants (182 non-concussed and 9 concussed) with a total of 77,140 recorded impacts during the 2015 football season. Head impact history was compared between concussed and non-concussed by evaluating the distribution of head impacts based on magnitude of peak linear acceleration (PLA) and peak rotational acceleration (PRA) (Figure 1).

Copyright 2016 The Organizing Committee for the 2016 Summer Biomechanics, Bioengineering and Biotransport Conference

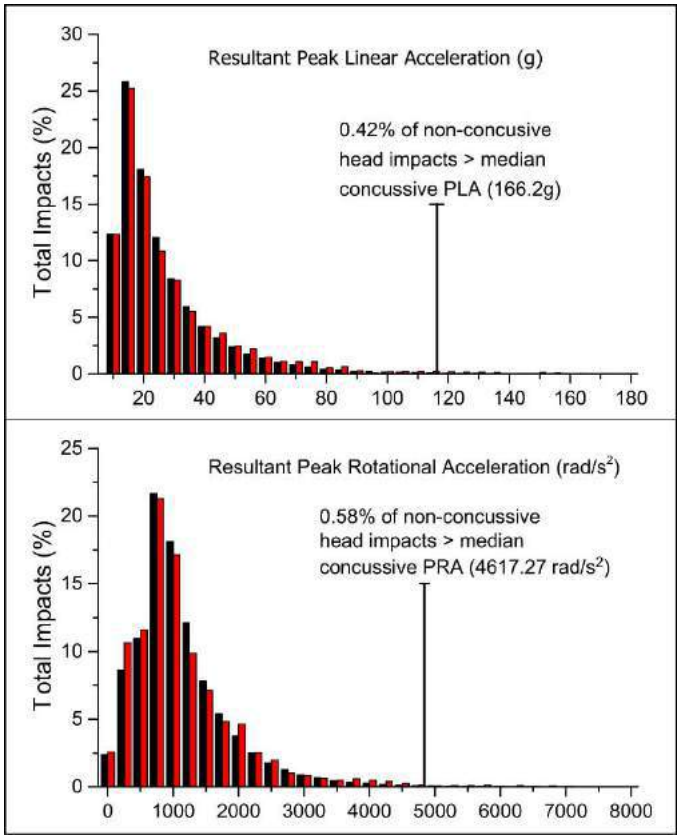

Figure 1: Distribution of peak linear and rotational accelerations between concussed(red) on non-concussed(black) players.

The mean PLA and PRA for all non-concussed players were 26.27g and 1134.05 rad/s^2 respectively. The mean PLA and PRA for all concussive impacts were 107.57g and 4840.05 rad/s^2 respectively.

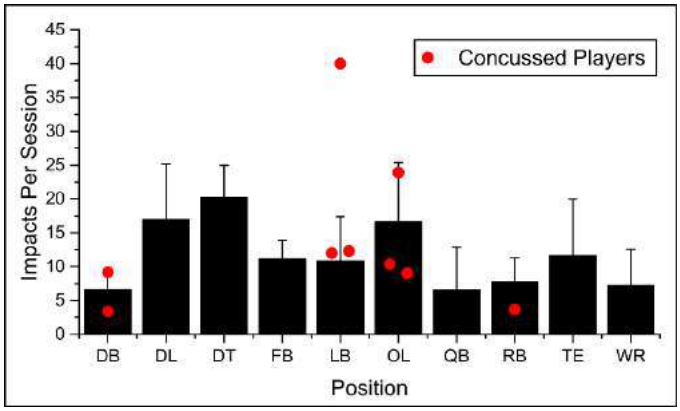

Figure 2: Number of impacts per session grouped by position. Position-matched data are provided for each concussed player.

Head impact history was also compared between position groups for non-concussed players by evaluating the average number of head impacts sustained by players per session (i.e., game, practice, or scrimmage). A one-way analysis of variance (ANOVA) of the average number of head impacts per session for non-concussed players was significantly different ($p < 0.05$) based on player's position. Bonferroni post-hoc analysis revealed that Defensive Back (DB) position had a significantly lower number of head impacts per session when compared to Defensive Line (DL), Defensive Tackle (DT) and Offensive Line (OL) positions. DL was also significantly different from Quarterback (QB), Running Back (RB) and Wide Receiver (WR). DT was significantly different from QB, RB and WR positions. OL was also significantly different from QB, WR positions.

Average PLA or PRA showed no significant differences between concussed and non-concussed players.

DISCUSSION

The goal of this study was to record and evaluate head impact history in collegiate football athletes over the course of a season. The frequency and magnitude of head impacts were compared between concussed and non-concussed players. Distribution of head impacts showed that concussed players sustained marginally more impacts at higher magnitudes for PLA and PRA compared to non-concussed players. Similar to other studies, the current study showed a significant difference in impacts per session based on player position. However, there were no significant differences in the magnitude of impacts between positions. A majority of concussed players had similar numbers of head impacts per session compared to non-concussed players, with the exception of two players that had remarkably more head impacts per session than their position-matched controls.

Data for current study show significantly different head impact history between football positions, with linemen generally sustaining more impacts per session. Comparison of concussed to non-concussed players shows somewhat of a shift toward higher magnitude impacts and primarily similar number of impacts per session, with two exceptions. This may point to a differing effect of head impact history on concussive onset, with some concussed players regularly sustaining higher magnitude head impacts and other concussed players sustaining a higher number of impacts. This important distinction will continue to be explored in this ongoing study.

ACKNOWLEDGEMENTS

This publication was supported by the National Center for Advancing Translational Sciences, National Institutes of Health, through Grant Number 8UL1TR000055. Its contents are solely the responsibility of the authors and do not necessarily represent the official views of the NIH. This work was supported by the US Army Medical Research and Materiel Command under Award No. W81XWH-12-1-0004 and by the Defense Health Program under the Department of Defense Broad Agency Announcement for Extramural Medical Research through Award No. W81XWH-14-1-0561. Opinions, interpretations, conclusions and recommendations are those of the author and are not necessarily endorsed by the Department of Defense.

REFERENCES

[1] "Sports-related recurrent brain injuries--United States.," *MMWR. Morb. Mortal. Wkly. Rep.*, vol. 46, no. 10, pp. 224–7, Mar. 1997.
[2] R. Graham et al., *Sports-Related Concussions in Youth*. Washington, D.C.: National Academies Press, 2014.
[3] T. W. Mcallister et al., *Neurology*, 79: 393–393 2012.
[4] B. I. Omalu et al., *Neurosurgery*, 59: 1086–922006.
[5] J. G. Beckwith et al., *Med. Sci. Sports Exerc.*, 45: 737–46, 2013.
[6] J. J. Crisco et al., *J. Biomech. Eng.*, 126: 849–54, 2004.
[7] J. G. Beckwith et al., *Ann. Biomed. Eng.*, 40: 237–48, 2012.

Copyright 2016 The Organizing Committee for the 2016 Summer Biomechanics, Bioengineering and Biotransport Conference

SB^{3}C2016
Summer Biomechanics, Bioengineering and Biotransport Conference
June 29 –July 2, National Harbor, MD, USA
SB^{3}C2016-709

A COMPUTATIONAL MODEL OF THE EYE FOR PRIMARY BLAST INJURY

B. Notghi [1], R. Bhardwaj [2], T.D. Nguyen [1]

(1) Department of Mechanical Engineering,
Johns Hopkins University
Baltimore, MD, USA

(2) Department of Mechanical
Engineering Indian Institute of Technology
Bombay Mumbai, MH, India

INTRODUCTION

The increase use of explosive weaponry in military conflict and terrorist attack in recent years, has increased the number of combat related injuries sustained by soldiers and civilian induced by the blasts [1]. Ocular trauma is one of the most common types of combat injuries resulting from the interaction of military personnel with improvised explosive devices. Ocular blast injury mechanisms are complex, and trauma may occur through various injury mechanisms. However, the injury mechanism associated with the primary blast wave, which can result in significant damage to internal ocular tissues and visual impairment, is unknown. Recently, the use of computational models have been extended from modeling blunt object impact to understand the mechanism of the primary blast injuries of the eye, induced by blast overpressure [2, 3]. However, there is still a gap in the literature for a model which simulate the deformation of anatomically accurate eye model exposed to blast overpressure and calculate the corresponding risk of injuries.

An experimentally validated computational model which include the main internal ocular structures of the eye, spatially varying thickness of cornea-scleral shell and tissue properties, have been utilized to help us in understanding the mechanism of primary injuries and also provide a measurable estimation of risk of injuries by using the risk of injuries available in literature.

METHODS

In order to investigate the effect of the overpressure on human eye, a computational model which are composed of three dimensional deformable eye, rigid skull and fluid domain have been used. The flow field around the structure is compressible, and pressure fields on the structure are non-uniform and highly transient. The fluid-structure interaction (FSI) solver [3] that employ the following methods have been used:

- Finite difference compressible flow solver for the propagation of the blast wave.
- Finite element elastodynamic solver with finite deformation of the human eye.
- Sharp-interface immersed boundary method for fluid-structure interaction.

The model includes detailed descriptions of the facial features of an average 21 year old male [3], the internal ocular structures, spatially varying thickness and anisotropic properties of the cornea and sclera. The internal ocular which have been considered in our model is shown in Figure (1). The local thickness variations of important load-bearing ocular components (cornea and sclera) were obtained from published histological measurements. In addition, a distributed fiber model was applied to describe the anisotropic elastic behavior of the sclera and cornea. The model directly incorporated published wide-angle X-ray scattering measurements of the anisotropic collagen structure. Furthermore, the effect of the local thickness variations and anisotropy of the important load-bearing ocular components on the deformation and stress response of the intraocular components was investigated and the risk for injuries such as lens dislocation, retinal detachment, globe rupture, and hyphema was calculated based on experimental data for blunt impact available in the literature. In addition, a sensitivity analysis with using analysis of variance method was performed to determine the statistical significant of change in different ocular components material properties of isotropic model on the stress distribution.

Copyright 2016 The Organizing Committee for the 2016 Summer Biomechanics, Bioengineering and Biotransport Conference

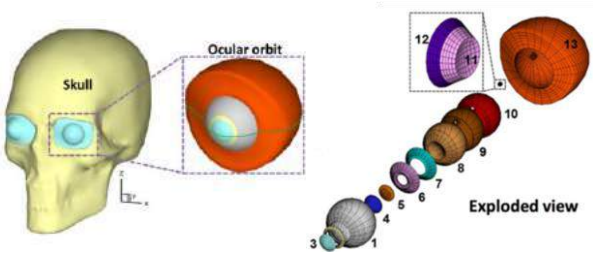

Figure 1: (onset) Assembled view of the eye depicting the extraocular tissues, sclera, limbus and cornea inside the skull. (inset) Ocular components in exploded view with associated zone numbers as follow (1) sclera,(2) limbus,(3) cornea,(4) aqueous, (5) lens (nucleus, cortex), (6) ciliary zonule, (7) ciliary muscle,(8) vitreous, (9) retina, (10) choroid, (11), Pre-laminar Neural Tissue (PLNT), (12) lamina cribrosa (LC), (13) extraocular tissue.

RESULTS

As it can be seen from Figure (2), the overall increase in maximum principal stress and IOP are due to the time-varying pressure loading boundary condition, and the periodic behavior of the stress and IOP for ocular components forming the posterior wall of the globe can be explained by the wave propagation inside the orbit. Ocular components forming the posterior wall of globe, experience higher oscillatory tensile and compressive stress (Figure 1-a) and ocular components forming the anterior structures of globe quickly reached their peak principal stress and quickly decayed (Figure 1-b). The von Mises stresses caused by tissue shear were largest in the scleral wall at the site of muscle attachments (Figure 1-c).

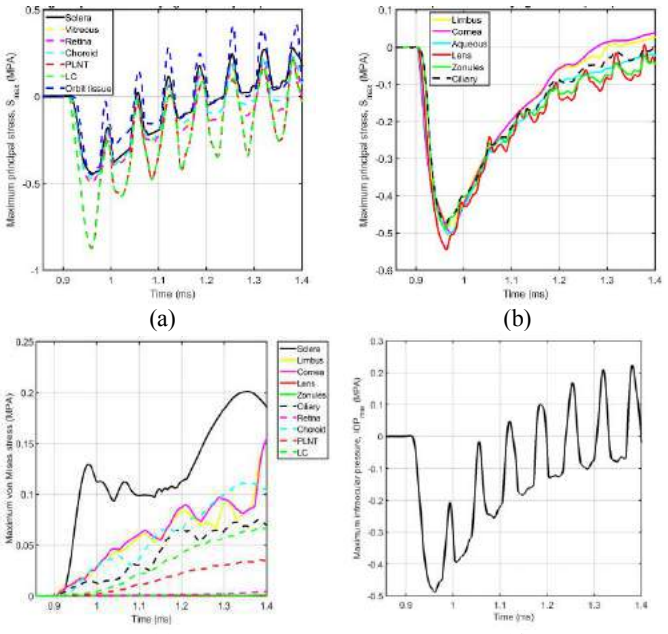

Figure 2: (a)High amplitude time varying maximum principal stress (b) Low amplitude time varying maximum principal stress (c) Time varying maximum von Mises stress (d) Time-varying maximum intraocular pressure (IOP)

In order to show the effect of considering an anisotropic material model to represent the cornea-scleral shell on the response of the structure, maximum principal stress (S_1) and maximum von Mises stress of the model with anisotropic material model ("anisotropic model") is compared to model with isotropic material properties with equivalent shear modulus for sclera and cornea to those in anisotropic model (Figure 3).

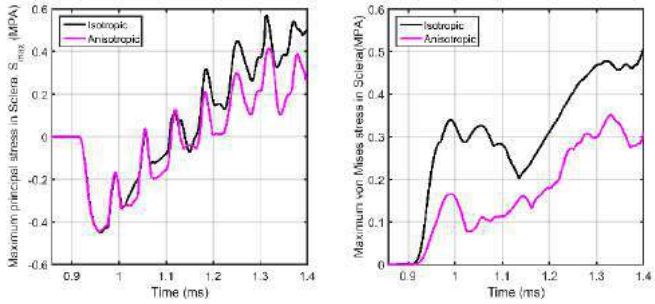

Figure 3: Comparison of anisotropic model and equivalent isotropic model (isotropic model) for cornea, limbus and sclera for time-varying (A) Maximum principal stress and (B) maximum Von Mises stress.

DISCUSSION

The stress analyses in our study correlate with the observed primary blast injuries in animal and cadaveric tissue studies, including retinal and scleral delamination, and lens detachment. Both trend of stress behavior agree with results reported by Rossi et al [4]. As shown in Figure 1-d, the maximum IOP inside the globe reached 0.22 MPa, corresponding to around 1650 mmHg, which is two orders of magnitude larger than the 15 mmHg physiologic IOP for a healthy eye. In addition, the maximum principal stress and maximum von Mises stress in sclera, choroid, retina, and ciliary zonlues showed the possibility of internal scleral delamination, chorioretinal detachments, and lens dislocation.

The blast wave loading may generated significant risk of corneal abrasions, hyphema injury. For a 2kg TNT blast at a standoff distance of, 2.5 meters we evaluated a 5% risk of Corneal Abrasions, 0.2% risk of hyphema and less than 0.01% risk of lens damage, retinal damage and globe rupture based on the maximum intraocular pressure. It should be noted that the injury risks were significantly reduced when calculated based on the maximum principal stress which show that, blast specific injury experiments are needed to more accurately evaluate the risk of injury. The anisotropic results shows that both isotropic and anistropic model have similar trends in stress. However, considering the isotropic material model can lead to overestimating both the von Mises and principal stress. Our sensitivity analysis for isotropic material model showed that the variation of the cornea-scleral shell have a significant effect on maximum principal stress of several main components of the eyes such as sclera, cornea, limbus, choroid, PLNT and LC.

ACKNOWLEDGEMENTS

This research was supported by US Army Medical Research, Vision Research Program under grant number W81XWH-10-1-0766.

REFERENCES

[1] STONE W. JAMA, 142(3):151–152, 1950.
[2] Esposito L. et al., CMBBE , 18(2):107–115, 2015.
[3] Bhardwaj R. et al., Biomechanics and modeling in mechanobiology, 13(1):123–140, 2014.
[4] Rossi T. et al, Ophthalmol. Visual Sci, 53(13):8057–8066, 2012.

Copyright 2016 The Organizing Committee for the 2016 Summer Biomechanics, Bioengineering and Biotransport Conference

SB^{3}C2016
Summer Biomechanics, Bioengineering and Biotransport Conference
June 29 –July 2, National Harbor, MD, USA
SB^{3}C2016-710

CORRELATION OF SUPRASPINATUS TENDON DEGENERATION AND QUANTITATIVE ULTRASOUND MEASURES

Gerald A. Ferrer (1), R. Matthew Miller (1), Masahito Yoshida (2), Amir A. Rahnemai-Azar (2), Volker Musahl (2,1), Richard E. Debski (1,2)

(1) Department of Bioengineering
University of Pittsburgh
Pittsburgh, PA, United States

(2) Department of Orthopaedic Surgery
University of Pittsburgh
Pittsburgh, PA, United States

INTRODUCTION

Rotator cuff tears are a significant clinical problem with an incidence rate over 30% in the general population [1]. Ultrasound (US) has become a common modality for detecting rotator cuff tears [2] and recently, quantitative ultrasound measures (QUS) have shown to be a reliable technique for quantifying tendon quality by analyzing ultrasound image grayscale values [3]. QUS has been established to quantify overall tendon quality [4], not the specific factors that can affect tendon quality such as by collagen fiber organization, tenocyte nuclei shape, tenocyte cell number, and lipoid degeneration. Histology has been used to investigate the specific factors responsible for tendon degeneration [5]. Therefore, the objective of this study is to assess the relationships between QUS of tendon quality and actual degeneration in tendons as quantified by histology. It is hypothesized that QUS will be correlated to structural parameters of the tendon such as collagen fiber organization.

METHODS

Four intact fresh-frozen cadaveric shoulders (55 ± 12 years) and four shoulders with a small supraspinatus tendon tear (71 ± 9 years) were used. Prior to dissection, US images were obtained in the transverse view of the widest part of the supraspinatus tendon near its insertion to the humerus, while using the cross-sectional view of the long head of biceps tendon (LHBT) as a consistent reference point between specimens [5]. Images were taken by an expert in musculoskeletal US for rotator cuff tear detection, using the same parameters for all images. A 1 cm wide region of interest (ROI) was measured 1 cm away from the posterior margin of the LHBT (Fig 1). Skewness, kurtosis, variance and mean echogenicity were calculated from a histogram that describes the grayscale value distribution, or echotexture, in the tendon ROI as a measure of tendon quality. Increased tendon degeneration has been reported to be associated with higher skewness and kurtosis as well as lower variance and echogenicity [3]. This type of quantitative analysis of regular US images provides different information than ultrasound elastography.

Following US imaging, all shoulders were dissected to isolate the supraspinatus tendon to obtain tissue biopsies (~2 x 4 mm) for histology. Biopsies were taken from each tendon near the myotendinous junction, mid-substance, and insertion site. All images were graded on four main parameters in a blinded fashion by two independent observers using a semi-quantitative scale (ICC = 0.89). The four parameters chosen to evaluate tendon degeneration were: collagen fiber organization, tenocyte nuclei shape, tenocyte cell number, and lipoid degeneration [4]. The grading scale was modified from Sano et al to create a 4-point scale of degeneration (0 = no change, 1 = slight localized change < 25% of tendon area, 2 = multifocal change 25-50% of tendon area, 3 = diffuse or global change > 50% of tendon area) [4]. For each parameter, the average grade between all three biopsy sites was used as a measure of the entire tendon. Total degeneration was determined as the summation of the score for all four parameters. QUS and histological findings were compared at the three biopsy sections and the entire tendon.

Pearson or Spearman's rho correlations were calculated between QUS and histological parameters with significance set at $p < 0.05$. Correlation strength was classified as negligible for r/rho = ±0.00-0.30, low for ±0.30-0.50, moderate for ±0.50-0.70, strong for ±0.70-0.90 and very strong for ±0.90-1.00 [6]. Independent samples t-tests or Mann Whitney U tests were conducted with significance set at $p < 0.05$ to compare QUS and histology grades between the intact and torn tendons.

RESULTS

A total of 3 significant correlations between QUS and histology grades were found. A strong correlation was found at the insertion site

Copyright 2016 The Organizing Committee for the 2016 Summer Biomechanics, Bioengineering and Biotransport Conference

between kurtosis and increased tenocyte cell number ($r = 0.724$, $p < 0.05$) (Fig 1). At the myotendinous junction, there was a strong inverse correlation between variance and lipoid degeneration ($rho = -0.843$, $p < 0.01$) (Fig 2). For the whole tendon, a strong inverse correlation was found between variance and lipoid degeneration ($rho = -0.826$, $p < 0.05$) (Fig 2). No significant differences of the QUS parameters were found between the intact and torn tendons ($p > 0.05$). For the histology grades, only a significant difference between the intact and torn tendons were found in lipoid degeneration at the midsubstance and the whole tendon ($p < 0.05$), and total degeneration for the whole tendon ($p < 0.05$).

DISCUSSION

All correlations found agree with prior studies that showed that increased kurtosis and decreased variance are associated with poor tendon health [4]. An increase in kurtosis implies that there was a sharp peak in the distribution of grayscale values of the ROI histogram, possibly resulting from the hypercellular regions found in the tendon. Variance measures the spread of the grayscale values, while lipoid degeneration indicates the amount of fatty infiltration. While the results did not support our hypothesis, our findings show that certain degenerative changes can be detected because of their effect on the echotexture of an image (eg. fatty infiltration due to lipoid degeneration will make the US image have hyperechoic regions). A limitation of this study is that the US image used for analysis corresponds most closely to the insertion site of the supraspinatus tendon. Interestingly, no significant differences of QUS and few significant histological differences were found between intact and torn tendons. This indicates that intact tendons show similar degenerative changes as the torn tendons and supports the reasoning that increased age increases the likelihood of a rotator cuff tear (Intact = 55, Torn = 71) [7]. However, a post-hoc power analysis for kurtosis showed only 4 additional samples in each group were needed to achieve a significant difference.

Overall, our results show that QUS can be used to assess some of the factors of tendon quality that can otherwise only be determined through histology in order to provide clinicians further insight on the degeneration of rotator cuff tendons and ultimately improve rotator cuff repair surgery. In the future, additional correlations will be performed using QUS and tendon tensile properties as determined from mechanical testing. This study provides information about how clinicians can use ultrasound as a diagnostic tool to non-invasively evaluate tendon degeneration.

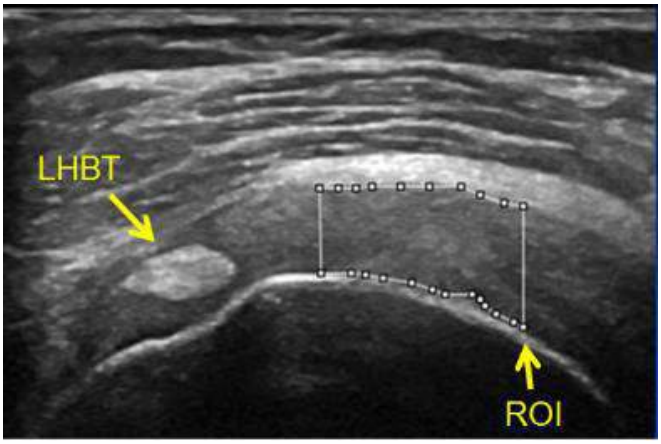

Figure 1: Transverse view of the supraspinatus tendon. A 1cm wide region of interest (ROI) was measured 1cm away from the posterior margin of the long head of biceps tendon (LHBT).

Table 1: QUS and histology grades for correlations found

Specimen	Kurtosis	Variance	Cell Number (Insertion)	Lipoid (Junction)	Lipoid (Whole)
1 (Intact)	0.17	376	0.5	1.0	0.3
2 (Intact)	-0.37	1343	1.0	0.4	0.1
3 (Intact)	-0.77	1414	0.3	0.2	0.1
4 (Intact)	0.44	481	0.5	0.2	0.2
5 (Torn)	0.19	275	0.6	2.1	1.2
6 (Torn)	1.46	404	0.9	1.7	0.7
7 (Torn)	1.01	376	0.5	1.4	0.6
8 (Torn)	3.61	476	1.3	0.4	0.4

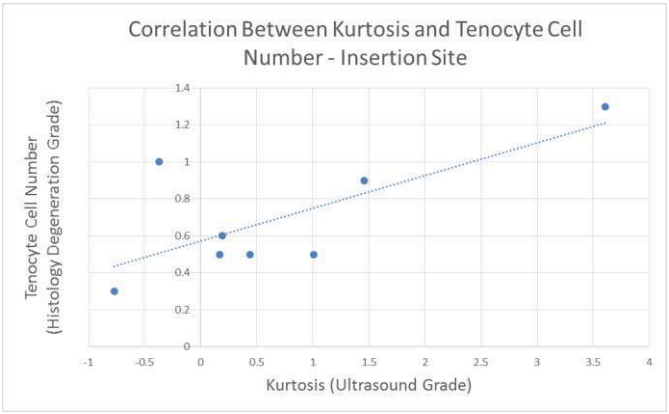

Figure 2: A strong positive correlation was found between kurtosis and increased tenocyte cellularity at the insertion site of the supraspinatus tendon.

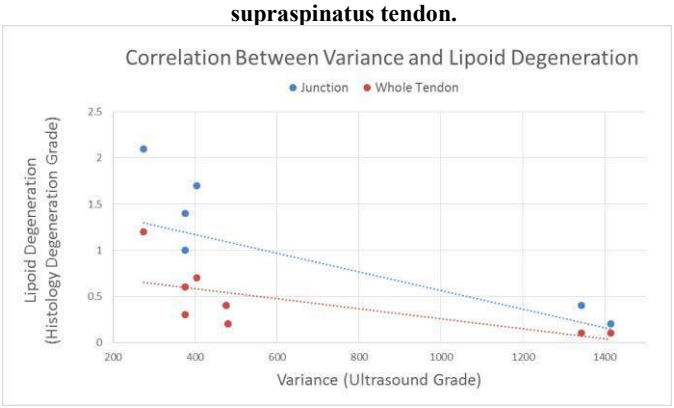

Figure 3: Strong inverse correlation between variance and lipoid degeneration for the myotendinous junction and the whole tendon.

ACKNOWLEDGEMENTS

Support from The Albert B. Ferguson, Jr., M.D. Orthopaedic Fund of The Pittsburgh Foundation (AD2-14-73915-04), the Department of Orthopaedic Surgery, Pittsburgh Chapter of the ARCS Foundation, and NSF Fellowship Grant No. 1247842 is gratefully acknowledged. Assistance with histology from Dr. James H-C Wang is appreciated.

REFERENCES

[1] Yamamoto et al., *JSES.*, 2010 Jan;19(1):116-20 [2] Lenza et al., *Coch Database Syst Rev*., 2013 Sep 24; 9:CD009020. [3] Collinger et al., *Am J Phys Rehab.*, 2010 May;89(5):390-400. [4] Collinger et al., *Acad Radiol.*, 2009 Nov;16(11):1424-32 [5] Sano H et al., *JSES.*, 1999 Nov-Dec;8(6):574-9. [6] Mukaka et al., *Malawi Med J.* 2012 Sep;24(3):69-71. [7] Oh JH et al. *AJSM.* 2010; 38(4):672-678.

Copyright 2016 The Organizing Committee for the 2016 Summer Biomechanics, Bioengineering and Biotransport Conference

SB^{3}C2016
Summer Biomechanics, Bioengineering and Biotransport Conference
June 29 –July 2, National Harbor, MD, USA
SB^{3}C2016-711

CT-BASED ESTIMATION OF STRUCTURAL INTERACTIONS OF THE VESSEL WALL AND STENT GRAFT IN ENDOVASCULAR REPAIR OF ABDOMINAL AORTIC ANEURYSM

Ryan J. Pewowaruk (1), Victor H. Barocas (1)

(1) Biomedical Engineering
University of Minnesota – Twin Cities
Minneapolis, MN, United States

INTRODUCTION

Abdominal aortic aneurysms (AAA, Figure 1A) are a pathological widening of the abdominal aorta, often treated by the placement of an endovascular stent graft (Figure 1B). The stent graft manages the blood flow, decreasing pressure in the aneurysm and in turn decreasing the likelihood of the rupture [1]. Aneurysms near the renal arteries present a challenge for the surgeon, as flow to the kidneys must not be obstructed [2]. This problem is solved by cutting holes in the side of the stent graft and then anchoring it to the renal arteries (Figure 1C). When the stent is deployed in the artery, however, it deforms the vessel wall. This deformation can change the location of the renal arteries, which means that the surgeon cannot know *a priori* which stent hole locations will be coincident with the renal arteries [3]. Aortic aneurysm deformation due to stent placement is not yet well understood, with both the irregular geometry of the aneurysm and the changing mechanical properties due to calcification and atherosclerotic plaques affecting the response [4, 5].

The goal of this project is to understand better how placing a stent in an AAA mechanically affects the vessel wall of the aorta and surrounding tissues. This was accomplished by calculating displacements and strains around the stent from before and after CT scans of a patient with an AAA.

METHODS

As part of standard care, a CT scan was taken of a patient with an AAA prior to treatment with a stent-graft. After the procedure was performed, another CT scan was taken using the same. A three-dimensional rendering of the aneurysm before and after stenting is shown in Figure 2 on the next page.

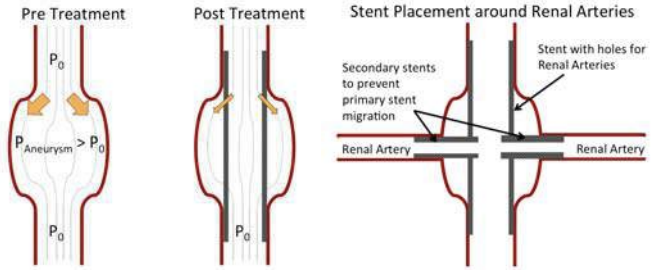

Figure 1: A. Abdominal aortic aneurysm. B. Endovascular stent graft, C. Modified stent graft to maintain renal blood flow

Matlab-based volume correlation software [6] was used to calculate the displacement field of the aorta and surrounding tissues as they deformed after the stent was placed. The software works by taking a volume of voxels from the first image stack and then iteratively finding the best match based on voxel intensities in the second stack of images, accounting for the fact that the volume can rotate, dilate, and shear. The displacement field was then numerically differentiated along each direction using a forward finite difference algorithm in MATLAB to obtain the deformation gradient at each point. From the deformation gradient at each point, the Green strain tensor was calculated using Equation 1, in which E_{ij} is the Green Strain tensor, F_{ij} is the deformation gradient tensor, and δ_{ij} is the Kronecker delta.

$$E_{ij} = \frac{1}{2}(F_{ki}F_{kj} - \delta_{ij}) \quad (1)$$

Copyright 2016 The Organizing Committee for the 2016 Summer Biomechanics, Bioengineering and Biotransport Conference

Figure 2: 3-D representation of stented aneurysm reconstructed from CT scans. Kidneys are shown in red.

RESULTS

A coronal cross-section of the aneurysm is shown in Figure 3. The arrows indicate the displacement of the aneurysm and surrounding tissue from before the stent was placed to after the stent was place. Throughout the middle of the aneurysm, the displacement vectors point to the left but at the distal end of the aneurysm, near the femoral bifurcation, the displacement vectors change direction and point the right. At the proximal end of the aneurysm, the vectors begin to point upwards and to the left.

Strain plots calculated in the same plane as the CT scan slice are also shown in Figure 3. In the anterior-posterior direction, peak in the tissue strain field is observed near the distal end of the aneurysm, with a Green Strain of 0.15 while surrounding tissues have strains in the range 0.05 to -0.05. An asymmetric effect is also seen at the proximal end of the aneurysm, near the junction with the renal arteries. To the left of the aorta, the tissue is in tension with Green strains ranging from 0.1 to 0.15, while tissue to the right of the aorta is unstrained.

In the left-right direction, the tissue on the right side of the patient's aneurysm is in tension while tissue on the left side of the patient's aneurysm is in compression. On the right side of the aneurysm, tensile strains in the left-right direction are highest near the renal arteries and lowest near the femoral bifurcation Green strains dropping from approximately 0.5 to 0.3. Conversely, on the left of the aneurysm, the compressive strains in the left-right direction are highest near the femoral bifurcation and lowest near the renal arteries with Green strains changing from approximately -0.25 to -0.1.

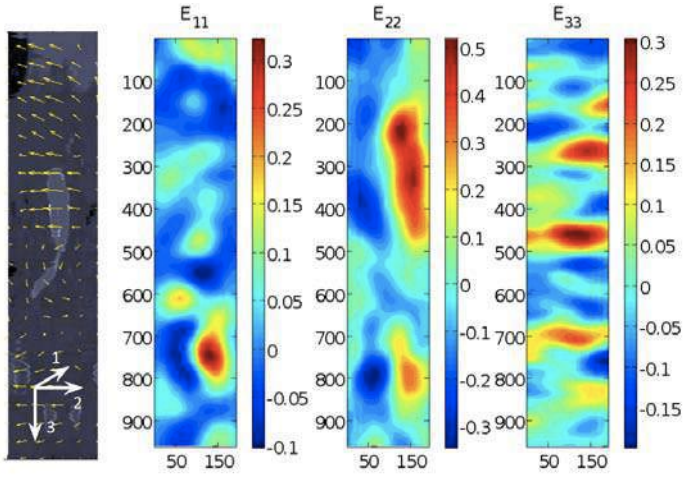

Figure 3: Coronal plane from CT image and strain plots. Aneurysm is in center above femoral bifurcation with arrows indicating displacements from pre to post operation (arrows not shown to scale). Directions are (1) anterior-posterior, (2) left-right, and (3) superior-inferior

Two peaks near the aneurysm appear on the strain plot showing strains in the superior-inferior direction. One peak is near the junction of the renal arteries, at the top of the stent at a vertical direction value of approximately 250. The second peak is at the distal end of the stent near the femoral bifurcation at a vertical direction value of approximately 500. At both peaks the maximum tensile strain in the vertical direction is approximately 0.25. In the areas immediately surrounding these peaks the Green Strain is closer to 0.1.

DISCUSSION

The calculated strains from before-and-after CT scans of a patient with an AAA provide two main insights into the mechanical interactions between the stent graft and the aortic wall and surrounding tissues. The first point is that the resulting deformation of the tissue is strongly dependent on aneurysm geometry. The original shape of the aneurysm is highly tortuous, and its mechanical properties likely vary with position. The tissue deforms when the straight cylindrical stent graft is deployed. The stent graft is rigid compared to the tissue, so the aneurysm must deform to accommodate it. This effect is clearly shown in the left-right direction strain plot, where tissue on the right side of the aneurysm is in tension and tissue of the left side of the aneurysm is in compression. This asymmetric effect is likely caused by the straight stent being expanded in the asymmetric aneurysm. A similar asymmetric effect is seen at the left side of the top of the aneurysm in the anterior-posterior direction strain plot.

The second trend observed in the strain plots is that strain is concentrated at the renal artery junction at the proximal end of the stent and also the femoral bifurcation at the distal end of the stent. In the superior-inferior direction strain (E_{33}) plot in Figure 3, peaks are seen at both ends of the aneurysm, where the stent begins and ends. Another peak in the strain field is seen at the femoral bifurcation in the anterior-posterior direction strain plot. It is important to recognize that the strains calculated in this work are based on the image stack and do not necessarily represent strain in the tissue proper.

By analyzing the strains calculated from before and after images of a patient treated with a stent graft for an AAA, it was determined that the strain varies spatially in the tissue around the aneurysm and that strain concentrations are present at the top and bottom of the aneurysm. It is speculated that asymmetries in the strain field are caused by the tortuous aneurysm conforming to the stent.

ACKNOWLEDGEMENTS

Thank you to Dr. Rumi Faizer of the University of Minnesota – Twin Cities for providing the clinical data presented in this abstract and his insight on endovascular repair. This work was supported with resources from the Minnesota Supercomputing Institute and by funding from the University of Minnesota Undergraduate Research Opportunities Program.

REFERENCES

[1] Krashram, M et al., *Vascular*. 10: 1155-1177, 2015
[2] Sugimoto, M et al., *Eur J Endovasc Surg*. 10:1016-1028, 2015
[3] Saratzis, A et al., *J Endovasc Ther*. 20:889-896, 2015
[4] Rodriguez, J et al., *J Biomech Eng.* 2:130-140, 2008.
[5] Maier, A et al., *Biomech Model Mechanobiol.* 9:511-521, 2010
[6] Bar-Kochba, E et al., *Experimental Mech,* 1:261-274, 2015

Copyright 2016 The Organizing Committee for the 2016 Summer Biomechanics, Bioengineering and Biotransport Conference

SB^{3}C2016
Summer Biomechanics, Bioengineering and Biotransport Conference
June 29 –July 2, National Harbor, MD, USA
SB^{3}C2016-712

SHEAR TESTING OF HUMAN ARICULAR CARTILAGE: ANISOTROPY APPARENT AT LARGE BUT NOT SMALL SHEAR STRAINS

Franz S. Maier (1), M. Hicham Drissi (2), David M. Pierce (1)

(1) Biomedical Engineering & Mechanical Engineering
University of Connecticut
Storrs, CT, USA

(2) Orthopaedic Surgery
University of Connecticut Health Center
Farmington, CT, USA

INTRODUCTION

Articular cartilage is a mechanically multiphase tissue consisting of fluid (water and dissolved ions) and solid (collagen, proteoglycans and chondrocytes) constituents. The interaction of water, proteoglycans and the collagen network creates the remarkable mechanical responses of cartilage under load. The principal alignment of collagen through the thickness is described by characteristic zones: superficial (SZ), middle (MZ) and deep (DZ). With respect to the articular surface, collagen fibers are principally orientated parallel in the SZ, random (isotropic) in the MZ and perpendicular in the DZ. In the SZ this orientation can easily be visualized as the so called split-line direction [1]. The mechanical properties of cartilage are strongly heterogeneous, varying both through the thickness and throughout the joint (e.g. load bearing vs. non load bearing regions) [2].

Cartilage experiences complex loading *in vivo*, combining compression, tension and shear. Relatively little is known about the shear response of cartilage although shear loads play a critical role in the development and progression of cartilage degeneration, e.g. Osteoarthritis (OA) [3]. Most studies on the shear properties of cartilage report torsion or simple shear tests under small strains and neglect the split-line direction, thus neglecting potential anisotropies.

In this study we seek to investigate the large shear strain response of human articular cartilage and its dependence on both the local split-line direction and location within the joint. Given the structure of the collagen network we hypothesize that the shear response of cartilage is strongly anisotropic. Toward this hypothesis we test location-matched human cartilage samples under multi-axial, large shear strains.

METHODS

We prepared samples from six human donors (30.2 ± 8 yrs old, mean ± std) from the Musculoskeletal Transplant Foundation. Using histology we verified the healthy condition of our samples [4]. We tested samples from both the lateral condyle and the patellar surface using seven representative locations within the joint (Fig. 1). We determined the split-line direction using India ink and extracted square samples (3x3 mm^2, full thickness) with one side parallel to the local split line. Using our triaxial shear testing device (Messphysik, Fuerstenfeld, AT) we completed large strain, simple shear tests at a quasi-static displacement rate (75 μm/min). First, we applied a pre-compression of 1% of the undeformed thickness and allowed the samples to equilibrate for 4000 sec. Next we applied cyclic simple-shear displacements parallel and perpendicular to the local split-line directions (six cycles per direction) at magnitudes ±5, ±10, ±15 and ±20% (with respect to the undeformed thickness) and measured the corresponding forces. When switching displacement directions we allowed the sample to equilibrate for 3000 sec. We completed all tests in a PBS bath at 37°C including antibiotics (100 U/ml penicillin and 100 μg/ml streptomycin) and protease inhibitor (Sigma Aldrich).

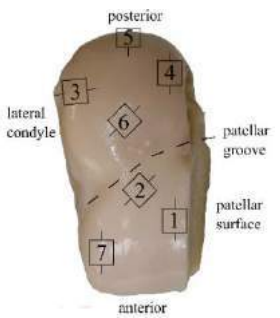

Figure 1: Locations within the femoral condyle where lines indicate the typical local split-line direction.

Copyright 2016 The Organizing Committee for the 2016 Summer Biomechanics, Bioengineering and Biotransport Conference

We calculated the peak-to-peak Cauchy stress and the strain-energy dissipation density at each applied strain considering only the last three applied cycles (to avoid preconditioning effects) using MATLAB (The MathWorks Inc., Natick, MA). To determine inter- and intra-patient variability we conducted a one-factor analysis of variance (ANOVA), with patient number (1-6) and location (1-7) as variables, followed by post-hoc tests using Tukey's Honest Significant Difference (HSD) to test for significance of relations. We used a paired *t*-test to compare the mechanical responses parallel and perpendicular to the split-line direction. Finally, we assessed the influence of age and thickness using Pearson's correlation coefficient. We completed all statistical analyses using SAS 9.4 (SAS Institute Inc., Cary, NC) with a significance level of 0.05.

RESULTS

The mechanical responses of all cartilage samples in shear were nonlinear and showed distinct hysteresis. Figure 2 shows representative stress-strain responses for donor 3, location 7.

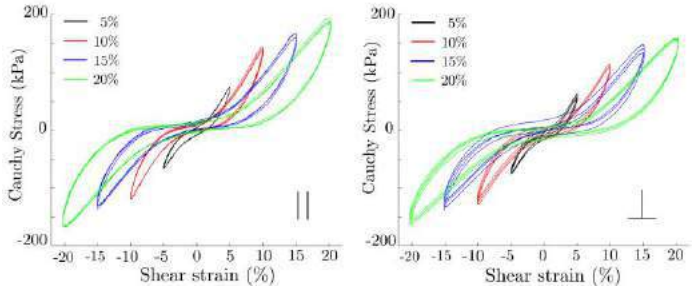

Figure 2: Representative stress-strain responses parallel (‖) and perpendicular (⊥) to the split-line direction (donor 3, location 7).

Table 1 shows the mean values and standard deviations for both the Cauchy stresses and energy dissipations (as a function of applied strain) summarizing all patients and locations. We report the strain-energy (density) dissipation in units of kPa, equivalent to $\mu J/mm^3$.

Table 1: Peak-to-peak Cauchy stresses and energy dissipations for all patients (mean ± std).

Strain (%)	Stress (kPa)		Energy dissipation (kPa)	
	‖	⊥	‖	⊥
5	107 ± 35	102 ± 35	1.56 ± 0.44	1.53 ± 0.46
10	216 ± 63	200 ± 57	5.86 ± 1.7	5.62 ± 1.7
15	302 ± 81	275 ± 71	12.8 ± 3.6	12.1± 3.6
20	355 ± 99	318 ± 93	21.9 ± 6.6	20.5 ± 6.3

There was no significant directional dependence for stresses at small strains (5%) but there was pronounced anisotropic behavior at larger strains, with the split-line direction being stiffer. Energy dissipation showed the same trend but initiated at larger strains, between 10-15%. Table 2 shows the mean difference δ between stresses and energies parallel and perpendicular to the split line, and the corresponding *p*-values from a paired *t*-test. A positive δ suggests that the split-line direction was stiffer and dissipated more energy.

Joint location did not significantly correlate with peak-to-peak stresses at 5% and 10% strain parallel to the split line. Location 6 was stiffest at 15% applied strain both parallel and perpendicular to the split line. Correspondingly, the most energy was dissipated at location 6 at all applied strains and in both directions. Donor age and sample thickness did not correlate significantly with the mechanical responses.

Table 2: Mean differences (δ) in peak-to-peak Cauchy stresses and energy dissipations between ‖ and ⊥ direction (* indicates $p<0.05$).

Strain (%)	Stress		Energy dissipation	
	δ (kPa)	*p*	δ (kPa)	*p*
5	4.8	0.1134	0.03	0.5696
10	16.0	0.0023*	0.24	0.1319
15	27.6	< 0.0001*	0.71	0.0150*
20	11.5	0.0013*	1.59	0.0060*

DISCUSSION

Our results showed a nonlinear stress-strain relation for large strains consistent with the nonlinear stiffening of collagen fibers, the main active load bearing component [5]. Tissue stiffening was more pronounced at 5% and 10% applied strain than at higher strains. This may suggest that the solid matrix adapts to external loads by rearranging the collagen fibers, or collagen-collagen and collagen-proteoglycan cross-links, within the matrix. It could also indicate that irreversible damage was induced. Equilibrating the specimen prior to each cycling of applied displacements eliminated reversible effects.

Our results showed pronounced anisotropy at strains larger than 5% for both stresses and energy dissipated. Dissipation effects due to fluid flow can be neglected due to our quasi-static loading, and thus the energy dissipation reported was due to the intrinsic viscoelastic response of the collagen and proteoglycan constituents. The correlation with direction, visualizable in the directionality of the SZ, may be a result of long-term adaptation of the tissues' load bearing components, mainly the collagen network, to *in vivo* loading.

Tissue from location 6, which dissipated the most energy at all strain levels, corresponds to the location with the highest loading *in vivo* [6]. The same location was only stiffest at 15% strain. Nine tests provided insufficient results at 20% applied strain (currently being retested) and were thus excluded in the statistical analyses. This may explain why the stresses at 20% applied strain did not follow the same trend. The relatively narrow age range of our donor group and the healthy state of the cartilage tested explain the lack of correlation among age and mechanical responses. Only tissue samples with an OARSI score of 0 (healthy tissues) were considered for this study [4]. Our finding that sample thickness did not correlate with peak-to-peak stress nor energy dissipation highlights the importance of structural integrity of the collagen network to the mechanical response [7].

Investigations on the mechanical response of cartilage to small shear deformations typically show linear, isotropic behavior, consistent with our study. To the best of our knowledge no study has previously shown the mechanical responses of cartilage under multi-axial, large-shear deformations. Interestingly, mechanical anisotropy only becomes apparent at large shear strains. In the future we aim to investigate the role of cartilage's zonal architecture on large shear response. We further aim to apply such results to mechanistically understand the mechanical behavior of cartilage and to inform computational models of the tissue's mechanics.

ACKNOWLEDGEMENTS

We thank the Musculoskeletal Transplant Foundation (MTF).

REFERENCES

[1] Below, S., et al., *J Arthr. & Related Surgery*, 18:613-617, 2002.
[2] Cohen, N., et al., *J Orthop & Sports Phys Ther*, 28:203-215, 1998.
[3] Atkinson, T., *J Biomech. Eng.,* 120:181-187, 1998.
[4] Pritzker, K., et al., *OsteoArthritis and Cartilage*, 14: 13-29, 2006.
[5] Zhu, W., et al., *J Orthop Res*, 11: 771-781, 1993.
[6] Blankevoort, L., et al., *J Biomech,* 24:1019-1031, 1991.
[7] Silverberg, J., et al., *J Orthop Res*, 31: 686-691, 1993.

Copyright 2016 The Organizing Committee for the 2016 Summer Biomechanics, Bioengineering and Biotransport Conference

SB³C2016
Summer Biomechanics, Bioengineering and Biotransport Conference
June 29 – July 2, National Harbor, MD, USA
SB³C2016-713

ROLE OF INTRACRANIAL PRESSURE IN OPTIC NERVE HEAD BIOMECHANICS

Yi Hua (1), Junfei Tong (1), Deepta Ghate (2), Sachin Kedar (2,3), Jeff Hawks (1,4), Linxia Gu (1,4,5)*

(1) Department of Mechanical and Materials Engineering
University of Nebraska-Lincoln
Lincoln, Nebraska, United States

(2) Stanley Truhlsen Eye Institute
University of Nebraska Medical Center
Omaha, Nebraska, United States

(3) Department of Neurological Sciences
University of Nebraska Medical Center
Omaha, Nebraska, United States

(4) Center for Advanced Surgical Technology
University of Nebraska Medical Center
Omaha, Nebraska, United States

(5) Nebraska Center for Materials and Nanoscience
Lincoln, Nebraska, United States

INTRODUCTION

Glaucoma, one of the leading causes of blindness worldwide, is characterized by gradual and progressive damage to the optic nerve [1]. Although elevated intraocular pressure (IOP) is widely accepted as an important risk factor for glaucoma, recent studies have demonstrated that an elevated IOP does not necessarily cause the development of this disease [2, 3]. The optic nerve head (ONH), which is the portion of the optic nerve clinically visible on examination, is exposed not only to the IOP within the eye, but also to the intracranial pressure (ICP), as it is surrounded by the cerebrospinal fluid in the retro-orbital subarachnoid space. These pressure regions are separated by the laminar cribrosa (LC) and thus influence the LC behaviors. Recent experimental data derived by using a postmortem, 3D histomorphometric technique show that the LC could move either posteriorly or anteriorly after acute IOP elevation (from 10 to 30 or 45 mmHg) in six adult normal monkeys [4]. It is speculated that the anterior movement of the LC is caused by the IOP, and its posterior movement is linked to the ICP. Mechanical strains in the ONH subjected to IOP have been well characterized [5]. However, the influence of ICP is lacking and needs to be elucidated for better detection and management of glaucoma.

In this work, the influence of ICP on the biomechanical responses of the ONH was systematically investigated. Specifically, a finite element (FE) model of the ONH with anatomical details was developed to elucidate how incorporation of the ICP would alter the strain distributions in the LC and post-laminar neural tissue (PLNT).

METHODS

An axially symmetric FE model of the ONH (Figure 1) was constructed with geometric dimensions estimated from histologic sections [5]. All tissues were assumed as isotropic, linear elastic, and incompressible materials with a Poisson's ratio $\upsilon = 0.49$. The Young's modulus for each tissue was adopted from the literatures [6-8], i.e., 3 MPa for sclera, 0.03 MPa for both pre and post-laminar neural tissues, 0.3 MPa for LC, 3 MPa for pia mater, and 9 MPa for dura mater. An ICP of 12 mmHg was applied to the subarachnoid space, representing the normal ICP measured in adults [9]. An IOP of 15 mmHg was applied on the interior of the eye, i.e., pre-laminar neural tissue [10]. A constant arterial pressure of 55 mmHg was considered [11]. The ONH model was meshed using 4-node bilinear axisymmetric quadrilateral shell elements with reduced integration and hourglass control (CAX4R). A mesh convergence test was conducted and the minimum mesh size of 20 μm was chosen. The model consisted of a total of 57,757 nodes and 56,673 elements. All simulations were carried out using ABAQUS/Standard 6.13 (Simulia, Providence, RI, USA).

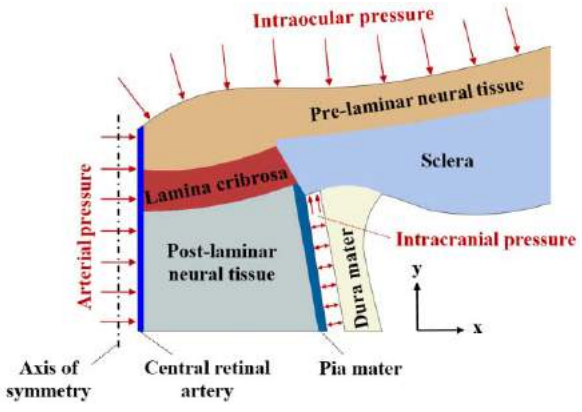

Figure 1: Finite element model of the optic nerve head.

Copyright 2016 The Organizing Committee for the 2016 Summer Biomechanics, Bioengineering and Biotransport Conference

RESULTS

The role of ICP in ONH biomechanics was estimated by comparing cases with/out the enforcement of the ICP. The contour plots of maximum principal strain (MPS) in the LC and PLNT were compared in Figure 2. It is clear that incorporation of the ICP did not alter the strain patterns much in the LC, i.e., the peak strains were located at the regions interfacing with the central retinal artery, and gradually decreased towards the LC edges. Moreover, the ICP relieved the strains sustained by the LC. The strain distributions in the PLNT were more sensitive to the ICP. For the case without considering the ICP, the peak strains were mainly concentrated at the top region of the PLNT. After considering the ICP at a magnitude of 12 mmHg, the peak strains shifted towards the bottom region in the PLNT.

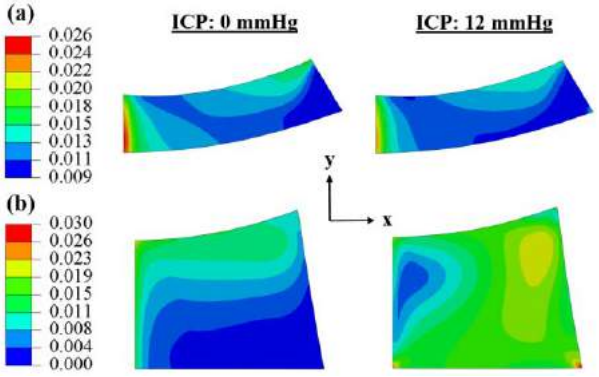

Figure 2: Contour plots of maximum principal strain in (a) lamina cribrosa and (b) post-laminar neural tissue.

The probability distributions of MPS in both LC and PLNT were further depicted in Figure 3. It is observed that the probability curves for both cases were almost overlapped in the LC. However, there was a profound right-shift for the PLNT after considering the ICP at the physiological level of 12 mmHg. For better characterization, the peak MPS was calculated as the average value in area sustained above 95% of the highest strain. After considering the ICP, the peak MPS in the LC decreased by 9.5% and the average MPS in the LC decreased by 5.7%. For PLNT, the peak MPS increased by 58.3% and the average one increased by 145.9%.

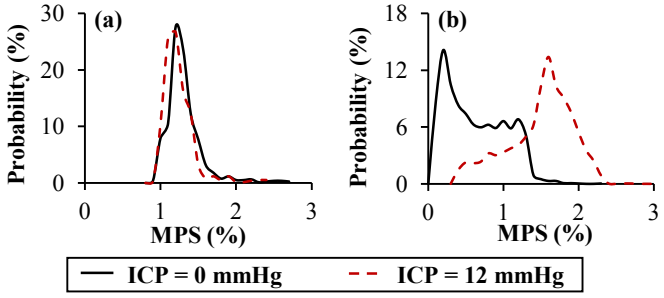

Figure 3: Probability distributions of maximum principal strain in (a) lamina cribrosa and (b) post-laminar neural tissue.

DISCUSSION

In this work, the influence of ICP on ONH biomechanics was investigated through a numerical model of the ONH. The MPS was chosen as the outcome measurement since strains have been speculated to correlate with ONH damages [12]. Our results showed that incorporation of the ICP in the retro-orbital subarachnoid space had less effect on strain distributions in the LC than those in the PLNT. The consideration of ICP altered peak strain locations in the PLNT from the upper region to the bottom region (Figure 2(b)). This could be explained by the enforcement of the ICP resulted in the deformation of the pia mater. To monitor the pia mater deformation, the x-displacement for the inner surface of the pia mater at the ICP levels of 0 and 12 mmHg was extracted (Figure 4). We found that the displacement at the top and bottom ends of the pia mater were along opposite directions. The top end displacement could be attributed to the domination of the IOP at 15 mmHg, and the bottom end displacement was most influenced by the ICP. As ICP varied from 0 to 12 mmHg, the displacement at the bottom end increased. The displacement of the pia mater would squeeze its adjacent PLNT, and has minimal impact on the LC since LC located above the pia mater.

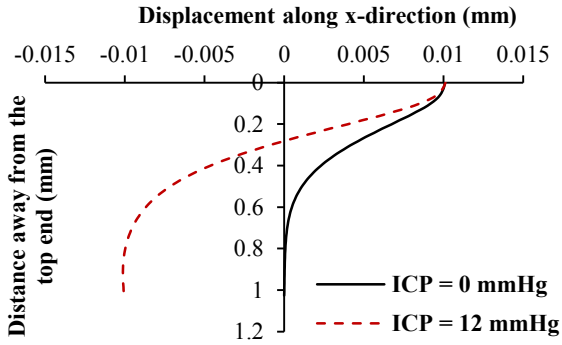

Figure 4: Displacement of the pia mater at different intracranial pressure levels.

This work could be enhanced by considering individual-specific models that could reproduce detailed anatomy of human ONH tissues. In addition, tissue properties were assumed as linear, isotropic, and homogeneous solids due to limited data in the literature. The viscoelastic nature of ocular tissues [13] will be considered in the future work through in-house characterizations.

In summary, we used numerical techniques to inspect the influence of ICP on the biomechanical responses of the ONH. Our results showed that incorporation of the ICP altered strain distributions in the PLNT, and this alternation was less in the LC. This work is clinically important since accurate characterization of the biomechanical environment within the ONH could be coupled to studies of the cellular and molecular responses to mechanical insults in glaucomatous eyes.

ACKNOWLEDGEMENTS

The authors gratefully acknowledge the seed grant from Department of Ophthalmology & Visual Sciences, College of Medicine, University of Nebraska Medical Center.

REFERENCES

[1] Quigley, H. A. et al., *Br J Ophthalmol*, 90: 262-267, 2006.
[2] Mi, X. S. et al., *Clin Interv Aging*, 9: 1563, 2014.
[3] Ren, R. et al., *Graefes Arch Clin Exp Ophthalmol*, 250: 445, 2012.
[4] Yang, H. et al., *Invest Ophth Vis Sci*, 50: 5785, 2009.
[5] Sigal, I. A. et al., *Invest Ophth Vis Sci*, 45: 4378-4387, 2004.
[6] Woo, S. Y. et al., *Exp Eye Res*, 14: 29-39, 1972.
[7] Jones, I. et al., *Eye*, 6: 556-559, 1992.
[8] Ozawa, H. et al., *J Neurosurg Spine*, 1: 122-127, 2004.
[9] Berdahl, J. P. et al., *Invest Ophthalmol Vis Sci*, 49: 5412, 2008.
[10] Medeiros, F. A. et al., *Ophthalmology*, 120: 1533-1540, 2013.
[11] Lam, C. S. et al., *Eur J Heart Fail*, 13: 18-28, 2011.
[12] Fazio, M. A. et al., *Biomech Model Mechanobiol*, 13: 551, 2014.
[13] Downs, J. C. et al., *Invest Ophth Vis Sci*, 46: 540-546, 2005.

Copyright 2016 The Organizing Committee for the 2016 Summer Biomechanics, Bioengineering and Biotransport Conference

SB^{3}C2015
Summer Biomechanics, Bioengineering and BIotransport Conference
June 17-20, 2015,Snowbird Resort, Utah, USA
SB^{3}C2016-714

CELLULAR CHOLESTEROL CONTENT MODULATES MONOCYTE INTERACTION WITH E-SELECTIN

Amit K. Saha (1), Anand K. Ramasubramanian (2)

(1) Department of Biomedical Engineering
The University of Texas at San Antonio
San Antonio, Texas, USA

(2) Department of Biomedical Engineering
The University of Texas at San Antonio
San Antonio, Texas, USA

INTRODUCTION

The plasma membrane is segregated into lipid rafts, which are dynamic, heterogeneous regions, rich in gangliosides, cholesterol and glycosphingolipids. Lipid rafts regulate a variety of cellular processes such as protein trafficking and signal transduction [1]. Cholesterol is a major constituent of the lipid rafts and is vital in maintaining their integrity[2]. The effect of cholesterol content has been studied in a variety of cell types such as neutrophils[3], fibroblasts[4] and erythrocytes[5], among others. The impact of cholesterol on monocyte biomechanics remains understudied despite the well-established link between both cholesterol and monocytes/macrophages in atherosclerosis and other diseases. We modified the cellular cholesterol content and tested for differences in monocyte biophysical response. We altered the baseline cholesterol and studied the differences in the rolling and adhesion properties of monocytes on e-selectin, and observed significant changes in the instantaneous and short term response. As a causative agent for the observed changes, we investigated the changes in membrane lipid rift distribution and expression levels, and also changes in the membrane fluidity due to changes in the cholesterol content. We also studied the consequential distribution and expression of the receptors to e-selectin present on monocytes. Apart from this, we examined changes in cellular deformability as a possible contributing factor to the changes in the rolling and adhesion dynamics.

METHODS

Cell Culture. Primary human monocytes were isolated from buffy coat using monocyte isolation kit II by indirect magnetic labeling, and the purity of the monocytes was determined by flow cytometry using FITC-conjugated anti-CD14 antibody and a suitable isotype control. The monocytes were resuspended in RPMI 1640 with 10% FBS at required concentration depending on the assay.

Cholesterol treatment. Cholesterol depletion was performed using 10 mM Methyl-β-cyclodextrin (MβCD). For cholesterol enrichment, 0.5 mM MβCD –cholesterol complex was used with cholesterol concentration of 40mg/gm. In both cases, the cells were incubated for 30 mins. at 37° C and 5% CO_2. Cholesterol content was measured using Amplex Red Cholesterol Assay Kit, as per the manufacturer's protocol.

Fabrication of custom microfluidic platform. A silicon mold was made using standard photolithographic techniques. These silicon molds wre used as a master to make polymeric micro-channels in polydimethylsiloxane (PDMS), and final devices were assembled by bonding with clean glass slides using oxygen plasma treatment.

Lipid raft and receptor distribution and expression levels. Lipid rafts and e-selectin receptors were studied for their expression levels and distribution patterns using multispectral imaging flow cytometry.

Membrane fluidity. Membrane fluidity was assessed using pyrenedecanoic acid fluorescence intensity measurements.

Perfusion studies. For rolling and adhesion analysis, the micro-channel slide was coated with e-selectin assembled on top of an inverted microscope attached to a time-lapse digital camera A monocyte suspension was then perfused through the micro-channels using a syringe pump at a constant flow rate corresponding to a wall shear stress of 1 dyn/cm^2. Videos were captured at 20X magnification, followed by subsequent image analysis. For deformability studies, the microfluidic device was assembled on top of an inverted microscope attached to a high speed camera. We used a custom nitrogen based cell delivery system to deliver the cell suspension at a pressure of 2 psi. The videos were taken at a magnification of 20X using the proprietary software for the camera, followed by subsequent image analysis.

Statistics. All experiments were performed in triplicate, and each experiment was repeated at least thrice under independent conditions. The results are represented as mean ± SEM from one representative experiment. Statistical differences between treatments were evaluated using one way ANOVA with Tukey's post-hoc test, and significance was reported at α=0.05. * and ϕ represent

Copyright 2016 The Organizing Committee for the 2016 Summer Biomechanics, Bioengineering and Biotransport Conference

significance as compared to cholesterol depleted and untreated monocytes. Consistent for all experiments (unless otherwise mentioned).

RESULTS

Changes in rolling and adhesion behavior due to cholesterol content. Alteration of cellular cholesterol significantly impacted the rolling and adhesion behavior of monocytes. Cholesterol depletion led to more cells rolling on the e-selectin coated surface (Fig. 1 a). However, only a small fraction was able to convert the transient rolling into sustained adhesion, as compared to cholesterol enrichment and untreated controls (Fig. 1 b). It also led to longer pause time and shorter rolling duration in cells. Cholesterol depletion led to the cells rolling in a faster (Fig. 1 c) and more erratic fashion (Fig. 1 d). Enrichment led to antithetical effects.

Changes in membrane properties. In order to have a better understanding of the changes in the rolling behavior, we investigated changes in lipid raft expression and distribution as a consequence of cholesterol treatment. We observed that cholesterol depletion results in decreased expression and a more uniform distribution. We probed into the changes in membrane fluidity due to cholesterol treatment. Cholesterol depletion significantly enhanced the plasma membrane fluidity (Fig. 2). We also observed significant changes in the expression levels of receptors of e-selectin on monocytes (CD44 and CD15) due to cholesterol treatment.

Changes in cellular deformability. We probed the changes in cellular deformability as a function of cholesterol load and also to understand possible links with the changes in rolling and adhesion dynamics. Cholesterol depletion was observed to decrease the cellular deformability (Fig. 3).

DISCUSSION

This work establishes a link between cellular cholesterol load and biophysical response in monocytes. We observed significant changes in rolling and adhesion behavior of monocytes due to altered cholesterol loads. And as probable reasons for the observed changes in rolling and adhesion dynamics, we investigated the changes in membrane properties and cellular deformability.

Since cholesterol is responsible in maintaining the integrity of the plasma membrane, disturbance in its natural balance alters the membrane fluidity and the lipid raft distribution and expression. Consequently, the receptors on the membrane also show altered expression levels and distribution. These can greatly influence the rolling and adhesion behavior of monocytes.

There is evidence linking cellular deformability to rolling, with stiffer cells having higher velocities[6]. The changes observed in rolling can hence partly be considered as an effect of the change in deformability.

It has been shown that monocytes in circulation can be considered as suitable representatives of cholesterol loaded macrophages[7]. Hence, our results can provide the foundation for an enhanced understanding of mechanistic features of diseases like atherosclerosis.

ACKNOWLEDGEMENTS

We gratefully acknowledge the help of Dr. Shatha Dallo, Dr. Chiungyu Hung, Dr. Marylene Palard (Microelectronics Research Center, UT Austin) and Shankar J. Evani. This work was supported by NIH HL112629. This work received technical and instrument support from The Immunology Defense Core at UTSA, funded by the National Institute on Minority Health and Health Disparities from the National Institutes of Health.

REFERENCES

1. Lundbaek, J.A., et al., Biophys J, 2003. **84**(3): p. 2080-9.
2. Roduit, C., et al., Biophys J, 2008. **94**(4): p. 1521-32.
3. Kannan, K.B., D. Barlos, and C.J. Hauser, Journal of Immunology, 2007. **178**(8): p. 5253-5261.
4. Kwik, J., et al., Proc Natl Acad Sci U S A, 2003. **100**(24): p. 13964-13969.
5. Forsyth, A.M., et al., Microvasc Res, 2012. **83**(3): p. 347-51.
6. Jadhav, S., et al., Biophys J, 2005. **88**(1): p. 96-104.
7. Devaraj, S. and I. Jialal, Arch Pathol Lab Med, 2008. **132**(9): p. 1432-5.

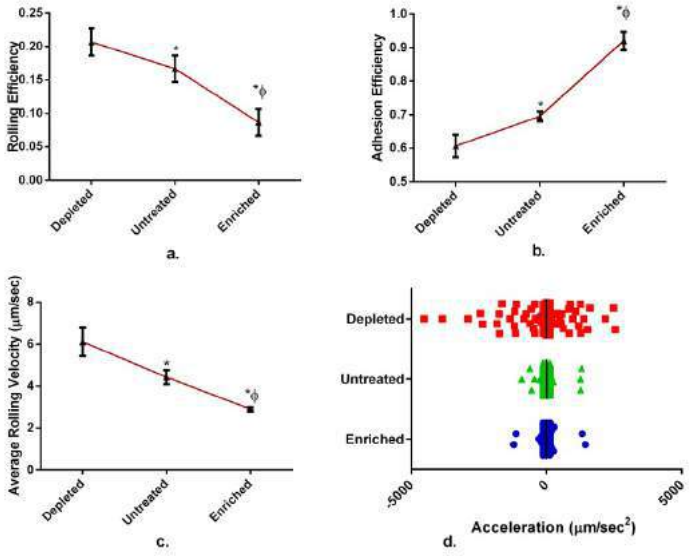

Fig. 1. Monocyte rolling and adhesion dynamics.

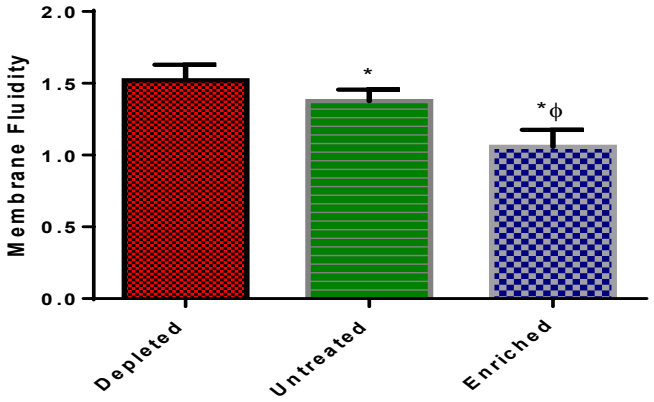

Fig. 2. Changes in membrane fluidity of human monocytes

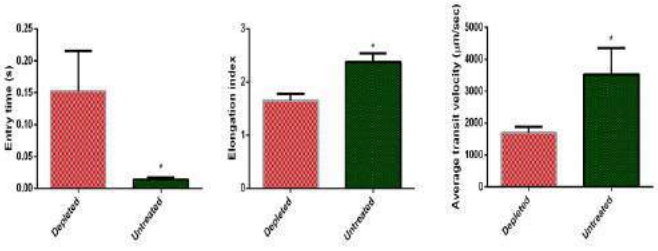

Fig. 3. Effect of cholesterol depletion on cellular deformability. Students' t-test. α = 0.05. n = 2.

Copyright 2016 The Organizing Committee for the 2016 Summer Biomechanics, Bioengineering and Biotransport Conference

SB^{3}C2016
Summer Biomechanics, Bioengineering and Biotransport Conference
June 29 –July 2, National Harbor, MD, USA
SB^{3}C2016-715

CONTINUOUS ON-CHIP HUMAN CELL SEPARATION BASED ON CONDUCTIVITY-INDUCED DIELECTROPHORESIS WITH SELF-ASSEMBLED IONIC LIQUID ELECTRODES

Mingrui Sun (1), Xiaoming He (1)

(1) Department of Biomedical Engineering
The Ohio State University
Columbus, OH, United States

INTRODUCTION

Cell separation is widely used in water analysis and diagnosis and treatment of diseases. [1, 2] Dielectrophoresis (DEP) is an attractive separation technique, which is capable to separate cells with low damage, no label, and high efficiency. [3, 4] There are various DEP devices, which can be divided into DC DEP devices and AC DEP devices, depending on the electric field used. The DC DEP devices can separate cells based on their conductivity and size. The electric gradient is generated by the patterns in the channels, and no deposition of metal electrodes is required. [5, 6] However, the DC DEP devices only can separate cells using negative DEP force, due to the lower conductivity of cells compared to the DEP buffer, which impedes the optimization of the separation. The AC DEP devices have the ability to separation cells based on the conductivity and size, as well as the permittivity and inner structures. [3, 4, 7] However, typically, the AC DEP devices need deposited metal electrodes. Moreover, even though the frequency can be adjusted, continuous positive DEP separation is also difficult to be achieved, because the positive DEP force attracts the cells towards the stronger electric field, where typically is close to the electrodes, which makes the cells attach to the electrodes. Besides, high voltage is required by the continuous DEP separation without solid electrodes. [8]

In this study, a continuous positive DEP separation is conducted using 3D self-assembled ionic liquid electrodes. The ionic liquid with higher conductivity than DEP buffer can form stable interface with the DEP buffer in the electrode regions. In addition, two types of DEP buffers with different conductivities were used to generate the electric field gradient in the electrode regions. In this study, the DEP device was used to separate live and dead PC-3 cells, and human ADSCs and MDA-MB-231 cancer cells.

METHODS

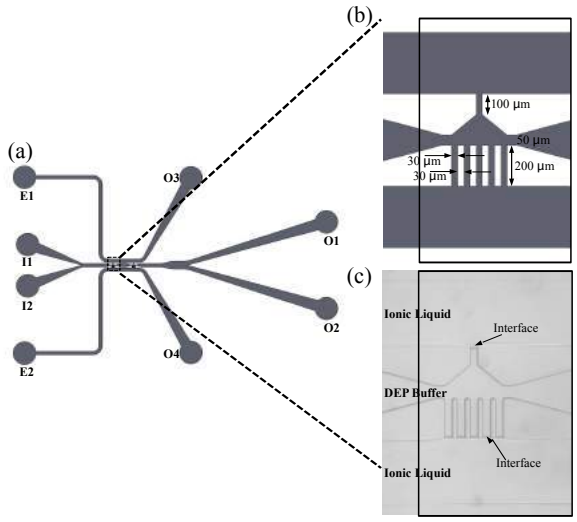

Figure 1: The structures of the DEP device and ionic liquid electrodes.

The DEP device was fabricated using the soft lithograph method and was made of PDMS. As shown in Figure 1, the modified DEP buffer (10% (w/v) sucrose, 0.3% (w/v) glucose, and 0.8% (v/v) cell culture medium in deionized water) with cells was introduced from I1 (100 μL/hr), and the original DEP buffer (10% (w/v) sucrose, 0.3% (w/v) glucose in deionized water) was introduced from I2 (400 μL/hr). The ionic liquid, [BMIM][PF_6], was used as the electrodes, and introduced from E1 and E2 (15 μL/hr). The samples after separation were collected from O1 and O2.

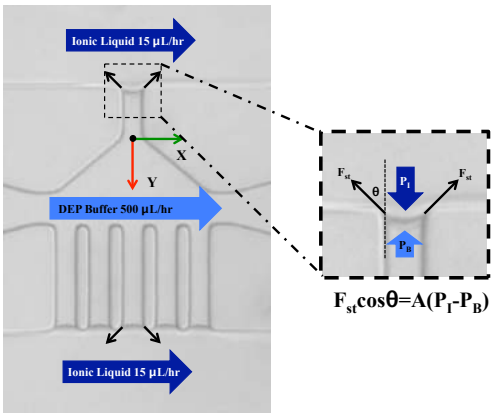

Figure 2: The formation of the stable interface between the ionic liquid electrodes and DEP buffer.

The interface between ionic liquid and DEP buffer experiences three forces: the pressure force from the ionic liquid, the pressure force from the DEP buffer, and the surface tension force (Figure 2). When three forces reach a balance, the stable interface forms.

In this study, the DEP device was used to separate live and dead PC-3 human prostate cancer cells, and human adipose-derived stem cells (ADSC) and MDA-MB-231 human breast cancer cells. Before separation, the cells were suspended in modified DEP buffer.

RESULTS

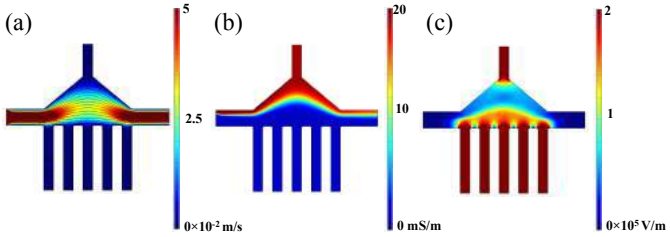

Figure 3: The simulated distributions of (a) velocity field, (b) conductivity field and (c) electric field in the electrode regions.

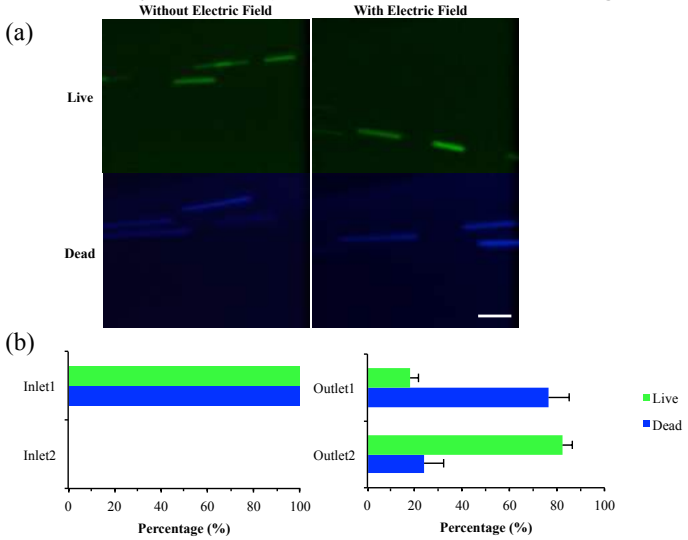

Figure 4: The separation of live and dead PC-3 cells. The error bars represent SD. Scale bar: 100 µm.

The distributions of velocity field, conductivity, and electric field were simulated using COMSOL Multiphysics (version 5.1), as shown in Figure 3. The conductivities of the modified DEP buffer and original DEP buffer are about 18 mS/m and 1 mS/m, respectively. Because the diffusion of the electrolytes between the modified DEP buffer and original DEP buffer, the gradual gradient of the conductivity is generated in the electrode regions. As a result, the gradient of electric field is induced by the gradient of the conductivity. In the frequency range used in this study, the cells experience positive DEP force, and are repelled towards the stronger electric field region.

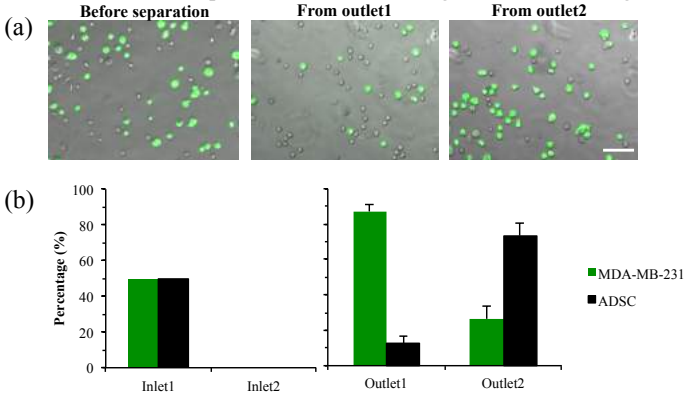

Figure 5: The separation of ADSC and MDA-MB-231 cells. The error bars represent SD. Scale bar: 100 µm.

As shown in Figure 4, the separation of live (green fluorescence) and dead (blue fluorescence) PC-3 cells was conducted. The live cells experience strong positive DEP force (83% deflected), and are defected more than the dead cells (23% deflected), when 150 Vpp at 100 kHz is applied to the electrodes. The separation of ADSC (green fluorescence) and MDA-MB-231 cells was also achieved (Figure 5). The ADSC experience stronger positive DEP force, and the purity of ADSC in the collection is about 74% and the purity of MDA-MB-231 is about 88%, when 75 Vpp at 50 kHz was applied to the electrodes.

DISCUSSION

In the separation of live and dead PC-3 cells, compared to the dead cells, the live cells have a lower conductivity and a higher permittivity of the membrane, and a higher conductivity of the cytoplasm, which lead to a stronger positive DEP response of the live cells than the dead cells. [9, 10] In the separation of ADSC and MDA-MB-231 cells, the ADSC, which are stem cells, have different electric properties from the cancer cells, MDA-MB-231. [4, 11] Moreover, the average size of the ADSC is larger than that of the MDA-MB-231 cells. Therefore, the DEP response of the ADSC is different from that of MDA-MB-231 cells.

ACKNOWLEDGEMENTS

This work was supported by an American Cancer Society (ACS) Research Scholar Grant (No. 120936-RSG- 11-109-01-CTDD) to X.H.

REFERENCES

[1] Armstrong, D et al., *Fems Microbiology Letters,* 194:33-37, 2001.
[2] Nagrath, S et al., *Nature*, 450:20-27, 2007.
[3] Shafiee, H et al., *Lab on a Chip*, 10:438-445, 2010.
[4] Salmanzadeh, A et al., *Lab on a Chip*, 12:182-189, 2012.
[5] Zhu, J et al., *Electrophoresis*, 31:1382-1388, 2010.
[6] Barbulovic-Nad, I et al., *Lab on a Chip*, 6:274-279, 2006.
[7] Li, H et al., *Sensors and Actuators B-Chemical*, 86:215-221, 2002.
[8] Sano, M et al., *Biosensors and Bioelectronics*, 30:13-20, 2011.
[9] Davey, C et al., *Pure and Applied Chemistry,* 65:1921-1926, 1993.
[10] Vahey, M et al., *Analytical Chemistry*, 80:3135-3143, 2008.
[11] Pethig, R et al., *Journal of Biomedicine and Biotechnology,* 2010.

SB^{3}C2016
Summer Biomechanics, Bioengineering and Biotransport Conference
June 29 –July 2, National Harbor, MD, USA
SB³C2016-716

A VIRTUAL COILING ALGORITHM TO SIMULATE ENDOVASCULAR COIL DEPLOYMENT IN CEREBRAL ANEURYSM USING SPRING BASED GEOMETRIC CONSTRAINT MODEL

Rahul Sanal (1, 3), Robert J. Damiano (1, 3), Adnan. H. Siddiqui (3, 5, 6), Jinhui Xu (4), Hui Meng (1, 2, 3)

(1) Department of Mechanical and Aerospace Engineering
State University of New York at Buffalo
Buffalo, NY

(2) Department of Biomedical Engineering
State University of New York at Buffalo
Buffalo, NY

(3) Toshiba Stroke and Vascular Research Center
State University of New York at Buffalo,
Buffalo, NY

(4) Department of Computer Science and Engineering
State University of New York at Buffalo
Buffalo, NY

(5) Department of Neurosurgery
State University of New York at Buffalo,
Buffalo, NY

(6) Department of Radiology
State University of New York at Buffalo,
Buffalo, NY

INTRODUCTION

Endovascular coil embolization is the most popular minimally invasive treatment option for treating intracranial aneurysms (IAs). Despite the wide adoption of this treatment, up to 30% of cases experience poor outcome. Since coils induce thrombotic occlusion by modifying aneurysmal hemodynamics, treatment outcome was thought to depend on these blood flow modifications. Treatment simulations prior to actual treatments could help identify possible outcomes for patient-specific aneurysms. However such simulations require accurate and efficient model for simulating coil deployment. We present a novel algorithm that utilizes a coil's tendency to restore its pre-shaped geometry to simulate deployment of coils inside IAs. We represent a coil as a set of discrete ordered points that seek to assume its reference positions, based on geometric constraints that are modelled as spring forces. We validated this algorithm by comparing simulation results against physical experiments of coil deployment and found excellent agreement. In the future, this method, combined with CFD, could be used in a real-time clinical setting to assess the potential hemodynamic impact of coil embolization prior to treatment.

METHODS

We model the mechanics of the coil points as a discrete, pseudo-structural system based on the equation of motion. The dynamics of the system is simplified, we assume coil deployments to be a quasi-static process, and the damping constant is equal to 1. We use finite differencing to discretize the equation of motion:

$$p^{k+1} = p^k + (F_e - F_i) \quad (1)$$

where p is the position coil point.

In general, the progression of coil points inside an IA geometry can be interpreted as the interaction difference between the sum of all the internal forces (F_i) and the external force (F_e) acting on the coil nodes when the coil is fully deployed. The internal forces are modeled using spring forces, which drive the motion of points seeking to restore the pre-shape, whereas the restriction due to the collision with the IA vessel wall and other coils is modeled by the external force.

As input to our algorithm, we used previously-derived 3D parametric equations to describe the centerline of a pre-shaped, tubular, coil geometry with a fixed length [1]. We discretized this coil centerline from end-to-end with a set of equidistant, ordered points.

Internal Forces To ensure that the final deployed coil geometry resembles the manufacturer's specifications of coil shape, size, and length, we imposed three geometric constraints which the coil points were required to adhere to during deployment. $\boldsymbol{f_{restore}}$, $\boldsymbol{f_{length}}$, and $\boldsymbol{f_{smooth}}$. The rationale for these geometric constraints is described as follows:

1. **"Free" state configuration:** When deployed released from the catheter inside an IA sac, coils attempt to recapture recover their pre-shaped configuration. This behavior is imposed by a restoration force, or $\boldsymbol{f_{restore}}$. In our algorithm, the user defined pre- shaped input coil geometry serves as the resting configuration of the coil.

   $$\boldsymbol{f_{restore}} = k_{restore}(r_i - \boldsymbol{p_i}^{\boldsymbol{k+1}}) \quad (2)$$

   Here, r_i is the coil point's position in the reference configuration, p_i is the point's current position, and $k_{restore}$ is the stiffness constant of the spring which connects the current coil point to its reference position in the "free" state geometry, which is computed as:

   $$k_{restore} = \frac{AE}{r_i} \quad (3)$$

   Here, A is the circular cross-sectional area of the coil and E is the Young's modulus of the spring. For the purposes of testing our

Copyright 2016 The Organizing Committee for the 2016 Summer Biomechanics, Bioengineering and Biotransport Conference

algorithm, we chose E to be 0.5 N/m^2 for each spring, as defined previously [2].

2. **Coil length:** The total length of the virtual coil should not deviate from its actual physical length. This is imposed by a spring along the length of the coil. The stiffness of each spring, $\boldsymbol{k_{length}}$, is defined to be inversely proportional to the distance between the two points it connected as follows:

$$\boldsymbol{f}_{length} = \begin{cases} -k_{length}(p_i - p_{i-1}), & \Delta l > \epsilon \\ k_{length}(p_i - p_{i-1}), & \Delta l < \epsilon \end{cases} \quad (4)$$

where,

$$\Delta l = p_i - p_{i-1} \quad (5)$$

Here, Δl is the Euclidean distance between two points in the current coil configuration.

3. **Coil bending:** To not produce any unrealistic final coil configuration which is unphysical a smoothing force is applied. This constraint is imposed by a smoothing force, $\boldsymbol{f_{smooth}}$, which is implemented by moving averages.

Together, these three constraints are imposed as internal forces onto all coil points to drive its deployment. The combined internal force is denoted by Thus the sum of all internal forces F_i becomes:

$$F_i = (\boldsymbol{f_{length}} + \boldsymbol{f_{length}} + \boldsymbol{f_{smooth}}) \quad (6)$$

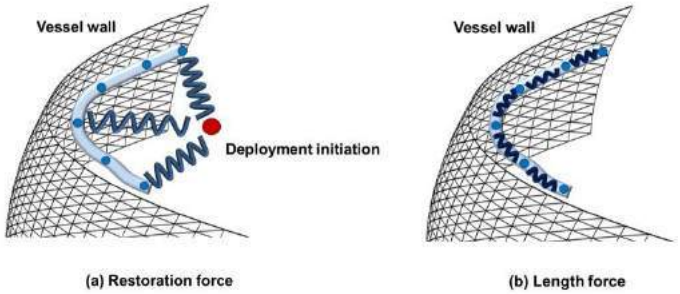

FIGURE 1: ILLUSTRATION OF INTERNAL SPRING FORCES USED IN OUR ALGORITHM.

External Forces During coil deployment, the patient-specific IA sac and the coils themselves act as external restrictions to the above-mentioned internal forces. To models these external force, coil points are deployed until they encountered the IA wall and/or other coil points, which act as external force.

Thus, the evolution of coil points is described by:

$$p^{k+1} = p^k + (\boldsymbol{F_e} - \boldsymbol{f}_{restore}(p^k) - \boldsymbol{f}_{length}(p^k) - \boldsymbol{f}_{smooth}(p^k)), \quad (7)$$

Where p^{k+1} describes the position of p node in the $k+1$ iteration. This equation is iterated across the coil mesh until the RHS of Equation (7) becomes equal to LHS.

RESULTS

We applied our algorithm to simulating coil deployment in internal carotid artery (ICA) sidewall patient-specific aneurysm geometry. To test our method, the aneurysm model was virtually coiled with 1-8 coils deployed sequentially to achieve 3.8%-29% packing density (PD, defined as the percentage of space occupied by coils in an IA). At 8 coils the IA approaches 30% which is the clinical goal. The entire simulation required 67-74 sec to deploy each coil, running on our workstation.

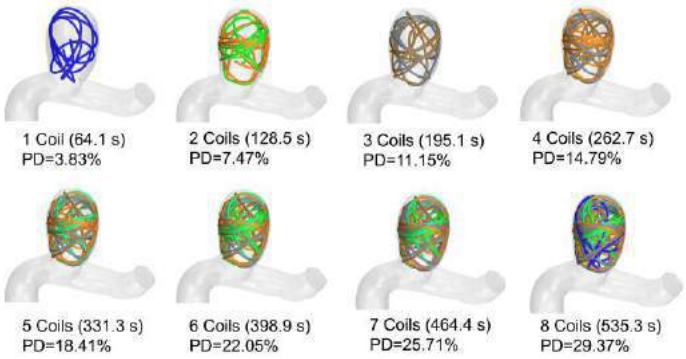

FIGURE 1: VIRTUAL COIL DEPLOYMENT IN A PATIENT SPECIFIC ANEURYSM USING OUR ALGORITHM.

In Vitro Validation: In a series of *in vitro* experiments we deployed a real 5 mm x 15 cm complex-shaped coil (Axium™ Detachable Coil, Medtronic, Dublin, Ireland) into an optically-transparent 8 mm x 8 mm x 3 mm hexahedron phantom. The deployments demonstrated that the simulated (Figure 2B) and experimentally deployed coils (Figure 2A) shared three key features. In both groups, the corners of the hexahedron geometry remained void of any coils, the center of the geometry contained a mass of coils, and the coils made large loops opposing to the walls of the models.

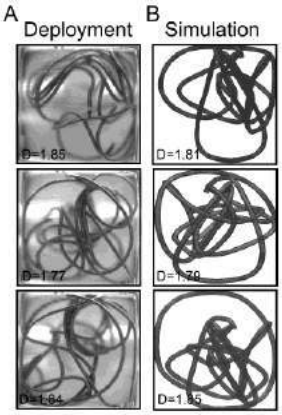

FIGURE 2: COMPARISON OF SIMULATED AND IN VITRO COIL DEPLOYMENTS IN PATIENT SPECIFIC ANEURYSM.

CONCLUSION

We developed a novel algorithm for virtually deploying endovascular coils in patient-specific aneurysms using a spring-based geometric constraint model.. Our validation studies demonstrate that this computational method closely matches with coils deployed experimentally *in vitro*. The accuracy and efficiency of our technique highlights its potential for implementation into a real-time clinical setting as a tool to investigate specific coil treatments prior to actual IA intervention.

ACKNOWLEDGEMENTS

This study is funded by the National Institute of Health (R01 NS 091075).

REFERENCES

[1] Babiker et al., *J Biomech*, 46.16: 2809-2816.2013

[2] Larrabide et al., *Medical image analysis* 16.3: 721-730.2012

Copyright 2016 The Organizing Committee for the 2016 Summer Biomechanics, Bioengineering and Biotransport Conference

SB³C2016
Summer Biomechanics, Bioengineering and Biotransport Conference
June 29 –July 2, National Harbor, MD, USA
SB³C2016-717

THE USE OF INDIVIDUAL MOTION UNITS TO ANALYZE *IN VIVO* TOTAL THORACOLUMBAR MOTION IN HEALTHY OLDER ADULTS

E. Cadel (1), S. Galvis (1), W. Eboch (2), P. Arnold (3), S. Wilson (2), E. Friis (2)

(1) Bioengineering Graduate Program
University of Kansas
Lawrence, Kansas, USA

(2) Mechanical Engineering
University of Kansas
Lawrence, KS, USA

(3) Department of Neurosurgery
University of Kansas Medical Center
Kansas City, KS, USA

INTRODUCTION

More than 65% of all adults over 60 years of age are affected by spinal deformity [1]. These deformities are most common in the thoracic region of the spine and can result in pain, poor balance, and reduced spinal mobility, the most common biomechanical measure presented in cadaveric and *in vivo* studies [2]. Corrective surgeries utilizing multilevel fusion systems are often recommended to alleviate patients' symptoms and regain spinal function.

In order to retain the most spinal mobility, the benefit of maximizing the number of unfused motion segments in the spine has been recognized [3]. However, it is difficult to quantify how much each individual motion unit contributes to *in vivo* spinal mobility because motion data is typically presented in segments comprised of multiple individual motion units due to anatomical constraints. These constraints are not present in cadaveric mobility studies resulting in the ability to present spinal mobility in terms of individual motion units [4], [5]. This inconsistency makes it difficult to compare data between these two models. The ability to compare cadaveric and *in vivo* motion is extremely beneficial for the clinical community because it allows for improved surgical planning.

The objective of this study is to develop a method that allows researchers to investigate the contribution of individual motion units to *in vivo* motion and frame it in a way that is more meaningful to surgeons. This method will allow for the comparison of individual thoracic and lumbar motion units in different physiological models and will be validated by comparing the calculated motion to different spinal mobility studies presented in the literature. With this new methodology, differences in percent contribution of individual motion units in various bending tasks and differences based on their location in the spine can both be investigated. The impact that individual motion units have on spinal mobility may aid clinicians in critical surgical planning decisions when using multilevel fusion systems.

METHODS

Spinal range of motion (ROM) in eighteen older adults, 70.0 ± 8.3 years (55-81 years), was measured using a TrakSTAR electromagnetic motion monitoring system (Ascension Technologies, Burlington, VT, USA) with sensors placed at the manubrium, at the spinous processes of T1, T3, T6, T10, L1, L3, and at the sacrum. After completing ten iterations of three trunk stretches, subjects performed a series of six bending tasks starting from a defined neutral standing position going to each subject's voluntary maximally bent position: flexion, extension, right and left lateral bending, right and left 45° anterior-lateral flexion. The order of the bending tasks was randomized for each subject and each task was repeated for five consecutive trials. Tasks with at least three acceptable trials were approved for analysis and the last acceptable trial was used for analysis.

Mean angular ROM was calculated for five segments: upper thoracic (T1-T3), middle thoracic (T3-T6), lower thoracic (T6-T10), thoracolumbar (T10-L1), and upper lumbar (L1-L3). Normalized ROM (nROM) was calculated by dividing the segmental ROM by the number of motion units in each segment. Percent contribution ROM (%ROM) was calculated by dividing each nROM value by the total ROM from T1-L3. Both nROM and %ROM represent the average motion and contribution of a single motion unit within a given segment, respectively. The first set of comparisons investigated the %ROM for all six bending tasks in a single normalized segment. The second set of comparisons investigated the %ROM for all five normalized segments in a single bending task. ANOVAs ($\alpha = 0.05$) were used followed by a Tukey-Kramer post hoc test to determine which combinations had significance.

Copyright 2016 The Organizing Committee for the 2016 Summer Biomechanics, Bioengineering and Biotransport Conference

All participants signed consent forms and this study was approved by the Institutional Review Board at the University of Kansas.

RESULTS

The nROM values calculated in this study were compared to *in vivo* and cadaveric studies found in literature. One *in vivo* study defined segments at different vertebrae than the current study [5]. To assess data for each motion unit, the same normalization methods were implemented on the data from this previous study. Another *in vivo* study used a Spinal Mouse system to measure ROM for each motion unit [6]. The motion unit data from all three studies indicated that ROM remains relatively constant through the thoracic spine and that there is a significant increase in ROM in the lumbar spine. The same trends were also present in cadaveric thoracolumbar mobility studies [4].

Based on the ANOVA results from the first set of comparisons, the percent contribution for all normalized spinal segments remained consistent, regardless of the bending task (Figure 1). The only significant difference in %ROM for a segment across bending modes was an increase in middle thoracic segment %ROM between right lateral bending and extension ($p < 0.01$).

Based on the ANOVA results from the second set of comparisons, the percent contribution of each sub-segmental region within a single bending mode was seen as consistent across the thoracic spine. The %ROM in the upper thoracic, middle thoracic, lower thoracic, and thoracolumbar segments were all statistically similar in flexion, extension, right lateral bending, and right and left 45° anterior-lateral flexion. However, for each given bending task, the upper lumbar %ROM was significantly greater than the %ROM in every other segment ($p < 0.02$).

DISCUSSION

Individual motion units are difficult to measure using traditional *in vivo* spinal mobility methods due to limited space between spinous processes and limitations in the resolution of external measures of the spine. This study developed a method to investigate the contribution of representative motion units within spinal segments during *in vivo* bending tasks.

The results from the first ANOVA set indicated motion contributed by a representative motion unit is independent of the bending task being performed. The second ANOVA set indicated the motion contributed by a representative upper lumbar motion unit is larger than its superior units and is also independent of the bending task being performed. The large nROM from the upper lumbar segment is supported by previous studies, signifying that the majority of total thoracolumbar spinal mobility originates in the lumbar spine. While results from this study indicate thoracic segments do not contribute as much to total thoracolumbar motion as lumbar segments, the upper, middle, and lower thoracic segments each contribute nearly 10% to overall trunk motion.

As with all *in vivo* data collected using motion sensors, soft-tissue artifact of the skin's movement over the spinous process during bending cannot be avoided. However, this artifact is less in the spine than in other areas of the body due to the firm attachment of the fascia to the spinous processes [7]. Limitations in analysis methods to transform position data into angular ROM prevented the ability to calculate ROM for the lower lumbar segment, L3-sacrum. Additionally, the developed method assumes that the contribution across a segment is equal for each motion unit.

The method presented is beneficial because it allows for an improved comparison of spinal mobility between different physiological models. It also provides surgeons with specific biomechanical information regarding the movement of motion units in the living spine. This information may become an important surgical tool for the planning of where spinal fusion constructs begin and end for patients with adult deformities. Understanding how much each motion unit contributes in a living spine can only help to better inform surgeons and spinal device designers.

ACKNOWLEDGEMENTS

This study was supported by The University of Kansas Doctoral Student Research Fund and the Self Graduate Fellowship at the University of Kansas. The authors would like to thank Hadley L. Sis, Benjamin M. Wong, and Joshua H. Arnold for their assistance with data collection, Matthew H. Dickinson for his assistance with data processing and analysis, and Nicole M. Speckin for her assistance with literature review.

REFERENCES

[1] Schwab, F et al., *Spine*, 35:2224-2231, 2010.
[2] Bess, S et al., *Spine*, 34:2186-2190, 2009.
[3] Auerbach, J et al., *Spine*, 37:359-366, 2012.
[4] White, A, Panjabi, M, *Clinical Biomechanics of the Spine*, 1990.
[5] Alqhtani, R et al., *J Manipulative Physiol Ther*, 38:275-281, 2015.
[6] Mannion, A et al., *Eur Spine J*, 13:122-136, 2003.
[7] Lundberg, A, *Hum Mov Sci*, 15:411-422, 1996.

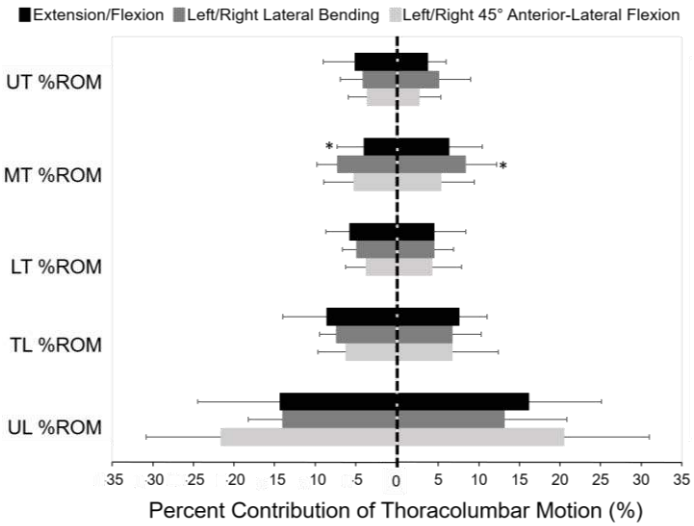

Figure 1: Segmental Range of Motion Comparisons. ROM for the contribution of a representative FSU in each spinal segment: upper thoracic from T1-T3 (UT), middle thoracic from T3-T6 (MT), lower thoracic from T6-T10 (LT), thoracolumbar from T10-L1 (TL), and upper lumbar from L1-L3 (UL). All values are reported as magnitudes of percent total motion from T1 to L3. * Denotes statistical difference between bending tasks ($p < 0.05$)

Copyright 2016 The Organizing Committee for the 2016 Summer Biomechanics, Bioengineering and Biotransport Conference

SB^{3}C2016
Summer Biomechanics, Bioengineering and Biotransport Conference
June 29 –July 2, National Harbor, MD, USA
SB^{3}C2016-718

CONFORMAL NANOENCAPSULATION OF ALLOGENEIC T CELLS MITIGATE GRAFT-VERSUS-HOST DISEASE BUT RETAIN GRAFT-VERSUS-LEUKEMIA ACTIVITY

S. Zhao (1, *), L. Zhang (2, *), J. Han (2), J. Chu (2), H. Wang (1), X. He (1,2) and J. Yu (2).

(1) Department of Biomedical Engineering,
The Ohio State University,
Columbus, OH, USA

(2) Comprehensive Cancer Center,
The Ohio State University,
Columbus, OH, USA

* These authors contributed equally to this work.

INTRODUCTION

Due to a graft-versus-leukemia (GVL) effect, allogeneic hematopoietic stem cell transplantation (HSCT) is an effective adoptive immunotherapy with cure potential. However, GVL is typically accompanied with graft-versus-host disease (GVHD), one of major complications of allogeneic HSCT that can lead to patient death [1]. GVHD can be divided into acute GVHD (aGVHD) and chronic GVHD (cGVHD). aGVHD occurs within 100 days of transplantation and aGVHD generally affects the skin, liver and intestinal tract of patients, leading to severe complications.

Activation of donor T cells and recipient antigen-presenting cells (APCs) plays critical roles in the aGVHD initiation [2]. Activation of APCs occurs in the first phase of pathophysiology of aGVHD, in which tissue damage is induced by chemotherapy preceding HSCT. Recently studies indicated that prior to HSCT, irradiation and/or chemotherapy damage the epithelia that line the mucosal barriers of skin and gastrointestinal tract. Disrupted barrier function leads to translocation of commensal microbiotas present on the skin and in the gastrointestinal tract, which fuels continuous activation of innate immune cells, creating and maintaining an inflammatory milieu permissive for subsequent activation of deleterious adaptive immunity. This allows microbial products, such as lipopolysaccharide, to translocate to the circulation, which stimulates the secretion of pro-inflammatory cytokines, such as interleukin (IL)-1 and tumor-necrosis factor (TNF). These pro-inflammatory cytokines stimulate the activation of host APCs, and then host APCs present antigens via MHC class II to CD4 T cells, resulting in activation, proliferation, and differentiation of donor T cells. Additionally, donor CD8+ T cells are also potent for inducing aGVHD. Donor CD8+ T cells preferentially damage recipient medullary thymic epithelial cells and impair negative selection, resulting in production of autoreactive CD4+ T cells that perpetuated damage to the thymus and augmented the development of aGVHD. Therefore, blockade of donor T cell activation is a common approach to suppress or prevent aGVHD.

While there are no reports regarding use of encapsulation in the setting of GVHD, this technology is promising in other applications through encapsulating grafted cells, islets, and tissue in biomaterials. Biocompatible biomaterials are used to form a micro or nano-scale semi-permeable membrane that conformally cover cells, allowing free transportation of oxygen, nutrients, and metabolic wastes, while limiting direct contact between grafted cells and host cells including immune cells [3]. Specifically, nanomaterial encapsulation via layer-by-layer deposition of cationic and anionic biomaterials is attractive because it can generate a multi-layer membrane on the surface of cells that potentially block direct contact between host antigen-presenting cells (APCs) and donor T cells in the setting of allogeneic transplantation with no change of the size, which may prevent the activation of donor T cells and in turn to reduce GVHD severity.

METHODS

In this study, we designed a layer-by-layer nano scale-coating on T cells. The cationic chitosan was deposited on the negatively charged cell membrane, forming a uniform nano-scale layer. Subsequently, negatively charged alginate was then coated on chitosan layer based on electrostatic deposition. Overall, the coating repeats one time, to achieve a four-layer coating on the surface of T cells. To assess successful coating, alginate labeled with fluoresceinamine was used to show the deposition of layer-by-layer coating and encapsulated cells showed strong green fluorescence on the surface. In addition, scanning electron microscope (SEM) was utilized to further visualize the cell morphology before and after encapsulation. There were many microvillies on the surface of non- encapsulated T cell, while the surface of encapsulated T cell became relatively smooth with porous structure.

Copyright 2016 The Organizing Committee for the 2016 Summer Biomechanics, Bioengineering and Biotransport Conference

The encapsulation efficiency was further evaluated by the population of fluoresceinamine-FITC-positive cells assessed by flow cytometry, indicating that 85.7% cells were encapsulated. Since the cationic and anionic polysaccharides could alter the surface charges, we also measured the cell surface zeta potential during the coating process. The zeta potential was about -19.5 mV before coating, while after first chitosan layer, the zeta potential shifted to -0.3 mV, indicating the successful deposition of cationic chitosan on the cell membrane. The following coating step of alginate on chitosan layer gave the overall surface zeta potential back to -24.6 mV. Then the third layer of chitosan and the fourth layer of alginate changed the zeta potential to 27.4 mV and -26.9 mV, respectively.

After the encapsulation, donor T cells were characterized in vitro, and their ability to inhibit GVHD and retain GVL was determined in vivo after being transplanted together with non-encapsulated donor bone marrow (BM) cells in a C57BL/6 → BALB/c HSCT mouse model.

RESULTS

After encapsulation, we investigated T cell proliferation in vitro by observing the growth curves after 48 h, 72 h, 96 h, and 120 h culture, and the results showed the similar proliferation rate between control and encapsulated T cells. In addition, we tested the ability of those encapsulated cells binding to CD3, a typical T cell marker, and we found that there is no evident difference before and after encapsulation.

To examine the cytotoxicity of encapsulated T cells against tumor cells, effector encapsulated T cells were induced under the stimulation of CD3-CD28 beads and were incubated with A20 or P815 tumor cells. Encapsulated T cells were able to lyse A20 and P815 tumor cells. No significant difference was observed between encapsulated T cells and non-encapsulated T cells. IL-2 secretion was moderately decreased at 48 hours after stimulation with CD3-CD28 beads, but no significant difference was observed at 96 hrs, indicating the coating was gradually degraded over time.

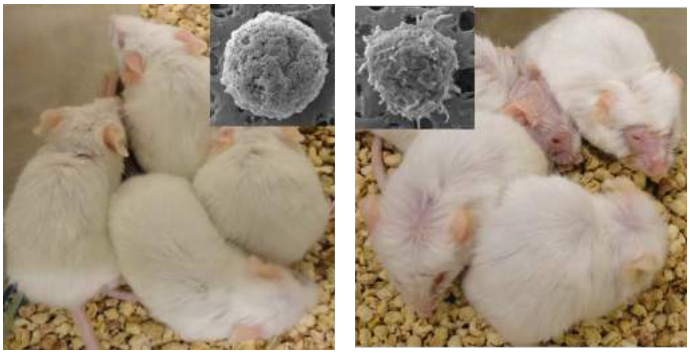

Figure 1: SEM images showing donor T cell after encapsulation has a smooth and porous surface (left inset) when comparing with non-coated one with microvilli (right inset). After transplantation, mice injected with encapsulated T cells have significantly less hair loss, weight loss and eye infection due to GVHD (left) than those injected with non-encapsulated ones (right).

To evaluate the potential of this encapsulation reducing GVHD, we transplanted encapsulated donor T cells into recipient mice. Compared to mice transplanted with allogeneic encapsulated T cells, the mice transplanted with control (non-encapsulated) cells developed more severe GVHD characterized by weight loss, hunching, reduced activity, ruffled fur and fur lost, and diarrhea. From day 21 to day 50, the clinical symptom scores of mice transplanted with encapsulated T cell group were significantly lower than those of mice in the non-encapsulated T cell group. Transplantation with encapsulated T cell significantly prolonged the survival of mice when compared with control donor T cells. A lymphoma A20 model were used to compare GVL effects of encapsulated and non-encapsulated T cells. Obvious tumor growth was observed in the mice engrafted with tumor cells alone 2 weeks post transplantation, while no tumor cells grew in the mice engrafted with BM cells together with either encapsulated T cells or non- encapsulated T cells throughout the 70-day observation period, demonstrating that the GVL effect of encapsulated T cells was not compromised. Consistent with these data, flow cytometric analyses indicated that there was no evidence of lymphoma in the spleen tissue in mice engrafted with encapsulated T cells or non-encapsulated T cell mice together with BM, but a tumor population were detected in mice transplanted with BM alone. In this model with both GVL and GVHD, transplantation with encapsulated T cell significantly prolonged the animal survival (63% at day 70, p = 0 .05 compared with T cell controls).

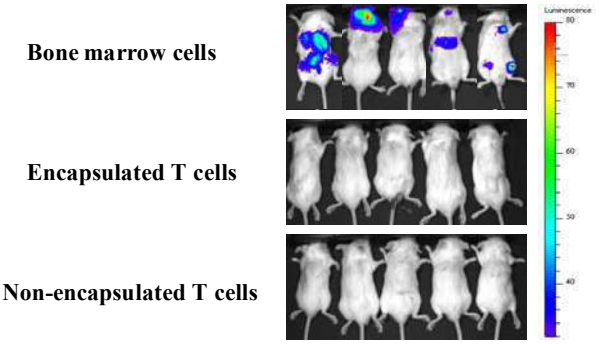

Figure 2: GVL activity was detected by biolumniscence imaging. Both encapsulated and non-encapsulated T cells treated mice had no evidence of lymphoma throughout the 70-day observation period, comparing with mice injected with bone marrow cells only.

DISCUSSION

In this study, we firstly adopted a nanomaterial encapsulation technology using chitosan and alginate to form multilayer semi-permeable membrane on the surface of T cells, which could contribute to the similar proliferation, secretion and cytotoxicity in vitro after encapsulation, which suggest that the function of T cell do not change after encapsulation. In addition, Encapsulated T cells reduce GVHD severity and prolong survival of mice with GVHD and retains the GVL activity of T cells. Therefore, we believe that the nano-encapsulated T cell in chitosan and alginate could attenuate GVHD through reducing the direct contact between donor T cells and host APCs, leading to inhibition of T cell activation by host APCs. These results indicated that nano-scale biomaterials could be used to encapsulate transplant cells aiming to reduce immune response while no significant increase of the size of cell itself.

ACKNOWLEDGEMENTS

This work was partially supported by grants from US National Institutes of Health (CA155521, OD018403, and CA185301 to J.Yu) and by an American Cancer Society (ACS) Research Scholar Grant (#120936-RSG-11-109-01- CDD to X. He).

REFERENCES

[1] R. Das, R et al., Blood, 115: 5249-5258, 2010.
[2] M.G. Roncarolo et al., Nat Rev Immunol 7: 585-598, 2007.
[3] P. de Vos et al., Biomaterials 27: 5603-5617, 2006.

Copyright 2016 The Organizing Committee for the 2016 Summer Biomechanics, Bioengineering and Biotransport Conference

SB^{3}C2016
Summer Biomechanics, Bioengineering and Biotransport Conference
June 29 –July 2, National Harbor, MD, USA
SB^{3}C2016-719

A NOVEL SELF-EXPANDABLE RETRACTOR FOR NEUROENDOSCOPY

Y. Xia (1), P. Plaha (2), J. Yang (3), Z. You (1)

(1) Department of Engineering Science
University of Oxford
Oxford, United Kingdom

(2) Department of Neurosurgery
John Radcliffe Hospital
Oxford, United Kingdom

(3) School of Pharmacy
Liaoning University of Traditional Chinese Medicine
Dalian, Liaoning, China

INTRODUCTION

To treat deep seated brain lesions, a current neuroendoscopy procedure typically inserts rigid tubular retractors into patient's brain to create clear passages. Although most literature reported positive results with the tubular retractor systems, such devices still have two inherent drawbacks. Firstly, because of the rigidity and relative large size of such retractors, they pose potential risks to surrounding healthy brain tissue. White matter damage along the surgical trajectory[1] and cytotoxic edema and cellular damage[2] have all been reported. Secondly, the long and thin cylindrical corridor created by the rigid retractor obstructs endoscope and surgical knife's movements.

In light of existing inadequacies, we propose a novel self-expandable retractor system that not only minimizes tissue injury but also improves surgery capacity. Inspired by self-expanding stent graft concepts[3], the retractor is made of Z-shaped Nitinol (NiTi) rings and a layer of Dacron fabric. As illustrated in Fig.1, the retractor would be first compressed and confined in a rigid outer sheath, and then inserted into the brain as its dilator penetrates. When inside the brain, the outer sheath would be extracted, deploying the retractor and allowing it to expand. Once the retractor fully self-expands to a desirable diameter, the dilator is also extracted, creating a clear corridor to the lesion site.

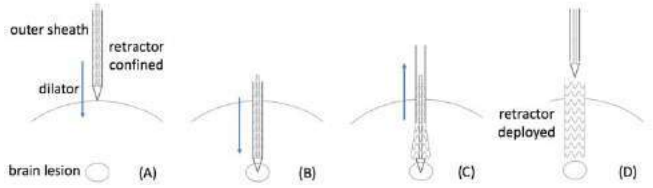

Figure 1 – Schematic drawing of self-expandable retractor deployment into brain tissue

The main objective of this paper is to find a functional design capable of self-expanding to a desired diameter when inside brain tissue.

METHODS

To develop such a self-expandable retractor, computational models have been made in ABAQUS/Explicit and finite element analysis has been conducted to study its mechanical behaviors and deployment inside brain tissue phantom. Then, based on the results of numerical design, prototypes have been made and experiments have been conducted to deploy the retractor in porcine brain *in vitro*.

In the finite element model, as an initial design, the self-expandable retractor has original diameter of 18mm and length of 30mm. It composes of 2 Z-shaped NiTi rings and a layer of Dacron fabric. It would be crimped and confined into an outer sheath of diameter 7mm before deployment. After being deployed inside brain tissue, it aims to self-expand to a minimum diameter of 16mm. The geometry of NiTi ring is first written in a Python script and imported into ABAQUS. Dacron fabric is fixed to NiTi rings using tie constraints. Rings with different geometries are modelled and flat plat compression tests are conducted to analyze their stiffness in order to find a functional design. Then, Coupled Eulerian Lagrangian method is used to model deployment of self-expandable retractor in brain tissue phantom, with brain tissue as Eulerian and retractor as Lagrangian. General contact is used in this model, frictions between parts are assumed to have coefficient of 0.1. Material properties for NiTi, Dacron and brain tissue are all taken from literature.

Based on our computational model, prototypes have been made using NiTi wires and Dacron fabrics. A set of jigs are custom made in order to heat treat NiTi wires to form the rings. The two free ends of the wire are connected using a thin stainless steel tube. Flat plate compression tests are also conducted experimentally. NiTi rings are

Copyright 2016 The Organizing Committee for the 2016 Summer Biomechanics, Bioengineering and Biotransport Conference

then stitched onto Dacron fabrics to form the retractors. A set of delivery device is also designed and 3D printed (Fig.2). To prepare for an experimental deployment of the retractor, porcine brains are obtained 6 hours post mortem and placed in a small container with open top. The retractor is then deployed and X-Ray images are taken.

Figure 2 - (left) A sample NiTi ring, (middle) some sample retractors and (right) a set of delivery device.

RESULTS

The deployment of retractor in brain tissue phantom is illustrated in Fig.3. Contour of strains on brain tissue is also shown. With an original diameter of 18mm, the retractor self-expands to a diameter of 15.9mm at the end of simulation. Current design features two rings with diameters of 18mm, heights of 12mm, wire diameters of 0.28mm and 5 crowns. Dacron fabric has thickness of 0.1mm. The retractor is 30mm in length, with 2mm space between each ring and 1mm at each end.

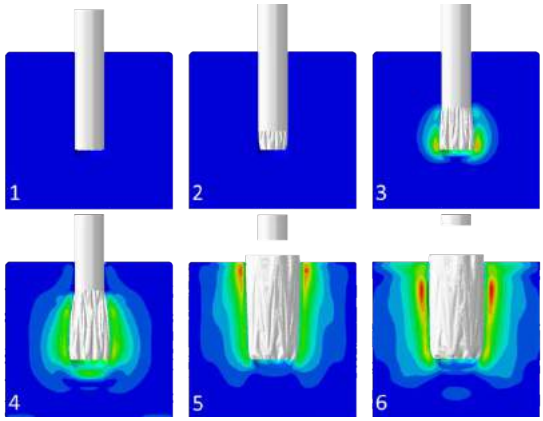

Figure 3 - FE simulation of a self-expandable retractor being deployed in brain tissue phantom.

Prototype with same parameters as the above mentioned numerical design is made and deployed into porcine brain *in vitro*. As revealed in the X-Ray image, the retractor self expands to a diameter of 16.2mm after deployment, which agrees well with the computational model.

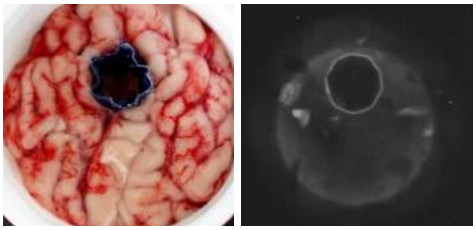

Figure 4 – (left) Experimental deployment in porcine brain *in vitro.* (right) X-Ray image of a deployed retractor

In both numerical analysis and experimental study, the current design proves to be functional as it successfully self-expands to desired diameter after deployment and creates a viable corridor for subsequent neuroendoscopy surgery. The concept of this novel retractor has been proved.

Flat plate compression test results further prove that the agreement in numerical and experimental deployments is not a coincidence. As shown in Fig.5, for NiTi rings with different geometries, experimental and numerical force vs compression distance results agree well.

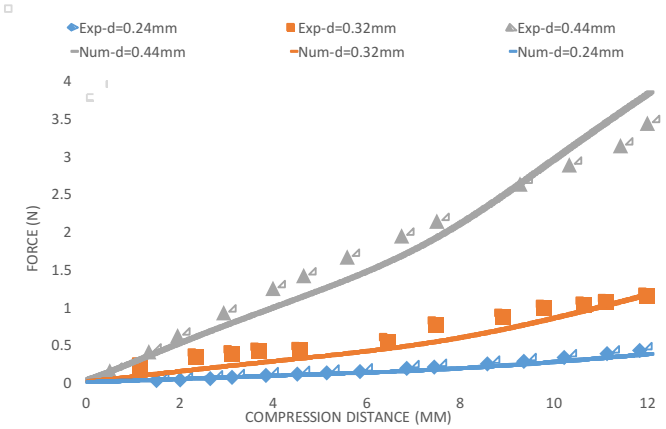

Figure 5 –Experimental and numerical results of flat plate compression of NiTi rings with different geometries.

DISCUSSION

A novel self-expandable retractor to assist treating deep brain lesion during neuroendoscopy has been presented. A coupled Eulerian Lagrangian model has been made and finite element analyses have been conducted to investigate interactions between brain tissue and surgical tools. The model is capable of simulating extreme deformations and thus is a sufficient tool to further develop this retractor. Prototypes of proposed retractor have also been made. The mechanical behaviours of the retractor in numerical and experimental analysis agree well. The concept of this novel self-expandable retractor has been proved.

However, the design of this novel retractor is still at its early stage. Current design is functional, but yet optimal. This study focused on mechanical behaviours of the retractor so that it is capable of self expanding to a desired diameter. The brain tissue is treated as a continuum solid at the moment. Though the computational model is capable of outputting stress/strain inside the phantom, it is unable to predict how much injury might occur in brain tissue.

Future work on this novel retractor will be dedicated to finding an optimal design that further minimizes brain tissue injury. More retractor designs will be explored, with different geometries and cover layer material choices. Biased stiffness[4] of NiTi rings will be considered so that the outward force acting on brain tissue is reduced, while the retractor is still capable of expanding to target diameter. Furthermore, an injury criteria of brain tissue will be added so that the finite element model becomes a comprehensive tool for designing, modelling, evaluating, and improving this novel retractor.

REFERENCES

1. Raza, S. M. *et al. Minim. Invasive Neurosurg.* **54,** 5–11 (2011).

2. Bander, E. D.*et al. J. Neurosurg.**October,*** 1–8 (2015).

3. Stoeckel, D. *et al. Eur. Radiol.* **14,** 292–301 (2004).

4. Duerig, T. *et al. Minim. Invasive Ther.* **9,** 235–46 (2000).

Copyright 2016 The Organizing Committee for the 2016 Summer Biomechanics, Bioengineering and Biotransport Conference

SB³C2016
Summer Biomechanics, Bioengineering and Biotransport Conference
June 29 –July 2, National Harbor, MD, USA
SB³C2016-720

ELECTROMECHANICAL COUPLING BEHAVIOR OF AXON MICROTUBULES

[1]Khashayar Teimoori, [2]Ali M. Sadegh, [3]Marom Bikson

[1,2] Department of Mechanical Engineering
The City College of the City University of New York
New York, NY 10031, USA

[3] Department of Biomedical Engineering
The City College of the City University of New York
New York, NY 10031, USA

INTRODUCTION

The axon is composed of both long and short Microtubules (MTs), the largest and stiffest component of the axon that form the internal cytoskeleton, and allow the axon to stretch in response to tensile and/or compressive strains. These MTs can be stretched and shrunk through regulation of tau proteins. Tau proteins are the connective parts that bind the MTs in the axon using an electrostatic zipper bond as shown in Figure 1. [1]

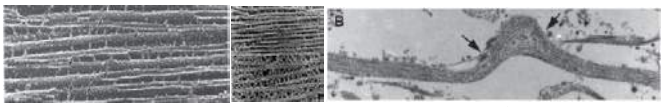

(a) (b)

Figure 1: (a) Electron microscopy image of porcine brain MTs with tau protein connections [1] (b) Experimental results for injury of cultured 2-mm-long axons [1,2]

Specifically, the proline-rich region of a tau protein forms this bond with the negatively charged N-terminus of another tau protein. Because of their viscoelastic behavior, tau proteins dynamically bind and unbind with each other when exposed to a tensile strain. Inside of the axon is a gel-like fluid called axoplasm, composed of molecules that conduct electrical neural impulses. This conductive fluidic substance has an electrical resistance that can affect the travel rate of any applied electric field across the axon. Recent numerical studies developed a computational model of MTs to examine a rate-dependent behavior of the MTs relative to their dynamic interactions and the tau protein under different strains as well as strain rates. In a study conducted by Ahmadzadeh et al. [1], the breaking of the tau connections and microtubules during axonal stretch injury was examined using a COMSOL model. Tau proteins act as an electrostatic zipper bond, which can reform after breaking. The proportion of free to connected tau proteins in strain-rate dependent breaking was analyzed to determine the effects of fast loading on the permanence of axonal deformation. It was observed that fast loading rates contributed to the breaking of tau proteins observed in traumatic brain injury, and the rupturing of microtubules that deforms the axon. Dynamic strain rates of 1-50 sec^{-1} damaged the axon at very small strains. [3] This study proposes that by applying an electric field to the Axon, when tau connections are fully disconnected, the axoplasm fluid will be stiffer, thereby the damaged axon as well as disconnected tau connections can be reformed faster. This process is behaving like a cast in order to hold the broken tau connection which would make the process of improving the axon, MTs and their connections faster.

METHODS

Using a localized model, we performed unit cell simulations, where a unit-cell contains three microtubules connected with two tau proteins. When an electric field is applied to a specific region across an axon, a bulk fluid motion is observed. In this case, the velocity of this motion is linearly proportional to the intensity of the applied electric field and it is dependent on both the material used to construct the axon as well as the solution in contact with the channel wall. This flow in the channel is called an Electroosmotic Flow. The simulated model and the geometry used in this study are depicted in Figure 2 in order for better understanding on what is going on the present study.

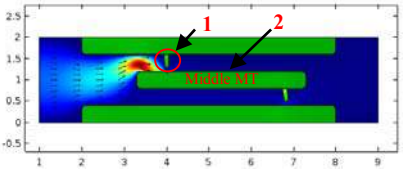

Figure 2: Geometry and simulation of the model, (1) the Upper tau connection (2) Middle short microtubule

Copyright 2016 The Organizing Committee for the 2016 Summer Biomechanics, Bioengineering and Biotransport Conference

While Ahmadzadeh et. al. [1], only focused on strain rate and therefore only required a mechanical model, we created a very first fluid structure interaction model of axon including MTs as well as tau connections and introduced the axoplasm as a fluid into the axon channel. First, by applying a velocity profile induced flow as an inlet, we measured flow and VonMises stress applied to the MTs without any applied electric field. The fluid flow is described by the incompressible Navier-Stokes equations for the velocity field, where $\mathbf{u} = (u, v)$, $\mathbf{u}_m = (u_m, v_m)$, and the pressure, p, in the spatial (deformed) moving coordinate system is stated in equations (1) and (2), respectively.

$$\rho\frac{\partial \mathbf{u}}{\partial t} - \nabla.[-p\mathbf{I} + \eta(\nabla\mathbf{u} + (\nabla\boldsymbol{u})^T)] + \rho\big((\mathbf{u} - \mathbf{u}_m).\nabla\big)\mathbf{u} = \mathbf{F} \quad (1)$$

$$-\nabla \cdot \mathbf{u} = 0 \quad (2)$$

Where, $\mathbf{I}$ denote the unit diagonal matrix and $\mathbf{F}$ is the volume force affecting the CSF flow. It is assumed that there is no gravitation or other volume forces affect the axoplasm, so that $\mathbf{F} = 0$.

At the channel entrance on the left, the flow has fully developed laminar characteristics with a parabolic velocity profile but its amplitude changes with time. At first, flow increases rapidly, reaching its peak value at 0.215s; thereafter it gradually decreases to a steady-state value of 0.01cm/s as depicted in Figures 4 and 6. The velocity in the x direction, u_{in} with the steady-state amplitude U comes from the equation (3);

$$\boldsymbol{u}_{in} = \frac{U.t^2}{\sqrt{(0.04-t^2)^2+(0.1t)^2}} \quad (3)$$

Where, t is the time expressed in seconds and U is the mean velocity at steady state and is equal to 1[cm/s] due to a very small movement of the axoplasm in Axon. [2] Afterwards, we applied both electric field and the velocity profile induced flow as an inlet. An electroosmotic induced flow was simulated by using COMSOL Muliphysics 5.2 (Palo Alto, CA 94304 USA) Software. Therefore, a very first novel steady state electro-Fluid-Solid-Interaction (eFSI) numerical analysis performed in order to investigate the effects of the applied electric field on the axoplasm fluid and thereby the stress as well as FSI interactions between MTs and the tau connections. The geometry is meshed using extremely fine mesh for the fluid dynamics analysis and the process of simulation was done within 11min and 4 secs in order to get the final eFSI results. The dimensions of each part of the model is illustrated in Table 1 and the final results are depicted in Figures 3 to 6 to be discussed in the Results section.

Dimension	Width (μm)	Height (μm)
Axon Channel	10	2
Upper Long MT	6	0.4
Lower Long MT	6	0.4
Middle short MT	4	0.4
Tau Proteins	0.1	0.4
Fillet Radius	r =0.1 (μm)	

Table 1: Information of the model [1,3]

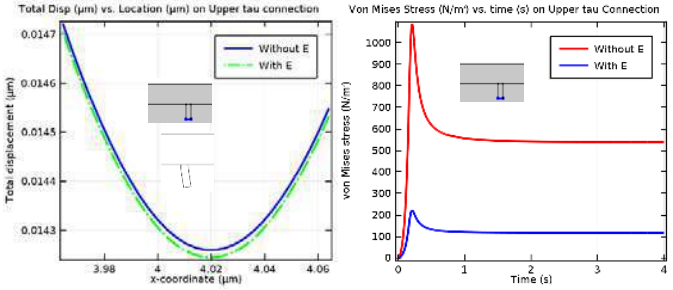

(3) (4)

Figures 3 and 4: Displacement and Von Mises stress changes of the upper tau protein connection with and without E field.

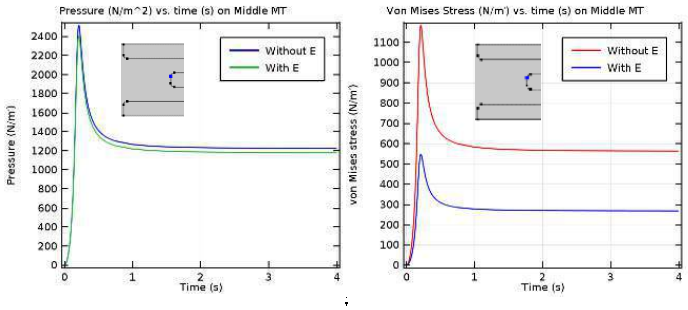

(5) (6)

Figures 5 and 6: Pressure and Von Mises stress changes of the MTs with and without E field.

RESULTS

The results demonstrated that the applied electric field in conjunction with the induced velocity can reform the axon after the separation and broken connections of tau proteins with MTs in a traumatic brain injury. The results of this study reveal that the pressure and Von Mises stresses on the tau protein and MTs are reduced when the axon is subjected to an electric field. The analysis of this study was based on the coupling of electromechanical and FSI in conjunction with fluid mechanics' theories. Specifically, by looking at Figures 3 and 4, it can be found that the applied electric field decreased the amount of the total displacements on the upper tau protein while significantly reduces its Von Mises stress. Note that in Figure 3 there is not much difference between the cases with and without electric field until the simulation reaches its steady state position. Similarly, Figures 5 and 6 reveal that applied electric field decreased the amount of the total pressure on the MT while significantly reduces its Von Mises stress. Hence, it is concluded that the axoplasm fluid is influenced by the induced electric field and therefore it acts as a stiffer fluid that the axon's MTs as well as the broken tau protein connections can regain their original forms.

Finally, by looking at both MTs and the tau protein connections between them, this study showed that an applied Electric field can reduce the displacement and the von Mises stresses on the tau protein and MTs thereby leading to repairing a damaged axon where tau protein connection is broken, as shown in Figures 3 to 6. Therefore, it is hypothesized that by applying an electric field, a damaged axon can repair itself through regaining the original morphology of its tau proteins and MTs. Further 3-D studies of the axon and its tau protein and MTs are needed to quantify the effect of electric field on the damaged axon.

REFERENCES

[1] Ahmadzadeh, Hossein, Douglas H. Smith, and Vivek B. Shenoy. "Viscoelasticity of tau proteins leads to strain rate-dependent breaking of microtubules during axonal stretch injury: predictions from a mathematical model." Biophysical journal 106, no. 5 (2014): 1123-1133.

[2] Hirokawa, N., Y. Shiomura, and S. Okabe. 1988. Tau proteins: the molecular structure and mode of binding on microtubules. J. Cell Biol. 107:1449–1459.

[3] Ahmadzadeh, H., Smith, D. H., & Shenoy, V. B. (2015). Mechanical Effects of Dynamic Binding between Tau Proteins on Microtubules during Axonal Injury. Biophysical journal, 109(11), 2328-2337.

Copyright 2016 The Organizing Committee for the 2016 Summer Biomechanics, Bioengineering and Biotransport Conference

SB^{3}C2016
Summer Biomechanics, Bioengineering and Biotransport Conference
June 29 –July 2, National Harbor, MD, USA
SB^{3}C2016-721

STIFFNESS-INDEPENDENT ON-CHIP EXTRACTION OF CELL-LADEN HYDROGEL MICROCAPSULES FROM OIL EMULSION INTO AQUEOUS SOLUTION BASED ON DIELECTROPHORESIS

Mingrui Sun (1), Haishui Huang (2), Xiaoming He (1)

(1) Department of Biomedical Engineering, The Ohio State University, Columbus, OH, United States

(2) Department of Mechanical Engineering, The Ohio State University, Columbus, OH, United States

INTRODUCTION

Cell microencapsulation is a technique to use biocompatible polymer to encapsulate single cell or cell clusters, which is widely used in 3D cell culturing, stem cell therapy, cell cryopreservation, drug delivery, and tissue engineering. [1-4] The hydrogel microcapsules allow the essential metabolism substances to pass through the capsules, while they block the immune cells and antibodies, and protect the encapsulated cells. [5] Recently, microfluidics has been an attractive technique for microencapsulation, which is well controllable and does less damage to cells than other techniques, such as emulsification and electrospray. [6-8] However, one challenge of microfluidics is that the cell microcapsules usually form in oil phase, but need to be transferred to aqueous phase for further applications. The conventional transfer process based on centrifuge and washing is complex and may damage the cells [9]. In addition, prolonged exposure to the oil phase decreases the cell viability in microcapsules significantly. As a result, timely extraction from the oil phase to the aqueous phase is required to improve the cell microencapsulation applications. There are many methods used to extract microcapsules from the oil phase into the aqueous phase, such as interfacial tension methods. [9, 10] However, these methods depend on the strength of the microcapsules, and if the microcapsules are too soft, they can't work.

This study reports a stiffness-independent and dielectrophoresis (DEP)-based approach for on-chip extraction of hydrogel microcapsules. Liquid electrodes are used in the DEP device instead of metal electrodes. Hydrogel microcapsules are generated in oil emulsion using flow-focusing junction. When the microcapsules pass through the electrode regions, the DEP force can deflect them towards the aqueous phase regardless of their mechanical strength. Complete extraction can be achieved when the electric field is higher than 1700 V. Moreover, the DEP extraction does not compromise the viability of the microencapsulated cells.

METHODS

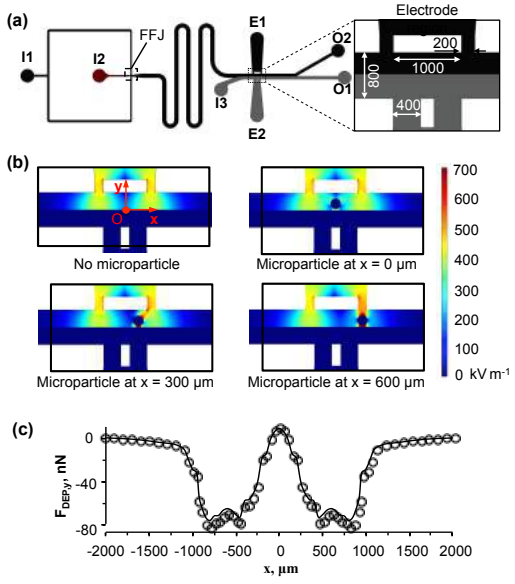

Figure 1: (a) The schematic figure of the DEP device. (b) The simulated electric field distribution in the electrode regions. (c) The calculated DEP force the microcapsules experience in the electrode regions.

As shown in Figure 1(a), the device was made of PDMS using soft lithograph. The alginate droplets, which were made of 0.5% or 2% (w/v) sodium alginate in saline without or with cells (introduced from I2, 100 µL/hr) were generated in the oil emulsion (introduced from I1, 5 mL/hr) at the flow-focusing junction (FFJ), and then formed hydrogel microcapsules in the microchannels. The oil emulsion was prepared by mixing mineral oil with $CaCl_2$ in deionized water using ultrasound. 1.3% (w/v) medium-viscosity carboxymethyl cellulose in saline was introduced via I3 (5 mL/hr). In the main extraction channel, a two-phase interface forms between the oil emulsion and cellulose solution. In addition, the electric field was applied to E1 and E2.

The electric field distributions in the electrode regions without and with microcapsule were simulated using COMSOL Multiphysics (version 4.3), as shown in Figure 1(b). The microcapsule affects the electric field distribution significantly in the electrode regions, and the electric field inside the microcapsule is much lower than that outside. In addition, the DEP force a microcapsule experiences at various locations in the electrode regions also was calculated. The results indicate that the DEP force is in the negative Y direction, and drives the microcapsules towards the aqueous phase.

Human C3H10T1/2 mesenchymal stem (C3) cells were suspended in 2% alginate in saline for cell viability study.

RESULTS

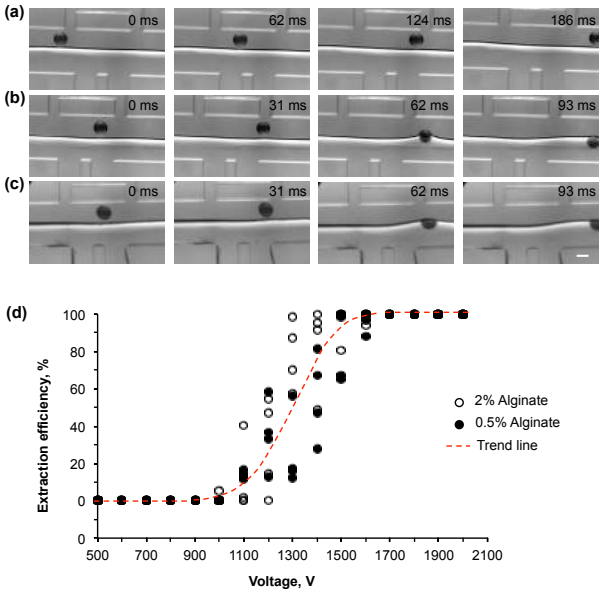

Figure 2: (a-c) Movement of hydrogel microcapsules in the electrode regions without and with electric field (moving from left to right). Scale bar: 200 µm. (d) The DEP extraction efficiency of alginate hydrogel microcapsules under various electric fields.

The behavior of an alginate (2%) hydrogel microcapsule in the electrode regions without electrical field is shown in Figure 2(a). The microcapsule moves without extraction. Figure 2(b) and (c) show the extraction of 2% and 0.5% alginate hydrogel microcapsules with electric field 1700 V, respectively. In the electrode regions, the DEP force drives the microcapsules towards the aqueous phase. Once the microcapsules touch the interface between the oil emulsion and aqueous solution, the microcapsules will be extracted by the surface tension force into the aqueous solution due to the hydrophilic property of the microcapsules. Figure 2(d) shows the extraction efficiency of the microcapsules in various electric fields. When the applied voltage is above 1700 V, 100% extraction can be achieved.

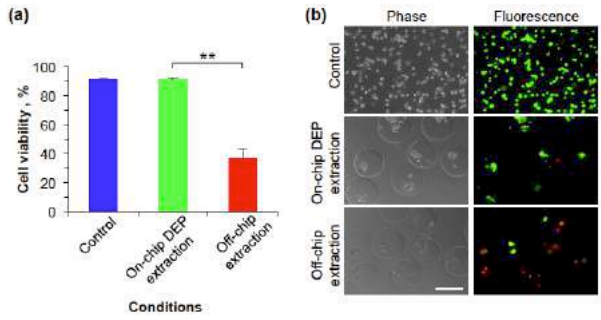

Figure 3: (a) The cell viability of the microencapsulated C3 cells in on-chip and off-chip extraction. (**): $p < 0.01$. The error bars represent SEM. (b) The phase and fluorescence images showing cell viability of different groups. Scale bar: 200 µm.

The cell viability results are shown in Figure 3. The cell viability of the on-chip DEP extraction (2000 V) group is 91.1%, which is similar with the control group (cells suspended in alginate solution without any treatment), while the cell viability of the off-chip extraction group (conventional centrifuge and washing method) is much lower (36.7%). These results indicate that the high electric field outside the microcapsule does no harm to the cells in the microcapsules when they pass through the electrode regions.

DISCUSSION

Based on the theory of dielectrophoresis, a microcapsule in a conductive medium can experience a DEP force in an electric field when the gradient of the electric field exists. In this study, as the size of the microcapsules is comparable to that of the microchannel, the microcapsules have a significant effect on the electrical field distribution in the electrode regions, as shown in Figure 1(b). Therefore, the microcapsules should be considered in the evaluation of the DEP force the microcapsules experience, which can be calculated using COMSOL Multiphysics based on the theory of the Maxwell stress tensor. As the DEP force depends on the electric properties of the microcapsules, but not the stiffness, the DEP device can achieve the stiffness-independent extraction of the microcapsules.

Due to the electrolyte (NaCl) in the microcapsules, the electric field intensity inside the microcapsules is much lower than that in the oil emulsion as a result of the Faraday cage effect. This can protect the cells in the microcapsules from the damage of the high electric field outside when the microcapsules move in the oil emulsion before extraction.

.

ACKNOWLEDGEMENTS

M.S. and H.H. contributed equally to this work. This work was partially supported by grants from NSF (CBET-1154965) and NIH (R01EB012108) to X.H.

REFERENCES

[1] Agarwal, P et al., *Lab Chip*, 13:4525, 2013.
[2] Choi, J et al., *Biomaterials*, 35:5122, 2014.
[3] Zhang, W et al., *Biomed. Microdevices*, 12:89, 2010.
[4] Kim, C et al., *Lab Chip*, 11:246, 2011.
[5] Chang, T, *Science*, 146:524, 1964.
[6] Zhang, W et al., *Chem. B*, 1:1002, 2013.
[7] Serra, M et al., *PloS One*, 6:e23212, 2011.
[8] Mumaw, J et al., *Int. J. Biomater.*, 2012:861794, 2012.
[9] Huang, H et al., *Appl. Phys. Lett.*, 105:143704, 2014.
[10] Deng, Y et al., *Lab Chip*, 11:4117, 2011.

SB^{3}C2016
Summer Biomechanics, Bioengineering and Biotransport Conference
June 29 –July 2, National Harbor, MD, USA
SB^{3}C2016-722

FLUID DISPLACEMENT DURING DROPLET FORMATION AT MICROFLUIDIC FLOW-FOCUSING JUNCTION

H. Huang (1,2), X.He (1,2)

(1) Department of Mechanical Engineering
The Ohio State University
Columbus , OH, USA

(2) Department of Mechanical Engineering
The Ohio State University
Columbus , OH, USA

INTRODUCTION

Microdroplets and microcapsules have been widely produced using microfluidic flow-focusing junction for biomedical and chemical applications. However, the multiphase microfluidic flow at the flow-focusing junction has not been well investigated. In this study, the displacement of two (core and shell) aqueous fluids that disperse into droplets altogether in a carrier oil emulsion was investigated both numerically and experimentally. It was found that extensive displacement of the two aqueous fluids within the droplet during its formation could occur as a result of the shear effect of the carrier fluid and the capillary effect of interfacial tension. We further identified that the two mechanisms of fluid displacement can be evaluated by two dimensionless parameters. The quantitative relationship between the degree of fluid displacement and these two dimensionless parameters was determined experimentally. Finally, we demonstrated that the degree of fluid displacement could be controlled to generate hydrogel microparticles of different morphologies using planar or nonplanar flow-focusing junctions. These findings should provide useful guidance to the microfluidic production of microscale droplets or capsules for various biomedical and chemical applications.

METHODS

Numerical simulation: The numerical simulation of the flow in multiphase flow in microfluidics with flow focusing junction can be modelled by commercial software COMSOL Multiphysics 4.3 by combining two independent level set functions($\emptyset_1$ and $\emptyset_2$). It solves the partial differential equations via finite element method (FEM) and transforms them into their weak forms. The discretization type for velocity components, pressure field, Level Set variables are second-order, linear and quadratic elements, respectively. Both the streamline diffusion and crosswind diffusion are turned on for the Navier-Stokes equations and Level Set equations for consistent stabilization with tuning parameter $C_k = 0.5$. Considering the complexity of numerically solving equatio, backward differentiation formulas (BDF) has been used to discretize the time steps with maximum order being 2 to further stabilize the computation. The governing equation set is shown as follows:

$$
\begin{cases}
\nabla \cdot \vec{u} = 0 \\
\rho \dfrac{\partial \vec{u}}{\partial t} + \rho(\vec{u} \cdot \nabla)\vec{u} = \nabla \cdot [-p\boldsymbol{I} + \mu(\nabla\vec{u} + (\nabla\vec{u})^T)] + f_{it} \\
\dfrac{\partial \emptyset_1}{\partial t} + \vec{u} \cdot \nabla\emptyset_1 = \gamma_{ls}\nabla \cdot \left(\epsilon_{ls}\nabla\emptyset_1 - \emptyset_1(1-\emptyset_1)\dfrac{\nabla\emptyset_1}{|\nabla\emptyset_1|}\right) \\
f_{it} = \nabla \cdot \left(\gamma\left(\boldsymbol{I} - (\vec{n}\vec{n}^T)\right)\delta\right) \\
\vec{n} = \dfrac{\nabla\emptyset_1}{|\nabla\emptyset_1|} \\
\delta = 6|\nabla\emptyset_1||\emptyset_1(1-\emptyset_1)| \\
\dfrac{\partial \emptyset_2}{\partial t} + \vec{u} \cdot \nabla\emptyset_2 = \gamma_{ls}\nabla \cdot \left(\epsilon_{ls}\nabla\emptyset_2 - \emptyset_2(1-\emptyset_2)\dfrac{\nabla\emptyset_2}{|\nabla\emptyset_2|}\right) \\
\rho, \mu, \gamma = f(\emptyset_1, \emptyset_2)
\end{cases}
$$

Experimental setups: All the fluids were irrigated into BD syringes before being introduced into microchannels by syringe pumps (Harvard Apparatus). To check the trajectory and distribution of dispersed fluids within droplets, we took fluorescence rather than bright field time-lapse images of the shell fluid. This is because the refraction indices of the fluids and materials of channel walls are required to be matched for the bright field or phase images to accurately capture the flow within droplets near the liquid-liquid interface and near the channel walls. The fluorescence time-lapse images were taken by a Zeiss AxioCam HSm fast-speed CCD camera equipped on a Zeiss Axio Observer.Z1 microscope under a 2.5X objective. The image size was set as 462 × 346 pixels and the exposure time was 2 ms, resulting in imaging frequency ~ 64 Hz. On the other hand, static images of hydrogel particles were taken using a Zeiss

Copyright 2016 The Organizing Committee for the 2016 Summer Biomechanics, Bioengineering and Biotransport Conference

AxioCam MR3 CCD camera under phase contrast field of a 10X objective. The corresponding resolution was 1388 × 1040 pixels.

RESULTS

As shown in Figure 1, numerical simulation revealed two mechanisms of fluid displacement during droplet formation. During droplet growth stage, the dispersed fluids still attach to the inlets and the carrier fluid flows over the pendent droplet, which induces shear stress and two counter-rotating vortices (arrows in the velocity field) within the growing droplets. During droplet pinch-off stage, one of two the aqueous tails recoils back to the inlet from the pinching point with the capillary velocity. The other aqueous tail recoils forward in the droplet that has pinched off. The recoiling could cause redistribution of the dispersed fluids in both the droplet that has pinched off and the next droplet to form. Of note, as the pinched-off droplet moves downstream in the same direction as the recoiling velocity, it causes less fluid displacement within the pinched-off droplet than the pendent one.40 The counter-rotating vortices and the capillary recoil can significantly disturb and transfer the aqueous core and shell fluids in the droplets, which could displace them off their desired and ideal positions (the shell fluid locates on the peripheral and core fluid in the inner area of the droplets). This phenomenon was referred as fluid displacement in this study.

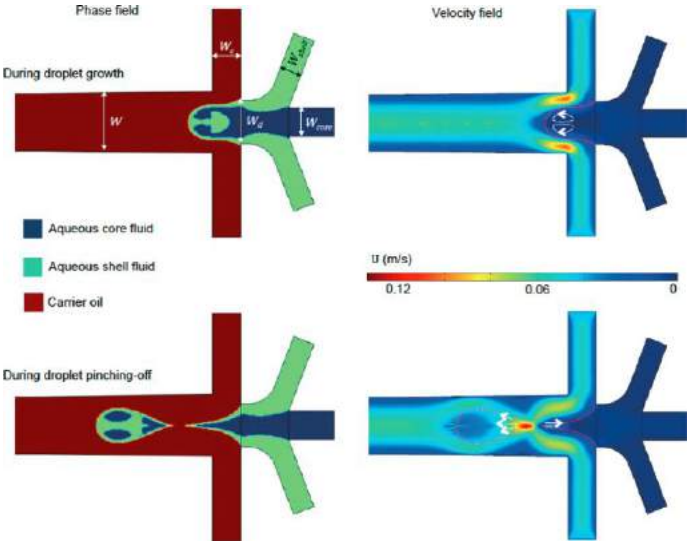

Figure 1: Numerical simulation of droplet formation at a planar flow-focusing junction for a typical flow condition. The arrows on the images of velocity field represent velocity vectors in the dispersed phase. Numerical settings: σ = 30 mN m^{-1}, $\mu_{core} = \mu_{shell}$ = 200 mPa s, μ_c = 30 mPa s, $q_{core} = q_{shell}$ = 0.4 ml hr^{-1}, and q_c = 10 ml hr^{-1}. Geometries: W = 400 µm, W_d = 300 µm, W_c = 200 µm, W_{shell} = 150 µm, and W_{core} = 200 µm.

The ratio I_{in}/I_{out} was used to evaluate the degree of fluid displacement within the droplets. A higher I_{in}/I_{out} suggests more shell fluid is displaced to the inner region. As shown in Figure 1, shear stress applied on the pendent droplet by the continuous carrier oil could induce vortices and fluid displacement during droplet formation, which however, could be balanced (with damping) by the viscous effect of the dispersed fluids. Therefore, a shear stress ratio ζ can be used to represent the shear effect on the fluid displacement within a droplet. On the other hand, the recoiling of the dispersed tail during and after droplet pinch-off is caused by interfacial tension between dispersed and carrier fluids. This deformation and the resultant displacement of dispersed fluids are also balanced (with damping) by viscous effect although the duration may not span over the whole droplet formation period. As a result, the capillary effect on fluid displacement can be evaluated by parameter λ.

As shown in the upper left inset of Figure 2, for constant λ, the slope between I_{in}/I_{out} and log10(ζ) is 0.55. While for constant ζ, the slope between I_{in}/I_{out} and log10(λ) is -0.82. As a result, the combined effect of these two mechanisms gives rise to the following relationship:

$$I_{in}/I_{out} = 0.55\log_{10}(\zeta) - 0.82\log_{10}(\lambda) = \log_{10}(\zeta^{0.55}/\lambda^{0.82})$$

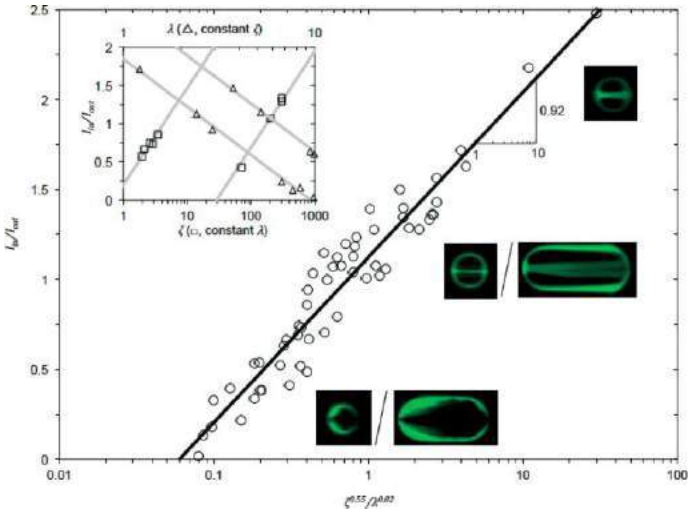

Figure 2: Experimental data showing the dependence of I_{in}/I_{out} on the two dimensionless parameters: shear stress ratio ζ and relative droplet size λ. The slope of the least square fitting line (black line) between I_{in}/I_{out} and $\log_{10}(\zeta^{0.55}/\lambda^{0.82})$ is 0.92. The ratio of q_{shell}/q_{core} = 0.2 for all experiments. Upper left inset: $I_{in}/I_{out} \sim 0.55\log_{10}(\zeta)$ for constant λ, $I_{in}/I_{out} \sim -0.82\log_{10}(\lambda)$ for constant ζ. Insets of fluorescence images: microdroplets generated with various combinations of ζ and λ.

The slope of the least square fitting line between I_{in}/I_{out} and $\log_{10}(\zeta_{0.55}/\lambda_{0.82})$ is 0.92, which is close to 1. The fitting goodness R^2 = 0.92. The insets of fluorescence micrographs show microdroplets of different I_{in}/I_{out} (i.e., different morphologies) for various combinations of ζ and λ.

ACKNOWLEDGEMENTS

This work was partially supported by grants from NSF (CBET-1154965) and NIH (R01EB012108). The authors would like to thank Dr. Mark Ruegsegger and Mr. Robert Jones for their help with measuring interfacial tension.

REFERENCES

Huang, H et al., *Lab Chip.*, 15: 4197–4205, 2015.

Copyright 2016 The Organizing Committee for the 2016 Summer Biomechanics, Bioengineering and Biotransport Conference

SB^{3}C2016
Summer Biomechanics, Bioengineering and Biotransport Conference
June 29 –July 2, National Harbor, MD, USA
SB^{3}C2016-724

ENHANCED MICROWAVE HYPERTHERMIA OF CANCER CELLS WITH FULLERENE

Mingrui Sun (1), Xiaoming He (1)

(1) Department of Biomedical Engineering
The Ohio State University
Columbus, OH, United States

INTRODUCTION

Hyperthermia is a widely used method for cancer treatment, which utilizes various energy sources, such as ultrasound, laser, or microwave to heat and damage the tumor. [1, 2] Among them, microwave hyperthermia has been commonly studied. The microwave field can be generated using antennas and heat the tumor effectively due to its high water content. However, only by designing the antennas to control the intensity distribution of the microwave field, the heating cannot be well targeted and the normal tissue adjacent to the tumor also may be damaged, [3-5] In order to improve the therapeutics and targeting property, nanoparticles are utilized as agents in the microwave hyperthermia. For instance, carbon nanotubes (CNTs) have been used to absorb the microwave energy and generate heat, enhancing the treatment of the tumors. [6, 7]

Fullerene (C60) is a carbon isotope with CNTs, and has been studied on its photodynamic effect. However, the poor water dissolvability limits its applications. Therefore, various methods have been developed to use chemical functionalization to improve the dissolvability of the fullerene. [8, 9] But the chemical modification may alter the properties and behaviors of the fullerene in the biological systems. [10-12] In addition, the fullerene has been demonstrated to absorb the microwave energy and generate heat, which makes it a promising agent in the microwave hyperthermia. [13]

In this study, a novel type of water-dissolvable nanoparticles, fullerene Pluronic F127-chitosan nanoparticles (C60-PCNPs), was synthesized by using Pluronic F127-chitosan nanocapsules (PCNPs) to encapsulate the free fullerene without any chemical modification, which can be utilized in microwave hyperthermia as the thermal agents. In addition, a microwave dish with an antenna was fabricated to heat the PC-3 cells with and without C60-PCNP treatment. The results demonstrate that the C60-PCNPs have great potential to enhance the cancer treatment by microwave hyperthermia.

METHODS

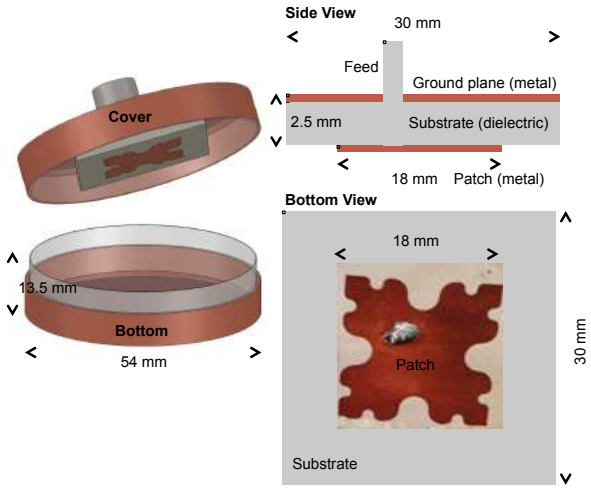

Figure 1: The structures of the microwave dish and antenna.

As shown in Figure 1, the microwave dish was fabricated by covering the 60 mm polystyrene petri dish using copper. The antenna was designed to heat 3 ml cell culture medium with cells in the microwave dish, and the frequency of microwave was about 2.4 GHz.

The PNCPs were synthesized as reported in the previous study, and then were used to encapsulate the fullerene to synthesize the C60-PCNPs. [14] Firstly, 5 mg PCNPs were dissolved in 2 ml DI water and

Copyright 2016 The Organizing Committee for the 2016 Summer Biomechanics, Bioengineering and Biotransport Conference

1 mg fullerene was dissolved in 1 ml toluene. Two solutions were then mixed using Vortex mixer for 3 hours. The mixture was rotatory evaporated to remove the toluene, filtered using 450 nm filters and then freeze-dried overnight to gain the dry C60-PCNPs.

PC-3 human prostate cancer cells were used in this study. 6×10^4 PC-3 cells in 300 µl medium were cultured at the central region of the dish for 1 day. 3 mg/ml of C60-PCNPs in cell culture medium was used to treat the cells (if needed) for 2.5 hours at 37 °C. Before the heating, cells were washed using cell culture medium, and 3 ml cell culture medium was added into the dish with cells for heating.

In the microwave heating, the cell samples were heated by microwave and cooled down at room temperature, and then incubated for 48 hours at 37 °C before the cell viability measurement. In the water-bath heating, the cell samples in the dish were floated on DI water in a beaker and heated on a hot plate, and cooled down at room temperature, and then incubated for 48 hours at 37 °C before the cell viability measurement. The thermal history in the water-bath heating is controlled to be the same with that in the central region of the microwave dish in the microwave heating.

RESULTS

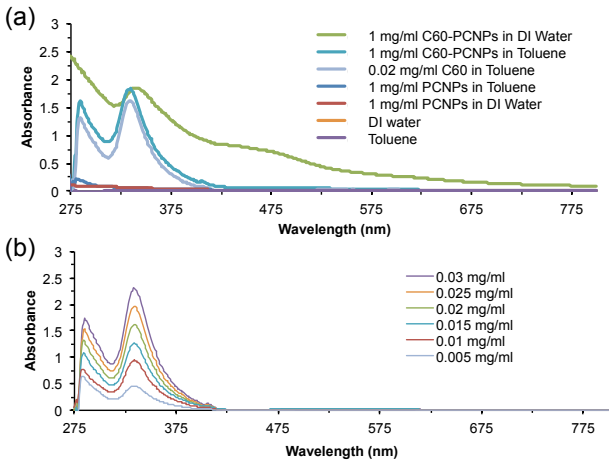

Figure 2: The absorbance spectra of various solutions.

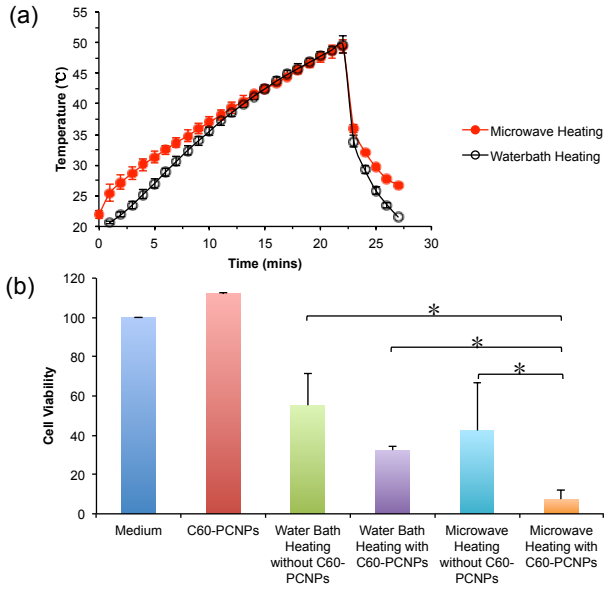

Figure 3: (a) The thermal process of the center of the dish with microwave heating and water bath heating. (b) PC-3 cell viability of different groups. (*): p<0.05..

As shown in Figure 2(a), the absorbance spectra of C60-PCNPs dissolved in DI water and toluene have a high peak at 334 nm, which is significant different with that of PCNPs in DI water and toluene. Additionally, the spectrum of C60-PCNPs in toluene has a similar profile with C60 in toluene. All these results indicate that the fullerene has been encapsulated into the nanocapsules in the C60-PCNPs. Moreover, as shown in Figure 2(b), the peak value at 334 nm is almost linearly related to the concentration of the fullerene in toluene. In addition, the diameter of the C60-PCNPs in DI water was measured around 340 nm at both 22 °C and 37 °C, while the diameter of the empty PCNPs is about 350 nm at 22 °C and 20 nm at 37 °C.

As shown in Figure 3, the thermal histories in the microwave heating and water-bath heating have no significant difference above 43 °C. The cell viability in C60-PCNPs group shows that the C60-PCNPs are not toxic to the PC-3 cells. The cell viability in the microwave heating with C60-PCNPs group is lower than that in any other groups, which indicates that the C60-PCNPs have the thermal effect (absorbing the microwave energy and generating heat in the microwave field) and can enhance the damage of the microwave to the PC-3 cells. Moreover, the viability in the microwave heating without C60-PCNPs group is similar with that in the water-bath heating without C60-PCNPs group, which shows that the damage of the microwave heating to the PC-3 cells mainly comes from the high temperature of the cell culture medium as the water-bath heating does.

DISCUSSION

The empty PCNPs can shrink when the temperature increases from 22 °C to 37 °C, but the diameter of the C60-PCNPs is not significant different in 22 °C with that in 37 °C, which indicates that the fullerene is encapsulated into the nanocapsules, and it is the fullerene inside the nanocapsules that impedes the shrinking of the C60-PCNPs. In addition, based on the linear relationship between the absorbance peak value at 334 nm and the concentration of the C60-PCNPs in toluene, and the peak values of the C60, PCNPs, and C60-PCNPs in toluene, the loading content of the C60 in the C60-PCNPs is calculated to be 23.0 ± 0.4 µg/mg.

ACKNOWLEDGEMENTS

This work was supported by an American Cancer Society (ACS) Research Scholar Grant (No. 120936-RSG- 11-109-01-CTDD) to X.H.

REFERENCES

[1] Wust, P et al., *The Lancet. Oncology*, 3:487-97, 2002.
[2] Skinner, M et al., *Phys Med Biol*, 43:3535-3547, 1998.
[3] He, X et al., *Int J Hyperthermia*, 20:567-593, 2004.
[4] Liu, J et al., *J Biomech Eng*, 122:372-9, 2000.
[5] Gilstrap, K et al., Am J Cancer Res, 1:508-20, 2011.
[6] Imholt, T et al., *Chemistry of Materials*, 15:3969-3970, 2003.
[7] Mashal, A et al., *IEEE Trans Biomed Eng*, 57:1831-4, 2010.
[8] Detrembleur, C et al., *Macromolecular Rapid Communications*, 27:498-504, 2006.
[9] Iwamoto, Y et al., *Chem Commun (Camb)*, 4805-7, 2006.
[10] Markovic, Z et al., *Biomaterials*, 29:3561-73, 2008.
[11] Chen, Z et al., *Current Drug Metabolism*, 13:1035-1045, 2012.
[12] Chen, Z et al., *Theranostics*, 2:238-250, 2012.
[13] Kiourti, A et al., *Journal of Electromagnetic Engineering and Science,* 14:267-272, 2014.
[14] Rao, W et al., *Acta biomaterialia*, 10:831-842, 2014.

SB^{3}C2016
Summer Biomechanics, Bioengineering and Biotransport Conference
June 29 –July 2, National Harbor, MD, USA
SB^{3}C2016-725

A NOVEL CRYOPRESERVATION APPROACH WITHOUT PENETRATING CRYOPROTECTANTS

H. Huang (1,2), X.He (1,2)

(1) Department of Biomedical Engineering
The Ohio State University
Columbus , OH, USA

(2) Department of Mechanical Engineering
The Ohio State University
Columbus , OH, USA

INTRODUCTION

Cryopreservation of mammalian cells is an enabling technology in cell line maintenance, assisted reproduction1, regenerative medicine and tissue engineering. It is achieved by first cooling cells into deep sub-zero temperatures (e.g. -196 ºC), under which all the biophysical and biochemical activities are arrested in the state of suspended animation, followed by warming back to normal temperatures (e.g. 37 ºC) for future use at a desired time and place. Nevertheless, it induces substantial cellular damages through intracellular ice formation (IIF), unduly dehydration and/or osmotic shock (freezing concentration)2. To alleviate the cryoinjuries, two conventional approaches have been adopted with the assistance of penetrating cryoprotective agents (pCPA, such as dimethylsulfoxide (DMSO) and 1,2-propanediol (PROH)), slow freezing and vitrification. Slow freezing (usually requires 1.5 – 2 M pCPA) would progressively dehydrate cells due to exosmosis driven by elevated extracellular osmolality as the extracellular water gradually transform into ice during freezing at a slow cooling rate (typically < 5 ºC/min), which permits intracellular water to emigrate across plasma membrane before freezing3. On the other hand, vitrification (usually requires 6 – 8 M pCPA) can deliver samples into amorphous or vitreous state without ice formation with ultra-rapid cooling rate (typically > 10,000 ºC/min) so that water molecules do not have time to rearrange their positions and orientations for crystallization before the loss of translational and rotational degrees of freedom4.

METHODS

Cryomicroscopy: Cryomicroscopy were undertaken using a Linkam (Waterfi eld) FDCS196 freeze-drying stage mounted on an Olympus BX 51 microscope. Real-time images were recorded using a QImaging Retiga CCD color camera. In each experiment, 5 µL cell suspension was loaded into the sample crucible and sandwiched with a coverslip (9 mm in diameter) to obtain clear images during both cooling and warming. The samples were cooled to −80 ºC (or -130 ºC) at 60 ºC min−1, held for 2 min, and warmed back at 60 ºC min−1 to room temperature (22 ºC). For the scenarios with IS, the samples were cooled to -4 ^{0}C and held for 2 min, during which ice seeding was performed by touching a LN_2-cooled steel onto the periphery of the crucible. Ice crystal would nucleate around the deeply-cooled spot, then proliferate to occupy the whole sample in a flash of second.

IR assessment: To investigate the IR activity during warming phase of cryopreservation, cryomicroscopy studies were conducted to visualize the possible ice growth in annealing. 5 µl PBS (or including trehalose), with or without IS at -4 ^{0}C, was cooled to -80 ^{0}C, and then warmed to -6 ^{0}C. The warming and cooling rates are the same as cryomicropic study (60 ^{0}C min−1). The icy samples were held at -6 ^{0}C for 15 min for annealing, during which real-time polarized images were taken to track the crystalline changes of size, morphology and orientation. The information of ice crystals, such as area and circularity, were measured by ImageJ, and the average entropy of polarized images was calculated by MATLAB (MathWorks).

Pre-dehydration by trehalose: For 3T3 cells, 5 µl coverslip-sandwiched sample (cell suspension with or without trehalose pre-dehydration) was cooled -6 ^{0}C, followed by IS and holding for 5 mins before warming back to 22 ^{0}C. The choice of -6 ^{0}C as IS temperature is due to the fact that IS at -6 ^{0}C can achieve similar dehydration level for cells suspended in PBS as the pre-dehydration of 0.33 M trehalose at room temperature. Cell size and viability were recorded prior, during and post dehydration and/or cooling. 5-min holding is of similar icy period for the cells in cryomicroscopy. For hRBCs, 100 µl sample with or without 0.33 M trehalose pre-dehydration was cooled to -6 ^{0}C and seeded with ice crystals around the periphery of the crucible. After holding for 5 min, it was warmed back to 22 ^{0}C. Then it was centrifuged at 1000 g for 5 min before measuring hRBCs hemolysis and recovery rates.

RESULTS

Cryomicroscopic study was performed to mimic the cryopreservation procedures of 3T3s as illustrated in Figure 1. Being consistent with mouse embryonic stem cells (mESCs) and human adipose-derived stem cells (hADSCs) in previous study[11], 3T3s are subjected to extensive IR and concomitant IIF during warming, which is a lethal event for either slow freezing or vitrification. Without IS,

Copyright 2016 The Organizing Committee for the 2016 Summer Biomechanics, Bioengineering and Biotransport Conference

ice crystals nucleate stochastically between -20 ^{0}C and -30 ^{0}C during cooling and propagate to occupy the whole sample instantaneously in this deeply metastable state (first three rows in Figure 1(A)). Only minority of suspended cells (< 30%) are captured by IIF during ice nucleation and further cooling to -80 ^{0}C (Figure 1(B)). However, all 3T3s experience intensive IIF during warming (darkening cells) and none of them can survive post thawing (Figure 1(C)). However, IS at -4 ^{0}C during cooling can dramatically eliminate IIF during warming (bright cells in last three rows of Figure 1(A)) and high cell viability ensues (Figure 1(C)), especially with 0.33 M trehalose predehydration at room temperature.

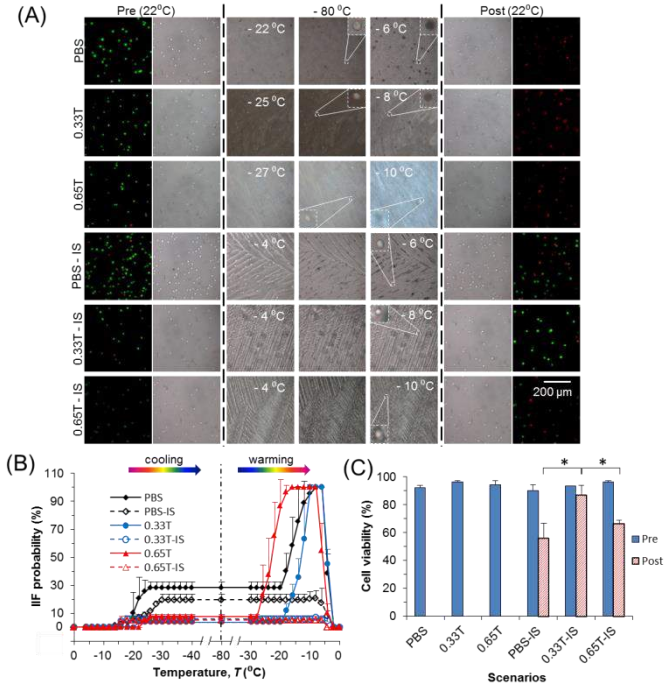

Figure 1: Intracellular Ice Formation (IIF) and viability of 3T3 cells during the cryopreservation. (A) Phase and fluorescence images of 3T3 cell in various scenarios. "PBS", "0.33T" and "0.65T" represent the cells are suspended in Phosphate-Buffered Saline (PBS), 0.33 M trehalose solution (dissolved in PBS) and 0.65 M trehalose solution (dissolved in PBS), respectively. IS stands for Ice Seeding. "Pre" and "Post" indicate the cases before and after cryopreservation. 5 μl samples were sandwiched by cover slip (diameter: 9 mm) in silicon crucible on the cryostage, and were cooled to -80 ^{0}C. Both cooling and warming rates were 60 ^{0}C/min. (B) IIF probabilities of 3T3 cells during cooling and warming phases in cryopreservation. (C) Vaiblities of 3T3 cells before and after cryopreservation. Each condition was performed by three independent runs. Error bar: standard deviation, *: $p < 0.05$.

The IRI mechanism of IS was investigated by polarized light cryomicroscopy. Without IS, the fine ice crystals nucleating between -20 ^{0}C and -30 ^{0}C during cooling undergo remarkable growth during warming through the reprecipitation of more stable crystals at the expense of the dissolution of unstable crystals and/or self-assembly-based aggregation and coalescence by oriented attachment. As a result, when the front of ice growth penetrates through the cell membrane, significant IIF is triggered to disrupt intracellular integrity as indicated by darkening region (Figure 2(A)).

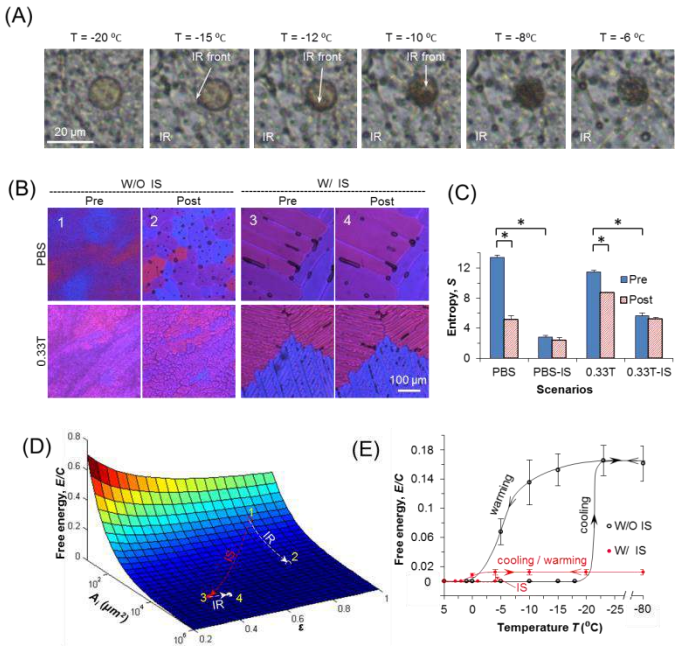

Figure 2: Inhibition of ice recrystallization (IR) and associated IIF by IS. (A) IIF induced by extracellular IR during warming phase. Significant IIF is triggered when the extracellular IR front penetrates the cell membrane, which precipitates the solutes and organelles from ice crystals and thus darkens the cells. (B) Polarized cryomicroscopic images of PBS solutions (with or without trehalose) before and after annealing at -6 ^{0}C for 15 min. (C) Entropies of polarized cryomicroscopic images before and after annealing. It shows that IS can dramatically decrease the entropy of overall icy samples and nearly eliminate IR in annealing. (D) Free energy of overall icy samples. A_i and ε are the area and circularity of ice crystals. Points 1, 2, 3 and 4 correspond to image 1, 2, 3 and 4 in (B), respectively. (E) Free energy of overall samples during cryopreservation. The free energy of isotropic solution at equilibrium state before and after ice melting is assume to be ground (zero). Error bar: standard deviation.

The polarized images during annealing at -6 ^{0}C are displayed by Figure 2(B). The IR can be illuminated by the entropy (S) change of these image of the sandwiched samples as IR would reorganize the orientations and positions of local crystals into a uniform pattern (Figure 2(C)), which implies IR during warming can be effectively prevented or even completely eliminated by IS during cooling. The corresponding free energy is plotted by Figure 2(D). While the overall energy change path is demonstrated by Figure 2(E), which shows a giant hysteresis loop of free energy with a precipitous rise and fall during freezing and thawing, respectively, when IS is absent, and marginal variation when IS present at -4 ^{0}C. In other words, IS at high subzero temperature can release the enormous free energy that otherwise would be engendered and stored in frozen samples during cooling and released to drive significant IR and IIF during warming

ACKNOWLEDGEMENTS

This work was partially supported by grants from NSF (CBET-1154965) and NIH (R01EB012108).

Copyright 2016 The Organizing Committee for the 2016 Summer Biomechanics, Bioengineering and Biotransport Conference

SB³C2016
Summer Biomechanics, Bioengineering and Biotransport Conference
June 29 –July 2, National Harbor, MD, USA
SB³C2016-726

ASSOSIATION OF HEMODYNAMIC STRESSES WITH THICKNESS OF ANEURYSM WALL: A CASE STUDY

Hamidreza Rajabzadeh Oghaz [1,2], Jaco J.M. Zwanenburg [3], Hui Meng [1,2,4]

**(1) Department of Mechanical and Aerospace Engineering
State University of New York at Buffalo
Buffalo, New York, USA**

**(2) Toshiba Stroke and Vascular Research Center
State University of New York at Buffalo,
Buffalo, New York, USA**

**(3) Department of Radiology
University Medical Center Utrecht
Utrecht, Utrecht, Netherlands**

**(4) Department of Biomedical Engineering
State University of New York at Buffalo
Buffalo, New York, USA**

INTRODUCTION

Intracranial aneurysms (IAs) are pathological outpouchings of cerebral arteries, which, if ruptured, often lead to death or permanent disability. Rupture risk stratification is critical for treatment decision. As potential biomarkers for rupture risk, aneurysm hemodynamics has been explored, since patient-specific Computational Fluid Dynamics (CFD) simulations can be implemented based on routine clinical rotational angiography or CT Angiography (CTA). Past CFD studies have shown both low Wall Shear Stress (WSS) and high WSS being correlated with rupture [1-3]. Towards this controversy, we have proposed two different hemodynamic-biological pathways, mediated by inflammatory infiltrates and mural cells, respectively [4]. Furthermore, it has been speculated that these two pathways could lead to different aneurysm wall phenotypes, from translucent thin walls that are almost cell-free to thick walls with atherosclerosis and inflammatory cell infiltration [4].

In our study of 204 aneurysms at the Gates Vascular Institute in Buffalo, we have statistically found that low WSS and high Oscillatory Shear Index (OSI) predict rupture status, although some ruptured aneurysms had high WSS [3]. We wish to explore possible relationship between these hemodynamic stresses and IA wall by directly observing patient aneurysm images, provided that we could simultaneously obtain the aneurysm 3D geometry (and thus CFD) and the wall thickness distribution.

Recent advancement in high-resolution MRI image has made it possible to image aneurysm wall [5]. Thus the objective of this study is to test the feasibility of combining hemodynamics based on CTA (which provides the accurate geometry and thus CFD) with aneurysm wall thickness distribution derived from high-resolution MRI vessel wall imaging performed on the same patient. This will pave the way for future exploration of association between hemodynamics and aneurysm wall phenotypes, so as to improve aneurysm rupture risk prediction.

METHODS

We analyzed high-resolution (0.8 mm isotropic resolution) 7.0 Tesla MRI images and CT Angiography images of a 5 mm unruptured aneurysm located at the left middle cerebral artery of a 55-year-old female patient. The images were taken at University Medical Center Utrecht, for detailed methods of MR imaging, refer to Kleinloog et al. [5].

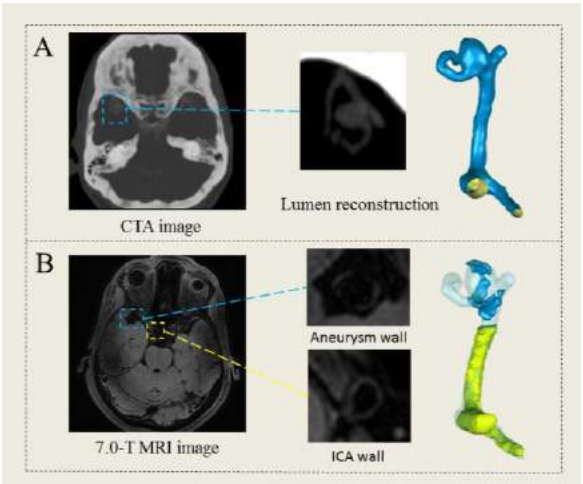

Figure 1: A) CT Angiography images and 3D reconstruction of lumen surface B) 7.0-Tesla MRI images for 3D reconstruction of thick wall regions around aneurysm and parent arteries. Blue and Yellow regions represent aneurysm wall and parent artery wall, respectively

Copyright 2016 The Organizing Committee for the 2016 Summer Biomechanics, Bioengineering and Biotransport Conference

Image Processing

We reconstructed the 3D luminal geometry of the aneurysm from CTA and the 3D geometry of the aneurysm wall through high-resolution MRI images, as shown in Fig. 1, and spatially co-registered the two 3D images for comparison. The 3D geometry of the lumen was reconstructed from DICOM images using an open-source visualization tool, The Vascular Modeling Toolkit. This lumen surface (inner surface of vasculature) represents the domain of blood flow.

The 3D reconstruction of MRI images was more challenging, because of the low signal-to-noise ratio and the small thickness of the aneurysm wall, surrounded by brain tissue. In order to distinguish and separate the aneurysm wall from the surrounding brain tissue, we used the 3D geometry of the aneurysm obtained using CTA images to determine the location of the aneurysm wall in MRI images. In this approach, since the MRI images of the parent arteries had better definition than aneurysm sac, we reconstructed the parent arteries wall and mapped it on the parent arteries reconstructed from the CTA images, as shown in Fig 1.B. This method helped us to identify the aneurysm wall location in MRI images. The process of removing the tissue around the aneurysm was done under supervision of a clinician who is familiar with medical images. As previously shown [5], thin portions of the aneurysm wall yield insufficient MRI signal to be visible. Therefore, we selected the regions that where visible as thick wall regions, see Fig 1.B.

CFD simulation

We assumed incompressible and laminar flow and conducted pulsatile CFD simulation using ANSYS FLUENT package. Patient-specific velocity inlet waveform, zero pressure outlet and rigid wall assumptions were adopted for numerical simulation. Viscosity and density of blood were taken as 0.0035 *Pa.s* and 1056 kg/m^3, respectively. We performed a sensitivity study of the effects of different assumptions frequently used in vascular CFD, such as neglecting the wall compliance, different outlet boundary conditions, and non-Newtonian behavior of the fluid. We found that the general distribution of hemodynamic parameters such as WSS and OSI are insensitive to these different simulation assumptions [6].

RESULTS

Figure 2 shows results from both CFD (distributions of WSS and OSI) on the luminal surface and MRI (wall thickness). Distribution of the WSS (Fig. 2A) shows that most parts of the aneurysm were exposed to low WSS (less than 1 *Pa*), except for the regions subjected to an inflow jet coming from the parent artery. Figure 2.B shows the distribution of OSI. The flow was not highly oscillatory, and only two small regions (one on the aneurysm and one on parent artery) had OSI values more than 0.1. This was expected because of the saccular and smoothly rounded shape of the aneurysm. Figure 2.B also shows that the location of regions with highest OSI value were located within low WSS regions. Figure 2.C shows that the thick wall regions were co-localized with low WSS regions. Likewise, the thin walls regions (not visible on 7.0-Tesla MRI images), were co-localized with high WSS regions (WSS higher than 0.2 *Pa*).

Based on this preliminary analysis, we hypothesize that a thicker wall (which is more visible on the MRI images) correlates with low WSS and high OSI value.

DISCUSSION

In this study we have demonstrated the feasibility of combining CFD simulation with direct imaging of aneurysm wall to study the association of hemodynamics and aneurysm wall thickness. Our preliminary results show that the thick wall regions are co-localized with low WSS, high OSI regions. This finding is in agreement with a previously described view [4]: low WSS is known to increase the thickness of the aneurysm wall by increasing inflammatory cell infiltration, atherosclerotic plaque, and formation of luminal thrombus. However, our result is opposite to findings by Kadasi et al. [7], who observed a positive correlation between WSS and thickness of the wall. This difference could be attributed to the different hemodynamic-biological pathways to aneurysm growth and rupture [4].

Even though we have analyzed only one case at this point, our approach paves the way for a more comprehensive study with more IA cases. A more advanced and computerized method for distinguishing and separating the thick wall regions will be developed to reduce human errors.

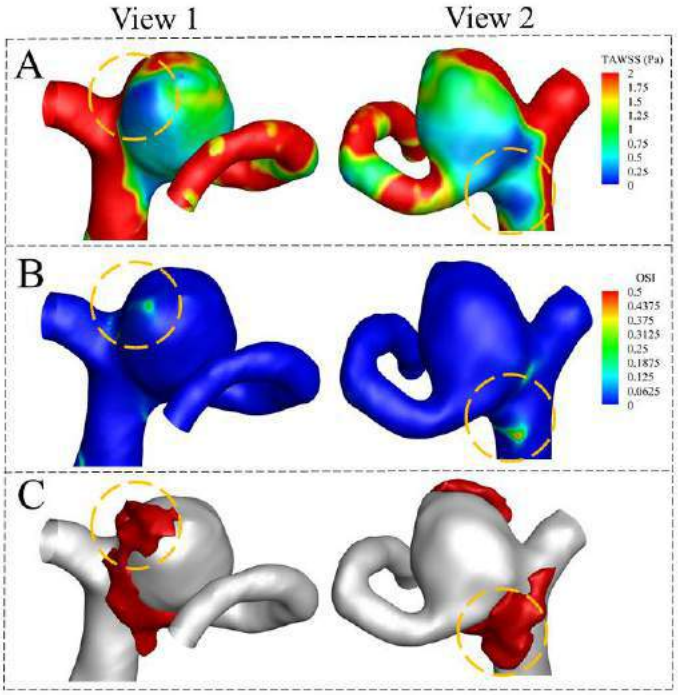

Figure 2: Distribution of: A) Wall Shear Stress B) Oscillatory Shear Index C) Thick-wall regions. Dashed-circles on the images indicate the approximate location of low WSS regions.

ACKNOWLEDGEMENTS

We would like to thank Ferdinand Schweder (University at Buffalo) for his assistance in processing the images. This study is partially funded by the National Institutes of Health (R01 NS 091075) and by the European Research Council (ERC grant agreement n°337333).

REFERENCES

[1] Xiang, J et al., Stroke, 42:144-152, 2011.
[2] Xiang, J et al., J Neurointerv Surg, 7:490-5, 2014.
[3] Xiang, J et al., J Neurointerv Surg, 8:104-10, 2014.
[4] Meng, H et al., Am J Neuroradiol, 35: 1254-62, 2014.
[5] Kleinloog, R et al., Neurosurgery, 75:614-22, 2014.
[6] Rajabzadeh Oghaz, H et al., Bulletin of the APS, 60, 2015.
[7] Kadasi, L.M et al., J Neurosurg, 119:172-9, 2013.

Copyright 2016 The Organizing Committee for the 2016 Summer Biomechanics, Bioengineering and Biotransport Conference

SB³C2016
Summer Biomechanics, Bioengineering and Biotransport Conference
June 29 –July 2, National Harbor, MD, USA
SB³C2016-727

DEVELOPMENT OF AN *INVITRO* MODEL FOR LIGAMENT WOUND HEALING

Stephanie M. F. Tuft (1), Julia T. Oxford (1), Erica E. Morrill (2), Raquel J. Brown (1), Trevor J. Lujan (2)

(1) Department of Biological Sciences
and Biomolecular Research Center
Boise State University
Boise, ID, USA

(2) Department of Mechanical
and Biomedical Engineering
Boise State University
Boise, ID, USA

INTRODUCTION

Ligaments provide joint stability through a dense network of collagen fibers that align along the primary loading direction. When a ligament is torn, fibroblasts at the wound site repair the tissue by forming scar tissue, a disorganized or multiaxial network of collagen fibers. Over time, repaired tissue achieves only modest fiber realignment, and after one year its strength is less than half that of healthy tissue. This diminished strength can lead to recurrent ligament sprains, pain, and abnormal stress patterns on the articular surface that can trigger irreversible cartilage degeneration. In order to develop clinical techniques that improve the structural and functional restoration of torn ligament, the mechanical and chemical factors that stimulate matrix remodeling must be identified. A challenge to identifying these factors is the absence of an *in vitro* model for ligament wound healing. The development and validation of an *in vitro* model would enable the study of mechanical and chemical factors that instruct fibroblasts to align the disorganized scar tissue and strengthen the ligament.

Prior studies have used cross-shaped (cruciform) molds to develop fibroblastic collagen gels with variable collagen networks.[1, 2] Although the center of these cruciform gels has a multiaxial fibrillar microstructure similar to scar tissue, no study has measured the gene expression of these gels to determine if they are suitable as an *in vitro* wound healing model. The objective of this study is to determine if gels that exhibit a multiaxial fiber architecture will promote the expression of genes associated with healing ligament.

METHODS

Overview. Collagen gels seeded with murine fibroblasts were incubated for 1, 2 or 3 weeks under three loading conditions: stress-free, uniaxial, or biaxial. At each time point, five genes associated with ligament wound healing were measured. Confocal microscopy and imaging software measured fiber alignment. In total, 90 collagen gels were synthesized and tested.

Collagen Gels: Collagen gels were produced by adding Purecol (bovine type I collagen), 10x DMEM, and suspended NIH/3T3 mouse embryonic fibroblast cells in culture media. The collagen gel solution was then neutralized to physiological pH with 0.1 M NaOH and brought to a final volume with 1x PBS. This gave a final cell density of 0.83 x 10^6 cells/mL per gel and a final type 1 collagen density of 1.5 mg/mL.

Teflon cruciform molds were machined with a channel aspect ratio of 1:0.5 (Fig. 1A). The cruciform design generates stress in the gel by resisting gel contraction with fixed glass rods (Fig. 1B).[1, 2] The stress environment at the cruciform channel arms (uniaxial stress) differs from the cruciform center (biaxial

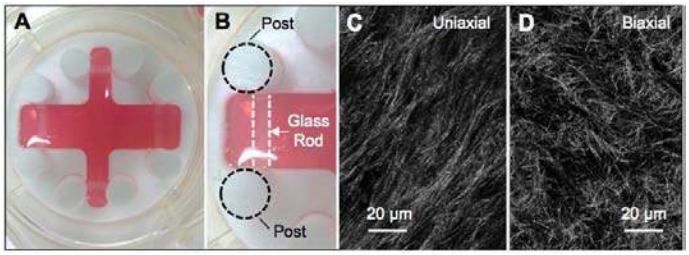

Figure 1: Collagen gels. A) Cruciform. B) Mechanical constraint, C) confocal image of cruciform center and D) cruciform arm.

Copyright 2016 The Organizing Committee for the 2016 Summer Biomechanics, Bioengineering and Biotransport Conference

stress). The gel solution was cast into the cruciform molds at 1.2 mL per mold, and at 2 mL per well in a six-well plate (stress-free). Cells were passaged at 60% confluency using trypsin/EDTA, and the collagen solution was allowed 120 minutes to gel at 37^{0}C. Cell culture media was exchanged every three days. 54 cruciform-shaped cellular gels and 36 stress-free discs were created to allow for a 1 week, 2 week and 3 week time course experiment.

Gene Expression. RNA was extracted from the molds via the TRIzol protocol [W.M. Keck Foundation, New Haven, CT], which required 16-18 cruciform gels to yield enough RNA for PCR analysis. The control specimens consisted of extracting RNA from NIH3T3 cells in a 2D tissue culture flask via the TRIzol method. RNA concentration was determined by measuring the absorbance at 260 nm. Messenger RNA (mRNA) was amplified by RT-PCR (40 cycles). Genes of interest were contained within the RT² Profiler™ PCR Array Mouse Extracellular Matrix & Adhesion Molecules. All results were normalized to GAPDH, and are expressed as positive fold-changes by comparing to results from the 2D tissue culture flask (data not shown).

The genes targeted for analysis include: collagen type I alpha I (Col1a1), collagen type III alpha I (Col3a1), collagen type V alpha I (Col5a1), integrin alpha 5 (Itga5), and tenascin-C (TnC). The rationale for selecting these genes is that previous animal studies on ligament wound healing found scar tissue at three weeks had a 2.6-fold increase in collagen I and a 1.9-fold increase in collagen III[3], and scar tissue at six weeks had a 4.2 fold increase in collagen V[4] and an increase in TnC[5]. In human ruptured ACL, Itga5 showed a 1.7 fold decrease[6].

Imaging. Confocal microscopy was used to evaluate the collagen fibril alignment in the stressed and stress-free gels at each time point. The collagen gels were auto-fluoresced at 63x using the 405 nm laser of a confocal microscope and ZEN imaging software (Fig 1C-D). FiberFit software was used to apply a fast-Fourier transform that measured fiber dispersion (fiber disorder) in the confocal images.[9] A trypan blue/calcein AM assay for live/dead cells was used to determine cell viability via the EVOS microscope's cell counting function.

RESULTS

A gradual increase in collagen was observed for all gels over time (Fig. 2). At three weeks, the stress-free gels had the greatest increase in Col1a1 expression (5.4 fold) and Col5a1 expression (4.8 fold), while the biaxial stressed gels had the greatest increase in Col5a1 expression (12.2 fold). The ratio of Col3a1 to Col1a1 had the greatest increase with time in the stress-free and biaxial gels (Fig. 2D). For all gels, only minor changes occurred over time in the ratio of Col5a1 to Col1a1 (Fig. 2D).

The increase in expression of Itga5 was lowest (2.7 fold) in the uniaxial stressed gels at two weeks and highest (4.2 fold) in stress-free gels at three weeks. The expression of TnC was greatest in the stress-free gels at week 2 (7.8 fold).

Image analysis found the uniaxial stressed gels had greater fibril alignment than the biaxial stressed gels (Fig. 1C-D; $p<0.001$). A significant interaction existed, where fibril alignment increased over time in the uniaxial gels and decreased over time in the biaxial gels ($P = 0.02$). Cell viability was a robust 100%.

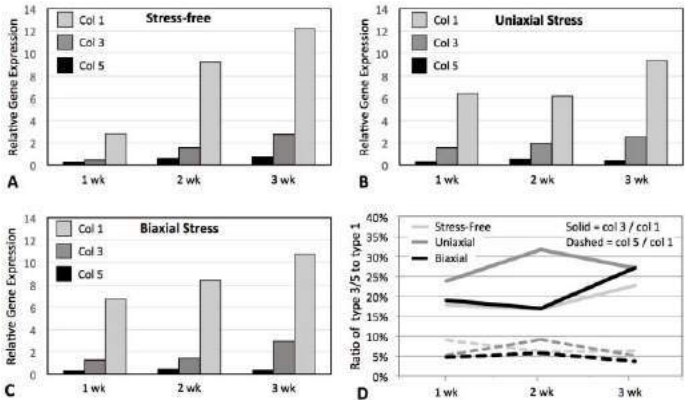

Figure 2: Gene expression when gels are exposed to A) stress-free, B) uniaxial and C) biaxial loads. D) Collagen ratios over time.

DISCUSSION

This study investigated whether growing NIH/3T3 cells in 3D bovine collagen gels could replicate the gene expression observed during ligament wound healing. Based on literature values[3, 4, 6, 7, 8], our results indicate that the stress-free gels have a gene expression profile most similar to healing ligament. For example, the stress free gels had gene expressions of Col1a1 and Col5a1 very near to *in vivo* studies. A close second to the healing ligament profile were the biaxial constructs based on the increase in expressions of the Col1a1, Col3a1, Itga5 genes and their disordered collagen fibril alignment. The uniaxial stressed constructs were least like the healing ligament gene profile and had the most aligned network of collagen fibrils.

Limitations of this work include an RNA sample size that precluded statistical analysis. Although eighteen gels were created for each loading group, all gels were required to extract sufficient RNA for analysis. Another limitation is that comparable animal studies use different molecular biology techniques. Also, the gel protein composition was not measured, but future work will characterize the molecular constituents using proteomics.

To our knowledge, this is the first study to focus on validating an *in vitro* model for ligament wound healing by examining mRNA expression and collagen fibril alignment in multiaxial collagen gels. Previous animal studies have compared differences in gene expression in fibroblasts from injured and healthy ligament *in vivo*. Also, studies have mechanically stressed cellular gel constructs but not with the aim of a healing ligament model. Once an *in vitro* healing ligament model has been validated, it can be used to test the effect of mechanical loading regimes and chemical stimuli on the remodeling and strengthening of the fiber network during healing. This could potentially aid in the development of clinical techniques that restore collagen organization and strengthen the healing ligament.

ACKNOWLEDGEMENTS

Kind support from the NIH (NIGMS P20GM109095).

REFERENCES

[1] Jhun, C. et al, *J Biomech Eng.*, 131(8): 1-21, 2009. [2] Sander, E. A. et al, *PNAS*, 106 (42): 17675-17680, 2009. [3] Frank, C. B. et al, *Osteoarthritis and Cartilage*, 7: 130-140, 1999. [4] Niyibizi, C. et al, *Knee Surg, Sports Traumatol, Arthrosc*, 8: 281-286, 2000. [5] Haslauer, C. M. et al, *Wound Repair Regen.*, 22(1): 103-110. [6] Brune, T. et al, *European Cells and Materials*, 14: 78-91, 2007. [7] Chao P. G. et al, *Biofabrication*, 6: 1-10, 2014. [8] Neurath M., *Zeitschrift fur Orthopadie und Ihre Grenzgebiete*, 131(2): 168-172, 1993. [9] Morrill EE et al., 2015 Proceeding of SB3C, Salt Lake City, UT.

Copyright 2016 The Organizing Committee for the 2016 Summer Biomechanics, Bioengineering and Biotransport Conference

SB^{3}C2016
Summer Biomechanics, Bioengineering and Biotransport Conference
June 29 –July 2, National Harbor, MD, USA
SB^{3}C2016-728

MECHANICAL BEHAVIOR AND GENETIC SIGNALING IN AORTIC ANEURYSMS IN NEWBORN LYSYL OXIDASE KNOCKOUT MICE

Marius C. Staiculescu (1), Robert Mecham (2), Jessica E. Wagenseil (1)

(1) Department of Mechanical Engineering and Materials Science
Washington University
Saint Louis, MO, USA

(2) Department of Cell Biology and Physiology
Washington University
Saint Louis, MO, USA

INTRODUCTION

The large elastic arteries provide reversible extensibility during the cardiac cycle and reduce the workload on the heart. This is made possible by the protein elastin, which is only present in the cardiovascular system of vertebrate animals [1]. Elastin is secreted from cells as the soluble protein tropoelastin, which is crosslinked by lysyl oxidase enzymes into insoluble elastic fibers [2]. In humans, lysyl oxidase (LOX) deficiency is associated with Ehlers-Danlos syndrome type IX and Menkes syndrome. LOX is an extracellular copper enzyme that initiates crosslinking of collagens and elastin by catalyzing oxidative deamination of the epsilon-amino group in certain lysine residues. Lox-knockout mice (Lox KO) die perinatally, exhibiting cardiovascular instability with abnormal lengthening and tortuosity of the descending aorta (DA), ruptured arterial aneurysms and diaphragmatic rupture [3]. Most aneurysms and vascular abnormalities occur in the DA. Therefore, Lox KO mice are a unique model to investigate locational differences in aneurysm susceptibility. We hypothesize that in Lox KO mice, mechanical properties, altered by deficient elastin crosslinking, and genetic signaling, are linked with DA aneurysms and tortuosity. To test our hypothesis we measured arterial mechanical behavior using a pressure myograph. Ongoing work includes imaging structural changes of the vascular wall using confocal microscopy and gene array analysis.

METHODS

To test vascular mechanics we isolated ascending aortas (AAs) and DAs from newborn wild type (WT) and Lox KO pups. The vessels were cannulated and pressurized in a pressure myograph (DMT) and subjected to a series of inflation and stretching protocols. The changes in outer diameter, pressure and axial force were recorded to determine the mechanical behavior of the WT and KO vessels (Figure 1).

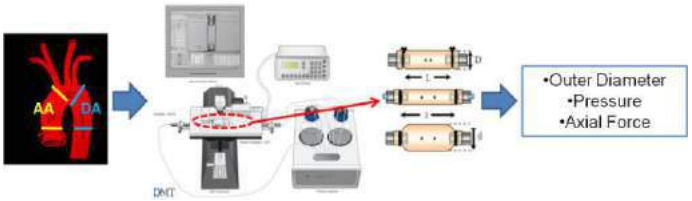

Figure 1. Schematic representation of the mechanical testing protocol.

For mechanical data analysis, we examined pressure–diameter and -compliance curves at the in vivo length. Compliance represents a structural property of the wall (depends on geometry and material). Diameter compliance (C) at each pressure (P_i) was calculated by,

$$C_{P_i} = \frac{\partial d_0}{\partial P}\Big|_{P=P_i} \quad (1)$$

where $d_0 = a_1 + a_2\left\{1 - exp\left(-\frac{P^{a_3}}{a_4}\right)\right\}$ (2)

is the outer diameter of the aorta [4], P is the lumen pressure, and a_i are constants determined by regression in Matlab (Mathworks). Material properties of the wall, such as stress, strain, and tangent modulus, under different loading conditions were also measured, but are not reported here.

To determine compositional and microstructural differences between Lox WT and KO vessels, images of pressurized arteries and arterial cross-sections were acquired with a Zeiss LSM 710 inverted confocal microscope. Imaging was performed with a Zeiss 20X air objective lens (NA 0.8) and a Zeiss 40X oil

Copyright 2016 The Organizing Committee for the 2016 Summer Biomechanics, Bioengineering and Biotransport Conference

immersion objective (NA 1.3). Prior to imaging, the vessels were stained with Alexa Fluor633 Hydrazide (elastin), Oregon Green488 conjugated CNA35 (collagen) and Hoescht 34580 (cell nuclei) for 20 – 30 min.

Microarray data will be obtained from an Affymetrix mouse Gene 2.0 array run by the Genome Technology Access Center at Washington University. We dissected the AA and DA from individual newborn pups. We pooled in groups of eight like-genotypes to obtain enough tissue for the array analysis. We currently have enough samples and are isolating the RNA.

RESULTS

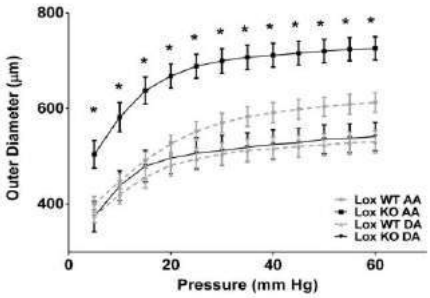

Figure 2. The arterial outer diameter increases nonlinearly with applied pressure in all groups. Lox KO AA (n=6) has a 20 – 25% larger outer diameter than Lox WT AA (n=8) at all pressures. However, in DAs from Lox KO (n=6) and Lox WT (n=6), the outer diameters are not significantly different. Data are means ± SEM. (*) P<0.05 (t-test, two tailed, equal variance) between Lox KO and WT AAs.

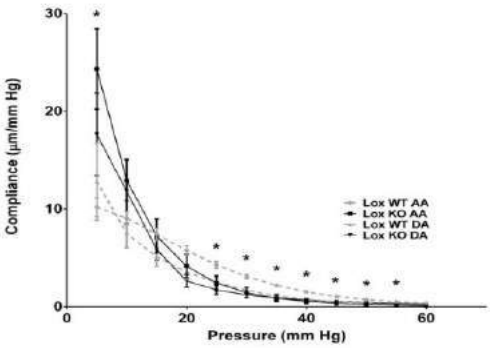

Figure 3. Compliance for both genotypes is high at low pressures, and very low at high pressures. Compared with WT AA (n=8), compliance is significantly higher in Lox KO at 5 mmHg (n=5), whereas between 25-55 mmHg the compliance is significantly lower. In DA, the compliance is not different between Lox KO (n=5) and WT (n=5). Data are means ± SEM. (*) P<0.05 (t-test, two tailed, equal variance) between Lox KO and WT AAs.

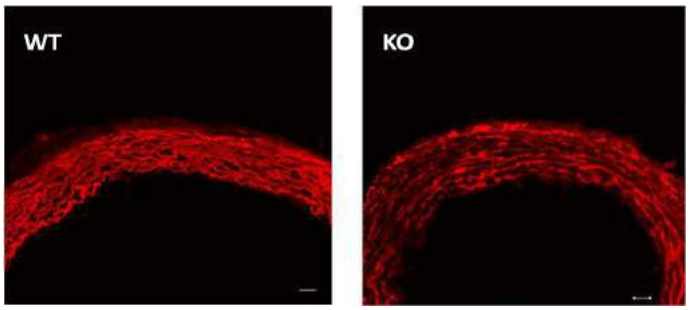

Figure 4. Cross-sections of AAs stained for elastin. Elastic lamellae in Lox WT AA are uninterrupted while in Lox KO the lamellae are discontinuous, revealing defects in elastin crosslinking. The scale bar is 10 μm.

DISCUSSION

Lox KO mice have thicker walls and fragmented elastic lamellae. Improper elastin fiber crosslinking due to Lox deficiency is probably the main cause of elastic lamellae fragmentation. AAs from Lox KO mice have larger outer diameters at all measured pressures. In contrast, DAs from Lox KO mice have similar outer diameters to WT mice. Despite the presence of aneurysms and tortuosity in the DA of Lox KO mice, the compliance is not significantly different from WT mice. However, the compliance is significantly lower in AA Lox KO mice between 25 and 55 mmHg. Our initial results do not explain the differences in the development of aneurysms and tortuosity mainly in the DA of Lox KO mice. Therefore, future research will concentrate on further characterizing wall material properties through stress/stain analysis under different loading conditions and examining genetic signaling through gene array analysis.

Our study of vascular mechanics and gene expression in a newborn Lox deficient mouse model is novel. There are currently no approved pharmaceutical treatments to prevent aneurysm growth. Large aneurysms can dissect and rupture, which is often fatal. Rupture and dissection depend on the mechanical properties of the aneurysmal wall. Thus, establishing a link between vascular mechanics and genetic signaling may lead to new therapeutic approaches to prevent aneurysm growth and rupture.

ACKNOWLEDGEMENTS

This work was supported, in part, by the National Institutes of Health grants R01HL115560 (JEW), R01HL105314 (JEW).

REFERENCES

1. Sage, H. and W.R. Gray, *Studies on the evolution of elastin--I. Phylogenetic distribution.* Comp Biochem Physiol B, 1979. **64**(4): p. 313-27.
2. Yanagisawa, H. and E.C. Davis, *Unraveling the mechanism of elastic fiber assembly: The roles of short fibulins.* Int J Biochem Cell Biol, 2010. **42**(7): p. 1084-93.
3. Hornstra, I.K., et al., *Lysyl oxidase is required for vascular and diaphragmatic development in mice.* J Biol Chem, 2003. **278**(16): p. 14387-93.
4. Fonck, E., et al., *Effect of elastin degradation on carotid wall mechanics as assessed by a constituent-based biomechanical model.* Am J Physiol Heart Circ Physiol, 2007. **292**(6): p. H2754-63.

Copyright 2016 The Organizing Committee for the 2016 Summer Biomechanics, Bioengineering and Biotransport Conference

SB^{3}C2016
Summer Biomechanics, Bioengineering and Biotransport Conference
June 29 –July 2, National Harbor, MD, USA
SB³C2016-731

MICROMATRIX-ENCAPSULATION OF CELL AGGREGATES FOR INJECTABLE DELIVERY AUGMENTS STEM CELL THERAPY OF MYOCARDIAL INFARCTION

S. Zhao (1, *), Z. Xu (2, *), H. Wang (1), N. Weisleder (1, 2), X. He (1).

(1) Department of Biomedical Engineering, The Ohio State University, Columbus, OH, USA

(2) Department of Physiology and Cell Biology, The Ohio State University, Columbus, OH, USA

* These authors contributed equally to this work.

INTRODUCTION

Heart attack or myocardial infarction (MI) is the leading cause of death globally [1]. This is due in part to the facts that the human heart has a very limited capacity of self-repair and there is no effective treatment for the loss of cardiac tissue, particularly cardiomyocytes (CMs), following MI. SCT has been explored as a promising option for treating MI, for which various types of stem cells have been investigated with both pros and cons and pluripotent stem cells (PSCs) including embryonic stem cells (ESCs) and induced pluripotent stem cells (iPSCs) are well established to be capable of differentiating into functional CMs3-6. However, the delivery of stem cells needs significant further improvement regardless of which types of stem cells are used. The retention of single or individual stem cells in the infarct zone delivered in suspension has been dismal and most of the retained cells die due to the hostile inflammatory microenvironment of MI (that could be exacerbated by the implanted cells to trigger immune reaction), leading to often as low as 1% or less viable cells in the heart within a few hours to days post injection. Delivery of stem cells in tissue-engineered constructs in the form of macroscale (up to a few centimeters) hydrogel, porous scaffold, or cell sheet/patch has improved cell retention. However, because there is significant cell death inside the constructs due to the limited diffusion length (less than ~100 um) of oxygen in vivo, it may require multiple surgeries (for cell sheet/patch less than ~100 um thick as 1D microscale constructs) to overcome the diffusion limit of oxygen in vivo.

METHODS

Here we produced 3D microscale stem cell constructs that allow for implantation by injectable delivery. This is achieved by first microencapsulating single pluripotent mouse embryonic stem cells (ESCs) in microcapsules with a liquid core and a semipermeable alginate hydrogel shell for culture to obtain the ESC aggregates with high (>90%) cell viability using novel coaxial electrospray technology [2]. The core-shell architecture of the microcapsule mimics the physical configuration of pre-hatching embryos during early embryo development with a hydrogel-like shell known as the zona pellucida and a permissive core, where stem cells from the totipotent to pluripotent stage are grown in vivo. The one integrated ESC aggregate formed in each microcapsule on day 7 resembles the single integrated cell aggregate in each pre-hatching embryo at the morula stage. Probably because of the biomimetic nature, our previous studies show that miniaturized, semi-closed culture in the core-shell microcapsules is inductive to stemness of both pluripotent and multipotent stem cells compared to the conventional open bulk culture. To bypass teratoma formation18,19 associated with using PSCs in their pluripotent state for tissue regeneration, we pre-differentiated the aggregated ESCs before implantation for 3 days using BMP-4 and bFGF to direct them to the early cardiac lineage as confirmed by qRT-PCR data and flow cytometric data.

After pre-differentiation, we released the aggregates from the core-shell microcapsules using isotonic sodium citrate solution. Next, we re-encapsulated the released aggregates in an alginate-chitosan micromatrix (ACM) by soaking the aggregates first in chitosan (and then in a solution of oxidized alginate. Chitosan is a positively charged polymer that can be attracted to the cells in the aggregate because the cell plasma membrane is negatively charged. The same electrostatic interaction applies to the complexation of alginate with chitosan and vice versa (alginate is negatively charged). As shown in the first two columns of Fig. 1, individual cells on the surface of bare pre-differentiated aggregate (Bare-A, top) are clearly visible while the aggregate with ACM encapsulation (ACM-A, bottom) is covered with materials. Furthermore, the elastic modulus of ACM-A is significantly

Copyright 2016 The Organizing Committee for the 2016 Summer Biomechanics, Bioengineering and Biotransport Conference

higher than that of Bare-A determined by atomic force microscopy (AFM) nanoindentation.

To investigate the safety and efficacy of ACM-A as compared to Bare-A, saline, and materials only (i.e., ACM) for treating MI, we conducted intramyocardial injection of $2x10^5$ cells/animal in 20 ul saline into the peri-infarct zone at 3 different sites using a 28 gauge syringe needle. This was done immediately following permanent ligation of the LAD at its proximal location to create a large-area MI in 8-12 week old male C57Bl6/J mice that are either wild-type (WT) with a normal immune system or CARD9 knockout (KO) with deficient macrophage function. After 4 weeks, all the characterization of heart dunction and cardiac tissue regeneration were performed.

RESULTS

The treatment with Bare-A and bare single cells differentiates themselves from the others with the formation of a large mass of tissue that grows out of the heart. It was observed in 60% WT mice with the bare single cells treatment and 57% with Bare-A treatment while it was not detected in WT mice with any of the other treatments including 30 WT mice treated with ACM-A. Further microscopic examination of the gown-out tissue revealed that it is a typical granuloma that contains inflammatory cells (mainly macrophages) with a loose tissue matrix, indicating that the outgrowth results from inflammatory reaction. More importantly, the MI mice treated with Bare-A started to die at as early as 2 days post injection while mortality was not observed for the single cells, saline and materials only (ACM) treatments until 5 days and for the treatment of ACM-A until 7 days after injection. Nearly 40% of the MI mice treated with Bare-A died during the first 4 days, a known time frame of acute inflammatory reaction to implanted bare single cells. Interestingly, although WT mice treated with single cells have higher occurrence of granuloma, the overall size of granuloma is smaller, compared to those treated with Bare-A, which might result relatively alleviated mortality in early time frame.We therefore reason that the biodegradable ACM should temporarily isolate the aggregated cells from contacting the host cells including macrophages and possibly NK cells and T cells to achieve a temporary immunoisolation (or "local immunosuppression") effect, which contributes to the significantly higher survival (~80% after 15 days of injection) and elimination of granuloma in WT mice treated with ACM-A.

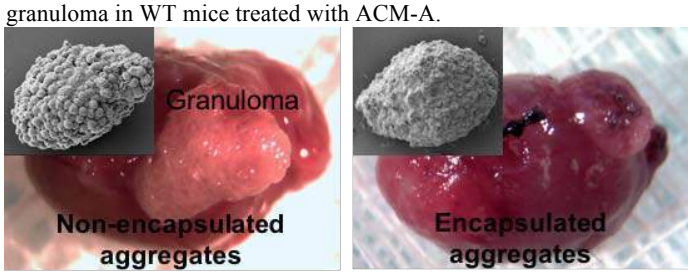

Figure 1: SEM images showing mESC aggregates after encapsulation has a smooth and porous surface (right inset) when comparing with non-coated one with visible single cells (left inset). After transplantation, the hearts of mice injected with Bare-A has large granulomas (left), but no for the ACM-A treated ones (right).

The ACM-A treatment also significantly improved heart function indicated by ejection fraction measured by PV-loops and ECG when compared to saline, Bare-A and ACM treatment. In addition, all cell treated groups (single cells, Bare-A and ACM-A) have partially restored the maximum and minimum rate of pressure change in left ventricle. ACM-A treatment significantly improved stroke volume and cardiac output compared to saline and ACM, and the time constant of isovolumic pressure relaxation (tau) when compared to saline treated ones, as well as the volume of left ventricle of LV end-systolic volume and end-diastolic volume compared to Bare-A and ACM. Noticeably, the measurements of those parameters indicated that ACM-A treated mice have more consistent recovery when comparing to those treated with single cells or Bare-A which have large variations, probably due to the existence of granuloma and resultant immune response in over half of the mice.

Furthermore, the ACM-A treatment significantly reduces fibrosis and inflammation compared to all other treatments 28 days after injection, which in turn should contribute to the high survival of WT MI mice with the ACM-A treatment. To find out if the significantly improved survival and the therapeutic benefit with the ACM-A treatment are partially a result of cardiac regeneration of the aggregated cells in situ, we injected the ACM encapsulated, pre-differentiated GFP-mESC aggregates into WT MI mice. Extensive fluorescence of GFP is evident in and beyond the whole MI zone 28 days post injection, suggesting the implanted cells survived, detached from the aggregates, and migrated throughout the MI zone and to proximal areas. By counting the GFP cells, it is determined that 47% of injected cells are retained in the heart 28 days post injection. This is much higher than single cells (7.3%) and Bare-A (17.6%) as well as that reported in previous studies5. Moreover, CM-like cells with green fluorescence are observed in the MI zone, indicating direct differentiation of the implanted cells into CMs. Furthermore, the green fluorescent CMs integrated with the neighboring non-fluorescent native CMs (Fig. 2), indicating the micromatrix was biodegraded allowing for timely integration of the implanted cell derived CMs and native ones. This is further supported by the expression of three typical markers of CMs including cTnI, connexin 43, and alpha-actinin in the green fluorescence CM-like cells derived from the implanted cells.

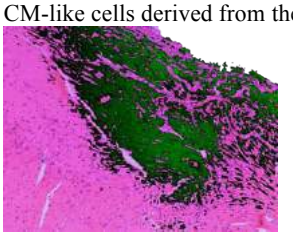

Figure 2: Low magnification GFP merged views of H&E stained tissue from left ventricle of MI heart of WT mice 28 days after treated with ACM aggregates, showing their integration with the neighboring non-fluorescent native host tissue.

DISCUSSION

ACM encapsulation of pre-differentiated microscale mESC aggregates improves the cell retention after intramyocardial injection and provides a temporary "local immunosuppression" for the aggregated cells to prevent early animal death due to acute inflammatory and immune reactions. The implanted cells have superb capability of regenerating cardiac tissue in situ via direct differentiation into not only CM- but also endothelial-like cells, to significantly reduce fibrosis and enhance cardiac function, which ultimately contributes to the significantly improved animal survival. Considering the proven biocompatibility of alginate and chitosan in the ACM, the micromatrix encapsulation technology may be valuable to facilitate clinical applications of SCT for treating MI and possibly many other diseases.

ACKNOWLEDGEMENTS

This work was partially supported by grants from NSF (CBET-1154965) and NIH (R01EB012108) to X.H., a Med to Grad School Fellowship from HHMI to S.Z., and a grant from NIH (R01AR063084) to N.W.

REFERENCES

[1] AS Go et al., Circulation 127(1): e6-e245, 2013.
[2] S. Zhao et al., Integrative Biotechnology 6: 874-884, 2014.

Copyright 2016 The Organizing Committee for the 2016 Summer Biomechanics, Bioengineering and Biotransport Conference

SB^{3}C2016
Summer Biomechanics, Bioengineering and Biotransport Conference
June 29 –July 2, National Harbor, MD, USA
SB^{3}C2016-733

A NOVEL DISTRACTIVE AND MOBILITY-ENABLING LUMBAR SPINAL ORTHOSIS

Daniel C. Hillyard (1), Denis J. DiAngelo (1)

(1) Department of Orthopedic Surgery and Biomedical Engineering
University of Tennessee Health Science Center
Memphis, TN, U.S.A.

INTRODUCTION

Low back pain (LBP) affects 60% to 90% of individuals at some point in their life[1], and as many as 5.4 million Americans are disabled annually as a result of LBP[2]. Most lumbar orthoses are marketed to treat LBP and provide amounts of immobilization, stabilization, or spinal decompression. Studies have suggested that with adequate frequency and duration of treatment, conservative treatments that decompress the spine and allow movement, such as water therapy, can be beneficial in the treatment of LBP[3-4]. More recently, dynamic orthoses that claim to axially decompress the spine have been introduced, but no supportive data exist. The objective of the study was to design a distractive mobility-enabling orthosis that applied a distractive load across the lumbar spine while allowing the user to move with minimal resistance.

METHODS

Distractive Mobility-Enabling Orthosis (DMO). The DMO (Fig. 1A) consisted of a distractive force component (DFC) and a mobility-enabling component (MEC). The DFC (Fig. 1B) was comprised of a flexible rod (anchored to the pelvic belt), a rod clamp, a non-deformable ring (attached to the upper torso glove), and a cable pulley array system. The cable system was connected between the lower part of the ring and the upper part of the flexible rod. As the user applied tension to the cable system the rod deformed downward creating an upward force on the ring. As cable tension increased more distractive force was applied between the the upper torso glove and the belt. The MEC (Fig. 1C) consisted of three tie rod ends attached to an interface plate mounted to the torso glove. The tie rod ends were guided by the ring to provide flexion and extension. The location of the ring was adjustable with the design goal of aligning the center of the ring with the center of rotation (CoR) of the lumbar spine.

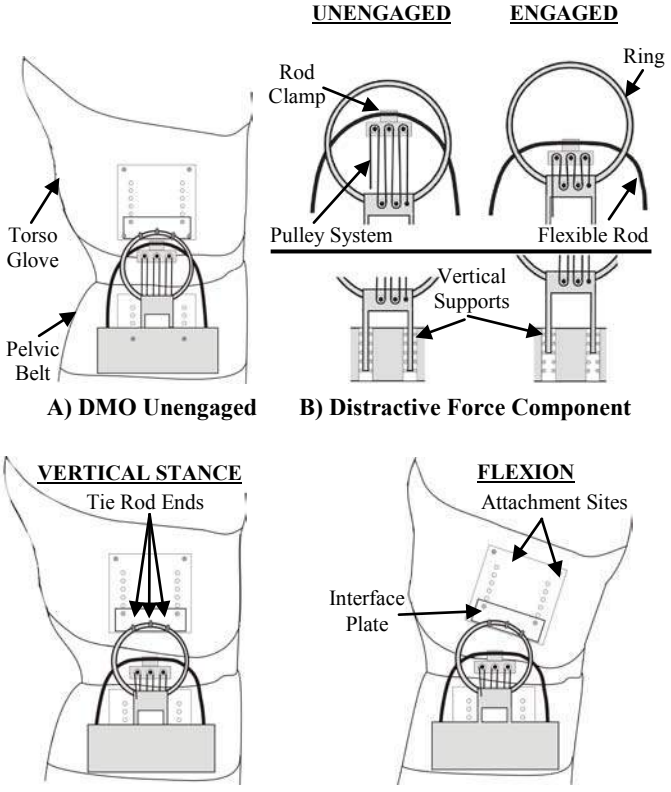

Figure 1: The Distractive Mobility-Enabling Orthosis.

Copyright 2016 The Organizing Committee for the 2016 Summer Biomechanics, Bioengineering and Biotransport Conference

Robotic Testing Platform and the Human Mechanical Analog. A robotic testing platform[5] (RTP) was used that provided four programmable degrees of freedom and included two load cells: an upper load cell (ULC) and a bottom load cell (BLC). The ULC measured applied loads and moments and the BLC measured loads and moments transferred through the spine. A previously validated human mechanical analog of the upper torso, lumbar spine, and pelvic girdle was mounted in the RTP and used for simulation testing[5].

Testing Protocol and Force Analysis. The DMO was placed on the mechanical analog with the ring CoR aligned with the previously determined CoR of the lumbar spine[6]. This step minimized any off-axis loads from being applied to the orthosis (Fig. 2A). If the alignment of the ring is poor, the brace load will enduce additional resistance to bending (brace load force component multiplied by its respective distance from the CoR of the lumbar spine). Two test conditions were simulated: vertical stance and extended ranges of flexion (25deg) and extension (10deg). An upper torso load of 300 N was applied during both tests. The ULC and BLC loads and moments were transformed to the sacral disc plane. Differences between them represented the spinal off-loading (or brace load, Fig. 2B) and resistance to bending (brace moment effect, Fig. 2C) of the DMO.

RESULTS

The off-loading capacity of the DMO is shown in Fig. 3. The DMO supported 98%, 99%, and 102% of the 300N applied vertical torso load during vertical stance, at 25 degrees of flexion, and at 10 degrees of extension, respectively. The DMO contributed 6.6 Nm of the 21.7 Nm (about 30%) and 4.4 Nm of the 10.9 Nm (about 40%) of the bending moment required for 25 degrees of flexion and 10 degrees of extension, respectively (Fig. 4).

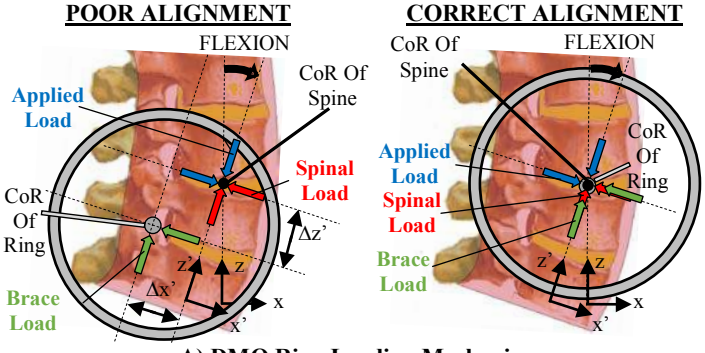

A) DMO Ring Loading Mechanics

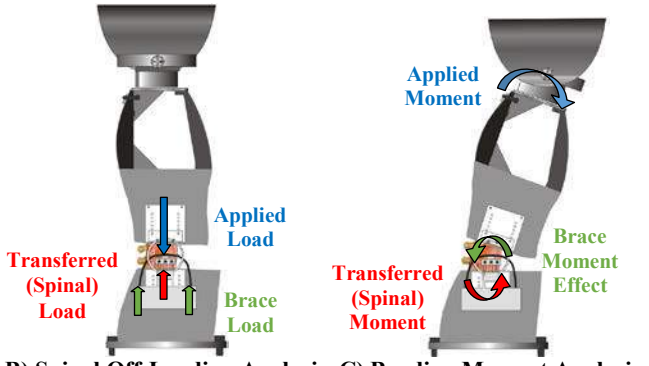

B) Spinal Off-Loading Analysis C) Bending Moment Analysis

Figure 2: Force Analysis of the DMO

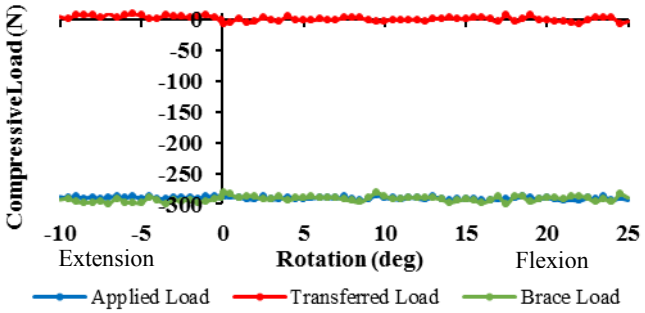

Figure 3: Spinal Off-Loading of the DMO.

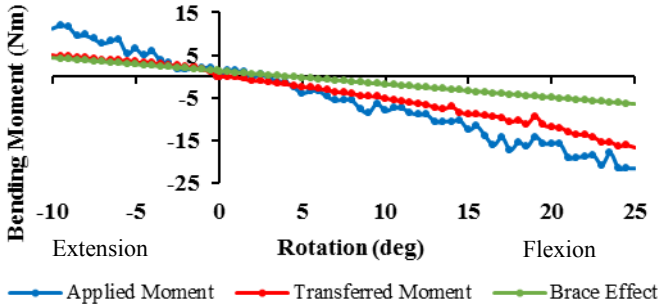

Figure 4: Resistance to Bending of the DMO.

DISCUSSION

The DMO reduced all spinal loading in upright stance and continued off-loading throughout extended ranges of flexion and extension with minimal brace bending resistance required. No literature has been found that contains laboratory data that demonstrates the efficacy of a dynamic lumbar orthosis. A 300 N torso load simulated an upper body weight of a 170lb person[7]. Aligning the center of the ring close with the CoR of the lumbar spine minimized additional bending moment required to move. The vertical torso load and the brace load act through approximately the same point of rotation minimizing the effect of off-axis force contribution to the effort required to bend. Lower brace effect moments compared to the moments transferred to the spine demonstrated that the DMO's resistance to bending was much lower than the spine's contribution; a desired outcome. Some limitations of the study were that the in vivo spinal bending moments were ignored, motion was limited to the sagittal plane, and flexion and extension ranges were limited by the physical size of the RTP.

ACKNOWLEDGEMENTS

John Simmons completed an initial DMO prototype and developed the testing protocol with assistance from Daniel Wido. Denis DiAngelo and John Simmons have a patent (U.S. Patent Application Serial No. 14/209,925) entitled "Lifting Distraction Back Support Device" on this device.

REFERENCES

[1] Fritz, JM et al., *Spine*, 33(16):1800-1805, 2008.
[2] Akay, J et al., *Hum Factors Ergon Manuf*, 19(1): 1-14, 2008.
[3] Baena-Beato, PA et al., *Pain Med* 14(1): 145-158, 2013.
[4] Cuesta-Vargas, AI et al. *Clin Rheumatol* 31(7): 1073-1078, 2012.
[5] Kelly, BP et al. *J Med Devices* 7(3):7, 2013.
[6] Simmons, JC. Doctoral Dissertation. *UTHSC*, 2014.
[7] Winter, DA. *Biomechanics of Human Movement*. New York, 1979.

Copyright 2016 The Organizing Committee for the 2016 Summer Biomechanics, Bioengineering and Biotransport Conference

SB³C2016
Summer Biomechanics, Bioengineering and Biotransport Conference
June 29 –July 2, National Harbor, MD, USA
SB³C2016-734

DIRECTION-DEPENDENT COLLAGEN DISRUPTION IN OVERSTRETCHED CEREBRAL ARTERIES

Matthew I. Converse (1), Justin T. Ingram (2), Raymond G. Walther (1), Kenneth L. Monson (1,2)

(1) Department of Mechanical Engineering
University of Utah
Salt Lake City, UT, USA

(2) Department of Bioengineering
University of Utah
Salt Lake City, UT, USA

INTRODUCTION

Traumatic brain injury (TBI) is a devastating cause of death and disability. Although damage to brain tissue is the fundamental concern in TBI, nearly all significant traumatic brain injuries include some element of injury to the blood vessels [1, 2], and any injury or dysfunction of the vasculature puts neural tissue at risk. Cerebrovascular dysfunction is a common outcome of TBI and can occur even in the absence of brain hemorrhage. Much is unclear about the mechanisms behind vascular impairment; however, we hypothesize that it is in part due to subfailure damage of the vascular wall.

Little is known about the nature of damage that arteries incur as a result of overstretch. We recently presented the novel application of collagen mimetic peptide (CMP) to characterize collagen disruption in axially overstretched cerebral arteries [3]. Results showed that damage occurred primarily among the axially oriented fibers within the adventitia. Furthermore, we demonstrated that the strength of the CMP signal was correlated with overstretch magnitude.

The objective of the present study was to characterize the nature of collagen damage following overstretch in different directions. Isolated sheep cerebral arteries were subjected to circumferential overstretch. CMP was again used to identify mechanically disrupted collagen. Results were compared to the axial overstretch case.

METHODS

Dissection and Sample Prep: A sheep head was obtained from a collaborating lab on campus. Immediately after death, the brain was removed and middle cerebral arteries (MCA) were dissected from the brain. Straight lengths of the MCA were cut into 3-5 mm segments (n=2) and branches ligated with unwound 6-0 suture.

Mechanical Testing: Mechanical testing was performed with an apparatus and methods similar to those described previously [4]. Briefly, each segment was cannulated with hypodermic needles and secured with 6-0 suture and cyanoacrylate glue. Samples were preconditioned to determine the *in vivo* configuration through a series of pressure cycles at varying axial stretches. Segments were then removed from the needles and cut into rings approximately 1 mm long (n=14). Two 28 gauge hypodermic needles were fed through the lumen of each ring and separated to circumferentially distend it beyond *in vivo* diameter (strain rate ≈ 0.025/s). Five of the samples were stretched to failure. Control rings (n=4) were not overstretched.

Staining for Collagen Fiber Damage: Immediately after overstretch, samples were removed from the testing needles and incubated for 1 hr in a PBS solution containing 20 μM of CF-CMP (CMP with a carboxyfluorescein tag for visualization) at 4°C. Following incubation, samples were rinsed in PBS (3x, 10 min also at 4°C), cut open circumferentially, and laid flat on a glass slide for imaging.

Confocal Imaging and Analysis: Samples were imaged at 10x (512 x 512 pixels) using a laser scanning confocal microscope (Fluoview 1000; Olympus). Serial slices were taken through the vessel wall in 2 μm increments. Using a custom MATLAB script, adjacent stacks were stitched together to form a single montage covering the full circumference of the vessel.

The CMP signal was quantified by calculating the average pixel brightness of the tissue and normalizing it relative to its control. The local strain associated with each imaged region was calculated based on the motion of the microspheres enveloping it. In the case that a sample was stretched to failure, the CMP signal and maximum strain were quantified away from the failure site.

Copyright 2016 The Organizing Committee for the 2016 Summer Biomechanics, Bioengineering and Biotransport Conference

RESULTS

CMP binding to mechanically damaged collagen: The CMP effectively bound to mechanically damaged collagen following circumferential overstretch. Figure 1 shows the strong fluorescent CMP signal in a sample stretched to failure compared to the negligible signal of a control.

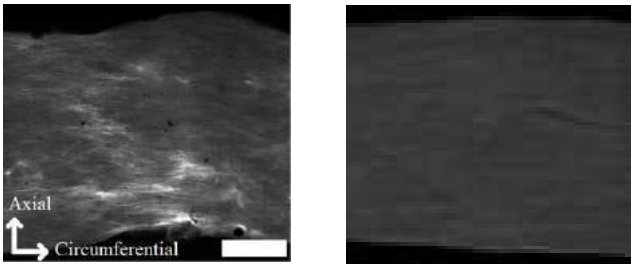

Figure 1: CMP fluorescence in the media of an artery stretched to failure (left) and control (right). Legend and scale bar (200 µm) apply to both images.

Location and Orientation of Damaged Fibers: In addition to increasing the fluorescence of damaged samples, the CMP signal localized the damaged fibers within the wall. The signal was found to primarily originate in the media and have a circumferential orientation (Fig 1).

Increased Signal with Overstretch Severity: The CMP signal was also found to increase with circumferential overstretch severity (Fig 2). The reported damage was calculated for a single slice within the media.

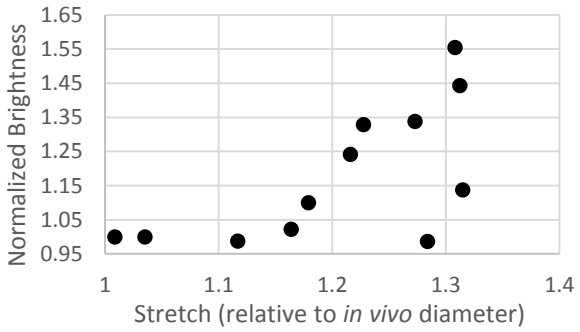

Figure 2: Normalized brightness of tissue within the media vs. stretch following circumferential loading.

DISCUSSION

Binding of CMP to mechanically damaged collagen in arteries is a novel discovery for the field of soft tissue biomechanics. CMP provides a non-destructive approach for localizing damaged collagen within the arterial wall. This is in contrast to SEM, TEM, and histological methods which require serial slicing to reveal subsurface damage. Furthermore, this approach effectively reveals the orientation and depth of the damaged fibers as well as strain-damage relationships.

First, the CMP bound along the length of the damaged fibers – revealing that the orientation of the damaged fibers aligned with the direction of loading. This was also true in our previous investigation of axial loading where the damage was found primarily among the axially oriented fibers. These finding are in agreement with the well-established role of collagen as the primary load bearing constituent in arteries [5].

Second, as in the previous study, the CMP bound in a depth-specific manner – revealing that circumferential loading primarily damages collagen within the media. In contrast, axial loading resulted in damage within the adventitia. Both of these findings are supported by the fact that longitudinally oriented collagen fibers are primarily found in the adventitia and that the media is rich with circumferentially oriented fibers [5].

Finally, the quantitative results in this study shed light on the threshold and distribution of collagen damage. Figure 2 shows that CMP intensity first rose above control values when stretched at least 15% beyond the in vivo diameter. Additional analysis needs to be done to understand the outliers in the graph as well as to compare this trend to that previously reported for axial loading.

These findings have significant implications for better understanding the nature of vascular damage in TBI. Vessels resected following TBI can be stained with CMP to characterize collagen damage and elucidate additional mechanisms at play in vascular dysfunction. Furthermore, the reported direction-dependent nature of vascular damage (and the CMP signal) may also increase understanding of the modes of vascular loading if observed following TBI.

ACKNOWLEDGEMENTS

Yang Li and S. Michael Yu for providing and assisting with CMP solutions.

REFERENCES

1. DeWitt, D., Prough, DS, *Traumatic cerebral vascular injury: the effects of concussive brain injury on the cerebral vasculature.* Journal of Neurotrauma, 2003. **20**(9): p. 795-825.
2. Graham, D.I., *Neuropathology of head injury*, in *Neurotrauma*, R.K. Nrayan, J.E. Wilberger, and J.T. Povlishock, Editors. 1996, McGraw-Hill: New York. p. 43-59.
3. Walther, R.G. *Collagen Mimetic Peptide as a Marker of Mechanical Damage in Lamb Middle Cerebral Arteries*. in *Summer Biomechanics, Bioengineering, and Biotransport Conference*. 2015. Snowbird Resort, Utah, USA.
4. Bell, E.D., J.W. Sullivan, and K.L. Monson, *Subfailure overstretch induces persistent changes in the passive mechanical response of cerebral arteries.* Frontiers in Bioengineering and Biotechnology, 2015. **3**.
5. Humphrey, J.D., *Mechanics of the arterial wall: review and directions.* Crit Rev Biomed Eng, 1995. **23**(1-2): p. 1-162.

Copyright 2016 The Organizing Committee for the 2016 Summer Biomechanics, Bioengineering and Biotransport Conference

SB^{3}C2016
Summer Biomechanics, Bioengineering and Biotransport Conference
June 29–July 2, National Harbor, MD, USA
SB^{3}C2016-735

A NOVEL NUMERICAL-EXPERIMENTAL INVERSE MODELING APPROACH TO INVESTIGATE THE TIME-EVOLVING THREE-DIMENSIONAL MECHANICAL PROPERTIES OF INFARCTED MYOCARDIUM

David S. Li (1), João S. Soares (1), John G. Lesicko (1), Reza Avazmohammadi (1), Joseph H. Gorman III (2), Robert C. Gorman (2), Michael S. Sacks (1)

(1) Center for Cardiovascular Simulation
Institute for Computational Engineering and Sciences
The University of Texas at Austin
Austin, Texas, USA

(2) Gorman Cardiovascular Research Group
Perelman School of Medicine
University of Pennsylvania
Philadelphia, Pennsylvania, USA

INTRODUCTION

Characterizing the evolution of the structural and mechanical properties of cardiac tissue after myocardial infarction (MI) is critical toward understanding the disease and creating better treatment strategies. Comprehensive biomechanical models of the infarcted heart can improve virtual surgery technologies and medical device development, as well as provide quantitative risk stratification tools for these interventions. However, cardiac tissue is highly heterogeneous, containing a complex mixture of cellular and matrix components that span several length scales. Moreover, due to its fiber structure, myocardium is distinctly anisotropic and highly nonlinear, requiring the acquisition of three-dimensional stress-strain relations in order for its mechanical properties to be properly characterized. These factors make creating physiologically realistic models of the behavior of myocardium especially challenging. Existing models of myocardium are based on very limited sets of extant biomechanical data, most often obtained from biaxial testing. Many underlying assumptions are necessary for three-dimensional generalization due to the utter lack of three-dimensional data. In addition to rigorous characterization of the behavior of normal myocardium, there is also a need to optimize the deployment of MI treatments (e.g., degradable hydrogels injected into the infarct site). This is severely hindered by not only the shortcomings of current models, but also the lack of understanding of the evolving mechanical properties of the infarct region over time.

Herein we propose a unified framework that utilizes an integrated numerical-experimental approach to investigate changes in the mechanical behavior of infarcted ovine myocardium from early to fully developed states. This work serves as a basis to advance and motivate more realistic mechanical models of myocardium for effectively evaluating future treatment strategies after MI.

METHODS

Preparation of Infarcted Ovine Myocardium Samples

Three adult 40-kg Dorset sheep were subjected to coronary ligation of the left anterior descending and second diagonal coronary artery, causing infarctions located around the apex of the left ventricle [1]. The hearts were explanted at 2, 4, and 8 weeks after the initial infarction, one sheep per time point, and the size and location of the infarcts were assessed. A sheep with no induced infarct was used as a healthy negative control and considered as a 0 week time point.

Bulk fiber orientation was estimated throughout the infarct region, and adjacent ~1x1x1 cm cuboidal samples were cut out in which the bulk fiber orientation was orthogonal with a cube edge (Figure 1). Samples were sectioned for both structural measurements and testing for mechanical properties (see below).

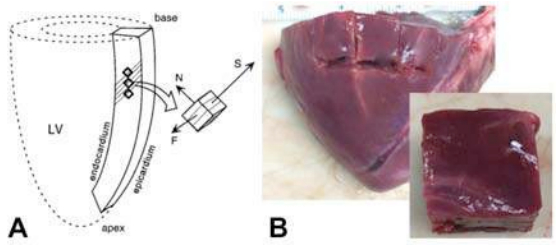

Figure 1: (A) Schematic of strategy for obtaining myocardium samples [2]**. (B) Sample collection (non-infarcted tissue shown).**

Three-Dimensional Mechanical Testing of Infarcted Myocardium

We have constructed a novel triaxial loading device (Triaxial EXperimental Analysis and Simulation, TEXAS) for acquiring the experimental data necessary to represent the three-dimensional mechanical properties of soft fibrous tissue (Figure 2A). The TEXAS

Copyright 2016 The Organizing Committee for the 2016 Summer Biomechanics, Bioengineering and Biotransport Conference

is capable of simultaneously applying a full range of three-dimensional deformation modes on cuboidal tissue samples, and it has been previously validated in determining the stiffness of synthetic gels in individual tensile, compressive, and simple shear.

The infarct samples were mounted using a nine pin attachment arrangement on each face of the cube (Figure 2B), and a set of tension, compression, and shear deformations was performed, both along the major axis direction of the tissue (aligned with the mean fiber direction) and along the two orthogonal cross-fiber directions. The data was then utilized to determine orthotropic constitutive relations of the infarct samples with an inverse modeling approach (see below).

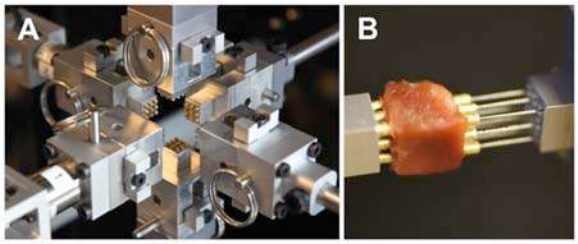

Figure 2: (A) Close-up of actuators and attachment pads of the TEXAS. (B) Myocardium sample attached.

Fiber Structure from Transmural Small Angle Light Scattering (SALS)

Transmural SALS employs a low power laser beam to raster scan planar sections of soft tissue [3], then computationally reconstructs the original three-dimensional tissue structure with unique rank tensors at each position that determine the overall directions of alignment for each plane, as well as boundaries of high-alignment regions [4].

Samples for structural characterization were first histologically analyzed. Subsequently, each cube was sectioned into ~40 planes along the transmural axis, approximately normal to the principal fiber planes. Using transmural SALS, we analyzed the samples with circumferentially varying fiber directions for each plane and compounded the three-dimensional local arrangement of the fibers to be utilized in our previously developed inverse modeling approach [5].

Inverse Modeling with Finite Element Simulations

The mechanical behavior of healthy and infarcted myocardium can be characterized by a stored energy density function $W(\mathbf{F})$, where $\mathbf{F}$ is the deformation gradient. The relation for the first Piola-Kirchhoff stress tensor $\mathbf{P}$ in terms of W is written as:

$$\mathbf{P} = \frac{\partial W}{\partial \mathbf{F}} - p\mathbf{F}^{-\mathrm{T}} \tag{1}$$

where p is the hydrostatic pressure. The orthotropic Fung-type material was employed:

$$W(\mathbf{E}) = \frac{1}{2}c_0\left[e^{Q(\mathbf{E})} - 1\right] \tag{2}$$

where $\mathbf{E} = (\mathbf{F}^{\mathrm{T}}\mathbf{F} - \boldsymbol{I})/2$, $\boldsymbol{I}$ is the identity tensor, c_0 is a positive constant, and Q is given by:

$$Q = c_1E_{11}^2 + c_2E_{22}^2 + c_3E_{33}^2 + 4c_7E_{12}^2 + 4c_8E_{13}^2 + 4c_9E_{23}^2 \tag{3}$$

Our inverse modeling approach is based on finite element (FE) simulations corresponding to the deformations performed in the TEXAS experiment. In the simulations, the stress-strain data collected from the TEXAS and the local fiber directions obtained from transmural SALS were incorporated into the inverse modeling FE problem and the mechanical properties of the infarct samples at the 0, 2, 4, and 8 week time points were determined through nonlinear least-squares regression (Figure 3).

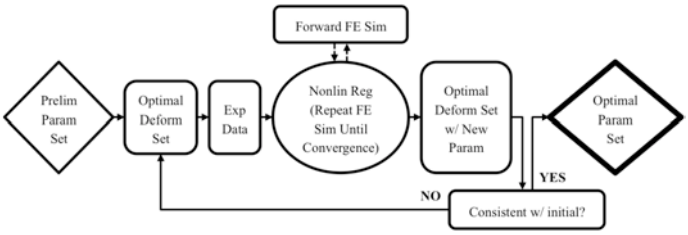

Figure 3: Overall combined numerical-experimental approach. FE simulations are repeated until convergence is reached.

RESULTS

Our inverse modeling analysis confirmed that the transient stiffness properties of the infarct samples increased nonlinearly over 8 weeks. Representative stress-strain plots for tension and shear also showed strongly nonlinear behavior (Figure 4A). From the local fiber orientation distribution functions, we obtained the planar fiber distributions (Figure 4B) to develop the FE simulations for our inverse model (Figure 4C).

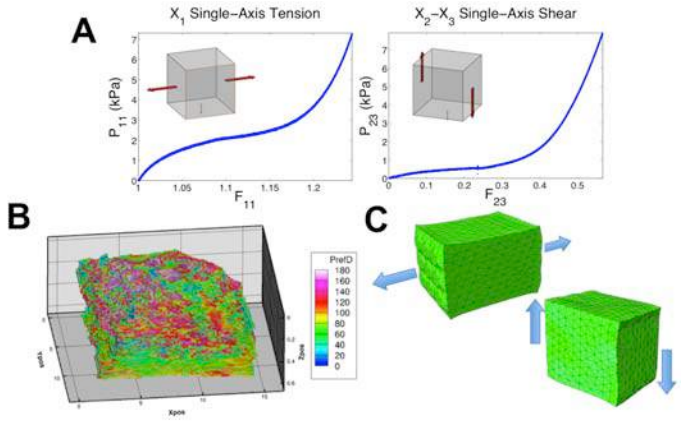

Figure 4: (A) Representative tension and shear stress-strain curves for healthy ovine myocardium. (B) Three-dimensional preferred fiber direction of collagen in an ovine infarct sample. (C) Corresponding FE simulations.

DISCUSSION

We have been able to successfully integrate structural and mechanical experimental components into a simple mechanical model for infarcted myocardium that shows the evolution in the mechanical properties of the infarct over time. Our next steps are to continue increasing the detail of our material modeling and expand the complexity of deformations performed in the TEXAS. This information will lead to more fully realistic models of healthy and infarcted myocardium to be incorporated in organ-level modeling of heart function and to aid in the *in silico* development and optimization of treatment interventions after heart attack.

ACKNOWLEDGEMENTS

Funding was provided by the NIH (R01 HL068816, HL089750, HL070969, HL108330, HL063954, and T32 EB007507).

REFERENCES

[1] Markovitz, LJ et al., *Ann Thorac Surg*, 48:838-845, 1989; **[2]** Dokos, S et al., *Am J Physiol Heart Circ Physiol*, 283(6):H2650-9, 2002; **[3]** Sacks, MS et al., *Ann Biomed Eng*, 25:678-689, 1997; **[4]** Advani, SG, Tucker, CL, *J Rheol*, 31:751-784, 1987; **[5]** Sacks, MS, *J Biomech*, 125(2):280-287, 2003.

Copyright 2016 The Organizing Committee for the 2016 Summer Biomechanics, Bioengineering and Biotransport Conference

SB³C2016
Summer Biomechanics, Bioengineering and Biotransport Conference
June 29 –July 2, National Harbor, MD, USA
SB³C2016-736

QUANTIFICATION OF SCLERAL STIFFENING IN RAT EYES AS A FUNCTION OF GLYCERALDEHYDE CONCENTRATION AND AGE

Ian C. Campbell (1,2), Bailey G. Hannon (3), A. Thomas Read (2), Joseph M. Sherwood (4), Pedro Gonzalez (5), and C. Ross Ethier (1,2,3,4)

(1) Center for Visual and Neurocognitive Rehabilitation
Atlanta VA Medical Center
Decatur, GA 30033

(2) Biomedical Engineering
Georgia Institute of Technology and Emory University
Atlanta, GA 30332

(3) Mechanical Engineering
Georgia Institute of Technology
Atlanta, GA 30332

(4) Bioengineering
Imperial College London
London, UK SW7 2AZ

(5) Ophthalmology
Duke University
Durham, NC 27705

INTRODUCTION

Glaucoma is a debilitating cause of vision loss affecting millions of people worldwide, and although treatments exist, they unfortunately do not work for all individuals. A large body of evidence suggests that ocular biomechanics is intimately involved in the development and progression of glaucoma, particularly evidenced by the causative risk factor of elevated intraocular pressure (IOP) [1]. All clinical treatments operate on the paradigm of lowering IOP, and there is presently no alternative when this approach fails.

Some have suggested [2] benefit in stiffening the sclera (the white outer coat of the eye) to help counteract the biomechanical consequences of elevated IOP. Animal models of glaucoma can be used to screen such an approach. One such model uses the rat, which has been extensively employed to study the pathogenesis of glaucoma [3]; however, the biomechanics of rat sclera has not been tested, nor has its response to stiffening agents. Here we used inflation testing of rat eyes treated with the stiffening agent glyceraldehyde [4] to study the effects of dose and age on the magnitude of scleral stiffening achieved. We hypothesized that glyceraldehyde would induce a dose-dependent stiffening of rat sclerae and that age would not significantly impact this effect in adult rats. Such characterization is important as we evaluate glyceraldehyde and other agents in modulating scleral biomechanics in the rat model of glaucoma.

METHODS

Eyes from freshly-euthanized Brown Norway rats were incubated overnight in either PBS or glyceraldehyde solution (either 0.25M or 0.125M, made in from a 0.5M solution in PBS diluted with deionized water to approximate physiological osmolarity in the final solution). Two different age groups of female, retired breeder rats purchased from Charles River were used in this study: Group A rats were 6-9 months old (exact ages unknown, as retired breeder dates of birth are not routinely transmitted upon purchase), and Group B rats were approximately 1.5 years old. Using 3D digital image correlation (DIC) techniques, we quantified the relative magnitude of stiffening by inflating whole eyes to simulate conditions of normal and elevated IOP. Eyes with sclera cleaned of all loose connective, fat, and muscle tissue were mounted on a custom-milled acrylic block that cradled the eye and incorporated an access channel for IOP modulation (Figure 1). We glued eyes cornea-side down using a thin coat of gel-style super glue and applied a speckle pattern of graphite powder to the exposed sclera using a fine mesh flour sifter and air brush. After waiting approximately 3 minutes for the eye to dry, it was rinsed in PBS to rehydrate and wash away excess graphite. Next, a 1mm diameter biopsy punch was inserted through the access channel to puncture the cornea. The biopsy punch was retracted and a Luer fitting was glued to the channel, which was purged of air by flushing with PBS. This mounting block was subsequently attached to a hydrostatic pressure reservoir set initially to 5 mmHg, and was immersed in a room temperature saline bath.

Using a pair of calibrated stereo cameras (AVT Stingray 504B) fitted with 50 mm lenses, we acquired 3D images of the surface of the posterior sclera over a period of 10 minutes per pressure step from 5 to 30 mmHg in increments of 5 mmHg. Images were correlated using Istra 4D 4.1.1 software (Dantec Dynamics), and first principal strain values were exported to Matlab R2016a for further processing. We computed the average strain magnitude of facets falling between the 25th and 75th percentiles to eliminate outliers, and we estimated the average stress in the posterior sclera using the assumption of a thin-walled spherical pressure vessel with a diameter of 6.5 mm and a thickness of 100 μm. Assuming transversely isotropic material properties with negligible radial stress and near incompressibility (ν=0.49), initial estimates of Young's modulus were obtained at 15 mmHg from the estimated

Copyright 2016 The Organizing Committee for the 2016 Summer Biomechanics, Bioengineering and Biotransport Conference

principal stresses (assuming first and second principal stresses are equal and third is negligible [5]) and the average first principal strain at this pressure for each eye, as:

$$E = (\frac{\sigma(1-\nu)}{\varepsilon_1}$$

This is a simplification of the material properties of this complex biological tissue but is sufficient for this initial comparative study investigating the relative magnitudes of stiffening.

One eye's strain decreased with increasing pressure (Group A, PBS) and was excluded as a technical failure. Finally, using R 3.2.2, we computed statistical likelihoods of differences using ANOVA. To differentiate between Young's modulus, we used a 3-factor split-plot model accounting for age, subject, control or treated eye, and dose. To differentiate between relative stiffening, we used a two-factor cross-factored model for both age and level of stiffening.

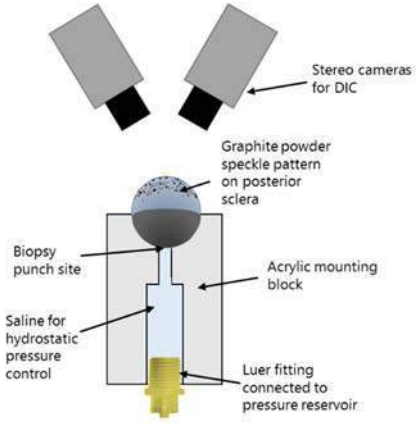

Figure 1: Rat eyes were mounted in an acrylic holder, corneas were punctured with a biopsy punch, and intraocular pressure was modulated with a hydrostatic pressure reservoir while stereo cameras imaged the posterior sclera.

RESULTS

Treating eyes overnight with glyceraldehyde significantly reduced mechanical strain at all pressure levels (Figure 2). At an inflation pressure of 15 mmHg, the estimated Young's modulus was increased by a factor of 2.24 ± 0.40 (mean ± SD) for 0.125M and 4.51 ± 2.49 for 0.25M when compared to PBS controls ($p = 0.011$) (Figure 3). When comparing relatively younger adult rats (Group A) to very old rats (Group B), we did not detect a significant difference between control eyes and eyes stiffened at 0.125M or eyes stiffened at 0.25M ($p = 0.26$).

DISCUSSION

Glyceraldehyde has a powerful stiffening effect on rat sclera, consistent with prior findings in mice [4], and even at moderate doses can more than double the relative stiffness of the sclera. This finding is important because high concentrations of stiffening agents could have off-target biological consequences if delivered clinically, while even relatively lower doses may have a strong stiffening effect. Further, we did not see a difference in either baseline stiffness or in susceptibility to glyceraldehyde stiffening between young adult rats and very old rats, increasing our flexibility for using this animal model of a disease strongly associated with advanced age in humans. Future steps to characterize the ocular biomechanics of the rat will include investigation of additional stiffening agents and concentrations as well as fitting the stress-strain relationship to nonlinear models of mechanical stiffness, as the modulus at a single magnitude of IOP provides only a limited description of rat ocular biomechanics.

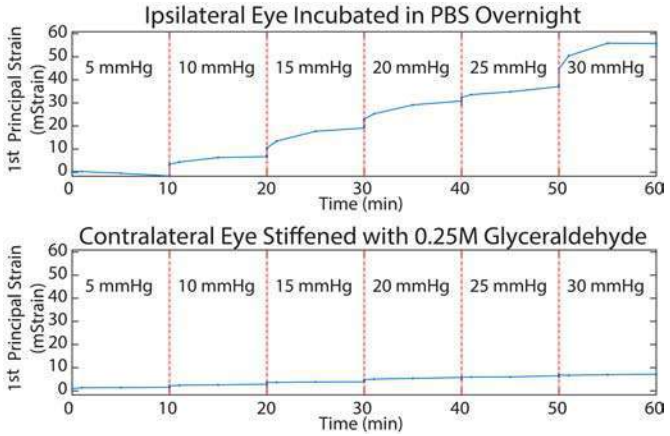

Figure 2: Representative strain vs. time at 6 pressure increments for a single rat from Group A. Scleral strain is much higher in the control eye than the contralateral stiffened eye, indicating that glyceraldehyde has a strong stiffening effect in the rat eye.

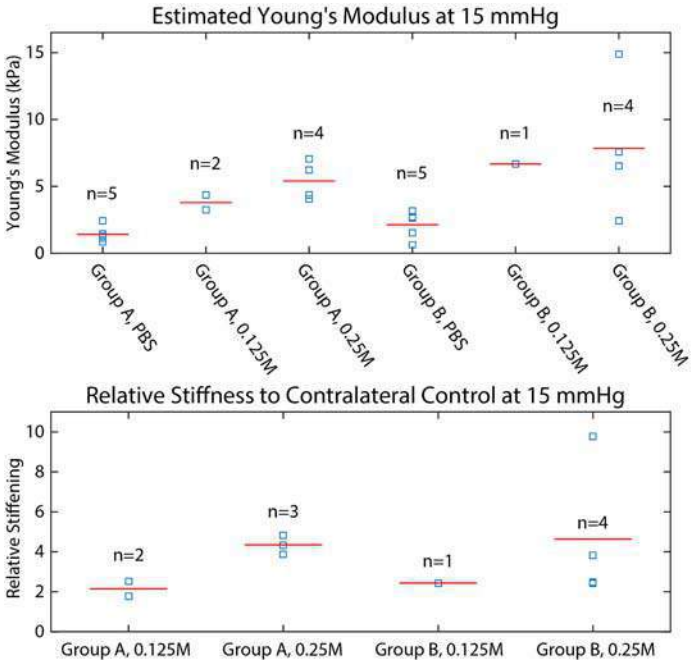

Figure 3: Glyceraldehyde increased the estimated Young's modulus at 15 mmHg in both ages of rats (Group A and Group B, top) relative to contralateral eyes incubated in PBS (bottom). Red lines are means for each group.

ACKNOWLEDGEMENTS

The authors gratefully acknowledge research support from the Department of Veterans Affairs (Career Development Award IK1 RX001791 to ICC), the National Institutes of Health (R01 EY025286 to CRE), and the Georgia Research Alliance (CRE).

REFERENCES

[1] Campbell, IC et al., *J Biomech*, 136:021004, 2014.
[2] Thornton, IL et al., *IOVS,* 50:1227-33, 2009.
[3] Morrison, JC, et al. *Exp Eye Res,* 64:85-96, 1997.
[4] Kimball, EC, et al. *Exp Eye Res,* 128:129-140, 2014.
[5] Rossman et al., *Intro to Eng Mech*. CRC Press, 2015.

Copyright 2016 The Organizing Committee for the 2016 Summer Biomechanics, Bioengineering and Biotransport Conference

SB^{3}C2016
Summer Biomechanics, Bioengineering and Biotransport Conference
June 29 –July 2, National Harbor, MD, USA
SB^{3}C2016-737

PHYSIOLOGICAL BASIS FOR RATIONAL CRYOTHERAPY PROTOCOL DESIGN

Sepideh Khoshnevis (1), R Matthew Brothers (2), Kenneth R Diller (1)

(1) Department of Biomedical Engineering
The University of Texas at Austin
Austin, Texas, USA

(2) Department of Kinesiology and Health Education
The University of Texas at Arlington
Arlington, Texas, USA

INTRODUCTION

Cryotherapy is used widely to manage the pain, swelling, and inflammation associated with soft tissue injury [1]. Many methods are based on the melting temperature of ice, either by direct application of an ice bag or by circulation of melted water from a cryotherapy unit (CTU) and do not accommodate protocol design based on a scientific understanding of the tissue response to low temperatures. A second major protocol parameter is the length of time and the frequency of application of cold to tissue. Cryotherapy practice varies dramatically among various practitioners [2], and may be recommended for use intermittently [3] or continuously [4], with each episode lasting for as briefly as 10 minutes to as long as multiple days. There are numerous publications that present anecdotal observations of the clinical benefits of cryotherapy as well as many reports on complications arising from its use [5–9]. The resulting injuries may range from nerve damage [9] to full thickness skin necrosis [5], typically as a consequence of the prolonged diminution of local blood flow in conjunction with the low temperature [10]. Most CTUs can and do produce temperatures far below the range for which significant diminution in blood flow occurs.

The surface application of cooling causes a reduction of skin temperature that gradually penetrates into the tissue. The extent to which the cooling penetrates depends on tissue type and its degree of perfusion and metabolism. This reduction in tissue temperature results in localized vasoconstriction and a profound reduction in perfusion to the area under treatment. Upon cessation of surface cooling, the skin temperature begins to increase while the deeper cold front is still propagating into the tissue. This increase in skin temperature does not directly translate into a rise in tissue perfusion. To clarify, the relationship between perfusion and tissue temperature shows a hysteresis effect such that the reduction in tissue temperature during surface cooling causes a direct decline in tissue perfusion, but the subsequent increase in temperature is not necessarily accompanied by an equivalent increase in perfusion [11]. This sustained vasoconstriction after removal of localized cooling can last for an extended period of time (hours), resulting in a reduced state of tissue perfusion at elevated tissue temperatures.

Cold-depressed skin perfusion can be enhanced by active surface heating. This understanding of the physiological response to localized heating or cooling may be applied to manipulate cryotherapy outcomes. Cold-induced vasoconstriction causes tissue starvation of nutrients and oxygen, plus a buildup of metabolic byproducts. Heat-induced vasodilation has the opposite effects. Therefore, inclusion of intermittent heating episodes during cryotherapy can be applied to modulate the time progression of blood flow to ensure adequate tissue nutrition. Accordingly, a cryotherapy protocol that includes intermittent cooling and warming episodes is anticipated to combine cooling therapy benefits with improved tissue healing.

METHODS

Experimental Procedure: Each subject was instrumented by applying multiple thermocouples, heat flux gauges (Omega) and Laser Doppler flowmetry probes (LDF, Moor Instruments) to his/her thigh. A flexible silicone heater (Chromalox) was used to allow active warming during the heating portion of the protocol. Heaters had built-in holes to allow application of perfusion probes through them during the experiment. The cryotherapy pad was applied at the treatment site such that it completely covered the heater in addition to a segment of the skin adjacent to the heater. This allowed for an area of the skin to be only cooled (control region) while another segment could be either cooled or heated (experimental region) based on the portion of the protocol. At each point of time during the active heating or cooling either the heater (heating) or CTU (cooling) was on. A perfusion probe

Copyright 2016 The Organizing Committee for the 2016 Summer Biomechanics, Bioengineering and Biotransport Conference

was applied to the region that only experienced active cooling (control probe) and two more probes were applied to the area that experienced both active heating and cooling (experimental probes). Data was collected using the National Instruments thermocouple (NI9213) and voltage (NI9215) modules, a data acquisition chassis (NI 9174) and a host computer and was analyzed using Matlab. Each experiment started with a baseline period where no water ran through the cooling pad followed by active cooling. The active cooling was intermittently interrupted by the inclusion of an active warming episode into the protocol.

Data Processing: Area under the curve was calculated for perfusion measured in both the experimental and control regions. This area was calculated in relation to an average baseline of zero and was considered to signify a deficit in perfusion in response to cooling and in respect to a continuation of baseline condition if cooling had not taken place. The total deficits were compared between the two regions (control and experimental). Additionally, recovery was defined as the area under the curve in respect to the minimum perfusion at the end of cooling for the active heating segment and compared to the deficit for the cooling episode prior to it.

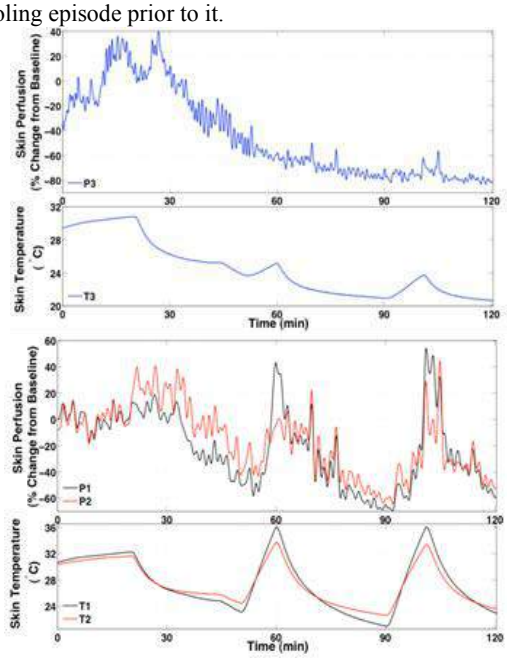

Figure 1: Plots of temperature and perfusion during cryotherapy trials. The upper data in blue show cooling interrupted for 10 min at 50 and 90 min with only passive rewarming. Lower plots in red and black substitute 10 min of active rewarming at 50 and 90 min.

RESULTS

Figure 1 illustrates surface skin temperature (bottom panels) and skin perfusion (top panels) from an exemplar experiment showing data from a perfusion probe in the control (top figure, blue) and experimental region (bottom figure, red and black). This experiment included a baseline, three cooling and two heating episodes. The first two cooling episodes lasted for 30 min each and the 3rd for 20 min while each heating episode was 10-min long. The control region, in the absence of active heating, experienced passive rewarming between each two consecutive cooling phases. As it can be seen with the control probe the skin temperature dropped considerably with active cooling and increased with its termination. As expected, the skin temperature increased more profusely with active heating in experimental region. During active cooling, perfusion encountered a significant reduction in both experimental and control regions while an increase in skin perfusion was only observed when active heating was present (experimental site). For this exemplar experiment, the total deficit was an order of magnitude higher for the control probe compared to the experimental probes. Additionally, the deficit and the recovery for the experimental probes were in the same order of magnitude. So even though the perfusion remained depressed during the duration of experiment, the inclusion of intermittent heating into the protocol allowed replenishment of oxygen and nutrients and removal of metabolic byproducts for brief time intervals.

DISCUSSION

There is now emerging a scientific basis for the rational design of cryotherapy protocols based on a coordinated manipulation of time and temperature of exposure. Although many variations are possible, the objective is to balance the benefits of low temperatures on reducing pain with the potential risk of inducing ischemic driven injury resulting from low temperature. The key to achieving an acceptable balance is intermittent rewarming at the treatment site. This type of protocol is difficult, although not impossible, to produce with a CTU that operates based on melting temperature of ice. An alternative that offers multiple advantages is to apply thermoelectric coolers (TEC) in the design of a CTU. TEC allows modulation of the active CTU temperature by regulating the magnitude and polarity of applied voltage. The result is the ability to change the therapeutic temperature continuously between values far below to far above the physiological range independently as a function of time and with a single CTU. When combined with a quantitative understanding of how blood flow can be manipulated by the applied temperature, the opportunity now exists for rationally designing and applying cryotherapy protocols to produce targeted therapeutic outcomes with minimized risk of ischemic injury side effects.

ACKNOWLEDGEMENTS

This research was sponsored by National Science Foundation Grants CBET 0828131, CBET 096998, and CBET 1250659, National Institutes of Health Grant R01 EB015522, and the Robert and Prudie Leibrock Professorship in Engineering at the University of Texas at Austin.

CONFLICT OF INTERST

Patent applications for cryotherapy devices and methods have been submitted by Dr. Khoshnevis and Dr. Diller to the United States Patent and Trademark Office. Ownership rights to this IP reside with The University of Texas System. Dr. Diller has served as an expert witness for both plaintiff and defendant counsel since 2000 in numerous legal cases regarding the safety and design of existing cryotherapy devices.

REFERENCES

[1] Swenson, C et al., *Scand. J. Med. Sci. Sports*, 6:193–200, 1996
[2] MacAuley, D, *Clin. J. Sport Med.*, 11:67–72, 2001
[3] Bleakley, C M et al., *Br. J. Sports Med.,* 40:700 –705,2006
[4] Barber, F A et al., *J. Arthrosc.,* 14:130–135, 1998
[5] Brown, W C et al., *J. Foot Ankle Surg,* 48:577–580, 2009
[6] Lee, C K et al., *Orthopedics,* 30:63–64, 2007
[7] Cuthill, J et al., *Physiotherapy,* 92:61–65, 2006
[8] Selfe, J et al., *Phys. Ther. Sport,* 8:153–158, 2007
[9] Babwah, T et al., *Res. Sports Med.*, 19:66–71, 2011
[10] Jia, J et al., *Brain*, 121:989–1001, 1998
[11] Khoshnevis, S et al., *J. Biomech. Eng*, 138:1-8, 2015

Copyright 2016 The Organizing Committee for the 2016 Summer Biomechanics, Bioengineering and Biotransport Conference

SB³C2016
Summer Biomechanics, Bioengineering and Biotransport Conference
June 29 –July 2, National Harbor, MD, USA
SB³C2016-738

SUSTAINED PRESENTATION OF NEUROTROPHIC CUES FOLLOWING TRAUMATIC BRAIN INJURY THROUGH MATRIX IMMOBILIZED BDNF FRAGMENT PEPTIDES

Christopher J. Lowe (1), David I. Shreiber (1)

(1) Department of Biomedical Engineering
Rutgers, the State University of New Jersey
Piscataway, NJ, United States

INTRODUCTION

Traumatic Brain Injury (TBI) is a devastating condition that often has long-lasting and life-altering effects. The initial, physical, primary injury is followed by a persistent, inflammatory secondary injury cascade. Cellular damage and death from primary injury occur instantaneous to the injury, but secondary injury persists for weeks and months after the initial insult, offering a potential opportunity for treatment. An obstacle to treatment is the complex, hostile nature of the secondary injury environment, which includes oxidative stress from free radicals, glutamate induced excitotoxicity, mitochondrial dysfunction, and cell death. Delivery of neurotrophic factors to the site of TBI has shown some promise in alleviating these symptoms, particularly with brain derived neurotrophic factor (BDNF). BDNF is critical to neuronal development and survival, but is rapidly cleared in vivo and it is unable to cross the blood-brain barrier at a therapeutically relevant rate, which limits its therapeutic potential. Recently, Cardenas-Aguayo et al identified short peptide fragments derived from BDNF's sequence that mimicked the activity of the full length growth factor [1]. Our laboratory has routinely created functional biomaterials by covalently grafting peptides and small molecules to collagen [2,3]. In this report, we seek to enhance the efficacy of these BDNF fragment peptides by covalently immobilizing them to a polymer matrix for sustained presentation at the injury site.

METHODS

Peptide Grafting to Collagen

The BDNF fragment peptide, IKRG, was synthesized commercially by Genscript (Piscataway, NJ). Type-I bovine collagen (Elastin Products Company, Owensville, MO) was reconstituted in 0.02N acetic acid at 3mg/mL. Peptides were coupled to amines on lysine residues in the collagen backbone via a zero length crosslinker, 1-ethyl-3-(dimethylaminopropyl) carbodiimide. The resulting solution was dialyzed to remove un-grafted peptide, lyophilized, and reconstituted at 3mg/mL in 0.02N acetic acid [2].

Hydrogel Preparation

Buffered hydrogel solutions from native or IKRG-grafted collagen were prepared using the following ratios: 20µL HEPES:130µL 0.15N NaOH:100µL 10x MEM: 53µL M199: 10µL L-glutamine: 10µL penicillin/streptomycin: 677µL 3.0mg/mL collagen solution. Hydrogels with varied peptide concentration were created by admixing grafted and native collagen hydrogel suspensions at target ratios. Hydrogel suspensions were placed in multiwell plates and allowed to self-assemble at 37°C for one hour.

Cerebellar Neuron Culture

Cerebellar Granule Neurons (CGNs) were isolated from day 6 rat pups. For neurite outgrowth assays, cells were cultured on collagen hydrogels at ~50,000 cells/cm^2 for 7 DIV in Neurobasal Medium (Life Technologies) containing 0.5% L-glutamine, 1% penicillin/streptomycin, 2% B27 supplement, and 1% potassium chloride. Soluble IKRG and BDNF were included at 1µM and 20ng/mL, respectively in requisite controls. For cellular activity assays, CGNs were plated onto poly-L-lysine (PLL) coated tissue culture plastic at ~200,000 cells/cm^2 using the same media compositions and maintained in culture for 9 DIV.

Immunocytochemistry for Neurite Outgrowth

CGN cultures were fixed on DIV 7 and stained immunohistochemically for β-III tubulin (TUJ1) and DAPI before being observed with fluorescent microscopy. Neurite outgrowth of CGNs was quantified from TUJ1 images using ImageJ.

Glutamate Induced Excitotoxicity

Glutamate induced excitotoxicity was modeled in vitro by adding 300µM or 500µM glutamic acid to the culture media for 1 hour.

Copyright 2016 The Organizing Committee for the 2016 Summer Biomechanics, Bioengineering and Biotransport Conference

Glutamate containing media was then removed and replaced with fresh media containing recovery treatments. Recovery treatments included native and IKRG grafted collagen at 0.33mg/mL, soluble IKRG or BDNF, as well as a no treatment control (media only).

Free Radical Induced Injury

Free radical injury was modeled via addition of rotenone, an inhibitor of the electron transport chain, which causes mitochondrial dysfunction and production of free radicals in a physiologically relevant way. 10µM rotenone was added to CGN cultures for 1 hour, and then replaced with fresh media containing recovery treatments described in the glutamate excitotoxicity studies.

Cellular Activity

Cellular activity for both glutamate and free radical studies was examined via Vybrant MTT Cell Proliferation Assay (ThermoFisher) using the manufacturer's instructions.

RESULTS

Neurite Outgrowth Assay

Neurites extending from CGNs cultured on IKRG-grafted hydrogel conditions tended to grow longer than those on native collagen (NC) (Figure 1). Increasing concentrations of grafted peptide corresponded to longer neurite outgrowth. CGNs cultured on IKRG-100 hydrogels, the highest peptide concentration tested, compared well with outgrowth from controls with soluble BDNF or IKRG.

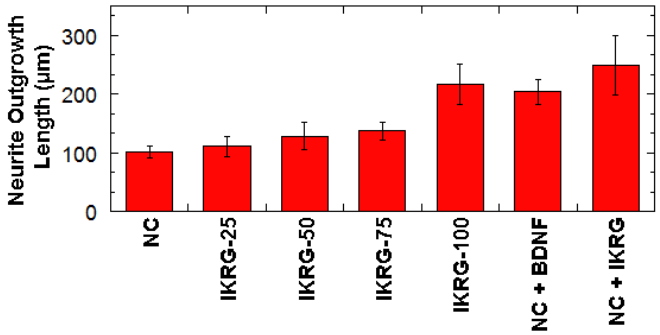

Figure 1: CGN Neurite Outgrowth on IKRG Grafted and Native Collagen (NC) Hydrogels

Glutamate Induced Excitotoxicity

CGN cultures demonstrated ~60% reduction in cellular activity following injury with glutamate. CGN cultures treated with native collagen (NC) following injury experienced a further reduction in cellular activity. CGN cultures treated with 100% IKRG grafted collagen following injury saw a twofold increase in cellular activity as compared to native collagen treated cultures, but the increase over untreated conditions was minimal (Figure 2).

Free-Radical Induced Injury

CGN cultures injured with rotenone exhibited a ~80% reduction in cellular activity. CGN cultures treated with native collagen following rotenone induced injury showed a greater than twofold increase in cellular activity. All IKRG grafted conditions showed a similar increase in cellular activity following injury as the native collagen condition. Soluble IKRG peptide induced the greatest recovery, a greater than three-fold increase in average cellular activity (Figure 2).

DISCUSSION

IKRG grafted collagen induced an observable increase in neurite outgrowth in CGN cultures. This confirms that IKRG was successfully grafted to the collagen backbone, and that the IKRG peptides retain their bioactivity following covalent coupling to collagen.

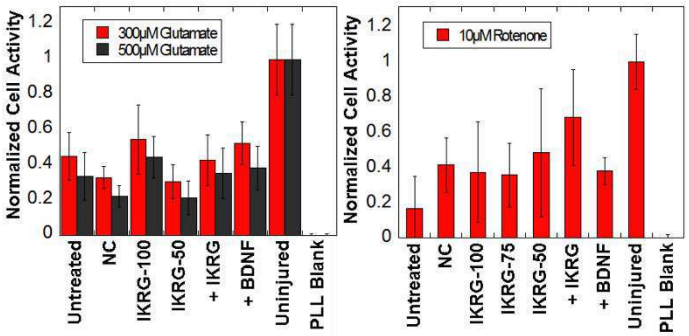

Figure 2: CGN Viability Following Glutamate Injury (Left) and Free-Radical Injury (Right) with Subsequent Recovery Treatments

Cells subjected to secondary injury were treated with native or grafted collagens at 0.33mg/mL in culture media. This concentration is too low for the collagen to self-assemble into a fully formed hydrogel network, however individual collagen molecules will partially self-assemble to generate higher molecular weight fibers. These fibers aggregate at the bottom of the culture well forming a viscous slurry, thereby presenting the grafted peptide cues in close proximity to the CGNs in a sustained manner.

Preliminary studies of glutamate-induced excitotoxicity revealed that treatment with collagen seems detrimental to CGN activity, as native collagen treatment further exacerbated the effects of the glutamate injury. IKRG grafted collagen at the highest concentrations showed a substantial increase in cellular activity as compared to native collagen, but the gains were minimal when compared to the untreated condition. This suggests that the negative effects collagen seems to be inducing in the CGNs are masking the full benefit of the grafted IKRG peptide to combat glutamate induced excitotoxicity.

Preliminary studies with free-radical injury induced by rotenone seemed to respond in an opposite manner. CGN cultures treated with native collagen following injury showed a strong improvement in cellular activity. It is possible that the collagen is serving as a sink for free radicals generated by the rotenone, sequestering the radical species away from the cells reducing the potential for further injury. No increase was observed in cellular activity as a result of incorporating the grafted IKRG peptides as compared to the native collagen conditions, indicating that the immobilized peptides may not be influencing CGN activity. The soluble IKRG peptide induced a very large recovery in cell viability following rotenone injury.

Secondary injury following TBI is inherently complex, which is highlighted by the injury-dependent responses of the CGNs to collagen treatment. Despite this, benefits to delivering IKRG were observed in both studies. Ongoing studies are examining the potential for a bio-inert matrix to serve as a carrier for the IKRG peptides, possibly eliminating the negative effects of collagen observed in glutamate studies.

ACKNOWLEDGEMENTS

This work is supported by the New Jersey Commission on Brain Injury Research (NJCBIR) through a graduate research fellowship (CBIR14FEL004)

REFERENCES

[1] Cardenas-Aguayo, M et al., *PLOS One*, 8:e53596, 2013.
[2] Masand, S et al., *Biomaterials*, 33: 8353-8362, 2012.
[3] Drzewiecki, K et al., *Langmuir*, 30: 11204-11211, 2014

Copyright 2016 The Organizing Committee for the 2016 Summer Biomechanics, Bioengineering and Biotransport Conference

SB^{3}C2016
Summer Biomechanics, Bioengineering and Biotransport Conference
June 29–July 2, 2016, National Harbor, Maryland, USA
SB³C2016-739

NEAR-WALL STAGNATION IN LARGE ARTERIES: IS WALL SHEAR STRESS MAGNITUDE SUFFICIENT?

Amirhossein Arzani (1), Alberto M. Gambaruto (2), Guoning Chen (3), Shawn C. Shadden (1)

(1) Department of Mechanical Engineering
University of California, Berkeley
Berkeley, CA, USA

(2) Department of Mechanical Engineering
University of Bristol
Bristol, UK

(3) Department of Computer Science
University of Houston
Houston, TX, USA

INTRODUCTION

Wall shear stress (WSS) is the most common parameter used to correlate blood flow with cardiovascular disease. WSS quantifies the frictional drag force on the vessel wall, and WSS vectors provide insight on near-wall transport, with the latter influencing key process including atherosclerosis and thrombosis. Likewise, near-wall stagnation is an important measure of hemodynamics, and relative residence time (RRT), defined as the inverse of time-average WSS (TAWSS) vector magnitude, is the traditional measure used to quantify near-wall stagnation. Due to the high Schmidt number in intravascular transport problems, there often exists thin concentration boundary layers next to the vessel wall and the WSS vector field can be scaled to obtain an accurate estimate of the flow velocity in these boundary layers. Using this approach, we recently introduced Lagrangian WSS structures as the organizing structures of near-wall transport and WSS exposure time (WSSET) [1]. This study investigates and compares RRT, surface concentration, WSSET, and Lagrangian WSS structures in different vascular pathologies to determine how to best quantify near-wall hemodynamics.

METHODS

WSS data were obtained from patient specific computational fluid dynamics simulations in abdominal aortic aneurysms (AAA), coronary artery aneurysms (CAA), and carotid arteries (CA). Briefly, Linear tetrahedral elements with a next to wall edge size of 200 μm (50 μ m) were used, and the time step divided the cardiac cycle into 1000 (5000) time steps in the AAA (carotid artery) models. The CAA data were used from a previous study [2] and obtained from vascularmodel.org. All the simulations were done in the open source SimVascular software (simvascular.org), based on a stabilized finite element method.

Next, near-wall transport measures were computed. RRT is computed as

$$\mathrm{RRT} = \frac{1}{\|\frac{1}{T}\int_0^T \tau dt\|}\ , \tag{1}$$

where τ is the WSS vector and T is the cardiac cycle duration. Lagrangian particle tracking of surface-bound tracers were used to generate WSS pathlines, using the near-wall velocity $\boldsymbol{u}_\pi = \frac{\boldsymbol{\tau}\delta n}{\mu} + O(\delta n^2)$, where δn is a small normal to wall distance chosen inside the concentration boundary layer and μ is the dynamic viscosity. Subsequently, WSSET was computed for each surface element as the accumulated amount of time that all the WSS trajectories spend inside the element

$$\mathrm{WSSET}(e) = \tfrac{1}{\mathcal{T}}\sqrt{\tfrac{A_m}{A_e}}\sum_{p=1}^{N_t}\int_0^{\mathcal{T}} H_e(p,t)\ \mathrm{d}t \tag{2}$$

$$H_e = \begin{cases} 1 \text{ if } \boldsymbol{x}_p(t) \in e \\ 0 \text{ if } \boldsymbol{x}_p(t) \notin e \end{cases}\ ,$$

where A_e is the area of the surface element, A_m is the average surface element area, $\mathbf{x}_p(t)$ is the position of the WSS trajectory, N_t is the total number of trajectories released, and $\mathcal{T}$ is the integration time. The WSS Lagrangian coherent structures (WSS LCS) [1] were also computed to provide insight on the near-wall flow topology. In this study, invoking the quasi-steady nature of near-wall transport the WSS LCS were directly computed from the saddle type fixed points of the time-average WSS vector field. Figure (1) depicts the procedure used in the computation of WSSET and WSS LCS.

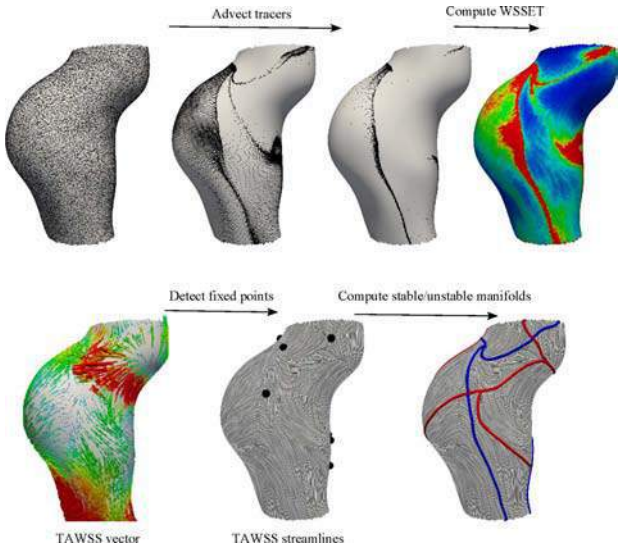

FIGURE 1: THE LAGRANGIAN APPROACHES USED TO COMPUTE WSSET (TOP) AND WSS LCS (BOTTOM).

Copyright 2016 The Organizing Committee for the 2016 Summer Biomechanics, Bioengineering and Biotransport Conference

Surface concentration was computed from the solution of 3D Eulerian advection-diffusion equation

$$\frac{\partial c}{\partial t} + \boldsymbol{u} \cdot \nabla c = D \nabla^2 c \,, \tag{3}$$

where c is a non-dimensional concentration, $\boldsymbol{u}$ is the velocity, and $D = 1 \times 10^{-5} \frac{cm^2}{s}$ is mass diffusivity. A constant Neumann boundary condition was prescribed at the vessel wall representing a uniform flux of concentration into the lumen. Zero Dirichlet boundary conditions were used for inlet and outlets with the outlets extended. The equation was solved using a finite element method with second order tetrahedral elements and boundary layer meshing implemented in FEniCS software.

RESULTS

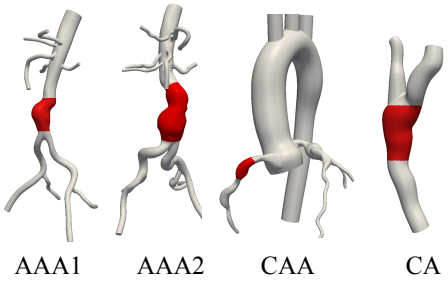

FIGURE 2: TWO ABDOMINAL AORTIC ANEURYSM (AAA1 AND AAA2), CORONARY ARTERY ANEURYSM (CAA), AND CAROTID ARTERY (CA) MODELS .

Representative results are presented in this section. Figure (2) shows the patient-specific models where the highlighted region shows the region where near-wall transport was studied. Figure (3) compares RRT, WSSET, Eulerian surface concentration, and WSS LCS. Comparison of RRT and WSSET to surface concentration reveals that WSSET has a higher correlation to surface concentration. This improvement is more pronounced in complex flows such as AAAs. RRT only considers the magnitude of the average near-wall velocity (a scale of TAWSS vector), whereas WSSET takes into account the complete tangential convective nature of near-wall transport.

The WSS LCS provides a template for near-wall transport and could be used to predict the regions where high concentration and stagnation occur. The attracting WSS LCS show the regions where near-wall tracers accumulate leading to high stagnation and concentration. The repelling WSS LCS mark the boundaries for the basins of attraction. Therefore, the repelling WSS LCS could be used to qualitatively infer how much an attracting WSS LCS will lead to high concentration. Moreover, the repelling WSS LCS partition the near-wall transport and provide transport barriers to convective transport [1].

DISCUSSION

Near-wall transport is an important aspect of cardiovascular mass transfer problems. This is manifested in the transport of thrombogenic, atherogenic, and atheroprotective biochemicals near the arterial wall. Moreover, near-wall transport of certain biochemicals influences endothelial cells mechanotransduction. Near-wall stagnation and concentration are both essential for these processes to be effective. For instance, it has been demonstrated that monocyte adhesion to endothelial cells occurs in regions of high concentration and stagnation [3]. In this study we compared RRT and recently proposed Lagrangian WSS metrics to surface concentration. WSSET demonstrated superior correlation with surface concentration. RRT only quantifies near-wall stagnation while WSSET quantifies near-wall stagnation, concentration, and takes into account the origin of the near-wall trajectories. The WSS LCS computed from the stable and unstable manifolds of TAWSS vector field provided a framework for studying the topology of near-wall transport and explaining the surface concentration results. Our results demonstrate that as the flow topology becomes more complex, the importance of considering the near-wall flow induced by the WSS vector fields in quantification of near-wall stagnation becomes more significant. Future work includes extending these comparisons to more aortic pathologies such as cerebral aneurysms.

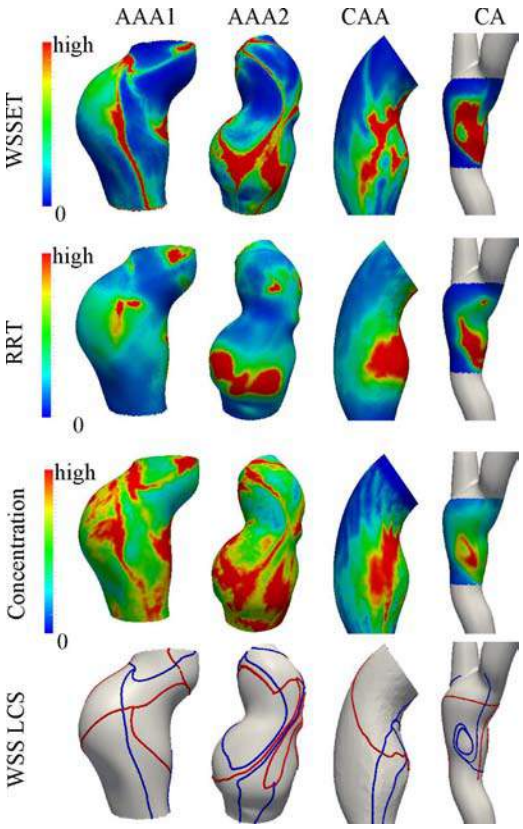

FIGURE 3: COMPARISON OF RRT, WSSET, SURFACE CONCENTRATION AND WSS LCS. THE UNSTABLE MANIFOLDS (ATTRACTING WSS LCS) AND THE STABLE MANIFOLDS (REPELLING WSS LCS) ARE SHOWN WITH BLUE AND RED LINES, RESPECTIVELY.

ACKNOWLEDGEMENTS

This work was supported by an NSF CAREER award (1354541).

REFERENCES

[1] Arzani A, Gambaruto AM, Chen G, Shadden SC. Lagrangian wall shear stress structures and near-wall transport in high-Schmidt-number aneurysmal flows. *Journal of Fluid Mechanics*, in press, 2016.

[2] Sengupta D, Kahn AM, Andrew M, Burns JC, Sankaran S, and Shadden SC, Marsden AL. Image-based modeling of hemodynamics in coronary artery aneurysms caused by Kawasaki disease. *Biomechanics and modeling in mechanobiology*, **11**(6), 915–932, 2012.

[3] Chiu JJ, Chen CN, Lee PL, Yang CT, Chuang HS, Chien S, Usami S. Analysis of the effect of disturbed flow on monocytic adhesion to endothelial cells. *Journal of Biomechanics*, **36**(12), 1883–1895, 2003.

Copyright 2016 The Organizing Committee for the 2016 Summer Biomechanics, Bioengineering and Biotransport Conference

SB³C2016
Summer Biomechanics, Bioengineering and Biotransport Conference
June 29 –July 2, National Harbor, MD, USA
SB³C2016-740

3D *in vitro* PLATFORM TO ISOLATE DORMANCY-CAPABLE CANCER CELLS

Julian A. Preciado[1], Eduardo Reategui [1], Molly Lefebvre[1], Samira Azarin[2], Emil Lou[3], Alptekin Aksan[1]
[1]Department of Mechanical Engineering, [2]Department of Chemical Engineering, [3]Hematology, Oncology and Transplant, Department of Medicine, University of Minnesota, Twin Cities
Minneapolis, USA

INTRODUCTION

Metastatic cancers account for approximately 90% of cancer-related deaths[1]. Certain metastatic cells undergo dormancy, a stage in tumor progression when cancer cells cease proliferating but remain alive in a quiescent state as a result of delayed adaptation to the new microenvironment. Recent studies suggest that metastasis-initiating cells enter into dormancy in response to signals within their new microenvironment and can remain dormant for years to decades, after which they regain a tumorigenic phenotype due to various not well understood reasons[1]. Therapeutic targeting of dormant cancer cells is difficult because the majority of cancer treatments target only rapidly proliferating cells. Therefore, understanding the microenvironmental niches that lead to dormant cell deactivation and reawakening is crucial in developing therapeutics to kill dormant cells, awaken in a controlled fashion so that they can be targeted by chemotherapeutic agents, or sustain dormancy to convert cancer into a manageable chronic disease.

Current methods to induce cancer cell lines into dormancy include serum starvation in 2D cell cultures and *in vivo* injections with cancer cell lines that exhibit dormant behavior. Several studies have shown that 2D cell culture does not recapitulate 3D *in vivo* cell behavior. In fact, it had been shown that serum starvation of 2D cell culture does not differentiate between cancer cell lines that have been shown to undergo dormancy in vivo (dormancy-capable) vs. those that do not (dormancy-incapable)[2]. *In vivo* models are problematic due to low dormant cell recovery for downstream processing, *in vivo* therapeutic experimentation and expense of animal studies. More recently, 3D *in vitro* encapsulation within a basement membrane extract system was proposed in order to drive cells into dormancy[2]. This was a successful model in differentiating dormancy-capable cell and dormancy-incapable cell lines. However, biological-based hydrogels such as basement membrane extract present challenges due to the presence of bioactive molecules such as fibrin, which has been shown to awaken dormant cells. Additionally, animal-derived products have an inherent batch-to-batch variability, leading to reproducibility challenges.

Recently, there has been an interest in encapsulating mammalian cells in silica hydrogels due to their biocompatibility, mechanical properties fine tuning and high permeability[3]. Controlling stiffness in particular allows production of gels where proliferation is controlled. Additionally, silica being a synthetic material ensures no unintended microenvironment-induced cell signaling cascades that occur in other 3D platforms such as basement membrane extract hydrogels.

We have developed stiff but reversible, highly permeable silica-PEG hydrogels where stiffness can be manipulated to control cell migration and proliferation. Reversibility of these hydrogels allows high cell recovery for downstream processing and analysis. We hypothesize that the stiffness of our hydrogel platform creates a biphasic, stress-inducing stimulus where dormancy-capable cancer cell lines can enter quiescence meanwhile highly invasive, dormancy-incapable cells become frustrated, enter senescence and eventually apoptosis. To our knowledge, we are the first group to use physical proliferation inhibition as a means to induce cancer cell dormancy.

METHODS

Gel synthesis: Tetraethylorthosilicate (TEOS) was hydrolyzed in 0.5 M acetic acid (AA) at a ratio of 1:9 for 30 min. 10 wt. % fumed silica (FS) was mixed separately with 4-arm PEG. TEOS-AA and FS-PEG solutions were then mixed at a ratio of 3:5. pH was then neutralized using 0.5 M ammonium hydroxide and gels are aged for 72 hrs. Gels were then particulated via sonication, washed with media 3 times and centrifuged at 1500 RPM for 5 min.

Cell encapsulation: Gel aliquots were vortexed, cells were added to the liquid gel at a concentration of $2x10^5$ cells/mL of gel and transferred into a well. After 5 min, culture media was added to the well.

Scanning Electron Microscopy: SEM conducted with a Hitachi S-900 FESEM. FIJI was used to measure pore size from images.

Live/dead staining: Calcein AM and propidium iodide were used as a live/dead kit, respectively, at optimized concentrations.

Alamar blue metabolic assay: 10 µL of Alamar Blue solution was added to 100 µL of gel and media. Abs_{570} and Abs_{600} were measured 12 hrs. later. Live, 2D cultured cells were used as positive controls and dead encapsulated and 2D cultured cells as negative controls.

Ki-67 staining and counting: Cells were fixed and permeabilized with 4% paraformaldehyde and 0.3% triton x-100, respectively. Encapsulated cells (for 30 min. and 2 days) were stained for proliferating marker Ki-67. Nuclei were counterstained with DAPI. 2D cultured serum-fed and serum-starved cells were used as a positive and negative controls, respectively.

RESULTS

Scanning Electron Microscopy: Fig. 1 shows a highly porous hydrogel structure with 1-5 µm size pores.

Live/Dead staining: A high number of encapsulated cells remained alive past 5 days of encapsulation as seen in **Fig. 2 (a) & (b)**, with very few staining dead.

Metabolic Activity: Metabolic activity data showed a clear distinction in cell viability between dormancy-capable cell lines (DCIS.COM, LNCaP, and MCF-7) from dormancy-incapable cell lines (OVCar-5 MDA-MB-468, and SKOV-3) with results summarized in **Table 1**. Dormancy-capable cell lines

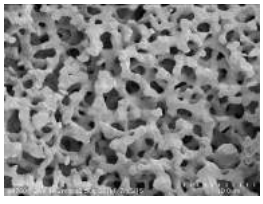

Figure 1. Silica-PEG hydrogel

Copyright 2016 The Organizing Committee for the 2016 Summer Biomechanics, Bioengineering and Biotransport Conference

had a $t_{50\%}$ and $t_{0\%}$ (time to 50% and 0% metabolic activity, respectively) of 7 and 21 days, respectively. On the other hand, nontumorigenic cell lines had a $t_{50\%}$ and $t_{0\%}$ of 1-4 and 3-7 days, respectively. **Fig. 3** shows this difference between dormancy-capable (MCF-7) and dormancy-incapable (MDA-MB-468), where the former has a slight decrease in metabolic activity meanwhile the latter has a sharp drop over 7 days of encapsulation.

Table 1. Cell lines encapsulated and their $t_{50\%}^{*}$ and $t_{0\%}^{**}$.

Cell Line	Time to 50% MA (days)*	Time to 0% MA (days)**
Human Ovarian Epithelial Cells (OVCar-5)	4.0	7.0
Human Mammary Gland Epithelial Cell (MDA MB-468)	<1	1
Human Ovarian Epithelial Cells (SKOV-3)	1.0	3.0
Human Mammary Gland Epithelial Cell (DCIS.COM)	>7	>21
Human Prostate Epithelial Cells (LNCaP)	>7	>21
Human Mammary Gland Epithelial Cells (MCF-7)	>7	>21

* and ** Time for in-gel metabolic activity of the encapsulated cells to drop down to 50% of its initial (day 0) value and zero, respectively.

Ki-67 expression: Immunofluorescent staining (**Fig. 1 (c)-(f)**) showed MCF-7 cells encapsulated for 5 days and serum-starved cells had a similar decrease in Ki-67 expression when compared to cells encapsulated for 30 min and serum-fed cells, respectively.

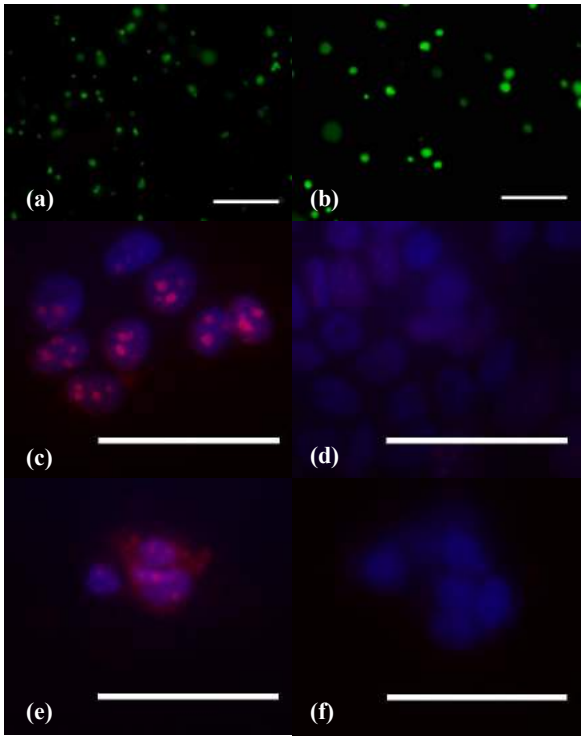

Figure 2. Live/Dead staining of MCF-7 cells encapsulated for **(a)** 30 min and **(b)** 5 days; scale bar = 200 µm. Ki-67 and DAPI staining of 2D cultured **(c)** serum-fed cells, **(d)** serum-starved cells, **(e)** cells ecapsulated for 30 min and **(f)** 5 days; scale bar = 100 µm.

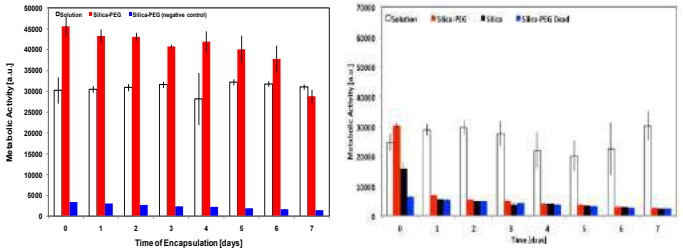

Figure 3. Metabolic activity data for dormancy-capable MCF-7 (left) cell line and dormancy-incapable MDA MB 468 (right).

DISCUSSION

SEM images show a highly porous structure with pores small enough to prevent cell migration and proliferation but large enough to allow nutrient and gas diffusion required for cellular metabolism.

Live/Dead staining and metabolic activity assay confirmed that MCF-7 cells remain alive and metabolically active when encapsulated for extended periods of time. Furthermore, metabolic activity data showed a stark contrast between dormancy-capable and dormancy-incapable cell lines. MDA-MB468, a highly-invasive, dormancy-incapable cell line had the sharpest decline in metabolic activity when encapsulated, with a $t_{50\%}$ and $t_{0\%}$ of <1 and 1 days, respectively. Conversely, MCF-7 cells only saw a modest drop in metabolic activity over 7 days. A sharp decrease in metabolic activity was attributed to cell death meanwhile a modest drop in metabolic activity was attributed to cells entering quiescence. During quiescence, metabolic activity is lowered given cells are not proliferative active and metabolic pathways are downregulated[1]. This biphasic response between MCF-7 and MDA-MB-468 can be credited to the physical constrains of our encapsulation platform, where cell migration and proliferation are inhibited, leading to cellular frustration and arrest (G0 phase of the cell cycle). In response to this stimulus, we believe if a cell cannot enter quiescence, it is forced into senescence and eventually apoptosis. Our platform differs from other dormancy-inducing methods such as serum-starvation because it contains an inherent specificity for dormancy-capable cells.

Ki-67, a cellular marker indicative of proliferation, was used to assess if encapsulated MCF-7 cells are in a quiescent state (G0). A similar decrease in Ki-67 expression can be seen between serum-fed **(c)** and serum-starved **(d)** cells and cells encapsulated for 30 min **(e)** and 5 days **(f)**. This concludes that encapsulated cells have indeed entered quiescence and are no longer proliferative active in a similar fashion as 2D serum-starved cells, the predominant method of inducing cell dormancy.

These findings conclude that this platform successfully and specifically drives dormancy-capable cell lines into quiescence. The platform's biocompatibility, high permeability to nutrients, and specificity for dormancy-capable cell lines make it an improved method to induce cancer cell dormancy compared to current approaches. Further studies will focus on the clinical applications of this platform to study cancer cell dormancy and potential treatments.

REFERENCES

1 Sosa MS, Bragado P, Aguirre-Ghiso JA. Mechanisms of disseminated cancer cell dormancy: an awakening field. *Nature reviews Cancer*. 2014;14(9):611-622.

2 Barkan D, Kleinman H, Simmons JL, et al. Inhibition of Metastatic Outgrowth From Single Dormant Tumor Cells by Targeting the Cytoskeleton. *Cancer research*. 2008;68(15):6241-6250.

3 Avnir, D, Coradin T, Lev O. et al. Recent bio-applications of sol–gel materials. *J. Mater. Chem.*, 2006, **16**, 1013-1030.

Copyright 2016 The Organizing Committee for the 2016 Summer Biomechanics, Bioengineering and Biotransport Conference

SB^{3}C2016
Summer Biomechanics, Bioengineering and Biotransport Conference
June 29 –July 2, National Harbor, MD, USA
SB^{3}C2016-741

SMOKING AND SMOKING CESSATION: IMPLICATIONS ON THE DEGENERATION OF THE INTERVERTEBRAL DISC

S. Elmasry (1), S. Asfour (1), J. P. de Rivero Vaccari (2), F. Travascio (1)

(1) Department of Industrial Engineering
University of Miami
Coral Gables, FL, USA

(2) Department of Neurological Surgery
University of Miami
Miami, FL, USA

INTRODUCTION

Tobacco smoking is still a popular habit in the United States, interestingly, 20% of the adult population smoke tobacco [1]. Epidemiological studies demonstrated an association between smoking and low back pain, a pathological condition strongly linked to the degeneration of the intervertebral disc (IVD) [2]. It is hypothesized that tobacco-smoking affects IVD health via two distinct mechanisms: (1) through nicotine, which reduces cell proliferation and biosynthesis of extracellular matrix (ECM) components; and (2) through constriction of the capillaries surrounding the IVD, thus hindering nutrient transport to the disc.

Disc homeostasis is complex and involves a series of intertwined metabolic processes which are difficult to control and study during *in vivo* experimental investigations. Hence, in this study, a computational model describing the homeostasis of IVD is used for quantifying how tobacco-smoking affects disc health, and for determining if and to which extent the process of disc degeneration due to tobacco-smoking can be reverted by cessation of smoking.

METHODS

The computational framework used in this analysis describes IVD homeostasis *via* the diffusive-reactive transport of nutrients, metabolites and growth factors [3, 4], see Figure 1. The effect of smoking on IVD homeostasis is accounted for in this model in two ways: (1) nicotine diffusing in IVD from the surrounding vascular network reduces the rate of glycosaminoglycan (GAG) production and cell proliferation in a dose-dependent manner [5, 6]; and (2) smoking impairs transvascular transport of solutes, thus reducing nutrient supply to IVD [7]. Based on the amount of nicotine delivered to the disc and the extent of nutrient deprivation, 'light smoking' and 'heavy smoking' scenarios were simulated, and the results were compared to a 'non-smoking' scenario.

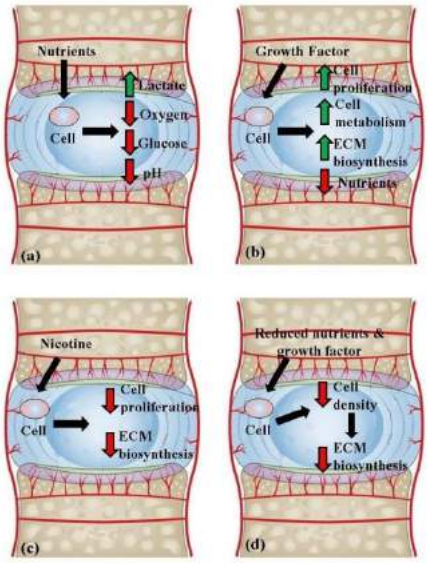

Figure 1: (a) Nutrients regulate cell metabolism. (b) Growth factor up-regulates IVD anabolism. (c) Nicotine down-regulates IVD anabolism. (d) Vasoconstriction deems IVD cell metabolism and anabolism

Copyright 2016 The Organizing Committee for the 2016 Summer Biomechanics, Bioengineering and Biotransport Conference

RESULTS

Due to smoking, cell density in the annulus fibrosus (AF) and nucleus pulposus (NP) decreased to 82% and 72% ('light smoking' scenario) and 58% and 43% ('heavy smoking' scenario) of normal levels, while no changes were observed at the cartilage endplate (CEP). Levels of GAGs decreased in all disc regions, with the largest reductions observed at the NP approaching 72% ('light smoking' scenario) and 38% ('heavy smoking' scenario) of that attained in a 'non-smoking' scenario, see Figure 2.

Smoking cessation was simulated by restoring the normal physiological supply of solutes and by eliminating nicotine delivery to a disc degenerated by tobacco-smoking. Changes in cell density and GAG levels in the IVD were observed over the time frame of one year, and it was discovered that GAG levels suddenly increased in all disc regions within a few days after quitting smoking. However, at the end of the year, cell density in the AF and the NP only attained 87% and 74% (light smoking), and 70% and 55% (heavy smoking) of the values corresponding to normal physiological conditions. Similar recovery patterns were observed for GAG levels, see Figure 3.

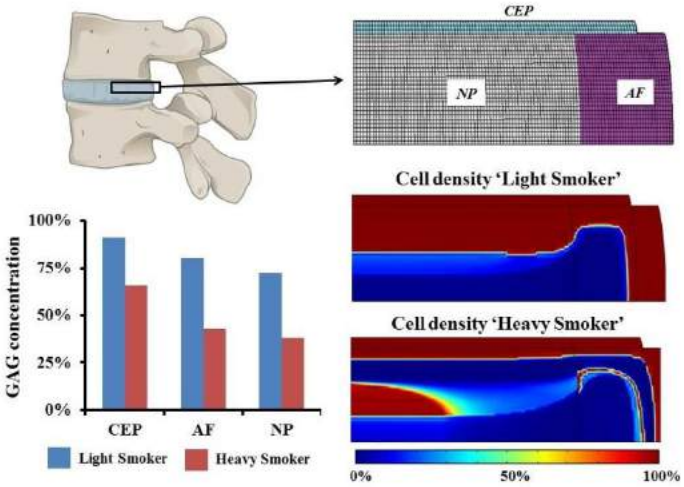

Figure 2: Effect of smoking on IVD homeostasis. The computational domain is shown together with cell density distribution and GAG levels in the disc. Data are normalized with respect to the 'non-smoking' scenario.

DISCUSSION

Depletion of GAG content across all disc regions, and reduction of cell density in both AF and NP found in this analysis are consistent with experimental studies reporting signs of disc degeneration at the NP, and at the inner and intermediate AF of rats and rabbits [8, 9].

In agreement with previous studies [9], our model shows that the benefits to disc health associated with cessation of smoking are limited. Quitting smoking has been associated with mitigation of low back pain [10]. Hence, it may be plausible that the inflammatory cytokines produced by disc cells upon exposure to nicotine would migrate outside the disc and interact with nociceptors responsible for low back pain [11]. Hence, upon cessation of smoking, also the nicotine-mediated expression of inflammatory cytokines would stop, and low back pain could be attenuated despite the fact that the disc is still degenerated.

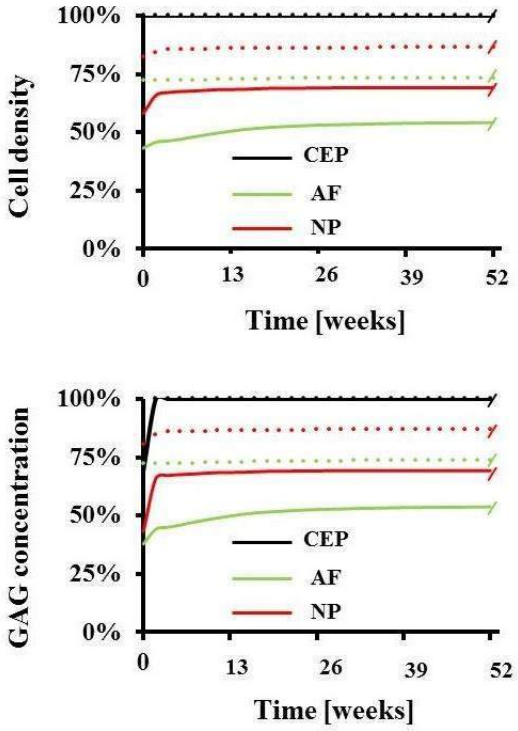

Figure 3: Effect of cessation of smoking. Both 'light smoking' (dotted lines) and 'heavy smoking' (solid lines) scenarios are reported. Data are normalized with respect to the 'non-smoking scenario'.

ACKNOWLEDGEMENTS

Study supported by funds donated to the Biomechanics Research Group of the University of Miami.

REFERENCES

[1] King et al., *Morb. Mortal. Wkly. Rep.,* 60:1207-1212, 2011.
[2] Battie et al., *Spine,* 16:1015-1021, 1991.
[3] Travascio et al., *J. Biomech,* 47: 2269-2276, 2014.
[4] Asfour et al., *J. Biomech,* 48: 332-339, 2014.
[5] Akmal et al., *Spine,* 29:568-575, 2004.
[6] Vo et al., *J. Orthop. Res.,* 29:1585-1591, 2011.
[7] Holm and Nachemson, *Clin. Orthop. Relat. Res*.,169:234-258, 1982.
[8] Uematsu et al., *J. Orthop. Sci.,* 6:177-182, 2001.
[9] Nemoto et al., *J. Orthop. Sci.,* 11:191-197, 2006.
[10] Behrend et al., *J. Bone Joint Surg.,* 94:2161-2166, 2012.
[11] Nadeau et al., *J. Neurosci.,* 31:12533-12542, 2011.

Copyright 2016 The Organizing Committee for the 2016 Summer Biomechanics, Bioengineering and Biotransport Conference

SB^{3}C2016
Summer Biomechanics, Bioengineering and Biotransport Conference
June 29 –July 2, National Harbor, MD, USA
SB^{3}C2016-742

SIMILARITIES AND DIFFERENCES BETWEEN FLOW MODE OF A LEUKOCYTE AND CIRCULATING TUMOR CELL IN MICROVESSELS

Naoki Takeishi (1), Yohsuke Imai (2), Takami Yamaguchi (1), Takuji Ishikawa (2)

(1) Graduate School of Biomedical Engineering
Tohoku University
Sendai, Japan

(2) Division of Mechanical Engineering
Tohoku University
Sendai, Japan

INTRODUCTION

We have numerically investigated the marginations of leukocyte and circulating tumor cell (CTC). Here, we review our recent works [1-2]. Leukocyte/CTC has to marginate to establish the adhesion to endothelial cells by the interaction with red blood cells (RBCs). Leukocyte/CTC has different physical properties, particularly in size, where a leukocyte is around 8 μm in diameter and a CTC is around 12-16 μm in diameter [3-4]. Despite previous experimental and numerical attempts [5-7], the interaction behavior between leukocyte/CTC and RBCs has not been yet understood in detail. The behaviors of leukocytes/CTCs are of fundamental importance in design of microfluidic devices, which help us to diagnose the progress of disease and to evaluate the efficacy of anticancer drugs. Hence, understanding the flow modes of leukocytes/CTCs in microvessels, including the cell velocities, is helpful in the design of novel microfluidic devices. The objective of this study, therefore, is clarifying the detailed interaction between single leukocyte/CTC and RBCs in microvessels, and also identifying the similarities and differences between flow mode of leukocyte and CTC.

We found that the flow mode of the leukocyte/CTC with RBCs underwent a transition from train formation to margination as the diameter of the vessel increased, although the motion of RBCs differed. We also found that both leukocytes and CTCs flowed faster than the mean blood velocity.

METHODS

Consider a cellular flow consisting of plasma, RBCs, and a leukocyte or CTC in a microvessel, which was modeled as a cylindrical channel of radius R. The periodic boundary conditions were employed. The plasma was assumed to be a Newtonian fluid with a viscosity of $\mu^P = 1.2 \times 10^{-3}$ Pa·s. The RBCs were modeled as biconcave capsules with a radius of $a^R = 4$ μm and a thickness of $t^R = 2$ μm, filled with a Newtonian fluid of viscosity $\mu^R = 6 \times 10^{-3}$ Pa·s, and enclosed by a hyperelastic membrane. The membrane was assumed to follow the constitutive law proposed by Skalak et al. (1973)[8], i.e.,

$$w = (I_1^2 + 2I_1 - 2I_2 + C\,I_2^2)(G/2) \qquad (1)$$

where w is the strain energy density function, G is the surface shear elastic modulus, C is the coefficient of the area dilation modulus, and I_1 and I_2 are the invariants of the strain tensor.

The leukocyte and CTC were modeled as spherical capsules with a radius of $a = 4$ μm for leukocyte, and $a = 8$ μm for CTC [3-4]. Because of cytoskeleton networks, the leukocyte/CTC are known to be less deformable than the RBCs, and hence we set to be $R_G = G/G^R = 10^2$. The other parameters remained the same (i.e., $C = C^R$ and $\mu = \mu^R$). The problem was characterized by the capillary number $Ca = \mu^P \dot{\gamma} a^R / G^R$, where $\dot{\gamma} = U_m/2R$ is the mean shear rate and U_m is the mean velocity. A fixed capillary number of $Ca = 0.2$ was used to mimic microcirculation. All data was for 20% volume fraction of RBCs (i.e., $Hct = 0.2$).

The finite-element method for the membrane mechanics and the lattice-Boltzmann method for the fluid mechanics were coupled by an immersed-boundary method. All procedures were implemented on a graphics processing unit (GPU) to accelerate the numerical simulation. The precise description of numerical method was documented in our previous works [1-2].

RESULTS AND DISCUSSION

Figure 1 shows snapshots of typical numerical results for different vessel sizes, where the channel size relative to the

Copyright 2016 The Organizing Committee for the 2016 Summer Biomechanics, Bioengineering and Biotransport Conference

leukocyte/CTC is normalized by the thickness of RBC, i.e., $(R - a)/t^R$. In the smallest vessel, $(R - a)/t^R = 0.5$, the leukocyte/CTC and RBCs formed train formation, where the leukocyte and RBCs exhibited single-file flow (Fig.1A1), while the CTC and RBCs exhibited a recirculating motion, whereby as an RBC approached the CTC in the center of the vessel, it retuned to the wall (Fig.1A2). When the vessel size was increased to $(R - a)/t^R = 1.5$, the leukocyte/CTC began to marginate by passing motion of RBCs, where the leukocyte was overtaken by RBCs (Fig.1B1), while the CTC overtook the RBCs (Fig.1B2). As the vessel size was further increased to $(R - a)/t^R = 2.5$, the passing motion of RBCs continuously occurred, and hence the leukocyte/CTC remained to be marginated. Although the CTC was faster than most RBCs, some RBCs passed forward (Fig.1C2).

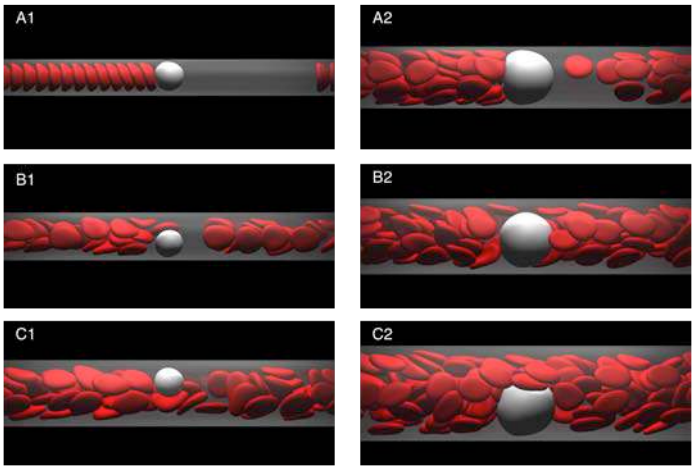

Figure 1: (A1, A2) Train motion of a leukocyte (a = 4 μm) and CTC (a = 8 μm) with RBCs (a^R = 4 μm, t^R = 2 μm) for $(R - a)/t^R$ = 0.5. (B1, B2) margination of leukocyte/CTC for $(R - a)/t^R$ = 1.5. (C1, C2) Margination of leukocyte/CTC for $(R - a)/t^R$ = 2.5.

We examined velocities of three different sized cells (a = 4, 6 and 8 μm). Figure 2 shows the numerical results of cell velocity together with an analytical result of rigid spheres with $R/a \approx 1$ [9], where the cell velocity V_C was normalized to the average blood velocity V_B. As shown in Fig.2, $V_C/V_B > 1$ for all values of R/a. With train formation, for small R/a values, the normalized cell velocity was similar to the analytical result for all cell sizes. When the cell marginated, the cell velocity diverged from the analytical result, but it remained higher than the average blood velocity.

To describe the flow modes of the leukocyte and CTCs quantitatively, we plotted a diagram showing the flow modes, which indicates the cell velocity relative to the average velocity of the RBCs, i.e., $(V_B - V_R)/V_B$ (Fig. 3). When a cell forms a train with the RBCs, the relative velocity should be almost zero. When the leukocyte is marginated and is overtaken by RBCs, the relative velocity is negative; when the CTC overtakes the RBCs, the relative velocity is positive. The relative velocity during train formation was assumed to be negligibly small, $|V_B - V_R|/V_B < 0.005$. The small CTC (a = 6 μm) first overtook the RBCs and was then overtaken by the RBCs over the range of vessel sizes investigated. Figure 3 also shows that the CTCs flowed faster than the RBCs; in constant, the velocity of the leukocyte was always smaller than the average RBC velocity.

In conclusion, we found that the flow mode of a CTC with RBCs in microvessels was similar to that of a leukocyte with RBCs. A transition from train formation to margination occurred at $(R - a)/t^R \approx 1$. The cell velocities of CTCs and leukocytes were larger than the average blood velocity, even when they were marginated. Moreover, only CTCs moved faster than RBCs.

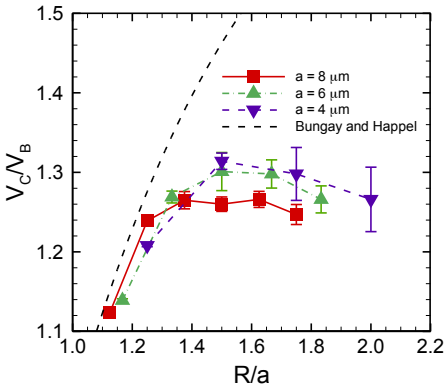

Figure 2: Ratio of cell velocity to the average blood velocity for various diameter microvessels. Analytical solutions are also shown using the expression reported by Bungay and Brenner [9], with $R/a \approx 1$.

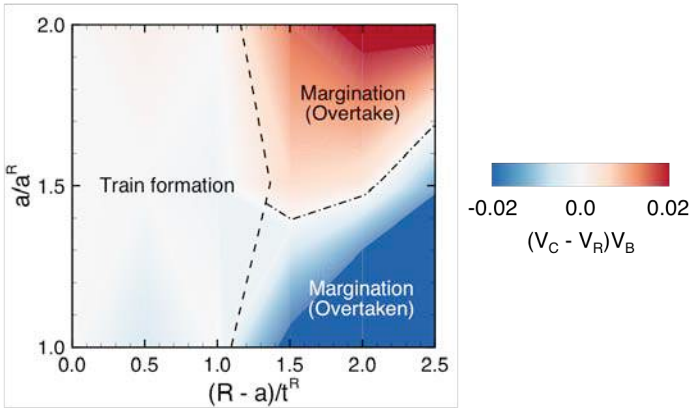

Figure 3: Comparison of flow modes. The flow modes as functions of $(R - a)/t^R$, and a/a^R. The color contours represent the cell velocity relative to the average velocity of the RBCs (i.e., $(V_C - V_R)/V_B$), and dashed lines show $|V_C - V_R|/V_B < 0.005$, and the dash-dot lines show $(V_C - V_R)/V_B < 0$.

ACKNOWLEDGEMENTS

This research was supported by JSPS KAKENHI Grant Nos. 24680048, 25000008, 26107703, and 14J03967. We also acknowledge support from the Tohoku University Division for International Advanced Research and Education Organization.

REFERENCES

[1] Takeishi, N et al., *Physiol Rep*, 2:e12037, 2014.
[2] Takeishi, N et al., *Phys Rev E*, 92:063011, 2015.
[3] Stott S et al., *Proc Natl Acad Sci USA*, 107:18392, 2010
[4] Harouaka R et al., *J Lab Automat*, 18:455-468, 2013.
[5] Schmid-Schönbein, G et al., *Microvasc Res*, 19:45-70, 1980.
[6] Freund, J., *Phys Fluids*, 19:023301, 2007.
[7] Fedosov, D et al., *Phys Rev Lett*, 108:028104, 2012.
[8] Skalak, R et al., *Biophys J*, 13:245-264, 1973.
[9] Bungay P and Brenner H, *Int J Multiphase Flow*, 1:25-56, 1973.

Copyright 2016 The Organizing Committee for the 2016 Summer Biomechanics, Bioengineering and Biotransport Conference

SB^{3}C2016
Summer Biomechanics, Bioengineering and Biotransport Conference
June 29 –July 2, National Harbor, MD, USA
SB^{3}C2016-743

SEX DIFFERENCES IN THE DYNAMIC BRAIN RESPONSE TO A MILD ANGULAR HEAD ACCELERATION

Deva D. Chan (1), Andy K. Knutsen (2), Yuan-Chiao Lu (1), Sarah Yang (1), Philip V. Bayly (3), John. A. Butman (4), Dzung L. Pham (1)

(1) Center for Neuroscience and Regenerative Medicine
Henry Jackson Foundation
Bethesda, Maryland, United States

(2) Institute for Defense Analyses,
Alexandria, VA, United States

(3) Mechanical Engineering and Materials Science
Washington University at St. Louis
St. Louis, Missouri, United States

(4) Radiology and Imaging Sciences
National Institutes of Health Clinical Center
Bethesda, Maryland, United States

INTRODUCTION

Traumatic brain injury (TBI) is prevalent in both the civilian and military populations [1]. Although it is clear that non-penetrating forms of TBI results from rapid forces or accelerations applied to the head, the factors that contribute to the mid- to long-term repercussions of TBI have yet to be fully elucidated. Recent work has implicated metabolic changes in even sub-concussive events of the brain [2], substantiating the need for further research in the brain's response to various levels of trauma.

Since the mechanics of TBI can not be studied *in vivo* in humans, computational models may lead to improved understanding of this process. However, experimental data of human brain mechanics remain required for model validation. Understanding how brain biomechanics may differ with demographic factors like race, age, and sex also informs the design of appropriate computational models.

Previous work by our group to assess brain biomechanics in living subjects has shown that accelerations of the living brain at sub-injury levels can be measured reliably with tagged magnetic resonance imaging (MRI) [3]. In this study, we acquired tagged MRI data in healthy volunteers to assess whether there is a sex-linked difference in the shear response of the brain to mild angular acceleration.

METHODS

Twenty healthy adult subjects (10 females, 10 males) were consented under an IRB-approved protocol and enrolled in this study. Subjects lay with their heads secured within an MRI-compatible head support [4] and voluntarily released a latch that permitted a head rotation of ~32° about the inferior-superior axis toward the left shoulder, aided by a counterweight and generating a rapid deceleration of the head when it rotates into a padded stop. Multiple repetitions of the motion were required to reconstruct multiple image slices with tag lines in orthogonal directions.

MR images were acquired using a Siemens 3.0T mMR Biograph scanner (Siemens, Munich, Germany) with a tagged image sequence that has been previously validated with this head rotation device [3]. Briefly, a 1-1 SPAMM tagging pulse [5] was followed by a segmented cine gradient echo acquisition at 18.06 ms temporal resolution, 1.5 mm x 1.5 mm spatial resolution, and 8 mm slice thickness. A position-controlled double-trigger system permitted the application of tag lines after the initiation of the head rotation to ensure repeatable synchronization of the image acquisition [3]. Motion between tagged image frames was tracked using harmonic phase (HARP) analysis [6] with the shortest-path HARP refinement algorithm [7]. Displacement vectors were computed between each voxel center in the first image (reference) to their locations in subsequent image frames and permitted the calculation of 2D Lagrangian strains. Maximum shear strain, γ_{max}, was then computed from principal strains.

To compare between subjects, area fraction (AF) was defined as the proportion of voxels of interest in which the shear strain exceeded a specified threshold. Brain tissues were segmented from a 1-mm isotropic MPRAGE anatomical scan using the S3DL technique [8] and registered to the tagged images. AF was computed at γ_{max} thresholds of 1% to 6% in the whole brain, cortical gray matter (CGM), deep gray matter (DGM), and white matter (WM). Differences between male and female groups were tested at each strain cutoff and time point using a Wilcoxon rank sum test at a significance level of 0.05.

RESULTS

One female subject was excluded from analysis due to image artifacts that prevented reliable calculation of strains and AFs. The

Copyright 2016 The Organizing Committee for the 2016 Summer Biomechanics, Bioengineering and Biotransport Conference

remaining female (n = 9) and male (n =10) subjects did not vary significantly in age or estimated brain volume (Table 1).

	Age	Brain	CGM	DGM	WM
	[years]	Estimated tissue volume [cm^3]			
Females (n = 9)	28.44 ± 5.64	1127.5 ± 125.3	537.0 ± 51.2	54.7 ± 5.7	391.5 ± 57.7
Males (n = 10)	28.30 ± 5.36	1175.4 ± 100.6	576.7 ± 43.3	55.7 ± 4.3	418.3 ± 39.3
P =	0.96	0.40	0.10	0.69	0.28

Table 1: Age and brain tissue volumes (mean ± S.D.) did not differ (Student's *t* test) between female and male groups.

AFs were computed for strain cutoffs of 1% to 6% in all subjects for whole brain, CGM, DGM, and WM (Figure 1). AFs peaked at the cine frame acquired at 45 ms, around the time of initial impact. A smaller and longer peak occurred in most subjects after impact, although the amplitude and timing of that peak varied by individual (not shown) and accounted for the increased variation of AFs after the impact. Significant differences in γ_{max} AFs were found in the whole brain and CGM (Figure 2) but not DGM and WM (not shown) after impact. Female AFs were higher than male AFs at each strain cutoff and time point pair for which significant differences were detected.

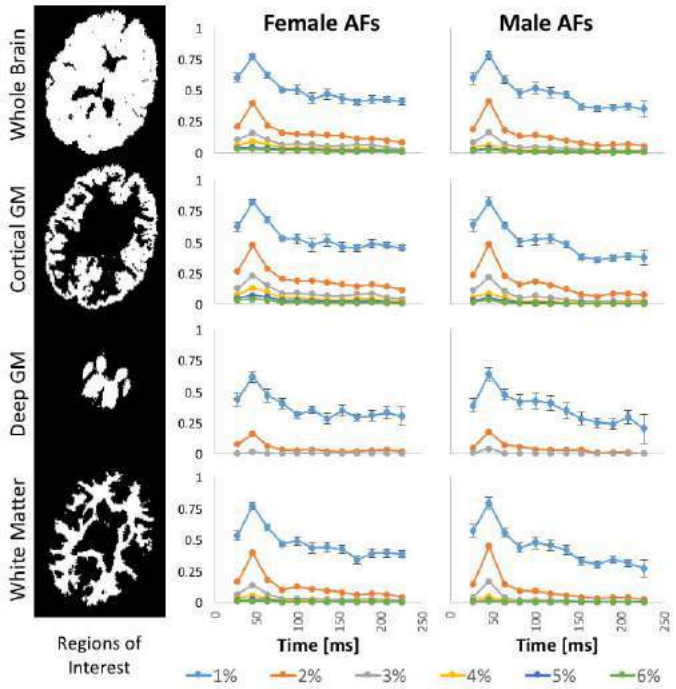

Figure 1: Segmented tissues of interest are shown through a single slice of the brain of a representative female subject. Median AFs are shown for each γ_{max} strain cutoff and time in tissues of interest, except where AFs are ~0 (i.e., DGM at 4%+). SEM is only shown for AFs at 1%, as they are larger than AFs at 2%+.

DISCUSSION

This study showed that shear strains were the highest at the initial impact (~45 ms), and that higher shear strains are more prevalent in the cortical gray matter than white and deep gray matter (Figure 1). However, no statistically significant differences were detected at the times that coincided with the height of the shear strain response. Comparisons at later time points show that there may be sex-linked differences in the shear strain within the cortical gray matter after the initial impact (Figure 2), with AFs at these times consistently greater in females than males. This difference may be the result of the inertial response of the brain after the skull has ceased motion, since sex-specific anatomic differences in overall head mass or size may affect the moment of inertia despite the similar brain size between males and females. These differences in the inertial response, which plays out across a longer time frame after impact, may also reflect sex-related differences in the dissipation of mechanical energy.

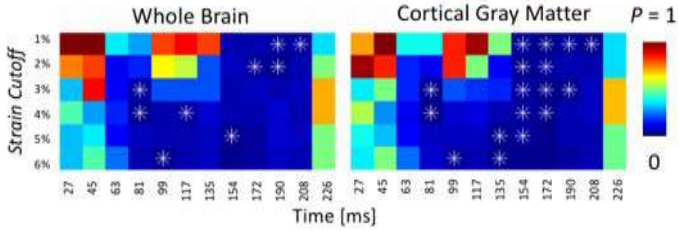

Figure 2: Differences in AFs between female and male groups were compared with a Wilcoxon rank sum test and P values are shown for each γ_{max} strain cutoff and time combination in whole brain and cortical gray matter (✳ $P < 0.05$).

Although this study compares males and females, it does not examine *why* this difference may be associated with sex, nor whether other factors – including subject compliance, age, or hormonal variations – may result in this difference. A major limitation of voluntary and subject-initiated motion is that subject compliance and consistency affect head accelerations, which in turn will influence image acquisitions that require at least 120 head rotations for multiple orthogonal slices through the whole brain. The sensitivity of such imaging measurements is dependent on multiple factors, and work is ongoing to quantify these effects *in vivo*. Future work will also include larger subject pools, allowing for an examination of the effect of age group, and a deeper examination of the various factors that effect the spatiotemporal response of the brain after impact.

Work to identify sex-linked differences in TBI remains unclear, with research showing that males have more severe disruption of the white matter and longer times to symptom resolution than females [9] but that females are more likely to report post-concussive symptoms [10] and show slower recovery of working memory [11]. This study represents a key step towards elucidating differences in brain biomechanics with sex and other demographic markers. Such work will enhance understanding of the factors that lead to brain injury and its costly long term effects and inform computational models of the brain that are applicable to a diverse civilian and military population.

ACKNOWLEDGEMENTS

This work was partially supported by grant NIH NINDS R01 NS055951, the Department of Defense in the Center for Neuroscience and Regenerative Medicine, and NIH Intramural Research Program.

REFERENCES

[1] Meaney, et al., *J Biomech Eng*, 136:021008, 2014.
[2] Poole, et al., *Dev Neuropsychol*, 40:12-17, 2015.
[3] Knutsen, et al., *J Biomech*, 47:3475-3481, 2014.
[4] Sabet, et al., *J Biomech*, 41:307-315, 2008.
[5] Axel & Dougherty, *Radiology*, 171:841-845, 1989.
[6] Osman & Prince, *Phys Med Biol*, 6:1665-1682, 2000.
[7] Liu & Prince, *IEEE Trans Med Imaging*, 29:1560-1572, 2010.
[8] Roy, et al., *IEEE J Biomed Health Inform*, 19:1598-1609, 2015.
[9] Fakhran, et al., *Radiology*, 272: 815-823, 2014.
[10] Brown, et al., *Sports Med*, 45:1027-1040, 2015.
[11] Hsu, et al., *Radiology*, 276:828-835, 2015.

Copyright 2016 The Organizing Committee for the 2016 Summer Biomechanics, Bioengineering and Biotransport Conference

SB³C2016
Summer Biomechanics, Bioengineering and Biotransport Conference
June 29 –July 2, National Harbor, MD, USA
SB³C2016-744

AN ALTERNATIVE METHOD TO CHARACTERIZE THE QUASI-STATIC MATERIAL PROPERTIES OF MURINE ARTICULAR CARTILAGE

Alexander Kotelsky (1), Chandler Woo (1), Mark R. Buckley (1)

(1) Department of Biomedical Engineering
University of Rochester
Rochester, NY, USA

INTRODUCTION

Articular cartilage is a load bearing structure that transmits forces across diarthrodial joints. A key feature of osteoarthritis (OA) – the leading cause of disability in the United States [1] – is cartilage degeneration. In the mouse, OA is easily induced through genetic or surgical means. Thus, murine models provide a valuable, low-cost research platform to study the progression of articular cartilage degeneration in OA. However, alterations in the mechanical properties of murine articular cartilage are challenging to measure due to its small size (thickness ~ 50 microns). A few research groups have quantified the mechanical properties of murine cartilage through nano- and micro-indentation techniques [2, 3]. Though effective, these techniques are somewhat indirect, as they require assumptions regarding the 3D geometry of the tissue and how it deforms due to a prescribed indenter displacement. We propose an alternative, more direct method of measuring the mechanical properties (Young's modulus and Poisson's ratio) of intact murine cartilage through inverse finite element modeling and confocal microscope-based 3D strain mapping of intact specimens subjected to compression.

METHODS

Distal femurs with fully intact cartilage (n=3) from 8-10 weeks-old BALB/c female mice were carefully dissected immediately after sacrifice and stored at -20°C until testing. The cartilage covering the distal femoral condyles was tested mechanically. For every experimental test, the femurs, hydrated in phosphate buffer saline solution, were placed onto the glass slide of a custom microscope-mounted device and loaded with 0.07N on the anterior side (on top of the patellofemoral groove) such that cartilage on the posterior femoral condyles was compressed against a cover glass (Figure 1). The experiments were performed at room temperature.

Characterization of material properties (E, ν) involves multiple experimental and computational methods. These methods and their sequence are as follows: 1) confocal microscope-based mapping of compressive strains in 3D; 2) implementation of inverse finite element analysis (iFEA) based on experimentally measured specimen displacement and strain distribution for calculation of the Poisson's ratio; 3) characterization of the boundary forces exerted on articular cartilage on a single condyle; and 4) implementation of iFEA based on specimen displacement and condylar boundary forces to characterize Young's modulus at equilibrium (E). A schematic diagram of the methods is depicted in Figure 1.

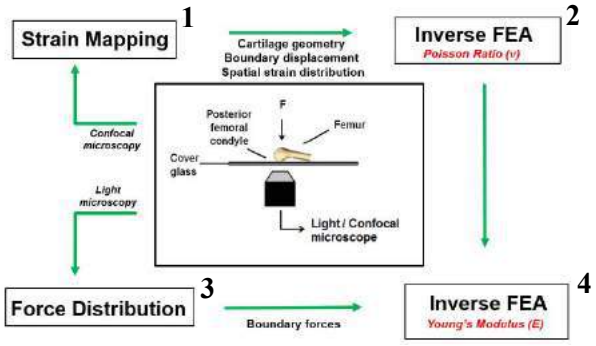

Figure 1. Schematic diagram of the experiments.

1. Strain mapping. Prior to testing, each specimen was fluorescently stained for 1h with 5-DTAF (10 µg/mL) (Sigma-Aldrich, Milwaukee, WI, USA) at room temperature to enable visualization of the extracellular matrix. Two femoral condyles in each of the stained murine cartilage samples were imaged with a 40X dry lens (LUCPLFLN, NA 0.6) on an Olympus FV1000 laser scanning confocal microscope (Olympus America, Center Valley, PA). 3D

Copyright 2016 The Organizing Committee for the 2016 Summer Biomechanics, Bioengineering and Biotransport Conference

image stacks were taken before compression and after the cartilage reached its post-compression equilibrium (i.e., 5 minutes after compression) (Figure 2 a-b). From the acquired image sets, spatially-varying compressive strain E_{33} (where E is the Green-Lagrange strain tensor) was quantified using custom MATLAB software (The MathWorks Inc., Natick, Massachusetts, USA) (Figure 2c).

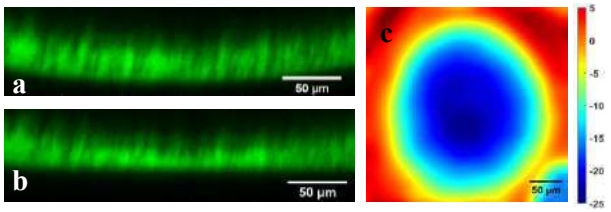

Figure 2. Representative confocal micrographs of murine articular cartilage in sagittal view (a) before and (b) after specimen compression; and (c) resultant compressive strain (E_{33}) map.

2. iFEA to determine Poisson's ratio. A 3D finite element model (FEM) of murine cartilage on a distal femoral condyle was created using FEBio software [4] (Figure 3a). The cartilage on a femoral condyle was approximated as an ideal hemispherical shell with outer radius of 826.5 ± 63.1 μm and a thickness of 45.9 ± 4.9 μm. The radius and thickness of each specific model was based on the 3D confocal micrograph used for step 1 (Figure 2a). The top surface (cartilage-bone interface) was constrained to be stationary, and a rigid wall contact was applied at the bottom surface and translated in the vertical direction with a prescribed displacement corresponding to the displacement measured in the strain mapping experiment. Although articular cartilage is a poroelastic/biphasic material, the cartilage was taken to be a neo-Hookean hyperelastic material, simulating the mechanical response of articular cartilage at equilibrium.

A FEM-based sensitivity study simulating the effect of Poisson's ratio ranging from 0 to 0.49 in increments of 0.025 on spatially-varying strain distribution was performed. Importantly, no effect on strain distribution was found for Young's moduli ranging from 1 to 14 MPa (data not shown). A Poisson's ratio was determined by matching spatially averaged strains in 4 regions along the radial direction between experiments and FE simulations (Figure 3b-e). The radial direction of a strain pattern was defined to originate from the maximum compressive strain observed. The Poisson's ratio was found by minimizing the root of sum of squared error (SSE) between compressive strains (E_{33}) obtained from the strain map experiment and FE simulations.

3. Measurement of boundary forces. Applying a force to the anterior side of the femur (Figure 1) produces three specimen-glass contact points: one cartilage contact on each distal femoral condyle and one bone-glass contact on the proximal end of a femur. Therefore, it is important to analyze the distribution of loading between two femoral condyles as a result of applied load of 0.07N on top of the patellofemoral groove of a specimen. The calculation of loading distribution on articular cartilage was performed by implementing principles of static mechanics. The approach includes identification of contact force locations on intact specimens through microscopic imaging and implementation of equilibrium moment balance in order to calculate the force distribution between femoral condyles.

4. Inverse finite element analysis to determine Young's modulus. The models from step 2 with pre-determined Poisson's ratios were used to estimate the Young's modulus of articular cartilage. An iterative optimization algorithm implemented in FEBio [4] was used to match boundary forces, which were determined from step 3.

Compressive stresses were obtained from forward FEA with pre-determined Poisson's ratio and Young's modulus from steps 2 and 4.

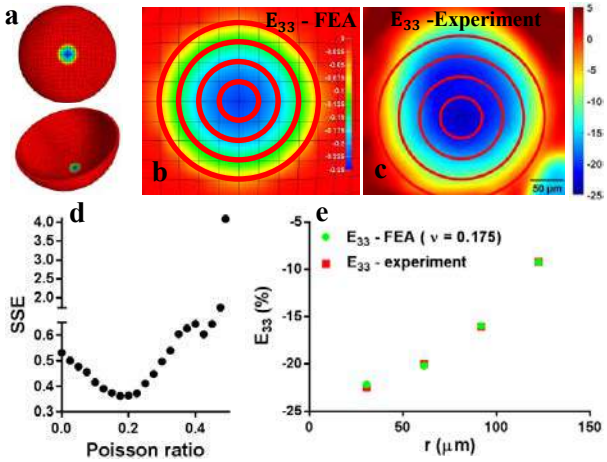

Figure 3. Representative (a,b) FEA of cartilage on murine femoral condyle, (c) strain map from step 1 with defined 4 regions, (d) SSE and (e) E_{33} comparison between FEM and experimental data.

RESULTS

Reaction forces (F), compressive strains (E_{33}), material properties (E, ν) and compressive stresses (σ) were calculated for the medial and lateral femoral condyles of all tested specimens using the methods described above. The mean Young's modulus across all medial and lateral specimens was 2.07 MPa, and the mean Poisson's ratio was 0.26.

Table 1: Parameters for murine cartilage on medial and lateral femoral condyles (mean ± standard deviation)

	F (mN)	E_{33} (%)	ν	E (MPa)	σ (MPa)
Medial	23.5 ± 1.5	-25.8 ± 2.3	0.28 ± 0.15	1.53 ± 0.94	-0.75 ± 0.08
Lateral	33.5 ± 3	-22.3 ± 1.1	0.24 ± 0.21	2.61 ± 1.16	-1.02 ± 0.11

DISCUSSION

In this study we developed an alternative method to quantify the material properties of murine articular cartilage at equilibrium. The method provides direct measurements of tissue deformation, and material properties are determined separately based on distinct measurement (strain distribution for Poisson's ratio and boundary force for Young's modulus). Mechanical properties found in this study are consistent with the values reported in the literature [2]. The applied compressive strains and stresses were below injurious levels [5, 6], such that material properties of articular cartilage were found without damaging the extracellular matrix during mechanical testing.

One limitation of the proposed study is that nonlinear material properties and biphasic material properties (e.g., hydraulic permeability) responsible for the transient deformation of articular cartilage were not assessed. Future studies will expand the proposed method to incorporate measurements of these parameters, and will apply this method to the assessment of material properties of murine cartilage at different stages of experimentally-induced OA.

ACKNOWLEDGEMENTS

The authors would like to acknowledge URSMD Confocal and Conventional Microscopy Core.

REFERENCES

[1] Murphy, L. et al., *Arthritis Rheum*, 59:1207-13, 2008. [2] Cao, L. et al, *J Biomech Eng*, 128:766-71, 2006. [3] Han, L. et al., *Annu Rev Mater Res*, 41:133-68, 2011. [4] Maas, S et al., *J Biomech Eng*, 134:1-10, 2012. [5] Wan, L et al., *J Orthop Res*, 1081-89, 2008. [6] Brand, R et al., *Hip Intl*, 11(3):117-26, 2001.

Copyright 2016 The Organizing Committee for the 2016 Summer Biomechanics, Bioengineering and Biotransport Conference

SB^{3}C2016
Summer Biomechanics, Bioengineering and Biotransport Conference
June 29 –July 2, National Harbor, MD, USA
SB^{3}C2016-745

NANOSECOND PROTEIN THERMAL INACTIVATION BY PLASMONIC NANOPARTICLE LASER HEATING

Peiyuan Kang (1), Zhenpeng Qin (1,2)

(1) Department of Mechanical Engineering
University of Texas at Dallas
Richardson, TX, USA

(2) Department of Bioengineering
University of Texas at Dallas
Richardson, TX, USA

INTRODUCTION

Plasmonic gold nanoparticles (GNP) have received broad interest in biomedical applications due to their unique optical and thermal properties [1]. Specifically, GNP can be designed to strongly absorb or scatter optical energy at different wavelengths of interest. The laser energy absorption can lead to significant temperature changes on the nanoparticle as well as the surrounding biological environment. Among the molecular components in the biological system, proteins are extremely thermally sensitive and play a critical rule in performing biological functions. The thermal effect on proteins are well understood in low temperatures (below 100˚C) and longer time scale (seconds to minutes) and the rate of protein thermal inactivation or denaturation is highly dependent on temperature. Several emerging applications (such as photoacoustics, nanophotothermolysis) involve laser heating of GNPs with ultra-short laser pulses (nanosecond to femtosecond) and the resulting temperature adjacent to GNP can be well above 100˚C without vaporization, for example up to 140 K overheating has been observed [2]. Although molecular dynamic simulations [3] and preliminary experiments [4] have shown protein inactivation, systematic investigation of the fate of proteins adjacent to GNPs under nanosecond laser heating is lacking.

In this research, we investigated on the effect of GNP heating on adjacent proteins in the nanosecond scale. Specifically, we experimentally measure protein inactivation as function of laser pulse energy, pulse number, and distance between the protein and GNP. Our research suggests a novel method to target and selective inactivate proteins of interest for biomedical applications.

METHODS

Protein conjugation to GNP: Protein inactivation was studied experimentally by conjugating an enzyme (α-chymotrypsin or α-CT) to 15nm GNP with a polyethylene glycol (PEG) spacer. Specifically, heterobifunctional PEG (Thiol-PEG-COOH with molecular weights 400, 600, 1000 and 3400Da) was first conjugated to GNP. Then we modified the carboxylic group by EDC and sulfo-NHS to replace the carboxylic group with sulfo-NHS ester intermediate which can react with amine groups in protein [5]. The reacted complex was then cleaned by centrifugation.

Protein inactivation by nanosecond laser: The prepared GNP-protein complex was then irradiated by an Nd:YAG nanosecond pulsed laser at 532nm (Quantel USA, 6 ns, beam diameter D = 9 mm), shown schematically in Figure 1A. The laser pulse energy is varied from 0 to 200mJ and the pulse number is from 1 to 20. The laser beam diameter is 9 mm. 40 μL sample was loaded in the cuvette and tested each time. The optical density (OD) of the sample was adjusted to be less than 0.1 in order to make sure that the sample was exposed to a uniform laser intensity.

Protein activity measurement: The protein inactivation was measured by a colorimetric enzyme assay. Specifically, α-chymotrypsin (α-CT) is a protein of molecular weight 24800 [6], and the a-chymotrypsin-catalyzed substrate hydrolysis is well known process. We used N-succinyl-L-alanyl-L-alanyl-L-prolyl-L-phenylalanine-4nitroanilide (Suc-Ala-Ala-Pro-Phe-pNA, Sigma-Aldrich) as the substrate, due to the high affinity (i.e. low K_m value) and high reactivity (i.e. high k_{cat}) [7-8]. The hydrolysis of Suc-Ala-Ala-Pro-Phe-pNA leads to a color change which can be monitored by the absorption value at 410nm (Figure 1 B&C). The enzymatic activity of α-CT was determined by measuring the rate of hydrolysis of the substrate Suc-Ala-Ala-Pro-Phe-pNA [9].

Copyright 2016 The Organizing Committee for the 2016 Summer Biomechanics, Bioengineering and Biotransport Conference

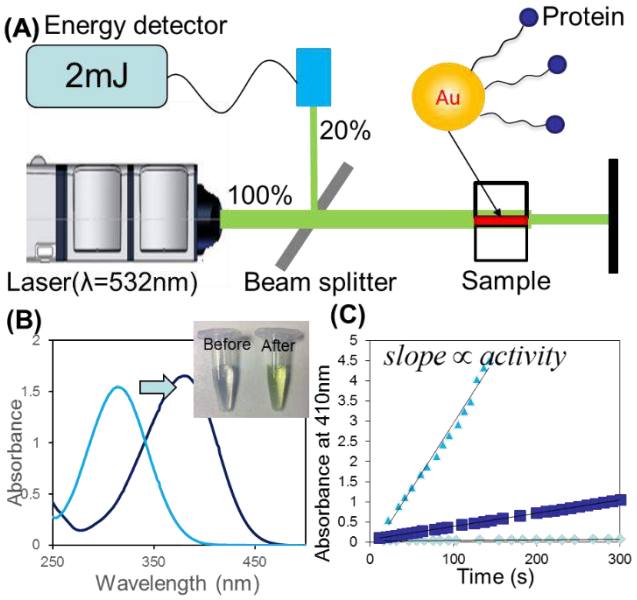

Figure 1: Schematic of experimental setup (A) and protein activity measurement using a colorimetric enzyme assay (B – C). B inset shows the color change after adding substrate to the enzyme.

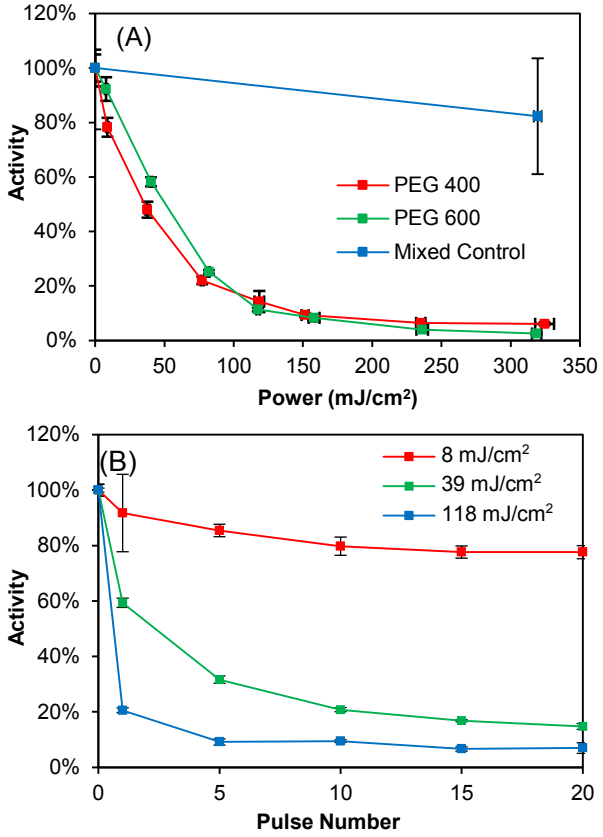

Figure 2: Preliminary experimental results of nanosecond protein inactivation. (a) Protein activity as a function of laser pulse energy (pulse width = 6 ns) for conjugated (PEG400 and 600) and free protein (Mixed control). PEG 400 refers to a 400 Da PEG spacer, mixed control refers to mixing PEG-coated GNP with α-CT directly without conjugation. (b) Effect of pulse number for PEG 600 sample.

RESULT

The experiment results are shown in Figure 2. The protein inactivation is dependent on laser pulse energy and complete inactivation (> 90%) is possible under one laser pulse with beam width of 6 ns (Figure 2A). Higher pulse energy leads to more reduction in protein activity. When pulse energy is higher than 116 mJ/cm^2, one pulse leads to more than 80% inactivation of α-CT. When the protein is not attached to the protein, shown as mixed control in Figure 2A, no obvious inactivation was observed, suggesting a highly selective and localized effect.

Further investigation is needed to determine the spatial extent of the protein inactivation. Preliminary results comparing PEG 400 and PEG 600 activity shows slight difference at low laser pulse energies, with PEG400 leading to more reduction in protein activity (Figure 2A). PEG spacers with higher molecular weight lead to longer distance between α-CT and GNP. As a result, the heating of protein is less intensive with longer PEG spacers.

The protein inactivation is strongly dependent on pulse number, shown in Figure 2B. The activity decreases dramatically in first five pulses and does not change significantly when further increasing the pulse number. After 5 laser pulses, the final activity is only strongly dependent on the laser pulse energy.

DISCUSSION

In summary, this study proves the selective protein inactivation adjacent to gold nanoparticles during nanosecond pulsed laser heating and establishes an experimental approach to investigate and understand this important phenomenon. The protein inactivation can be further controlled in the nanometer scale by laser energy, nanoparticle size, distance between protein and nanoparticle, and thermal interface resistance. Importantly, our study suggests a novel protein inactivation method with broad biomedical applications, such as investigating and designing novel nano-surgical tools to target and selectively inactive proteins of interest in living systems.

ACKNOWLEDGEMENTS ZQ would like to thank Qi Shao (University of Minnesota) and Dr. Stephen Leven (University of Texas at Dallas) for helpful discussions.

REFERENCES

[1] Kelly, K.L. et al. J. Phys. Chem. B. 107:3, 668-677, 2003
[2] Siems, A. et al. New J. Physics. 13, 043018, 2011
[3] Yan C. et al. J. Mol. Graph. Model. 29, 2012, 2010
[4] Huttmann G. et al. Proc. SPIE, 5142, 2003
[5] Hermanson G.T., Bioconjugate Techniques, Third Edition. *Elsevier* 263-265
[6]Myron L, B et al., *Journal of Chemical Education* 44:2 84-88, 1967.
[7] Bru P. et al. Eur. J. Biochem. 199, 95-103, 1991.
[8] DelMar, E. G. et al, *Anal. Biochem.* 99, 316-320. 1979
[9] Rodríguez-Martínez, J.A. et al. *Biotechnol Lett*., 31:6: 883–887 2009.

Copyright 2016 The Organizing Committee for the 2016 Summer Biomechanics, Bioengineering and Biotransport Conference

SB^{3}C2016
Summer Biomechanics, Bioengineering and Biotransport Conference
June 29 –July 2, National Harbor, MD, USA
SB^{3}C2016-746

TREATMENT OF THORACOLUMBAR BURST FRACTURE: A BIOMECHANICAL ANALYSIS OF THREE DIFFERENT FIXATION CONSTRUCTS

S. Elmasry (1), S. Asfour (1), J. Gjolaj (2), L. Latta (2,3), F. Eismont (2), F. Travascio (1)

(1) Department of Industrial Engineering
University of Miami
Coral Gables, FL, USA

(2) Department of Orthopaedic Surgery
University of Miami
Miami, FL, USA

(3) Max Biedermann Institute
Mount Sinai Medical Center
Miami Beach, FL, USA

INTRODUCTION

Thoracolumbar fractures represent approximately 90% of fractures found at spine, and nearly 20% of such injuries are burst fractures [1]. Surgical correction with corpectomy and subsequent fusion of neighboring levels is a well-known treatment, which can be performed with different fixation techniques. The objective of fixation is to correct angular deformity, stabilize fracture, decompress neural elements, and restore vertebral body height [2]. The stiffness of the construct plays a key role in the success of achieving these goals by re-stabilizing the anterior and middle spinal column. Accordingly, several biomechanical studies have been performed to analyze the stiffness of the different fixation constructs at the thoracolumbar junctions [2, 3].

There are many procedures for burst fracture treatment, and they generally involve corpectomy, which consisted in the dissection of the affected vertebral body and the adjacent intervertebral discs (IVDs). Often, an expandable cage is placed between the superior and inferior vertebral bodies to stabilize the anterior column of the spine. However, expandable cages alone are not enough to fuse the junction. In some cases, pedicle screws and rods are implanted through posterior approach to increase the stiffness of the fusion [4, 5]. Alternatively, aiming to achieve less invasive type of procedure, a lateral (transverse) plate can be used as a hardware component to fix the segment through a posterolateral approach [6]. Whether one family of procedures is better than the other is yet to be determined.

In order to try to answer this question, we deployed a computational model for spine biomechanics to simulate the biomechanical behavior operated segments (T12-L2) under physiologically relevant mechanical loads. More specifically, we investigated the biomechanics of three different constructs using (1) pedicle screws and rods, (2) transversal plate, and (3) a hybrid construct including both screws and plate. The different constructs were compared in terms of their stiffness, which is considered a quantitative metric to measure the quality of a fixation construct.

METHODS

A 3D nonlinear finite element model of the thoracolumbar junction (T12-L2) was constructed from CT scan of a healthy male subject (Visible Human Project®) via commercially available image processing software (Mimics; Materialise, Louvain, Belgium). The model included the cortical and cancellous bones of T12 and L2, the posterior element of L1, facet joints, and the major spine ligaments except the anterior and posterior longitudinal ligaments. All material properties were taken from the literature [7, 8], and a gap of 0.4 mm was specified between cartilage layers with a sliding interface between the superior and inferior cartilage [9].

To obtain the constructs, complete corpectomy was performed at L1 level by removing L1 vertebral body and the adjacent IVDs. A total of three different fusion constructs at the thoracolumbar junction were investigated: (1) expandable cage with a transverse plate and one posterior pedicle screw (1RPC), (2) expandable cage with two posterior pedicle screws (2RC), and (3) expandable cage with transverse plate (PC), see Figure 1. All the hardware material was assumed to be of titanium with 110 GPa elastic modulus and 0.3 poisson's ratio [10]. Sliding interfaces were defined between the expandable cage and the surfaces of the vertebral bodies of T12 and L2, with friction coefficient of 0.8 to prevent the cage from slipping [11]. The pedicle screws were placed posteriorly and connected with

Copyright 2016 The Organizing Committee for the 2016 Summer Biomechanics, Bioengineering and Biotransport Conference

posterior rods by a tied contact. The transverse plate was connected via four lateral screws to T12 and L2 vertebral bodies, and a sliding contact with 0.1 friction coefficients was assumed between plate and vertebrae [12]. Four-node solid elements were used to discretize the model, and non-commercial software FEBio (FEBio 2.2.0, Musculoskeletal Research Laboratory, University of Utah, Salt Lake City, UT) was employed to solve the FE model.

For all the constructs, bending moments of 5 Nm were applied at T12 on the three major anatomical planes, to obtain loading conditions of Flexion-Extension, Lateral Bending, and Axial Rotation. The base of L2 was fixed. The stiffness (Nm/deg) for each loading condition was measured by dividing the applied moment by the amount of rotation of T12 relative to L2. Also, for each loading condition, we measured the coupled motion (i.e., rotation in the anatomical planes where the moment is not applied).

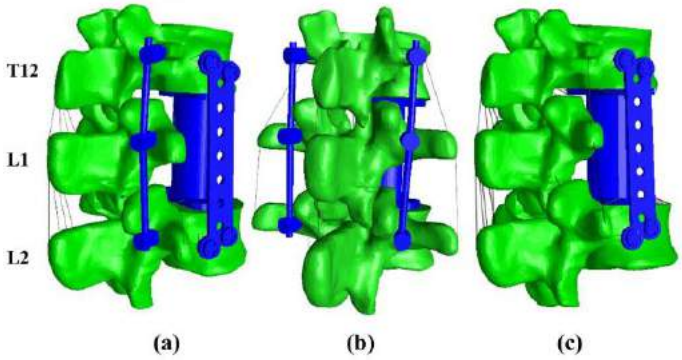

Figure 1: Thoracolumbar spine FE model with performed corpectomy at L1: (a) 1RPC construct, (b) 2RC construct, (c) PC construct

RESULTS

Stiffness values are reported in Figure 2. It is shown that the 1RPC construct was the stiffest, while the PC construct was the most compliant for all loading conditions. The only exception was for the case of left lateral bending, where the PC construct yielded higher stiffness than 2RC. Moreover, for all the constructs, the largest values of stiffness were attained during left lateral bending. In contrast, the lowest values were found during axial rotation. Table 1 shows the coupled motion for all the constructs. For almost all the cases investigated, the PC construct produced a coupled motion nearly one order of magnitude larger than that found in the other constructs. Also, 1RPC almost always generated the lowest coupled motion.

Table 1: Coupled motion during the six loading conditions for all constructs in degrees. Table abbreviations: Lateral Bending (LB); Flexion-Extension (FE); Axial Rotation (AR)

	Flexion		Extension		Right Lat. Bend.	
	LB	AR	LB	AR	FE	AR
1RPC	0.0868	0.0189	0.039	0.0387	0.1082	0.006
2RC	0.0127	0.015	0.0239	0.0167	0.124	0.0623
PC	0.598	0.278	0.19	0.086	0.484	0.045
	Left Lat. Bend.		Right Axial Rot		Left Axial Rot	
	FE	AR	FE	LB	FE	LB
1RPC	0.058	0.038	0.02	0.1	0.052	0.037
2RC	0.114	0.069	0.142	0.071	0.172	0.0793
PC	0.001	0.0251	0.096	0.208	0.062	0.721

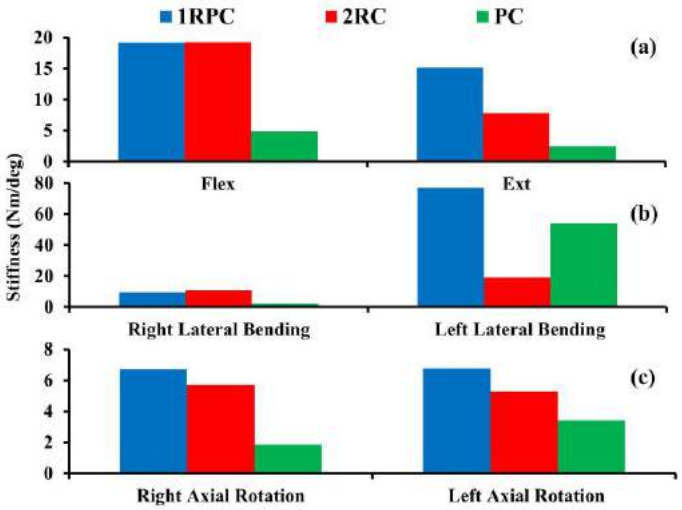

Figure 2: Stiffness of the three constructs for all the loading conditions: (a) Flexion-Extension, (b) Lateral Bending, (c) Axial rotation.

DISCUSSION

Several studies reported high failure rates of fusion techniques applied to treat burst fracture at the thoracolumbar junction due to poor anterior column support, and insufficient points of fixation [10, 11]. Hence, the choice of the fixation hardware is crucial to guarantee the success of such surgeries. In this study, three different short segment constructs were biomechanically compared to investigate their stiffness under different loading conditions. The results show that using pedicle screws increase the stiffness during flexion-extension moments when compared to lateral plate only, see Figure 2a. However, during left lateral bending, the main load was supported by the transverse plate. Accordingly, 1RPC and PC produced higher stiffness than 2RC. Consequently, the stiffness of 1RPC and PC reduced significantly at the right lateral bending, due to the lack of a transverse plate, see Figure 2b. These findings emphasize the non-symmetric behavior of the transverse plate in stiffening the junction when loaded in the coronal plane. These results were corroborated by the higher coupled motion for the PC construct in all loading condition, except for the case of left lateral bending. In conclusion, the results of this analysis suggest that pedicle screws are very important in supporting the spine during flexion, extension and axial rotation, and also suggest not using the transverse plate alone.

ACKNOWLEDGEMENTS

Study supported by funds donated to the Biomechanics Research Group of the University of Miami.

REFERENCES

[1] Dai et al., *Surgical neurology,* 67: 221-231, 2007.
[2] Been & Bouma, *Acta Neurochirurgica,* 141: 349-357, 1999.
[3] Scheer et al., *Global spine journal,* 5: 73, 2015.
[4] Mahar et al., *Spine*, 32: 1503-1507, 2007.
[5] Norton et al., *The Spine Journal*, 14: 1734-1739, 2014.
[6] Kim et al., *Spine*, 2: 62-68, 2005.
[7] Pintar et al., *Journal of biomechanics*, 25: 1351-1356, 1992.
[8] Cowin, *Bone mechanics handbook*, 2001.
[9] Schmidt et al., *European Spine Journal,* 21: 663-674, 2012.
[10] Kim, *Spine*, 32: 2558-2568, 2007.
[11] Polikeit et al., *European Spine Journal*, 12: 413-420, 2003.
[12] Park et al., *Journal of Orthopaedic Science,* 14: 443-449, 2009.

Copyright 2016 The Organizing Committee for the 2016 Summer Biomechanics, Bioengineering and Biotransport Conference

SB³C2016
Summer Biomechanics, Bioengineering and Biotransport Conference
June 29 –July 2, National Harbor, MD, USA
SB³C2016-747

IN-SITU HEAD ACCELERATION MEASUREMENTS FOR PLAYGROUND IMPACTS RELATIVE TO HEAD INJURY METRICS

Eric A. Kennedy, Greg P. Danchik, Chris D. DiDomenico

Department of Biomedical Engineering
Bucknell University
Lewisburg, PA, USA

INTRODUCTION

Recent scientific efforts to better understand the risk of traumatic brain injury (TBI) – particularly as a result of head impact in sports and play [1, 2] – have led to increased societal awareness, changes in gameplay and practice rules, and new initiatives in the evaluation of helmets. Additionally, campaigns such as the federal government's "Let's Move" initiative encourage a rediscovery of physical activity, particularly for children. While the benefit of an active lifestyle is hardly disputed, the need for injury prevention strategies does increase.

Playground injuries account for 200,000 emergency room visits every year [3]. Approximately 70% of these injuries come from falls onto the surface [4], with the vast majority of injuries (75%) occurring on public playgrounds [5]. Of those emergency room visits, approximately 30% of those injuries were to the head and neck area [6]. This is critical as a childhood head injury can have a lasting impact throughout life. Head injuries have a variety of side effects; some of the most common side effects are headaches and behavioral changes [7, 8, 9] but head injuries have also been linked with educational lag and psycho-social challenges from one year after the injury to even two decades later in life [10, 11].

Little research exists regarding in-situ surface data and assessment of the variability of surface performance in different locations on the playground (swings, slides, etc.). The research that does exist supports that in-situ surface erosion caused by foot traffic and other factors, as well as the location within the playground, play a significant role in head injury potential [12]. It is evident that the locations within the playground that have the most amount of surface erosion pose the highest risk in general, but this risk is not yet quantified.

With that context, the purpose of this study was to perform on-site (in-situ) evaluation of playground surfacing – particularly high-maintenance surfaces, such as wood-chip mulch – to evaluate the impact attenuation characteristics between maintenance cycles. Additionally, in-situ results are compared to established limits for head injury, such as automotive head injury metrics and limits utilized by US federal regulations and the Insurance Institute for Highway Safety (IIHS).

METHODS

To assess various playground surfaces, a Playground Impactor Missile (PIM) and test protocol was developed in conformance with standard ASTM F1292-13 [13]. The PIM was instrumented with three accelerometers in a triaxial configuration located at the missile's center of gravity. The testing height from the bottom of the PIM to the playground surface for the tests was 1.50 ± 0.08 meters. Four playgrounds, municipal and private, with various ground covers (mulch, grass, unitary surface) served as the test sites. The locations that were assessed included the surface under the swings, slides, monkey bars, and on several low traffic areas (open, non-specific locations) with the appearance of high quality ground cover. The PIM was then dropped three times at each location. Thickness of the ground cover was determined by measuring the depth of the wood chips to the geotextile fabric beneath the surface after three tests were conducted at each location.

Head injury risk assessment was performed by calculating the Head Injury Criteria (HIC_{15}) for each test location and categorizing the risk level for an Abbreviated Injury Scale (AIS) level 2 ("moderate") head injury. AIS 2 was the head injury risk level chosen because the injuries classified as AIS 2 head injuries are most closely related to mild traumatic brain injury events, such as concussion. Similarly, the AIS 2 risk curve is also closely related to other biomechanical risk estimates for concussive injuries [14].

The risk levels were based on the severity of head injury risk and were divided into six different levels: *Risk Level 1* (<10% of AIS 2 head

Copyright 2016 The Organizing Committee for the 2016 Summer Biomechanics, Bioengineering and Biotransport Conference

Table 1: The average HIC_{15} scores, with associated AIS 2 head injury risk, and head accelerations for each surface type and depth.

Surface	Average HIC_{15}	Avg. Peak Accel. (g)	AIS 2 Injury Risk
Bare Soil	1612 ± 563	261 ± 59	99% (92% - 100%)
2.5 cm Mulch	679 ± 94	135 ± 13	62% (50% - 73%)
7.5 cm Mulch	346 ± 62	87 ± 10	20% (14% - 27%)
10.0 cm Mulch	283 ± 34	73 ± 5	14% (11% - 17%)
12.5 cm Mulch	236 ± 30	66 ± 5	10% (8% - 12%)
15.0 cm Mulch	178 ± 58	53 ± 12	6% (3% - 10%)
Grass	1238 ± 336	197 ± 34	97% (84% - 99%)
Unitrary Surface	567 ± 72	113 ± 12	47% (38% - 57%)

injury), *Risk Level 2* (10%-20%), *Risk Level 3* (20%-30%), *Risk Level 4* (30%-40%), *Risk Level 5* (40%-89%), and a *Critical Limit* risk level (89+%), which is the current threshold limit established by the ASTM (HIC_{15}<1000). Due to the non-linear relationship between HIC_{15} and predicted injury risk, the risk level divisions were determined by percentage of head injury risk rather than the calculated HIC_{15} value. The 40% risk threshold was chosen to serve as a cutoff for acceptable surfaces (*Risk Level 4* or below) versus poor performing or incompliant surfaces (*Risk Level 5* – *Critical Limit*). The *Critical Limit* was identified in accordance to ASTM's standard for impact attenuation on playground surfaces; if the HIC_{15} score exceeds 1000, the test exceeds the ASTM's critical limit [13].

RESULTS

The tests were performed at four different test sites, i.e. different playgrounds. The test locations (41) were selected from high and low traffic areas and were found to have surface types of 15 cm of mulch (10 locations), 12.5 cm (2 locations), 10 cm (3 locations), 7.5 cm (3 locations), 2.5 cm (1 location), grass (13 locations), unitary surface (5 locations) and bare soil (4 locations). The three HIC_{15} scores and g-max scores at each location were averaged together to determine the average HIC_{15} and g-max at each location (Table 1). The average HIC_{15} scores ranged from 178 with 15 cm of mulch and 1612 at bare soil, while average peak accelerations ranged from 53-261 g. The HIC_{15} scores were also plotted along the AIS 2 injury risk curve (Figure 1).

DISCUSSION

ASTM standard F1292-13 is the preeminent standard for impact attenuation on playgrounds. This study followed this standard with surface preparation, data analysis, and the identification of the critical limit (HIC_{15}<1000 and g-max<200). In ASTM F1292-13, the height at which the critical limit is reached is defined as the critical height. The critical height is then compared to the fall height of the equipment as determined by ASTM F1487-07 and is generally defined as the highest point at which a child could fall off that piece of equipment [16]. While determination of the critical height was not the focus of this study, the ASTM critical limit was exceeded on two surface types: bare soil and grass – both located directly underneath swings, one of the highest risk pieces of playground equipment. Based on current ASTM F1292-13 limits, all other surfaces remained below the ASTM critical limit (from a drop height of 1.5 m).

This study found that areas with decreased surface quality had a decrease in impact attenuation and an increase in head injury risk, which is consistent with other studies that have shown head injuries to occur most frequently around high-use playground equipment [4, 5, 12]. This

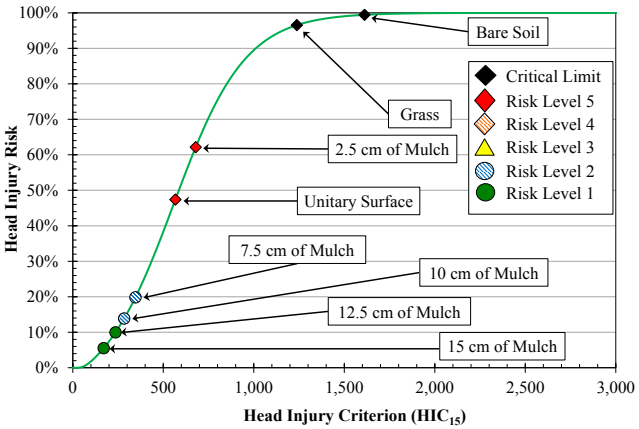

Figure 1: The average HIC_{15} scores of each surface depth and type are plotted on the AIS 2 head injury risk curve.

underscores the importance of regular maintenance, and the data particularly shows the benefits of strict adherence to a minimal mulch depth (7.5 cm or greater) as a potential maintenance guideline for loose fill surfaces.

It is interesting to note that the ASTM limit of HIC_{15}<1000 allows for a tolerable head injury risk (AIS 2) of <89%, while contemporary automotive crash test standards have evolved to lower injury metrics, with a HIC_{15} limit of 700 (<65%) for US crash test regulations [15] and HIC_{15} thresholds of 840 (<79%) for *Marginal-Poor*, 700 (<65%) for *Acceptable-Marginal*, and 560 (<46%) for *Good-Acceptable* performance classifications within the IIHS testing protocols [17]. While the ground covers were found to be compliant with current playground standards (outside of bare soil and grass), several passing surfaces would otherwise approach head impact performance thresholds for automotive safety testing. Due to the high observed risk of AIS 2 head injury and associated potential long-term consequences, it is suggested that current playground standards should be revisited in relation to standards in other industries, such as the automobile industry.

ACKNOWLEDGEMENTS

The authors wish to thank the Bucknell University Program for Undergraduate Research for its support of this program.

REFERENCES

[1] Daniel R (2012) Ann Biomed Eng 40: 976-981
[2] Rowson S (2011) Ann Biomed Eng 39: 2130-2140
[3] Phelan KJ (2001) Ambul Pediatr 1:227-233
[4] National Program for Playground Safety (2013) Fall Surfacing
[5] CDC (2009) Playground Injuries
[6] Loder R (2008) J of Pediatr Surg 43: 691-699
[7] Hamilton NA (2010) Semin Pediatr Surg 19: 271-278
[8] Savola O (2003) Eur J Neurol 10: 175-181
[9] Eisenberg MA (2014) Pediatrics 133: 999-1006
[10] Klonoff H (1993) J Neurol Neurosurg Psychiatr 56: 410-415
[11] Daneshvar DH (2011) Phys Med Rehabil Clin N Am 22: 683-700
[12] Sherker S (2005) Int J Inj Contr Saf Promot 12: 63-66
[13] ASTM F1292 (2013)
[14] Funk JR (2007) 51st Annual Proceedings of 13M. 343-361
[15] Eppinger RH (2000) Supplement: Dev. Improved Injury Criteria
[16] ASTM F1487 (2007)
[17] IIHS (2014) Mod. Overlap Frontal Crashworthiness Evaluation

Copyright 2016 The Organizing Committee for the 2016 Summer Biomechanics, Bioengineering and Biotransport Conference

SB^{3}C2016
Summer Biomechanics, Bioengineering and Biotransport Conference
June 29 –July 2, National Harbor, MD, USA
SB^{3}C2016-748

MODELING AND SENSITIVITY ANALYSIS OF THE WIAMAN ATD HEAD AND NECK: A FINITE ELEMENT STUDY

Matthew L. Davis (1), Jeremy M. Schap (1), Michael P. Boyle (2), Robert S. Armiger (2), Mostafiz Chowdhury (3), F. Scott Gayzik (1)

(1) Wake Forest University School of Medicine
Winston-Salem, NC, USA

(2) Johns Hopkins Applied Physics Laboratory
Laurel, MD, USA

(3) U.S. Army Research Laboratory
WIAMan Engineering Office
Aberdeen Proving Ground, MD, USA

INTRODUCTION

Under body blast (UBB) events in theater are frequently the cause of injuries sustained by the modern warfighter. According to Owens et al., explosion-related injuries have increased from 7% to 81% from World War I to recent conflicts [1]. The U.S. Army Warrior Injury Assessment Manikin (WIAMan) program is seeking to mitigate injuries from UBB events through the development of a soldier-representative, biomechanically-validated anthropomorphic test device (ATD). The WIAMan ATD will be used to enhance human risk assessment in the UBB environment (e.g. live-fire test and evaluation) and to improve safety mitigation technology. This effort includes the development of a computational model of the pre-generation 1 design of the WIAMan ATD. The current study focuses on the head and neck of the computational model. The objective of this study is to use the model of the WIAMan head and neck to predict its response in two UBB-related simulations and to analyze geometrical sensitivity in this regime. This study leverages the strength of finite element models (FEMs) as a predictive tool to better inform the development of the physical ATD.

METHODS

The geometries used for this study were based on computer aided designs of the pre-generation 1 WIAMan head-form and neck. The molded head flesh and skull were tetrahedrally meshed and were modeled as Shore 55A PVC and Shore 75D polyurethane respectively. The molded neck was hexahedrally meshed and modeled as a Shore 75A rubber. Physical instrumentation and connection plates included in the designs of the pre-generation 1 ATD were also meshed and included in the model. The assembled head-form and neck can be seen in Figure 1.

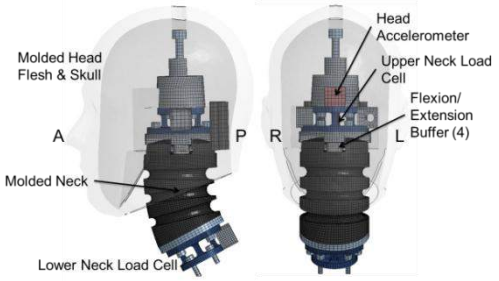

Figure 1. WIAMan Pre-Gen 1 ATD head and neck design.

For this study, two experimental loading conditions were simulated with the FEM. The first was based on a controlled vertical compression of the neck (MTS experiments performed by Bass et al. Duke University, Figure 2a). The second scenario simulated was based on a vertical acceleration of the head and neck components together (experiments performed by Pintar and Yoganandan et al., Medical College of Wisconsin, Figure 2b). In this simulation, the full head-neck was accelerated vertically towards a barrier representing a simplified vehicle roof. As in the experiments, the head of the model was also outfitted with a helmet. Each simulation was run at various speeds and all simulations were run using MPP LS-Dyna (v. 6.1.1, LSTC, Livermore, CA). Filtering was performed using SAE filters in LS-Prepost. Following simulation, model results were compared to physical tests and objectively evaluated using CORrelation and Analysis (CORA). For the neck-only compression tests, additional simulations were also performed to evaluate the sensitivity of the WIAMan neck to curvature changes, geometry modifications, and load cell alignment.

Copyright 2016 The Organizing Committee for the 2016 Summer Biomechanics, Bioengineering and Biotransport Conference

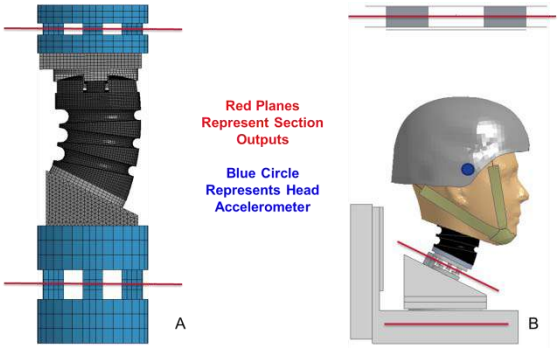

Figure 2. Primary test setups.

RESULTS

In the neck-only compression simulations, the molded neck had upper neck peak loads of 5.6 kN, 7.1 kN and 8.7 kN for compression velocities of 200 N/ms, 400 N/ms, and 600 N/ms respectively. CORA [2] scores comparing the simulated compression tests to the physical tests can be seen in Table 1. Additionally, the percent difference in peak load can also be found in Table 1. For both the CORA score and peak differences, the scores were weighted to emphasize the primary responses (compressive load and primary moment) over off-axis loading. Plots of two representative traces can be seen in Figure 3. These plots are representative of the upper load cell compressive load (Z Force) along the vertical axis and the primary moment at the upper load cell in the sagittal plane (Y Moment).

Table 1. CORA Scores

	200 N/ms	400 N/ms	600 N/ms
Weighted CORA Score	**0.82**	**0.81**	**0.81**
Weighted Peak Difference	**0.11**	**0.09**	**0.10**

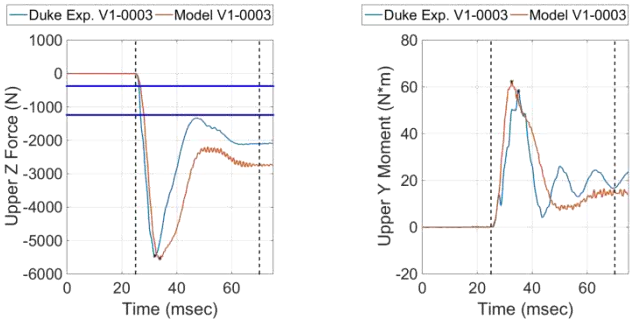

Figure 3. Primary responses at 200 N/ms. Data shown were measured at the upper load cell.

With regards to sensitivity analysis, the base of the molded neck was translated ± 15 mm in the anterior-posterior direction to evaluate the effect of neck curvature on the peak loads. From this, 15 mm of posterior translation was found to decrease the peak compressive load by 11% and increase the moment by 12%. Anterior shift had little effect on the compressive load, but reduced peak moment by 18%.

The effect of load cell alignment was evaluated by translating the upper load cell ± 5 mm in the anterior-posterior direction. Following these translations, the model was found to show no sensitivity in peak compressive load, but showed a 64% increase in moment for posterior shift and a 57% decrease in moment for anterior shift.

Lastly, the effects of volume change due to geometry modifications were evaluated. Based on these simulations, reductions in volume led to a linear decrease in compressive forces (Figure 4).

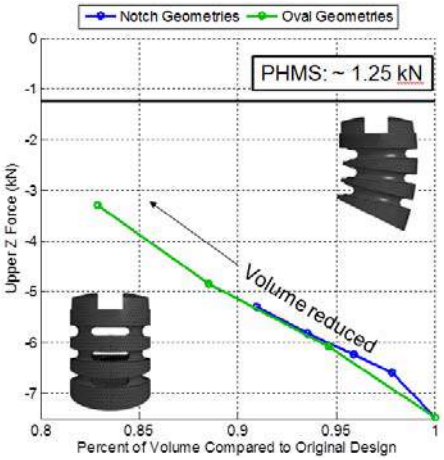

Figure 4: Sensitivity to design modifications. Typical notched and oval modifications shown. Plot shows typical peak value for PMHS testing.

The helmeted head-neck simulations were run at 3 speeds: 1m/s 2m/s and 3m/s. Of these, only the 3m/s simulation had head-to-roof contact. In this simulation, the peak roof contact force was 13.5 kN. In general moments were greater for the roof contact case than in the neck-only compression tests.

DISCUSSION

In this study, the pre-generation 1 design of the WIAMan neck was evaluated in two conditions. It has been validated in axial compression. Next steps will focus on continued validation in the roof impact scenario which are pending physical testing. It is known from the physical tests (and supported in virtual evaluation) that the neck is stiffer than cadaveric cervical spine tests conducted for the program. Therefore, the sensitivity analyses were run to evaluate where design modifications can have the most impact in aligning the ATD response to the PMHS tests. From these, the neck (particularly moment) was found to be most sensitive to load cell alignment and volume changes induced by removing material from the molded neck had the greatest effect on lower the force. Thus, Modeling and Simulation (M&S) activities are informing the design, evaluating design modifications and assessing strength of design for the WIAMan program.

ACKNOWLEDGEMENTS

This work was supported under contract #N00024-13-D-6400, sponsored by the United States Army Research Lab in support of the Warrior Injury Assessment Manikin (WIAMan) program. WFU was funded through subcontracts 117216 from John Hopkins University Applied Physics Lab. The authors gratefully acknowledge input from all members of the M&S team; Kevin Lister and Cameron Bell of Corvid Technologies, Matt Shanaman, Connor Pyles, Nicholas Vavalle and Christian Lomika of JHU APL. Experiments modeled were conducted by Drs. Pintar and Yoganandan of the Medical College of Wisconsin and Dr. Dale Bass of Duke University. The M&S team gratefully acknowledges the support of the program lead Ken Tarcza and JHU APL lead, Andrew Merkle.

REFERENCES

[1] Owens, B.D. et al., *J Trauma and Acute Care Surgery*, 2008, vol. 64: pp.295-299

[2] Ghere C. et al. *21st Enhanaced Safety of Vehicles*, Stuttgart, Germany, 2009

Copyright 2016 The Organizing Committee for the 2016 Summer Biomechanics, Bioengineering and Biotransport Conference

SB³C2016
Summer Biomechanics, Bioengineering and Biotransport Conference
June 29 –July 2, National Harbor, MD, USA
SB³C2016-749

ISOLATION OF RARE TUMOR CELLS USING ADHESION ROLLING IN A MICROFLUIDIC CHIP WITH INCLINED WAVY SURFACES

Shunqiang Wang (1), Roy Ghosh (1), Ran He (1), Jie Yang* (2) Yaling Liu* (1,3)

(1) Department of Mechanical Engineering & Mechanics
Lehigh University
Bethlehem, PA, USA 18015

(2) School of Mechanics and Engineering
Southwest Jiaotong University
Chengdu, China 610031

(3) Bioengineering Program
Lehigh University
Bethlehem, PA, USA 18015

INTRODUCTION

Circulating tumor cells (CTCs) have been recognized as the precursor to metastasis in many cancers. These cells are rare in the bloodstream, and, if isolated, can provide details on the diagnosis of non-hematologic and epithelial cancers, along with furthering the research on metastatic cancers and their origins. The ultimate goal in this field is to isolate CTCs from normal blood cells with a high efficiency, high purity and high viability [1]. Various technologies have been developed which fall into two main categories: physical property based and immuno-affinity based approaches. Due to the complexity of cell biology, there is currently no definite method,yet, to achieve the above-mentioned goal yet. Most of the methods on the separation of CTCs from whole blood require complex blood processing and complex approaches to detach captured CTCs, thus yielding a low viability. As a result, there is an urgent need to develop a technique to isolate CTCs from blood samples in a convenient and reliable manner.

In literature, it was found that E-selectin is present on endothelial cells when chemotaxis of leukocytes (leukocyte migration) occurs [2]. The ligand-receptor attraction allows for the rolling of leukocytes due to a relatively weak bond. A similar interaction is noted with tumor cells. Through their binding to E-selectin, tumor cells are able to travel along blood vessels to different organs and cause metastasis. In a previous study, CTC rolling on E-selectin was compared to white blood cells (WBCs). The WBCs exhibited a stronger interaction with stable, more numerous bonds. Conversely, CTCs maintained a weaker bond [3]. By taking advantage of this adhesion force difference, we aim to develop a novel microfluidic chip coated with E-selectin to isolate CTCs from normal blood cells.

In the following contents, the working mechanism of the device is first discussed. Then our preliminary experimental results are used to support the proposed idea.

METHODS

Working Mechanism

The overall strategy to isolate tumor cells from normal blood cells is described below. After designing an E-selectin coated microfluidic chip with inclined wavy patterns, blood samples spiked with tumor cells are injected through the chip. Different cells either flow or roll along different pathways, as sketched in Fig. 1(a) and explained in the following paragraphs The experimental test system is shown in Fig. 1(b). For the preliminary flow test, RBCs are lysed so that isolation of only WBCs and CTCs are tested.

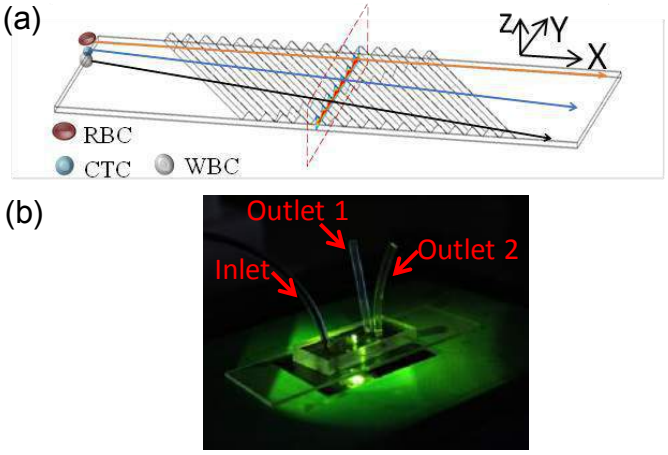

Fig. 1 (a) The proposed concept of different cells flowing or rolling along different pathways. (b) Experimental setup for the tumor cell isolation.

To achieve the cell adhesive rolling based cell isolation mentioned above, the device performance was evaluated from two aspects. First, with the inclined wavy pattern, the flow presents velocity components in the cross-section as shown in Fig. 2(a). Due to the fluid mass conservation and the inclined wavy direction, a large looped flow pattern with a clockwise direction is formulated as shown in Fig. 2(b). Regarding the forces, cells experience same gravity force and buoyant force everywhere while drag forces exhibit different directions in different locations. With Since the densities of both CTCs and WBCs are larger than that of the fluid medium, cells undergo an unstable force balance and shift following the flow loop pattern. They

Copyright 2016 The Organizing Committee for the 2016 Summer Biomechanics, Bioengineering and Biotransport Conference

finally focus at the interfaces where buoyant force and drag force balance with the gravity [4].

After the cells focus to one side of the channel, subsequent cell isolation is achieved based on different adhesive force for CTCs and normal blood cells. As shown in Fig. 2(c), it was found that RBCs have no interaction with the E-selectin coated surface, thus following the straight flow stream. Both CTCs and WBCs perform adhesive rolling on E-selectin while stronger adhesion force exists for WBCs. In combination with an inclined wavy pattern, which provides a guiding direction, it is expected that CTCs and WBCs will roll on the E-selectin coated surface following different pathways.

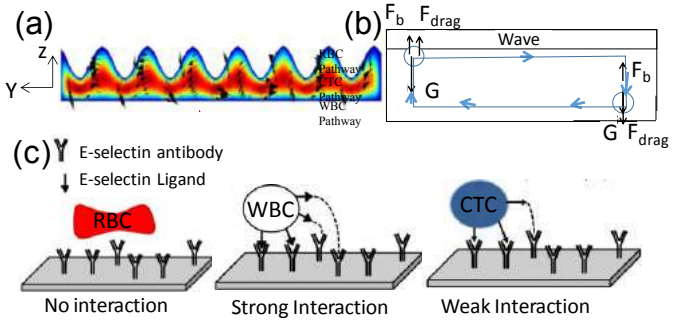

Fig. 2 (a) The velocity contour in the cross-section of Fig. 1(b). (b) A schematic image of the looped flow pattern and the forces acting on a flowing cell. (c) A schematic image indicates the interaction between cells and E-selectin coated surfaces.

Fabrication Approach

A reflow approach was used to fabricate the inclined wavy pattern. Briefly speaking, a traditional grooved pattern was first fabricated. After replicating an uncured photoresist mold by the nano-imprint approach, the photoresist was melted to form waves at 65 ^{o}C.

Cell Isolation Test

PC3 cells were cultured and used as a model CTC cell line. PC3 cells were pre-stained with cell-tracker and then spiked into human whole blood or RBC lysed blood. Cell solution was then injected into the E-selectin coated microfluidic chip. Regular and fluorescent microscopes were used to observe the cell rolling and isolation process. To quantify the cell rolling velocities, the cell rolling process was recorded and then analyzed by ImageJ.

RESULTS

To demonstrate the focusing effect brought by the inclined wavy pattern, we then performed a cell flowing test in a microfluidic chip with no E-selectin coating, as shown in Fig. 3. It was clearly observed that all cells are focused to the side channel with a narrow focusing band. This observation shows that all cells are first focused to one side, and are then isolated based on the adhesion force difference mentioned above.

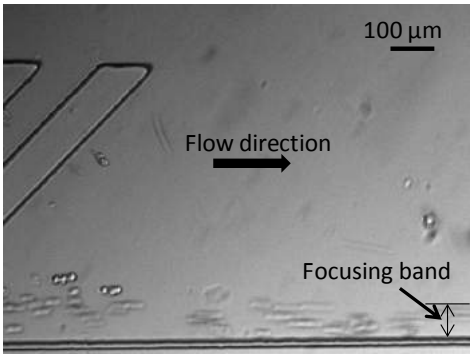

Fig. 3 Optical image indicates cell focusing effect in a microfluidic chip with inclined patterns.

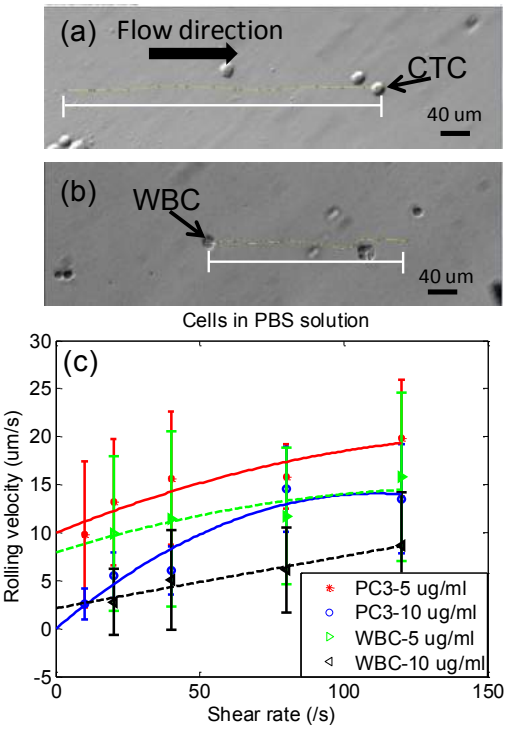

Fig. 4 Transient cell rolling image for (a) CTC and (b) WBC. (c) Rolling velocity for PC3 cells and WBCs under different shear rates and different E-selectin coating density.

To demonstrate the adhesion difference for CTCs and WBCs, Fig. 4(a) and (b) show time series of CTCs and WBCs rolling on an E-selectin coated flat surface. It indicates that CTCs roll faster than WBCs. Fig. 4(c) shows a further quantitative analysis of cell rolling velocities for CTCs and WBCs under different shear rates and different coating densities. In comparison to WBCs, the larger rolling velocity for CTCs suggests a smaller adhesion force between CTC and E-selectin. This supports our hypothesis that CTCs and WBCs will be geared towards different pathways, as sketched in Fig. 1(a).

DISCUSSION

Our preliminary results demonstrate the cell focusing effect and adhesive force difference in the proposed microfluidic chip coated with E-selectin. This suggests that the proposed cell adhesive rolling based approach for tumor cell isolation is feasible. This approach provides a convenient strategy to isolate tumor cells from whole blood without any blood processing and cell detachment operation, thus presenting a convenient platform which is essential for tumor cell profiling and genomic analysis. Future work will be performed to validate the full functionality of this device.

ACKNOWLEDGEMENTS

This work is supported by NSF grant CBET-1264808 and DMS-1516236.

REFERENCES

[1] Yu, M. et al., *The Journal of cell biology,* 192: 373-382, 2011.
[2] Ye, C. et al., *International journal of cancer,* 61: 455-460, 1995.
[3] Myung, J. et al., *Langmuir*, 26: 8589-8596, 2010.
[4] Hsu, C. et al., *Lab on a Chip*, 8: 2128-2134, 2008.

Copyright 2016 The Organizing Committee for the 2016 Summer Biomechanics, Bioengineering and Biotransport Conference

SB^{3}C2016
Summer Biomechanics, Bioengineering and Biotransport Conference
June 29 –July 2, National Harbor, MD, USA
SB^{3}C2016-750

ANISOTROPICALLY STIFF MICROPILLAR SUBSRATE FOR CONTROLLING CELLULAR ALINGMENT AND ELONGATION

Y. Alapan (1), M. Younesi (2), O. Akkus (1,2,3), U. Gurkan (1,2,3)

(1) Mechanical and Aerospace Engineering Department
Case Western Reserve University
Cleveland, OH, USA

(2) Biomedical Engineering Department
Case Western Reserve University
Cleveland, OH, USA

(3) Orthopaedics Department
Case Western Reserve University
Cleveland, OH, USA

INTRODUCTION

Substrate properties, such as stiffness, control cell morphology, elongation, alignment (spatial orientation), and anisotropy of cell and nucleus shape, which partially direct the cell fate. Thus, it is of utmost importance to achieve elongated and aligned cellular organization *in vitro* for functional and hierarchical study of cell behavior. Even though methods exploiting substrate topography were previously utilized to achieve cellular alignment, they were limited to two dimensional (2D) planar substrates. In native tissues, extracellular matrix and other cells confine cells, which result in different morphology, adhesion, migration, and cytoskeletal arrangement in comparison to cells in 2D. Thus, there is a need for engineered 3D microenvironments with precise control over topography and stiffness.

Microengineered substrates allow simplification and decoupling of the complex in vivo 3D environment by mimicking key physical characteristics, such as stiffness and directionality. Micropillar arrays have been utilized as 2D semi-continuous substrates for studying the relationship between focal adhesion size and traction forces, and cell differentiation [1]. Micropillars can be used as 3D microenvironments with controlled mechanical, chemical, and biological features.

Here, we have designed and fabricated, anisotropically stiff micropillar array substrates to confine, align, and elongate single mesenchymal stem cells (MSCs) and cardiomyocytes in a 3D microenvironment (Fig. 1a-c). We present for the first time, to the best of our knowledge, control of cell elongation and alignment in a 3D microenvironment by systematically modulating the stiffness anisotropy of the microfabricated substrate. We discovered that anisotropically stiff micropillar substrates provide cellular confinement in 3D, aligning cells in the stiffer direction with extraordinary elongation of both MSCs (≈ 600 μm) and cardiomyocytes (≈ 500 μm).

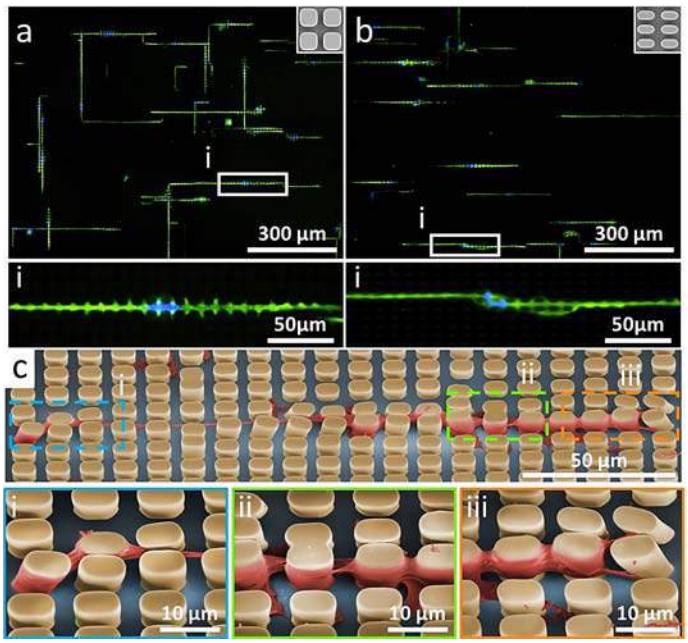

Figure 1. Unidirectional cell elongation in anisotropically stiff micropillar arrays. (a, b) Entrapped cells (F-actin, green) and their nuclei (DAPI, blue) display elongation in both **(a)** isotropic, and **(b)** anisotropic 3D micropillar environment. **(c)** Scanning electron microscope (SEM) image (pseudo-colored, cells: red, pillars: brown, substrate bottom surface: gray) of an elongated cell entrapped within an anisotropic inter-pillar space.

Copyright 2016 The Organizing Committee for the 2016 Summer Biomechanics, Bioengineering and Biotransport Conference

METHODS

Micropillar arrays were fabricated in both isotropic and anisotropic configurations with stiffness anisotropies (SA) ranging from 1 to 3.7 (Fig. 2a-d). Poly(dimethylsiloxane) (PDMS) replica-molding was used to fabricate negative template by casting PDMS over SU-8 micropillar master. After curing and peeling off, micropillar arrays were obtained by casting PDMS over the negative template. Afterwards, MSCs and cardiomyocytes were seeded on isotropic and anisotropic micropillar arrays. Overnight cultured cells were labeled with cytoskeletal F-Actin and nuclear staining to analyze cell alignment, elongation, and entrapment in 3D anisotropically stiff micropillar environment. A fluorescent cell tracking stain was used for time lapse live cell imaging.

RESULTS

Isotropic micropillar arrays showed random cell alignment in both horizontal and vertical directions, whereas cells in anisotropic micropillar arrays unidirectionally aligned in the stiffer (horizontal) direction. We observed higher degree of unidirectional cell alignment with increasing SA of the micropillar arrays both for MSCs and cardiomyocytes (Fig. 2d). In time lapse analysis, cells settled down and migrated into inter-pillar space within 0.6 hours and elongated in both directions within 5 hours (Fig. 3a-d). Cells were completely elongated and aligned in the stiffer direction within 15 hours (Fig. 3e).

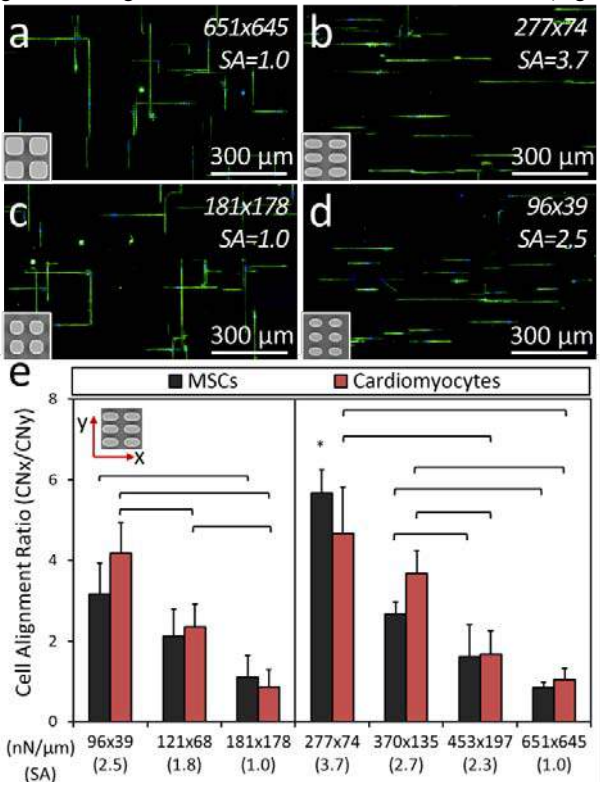

Figure 2. Functionalized anisotropic micropillar arrays control cell morphology and alignment. (a-d) Cell alignment in isotropic **(a)** and anisotropic **(b-d)** micropillar arrays was observed, indicated by cytoskeletal F-Actin staining. **(e)** Higher cell alignment ratios (CNx/CNy; number of cells aligned in x- direction, CNx, divided by number of cells in y- direction, CNy) were observed with increasing stiffness anisotropy of the micropillar arrays for both MSCs and cardiomyocytes. The horizontal lines between individual groups represent statistically significant difference based on one way ANOVA test ($p<0.05$).

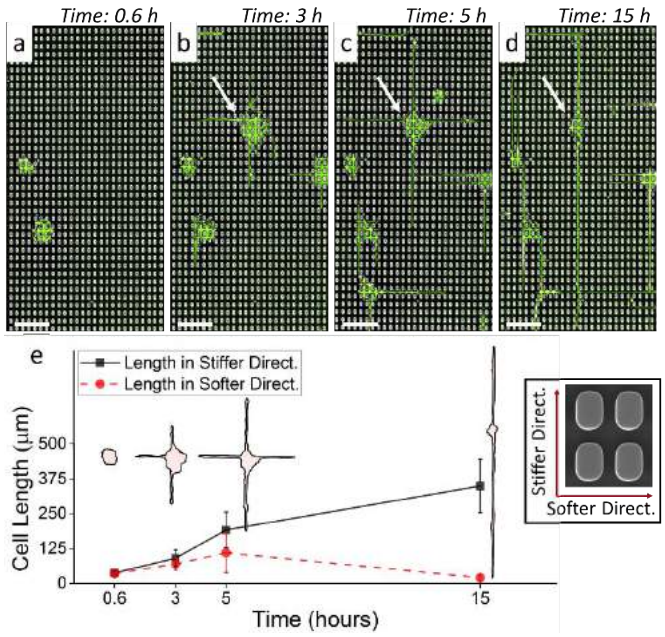

Figure 3. Time lapse analysis of cell entrapment and elongation in inter-pillar space. (a) Seeded MSCs settled down on anisotropically stiff micropillar arrays (SA=2.3) and started migrating into the inter-pillar space. **(b, c)** Cell elongation in inter-pillar space began within 3 to 5 hours after cell seeding. **(d)** Cells were fully elongated and aligned in the stiffer direction (vertical) within 15 hours after cell seeding. White arrows points to a typically elongated cell. Scale bars indicate 50 µm of length. **(e)** Cell length in softer direction increased within 0.6 hours to 5 hours, but decreased from 5 to 15 hours after seeding. On the other hand, cell length in stiffer direction displayed a continuous increase within 15 hours after seeding. Schematic of a typical cell morphology over time is displayed in the plot.

DISCUSSION

Here we present a new approach and platform that would allow the study of cell behavior in a precisely controlled 3D microenvironment. The described microfabricated pillar system can be utilized for the study of cell-ECM interactions and cell behavior in a mechanically controlled 3D environment. The micropillar platform allows precise control over substrate stiffness and stiffness anisotropy, which induces different degree of cell alignment and elongation. The presented microengineered approach induces cells to elongate and align along the stiffer axes of micropillars while confining cells in a 3D environment. Cultivation of highly elongated and aligned cardiomyocyte constructs can potentially lead to a highly organized and functional cardiac tissue. Furthermore, highly organized cell arrays can be utilized in other tissues with elongated cell phenotypes, such as nerves, tendons and ligaments.

ACKNOWLEDGEMENTS

This work was supported in part by Grant # 2013126 from the Doris Duke Charitable Foundation, Grant # R01 AR063701 from the National Institute of Health, and Grant # DMR-1306665 from the National Science Foundation. Authors acknowledge Grace Gongaware from Case Biomanufacturing and Microfabrication Laboratory and Cleveland Institute of Art for pseudo-coloring the SEM images.

REFERENCES

[1] Alapan, Y et al., *Biotechnol. Adv.*, 33:1727-1743, 2015.

Copyright 2016 The Organizing Committee for the 2016 Summer Biomechanics, Bioengineering and Biotransport Conference

SB³C2016
Summer Biomechanics, Bioengineering and Biotransport Conference
June 29 –July 2, National Harbor, MD, USA
SB³C2016-751

ANALYSIS OF CHROMATIN MECHANICS DURING CARDIOMYOCYTE CONTRACTION USING NUCLEAR SPATIAL STRAIN MAPS REVEALS NEW PROTECTIVE MECHANISM

Benjamin Seelbinder (1), Soham Ghosh (1), Sarah Calve (2), Corey P. Neu (1,2)

(1) Mechanical Engineering
University of Colorado Boulder
Boulder, CO, USA

(2) Biomedical Engineering
Purdue University
West Lafayette, IN, USA

INTRODUCTION

The cell nucleus is known to contain, maintain, and interpret the genomic information that forms the basis of every individual. In addition, it experiences an enormous amount of deformation in everyday tasks, especially in mechanically challenged tissues like the heart, muscles, skin and tendons. Elevated nuclear strain can lead to extensive DNA damage [1]. Genomic instability due to altered chromatin structuring factors is one of the suspected main mechanism for the accumulation of mutations necessary for cancer development [2]. Understanding how the nucleus reacts to high nuclear strains and protects the integrity of its genome can open new perspectives on diseases ranging from cancer to conditions with pathological stiffened tissues, e.g. in the heart due to aging, malnutrition or post-infarction.

In differentiated cells, chromatin shows a distinct architecture with areas of different chromatin densities. This structure is achieved through histones: DNA is wound around a histone core at regular intervals (200±40 bp) and histone modifications control chromatin density by changing DNA-histone and histone-histone interactions [3]. Functional evaluation of this architecture mostly focuses on transcriptional accessibility. However, it can also serve a physical purpose as shown for photoreceptor cells of nocturnal animals which utilize a centralized dense chromatin core to focus light into receptor areas like a lens [4]. Here we propose a similar role for the chromatin architecture of mechanically challenged cells in which areas of loose non-coding and/or inactive DNA could be used as a strain relief system to protect active genes and reduce DNA breakage.

To test for our hypothesis, we analyzed the relation between strain and architecture of cardiomyocyte (CM) nuclei during contraction. We utilized a novel algorithm that determines spatial strain maps from an undeformed and deformed image input [5] in combination with fluorescently-labeled histones to assess chromatin architecture (Figure 1b). Additionally, we took advantage of the observation that

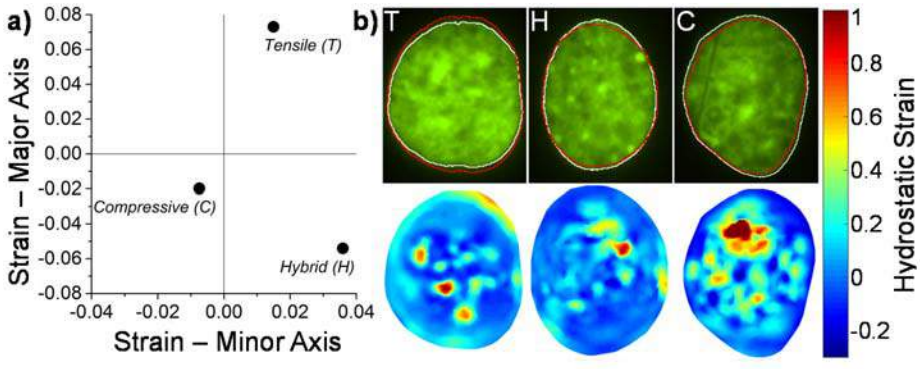

Figure 1. Nuclear loading modes of CM nuclei during contraction. Image stacks of nuclear deformation during CM contraction were recorded. **a)** Image stacks were reoriented along the major axis and the relative size difference (strain) before and after contraction was determined for each axis. Displayed are 3 nucleus that represent the 3 major loading modes: Tensile, Compressive and Hybrid. **b)** Upper panel: Chromatin intensity pictures (H2B-EGFP); nuclear borders, white: resting state, red: peak contraction. Lower panel: Spatial nuclear strain maps between resting state and peak contraction.

Copyright 2016 The Organizing Committee for the 2016 Summer Biomechanics, Bioengineering and Biotransport Conference

cultured CMs show different nuclear loading modes that range from biaxial tensile to biaxial compressive to hybrid modes with mixed tensile and compressive features along the main axis (Figure 1a). Comparing chromatin mechanics in different loading modes enabled us to identify consistent features that further supported our theory.

METHODS

Cardiomyocytes (CM) were derived from embryonic mice 16.5 days post conception which harbored an EGFP-tag at the H2B histone protein (JaxMice #006069). Isolated CMs were cultured on thin (500 µm) layers of polydimethylsiloxane (Sylgard® 527) with a stiffness of ~15 kPa and coated with Matrigel. 4 days after plating, image stacks of nuclear deformations during CM contractions were acquired using epi-fluorescence microscopy with a EMCCD camera at ~6.4 fps. Chromatin density was determined from EGFP-H2B fluorescence intensity pictures.

High resolution intra-nuclear strain fields were determined from an undeformed nuclear image during resting state and deformed image during peak contraction using a Hyperelastic Warping-based set of custom-written algorithms [5].

RESULTS

Chromatin intensity distributions followed the pattern of a multi-term Gaussian distribution with a distinct peak at mid-density chromatin (MDC) regions (Figure 2a). Notably, absolute strain values for all loading modes tended to decrease towards this peak. In the tensile loading mode strain values were highly tensile for low density chromatin (LDC), decreased towards the chromatin peak and become compressive towards high density chromatin (HDC). Interestingly, in the compressive case this observation was reversed. The hybrid loading mode in turn revealed an overlay of both before described cases with high tensile and compressive strains in both LDC and HDC and decreased strains at MDC where chromatin distribution is peaked. Analysis of 10 nuclei with mixed loading modes confirmed the trend of decreased absolute strains at MDC (Figure 2b). Segmenting the nuclei intensity pictures into LDC, MDC and HDC regions using the chromatin distributions, respectively, revealed a distinct pattern of a MDC core surrounded by LDC and MDC distributed throughout the interface of both (Figure 2c). Population analysis (n=10) confirmed that observation with LDC residing close the nuclear border, HDC close to the center and MDC being distributed in between (Figure 2d).

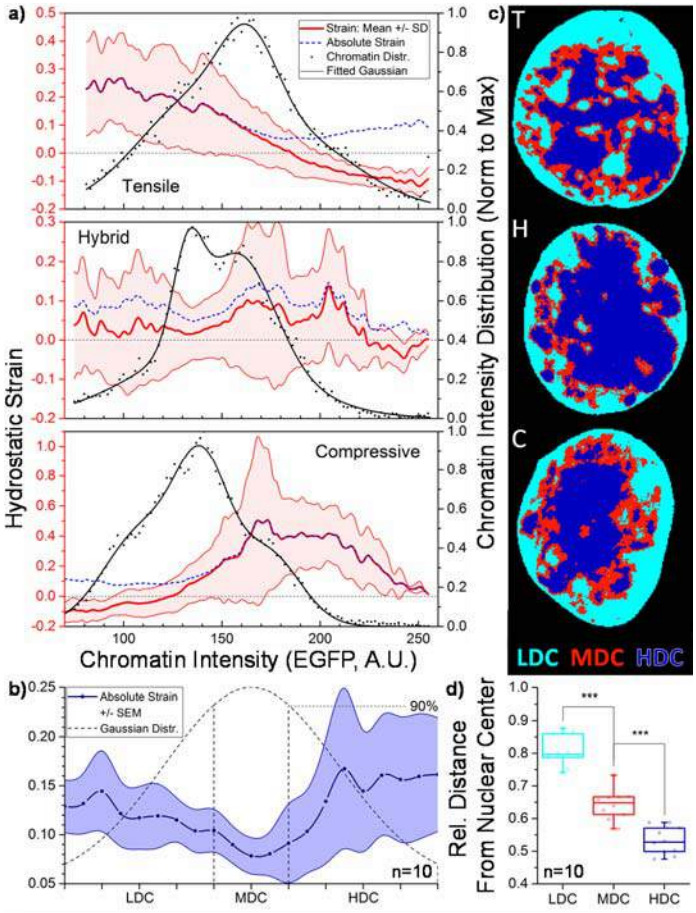

Figure 2. Relation between nuclear strain and architecture. Spatial relation of chromatin intensity images and strain maps shown in Figure 1 were analyze. **a)** *Left axis*: For each intensity value (grey values 0-255) the spatially correspondent strain values have been averaged. *Right axis*: Chromatin intensity histogram. The distribution followed a 3-term Gaussian distribution (R^2>0.98). **b)** Chromatin intensity values were normalized using Gaussian fits and absolute strain values were averaged. **c)** Intensity maps were segmented into LDC, MDC and HDC regions via histograms. **d)** Average relative distance [0-1] to nuclear center was determined for LDC, MDC and HDC regions for 10 nuclei; *** p<0.0001.

DISCUSSION

We hypothesized that chromatin architecture can serve a mechanical purpose in mechanically challenged cells to protect important genes from strain-induced damages. In such a system, soft LDC could act as an elastic element and cushion incoming strains. In accordance to that, strain values in LDC followed the main loading mode in all three nuclei, as would be expected from a spring-like element. Additionally, LDC was primarily found at the nuclear border which would be the best location to place a cushioning element. In contrast, ridged HDC was expected to display higher stiffness with only minor strains, however, absolute strain values where even higher than in LDC regions and showed a reversed relationship to the loading mode being tensile in the compressive case and compressive in the tensile case. One explanation could be, that HDC rather acts as a chromatin reservoir. During nuclear tension, chromatin would be withdrawn from HDC regions and the image-based algorithm would register the optical shrinking as compressive strains. Also during nuclear compression, more chromatin would be pressed into HDC regions during compressive loads. In accordance with our hypothesis, chromatin withdraw from this reservoir would also provide strain relief for adjacent MDC regions during tensile strains. We observed that absolute strain values are lowest for MDC where chromatin distribution peaked. It is reasonable to assume that such regions may also harbor most of the actively transcribed genes, though further investigation is needed to explore this.

In summary, using a novel imaging algorithm we provided first data that the distinct chromatin architecture of differentiated cells may provide a protective mechanism to maintain genomic integrity and enable proper gene transcription even under high nuclear strain burdens.

ACKNOWLEDGEMENTS

The authors acknowledge funding from NSF CAREER 1349735.

REFERENCES

[1] Harada, T et al, *J. Cell Biol.*, 204:669–82, 2014.
[2] Morgan, MA et al, *Genes Dev.*, 29:238–249, 2015.
[3] Lawrence, M et al, *Trends Genet.*, 32:42–56, 2016.
[4] Solovei, I et al, *Russ. J. Genet.*, 46:1029–1032, 2010.
[5] Henderson, JT et al, *Biophys. J.*, 105:2252–61, 2013.

Copyright 2016 The Organizing Committee for the 2016 Summer Biomechanics, Bioengineering and Biotransport Conference

SB^{3}C2016
Summer Biomechanics, Bioengineering and Biotransport Conference
June 29 –July 2, National Harbor, MD, USA
SB^{3}C2016-752

OBJECTIVE IDENTIFICATION OF THE YIELD POINT FROM TENSILE TESTING OF AORTIC TISSUES

Madhavan L. Raghavan, Timothy K. Chung, Chaid D. Schwarz

Biomedical Engineering
University of Iowa
Iowa City, IA, USA

INTRODUCTION

Identifying the yield point in the elastic curves from uniaxial extension failure testing of biological soft tissues is useful for two purposes – demarking the elastic region for determining elastic parameters and for determining the yield strength, a conceivable metric of the specimen's susceptibility to failure. Unlike ultimate point (the peak point in the curve), the identification of the yield point is not straightforward for biological soft tissues. For these tissues, the definition of the yield point itself is mixed, further aggravated by the nonlinear force-extension response, the micromechanics of gradual collagen recruitment, the not-so-uncommon presence of seemingly multiple yield points and the inevitable noise in acquired data. Due to these challenges, approaches for yield point identification in the elastic curves of classical structural materials are not applicable for soft tissues. In tissue biomechanics literature, the yield point is typically identified visually by subjective discretion. While expedient, subjective visual approaches to yield point identification, especially in the absence of precise *a priori* definitions, can adversely impact reliability of inferences drawn. The goal of this study was to develop an objective method for identifying the yield point from elastic curves generated from uniaxial testing of aortic wall tissue. Specifically, we sought to: 1) develop algorithms for determining yield point based on multiple definitions; 2) apply algorithm and determine yield points on a study population of force-extension curves obtained during uniaxial extension testing of aortic tissue samples from 100 study subjects; 3) Identify the optimum yield point identification method by comparing algorithm-based estimates of yield points with subjective adjudicated consensus of three human experts.

METHODS

The definition of yield point, unlike the ultimate point, requires nuanced consideration. The theoretical definition for classical structural materials – isotropic, following Hooke's law – is easy and straightforward enough. It is the point where the material starts to behave inelastically or undergoes irreversible deformation. In practice, for such materials, this coincides with the point where the linear stress-strain relationship is breached and the slope starts to decrease. But even here, the operational definition requires additional consideration such as an allowance for noise in measurements. How much decrease in slope is decrease enough such that the inevitable noise does not affect the determination? For isotropic Hooke's law materials, Christensen [1] defines the yield point as the point at which *the actual strain is 5% greater than that of the linear elastic projection* – presumably 5% is low enough not to adversely impact the theoretical definition while being high enough to ensure the yield point pick does not succumb to measurement noise. Even this operational definition is problematic for biological soft tissues mainly because the slope itself is changing incrementally (albeit increasing) prior to yield requiring us to further define, ad hoc, a predefined range of strain over which the incremental slope is determined resulting in a strong sensitivity to such choices. But a further complication is the not-so-uncommon presence of multiple local minimas in slope between the first occurrence of a yield point candidate and the ultimate point. For these reasons, slope calculations were unsuitable for our methods. Instead, we used the stress/strain ratio as its proxy. While the stress/strain ratio is certainly not the slope for nonlinear curves, because of the

Copyright 2016 The Organizing Committee for the 2016 Summer Biomechanics, Bioengineering and Biotransport Conference

strain stiffening behavior of biological soft tissues, a drop in stress/strain ratio would reflect the beginning of the underlying structural damage that the yield point would signify. Because it is evaluated independently point-by-point, its calculation does not require a smooth curve. We evaluated two yield point definitions and identified the optimal definition by comparing against the consensus picks among three human users. The 'elastic yield point' (Y_e) was defined as the first instance where the stress/strain ratio drops by 3% (with additional criteria for filtering noise described subsequently). the peak yield point (Y_p) was defined as the point where the stress/strain ratio reaches its peak (with no noise filtering).

Figure 1. Yield point on elastic curves

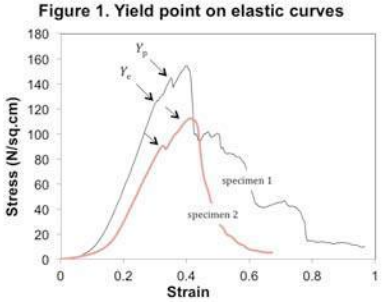

An algorithm was developed for identifying Y_e and Y_p based on the stress-strain curve in MATLAB. First, the stress/strain ratio (k), which is the slope of the line joining the origin to each datapoint prior to the ultimate point was calculated. To identify the local maxima of k without using derivatives (which are highly sensitive to noise), a two-pass filtering approach was taken: a coarse filtering approach to identify the neighborhood where a local maxima occurs and a fine filter to identify the precise point of the local maximum within that neighborhood. k at each point is first compared to that at its coarse neighbor before and after it. The coarse neighborhood around a point was defined as a window that is 3% of the ultimate strain for a specimen. The points whose k is larger than both its coarse neighbors on either side pass this filter. Next, k at the points that pass the coarse filter is compared to that at its immediately neighboring point. Again, only the points whose k is larger or equal to its neighbor on it left (lower strain) and larger to its neighbor on its right (higher strain) pass this filter and hence assigned as a yield point candidate. Among all the yield point candidates, the point corresponding to the lowest strain is designated as Y_e and that corresponding to the highest value of k is designated as Y_p. The algorithm was used to determine Y_e and Y_p in a study population of 100 elastic curves obtained from uniaxial testing of 100 aortic wall tissue specimens. These specimens were harvested from human cadavers and from patients ranging in ages from 30 through 70 years. The specimens were all cut into rectangular strips of approximately, 4 mm wide and 20 mm long. Upon measurement of its dimensions, the specimens were clamped and extended uniaxially at a constant strain rate until they tore and separated into two pieces. The recorded force and extension data was then used to calculate the incrementally varying stress and strain to obtain the elastic curves [2]. The stress-strain data was then analyzed by our developed algorithm without any human intervention to identify the Y_e and Y_p for each curve.

To assess the reliability of our algorithm, three human users who had prior experience with elastic curves of biological soft tissues were chosen. First, a training set of 10 randomly chosen curves were used to ensure the three users understand the yield point definitions. Subsequently, they individually visualized each of the remaining 90 curves and demarked manually their subjective picks for Y_e and Y_p per their respective definition. The three users picks were then compared to identify the curves where discrepancy in picks existed. These were then adjudicated and a consensus was reached. Thus, a single set of consensus yield point picks became available for the human users. These were then compared to the algorithm picks.

RESULTS

Figure 2. Yield strain estimates

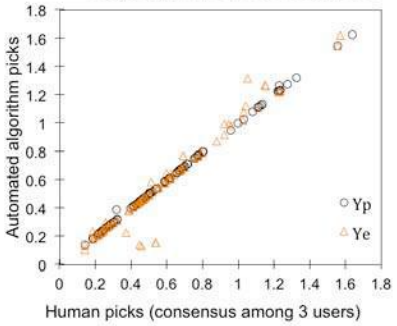

The algorithm found the yield points for all the curves in the study population. The algorithm-estimated yield points matched quite well with the human consensus-based estimates with the r^2 values for stress (0.995) and strain (0.999) at Y_p being higher than the r^2 values for stress (0.930) and strain (0.927) at Y_e (Figure 2).

DISCUSSION

The elastic curve obtained during tensile testing of biological soft tissues is a window into its structural mechanical caliber. Traditionally, key inferences drawn from such curves tend to be the elastic parameters and the ultimate strength. The yield point is rarely focused on because of legitimate concerns about the consistency in its determination even though it may just signify a key milestone for failure, perhaps even more so than the ultimate point. We report here definitions for two yield point definitions, developed an algorithm to determine them objectively, used it to make picks in a large population of elastic curves for aortic wall tissue, and compared it to the gold standard of visual identification that had consensus of three users. An automated approach to yield point identification allows for analysis of large population of elastic curves rapidly while also being devoid of human subjectivity. But first, such an automated approach has to be shown to be reliable and consistent with a gold standard - human users consensus. By that yardstick, in our study, the algorithm picked peak yield point (Y_p) was the most reliable. When using the algorithm, we propose that Y_p be used as the yield point, while individualized attenstion be paid to cases where there is a large difference between Y_p and Y_e. One limitation of our approach is that the very notion that the curve would inflect when the elastic region is breached (revealing a yield point) remains unproven owing to a poor understanding of the failure mode of these tissues. Still, the first and final points of inflection in the pre-failure regions of the elastic curve (referred to here as yield points) likely signify breach of some micromechanical milestones under tension for these tissues and therefore, our proposed objective automated methodology can help improve inferences drawn from tensile testing of biological soft tissues.

ACKNOWLEDGEMENTS

We are grateful to Drs. Erasmo Simao da Silva and Otavio Ninomiya, University of São Paulo, for sharing tensile test data.

REFERENCES

[1] Christensen, R. M., Acta Mech. 196, 239-244, 2008
[2] Ninomiya et al., J Vasc Res., 2016

Copyright 2016 The Organizing Committee for the 2016 Summer Biomechanics, Bioengineering and Biotransport Conference

SB^{3}C2016
Summer Biomechanics, Bioengineering and Biotransport Conference
June 29 –July 2, National Harbor, MD, USA
SB^{3}C2016-753

EFFECT OF TRANSCATHETER AORTIC VALVE POSITIONING ON PARAVALVULAR LEAKAGE: A PATIENT-SPECIFIC NUMERICAL MODEL

Matteo Bianchi, Ram P. Ghosh, Gil Marom, Danny Bluestein

Department of Biomedical Engineering
Stony Brook University
Stony Brook, NY, USA

INTRODUCTION

Calcific aortic stenosis (CAS) is a formation of calcium deposits that thickens and stiffens the aortic valve's leaflets, thus causes a significant obstruction to blood flow during systole and limits the closure during diastole. Currently, replacement of the stenotic valve with a prosthetic valve is the only effective treatment. In recent years, a minimally invasive option of transcatheter aortic-valve replacement (TAVR) is available for high-operative-risk patients. The prosthetic valve is comprised of a bio-prosthetic leaflets mounted on a metal stent that is deployed on the diseased leaflets and therefore 'anchored' only by contact between the native root and the stent. A possible suboptimal deployment location can cause longitudinal shift of the prosthesis during the deployment [1] or post-procedural migration [2] as a result of paravalvular leakage (PVL). Currently, despite several modeling attempts to replicate the procedure, few studies investigated different stent positioning. However, these models employed either a not calcific aortic root (AR) geometry [3] thus neglecting the effect of the calcifications on the deployment outcome, or a self-expandable TAVR valve [4]. None of them modeled the influence on the PVL hemodynamics.

The aim of this work is to evaluate the effect of different TAVR deployment positions on the procedural outcome by specifically assessing risk for migration phenomena. As a first stage toward this goal, a finite element analysis (FEA) of Edwards SAPIEN valve crimping, with the prosthetic leaflets, was performed. Then, the crimped TAVR stent was deployed via balloon-inflation in a patient-specific calcified AR in three and in various locations. After a recoiling period, when the stents achieved their final position, the PVL will be evaluated by employing computational fluid dynamics (CFD) models of these configurations. Thrombogenic potential will be calculated from platelets particle flow through the paravalvular gaps.

METHODS

An 88-year-old male patient with annulus diameter of 23 mm was implanted with 26 mm Edward SAPIEN TAV in Stony Brook University Hospital. The valve was deployed via transfemoral approach and migration of the prosthesis into the LV cavity occurred after retrieval of the delivery system. The CTA scans of this case were collected after obtaining approval from IRB. The DICOM files were processed in the open source segmentation tool ITK-SNAP v3.2 to extract the blood lumen and the calcifications domains. The aortic vessel wall was extruded with a homogenous thickness while for the AV leaflets thickness varied proportionally to the radial location, resulting in thinner leaflets toward the free edge. The soft tissue thickness was then modified by to assure that the deposits are fully embedded in it. The shape and area of the AV opening were determined from the CT and echocardiography measurements.

The stent of the balloon-expandable Edwards SAPIEN is made of stainless steel (AISI 316 LVM) and was modeled as elastic material [5], whereas the bioprosthetic leaflets were modeled as hyperplastic [6]. The crimping process was simulated by radially displacing a cylindrical crimper in Abaqus Explicit 6.14 (SIMULIA, Dassault Systèmes, Providence, RI). The stent was meshed with 69,876 brick elements and the bioprosthetic leaflets with triangular-shell elements The stent was fully crimped to outer diameter of 8 mm. The balloon was meshed with 216,960 quadrilateral elements, its thickness was 0.06 mm, and its material was linear elastic [5]. The balloon deflation was modeled to fit inside the crimped stent.

The AR mesh was smoothed with ANSYS 15 Fluent Meshing obtaining a tetrahedrons-based mesh that can facilitate large deformations. The AR sinus, calcifications and each leaflet were modeled with independent material models. Three deployment configurations were simulated by placing the stent centroid in the AV

Copyright 2016 The Organizing Committee for the 2016 Summer Biomechanics, Bioengineering and Biotransport Conference

annulus plane, 30% shifted toward the aorta, and 30% shifted toward the left ventricle (LV) cavity and referred to as midway, distal and proximal, respectively (first row of Figure 1). In every model, the balloon was gradually inflated to a pressure of 1.38 atm and, once reached the full deployment, the stent was allowed to recoil.

The blood domain was extracted from each deployed configuration and the hemodynamics through the paravalvular gaps was investigated. Thrombogenicity is calculated from stress accumulation along the trajectories of platelets passing through these gaps. As a preliminary study, a novel TAVR valve's model was employed. The fluid domain geometry was obtained from the Living Heart Model (SIMULIA, Dassault Systèmes, Providence, RI), inclusive of a healthy AR, ascending aorta and aortic arch. The pressure and flow boundary conditions were obtained from Olufsen et al. [7] and the CFD simulations were carried out in ANSYS Fluent 16.2.

RESULTS

Similar stress distribution patterns and magnitudes were observed in the distal and the midway cases, where the maximum value were in the contact region (Figure 1). The embedded calcifications experience higher stresses than the surrounding soft tissue (for example, 3.4 MPa vs. 0.5 MPa), as a result of the stiffer material properties. The proximal deployment resulted in higher stress magnitudes at the middle of the deployment and in overall lower stresses at the end of the deployment.

The anchorage strength and the landing zone of the three configurations were quantitatively assessed based on the contact between the stent and the AR in the final recoiled configuration. Spatial maximum contact pressures at the end of the recoil were then calculated, with the distal deployment resulting in the highest magnitude of 10.38 MPa, compared to the midway and proximal cases (6.26 MPa and 3.84 MPa, respectively). In the first period of the deployment (until 80%), the inflated balloon develops the characteristic "dog-bone" configuration and then it expanded rapidly. It can be seen from the quick increase in the area. At the beginning of the recoil, when the contact with the balloon stopped, a sudden drop of the contact area can be seen. The proximal deployment experienced a loss of almost 75% of the contact area at the end of the recoil when the stent dislocated to the LV (Figure 2).

The preliminary CFD analysis demonstrates that the strong systolic jet leads to a maximum wall shear stress on the aortic wall in front of the valve (Figure 3). The ascending aorta creates a right-handed helical flow. The wall shear stress magnitude on the aortic side of prosthetic leaflets was found to be the highest on the valve surface (90 Pa). Based on the final deployed configurations in the patient-specific AR, the diastolic flow in the distal and midway positions is being evaluated. Regurgitations through the paravalvular gaps appear to be more pronounced in the midway configuration. Higher thrombogenic potential is expected to be found in the gaps with higher flow rate.

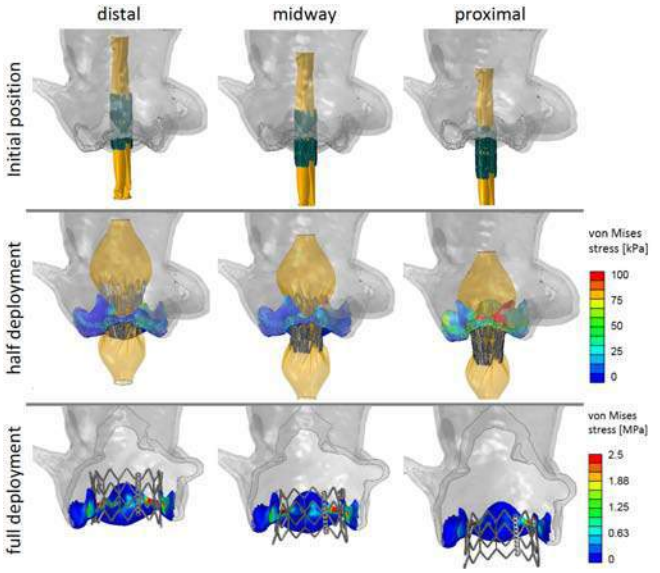

Figure 1: Various stages of the stent deployment in the three deployment locations with von Mises contours plots.

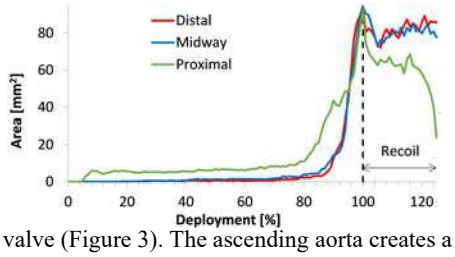

Figure 2: Total contact area in the deployment and recoil phases.

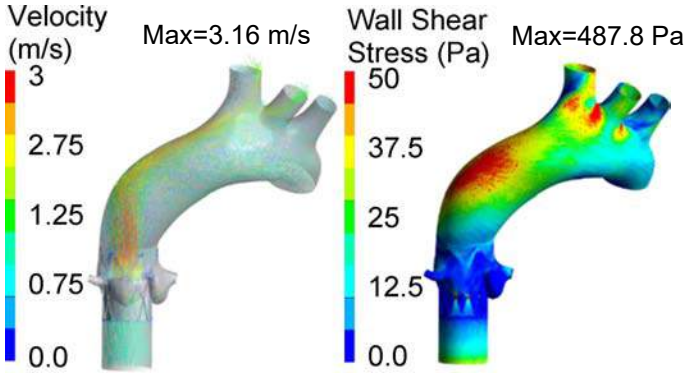

Figure 3: Flow velocity field in the TAVR valve and the aortic arch (left) and wall shear distribution on the vessel wall (right).

DISCUSSION

This study investigated the impact of TAVR deployment position on the procedural success with a focus on the risk of device migration. The comparison of the three positions showed that proximal deployment could lead to migration into the LV. This case resulted in lower contact area, which led to higher localized contact pressure and higher stress levels in the native tissue. The distal and midway configurations had comparable outcomes that would probably lead to similar performance. The influence of the TAVR valve on the hemodynamics in the anatomical aortic arch was numerically modeled for the first time. We plan to model the flow through the paravalvular gaps with fluid-structure interaction and estimate the thrombogenicity of the various configurations. After further validation of the current methods, the proposed approach might be used as a predictive tool for procedural planning in order to ultimately prevent prosthesis migration. In addition, the calculated thrombogenic potential may help design better procedure, by reducing the risk for thrombus formation and stroke events.

ACKNOWLEDGEMENTS

This study is supported by the NIH-NIBIB Quantum Award Phase II-1U01EB012487 (DB). The geometry of the aorta was adapted from The Living Heart Project (Dassault Systèmes). ANSYS, Inc. is in an academic partnership with Stony Brook University.

REFERENCES

[1] Dvir, D, et al., *JACC Cardiovas Interv*, 5:563-570, 2012.
[2] Cao, C, et al., *Ann Cardiothorac Surg*, 1:243-4, 2012.
[3] Capelli, C, et al., *Med Biol Eng Comput*, 50:183-92, 2012.
[4] Morganti, S, et al., *J Biomech*, 2015.
[5] Tzamtzis, S, et al., *Med Eng Phys*, 35:125-30, 2013.
[6] Sacks, M, *J Elast*, 61:199-246, 2000.
[7] Olufsen, MS, et al., *Ann Biomed Eng*, 28:1281-99, 2000.

Copyright 2016 The Organizing Committee for the 2016 Summer Biomechanics, Bioengineering and Biotransport Conference

SB^{3}C2016
Summer Biomechanics, Bioengineering and Biotransport Conference
June 29 –July 2, National Harbor, MD, USA
SB^{3}C2016-754

EFFECT OF HYDRATION ON INTERVERTEBRAL DISC RECOVERY

Semih E. Bezci, Grace D. O'Connell

Department of Mechanical Engineering
University of California, Berkeley
Berkeley, CA, USA

INTRODUCTION

Intervertebral disc mechanics are largely dependent on its structure and biochemical composition. The disc consists of a collagen-rich annulus fibrosus (AF), which surrounds a gel-like core, the nucleus pulposus (NP). The high water content of these subcomponents (NP: 80-85%, AF: 70-80%) allows the disc to resist large compressive loads while maintaining spinal flexibility and mobility [1,2]. External loads induce fluid flow out of the disc while negatively charged proteoglycans attract water during bed-rest recovery. Previous studies, including work from our own laboratory, have used osmotic loading to evaluate the effect of tissue hydration (i.e. water absorption) on mechanical function. Recently, we demonstrated that an increase in disc hydration decreases disc joint compressive stiffness [3]. This previous study only considered disc mechanics once a steady-state condition was achieved; therefore, the time-dependent response to achieve a steady-state condition under osmotic loading is not well understood.

Water re-absorption into the disc increases internal pressure; however, water flow into the disc is not trivial, due to porosity differences in the NP, AF, and endplate [4]. The first objective of this study was to analyze the time-dependent response of disc components (i.e., NP, AF and whole disc) under free-swelling conditions. Swelling response of the NP and AF were evaluated as tissue samples and under in situ conditions to account for differences in tissue swelling behavior and boundary conditions. The second objective of this study was to evaluate time-dependent recovery behavior under osmotic loading.

METHODS

Skeletally mature bovine spine sections were acquired from the local abattoir (n = 14 spines, age = ~18 months). Bone-disc-bone segments were prepared by removing the surrounding muscles and posterior elements for Studies 1 and 2 (n = 31). In Study 1, discs were dissected from the superior and inferior vertebral bodies using a scalpel to assess swelling behavior of the whole disc (n=10), NP (n=6) and AF (n=6). Whole disc or tissue samples were immersed in phosphate buffered saline (PBS) solution (0.15 M or 1.5 M PBS) until equilibrium swelling was attained, which was defined as a change in wet weight of less than 0.02 g/hr. The swelling ratio was calculated as the differences between pre- and post-swollen wet weights, normalized by the pre-swollen wet weight. A stretched exponential function was used to describe the swelling ratio as a function of time (Eq. 1), with model parameters to describe equilibrium swelling ratio (Q_∞), time constant (τ), and stretch parameter (β) where $0 < \beta \leq 1$. The stretch parameter, β, describes the rate of change of tissue-swelling with respect to an exponential curve, where the response is faster than an exponential description for $t < \tau$ and slower than exponential curve for $t > \tau$ [5]. A Student's t-test was performed to determine differences in swelling behavior of the 0.15 M and 1.5 M PBS groups.

$$Q(t) = Q_\infty \left(1 - e^{-(t/\tau)^\beta}\right) \quad (1)$$

In Study 2, unloaded recovery of bone-disc-bone motion segments was assessed with respect to osmotic loading. Motion segments were potted in bone cement to ensure parallel loading and hydrated in 0.15 M PBS solution prior to mechanical testing. A 300 N creep load was applied and held for two hours. At the end of the creep portion of the test, the water bath was replaced with fresh saline (0.015 M, 0.15 M, 0.75 M and 1.5 M PBS). Then, motion segments were allowed to recover at a nominal load (20 N) to ensure the platen was in contact with the sample during recovery (12 hours). Each sample was re-hydrated between tests and tested in a random order. Force and displacement were measured. The displacement during recovery was

Copyright 2016 The Organizing Committee for the 2016 Summer Biomechanics, Bioengineering and Biotransport Conference

curve fit to a 5-parameter rheological model (lsqcurvefit function, Matlab Inc.) shown in Eq. 2 [6].

$$d = \mathrm{L}\left[\frac{1}{S_1}\left(1 - e^{-(t/\tau_1)}\right) + \frac{1}{S_2}\left(1 - e^{-(t/\tau_2)}\right) + \frac{1}{S_E}\right] \quad (2)$$

The model is composed of two Voigt solids with a spring in series and allows for the characterization of the fast response (S_1 and τ_1), the slow response (S_2 and τ_2), and the elastic response (S_E). To simplify the model, the elastic response (S_E) was set as the instantaneous displacement during recovery. The model also provided parameters for equilibrium distance (d_{eq}) and equilibrium time (t_{eq}). To validate the equilibrium time predicted by the model, additional samples were loaded under the same conditions and allowed to recover for 48 hours (n = 5). A one-way ANOVA with Tukey post-hoc test was used to determine the effect of bath osmolality on recovery properties. The 0.15 M PBS group served as the control. Significance was assumed at $p \leq 0.05$.

RESULTS

The stretched exponential function described the swelling ratio well for all groups (Fig. 1; $R^2 > 0.98$). Equilibrium swelling ratio of whole discs hydrated in 0.15 M PBS was 18% greater than the 1.5 M PBS group (Fig. 2 – '*'; $p < 0.015$). There was no difference in the time constant and the stretch parameter (Fig. 2; $p > 0.07$). Tissue swelling of the NP and AF separately (0.15 M PBS only) resulted in a significant difference in swelling ratio and the stretch parameter, as expected (Fig. 2 – '^'; $p < 0.02$).

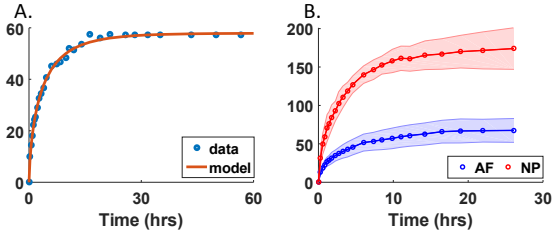

Figure 1: A) A representative AF sample showing the swelling ratio, Q (%), with model fit and B) swelling ratio for NP and AF - whole disc data not shown. Circles indicate the experimental data.

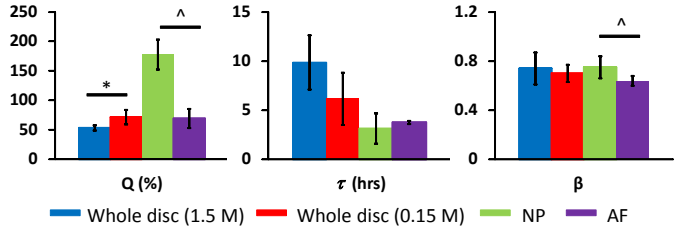

Figure 2: The parameters for the stretched exponential function.

Full recovery was not observed within 12 hours for any group, but there was a decrease in recovery with osmotic loading ($p < 0.001$; Fig. 3A). Recovery in a hyperosmotic saline (≥ 1.5 M PBS) demonstrated a reverse trend in disc height after ~3 hours, such that the disc exhibited features of loading rather than recovery (Fig. 3A – purple line). The 5-parameter model fit well to the experimental data (Fig. 3B, $R^2 > 0.99$) except in 1.5 M due to the decrease in disc height during recovery. The instantaneous displacement (elastic response) during recovery was 0.52 ± 0.12 mm (pooled average across all osmotic loading conditions). The equilibrium displacement predicted by the model agreed well with the results obtained from samples tested for 48h (Fig. 3B). The fast response behavior (S_1 and τ_1) was altered with osmotic loading ($p < 0.05$), while the slow response behavior (S_2 and τ_2) was not dependent on the osmotic loading condition (Fig. 4, S_2 = 1620 ± 422 N/mm and τ_2 = 26.7 ± 8.76 min, pooled average across all osmotic loading conditions).

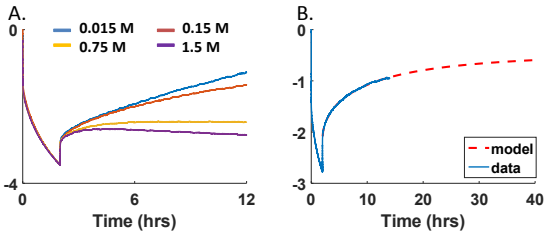

Figure 3: A) Disc height recovery for each osmotic loading group (PBS solution). B) A representative sample of data and model fit.

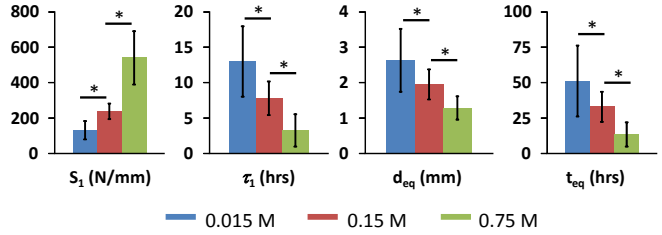

Figure 4: The results obtained from the 5-parameter model. Only statistically significant results are shown.

DISCUSSION

The disc needs to maintain adequate hydration in order to preserve flexibility, mobility, and resistance to external loads. This study evaluated the effect of osmotic loading on disc recovery behavior. In Study 1, swelling ratios of NP and AF tissue structures were evaluated separately and as a composite material (i.e. whole disc). The swelling ratio of excised discs decreased with hyperosmotic loading, which agreed well with disc joint recovery measured in Study 2. As expected, swelling behavior was greatly altered by the boundary conditions. The swelling ratio of the whole disc was closer to the AF swelling ratio, even when accounting for differences in the initial volume of each subcomponent (Fig. 2; NP volume ≅ 30% of disc volume) [7].

In hyperosmotic saline (≥ 1.5 M PBS), disc height recovery did not follow the expected behavior. After approximately 3 hours of recovery, disc height recovery reversed, suggesting a shift between recovery from mechanical loading and loading from the osmotic environment. To estimate the balance between mechanical loading and osmotic loading, the displacement at 12 hours (d_t=12hrs) was compared to the elastic displacement (S_E). The findings reported here suggest that the disc is in osmotic equilibrium in a saline bath with a concentration of ~1.0 M.

The intervertebral disc loses a significant amount of water during diurnal loading. Rehydration plays a crucial role in the disc mechanics and tissue maintenance. In conclusion, changes in the disc's external osmotic environment greatly alters disc recovery following mechanical loading, which may result in long-term degenerative like changes in composition and mechanical function.

ACKNOWLEDGEMENTS

This study was supported by the Hellman Fellows Fund (Hellman Foundation, San Francisco, CA).

REFERENCES

[1] Beckstein, JC et al., *Spine,* 33(6):E166-E173, 2008. [2] Urban, JP et al. *Spine*, 13(2), 179-187, 1988. [3] Bezci, SE.et al. *J Biomech*, 137(10):101007, 2015. [4] Stokes IAF et al. *Ann Biomed Eng*, 39(1):122-131, 2011. [5] van der Veen AJ et al. *J Biomech*, 46(12):2101-3, 2013. [6] O'Connell GD et al. *J Mech Behav Biomed Mater*, 4(7):933-942, 2011; [7] O'Connell GD et al. *Spine*, 32(3):328-33, 2007.

Copyright 2016 The Organizing Committee for the 2016 Summer Biomechanics, Bioengineering and Biotransport Conference

SB³C2016
Summer Biomechanics, Bioengineering and Biotransport Conference
June 29 –July 2, National Harbor, MD, USA
SB³C2016-755

DETAILED FINITE ELEMENT MODELING OF FIBER-REINFORCED TISSUES

Bo Yang, Minhao Zhou, Grace D. O'Connell

Mechanical Engineering
University of California, Berkeley
Berkeley, CA, United States

INTRODUCTION

Fiber-reinforced tissues, including tendons, ligaments, and the annulus fibrosus (AF) of the intervertebral disc, sustain large tensile stresses during physiological loading. These materials consist of collagen fibers embedded within a proteoglycan rich matrix, and previous constitutive models have shown that fiber-matrix interactions may play an important role in stress distribution; however, these properties are difficult to measure experimentally [1, 2].

Finite element modeling (FEM) is widely used as a complementary approach to experiments. FEMs provide detailed information of stress strain distributions that are difficult to measure directly, including stress distributions and failure behavior throughout complex tissues [3, 4]. For fiber-reinforced biological tissues, most FEM methods describe the fibers and matrix components as either fibers fixed within a matrix [5, 6] or a homogenized volume [7, 8]. However, these two methods cannot provide information about the fiber-matrix interactions, which may be crucial for understanding failure mechanics [9]. Alternatively, a more intuitive and biomechanically correct method describes collagen fibers as a separate material from the extrafibrillar matrix. Separation of fibers and matrix materials has been rarely used, likely due to difficulties of fiber bundle modeling and computational time.

The objective of this study was to compare the mechanical behavior of AF tissue under uniaxial tension using the three FEM methods described above. We based the model architecture on the AF due to the complex fiber architecture, where collagen fibers are oriented at ±45-65º to the vertical axis of the spine (Fig. 1). However, the methods applied here are easily applicable to understanding fiber-matrix interactions of other fiber-reinforced tissues, such as tendons and ligaments.

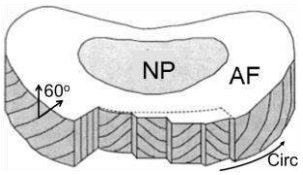

Fig. 1: Schematic of disc.

METHODS

Single lamella models were developed based on AF anatomy reported in Marchand *et al.* [10]. Specifically, each lamella is 0.2 mm thick with fibers described as cylinders through the length of the tissue (radius = 0.059 mm & 0.22 mm between fibers). Three FEM descriptions were assessed, including (1) embedded smeared (EMB), (2) homogenized hyper-elastic (HOM), and (3) fiber-matrix separated (SEP).

The solid matrix for all three models was described using a Mooney-Rivlin material description and all fibers were described as tension-only materials (Table 1). In the EMB model, the fibers were described as being an embedded rebar layer (material coefficients: E = 500 MPa, ν = 0.3, which was first reported in [5] and latter widely used in [6, 11, 12]). In the HOM and SEP models, an exponential-linear description was employed for the fibers, where the stress-stretch response increases exponentially at lower strains, then increases linearly past a defined strain threshold. Single lamellae tensile testing data in [13] was used to determine material coefficients for HOM and SEP models.

The EMB model was developed and solved by Abaqus (6.11) using model parameters reported in the literature for the AF [5]. The HOM model was developed using Preview. The SEP model was developed in SolidWorks (2015) and meshed by Abaqus and Ansa

Copyright 2016 The Organizing Committee for the 2016 Summer Biomechanics, Bioengineering and Biotransport Conference

(v16.0.0), and then imported into Preview. HOM and SEP models were evaluated using the FEBio solver.

	EMB(Matrix)	HOM	SEP(Matrix)	SEP(Fiber)
C_1 (MPa)	0.7	0.5	0.75	0.75
C_2 (MPa)	0.2	0.1	0.1	0.1
K (MPa)	N/A	50	50	50
D	~0	N/A		
C_3 (MPa)	N/A	0.05	N/A	0.21
C_4		78		98
C_5 (MPa)		70		380
λ		1.017		1.025

Table 1: Material parameters for FEM models.

Once material coefficients were determined, uniaxial tensile simulation results of double-layer models with fibers in ±65° orientation were compared to multi-layered uniaxial tensile data reported by Ebara *et al.* [14]. HOM and EMB double-layer models had ~20,000 elements, while SEP has ~2-3 x 10^6 elements. Finally, the SEP model was used to evaluate the effect of fiber orientation on tissue-level mechanics. Fiber bundles were arranged at ±45º, ±50º, ±55º, or ±60º, representing the change in fiber orientation from the inner to the outer AF.

RESULTS

Material properties for the HOM and SEP models were able to closely match single-lamella data (Fig. 2A) [13], while the linear description of fibers in the EMB model resulted in a poor fit to the data (Fig. 2 – green line). Model validation of the HOM and SEP models using a multi-layered description with alternating fiber orientation showed a close fit to experimental data (Fig. 2B; $R^2 = 0.64$ and 0.99, respectively) [14], and EMB almost had a linear behavior.

Once validated, the SEP model was used to describe uniaxial tensile with fiber orientation varying from ±45º to ±65º. A decrease in fiber orientation reduced tissue modulus by approximately 64% (Fig. 3A – slope of purple line *versus* blue line). Tensile stress resulted in fiber re-orientation along the direction of loading (Fig. 3B), which matched well with experimental data of fiber re-orientation [15].

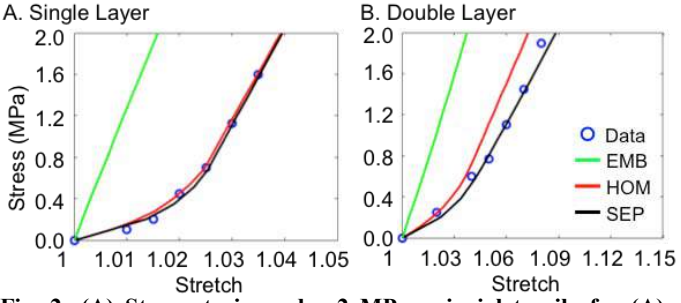

Fig. 2: (A) Stress-strain under 2 MPa uniaxial tensile for (A) single-lamella models and (B) double-lamella models (fiber orientation = ±65°).

DISCUSSION

In this study, we developed a separated fiber-matrix model description (SEP) and compared it to more commonly used FEM for fiber-reinforced tissues (EMB and HOM). Describing collagen fibers as a separate material from the extrafibrillar matrix is more consistent with the disc anatomy, but is rarely used due to computational requirements (run time: 2 minutes for HOM, 30 minutes for SEP). Recent work has demonstrated the importance of fiber-matrix interactions under physiological loading conditions [2, 16], and it is likely that these interactions play an important role in understanding the failure mechanics. SEP model demonstrated inhomogeneous stress distribution between the matrix and fibers, due to the large differences in material properties (Fig. 4)

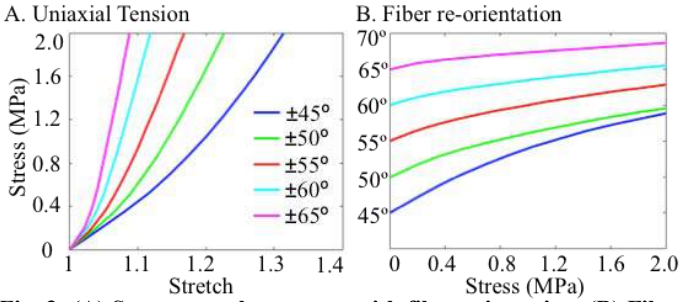

Fig. 3: (A) Stress-stretch response with fiber orientation. (B) Fiber re-orientation under tension.

The healthy AF is noted by transition of collagen fiber orientation and collagen composition (type I to II) from the outer AF to the inner AF. We used the SEP model to evaluate the effect of collagen fiber orientation while maintaining fiber strength. As expected, decreasing the fiber's initial orientation from ±65º (i.e. more aligned with the direction of loading) to ±45º resulted in a decrease in tissue stiffness. The decrease in Young's modulus from 21.8 MPa to 7.5 MPa in the inner AF follows a similar trend to experimental values (17.22 ± 7.69 MPa and 2.65 ± 1.03 MPa, respectively) [17]. However, the predicted Young's modulus of the inner annulus was 3X greater than reported values, which is likely due to the differences in collagen type.

Most embedded model descriptions for fiber-reinforced biological tissues use the linear elastic model description for collagen fibers (i.e. EMB model), with disc joint nonlinearity in compression provided by the disc geometry with fibers of various orientations [5]. However, both our single-lamella and double-layer embedded model showed an approximately linear behavior under a physiological level of strain (Fig. 2). This implies that geometric nonlinearity is not significant enough to cause stress-stretch nonlinearity in tension.

In conclusion, the findings of this study demonstrate that the SEP model has advantages over the EMB and HOM models and will be valuable for studying tissue failure. Future work will incorporate tissue-swelling behavior of the extrafibrillar matrix. Few FEMs of disc tissue include tissue swelling; however, it is likely that matrix swelling will allow for more homogenized stress distributions during loading [18].

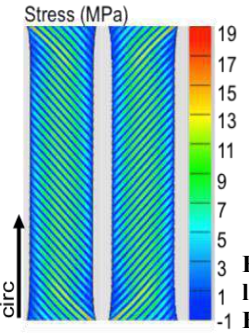

Fig. 4: Circumferential stress in multi-lamellae AF (±65°, 2 MPa applied stress). Higher stresses observed in fibers (blue).

ACKNOWLEDGEMENTS

This study was supported by the Hellman Fellows Fund (Hellman Foundation, San Francisco, CA).

REFERENCES

[1] Guerin, et al., *J Orthop Res*, 2007; [2] O'Connell, G.D., *J Biomech Eng*, 2009; [3]Schmidt, H., et al., *J Biomech*, 2013; [4] Hadi, M.F., *J Biomech Eng*, 2012; [5] Ueno, K & Liu, Y.K., *J Biomech Eng*, 1987; [6] Adam, C. et al., *J Biomech*, 2015; [7] Nathan, T.J., et al., *J Biomech*, 2014; [8] Ayturk, U.M., et al., *J Biomech Eng*, 2010. [9] Latridis, J.C., *J Biomech,* 2004. [10] Marchand, F. et al., *Spine,* 15.5, 1990; [11] Little, J.P., et al., *Comput Methods Biomech Biomed Engin*, 2008; [12] Kiapour, A., et al., *Spine,* 2012. [13] Holzapfel, G.A. et al., *Biomech Model Mechan,*, 2005; [14] Ebara, S. et al., *Spine,* 1996; [15] Guerin, H.A.L. & Elliott, D.M., *J Biomech*, 2006. [16] O'Connell, G.D., *Biomech Model Mechanobiol,* 2011. [17] Mow, V.C., Huiskes R., *Basic orthopaedic biomechanics & mechano-biology*, 2005. [18] Roccabianca, S., et al., *Biomech Model Mechanobiol*, 2014.

Copyright 2016 The Organizing Committee for the 2016 Summer Biomechanics, Bioengineering and Biotransport Conference

SB^{3}C2016
Summer Biomechanics, Bioengineering and Biotransport Conference
June 29 –July 2, National Harbor, MD, USA
SB^{3}C2016-756

HEMODYNAMIC REGULATION OF TIE1 IN AORTIC VALVE ENDOTHELIAL CELLS

Camryn L. Johnson (1) and W. David Merryman (1)

(1) Biomedical Engineering
Vanderbilt University
Nashville, Tennessee, U.S.

INTRODUCTION

Throughout each cardiac cycle, the aortic valve is subjected to a variety of mechanical forces. During systole, blood is ejected from the left ventricle through the aortic valve, exposing the ventricularis, the side of the valve facing the ventricle, to pulsatile flow with high magnitude shear stress (~20 dynes/cm^2). Following systole, the valve closes, and the fibrosa, the side of the valve facing the aorta, is exposed to recirculatory flow patterns with low magnitude shear stress (~2-5 dynes/cm^2). These two sides of the valve have different transcriptional profiles, indicating unique phenotypes. It is suspected that many of these differences arise from the distinct flow patterns to which each side is exposed [1].

Tie1 is an orphan tyrosine kinase receptor found almost exclusively in endothelial cells. Not much is known about its direct signaling, though Tie1 has been associated with several diseases, including atherosclerosis and rheumatoid arthritis [2]. Although there is no known ligand for Tie1, it has been shown to respond to mechanical stimuli and is expressed more highly in regions of disturbed flow. Tie1 is also frequently associated with Tie2, another tyrosine kinase receptor with key functions in endothelial cell survival and angiogenesis. Angiopoietin-1 (Ang1) is a known agonist of Tie2, although the association between Tie1 and Tie2 has been shown to mediate the response of Tie2 to ligand binding. While Tie1 is bound to Tie2, the extracellular domain of Tie2 is not available for binding to a ligand. In response to certain signals, including shear stress, Tie1 is cleaved into its ectodomain and endodomain, which contains the intracellular and transmembrane domains. Upon cleavage, the endodomain remains bound to Tie2, but frees the extracellular portion of Tie2 for ligand binding. Additionally, the endodomain of Tie1 can phosphorylate Tie2 independent of ligand, and Tie2 can phosphorylate the endodomain of Tie1 [3].

Although studies have previously demonstrated the effects of shear stress on the cleavage of Tie1, none have focused on the aortic valve endothelial cells. Though very similar in morphology to vascular endothelial cells, valve endothelial cells demonstrate distinct gene expression profiles. One important difference is that while aortic endothelial cells align parallel to flow, valvular endothelial cells align perpendicularly [1]. The change in expression of Tie1 in response to mechanical stimuli in the valve could reveal more phenotypic differences between vascular and valvular endothelial cells and could be crucial to understanding the effects of the distinct hemodynamic profiles on each side of the aortic valve.

METHODS

Porcine aortic valves were excised and digested in 600 U/mL collagenase for 10 minutes. The fibrosa and ventricularis were identified and endothelial cells were isolated from each. Populations of porcine aortic valvular endothelial cells (pAVECs) were purified using clonal expansion, with an initial concentration of 0.3 cells/well. Pure populations were combined following immunostaining for CD31 and aSMA to confirm that there was no fibroblast contamination.

Strain experiments were performed using the Flexcell FX-4000 Tension System. Cells were plated onto the flexible bottom of Flexcell plates coated with collagen IV. The plates were placed onto loading posts and a vacuum was applied, resulting in equibiaxial strain of the cells. In order to simultaneously apply shear stress and strain to the pAVECs, an insert for the Flexcell plates was designed and 3D printed. These inserts (**Figure 1A**) were placed into the Flexcell plate wells, replacing the cover. A barb on each side was attached to tubing, which was connected to a peristaltic pump programmed using an Arduino Uno microcontroller. Media flowed into the barb through the insert and out via a small notch (0.6 mm in height) at the base of the

Copyright 2016 The Organizing Committee for the 2016 Summer Biomechanics, Bioengineering and Biotransport Conference

insert (**Figure 1B**). During pulsatile unidirectional flow, media entered the well through one side of the insert and exited through the other side. This repeated with a frequency of 0.5 Hz. During pulsatile bidirectional flow, the notches on each side of the insert alternated as the entrance and exit for media. The entire cycle repeated with a frequency 0.25 Hz (**Figure 1C**). This setup resulted in flow over the cells, and the applied shear stress was calculated using the flow rate from the pump. For combined strain and shear experiments, strain was applied during the periods without flow. Protein expression was quantified via Western blots.

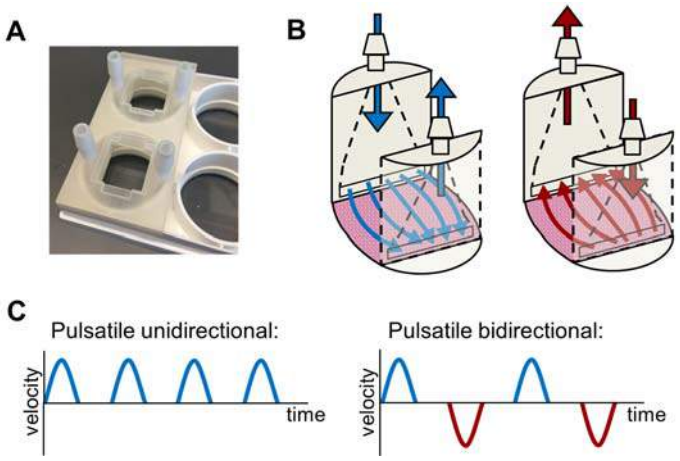

Figure 1. A) Flow insert placed into Flexcell plate. B) Illustration of the flow direction within the inserts. C) Velocity profiles for the two types of flow used.

RESULTS

Full length Tie1 protein expression in pAVECs decreased ~40% in response to 15% strain over 24 hours, while Tie1 endodomain levels increased (**Figure 2A**). Additionally, qPCR results showed that Tie1 mRNA levels did not decrease this dramatically, further indicating that Tie1 is cleaved in response to cyclic strain. Full length Tie1 protein expression in pAVECs also decreased ~60% in response to 7 hours of 10 dynes/cm^2 pulsatile bidirectional shear stress and decreased ~90% in response to 24 hours of 15% strain combined with 2 dynes/cm^2 pulsatile bidirectional shear stress (**Figure 2B and 2C**). Akt, a protein kinase downstream of Tie2 activation, shows increased phosphorylation after 15 minutes of strain (**Figure 2D**), demonstrating that Tie1 is being cleaved and activating Tie2.

DISCUSSION

These results demonstrate the importance of mechanical stimuli to Tie1 expression in the aortic valve. The finding that 15% strain decreases full length Tie1 expression contradicts studies in microvascular endothelial cells that indicate strain increases Tie1 expression [4]. Given the different flow patterns, gene expression profiles, and response to flow of valvular endothelial cells compared to vascular endothelial cells, it is important to better understand the signaling of this cell type and particularly the influence of mechanical stimuli. Despite an increasing understanding of Tie2 signaling, there is a lack of sufficient understanding of Tie1, and even less is known about its particular role in the aortic valve. The varying responses in Tie1 expression to different shear stresses and strains further demonstrate that mechanical regulation plays an important role in its signaling and warrants further investigation.

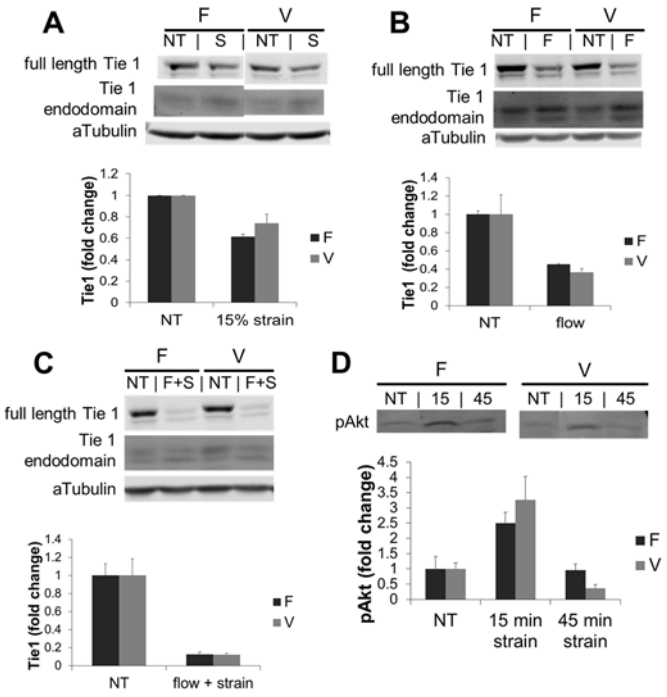

Figure 2. A) 24 hours of 15% cyclic strain (S) resulted in ~40% reduction in Tie1 expression in fibrosa (F) and ventricularis (V). B) 7 hours of 10 dynes/cm^2 shear stress with pulsatile bidirectional flow (F) resulted in ~60% reduction in Tie1 expression. C) 24 hours of 15% cyclic strain combined with 2 dynes/cm^2 shear stress with pulsatile bidirectional flow (F+S) resulted in ~90% reduction in Tie1 expression. D) 15 minutes of cyclic strain resulted in increased phosphorylation of Akt.

ACKNOWLEDGEMENTS

This work was supported by a National Science Foundation Graduate Research Fellowship (DGE-1445197).

REFERENCES

[1] Butcher, Jonathan T., et al. *J Heart Valve Dis* 17.1 (2008).

[2] Woo, Kel Vin, et al. *Trends in c ardiovascular medicine* 21.4 (2011): 118-123.

[3] Singh, Harprit, et al. *Cellular signalling* 21.8 (2009): 1346-1350.

[4] Zheng, Wei, et al. *American Journal of P hysiology-Heart and Circulatory Physiology* 287.6 (2004): H2739-H2745.

Copyright 2016 The Organizing Committee for the 2016 Summer Biomechanics, Bioengineering and Biotransport Conference

SB^{3}C2016
Summer Biomechanics, Bioengineering and Biotransport Conference
June 29 –July 2, National Harbor, MD, USA
SB^{3}C2016-757

PATIENT-SPECIFIC IN-VITRO MODELS FOR HEMODYNAMIC ANALYSIS OF CONGENITAL HEART DISEASE - ADDITIVE MANUFACTURING APPROACH

R. Medero (1,2), S. García-Rodríguez (2), P.V. Anagnostopoulos (3), C.J. François (2), A. Roldán-Alzate (1,2)

(1) Department of Mechanical Engineering
University of Wisconsin
Madison, WI, United States

(2) Department of Radiology
University of Wisconsin
Madison, WI, United States

(3) Department of Pediatric Cardiothoracic Surgery
University of Wisconsin
Madison, WI, United States

INTRODUCTION

Altered hemodynamics in total cavo-pulmonary connection (TCPC), a palliation of single ventricle defects, results in long-term complications, such as decreased exercise capacity, arrhythmia, and ventricular failure [1]. Patient-specific anatomy hinders a general solution for all patients. Although flow-sensitive magnetic resonance imaging (4D flow MRI) has been used to assess flow in TCPC *in vivo*, this approach is limited in its ability to predict flow behavior under extreme conditions or to evaluate effects of varying surgical procedures. Computational fluid dynamics (CFD) helps to understand hemodynamic phenomena and to virtually explore variations in physiological conditions, anatomy and tissue properties. Limitations due to simplifications and lack of validation have hindered clinical use of this potentially powerful tool [2]. The use of 3D printing to create patient-specific models is becoming more widely adopted, including complex congenital heart disease [3], as the technology becomes more ubiquitous and less expensive. There are now a variety of 3D printing techniques commercially available, including stereolithography (SLA), selective laser sintering (SLS), and fused deposition modeling (FDM) [4, 5]. There are substantial differences between each of these technologies with respect to their printing resolution, material properties, and costs. The impact of different printing resolutions and material properties on quantitative 4D flow MRI measurements in TCPC are unknown. In this study, we compared in vitro 4D flow MRI measurements in three models, each fabricated with a different 3D printing technique, to determine if there are any significant differences in hemodynamics due to manufacturing method.

METHODS

Patient-specific models: Three physical models of TCPC were created using 3D printing according to an IRB-approved and HIPAA-compliant protocol. The TCPC was segmented from images acquired as part of a clinical cardiac MRI study in MIMICs (Materialise, Leuven, Belgium) (Fig. 1A). The segmented TCPC volume was exported in STL format and printed using an SLA (Formlabs), an SLS (DTM Sinterstation 2500CI ATC), and an FDM (Makerbot Replicator) 3D printer (Fig. 1B). Internal support was removed from the SLA and FDM models. The FDM model was treated with acetone to remove remaining support material and smooth the internal surfaces.

In vitro MRI: Polyethylene tubing was attached to the inlets and outlets of the TCPC and then connected to a perfusion pump (Stockert SIII Heart-Lung Machine). MRI was performed on a clinical 3T scanner (GE Discovery MR 750, Waukesha, WI) with a 32-channel phase array body coil. 4D flow MRI was performed with a 5-pt radial-undersampled technique (PC-VIPR with following parameters: FOV = 32 x 32 x 32 cm^3, TR/TE = 5.5/2.3 ms, α = 15°, Venc = 150 cm/s, projection number ≈ 22000, 16 reconstructed cardiac time frames, scan time: 5 minutes 15 seconds. Each TCPC model was imaged separately while secured in agar, as water was pumped through the TCPC models at three different flow rates (1, 2, and 3 L/min).

Analysis: 4D flow MRI data sets were segmented, visualized and quantified in Ensight (CEI, Inc., Apex, NC). Velocity streamlines were generated to visualize flow trajectories (Fig. 1C). Flow (L/min), kinetic energy (mJ) and vorticity (s^{-1}) in the inferior vena cava (Fontan), superior vena cava (Glenn), left pulmonary artery (LPA), and right pulmonary artery (RPA) were quantified at each flow rate. Flow measurements were compared with flows experimentally measured using a clamp-on flow sensor (Transonic, Ithaca, NY). Flow values measured in each vessel were compared between different models using paired Student t-test. A p-value of 0.05 was chosen to indicate statistical significance. Finally, flow distributions (ratios) to the LPA and RPA were calculated.

Copyright 2016 The Organizing Committee for the 2016 Summer Biomechanics, Bioengineering and Biotransport Conference

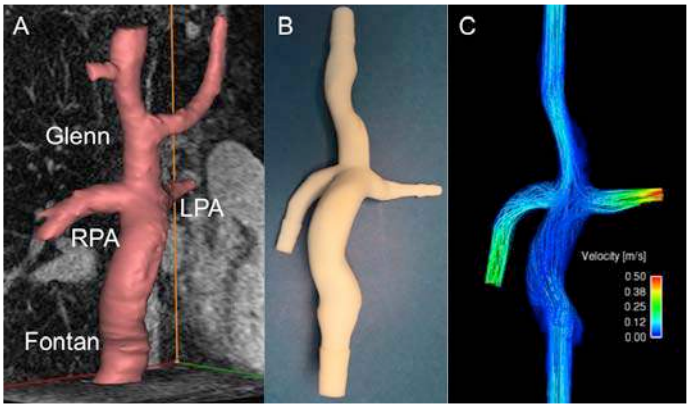

Figure 1: 3D patient-specific geometries generated from PC angiograms. A. Computational 3D model of extra-cardiac TCPC. B. TCPC model fabricated with SLS. C. Velocity streamlines.

RESULTS

4D flow MRI data was successfully acquired at each flow rate in all three models. Qualitative analysis of the velocity streamlines (Fig. 1C) revealed similar flow structures in the three models. Increase in flow rate did not substantially change the flow profiles and streamline distributions in any of the models. Excellent correlation between MRI and direct flow measurements was found (R^2 = 0.96) (Fig. 2). Differences in net flow measured with 4D flow MRI in the different models were not statistically significant ($p > 0.05$). Figure 3 shows vorticity and kinetic energy in the Fontan measured at the three different flow rates. Table 1 summarizes the flow distribution (%) to the LPA and RPA for the models at the three different flow rates.

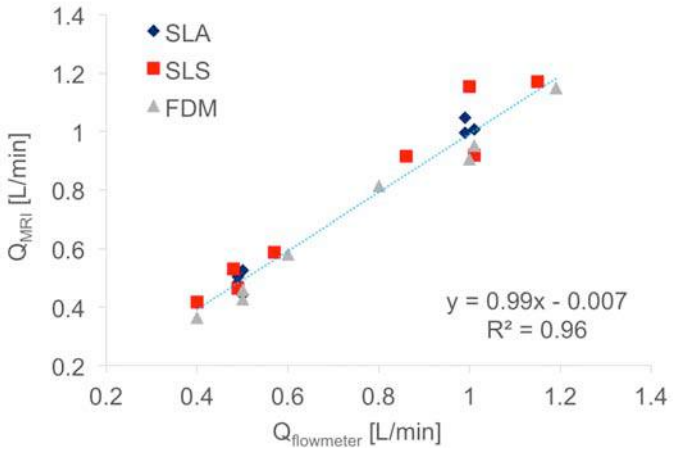

Figure 2: Linear correlation between MRI and direct flow measurements in TCPC in vitro models fabricated using SLA, SLS and FDM.

DISCUSSION

In-vitro systems, using SLA, SLS and FDM technologies, were developed using patient-specific models as a tool not only to control flow parameters but also to compare with CFD simulations. The three technologies showed similar flow measurements. Although not statistically significant, a trend can be noted at a flow of 3 L/min, where kinetic energy and vorticity show lower flow values for the FDM technique. Further analysis on surface roughness may add more insight into its effects on hemodynamics. Flow measurements performed with the flowmeter highly correlate with those done by 4D flow MRI, showing the accuracy of the latter as a technique to quantify flow. Using agar to fix the model substantially improved the signal-to-noise ratio in the MR images and significantly decreased motion artifacts when compared to the model submerged in water. The combination of additive manufacturing techniques and advanced MRI allows the in vitro hemodynamic assessment of highly complex anatomical variations in several cardiovascular pathologies.

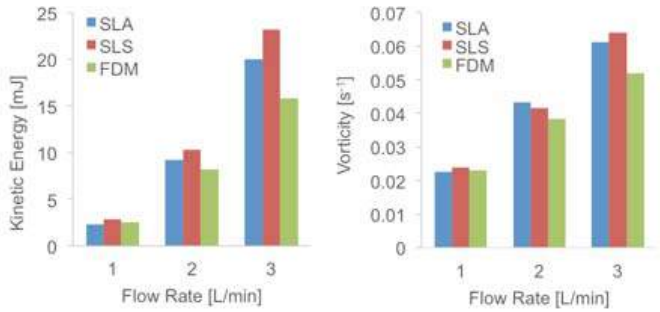

Figure 3: Comparison of kinetic energy (left) and vorticity (right) in the Fontan with respect to flow rate.

Table 1: Flow distribution (%) to the LPA and RPA for the different models at the three flow rates. Streamlines and arrows show the flow distribution and direction respectively.

		Outlet Flow %	
		LPA	RPA
1 L/min	SLA	51.08	48.92
	SLS	41.59	58.41
	FDM	38.55	61.45
2 L/min	SLA	48.73	51.27
	SLS	43.90	56.10
	FDM	41.42	58.58
3 L/min	SLA	47.86	52.14
	SLS	43.69	56.31
	FDM	39.65	60.35

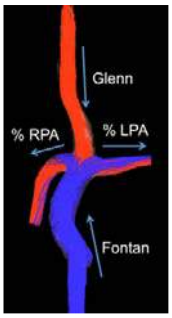

ACKNOWLEDGEMENTS

We are grateful to the American Heart Association for the Scientist Development Grant (AR) and to GE Healthcare for its support.

REFERENCES

[1] Khairy P et al., Circulation, 117:85-92, 2008.
[2] Haggerty CM et al., Ann Biomed Eng, 40:2639-51, 2012
[3] Roldán-Alzate, A et al., Journal of Biomechanics, 48:1325–1330, 2015
[4] Gibson, I et al., *Additive Manufacturing Technologies*, 5:103-161, 2010.
[5] Gebhardt, A et al., *Understanding Additive Manufacturing: Rapid Prototyping, Rapid Tooling, Rapid Manufacturing,* 2:34-40, 2012.

Copyright 2016 The Organizing Committee for the 2016 Summer Biomechanics, Bioengineering and Biotransport Conference

SB^{3}C2016
Summer Biomechanics, Bioengineering and Biotransport Conference
June 29 –July 2, National Harbor, MD, USA
SB^{3}C2016-758

SHEAR STRESS MAINTAINS ENDOCARDIAL PHENOTYPE IN INDUCED PLURIPOTENT STEM CELL DERIVED ENDOCARDIAL CELLS

Mark J. Vander Roest (1), Camryn L. Johnson (1), H. Scott Baldwin (2), W. David Merryman (1,2)

(1) Biomedical Engineering and (2) Pediatric Cardiology
Vanderbilt University
Nashville, TN, USA

INTRODUCTION

Tissue engineered heart valves (TEHVs) are an unmet medical need that have not been able to achieve long term viability post-implantation. Previous TEHV models using cell sources such as mesenchymal stem cells or arterial fibroblasts have failed due to valve calcification, stenosis, and fibrosis [1]. These outcomes suggest a failure of the cells to respond to the dynamic environment of the valve appropriately. Potentially, these problems may be addressed by using patient specific induced pluripotent stem cells (iPSCs) that are differentiated into endocardial cells and subsequently guided *in vitro* to the cell types of the mature cardiac valves.

Endocardial cells are a unique subtype of endothelial cells which line the chambers of the heart. During embryonic development, a select population of endocardial cells overlaying localized swellings in the primitive heart tube called endocardial cushions undergo endothelial to mesenchymal transformation (EMT) to become valve interstitial cells (VICs). These cells invade the cushion and remodel the extracellular matrix to form the atrioventricular valves. In mature valves, VICs function to maintain the structure and integrity of the valve, making them an ideal cell source for TEHVs. Unfortunately, these cells are often defective in patients needing valve replacements, and no stem cell based method to generate them currently exists.

Current biochemical strategies of stem cell differentiation use static culture, which does not represent the dynamic mechanical environment of the developing heart. Contraction of the myocardium and blood flow over the endocardium impart mechanical stretch and fluid shear respectively, which are known to affect endocardial EMT and valve development [2]. We hypothesize that incorporating these mechanical stimuli in the differentiation of endocardial cells will create a more physiologically relevant environment, enabling the generation of an alternative cell source for tissue engineered heart valves. Herein, we demonstrate that we can utilize mechanical stimulation to drive endothelial progenitor cells (CD34+) derived from human iPSCs down an endocardial lineage (Nfatc1+). These cells may be an essential cell source for patient-specific TEHVs.

METHODS

iPSCs were maintained on Matrigel in mTeSR, changed daily. Endothelial progenitors were generated following a previously published differentiation protocol [3]. iPSCs were dissociated to single cells and seeded at 50,000 cells/cm^2 onto Matrigel coated six-well culture dishes in mTeSR with 10 μM ROCK inhibitor (Y-27632) for 24 hours, after which they were cultured for an additional two days in mTeSR. After three days in culture, media was changed to a basal media consisting of Advanced DMEM/F12 with 2.5 mM Glutamax and 60 μg/mL ascorbic acid with 6 μM GSK3 inhibitor (CHIR99021). After two days in culture, media was replaced with basal media without additional CHIR and cells were cultured for an additional 3 days.

Endothelial progenitors were purified by MACS cell separation with a CD34 MicroBead kit (Mitenyi Biotec). Cells were immediately seeded onto collagen IV coated BioFlex culture plates (FlexCell) in EGM-2 MV (Lonza). Cells were allowed to adhere and grow to confluency (3-4 days). Confluent monolayers of endothelial progenitors were subjected to either equibiaxial strain using the FlexCell-4000 tension system or fluid shear using a custom built bioreactor (**Figure 1**). A strain regimen was created to approximate physiological values (10% strain, 1Hz) and carried out for 24 - 48 hours. Likewise, shear testing was performed at physiologically relevant values of 10-15 dyne/cm^2 in either pulsatile, unidirectional flow, or bidirectional flow. Following mechanical stimulation, cells were lysed for analysis. RNA was isolated from cell lysates using TRIzol and reverse transcribed to cDNA using a

Copyright 2016 The Organizing Committee for the 2016 Summer Biomechanics, Bioengineering and Biotransport Conference

SuperScript IV Reverse Transcriptase kit. qPCR was performed with an iQ SYBR Green kit and BioRad CFX96 themocycler.

RESULTS

Endothelial differentiation was demonstrated via qPCR throughout the differentiation protocol and CD31 immunostaining of differentiated cells following one week of culture in endothelial media. The results indicate successful generation and efficient purification of endothelial progenitors (CD34+) at day eight of the protocol (**Figure 2**). HUVECs were used as an endothelial control for comparison. Notably, expression of endocardial marker Nfatc1 was higher in the differentiated cells than in the HUVECs, indicating the presence of cells with an endocardial expression profile (**Figure 2D**).

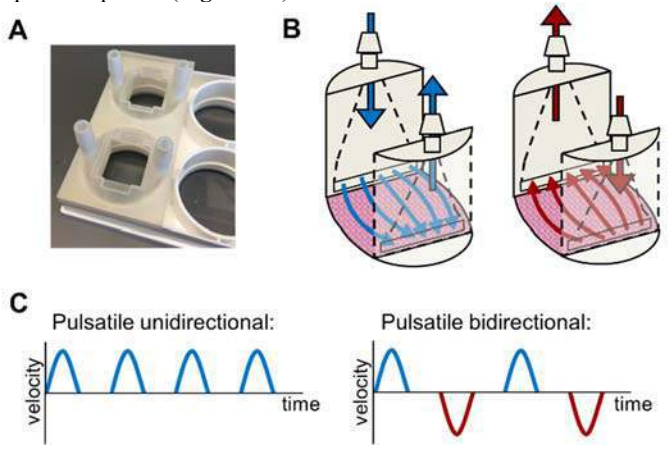

Figure 1: Photograph (A) and schematic (B) of fluid shear device designed for use with BioFlex culture plates. (C) Flow pattern for unidirectional and bidirectional flow.

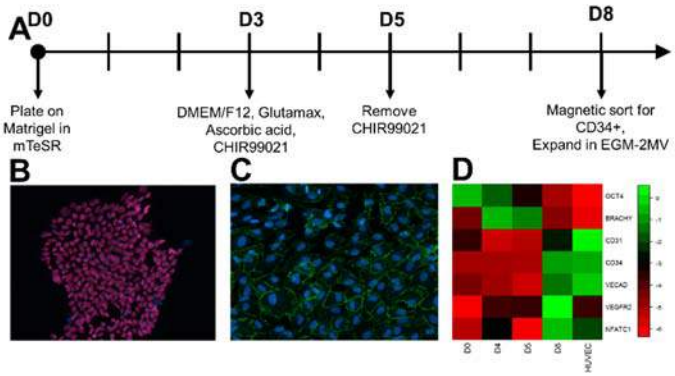

Figure 2: (A) Timeline of endothelial differentiation of iPSCs. (B-C) Immunostaining of D0 iPSCs (B. Oct4-red, DAPI-blue) and iPSC-endothelial cells (C. CD31-green, DAPI-blue). (D) Heatmap showing transition from pluripotency through mesoderm (Brachyury), to an endothelial precursor. Color bar in log10 scale.

Shear testing of the cells revealed differential gene expression response to unidirectional versus bidirectional flow (**Figure 3**). While uni-directional flow increased expression of Nfatc1, bidirectional flow caused a slight decrease. This decreasing Nfatc1 expression was accompanied by a dramatic increase in expression of Snai2, an EMT inducing transcription factor, and BMP2, an EMT associated protein known to be required for endocardial EMT [4]. These changes to EMT markers were not seen to nearly the same extent in cells sheared unidirectionally. Finally, cyclic strain was found to down-regulate both endocardial and EMT markers. Together, these data indicate a role of pulsatile unidirectional shear stress in maintaining an endocardial phenotype while bidirectional shear induces EMT.

DISCUSSION

This study shows fluid shear stress to be a potential regulator of endocardial cell phenotype and that the pattern of the shear stress may be a source of further control. Several genes were differentially regulated in unidirectional versus bidirectional shear stress, including endocardial marker Nfatc1 and EMT inducing transcription factors Snai2 and BMP2. The inverse effects of the two shear conditions could provide a tool with which to both maintain an endocardial population (uni-directional flow) and induce EMT to generate VICs (bidirectional flow). This type of control over cell fate would be extremely beneficial in creating a novel cell source for tissue engineered heart valves.

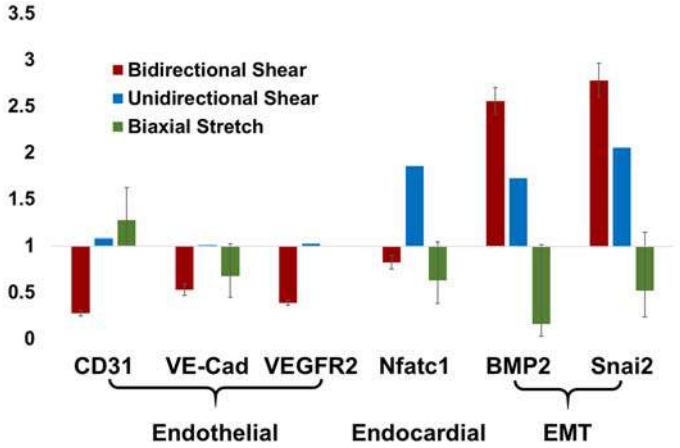

Figure 3: qPCR quantified expression of endocardial and EMT markers in endothelial progenitors exposed to unidirectional or bidirectional shear, or mechanical strain relative to endothelial progenitors in static culture.

ACKNOWLEDGEMENTS

This work was supported by the NIH (5T32HL007411-34).

REFERENCES

[1] R. a. Rippel, H. Ghanbari, and A. M. Seifalian, "Tissue-engineered heart valve: Future of cardiac surgery," *World J. Surg.*, vol. 36, no. 7, pp. 1581–1591, 2012.

[2] M. K. Sewell-Loftin, D. M. DeLaughter, J. R. Peacock, C. B. Brown, H. S. Baldwin, J. V Barnett, and W. D. Merryman, "Myocardial contraction and hyaluronic acid mechanotransduction in epithelial-to-mesenchymal transformation of endocardial cells.," *Biomaterials*, vol. 35, no. 9, pp. 2809–15, Mar. 2014.

[3] X. Lian, X. Bao, A. Al-Ahmad, J. Liu, Y. Wu, W. Dong, K. K. Dunn, E. V. Shusta, and S. P. Palecek, "Efficient Differentiation of Human Pluripotent Stem Cells to Endothelial Progenitors via Small-Molecule Activation of WNT Signaling," *Stem Cell Reports*, vol. 3, no. 5, pp. 804–816, 2014.

[4] L. Ma, M.-F. Lu, R. J. Schwartz, and J. F. Martin, "Bmp2 is essential for cardiac cushion epithelial-mesenchymal transition and myocardial patterning.," *Development*, vol. 132, no. 24, pp. 5601–11, Dec. 2005.

Copyright 2016 The Organizing Committee for the 2016 Summer Biomechanics, Bioengineering and Biotransport Conference

SB^{3}C2015
Summer Biomechanics, Bioengineering and BIotransport Conference
June 29 –July 2, National Harbor, MD, USA
SB^{3}C2016-759

DETERMINATION OF THE TENSILE MECHANICAL PROPERTIES OF THE SEGMENTED TRICUSPID VALVE ANNULUS

Fatima Al-Quaiti (1), Evelia Salinas (1), Lori Boies (1), Edward Sako (2), Shamik Bhattacharya (1)

(1) School of Science, Engineering and Technology
St. Mary's University
San Antonio, Texas, United States

(2) Cardiothoracic Surgery
University of Texas Health Science Center at San Antonio
San Antonio, Texas, United States

INTRODUCTION

The tricuspid valve apparatus consists of the tricuspid annulus, leaflets, and chordae. The valve is located between the right atrium and right ventricle of the heart and prevents the back flow (regurgitation) of blood into the right atrium. The tricuspid annulus (TA) is defined as the hinge point of the leaflets (Figure 1A); surgically it is identified as the apparent transition between the right atrial tissue and the tricuspid leaflet.

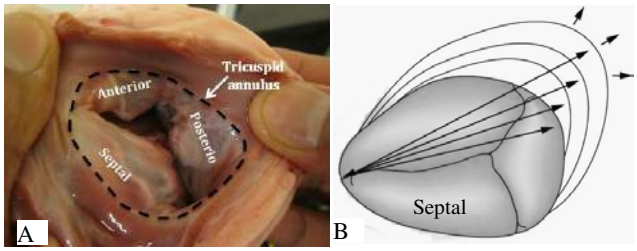

FIGURE 1 – (A) THE NATIVE TRICUSPID VALVE ANNULUS AND (B) TRICUSPID ANNULUS DILATION

Functional tricuspid regurgitation (FTR) is increasingly recognized as a source of morbidity in patients, particularly those with chronic mitral valve regurgitation [1]. Asymmetrical tricuspid annulus dilation (Figure 1B) is a major feature in FTR. The mechanism of this asymmetric dilation is not understood clearly. Tricuspid ring annuloplasty (TRA) is the most preferred surgical therapy to repair FTR. In TRA, a partial ring is sutured to the annulus, which cinches the dilated annulus and restores the native shape. However, the ring only partially covers the annulus, keeping the septal segment untouched due to the presence of the AV node. After TRA, instances of recurrent regurgitation, septal dilation, and ring separation have occurred [2]. Differing strengths between the free and septal annulus segments can contribute to the asymmetrical annulus dilation or to the septal dilation after TRA. The hypothesis is that the annulus segments may not have same mechanical properties. To date, there has been no quantification of the mechanical properties of the tricuspid valve annulus. This study aims to quantify the tensile mechanical properties of the segmented tricuspid annulus. The data collected will be used to identify the differences in the tensile mechanical properties between the septal and free wall regions across species. The findings of this study may potentially enhance our understanding of asymmetrical tricuspid annulus dilation and may contribute to the durability of the TRA technique.

METHODS

This method was modeled after a previous tensile test study of the mitral valve annulus [3]. Ovine and porcine hearts were collected from local slaughterhouses and transported in coolers. Hearts were cryopreserved until the day of the experiment upon which hearts were thawed in a saline bath at 37.5°C. To carry out the experiment, we used the UStretch Tissue Tensile Test system (Cellscale). The TA was cut into a free wall segment and a septal wall segment. The free wall segment consisted of the anterior and posterior sections. The tissues were then isolated and trimmed to an approximate length of 30.0 mm, width of 6.0 mm, and thickness of 1.2 mm. The tissues were then marked with 4 graphite markers placed in a square at the center of the tissue. We secured 6.0 to 7.0 mm of the tissue on both sides between two grips (Figure 2).

Copyright 2016 The Organizing Committee for the 2016 Summer Biomechanics, Bioengineering and Biotransport Conference

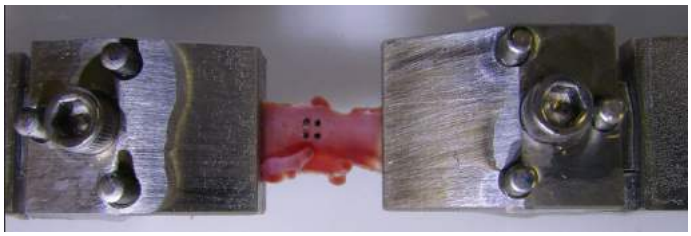

FIGURE 2 – TENSILE TEST SET-UP OF TRICUSPID ANNULUS SEGMENTS

The experiment was carried out at 37.5°C. Samples first underwent a preconditioning phase in which the tissues were stretched by 7.5 mm at a speed of 2.0 mm/min and then recovered to their original length. After the completion of the preconditioning phase, the tissues were stretched at a speed of 2.0 mm/min until they presented the first sign of failure, which was indicated by a drop in the magnitude of force required to stretch the tissue.

To calculate stress, the force was divided by the product of the thickness and width of the tissue. Stress was analyzed through a calculation of force divided by the product of tissue thickness and width. The percent strain was quantified using UStretch image analysis. As shown in Figure 3, the trackers were placed at the center of each marker, and the percent strain was measured for each movement between images as a 4-point average.

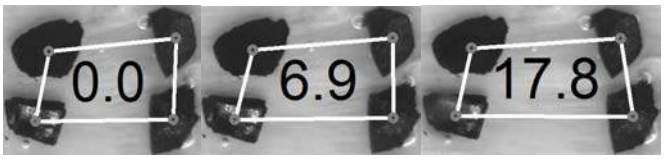

FIGURE 3 – CALCULATED PERCENT STRAIN USING POSITIONED TRACKERS

RESULTS

The results are based on two ovine hearts and two porcine hearts. In the preconditioning (Figure 4) and stretch to failure curves (Figure 5), we found that as the tissues were stretched, the stress and strain also both increased. Variation of mechanical properties between the septal and free wall regions was greater for the porcine hearts compared to the ovine hearts.

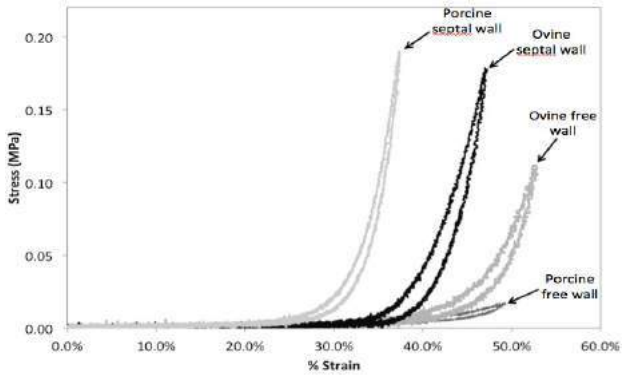

FIGURE 4 – PRE-CONDITIONING CURVES FOR OVINE AND PORCINE TRICUSPID ANNULUS SEGMENTS

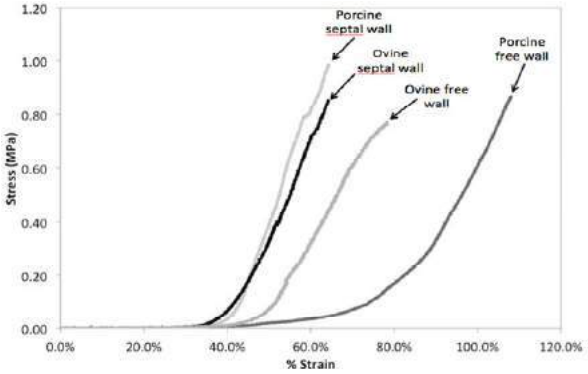

FIGURE 5 – STRETCH TO FAILURE CURVES FOR OVINE AND PORCINE TRICUSPID ANNULUS SEGMENTS

The porcine septal wall tissue samples had an average stress and strain of 0.983 MPa and 64.4%, respectively. The porcine free wall tissue samples experienced an average stress of 0.868 MPa and an average strain of 108.1% at the first sign of failure. The ovine septal wall tissue samples had an average stress and strain of 0.854 MPa and 64.2%, respectively. The ovine free wall tissue samples experienced an average stress of 0.771 MPa and an average strain of 78.4% at the first sign of failure.

DISCUSSION

The mechanical properties of the TA have not been investigated. The purpose of this study is to build a database for the mechanical properties of the TA. In both species, it appears that the septal wall can withstand a larger stress, but lower strain than the free wall before failing. We found that the septal walls of the porcine hearts could withstand a greater amount of stress and lower amount of strain than the ovine hearts before exhibiting the first sign of failure. The free wall tissues of the porcine hearts experienced lower stress and lower strain than the free wall tissues of the sheep hearts.

Although the stress increases with strain and strain and vice versa, their values at the first sign of failure for the porcine septal wall tissue were lower than the values shown at the first sign of failure for the septal tissue in the ovine hearts, indicating that the two species do not exhibit the same stress and strain over the same amount of tissue.

The preliminary experiment showed a difference in the mechanical properties between the septal and free wall regions of porcine and ovine TA. More experiments need to be done to validate these findings. The variation in mechanical properties across different segments of the TA and across the species may help us understand the mechanics of asymmetrical tricuspid annulus dilation. The results can also enhance our understanding of the cause of septal dilation following TRA. This can lead to a better ring design, increase the durability of TRA, or the development of a percutaneous TRA technique.

ACKNOWLEDGEMENTS

The work is supported by St. Mary's Research grant, IIMS-CTSA grant (UTHSCA), and MARC fellow training aid. We thank Daniel Gerdin for his help in this work and appreciate all the support given by Dr. Tim Raabe.

REFERENCES

[1] Izumi, C., K. Iga, and T. Konishi, *Progression of isolated tricuspid regurgitation late after mitral valve surgery for rheumatic mitral valve disease.* J Heart Valve Dis, 2002. **11**(3): p. 353-6.

[2] Isomura, T., et al., *Tricuspid annuloplasty with the MC3 ring and septal plication technique.* Asian Cardiovasc Thorac Ann, 2015. **23**(1): p. 5-10.

[3] Gunning, G.M. and B.P. Murphy, *Determination of the tensile mechanical properties of the segmented mitral valve annulus.* J Biomech, 2014. **47**(2): p. 334-40.

Copyright 2016 The Organizing Committee for the 2016 Summer Biomechanics, Bioengineering and Biotransport Conference

SB^{3}C2016
Summer Biomechanics, Bioengineering and Biotransport Conference
June 29 –July 2, National Harbor, MD, USA
SB^{3}C2016-760

CHANGES IN NUCLEAR STIFFNESS OF NESPRIN-1 DEPLETED FIBROBLASTS EXPOSED TO CYCLIC STRETCHING

Naoya Sakamoto (1), Kiyomi Sadamoto (2), Mai Ogawa (2), Masaki Takeuchi (2), Noriyuki Kataoka (3)

(1) Department of Intelligent Mechanical Systems
Tokyo Metropolitan University
Hachioji, Tokyo, Japan

(2) Department of Medical Engineering
Kawasaki University of Medical Welfare
Kurashiki, Okayama, Japan

(3) Department of Mechanical Engineering
Nihon University
Koriyama, Fukushima, Japan

INTRODUCTION

The nucleus is the largest organelle in the cell and its primary functions are maintaining hereditary information and controlling cell activities. Alternations of nuclear functions and components thus have been implicated in disease pathogenesis. Recently, mechanical condition of the nucleus in a cell and its mechanical properties have also received increasing attention, because changes of nuclear mechanical properties are found as features of cancer cells and "laminopathies" patient cells, which are genetic disorders caused by mutations in genes encoding nuclear membrane proteins [1, 2].

Previous studies have shown that mechanical stimuli such as fluid shear stress and mechanical cyclic strain induce changes in mechanical properties of the nuclei of cells [3, 4]. Mechanical stimuli are now recognized as important cues for cell physiology and pathology, and known to cause morphological changes concomitant with actin cytoskeletal reorganization. Mechanical forces acting on the surface of a cell are transmitted through actin cytoskeletons to intracellular mechano-sensor regions such as focal adhesions and intercellular junctions where mechanical signals are sensed and transduced into biochemical signals. Since actin cytoskeletons are bound to the nucleus in the cell with LINC (linker of nucleoskeleton and cytoskeleton) complex, which is composed of nesprins and SUN proteins, and mechanical forces are also transmitted to the nucleus and believed to play important roles in cell morphology and functions. Indeed, previous studies reported that knockdown of nesprin-1, which is a component of LINC complex and directly bind to actin cytoskeletons in cells, causes suppression of the cell morphological responses to mechanical stimuli [5, 6]. However, the detailed relationship between the force transmission to the nucleus and nuclear mechanics are still unclear.

To address the underlying mechanisms, we explored the effect of knockdown of nesprin-1, a key component of LINC complex for the force transmission to nucleus, on nuclear mechanical properties of cells exposed to cyclic stretching.

METHODS

Cell culture and siRNA transfection

Human skin fibroblasts (Riken Bioresource Center, Japan) were used in the present study. For siRNA knockdown of nesprin-1, cells were transfected with 100 nM siRNA targeting human nesprin-1 (Dharmacon, USA) according to manufacturer's protocol. To confirm reduction of nesprin-1 expression, cells were fixed, stained with an antibody for nesprin-1 (Abcam) and Hoechst33342 (Life Technologies), and examined by fluorescence microscopy (Olympus).

Cyclic stretching experiment

Fibroblasts treated with siRNA were detached form a cell culture flask with tryspin-EDTA, seeded in a collagen-coated stretching chamber (Strex, Japan), and then subjected to 10 % uniaxial cyclic stretching at 1 Hz for 24 h.

AFM measurement

After the cyclic stretching experiment, atomic force microscopy (AFM) indentation (Olympus, Japan) was performed to assess the nuclear mechanical properties in cells. Force-indentation curves were captured at the center of single intact cell (i.e., over the nucleus). Curves obtained were then fitted to the Seddon model (eq. 1) to calculate apparent nuclear elastic moduli.

$$F = \frac{2E\tan\alpha}{\pi\left(1-\nu^2\right)}d^2 \quad , \qquad (1)$$

Copyright 2016 The Organizing Committee for the 2016 Summer Biomechanics, Bioengineering and Biotransport Conference

where F is the loading force, E is the elastic modulus of the sample, d is the indentation depth, ν is the poisson ratio of the sample, and α is the half cone effective angle. It should be noted that in preliminary experiments (data not shown), we confirmed that changes of nuclear mechanical properties in intact cells can be assessed by this method.

RESULTS

Fluorescence microscopy showed that localization of nesprin-1 to the nuclear envelope observed in non-treated wild type cells (WT cells) was depleted in fibroblasts transfected with siRNA targeting nesprin-1 (siNes1 cells) (Fig. 1). This result indicates that the expression of nesprin-1 in fibroblasts was depleted by transfection of nesprin-1-specific siRNA.

Typical force-indentation curves are shown in Fig. 2. There is no obvious difference in curves for statically cultured WT cells and siNes1 cells. For the WT cells, similar force-indentation curves were obtained after exposure to cyclic stretching for 24 h. In contrast, curves for cyclic-stretched siNes1 cells have lower slope than those for static cells.

Fig. 3 indicates apparent elastic moduli of nuclei for WT and siNes1 cells. No significant differences in the elastic modulus of nuclei were found between static WT cells and static siNes cells. The elastic modulus for siNes1 cells exposed to cyclic stretching was significantly lower than those for static siNes1cells and cyclic-stretched WT cells.

DISCUSSION

The result of this study suggests that nesprin-1 plays an important role in maintenance of nuclear mechanical stiffness in cells under mechanical condition. Lamins, the major components of nuclear lamina, are known to provide mechanical stiffness of the nuclei, but nuclear lamin-associated proteins are also thought to contribute the nuclear mechanical properties. A recent study reported that a mechanical force applied via nesprin-1 caused an increase in phosphorylation of emerin, one of the lamin-associated proteins [2], which may lead structural reorganization of nuclear lamina. We need to investigate changes in protein expression and structures of nuclear lamina in cells exposed to cyclic stretching as a next step.

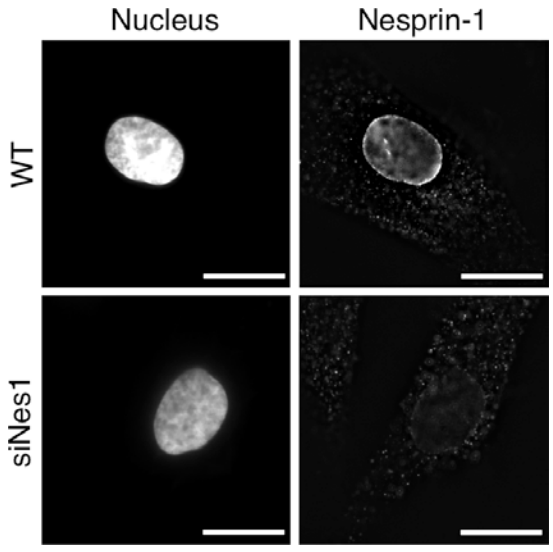

Figure 1: Typcical fluorescence images of nucleus and nesprin-1 in wild type (WT) and siRNA-transfected (siNes1) fibroblasts. Bars = 20 μm.

ACKNOWLEDGEMENTS

This study was supported in part by Grants-in-Aid for Scientific Research by the MEXT of Japan (No. 15K01304).

REFERENCES

[1] Scaffidi, P et al., *PLos Biol*, 3: 1885-1895, 2005.
[2] Dahl, KN et al., *Microcirculation*, 17: 179-191, 2010.
[3] Deguchi, S et al., *J Biomech*, 38: 1751-1759, 2005.
[4] Guilluy, C et al., *Nat Cell Biol*, 4: 376-381, 2014.
[5] Chancellor, TJ et al., *Biophys J*, 99: 115-123, 2010.
[6] Anno, T, et al., *Biochem Biophys Res Commun*, 424: 94-99, 2012.
[7] Seddon IN, *Int J Eng Sci*, 3: 47-57, 1995.

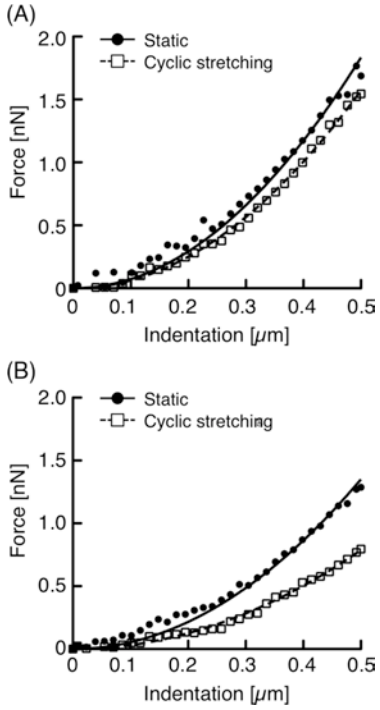

Figure 2: Typical force-indentation curves obtained by AFM indentation tests for nuclei of wild type (A) and siRNA-transfected (B) fibroblasts.

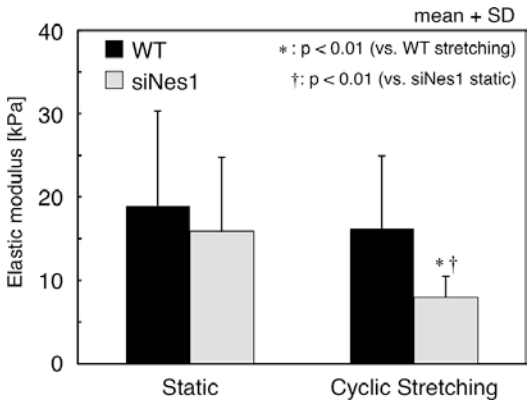

Figure 3: Elastic moduli of nuclei of wild type (WT) and siRNA-transfected (siNes1) fibroblasts. n = 30.

Copyright 2016 The Organizing Committee for the 2016 Summer Biomechanics, Bioengineering and Biotransport Conference

SB^{3}C2016
Summer Biomechanics, Bioengineering and Biotransport Conference
June 29 –July 2, National Harbor, MD, USA
SB^{3}C2016-761

INTRAOCULAR PRESSURE MEASUREMENT THROUGH THE LASER INDUCED CAVITATION BUBBLES DYNAMICS.

Luis F. Devia-Cruz[1], Santiago Camacho-López[1]

(1) Departamento de Óptica, Centro de Investigación Científica y de Educación Superior de Ensenada, Carretera Ensenada-Tijuana No. 3918, Zona Playitas, C.P. 22860, Ensenada, B. C., Mexico.

INTRODUCTION

The Intraocular pressure (IOP) is a mechanical property of the intraocular fluids in the eyeball. One of the main eye diseases that affect the IOP is the so called Glaucoma, it alters the intraocular aqueous humor balance, causing an elevation of the intraocular pressure, and therefore irreversible damage to the optic nerve terminal fibers. Currently, the IOP measurement is performed by using techniques based on the Imbert-Fick principle (Chihara 2008); which states that the pressure of a liquid inside a thin-walled sphere is proportional to the force required to flatten part of its surface, divided by the area of flattening. This type of measurement requires physical contact to directly induce a mechanical deformation of the human eyeball. Several ophthalmologist reports point out the fact that patient movements, blood pressure changes, and the cornea physical characteristics which are distinct person to person, directly affect the IOP measure accuracy and precision.

The study of the laser-induced cavitation phenomenon in biological media began with the use of Q- switched lasers in therapeutic applications in the mid 60's Lee &Gojani [1]. With the advent of lasers in medicine, it is possible to cut and remove material at a few microns scale; these new techniques were based on the mechanism of breaking of molecular bonds due to high energy lasers that provided UV ranges and high absorption of the tissue to such wavelengths Niemz [2].

Cavitation bubbles are well characterized through their maximum radius and collapse time; however them both are elaborated and expensive to determine. The traditional laser-photographic techniques require several laser shots and bubbles generated in order to recreate a whole bubble event and its dynamics Gregorčič[3], Evans [4]. An immediate disadvantage is the fact that even when the shot to shot energy per pulse does not fluctuate much, the stochastic nature of the laser-induced plasma produces a slightly different cavitation bubble from shot to shot making it somehow hard to fully recreate a single cavitation bubble event from a series of many laser shots. The use of high-speed cameras, say over 300.000 frames per second,is expensive and no matter this speed it still happens many times to miss either the maximum radius or the exact time collapse frames. This is a significant inconvenience since those data are quite important for the study and applications of the cavitation bubble phenomenon.

METHODS

The experimental part of this work is based on a recently reported cavitation characterization technique called Transmittance Spatial Modulation (TSM), Devia et Al. 2012 [5] , where the modulation of the spatial intensity profile of a probe CW beam is generated by the cavitation bubble itself. A HeNe laser (@632.8 nm) was used as probe beam, it passed co-linearly (see Figure 1) with the pump (@532nm) beam and then it is collimated throughout the sample. When the pump pulse arrives and the cavitation process starts, the bubble grows to its maximum size, and then it collapses to start it over again.

The bubble acts as a negative lens, therefore the (collimated probe) light incident onto the bubble is deflected or/and scattered sideways and the total amount of light detected is inversely proportional to the bubble size. All the transmitted light was collected through a lens onto a fast (1 ns rise time) photo diode, whose signal was visualized and recorded using an oscilloscope (1GHz, Tektronix DPO). Figure 2 shows a typical trace of the time evolution of the whole cavitation event. The collapse time for the first bubble depends

Copyright 2016 The Organizing Committee for the 2016 Summer Biomechanics, Bioengineering and Biotransport Conference

on both the pump pulse energy and on the actual liquid pressure. It is then possible, to infer the actual liquid pressure by just measuring the first collapse time for a given pump pulse energy.

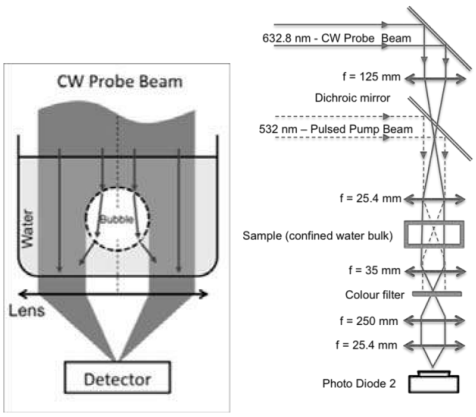

Figure 1.STM technique operation principle and experimental setup.

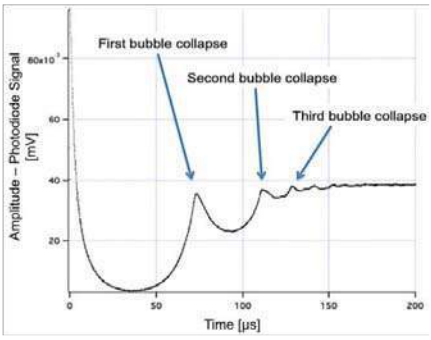

Figure 2. Trace from the transmitted light that propagates through the cavitation Bubble plane. The collapse times can be measured off from this trace with a high time resolution, since the trace is obtained by using a very fast photo diode.

RESULTS

The collapse time was measured under several liquid pressure values and pulse energy conditions. Parametric curves of the collapse time dependence on the liquid pressure were obtained and are shown in Figure 3.

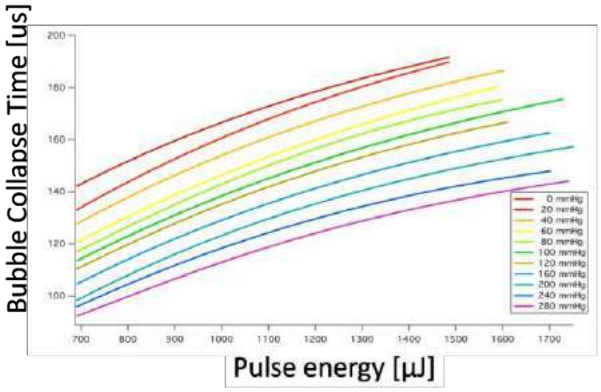

Figure 3. Cavitation bubble collapse time dependence on the liquid pressure and pump pulse energy.

DISCUSSION

The first collapse time in a laser-induced cavitation bubble event depends clearly on both the external liquid pressure and on the laser pulse energy. For well-known pulse energy, it is possible to infer the actual liquid pressure by precisely measuring the bubble collapse time. The presented STM technique seems to be a feasible way of implementing an IOP sensor. By using this technique the IOP measurement is expected to be more accurate than traditional tonometry measurements. Some advantages of the laser- induced cavitation and STM based sensor, among other,are that the in this case the IOP measurements would not depend on person to person factors as: patient age, gender, patient eye ball movements during measuring and/or corneal thickness. This is so due to the fact that the through the scheme proposed here the IOP measurement takes only a few tens of microseconds and the sensor measures the IOP directly inside the anterior chamber, avoiding all the above mentioned factor as sources of uncertainty on the measurements.

ACKNOWLEDGEMENTS

LFDC acknowledges CONACyT support through PhD scholarship. Authors acknowledge partial support to this research work by Oftálmica Internacional.

REFERENCES

[1] Lee, H., et al., Dynamics of laser-induced bubble collapse visualized by time-resolved optical shadowgraph. Journal of Visualization, 2011. 14 (4): p. 331-337.

[2] Laser Tissue Interactions Fundamentals and Applications. Markolf H.Niemz. Third ed. Biological and medical physics, biomedical engineering. 1996, Springer: Germany.

[3] Gregorčič, P., et al., Measurements of cavitation bubble dynamics based on a beam-deflection probe. AppliedPhysics A, 2008. 93 (4): p. 901-905.

[4] Evans, R. and S. Camacho-López, Pump-probe imaging of nanosecond laser-induced bubbles in distilled watersolutions: Observations of laser-produced-plasma. Journal of Applied Physics, 2010.108(10): p. 103106.

[5] Devia-Cruz, Luis F., Santiago Camacho-López, Rodger Evans, et al. 2012. Laser-induced cavitation phenomenon studied using three different optically-based approaches – An initial overview of results. Photonics and Lasers in Medicine. 1(3): 143-229.

Copyright 2016 The Organizing Committee for the 2016 Summer Biomechanics, Bioengineering and Biotransport Conference

SB^{3}C2016
Summer Biomechanics, Bioengineering and Biotransport Conference
June 29 –July 2, National Harbor, MD, USA
SB^{3}C2016-762

SIMULATION OF AIRFLOW IN REALISTIC MODEL PULMONARY ACINUS

Y. Inagaki (1), K. Yamanaka (1), G. Tanaka (1), T. Sera (2)

(1) Department of Mechanical Engineering,
Chiba University
Chiba, Chiba, Japan

(2) Department of Mechanical Engineering,
Kyushu University
Fukuoka, Fukuoka, Japan

INTRODUCTION

Many diseases occurring within a lung are caused by deposition of inhaled particle. Therefore, predilection sites of lung diseases are closely related to airflow in lung. In development of drag delivery system for lung, drug accessibility has a close relation with airflow in a lung. Especially, as a pulmonary acinus is complex shape, airflow in a lung can be much influenced by the complex acinus shape.

Since airflow in a pulmonary acinus has low Reynolds number, it was considered that molecular diffusion contributes to substance transportation. However, recently, it is reported that complex flow induced by expansion and contraction of acinar associated with respiratory enhances gas transportation [1]. Moreover, according to a previous report, as a result of experimental visualization of mixing in rat lungs, stretch and folding mixing pattern was observed in the lung [2]. On the other hand, in numerical simulation, characteristic of chaos mixing was observed in pulmonary airway, nevertheless, that was not observed in bronchiole [3]. This difference can be closely related to complex geometry of pulmonary acinus. Although several studies about pulmonary acinus were reported, characteristic of mixing in pulmonary acinus and mixing mechanism is not clear.

The objective of this study is to evaluate characteristic of chaos mixing in a realistic pulmonary acinus model in terms of streamline, distribution of scalar concentration and lyapunov exponent.

METHODS

A realistic 3D model of pulmonary acinus was reconstructed from synchrotron radiation-CT images of a closed-chest mouse. Model construction method is as previously reported [4]. Figure 1 depicts the realistic pulmonary acinus model. The volume size was 893×727×930μm^3, and the inlet was of 79.7 μm diameter. The computational mesh was generated using enGrid (enGits GmbH) and Amira 5.4.0 (Visualization Science Group). An unconstructed mesh with tetrahedron was created for the whole. The mesh comprised 1,079,407 cells.

The working fluid was air (density: ρ=1.140 kg/m^3, kinematic viscosity: ν=1.713×10^{-5}m^2/s) under body temperature (310K). The flow in the model was assumed to be 3D, laminar, unsteady, and incompressible. The governing equations were expressed as

$$\frac{\partial u_i}{\partial x_i} = 0 \quad (1)$$

$$\frac{\partial u_i}{\partial t} + \left(u_j - u_{gj}\right)\frac{\partial u_i}{\partial x_j} = -\frac{1}{\rho}\frac{\partial p}{\partial x_i} + \nu\frac{\partial^2 u_i}{\partial x_j x_j} \quad (2)$$

$$\frac{\partial \theta}{\partial t} + u \cdot \nabla\theta = a\nabla^2\theta \quad (3)$$

Where, u_g is the moving grid velocity. These equations were solved using non-commercial CFD library (OpenFOAM 2.3.x, OpenFOAM Foundation), with flow solver based on the PIMPLE method.

The overall configuration of the model was assumed to remain self-similar throughout the expansion and contraction cycle. The volume change *V(t)* was taken as a moving boundary problem given by the sinusoidal function of Eq.(4). The dynamic mesh function of OpenFOAM software was used to model the expansion and construction, with all grid velocity (u_g v_g w_g) given by Eqs.(5)-(7) based on the coordinate system with its origin (x_0 y_0 z_0) at the cross-sectional center of the artificial inlet.

$$\mathrm{V(t)} = V_{FRC} + V_T\left(\frac{1-cos\omega t}{2}\right) \quad (4)$$

$$u_g(t) = \left(x_g - x_0\right)\left(\frac{\sqrt[3]{V_{ratio}}-1}{2}\right)\omega sin\omega t \quad (5)$$

$$v_g(t) = \left(y_g - y_0\right)\left(\frac{\sqrt[3]{V_{ratio}}-1}{2}\right)\omega sin\omega t \quad (6)$$

$$w_g(t) = \left(z_g - z_0\right)\left(\frac{\sqrt[3]{V_{ratio}}-1}{2}\right)\omega sin\omega t \quad (7)$$

Copyright 2016 The Organizing Committee for the 2016 Summer Biomechanics, Bioengineering and Biotransport Conference

Here, V_{FRC} is functional residual capacity, V_{TLC} is total lung capacity, $\omega = 2\pi/T$ is angular frequency, and x_g, y_g, z_g are grid coordinates at t = 0. In this study, we set V_{FRC} and V_{TLC} as 4.94×10^{-11} and 18.7×10^{-11} m^3 respectively. Breathing period T was 4.0s.

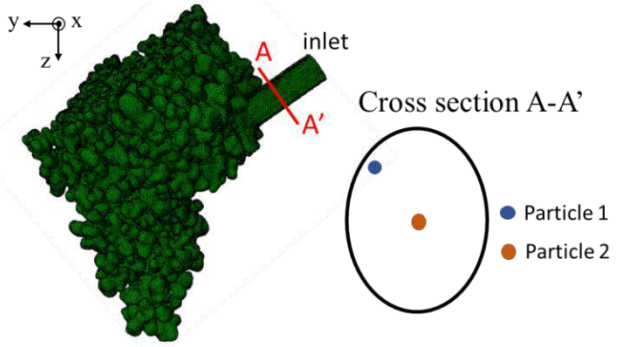

Figure 1: Pulmonary acinar model

The lyapunov exponent was calculated based on the particle tracking in order to judge the occurrence of the chaos [5]. Although the lyapunov exponent is strictly defined as a spectrum having dimensions of the phase space, practically the largest value among them is important. The largest lyapunov exponent λ is defined by the following Eq. (8).

$$\lambda = \lim_{t\to\infty}\left[\left(\frac{|dx(T)|}{|dx(0)|}\right)\right] \qquad (8)$$

Here $x(T)$ and $x(0)$ is the distance between two particles at time $t=T$ and t = 0, respectively. When λ is positive, the flow is chaotic. In the present study, λ was calculated from the distance between two neighboring particles during t/T = 0 - 7.0.

RESULTS

Figure 2 shows streamline in one of alveolus during one respiratory period at phase intervals of t/T= 0.25. The flow condition are Re_{max}=0.123 and Womersley number α=0.0129 in artificial inlet. The completion of inspiration at t/T=0.5 and the completion of respiration at t/T=1.0 correspond to the times of maximum and minimum volume, respectively. The phase of t/T=0.25 and the phase of t/T=0.75 correspond to the times of maximum and minimum grid velocity. A recirculating flow was observed at t/T=0.25, 0.75, however, a recirculating flow was not observed at t/T=0.5,1.0. Formation and elimination of vortex during one respiratory cycle was suggested.

The effect of the complicated flow on substance transportation was evaluated using advection-diffusion equation. We set thermal diffusion coefficient a as approximately zero to visualize scalar transportation lead to advection. Figure 3 (a) (b) shows distribution of scalar concentration in y-z plane passing the origin (x_0 y_0 z_0) at t/T=0, 2.0. The distribution at t/T=0 was totally different to the distribution at t/T=2.0. Especially, distribution of scalar concentration in alveolus was high.

Chaotic mixing was quantitatively evaluated using lyapunov exponent. Figure 3 shows lyapunov exponents in any two particles in a cross section A-A' (Figure 1). As a result, in seventh period, both of the lyapunov exponents show 0.14.

DISCUSSION

According to the previous report, in axial oscillatory flow through a furrowed channel, formation and elimination of unsteady vortex in furrowed part was observed [6], which was reported as chaotic mixing typical example [7]. It is presumed that a recirculating flow in this study was occurred owing to this phenomenon. This reason why distribution of scalar concentration in alveolus was high is that a fluid in an alveolus part was trapped by vortex.

Lyapunov exponent of Lorenz attractor and Rossler attractor, which was known for typical chaos example, was 0.1~1.5 [8]. Therefore, it is suggested that flow in a pulmonary acinus model has characteristic of chaotic mixing.

REFERENCES

[1] Henry, F. S. et al., *J. Appl. Phisiol.,* 92:835-845, 2002
[2] Tsuda, A. et al., *Proc. Natl. Acad. Sci.*, 99:10173-10178, 2002.
[3] Tanaka, G. et al., *Int. J. Heat Mas Transf*, 55;1873-1880, 2012.
[4] Sera, T. et al., *J. Appl. Physiology,* 115; 219-228, 2013
[5] Wolf, A., et al., *physica 16D*, 285-317, 1985.
[6] Sobey, I.J. et al., *Engeering Science*, 44; 2129-2134, 1985.
[7] Ottino, J.M., "The kinematics of mixing: stretching, chaos, and transport", Cambridge University, 252-256, 1989
[8] Sato, S. et al., *Prog. Theor. Phys*., 77(1); 1-5, 1987.

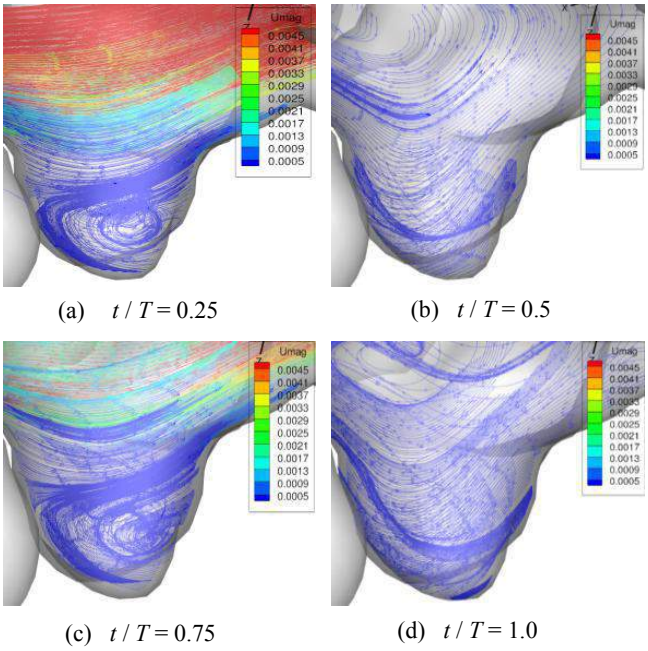

Figure 2: Streamline in pulmonary acinar model

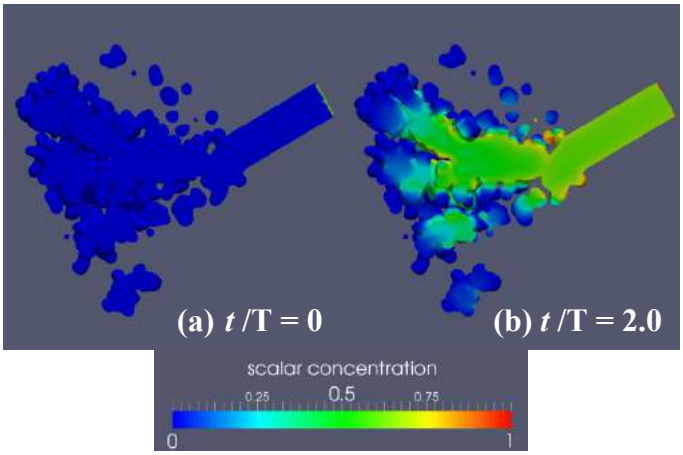

Figure 3: Distribution of scalar concentration

Copyright 2016 The Organizing Committee for the 2016 Summer Biomechanics, Bioengineering and Biotransport Conference

SB³C2016
Summer Biomechanics, Bioengineering and Biotransport Conference
June 29 –July 2, National Harbor, MD, USA
SB³C2016-763

EFFECT OF DEFORMATION ON CEREBRAL ANEURYSM IN MIDDLE CEREBRAL ARTERY

S. Omachi (1), G. Tanaka (1), H. Liu (1), R. Yamaguchi (1)

(1) Graduate School of Engineering
Chiba University
Chiba, Japan

INTRODUCTION

The middle cerebral artery MCA is one of predilection vessels of aneurysm in circle of Willis. In the present study, the flow model simulates an ideal aspherical aneurysm model located at the apex of bifurcation in middle cerebral artery (MCA: M1, M2 and M3). The effect of elasticity on flow pattern around aneurysm induced at the apex of middle cerebral artery was experimentally examined by particle image velocimetry *in vitro*. Flow structure was examined for elastic model 3 folds as large as real aneurysm size. The effect of wall deformation on flow structure was examined at several phases in pulsatile blood flow wave.

METHODS

In the present study, flow behavior inside aneurysm induced at the apex where middle cerebral artery MCA: M1 bifurcates to M2 and M3 was examined for both elastic and rigid models as shown in Figure 1 [1]. There is an aneurysm with width of N= 6 mm and depth of D= 12 mm (AR= D/N= 2.0). We experimentally examined the flow behavior inside aneurysm wall and wall deformation in PIV. Aneurysm wall is made from silicone resin with the wall thickness of 0.4 mm.

In PIV, the measurement conditions are interrogation window size 32 pixels× 32 pixels and 50% overlapping.

The working fluid is 51.5% aqueous glycerin with a refractive index of 1.41 identical to that of silicone resin (KE-1606, Shin-Etsu Chemical Ltd., Tokyo, Japan), a density of $\rho = 1.13$ g/cm^3, and a kinematic viscosity of $\nu = 6.33 \times 10^{-6}$ m^2/s at 293 K (26°C). The working fluid flows into the model through the 320-mm-long straight inlet tube. The working fluid flows through an ultrasonic flow meter (TS410, Transonic System Co. Ltd.).

As the boundary condition, the pulsatile blood flow wave which simulates that by Valen-Sendstad, et al [2] is assumed at inlet M1 as

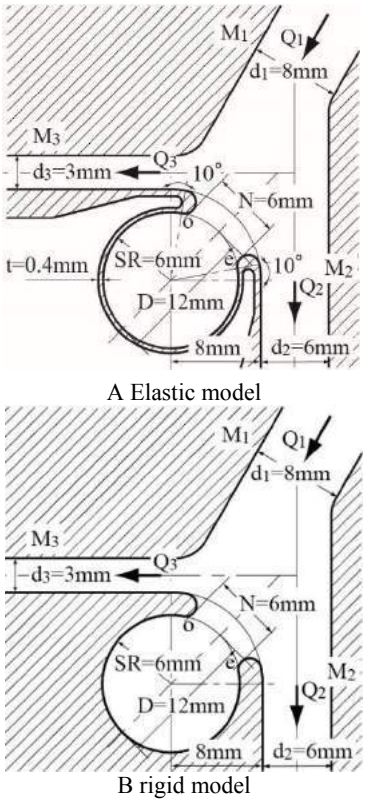

Figure 1: Patient-specific aneurysm model in MCA

Copyright 2016 The Organizing Committee for the 2016 Summer Biomechanics, Bioengineering and Biotransport Conference

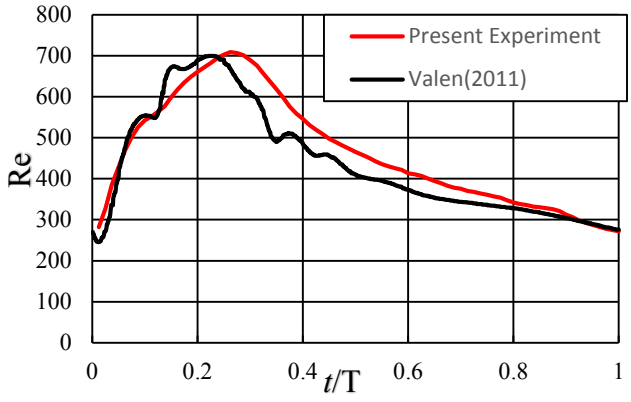

Figure 2: Pulsatile flow wave form by Reynolds number (α=1.41)

shown in Figure 2 and flow rate at both outlets is even.

The experiment was carried out in the laminar pulsatile blood flow wave form with a Womersley number of $\alpha = (d_0/2)\,(\omega/\nu)^{(1/2)} = 1.41$, a mean Reynolds number of $Re_m = d_1 U/\nu = 400$, where ω, d_1 and U are the pulsatile angular velocity, the diameter of MCA: M1 vessel and the mean velocity through it.

The light source was a 15 Hz dual-pulse YAG laser with 30 mJ output and a pulse interval ranging from 350–1600 μs. A cylindrical lens produces a laser sheet thickness of 0.3 mm that is irradiated parallel to the median plane of aneurysm model. The scatter material comprises fluorescent particles of 14 μm in diameter. Scattered radiation from tracer particles was recorded using the Image Intense CCD camera (1376 × 1040 pixels, GmbH) fitted with an AF NIKKOR lens (Nikon) positioned perpendicularly to the median plane of aneurysm. Digital images were processed using DaVis 7 software (LaVision, GmbH).

RESULTS

At three typical phases, i.e. early systole (t/T=0.125), peak systole (0.25) and mid-diastole (0.375), the velocity vector inside the aneurysm are shown in Figure 3, 4. In elastic model, as the flow rate increases, the inflow velocity along the aneurysm wall in M2 vessel side steeply increases as shown in Figure 3 at peak systolic phase. In rigid model, the inflow velocity is smaller than that in elastic model.

The deformation phase in elastic model is similar to that of pulsatile flow wave because the Womersley number is not so high (α=1.41). As shown in Figure 5, the deformation defined as the ratio of difference maximum and minimum to minimum diameter is comparable to 5.0% indicated by Weber [3].

The distribution of WSS along aneurysm wall at peak systolic phase as a typical result is shown in Figure 6. From θ=0 to 90, WSS in elastic model is smaller than that in rigid model. On the other hand, from θ= 90 WSS is a little larger than that in rigid model. This difference might be related to inertial flow of high penetrating velocity into elastic model.

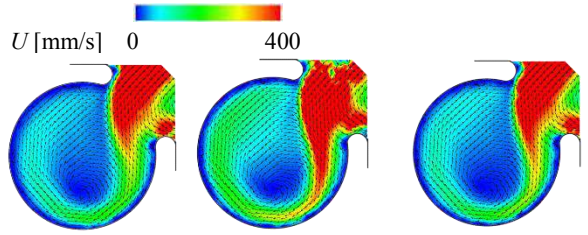

(a) *t*/T=0.125 (b) *t*/T=0.25 (c) *t*/T=0.375

Figure 3: Velocity distributions in aneurysm elastic model

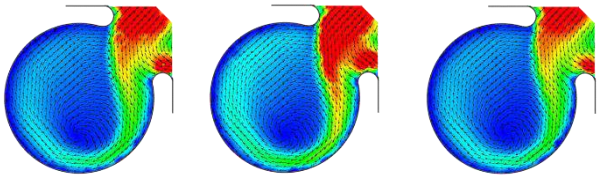

(a) *t*/T=0.125 (b) *t*/T=0.25 (c) *t*/T=0.375

Figure 4: Velocity distributions in aneurysm rigid model

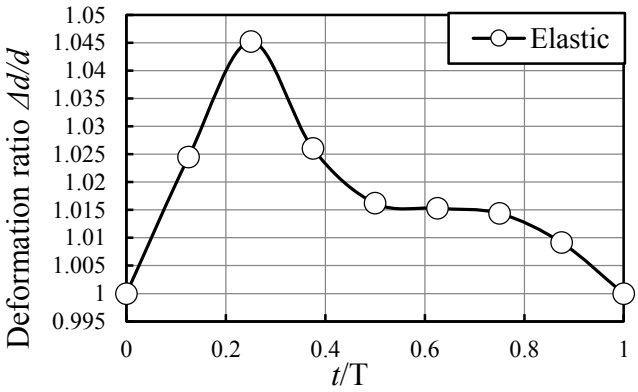

Figure 5: Deformation ratio in aneurysm model

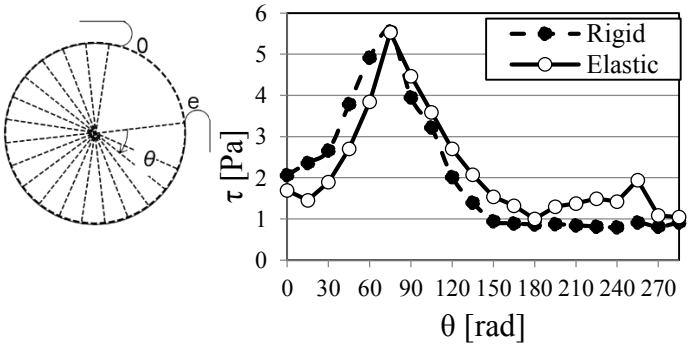

Figure 6: Wall shear stress along aneurysm wall

ACKNOWLEDGEMENTS

We are grateful for support by Mr. Takeshi Shibayama.

REFERENCES

[1] Xu, L, Yamaguchi, R., et al, 2016, Effect of elasticity on wall shear stress inside cerebral aneurysm at anterior cerebral artery." Tech & Health Care." in press.

[2] Valen-Sendstad, K., et al. 2011, Direct numerical simulation of transitional flow in a patient-specific intracranial aneurysm. "J. Biomechanics." 44; 2826 –2832.

3. Meyer, F. B., et al, 1993, Pulsatile increases in aneurysm size determined by cine phase-contrast MR angiography. "J. Neurosurg." 78; 879-883.

Copyright 2016 The Organizing Committee for the 2016 Summer Biomechanics, Bioengineering and Biotransport Conference

SB³C2016
Summer Biomechanics, Bioengineering and Biotransport Conference
June 29 –July 2, National Harbor, MD, USA
SB³C2016-765

CONTRIBUTION OF ULTRASOUND ABSORPTION IN NANOPARTICLES FOR HYPERTHERMIA APPLICATION

V. Kumar (1), S. B. Devarakonda (2), R. K. Banerjee (2), A. K. Ganguli (1, 3), C. Bera (1)

(1) Institute of Nano Science and Technology, Mohali, Punjab 160062, India

(2) Mechanical and Materials Engineering Department, University of Cincinnati, Cincinnati, OH, USA

(3) Department of Chemistry, Indian Institute of Technology, New Delhi 110016, India

INTRODUCTION

There is a renewed interest in the thermal properties of ferrofluids due to the biomedical application of heating effect of magnetic nanoparticles (mNPs) [1] and application of focused ultrasound therapy for ablation of malignant tumors [2]. The ultrasound based treatment is a non-invasive alternative to conventional surgical procedures. However, one of the major problem in the field has been controlling accurate delivery of heat (energy) to the disease site, while minimizing collateral damage to the surrounding healthy tissue. One of the most important requirement for ultrasound therapy for clinical planning is to determine heat generated in tissue due to acoustic energy transfer to heat energy. These lead us to investigate the reason of temperature rise in mNPs in presence of ultrasound. Although most of the experimental investigations have predicted that the main reason behind the temperature rise is ultrasonic attenuation [3-6], there is a lack of fundamental knowledge based on either experimental or theoretical investigation on the contribution of attenuation to temperature rise in media such as ferrofluids or mNPs infused tissue mimicking materials (TMM). Few theoretical investigations have been made based on fluid dynamics and "streaming theory" to study acoustic attenuation [6-9]. Following Ref. [10], we develop a simple model based on acoustic mean free path to calculate temperature rise due to ultrasound attenuation in ferrofluids. From this model it is possible to calculate contribution of different media on temperature rise by changing volume fraction (x) of nanoparticles, viscosity of ferrofluid medium, etc.

METHODS

Acoustic wave propagated in a medium interacts with the thermal phonons and as a result of this acoustic wave is absorbed [10]. Due to this absorption, the momentum of thermal phonons increase which tends to set up heat flow in the direction of ultrasound propagation and generates a temperature gradient. Following Ref. [10], the increase in temperature with time is given by,

$$\Delta T = \int_0^t \frac{3N\hbar\omega v_{nf}}{\lambda_{nf} C_{nf} V}\, dt \qquad (1)$$

where λ_{nf} is the acoustic mean free path for ferrofluids, C_{nf} is the heat capacity, v_{nf} is the velocity of ultrasound, V is the total volume of medium, N is the number of phonons in acoustic mode, $(N\hbar\omega/V)$ is the energy density in the medium which we can calculate from the power of ultrasound wave, $\hbar$ is the reduced Planck constant and ω is the ultrasound frequency.

Acoustic mean free path of the media is calculated from absorption coefficient, $\lambda_{nf} = (((\frac{x\alpha_{np}}{\rho_{np}} + \frac{(1-x)\alpha_f}{\rho_f})(\rho)^{-1}$ where ρ is the total density.

Absorption coefficient α_f of ultrasound for fluid is calculated using theory of Stokes [11]

$$\alpha_f = \frac{2\eta\omega^2}{3\rho_f v_f^3} \qquad (2)$$

Where η is the viscosity of base fluid, ρ_f is density of fluid, v_f is the speed of sound in base fluid

The absorption coefficient, α_{np} for nanoparticle can be written as, [12]

$$\alpha_{np} = 1.1\frac{\gamma^2\omega^2\tau C_{np}T}{v_{np}^3} \qquad (3)$$

C_{np} is the heat capacity of nanoparticle, v_{np} is the speed of ultrasound in nanoparticle, ρ_{np} is the density of nanoparticle at absolute temperature, γ is the Gruneisen parameter, τ is the phonon relaxation time which is calculated as, $\tau^{-1} = (\frac{1}{\tau_b} + \frac{1}{\tau_{np}}$. τ_b is the bulk phonon relaxation time, $\tau_b = \frac{3\kappa}{C_{np}\rho_{np}v_{np}^2}$, where κ is the heat conductivity and

Copyright 2016 The Organizing Committee for the 2016 Summer Biomechanics, Bioengineering and Biotransport Conference

$\tau_{np} = \frac{l}{v_{np}}$ is the relaxation time for boundary scattering, *l=10nm* is the nanoparticles diameter. The values of different physical parameters for Eqn. 1-3 are listed in Table. 1.

Table 1: List of physical parameter used in Eqn. 1-3.

	Water	**Fe_2O_3**
Specific Heat, C_p	4175 J/Kg-K [13]	650.6 J/Kg-K [14]
Density, ρ	995.64 Kg/m^3 [15]	5.26×10^3 Kg/m^3 [16]
Thermal Conductivity, κ		11.3 W/m-K [17]
Velocity, v	1509 m/s. [18]	6273 m/s [19]
Bulk Modulus, B		2.07×10^{11} Pa [19]
Gruneisen parameter, γ		1.51 [20]
Viscosity, η	797.3×10^{-6} Pa-s [21]	

RESULTS

Fig. 1 represents the acoustic wave mean free path calculated for different volume fraction (x), and Fig. 2 represents the temperature rise due to ultrasound attenuation. Supplied power (P) to the ferrofluids medium is calculated from experimental temperature rise as,$P = \frac{dT}{dt} MC_{nf}$, where M is the total mass, $\frac{dT}{dt}$ is calculated from the linear region of experimental temperature rise(Fig.2). The calculated P for x values of 0.5%, 1% and 2 % is 1.8 J/s.

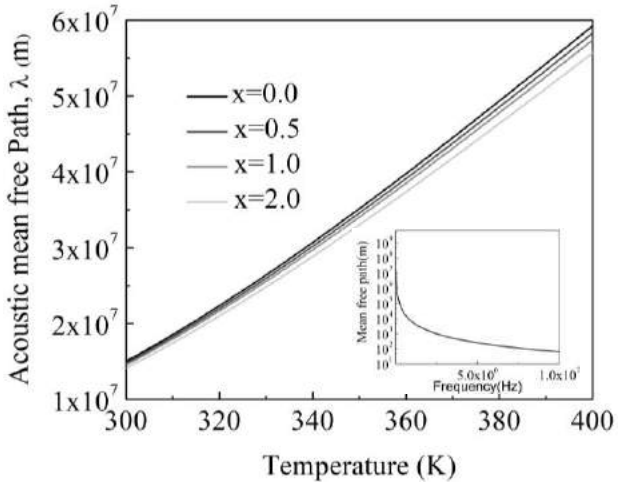

Figure 1: Acoustic mean free path for different volume fraction of ferrofluids for 20 KHz frequency. Here, *x* is the volume fraction of Fe_2O_3. (Inset) mean free path for different frequencies.

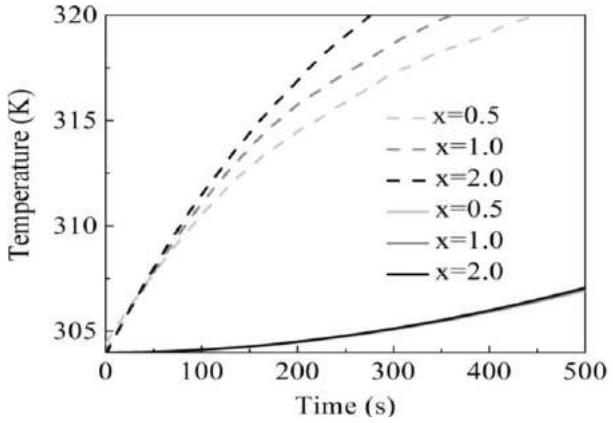

Figure 2: Temperature rise for ultrasound propagation time. Dashed lines are experimental values of total temperature rise for 20 KHz ultrasound frequency, solid lines are theoretical calculation for ultrasound attenuation. *'x'* is the volume fraction.

DISCUSSION

Here, we have shown that the theoretical temperature rise in ferrofluids due to purely ultrasound attenuation is very low (1.7 °C after 400s at x= 0.5%). However, for highly viscous medium the temperature rise is faster and higher compared to ferrofluids. Only by changing the viscosity of base fluid to 3.4 cp and 10 cp, we observed temperature rise of 3.6°C and 10.2°C respectively for x =1%, after 300s. It has been observed that change in acoustic mean free path in ferrofluids is smaller after 1.5MHz frequency, so the change in frequency will not have a dominant effect on temperature change at very high frequencies. This model can also be used for the temperature calculations in TMM and it can be further improved by incorporating other phenomena for temperature increase such as phonon-electron interaction in NPs, viscous heating and temperature rise due to fluid momentum.

ACKNOWLEDGEMENTS

VK and CB acknowledge computing facility of PARAM Yuva-II. Also, partial financial support (time spent by co-investigators) from the National Science Foundation (Grant No. 1403356) is gratefully acknowledged.

REFERENCES

[1] Lee, L., Simon, C., Bove, E. *et al.*, Echocardiography, 17(6), 563-566 (2000).

[2] S. A. R. Dibaji et al, J Nanotechnology in Engineering and Medicine, 4: 041003, 2013.

[3] Curra, F. P., and Crum, L. A., Acoust. Sci. Technol., 24(6), 343–348, 2003.

[4] Ter Haar, G., Phys. Today, 54(12), 29–34, 2001.

[5] Wu, J., and Du, G., Ultrasound Med. Biol., 16(5), 489–498, 1990.

[6] Curra, F. P., Mourad, P. D., Khokhlova, V. A., Cleveland, R. O., and Crum, L.A., IEEE Trans. Ultrason. Ferroelectr. Freq. Control, 47(4), 1077–1089, 2000.

[7] Soneson, J. E., AIP Conf. Proc., 1113(1), 165–169, 2009.

[8] Myers, M. R., and Soneson, J. E., J. Acoust. Soc. Am., 126(1), 425–433, 2009.

[9] Dibaji, S. A. R., Banerjee, R. K., Soneson, J. E., and Myers, M. R., J. Acoust. Soc. Am., 134(5), 3435–3445, 2013.

[10] Simons, S., Proc. Phys. Soc., 83, 645-657, 1964

[11] Pinkerton, J. M. M., Proc. Phys. Soc., 62, 129-141, 1949

[12]Brawer, Steven, Phys. Rev. B, 7(4), 1712-1717, 1973

[13]Bousfield, W. R., and Bousfield ,W. E., Proc. R. Soc. Lond. A, 85, 302-304, 1911.

[14]Lide D. R., CRC Handbook of Chemistry and Physics, CRC Press, 2009.

[15]Bigg, P. H., Br. J. Appl. Phys,18, 521-525, 1967.

[16]Schwertman, U., and Cornell, R. M., Iron Oxides in the Laboratory Preparation and Characterization, Wiley-Vch, 2nd Edition, 2000, pp. 7

[17]Toher, Cormac, Physical Review B, 90, 174107, 2014.

[18] Greenspan, Martin and Tschiegg, Carroll E., The Journal of the Acoustical Society of America, 31(1), 75-76 1959

[19]Anderson, Don L., and Anderson, Orson L., Journal of Geophysical Research, 75(17), 3494-3500, 1970

[20]Shim, Sang-Heon, and Duffy, Thomas S., American Mineralogist, 87, 318-326, 2001

[21] Kestin, J., *et al*, Phys. Chem., 7(3), 941-948, 1978.

Copyright 2016 The Organizing Committee for the 2016 Summer Biomechanics, Bioengineering and Biotransport Conference

SB³C2016
Summer Biomechanics, Bioengineering and Biotransport Conference
June 29 –July 2, National Harbor, MD, USA
SB³C2016-766

CAN WE USE APPARENT THERMAL CONDUCTIVITY TO INCLUDE THE EFFECT OF BLOOD PERFUSION? AN ATTEMPT TO PREDICT FROZEN REGION DURING CRYOSURGERY

Mohammed M. Shurrab (1), Haidong Wang (1), Takanobu Fukunaga (1), Kosaku Kurata (1), Hiroshi Takamatsu (1)

(1) Department of Mechanical Engineering
Kyushu University
Fukuoka, Japan

INTRODUCTION

Prediction of temperature distribution in tissues and organs is important for treatments such as hyperthermia, radiofrequency ablation, high-frequency focused ultrasound and cryosurgery, which induce a change of temperature from their physiological state. Many types of models and equations have been therefore developed to take into account the effect of blood perfusion that often has a significant effect on the heat transport in tissues. However, they have introduced many parameters associated with blood perfusion and, in some cases, anatomical information, which are not available in many cases. In addition, from the practical point of view, the result of using complicated models was not significantly different from that of simple bioheat equation proposed by Pennes [1]. These were the reasons why the conventional Pennes bioheat equation has been used for many applications in spite that it has intrinsic problems. However, even in the case of using Pennes bioheat equation, the blood perfusion, which is defined by the rate of blood flow per unit volume of tissue, is not available in many cases particularly for human tissues and organs. This leads us to come up with a practical idea of using apparent thermophysical properties that include the effect of blood perfusion. The objective of this study is to examine the feasibility of introducing our idea to cryosurgery for predicting the size of ice ball.

METHODS

Simulation was carried out for cryosurgery operated with a 1.5-mm-dia. cryoprobe. We assumed that a single probe was placed in a uniform tissue. The bioheat equation that neglects the effect of metabolic heat generation and takes into account the freezing process as a source term is expressed by

$$\rho\left(c-L\frac{\partial g_s}{\partial T}\right)\frac{\partial T}{\partial t}=\frac{1}{r}\frac{\partial}{\partial r}\left(kr\frac{\partial T}{\partial r}\right)+\frac{\partial}{\partial z}\left(k\frac{\partial T}{\partial z}\right)+\rho_b c_b \omega_b (T_b-T) \qquad (1)$$

where T is the temperature, ρ is the density, c is the heat capacity, k *is* the thermal conductivity, L is the latent heat of freezing, g_s is the solid fraction, and ω is the blood perfusion rate. Subscript b stands for the blood. We assumed that the tissue is equivalent with a 0.9 % sodium chloride aqueous solution, and no blood flow takes place in the frozen region. The temperature at the probe surface of a Joule-Thomson cryoprobe measured by an experiment [2] was used as a boundary condition. The probe temperature decreased to ~–95 °C when the argon gas was supplied at 27.4 MPa, ~–85 °C at 25.2 MPa, and ~–75 °C at 22.4 MPa. It was assumed that the probe surface 32 mm from the tip was uniform but adiabatic at the rest.

Solutions of the bioheat equation and the normal heat conduction equation were compared with each other. The bioheat equation, Eq. (1), was solved for given values of thermal perfusion rate B (= $\rho_b c_b \omega_b$) as a parameter. The heat conduction equation that neglected the perfusion term in Eq. (1) was solved using apparent thermal conductivity k_{ap} as a parameter. We defined the enhancement factor ε by $k_{ap}=\varepsilon k$ to express the increase in apparent thermal conductivity due to blood perfusion. Based on the literature survey, we used B = 17 kW/(m^3·K) as a typical value for soft tissues [3], and examined the perfusion effect within the range of B < 50 kW/(m^3·K).

RESULTS

Figures 1 and 2 respectively show the effect of B and ε on the radial temperature distribution at 16 mm from the tip at 600 s after the start of cooling. The radius of ice ball, which is identified by the place where T = –0.5 °C, is smaller for larger B (Fig. 1) and larger ε (Fig. 2), while the temperature gradient at the unfrozen part near the ice front is larger for larger B but smaller for larger ε.

Since the effects of B and ε on the size of ice ball were qualitatively the same, we tried to determined ε that gave the same ice-ball size with that obtained for a given B. Figure 3 demonstrates that

Copyright 2016 The Organizing Committee for the 2016 Summer Biomechanics, Bioengineering and Biotransport Conference

the simulation with $\varepsilon = 1.9$ agrees well with that obtained for $B = 17$ kW/(m^3·K) not only in the size of ice ball but also in the temperature distribution inside the ice ball irrespective of the freezing time.

The value of ε determined for given B is shown as a function of B in Fig. 4. The ε value increases with B, which is reasonable from the physical point of view. In addition, the value determined for three different gas pressures, *i.e.* different probe temperatures, agreed well with one another, and overlapped in Fig. 4.

Figure 5 compares the growth of ice ball between $B = 17$ kW/(m^3·K) and $\varepsilon = 1.9$. They agree well with each other irrespective of time and the gas pressure.

DISCUSSION

Prior to the simulation of cryosurgery, we examined the effect of B and k_{ap} on the temperature distribution for a non-freezing case where the temperature at the probe surface was decreased to 7 °C. At a given time the temperature-changed area was smaller, *i.e.* the temperature gradient near the probe surface was larger, for larger B or smaller k_{ap}. This indicates that the increase of blood perfusion does not correspond to the increase of apparent thermal conductivity from a perspective of temperature distribution, which was also suggested by Figs. 1 and 2. Therefore, the apparent thermal conductivity does not work for predicting temperature distribution in tissues with blood perfusion.

However, the apparent thermal conductivity does work for predicting the size of ice ball during cryosurgery. We determined the apparent thermal conductivity for a given rate of blood perfusion. The enhancement factor ε, which expresses the increase of apparent thermal conductivity from the intrinsic value, was determined to give the same size of ice ball as that for a given perfusion rate. Thus determined ε was independent of cooling time and also the probe temperature that depends on the pressure of supplied gas. It was reasonable from the physical point of view that ε increased with the thermal perfusion rate B. The result shown by Fig. 4 demonstrates that freezing of tissue with blood perfusion of $B = 20$ kW/(m^3·K) is equivalent to freezing of material that has the thermal conductivity twice larger than the tissue. The fact that the temperature distribution inside the ice ball also agreed well indicates that using apparent thermal conductivity is also useful for predicting a safety margin of ice ball that should be made larger than a tumor to completely kill all cancer cells.

REFERENCES

[1] Pennes H., *J. appl. physiol.*, 1:93-122, 1948.
[2] Shurrab M., et. al., *Int. J. Refrig.*, (under review), 2016.
[3] Zhao G., et. al., *Med. Eng. Phys.*, 29: 205-215, 2007.

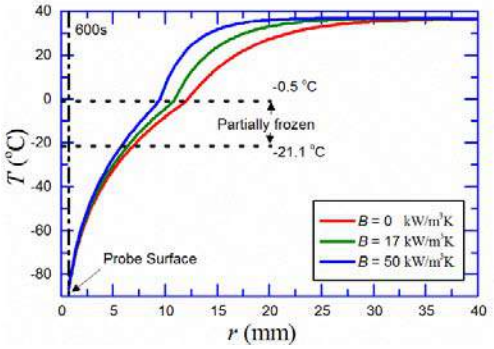

Figure 1: Radial temperature distribution at different blood perfusion rates.

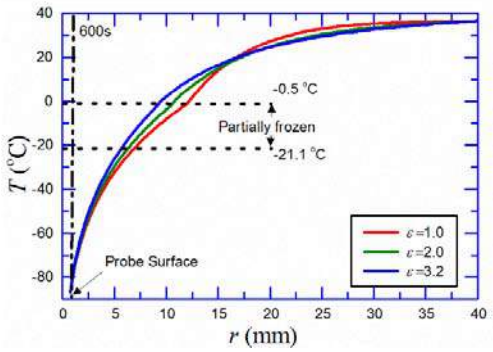

Figure 2: Radial temperature distribution at different apparent thermal conductivities.

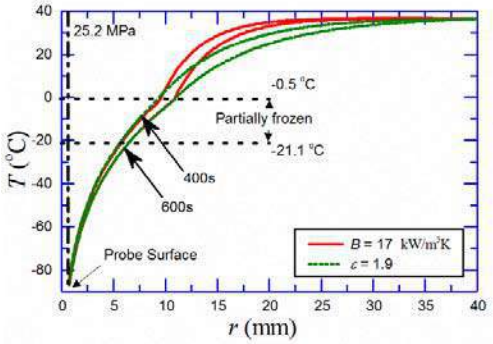

Figure 3: Comparison of the temperature distributions between $B = 17$ kW/(m^3·K) and $\varepsilon = 1.9$.

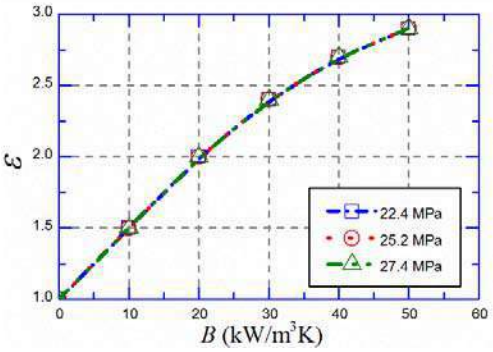

Figure 4: Enhancement factor as a function of thermal perfusion rate.

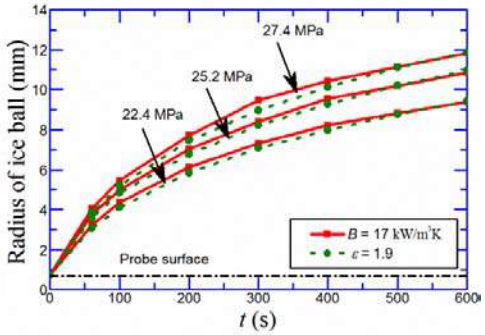

Figure 5: Comparison of ice ball size between $B = 17$ kW/(m^3·K) and $\varepsilon = 1.9$ at different gas pressures.

Copyright 2016 The Organizing Committee for the 2016 Summer Biomechanics, Bioengineering and Biotransport Conference

SB³C2016
Summer Biomechanics, Bioengineering and Biotransport Conference
June 29 –July 2, National Harbor, MD, USA
SB³C2016-767

DYNAMIC BUBBLE FORMATION IN ADV ASSISTED HIFU WITH PREEXISTING BUBBLE WALL

Y. Xin (1), A. Zhang (1*), L. X. Xu (1), J. B. Fowlkes (2)

(1) School of Biomedical Engineering
Shanghai Jiao Tong University
Shanghai, China

(2) Department of Radiology
University of Michigan
Ann Arbor, Michigan, USA

INTRODUCTION

High intensity focused ultrasound (HIFU) is a promising noninvasive treatment for tumor. Ultrasound energy is focused in a tiny region inside the body where the temperature can reach above 56 ℃ within several seconds, leading to thermal necrosis of the tumor tissue.

The acoustic droplets vaporization technique are shown to be able to greatly increase the lesion size and thus accelerate the treatment process [1]. During the treatment, the acoustic droplets instead of the bubbles are injected, only when they are exposed to the ultrasound of certain frequency and pressure, these droplets are vaporized into bubbles. Experiments have shown that the introduction of ADV droplets in HIFU would significantly shorten the treatment time [2].

Injected droplets accumulate at the periphery of the tumor where there are plenty of vessels. Usually the bottom of tumor would be treated first. HIFU lesions are created within tumor along the bottom face, while all the ADV droplets are vaporized in this region, forming a bubble wall along the tumor bottom edge. The existing bubble wall would greatly reshape the followed acoustic field and thus result in very different lesion shape for each focus used. However, this process is highly dynamic and it hard to image at the same time for a safe planning of the treatment. A simulation model which can precisely predict the influence of the bubble wall on the following evaporation of droplets is necessary for acoustic parameter selection and treatment pathway planning. Current models have successfully predicted the acoustic field and correspondent temperature distribution during HIFU treatment, but none of the models is suitable for this study.

In this paper, a model is proposed to mathematically describe the droplets evaporation conditions and correspondent acoustic field and bubble formation in ADV assisted HIFU treatment in the presence of preexisting bubble is studied numerically. The highest pressure in front of a plane wall or a curved wall as function of the location of the wall is obtained.

METHODS

Both plane wall and curved wall are employed in the simulation as shown in Fig.1

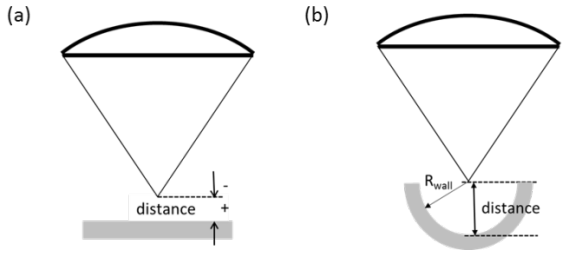

Figure 1: Geometry for simulation of the highest pressure in front of a plane wall (a) and a curved wall (b).

Acoustic field is calculated using linear sound propagation equation. It is solved in frequency domain by the following equations.

$$\nabla \cdot \frac{1}{\rho_c} \nabla p - \frac{k^2 p}{\rho_c} = 0 \tag{1}$$

$$k = \frac{\omega}{c} - i\alpha, c_c = \frac{\omega}{k}, \rho_c = \frac{\rho c^2}{c_c^2} \tag{2}$$

Where p is pressure, ρ is density, k is wave number, ω is angular frequency, and c is sound speed. Subscription c indicates the parameter is complex number. The presence of bubbles in the medium leads to the variation of parameters. Bubble void fraction is defined by f_G, on which density, sound speed and sound attenuation coefficient α

Copyright 2016 The Organizing Committee for the 2016 Summer Biomechanics, Bioengineering and Biotransport Conference

all depend. Subscription p and G refer to parameters of phantom and gas, respectively.

$$f_G = \begin{cases} 0 & \text{, no bubble} \\ \frac{4}{3}\pi n_G R_0^3 & \text{, with bubbles of number density } n_G \text{ in medium} \end{cases} \quad (3)$$

$$f_P = 1 - f_G \quad (4)$$

$$\rho = f_P \rho_P + f_G \rho_G \quad (5)$$

$$\frac{c_P^2}{c_c^2} = 1 + 4\pi c_P^2 \int_0^\infty \frac{R_0 n_G(R_0)\, dR_0}{\omega_0^2 - \omega^2 + i\frac{4\mu\omega}{\rho_P R_0^2}} \quad [3] \quad (6)$$

$$\omega_0^2 = \frac{1}{\rho_P R_0^2}\left(3\kappa P_0 - \frac{2\sigma}{R_0}\right) \quad [3] \quad (7)$$

$$c = \frac{c_P}{real\left(\frac{c_P}{c_c}\right)}, \quad \alpha = \frac{imag\left(-\frac{c_P}{c_c}\right)\omega}{c_P} \quad [3] \quad (8)$$

ADV droplets would be vaporized under certain conditions, which are related to ultrasound frequency, diameter of the droplets, super heat degree and total ultrasound 'on time'. The following assumptions are used to decide how much bubbles will form in certain acoustic field:

(i) Threshold for droplets in phantom gel exposed to 750 kHz ultrasound is found to be 7.4 MPa as was found in experiment [4].

(ii) The probability of droplets vaporized increases linearly with pressure in a range, which is defined as 1.6 MPa as found in one of the experiment [5].

(iii) The phase shifted threshold decreases as the total ultrasound 'on time' increases. The relationship between the threshold and the ultrasound 'on time' is obtained by averaging the findings from three different approaches [5].

(iv) The threshold is lowered when there are bubbles coexist as has been found experimentally [5].

RESULTS

The bubble area created in after 200 pulses with preexisting of a plane wall is shown in Figure 2. All the bubbles vaporized are in the proximal side of the bubble wall, which indicates the shielding effect of the wall. This character of bubble wall can be employed to protect normal tissue in distal area in practical. The shape and size of the created bubble area are similar to the one created in the experiment [4] which used the same parameters of ultrasound and droplets. Comparing to the bubble area formed when there is no preexisting bubble wall as also shown in Fig.2(b), the preexisting bubble have caused a lot more bubbles formation in the region close to the bubble wall, and the bubble area formed are shorter with a larger head.

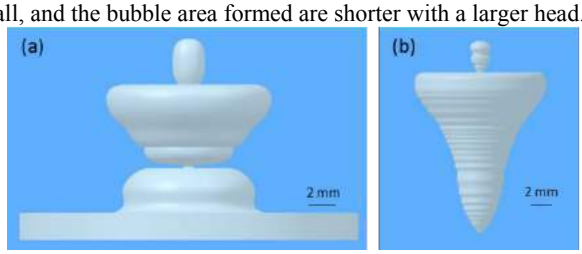

Figure 2: (a) Bubble area created in the presence of 2 mm bubble wall after 200 pulses (pulse duration 20 μs) of ultrasound exposure. The HIFU is focused on the upper surface of wall with focal pressure of 14.7 MPa. The frequency is 750 kHz. (b) Bubble area created without bubble wall for the same condition.

Fig. 3(a) and (c) are the pressure field and the relationship of the highest pressure achieved with the distance between the HIFU focus and the front surface of the plane bubble wall. Fig.3 (b) and (d) are the same results when the bubble wall is a curve. It is found that the pressure in front of a plane bubble wall can be as high as 6.66 dB. Almost all the highest pressure in front of the wall are higher than 0 dB in location range from -2.8 mm to 4.3 mm. The highest pressure achieved in front of a curved wall is 4.07 dB.

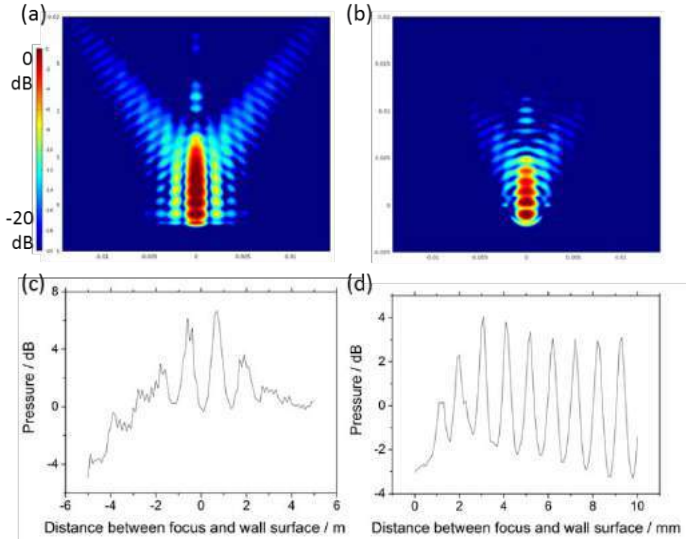

Figure 3: Pressure distribution in front of a plane wall (a) and a curved wall (b) when the front surface of the wall is at 2 mm. Highest pressure as function of wall location in front of a plane wall (c) and a curved wall (d). The frequency was 750 kHz, the focal pressure was 14.7 MPa.

DISCUSSION and CONCLUSION

By comparing to others experiment study, the current model could give a good prediction of bubble area in ADV droplets assisted HIFU therapy with the influence of the preexisting bubble wall being discussed. The model can be further used for study of irregular shape of the bubble wall as real tumor edge. In this study, a linear sound propagation equation has been used, which excludes the nonlinearity in the treating process and may have underestimated the size of the bubble area. Further work is needed to couple the heat transfer model with this proposed model to simulate the thermal lesion in this therapy, which may have greater potential to be used as a tool for design of path and parameters before treatment.

ACKNOWLEDGEMENTS

This work is supported by Natural Science Foundation of China (NSFC51476101, NSFC 51521004), the Chinese government "111 Project" (B08020), the Shanghai Physical Therapy of Major Disease and Detection Equipment Engineering Research Center, Med-X Institute.

REFERENCES

[1] Kripfgans, O. et al., *Ultrasound in Med. & Biol.*, 26(7):1177-1189, 2000

[2] Zhang, M. et al., *Acad. Radiol.*, 18:1123-1132, 2011

[3] Church, C., *J. Acoust. Soc. Am.*, 97(3):1510-1521, 1995.

[4] Lo, A. et al., *Ultrasound in Med. & Biol.*, 32(1):95-106, 2006.

[5] Lo, A. et al., *IEEE Trans. Ultrason. Ferroelectr. Freq. Control*, 54(5):933-946, 2007.

Copyright 2016 The Organizing Committee for the 2016 Summer Biomechanics, Bioengineering and Biotransport Conference

SB^{3}C2016
Summer Biomechanics, Bioengineering and Biotransport Conference
June 29 –July 2, National Harbor, MD, USA
SB^{3}C2016-768

LONGITUDINAL STUDY OF WALL SHEAR STRESS OVER SURGICALLY-INDUCED ATHEROSCLEROTIC PLAQUES IN MICE

R Xing (1), A. Moerman (1), R.Y. Ridwan (2), A. van der Steen (1), F.J.H. Gijsen (1), K. Van der Heiden (1)

(1) Department of Biomedical Engineering and Cardiology, Erasmus Medical Center, Rotterdam, The Netherlands

(2) Department of Genetics, Erasmus Medical Center, Rotterdam, The Netherlands

INTRODUCTION

Wall shear stress (WSS) is the frictional force that blood flow exerts on the endothelium of the vessel wall. It is known to initiate atherosclerotic plaque growth, which is the accumulation of lipids, fibrous tissue and inflammatory cells in the arterial wall.

As the disease advances, plaques can progress into two distinctive types: a stable or a vulnerable plaque. Vulnerable plaques are characterized by thin fibrous cap, large lipid pool and increased plaque inflammation. Rupture of a vulnerable plaque is the main cause of stroke and myocardial infarction. However, factors determining plaque progression and plaque vulnerability remain unclear.

We hypothesized that WSS plays a role in atherosclerotic plaque progression and plaque stability [1]. We want to study this hypothesis using a WSS-manipulated atherosclerotic mouse model, in which both a stable and a vulnerable plaque are present in the same vessel [2]. In this study, we demonstrate for the first time how WSS patterns change over time during plaque progression in this mouse model.

METHODS

A tapering cast was placed around the right common carotid artery (RCCA) of female ApoE$^{-/-}$ mice (n=7). The cast has a tapering lumen (diameter from 400 µm to 200 µm over 1.5 mm) which changed the blood flow in the RCCA. The cast induces a low WSS region upstream of the cast, high WSS in the cast, and oscillatory WSS area downstream of the cast. It was previsouly shown that vulnerable plaques develop in the region upstream of the cast [2]. We followed plaque progression over time at 5, 7, 9 weeks after cast placement. In order to calculate WSS, blood flow and detailed 3D geometry of the RCCA is required.

First, we measured the blood velocity and vessel diameter in the RCCA by Doppler Ultrasound (Vevo 2100). The two measurements were captured at the same location to determine the flow rate. Next, RCCA vessel geometry was obtained using the contrast-enhanced micro-CT imaging system (Quantum FX) with a resolution of 40 µm. RCCA vessel surface was then reconstructed using an in-house developed segmentation protocol. Finally, computational fluid dynamics (Fluent 14.5) was applied to compute the velocity field and WSS distribution in the RCCA at three time points during plaque progression. Quantitative analysis was performed using Matlab (Matlab 2011b).

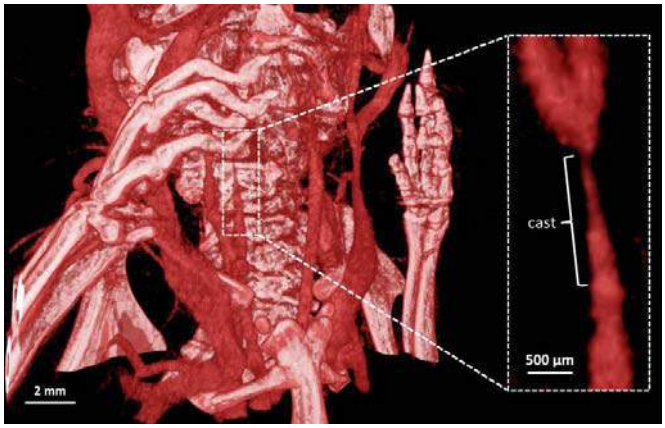

Figure 1: 3D volume rendering of the murine vascular network. The box shows the zoomed-in area of the narrowing carotid artery caused by the tapering

Copyright 2016 The Organizing Committee for the 2016 Summer Biomechanics, Bioengineering and Biotransport Conference

RESULTS

CT-imaging: A 3D volume rendering of the contrast enhancement vasculature is shown in Figure 1. Next to the arteries, bone tissues including vertebrae, sternum and ribs were also visualized. The common carotid arteries are located close to the vertebrae. They travel parallel along the vertebrae, at both sides of the neck. The narrowing of the RCCA caused by the tapering cast and the carotid bifurcation are clearly visible (Figure 1, zoomed-in box).

Flow data: Diameter and velocity measurements were performed in all mice successfully. The resulting flow data (figure 2), reveal an immediate reduction in the flow after cast placement of approximately 66%, followed by a further decrease to 20% at week 5. After that time point, the flow stabilized.

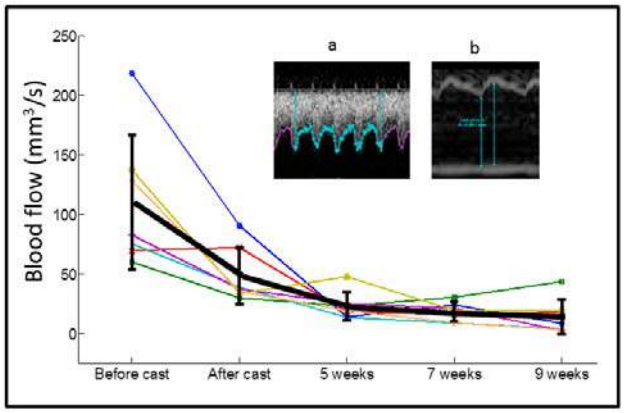

Figure 2: The blood flow at 5 different time points derived from (a) blood velocity measurements upstream to the cast using Doppler Ultrasound and (b) vessel diameter measurements using M-mode at the same location.

Geometrical data: The average diameter of the upstream part of the common carotid artery was 480±51 µm, 473±27 µm and 450±43 µm at week 5, 7 and 9 respectively. The minimum diameter decreased from 386±79 µm to 303±82 µm. The average area stenosis was 51±16%, 67±9% and 72±13%. Two examples of the reconstructed lumen for two different animals are shown in figure 3. They illustrate that significant differences can be found between individual animals.

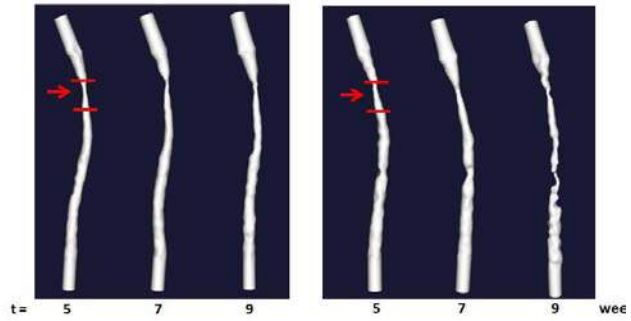

Figure 3: The reconstructed lumen from two animals at three different time points during plaque development. The cast region is indicated by the red lines. The differences between the animals are evident: while disease progression is slower for the mouse in the left panel, the carotid artery of the animal in the right panel shows severe plaque progression, leading to an irregular lumen narrowing.

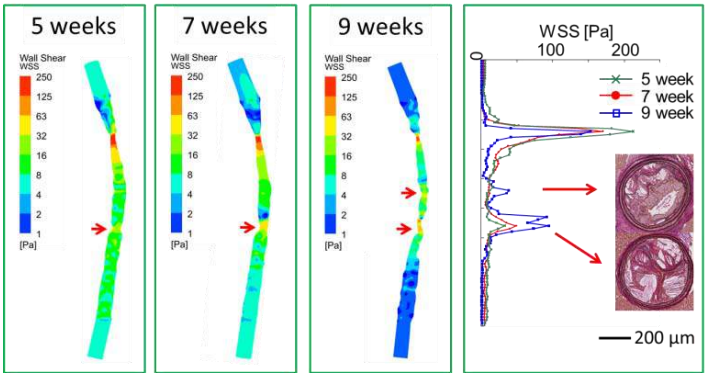

Figure 4: The WSS patterns at three different time points in a severly diseased animal. The appearance of heterogeneous WSS distributions due to lumen intruding plaques (red arrows) is obvious. After registration, averaged WSS patterns can be related to histology (right panel).

Shear stress data: An example of the time averaged WSS distribution in a severely diseased animal is shown in left three panels in figure 4. Five weeks after cast placement, WSS was low upstream of the cast, while maximum WSS was observed inside the cast region. Asymmetrical WSS patterns were present downstream of the cast. Seven weeks after cast placement, WSS slightly increased upstream of the cast while flow recirculation appeared downstream of the cast. A distinct stenosis with high WSS upstream and low WSS downstream developed upstream of the cast. An increasingly complex pattern with multiple focal lesions appeared at week 9. After averaging the WSS in the circumferential direction, the WSS data was co-registered with histology. The preliminary analyses show that plaque composition was different at the different location: a larger necrotic core was present at the upstream plaque, indicating a potential role of WSS.

DISCUSSION

Genetically modified mice are frequently used to study the initiation and progression of atherosclerosis. The relationship between atherosclerosis and WSS was hardly studied in mice before, mainly due to the size of the arteries. Imaging them with sufficient spatial resolution for WSS computations, especially in a longitudinal study design, is a real challenge. In this study, we used contrast-enhanced µCT to monitor WSS patterns in a diseased mouse carotid artery over time.

We analyzed the effect of plaque growth on WSS and we were able to demonstrate that there were significant variations in the rate of plaque progression, leading to significant differences between both geometry and flow ratess. Animal-specific measurements are therefore required to accurately assess WSS patterns in vivo. A second consequence of these data is that longitudinal studies within a single animal are required to establish causal relationships between biomechanical indices and plaque composition and progression.

Future work will focus on establishing causal relationship between (changes in) WSS and plaque composition.

ACKNOWLEDGEMENTS

The research for this paper was financially funded by a fellowship from the Erasmus MC Foundation.

REFERENCES

[1] Wentzel,et al., Cardiovascular

[2] Cheng et al, Circulation, 2006 Jun 13;113(23)

Copyright 2016 The Organizing Committee for the 2016 Summer Biomechanics, Bioengineering and Biotransport Conference

SB³C2016
Summer Biomechanics, Bioengineering and Biotransport Conference
June 29 –July 2, National Harbor, MD, USA
SB³C2016-769

MORPHOLOGICAL MEASUREMENT AND THE OXYGEN DIFFUSION ANALYSIS IN MOUSE ACINAR CLUSTER OBTAINED FROM MICRO-CT

Luosha Xiao (1), Toshihiro Sera (2), Kenichiro Koshiyama (1), Shigeo Wada (1)

(1) Graduate School of Engineering Science
Osaka University
Toyonaka, Osaka, Japan

(2) Faculty of Engineering
Kyushu University
Fukuoka, Japan

INTRODUCTION

As the main site of gas exchange, pulmonary acini play an important role in respiratory functions. The acini consist of tree-like ducts and alveoli, which form highly fine and heterogeneous structure. An acinar cluster is a peripheral unit of the acini belong to the same terminal conducting airway. The oxygen in inhaled air has not been exchanged yet before it arrive to the entrance of the acinar cluster. To understand the effects of heterogeneity on respiratory functions, it is necessary to estimate the heterogeneous features of acini and subsequently to perform biomechanical analysis of gas exchange in a cluster. In this paper, we performed morphological measurements and the oxygen diffusion analysis with the measured data of the mouse acinar cluster.

METHODS

A semi-automatic segmentation method was used to collect mouse acinar clusters from synchrotron micro-CT images of the mouse lungs [1, 2]. The acinar volume and surface area of the segmented acini were estimated based on the voxel and surface meshes. The locational information of individual acini in the cluster was imparted by estimating the skeleton of each airway branch. 31 acini in three acinar clusters were analyzed.

To describe the oxygen transport in the acinar cluster, a three-compartment model (the airway side, the acinar wall tissue, and the blood side) was used with considering the conservation of oxygen flux between the compartments (Figure 1) [3].

The airway side includes the terminal conducting airway and the acinus. The averaged oxygen concentration C (dimensionless volume fraction) in the airway is considered by the diffusion equation for the one-dimension and the steady state. The oxygen flux J_{air} in the airways is

$$J_{air} = AD\frac{C_{in}-C_w}{L}, \quad (1)$$

where A is the apparent cross-sectional area of the airway to an acinus, D is the diffusion coefficient of oxygen in air, C_{in} is the constant concentration at the entrance of the terminal conducting airway, L is the averaged distance from the entrance to the acinar wall, and C_w is the averaged oxygen concentration at the wall.

The blood side includes blood capillaries. The oxygen concentration C in a capillary is considered by the advection equation for the one-dimension and the steady state. The oxygen flux J_{blood} in the blood capillary is

$$J_{blood} = Q_b\left(C_{b_{out}} - C_{b_{in}}\right), \quad (2)$$

where Q_b is the averaged blood flow in the capillary, C_{bout} is the averaged concentration at the capillary exit, and C_{bin} is the constant concentration at the capillary entrance.

In the airway, the oxygen concentration can be converted to the partial pressure by using Henry's law. In the blood capillary, the relationship between the oxygen partial pressure and the oxygen concentration can be written as the following set of equations [4];

$$\begin{gathered} C_b = S_{O_2}\cdot H_{max} + 3.0\times 10^{-5}\cdot P_b, \\ S_{O_2} = \frac{u}{u+1}, \\ u = 0.925v + 2.8v^2 + 30v^3, \text{ and} \\ v = \left(0.004273 + 0.04326\cdot {P_{b_{co_2}}}^{-0.535}\right)\cdot P_b, \end{gathered} \quad (3)$$

where S_{O_2} is the hemoglobin saturation that can be pre, H_{max} is the maximum amount of oxygen blood unit volume saturated with the

Copyright 2016 The Organizing Committee for the 2016 Summer Biomechanics, Bioengineering and Biotransport Conference

oxygen, and $P_{b_{co_2}}$ is the partial pressure of carbon dioxide in blood. C_{bout} in Eq. (2) can be obtained from Eq. (3) by assuming $P_b = P_w$.

In this model, the morphological parameters, A, S, L, and Q_b were obtained from our experimental data. A is estimated by averaging the cross-sectional area of the terminal conducting airway from the entrance of the terminal conducting airway to the entrance of the individual acinus. S is the surface area of the individual acinus. L is estimated by the sum of L_{acinus} and L_{airway}, where L_{acinus} is the characteristic length of the individual acinus estimated by taking cubic root of the acinar volume, and L_{airway} is estimated based on the centerline of the terminal conducting airway. For each individual acinus, Q_b is estimated by volume-dependent scaling based on the pulmonary blood flow in healthy human lungs. Other constant parameters are obtained from the healthy human lung conditions e.g. Ref. [5, 6], and the value of the parameters are summarized in Table 1. The morphology-dependent C_w were determined self-consistently.

Table 1: Parameter settings of the three-compartment model.

Parameter	Value
D [mm^2/s]	20
C_{in} [-]	0.132
$P_{b_{co_2}}$ [mmHg]	40
$P_{b_{in}}$ [mmHg]	40
H_{max} [cm^3/cm^3]	0.197

RESULTS AND DISCUSSION

Figure 2 shows the relationship between the volume and the location of each acinus from the entrance of the terminal conducting airway. The location of each acinus was normalized using the overall length of the terminal conducting airway as a measure of scale. The mean acinar volume and surface area were 0.07 ± 0.05 mm^3 and 6.13 ± 3.78 mm^2 (mean ± standard deviation), respectively. The largest acinus of each cluster was found in the distal region of the terminal conducting airway.

In above three clusters, the oxygen concentrations at acinar wall of each acinus were analyzed using the self-consistent model described above. Figure 3 shows the relationship between the oxygen concentration at acinar wall and L, for C_{in} = 0.132 (corresponding to 100 mmHg). The acinus at the distal region in the cluster shows a lower oxygen concentration comparing with that of the closer acini, but it is still in a larger range (>90 mmHg).

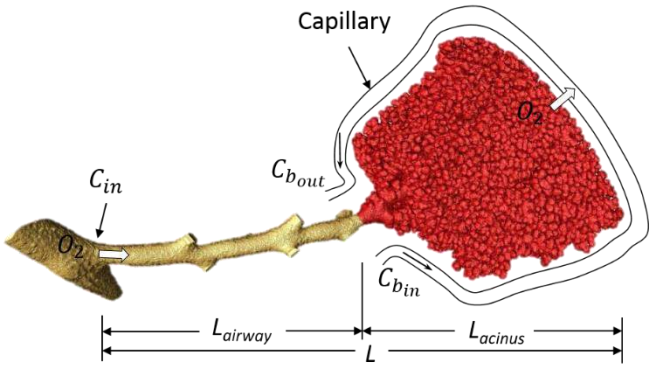

Figure 1: Model schematic of the oxygen transport for an individual acinus in an acinar cluster.

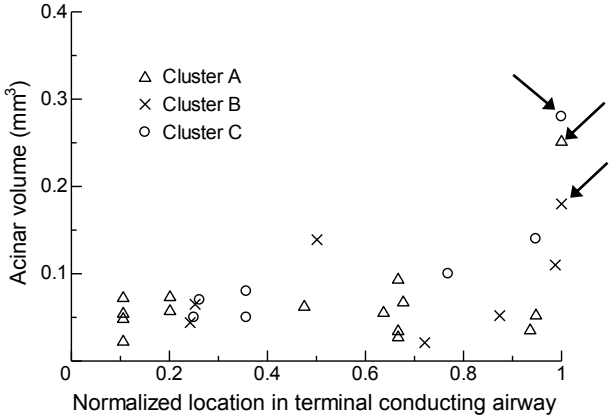

Figure 2: Acinar volume vs. location in the terminal conducting airway. Arrow indicates the largest acinus in each cluster.

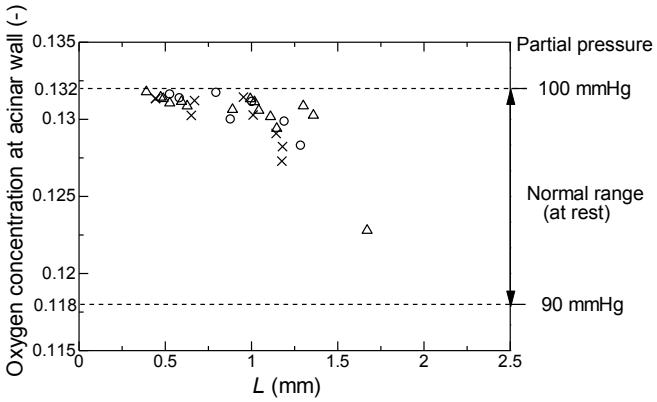

Figure 3: Oxygen concentration at acinar wall vs. distance from the entrance to the acinar wall (L).

SUMMARY

This study investigated the oxygen diffusion based on the acinar cluster morphology using a three-compartment model. Considering the gas transport at acinar cluster level, in spite of the large-volume acinus at distal region, the oxygen transport ability is enough to cover the large volume. In the future, the analysis with more sophisticated model should be conducted and it may be interesting to analyze the effects of the heterogeneity on respiratory functions for diseased lung conditions.

ACKNOWLEDGEMENTS

This work was supported in part by JSPS Grants-in-Aid for Scientific Research (No. 24240073) and the grants for excellent Graduate Schools Program, Department of Mechanical Science and Bioengineering, Osaka University.

REFERENCES

[1] Sera, T et al., *J. of Appl. Physiol*, 115(2):219-28, 2013.
[2] Xiao, L et al., *Comput Math Methods Med*, 2013:575086, doi:10.1155/2013/575086, 2013.
[3] Wada, S et al., *Comput. Biomech*, pp 247-269, 1996.
[4] Gomez, MD, *Am. J. Physiol*, 200:135-142, 1961.
[5] Wagner, PD et al., *J. of Appl. Physiol*, 33:62-71, 1972.
[6] Mines, AH, *Raven Press (New York)*, 1986.

Copyright 2016 The Organizing Committee for the 2016 Summer Biomechanics, Bioengineering and Biotransport Conference

SB³C2016
Summer Biomechanics, Bioengineering and Biotransport Conference
June 29 –July 2, National Harbor, MD, USA
SB³C2016-770

IN VITRO AND IN VIVO MODEL FOR ASSESSING IRREVERSIBLE ELECTROPORATION ON PANCREATIC CANCER

Qi Shao(1), Connie Chung(2) Feng Liu(2), Kianna Elahi(1), Paolo Provenzano(1), Bruce Forsyth(3), John. C. Bischof(1,2)

(1) Biomedical Engineering
University of Minnesota
Minneapolis, MN, USA

(2) Mechanical Engineering
University of Minnesota
Minneapolis, MN, USA

(3) Boston Scientific
Maple Grove, MN, USA

INTRODUCTION

Pancreatic cancer of all types was the 4th most common cause of cancer death in the United States in 2015 with few effective treatments available. Clearly, there is a need to find more effective approaches including possibly focal therapies that can be applied directly or under image guidance to treat this devastating disease.

One promising new focal therapy is irreversible electroporation (IRE) which has increased during the past decade due to many advantages over other focal therapies including being simple, fast and minimally invasive[1]. Compared to other thermal therapies, IRE has two important advantages if properly deployed: (1) reduction of collateral and thermal damage (e.g. over-treatment and thermal effects [2]) and (2) lack of dependence on blood perfusion (i.e. no blood sink or source thermal effects). The new application of IRE as an independent cancer therapy and its unique advantages has led to widespread interest from the scientific community [3-5].

This work presents preliminary data on the assessment of the impact of IRE on pancreatic cancer in *in vitro* and *in vivo* models. A series of IRE parameters (electric field and number of pules) were applied to cell suspensions in the *in vitro* model, and outcome is presented in terms of viability. Different treatment strategies with the same voltage, pulse number and pulse width but different in timing were applied to vivo tumor model, and the efficacy was evaluated by tumor growth delay after treatment.

METHODS

In Vitro Experiments:

In vitro experiments were performed with human adenocarcinoma cells (AsPC-1) and murine pancreatic ductal adenocarcinoma cells (KPC). For each *in vitro* electroporation test, 400 µl of the prepared cell suspension (0.5~0.6 million cells/ml) was pipetted into the electrode gap (2 mm) in an electroporation cuvette (FB102, Fisher Scientific), which was then placed in an external electric field created by an electric pulse generator (BTX ECM 830, Harvard Apparatus). The pulsing frequency was set to 10 Hz and the pulse duration was 50 µs. Cells were subjected to 10, 50, and 99 pulses at electric fields between 500, 750, 1000 and 1250 V/cm.

Viability after pulsing was evaluated using a Tetrazolium-based Cell Counting Kit-8 (CCK-8) assay. It is a metabolic-based assay that measures the dehydrogenase activity within cells. A clear, flat-bottomed 96-well plate was loaded with 100 µL of cell suspension and 10 µL of CCK-8 dye per well. The plate was then incubated at 37 degrees C and 5% CO_2 for 3 – 4 hours depending on the cell concentration. After incubation, the optical absorption of the samples was read in a spectrophotometer at a wavelength of 450 nm.

In Vivo Experiments:

In vivo tumors were grown using AsPC-1 cells grown in a nude mouse hind limb model. All animal usage and experimental procedure protocols were reviewed and approved by the Institutional Animal Care and Use Committee of the University of Minnesota. 100 µL of the suspension of 1 million cells was injected subcutaneously over hind limb of mice under general anesthesia.

Tumors were treated with IRE 15 days after implantation, with average size of 100 mm^3 (on average 9 mm by 7 mm). Treatments were delivered by a pair of customized needle electrodes connected to an electrical pulse generator (BTX ECM 830, Harvard Apparatus). The needles (OD = 0.7 mm) were fixed on a plastic block with a center-to-center distance of 4 mm. An insulating layer was coated outside each needle with heat shrink tubing leaving a 3 mm tip for treatment. The needle electrodes were inserted symmetrically to the center of the tumor through the skin. Effective treatment depth is determined by the exposed needle length (3 mm).

The animals were randomly divided into four group with each group receiving a different treatment plan. Group 1 received sham procedure without any electric pulses. Groups 2 and 3 were applied

Copyright 2016 The Organizing Committee for the 2016 Summer Biomechanics, Bioengineering and Biotransport Conference

with 51 IRE pulses at pulse strengths of 600 V (potential between two electrodes), durations of 50 µs and pulse repetition rates of 10 Hz. However, for group 3, the 51 pulses were delivered in three trains of 17 pulses with delays of 30 s in between trains. Group 4 have the same pulses as group 2, but the repetition rate was set to 1 Hz.

After IRE treatment, the mice were returned to their cages and monitored for any complications. Tumor growth measurements were taken twice a week using a caliper. The sizes of the major axis (L) and minor axis (S) of the tumors were measured and used to calculate tumor volumes (V) by using V=1/2*L*S^2. All tumors were monitored for at least 40 days after the IRE treatment.

RESULTS

The *in vitro* result of cell viability after IRE with different parameters are shown in Figure 1 (AsPC-1) and Figure 2 (KPC). The AsPC-1 cells can be seen to be more sensitive for the same IRE conditions than KPC. For instance, field strength (V/cm) had relatively little impact on AsPC-1 (all above 90%) at 10 pulse repetitions where KPC dropped to 85% and 64% at 750 and 1250 V/cm. Reductions were more dramatic at higher pulse numbers.

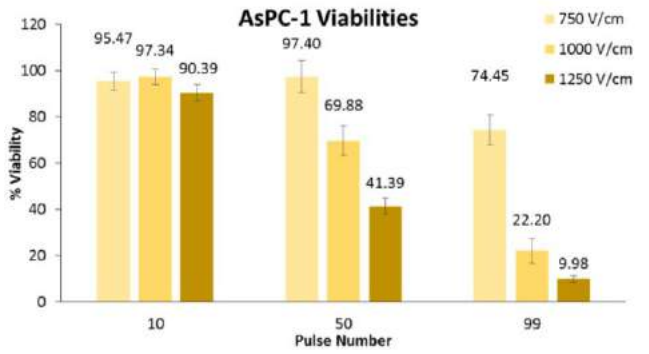

Figure 1: AsPC-1 viabilities after 10, 50, and 99 pulses and electric fields of, 750, 1000, and 1250 V/cm.

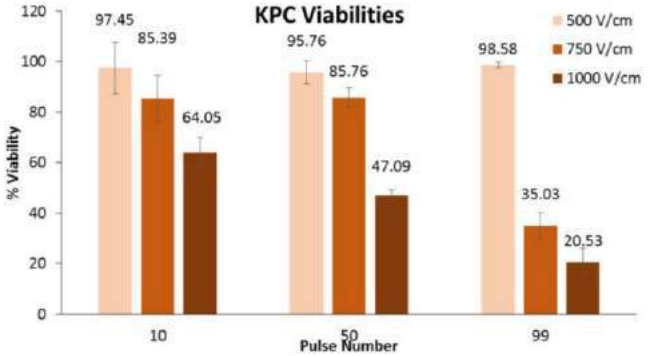

Figure 2: KPC cell viabilities after 10, 50, and 99 pulses and electric fields of 500, 750, and 1000 V/cm.

The *in vivo* tumor growth demonstrates that pulse timing can have a dramatic impact on tumor growth delay. The in vivo tumor growth is being collected as of the deadline of this abstract submission.

DISCUSSION

Our *in vitro* and *in vivo* data sets can help in protocol development for pancreatic and other cancer treatments by IRE. For instance, in vitro testing can demonstrate relative susceptibility of different cancer types to IRE. In the cell types tested were found that the human line (AsPC-1) was less susceptible for the same IRE

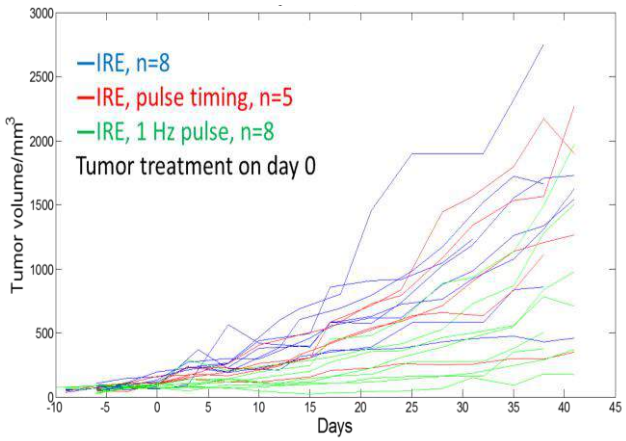

Figure 3: Partial results from *in vivo* IRE tumor ablation study.

conditions as the KPC (murine line). Further, we were able to define the conditions where viability dropped between 10% for the cell type. In the case of *in vivo* testing, the pulse timing and delivery methods were also explored to improve the destructive potential or IRE. In this case, for the same energy applied, waiting between pulses (Pulse timing group) improves outcomes over IRE pulsing at 10 Hz. This agrees with previous work on pulse timing presented both in vitro and *in vivo* in a prostate cancer model with IRE[5]. By extending this pulse timing out to as long as a second between pulses improves this result even further. It is not clear whether there is a limit to this effect in the pancreatic lines tested. The time frame of 1 second between pulses during timing is interesting because it suggests that IRE can be gated along with the heartbeat in the clinic. Together, these results suggest that further IRE protocol design and parameter setting exploration is warranted. In the future, this information can perhaps help in the effective design and translation of a clinical IRE device for the treatment of pancreatic cancer.

ACKNOWLEDGEMENTS

The work is supported by Boston Scientific and the IEM Cancer Animal Core lab.

REFERENCES

[1] R. V. Davalos, L. M. Mir, and B. Rubinsky, "Tissue ablation with irreversible electroporation," *Annals of Biomedical Engineering,* vol. 33, no. 2, pp. 223-231, Feb, 2005.

[2] C. L. Jiang, R. V. Davalos, and J. C. Bischof, "A Review of Basic to Clinical Studies of Irreversible Electroporation Therapy," *Ieee Transactions on Biomedical Engineering,* vol. 62, no. 1, pp. 4-20, Jan, 2015.

[3] C. L. Jiang, Z. P. Qin, and J. Bischof, "Membrane-Targeting Approaches for Enhanced Cancer Cell Destruction with Irreversible Electroporation," *Annals of Biomedical Engineering,* vol. 42, no. 1, pp. 193-204, Jan, 2014.

[4] Z. P. Qin, J. Jiang, G. Long, B. Lindgren, and J. C. Bischof, "Irreversible Electroporation: An In Vivo Study with Dorsal Skin Fold Chamber," *Annals of Biomedical Engineering,* vol. 41, no. 3, pp. 619-629, Mar, 2013.

[5] C. L. Jiang, Q. Shao, and J. Bischof, "Pulse Timing During Irreversible Electroporation Achieves Enhanced Destruction in a Hindlimb Model of Cancer," *Annals of Biomedical Engineering,* vol. 43, no. 4, pp. 887-895, Apr, 2015.

Copyright 2016 The Organizing Committee for the 2016 Summer Biomechanics, Bioengineering and Biotransport Conference

SB^{3}C2016
Summer Biomechanics, Bioengineering and Biotransport Conference
June 29 –July 2, National Harbor, MD, USA
SB^{3}C2016-771

NUMERICAL MODELING OF FLOW DIVERTER STENT IN GIANT CEREBRAL ANEURYSM

A. F. Sanches (1), E. Gutheil (1)

(1) Interdisciplinary Center for Scientific Computing, University of Heidelberg, Heidelberg, Germany

INTRODUCTION

Cerebral aneurysm is a vascular disease characterized by the local dilatation of arterial walls in the intracranial space. The aneurysm may rupture and cause sub arachnoid hemorrhage, associated with high mortality and morbidity. Due to widely used imaging methods in clinical surgery, the detection of cerebral aneurysms that are not ruptured becomes more and more frequent. In order to reduce the risk of rupture and hemorrhage and to identify highly effective treatment options, the understanding of the hemodynamic mechanisms involved is of great importance [1-2] and numerical tools may provide excellent support of the medical treatment of cerebral aneurysms.

Endovascular intervention is one of the treatments of choice for cerebral aneurysms because of both its safety and efficacy. Large, giant, wide-necked, and fusiform aneurysms are considered more challenging and less tractable to traditional endovascular coil embolization. The flow diverter stent is a promising method of endovascular reconstruction for large and complex intracranial aneurysms, with an overall porosity metallic mesh placed in the parent artery to reduce blood flow in the aneurysm to the point of stagnation and gradual thrombosis [3].

Computational techniques offer new capabilities in the healthcare provision for intracranial aneurysms. The availability of a simulation tool for virtual flow diverter is extremely useful to support the decisions of treatment options by medical experts and to develop and optimize new implant designs [4-5]. In this project, the development of a computational tool for the modeling and simulation of the hemodynamic effects of the endovascular stents with different porosities are performed. A flow diverter and a regular stent are modeled and analyzed taking into account their design, porosity, and the flow reduction through the giant sidewall cerebral aneurysm is studied.

METHODS

An idealized giant sidewall cerebral aneurysm with a diameter of 33 mm is modeled based on a three-dimensional cerebral rotational angiography image provided by the Heidelberg Medical School. Two stents with regular meshes made of cylindrical wires are considered which fit the shape of the parent artery. Their geometrical properties are summarized in Table 1 in terms of a stent unit cell. The stent with a low metal coverage proportion is called regular stent (RS) and that with high metal coverage proportion is known as flow diverter (FD).

The computational grids for the simulations were generated using the software ICEM-CFD v.11 (Ansys Inc.). The laminar flow is described by three-dimensional incompressible equations, which are solved using the software platform OpenFoam v2.3. The non-Newtonian flow is modeled with Carreau-Yasuda's fluid model [6]. A uniform velocity profile of 0.14 m/s for the late diastole, and 0.56 m/s for the peak systole is prescribed at the inlet, and the pressure gradient at the outlet is zero. All the vascular walls are assumed rigid with a no-slip boundary condition. The elasticity of the stent is neglected.

Table 1: Geometrical dimensions of the assumed stent unit cell [5]

Unit cell	Dimension	RS	FD
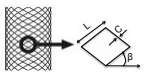	C (μm)	0.94	0.30
	L (mm)	60	42
	β	49°	55°
	ε (porosity)	0.88	0.73

RESULTS AND DISCUSSION

Figures 1 and 2 show a comparison of the velocity and its streamlines for the pure aneurysm, the regular stent, and the flow diverter during the systolic and diastolic cardiac flow, respectively.

Copyright 2016 The Organizing Committee for the 2016 Summer Biomechanics, Bioengineering and Biotransport Conference

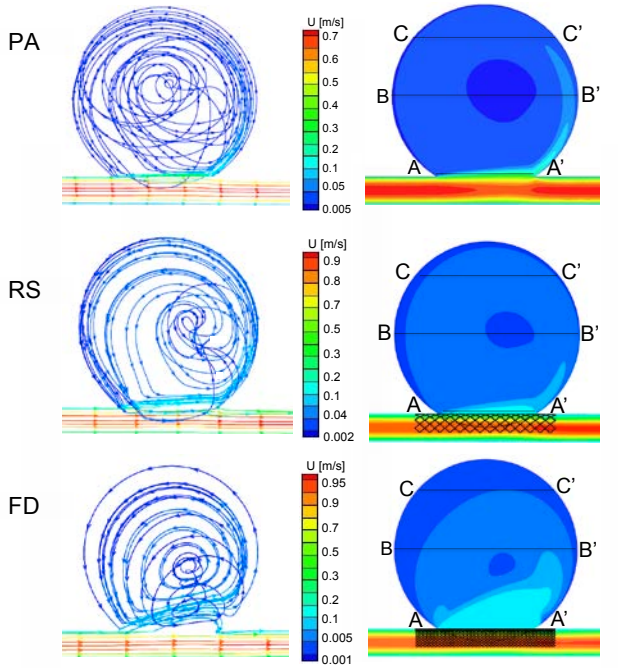

Figure 1: Velocity streamlines (left), velocity contour at the mid plane (right) for systolic cardiac flow, of pure aneurysm (PA), regular stent (RS), and flow diverter (FD)

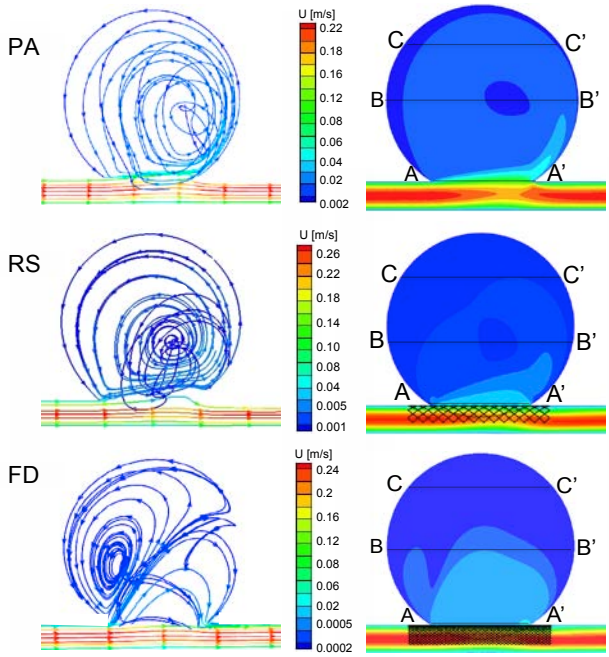

Figure 2:Velocity streamlines (left), velocity contour at the mid plane (right) for diastolic cardiac flow, of pure aneurysm (PA), regular stent (RS), and flow diverter (FD)

In the pure aneurysm and for the regular stent, the flow pattern at the aneurysm neck consists of a main clockwise distal inflow jet. A possible physical mechanism to describe this phenomenon involves both shear stress and pressure [5]. The shear stress transmitted at the cerebral aneurysm neck, induced by a strong velocity gradient in the parent artery, drives a counter-clockwise intra-aneurysmal flow. The use of the flow diverter causes the flow to transfer to a clockwise streamline from the proximal to distal side of the neck, driving a low motion swirl to the aneurysm's dome. The implantation of the FD impedes the flow at the aneurysm's neck, resulting in both a lower shear stress transmission and an increase of pressure gradient along the parent artery. The latter pushes the circulating fluid inward and outward the cerebral aneurysm at the proximal and distal sides of the neck, respectively. The magnitude of flow velocity inside the aneurysm is strongly reduced due to the use of the RS and even more due to the FD as shown in Fig. 1, note the different scales in the different parts of the figure.

The reduction of the aneurysm inflow and the flow activity after the implantation of a stent or flow diverter is a key factor for thrombus formation inside the aneurysm. As flow activities decrease, the turnover time increases in an inverse proportion, and therefore the chance of aneurysm thrombotic occlusion is likely to increase.

Tables 2 and 3 show the wall shear stress (WSS) for the PA, the RS, and the FD, for the systolic and diastolic cardiac flow, respectively. A strong reduction of the WSS for the different cross sections for both the regular stent and flow diverter is noted. However, the WSS reduction of the flow diverter during the peak systole is more significant, especially in the dome of the aneurysm.

CONCLUSIONS

The flow diverter effectively reduces the wall shear stress, the blood flow velocity and provides a structure to support endothelialization and reconstruction of the parent artery. This device also relocates the center of the vorticity in the intracranial aneurysm. The use of the flow diverter greatly improves the performance compared to the regular stent, and flow separation at the distal side of the neck is observed, promoting thrombosis.

Table 2: Wall shear stress for the systolic cardiac flow

	PA	RS	FD
A-A'	13.2 Pa	2.6 Pa (-80.3%)	1.3 Pa (-90.1%)
B-B'	0.45 Pa	0.066 Pa (-85.3%)	0.04 Pa (-91.1%)
C-C'	0.18 Pa	0.031 Pa (-82.7%)	0.0015 Pa (-99.2%)

Table 3: Wall shear stress for the diastolic cardiac flow

	PA	RS	FD
A-A'	1.6 Pa	0.88 Pa (-45%)	0.24 Pa (-85%)
B-B'	0.038 Pa	0.0043 Pa (-88.7%)	0.0043 Pa (-88.7%)
C-C'	0.013 Pa	0.0018 Pa (-86.1%)	0.0001 Pa (-99.2%)

ACKNOWLEDGEMENTS

The authors thank Prof. Dr. Bendszus and Dr. Möhlenbruch from Neuroradiology Department of Heidelberg Medical School for providing the medical images and data. They gratefully acknowledge the financial support of the Graduate School "MathComp".

REFERENCES

[1] Wong, G K C et al., *J Clinical Neuroscience*, 18:737-740, 2011.
[2] Xiang, J et al., *J Neurointerventional Surgery*, 0:1-7, 2014.
[3] Möhlenbruch, M A et al., *AJNR*, 6:1155-61, 2015.
[4] Poon, W S et al., *J Clinical Neuroscience,* 18:1285-1288, 2011.
[5] Bouillot, P, et al., *PLoS One,* 9: 1-17, 2014.
[6] Gambaruto, A, et al, *Math Bio and Engineering*, 3: 649-665, 2013.

Copyright 2016 The Organizing Committee for the 2016 Summer Biomechanics, Bioengineering and Biotransport Conference

SB^{3}C2016
Summer Biomechanics, Bioengineering and Biotransport Conference
June 29 –July 2, National Harbor, MD, USA
SB^{3}C2016-772

ACUTE EFFECTS OF CELL FREE HEMOGLOBIN AND SICKLED RED BLOOD CELLS ON PULMONARY VASCULAR IMPEDANCE IN OTHERWISE HEALTHY MICE

David A. Schreier (1), Timothy A Hacker (2), Diana Tabima (1), and Naomi C Chesler (1,2)

(1) Department of Biomedical Engineering, University of Wisconsin-Madison, 2146 ECB, 1550 Engineering Dr., Madison, WI 53706

(2) Department of Medicine, University of Wisconsin-Madison,1685 Highland Avenue, 5158 Medical Foundation Centennial Building, Madison, WI 53705

INTRODUCTION

Patients with sickle cell disease (SCD)-related pulmonary hypertension (PH) have a substantially increased risk of sudden death compared to those with SCD alone, as high as a 50% within 2 years [1, 2]. The prevalence of PH in adults with SCD is high--about 30%, while the percentage of SCD patients with evidence of PH via lung histology at the time of death is even higher--75% [3-5]. SCD red blood cells (RBC) are more rigid, dense and frequently trapped in the microcirculation, thereby interrupting blood flow and causing ischemia, thrombotic events, increased oxidative stress, and reperfusion injury [6]. SCD RBCs also lyse easily, releasing cell-free hemoglobin, which itself causes depletion of nitric oxide, vasoconstriction and is a major contributor to endothelial cell dysfunction in SCD. All of these consequences of SCD can and often do have drastic effects on hemodynamics including increasing pulmonary vascular resistance (PVR) [6] and systemic arterial wave reflections [7].

In this study, we sought to investigate the impact of SCD RBCs and cell free hemoglobin, independent of other SCD-related abnormalities, on the hemodynamic changes that ultimately cause PH and increase mortality in SCD. We chose to use pulmonary vascular impedance (PVZ) to measure these changes as it provides a comprehensive view of the both static and dynamic components of right ventricular (RV) afterload in the pulmonary vasculature. That is, in addition to PVR, PVZ relays information about characteristic impedance and wave reflections, which are affected by changes in pulmonary arterial stiffness, which has been shown to be a predictor of morbidity and mortality in patients with pulmonary hypertension alone [8]. We hypothesized that SCD RBCs, especially when exposed to acute hypoxia (AH), and cell free hemoglobin will increase PVR and wave reflections in the pulmonary circulation in otherwise healthy lungs.

To test this hypothesis, we infused RBCs from control mice (cRBCs), RBCs from SCD mice (SCD RBCs), or cell free hemoglobin in solution into the jugular vein of mice. We measured PVZ in vivo at baseline, after each injection, and also after 5 minutes of 10% O2 ventilation, which has been shown to lower blood oxygen levels in mice [9]. Our results confirmed that cell free hemoglobin increases both PVR and wave reflections, with a further increase with exposure to AH, while SCD RBCs increase PVR and wave reflections only after exposure to AH, suggesting that increased cell free hemoglobin and lowered blood oxygen levels are key to poor outcomes in SCD-related PH.

METHODS

Whole blood was drawn from donor male SCD mice, or C57Bl6 mice (14 weeks-old) to obtain RBCs. Cell free hemoglobin was purchased commercially. Using established techniques from our lab [10-12], male C57BL6 (14-16 weeks old) mice underwent catheterization of the main pulmonary artery (PA) to obtain pressure with simultaneous echocardiography to obtain PA flow. Once baseline measurements were recorded, 200 uL of blood (Hct~45%) was drawn from each mouse and replaced with an equal volume of a 45%-by-volume suspension of SCD RBCs, cRBCs or cell free hemoglobin in physiological saline solution (200 μM). All pressure and flow measurements were repeated and the cycle was repeated 1 more time, thereby introducing a total of 400 uL of SCD RBCs, cRBCs or cell free hemoglobin in solution. After all transfusions were performed, the animal was exposed to 5 minutes of AH (10% O_2), and then pressure and flow measurements were repeated.

Copyright 2016 The Organizing Committee for the 2016 Summer Biomechanics, Bioengineering and Biotransport Conference

Simultaneously obtained pressure and flow waveforms were analyzed using both time and frequency domain techniques as each method can relay important information about the state of the pulmonary vasculature. Metrics of PVZ were calculated in the time domain using wave intensity analysis as previously described [13]. Total PVR (Z_0) is calculated as mPAP divided by Q averaged over the cardiac cycle. The pulmonary arterial pressure waveform is separated into forward (Pf) and backward (Pb) traveling components using the linear wave separation method [14]. The index of global wave reflections (RQ) is calculated as the ratio of the amplitude of Pb to Pf. The characteristic impedance (Z_C) is calculated as the derivative of pressure with respect to the flow at 95% max flow in early systole.

In the frequency domain, P and Q are decomposed into sinusoids at harmonics of the heart rate using a Fourier transform, which expresses the data as the sum of series of sine and cosine waves. Z_0 is obtained as the magnitude of PVZ (Z) at 0 Hz; characteristic impedance (Z_C) is obtained by averaging Z from the 4th to 10th harmonics.

RESULTS

Infusion of cell free hemoglobin (Hb+) did not affect mPAP but did increase PVR and wave reflections after the 2nd infusion. These increases were maintained with exposure to acute hypoxia (AH). Hb+ with or without acute hypoxia did not affect Z_C. Infusion SCD RBCs did not affect mPAP, PVR or wave reflections until the animals were also made acutely hypoxia. As with Hb+, SCD RBCs with or without acute hypoxia did not affect Z_C. Infusion of cRBCs did not alter mPAP, PVR, wave reflections or Z_C after either infusion with or without acute hypoxia.

Table 1. Hemodynamic values: mean pulmonary artery pressure (mPAP: mmHg), pulmonary vascular impedance (Z_0) and characteristic impedance (Z_C: mmHg*min/ml), and wave reflections RQ (dimensionless).

	mPAP	Z_0	RQ	Z_C
cRBCs	13.3±1.3	1.6±0.2	0.32±0.03	0.26±0.02
2nd	12.0±2.2	1.6±0.4	0.29±0.03	0.28±0.01
AH	10.3±2.5	1.5±0.3	0.32±0.04	0.30±0.05
Hb+	13.2±1.0	1.2±0.1	0.33±0.02	0.20±0.03
2nd	13.7±1.0	1.4±0.1*	0.38±0.03*	0.24±0.03
AH	13.2±1.3	1.5±0.1*	0.44±0.04*	0.20±0.02
SCD RBCs	15.5±0.6	1.3±0.1	0.31±0.04	0.21±0.02
2nd	14.2±0.4	1.6±0.1	0.32±0.02	0.21±0.01
AH	12.2±0.7*	1.9±0.2*	0.37±0.05*	0.21±0.02

Note: values are ±SE, n=4 for cRBCs (animals injected with control RBCs), n= 5 for Hb+ and SCD RBCs (animals injected with cell free hemoglobin or SCD RBCs). *P<0.05 versus baseline, represented by cRBCs, Hb+, and SCD RBCs.

DISCUSSION

Our results confirm that infusion of cell free hemoglobin and sickled SCD RBCs alter RV afterload and further suggest that release of cell free hemoglobin, as occurs in SCD due to hemolysis of fragile RBCs, increases wave reflections. Additionally, acute hypoxia, which has previously been shown to cause hypoxemia, increases wave reflections after multiple transfusions of SCD RBCs, suggesting that decreased oxygen levels in SCD increases wave reflections. The increases in pulmonary vascular resistance with no change in mPAP can be explained by significant decreases in cardiac output. Interestingly mPAP actually significantly decreased with transfusions of SCD RBCs after exposure to acute hypoxia. Since both heart rate and systemic pressure also decreased with exposure to AH in animals with SDC RBCs, it is possible the combination hampered the ability of the left ventricle to increase CO, which ultimately decreased pulmonary artery pressure. Additionally, endothelial cells in these otherwise healthy lungs could have released NO in response to SCD RBCs and AH, which would also explain the decreased mPAP. We also note that mPAP and Z_0 were not increased by AH as might be expected due to hypoxic pulmonary vasoconstriction. Since the lungs were healthy and hematocrit was normal, we anticipate release of NO from healthy endothelial cells counteracted any vasoconstriction induced by AH.

In conclusion, our results suggest that SCD increases both steady (Z_0) and unsteady (wave reflections) components of RV afterload. Further, release of cell free hemoglobin from lysed SCD RBCs may contribute to increased risk of sudden RV failure in SCD.

ACKNOWLEDGEMENTS

This work was supported by NIH grant 1R01HL086939 (NCC), and NIH F31 HL128088-01 (DAS). The authors also would like to acknowledge Gaoussou Diarra for his surgical expertise.

REFERENCES

1. Castro, O., M. Hoque, and B.D. Brown, Blood, 2003. **101**(4): p. 1257-61.
2. Charache, S., J Lab Clin Med, 1994. **124**(4): p. 473-4.
3. Ataga, K.I., et al., Am J Med, 2004. **117**(9): p. 665-9.
4. De Castro, L.M., et al., Am J Hematol, 2008. **83**(1): p. 19-25.
5. Haque, A.K., et al., Hum Pathol, 2002. **33**(10): p. 1037-43.
6. Machado, R.F. and H.W. Farber, Clin Chest Med, 2013. **34**(4): p. 739-52.
7. Aessopos, A., et al., Atherosclerosis, 2007. **191**(2): p. 427-32.
8. Hunter, K.S., et al., Am Heart J, 2008. **155**(1): p. 166-74.
9. Schreier, D., et al., J Biomech Eng, 2013. **135**(2): p. 021018.
10. Schreier, D.A., et al., J Biomech Eng, 2015.
11. Schreier, D.A., et al., J Appl Physiol (1985), 2014. **117**(8): p. 833-9.
12. Tabima, D.M., et al., J Biomech, 2012. **45**(5): p. 799-804.
13. Mitchell, G.F., et al., Am J Physiol, 1994. **267**(5 Pt 2): p. H1907-15.
14. Westerhof, N., et al., Cardiovasc Res, 1972. **6**(6): p. 648-56.

Copyright 2016 The Organizing Committee for the 2016 Summer Biomechanics, Bioengineering and Biotransport Conference

SB^{3}C2016
Summer Biomechanics, Bioengineering and Biotransport Conference
June 29 –July 2, National Harbor, MD, USA
SB^{3}C2016-773

A COMPUTATIONAL INVESTIGATION OF THE POSITIONING OF TRANSCATHETER AORTIC HEART VALVES TO ENHANCE LONG TERM PERFORMANCE

McGee, O. M. (1), Gunning, P. S (1), McNamara L. M. (1)

(1) Biomedical Engineering,
College of Engineering and
Informatics, NUI Galway, Ireland

INTRODUCTION

Aortic Stenosis (AS) is an age related degenerative disease of the aortic valve that causes progressive narrowing of the valve and aortic regurgitation. The current gold standard of treatment requires open heart surgery to replace the stenotic valve with a surgically implanted prosthetic valve. However, approximately 30% of the patients are refused this highly invasive surgery because of the high preoperative mortality risk [1]. Transcatheter Aortic Valve Implantation (TAVI) is a minimally invasive alternative to open heart surgery. TAV's consist of an expandable metallic frame onto which animal derived tissue leaflets are attached, and then crimped onto a catheter for minimally invasive delivery to the site of the native stenotic valve. The valve stent is positioned at the site of the native valve using radiopaque markers under fluoroscopy and then expanded radially, using a balloon or by means of self-expanding stent material.

The first generation TAVR's in clinical use were the Edwards Sapien® Valve (a balloon expanding stent) and the Medtronic CoreValve® (a self-expanding Nitinol stent) [2]. For these valves, the final deployment position of TAVR's varies changing over time depending on operator experience [3]. Incorrect positioning of TAVR's, for example a valve extending excessively into the ventricle or the aorta, can cause adverse effects such as mitral insufficiency, arrhythmias or aortic injury [4]. Precise positioning of TAV's might overcome the need for revision surgery and enhance the long term mechanical performance. Second generation TAVR's have been developed to allow for repositioning of the TAV directly after deployment (TRINITY TA, Evolut R^{TM}, Lotus$^{TM)}$. However, it remains that optimal positioning of TAVR's has not been defined.

Finite element models have been applied to model the performance of TAV's in particular to understand the role of the interaction of the valve with the native anatomy in device performance [5-7]. However such methods have not been applied to predict the role of valve positioning. In this study finite element techniques will be used to compare a first generation self- expanding laser cut stent to a second generation self-expanding braided stent with a repositionable locking mechanism. This research will derive an understanding of the role of positioning on the mechanical performance on both TAV's.

METHODS

A patient specific aortic root geometry was generated from Multi-slice computed tomography (MSCT) images of an 89 year old male with a stenosed aortic valve. The images taken pre-TAVR at peak diastole (slice thickness = 0.625 mm, slice dimensions = 512 9 512 and pixel spacing = 0.5 mm) were manually thresholded between Hounsfield units of 250 to 700 using Mimics 14.1 Imaging Software (Materialise, Leuven, Belgium) [6]. This aortic root was meshed using 43296 shell elements (S4R), with reduced integration and hourglass control, and implemented into a finite element model created in ABAQUS. Crimping and deployment of two different self-expanding Nitinol TAV stents (a braided stent and a laser cut stent) into the aortic root was modelled. The braided stent was modelled using 3 node quadratic beam elements (B32). The laser cut stent was modelled using 8 noded linear brick elements (C3D8R) with reduced integration and hourglass control. Both stents were modelled using a self-expanding superelastic Nitinol inbuilt material model (VUMAT). The aortic root was modelled as isotropic hyperelastic. Before the valve stents were deployed they were reduced radially inward by 12 mm using a rigid cylindrical surface (crimper). Boundary conditions were placed on the rigid surface to reduce the diameter. Surface-to-surface contact with a coefficient of friction of 0.1 was implemented between the crimper (master) and stent (slave). The stents were deployed annularly such that the TAVR was positioned with an equal distribution of the TAVR

Copyright 2016 The Organizing Committee for the 2016 Summer Biomechanics, Bioengineering and Biotransport Conference

stent above and below the annulus using surface-to-surface contact between the stent (master) and aortic root (slave) with coefficient of friction of 0.1. A final locking step was applied to the braided stent to simulate locking, which is representative of commercial repositionable TAVI devices.
This approach was also undertaken for stents positioned 5mm above the annulus (supra-annular) and 5mm below the annulus (sub-annular).

RESULTS

Laser Cut Stent:
The 99th percentile maximum von Mises stresses in the aortic tissue were taken to eliminate possibly eschewed elements. Higher stresses were observed in the supra annular and annular positions with 99th percentile maximum von Mises stresses of 0.1254 MPa and 0.1136 MPa respectively. The lowest maximum stress of 0.1056 MPa was observed at the sub annular position. The stent experienced a maximum von Mises stress of 2409 MPa (Figure 1) when deployed at the aortic annulus. The maximum von Mises stresses of 909.3MPa and 710.72MPa were predicted for stents deployed at 5mm supra and sub annular positions.
Fig. 2 shows percentage volume vs. stress graph showing the percentage stress distribution in the aortic root for the laser cut stent. The supra annular position had larger percentages of the aortic root volume experiencing high stress, whereas at the sub annular position larger percentages of the tissue volume were at a low stress (MPa).

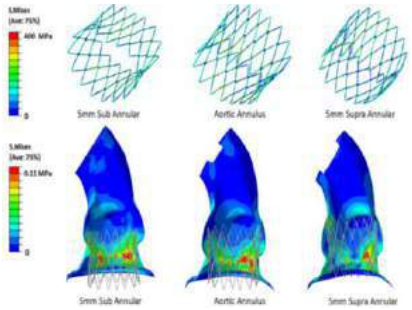

Figure 1: Contour plots of Von Mises stresses (MPa) in the aortic root and the laser cut stent in three different positions

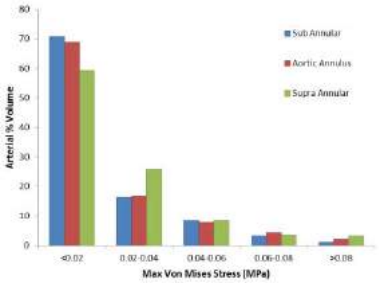

Figure 2: Percentage Volume plots of Von Mises stresses (MPa) in the aortic root deployment of laser cut stent.

Braided Stent:
Higher stresses were observed in the supra annular and sub annular positions with 99th percentile von Mises stresses of 0.8635 MPa and 0.8887 MPa respectively. The lowest stress of 0.7012 MPa was observed at the annular position. The stent experienced a maximum stress of 405.453 MPa (Figure 3) when deployed sub annularly. Stresses of 284.31 MPa and 261.29 MPa were predicted for stents deployed at the annular and 5mm supra annular positions.

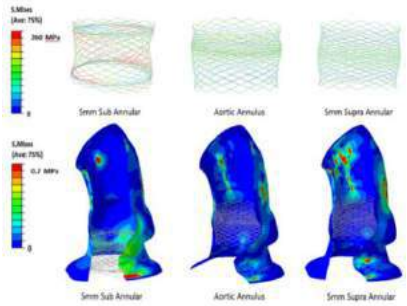

Figure 3: Contour plots of Von Mises stresses (MPa) in the aortic root and the braided stent in three different positions

Fig. 4 shows a percentage volume vs. stress graph showing the percentage stress distribution in the aortic root for the braided stent. There were larger percentages of the aortic root volume at high stress sub annularly, whereas at the sub annular and annular positions large percentages of the tissue volume were at a low stress (MPa).

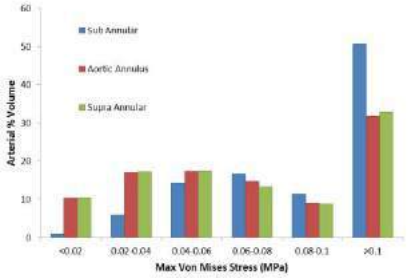

Figure 4: Percentage Volume plots of Von Mises stresses (MPa) in the aortic root after deployment of braided stent.

DISCUSSION

These results show that valve positioning influences the maximum stresses in the aortic tissue and in the valve stent. The results also suggest that the optimal position is dependent on valve design. Recommendations for the optimal positioning vary with the design of the valve [3]. However, this has never been investigated while examining the impact of stress. For the braided stent the optimal position appears to be between the aortic annulus and sub annular positions, as this is where the lowest aortic and stent stresses were seen. The maximum Von Mises stresses predicted for all three deployment positions for both the braided stent and the laser cut stent are well below the rupture stress of the aortic tissue (1.75MPa [8]). Although the lowest stresses for the braided stent were seen at the supra annular position, positioning of the valve stent too high can lead to obstruction of the coronary arteries [3]. The exclusion of the native leaflets and calcifications from the aortic root is a limitation of the study, but will be included in future work. Secondly, the laser cut stent design is not representative of any commercially available stent, but was used to develop the computational approach.

ACKNOWLEDGEMENTS

This study was funded by an Enterprise Partnership Scheme Postgraduate Scholarship.

[1]Iung, B. et al 2003. Eur Heart J, 24(13), 1231-43
[2]Padala, M., et al. (2010). Cardiovasc Eng Technol 1(1): 77-87.
[3] Piazza, N., et al. (2008). Circ Cardiovasc Interv 1(1): 74-81.
[4]Masson, J.-B. et al (2009). JACC: Cardiovascular Interventions, 2, 811-820.
[5] Capelli, C., et al (2012), Med Biol Eng Comput, 50(2), 183-92.
[6] Wang, Q., et al. (2012), J Biomech, 45(11), 1965-71.
[7] Gunning, P. S., et al (2014), Ann Biomed Eng, 42(9), 1989-2001.
[8] Vorp, D.A., et al. (2003) The Ann Thorac Surg,. 75(4): p. 1210-1214.

Copyright 2016 The Organizing Committee for the 2016 Summer Biomechanics, Bioengineering and Biotransport Conference

SB^{3}C2016
Summer Biomechanics, Bioengineering and Biotransport Conference
June 29 –July 2, National Harbor, MD, USA
SB^{3}C2016-774

WINDKESSEL APPROACH FOR BLOOD FLOW RESPONSES: APPLICATION IN VENOUS ULCER RISK ASSESSMENT

W. Pan (1), S. Baek (1), TR. Bush (1)

(1) Mechanical Engineering
Michigan State University
East Lansing, MI, USA

INTRODUCTION

Venous ulcers, or stasis ulcers are severe skin wounds that make up 90% of all lower extremity ulcers [1]. Venous ulcers are a global problem affecting 2.5 million people in the US, 6 million in Brazil, and approximately 14 million in Europe [2], [3]. A venous ulcer is usually caused by chronic venous insufficiency which results in an inability to effectively move the blood back to the heart [1]. These ulcers are painful and can become infected and result in amputation. Therefore, it is important to understand the blood flow in the lower leg and to be able to identify populations at risk of developing venous ulcers prior to their formation.

One of the classical models for studying blood flow is the "Windkessel" method, in which the hemodynamic characteristics of cardiovascular blood flow are modeled using electrical circuit elements [4]. The blood pressure and flow are equalized with circuit voltage and current, while the vessel resistance and compliance are represented with resistors and capacitors. However, none of the Windkessel-based models have considered the effects of external loads on perfusion, nor have they addressed patient-specific parameters for the potential of risk assessment.

The goal of this study was to develop a model that represents the blood flow responses of locally-induced loading and to compare model parameters across samples of healthy individuals and those with venous ulcers.

METHODS

Experimental data were collected by performing a perfusion test among eighteen participants with venous ulcers on one or both of their legs and twenty healthy participants. In the perfusion test, external normal (perpendicular to skin) load and combined normal and shear (parallel to skin) load were applied on the lateral side of the participants' lower legs (Figure 1) [5]. Each test started with a one minute baseline (no loading); then one minute of either normal or combined loading; followed by a recovery period after the load was removed. Every leg of every participant was tested with the two different loading conditions and the skin perfusion was monitored continuously.

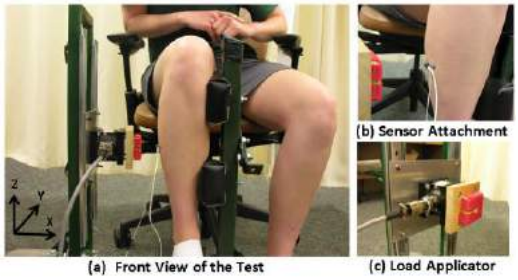

Figure 1: Leg perfusion test set up (a) front view of the test (b) perfusion sensor attachment (c) load applicator with load cell implemented

The magnitude of the load was measured with a 6 axis load cell (AMTI, USA) and the regional blood perfusion was recorded with a non-invasive Laser Doppler Perfusion sensor (Perimed, Sweden).

Meanwhile, a circuit model based on the Windkessel approach was developed. The proposed model consisted of two resistors (where R_1 represented the global vascular resistance and R_2 represented the local vascular resistance), one capacitor (C) that represented the capillary compliance and two voltage sources V_{ext} that represented the external pressure and V_0 represented the hydrostatic pressure (Fig 2). The voltage source V_{ext} was placed in series with R_2 to represent the external pressure applied locally by the loading on the participants'

Copyright 2016 The Organizing Committee for the 2016 Summer Biomechanics, Bioengineering and Biotransport Conference

legs. The voltage source V_0 represented the hydrostatic pressure at the testing site on the lower leg, which was determined by the pressure at the heart and the vertical distance between the heart and the test site.

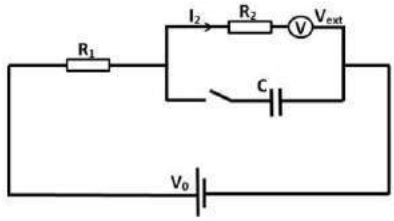

Figure 2: Model to simulate the blood flow of lower leg under normal and shear external loadings

A switch was added in series with the capacitor so that the effect of the capacitor could be controlled to be open during the reperfusion period (after load removal). This feature was designed based on the capacitor's time-history characteristic during discharging. The model was then built in Simulink (MATLAB, USA) and simulation output was brought into MATLAB for comparison with the experimental data.

During the iteration process, R_1, R_2 and C values (RCR values) were adjusted so that the model output fit the experimental data. Two individual observers performed the model iterations for all trials. The subject-specific RCR values for both observers were then analyzed statistically within each observer.

RESULTS

The legs from test participants were categorized into three groups: legs with open ulcers ("wounded"), legs without ulcers but from the same patients who had an ulcer ("non-wounded"), and legs from healthy participants ("healthy"). This categorization resulted in 20 wounded legs, 15 non-wounded legs (some participants had wounds on both legs or only on one leg) and 40 healthy legs.

Figure 3 displays an example of the comparison between the model output and experimental data for one participant. The initial spike in the plot was an experimental artifact caused by the contact of the load cell with the perfusion sensor as load was applied.

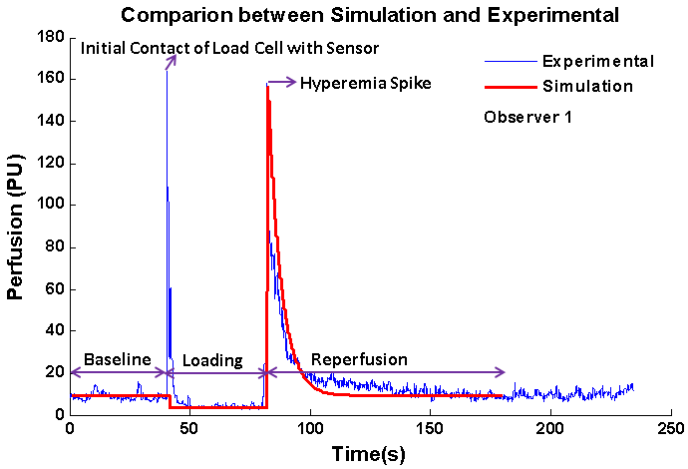

Figure 3: Comparison between model simulation output and experimental data. The experimental artifact was due to the contact of the load cell with the perfusion sensor during initiation of force application

The parameters of R_1, R_2 and C values from the model simulation are listed in Table 1.

Table 1: R_1, R_2 and C values from two individual observers that yielded model outputs representing each patient's experimental data set.

	Observer 1	Observer 2
R1		
Wounded	8.85 ± 4.56	5.02 ± 3.46
Non-Wounded	9.25 ± 4.93	6.91 ± 4.65
Healthy	9.21 ± 4.36	6.36 ± 3.93
R2		
Wounded	2.05 ± 3.21	4.97 ± 3.61
Non-Wounded	2.61 ± 3.25	4.14 ± 3.70
Healthy	3.64 ± 1.58	6.24 ± 2.59
C		
Wounded	26.76 ± 46.59	11.65 ± 27.51
Non-Wounded	6.86 ± 8.15	5.49 ± 9.70
Healthy	7.30 ± 10.30	4.28 ± 4.85

Note: Data refer to average of all subjects ± standard deviations

A one-way ANOVA showed that significant differences existed in R_2 ($p=0.0033$ for Observer 1 and $p=0.0044$ for Observer 2) and C ($p=0.00027$ for Observer 1 and $p=0.044$ for Observer 2) between the three groups. However no significant differences were found by either observer for R_1. These results indicate that the global vessel resistance did not differ between the three groups; however, the localized resistance and compliance were significantly different between wounded legs and healthy legs.

DISCUSSION

The model demonstrated its capability for replicating the blood perfusion during a loading and unloading process, as well as the reperfusion period; further we were also able to use it to identify patient-specific RCR parameters. Of particular interest is that smaller R_2 values were found for individuals with wounds, regardless of whether a wound had formed or if was on the leg without a wound. Further, the C value was much higher for those who already had a wound. This suggests that there are thresholds for these values which could be identified and used to determine when a person moves to a high risk category for wound formation. If this threshold could be established then a "just-in-time" prevention strategy could be utilized. Such a strategy would be a vast improvement from the current state, where treatment occurs *after* the wound is present. This approach would be to *prevent* the wound all together.

Future work will be to increase the sample size so that ranges of RCR values can be identified for patient sub-groups and these thresholds for the parameters can be developed to determine when a person is at high risk for developing a venous ulcer.

The modeling of skin perfusion will help us better understand the blood flow behavior pre- and post- venous ulcers, advancing our biomechanics knowledge on wound formation.

ACKNOWLEDGEMENTS

The authors would like to thank Kelly Patterson, Yifan Men, Josh Drost and Amy Lenz in their assistance with this work.

REFERENCES

[1] Abbade, L. P. F. et al., *Int. J. Dermatol.*, 44 (6), 449–56, 2005.
[2] Margolis, D. J. W. et al., *J. Am. Acad. Dermatol.*, 46 (3),381–386, 2002.
[3] Salomé G. M.et al., *World J. Surg.*,37 (6),1438–45, 2013.
[4] Sagawa, K. et al., *J. Mol. Cell.* Cardiol.,22 (3), 253–277, 1990.
[5] Pan, W et al., *Clin. Biomech.*, 30 10),1218–1224, 2015.

Copyright 2016 The Organizing Committee for the 2016 Summer Biomechanics, Bioengineering and Biotransport Conference

SB^{3}C2016
Summer Biomechanics, Bioengineering and Biotransport Conference
June 29 –July 2, National Harbor, MD, USA
SB^{3}C2016-775

HOW MUCH ADDITIONAL MATERNAL SPATIAL CAPACITY DO FORCEPS REQUIRE WHEN DELIVERING THE FETAL HEAD DURING VAGINAL BIRTH?

Paige V. Tracy (1), John O. DeLancey (2), James A. Ashton-Miller (1,3)

(1) Department of Biomedical Engineering
University of Michigan
Ann Arbor, MI, USA

(2) Department of Obstetrics and Gynecology
University of Michigan
Ann Arbor, MI, USA

(3) Department of Mechanical Engineering
University of Michigan
Ann Arbor, MI, USA

INTRODUCTION

Approximately 11% of U.S. women undergo surgery for pelvic organ prolapse or fecal and urinary incontinence [1]. Injury that occurs during vaginal birth is the leading risk factor for causing these pelvic floor disorders [2]. Pelvic organ prolapse is found most often in women who sustain levator ani muscle injuries during delivery. Indeed, ~13% of women delivering vaginally for the first time sustain these injuries [3]. A (maternal) geometric capacity – (fetal head) demand model was developed to examine these issues [4]. The model was used to examine the role of four potential risk factors for levator ani muscle injury during a typical occiput-anterior vaginal delivery: the subpubic arch-angle, levator hiatus length, levator origin location on the pelvis, and fetal head size. The model allows one to estimate the degree of cephalo-levator disproportion, represented by the variable *g*, the ratio of maternal capacity divided by fetal head demand, which indicates the risk for levator injury.

During difficult vaginal deliveries when labor is obstructed, it is sometimes necessary to deliver the fetal head by attaching obstetrical forceps on either side of the head and pulling. The risk is that, even though the fetal head is delivered safely, up to 49% of forceps-assisted deliveries are associated with maternal levator muscle injuries [5]. Two hypotheses have been proposed to explain this injury: 1) the space occupied by the forceps themselves causes increased maternal levator muscle stretch, and 2) excessive traction force on the forceps and too little time to allow for levator tissue stress relaxation [5].

The purpose of this analysis was to test the first hypothesis.

METHODS

Sequential 2 mm thick MRI scans were acquired of a 50th percentile female pelvis in the axial, sagittal, and coronal planes. These images were imported into 3D Slicer (Brigham and Women's Hospital, Boston, MA, USA), and 3D models were generated using the segmentation editor tool. These models included the pelvis, the internal anal sphincter, the perineal membrane, and the puborectal and pubococcygeal portions of the levator ani muscles.

From this model, the length of the soft tissue loop that forms the maternal birth canal was determined. Maternal capacity, C_M, was then calculated as the sum of the soft tissue loop length, SL, and the arch length of the portion of the fetal head not in contact with the soft tissue loop (D_{head} = diameter of fetal head), less the portion of the soft tissue loop not in contact with the fetal head, L_{wrap} (Eqn. 1, Fig. 1). Here, maternal capacity refers to the largest diameter spherical head the pelvic floor can accommodate without injury. Soft tissue loop length reflected a 1.6x striated muscle stretch ratio prior to injury as well as 1.37x muscle fiber lengthening reported to occur during pregnancy [6].

$$C_M = SL + \pi * D_{head} * \left(\frac{180-\theta}{360}\right) - L_{wrap,left} - L_{wrap,right} \quad (1)$$

Here, we modify our previous assumption [4] that the presenting fetal head cross section is circular so that we may also include the cross-section of both forceps blades in the birth canal. The cross-section of the blades is actually rather small compared to that of the fetal head. For example, in the case of the Simpson forceps, which have open spoon-shaped steel frames, we measured the total cross-section of the blades frames to be 1.2 cm^2 compared to the 62 cm^2 of a 50 percentile male fetal head. Hence the cross-sectional area occupied by the forceps is less than 2% of that of the fetal head.

Clinically, it has been observed that use of Simpson forceps results in noticeable indentations on the sides of the fetal head

Copyright 2016 The Organizing Committee for the 2016 Summer Biomechanics, Bioengineering and Biotransport Conference

following delivery. So, we calculated the fetal head demand for three cases (Fig. 1). Case 1, in which no forceps are applied (the control case). Case 2, in which the forceps blades' frames have just been placed with the blades standing proud of the fetal skin surface, the maternal levator muscles is stretched across them, yet no indentation of the skin by the forceps has occurred. Case 3, in which pressure has been applied to grip the head and the forceps have fully indented the fetal head skin. We then calculated *g*, the ratio of maternal capacity divided by fetal head demand, for the three cases.

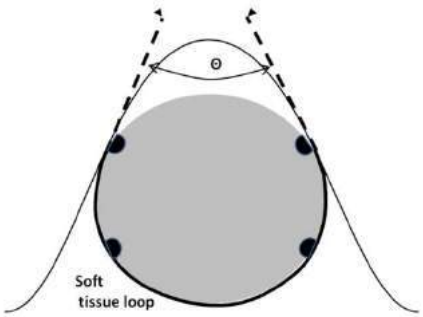

Figure 1: Caudal view of anterior pelvis with variables used in the maternal capacity calculations. The soft tissue loop originates high on the pelvis (filled arrow heads) and wraps around the fetal head (grey circular structure). The portion of the soft tissue loop in contact with the fetal head is represented by the thick black band, while the portion not in contact with the fetal head is represented by the dashed lines. Θ = subpubic arch angle. The left and right pairs of small filled black semicircular shapes represent the cross-section of the open frame spoon-shaped forceps blade fully indenting each side of the head (Case 3).

RESULTS

In Case 2, the attachment of Simpson forceps with zero indentation, resulted in increases in fetal demand of 1.7% compared to the 'no forceps' case across all combinations of fetal head circumference and maternal capacity (Case 1). However, in Case 3, when forceps fully indented the fetal head, this increase in fetal demand was reduced to 0.8 – 1.1%.

The application of Simpson forceps was sufficient to cause a decrease in the predicted value of *g (*cephalolevator disproportion) from ≥1 (no injury predicted) to <1 (injury predicted) in 2.5% of maternal-fetal pairings for the no indentation (Case 2), and 1.2% of maternal-fetal pairings for the full indentation (Case 3).

DISCUSSION

The application of Simpson forceps was found to change the predicted levator injury outcome by no more than 3% in the at-risk maternal population, a value much less than the 49% increase in the rate of levator ani injury reported when forceps are used (see Introduction). Hence, we reject the hypothesis that it is the space taken up by the forceps in the birth canal that is the primary factor that causes maternal levator injury. Instead, the alternative hypothesis, excessive traction force, would seem to be a more tenable argument [5]. Since the smallest women with the largest babies will require Caesarian (C) section, it is the smaller women with larger babies not requiring C section who are at greatest risk for forceps-related injuries.

ACKNOWLEDGEMENTS

We thank Dr. Janis Miller for access to the EMRLD MRI data. We gratefully acknowledge financial support from the Public Health Service and the Office for Research on Women and Gender grant # P50 HD044406-07 (Project 1).

Table 1: Predicted maternal capacity-to-fetal head demand ratio, *g*, for Case 1 – no forceps. In this *and the following tables*, the intensity of red shading indicates the degree of cephalo-levator disproportion.

CAPACITY (Maternal Circumference, in Percentile)	DEMAND (Fetal Head Circumference, in Percentile)								
	10	20	30	40	50	60	70	80	90
10	0.94	0.92	0.91	0.90	0.89	0.88	0.87	0.86	0.85
20	1.07	1.05	1.04	1.03	1.02	1.01	1.00	0.99	0.97
30	1.17	1.15	1.13	1.12	1.11	1.10	1.09	1.08	1.06
40	1.25	1.23	1.21	1.20	1.19	1.17	1.16	1.15	1.13
50	1.32	1.29	1.28	1.26	1.25	1.24	1.23	1.21	1.19
60	1.39	1.36	1.35	1.33	1.32	1.31	1.29	1.28	1.26
70	1.46	1.43	1.42	1.40	1.39	1.37	1.36	1.34	1.32
80	1.54	1.52	1.50	1.48	1.47	1.45	1.44	1.42	1.40
90	1.65	1.63	1.60	1.59	1.57	1.56	1.54	1.52	1.50

Table 2: Predicted maternal capacity-to-fetal head demand ratio, *g*, for Case 2 – forceps without indentation. In this *and the following table*, each cell with a black margin indicates a change in predicted injury outcome following the introduction of Simpson forceps.

CAPACITY (Maternal Circumference, in Percentile)	DEMAND (Fetal Head Circumference, in Percentile)								
	10	20	30	40	50	60	70	80	90
10	0.92	0.91	0.89	0.88	0.88	0.87	0.86	0.85	0.83
20	1.06	1.04	1.02	1.01	1.00	0.99	0.98	0.97	0.96
30	1.15	1.13	1.11	1.10	1.09	1.08	1.07	1.06	1.04
40	1.23	1.21	1.19	1.18	1.17	1.15	1.14	1.13	1.11
50	1.30	1.27	1.26	1.24	1.23	1.22	1.21	1.19	1.17
60	1.36	1.34	1.32	1.31	1.30	1.28	1.27	1.26	1.23
70	1.44	1.41	1.39	1.38	1.36	1.35	1.34	1.32	1.30
80	1.52	1.49	1.47	1.46	1.44	1.43	1.41	1.40	1.37
90	1.63	1.60	1.58	1.56	1.55	1.53	1.52	1.50	1.47

Table 3: Predicted maternal capacity-to-fetal head demand ratio, *g*, for Case 3 – forceps with full indentation.

CAPACITY (Maternal Circumference, in Percentile)	DEMAND (Fetal Head Circumference, in Percentile)								
	10	20	30	40	50	60	70	80	90
10	0.93	0.91	0.90	0.89	0.88	0.87	0.86	0.85	0.84
20	1.06	1.04	1.03	1.02	1.01	1.00	0.99	0.98	0.96
30	1.16	1.14	1.12	1.11	1.10	1.09	1.08	1.07	1.05
40	1.23	1.21	1.20	1.19	1.17	1.16	1.15	1.14	1.12
50	1.30	1.28	1.27	1.25	1.24	1.23	1.22	1.20	1.18
60	1.37	1.35	1.33	1.32	1.31	1.29	1.28	1.27	1.24
70	1.44	1.42	1.40	1.39	1.37	1.36	1.35	1.33	1.31
80	1.53	1.50	1.48	1.47	1.45	1.44	1.42	1.41	1.39
90	1.64	1.61	1.59	1.57	1.56	1.54	1.53	1.51	1.48

REFERENCES

[1] J. A. Ashton-Miller and J. O. DeLancey, *Annual Review of Biomedical Engineering,* vol. 11, pp. 163-176, 2009.

[2] J. Mant, R. Painter and M. Vessey, *British Journal of Obstetrics and Gynaecology,* vol. 104, no. 5, pp. 579-85, 1997.

[3] K. Shek and H. Dietz, *BJOG An International Journal of Obstetrics and Gynecology,* vol. 117, no. 12, pp. 1485-1492, 2010.

[4] P. V. Tracy, J. O. L. DeLancey and J. A. Ashton-Miller, *Journal of Biomechanical Engineering,* pp. e1-e54, 2016.

[5] H. U. Memon, J. L. Blomquist, H. P. Dietz, C. B. Pierce, M. M. Wienstein and V. L. Handa, *Urogynecology: Original Research,* vol. 125, no. 5, pp. 1080-1087, 2015.

[6] M. Alperin, D. M. Lawley, M. C. Esparza and R. L. Lieber, *American Journal of Obstetrics and Gynecology,* vol. 213, no. 2, pp. 191 - 197, 2015.

Copyright 2016 The Organizing Committee for the 2016 Summer Biomechanics, Bioengineering and Biotransport Conference

SB^{3}C2016
Summer Biomechanics, Bioengineering and Biotransport Conference
June 29 –July 2, National Harbor, MD, USA
SB^{3}C2016-776

EVALUATING LEFT VENTRICULAR FUNCTION USING CARDIAC AND RESPIRATORY-GATED VOLUMETRIC MURINE ULTRASOUND

Arvin H. Soepriatna (1), Frederick W. Damen (1,2), Pavlos P. Vlachos (1,3), Craig J. Goergen (1)

(1) Weldon School of Biomedical Engineering
Purdue University
West Lafayette, Indiana, USA

(2) School of Medicine
Indiana University
Indianapolis, Indiana, USA

(3) Department of Mechanical Engineering
Purdue University
West Lafayette, Indiana, USA

INTRODUCTION

Conventional ultrasound techniques for evaluating left ventricular (LV) health are dependent on geometric assumptions from 2D images.[1] These assumptions often yield inaccurate measurements with large variability, especially in patients with remodeled hearts or cardiac deformities.[2] Recently, there is also a growing interest in characterizing 3D myocardial strain to study regional myocardial function, dyssynchrony, and cardiac remodeling.[3] However, to evaluate 3D myocardial strain, we need a 4D imaging technique that captures a pulsating 3D structure with high spatiotemporal resolution. The purpose of this study was to develop a cardiac and respiratory-gated volumetric (4D) ultrasound technique that can reconstruct exact 3D geometries of a mouse's LV throughout the cardiac cycle.

METHODS

Animal Preparation: We used 51.6 ± 22.3 weeks old, wild-type, C57BL/6 mice (n=5) for this experiment. The mice were anesthetized with 2-3% isoflurane and medical grade air at 1.5 L/min. We removed hair from the left ventral thorax of each mouse using a depilatory cream and secured its paws to gold-plated ECG and respiratory leads while lying supine on a heat-modulated stage. Throughout image acquisition, isoflurane levels were adjusted to maintain a stable heart rate and respiration rate.

Image Acquisition: We acquired cardiac datasets using the small animal Vevo2100 ultrasound system (FUJIFILM, VisualSonics Inc.) with a MS550D probe (40 MHz central frequency) attached to a linearly translating 3D motor. All datasets were obtained at 1000 frames-per-second using the VisualSonics ECG-gated kilohertz visualization (EKV) module, which collects a series of images taken at consecutive time points across the cardiac cycle **(Figure 1, Step 1)**. The ultrasound probe was positioned on the left ventral thorax to acquire cross-sectional cine loops of the left ventricle, and the probe was translated from the apex to the base of the left ventricle with step sizes ranging from 80 to 200 μm **(Figure 1, Step 2)**.

Data Reconstruction: Using MATLAB (MathWorks), spatially adjacent EKV cine loops were concatenated and temporally matched to reconstruct a volume representing one synchronized time-point in the cardiac cycle **(Figure 1, Step 3)**. The series of time-dependent volumetric datasets were then temporally merged to create a 4D dataset **(Figure 1, Step 4)**. Gaussian smoothing was implemented temporally and spatially to remove speckle artifacts.

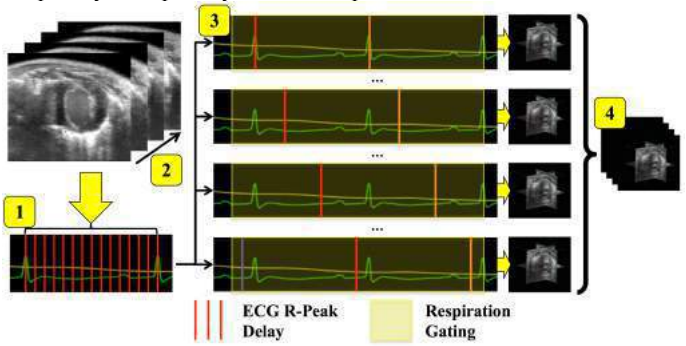

Figure 1: A schematic of the 4D imaging technique from image acquisition to volumetric rendering.

Data Analysis: The data were resampled to isotropic voxels and were exported to FSL, a functional MRI software, to nonlinearly register successive temporal volumes together.[4,5] Nonlinear transformations **(Equation 1)** were calculated in FSL using a sum-of-

Copyright 2016 The Organizing Committee for the 2016 Summer Biomechanics, Bioengineering and Biotransport Conference

squared, intensity-based, residuals cost function **(Equation 2)** to optimize a 3D warping field represented by cubic B-spline functions.[6]

$$\begin{bmatrix} x' \\ y' \\ z' \\ 1 \end{bmatrix} = A \begin{bmatrix} x \\ y \\ z \\ 1 \end{bmatrix} + \begin{bmatrix} d_x(x,y,z) \\ d_y(x,y,z) \\ d_z(x,y,z) \\ 0 \end{bmatrix} \quad (1)$$

$$O(w) = \sum_{i=1}^{N} \left(g\left(x_i'(x_i, w)\right) - f(x_i) \right)^2 \quad (2)$$

In **Equation 1**, $(x', y', z', 1)$ is the nonlinear transformation, A is a 4x4 transformation matrix, and $d_i(x,y,z)$ is the warping field represented by cubic B-splines. In **Equation 2**, $O(w)$ represents the optimization function, g denotes the image we want to warp to, and f denotes the reference image. Once the nonlinear transformations between successive time points have been calculated, they are applied to the manually segmented binary masks of the LV endocardial and epicardial walls to deform the masks and track their motion across the cardiac cycle. Volume quantifications of the binary masks at each time point were used to evaluate LV function **(Table 1)**.

RESULTS

The proposed ultrasound technique can be used to capture the geometries of a beating mouse left ventricle, independent of geometric assumptions. **Figure 2** and **Figure 3** demonstrate the changing left ventricular geometries during end-diastole and peak-systole in 2D and 3D, respectively. To obtain true measurements of LV lumen volumes, the papillary muscles were excluded from the quantification of chamber volumes. Although a significant decrease in end-diastolic volume (EDV) and peak-systolic volume (PSV) was observed (EDV=41±9 µL vs. PSV=13±4 µL; $p<0.01$), myocardial wall volumes remained relatively constant with a slight increase (2.5%) from 118±7 mm^3 during end-diastole to 121±14 mm^3 during peak-systole. **Table 1** summarizes the different cardiac parameters that we calculated to evaluate left ventricular function.

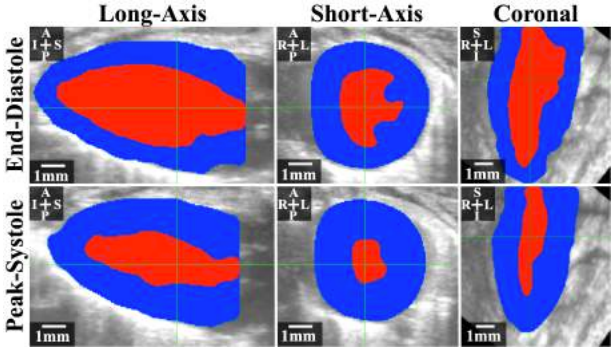

Figure 2: Three axis views of a representative mouse LV at both end-diastole and peak-systole. Masks of the LV lumen (red) and myocardial wall (blue) are shown overlaid to the ultrasound data.

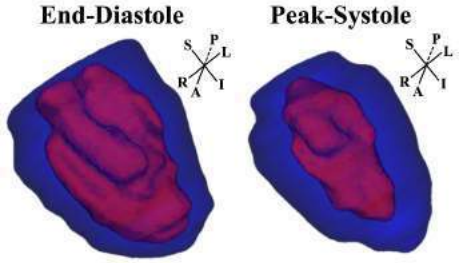

Figure 3: 3D representations of a mouse LV lumen (red) and myocardial wall (blue) at end-diastole and peak-systole (right).

Table 1: Comparisons of LV function measurements acquired from the reconstructed 4D data and those reported from literature. Data are shown as mean ± standard error.

Table 1. Evaluation of LV Function		
Parameter	**Measured**	**Literature**
EDV (µL)	41 ± 9	50 ± 8 [7]
PSV (µL)	13 ± 4	20 ± 6 [7]
SV (µL)	28 ± 7	30 ± 6 [7]
EF (%)	68 ± 6	60 ± 9 [7]
HR (bpm)	526 ± 47	331 ± 35 [7]
CO (mL/min)	14 ± 3	10 ± 2 [7]
LV mass (mg)	126 ± 12	122 ± 6 [8]
LV Mass/BW (mg/g)	3.0 ± 0.5	3.4 ± 0.1 [9]

DISCUSSION

The results of this study show that our ultrasound technique is capable of acquiring evolving 3D geometries with high temporal resolution. When applied to the LV, we can quantify its motion across the cardiac cycle and evaluate cardiac health more accurately, independent of geometrical assumptions. As seen in **Table 1**, our measured end-diastolic and peak-systolic volumes were smaller than previously reported values because we excluded the papillary muscles from the measurements of LV lumen volumes. Despite these differences, our measured stroke volumes of 28±7 µL and ejection fractions of 68±6 % were very similar to those reported in literature.[7] Furthermore, similar to results depicted in literature, the measured LV myocardial wall volume is for the most part constant throughout the cardiac cycle.[10] The slight increase (2.5%) in myocardial wall volume during peak-systole may be attributed to LV wall thickening during contraction.

The application of the proposed 4D ultrasound technique goes beyond the evaluation of cardiac function. Since we can accurately extract 3D LV geometries with high temporal resolution (1 ms), the proposed technique is capable of capturing both three-dimensional global and regional wall motion and contractility of the LV to study myocardial wall dynamics. This technique is particularly useful in studying the dynamics of diseased or remodeled hearts, as the geometric assumption that the left ventricle can be modeled as a stack of elliptical discs is often incorrect. Future work will focus on utilizing the proposed 4D ultrasound technique to study how 3D myocardial strain evolves throughout cardiac remodeling.

ACKNOWLEDGEMENTS

This work was supported by funds from the American Heart Association (14SDG18220010 to CJG).

REFERENCES

[1] Lang, R *et al.*, *J Am Soc Echocardiogr*, 18:1440-1463, 2005.
[2] Folland, E *et al.*, *Circulation*, 60:760-766, 1979.
[3] Gorcsan III, J *et al.*, *J Am Coll Cardiol*, 58:1404-1413, 2011.
[4] Woolrich, M *et al.*, *Neuroimage*, 45:S173-186, 2009.
[5] Jenkinson, M *et al.*, *Neuroimage*, 62:782-790, 2012.
[6] Andersson, J *et al.*, Technical Report TR07JA2, 2007.
[7] Constantinesco, A *et al.*, *J Nucl Med*, 46:1005-1011, 2005.
[8] Lygate, C *et al.*, *Basic Res Cardiol*, 107:276, 2012
[9] Deschepper, C *et al.*, *J Appl Physiol*, 97:369-376, 2004.
[10] Carlsson, M *et al.*, *Am J Physiol Heart Circ Physiol*, 292:H1452-9, 2007.

Copyright 2016 The Organizing Committee for the 2016 Summer Biomechanics, Bioengineering and Biotransport Conference

SB^{3}C2016
Summer Biomechanics, Bioengineering and Biotransport Conference
June 29 –July 2, National Harbor, MD, USA
SB^{3}C2016-777

DEPLOYMENT AND DEGRADATION OF A BIORESORBABLE STENT: A COUPLED COMPUTATIONAL MODEL BETWEEN STENT AND ARTERY

J. Mensah-Gourmel (1), F. Cornat (1), A. Lafont (2), A.I. Barakat (1)

(1) Hydrodynamics Laboratory
Ecole Polytechnique
Palaiseau, France

(2) Georges Pompidou European Hospital,
Cardiology department, APHP
Paris Descartes University
Paris, France

INTRODUCTION

Today, sent deployment is the most common treatment for symptomatic atherosclerosis. Bioresorbable stents (BRS), the latest concept in stents, are based on the premise that a stent is needed only until arterial wound healing occurs after which it would be desirable for the stent to degrade so that the arterial wall recovers its natural compliance. Deployment of a stent profoundly alters the mechanical environment in the arterial wall, and these alterations play an important role in regulating the incidence of complications such as restenosis and neointimal hyperplasia [1]. In the case of a BRS, the mechanical stresses in both the stent and the arterial wall evolve as the stent degrades. Furthermore, the hydrolysis-driven degradation of the stent can be accelerated by mechanical stresses in the stent, an additional coupling that needs to be taken into account. We are interested in determining the evolution of stresses in both the stent and the arterial wall during the stent degradation process and in elucidating the effect of these stresses on remodeling processes in the wall. To this end, we have developed a 3D finite element model of the deployment and degradation of a polylactic acid (PLA) BRS that integrates the coupling between the stent and the artery.

METHODS

A two-step model of stent deployment and degradation was developed using the commercial finite element multi-physics code COMSOL 5.1. A 3D model of a 160 µm-thick BRS with a closed-cell design is first subjected to pressure-driven deployment within an artery. The deployment is arrested when the average internal radius of the stent attains a desired value. The stent remains open after expansion due to plastic deformation. Residual stresses in the stent are computed and used as initial conditions for the degradation step. Both artery and stent are modeled as hyperelastic materials. Parameters for the incompressible artery are taken from literature. The stent is assumed to be nearly incompressible, and we model its hyperelastic behavior using a neo-Hookean strain energy density function W given by:

$$W = \mu(t).(I_1 - 3) \tag{1}$$

where µ is the shear modulus and I_1 is the first invariant of the right Cauchy-Green deformation tensor. Hydrolysis-driven stent degradation is modeled through the time evolution of mechanical properties as:

$$\mu(t) = \frac{1}{2}\mu_0 e^{-k_h t} \tag{2}$$

where $1/k_h$ is a degradation characteristic time [2,3] and μ_0 is the initial value of the shear modulus, considered to a first approximation equal to one third of the Young's modulus of PLA. Literature values for PLA Young's modulus are 3-5 GPa; however, due to computational issues in limiting the recoil of the stent post deployment, we used a value of 20 GPa. Water diffusion is considered instantaneous; thus, water concentration is uniform in the stent and hydrolysis-driven degradation is spatially homogeneous. In light of evidence that PLA mechanical properties and molar mass evolve in a similar manner [2], k_h can be deduced from the evolution of molar mass. Because mechanical loading – in this case both residual loads and loads induced by the artery – accelerate the degradation of polymers, we added load-induced degradation to the model. Thus, the overall mechanical behavior of the stent is described as:

$$\mu(t) = \frac{1}{2}\mu_0 e^{-(k_h + k_l(load)).t} \tag{3}$$

Copyright 2016 The Organizing Committee for the 2016 Summer Biomechanics, Bioengineering and Biotransport Conference

with k_l(load) a stepwise function of the load, taken as the von Mises stress within the stent. The function is assumed to evolve linearly with load up to a prescribed threshold beyond which it saturates.

The finite element model yields the evolution of stresses in the stent and the artery as well as information on the evolution of stent mechanical characteristics. In future work, the stresses in the arterial wall will be combined with a model of wall remodeling to gain insight into the biological ramifications of the altered mechanical stress field.

RESULTS

Figure 1 depicts the time evolution of the internal radius of the stent (Fig. 1a) and the average von Mises stresses in both the stent and the arterial wall (Fig. 1b) during stent degradation (t=0 denotes the end of stent deployment). As can be seen from the stent radius data (Fig. 1a), the stent undergoes rapid recoil immediately after deployment. In this simulation, the recoil is 7.9% of the maximum radius reached during deployment, comparable to reported recoil of BRS in vivo (vascular surgeons; personal communication). During the degradation phase, the stent radius decreases progressively; the decrease is ~2% of the post-recoil radius at t=100. The average von Mises stresses in the stent and in the arterial wall exhibit largely similar time evolution: they increase with deployment and reach a peak at the end of it (not shown), decrease sharply with the plastic recoil, and then decrease more slowly during degradation (Fig. 1b). Between the beginning and end of degradation, the average von Mises stresses in the present simulation are reduced by a factor of 3.7 and 4.8 for the artery and the stent, respectively, and the maximal von Mises stresses are reduced by a factor of 1.9 and 1.03. Not surprisingly, the decrease in stent radius and in the stresses within both the stent and the arterial wall are larger when the degradation is both hydrolysis- and load-driven compared to when it is solely hydrolysis-driven. The magnitude of the difference between the two scenarios naturally depends on the saturation threshold chosen for the k_l(load) function.

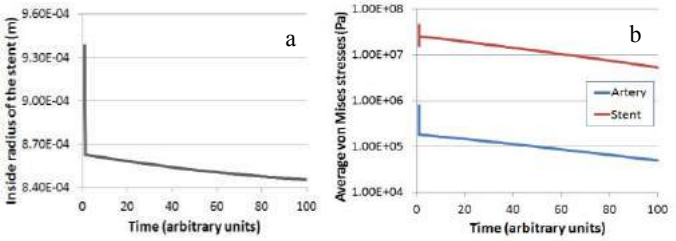

Figure 1 – Time evolution of a: the inside radius of the stent, b: the average von Mises stresses within the stent and the artery during stent degradation. Note the logarithmic scale for the stresses.

BRS degradation is modeled here as a progressive decay in stent mechanical properties driven by both polymer hydrolysis and the mechanical stresses within the polymer. The spatially heterogeneous mechanical stress field within the stent thus induces inhomogeneous degradation within the stent, as can be clearly seen in Fig. 2a which depicts the distribution of the shear modulus μ at the end of degradation (the initial shear modulus is spatially uniform and has the value μ_0). The effect of mechanical loading is most pronounced at strut intersections corresponding to the stent areas subjected to the highest stresses. A plot of the standard deviation of μ (normalized by its average value), a measure of the spatial heterogeneity of stent degradation, reveals that this heterogeneity increases until t=60 and then begins to decrease beyond that point (Fig. 2b). The areas of the stent whose μ decreases the fastest are those subjected to the highest stresses, thus leading to not only a decrease in mechanical properties but also a reduction of the stresses in those areas. Thus, a homogenization of the stresses within the stent ultimately occurs. This may explain the behavior in Fig. 2c.

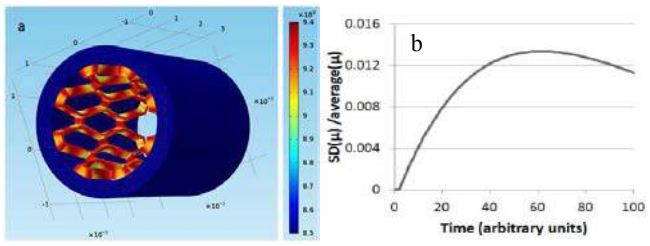

Figure 2 – contour map of the stent shear modulus μ at the end of degradation (a); standard deviation of μ normalized by μ (b)

DISCUSSION

Inserting a stent into an artery disturbs the mechanical environment within the arterial wall and can lead to pathological responses. In the case of a BRS, the stresses in the stent both due to deployment and contact with the arterial wall can accelerate stent degradation and dismantling. Understanding the coupling between stent and artery is thus fundamental to predict the behavior of the inserted device and the remodeling of the vessel. Our model enables us to follow the evolution of stresses both in the stent and the arterial wall with deployment and degradation. Previous studies modeled the deployment of a stent in an artery stenosed by an atherosclerotic plaque [1] or the evolution of mechanical properties during the deployment and degradation of the stent alone [4]. To our knowledge, the dynamic coupling of the stent and the artery during both deployment and degradation has not previously been studied. Residual stresses and artery-induced stresses in the stent lead to an inhomogeneous degradation within the device. This could be used to predict the location of the weakest points of the stent which are expected to be the first to break during stent dismantling. The present results will be combined with a model of stress-induced arterial wall remodeling in order to better understand the mechanobiological ramifications of BRS implantation.

A major limitation of the present work is that stent dismantling is not taken into account. The stent struts may certainly break before the end of the modeled degradation, thus modifying the complex interaction between stent and artery and potentially allowing positive remodeling of the vessel. Another limitation is that the model only considers a healthy artery; further studies should take into account an atherosclerotic plaque. Lastly, the degradation dynamics are very sensitive to the composition of the stent polymer. This model would benefit from more detailed experiments on the degradation dynamics of the polymeric stent to complement the behavior assumed in the present study. Incorporating such measurements into the modeling promises to allow the optimization of BRS design and properties.

ACKNOWLEDGEMENTS

JMG is supported by an Ecole Polytechnique doctoral fellowship. FC is supported by an Ecole Normale Superieure doctoral fellowship. Research supported in part by an endowment in cardiovascular cellular engineering from the AXA Research Fund.

REFERENCES

[1] Lally, C et al. *Journal of Biomechanics*, 38:1574-1581, 2005.
[2] Vieira, AC et al. *J Mech Behav Biomed Mater*, 4(3):451-460, 2010.
[3] Soares, JS et al. *ASAIO Journal*, 54(3):295-301, 2008.
[4] Soares, JS et al. *Ann of Biomed Eng*, 2015.

Copyright 2016 The Organizing Committee for the 2016 Summer Biomechanics, Bioengineering and Biotransport Conference

SB^{3}C2016
Summer Biomechanics, Bioengineering and Biotransport Conference
June 29 –July 2, National Harbor, MD, USA
SB^{3}C2016-778

SIMVASTATIN DOES NOT ADVERSELY AFFECT THE MECHANICAL AND HISTOLOGICAL PROPERTIES OF THE ACHILLES TENDON IN A DIET INDUCED HYPERCHOLESTEROLEMIA RAT MODEL

Daniel S. Choi (1), Jennica J. Tucker (1), Louis J. Soslowsky (1)

(1) McKay Orthopaedic Research Laboratory
University of Pennsylvania
Philadelphia, PA, USA

INTRODUCTION

Hypercholesterolemia affects more than 27% of adults over the age of 20 in America [1]. In addition to increasing the risk for heart disease, stroke, and peripheral artery disease, previous studies have shown hypercholesterolemia to be a risk factor for tendon ruptures in both the supraspinatus and Achilles tendons [2]. For example, elevated cholesterol levels were identified in 83% of patients with Achilles tendon ruptures [3]. Although statins are widely administered for the treatment of hypercholesterolemia, their effect on the musculoskeletal system, subjected to the systemic influence of high cholesterol, is relatively unknown. Therefore, the purpose of this study was to elucidate the effects of statins on diet-induced hypercholesterolemic rat Achilles tendons [4]. We hypothesized that statin treatment in rats with hypercholesterolemia would improve the mechanical and histological properties of their Achilles tendons.

METHODS

30 adult male age-matched Sprague-Dawley rats (400-450g) were used in this IACUC approved study. Over the course of nine months, 20 rats received a high cholesterol diet to induce hypercholesterolemia [4] and 10 rats received a standard diet. All rats had free access to food and water and underwent weekly weight measurements. After the initial six months, a subset of the high cholesterol diet rats was orally administered a daily dose of simvastatin (20mg/kg) for the final three months while maintaining a high cholesterol diet (HC+S, n=10). The remaining rats did not receive statin, but remained on their high cholesterol diets for the final three months (HC, n=10). Blood samples were taken from all rats at six and nine months to measure their levels of total cholesterol (TC), high-density lipoprotein (HDL), triglycerides (TG), and TC to HDL ratios (TC/HDL) in order to assess hypercholesterolemia. All rats were sacrificed at the end of the nine months, and their right Achilles musculotendinous units were dissected and processed for histological analysis. Prior to mechanical testing, the specimens were thawed and their left Achilles tendon-foot complexes were removed and fine dissected [5,6]. Tendons were uniaxially loaded until failure in fixtures that held the tissue in a configuration resembling physiological conditions (Figure 1). Comparisons were made between all groups for both mechanical and histological assays. Mechanical parameter comparisons were made using one-way ANOVAs with significance set at $p \leq 0.05$ and trends at $p \leq 0.1$. Post hoc t tests with Bonferroni corrections were used to determine directionality. Non-parametric Kruskal-Wallis ANOVAs with significance at $p \leq 0.05$ and trends at $p \leq 0.1$ were used for tendon histological comparisons. Post hoc Mann-Whitney *U* tests with Bonferroni corrections were used to determine directionality.

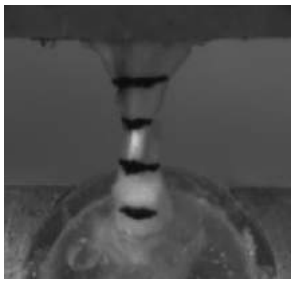

Figure 1: Rat Achilles tendon in fixtures for mechanical testing. The calcaneus is embedded in PMMA (bottom) perpendicular to the loading axis. Stain lines 1 and 2 (from the bottom up) represent the insertion region. Stain lines 2 to 4 define the mid-substance region.

Copyright 2016 The Organizing Committee for the 2016 Summer Biomechanics, Bioengineering and Biotransport Conference

RESULTS

While rats on the high cholesterol diet weighed significantly less than those on the regular diet, no differences in weight were found between the HC and HC+S groups. Serum lipid analysis found significantly elevated levels of TC, HDL, and TC/HDL with significantly decreased levels of TG in the high cholesterol groups compared to the control group at six months. At nine months, the HC+S group exhibited a trend toward decreased TC, significantly decreased HDL, and no significant differences in TG or TC/HDL ratio compared to the HC group.

Mechanical Testing: No significant differences were found in cross-sectional area (Figure 2A), maximum load (Figure 2B), maximum stress (data not shown), percent relaxation (data not shown), or elastic modulus (Figure 2D). A trend towards increased stiffness was found in the HC group when compared to the CTL group. Significantly decreased stiffness was found in the HC+S group when compared to the HC group (Figure 2C).

Histological Assays: At the insertion, there were significantly rounder cells in the HC+S group compared to the HC group with no significant changes in cellularity. At the mid-substance, a trend towards increased cellularity in the HC group compared to the CTL group was found with no significant changes in cell shape (Figure 3).

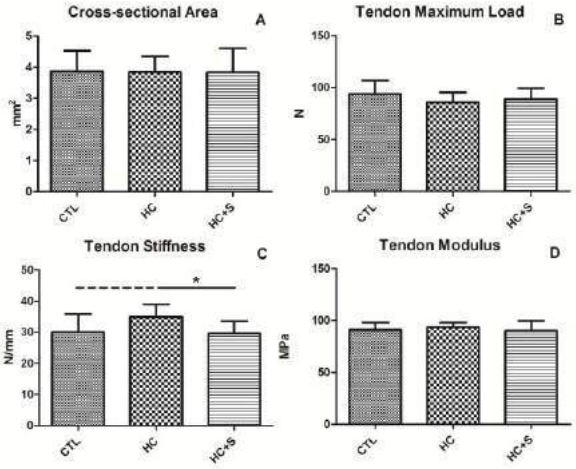

Figure 2: (A) No differences in cross-sectional area. (B) No differences in tendon maximum load. (C) Significant differences in stiffness (p=0.04). (D) No differences in tendon modulus of elasticity. Data presented as mean±SD.

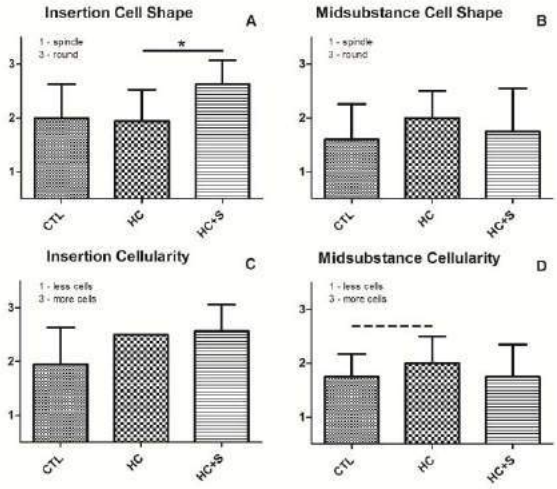

Figure 3: (A) Trend towards cell shape differences at insertion (p=0.06). (B) No differences in cell shape observed at mid-substance. (C) No differences in cellularity at insertion. (D) Trend towards cellularity differences at mid-substance (p=0.09). Data presented as median±IQR.

DISCUSSION

This study investigated the effects of statin treatment in a diet induced hypercholesterolemia model of the rat Achilles tendon. After 3 months of simvastatin treatment following a high cholesterol diet, the stiffness values of tendons in the HC+S group decreased to stiffness values similar to that of the CTL group. All other mechanical parameters were unchanged by statin treatment. From the histological assays, it appears that the statin treatment may cause a rounding of the cells in the insertion region when compared to both the CTL and HC groups. Rounding of cells could potentially be indicative of tendinopathy or chondrogenesis [7]. At the mid-substance region, a trend towards an increase in cell density was found in the HC group compared to the CTL group. The HC+S group did not have such a trend for increased cell density and had cellularity comparable to that of the CTL group which could be a result of the statin treatment. Lower cell density may be indicative of an aging tendon [8]. Previous studies have found decreased mechanical properties and higher predisposition to rupture in non-hypercholesterolemic rats treated with statins [9]. However, in general, our results suggest that statin treatment neither improves nor worsens the mechanical and histological properties of Achilles tendons in hypercholesterolemic rats. Additional studies examining tendon properties at additional time points or examining various dosages of statin treatment may help to more clearly elucidate the effects of statin on tendons present in a hypercholesterolemic environment. A limitation to the current study was the use of a diet-induced model of hypercholesterolemia, which did not take familial causes into account. In addition, the statin treatment did not have the pronounced effect of reducing cholesterol levels to the extent expected. However, the drug was administered at pharmacological doses and any evidence suggesting an adverse effect due to such treatment in either the mechanical or histological properties of the Achilles tendon was not found. While recognizing the study limitations, the results support that statin treatment may be prescribed to hypercholesterolemic individuals without major compromises to Achilles tendon health.

ACKNOWLEDGEMENTS

The authors thank D.J. Rader and D. Cromley for the lipid panel measurements. This study was partially supported by the Penn Center for Musculoskeletal Disorders (P30 AR050950).

REFERENCES

[1] Centers for Disease Control and Prevention, Health, United States, 2014. [2] Klemp P, et al. Ann Rheum Dis, 52:44-48, 1993. [3] Mathiak G, et al. Arch Orthop Trauma Surg, 119:280-284, 1999. [4] Beason DP, et al. J Shoulder Elbow Surg, 23:867-872, 2014. [5] Bey MJ, et al. J Biomech Eng, 124:253-258, 2002. [6] Huang TF, et al. Ann Biomed Eng, 32:336-341, 2004. [7] Soslowsky LJ, et al. J Shoulder Elbow Surg, 9:79-84, 2000. [8] Mazzone MF, et al. Am Fam Physician, 65:1805-1810, 2002. [9] de Oliveira, et al. Food Chem Toxicol, 77:50-57, 2015

Copyright 2016 The Organizing Committee for the 2016 Summer Biomechanics, Bioengineering and Biotransport Conference

SB³C2016
Summer Biomechanics, Bioengineering and Biotransport Conference
June 29 –July 2, National Harbor, MD, USA
SB³C2016-779

ON MECHANICS AND STRUCTURE OF 3D RANDOMLY CROSS-LINKED FIBROUS NETWORKS

H. Hatami-Marbini (1)

(1) Department of Mechanical & Industrial Engineering, University of Illinois at Chicago, Chicago, Illinois 60607

INTRODUCTION

A large number of biological materials, such as cytoskeleton and extracellular matrix, are composed of a randomly cross-linked fibrous solid skeleton. For instance, the cytoskeleton is a complex network of F-actin, microtubules, intermediate filaments, binding proteins, and different cross-link filaments [1]. Similarly, the extracellular matrix of soft tissues is a three-dimensional network of collagen fibers. Therefore, it is important to determine the mechanical properties of random fibrous structures and understand physical origins of their mechanics. Although random fibrous materials often appear as three-dimensional structures, a majority of previous computational studies in the field have focused on modelling them as a two-dimensional intertwined fibrous networks [2-4]. For instance, Hatami-Marbini and Picu [5] constructed 2D networks by randomly placing fibers of a given length and orientation in a square domain. They defined rigid connections at all points where the fibers cross. The fibers were assumed to have both a bending and a stretching stiffness. Using this model, they studied their mechanical behavior at different length scales and concluded that the mechanics of random fiber networks is controlled by nonaffine deformation on all length scales and their nonaffinity scales as a power law with the scale of observation. It yet remains to determine whether these conclusions hold for three-dimensional networks. The primary objective of the present study is to construct 3D random fiber networks and investigate their non-affine behavior. For this purpose, we extend our 2D strain-based non-affinity measure [5] to 3D and investigate the influence of the characteristic length scales on non-affine behavior of 3D networks.

METHODS

Different realizations of 3D fiber networks are generated by randomly placing fibers of length L_0 with random orientation in a cubic domain of linear dimension L, Figure 1.

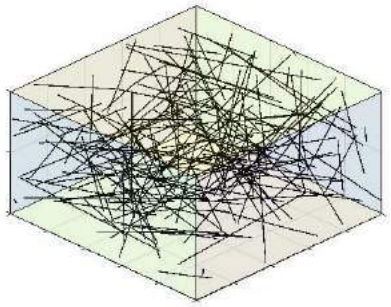

Figure 1: A typical three-dimensional random fiber network generated by depositing straight lines with random orientation in a cubic box.

Rigid connections are assumed between all fibers which are closer than a critical value. The mechanical properties of individual fibers are characterized by axial, bending, shear, and torsional stiffness. The total energy of the system is written as the sum of the strain energies caused by the deformation of all fibers. The energy of a single filament is given by

$$U_f = \frac{1}{2}\int \mu\left(dl/ds\right)^2 ds + \frac{1}{2}\int \kappa_w \left(d^2v/ds^2\right)^2 ds + \frac{1}{2}\int \kappa_v \left(d^2w/ds^2\right)^2 ds + \frac{1}{2}\int \kappa_\phi \left(d\phi/ds\right)^2 ds \quad (1)$$

where v and w are transverse displacements, ϕ is the angle of rotation, κ_w and κ_v are bending moduli, κ_ϕ is the torsional modulus, and μ is the

Copyright 2016 The Organizing Committee for the 2016 Summer Biomechanics, Bioengineering and Biotransport Conference

stretching modulus. The above energy equation for fibers with circular cross-section gives three unique characteristic length scales: the fiber length, L_0, the mean segment length, l_c, and the square root of the ratio of bending stiffness and axial stiffness, l_b [6].

The deformation of the network subjected to a uniform strain field is found using an energy minimization procedure. Strains are computed on various probing length scales by choosing a quadruplet of network nodes such that they form approximately an equilateral tetrahedron. The displacement field u_i within a tetrahedron is written in terms of its nodal displacements using the finite element interpolation functions. The uniform strain field ε_{ij} associated with each tetrahedron is obtained from the strain-displacement relation. After calculating the three-dimensional strain field, the non-affinity measure is defined in terms of the fluctuations of the deformation gradients relative to their affine estimates, i.e.

$$h_{jk} = \left\langle \left(\varepsilon_{jk}^{\text{nonaffine}} - \varepsilon_{jk}^{\text{affine}} \right)^2 \right\rangle_l \Big/ \left(\varepsilon^{\text{applied}} \right)^2 \qquad (2)$$

In the above equation, $< >_r$ denotes the average of the quantity over all possible length scale r. The above strain-based non-affinity measure is independent of the applied far-field loading and will characterize the average of the displacement gradients over different length scales. This 3D non-affinity measure can be used to investigate the influence of the characteristic length scales on non-affine mechanical behavior of three-dimensional fibrous structures.

RESULTS

In Figure 1, different components of non-affinity measure are plotted for a network with fiber number density of 200 when subjected to uniform uniaxial tensile strain in the x_1-direction. From this plot, it is clear that all components of the non-affinity measure are non-affine and follow the similar scaling.

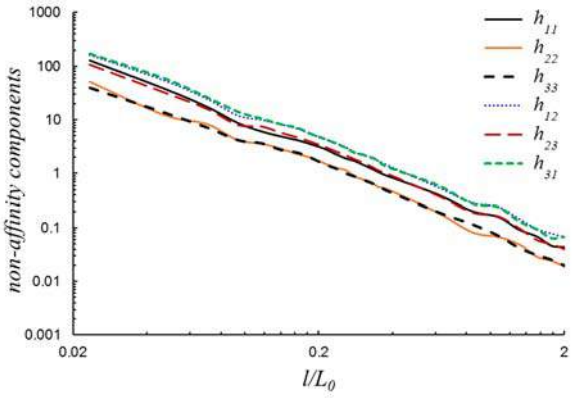

Figure 1: Components of the normalized non-affinity measure as a function of normalized probing length scale for a network with fiber number density of 200. It is seen that all components of the non-affinity measure are non-affine and follow the similar scaling

DISCUSSION

The primary objective of the present work was to develop a new non-affinity measure for characterizing the non-affinity of three-dimensional fiber networks. Previous studies on mechanics of random fiber networks are mainly focused on two-dimensional random fiber networks because 3D simulations are computationally very expensive [2-5]. In this work, we have created 3D networks by depositing random lines with arbitrary orientation in a simulation box. The solution of the system subjected to a uniform far-filed load is then obtained by minimizing the total energy of the system. A new non-affinity measure was constructed such that the mechanical response of the network can be investigated at different length scales. The proposed measure is independent of the applied far-field and has a one-to-one relation with the average (i.e. homogenized) mechanical behavior of the network. Using this measure, it was observed that all components of the non-affinity measure follows a power law scaling with probing length scale, Figure. 2. The exponent of this power-law is almost independent of the far-filed loading. The influence of fiber number density and stiffness was also investigated (results not shown). The differences between the behaviors of 2D and 3D networks were also characterized. It was concluded that although there are certain similarities in the behaviors of 2D and 3D networks, the behavior of 3D networks are more non-affine. Furthermore, the results of numerical models based on 3D fiber networks are closer to those observed in previous experimental studies [6, 7].

ACKNOWLEDGEMENTS

This study was supported in part by National Science Foundation (1351461).

REFERENCES

[1] Hatami-Marbini, H, Mofrad, M, Rheology and Mechanics of the Cytoskeleton, in *Complex Fluids in Biological Systems: Experiment, Theory, and Computation*, 187-205, 2015

[2] Head, DA, Levine AJ, MacKintosh, F, Deformation of crosslinked semiflexible polymer networks, *Physical review letters* 91, 108102, 2003.

[3] Chandran PL, Barocas, VH, Affine vs. non-affine fibril kinematics in collagen networks: theoretical studies of network behavior, *Journal of biomechanical engineering* 128, 259, 2006.

[4] Hatami-Marbini, H, Picu, RC, Modeling the mechanics of semiflexible biopolymer networks: non-affine deformation and presence of long-range correlations, in *Advances in Soft Matter Mechanics* Springer Berlin Heidelberg, 2012.

[5] Hatami-Marbini, H, Picu, RC, Scaling of nonaffine deformation in random semiflexible fiber networks, *Physical Review E* **77**, 062103, 2008.

[6] Hatami-Marbini, H, Non-affine behavior of three-dimensional semiflexible polymer network, under review.

[7] Liu, J, Koenderink, G, Kasza, K, MacKintosh, F, Weitz, D, Visualizing the strain field in semiflexible polymer networks: strain fluctuations and nonlinear rheology of F-actin gels, *Physical review letters* 98, 198304, 2007.

Copyright 2016 The Organizing Committee for the 2016 Summer Biomechanics, Bioengineering and Biotransport Conference

SB³C2016
Summer Biomechanics, Bioengineering and Biotransport Conference
June 29 –July 2, National Harbor, MD, USA
SB³C2016-780

EXPERIMENTAL INVESTIGATION OF FUNCTIONAL FORMS REQUIRED FOR MODELING DEGRADING ACELLULAR TISSUE ENGINEERED VASCULAR GRAFTS IN A PREDICTIVE GROWTH AND REMODELING FRAMEWORK

Piyusha Gade (1), Keewon Lee (1), Blaise N. Pfaff (4), Yadong Wang(3), Anne M. Robertson (1,2)

(1) Department of Bioengineering
University of Pittsburgh
Pittsburgh, PA, USA

(2) Department of Mechanical Engineering and Materials Science
University of Pittsburgh
Pittsburgh, PA, USA

(3) Department of Chemical and Petroleum Engineering, Bioengineering, Surgery
University of Pittsburgh, PA, USA

(4) Department of Chemical Engineering
Pennsylvania State University
Philadelphia, PA, USA

INTRODUCTION

Cell-free tissue engineered vascular grafts (TEVGs) that harness in-host growth and remodeling (G&R) capabilities represent an emerging technology that provides an alternate solution to the problems faced by autografts and cell-seeded TEVGs [1]. Despite the remarkable success of this technology in animal models [2], much of its development is based on a trial and error investigation which calls for a more rational design of TEVGs for accelerated development. Our in-house computational G&R tool is one such tool that is being used for numerical hypothesis testing [3] to guide rational design of bi-layered composite grafts: a porous poly-glycerol sebacate (PGS) core and electrospun polycaprolactone (PCL) outer sheath which have shown mature elastin and nerve regeneration in small animals [2].

The main requirement for successful neoartery formation is the effective interplay between PGS degradation and cell proliferation with extracellular matrix (ECM) deposition. Since it has been postulated that one of the main mechanisms of ECM deposition is through the stress driven mechanobological response of synthetic cells, accurate modeling of load transfer from the graft to cells is crucial. Currently there is little experimental data to guide even the qualitative features of the degradation models needed for such analysis.

The G&R theory models the evolving neoartery using a constrained mixture model where each of the constituents is modeled as hyperelastic [4],

$$W(s) = \Sigma W^{\alpha}(s) = \frac{\rho^{\alpha}}{\rho(s)} Q^{\alpha}(s) \widehat{W}^{\alpha} \boldsymbol{C}^{\alpha}_{n(0)}(s) + \int_0^s \frac{m^{\alpha}(\tau)}{\rho(s)} q^{\alpha}(s-\tau) \widehat{W}^{\alpha}(\boldsymbol{C}^{\alpha}_{n(\tau)}(s)) d\tau$$

where, $Q^{\alpha}(s)$ represents the survival fraction of the originally existing material. The superscript α designates the constituents (e.g. components of the evolving ECM and PGS core). In this work, we aim to characterize PGS degradation and use this data to determine an appropriate functional form of the survival function ($Q^{\alpha}(s)$) as well as the degrading strain energy function for the PGS core.

METHODS

Tubular porous PGS vascular grafts with an outer diameter of (1.708 ± 0.039 mm) and thickness of (0.289 ± 0.026 mm) were fabricated using a salt-leaching technique [2]. Since hydrolysis, which can be catalyzed by enzymes, is the main mechanism of PGS degradation, n = 7 samples each were used for hydrolytic and enzymatic degradation. Samples were immersed in 1 ml tubes containing pH 7 adjusted phosphate buffered saline (PBS) kept at 37 °C. Since esterase has been reported to be the primary enzyme responsible for polymer degradation *in-vivo* [5], cholesterol esterase (Sigma-Aldrich) with a concentration of 0.2 units/µg PGS in 1 ml PBS kept at 37 °C was used for enzymatic degradation. The media was replaced every 2 days to maintain enzyme activity. The pH of the media was controlled to be 7.4. In order to understand the degradation characteristics of porous PGS grafts, we examined weight loss and mechanical properties. Dry weight loss was measured by lyophilizing each sample post-degradation. Uniaxial mechanical testing was performed by stretching samples in the longitudinal direction while submerged in PBS. Mechanical properties are expected to be isotropic due to the nature of the manufacturing process. The samples were stretched to failure at a strain rate of 0.005 mm/s. Each sample was also scanned with a resolution of at least 4 µm, before and after degradation using micro computed tomography (Micro-CT; Bruker Corporation – SKYSCAN 1272). This was done to assess the change in porosity during degradation and the average baseline porosity was evaluated to be 75.27%. The samples were evaluated at time points of

Copyright 2016 The Organizing Committee for the 2016 Summer Biomechanics, Bioengineering and Biotransport Conference

1, 4, 7, 14, 21 and 28 days since previous *in-vivo* work showed complete degradation of a solid PGS core by one month [6].

RESULTS

The rate of mass loss is of fundamental importance in studying the degradation characteristics of these constructs. Fig. 1 shows the nearly linear rate of mass loss with almost 85% loss at day 21 for enzymatic degradation. This is higher than the 70% mass loss reported at day 35 for solid PGS [6] which is conjectured to be a result of the high porosity of the PGS grafts.

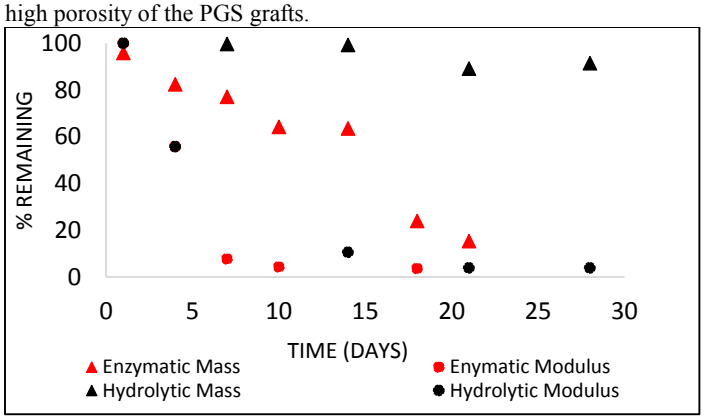

Figure 1: Percent change in mass and modulus of porous PGS in enzymatic and hydrolytic degradation.

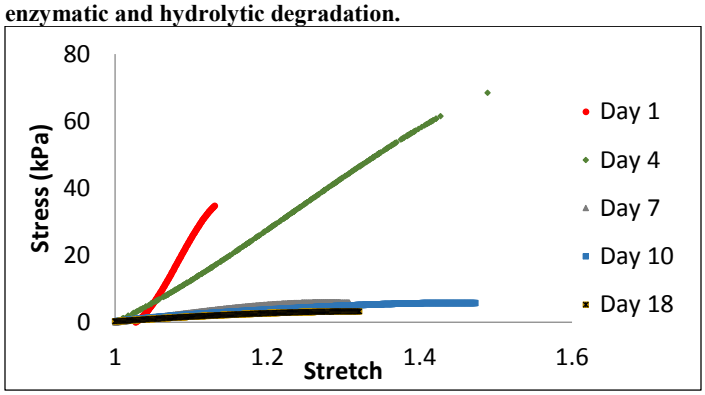

Figure 2: Stress (Piola-Kirchoff) – stretch curve for uniaxial failure test of the PGS scaffold as a function of exposure time to enzymatic degradation.

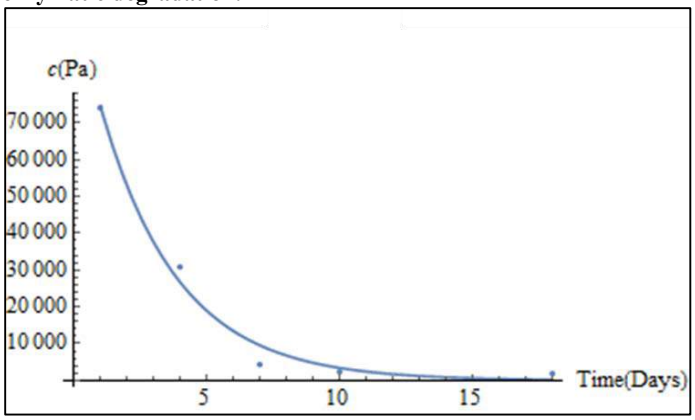

Figure 3: Damage-like function for scaling mechanical properties as a function of exposure time during enzymatic degradation. 'c' is the instantaneous material parameter in the Neo-Hookean model.

Another important functional form required for modeling degradation of the PGS core, is the time dependent mechanical response of the degrading graft. Figures 2 and 3 highlight the rapid loss in stiffness (about 40% at day 4) for both degradation mechanisms at early time points suggesting rapid transfer in load to the developing ECM and outer PCL sheath. A Neo-Hookean model [$W(t) = c(t)\,(I_1 - 3)$] was fit to the enzymatic time-varying mechanical response followed by fitting 'c(t)' as a function of exposure time to enzymatic degradation, Fig. 3. The resulting function $c(t) = C_1 e^{-C_2 t}$, where $C_1 = 212\ kPa, C_2 = 1.04\ 1/sec$ with R^2 of 0.99, represents a damage model for scaling mechanical properties as a function of exposure time.

DISCUSSION

Successful G&R elicited by porous acellular TEVGs as considered in this case rests on balance between porosity induced cell-infiltration and degradation of polymer material. Computational G&R models have proven to be sources of predictive capabilities which can aid in design of these TEVGs. However, sensitivity analysis of these models has shown that their predictive capability is highly dependent on various key parameters like half-life and time dependent mechanical behavior of the scaffold material [3].

This work provides much needed experimental data on the degradation characteristics of TEVGs and will be used to prescribe the survival function for the PGS scaffold. Various models assume a sigmoidal loss in mass [7] while Fig. 1 shows a linear loss in mass for this construct. This trend has also been observed in the *in-vivo* report for a solid block of the same material [6]. This difference in trend from sigmoidal to linear changes the functional form of the survival function and will likely affect G&R predictions. This also demonstrates the need for experimental validation of assumed functional forms used in G&R simulations. While a linear loss of mechanical properties was found during degradation of solid PGS [6], an exponential decrease was observed for our porous grafts. We conjecture this is due to the high porosity of these samples and the mechanisms driving this dependence are currently under investigation.

The current data enables development of an experiment-driven functional form of the survival function and changing mechanical properties during scaffold degradation. This data is crucial for predicting mass kinetics and changing load bearing contributions of the constituents during scaffold degradation. Hence, these findings are essential for appropriately modeling the stress-driven mechanobiological response of recruited ECM-producing cells in degrading acellular TEVGs.

ACKNOWLEDGEMENTS

This work is supported by NIH/1R21HL124479-01: In Host Remodeling of Grafts to Functional Arteries – Translation to Mature Animals.

REFERENCES

[1] Kannan, R. Y. et al., *J. Biomed. Mater. Res. Part B Appl. Biomater.*, 74: 570-581, 2005.

[2] Wu, W et al., *Nat Med*, 18: 1148-1153, 2012.

[3] Valentin, A et al., *The 4th Canadian Conference on Nonlinear Solid Mechanics*, 2013.

[4] Humphrey, J.D. et al., Mathematical models and methods in applied sciences., 12.03: 407-430, 2002.

[5] Scott, G. *Degradable polymers: principles and applications*, 2002.

[6] Yadong, W et al., *Journal of biomedical materials research Part A* 66.1: 192-197, 2003.

[7] Miller, K.S., *Journal of biomechanics* 47.9: 2080-2087, 2014.

Copyright 2016 The Organizing Committee for the 2016 Summer Biomechanics, Bioengineering and Biotransport Conference

SB^{3}C2016
Summer Biomechanics, Bioengineering and Biotransport Conference
June 29 –July 2, National Harbor, MD, USA
SB^{3}C2016-781

CHARACTERISTIC X-RAY DIFFRACTION METHOD FOR MECHANICAL ANALYSIS OF MINERAL AND COLLAGEN PHASES IN BONE TISSUE

Masahiro Todoh (1), Shigeru Tadano (1)

(1) Faculty of Engineering
Hokkaido University
Sapporo, Hokkaido, Japan

INTRODUCTION

Bone is often regarded as a composite material consisting of mineral particles and organic matrix (mostly Type I collagen) on a microscopic scale [1-3]. The mechanical properties of bone tissues at a macroscopic scale depend on the structural organization and properties of constituents in the microscopic scale. Considerable attempts have been made to investigate the effect of the microscopic constituent on the mechanical properties of bone. It is the interaction between the mineral and organic material that determines the mechanical properties. However, both mechanical behaviors of mineral and collagen phases are not clear yet.

Because of non-destructive and non-invasive advantages of X-rays and predictive diffraction patterns with crystals or polymers, it has been widely applied to reveal various aspects of materials and in few approaches in the case of biological tissues like bone. In this study, to clear both mechanical behaviors of collagen matrix and apatite crystals in bone, the cortical bone samples were collect from bovine femoral diaphysis. The microscopic mechanical behaviors of both mineral particles of apatite and collagen matrix in bone tissues were observed by wide angle X-ray diffraction (WAXD) and small angle X-ray scattering (SAXS), respectively. In combination with micro-tensile device, both strains of mineral and collagen phases were measured. From those results, the mechanical effect of both components in bone tissues were discussed.

METHODS

Five cortical bone specimens with average sizes of about 10.0 (long) × 2.0 (wide) × 0.2 (thick) mm were cut out from the bovine femoral diaphysis (Age: 23 months old) , where the longer edges of specimens are aligned to the parallel and perpendicular to the bone axis. Rough cuts were done by using a band saw and fine cuts by using a low-speed diamond saw (SBT650, South Bay Technology, Inc. USA). Both ends in 3.5mm length of specimen were bonded to metal plates for fixation to the micro-tensile device by the adhesive.

In this study, the microscopic mechanical behaviors of both mineral particles of apatite and collagen matrix in bone are observed by wide angle X-ray diffraction (WAXD) caused by the lattice structure of apatite crystals and small angle X-ray scattering (SAXS) caused by the periodic structure of collagen molecules, respectively.

The Bragg's law relates the Bragg angle θ to the interplanar spacing d. The microscopic strain ε^H of mineral phase and ε^C of collagen phase can be calculated as the ratio of interplanar spacing d^H and d^C at the deformed state to $d_0{}^H$ and $d_0{}^C$ at the non-deformed state, as Eqs. (1) and (2).

$$\varepsilon^H = \frac{d^H - d_0^H}{d_0^H} = \frac{\sin\theta_0^H - \sin\theta^H}{\sin\theta^H} \quad (1)$$

$$\varepsilon^C = \frac{d^C - d_0^C}{d_0^C} = \frac{\sin\theta_0^C - \sin\theta^C}{\sin\theta^C} \quad (2)$$

where θ_0 and θ are Bragg angles of non-deformed state and deformed state, respectively. Each strain of mineral and collagen phases was calculated by

The X-ray diffraction measurements were performed by X-ray diffractometer (NANO-Viewer, Rigaku Corp., Japan). Characteristic X-ray (Cu-Kα) was generated. The diffraction images were recorded by imaging plates mounted on 81.5 mm and 622.5 mm camera length at WAXD and SAXS experiments as shown in Fig. 1. The specimens were loaded by the micro-tensile device during X-ray diffractions. This device had a load cell (LUX-B-200N-ID-P, Kyowa Electric Instruments Co., Ltd., Japan; Capacity 200 N) and uni-axial stage (TSDM40-15, Sigma Koki Co., Ltd., Japan). The specimens were loaded from 0, 25,

Copyright 2016 The Organizing Committee for the 2016 Summer Biomechanics, Bioengineering and Biotransport Conference

50 MPa at bone axial direction and from 0, 10, 20 N at circumferential direction, respectively. Each irradiation time was 30 min.

RESULTS

As the results of WAXD and SAXS, each diffraction image from mineral and collagen phases was recorded as shown in Fig. 2 (a) and (b), respectively. In the WAXD image, (002) and (211) diffractions were strong. In SAXS image, 3rd order diffraction from d =22.6 nm as specific periodic length of collagen molecules. SAXS image also contained a diffuse scattering perpendicular to the bone axial direction.

As the results of WAXD and SAXS with bone axial and circumferential tensile loading, the strains of mineral and collagen phases increased with macroscopic bone tissue strain as show in Fig. 3 (a) and (b), respectively. The strain of mineral and collagen phases were different in the bone axial and circumferential directions. The mineral strain for circumferential direction was 74.3% of axial direction. The collagen matrix strain for circumferential direction was 74.5% of axial direction.

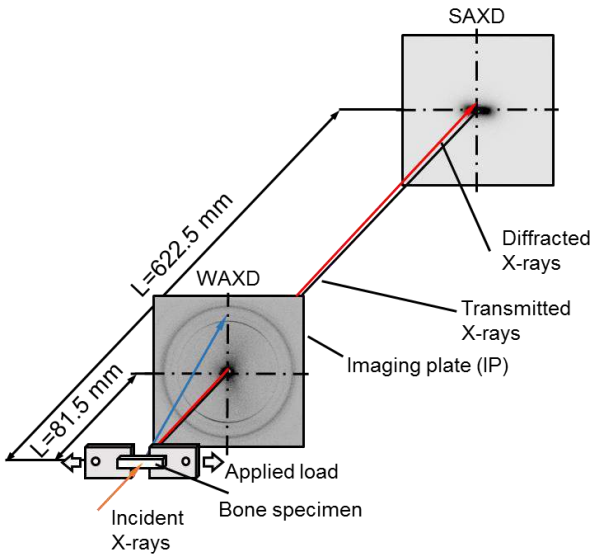

Figure 1: X-ray diffraction system for WAXD and SAXS imaging for bone specimen under tensile loading.

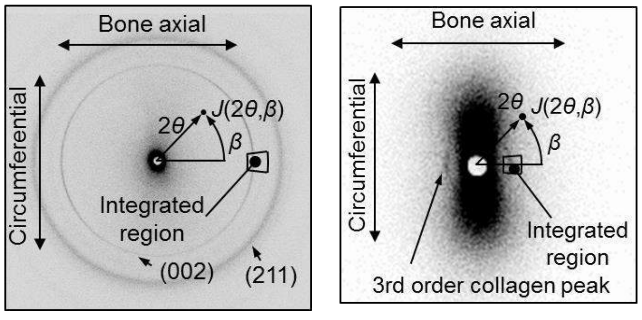

(a) WAXD image (b) SAXS image

Figure 2: X-ray diffraction images by WAXD (a) and SAXS (b) from cortical bone specimen.

DISCUSSION

The microscopic mineral strains were lower than collagen strains. This shows the collagen matrix strain allowed tensile deformation as compared with mineral phase. The strain of mineral and collagen matrix were different in the bone axial and circumferential directions. As the results of tensile tests, the elastic modulus were 11.0 and 8.2 GPa in bone axial and circumferential directions, respectively. This mechanical anisotropy may relate to the differences of microscopic responses of each constituent. In summary, this study could suggest that macroscopic mechanical properties of bone tissue depend on the degree of deformation of mineral and collagen matrix quantitatively.

ACKNOWLEDGEMENTS

The characteristic X-ray diffraction was carried out with X-ray diffractometer (NANO-Viewer, Rigaku Corp., Japan) at the OPEN FACILITY, Hokkaido University Sousei Hall.

REFERENCES

[1] Rho, JY et al., *Med Eng & Phys*, 20:92-102, 1988.
[2] Fratzl, P et al., *J Mater Chem*, 14:2115-2123, 2004.
[3] Yamashita, J et al., *J Biomed Mater Res*, 63:31-36, 2002.

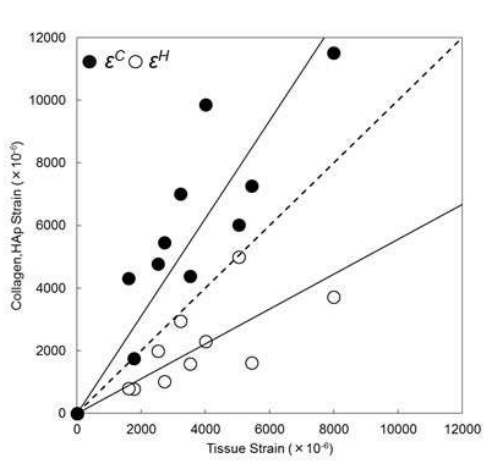

(a) Bone axial tensile loading

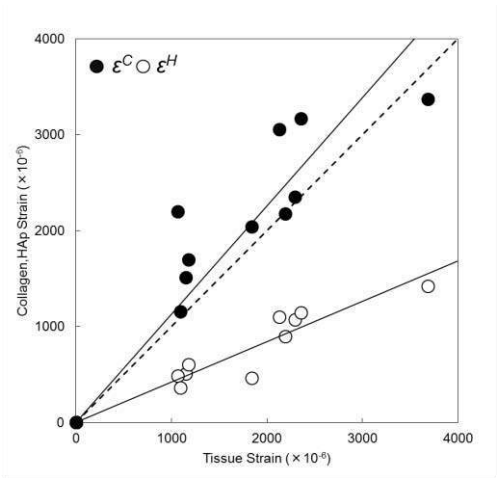

(b) Circumferential tensile loading

Figure 3: Relationships between microscopic strains of collagen and mineral phases vs macroscopic tissue strain of cortical bone.

Copyright 2016 The Organizing Committee for the 2016 Summer Biomechanics, Bioengineering and Biotransport Conference

SB³C2016
Summer Biomechanics, Bioengineering and Biotransport Conference
June 29 –July 2, National Harbor, MD, USA
SB³C2016-782

MRI BASED CAP THICKNESS AND PEAK CAP STRESS PREDICTION: MAN VERSUS MACHINE

Annette M. Kok (1), Aad van der Lugt (2), Antonius F.W. van der Steen (1), Jolanda J. Wentzel (1), Frank J.H. Gijsen (1)

(1) Biomedical Engineering
Erasmus MC
Rotterdam, The Netherlands

(2) Radiology
Erasmus MC
Rotterdam, The Netherlands

INTRODUCTION

A most common cause of ischemic stroke is carotid plaque rupture. A rupture prone plaque was found to be associated with intraplaque hemorrhage, expansive remodeling, and a large and soft lipid rich necrotic core (NC) covered by a thin fibrous cap [1].

From a biomechanical point of view, the cap will rupture when the stresses in the cap exceed the strength of the cap. Cap stresses can be calculated with Finite Element Analysis (FEA). In carotid arteries, Magnetic Resonance Imaging (MRI) is often used to obtain the geometric input for FEA. MRI has many advantages (e.g. high contrast, large field of view, and non-invasive), but the main drawback is that the MRI resolution is often lower than the thickness of the cap [2]. A recent study showed that median cap thickness of ruptured plaques was only 80 µm (70 – 100 µm), which is roughly six times smaller than the MRI resolution [3]. Nieuwstadt et al. showed that when the cap thickness is lower than the MRI resolution, the manual segmentation performed by a reader overestimates the cap thickness significantly, leading to a gross underestimation of the peak cap stress [2].

Instead of manual segmentation, a model could potentially help to estimate the minimum cap thickness, and thus also peak cap stress. This is especially relevant for thin caps that fall below or are close to the image resolution. The aim of this study is twofold 1) reconstruct the cap based on a model that estimates the minimum cap thickness based on geometric plaque features 2) compare the cap thickness and peak cap stress of readers and the reconstructed geometries with the ground truth to investigate if the model outperforms the reader.

METHODS

A schematic overview of the methods is given in Figure 1. Plaque material was obtained from 34 patients who underwent an endarterectomy. The plaques were sliced at 1 mm interval resulting in 76 carotid cross-sections with 148 NCs. After histological staining, lumen, vessel, and NC contours were manually delineated and these contours are considered to represent the ground truth.

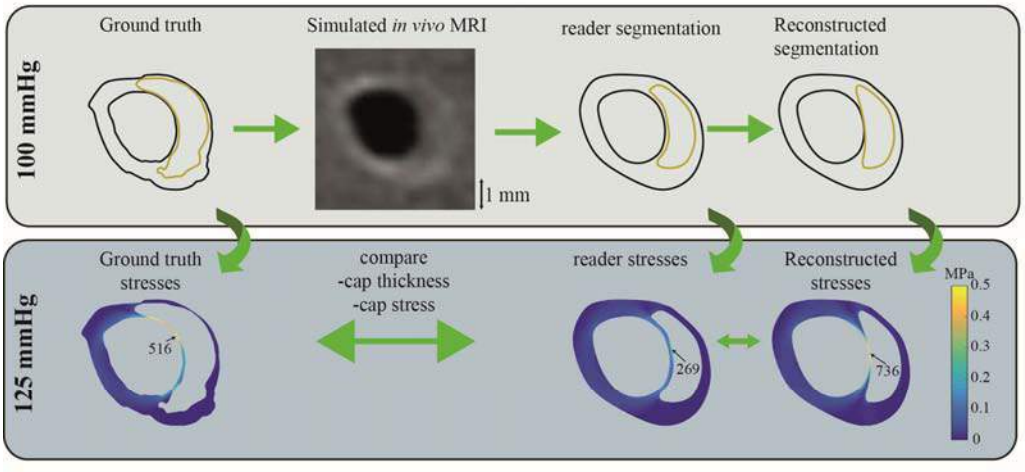

Figure 1: Schematic overview of the methods, each horizontal block represent the state of the geometric at 100 and 125 mmHg.

Copyright 2016 The Organizing Committee for the 2016 Summer Biomechanics, Bioengineering and Biotransport Conference

In order to estimate the minimum cap thickness a Generalized Estimation Equation model (GEE) was used. The input parameters for this model were NC angle, NC thickness and the distance from lumen to the NC centroid (CentroidDistance), whereas the minimum cap thickness served as the output parameter, see Figure 2. All the listed parameters (except the NC angle) were normalized with respect to vessel wall thickness, in order to correct for plaque size. The normalized cap thickness was estimated at three positions along the NC angle, 25, 50 and 75%. In the model, we assume that the cap is symmetrical around the center of the NC angle, therefore two relationships can be derived for the normalized minimum cap thickness: one for the midcap (CT_{50}) and one for the combined sidecap (CT_{25}/CT_{75}) positions.

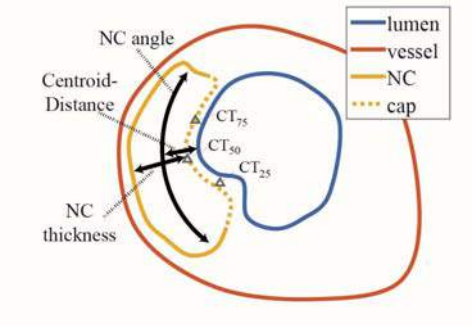

Figure 2: Schematic overview of the input parameters for the GEE model: Necrotic Core (NC) angle, Centroid Distance and NC thickness. The triangles indicate the cap thickness (CT) as estimated by the model. The dotted line represent the cap that is removed, and reconstructed bases on the model.

From a subset (33 cross-sections), containing 44 necrotic cores, the ground truth contours were then used to simulate *in vivo* MRI images with an in-plane resolution of 0.62 mm x 0.62 mm. The protocol is described in more detail by Nieuwstadt et al. [2]. Three experienced MRI readers manually delineated the simulated MRI images. Since, the manual cap contours are not reliable, caps thinner than 0.62 mm from the lumen were removed, see the dotted line in Figure 2. Subsequently, the cap was reconstructed using the CT_{50}, CT_{25} and CT_{75} and a non-uniform rational b-spline.

Abaqus (Dassault Systemes Simulia Corp., Providence, RI, USA) was used for the FEA. A Neo-Hookean, non-compressible, isotropic material model was used, with Young's moduli for the intima and lipid of 1 MPa and 6 kPa, respectively [4]. Peak cap stress was defined as the 99 percentile von Mises stress in front of the necrotic core or in the 15° shoulder region. For analysis, we divided our data into two groups 1) ground truth CT < 0.1 mm (thin caps) and 2) > 0.1 mm (thick caps). The maximum peak cap stress and (error in) peak cap stress are not normally distributed, therefore median and interquartiles were reported.

RESULTS

The GEE model estimated the CT_{50}[-] as: -0.03*NC angle [rad] - 0.35 * NC thickness[-] + 0.82 * CentroidDistance[-] (r^2=0.89 and p<0.05). Similarly, $CT_{25/75}$[-] = -0.03*NC angle[rad] - 0.28*NC thickness[-] + 0.54*CentroidDistance[-] + 0.12 (r^2 = 0.46 and p<0.05).

The minimum cap thickness of the ground truth, reader and reconstructed model geometries were 0.07 mm (0.06 – 0.11 mm), 0.23 mm (0.18 – 0.29 mm), 0.12 mm (0.03 – 0.22 mm), respectively. The cap thickness error (with respect to the ground truth) of the readers is 0.14 mm (0.08 – 0.24 mm). This error was significantly (p<0.01) reduced to 0.07 mm (0.04 – 0.13 mm), when the model was used to reconstruct the cap. For thin caps, the model predicts the minimum cap thickness better than the reader, in contrast to thick caps where the cap thickness estimation does not improve, see Figure 3.

The total peak cap stresses (n=17) of the ground truth, reader and reconstructed model geometries were 516 kPa (336 – 554 kPa), 124 kPa (104 – 269 kPa), 342 kPa (162 – 540 kPa), respectively. The error of the peak cap stress (with respect to the ground truth) for the reader and model was not significantly different (p=0.27), 136 kPa (81.0 – 247 kPa) and 183 kPa (79.3 – 322 kPa) , respectively. For thin and thick caps, no improvement in terms of peak cap stress of the model vs. the reader was observed, see Figure 3.

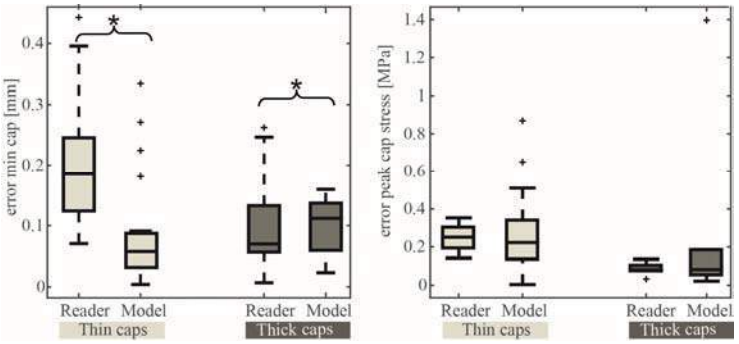

Figure 3: Boxplot of the error of minumum cap thickness (left) and the error of peak cap stresses (right) of reader vs. Model. Light grey depicts the thin caps (<0.1 mm) and dark grey the thick caps (>0.1 mm). The asterisk (*) indicates significant difference (p<0.05).

DISCUSSION

The main finding of this study is that for thin plaques caps the model estimates the minimum cap thickness better than the reader, but does not improve prediction of the peak cap stress.

The cap thickness improvement by the model shows that there is a strong relation between minimum cap thickness and geometric parameters. Although it might be intuitively clear that there might be such a relationship, this relationship was not quantified before and was not reported in the literature. Some clinical studies use cap thickness alone to estimate rupture risk of carotid plaques [3], and this model can potentially be used to improve cap thickness estimation for thin caps.

Interestingly, the minimum cap thickness improvement did not improve the peak cap stress prediction. Previous studies showed that in addition to the cap thickness, lumen curvature and necrotic core shape are important stress predictors [5-6]. In MRI segmented images not all of these features are captured, and important stress predictors might be smoothed and consequently stresses are underestimated. So caution is required when calculating peak cap stresses in the thin caps (<0.1mm) obtained with manually segmented MRI images.

ACKNOWLEDGEMENTS

The research leading to these results has received funding from the European Research Council under the European Union's Seventh Framework Programme / ERC Grant Agreement n. 310457.

REFERENCES

[1] Schaar, JA et al., *J. Eur Heart J,* 25 (12), 1077–82, 2004.
[2] Nieuwstadt, HA et al., *Magn Reson Med,* 72 (1),188–201, 2014.
[3] Shindo, S et al., *AJNR Am J Neuroradiol,* 36 (11), 2140–6, 2015.
[4] Kok, AM et al., *Biomed Eng Online,* submitted.
[5] Akyildiz, AC et al., *Comput Methods Biomech Biomed Engin*, Epub ahead of print, 2015.
[6] Teng, Z et al., *J Biomech Eng,* 133(3), 2011.

Copyright 2016 The Organizing Committee for the 2016 Summer Biomechanics, Bioengineering and Biotransport Conference

SB^{3}C2016
Summer Biomechanics, Bioengineering and Biotransport Conference
June 29 –July 2, National Harbor, MD, USA
SB^{3}C2016-783

A NEW APPROACH FOR ABDOMINAL AORTIC ANEURYSM LOCAL GROWTH QUANTIFICATION

Eleni Metaxa (1), Iordan Iordanov (1), Emmanuel Maravelakis (2), Yannis Papaharilaou (1)

(1) Institute of Applied and Computational Mathematics
Foundation for Research and Technology
Her, State, Country

(2) Department of Environmental and Natural Resources Engineering
Technological Educational Institute of Crete, Chania, Greece

INTRODUCTION

Abdominal aortic aneurysm (AAA) growth rate is a marker for rupture risk as it potentially reflects undesirable wall remodeling that leads to wall weakening. Currently, expansion rate is measured as change in maximum diameter over time. However, expansion is not uniform and is therefore questionable if measurement of maximum diameter change over time is adequate to capture an increased localized remodeling activity. Therefore, a paradigm shift is needed for a more sensitive quantification of AAA growth, which would not only identify small non-symptomatic aneurysms at high risk and prevent rupture thus saving lives, but also reduce the cost of emergency surgeries.

One of the difficulties in quantifying regional wall growth is that as the aneurysm grows it may elongate, become tortuous, and shift towards one side. Therefore, establishing correspondence of wall regions between follow up scans is not trivial. Even if the AAA is manually co-registered with its follow-up image, using landmarks such as renal arteries [1], the distance between wall surfaces obtained cannot be directly translated into regional growth.

In contrast to vascular disease follow-up studies, ongoing research in other medical fields that deal with regional growth quantification in the presence of shape alteration (e.g. cancer tumors) have exploited non-rigid registration methods. The present study aims at introducing a new, more sensitive method of AAA growth rate estimation based on regional wall surface area change. The proposed methodology is based on iterative closest point (ICP) algorithm and is validated using patient-specific AAAs and their artificially deformed follow-up models. Original and deformed surfaces were discretized into triangular surface meshes and were matched by the algorithm. A new measure of local surface growth is then computed from the distribution of element surface area change. To the best of authors' knowledge, this is the first work that exploits vascular non-rigid registration for AAA disease follow-up.

METHODS

The method is based on open source non-rigid point cloud registration code that implements ICP algorithm for bone surface registration [2]. The code has been adapted to capture smaller deformations that may be present during arterial disease follow-up, has been validated, and evaluated. Input to the code are the triangulated surfaces referred to as Source (surface to be deformed) and Target (surface to be matched by Source). The goal is to obtain a measure of local wall surface deformation based on element area change of the registered Source surface. The code is split into two distinct phases: **Phase 1:** Surfaces are prealigned and a general deformation of the Source surface is performed to best match the Target using Procrustes algorithm. **Phase 2:** Surfaces are finely matched through local non-rigid deformation: for every point p on the Source surface, the K-nearest neighbors are considered, and each neighbor influences the displacement of p based on a Gaussian radial basis centered on p acting as weight function.

To evaluate the method, three dimensional computed tomography (CT) scans of 12 aneurysmatic aortas were used. The aortic luminal and external surfaces were segmented, reconstructed and tetrahedral volumetric mesh of wall and thrombus were obtained. Wall deformation was obtained by applying a uniform pressure in ANSYS. The displacement computed at each node of the external surface was used as reference displacement. By applying a wrap-by-vector with a scale factor from 0.5 to 7 in ParaView, a range of surface deformations were obtained for each AAA model. The Source surface was co-registered with each of the multiple Target surfaces, and results were evaluated

Copyright 2016 The Organizing Committee for the 2016 Summer Biomechanics, Bioengineering and Biotransport Conference

using the following metrics:

- The Overlap coefficient was defined as the percentage of points on Source whose Euclidean distance from the Target is smaller than 1 mm.
- The local registration error (Reg_{err}) is defined as:

$$Reg_{err} = LAC_{real} - LAC_{est}.$$

where LAG: the Local Area Change of each surface element a) due to application of nodal displacements (provided by ANSYS), LAC_{real}, and b) due to registration, LAC_{est}.

- To obtain a global measure of registration error for each case, an Error Index (EI) was defined as the mean plus the standard deviation of Reg_{err}.

Mesh, Initial Distance, and Rotation Sensitivity Analysis

a) The effect of mesh density on overlap coefficient was evaluated using one of the AAA models. b) To assess the effect of initial distance distribution (after prealignment) between Source and Target surfaces on registration accuracy, a Distance Index (DI) was defined as the mean value plus the standard deviation of the distance of each node between Source and Target Surfaces. c) The stability of the method with respect to rigid body motion was assessed. Towards this the Source surface of all cases was first rotated with respect to X-, Z- and both X- and Z-axes for various angles (3º-24º) and then registered to the Target surface.

RESULTS

Mesh sensitivity analysis showed that when mesh density was above 0.75 mm^{-2}, the overlap coefficient was < 0.60, while for mesh densities ranging between 0.15 mm^{-2} and 0.75 mm^{-2} overlap was > 0.94. Furthermore, the EI did not increase with increase of angle rotation, but presented negligible discrete fluctuations.

Initial distance between Source and Target surfaces was, as expected, inversely related to registration accuracy. As distance increased, less surface elements after registration changed their area in accordance with the computed value (from ANSYS). In order to obtain an estimate of error associated with DI, 12 test cases were registered to each of their follow-ups of different Distance Index producing a database of 157 registrations. The cases were grouped per DI range (in 1 mm intervals) with 16 to 23 cases in each group, and the mean and range of EI is presented (Fig. 1).

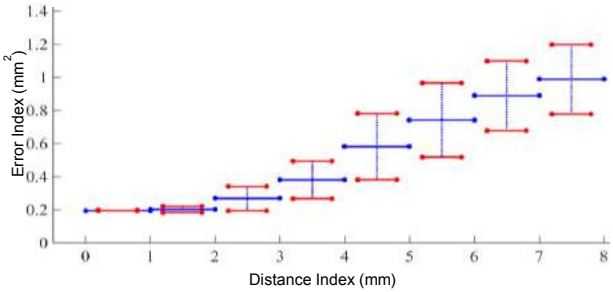

Figure 1: Effect of initial distance between surfaces to the registration error. For every 1 mm of Distance Index, the mean and range (min, max) of error index are presented.

Application on patient-specific follow-ups

The method was applied to surfaces generated from clinical follow-up CT scans of two AAA patients and results obtained are presented (Fig 2). The maximum diameter of the first AAA (Fig. 2A) increased from 35 to 45 mm in 29 months, and the maximum LAC was found at the surrounding area of maximum diameter at the anterolateral region, and equal to 5.6 ± 0.2 mm^2 (DI=1.72 mm, suggesting an EI=0.2 mm^2), or in terms of percentile growth 86.2 ± 3.6 %. The maximum distance between the initial and follow-up image (correspondence) at this location was 8.3 mm. Maximum diameter of the second AAA (Fig. 2B) increased from 50 to 52 mm in 12 months, and the maximum LAC was found at the distal end of the sac, below the region of maximum diameter, and equal to 2.8± 0.2 mm^2, or in terms of percentile growth 34.3 ± 3.6 %. The maximum distance between the initial and follow-up image (correspondance) at this location was 5.5 mm.

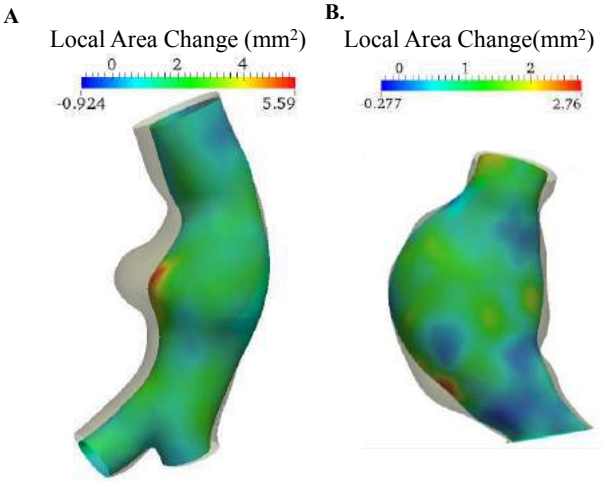

Figure 2: Application of method on two real AAA cases (A, B). Initial surface with distribution of local element area change and follow-up surface (grey, semi-transparent) shown.

DISCUSSION

We propose a methodology based on non-rigid registration in order to obtain a detailed distribution of local vascular growth. Our results suggest that the method can offer a meaningful measure for local area change of AAA wall surface, and provide a useful tool in vascular follow-up studies.

The method was applied for two real patient cases. In the first case, maximum surface growth occurred at the region of maximum diameter. In such cases, the growth rate based on maximum diameter would capture the maximum AAA growth rate. However, in the second case, the maximum surface growth did not spatially coincide with maximum diameter change. In such case the proposed methodology offers accurate growth rate estimates based on local surface deformation analysis.

In contrast to maximum diameter based growth estimation, surface area change based growth estimates cannot be clinically interpreted and evaluated as yet. Based on the two cases analyzed here 5.6 and 2.8 mm^2 surface area change correspond to local surface displacements of 8.3 and 5.5 mm respectively. It is anticipated that multicenter, large cohort clinical studies will assist in providing clinical guidelines based on both local and global surface growth values for improved rupture risk stratification.

ACKNOWLEDGEMENTS

Financially supported by the Action «Supporting Postdoctoral Researchers», co-financed by the European Social Fund (ESF) and the Greek State (LS7_2224).

REFERENCES

[1] Baek, et al. *11th. World Congress on Computational Mechanics*. Barcelona, Spain. 2014

[2] Audenaert. *Matlab Central*. http://www.mathworks.com/matlabcentral/fileexchange/41396-nonrigidicp 2013

Copyright 2016 The Organizing Committee for the 2016 Summer Biomechanics, Bioengineering and Biotransport Conference

SB^{3}C2016
Summer Biomechanics, Bioengineering and Biotransport Conference
June 29 –July 2, National Harbor, MD, USA
SB^{3}C2016-785

INVESTIGATION OF BIOTRANSPORT IN A TUMOR WITH NON-HOMOGENEOUS PERMEABILITY USING A NON-INTRUSIVE POLYNOMIAL CHAOS APPROACH

Miao Lu (1), Liang Zhu (1), Ronghui Ma (1), Maher Salloum (2), and Meilin Yu (1),

(1) Dept. of Mechanical Engineering, University of Maryland Baltimore County, Baltimore, MD 21250, USA

(2) Scalable and Secure Systems Research Department, Sandia National Labs, Livermore, CA 94550, USA

INTRODUCTION

Modeling drug transport in tissues has recently gained much attention in the bioengineering community due its vast areas of applications [1]. Such injections often employ a positive pressure infusion directly in the target tissue. It is often referred to as convection enhanced delivery. There are several studies that addressed this problem in the literature. These studies rely on mathematical models of flow in porous media (e.g., Darcy, Brinkman) and are successful in accounting for the existence of capillaries, tissue metabolism, etc. However, these models rely on the assumption that the tissue properties (e.g. permeability) are uniform inside tumors. MicroCT imaging following nanofluid infusion often reveals highly irregular distributions due to the spatial heterogeneity of the tissue [2].

It is of clinical significance to model enhanced convection drug delivery to tissues and accounting for the uncertainty resulting from the structural randomness in the tissue. In the current study, a non-intrusive polynomial chaos (NIPC) approach [3] is used to investigate the effect of random permeability on the positive pressure infusion in a tumor. We note that in the NIPC approach, no modification is needed for the available deterministic simulation tool. This can take full advantage of the contemporary development of high-fidelity computational fluid dynamics (CFD) methods. The information collected from this study can be used to study concentration and temperature field in biological systems with uncertain permeability and porosity.

METHODS

Governing Equations Consider the two dimensional (2D) Darcy's equation in the spherical coordinate system without change in the azimuthal direction,

$$\frac{\partial}{\partial r}\left(\frac{\kappa r^2}{\mu\phi}\frac{\partial p}{\partial r}\right)+\frac{1}{sin\theta}\frac{\partial}{\partial\theta}\left(\frac{\kappa sin\theta}{\mu\phi}\frac{\partial p}{\partial\theta}\right)=0, \quad (1)$$

where p is the gauge pressure, κ is the permeability, μ is the fluid viscosity, and ϕ is the porosity. The boundary conditions are specified as follows:

$$\begin{cases} p=0, & r=R_{tumor} \\ \dfrac{dp}{dr}=\dfrac{-Q\mu\phi}{4\pi R^2\kappa}, & r=R_{needle} \end{cases}. \quad (2)$$

Eq. (1) is discretized with the 2nd order finite difference scheme, and then solved using the Gauss-Seidel iteration.

Non-Intrusive Polynomial Chaos (NIPC) Following the polynomial chaos theory, the pressure p in Eq. (1) is decomposed into separable deterministic and stochastic components as follows:

$$p(\vec{x},\vec{\xi})\approx\sum_{j=0}^{N-1}p_j(\vec{x})\,\psi_j(\vec{\xi}), \quad (3)$$

where $p_j(\vec{x})$ is the jth deterministic component associated with the jth random basis function $\psi_j(\vec{\xi})$. In the generalized polynomial chaos theory, different types of polynomials are used to provide an optimal basis for different continuous probability distribution types. For example, Hermite polynomials are adopted as basis functions for the normal distribution.

In the current study, the point collocation NIPC is adopted. Specifically, N sampling points, i.e., $\vec{\xi}$, are chosen in the random space, and the basis functions $\psi_j(\vec{\xi}), j=1,\cdots,N$, are evaluated on these points. The deterministic numerical solver for Eq. (1) is then used to generate outputs on these sampling points. Finally, the deterministic components $p_j(\vec{x}), j=1,\cdots,N$, can then be computed by solving the following linear system:

Copyright 2016 The Organizing Committee for the 2016 Summer Biomechanics, Bioengineering and Biotransport Conference

$$\begin{pmatrix} \psi_0(\vec{\xi}_0) & \cdots & \psi_{N-1}(\vec{\xi}_0) \\ \vdots & \ddots & \vdots \\ \psi_0(\vec{\xi}_{N-1}) & \cdots & \psi_{N-1}(\vec{\xi}_{N-1}) \end{pmatrix} \begin{pmatrix} p_0(\vec{x}) \\ \vdots \\ p_{N-1}(\vec{x}) \end{pmatrix} = \begin{pmatrix} p(\vec{x},\vec{\xi}_0) \\ \vdots \\ p(\vec{x},\vec{\xi}_{N-1}) \end{pmatrix}. \quad (4)$$

The mean of the random variable p can then be calculated as

$$E[p(\vec{x},\vec{\xi})] = \int_{\Omega} p(\vec{x},\vec{\xi}) w(\vec{\xi}) d\vec{\xi} = p_0(\vec{x}), \quad (5)$$

where $w(\vec{\xi})$ is the probability density function. The variance of the distribution can be calculated as

$$\begin{aligned} Var[p(\vec{x},\vec{\xi})] &= \int_{\Omega} \left(p(\vec{x},\vec{\xi}) - E[p(\vec{x},\vec{\xi})]\right)^2 w(\vec{\xi}) d\vec{\xi} \\ &= \sum_{j=1}^{N-1} p_j^2(\vec{x}) \int_{\Omega} \psi_j(\vec{\xi}) \psi_j(\vec{\xi}) w(\vec{\xi}) d\vec{\xi}. \end{aligned} \quad (6)$$

The permeability κ is assumed to follow a log-normal distribution, which is expressed as

$$log(\kappa) = \hat{\kappa} = \hat{\kappa}_{ave} + \xi\sigma, \quad (7)$$

where $*_{ave}$ stands for the mean value, and σ is the standard derivation. In the current study, only one stochastic variable ξ (i.e., one random dimension) is investigated.

RESULTS

The physical parameters in the simulation are tabulated in Table 1. Three types of numerical simulations, namely, those with deterministic permeability, random permeability with small variance, and random permeability with large variance are carried out on a 101×51 mesh as shown in Figure 1(a). The pressure contours for the cases with constant permeability of 0.5 md, random permeability with mean value of 0.5 md and $\sigma = 0.2\hat{\kappa}_{ave}$, and random permeability with mean value of 0.5 md and $\sigma = 2\hat{\kappa}_{ave}$ are displayed in Figure 1(b)-(d), respectively. It is clear that if the permeability is constant, the shape of the pressure contour is symmetric about the center. Large randomness in permeability can result in shape asymmetry. The distributions of the random permeability for the cases presented in Figure 1(c) and (d) are displayed in Figure 2(a) and (b), respectively. The statistic information, i.e., the mean and variance of the pressure, for the case with mean permeability of 0.5 md and $\sigma = 2\hat{\kappa}_{ave}$ from the point collocation NIPC analysis is presented in Figure 3.

Parameters	Value
Mean Tumor Permeability, κ	0.5 *md*
Tumor Porosity, ϕ	0.2
Fluid Viscosity, μ	8.9×10^{-4} Pa·s
Infusion Rate, Q	5 μL/min
Needle Diameter	0.5 mm
Tumor Diameter	10 mm

Table 1: Physical parameters in the numerical simulation.

DISCUSSION

From Figure 3 it is observed that if the permeability is a random variable with log-normal distribution, large variation of pressure will occur in the region with large pressure gradient (i.e., the region near the needle). This feature is further confirmed by the random pressure distribution as shown in Figure 1(d). From the simulation results, it is concluded that if all other physical processes are assumed perfect, large variation of the tumor permeability can result in pressure shape asymmetry. This can further induce the asymmetry in the particle concentration field as observed in Ref. [2].

ACKNOWLEDGEMENT

This work is supported by UMBC.

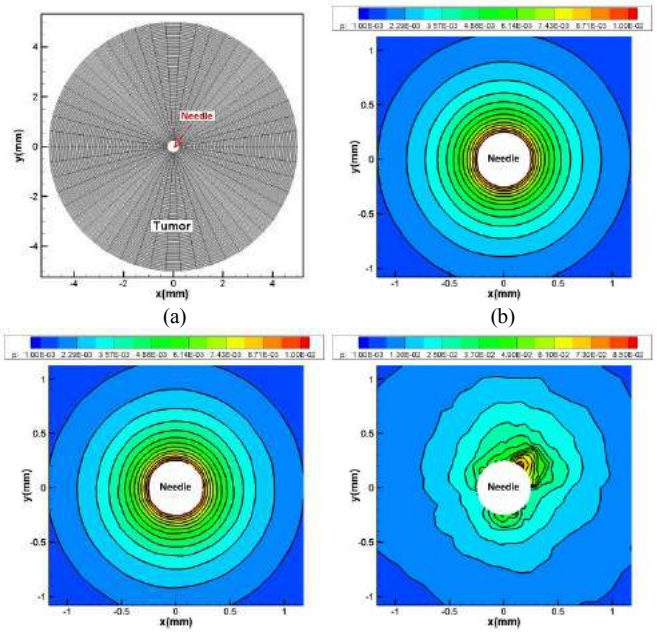

Figure 1: (a) Mesh of size 101×51; pressure contour with (b) constant permeability of 0.5 md; (c) mean permeability of 0.5 md, and $\sigma = 0.2\hat{\kappa}_{ave}$; (d) mean permeability of 0.5 md, and $\sigma = 2\hat{\kappa}_{ave}$.

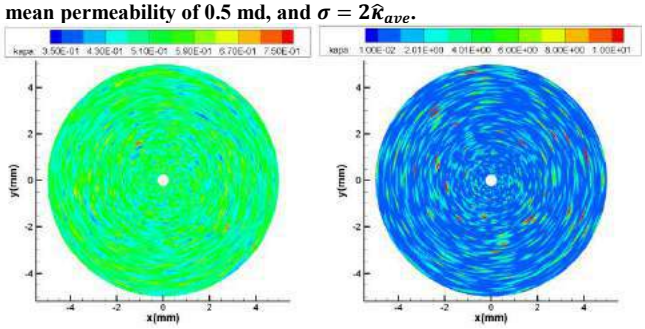

Figure 2: Contours of random permeability. (a) Mean permeability of 0.5 md with $\sigma = 0.2\hat{\kappa}_{ave}$; (b) mean permeability of 0.5 md with $\sigma = 2\hat{\kappa}_{ave}$.

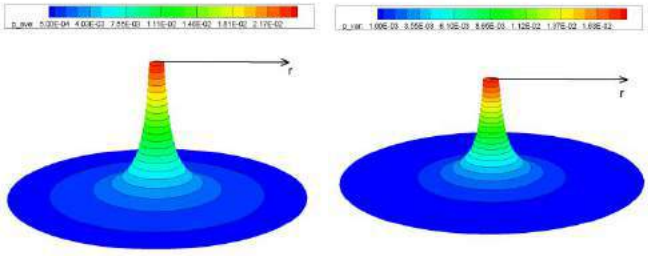

Figure 3: Statistic information from the point collocation NIPC analysis of the case with mean permeability of 0.5 md and $\sigma = 2\hat{\kappa}_{ave}$. (a) Mean value of the pressure; (b) variance of the pressure.

REFERENCES

[1] Barat, A et al., *Simulation Modelling Practice and Theory*, 14: 843-856, 2006.

[2] Attaluri, A et al., *Int. J. Hyperthermia*, 27:491-502, 2011.

[3] Xiu, D. and Hesthaven, *SIAM J. Sci. Comput.*, 27:1118-1139, 2005.

Copyright 2016 The Organizing Committee for the 2016 Summer Biomechanics, Bioengineering and Biotransport Conference

SB³C2016
Summer Biomechanics, Bioengineering and Biotransport Conference
June 29 –July 2, National Harbor, MD, USA
SB³C2016-786

LAMINA CRIBROSA DISINSERTIONS AS A MECHANOPROTECTIVE STRATEGY

**Andrew P. Voorhees (1), Ning-Jiun Jan (1,2),
John G. Flanagan (3), Jeremy M. Sivak (4), Ian A. Sigal (1,2)**

(1) Ophthalmology
University of Pittsburgh
Pittsburgh, PA, USA

(2) Bioengineering
University of Pittsburgh
Pittsburgh, PA, USA

(3) Optometry and Vision Science
University of California Berkeley
Berkeley, CA, USA

(4) Ophthalmology and Vision Sciences
University of Toronto
Toronto, ON, Canada

INTRODUCTION

Damage to the retinal ganglion cell (RGC) axons in glaucoma is believed to initiate at the lamina cribrosa (LC) in the back of the eye (Fig 1A). The LC is a meshwork of collagenous beams thought to provide mechanical support to the RGC axons. A clinical observation in some glaucoma patients is regions of the LC (primarily at the LC-sclera interface) with missing collagen beams (Fig. 1B-C) [1]. This phenomenon is called a disinsertion. It is assumed that disinsertions weaken the LC and leave RGC axons in the region more susceptible to mechanical trauma from elevated intraocular pressure.

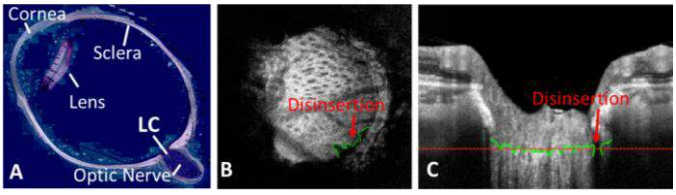

Figure 1: (A) Cross section of the eye showing the location of the LC and Optic Nerve. (B) En face OCT image of a glaucomatous human LC with a large disinsertion (C) Axial view from the same OCT scan. (B-C Adapted from [1]).

In this abstract we investigate the effects a LC disinsertion might have on the IOP induced strains experienced by the neural tissues. Since it is unfeasible to test these effects experimentally, we use a specimen-specific microstructure-based non-linear finite element model (Fig 2).

METHODS

To study the effect that the loss of LC beams has on the mechanics of the neural tissue we tested three different cases: 1) The original, unmodified structure, 2) A model of the same region, with a large disinsertion at the LC-sclera interface and 3) A model of the original region with a central LC beam removed (Fig. 3).

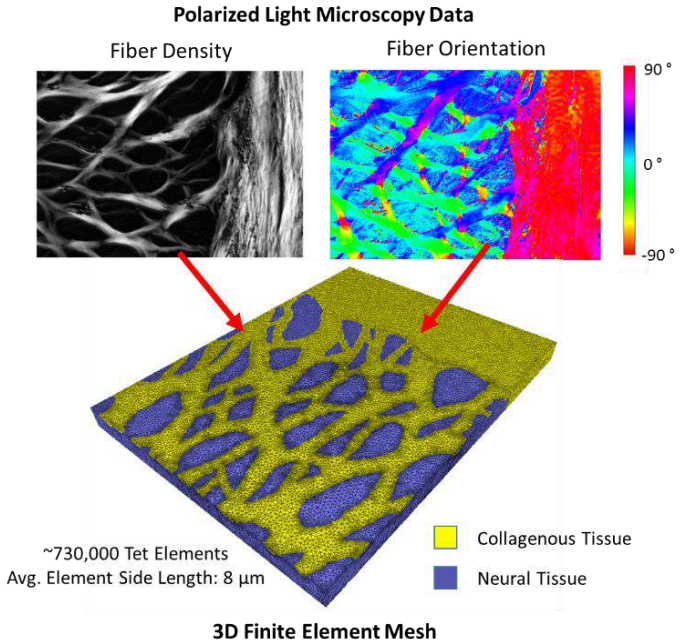

Figure 2: Polarized light microscopy data from a 30 µm thick section of sheep optic nerve head were used to generate the finite element mesh.

Copyright 2016 The Organizing Committee for the 2016 Summer Biomechanics, Bioengineering and Biotransport Conference

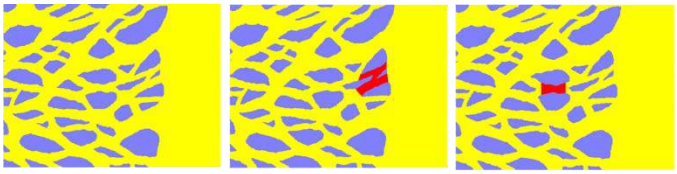

Figure 3: We used three different models to investigate the effects that the loss of laminar collagen beams might have on the neural tissues of the LC. Red regions denote the location of removed beams. Removed regions were considered to have the same material properties as the ground matrix of the neural tissue.

As pictorially described in Fig 2, the model geometry is a 3D reconstruction of a small temporal region of a section of a sheep optic nerve head. Collagen beams and scleral tissues were modeled as nearly incompressible Neo-Hookean solids with a 3D Von Mises distribution of fibers with an exponential-power law strain energy density function. The neural tissue was modeled as a compressible Mooney-Rivlin solid with a perfectly aligned distribution of fibers with an exponential-power law strain energy density function. All parameters of the constitutive formulations were based on literature values [2-3]. Mean collagen fiber orientation was calculated from the polarized light images while the orientation of fibers in the neural tissue was assumed to be along the direction of the axons (out of the plane of the image). A planar, equibiaxial load of 100 kPa (corresponding to an IOP of roughly 28 mmHg [2]) was applied. Finite element analysis was conducted using FEBio v2.3 [4]. To avoid edge effects, only central regions of the models were analyzed.

RESULTS

IOP-induced stresses and strains predicted in the original model varied greatly between the neural tissue pores and the beams, and from pore to pore (Fig 4). Average Green strains were 0.15 in the naso-temporal direction (left-right) and 0.09 in the inferior-superior direction (top-bottom) was 0.09.

A disinsertion reduced maximum strains in the pores adjacent to the removed tissue, however some nearby pores did experience a slight elevation in strain. Interestingly, the disinsertion also seemed to reduce the stresses in beams far from the disinsertion site.

A central defect substantially increased strains in the regions adjacent to the defect, but had little effect on more distant pores. The removal of the central beam reduced the stresses in some smaller beams, and slightly increased stress in the large beams running parallel to the removed beam.

DISCUSSION

Our study suggests that LC disinsertions at the LC-scleral boundary may actually be mechano-protective, reducing peak strains within the adjacent neural tissue. This surprising finding challenges the common assumption that increased collagen content must reduce tissue strain. Instead, removing peripheral LC beams transferred mechanical load to other regions of the LC, potentially protecting the RGC axons in vulnerable regions at the expense of axons in more robust regions. A central defect, however, had a different effect, causing the expected increased mechanical insult in the neural tissues. Further study is needed to determine exactly how the location, organization, and geometry of the beams influence this behavior.

Our model explicitly incorporates both detailed image-based LC beam geometries and complex non-linear material properties which previous models have not wholly accounted for [5]. As a consequence, the IOP-induced strains predicted by our model are very large and inhomogeneous compared with most previous models of the optic nerve head [5]. We have recently observed large IOP-induced strains and wide pore to pore variability in human donor eyes [6]. These findings are in agreement with our model and give us confidence in the results.

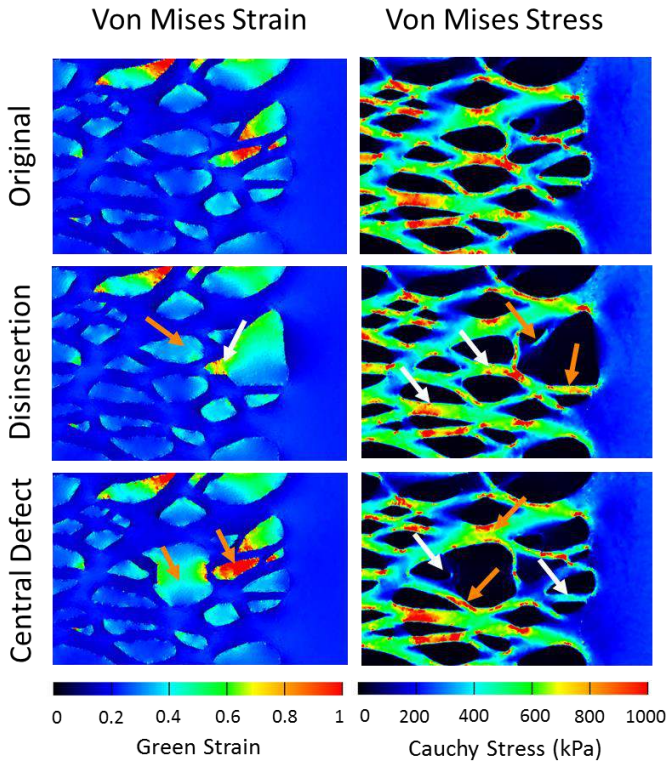

Figure 4: Von Mises strains (left column) and Von Mises stresses (right column) were calculated for each of the three cases. Orange arrows mark locations where stress or strain were increased (compared to original), while white arrows denote a decrease.

Despite this agreement, there are several limitations to this study. While the material properties we use include specimen specific fiber alignment and non-linear stress-strain behavior, they are still derived from non-sheep models [2-3]. Our model also treats the neural tissue and collagen beams as a continuum ignoring the fragile biochemical connections that exist in vivo. Lastly, due to computational expense, our model was limited to a small region of the LC and sclera. We hope to address these issues in our future work.

In summary, LC beam disinsertions may serve as a mechanism for transferring mechanical insult from an IOP-sensitive region to other less susceptible regions, thereby protecting local RGC axons.

ACKNOWLEDGEMENTS

Funding: NIH R01-EY023966, NIH P30-EY008098 and NIH T32-EY017271, the Eye and Ear Foundation (Pittsburgh, PA). CIHR MOP123448.

REFERENCES

[1] Kim, KK et al., *Acta Ophthalmol,* (In Press) 2016.
[2] Zhang, LJ et al., *IOVS,* 56:2031-2042, 2015.
[3] Galle, BH et al., *J Biomech,* 43: 2839-2843, 2010.
[4] Maas, SA et al., *J Biomech Eng,* 134: 011005, 2012.
[5] Sigal, IA et al., *Exp Eye Res*, 88:799-807, 2009.
[6] Sigal, IA et al., *IOVS*, 55:1-15,2015.

Copyright 2016 The Organizing Committee for the 2016 Summer Biomechanics, Bioengineering and Biotransport Conference

SB^{3}C2016
Summer Biomechanics, Bioengineering and Biotransport Conference
June 29 –July 2, National Harbor, MD, USA
SB^{3}C2016-787

IN SILICO AND IN VITRO MODELLING OF FLOW BEHAVIOUR IN LYMPHATIC VESSELS

Sinéad T. Morley (1,2), David T. Newport (1), Michael T. Walsh (1,2)

(1) Centre for Applied Biomedical Engineering Research (CABER), Dept. of Mechanical Aeronautical & Biomedical Engineering, University of Limerick, Limerick, Ireland.

(2) Health Research Institute (HRI) and Material and Surface Science Institute (MSSI), University of Limerick, Limerick, Ireland.

INTRODUCTION

Breast cancer is the most common cancer form in women, with an estimated 1.2 million new cases worldwide each year [1]. Tumour metastasis to regional lymph nodes is a crucial step in the progression of breast cancer and approximately 90% of cancer related deaths are due to metastasis [2]. It is not yet known why some cancerous cells metastasize from the lymph nodes and others do not, therefore, a fundamental understanding of the response of cells to the forces in the lymph vessels needs to be established. Lymph contains cells that are approximately 6μm and the diameter of breast cancer cells varies from 20-40μm [3]. The dynamics by which breast cancer cells travel through the lymphatic system to distant sites, and eventually establish metastatic tumours, remains poorly understood. There is a considerable wealth of research that examines transport properties of biological cells/particles in microfluidic channels [3-5]. However, the majority of these studies examine very small particles (0.2-1μm) under typical inertial focusing flow rates (30< Re <300) and very limited data is available on the response of large particles (20-50% the channel width) to low Reynolds number Poiseuille flow such as that seen in the lymphatic vessels. Inertial focusing of biological cells/particles in channels is dependent on properties such as particle size, shape and deformability. However, when the channel height approaches the same order of magnitude as the cells, the cells are influenced by the channel walls and the assumption that the cells travel with the local fluid velocity is no longer valid. It has been shown that larger particles tend to lag the fluid velocity but the exact forces that these particles are subjected to are not yet fully understood.

Using both numerical and experimental methods, the effect of breast cancer cells within the lymph vessels and how they respond to the forces generated by the flow field is investigated in this study. Cancer cells can change morphologically in response to local flow conditions. The objective is to determine whether such cells migrate due to morphological changes imposed by the local flow environment. This paper models the fluidic transport behaviour of breast cancer cells through lymphatics by investigating both cell flow (MCF-7's and MDA-MB-231 cells) and particle flow (Microparticles GmbH and Cospheric) in a microchannel at low flow rates (by HTS / LoC standards) which are representative of *in-vivo* conditions in the collecting lymphatics. The longer term goal of this work is to expose metastatic breast cancer cells to an appropriate fluidic context, mimicking their migration through the collecting lymphatics to the sentinel nodal sites downstream of a cancerous tumour.

METHODS

Experimental Methods: Experimental methods, using micro-Particle Image Velocimetry (μPIV) techniques, have been employed to model the flow behaviour of microparticles and breast cancer cells in a polymer 100x100μm channel. Microparticles have been used to simulate the flow of various immune cells contained within the lymph. A range of separate particle sizes and cell sizes are exposed to a low Reynolds number Poiseuille flow and their response to the flow in terms of speed and spatial distribution are analysed and compared. The Reynolds number is 0.08 which is considerably lower than that used in inertial sorting devices, and the particle/cell concentration is representative of that experienced in the collecting lymph *in-vivo*.

The experimental set-up consists of a high speed CCD camera (Imager LX 2M; LaVision, Germany) connected to an inverted microscope (IX73; Olympus, Tokyo) with illumination provided by dual Nd: YAG lasers (New Wave Research, UK). The channel was placed on the stage of the microscope and the flow rate was kept constant at 0.233 μL/min using a syringe pump (Harvard Apparatus, Holliston, MA). Microparticles of diameter; 5μm, 10μm, (Microparticles GmbH, Germany) and 27-32μm (Cospheric, CA) were

Copyright 2016 The Organizing Committee for the 2016 Summer Biomechanics, Bioengineering and Biotransport Conference

mixed at a 0.08% wt fraction. These particle sizes and their density were chosen to correspond to the cell sizes and density seen in the lymph vessels *in vivo* [8]. The breast cancer cells were cultured in Dulbecco's Modified Eagle's medium and incubated at 37°c in 5% CO_2 until near confluence before testing.

The μPIV images were processed using the DaVis software (version 8.2.3) from LaVision. The images were evaluated using a cross-correlation method and using a multi-pass interrogation algorithm with a 50% overlap the corresponding velocity fields were obtained. In order to individually track the large particles/cells Particle Tracking Velocimetry (PTV) techniques were employed. Using a combination of μPIV and PTV techniques the disturbed flow field around large particles/cells was investigated.

Computational Methods: Numerical simulations were performed using the commercially available software Star CCM+ Version 10.06.009 (CD-adapco, NY). A three-dimensional model of the microchannel used in the experiments was created and computational fluid dynamic analysis was carried out. The Dynamic Fluid Body Interaction (DFBI) model was employed to model the motion of a cancer cell through a microchannel. The DFBI module enables the implicit unsteady solver to calculate the hydrodynamic forces and moments acting on the cancer cell and solves the governing equations of motion to find the new position of the cancer cell as it travels through the microchannel. The supercomputer facilities of the Irish Centre for High end Computing (ICHEC) were utilized to run these DFBI simulations. An overset meshing strategy was employed and a grid independence study was carried out. The mesh was refined in the area near the particle-fluid interface in order to improve the accuracy of the results whilst simultaneously providing faster computational solving times. Using the DFBI model it is possible to follow a cancer cells progression through a channel due to the applied fluidic forces generated from the lymphatic environment.

RESULTS

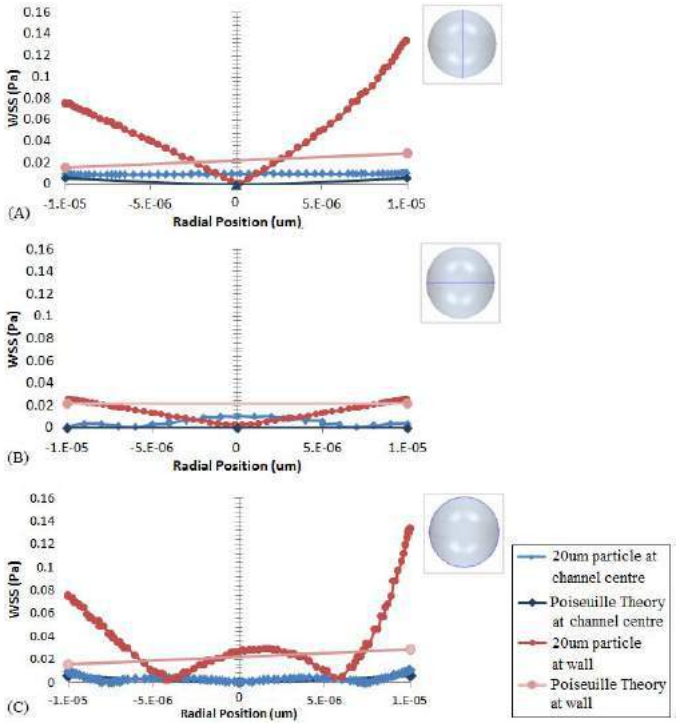

Figure 1: WSS magnitude plotted along the 20μm cell surface in the (A) YZ plane, (B) XY plane, (C) XZ plane.

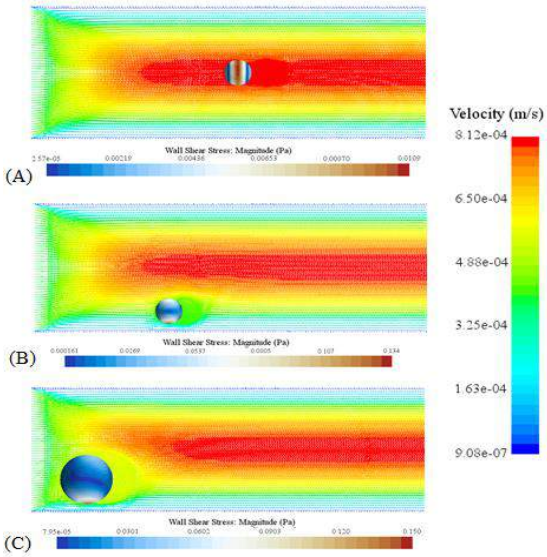

Figure 2: WSS magnitude on cell surface and the disturbed velocity plots, for both 20μm (A) + (B), and 40μm diameter cells (C), at different positions and time points in the flow.

DISCUSSION

The work carried out in this study investigates the migration behaviour of MCF-7 and MDA-MB-231 breast cancer cells to Poiseuille flow within a 100μm square channel. The objective is to determine whether such cells migrate due to morphological changes imposed by the local flow environment, and are compared to solid particles of different sizes as a reference case. The flow behaviour of the cells is largely dispersed and observations indicate that the size of the cell plays an important role in cell motility. Results indicate that cells travelling at the channel centre are subjected to a far lower, more uniform shear stress level than cells travelling close to the channel walls, where high WSS gradients can be seen, as illustrated in Fig. 1.

Figure 2 illustrates the WSS magnitude experienced by cells, of diameter 20μm and 40μm, both at the channel centre and 5μm from the channel wall. The size and position of the cell within the vessel affects the lymphatic fluidic environment to varying degrees. When the vessel height approaches the same order of magnitude as the cells, the cells are influenced by the vessel walls and the assumption that the cells travel with the local fluid velocity is no longer valid. It has been shown that larger cells tend to lag the fluid velocity but the exact forces that these cells are subjected to are not yet fully understood. Further analysis is needed to quantify this effect. Good correlation between measured and predicted velocity profiles was seen with the accuracy of the prediction decreasing with radius. Particle sizes (5-40μm) corresponding to different cell types did affect the results suggesting that cell size, relative to lymph vessel diameter, is an important factor in cell behavior in the flow. This finding could potentially have very important consequences, as it may be possible to elucidate if a particular cancer cell size exists that encourages metastasis within these vessels. Knowledge of this fact could potentially lead to improved screening/treatment methods for patients.

ACKNOWLEDGEMENTS

EMBARK from the IRC and Mid-Western Cancer Foundation.

REFERENCES

[1] Lee, J. H. and Nan A., *Journal of Drug Delivery*, 2012.
[2] Chandrasekaran, S., *et al*., *Lab on a Chip*, 14(1):118-127, 2014.
[3] Faivre, M., *et al*., *Biorheology*, 43(2):147-159, 2006.
[4] Peng, Z., *Mechanical Engineering*, 126, 2011.
[5] Hur, S. C., *et al*., Biomicrofluidics, 5(2):022206, 2011.
[6] Rahbar, E. & Moore, J. E., *Journal of Biomechanics*, 44, 2011.

Copyright 2016 The Organizing Committee for the 2016 Summer Biomechanics, Bioengineering and Biotransport Conference

SB^{3}C2016
Summer Biomechanics, Bioengineering and Biotransport Conference
June 29 –July 2, National Harbor, MD, USA
SB^{3}C2016-788

VELOCITY-DILATATION FORMULATION FOR COMPUTATIONAL FLUID DYNAMICS IN FEBIO

Gerard A. Ateshian (1), Jay J. Shim (1), Steve Maas (2), Jeffrey A. Weiss (2)

(1) Department of Mechanical Engineering
Columbia University
New York, NY, USA

(2) Department of Bioengineering
University of Utah
Salt Lake City, UT, USA

INTRODUCTION

The mechanics of biological fluids is an important topic in biomechanics, most notably for the study of blood flow through the cardiovascular system and related biomedical devices, cerebrospinal fluid flow, airflow through the respiratory system, biotribology by fluid film lubrication, and flow through microfluidic biomedical devices. Biological fluids are generally modeled as nearly incompressible, though compressible flow may be needed to analyze wave propagation as required for example in acoustics (airflow through vocal folds) and the analysis of ultrasound propagation for imaging blood flow.

FEBio is a free finite element software designed to meet the computational needs of the biomechanics and biophysics communities (febio.org)[3]. This study describes the formulation of a novel finite element framework for computational fluid dynamics and its implementation and verification in FEBio. Conventional computational fluid dynamics implementations typically model either isothermal incompressible flow or anisothermal compressible flow. Computational analyses of incompressible flow typically enforce the incompressibility condition using either mixed formulations (where the finite element interpolation of fluid pressure is lower order than that of the fluid velocity) or the penalty method (where the fluid pressure is proportional to the divergence of the fluid velocity via a penalty factor)[4]. These formulations suffer from ill-conditioning of the tangent (stiffness) matrix as the incompressible limit is approached[5] and require methods such as the streamline upwind Petrov-Galerkin stabilization[6] to produce reliable results. Anisothermal compressible flow analyses typically need an equation of state between pressure, density and volume and require the additional solution of the energy balance equation to solve for the spatio-temporally varying temperature.

We propose to overcome these constraints by employing a novel yet straightforward approach to analyze isothermal compressible flow using fluid dilatation (instead of fluid pressure) as an essential variable. Just like fluid velocity, dilatation is a kinematic quantity that can serve as a state variable in the formulation of functions of state (such as viscous stress and elastic pressure). Another benefit of this approach is that the dependence of density on dilatation is obtained by analytically integrating the mass balance equation, as conventionally done in finite elasticity. In effect, we propose to use a finite elasticity approach to describe the elastic compressibility of the fluid, using the dilatation as the only required component of the strain tensor. In this approach, fluid velocity and dilatation are obtained by satisfying the momentum balance equation as well as the fundamental kinematic relation between the time rate of change of the dilatation and the divergence of the velocity.

METHODS

In a spatial frame the momentum balance is $\rho\mathbf{a}=\mathrm{div}\mathbf{T}+\rho\mathbf{b}$, where ρ is the density, $\mathbf{T}$ is the Cauchy stress, $\mathbf{b}$ is the body force per mass and $\mathbf{a}$ is the acceleration, given by the material time derivative of the velocity $\mathbf{v}$ in the spatial frame, $\mathbf{a}=(\partial\mathbf{v}/\partial t)+(\mathrm{grad}\mathbf{v})\cdot\mathbf{v}$. The kinematic relation between the Jacobian of the deformation, $J=\det\mathbf{F}$ (where $\mathbf{F}$ is the deformation gradient) and the velocity is $\partial J/\partial t+\mathrm{grad}J\cdot\mathbf{v}=J\,\mathrm{div}\mathbf{v}$. The virtual work δW used in our finite element formulation is

$$\begin{aligned}\delta W = &\int_\Omega \delta\mathbf{v}\cdot\left(\mathrm{div}\mathbf{T}+\rho\left(\mathbf{b}-\mathbf{a}\right)\right)dv \\ &+\int_\Omega \delta J\left(\frac{\partial J}{\partial t}+\mathrm{grad}J\cdot\mathbf{v}-J\,\mathrm{div}\mathbf{v}\right)dv\end{aligned} \tag{1}$$

where $\delta\mathbf{v}$ is a virtual velocity and δJ is a virtual energy; Ω is the fluid domain and dv is a differential volume in Ω. From the mass balance it

Copyright 2016 The Organizing Committee for the 2016 Summer Biomechanics, Bioengineering and Biotransport Conference

follows that $\rho=\rho_r/J$, where ρ_r is the fluid density in the reference configuration. The Cauchy stress is split into a hydrostatic elastic pressure p and a viscous stress $\mathbf{T}^v$, $\mathbf{T}=-p\mathbf{I}+\mathbf{T}^v$, where p only depends on J, e.g., according to ideal gas law or alternatively $p=\kappa(1-J)$ where κ is the fluid bulk modulus. Typically, $\mathbf{T}^v$ describes a Newtonian fluid. This formulation was implemented into FEBio using the standard approach for linearizing δW along increments in $\mathbf{v}$ and J and discretizing the resulting nonlinear system using Newton's method.

RESULTS

We verified this implementation for a wide range of test problems, including closed form solutions for incompressible Newtonian fluids such as planar and circular Poiseuille flow, planar and circular Couette flow, Blasius boundary layer, and Womersley reciprocal flow. Results for lid-driven cavity flow (Fig. 1) compared favorably to the results of Ghia et al.[2] and others [6,7]. Flow past a backward facing step was verified against the CFD analysis of Zienkiewicz et al.[7] (Fig. 2) and validated against the experimental results of Denham and Patrick [1] (Fig. 3). Finally, we illustrate transient flow past a cylinder at Re=100, demonstrating an initial metastable state, which spontaneously breaks into eddies, eventually settling to a cyclical response producing a Karman vortex street (Fig. 4). The average drag coefficient evaluates to C_D=1.26, consistent with experimental observations.

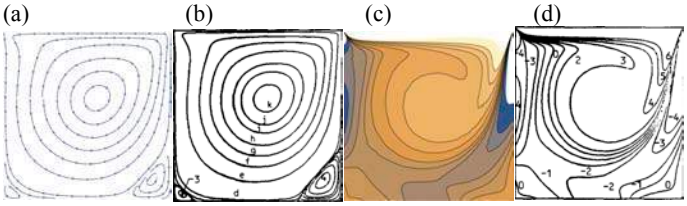

Figure 1: Lid-driven cavity flow in 2D at Re=400. Comparison of (a) FEBio results with (b) Ghia et al.[2] for fluid velocity streamlines. Vorticity contour plots from (c) FEBio and (d) Ghia[2].

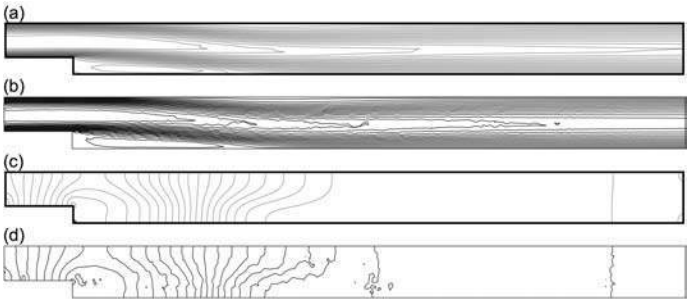

Figure 2. Flow past a backward facing step (left to right) at Re=229, comparing FEBio (a & c) and CFD analysis of Zienkiewicz et al. [7] (b & d): Contour plots of horizontal velocity component (a, b) and pressure (c, d).

DISCUSSION

This study describes the implementation of a computational fluid dynamics framework in FEBio. Though numerous CFD approaches have been described for incompressible flow in the prior literature[4,7], we believe that our approach, which employs the kinematic constraint between J and $\mathbf{v}$, is novel. In effect, we are able to solve isothermal compressible flows without using the energy balance, yielding the elastic pressure p based on its dependence on J. Nearly-incompressible flow is modeled by employing physically realistic values of the fluid bulk modulus. This formulation uses the same number of nodal degrees of freedom as standard $\mathbf{v}$-p formulations. This implementation extends the modeling capabilities of FEBio to allow investigations relevant to fluid flow in biological systems. It also sets the stage for the future implementation of fluid-solid interactions, which are particularly important in biomechanics.

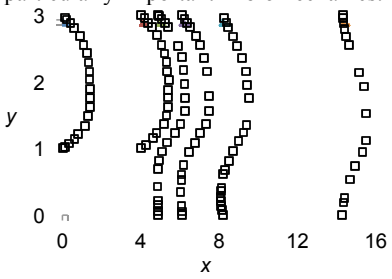

Figure 3. Flow past a backward facing step at Re=229, comparing horizontal velocity profiles from FEBio (solid curves) against experimental results (symbols) [1].

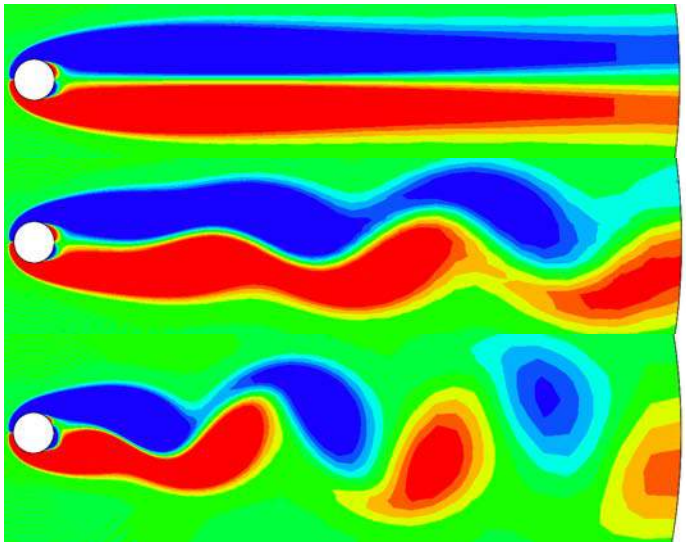

Figure 4. Vorticity contours at increasing time points for transient flow past a cylinder at Re=100, analyzed with FEBio. An initial metastable profile starts to shed eddies, then settles into a periodic response producing a Karman vortex street.

ACKNOWLEDGEMENTS

National Institutes of Health, R01GM083925.

REFERENCES

[1] Denham MK, Patrick MA: Laminar flow over a downstream-facing step in a two-dimensional flow channel. *Trans. Inst. Chem. Eng.*, 52(4): 361-367, 1974.

[2] Ghia U, Ghia KN, Shin C: High-Re solutions for incompressible flow using the Navier-Stokes equations and a multigrid method. *J. Comput. Phys.*, 48(3): 387-411, 1982.

[3] Maas SA, Ellis BJ, Ateshian GA, Weiss JA: FEBio: finite elements for biomechanics. *J. Biomech. Eng.*, 134(1): 011005, 2012.

[4] Reddy JN, Gartling DK, 2001, The finite element method in heat transfer and fluid dynamics, CRC Press, Boca Raton, FL.

[5] Ryzhakov PB, Rossi R, Idelsohn SR, Onate E: A monolithic Lagrangian approach for fluid-structure interaction problems. *Comput. Mech.*, 46(6): 883-899, 2010.

[6] Tezduyar TE, 1992, Stabilized finite element formulations for incompressible flow computations, Academic Press.

[7] Zienkiewicz OC, Taylor RL, Nithiarasu P, 2014, The finite element method for fluid dynamics, Butterworth-Heinemann, Oxford.

Copyright 2016 The Organizing Committee for the 2016 Summer Biomechanics, Bioengineering and Biotransport Conference

SB³C2016
Summer Biomechanics, Bioengineering and Biotransport Conference
June 29 –July 2, National Harbor, MD, USA
SB³C2016-789

ASSESSMENT OF 4D FLOW ACCURACY FOR QUANTIFICATION OF CEREBROSPINAL FLUID DYNAMICS IN THE CERVICAL SPINE: COMPARISON OF IN VITRO MEASUREMENTS AND NUMERICAL SIMULATION

S. Heidari Pahlavian (1, 2), F. Loth (1, 2), S. Thyagaraj (1, 2), A. C. Bunck (3), D. Giese (3), B. A. Martin

(1) Conquer Chiari Research Center, The University of Akron, Akron, OH, USA.

(2) Department of Mechanical Engineering, The University of Akron, Akron, OH, USA.

(3) Department of Radiology, University Hospital of Cologne, Cologne, Germany

(4) Department of Biological Engineering, The University of Idaho, Moscow, Idaho, USA.

INTRODUCTION

Cerebrospinal fluid (CSF) has several important functions in the central nervous system (CNS) and abnormal alterations in its production, absorption, and dynamics are thought to be linked with a number of CNS disorders including Alzheimer's disease [1], hydrocephalus [2], and Chiari malformation [3]. *In vivo* measurement techniques including phase contrast magnetic resonance imaging (PC MRI) and intraoperative ultrasound [4] have contributed to the understanding of CSF hydrodynamics. More recently, faster and more detailed assessment of CSF velocities has been achieved using time-resolved three directional PC-MRI sequences (4D Flow) [3]. 4D Flow has enabled the simultaneous measurement of velocities in through-plane and in-plane directions and allows for attaining higher spatio-temporal resolution compared with conventional 2D PC MRI methods within a clinically feasible time-frame. Despite these advantages, 4D Flow measurements of CSF velocities are subject to a number of potential errors and prior to further implementation of this technique, its accuracy must be evaluated. The objective of this work was therefore to assess the accuracy of 4D Flow measurements of CSF dynamics, in terms of velocity magnitude and distribution using an MRI-compatible experimental platform.

METHODS

An anatomically-detailed 3D geometry of the cervical spinal SAS was created based on manual segmentation of T2-weighted MRI images of an adult volunteer and addition of idealized dorsal and ventral spinal cord nerve rootlets [5] (Figure 1 (a)). A phantom model was constructed based on this geometry using the stereolithography technique (Viper si2 SLA system, 3D System Corp., Valencia, CA) and was implemented in an *in vitro* flow system as shown in Figure 1(b). The experimental

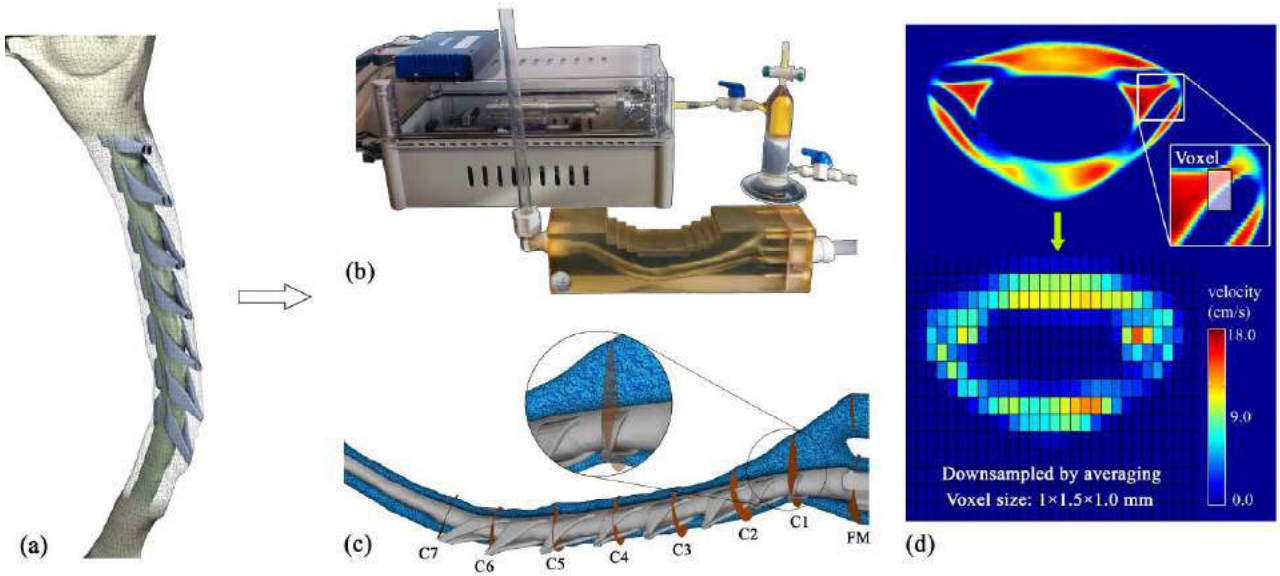

Figure 1. a) Rendering of the reconstructed geometry of the cervical spinal subarachnoid space including spinal cord nerve rootlets. b) Experimental platform including computer controlled pump, custom designed oil-water interface, and phantom 3D printed model c) Computational grid used in the numerical simulation. Also, shown are the location of the axial planes on which the results were compared against *in vitro* 4D Flow. (FM = foramen magnum, C7 midline of the seventh cervical vertebra). d) Spatial averaging of CFD velocities onto a coarse structured grid with voxel size equal to the 4D Flow data.

Copyright 2016 The Organizing Committee for the 2016 Summer Biomechanics, Bioengineering and Biotransport Conference

platform consisted a computer-controlled pulsatile syringe pump which was connected to the model thorough a custom designed oil-water interface and 7.6 meters of rigid tubing. *In vitro* 4D Flow measurements were performed on a 1.5 T MRI (Achieva, Philips Healthcare, Best, Netherlands) with in-plane and through-plane resolutions of 1.0 and 1.5 mm, respectively. The encoding velocity (V_{ENC}) was set to 15 cm/s and the flow cycle was temporally encoded in 16 phases, corresponding to an acquired temporal resolution of 52 ms. GTFlow software (Gyrotools Ltd., Zurich, Switzerland) was used for the post-processing of 4D Flow data. Computational fluid dynamic (CFD) simulation of CSF flow was carried out based on the same composite geometry and flow boundary conditions using ANSYS FLUENT (ANSYS Inc., Canonsburg, PA) and its results were spatially averaged to match the resolution of 4D Flow measurements (Figure 1(d)). CSF velocities obtained from *in vitro* measurements and CFD were compared in terms of peak values, distribution, and pixel-by-pixel correlation.

RESULTS

Good agreement was observed between CFD and *in vitro* 4D Flow, in terms of spatial distribution and peak magnitude of through-plane velocities with an average difference of 7.5% and 10.6% for peak systolic and diastolic velocities, respectively. Both methods showed anterior dominance of the CSF flow in the axial planes near the cranial end of the geometry (C1) and also regions of elevated flow between nerve rootlets. The discrepancies in velocity magnitude were more pronounced near the nerve rootlets and the edges of the axial planes (red arrows in Figure 2(a)). Pixel-by-pixel comparison of through-plane velocities using linear regression analysis revealed a good correlation between CFD and 4D Flow measurements ($r>0.75$) at most axial planes and timeframes (Figure 2 (b)). Weaker correlation between CFD and 4D Flow were observed at the timeframes corresponding to near zero CSF flow rate and near the cranial end of the geometry, where velocities were smaller due to the larger cross-sectional areas. Much larger discrepancies of in-plane velocities were observed between CFD and 4D Flow compared to those of through-plane velocities. The maximum values of mean correlation coefficients averaged over all axial planes and all timeframes were 0.52±0.19 and 0.50±0.10, respectively for in-plane velocities.

DISCUSSION AND CONCLUSION

The developed experimental platform provided a controlled flow environment, suitable for the assessment of 4D Flow accuracy in measuring CSF velocities. The findings of this study showed a good qualitative and quantitative agreement between *in vitro* 4D Flow measurements and numerical simulation, in terms of through-plane velocities, reflecting the good accuracy of 4D Flow for through-plane velocity quantification. As such, our results support that the previously reported large discrepancies between *in vivo* 4D Flow measurements and CFD [6] were likely due to the modeling simplification of the numerical models and not 4D Flow measurement error. The lower accuracy of 4D Flow in measuring low-magnitude thorough-plane and in-plane velocities is possibly due to the lower signal-to-noise ratio in the low velocity flow regions caused by the high V_{ENC} parameter utilized in the 4D Flow sequence. Improvement of 4D Flow sequences through acquisition of lower V_{ENC} for in-plane velocities or multiple V_{ENC} acquisitions should be performed prior to further consideration of this technique for quantification of low through-plane velocities or secondary flow components.

ACKNOWLEDGEMENTS

The authors acknowledge Conquer Chiari, Swiss National Science Foundation and American Syringomyelia Alliance Project for support of this work.

REFERENCES

[1] Silverberg G, et al., *Cerebrospinal Fluid Res*, 3:7, 2006.
[2] Bradley WG, et al., *Radiology*, 198(2):523-529, 1996.
[3] Bunck AC, et al., *European Radiology*, 22(9):1860-1870, 2012.
[4] Lagana MM, et al., *Curr Neurovasc Res,* 11(4):349-358, 2014.
[5] Heidari Pahlavian S, et al., *PLoS ONE*, 9(4):e91888, 2014.
[6] Yiallourou TI, et al., *PLoS ONE*, 7(12):e52284, 2012.

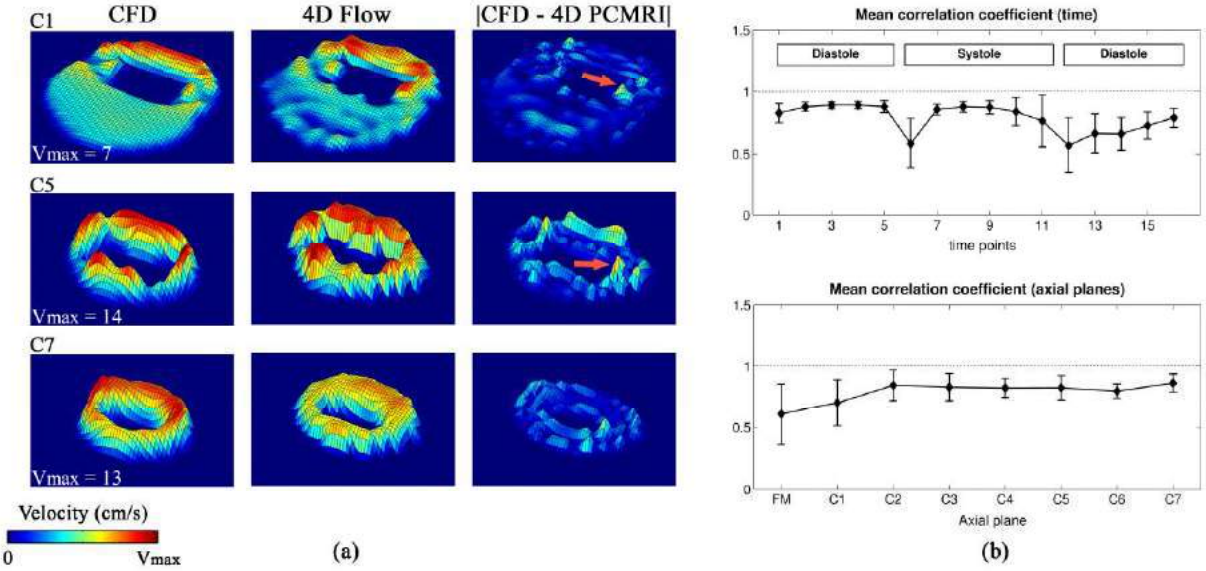

Figure 2. a) Surface plot comparison of through-plane velocities simulated by CFD and measured by *in vitro* 4D Flow on three representative axial planes. b) Mean correlation coefficients obtained from pixel-by-pixel comparison of through-plane velocities, averaged over all axial planes (top) and over all flow cycle timeframes (bottom). Systole and diastole corresponds to craniocaudal and caudocranial CSF flows, respectively.

Copyright 2016 The Organizing Committee for the 2016 Summer Biomechanics, Bioengineering and Biotransport Conference

SB³C2016
Summer Biomechanics, Bioengineering and Biotransport Conference
June 29 –July 2, National Harbor, MD, USA
SB³C2016-791

EFFECT OF PENTA-GALLOYL GLUCOSE ON MURINE AAA: MATERIAL PARAMETER OPTIMIZATION AND FINITE ELEMENT IMPLEMENTATION

Mirunalini Thirugnanasambandam (1), Dan T. Simionescu (2), Eugene Sprague (1, 3), Beth Goins (4), Geoffrey D. Clarke (4), Hai-Chao Han (1, 5), Krysta L. Amezcua (1), Oluwaseun Rita Adeyinka (1), Ender A. Finol (1)

(1) Department of Biomedical Engineering
University of Texas at San Antonio
San Antonio, Texas, USA

(2) Department of Bioengineering
Clemson University
Clemson, South Carolina, USA

(3) Department of Medicine
University of Texas Health Science Center at San Antonio
San Antonio, Texas, USA

(4) Department of Radiology
University of Texas Health Science Center at San Antonio
San Antonio, Texas, USA

(5) Department of Mechanical Engineering
University of Texas at San Antonio
San Antonio, Texas, USA

INTRODUCTION

Abdominal aortic aneurysms (AAA) are characterized by the dilatation of the abdominal aorta by more than half of its original diameter. The pathogenesis of AAAs is mainly based on the evolution of the mechanobiology of the aortic wall caused by variation in its composition due to proteolytic degradation. Being the 13th leading cause of death in the United States and given the asymptomatic nature of the disease, AAAs have a mortality rate of about 90%. Current methods of clinical treatment of AAAs include Endovascular Repair (EVAR) and open abdominal surgery. Few clinical trials have tested the effects of non-specific drugs on AAA growth. The objective of this study was to evaluate the effects of Penta-galloyl glucose (PGG), an elastin and collagen-binding polyphenol, on the growth of murine AAA. The biomechanical evolution of the AAA was studied by evaluating the peak von Mises stress and the biological evolution of AAA was studied by evaluating the MMP-9 activity, which indicates inflammation and degradation of the extracellular matrix.

METHODS

2.1 Animal study

In this study, six Sprague-Dawley rats were used. μMR images and in-vivo molecular images of the rats' abdominal aorta were acquired initially. The rats were divided into control and treated groups. A survival surgery was performed on all subjects, during which aneurysm formation was induced using a calcium chloride ($CaCl_2$) model. A gauze, soaked in 0.5M $CaCl_2$, was applied in the suprarenal location. PGG at body temperature (37 °C) was applied peri-adventitially to the treatment group before the application of 0.5 M $CaCl_2$. During the first follow-up phase, IVIS *in vivo* imaging was done on all the rats after injecting a probe (MMPSense 750 FAST) in the tail vein. MMPSense 750 FAST is an MMP activatable agent that is optically silent upon injection but fluoresces on cleavage by disease-related MMPs. During the second follow-up phase, μMRI was used again to acquire images of the abdominal aorta. *In vivo* imaging was also repeated and fluorescent maps of MMP activity were generated. All the rats were sacrificed and the aortas were harvested for further testing. The thoracic, abdominal aortic and aneurysmal tissues were cut into 25mm^2 square specimens and were then tested using the Cellscale planar biaxial tensile tester.

2.2 Material model parameters

Force-displacement data obtained from the biaxial tests was analyzed to obtain the stress-strain curves for each rat in the thoracic, abdominal and aneurysmal regions of the aorta. The least squares error between experimentally calculated Cauchy stress and its theoretically evaluated value was minimized using a genetic algorithm. The Levenberg-Marquardt algorithm was used to evaluate the Fung material model parameters that define the strain energy density (SED) function as follows:

$$\Psi = \frac{c}{2}(e^{Q} - 1), \tag{1}$$

where $Q = c_2 {E_{\theta\theta}}^2 + c_3 {E_{zz}}^2 + 2 * c_5 E_{\theta\theta} E_{zz} + 2 * c_8 {E_{\theta z}}^2$.

Convexity of the SED function was imposed as a constraint in the optimization procedure according to $c > 0$; $c_2, c_3 > 0$; $c_2 * c_3 > {c_5}^2$. The parameter c_8 was evaluated using the equivalence of the spatial elasticity tensor and stiffness matrix for orthotropic materials, as described in [1]. Thus, $c_8 = \frac{2G_{12}}{c}$. The shear modulus for the rat aorta was obtained from [2] as G_{12}= 137 kPa. These parameters were used to plot the individual Cauchy stress-Green Lagrangian strain plots. The pointwise averaged curve was then obtained for each region of the aorta, from which the corresponding Fung model parameters were

Copyright 2016 The Organizing Committee for the 2016 Summer Biomechanics, Bioengineering and Biotransport Conference

evaluated. The average parameter values for each region are presented in Table 1.

Table 1: Fung material model parameters by region (TA: thoracic aorta; AAA: aneurysmal abdominal aorta; AA: abdominal aorta).

Location	c (kPa)	c_2 (kPa)	c_3 (kPa)	c_5 (kPa)
TA (by pointwise average)	299.5	0.5091	0.3502	0.0374
TA (by c-wise average)	898.2	0.5094	0.3290	0.0852
TA (by c-wise average without outliers)	336.3	0.3627	0.2014	0.0852
AAA (by pointwise average)	13.27	3.413	2.878	0.3959
AAA (by c-wise average)	45.37	2.867	1.643	0.7817
AAA (by c-wise average without outliers)	45.37	2.867	1.643	0.7817
AA (by pointwise average)	11.49	2.799	2.454	0.5066
AA (by c-wise average)	38.65	2.118	1.471	0.7897
AA (by c-wise average without outliers)	20.59	2.118	1.471	0.7897

2.3 Biomechanical image analysis

The μMR images of the rats were segmented using in-house segmentation and geometry quantification code (AAAVASC). The contours generated from the segmentation were used to create an STL file of the outer wall by lofting the surface on them using Solidworks. The STL geometry was then smoothened locally and an inner offset surface was created using 3-Matic. The geometry was then imported into ANSYS ICEM, where the finite element mesh was generated and later input into FEBio, an open-source FEA solver, as shown in Fig. 1. The material parameters obtained from biaxial tensile testing were used to evaluate the Young's modulus and shear moduli. The boundaries were fixed and an internal pressure of 120 mmHg was applied to the endoluminal surface. The von Mises stress was quantified using Postview. The same procedure was repeated to evaluate the evolution of wall stress with time and with the growth of AAA.

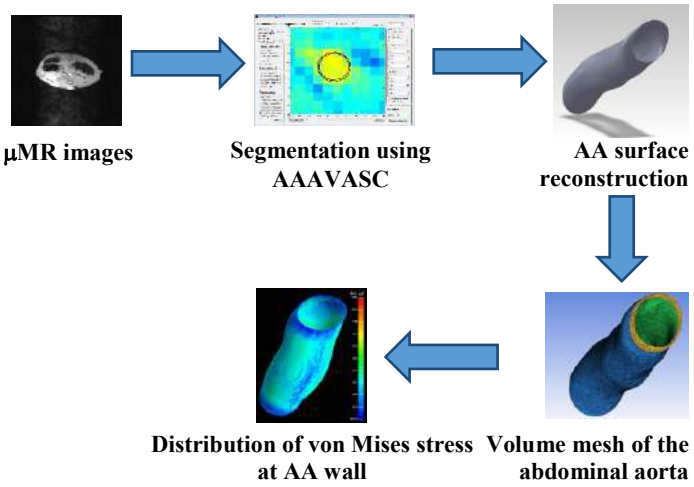

Figure 1: Flowchart for evaluation of stress distribution from μMRI images of the rat aorta.

RESULTS

The distribution of von Mises stress on the wall of exemplary abdominal aortas is presented in Fig. 2. The peak von Mises stresses are 800 kPa for the control (prior to AAA induction surgery), 1.88 MPa for the control (post AAA induction surgery), 904 kPa for the PGG-treated AA (prior to AAA induction surgery), and 1.47 MPa for the PGG-treated AA (post AAA induction surgery). The images from the IVIS microscope after injection of the probe are shown in Fig. 3. The fluorescence intensity map represents the distribution of MMP activity and matrix degradation.

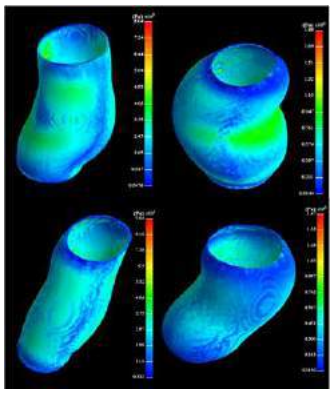

Figure 2: Distribution of von Mises stress (Pa) on the wall of a control (top) and PGG-treated (bottom) abdominal aorta pre- (left) and post- (right) AAA induction surgery.

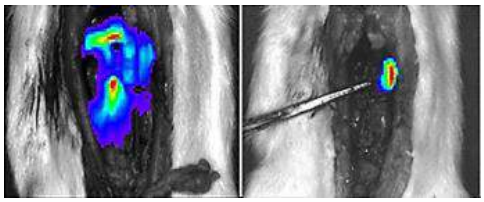

Figure 3: MMPSense Fluorescence intensity map obtained from IVIS images for control (left) and PGG-treated (right) rats.

DISCUSSION

The percentage increases in peak von Mises stress in the control and PGG-treated rats are 134% and 63%, respectively, between pre- and post-AAA induction procedures. Previous studies established that PGG binds specifically to arterial elastin and, in doing so, preserves elastic laminar integrity and architecture. However, this conclusion was based on a low percentage increase in maximum diameter in PGG-treated rats [3]. While the same observation holds true in this study, we also noticed a small percentage increase in peak von Mises stress in PGG-treated rats compared to controls, thus implying potential AAA stabilization. Antibiotics, statins and beta-blockers have been used in clinical trials, but there is limited evidence of their stabilization effects. The limitation of this study, however, is the small sample size of animal subjects. Future studies should focus on the effect of geometry and material parameters on the wall stress.

ACKNOWLEDGEMENTS

This work was supported in part by The University of Texas System Board of Regents - Science and Technology Acquisition and Retention (STARS) program.

REFERENCES

[1] Ateshian, Gerard A., and Kevin D. Costa., *Journal of biomechanics* 42.6 (2009): 781-785.

[2] Deng, S. X., et al., *American Journal of Physiology-Heart and Circulatory Physiology* 266.1 (1994): H1-H10.

[3] Isenburg, Jason C., et al., *Circulation* 2007; 115:1729-1737.

Copyright 2016 The Organizing Committee for the 2016 Summer Biomechanics, Bioengineering and Biotransport Conference

SB^{3}C2016
Summer Biomechanics, Bioengineering and Biotransport Conference
June 29 –July 2, National Harbor, MD, USA
SB^{3}C2016-792

A 3-D MODEL OF BREAST TUMOR - ENDOTHELIAL CELL INTERACTIONS

Swathi Swaminathan (1), Olivia Ngo (2), Alisa Morss Clyne (1,2)

(1) Mechanical Engineering and Mechanics, Drexel University Philadelphia, PA, USA

(2) School of Biomedical Engineering, Science, and Health Systems, Drexel University Philadelphia, PA, USA

INTRODUCTION

Tumor vasculature is tortuous and hyperpermeable, with increased angiogenesis and inflammation.[1] Blood vessels lined with endothelial cells orchestrate a number of biological processes, most importantly providing the tumor with essential nutrients and oxygen for rapid growth.[2, 3] In the last few decades, the predominant theory has been that tumor progression can be slowed by inhibiting regional angiogenesis and thereby depriving the tumor of essential oxygen and nutrients.[4, 5] However, recent research has shown that increasing blood flow in vivo in the tumor microenvironment through exercise may impede tumor growth and salvage tumor dormancy.[6, 7] Studies have shown that increasing blood flow in tumor vessels reduces abnormalities in microvascular function by normalizing the local angiogenesis and endothelial cell proliferation as well as down-regulating inflammatory processes.[8] It is thus important to understand how blood flow through endothelial cells influence the proliferation of the breast tumors. [9-11]

We hypothesize that increased blood flow to the breast tumor microvasculature normalizes vascular structure and endothelial cell barrier function, which in turn inhibits breast tumor growth. As an initial step in examining this hypothesis, we created a 3D model of endothelial tube – breast spheroid interactions. This was accomplished by allowing the breast cancer cells to form spheroids and the endothelial cells to form tubes on an extra-cellular matrix (ECM). Then, the endothelial tubes were co-cultured with the spheroids.

METHODS

Cell culture

The breast cancer cell line MCF-10A was a generous gift from Dr. Mauricio Reginato (Drexel College of Medicine). MCF10A cells were maintained in DMEM/F12 50/50, 5% horse serum, 20 ng/ml epidermal growth factor (EGF), 500 ng/ml hydrocortisone, 10 ng/ml cholera toxin, 10 μg/ml bovine insulin and 1% penicillin-streptomycin. 3D medium was based on the same recipe without the EGF. Human umbilical vein endothelial cells (HUVEC, Cell Applications) were maintained in EBM-2 (Endothelial Basal Medium) supplemented with 10% fetal bovine serum and EGM-2 Bulletkit. HUVEC medium was changed every two days and cells were used up to passage 12.

3D Breast Cancer Spheroid Formation

60 μL Matrigel (growth factor reduced, Corning) was added to each well of a Falcon 8 chamber polystyrene vessel affixed to a tissue culture treated glass slide and incubated at 37°C for 15-20 minutes to solidify the Matrigel. MCF-10A cells were resuspended in 3D medium with 20% Matrigel and 10 μg/ml EGF at 10,000 cells/ml. 400-450μl of this mixture was added to each chamber well. Medium was replaced every 4 days for the 10-12 days required to obtain hollow spheroids.

Endothelial Tube Formation

Matrigel was prepared as for the MCF-10A cells. 5-10,000 HUVEC were added to each well in EBM-2 (serum and supplements free). Cells were allowed to form tubes overnight (~15 hours).

Co-culturing Spheroids on Endothelial Tubes

Spheroids in 3D medium were carefully pipetted out of their wells and added on to the HUVEC tubes. The co-culture was maintained in 3D medium containing 20% Matrigel and EGF (10 μg/ml) and the interaction between the spheroids and endothelial tubes was observed.

Co-culture Confocal Microscopy

Mono- and co-cultures were fixed with 4% paraformaldehyde, blocked in 10% goat serum + 1:100 F(ab)2 fragment, and then incubated with primary antibodies (1:100) overnight at 4°C. After thorough washing, samples were incubated with secondary antibodies (1:200) for 1 hour in the dark. See Table 1 for primary and secondary antibodies Wells were detached from the slides and sealed with PBS-Glycine and

Copyright 2016 The Organizing Committee for the 2016 Summer Biomechanics, Bioengineering and Biotransport Conference

coverslips. The labelled samples were then imaged using an Olympus FV1000 confocal microscope.

Table 1: Table of Primary and Secondary Abs

LABELLING COMPONENT	PRIMARY AB	SECONDARY AB
Integrin α6 (MCF-10A)	Rat Hu mab CD 49f	Anti- rat Alexa fluor 488
Nuclei (MCF-10A and HUVEC)	N/A	Hoechst
PECAM (HUVEC)	PECAM1 mouse polyclonal	Anti-mouse Alexa Fluor 647

RESULTS

MCF10A cells cultured on matrigel in the 3D medium gave rise to spheroids after 5-6 days. When the spheroids were allowed to grow for 8-10 days, they underwent a series of morphological changes that resulted in acini-like spheroids with a hollow center, similar to the glandular epithelium *in vivo* (Figure 1a.) After overnight incubation on Matrigel, HUVECs formed capillary–like architectures (Figure 1b). After 24 hours of MCF-10A spheroid and HUVEC tube co-culture, most of the spheroids were observed to be associated with HUVEC tubes as indicated by phase contrast and confocal microscopy (Figure 1c). Co-culture phase contrast images after 48 and 72 hours showed the spheroids seeming to merge with some endothelial tubes, although some tubes remained visible under the spheroid layer (Figure 1d).

DISCUSSION

In this study, we showed that endothelial cells, when grown into tube-like structures, can be co-cultured effectively with breast tumor cells over a short period of time. This method proved successful, whereas other techniques did not. When suspended HUVEC were added to spheroids already in Matrigel, the HUVECs did not adhere well and were often rinsed away in the subsequent labeling process. Previous studies of co-culture showed that endothelial cells became apoptotic or destroyed the spheroids when co-cultured.[2, 3] However, this was not the case in our study.

This model provides a promising method for examining endothelial tube interaction with breast cancer spheroids in 3D co-culture. However, we still must determine how the co-culture is best maintained over time. While this model can provide a better understanding of the organizational and functional endothelial cell–breast cancer interactions *in vitro*, the current model cannot account for flow effects. In the future, we will develop a microfluidic version of the endothelial tubes to assess how blood flow rate impacts endothelial cell – breast cancer interactions. This will pave the way to develop novel treatment methods that disrupt the vessel milieu housing these breast cancer cells

ACKNOWLEDGEMENTS

We thank Dr. Reginato for providing us with the breast cancer cell lines and spheroid culture protocols.

REFERENCES

1. Fukumura, D.; Jain, R. K. *Journal of cellular biochemistry* **2007,** 101, (4), 937-49.
2. Zamora, P. O *et al*. *Cancer Res* **1980,** 40, (12), 4631-9.
3. Jahroudi, N.; Greenberger, J. S. *J Neurooncol* **1995,** 23, (2), 99-108.
4. Jain, R. K. *Nat Med* **2001,** 7, (9), 987-989.
5. Saaristo, A *et al*. *Oncogene* **2000,** 19, (53), 6122-6129.
6. Betof, A. S. *et al Journal of the NCI* **2015,** 107, (5).
7. Goh, J. *et al*. *PloS one* **2013,** 8, (11), e80123.
8. Folkman, J. *et al*. *The Journal of experimental medicine* **1971,** 133, (2), 275-88.
9. Ghajar, C. M. *et al Nat Cell Biol* **2013,** 15, (7), 807-17.
10. Kim, J. B. *et al*. *Breast Cancer Res Treat* **2004,** 85, (3), 281-91.
11. Oudar, O. *Crit Rev Oncol Hematol* **2000,** 36, (2-3), 99-106.

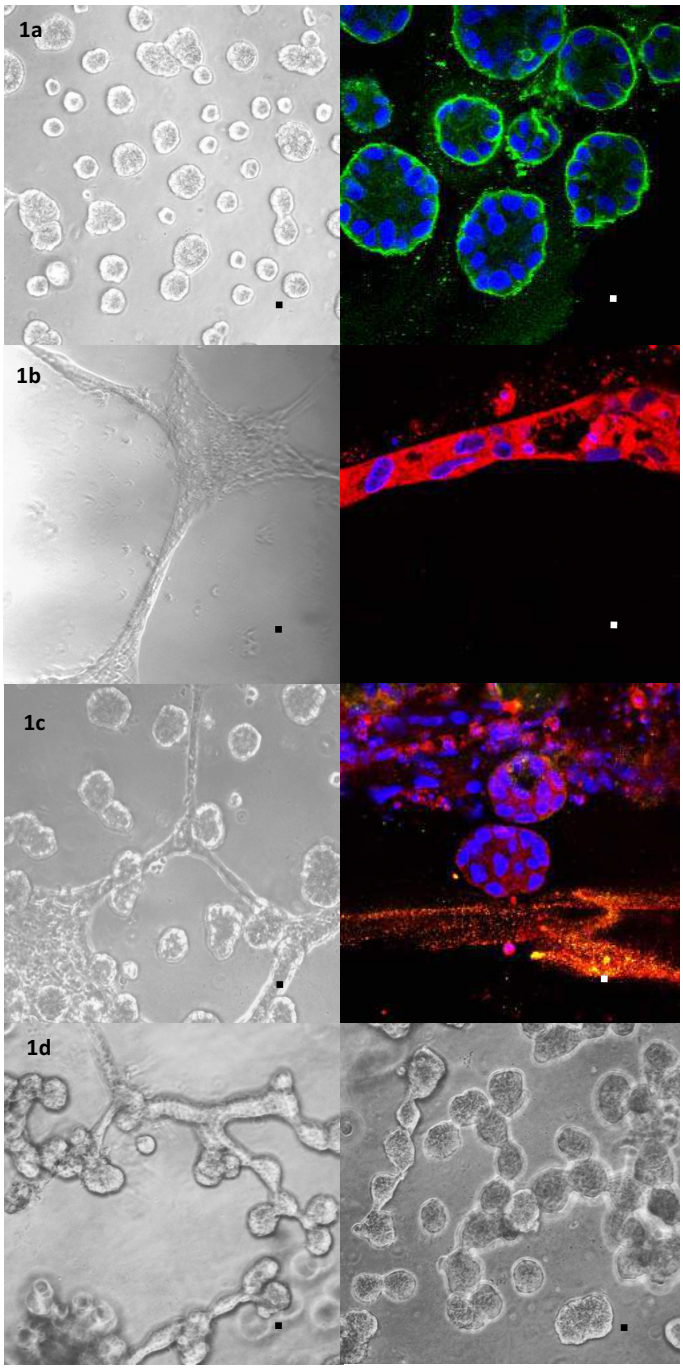

Figure 1. a) Spheroids; b) Endothelial tubes; c) spheroids co-cultured with endothelial tubes after 24h d) co-cultures after 48 h (left) and 72 h (right). Images a-c are by phase contrast (left) and confocal (right) microscopy. PECAM=red, Integrin α6=green and nuclei=blue. Scale Bar: 10 μm.

Copyright 2016 The Organizing Committee for the 2016 Summer Biomechanics, Bioengineering and Biotransport Conference

SB^{3}C2016
Summer Biomechanics, Bioengineering and Biotransport Conference
June 29 –July 2, National Harbor, MD, USA
SB^{3}C2016-793

DIFFERENTIATING STEM CELLS EXHIBIT MOLECULAR AND MICROENVIRONMENTAL HETEROGENEITY AT THE SINGLE CELL LEVEL

Claire M. McLeod (1,2,3), Allison J. Cote (1), Arjun Raj (1), Robert L. Mauck (1,2,3)

(1) Department of Bioengineering
University of Pennsylvania
Philadelphia, PA, USA

(2) Department of Orthopaedic Surgery,
University of Pennsylvania,
Philadelphia, PA 19104, USA

(3) Translational Musculoskeletal Research Center,
Philadelphia VA Medical Center,
Philadelphia, PA, USA.

INTRODUCTION

The extracellular matrix (ECM) of articular cartilage provides mechanical resilience over a lifetime of load-bearing use. However, traumatic injury and degenerative processes compromise these mechanical functions, and damaged joint surfaces often require replacement. Tissue engineered constructs can mimic native cartilage, but their clinical use is complicated by cellular heterogeneity [1]. Such cell-to-cell variation is particularly pronounced in mesenchymal stem cell (MSC) populations: within a single MSC population, cells will undergo chondrogenesis to varying extents and over different timescales.

Despite this acknowledged phenotypic heterogeneity in MSCs, many studies investigating the molecular basis of their chondrogenic phenotype rely on bulk assays that average transcription and protein synthesis over an entire tissue-engineered construct. Single cell techniques now allow us to observe these systems with greater biological resolution and to parse cell-to-cell variation. Here, we employ quantitative single-cell methods to answer two principle questions: does transcriptional variation distinguish strongly chondrogenic cells from weakly chondrogenic cells, and how do temporal dynamics in matrix synthesis contribute to chondrogenic heterogeneity? To address these issues, we used single molecule RNA FISH to measure the absolute abundance of traditional differentiation markers, including the matrix protein aggrecan. We paired this analysis with immunofluorescent quantification of pericellular matrix accumulation, and found that, in this case, mRNA abundance is a poor predictor of protein abundance. Additionally, using a novel method to metabolically label nascent proteins with artificial methionine analogs, we traced the process of early matrix deposition, and found that both MSCs and chondrocytes produce matrix heterogeneously, and that the dynamics of matrix secretion differ by cell type.

METHODS

Cell culture: Juvenile bovine MSCs and chondrocytes were isolated as in [2]. Passage 1 cells were encapsulated in 2% agarose micro-gels (μ-gels, ~400 μm in thickness) at $2x10^6$ cells/mL. These μ-gels were cultured in a chemically defined media containing 10 ng/mL TGFβ-3 for up to 21 days. For studies examining nascent matrix synthesis, a methionine-free media formulation was supplemented with either 50 mM of the methionine analog homopropargylglycine (HPG), or 50 mM methionine as a control. RNA FISH: Single molecule RNA FISH was performed as in [3]. μ-gels were simultaneously stained with DAPI and oligonucleotide probes directed against aggrecan and GAPDH. From images, a custom MATLAB script quantified absolute mRNA expression at the single cell level (n=39-113 cells/condition). Matrix accumulation was simultaneously assessed via immunofluorescent staining for aggrecan core protein (Abcam ab3778). Nascent Protein Visualization: Following fixation, Alexa488-azide was reacted with HPG to label proteins that had incorporated the methionine analog during culture [4]. Nuclei and cell membranes were stained with Hoechst and CellMask Orange respectively. For imaging, individual cells were located via nuclear staining, and confocal sections of the cell mid-plane were captured at 100X (n=20-30 cells/group). For each cell, 20 radial intensity profiles emanating from the cell center were mapped, truncated to include only the extracellular domain, and averaged over each cell. Total matrix intensity was calculated by integrating intensity over distance from the cell membrane. Statistics: To compare single cell RNA counts, we constructed a generalized linear mixed model with a log-link function and by-donor random intercepts. Estimated means were compared using t-distributions with Satterthwaite approximations and simulated

Copyright 2016 The Organizing Committee for the 2016 Summer Biomechanics, Bioengineering and Biotransport Conference

adjustment for multiple comparisons. Matrix radius and total intensity were compared via t-test.

RESULTS

Mean single cell aggrecan mRNA abundance rose sharply in the first day following exposure to TGFβ and remained high for the duration of culture (day 1 vs 21, not shown). MSCs showed striking cell-to-cell variation in mRNA abundance, with aggrecan mRNA copy number per cell spanning three orders of magnitude (10^0 - 10^2, Fig 1A). Cell-to-cell variation in mRNA abundance was also similar between days 1 and 21 of TGFβ exposure (as measured by coefficient of variation, 0.69 vs 0.72). Thus, gene expression heterogeneity neither emerged nor attenuated with differentiation culture. Other differentiation markers including COMP and Sox9 behaved similarly.

Simultaneous RNA FISH and immunofluorescence for aggrecan RNA and the corresponding aggrecan core protein revealed that, at day 7, ~34% of MSCs had accumulated extracellular aggrecan protein (Fig 1B). While these high chondro-potential cells exhibited greater mean aggrecan transcript abundance than their low chondro-potential counterparts, the shift in mean aggrecan RNA number was small (Fig 1C, 1.35 fold change). Due to the poor separation in mRNA abundance distributions between these two groups, aggrecan mRNA copy number was unable to strongly predict the chondro-potential of individual cells.

One possible explanation of this disconnect between transcript and protein abundance in individual cells is that transcription is a stochastic process comprised of long 'silent' periods punctuated by short transcriptional bursts. In contrast, matrix accumulation reflects the integration of a cell's gene expression history. Towards the goal of linking an individual cell's transcriptional history with its protein output, we utilized amino acid tagging to label nascent extracellular matrix proteins [4]. Methionine analogs metabolically labeled intracellular proteins as well as proteins incorporated into the forming ECM (Fig 2A). After one day in HPG media, both chondrocytes and MSCs demonstrated intracellular labeling, but showed little extracellular labeling. During the next 7 days, ECM progressively extended from the cell border and into the extracellular space (Fig 2B-C). By day 7, both cell types had accumulated a metabolically labeled extracellular matrix comprised of discrete fibers (Fig 2D). The chondrocyte matrix was both more extensive (radius=19.8 vs 3.1 μm, $p<0.01$) and more intensely labeled (total intensity= 165 vs 49 a.u., $p<0.01$) than the MSC matrix. To compare the relative variability of the matrix, we computed CV of total matrix intensity. On day 7, MSCs demonstrated greater matrix variability than chondrocytes (MSC CV =1.84, chondrocyte CV=1.24), likely reflecting MSC's characteristic heterogeneity and slower differentiation kinetics. Intriguingly, by day 9, almost all HPG-labeled chondrocytes exhibited a pericellular ring of low HPG intensity immediately adjacent to the cell membrane. This ring co-localized with pericellular staining of aggrecan core protein, and seemed indicative of cells with a maturing cartilage-like matrix (Fig 2E). Strikingly, such a ring was rare amongst MSCs at the same time point, occurring in only ~5% of MSCs.

DISCUSSION

Here, quantitative single cell analysis of gene expression provided evidence that mRNA abundance of the chondrogenic marker aggrecan is only weakly linked to aggrecan protein expression and the chondrogenic phenotype of an MSC. These cells showed high transcriptional heterogeneity that failed to attenuate with prolonged differentiation. Interestingly, this transcriptional variability was unable to predict the heterogeneity observed in matrix accumulation; that is, cells expressing high elvels of aggrecan mRNA did not necessarily produce the most matrix. Nascent protein labeling via HPG incorporation into methionine-containing proteins (e.g. Col2, aggrecan) confirmed that matrix accumulation varied between cells in both MSC and chondrocyte populations. These results were also consistent with the expectation that ECM accumulates with culture time, and that MSCs and chondrocytes differ in their trajectory and rate of matrix accumulation. Future studies will pair RNA FISH and nascent matrix labeling to more directly link transcriptional abundance with protein deposition into the pericellular space, and may indicate that while instantaneous gene expression does not correlate with total protein accumulation, it can predict short-term matrix production.

ACKNOWLEDGEMENTS

This work was supported by the NIH (New Innovator 1DP2OD008514, R01 EB008722, R01 EB02425) and the NSF (DGE-0822).

REFERENCES

[1] Phinney+ J. Cell Biochem, 113:2806-2812, 2012.
[2] Farrell+ *J Biomech,* 1:134-42, 2015.
[3] Raj+ *Nat Methods*, 5:877-879, 2008.
[4] Dieck+ *Curr Protoc Cell Biol*, 7: Unit7.11, 2012.

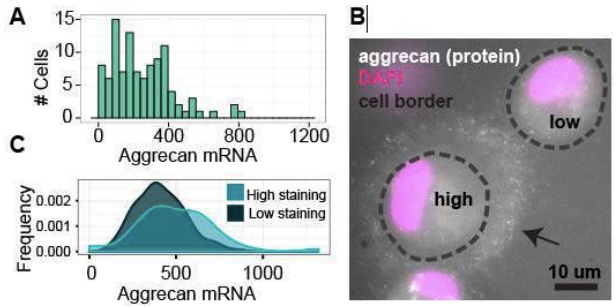

Figure 1: A) MSCs express aggrecan and other mRNAs heterogeneously. B) MSCs with high and low chondro-potential are identified by differences in extracellular aggrecan core protein accumulation. C) Aggrecan mRNA abundance does not robustly separate high from low chondro-potential cells.

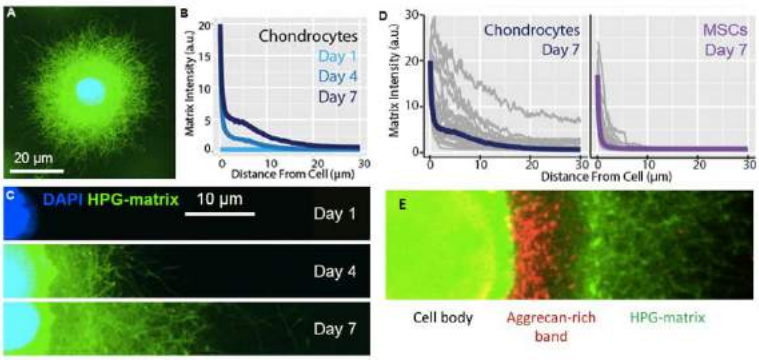

Figure 2: Metabolic labeling of ECM. A) Day 7 chondrocyte labeled with HPG. B) Radial profiles and C) morphology of chondrocyte ECM with time. D) Individual (grey) & average (blue/purple) profiles. E) Day 9 chondrocyte surrounded by an aggrecan-rich band within the HPG-labeled matrix.

Copyright 2016 The Organizing Committee for the 2016 Summer Biomechanics, Bioengineering and Biotransport Conference

SB^{3}C2016
Summer Biomechanics, Bioengineering and Biotransport Conference
June 29 –July 2, National Harbor, MD, USA
SB^{3}C2016-794

MICROFLUIDICS FOR THE STUDY OF OXYGEN GRADIENTS AT THE MATERNAL FETAL INTERFACE

Yassen Abbas (1,2), Carolin Oefner (2,3), Graham J. Burton (2,4), Ashley Moffett (2,3), Michelle L. Oyen (1,2)

(1) Department of Engineering
University of Cambridge
Cambridge, UK

(2) Centre for Trophoblast Research
University of Cambridge
Cambridge, UK

(3) Department of Pathology
University of Cambridge
Cambridge, UK

(4) Department of Physiology,
Development and Neuroscience
University of Cambridge
Cambridge, UK

INTRODUCTION

Pregnancy disorders such as pre-eclampsia, Intrauterine Growth Restriction (IUGR) and recurrent miscarriage are detrimental to the health of women and their offspring. Regardless of the underlying mechanisms of these diseases, the common histological observations point to abnormalities in the development of the placenta, characterized by inadequate trophoblast invasion and incomplete remodeling of the spiral arteries. The trophoblast is the unique cell type of the placenta and it invades and remodels the maternal spiral arteries to form highly dilated vessels that reduce maternal blood flow resistance and increase uteroplacental perfusion to meet the requirements of the developing fetus. When invasion is inadequate arteries remain, narrow at the opening into the intervillous space and result in disturbed blood flow patterns. This leads to reduced growth of the branches of the placental villous tress and reduced uteroplacental blood flow.

A large variety of factors are thought to influence the migratory behavior of trophoblasts. There is evidence that oxygen mediates trophoblast invasion, although this evidence is conflicting with claims that hypoxia both stimulates [1] and inhibits trophoblast invasion [2]. The disagreement in literature may be due to the different cell types, oxygen concentrations and whether the culture medium was supplemented with growth factors or not. Furthermore, these studies were conducted in static cultures in a single oxygen environment which is one of the limitations of the current *in vitro* models used to study the role of oxygen in placental biology.

In this work, the aim is to create a microfluidic cell invasion assay with a dynamic oxygen gradient to study the migration and invasion of primary human trophoblast cells. We demonstrate the working principle of this device with primary trophoblasts under a chemical gradient of Granulocyte Macrophage Colony-Stimulating Factor (GM-CSF). GM-CSF is a cytokine secreted by uternine Natural Killer (uNK) cells and is known to promote trophoblast migration [3]. We describe how the device is adapted to be representative of the oxygen tension at the maternal fetal interface. From <20 mm Hg at the placental villi (fetal) to approximately 60-80 mm Hg at the decidua (maternal) in the first trimester of pregnancy (Figure 1a). The device used for this study is made up of three channels - a central channel for cell culture and two side channels for cell medium delivery [4] and chemical and oxygen gradient generation (Figure 1b). The device will be used to determine if hypoxia (or low oxygen concentration) inhibits or stimulates trophoblast invasion.

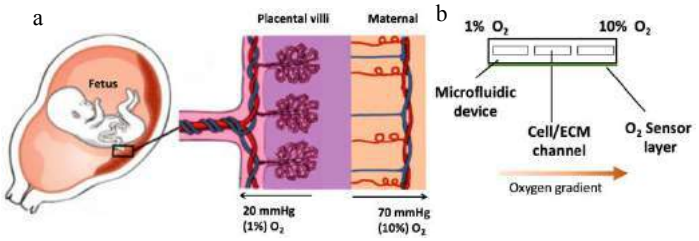

Figure 1: The oxygen gradient in (a) the first trimester of pregnancy and (b) in the microfluidic device.

METHODS

The design of the device is imprinted onto a silicon wafer using soft lithography which acts as a mold to manufacture the device using polydimethylsiloxane (PDMS) [4]. Primary trophoblast cells are encapsulated in matrigel extracellular matrix (ECM) protein and loaded into the central channel of the device 24 hrs before the beginning of the invasion assay. The cells are isolated from first trimester placental and

Copyright 2016 The Organizing Committee for the 2016 Summer Biomechanics, Bioengineering and Biotransport Conference

decidual samples taken from routine terminations of pregnancy (6-12 weeks) and tagged with a fluorescently labelled cell tracker. Cell migration is tracked using a LSM700 confocal laser scanning microscope (Zeiss, Oberkochen, Germany) over 12 hrs. Z-stacks of multiple positions are taken and the images are processed using the imaging software Fiji and the built-in plugin TrackMate. Data is generated on the the speed and directionality of cell movement.

For GM-CSF gradient generation, 10 ng/mL was added to cell medium in one channel with no GM-CSF in the other medium channel. To generate an oxygen gradient cell medium is preequlibriated in nitrogen gas in a specially made gas tight vessel coiled with gas permeable tubing. The dissolved concentration of oxygen entering the device is set by the flow rate of liquid through the system which controls the gas diffusion time. The gradient is validated using optical oxygen sensors (Presens, Regensburg, Germany) which records the oxygen concentration at the inlet and outlet of each channel. In addition, a thin film oxygen sensor is fabricated from the oxygen sensitive dye platinum(II) meso-tetrakis(penta uorophenyl)porphyrin (PtTFPP) and bonded to the base of the device. The sensor allows real-time visualization of the gradient by imaging using a fluorescent microscope.

RESULTS

Primary trophoblasts cells were found to migrate towards an increasing concentration of GM-CSF. The direction of cell movement is obtained by analyzing the cell tracks generated by TrackMate. A polar histogram is generated giving the number of cells (inner radial axis) and direction (outer radial axis). The polar histogram for primary trophoblasts cultured with a gradient of GM-CSF and without is shown in Figure 2a and Figure 2b respectively.

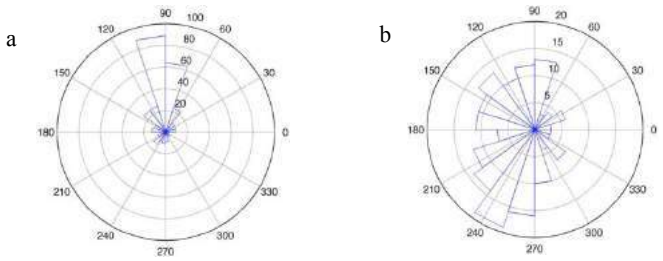

Figure 2: Polar histograms of primary trophoblasts show directed migration under (a) a gradient of GM-CSF compared to random movement with (b) no gradient. Note: difference in inner radial axis scale between (a) and (b).

Generation of an oxygen gradient along the device is confirmed visually using the thin film oxygen sensor (Figure 3a) and by taking an intensity profile along the width of the image (Figure 3b).

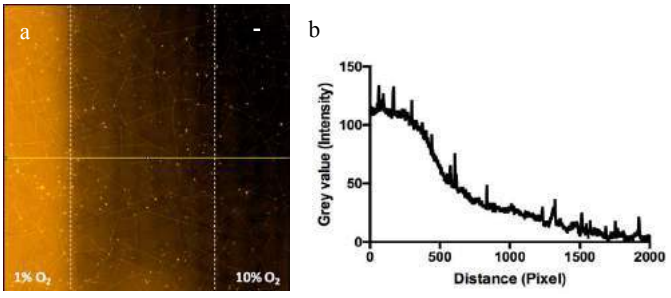

Figure 3: Confirmation of an oxygen gradient generated (a) visually and (b) its subsequent intensity profile. Scale bar: 200 µm.

The oxygen concentration entering and exiting each channel is easily controlled by adjusting the flow rate of liquid (Figure 4). There was no difference between using a syringe pump and operating the flow in a closed loop using a peristaltic pump. As PDMS is gas permeable oxygen readily defuses into the device resulting in higher oxygen concentrations measured at the outlet. An oxygen gradient therefore exists along the device as well as across the device and this gradient was found to be dependent on the flow rate of liquid through the system. This provides a greater range of oxygen gradients which can be studied in a single device.

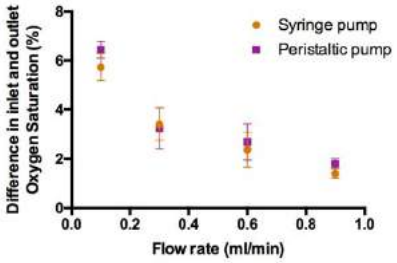

Figure 4: Oxygen concentration at the inlet and outlet of each channel is proportional to the flow rate of liquid.

DISCUSSION

Insufficient trophoblast migration and remodeling of the uterine spiral arteries is associated with poor placental development and outcomes in pregnancy. Methods to study trophoblast migration have mainly used trophoblast cell lines and simple 2D assays. Here, we present a microfluidic device to study primary trophoblast motility in a physiologically relevant microenvironment and in real time. We show that under a chemical gradient of GM-CSF primary trophoblasts migrate towards increasing concentrations of the cytokine when compared to the control. GM-CSF is one of the large variety of factors which are thought to influence trophoblast migratory behavior. Another is oxygen, for which there is inconclusive evidence on its importance on whether hypoxia (physiologically low oxygen) stimulates or inhibits trophoblast migration. Despite a dynamic oxygen gradient between the placental bed and the maternal decidua most *in vitro* studies use single oxygen concentrations, static cultures and assays used are 2D. Here, a microfluidic device is used to recreate the oxygen gradient at the maternal/fetal interface. The gradient demonstrated is dynamic which avoids stratification of oxygen within unstirred medium as in traditional well plate assays. A thin film oxygen sensor allows real time validation of the oxygen gradient using a fluorescent microscope. The oxygen concentration at the cell-medium interface can be determined using the Stern-Volmer relationship. Experiments with primary trophoblast cells under a dynamic gradient of oxygen are ongoing.

ACKNOWLEDGEMENTS

This study was funded by the EPSRC.

REFERENCES

[1] Graham, C. H et al., *Placenta*, 21:443-450, 2000.

[2] Caniggia, I. & Winter, J. L. *Placenta*, 21Suppl A: S25-S30, 2000.

[3] Xiong, S et al., *J Clin Invest*, 123: 4264-4272, 2013.

[4] Zervantonakis, K et al., *PNAS,* 109: 13515-13520.

Copyright 2016 The Organizing Committee for the 2016 Summer Biomechanics, Bioengineering and Biotransport Conference

SB³C2016
Summer Biomechanics, Bioengineering and Biotransport Conference
June 29 –July 2, National Harbor, MD, USA
SB³C2016-795

EVALUATION OF THE BIODENT REFERENCE POINT INDENTATION (RPI) PLATFORM TO MEASURE THE ELASTIC MODULUS IN MOUSE BONES

Mark T. Begonia (1), Mark Dallas (2), Sravan K. Kola (1), Nuria Lara-Castillo (2), Vladimir Dusevich (2), Mark L. Johnson (2), Ganesh Thiagarajan (1)

(1) Department of Civil and Mechanical Engineering
University of Missouri-Kansas City
Kansas City, MO, USA

(2) Department of Oral and Craniofacial Sciences
University of Missouri-Kansas City
Kansas City, MO, USA

INTRODUCTION

Elastic modulus (i.e. Young's modulus) is a parameter used to characterize a b one's ability to deform without experiencing permanent damage. Three-point bending is the traditional method used to measure the elastic modulus in mouse bones. However, three-point bending is a destructive technique and thus cannot be used for *in vivo* longitudinal studies to examine bone quality in mice. Another technique known as reference point indentation (RPI) has emerged recently due to its ability to measure localized bone properties in a non-destructive manner [1].

In this study, we developed a technique to determine the elastic modulus using RPI data collected from the BioDent™ testing platform [2]. We analyzed multiple groups of mouse bones to: (1) assess the sensitivity of the BioDent™ to various factors such as genotype, gender, and age and (2) compare elastic moduli obtained from three-point bending versus RPI testing. This work will contribute toward developing an *in vivo* experimental approach to study bone quality in mouse models of aging as well as developing finite element (FE) models that incorporate the heterogeneous properties of bone.

METHODS

BioDent™ studies were conducted on three different sets of mouse bones. The first study analyzed ulnas that were harvested from 6-month old female TOPGAL mice. These mice were maintained in our colony on a mixed C57Bl/6 x CD1 background and served as a reporter for the β-catenin signaling pathway. Scanning electron microscopy (SEM) was also performed on the ulnas to assess surface defects created by each indentation. The second study was conducted on femurs collected from 4-5 month old β-catenin heterozygous conditional knockout (HETcKO) mice and their littermate controls. The third study examined both gender and age effects in femurs that were collected from C57Bl/6 mice [3] at 6, 12, and 22 months.

RPI tests were conducted on polymethyl methacrylate (PMMA) before and after they were performed on m ouse bones to ensure the quality and stability of the test probe. D uring RPI testing of bones, each sample was secured onto a custom stage and submerged in PBS while a dissection microscope was used to position the reference probe over each indentation site. Multiple sites were selected on the shaft of each bone to investigate regional differences in mechanical properties. For each indentation, a 2 N load was applied for one cycle. Only one cycle was applied because single indentations are sufficient to obtain the elastic modulus [4,5] and because 80-90% of the Total Indentation Distance (TID) can be attained in the first indentation cycle [7].

The elastic modulus was calculated from RPI measurements using two different methods: (1) Oliver-Pharr and (2) Geometric. The Oliver-Pharr (O/P) method was developed by W.C. Oliver and G.M. Pharr to determine the elastic modulus of a material using data from a single cycle. T he accuracy of the elastic modulus depends on the maximum load, maximum displacement, and elastic unloading stiffness (i.e. contact stiffness) [7]. Th e Geometric method is similar to the O/P method but utilizes different values for the area and area function. We also determined the elastic modulus of bones by using a biomechanical analysis procedure that employed three-point bending, microCT, and ImageJ [3]. T he objective was to validate the RPI methodology by comparing the elastic moduli with those obtained from the widely accepted three-point bending method.

RESULTS

Table 1 summarizes the elastic moduli obtained from the TOPGAL ulna based on the location of the indentation site as well as the BioDent™ analysis method employed. RPI testing captured

Copyright 2016 The Organizing Committee for the 2016 Summer Biomechanics, Bioengineering and Biotransport Conference

regional differences on the ulna surface as evidenced by higher elastic moduli for the midshaft compared to either the distal or proximal locations. In addition, the O/P method reported higher elastic moduli at the proximal (9%), midshaft (12%), and distal (10%) indentation sites when compared to the Geometric method.

Table 1: Elastic Moduli Obtained through Both BioDent™ Analysis Methods in the TOPGAL Ulna.

Indentation Site	O/P Method (GPa)	Geometric Method (GPa)
Proximal Ulna	4.66	4.24
Ulna Midshaft	5.71	5.08
Distal Ulna	4.97	4.51

Figure 1 shows SEM micrographs from the surface of the TOPGAL mouse ulna at (A) 100x and (B) at 1000x after applying a 2 N load for 1 cycle. The indentation site (indicated by red arrow) was positioned centrally along the longitudinal axis of the ulna. The corresponding microcracks were approximately 25-30 μm wide. Figure 2 shows the elastic moduli for the femurs of (A) HETcKO mice and (B) their littermate controls. C omparisons are also shown according to gender and the BioDent™ analysis method applied. Statistical analysis [8] using one-way analysis of variance (ANOVA) and Tukey HSD test for post-hoc comparisons indicated that there were no s ignificant differences in the elastic moduli obtained from three-point bending versus RPI testing.

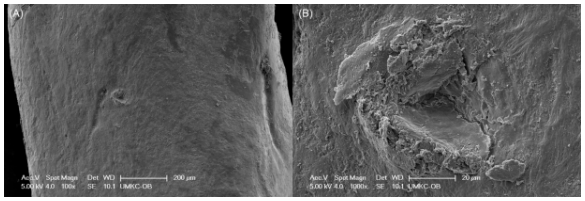

Figure 1: SEM micrographs showing an indentation site and microcracks at (A) 100x and (B) 1000x on the TOPGAL ulna.

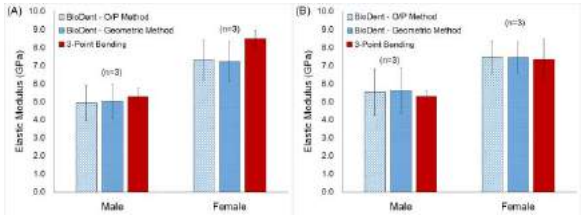

Figure 2: Femur analysis of (A) HETcKO mice and (B) their littermate controls revealed no significant differences in the elastic moduli regardless of the BioDent™ analysis technique used.

Figure 3 shows the elastic moduli for the femurs of (A) male and (B) female C57Bl/6 mice at three different ages. For all age groups, two-way ANOVA revealed that there was no significant difference between the elastic moduli obtained from the O/P and Geometric methods. RPI also exhibited a generally higher variability compared to three-point bending data. In addition, gender based differences in three-point bending data were only found at 6-months (i.e. females with 53% higher elastic modulus than males). However, neither the O/P nor the Geometric method was sensitive to gender based differences in the elastic modulus for all age groups.

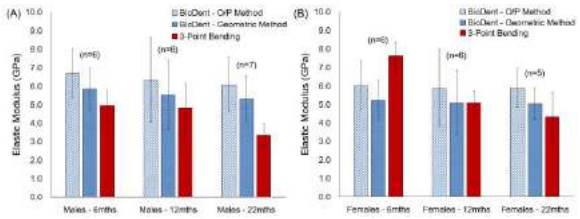

Figure 3: Comparison of elastic moduli obtained from three-point bending and RPI tests of (A) male and (B) female C57Bl/6 femurs.

DISCUSSION

The microcracks observed via SEM on the surface of the TOPGAL mouse ulna (Fig. 1) were also found in previous studies [6,9]. More importantly, RPI testing on the TOPGAL mouse ulna also demonstrated the ability of the BioDent™ to capture localized bone properties (Table 1). Although these findings correspond to *ex vivo* experiments, they are nonetheless encouraging for researchers who may be investigating the applicability of the BioDent™ for mouse bones as small as the ulna.

Elastic moduli measured using the Oliver-Pharr and Geometric methods were not significantly different from those measured by traditional three-point bending (Fig. 2). This finding indicates that the non-destructive RPI technique is equally effective at determining the elastic modulus as the widely established yet destructive three-point bending procedure. Furthermore, these results highlight the potential use of the femur rather than the ulna for *in vivo* assessments of bone quality since the femur possesses a naturally larger surface area and thickness compared to the ulna. However, RPI testing must also be performed on femurs with soft tissue intact to assess the effectiveness of the BioDent™ platform under *in vivo* conditions.

For the C57Bl/6 femurs, both the O/P and Geometric methods produced elastic moduli with higher variability compared to the elastic moduli obtained from three-point bending. The main reason for these differences is most likely due to the inclusion of RPI measurements collected from multiple femur sites to calculate the elastic moduli. As shown in Table 1, RPI testing can already detect regional differences in mouse bones the size of the ulna. Therefore, it is reasonable that larger mouse bones such as the femur would also produce higher variations in the localized bone properties. Conventional three-point bending may be more sensitive to gender and age based differences in the elastic modulus for the C57Bl/6 femur. However, this work shows that a n on-destructive technique for measuring the elastic modulus is achievable for certain mouse bones.

ACKNOWLEDGEMENTS

This work was funded by a grant from the National Institutes of Health – NIA P01 AG039355 (LF Bonewald-PI) and NIAMS R01 AR053949 (ML Johnson – PI).

REFERENCES

[1] Allen, MR et al., *J Bone Miner Res*, 30(9):1539-1550, 2015.
[2] ActiveLife Scientific, Inc., Santa Barbra, CA
[3] National Institutes of Health, Bethesda, MD.
[4] Thurner, PJ, *Wiley Interdiscip Rev Nanomed Nanobiotechnol*, 1(6):624-649, 2009.
[5] Zysset, PK, *Osteoporos Int* 20(6):1049-1055, 2009.
[6] Beutel, BG and Kennedy, OD, *Bone* 75:1-7, 2015.
[7] Oliver, WC and Pharr, GM, *J Mater Res*, 7:1564, 1992.
[8] IBM SPSS Inc., Chicago, IL.
[9] Yassen, GH et al., *Eur J Dent* 8:521-527, 2014.

Copyright 2016 The Organizing Committee for the 2016 Summer Biomechanics, Bioengineering and Biotransport Conference

SB^{3}C2016
Summer Biomechanics, Bioengineering and Biotransport Conference
June 29 –July 2, National Harbor, MD, USA
SB^{3}C2016-796

IOP-INDUCED STRAINS IN THE OPTIC NERVE HEAD USING ULTRASOUND SPECKLE TRACKING

Elias Pavlatos (1), Xueliang Pan (1,2), Richard T. Hart (1), Paul A. Weber (3), Jun Liu (1,3)

(1) Department of Biomedical Engineering
The Ohio State University
Columbus, OH, USA

(2) Center for Biostatistics
The Ohio State University
Columbus, OH, USA

(3) Department of Ophthalmology
The Ohio State University
Columbus, OH, USA

INTRODUCTION

Glaucoma is an ocular disease that is associated with irreversible optic nerve damage and loss of vision. Evidence has shown that glaucomatous optic nerve damage initiates within the optic nerve head (ONH) [1], where the retinal ganglion cell axons exit the back of the eye en route to the brain. The stresses and strains within the ONH resulting from the intraocular pressure (IOP) are thought to play an important role in axonal health and disease. However, the exact mechanism by which mechanical insult can lead to optic nerve damage remains largely unknown.

Many studies have investigated the mechanical response of the posterior sclera during increases in IOP. Recently, there has been an increased effort to directly measure the mechanical response of the ONH to IOP elevation. Deformation within the ONH has been measured using various techniques including confocal microscopy [2], optical coherence tomography (OCT) [3], micro-computed tomography (μCT) [4], and second harmonic generated (SHG) imaging [5, 6]. Such studies have focused mainly on the lamina cribrosa (LC), a mesh-like matrix of collagen fibers through which axons pass through the scleral canal. It is hypothesized that high levels of strain experienced by ONH tissues such as the LC can damage the traversing nerve fibers, impair blood flow, and lead to optic nerve pathology.

Our laboratory has previously used a high-resolution ultrasound speckle tracking method to measure strains within the sclera and cornea [7]. In this study, the technique was used to measure strains within the ONH during increases in IOP. The goal of the study was to map the mechanical response of a transverse ONH cross-section to IOP elevation. We also evaluated the correlation between strain behavior and tissue morphology using histological analyses. Better understanding the IOP-induced strains within the ONH may provide insight into the potential biomechanical mechanisms of glaucomatous optic nerve damage.

METHODS

Thirteen porcine globes and one globe from a human donor (75 years old, Caucasian, male) were tested within 72 hours postmortem. The optic nerve was trimmed to the outer surface of the peripapillary sclera. The anterior portion of the globe was removed using a 7.5 mm trephine. The globe was mounted on a customized pressurization chamber and immersed in 0.9% saline. The chamber was connected to a programmable syringe pump (PHD Ultra, Harvard Apparatus) and a pressure sensor (P75, Harvard Apparatus) to continuously control and monitor IOP.

Each globe was preconditioned using twenty pressure cycles from 5 to 30 mmHg followed by an equilibration period of 30 minutes at 5 mmHg. Inflation testing was then performed by increasing IOP from 5 to 30 mmHg, with 0.5 mmHg pressure steps every 15 seconds. During inflation, a 55 MHz ultrasound probe (Vevo 660, VisualSonics Inc.) was positioned to acquire images along the nasal-temporal meridian of the ONH. At each pressure level, 2D cross-sections of radiofrequency data were obtained. The IOP and data acquisition were controlled using a customized LabView interface (National Instruments).

The acquired RF data was analyzed using a 2D ultrasound speckle tracking algorithm [7]. A grid of points was defined throughout the tissue cross-section, and displacement vectors were calculated for each point during inflation. Least squares strain estimation and coordinate transformation methods were used to calculate through-thickness and in-plane strains.

Histological analyses were performed for the human donor globe and three of the tested porcine globes. All eyes were immersed in a 10% formalin solution for 24 hours prior to histological processing.

Copyright 2016 The Organizing Committee for the 2016 Summer Biomechanics, Bioengineering and Biotransport Conference

The human globe was fixed at an IOP of 15 mmHg, and the three porcine globes were fixed at 5, 15, and 30 mmHg. A tissue section was prepared from each eye along the nasal-temporal meridian, corresponding to the cross-section imaged using ultrasound. The sections were stained using haemotoxylin and eosin staining. The histology images were compared to strain maps to assess the large-scale correspondence between tissue structures and the strain response within the ONH.

RESULTS

Strain maps in the scanned cross-section were obtained at each pressure level for each eye. To quantify the strain magnitudes, the through-thickness and in-plane strains were averaged over the entire ONH cross-section for each eye. At 30 mmHg, the porcine ONH exhibited an overall through-thickness compressive strain of -0.053 ± 0.015 and an in-plane tensile strain of 0.018 ± 0.008 (n=13). The human ONH strains were lower in magnitude compared to the average strains in the porcine eyes, with through-thickness and in-plane strains of -0.012 and 0.006 respectively.

The ONH cross-section was further split into two equal thickness layers to compare the mechanical response of the anterior and posterior regions of the ONH (Figure 1). In the porcine globes, the through-thickness compressive strains at 30 mmHg were approximately 4.4 times larger in the anterior layer compared to the posterior layer (-0.088 ± 0.019 vs. -0.020 ± 0.011, $p<0.001$). The in-plane tensile strains were slightly but significantly higher in the posterior layer (0.015 ± 0.011 vs. 0.021 ± 0.007, $p=0.025$), where substantial strain heterogeneity was also present. Similar trends were found at 15 mmHg. In agreement with the measurements in porcine eyes, larger through-thickness compressive strains were also observed in the anterior human ONH.

A histological section for a porcine eye fixed at 30 mmHg showed a layer of prelaminar neural tissue at the anterior ONH, with a visible LC layer situated between the prelaminar and retrolaminar neural tissue (Figure 2).

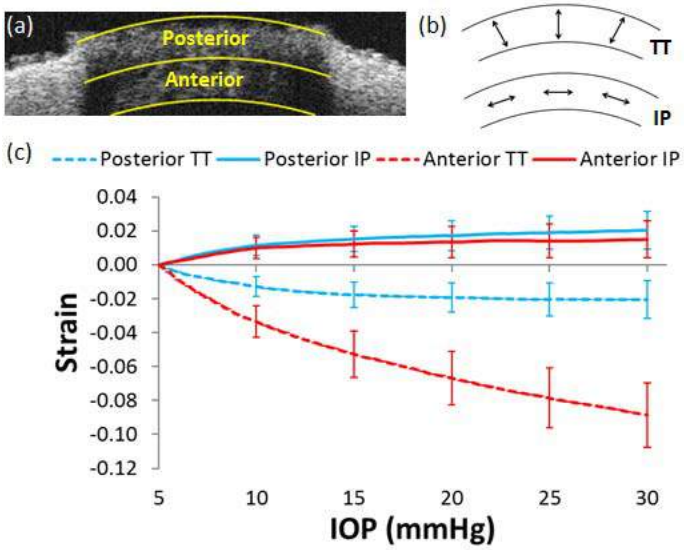

Figure 1: (a) An ultrasound cross-sectional image of a porcine ONH divided into two equal thickness layers, (b) the through-thickness (TT) and in-plane (IP) directions, and (c) the average TT and IP strains in the anterior and posterior layers of porcine ONH (n=13, error bar: standard deviation).

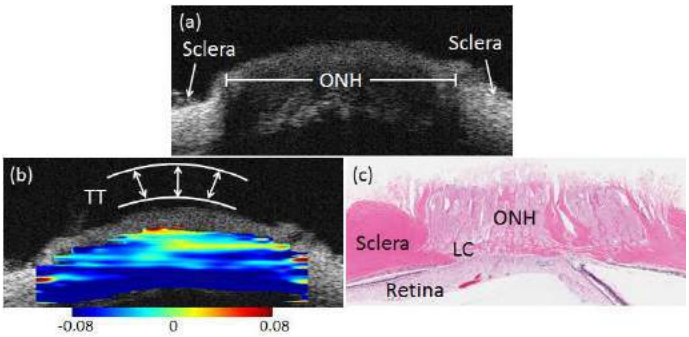

Figure 2: (a) An ultrasound image, (b) a map of through-thickness strain, and (c) a histology image of a representative porcine ONH at 30 mmHg. The region of large through-thickness compression appears to correspond to the prelaminar neural tissue.

DISCUSSION

The strain measurements presented in this study showed the expected through-thickness compression and in-plane tension in the ONH tissue during IOP elevation. A substantially larger through-thickness compressive strain was observed in the anterior ONH, showing a marked difference in the mechanical responses comparing the anterior and posterior ONH.

Histological analyses indicated a potential correspondence between the strain response and anatomical structures. Based on a comparison of the strain map and the histology image from the same eye (Figure 2), it appeared that the largest compression was in the region of the prelaminar neural tissue, whose in-plane stretch was moderate (Figure 1c, red curves). This experimental data provides support to the notion that prelaminar neural compression may play an important role in the onset of glaucoma, resulting in IOP-related axonal transport blockage and neural damage [8]. The mechanical deformation of the LC and retrolaminar neural tissue during inflation appeared to be more heterogeneous and smaller in magnitude than that of the prelaminar neural tissue. Others have also reported considerable strain heterogeneity within the trabecular beams of the LC in response to elevated IOP [5].

The current study was limited to 2D measurements of ONH strain. Future work will extend the strain measurements to 3D to obtain a more complete characterization of ONH deformation, including the measurement of principal and shear strains. The direct measurement of deformation within the ONH tissue volume in its physiological configuration will provide a better delineation of the in vivo mechanical loading and insult experienced by ONH structures and cells during IOP elevations, and help us better understand the mechanical pathways of glaucomatous neural damage.

ACKNOWLEDGEMENTS

NIH Grant R01EY020929

REFERENCES

[1] Nickells, RW et al., *Annu Rev Neurosci*, 35:153-79, 2012.
[2] Albon, J et al., *Br J Ophthalmol*, 84(3):318-23, 2000.
[3] Girard, M et al., *ASME Proc*, 423-4, 2012.
[4] Coudrillier, B et al., *Invest Ophthalmol Vis Sci*, 56(7):6149, 2015.
[5] Sigal, I et al., *Invest Ophthalmol Vis Sci*, 55:1-15, 2014.
[6] Midgett, D et al., *Invest Ophthalmol Vis Sci*, 56(7):6145, 2015.
[7] Tang, J et al., *J Biomech Eng*, 134(9):091007, 2012.
[8] Quigley, H et al., *Invest Ophthalmol Vis Sci*, 19(5):505-17, 1980.

Copyright 2016 The Organizing Committee for the 2016 Summer Biomechanics, Bioengineering and Biotransport Conference

SB³C2016
Summer Biomechanics, Bioengineering and Biotransport Conference
June 29 –July 2, National Harbor, MD, USA
SB³C2016-797

STRAIN DETERMINATION IN THE OSTEOCYTE LACUNAE USING FINITE ELEMENT ANALYSIS

Sravan K. Kola (1), Mark T. Begonia (1), LeAnn M. Tiede-Lewis (2), Sarah L Dallas (2), Mark L. Johnson (2), Ganesh Thiagarajan (1)

(1) Department of Civil and Mechanical Engineering
University of Missouri-Kansas City
Kansas City, MO, USA

(2) Department of Oral and Craniofacial Sciences
University of Missouri-Kansas City
Kansas City, MO, USA

INTRODUCTION

Osteoporosis is an age-related disease characterized by low bone mass, which leads to a compromised skeletal structure and increased risk of fracture. This disease causes more than 8.9 million fractures worldwide each year with an osteoporotic fracture occurring every 3 seconds [1]. Bone is a dynamic organ that adapts its composition and structural properties in response to its loading environment [2, 3]. Therefore, researchers have sought to better understand both the mechanical and biological mechanisms of increased bone formation to treat osteoporosis [4]. Osteocytes, which constitute the majority of bone cells and are located within the mineralized bone matrix, have been postulated to be the primary mechanosensory cells in bone [5, 6] and would be suitable cellular targets for drug therapies or individualized exercise regimens. However, the precise mechanism in which osteocytes convert mechanical stimuli into biological signals (i.e. mechanotransduction) is not fully understood.

In this study, we developed a 2-D finite element (FE) model to examine the strain response in the osteocyte lacunae and perilacunar regions. We analyzed the variations in lacunar strain based on the perilacunar modulus as well as the osteocyte position and orientation. A 3-D microscale FE model was then developed to analyze lacunar strains in realistic osteocyte geometries rather than idealized ellipsoids. This work is part of a multiscale FE modeling approach that will be used to determine if heterogeneous osteocyte activation corresponds to a minimum strain threshold required to initiate mechanotransduction.

METHODS

FEBio Software Suite [7] was used to create a 2 -D model consisting of the bone matrix, osteocyte lacunae, and perilacunar region. A sinusoidal load was applied to the top surface of the model and a fixed boundary condition was assigned to the bottom surface. As shown in Fig. 1A, six osteocytes were created with two osteocytes oriented horizontally (H1 and H2), two oriented vertically (V1 and V2), and two oriented diagonally (D1 and D2). Strains were analyzed in the three osteocyte subregions as a function of the perilacunar modulus: inner lacunae (Fig. 1B), outer lacunae (Fig. 1C), and perilacunar region (Fig. 1D). Strain ratios were also calculated to compare the maximum strains in the osteocyte subregions to the global strain in the surrounding bone.

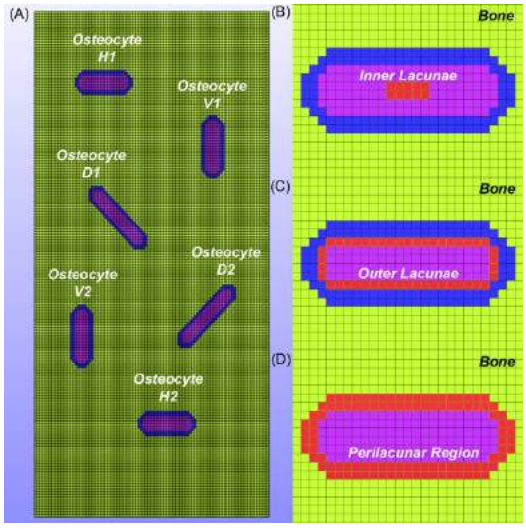

Figure 1: (A) 2-D FE model showing each osteocyte and the (B) inner lacunae, (C) outer lacunae, and (D) perilacunar region.

Copyright 2016 The Organizing Committee for the 2016 Summer Biomechanics, Bioengineering and Biotransport Conference

The 3-D model was developed by importing confocal microscope image stacks of osteocytes into Mimics® Innovation Suite [8] to generate a volume mesh composed of 10-node tetrahedral elements. A sinusoidal load was applied to the top surface of the model and a fixed boundary condition was assigned to the bottom surface. The 3-D model contained seventeen osteocytes of various sizes (Fig. 2A). Strain ratios (i.e. lacunae/bone) were calculated for each osteocyte shown in Fig. 2B.

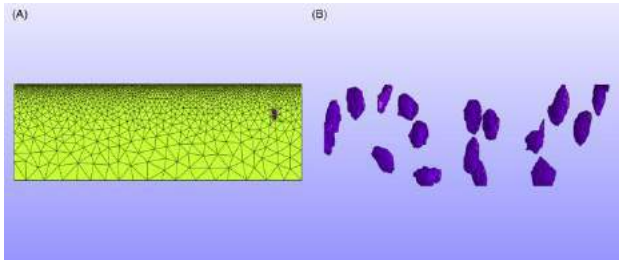

Figure 2: (A) Front view of 3-D FE model with a single osteocyte selected. (B) 3-D FE model showing only the osteocytes analyzed.

RESULTS

Strain ratios of the inner lacunae, outer lacunae, and perilacunar region to the bone matrix are summarized in Tables 1, 2, and 3, respectively. For each osteocyte and their three subregions, the strain ratios decreased as the perilacunar modulus increased. Differences in position also led to lower strain ratios in Ocy H2 compared to Ocy H1 and in Ocy V2 compared to Ocy V1. Conversely, the increased distance from the applied load produced higher strain ratios in Ocy D2 compared to Ocy D1. Finally, osteocyte orientation (e.g. Ocy H1 versus Ocy V1) was found to decrease strains in the inner (~18%) and outer (~24%) lacunae but not the perilacunar tissue.

Table 1: Ratios of Maximum Inner Lacunae Strain to Global Bone Strain (2000 με) for each Osteocyte (Ocy).

Perilacunar Modulus	Ocy H1	Ocy H2	Ocy V1	Ocy V2	Ocy D1	Ocy D2
5 GPa	10.31	9.25	1.92	1.70	9.98	10.86
10 GPa	9.77	8.86	1.80	1.60	9.39	10.16
15 GPa	9.35	8.56	1.69	1.51	8.94	9.64
20 GPa	9.02	8.31	1.59	1.43	8.57	9.21

Table 2: Ratios of Maximum Outer Lacunae Strain to Global Bone Strain (2000 με) for each Osteocyte (Ocy).

Perilacunar Modulus	Ocy H1	Ocy H2	Ocy V1	Ocy V2	Ocy D1	Ocy D2
5 GPa	8.67	7.78	2.11	1.98	6.18	6.66
10 GPa	8.08	7.32	1.96	1.85	5.70	6.11
15 GPa	7.63	6.98	1.85	1.74	5.34	5.71
20 GPa	7.28	6.70	1.75	1.65	5.06	5.40

Table 3: Ratios of Maximum Perilacunar Strain to Global Bone Strain (2000 με) for each Osteocyte (Ocy).

Perilacunar Modulus	Ocy H1	Ocy H2	Ocy V1	Ocy V2	Ocy D1	Ocy D2
5 GPa	1.27	1.11	1.53	1.42	1.10	1.14
10 GPa	1.10	0.99	1.41	1.30	0.96	1.30
15 GPa	0.98	0.87	1.31	1.22	0.86	1.22
20 GPa	0.89	0.79	1.22	1.14	0.78	1.14

Osteocytes in the 3-D model were divided into four subgroups: top surface (n=3), side surface (n=2), bottom surface (n=3), and internal (n=9). Strain ratios for osteocytes found in the top, side, and bottom surfaces fell within ranges of 2.09-6.24, 2.35-3.03, and 1.49-2.63, respectively. Meanwhile, the internal osteocytes yielded strain ratios as low as 1.74 and as high as 2.91.

DISCUSSION

The 2-D model confirmed that the maximum strains in the inner lacunae, outer lacunae, and perilacunar tissue all increased due to their proximity to the applied load. In addition, strains in all three osteocyte subregions were influenced more predominantly by the horizontal and vertical orientations than the diagonal orientation. These findings indicate that the strain response not only depends on the alignment of the osteocyte, but also the osteocyte subregion examined. A better understanding of how mechanical stimuli directly affects the inner lacunae, outer lacunae, and perilacunar tissue may provide evidence that can be used to identify the minimum strain threshold required for osteocyte activation.

The 3-D model presented data similar to the 2-D model in that the lacunae strains varied based on the osteocyte positioning relative to the applied load. When comparing osteocytes near the top surface versus those near the bottom surface, we found that lacunar strains were 28-57% lower in the osteocytes positioned farthest from the applied loading. Furthermore, one of the osteocytes at the top surface exhibited a strain ratio (6.24) that was approximately 3x larger than the others in its subgroup. This finding could be explained by its proximity to the applied load, but the exact coordinates of each osteocyte would be needed for confirmation. Although the 3-D model did not possess any osteocyte subregions that represented the perilacunar tissue, the 2-D model exhibited decreases in lacunae strain as a result of an increased perilacunar tissue modulus. This finding has been observed in previous work [9,10], which examined the strain response in idealized, ellipsoidal osteocyte geometries. However, a key difference between the two aforementioned studies and this work is that our 3-D model comprises a more realistic representation of the typical osteocyte structure and arrangement. Therefore, the strains observed in the lacunar regions should provide a more accurate depiction of the strain distributions found throughout the osteocyte architecture. Future studies will utilize these FE models to correlate strains observed in the osteocyte lacunae with the heterogeneous activation of biological pathways associated with both mechanical loading and bone formation (e.g. Wnt/β-catenin signaling pathway).

ACKNOWLEDGEMENTS

This work was funded by a grant from the National Institutes of Health – NIA P01 AG039355 (LF Bonewald-PI) and NIAMS R01 AR053949 (ML Johnson – PI).

REFERENCES

[1] Johnell O and Kanis JA, *Osteoporos Int*, 17:1726, 2006.
[2] Carter, DR et al., *Acta Orthpaedica*, 52(5):481-490, 1981.
[3] Turner, CH et al., *Bone*, 13(6):417-422, 1992.
[4] Cowin, SC et al., *J Biomech Eng*, 113:191, 1991.
[5] Lanyon, LE et al., *J Biomech*, 15(3):141-154, 1982.
[6] Klein-Nulend J, et al., *The FASEB Journal*, 9(5):441-445, 1995.
[7] Maas, SA et al., *J Biomech Eng*, 134(1), 2012.
[8] Mimics® Innovation Suite, Materialise, Plymouth, MI.
[9] Bonivtch, AR et al., *J Biomech*, 40:2199-2206, 2007.
[10] Wang, L et al., *Biomed Res Int*, 2015, 2015.

Copyright 2016 The Organizing Committee for the 2016 Summer Biomechanics, Bioengineering and Biotransport Conference

SB^{3}C2016
Summer Biomechanics, Bioengineering and Biotransport Conference
June 29 –July 2, National Harbor, MD, USA
SB^{3}C2016-798

HEMODYNAMIC MODIFICATIONS AND ITS ASSOCIATION WITH OUTCOME IN INTRACRANIAL ANEURYSMS TREATED USING FLOW DIVERTERS

Nikhil Paliwal (1, 2), Jason Davies (3), Adnan H. Siddiqui (2, 3), Hui Meng (1, 2, 3, 4)

(1) Mechanical and Aerospace Engineering
University at Buffalo, the State University of New York, Buffalo, NY, USA

(2) Toshiba Stroke and Vascular Research Center
University at Buffalo, the State University of New York, Buffalo, NY, USA

(3) Neurosurgery
University at Buffalo, the State University of New York, Buffalo, NY, USA

(4) Biomedical Engineering
University at Buffalo, the State University of New York, Buffalo, NY, USA

INTRODUCTION

Endovascular intervention using Flow Diverter (FD) – a densely woven stent with high metal coverage rate and low porosity – is the prevalent treatment modality in intracranial aneurysms (IAs), especially among the traditionally challenging wide-necked and fusiform aneurysms. FDs are implanted to occlude the aneurysm and facilitate endoluminal reconstruction of the parent artery. Despite good clinical success of FDs, complications like incomplete occlusion and post-treatment rupture leading to subarachnoid hemorrhage have been reported [1]. Implantation of a FD disrupts the flow of blood in the aneurysm, inducing pro-thrombotic conditions. However, for patients with incomplete occlusion these pro-thrombotic environments could not be attained. Therefore to understand the relationship of FD deployment and treatment outcome it is important to gain insight on the flow modifications associated with the pro-thrombotic conditions. Computational fluid dynamic (CFD) analysis of pre- and post-treatment aneurysms can provide flow modifications by FD deployment, and can identify parameters that are associated with the treatment outcome.

In the current study an efficient virtual stenting method was used to mimic the clinical intervention on the patient-specific aneurysm geometries treated with the commercially available flow diverter: the Pipeline embolization device (PED, Covidien/Medtronic). CFD simulations were then performed on these geometries to obtain pre- and post- treatment hemodynamics. Modifications in hemodynamic parameters were calculated and correlated with 12 months clinical outcome.

METHODS

Five patient-specific aneurysms were selected for this study with the approval from the IRB at our institution. All the patients were treated using 1 PED. The following clinical information was collected for each patient (1) 3D digital subtraction angiographic (DSA) image, (2) PED device specification and landing zone and (3) 12 months clinical follow-up information. At the clinical follow-up after 12 months, 3 aneurysms were completely occluded and 2 were partially occluded.

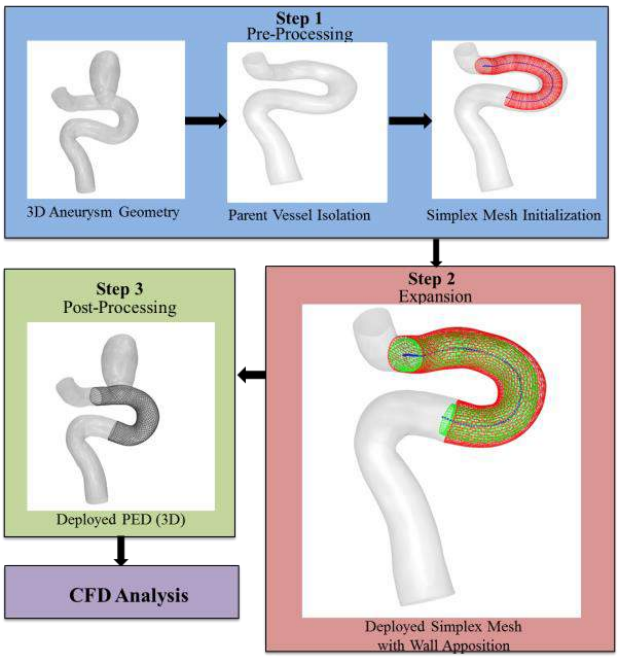

Figure 1: Virtual stenting workflow.

Copyright 2016 The Organizing Committee for the 2016 Summer Biomechanics, Bioengineering and Biotransport Conference

3D vessel reconstruction of the DSA images was performed using vascular modeling toolkit (vmtk). We then used an efficient virtual stenting workflow [2] to simulate the process of PED implantation in in each aneurysm. The workflow (Figure 1) is divided into three steps: (1) pre-processing, where the parent vessel is isolated and a generalized simplex mesh structure is generated to fit the vessel along its centerline using vessel-specific initialization, (2) expansion, to achieve good apposition of the simplex mesh with the vessel wall and (3) post-processing, where the PED pattern is mapped on the deployed simplex mesh and wires swept into a 3D structure. We improved the existing fast virtual stenting [3] algorithm by integrating the vessel-specific rapid initialization and adaptive expansion force, which led to better efficiency and accuracy of the PED deployment compared to the previous algorithm. The deployed PED was then incorporated into the aneurysm geometry.

CFD simulations were then performed on the pre- and post-treated geometries on STAR-CCM+ v10.02 (CD-adapco, Melville, NY) under steady-state conditions. Blood was modeled as Newtonian fluid, with density 1056 kg/m^3 and dynamic viscosity as 0.0035 Pa-s. The hemodynamic parameters calculated were inflow rate, aneurysmal velocity, vortex coreline length and energy loss (EL) by the PED.

RESULTS

Figure 2 shows the velocity streamlines and vortex corelines for one completely occluded and one partially occluded case. For the completely occluded case, a larger number of vortex corelines are present in the aneurysm before treatment, which are diminished by the implantation of the PED. For the partially occluded case, the vortex corelines are fewer prior to the treatment, but the PED failed to diffuse the vortices, giving a similar distribution of the vortex corelines even after the treatment.

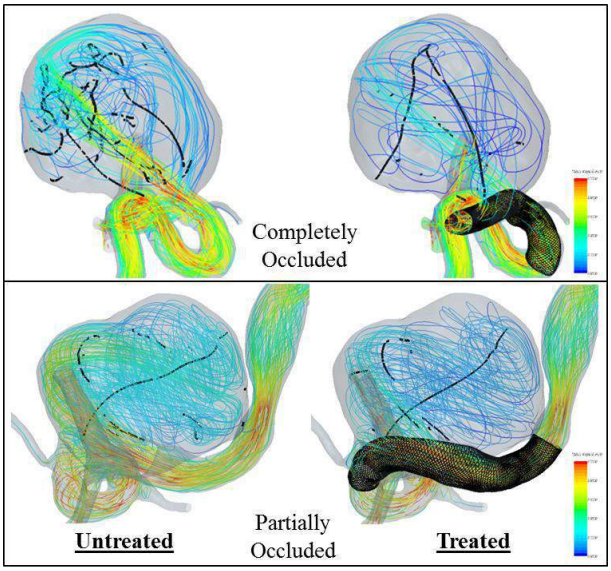

Figure 2: Pre- and post-treatment velocity streamlines and vortex corelines (black) for one aneurysm with complete occlusion and one aneurysm with incomplete occlusion after 12 months clinical follow-up.

Quantification of hemodynamic parameters (Figure 3) showed an average inflow rate reduction of 42.3% in completely occluded cases as compared with 33.7% in partially occluded cases. There was a reduction of 54.5% in aneurysmal average velocity in cases occluded within 12 months, whereas the patent cases had a reduction of 45.6%.

There was a substantial reduction in vortex coreline length and EL for completely occluded cases with a reduction of 45.1% and 29.1% respectively as compared to 21.7% and 9.8% for the partially occluded cases (Figure 3: red dotted box).

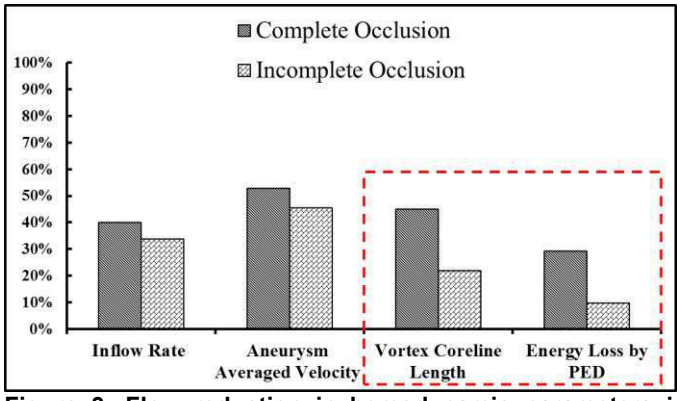

Figure 3: Flow reduction in hemodynamic parameters in aneurysms occluded within 12 months versus aneurysm with incomplete occlusion after 12 months clinical follow-up.

DISCUSSION

The results demonstrate that the bulk flow is reduced in the aneurysm for all the patients treated using the PED. But the reduction in flow parameters like inflow rate and average velocity was comparable in all the patients. However as shown in Figure 3 in red dotted box, there is a noticeably higher reduction of vortex coreline length and EL for aneurysms that occluded within 12 months. This suggests that bulk flow parameters like inflow rate and aneurysmal average velocity may not be linked with the occlusion times. On the other hand, substantial reduction of vortex coreline length and EL in the occluded cases suggest that the localized complex flow in the aneurysm was substantially dispersed into simple flow for completely occluded treated cases, whereas in patent cases the PED was unable to reduce the complex flow inside the aneurysmal sac (e.g. see Figure 2).

Although the patient population is very small to draw any clinically significant conclusion, results do suggest that higher reduction in localized flow into the aneurysm can be associated with the occlusion rate, and eventual outcome of the treatment.

The current study shows preliminary results of an ongoing study which aims at prospectively predicting outcome of different treatment strategies using flow diverters. We plan to increase the sample size of our current study and identify hemodynamic parameters that can predict the outcome of IAs treated using FDs. Based on these parameters a predictive model can be built which can prospectively predict the treatment outcome and aid the clinicians in *a priori* assessment of the outcome of different treatment strategies.

ACKNOWLEDGEMENTS

This study is funded by the National Institutes of Health (R01 NS 091075). The authors would like to acknowledge Dr. Jianping Xiang, Robert Damiano and Nicole Varble for their technical assistance.

REFERENCES

[1] Siddiqui, A et al., *J Neurosurg*, 116:1258-1266, 2012.

[2] Paliwal, N et al., *ASME IDETC-CIE* (pp. V003T12A014-V003T12A014), 2014.

[3] Larrabide, I et al., *Med. Image Anal.*, 16(3), 721-730, 2012.

Copyright 2016 The Organizing Committee for the 2016 Summer Biomechanics, Bioengineering and Biotransport Conference

SB^{3}C2016
Summer Biomechanics, Bioengineering and Biotransport Conference
June 29 –July 2, National Harbor, MD, USA
SB^{3}C2016-799

RIBOFLAVIN/UVA COLLAGEN CROSS-LINKING EFFECTS ON TENSILE AND COMPRESSIVE PROPERTIES OF THE CORNEA

H. Hatami-Marbini (1)

(1) Department of Mechanical & Industrial Engineering, University of Illinois at Chicago, Chicago, Illinois 60607

INTRODUCTION

Keratoconus is an eye disorder affecting almost one to five people in every 10,000. In this disease, the progressive non-inflammatory stromal thinning and softening causes the cornea to bulge out due to the intraocular pressure. This changes the normal curvature of the cornea and results in serious vision disorders such as astigmatism and myopia. It has been shown that the riboflavin/UVA collagen cross-linking process can be used to improve the biomechanical properties of keratoconus corneas and stop the progression of the disease [1-2]. In this treatment procedure, cross-links are introduced into the stroma by continuous application of riboflavin solution along with the UVA irradiation. The influence of various parameters of this treatment option, such as the wavelength and intensity of the UVA, is often assessed by the changes that they cause in corneal biomechanical properties. The uniaxial tensile tests are among the most commonly used experimental techniques for this purpose. Using this testing technique, it has been concluded that maximum tensile stress in the riboflavin/UVA treated rabbit, porcine, and human corneas significantly increased [1-3]. We have recently shown that hydration plays an important role in defining the biomechanical properties of the cornea [4-5]. In particular, swollen corneal samples had softer mechanical properties compared with the dehydrated corneas. The present study was designed to extend these previous studies and investigate possible effects of hydration on corneal stiffening due to the riboflavin/UVA collagen crosslinking treatment.

The cornea is a hydrated soft tissue which transmits the incident light while acting as a resilient barrier to the mechanical forces. The cornea is composed of different layers but the stromal layer, is known to be primarily responsible for its mechanical properties. The stroma consists of thin parallel-to-the-surface collagen lamellae embedded in a proteoglycan matrix. In experimental techniques such as inflation and uniaxial tensile experiments, the corneal samples are immersed in ionic solutions to avoid dehydration. Due to the presence of the proteoglycans, this will cause the specimens to imbibe the fluid and swell. The change in fluid content has important effects on the measured properties as shown in recent publications [4-6]. In the present research, we extend these previous studies and characterize the influence of hydration on both compressive and tensile properties of the collagen cross-linked corneas.

METHODS

Fresh bovine and porcine sample were obtained from a local slaughterhouse and transferred to the laboratory on ice. Bovine samples were used for uniaxial tensile tests and porcine samples were used for unconfined compression experiments. From each eye globe, a corneal scleral ring was dissected with a scissor. Corneal scleral rings were divided into control and collagen cross-linked groups [7]. The collagen cross-linked groups were cross-linked using a custom-made cross-linking device. Prior to UVA/riboflavin collagen crosslinking, all samples were placed in 0.1% riboflavin with 20% dextran T500 solution until they reached an equilibrium swelling state. A Pachymeter (DGH Pachette 3, DGH Technology, Inc., Pennsylvania, USA) was used to measure the thickness of samples and ensure that they reached equilibrium. The specimens were placed on a semi-sphere surface in order to mimic their natural in-vivo curvature and were subjected to the UVA irradiation with an irradiance of 3 mW/cm^2 for 30 minutes. During this period, drops of riboflavin solution were added on their surface every five minutes. After the UVA/riboflavin crosslinking treatment, a double blade cutting device and trephine were used to punch either a rectangular strip or a disk from corneal sclera rings. The strips were prepared from nasal-temporal orientation and were used in uniaxial

Copyright 2016 The Organizing Committee for the 2016 Summer Biomechanics, Bioengineering and Biotransport Conference

tensile tests while the corneal disks were used to character size the unconfined compression behavior [7-8].

The uniaxial tensile tests were done using a dynamic mechanical analyzer (RSA-G2, TA instrument, Delaware, USA). First, the cross-linked specimens were soaked in the Ophthalmic Balanced Salt Solution or being dehydrated in air until their thickness reached the thickness of one of the three thickness groups, i.e. 500, 700, 900, 1100, and 1500 µm. The strips were then secured between the clamps of the DMA machine and the immersion chamber was filled with mineral oil in order to prevent any swelling/deswelling during the experiments. All samples were subjected to a preconditioning step for creating a similar stress-strain history in them. The preconditioning procedure included five rapid loading/unloading cycles followed by three short stress-relaxation steps. The experiments were done by applying 5% axial strain with a displacement rate of 2 mm/min. During the experiments, the applied force was measured and the stress was calculated from dividing the recorded force by the initial cross-sectional area of the strips. Similar experiments were done on untreated samples. For unconfined compression experiments [8], a compressive tare stress was used to determine the initial thickness of the corneal disks and successive stress-relaxation tests were conducted by bringing the head down. Compressive strain steps of 5% with a given displacement rate. The experimental data was modelled using a transversely isotropic material model in order to determine the material properties at different levels of hydration.

RESULTS

Figures 1 and 2 show the tensile stress-strain behavior of untreated and riboflavin/UVA collagen crosslinked corneal strips at different thicknesses, respectively. In both treated and untreated groups, it is seen that tensile properties became stiffer with decreasing thickness (hydration). Furthermore, it is seen that within a specific thickness group, the collagen cross-linking procedure significantly increased the tensile strength of the cornea. It is noted that the hydration of the samples can be estimated using the hydration-thickness relation, H_w=3.7ln(t/0.295) [6]. This relation gives average hydration of 2.0, 3.2, 4.1, 4.9, and 6 mg water/ mg dry tissue for samples with average thickness of 0.5, 0.7, 0.9, 1.1, and 1.5 mm respectively..

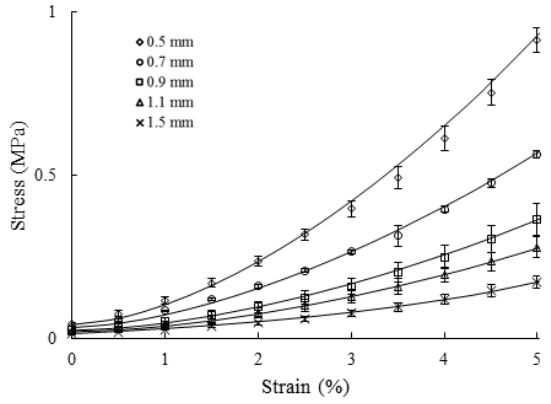

Figure 1: Stress-strain of untreated bovine cornea at different levels of thickness (hydration).

DISCUSSION

The primary objective of the present work was to determine the influence of hydration on tensile and compressive properties of the riboflavin/UVA collagen cross-linked cornea. Figures 1 and 2 show that the riboflavin/UVA collagen crosslinking procedure has strengthened the tensile properties of the bovine cornea, which is similar to the effect of this procedure on porcine, human, and rabbit corneas. Furthermore, this plot shows that the stiffening effect of the collagen cross-linking treatment, as measured by uniaxial tensile testing method, is hydration dependent. In Figure 3, we plotted the tangent modulus of the collagen cross-linked corneal strips at different levels hydration and compare them with the tangent modulus of the untreated bovine corneas.

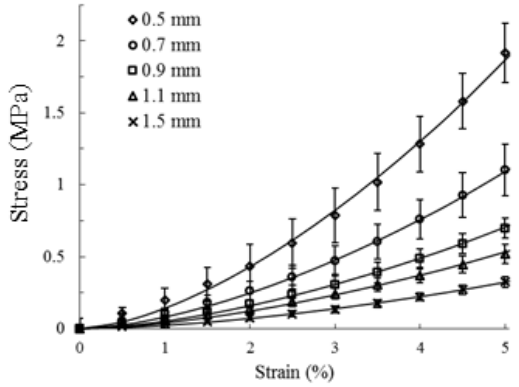

Figure 2: Stress-strain of the collagen cross-linked bovine corneal strips at different levels of thickness (hydration).

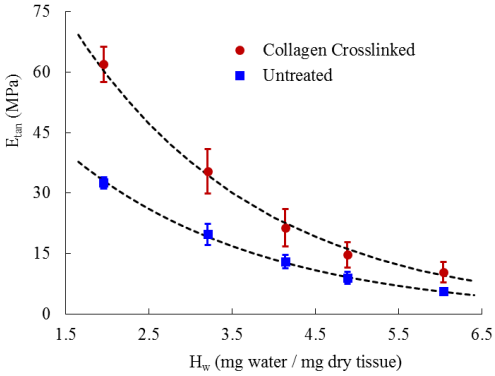

Figure 3: Tangent modulus of the collagen cross-linked and untreated corneal strips at different levels hydration.

Figure 3 clearly shows that an accurate estimate of the stiffening effects of collagen crosslinking is only possible if the tensile behavior of treated and untreated specimens is measured at the same level of hydration. The presentation will expand on these studies and discuss the behavior of the specimens in unconfined compression (results not shown here).

REFERENCES

[1] Spoerl, E, Huhle, M, Seiler, T, Exp Eye Res 66:97-103, 1998.
[2] Wollensak, G, Spoerl, E, Seiler, T, Am J Ophthalmol, 135:620-627, 2003.
[3] McCall, AS, et al., Invest Ophthalmol Vis Sci 51:129-138, 2001.
[4] Hatami-Marbini, H, Etebu, E, *Biorheology*, 50:133–147, 2012.
[5] Hatami-Marbini, H, Rahimi, A, J Mech Behav Biomed Mater 36:90-97, 2014.
[6] Hatami-Marbini, H, Ann of Biomed Eng, 42:1740-1748, 2014.
[7] Hatami-Marbini, H, Rahimi, A, J Biomech 48:1052-157, 2015.
[8] Hatami-Marbini, H, et al, under preparation.

Copyright 2016 The Organizing Committee for the 2016 Summer Biomechanics, Bioengineering and Biotransport Conference

SB³C2016
Summer Biomechanics, Bioengineering and Biotransport Conference
June 29 –July 2, National Harbor, MD, USA
SB³C2016-800

ELUCIDATING MECHANISMS OF TENDON DAMAGE BY MEASURING MULTISCALE UNLOADED RECOVERY FOLLOWING TENSILE LOADING

Andrea H. Lee (1), Spencer E. Szczesny (2), Kristen L. Fetchko (1), Michael H. Santare (3), Dawn M. Elliott (1)

(1) Department of Biomedical Engineering
University of Delaware
Newark, DE, USA

(2) Department of Orthopaedic Surgery
University of Pennsylvania
Philadelphia, PA, USA

(3) Department of Mechanical Engineering
University of Delaware
Newark, DE, USA

INTRODUCTION

Microscale tensile testing demonstrates that tendon loads are transferred between discontinuous fibrils via shear of the interfibrillar matrix [1]. Moreover, tendon exhibits macroscopic strain-softening at strains beyond the elastic limit [1, 2], which can be explained by plastic deformation of the interfibrillar matrix [3]. However, the mechanisms of recovery at the microscale (e.g., fibril strain and interfibrillar sliding) and their relationship to macroscale mechanics (e.g., nonlinearity and modulus) are unknown. Specifically, it is unclear whether the observed plastic deformation of the interfibrillar matrix contributes non-recoverable tendon damage. Here, we (1) measured the unloaded recovery of tendon following tensile loading, (2) quantified microscale deformations and classified them as elastic, viscoelastic, or non-recoverable (i.e., plastic/permanent), and (3) established relationships between macro- and micro-scale recovery. Thus, the objective of this study was to elucidate mechanisms of tendon damage at multiple length scales.

METHODS

Sample Preparation: Tail tendon fascicles from 6-7 month Sprague-Dawley male rats were dissected, stained with 10 μg/ml 5-DTAF (Life Technologies), and tested on a custom-made uniaxial testing device mounted on an inverted confocal microscope (LSM 5 LIVE) as previously described [1]. Macroscale tissue strain was measured using applied ink markers and a CCD camera. Microscale deformation, including fibril strain and fibril sliding, was measured using four photobleached lines separated by 125 μm.

Multi-scale Mechanical Testing: Samples were preloaded to 0.5g to define the reference length, preconditioned (5 cycles of 4% grip strains), and loaded to either 2, 4, 6, or 8% grip strain, defined as the "baseline" (Fig 1). Strain was held constant for a 15 min relaxation period and then unloaded to the reference length (Fig 1). Each fascicle was assigned to a rest or no rest group. The no rest group was immediately loaded to failure, whereas the rest group was held at its reference length for 60 min before loading to failure. Microscale images were acquired only for the rest group including: reference image before loading, at the beginning and at the end of the relaxation period, and every 10 minutes during the 60 min rest. Finally, each fascicle was ramped to failure, defined as the "diagnostic" (Fig 1). The strain rate was 1%/s for all loading. In all, we performed multiscale mechanical testing on 8 groups (2, 4, 6, and 8% strain, each with rest or no rest, with n=7 fascicles per group).

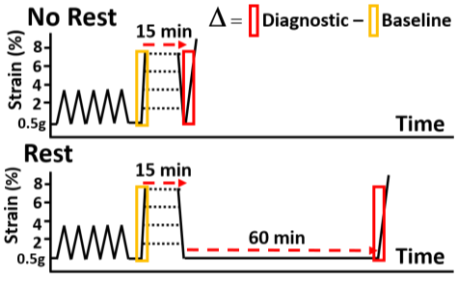

Fig. 1: Mechanical testing protocol

Data Analysis: Macroscale stress-strain response was fit with a nonlinear model [4] that optimized for the transition strain (the end of toe-region) and linear region modulus. These properties were calculated for the baseline and diagnostic ramps, and change in each property was determined, Δ = Diagnostic – Baseline (Fig 1). A linear regression was performed between macroscale parameters and tissue strain. An extra-sum-of-squares F-test was performed to test significant differences between rest and no rest groups. The 2% strain group was excluded for macroscale analysis because transition strain and linear modulus are not evident at this low strain level.

Microscale mechanical properties (fibril strain and interfibrillar sliding) were determined from confocal microscope images [1]. Fibril

Copyright 2016 The Organizing Committee for the 2016 Summer Biomechanics, Bioengineering and Biotransport Conference

strain was defined as the change in distance between pairs of photobleached lines, and interfibrillar sliding was the averaged tortuosity of these lines. Microscale deformations were then decomposed into the recoverable (elastic and viscoelastic) and non-recoverable portions, where recovery is defined as the time dependent return of microscale properties during the rest period. A linear regression was performed between the microscale parameters and tissue strain and also between the macro- and microscale parameters. Significance was set at the 95% confidence level for all analyses.

RESULTS

The macroscale Δ transition strain increased with tissue strain (Fig 2A, rest group $R=0.62$, $p<0.005$; no rest group $R=0.22$, $p=0.36$), suggesting damage related to tendon elongation. In addition, the Δ linear region modulus decreased with tissue strain (Fig. 2B, rest group $R= -0.73$, $p<0.005$; no rest group $R= -0.50$, $p<0.05$), which suggests strain dependent damage. Notably, there was no difference between the rest and no rest groups for transition strain slope (rest group: 0.23; no rest group: 0.18, $p>0.8$) or modulus slope (rest group: -6827MPa; no rest group: -6537MPa, $p>0.9$), suggesting non-recoverable macroscale changes and permanent damage to the tissue.

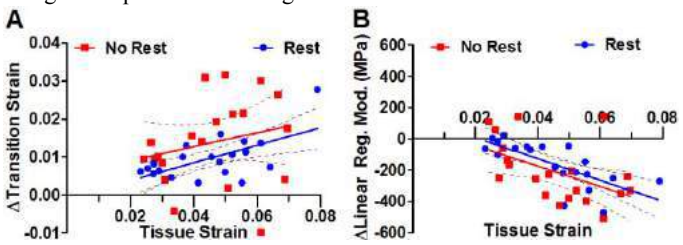

Fig. 2: Correlations between Δ transition strain (A) and Δ linear region modulus (B) with strain. No difference between no rest and rest group indicate non-recoverable permanent damage.

Microscale mechanical testing was used to investigate the structural source of the observed macroscale damage. Fibril strain elastically recovered in all strain groups with total recovery greater than 99.5% (Fig 3A). These findings suggest no fibril damage. Conversely, the interfibrillar sliding did not fully recover, with up to 50% non-recoverable sliding (Fig 3B), suggesting permanent damage. Fibril sliding recovery was also time-dependent, composed of both elastic (instantaneous) and viscoelastic recovery (Fig 3B).

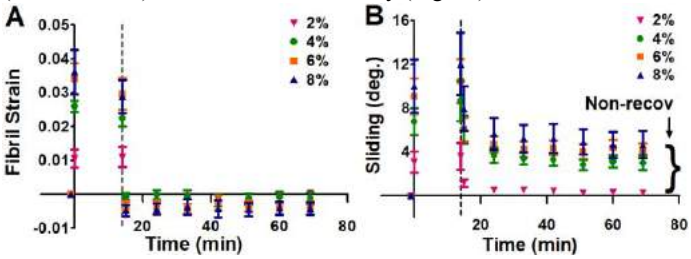

Fig. 3: Time course shows fibril strain fully recovered (A), but interfibrillar sliding recovery was incomplete (B). The dotted line represents when samples were unloaded. Error bars in SEM.

Surprisingly, while elastic sliding recovery was strain dependent (Fig 4A, $R= -0.53$, $p<0.005$), viscoelastic sliding recovery was not correlated with strain, and averaged 27.5± 8.9% across all strains (Fig 4B). This implies that the increase in non-recoverable sliding with tissue strain (Fig 4C, $R=0.64$, $p<0.0005$) was due to elastic sliding recovery. When relating the macro to micro parameters, non-recoverable sliding correlated with Δ transition strain (Fig 4D, $R= 0.57$, $p<0.005$), which suggests that the change in tissue transition strain may be caused by microscopic non-recoverable interfibrillar sliding.

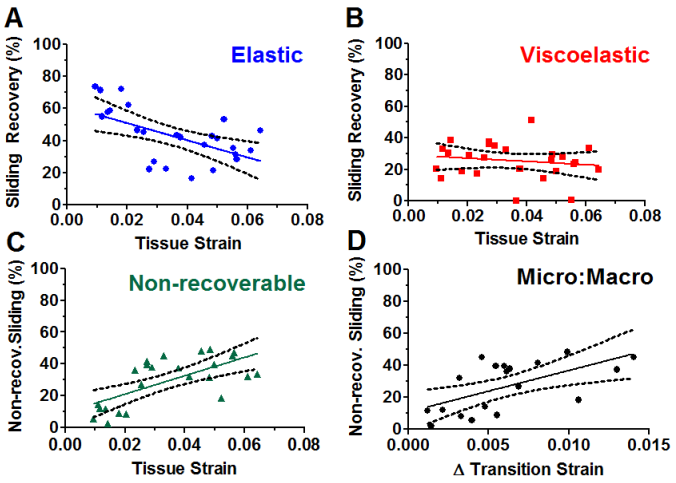

Fig. 4: Interfibrillar sliding is composed of elastic sliding recovery (A), viscoelastic sliding recovery (B), and non-recoverable sliding (C). The non-recoverable sliding contributed to the increase in translation strain (D).

DISCUSSION

This study elucidates mechanisms of tendon damage by measuring multiscale unloaded recovery following tensile loading. At the macroscale level, stretching past the elastic limit produces permanent damage (Fig 2), as expected. At the microscale level, the complete elastic recovery of the fibril strain suggests no damage to the primary load bearing collagen fibrils (Fig 3A). However, non-recoverable sliding increases with tissue strain due to a decrease in elastic sliding recovery (Fig 4A). This suggests that permanent elongation in tendon is primarily due to damage in the interfibrillar matrix, which is consistent with the assumption of plastic interfibrillar sliding within our shear lag model [1, 3]. In addition, non-recoverable sliding correlates with Δ transition strain (Fig 4D), suggesting that the observed permanent increase in transition strain can be explained by interfibrillar matrix damage at the microscopic level.

Although molecular structures responsible for matrix recovery are unknown, we hypothesize small diameter collagen fibrils may be a major contributor in elastic sliding recovery. Previously, our lab confirmed a network of small diameter fibrils connecting larger fibrils and these smaller fibrils may transfer loads between larger diameter fibrils [5]. At low strain, these undamaged elastic small fibrils may drive elastic sliding recovery but at high strain may lose helicity and destabilize [6]. Furthermore, we hypothesize that the non-collagenous matrix may be a major contributor in viscoelastic sliding recovery.

This study makes important advances on previously reported permanent elongation in overloaded tendon [7] and observations of microscale elastic recovery in tendon [8] by quantifying the time-dependent recovery and non-recoverable damage at multiple length scales. These findings are important in gaining insight into musculoskeletal injuries and designing rehabilitation strategies.

ACKNOWLEDGEMENTS

The National Institutes of Health grant R01 EB02425.

REFERENCES

[1] Szczesny, S et al., *Acta Biomat*, 2014. [2] Torp, S et al., *Colston Research Society* 1975. [3] Szczesny, S et al., *J Mech Behav Biomed Mater,* 2015. [4] Tanaka, M et al., *J Biomech Eng,* 2011. [5] Szczesny, S et al., *SB³C Proceeding,* 2015. [6] Veres, S et at., *J Orthop Res,* 2013. [7] Fung, D et al., *J Orthop Res*, 2008. [8] Thorpe, T et al., *Acta Biomat*, 2013.

Copyright 2016 The Organizing Committee for the 2016 Summer Biomechanics, Bioengineering and Biotransport Conference

SB^{3}C2016
Summer Biomechanics, Bioengineering and BIotransport Conference
June 29–July 2, National Harbor, MD, USA
SB^{3}C2016-801

TRACTION FORCE MEASUREMENT OF MIGRATING CELLS IN MULTICHANNEL MICROPILLAR DEVICE

Toshiro Ohashi (1), Akito Sugawara (2)

(1)Faculty of Engineering
Hokkaido University
Sapporo, Hokkaido, Japan

(2) Graduate School of Engineering
Hokkaido University
Sapporo, Hokkaido, Japan
(Present: JFE Steel Corporation)

INTRODUCTION

Cell migration is known to play an important role in a number of physiological events in living body such as morphogenesis, wound healing, and tumor metastasis. In the majority of such events, cells move as a group, called collective cell migration. Compared to a single cell migration, the mechanism of collective cell migrations has not been understood well and attempts have been made in simple experimental setups exemplified by "wound healing" assay [1, 2]. However, this technique is vulnerable to artefacts associated to the creation of the wound. To overcome such limitations, Doran et al. [3] have proposed a new experimental device using MEMS techniques. A significant advantage of the device was the ability to maintain an intact surface prior to the commencement of the analysis of collective cell migration.

MEMS techniques have also been employed to measure cellular behaviours at micro- and nano-scales. One of such applications is an array of micropillars, where cellular traction forces can be determined from the deflection of the micropillars [4]. The purpose of the present study is to clarify the mechanism of collective cell migration at single cell level. To do this, we adopted the micropillar technology and integrated the micropillar arrays into a novel multichannel device [3]. With such novel experimental setup, traction force distribution within a cell collectivity was evaluated, which may reflect positional differences in mechanical roles of individual cells in collective cell migration.

METHODS

Mouse NIH 3T3 fibroblasts were cultured in DMEM (Gibco, USA) supplemented with 10% of FBS (Gibco) (DMEM + 10%FBS) at 37°C/5% CO_2 and used for experiments described below. A PDMS-made cell migration device was designed based on a device previously reported [3] and fabricated by standard photolithography and soft-lithography [4]. The current device consists of a reservoir (15.5 mm x 16.8 mm) with a flat surface for establishing a confluent cell monolayer, attached with microchannels for cell migration (Fig. 1). Each set of six microchannels branching off the reservoir converges at a single syringe port. Of six channels, four channels have arrays of micropillars (2 - 3 μm in diameter, 6.5 μm in height) at the bottom surface for the measurement of cell traction forces during migration, whereas the remaining two channels have a flat surface and serve as reference channels.

As shown in Fig. 1, a suspension of NIH 3T3 cells at a concentration of 5 x 10^5 cells/mL in DMEM + 10%FBS was loaded to the reservoir from the open top, following the sealing of the top of microchannels with the thin PDMS film. Due to the surface tension at the interface between the reservoir and the microchannels, the medium did not enter the channels. The cells were incubated at 37°C/5% CO_2 until a confluent monolayer was formed within the reservoir.

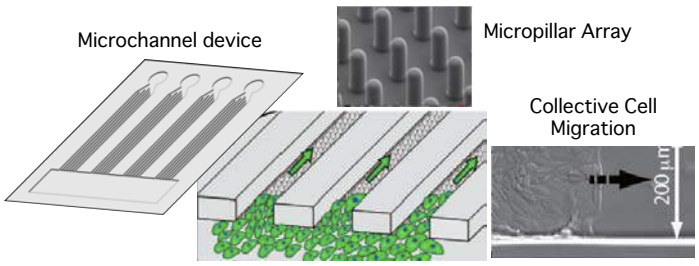

Fig. 1 Microchannel device with micropillar arrays.

Copyright 2016 The Organizing Committee for the 2016 Summer Biomechanics, Bioengineering and Biotransport Conference

At the day of experiments, the device containing a confluent cell monolayer was set on a microscope stage. Cell migration was initiated when the microchannels were backfilled with the medium from the syringe port. A set of microscopic images of the top of micropillars including cells and the bottom of the same micropillars was obtained every 10 minutes with a x10 objective lens attached to an inverted microscope (IX81, Olympus, Japan). To determine traction forces for individual cells in a monolayer that demonstrated a collective migration, each individual cells was identified from microscopic images. Cellular traction forces were determined by measuring the deflection of the top of the micropillars [4]. Bright-field images were acquired using a CCD camera (ORCA-R2, Hamamatsu Photonics K.K., Japan) and the deflection was obtained through an image analysis using Image J (NIH). For small deflections, the micropillars behave like simple springs such that the bending force is directly proportional to the deflection of the micropillars. The spring constant of the micropillars was indirectly determined by cross-calibration.

RESULTS AND DISCUSSION

After the onset of cell migration experiment, the cells migrated into microchannels with both flat surface and micropillar substrates throughout a 26 h experimental period. Traction force microscopy was performed for the migrating cells (Fig. 2). In the analysis, cells on the moving front (leading cells) and those behind the leading cells (submarginal cells), particularly cells on the second and third rows, were chosen, as it was reported previously that cells within a certain distance from the moving front mainly committed to the forwarding movement of a cell collectivity [1]. It was observed that all the cells analysed generated traction forces but with different degrees. The leading cells generated traction forces over 10 nN at their leading edges, directing the backward of the moving direction. Cells on the second row generated smaller magnitude of traction forces. Most of traction force vectors directed the backward as in the case of the leading cells. Further small magnitude of traction forces was observed in cells on the third row, and the directions of these forces were varied compared to those from the cell on the first and second rows.

The present study demonstrated mechanical behaviour of cells within a moving collectivity at single cell level using a newly fabricated device combining elastic micropillar and microchannel structure. The results obtained demonstrate that cells consisting of collective cell migration generate traction forces with different magnitudes and directions depending on their relative positions, possibly reflecting positional differences in mechanical roles within a moving cell group. In particular, a gradual increase in the magnitude of traction forces towards the moving front may suggest reductions in the degree of cell-cell mechanical connections. Because cells near the moving front need to move forward and tug the rest of the cells within the collectivity, these cells may need to loosen cell-cell interactions and actively migrate like single cells. It remains to study how cells recognize their relative positions to modulate cell-cell and cell-matrix interactions and how mechanical/biochemical signals are transmitted between cells to achieve such coordinated cellular behaviours.

CONCLUSIONS

Measurement of traction forces, generated by cells to their local environment, has been proposed as a quantitative way to study mechanical behavior of collective cell migration. We measured the traction forces exerted by mouse NIH 3T3 fibroblasts during migration using a multichannel migration device with micropillars. It is assumed that cells on the front line generated large traction forces and migrated actively as single cells, pulling adjacent cells forward, whereas the movement of cells after the third row was restricted by mechanical linkages between their neighboring cells that generated smaller traction forces.

ACKNOWLEDGEMENTS

The present study was partially supported by JSPS Bilateral Joint Research Project (Japan-Australia, in collaboration with Prof. Justin Cooper-White). The device was fabricated at Creative Research Institution 'Sousei', Catalysis Research Center and Nanotechnology Research Center of Research Institute for Electronic Science at Hokkaido University.

REFERENCES

[1] Fenteany, G et al., *Curr Biol*, 10: 838- , 2000.
[2] Farooqui, R and Fenteany, G, *J Cell Sci*, 118: 63- ,2005.
[3] Doran, MR et al., *Lab Chip*, 9: 2369- ,2009.
[4] Tan JL et al., *Proc Natl Acad Sci*, 100:1484-1489, 2003.

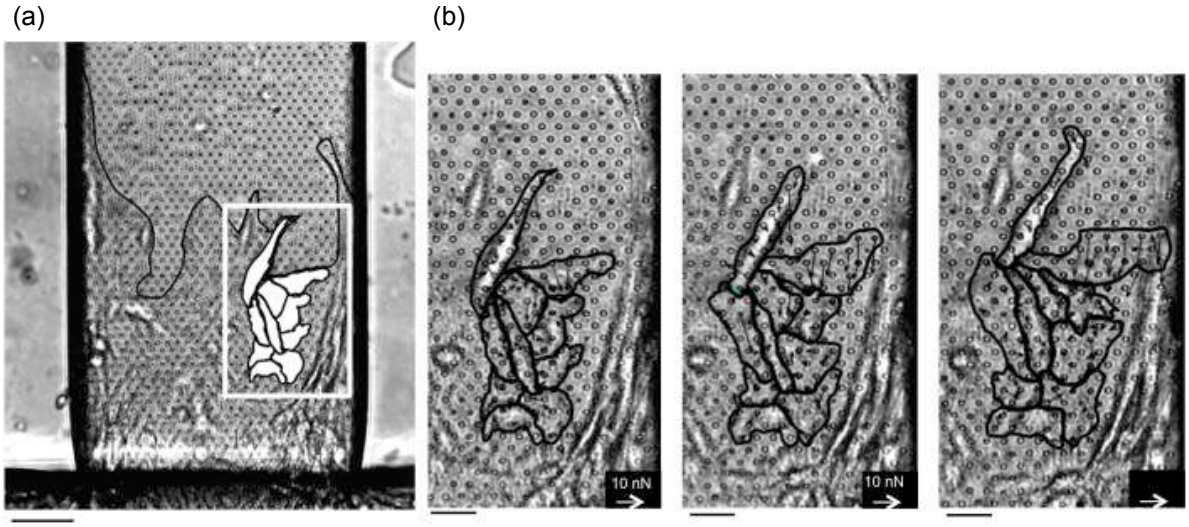

Fig. 2 (a) Cell migration of at 24 h. Bar = 50 μm. (b) Magnified views of the rectangular region in (a), superimposed with traction forces (arrows) at 24, 25 and 26 h. Bars = 20 μm.

Copyright 2016 The Organizing Committee for the 2016 Summer Biomechanics, Bioengineering and Biotransport Conference

SB^{3}C2016
Summer Biomechanics, Bioengineering and Biotransport Conference
June 29 –July 2, National Harbor, MD, USA
SB^{3}C2016-802

LINKING MITRAL VALVE INTERSTITIAL CELL DEFORMATION TO BIOSYNTHETIC RESPONSE: IMPLICATIONS FOR MITRAL VALVE REPAIR

Salma Ayoub (1), Chung-Hao Lee (1), Connor T. Hughes (1), Giovanni Ferrari (2), and Michael S. Sacks (1)

(1) Center for Cardiovascular Simulation
Institute for Computational Engineering & Sciences
Department of Biomedical Engineering
The University of Texas at Austin
Austin, TX, USA

(2) Department of Surgery
Gorman Cardiovascular Research Group
University of Pennsylvania
Philadelphia, PA, USA

INTRODUCTION

In the US, nearly 40,000 patients undergo mitral valve (MV) repair or replacement each year due to mitral regurgitation [1]. Due to the complications associated with mechanical and bioprosthetic valve replacement, the procedure of choice has become MV repair. However, recent studies have indicated that the long-term durability of surgical repair is significantly less than previously thought [2-4]. Patients undergoing MV repair for myxomatous disease had a 10% to 16% recurrence rate of MR that required reoperation within 10 years of surgery and patients with functional MR had a 30% recurrence rate at 6 months post-surgery and up to 60% after 3 to 5 years [2-4]. Repair failure was linked to the excessive tissue stress imposed by the sutures and the annuloplasty ring—non-physiological stresses on the tissue lead to suture dehiscence in both leaflets and annulus. Understanding the underlying mechanobiology of the compensatory response of mitral valve interstitial cells (VICs) to stress overload is necessary for developing better modeling tools and improving surgical repair. This study uses an *in vitro* system to answer specific questions on MV mechanobiology and provides insight into the micromechanics of surgically repaired MV by identifying cellular deformation as a potential mechanical basis for surgical repair failure.

METHODS

Bioreactor design & validation: The tissue strip bioreactor used is a modified version of the one previously described [5]. Cyclic stretch is applied with a stepper motor linear actuator. An in-house LabVIEW virtual instrument (VI) is used to control both the linear actuator and the load cell and collect load data and actuator displacement.

Tissue preparation and Bioreactor Treatment: For each bioreactor treatment group, n = 8 MVs were used (Fig. 1). Fresh porcine hearts were collected from young hogs from a local USDA approved abattoir. Rectangular strips (11.5 mm x 7.6 mm) were dissected from the clear zone of the anterior leaflet, sutured, mounted into the cyclic stretch bioreactor, then cyclically stretched for 48 hours (at either 0%, 10%, or 30% stretch) at 1.17 Hz within an incubator maintained at 37°C and 5% CO_2. At the end of each treatment, samples were either fixed or snap-frozen for further analysis as described below.

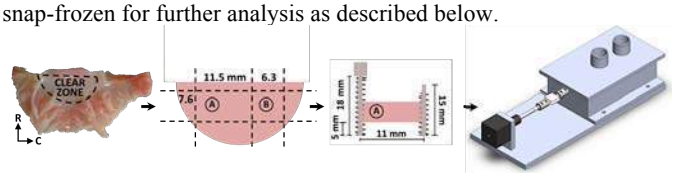

Figure 1: MVAL samples for bioreactor treatment. Rectangular samples are sutured on the sides using springs and mounted into the load-sensing tissue strip bioreactor.

Cell and tissue deformation: A group of n = 9 valves was used for microenvironment and cell deformation analysis. Briefly, MVAL samples were mounted on the bioreactor, subjected to a single extension of 10, 20, or 30% strain, and fixed along the circumferential direction with 2.5% EM grade glutaraldehyde for 4 hours. The fixed tissue was prepared using standard protocol, sectioned (70 nm), and imaged using transmission electron microscopy. VIC cytoplasmic and nuclear aspect ratios were calculated by measuring the major and minor axes of the cytoplasm and nucleus, respectively. *Tissue Deformation:* A second group of fixed tissue was used for collagen fiber alignment. Briefly, the fixed samples were dehydrated, cleared in a graded glycerol/water solution and stored in 100% glycerol. A non-polarized laser was passed through the tissue. The normalized orientation index (NOI) was used to quantify tissue deformation.

ECM Biosynthesis and Cell activation: Samples were fixed with formalin, embedded in paraffin, sectioned (5μm), and stained with

Copyright 2016 The Organizing Committee for the 2016 Summer Biomechanics, Bioengineering and Biotransport Conference

Movat pentachrome to analyze layer-specific morphological changes. Staining for α -SMA was performed to quantify VIC activation. Collagen, elastin, and glycosaminoglycan content were quantified using the Sircol, Fastin, and Blyscan assays, respectively.

Finite Element Numerical Prediction of VIC deformation: Using our macro-micro finite element (FE) model of the MVAL [6], a representative volume element of the fibrosa layer that takes into account microstructural composition was constructed. Displacements imposed by the bioreactor on the tissue were used as the boundary displacements of the RVE. MVIC deformation in the fibrosa layer was simulated and quantified by the ratio of the cytoplasmic over the transmural dimensions, defined as the nuclear aspect ratio (NAR).

RESULTS

Tissue micromechanics increase nonlinearly with strain: The collagen fiber alignment data shows that overall tissue alignment remains the same at 10% and 20%, indicating that the collagen fibers do not undergo any major changes at physiological strains. This said, at the 30% strain, there is a substantial increase in fiber alignment, highlighting the non-linear MVAL micromechanics (Fig. 2). Interestingly, VIC deformation shows a similar trend, whereby cytoplasmic deformation decouples from nuclear deformation at hyper-physiological strain levels and increases sharply.

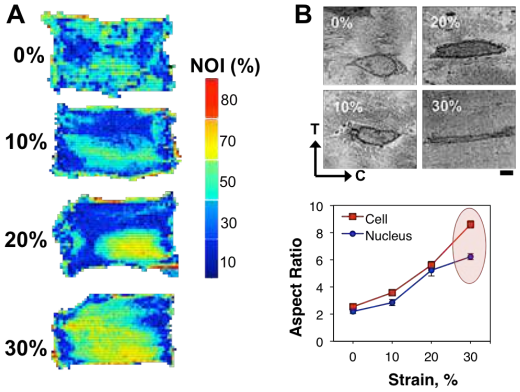

Figure 2: (A) Collagen fiber alignment maps. (B) Representative MVIC from samples at different strain levels. Scale bar: 5 µm.

Cellular activation initiates in the outer layers of the MV: In non-diseased valves, VICs have a quiescent, fibroblast-like phenotype. When activated, the VIC phenotype changes as they begin to exhibit myofibroblast properties, mainly an upregulation in α-smooth muscle actin (α-SMA). Immunohistochemistry of α-SMA shows that the cells in the outer layers, thus, the atrialis/spongiosa and ventricularis, begin to express α-SMA before the cells in the fibrosa layers at 20% strain level. At 30% strain, cells across all layers of the MV express α-SMA.

Biosynthetic activity increases at hyper-physiological levels: When activated to their myofibroblast phenotype, VICs exhibit increased biosynthetic activity. Results from the Sircol colorimetric assay show a significant increase in collagen biosynthesis at hyper-physiological levels. This is in line with not only the increased α-SMA expression, but also the changes observed in tissue micromechanics and cellular deformation (Fig. 3). Results from the Blyscan assay reveal sulfated-glycosaminoglycan (s-GAG) leaching into the media, which is characteristic of valve tissue that undergoes physiological cyclic stretch *in vitro*. This said, the level of leaching decreases at hyper-physiological levels, suggesting an upregulation of s-GAG synthesis at these levels. The repeated measures design allows us to analyze the data sample-by-sample and identify outliers.

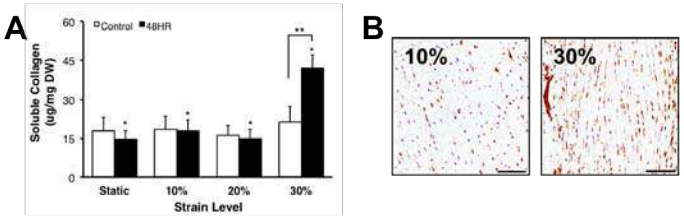

Figure 3: (A) Acid-Pepsin soluble collagen before and after cyclic stretch treatment at different strain levels. B) α-SMA expression in samples subjected to 10% and 30% strain. Scale bar: 250 µm

MVIC NAR can be used as a tool to link the current uniaxial bioreactor to physiological deformation modes: Simulations of MVIC NAR in the fibrosa layer using the macro-micro MV FE model were in agreement with the experimental measurements. Under physiological biaxial deformation modes (ranging from 0 to 150 N/m), MVICs in the fibrosa have an NAR that ranges from 2.5 to 3.5, respectively. When linked to the uniaxial deformation mode, such a NAR occurs when the tissue is strained by ~12.5% in the circumferential direction. When deformed above the physiological range (NAR>3.5), MVICs appear to be activated and exhibit substantial biosynthetic activity as indicated by the colorimetric assay results.

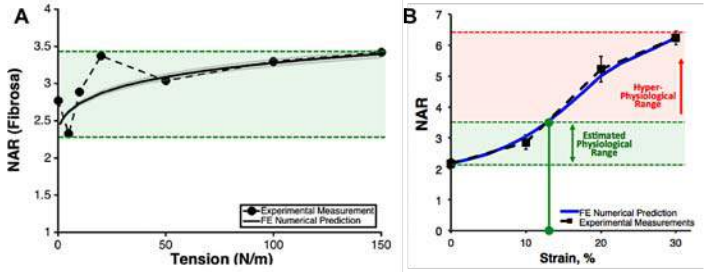

Figure 4: (A) NAR under equibiaxial deformation modes. (B) Simulated vs. Experimental NAR under uniaxial stretch. The MVIC NAR from the biaxial system can be used to link the uniaxial system to physiological and hyper-physiological deformation modes.

DISCUSSION

Results from this study reveal an important link between MV micromechanics and MVIC biosynthetic response, primarily an increase in VIC activation and biosynthetic activity at NAR>3.5. This study provides important insights into the micromechanics of surgically repaired MVs by identifying cellular deformation as a potential mechanical basis for surgical repair failure**.** Though novel and a first attempt to link MVIC deformation to biosynthetic response, this tissue strip bioreactor does not replicate the micromechanics of the physiological environment, which impose strains on both radial and circumferential directions. Future work will focus on improving the *in vitro* system by designing a more physiologically realistic bioreactor that imposes biaxial deformation modes on the valve tissue.

ACKNOWLEDGEMENTS

National Institute of Health (NIH) Grant R01HL119297.

REFERENCES

[1] Flameng, W. et al., *Circulation*, 107: 1609-1613, 2003.
[1] Gillinov, AM et al., *J Thorac Cardiovas Surg*, 135: 885-593, 2008.
[4] Bouma, W et al. *Ann Thorac Surg*, available online first (In press), doi: 10.1016/j.athoracsur.2015.09.076, 2015.
[5] Merryman, WD et al. *Cardiovascular Path* 16: 268-276, 2007.
[6] Lee, CH et al., *J Theor Biol*, 373: 26-39, 2015.

Copyright 2016 The Organizing Committee for the 2016 Summer Biomechanics, Bioengineering and Biotransport Conference

SB^{3}C2016
Summer Biomechanics, Bioengineering and Biotransport Conference
June 29 –July 2, National Harbor, MD, USA
SB^{3}C2016-803

MITRAL VALVE LEAFLET REMODELING DURING PREGNANCY: IMPLICATIONS FOR MODELING VALVULAR ADAPTATION

Bruno V. Rego (1), Sarah M. Wells (2), Michael S. Sacks (1)

(1) Center for Cardiovascular Simulation
Institute for Computational Engineering and Sciences
Department of Biomedical Engineering
The University of Texas at Austin
Austin, TX, USA

(2) School of Biomedical Engineering
Dalhousie University
Halifax, NS, Canada

INTRODUCTION

The mitral valve (MV) is an integral part of the left ventricle (LV), connected via the papillary muscles (PMs) and annulus. Changes to the geometry or contractile motion of the LV thus affect the external boundary conditions of the MV, which in turn place the MV leaflets in a state of altered strain. In response to this, the MV undergoes a complex process of growth and remodeling (G&R) in an attempt to adapt to its new ventricular environment.

Pregnancy represents a non-pathological, LV volume overload paradigm for increased MV loading. It has been shown to produce rapid, dramatic changes in the mechanical behavior and structure of MV leaflet tissue [1,2]. Interestingly, the mechanical behavior of the MV anterior leaflet undergoes a biphasic change during pregnancy; with the apparent stiffness of the leaflet increasing significantly in early pregnancy but returning to normal by the end of pregnancy [1]. In contrast, a more recent investigation into structural changes of MV collagen during pregnancy uncovered no biphasic changes, but instead found only monotonic changes in mass fraction, fiber direction, and fiber alignment [2].

The objective of the present study was to reconcile these two sets of seemingly contradictory results by using a structural constitutive modeling approach that could unify the biphasic mechanical and monotonic structural trends of these previous studies. This goal sets the stage for developing a comprehensive G&R model of MV tissues.

METHODS

Data Collection and Processing. Experimental methods for tissue harvest and mechanical testing have been described previously [1]. Briefly, fresh MV anterior leaflets from 5 never-pregnant heifers (NP) and 10 pregnant cows (P) at a variety of post-conception time points were excised, and their dimensions were measured. A rectangular specimen from the belly region of each anterior leaflet was mechanically preconditioned and loaded under a membrane tension-controlled equibiaxial protocol to a peak tension of 60 N/m in both directions. The Green-Lagrange strain ($\mathbf{E}$) and second Piola-Kirchhoff stress tensors ($\mathbf{S}$) were calculated at each loading state, referenced to the current excised state. To establish direct correspondence between NP and P material behaviors, the constitutive relation for all specimens was expressed with respect to a single pre-pregnant reference configuration, estimated from dimensional changes for P specimens.

Constitutive Model. We utilized a meso-scale structural constitutive model (MSSCM) for MV leaflet tissues [3]. Under this formulation, the total stress in the leaflet was assumed to be the weighted linear sum of the stresses borne by the underlying collagen and elastin fiber networks. The collagen phase is modeled at the level of an undulated fiber ensemble, which exhibits the properties of a unidirectional population of collagen fibers having a bounded distribution of slack strains with lower bound E_{lb} and upper bound E_{ub}. We modeled the distribution of slack strains D with mean μ_D and standard deviation σ_D using a beta distribution to describe the recruitment of fibers in an ensemble.

We defined a beta-distributed orientation distribution function (ODF) $\Gamma(\theta)$ mapped onto $\left[-\pi/2, \pi/2\right]$ with mean μ_Γ and standard deviation σ_Γ, which describes the directional density of fibers at any angle θ from the circumferential axis. The total stress in the collagen network is the sum of stresses along all ensemble directions, weighted by the ODF.

In accordance with previous findings, the elastin phase was modeled as the superposition of two orthogonal populations. Skipping several derivation steps, the sum of the stresses borne by collagen and elastin, weighted by mass fractions ϕ_c and ϕ_e respectively, yields the total tissue-level $\mathbf{S}$ as

Copyright 2016 The Organizing Committee for the 2016 Summer Biomechanics, Bioengineering and Biotransport Conference

$$\mathbf{S}(\mathbf{E}) = \phi_c \eta_c \int_{-\pi/2}^{\pi/2} \Gamma(\mu_\Gamma, \sigma_\Gamma, \theta) \left[\int_0^{E_{ens}} \frac{D(\mu_D, \sigma_D, E_{lb}, E_{ub}, x)}{2x+1} \left(1 - \sqrt{\frac{2x+1}{2E_{ens}+1}}\right) dx \right] (\hat{N} \otimes \hat{N}) d\theta + \phi_e \left[\eta_e^C (I_4 - 1)(\hat{N}_C \otimes \hat{N}_C) + \eta_e^R (I_6 - 1)(\hat{N}_R \otimes \hat{N}_R) \right] \quad (1)$$

where $\{\eta_c, \eta_e^C, \eta_e^R\}$ are the effective stiffness moduli of collagen, circumferential elastin, and radial elastin, respectively; $E_{ens} = \hat{N}^T \mathbf{E} \hat{N}$ is the strain for an ensemble pointing in $\hat{N}$; $\{\hat{N}_C, \hat{N}_R\}$ are the circumferential and radial direction vectors, respectively; $I_4 = \hat{N}_C{}^T (\mathbf{F}^T \mathbf{F}) \hat{N}_C$; and $I_6 = \hat{N}_R{}^T (\mathbf{F}^T \mathbf{F}) \hat{N}_R$. The contributions of the collagen and elastin terms can be easily decomposed.

Parameter Estimation. Collagen and elastin moduli were fixed and volume fractions were taken from previous findings [2]. The remaining structural parameters of the recruitment function D and ODF Γ were estimated using a Differential Evolution search algorithm implemented in Wolfram Mathematica [3].

RESULTS

Leaflet Dimensions. Reanalysis of previous dimensional results from [2] showed that circumferential and radial leaflet lengths increase monotonically with fetal age, reaching growth stretches of 1.4 and 1.2 respectively by term (Figure 1; $R^2 = 0.510$ and 0.226, $p < 0.01$).

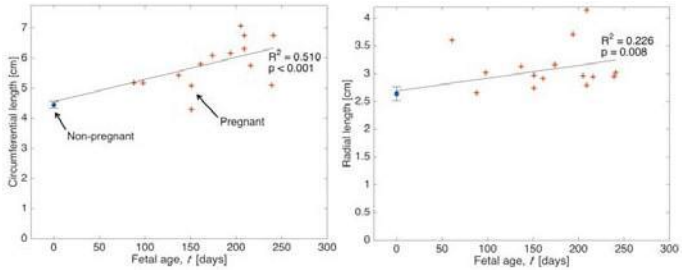

Figure 1: Circumferential (left) and radial (right) leaflet lengths versus fetal age, showing a monotonic increase in both.

Model Fitting. The MSSCM generated excellent fits to the mechanical data, achieving $R^2 = 0.940$ on average (Figure 2).

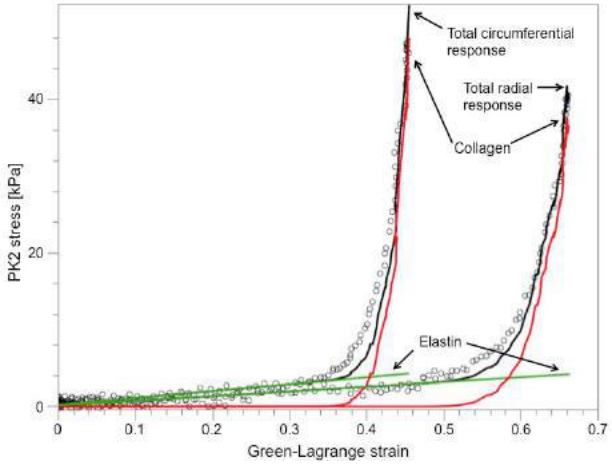

Figure 2: Sample fit, showing collagen and elastin contributions.

Collagen Fiber Orientation. The preferred fiber angle μ_Γ increased significantly in pregnancy (7° in P specimens compared to 3° in NP, $p = 0.035$). In addition, the splay of collagen fibers σ_Γ decreased modestly in early pregnancy but then increased continuously beyond its NP value ($p = 0.036$).

Collagen Fiber Recruitment. The mean stretch value at which collagen fibers were recruited (calculated from μ_D) was found to correlate strongly with fetal age (Figure 3; $R^2 = 0.572$, $p = 0.006$). Specifically, the results show a sharp drop from NP in early pregnancy, followed by a gradual return to NP range during middle and late pregnancy. In contrast to the results, passive stretching to match the dimensional changes would have caused recruitment stretch to decrease monotonically, since fibers would become progressively less crimped. Our results are thus evidence of the significant role that G&R play in actively changing the fiber structure of the MV.

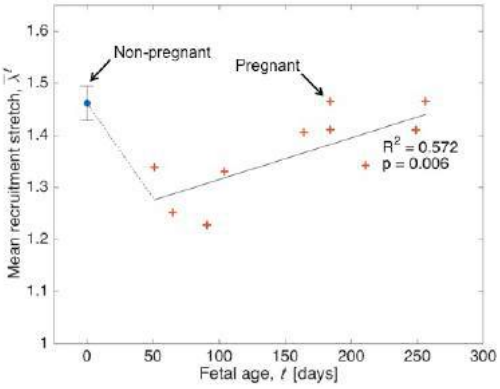

Figure 3: Mean recruitment stretch for both NP and P specimens, showing a trend that mirrors that of the leaflet's extensibility.

DISCUSSION

In this study, we have used a structural constitutive model to directly deduce changes in collagen fiber architecture during pregnancy. Our results provide the first detailed structural information of MV remodeling *in vivo*. While the changes in ODF parameters are primarily monotonic, continual G&R bring about a biphasic trend in mean recruitment stretch mirroring that of the mechanical response of the leaflet, which exhibits decreased extensibility in early pregnancy and a full recovery of the pre-pregnant response by term [1].

While early pregnancy parameter results are consistent with what would be expected under passive stretching (i.e. no G&R), the results deviate significantly from that trend after about 80 days. We hypothesize that G&R in the MV is mediated by deformations of the embedded interstitial cells [4], which would suggest that there is a threshold of abnormal cellular deformation beyond which G&R is triggered in an effort to restore homeostasis and physiological function. Future studies must aim to draw a more intimate connection between these mechanical and biological realms of valvular G&R under overload-induced conditions of increased leaflet strain.

ACKNOWLEDGEMENTS

NIH grants R01HL119297 and R01HL108330. Rego is supported by the NSF Graduate Research Fellowship Program.

REFERENCES

[1] Wells, SM et al., *Am J Physiol*, 303(7):H878-H892, 2012.
[2] Pierlot, CM et al., *Ann Biomed Eng*, 40(10):2058-2071, 2014.
[3] Zhang, W et al., *Acta Biomater*, doi:10.1016/j.actbio.2015.12.001.
[4] Lee, CH et al., *J Theor Biol*, 373:26-39, 2015.

Copyright 2016 The Organizing Committee for the 2016 Summer Biomechanics, Bioengineering and Biotransport Conference

SB^{3}C2016
Summer Biomechanics, Bioengineering and Biotransport Conference
June 29 –July 2, National Harbor, MD, USA
SB^{3}C2016-804

REGIONAL VARIATIONS IN THE MECHANICAL STRAINS OF THE HUMAN OPTIC NERVE HEAD

D.E. Midgett (1)

M.E. Pease (2), H.A. Quigley (2), M. Patel (3), C. Franck (3)
T.D. Nguyen (1)

(1) Mechanical Engineering
Johns Hopkins University
Baltimore, MD, United States

(2) Wilmer Eye Institute
Johns Hopkins University
Baltimore, MD, United States

(3) School of Engineering
Brown University
Providence, RI, United States

INTRODUCTION

In glaucoma, the progressive loss of the retinal ganglion cells (RGCs) in the optic nerve head leads to permanent vision loss and eventual blindness. The intraocular pressure (IOP) is associated with the prevalence and severity of glaucoma damage, and the level of IOP is used to screen for the disease. Animal studies have shown that a chronic increase in IOP causes glaucoma damage, and lowering pressure slows the progression of damage in the majority of patients. However, there is a wide distribution of IOP among glaucoma patients and among those without glaucoma. While glaucoma patients on average have higher IOP, nearly half of those with glaucoma damage have IOP in the normal range. Moreover, a significant number of those with higher IOP do not have glaucoma damage [1-4]. These observations suggest that the susceptibility of the ONH to glaucoma damage might depend on its mechanical response of the ONH and surrounding sclera. Computational modeling studies of the posterior sclera have suggested that the elastic modulus of the LC and sclera strongly correlates with the strains experienced in the LC [5].

Both clinical and laboratory studies have measured differences in the mechanical behavior and structure of the posterior sclera, LC and ONH of glaucoma and normal eyes. Structural changes in glaucoma include the remodeling of the anisotropic collagen fiber and elastin structure at the lamina cribrosa [4] and axial elongation and thinning of the sclera [6-8]. Hommer et al [9] measured an increase in ocular rigidity with the progress of open-angle glaucoma. Downs et al [10] found a larger relaxation modulus for scleral strips from monkey eyes with experimentally induced early glaucoma. Girard et al measured a stiffening of the sclera [11]. Coudrillier et al [12] reported a thickening of the peripapillary sclera, slower circumferential creep rates, and a stiffer behavior in the meridional direction of the peripapillary sclera in human eyes with glaucoma. Few studies have measured the mechanical behavior of the lamina cribrosa. In this study, we present a method to measure the three-dimensional deformation field in the lamina cribrosa under controlled inflation. The method uses laser-scanning second harmonic generation microscopy to image the collagen structures of the deforming volume of the lamina cribrosa and digital volume correlation for deformation mapping.

METHODS

Six human eyes from 5 donors (ages 26-71) obtained within 48 hours post-mortem had the choroid and retina removed, the optic nerve removed at the sclera (the myelin line), and the posterior sclera mounted on a custom inflation chamber. The pressure was raised to 5, 10, and 45 mmHg. A Zeiss LSM 710 NLO microscope, tuned to 790nm with a band pass 390-410nm filter, was used to acquire two duplicate stacks of the LC structure using second harmonic generation (SHG) imaging at each pressure. The SHG stacks were treated with Huygens Essential deconvolution algorithm using a theoretical point spread function (SVI) and local adaptive histogram equalization (FIJI) to enhance contrast. The Fast Iterative Digital Volume Correlation (DVC) algorithm [14] was used to post-process the SHG stacks to calculate the 3D displacement fields and correlation error. The correlation coefficient was used to remove poorly correlating subsets and Gaussian filtering was used to remove local error spots. Strains were calculated by fitting a high order polynomial function to the displacement field and taking the gradient locally. The LC was divided into 4 quadrants surrounding the central retinal artery and vein (inferior-nasal (IN), inferior-temporal (IT), superior-nasal (SN), superior-temporal (ST). The principal strains were averaged and analyzed for regional differences.

Copyright 2016 The Organizing Committee for the 2016 Summer Biomechanics, Bioengineering and Biotransport Conference

RESULTS

Displacements and strains in the LC exhibited substantial variation in the plane but not through the thickness (Figure 1). The average shear strains (in plane: -0.15±0.14%, out of plane: -0.22±0.23%, 0.19±0.34%) were significantly smaller than the normal strains. For nearly all eyes, the strain at 45mmHg along the inferior-superior axis (3.02±1.09%) was larger than along the nasal-temporal axis (2.03±0.75%). The maximum principal strain was largest in the IT quadrant and smallest in the IN quadrant. In paired t-tests, the maximum principal strain in IT was significantly larger than in IN (p=0.026) and nearly significantly larger than in SN (p=0.067) and IT (p=0.076).

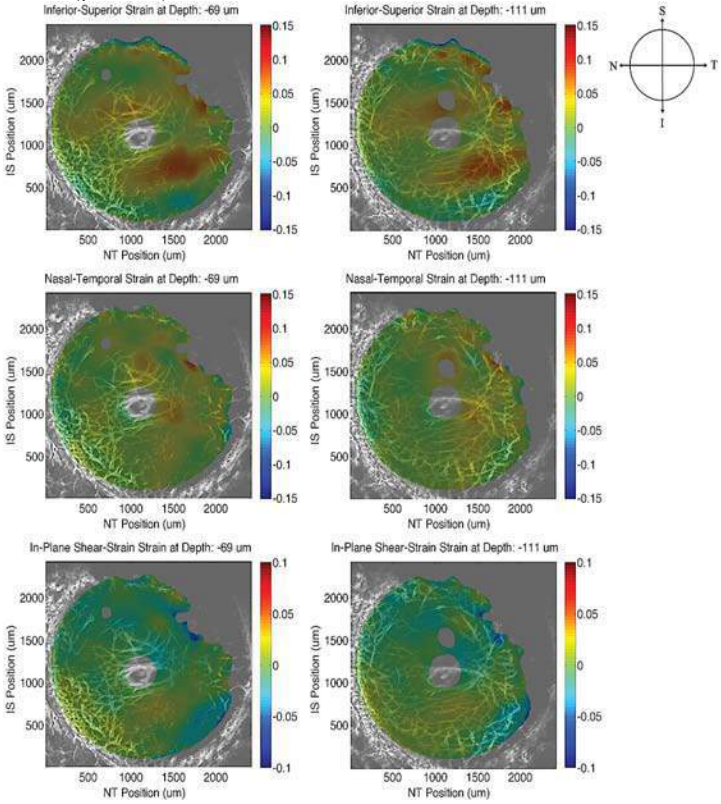

Figure 1, Contour plots of the in-plane normal and shear strains for the LC of a 57-year old Caucasian male

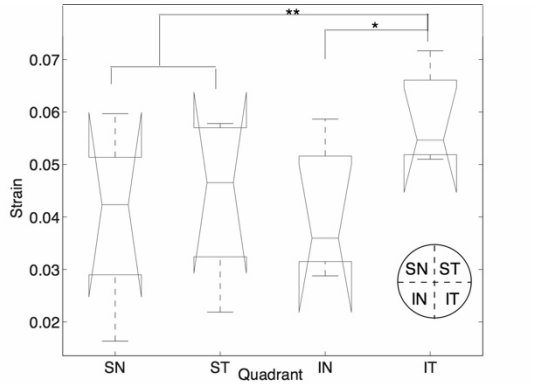

Figure 2, Maximum principal strain in the human LC at 45 mmHg. The IT quadrant was statistically larger than the IN (*p<0.05), SN and ST (p<0.1) quadrants.**

DISCUSSION

This study demonstrates that the configuration of collagen in the human LC, imaged by SHG in an inflation experiment, can be correlated using DVC. This allows for the calculation of 3D displacement and strain fields at high resolution for in-vivo LC tissues as a function of applied pressure. Preliminary data suggests strong anisotropy in the strain response of the LC, which may help to explain the progression of axonal damage in glaucoma. The current body of research indicates that glaucoma pathologically remodels the tissues of the ONH in a way that causes constriction of the nerve cross-section and "cupping" at the ONH, a phenomenon where the rim of the tissue making up the ONH narrows and deepens. RGCs with larger diameter are damaged first indicating straining of the nerves may be a major cause of damage. The injury pattern typically expresses in an hourglass shape with preferentially greater injury at the superior and inferior poles. [1] Our results indicated greater strains in the inferior-superior direction which would lead to warping of the ONH cross section and greater strains on the RGCs at the inferior and superior poles, which agrees with known glaucoma damage patterns. The main limitation of the study is insufficient resolution to calculate accurate out of plane strains.

ACKNOWLEDGEMENTS

Grants supporting this project: NSF CAREER Award #1253453, PHSR Grant EY021500, EY02120, EY01765

Equipment and Facilities: Wilmer Eye institute laboratories and microscopes

Wilmer Eye Institute Personnel: Cathy Nguyen, Rhonda Grebe, Lizzie Kimball

REFERENCES

[1] Quigley HA, *Prog in Ret and Eye Res*, 1997;18:39–57.
[2] Burgoyne CF, et al, *Prog Retin Eye Res,* 2005;24:39–73.
[3] Morrison JC, et al, *Prog Retin Eye Res*, 2005;24:217–240.
[4] Hernandez MR, et al, *Arch Ophthalmol*, 1997;115:389–395.
[5] Sigal IA, et al. *Invest Ophthalmol Vis Sci*, 2005;11:4189–4199.
[6] Cone FE, et al, *Exp Eye Res*, 2010;91:415–424.
[7] Nguyen C, et al. *Invest Ophthalmol Vis Sci*, 2013;54:1767-1780.
[8] Elizabeth CK, et al, *Molecular Vision,* 2013; 19:2023-2039
[9] Hommer A, et al, *Invest Ophthalmol Vis Sci*, 2008;49:4046–4050.
[10] Downs JC, et al, *Invest Ophthalmol Vis Sci*, 2005;46:540–546.
[11] Girard MJA, et al, *Invest Ophthalmol Vis Sci,* 2011;52:5656–5669.
[12] Coudrillier B, et al, *Invest. Ophthalmol. Vis. Sci,* 2012:53:1714-1728.
[13] Bar-Kochba E, et al, *Experimental Mechanics*, January 2015: 55:261-274.

Copyright 2016 The Organizing Committee for the 2016 Summer Biomechanics, Bioengineering and Biotransport Conference

SB^{3}C2016
Summer Biomechanics, Bioengineering and Biotransport Conference
June 29 –July 2, National Harbor, MD, USA
SB^{3}C2016-805

WHEN THEATRE COMES TO CAPSTONE DESIGN: OH HOW CREATIVE THEY CAN BE…

Ferris M. Pfeiffer, PhD (1,2), Suzanne Burgoyne, PhD (3), Rachel E. Bauer, MA (3)

(1) Department of Bioengineering
University of Missouri
Columbia, MO, USA

(2) Department of Orthopaedic Surgery
University of Missouri
Columbia, MO, USA

(3) Department of Theatre
University of Missouri
Columbia, MO, USA

INTRODUCTION

The creative process is fun, complex, and sometimes frustrating, but it is critical to the future of our nation and progress in science, technology, engineering, mathematics, as well as a multitude of other fields. Part artist and part scientist, successful innovators and entrepreneurs are fueled by a passion to find a solution. A pursuit of innovation can be instilled at an early age and, properly fostered, can help develop students into 21st century creative scientists, engineers, and innovators [1]. It may seem quite unconventional to some, but successful engineers and artists share many qualities particularly in areas of creativity. How this creativity is manifested in the engineer and artist sometimes varies widely. Engineers often create with more tangible materials such as metal and plastic while artists may create with more abstract materials (e.g. paint, voice, instrument, body, etc). This divergence in creative expression is due in part to the educational experience of each discipline. By the time most engineers and artists reach undergraduate education they are on very different paths in how they acquire, interpret, and present knowledge. As a teacher and mentor of many engineering students, I see the value of having innovative, creative, self-motivated, and sometimes fearless individuals who can develop unique solutions. We often hear this referred to as "thinking outside the box". It turns out, that most artists are innovative, creative, self-motivated, and mostly fearless in their craft. Thus, we set out to see if implementing methods of active learning typical to the theatre department could impact the creativity of senior capstone design students in the Bioengineering department.

METHODS

Senior Bioengineering (BE) capstone design students (n=45) were allowed to self-select into groups (n=5 per group) based upon capstone design projects pre-identified by the faculty mentors facilitating the class. A sub-set of these students (3 groups; n=15 total students) were randomly assigned to be in the experimental (E) group. All other students were assigned to be in the control (C) group.

Prior to the beginning of coursework, all students completed a validated survey measuring engineering design self-efficacy [2]. Albert Bandura's theory of self-efficacy proposes that people's beliefs in their capability to achieve a task affect their actual ability to achieve that task--if they have the requisite skills. Noted psychologist Bandura points to numerous studies showing that people who rate their self-efficacy high for a particular task will be more motivated, and will perform better, than people with more ability who rate their self-efficacy lower [3]. Self-efficacy theory is very relevant to creativity, since experts point out that a system designed to educate students for the industrial age squashes the creativity out of them. Students are conditioned to believe they inherently lack creativity, and any approach to creativity education must address this issue and help students to rediscover their innate creative potential [4].

The control and experimental groups both received standard instruction, but in addition the experimental group received one hour per week of creativity training developed by a theatre professor. Having taken a faculty development leave in 2010/2011 to design a course in creativity for non-arts majors which she has since taught annually, the professor and a graduate assistant led the engineering students in a condensed version of her creativity course. This active learning process integrated techniques drawn from actor training, improvisation, and theatre of the oppressed [**5]** with creative problem-solving methods drawn from multiple research-based sources [6]. For instance, a short lecture comparing convergent and divergent thinking was immediately followed by a theatre exercise in which the class, divided into two

Copyright 2016 The Organizing Committee for the 2016 Summer Biomechanics, Bioengineering and Biotransport Conference

groups, put divergent thinking into action by quickly inventing forty ways to cross a room. Theatre games helped the students develop a safe, supportive environment in which students could begin to venture outside their comfort zones. Unless one is willing to risk trying something new—and making mistakes--one can't be creative. Theatre exercises also enabled students to open their minds, question assumptions, and see things differently, since creativity is more about seeing things differently than seeing different things. Other exercises involved active listening, framing and reframing their creative problems, using analogies to brainstorm solutions, and evaluating and refining solutions.

Following the semester, the students again completed the self-efficacy survey. The surveys were examined to identify differences in the initial and final self-efficacy as well as to compare change in the experimental and control groups over the course of the semester. An analysis of variance was used to compare the experimental and control groups with $p<0.05$ considered significant.

RESULTS

Students in the experimental group reported more than a two-fold (4.8 (C) vs 10.9 (E)) increase of confidence in their ability to perform engineering design following a single semester of creativity education (Figure 1 column a). Substantial increases in student confidence were seen in other surveyed areas as well with the exception of prototype development (Figure 1 column f) and design evaluation (Figure 1 column g). Additionally, students in the experimental group were more motivated (4.2 (E) vs 0.2 (C)) (Figure 2) and less anxious (-7 (E) vs -6.2 (C)) (Figure 3) when engaging in engineering design following the semester of creativity instruction.

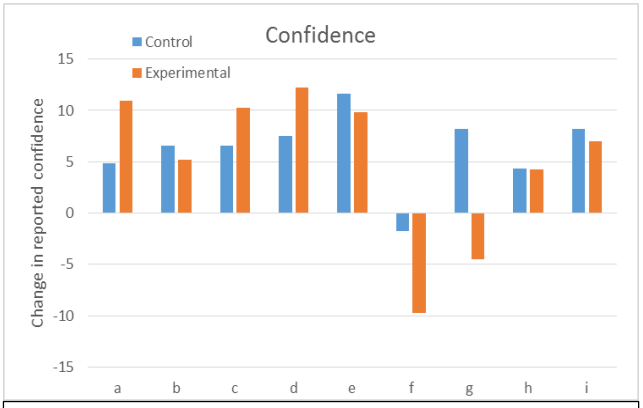

Figure 1. Student self-reported change in confidence in the engineering design process following a semester using a "curriculum of creativity".

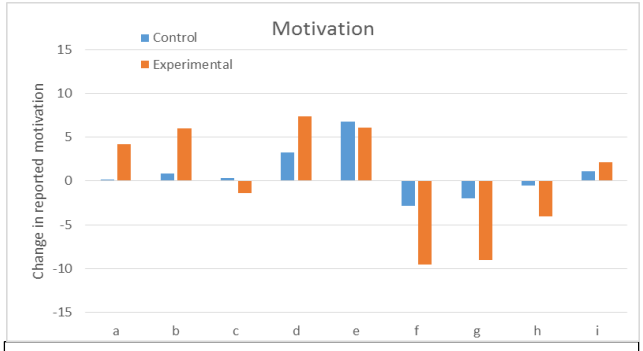

Figure 2. Student self-reported change in motivation in the engineering design process following a semester using a "curriculum of creativity".

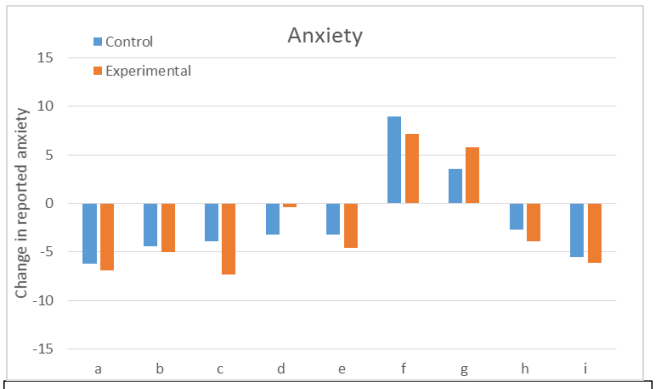

Figure 3. Student self-reported change in anxiety in the engineering design process following a semester using a "curriculum of creativity".

The only surveyed area in which students in the experimental group were significantly less confident and motivated as well as more anxious than students in the control group was in the area of constructing a prototype and evaluating their design (Figures 1-3 columns f and g). Prototyping and design evaluation were not a focus of the class in general and such tasks were not covered in the creativity curriculum. However, plans are underway to include activities to strengthen these areas in future classes.

DISCUSSION

The results of this pilot study indicate there is significant potential to improve engineering students' creative self-efficacy through the implementation of a "curriculum of creativity" which is developed using theatre methods. Further research is needed to evaluate the long term effects of such instruction. We also intend to investigate if this type of instruction can be deployed throughout other courses along the spectrum of the engineering undergraduate education. This pilot work provides promising initial data which can help refine methods and shows the potential for increasing student creativity using an unconventional approach.

ACKNOWLEDGEMENTS

This work was supported by the Comparative Orthopaedic Lab and the Center for Applied Theatre and Drama Research.

REFERENCES

1. Zenios, S., et al., *Biodesign: The Process of Innovating Medical Technologies*. 2010, New York: Cambridge University Press.
2. Carberry, A.R., H.-S. Lee, and M.W. Ohland, *Measuring Engineering Design Self-Efficacy*. Journal of Engineering Education, 2010. **99**(1): p. 71-79.
3. Bandura, A. *Self-Efficacy: The Exercise of Control.* 1997. New York: Freeman.
4. Robinson, Sir K. *Out of Our Minds: Learning to Be Creative*, rev. ed. 2011. Chichester, U.K.: Capstone.
5. Boal, A. *Games for Actors and Non-actors,* 2nd ed. 2002. Trans. A. Jackson. London: Routledge.
6. Sawyer, K. *Zig-Zag: The Surprising Path to Greater Creativity*. 2013. San Francisco: Jossey-Bass.

Copyright 2016 The Organizing Committee for the 2016 Summer Biomechanics, Bioengineering and Biotransport Conference

SB^{3}C2016
Summer Biomechanics, Bioengineering and Biotransport Conference
June 29 –July 2, National Harbor, MD, USA
SB^{3}C2016-807

CHONDROCYTE DEATH AND MITOCHONDRIAL DYSFUNCTION ARE MEDIATED BY CARTILAGE FRICTION AND SHEAR STRAIN

Edward D. Bonnevie (1), Michelle L. Delco (2), Naveen Jasty (1), Lena R. Bartell (3), Lisa A. Fortier (2), Itai Cohen (3), Lawrence J. Bonassar (1,4)

(1) Sibley School of Mechanical and Aerospace Engineering
Cornell University
Ithaca, NY, USA

(2) Comparative Biomedical Sciences
Cornell University
Ithaca, NY, USA

(3) Applied Engineering Physics
Cornell University
Ithaca, NY, USA

(4) Meinig School of Biomedical Engineering
Cornell University
Ithaca, NY, USA

INTRODUCTION

Both injury and disease reduce synovial fluid's ability to lubricate articular cartilage, and recently, inferior lubrication has been linked to chondrocyte apoptosis [1]. However, the specific biological mechanisms and mechanical thresholds that lead to this cell death remain unknown. Both cell death and mitochondrial (MT) dysfunction within articular chondrocytes can accompany impact injuries, and both are correlated with tissue strain [2-3]. Additionally, tissue strain during articulation is a function of both lubricant composition (i.e., friction coefficient) and depth from the tissue surface [4-5]. Thus, the goals of this study were: 1) to measure the depth-dependent shear strains of cartilage for friction coefficients that span the range between injury and disease, and 2) to connect these results to cellular changes within articular cartilage including cell death and MT dysfunction. Collectively, these data will help to describe what role inferior lubrication may play in the progression of cartilage damage.

METHODS

Cartilage was obtained from the femoral condyles of 1-3 day old bovids. Friction coefficients were measured against glass under 15% normal strains while lubricated by either PBS or equine synovial fluid (ESF). Samples were articulated for 30 cycles at 1 mm/s (Fig 1A) then allowed to reequlibrate in DMEM for 90 minutes. This set-up was mounted in parallel on an inverted confocal microscope, and local shear strains of 5-DTAF stained cartilage were measured by tracking the displacements of photobleached lines (Fig 1B). Slid samples and controls without 5-DTAF were stained with either calcein AM and ethidium homodimer (for live and dead cells, respectively) or MitoTracker Green (MTrG) and tetramethylrhodamine methyl ester (TMRM) (for all MT and functional MT, respectively). Percent cell death and MT dysfunction were calculated through image analysis conducted using ImageJ.

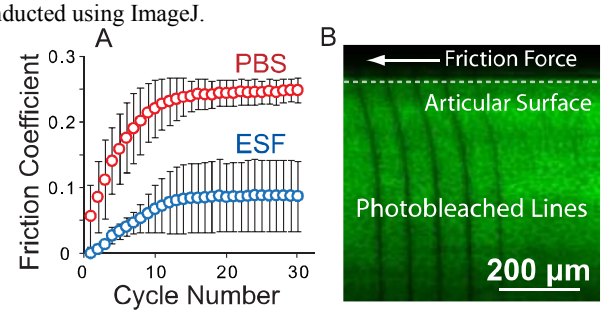

Figure 1: (A) Friction coefficients for PBS- and synovial fluid-lubricated cartilage (n=4). (B) Frictional shear strains are tracked on a confocal microscope.

RESULTS

The friction coefficient of cartilage lubricated by ESF was 70% lower than PBS (0.08 to 0.26, Fig 1A), and depth-dependent shear strain profiles scaled similarly (Fig 2). In the ESF lubricated cartilage, shear strains near the surface were ~4% and leveled off to ~1% in deeper tissue, but for the PBS group, shear strains were over 9% near the surface and under 5% in deeper tissue. In non-slid control tissue, minimal cell death was found (Fig 3CD). For ESF-lubricated cartilage, cell death was localized to the region less than 50 μm from the surface, within the two most superficial cell layers (Fig 3BD). However, for PBS-lubricated cartilage, cell death extended over 100 μm from the articular surface (Fig 3AD). In contrast to cell death data, sliding in both PBS and ESF caused MT dysfunction in the superficial zone (top most 100 μm).

Copyright 2016 The Organizing Committee for the 2016 Summer Biomechanics, Bioengineering and Biotransport Conference

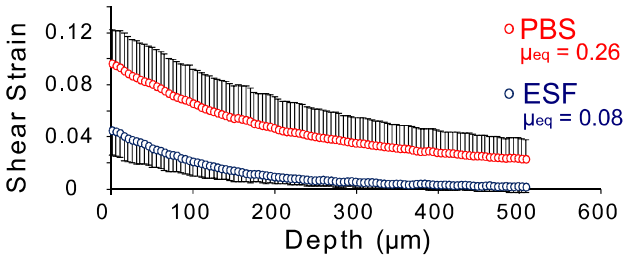

Figure 2: Frictional shear strains are dependent on lubricant composition, friction coefficient (μ_{eq}), and tissue depth (n=6-7).

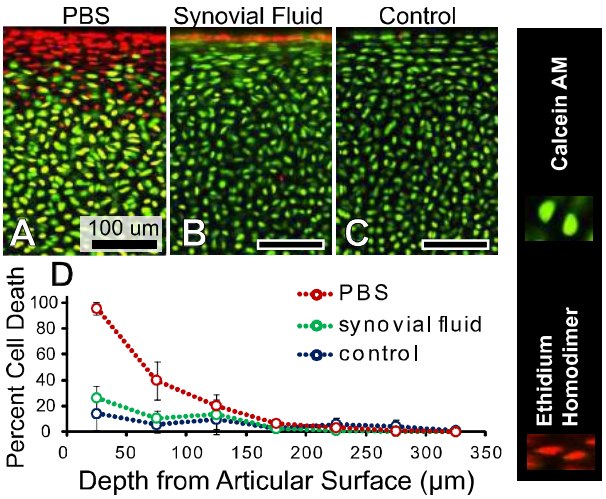

Figure 3: (A-C) Live dead staining of cartilage with different friction conditions. (D) Cell death was most pronounced in the superficial 100μm of PBS-lubricated cartilage (n=4).

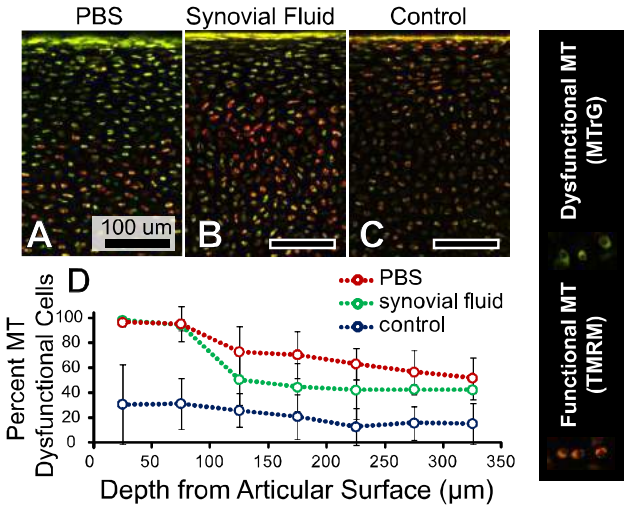

Figure 4: (A-C) MT staining of cartilage with different friction conditions. (D) MT dysfunction was most pronounced in the superficial 100μm of PBS- and ESF-lubricated cartilage (n=4).

For the control tissue, colocalization of MTrG (staining all MT) and TMRM (staining only polarized MT) occurred within functional chondrocytes near the surface (within 100 μm) (Fig 4CD). However for both ESF and PBS, colocalization of both MTrG and TMRM was rare within the superficial tissue (Fig 4).

DISCUSSION

This study connected cartilage friction coefficient with depth-dependent shear strains in cartilage to understand mechanical cues that lead to both cell death and MT dysfunction (Fig 5). We revealed significant cell death within the superficial 100 μm of cartilage lubricated by PBS where shear strains ranged from 7% to 9% (Fig 5A). This region is known to have increased apoptosis in joints with high boundary friction [1]. Conversely, minimal cell death was detected in the ESF-lubricated tissue, likely due to the lower shear strains (~4%, Fig 5B). Interestingly, both ESF- and PBS-lubricated cartilage displayed mitochondrial dysfunction within the superficial 100 μm of tissue. While this result can be attributed to cell death in the PBS group, it is likely that live cells in the ESF group may be destined for MT-mediated apoptosis. Notably, although the deeper chondrocytes in the PBS group were exposed to high shear strains (~4%) there was little evidence of MT dysfunction (Fig 5C). However, superficial cells in the ESF group experience similar shear strains but displayed pronounced MT dysfunction (Fig 5D). This phenomenon may indicate that the chondrocytes in the different regions of articular cartilage respond differently to mechanical signals regarding both necrosis and apoptosis, and that dysfunctional cells may be an important target for restabilization and ultimate prevention of PTOA.

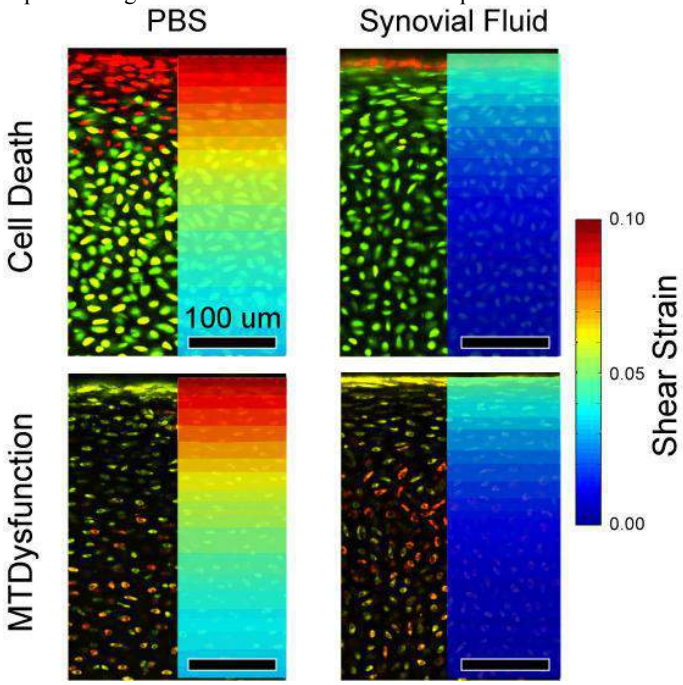

Figure 5: Strain field overlays reveal the relationships between shear strain and both cell death and MT dysfunction. For PBS-lubricated tissue, cell death and MT dysfunction were localized to high strain regions. For ESF-lubricated tissue, minimal cell death, but significant MT dysfunction were localized to superficial tissue.

ACKNOWLEDGEMENTS

This study was supported by the NSF GRFP and the NIH.

REFERENCES

[1] Waller, K. et al., *P NATL ACAD SCI USA,* 110:5852-5857, 2013.
[2] Bartell, L. et al., *J Biomech*, 48:3440-3446, 2015.
[3] Delco, M. et al., *Osteoarth Cart,* 23:A288-A289, 2015.
[4] Bonnevie, E. et al., *PloS ONE,* 10.11, 2015.
[5] Wong, B. et al. *Arthritis Rheum,* 58.7: 2065-2074, 2008.

Copyright 2016 The Organizing Committee for the 2016 Summer Biomechanics, Bioengineering and Biotransport Conference

SB^{3}C2016
Summer Biomechanics, Bioengineering and Biotransport Conference
June 29 –July 2, National Harbor, MD, USA
SB^{3}C2016-808

THE INFLUENCE OF GEL STIFFNESS ON GROWTH FACTOR GENE EXPRESSION OF SCHWANN CELLS

Carlisle R. DeJulius (1), Rebecca Kuntz Willits (1)

(1) Department of Biomedical Engineering
The University of Akron
Akron, Ohio, U.S.A.

INTRODUCTION

There are an estimated 360,000 instances of injury to peripheral nerves per year in the United States. These injuries can be very debilitating to patients, causing paralysis in the worst cases. If regeneration is possible, the unaided rate of neuronal repair is 1mm/day[1]. Schwann cells are glial cells in the peripheral nervous system that provide support to neurons. Under normal conditions, Schwann cells insulate axons to protect them while secreting neural growth factors such as glial cell line-derived neurotrophic factor (GDNF) and neurotrophin-3 (NT-3)[2]. When nerves are damaged, Schwann cells serve to break down debris and encourage regeneration of the neurons. Studies of nerve regeneration seek a method to speed the growth rate of injured neurons. One option is to use a three-dimensional scaffold to act as a bridge between the severed ends. This study makes use of poly(ethylene glycol) (PEG) hydrogels as an eligible material. PEG is suitable because both the mechanical and chemical properties of PEG gels can be easily modified[3].

Because Schwann cells are vital to neuronal health, this project aims to investigate the gene expression of these cells with particular focus on key growth factors. Previous work has shown increased proliferation of Schwann cells within 3D scaffolds with modulus of ~500 Pa[2]. Therefore, we hypothesized that the expression of growth factors in Schwann cells are up-regulated gels of similar stiffness to maximum proliferation.

METHODS

Isolating RNA from Cells Cultured in PEG Hydrogels: Primary rat Schwann cells were isolated for other studies to ~100% purity (via S-100). PEG gels were prepared using 3kDa PEG diacrylate (PEGDA) at a concentration of 5% by mixing PEGDA, 0.5% Irgacure (photoinitiator), and phosphate-buffered saline (PBS). Cells were encapsulated in the gels at a concentration of 400,000 cells/mL. Trizol was added to the gels, and after centrifugation, the Trizol-cell solution was removed to a new tube and chloroform was added to enhance phase separation. The RNA was precipitated using 100% isopropanol. The pellet was washed 3 times with 75% ethanol and resuspended in molecular biology-grade water. A DNA digestion was performed using PerfeCTa DNase I Kit (Quanta Biosciences). RNA quality was evaluated using gel electrophoresis and spectroscopy.

Testing Stiffness of PEG Hydrogels: Oscillatory shear rheometry (8mm parallel plate) was used to measure the shear modulus (G*) of the hydrogels (n=4 for each test). The strain was kept constant at 5% and moduli were taken at 10rad/s. The goal G* were selected to match a previous study[2] at 130Pa, 240Pa, 560Pa, and 720Pa. ANOVA was used to test significance of results ($p<0.05$).

Evaluating Gene Expression of Schwann Cells: RNA of sufficient quality was reverse transcribed to cDNA using qScript cDNA Synthesis Kit (Quanta Biosciences). Amplitaq Gold 360 Mastermix was used to perform PCR, and gene expression was evaluated with gel electrophoresis. The genes of interest are listed in **Table 1** and include growth factors and growth factor receptors. The intensity of the gel electrophoresis bands was analyzed using ImageJ software. All gene expression was normalized to the housekeeping gene β-actin. ANOVA was used to test significance of results ($p<,0.05$).

RESULTS

Isolating RNA from Cells Cultured in PEG Hydrogels: Several changes were made when optimizing the Trizol RNA isolation procedure for cells cultured in 3D gels. First, the gels were incubated in Trizol for 15 minutes instead of the manufacturer suggested 5 min to allow for complete lysing. The Trizol-cell solution then had to be separated from the gel, as stated previously. At this point, the isolation procedure continued as it would for cells cultured on 2D substrates. During RNA quality testing, it was determined that soluble PEG

Copyright 2016 The Organizing Committee for the 2016 Summer Biomechanics, Bioengineering and Biotransport Conference

interfered with absorbance, so gel electrophoresis was solely used to check quality. Further work determined that PEG contamination did not interfere with subsequent reverse transcription or PCR.

Testing Stiffness of PEG Hydrogels: G* for 12 PEG concentrations were obtained (**Figure 1, n=4**). Using this curve, the PEG concentrations needed for the desired stiffnesses fell between 3.5 to 4.5%. However, the lower concentrations of PEG (**Figure 2**) followed a different trend when separated from the higher concentrations. More data will be collected within this range of PEG concentrations to determine the correct concentrations of PEG.

Evaluating Gene Expression of Schwann Cells: The quality of the housekeeping gene primer and the other primers used has been confirmed; the products show single bands on an agarose gel at the correct molecular weight. Preliminary work has investigated the gene expression of Schwann cells cultured in 2D on PEG gels. Results indicated that mRNA for *TrkB* and *p75* is significantly up-regulated in 3% gels (n=4) when compared to 5% gels (n=4), with no significant difference between 3% and 7% gels (n=1). mRNA for *TrkC* was significantly up-regulated in 3% gels when compared to 5% and 7% gels. In contrast, the mRNA for *GDNF, NT3* and *TrkA* was significantly up-regulated in 5% gels when compared to 3% and 7%. However, it is clear that n must be increased for 7% gels to truly determine significance.

DISCUSSION

Schwann cells are vital to the healing and maintenance of nerves. Manipulation of the cells' gene expression could lead to important clues to optimal conditions for nerve regeneration. This study focused on plain PEG hydrogels because their mechanical properties can be easily varied by changing PEG concentration. It was shown that the stiffness of the PEG gels increases with increasing PEG concentration (**Figure 1**), agreeing with expectations and other work.

Marquardt and Willits obtained a shear modulus of 69.23±4.27Pa for 3% gels, 479.49±9.79Pa for 4% gels, and 992.24±36.07Pa for 5% gels[3]. Their result for 4% gels agreed with the results presented here. However, the result for 5% gels obtained was over twice as high as their result. Minor differences existed between the protocols; e.g., Marquardt and Willits prepared their solutions using DI H_2O instead of PBS[3]. However, potentially more significant was that they tested the gels using 25-mm parallel plate oscillatory shear rheometry as opposed to 8-mm parallel plate. The size difference may be of particular note because the smaller surface area of 8-mm tests could lead to more drying, and thus increased modulus. This outcome will be explored in future work.

Our preliminary results indicated that *GDNF* expression was up-regulated in 5% gels when compared to 3% and 7% gels. Therefore, we are interested to determine if there is a parallel increase in glial growth factor expression in 3D. Zhou et al found Schwann cell proliferation was maximum in 3D gels with a 5x lower modulus than previous 2D studies[4]. Extrapolating this result to the work here, a 5% gel is approximately 5x higher than the 3D modulus that Zhou reported to be optimal for proliferation (563.8 ± 66 Pa)[2]. Therefore, gels of this modulus will be of interest as we continue to gather gene expression data, particularly as both *GDNF* and *NT3* expression was increased in 2D. The up-regulation of these two key growth factors could help to explain why Zhou saw increased proliferation at this modulus.

To date, we have obtained an efficient and effective method of extracting RNA from Schwann cells cultured in 3D. This method could be extended in the future to other cell types or materials. A curve for the shear modulus of PEG gels has been constructed and will be used to determine concentrations to match the target moduli. The gene expression of Schwann cells at these different moduli will be evaluated for information about how a 3D environment influences these cells' behavior, with particular focus on supporting nerve regeneration.

ACKNOWLEDGEMENTS

Funding was provided by Choose Ohio First for Bioinformatics Scholarship and the Margaret F. Donovan Endowed Chair for Women in Engineering.

REFERENCES

[1] Kontoveros, D. (2015). *Schwann Cell Proliferation and Migration in Response to Surface Bound Peptides for Nerve Regeneration*. (Electronic Thesis). Retrieved from https://etd.ohiolink.edu

[2] Zhou, W., J.M. Stukel, and R.K. Willits. Tuning the mechanical properties of poly(ethylene glycol) microgel-based scaffold to increase 3D Schwann cell proliferation. Macromolecular Bioscience, In press, November 2015.

[3] Marquardt, L. and R.K. Willits. Neurite growth in PEG gels: effect of mechanical stiffness and laminin concentration. Journal of Biomedical Materials Research, Part A. 98A: 1-6, 2011.

[4] Gu, Y., et al., *The influence of substrate stiffness on the behavior and functions of Schwann cells in culture.* Biomaterials, 2012. **33**(28): p. 6672-81.

Table 1: Genes of Interest

Gene	Function
β-actin	Housekeeping
Nerve Growth Factor (NGF)	Growth factor
Neurotrophin-3 (NT-3)	Growth factor
Glial-Derived Neurotrophic Factor (GDNF)	Neuronal support
TrkA	NGF receptor
TrkB	NT-3 receptor
TrkC	NT-3 receptor
P75	Low-affinity NGF receptor
GDNF receptor α1 (GRα1)	GDNF receptor

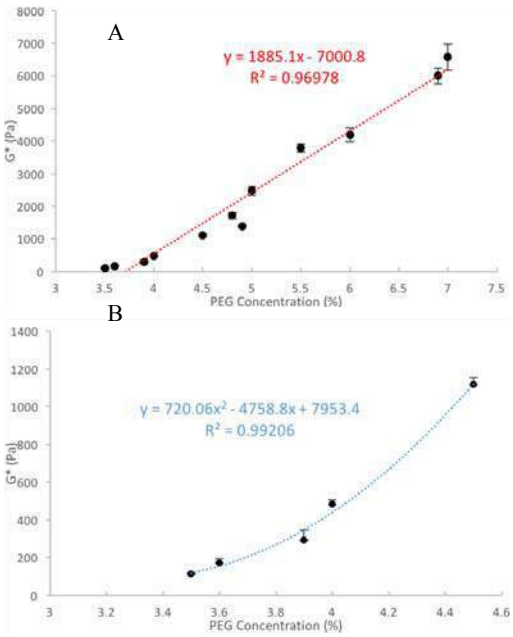

Figure 1: G* (Pa) values plotted against PEG concentration (%) for A) concentrations ranging from 3.5-7% and B) concentrations ranging from 3.5-4.5%. Error bars represent standard error (n varies for each sample, between 3 and 11).

Copyright 2016 The Organizing Committee for the 2016 Summer Biomechanics, Bioengineering and Biotransport Conference

SB³C2016
Summer Biomechanics, Bioengineering and Biotransport Conference
June 29 –July 2, National Harbor, MD, USA
SB³C2016-809

MOLECULAR LEVEL DETECTION AND QUANTIFICATION OF COLLAGEN MECHANICAL DAMAGE USING COLLAGEN HYBRIDIZING PEPTIDES

Jared L. Zitnay (1,2), Yang Li (1), Zhao Qin (3), Baptiste Depalle (3), Shawn P. Reese (1,2), Markus J. Buehler (3), S. Michael Yu (1), Jeffrey A. Weiss (1,2,4)

(1) Department of Bioengineering
University of Utah
Salt Lake City, Utah, USA

(2) Scientific Computing and Imaging Institute
University of Utah
Salt Lake City, Utah, USA

(3) Department of Civil and Environmental Engineering
Massachusetts Institute of Technology
Cambridge, Massachusetts, USA

(4) Department of Orthopaedics
University of Utah
Salt Lake City, Utah, USA

INTRODUCTION

Many painful and physically debilitating conditions involve subfailure damage to connective tissues. As collagen is the major structural component of connective tissues, tissue injury and disease due to over-use, repeated subfailure injury, and trauma presumably involve damage to the hierarchical structure of collagen at one or more physical scales. While previous studies have documented clinically relevant mechanical damage to connective tissues following subfailure loading [1, 2], the exact nature of damage to collagen across its hierarchy of structure is poorly understood. A handful of indirect studies have indicated molecular level collagen damage occurs during overloading [3, 4], but there is no conclusive experimental evidence to indicate the extent, location, or mechanism of molecular level failure of collagen during subfailure loading.

A tissue-level imaging technique capable of directly detecting collagen damage at the molecular level would be highly useful for understanding the relationship between tissue injury and molecular damage. Collagen hybridizing peptide (CHP), a small synthetic peptide consisting of Gly-Pro-Hyp amino acid repeats, mimics the triple-helical molecular structure of natural collagens [5] and binds to unfolded collagen strands [6]. Considering the ability of CHP to hybridize with the unfolded collagen triple helix, we hypothesized that carboxyfluorescein (CF) labeled CHP (CF-CHP) could be used to detect and quantify molecular level damage to collagen caused by mechanical loading. Steered molecular dynamics (MD) simulations allowed us to investigate the molecular response of the collagen triple helix under loading with atomic resolution, enabling identification of the dominating molecular mechanism of permanent mechanical damage to fibrous collagens in load bearing tissues.

METHODS

Tail tendon fascicles were dissected from Sprague-Dawley rat tails. Individual fascicles were separated and tested by a single or cyclic fatigue tensile stretch protocol on a custom material test system. Single stretch samples were preloaded to 0.03 N then strained at 0.5 % per second to 1.0, 2.5, 5.0, 7.5, 9.0, 10.5, 12, 13.5, or 15% clamp strain (n=3 samples per group). Unloaded samples were used as a negative control (n=5). For cyclic stretching, preconditioned samples were preloaded to 0.03 N then loaded at 1 Hz from 1-5% clamp strain for 10, 100, or 1000 cycles or at 0.1 Hz from 1-5% clamp strain for 10 or 100 cycles (n=3 samples per group). Control groups for cyclic testing consisted of unloaded and preconditioned-only samples (n=3 each group). All tests were performed with samples immersed in 1× PBS.

Following testing, samples were unloaded from the test system and stained using CF-CHP of sequence CF-G_3-$(GPO)_9$ [7]. Individual samples were incubated overnight at 4 °C in 500 µl of 7.5 µM monomeric CF-CHP in 1× PBS. Following staining, samples were washed three times with 1 ml of 1× PBS for 30 minutes at room temperature to remove unbound CHP. Samples were stored in 1× PBS at -20 °C until imaging.

Entire stained fascicles were imaged for CF fluorescence using an automated widefield fluorescence microscope. Fascicles were mounted in 1× PBS and imaged at 4× magnification using the FITC channel and 488 nm excitation. Fluorescence intensity was measured by a thresholding segmentation method. For single stretch samples, the stained region was isolated by thresholding using Otsu's method [8]. Cyclically stretched samples were thresholded by subtracting the average pixel intensity of the unloaded control samples and using the positive valued pixels for intensity measurement. The mean pixel intensity of the identified regions was calculated and used as the measurement of CF-CHP staining intensity.

Copyright 2016 The Organizing Committee for the 2016 Summer Biomechanics, Bioengineering and Biotransport Conference

Steered MD simulations were performed using a representative homotrimeric Type-I α-1 collagen molecule comprised of ten [Gly-X-Y] triplets from a location near the 930-Lys intermolecular crosslink in *Mus musculus* [9]. Periodic boundary conditions were applied to all directions. Each simulation was performed in the isothermal-isobaric ensemble (pressure = 1 atm and temperature = 310 K) with 2 fs simulation time step using a rigid bonds model for all of the covalent bonds between hydrogen atoms and other heavy atoms. Energy minimization and equilibrium simulation was performed before mechanical test. The steered MD method was used to deform the molecule to a specified strain with a constant loading speed of 0.002 Å/ps. Simulations were performed with either tension dominant loading that stretches the whole triple-helical collagen molecule or shear dominant loading that corresponds to pulling a single strand out of the triple helix. Following removal of the tensile load, the structure was allowed to stress relax for 40 ns. Solvent accessible surface area (SASA), a measure of molecular unfolding, was computed during the last 20 ns of the relaxation simulation.

RESULTS

There was a significant effect of applied strain on measured fluorescence intensity ($p < 0.001$) of single tensile stretch samples with incrementally applied strain (Fig. 1a). Statistical analysis separated the samples into three groups: the samples tested to strains between 0 and 7.5%, a second group containing 9 and 10.5% strain samples, and a final group containing 12-15% strain samples. Comparison of mechanical testing and fluorescence intensity data (Fig. 1a) revealed that onset of significant CHP binding, which took place between 7.5-9% strain, corresponded to the onset of microstructural tissue damage, indicated by a decrease in material tangent modulus (red line in Fig. 1a).

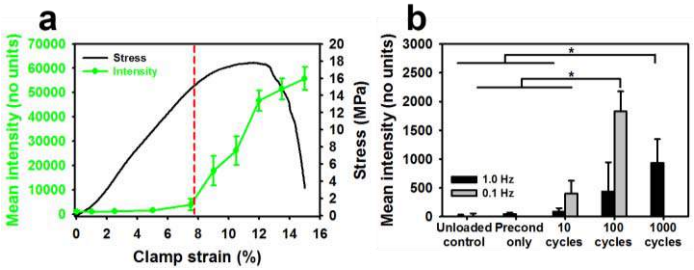

Figure 1. (a) Mean pixel intensity (n=5 0% strain, n=3 1-15% strain, mean ± std) and average strain vs. strain plot for the 15% strain group (n=3). (b) Mean fluorescence intensity vs. fatigue loading condition for samples loaded between 1-5% strain at 0.1 and 1.0 Hz (n=3, mean ± std, * p<0.05).

For cyclically stretched samples, there was a significant effect of the number of cycles on fluorescence intensity ($p<0.001$, 0.1 Hz loading; $p=0.014$, 1.0 Hz loading), with both frequency groups displaying statistically significant fluorescence increase with increased loading cycles (Fig. 1b).

Computational MD simulations revealed that shear dominant loading leads to failure at 12.7% strain, while tension dominant loading showed no signs of failure up to 20% strain. Failure in the shear dominant loading also led to irreversible unfolding of the triple helical collagen model starting at 13.6% strain, observable both by a visible structural change (Fig. 2a) and increased SASA (Fig. 2b).

DISCUSSION

Using CHP, we demonstrated for the first time that irreversible unfolding of collagen molecules is a critical feature of the mechanical failure process in tendon fascicles. In addition, computational simulations indicated that shear-dominant stress transfer, which results in pulling one strand out of the collagen triple helix, is the most likely mechanism of collagen unfolding during tensile overload. Recently, Veres et al. reported that mechanical overloading causes permanent denaturation of collagen molecules in tendon even under subfailure tissue loading, as measured by the enthalpy of thermal unfolding and trypsin digestion [10]. The computational simulations revealing collagen triple helix unfolding due to shear dominant loading, which occurs by stress transfer through molecular sliding and intermolecular crosslinks, are consistent with the collagen deformation mechanisms of molecular stretching and intermolecular sliding proposed by Sasaki and Odajima [11]. In addition, this sliding and shear dominant damage mechanism is in agreement with the gradual accumulation of molecular damage revealed by CHP binding, as breaking of covalent bonds in the peptide backbone or intermolecular crosslink is a highly energetic process that is expected to result in catastrophic tissue failure.

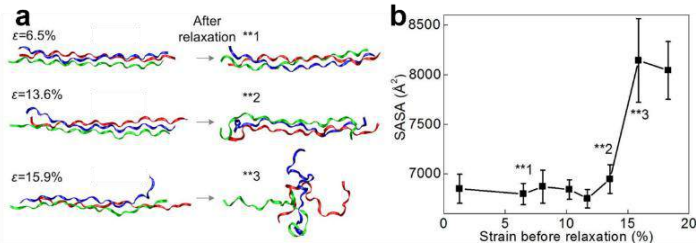

Figure 2. (a) Simulation snapshots taken before and after relaxation simulation for shear-dominant loading to 6.5, 13.6, and 15.9% strain. (b) SASA vs. applied strain (mean ± std) computed during the last 20 ns of relaxation. Increased SASA corresponds to the unfolding observed in the simulation snapshots.

Our results provide an explanation for the progression of mechanical damage in collagen-rich tissues, as well as implications for initiation of the inflammatory response and subsequent healing. Collagen molecular damage prior to fiber-scale tissue disruption and CHP binding to fatigue loaded samples suggest that subfailure damage initiates as collagen triple helix unfolding long before progressing to disruption or damage of structures at larger physical scales. This unfolding of collagen molecules can expose cryptic cell binding domains that are known to elicit healing responses including cell recruitment, damaged collagen removal, and new collagen production [12]. Thus, CHP binding provides an unprecedented tool for detecting collagen mechanical damage in connective tissues, and offers an exciting potential for translational application to the diagnosis, staging, and treatment of connective tissue disorders and injury.

ACKNOWLEDGEMENTS

Financial support from NIH R01EB015133 and R01AR047369 awarded to J.A.W, NIH R01AR060484, R21AR065124; DOD W81XWH-12-1-0555 awarded to S.M.Y; ONR-PECASE N000141010562 and AFOSR FA95501110199 awarded to Z.Q, and M.J.B; and Wellcome Trust grant WT097347MA awarded to B.D.

REFERENCES

[1] Cheng, Vinton W. T. et al., *J Mater Sci,* 42: 8957-8965, 2007. [2] Fung, D. T. et al., *J Biomech,* 43: 274-279, 2010. [3] Bank, R. A. et al., *Matrix Biol,* 16: 233-243, 1997. [4] Uzel, S. G. et al., *J Mech Behav Biomed Mater,* 4: 153-161, 2011. [5] Li, Y. et al., *Curr Opin Chem Biol,* 17: 968-975, 2013. [6] Li, Y. et al., *Proc Natl Acad Sci U S A,* 109: 14767-14772, 2012. [7] Li, Y. et al., *Bioconjug Chem,* 24: 9-16, 2013. [8] Otsu, Nobuyuki, 9: 62-66, 1979. [9] Reiser, K. et al., *Faseb J,* 6: 2439-2449, 1992. [10] Veres, S. P. et al., *Matrix Biol,* 33: 54-59, 2014. [11] Sasaki, N. et al., *J Biomech,* 29: 1131-1136, 1996. [12] Davis, George E. et al., 156: 1489-1498, 2000.

Copyright 2016 The Organizing Committee for the 2016 Summer Biomechanics, Bioengineering and Biotransport Conference

SB³C2016
Summer Biomechanics, Bioengineering and Biotransport Conference
June 29 –July 2, National Harbor, MD, USA
SB³C2016-810

EFFECT OF SHEAR STRESS ON GLUCOSE METABOLISM IN PULMONARY ARTERIAL HYPERTENSION

Sarah E. Basehore (1), Alisa Morss Clyne (2)

(1) School of Biomedical Engineering, Science, and Health Systems
Drexel University
Philadelphia, PA, USA

(2) Mechanical Engineering and Mechanics
College of Engineering
Drexel University
Philadelphia, PA, USA

(3) College of Medicine
Drexel University
Philadelphia, PA, USA

INTRODUCTION

Pulmonary arterial hypertension (PAH) is a life-threatening disease characterized by increased pressure in the right heart and arteries supplying blood to the lungs[1]. In PAH, the pulmonary arteries remodel and constrict, decreasing luminal cross section and increasing vascular resistance. Eventually, the increased pressure results in right ventricular failure, which compromises cardiac output and portends a poor prognosis.

Various studies have demonstrated links between altered cellular glucose metabolism and PAH[2,3]. PAH patients showed increased pulmonary uptake of 18 F-labeled deoxyglucose on PET/CT when compared to healthy controls, indicating increased glucose uptake in the lung[4]. Increased glucose metabolism can elevate hexosamine biosynthetic pathway (HBP) flux, which increases the post-translational protein modification O-GlcNAcylation.

In O-GlcNAcylation, a single sugar is added to serine and threonine residues of nuclear and cytoplasmic proteins[5]. Protein O-GlcNAcylation is important in cellular processes such as transcription, stress response, apoptosis, glucose sensing, and cell signaling in a variety of diseases including diabetes, Alzheimer's, and cancer[1,6]. In PAH, pulmonary aortic smooth muscle cells showed increased HBP flux and enhanced O-GlcNAc transferase (OGT), the enzyme which catalyzes protein O-GlcNAcylation. In endothelial cells, high glucose and elevated HBP flux increased endothelial nitric oxide synthase (eNOS) O-GlcNAcylation and thereby decreased eNOS phosphorylation and nitric oxide (NO) bioavailability at baseline and in response to insulin and blood flow[7-10]. However, the effect of increased glucose metabolism on pulmonary arterial endothelial cell NO production in response to changes in blood flow has not yet been investigated. The goal of this study is to determine how altered glucose metabolism in human PAEC impacts NO production in response to flow.

METHODS

Human umbilical vein endothelial cell (HUVEC) and human pulmonary artery endothelial cells (HPAEC) response to chronic flow was assessed using a parallel plate flow chamber. Cells were seeded at 17,000 cells/cm^2 on collagen coated 25 x 75 mm glass slides for 48 hours and then subjected to 24 hours of 20 dynes/cm^2 shear stress. Glass coverslips were coated with 10 mg/ml of collagen Type 1at 37^{o}C for 3 hours prior to cell seeding.

Endothelial cell morphological response to chronic flow was determined by actin fiber alignment. Cells were fixed in 4% paraformaldehyde and permeabilized with 0.1% Triton X-100. Actin fiber alignment was assessed by labeling actin filaments and nuclei with 165 nM rhodamine phalloidin and 0.2 mg/mL bisbenzimide, respectively. Samples were imaged with a 20x objective in an Olympus 1X81 inverted confocal microscope. Actin fiber alignment was analyzed using a custom edge detection Matlab program developed[11].

For glucose studies, HUVECs and HPAECs were seeded at 17,000 cells/cm^2 on 60 x 15 mm culture dishes for 48 hours and then incubated in high glucose (30 mM), D-mannitol (osmotic control) or glucosamine (2-5 mM) for 0 to 4 hours under static conditions.

Endothelial cell protein O-GlcNAcylation in response to glucose or glucosamine was determined by Western Blot. Samples were prepared by scraping cells off the surface in ice-cold lysis buffer (20 mM Tris, 150 mM NaCl, 1% Triton X-100, 2 mM EDTA, 2 mM PMSF, 0.1% SDS, 2 mM Na_3VO4, 50 mM mM NaF, 10% glycerol, complete protease inhibitor, pH 7.4). Samples were then centrifuged for 10 min at 10,000g, 4^{o}C to remove insoluble material. Cell lysates were normalized for protein content, separated by SDS-PAGE on a 4–12% Bis-Tris gel, and transferred to a nitrocellulose membrane.

Copyright 2016 The Organizing Committee for the 2016 Summer Biomechanics, Bioengineering and Biotransport Conference

After blocking in 5% Bovine Serum Albumin (Sigma), membranes were incubated with primary GlcNAc antibody (Cell Signaling) overnight at 4ºC followed by a secondary horseradish peroxidase-conjugated antibody for 2 hours at room temperature. GAPDH was used as the loading control. Protein bands were detected using an enhanced chemiluminescence kit (Western Lightning, PerkinElmer), and visualized with a Fluorchem digital imager (Alpha Innotech). Band intensity was quantified using AlphaEase FC software.

Statistical analysis was performed with GraphPad Prism. Each experiment was performed in duplicate or triplicate and repeated three times. Comparisons between two groups were analyzed by Student's t-test, and comparisons among multiple groups were analyzed by two-way analysis of variance with a Tukey post-hoc test. Statistical significance is indicated by *p<0.05, **p<0.01, or ***p<0.001.

RESULTS

HPAECs exposed to 24 hours of shear stress (chronic) in a parallel plate flow chamber showed a 17% increase in actin fiber alignment as compared to static controls (Figure 1), demonstrating that HPAECs respond morphologically to shear stress.

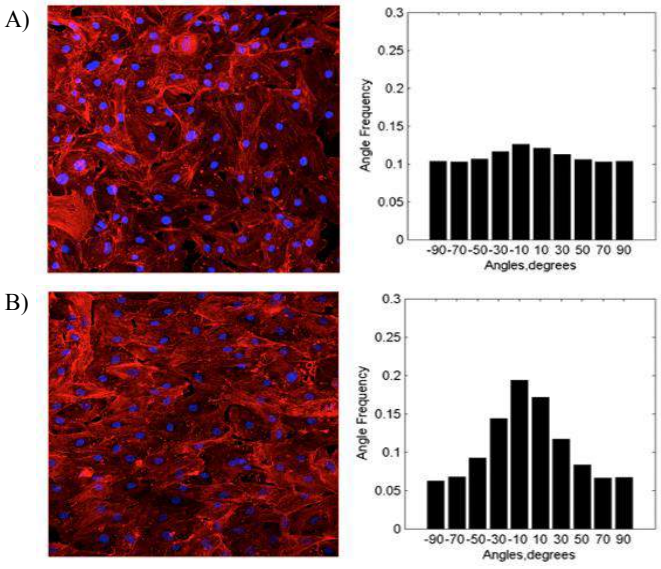

Figure 2: Actin Fiber Alignment of HPAECs

A) Static Healthy HPAECs B) Healthy HPAECs after 24 hour flow C) Percent Alignment of Healthy HPAECs: Static vs. Flow

O-GlcNAclyation increased when HUVECs were exposed to more than 3 hours of 30 mM glucose and 5 mM glucosamine (Figure 2).

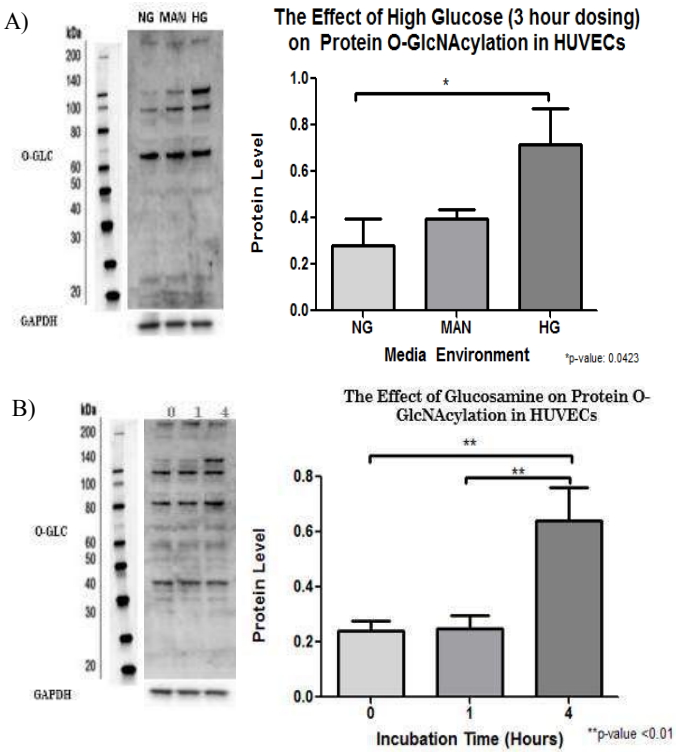

Figure 1: HUVECs in hyperglycemic environments

A) 30 mM high glucose B) 5 mM Glucosamine

DISCUSSION

These data suggest that HPAECs respond similarly to chronic shear stress as other macrovascular endothelial cell types. In addition, increased HBP flux increases protein O-GlcNAclyation in human endothelial cells. HPAECs have an altered glucose metabolism, yet little is known about how this affects other cell properties. We and other have shown that altered glucose environments can affect macrovascular endothelial cell mechanotransduction[12,13]. My findings may elucidate the links between altered glucose and altered HPAEC function in PAH, giving insight into pulmonary hypertension.

In the future, we will determine HPAEC protein O-GlcNAcylation in high glucose/glucosamine, examine the effects of acute flow on HPAEC protein O-GlcNAcylation and p-eNOS, and determine any changes in HPAEC protein O-GlcNAclyation with chronic flow.

ACKNOWLEDGEMENTS

This research was supported by a Drexel University seed grant.

REFERENCES

[1] Chatham JC. Biochim Biophys Acta 1800: 57– 66, 2010
[2] Barnes JW1, Circulation. 2015 Apr 7; 131(14):1260-8.
[3] Darrell D. Belke. Journal of Appl. Phys. 2011 Jul 1; 111: 1,157-162
[4] Marsboom, G., et al., Am J Respir Crit Care Med, 2012.
[5] Boglarka Laczy, American Journal of Phys., 2009 Jan 1; 296:1
[6] Hart GW, Annu Rev Biochem. 2011; 80:825-858
[7] Federici, M., et al., Circulation, 2002. 106(4): p. 466-72.
[8] Du, X.L., et al., J Clin Invest, 2001. 108(9): p. 1341-8.
[9] Beleznai, T., Vascul Pharmacol, 2012. 56(3-4): p. 115-21.
[10] Musicki, B., et al., Proc Natl Acad Sci, 2005. 102(33): p. 11870-5.
[11] Kemeny, Steven. Microsc. Microanal. 17, 156–166, 2011.
[12] Figueroa, D., et al., Cellular and Molecular Bioengineering, Vol. 4, No. 2, June 2011
[13] Kemeny, S., et al., Journal of Biomechanics 44 (2011) 1927–1935

Copyright 2016 The Organizing Committee for the 2016 Summer Biomechanics, Bioengineering and Biotransport Conference

SB^{3}C2016
Summer Biomechanics, Bioengineering and Biotransport Conference
June 29 –July 2, National Harbor, MD, USA
SB^{3}C2016-812

COMPUTATIONAL ANALYSIS ON POST-FUSION EFFECTS OF HARDWARE PRESERVATION OF REMOVAL ON OSTEOPOROTIC PROXIMAL TIBIA CARTILAGE AND SUBCHONDRAL BONE

A. Sori (1), R. Solomon (1), S. Asfour (1), R. Lindsey (2), A. Alhandi (3), L. Latta (3), F. Travascio (1)

(1) Department of Industrial Engineering
University of Miami
Coral Gables, FL, USA

(2) Department of Orthopaedic Surgery
University of Texas Medical Branch
Galveston, TX, USA

(3) Max Biedermann Institute for Biomechanics
Mount Sinai Medical Center
Miami Beach, FL, USA

INTRODUCTION

Tibia fractures in the proximal head require screws to be applied to the fracture site for proper fusion to occur without misalignment, at which point whether or not to remove the hardware is at the surgeon's discretion. Patients with osteoporosis are at a higher risk of fracturing bone. Literature is inconclusive if removal would benefit the patient, as complications from both screw removal and non-removal have been reported.[1-3] Screw removal may compromise bone integrity, whereas remaining screws risk migrating and proliferating microfractures.[1-4] Through computational analysis, this study investigates the effects of screw removal at the proximal tibia site in both healthy bone and osteoporotic bone, and its effect on the biomechanics of articular cartilage and surrounding tissue to better assist the surgeon's decision to remove hardware post-fusion.

METHODS

A generic bone model comprising of cortical and cancellous bone was used for this study, and its 3D geometry was reconstructed using 3-matic and Mimics software (Materialise, Belgium). The material properties for bone were taken from previous studies.[1] The simulated properties of the bone material were then altered to represent biological data of osteoporotic bone found in studies.[8,9] A layer of 3mm of articular cartilage was added to the two tibia condyles and modeled as a biphasic material.[10] A total of four scenarios were simulated: intact tibia (I), tibia with titanium screws (S), tibia with holes (H), and tibia with holes filled with calcium sulfate polymer (P) (figure 1). As per instructions of a surgeon, screws were inserted into the subchondral bone. A mechanical load simulating the gait of a 70 kg 30 year old man was applied to the bone model, and a computational analysis was conducted with FEBio Suite (University of Utah) to yield stresses in the cartilage and subchondral bone.[11]

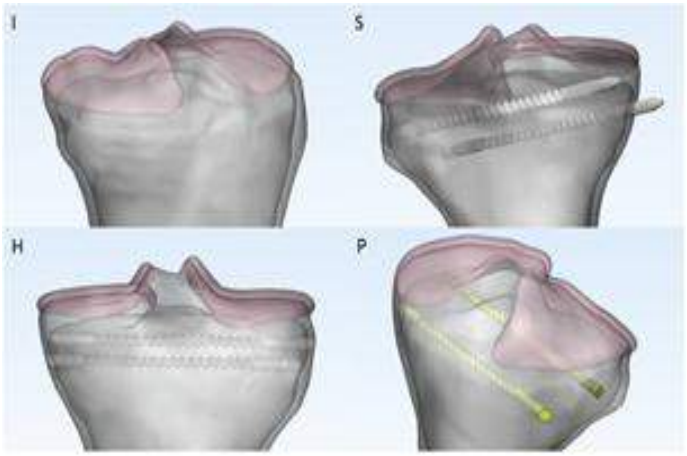

Figure 1: Models of the generic bone with cortical and cancellous bone and cartilage. (I) Intact tibia (S) Tibia with titanium screws (H) Tibia with the screw removed with unfilled holes (P) Tibia with a calcium sulfate polymer filling the holes.

Copyright 2016 The Organizing Committee for the 2016 Summer Biomechanics, Bioengineering and Biotransport Conference

RESULTS

Effective stress and effective fluid pressure in the cartilage were identical among the models (data not shown). In contrast, the effective stress in the subchondral bone changed according to the simulated scenario (figure 2), with healthy bone not differing significantly from osteoporotic bone except with the polymer filling. The tibia with unfilled holes produced the largest peak stress of 1.64 MPa in healthy bone, and 1.61 MPa in osteoporotic bone at the cortical/cancellous interface at the holes sites. This suggests that holes compromise the integrity of the bone. The calcium sulfate had the largest difference of peak stresses between healthy and osteoporotic bone; it induced peak stresses of 1.21 MPa in healthy bone and 1.09 MPa in osteoporotic bone at the cortical/cancellous interface at the polymer site. This is outside the range of the intact tibia, which has peak stresses of 1.14 MPa for healthy bone and 1.11 MPa for osteoporotic bone. Screws induced the second highest peak stresses, with 1.29 MPa for healthy bone and 1.34 MPa for osteoporotic bone.

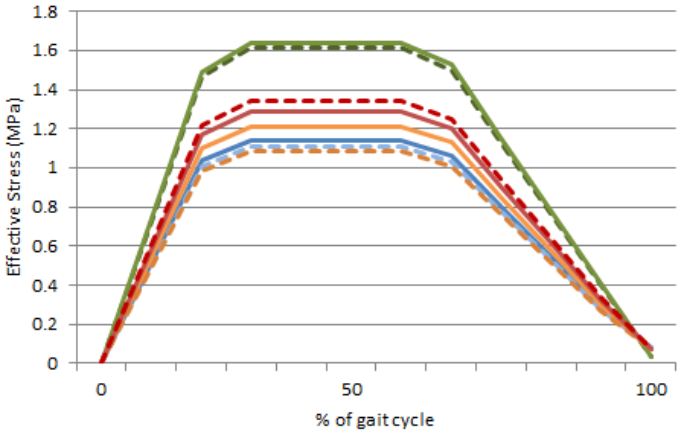

Figure 2: Peak values of effective stress computed at screw holes during gait. (Blue) Intact tibia. (Red) Titanium screws. (Green) Unfilled holes. (Orange) Holes filled with a calcium sulfate polymer. Solid lines represent healthy bone; dotted represents osteoporotic bone.

DISCUSSION

The results of this study suggest that the geometric and mechanical alterations that screws cause in the bone in both healthy and osteoporotic bone may not directly affect cartilage. Different outcomes are observed in the subchondral bone. It is observed that screw holes produce higher levels of mechanical stress at the cortical/cancellous interface when compared to those scenarios including the presence of screws or polymer filling in both cases. This is because both cancellous and cortical bones tend to collapse at the screw holes thus increasing the Lagrange strains (data not shown). In contrast, when holes are filled with polymer whose mechanical properties are similar to that of cancellous bone, stresses in the subchondral bone most closely match those found in the intact tibia scenario. However, the difference between healthy and osteoporotic bone is most significant with polymer fillings. The similar values between osteoporotic and healthy bone are expected; the simulated trials were with a single step, where the mechanical instabilities in osteoporotic bone are unlikely to affect stress levels.

This study suggests that the presence or absence of the hardware in the tibia may not directly cause post-fracture cartilage complications such as osteoarthritis. Also, hardware removal post-fracture fusion should be accompanied by filling the holes with polymer whose mechanical properties resemble those of the natural cancellous bone in both healthy bone and osteoporotic bone in order to preserve subchondral bone integrity.

ACKNOWLEDGEMENTS

Study supported by funds donated to the Biomechanics Research Group of the University of Miami.

REFERENCES

[1] Honkonen SE, Journal of Orthopedic Trauma, 9 (1995).
[2] Mehin R, et al. Can J Surg, 55 (2012) 87-94.
[3] Cowie J, et al. Bone & Joint, (2015).
[4] Cho W, Springer, (2014).
[5] Asaid R, et al. Eur J Orthop Surg Traumatol, 22 (2012) 211-213.
[6] Citak M, et al. Arch Orthop Trauma Surg, 131 (2011) 1405-1408.
[7] Keaveny TM, et al. Bone Meachanics, (2004).
[8] Tjhia C, et al. Bone 49(6): 1279-1289 (2011).
[9] Tsouknidas A, et al. Journ of Biomechanics, 45 (2012).
[10] Lu J, et al. Med Sci in Sports Exercise, 40 (2015) 193-9.
[11] Zhao D, et al. Journ of Orthopaedic Research, 10 (2007) 593-602.

Copyright 2016 The Organizing Committee for the 2016 Summer Biomechanics, Bioengineering and Biotransport Conference

SB³C2016
Summer Biomechanics, Bioengineering and Biotransport Conference
June 29 –July 2, National Harbor, MD, USA
SB³C2016-813

EMULATION OF MUSCULAR THIN FILM DEFLECTION USING THERMAL CONTRACTION: COMPARISON OF CONSTITUTIVE MODELS

Victoria A. Webster (1), Santiago G. Nieto (1,2), Anna Grosberg (3), Ozan Akkus (1,2,4), Hillel J. Chiel (2,5,6), Roger D. Quinn (1)

(1) Dept. of Mech. and Aero. Engineering
Case Western Reserve University
Cleveland, OH, USA

(2) Dept. of Biomedical Engineering
Case Western Reserve University
Cleveland, OH, USA

(3) Dept. of Biomedical Engineering
University of California, Irvine
Irvine, CA, USA

(4) Dept. of Orthopaedics
Case Western Reserve University
Cleveland, OH, USA

(5) Dept. of Biology
Case Western Reserve University
Cleveland, OH, USA

(6) Dept. of Neurosciences
Case Western Reserve University
Cleveland, OH, USA

INTRODUCTION

This research details an improved modeling approximation technique for biohybrid devices using a widely available tool. Previous studies have shown that cellular contraction can be roughly approximated in finite element analysis (FEA) simulations using the built in thermal contraction capabilities [1]. While many models simulate cellular contraction using individual forces or cell-substrate interface traction forces, approximations using a calibrated thermal contraction model greatly reduce computational runtime. In order to approximate cellular contraction using thermal contraction, a relevant thermal expansion coefficient (TEC) is needed.

While a wide range of biohybrid actuators have been developed [2-5], many such devices are based on the actuation of a thin layer of cells on one side of a biocompatible substrate [6]. This results in a device that functions as a cantilever. Previously, we have used a modified Stoney's approximation to calculate the stress in the cell layer, and subsequently calculated the TEC based on a linear thermal stress-strain relationship [7]. However, this technique resulted in a wide range of TEC values, and required experimental calibration of a correction factor. In the current study, we instead treat the deformed cantilever as a bi-layer beam with two thermal contraction coefficients (as in a thermostat). Using this technique, the current study identified an improved range of TEC values for approximating cellular contraction using native thermal contraction capabilities in FEA software packages.

METHODS

In this study, the deflections of 13 muscular thin films (MTFs) [8] as the result of cellular contraction were used to calibrate or validate TEC variables α and ΔT for use in FEA simulations. The coefficient of thermal contraction along the cell contraction direction is denoted as α and the driving temperature was denoted as ΔT. Six samples were used for calibration while 7 samples were saved and used as a test set for comparing the simulation to experimental values.

Model Calibration

For this study two calibration methods have been compared. First, the TEC was calibrated based on a calculated stress in the cell layer, which can be calculated based on the deflection or radius of curvature (ROC) of the device during contraction. Based on this approximation, a model was developed to reproduce the experimental contraction force. The first method for approximating the cell stress is to apply Stoney's equation [9]:

$$\sigma_c = \frac{1}{6Rt_c}\left(\frac{E_s {t_s}^3}{\left((1-\nu)(t_s+t_c)\right)} + \frac{E_c {t_c}^3}{\left((1-\nu)(t_s+t_c)\right)}\right) \quad (1)$$

where R is the experimentally measured radius of curvature of the beam, ν is the poisson's ratio, t_c and t_s are the thicknesses of the cell and substrate layers, respectively, E_c and E_s are the moduli of the cells and substrate, respectively. The TEC was then determined using the linear thermal stress-strain relationship:

$$\alpha\Delta T = \frac{\sigma_c}{E_c} \quad (2)$$

The second method for model calibration is to calculate the TEC directly based on the ROC by treating the cantilever as a bi-layer beam with each material having different material and thermal properties [10]. By assuming that the TEC of the substrate is 0, this model was reduced to:

$$\alpha\Delta T = -\frac{1}{R}\frac{(E_s t_s^2 - E_c h_c^2 + 4E_s E_c t_s t_c (t_s+t_c)^2)}{6E_c t_c (E_s h_s h_c + E_s h_s^2)} \quad (3)$$

Copyright 2016 The Organizing Committee for the 2016 Summer Biomechanics, Bioengineering and Biotransport Conference

The TEC was determined for the minimum and maximum contraction states for 6 randomly selected MTF samples using both techniques, resulting in four TEC ranges.

Simulation

Muscular thin films were simulated in ANSYS Mechanical APDL using two dimensional plane strain elements. MTFs were comprised of a bi-layer cantilever with a fixed boundary condition on one end. Contraction in the cell layer was approximated using an orthotropic coefficient of thermal contraction. While the calibration technique results in a value for $\alpha\Delta T$, ANSYS requires α and ΔT to be entered separately. Therefore, $\Delta T = 1$ for the purposes of this study. In the direction of the desired contraction, the calculated α was implemented, while the TEC in all other directions was set to zero.

The 7 test sample geometries (Figure 1) were simulated using the average, average minus one standard deviation, and average plus one standard deviation for each of the four calibrated TEC cases, and the resulting deflections were compared to the experimental values.

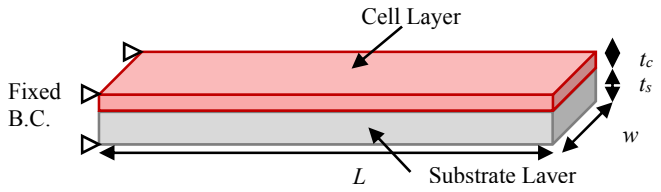

Figure 1 Schematic of cantilever MTF

RESULTS and DISCUSSION

TEC calibration using the basic Stoney's approximation resulted in a TEC range of -0.216 ± 0.024 for the minimum contracted state and -0.387 ± 0.11 for the maximum contracted state, while calibration using the thermostat model resulted in a minimum range of -0.145 ± 0.016 and a maximum range of -0.26 ± 0.075 (Figure 2).

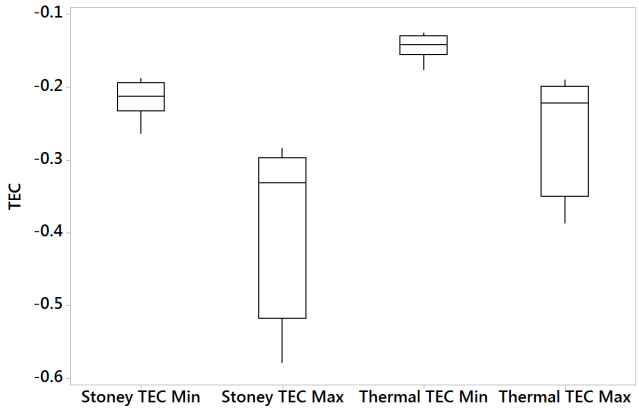

Figure 2. Box and whisker plot of the TEC ranges for the minimum and maximum contracted states calibrated using Stoney's approximation and the Thermal model on the six calibration samples.

Each MTF configuration was simulated across the projected range of TEC values. In both the minimum (Figure 3) and maximum (Figure 4) contracted states, the thermal model performed better than the calibration using Stoney's approximation when compared to the experimental deflection. In the case of the minimum contracted state there was no significant difference between the experimental deflection and the simulation using the Thermal calibration technique (T-test: p = 0.246). However, the Stoney's calibration technique in both cases, and the Thermal technique for the maximum contraction did vary significantly from the experimental deflection (T-test: $p<0.05$).

The use of the thermostat based model results in an improved simulated deflection over that provided by the uncorrected Stoney's calibration technique.

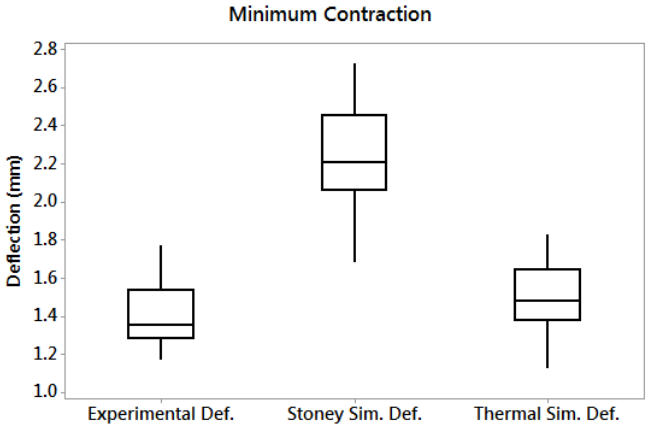

Figure 3. Box and whisker plot comparing the experimental and simulated MTF deflection in the minimum contracted state using the seven test samples.

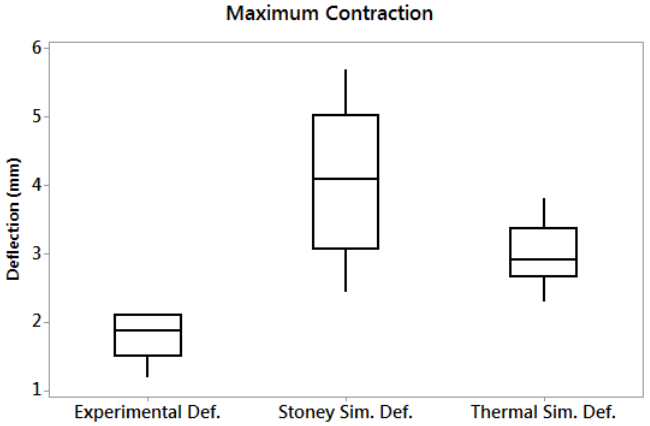

Figure 4. Box and whisker plot comparing the experimental and simulated MTF deflection during maximum contraction using the seven test samples.

ACKNOWLEDGEMENTS

This material is based upon work supported by the National Science Foundation Graduate Research Fellowship under Grant No. DGE-0951783. This study was also funded in part by grants from the National Science Foundation (Grant Number DMR-1306665) and National Institute of Health (Grant Number R01 AR063701).

REFERENCES

[1] K. Na et al. *NSTI-Nanotech*, 2008, vol. 3, pp. 737–740.
[2] W. Legant et al. *PNAS*, vol. 106, no. 25, pp. 10097–102, 2009.
[3] A. Feinberg et al. *Science*, vol. 317, pp. 1366–70, Sep. 2007.
[4] C. Cvetkovic et al. *PNAS*, vol. 111, no. 28, pp. 10125–30, Jun. 2014.
[5] V. Chan et al. *Lab Chip*, vol. 12, pp. 88–98, Jan. 2012.
[6] J. Park et al. *Anal. Chem.*, vol. 77, pp. 6571–80, Oct. 2005.
[7] V. Webster et al. SB^{3}C 2015. Snowbird, UT, USA. 2015
[8] A. Grosberg et al. *Lab Chip*, vol. 11, no. 24, pp. 4165-4173, Dec. 2011.
[9] K. Wilson et al. *PLoS One*, vol. 5, no. 6, p. e11042, Jan. 2010.
[10] N. Naotake. et al. Thermal Stresses. New York: Taylor and Francis. 2003.

Copyright 2016 The Organizing Committee for the 2016 Summer Biomechanics, Bioengineering and Biotransport Conference

SB³C2016
Summer Biomechanics, Bioengineering and Biotransport Conference
June 29 –July 2, National Harbor, MD, USA
SB³C2016-814

DRILL-SPECIFIC HEAD IMPACT EXPOSURE IN YOUTH FOOTBALL PRACTICE

Eamon T. Campolettano, Steve Rowson, and Stefan Duma

Biomedical Engineering and Mechanics
Virginia Tech
Blacksburg, VA 24060

INTRODUCTION

Youth football players represent 70% of all players in the United States, and yet the level of research into head impact exposure within this population is limited when compared to that of high school, collegiate, and professional football [1]. The prevailing thought for concussion mitigation today is to limit head impact exposures, primarily through proper teaching and rule modification [2].

Recently, researchers have begun to instrument youth football players with helmet-mounted accelerometer arrays to quantify head impact exposure and concussion tolerance [1, 3]. Daniel et al instrumented seven players on one team and reported that most high magnitude impacts occurred in practice, rather than games [1]. The findings from that study were part of the process that led to rule changes in the Pop Warner organization [3]. The following year, Cobb et al followed three youth football teams and found that teams adhering to the policy changes experienced a 40% reduction in overall impacts relative to those that did not [4].

While these studies provided valuable insight to head impact exposure in youth football players, they looked at practices and games as a whole, with little analysis quantifying the causation of high magnitude impacts. The objective of this study was to analyze youth football practices and determine which drills produced high magnitude impacts. The results of such analysis conducted on a larger scale could be useful for future research or further policy implementation to mitigate head impact exposure in youth football.

METHODS

This study investigated head impact exposure among youth football players. Two youth football teams composed of 9-11 year old players were included in this study approved by the Virginia Tech Institutional Review Board. Guardians provided written consent and the youth players verbally assented to participation. A total of 34 players (average age of 9.99 ± 0.74) chose to participate and received helmets instrumented with accelerometer arrays associated with the HIT System.

The HIT System consists of a six accelerometer array that is mounted inside of a Riddell Revolution or Speed helmet. The accelerometers are spring-mounted so that contact with the head is maintained for the duration of the impact. This ensures measurements of head acceleration, rather than helmet acceleration [5]. Players wore the instrumented helmets at each practice and game throughout the season. When an individual data channel exceeded a 14.4 g threshold, data acquisition automatically triggered, capturing 40 ms of data, including 8 ms of pre-impact data. Impact data were then wirelessly transmitted from the helmets to the sideline computer, where the data were processed to compute linear and rotational resultant accelerations according to previous research [6, 7].

Games and practices were filmed to facilitate video verification of head impacts. For every impact greater than or equal to 40 g in practice, video was used to identify the specific drill/activity associated with impact. Each of these impacts was assigned one of nine classifications corresponding to the drill that resulted in the impact (Table 1). Furthermore, practice film and activity logs kept for each day of practice were used to determine the total time spent practicing each drill type and to assess the relative severity of drills to each other.

Impact rates were computed on a per hour basis. Byar's method, which retains high levels of accuracy for both small and large counts, was used to compute 95% confidence intervals for these rates [8]. Empirical cumulative distribution functions (CDF) were also determined for each drill for linear resultant acceleration.

Copyright 2016 The Organizing Committee for the 2016 Summer Biomechanics, Bioengineering and Biotransport Conference

Table 1. Each impact over 40 g was classified as being associated with one of the following drills. Most drills resulted in tackling. Most time was devoted to drills with game situation fidelity.

Practice Drill	Description
Blocking Drill	Drills focused on teaching blocking
Tackling Drill – Blocker Present	Tackling drill with at least one blocker present as well as a ball carrier and tackler.
Tackling Drill – No Blocker Present	Tackling drill where only a ball carrier and tackler participate
King of the Circle	Player in middle of circle rushes at player on perimeter of circle.
Scrimmage	Full 11 vs. 11 offense vs defense
Offense vs. Defense	Small scale (5 v 5 up to 8 v 8) offense vs. defense
Offense or Defense	11 offensive or defensive players with 3-4 proxy players on the other side
Passing or Running Drills	Pass catching or rushing drills
Other	All other activities

RESULTS

For the season, 408 impacts that exceeded the 40g threshold were video verified, with 314 (77%) occurring in practice and the remaining 94 (23%) in games. The number of impacts, as well as time spent, for a particular drill varied greatly over the course of the season, necessitating the use of a normalized impact rate for comparisons to be made. Impacts per hour for each drill were computed with 95% confidence intervals for thresholds of increasing linear acceleration severity (Fig. 1). Drills involving tackling resulted in a higher rate of impact than those that did not. Increasing severity thresholds resulted in lower rate of impact across all drills. No players in the study sustained a concussion.

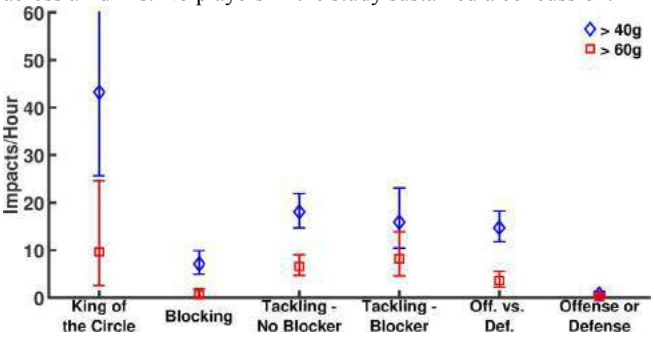

Figure 1. The heavy contact and rapid nature of King of the Circle led to the highest impact rate of all practice drills. Drills resulting in a tackle were found to lead to higher impact rates as well.

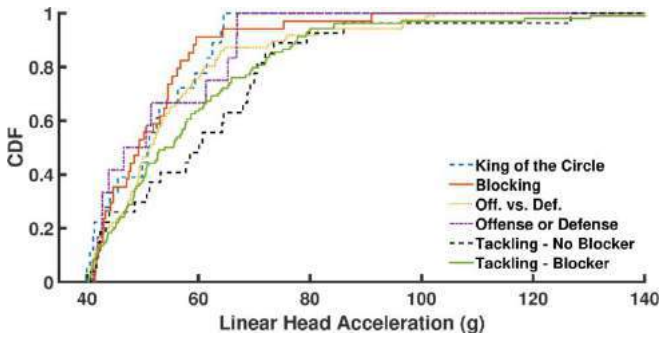

Figure 2. Tackling drills were found to have the largest proportion of impacts over 70 g.

CDFs were determined for linear acceleration magnitudes for the selected drill types (Fig. 2). Though consistent up to 60 g, the non-tackling drills were less frequently associated with accelerations of greater magnitude. Tackling drills were associated with greater severity head impacts than non-tackling drills.

DISCUSSION

Previous work into youth football head impact exposure has investigated magnitude and frequency of impacts, as well as the effect of style of play on those values [4, 6]. The proportion of high magnitude head impacts in youth practices (77%) was found to be consistent with the 79% found by Daniel et al [1]. Looking at practices in more detail, impact rate differed markedly between drills with and without tackling for all severity levels. Those without tackling resulted in fewer than 10 impacts above 40 g per practice-hour while drills involving tackling exceeded this. King of the Circle produced high magnitude impacts more frequently than any other activity because of the speed at which it is performed (Fig. 1). Each player rushes three times at a different defender and the drill continues until all have the opportunity. Notably, this drill was carried out for the shortest amount of time of all those assessed. Further, no impact from King of the Circle exceeded 70 g (Fig. 2). Tackling drills, with or without blockers, were associated with the highest proportion of impacts over 70 g. With a high impact rate and magnitude, these drills, as carried out by the teams in this study, expose players to heightened head impacts. Of note is that the two teams in the study spent the most time conducting either Offensive or Defensive drills. These drills resulted in a very low rate of impact and closely mimicked game play. Off. vs. Def. also exhibited fidelity to game situations, and the high impact rate observed there stems from the smaller number of players involved. This enabled players to achieve greater momentums and produce higher magnitude impacts.

Certain limitations pertaining to this study should be noted. The HIT System is associated with random error up to 15.7% for individual acceleration measurements, but the average error is only 1% [9]. Variations in head impact exposure data between the two teams in this study were present.

Head impact kinematic data for two youth football teams of players 9-11 years old were collected in order to assess the effect of specific practice drills on impact exposure. Much of practice time was spent in non-contact scenarios, but contact drills presented high rates of exposure to the athletes. Coaches and league organizers can use these data to structure practices in ways that work to mitigate high magnitude impacts. Further research into practice drill impact exposure at all levels of football is necessary to further player safety and characterize exposure on a larger scale.

ACKNOWLEDGEMENTS

The authors gratefully acknowledge the NIH-NINDS under award number R01NS094410 for supporting this work and the Blacksburg Juniors football teams for their participation in this study.

REFERENCES

[1] Daniel, R. et al., *Ann. Biomed. Eng.*, 40(4):976– 981, 2012.
[2] Crisco, J. J., *Curr. Sports Med. Rep.*, 10:7–9, 2011.
[3] Rules changes regarding practice & concussion prevention. Pop Warner, 2012.
[4] Cobb, B. et al., *Ann. Biomed. Eng.,* 41(12): 2463-2473, 2013.
[5] Manoogian, S. et al., *Biomed. Sci. Instrum.*, 42:383–388, 2006.
[6] Rowson, S. et al., *Ann. Biomed. Eng.,* 40(1):1–13, 2012.
[7] Crisco, J. J. et al., *J. Biomech.*, 126(6):849–854, 2004.
[8] Breslow, N. E., *IARC Scientific Publications,* 82, 1993.
[9] Beckwith, J. G. et al., *Ann. Biomed. Eng.*, 40(1):237–248, 2012.

Copyright 2016 The Organizing Committee for the 2016 Summer Biomechanics, Bioengineering and Biotransport Conference

SB^{3}C2016
Summer Biomechanics, Bioengineering and Biotransport Conference
June 29 –July 2, National Harbor, MD, USA
SB^{3}C2016-815

EFFECTS OF MENISCAL TRANSPLANTATION ON KNEE JOINT CONTACT MECHANICS AND POSTOPERATIVE ARTICULAR CARTILAGE IMAGING

Hongsheng Wang (1), Matthew Koff (2), Hollis Potter (2), Scott Rodeo (3), Suzanne A. Maher (1)

(1) Department of Biomechanics
Hospital for Special Surgery
New York, NY, USA

(2) Magnetic Resonance Imaging Laboratory
Hospital for Special Surgery
New York, NY, USA

(3) Sports Medicine and Shoulder Service
Hospital for Special Surgery
New York, NY, USA

INTRODUCTION

Meniscal allograft transplantation, MAT, is a salvage procedure intended to replace extensively degenerated menisci [1]. Although MAT is successful in alleviating symptoms and improving knee function in the short- to medium-term, long-term outcomes are highly variable. It is generally believed that the magnitude of change in joint contact mechanics has a relationship with the onset and progression of cartilage degeneration [2]. While changes in contact mechanics after meniscal injury have been quantified in cadaveric studies [3, 4] the biological response of articular cartilage to those changes have not been explored.

The primary objective of this study was to determine the effect of MAT on *in vivo* patient-specific knee joint contact mechanics. The secondary objective was to explore the relationship between pre- to post-MAT changes contact mechanics and early biological changes to knee joint articular cartilage. To satisfy these objectives we developed a platform of tests consisting of: an *intraoperative* protocol for the direct measurement of knee joint contact stress, and a *pre- and post-operative* quantitative magnetic resonance imaging (qMRI) for the evaluation of changes in cartilage thickness, composition and collagen structural organization of cartilage matrix.

METHODS

Five subjects (2M/3F, age: 21 ± 4 years, weight: 71.8 ± 14.3 kg) scheduled to undergo meniscal transplantation were enrolled in this study following IRB approval. All patients had undergone prior total meniscectomy, and showed no signs of advanced chondral degeneration on preoperative MRIs. Two subjects (*subjects 4, 5*) underwent isolated meniscal transplantation, while the remaining three subjects underwent MAT in addition to ACL reconstruction (*subject-1*), revision ACL reconstruction (*subject-2*), and osteochondral allograft transplantation (OATS) in the weight-bearing zone of the femoral condyle (*subject-2, 3*).

Imaging: All subjects underwent imaging of the knee prior to surgery and at their follow-up visits (3 to 6 months) on a clinical 3.0 T scanner (GE Healthcare, Waukesha, WI). Cartilage thickness was assessed using a coronal 3D high-resolution spoiled gradient echo (SPGR) sequence, with voxel dimensions = $1.5\times0.27\times0.27$ mm^3. Proteoglycan content was assessed using T1ρ mapping, with the acquisition parameters: 4 time of spin lock (0, 20, 40, 60 ms), and voxel dimensions = $3\times0.58\times0.58$ mm^3. Collagen fiber organization and water content was assessed by T2 mapping, with echo time = 7.2, 14.4, 21.6, 28.8, 36.0, 43.2, 50.4, 57.6 ms, and voxel dimensions = $3\times0.58\times0.58$ mm^3. SPGR images were manually segmented to create a 3D model of articular cartilage and bone. T2 and T1ρ relaxation times within the tibial cartilage were calculated by fitting a mono-exponential decay equation. The T1ρ and T2 values on 2D slices were then overlaid on the 3D anatomical surface model of the tibial plateau to create the 3D mapping (Fig. 1) [5].

Intra-operative contact stress measurement: During surgery, contact stress on the tibial plateau surface was quantified using a thin-electronic sensor (Tekscan Inc., Boston, MA). The sensor was calibrated and trimmed to accommodate to the shape of the tibial plateau, then sterilized using ethylene oxide. The sensor was passed through a small arthrotomy from anterior to posterior by pulling the posterior tab via a passing suture placed through a posterolateral incision (Fig. 2A), and its position was adjusted arthroscopically to cover the entire tibial plateau. A custom designed surgical boot was used to manually apply an axial force to the foot until 50% body weight was reached (Fig. 2B). The boot was equipped with a load cell (Model: 31/1432-04, Honeywell Inc.) to monitor the applied force in real-time. Contact stress and contact area were evaluated before

Copyright 2016 The Organizing Committee for the 2016 Summer Biomechanics, Bioengineering and Biotransport Conference

(meniscectomy condition) and after allograft placement (transplanted condition).

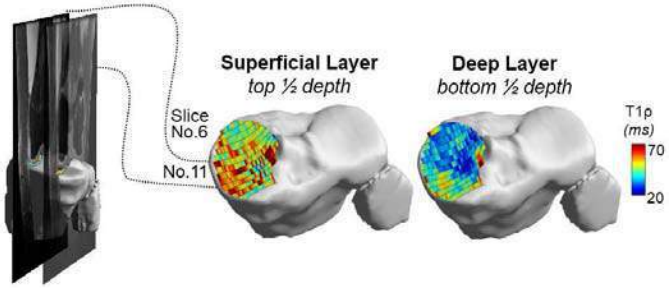

Figure 1. Reconstruction of 3D T1ρ mapping of the tibial cartilage

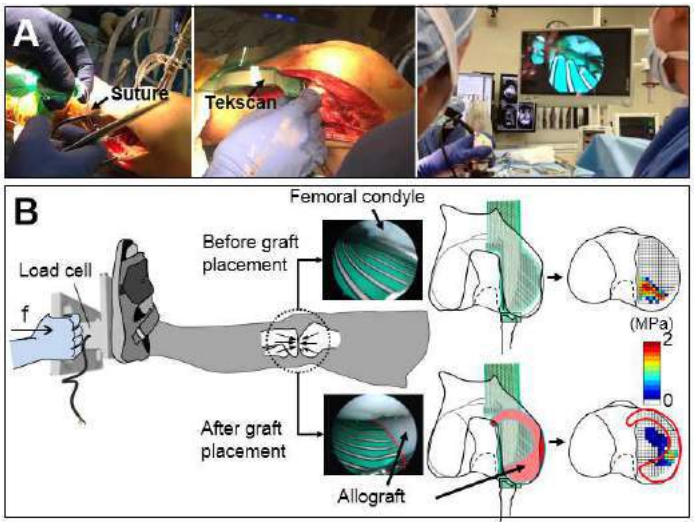

Figure 2. (A) Photo and schematic (B) of intraoperative measurements

RESULTS

For the meniscectomized condition, tibial plateau peak contact stresses of 1.96 ± 0.39 MPa (range: 1.67 MPa to 2.64 MPa) and contact areas of 160 ± 44 mm^2 (range: 120 mm^2 to 225 mm^2) were quantified. Following meniscal transplantation, increases in contact area of 29% and decreases in peak contact stress of 17%, on average occurred compared to the meniscectomy condition.

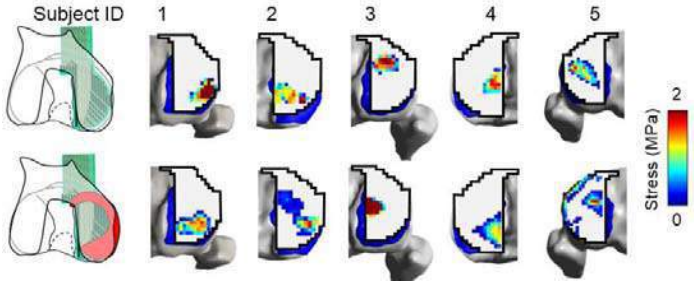

Figure 3. Contact stress at meniscectomy condition (top row), and after graft placement (bottom row)

Follow-up scans were obtained for subjects #1, 2 & 3 at 6 months, for subject #4 at 5 months and for subject #5 at 5 months. Our analysis was focused on the tibial cartilage of the affected compartment. There were minimal changes (< 1%) in average cartilage thickness at follow-up scans within both cartilage-cartilage (CC) and cartilage-meniscus (CM) contact zones (Fig. 4C). At follow-up scans, the average T1ρ were shorter than their preoperative levels within the CM values zone (superficial layer: -11% ± 17%, deep layer: -6% ± 14%, Fig. 4A). In contrast, changes were less remarkable within the CC zone (superficial layer: -3% ± 17%, deep layer: 0% ± 14%). We observed prolonged T2 values within the CC zone of the deep layer (8% ± 23%, Fig. 4B) while there were smaller increases (< 3%) within the CM zone and in the superficial layer.

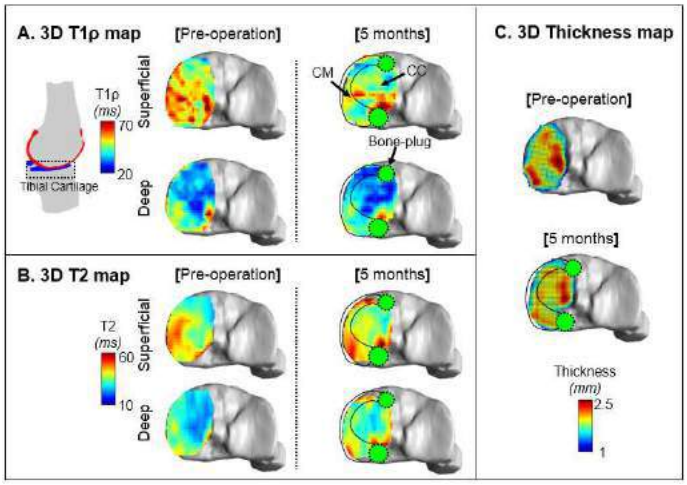

Figure 4. Preoperative and postoperative (A) T1ρ, (B) T2 and (C) thickness map of tibial cartilage of a representative subject (*subject 4*)

DISCUSSION

We have applied a newly developed platform technology to quantify the effect of MAT on intra-operative knee joint contact stresses and the subsequent biological response of articular cartilage in a pilot cohort of 5 patients. The majority of patients (4/5) exhibited decreased peak contact stress and increased contact area, suggesting that meniscal transplantation plays an important role in redistributing joint loads, at least in the immediate post-operative environment. Follow-up MRI taken at 3 to 6 months demonstrated decreased T1ρ values in tibial articular cartilage, specifically in the region beneath the meniscal allograft, suggesting increases in proteoglycan content and decrease in water content within the zone. A concomitant prolongation of T2 values was found primarily within the central region of the tibial plateau, suggesting moderate increased disorganization of the collagen network within this region. Minimal differences in cartilage thickness were found over the short time frame of this preliminary study. In summary, our pilot study indicates that the contact mechanics of MAT are highly patient-specific. But irrespective of patient-to-patient variability, MAT results in a chondro-protective effect, even at short follow-up [6]. Longer follow-up imaging data in a larger cohort will be required to determine if immediate post-operative patient-specific changes in joint contact mechanics after MAT are predictive of outcome.

ACKNOWLEDGEMENTS: This study was supported by American Orthopaedic Society for Sports Medicine.

REFERENCES: [1] Rodeo, S. A., 2001, *The American journal of sports medicine*, 29(2), pp. 246-261. [2] Andriacchi, T. P., Mundermann A, Smith RL, et al, 2004, *Ann Biomed Eng*(32), pp. 293-298. [3] Wang, H., et al., 2014, *The American journal of sports medicine*. [4] Bedi, A., et al., 2010, *The Journal of bone and joint surgery. American volume*, 92(6), pp. 1398-1408. [5] Shiomi, T., et al., 2013, *Skeletal Radiol*, 42(3), pp. 363-370. [6] Akella, S. V., et al., 2001, *Magn Reson Med*, 46(3), pp. 419-423.

Copyright 2016 The Organizing Committee for the 2016 Summer Biomechanics, Bioengineering and Biotransport Conference

SB^{3}C2016
Summer Biomechanics, Bioengineering and Biotransport Conference
June 29 –July 2, National Harbor, MD, USA
SB³C2016-816

FUNCTIONAL EVALUATION OF EXOSKELETON CONTROL STRATEGIES FOR TREATING CROUCH GAIT IN CEREBRAL PALSY

Zachary F. Lerner, Diane L. Damiano, Thomas C. Bulea

Rehabilitation Medicine Department
Clinical Center
National Institutes of Health
Bethesda, Maryland, USA

INTRODUCTION

Cerebral palsy (CP) is the most common chronic motor disability in children, with a reported prevalence of 2-2.5 per 1,000 births [1]. More than 50% of individuals with CP exhibit crouch gait [2], a pathological walking pattern characterized by excessive bilateral knee flexion and elevated knee extensor joint moments [3]. Orthopaedic surgery may result in short-term improvements in crouch that often did not persist with time and growth and may exacerbate weakness, excessive anterior pelvic tilt or knee hyperextension. More effective treatment strategies that can preserve or augment strength for those with CP, and thereby help to maintain gait function, are needed.

Powered exoskeletons as well as some orthoses have the potential to assist gait in children with neurological deficits and restore or improve their joint biomechanics while worn [4]. However, we not aware of any orthotic or robotic assistance devices that specifically seek to "treat" crouch gait, i.e. lead to improved gait function when the device is removed. The potential contributors to crouch gait, including spasticity, contracture, poor motor control, and muscle weakness, pose challenges for the design and control of such devices in individual patients. More research is needed to determine appropriate exoskeleton control strategies that successfully treat this heterogeneous gait disorder.

Individuals with crouch gait have excessive knee flexion at initial foot contact and throughout stance. Therefore, in treating crouch gait, it may be useful for a powered knee exoskeleton to provide assistance either during the swing phase, acting to extend the knee prior to initial contact, during the stance phase, acting to support the body, or both.

The goal of this study was to evaluate the ability of our custom exoskeleton to provide knee extension assistance during the stance and swing phases of gait, and how the different modes of assistance affect knee joint angles in a child with crouch gait from CP.

METHODS

Exoskeleton Design & Control Strategies

We developed a novel exoskeleton to provide knee extension assistance that integrated custom-molded orthotic braces, motors, transmissions, and sensors (Fig. 1). Our motor controller implemented a finite state machine that divided the gait cycle into stance, early swing, and late swing phases. We evaluated three modes of assistance (Figure 2); a **swing assist** condition that specified a constant extensor torque during the late swing state (3.5 Nm), a **stance assist** condition that specified constant extensor torque during the stance state (3.5 Nm), and a **stance & swing assist** condition that specified extensor torque during stance and late swing states.

Figure 1. The subject walking assisted by our exoskeleton.

Copyright 2016 The Organizing Committee for the 2016 Summer Biomechanics, Bioengineering and Biotransport Conference

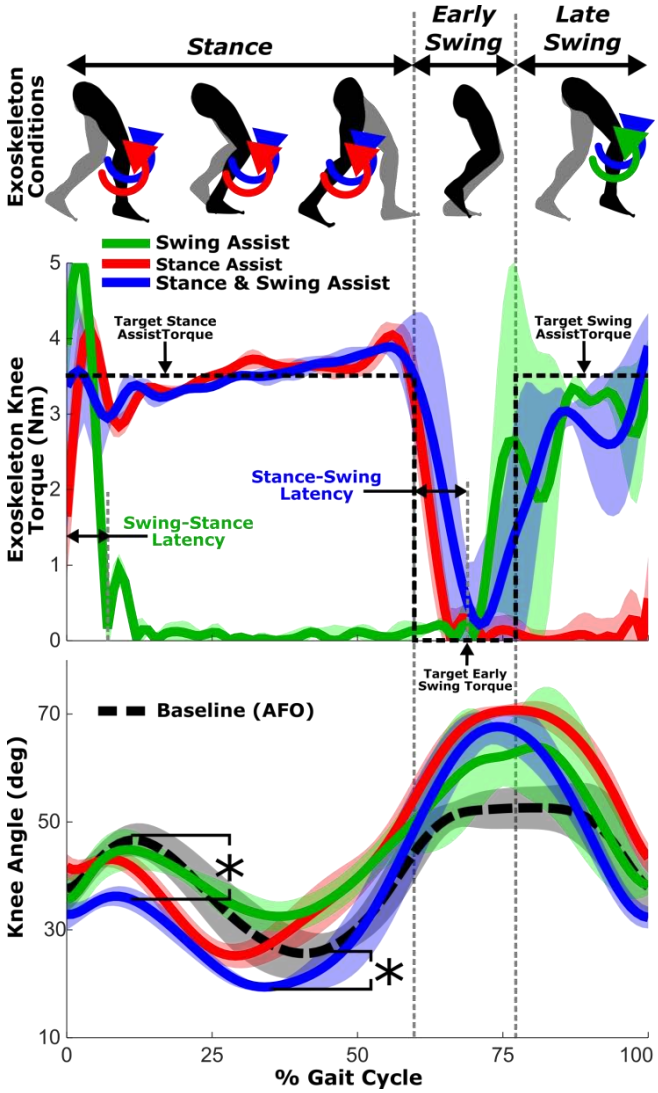

Figure 2. Exoskeleton conditions (top), measured torques (middle) and knee angles (bottom) for the right leg. Shaded regions represent ±1SD from the mean. * Indicates (p<0.05).

Participant Information

We recruited a 6 year old boy with CP and crouch gait, and obtained written informed consent and assent from the parent and the child, respectively. The Institutional Review Board at the National Institutes of Health approved this study.

Gait Analysis

The participant acclimated to the exoskeleton over 4 visits. On the 5th visit, he first walked over ground using his own AFOs (baseline condition), and then with the powered exoskeleton under the three exoskeleton conditions. We used a full-body marker set and 10 motion capture cameras (Vicon, Oxford, UK) to collect kinematic data. Joint angles were computed in Visual 3D (C-Motion, Germantown, MD). Torque from each of the exoskeleton's motors were measured by a sensor mounted on the drive shaft at the knee and was synchronized with the motion capture system.

Functional Exoskeleton Evaluation

The performance of our motor control algorithm was evaluated by comparing the desired (specified) assistive torque to the actual assistive torque measured from the torque sensor. We also evaluated how walking with the different exoskeleton conditions affected knee joint kinematics compared to the participant's baseline gait pattern, statistically analyzed via one-factor ANOVA procedures.

RESULTS

Measured assistive knee torques and computed knee joint angles across the conditions for the right (more affected) leg are shown in Fig. 2. The average root mean square error (RMSE) between the specified (target torques depicted in Fig. 2) and measured assistive torques was 0.91 Nm across all of the exoskeleton conditions. The average latency from when the controller changed state to when the specified torque setting was reached (as depicted in Fig. 2) was 52 ms. The shortest latency occurred during the transition to stance phase in the stance assist condition; the longest latency was from stance to early swing.

Maximum knee flexion during stance was reduced by 10.2° (right limb, $p<0.001$) and 5.3° (left limb, $p=0.003$) in the stance & swing assist condition compared to baseline; peak knee extension during stance increased by 5.4° (right limb, $p=0.002$) and 8.5° (left limb, $p<0.001$) in this condition as well. Knee range of motion increased for all of the exoskeleton conditions compared to baseline.

DISCUSSION

Motorized exoskeletons have the potential to provide customizable and adaptable control strategies to assist individuals with crouch gait. In this study, we evaluated the ability of our exoskeleton to provide assistance during different phases of the gait cycle because the many potential contributors of crouch gait suggest that the same level and timing of assistance is unlikely to be ideal for every patient. Our results suggest that the performance of the exoskeleton motor control conditions were adequate for providing assistance during each of the specified gait phases. Motor latencies were of similar duration to those of biological processes (e.g. muscle contractions), and therefore likely appropriate for human-machine interactions.

Our primary finding is that the powered assistance successfully reduced the amount of crouch in our participant. Overall, the stance & swing assist condition yielded the largest improvement in knee extension, followed by the stance assist condition. Peak knee flexion during swing was greater during all exoskeleton conditions compared to the baseline condition, representing a more normal kinematic pattern. A consequence of this was that while the exoskeleton was able to assist knee extension during terminal swing in the swing and stance & swing conditions, the limb needed to travel through a greater range of motion. Therefore, the potential benefit of the swing assistance may have been mitigated.

The results of this study are encouraging; we are currently evaluating how our exoskeleton and assistive conditions affect muscle activity, neuromuscular control, and gait mechanics in a larger cohort of children with crouch gait caused by CP. Areas of continued and future research include the development of adaptive control algorithms that may be used in long-term rehabilitation to reduce crouch while maintaining or improving strength.

ACKNOWLEDGEMENTS

This work was supported by the Intramural Research Program of the NIH Clinical Center (protocol # 13-CC-0210).

REFERENCES

[1] Berker, A et al., *Ped Clin North Am*, 55:1209-1225, 2008.
[2] Wren, T et al., *J Ped Orhtop*, 25:79-83, 2005.
[3] McNee, A et al., *Gait Posture*, 20:171-176, 2004.
[4] Borggraefe, I et al., *Eur J Paediatr Neurol*, 14:496-502, 2014.

Copyright 2016 The Organizing Committee for the 2016 Summer Biomechanics, Bioengineering and Biotransport Conference

SB³C2016
Summer Biomechanics, Bioengineering and Biotransport Conference
June 29 –July 2, National Harbor, MD, USA
SB³C2016-817

LOCALIZED HISTOLOGICAL DIFFERENCES IN TENDON DEGENERATION BETWEEN TORN AND INTACT SUPRASPINATUS TENDON

R. Matthew Miller (1), Gerald A. Ferrer (1), Masahito Yoshida (1,2), Leanna Sullivan (1), James H-C. Wang (2), Volker Musahl (1,2), Richard E. Debski (1,2)

(1) Department of Bioengineering
University of Pittsburgh
Pittsburgh, PA, USA

(2) Department of Orthopaedic Surgery
University of Pittsburgh
Pittsburgh, PA, USA

INTRODUCTION

Rotator cuff tears are a significant clinical problem with an incidence greater than 30% in the general population [1]. Age-related degeneration has been proposed as a significant intrinsic factor likely related to the development of rotator cuff tears [2]. Furthermore, in the case of re-tears of surgically repaired degenerative rotator cuff tears, failure typically occurs at the tendon-suture interface [3], thus indicating poor tissue quality in these regions likely due to tendon degeneration. Previous studies assessing tendon degeneration of intact and torn rotator cuff tendon through histological analysis [4-6] found a strong relationship between age and degeneration; i.e. tendon degeneration increased with age. Additionally, regions with greater tendon degeneration were localized to areas adjacent to chronic rotator cuff tears. However, these studies typically take samples only from a single region of the tendon, and do not account for localized degeneration that may exist elsewhere in the tendon.

Recent findings using computational models of supraspinatus tendon tears indicate that different regions of a tendon may experience different magnitudes of mechanical strain relative to the location of a tear [7]. Similarly, differences in localized degeneration may relate to the ability of tendon tissue to resist tear propagation or suture pull-out during or after repair. Therefore, the objective of this study was to investigate histological differences in localized rotator cuff tendon degeneration in tendons with and without chronic rotator cuff tears. It was hypothesized that 1) degeneration would be worst at the insertion of the supraspinatus tendon to the humerus, the most common location for tears, and 2) degeneration around the tear will be worst in the stress-shielded region medial to the rotator cuff tear.

METHODS

Four intact fresh-frozen cadaveric shoulders (55 ± 12 years, 3 female, 1 male) and four shoulders with small rotator cuff tears isolated to the supraspinatus tendon (70 ± 9 years, 3 female, 1 male) were procured with permission from the University ethical oversight board. Supraspinatus and infraspinatus tendons were split into anterior and posterior halves of approximately equal width using a No. 11 scalpel blade. Tendon biopsies (dimensions of ~2 x 4 mm) were then taken near the myotendinous junction, tendon mid-substance, and the insertion for each tendon half. For tendons with an existing chronic tear, three samples were taken from around the tear: one sample from the medial edge of the tear, one from the anterior edge of the tear, and one from the posterior edge of the tear. All samples were fixed in 10% buffered formalin solution for at least three days, embedded in paraffin, and sectioned at a thickness of 5 µm. All slides were stained with H&E to visualize tendon morphology, and then imaged using a light microscope with a 20x objective lens across the full tendon thickness.

All histological images were graded by three independent observers for tendon degeneration using a semi-quantitative scale. Four main parameters were chosen to evaluate tendon degeneration: collagen fiber organization, tenocyte nuclei shape, tenocyte cell number, and lipoid degeneration [5, 8]. The chosen grading scale was modified from Sano et al. to create a 4-point scale of degeneration (0 = no change, 1 = slight localized change <25% of tendon area, 2 = multifocal change 25-50% of tendon area, 3 = diffuse or global change >50% of tendon area) [4]. Each histological image was graded by each observer using this 4-point scale for the four degeneration parameters, and the scores of the parameters were summed to generate an "overall" degeneration score. The scores of the three observers were then averaged to determine an overall degeneration score for the degeneration parameters for each sample.

Copyright 2016 The Organizing Committee for the 2016 Summer Biomechanics, Bioengineering and Biotransport Conference

Degeneration was compared for the three locations along the proximal-distal tendon length and the three locations around the chronic tear using ANOVA with post-hoc Games-Howell test with significance set at $p < 0.05$. Degeneration between tendons with and without chronic tears was compared using independent samples Mann-Whitney U tests.

RESULTS

In the shoulders with a tear, the anterior-posterior tear width was 14.8 ± 11.8 mm, and the medial-lateral tear width was 11.0 ± 7.0 mm. All tears exhibited a classic "crescent" shape. All tendons showed various stages of tissue degeneration, with some intact tendons showing nearly no degenerative changes (Figure 1A) and others showing significant fatty infiltration (Figure 1B) and loss of fiber organization (Figure 1C). Qualitatively, the worst degeneration was located around the chronic supraspinatus tear (Figure 1C). Grading among the three examiners showed good inter-rater reliability (ICC = 0.89).

No statistically significant differences were found in total degeneration, fiber organization, nuclei shape, or cellularity by location. However, the myotendinous junction showed a greater amount of lipoid degeneration compared to the tendon mid-substance or insertion ($p < 0.001$) (Table 1, Figure 1B). Similarly, lipoid degeneration was the only parameter to show a statistically significant difference between tendons with and without rotator cuff tears (Table 1). The medial edge of the rotator cuff tears showed small increases in most degeneration parameters compared to the anterior and posterior edges, especially for cell shape and total degeneration (Table 2). However, these differences were not statistically significant.

DISCUSSION

The results of this study indicate that age-related degeneration is a wide-spread phenomenon for intact tendons and those with small rotator cuff tears, and is not localized to the tendon insertion, refuting the hypothesis under study. However, lipoid degeneration in the tendon was found to be much greater near the myotendinous junction, indicating that muscle fatty infiltration may also result in tendon degeneration. Therefore, the clinical relevance of these results is that the risk of suture pull-out may be greater when this region is mobilized for rotator cuff repair. Although tears typically occur at the tendon insertion, degeneration does not appear to be worse there. Other factors such as biological processes or local strain distributions may more likely influence the location of tear initiation and propagation.

Interestingly, between the intact and torn tendons, lipoid degeneration was the only parameter that showed a statistically significant difference. This supports the notion that age-related tendon degeneration likely occurs prior to the development of a rotator cuff tear. Conversely, when the material properties of the tissue are reduced due to degeneration, tissue strains become sufficient to initiate a tear that can grow over time and result in further degeneration. Additionally, no statistically significant differences were found between the medial and anterior/posterior edges of the tear, indicating that although the medial edge of the tear becomes unloaded, it does not become more degenerated than the rest of the tissue surrounding the tear.

A limitation of this study was that only H&E staining was performed to assess degeneration based on changes in tendon morphology. While H&E staining was sufficient to find significant differences in key degenerative parameters, future work will include more rigorous biochemical procedures, including stains specific to collagen, fat, GAGs to better quantify degeneration.

This study provides insights on age-related degeneration in intact and torn rotator cuff tendons. Such tendon degeneration is not always macroscopically visible to surgeons, leading to overestimation of the quality of rotator cuff tissue during repair. The long-term goal of this work is to better quantify the etiology of rotator cuff tear progression and provide a guide for orthopaedic surgeons by defining a "danger zone" of poor tissue around a rotator cuff tear.

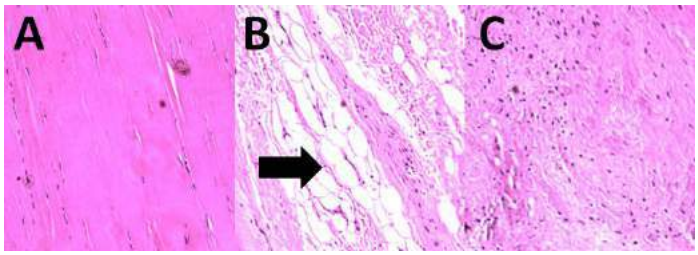

Figure 1: Histology of rotator cuff tendons. A) Intact infraspinatus tendon with well-aligned collagen fibers and normal cells. B) Intact supraspinatus tendon near the myotendinous junction showing lipoid degeneration (black arrow). C) Chronic supraspinatus tendon tear showing complete loss of fiber organization and hypercellularity.

Table 1: Degeneration Parameter Values (Mean ± SD) for Fiber Organization (Fiber), Cell Shape (Shape), Cellularity (Number), Lipoid Degeneration (Lipoid), and Total Degeneration (Sum)

	Fiber	Shape	Number	Lipoid	Sum
Insertion	2.5 ± 0.3	2.5 ± .03	0.6 ± 0.3	0.2 ± 0.2	5.9 ± 0.7
Mid-substance	2.4 ± 0.4	2.4 ± 0.4	0.6 ± 0.2	0.3 ± 0.3	5.6 ± 0.9
Junction	2.4 ± 0.3	2.4 ± 0.3	0.8 ± 0.4	0.9 ± 0.6	6.4 ± 1.1
p	0.349	0.168	0.616	**< 0.001**	0.051
Intact	2.5 ± 0.2	2.5 ± 0.3	0.6 ± 0.2	0.3 ± 0.3	5.9 ± 0.7
Chronic	2.3 ± 0.4	2.4 ± 0.4	0.8 ± 0.3	0.6 ± 0.6	6.1 ± 1.2
p	0.328	0.546	0.163	**0.033**	0.476

Table 2: Degeneration Parameter Values around Chronic Rotator Cuff Tears (Mean ± SD)

	Fiber	Shape	Number	Lipoid	Sum
Anterior	2.6 ± 0.4	2.7 ± 0.4	0.9 ± 0.4	0.2 ± 0.3	6.3 ± 1.0
Posterior	2.6 ± 0.2	2.1 ± 0.6	0.4 ± 0.3	0.3 ± 0.5	5.4 ± 1.3
Medial	2.8 ± 0.2	2.9 ± 0.1	1.1 ± 0.6	0.5 ± 0.4	7.3 ± 0.8
p	0.575	0.096	0.159	0.583	0.096

ACKNOWLEDGEMENTS

Support from The Albert B. Ferguson, Jr., M.D. Orthopaedic Fund of The Pittsburgh Foundation (AD2014-73915-04), the Department of Orthopaedic Surgery, the Pittsburgh Chapter of the ARCS Foundation, and NSF Fellowship Grant No. 1247842 is gratefully acknowledged.

REFERENCES

[1] Yamamoto et al. J Shoulder Elbow Surg. 2010;19(1):116-20.
[2] Thomopoulos et al. J Orthop Res. 2015;33(6):832-9.
[3] Ponce et al. Am J Sports Med. 2013;41(10):2256-61.
[4] Sano et al. J Shoulder Elbow Surg. 1999;8(6):574-9.
[5] Longo et al. Am J Sports Med. 2008;36(3):533-8.
[6] Matthews et al. J Bone Joint Surg Br. 2006;88(4):489-95.
[7] Thunes et al. J Biomech Eng. 2015;137(8):081012.
[8] Hashimoto et al. Clin Orthop Relat Res. 2003(415):111-20.

Copyright 2016 The Organizing Committee for the 2016 Summer Biomechanics, Bioengineering and Biotransport Conference

SB³C2016
Summer Biomechanics, Bioengineering and Biotransport Conference
June 29 –July 2, National Harbor, MD, USA
SB³C2016-818

STRESS FIBER CONTRACTILE BEHAVIOR IN AORTIC VALVE INTERSTITIAL CELLS

Yusuke Sakamoto (1), Rachel M. Buchanan (1), Johannah S. Adams (2), Farshid Guilak (3), Michael S. Sacks (1)

(1) Center for Cardiovascular Simulation
Institute for Computational Engineering and Sciences
Department of Biomedical Engineering
Austin, TX USA
The University of Texas at Austin
Austin, Texas USA

(2) Departments of Orthopaedic Surgery and Biomedical Engineering
Duke University Medical Center
Durham, North Carolina USA

(3) Departments of Orthopaedic Surgery, Biomedical Engineering, and Developmental Biology
Washington University, St. Louis USA

INTRODUCTION

Valve interstitial cells (VICs) reside in heart valve tissues and play critical roles in tissue maintenance, but also contribute to heart valve diseases [1]. VICs are myofibroblast-like cells with tissue remodeling activity due to collagen production and contraction activities mediated by α-smooth muscle actin (α-SMA) stress fibers. The VICs are activated by mechanical stimuli during tissue repair, development, and remodeling, and removed as they complete their role. The VICs are sensitive to their surrounding microenvironments, and excessive and persisting environmental changes cause the improper regulations of VICs, contributing the progression of valve disease. Thus, it is important to characterize how the external mechanical stimuli translate into and activate the VICs, and how the different activation levels affect the VIC's internal mechanics and their mechanical response to the surrounding tissues.

Contractile properties of the VICs are connected to their valve tissue remodeling and repair capabilities, as well as initiation of pathological process. However, their contractile mechanism are not well understood. Thus, in order to understand the complex biomechanical behaviors of the VICs in cellular and subcellular levels, we need to develop a computational model of the VICs that is capable of capturing their responses to mechanical stimuli from surrounding tissues under wide range of activation states. Such a model can integrate the various and often disparate experimental findings by deciphering the underlying mechanisms and provide us with insight that would otherwise be difficult or impossible to obtain from experimental data and observations alone.

The objective of this study is to develop an improved computational model of a VIC by incorporating a more realistic stress fiber model. Then, by integrating the experimental data of the AVICs into the model, we studied how the stress fibers in the AVICs adapt to different activation states, and how the different components of the stress fibers, F-actin and α-SMA, affect the stress fiber biomechanics.

METHODS

We carried out the microindentation experiment on AVICs cultured on a flat thin-layered collagen substrate over a glass. We used a spherical indenter with 5 μm diameter. We controlled the activation states of the AVICs with different chemical reagents to alter the biomechanical properties of the stress fibers. Then, using the experimental data from different experimental groups, we studied how the different components of the stress fibers (α-SMA and F-actin) influenced the stress fiber biomechanics, such as their stiffness and contractile strength. We have five experimental groups: Cytochalasin D pretreated group (CytoD), Control groups with 5 mM and 90 mM KCl treatments (C5 and C90 groups, respectively), and transforming growth factor-beta1 (TGF-β1) pretreated groups with 5 mM and 90 mM KCl treatments (T5 and T90 groups, respectively). For each group, we extracted the indentation depth vs force curves, which were later fit to the computational model.

Immediately following the microindentation, α-SMA, F-actin, and nucleus were stained with and fluorescent images were taken to quantify the expression levels of α-SMA and F-actin for each group. Z-stacks were also taken using confocal microscopy to determine the appropriate AVIC and nucleus geometries and stress fiber orientations for each activation state. The expression levels of α-SMA and F-actin, AVIC and nucleus dimensions, and stress fiber orientations were averaged for each group and used for the input for the computational model.

The computational model of an AVIC was developed by extending the "basic" model of a VIC from our previous study [2]. The improved model can capture more realistic stress fiber mechanical responses. The main improvements are: 1) more realistic stress fiber geometry taken

Copyright 2016 The Organizing Committee for the 2016 Summer Biomechanics, Bioengineering and Biotransport Conference

from experiments, 2) more realistic stress fiber contraction model. The computational domain consists of three subdomains: Ω_{cyto}, Ω_{nuc}, and Ω_{ind}, which describe the cytoplasm, nucleus, and rigid spherical indenter, respectively (Figure 1). The cytoplasm was considered as a solid mixture of basal cytoplasm and oriented stress fibers. The basal cytoplasm was modeled as a nearly-incompressible neo-Hookean material. The stress fibers were modeled as the ensemble of oriented 1D fibers with passive elastic and active contractile responses with their orientation described by a continuum orientation density function. The active contraction of the stress fibers were modeled by length-tension relationship (f_l) multiplied by the maximum contraction strength (f_0):

$$f(\bar{\phi}_{\alpha-SMA}, \bar{\phi}_{F-actin}, \lambda) = f_0(\bar{\phi}_{\alpha-SMA}, \bar{\phi}_{F-actin}) f_l(\lambda)$$
$$f_0(\bar{\phi}_{F-actin}, \bar{\phi}_{\alpha-SMA}) = f_{F-actin}\bar{\phi}_{F-actin} + f_{\alpha-SMA}\bar{\phi}_{\alpha-SMA} \quad (1)$$

where f_l only depends on 1D stretch (λ) and f_0 is a linear combination of expression levels of F-actin and α-SMA ($\bar{\phi}_{F-actin}$ and $\bar{\phi}_{\alpha-SMA}$, respectively). Two constants: $f_{F-actin}$ and $f_{\alpha-SMA}$, were determined using experimental data. The AVIC and nucleus dimensions, F-actin and α-SMA expression levels, and stress fiber orientation density were determined from the experiments and fed into the computational model. Then, using the indentation depth vs force curves from the simulations and experiments, the model parameters were determined.

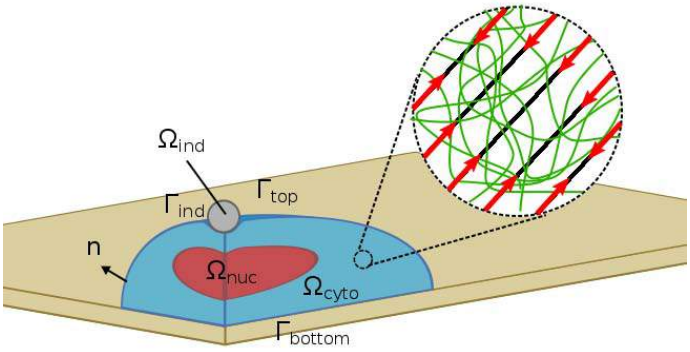

Figure 1: AVIC model framework.

RESULTS

The primary result in this study is that we separated the contributions of the F-actin and α-SMA to the overall contractile strength of the stress fibers (Figure 2). In Figure 2, green and blue columns represent the contributions of the F-actin and α-SMA to the contractile strength of the stress fibers within AVICs for each group determined by (1). The treatment with 90 mM KCl and pre-treatment with TGF-β1 activated the AVICs, enhancing the contractile strength of the stress fibers. In addition, the overall contractile strength of the stress fiber was dominated by the α-SMA contribution, which is consistent with the previous experimental observations that incorporation of the α-SMA into stress fiber significantly enhances the contractile activity of the VICs [3].

To better understand the interaction between the AVICs and substrates, we calculated the total force that the AVIC exerts on the substrate for each group. The calculated total forces are: 0 nN, 71.8 nN, 86.6 nN, 142.6 nN, and 158.5 nN for CytoD, C5, C90, T5, and T90 groups, respectively. The total force calculated from the TFM experiments are: 35.2±9.6 nN (n=15), 544.9±114.5 nN (n=13), and 932±393.5 nN (n=8), respectively for Blebbstatin treated, control, and TGF-β treated groups (unpublished data from Dr Billiar's lab). Note that Blebbstatin disrupts the stress fiber structure, just as CytoD does. Although the total forces calculated in this study were smaller than the TFM data, the trends stayed the same: the relative increase of the total force from the C5 to T5 group in this study was 2.0 while the relative increase of the total force measured by TFM from the control to TGF-β treated group was 1.7. Thus, our model can be used to capture the trend in the total force that AVICs exert on the surrounding substrates. The larger total forces in the TFM experiment may be resulted from the stronger contractile force near the ends of the AVIC, as observed for fibroblasts [4].

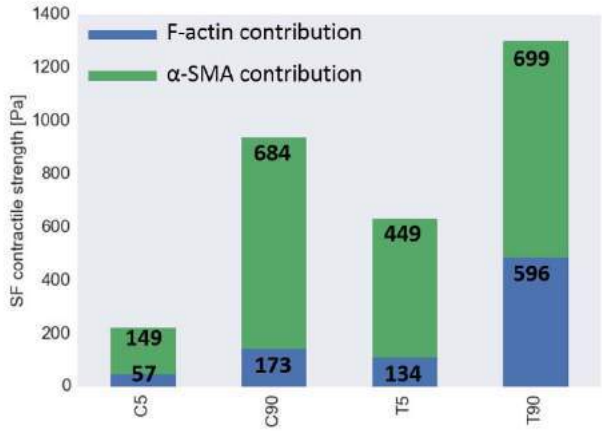

Figure 2: Contributions of the F-actin and α-SMA to the maximum SF contraction strength (f_0) for each group.

DISCUSSION

We have developed the improved computational model of the AVICs that consists of the different mechanical constituents of the stress fibers. We have incorporated the detailed data of the AVIC under microindentation experiment into our model to derive the insight in the stress fiber biomechanics, which was previously unable to obtain due to the complexity of the mechanisms and difficulty of directly analyzing the subcellular mechanics. We have found that the both F-actin and α-SMA contribute to the stress fiber force generation. However, as previously reported, the incorporation of α-SMA into the stress fibers have dominant effect on the increase in the stress fiber contractile strength. This increase in the stress fiber contractile strength also influenced the traction force that the AVICs exert on the substrates. Thus, in order to understand how the AVICs interact with the surrounding environment, it is critical to model the stress fiber mechanics with the α-SMA component. We hope that our study can provide an improved view of the stress fiber force generation mechanics within the AVICs.

ACKNOWLEDGEMENTS

- We would like to thank Dr Ferrari at the University of Pennsylvania for donating AVICs used in this study.
- We would like to thank Dr Billiar and Heather Cirka at Worcester Polytechnic Institute for providing the TFM data of AVICs.
- This study was supported by NIH Grant R01 HL-68816-01 and R01 HL119299.

REFERENCES

1. Sacks, M.S., et al. *J Biomech*, 2009. **42**(12): p. 1804-24.
2. Sakamoto, Y., et al. *J Mech Behav Biomed Mater*, 2016. **54**: p. 244-58.
3. Hinz, B., et al. *American Journal of Pathology*, 2012. **180**(4): p. 1340-1355.
4. Peterson, L.J., et al. *Molecular Biology of the Cell*, 2004. **15**(7): p. 3497-3508.

Copyright 2016 The Organizing Committee for the 2016 Summer Biomechanics, Bioengineering and Biotransport Conference

SB^{3}C2016
Summer Biomechanics, Bioengineering and Biotransport Conference
June 29 –July 2, National Harbor, MD, USA
SB^{3}C2016-819

MECHANICAL TRAUMA IN ARTICULAR CARTILAGE INDUCES RAPID, LOCATION-DEPENDENT CHONDROCYTE DYSFUNCTION

Lena R. Bartell (1), Michelle M. Delco (2), Lawrence J. Bonassar (3,4), Itai Cohen (5), Lisa A. Fortier (2)

(1) School of Applied and Engineering Physics
Cornell University
Ithaca, NY, USA

(2) Department of Clinical Sciences
Cornell University
Ithaca, NY, USA

(3) Sibley School of Mechanical and Aerospace Engineering
Cornell University
Ithaca, NY, USA

(4) Meinig School of Biomedical Engineering
Cornell University
Ithaca, NY, USA

(5) Department of Physics
Cornell University
Ithaca, NY, USA

INTRODUCTION

In this study we investigate the earliest signs of damage in articular cartilage (AC) following mechanical trauma and thus inform the development of treatments for osteoarthritis (OA).

OA is a painful and debilitating joint disease that develops when AC degrades, exposing the underlying bone. Today, OA is one of the leading causes of disability in the United States. Moreover, at least 12% of OA develops after a distinct, mechanically traumatic event, such as a sports injury [1]. Current research recommends that OA interventions target the disease early, in what may be thought of as pre-OA. At this early stage, the AC has been damaged but true clinical OA has yet to develop [2-3]. Thus, in the search for a treatment, it is critical to understand the early pathogenesis of OA. However, little is known about the earliest stages of AC degeneration, especially in the minutes to hours after trauma [4]. Recent studies show that chondrocyte respiratory dysfunction and death are early indicators of AC damage [4-6]. In particular, mitochondrial depolarization may be a key precursor to cell death and the eventual onset of OA.

Therefore, in this study, we investigate how chondrocyte dysfunction and death develop in the minutes to hours after impact trauma.

METHODS

To study the kinetics of chondrocyte dysfunction after mechanical trauma, we used a custom rapid impact device combined with a novel direct-imaging method to monitor individual cells over time in whole tissue. Cylindrical explants (n=3, 6 mm diameter, 3 mm deep) were extracted from the medial condyle of 1-3 day old bovines. Samples were cut perpendicular to the articular surface, creating two opposing hemiclyinders (Fig. 1A). Hemicylinders were then stained with Hoechst 33342 (1 µg/mL for 50 min) to highlight dead cell nuclei, MitoTracker Green (MTG, 200 nM for 50 min) to highlight all mitochondria, and Tetramethylrhodamine (TMRM, 10 nM for 30 min) to highlight polarized (healthy) mitochondria only. The two samples were mounted to the impactor's backplate and then loaded into the PBS bath of the impactor, as described previously [7]. One of the two hemicylinders was impacted at approximately 1 MPa over 5-10 ms using a 0.8 mm diameter rod. The second sample served as an unimpacted control. Samples were imaged using confocal fluorescence

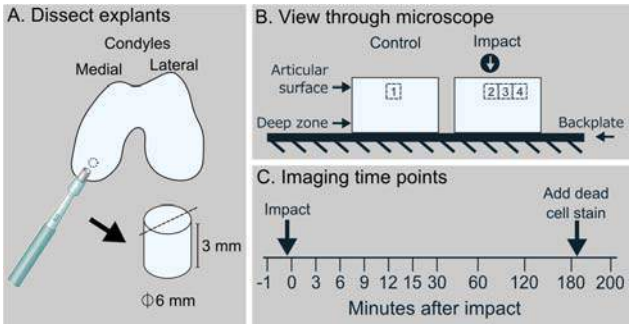

Figure 1. Experimental design. Samples were (A) dissected from medial condyle and stained with Hoechst, MTG, and TMRM, and then (B) mounted in the impactor on a confocal microscope. Control samples were imaged at one position and impact samples at 3 positions. (C) Positions were imaged before and for 3 h after impact. Samples were then stained with EthD and imaged again.

microscopy with 20× magnification (424 µm field of view) at different positions relative to the impact, as depicted in Fig. 1B. All imaging positions were centered 424 µm below the articular surface, to avoid artifacts from imaging at the surface. Positions 2-4 were adjacent fields of view, with position 2 centered under the impact. Samples were imaged at these positions before and for multiple time-points after impact, as described in Fig. 1C. Then, at 3 h after impact, samples were additionally stained with ethidium homodimer (EthD, 2 µM for 20 min) to highlight dead cells, and imaged again to determine the fate of each cell.

Images were processed in MATLAB to extract cellular changes after impact. Images were first registered to align them over time and then thresholded to segment individual cells. The average TMRM signal of each cell was tracked over time and cells that lost more than 75% of their initial TMRM signal were marked as depolarized. The difference between TMRM images before impact and at 15 min after impact was also calculated.

RESULTS

After impact, mitochondria depolarized rapidly (Fig. 2, 3). Confocal images revealed dramatic mitochondrial depolarization

Copyright 2016 The Organizing Committee for the 2016 Summer Biomechanics, Bioengineering and Biotransport Conference

within the first 15 minutes after impact, especially directly under the impact (position 2, Fig. 2). This rapid depolarization was confirmed by survival curves based on each cell's decrease in TMRM signal over time (Fig. 3).

Confocal images further revealed that rapid mitochondrial depolarization and cell death were linked. Cells that showed mitochondrial depolarization within 15 minutes after impact stained for cell death at 200 min, while cells that depolarized later did not (Fig. 2).

Moreover, mitochondrial depolarization and cell death varied based on distance from the impact (Fig. 2, 3). Directly under the impact (position 2), there was widespread mitochondrial depolarization and cell death. Further away from the impact (positions 3-4), there was some depolarization and death, but less than at position 2. In comparison, images at position 1 revealed little to no depolarization or death in the control sample.

DISCUSSION

Using a novel direct-imaging method to track individual chondrocytes in whole AC, we revealed that, near the impact location, mitochondria begin to depolarize immediately after trauma. Furthermore, only cells whose mitochondria depolarize by 15 min after impact have died by approximately 3 hours after impact. These effects are strongest closest to the impact and weaker further away.

These cells that depolarize and die quickly after impact may initiate the biological instability and feed-forward loop that drives cartilage degradation and OA development. As such, this subset of damaged cells may be a key target for mitoprotective therapies or other treatments that interrupt cellular deterioration. These results further emphasize that potential OA treatments should be focused very early after trauma, perhaps within the first hour.

The location-dependence of cellular dysfunction also provides insight into OA initiation after trauma. Recent studies have shown a similar position-dependence in the cell death that develops immediately after impact injury [7]. In particular, the mitochondrial dysfunction observed in this study appears to correlate with the impact-induced strain profile described in Bartell, et al [7]. This implies that strain during rapid impact leads to mitochondrial dysfunction, cell death, and the ultimate development of OA.

Overall, this method expands the current ability of the field, enabling us to study the earliest changes in AC after mechanical trauma. In particular, these results provide a detailed understand of how AC degrades and how potential therapies may prevent OA from developing.

ACKNOWLEDGEMENTS

This work was funded by in part by the NIH (R21-AR062677), the NSF (CMMI-1536463), and the Harry M. Zweig Fund for Equine Research. L.R.B. was also supported by the NSF GRFP (DGE-1144153). Imaging data was acquired through the Cornell University Biotechnology Resource Center, with NYSTEM (CO29155) and NIH (S10OD018516) funding for the shared Zeiss confocal microscope.

REFERENCES

[1] Brown, T. et al. *J Orthop Res*, 20:739-44, 2006.
[2] Anderson, D. et al. *J Orthop Res*, 29:802-9, 2011.
[3] Chu, C. Et al. *J Orthop Res*, 33:939-947, 2015.
[4] Lotz, M. et al. *Osteoarth Cart*, 7:389-91, 1999.
[5] Delco, M. et al. *Osteoarth Cart*, 23:A288–89, 2015.
[6] Huser, C. et al. *Arth Rheum*, 56:2322-34, 2007.
[7] Bartell, L. et al. *J Biomech*, 48:3440-46, 2015.

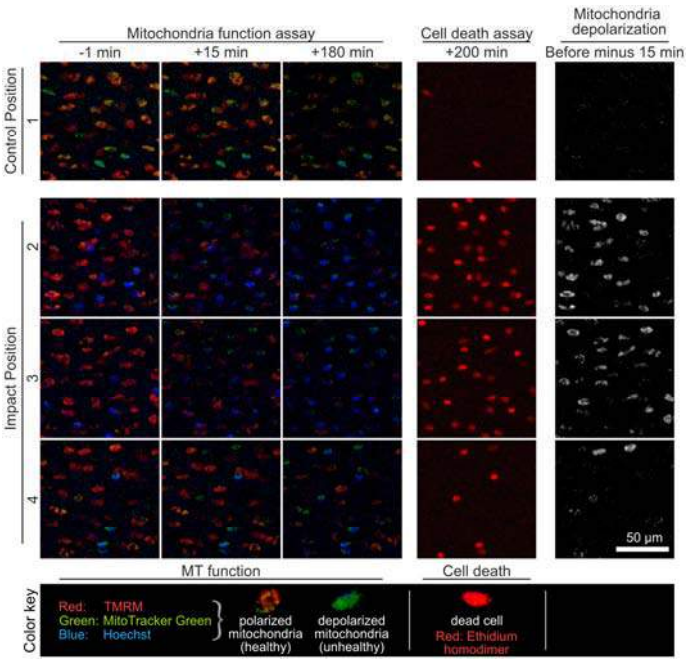

Figure 2. <u>Impact causes rapid, location-dependent mitochondrial dysfunction</u>. Example confocal images show mitochondria function (columns 1-3) and cell death (column 4) at the different sample positions in the control (row 1) and impact (rows 2-4) samples. The difference between TMRM signal before impact and at 15 mins after impact is also shown (column 5). The mitochondria assay is shown before impact, 15 min after impact, and 180 min after impact. For mitochondria function images, red (TMRM signal) indicates polarized mitochondria, while a loss of red over time (exposing the underlying green stain) indicates depolarization. For cell death images (column 4), red indicates dead cells. Images in the same row are from identical locations.

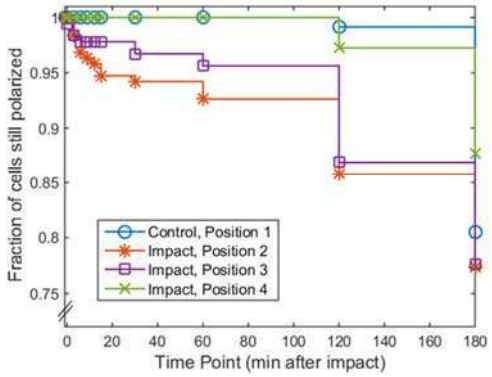

Figure 3. <u>Survival curve quantifies rapid, location-dependent mitochondrial dysfunction after impact</u>. This plot shows the fraction of polarized mitochondria over time in control (position 1) and impact (position 2-4) samples. Cells that lost more than 75% of their initial TMRM signal were marked as depolarized. Overall, cells depolarize rapidly, with more depolarization closer to the impact location.

Copyright 2016 The Organizing Committee for the 2016 Summer Biomechanics, Bioengineering and Biotransport Conference

SB³C2016
Summer Biomechanics, Bioengineering and Biotransport Conference
June 29 –July 2, National Harbor, MD, USA
SB³C2016-820

EXPERIMENTAL VALIDATION OF A SUBJECT-SPECIFIC ANISOTROPIC MODEL OF THE ROTATOR CUFF TO PREDICT TEAR PROPAGATION

R. Matthew Miller (1), James Thunes (1), Volker Musahl (1,2)
Spandan Maiti (1), Richard E. Debski (1,2)

(1) Department of Bioengineering
University of Pittsburgh
Pittsburgh, PA, USA

(2) Department of Orthopaedic Surgery
University of Pittsburgh
Pittsburgh, PA, USA

INTRODUCTION

The initiation and propagation of rotator cuff tears are poorly understood, despite an incidence of over 30% [1]. Numerous studies have shown the importance of tendon surface strains on the initiation and propagation of rotator cuff tears [2, 3]. Additionally, computational models have been developed to further investigate the mechanical environment of the rotator cuff [4,5]. However, these models use simplified geometry or isotropic elastic material properties, which are not representative of the true properties of tendon tissue and can have a drastic effect on the predicted strains. Therefore, the objective of this study was to develop and experimentally validate a three-dimensional finite element model of supraspinatus tendon using subject-specific geometry and anisotropic material properties to predict strains in intact supraspinatus tendon at multiple joint angles. The model was considered valid if the difference between experimental and predicted strains was less than the experimental repeatability of 3%.

METHODS

An intact, cadaveric shoulder (male, 70 y.o.) was dissected to isolate the rotator cuff tendons. A 6 x 4 array of markers was affixed to the bursal and articular surfaces of the tendon (Figure 1). The humerus was potted in epoxy putty and loaded into a custom jig that allowed for positioning of the tendons. Geometry of the shoulder and markers were obtained using a soft-tissue CT scanning protocol at 70 degrees of glenohumeral abduction (GE Lightspeed 16, Milwaukee, WI).

Next, the humerus was secured to a materials testing machine (Instron, Model 5965) and the supraspinatus tendon was clamped to the crosshead for loading at 70 degrees of abduction (Figure 1). The infraspinatus was loaded with 22 N to simulate load sharing with the supraspinatus. A 4-camera video tracking system was used to track marker positions during testing (Spica Technology, Kihei, Maui HI). After 5 N preload and preconditioning (5-50 N, 10 cycles), the preload was reapplied and the reference strain configuration was recorded. Next, cyclic loading was performed (5-200 N, 50 cycles, 20 mm/min) and marker locations were recorded at the peak of the final load cycle. This process was repeated at 90 degrees. Maximum principal Green-Lagrange strain was calculated at the centroid of each element created from sets of four surface markers (total of 30 elements). Calculations were performed by inputting the reference and strained configurations of the surface markers into ABAQUS (ABAQUS/CAE 6.4) [6].

Next, the tendon was split into thirds of equal anterior-posterior width to determine material properties. After measurement of cross-sectional area with 2% accuracy (NextEngine 3D Scanner HD), each third was loaded to failure and stress-strain curves were generated. A transversely isotropic fiber reinforced Neo-Hookean model was chosen to represent the behavior of the tendon [7], and a set of material constants were calculated using a least squares approach (MATLAB). The humerus and cartilage were represented as fixed rigid bodies.

Humerus and tendon geometry were segmented from CT data (Mimics 15, Materialize) and converted to a solid model. The mesh for finite element modeling (Hypermesh, Altair Engineering) consisted of 14350 nodes and 63439 tetrahedral elements. This mesh was chosen after testing convergence with a change in strain of less than 1%. Displacement-driven finite element analyses were performed for each joint angle using custom non-linear code [8] and displacements recorded at 200N. A 22N load was applied to the infraspinatus to mimic experimental conditions. Inhomogeneous material properties were assigned to the supraspinatus by varying material parameters in the anterior-posterior direction based on experimental data.

Maximum principal Green-Lagrange strains for each element were computed. The nodes nearest to the center of each marker were recorded to make comparisons within the same regions of interest as

Copyright 2016 The Organizing Committee for the 2016 Summer Biomechanics, Bioengineering and Biotransport Conference

experimental conditions. The strains of all tetrahedral elements bounded within each experimental strain element were recorded and averaged to determine an average strain for each region. This value was compared to the strains for each experimental surface element [6]. For validation, the average difference in strain between model and experiment must be less than the experimental repeatability of 3% strain.

RESULTS

Experimentally, the largest maximum principal strains were found on the articular side of the tendon, with the largest strain observed being 13.4% at 90 degrees of abduction (Figure 2A). On the bursal side, the largest strain was 11.7%, also at 90 degrees of abduction (Figure 2B). On average, maximum principal strain was 2% strain higher at 90 degrees of abduction than at 70 degrees. Strains increased in magnitude further away from the tendon insertion, and decreased in magnitude on the articular side from anterior to posterior. On the bursal side, strains decreased from posterior to anterior in reverse of the articular side.

Qualitatively, the model predicted a similar pattern of strain as the articular side of the supraspinatus, with strains decreasing closer to the insertion (Figure 2A). On the bursal side, the model predicted a pattern more similar to the experimental strains on the articular side (Figure 2B) Predictions of average strains at 90 degrees were within 3.6% strain of experimental values for the bursal side and 3.1% strain for the articular side. At 70 degrees, predictions for the bursal side were within 2.2% strain and for the articular side were within 3.6% strain. On the bursal side, strain predictions were most different from experimental closer to the insertion (Table 1). On the articular side, predictions were most different in the middle row of markers. Strains in the anterior-posterior direction were most different closer to the infraspinatus.

DISCUSSION

This study developed and validated a subject-specific 3D finite element model for prediction of tendon strains at two glenohumeral joint angles. Bursal and articular surface strains predicted by the model were close to within 3% strain of the experimentally determined values, but the model had difficulty predicting experimental strains near the insertion and infraspinatus tendon, indicating potential boundary effects that are currently not accounted for by the model. Additionally, experimental measures and model predictions were similar to previous studies that have shown similar patterns and magnitudes of strain [9,10]. Previous models of intact rotator cuff tendon using simplified geometry and isotropic elastic material properties found highest stresses to be located on the articular side of the tendon and that the magnitude of stress increased with joint angle, similar to the predictions of the model in the present study for strain [4,5].

Unlike previous models of the rotator cuff, this model uses experimental validation with subject-specific geometry and anisotropic, inhomogeneous material properties that better represent the behavior of the tendon. Overall, this model establishes a framework to predict the effect of loading on tendon strain, providing a useful tool to better evaluate the mechanical environment of the supraspinatus tendon as it relates to rotator cuff injury. Based on the validation data, this model will be improved by varying material parameters at the tendon insertion and where fibers from the infraspinatus merge with the supraspinatus to better account for local differences in material properties. Ultimately, by introducing "tears" of different geometry, location, and chronicity into the intact tendon geometry, this model can be used to predict tendon strains for investigating risk factors for rotator cuff tear initiation and propagation.

The model has been only validated for the region medial to the tendon insertion. However, the goal of this model is to predict tear propagation within the region most common to rotator cuff tears, and therefore it can serve as a basis for further studies. Future directions for the model include contact boundary conditions between tendon and cartilage to validate the model at lower abduction angles. This information will provide surgeons with updated guidelines for proper management of rotator cuff tears to minimize the time and costs associated with rotator cuff tear treatment.

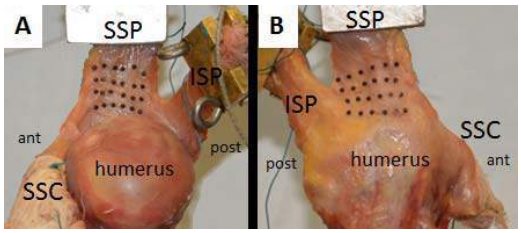

Figure 1: Experimental setup for A) articular and B) bursal surfaces. SSP: Supraspinatus; ISP: Infraspinatus; SSC: Subscapularis

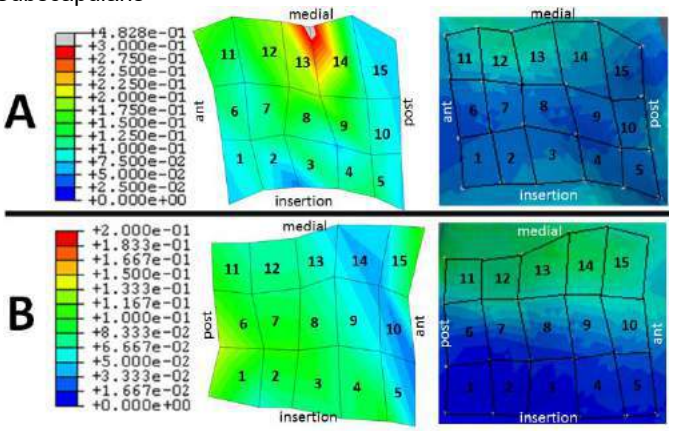

Figure 2: Experimental and predicted surface strain contour plots at 90 degrees of abduction for A) articular and B) bursal surfaces

Table 1: Differences in % Strain between Experiment and Model Predictions by Marker Row (Avg ± SD)

Marker Row	90° Bursal	90° Articular	70° Bursal	70° Articular
Medial (11-15)	1.7% ± 1.5%	2.7% ± 2.2%	1.6% ± 0.8%	2.2% ± 2.7%
Middle (6-10)	4.3% ± 4.1%	4.1% ± 1.7%	2.2% ± 2.2%	5.8% ± 3.0%
Insertion (1-5)	4.9% ± 3.5%	2.5% ± 1.4%	2.8% ± 2.2%	2.8% ± 3.0%

ACKNOWLEDGEMENTS

Support from The Albert B. Ferguson, Jr., M.D. Orthopaedic Fund (AD2015-1765-23), the Department of Orthopaedic Surgery, and ARCS Foundation is gratefully acknowledged.

REFERENCES

[1] Yamamoto J Shoulder Elbow Surg. 2010 Jan;19(1):116-20. [2] Andarawis-Puri et al. J Biomech. 2009 Jan 19;42(2):158-63. [3] Miller et al. J Orthop Res. 2014 Oct;32(10):1283-9. [4] Inoue et al. Knee Surg Sports Traumatol Arthrosc. 2013 May;21(5):1151-7. [5] Seki et al. J Orthop Sci. 2008 Jul;13(4):348-53 [6] Moore et al. Ann Biomed Eng. 2010 Jan;38(1):66-76. [7] Weiss et al. Comput. Methods Appl. Mech. Engrg. 135 (1996) 107-128 [8] Thunes et al. J Biomech Eng. 2015 Aug;137(8):081012. [9] Reilly et al. J Bone Joint Surg Br. 2003 85-B:594-9. [10] Bey et al. J Orthop Res. 2002 20:869-874.

Copyright 2016 The Organizing Committee for the 2016 Summer Biomechanics, Bioengineering and Biotransport Conference

SB³C2016
Summer Biomechanics, Bioengineering and Biotransport Conference
June 29 –July 2, National Harbor, MD, USA
SB³C2016-821

EXPERIENCES WITH INTRODUCING STEM CLUBS TO K-12 STUDENTS: PERILS, PITFALLS, AND PEARLS OF WISDOM?

Ferris M. Pfeiffer, PhD (1,2)

(1) Department of Bioengineering
University of Missouri
Columbia, MO, USA

(2) Department of Orthopaedic Surgery
University of Missouri
Columbia, MO, USA

INTRODUCTION

The importance of engaging and inspiring young scientists and innovators cannot be understated. The future of technological advancement is critical to advancing an ever more complex society, and without new ideas and new innovators, we will swiftly be left behind. Therefore, there are numerous efforts underway to increase participation in science, technology, engineering and math (STEM). However, for individuals who are not trained in developing curriculum or teaching at the elementary school level, it is daunting and often discouraging to embark on such an endeavor no matter how important it may be. One avenue which allows University level scientists and engineers to disseminate their research to elementary school children is the STEM club. STEM clubs can be simple and informal with limited required resources to well-funded outreach programs with strong ties to one's University. In this pilot work, I wish to share some of the experiences in implementing a rather informal STEM club at my hometown elementary school. A fun and active program was introduced and implemented as a curriculum of instruction for students in the area of creativity and innovation of new solutions using a translational analysis approach which involved the use of technology including 3D printing. The instruction was based in part on the "Biodesign" textbook [1], findings on creativity in the classroom [2], along with other resources. Over the course of two weeks, students were be facilitated through a process of 1) observing physical phenomena which was of interest, 2) identification of needs, 3) brainstorming solutions, 4) concept generation in an *in silico* (virtual) environment, and 5) design optimization. Students were provided access to the necessary *in silico* technology (i.e. Solidworks) as well as 3D printing technology (ZCorp 3D printer) which were made available from my research lab.

METHODS

Self-identified interested elementary students (n=10 3rd-5th grade) were selected from math and science classes of a local elementary school. Students were polled (scale 1-10 with 10 being high interest and or efficacy) to determine their initial self-efficacy and interest in science and math (Figure 1). Students were then instructed to seek out any problem that interested them and which may have a technological solution (a few examples were provided as guidance). Students were to watch the news, read newspapers or magazines, and/or poll their friends and families. After one night of research, two potential problems were

Figure 1. Self-reported interest and self-efficacy in math and science

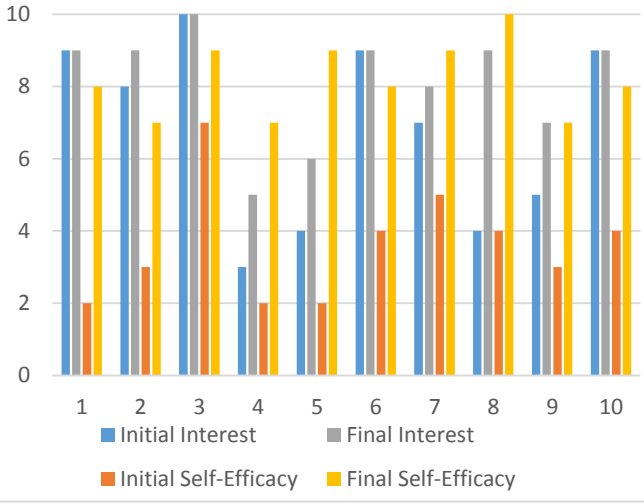

Copyright 2016 The Organizing Committee for the 2016 Summer Biomechanics, Bioengineering and Biotransport Conference

identified for further analysis from the long list of possibilities compiled. The first was the development of a new water filter (perhaps for use in underdeveloped countries or in water bottles), and the second was a heatsink to keep computers and/or game consoles cooler. General and specific needs for each were discussed such as size requirements, costs, surface area, and materials. A brainstorming session was facilitated to develop as many creative solutions to the problems as possible. Minimal input from the PI was included in an attempt to avoid stifling creativity and thinking. Next, students were asked to translate their ideas into *in silico* computer models using computer aided design (CAD) methods. Students were given an introduction to Solidworks (Dassault Systèmes, Waltham, Massachusetts, USA), and then asked to create a model which was no more than 1" in dia and 5" in length which had a maximum surface area for filtration and/or heat transfer. Initial designs ranged from the simplistic to the very complicated (Figure 2). Each student presented their designs and explained their rationale to the group. Alternative strategies were discussed in the context of design improvement/optimization. Finally, students were facilitated through a process of design refinement until they reached their self-identified "optimal" solution (Figure 3). Students were again polled (scale 1-10 with 10 being high interest and or efficacy) to determine their self-efficacy and interest in science and math following the exercises and instruction (Figure 1).

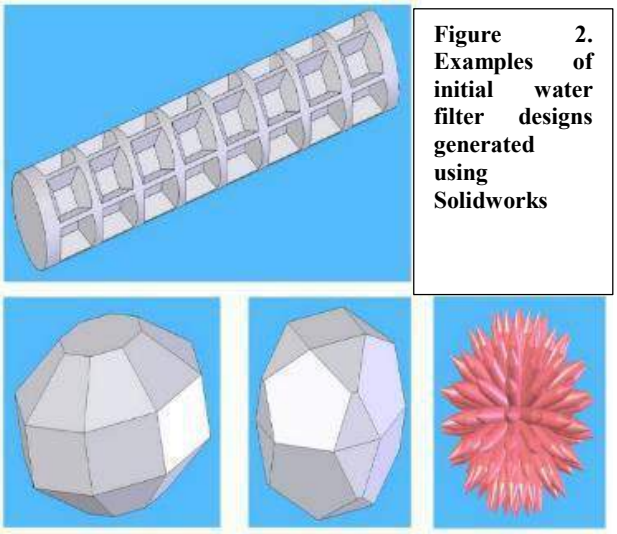

Figure 2. Examples of initial water filter designs generated using Solidworks

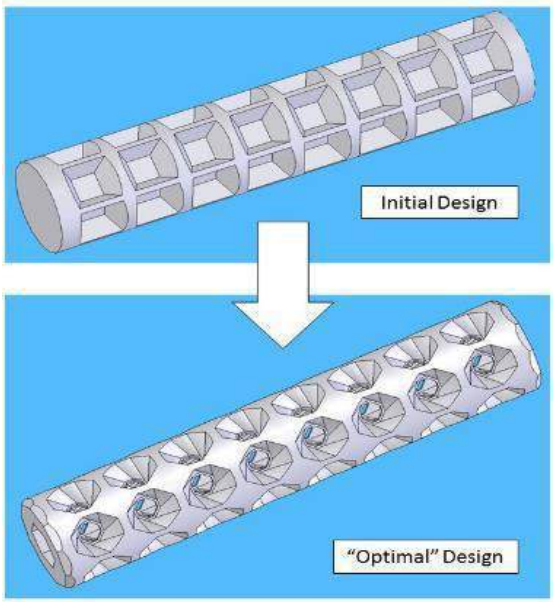

Figure 3. Examples of initial water filter designs and "optimal" final design

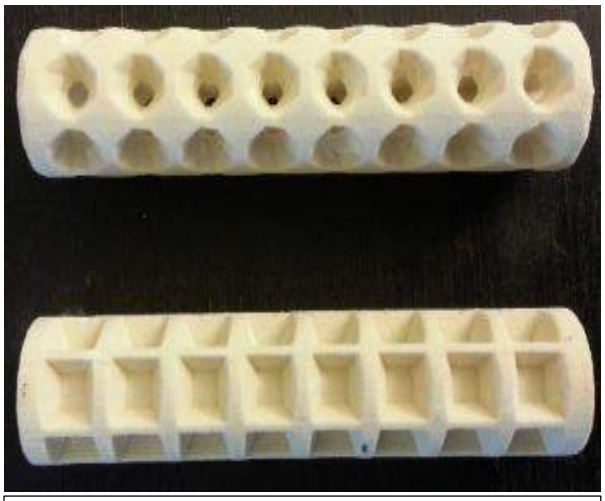

Figure 4. Examples of 3D printed water filter designs

RESULTS

In general, student interest in math and science remained the same although there was a trend toward an increase in interest following the exercises. Student's perceived self-efficacy was substantially increased following the active learning activities indicating the potential for improvement using similar methods.

*S*tudents were provided the opportunity to 3D print their designs, including initial and "optimal" final designs (Figure 4), using a ZCorp Z400 3D printer currently in use for research purposes at the PIs lab.

DISCUSSION

The opportunity for hands-on active learning including generating *in silico* and 3D printed solutions had a tremendous impact on the students involved. Additionally, the process was very fulling to the instructor and the faculty contacts. The implementation of STEM clubs need not be so complex as to stifle implementation. Even an informal implementation such as was seen in this exercise has measurable and lasting impact on student's passion for STEM.

ACKNOWLEDGEMENTS

This work was supported by the Comparative Orthopaedic Lab

REFERENCES

1. Zenios, S., et al., *Biodesign: The Process of Innovating Medical Technologies*. 2010, New York: Cambridge University Press.
2. Beghetto, R., *Killing Ideas Softly? The Promise and Perils of Creativity in the Classroom*. 2013: Information Age Publishing, Inc.

Copyright 2016 The Organizing Committee for the 2016 Summer Biomechanics, Bioengineering and Biotransport Conference

SB^{3}C2016
Summer Biomechanics, Bioengineering and Biotransport Conference
June 29 –July 2, National Harbor, MD, USA
SB^{3}C2016-822

MATRIX STIFFNESS ENHANCES VASCULOGENESIS THROUGH CYTOSKELETAL ACTIVATION OF YAP AND TAZ MEDIATED GENE EXPRESSION

Devon E. Mason (1), Sherry L. Voytik-Harbin (2), Mervin C. Yoder (3), Joel D. Boerckel (1)

(1) Aerospace and Mechanical Engineering,
University of Notre Dame,
Notre Dame, Indiana, US

(2) Weldon School of Biomedical Engineering and
Dept. of Basic Medical Sciences,
Purdue University,
West Lafayette, Indiana, US

(3) Herman B Wells Center for Pediatric Research,
Indiana University School of Medicine,
Indianapolis, Indiana, US

INTRODUCTION

Blood vessel formation is essential for tissue development and regeneration and contributes to tumor growth and metastasis [1]. Physical cues such as the mechanical properties of the extracellular matrix are known to modulate vessel formation [2], but the mechanisms by which vessels respond to these mechanical signals are poorly understood [1].

Yes-associated protein (YAP) and transcriptional activator with PDZ-binding domain (TAZ) were recently identified as potential key mediators of cellular mechanotransduction [3]. These paralogous transcriptional co-activators translocate to the nucleus and activate the TEA-domain (TEAD) family of transcription factors to promote transcription of pro-proliferative and anti-apoptotic genes [4]. YAP and TAZ are regulated by two opposing pathways: cytoskeletal tension [3], which promotes YAP/TAZ activation through nuclear translocation, and cell-cell contact-mediated inhibition through the Hippo pathway Ser/Thr kinases, large tumor suppressor 1 and 2 (Lats1/2), which restrict YAP and TAZ to the cytosol [4]. YAP and TAZ regulate organ size and cell differentiation [3-4], and YAP, but not TAZ, has been reported to promote angiogenesis and embryonic vasculogenesis [5-6]. However the roles of YAP and TAZ in neovascular mechanotransduction are unknown.

We hypothesize that YAP and TAZ are essential mediators of endothelial progenitor cell mechanotransduction of extracellular matrix rigidity. We used endothelial colony forming cells (ECFCs), circulating endothelial progenitor cells capable of undergoing post-natal vasculogenesis, the *de novo* formation of vessels, *in vivo* [7]. ECFCs enhance vessel formation in response to matrix stiffness [8], however a mechanism has yet to be identified.

METHODS

ECFCs isolated from umbilical cord blood were cultured in endothelial growth medium (EGM-2) with 10% FBS. YAP and TAZ were depleted using either YAP, TAZ, YAP and TAZ, or non-targeting siRNA, and efficiency of depletion was assessed by Western blot (data not shown). YAP and TAZ mechanosensitivity in ECFCs was assessed on soft and stiff 2D substrates using tunable polydimethylsiloxane (PDMS). ECFC migration and vasculogenesis were evaluated in wound migration, 2D Matrigel tube formation, and 3D collagen matrix vasculogenesis assays. YAP and TAZ activation during ECFC migration was assessed by immunofluorescence in the wound migration assay. YAP and TAZ subcellular distribution was quantified in regions of interest (ROI) of 957 μm by 100 μm. YAP and TAZ intensity in each ROI was normalized to cell number and basal expression, and data were fit to an exponential decay function by least squares regression. Mechanical control of YAP and TAZ localization during 3D vasculogenesis was evaluated in collagen fibril matrices of defined architecture, enabling control of matrix rigidity independent of matrix density, as described previously [8]. Matrices formulated from oligomeric collagen fibrils contain native cross-links that form stiffer matrices (G'=1049 Pa) than monomeric collagen (G'=305 Pa), while maintaining the same ligand density [6]. ECFCs embedded in oligomeric matrices and transplanted into immunocompromised mice were recovered and stained for YAP, TAZ, human cysteine rich angiocrine-61 (Cyr61), connective tissue growth factor (CTGF), and human CD31.

RESULTS

ECFC YAP and TAZ exhibited matrix mechanosensitivity on stiff PDMS, with nuclear localization of stiff (130 kPa) and cytosolic localization on soft (5 kPa) PDMS (Fig. 1). ECFC migration was significantly impaired by YAP and/or TAZ depletion though TAZ

Copyright 2016 The Organizing Committee for the 2016 Summer Biomechanics, Bioengineering and Biotransport Conference

knockdown had a more pronounced effect that was statistically identical to YAP/TAZ co-depletion (Fig. 2AB). Both YAP and TAZ were activated in migrating ECFCs in a position-dependent manner; both nuclear localization and total YAP/TAZ expression follow an exponential decay from the migrating front (Fig. 2C, D, and E). Migration-dependent nuclear localization correlated with increased cell density and decreased cell area, readouts for contact inhibition and cytoskeletal activation, respectively (data not shown).

YAP and/or TAZ depletion significantly reduced 2D tubular network formation on matrigel in a dose-dependent manner, with loss of both YAP and TAZ abrogating tube formation at all time points (Fig. 3A). ECFCs embedded in oligomeric collagen readily formed large tubes whereas monomeric matrices form smaller tubes with less extensive networks (data not shown). Depletion of YAP and TAZ decreased cell spreading and abrogated vessel formation in oligomer matrices (Fig. 3B). Embedding cells in stiff oligomer collagen matrices resulted in nuclear localization of YAP (Fig. 3C) and TAZ (data not shown), and nuclear exclusion in soft matrices (Fig. 3C).

Collagen matrices laden with human ECFCs implanted *in vivo* were stained for hCD31, YAP, TAZ, Cyr61, and CTGF (Fig.4). ECFCs formed a functional human neovascular plexus that integrated with the host vasculature, and exhibited strong expression and nuclear localization of YAP and TAZ. Downstream targets of YAP and TAZ, Cyr61 and CTGF, were expressed throughout matrices but primarily at vessel walls.

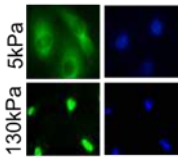

Figure 1: ECFCs seeded on soft (5 kPa) and stiff (130 kPa) PDMS and stained for TAZ (green) and DAPI (nuclei; blue).

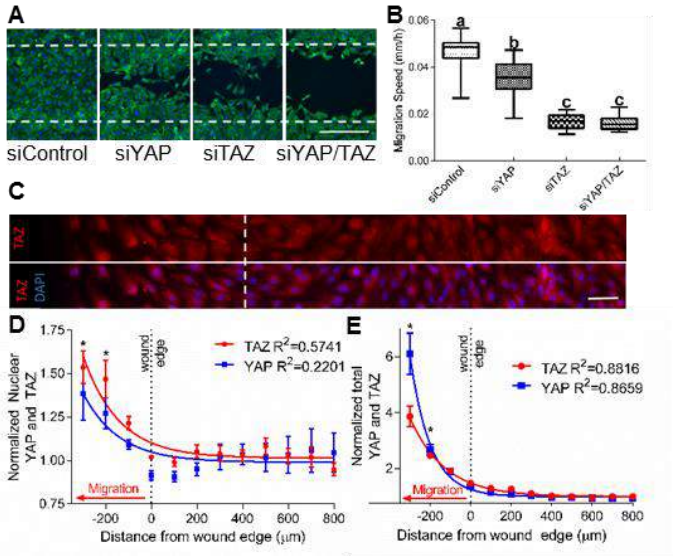

Figure 2: A) ECFC migration images 12 hours post-wounding, stained with phalloidin (F-actin; green) and DAPI (nuclei; blue), scale bar = 250 µm. B) Migration speed mean with SD, Significance indicators denote significant differences p < .0001. C) TAZ in migrating ECFCs, TAZ (red) and DAPI (blue), dotted line is the initial wound edge, scale bar =50µm. D&E) Normalized nuclear and total YAP and TAZ versus distance from the wound edge with exponential decay fit, data points are mean with SEM, * indicates significant differences compared to basal levels, p<.0001.

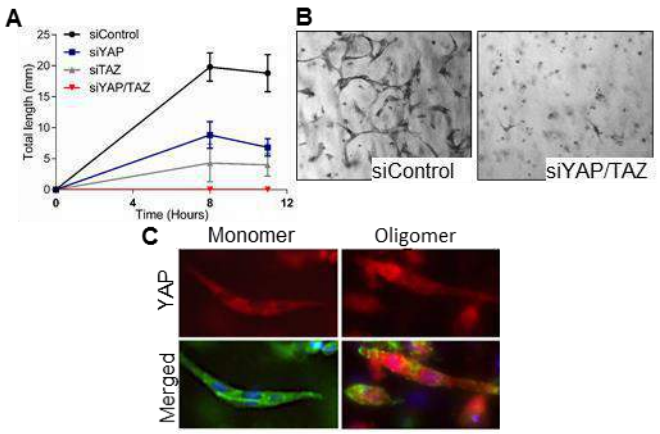

Figure 3: A) Total tube length of ECFCs plated on matrigel, displayed as mean with SD. B) Images of ECFCs embedded in oligomeric collagen matrices (G'=132 Pa). C) ECFCs embedded in monomeric or oligomeric collagen and stained for YAP (red), actin (green), and DAPI (blue).

Figure 4: Collagen matrices implanted in vivo stained for human CD31, YAP, TAZ, CTGF, and human Cyr61.

DISCUSSION

Taken together, these data suggest that YAP and TAZ are essential for mechanical regulation of ECFC vasculogenesis. YAP and TAZ were expressed and regulated by matrix rigidity in ECFCs, in both 2D and 3D. Depletion of YAP and/or TAZ impaired ECFC migration, tubular network formation and vasculogenesis in 2D and 3D. Loss of YAP resulted in a mild phenotype, suggesting a potential compensatory function for TAZ, which may indicate a more dominant role than YAP in vasculogenesis; ether because TAZ is more highly expressed or a more potent transcriptional activator in ECFCs.

YAP and TAZ expression and nuclear localization correlated inversely with cell density and proportionally with cell area, indicating that Hippo and cytoskeletal activation may act in concert to regulate YAP and TAZ activation during migration of initially confluent ECFCs, with regulation of both total expression and subcellular distribution. This may be attributable to increased transcription and/or reduced degradation of both YAP and TAZ in migrating ECFCs.

These results indicate that YAP and TAZ are essential for ECFC vasculogenesis and mechanotransduction, and based on *in vivo* YAP and TAZ target gene expression we hypothesize that YAP and TAZ mediate ECFC vasculogenesis through Cyr61 and CTGF expression.

ACKNOWLEDGEMENTS

This work was supported by grants from the Advanced Diagnostics and Therapeutics Initiative (to JDB) and the Indiana CTSI (NIH/NCRR UL1TR001108 to JDB).

REFERENCES

[1] Auger, FA et al. Annu. Rev. Biomed. Eng., 15:177-200, 2013
[2] Boerckel, J et al. PNAS, 108: 674-680, 2011
[3] Dupont, S et al. Nature, 474: 179-183, 2011
[4] Zhao, B et al. Nat. Cell Bio, 13: 877-883, 2011
[5] Choi, H et al. Nat. Comm., 6: 6943, 2015
[6] Morin-Kensicki, E et al. Mol. Cell Biol., 26: 77-87, 2006
[7] Critser, P et al. Curr Opin Organ Transplant, 15: 68-72, 2011
[8] Bailey, J et al. Biopolymers, 95: 77-93, 2011

Copyright 2016 The Organizing Committee for the 2016 Summer Biomechanics, Bioengineering and Biotransport Conference

SB^{3}C2016
Summer Biomechanics, Bioengineering and Biotransport Conference
June 29 –July 2, National Harbor, MD, USA
SB³C2016-823

ELASTIN FIBER NETWORK IN PORCINE EPICARDIUM: 3D VISUALIZATION AND QUANTIFICATION

Xiaodan Shi (1), Bryn Brazile (1), David Lee (1), Sourav S. Patnaik (1), Jim Cooley (3), Raj Prabhu (1), Lakiesha N. Williams (1), Song Zhang (2), Jun Liao (1)

(1) Department of Biological Engineering
Mississippi State University
Mississippi State, MS, United States

(2) Department of Computer Science and Engineering
Mississippi State University
Mississippi State, MS, United States

(3) Department of Pathology and Population Medicine
Mississippi State University
Mississippi State, MS, United States

INTRODUCTION

Heart disease has become the number one leading cause of death in the US with around 6 million deaths each year. To better understand the global heart contraction and relaxation, it is essential to obtain the knowledge in heart muscle organization, as well as how the complex multilayered helical architecture is mediated by 3D cardiac extracellular matrix (ECM) that spans from epicardium, to myocardium, to endocardium. However, the majority of the previous research on cardiac ECM has mainly focused on collagen in heart, while little has been done to study elastin, another important component in the heart ECM [1-2]. In this study, we aim to delineate and quantify the 3D elastin network in the epicardium of the porcine left ventricle.

METHODS

Fresh porcine hearts (~6 months old) were obtained from a local abattoir. To acquire the 3D image of the elastin network, epicardium samples (12 mm × 12 mm × 1 mm) were dissected from the base, middle and apex regions of the left ventricle in both the anterior and posterior locations (Figure 1).

Laser scanning confocal microscopy (LSCM) was applied to visualize and image the 3D elastin network under red channel (elastin autofluorescence, CY3, Ex = 543 nm) with z-stack imaging technique. The 3D z-stack images covered a thickness range from 40 to 70 μm at ~1 μm interval. All images were acquired with a 12-bit gray scale and a dimension of 1024 × 1024 pixels. ImageJ (NIH, Bethesda, MD) was used to create a 3D projection of the first 15 μm thick layer, the last 15 μm layer, and the full thickness of image stack. Elastin fiber orientation and distribution in different layers were then quantified using OrientationJ plugin. For histological assessment, tissue samples were fixed in 10% formalin for 72 hours and stained with Movat's pentachrome, in which elastin is stained black, heart muscle stained red. In-house custom written software was also used to reveal other 3D features of the epicardial elastin network.

Copyright 2016 The Organizing Committee for the 2016 Summer Biomechanics, Bioengineering and Biotransport Conference

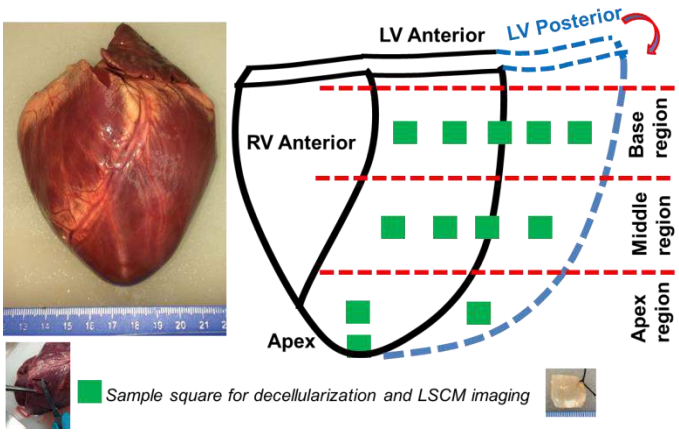

Figure 1: Schematic illustration of the left ventricle showing locations of sample dissection.

RESULTS

We first validated that the fiber image signals in LSCM images are elastin specific since under the same condition the decellularized myocardial layer, which dominantly consists of collagen network, produces no detectable signals (Figure 2B). On the other hand, elastin fiber signals were detected not only in the decellularized epicardial layer (Figure 2A) and the decellularized endocardial layer (Figure 2C), but also around vascular wall (Figure 2D) which is primarily composed of elastin fibers.

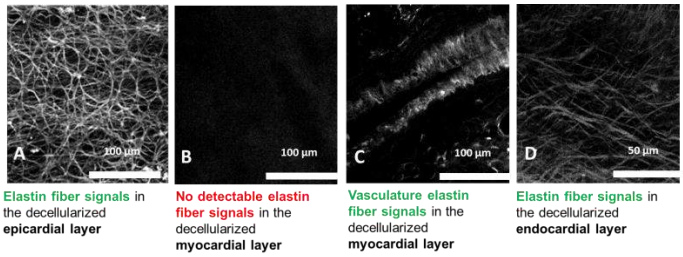

Figure 2: LSCM image signals are elastin specific.

We were able to create a first-order mapping of the elastin network in the epicardium of the left ventricle. Elastin fibers were found to be abundant in the epicardium and exhibit certain patterns, which were highly correlated to their anatomical location in the left ventricle. The elastin fiber orientation and fiber alignment were found to often take one pattern/orientation at the surface layer, but change to another pattern/orientation when reaching to the deep layer. As an example, Figure 1 showed an epicardial elastin fiber pattern observed in the left ventricle apex region, in which we noticed a 3D meshwork in the surface of the epicardium (first 15 µm depth) and a highly oriented wave elastin fiber arrangement in the last 15 µm thick of the epicardium (Figure 3).

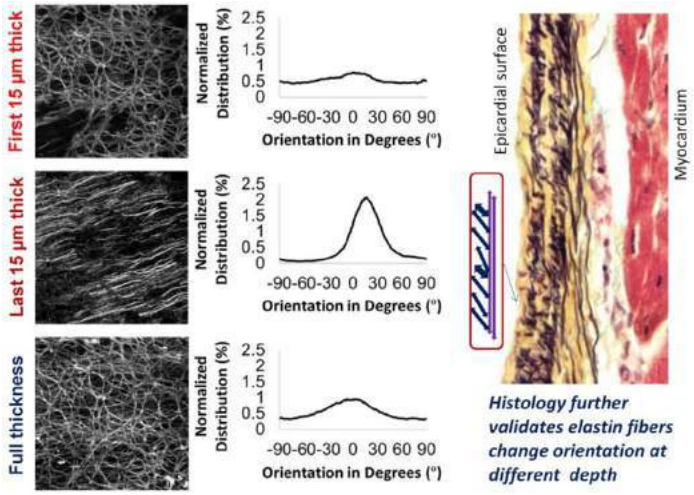

Figure 3: Epicardial elastin network shows depth-dependence in the apex section. The depth-dependence is also verified by histological observation.

DISCUSSION

Our study revealed a first-order mapping of the epicardial elastin network in the left ventricle. We found that the elastin network in the left ventricle showed certain patterns that were correlated to their anatomic locations. Besides the location variation, epicardial elastin network also showed a 3D structural alteration from the surface layer to the deep layer. Overall, the observed elastin fiber pattern, fiber orientation, and fiber alignment might serve certain mechanical function that helps coordinating the heart contraction and relaxation. Future work will be focusing on understanding the structural-functional relationship of this 3D elastin design in the left ventricle.

ACKNOWLEDGEMENTS

This work is supported by AHA (13GRNT17150041) and MAFES CRIS (#MIS-351070).

REFERENCES

[1] Jöbsis, P.D., et al., *Am J Physiol Heart Cir Physiol*, 293(6): H3379-H3387, 2007.

[2] Fomovsky, G.M., et al. *Journal of molecular and cellular cardiology*, 48(3):490-496, 2010.

Copyright 2016 The Organizing Committee for the 2016 Summer Biomechanics, Bioengineering and Biotransport Conference

SB^{3}C2016
Summer Biomechanics, Bioengineering and Biotransport Conference
June 29 –July 2, National Harbor, MD, USA
SB^{3}C2016-824

DECELLULARIZED EXTRACELLULAR MATRIX ELECTROSPUN SCAFFOLD FOR A NOVEL AIRWAY SMOOTH MUSCLE MODEL

Bethany M. Young (1), Bryan A. Blakeney (2), Brittany P. Allen (1), Gretchen E. Schreyack (1), Robert A Pouliot (1), Rebecca L. Heise (1,2)

(1) Biomedical Engineering, Virginia Commonwealth University, Richmond, Virginia, USA

(2) Physiology and Biophysics, Virginia Commonwealth University, Richmond, Virginia, USA

INTRODUCTION

Airway smooth muscle plays a key role in lung homeostasis and disease pathologies. Lung diseases such as COPD and asthma exhibit increased airway smooth muscle (ASM) mass as compared to healthy individuals with varying levels of ASM density and key differences between inflammatory responses [1]. Current studies associated with COPD and asthma lack good animal models leading to a poor understanding of the cellular and molecular mechanisms driving airway remodeling. Recent data focuses on testing with whole airways or isolated ASM cells. These approaches are limited due to the lack of biological insight with whole airway samples and the lack of structural and environmental cues in isolated cells. It is important to find a physiologically and anatomically correct airway model to achieve an accurate, controllable, and highly observable in vitro platform to study intracellular pathways in normal tissue remodeling and diseased states.

To successfully create an in vitro airway model requires mimicking the biological and architectural cues on the micro and nano levels. A strong biologically active material is achieved by combining a naturally derived substance with a synthetic polymer possessing superior mechanical strength. Natural materials offer more benefits than exclusively synthetic scaffolds because of cellular-extracellular matrix (ECM) interactions including tissue-specific signaling with proteins (i.e. collagen, elastin, fibronectin, and laminin) [2]. Specifically using ECM derived directly from lung parenchyma ensures the scaffold will have the appropriate ratio of structural proteins for the proper signaling and maintenance of lung cell phenotypic expression [3].

The architecture of the natural ECM can further be mimicked by fabricating the scaffold with a nanofiber structure similar to that of natural ECM with the use electrospinning. Electrospinning is a highly controllable and versatile technique using high electric potentials to develop nanofibers mimicking the natural fibers throughout the human body [4]. When layered randomly into a three dimensional mat, the resulting scaffold has a highly porous architecture allowing nutrient movement, cell infiltration, and a mechanical strength closer to natural tissue. The goal of this study was to create an airway smooth muscle construct utilizing a scaffold electrospun with PLLA and decellularized pig lung ECM (DPLECM).

METHODS

Scaffold Fabrication: Pig lungs (donated from Smithfield Hams) were decellularized by established protocol [5] using detergents and ionic solution, lypholized at -80^{0}C, then freezer milled using SPEX 6700 to a fine powder. 140mg and 70 mg of powdered PLECM were combined with 3 mL Hexafluoro-2-propanol (HFP) and mixed for 24 hours on a vortexer. 400 mg PLLA in 1 mL of HFP was mixed for the same period of time. The PLECM solution was poured into a syringe and pushed through a 150x150 mesh count stainless steel type 304 wire cloth into the PLLA solution and vortexed again for an hour to create the final PLLA/PLECM/HFP solution. Solutions with 35 mg, 17.5 mg, and 0 mg PLECM with 100mg PLLA per mL HFP were electrospun onto a rectangular or cylindrical mandral using the parameters in Table 1 which were arrived at by the establishment of a stable Taylor cone.

Table 1.

[PLECM]	Flow Rate	Voltage	Distance
35 mg/mL	4 mL/hr	27 kV	27 cm
17.5 mg/mL	4 mL/hr	27 kV	27 cm
0 mg/mL	4 mL/hr	15 kV	27 cm

Scaffold Characterization: Scaffold hydrophobicity testing by water contact angle was done using the sessile drop method with 5 µL dH2O. Elastic properties of PLLA scaffolds with varying amounts of PLECM (17.5 mg/mL, 35 mg/mL, and 0 mg/mL) under wet and dry conditions were determined using MTS Bionix 200 with TestWorks 4.0 Software, using established tensile testing protocols. Scaffolds with various concentration of ECM were fixed for Scanning Electron Microscopy (SEM, JEOL LV-5610)imaging to show fiber size and architecture. To verify the precence of ECM protiens post electrospinning, Mason's Trichrome staining of all scaffolds were done to compare ECM protien staining density.

Biocompatability: 35mg/mL and PLLA only scaffolds were seterilized and seeded with human airway smooth muscle cells (HASMCs, Lonza) for 1 week and imaged by SEM. All samples were dried using a Tousimis Critical point dryer, carbon coated, and imaged using SEM. PLECM/PLLA scaffolds of different concentrations were placed in a 24-well TC plates and sterilized. A

Copyright 2016 The Organizing Committee for the 2016 Summer Biomechanics, Bioengineering and Biotransport Conference

Live/Dead cell viability assay (Thermo Fisher Scien tific) was performed to quantify the number living and dead cells after 48 hours. HASMCs were also seeded on coatings of 35 mg/mL PLECM without any PLLA, 35 mg/mL PLECM with 100 mg/mL of PLLA, 100 mg/mL PLLA without PLECM, and TCP for one week to assess gene expression using qPCR.

Statistical Analysis: All experiments with a m inimum of N=3. One way ANOVAs with Tukey post hoc were performed with GraphPad software. P<0.05 was considered significant.

RESULTS

Electrospinning PLLA and PLLA/PLECM composite scaffolds created a nanof ibrous scaffold with the diameter and morphology visualized with a JEOL LV-56-10 SEM. Figure 1 shows an average fiber thickness of 409.64nm and an aver age scaffold thickness of 0.2 5mm at (A) 250 0x and (B) 1000x magnification. To assess the h ydrophobicity of the PLLA and PLECM scaffolds, the water contact angle w as determined to have dropp ed significantly by 17.78° with addition of 35 mg/mL PLECM compared to P LLA only (data not shown).

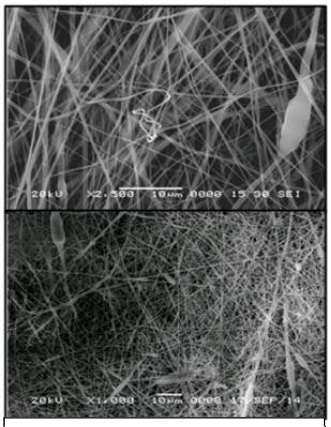

Figure 1. SEM of electrospun Fibers of 100 mg/mL PLLA + 35 m g/mL

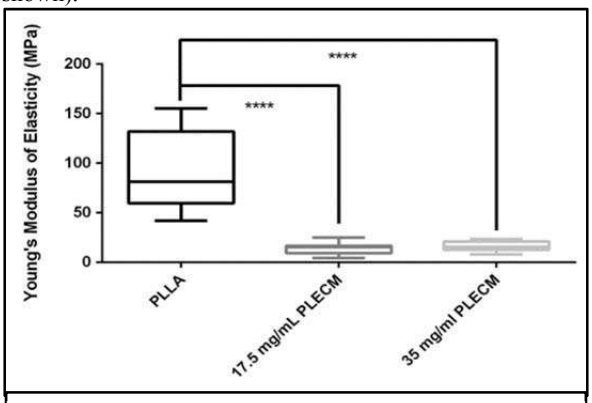

Figure 2. Tensile Testing of PLLA scaffolds with various amounts of PLLA under wet conditions.

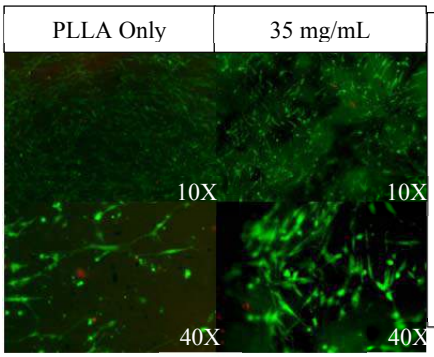

Figure 3. Liv e/Dead cell viability assay of HASMCs on PLLA only and 35 mg/mL PLLA/PLECM scaffolds for 48 hours after attachment. Green is live and red is dead.

The presence of PLECM in the scaffold significantly decreased the elastic modulus of th e electrospun scaffold closer to that of native tissue (0.17-2 MPa, [6]) as compar ed to a fully synthetic PLLA scaffold (Fig. 2).

HASMCs were then seeded onto the surface of the scaffolds with various PLECM concentrations for 1 week and imaged with SEM. HASMC behavior s howed a qualit ative increase in confluen cy over the scaffolds that contained PLECM over those that were composed of only PLLA (data not shown). A 48 hour Live/Dead cell viability assay results shown in figure 3 revealed support of HASMCs on both scaffolds with increased cell death (red) on PLLA only scaffolds.

DISCUSSION

The importance of ECM in promoting complex biolog ical signaling both in vitro and in vivo has be en confirmed in pr evious research [7]. These earlier studies showing ben efits of incorporating various other d ecelularized ECM tissue into regener ative scaffolds supported our hypothesis that incorporation of PLECM into a synthetic electropsun scaffold will be an ideal m aterial for in vitro airwa y smooth muscle. Electrospinn ing a fibrous scaffold with and without PLECM allowed us to contro l alignment, filament size, and thickness of the filament matrix to develop a nanofibourous mat that mimics the natural structure of the lung. The nanofiber diameter and stru cture we have achieved are within rang e of the optim al fiber diam eter to represent natural ECM arch itecture, allowing for proper m echanical and structural stimulation for natural cell differentiation.

By creating an in vitro environ ment that closely resembles the in vivo environment we can more e fficiently and controllably study airway smooth muscle phenotype. The advantages that n atural ECM offer have been exploited in this study to develop a customizable nanostructure, mechanical profile, and degrad ation properties with practical biological signaling. O ur scaffold has been optimized for an accurate human analog for s mooth muscle function in the airwa ys. In vivo, SMCs exhibit a specific str ucture and organization modulated by mechanical forces transferred to ce ll cytoskeletal filaments thr ough ECM proteins. SMCs will rem odel the ECM around it, attaching in a highly organized 3D structure to for unified baseline contractile forces with the ability to perform more extreme contractions. Smooth muscle ECM remodeling and ke y contractile and relaxing proteins detection make this model physiologically relevant.

In conclusion, the addition of PLECM to a P LLA electrospun scaffold will offer characteristics similar to that of native lung tissue. The data suggests that the extracellular matrix allows for increased cell attachment and proliferation through biological signaling and mechanical stimulation. These similarities allow this structure to become a model for normal smo oth muscle behavior, eliminating the need for inadequate animal models for studying airway remodeling.

ACKNOWLEDGEMENTS

NSF CAREER CMMI 135162, CHRB 236-05-13, VC U Nanomaterials Core Character ization Facility, VCU Micros copy Facility Dr. Zhao for con tact angle measurement, Dr. Yan g for electrospinning equipment

REFERENCES

[1] Postma, D.S et al., *AJRCCM,* 158:187-192, 1998.
[2] Londono, R et al., *Annals BME.*43:577-592, 2015.
[3]England, K.A., *Tissue Engineering*. 16:2581-2591,2010.
[4]Badylak, S.F et al., *Transplant. Immunology.* 12:367-377, 2004.
[5] Bosworth, L et al., *Electrospinning for Tissue Regeneration.* 2011.
[6] Wang, J.Y et al., *arXiv:1111.5645.* 2011
[7] Gibson, M et al., *BioMed Research International.* 2014:1-13, 2014.

Copyright 2016 The Organizing Committee for the 2016 Summer Biomechanics, Bioengineering and Biotransport Conference

SB^{3}C2016
Summer Biomechanics, Bioengineering and Biotransport Conference
June 29 –July 2, National Harbor, MD, USA
SB^{3}C2016-825

DAMAGE MODELING OF A HUMAN TIBIA AND FIBULA FRACTURE CAUSED BY A MIXED MARTIAL ARTS KICK

A. Lamont (1), V. Nguyen (1, 2), R. Bertucci (1), Y. Hammi (1), M.F. Horstemeyer (1), J. Liao (1,2), H. Rhee (1), L. Williams (1,2), R. Prabhu (1,2)

(1) Center of Advanced Vehicular Systems
Mississippi State University
Starkville, MS, United States

(2) Department of Agricultural and Biological Engineering
Mississippi State University
Mississippi State, MS, United States

INTRODUCTION

Mixed Martial Arts (MMA) is a sport in which two athletes engage in combat with their hands and feet, each seeking to defeat the other by knock out, submission, or by the unanimous decision of judges. On December 28, 2013 during the Ultimate Fight Championship (UFC) 168 event at the MGM Garden Arena in Las Vegas, Nevada, MMA and UFC athlete Anderson Silva suffered a compound fracture of his left tibia and fibula bones in a location above the ankle[1]. While common for MMA artist to sustain lower extremity injuries[2,3], such extent of a leg injury does not occur often on the professional level. Studies show that damage to the lower extremities are fairly common, occurring in roughly 30.4% of the studied cases[4]. More specifically, damage to the lower leg was determined to occur in 4.3% of the studied cases[4].

The objective of this study was to analyze the bone fracture damage caused by the kick through a finite element analysis (FEA) to further understand the biomechanics of the compound fracture. The study also provides additional verification of the simulation through comparison with Von Mises stress data from previous results and literature.

METHODS

GIMP[5] and Windows Live Movie Maker (Microsoft Inc., WA, USA) were implemented to perform image analysis of the injury. A video was obtained that offered a front and side view of the kick[6] and images were collected in a frame by frame manner at both viewing angles. The displacement, velocity, and acceleration of the legs were calculated from images to obtain an initial estimation of the force.

Next, Adams/View^{TM} rigid body dynamics software by MSC was used to design a low-fidelity macro-scale rigid body model of the kick. After measuring the length of the legs and hips of Silva and the initial locations of his ankle, knee, and hip joints, a model was able to be developed representing Silva's lower body. Additionally, the defending leg of Chris Weidman was measured and added to the rigid body model. Each joint of each athlete model was given a rotational motion function that represented the rotational displacement and velocities calculated in the image analysis. After changing the material description of the model to bone,=, Adams/Post Processor was used to produce graphical data to determine the maximum force of the kick. This kicking force was then compared to kicking forces found in other studies to determine its relative strength.

Abaqus/CAE^{TM} FEA software by Dassault Systemes was implemented to perform a FEA on the injury. A lower extremity orphan mesh was imported for both Silva and Weidman. After placing the meshes and defining the material characteristics for skin, muscle, and bone as elastic materials [7,8,9,10,11] rotational velocity BCs were produced according to the data collected in the image analyses and rigid body dynamics model.

Then damage criteria was added to the material model in the FEA. Assuming the failure model of the bone has two components, plastic and ductile damage. Plastic behavior depends on the progression of yield stress with plastic strain, while modeling ductile damage requires certain constants. From literature, the constants used were a fracture strain of 0.035 and a stress triaxiality, a ratio of hydrostatic to deviatoric stress that constraints plastic deformation, of 0.333[12]. Using the criteria above, the simulation calculated the ductile damage caused by the kick.

Animations of the FEA results were created and analyzed to determine the magnitude and location of the damage in both the tibia and fibula from contact to the end of the simulation at 0.09 seconds. We developed failure causation conclusions by comparing the time of failure in the simulations to published data on the biomechanical properties of human bone.

UNCLASSIFIED:
Distribution Statement A. Approved for public release
Copyright 2016 The Organizing Committee for the 2016 Summer Biomechanics, Bioengineering and Biotransport Conference

RESULTS

The FEA simulations revealed information regarding the location and development of damage in Anderson Silva's tibia and fibula. Figure 1 shows the ductile damage initiation for the tibia and fibula in addition to damage at maximum Von Mises stress, pressure, and strain.

a)

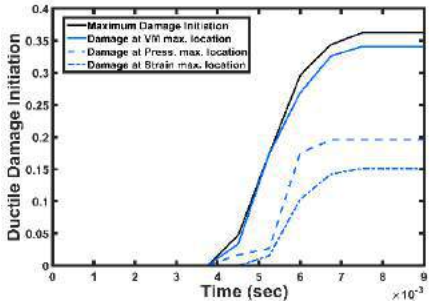

b)

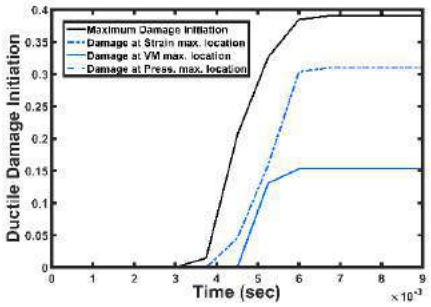

FIGURE 1: THE DUCTILE DAMAGE INITIATION, DAMAGE AT OVER TIME AT THE MAXIMUM LOCATION FOR (A) TIBIA AND (B) FIBULA. THE GRAPHS SHOW THE EVOLUTION OF PEAK DAMAGE VS. TIME AT STRAIN COMPARED TO DAMAGE AT PEAK PRESSURE AND VON MISES LOCATIONS.

The damage of the tibia can be indicated to occur in Figure 2(a), and the damage of the fibula in Figure 3(a). Figure 3(b) and Figure 3(b) show the maximum damage caused by the kick. The locations of peak damage in Figures 2 and 3 correlate well.

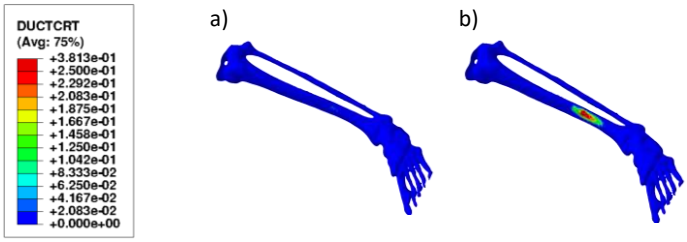

FIGURE 2: THE DUCTILE DAMAGE CRITERIA FROM THE FEA IS DEPICTED AS A FRACTION OF DAMAGE CRITERIA INITIATION. IN (A) and (B) A VIEW OF THE TIBIA AT 0.045 AND 0.09 SECONDS.

DISCUSSION

The objective of the study was to calculate damage and to validate the simulation model. In comparison to the damage occurred at the point-of-contact and location of either maximum pressure or Von Mises. As shown by the damage initiation graph and the FEA animation, the damage began to occur in the tibia and fibula approximately 0.04 seconds, and Figure 1 shows damage in the tibia is mostly caused by Von Mises stress while damage in the fibula is caused by strain.

The FEA simulations offer data to support the following conclusion: After the initial contact of the legs, Silva's bone began to bend as his foot continued to rotate. The bending of the tibia concentrated stress at the apex of the bend which ultimately caused the bone to yield and fracture. The continuation of motion in the foot caused the fibula to bend just above its connection to the foot. Like the tibia, this bending caused the fibula to fail.

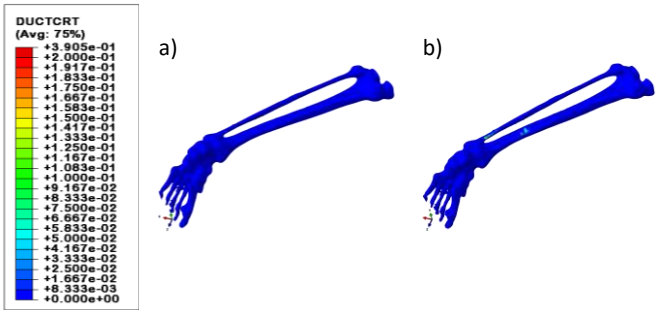

FIGURE 3: THE DUCTILE DAMAGE CRITERIA FROM THE FEA IS DEPICTED IN FRACTION OF DAMAGE CRITERIA INITIATION. IN (A) AND (B) A VIEW OF THE FIBULA AT 0.045 SECONDS AND 0.09 SECONDS.

Using this model, future studies could include effect of certain safety equipment such as a shin guard in lack of damage and/or of modified velocities or rotation of the kicking leg simulating difference between improper and proper technique. These studies would benefit new MMA students, or even skilled MMA fighters, perfecting the technique to avoid severe injuries seen here.

ACKNOWLEDGEMENTS

The above material is based on work supported by the Department of Agricultural and Biological Engineering and the Center for Advanced Vehicular Systems at Mississippi State University through a subcontract funded by the US Army. This material is based upon work supported by the U.S. Army TACOM Life Cycle Command under Contract No. W56HZV-08-C-0236, through a subcontract with Mississippi State University, and was performed for the Simulation Based Reliability and Safety (SimBRS) research program. Any opinions, findings and conclusions or recommendations expressed in this material are those of the author(s) and do not necessarily reflect the views of the U.S. Army TACOM Life Cycle Command.

REFERENCES

[1] Schlinsky, A. http://fansided.com/2014/01/01/ufc-168-dr-sanders-explains-anderson-silvas-surgery/#!BnwLo (3/25/2014).
[2] Bledsoe et al., *J. of Sports Sci. and Med.,* 5:136-142, 2006.
[3] Ngai et al., *Br. J. of Sports Med.,* 42(8):686-689, 2008.
[4] Rainey et al., *N. Am. J. of Sports Phys. Ther.*, 4(4):190-199, 2009.
[5] GNU Image Manipulation Program, http://www.gimp.org/ (accessed 3/27/2014)
[6] Paki Fighter., https://www.youtube.com/watch?v=ddWOhKWhsXk (accessed 2/15/2014).
[7] Diridollou et al., *Skin Research & Tech.*, 6(4): 214-221, 2000
[8] Li et al., *J. of the Royal Soc. Interface*, 9(70): 831-841, 2012
[9] Levinson et al., *J. of Biomech.*, 28(10): 1145-1154, 1995
[10] Kim et al., *BioMed Research International*, ID 197479, 2013
[11] B. LaVeau, *Biomech. of Human Motion*, 3, 1992
[12] McElhaney, J.H., (1966). "Dynamic response of bone and muscle tissue. *J. of Appl. Phys*. 21(4).
[13] Taylor, G.I., Quinney, H. (1931) "The Plastic Distortion of Metals," Phil. Trans. R. Soc., London, Vol. A230, pp. 323.
[14] Lalaji, A. http://insideinjuries.com/anderson-silva-broken-tibia-fibula/ (accessed 4/29/2014).
[15] Gray, L., *J. of Biomech.,* 12(8): 636-637, 1979

Copyright 2016 The Organizing Committee for the 2016 Summer Biomechanics, Bioengineering and Biotransport Conference

SB^{3}C2016
Summer Biomechanics, Bioengineering and Biotransport Conference
June 29 –July 2, National Harbor, MD, USA
SB^{3}C2016-826

"CONTEMPORARY ISSUES IN …. BIOENGINEERING": A NEW REQUIRED COURSE ADDRESSING SEVERAL CURRICULAR CONCERNS

Steven W. Day (1, 2), Robert J. Stevens (1)

(1) Department of Mechanical Engineering
Rochester Institute of Technology
Rochester, NY, USA

(2) Department of Biomedical Engineering
Rochester Institute of Technology
Rochester, NY, USA

INTRODUCTION

We present the design and implementation of an online course called "Contemporary Issues in …" (herein called CI) that addresses significant teaching/learning/assessment issues within the Department of Mechanical Engineering in the College of Engineering at Rochester Institute of Technology. Specifically, we have: *1) The desire to relate student co-op experiences to coursework.* 2) *A Need to satisfy Institute and ABET writing Requirements* and 3) *A need for delivery and assessment of content related to contemporary issues, ethics, economics, life long learning, and societal impact*. It has historically been particularly difficulty to demonstrate delivery and assessment of related ABET program outcomes (f, h, i, and j) as they are generally not the central topic in core engineering courses that are required of all students.

This course helps address the "hard-to-reach" program outcomes, draw on students co-op experiences, and have had some writing requirements that help to satisfy ABET and Institute policy. We believe our model of a standardized, but customizable course is innovative and helps address the issues described above.

METHODS

We applied a design methodology to create this course. We first identified the overall goals that we hoped to accomplish. We then identified specific course outcomes. Lastly, we designed a method of delivering content in a way that ensured some uniformity across offerings, but allows the instructor to customize the section to a particular interests. Lastly, assignments were designed to assess the achievement of these outcomes

Some of the overall goals of the course stem from the following:
Feedback from our Industrial Advisory Committee: The most common requests from employers are related to "soft" skills, including the ability to effectively communicate technical material to management, justify the value proposition of engineering investments and alternatives, awareness of the context of an engineering solution (both from a society and company market perspective).
ABET: We had some experience with elective courses taught within the department that provided a meaningful way for us to address ABET f, g, h, i, and j (professional and ethical responsibility, effective communication, impact of engineering solutions in a broad context, lifelong learning, and contemporary issues) for a small subset of students. We wanted to integrate these aspects into this required course.
Professionalism: All students are required to complete one full year of paid work experience before graduating. We want this course to serve as a way to better link student co-op experiences to their coursework on campus.
RIT required Writing Intensive Course: Institute Policy requires that each department offer at least once course for which the evaluation of the quality of writing is a substantial (>20%) of the grade for that course.
KGCOE Ethics Curriculum: The College of Engineering Ethics Committee has proposed 5 learning objectives to be incorporated into a 3rd year course. Integration of these into the Contemporary Issues family of courses would ensure that all students satisfy these requirements.
FE Exam and licensure: The FE exam includes some topics, such as economics and professional licensure that are not covered in any of our other required courses. We wish to address those in this class.

Copyright 2016 The Organizing Committee for the 2016 Summer Biomechanics, Bioengineering and Biotransport Conference

RESULTS

This process described here resulted in a course that contains common content, but that can be "flavored" to appeal to specific interests of students and faculty by including three types of content: 1) Common Lecture 2) Material common to sections, but customized for flavor, and 3) Flavor specific (Fig 1). The common content (e.g. ethics, economics, writing,) and assessment activities are the same for all sections, but the flavoring of the course helps students engage and to recognize the potential application of the common material to their specific interests. To date, we have offered seven sections of the course over the past three semesters. Four flavors of the course (Energy and the Environment, Bioengineering, Automotive, and Aerospace) have been offered. Table 1 includes the key elements of the course.

Table 1: Course Elements. Except for the feasibility report, each of these is repeated on a weekly basis. The content included is a typical weekly example, but actual content certainly varies from week to week.

	Example of Content	Method
Common Lecture	Ethical Decision making tools, including line-drawing and flow charting.	Monday lecture. All sections/flavors in attendance
Flavored Lecture	Medical and health-care related Ethics	Wednesday lecture, sections meet separately
Discussion	Ethical and economic considerations of Medicare approval of a new medical device	Online in small discussion groups throughout week with one in-class discussion.
Quiz	Multiple choice questions on readings and lectures for both common and flavored content.	Online
Problem Sets	Students implement methods from general and flavor content in a typical problem set format.	Weekly and submitted online.
Feasibility Assessment	Evaluate the technical feasibility as well as economic and societal impact of an emerging technology.	Staged assignments throughout semester culminate in a technical brief.

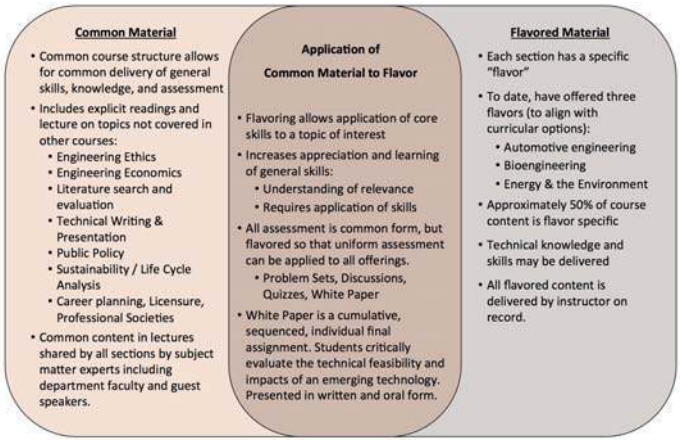

Figure 1: Schematic of the types of course content, including content common to all sections, content unique to each section (flavored) and that the common material is applied to the flavor.

Results of student self-reported learning indicates that the course is generally effective in all stated learning outcomes (Fig 1).

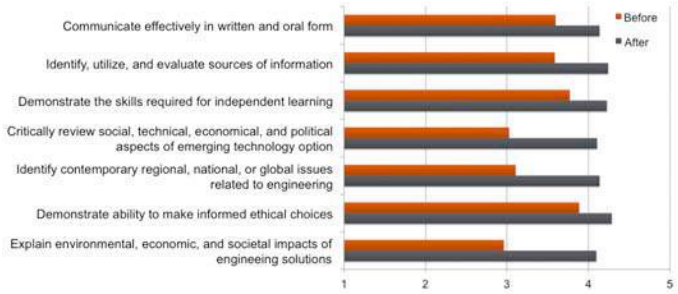

Figure 1: Follow directions for Figures in the instructions document. Figure captions are centered below the graphic.

DISCUSSION

This course as a required course very clearly ensures exposure of the undergraduates to each of these critical topics. Student self-reported learning indicates that it is effective in most or all of the stated course outcomes, but we do not have more rigorous evaluation of student learning.

There has been some variation in the way that the course was delivered over the past two years, including two sections offered online, and inter-instructor variability. This seems to greatly affect student perceptions of the course, although we don't currently have enough information to be certain what the most effective mode of delivering this course is.

ACKNOWLEDGEMENTS

The authors wish to acknowledge collaborating instructors for providing us with student learning outcomes data.

Copyright 2016 The Organizing Committee for the 2016 Summer Biomechanics, Bioengineering and Biotransport Conference

SB^{3}C2016
Summer Biomechanics, Bioengineering and Biotransport Conference
June 29 –July 2, National Harbor, MD, USA
SB^{3}C2016-827

BIOMECHANICAL PROPERTIES OF THE NEONATAL BRACHIAL PLEXUS

Shania Shaji (1), Malaeb Shadi (2), Maria Delivoria (2), Anita Singh (1)

(1) Biomedical Engineering
Widener University
Chester, PA, USA

(2) Pediatrics, Obstet. & Gynecol.
Drexel College of Medicine
Philadelphia, PA, USA

INTRODUCTION

Neonatal Brachial Plexus Palsy (NBPP) continues to occur in 1.1-2.2 out of 10,000 births [1]. The brachial plexus (BP) is a network of nerves that originate in the neck and run through the shoulder to the arm [2]. Stretching of the BP or avulsion of the roots can occur during birth when the infant's shoulder impacts with the bony pelvis of the mother due to maternal (endogenous) forces as well as clinician-applied (exogenous) forces [2,3]. Since *in vivo* measurements of the endogenous and exogenous forces, fetal shoulder deformation, and the response of the BP are difficult to assess during delivery, computational and physical models are used. However, a complete lack of biomechanical properties and data on the neonate BP limits the correct assessment of the risk of injury using these models. The goal of this study is to determine the biomechanical properties of the BP using a neonatal porcine model (piglets).

METHODS & MATERIALS

Samples: 133 fresh neonatal (3-5 days old) piglet BP cord segments (Chord, Division and Nerve) were harvested from 9 piglets and immediately preserved in 1% BSA (bovine serum albumin) until testing. The BP segments were divided into two groups based on tensile displacement rate. Group A (n=54) specimens were subjected to a stretch rate of 0.01 mm/s and those in Group B (n=79) were subjected to a stretch rate of 10 mm/s.

Testing Apparatus: An ADMET material testing machine (eXpert 7600, ADMET Inc., Norwood, MA) was used to stretch the BP Segments (Fig. 1). Stretch rates were controlled by built-in GuageSafe software (ADMET Inc., Norwood, MA). Each BP segment was anchored by specially designed and fabricated clamps (Fig. 2). The padded side facing the segment helped minimize the stress concentration at the clamping site [4,5,6]. A digital microscope was used to obtain images of harvested BP segments before stretch (5X; Digital Microscope, Elmwood Park, NJ). A 2mm scale (Leitz,Ernst-Leitz-Wetzlar GmbH, Germany) at the same magnification measured the segment diameter.

The segments were clamped with no initial tension prior to stretch. Each BP segment was stretched at the assigned rate (0.01 mm/s or 10 mm/s) until complete failure. During this test, the load and displacement data was acquired. Failure site was recorded and the clamps were checked for the presence of BP tissue. No tissue in the clamps implied that the tissue had completely slipped, and the results of those experiments were disregarded.

Data Analysis: Maximum stress and corresponding strain were calculated from the obtained load-displacement data during tensile testing. Load data and the cross sectional area was used to calculate nominal stress.

Copyright 2016 The Organizing Committee for the 2016 Summer Biomechanics, Bioengineering and Biotransport Conference

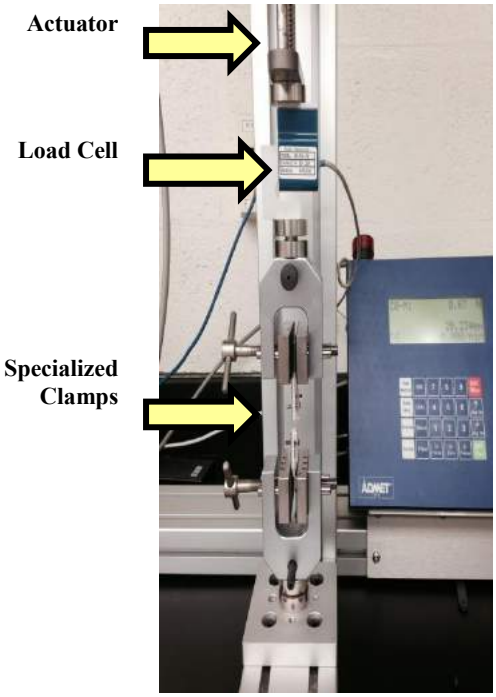

Figure 1: Biomechanical Testing Machine

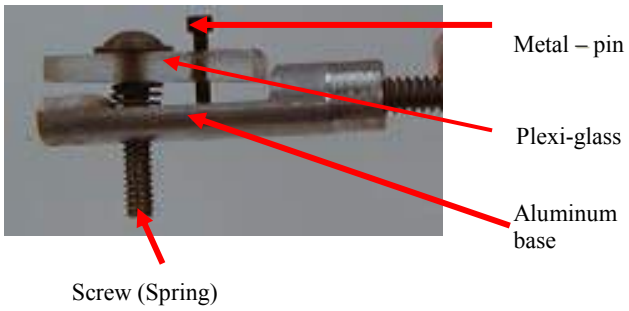

Figure 2: Clamp Fabrication

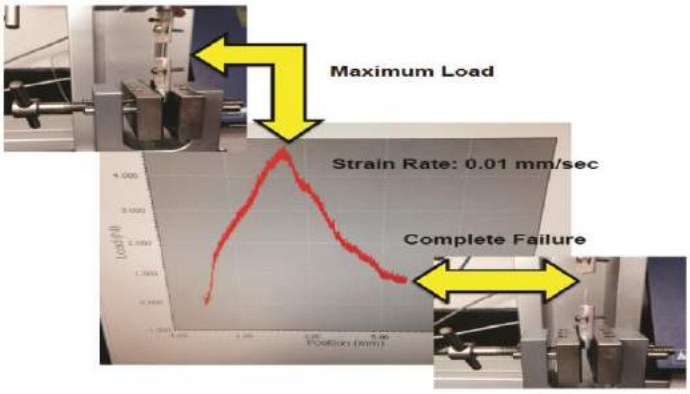

Figure 3: Preliminary Testing of BP Cord Segment at 0.01 mm/sec

RESULTS

Nerve rupture typically occurred immediately after reaching the proportional limit as shown in Fig. 3. Table 1 contains experimental data for brachial plexus segments tested at both quasistatic and dynamic rates.

Table 1: Mechanical Data of BP Segments

	Root/Cord		Division/Trunk		Nerve	
Rate	0.01 mm/s	10 mm/s	0.01 mm/s	10 mm/s	0.01 mm/s	10 mm/s
Stress (MPa)	1.1 ± 0.1	2.5 ± 0.1	4.9 ± 0.1	7.8± 0.2	15.6+ 0.9	24 + 1
Strain (%)	25 ± 3	23 ± 1	32± 1	31 ± 1	35 ± 3	36 ± 1.5
n	18	28	25	24	11	27

DISCUSSION

- Failure Stress and Strain were highest in the Nerve segment, followed by Division/Trunk and lowest in the Root/Cord segment
- Strain rate effect was observed with a lower failure stress at the quasistatic rate than at the dynamic rate for all BP segments. This is because the nerve tissue acts in a viscoelastic manner and becomes stiffer at a faster strain rate.

Overall, the experiment data provides detailed biomechanical properties of the BP tissue. The data obtained from studying the BP at these two rates helps better understand the associated injury mechanisms since this information can be used to develop a biofidelic computational model that accurately illustrates the predisposing risk factors for BP injury.

ACKNOWLEDGEMENTS

We would like to acknowledge the help of Dylan Lawrence and Bridgette Saverine.

REFERENCES

[1] Chauhan, SP, Blackwell SB, Ananth CV. Seminars in Perinatology, 2014, 8(4):210-218.
[2] N. Zhang, B. Gonik, and M. Grimm, Summer Bioengineering Conference, 2003.
[3] M. Grimm, R. Costello, B. Gonik, Am J Obstet Gynecol 2010; 203:339.e1-5.
[4] Singh, A, Lu Y, Chen, CY, Kallakuri, S, Cavanaugh, JM. 2006, 50: 601-623. SAE Paper # 2006- 22-0023.
[5] Singh, A, Lu, Y, Chen, C, Cavanaugh, JM. J of Biomechanics, 2006, 39: 1669- 1676.
[6] Singh, A, Kallakuri, S, Chen, CY, Cavanaugh, JM. 2009, Journal of Neurotrauma, 26:1-14.

Copyright 2016 The Organizing Committee for the 2016 Summer Biomechanics, Bioengineering and Biotransport Conference

SB³C2016
Summer Biomechanics, Bioengineering and Biotransport Conference
June 29 –July 2, National Harbor, MD, USA
SB³C2016-828

INVESTIGATION OF THE PRESSURE-LENGTH RELATIONSHIP ALONG A LYMPHATIC CHAIN WITH MODELING AND EXPERIMENTS

Mohammad S. Razavi (1), Tyler S. Nelson (1), Rudolph L. Gleason (1,2), J. Brandon Dixon (1,2)

(1) Woodruff School of Mechanical Engineering
Georgia Institute of Technology
Atlanta, GA, USA

(2) Coulter Department of Biomedical Engineering
Georgia Tech and Emory University
Atlanta, GA, USA

INTRODUCTION

The lymphatic system is fundamental to fluid hemostasis, cell trafficking and immune responses. The dysfunction of lymphatic system is associated with a wide range of pathologies like lymphedema. The lymphatic vessels transport lymph from the interstitium back to the great veins in the venous system through a series of contractile units, known as lymphangions, and one-way valves to prevent back flow. The lymphatic system must impart energy on the fluid to transport flow up the adverse pressure gradients that occur in vivo from gravitational forces and unfavorable pressure difference between the interstitium and central venous pressure. The required energy to sustain lymph flow is mainly provided by rapid/phasic contraction of unique lymphatic smooth muscle cells that has functional features and myosin isoforms found in both vascular smooth muscle cells and cardiac muscles. It has been shown that both active (e.g., myogenic and tonic contractions) as well as passive (e.g., distension of vessel) mechanical properties of the wall regulate lymph transport. Hence, a series of pumps and valves are utilized to propel flow and overcome opposing pressure gradient across the network. Recently, models of the lymphatic system have been developed to shed insight on the influence of various morphological features, mechanical properties, and biological parameters on lymphatic pump performance [1, 2]. Here, we adapt our previously published constitutive model of a lympangion to support a series of lymphangions to establish a framework for studying the maximum pressure generation of a lymphangion chain in series [2]. Using a previously developed NIR imaging technique developed in our lab for measuring lymphatic pumping pressure non-invasively in vivo [3], we compare our computational model (developed with geometric and mechanical data taken from the rat thoracic duct) with in vivo measurements from rat tail lymphatic.

METHODS

Mathematical Model. To model mechanical behavior of the lymphatic vessels, a constitutive framework is used to obtain both active (contractile) and passive mechanical parameters (e.g., distension) in response to mechanical stimuli (e.g., transmural pressure). The framework is based on a microstructurally motivated four fiber model for lymphatic vessels. In this framework, the Cauchy stress consists of active stress (due to action of smooth muscle cells) and passive stress (due to mechanical passive behavior or vessel morphology) as

$$\mathrm{T}^{\mathrm{pas}} = -\mathrm{pI} + \frac{2}{\det(\mathrm{F})}\mathrm{F}\frac{\partial \mathrm{W}}{\partial \mathrm{C}}\mathrm{F}^{\mathrm{T}} \quad (1)$$

where $\mathrm{T}^{\mathrm{pas}}$ is passive stress, F is the elastic deformation gradient, W is the strain energy density function originally proposed by Holzapfel, C is the right Cauchy-Green, I is the identity tensor, and p is the Lagrange multiplier. The active contractile behavior was also adopted from Rachev and Hayashi [4] as

$$T^{act} = 0.5 * T_{act}^{sys} * \lambda_\theta \left[1 - \cos\left(\frac{2\pi}{t_c}(t)\right)\right]\left[1 - \left(\frac{\lambda_M - \lambda_\theta^e}{\lambda_M - \lambda_0}\right)^2\right] \quad (2)$$

where $\mathrm{T}^{\mathrm{act}}$ is active, $\mathrm{T}_{\mathrm{act}}^{\mathrm{sys}}$ is a parameter dependent on the activation of the smooth muscle, λ_θ is the circumferential stretch of the vessel, λ_M is the stretch at which the contraction is maximum, $\mathrm{T}_{\mathrm{act}}^{\mathrm{sys}}$ regulate the magnitude of maximum spontaneous contraction, λ_0 is the stretch at which force generation ceases, t_c is contraction period, and t is time. The passive and active model's parameters were chosen from Caulk et

Copyright 2016 The Organizing Committee for the 2016 Summer Biomechanics, Bioengineering and Biotransport Conference

al [2], in which experimental data from rat thoracic duct was fit to the model. The contraction time is assumed to be 2 seconds. To model the valve function in a chain, we used a valve-resistance model by Bertram et al [1], which accounts for the valve resistance as function of pressure drop across the valve as

$$Q_V = \frac{\Delta p_V}{R_V} \tag{3}$$

$$R_V = 600 - 12 * 10^7 \left[\frac{1}{1 + exp(-0.02(\Delta p_V))} - 1\right] \tag{4}$$

where Q_V is flow rate, Δp_V is pressure drop, and R_V is resistance across the valve. Using an optimization algorithm in Matlab, the constitutive and fluid models are solved simultaneously to satisfy mass conservation in the chain of vessels. In the process, the inlet pressure is assumed to be 2 cm_H2O and the outlet pressure is increased up to the pressure at which flow rate decrease below 10% of the flow rate at an outlet pressure equal to 2 cm_H2O. The simulations are repeated with various lymphangion numbers in the chain. The geometrical parameters of a single lymphangion and active parameters associated with the lymphatic smooth muscle cells are summarized in Table 1.

In vivo-Experiments. Utilizing an occlusion cuff on the rat tail with near-infrared (NIR) imaging we were able to measure the maximum occlusion pressure at various locations along the rat tail at which flow can be detected. The procedures involve the intradermal injection of an appropriately sized NIR probe near the distal tip of the tail, which is subsequently transported from the injection site by the lymphatic. Occlusion is achieved through feedback control of a pressure cuff, placed at various locations proximal to the injection site, with a customized VI written in LabView. The pressure reading from the experiment, which we refer to as the effective pumping pressure, is equivalent to the maximum back pressure in the model in which the last valve can be opened and flow achieved.

RESULTS

Figure 1 depicts the relationship between maximum outlet pressures which can be overcome by a chain of lymphatic vessels as a function length. The maximum back pressure was calculated for chains with different number of working lymphangions in series. As shown, the maximum outlet pressure increases with the number of lymphangions in the chain.

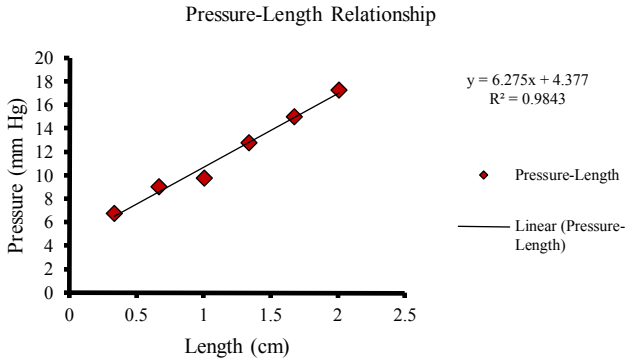

Figure 1 The pressure-length relationship along lymphatic chains of rat thoracic duct using the computational framework.

Table 1 Constant parameters associated with lymphangion's geometry and constitutive model for active mechanical behavior [2].

parameter	*unit*	*value*
Diameter of lymphangion	μm	252
Thickness of lymphangion	μm	33.7
Length of lymphangion	cm	0.335
T_{act}^{sys}	Dyne/cm^2	118620
λ_M	-	1.7636
λ_0	-	0.6119

Figure 2 shows the pressure-length relationship along rat model. The length refers to the distance from the tip of tail. This figure demonstrates that along a lymphatic chain the maximum occlusion pressure in which flow can be achieved increases.

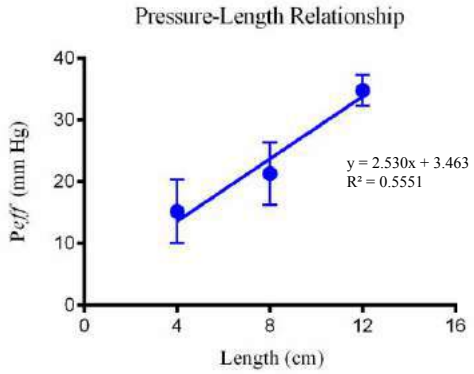

Figure 2 The pressure-length relationship along rat tail lymphatics using NIR imaging technique.

DISCUSSION

Both the computational and the experimental results provide evidence that adverse pressure gradients can be overcome by increasing the overall pumping capacity of the chain through the addition of lymphangions. Interestingly the rat thoracic duct is on average about 3-times larger than the collecting lymphatics in the rat tail, which could explain the greater slope in the computational data when compared to the experimental. Whether there is a scaling law that determines the pumping capacity of a lymphangion chain is an important area of future work. However the overall similarity of the results is encouraging given that mechanical and geometric properties of rat tail lymphatics are largely unknown and difficult to assess experimentally. Further elucidation of the mechanical properties of lymphatic vessels from various anatomies and disease states will be important for understanding how these factors lead to pump failure in lymphedema.

ACKNOWLEDGEMENTS: This work was supported by NIH R01 HL113061

REFERENCES

1. Bertram, C., et al., *Development of a model of a multi-lymphangion lymphatic vessel incorporating realistic and measured parameter values.* Biomechanics and modeling in mechanobiology, 2014. **13**(2): p. 401-416.
2. Caulk, A.W., et al., *Quantification of the passive and active biaxial mechanical behaviour and microstructural organization of rat thoracic ducts.* Journal of The Royal Society Interface, 2015. **12**(108): p. 20150280.
3. Nelson, T.S., et al., *Minimally invasive method for determining the effective lymphatic pumping pressure in rats using near-infrared imaging.* American Journal of Physiology-Regulatory, Integrative and Comparative Physiology, 2014. **306**(5): p. R281-R290.
4. Rachev, A. and K. Hayashi, *Theoretical study of the effects of vascular smooth muscle contraction on strain and stress distributions in arteries.* Ann Biomed Eng, 1999. **27**(4): p. 459-68.

Copyright 2016 The Organizing Committee for the 2016 Summer Biomechanics, Bioengineering and Biotransport Conference

SB^{3}C2016
Summer Biomechanics, Bioengineering and Biotransport Conference
June 29 –July 2, National Harbor, MD, USA
SB^{3}C2016-829

FLOW-RATE-CONTROLLED REMODELING OF GLOMERULAR CAPILLARIES

Lazarina I. Gyoneva (1), Daniel J. Goodman (1), Yoav Segal (2,3), Kevin D. Dorfman (4), Victor H. Barocas (1)

(1) Biomedical Engineering
University of Minnesota
Minneapolis, MN, United States

(2) Medicine
University of Minnesota
Minneapolis, MN, United States

(3) VA Medical Center
Minneapolis, MN, United States

(4) Chemical Engineering and Materials Science
University of Minnesota
Minneapolis, MN, United States

INTRODUCTION

The maintenance of normal permeability through the renal glomerular capillaries is a vital and tightly regulated process ensuring the proper filtration of blood. The capillary wall ultrafilter, however, is also subjected to large hydrostatic pressures, meaning that it must be stiff enough to oppose distension but still be porous enough to allow filtration. The glomerular capillaries are well adapted to their function. They are composed of a basement membrane (GBM) with specialized cells on the inner and outer surfaces. The GBM is mostly composed of type IV collagen, laminin, and proteoglycans, of which collagen IV is the primary component responsible for the mechanical stability of the capillaries. The GBM is also responsible for at least 50% of the capillary wall's resistance to plasma filtration [1, 2].

The opposing challenges of mechanical stability and high permeability must remain in balance, even as the capillaries are growing, remodeling, or responding to abnormal conditions [3]. Without tight regulation of transcapillary flow, the capillaries could enter a dangerous positive feedback loop. For example, an increase in pressure in the glomerular capillaries could increase the stresses and strain on the epithelial cells. In response, the cells would deposit more material into the GBM, but that would have the side effect of reducing permeability and again increasing the hydrostatic pressure. Clinically, patients with chronic hypertension present with leaky capillaries, thicker basement membrane, abnormal glomerular filtration rate, and damage to the epithelial cells [4]. Our goal is to investigate how a GBM remodeling scheme would function when subjected to the constraint that capillary pressure increases to maintain constant filtration rate in response to changes in GBM permeability.

METHODS

The GBM was simulated in a multiscale model (Fig. 1) that allows us to link the nanoscale structure of the collagen IV network with the response of the capillaries on the microscale [5]. Collagen IV networks were modeled as three-dimensional networks of rods with connectivity of 4. The glomerular capillary was modeled as a ring section of a thin cylindrical tube. Normally, the hydrostatic pressure acting on the capillary wall is approximately 40 mmHg. We examined two scenarios that involved an increase from nominal pressure by 7 mmHg and 10 mmHg, which inflates the capillary ring from its resting state. The transcapillary flow, Q, through the deformed collagen IV networks is the target filtration rate which must be maintained constant during the remodeling process. The permeability of the fibrous network was calculated by modeling the media as a spatially periodic array of cylinders with defined drag parallel and perpendicular to the cylinders [6].

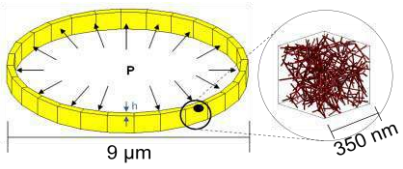

Figure 1: Multiscale model of glomerular basement membrane.

Remodeling, that is deposition and removal of collagen IV, was simulated by changing the radius of the already existing collagen fibrils based on specific rules. From the work of Bhole et al., 2009 [7], it is known that collagen fibers under tension are protected from degradation. Therefore, the rate of collagen removal was defined as in Eq. 1:

Copyright 2016 The Organizing Committee for the 2016 Summer Biomechanics, Bioengineering and Biotransport Conference

$$\left(\frac{dr}{dt}\right)_{removal} = -k_1 exp\left(-k_2\left(\lambda_{fibril} - 1\right)\right) \quad (1)$$

where k_1 and k_2 are constants taken from [8] and λ_{fibril} is the stretch ratio of the collagen IV fibril.

Two cases were considered for the addition of collagen IV material: (1) material added at a constant rate; (2) the rate of addition was dependent on the circumferential strain of the capillary (Eq. 2).

$$\left(\frac{dr}{dt}\right)_{addition} = k_3 exp\left(k_2\left(\lambda_{capillary} - 1\right)\right) \quad (2)$$

where k3 is also a constant from [8] and $\lambda_{capillary}$ is the circumferential stretch ratio of the capillary. The net change in collagen fibril radius at each remodeling step is then the sum of the addition and removal rates.

The GBM was remodeled over 500 time steps and the transcapillary flow was held constant during remodeling, representing the physiological needs of the capillary. For comparison, a case was also considered where remodeling was performed at constant hydrostatic pressure.

RESULTS

Over the 500 remodeling steps, the transcapillary flow was held constant (not shown). As seen in Figure 2, when the filtration rate is maintained and the deposition of collagen IV material is dependent on the strain of the system, the hydrostatic pressure increases for ~100 steps and then levels off, for an increase of between 20% and 40% (the increase was larger with the higher initial pressure). In the case of constant rate of collagen addition, the pressure did not fully equilibrate in the provided remodeling time. In all cases, there was net positive deposition of material, though the amount was twice as large in the strain-dependent addition case for both inflation pressures. The diameter of the capillary decreased significantly, almost returning to the initial resting diameter of 9 um. In the strain-dependent cases, the decrease was slightly larger than in the constant deposition case. Finally, circumferential stress in the capillary increased by a different amount for all cases. The largest increase was for the GBM remodeled at constant addition rate and initially inflated by 10 mmHg. The smallest increase in stress was observed for the opposite remodeling case.

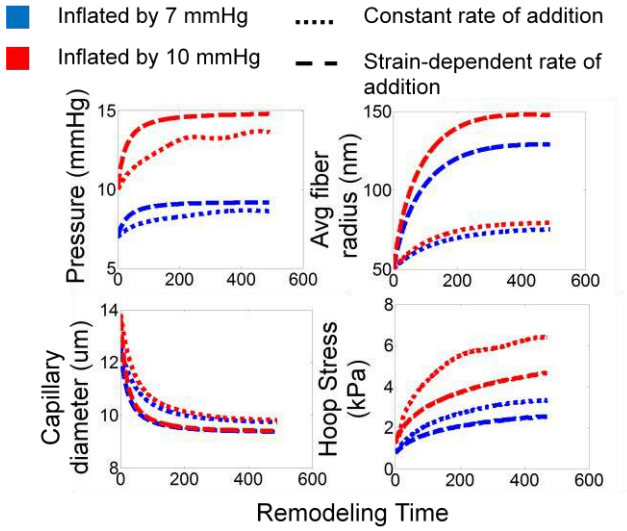

Figure 2: Response of the glomerular capillary system to remodeling at constant transcapillary flow.

In comparison to the constant transcapillary flow remodeling case, as seen in Figure 3, remodeling performed at constant pressure (initial inflation of 10 mmHg, constant rate of addition) results in a decrease in the transcapillary flow, a small decrease in the amount of newly deposited collagen IV, the same diameter decrease, and a decrease in the circumferential stress by half.

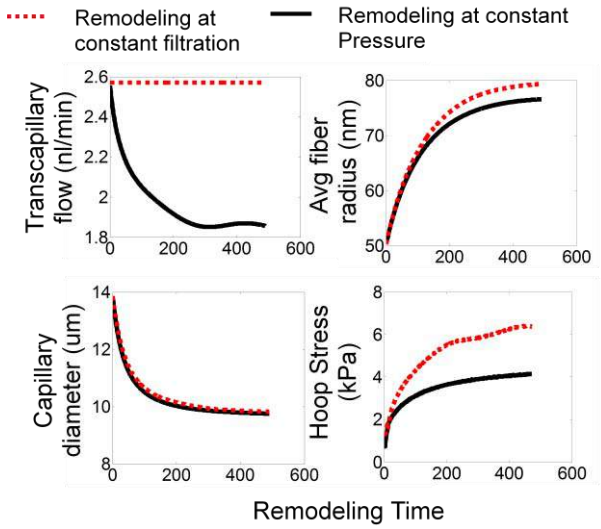

Figure 3: Comparison of remodeling at constant transcapillary flow and constant pressure. Both are done at 10 mmHg initial inflation and constant rate of collagen IV addition.

DISCUSSION

Generally, remodeling done at constant flow rate protected the system, which was not possible with remodeling at constant pressure. Inflating the capillary resulted in increased deposition of collagen IV. To maintain constant filtration rate, the hydrostatic pressure had to increase, but at the same time, the diameter of the capillaries reduced back to normal, lowering the strain of the epithelial cells. The stress on the GBM did increase, but the increased amount of collagen would stiffen the GBM, allowing it to withstand the higher stresses. In contrast, remodeling performed at constant pressure also resulted in increased deposition of collagen IV and reduction in the capillary diameter, but the large reduction in filtration would significantly hinder the kidneys ability to filter blood plasma.

We saw that when the glomerular cells had the ability to sense and respond accordingly to changes in their environment, the response was quicker and stresses were lower. In the simpler case of the system having a constant addition rate of collagen IV material, the response was not always stable and it resulted in larger stresses

ACKNOWLEDGEMENTS

This work was carried out in part using computing resources at the University of Minnesota Supercomputing Institute and was supported by the National Science Foundation Graduate Research Fellowship and Grant No. NSF CMMI 1300649.

REFERENCES

[1] Haraldsson, B et al., *Physiol Review*, 88:451-487, 2008. [2] Deen, WM et al., *Am J Physiol Renal Physiol*, 281:F579-F596, 2001. [3] Kriz, W et al., *Kidney Int*, 49:1579-1574, 1996. [4] Iversen, BM et al., *Microvasc Res*, 34:137-151, 1987. [5] Chandran, PL et al., *J Biochem Eng*, 129:137-147, 2007. [6] Stylianopoulos, T et al., *Phys Fluids*, 20:123601, 2008. [7] Bhole, A et al., *Phil Trans R Soc*, 367:3339-3362, 2009. [8] Gyoneva, L et al., *Interface Focus*, 6:20150069, 2016.

Copyright 2016 The Organizing Committee for the 2016 Summer Biomechanics, Bioengineering and Biotransport Conference

SB³C2016
Summer Biomechanics, Bioengineering and Biotransport Conference
June 29-July 2, National Harbor, Maryland, USA
SB³C2016-830

FOLD-AND-GO SINGLE KNEE SCOOTER

Kevin R. Mozurkewich
Lawrence Technological University
Southfield, Michigan, United States

Nicholas Colarossi
Lawrence Technological University
Southfield, Michigan, United States

Muntha Issa
Lawrence Technological University
Southfield, Michigan, United States

Faculty Advisor(s)

Eric G. Meyer
Technical Advisor
Biomedical Engineering
Southfield, Michigan, United States

Mansoor Nasir
Faculty Advisor
Biomedical Engineering
Southfield, Michigan, United States

INTRODUCTION

Single lower leg injuries such as a sprained ankle or a fractured foot area common occurrence. According to the Cleveland Clinic there are over 23,000 reported ankle sprains in the United States each day [1]. The patients may be recommended to use a wheelchair, rollator, crutches single knee scooters or other types of assistive devices based on their age, nature of the injury and the general health of the user.

There are many products on the market to provide mobility to people with single leg injuries or conditions. According to medical device distributors [Binson's, Livonia MI] however; there is a shift from conventional mobility devices like crutches and canes, to more mobile and innovative devices like single knee scooters [**Figure 1**].

Although there are more single knee scooters being used today than ever before, many patients do not choose this device because it is expensive, heavy and difficult to place in the vehicle when not in use. This project focuses on improving the portability of the single knee scooter.

"There is a need to create a single leg mobility device that is lightweight, compact and inexpensive, giving all users the ability to handle and store the device when not in use."

Figure 1 –A common knee scooter has four wheels and weighs approximately 30 lbs.

PRODUCT DESIGN

The "*Fold-and-Go*" scooter design was developed in order to create an innovative new solution that reduces weight, cost, and bulk of current scooter designs while adding an increase in portability. While some current designs on the market are labeled as "folding," the space saving is minimal and the devices often only include features such as collapsible handlebars. As shown in Figure 1, the *"Fold and Go"* knee scooter features a fully collapsible frame as well as retractable handlebars which allows the device to easily fold into a compact shape.

In addition to the folding frame, the device is constructed from lightweight aluminum tubing while featuring a significant reduction in size and weight achieved by the simple and compact design. This allows the device to be easily folded and carried or stored in the back of a vehicle, for example.

In order for the device to be easily foldable and user friendly, a four bar linkage system is used to allow the main lower wheel platform to fold up while simultaneously folding the knee rest and vertical support post up. The design features a foldable knee pad located above a vertical tube that supports the weight of the user as well as aid in the folding mechanism of the device. At the base of the main vertical handlebar post, a simple two position locking mechanism allows the user to transfer the device from the open to folded position. Once the locking mechanism switch is pressed, the user simply folds the knee brace upwards which utilizes the four bar linkage system to pull up the base of the scooter and lock it in position. From there, the handlebars can be collapsed for additional reduction in package space. The device features a knee pad height adjustment option allowing the user to adjust the height in one inch increments. This adjustment will be achieved by a series of mounting holes spaced 1" apart in the vertical support sections of the device. See Figure 2 below for a profile view rendering of the knee scooter in fully open, half folded, and fully folded position.

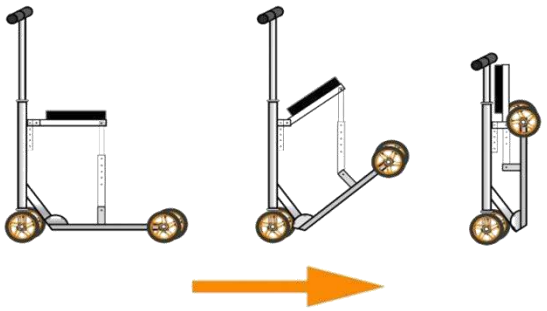

Copyright 2016 The Organizing Committee for the 2016 Summer Biomechanics, Bioengineering and Biotransport Conference

Figure 2 - Side profile progressive image showing how the device is going to fold flat when not in use.

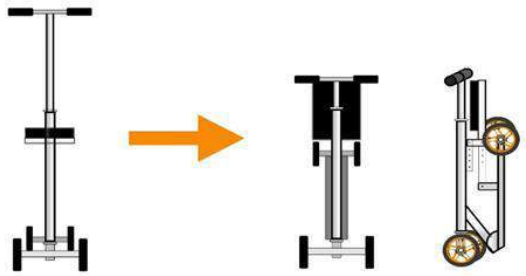

Figure 3 – Front profile progressive image showing how the device is going to fold flat when not in use.

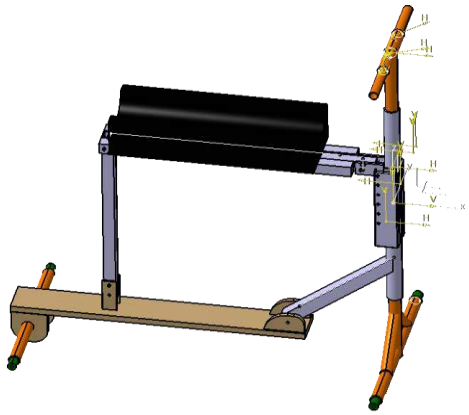

Figure 4 – Preliminary prototype CAD model of the device.

MARKET ANALYSIS & BUDGET

Currently, Over 6.8 million people use personal mobility devices and of those, 40% are estimated to be unable to perform their desired daily activities. We are looking to target any patient 12 years and older who has a single lower leg injury or condition. This device is specially designed to aid in the recovery from injuries, conditions and surgical procedure of the lower limb. Unlike Crutches this device allows the affected limb to be supported which is a key part of the healing process. Furthermore, this device helps to keep the patient from straining the knee of the uninjured leg.

According to the Cleveland clinic, 23,000 people in the United States sprain or strain their ankle every day[1]. According to twin city press, ten million sets of crutches are sold in the US each year. According to Grandview Research, the market for premium rollators and scooters is going to grow nearly 15% from 2014 to the year 2020[3].This projected growth is greater than the growth expected in walking aids over the same time frame. This growth is estimated to increase from 4.5 billion in 2012 to roughly 8 billion in 2018 [**Figure 5**].

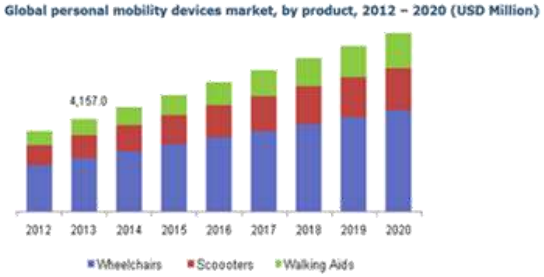

Figure 5- Estimated market broken down by current mobility devices

Below is an itemized budget with justification for each item. **[Table 1].**

Table 1- Itemized budget for development of this product.

Senior Design Budget Break Down			
Item	**Break Down**	**Cost**	**Justification**
Materials	Aluminum Tube	$200.00	Enough aluminum tube to account for multiple iterations of the final design
	Aluminum stock	$75.00	Enough aluminum stock for multiple iterations of the final bracketry design
	Welding rods	$25.00	Package of aluminum welding rods
	Casters w/ bearings	$50.00	4 polyurethane casters with bearings
	Hand Grips	$25.00	Ergonomic hand grips
	Paint	$25.00	Finish
	Razor Scooters	$100.00	Used razor scooters for evaluation and scrap parts
Machining	Machine Shop Labor	$150.00	If necessary to source out the machining of brackets due to time constraints with our equipment. If sourcing is required, request for donations from the machine shop (in the form of materials, labor or both) would be made.
	Machine Shop Parts	$200.00	
Testing	Additional Sensors / Markers	$100.00	Any additionally markers or sensing devices to collect data accurately
	Testing set up	$50.00	Material for making any testing fixture or stand that will be needed
Other	Fasteners	$25.00	High grade fasteners for assembly
	Bushings	$25.00	Bushings and or bearings to decrease handle bar turning efforts
	Weld Fixture	$100.00	May be necessary to ensure the components do not warp during the welding process
	Gas Mileage	$100.00	Gas mileage for picking up parts, materials etc.
Total		**$1,250.00**	

ACKNOWLEDGEMENTS

We would like to thank our advisors, Eric Meyer and Mansoor Nasir with their help with this project. Additionally, we would like to thank Binson's (Livonia, Michigan) for feedback on current devices and Alro Steel (Livonia, Michigan) for material and service donations.

REFERENCES

[1] Cleveland Clinic, "Ankle Injuries," Web, October, 2015

[2] Twin City Press, "Bloomington Startup committed to building a better crutch." Christopher Snowbeck, October, 2012.

[3] Grand view Research, "Market Research & Consulting". Web. March 2015.

Copyright 2016 The Organizing Committee for the 2016 Summer Biomechanics, Bioengineering and Biotransport Conference

SB^{3}C2016
Summer Biomechanics, Bioengineering and Biotransport Conference
June 29 –July 2, National Harbor, MD, USA
SB^{3}C2016-831

ADDRESSING IATROGENIC INJURY DUE TO TRAUMATIC URETHRAL CATHETERISATION

Eoghan M. Cunnane (1), Niall F. Davis (2), Connor V. Cunnane (1), Rory O'C. Mooney (1), John A. Thornhill (2), Michael T. Walsh (1),

(1) Centre for Applied Biomedical Engineering (CABER), Health Research Institute (HRI), Materials and Surface Science Institute (MSSI), Mechanical, Aeronautical and Biomedical Engineering (MABE) Department, University of Limerick, Limerick, Ireland.

(2) Department of Urology, Tallaght Hospital, Dublin, Ireland.

INTRODUCTION

Urethral catheterization is frequently performed in health care settings. Almost 25% of hospitalized patients are catheterized during inpatient stay[1]. The estimated incidence of iatrogenic catheter related urethral injury is 0.3% to 3% but this may underrepresent the true incidence[2,3]. Urethral injury typically occurs in men when the anchoring balloon of a Foley catheter is inadvertently inflated in the urethra[4]. Urethral rupture can lead to the long-term complication of urethral stricture disease and may require urethral reconstruction in severe cases[5]. This study seeks to address this issue by quantifying the cost of this problem on a sample of Irish hospitals, characterising the key urethral tissue mechanical properties pertaining to this mechanism of injury and characterising the user and manufacturer variability of urethral catheter inflation properties. This information is then utilised to develop a novel medical device aimed at eliminating this clinical issue.

METHODS

The incidence and cost of iatrogenic urethral injuries was prospectively monitored in Tallaght Hospital and surrounding district hospitals over a 5 month period. The cost of managing catheter related injuries was recorded to determine the economic impact of this issue on the healthcare system. This cost was estimated by adding the cost of resources utilised to treat the injured patient.

The key mechanical properties of urethral tissue pertaining to catheter related injury are the distension that the urethra can undergo prior to rupture and also the corresponding pressure in the catheter at rupture. To characterise these properties and identify the values pertaining to urethral injury, the anchoring balloons of urethral catheters were intentionally inflated in the bulbar region of porcine urethras maintained *ex vivo* (n=21). Catheter pressure was monitored during inflation using a pressure transducer. Retrograde urethrography was performed to identify urethral injury and also to measure internal urethral diameter.

The user and manufacturer variability of commercially available urethral catheters was investigated by characterising the inflation properties of catheters from several manufactures. Inflation of anchoring balloons was performed at atmospheric pressure by different users (n=8). A pressure transducer was used to measure inflation pressures and video extensometry was used to measure balloon inflation profiles. Manufacturer variability was investigated by applying constant forces to the plunger of syringes attached to the anchoring balloon. These forces are designed to mimic 'heavy-handed', 'intermediate' and 'light-handed'. Three brands of commercially available urethral catheters were investigated (n=3 per brand). The potential to mitigate the identified user and manufacturer variability using a flow resistance approach was then investigated. Flow resistance to the anchoring balloon during inflation was increased by reducing the cross sectional area of the syringe outflow and the impact of this resistance on user and manufacturer variability was examined.

RESULTS

Prospective monitoring of iatrogenic urethral injuries in Tallaght Hospital and surrounding district hospitals over a 5 month period revealed 11 iatrogenic urethral injuries that required invasive urological intervention. 6 of these injuries were recorded in Tallaght Hospital and the remaining 5 injuries were recorded in the district hospitals. 10 of these injuries related to balloon dilation in the urethra. The remaining injury was a bladder rupture. As 6,500 urethral catheterisations are performed annually in Tallaght Hospital, this extrapolates to an incident rate of 0.3% which corresponds with

Copyright 2016 The Organizing Committee for the 2016 Summer Biomechanics, Bioengineering and Biotransport Conference

previously reported rates[2]. The cost of injury acute management, excluding litigation, during this 5 month period was €80,000. This extrapolates to an annual cost of €192,000 to treat iatrogenic urethral catheter injury in a single Irish hospital. A device that could completely prevent this injury, and that cost the hospital €4 per device, would cost the Tallaght Hospital €26,000. This would result in a saving for this particular hospital of €166,000 or over 85% of the cost currently spent on treating this preventable incident.

Urethral injury was observed in 5 of the porcine samples tested following retrograde urethrography. Further analysis of catheter pressure and internal diametric strain revealed that samples remained free from rupture bellow an internal diametric strain vale of 50% and a catheter balloon pressure of 150kPa, Figure 1. The threshold above which urethral injury occurs is 150kPa catheter pressure or 50% diametric strain. Such values can be utilised to design a safety device that eliminates the potential for iatrogenic urethral catheter balloon dilation injuries.

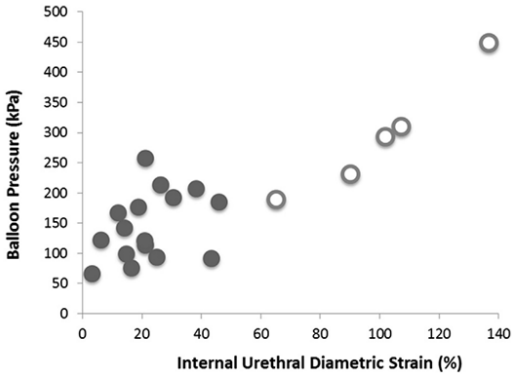

Figure 1: Maximum catheter balloon/urethral pressure and internal diametric strain recorded for each of 21 urethral samples tested. Open circles indicate ruptured urethral samples. Filled circles indicate unruptured samples. Figure clearly demonstrates safety cutoff of 50% internal urethral diametric strain and/or maximum balloon pressure cutoff of 150 kPa before urethral rupture.

During user variability investigation, variations in maximal inflation pressures ranged from 75 to 355 kPa and variations in average flow rates ranged from 19.94-69.08 ml/min. During manufacturer variability investigation, the maximum 'light-handed' inflation pressures ranged from 175kPa to 197kPa for each catheter brand while maximum 'heavy-handed' inflation pressure range increased from 563kPa to 634kPa. Increasing the flow resistance by reducing the cross sectional area of the syringe outflow reduced maximum inflation pressure to below the rupture threshold of 150kPa.

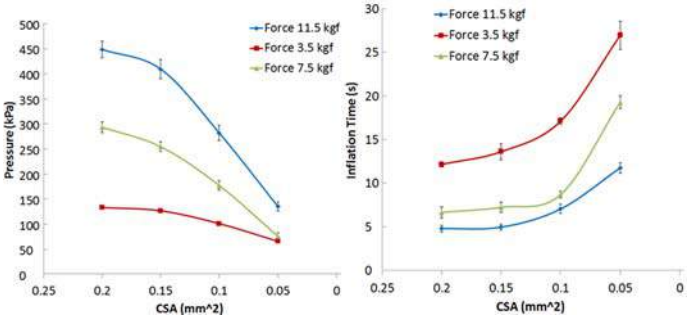

Figure 2: Pressure and inflation time versus flow resistance for the three weights that correspond to high (11.5kg), intermediate (7.5kg) and low (3.5kg) forces applied by different users.

DISCUSSION

A safer urethral catheter system to eliminate the potential for iatrogenic urethral catheter balloon dilation injuries was designed based on the parameters characterized in this study. The novel syringe system is composed of a safety valve that activates at 150 kPa to prevent trauma and an orifice that restricts flow to eliminate user and manufacturer variability. This device has been studied in male cadavers and operated reliably, Figure 3. The device is scheduled to undergo clinical trial in March of this year.

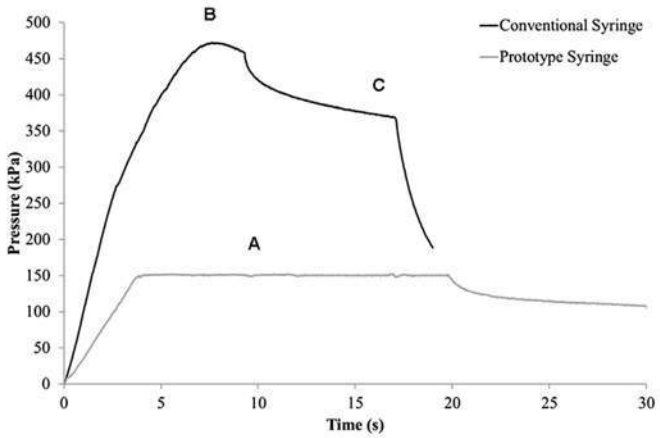

Figure 3: Pressure profiles of catheter inflated in cadaveric urethra using flow resistance technique with syringe pump at infusion rate of 30 ml per minute. Testing was performed with standard (black curve) and prototype (gray curve) syringes. Prototype curve clearly shows safety of novel prototype safety syringe as maximum inflation pressure was limited to safe plateau pressure of 150 kPa up to 20 seconds (s), when inflation process was completed (A). In contrast, flow resistance approach with standard syringe achieved inflation pressure of 450 kPa (B). Inflation pressure decreased at approximately 8 seconds, indicating that urethral threshold pressure was breached. Pressure continued to decrease until inflation was discontinued at approximately 16 seconds (C).

ACKNOWLEDGEMENTS

Supported by an Enterprise Ireland Commercialisation Fund grant with the assistance of Ireland's European Structural and Investment Funds Programme, and the European Regional Development Fund, and the Biomedical Engineering and Regenerative Medicine (BMERM) Structured PhD programme, the framework of the Irish Government's Programme for Research in Third Level Institutions Cycle 5, and the Irish Research Council under the EMBARK Initiative.

REFERENCES

[1] Chenoweth et al., Crit Care Clin 2013; 29: 19.
[2] Trout et al., RN 1993; 56: 52.
[3] Davis et al., Ir J Med Sci 2015; 184: 365.
[4] Thomas et al., BJU Int 2009; 104: 1109.
[5] Kashefi et al., J Urol 2008; 179: 2254.

Copyright 2016 The Organizing Committee for the 2016 Summer Biomechanics, Bioengineering and Biotransport Conference

SB^{3}C2016
Summer Biomechanics, Bioengineering and Biotransport Conference
June 29 –July 2, National Harbor, MD, USA
SB^{3}C2016-832

MOLECULAR CONTROL OF DIFFERENTIAL GROWTH DURING LOOPING OF THE EMBRYONIC SMALL INTESTINE

Nandan L Nerurkar, Cliff J Tabin

Department of Genetics
Harvard Medical School
Boston, MA, USA

INTRODUCTION

The dramatic changes in tissue shape that underlie embryogenesis necessitate precise, stereotyped regulation of physical forces. To ensure that these forces arise at the right location and time with the right orientation and magnitude, they must be prescribed by genetic and molecular cues. We know very little about how this is accomplished during development. Here we investigate the molecular signals responsible for coiling of the small intestine, a process driven by mechanical buckling due to differential growth of adjoined tissues [1]. This process allows the human gut to achieve four times the adult height, and is essential to intestinal function. Errors in looping are associated with a wide range of congenital gastrointestinal defects.

The vertebrate gut begins as a straight, simple tube that is anchored dorsally to the body wall by a thin membranous tissue, the dorsal mesentery. In the chick embryo, looping of the small intestine begins at embryonic day (E) 5, and is completed by E16 (Fig. 1A). Previous work from our group demonstrated that looping occurs due to rapid elongation of the gut tube against the dorsal constraint of the mesentery, which elongates much slower [1]. This results in compressive forces that buckle the tube into its looped configuration; when the tube and mesentery are separated, the loops disappear (Fig. 1B). This mechanism has been supported by both physical and computational models of strain mismatch between a thin membrane and a long tube (Fig. 1C-E). Despite a clear physical understanding of gut looping, it is unknown how tissue growth and stiffness are ascribed at the molecular level to regulate this process. In any context, at present we lack an integrated understanding of how the intracellular signaling events that drive development relate to the physical properties that define tissue shape during morphogenesis. Here we identify BMP signaling as the key signal regulating differential growth and therefore looping morphogenesis of the small intestine.

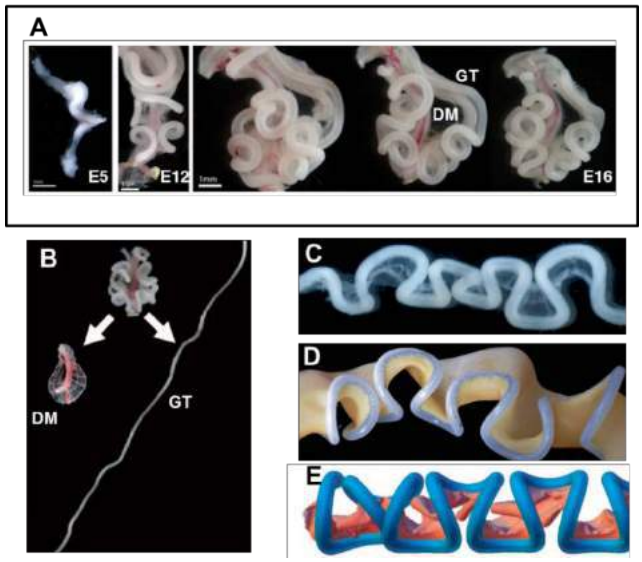

Fig. 1: A) gut tube transforms from straight at E5 to looped by E16; looping is highly stereotyped (GT=gut tube, DM = dorsal mesentery). B) Separation of GT amd DM causes loss of loops. C) Intestinal loops at E16. D) tubing stitched to prestretched rubber membrane following release of prestretch. E) Computational model of differential growth. Fig. 1 adapted from [1].

METHODS Chicken eggs were incubated to the desired stage as described [2]. Gene expression was visualized by frozen section *in situ*

Copyright 2016 The Organizing Committee for the 2016 Summer Biomechanics, Bioengineering and Biotransport Conference

hybridization using established protocols. To misexpress genes in the developing chick gut *in ovo*, eggs were windowed at E5, and a replication competent avian retrovirus, RCAS, was injected at the base of the yolk stalk. Using established methods, *GFP*, *noggin*, and *bmp2* were cloned into the RCAS vector [3]. Infected guts were collected from E12 to E16 to assess BMP activity (phospho-smad 1/5/8 immunofluorescence), cell proliferation (Edu incorporation), and morphometry and residual strain.

RESULTS

To identify candidate genes, we first screened for the expression of key developmental genes in the small intestine, looking for expression patterns that favor either the gut tube (elongates rapidly) or the attached dorsal mesentery (elongates slowly). The BMP pathway showed a strong dorsal bias in expression, with *bmp2* strongly expressed in the dorsal mesentery and its attachment to the gut tube (i.e. the inner curvature of loops), but absent from the ventral gut tube (outer curvature, Fig. 2A). Expression of BMP receptors *bmpr1b* and *bmpr2* was also dorsally biased (not shown).

We next developed a viral misexpression strategy to disrupt BMP activity in the gut. Specificity and robustness of infection were confirmed by RCAS-GFP infection (Fig. 2B). To broadly disrupt BMP activity, we overexpressed the BMP antagonist *noggin*; this effectively diminished endogenous BMP signaling (Fig. 2C, D). Strikingly, BMP inhibition resulted in a dramatic decrease in intestinal loops (Fig. 3A, B). This was accompanied by an increase in dorsal mesentery perimeter (Fig. 3C-E), despite no change in gut tube length (Fig. 3F). As a result the residual strain between tube and mesentery was reduced by 2-fold (Fig. 3G). We next misexpressed *bmp2* to observe whether activation of the BMP pathway will result in more loops. RCAS-Bmp2 infection resulted in a robust increase BMP signaling (Fig. 2E), and had a striking effect on looping morphology. The number and tightness of coils increased with *bmp2* misexpression (Fig.4). In particular, regions of 'hyperlooping', or nesting of loops within loops, were observed with *bmp2* over expression. Such hyperloops were never observed in wildtype or RCAS-GFP infected guts.

These findings suggest that differential growth in the looping small intestine is modulated by BMP signaling. Specifically, we propose that bmp2 in the dorsal mesentery suppresses cell proliferation and therefore elongation. This is why inhibition and activation of the pathway result respectively in a decrease and increase in differential growth. To test this, we looked next at the effect of BMP signaling on cell proliferation in the mesentery. As expected, inhibition caused a significant increase in proliferating cells while *bmp2* overexpression decreased the number of proliferating cells in the dorsal mesentery.

DISCUSSION

The physics of intestinal looping have been recently elucidated [1]. Here we exploit this detailed understanding of buckling morphogenesis in the gut to ask the question of how molecular signals modulate physical forces during development. We identified BMP signaling, and bmp2 in particular, as key regulators of differential growth in the small intestine. While we have demonstrated that cell proliferation, and consequently elongation rate, are inversely related to BMP activity, it is unclear to what extent looping phenotypes are the result of other changes, such as the mechanical properties of gut tube and mesentery, or changes in tissue geometry. To test this, we are currently performing tensile testing experiments to measure the effects of BMP activity, and will incorporate these findings into a previously developed computational model of gut buckling. This will allow us to precisely determine the physical determinants of looping morphogenesis that are determined by BMP signaling. Finally, we are examining the natural variation in intestinal loop morphology among closely related avian species to determine whether evolutionary modulation of morphogenetic forces in the gut can be explained by differential regulation of the BMP signaling pathway.

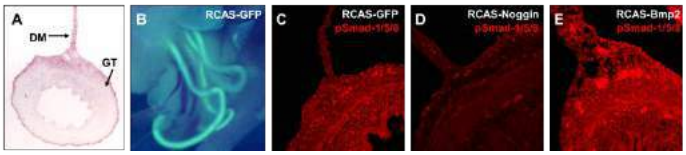

Fig. 2: A) in situ hybridization for *bmp2* in the E12 chick midgut. B) E12 whole mount GFP signal following RCAS-GFP infection. C-E) Phospho-smad 1/5/8 immunofluorescence at E14 following GFP (C), Noggin (D), and Bmp2 (E) misexpression.

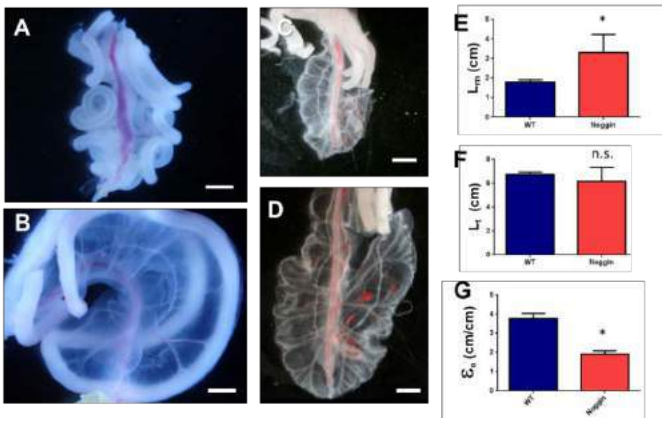

Fig. 3 E14 Small intestine infected with RCAS-GFP (A) and RCAS-Noggin (B). E14 Dorsal mesentery following removal of gut tube with RCAS-GFP (C) and RCAS-Noggin (D). Length of mesentery (L_m, E) and gut tube(L_t, F) following infection. G) Residual strain ($\varepsilon_0=L_t/L_m$) following infection.

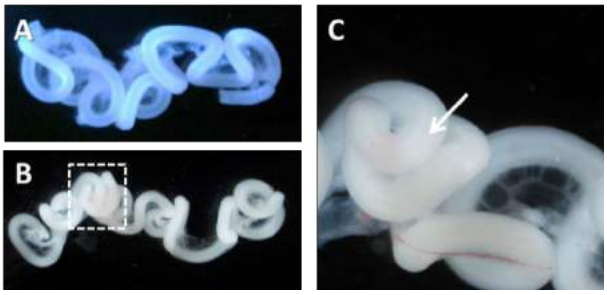

Fig. 4 RCAS GFP (A) and Bmp2 (B) infected E14 small intestine. Boxed region enlarged in (C); arrow indicates hyper-looping.

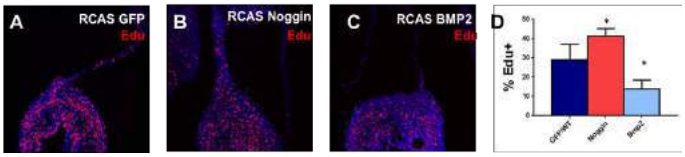

Fig. 5: Edu incorporation labels proliferating cells in the mesentery following misexpression of GFP (A), Noggin (B), and Bmp2(C), quantified in (D).

ACKNOWLEDGEMENTS Work supported by NIH grants R01HD047360 (CJT) and F32HD069074 (NLN).

REFERENCES [1]Savin+, *Nat.*, 476(7358):57, 2011. [2] Hamburger+, *J Morph*, 88(1):49, 1951. [3] Logan+, *Methods*, 14(4):407-20, 1998.

Copyright 2016 The Organizing Committee for the 2016 Summer Biomechanics, Bioengineering and Biotransport Conference

SB^{3}C2016
Summer Biomechanics, Bioengineering and Biotransport Conference
June 29 –July 2, National Harbor, MD, USA
SB^{3}C2016-833

KINEMATIC EVALUATION OF A WEARABLE SOFT ROBOTIC SYSTEM FOR CONTINUOUS PASSIVE MOTION IN POST STROKE HAND REHABILITATION

Rita M. Patterson (1), Nicoleta Bugnariu (2), Timothy Niacaris (3), Mahdi Haghshenas-Jaryani (4), Wei Carrigan (4), Caleb Nothnagle (4), Muthu BJ. Wijesundara (4)

(1) Family Medicine and Osteopathic Manipulative medicine
University of North Texas Health Science Center
Fort Worth, TX, USA

(2) Physical Therapy
University of North Texas Health Science Center
Fort Worth, TX, USA

(3) Orthopaedic Surgery
University of North Texas Health Science Center
Fort Worth, TX, USA

(4) UTA Research Institute
University of Texas at Arlington
Fort Worth, TX, USA

INTRODUCTION

Approximately 800,000 people in the United States have a stroke each year of which 30% to 66% of all stroke survivors have impaired hand functions [1-3]. Hand impairments are mostly recognized by spasticity, inability to open/close hands, inaccurate finger and hand movements, and poorly modulated fingertip forces [4]. Continuous Passive Motion (CPM), and Patient Assisted Movement (PAM) are two common therapeutic interventions, which capitalize on the brain's inherent neuroplasticity to increase adaptation to stroke [5-7]. For these therapeutics to be effective, the duration, intensity, and consistency of therapy as well as patient compliance are all vital factors. However, a shortage of resources and compliance will hinder the return of hand functionality. While it has been shown that robotic motion can provide many of these attributes, no dedicated system has been made which can effectively apply post-stroke hand therapy. To address this need, a soft robotic rehabilitation system (Fig. 1) capable of monitoring and assisting hand motion for post-stroke patients has recently been developed [8, 9]. To apply this system to the clinical population, it is vital to understand the kinematic interaction between such a robotic glove and the human hand to ensure patient safety and performance. This abstract compares simulation and experimental data on a human finger with a corresponding robotic digit to evaluate the viability of the current design for rehabilitation purposes.

METHODS/RESULTS

Glove and Soft Robotic Digits:

This system consists of five sensorized robotic digits and a wearable fixture along with a programmable control unit that monitors and modulates the trajectory of the fingers (Fig. 1(a)). CPM can be applied through this system by setting the motion parameters of the control unit.

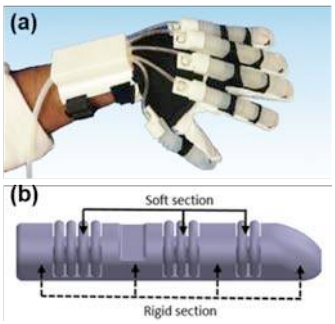

Figure 1: (a) Prototype of the robotic glove, (b) CAD model of a single robotic digit.

Finger motion is accomplished by pneumatically actuated soft robotic digits based on a hybrid soft-and-rigid actuator technology which uses inflatable and deflatable bellows to produce a bending movement along the joints (Fig. 1 (b)) [8]. As shown in Fig. 1(b), the robotic digit consists of three bellow-shaped soft sections and four rigid sections (in an alternative order) in correspondence to three joints, three phalanges with the metacarpal. Computer simulations of the soft robotic digit have been examined for finger range of motion (ROM) at each joint: metacarpal phalangeal (MCP), proximal interphalangeal (PIP), and distal interphalangeal (DIP) (Fig. 2). The numerical simulation studies of the soft robotic digit have shown that the resulting relative angles between rigid sections at MCP, PIP, and DIP (Fig. 2(a)) can reach full anatomical ROM (MCP: 0-90º; PIP: 0-100º, DIP: 0-70º [10,11]) at a single actuation pressure of 24.3kPa, as shown in Fig. 2(b).

Copyright 2016 The Organizing Committee for the 2016 Summer Biomechanics, Bioengineering and Biotransport Conference

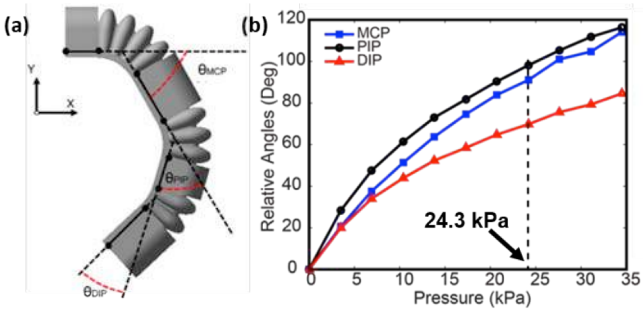

Figure 2: (a) Relative angles between MCP, PIP, and DIP sections, (b) ROM for each joint with respect to actuation pressure.

Kinematic study:

A kinematic study was carried out to compare one subject's index finger with a robotic digit using a motion capture system (Motion Analysis Corp, Santa Rosa, CA). The motion capture system is capable of detecting the position of markers placed along the digit to within 0.25mm and angular positions to within 5˚. This study determined the functional anatomical ROM requirements at each joint for both the robotic digit and index finger. To identify the motion parameters, reflective markers were placed on the joints and phalanges (Fig. 3(a) and (b)). Both the subject and robotic digit moved the finger for flexion/extension while the x, y, and z coordinates of the markers were recorded. Figure 4(a) shows the robotic digit's angular data for the DIP, PIP and MCP joints while Fig 4(b) shows this data for a human finger.

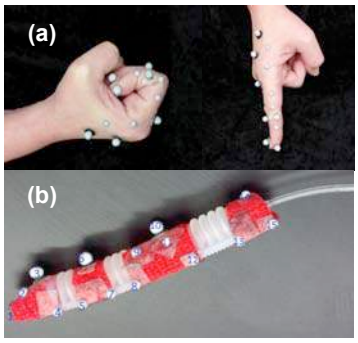

Fig 3: Marker placement on (a) a subject's finger index and (b) a single soft robotic digit.

The achieved ROM for MCP, PIP, and DIP joints of the robotic digit are 85˚, 96˚, and 53˚, respectively, which are in good agreement with the full anatomical ROM. It should be noted that the human finger (MCP: 45˚, PIP: 75˚, and DIP: 45˚) did not quite reach its full ROM during testing due differences in functional range of motion versus isolated joint range of motion. However, these robot achieved ROM are consistent with the functional ROM of the human fingers.

DISCUSSION

A hand therapy glove has been designed to provide flexion and extension of the fingers as an adjunct to hand therapy. A prototype has been fabricated based on initial design parameters and is able to provide joint ROM based on the literature. Functional grasp parameters have been experimentally measured in a human finger and will be used for future design improvements.

Future work: Experimental data will be collected with the robot on the hand to provide optimal control parameters for passive motion of the digits. Other important kinematic parameters include the center of rotation (COR) and dorsal skin lengthening of the human finger. The COR of the robot finger will need to coincide with the corresponding finger joint to ensure proper motion in the hand [12]. The dorsal skin of the human finger stretches during finger flexion, for example 12 mm of lengthening has been reported when the PIP is at 90˚ of flexion [13]. This lengthening effects the joint location of the corresponding robotic digit, causing misalignment. To accommodate for this, the robotic digits will be designed to match this lengthening. Once improved design parameters are obtained, these data will be used to modify the robotic glove for clinical evaluation.

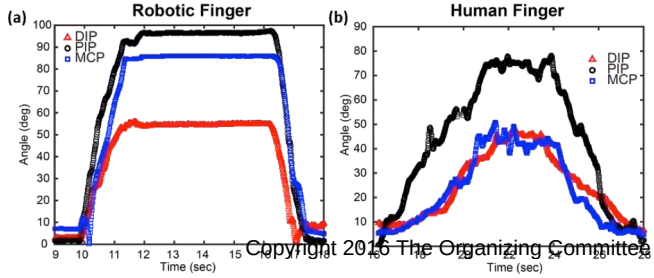

Figure 4: Robotic and Human finger joint angles.

ACKNOWLEDGEMENTS

This work is supported by the Texas Medical Research Collaborative (TexasMRC). The authors wish to thank the staff at the UTARI and UNTHSC.

REFERENCES

[1] Adamson, J., et al, J Stroke and Cerebrovascular Diseases, 13(4), pp.171-177, 2004.
[2] Rosamond, W., et al. American Heart Association Statistics Committee, vol117, pp 25-146, 2008.
[3] American Heart Association Heart Disease and Stroke Statistics 2014 Update-http://www.americanheart.org
[4] Kwakkel, G., et al, Physiotherapy, 85(7), pp.377-391, 1999.
[5] Dobkin, B.H., The Lancet Neurology, 3(9), pp.528-536, 2004.
[6] Bayona, NA, et al, Topics in Stroke Rehab. 12(3), pp. 58–65, 2005.
[7] Wolf, S.L., et al, Jama, 296(17), pp.2095-2104, 2006.
[8] Haghshenas-Jaryani M., et al, Proc Int Design Engr Tech Conf and Computers and Info in Engr Conf, Boston, MA, ASME, 2015.
[9] Wijesundara M. BJ., et al, U.S. Patent Application No. 14/990,257, (Pending), 2016.
[10] Hume, M.C., et al, J hand surgery, 15(2), pp.240-243, 1990.
[11] Kawasaki, H., IEEE Rehab Robotics Conf. (pp. 234-240), 2007.
[12] Heo, P.,et al Int J Precision Engr & Manufacturing, 13(5), pp.807-824, 2012.
[13] Rath, S., Indian J plastic surgery, 44(2), p.178, 2011.

Copyright 2016 The Organizing Committee for the 2016 Summer Biomechanics, Bioengineering and Biotransport Conference

SB³C2016
Summer Biomechanics, Bioengineering and Biotransport Conference
June 29-July 2, National Harbor, Maryland, USA
SB³C2016-834

REACHING AID FOR SPINAL FUSION RECIPIENTS

Maryssa Mercer
Wayne State University
Detroit, Michigan, United States

Bijal Patel
Wayne State University
Detroit, Michigan, United States

Casey Schiner
Wayne State University
Detroit, Michigan, United States

Celia Staniak
Wayne State University
Detroit, Michigan, United States

Faculty Advisor(s)

Michele Grimm
Wayne State University
Detroit, Michigan, United States

Brian Mundo
Wayne State University
Detroit, Michigan, United States

INTRODUCTION

Osteoporosis is a medical condition affecting the bones, causing them to become brittle and fragile. The condition affects a large number of people worldwide, including over 200 million women; about one-tenth of women over 60 years-of-age and about two-thirds of women over 90 years-of-age are diagnosed with osteoporosis [1]. Osteoporosis can lead to various medical problems, including fractures and kyphosis. More than 8.9 million fractures occur annually from osteoporosis [2]. Those who develop vertebral fractures from osteoporosis have a higher risk of fracture within the next 1-2 years [3]. In order to help prevent fractures, the National Osteoporosis Foundation recommends a 10 lb. lifting limit [4].

Several vertebral fractures can cause a curve in the spine, known as kyphosis, resulting in forward curving of the spine and hunching of the back. Kyphosis can cause serious pain and complications due to muscles, tendons, and ligaments being strained from the curve of the spine [5]. Kyphosis affects approximately 4-8% of the general population and is most commonly caused by osteoporosis [6, 7].

Criteria taken into consideration for surgical treatment of kyphosis include the severity of the curve, the balance of the patient, and neurological symptoms of the patient [8]. According to the Scoliosis Research Society, surgical treatment is recommended if the curve of the spine becomes greater than 80° and the patient is experiencing pain [9]. Spinal fusion is the most common solution for severe cases of kyphosis. Although the patient may experience a feeling of the same or greater mobility after surgery, such motions are accomplished by overcompensation in spinal discs and/or the hip joint adjacent to the fusion site [10]. Often, medical professionals provide the advice of avoiding the B.L.T.'s (bending, lifting, and twisting) immediately post-surgery [11]. As the healing process continues, lifting and twisting are generally accepted movements; however, due to the mechanics of the spine, bending remains a post-operative restriction. If osteoporosis was the original cause of the kyphosis, the lifting limit of 10 lb. also remains as a restriction for the patient.

With the restrictions of being unable to bend the spine and a 10 lb. lifting limit, patients may find it a challenge to maintain their independence. Through interviews and clinical observations with spinal fusion patients with and without osteoporosis, the most common and difficult tasks to perform were recorded. Further insight regarding the most significant needs of spinal fusion recipients in their postoperative lifestyle was gained through interviews with technical experts including orthopedic surgeons, neurosurgeons, research engineers, physical therapists, and occupational therapists. The following user needs statement was developed from these observations and interviews with patients and clinicians:

> Spinal fusion recipients require a means to increase ability to perform activities of daily living that require bending, while minimizing bending torque and compressive stresses on the spine. Patients with osteoporosis must take further caution to prevent bone fractures elsewhere in the body.

Our ultimate goal is to prevent the need for subsequent surgeries due to compression fractures by minimizing the most significant post-operative injury risk factor. We hope to eliminate the tendency for spinal fusion recipients to perform the risky, habitual behavior of spinal flexion in order to accomplish a variety of daily tasks. Our team aims to design an assistive device that reduces the bending torque and anterior axial compression on the vertebrae near the fusion region while allowing patients to perform lifting activities and tasks that would traditionally require truncal bending.

PRODUCT DESIGN

The goal of the design was to create a simple reaching aid that was more functional and user friendly than devices currently available on the market. After an analysis of current reaching aids, three main areas were of issue. These were support on the arm, required grip strength, and device length (reach). This design eliminates these three problems.

The CAD model of the assistive reaching device is shown in Figure 1. The device consists of four parts, as labeled in Figure 1: 1. Wrist brace, 2. Handle, 3. Body, 4. Grippers. The wrist brace is broken down into a C-shaped cuff and a support piece. Together, these attach to the body of the device using a clamp with a wingnut. The wrist brace can be adjusted in length to fit all sizes of users. The handle consists of a frame, two locks, and a pulling mechanism. The frame is used to support the hand and allow for control of the device. The pulling mechanism is used to operate the grippers and secure objects. The locks are used to lock the pulling mechanism in place so the user does not have to transmit a continuous pull. Inside of the pulling mechanism is a retraction mechanism that allows the device to be operable at any length. The body of the device is a twist to lock pole. The body can be adjusted in length for use or for storage. Lastly, the

Copyright 2016 The Organizing Committee for the 2016 Summer Biomechanics, Bioengineering and Biotransport Conference

grippers are similar to standard reaching aids. This portion of the design is a 2 arm gripping system. It will have a component on the end of each arm to create more friction between the device and the object for a more secure connection.

The operation of this device is as follows: The user must insert their hand and lower arm into the wrist brace and secure it to the arm. The user then places their palm against the most superior portion of the handle with their fingers reaching down, touching the pulling mechanism. From here the user may reach towards an object they want to retrieve. Once the object is between the grippers, the user will pull the pulling mechanism towards the superior portion of the handle frame. Once the user has a secure grip on the object, they will use their thumb to turn the lock on the top portion of the handle. This locks the handle in place so that no more grip force is needed to operate the device. From here, the user may bring the grips towards them and grab the object while unlocking the pulling mechanism.

By creating a design that is as simple as possible, not only is it effective, but it is very reliable. This design combines aspects of support, ease of use, and dynamics to create an optimized device. The wrist brace transfers a significant portion of the load along the forearm rather than concentrating forces at the wrist in order to reduce the risk of distal radial fracture in users with osteoporosis [17]. The locking mechanism allows for an easier-to-use device with better control than the current market's devices. The extendable and retractable body also allows for a dynamic, portable, and multifunctioning device. This combination of designs will boost the device above all current market options.

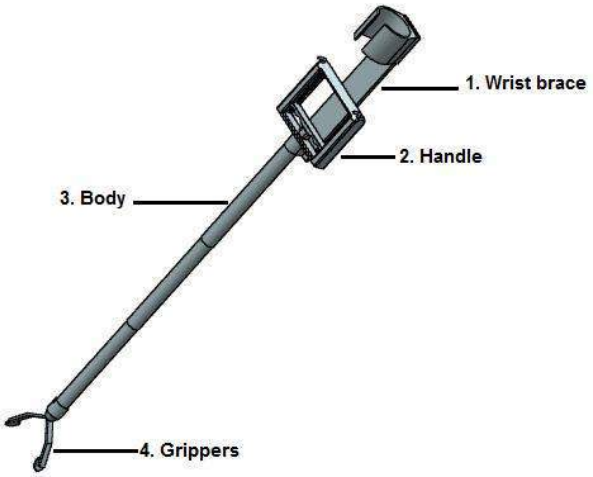

Figure 1. CAD model of the design with parts labeled

BUDGET & MARKET ANALYSIS

As this is a simple design and is operated mechanically, the design budget is fairly small. Materials to create each component of the device are inexpensive. The functional prototype will only be needed to ensure the overall concept of the device will work. We estimate a prototyping cost of $400 for materials, manufacturing, and assembly. Fatigue and strength testing will be done on the materials of the final device to ensure that the device will not fail under expected loads or during normal use patterns. Fatigue and strength testing of components will add another $500 to the budget, for a total of $900.

Because similar devices are currently sold in the market at very low costs (typically under $20 [18]), our device will have to compete with these low costs. The early prototyping costs were in the range of buying a reaching aid from an online source. When manufacturing is scaled up, the costs will similarly be very low. We will aim for a competitive sales price, hopefully achieving as low as $20. While this is more expensive than some similar devices on the market, features of this device and the longer expected lifetime make up for the higher cost. Because this device has components such as the wrist brace and locking mechanism, it has the ability to pick up a wider range of objects than current devices. Also, since the device is adjustable in length, it will be able to be used in various environments and is easier to transport compared to current devices. This device is a new and improved reaching aid; it addresses all of the needs identified by users, creating the best version to date.

This device will be beneficial to anyone with problems performing tasks that require a bending of the spine. This includes, but is not limited to, spinal fusion patients, patients that are wheelchair bound, users of mobility assist devices, and the elderly. There are over 400,000 spinal fusions performed in the US annually [16]. According to the CDC in 2010, roughly 3.6 million people in the United States, about 1.5% of the total population, used wheelchairs or similar device, and 11.6 million people, about 4.8% of the total population, usde assistive mobility devices such as canes, crutches or walkers [15]. In these cases, potential users need a means of performing activities of daily living that require bending while still using their mobility assist device. Thus, the potential market size for this device is large; it is also not likely that the demand for this type of device will significantly drop from its current point.

ACKNOWLEDGEMENTS

We would like to thank Dr. Michele Grimm, Dr. Heather Lai, and Professor Brian Mundo for their advising on this project. We would also like to thank Wayne State University for the funding provided to us. Partial support of the BME Design Program is provided by NIH R25EB014772-03 with additional funding from Life Beyond Barriers LLC.

REFERENCES

[1] J, K., 2007. WHO Technical Report.
[2] J., J.O.a.K., 2006. An estimate of the worldwide prevalence and disability asscociated with osteoporosis fractures. Osteoporosis International 17.
[3] C., R., 2007. Mild prevalent and incident vertebral fractures are risk factors for new fractures. Osteoporosis International 18.
[4]2015b. Exercise Examples. National Osteoporosis Foundation.
[5] 2015c. Osteoporosis and Your Spine. National Osteoporosis Foundation.
[6] Spivak, J., 2010. Kyphosis Causes and Treatment Spine-health.
[7] Clark, K.a., 1998. Kyphosis (Scheuermann's disease; Roundback; Hunchback; Postural kyphosis). Clinical Medicine, 4th edition Medline Plus
[8] Highsmith, J., 2015. Surgery for Kyphosis Scoliosis Research Society.
[9] 2015a. Developmental Kyphosis, Surgical Treatment. Scoliosis Research Society.
[10] Health, S., 2015. Evaluating Spinal Fusion Surgery Spine Health.
[11] Yee, A., 2008. Do Patient Expectations of Spinal Surgery Relate to Functional Outcome?, Clinical Orhtopaedics and Related Research 466.5 pp. 1154-1161.
[12] Nachemson AF, M.J.D., 1964. A method for the determination of pressure in the lower lumbar discs. J Bone Joint Surg Am 46 (5): 1077 -1092).
[13] Edwards WT, H.W., Posner I, 1987. Variation of lumbar spine stiffness with load Journal of Biomechanics, Trans ASME 109:35-42.
[14] Jayaraman G, Z.H., Jacobs RR 1989. Biomechanical analyses of surgical correction techniques in idiopathic scoliosis: significance of biplanar characteristics of scoliotic spines. Journal of Biomechanics 22:427-438.
[15] Brault, M.W., 2012. Americans With Disabilities: 2010 Census P70-131.
[16] Rajaee, SS et al., *Spine (Phila Pa 1976)*, 37(1):67-76, 2012.
[17]. Oyen J. et al., 2011. Osteoporosis as a risk factor for distal radius fractures: a case-control study. J Bone Joint Surg Am. 2011, 93(4):348-56.
[18] Reachers, Mobility Aids. 2015 Medline Industries

Copyright 2016 The Organizing Committee for the 2016 Summer Biomechanics, Bioengineering and Biotransport Conference

SB^{3}C2016
Summer Biomechanics, Bioengineering and Biotransport Conference
June 29 –July 2, National Harbor, MD, USA
SB^{3}C2016-835

MECHANISMS OF CERVICAL SPINE DISC INJURY UNDER CYCLIC LOADING: EXPERIMENTS AND FINITE ELEMENT ANALYSIS

Sagar Umale (1), Narayan Yoganandan (1), Mike Arun (1), Brian Stemper (1), Brian Snyder (2)

(1) Department of Neurosurgery,
Medical College of Wisconsin,
Milwaukee, WI, USA

(2) Beth Israel Deaconess Medical Center,
Harvard Medical School,
Cerebral Palsy Clinic Children's Hospital,
Boston, MA, USA

INTRODUCTION

Military helicopter pilots, soldiers, heavy duty vehicle drivers and others working in vibratory environments sustain cyclic loading as a part of their activities [1]–[3]. Many studies have been conducted to understand the mechanical response of the lumbar spine under cyclic loading, with a primary focus on experiments from human cadaver spines [4]–[6]. While finite element modeling (FEM) to understand the internal responses of disc components have primarily concentrated on acute loading of lumbar and cervical spines [7], some repeated loading simulations are also published on the lumbar spine [8]. However, cyclic loading studies on the human cervical spine combining experimental data and FEM are limited. The objective of this study is to develop and validate a three-dimensional FEM of the human C4-C5 intervertebral disc using in-house experiments and determine the stress strain distributions within its components in an attempt to explain the potential mechanisms of disc injury.

METHODS

The finite element model of the C4-C5 disc with the associated superior and inferior end plates was developed from CT images. The nucleus pulpous and annulus ground substance were modeled using solid hexahedral elements. The annular fibers were modeled with five pairs of concentric quadratic shell layers embedded in the ground substance [7]. The superior and inferior cartilaginous and bony endplates were modeled using shell elements. The element size was 0.5 mm, and the model was composed of 8,740 solid hexahedral elements and 18,636 quadratic shell elements. The geometry represented the average area and disc height of the C4-C5 disc segments tested at 2 Hz for 10,000 cycles. The material properties for the ground substance were obtained from in-house experiments, performed on disc segments before cyclic loading, described later.

The material properties for the endplates, nucleus and annular fiber components were obtained from literature [7]–[9]. The annular ground substance was modeled as a hyper-viscoelastic material. The nucleus was modeled with an elastic modulus of 1 MPa and a Possion's ratio of 0.45. The annular fibers were modeled as hyper-elastic (Aruda-Boyce) material, and tension-only material properties were varied from the inner most layer to the outer most layer. The bony endplates were modeled with an elastic modulus of 5,600 MPa and a Poisson's ratio of 0.3, and uniform thickness of 1 mm. The cartilaginous endplates were modeled with an elastic modulus of 24 MPa and a Poisson's ratio of 0.4, and uniform thickness of 0.8 mm. The cyclic loading was applied in two steps: (1) a uniform load of 150 N at 2 Hz was applied to the superior end plate, and (2) a direct cyclic step simulating 10,000 compression cycles based on the previous step history.

The model was validated by conducting experiments with two female (mean age 47±23years) C4-C5 disc segments. Pre-test antero-posterior and lateral radiographs and computed tomography (CT) scans of the spinal columns were obtained. All tests were done in a physiologic chamber by maintaining the specimen in a heated water bath during the entire loading period. Tension-compression and viscoelastic tests were conducted, and this was followed by subjecting the specimens to 150 N of compressive force at a frequency of 2 Hz for 10,000 cycles. Tension-compression and viscoelastic tests were repeated after the cyclic loading. The specimens were x-rayed after the loading period.

The initial output of the FEM was used to extract displacement-time responses and compare with the experimental corridors, expressed as mean and plus and minus one standard deviation. Stress analysis outputs consisted of determining profiles of maximum and minimum principal stresses and strains, vector directions, and Von Mises stresses

Copyright 2016 The Organizing Committee for the 2016 Summer Biomechanics, Bioengineering and Biotransport Conference

in the constituents of the disc and endplates. Patterns of these internal distributions were used to infer the potential mechanisms of load transfer within the disc components under cyclic loading.

RESULTS

The displacement-cycle responses from the model were within the experimental mean plus minus one standard deviation corridors (Figure 1). The displacement was greater during the initiation of the loading process and reduced exponentially in the first 2,000 cycles, followed by a plateau showing the effect of viscoelasticity in this first 2,000 cycle period. The Von Mises stress distribution in the disc at the end of the step 2, that is, 10,000 cycles is shown (Figure 2). The residual stress was maximum in the annulus and concentrated along the periphery. The residual Von Mises stress in the nucleus was approximately one-tenth of the annulus and was concentrated along the outer circumference. As expected, the annular fibers had the least residual stress, concentrated in the innermost layer.

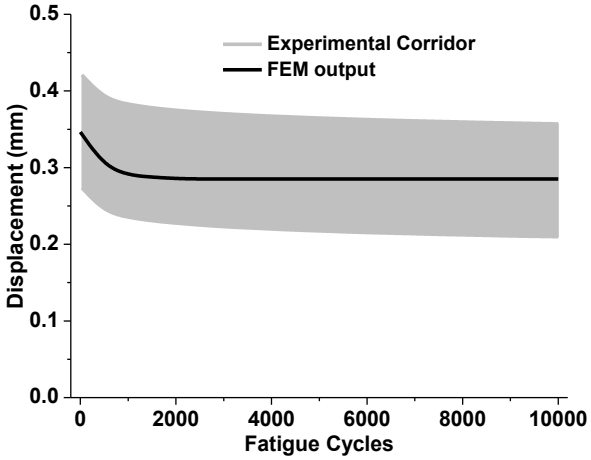

Figure 1: Comparison of the cyclic response from FEM with experimental corridor (Shaded region)

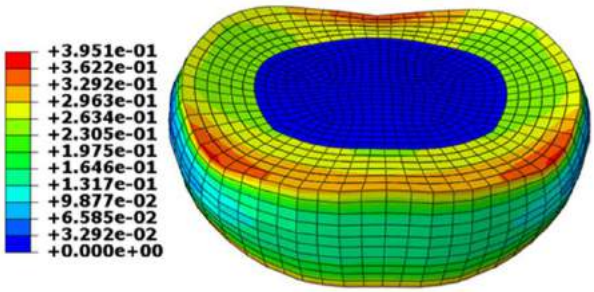

Figure 2: Von Mises stress distribution

The principal stresses were considerably lower than the Von Mises stresses, indicating the development of the shear stress during the cyclic loading process. This was also evident from the direction vectors of the principal stresses. The principal strains were found to be maximum in the annulus ground substance and fibers. The tensile stresses and strains occurred in the radial direction, whereas the compressive stresses and strains occurred in the axial direction.

DISCUSSION

This is the first study to conduct cyclic loading experiments simulating physiological situations and use its inputs and outputs to develop and validate a three-dimensional FEM of the C4-C5 disc. Following validation, the internal responses of the components of the discs were extracted from stress analysis. Although the external cyclic loading was axial, the response of the cervical disc was multi-modal: compressive and shear stresses were developed due to anisotropy. The concentration of the minimum principal stresses at the annulus nucleus boundary along the anterior and posterior direction can lead to circumferential tears, and the maximum principal stresses concentrated at the annulus and cartilaginous endplate boundary can lead to radial tears in the disc, thus explaining a mechanism of internal disc failure due to cyclic loading and correlating with clinical observations of radial and circumferential tears [10]. The development of the shear stresses in association with the peak principal stresses may lead to delamination of the disc under cyclic loading in human cervical spines. It is known that the posterior annulus is supplied by the sinuvertebral nerves, and the anterior and lateral regions are supplied by autonomic nerves [11]. The compression of the annulus and the presence of the nerves in these regions may elicit discogenic pain in patients sustaining cyclic loading from occupational and military activities. The present study offers an explanation for these clinical phenomena.

ACKNOWLEDGEMENTS

This work was supported in part by the U.S. Army Medical Research and Materiel Command Fort Detrick, Maryland (01026018, Contract No. W81XWH-13-1-0050). This material is a result of work supported with resources and use of facilities at the Zablocki VA Medical Center, Milwaukee, Wisconsin. NY and BDS are part-time employees of the Zablocki VA Medical Center, Milwaukee, Wisconsin. The content included in this work does not necessarily reflect the position or policy of the U.S. Government.

REFERENCES

[1] S. P. Cohen et. al., "Spine-area pain in military personnel: a review of epidemiology, etiology, diagnosis, and treatment," *Spine J.*, vol. 12, no. 9, pp. 833–842, 2012.

[2] V. De Loose et. al., "Individual, work-, and flight-related issues in F-16 pilots reporting neck pain," *Aviat. Space Environ. Med.*, vol. 79, no. 8, pp. 779–783, 2008.

[3] M. Mangnusson et. al., "Are occupational drivers at an increased risk for developing musculoskeletal disorders," *Spine*, vol. 21, pp. 710–7, 1996.

[4] J. McElhaney et. al., "Cervical Spine Compression Responses," in *STAPP car crash conference*, 1983.

[5] M. A. Adams and W. C. Hutton, "The effect of fatigue on the lumbar intervertebral disc," *J. Bone Joint Surg. Br.*, vol. 65, no. 2, pp. 199–203, 1983.

[6] C. E. Gooyers et. al., "The Impact of Posture and Prolonged Cyclic Compressive Loading on Vertebral Joint Mechanics," *Spine*, vol. 37, no. 17, pp. E1023–E1029, 2012.

[7] M. B. Panzer and D. S. Cronin, "C4–C5 segment finite element model development, validation, and load-sharing investigation," *J. Biomech.*, vol. 42, no. 4, pp. 480–490, 2009.

[8] M. Qasim et. al., "Initiation and progression of mechanical damage in the intervertebral disc under cyclic loading using continuum damage mechanics methodology: A finite element study," *J. Biomech.*, vol. 45, no. 11, pp. 1934–1940, 2012.

[9] T. Pitzen et. al., "Variation of endplate thickness in the cervical spine," *Eur. Spine J.*, vol. 13, no. 3, pp. 235–240, 2004.

[10] M. A. Adams and P. J. Roughley, "What is intervertebral disc degeneration, and what causes it?," *Spine*, vol. 31, no. 18, pp. 2151–2161, 2006.

[11] N. Bogduk et. al., "The nerve supply to the human lumbar intervertebral discs." *J. Anat.*, vol. 132, no. Pt 1, p. 39, 1981.

Copyright 2016 The Organizing Committee for the 2016 Summer Biomechanics, Bioengineering and Biotransport Conference

SB^{3}C2016
Summer Biomechanics, Bioengineering and Biotransport Conference
June 29 –July 2, National Harbor, MD, USA
SB^{3}C2016-836

APICAL INFLOW CANNULA ANGLE AND LEFT VENTRICULAR SIZE IMPACT LVAD THROMBOSIS RISK

Venkat Keshav Chivukula (1), Patrick McGah (1), Anthony R. Prisco (2), Jennifer A. Beckman (3), Guilherme J.M. Garcia (2), Claudius Mahr (3) & Alberto Aliseda (1)

(1) Department of Mechanical Engineering
University of Washington
Seattle, WA, USA

(2) Biotechnology and Bioengineering Center
Medical College of Wisconsin
Milwaukee, WI, USA

(3) Division of Cardiology
University of Washington
Seattle, WA, USA

INTRODUCTION

In the US alone, heart failure (HF) affects 2.4% of the population (> 5 million) and ~ 1 million new HF cases are reported annually, incurring annual direct expenditures of $31 billion in 2012 [1]. Due to the dearth of donor hearts and the increasing number of end-stage HF patients, left ventricular assist devices (LVAD) are increasingly being utilized as long-term destination-therapy (DT) devices [2]. However, neurologic events (especially embolic) continue to be one of the primary causes of mortality and morbidity in LVAD patients [3]. Blood flow through the inflow cannula and outflow graft is largely inertia-driven; consequently, hemodynamics in the left ventricle (LV) vary substantially between different surgical configurations.

While LVADs vary in their design (axial/ centrifugal flow), innovation in surgical LVAD inflow cannulation has remained stagnant, and implantation strategies vary widely among surgeons. The LVAD is connected to the heart and the circulatory system via an inflow cannula and outflow graft, with the inflow cannula typically placed in an apical orientation in the left ventricle. Thrombotic events from LVADs can be attributed to mechanisms such as non-physiological blood flow, hemolysis and subsequent platelet activation. A potential putative etiology of LVAD thrombosis is misalignment of the inflow cannula which has been described clinically but until now not quantified.

This project aims at elucidating the influence of LVAD inflow cannula angle configuration and the impact of LV size, on LVAD thrombogenicity, agnostic of LVAD design.

METHODS

This study used unsteady computational fluid dynamics (CFD), virtual surgery, in-vitro patient-specific flow visualization and PIV and Lagrangian analysis on 3D patient-specific models of the left ventricle to evaluate thrombogenic potential of LVAD inflow cannula orientation and LV size.

Virtual Surgery: Using a CT-derived, 3D patient-specific model of the LV, virtual surgery was performed via SOLIDWORKS and Vascular Modeling Toolkit software by implanting the LVAD inflow cannula at various orientations (-14^0, -7^0, 0^0, 7^0 and 14^0) with respect to surgical 0^0 (line connecting the mitral valve to the apex of the LV) (See Figure 1). LV size was varied by creating larger / smaller LV models and implanting a standard-sized LVAD inflow cannula at the apical location of the LV, with zero angle orientation.

CFD and boundary conditions: Tetrahedral meshes were created for all patient models using ANSYS ICEM CFD. Unsteady CFD was performed in ANSYS FLUENT (Ansys Inc., Canonsburg, PA) modeling blood as an incompressible Newtonian fluid with density ρ = 1060 kg/m^3 and dynamic viscosity μ = 0.0035 Pa-s, as well as a shear-thinning non-Newtonian fluid [4]. Platelet (particle) motion and behavior was analyzed using FLUENT's multi-phase simulation option (discrete phase for platelets). Inertialess platelets (particles) were released periodically from the mitral valve. Patient-specific pulsatile mitral valve flow (obtained from Echo Doppler measurements) was prescribed as inflow conditions, and was modulated based on cardiac output (Figure 1(b)). A pressure-implicit with splitting of operators (PISO) scheme was used for spatial calculations and a second-order implicit scheme was used for temporal calculations. Grid convergence was performed, and the resulting meshes contained between 2 and 3 million grid points, depending on the LVAD and LV configuration.

Copyright 2016 The Organizing Committee for the 2016 Summer Biomechanics, Bioengineering and Biotransport Conference

Minimum thrombogenic performance (MTP) evaluation: In addition to Eulerian parameters such as pressure and wall shear stress (WSS), Lagrangian tracking was performed on all platelets traversing through the computational domain. The particle stress history (SH) was obtained as SH = $\int_{t_0}^{t} \tau(X(t'), t')dt'$, where τ is the local instantaneous shear stress magnitude at time t' and $X(t')$ is the platelet's location at that time instance. Additionally, the residence time (RT) of the platelet was also recorded. MTP for each configuration was evaluated based on the SH and RT to determine levels of platelet activation.

RESULTS

Trajectories for neutrally-buoyant particles (surrogates for blood-suspended cells) were computed for 10 cardiac cycles. Comparison of the results for both particle RT and SH demonstrated that residence times and integrated shear-histories of particles that have exited the ventricle within 3 cardiac cycles was statistically the same, regardless of the inflow cannula position, within the middle of the range studied thus far [-7^0,$+7^0$]. After three cardiac cycles, a large number of stagnated platelets were found recirculating in the ventricle. A large increase of stagnated particles was found for the largest inflow cannula angles (-14^0 and $+14^0$), with the surgical 0^0 configuration presenting the lowest apparent thrombogenicity. Investigation of the effect of LV size revealed increased stagnation, higher cumulative shear history along the trajectories and increased global WSS for smaller ventricles.

DISCUSSION

Despite the LVAD throughput being many times the volume of the fully distended LV, a very large percentage (~ 40%) of blood-suspended particles entering the ventricle lingered even after 3-5 cardiac cycles. Stagnation zones (Figure 1 (c), (d) and (e)) indicate the possibility of some of these particles being trapped for much longer times (investigation is underway for further quantification), with increased potential of platelet activation, prior to entering the LVAD. Results thus far indicate that deviation away from the surgical 0^0 configuration is unfavorable and may have serious implications for thrombosis.

ACKNOWLEDGEMENTS

The authors thank Professor John LaDisa for assistance with this work. There are no financial disclosures to report.

REFERENCES

[1] Go, AS et al., *Circulation*, 129(3):399, 2014.
[2] Mancini, D and Colombo, PC, *J Am Coll Cardiol*, 65(23): 2542-55, 2015
[3] Najjar, SS et al., *J Heart Lung Transplant*, 33(1):23-34, 2014
[4] Chandran, KB et al, CRC Press, 2nd ed., 2012

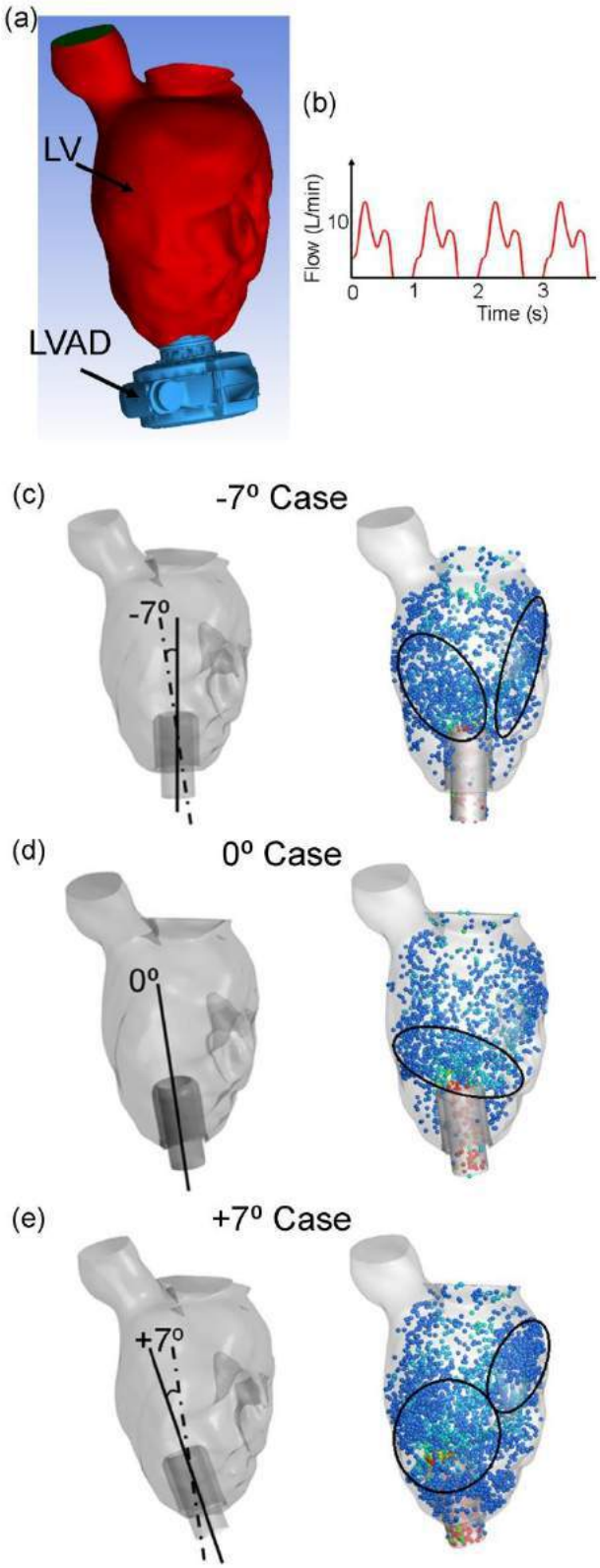

Figure 1 : (a) Patient-specific model of the LV (red) and LVAD (blue), (b) Unsteady blood flow rate obtained from patient measurements used as input to the model, (c), (d) and (e) Results for inflow graft placement simulations, (c) -7º case, (d) 0º case and (e) +7º case (Angles measured from surgical 0º). Shown on the left are the computational geometries, while on the right are platelet distributions in the ventricle one cardiac cycle after injection from the mitral valve. Note the increased accumulation of platelets near the walls and bottom of the ventricle for the -7 and +7 cases. Platelets so trapped in these regions have the potential to get activated, initiating a thrombus. LV: Left Ventricle, LVAD: Left Ventricular Assist Device

Copyright 2016 The Organizing Committee for the 2016 Summer Biomechanics, Bioengineering and Biotransport Conference

SB^{3}C2016
Summer Biomechanics, Bioengineering and Biotransport Conference
June 29 –July 2, National Harbor, MD, USA
SB^{3}C2016-837

EFFECT OF COMPACTION ON STRETCH SENSITIVITY IN FIBROBLAST-POPULATED COLLAGEN GELS

Kellen Chen (1), Jeffrey W. Holmes (1,2,3)

(1) Department of Biomedical Engineering
University of Virginia
Charlottesville, VA, USA

(2) Department of Medicine
University of Virginia
Charlottesville, VA, USA

(3) Robert M. Berne Cardiovascular Research Center
University of Virginia
Charlottesville, VA, USA

INTRODUCTION

Many cell types align in response to cyclic stretch, and this alignment response is thought to play an important role in function, such as shear stress sensing in endothelial cells and anisotropic scar tissue formation in skin, tendon, and heart. Interestingly, although most 2D *in vitro* stretch experiments cause cells to align perpendicular to applied cyclic stretch, *in vivo* fibroblasts and collagen in healing scar typically align parallel to stretch. Recently, Obbink-Huizer et al. proposed a hypothesis to explain this discrepancy [1]. They postulated that in tissue or in 3D culture systems, compaction transverse to the loading direction outweighs the cyclic stretching – in other words, cells still avoid strain, but they avoid the (larger) compaction strain more strongly than the (smaller) applied stretch.

To date, only limited experimental data are available to assess this hypothesis. Foolen et al. designed a collagen gel loading system that allowed them to perform either uniaxial cyclic stretching (in x_1 with x_2 left free to compact) or *strip* uniaxial cyclic stretching (in x_1 with x_2 constrained) [2]. In the gels that underwent uniaxial cyclic stretching, cells aligned parallel to the constraint, per previous studies. In the gels that underwent strip uniaxial cyclic stretching, most cells showed no alignment response. Foolen also found that alignment responses changed as gels were cultured longer prior to stretching, but the role of compaction in this phenomenon was unclear. In order to better separate the alignment responses of rat cardiac fibroblasts to compaction vs. stretch in 3D culture, we developed a system that allows us to independently prescribe compaction in the loading and transverse directions, prior to and during the application of cyclic uniaxial stretch.

METHODS

Adult rat cardiac fibroblasts were isolated from Sprague-Dawley rats and used to populate collagen gels using published methods [3]. Gels were poured into negative PDMS (Dow Corning, Sylgard 184 Silicone Elastomer Kit) cruciform molds with small sponges at the arms and allowed to polymerize for 4h in the incubator in a 100mm X 15 mm Petri dish. Petri dishes were pre-coated with a 1-2mm layer of PDMS to prevent collagen from adhering to the surface of the dish. Then, the gel was either isotropically restrained for 24h (prerestrain) by pushing two small pins through each sponge into the PDMS layer, or the gel was allowed to float free and isotropically compact (precompact) for 24h.

An overview of all loading conditions can be found in Table 1. Nineteen prerestrained gels were fabricated. Three gels were fixed after the initial 24h period to serve as controls. The remaining gels were transferred to CellScale MechanoCulture B1 devices (for pictures and videos of the devices, see [4]). In the devices, four gels were uniaxially constrained in the x_1 direction, four were subjected to uniaxial cyclic stretch in the x_1 direction, four were equibiaxially constrained, and four were subjected to strip uniaxial cyclic stretch (stretch applied in the x_1 direction and x_2 direction held fixed). Thirteen precompacted gels were fabricated. Three gels served as control gels, five gels were uniaxially constrained in the x_1 direction, and five were subjected to uniaxial cyclic stretch in the x_1 direction. Cyclic stretch was performed at 10% amplitude and 0.5Hz.

After the stretch protocols, the gels were fixed in 10% formalin for 24h and the F-actin was stained using Alexa Fluor 488 Phalloidin (Thermo Fisher Scientific, A12379). A confocal microscope captured z-stacks through the entire thickness at three different xy-locations in the center of each gel. The resultant images were converted to binary (fluorescent pixels = white, dark pixels = black), and white pixel clusters above a certain size threshold were identified as cells. Using MATLAB, each cell's centroid and boundary were identified, and vectors originating from the centroid and ending around the cell

Copyright 2016 The Organizing Committee for the 2016 Summer Biomechanics, Bioengineering and Biotransport Conference

boundary were created. The radius and angle of each vector was used to compute the direction (mean angle, MA) and the degree of cell alignment (mean vector length, MVL).

Table 1: Summary of gel culture and mechanical loading conditions. Prerestrain: 24h control (green), uniaxial constraint/cyclic (blue), equibiaxial constraint/strip uniaxial cyclic (light blue). Precompact: 24h control (orange), uniaxial constraint/cyclic (red). Numbers in parenthesis indicate the number of gels.

Culture Conditions before load t=0h → 24h	Mechanical Loading Conditions t=24h → 48h
Prerestrained gels (19)	None, fixed after initial 24h (3)
	Uniaxial constraint (4)
	Uniaxial 10% cyclic (4)
	Equibiaxial constraint (4)
	Strip uniaxial 10% cyclic (4)
Precompacted gels (13)	None, fixed after initial 24h (3)
	Uniaxial constraint (5)
	Uniaxial 10% cyclic (5)

Cells with MVL ≤ 0.3 were classified as circular (unaligned), cells with MVL > 0.3 and $-45^o < MA < 45^o$ were classified as parallel, and cells with MVL > 0.3 and $45^o < MA < 90^o$ or $-90^o < MA < -45^o$ were classified as perpendicular. Note that stretch was always applied in the x_1 direction, which corresponds to 0^o. The MVL threshold was determined by visual assessment of the MVLs assigned to differently shaped cells. Differences in the fraction of circular cells and parallel cells were each assessed with one-way ANOVA followed by Tukey multiple comparisons post hoc tests (Prism, GraphPad Software, San Diego, CA).

RESULTS

Prerestrained control gels showed similar numbers of circular, parallel, and perpendicular cells after 24h of culture (Fig. 1). Uniaxial cyclic stretching for an additional 24h induced a significant increase in the fraction of circular cells compared to control ($p<0.001$, Fig. 1); these uniaxially stretched gels also contained more circular cells and fewer cells aligned parallel to the loading axis than gels constrained uniaxially but not stretched ($p<0.01$, Fig. 1).

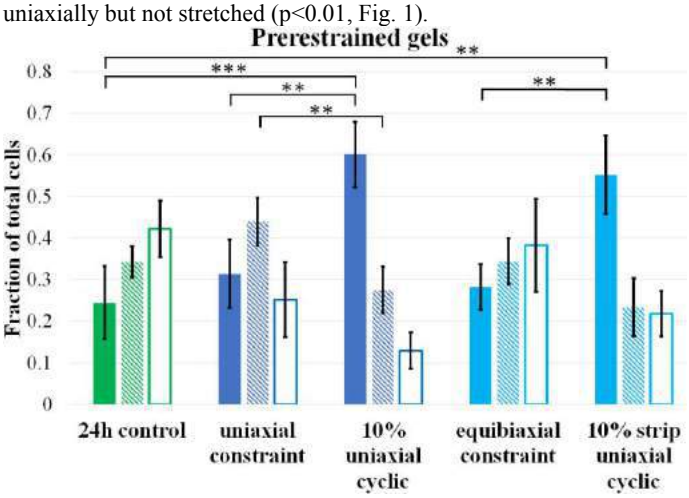

Figure 1: Fraction of circular (solid), parallel (striped), and perpendicular (open) cells in prerestrained gels following mechanical loading. Bars are color coded to match Table 1.

Gels undergoing either uniaxial constraint or uniaxial cyclic stretch were free to compact transversely; we next performed equibiaxial constraint and strip uniaxial stretch tests to eliminate this transverse compaction and isolate the effects of stretch. In these tests, the fraction of circular cells still increased during cyclic stretch compared to equibiaxial constraint ($p<0.01$) and control ($p<0.01$), with no significant changes in number of parallel cells (Fig. 1).

Finally, we examined the effect of precompaction. About half the cells in precompacted, uniaxially constrained gels aligned parallel to the direction of constraint (Fig 2). In contrast to prerestrained gels, precompacted gels subjected to uniaxial cyclic stretch showed no significant change in cell distributions compared to gels under uniaxial constraint. Thus, allowing the gels to compact before mechanical loading appeared to reduce cell responsiveness to stretch.

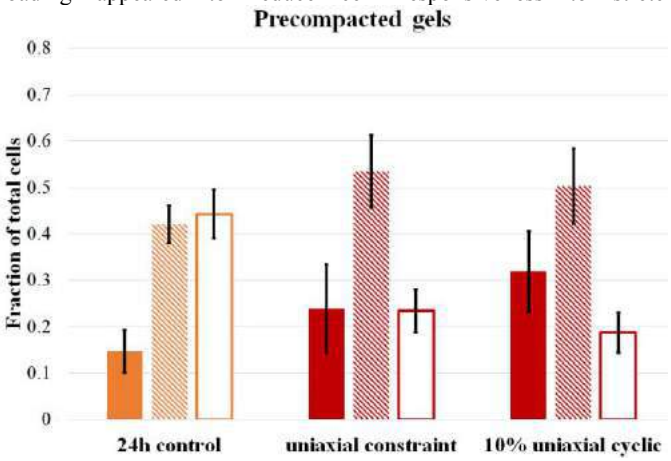

Figure 2: Fraction of circular (solid), parallel (striped), and perpendicular (open) cells in precompacted gels following mechanical loading. Bars are color coded to match Table 1.

DISCUSSION

We performed tests aimed at separating the effects of compaction and applied stretch. Gels that were restrained for 24h (prerestrained) showed significant changes in cell alignment in response to 10% cyclic stretch, compared to gels that were constrained but not stretched. Unexpectedly, these responses did not depend strongly on whether the direction transverse to the stretching axis was free to compact (uniaxial cyclic case) or prevented from compacting (strip uniaxial cyclic case). Regardless of transverse boundary conditions, cyclic stretch in the x_1 direction induced a significant increase in the number of circular cells. The reason for the large number of circular cells observed in these experiments is unclear. One possibility is that this represents a transition state for cells that are changing alignment in response to mechanical stretch; experiments to evaluate the evolution of this response at later time points are underway. Because we saw similar responses at 2.5% and 5% cyclic stretch (data not shown), it seems unlikely that the increase in number of circular cells reflects stretch-induced cell damage.

In contrast to prerestrained gels, gels that were allowed to compact for 24h (precompacted) prior to stretch showed no difference in cell alignment when stretched cyclically or simply constrained. Thus, we conclude that compaction of fibroblast-populated collagen gels alters the fibroblast alignment response to cyclic stretch. We hypothesize that compaction may decouple macroscopic and microscopic (cell-level) strains by altering collagen gel structure.

ACKNOWLEDGMENTS

This study was supported by the National Science Foundation (CMMI 1332530, JWH) and the National Institute of General Medical Sciences (5T32 GM008715, KC).

REFERENCES

[1] Obbink-Huizer, C, *Biomech Model Mechanobiol*, 13:227–36, 2014 [2] Foolen, J, *Biomaterials*, 33:7508–7518, 2012 [3] Thomopoulos, S, *J Biomech Eng*, 129:642–50, 2007 [4] http://cellscale.com/products/mechanoculture-specimens/

Copyright 2016 The Organizing Committee for the 2016 Summer Biomechanics, Bioengineering and Biotransport Conference

SB^{3}C2016
Summer Biomechanics, Bioengineering and Biotransport Conference
June 29 –July 2, National Harbor, MD, USA
SB^{3}C2016-838

NATIVE CARDIAC OUTPUT AND SURGICAL IMPLANTATION CONFIGURATION MAY INFLUENCE LVAD THROMBOSIS RISK

Venkat Keshav Chivukula (1), Patrick McGah (1), Anthony R. Prisco (2), Jennifer A. Beckman (3), Guilherme J.M. Garcia (2), Claudius Mahr (3) & Alberto Aliseda (1)

(1) Department of Mechanical Engineering
University of Washington
Seattle, WA, USA

(2) Biotechnology and Bioengineering Center
Medical College of Wisconsin
Milwaukee, WI, USA

(3) Division of Cardiology
University of Washington
Seattle, WA, USA

INTRODUCTION

Heart failure (HF) affects 2% of the US population, and over 1 million new cases are reported annually, incurring an annual treatment cost of over $30 billion [1]. Dearth of donor hearts and increasing HF cases have led to left ventricular assist devices (LVAD) transitioning from their original intended purpose of bridge-to-transplant (BTT) to long-term destination therapy (DT) devices [2]. VAD patients remain at elevated risk for cerebrovascular events, with high incidence of ischemic stroke, one of the most devastating complications of this therapy [3]. In the light of increasing use of LVADs as DT devices, focus is shifting to reduce thrombogenicity of LVADs and to re-evaluate implantation strategies.

The LVAD is surgically connected to the heart and circulatory system via an inflow cannula and outflow graft, with the outflow graft typically anastomosed to the aortic arch, proximal to the brachiocephalic artery and distal to the aortic sinus.. Primarily previous studies have focused on flow across the LVAD with little emphases on other factors such as; implantation, blood pressure and native cardiac output management. Additionally, in most studies, focus was only on global flow parameters in an Eulerian frame of study such as wall shear stress.

This project aims at elucidating the influence of LVAD outflow graft anastomosis configuration, and the coupling of intermittent aortic valve opening, on LVAD thrombogenicity, agnostic of LVAD design.

METHODS

This study used unsteady computational fluid dynamics (CFD), virtual surgery and Lagrangian analysis on 3D patient-specific models of the aortic arch and great vessels to determine efficient LVAD implantation and blood pressure management strategies.

Virtual Surgery: Using a CT-derived, 3D patient-specific model of the aortic arch and great vessels, virtual surgery was performed by anastomosing LVAD outflow grafts at different configurations (45^0, 60^0 and 90^0) to the aortic root (Figure 1 (a)). Virtual surgery was performed using software such as SOLIDWORKS and Vascular Modeling Toolkit.

CFD and boundary conditions: Tetrahedral meshes were created for all patient models using ANSYS ICEM CFD. Unsteady CFD was performed in ANSYS FLUENT (Ansys Inc., Canonsburg, PA) modeling blood as an incompressible Newtonian fluid with density ρ = 1060 kg/m^3 and dynamic viscosity μ = 0.0035 Pa-s. Platelet (particle) motion and behavior was analyzed using FLUENT's multi-phase simulation option (discrete phase for platelets). Inertialess platelets (particles) were released periodically from the LVAD outflow graft and intermittently from the aortic valve (see below, Figure 1 b and c). A continuous flow boundary condition was used for the inlet (LVAD outflow graft), and physiologically relevant peripheral vascular resistances were used in a lumped parameter model at the outlets. A pressure-implicit with splitting of operators (PISO) scheme was used for spatial calculations and a second-order implicit scheme was used for temporal calculations. Grid convergence was performed, and the resulting meshes contained between 2 and 3 million grid points, depending on the LVAD configuration.

Native cardiac output management: To investigate the influence of intermittent aortic valve opening, unsteady flows at different frequencies and ejection fractions were integrated into a left ventricle inflow model. The ejection frequency was programmed for one partial ejection every 2 – 6 cardiac cycles. Platelets (particles) were ejected from the aortic valve inlet during every ventricular ejection.

Copyright 2016 The Organizing Committee for the 2016 Summer Biomechanics, Bioengineering and Biotransport Conference

Minimum thrombogenic performance (MTP) evaluation: In addition to Eulerian parameters such as pressure and wall shear stress (WSS), lagrangian tracking was performed on platelet surrogates traversing through the computational domain. The particle stress history (SH) was obtained as SH = $\int_{t_0}^{t} \tau(X(t'), t')dt'$, where τ is the local instantaneous shear stress magnitude at time t' and $X(t')$ is the platelet's location at that time instance. Additionally, the residence time (RT) of the platelet was also recorded. MTP for a particular configuration was evaluated based on the SH and RT to determine levels of platelet activation and accumulation.

RESULTS

LVAD outflow graft configurations: Global WSS was reduced for acute angles at one location (aorta near the root of the brachiocephalic branch), but no configuration globally minimized the WSS on the arterial walls. However, Lagrangian tracking of suspended platelets (discrete particles) revealed significant hemodynamic changes for the various configurations. The particles' SH and RT indicated that the percentage of particles with long RT and elevated SH decreased strongly for acute angles (Figure 1, (d) and (e)).

Intermittent aortic valve opening: Maximum global WSS resulting from the impingement of the jet from the LVAD outflow graft was reduced due to aortic valve opening, as the aortic flow coupled with the impinging jet, reducing the stagnation point flow on the contralateral wall. Here, too, suspended platelet tracking analysis revealed reduced SH and RT for acute configurations with the aortic valve opening once every 5 cardiac cycles. More importantly, the intermittent aortic flow aided in the early transport of stagnated particles just distal to the aortic valve, thereby reducing the time for platelet activation.

DISCUSSION

Optimal outflow graft configuration analysis can be performed based on suspended cell tracking computations. This study suggests that acute graft angle configurations minimize thrombogenicity by lowering the integrated shear stress 'felt' by the platelets and their residence times. Aortic valve opening, even at low cardiac output and low frequency (half the natural ejection volume occurring once every 5 cardiac cycles) reduced Wall Shear Stress compared to no Aortic Valve opening. Thus, a VAD management strategy permitting intermittent aortic valve opening coupled with acute angle (~45^0 - 60^0) LVAD outflow graft implantation could potentially reduce stroke risk.

ACKNOWLEDGEMENTS

The authors thank Professor John LaDisa for assistance with this work. There are no financial disclosures to report.

REFERENCES

[1] Go, AS et al., *Circulation*, 129(3):399, 2014.
[2] Mancini, D and Colombo, PC, *J Am Coll Cardiol*, 65(23): 2542-55, 2015
[3] Najjar, SS et al., *J Heart Lung Transplant*, 33(1):23-34, 2014

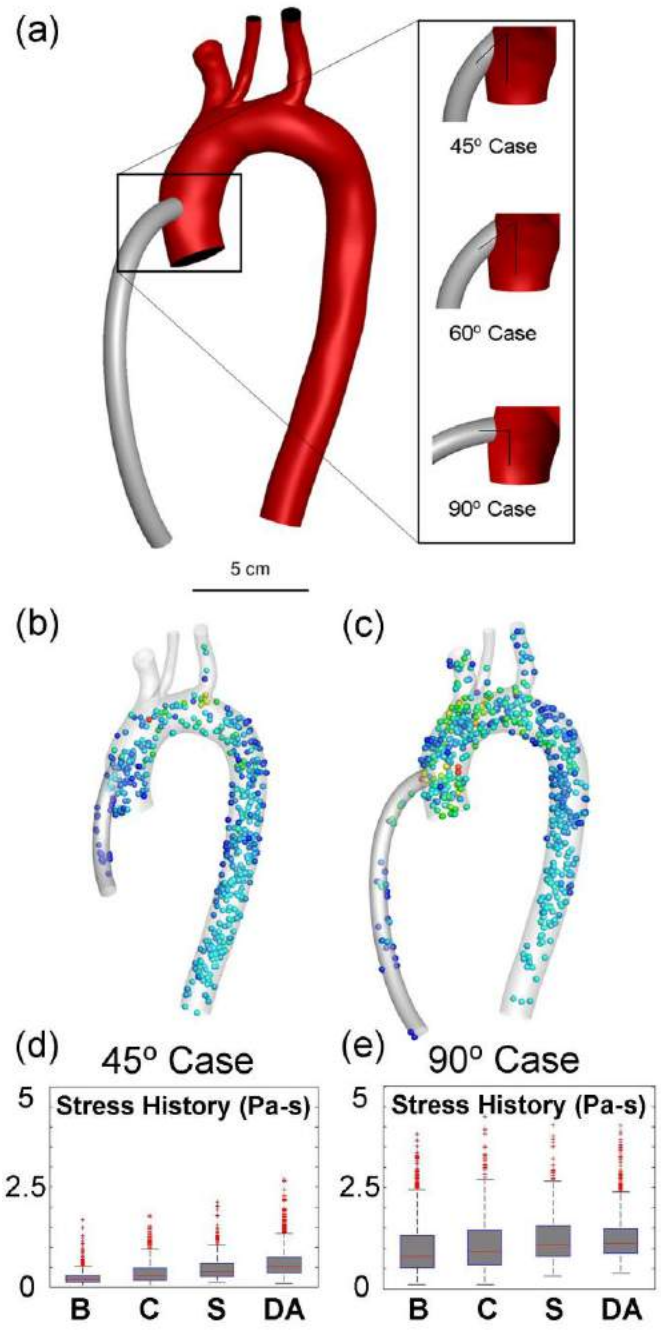

Figure 1: Preliminary results for outflow graft placement simulations (a) Three virtually anastomosed configurations of the LVAD outflow graft, (b) and (c) Snapshots of platelet locations 1 second after ejection from outflow graft for 45° and 90° cases, respectively, (d) and (e), Box-and-whisker plots of cumulative platelet stress histories after 3 cardiac cycles for 45° and 90° cases, respectively. Note the reduced cumulative shear stress histories and tighter distributions for the acute (45°) case. B: brachiocephalic, C: common carotid, S: subclavian and DA: descending aorta.

Copyright 2016 The Organizing Committee for the 2016 Summer Biomechanics, Bioengineering and Biotransport Conference

SB^{3}C2016
Summer Biomechanics, Bioengineering and Biotransport Conference
June 29 –July 2, National Harbor, MD, USA
SB^{3}C2016-839

DEVELOPMENT OF AN ISOTHERMAL VITRIFICATION MATRIX AND METHOD FOR THE ROOM TEMPERATURE STABILIZATION OF PROTEINACEOUS CANCER BIOMARKERS IN ARCHIVAL HUMAN SERA

Morwena J. Solivio, Ph.D., Goeun Heo, M.S., Alptekin Aksan, Ph.D.

Biostabilization Laboratory, Department of Mechanical Engineering, University of Minnesota, Minneapolis, MN 55455, USA

INTRODUCTION

There are approximately 600 million liquid biospecimens including serum and plasma collected from patients, currently stored in biorepositories across the U.S. and the world, with the number increasing at a rate of 20 million samples per year **(1)**. These biospecimens are generally stored for future biomarker research and verification, where the availability of high quality biospecimens is integral. However, even when best practices are followed, and the biospecimens are frozen immediately after collection and processing, cryogenic storage, and freeze-thaw alone, can impose harsh chemical and mechanical stresses that can damage proteinaceous biomarkers and significantly compromise sample quality. Additionally, cryogenic storage is costly, with an estimated cost of $100 million annually **(2)**.

This research focuses on developing a room temperature stabilization technology for storing achievable serum and plasma samples. A sugar based electrospun matrix is designed to adsorb and isothermally vitrify liquid biospecimens. When vitrified, all biochemical reactions in the biospecimen can be stopped without exposure to extreme stresses induced by cryogenic storage and freeze-thaw **(3)**. The removal of water during isothermal vitrification will significantly reduce sample volume and storage requirement, while room temperature stabilization will not only reduce storage cost but also make the samples less vulnerable to failures such as power shortage, equipment breakdown and human error that can occur in cryogenic storage facilities. Additionally, this technology will eliminate the need for thawing, re-aliquoting and re-freezing of large samples (which are known to introduce sample modifications), since dried samples can be readily divided by breaking them into smaller pieces.

METHODS

To produce the sugar-based electrospun matrix, a solution containing 1.2 M trehalose (TRE) and 0.025 M dextran (DEX) was rigorously mixed for 24 hours. The solution was then electrospun at a flowrate of 0.003 mL/min through a 15 kV gradient across a 15 cm gap. Electrospun woven matrices were then stored into disks, placed in 24-well plates and stored in a vacuum chamber before use. Five low concentration excipients, known to impede various protein denaturation mechanisms were added at their identified optimum concentration. The selected excipients and their concentrations are: 1.5% glycerol, 1% PEG, 0.1% Tween 20, 0.3% gluconic acid and 0.2% glucamine.

Lactate dehydrogenase (LDH), a known freeze-thaw sensitive cancer biomarker was used for matrix optimization. A model serum solution containing 50 mg/mL bovine serum albumin (BSA) was spiked with 8 μg/mL LDH and 150 μL was added to 250 mg electrospun matrix. The samples were then dried in a vacuum chamber prior to re-suspension and subsequent enzymatic activity analysis. Enzymatic activity of treated samples was compared with values obtained for the untreated (fresh) control (taken as 100%).

The optimized matrix was further validated using four additional biomarkers: C-reactive protein (CRP), prostate specific antigen (PSA), matrix metalloproteinase-7 (MMP-7), and C3a, representing various storage sensitivities. The upper limit concentrations of the test biomarkers were spiked into the model serum prior to isothermal vitrification. Enzyme-linked immunosorbent assay (ELISA) was conducted to measure protein recovery. All experiments were conducted in at least 3 replicates. A two-tailed student's t-test was used to measure statistical significance of recovery between desiccated samples and the fresh control.

Copyright 2016 The Organizing Committee for the 2016 Summer Biomechanics, Bioengineering and Biotransport Conference

RESULTS

To produce the electrospun isothermal vitrification matrix, a high voltage differential was utilized to extrude the viscous lyoprotectant cocktail to form fibers of 4-5 µm in diameter (***Figure 1A,B***). Multiple layers of fibers were woven together and dried to produce a very adsorbent and porous matrix (the sponge) (***Figure 1C***). Electrospun matrices were compacted in 24-well plates (250 ± 5 mg/well) and vacuum dried for 24 hours to reduce their water content, which helped increase the glass transition temperature (T_g). Using LDH as the model protein, the matrix was further optimized to include low concentration excipients known to inhibit various protein denaturation mechanisms. The excipients, glycerol, PEG, Tween 20, gluconic acid and glucamine were included in the optimized matrix at the concentration that results to the maximum LDH stabilization. LDH in the model serum subjected to isothermal vitrification in the basic matrix, exhibited 92±2% activity compared to the un-treated, fresh control set at 100% **(Figure 2)**. Addition of all five excipients to the matrix at their optimum concentration, resulted to a recovery of 104±3% (P = 0.14). To validate these results, the optimized matrix was further tested using four additional biomarkers selected for their sensitivities to various storage conditions. **CRP** is a biomarker exhibiting remarkable stability to freezing, freeze-thaw, refrigeration and room temperature storage (**Figure 3A)**. Desiccation of the model serum solution in the basic matrix resulted in 82 ±5 % recovery, while desiccation with the optimized matrix enabled complete stabilization of the protein with 99 ± 3% recovery (P = 0.58). **PSA** is a biomarker that is relatively stable during cryogenic and refrigerated storage, and during repeated freeze/thaw (**Figure 3B**). Desiccation of PSA in the basic matrix resulted to a significantly reduced protein level of 59 ± 16% compared to the control. Isothermal vitrification in the optimized matrix increased post re-hydration recovery to 99 ± 4% (P = 0.47). **MMP-7** is highly sensitive to freeze/thaw (**Figure 3C**). A recovery of 84 ± 4% was obtained when the biomarker was desiccated in the basic matrix. Recovery increased to 94 ± 3% (P = 0.00154) when the sample was isothermally vitrified in the optimized matrix. **C3a** is freeze-stable, however is sensitive to refrigerated storage and against repeated freeze/ thaw (**Figure 3D)**. Samples desiccated in the basic matrix resulted in 82 ± 3% recovery, while samples isothermally vitrified in the optimized matrix had a recovery of 106±1% (P = 0.003). Similar to MMP-7, C3a is among the more vulnerable biomarkers and the p-value showed significant difference in the recovery of samples desiccated in the optimized matrix compared to fresh control.

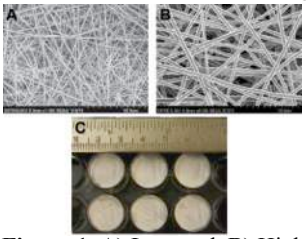

Figure 1. A) Low and, **B)** High magnification SEM images of the electrospun adsorbing/dissolving matrix, **C)** The matrix packaged in a 24-well plate, ready for us

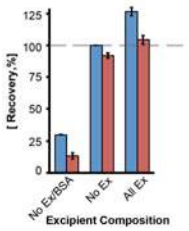

Figure 2. Matrix optimization. LDH activity after desiccation in the basic matrix resulted to 92±2% recovery. Addition of low concentration excipients resulted to complete stabilization of the enzyme (n=3).

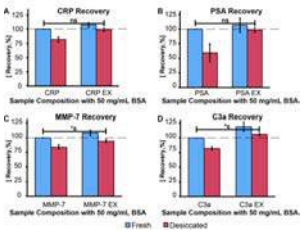

Figure 3. Validation of stabilization by the optimized matrix with selected proteinaceous biomarkers representing various storage sensitivities. A) CRP, B) PSA, C) MMP-7, and **D) C3a**. Error bars represent standard deviation from at least three independent experiments. Statistically significant and significant difference based on p-value calculations are denoted by ***s** and **ns, respectively.**

DISCUSSION

Cryogenic storage is currently the most ubiquitously adopted method of biospecimen preservation in biobanks and biorepositories **(2)**. Many biospecimens are stored at -20, -40, -80^{o}C or in liquid nitrogen without following any optimized biopreservation protocols, imposing harsh stresses, and damaging proteinaceous biomarkers by mechanisms such as cold denaturation, binding and aggregation at the ice interface, degradation due to ionic gradients and pH swings (**4-6)**, in addition to the high cost associated with cryogenic storage facilities.

In this work, developed a stabilization material (an electrospun matrix containing an optimized lyoprotectant cocktail) and methodology for room temperature storage of liquid biospecimens as a potential alternative to cryogenic storage. The adsorbing/dissolving matrix developed here takes advantage of capillary action induced by the porous nature of the electrospun lyoprotectant matrix (**Figure 1B, C**) to bypass the challenges associated with mixing of high concentrations of lyoprotectants (1-2M), required to effectively stabilize biological samples by isothermal vitrification.

The composition of the lyoprotectant matrix has been optimized to protect a wide variety of cancer biomarkers to ensure that functional clinical assay values on the day of collection match the values post-storage within 5% of the measured value. A downside of isothermal vitrification is the long drying times, which can introduce modifications, since until the sample is vitrified, the biomolecules are mobile and can undergo processes such as unfolding, proteolytic degradation, and aggregation. To accelerate drying, we employed vacuum drying and achieved > 90% water removal within 4 hours. This matrix and method, resulted to a T_g of >4^{o}C after 4 hours of desiccation, allowing for storage in a regular refrigerator. Furthermore, we demonstrated stabilization of test proteins LDH, CRP, PSA, MMP-7 and C3a, with a minimum recovery of 94%, making this a promising method to target stabilization of an expanded number of protein biomarkers and an excellent alternative to cryogenic storage.

ACKNOWLEDGEMENT

This research is funded by an NIH IMAT grant (5R21CA157298-03)

REFERENCES

[1] Shabikani, M et al., *Clin Biochem*, 47:258-266, 2014.
[2] Vaught, JB et al., *Cancer Epidemiol Biomarkers Prev*, 21:253-255, 2012.
[3] Less, R et al., *Cryobiology,* 66:176-185, 2013.
[4] Lopez, CF et al., *J of Phys Chem B*, 112:5961-5967, 2008.
[5] Twomey, A et al., *J of Phys Chem B*, 117:7889-7897, 2013.
[6] Twomey, A et al., *Int J Pharm*, 487: 91-100, 2015.

Copyright 2016 The Organizing Committee for the 2016 Summer Biomechanics, Bioengineering and Biotransport Conference

SB^{3}C2016
Summer Biomechanics, Bioengineering and Biotransport Conference
June 29 –July 2, National Harbor, MD, USA
SB^{3}C2016-840

ADVENTITIAL REMODELING IN HYPERTENSION LEADS TO AORTIC MALADAPTATION AND LOSS OF FUNCTION

Matthew R. Bersi (1), Chiara Bellini (1), Jing Wu (2), Kim Ramil C. Montaniel (2), David G. Harrison (2), Jay D. Humphrey (1)

(1) Department of Biomedical Engineering
Yale University
New Haven, Connecticut, USA

(2) Departments of Medicine and Pharmacology
Vanderbilt University
Nashville, Tennessee, USA

INTRODUCTION

Hypertension has long been identified as a clinical risk factor for chronic vascular disorders such as heart attack, stroke, and renal failure [1]. Increased understanding of the relationship between hypertension and arterial mechanics suggests that increased large artery stiffness can lead to essential hypertension and increased pulse pressure [2]. Conversely, arteries have been long known to stiffen in response to the increases in intramural stresses that arise as a result of increased blood pressure [3]. Thus, central artery stiffening can be both a cause and consequence of hypertension, likely occurring through a complex relationship between local wall mechanics and global hemodynamics. One emerging concept is the critically important role of inflammation in hypertension. In particular, although mechanical factors are fundamental to both aortic wall structure and hemodynamics, little attention has focused on characterizing the aortic mechanical properties in the pro-inflammatory angiotensin II (Ang II) infusion model of hypertension. Toward this end, the current study presents a detailed analysis of biaxial wall mechanics following 2 or 4 weeks of Ang II infusion. In particular, we quantified both the transmurally averaged and layer-specific (media and adventitia) mechanical properties in order to identify the bulk mechanical behavior of the aorta as a whole, as well as understand the differential loads experienced by medial and adventitial cells. Our analyses suggest that early hypertensive remodeling is mechanically maladaptive and ultimately compromises the ability of the aorta to store elastic energy during systole, which is the primary mechanical function of large elastic arteries.

METHODS

Animal Model - Hypertension was induced in 3 month old male wild-type (C57BL/6) mice by Ang II infusion (490 ng/kg/min). Age-matched controls underwent a Sham procedure and were infused with normal saline [4]. Blood pressure was measured at regular intervals over the 4-week study period by telemetry. At the designated experimental time point, mice were euthanized and the descending thoracic aorta (from the left subclavian to the third pair of intercostal branches) was excised for mechanical testing.

Biaxial Mechanical Testing and Analysis – Excised samples were cleaned, branches ligated, and cannulated onto glass micropipets for mechanical testing using a custom computer-controlled biaxial device [5]. Specimens were placed in a Hanks buffered physiologic solution at 37^{o}C and subjected to mechanical preconditioning (cyclic pressurization near the *in vivo* axial stretch). The unloaded configuration (outer diameter, axial length, and wall thickness) was then recorded, the *in vivo* axial stretch was estimated based on the force-pressure relationship, and vessels were subjected to a series of 3 cyclic pressure-diameter protocols (from 10 to 140 mmHg at 0.95, 1.0, and 1.05 times the *in vivo* axial stretch) and 4 cyclic axial force-length protocols (from 0 to 40 mN at 10, 60, 100, and 140 mmHg), with data points continuous recorded on-line for the 7 protocols [6]. Material property characterization was then performed using an appropriate constitutive equation for describing either the bulk or layer-specific behaviors [7]. For example, the constitutive equation W (Eq.1) was used to describe the contribution of elastin (c) and four families of locally parallel collagen fibers (c_1^j, c_2^j) to the transmurally averaged material properties of the aortic wall.

$$W\left(\mathbf{C}, \mathbf{M}^j\right) = \frac{c}{2}(I_\mathbf{C} - 3) + \sum_{j=1}^{4} \frac{c_1^j}{4c_2^j}\left\{\exp\left[c_2^j\left(IV_\mathbf{C}^j - 1\right)^2\right] - 1\right\}, \qquad (1)$$

Following mechanical testing, aortas were fixed overnight in a 10% neutral buffered formalin solution, embedded in paraffin, sectioned

Copyright 2016 The Organizing Committee for the 2016 Summer Biomechanics, Bioengineering and Biotransport Conference

serially, and stained for structural proteins of interest, namely collagen, elastin, and smooth muscle cells. Complete cross-sections were imaged at 40x magnification and a custom MATLAB script was used to extract areal wall composition and the percentage of the wall occupied by media or adventitia. Metrics of interest were compared across all three study groups (n = 5; Sham, 2-week Ang II, and 4-week Ang II) using a one-way ANOVA followed by a post-hoc Bonferroni correction with a value of $P < 0.05$ considered significant.

RESULTS

Ang II infusion increased blood pressure from 121/99 mmHg (Sham) to 167/133 mmHg at 2 weeks and 172/129 mmHg at 4 weeks (Figure1A). This induced hypertension resulted in dramatic vascular remodeling that was biaxial in nature. Namely, thoracic aortas at both 2 and 4 weeks exhibited a similar reduced capability to circumferentially distend in response to changes in pressure and reduced capability to axially extend in response to changes in axial force. Importantly, it is this biaxial reduction in distensibility and extensibility that lead to a reduction in elastic energy storage capability upon biaxial loading (Figure 1B). Biaxial wall stresses were also was significantly reduced following hypertension, primarily due to increased wall thickness (>100 vs. 39 μm, P<0.001) and a reduced *in vivo* axial stretch (<1.35 vs. 1.62, P<0.001) leading to a decrease in *in vivo* axial force. Circumferential material stiffness was not statistically different after hypertension, whereas axial material stiffness was significantly lower (<2.45 vs. 3.84 MPa, P<0.001) due to the reduced axial stretches. Layer-specific histological analysis revealed that, on average, Ang II samples had an increased adventitial burden (30% in Sham versus 56% in Ang II, Figure 1C). Using a bilayered modeling approach, hypertension was found to increase both circumferential stress and material stiffness in the adventitia, relative to Sham. Furthermore, simulation of acute pressure increase predicted a greater percent increase in biaxial stress in the adventitia versus the media, illustrating the protective mechanical role of the adventitia. Despite a striking maintenance of overall circumferential stiffness, hypertension ultimately resulted in early maladaptive geometric, material, and structural changes in the descending thoracic aorta, primarily through excessive adventitial remodeling, that results in a loss of vascular function.

DISCUSSION

This study demonstrates, for the first time, that angiotensin-induced hypertension has a marked effect on both the circumferential and axial wall properties, and that the observed remodeling is preferentially adventitial. Additionally, the remodeling appears to be established as early as 2 weeks after infusion and is maintained for at least 4 weeks. The primary mechanical function of large arteries – to sustain blood flow during diastole [8] – is thus compromised due to the inability to effectively store elastic energy. Nonetheless, increasing evidence suggests that intramural cells seek to maintain local wall properties near homeostatic values [9]. Interestingly, the observed axial stretch reduction tends to maintain the circumferential material stiffness near the mechanobiologically preferred Sham values.

The excessive adventitial fibrosis following hypertension could be a result of either dysfunctional mechanosensing [10] or any number of contributors leading to collagen production. Indeed, the adventitia is a biologically complex layer that is both a source of progenitor and inflammatory cells and is involved in arterial remodeling and injury responses [11,12]. Interestingly, both pressure-induced mechanical stresses and angiotensin-induced inflammation via the activation of the AT_1 receptor are synergistic in their production of extracellular matrix [13], and, consistent with the current observations, it is likely the combination of the two that is contributing to the exuberant adventitial matrix production. Of note, several models of hypertension report similar adventitial collagen deposition, thus the current findings of maladaptive wall mechanics are likely not specific to Ang II, but rather are generally relevant to models of hypertension.

In summary, the present experimental findings and computational results suggest that hypertension preferentially increases circumferential stress within the adventitial layer, the primary site of matrix deposition and remodeling. Because the bulk aortic response is mechanically maladaptive, the production of adventitial collagen appears to likely result from a combined inflammatory response. Although current clinical assessments of arterial stiffening focus on intimal-medial thickening, our results suggest a need to shift the focus to the adventitia, and in particular adventitial inflammation, which we show can compromise the vascular function of an otherwise competent aortic media.

ACKNOWLEDGEMENTS

This work was supported, in part, by grants from the NIH (R01-HL105294, R01-HL105297) and NSF (CMMI-1161423).

REFERENCES

[1] O'Rourke, MF et al., *J Am Coll Cardiol*, 50(1):1-13, 2007. **[2]** Laurent, S et al., *Eur Heart J*, 27(21):2588-2605, 2006. **[3]** Vogt, M et al., *Circulation*, 111(24):3269-3273, 2005. **[4]** Wu, J et al., *Circ Res*, 114(4):616-625, 2014. **[5]** Gleason RL, et al., *J Biomech Eng,* 126(6):787, 2004. **[6]** Ferruzzi, J et al., *Ann Biomed Eng,* 41(7):1311-1130, 2013. **[7]** Bellini, C et al., *Ann Biomed Eng,* 42(3):488-502, 2014. **[8]** Ferruzzi, J et al. *J Biomech Eng, 1*37(3):031007, 2015. **[9]** Shadwick, RE, *J Exp Biol*, 202(23):3305-3313, 1999. **[10]** Humphrey, JD et al., *Nat Rev Mol Cell Biol,* 1-11, 2014. **[11]** Majesky, MW et al., *Arterioscler Thromb Vasc Biol,* 31(7):1530-39, 2011. **[12]** Maiellaro, K et al., *Cardiovasc Res*, 75(4):640-648, 2007. **[13]** Bardy, N et al., *Circ Res,* 79(1):70-78, 1996.

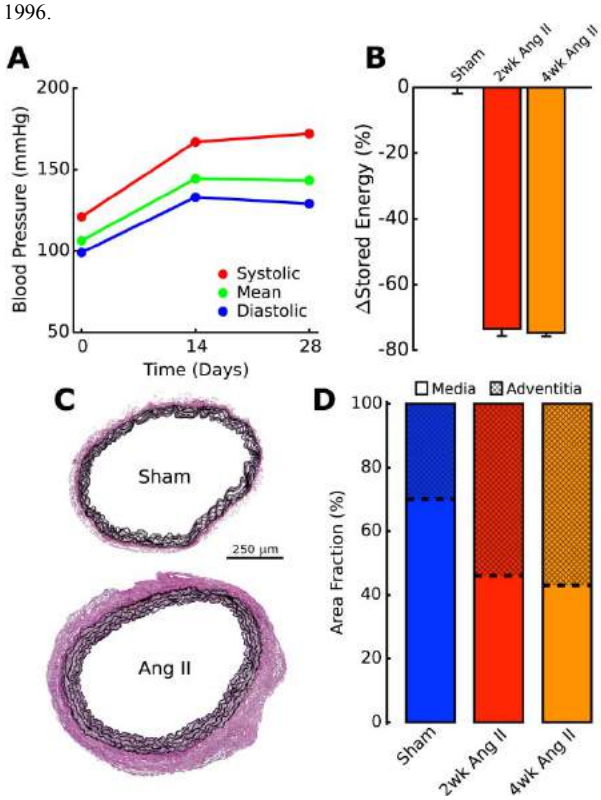

Figure 1: Vascular remodeling in Ang II induced hypertension. (A) Average blood pressure measurements, (B) percent change in stored energy, (C) representative histological sections, and (D) wall layer percentage after Sham, 2 or 4 weeks of Ang II infusion

Copyright 2016 The Organizing Committee for the 2016 Summer Biomechanics, Bioengineering and Biotransport Conference

SB^{3}C2016
Summer Biomechanics, Bioengineering and Biotransport Conference
June 29 –July 2, National Harbor, MD, USA
SB^{3}C2016-841

CARDIAC CONTRACTILITY AS A FUNCTION OF GLOBAL TISSUE ORGANIZATION

Meghan Knight (1), Nancy Drew (1, 2, 4), Linda McCarthy (2), Anna Grosberg (1, 2, 3, 4)

(1) Department of Biomedical Engineering
University of California, Irvine
Irvine, CA, USA

(2) The Edwards Lifesciences Center for Advanced Cardiovascular Technology
University of California, Irvine
Irvine, CA, USA

(3) Department of Chemical Engineering and Materials Science
University of California, Irvine
Irvine, CA, USA

(4) Center for Complex Biological Systems
University of California, Irvine
Irvine, CA, USA

INTRODUCTION

The heart is intricately organized on a wide range of length-scales. Multiple types of heart diseases are associated with remodeling of myofibrils and sarcomeres – the basic force producing unit of the heart. However, it is not fully understood how organization of cardiac tissues affects the contractility properties. To study this relationship, it is convenient to create *in vitro* models that can be well characterized and controlled. These *in vitro* platforms can be used to analyze the force production of differently organized engineered cardiac tissues, and it was found that disorganized (isotropic) tissues are significantly weaker than predicted based on the forces measured in organized (anisotropic) tissues [1, 2]. However, the prediction is based on a greatly simplified net force model, which has never been proven to accurately represent cardiac tissues because the change in organization is associated with downstream effects such as changes in gene expression levels that can further affect function [3]. As a result, the only way to truly understand the contribution of organization to change in force production is to create an experimental platform that decouples the direct and downstream effects of organizational changes. We hypothesized that these biological downstream effects could be muted if the cells were organized locally, even if the global organization was varied. Thus such locally aligned tissues could then be used to test force-global organization relationship models.

METHODS

We have adopted the "heart-on-a-chip" device to be used to study the relationship between cardiac muscle architecture and force production [2]. Organization of the cardiac tissue was controlled by a method of microcontact printing in which extracellular matrix was patterned onto a PDMS film (Figure 1). Neonatal rat ventricular myocytes were seeded onto these films and conformed to the extracellular matrix pattern. Force production of tissues was measured with the "heart-on-a-chip" device. Organization of the heart tissues was quantitatively characterized using an orientational order parameter metric based on the alignment of sarcomeres and actin fibrils. Gene expression of these tissues of varying organization was measured using qPCR.

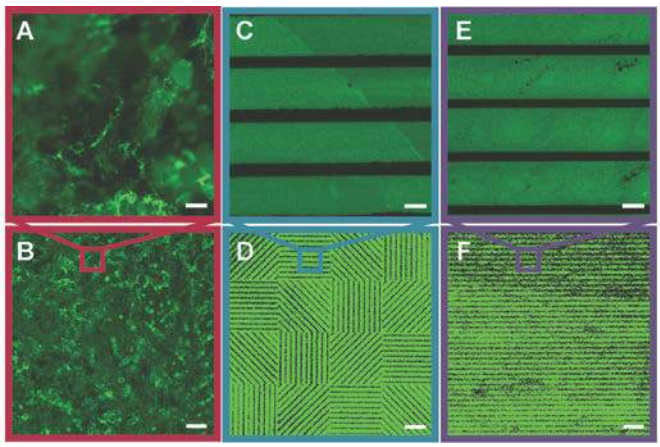

Figure 1: The extracellular matrix printed in various patters: (A,B) Isotropic, (C,D) Parquet, (E,F) Globally anisotropic. (A,C,E) scale bar = 100 μm, (B,D,F) scale bar = 10 μm

Copyright 2016 The Organizing Committee for the 2016 Summer Biomechanics, Bioengineering and Biotransport Conference

RESULTS

The relationship between global organization and force production was modeled parametrically assuming the following simplification for the angle distribution of the tissue's actin fibrils:

$$P = \begin{cases} 0 & -\frac{\pi}{2} \le \theta < -\theta_0 \\ \frac{1}{2\theta_0} & -\theta_0 \le \theta \le \theta_0 \\ 0 & \theta_0 < \theta \le \frac{\pi}{2} \end{cases} \quad \text{where } \lim_{\theta_0 \to 0} P = \delta(\theta = 0) \qquad (1)$$

The parameter θ_0 can be calculated from a measured orientational order parameter (OOP):

$$OOP = \langle \cos(2\theta) \rangle = \int_{-\theta_0}^{\theta_0} \frac{1}{2\theta_0} \cos(2\theta)\, d\theta = \frac{sin(2\theta_0)}{2\theta_0} \qquad (2)$$

The net stress produced by the tissue in a specified direction was then defined as:

$$\sigma = \sigma_0 \frac{\sin \theta_0}{\theta_0} \qquad (3)$$

Thus σ_0 is the only parameter of the formulized model.

The tissues were constructed based on the patters presented in Figure 1. The three types of tissues were characterized for actin fibril organization and gene expression profiles (Figure 2). The gene expression level results suggest that the "downstream" biological consequences of changing tissue organization were at least muted (Figure 2B).

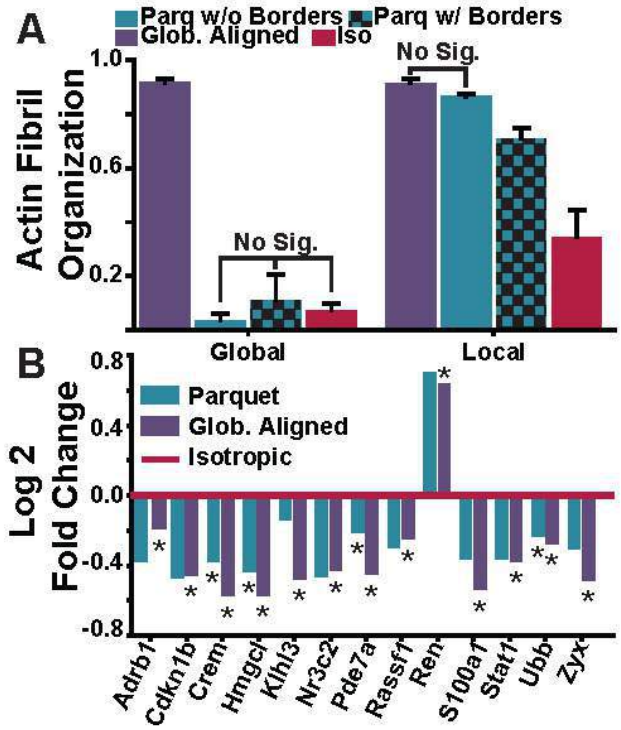

Figure 2: (A) Actin fibril OOP for the global and local spatial scales for the three tissue types. The parquet with borders, include the tissue regions in between parquet styles.

The parquet patterns were not only made with a global isotropic organization (Figure 2A), but also with a range of global organizations. All of these tissues were then tested using the "heart-on-a-chip" device to measure the global stress production.

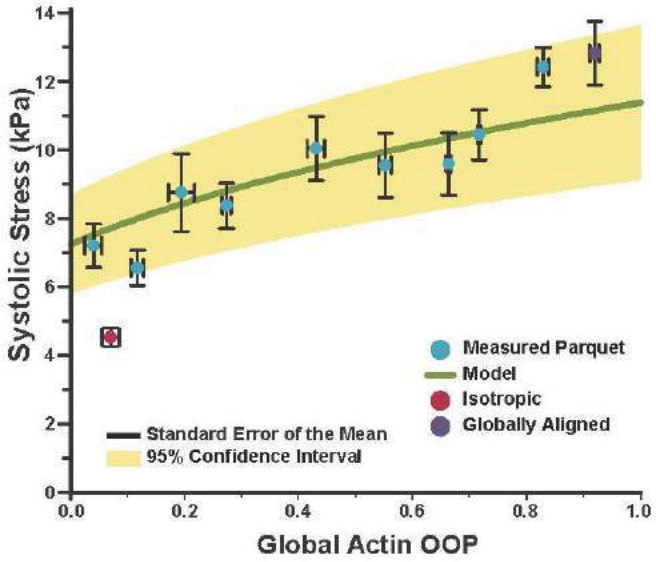

Figure 3: The systolic stress measured along the films as a function of global actin organization.

Thus we were able to show that all parquet tissues fall within the 95% confidence limit of the model presented in equations (2) and (3).

DISCUSSION

We have shown that with muted downstream effects, which are normally driven by local tissue organization, the global organization of the myofibrils is related to the net stress developed by a cardiac tissue through an single parameter analytical model. Consequently, it is now possible to estimate the contribution to force production of other factors that would normally be coupled to tissue organization. These results will lead to a better understanding of the normal and pathological hearts. Additionally, it is now possible to quantitatively analyze differences in various tissues (which inherently have different organizations), such as stem cell-derived cardiac monolayers. As more studies are performed on cardiac tissues, our results can be used to gain insight into the functional implications of a variety of biological factors; thus elucidating the underpinnings involved in heart development and disease.

ACKNOWLEDGEMENTS

We thank the BEAMS lab at UC, Irvine for aiding in the confocal imaging used in this work with particular recognition of Abishek Kurup, Mark Keating, Shreyas Raj Ravindranath, and Thi Nha Timothy Tran. We also thank Kelsey Fung for helping to establish the qPCR work used in this paper. This work was funded by the National Science Foundation EAGER award (Award No. 1338609).

REFERENCES

1. Feinberg, A.W., et al., Biomaterials, 2012. **33**(23): p. 5732-5741.
2. Grosberg, A., et al., Lab Chip, 2011. **11**(24): p. 4165-4173.
3. Chung, C.-y., et al., The FASEB Journal, 2011. **25**(3): p. 851-862.

Copyright 2016 The Organizing Committee for the 2016 Summer Biomechanics, Bioengineering and Biotransport Conference

SB^{3}C2016
Summer Biomechanics, Bioengineering and Biotransport Conference
June 29 –July 2, National Harbor, MD, USA
SB^{3}C2016-843

MAPPING HAND DYSFUNCTION: A MODEL FOR USE IN REHABILITATION

Joshua P. Drost (1), Hyokyoung Hong (2), Tamara Reid Bush (1)

(1) Mechanical Engineering
Michigan State University
East Lansing, Michigan, USA

(2) Statistics and Probability
Michigan State University
East Lansing, Michigan, USA

INTRODUCTION

Imagine not being able to use your hands – unlocking a door, holding a toothbrush, eating a meal and using your phone all become challenging if not impossible tasks. People use their hands each day and when their abilities change, it is imperative that we understand how much and what type of function was lost in order to provide the best possible treatment. Currently, surveys (which are subjective based) are used to assess hand function; a *pressing need exists to objectively detect and quantify changes in hand function.* [1, 2]. Changes in hand function include both changes in the motion and force abilities. A model that maps both the force and motion abilities will allow clinicians to easily compare changes in hand function and finger strength pre- and post- rehabilitation, treatment or surgical intervention.

Recently, we modeled the differences in kinematic finger space between hands with and without reduced functionality due to arthritis [3]. This model includes the full range of motions for each finger; however, the forces that each finger can produce are not available. *Both* motion and forces are necessary to generate a comprehensive hand model for clinical use.

Thus, to achieve this comprehensive hand model, the forces that can be applied over various finger postures must first be quantified and compared. The goal of this work was to determine forces associated with the index finger and map these to the kinematic workspace of participants with and without reduced hand functionality.

METHODS

Sixteen participants (7 female and 9 male, average age 25.6 years, SD 6.1 years) without any reported injury or arthritis, termed "Healthy", and fifteen participants (13 female and 2 male, average age 73.5, SD 4.8 years) with doctor diagnosed arthritis, termed "Arthritic", were included in this study.

The maximum forces of the index finger were measured in two conditions. 1) Forces due to changes in flexion/extension of the index finger (no adduction or abduction of the finger) were measured using a "U-shaped" metal bracket placed in seven trials along a line, each 12mm apart. In each position the participant was asked to press down on the bracket with his/her maximum load (called "Flexion/Extension Push"—Figure 1A) then pull the bracket with maximum load (called "Flexion/Extension Pull"—Figure 1B). 2) Second, maximum finger forces were measured at each of six trials to determine force differences related to abduction/adduction. Three of the trials were at maximum extension (called "Adduction/Abduction Push"—Figure 1C) and the other three trials were at a mid-range flexion (called "Adduction/Abduction Push"—Figure 1D) of the interphalangeal joints. During data collection participants were asked to continually grip a cylindrical handle with the other fingers to isolate the finger forces and to maintain a consistent orientation of the wrist.

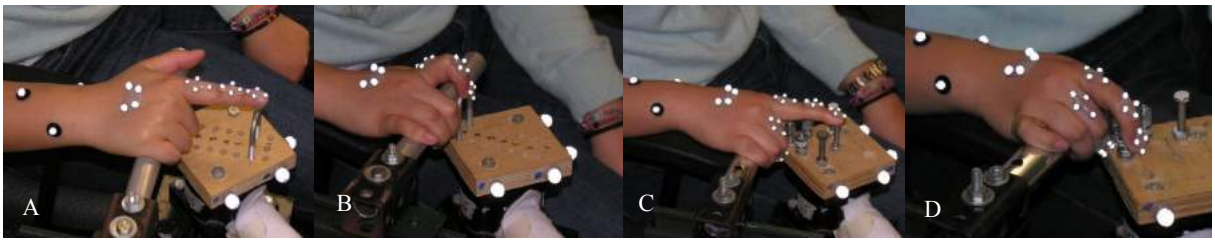

Figure 1: Experimental setup and force data for (A) flexion/extension push, (B) flexion/extension pull, (C) adduction/abduction push and (D) adduction/abduction pull trials

Copyright 2016 The Organizing Committee for the 2016 Summer Biomechanics, Bioengineering and Biotransport Conference

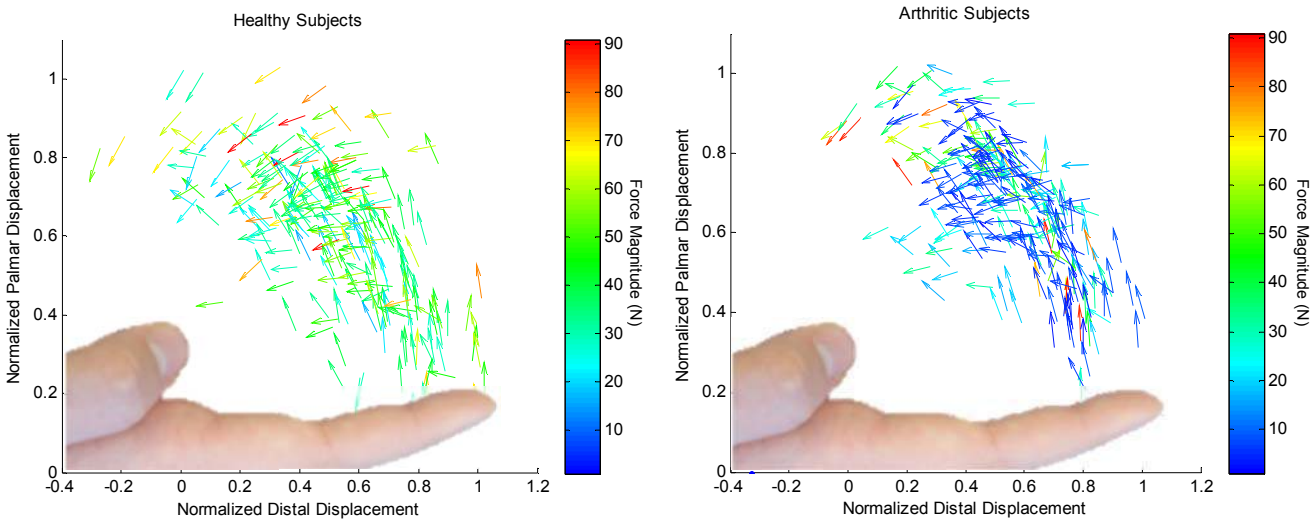

Figure 2: Sagittal projection of each force separated by groups healthy (left) and arthritic (right) individuals. Displacements are normalized based on participants finger length and are measured from the center of the second MCP joint.

After collection, the data were analyzed for each trial in terms of the 1) position (x,y,z coordinate) of the fingertip in 3D space, 2) the direction of the force applied and 3) the magnitude of the force applied. In order to compare between participants the position of the fingertip was normalized based on the participant's finger length. The force data were then compared in five different hypotheses:

1. The maximum force varies with regards to health condition (i.e. healthy or arthritic).
2. Position of the fingertip in 3D space affects the maximum force.
3. Direction of the applied force affects the maximum force.
4. Arthritis affects the range of positions used to apply forces.
5. Arthritis affects the range of directions used to apply forces.

Age and gender were also accounted for in the statistical analysis.

RESULTS

The force vectors for each trial, projected onto the sagittal plane, are presented in Figure 2. On the left are the healthy participants and on the right are the individuals with arthritis. Forces were plotted based on the finger position in 3D space and normalized based on the length of the individual's finger. The origin for all data was at the MCP (metacarpal phalange) joint of the index finger. The plots are oriented so that a fully extended index finger would sit along the horizontal axis with the pad of the index finger pointing in the positive vertical direction.

Analysis of covariance (ANCOVA), multivariate analysis of variance (MANOVA) and multiple linear regression methods were used to determine whether there were any significant differences between force magnitude, position and direction, and participant groups based on the five hypotheses. In all cases age and gender were accounted for.

1. The maximum amount of force varied significantly with regards to health condition (ANCOVA, $p<0.001$). Arthritic forces were significantly lower than healthy.
2. Position of the fingertip in the kinematic space significantly affected the amount of force applied when controlling for the health condition (ANCOVA, $p=0.01$). Maximum forces tended to be higher towards the center of the range of motion and smaller at the edges.
3. Direction of the force significantly affected the amount of force applied when accounting for health condition (Multiple Linear Regression, $p=0.0151$). Forces from pull trials (directed toward the wrist) tended to be higher than forces from push trials (directed perpendicular to the palm).
4. Health condition of the subjects significantly affected the range of motion used to apply forces in terms of the volume of space used to apply forces (MANOVA, $p<0.001$). The range of motion was also significantly affected by health in the palmer direction (ANCOVA, $p=0.01544$) and the in the medial lateral direction (ANCOVA, $p=0.00829$). Not only were forces lower for arthritic patients but the volume was lower than in healthy participants.
5. Health of the subjects significantly affected the range of directions used to apply forces (ANCOVA, $p=0.0199$). Arthritic subjects used a smaller range of force directions when applying force.

DISCUSSION

Arthritis limits the force abilities of the hand in measurable ways. The maximum force ability is significantly affected by arthritis over the entire range of motion. Subjects with arthritis not only used a smaller range of motion but also used a smaller range of directions to apply forces. These findings indicate that our model can objectively identify losses in hand function due to arthritis.

Also, regardless of health condition of the patient, the position of the finger in 3D space and direction of the applied force significantly affected the maximum force than was applied. Building on these relationships it will be possible to sample a few positions and create a continuous model of the force space based on finger position and force direction for groups with and without arthritis. Further, population models can be created that will show the average abilities for sub-populations and patient-specific models can be compared to these population models to determine the magnitude of their limitations as compared to a larger sample..

Next steps are to include the measurement of forces for all fingers, and these will be mapped to a 3D kinematic model of the entire hand..

Clinically, this model is highly innovative and useful. Measures of motion and force will be gathered prior to intervention, mid-way through rehabilitation and after rehabilitation is complete. Comparisons of these models will be able it determine what level of function was restored and what it consistent across all fingers.

ACKNOWLEDGEMENTS

The authors would like to thank the Pearl J. Aldrich Endowment in Aging Related Research for their funding as well as Sam Lietkam, Wu Pan, and Jessica Buschman for assistance in capturing data.

REFERENCES

[1] Chung K C., et al The Journal of Hand Surgery, 575-587. 1998.
[2] Katz S, et al. Journal of the American Medical Association, 914-919. 1963.
[3] Leitkam S, Bush TR. ASME Journal of Biomechanical Engineering. 2015.

Copyright 2016 The Organizing Committee for the 2016 Summer Biomechanics, Bioengineering and Biotransport Conference

SB^{3}C2016
Summer Biomechanics, Bioengineering and Biotransport Conference
June 29 –July 2, National Harbor, MD, USA
SB^{3}C2016-844

THE EFFECT OF LIGAMENT STIFFNESS ON SHOULDER CARTILAGE PRESSURE AND KINEMATICS

Hafizur Rahman (1), Mariana E. Kersh (1)

(1) Department of Mechanical Science and Engineering
University of Illinois at Urbana-Champaign
Urbana, Illinois, USA

INTRODUCTION

Rotator cuff tears are considered one of the primary causes of shoulder pain and dysfunction in adults. More than 50% of patients over the age of 60 and 80% of patients over the age of 80 experience a cuff tear [1]. Unfortunately, the success rate of rotator cuff repair is variable with many resulting in a re-tear. Revision surgeries can be as high as 30% for isolated supraspinatus tendon tears [2].

Rotator cuff tears not only decrease the mechanical properties of the cuff muscles, but also have secondary effects on the other tissues within the joint – specifically, ligaments and cartilage. In the presence of rotator cuff tears, the mechanical properties of the coracoacromial ligament have been shown to decrease, the area of glenohumeral (GH) cartilage degeneration increases, and glenoid cartilage thickness and modulus of elasticity decreases [3-6]. Thus, the overall shoulder joint stability and function would likely be affected by the change in these properties. However, the degree to which these changes affect function is not well understood.

There is a wide variation in the measured mechanical properties of shoulder joint ligaments [7-8]. It is essential to know how the variation of ligament stiffness affects the kinematics and cartilage pressure in the GH joint in order to understand why there is a high incidence of re-tears. To investigate this, we developed a three-dimensional finite element (FE) model of the shoulder joint.

METHODS

Computed tomography (CT) data files of a male shoulder (voxel size: 0.34 x 0.34 x 0.49 mm) were used to reconstruct the geometries of the humerus and scapula (Figure 1A) using image processing software (Amira v5.6, Visualization Sciences Group, Germany). Bones surfaces were created and exported into Geomagic Studio (v2014, Geomagic Inc., USA) to smooth, refine, and reduce noise in the solid computer-aided design models (Figure 1B).

Construction of the FE model and all simulations were performed using Abaqus (v6.13, Daussalt Systems, France). Shell elements were used for the humerus and scapula (elastic modulus, E = 17 GPa, poisson's ratio, v = 0.30) [9]. A layer of elements were offset from the proximal and distal ends of the humerus and scapula to model the articular cartilage. Humeral cartilage was defined as 0.5 mm thick and scapular cartilage as 1 mm thick and modeled using a neo-Hookean hyperelastic material model (shear modulus, G = 6.8 MPa, v = 0.45) [10]. Frictionless contact was defined between the humerus and scapula. Within the glenohumeral joint are four primary ligaments that provide stability: coracohumeral (CHL), superior glenohumeral (SGHL), middle glenohumeral (MGHL), and inferior glenohumeral (IGHL). These ligaments were modeled as axial springs (Figure 1C). Stiffness values from the literature for the CHL, SGHL, and IGHL were used to model the ligaments [7-8]. No stiffness values were available for the MGHL; therefore, the average of the SGHL and IGHL were used. A local coordinate system was defined corresponding to the medial-lateral (ML), superior-inferior (SI), and anterior-posterior (AP) directions.

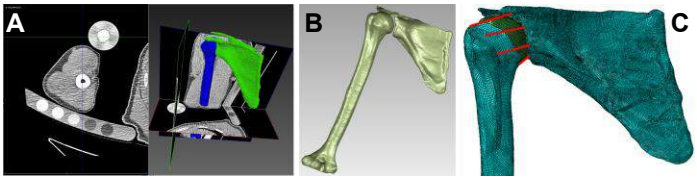

Figure 1: A) Geometry created in Amira, B) exported from Geomagic, C) FE model of shoulder joint with ligaments (red)

Copyright 2016 The Organizing Committee for the 2016 Summer Biomechanics, Bioengineering and Biotransport Conference

To simulate abduction, the humerus was rotated about the local AP axis. Rotations about the ML and SI axes were zero. Translational components of humerus were left unconstrained. During first 30° of abduction, the scapula was fixed and then followed a 2:1 relation for upward rotation with respect to the humerus [11].

Simulations were run for three different stiffness values (Table 1). Low stiffness was defined as the average stiffness minus one standard deviation, and high stiffness as the average stiffness plus one standard deviation. The kinematics of the humerus, peak and mean cartilage contact pressures were calculated. The relationship between contact pressures and abduction was analyzed using linear regressions. F-tests were used to test for significant differences in contact pressure as a result of changing the stiffness values ($\alpha = 0.05$).

Table 1: Ligament stiffness, K (N/mm) [7-8]

	CHL	SGHL	MGHL	IGHL
Low	30.8	15.9	15.6	15.4
Avg	36.7	17.4	21.4	25.4
High	42.6	18.9	27.1	35.4

RESULTS

With increasing abduction angle, both peak and mean scapula cartilage pressure increased regardless of stiffness value (R^2 range = 0.71 - 0.86) (Figure 2A, B). Similar trends were found for the humeral cartilage. Decreasing stiffness resulted in lower peak scapula contact pressure ($p=0.047$), but had no effect on the mean contact pressure. However, increasing stiffness did not change either peak or mean scapula cartilage pressure. Humerus cartilage pressure was also not changed by increasing ligament stiffness, but decreasing stiffness decreased both peak and mean humerus cartilage pressures ($p=0.014$ for peak, $p<0.001$ for mean).

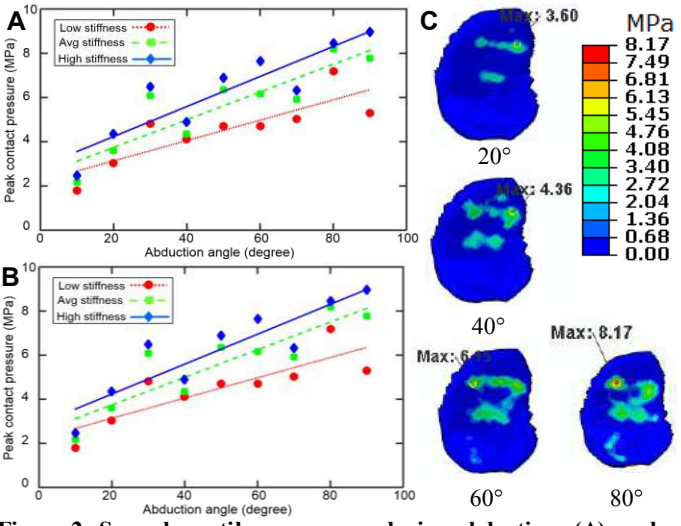

Figure 2: Scapula cartilage pressure during abduction: (A) peak, B) mean and C) pressure map for average stiffness at 20°, 40°, 60°, and 80° abduction

Decreasing ligament stiffness caused the humerus to move more posteriorly ($p=0.02$) whereas increasing stiffness resulted in no change (Figure 3). Superior-inferior translations were sensitive to both increasing ($p=0.012$) and decreasing stiffness ($p=0.0044$). However, changing ligaments stiffness did not change medial-lateral translations.

DISCUSSION

The purpose of this study was to investigate the influence of ligament stiffness on humerus kinematics and cartilage pressure. Our results indicate that cartilage pressure was only sensitive to decreases in ligament stiffness. Surprisingly, increasing stiffness contributed to changes in superior-inferior translations but did not result in changes in cartilage pressure.

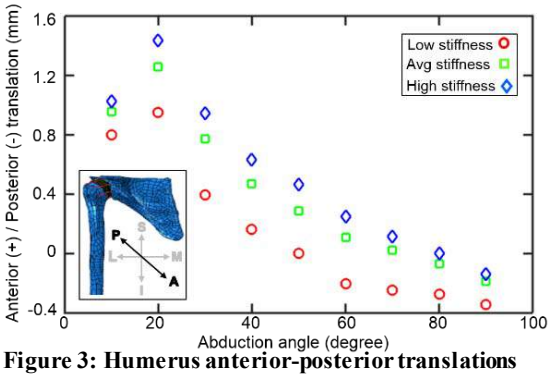

Figure 3: Humerus anterior-posterior translations during abduction

Since, there was no variation in medial-lateral translation, anterior-posterior translation may be the driving kinematic degree of freedom of cartilage contact pressure during abduction.

Our results show that humerus translation and cartilage pressure are sensitive to ligament stiffness. Others have shown that the mechanical properties of shoulder ligaments decrease due to rotator cuff tears [3-4]. If the injured rotator cuff tendons alone are treated during a repair, without regard for restoring ligament stiffness, the overall shoulder joint function may not be the same as the normal healthy shoulder. Moreover, the assessment of kinematics and muscle function as a metric of joint function (e.g. ability to lift the arm) may mask changes in cartilage pressure resulting in secondary consequences such as osteoarthritis.

Though our FE model has not been experimentally validated, our results are consistent with previous studies in the prediction of glenohumeral contact pressure. For example, others have reported mean cartilage pressure of 1.09±0.35MPa at 60° abduction [12], and our model results ranged from 1.02MPa - 1.44MPa. We report peak scapula cartilage pressure at 90° abduction ranging from 5.29MPa - 8.96MPa depending on ligament stiffness, and others have measured peak contact pressure of 4.2MPa for single arm weight and 9.2MPa for double arm weight at the same angle [13]. The anterior-posterior translation was also similar to previous findings [14-15].

In conclusion, our results indicate that ligament stiffness results in changes in contact pressure. Small kinematic changes resulted in significant changes in contact pressure suggesting that care should be taken when interpreting patient function. Altered ligaments stiffness may affect cartilage contact pressure even after rotator cuff repair.

ACKNOWLEDGEMENTS

We would like to thank Stu Warden for use of the CT data.

REFERENCES

[1] Milgrom, C et al., *J Bone Joint Surg [Br]*, 77(2):296-298, 1995 [2] Goutallier, D et al., *J Shoulder Elbow Surg*, 12(6):550-554, 2003 [3] Soslowsky, LJ et al., *Clin Orthop*, 304:10-17, 1994 [4] Fremerey, R et al., *Knee Surg Sports Trau Arthrosc*, 8(5):309-313, 2000 [5] Hsu, HC et al., *Acta Orthop Scand*, 74(1):89-94, 2003 [6] Reuther, KE et al., *J Orthop Res*, 30(9):1435-1439, 2012 [7] Boardman, ND et al., *J Shoulder Elbow Surg*, 5(4):249-254, 1996 [8] Bigliani, LU et al., *J Orthop Res*, 10(2):187-197, 1992 [9] Dalstra, M et al., *J Biomech Eng*, 117(3):272-278, 1995 [10] Park, S et al., *Osteoarthritis Cartilage*, 12(1):65-73, 2004 [11] Inman, VT et al., *J Bone Surg Am*, 26:1-30, 1944 [12] Hansen, ML et al., *53rd Annual Meeting of the ORS*, 1157, 2007 [13] Conzen, A et al., *J Shoulder Elbow Surg*, 9(3):196-204, 2000 [14] Massimini, DF et al., *J Orthop Surg Res*, 7(1):1-9, 2012 [15] Konrad, GG et al., *J Orthop Res*, 24(4): 748-756, 2006.

Copyright 2016 The Organizing Committee for the 2016 Summer Biomechanics, Bioengineering and Biotransport Conference

SB^{3}C2016
Summer Biomechanics, Bioengineering and Biotransport Conference
June 29 –July 2, National Harbor, MD, USA
SB^{3}C2016-846

SIMILITUDE ASSESSMENT METHOD FOR COMPARING PMHS RESPONSE DATA FROM IMPACT LOADING ACROSS MULTIPLE TEST DEVICES

Christopher J. Dooley[1], Francesco V. Tenore[1], F. Scott Gayzik[2], Andrew C. Merkle[1]

(1) Biomechanics and Injury Mitigation Systems
Johns Hopkins University Applied Physics Lab
Laurel, MD, USA

(2) School of Medicine
Wake Forest University
Winston-Salem, NC, USA

INTRODUCTION

One of the primary tools in the development of both physical models, such as anthropomorphic test devices (ATDs), and Finite Element (FE) models, in the field of injury biomechanics is the biofidelity response corridor or BRC. BRCs are used to encapsulate a range of responses for validation, as an alternative to the utilization of individual characteristic response. Multiple techniques have been used to develop BRCs in the past, whether by bounding the set of responses [1], finding the mean and standard deviation at each discrete time step [2], or using an objective tool such as the open source software "Correlation and Analysis" (CORA) to develop a corridor from a set of response curves [3]. Gayzik et al. [4] examined these techniques and proposed a modified method based on work published by Nusholtz et al. [5] for impact and accelerative loading applications. These modifications were part of an effort to better understand human body response to under body blast (UBB) loading, characterized by high rate, short duration impact events.

An ongoing study to determine the whole body post mortem human surrogate (PMHS) response to UBB loading has utilized the Gayzik [4] method to develop BRCs for model development. Due to the intensive nature of whole body PMHS testing under UBB conditions, and sample size necessary to create BRCs, experiments have been conducted on both horizontal and vertical test devices, including both accelerative and decelerative designs, with the intent to combine all responses into a representative BRC. To facilitate aggregation of these data, all input conditions and positioning requirements were tightly controlled to ensure that PMHS at multiple facilities were being exposed to similar inputs. With small tested populations from a variety of test devices, an objective method for assessing similitude of responses between test rigs was used as a metric for inclusion of a response in the resulting BRC. The goal of this method is to supply a statistically sound, objective method to assess the similitude of an individual response against a set of responses to ensure that the BRC created from the set is a consistent set of responses to a similar input. The method does not suggest removal of responses, but rather reevaluation by a biomechanist with an understanding of the test device and subject.

The goals of this method are to quantify the similitude of a set of responses, potentially from multiple test devices, by evaluating statistical differences in order to identify responses to reevaluate from a biomechanics or physical perspective.

METHODS

Nusholtz et al. [5] described a two-stage method to compare multiple tests with a single ATD against themselves and against tests from one or more ATDs of the same design in order to assess repeatability and reproducibility of the ATD, respectively. Here, a similar approach is followed, involving the modified point-wise normalization (PWN) technique developed by Gayzik et al [4], with some important distinctions.

First, given that each PMHS is employed only once, we use the term *intrarepeatability* to indicate the process of testing differences within a specific test condition (e.g. tests within an accelerative and vertical setup) using multiple (three or more) specimens. A test condition is found to be *intrarepeatable* if the following criteria are met: 1) the sample size consists of three or more tests; 2) the PWN value found is at least *50%* of the input signal correlation. This threshold was determined heuristically based on the examined data. If a test condition has a sample size smaller than 3, this step is not executed and the data are automatically inserted into the next stage. A test condition that is identified as non-repeatable is reviewed from a biomechanics and experimental perspective to potentially identify

Copyright 2016 The Organizing Committee for the 2016 Summer Biomechanics, Bioengineering and Biotransport Conference

faults in the test setup. If the test is discarded, or if intrarepeatability as a whole does not pass, then the intrarepeatability step is repeated by removing a single test to identify potential outliers in the data. This is repeated as long as the number of samples undergoing intrarepeatability analysis satisfies criteria 1.

Second, test conditions that pass intrarepeatability or that cannot undergo the intrarepeatability stage due to sample size limitations are directly fed to the *interrepeatability* and *reproducibility* stage. Here, we use a similar technique to identify potential outliers: one test at a time is removed from the set to examine how the PWN value distribution changes for the remaining response in the set (interrepeatability). We then calculate how the removed signal correlates to the set as a whole (reproducibility). Subsequently, a two-sample non-parametric statistical test (Wilcoxon rank-sum) is used to test the null hypothesis that the samples are from the same group. As a result of the small sample sizes involved in the data set, this statistical analysis aims at minimizing Type I errors through the use of a non-parametric Wilcoxon rank-sum test (in which test sizes of 0.05 and 0.01 are examined).

RESULTS

The results of this assessment are shown in Figure 1 on an sample data set at two different significance levels. The left figure shows a reduction in responses identified for reevaluation at the more conservative significance level ($p < 0.05$) with two responses being identified, while three responses are identified at a significance level of $p < 0.1$. The traces identified for reevaluation demonstrate a temporally shifted response, even though all responses are shifted for optimal correlation. One of the responses in the $p < 0.05$ case is likely excluded due to its lower peak amplitude relative to the set. The additional response identified at $p < 0.01$ represents the most extreme response of the set. Since these are acceleration responses, they are evaluated over the range of time from 0 sec to the peak velocity.

Figure 2 highlights the intermediate calculations performed upon each response in the set. The method creates a matrix of correlation values for each curve with respect to every other curve based on a point wise normalization calculation. The assessment of the similitude for each individual curve generates a distribution of correlation values for the curve under analysis compared to all of the remaining curves together (reproducibility) and all of the remaining curves against each other (repeatability). The three possible outcomes are shown in Figure 2. The first stage of analysis compares the repeatability and reproducibility. If these metrics are not statistically different, the curve is retained within the set (Fig. 2C). If these metrics are statistically different and the reproducibility is greater, the curve is also retained (Fig. 2B). If the reproducibility is less than the repeatability, then that response is identified for reevaluation (Fig. 2A).

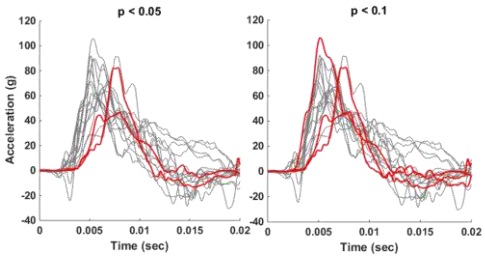

Figure 1. Example application of similitude analysis showing assessment at the $p < 0.05$ (Left) and $p < 0.1$ level (Right), blue traces passed through the analysis while the red traces were identified for reevaluation.

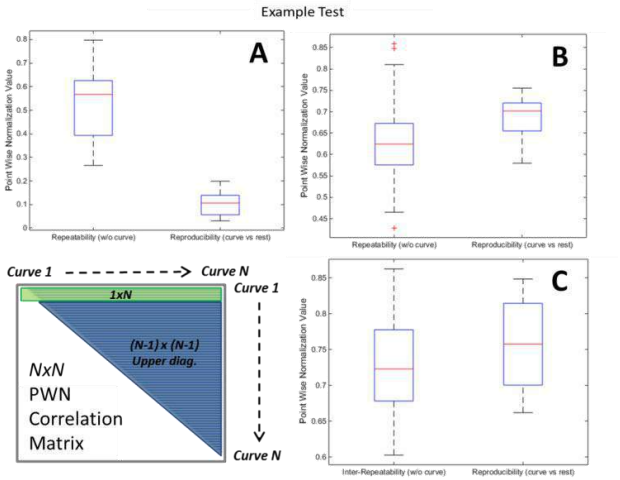

Figure 2. Visualization of correlation matrix showing repeatability, blue (n-1)x(n-1) upper diagonal, and reproducibility, green 1xn vector, and box plot depictions of possible outcomes of same different analysis. Repeatability and reproducibility statistically different with reproducibility lower than repeatability (A) and higher than repeatability (B). Repeatability and reproducibility not statistically different (C). Case A would be the only scenario in which a response would be identified for reevaluation.

DISCUSSION

The method proposed here for the evaluation of similitude consists of a non-parametric test chosen to minimize Type I errors, false positives. The key aspect of the data is the low number of samples, which necessitates ensuring that differences found are investigated further given the low power of the statistical test. The thresholds were empirically and heuristically determined based on the data. The method was able to conservatively assess the data and provide recommendations for reevaluation that consistently identified responses underlying biomechanical justification for exclusion, such as mount failures or local bony injury.

While the method showed promise there are caveats such as an extra stage of analysis was undertaken for responses from a single condition with $n > 3$ in contrast to those conditions with $n < 3$. Future work will include a more in-depth analysis of possible degradation functions for the analysis thresholds of responses observed further from the location of mechanical loading.

ACKNOWLEDGEMENTS

This effort was funded by contract #N00024-13-D-6400, U.S. Army Research, Development and Engineering Command in support of the Warrior Injury Assessment Manikin (WIAMan) project. The content included in this work does not necessarily reflect the position or policy of the U.S. government. The authors gratefully acknowledge the input of the principal investigators from each participating institution.

REFERENCES

[1] Kent, et al, *Journal of Auto. Eng.*, 2006.
[2] Yoganandan, et al, *Journal*, 2004.
[3] Gehre and Shahlschmidt, *Journal*, 2011.
[4] Gayzik, FS et al, *Journal of Biomechanics,* 2015.
[5] Nusholtz, GS et al, *SAE Int. J. Trans. Safety,* 2013.

Copyright 2016 The Organizing Committee for the 2016 Summer Biomechanics, Bioengineering and Biotransport Conference

SB³C2016
Summer Biomechanics, Bioengineering and Biotransport Conference
June 29 –July 2, National Harbor, MD, USA
SB³C2016-847

ON THE USE OF THE INVERSE FINITE ELEMENT METHOD TO ESTIMATE PELVIC FLOOR SUPPORT STRUCTURE IMPAIRMENTS IN WOMEN WITH PELVIC ORGAN PROLAPSE

Mark T. Gordon (1), James A Ashton-Miller (2), John OL DeLancey (3), Luyun L. Chen (2)

(1) Bioengineering and Mechanical Engineering
California Baptist University
Riverside, CA, USA

(2) Biomedical Engineering Department
University of Michigan
Ann Arbor, MI, USA

(3) Obstetrics and Gynecology Department
University of Michigan
Ann Arbor, MI, USA

INTRODUCTION

Pelvic organ prolapse is a prevalent and distressing female health problem. Unfortunately the results of standard care are sub-optimal. Pelvic floor dysfunction that is severe enough to require surgical repair affects 11% of women, a figure that is expected to increase with the burgeoning aging population (Olsen 1997). The anterior vaginal wall is both the most common site of pelvic organ prolapse (in what is called a 'cystocele') and the most frequent site of operative failure. That operative failure rates can reach 25% indicates the need to re-appraise current diagnostic and surgical strategies for this condition.

Most of the existing theories of cystocele formation are based on clinical observations and hypothesize a weakness (or defect) in isolated parts of the uterovaginal support system: apical support, paravaginal attachments, vaginal wall fascial tissues and/or levator ani muscle. And these theoretical postulates has been the associated with a surgical procedure designed to address specific defects. The available data suggest that each woman has her own unique problem; however satisfactory identification of defects in the clinic or operating room has not yet been possible. A framework and research tool is needed that can determine the specific status of the support system in each area and choose the operative approach most appropriate for specific women could greatly improve the treatment selection as well as improve outcomes.

Significant progress has made in better understanding the multi-factorial mechanism of pelvic organ prolapse. Women with pelvic organ prolapse were found to have decreased stiffness and resiliency in supporting structures (Cosson 2004). There has been a demonstrated link between levator ani muscle injury and pelvic organ prolapse (DeLancey 2007). A first 3-D computational model (Chen 2009) demonstrated interactions between the several different aspects of support. In addition, the development of the 3D "Stress MRI" (Larson 2010, 2011) has made it possible to measure the 3D deformations of vaginal wall in living women and to separately identify the site and location of structural failure in individual women. This progress has made it possible to identify the pre-operative impairment status in various supporting structures and to start to understand the impact of treatment on the pelvic support system.

The objective of this study was to utilize the 3D FEA model of cystocele, develop an inverse finite element modeling method to identify pre-operative impairments in women with pelvic organ prolapse. Then we investigate how the accuracy of the MRI measurements would affect the accuracy of the 'impairment status' prediction.

METHODS

Pre-operative FEA Model Development

Similar to Chen (2009), we started by mapping the pre-operative pelvic resting geometry observed on 3T MR images as the pre-operative FEA model geometry. The 3D anterior vaginal wall and its support system was imported into ABAQUS v6.11.1 to generate the mesh, assign contact constraints and boundary conditions. The normal material parameters for the structures in the model were based experimental measurements and the literature. We assumed zero initial displacements and displacement rates, displacements and rotations from the initial state configuration were finite, inertial loads were negligible, tissue incompressibility and contact between structures was frictionless. The ABAQUS explicit solver V6.11 was used to solve the equations.

Copyright 2016 The Organizing Committee for the 2016 Summer Biomechanics, Bioengineering and Biotransport Conference

Determining Patient Specific Structure Impairment Parameters Pre-operatively using the Inverse Finite Element Method

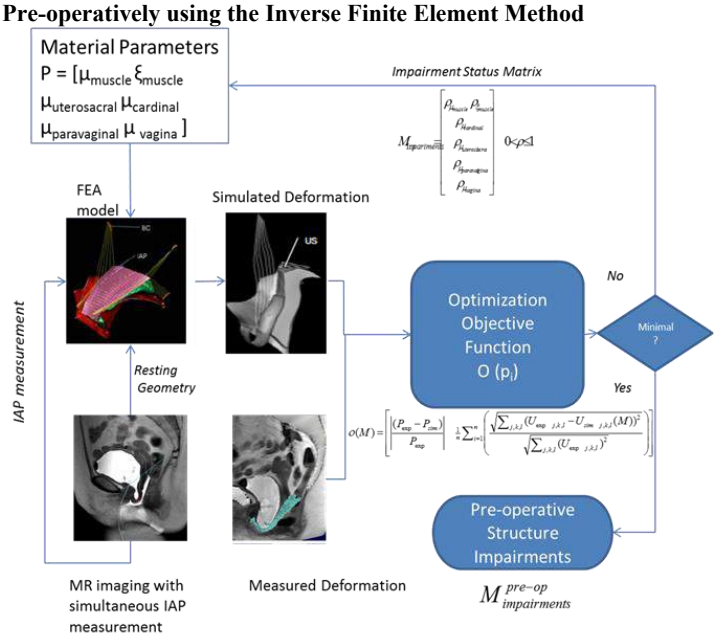

Figure 1: Schematic of inverse finite element modeling strategy

Impairments in the support structures were defined as the percent decrease in material stiffness (Chen 2009) shown as impairment status matrix $M_{\text{pre-op impairment}}$, which was determined using the inverse finite element modeling strategy shown in Figure 1.

An iteratively process was used to determine the pre-operative impairment status in all structures when the simulated Valsalva matched the stress MRI measurement by minimizing the user-defined cost function $o(M)$, which was calculated as the difference between simulated vaginal wall deformation and pre-operative MR-based measurements at maximal Valsalva.

In this phase of the study we mimicked MRI data by adding random noise to each coordinate of the finite element result. The noise was centered on 0 and the standard deviation was varied to determine how sensitive the inverse FEA prediction was to this noise. The FEA model was run for a full 3^3 design, treating the apical supports as one variable. Three levels were used to define if the tissue was healthy, had a minor impairment, or a major impairment. This yielded the data points that were used to determine the optimal match for the MRI data.

The Optimization Process

To determine $M_{\text{pre-op impairment}}$ that generated the closest data to the MRI data, each FEA data set was compared to the mimicked MRI data. First, for each point on the mimicked MRI data the three closest points in the FEA data set were determined. These points were then used to construct a plane and the distance from the MRI point to the constructed plane was determined. That distance was then raised to the second power. This process was completed for each of the MRI reference points and the distances were summed as a cost for that FEA parameter set. The FEA data set with the lowest cost was determined and the parameters that generated that FEA data set were predicted as the MRI parameters. In the current phase of the study, the predicted parameter set was compared with the parameter set that was used to generate the MRI data; if the parameters were the same then the optimization was deemed a successful prediction. This simple comparison was used to reduce the run time. Otherwise directly searching through the 36-dimensional space and running the FEA each time would have been too time intensive to complete for future, patient specific models.

The robustness of the method was determined by changing the size of the standard deviation. The simulation was run 100 times for each of the parameter sets (270 in total) at five different standard deviation levels (0.5 mm, 1 mm, 1.25 mm, 1.5 mm, and 2 mm). The percentage of the successful optimizations was recorded as the result.

RESULTS

The matching success rate was 97% when the standard deviation of the noise was set to 1 mm (Table 1). However, the success rate decreased markedly as the standard deviation of the noise was increased. It is important to note that the 1 mm standard deviation on each dimension results in mimic MRI points that are an average of approximately 1.6 mm from the FEA point.

The parameter that was most frequently incorrectly identified varied with the size of the standard deviation. For the lower standard deviation values the paravaginal tissue property was most frequently misidentified and was three times more likely to be predicted as healthier than more damaged as shown in Table 1. Above 1.25 mm in standard deviation the apical supports were more frequently misidentified. They were twice as likely to be identified as more damaged than healthier. The PVM was the least likely to be incorrectly identified regardless of the standard deviation size.

Table 1 The Standard Deviation of noise affect on the success of impairment status prediction.

SD (mm)	All	PVM			Paravaginal			Apical		
	S (%)	S (%)	H (%)	D (%)	S (%)	H (%)	D (%)	S (%)	H (%)	D (%)
0.5	100	100	0.0	0.0	100	0.0	0.0	100	0.0	0.0
1	97	100	0.1	0.0	98	1.5	0.4	99	0.5	0.9
1.25	91	99	1.0	0.1	94	4.0	1.8	94	2.1	3.4
1.5	79	96	2.2	1.7	87	7.9	4.8	86	4.4	9.6
2	53	86	9.0	4.9	72	16	12	68	9.7	23

All: all parameters; S: successful prediction; H: predicted healthier; D: predicted more damaged

DISCUSSION

Even a simple cost function such as determining how far the MRI points are from the FEA surface can yield high parameter matching if the noise on the MRI data is sufficiently low. This result emphasizes the importance of accurate MRI data if inverse FEA modeling is to be a success.

ACKNOWLEDGEMENTS

We appreciate Office for Research on Women's Health SCOR on Sex and Gender Factors Affecting Women's Health and the National Institute of Child Health and Human Development Grants 2 P50 HD044406, R01 HD 038665, R21HD079908 and BIRCWH K12 HD004438

REFERENCES

Olsen AL, et al *Obstet Gynecol.* 89(4):501-6.
Chen, L et al, *J Biomech* 42(10):1371-7
DeLancey, JOL et al, *Obstet Gynecol*. 109(2 Pt 1):295-302
Cosson. M et al *Eur J Obstet Gynecol Reprod Biol.* 112(2):201-5.

Copyright 2016 The Organizing Committee for the 2016 Summer Biomechanics, Bioengineering and Biotransport Conference

SB^{3}C2016
Summer Biomechanics, Bioengineering and Biotransport Conference
June 29 –July 2, National Harbor, MD, USA
SB^{3}C2016-848

ADHESION AND INVASION OF CIRCULATING CANCER CELLS ON INFLAMED ENDOTHELIUM

Taylor J. Thompson (1), Bumsoo Han (1,2,3)

(1) School of Mechanical Engineering
Purdue University
West Lafayette, IN, USA

(2) Birck Nanotechnology Center
Purdue University
West Lafayette, IN, USA

(3) Purdue Center for Cancer Research
Purdue University
West Lafayette, IN, USA

INTRODUCTION

Metastasis is the ultimate cause of death among the vast majority of cancer patients. One of the major modes of cancer metastasis is through the circulatory system, also known as haematogenous metastasis. Haematogenous metastasis is a highly inefficient process, with less than 0.01 % of circulating tumor cells forming metastases [1]. This low rate is largely due to the rapid destruction of cancer cells in the circulation by immune cells [2] or hemodynamic forces on immobilized cells [3]. This suggests that the rate-limiting steps in the metastatic cascade are the adhesion and eventual penetration of the vasculature of the target host organ. Many of these mechanisms of the haematogenous metastatic cascade remain poorly understood, including the adhesion and extravasation of circulating tumor cells in the vasculature of secondary target organs. Past research in this area has been hampered by poor control of pathophysiological conditions in animal models, and the failure to recapitulate an *in vivo*-like environment in *in vitro* models. In this work, a microfluidic device was developed to support the culture and observation of engineered microvasculature with systematic control of the environmental characteristics. This device was then used to study the adhesion of circulating cancer cells to an endothelium under varying conditions to delineate the effects of hemodynamics and inflammations. The resulting understanding will help to establish a quantitative and biophysical mechanism of interactions between cancer cells and endothelium.

METHODS

Cells and Reagents

Human **m**icro**v**ascular **e**ndothelial **c**ells (hMVEC, Lonza) were maintained in endothelial basal medium-2 supplemented with various growth factors and FBS as suggested by the vendor. These cells were harvested when confluence reached 80-85% utilizing 0.025% trypsin and EDTA. Cells of passage 7 to 11 were used in the experiments.

Human breast cancer cell line (MCF-7) was grown in Advanced DMEM/F12 basal medium (Invitrogen) supplemented with 5% FBS, L-glutamine, and Pen/Strep. MCF-7 cells were harvested when confluence reached 80-90%. To reduce the likelihood of enzymatic cleavage of potential membrane binding proteins during harvesting, a non-enzymatic chelator, Versene (Invitrogen), was used to gently detach cells from the culture flask prior to experiments.

In Vitro Endothelium-on-Chip

A microfluidic platform, as illustrated in **Figure 1A** and **B**, was fabricated by standard photolithography technique. The channel measuring 75 μm in height, 300 μm in width, and about 2 cm in length. Three ports were then drilled using a biopsy punch, one at each end of the channel and one about 2.5 mm off-center. The channel walls were coated with 1 mg/mL type I rat tail collagen.

Harvested hMVECs were slowly introduced through the channels utilizing a syringe pump (NE-4000x, New Era). Once cells occupied the area of interest of the channels (from the reservoir to the far port), the devices were moved to an incubator where cells were allowed to adhere to the channel surfaces for 45 minutes. Once hMVEC reached confluence in the channel (about 48 hours), the hMVEC were subjected to a 0.30 dyne/cm^2 shear stress for additional 24 hours utilizing a syringe pump. Exposure to this low shear stress maintains a cobble-stone morphology in which the hMVEC have no apparent alignment. This is consistent with venule morphology *in vivo* [4]. The confluence of the grown endothelial monolayers can clearly be seen in **Figure 1C**. When studying the effect of inflammatory cytokine stimulation, hMVEC monolayers were treated with 50 ng/mL TNF-α for 5 hours prior to experiments, as previously reported [5].

Copyright 2016 The Organizing Committee for the 2016 Summer Biomechanics, Bioengineering and Biotransport Conference

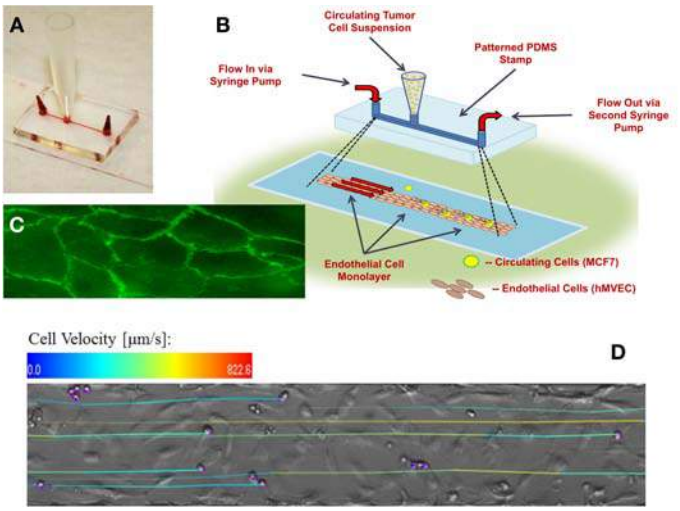

Figure 1: (A) Photograph of the fabricated chip. (B) Schematic of the chip configuration. (C) Morphology of hMEVC endothelium with tight cell-cell contact. (D) Microscopy analysis of cell motion.

Time-lapsed Microscopic Analysis

The prepared microfluidic platform was placed in an incubation stage (Okolab) on an inverted microscope (IX71, Olympus). The channel was perfused with hMVEC medium at physiologically relevant velocities. It has been reported that the mean blood velocity at human capillary beds and post-capillary venules ranges from approximately 250 to about 1400 μm/s [6]. Thus, the hydrodynamic velocities along the channel (v_{hyd}) are 300, 600, and 900 μm/s. Harvested MCF-7 cells were suspended in hMVEC culture medium at a concentration of 1.5 x 10^5 cells/mL, and then 50 μL of this suspension was then added to the center reservoir. Tumor cells from the reservoir then sedimented into the channel, allowing for a relatively constant stream of flowing cells in the observation area. The channel was imaged for cellular motion with a CCD camera (EXI Aqua, Q Imaging). The images were further analyzed to characterize cancer cell interaction with endothelium as shown in **Figure 1D**. The cancer cell behavior was quantified by separating them into different states of dynamic adhesion [7]. These dynamic states of adhesion can be divided into four as follows by use of the cell velocity - i) "no adhesion" describes a state where cells are moving at a velocity greater than $0.5v_{hyd}$; ii) "rolling" describes a state where cells move slower than $0.5v_{hyd}$, but without notable periods of immobilization; iii) "transient adhesion" describes cells moving slower than $0.5v_{hyd}$ with notable periods of immobilization; and iv) "firm adhesion" describes cells moving less than 0.2 μm within 0.5 seconds.

RESULTS AND DISCUSSION

Figure 2 depicts the percentage of MCF-7 cells exhibiting each of the four adhesion behaviors defined on unstimulated or TNF-α stimulated hMVEC. As expected, TNF-α stimulation significantly increased the amount of observable interaction occurring between circulating cancer cells and the endothelial monolayer. The majority MCF-7 cells on the unstimulated endothelium display no observable adhesion behavior, with virtually none becoming immobilized for any discernable amount of time. In addition, cells considered to be rolling traveled, on average, 20 percent faster on unstimulated endothelium than on the TNF-α stimulated one. These results are not surprising due to the lack of adhesion molecules in resting type endothelial cells. Once stimulated, however, interaction between the circulating cells and the endothelium became more prevalent, with the vast majority of cells exhibiting some form of adhesion. Nearly 30 percent of adhering cells became immobilized at some point with more than half of these becoming firmly adhered.

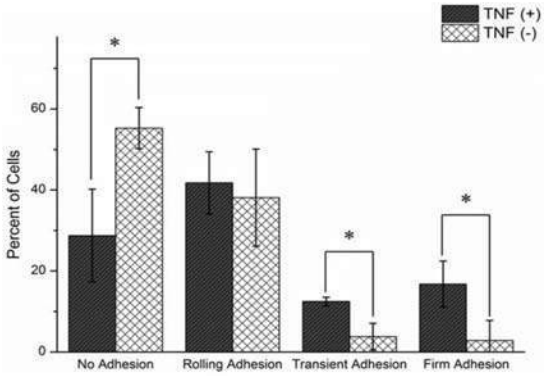

Figure 2: Effects of TNF-alpha on adhesion. Comparisons noted with symbol are statistically significant ($p < 0.05$)

Figure 3 shows the differences in the states of adhesion for adhesion assays performed at mean fluid velocities of 300, 600, and 900 μm/s. A clear and significant difference can be seen in the number of firmly adherent circulating MCF-7 cells between the experimental groups. There is a clear jump in the percent of non-interacting tumor cells as the fluid velocity increased. As the velocity increase to 900 μm/s, the vast majority circulating tumor cells failed to show any discernable interaction with the underlying endothelium. An interesting observation was the number of slowly rolling cells present in the 600 μm/s experimental group. This slow rolling was not observed in either the low or the high velocity groups.

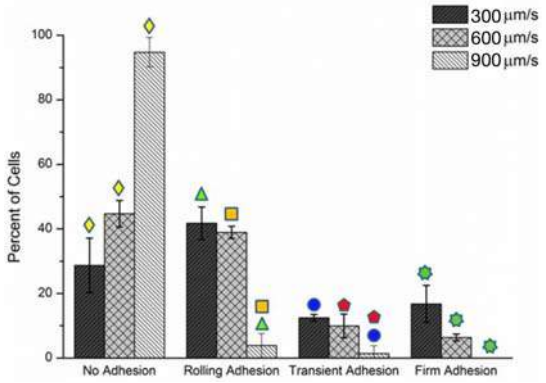

Figure 3: Effects of shear rate on adhesion. Comparisons noted with symbol are statistically significant ($p < 0.05$)

ACKNOWLEDGEMENTS

This work was partially supported by NCI Contract HHSN261201400021C and a CTR Award from Indiana CTSI funded in part by UL1 TR000006 from NIH, and a grant from Walther Cancer Foundation.

REFERENCES

[1] Chambers, AF et al, *Nat. Rev. Cancer*, 2:563-572, 2002.
[2] Hanna, N, *Metastasis Rev*, 1:45-64, 1982.
[3] Weiss, L, *Cancer Metastasis Rev*, 11:227-235, 1992.
[4] Zheng, Y et al, *PNAS*, 109:9342-9347,2012.
[5] Song, JW et al, *PLoS One*, 4:2009.
[6] Koutsiaris, AG et al, *Biorheology* 44:375-386, 2007.
[7] Chang, KC et al, PNAS, 97:11262-11267, 2000.

Copyright 2016 The Organizing Committee for the 2016 Summer Biomechanics, Bioengineering and Biotransport Conference

SB^{3}C2016
Summer Biomechanics, Bioengineering and Biotransport Conference
June 29 –July 2, National Harbor, MD, USA
SB^{3}C2016-849

DEVELOPMENT AND EVALUATION OF AN ARBORIZING CATHETER FOR CONVECTION ENHANCED DELIVERY

Egleide Y. Elenes (1), Christopher G. Rylander, PhD. (2)

(1) Biomedical Engineering
The University of Texas at Austin
Austin, TX, USA

(2) Mechanical Engineering
The University of Texas at Austin
Austin, TX, USA

INTRODUCTION

Malignant tumors of the central nervous system are the third leading cause of cancer-related deaths in adolescents and adults and the leading cause of death in children with a mean survival time of 15 months and a mortality rate exceeding 95% [1]. Despite intense medical research focused on improving treatment, survival statistics for patients with aggressive brain tumors such as glioblastoma, or GBM, have not changed satisfactorily in 80 years. One of the reasons for poor survival is that systemic treatment of GBMs is limited by insufficient delivery of drugs due to the blood-brain barrier (BBB). Additionally, glioma cells, which play a role in tumor progression and resistance to therapy, typically infiltrate up to 2 cm beyond the volume of visible tumor [1], making them difficult to detect and treat.

Convection-enhanced delivery (CED), pioneered at the NIH/NINDS, has emerged as a promising method for the delivery of high concentrations of macromolecules to larger regions of brain tissue [2]. The principle of CED involves the stereotactically-guided insertion of a small-caliber catheter into the brain. Through this catheter, high-molecular-weight proteins can be pumped into the brain parenchyma and is pushed primarily through the interstitial space. Experiments have shown that CED can deliver infusates 2 cm into the brain parenchyma after 2 hours of continuous infusion, an order of magnitude higher than the distances obtained with simple diffusion [3].

Although CED has achieved greater efficacy than traditional systemic chemotherapy, it amounted to inconsistent increases in patient survival during Phase III clinical trials [4]. This can be attributed to the limited ability of CED to uniformly distribute drug throughout the tumor and broadly disseminate drug to the infiltrative GBM cells residing in the primary tumor periphery, which correlate with tumor recurrence. Additionally, the anatomical heterogeneity of the brain complicates perfusion by CED. Portions of the brain are inherently difficult to saturate with drugs due to variations in permeability of white and gray matter, tumor tissue, cerebrospinal fluid tracts, and anatomy of vascular beds. Furthermore, the high lipid content of the white matter highly resists movement of aqueous drug formulations. Further limitations of CED involve the "off-label-use" of commercially available catheters designed for different medical applications to perform the therapy [5, 6]. These catheters do not possess the arborizing capability to effectively perfuse drugs over large tissue volumes, including margins surrounding tumors that contain more distant infiltrative cells responsible for regrowth of the tumor [7]. In effort to ascertain targeted delivery and infuse greater tumor volumes, CED often requires insertions of multiple catheters; thus, increasing the risk of trauma to healthy neurological tissue and increasing the probability of seeding the needle tract with cancer cells [8]. For these reasons, we developed a novel arborizing catheter for broad loco-regional delivery of therapeutics.

METHODS

Development of an Arborizing Catheter. The arborizing catheter (**Fig. 1A**) consists of a cannula (OD ~3 mm) that is manufactured using seven aligned biocompatible polyether ether ketone (PEEK) tubing bonded with light-cured acrylic adhesive. The distal end of the tubing is twisted. Once the acrylic is cured, the end of the cannula is filed to a smooth conical tip. The cannula houses seven flexible, hollow silica microneedles (375 μm OD; 180 μm ID) with their distal end polished to a smooth bevel tip (**Fig. 1B**) and their proximal end glued to a 22 G dispensing needle with a Luer lock adapter.

When deploying the microneedles, the twisting of the PEEK tubing allows the needles to branch at an angle of up to 30° (angle of peripheral needles from cannula axis). These individual microneedles can be deployed, arborizing from a single cannula, providing multiple infusion tracts per one primary cannula insertion tract. They can be fully retracted back into the cannula upon completion of the therapy; thus, the tumor-contacting surfaces of needles would remain completely within the primary cannula upon removal, thereby reducing the probability of tumor cell-seeding in healthy brain tissue and preventing mechanical damage to surrounded tissue when extracting the catheter.

Copyright 2016 The Organizing Committee for the 2016 Summer Biomechanics, Bioengineering and Biotransport Conference

Figure 1. A) Arborizing catheter prototype with deployed microneedles. B) Individual silica microneedle (arrow indicates air bubble at sharp beveled tip)

Infusion Experiments with Tissue Phantoms. The arborizing catheter was evaluated with infusion experiments using agarose tissue phantoms. Agarose gel (0.6% w/w), previously validated as a brain tissue phantom, [9] was made by mixing agarose powder (BioRad, Hercules, CA) and deionized water, then heated and stirred until clear. Then each microneedle's Luer lock adpater was connected to BD syringes, filled with a 0.04% solution of indigo carmine dye. The syringes were loaded into a programmable syringe pump (Harvard Apparatus Company, Holliston, MA), and each microneedle was primed. The cooled agarose mixture was then poured into a glass cube containing the arborizing catheter with each microneedle deployed 2 cm from the cannula tip and the gel was allowed to set.

Infusions in the congealed agarose were recorded using an optical shadowgraphy setup, which captures images of the infusion cross-section at multiple angles (front, side, and bottom) (**Fig 2A**). Each infusion was performed at a steady rate of 1 µl/min for 100 minutes while a digital camera (Canon USA, Rebel T1i, Melville, NY) positioned and secured at a fixed distance from the agarose-filled glass box, captured images every minute. For comparison, single needle infusions, analogous to infusion with a single-port catheter, were tested using similar experimental procedures.

Image Analyses to Quantify Mean Distribution Ratios. Final infusion images were processed using MATLAB (The Mathworks, Natick, MA), and Image J (NIH, Bethesda, MD). An algorithm was written in MATLAB to separate and scale each view (front, side and bottom) into separate images. Intensity of the each image was then normalized to an external reference file. Image J was used to convert the images into binary images and determine the best-fit ellipsoid for each view. The major and minor axes of each view's ellipsoid were recorded and mapped to the appropriate axes. The major axes of the front and side view were scaled and averaged to obtain the major axis for the calculated ellipsoid volume (**Fig 2B**). This value and the minor axes from the front and side view were taken to be the semi-axes of a representative 3-dimensional ellipsoid and the approximate volume distribution (V_d) was calculated using:

$$V_d = (4/3)\,\pi\, abc \qquad (1)$$

where a, b, and c are the semi-axes of the ellipsoid. Single-needle infusions were assumed to be spherical and V_d was calculated using the equation for volume of a sphere. The mean distribution ratio (volume distribution (V_d) / total volume infused (V_i)) was calculated for each infusion for comparison.

RESULTS

Using the shadowgraphy technique described above, the distribution profiles of the arborizing catheter were captured and compared to single needle distributions. **Fig. 3** demonstrates a representative infusion for the single needle versus the catheter after 100 minutes of continuous infusion. With the arborizing catheter, the distribution volume distribution was ~5-times greater than with a single needle. However, the mean distribution ratio, V_d/ V_i for the arborizing catheter was approximately 75% smaller than the distribution ratio for a single needle.

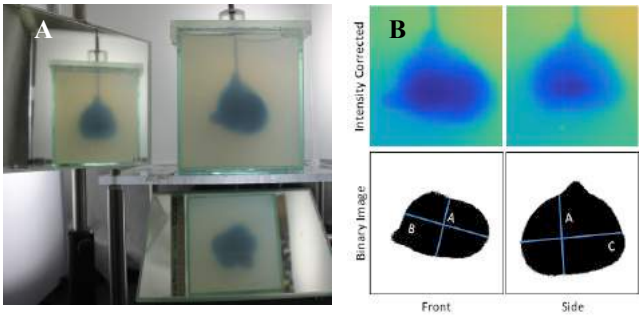

Figure 2. A) Shadowgraphy experimental setup showing three views of the infusion volume. B) Image processing and analysis to quantify dispersal volume and major/minor axes.

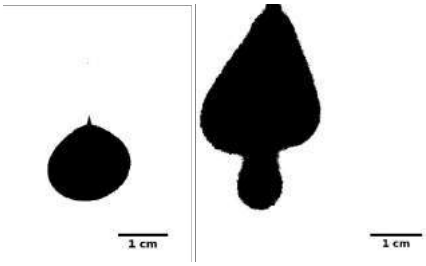

Figure 3. Binary images of infusion profiles for single needle (left) versus arborizing catheter (right) after t = 100 min.

Table 1: Mean distribution for the arborizing catheter versus single needle infusions

	Total V_d (ml)	Total V_i (ml)	V_d/V_i
Arborizing catheter	9.2	0.7	13.1
Single needle	1.8	0.1	17.6

DISCUSSION

Failure to targeting distant, infiltrating glioma cells limits CED efficacy, which may be overcome by achieving broader distribution of therapeutics. In this study, we found that the arborizing catheter achieved greater V_d than a single needle (analogous to a single-port catheter) for equal infusion times. Infusion duration is important as CED is often performed inside an MRI machine, which adds to the cost of the therapy. The V_d/ V_i for the arborizing catheter was only ~ 75% of the ratio for the single needle, which was smaller than we expected. However, the smaller mean distribution ratio may be due to overlap in the distribution volumes for individual needles of the catheter. However, the arborizing catheter did achieved a greater distribution ratio than other studies using reflux-preventing, single-port catheters which reported V_d/V_i of ~ 0.67-1.6 [10].

ACKNOWLEDGEMENTS

This work was funded by the Wallace C. Coulter Foundation.

REFERENCES

1. Morrison PF, et al., *Am J Physiol* 1994, **266**:R292-305.
2. Vandergrift WA, et al., *Neurosurg Focus* 2006, **20**(4):E13.
3. Berger MS, *Semin Oncol* 1994, **21**(2):172-185.
4. Fiandaca MS, et al., *Neurotherapeutics* 2008, **5**(1):123-127
5. Debinski W, Tatter SB, *Exp rev neurotherap* 2009, **9**:1519-1527.
6. Raghavan R, et al., *Neurosurg Focus* 2006, **20**(4):E12.
7. Denton KJ, et al., *Journal of clinical pathology* 1990, **43**(1):83.
8. Slywotzky C, Maya M, *Abdominal imaging* 1994, **19**(2):174-176
9. Chen Z-J, et al., *J Neurosurg* 2004, **101**:314-322.
10. Gill T, et al., *Journal of neuroscience methods* 2013, **219**(1):1-9.

Copyright 2016 The Organizing Committee for the 2016 Summer Biomechanics, Bioengineering and Biotransport Conference

SB^{3}C2016
Summer Biomechanics, Bioengineering and Biotransport Conference
June 29 –July 2, National Harbor, MD, USA
SB^{3}C2016-851

A METHOD FOR PREDICTING COMPLETE GROUND REACTION FORCES WITH PLANTAR PRESSURE INSOLES DURING LEVEL AND ANGLED WALKING

Andrew J. Crechiolo (1,3), Feng Wei (1,2,3), Roger C. Haut (1,2,3)

(1) Orthopaedic Biomechanics Laboratories
Michigan State University
East Lansing, MI, USA

(2) Department of Radiology
Michigan State University
East Lansing, MI, USA

(3) Department of Mechanical Engineering
Michigan State University
East Lansing, MI, USA

INTRODUCTION

Knowing the ground reaction forces (GRFs) during walking has various biomechanical applications such as injury prevention, gait analysis, and prosthetic and footwear design. The current study presents a method for predicting the GRFs during level and angled walking that can be used for various outdoor biomechanics studies geared towards the applications mentioned above, that does not require the use of a force plate or other environmental limiting factors.

To date, only force plates have been used to obtain ground reaction force data for studies involving walking over angled surfaces [1,2,3]. For outdoor biomechanics studies an embedded force plate would limit the number of consecutive steps for which data could be recorded, the validity of the foot-ground interaction surface, and the environmental versatility of the study.

A study by Forner-Cordero et al. [4] successfully obtained GRFs during level walking with the use of Pedar plantar pressure insoles combined with kinematic data from a motion capture system. The use of a motion capture system in an outdoor environment for extensive studies is not feasible since calibration is tedious, and the area of the study would still be limited to that which is visible to the motion capture cameras. A study by Fong et al. [5] successfully used Pedar plantar pressure insole data correlated with force plate data, using linear regression analysis, to predict GRFs during level walking. It was hypothesized in the current study that splitting foot contact force data into three phases: Heelstrike^1, Transition^2, Toeoff^3, with separate linear regression equations would both: increase the accuracy of predictions compared to the one-phase regression model developed by Fong et al. [5] as well as create a more versatile model that would allow for the prediction of GRFs during angled walking. This three-staged regression model was proposed because in pilot studies we observed contact loads shifting noticeably from a posterior to anterior location on the foot during level walking gait. The method presented in the current study may be used more effectively in the future for estimating GRFs in numerous original outdoor biomechanical environments such as during angled gait on mountainous terrain.

METHODS

Approval of human subject use was obtained from the IRB. Six healthy male subjects with no known pathology or major lower body injuries within the past ten years were recruited for this study. A 16' long, 0°-20° adjustable ramp with an embedded force plate was used for the level and angled walking trials. Each subject performed ten walking trials at angles 0°, ±5°, ±10°, ±15°, and ±20° while wearing a minimalist shoe outfitted with plantar pressure insoles.

Trial data were then trimmed to include only that from the subject's right foot. Since each subject performed ten walking trials at each angle, nine were used to generate the regression model for the given angle, and one trail was randomly chosen to later assess the accuracy of the model by comparing predicted values using the Pedar data against the force plate GRF data.

Trial data were then split in half at the midstance frame. An Excel macro was used to generate coefficients of determination (R^2 values) between each individual insole senor's pressure readings, and the force plate force measurements. Three insole sensors from each half of the footstrike (before and after midstance) that exhibited a high linear correlation (determined with R^2 values) between each respective GRF component were chosen to create pressure masks. The Heelstrike^1 and Toeoff^3 stages used these sets of correlated sensors as inputs for their respective linear regressions, while the Transition^2 stage used a combination of the two sets of correlated sensors.

Slope and intercept constants were then created between these pressure masks and the force plate measurements of GRF. This

Copyright 2016 The Organizing Committee for the 2016 Summer Biomechanics, Bioengineering and Biotransport Conference

process of creating a linear regression using pressure mask values as inputs was done for the anterior-posterior and medial-lateral components of the GRF.

The Pedar system's capacitance sensors allow it to directly measure the vertical force. Instead of using a pressure mask, the Pedar system's measurement of the vertical force was used as the input to the regression model for the vertical component.

The linear regressions generated from the first half of the footstrike were used to predict the GRFs from the first nonzero pressure reading until two frames before the midstance frame, forming the first segment of the model, Heelstrike^1. The linear regression generated from the second half of the footstrike was used to predict data from the fourth frame past midstance until the last non zero pressure reading, forming the third stage of the prediction model, Toeoff^3. The second stage of the model, Transition^2, used a weighted combination of both regression models and was inserted into the model to account for the gradual change in the location of the load bearing sensors from posterior to anterior. Equation 1.1 is a general format of the model. $M(P)^{\theta}_{x,y,z}$, is the model output which is a function of Pedar insole measurements, P. The model was dependent on the surface angle θ and the component of GRF being predicted denoted by *x,y,z*.

$$M(P)^{\theta}_{x,y,z} = \begin{cases} f(P) = m_1 * \left(\bar{P}_{\text{c,d,e}}\right) + b_1, & P_{HS} \le P \le P_{MS-3} \\ \begin{bmatrix} .9 \\ .7 \\ .6 \\ .4 \\ .3 \\ .1 \end{bmatrix} * f(p) + \begin{bmatrix} .1 \\ .3 \\ .4 \\ .6 \\ .7 \\ .9 \end{bmatrix} * g(p), & P_{MS-2} \le P \le P_{MS+3} \\ g(P) = m_2 * \left(\bar{P}_{\text{f,g,h}}\right) + b_2, & P_{MS+4} \le P \le P_{TO} \end{cases} \quad \textbf{(1.1)}$$

$f(P)$ is the linear regression used for the Heelstrike stage of the model with slope and intercept constants, m_1 and b_1. $\bar{P}_{\text{c,d,e}}$ arbitrarily represents the pressure mask input made from three sensors: *c, d,* and *e*. Similar to $f(P)$, $g(P)$ is the linear regression used for the Toeoff stage. $P_{HS} \le P < P_{MS-2}$ denotes the range of Pedar values used for the Heelstrike stage which was from the first non-zero Pedar value, P_{HS}, until three frames before midstance frame, P_{MS-3}. Likewise, the Transition stage used Pedar values from two frames before the midstance frame, P_{MS-2}, until three frames past the midstance frame, P_{MS+3}. Lastly, the Toeoff stage used Pedar values from four frames past midstance frame,P_{MS+4}, until the last nonzero Pedar value, P_{TO}.

RESULTS

For each of the six subjects on each walking surface angle the GRFs were predicted for one trial and the root mean square errors (RMSEs) of the predictions were averaged for each angle and presented in Table 1.1.

		GRF Prediction RMSE (N)		
		Vertical	Medial/Lateral	Anterior/Posterior
0°		26.95	10.05	20.12
5°	Incline	35.28	9.94	19.59
	Decline	35.23	14.01	30.87
10°	Incline	40.69	9.40	26.15
	Decline	31.64	14.56	38.59
15°	Incline	37.29	8.92	29.08
	Decline	33.46	12.47	42.30
20°	Incline	42.22	10.71	39.25
	Decline	38.09	12.52	40.35

Table 1.1: Averaged RMSE results of 6 subjects at angles 0°, ±5°, ±10°, ±15°, and ±20°.

There were slight increases in RMSEs as surface angle increased for the vertical and anterior/posterior directions (Table 1.1). Of the 99 pressure insole sensors, the three most highly correlated sensors were not always the same between any two angles for a subject. It was also found that the locations of the three most highly correlated sensors were not consistent between subjects.

DISCUSSION

Compared to studies from past literature, the relatively low RMSE values in the current study support the hypothesis that a three-staged model can be used to accurately predict GRFs for level and angled walking. The current study showed that a three-staged regression model improved prediction accuracies when compared to the one-staged regression model used in Fong et al. [5] by 11.48, 1.66, and 7.29 N or 29.87%, 14.18%, and 26.60% in the respective vertical, medial/lateral and anterior/posterior directions. The RMSEs of the three-staged regression model, when compared to the study of Forner-Cordero et al. [4] which also used Pedar insoles to generate GRFs curves, improved slightly in the vertical direction but not in the medial/lateral or anterior/posterior directions. Forner-Cordero et al., however, used a motion capture system to collect gait dynamics which assisted in the GRF calculations. The use of a motion capture system in an outdoor environment would be tedious due to calibration issues, and would limit the area of study. Thus, the method used by Forner-Cordero et al. might be less feasible than that of the three-staged regression model for use in outdoor environments. The slight increase in RMSEs for the vertical and anterior/posterior directions as the ramp angle increased may be due to a trend for increases in maximum values of the vertical and anterior/posterior GRF component as the surface angle increases, as observed by Lay et al. [3].

It should be noted that the three-staged regression model was angle and subject specific. Indicators of the model's specificity are the differences in location of the most highly correlated sensors between angles. The variation in location of the most highly correlated sensors across angles was most likely due to differences in gait, such as the ankle, knee and hip angles, which are caused by the changes in grade [3]. The difference in location of the most highly correlated sensors between subjects was also most likely due to differences in gait mechanics between subjects that caused the loading of different pressure sensors during walking. Future studies may involve more footwear designs and test if the model is also footwear specific.

The three-staged model developed in the current study was shown to be a viable tool for predicting the GRFs during walking in outdoor settings due to its small errors and its simplicity which requires only Pedar plantar pressure insoles and calibration trials. The three-staged model should allow for future studies dealing with injury prevention, gait analysis, as well as prosthetic and footwear design in diverse outdoor environments such as mountainous terrains. Future studies should also aim to assess the impact of surface texture on the accuracy of the model predicted GRFs.

ACKNOWLEDGEMENTS

The authors would like to thank Mr. Clifford Beckett and Mr. Jerrod Braman for their technical support in this study. The authors would also like to thank Wolverine WorldWide, Inc. for a financial gift to help support our laboratories.

REFERENCES

[1] Wannop et al., *Gait & Posture*, 40:118–122, 2014.
[2] McIntosh et al., *Journal of Biomechanics*, 39:2491–2502, 2006.
[3] Lay et al., *Journal of Biomechanics*, 39:1621–1628, 2006.
[4] Forner-Cordero et al., *Journal of Biomechanics* 37:1427–1432, 2004.
[5] Fong et al., *Journal of Biomechanics* 41:2597–2601. 2008.

Copyright 2016 The Organizing Committee for the 2016 Summer Biomechanics, Bioengineering and Biotransport Conference

SB³C2016
Summer Biomechanics, Bioengineering and Biotransport Conference
June 29 –July 2, National Harbor, MD, USA
SB³C2016-852

THE MITRAL VALVE CHORDAE TENDINEAE: A TOPOLOGICAL AND GEOMETRIC ANALYSIS

Amir H. Khalighi (1)(2), Andrew Drach (2), Charles H. Bloodworth IV (3), Eric L. Pierce (3) , Ajit P. Yoganathan (3), Robert C. Gorman (4), Joseph H. Gorman III (4), and Michael S. Sacks (1)(2)(5)

(1) Department of Mechanical Engineering,
The University of Texas at Austin
Austin, TX, USA

(2) Center for Cardiovascular Simulation,
Institute for Computational Engineering and Sciences,
The University of Texas at Austin
Austin, TX, USA

(3) Cardiovascular Fluid Mechanics Laboratory,
Wallace H. Coulter Department of Biomedical Engineering, Georgia Institute of Technology
Atlanta, GA, USA

(4) Gorman Cardiovascular Research Group,
University of Pennsylvania,
Philadelphia, PA, USA

(5) Department of Biomedical Engineering,
The University of Texas at Austin
Austin, TX, USA

INTRODUCTION

Mitral Valve (MV) regurgitation is the most common heart valve disease, afflicting more than 2.5 millions of people in the U.S. alone [1] with a fairly high mortality rate among the population. This pathologic condition is generally characterized by morphologic alterations or impaired interactions of the MV complex constituents (annulus, leaflets, chordae tendineae, and papillary muscles). While the MV annulus and leaflet geometry has been extensively studied [2], the chordae tendineae topology have never been quantitatively explored. Thus, an improved understating of MV chordae tendineae would facilitate the development of advanced surgical strategies and treatment planning.

Chordae Tendineae are cylindrical structures of collagenous connective tissue that protrude from the papillary muscle tips on the posterior left ventricular inner heart wall and insert on the MV leaflets. From a mechanical perspective, the chordae tendineae provide a suspension system that supports the MV leaflets and prevents them from swinging to the atrial cavity during ventricular contraction. MV repair, which is a widely practiced operation to treat regurgitant MVs [3], often benefits from modifying the chordal structure to restore the MV's functionality. This may include repair, reattachment, or rearrangement of the chordae tendineae, adding artificial chords, or even cutting existing normal chordae tendineae.

In this work, our methodology and results on the topological characterization and geometrical quantification of the MV chordae tendineae are presented. We wanted to find out if the chordal branching outline follows any pattern versus being purely random. Our findings, for the first time, provide a basis to predict the geometry of the MV chordae tendineae that ultimately allows developing a population-representative model of the healthy chordal structure.

METHODS

To acquire MV geometry, we imaged four ovine heart valves obtained from an USDA approved abattoir (Superior Farms, CA, USA) in the Georgia Tech Cylindrical Left Heart Simulator (CLHS) [4] as described in [5]. The valves were pressurized and imaged using micro computed-tomography in the simulated fully closed state to better resolve the fine features and geometric details of the chordal structure. Next, the four DICOM imaging data-sets were segmented in the ScanIP software suite (Simpleware Ltd., Exeter, UK) to acquire tessellated surface representations of the MV apparatus. To perform geometry modeling, we relied on the centerline modeling feature in ScanIP to extract a spline-based curve-skeleton representation of the chordae tendineae and the pointwise mean cross sectional area long the skeleton (Fig 1).

Next, we analyzed the curve–skeleton model of the chordae tendineae to develop the Reeb graph [6] representation of the chordal topology (c.f. Fig. 5). Furthermore, we extracted the chordae-to-leaflet and chordae-to-papillary muscle attachment locations, referred to as insertion and origin points respectively, by analyzing the rate of change in the cross sectional area along the chordae skeleton. To extract these anatomical landmarks, a threshold value of 0.15±0.05 was set on the normalized rate of change in the cross sectional area. The cut-off values were adjusted empirically according to our pilot studies which showed the transition zones between the MV chordae tendineae and surrounding structure can be characterized by the aforementioned threshold.

Copyright 2016 The Organizing Committee for the 2016 Summer Biomechanics, Bioengineering and Biotransport Conference

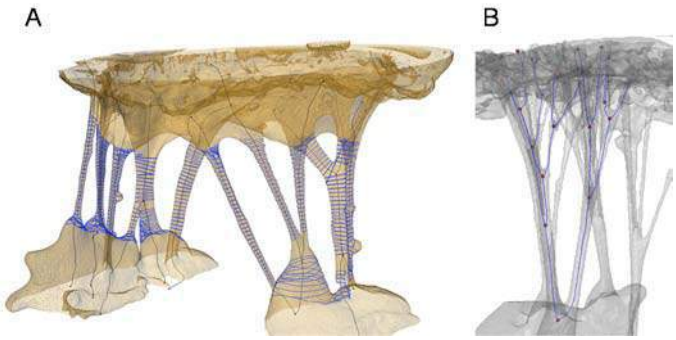

Fig. 1: (A) shows the curve-skeleton representation of chordae tendineae with the cross sectional area. (B) represents how this modeling approach captures the branching structure of chordae.

RESULTS

We developed well-defined geometric models of the MV chordae tendineae (Fig 2), which were used to analyze the chordal structure by extracting and classifying the chordal anatomical landmarks (Fig 4). The study of origin, branching, and insertion points in the chordal structure suggests that the number of these natural fiducial points increases almost linearly along the chordae tendineae (Fig 3).

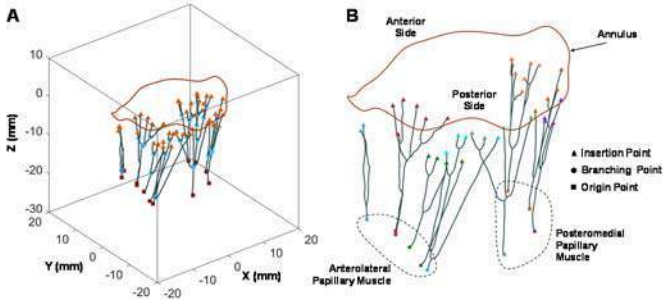

Fig. 2: (A) shows the B-spline representation of the chordae tendineae. In (B), we have classified the anatomical landmarks.

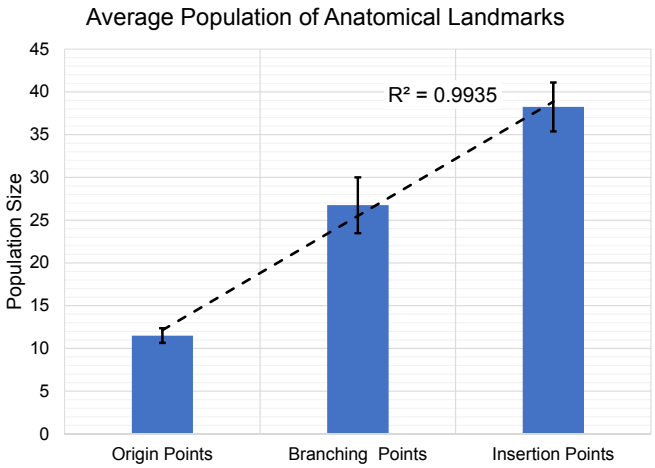

Fig. 3: The number of anatomic fiducial points in the chordal structure increases almost linearly

Interestingly, we observed that the branching pattern in the cylindrical chordal structure follows the full binary tree pattern (Fig 5). In other words, at every bifurcation location, only two outgoing segments emerge from an incoming branch. The same pattern was consistently observed across the studied population of ovine MVs.

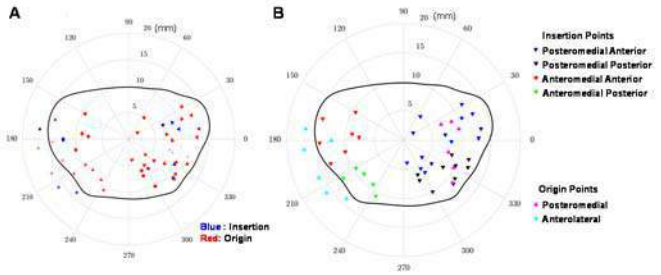

Fig. 4: (A) represents the distribution and (B) shows the classification of insertion and origin location

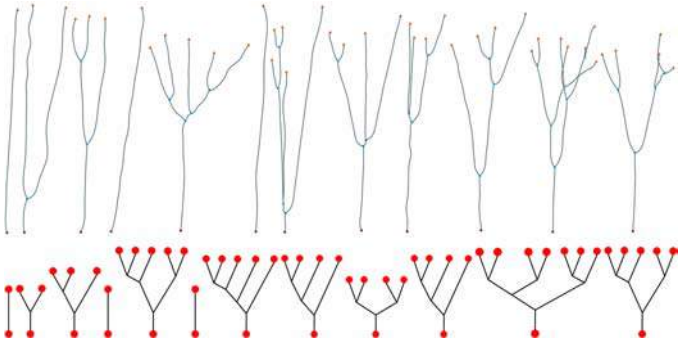

Fig. 5: The full binary tree branching pattern for a single MV. Top row signifies the unfolded geometry of the chordal structure. Bottom row is the collection of Reeb graphs representing the chordal topology

DISCUSSION

In this work, we presented a novel, robust approach to process pre-clinical images and build anatomically accurate geometric models of the MV chordae tendineae. Across a population, we observed that the branching pattern in the cylindrical structure of MV chordae tendineae mainly follows the full binary tree pattern except for very sparse interconnections between some chordae tendineae. From the modeling aspect, this emphasizes that computational models of the MV should respect this existing underlying structure in the chordal geometry to improve anatomical accuracy. Moreover, this interesting finding strongly suggests that the shape of MV chordae tendineae is not random, and, in fact, is tied to some specific fundamental factors. In addition, by extraction and classification of the anatomical landmarks in the chordal structure, we realized that these points are localized in anatomically distinct regions. We believe these regularities provide a basis to average the MV chordae tendineae across a population and develop a population-representative model of the chordal structure.

ACKNOWLEDGEMENTS

Research reported in this publication was supported by National Heart, Lung, and Blood Institute of the National Institutes of Health under award number R01HL119297. The content is solely the responsibility of the authors and does not necessarily represent the official views of the National Institutes of Health.

REFERENCES

[1] Enriquez-Sarano, M et al. *The Lancet*, *373*(9672), 1382-1394, 2009.
[2] Padala, M et al. *Ann. Thorac. Surg.* 1499-1504, 2009.
[3] Moss, R et al. *Circulation*, *108*(10 suppl 1), II-90. 2003.
[4] Rabbah, JP et al. *Ann. Biomed. Eng.* 41.2: 305-315, 2013.
[5] Khalighi, A et al. *Lecture Notes in Comput. Sci.*, 164-171, 2015.
[6] Biasotti, S et al. *Theor Comput Sci* 392.1:5-22, 2008.

Copyright 2016 The Organizing Committee for the 2016 Summer Biomechanics, Bioengineering and Biotransport Conference

SB³C2016
Summer Biomechanics, Bioengineering and Biotransport Conference
June 29 –July 2, National Harbor, MD, USA
SB³C2016-853

BACTERIAL GROWTH INSIDE REVERSIBLE CA-ALGINATE GELS ENCAPSULATED IN A THIN SILICA FILM

Goeun Heo (1), Jonathan K. Sakkos (1), Sujin Yeom (2), Lawrence P. Wackett (2,3), Alptekin Aksan (1,3)

(1) Department of Mechanical Engineering
University of Minnesota
Minneapolis, MN, USA

(2) Department of Biochemistry, Molecular Biology, and Biophysics
University of Minnesota
Minneapolis, MN, USA

(3) Biotechnology Institute
University of Minnesota
St Paul, MN, USA

INTRODUCTION

Bioremediation has been considered as a promising method to treat wastewater due to its low cost compared with physicochemical processes [1]. Encapsulation of enzymes or microorganisms, which are required for degrading toxic chemicals in water, is an efficient way to protect the organisms against predation, temperature extremes, and pH variations. While encapsulation is an effective way to increase stability, inherent characteristics of encapsulation prevent living organisms from reproducing within the system due to space limitation, limiting the longevity and adaptability of the biodegradation processes. One way of solving this problem is by generating a more pliable space within the encapsulation medium in which cells can replicate and replace dead cells.

A Ca-alginate composite is a hydrogel, which can be easily depolymerized when exposed to a chelating solution, such as citric acid. This process is cytocompatible and not negatively affect the viability of the encapsulated bacteria (data not included). The protectant silica gel coating deposited on the alginate keeps the bacteria from leaking out, and is permeable enough to allow diffusion of water and chemicals. Silica is a good material for encapsulation due to its relatively low cost, thermal and chemical stability, and easily tunable mechanical and transport characteristics. The methods to encapsulate bacteria containing alginate beads inside silica coating has been shown by Callone et al [2]. However, the irregular shape and fragility of the thin silica coating around the alginate microspheres cause issues.

Here, we developed a method to encapsulate spherical Ca-alginate gels, which contain bacteria in a thin silica film. The fast reaction time (less than 2 minutes) between SNP (silica nano-particles) and silica alkoxide precursors keeps microorganisms alive during the co-encapsulation process. The proposed method is expected to help us develop a reproducible, self-sustaining, and high efficient biomaterial encapsulation system, as depicted in Figure 1.

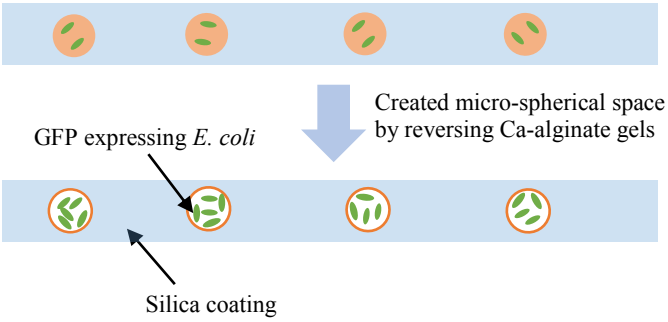

Figure 1: Silica micro-bioreactor

METHODS

Alginate Beads Electrospraying

Two percent (wt/wt) of alginate was dissolved in deionized water while stirring overnight. A small amount of GFP expressing *E. coli* was added into alginate solution, which was loaded into a 1 ml syringe. At a constant flowrate and a voltage differential (2.2 ml/hr, 4.5 kV/cm), the alginate solution was electrosprayed into 100 mM of $CaCl_2$ solution, producing Ca-alginate beads of homogeneous size (d~170μm).

Copyright 2016 The Organizing Committee for the 2016 Summer Biomechanics, Bioengineering and Biotransport Conference

Silica Synthesis and Coating Formation

TEOS (tetraethylorthosilicate) was hydrolyzed under acidic conditions as, detailed elsewhere [3]. SNP (TM40, 22 nm) were neutralized with the addition of 1M HCl. Four samples were prepared on top of cover slides attached to a petri dish with a 10 mm hole. The alginate gels were placed on the slides. Eighty µl of SNP and hydrolyzed TEOS at a ratio of 7:1 were added on top, which formed a thin film (thickness < 500µm). The Ca-alginate beads were floated onto the mixture solution, so after the silica polymerized, 30 µl of SNP + TEOS solution was added to prevent cell leakage. Citric acid (0.1 M) was neutralized with the addition of NaOH. Minimal media (M9) was prepared in deionized water.

Confocal Microscopy

Nikon A1Rsi Confocal with SIM Super Resolution microscopy was used to collect confocal images. Images of each sample were taken at 100 µm increments in the z direction, and stacked together.

RESULTS

0.1M of neutralized citric acid was added on top of the samples to depolymerize spherical Ca-alginate microspheres. Twenty mins later, the citric acid solutions were removed and minimal media (M9) was added and kept for 30 hours to allow cells to proliferate (Figure 2(d)). Controls were the beads in PBS (a), 0.1M citric acid + M9 (b), and M9 in the absence of citric acid (c). As expected, no growth was observed in the solid gel (a, PBS only and c, M9 only). However, when microspheres were reversed and with sufficient amount of nutrients, noticeable growth was obtained (b,d). The inset image of Figure 2(b,d)

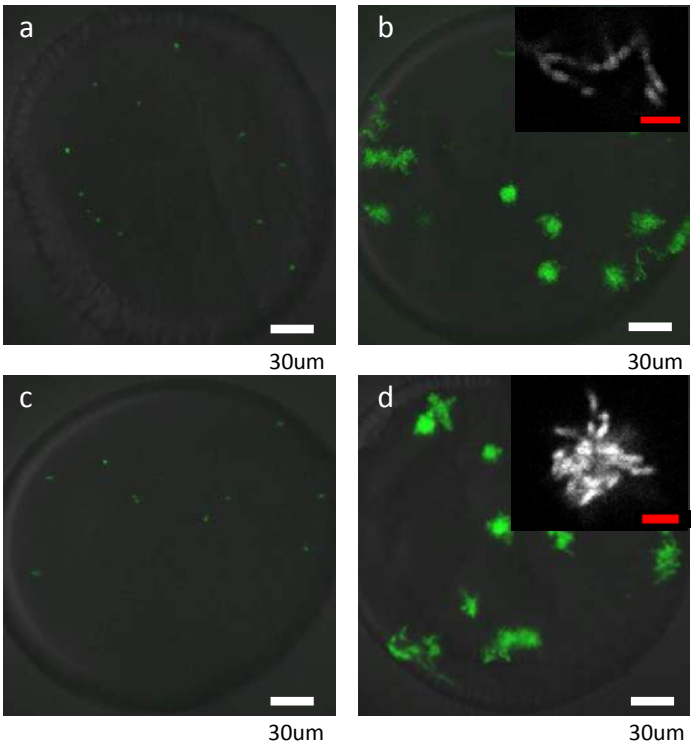

Figure 2: Confocal microscopy images of GFP expressing *E. coli* growth after 15hours incubated in (a) PBS, (b) 0.1M citric acid + M9, (c) M9, (d) 0.1M citric acid for 20 mins and replaced to M9 (for (b),(d): inset scale is 5µm)

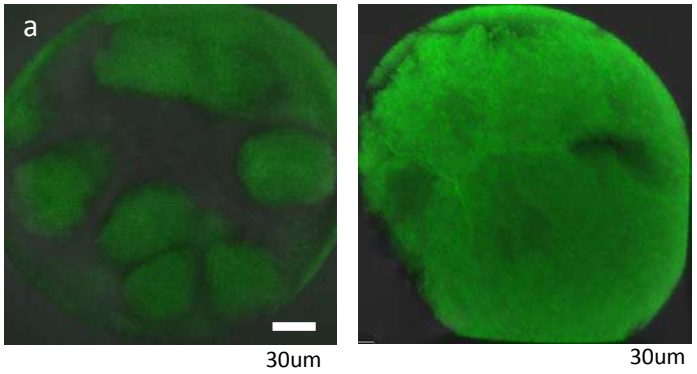

Figure 3: Confocal microscopy images of GFP expressing *E. coli* growth after 30hours incubated in (a) 0.1M citric acid + M9 (b) 0.1M citric acid for 20 mins and replaced to M9

shows the shape of bacterial colonies. When *E. coli* cells were exposed to citric acid for too long, the morphology of the colonies was unusual as the chelating solution also removed iron from the bacteria and iron is an essential nutrients for their growth [4].

Figure 3(a) shows the bacterial colonies in the presence of citric acid and media solution. When recombinant *E. coli* were exposed to citric acid for longer time periods (30 hours), necrotic regions developed. In Figure 3(b), Ca-alginate hydrogel microspheres were reversed and filled with media, the bacteria filled the free space, and stopped growing, presumably due to space limitation.

DISCUSSION

GFP expressing *E. coli* cells were encapsulated in Ca-Alginate beads embedded in a thin silica film. Divalent ions were taken out from the Ca-Alginate gels using chelator solution, and the spherical cavity that was generated was filled with media solution to promote bacterial growth. Confocal microscopy allowed observation of the growth of the bacteria. Thirty hours was sufficient time for bacteria to replicate and thus fill in the vacated cavity. The growth of bacteria was observed microscopically and morphology of individual bacteria and colonies were studied. This method shows promise for developing a sustainable, evolving bioreactor system for water remediation.

ACKNOWLEDGEMENTS

We ackowledge help of the UIC (University Image Center) at the University of Minnesota. This research is supported by Syngenta Inc. and a seed grant from the Biotechnology Institute.

REFERENCES

[1] Perullini, M et al., *J. Mater. Chem*., 20, 6479-6483, **2010**.
[2] Callone, E et al., *J. Mater. Chem*., 18, 4839-4848, **2008**.
[3] Mutlu, B et al., *J. Mater. Chem*. A, 1, 11051, **2013**.
[4] Appenzeller, B. M. R. et al., *Appl. Environ. Microbiol.* 71 no.9, 5621-5623, **2005**.

Copyright 2016 The Organizing Committee for the 2016 Summer Biomechanics, Bioengineering and Biotransport Conference

SB^{3}C2016
Summer Biomechanics, Bioengineering and Biotransport Conference
June 29 –July 2, National Harbor, MD, USA
SB^{3}C2016-854

FINITE ELEMENT MODELING OF CELL pH AND Ca^{2+} REGULATIONS FOR CHONDROCYTES WITH MIXTURE THEORY

Chieh (Jay) Hou (1), Eben G. Estell (2), Clark T. Hung (2), Gerard A. Ateshian (1)

(1) Mechanical Engineering
Columbia University
New York, NY, USA

(2) Biomedical Engineering
Columbia University
New York, NY, USA

INTRODUCTION

Chondrocytes, the single cell type within articular cartilage, are subjected to a challenging extracellular environment with high osmolarity, low pH and oxygen, and profound fluctuations, due to turnover of proteoglycan content and dynamic physiological loading of cartilage [1]. This environment is also inhomogeneous, with varying stiffness and composition from pericellular to territorial and extracellular matrix [2]. Such a challenging environment requires effective mechanisms for maintaining homeostasis of chondrocytes. In particular, cell volume, pH and Ca^{2+} regulation have been studied extensively in these cells [1].

There are similarly extensive mathematical modeling studies of cell physiology; most of these, however, are limited to 1D investigations of isolated cells in a homogeneous environment under isochoric conditions. Mixture theory is able to model solid stress and strain, transport of solvent and multiple solutes, and electrical potential within a mixture; with the implementation of mixture theory into the open-source finite element software FEBio [3], coupled with chemical reactions and active membrane transport [4,5], it becomes possible to model cell physiology within a 3D inhomogeneous environment, while accounting for cell and tissue deformation and interactions, and transport of solvent and solutes. As a first step, this study investigates whether the FEBio framework may reproduce basic models for cell pH and Ca^{2+} regulation (modeling of cell volume regulation has been described previously [5]).

SOLUTE-SELECTIVE MEMBRANE PATHWAY

Active membrane transport may be incorporated into mixture theory by adding an active momentum supply $\hat{\mathbf{p}}_a^\alpha$ into the linear momentum balance equation [5]; for solute-selective pathways the momentum balance reduces to

$$-\rho^\alpha \mathrm{grad}\tilde{\mu}^\alpha - \mathbf{f}^\alpha\left(\mathbf{v}^\alpha - \mathbf{v}^s\right) + \hat{\mathbf{p}}_a^\alpha = \mathbf{0} \tag{1}$$

where ρ^α is the apparent density, $\tilde{\mu}^\alpha$ the mechanoelectrochemical potential, $\mathbf{f}^\alpha$ the diffusive drag tensor, and $\mathbf{v}^\alpha$ the velocity, while the superscript α refers to solute α, and s is the solid. With the constitutive relation for $\tilde{\mu}^\alpha$ and the diffusivity $\mathbf{d}_m^\alpha = R\theta\varphi^w c^\alpha\left(\mathbf{f}^\alpha\right)^{-1}$ [6], where R is the universal gas constant, θ the absolute temperature, φ^w the solvent volume fraction, and c^α the solute concentration, Eq. (1) can be inverted to produce the molar flux of solute α

$$\mathbf{j}_m^\alpha = \mathbf{j}_a^\alpha - \frac{\varphi^w \mathbf{d}_m^\alpha}{R\theta}\cdot\left(c^\alpha z^\alpha F_c \mathrm{grad}\psi + R\theta\,\mathrm{grad}c^\alpha\right) \tag{2}$$

where z^α is the charge of solute α, F_c is Faraday's constant, and ψ the electrical potential; $\mathbf{j}_a^\alpha = \mathbf{d}_m^\alpha\cdot\hat{\mathbf{p}}_a^\alpha$ is the active part of $\mathbf{j}_m^\alpha$ and the remaining term is the passive component. Eq.(2) can be rewritten as

$$\mathbf{j}_m^\alpha = \mathbf{j}_a^\alpha - \varphi^w\tilde{\kappa}^\alpha\mathbf{d}_m^\alpha\cdot\mathrm{grad}\tilde{c}^\alpha \tag{3}$$

with the effective solute concentration $\tilde{c}^\alpha$ and the partition coefficient $\tilde{\kappa}^\alpha$ defined in FEBio. With Eq. (3), the implementation of solute-selective pathways into FEBio can be accomplished by adding $\mathbf{j}_m^\alpha$ to the total flux $\mathbf{j}^\alpha = \mathbf{j}_0^\alpha + \mathbf{j}_m^\alpha$, where $\mathbf{j}_0^\alpha$ is the original passive molar flux.

CELL pH REGULATION

Under an acidic extracellular environment (pH ~ 6.8), chondrocytes extrude their intracellular acid primarily via a H^+ pump and $Na^+\times H^+$ exchanger to maintain cytoplasmic pH ($pH_i \sim 7.1$) [1]. Weak acids, such as CO_2/HCO_3^- solution, and bases in the cytoplasm, act as buffers. Mathematical modeling of cell pH regulation, as in Leem's study [7], generally employ the law of mass action to model reactions of buffers, coupled with the buffering power defined within the Henderson-Hasselbalch equation to evaluate the cell pH; cell volume

Copyright 2016 The Organizing Committee for the 2016 Summer Biomechanics, Bioengineering and Biotransport Conference

regulation is normally not considered.

In this study, a 1D cell model previously created for cell volume regulation is used [5] (Fig. 1a), with Na^+, K^+, Cl^-, n (neutral solute) across the membrane, c^F (fixed charge density) in the protoplasm, and Na^+-K^+ pump on the membrane. Additionally, H^+, CO_2, HCO_3^- are allowed to permeate across the membrane, coupled with a CO_2/HCO_3^- reaction in the protoplasm; H^+ pump and $Na^+ \times H^+$ exchanger are incorporated in the membrane. The reaction is described by

$$CO_2 + H_2O \underset{k_{-1}}{\overset{k_1}{\rightleftarrows}} H^+ + HCO_3^- \tag{4}$$

where k_1 and k_{-1} are the reaction rates. The molar flux of H^+ pump is simplified from Eq. (3) and defined by

$$\mathbf{j}^{\mathrm{H}}_{\mathrm{Hp}} = j^{\mathrm{H}}_{\mathrm{Hp}}\mathbf{n} \tag{5}$$

where $j^{\mathrm{H}}_{\mathrm{Hp}}$ is the pumping flux for H^+. The molar flux of $Na^+ \times H^+$ exchanger is simplified from Eq. (3) and defined by

$$\mathbf{j}^{\mathrm{Na}}_{\mathrm{NaH}} = -\varphi^w d_{\mathrm{NaH}}\left(\tilde{\kappa}^{\mathrm{Na}}\mathrm{grad}\tilde{c}^{\mathrm{Na}} - \tilde{\kappa}^{\mathrm{H}}\mathrm{grad}\tilde{c}^{\mathrm{H}}\right) = -\mathbf{j}^{\mathrm{H}}_{\mathrm{NaH}} \tag{6}$$

where d_{NaH} is the diffusivity of Na^+ and H^+ for this pathway.

Analytical expressions from mixture theory can be similarly derived [5] and solved numerically in MATLAB. With the Henderson-Hasselbalch equation [7], pH_i is calculated according to

$$\mathrm{dpH}_i/\mathrm{d}t = Aj^{\mathrm{H}}/\varphi^w V\beta \tag{7}$$

where A is the area and V the volume of the cell, and j^{H} is the total H^+ flux; $\beta = 2.303\cdot[\mathrm{HCO_3^-}]_i$ is the buffering power of the CO_2/HCO_3^- buffer, where $[\mathrm{HCO_3^-}]_i$ is the HCO_3^- concentration in the protoplasm.

H^+ pump is required to maintain the cell pH while its inhibition will acidify the cell (Fig. 2b). Results from mixture theory agree with the equations of Leem's study [7], since the change in cell volume is minimal. The small difference between the MATLAB implementation and FEBio occurs because the former uses the approximate assumption of buffer equilibrium in Eq. (7).

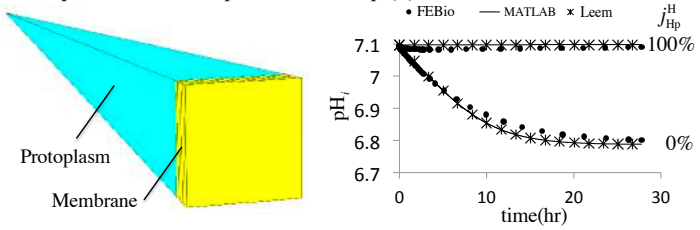

Figure 2: (a) 3D finite element model of spherical cell using spherical symmetry; (b) pH_i response with 0% and 100% H^+ pump flux, from FEBio, MATLAB, and Leem's study [7]**.**

CELL Ca^{2+} REGULATION

In common with all mammalian cells, chondrocytes have low free Ca^{2+} in the cytoplasm ($[Ca^{2+}]_i \approx 80\mathrm{nM}$), while most Ca^{2+} is bound and stored in organelles ($[Ca^{2+}]_{\mathrm{total}} \approx 1\mathrm{mM}$) [1]. Mechanisms that maintain low Ca^{2+} levels and induce potential oscillations include Ca^{2+} pump, inositol triphosphate (IP_3) -sensitive Ca^{2+} channel, and mechano-sensitive Ca^{2+} channel on the cell and organelle membranes, such as the endoplasmic reticulum (ER) membrane. The free Ca^{2+} level affects cell adhesion, aggregation, matrix synthesis, and differentiation [8]. Mathematical modeling of cell Ca^{2+} regulation, such as in LeBeau's study [9], generally considers the mass balance in the cytoplasm, with Ca^{2+} flux induced by constant-field electro-diffusion, Ca^{2+} pumps, and Ca^{2+} channel with several states coordinated by reactions. In this study we use a model similar to that proposed in LeBeau's study to examine Ca^{2+} regulation with FEBio.

The cell model for volume regulation is used again [5], while the protoplasm is divided into the ER, ER-membrane, and cytoplasm domains (Fig. 2a). Ca^{2+} is allowed to permeate across the ER-membrane; a fixed charge c^F is prescribed in the protoplasm (all three domains); a Ca^{2+} pump (Hill equation) and Ca^{2+} channel (LeBeau [9]) are modeled on ER-membrane. The Ca^{2+} pump molar flux is

$$\mathbf{j}^{\mathrm{Ca}}_{\mathrm{pH}} = k_{\mathrm{pH}}[\mathrm{C}_2]\mathbf{n} \tag{8}$$

where k_{pH} is constant and $[\mathrm{C}_2]$ is coordinated by the reaction

$$\mathrm{C}_1 \underset{k^{\mathrm{pH}}_{-1}}{\overset{k^{\mathrm{pH}}_{1}}{\rightleftarrows}} \mathrm{C}_2 \tag{9}$$

where the conformational states C_1, C_2 are solid-bound molecules on ER membrane, and $k^{\mathrm{pH}}_1 = V_p[Ca^{2+}]_i^2/(K_p^2 + [Ca^{2+}]_i^2)$ (Hill equation with constants V_p and K_p) and k^{pH}_{-1} are reaction rates. The molar flux of Ca^{2+} channel is

$$\mathbf{j}^{\mathrm{Ca}}_{\mathrm{cL}} = -d_{\mathrm{cL}}\varphi^w\tilde{\kappa}^{\mathrm{Ca}}\mathrm{grad}\tilde{c}^{\mathrm{Ca}} \tag{10}$$

where $d_{\mathrm{cL}} = k_{\mathrm{cL}}[\mathrm{O}]^4$ and $[\mathrm{O}]$ is coordinated by the reactions

$$\mathrm{S} \underset{k^{\mathrm{cL}}_{-1}}{\overset{k^{\mathrm{cL}}_{1}}{\rightleftarrows}} \mathrm{O} \overset{k^{\mathrm{cL}}_{2}}{\rightarrow} \mathrm{I}_1 \overset{k^{\mathrm{cL}}_{3}}{\rightarrow} \mathrm{S} \text{ and } \mathrm{I}_1 \overset{k^{\mathrm{cL}}_{4}}{\rightarrow} \mathrm{I}_2 \overset{k^{\mathrm{cL}}_{5}}{\rightarrow} \mathrm{S} \tag{11}$$

where the conformational states S, O, I_1, I_2 are solid-bound molecules on ER membrane; $k^{\mathrm{cL}}_1 = \alpha_1[Ca^{2+}]_i^3/(\beta_1^3 + [Ca^{2+}]_i^3)$ (constant α_1 and β_1), k^{cL}_{-1}, k^{cL}_2, k^{cL}_3, k^{cL}_4, k^{cL}_5 are reaction rates. Analytical expressions from mixture theory are similarly derived and solved in MATLAB.

$[Ca^{2+}]_i$ oscillations are observed (Fig. 2b). The signaling factor IP_3 in the cytoplasm may induce oscillations by increasing the value of k^{cL}_4. Results from FEBio agree with those from MATLAB. In LeBeau's study $[Ca^{2+}]_{\mathrm{ER}}$ in the ER is assumed to remain constant, producing oscillations different in period and amplitude compared to those from FEBio; they agree with those from MATLAB when the latter is modified to adopt that assumption.

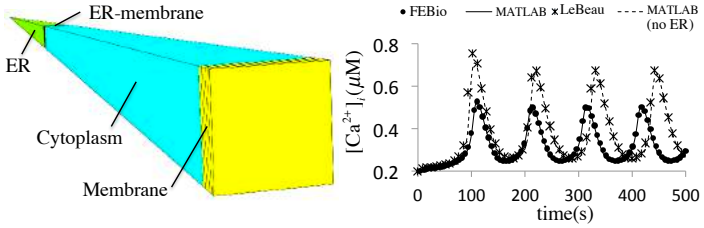

Figure3: (a) Cell finite element model showing four domains; (b) $[Ca^{2+}]_i$ oscillations from FEBio, MATLAB (with and without ER $[Ca^{2+}]_{\mathrm{ER}}$ fluctuations), and LeBeau's study [9].

SUMMARY. This study demonstrates that classical models of cell physiology may be reproduced with mixture theory using MATLAB and FEBio. The FEBio implementation relies on the incorporation of chemical reactions and active membrane transport pathways. FEBio predictions reproduced those of standard 1D cell models under constant volume; however, FEBio is also able to analyze fully 3D models of deforming cells and their surrounding matrix.

ACKNOWLEGEMENTS. NIH RO1 GM083925.

REFERENCES. [1] R.Wilkins, *J Membrane Biol*, 177:95-108, 2000. [2] R.E.Wilusz, *Matrix Biol*, 39:25-32, 2014. [3] S.A.Maas, *J Biomech Eng-T ASME*, 134, 2012. [4] G.A.Ateshian, *Biomech Model Mechanobiol*, 13:1105-1120, 2014. [5] C.Hou, *SB3C2015,* 356, 2015. [6] G.A.Ateshian, *Biomech Model Mechanobiol*, 6:91-101, 2007. [7] C.Leem, *J Physiol-London*, 509:471-485, 1998. [8] A.Gigout, *Osteoarthr Cartilage*, 13:1012-1024, 2005. [9] A.LeBeau, *J Gen Physiol*, 113:851-871, 1999.

SB^{3}C2016
Summer Biomechanics, Bioengineering and Biotransport Conference
June 29 –July 2, National Harbor, MD, USA
SB^{3}C2016-855

NONLINEAR CREEP BEHAVIOR OF UTEROSACRAL AND CARDINAL LIGAMENTS

Adwoa Baah-Dwomoh (1), Ting Tan (1), Raffaella De Vita (1)

(1) Mechanics of Soft Biological Systems Laboratory
Biomedical Engineering and Mechanics Department
330A Kelly Hall, Virginia Tech
Blacksburg, VA, USA

INTRODUCTION

It is estimated that pelvic organ prolapse (POP), the descent of organs into the vaginal cavity, affects approximately 3.3 million women annually in the United States [1]. Damage to the uterosacral (USL) and cardinal (CL) ligaments, two major supportive pelvic ligaments, is thought to be one of the major causes of POP [2]. These ligaments are used to surgically treat POP: they are either sutured to surrounding pelvic tissues or sutured to a synthetic mesh to help support the prolapsed organ. Both of these procedures are marred by complications, with almost as many as 25% of women who have had a corrective surgery experiencing a reoccurrence of organ prolapse [3]. Current surgical techniques and mesh materials for the treatment of POP have been developed without considering the mechanical properties of the native ligaments of the pelvic organ complex. Determining the biomechanical properties of the USL and CL is imperative to help develop improved surgical techniques and mesh materials. To date there are no studies that characterize the nonlinear creep properties of these ligaments, including the effect of multiple and consecutive constants loads. The goal of this study is thus to reveal nonlinearities in the creep behavior of swine USL and CL using planar biaxial testing and digital image correlation. Biaxial mechanical tests better represent physiologically the forces acting on these ligaments *in vivo* compared to uniaxial mechanical tests. Creep behavior is also physiologically important for the ligaments since they are subjected to constant loads in-vivo over time.

METHODS

USL and CL from three adult swine (3 to 4 years old, approximately 450 lbs) were obtained with approval from the Institutional Animal Care and Use Committee at Virginia Tech. Specimens were carefully dissected and were cut to be approximately 3 x 3 cm^2, then frozen at -20 °C before biaxial mechanical testing. A speckle pattern was created and applied to each specimen using methylene blue 1% and an aerosol fast dry gloss white paint to create contrast. The specimens were then gripped with 4 hooks on each side and mounted into a planar biaxial testing system (Instron, UK) equipped with four 20 N load cells. The two axial directions were selected to be the main in vivo loading direction of the ligaments and the direction perpendicular to it (Figure 1). Specimens (n=9) were split into three groups and each specimen was submerged in a PBS bath. Each specimen in group one was preloaded to 0.1 N and preconditioned from 0.1 N to 1 N at 0.05 N/s for 10 cycles equally along the two loading directions. After preconditioning, the specimen was unloaded, allowed to recover for 10 min and then subjected to three creep tests. The specimen was stretched at a rate of 0.05 N/s and held at a constant equi-biaxial load of 1 N for 20 min (1200 s), then unloaded and allowed to recover for 200 min (12000 s). A second creep test, followed by recovery, and a third creep test were performed on the specimen using equal load over equal time interval. Specimens in groups two and three followed a similar protocol as specimens in group one, however, specimens were preconditioned for 0.1 N to 2 N at 0.05 N/s for 10 cycles and creep testing at an equi-biaxial load of 2 N for group two and specimens were preconditioned for 0.1 N to 3 N at 0.05 N/s for 10 cycles and creep testing at an equi-biaxial load of 3 N for group 3. For all groups of specimens, a 3D digital image correlation system (Correlated Solutions, Inc., SC) was used to accurately measure the Langrangian strain.

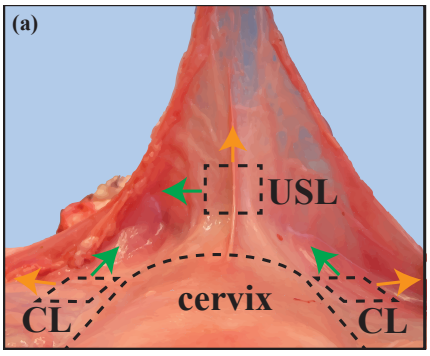

Figure 1: Image indicating the USL/CL complex. The arrows indicated the main *in vivo* loading direction (orange) and loading direction perpendicular to the main *in vivo* loading direction (green).

RESULTS

Specimens exhibited the highest increase in strain over time during the first creep test (Figure 2) in both loading directions. This

Copyright 2016 The Organizing Committee for the 2016 Summer Biomechanics, Bioengineering and Biotransport Conference

held true for the specimens in all 3 groups, that is for specimens subjected to 3 consecutive creep tests at 1 N (not shown), 2 N (Figure 2), and 3 N (not shown).

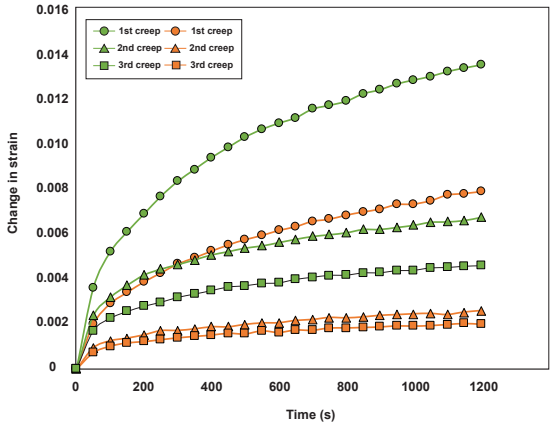

Figure 2: Creep data for one representative specimen in the main *in vivo* loading direction (orange) and perpendicular to the main *in vivo* loading direction (green) undergoing 3 consecutive creep tests at an equi-biaxial load of 2 N. For each direction, creep during the 1st test is the highest, followed creep in the 2nd and 3rd tests.

The mean stress for each test group was determined (Table 1). Mean isochronal stress strain data were calculated by selecting four time points during the first creep tests from each group (t=0 s, 100 s, 600 s, 1200 s), calculating the mean strain for each group at those time points during the first creep test, and plotting the mean stress vs the mean strain for each time point. The mean isochronal curves (Figure 3) show the nonlinear creep behavior in both the main *in vivo* loading direction and the perpendicular to the main *in vivo* loading direction.

Table 1: Calculated mean stress in the main *in vivo* loading direction and perpendicular to the main *in* vivo loading direction used for isochronal stress-strain plot (n=9)

	Mean stress (MPa) Main *in vivo*	Mean stress (MPa) Perp *in vivo*
Group 1	0.058	0.053
Group 2	0.097	0.101
Group 3	0.130	0.121

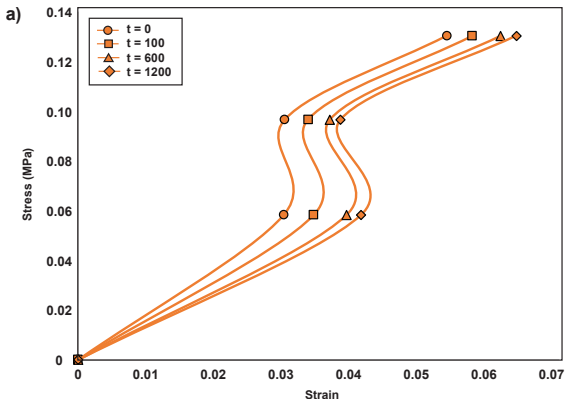

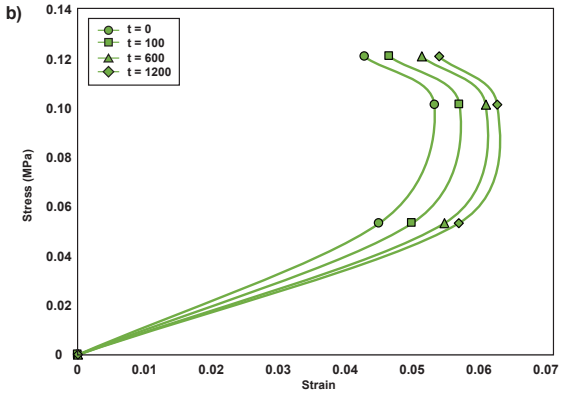

Figure 3: Mean isochronal stress strain data (a) along the main *in vivo* loading direction (orange) and (b) perpendicular to the main *in vivo* loading direction (green). These data show the nonlinear creep behavior of the USL/CL complex.

DISCUSSION

Specimens exhibited the highest creep during the first biaxial test and showed less creep behavior for each subsequent biaxial test for all test groups (Figure 2). We hypothesize that this occurs due to water vacating the USL/CL specimen during the first creep and a rearrangement of the collagen fibers, reducing the movement of collagen fibers during subsequent creep tests. Mean isochronal stress strain data show the nonlinear viscoelastic behavior of USL/CL in both the main *in vivo* loading direction and perpendicular to the main *in vivo* loading direction. The origin of the observed nonlinearity is currently unknown and is being investigated by our group.

This is the first study on the nonlinear biaxial viscoelastic behavior of pelvic floor ligaments. Quantifying the viscoelastic behavior of these ligaments in physiologically relevant loading conditions is important when performing reconstructive surgeries for POP. Such results are expected to greatly benefit future surgeons and researchers in material science by giving them the necessary data to create better surgical techniques and mesh materials. By understanding the mechanical properties of these ligaments, such as their viscoelastic behavior, mesh materials can be made to have similar properties as the native tissue so as to improve their current *in vivo* performance.

ACKNOWLEDGEMENTS

This research is supported by the National Science Foundation under PECASE Award No.1150397.

REFERENCES

[1] Price, Lane FL, Craig JB, Nistor G, Motakef S, Pham QA, Keirstead H. The effect of age and medical comorbidities on in vitro myoblast expansion in women with and without pelvic organ prolapse. *Female Pelvic Med Reconstr Surg*.20:281--286, 2014

[2] Petros. Springer, New York, NY, USA, 3rd edition, 2011.

[3] Whiteside JL, Weber AM, Meyn LA, Walters MD. Risk factors for prolapse recurrence after vaginal repair. *American journal of obstetrics and gynecology.* 191(5):1533-8, 2004

[4] Becker and De Vita, Biaxial mechanical properties of swine uterosacral and cardinal ligaments. *Biomech. Model. Mechanobiol.,* 14:549--560, 2015

Copyright 2016 The Organizing Committee for the 2016 Summer Biomechanics, Bioengineering and Biotransport Conference

SB³C2016
Summer Biomechanics, Bioengineering and Biotransport Conference
June 29 –July 2, National Harbor, MD, USA
SB³C2016-856

PORCINE SMALL INTESTINAL SUBMUCOSAL VALVE DYNAMICS IN THE AORTIC POSITION

Omkar V. Mankame[1] , Makensley Lordeus[1] , Lilliam Valdes-Cruz[2] , Steven Bibevski[2] , Frank Scholl[2] , Sarah M Bell[2] , Ivan Baez[2] , Sharan Ramaswamy[1]

(1) Department of Biomedical Engineering, Florida International University, Miami, Florida, United States

(2) Joe DiMaggio Children's Hospital, Memorial Regional Hospital, Hollywood, Florida, United States

INTRODUCTION

Critical congenital heart valve diseases have extremely limited treatment options. Lack of sizing options and an inability of a prosthetic valve to grow with the pediatric patient are the primary technical barriers. Tissue engineering is a concept which can provide for growth, self-repair and a permanent approach for replacing defective heart valves[1]. Recently cardiovascular substitutes made from extra cellular matrix derived from the porcine small intestinal submucosa (PSIS) has shown immense potential for *in vivo* tissue regeneration as the ECM-PSIS bioscaffold degrades[2, 3]. PSIS bioscaffold is a unique acellular, biodegradable soft tissue material which allows native cells to migrate on it and thus remodels into healthy tissue. In our group, PSIS-valves have been used in the treatment of compassionate care cases involving neonates suffering with critical valve defects. To our knowledge we are the first and only group to have employed this treatment in pediatric patients, with the valve observed (via echocardiography) to function flawlessly for over a year thus far.

Here we conducted an organized functional assessment of PSIS valves in order to define its opening and closing characteristics. To achieve this task, we utilized a dedicated Pulse Duplicator System (Vivitro Laboratories, Victoria, Canada), which has been modified to evaluate the valves in physiological conditions as that of the functioning heart[4]. Through this study we aim to determine functional effectiveness of **tri-leaflet** PSIS bioscaffold valve sutured in the **Aortic position** using a pulse simulator.

METHODS

Fresh porcine hearts were collected from a slaughterhouse which is USDA approved (Mary's Ranch Inc., Miami, FL). Aortic heart valves along with the aortic conduit were then harvested by isolating the aortic root, under sterile condition. These extracts were stored in a cocktail solution prepared by mixing PBS solution and Protease Inhibitor tablets (Sigma-Aldrich). The native aortic valve was excised and in its place, the PSIS bioscaffold assembled aortic valve construct was sutured into the valve location, within the porcine aortic conduit.

Once the Aortic Valves were constructed, they were then introduced in a Pulse Duplicator System (Vivitro Laboratories, Victoria, Canada). We have made use of this system in our previous experiments where we tested flexible-leaflet valve implants[2]. In order to assess hydrodynamic parameters of PSIS based valves, the normal physiological environment of the native human aortic valve was recapitulated. The mechanical unit of the pulse duplicatior comprises of a piston pump, various chambers which mimic those of the heart and an integrated software system. Tri-leaflet PSIS valves assembled from sheets of PSIS bioscaffold (Cormatrix, Roswell, GA) were mounted in the aortic position within the pulse duplicator. A 0.9% saline solution was introduced into the system through the atrial chamber, to fill the loop with fluid. . The heart rate was set to 70 beats/min. A physiological waveform representative of the pumping action of the left ventricle was selected (in the case of the Vivitro system the S50 waveform was chosen for all hydrodynamic tests) to drive flow through the loop. To facilitate the measurement of flowrates and pressure, external instrumentation namely a flowmeter and three pressure transducers were introduced into the system. Flow probe was positioned at the inlet of the aortic root and pressure transducers at ventricular, atrial and aortic locations. We first calibrated the machine to ensure correct flow and pressure output readings by using a pair of bi-leaflet mechanical valves of known performance, placed in the mitral and aortic positions respectively. Subsequently, the mechanical valve in the aortic position was replaced with the PSIS-valve. Commercially

Copyright 2016 The Organizing Committee for the 2016 Summer Biomechanics, Bioengineering and Biotransport Conference

available bioprosthetic valves (Medtronic Freestyle, Medtronic, Minneapolis, MN) were also tested to serve as a flexible control group.

The effective orifice area (EOA) and energy loss for the valve was defined as follows:

$$EOA = \frac{QRMS}{51.6 * \Delta P} \quad \text{..... (1)}$$

$$Energy\ Loss = \left(\frac{\rho * v2}{2}\right) * \left(1 - \left(\frac{EOA}{Aglass.tube}\right)\right)^2 * SV \quad \text{..... (2)}$$

RESULTS

Hydrodynamic evaluation of ECM aortic valves revealed that the resulting flow waveforms were physiologically-shaped (Fig. 1). Robust forward flow was observed in both the heart valves (Fig. 1). It was found that the EOAs of both the PSIS and Bioprosthetic valves were comparable making the bioprosthetic valves an objective control (Table 1). Between the PSIS and bioprosthetic valves, it was observed that both the energy loss and regurgitant fraction metrics were statistically different ($p < 0.05$) between the two groups.

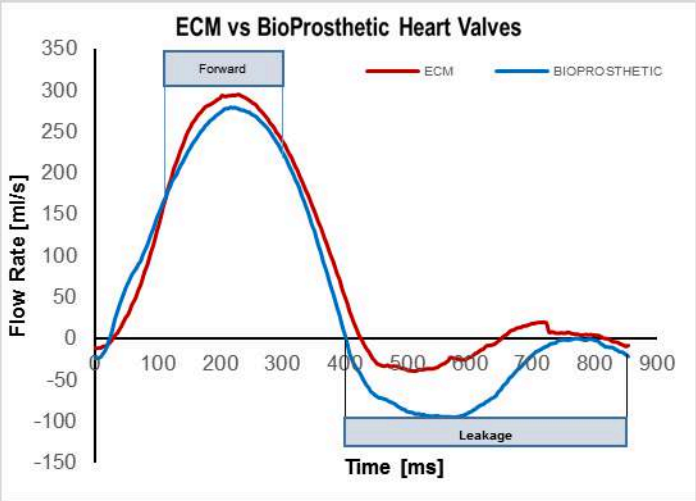

Figure 1: Flow waveforms of PSIS-ECM and Bioprosthetic valves tested in the aortic position using a Vivitro Pulse Duplicator System.

Table 1: Hydrodynamic Parameters of n=3 Aortic PSIS ECM Valves and n=2 Bioprosthetic Valves for Systolic Phase. Note: '*' indicates *statistically significant* (*P < 0.05*).

Aortic Valves	ΔP (mmHg)	Q_{rms} (ml/s)	EOA (cm^2)	Systolic Energy Loss (mJ)*	RF (%)*
PSIS ECM (n=3)	24.0 ± 2.4	239.9 ± 44.4	0.96 ± 0.21	36.4 ± 19.1	13.8 ± 9.8
Bioprosthetic (n=2)	18.1 ± 1.9	244.4 ± 3.6	1.12 ± 0.08	2.9 ± 0.7	51.3 ± 0.8

DISCUSSION

The *in-vitro* testing of the heart valves in the aortic location clearly demonstrates robust acute functionality of PSIS valves when compared to the bioprosthetic control valves thus validating further investigation of the PSIS valves for valve replacement. We believe that the greater leakage in the control valves was potentially due to paravalvular leakage in the bioprosthetic valve, probably due to greater size mismatch between bioprosthetic annulus and the valve holder that it was secured to; despite this, its forward flow rate was strong. . On the other hand the significantly greater energy loss in the PSIS valves ($p < 0.05$) was possibly due to its stiffer leaflet material properties. This may be an area of concern for the long term functionality of ECM valves, depending on its potential to support de novo valvular tissue growth *in vivo*. Hence, our next steps will involve further hydrodynamic testing and optimization of PSIS bioscaffold valves as well as *in-vivo* studies.

ACKNOWLEDGEMENTS

We would like to thank Vivitro Laboratories, Victoria, Canada for their valuable assistance.

REFERENCES

1. Stock UA, Vacanti JP, Mayer Jr JE, Wahlers T. Tissue engineering of heart valves -- current aspects. Thorac Cardiovasc Surg 2002;50(3):184-93.
2. Gerdisch MW, Shea RJ, Barron MD. Clinical experience with CorMatrix extracellular matrix in the surgical treatment of mitral valve disease. J Thorac Cardiovasc Surg 2014;148(4):1370-8.
3. Slachman FN. Constructive remodeling of CorMatrix extracellular matrix after aortic root repair in a 90-year-old woman. Ann Thorac Surg 2014;97(5):e129-31.
4. Ramaswamy S, Salinas M, Carrol R, Landaburo K, Ryans X, Crespo C, Rivero A, Al-Mousily F, DeGroff C, Bleiweis M and others. Protocol for relative hydrodynamic assessment of tri-leaflet polymer valves. J Vis Exp 2013(80):e50335.
5. Love JW; Cardiomend LLC, Santa Barbara, CA, assignee. Methods of Heart Valve Repair. USA. 1998.
6. Kirklin J, Smith D, Novick W, Naffel D, Kirklin J, Pacifico A, Nanda N, Helmcke F, Bourge R. Longterm function of cyropreserved aortic homografts: Ten year study. J Thorac Cardiovasc Surg 1993;106(154-166).

Copyright 2016 The Organizing Committee for the 2016 Summer Biomechanics, Bioengineering and Biotransport Conference

SB^{3}C2016
Summer Biomechanics, Bioengineering and Biotransport Conference
June 29 –July 2, National Harbor, MD, USA
SB^{3}C2016-857

A MODEL TO DETERMINE THE EFFECT OF AXIAL STRETCH ON LUMEN COLLAPSE OF ARTERIES

Fatemeh Fatemi Far, Hai-Chao Han

Department of Mechanical Engineering
The University of Texas at San Antonio
San Antonio, TX, USA

INTRODUCTION

Blood vessels collapse when the transmural pressure, the difference between the lumen pressure and external pressure, is highly negative [1, 2]. The lumen collapse is commonly seen in vein since vein walls are thinner and the lumen pressure is low. However, arteries may collapse under certain conditions such as peripheral arteries compressed by pressure cuffs or intramyocardial coronary arteries during left ventricle contraction [2, 3]. Also it has been reported that negative transmural pressure is induced at the throat of the stenosis in arteries under cyclic pressure that may cause critical conditions related to heart attack and stroke [2, 4].

Buckling equation have been developed by assuming the artery as a thin-walled cylindrical tube of linear elastic material subjected to transmural pressure [1]. This model does not account for thick, nonlinear arterial wall under axial stretch [2]. With the significant axial stretch in arteries and veins in vivo [5], it is important to understand its effects on mechanical stability of arteries.

Therefore, the objectives of this study were to develop and validate buckling equation that takes into account the nonlinear anisotropic material for thick-walled artery under various axial stretch ratios, and investigate the post-buckling behavior of arteries under negative transmural pressure using numerical simulations.

METHODS

Buckling Model Analysis: Arteries were modeled as thick-walled cylindrical tubes, under internal pressure p_i, external pressure p_e and axial stretch ratio λ_z. The arterial wall was assumed to be nonlinear elastic, incompressible, anisotropic material with an exponential Fung strain energy function [6].

Based on the curved beam bending theory and classic model for thin-walled elastic tube [1], we assumed that the curvature change κ for the initially circular vessel took the shape of a sinusoidal waveform when the collapse occurs at buckling.

$$\kappa = \frac{1}{\rho_m} - \frac{1}{r_m} = C.\sin(n\theta) \tag{1}$$

where C is a small-value constant, n is a positive integer and r_m and ρ_m are neutral axis radius in loaded and deformed conditions, respectively. Using the deformation gradient matrix in cylindrical coordinates and neglecting the higher order terms of C, the incremental circumferential strain at location (r, θ) becomes

$$\Delta E_\theta = -C\left(\frac{\pi r}{\Theta_0 R}\right)^2 n(r - r_m)cos(n\theta) \tag{2}$$

where (R, Θ) is the initial coordinates in the unloaded condition and $2\Theta_0$ is the opening angle of the artery (due to residual stress).

The incremental circumferential stress $\Delta\sigma_\theta$ was then determined based on the strain energy function and the bending moment M_θ was determined by integrating the moment generated by the incremental circumferential stress $\Delta\sigma_\theta$ across the arterial wall. Accordingly, the critical buckling pressure was obtained and can be expressed in form of:

$$p_{cr} = (p_e - p_i)_{critical} = \frac{3EI}{{r_m}^3} \tag{3}$$

Where EI is an "equivalent rigidity" that is an integral function of strain, material parameters and axial stretch ratios. Note that although the expressions are similar to the classic thin-walled tube buckling, both EI and r_m are complicated functions of material constants and strains, including axial strain.

Simulations based on the buckling equations were done for a set of five porcine coronary arteries with Fung strain energy function material constants reported by Wang et al.,[7]. We assumed the coronary arteries all have the same inner diameter of 0.8 mm, wall thickness of 0.5 mm and a length of 10 mm in the unloaded condition (for simplicity and because the dimension data was not reported in Wang et al.,[7]).

Finite Element Analysis of buckling: For comparison and post-buckling analysis, buckling analysis was conducted for the same set of five arteries using the commercial FEA package ABAQUS®. An initial imperfection (1% variance in the thickness) was used in our models to facilitate the buckling. Axial displacements were applied at both ends to create designated axial stretch ratios in the models. An external pressure was applied to generate buckling and keep increasing to reach post-buckling deformation. The lumen aspect ratio and lumen

Copyright 2016 The Organizing Committee for the 2016 Summer Biomechanics, Bioengineering and Biotransport Conference

area were determined to characterize the deformation and shape change due to pressure load and buckling.

RESULTS

Our results demonstrated that arteries were initially compressed by the external pressure and then buckled when the external pressure exceeded a critical value. This value depends upon the axial stretch ratio and material properties of arterial wall. FEA simulations showed that the aspect ratio of lumen increased dramatically post- buckling.

The critical buckling pressure of the coronary arteries obtained using both the theoretical model equation and FEM simulations matched well and changed with designated stretch ratios (Fig.1). Our simulations also captured the post buckling behavior of the arteries. It was seen that when the pressure continued to increase beyond the critical buckling pressure, the lumen aspect ratio continued to increase nonlinearly (Fig. 2).

DISCUSSION

We developed a buckling equation that described the critical buckling of nonlinear orthotropic arterial wall buckling under transmural pressure and validated with FEA simulations. Our simulation results showed that the lumen aspect ratio continued to increase nonlinearly with increasing the external pressure beyond the critical buckling pressure. Furthermore, the critical buckling pressures of arteries predicted by FEA were in good agreement with the theoretical predictions.

Compared with previous studies [1, 8], the advantage of the buckling equation obtained in this study lies in its capability to model nonlinear anisotropic material for thick-walled artery. A new finding from the current study is that the axial stretch ratio affects the critical buckling pressure.

There were a few limitations in this study. One limitation is that our analysis was limited to the arterial wall as a single layer anisotropic material, although arterial walls are multilayered structures. Another limitation in our simulation is that the boundary conditions were simplified with no surrounding tissue support.

Local collapse may occur in coronary arteries distal to stenosis or due to myocardial bridge. This causes vessel compression resulting in hemodynamic changes which probably lead to angina, myocardial ischemia, cardiac arrhythmias, syncope or even sudden cardiac death [3]. Thus understanding of artery cross section buckling (collapse) behavior is important in understanding these vascular disorders.

ACKNOWLEDGEMENTS

This work was supported by grant R01HL095852 from the National Institutes of Health and partially supported by grant 11229202 from National Natural Science Foundation of China.

REFERENCES

[1] Fung YC. Biomechanics: circulation. New York: Springer; 1997.

[2] Han HC, Chesnutt JK, Garcia JR, Liu Q, Wen Q. Artery buckling: new phenotypes, models, and applications. Ann Biomed Eng. 2013;41:1399-1410.

[3] Corban MT, Hung OY, Eshtehardi P, Rasoul-Arzrumly E, McDaniel M, Mekonnen G, et al. Myocardial BridgingContemporary Understanding of Pathophysiology With Implications for Diagnostic and Therapeutic Strategies. J Am Coll Cardiol. 2014;63:2346-2355.

[4] Tang D, Yang C, Kobayashi S, Ku DN. Steady flow and wall compression in stenotic arteries: a three-dimensional thick-wall model with fluid-wall interactions. J Biomech Eng. 2001;123:548-557.

[5] Han HC, Fung YC. Longitudinal strain of canine and porcine aortas. J Biomech. 1995;28:637-641.

[6] Fung YC. Biomechanics: Mechanical Properties of Living Tissues. 2nd ed. New YorK: Springer Verlag; 1993.

[7] Wang C, Garcia M, Lu X, Lanir Y, Kassab GS. Three-dimensional mechanical properties of porcine coronary arteries: a validated two-layer model. Am J Physiol Heart Circ Physiol. 2006;291:H1200-1209.

[8] Aoki T, Ku DN. Collapse of diseased arteries with eccentric cross section. J Biomech. 1993;26:133-142.

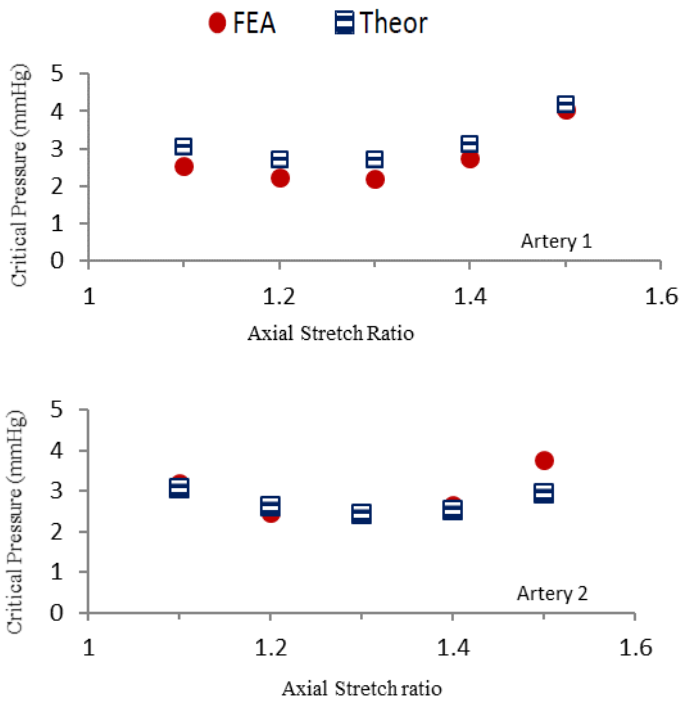

Figure 1: Comparison of the FEA predicted and theoretically measured critical buckling pressure at various axial stretch ratios.

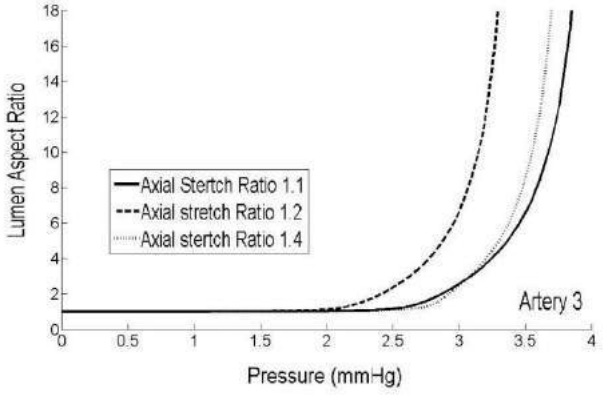

Figure 2: Aspect Ratio (major axis/minor axis) of the lumen plotted with external pressure for different axial stretch ratios.

Copyright 2016 The Organizing Committee for the 2016 Summer Biomechanics, Bioengineering and Biotransport Conference

SB^{3}C2016
Summer Biomechanics, Bioengineering and Biotransport Conference
June 29 –July 2, National Harbor, MD, USA
SB^{3}C2016-858

PULMONARY CONTUSION MODELING IN RECONSTRUCTIONS OF FRONTAL MOTOR VEHICLE COLLISIONS

James P. Gaewsky (1,2), Derek A. Jones (1,2), Ashley A. Weaver (1,2), Joel D. Stitzel (1,2)

(1) Wake Forest University School of Medicine, Winston-Salem, NC, USA

(2) Virginia Tech - Wake Forest Center for Injury Biomechanics, Winston-Salem, NC, USA

INTRODUCTION

Approximately 1.24 million motor vehicle crash (MVC) deaths occur annually worldwide, while an additional 20-50 million MVC occupants sustain non-fatal injuries [1]. MVCs are associated with approximately 60–70% of all blunt chest trauma and are the most common cause of PC [2, 3]. As the understanding of injury mechanisms in MVCs and the performance of occupant restraint systems improves, the risk of fatality and severe injury in MVCs will continue to decrease.

Currently, several methods are employed to study blunt trauma injury mechanisms in MVCs. To evaluate the ability of vehicles to protect occupants during crash events, controlled crash tests are performed using anthropomorphic test devices (ATDs). These ATDs were developed and instrumented based on post-mortem human subject (PMHS) impact tests. However, PMHS tests have several shortcomings, including an elderly population set and an inability to predict physiologic injury outcomes.

More recently, computational methods have been employed to study the mechanical responses of full human body models in impact events [4-6]. However, for many injury outcomes it is difficult to correlate the mechanical response to physiologic injuries. One common MVC injury that is difficult to characterize by the occupant's mechanical response is pulmonary contusion (PC).

The Crash Injury Research and Engineering Network (CIREN) and National Automotive Sampling System (NASS) survey motor vehicle crashes to assess occupant injury outcomes in real world crash events. Although these databases contain a wealth of crash injury information including radiology reports, occupant information, and case vehicle information from event data recorders (EDR), relatively few studies have computationally modeled these MVCs to assess occupant injuries. Previous studies have reconstructed side and oblique frontal impact crashes but were limited by the breadth and level of detail of crash injuries analyzed, the variability of vehicle models, or the number of cases analyzed [4-6].

This study analyzed four real world MVCs from the CIREN and NASS databases to correlate mechanical response data of the full human body finite element model to pulmonary contusion outcomes. Two cases with occupants who had PC and two cases with occupants who did not were analyzed. The study aims to estimate mechanical thresholds correlating to PC injury in real world MVCs.

METHODS

CIREN cases were reconstructed using finite element model (FEM) simulations in a three step process [7]. Two frontal case reconstructions with PC and two without PC were selected and summarized in Table 1. The severity of the crash is noted by the change in velocity of the vehicle during the crash event (delta-V). The injury cases selected from the CIREN and NASS databases had PC in at least one lung. The non-injury cases did not contain any moderate thorax injuries on the Abbreviated Injury Scale (AIS 2+).

Table 1: Case Summaries

		Occupant				Delta-V
	Vehicle	Sex	Age	Height (cm)	Weight (kg)	(kph)
PC	2007 Hummer	F	50	173	86	57
	2006 Cobalt	M	80	183	77	43
No PC	2012 Civic	F	67	165	66	56
	2007 Corolla	M	57	165	71	54

Step 1: A generic simplified vehicle model (SVM) containing the floor, seat, seatbelt, dashboard, steering wheel, and airbag was tuned to mimic the frontal crash response of the case vehicle for each reconstruction. Frontal New Car Assessment Program (NCAP) crash

Copyright 2016 The Organizing Committee for the 2016 Summer Biomechanics, Bioengineering and Biotransport Conference

test vehicle kinematics for each case were video tracked and then incorporated into crash test reconstruction simulations with a validated model of the Hybrid III ATD (Figure 1) [4].

For each case, vehicle restraint parameters (e.g. airbag inflation rate, belt pretensioner force) were varied using a Latin Hypercube Design (LHD) of experiments to find an optimal set of vehicle parameters that resulted in simulated ATD responses closely matching test data signals using the Sprague and Geers method to quantify magnitude and phase errors between corresponding data curves [8].

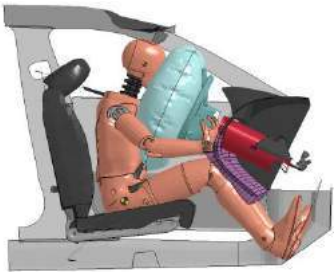

Figure 1: The SVM contains common vehicle restraint and safety systems such as seatbelts with load limiters and pretensioners, airbags, and a collapsible steering column.

Step 2: The THUMS v4.01 human body model was scaled and implemented into the tuned SVM using reported occupant data and positioning information. Additionally, a range of occupant positions were simulated to understand the influence of pre-crash occupant position. A 120 simulation LHD was performed to evaluate the effects of varying the seatback angle, longitudinal seat track position, D-ring height, and steering wheel position and angle within each case reconstruction.

Step 3: The case's EDR velocity pulse was applied to the tuned SVM to simulate the crash for each of the 120 THUMS occupant positions per case. Simulated THUMS instrumentation (i.e. accelerometers, load cells, and strain measurements) was implemented and used to measure injury metrics correlated to common frontal crash injuries. For each crash simulation, maximum principal stresses and strains (MPS) were evaluated in each of the 34,000 left lung and 44,000 right lung elements of THUMS. Subsequently, for each simulation the lung volume fraction exceeding threshold stress and strain values were evaluated and compared to existing literature [4, 9, 10]. The peak MPS threshold value selected was 0.343, as identified by Gayzik et al [9].

RESULTS

In the 2006 Chevrolet Cobalt reconstruction, the occupant's AIS 3 lung contusion (49% of lung contused: see Figure 2) was predicted since over 49% of the THUMS lung elements exceeded a 34.3% first principal strain threshold.

According to the MPS metric, the percentage of the Cobalt occupant's left lung volume estimated to be contused ranged from 5.0-55.0% (mean=35.3%) as a function of occupant position (Figure 3). The baseline case estimated 40.5% of the left lung to be contused, compared to 49% measured in the CIREN subject.

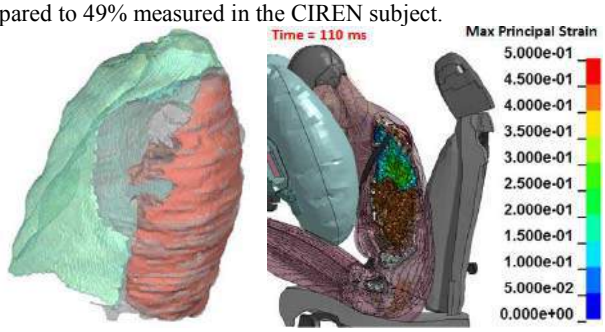

Figure 2: (Left) Case occupant lung segmentation from computed tomography: healthy (gray), contused (pink), and pneumothorax (blue-green). (Right) MPS distribution in the left lung of THUMS.

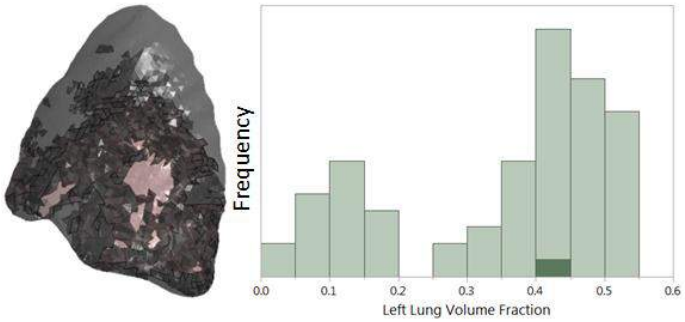

Figure 3: (Left) The distribution of left lung elements exceeding the MPS threshold in the baseline simulation. (Right) The distribution of threshold values estimated across all Cobalt Simulations.

DISCUSSION

The simulations predicting the highest volume fractions exceeding the MPS threshold were the simulations with the most rearward and reclined occupants. The mechanical responses of the chest and lungs in the PC and non-PC cases varied from each other. In the cases with PC, a greater portion of the lung volume exceeded threshold values. In most occupant positions simulated, the volume fraction of elements exceeding the MPS threshold value was less than the case occupant's injured tissue volume. This may indicate that the threshold value for THUMS should be lower than the 0.343 threshold previously identified. Future simulations may also explore the effects of lateral, vertical and pitching motions during the crash event simulations. Additionally, the material properties of the ribs may be modified as a function of age to evaluate the effect on PC risk.

By continuing to populate the data set with additional case reconstructions, and implementing other injury risk factors into the simulations, guidelines and injury risk curves can be established to determine whether THUMS predicts PC injuries in future impact simulations. This computational modeling approach will help researchers to understand and mitigate the likelihood of PC in severe MVCs. Ultimately, the ability to predict pulmonary contusion risk will lead to better occupant protection and a reduced burden on the trauma system.

ACKNOWLEDGEMENTS

Funding for this project was provided by Toyota's Collaborative Safety Research Center. Computations were performed on the Wake Forest University DEAC Cluster, a centrally managed resource with support provided in part by the University, and the Blacklight system at the Pittsburgh Supercomputing Center (PSC).

REFERENCES

1. WHO, *Global Status Report on Road Safety*. 2013.
2. Allen, G.S. and N.E. Coates. The American surgeon, 1996. 62(11): p. 895-900.
3. Cohn, S.M. Journal of Trauma and Acute Care Surgery, 1997. 42(5): p. 973-979.
4. Danelson, K.A. and J.D. Stitzel. Traffic injury prevention, 2015.
5. Golman, A.J., et al. Accident Analysis & Prevention, 2014. 64: p. 1-8.
6. Iraeus, J. and M. Lindquist. Traffic Inj Prev, 2014. 15 Suppl 1: p. S88-95.
7. Gaewsky, J.P., et al. Traffic injury prevention, 2015. 16(sup2): p. S124-S131.
8. Sprague, M. and T. Geers. International Journal for Numerical Methods in Engineering, 2004. 60(15): p. 2467-2499.
9. Gayzik, F.S., J.J. Hoth, and J.D. Stitzel. Biomechanics and modeling in mechanobiology, 2011. 10(4): p. 505-520.
10. Gayzik, F.S., et al. Stapp car crash journal, 2007. 51: p. 189-209.

Copyright 2016 The Organizing Committee for the 2016 Summer Biomechanics, Bioengineering and Biotransport Conference

SB^{3}C2016
Summer Biomechanics, Bioengineering and Biotransport Conference
June 29-July 2, National Harbor, Maryland, USA
SB^{3}C2016-859

ARK BRACE: AN ACTIVE REHABILATATIVE KNEE BRACE

Jarrel Bobb
Lafayette College
Easton, PA, USA

Kelly Chickering
Lafayette College
Easton, PA, USA

Patrick Donohue
Lafayette College
Easton, PA, USA

Mac Gallagher
Lafayette College
Easton, PA, USA

Shannon Hartzell
Lafayette College
Easton, PA, USA

Cole Lipman
Lafayette College
Easton, PA, USA

M. Jake Miorin
Lafayette College
Easton, PA, USA

Kailan Ottaway
Lafayette College
Easton, PA, USA

Faculty Advisor
Alexander Brown
Lafayette College
Easton, PA, USA

INTRODUCTION

Across the world, there are millions of knee surgeries performed on athletes of all competitive levels for various knee injuries. Common knee injuries include tears of the primary knee ligaments ACL, MCL, LCL, and the meniscus, all of which require the aid of a brace during recovery. Successful rehabilitation requires recuperation of flexibility, range of motion, and strength [1]. Braces in the current market focus on range of motion recovery; the strengthening of surrounding muscle is limited primarily to physical therapy exercises. As a result of this limitation, significant atrophy of the leg muscles often develops which can, in turn, increase the period in which patients are restricted to crutches.

According to a research report conducted by GlobalData, the 2014 global market for orthopedic braces and supports was $2.56 billion, a figure predicted to increase to approximately $3.5 billion by 2021 [2]. Knee braces alone make up approximately 71% of the total orthopedic bracing market, proving their dominant status in a market that is becoming increasingly commoditized due to strong price competition and discounting. Over $500M of annual healthcare costs stem from the yearly 250,000 to 300,000 ACL injuries alone, with patients being almost exclusively athletes [3]. To satisfy this market need, the authors are developing an active rehabilitative knee brace that will allow patients to walk without the aid of crutches sooner in the rehabilitation process at a competitive market value.

PRODUCT DESIGN

The proposed actuated device will assist patients in walking with crutches during recovery by amplifying muscle activity using an electric motor and Force sensitive resistors (FSRs). In its functionality, the proposed device sits between traditional braces that do not activate the knee joint [4], the Continuous Passive Motion (CPM) which moves the patient's knee while they recline, and fully actuated exoskeletons like the AlterG bionic leg which are too expensive for the average consumer (up to $20,000) [5]. By using low cost sensors and actuators to create a device that will have a target price point under $600, the ARK Brace, Active Rehabilitation Knee Brace, will be an affordable and safe alternative for patients in mid-stage recovery from major knee injuries. With an appropriately selected motor and sensor suite, the ARK could change the method of knee injury recovery for thousands of athletes. ARK's electric motor, chosen to reduce cost and complexity when compared with hydraulic or pneumatic actuators, will work *with* a patient's muscles and ligaments sensors to reduce ligament loads during early walking. A conceptual block diagram of ARK's design is shown in Figure 1.

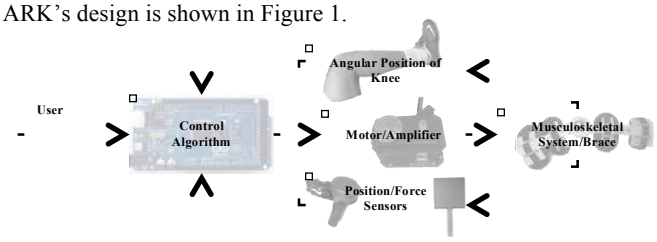

Figure 1. Block diagram of the ARK Brace exoskeleton.

The major sensing, decision-making, and actuation components of ARK must all work appropriately with the knee's physiology for the device to be successful. FSRs in the foot and a potentiometer attached to the knee joint will track a patient's position in his/her specific gait cycle, and EMG sensors will provide ARK's control algorithm, running on an Arduino Mega microcontroller, with muscle activity information. The ARK will use these sensors to calculate the required assistive torque at the knee joint. All sensing, decision-making, and actuation information and force flows are critical to ARK's goal of assisting knee ligament recovery during mid-stage recovery.

The ARK's brace structure will be built to conform to the motion constraints of a healthy knee. There are two major axes of movement within the knee: the longitudinal-rotational (LR) axis and the flexion-extension (FE) axis. A misalignment of the bones through this axis by an amount of as little as 2-3° can begin to compromise knee structure and increase risk of ligament injury within the joint [6,7]. ARK's bracing structure must provide at least that level of angular accuracy to be useful.

Copyright 2016 The Organizing Committee for the 2016 Summer Biomechanics, Bioengineering and Biotransport Conference

An IRB-approved gait study of recovering athletes at Lafayette's biomechanics lab is in ongoing to determine where in the gait cycle the athletes require extra assistance. In order to provide measurements for this study that go above and beyond the information available in Lafayette's motion-tracking biomechanics lab, the authors created a data collection and prototyping platform to test various biosensors, motors, and control architectures. Preliminary testing has been performed on healthy athletes to generate a baseline for a normal gait and determine the accuracy of the sensors shown in Figure 2a. The test and measurement platform uses all of the aforementioned sensors so that the final brace's configuration and layout can be optimized.

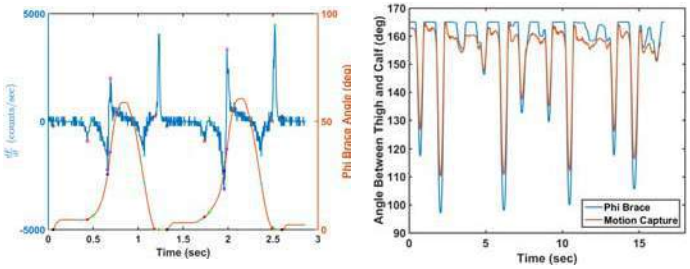

Figure 2: (a) Feature tracking of knee angular position against the first time derivative of the force applied by the heel of the foot identifies gait cycle percentage and (b) Knee angular position from potentiometer data and motion tracking system confirms the accuracy of the test platform's sensors.

ARK's motor, battery, and amplifier selection is also critical to the brace's ability to assist in ligament tear recovery. A motor that would fully replace knee function would have a stall-torque upwards of 60 N-m [8]. However, ARK's role is merely to augment existing muscle torque during normal gait to reduce ligament loads during mid-stage recovery through stress shielding. Stress shielding refers to the division of stress through a medium in order to reduce the stresses across a weakened or injured region. The ARK will reduce the tension in the knee ligaments by reducing the torque reacted through the joint. Based on data collected in the lab, the authors chose the Dynamixel MX-106T as the motor for use in the ARK Brace. The MX-106T at 12V has a stall torque of 8.4 N-m and no-load angular velocity of 4.71 rad/s. The MX-106T will provide a significant fraction of the required torque and nearly enough no-load speed to accommodate normal, healthy walking. It was chosen based on the competing requirements of size, weight, power, and cost.

ARK's control algorithm will use data from the gait study to select regions of the gait cycle (identified using a potentiometer on the ARK and FSRs under the foot as in Figure 2a) during which amplification of hamstring or quadriceps activity would provide the greatest assistance in lowering ligament forces during walking. The degree to which ligament forces will be reduced by active assistance will be user-selectable to comply with physician recommendations. An analysis of preliminary trials has revealed repeatable trends and correlation between the angular position of the knee and the change in the pressure applied by the heel and the ball of the foot. The rollover from heel to toe will help schedule the end of the stance phase and into the swing phase, allowing the control system to appropriately regulate knee motion and torque.

BUDGET & MARKET ANALYSIS

The current market for orthopedic bracing is expanding and is conducive to the introduction of an active knee brace into the space. Aside from the conglomerate DONJOY Global, which accounts for a quarter of the total market, the bracing market is largely fragmented with no other company accounting for greater than 10% of total market share allowing for relative ease in market entry [9,10]. Looking specifically at the products currently available in postoperative bracing there are three types of technologies that would compete with our active knee brace. The first of these technologies is the traditional, non-automated family of braces from companies such as DONJOY, Breg, Ossur and Bledsoe whose costs fall within the $250-500 range. Second, CPM machines, devices designed to gently extend and flex the knee joint following reconstructive surgery, are also widely used in the very early stages of recovery for range of motion recuperation. However, this device only works with a sedentary patient. Exoskeleton technology is relatively new to the market. Direct competition with the ARK includes devices like the Bionic Leg from AlterG, which is heavier, more expensive, and more powerful than the ARK, and is also designed with a specific portion of knee injury recovery in mind. ARK's projected sale price of $600 will result in a product costing less than CPMs or existing active braces, while remaining in a price range that provides a competitive alternative to traditional knee braces.

The brace will initially be marketed towards collegiate, professional, and certain high school sports medicine departments as well as physical therapy and rehabilitation centers. Roughly 460,000 student athletes currently compete at the NCAA Division I, II and III levels at approximately 1,200 colleges and universities, all of which have a sports medicine department [11]. In the United States alone, physical therapy jobs are slated to grow by 34% over the next decade, well above the 7% national average for occupation growth, which speaks to the increasing need for their services and product development in the industry [12].

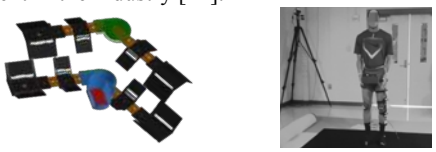

Figure 3: (a) CAD model of ARK Brace and (b) participant in Lafayette's biomechanics lab.

ACKNOWLEDGEMENTS

The authors would like to thank Matt Bayly, director of sports medicine at Lafayette College, and the doctors at Coordinated Health for their valuable input.

REFERENCES

[1] A. Phinit Phisitkul, 'MCL Injuries of the Knee: Current Concepts Review', *The Iowa Orthopaedic Journal*, vol. 26, p. 77, 2006.
[2] Qmed.com, 'Why Orthopedic Braces Are a Growing Market', 2015. [Online].
[3] Livestrong.com, 'Statistics on ACL Injuries in Athletes | Livestrong.com, 2013. [Online].
[4] FamilyDoctor.org, 'Knee Bracing: What Works?', 2015. [Online].
[5] Alter-G, 'Inquiry of Price for Bionic Leg', Telephone.
[6] Roland M, Hull ML, Howell SM. Virtual Axis Finder: A New Method to Determine the Two Kinematic Axes of Rotation for the Tibio-Femoral Joint. ASME. J Biomech Eng. 2009;132(1):011009-011009-9. doi:10.1115/1.4000163.
[7] Krackow, M.d. Kenneth A. The Measurement and Analysis of Axial Deformity at the Knee (n.d.): n. pag. Web.
[8] Martinez-Villapado S.M. J Rehab Res Dev 2009, 46: 361-371
[9] PRNewswire.com, "US Market for Orthopedic Braces and Supports", 2013. [Online].
[10] Djoglobal.com, 'DJO Global Brand & Products', 2015. [Online].
[11] Ncaa.org, "Membership", 2015. [Online].
[12] United States Bureau of Labor Statistics, "Physical Therapists", 2015. [Online].

Copyright 2016 The Organizing Committee for the 2016 Summer Biomechanics, Bioengineering and Biotransport Conference

SB^{3}C2016
Summer Biomechanics, Bioengineering and Biotransport Conference
June 29 –July 2, National Harbor, MD, USA
SB^{3}C2016-860

A NEW EDUCATIONAL APPROACH TO TEACHING SCIENCE AND ENGINEERING FOR K-12 STUDENTS

Kritsakorn Chaumpanich (1), Michelle Johnson (2), Yingcai Xiao (1), Philip A. Allen (3), Yang H. Yun (4)

(1) Department of Computer Science
University of Akron
Akron, Ohio, USA

(2) PLTW Biomedical Science
North High School
Akron, Ohio, USA

(3) Department of Physiology
University of Akron
Akron, Ohio, USA

(4) Department of Biomedical Engineering
University of Akron
Akron, Ohio, USA

INTRODUCTION

When teaching educational contents that are inherently graphical in nature, research has shown that learning is more efficient when stimulating the visual component of working memory (the visuo-spatial sketchpad) as compared to language-based approaches.[1,2] In the working memory model proposed by Baddeley and Hitch,[3] the central executive controls the flow of information to and from the phonological loop (verbal buffer), the visuo-spatial sketchpad (visual buffer), and the episodic buffer (where context is added to short-term-memory codes for storage in long-term memory). We know that both verbal and visual codes are stored in short-term memory because we can use these two types of codes to interfere with working memory performance.[2,3] Because of the "video game effect," there is accumulating evidence that individuals can use visual codes to help supplement verbal-code information in short-term or working memory.

Furthermore, there is evidence that humans use "embodied cognition" to improve performance.[2-4] That is, we encode the state of the body and use it as a "somatic marker" (or contextual cue) when storing working-memory information in long-term memory.[3] Using these assumptions, it is predicted that visual codes and motoric feedback from movements should improve the educational outcomes in learning science and engineering information.

The goal of this project is to refocus science and engineering education by introducing a new technology that is integrated with interactive, educational content that engages, inspires, and stimulates the visual center of the brain. To accomplish these goals, a new curriculum has be designed and implemented that engages students and interactively introduces visual information using the Microsoft Kinect^{TM} device. This device will be coupled to a computer system and will allow students, as an example, to actively explore a cell's anatomy and its functions using an interactive spatial interface instead of simply showing pictures with verbal descriptions. This approach also promotes active, rather than passive, learning by employing embodied cognition, where human movements could help improve both the short-term episodic and long-term memories of students. In our approach, both the visual/spatial information and the motoric interactions can be stored with a memory trace of the learning event (e.g., structures and functions of an eukaryotic cell and its organelles), thereby adding more efficient retrieval paths.

METHODS

Kinect^{TM} was adapted to capture the motion of students and track their gestures to allow them visually interact with the education contents. These contents were created as virtual 3D objects and developed into four learning modules (Cell, DNA, Immune System and Gene Therapy) and imported into a game engine (Unity3D) for animation and display. User movements captured by Kinect^{TM} were sent to the

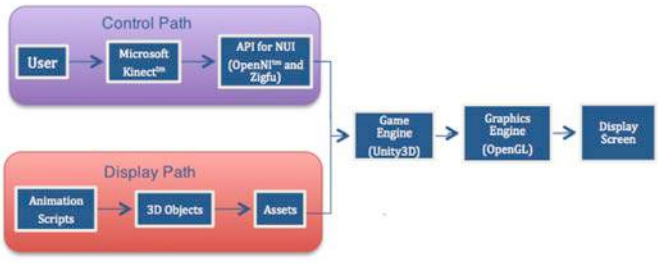

Figure 1. The architecture of the Kinect^{TM} based learning system

Copyright 2016 The Organizing Committee for the 2016 Summer Biomechanics, Bioengineering and Biotransport Conference

game engine through the application-programming interface provided by OpenNI and Zigfu. The students were able to rotate the virtual objects (cell and organelles) and zoom onto nano-sized molecules (DNA and ribosomes). They were able to study their structures as well as the functions through interactive animations. This "first person" perspective using embodied cognition should help students to learn more efficiently. Finally, the gestures to interact with objects were intuitive with a minor learning curve. Figure 1 depicts the architecture of our Kinect™ based system.

An experimental goal of the project is to compare the learning outcomes for K-12 students at low social economic settings (SES). The learning and understanding of educational materials related to each module was tested. The experimental design is given in Table 1. All students were exposed to either the traditional techniques or enhanced teaching using the Kinect™ system. The contents for Modules 1 - 2 reflect typical contents in K-12 textbooks and the tests require recall of knowledge. In contrast, modules 3-4 are more conceptual. The tests are understanding of concepts of acquired immunity and include engineering design, especially in module 4. The experimental design allowed for intragroup and intergroup comparisons. After each session, students were tested using a 20-point exam, and the results for the traditional and technology-enhanced teaching methods were averaged and compared using t-test or ANOVA with Tukey post hoc test.

Table 1 - Experiment groups

	Group 1	Group 2
Module 1 – Cell	Kinect™	Traditional
Module 2 – DNA	Kinect™	Traditional
Module 3 – Immune System	Traditional	Kinect™
Module 4 – Gene Therapy	Traditional	Kinect™

RESULTS

Individuals who received Kinect™-enhanced instruction performed significantly better on tests over the course material than did individuals who received only the traditional instruction (81.6 ± 3.1% vs. 70.2 ± 2.7%, $p < 0.05$, Figure 2). This pattern of results occurred even though all participants received two modules both types of instruction.

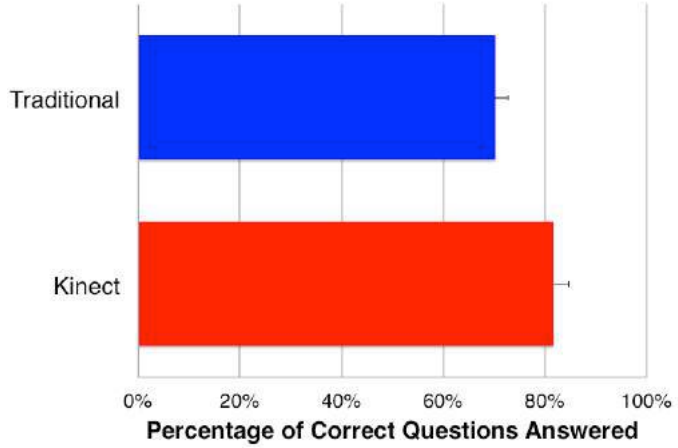

Figure 2. Test Results for Traditional vs. Kinect™ Instruction

When student's performance is examined for modules 1-2 verses 3-4, instruction with Kinect™ also shows a significant advantage (Figure 3). Overall, students performed better in modules 3-4, which contains conceptual information that is more difficult than in modules 1-2. However, no significance is observed when comparing Kinect™ vs. traditional instruction for modules 1-2 ($p > 0.05$). In contrast, significance differences are observed when comparing Kinect™ vs. traditional instruction for modules 3-4 ($P < 0.01$).

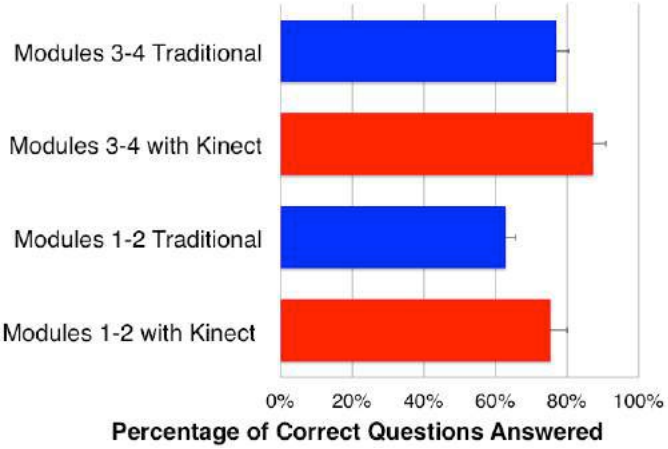

Figure 3. Test Results for Traditional vs. Kinect™ Instruction

DISCUSSION

"A picture is worth a thousand words." Teaching simultaneously with pictures and words is a standard practice in science and engineering but has been shown to be inefficient for learning. Until recently, technical challenges have limited our ability to teach visual information without a heavy reliance on language. If realized, complex scientific and engineering instructions can be learned more efficiently and quickly. This advantage may have added benefits of lowering students' apprehension toward science and engineering and encouraging them to choose a career in these fields. Our educational modules and technological equipment have been distributed North High School in Akron, Ohio. They have adopted our educational modules and tested the efficacy of technology-enhanced learning verses the traditional instructions. The comparison of learning was made for each student using both methods. Our preliminary results indicate students perform significantly better on tests using the Kinect™ interface than traditional instructional methods in which students do not actively manipulate visual objects. In addition, performance on test suggests that students are better at understanding conceptually changing topics using technology-enhancing instructions. The technology-enhanced learning also shows effectiveness in a school that is in a low SES setting.

ACKNOWLEDGEMENTS

The authors would like to acknowledge t National Science Foundation (RIGEE-1137052 and CBET-0954360) for providing the funding for this project.

REFERENCES

[1] Kraemer, DJ et al. *Neurosci.* 29(12):3792-3798. 2009.

[2] Yun, YH et al. *Proceedings of the International Conference e-Learning 2014.* IADIS Press: 394-398. 2014

[3] Baddeley A. *Science.* 255(5044):556-559. 1992

[4] Allen PA. et al. *Exp Aging Res.* 31(4):355-391. 2005.

Copyright 2016 The Organizing Committee for the 2016 Summer Biomechanics, Bioengineering and Biotransport Conference

SB³C2016
Summer Biomechanics, Bioengineering and Biotransport Conference
June 29 –July 2, National Harbor, MD, USA
SB³C2016-861

PHENOTYPIC CHANGES OF STROMAL VASCULAR FRACTION CELLS FOR USE IN A TISSUE ENGINEERED VASCULAR GRAFT

Darren G Haskett (1,4), Katelyn Bruce (2), Jeffrey T Krawiec (3,4), Justin S Weinbaum (3,4), Antonio D'Amore (1,3,4), William Wagner (1,3,4), Lauren Kokai (4,5), J. Peter Rubin (4,5), David A Vorp (1,3,4,6)

(1) Department of Surgery
University of Pittsburgh
Pittsburgh, PA, USA

(2) Department of Bioengineering
Carnegie Mellon University
Pittsburgh, PA, USA

(3) Department of Bioengineering
University of Pittsburgh
Pittsburgh, PA, USA

(4) McGowan Institute of Regenerative Medicine
University of Pittsburgh
Pittsburgh, PA, USA

(5) Department Plastic Surgery
University Pittsburgh
Pittsburg, PA, USA

(6) Department of Cardiothoracic Surgery
University of Pittsburgh
Pittsburgh, PA, USA

INTRODUCTION

Small diameter tissue engineered vascular grafts (TEVGs) containing adipose derived mesenchymal stem cells (ADMSCs) have been shown to promote remodeling and vascular homeostasis *in vivo* and offer a possible treatment solution for those suffering from cardiovascular disease [1-3]. However, the time needed for culture represents a large hurdle for such a treatment option, whereas TEVGs containing cells taken directly from the stromal vascular fraction (SVF) following liposuction would not suffer such an impediment. SVF is known to be comprised of multiple phenotypes of cells, and previous results have shown that TEVGs seeded, shortly cultured, and implanted with SVF from young healthy individuals will remain patent in rats and will undergo remodeling.

However, it is unknown which cell types are binding to the scaffold. Additionally, it is unknown if the short 2 day culture period currently used before implantation can be removed to have a quicker implementation of the SVF extraction, seeding, and implantation process in order to make the procedure more clinically relevant.

The current study aims to determine the phenotypes of the scaffold-binding cells from SVF (in comparison to the seeded pool) and how these phenotypes change up to four passages from harvest (which is the current standard for ADMSC TEVGs). Furthermore, this study aims to determine if SVF seeded TEVGs without a short period of culture will remain patent *in vivo* and remodel by studying the histological and functional changes as well as the fate of the SVF.

METHODS

SVF, obtained from adult adipose tissue, was seeded onto poly(ester urethane)urea (PEUU) bilayered scaffolds using a customized rotational vacuum seeding device and then cultured in spinner flask for 2 days. PEUU scaffolds were seeded with SVF immediately after acquisition and at each subsequent passage up to passage 4. Scaffolds were then incubated for a short period to allow cells to be incorporated into the scaffold and then either fixed immediately or cultured for 2 days in a spinner flask and then fixed using a 4% paraformaldehyde solution. Fixed sections were then analyzed using immunofluorescent chemistry (IFC) for markers that define difference phenotypes. These markers include CD31 for endothelial cells, CD34 for endothelial precursor cells, CD4 for T cells, CD20 for B cells, CD68 for macrophages, and CD90 for ADMSCs.

SVF seeded scaffolds seeded immediately after collection underwent 2 days of culture in a spinner flask were surgically implanted

Figure 1: Example image of TEVG implant in the abdominal aortic interposition in a rat is shown.

Copyright 2016 The Organizing Committee for the 2016 Summer Biomechanics, Bioengineering and Biotransport Conference

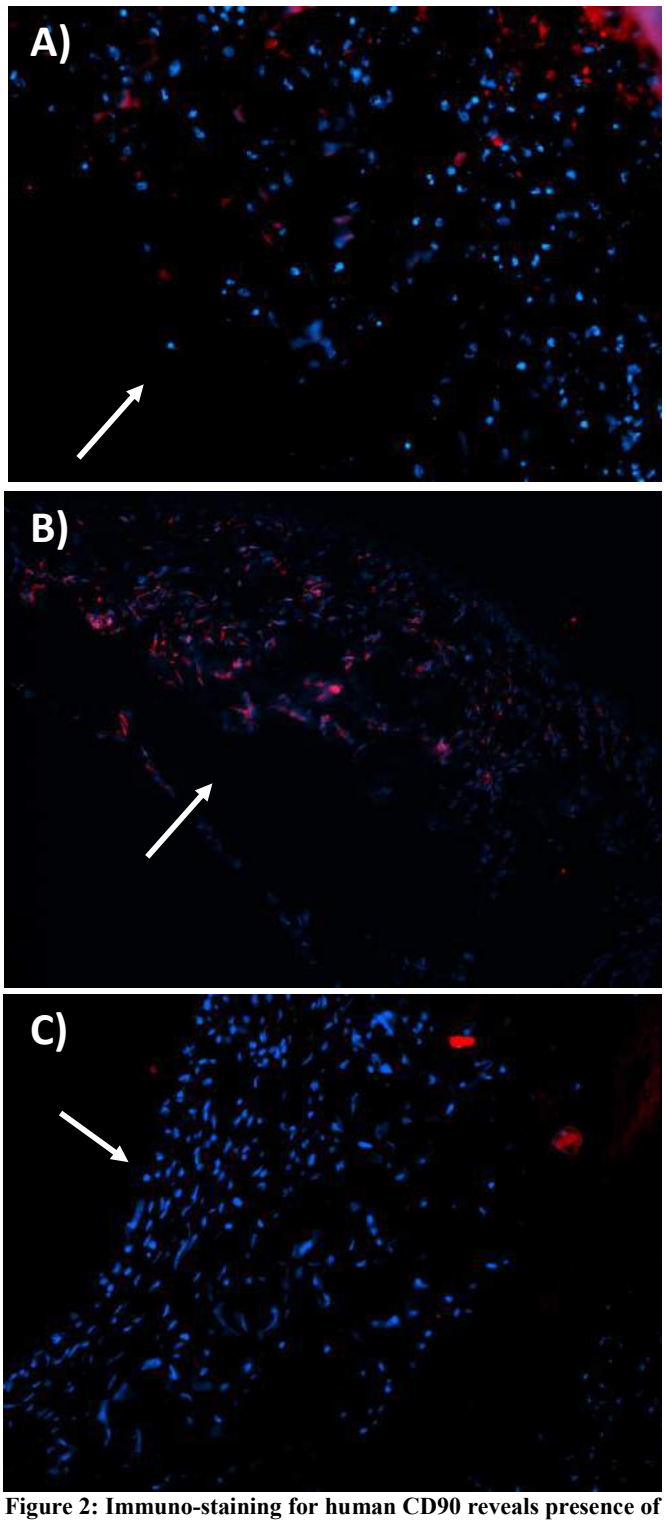

Figure 2: Immuno-staining for human CD90 reveals presence of implanted cells during short term implantations. Explanted TEVGs were stained with human specific CD90 (red; counterstained with DAPI (blue)) to identify the presence of implanted AD-MSCs in explants consisting of (A) a TEVG seeded with healthy AD-MSCs at 1 week, (B) non-implanted seeded TEVG positive control, (C) and a negative control. Arrows indicate luminal edge.

as abdominal aortic interposition grafts in rats, as well as seeded scaffolds that did not undergo a 2 day culture period (**Figure 1**) as described previously [1-3]. Implanted scaffolds were allowed to remodel for up to 8 weeks and the presence of patency and vascular components determined, along with any signs of inflammation using IFC.

RESULTS

IFC analysis shows positive staining for CD31 and CD34, markers of endothelial cells and endothelial precursor cells respectively, when SVF was directly seeded (without passage). Gradually the percent of cells staining for both CD31 and CD34 decreases over passage, until it is absent at passage 4 (**Table 1**). The presence of immune cells based on markers CD4 for T cells, CD20 for B cells, and CD68 for macrophages were not present in seeded scaffolds.

Table 1: Heterogeneity of SVF seeded scaffolds with increasing passage.

Cell Marker	CD31	CD34	CD4	CD20	CD68
Initial SVF	27%	28%	0%	0%	0%
Passage 1	41%	12%	0%	0%	0%
Passage 2	28%	5%	0%	0%	0%
Passage 3	41%	0%	0%	0%	0%
Passage 4	0%	0%	0%	0%	0%

In contrast, staining for CD90 (an MSC marker) was present in all samples that were tested including scaffolds after they were seeded with ADMSCs and implanted (**Figure 2**).

DISCUSSION

Initial findings show that both endothelial cells and endothelial precursor cells do attach to the PEUU scaffold and are present at the time of implantation of the TEVG. It was also found that ADMSC markers were present in scaffolds seeded with SVF at varying passages and within the TEVG after a week of remodeling *in vivo*.

As yet the fate of the different SVF cell types is unknown during *in vivo* remodeling. Previous work has shown that after a week, seeded cells are often present in greatly reduced numbers compared to initial seeding, and the presence of stem cells merely promoted ingrowth and cellular migration [4], thus it may not be as important to have grafts be seeded with ADMSCs which have the disadvantage of long incubation times.

Understanding differences between SVF and ADMSCs for seeding of TEVGs will allow for better clinical translation and swifter application.

ACKNOWLEDGEMENTS

The authors would like to acknowledge sources of support: Vascular Training Grant support to Dr. Darren Haskett (NIH T32 HL098036; Dr. Edith Tzeng, PI) and NIH grant to Dr. David Vorp (NIH R21 EB016138).

REFERENCES

1. He, W., et al., Cardiovascular Engineering and Technology, 2011. **2**(3): p. 149-159.
2. He, W., et al., Biomaterials, 2010. **31**(32): p. 8235-44.
3. Nieponice, A., et al., Tissue Eng Part A, 2010. **16**(4): p. 1215-23.
4. Kurobe, H., et al., Stem Cells Transl Med, 2012. **1**(7): p. 566-71.

Copyright 2016 The Organizing Committee for the 2016 Summer Biomechanics, Bioengineering and Biotransport Conference

SB^{3}C2016
Summer Biomechanics, Bioengineering and Biotransport Conference
June 29 –July 2, National Harbor, MD, USA
SB^{3}C2016-862

DOES TISSUE ARCHITECTURE MATTER TO BULK MECHANICS? SCRAMBLED EMBRYOS SUGGEST NOT.

Joseph H. Shawky (1) and Lance A. Davidson (1,2,3)

(1) Department of Bioengineering
University of Pittsburgh
Pittsburgh, PA 15260

(2) Department of Developmental Biology
University of Pittsburgh
Pittsburgh, PA 15260

(3) Department of Computational and Systems Biology
University of Pittsburgh
Pittsburgh, PA 15260

INTRODUCTION

During early animal development, large scale tissue movements facilitate the formation of complex tissue architectures and eventually the vertebrate body plan. Fine-grained control of mechanical properties and force production is critical to the successful placement of tissues within the embryo. An example can be seen in dorsal tissues within embryos of the aquatic frog *Xenopus laevis* which increase in modulus six-fold as they gastrulate to form the three germ layers, and neurulate to form the central nervous system [1]. The mechanisms that regulate these mechanical properties are not well understood but may be separated into changes in the composition of materials, such as newly assembled extracellular matrix or F-actin cortex that composes the embryo, and changes within the structural microanatomy, such as establishment of laminar cell sheets and the notochord at the embryo's midline.

Molecular factors controlling F-actin assembly and myosin activity are known to contribute to tissue stiffening [1,2] however changes in the cytoskeleton cannot account for all the modulus changes observed in the developing embryo. Bulk mechanical properties of biological tissues, like manufactured materials, depend not only on material properties of their components but also the microstructural organization in which the constituents are arranged [3].

Tissue movements during gastrulation and neurulation construct specific architectures (i.e. segmentation cavities and neural folds) with distinct tissue boundaries through individual and collective cell migration [4], cell shape change [5] and extracellular matrix deposition. Establishment of these architectures facilitates tissue morphogenesis in several ways including creating morphogen gradients across cells/tissues, and enabling zones of tissue morphogenesis for specific roles such as bottle cell contraction or tissue involution. However, the role of newly formed architectures on bulk tissue modulus has been neglected. To elucidate the source of bulk stiffening in these tissues, it is key to understand how the changing structures within the embryo contribute to bulk mechanical properties.

In this study, we decouple the role of tissue microarchitecture from the compositional contribution to bulk mechanical properties by disrupting this architecture in embryonic tissues (Figure 1A) and measuring the mechanical properties of reaggregated, hereinafter referred to as "scrambled", tissues. We find that, surprisingly, tissue architecture makes little contribution to the bulk mechanical properties but is critical to the continuing self-assembly of the dorsal axis.

METHODS

Embryos and Microsurgery *X. laevis* embryos were obtained by standard methods [6], fertilized in vitro, dejellied in 2 wt.% cysteine and cultured in 1/3× modified Barth's saline at 22 °C. Staging of embryos was performed according to the table of Nieuwkoop and Faber (1967). To isolate dorsal tissues, early neurula (stage 13) embryos were selected and transferred to culture media, Danilchik's for Amy (DFA). For mechanical testing, 3 clutches were used with at least 7 embryos per group.

Tissue Dissociation and Reaggregation Dorsal tissues were dissociated in Ca^{++} and Mg^{++} free DFA for 5 to 7 minutes and superficial epithelium discarded. Dissociated cells were transferred to custom wells. 50µl agarose was pipetted into each well to enable tissue reaggregation without attachment. Cells were centrifuged for 10 min at

Copyright 2016 The Organizing Committee for the 2016 Summer Biomechanics, Bioengineering and Biotransport Conference

5G to create disc shaped tissues and confirmed the top and bottom surfaces of the scrambled tissues were flat. After centrifugation, scrambled tissues were removed from the chamber and cultured in DFA for 30 minutes before microsurgery. Scrambled tissues were cut into regular shaped "bricks" approximately 200x400x600um for mechanical testing.

Mechanical Testing Time-dependent viscoelastic properties of embryonic tissues were measured using an unconfined uniaxial compressive stress-relaxation test described in detail previously (Davidson and Keller, 2007). In brief, the tissue sample is compressed ~20% along its anterior-posterior axis while the resistive force is measured by the deflection of the optical fiber force transducer. The tissue samples are visualized by stereomicroscopy during compression to obtain length measurements throughout testing. Immediately after testing, samples are fixed in 4% paraformaldehyde, bisected and imaged to obtain cross sectional areas. Young's modulus after 180 seconds of compression, E(180), is then calculated using measured resistive force, cross-sectional area and strain measurements as shown below:

$$\mathrm{E}(180) = {}^{\sigma}/_{\epsilon} = \left(\frac{F}{A}\right)/\left(\frac{\Delta \mathrm{L}}{\mathrm{L}_0}\right) \qquad (1)$$

where E is the time dependent elastic modulus, F is the resistive force measured during the stress-relaxation test, A is the cross-sectional area, L_0 is the length of samples before compression and ΔL is the change in length before and after compression. Statistical significance of treatments on E(180) over a set of different clutches was analyzed using 2-way ANOVAs using commercial statistical software (SPSS).

Confocal Microscopy Laser scanning confocal microscopy was used to acquire high-resolution image stacks of scrambled and native tissues immunostained for fibronectin (fn1) using the 4H2 monoclonal antibody. Stacks were collected using a confocal laser scan head (SP5 Leica Microsystems) mounted on an inverted compound microscope (DMI6000, Leica Microsystems) using acquisition software (LASAF, Leica Microsystems).

RESULTS

Loss of Tissue Architecture in Scrambled Tissues To create scrambled tissues, we isolated tissue samples from neurula stage embryos, dissociated them and reaggreagted them into regularly shaped samples. To assess the degree of bulk tissue architecture disruption, we fixed and stained scrambled tissues for fibronectin, the dominant extracellular matrix protein at this stage in development. In native dorsal tissues, germ layers are separated by a dense fibronectin matrix. Fibronectin staining revealed a complete loss of bulk tissue architecture (Figure 1B) however local tissue microdomains surrounded by fn1 containing ~2 to 20 cells remained. Scrambled tissues remain intact for several hours after aggregation however they do not undergo convergent extension movements or neural fold formation observed in control tissues.

Elastic Modulus is Unchanged in Scrambled Tissues To test if there is any change in the modulus of scrambled tissues, samples were loaded into the nanoNewton force measurement device. Reported modulus values are the elastic modulus after a 180 second stress/relaxation test. There was no significant difference in modulus between stage 16-equivalent scrambled tissues and native dorsal tissues (2-way ANOVA p-val = 0.29; Figure 1C).

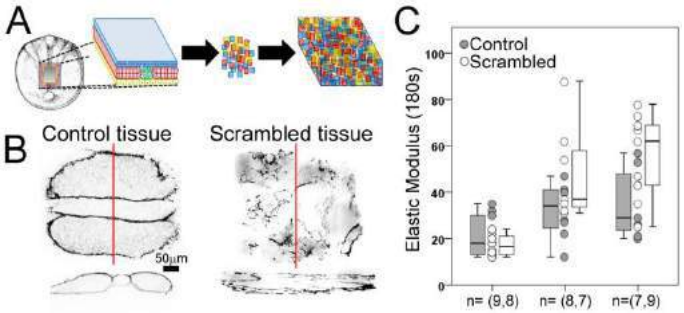

Figure 1: A) Schematic of bulk tissue architecture disruption. Tissues are isolated at early neurula stage, dissociated, and reaggregated into "scrambled" tissues. B) Fibronectin staining reveals loss of bulk architecture and stereotypic fibronectin organization. C) Mechanical testing results reveal that scrambled tissues have the same modulus as native control tissues.

DISCUSSION

In this study we investigated the contribution of tissue microarchitecture in embryonic tissues to bulk tissue mechanical properties. We find that scrambling tissues into random architectures does not alter the bulk mechanical properties of these tissues which suggests that the source of stiffness in these embryonic tissues resides within the stiffness of individual cells stiffness, rather than the architecture in which the cells are arranged. Our results in *X. laevis* may be extended to other tissues, either in embryos or during regeneration, where ECM does not significantly contribute to modulus. While modulus was unchanged in scrambled tissues these tissues were not competent to re-organize and drive convergent extension movements or neural fold formation. It remains unclear whether cell-cell or cell/extracellular matrix (ECM) signaling or cell sorting occurs after reaggregation to re-start morphogenetic programs. Since the architecture is not a regulator of embryonic bulk tissue mechanical properties at these stages, ongoing studies are underway to understand how cell identity contributes to tissue bulk properties.

ACKNOWLEDGEMENTS

This work has been supported by grants from the NIH (R01 HD044750 and R21 ES019259) and the NSF (CAREER IOS-0845775 and CMMI-1100515). JHS is supported by the NIH Biomechanics in Regenerative Medicine Training Grant (BiRM; T32 EB003392).

REFERENCES

[1] Zhou et al., *Dev,* 136:677:688, 2009.
[2] Zhou et al., *Dev,* 137: 2785-2794, 2010.
[3] Fung, YC. Biomechanics: Mechanical Properties of Living Tissues, 1993
[4] Aman, A and Piotrowski, T. *Dev. Biol.,* 341: 20-33, 2010.
[5] Paluch, E and Heisenberg, CP. *Curr Biol,* 19: R790-799, 2009.
[6] Kay, BK and Peng, HB. Practical Uses in Cell and Molecular Biology, 1991

Copyright 2016 The Organizing Committee for the 2016 Summer Biomechanics, Bioengineering and Biotransport Conference

SB³C2016
Summer Biomechanics, Bioengineering and BIotransport Conference
June 29-July 2, 2016, National Harbor, MD, USA
SB³C2016-863

FIBERFIT: A VALIDATED SOFTWARE APPLICATION TO MEASURE FIBER ORGANIZATION IN SOFT TISSUE

Azamat Tulepbergenov (1), Erica E. Morrill (3), Christina J. Stender (3), Roshani Lamichhane (1), Raquel J. Brown (2), Trevor J. Lujan (3)

(1) Department of Computer Science
Boise State University
Boise, ID, USA

(2) Biomolecular Research Center
Boise State University
Boise, ID, USA

(3) Department of Mechanical and Biomedical Engineering
Boise State University
Boise, ID, USA

INTRODUCTION

The mechanical function of biological tissue is primarily regulated by the underlying fibrillar architecture. In soft connective tissue, defects to the fibrillar collagen network are associated with acute and chronic disorder [1-3]. Therefore, an extensive amount of research has been devoted to characterizing fibrillar networks [4,5], and this requires the accurate extraction of descriptive structural parameters from imaging data [6]. For tissues with multiaxial fiber networks, relevant structural parameters include fiber dispersion and mean fiber orientation, which are both properties of the fiber orientation distribution and are measures of material anisotropy. Accurate quantification of the fiber orientation distribution can advance a mechanistic understanding of collagen networks and clarify the functional impact of soft tissue remodeling and repair.

Over the past decade, free software applications have been developed that enable researchers to use mathematical algorithms to measure fiber organization. Researchers can now generate fiber orientation distributions based on fast Fourier transformation (FFT) methods with Oval Profile Plot and Directionality software [7,8]; and by using structure tensor methods with OrientationJ software [9]. Although these software applications have assisted the quantification of fiber dispersion and mean fiber orientation, the accuracy of these software applications has not been characterized with validation studies. Moreover, the sensitivity of these image analysis programs to common image processing techniques is not well understood Therefore, uncertainty exists in the accuracy and physical meaning of the fiber organization parameters being computed by these software applications [6]. The objective of this research is to develop and validate a free software application to accurately and automatically measure fiber orientation distribution in soft connective tissue.

METHODS

Software Development. A portable software application, FiberFit, was developed in Python utilizing the FFT band-pass method (Fig. 1; free download at http://coen.boisestate.edu/ntm/fiberfit/). This software was designed to support fast and intuitive two-dimensional analysis of fiber networks. The image analysis code in FiberFit was created by using numpy and scipy libraries to port an FFT band-pass method we developed in Matlab into Python [10]. This code fits a von Mises distribution to the FFT generated fiber orientation distribution. Parameters for fiber dispersion, k, and mean fiber orientation, μ, are automatically calculated and displayed by the program. This FFT band-pass method was previously validated using known test images of fiber networks with variable density and organization [11]. The average error was less than 8% when measuring k, and less than 1 degree when measuring μ.

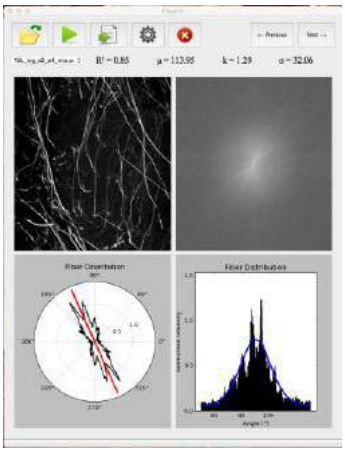

Fig. 1: FiberFit user interface

The FiberFit user interface (Fig. 1) is built using Qt bindings for Python. Users can analyze 8-bit images and export results and parameters (k and μ) as PDF and spreadsheet reports. Multiple images can be analyzed at a single time and users can implement different cut-off frequencies for the band-pass filter.

Copyright 2016 The Organizing Committee for the 2016 Summer Biomechanics, Bioengineering and Biotransport Conference

Software Validation. FiberFit software was evaluated using confocal images of ligament. Collagen fibril networks in five bovine ligament specimens were autofluoresced at 63× using the 405 nm laser of a confocal microscope and ZEN imaging software (Fig. 2a) [12]. ImageJ was used for image preprocessing prior to analysis with FiberFit.

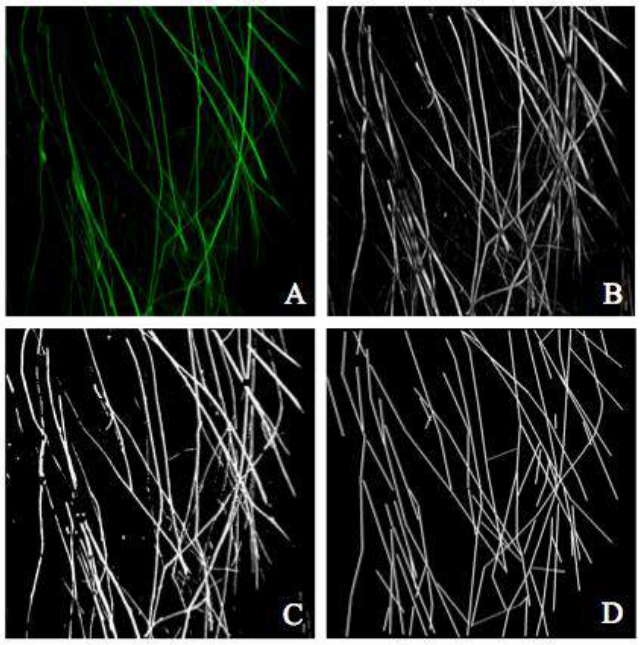

Fig. 2: Images of fiber network. A) original confocal image, B) grayscale, C) binary, and D) manually traced.

The first steps in image preprocessing included sharpening, filtering, smoothing, and normalizing the intensity values of all images. Each image was then converted into two formats: 8-bit grayscale (Fig. 2b) and binary (Fig. 2c). As a final noise removal step, a despeckle operation (3x3 median filter) was applied to all converted images. The grayscale and binary images were then analyzed using FiberFit to generate a fiber orientation distribution and calculate k and μ.

To determine the accuracy of using FiberFit to calculate k and μ, a third set of images was created by manually tracing the start and end points of the fibrils in the original confocal image (Fig. 2d). A discrete fiber orientation distribution, $f(\theta_i)$, was built for each of these manually traced images by using the total number of pixels for lines orientated along each angle θ_i. The mean (μ) and standard deviation (σ) of the discrete fiber orientation distribution were calculated using a multimodal, centrally symmetric approach [13]. A two-term exponential relationship between σ and k was then developed by fitting k to distributions with known σ values ($R^2 = 1.0$).

The k and μ parameters calculated from the discrete fiber orientation distributions ($k_{discrete}$, $\mu_{discrete}$) were used as a gold standard to determine the accuracy of calculating k and μ using FiberFit ($k_{FiberFit}$, $\mu_{FiberFit}$), where error in measuring μ was defined by the absolute mean difference ($|\mu_{FiberFit} - \mu_{discrete}|$), and error in measuring k was defined by the absolute mean percentage error ($|k_{discrete} - k_{FiberFit}|/ k_{discrete}$).

RESULTS

The FiberFit software quantified k and μ for all ligament confocal images with an average runtime of 3.1 ± 0.2 seconds on a 2.7 GHz processor. We found that using the grayscale preprocessing method gave the strongest correlation to the manual tracing method for measuring k ($R^2 = 0.95$; Fig. 3), and the binary preprocessing method gave the strongest correlation to the manual tracing method for measuring μ ($R^2 = 0.97$; Fig. 3). The average error in measuring k and μ with the grayscale method was 13.3 ± 8.2% and 3.3 ± 3.1 degrees, respectively, and for the binary method was 22.7 ± 15.1% and 2.1 ± 0.6 degrees, respectively.

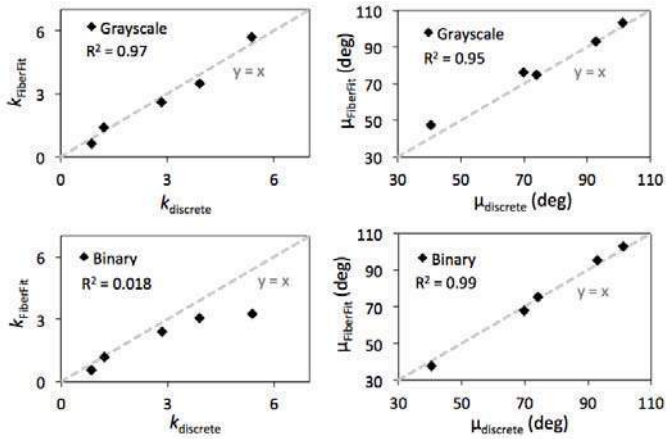

Fig. 3: Correlation of FiberFit results to known values when using (A, B) grayscale and (C, D) binary processing methods.

DISCUSSION

A free software application, FiberFit, was successfully developed to quickly, automatically, and accurately extract fiber dispersion and mean fiber orientation from fiber networks in ligament. We found that converting images to grayscale prior to using FiberFit gave good results. Converting images directly to binary gave less consistent results for highly aligned fiber networks. Both these techniques required background filtering to remove noise, otherwise mean fiber orientation error was almost two times greater (data not shown). In this study, we developed a validation strategy using discrete distributions and manual tracing to assess FFT accuracy in confocal images. This novel approach may be useful for evaluating and optimizing FFT with other imaging modalities and tissues.

The FiberFit software includes unique features that can support and expedite research in biomechanics and mechanobiology. A novel feature of FiberFit is the automated extraction of descriptive structural parameters (k and μ) based on the fitting of a semicircular von Mises distribution to the FFT generated fiber orientation distribution. The quantification of structural parameters from imaging data is a critical step to understanding the inter-relations between biological processes, such as collagen remodeling and repair, and the mechanical environment.

In conclusion, this study has provided guidelines, experimental methodologies and computational tools for researchers that are investigating the microstructure and mechanics of fibrillar networks in biological tissue. To our knowledge, FiberFit is the first free software to implement a band-pass filter for the FFT analysis of fiber networks.

ACKNOWLEDGEMENTS

Kind support provided by the NIH (NIGMS P20GM109095 and NIGMS P20GM103408).

REFERENCES

[1] Woo S.L. et al., *J. Biomech. Eng.*, 111(1):95, 1989. [2] Vogel et al., *Lab. Investig.*, 40(2):201-6, 1979. [3] Makareeva E et al., *J. Biol. Chem.*, 283(8):4787-98, 2008. [4] Polzer S et al., *Microsc. Microanal.*, 19:1395-1404, 2013. [5] Schriefl A et al., *J. R. Soc. Interface*, 9(76):3081-93, 2012. [6] D'Amore A et al., *Biomaterials*, 31(20):5345-54, 2010. [7] O'Connell B, "Oval Profile Plot plugin for ImageJ," 2012. [8] Tienevez J, "Directionality plugin for ImageJ," 2010. [9] Rezakhaniha R et al., *Biomech. Model. Mechanobiol.*, 11(3-4):461-73, 2012. [10] Jones T et al., "SciPy: Open Source Scientific Tools for Python," 2001-. [11] Morrill E et al., *SB³C2015-431*, Poster88, 2015. [12] Monici M, *Biotechnol Annu Review*, 11(11):227-56, 2005. [13] Mardia K et al., *Directional Statistics*, 2000

Copyright 2016 The Organizing Committee for the 2016 Summer Biomechanics, Bioengineering and Biotransport Conference

SB³C2016
Summer Biomechanics, Bioengineering and Biotransport Conference
June 29 –July 2, National Harbor, MD, USA
SB³C2016-864

ULTRASOUND MEASUREMENT OF SHAPE CHANGE DURING IN VITRO INFLATION OF AN ARTERIAL BIFURCATION

John P. Carruth (1), Ryan R. Mahutga (1), Christopher E. Korenczuk (1), Victor H. Barocas (1)

(1) Department of Biomedical Engineering
University of Minnesota – Twin Cities
Minneapolis, Minnesota, USA

INTRODUCTION

The arterial tree is a complex network containing millions of arterial branches [1]. The arterial wall is composed of the endothelium, smooth muscle, and elastic and collagen fibers. The components of the layers each contribute to the mechanical properties of the artery, and the interaction of those components, like the arterial structure itself, becomes more complex when the vessel geometry deviates from the cylindrical. An example of such an irregular geometry is a bifurcation. The bifurcation's structural and mechanical properties are different from and more complex than those of a straight artery [2,3,4]. Therefore, the bifurcation is an important area of interest in the study of arterial mechanics.

Bifurcations are, however, difficult to study experimentally because the complex architecture and geometry do not lend themselves to standard mechanical testing protocols. Planar biaxial testing is problematic because a planar section of the tissue is difficult to isolate and because properties vary with position within the sample. Inflation is a relatively simple experiment, but it is difficult to analyze the inflation of a bifurcation because the convenience of radial symmetry is lost.

In this work, we develop a test system for inflation of an arterial bifurcation with simultaneous ultrasound scanning, which can then be used to construct 3-D images of the bifurcating vessel at controlled internal pressures. Eventually, these data could be used in an inverse model to assess the mechanical properties of the bifurcation.

METHODS

Arterial inflation testing was performed on a porcine carotid artery obtained from the University of Minnesota's Visual Heart Lab. The sample was cleaned to remove as much of the surrounding connective tissue as possible. The two daughter branches of the sample were cut so that the total length of the sample was approximately 5 cm, ensuring that the sample would fit in the inflation device. The sample was attached to male Luer fittings with suture. The sample was flushed with PBS to ensure there were no clots. One of the daughter branches of the sample was capped to prevent flow out allowing pressurization of the system.

The sample was placed in the artery inflation device utilizing the attached Luers to connect into a closed fluid system (Figure 1A). The inflation device was submerged in a fluid bath. The system contained a bleed-off valve to release any trapped air, a non-torqueing connector, and a pressure monitor. Once the artery was secured in the device, the non-torqueing connector was adjusted to ensure that the artery was torque-free. The bath was filled with phosphate-buffered saline (PBS) solution to a level at least 1 cm higher than the artery. Using a syringe, the system was filled with PBS, the bleed-off valve was closed, and the pressure monitor was zeroed. The sample was stretched to 125% of its original length prior to inflation to simulate its in vivo length [5].

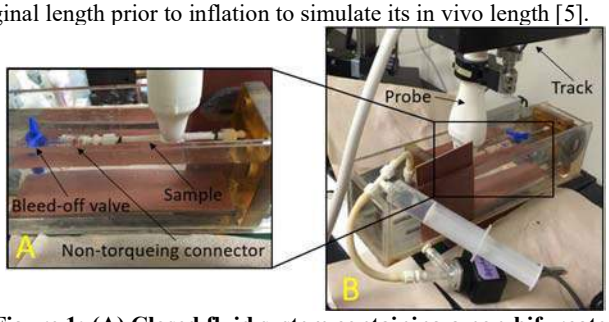

Figure 1: (A) Closed fluid system containing a non-bifurcated sample submerged in (B) the experimental setup.

The experimental setup can be seen in Figure 1B. A small-animal, 38 MHz ultrasound probe (Vevo 2100) attached to a track allowed

Copyright 2016 The Organizing Committee for the 2016 Summer Biomechanics, Bioengineering and Biotransport Conference

image slices to be obtained under constant motion along the long axis of the sample. The ultrasound probe was placed in the PBS in a position capturing a cross-sectional image of the sample. Rubber was placed below the sample to reduce echoing off the tank bottom. The probe and imaging software were adjusted until a clear ultrasound image was obtained. The sample was preconditioned by inflating the system from 5 to 100 mmHg 10 times. The pressure was then increased in increments from 0 to 300 mmHg. After each 20 mmHg pressure step, a cross-sectional ultrasound image stack was captured along the length of the sample. Images of 22px/mm resolution were captured 1.52 mm apart. The ultrasound image stacks were used to create a 3-D model of the sample using the software Seg3D [6].

The experimental protocol was also performed on a non-bifurcated (straight, roughly cylindrical) carotid artery. A pressure-diameter analysis was performed using three selected images from the ultrasound image stacks. The image at the center of the sample and images 30.4 mm from each end were used. Inner and outer sample diameters were measured at these points using imageJ.

RESULTS

Three cross-sectional images taken from the ultrasound image stack of a carotid bifurcation at 10 mmHg are displayed in Figure 2. The three images are of the mother vessel, the bifurcation, and the two daughter vessels.

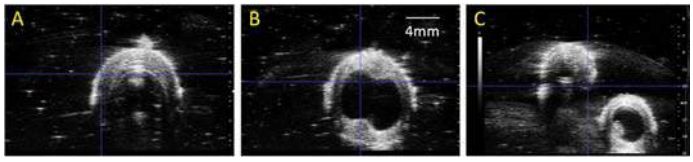

Figure 2: Cross-sectional ultrasound images of the (A) mother vessel, (B) bifurcation, and (C) two daughter vessels. Scale bar (4mm) applies to all images.

The branching of the carotid bifurcation can be seen in Figures 2 and 3. The image of the bifurcation in Figure 2B shows the complexity of the geometry occurring at the bifurcation. The manner in which the mother vessel splits into two daughter vessels determines the distribution of the arterial layers, and thus the mechanical properties, at the bifurcation. The 3-D model of carotid bifurcation (Figure 3) shows the split from the proximal mother vessel to the two distal daughter vessels.

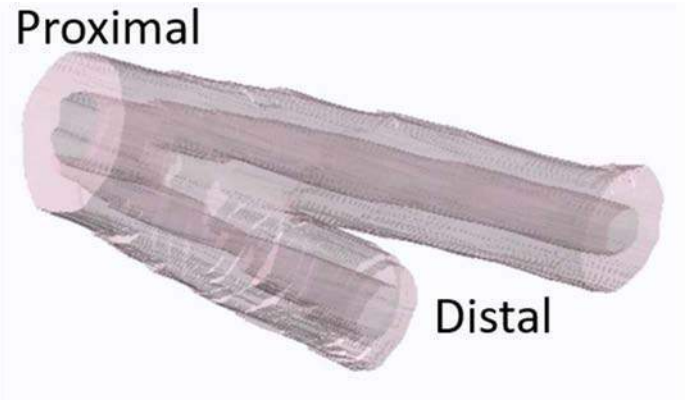

Figure 3: 3-D reconstruction of carotid bifurcation with proximal and distal ends labeled.

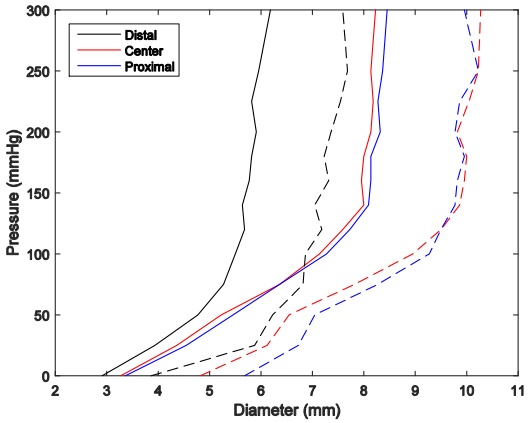

Figure 4: Pressure-diameter plot of non-bifurcated carotid artery. Dashed and solid lines correspond to the outer and inner diameters, respectively.

The lockout (i.e., the sharp upturn in the pressure-diameter curve) of the circumferential fibers can be seen in Figure 4. Lockout occurred at around 125 mmHg for the center and proximal slices and around 110 mmHg for the distal slice. Normal porcine systolic blood pressure occurs at 125-130 mmHg [7]. Blood vessels are very distensible at physiological pressures and due to fiber lockout become much less distensible at higher pressures [8]. Fiber lockout ensures blood vessels can be compliant at physiological pressures and offers protection against defects at higher pressures.

DISCUSSION

We have demonstrated the ability to perform an inflation test on a bifurcating vessel while concurrently imaging the full vessel geometry with ultrasound. Although there were challenges in constructing the test apparatus, preparing the vessel, and analyzing the ultrasound data, the resulting combination of pressure and detailed volume has the potential to provide a new level of understanding of bifurcation mechanics. Our data will serve as the input to an image-based finite-element model of bifurcation inflation, which in turn will provide insight into differences between the bifurcation's properties and those of the more cylindrical portions of the vessel. In addition, it may be possible to use 3-D volume correlation methods [9] to extract a detailed strain field from the experimental image stack.

ACKNOWLEDGEMENTS

We acknowledge the help and support of the Minnesota Supercomputing Institute, Professor Robert Tranquillo's Lab group especially Zeeshan Syedain, and the University of Minnesota – Twin Cities Undergraduate Research Opportunities Program. Tissue was provided by the Visible Heart Laboratory at the University of Minnesota.

REFERENCES

[1] Singhal, S et al., *Circulation Research*, 33:190-197, 1973.
[2] Debes, J and Fung, Y.C., *Am. J. Physiol,.* 269: H433-H442, 1995.
[3] Rowe, A et al., *Journal of Vascular Research*, 40: 406-415, 2003.
[4] Tong, J et al., *Annals of Biomedical Eng.*, 39: 1703-1719, 2011.
[5] Valentin, A and Huphrey, JD, *Medical & Biological Engineering. & Computing,* 47: 979-987, 2009.
[6] CIBC, Seg3D: Volumetric Image Segmentation and Visualization. Scientific Computing and Imaging Institute (SCI), 2015.
[7] Hannon, J.P et al., *Div. of Military Trauma Research*, 379, 1989.
[8] Kochova P et al., *Physiol. Meas.*, 33: 1335-1351, 2012.
[9] Bar-Kochba et al., *Exp. Mech.*, 55: 261-264, 2015.

Copyright 2016 The Organizing Committee for the 2016 Summer Biomechanics, Bioengineering and Biotransport Conference

SB^{3}C2016
Summer Biomechanics, Bioengineering and Biotransport Conference
June 29 –July 2, National Harbor, MD, USA
SB^{3}C2016-865

INFLUENCE OF SUBARACHNOID HEMORRHAGE FACTORS ON VASCULAR SMOOTH MUSCLE CELL FUNCTIONAL PHENOTYPE IN THE DEVELOPMENT OF CEREBRAL VASOSPASM

Eric S. Hald (1), Zaw Win (1), Justin Buksa (1), Connor Timm (1), Patrick W. Alford (1)

(1) Department of Biomedical Engineering
University of Minnesota-Twin Cities
Minneapolis, MN, USA

INTRODUCTION

Subarachnoid hemorrhage **(SAH)** is bleeding in the subarachnoid space of the brain, often a result of traumatic brain injury or intracranial aneurysm [1]. When SAH occurs, growth and clotting factors, such as TGF-β, PDGF, and thrombin, are released. Surrounding tissues exposed to abnormal levels of these factors can undergo a variety of mechanical and biochemical perturbations affecting both vascular and neural function. Cerebral vasospasm **(CV)** is a potentially lethal vascular disease that often occurs after SAH and is characterized by acute hypercontractile arterial behavior followed by extended remodeling, lumen occlusion, and ischemia over the course of 3-7 days after a bleed occurs [1]. It is unclear what initiates this characteristic functional behavior in CV progression, resulting in limited therapeutic options to reduce negative patient outcomes associated with CV.

Vascular smooth muscle cells **(VSMCs)** typically exist in a distribution between two functional phenotypes: contractile or synthetic (proliferative) [2]. During CV, the distribution of VSMC phenotypes is thought to relate to tissue-level mechanics in the cerebral vasculature [3]. Here, we utilize a traction force microscopy method to determine changes in VSMC mechanics resulting from differential treatment with SAH factors. We consider a distribution of VSMCs between synthetic and contractile functional phenotypes, how treatment with individual SAH-borne factors affects shifts in these distributions, and to what extent these factors may be critical in the pathologic mechanical progression of CV.

METHODS

Substrate Fabrication and VSMC Culture and Treatment

Polyacrylamide **(PA)** hydrogels were fabricated as in [4] and tuned to a Young's modulus of 13.5 kPa. A solution of 200-nm fluorescent microspheres was added to allow substrate displacement tracking. Gels were bound to 35-mm glass cover slips using bind silane. Glass cover slips were used to create PA gels with a diameter of 12 mm and thickness of 30-50 μm. PDMS rings (18-mm diameter) were attached to reduce cell seeding area and required medium volume. Sulpho-SANPAH (0.5 mg/mL) was used to crosslink fibronectin (50 ug/ml) to PA gels as in [5]. VSMCs were then seeded at a density of 5000 cells per gel. After attachment, each sample was treated with serum-free medium for 24h to induce a contractile functional phenotype characteristic of normal arterial wall conditions [6]. After 24h in serum-free medium, each sample was treated with serum-free medium

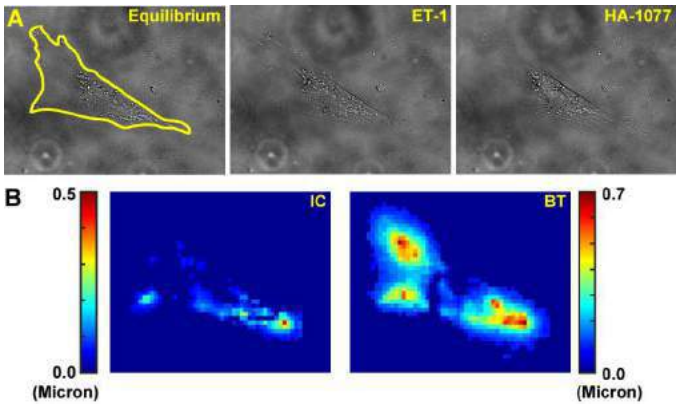

Figure 1. Traction force microscopy VSMC contractility assay. (A) Brightfield images of single VSMC at different treatment time points during assay. Outline: cell spread area at equilibrium. ET-1: endothelin-1-induced contraction. HA-1077: rho-kinase inhibited VSMC relaxation. **(B)** Associated displacement fields for induced contraction (IC, ET-1 – Equilibrium) and basal tone (BT, HA-1077 – Equilibrium).

Copyright 2016 The Organizing Committee for the 2016 Summer Biomechanics, Bioengineering and Biotransport Conference

containing one of three SAH factors (TGF-β, PDGF, or thrombin) at one of five physiologic or pathologic concentrations (including control). Solutions were refreshed every 24h for up to four days of treatment.

Traction Force Microscopy to Determine VSMC Traction Force

Traction force microscopy experiments were conducted to determine two important stress states: 1) basal tone via tissue relaxation with HA-1077, a rho-kinase inhibitor, and 2) induced contraction via stimulation with endothelin-1, a vasoconstrictor (Fig. 1A). Images of fluorescent microspheres within PA gels directly underneath single VSMCs were captured after experimental treatments to track displacements resulting from stress generation (Fig. 1B).

Strain Energy Calculation to Determine Shifts in VSMC Functional Phenotype Distribution

Bead displacement fields and corresponding calculated traction forces were computed for substrate changes between equilibrium and relaxed (basal tone) and induced contraction and equilibrium (induced contraction) time points using the ImageJ plugins developed in [7]. Strain energy (U) in the PA gel was calculated according to:

$$U = \frac{1}{2}\int \vec{T}\cdot\vec{u}\, dxdy \quad (1)$$

where $\vec{T}$ is the traction stress vector and $\vec{u}$ is the displacement vector.

Total strain energy for each cell was normalized by Day 1 control means for each set of experiments. A threshold of 1.0 (i.e. Day 1 control mean) was used to determine percentage of cells above functional phenotype threshold (contractile) and below functional phenotype threshold (synthetic). Differences between treatment conditions and same day controls were calculated as percent difference in fraction of contractile cells.

RESULTS AND DISCUSSION

Here, we present a traction force microscopy assay to determine effects of isolated SAH factor treatment on single VSMCs over physiologic and pathologic concentration ranges. Temporal changes in VSMC functional phenotype were measured as a function of strain energy in PA gels from single VSMC traction forces. TGF-β treatment initially resulted in fewer contractile cells, as measured in basal tone and induced contraction stress states. The percentage of contractile cells increased for both states by Day 4 (Fig. 2, Row 1). PDGF treatment resulted in increased contractile functional phenotype for basal tone, but decreased contractile phenotype for induced contraction across all time points (Fig. 2, Row 2). Thrombin yielded dose-dependent responses in functional phenotypes related to induced contraction (Fig 2, Row 3).

Basal tone and induced contraction are important stress states due to the mechanical responses they elicit. It has been hypothesized that tissues have a preferred local stress and that they grow to maintain this stress [8]. Changes in this target stress, as measured by changes in basal tone here, then result in growth rate changes. The initial decrease in functional basal tone induced by TGF-β (and thrombin), followed by increased functional basal tone over time (Fig. 2) may mirror the acute hypercontractile behavior in CV and the increased growth and remodeling experienced in prolonged CV. Similarly, PDGF appears to promote growth and remodeling at all times, possibly being critical in later stages of CV.

Endothelin-1-induced contraction is representative of VSMCs' ability to actively contract in maintenance of endothelial shear stress. In CV, shear stress increases due to luminal narrowing. This should result in decreased endothelin response, suggesting the decreases observed in PDGF induced contraction (Fig. 2) could be important in CV progression. Further work to rigorously predict the effects of pathologic

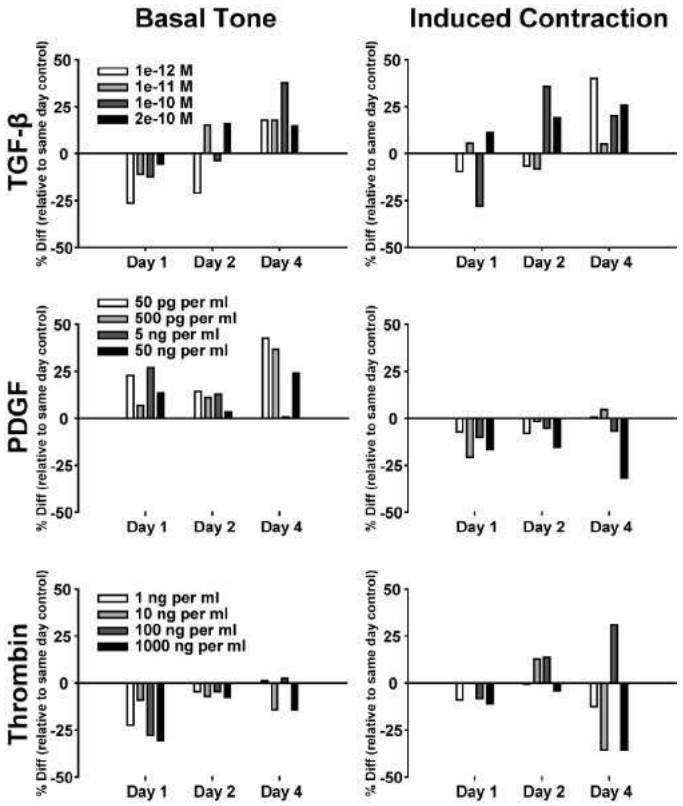

Figure 2. SAH factor-induced temporal functional phenotype distribution differences. Treatment of VSMCs with SAH factors TGF-β, PDGF, and thrombin induces different distributions of contractile and synthetic functional phenotypes. Left: Basal Tone. Right: Induced Contraction. Row 1: TGF-β. Row 2: PDGF. Row 3: Thrombin.

changes in functional phenotype distributions on tissue response and the downstream consequences for arterial blood flow in the brain can be accomplished via computational modeling.

These results represent behavior of sparse single VSMCs exposed to three factors known to increase in abundance as a result of SAH. VSMCs in native arteries experience much different architecture and surroundings, including cell-cell contacts and signaling. We can extend this work to investigate differences between "injured" solitary VSMCs and intact vascular architecture using a vascular muscular thin film technique as in [9], yielding a more complete understanding of the influence of SAH factors on cerebral vascular mechanics.

ACKNOWLEDGEMENTS

We thank financial support from the American Heart Association Scientist Development Grant, 13SDG14670062 (PWA) and the University of Minnesota Doctoral Dissertation Fellowship (ESH).

REFERENCES

[1] Humphrey, JD et al., *Ann Biomed Eng*, 35:1485-1497, 2007.
[2] Owens, GK et al., *Physiol Rev,* 84:767-801, 2004.
[3] Alford, PW et al., *PNAS,* 108:12706-12710, 2011.
[4] Tse, JR and Engler AJ, *Curr Protoc Cell Biol*, 47:10-16, 2010.
[5] Aratyn-Schaus, Y et al., *JoVE*, 46:2173, 2010.
[6] Han, M et al., *Am J Physiol Cell Physiol,* 291:C50-C58, 2006.
[7] Tseng, Q et al., *PNAS*, 109:1506-1511, 2011.
[8] Fung, YC, *Biomechanics*, pg. 530, 1990.
[9] Hald et al., *Biofabrication*, 6: 045005, 2014.

Copyright 2016 The Organizing Committee for the 2016 Summer Biomechanics, Bioengineering and Biotransport Conference

SB^{3}C2016
Summer Biomechanics, Bioengineering and Biotransport Conference
June 29 –July 2, National Harbor, MD, USA
SB^{3}C2016-866

DEVELOPMENT OF FINITE ELEMENT-BASED INJURY METRICS FOR HEAD INJURY PREDICTION

Derek A. Jones (1,2), Jillian E. Urban (1,2), Ashley A. Weaver (1,2) , Joel D. Stitzel (1,2)

(1) Wake Forest School of Medicine
Winston-Salem, NC, USA

(2) Virginia Tech – Wake Forest Center for Injury Biomechanics, Winston-Salem, NC, USA

INTRODUCTION

Over 1.7 million people sustain a Traumatic Brain Injury (TBI) each year, 52,000 of whom die. Motor vehicle crashes (MVCs) are the second leading cause of TBI (17.3%) and are responsible for the largest percentage of TBI-related deaths (31.8%) in the United States [1]. Basic mechanisms of TBI are becoming better understood including the understanding that head injury is primarily the result of direct contact to the head [2,3]. However, due to the complexity in loading conditions and crash configurations during a MVC, there is still much that is unknown about the mechanistic differences between different types of head injuries and how those injuries may be mitigated. The objective of this research study is to better understand the contact parameters and regional mechanisms that contribute to head injuries with an emphasis on describing scenarios that could be mitigated through limiting rotational versus linear accelerations (i.e., BrIC versus HIC). With better understanding of the correlations between ATD criteria (HIC and BrIC), contact surface stiffness, and finite element (FE) model metrics, we can better understand regional and organ level mechanisms of head injury and develop methods to better mitigate injuries in MVCs.

METHODS

Contact Surfaces and Injury Mechanisms

The Global Human Body Models Consortium (GHBMC) 50th percentile head and neck model was utilized to investigate contact surfaces associated with head injury and resulting mechanisms of injuries including cerebral contusion, diffuse axonal injury (DAI), intra-cerebral hemorrhage, intraventricular hemorrhage (IVH), subdural hematoma (SDH), subarachnoid hemorrhage (SAH), and epidural hematoma (EDH) [4]. The contact surfaces were defined as hard (i.e., pole, tree, bare sheet metal, striking vehicle's grille), compliant (i.e., door trim, A-pillar trim, instrument panel), and soft (i.e., airbag).

Simulation of Various Contact Types and Impact Locations

Four parameters (impact velocity, impactor stiffness, impact location, and impact orientation) were varied over a parameter range wide enough to simulate the response of the head from a large population of head impact cases. Impact velocities were chosen to represent approximate velocities seen in MVCs. Impactor stiffness estimation values were generated based on the three contact surface categories (hard, compliant, and soft) in order to capture the full range of possible head contact surfaces resulting from a MVC. A set of 24 locations around one side of the head were selected as starting impact locations. Five impact directions were then used for each of the 24 locations (Figure 1).

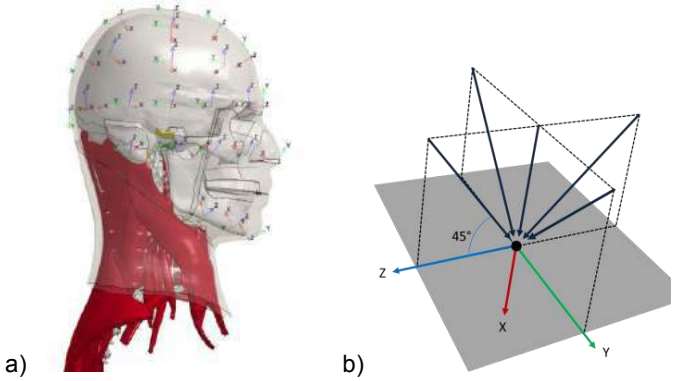

Figure 1: Impact locations (a) and directionalities (b) used to impact the GHBMC head and neck model. Positive X axis directed toward Head CG.

Copyright 2016 The Organizing Committee for the 2016 Summer Biomechanics, Bioengineering and Biotransport Conference

Development of Criteria for Evaluation of Brain Response

Previously, the GHBMC 50th percentile head model was developed to predict multiple Crash Induced Injuries (CIIs) including skull/facial/nose fracture, SDH, cerebral contusion, and DAI. This study aimed to develop metrics to predict region of interest (ROI)-based metrics of cerebral contusion (e.g., within the frontal and temporal lobes), EDH, SAH, intra-cerebral hemorrhage, IVH, and skull deformation. The development of these injury metrics was done by combining injury physiology understanding, contact simulations, and reported case outcomes from the CIREN and NASS databases. ROI-based injury metrics were developed based on ROI definitions of anatomic locations and geometrical locations with respect to the impact location were used for subsequent analysis (Figure 2). Conical ROIs were based on the angle between vectors defined by the vector between the brain CG and impact location as well as the vector between an element and the brain CG. Sets of elements were used for analysis based on four conical sections <30°, <60°, >90°, and >130° from impact. The first two sections represent coup region, while the latter two represent contre-coup. Blue, green, and red highlighted regions of Figure 2 represent the deep, intermediate, and outer subsections of the <30° conical ROI.

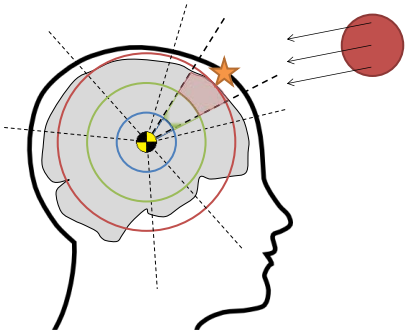

Figure 2: Spatially defined ROIs based on impact location and CG of the brain. Orange star represents impact location. Dotted lines represent conical sections spanning <30°, <60°, >90°, and >130° from impact.

Comparison of Head Injury Prediction for GHBMC to HIC and BrIC

The five sets of simulations performed were post-processed to obtain injury prediction values based on the newly developed injury predictors in terms of AIS 1-5 injury risk as well as the predicted AIS injury risk from HIC and/or BrIC. The predictions were then compared.

RESULTS

The simulations yielded a wide range of HIC and BrIC values as well as many different combinations of injury risk determined by each metric. Some simulations produced high risk values associated with BrIC (rotational velocity) coupled with low risk as predicted by HIC (linear acceleration). The risk was correlated to both impactor speed and stiffness (Figure 3). For a given simulation, the distribution of max principal strain was also calculated and separated by ROI. One of the more severe impacts to the top of the head resulted in a clearly distinguishable maximum principal strain distribution (Figure 4). Locations closer to the impact location (coup) reached higher levels of max principal strain than those on the opposite side of the head (contre-coup).

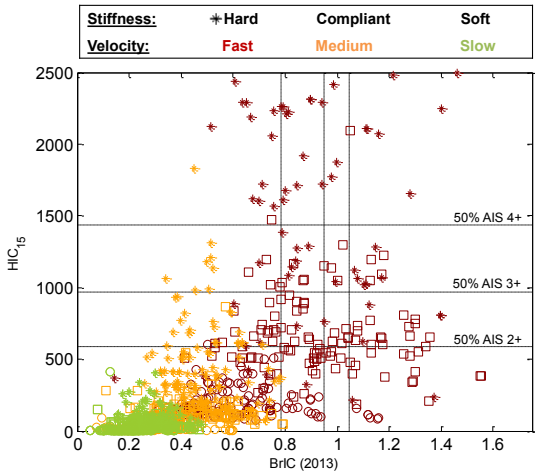

Figure 3: Distribution of impact simulations' HIC and BrIC values with respect to velocity and stiffness of impactor. Isoclines of 50% risk of AIS 2+, 3+, and 4+ overlaid on plot.

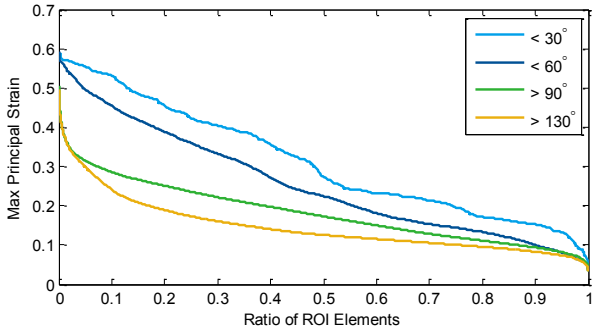

Figure 4: Maximum principal strain distribution in high stiffness, high velocity impact by conical section.

DISCUSSION

The parametric study of head impacts resulting in a wide range of HIC and BrIC values in conjunction with detailed injury metrics allows for the further understanding of specific injury risk and the correlation between ATD criteria. Preliminary results indicate in hard contact simulations, maximum principal strain is higher in coup regions than in contre-coup regions. High HIC values were more often seen with high impactor stiffness, while high BrIC values were observed with compliant materials. Simulations that produced high injury risk based on one metric (i.e., HIC or BrIC) did not always indicate high injury risk from the other, indicating the two are not tightly coupled.

ACKNOWLEDGEMENTS

This study was funded by the National Highway Traffic Safety Administration under Cooperative Agreement Number DTNH22-10-H-00294. Views expressed are those of the authors and do not represent the views of NHTSA. The authors would also like to acknowledge Matt Craig and Erik Takhounts for their involvement in the discussion of the study design.

REFERENCES

[1] Coronado, VG et al., *MMWR Surveill Summ*, 60:1-32, 2011.
[2] Nirula, R et al., *Acc Anal Prev*, 35:201-210, 2031.
[3] Yoganandan, N. et al., *Acc Anal Prev*, 42:1370-1378, 2010.
[4] Gayzik, FS et al., *Ann Biomed Eng*, 39:2568-2583, 2011.

Copyright 2016 The Organizing Committee for the 2016 Summer Biomechanics, Bioengineering and Biotransport Conference

SB^{3}C2016
Summer Biomechanics, Bioengineering and Biotransport Conference
June 29 –July 2, National Harbor, MD, USA
SB^{3}C2016-867

THE QUANTIFICATION OF BLOOD FLOW PATTERNS INDUCED BY ENDOVASCULAR STENT GRAFTS: AN EXPERIMENTAL INVESTIGATION OF THE EFFECTS OF OVERSIZING AND COMPLIANCE

Amanda Colella-Centazzo (1), Clifton R. Johnston (1)

(1) Department of Mechanical Engineering
Dalhousie University
Halifax, NS, Canada

INTRODUCTION

In current medical practice endovascular stents are the most common treatment used in the management of arterial disease, particularly to bridge blood flow through aneurysmal vessels. Despite their relative ease of implantation they have been shown incite harmful secondary issues long-term that negate these benefits, with additional interventions occurring at higher rates as compared to open repair surgery [1], while showing no significant difference in survival after 2 years [2]. The alterations to the fluid dynamic forces that are incited by the stent play an important role in tissue healing, stent migration and by extension stent efficacy.

More specifically, areas of low wall shear stress (WSS) have been shown to affect the progression of atherosclerosis, the proliferation of intimal hyperplasia and the formation of thrombi [3]. These fluid dynamic considerations directly affect the long-term patency of stent grafts and have therefore prompted investigation into how the presence of the stent alters the local hemodynamic environment.

An environment representing that of the human femoral artery was constructed with optical access to the blood analog as it exits an implanted stent graft. Using Particle Image Velocimetry (PIV) the flow patterns were imaged and the changes to the peak velocity and WSS induced by stent implantation were quantified for several stent-vessel cases, specifically examining the effect of stent sizing and the compliance of the treated vessel. Tests were conducted in a rigid acrylic test section and an elastic mock artery with a compliance within the clinically observed range.

METHODS

A closed flow loop was designed and constructed for visualization and measurement of flow through a 10 mm inner diameter tube, representing a simplified geometry of the femoral artery. A common non-Newtonian blood analog representative of physiological hemodynamic parameters and comprised of a mixture of glycerol (40%), xantham gum (0.04%) and water, was circulated through the test section [4]. The mixture was exposed to a 1Hz pulsatile flow profile typical of the human femoral artery (Figure 1) with a peak velocity of 47 cm/sec, the mean peak forward velocity in the femoral artery reported by Fronek et al. [5]. This corresponds to a Reynolds number at peak flow of 1033.5, which is within the physiologically observed range [6].

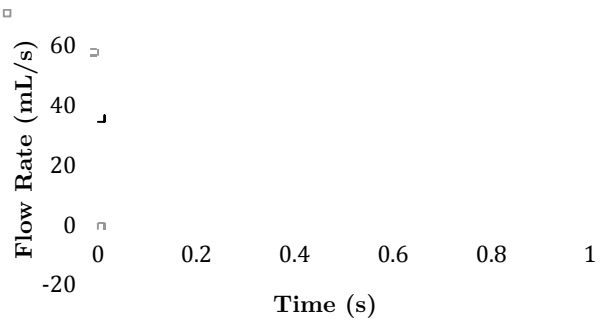

Figure 1 - 1 Hz Input waveform representing pulse profile typical of the human femoral artery.

Using PIV, cross-sectional velocity and wall shear stress immediately downstream of a Gianturco Zenith stent graft (Cook Medical, Inc., Bloomington, IN, USA) were quantified. The compliance of the elastic tube was tested in a modified PIV set-up and was found to be 7.77 % mm Hg^{-1x} x 10^{-2}, which is representative of a healthy human male femoral artery. The two stents of 20% and 40% oversizing were deployed in the test section and an identical test was performed in a rigid acrylic tube for comparison.

The test section was embedded in an acrylic flow chamber, which was filled with 100% glycerol to correct for the refraction index differences between the circulating fluid and the surrounding vessel and allow the laser sheet to reach the test area unaffected. The fluid was seeded using 10 µm silver coated hollow glass spheres, which were illuminated using a 1 mm thick laser sheet. Image frames were collected using a Photron mini UX100 at 4000fps with 20 image pairs collected per pulse, over 10 pulses.

RESULTS

Oversizing: Introduction of a full stent (3 wires in a polyester cover) had a substantial effect on flow velocities, particularly at peak pulse. The flow observed followed an asymmetric pattern due to variations in the folding and pillowing of the fabric between the stent wires. This

Copyright 2016 The Organizing Committee for the 2016 Summer Biomechanics, Bioengineering and Biotransport Conference

asymmetry was more pronounced in the 12 mm stent. This appears to be due to the fact that the 12 mm stent has seven wire peaks, while the 14 mm stent has eight. Although both were installed in the tube such that their wires were symmetric in the plane of the camera, the seven peaks allowed more intra-wire spacing and therefore allowed the fabric sheath and wires to deploy asymmetrically.

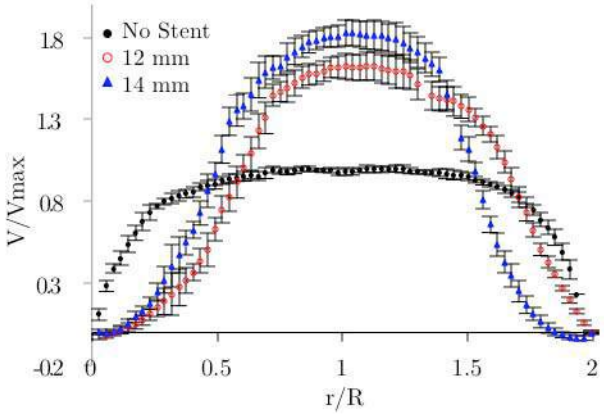

Figure 2 - Velocity profiles at peak pulse at x/R=0.5 downstream of a 12 mm and 14 mm Gianturco stent compared to the same acrylic vessel with no stent.

Both stents caused a considerable reduction in velocity close to the wall accompanied by an accelerated core flow (Figure 2). At 20% and 40% oversizing (12 mm and 14 mm stents) the centerline velocities at x/R=0.5 increased by 65.4% and 86.2%, respectively, as compared to the non-stented condition. At peak pulse, the 12 mm stent caused a velocity reduction from the wall to r/R = 0.5776 and r/R=0.7040 to the far wall, with flow reversal noted between the wall and r/R= 0.08664. A similar pattern was observed with the 14 mm stent, with reduced velocities occurring between the wall and r/R = 0.4621 and r/R= 1.5306. The largest absolute change for both stents occurred at r/R=0.2310 and was a decrease of 35.60 cm/s (85.0%) and 31.72 cm/s (75.8%) for the 12 mm and 14 mm stents, respectively

The wall shear stress saw a decrease upon introduction of both stents across the pulse cycle, with the most substantial changes in WSS occurring during acceleration of the fluid (Figure 4-11). Due to the asymmetry in the vessel, the WSS drop varied between the two walls. For comparison, the most severe case is considered. The drop observed at peak flow was found to be 82.1% for the 12 mm stent. The 14 mm stent saw a 120.7% in the WSS due to the flow reversal noted at the wall.

The cycle averaged WSS decreased from 0.920 Pa in the non-stented case to -0.832 Pa and -1.2675 Pa for the 12 mm and 14 mm stent. The change in sign of the cycle averaged WSS indicates a substantial flow reversal over the course of the pulse at the near wall. The OSI, surprisingly, decreased upon stent introduction from 0.4385 to 0.4182 and 0.3642 for the 12mm and 14mm stent, respectively. This is due to the fact that the flow was already pulsatile and therefore highly oscillatory to begin with, which is an important characteristic of flow in the peripheral arteries. The lowering of the WSS in both positive and negative flow direction, led to an overall WSS approaching zero, in turn lowering the OSI.

Compliance: Tests conducted in the compliant vessel showed similar trends to those in acrylic, however changes were more pronounced. Cross-sectional velocity profiles downstream of a single stent wire (Figure 3) showed a larger drop in velocities at the vessel periphery compared to the acrylic values (5.306 cm/s and 8.77 cm/s respectively). The centerline velocities increased more in the SYLGARD at 11.7%, compared to 4.65% in the acrylic. The WSS saw a drop at the peak with a 22.0% decrease in the acrylic and a 26.9% decrease in the SYLGARD.

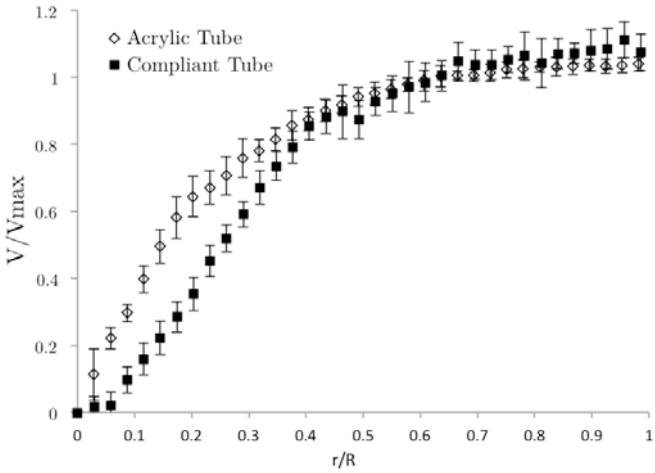

Figure 3 - Velocity profiles at peak pulse downstream of a Gianturco stent wire in acrylic and compliant vessels

DISCUSSION

The effect of oversizing was consistent across vessel compliances, with the larger 14 mm stent causing more substantial changes to the flow profiles as compared to the smaller 12 mm. The stents both caused an increase in the centerline velocities, accompanied by a drop at the vessel periphery. This incited a drop in the WSS, a feature that has been shown to promote re-stenosis. Oversizing of the stent is common practice clinically to ensure proper adhesion of the graft and to minimize stent migration, however this convention has important implications on the degree of disturbance introduced into the blood flow. These findings suggest that a graft with a diameter closer to the native vessel could be helpful in reducing the instances of stent re-occlusion.

Additionally the rigid tube was shown to lessen the velocity disturbances induced by the stents introduction, with centerline velocity increases more than double in the compliant vessel. This would imply that in more compliant vessels where the compliance mismatch is greater the stent has a larger effect on the fluid flow.

REFERENCES

[1] Greenhalgh, RM, *The Lancet*, 364: 843-848, 2004.

[2] De Bruin et al., *NEJM*, 362:1881-1889, 2010.

[3] Chiu and Chien, *Physiological Reviews*, 91: 327–387, 2011.

[4] Brookshields, K.A. et al., *J of Bioreheology*, 30:107-116, 1994.

[5] Fronek, A et al., *Circulation*, 53:957-960, 1976.

[6] C. Caro, *The Mechanics of the Circulation*, 2012.

Copyright 2016 The Organizing Committee for the 2016 Summer Biomechanics, Bioengineering and Biotransport Conference

SB^{3}C2016
Summer Biomechanics, Bioengineering and Biotransport Conference
June 29 –July 2, National Harbor, MD, USA
SB^{3}C2016-868

DEVELOPMENT OF A PLATFORM FOR STUDYING ASTROCYTE MECHANOBIOLOGY: COMPRESSION OF ASTROCYTES IN 3D COLLAGEN GELS

John J.E. Mulvihill (1,2), Lisa A. Schildmeyer (1), Julia Raykin (1), Eric J. Snider (1), Kavita Chinoy (1), Danny J. Kelly (2), C. Ross Ethier (1,3).

(1) Wallace H. Coulter Dept. of Biomedical Engineering
Georgia Institute of Technology
Atlanta, Georgia, USA

(2) Mechanical and Manufacturing Engineering
Trinity College Dublin
Dublin, Ireland

(3) Atlanta VA Medical Center,
Decatur, Georgia, USA

INTRODUCTION

Glaucoma is the second leading cause of blindness worldwide (World Health Organization), affecting more than 70 million people. As glaucoma is primarily a disease of aging, the burden is expected to increase, with the number of people affected by glaucoma set to rise to 80 million by 2020 [1].

Glaucoma is an optic neuropathy in which intraocular pressure (IOP) exceeds a threshold, leading eventually to damage to retinal ganglion cells (RGCs) that carry vision information to the brain [2]. RGC axons pass through a web of connective tissue ("the lamina cribrosa") as they exit the eye and converge to form the optic nerve. IOP deforms the delicate tissues of the optic nerve head (ONH), which is thought to predispose resident astrocytes to transition to a reactive phenotype; this transition is in turn believed to contribute to RGC dysfunction and eventual death, resulting in vision loss. The mechanisms of how astrocytes transition to the reactive phenotype due to stimulation from increased IOP is unclear. To date, ONH astrocyte mechanobiology has only been studied in 2D (monolayer) culture systems [2-4]. While 2D culture models have revealed important information, 2D culture primes astrocyte reactivity, confounding studies of astrocyte mechanobiology [3].

Accordingly, our overall aim is to better understand the mechanobiology of ONH astrocytes in a physiologically relevant 3D environment. In this preliminary study, we first hypothesize that a 3D culture system offers an improved environment for studying astrocyte reactivity. We analyze cell morphology and the change in protein levels that biomechanical loading, mimicking the effects of IOP, has on astrocytes grown in 3D collagen gels at different time points in comparison to static control 3D gels.

METHODS

This proof-of-principle study used the DI TNC1 (ATCC) immortalized cell line, derived from primary cultures of rat cortical astrocytes. The cells were maintained in Dulbecco's Modified Eagle Medium (DMEM, Cellgro, 10-013-CV) with 10% FBS (Hyclone, SH30910) and 1% 1X Pen/Strep (Hyclone, SV30010).

For 3D cell culture, cells were seeded at a density of 1 million cells/ml in a gel matrix consisting of 10% 0.1M NaOH, 10% 10X DMEM, 30% cell/1X media and 50% 2 mg/ml collagen type I (MP Biomedical, 150026). For each gel, 700µl of gel matrix was added to in a non-tissue culture treated 24-well plate for 15 minutes before addition of media, and gels were released from wells after 24 hours. The gels were left in static culture for 7 days prior to mechanical stimulation (Figure 1, left). For 2D cell culture, cells were seeded in a 75 cm^2 flask (Falcon PET, Fisher).

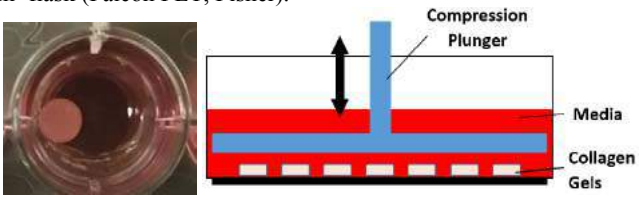

Figure 1: Top-down image of collagen gel prior to mechanical stimulation (left) and a diagram of the bioreactor system (right) to illustrate the compressive load applied to the collagen gels.

A bioreactor system was developed to apply a compressive mechanical load to the 3D collagen gels (Figure 1, right). The strains generated by the system were selected to correspond to those thought to be experienced by astrocytes under elevated IOP in the lamina cribrosa, where most ONH astrocytes reside [4]. Specifically, the 3D

Copyright 2016 The Organizing Committee for the 2016 Summer Biomechanics, Bioengineering and Biotransport Conference

collagen gels containing astrocytes were compressed, within the custom culture dish, by 10% for 0, 24, 48 and 72 hours at 1Hz [4]. An equal number of control gels were not subjected to compression and maintained in a replicate culture dish.

For protein level quantification, flow cytometry (FC) (BD Accuri C6) was used to assess the change in levels of key protein markers for astrocyte reactivity; GFAP (Millipore, MAB360, FC: 1:100 in FACS buffer, 5% FBS in PBS) and vimentin (Santa Cruz, sc6260, FC: 1:100). For each time point (n=3), gels were gently triturated for 10 mins in a solution of Accumax (Innovative Cell Technologies Inc.) and Trypsin (0.125%, Cellgro) at 37°C to dissociate the collagen and release the cells. For cell morphology examination, gels were permeabilized in 0.1% triton-X100 for 15 mins, after which phalloidin and DAPI stains were applied for 2 hours and 15 minutes, respectively. Gels were examined using confocal microscopy to acquire maximum intensity projections (MIP) of z-stacks from various sections of the gels to quantitatively analyze cell directionality and alignment (FIJI, NIH). Statistical analysis was carried out using one-way ANOVA to test differences in protein levels.

RESULTS

A significant difference in GFAP expression was found between 2D and 3D controls (Figure 2, p=0.03). Protein expression was significantly increased in compressed vs. control gels at 24 hour (p=0.03), 48 hour (p=0.05) and 72 hours (p=0.01). GFAP expression significantly increased between 24 and 72 hours (p=0.02).

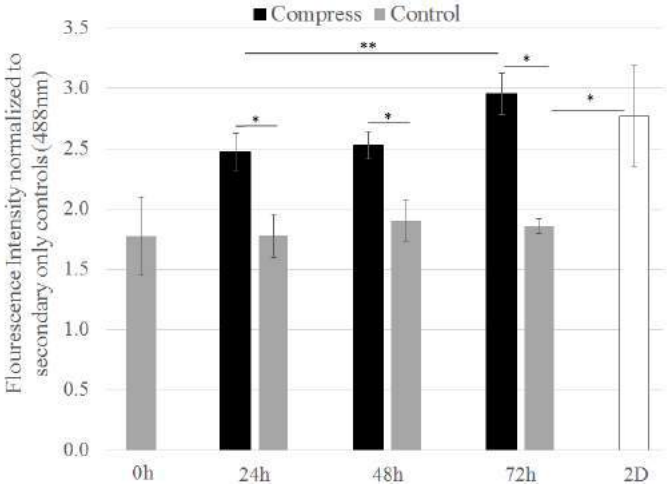

Figure 2: Mean fluorescence intensity for GFAP labelling from FC analysis for compressed (black) and control (grey) gels at 0, 24, 48 and 72 hours and for 2D culture (white). Error bars are standard deviations (*p≤0.05, **p≤0.001).

Similar significant trends were found for vimentin expression differences between 2D and 3D controls (Figure 3, p=0.01). Vimentin expression was significantly increased in compressed vs. control gels at 24 (p=0.01), 48 (p<0.001) and 72 hours (p<0.001). Vimentin expression levels significantly increased between 24 & 72 hours and 48 & 72 hours (both p<0.001). No increase in either GFAP or vimentin labelling was found between the control gels at each time point (0, 24, 48 and 72h).

Figure 4 represents MIP images from a control gel (left) and a compressed (right) gel to highlight the alignment of astrocytes due to mechanical stimulation. Cells in compressed gels were found to align in a preferred direction compared to the random alignment in static controls (p<0.001). An increase in the expression of vimentin (Figure 4) and GFAP (not shown) was found between compressed and control gels.

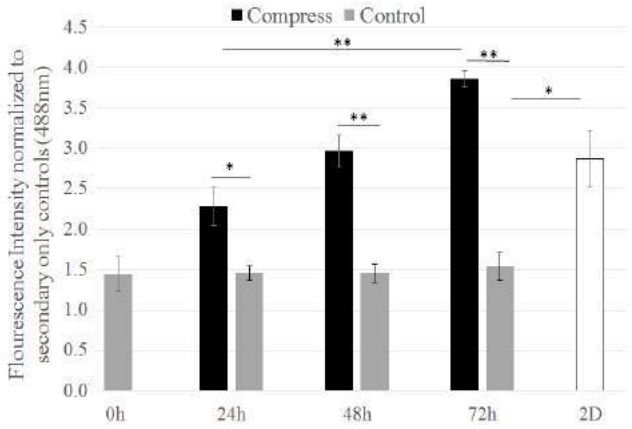

Figure 3: Mean fluorescence intensity for vimentin labelling from FC analysis for compressed (black) and control (grey) gels at 0, 24, 48 and 72 hours and for 2D culture (white) . Error bars are standard deviations (*p≤0.05, **p≤0.001).

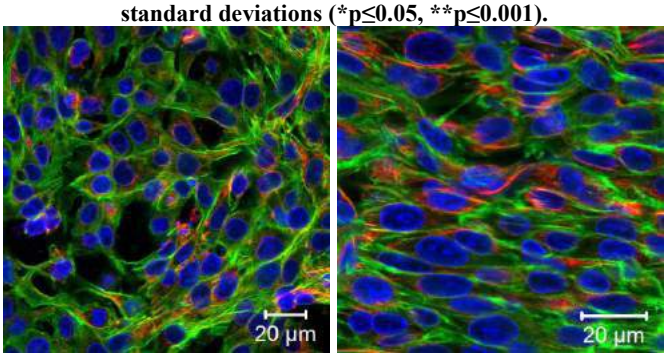

Figure 4: MIP image of control (left) and compressed (right) gels at 48 hours illustrating increased alignment of cells and expression of vimentin in compressed gel. DAPI: blue, phalloidin: green and vimentin: red.

DISCUSSION

The first hypothesis under investigation in this study is that a 3D environment is preferred for studying astrocyte mechanobiology over a 2D environment [3,4]. Our 3D platform is more realistic and leads to less basal astrocyte reactivity vs. 2D, as judged by lower GFAP and vimentin expression (Figure 2 and 3 respectively). Secondly, this study found that compression, mimicking certain aspects of IOP loading, significantly increased the level of both proteins at each time point vs. static controls, evidence for biomechanically-modulated astrocyte reactivity in our system. Further, no change in protein expression was found for the control 3D gels between each time point (0, 24, 48 and 72 hours) suggesting that the mechanical stimulation is instigating the change in protein levels rather than the 3D environment.

Astrocytes in the compressed 3D gels exhibited increased alignment vs. control 3D gels (Figure 4). This changed astrocyte morphology could be a factor in the transition of astrocytes to a reactive phenotype. Further work is necessary to quantitatively analyze the morphological difference between compressed and control 3D gels, particularly in primary human astrocytes from the ONH.

ACKNOWLEDGEMENTS

ELEVATE: Irish Research Council International Career Development Fellowship – co-funded by Marie Cure Actions; Georgia Research Alliance.

REFERENCES

[1] Quigley, HA, et al., *Br J Ophthalmol*, 90(3):262-7, 2006.
[2] Varma, R et al., *Am J Opthalmol*, 152(4): 515-22, 2011.
[3] East, E et al., *J Tissue Eng Regen Med,* 3:634-646, 2009.
[4] Rogers, RS et al., *Mol & Cell Proteomics*, 11(2), 2012.

Copyright 2016 The Organizing Committee for the 2016 Summer Biomechanics, Bioengineering and Biotransport Conference

SB^{3}C2016
Summer Biomechanics, Bioengineering and Biotransport Conference
June 29 –July 2, National Harbor, MD, USA
SB^{3}C2016-870

CUSTOMIZABLE SURFACE-COATING METHOD FOR BIOPROSTHETIC VALVE BIOCOMPATIBILITY

Monica M. Fahrenholtz (1), K. Jane Grande-Allen (1)

(1) Bioengineering
Rice University
Houston, TX, USA

INTRODUCTION

Each year, over 90,000 prosthetic heart valves are implanted in the U.S. and 280,000 worldwide, about half of which are bioprosthetic heart valves [1], and the share of bioprosthetic valves being used is growing, especially in younger patients, [2]. Complications involving thrombosis, inflammation, and calcification are still a major problem in bioprosthetic valve replacements, leading to a growing need for better technology. In particular, pediatric patients are at higher risk for these complications and would benefit greatly from improved replacement devices.

There is still much active research in the area of improving heart valve replacements. While most work has been done in the area of fully synthetic or tissue engineered valve replacements [3], a secondary focus in the field has been on the surface modification of currently available bioprosthetic heart valve devices to promote re-endothelialization. Targeting the modification of currently approved devices could lead to more rapid translation to the clinic. Toward this end, a few researchers have pioneered methods for modification of bioprosthetic valve surfaces with titanium [4], bioactive molecules (e.g. hyaluronic acid, heparin) [5,6], nanoparticles [7], or even polymer films [8] to produce an anti-fouling, non-immunogenic coating.

Unfortunately, many surface modification strategies require the use of harsh solvents or drying methods that may change the bulk structure of the valve device, potentially affecting its function. Additionally, some strategies meant to promote re-endothelialization are highly non-specific and may lead to additional acute surface fouling [8,9]. While these are serious challenges, the need for new technology to improve patient quality of life continues to motivate efforts to incorporate promising technologies into current practices on a shorter timescale.

Toward this end, we have developed a novel two-step surface coating method that can be easily incorporated into current bioprosthetic valve manufacturing processes, uses FDA-approved materials, and can be carried out under mild conditions with minimal risk of adverse effects from the processing steps. Here, we investigate this surface coating process for its controllability in terms of coating thickness and surface coverage, its effect on surface mechanical properties of the bioprosthetic tissue, and its anti-fouling properties.

METHODS

Initially, a previously developed bioprosthetic valve surface model (BVSM) was used to investigate multiple coating formulations [10]. In general, this coating was achieved by first converting reactive amine groups on the surface to acrylate groups via an n-hydroxysuccinimidyl-PEG(2000)-acrylate linker, then the surface coating was added by glucose oxidase-initiated free radical polymerization of PEGDA at the surface.

To measure coating thickness on the BVSM under various reaction conditions, the coating was doped with acryl-rhodamine dye and analyzed by confocal microscopy. From this data, it was determined that 6 kDa PEGDA resulted in the most consistent coating coverage and thickness for future studies.

Coated BVSMs were then analyzed by bioindentation to measure the effect of the coating on surface mechanical properties. The coatings were also exposed to rhodamine-labelled BSA to measure acute fouling of the surface.

Based on optimization of the coating on the BVSM, the coating method was then translated to porcine bioprosthetic tissue biopsies (porcine aortic valve leaflets fixed in 0.2% glutaraldehyde for 3 days). Changes in surface mechanical properties were measured by bioindentation, and coverage of the tissue surface was qualitatively

Copyright 2016 The Organizing Committee for the 2016 Summer Biomechanics, Bioengineering and Biotransport Conference

analyzed by SEM. Coating of the surface with PEGDA was also confirmed by XPS analysis of the C1s spectra, specifically comparing the component peaks at 286 eV (C-O, C-N) and 284.8 eV (C-C).

All results were analyzed using R statistical software (R Project) via an ANOVA and post-hoc Tukey's test for differences between groups, with a correction for repeated measures as appropriate.

RESULTS

Different PEGDA oligomer sizes and reaction conditions were analyzed for surface coating thickness, as demonstrated in Figure 1. Given the more consistent results obtained from 6 kDa formulations, 6 kDa PEGDA with a 2 min reaction time was chosen.

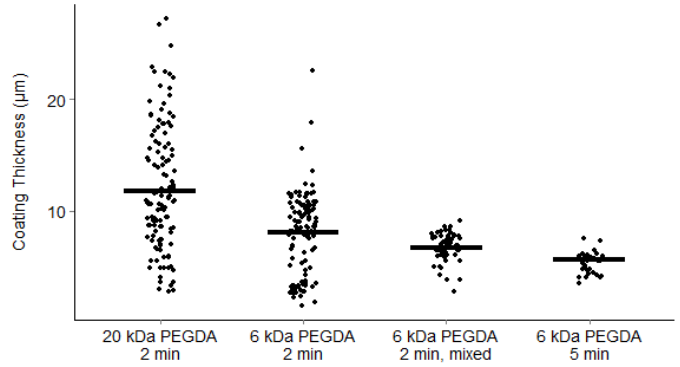

Figure 1: No significant change in surface coating thickness was observed; however, 20 kDa PEGDA showed more variable coating thickness as compared to 6 kDa formulations.

Next, the coatings were analyzed for percent fouling of the surface. The coating significantly decreased the acute fouling of the BVSM surface, such that the fouling of the coated surface was not significantly different from the protein-repellant PEGDA only control (Figure 2).

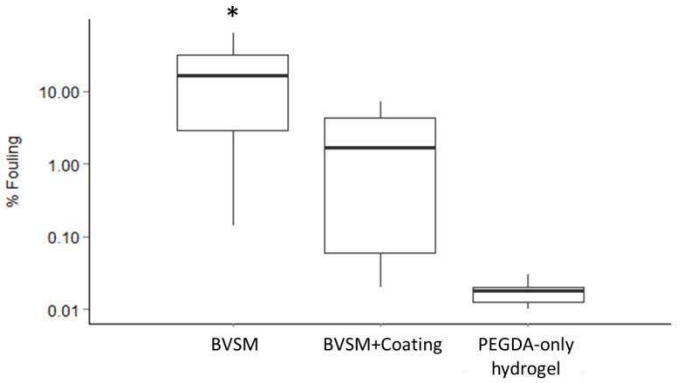

Figure 2: Fouling on BVSM surface was significantly greater than both the coated BVSM and PEGDA-only hydrogel control.

The coating method was again applied to the BVSM and also to porcine bioprosthetic tissue samples. Stiffness of the surface as determined by bioindentation (via Oliver & Pharr method) was not found to be significantly different among any of the groups, indicating that the coating method did not affect the surface stiffness and also confirming previous literature showing that the BVSM mimics bioprosthetic tissue stiffness [10].

SEM imaging was then used to qualitatively show that some coating of the tissue surface was obtained, and that increasing the reaction time increased the observable area of coverage (Figure 3). In the coated groups at 1000X magnification, the coating appears as darker, smoother spots on the valve tissue. At high magnification (10,000X), the coated regions become thicker and more continuous with increasing reaction time. Coverage also appeared to be increased by increasing glucose oxidase concentration (data not shown).

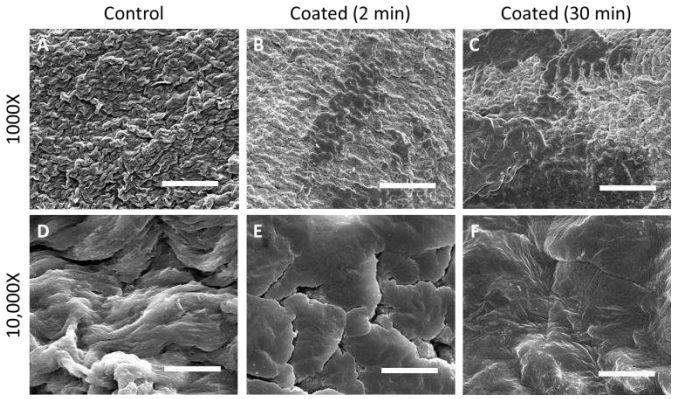

Figure 3. Representative SEM images of bioprosthetic tissue (A,D), tissue coated for 2 min (B, E) and tissue coated for 30 min (C, F). Scale bar = 40 µm (1000x), 4 µm (10,000x).

The observed areas assumed to be coating in the SEM images were confirmed to be the PEGDA coating by analysis with XPS, which showed an increasing contribution of the C-O peak (indicative of PEGDA) to the C1s spectra for all coated samples compared to uncoated tissues.

DISCUSSION

In this work, we have successfully optimized a two-step surface coating method using a previously-developed bioprosthetic valve surface model and translated the method to bioprosthetic valve tissue samples. We show that the thin coating formed on the BVSM is functional in preventing protein adhesion, and coatings on both the BVSM and tissue samples do not significantly influence surface mechanical properties. Translation of the coating method to bioprosthetic tissue resulted in a non-continuous surface coating of PEGDA, but area coverage could be significantly increased with increased reaction time and glucose oxidase concentration. Overall, this work demonstrates the feasibility of the proposed two-step coating method for modifying the surface of bioprosthetic tissue and sets the stage for future work to optimize coverage to produce a functional barrier and to add molecules to promote *in situ* endothelialization.

ACKNOWLEDGEMENTS

The authors would like to acknowledge funding from the March of Dimes Research Grant (6-FY13-86).

REFERENCES

[1] Pibarot P, Dumesnil JG, *Circulation,* 119:1034–48, 2009.
[2] Chan V, et al., *Circulation,* 124:S75–80, 2011.
[3] Li S, Henry JJD, *Annu Rev Biomed Eng*, 13:451–75, 2011.
[4] Guldner NW, et al., *Circulation,* 119:1653–60, 2009.
[5] Hahn SK, et al., *Biotechnol Bioprocess Eng*, 10:218–24, 2005.
[6] Lee WK, et al., *Biomaterials,* 21:2323–30, 2000.
[7] Ghanbari H, et al., *Int J Nanomedicine,* 6:775–86, 2011.
[8] Nogueira GM, et al. *Mater Sci Eng C*, 30:575–82, 2010.
[9] Dahm M, et al. *Biomed Mater Eng,* 14:419–25, 2004.
[10] Fahrenholtz MM, et al., *Acta Biomater*, 26:64–71, 2015.

Copyright 2016 The Organizing Committee for the 2016 Summer Biomechanics, Bioengineering and Biotransport Conference

SB^{3}C2016
Summer Biomechanics, Bioengineering and Biotransport Conference
June 29 –July 2, National Harbor, MD, USA
SB^{3}C2016-871

A PRELIMINARY STUDY TO DETERMINE IF ARTERIOVENOUS FISTULA CONFIGURATION GENERATES HELICAL FLOW AND IF HELICAL FLOW IS A SURROGATE MARKER OF EXPOSURE TO DISTURBED SHEAR

Connor V. Cunnane (1, 3), Leonard D. Browne (1, 3), Stephen P. Broderick (1, 3), Craig Dunlop (3), Graeme J. Houston (2, 3) Michael T. Walsh (1, 3)

(1) Centre for Applied Biomedical Engineering Research, Health Research Institute, Department of Mechanical, Aeronautical & Biomedical Engineering and Material & Surface Science Institute, University of Limerick, Limerick, Ireland

(2) Cardiovascular and Diabetes Medicine, Ninewells Hospital and Medical School, University of Dundee, Dundee, United Kingdom

(3) Vascular Flow Technologies, Dundee, United Kingdom

INTRODUCTION

End stage renal disease (ESRD) is a condition that affects the ability of the kidneys to filter blood effectively. Patients suffering from ESRD are often referred to hemodialysis as a replacement therapy for the lost function of their kidneys. In order to achieve efficient dialysis a vascular access (VA) capable of supplying high flow rates is required. The most commonly used VA type is an arteriovenous fistula (AVF), due to their superior patency rates over arteriovenous grafts. Following fistula creation there is a drastic change in local hemodynamics. This results in the venous segment of the AVF undergoing significant biological changes in a process known as maturation. Even though AVFs are the most commonly used access type, they suffer from poor primary patency rates ranging from 44-60%[1, 2]. Fistula non-maturation and venous stenosis are the two main contributors to these high failure rates. Intimal hyperplasia has been impleaded as the primary cause of these contributors.

Until recently Wall Shear Stress (WSS) parameters have been employed as the primary indicators regarding the progression of intimal hyperplasia. However, more recent studies suggest that WSS based parameters alone provide an incomplete analysis of the local hemodynamics and should be complimented by a quantitative description of the bulk flow. It is hypothesised that counter rotating helical structures within the bulk flow can result in the suppression of flow disturbances, which can lead to the development of intimal hyperplasia (IH)[3]. This study investigates the effect that the anastomosis angle between the arterial and venous segment of an AVF has on the development of such flow fields and if certain helicity-based bulk flow descriptors can act as a surrogate marker of exposure to disturbed shear.

METHODS

The idealised AVF geometries analysed as part of this study were adapted from the work conducted by Steinbuch, 2011. Each model is geometrically identical apart from the anastomosis angle which is varied to 10^o, 35^o, 50^o and 70^o (Figure. 1). Computational fluid dynamics simulations were carried out for each model applying a brachial artery wave form with an average flow rate of 600mL/min at the artery inlet in all models. Three seconds of flow was simulated which correlated to three cardiac cycles. All the results were averaged over the 3rd cardiac cycle.

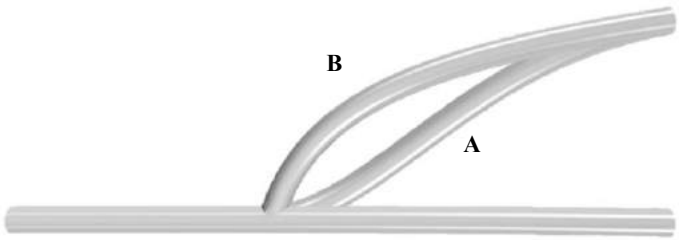

Figure 1: Idealised models of the AVF geometries analysed in this study, displaying the 10^o (A) and 70^o (B) models, the 35^o and 50^o models were omitted from the image for clarity purposes.

The distribution of the time-averaged wall shear stress (TAWSS), oscillatory shear index (OSI), relative residence time (RRT) and transverse wall shear stress (TransWSS) were computed at the AVF surface. Each of the WSS parameters were represented using threshold values to represent the 80th and 90th percentile values. Disturbed shear was characterised by the surface area exposed to OSI, RRT and TransWSS over (or TAWSS under) a threshold value.

The helicity, H(t), of a flow confined to a domain **D** of 3-dimensional Euclidean space $\mathbf{R}^3$ is given by

$$H(t) = \int_D v(\boldsymbol{x},t).\omega(\boldsymbol{x},t)dV = \int_D H_k(\boldsymbol{x},t)dV \qquad \text{(Eq. 1)}$$

A useful indicator of how the velocity vector is orientated with respect to the vorticity vector is the Localised Normalised Helicity (LNH) proposed by Shtilman et al., 1985, defined as

Copyright 2016 The Organizing Committee for the 2016 Summer Biomechanics, Bioengineering and Biotransport Conference

$$LNH = \frac{v(x,t).\omega(x,t)}{|v(x,t)||\omega(x,t)|} \quad \text{(Eq. 2)}$$

and has been proven to be a useful quantity for the visualisation of complex flow patterns in cardiovascular flows[6].

The helicity-based bulk flow descriptors utilised in this study to characterise the bulk flow were defined by Gallo et al., 2012. The descriptors h_1 and h_3 quantify the balance between counter rotating helical fluid structures in the flow field, while h_2 and h_4 quantify the helical intensity.

$$h_1 = \frac{1}{TV_i}\int_T \int_{V_i} H_k dV\, dt \quad \text{(Eq. 3)}$$

$$h_2 = \frac{1}{TV_i}\int_T \int_{V_i} |H_k| dV\, dt \quad \text{(Eq. 4)}$$

$$h_3 = \frac{h_1}{h_2} \quad \text{(Eq. 5)}$$

$$h_4 = |h_3| = \frac{|h_1|}{h_2} \quad \text{(Eq. 6)}$$

Multivariate regression analysis was performed to assess the potential for a combination of helicity parameters in indicating exposure to disturbed shear. The robustness of the regression analysis to different volumes of integration (V_{Artery} and V_{Vein}) for the helicity based bulk flow descriptors was analysed and the results obtained were compared to those generated by integrating over V_{Full}. The Akaike information criterion (AIC) was then applied to select the optimal combination of the helicity-based bulk flow descriptors to analyse the bulk flow.

RESULTS

The different topological flow features present in the bulk flow were visualised using the parameter LNH. Figure 2 displays the contour plots of LNH averaged over the 3rd cardiac cycle for all 4 models. A threshold of LNH_{avg} = ± 0.2 was adopted for the visualisation of helical flow structures present within the bulk flow.

The presence of helical fluid structures characterised the bulk flow in all 4 models. These helical fluid structures originated at the anastomosis region and propagated along the venous segment of the AVF. The flow field seen in the 10° model is predominantly dominated by a single counter clockwise helical structure (red) however as the anastomosis angle increases the flow field transitions to one in which there are two counter rotating helical structures, which is clearly evident in the 70° model (Figure. 2).

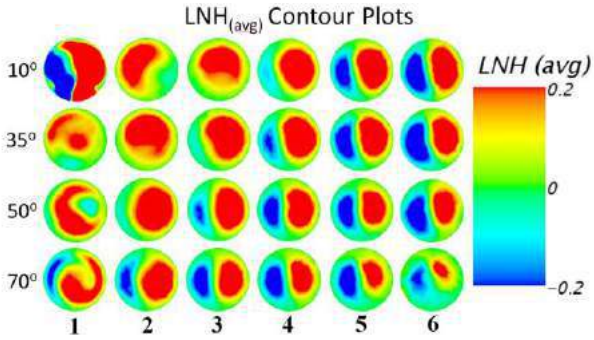

Figure 2: Circumferential slices taken at 1cm intervals from the anastomosis along the venous segment of all 4 AVF models. $LNH_{(avg)}$ contour plots display a flow field dominated by a single counter clockwise helical structure for the 10° model (red), while the 70° models displays a flow field with two counter rotating helical structures (red and blue).

Examining the WSS parameters when integrated over V_{Full} revealed a clear trend whereby as the anastomosis angle increases so too does the overall distribution of both TAWSS and OSI. However, in contrast to this, both RRT and TransWSS decrease in overall distribution.

Table 1: Best fitting models by AIC among the possible combination of helicity descriptors (Eq. 3-6) integrated over V_{Full}.

(P< 0.05)		10°	35°	50°	70°
WSS_{80}	Model	(h2)	(h2)	(h2)	(h2)
	R^2_{adj}	0.9842	0.9391	0.9129	0.8982
WSS_{90}	Model	(h2,h3)	(h2)	(h2)	(h2)
	R^2_{adj}	0.9526	0.9397	0.9083	0.8533
$TransWSS_{80}$	Model	(h2)	(h2)	(h2)	(h2)
	R^2_{adj}	0.8994	0.8851	0.8641	0.6933
$TransWSS_{90}$	Model	(h2)	(h2)	(h2)	(h2)
	R^2_{adj}	0.9369	0.9434	0.7843	0.4903

Multivariate regression analysis revealed a significant relationship between both TAWSS and TransWSS with the helicity based bulk flow descriptor h_2 when integrated over the V_{Full}. However, the relationships differed significantly for the different volumes of integration. When integrating over V_{Artery} each model displayed a discrete correlation with h_1 and when integrating over V_{Vein} each model displayed a completely arbitrary correlation with each of the helicity based bulk flow descriptors.

DISCUSSION

Gallo et al. analysed the potential benefit of helical flow in the carotid bifurcation. They found that high helical intensity is instrumental in suppressing flow disturbances within the bulk flow; however they also state that the potential benefit could be moderated if one direction of rotation is dominant in the flow field. This would suggest that the flow field displayed by the 70° model is the most beneficial at suppressing flow disturbances, evident by the fact that two counter rotating helical structures characterise the flow field.

Both TransWSS and TAWSS displayed a significant correlation with the helicity based bulk flow descriptor h_2 ($P<0.005$) when integrated over V_{Full}. TransWSS was selected as the sole indicator of disturbed shear as it incorporates TAWSS in its calculation. As the anastomosis angle increases the overall distribution of TransWSS decreases, which correlates to an overall reduction in the distribution of disturbed shear as well.

These findings answer both research questions outlined at the beginning of this study; to determine if AVF configuration can generate helical flow and if helical flow is a surrogate marker of exposure to disturbed shear. These preliminary results suggest that the benefit of helical flow that has been proven to suppress flow disturbances in the carotid bifurcation might also exhibit the same benefits in AVFs. These findings also provide preliminary data illustrating the importance of AVF configuration and its potential impact on AVF maturation. This could lead to a reduction in variability currently observed in AVF configuration by supplying quantitative data identifying the most beneficial AVF configuration in relation to maturation. However further studies conducted on realistic geometries are required before any concrete conclusions can be drawn.

ACKNOWLEDGEMENTS

The authors would like to acknowledge the Irish Research Council for their funding.

REFERENCES

1. Lee et al. J. Am. Soc. Nephrol. 18: 1936–1941, 2007.
2. Tordoir et al. Nephrol. Dial. Transplant. 18: 378–383, 2003.
3. Gallo et al., J. Biomech., 45(14): 2398–404, 2012
4. Steinbuch, Intern Report. 2011.
5. Shtilman et al. Physics Letters 113A: 32–37, 1985.
6. Morbiducci et al. J. Biomech., 40: 519-534, 2007.

Copyright 2016 The Organizing Committee for the 2016 Summer Biomechanics, Bioengineering and Biotransport Conference

SB^{3}C2016
Summer Biomechanics, Bioengineering and Biotransport Conference
June 29 –July 2, National Harbor, MD, USA
SB^{3}C2016-872

BIOMECHANICAL CHARACTERIZATION OF SIX MURINE MODELS OF THORACIC AORTIC ANEURYSM AND DISSECTION

Chiara Bellini (1), Matthew R. Bersi (1), Jacopo Ferruzzi (1), Jay D. Humphrey (1)

(1) Department of Biomedical Engineering
Yale University
New Haven, Connecticut, USA

INTRODUCTION

Thoracic Aortic Aneurysm and Dissection (TAAD) is the result of a pathological tissue degeneration process that leads to an abnormal dilation with possible rupture of the aortic wall. Between 1999 and 2013 more than 25,000 people lost their lives in the US alone due to TAAD. Patients suffering from TAAD often have a genetic predisposition, associated with either complex connective tissue syndromes (e.g. Marfan syndrome) or familial disorders (e.g. non-syndromic gene mutations). The documented conservation of these genes across species warrants the use of animal models for the study of TAAD, particularly at the early stages of the disease when human data is not available, and for longitudinal studies. Regardless of their specific etiology, all TAADs are characterized by both a compromised structural integrity of the aortic wall - including loss of elastic fiber integrity, dysfunction or loss of smooth muscle cells (SMCs), and local accumulation of mucoid material (GAGs/PGs) - and by changes in cell signaling; in particular, Angiotensin II (AngII) and Transforming Growth Factor beta (TGF-β) signaling. We present herein a comparison of the biaxial mechanical properties of six murine models of TAAD: (1) *Fbn1*$^{mgR/mgR}$ – a mouse model of Marfan syndrome, where fibrillin-1 deficiency causes fragmentation and loss of elastin [1]; (2) *Fbln5*$^{-/-}$ – a mouse model of arterial ageing, where the absence of fibulin-5 is responsible for the disorganization of the elastic laminae [2]; (3) *Myh11*$^{R247C/R247C}$ – a mouse model of familial TAAD, where a recurrent rare R247C variant is knocked-in the smooth muscle myosin heavy chain (*Myh11*) gene [3]; (4) *Tgfbr2*$^{f/f}$ – a mouse model of TAAD, where the reduced expression of TGF-β type II receptors in the aortic media leads to elastin fragmentation [4]; (5) *Fbln4*^{SMKO} – a mouse model of TAAD, where a significant reduction of fibulin-4 gives rise to disorganized elastic fibers and increased collagen content [5]; (6) AngII-*ApoE*$^{-/-}$ – a mouse model of TAAD similar to the fibrillin-1 deficient mouse, where a high-dose Ang II infusion in apolipoprotein-E null mice brings about focal disruption of elastic fibers and increased medial collagen deposition [6].

METHODS

All animal procedures complied with IACUC protocols at the appropriate Institution. Mutant and control mice were euthanized and the ascending aorta (ATA) excised from the chest cavity with the aid of microdissection tools and a dissection microscope. After removal of fat and excess perivascular tissue, the left carotid artery, left subclavian artery and distal portion of the arch were ligated with sutures. The ATA was then mounted on glass cannulae, through the openings of the aortic root and the brachiocephalic trunk, and secured with sutures for mechanical testing. After preliminary estimation of the unloaded geometry and of the *in vivo* axial stretch, each specimen was extended to the *in vivo* length, acclimated in Hanks buffered physiological solution for ~15 minutes under pulsatile flow between 80 and 120 mmHg, and preconditioned with four cycles of pressurization between 10 and 140 mmHg. Following re-estimation of the unloaded geometry and *in vivo* axial stretch, each ATA was exposed to three pressure-diameter tests (cyclic pressurization between 10 and 140 mmHg at the *in vivo* and ± 5% of the *in vivo* axial stretch) and four axial force-length tests (cyclic extension between 0 and ~50mN at 10, 60, 100 and 140 mmHg). Outer diameter, axial stretch, luminal pressure and axial force were recorded online throughout the mechanical tests. Unloaded wall thickness was measured using either an optical coherence tomography system on the mounted specimen or a dissection microscope on rings cut from each specimen after mechanical testing [7]. With the exception of the *Fbln4*^{SMKO} model, where only n=3 aneurysmal specimens were tested, data from at least n=5 specimens were collected for all the other mutants and their

Copyright 2016 The Organizing Committee for the 2016 Summer Biomechanics, Bioengineering and Biotransport Conference

controls. Mechanical data from specimens of the same genotype were combined with a consistent averaging procedure [7] to obtain a genotype-specific average mechanical response. A microstructurally-motivated four fiber family constitutive relationship was fit to the specimen-specific and averaged data sets by means of a nonlinear regression [7]. Estimated material parameters were used to predict mechanical metrics – stretch, stress, linearized stiffness, stored energy, and distensibility – at the genotype-specific *in vivo* axial length and systolic pressure.

RESULTS

Gross examination revealed significant phenotypic differences between the six genotypes. *Myh11*$^{R247C/R247C}$ mice manifested the mildest aortic phenotype, but they became vulnerable to TAAD when made hypertensive. Conversely, *Fbln5*$^{-/-}$ mice had elongated and tortuous arteries, but they did not show any propensity for aneurysm formation when made hypertensive. *Tgfbr2*$^{f/f}$ mice showed thickening, dilation and dissection of the thoracic aorta, with occasional intramural hematoma, intimal flaps and false lumens. Finally, *Fbn1*$^{mgR/mgR}$, *Fbln4*^{SMKO}, and AngII-*ApoE*$^{-/-}$ mice all developed large aneurysms of the ascending thoracic aorta, with tissue lesions visible under a dissection microscope.

Notwithstanding the phenotypic differences, the material behavior of the six genotypes was remarkably similar. Figure 1 reports the average circumferential (left panel) and axial (right panel) stretch/stress behavior for the six genotypes and the control. *Fbn1*$^{mgR/mgR}$, *Fbln4*^{SMKO}, and AngII-*ApoE*$^{-/-}$ exhibit the most prominent decrease in circumferential distensibility for the range of pressures between 10 and 140 mmHg. Similarly, the *in vivo* axial stretch is reduced in these genotypes, with the *Fbln4*^{SMKO} on average working at the lowest axial extension, followed by *Fbn1*$^{mgR/mgR}$ and AngII-*ApoE*$^{-/-}$.

DISCUSSION

The primary mechanical function of the aorta is to store elastic energy during systole and release it during diastole to ensure proper perfusion of peripheral tissues. Changes in either the axial or the circumferential mechanical properties alter the ability of the aorta to perform this function and increase the workload of the heart. This aspect is particularly relevant for the ATA, which, unlike the descending thoracic or the abdominal aorta, varies in length throughout the cardiac cycle due to the contraction of the heart. It is therefore necessary to evaluate the effect that TAADs have on both the circumferential and the axial behavior of the ATA. While *in vivo* measures can only provide circumferential information, *in vitro* biaxial tests on mouse models of TAAD offer the opportunity to collect otherwise unmeasurable data.

Although mechanical data on arteries from mouse models of TAAD have been reported in the literature [8-10], previous studies relied either on ring tests, which generate a complex state of stress difficult to analyze, or on *in vivo* pressure-diameter data, which do not provide enough information for a rigorous biaxial mechanical characterization [11-14]. We performed inflation-extension tests on the ATA from six murine models of TAAD and compared their estimated biaxial behavior with a suitable control. We showed that all aneurysmal phenotypes share common features, a decrease in circumferential distensibility and axial extensibility. There is a need, however, to identify appropriate mechanical metrics – both structural and material – that can reliably indicate the propensity for the development of TAADs and the vulnerability of a lesion.

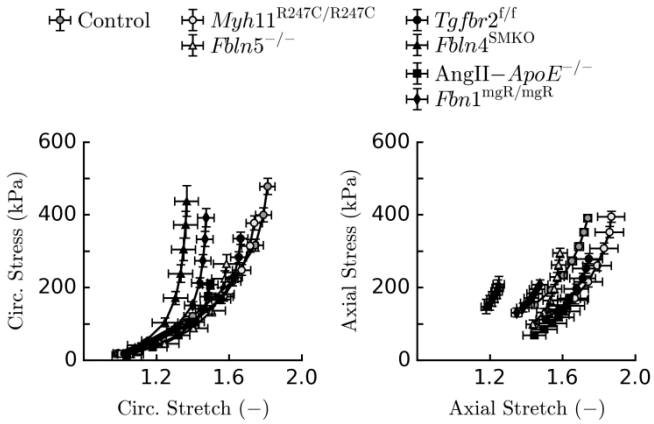

Figure 1: Average circumferential (left panel) and axial (right panel) stress/stretch plots for the six genotypes and the control.

Finally, the changes in structural, material and energy-related metrics that we observed in the aneurysmal phenotypes result from dysregulated mechanosensing induced by specific genetic mutations or pharmacological treatments [15]. Many questions regarding the mechanisms by which the cells probe their environment are yet to be answered and will provide insights on the initiation and progression of TAAD as well as on the interplay between macroscopic mechanics.

ACKNOWLEDGEMENTS

We kindly acknowledge Prof. Milewicz (University of Texas Health Center), Prof. Ramirez (Mt. Sinai School of Medicine), Prof. Rifkin (NYU Medical Center), Prof. Tellides (Yale school of Medicine), and Prof. Yanagisawa (University of Tsukuba) for providing either mouse breeding pairs or excised mouse arteries. This work was supported, in part, by grants from the National Institutes of Health (R01 HL105297 and U01 HL116323 to JDH) and the National Marfan Foundation (to JDH).

REFERENCES

[1] Pereira, L et al., *Proc Natl Acad Sci USA*, 96:3819-3823, 1999.
[1] Yanagisawa, H et al., *Nature*, 415:168-171, 2002.
[3] Kuang, S-Q et al., *Circ Res*, 110:1411-1422, 2012.
[4] Li, W et al., *J Clin Invest*, 124:755-767,2014.
[5] Huang, J et al., *Circ Res*, 106:583-592, 2010.
[6] Daugherty, A et al., *Clin Sci*, 118:681-689, 2010.
[7] Feruzzi, J et al., *Ann Biomed Eng*, 41:1311-1330.
[8] Wenstrup, RJ et al., *J Biol Chem*, 281:12888-12895, 2006.
[9] Chung, AWY et al., *Circ Res*, 101:512-522, 2007.
[10] Cooper, TK et al., *Vet Path*, 47:1028:1039, 2010.
[11] Hanada, K et al., *Circ Res*, 100:738:746, 2007.
[12] Carta, L et al., *ATVB*, 29:2083-2089, 2009.
[13] Mariko, B et al., *J Pathol*, 224:33-44, 2011.
[14] Huang, J et al., *Sci Trans Med*, 5:183ra58, 2013.
[15] Humphrey, JD et al., *Circ Res*, 116:1448-1461, 2015.

Copyright 2016 The Organizing Committee for the 2016 Summer Biomechanics, Bioengineering and Biotransport Conference

SB³C2016
Summer Biomechanics, Bioengineering and Biotransport Conference
June 29 –July 2, National Harbor, MD, USA
SB³C2016-873

DISORGANIZED LAYERS WITHIN AN OTHERWISE ALIGNED FIBROUS NETWORK PRESERVE BULK MECHANICS AND PROMOTE STRAIN RECONSTITUTION IN THE CONTEXT OF RADIAL TEARS

Sonia Bansal (1,2,3), Niobra M. Keah (1,3), Feini Qu (1,2,3,4), Spencer E. Szczesny (1,3), Alexander L. Neuwirth (1,3), Robert L. Mauck (1,2,3), Miltiadis H. Zgonis (1,3)

(1) McKay Orthopaedic Research Laboratory
University of Pennsylvania
Philadelphia, PA, 19104

(2) Department of Bioengineering
University of Pennsylvania
Philadelphia, PA, 19104

(3) Translational Musculoskeletal Research Center
Philadelphia VA Medical Center
Philadelphia, PA, 19104

(4) School of Veterinary Medicine
University of Pennsylvania
Philadelphia, PA, 19104

INTRODUCTION

Meniscal tears are one of the most common orthopedic injuries in the U.S. [1]. Radial tears, which interject perpendicularly and sever the circumferential fibers that make up the meniscus bulk, are thought to compromise mechanical function. As such, these tears are usually treated by partial meniscectomy (excision of the damaged region), with the assumption that severed fibers play no mechanical role. While this is common dogma, a recent study by Bedi et al. [2] suggested that radial tears do not increase knee contact stresses until they reach ~90% of meniscus width [3]. To resolve this contradiction, we reconsidered the role of radial elements ('tie fibers'). These fibers (and sheets) originate at the meniscus periphery and interdigitate amongst the circumferential fibers, binding these fibers together and potentially mediating strain transfer [4]. To query the role of these radial elements, we first quantified their density in the juvenile meniscus. Next, to test the role of radial elements in an aligned network, we utilized electrospinning to generate a meniscus analog. Here, we varied the speed of the collecting mandrel [6] to create scaffolds that were aligned, but contained a subset of non-aligned layers to create 'tie fiber-like' elements. We varied this 'tie fiber' fraction between 25-75% of the scaffold thickness, in seven discrete layers. Through tensile testing of intact scaffolds and those into which a 'radial' defect was introduced, our data suggest that these radial elements may play a critical role in preserving mechanical properties when aligned fibers are severed.

METHODS

Native Tissue Analysis: To determine the quantity of radial elements needed within synthetic constructs, we imaged juvenile bovine menisci at 10X magnification using second-harmonic generation (SHG, 840nm excitation). Three regions of interest were chosen to represent the outer, middle, and inner zones of each radial section along the meniscus circumference. Images were processed with a FIJI integral image filter plugin to decrease noise (**Fig. 1**) [8,9,10] and the area fraction with positive SHG signal computed. Mean fiber density was analyzed by 1-way ANOVA ($p \leq 0.05$) with Tukey's post hoc; data are presented as mean ± SEM.

Scaffold Fabrication and Mechanical Testing: Nanofibrous poly(ε-caprolactone) (PCL) scaffolds were electrospun [7]. For aligned (AL) scaffolds, a mandrel rotating at 10 m/s served as the collector. To form non-aligned (NA) scaffolds, the mandrel was slowed to ~3 m/s. To replicate radial tie elements, AL scaffolds were produced that included discrete NA layers by lowering the speed of the mandrel for set periods of time. These composite scaffolds had 7 alternating AL and NA layers (**Fig. 2**) to produce scaffolds with 25, 33, 50, and 75% NA content through the thickness. Scaffolds were cut to 30 mm length (in the AL direction) x 5 mm width for mechanical testing. Two conditions were tested: intact or defect, with the latter having a radial cut spanning 50% of the width at the middle of the sample height. Cross sectional area was measured with a laser-based device [7] prior to speckle coating. Samples were evaluated in tension in a ramp to failure test (0.5% strain/s), during which they were imaged for strain tracking using the Vic2D image correlation software. Stress versus strain data were curve-fit using a custom bilinear fitting program in MATLAB to define the 'toe' and 'linear' modulus, as well as the transition strain [11,12]. Significance (n=8/group) was analyzed using 1-way ANOVA ($p \leq 0.05$), with Tukey's post hoc; data are presented as mean ± SEM. Percentage change of linear modulus analyzed using 1-way ANOVA ($p \leq 0.05$), with Dunnett's post hoc.

Copyright 2016 The Organizing Committee for the 2016 Summer Biomechanics, Bioengineering and Biotransport Conference

RESULTS

Histological analysis showed that tie fiber density ranged from 1.36% in the inner zone of the body to 26.6% in the inner zone of the posterior horn (**Fig. 1**). Mean fiber density was higher in the inner zone (13.6%) compared to the middle and outer zones (11.1% and 8.3% respectively) and higher in the posterior horn compared to the anterior horn (12.3% and 10%, respectively, data not shown).

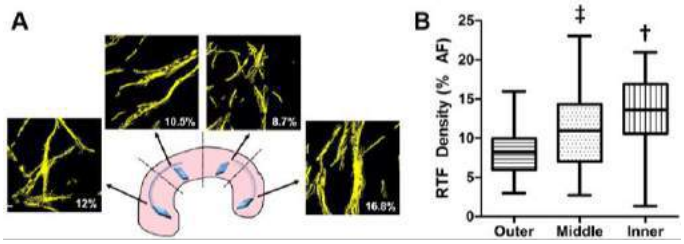

Figure 1: Radial tie fiber distribution varies by location. (A) Area fraction of radial tie fibers (yellow) in the middle zone across one juvenile bovine medial meniscus. Percentages indicate the RTF area fraction in image. Scale bar = 100 µm. (B) Radial tie fiber density, reported as Area Fraction (%) across the meniscus. Whiskers denote range. ‡, † = p≤0.05 vs. all other groups.

The toe and linear region modulus of AL scaffolds was ~2 and ~7X higher (5.5 and 18.8 MPa, respectively) than that of NA scaffolds (2.8 and 2.8 MPa, respectively). As the percentage of NA layers in composite scaffolds increased, the linear region modulus decreased. The toe region modulus showed smaller changes (**Fig 2**).

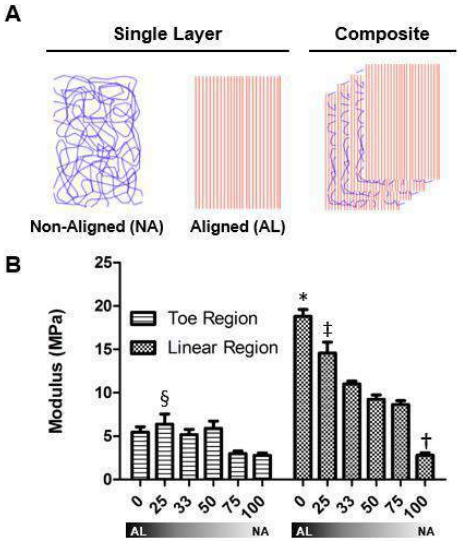

Figure 2: Radial elements alter mechanical properties of composite scaffolds. (A) Schematic of scaffold groups. (B) Toe and Linear moduli of intact scaffolds. § = p≤0.05 vs. 75%, TM. *, ‡, † = p≤0.05 vs. all other groups, LM.

When comparing the linear region modulus of intact scaffolds versus defect scaffolds, there was a trend towards a difference in the percent change for AL compared to composite scaffolds. That is, AL scaffolds lost ~50% of their apparent modulus (as expected with a defect spanning half of the width), while composite scaffolds with ≥33% NA content lost only ~20-30% of their apparent modulus (**Fig 3).** Preliminary studies mapping strain at the defect showed more rapid strain reconstitution in composite scaffolds compared to AL scaffolds (**Fig 3**).

DISCUSSION

This study developed a biomaterial analog of the meniscus radial tie fiber, namely a disorganized fibrous layer interspersed in an otherwise aligned fiber array. The linear and toe moduli of composite scaffolds generally followed expectations, with increasing NA content decreasing the linear modulus. Inclusion of NA layers also appeared to preserve scaffold mechanics in the context of a defect. That is, when a 50% radial cut was introduced, AL scaffolds showed the expected 50% decrease in apparent modulus, whereas the 33%, 50%, 75%, and 100% NA scaffolds all showed a less marked decline. This suggests that composite scaffolds, by virtue of the NA inclusions, provide some degree of strain transfer between layers, engaging aligned fibers adjacent to the defect that had been severed. This is consistent with our previous studies on the tensile response of non-orthogonally aligned nanofibrous layers [13,14] and with the shear lag mechanism reported for native tendon [15]. Collectively, these data imply that radial tie elements in native meniscus may be essential for enabling efficient load transfer in the context of tears that interrupt the circumferential fibrous architecture.

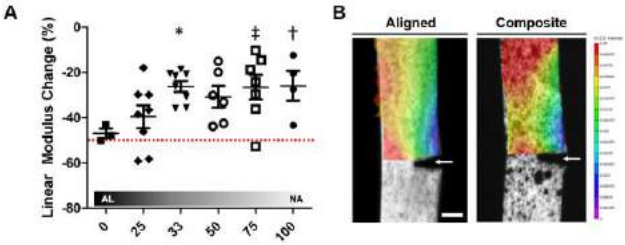

Fig. 3: Radial elements contribute to load transfer near a defect. (A) % change in modulus with defect. Red line indicates a 50% reduction. *, ‡, † = trending p≤0.10 vs. 0% (AL) group. (B) Local strain in Aligned and Composite (33% NA) scaffold with defect at 5% strain. Color bar from 0% (purple) to 5% strain (red). Scale: 2 mm.

It should be noted that our biomaterial model utilizes relatively high percentages of tie fiber elements (e.g., NA layers) while imaging suggests that native juvenile menisci have a lower (~11%) RTF density. This is in part due to the conservative processing steps involved in determining RTF density. Furthermore, RTFs have an organized, branched, collagenous structure that run perpendicular to circumferential fibers and may exhibit stronger molecular connections yet unknown. In contrast, our biomaterial analog utilized non-aligned fibers with little organization, and this likely led to less efficient engagement of the orthogonal fibers. Despite this limitation, our findings indicate that radial tie elements in the native meniscus may play a heretofore unappreciated role in enabling strain transfer around tears that interrupt the continuity of circumferential fibers. This new understanding may direct tissue engineering strategies aimed at producing functional replacements and could alter clinical practice with respect to partial meniscectomy.

ACKNOWLEDGEMENTS: This work was supported by the OREF New Investigator Grant, the NIH, and the VA.

REFERENCES: [1] Moran et al, *Sports Med Arthros*, *23*:156, 2015. [2] Harper et al, *Am J Roentgen,* 185:1429, 2005. [3] Bedi et al, *J Bone Joint Surg* 92:1398, 2010. [4] Skaggs et al, *J Orth Res,* 12:176, 1994. [5] Keah et al, *PCMD Symposium*, 2015. [6] Li et al, *J Biomech,* 40:1686, 2007. [7] Baker & Mauck, *Biomat,* 28:1967, 2007. [8] Saalfeld, FIJI 2012. [9] Dougherty, FIJI 2006. [10] Schindelin et al, *Nat Methods,* 2012. [11] Peloquin et al, *J Biomech Eng*, 2016. [12] Tanaka et al, *J Biomech Eng,* 133:074502, 2011. [13] Nerurkar et al, *Nat Mater,* 8:986. [14] Fisher et al, *Acta Biomater*, 9: 4496, 2013. [15] Szczesny & Elliott, *Acta Biomater,* 10:2582, 2014.

Copyright 2016 The Organizing Committee for the 2016 Summer Biomechanics, Bioengineering and Biotransport Conference

SB³C2016
Summer Biomechanics, Bioengineering and Biotransport Conference
June 29 –July 2, National Harbor, MD, USA
SB³C2016-875

DECREASED WALL SHEAR STRESS IN ISOLATED REGIONS OF THE PULMONARY ENDOTHELIUM COULD IMPACT PULMONARY VASCULAR DYSFUNCTION ON A GLOBAL AND CELLULAR LEVEL IN PULMONARY HYPERTENSION

Vitaly O. Kheyfets (1,2), Michal Schafer (1,2), Joyce D. Schroeder (1), Jamie Dunning (1), Chris A. Podgorski (2), James Browning(3), Jean Hertzberg (3), Kendall S. Hunter (1,2), J. Kern Buckner (2), Robin Shandas (1), Brett E. Fenster (2)

(1) Bioengineering/Medicine
University of Colorado Denver | Anschutz Medical Campus
Aurora, CO

(2) Department of Cardiology
National Jewish Health
Denver, CO

(3) Mechanical Engineering
University of Colorado Boulder
Boulder, CO

INTRODUCTION

Pulmonary hypertension (PH) is a disease characterized by progressive pulmonary vascular dysfunction, which gradually increases right ventricular afterload. Recent studies have shown that the wall shear stress (WSS) acting on the endothelium is reduced in hypertensive conditions [1], but the consequence of this phenomenon is poorly understood. Endothelial cells (ECs) subjected to pathologic WSS are shown to change morphology, alignment, and gene expression, but additional work is needed to investigate the system transients and cell-to-cell signaling in regional stress variations.

The objective of this study was: (1) to utilize velocity encoded 4D magnetic resonance imaging (4D MRI) to measure WSS in patients with PH; and (2) implement a mathematical model of cellular calcium metabolism to investigate transient and regional calcium deposition dynamics. Based on qualitative observations of pulmonary arterial blood flow and previous computational studies, the endothelium was subjected to decreased and inhomogeneous WSS in PH. The primary hypothesis of this study was that isolated regions of low WSS would correlate with global pulmonary vascular health. Therefore, the secondary hypothesis was that the biochemical consequence of inhomogeneous WSS would impact calcium distribution in stimulated and neighboring non-stimulated cells.

METHODS

Measuring WSS in PH Patients

17 adult PH patients and 5 controls with chronic obstructive pulmonary disease were prospectively recruited to undergo same day right heart catheterization (RHC), blood biochemistry analysis, and velocity encoded 4D MRI at National Jewish Health (Denver, CO).

RHC data was used to compute the index of wave reflection (Γ), which is a measure of the impedance mismatch between the proximal and distal vasculature. Γ has been shown to increase in PH [3].

4D cardiac MRI was performed on a 1.5T system (Siemens, Erlangen, Germany) with 3-dimensional velocity encoding (voxel volume=2.4-2.6 x 2.4-2.6 x 2.4-3.0 mm, α=14-15°, TE/TR=2.85/48.56 ms, VENC =150 cm/s, temporal resolution=42-48 ms). Flow data was used to measure the shear-rate at 8 locations around the circumference of the main pulmonary artery (MPA) (see Fig. 1), 1*cm* downstream from the pulmonic valve. WSS was computed according to the equation shown in Fig. 2. Patient specific viscosity was calculated based on blood hematocrit (Ht) at the time of RHC.

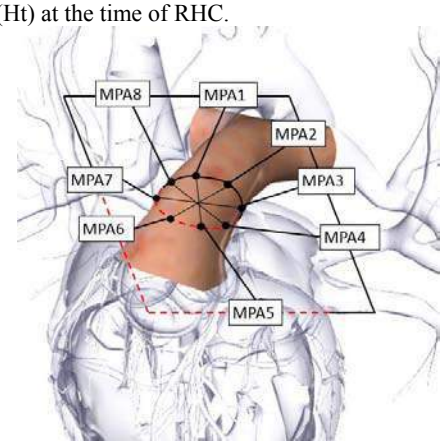

Figure 1: Schematic showing 8 locations along the circumference of the MPA where WSS was measured, positioned 1*cm* downstream from the pulmonic valve.

Copyright 2016 The Organizing Committee for the 2016 Summer Biomechanics, Bioengineering and Biotransport Conference

Computational Model of Calcium Dynamics in Endothelial Cells

A computational model of cytosolic and extracellular calcium dynamics was developed for 100 endothelial cells that share a common extracellular matrix. The model was executed for 1 second under two conditions: 20 out of 100 cells were subjected to a 20% and 80% decrease in WSS.

The major mechanisms that contribute to calcium homeostasis in a single cell were described using 5 coupled ordinary differential equations (not included for brevity) and kinetic conditions for receptor activation. This model was expanded from the experimentally validated derivation by Weisner *et al.* [2], by coupling the extra-cellular calcium concentration to the exchange of calcium across the cellular plasma membrane. Therefore, a 5th equation was included within the coupled ODE system to iteratively compute the extracellular calcium concentration. Coupling between neighboring cells was introduced by describing the total calcium concentration in a single computational node with a 1-D diffusion equation.

The system was integrated using an in-house code that utilized a 4th order Runge-Kutta method. At each iteration of time, calcium diffusion was discretized using an implicit finite difference method.

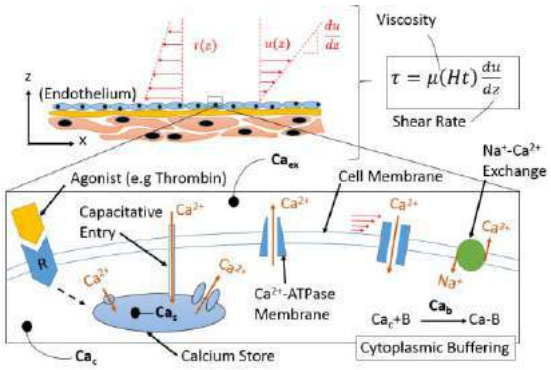

Figure 2: Schematic of WSS acting on endothelium with calcium regulation mechanisms. The computational model solves for calcium concentration in four regions: Ca_c: cytosolic concentration; Ca_s: calcium concentration in storage; Ca_b: calcium bonded to buffering proteins; and Ca_{ex}: calcium concentration in the extracellular matrix.

RESULTS

4D MRI

Qualitative analysis of streamlines consistently show a region of recirculation in the right inferior region of the MPA (see Fig. 3). This is seen in every PH patient (n = 17), but is not seen in any controls (n = 5).

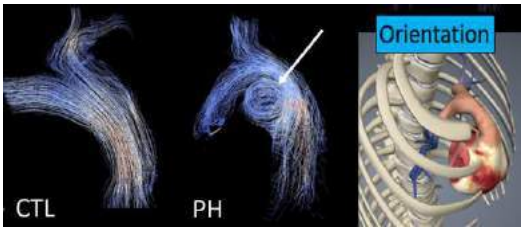

Figure 3: Typical flow streamlines in the MPA at peak systole. White arrow shows vortex formation in PH patients.

Decreased peak-systolic WSS in regions of perturbed flow (MPA 6 and 7) is linearly correlated with severity of vascular dysfunction across PH and CTL patients (see Fig. 4). However, the correlation was not seen for the other 6 points along the circumference of the main pulmonary artery.

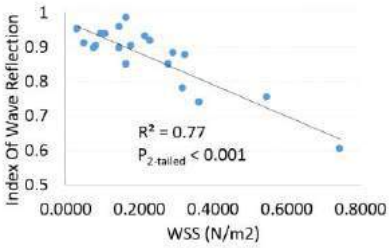

Figure 4: Negative correlation between WSS at points 6 and 7, and the index of wave reflections.

Endothelial Cell Model

Simulated temporal metabolic effects in a single endothelial cell take over 300 seconds to reach steady state in response to a step impulse in agonist concentration (0 to 1 U/mL) and WSS (extracellular calcium influx from 5 to 7.5 μM/s).

In a simulation of 100 cells, 20 cells in the middle were subjected to a steady state 20% decrease in WSS for 1second. The simulation was repeated with an 80% decrease. In the 20% scenario, all cells increased intracellular calcium. In the 80% scenario, non-stimulated cells increased intracellular calcium, but stimulated cells revealed a decrease (see Fig. 5).

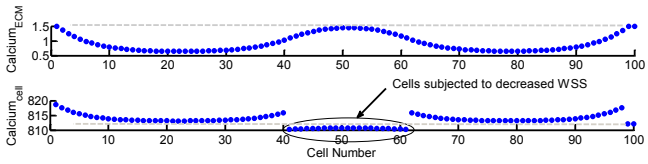

Figure 5: Extracellular (top) and intracellular (bottom) calcium concentration in 100 cells after 1 second of simulation. Dashed gray line indicated initial condition.

DISCUSSION

- The extent of WSS decrease in a small region of perturbed flow is correlated with an impedance mismatch between the distal and proximal pulmonary vasculature.
  - Index of wave reflections is increased in progressive pulmonary hypertension [3].
- 4D MRI results raise the following question: How does decreased WSS in a small region of endothelial cells impact neighboring cells?
- Preliminary simulations show extracellular calcium is uptaken by non-stimulated cells. However, stimulated cells expel intracellular calcium at extremely low WSS, but not in slightly lowered WSS.
  - Increase in intracellular calcium is linked to nitric oxide production and could impact other metabolic functions.
- Model results are preliminary: Additional work is needed to estimate proper model input parameters.

ACKNOWLEDGEMENTS

This work was supported by the Butcher Foundation Award and 3 NIH Awards: (1) IH NHLBI 5 T32 HL072738-10; (2) NIH R01 HL114753; (3) NIH K24 HL081506.

REFERENCES

[1] Kheyfets, V., M. Thirugnanasambandam, L. Rios, D. Evans, T. Smith, T. Schroeder, J. Mueller, S. Murali, D. Lasorda, J. Spotti, and E. Finol,. *Pulm Circ*, 2015. 5: 90-100.

[2] Wiesner, T.F., B.C. Berk, and R.M. Nerem,. *Am J Physiol*, 1996. 270: C1556-69.

[3] Wang, Z. and N.C. Chesler,. *Pulm Circ*, 2011. 1: 212-23.

Copyright 2016 The Organizing Committee for the 2016 Summer Biomechanics, Bioengineering and Biotransport Conference

SB^{3}C2016
Summer Biomechanics, Bioengineering and Biotransport Conference
June 29 –July 2, National Harbor, MD, USA
SB^{3}C2016-876

A RAMAN MICROSPECTROSCOPIC TECHNIQUE TO QUANTIFY RESIDUAL WATER IN DESICCATED SAMPLES

Quinn Osgood, Jason Solocinski, Nilay Chakraborty

Mechanical Engineering Department
University of Michigan Dearborn
Dearborn, MI, USA

INTRODUCTION

The ability to preserve biological material in a desiccated state above cryogenic temperatures is of great laboratory and clinical importance. Commonly known as lyopreservation, dry state preservation has many potential advantages over the more traditional approach of cryopreservation. Perhaps the most important being greater control over storage logistics and phase non-uniformity that can potentially arise at low temperatures during cryopreservation, which can damage the material being preserved. Non-uniformities are inherent in most methods of biopreservation due to changes in the thermodynamic state of the medium in which the preservation is taking place [1]. Such changes in thermodynamic state can be manifested through crystal formation, glass formation, or both happening in close spatial proximity, as is the case of cryopreservation. Lyopreservation can potentially avoid these problems if a spatially uniform glassy environment can be created. In absence of substantial water in the preservation matrix, arguably lyopreserved samples have the advantage of creating a more uniform and stable glassy environment.

Non-uniform water distribution following lyopreservation has the potential to cause significant damage to the preserved components [2]. Water content determines the state of molecular mobility and phase uniformity, which in turn controls the molecular reactivity and biological responses. Higher quantities of water impact determinants of biological stability including the viscosity and glass transition temperature of the preservation matrix [3]. Gravimetric determination of residual moisture in biological samples is a standard practice in lyopreservation. However, determination of trace amount of water using traditional gravimetric technique remains a problem due to uncertainties stemming from minimum detectable change of weight. Most desiccation protocols are inherently non-uniform and a standard gravimetric analysis is unable to quantify variations in trace amounts of residual water in the samples. Raman spectroscopy has been used to quantify water content in synthetic and geologic glass formations with high spatial resolution [4,5]. The protocol developed here utilizes similar technique of using spatially correlated Raman microspectroscopy to non-invasively quantify non-uniformities in the biological samples formed during lyopreservation.

METHODS

Two different desiccation techniques (spin drying and passive drying of droplets in sessile format) were employed to desiccate biologically relevant lyoprotectant medium containing high concentrations of trehalose (1.8 M) in a 20 mM HEPES buffered solution. The trace water quantification technique using Raman microspectroscopy was employed to evaluate water in the desiccated samples in both cases.

Spin Drying

750 µL of lyoprotectant solution was spin-dried using a spinning machine on. 22 mm glass coverslips in a controlled environment which is purged with ultra high purity Nitrogen gas. Spinning speeds to 1000RPM for 55s with a ramp up to 3000RPM for 5s was used to complete the drying process.

Droplet Drying

2.5µL droplets of the lyoprotectant formulation was deposited onto a 22mm glass coverslips in sessile droplets and was desiccated using passive diffusion technique in a controlled humidity chamber (dry box). The droplets were allowed to dry via natural convection for 90 minutes. The mass of the dried droplet roughly correlated with the desiccated spin-dried samples.

Raman Spectroscopy

Following desiccation, Raman spectra were gathered using a 532nm solid-state laser for excitation. Data for spin-dried samples was

Copyright 2016 The Organizing Committee for the 2016 Summer Biomechanics, Bioengineering and Biotransport Conference

collected at the center of the round coverslip then at 2mm increments until reaching the edge of the coverslip at 11mm. Data for droplet-dried samples were collected at the center of the droplet then at 0.30mm increments until reaching the edge of the plate at 1.5mm.

RESULTS

In the lyoprotectant solution studied here there are many distinct peaks in the Raman signature indicating quantitative presence of specific molecules including water. The ratio of the CH stretching peak, which is dominated by trehalose (centered around wave number 2955) to the asymmetric portion of the OH stretching band (centered around wave number 3435) was used for quantify residual water in the samples (Fig. 1). Note that these center values are approximate and subject to shift with varying states of dryness and crystallinity. As shown in Fig. 2, by creating various solutions of with a known concentration of trehalose (and water) and analyzing the corresponding Raman spectra a relationship between the mass fraction of trehalose [≈ (1-residual water content)] and the CH/OH ratio was determined. Since the relevant data comes from a ratio of peaks direct comparisons between samples are possible even if peak intensities are disparate.

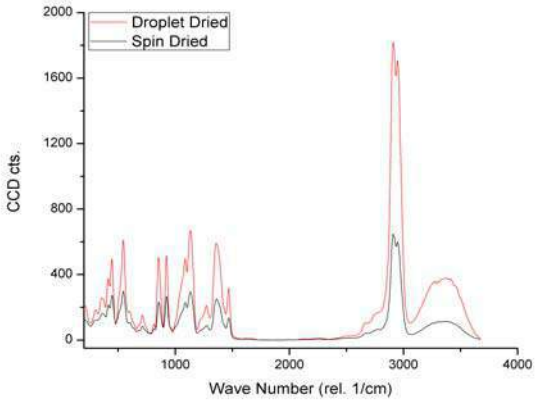

Figure 1. Comparison of Raman spectra gathered from a spin-dried sample and a droplet dried sample

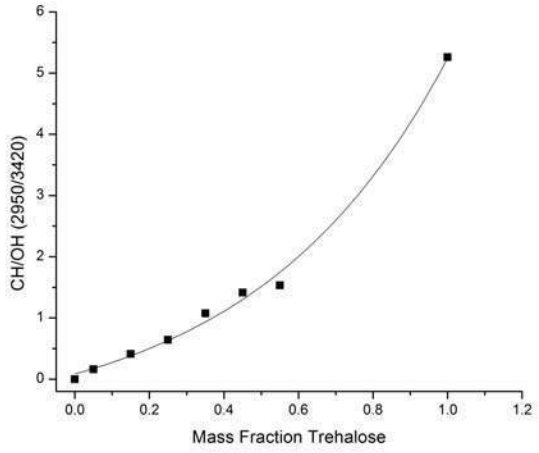

Figure 2. The exponential relationship between the mass fraction and CH/OH. This relationship can be used to quantify residual water content in desiccated samples.

It is important to note here that this relationship only holds for non-crystalline states. Hence the technique can be used to determine residual water non-invasively in an unknown sample. This technique was applied to compare the uniformity of the desiccated samples using two different drying techniques discussed here in.

The ratio of the CH stretching peak to the OH asymmetric stretching peak was determined for each Raman spectra obtained. These values were used in conjunction with the relationship determined in Fig. 1 to establish mass fraction of trehalose as a function of radius for both droplet and spin dried samples. For the droplet dried sample weight percent of trehalose ranges from 94% at the center to 100% near the edge. For the spin dried sample the weight percent for trehalose varies from 95% at the center to 97% near the edge.

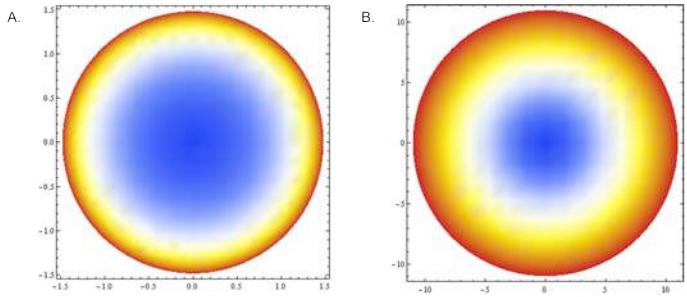

Figure 3. Map of trehalose content of A. droplet dried sample and B. spin dried sample. Red indicates higher weight percent.

DISCUSSION

The resulting plot in Fig. 3 demonstrate the differences in water content within the sample and allows of the direct comparison of the uniformity of different desiccation methods. It is clear in figures 3A and 3B that spin-drying results in a larger and more uniform area of dryness than droplet drying. It follows that spin-drying is a more favorable desiccation method because it greatly reduces the non-uniformities present after desiccation. Also, note the differences in scale between 3A and 3B, the total area show in 3B is 7.07mm^2 while the area shown in 3A is 380.13 mm^2.

This methodology can be extended to any desiccation method to determine the extent of the non-uniformities it produces. It provides a means to estimate the usefulness of a desiccation method prior to biological testing.

ACKNOWLEDGEMENTS

Authors would like to acknowledge the NSF Grant 60157 and startup fund from UM Dearborn.

REFERENCES

1. Ragoonanan, V. et al. *Biophysical journal*, *94*(6), 2212-2227, 2008.
2. Reátegui, E. E. et al. *Chemical Engineering Research and Design*, *86*(11), 1187-1195, 2008
3. Tomozawa, M. *Journal of Non-Crystalline Solids*, *73*(1), 197-204, 1985.
4. Thomas, R. *American Mineralogist*, *85*(5-6), 868-872, 2000.
5. Chabiron, A. et al. *Contributions to Mineralogy and Petrology*, *146*(4), 485-492, 2004.

Copyright 2016 The Organizing Committee for the 2016 Summer Biomechanics, Bioengineering and Biotransport Conference

SB³C2016
Summer Biomechanics, Bioengineering and Biotransport Conference
June 29 –July 2, National Harbor, MD, USA
SB³C2016-877

AGE-RELATED DIFFERENCES IN HUMAN DERMAL FIBROBLAST MECHANOSENSITIVITY TO HYALURONIC ACID DERMAL FILLER

Aribet M. De Jesús[1], Sathivel Chinnathambi[1], Mariam El-Hattab[1] Douglas K. Henstrom[2], Edward A. Sander[1]

[1]Department of Biomedical Engineering, University of Iowa, Iowa City, IA, 52242

[2]Department of Otolaryngology – Head and Neck Surgery, University of Iowa, IA 52242

INTRODUCTION

The aging of skin is accompanied by the appearance of wrinkles, increased fragility, and a loss of elasticity. In addition, the dermal extracellular matrix (ECM) become fragmented, and the resident fibroblasts become quiescent, most likely due to a reduction in homeostatic levels of ECM tension [1, 2]. The injection of cross-linked hyaluronic acid (HA) based dermal fillers, which are used cosmetically to increase suppleness and improve appearance, also have been shown to induce once quiescent human dermal fibroblasts (HDFs) to synthesize new collagen [3]. Changes in the local mechanical environment from HA injection might provide important mechanical cues that stimulate the fibroblasts to restore the ECM. In this study, we investigate this hypothesize and whether aging alters HDF mechanosensivity by using an *in vitro* collagen gel system as a model of the dermis.

METHODS

***In Vitro* Model:** An *in vitro* model of the dermis was prepared by culturing HDFs from patients between the ages of 14 and 93 years old at a concentration of 250,000 cells/mL in 2 mg/mL type I collagen gels. Cells were maintained in DMEM supplemented with 10% FBS, 1% P/S, and 0.1% amphotericin B and in a humidified incubator at 37°C for 24 hours before releasing the gels from their attachments. The gels were kept free-floating for 24 hours in order to simulate a tension-free, fragmented dermis. Next, 15 µL of dermal filler or 1x PBS (control) were injected into the gel center. **Gene Expression:** Changes in the expression of genes that encode for key mechanoresponsive proteins and components of the Rho/ROCK pathway were examined five minutes and 24 hours after treatment (n=3 per age, per time-point) by performing qPCR. Fold-changes in the expression of RhoA, ROCK1, ROCK2, and COL1 mRNA were determined using the $\Delta\Delta C_T$ method.

Characterization of HA Swelling: The swelling properties of the cross-linked HA-based dermal filler (Juvederm Ultra XC, Allergan, Irvine, CA) were measured by performing osmotic pressure tests. 100 µL of HA (n=4) was injected into the opening of a 1 mL pipette and separated from a solution of 1x PBS by a dialysis membrane. The height of the water column within the pipette was measured every hour during the first eight hours, followed by every 12 hours until 72 hours had passed. The change in water height was used to calculate the swelling pressure of the HA filler and the swelling ratio (i.e., current gel volume to initial gel volume). This ratio was used to estimate the stress imparted by the swelling HA filler on the surrounding collagen gel. This estimate was made by injecting 10 µL of HA filler into the center of an acellular collagen gel and acquiring time-lapse images using differential interference contrast (DIC) microscopy every hour for 24 hours. The change in filler area was used to calculate a swelling ratio that could be related back to the swelling pressure and an average resistive stress in the surrounding collagen gel.

RESULTS

The swelling potential of cross-linked HA used in this study was characterized by defining its swelling ratio when directly exposed to a solution of 1x PBS and when injected into a collagen gel. The hygroscopic behavior of HA caused the filler to imbibe 30.7 ± 9.2 µL of PBS after two days of contact with 1x PBS. This added fluid resulted in a swelling ratio of 1.31 ± 0.09 and a swelling pressure of 28.57 ± 6.98

Copyright 2016 The Organizing Committee for the 2016 Summer Biomechanics, Bioengineering and Biotransport Conference

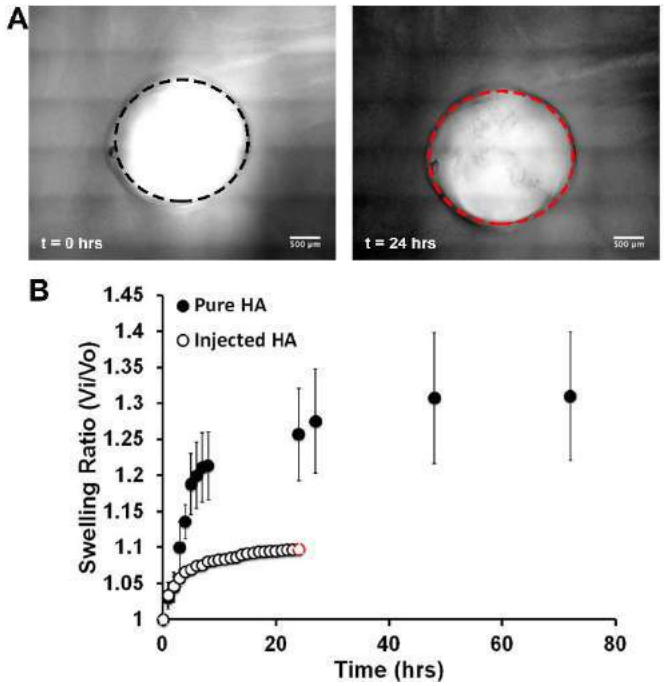

Fig. 1. (A) DIC images of HA dermal filler injected into a collagen gel 0 and 24 hours after exposure to 1x PBS. Dotted circles represent the gel area and are represented in B. (B) Swelling ratio of pure HA and of HA injected into a collagen gel in a 1x PBS solution. The difference in the swelling ratio provides an estimate of the stress in the collagen gel.

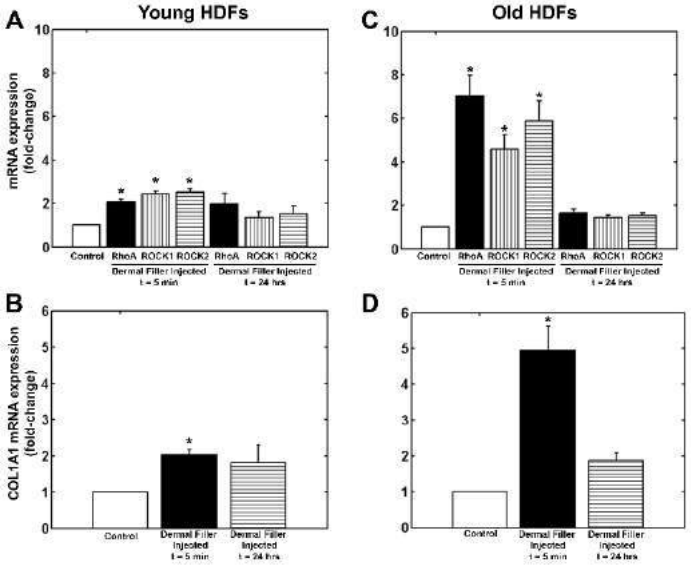

Fig. 2 Gene Expression in (A, B) young and (C, D) old HDFs in response to treatment with HA dermal filler. 1x PBS served as controls. Asterisks indicate a significant difference compared to control ($p < 0.05$).

Pa. When injected into a collagen gel, the surrounding fibrous network resisted swelling of the cross-linked HA. As a result, the equilibrium-swelling ratio was found to be 1.1, which resulted in an average resistive stress of 20.7 Pa in the collagen gel.

Injection of HA dermal filler into released collagen gels caused a significant increase in gene expression for RhoA, ROCK1, ROCK2, and COL1A1 five minutes after treatment ($p<0.05$) in both old and young HDFs (Fig 2.A-D). Fold-changes in the expression of these genes were found to be greater in old HDFs than in young HDFs. Expression levels remained slightly elevated 24 hours after treatment but were not significantly different from PBS controls.

DISCUSSION

The injection of dermal filler into a model of the aged dermis caused noticeable deformations in the collagen due to swelling of cross-linked HA. These deformations introduced a heterogeneous stress in the gel that induced increased expression of key genes in the mechanosensitive pathway Rho/ROCK and in the production of collagen. The gene expression patterns followed the changes in swelling behavior of the injected dermal filler. The largest changes in the swelling ratio were observed during the first 30 to 60 minutes after filler injection. By 24 hours, the HA swelling ratio was reaching a plateau. Similarly, a large increase in the expression of RhoA, ROCK1, ROCK2, and COL1A1 was observed after five minutes with a return to nearly basal levels by 24 hours. These results indicate that the HDFs responded mechanically to the injection of HA, although it remains unclear to what extent gene expression translated to downstream collagen production. Surprisingly, and contrary to our initial expectations, the HDFs from older patients demonstrated a significantly elevated response compared to HDFs from younger patients when compared to control. It may be that baseline expression in old HDFs is lower than in younger HDFS and so mechanical stimulation produces what appears to be greater sensitivity in older cells. Ongoing studies are measuring total collagen production to help clarify this issue.

ACKNOWLEDGEMENTS

This study was supported by the Carver Charitable Trust Grant #14-4384 and the Graduate Assistance in Areas of National Need Fellowship (GAANN) P200A120071. We also thank Victor Lai for advice on conducting the swelling tests.

REFERENCES

[1]. Fisher, G.J., et al., *Archives of dermatolo*gy. 138(11): p. 1462-1470, 2002.

[2] Fisher, G.J., et al., *New England Journal of Medicine*, 337(20): p. 1419-1429, 1997.

[3] Quan, T., et al.,*Journal of Investigative Dermatology*, 133(3): p. 658-667, 2012.

Copyright 2016 The Organizing Committee for the 2016 Summer Biomechanics, Bioengineering and Biotransport Conference

SB³C2016
Summer Biomechanics, Bioengineering and Biotransport Conference
June 29 –July 2, National Harbor, MD, USA
SB³C2016-878

OPTIMIZATION OF *IN VITRO* ENDOTHELIAL CELL SELF-ASSEMBLY FOR MILLIMETER SCALE VASCULOGENESIS

Joshua T. Morgan (1), Jasmine Shirazi (1), Erica M. Comber (1), Peter A. Sariano (1), Jason P. Gleghorn (1)

(1) Department of Biomedical Engineering
University of Delaware
Newark, DE, USA

INTRODUCTION

During embryogenesis, endothelial precursor cells distributed throughout the mesenchyme self-organize into an initial network called the vascular plexus [1]. This process, termed vasculogenesis, provides the early vascular system of every tissue and organ in the body. As the plexus is perfused by the beating heart, the initial stochastic architecture is extensively remodeled into a hierarchy of vessels that compose the mature vascular system [2]. An example of vasculogenesis is the plexus formed around the developing airway tree in embryonic lung, where vessels formed on cellular length scales assemble into a network that spans the entire organ (Figure 1). Importantly, this network emerges stochastically but is sufficient to fully vascularize developing organs. Understanding the microenvironmental factors that guide formation of functional 3D networks remains a central question in development and morphogenesis. Modeling the formation of the vascular plexus *in vitro* can provide an important tool for understanding how tissue biophysical and biochemical properties guide self-assembly in developing tissues.

Previous research has demonstrated that endothelial cells randomly dispersed throughout the bulk of various hydrogels can be induced to form multicellular structures, including primitive networks. However, these studies often focus on specific aspects of network formation at cellular length scales, such as lumen formation or branch extension. Whereas these experiments elucidate local cellular interactions, they have yet to fully address the self-assembly of vascular networks that connect across physiological tissue length scales. Further, culture conditions vary among research groups, making it difficult to assemble a cohesive understanding of the vascular self-assembly process.

To directly address this knowledge gap, we have developed a 3D endothelial culture model to assay large-scale network formation within collagen gels. This culture model was systematically tested to determine the influence of collagen concentration (regulating stiffness and pore size) and cell density (regulating cell-cell distance) on self-assembly. We identified ideal culture conditions for the robust formation of stable, millimeter-scale plexuses. Further, we developed methods to characterize the morphology and connectivity of these networks for comparison to plexus formation in embryonic lung explants.

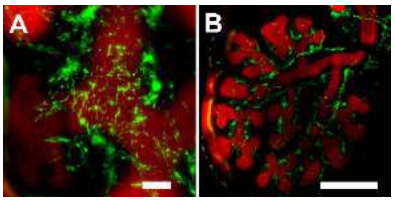

Figure 1: Plexus formation in developing mouse lung. (A) Blood vessels (CD-31; green) form on cellular length scales around the airways (E-cadherin; red). (B) Networks are connected across the entire organ (E12). Scale bars are (A) 50 and (B) 500 μm.

METHODS

Lung explants: Timed pregnant CD-1 mice were humanely euthanized using CO2 asphyxiation under an Animal Use Protocol approved by the University of Delaware IACUC. Lung explants (embryonic day 12; E12) were isolated and either cultured for 48 h in floating membrane culture or immediately fixed and stained for E-cadherin (epithelium) or CD-31 (endothelium) using standard protocols.

Human umbilical vein endothelial cells (HUVECs) were cultured in EGM-2 medium. Collagen was freshly isolated from rat tails [3]. Collagen hydrogels with HUVECs dispersed throughout the bulk were constructed in PDMS molds treated with 2% (poly)ethylenimine and 0.2% glutaraldehyde. The cylindrical gels (7 mm dia. × 3 mm tall) were

Copyright 2016 The Organizing Committee for the 2016 Summer Biomechanics, Bioengineering and Biotransport Conference

chemically crosslinked to the PDMS sidewalls while keeping the upper and lower surfaces free (Figure 2A). Collagen of varying weight percent was prepared with suspended HUVECs and polymerized as previously described. Gels were maintained in EGM-2 with 50 ng /mL tetradecanoylphorbol acetate and 50 µg/mL sodium ascorbate. For each condition 3-4 technical replicates and 2-3 experimental replicates were performed. Gels were fixed and stained with DAPI (to label nuclei) and phalloidin (to label actin). Samples were imaged with a Zeiss widefield AxioObserver Z1 (for gross characterization) and a Zeiss confocal LSM880 (for reflectance and detailed analysis). Confocal images were filtered and segmented using custom algorithms (MATLAB 2015b).

RESULTS

To determine which culture conditions were optimum for network formation, we cultured HUVECs in collagen gels for 7 days at a range of cell densities (0.5e6, 1e6, 1.5e6, 2e6 cells/mL) and collagen densities (0.2, 0.3, 0.4, 0.5, 0.6%). After fixation and staining, a trained observer scored gross cell viability and network formation on a scale of 1-4, with 3 and 4 representing network formation. Network formation was supported in a subset of conditions (Figure 2B).

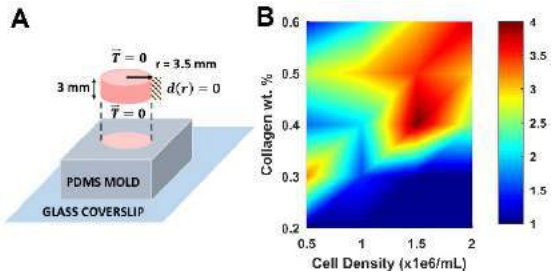

Figure 2: Development of an *in vitro* model of vasculogenesis. (A) Schematic of culture geometry. Displacement *d* is fixed at radial boundary while the top and bottom have zero traction forces (*T*) (B) At 7 days, some conditions resulted in robust (≥3) networks.

Importantly, these primitive vascular networks were 3D and spanned the entire 7 mm construct (Figure 3A). To investigate morphological parameters of the plexus, we used confocal and reflectance microscopy to identify cellular morphology and the presence of lumens within the collagen gel (Figure 3B). Further, after segmenting the images as shown in Figure 3C, we constructed 3D volumes of the vascular networks (Figure 3D). From these volumes we determined the network volume fraction as well as the connectivity, which we defined as the median percentage of network accessible from 50 random points. As an example, networks formed with 1e6 and 1.5e6 cells/mL embedded within 0.5% collagen had network volume fractions of 14.15±1.82% and 24.03±6.64%, respectively, while connectivity was 88.75±4.17% and 75.02±0.81%, respectively.

Having identified a range of conditions suitable for network formation, we tested their long-term stability. Using 0.5% collagen and 1.5e6 cells/mL as a representative case, we fixed samples at 3, 7, 14, and 21 days. By gross inspection, some connectivity was observable by day 3, full networks were apparent by day 7, and no changes to the gross network morphology were observed at the 14 and 21 day timepoints.

Lastly, to test whether network formation was sensitive to fluidic forces, we fabricated our construct within a microfluidic device and applied perfusion through the hydrogel for 48 h at approximately 0.05 dyne/cm^2. Preliminary findings demonstrate visible alignment of the network braches parallel to flow, demonstrating this methodology can be used to test the role of mechanics in vascular maturation.

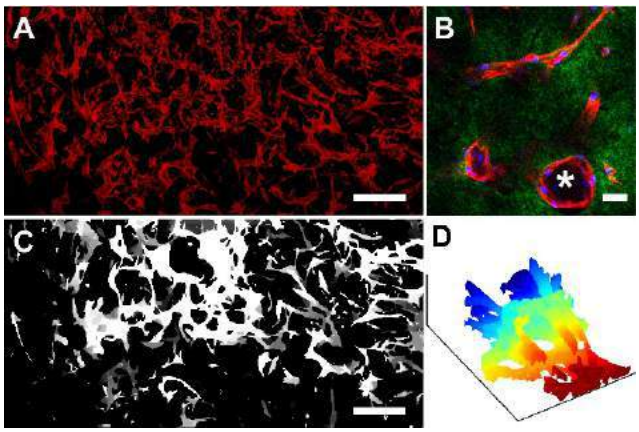

Figure 3: Self-assembled networks are large, interconnected, and have lumens. (A) Maximum projection of 4x2x0.2 mm region of a plexus (B) HUVECs labeled with phalloidin (red) and DAPI (blue) permeate the collagen gel (green). Cell-lined lumens (*) are observed. (C) Networks were automatically segmented and (D) constructed into volumes. Scale bars are (A, C) 500 and (B) 50 µm.

DISCUSSION

We performed a p arametric study of the *in vitro* conditions necessary for the culture of millimeter-scale vascular networks similar to those observed in the embryonic mouse lung. Having identified conditions ideal for self-assembly, we characterized the stability and morphology of a subset of culture conditions. Additionally we demonstrated that these networks respond to flow, providing a novel platform to interrogate the role of fluid cues on t he maturation of vascular networks. This *in vitro* vasculogenesis model enables future biophysical and molecular studies to elucidate the regulators of plexus formation that would not be possible in developing embryonic organs.

Further, this model has potential translational applications in tissue engineering. The ability to vascularize engineered graft tissues remains a fundamental challenge in tissue engineering. As the size of the required graft grows, providing nutrients and oxygen to metabolically active tissue necessitates the incorporation of vascular and lymphatic networks [4-5]. By exploiting the self-assembly of vascular cells to create large-scale and stable networks, as we do here, we may enable the fabrication of larger graft tissues for reconstructive uses.

In summary, we have developed a robust methodology for creating large-scale vascular networks for fundamental studies of micro-environmental regulation and mechanotransduction in vasculogenesis and potential translational applications of engineering large vascularized tissue grafts. Ongoing studies are focused on understanding the molecular regulators of plexus scaling, incorporation of mesenchymal cells, and determining the impact of fluid shear forces on vascular network remodeling and maturation.

ACKNOWLEDGEMENTS

Funding for this research was provided by National Science Foundation (1537256), University of Delaware Research Foundation Pilot Grant, ORAU Ralph E. Powe Junior Faculty Enhancement Award, and the National Institutes of Health (1 P30 GM110759-01).

REFERENCES

[1] Risau, W & Flamme, I, *Annu Rev Cell Dev Bio*, 11:73-91, 1995.
[2] le Noble, F et al., *Cardiovasc Res*, 65(3):619-28, 2005.
[3] Cross, VL et al., *Biomaterials*, 31(33):8596-607, 2010.
[4] Auger, FA et al., *Annu Rev Biomed Eng*, 15:177-200, 2013.
[5] Novesel, EC et al., *Adv Drug Deliv Rev*, 63(4-5):300-11, 2011.

Copyright 2016 The Organizing Committee for the 2016 Summer Biomechanics, Bioengineering and Biotransport Conference

SB³C2016
Summer Biomechanics, Bioengineering and Biotransport Conference
June 29 –July 2, National Harbor, MD, USA
SB³C2016-879

DESIGN OPTIMIZATION OF A HYALURONAN-BASED DRUG DELIVERY DEVICE TO IMPROVE OCULAR RETENTION

Jourdan Colter (1), Nathaniel Cady (2), Hee-Kyoung Lee (3), Brenda Mann (3), Barbara Wirostko (3), Brittany Coats (1)

(1) Mechanical Engineering
University of Utah
Salt Lake City, Utah, USA

(2) Colleges of Nanoscale Science and Engineering
SUNY Polytechnic Institute
Albany, New York, USA

(3) Jade Therapeutics Inc.
Salt Lake City, Utah, USA

INTRODUCTION

Novel carboxymethylated hyaluronic acid based hydrogel polymers (CMHA-S, Jade Therapeutics Inc., SLC) are emerging as controlled and localized means for drug-delivery in the treatment of ophthalmic conditions, such as corneal ulcers, injuries and infections. These bio-erodible hydrogels offer improved drug bioavailability, safety, and therapeutic effectiveness from existing therapies, as hyaluronic acid (HA) is a naturally occurring polysaccharide already found in the eye [1]. However, retention of these hydrogel films in the ocular environment is poor due to the high lubricating properties of HA, thereby reducing the efficacy of the hydrogels in long-term drug delivery application.

In this study, we use a computational finite element model of the eye to: (1) define optimal surface friction ratios of the hydrogel to the sclera and eyelid that minimize displacement, and (2) evaluate multiple geometrical designs capable of achieving these ratios. The improved length of retention of the optimized design was verified using *in vivo* rabbit studies.

METHODS

The FE model represented a hydrogel film placed in the inferior fornix of the adult human eye. Model components consisted of a simplified eye with a radius of 11mm, a lower eyelid depicting the inferior fornix, and the hydrogel film. The hydrogel film was placed between the globe and lower eyelid in the first step allowing the eyelid to deform around the hydrogel (Fig. 1A). Then, an upward eye rotation that was replicative of a physiological eye movement was applied so that the displacement of the film due to the globe movement could be measured [2]. The material models and coefficients are provided in Table 1. The optimal friction ratio between the surfaces of the hydrogel and the globe/lid was found by iteratively sweeping through coefficients of friction (0-0.2) on each side of the hydrogel. In order to find the optimal geometry design, eight different hydrogel geometries varying in size and cross-section were implemented into the model (Fig. 1B). The friction on the globe side of the hydrogel was held at 0.05, and each of the eight geometries was simulated at lid-side frictions of 0.1 and 0.15. The best performing geometry influenced the design of the geometries that were mold-manufactured, developed and tested *in vivo*. Thickness measurements were taken from the molded

Table 1: Material models and coefficients used in the simulations.

		Viscoelastic Coefficients			Hyperelastic Coefficients			
Material	**Constitutive Model**	G_1	**K**	τ	**D**	C_{i0}	C_{0i}	C_{ii}
Globe (sclera)	Hyperelastic Polynomial N=2 Viscoelastic Prony-series ρ = 1243 kg/m ν = 0.49	0.20 0.15	0 0	7.52 77.23	0 0	2.4e8 1.6e10	-2.1e8 2.6e10	-4.1e10 0
Hydrogel	Elastic E = 4.06 MPa Viscoelastic Prony-series ρ = 1000 kg/m ν = 0.49	.0334	0	4.79				
Eyelid	E = 58.2 MPa ρ = 1000 kg/m ν = 0.49							

Copyright 2016 The Organizing Committee for the 2016 Summer Biomechanics, Bioengineering and Biotransport Conference

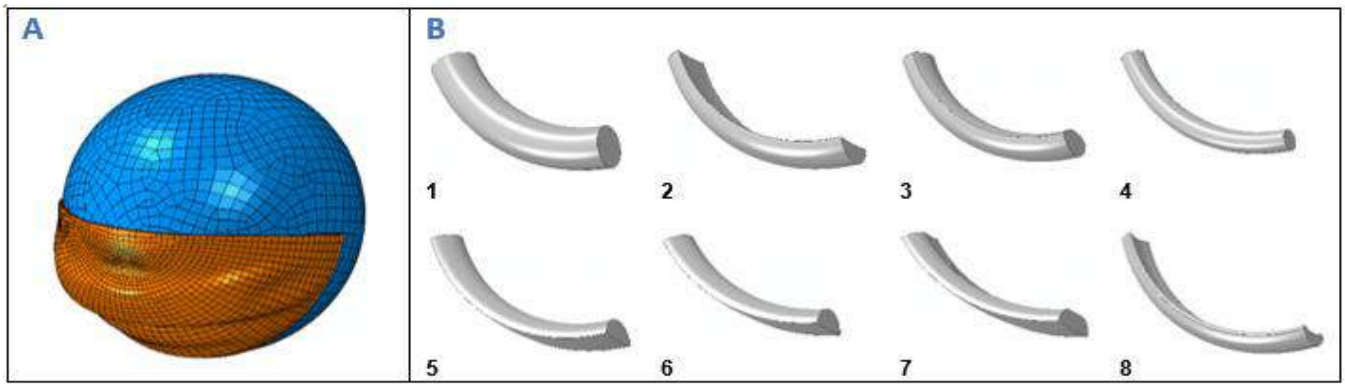

Figure 1: (A) Whole eye finite element model used to identify optimal friction ratio and geometry design to minimize film displacement.

films from both hydrated and dehydrated sections, so that these values could be compared to the design target thicknesses to verify the *ex vivo* geometry. The films produced from the molds were tested in an *in vivo* rabbit model. Based on the results of the simulations, three shapes were selected for evaluation in the inferior fornix of New Zealand White Rabbits (N=3 for each shape). Hydrogel retention and tolerability in the rabbit eyes were observed for 8 days.

RESULTS AND DISCUSSION

The ratio of friction between the hydrogel/globe interface and hydrogel/lid interface that results in immobilization during normal eye movement can be defined by the linear relationship shown in Fig. 2. Specifically, the coefficient of friction on the globe side of the hydrogel must be approximately 1.4 times larger than the lid side for adequate immobilization. Assuming that the interaction between the globe and the hydrogel is frictionless, the ideal friction coefficient between the lid and hydrogel is approximately 0.07. In the geometry optimization, Geometries 1 and 4 completely dislodged from the eye and were excluded from further analysis. The geometry that yielded the least amount of displacement for both simulated coefficients of friction on the lid side was Geometry 7 (Fig. 3). During the fabrication process, hydrogel films retract in molds when they are dried. The rehydrated film thicknesses averaged approximately 50% thicker than the target geometry. Future refinements to mold geometry will need to account for the increased swelling thickness. Geometries 7, 8, and a new rectangular film shape were selected for evaluation in the rabbits. As predicted, Geometry 7 had the best retention with 2 of the 3 films lasting up to 3-4 days. Geometry 8 had 1 of the 3 films last up to 3-4 days. The rectangular film performed the worst, and was dislodged within a day.

CONCLUSION

Finite element analysis is a powerful tool that can optimize drug delivery systems for better interaction with the eye. The novel HA-based hydrogel film is a viable topical ophthalmic drug delivery device if the 1.4:1 ratio of frictional properties against the surface of the lid and globe is maintained. This variance can be achieved through surface modifications of the hydrogel or using geometrical features to create larger frictional forces against the lid. Future studies will investigate micropatterning of the film as a means to better control frictional interactions with the eye.

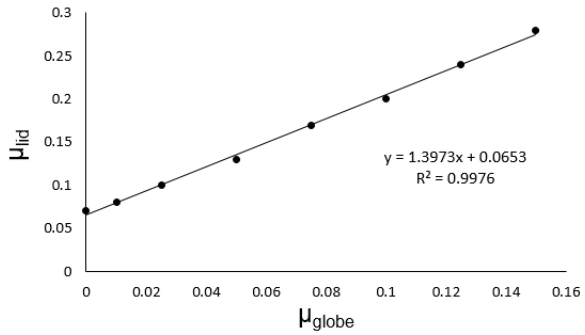

Figure 2: (A) Relationship between friction of the hydrogel with the lid (μlid) and globe (μ_{globe}) that is required to retain the film in the lower fornix of the eye during regular eye movement.

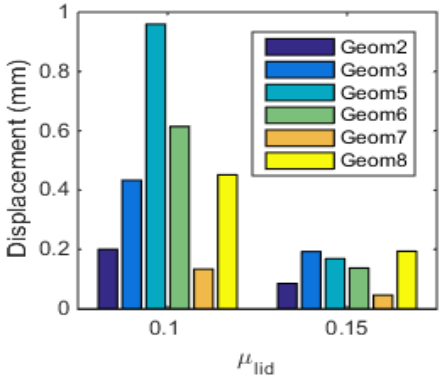

Figure 3: Maximum nodal displacement of film geometries. Geometries 1 and 4 were excluded from the analysis because they completely displaced from the lower eyelid.

ACKNOWLEDGEMENTS

The authors would like to thank the financial support from NSF SBIR Phase II Grant IIP-1430921 and DoD Phase II SBIR Grant W81XWH-14-C-0025.

REFERENCES

[1] Toole, BP et al., *Semin Cell Dev Biol*, 12:79-87, 2001.
[2] Hyde, JE, *Am J Ophthalmol,* 48:85-94, 1959.

Copyright 2016 The Organizing Committee for the 2016 Summer Biomechanics, Bioengineering and Biotransport Conference

SB^{3}C2016
Summer Biomechanics, Bioengineering and Biotransport Conference
June 29 –July 2, National Harbor, MD, USA
SB^{3}C2016-880

POLYCAPROLACTONE FIBROUS SCAFFOLDS TO NAVIGATE NEURAL STEM CELLS

Nastaran Hashemi (1)

(1) Department of Mechanical Engineering
Iowa State University
Ames, Iowa, USA

INTRODUCTION

Tissue engineering is an interdisciplinary area that combines engineering and biology in order to improve or replace biological functions. A prominent area of tissue engineering is related to regenerative medicine and neurorepair.. The discovery of effective therapeutic interventions targeted towards neurodegenerative conditions and nerve injuries has proven challenging. Scientists and engineers with various backgrounds have been drawn into the field of neural tissue engineering due to its importance for development of novel therapeutic strategies. For example, peripheral nerve regeneration is a complicated phenomenon which is often successful as long as the injuries are small. With more severe nerve injuries such as a nerve gap, however, interposition of a nerve graft or nerve regeneration conduit is usually required. Complexity in the spinal cord injury is more serious since, for the most part, regeneration is prohibited. Fortunately, neural tissue engineering provides extraordinary promise to combat this injury. Fibrous scaffolds have shown tremendous promise to build hierarchical structures and enhance the cellular behavior due to their high surface-area-to-volume ratio. The orientation of the fibers in these kinds of scaffolds are important because the aligned fibers play a predominant role in directing the cells to grow in a desirable direction. In this paper, we fabricated Poly (ε-caprolactone) (PCL) microfibers using a microfluidic approach in order to create a 3D environment to direct the growth and differentiation of neural stem cells and control the cellular microenvironment. The phase inversion strategy was chosen for fiber solidification because the fibers are used as a scaffold and it is not desirable to decrease the degradability of the polymer by cross-linking. PCL is a biocompatible and biodegradable polymer widely applied in biomedical area. However, this is the first time that adult neural stem cells were cultured on PCL fibers. In this paper, polycaprolactone fibers are fabricated in different sizes using a microfluidic platform. By using this approach, we show large degree of flexibility in the control of the size of the fibers. We have cultured green fluorescent protein-expressing (GFP) Adult Hippocampal Stem/Progenitor Cells (AHPCs) on PCL microfibers and investigated their ability to adhere, survive, proliferate and differentiate. It was shown that the cells attach to and align themselves on the microfiber substrates. The microfluidic microfabrication platform was able to create a biocompatible scaffold out of fibers to provide a desirable growth environment for the neural stem cells. It was demonstrated that cell death is minimal, and cell proliferation may be affected by changing the features of the fibrous scaffold.

METHODS

Phase inversion (solvent extraction) strategy was used to solidify PCL and fabricate microfibers. In this process, 2,2,2- trifluoroethanol (TFE) in the core fluid is replaced by the ethanol and water in the sheath fluid at the interface between the sheath and core solution. This exchange results in PCL solidification because the sheath fluid is miscible to TFE, but not solvent to PCL.

RESULTS

Two fluids, i.e. the core and sheath fluids, are introduced into the microchannel and diffusion occurs only at the core/sheath fluid interface due to the laminar flow regime. In order to have a continuous fiber fabrication process, a core/sheath flow profile is required. The sheath fluid focuses the core fluid laterally after the two fluids are introduced at the upstream of the channel and changes the shape of the core fluid to a thin vertical strip. Chevron grooves in the downstream of the channel decrease the hydrodynamic resistance perpendicular to the flow direction. The sheath flow rate is higher than the core flow

Copyright 2016 The Organizing Committee for the 2016 Summer Biomechanics, Bioengineering and Biotransport Conference

rate in order to provide the force needed to keep the core fluid at the center of the microchannel. Because the hydrodynamic resistance is inversely proportional to flow rate, the sheath fluid fills the grooves, wraps around the core fluid, and pushes it to the center of the channel.

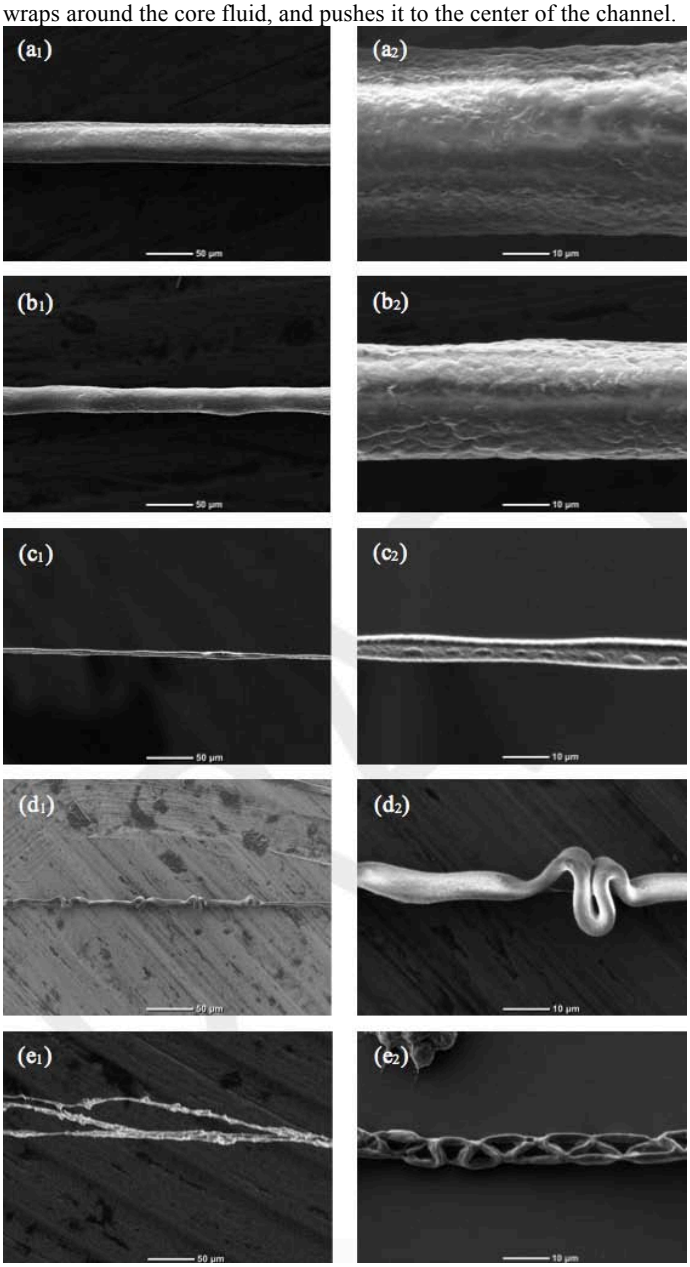

Figure 1: SEM images of PCL microfibers at sheath-to-core flow rates of (a) 20:5; (b) 60:5; (c) 200:4; (d) 300:2, and (e) 400:1.

Sheath fluid and chevron grooves exert lateral and vertical hydrodynamic focusing forces on the core fluid. The lateral and vertical hydrodynamic focusing, which is originated from the shear force between the core and sheath fluids, plays a pivotal role to keep the core fluid at the center, align the polymer chain, and change the shape of the microfibers. The hydrodynamic force depends on the viscosity and relative velocity of the core and sheath fluids. By adding polyethylene glycol (PEG) to the sheath fluid, the viscosity of core and sheath solutions match and there is no need to use high relative velocities to focus the core fluid when fabricating the fibers. Additionally, there is a possibility of flow instability in the channel at high relative velocities that results in changing the flow regime to transient from laminar. Figure 1 shows the field emission scanning electron microscopy images of the fibers fabricated using the flow rate ranges of 1-5 μL min^{-1} and 20-400 μL min^{-1} corresponding to the core and sheath fluids, respectively. The concentration of the PCL in TFE and PEG in the water/ethanol was kept at a constant value of 5%. Ki-67 immunolabeling was used to evaluate whether the PCL microfibers would support proliferation of the AHPCs. Expression of the Ki-67 antigen occurs during the cell cycle (not detected in cells in the resting phase) and therefore is commonly used as a cellular marker for cell proliferation. Ki-67 immunolabeled cells were present on all microfibers examined. Figure 2 (A-C) illustrates an example of Ki-67 immunolabeled cells growing on microfluidic spun PCL microfibers at a sheath-to-core flow rate of 60:5. [1]

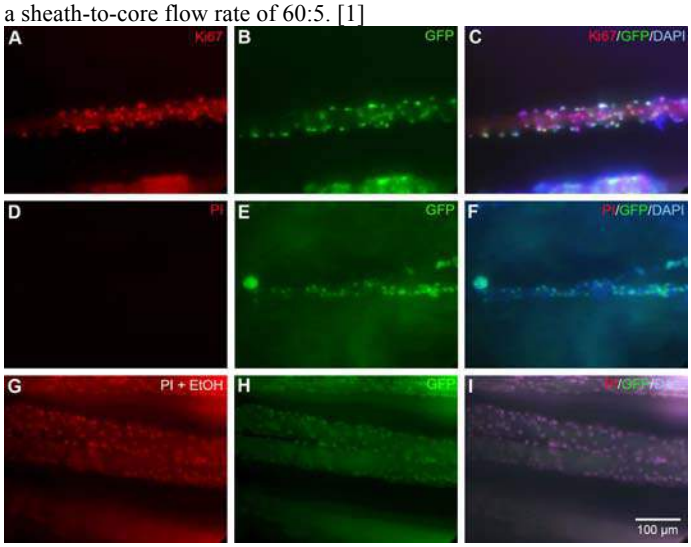

Figure 2: Attachment, proliferation and survival of AHPCs cultured on PCL microfibers. Fluorescence images of AHPCs immunolabeled for Ki-67, cell proliferation marker (A-C) or Propidium Iodide (PI) staining.

DISCUSSION

Polycaprolactone microfibers with different features were fabricated in this work using microfluidic fiber fabrication with the solidification strategy of phase inversion. The mean diameter of the fabricated fibers ranged from 2.6-36.5 μm by selecting the sheath-to-core flow rate ratio from 400 to 4. The fibers were chemically modified with extracellular matrix molecules to facilitate cell attachment and for guiding the direction of AHPC growth in vitro. The results showed that the PCL fiber can be used as a fibrous scaffold which is not cytotoxic to the AHPCs, and supports cell adhesion, differentiation, and proliferation. Additionally, it was shown that the clusters of these adult neural stem cells can be aligned using the PCL microfibers. Integration of multiple cues within a 3D context is important for gaining a better understanding in regulating neural stem cell differentiation and in designing scaffolds for neural tissue engineering. In addition, the PCL fibers can be applied in regeneration of other tissues such as muscle, tendons, and blood vessels.

ACKNOWLEDGEMENTS

We acknowledge the Office of Naval Research and ISU PIIR for support of this work.

REFERENCES

[1] Sharifi, F et al., *JMBBM*, to appear, 2016.

Copyright 2016 The Organizing Committee for the 2016 Summer Biomechanics, Bioengineering and Biotransport Conference

SB^{3}C2016
Summer Biomechanics, Bioengineering and Biotransport Conference
June 29 –July 2, National Harbor, MD, USA
SB^{3}C2016-881

DEVELOPING COMPUTATIONAL FLUID-STRUCTURE MODELS FOR THE LYMPHATIC VALVE

John T. Wilson (1), Lowell T. Edgar (1), Raoul van Loon (2), James E. Moore Jr. (1)

(1) Department of Bioengineering
Imperial College London
South Kensington Campus
London, United Kingdom

(2) College of Engineering
Swansea University
Bay Campus
Swansea, United Kingdom

INTRODUCTION

The lymphatic system is an expansive vascular network running parallel to the venous system that plays a vital role in fluid homeostasis within the body as well as immune cell transport. It takes up fluid from the interstitial spaces in the body and transports it to the venous return. Unlike the cardiovascular system, the fluid within this network of vessels is not driven by a central pump, but rather by extrinsic and intrinsic mechanisms that take the lymphatic fluid (lymph) from a lower pressure environment to a higher one. Extrinsic mechanisms influence the flow of lymph via outside forces including arterial pulsations, skeletal muscle contractions and diaphragmatic movement. Intrinsic forces transport lymph via the contraction of lymphatic muscle cells (LMCs) that line the lumen of the lymphatic vessel.

Bi-leaflet check valves are frequent throughout the vessels and serve to prevent retrograde flow. Valve defects have been shown to underlie the pathogenesis of lymphatic distichiasis, a dominantly inherited form of primary lymphedema [1,2]. Physical injury to valves occurs in lymphatic filariasis [3], which is the most common cause of lymphedema in the world affecting over a hundred million people worldwide [4,5]. Once the healthy valve behavior is understood, the disease states can begin to be investigated.

Experiments involving the lymphatic valves are difficult due to the extremely low lymph flow rates within the vessels (13.95 ± 5.27 μL/hr) and small diameters (91 ± 9 μm) [6]. The computational work here builds on our previous models of the rat mesenteric lymphatic valve, which used an image-based computational fluid dynamics (CFD) approach [7] and uncoupled fluid-structure interaction (FSI) approach [8], respectively. The present study implements a coupled FSI approach with an idealized geometry of a rat mesenteric lymphatic valve to understand the transient fluid and solid mechanical behavior of the valve. This work forms the framework of future lymphatic FSI studies implementing more complex boundary conditions and image-based geometries.

METHODS

Idealized Geometry and FSI Approach. An idealized geometry of a rat mesenteric lymphatic valve described previously [8] was used as the computational domain for simulations. Due to the expected high degree of leaflet deflection over short time scales (e.g. complete opening in less than 1 second), a strong coupling between the fluid and structural equations is necessary. A two-way iteratively implicit method was employed using ANSYS Fluent as the fluid solver and ANSYS Mechanical APDL as the structural solver. The equations of the solid and fluid are solved separately but data is exchanged within a time step. Each iteration within a time step is known as a coupling iteration. The ANSYS platform (v16.1, Canonsburg, PA, USA) was chosen because of its mesh proficiencies and ability to remesh the fluid region at every time step. Only ¼ of the valve was modeled in order to reduce computational cost (Fig. 1).

Structural Boundary Conditions. The ½ -leaflet was meshed using the SOLID187 element, which is a 3D, 10-node element well-suited to modeling irregular meshes with second order accuracy in space. The valve leaflets were fixed at the annulus (edge where the leaflets attach to the wall of the vessel) and geometric non-linearities were taken into account, which allows for large deflections of the leaflets. A Hilber-Hughes-Taylor

Copyright 2016 The Organizing Committee for the 2016 Summer Biomechanics, Bioengineering and Biotransport Conference

(HHT) time integration method, which allows for energy dissipation and second order accuracy in time, was used to discretize the equations of motion and the Newton Raphson Method was applied to solve the discretized equations. For the material behavior, a Neo-hookean model was employed. A value of 20 kPa was used for the shear modulus, G, which is slightly lower than that of arterial elastin [9, 10, 11], whilst a Poisson's ratio of 0.45 was chosen (nearly incompressible).

Flow Conditions. The fluid domain was imported into the commercial CFD software, ANSYS Fluent, and meshed using tetrahedral elements resulting in a computational mesh of approximately 156,500 volumetric elements. A fluid with dynamic viscosity, μ, of 1.5 cP [12] and density, ρ, of 1 g/cm^3 was used to model lymph. An unsteady and increasing pressure boundary condition with a maximum pressure of 50 Pa was applied at the inlet of the geometry and the outlet was kept constant at 0 Pa.

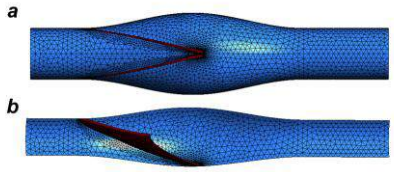

Figure 1: Lymphatic valve geometry: a) 3D view of the model with computational domain reflected and rotated and b) skewed 3D view of the actual ¼-valve model.

Symmetry boundary conditions were applied at the regions where the full valve leaflet had been divided into quarters to model mirror symmetry at these locations. Diffusion-based mesh smoothing, local cell remeshing and local face remeshing were applied to rectify irregularities in the fluid mesh resulting from the deformations. The simulation was allowed to run for 0.45s using a minimum time step of 2 ms. Three coupling iterations per time step were implemented in ANSYS Fluent with a maximum number of coupling iterations of 300.

RESULTS

The leaflet deflection increases in an apparently linear fashion until approximately 0.3 s, where the deflection at the leaflet tip, δ_y, reaches 4 µm (Fig. 2.).

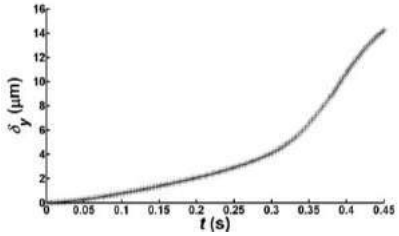

Figure 2: Deflection at the leaflet tip, δ_y, versus time, t.

From 0.3 s, δ_y increases to 14 µm (t = 0.45 s) in a non-linear monotonic fashion. Representative velocity streamlines revealed a peak velocity value of approximately 39 mm/s at 0.45 s (Fig. 3).

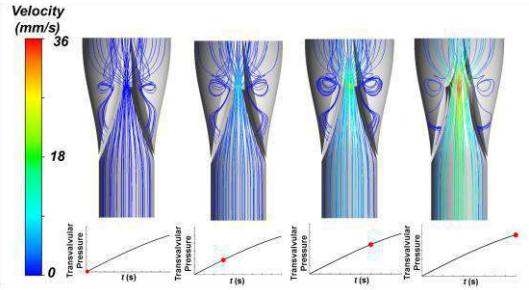

Figure 3. Representative velocity streamlines. Plots below the streamline figures represent the location on the transvalvular waveform at which the data were extracted.

Streamlines revealed apparent regions of recirculation between the valve leaflets and the sinus wall. However, the velocities in these regions are essentially negligible compared to central lymph flow.

DISCUSSION

In this study, an FSI model of a rat mesenteric lymphatic valve was developed. The peak velocity was 39 mm/s and regions of apparent recirculation were observed adjacent to the valve leaflets. One limitation of this study includes the simplification of the geometry to ¼ of the full valve and sinus using symmetry boundary conditions. Due to the low flow rates (Re<1), and the fact that our previous work [8] has shown that asymmetric openings tend to occur only at lower values of sinus-to-root ratio (which is unlikely to occur physiologically), there is strong indication that the assumption is reasonable. Future studies will include implementing a sinusoidal inlet pressure to open and close the valve leaflets as well as modeling the full geometry to understand whether the symmetric assumption is valid. Overall, this work has created a foundation for the future development of FSI models of the lymphatic valve.

ACKNOWLEDGEMENTS

We would like to acknowledge NIH for, in part, funding this study (Grant R01 HL094269 and U01 HL123420) and the Royal Academy of Engineering and Royal Society for funding J.E. Moore Jr.

REFERENCES

[1] Mellor, R.H. et al., *Circulation,* 115(14):1912-1920, 2007.
[2] Petrova, T.V., et al., *Nature Medicine*, 10(9):974-981, 2004.
[3] Case, T. et al., *Lymphology*, 24(4):174-183, 1991.
[4] Pfarr, K., et al., *Parasite Immunology,* 31(11):664-672, 2009.
[5] Chakraborty S., et al., *Microcirculation*, 20(5): 349-364, 2013.
[6] Dixon B., et al., *Microcirculation*, 13(7):597-610, 2006.
[7] Wilson J.T., et al., *J Biomech Eng*, 135(5):51005, 2013.
[8] Wilson J.T., et al., *J Biomech*, 48(13):3593-3599, 2015.
[9] Mithieux, S.M., et al., *Advances in Protein Chemistry*, 70:437-461, 2005.
[10] Nivison-Smith, L. & Weiss, *Regen Med Tissue Engr Biomater InTech*, 323-340, 1997.
[11] Zou, Y., & Zhang., *Ann Biomed Eng*, 37(8):1572-1583, 2009.
[12] Swartz M.A. & Fleury, *Annu Rev Biomed Eng*, 9:229-256, 2007.

Copyright 2016 The Organizing Committee for the 2016 Summer Biomechanics, Bioengineering and Biotransport Conference

SB³C2016
Summer Biomechanics, Bioengineering and Biotransport Conference
June 29 –July 2, National Harbor, MD, USA

SB³C2016-882

COMPUTATIONAL MODELING OF OPTIMIZATION OF DRUG-ELUTING STENTS UNDER MULTIPLE MECHANICAL CRITERIA

François M. Cornat, Franz Bozsak, Abdul I. Barakat

Hydrodynamics Laboratory (LadHyX)
Department of Mechanics
Ecole Polytechnique
Palaiseau, France

INTRODUCTION

Atherosclerosis is the leading cause of mortality in the world. The most common treatment for atherosclerosis today is the implantation of a stent. The earliest stents were bare metal stents (BMS); however, the unacceptably high restenosis rates associated with BMS led to the development of drug-eluting stents (DES). Although highly effective in preventing restenosis, DES appear to be associated with an increased risk of late stent thrombosis (LST) which, though rare, is often fatal when it occurs. LST following DES implantation is attributable to delayed endothelial wound healing following the extensive endothelial damage induced by the high pressure deployment of a stent [1]. The delayed endothelial healing has multiple causes: 1) the drugs eluted by DES inhibit not only smooth muscle cell proliferation but also endothelial cell proliferation, thereby slowing down vascular wound healing, 2) stents induce arterial flow disturbance which can impair endothelial cell migration [2], and 3) the stresses induced by stenting in the arterial may compromise vascular healing. We are interested in optimizing DES design and performance with the overall goal of controlling restenosis while simultaneously allowing endothelial healing. Accomplishing this goal requires a sufficiently high drug concentration in the arterial media to prevent restenosis while maintaining drug concentration at the endothelium as low as possible. Furthermore, the stent needs to induce minimal arterial blood flow disturbance as well as minimal stress excursions in the arterial wall.

We recently developed a computational model that describes the transport within the arterial wall of drugs eluted from DES [3]. We subsequently used this model to optimize drug release from DES to define a cost function whose minimization allowed us to determine the optimal combination of initial drug concentration loaded onto the DES and drug release kinetics [4]. The minimization of the cost function was performed using a surrogate management framework-based gradient-free optimization algorithm. We now wish to extend the optimization to account for stresses in the stent and the arterial wall as well as stent-induced arterial flow disturbance. Thus, the specific goal of the present work is to develop a computational model and associated optimization scheme to minimize stent-induced arterial blood flow disturbance as well as the stresses in the arterial wall while simultaneously ensuring stent integrity during deployment and limiting contact pressure between the stent and the artery in order to minimize arterial wall damage.

METHODS

We developed a fully parameterized three-dimensional model of a closed-cell stent design (Fig. 1). This approach provides the ability to systematically evaluate the effect of each parameter on the optimization results. Here, we focus specifically on stent strut dimensions; thus the two optimization parameters are ‘a’ and ‘b’ in Fig. 1 which represent the strut semi-height and semi-width, respectively.

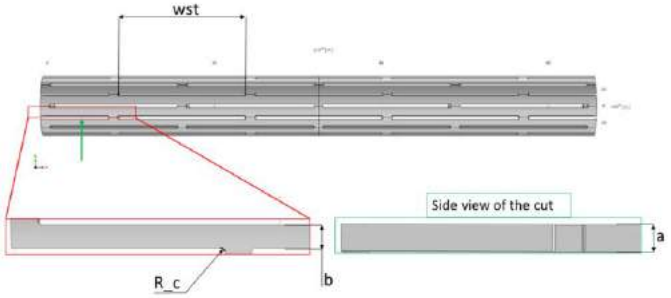

Figure 1: Stent design and parameters definition

The stent is assumed to be made of cobalt-chromium (CoCr). The initial

Copyright 2016 The Organizing Committee for the 2016 Summer Biomechanics, Bioengineering and Biotransport Conference

crimped stent diameter is 0.5 mm, and it is expanded to a final diameter of 4 mm, typical of a human coronary artery. The stent is expanded by applying a pressure to its inside surface. Instead of applying a constant pressure until the stent radius reaches the arterial radius, the computational expansion of the stent was accomplished via a step-by-step increase in the applied pressure. At every step, the stent radius was monitored, and pressure augmentation was arrested when the desired radius (corresponding to the arterial inner radius) was attained. At that point, the pressure was removed to obtain the final stent configuration. With this method we can precisely control the expansion of the stent at each step and evaluate the critical steps. The total expansion time is 1 sec.

We use the commercial finite element Multiphysics code COMSOL 5.1 to evaluate the stresses within both the stent and the arterial wall as the stent is expanded from the crimped configuration to its fully expanded state. The stent is assumed to exhibit elasto-plastic mechanical behavior with strain hardening. The artery is assumed to exhibit purely elastic behavior. The contact phase between the stent and the artery is simulated with the Lagrangian method and allows determination of the contact pressure and the contact surface area. We also solve the Navier-Stokes equations in the arterial lumen to evaluate stent-induced flow disturbance.

For the optimization, we use the surrogate management framework as described in our previous work to determine the combination of 'a' and 'b' that minimizes an overall cost function J that combines the effects of stresses in the stent, stresses in the arterial wall, stent-wall contact pressure, stent-wall contact surface area, and flow disturbance. Each of these five quantities are assumed to contribute equally to J so that:

$$J = \frac{1}{5} * (J_{MSS} + J_{MSA} + J_{CP} + J_{CS} + J_{FDI})$$

In this expression, J_{MSS} is the "Mechanical Stress in the Stent" score which describes the normalized average von Mises stress in the stent and is defined as:

$$J_{MSS} = \frac{1}{V_S}\int_{V_S} \frac{\sigma_{VonMises}}{\sigma_{CoCr}} dV \; (and \; (\frac{\max(\sigma_{VonMises})}{\sigma_{CoCr}} < 1$$

where V_s is the stent volume and σ_{CoCr} is the tensile strength of CoCr. J_{MSA} is the "Mechanical Stress in the Artery" score which denotes the average von Mises stress in the arterial wall and is defined as:

$$J_{MSA} = \frac{1}{V_A}\int_{V_A} \frac{\sigma_{VonMises}}{\sigma_{crit}} dV$$

where V_A is the volume of the arterial wall and σ_{crit} denotes a maximum arterial wall stress beyond which complications in re-endothelialization develop [5]. J_{CP} and J_{CS} are respectively the "contact pressure score" and the "contact surface area" score and are defined as:

$$J_{CP} = \frac{\max(P_{contact})}{P_0} \; (and \; J_{CS} = \frac{S_{contact}}{S_A}$$

where P_0 is the maximum pressure that can be supported by an artery and S_A is the arterial surface area. Finally, J_{FDI} denotes the "Fluid Disturbance Index" which describes the extent of stent-induced flow disturbance and is defined as:

$$J_{FDI} = \frac{1}{S_S}\int_{S_S} \left|\frac{\tau - \tau_0}{\tau_0}\right| dS$$

where τ is the local wall shear stress, τ_0 is the wall shear stress that would exist in the artery in the absence of a stent, and S_s, is the surface area of the stent exposed to the blood flow.

The optimization was performed in MATLAB using the function evaluations obtained from the COMSOL solid mechanics and fluid mechanics simulations.

RESULTS

Figure 2 depicts the dependence of the cost function J on the strut dimensions in the ranges 60≤a≤120 μm and 60≤b≤140 μm during the 1 second-long stent expansion process. The results indicate that very small dimensions need to be avoided while large b is generally desirable. In the present simulation, the global optimum (denoted by a red cross) is obtained for a=83 μm and b=140 μm. A secondary optimum (blue cross) is obtained for a=120 μm and b=140 μm. Future simulations will extend the range of dimensions studied.

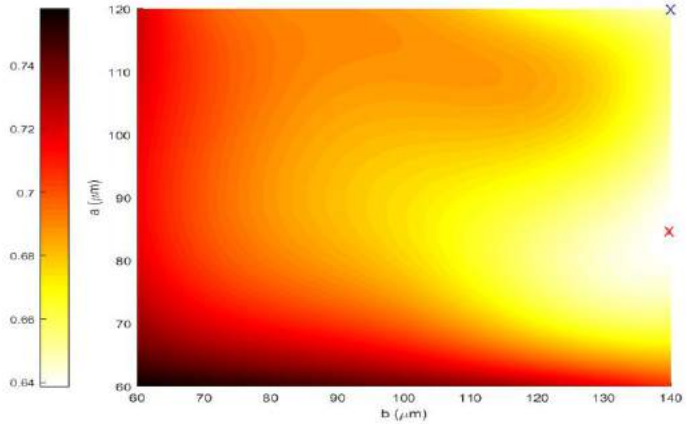

Figure 2: Cost function dependence on strut dimensions. Red and blue crosses respectively denote the global and secondary optima.

DISCUSSION

Mechanical evaluation of the interplay between the stent and the artery during stent deployment as performed in this study is an important consideration in the process of optimization of stent design and performance. While the goal of minimizing stent-induced flow disturbance in the arterial lumen pushes stent design towards thinner struts, the need for the struts to withstand the large mechanical stresses during the violent stent expansion process pushes the design towards thicker struts. The overall optimal strut design obtained in the present simulation is consistent with this notion as its dimensions are sufficiently large to ensure mechanical resistance but also minimize arterial flow perturbation. A secondary optimum is identified corresponding to struts sufficiently large to drastically minimize stresses in the stent but come at the expense of a certain level of flow disturbance. Performing similar simulations for larger range of strut dimensions will allow us to determine the optimal strut design. Moreover, a sensitivity study on local strut curvature ('R_c' in Fig. 1) and the length of bars between two nodes ('wst') will provide an assessment of a complete optimal stent design. All the simulations thus far have been performed on a closed-cell stent design. It would be important to expand the scope to also include open-cells stents.

ACKNOWLEDGMENTS

Francois Cornat is supported by a doctoral fellowship from *Ecole Normale Superieure.* This work was supported in part by a permanent endowment in Cardiovascular Cellular Engineering from the AXA Research Fund.

REFERENCES

1] Edelman, R. E., *Circ Res.* 84:378-383;1999
[2] Gojova, A. *J Appl Physiol* 98:2355-2362;2005.
[3] Bozsak, F. *Biomech Model Mechanobiol* 13:327-347;2014.
[4] Bozsak F. *PlosONE* 10(6):60130182; 2015
[5] Timmins, L. H. *Lab Invest.* 91 :955-697 ;2011

Copyright 2016 The Organizing Committee for the 2016 Summer Biomechanics, Bioengineering and Biotransport Conference

SB³C2016
Summer Biomechanics, Bioengineering and Biotransport Conference
June 29 –July 2, National Harbor, MD, USA
SB³C2016-883

BUCKLING CONFIGURATIONS OF THE EXTRACARDIAC TOTAL CAVOPULMONARY CONDUIT

Gokce N. Oguz (1), Senol Piskin (1), Erhan Ermek (1), Naz Altekin (1), Ahmet Arnaz (2), Kerem Pekkan(1)

(1) Department of Mechanical Engineering
Koc University
Sariyer, Istanbul, Turkey

(2) Department of Cardiovascular Surgery, Acıbadem Bakırköy Hospital,
Bakirkoy, Istanbul, Turkey

INTRODUCTION

Congenital heart defects impact nearly 1 in 100 newborns worldwide [1]. The palliative surgical repair of single-ventricle congenital heart defects is achieved through the total cavopulmonary connection (TCPC), introduced by de Leval et al. in 1988. Extracardiac (EC) TCPC is a common surgical template where the superior vena cava (SVC) is connected to the superior aspect of the right pulmonary artery (RPA) and inferior vena cava (IVC) is anastomosed to the RPA by using a thin artificial conduit [2]. The typical conduit material, Polytetrafluoroethylene (PFTE; Gore-Tex, WL Gore & Associates, Newark), is widely used, in addition to the porcine pericardium and Dacron grafts. Earlier studies have shown that the geometric configuration of TCPC is the main factor in determining the hemodynamic efficiency and the total cardiac output [3]. Both *in vitro* experiments and computational fluid dynamics (CFD) studies have been conducted to investigate the patient-specific flow fields and efficiency in different TCPC templates [4-6].

Patient-specific studies that focused on TCPC hemodynamics are conducted entirely on "functional" conduits, which are acquired from patients having an optimal single-ventricle physiology. The severely kinked EC TCPC anatomical conduits are usually associated with patients at critical conditions and not recruited for research purposes due to the practical or ethical concerns. *In-silico* compressed and kinked conduit geometries are studied nevertheless through hypothetical buckling configurations [7] and attracted wide clinical attention [8]. Therefore the actual, less-than-optimal TCPC pathways can also lead to significant blood flow resistance and deserve a systematic analysis.

In this manuscript we designed a mock-up EC TCPC circuit to replicate the mechanically failed IVC anastomosis morphologies under static physiological venous pressure loading first time in literature. The sensitivity of hemodynamic performance to torsional buckling and conduit kink due to caval offset are digitized in three dimensions (3D) and employed in CFD simulations for efficiency estimates.

METHODS

The 3D shapes of possible EC TCPC conduit failure modes are generated under physiological systemic venous pressure conditions (9, 12, and 15 mmHg) using a static pressure mock circuit (Figure 1). The experimental set-up consists of articulated arms and allowed the replication of both the intraoperative caval offset and anastomosis twist angle simultaneously.

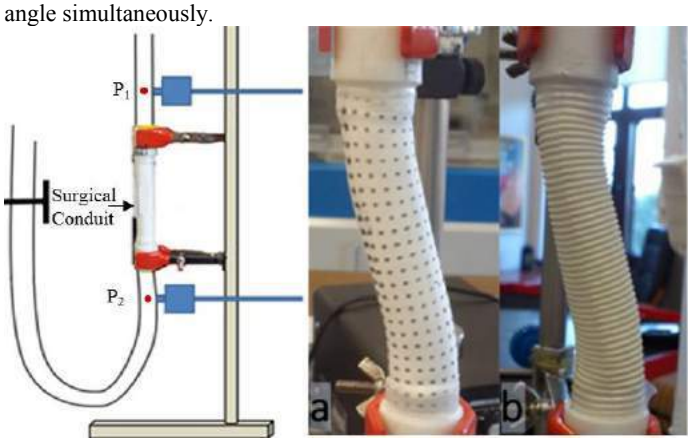

Figure 1. (Left) The static pressure mock-up setup for acquiring the 3D surgical pathway deformations (Right) PTFE (a) and Dacron (b) conduits at 0° twist and half diameter (0.5D) offset.

The mechanical behavior of all the three commonly used surgical materials, PTFE, Dacron and Porcine Pericardium, is studied in this mock circuit. Mechanical properties of the surgical materials are

Copyright 2016 The Organizing Committee for the 2016 Summer Biomechanics, Bioengineering and Biotransport Conference

measured using a biaxial test system (Bose). For the conduit-to-pulmonary artery anastomosis, three twist angles (0°, 30° and 60°) and three caval offset configurations (0, 0.5D, and 1D) resulted a total of 81 cases. However, for brevity, in this abstract we presented only 6 kinked conduit geometries of the PTFE material. Among these 6 geometries 2 of them are specifically selected by the pediatric cardiovascular surgeon due to their close resemblance to the real post-operative conduit geometries as observed intraoperatively.

3D scanned (Breuckmann SmartScan R5) geometries are reconstructed using Geomagic Studio (Raindrop Geomagic Inc). High-quality tetrahedral meshes are generated in Pointwise V16.04 (Pointwise, Inc.). The inlet and outlet boundaries of the CFD models are extended by 5 and 10 diameters, respectively. 3D, laminar, incompressible, and steady flow simulations are conducted using OpenFOAM (www.openfoam.org). All simulations are run until convergence to a steady-state solution (for a residual of 1E-6 in pressure, velocity and continuity). Parabolic velocity profile boundary condition is specified at the inlet extension of conduit with maximum velocity magnitude of 0.09136 m/s. [4]. Mesh convergence tests are done using the most buckled conduit geometry and the resulting mesh density is used for all geometries.

RESULTS

The observed buckling and kinked structures are considerably different for each surgical material. In PTFE, buckling is initiated proximal to the anastomosis locations of the conduit, which is different than Dacron and Porcine Pericardium grafts.

In order to analyze the effect of caval offset on IVC conduit buckling, 3 different offsets (0D, 0.5D and 1D) are specified under 15 mmHg pressure and 60° PA anastomosis twist angle (Figure 2). Clinically this pressure level corresponds to a problematic venous pressure state representing the maximum possible internal loading. In addition, configurations with 3 different twist angles (30°, 60°, and 90°) under 9 mmHg pressure having 0.5D offset are studied to illustrate the effect of anastomosis twist angle for the functional single-ventricle circulation (Figure 3).

For comparison the pressure drop values are reported relative to the ideal straight IVC conduit Poiseuille pressure drop levels (0.9Pa) along with the computed flow streamlines (Figure 2 and 3). The pressure drop increases nonlinearly with increasing offset level or angle of twist due to the buckling associated cross sectional narrowing. Also visible differences are observed in the flow field at 1D offset inside 15 mmHg pressure with 60° PA anastomosis twist angle (Figure 2) and 60° PA anastomosis twist angle under 9 mmHg pressure with 0.5D offset (Figure 3). In both cases fluid particles gathered momentum in radial direction and centerline velocity increased due to buckling.

DISCUSSION

An abrupt change in the pressure trend is observed between 0,5D and 1D offset configurations as displayed in Figure 2. 1D offset level resulted an increase in pressure drops up to 3 times compared to the 0D. Due to nonlinear relation between offsets, pressure drop for higher offset levels are ambiguous. It is also interesting to note that the configuration selected by the cardiovascular surgeon resulted the highest pressure drop for the offset level trend but not for the twist angle. Especially the surgeon's selected configuration for offset level may need to be revised in terms of our ongoing runs. Surgeon's selected configuration for twist angle can be accepted as consistent with relatively low pressure drop although it did not result the best.

IVC energy loss is calculated as %9 of total loss in an optimal TCPC flow with Poiseuille flow assumption. [3] Failed Fontan configurations with buckling and kinking produced more energy loss than expected which may be main source of energy loss in total TCPC configuration. Finally the relative twist and offset directions are an important factor, which affects final buckling severity significantly.

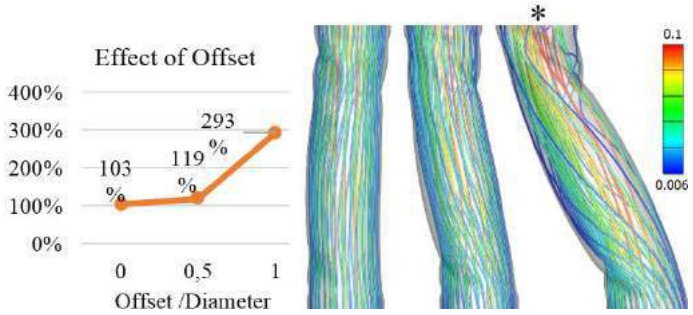

Figure 2. (Left) Pressure percent differences relative to straight conduit pressure drop for 3 different offsets under 15 mmHg venous pressure and 60° twist (Right) Coronal view of velocity magnitude (m/s) stream traces inside 15 mmHg pressure and 60° twist for 0D offset, 0.5D offset and 1D offset conduits are given respectively from left to right. The case identified by the surgeon is marked with a *.

In summary, we presented our recent results on the conduit failure modes. Ongoing studies include solving flow fields due to different conduit materials under variable buckling configurations. This way the effect of material and texture of conduit on pressure drop and flow characteristics will be disclosed. The simulations, in this study, were realized for rigid wall and steady state flow conditions. Repeating the simulations for compliant material under pulsatile flow would also contribute to more realistic results.

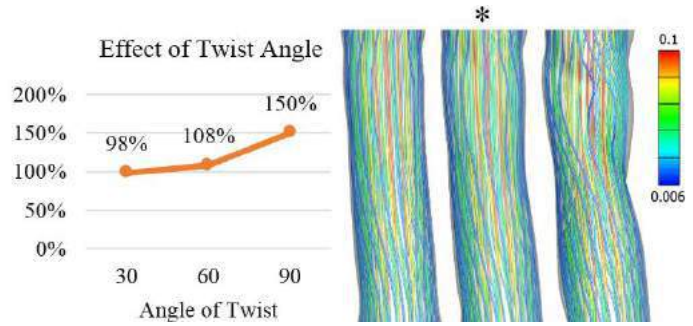

Figure 3. (Left) Pressure percent differences relative to straight conduit pressure drop for 3 different twist angles under 9 mmHg venous pressure and 0.5D offset (Right) Sagittal view of velocity magnitude (m/s) stream traces inside 0.5D offset with 9 mmHg pressure for 0° twist, 30° twist and 60° twist conduits are given respectively from left to right. The case identified by the surgeon is marked with a *.

ACKNOWLEDGEMENTS

Funding was provided by grants EU FP7 293931-*CardioFluidMechanics*

REFERENCES

[1]Boneva, R et al., *Circulation*, 103: 2376-2381, 2001.
[2] Liu, Y et al., *Journal of Biomedical Engineering,*126: 594-603, 2004.
[3] Ryu, K et al., *Annals of Biomedical Engineering,* 29:844-853, 2001.
[4]Pekkan, K et al. *Annals of Biomedical Engineering,* 33:284-300, 2005.
[5]Sharma, S et al., *JACC*, 27(5):1264-69, 1996.
[6] Ensley, AE et al. *Annals of Thoracic Surgery,* 68(4):1384-90,1999.
[7] Yoshida, M et al. *Journal of Cardio-Thoracic Surgery*, 44:e46-e52,2003.
[8] De Leval, M, *Journal of Cardio-Thoracic Surgery*, 44: e52,2003.

Copyright 2016 The Organizing Committee for the 2016 Summer Biomechanics, Bioengineering and Biotransport Conference

SB^{3}C2016
Summer Biomechanics, Bioengineering and Biotransport Conference
June 29 –July 2, National Harbor, MD, USA
SB^{3}C2016-884

VISCO-HYPERELASTIC MODELING OF THE PENN STATE PULSATILE PNEUMATIC PEDIATRIC VAD MEMBRANE

Bryan C. Good (1), Keefe B. Manning (1, 2)

(1) Department of Biomedical Engineering
Pennsylvania State University
University Park, PA, USA

(2) Department of Surgery
Penn State Hershey Medical Center
Hershey, PA, USA

INTRODUCTION

Despite the highest wait-list mortality in all of transplantation medicine (23% dying within 6 months of being added [1]), only recently has a pediatric ventricular assist device (PVAD), the Berlin Heart EXCOR, been approved for use in the United States for children of various sizes with congenital heart disease [2]. In 2004, the Pennsylvania State University was awarded one of five contracts by the National Institutes of Health (NIH) with the goal of creating a mechanical circulatory support device for children based on the successful adult pneumatic Pierce-Donachy/Thoratec device [3]. As part of developing a reliable PVAD, it is necessary to accurately predict the hemodynamics within the device due to higher hemolysis and thrombosis rates in PVADs compared to adult left ventricular assist devices (LVADs) [4].

To accomplish this, a tightly coupled fluid-structure-interaction (FSI) solver is required to accurately model the interactions of the air, a membrane and blood in the pneumatic pump. As a first step towards a full FSI model, an accurate representation of the PVAD's segmented poly-(ether polyurethane urea) (SPEUU) membrane needs to be developed. Polyurethanes are randomly segmented copolymers that consist of both hard and soft structural segments. This composition of polyurethane leads to unique mechanical properties including hyperelasticity, cyclic softening (the Mullins' effect), hysteresis, and time dependence [5]. Previous work has been done on the characterization of other polyurethane materials including polyurethane nanocomposites [6] and polyurethane foams [7]. However, due to the unique mandrel-layering process in which the Penn State PVAD SPEUU membranes are fabricated, specific material characterization needs to be performed and an appropriate constitutive model developed.

METHODS

To determine the hyperelastic and viscoelastic parameters of the PVAD membrane, two sets of tensile tests are conducted on "dog-bone" shaped samples cut from manufactured PVAD membranes according to ASTM D638 Standard Test Method for Tensile Properties of Plastics. According to the ASTM standard, all dimensions must be directly scaled when using a smaller sample, which was necessary due to the small size of the PVAD membrane (scale factor of 55/115 was used) (Fig. 1A). The PVAD membranes are manufactured to a thickness of 0.012'±0.002'. Therefore, digital calipers were used to measure the exact sample thicknesses prior to testing.

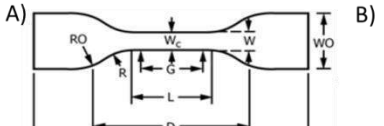

Dimension (in mm)	ASTM Standard	Actual
W-Width of narrow section	6	2.9
L-Length of narrow section	33	15.8
WO-Width overall	19	9.1
LO-Length overall	115	55
G-Gage length	25	12
D-Distance between grips	65	31.1
R-Radius of fillet	14	6.7
RO-Outer radius	25	12

Figure 1: A) Dog-bone sample test dimensions. B) Lloyd tensile device with SPEUU sample loaded.

All tests were performed on a Lloyd tensile testing machine with a load cell of 5N (Fig. 1B). Prior to data collection, 4 loading cycles were applied to each sample to eliminate the effects of cyclic softening and achieve a converged hysteresis loop (Fig. 2A).

Copyright 2016 The Organizing Committee for the 2016 Summer Biomechanics, Bioengineering and Biotransport Conference

To determine the correct hyperelastic constitutive model for this material, uniaxial tensile tests were performed on 5 samples (Fig. 2B). The samples were loaded at a strain rate of 0.01 s^{-1} to a maximum strain of 0.25. The resultant stress vs. strain data were fit to six well established hyperelastic models (St. Venant-Kirchhoff, Neo-Hookean, Mooney-Rivlin, Yeoh, and both 2 and 3-constant Ogden models) using an in-house Matlab code (Fig. 2C). For non-linear visco-hyperelastic materials, the stress depends on both the time and strain (Eq. 1):

$$S(\lambda, t) = S(\lambda) * g(t) \qquad (1)$$

Where $S(\lambda)$ is the strain-dependent function determined later and g(t) is a time dependent function defined using a Prony series (Eq. 2):

$$g(t) = g_\infty + \sum_{i=1}^{n} g_i \cdot e^{-\frac{t}{\tau_i}} \qquad (2)$$

Where g_i represents characteristic amplitudes, τ_i relaxation times and n the number of relaxation times and amplitudes needed to describe the visco-hyperelastic response. To determine the amplitudes and relaxation times, stress relaxation tests were performed where each sample was loaded quickly (1 s^{-1}) to a strain of 0.25 and held fixed for 3 minutes (Fig 3A). The resultant stress vs. time data were fit to a Prony series using an in-house Matlab code (Fig. 3B).

RESULTS

The Mooney-Rivlin model (Eq. 3) was shown to have the best fit to four of the five SPEUU samples stress vs. strain loading data based on a least squares regression analysis and was chosen as the hyperelastic model for this material:

$$S_{MR}(\lambda) = \frac{2}{\lambda}(C_{10}\lambda^4 + C_{01}\lambda^3 - C_{10}\lambda - C_{01}) \qquad (3)$$

Where S is the second Piola-Kirchhoff stress and λ is the uniaxial stretch ratio. The constitutive coefficients, C_{10} and C_{01} were fit for each sample and averaged (3.58 and -2.34 MPa, respectively).

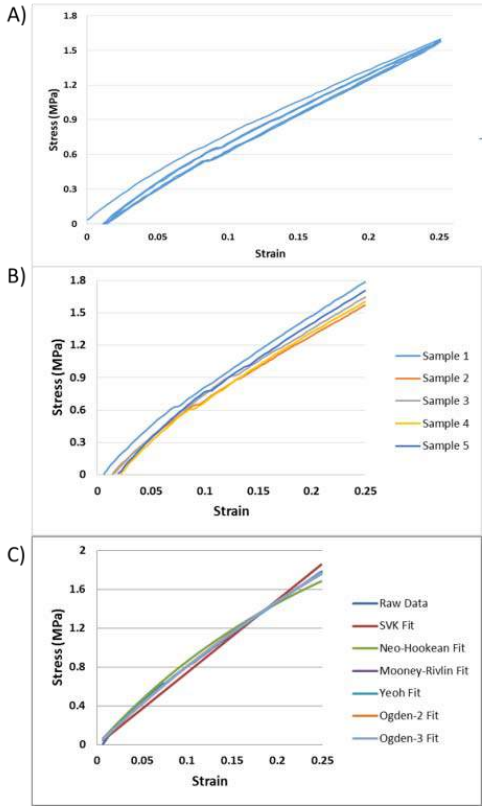

Figure 2: A) Example of SPEUU cyclic softening and hysteresis. B) Raw loading data of 5 SPEUU samples to a strain of 0.25. C) Hyperelastic model fits to single SPEUU loading curve.

A 4-term Prony series was chosen to fit the stress relaxation data and the characteristic amplitudes (1.65, 0.051, 0.050, 0.049 MPa) and relaxation times (1.11, 8.45, 110.91 s) were found individually for each sample and averaged.

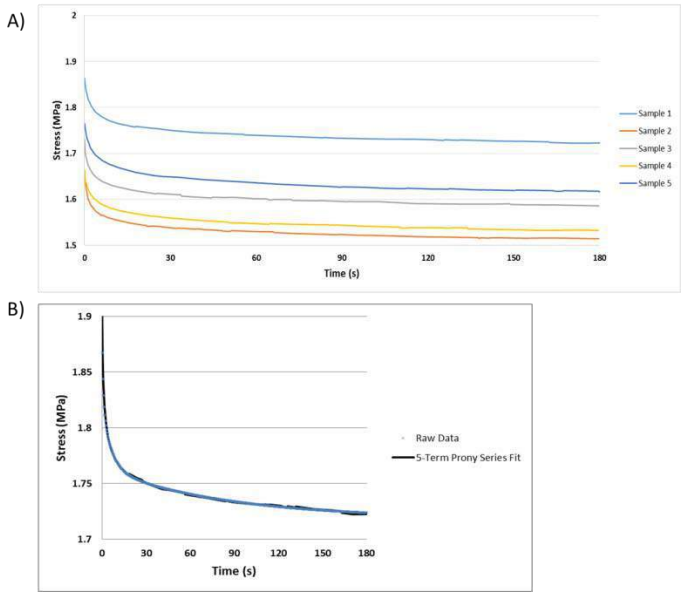

Figure 3: A) Raw stress relaxation data of 5 SPEUU samples held at a strain of 0.25. B) 4-term Prony series fit to a single sample's stress relaxation data.

DISCUSSION

The Penn State PVAD SPEUU membrane is a visco-hyperelastic material that can be accurately described using a Mooney Rivlin hyperelastic model and a 4-term Prony series model. Mooney-Rivlin hyperelastic models have been used previously by Donahue *et al.*[8] and Pawlikowski [6] for other polyurethane materials with coefficients of similar magnitude (~9 and -5 MPa for C_{10} and C_{01}, respectively). Prony series have also been used by many [6][9] to describe the time-dependent relaxation behavior of polymer materials in a similar manner and combined with a constitutive hyperelastic model. The constitutive visco-hyperelastic developed here will be used in a computational finite volume solid mechanics solver to simulate actual Penn State PVAD membrane dynamics. The cyclic stress-strain loading/unloading data from the five SPEUU samples will be used to validate the solid solver and constitutive model with the same dog-bone geometry prior to incorporation into a tightly-coupled FSI computational solver of the entire PVAD.

ACKNOWLEDGEMENTS

This work was supported through NIH NHLBI HL108123.

REFERENCES

[1] Mah D, et al. *J Heart Lung Transpl*, 28(12), 2009.
[2] Almond C, et al. *Circulation*, 127(16), 2013.
[3] Baldwin J, et al. *Circulation*, 113(1), 2006.
[4] Bachmann C, et al. *Artif Organs*, 24(5), 2000.
[5]Qi and Boyce. *Mechanics of Materials*, 37:817-839, 2005.
[6] Pawlikowski, M. *Mech Time-Depend Mater*, 18:1-20, 2014.
[7] Mills, N. *Cellular polymers*. 25(5):293-316, 2006.
[8] Donahue TL, et al. *Medical engineering & physics*, 31(4), 2009.
[9] Goh S, et al. *Mechanics of Time-Dependent Materials*, 8: 2004.

Copyright 2016 The Organizing Committee for the 2016 Summer Biomechanics, Bioengineering and Biotransport Conference

SB^{3}C2016
Summer Biomechanics, Bioengineering and Biotransport Conference
June 29 –July 2, National Harbor, MD, USA
SB^{3}C2016-885

EFFECTS OF REPRODUCTION AND LACTATION ON MATERNAL BONE TISSUE MECHANICAL PROPERTIES AT DIFFERENT LENGTH SCALES

Y. Li (1), G. Peng (1), W.J. Tseng (1), C.M.J. de Bakker (1), P. Chandrasekaran (2), Y. Jeong (3), D.G. Kim (3), L. Han (2), X.S. Liu (1)

(1) Department of Orthopaedic Surgery,
Perelman School of Medicine
University of Pennsylvania
Philadelphia, PA, USA

(2) School of Biomedical Engineering,
Science and Health Systems
Drexel University
Philadelphia, PA, USA

(3) College of Dentistry,
The Ohio State University
Columbus, OH, USA

INTRODUCTION

The fetal/infant bone growth that occurs during pregnancy and lactation exert remarkable pressure on maternal calcium homeostasis, resulting in substantial loss of bone mineral density. Although bone formation dramatically increases following weaning, bone mass nevertheless cannot be fully recovered. This partially recovery has been demonstrated in the rat skeleton. Our previous studies show that compared to age-matched virgin rats, post-weaning rats had 60% lower trabecular bone volume fraction (BV/TV) in the proximal tibia and 10% lower cortical bone area in the femur midshaft. However, multiple studies indicate that the number of pregnancies and the duration of lactation have a neutral or even positive effect on long-term fracture risk [1-3]. This paradox implies that reproduction and lactation may lead to a functional adaption of the maternal skeleton in bone's structure and mechano-sensitivity, generating balanced skeletal responses to improve bone quality beyond bone quantity across different length scales. A few recent studies suggest that osteocytes can actively remodel their peri-lacunar matrix during lactation [4], which may alter material properties of peri-lacunar bone matrix, thus affecting skeletal mechano-sensitivity. Therefore, we hypothesized that bone tissue mechanical properties could be modulated by osteocyte peri-lacunar remodeling during female reproduction. The first objective of this study was to compare both short-term and long-term changes in mechanical properties of bone tissue at different length scales in response to reproduction and lactation. The second objective was to investigate the roles of osteocytes in modulating these changes and define changes in the osteocyte micro-mechanical environment during different reproductive stages.

METHODS

All animal experiments were approved by IACUC. *6-Month Old Rats:* Female, SD rats were assigned to 3 groups: Virgin (n=5), Lactation (n=5, euthanized 2-week post lactation), and Recovery (n=5, euthanized 2-week post weaning). All animals were sacrificed at age 6 months. *14-Month Old Rats:* Female, SD rats were assigned to 2 groups: Virgin (n=3), and Reproduction (n=3). Reproductive rats underwent 3 repeated cycles of pregnancy, lactation, and weaning. All animals were sacrificed at age 14 months. *μCT Scan:* Femurs were harvested from each rat at euthanasia and subjected to *ex vivo* μCT scanning (vivaCT40, Scanco, 10.5 μm voxel size) to assess cortical bone area (Ct.Area) at the mid-shaft. *3-Point Bending Test* was performed at the femur mid-shaft region (Instron 5542). The load-displacement curve was used to calculate whole bone stiffness. Combining the geometric and mechanical information, corrected Young's modulus was calculated with Timoshenko's correction factors to avoid shearing error. *Nanoindentation Test:* A ~3mm thick specimen was cut from the midshaft of the bended femur along transverse plane by using low speed diamond saw under irrigation. The specimen surface was manually polished with grain size 1 μm, 0.3 μm, until 0.06 μm in wet condition. Indentation tests were performed using a nanoindenter (Nano-XP, MTS) in a wet chamber with Berkovich tips (speed 10nm/s; indentation depth 500nm; 30-second holding time). The elastic modulus (E) and hardness (H) were calculated based on the unloading portion of the load-displacement

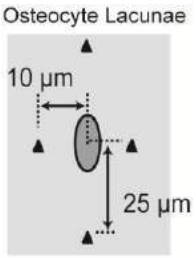

Fig 1. Indentations at 10μm vs. 25μm from the center of osteocyte lacunae.

Copyright 2016 The Organizing Committee for the 2016 Summer Biomechanics, Bioengineering and Biotransport Conference

curve by Oliver-Pharr method. 8-10 osteocyte lacunae were chosen for each specimen. 2 indents were applied at 10-µm and 2 at 25-µm distance to the center of each osteocyte lacuna (Fig 1). *Statistics:* 2-way ANOVA with Bonferroni corrections was applied to compare groups and indentation distances in both 6-month rats and 14-month rats. Differences were considered significant when $p<0.05$.

RESULTS

6-month-old rats: Ct.Area were 13% and 10% lower in the Lactation and Recovery groups, respectively, compared to the Virgin group (Fig 2A), indicating that the femoral cortical bone volume was significantly reduced by reproduction. However, 3-point bending tests indicated no reproductive effect on the whole bone stiffness between Virgin, Lactation, and Recovery rats (Fig 2B). Interestingly, nano-indentation tests revealed that bone matrix tissue modulus in the Lactation group was 5% and 10% higher than Virgin and Recovery groups, respectively (Fig 2C), while the indentation hardness in the Lactation group was 5% higher than both Virgin and Recovery groups ($p < 0.05$). By stratifying indentation modulus based on their distance to the center of lacunae, we found that elastic moduli at 10 µm ($E_{10\mu m}$, within peri-lacunar space) and 25 µm ($E_{25\mu m}$, interstitial bone region) had no difference in the virgin group. In contrast, $E_{10\mu m}$ was 3% lower than $E_{25\mu m}$ in the lactation group, while in the recovery group, $E_{10\mu m}$ was 7% greater than $E_{25\mu m}$. Furthermore, the ratio of $E_{10\mu m}$:$E_{25\mu m}$ in the recovery group was significantly greater than those in the Virgin and Lactation groups (Fig 2D). No difference of hardness (H) or brittleness (E/H) was found in different distances. *14-month-old rats:* No difference was found in the femoral Ct.Area and whole bone stiffness between the virgin rats and rats with reproduction history (Fig 2A-B). However, average indentation modulus was 4% higher in the Reproduction group than the Virgin group (Fig 2C), while the indentation hardness was not different in these two groups. No difference between $E_{10\mu m}$ and $E_{25\mu m}$ was found in Virgin or Reproduction group. Furthermore, the ratio of $E_{10\mu m}$:$E_{25\mu m}$ was not different between two groups (Fig 2D). No difference of hardness (H) or brittleness (E/H) was found either in two groups or different distances.

DISCUSSION

This study investigated both short-term and long-term changes in bone mechanical properties in response to reproduction and lactation. Lactation dramatically reduced cortical bone area in rat femur, and this reduction persisted after weaning. However, whole bone stiffness was preserved in both lactating and post-weaning rats, likely through altered material properties of bone tissue. Further tests by nanoindentation suggested that nano-scale bone tissue modulus and bone tissue hardness significantly increased during lactating, which may compensate for the reduced bone area to preserve whole bone mechanical properties. Despite smaller bone area and lower nano-scale elastic modulus, whole bone stiffness of post-weaning rats was not different from that of the virgin rats. Therefore, further tests at different length scales, such as microindentation tests, may be necessary to elucidate tissue level mechanisms to preserve whole bone mechanical properties in post-weaning bone. Moreover, our study also demonstrated significant tissue-level changes in rats with multiple reproduction cycles, suggesting reproduction history may exert long-term effect on bone tissue composition and mechanics. Additionally, the decrease of $E_{10\mu m}/E_{25\mu m}$ over the course of lactation and the increase of $E_{10\mu m}/E_{25\mu m}$ over the course of recovery suggest that osteocyte may have ability to directly remodel its local surrounding bone tissue to generate positive or negative gradient of material properties during different stages of a reproductive cycle. For example, during lactation, the peri-lacunar material properties would temporarily decrease. This could be caused by fast release of calcium ions from peri-lacunar matrix, mediated by osteocyte remodeling. In contrast, during weaning, the osteocytes may actively deposit minerals and accelerate mineralization at the peri-lacunar region, causing higher material properties. This alteration may have influence on the tissue deformation and strain distribution in the peri-lacunar bone region [5], thus affecting osteocyte signaling. However, even though osteocyte remodeling has an important influence on the heterogeneity of bone tissue properties, this local mediation itself cannot account for the overall changes in tissue-level mechanical properties, *e.g.*, increased elastic modulus during lactation. Further explorations are required to uncover the mechanism behind bone tissue adaptation to reproduction and lactation.

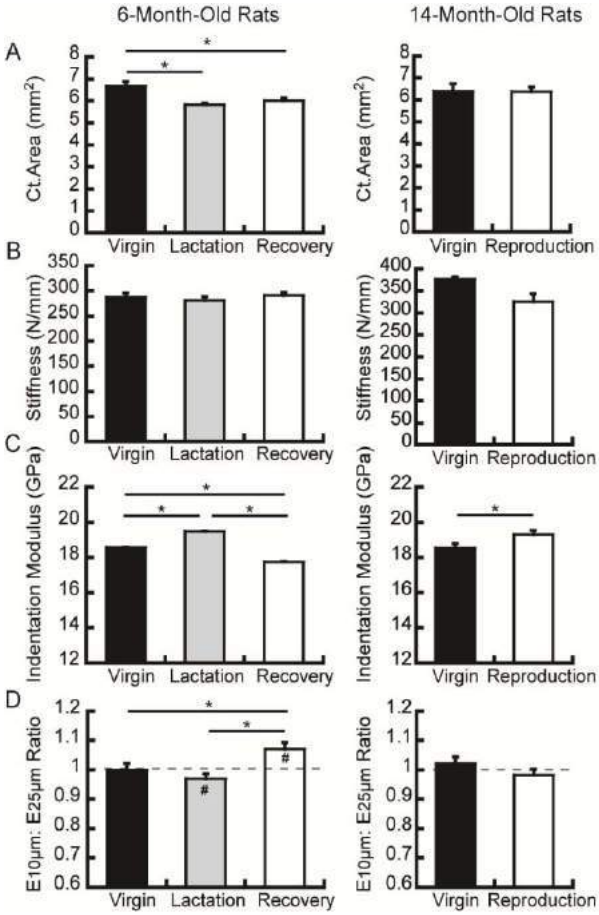

Fig 2. Mean±SEM of (A) Ct.Area, (B) Whole bone stiffness, (C) Nano-scale elastic modulus, and (D) Ratio of E10µm:E25µm of (Left) 6-month-old rats and (Right) 14-month-old rats. * difference between groups; # difference between E10µm and E25µm.

ACKNOWLEDGEMENTS

This study is supported by NIH/NIAMS P30-AR050950, R03-AR065145, and NSF Graduate Student Research Fellowship.

REFERENCES

[1] Paton, LM et al., *Am J Clin Nutr*, 77:707-714, 2003;
[2] Kovacs, CS and Ralston, SH., *Osteoporos Int*, 26:2223-2241, 2015;
[3] Melton, LJ et al., *Osteoporos Int.,* 1993;
[4] Qing, H et al., *J Bone Miner Res*, 27(5): 1018-1029, 2012;
[5] Bonivtch, AR et al., *J Biomech*, 40:2199-2206, 2007.

Copyright 2016 The Organizing Committee for the 2016 Summer Biomechanics, Bioengineering and Biotransport Conference

SB³C2016
Summer Biomechanics, Bioengineering and Biotransport Conference
June 29 –July 2, National Harbor, MD, USA
SB³C2016-887

LABORATORY EVALUATION OF WEARABLE HEAD IMPACT SENSORS

Abigail M. Tyson, Steven Rowson, and Stefan M. Duma

Department of Biomedical Engineering and Mechanics
Virginia Tech
Blacksburg, VA, USA

INTRODUCTION

As many as 3.8 million sports-related concussions are estimated to occur each year in the United States [1]. While acute symptoms may persist for days to weeks following a concussion, recent research has suggested repetitive concussive and subconcussive impacts may result in long-term neurodegeneration [2]. Diagnosis is dependent upon an athlete's self-reporting of symptoms, yet over 50% of athletes fail to do so after a concussion [3]. To provide an objective measure of head impact magnitudes, companies have developed wearable head impact sensors for on-field play. Although sensors themselves cannot diagnose a concussion, they can provide additional information on impact severity to a medical professional who can properly assess for injury.

Researchers are also interested in wearable head impact sensors to shed further light on the biomechanics of concussions. Men's football has been extensively studied over the past 13 years using a helmet-mounted sensor system, yet little work has investigated head impacts in women and children [4]. The introduction of new sensors for unhelmeted sports have the potential to provide valuable data on these understudied populations.

With a surge in wearable impact sensors coupled with increasing knowledge of the potential risks of sport-related concussions, it's possible that most athletes will be wearing sensors within the next five to ten years. Unfortunately, the accuracy and reliability of these sensors are not regulated. The objective of this study was to define and implement laboratory methods as the initial phase of a head impact sensor evaluation program. Sensors with minimal error in ideal conditions as shown by these tests will be further evaluated in more realistic scenarios: on-field and cadaver tests. The combination of both ideal and realistic testing phases will be used to provide an overall sensor evaluation for both researchers and consumers.

METHODS

Impacts were performed to both an unhelmeted and helmeted NOCSAE head, custom fit to a Hybrid III neck, mounted on a linear slide table. Tests were conducted with a pendulum impactor having a flat impactor face made of 40 mm vinyl nitrile for the unhelmeted condition and flat, rigid nylon for the helmeted condition. A large Riddell Speed helmet (Elyria, OH) was worn during helmeted tests. Impacts were performed to the front, front boss, rear boss, and rear locations of the headform (Figure 1) at targeted linear head accelerations of 25, 50, 75, and 100 g.

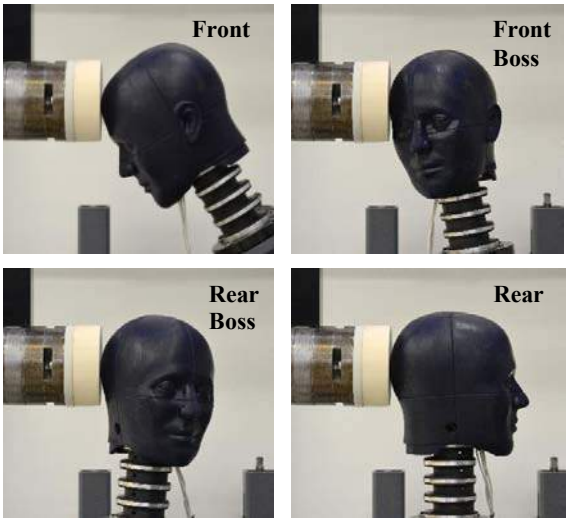

Figure 1: Headform orientations for the four impact locations. Only the unhelmeted setup is shown.

Copyright 2016 The Organizing Committee for the 2016 Summer Biomechanics, Bioengineering and Biotransport Conference

Impact locations were chosen based on frequency of occurrence in sports [5], variability in elevation, and equal spacing in azimuth. Impact magnitudes were chosen to represent the range of impacts in sports [6]. For consistency, reference values were verified to remain within ± 5 g of the target acceleration value. Each test configuration was repeated four times, totaling 64 tests per sensor.

Six commercially-available wearable head impact sensors were tested under this protocol: xPatch (X2 Biosystems, Seattle, WA), Vector Mouth Guard (i1 Biometrics, Kirkland, WA), SIM-G (Triax Technologies, Norwalk, CT), gForce Tracker (gForce Tracker, Markam, ON), Shockbox (i1 Biometrics, Kirkland, WA), and HeadsUp Headband (Integrated Bionics, Houston, TX). Hereafter, the sensors will be referred to as X2, Vector MG, Triax, GFT, Shockbox, and HeadsUp. Sensor acceleration and velocity measurements were compared to reference data measured by three linear accelerometers and three angular rate sensors (6DX Pro 2k-18k 6DOF sensor package DTS, Seal Beach, CA) located in the headform center of mass.

Sensors were positioned on the headform or helmet according to manufacturer instructions except for the Vector MG. Since the NOCSAE headform is not currently adapted for a mouth guard, the sensor was firmly adhered to the front of the headform at a 90° angle. However, this rotation was insignificant to results since only resultant data were used. Sensors were only tested under helmeted or unhelmeted conditions corresponding to sports recommended for use by the manufacturer. All sensors output at least peak linear acceleration. X2, Vector MG, Triax, and GFT also measured peak rotational kinematics and time-varying responses for each impact.

Reference headform kinematics were processed using MATLAB 2014a and filtered at CFC 1000 for linear acceleration and CFC 155 for rotational velocity. Comparisons between sensors and reference were obtained by fitting least squares linear regressions to peak values and obtaining the slope and R^2 coefficient of determination for each kinematic variable. To equally compare slope and R^2 values among sensors, regressions were constrained through the origin.

For the sensors that also record a time-varying kinematic response, comparisons were made at each time point. Sensor and reference curves were aligned by minimizing the root mean square (RMS) error:

$$RMS = \sqrt{\frac{\sum\left(x_{ref} - x_s\right)^2}{n}} \quad (1)$$

where x_{ref} is the kinematic value for the reference, x_s is the kinematic value for the wearable sensor, and n is the number of points in the time series. RMS error was then normalized by the peak reference value of the curve to compare sensors equally. Average and standard deviations of normalized RMS error (NRMSE) were calculated for each test condition. All calculations were made in MATLAB 2014a.

RESULTS

Results from linear regressions for each kinematic variable are shown for each sensor and test condition (Table 1). Perfect accuracy and correlation would result in a slope of 1.00 and R^2 of 1.00. Most sensors performed best in rotational velocity and worst in rotational acceleration. The variables for X2, Vector MG, and Helmeted GFT with low overall R^2 values had high individual location correlations above 0.9. The remaining sensors had low correlations overall and by location. Shockbox and Heads Up also failed to record 14% and 25% of the 64 tests, respectively.

NRMSE followed similar trends to the slope and R^2 values, with rotational velocity having the lowest error and rotational acceleration having the highest. X2 and Vector MG remained within 15% error for most test conditions. The remaining sensors had test conditions exhibiting mostly within 10-50% error, with some reaching over 100%.

Table 1: Slope (m) and R^2 coefficient of determination for the least squares linear regressions for each kinematic variable.

Sensor	LA		RV		RA	
	m	R^2	m	R^2	m	R^2
Unhelmeted X2	1.05	0.98	1.01	1.00	1.65	0.61
Helmeted X2	1.02	0.86	0.99	0.95	1.41	0.13
Vector MG	0.80	0.70	1.04	1.00	1.47	0.73
Unhelmeted Triax	1.06	0.25	1.12	0.93	0.46	-0.56
Helmeted Triax	0.94	0.15	1.15	0.79	0.72	0.19
Unhelmeted GFT	0.73	-0.24	0.65	0.42	-	-
Helmeted GFT	0.38	0.39	1.06	0.89	-	-
Shockbox	1.60	-1.19	-	-	-	-
HeadsUp	0.54	-0.73	-	-	-	-

DISCUSSION

These laboratory methods make up Phase I of a two-phased approach to evaluate wearable sensors. Phase II consists of on-field tests and cadaver tests that will better evaluate each sensor under more realistic conditions which have been shown to affect sensor performance [7].

There were several factors that increased the error of these sensors. Physical factors included sensor-helmet interactions for X2 and Triax and poor coupling between the headband and headform for GFT. Computational factors included low sampling rates introducing error throughout the calculations of rotational acceleration from differentiated rotational velocity. Imperfect rotational accelerations were then used to transform linear accelerations to the headform center of gravity, decreasing the accuracy in those measurements as well.

Although all sensors will always have some inherent error, data can still be valuable in quantifying concussive head accelerations and defining head impact exposure in sports. This is especially true for analyses that take into account the error measured in this study and are applied across the vast amount of data that could be collected.

This study demonstrates that head impact sensor accuracy and reliability vary greatly between commercially available products, and highlights the need for objective and public data characterizing sensor quality. By creating an objective two-phased evaluation of these sensors, consumers and researchers can be informed of their differences and manufacturers can be encouraged to create a product that will become a valuable tool to aid in the identification of head impacts in sports.

ACKNOWLEDGEMENTS

The authors gratefully acknowledge the Lewis Family Foundation for supporting this work.

REFERENCES

[1] Langlois JA, et al., *J Head Trauma Rehabil.* 21(5):375-378, 2006.
[2] Omalu BI, et al. *Neurosurgery*. 57(1):128-134, 2005.
[3] McCrea M, et al. *Clin J Sport Med.* 14(1):13-17, 2004.
[4] Hootman JM, et al. *J Athl Train.* 42(2):311-319, 2007.
[5] Rowson S, et al. *J Biomech Eng.* 131(6):061016, 2009.
[6] Wu LC, et al. *arXiv preprint arXiv:1503.03948.* 2015.
[7] Rowson S, et al. *Ann Biomed Eng.* 39(8):2130-2140, 2011.

Copyright 2016 The Organizing Committee for the 2016 Summer Biomechanics, Bioengineering and Biotransport Conference

SB^{3}C2016
Summer Biomechanics, Bioengineering and Biotransport Conference
June 29 –July 2, National Harbor, MD, USA
SB^{3}C2016-888

INTEGRATION OF A BAROREFLEX MODEL INTO A WHOLE BODY PHYSIOLOGY ENGINE

Rachel B. Clipp, PhD, M. Cameron Thames, MS, Jeffrey B. Webb, MS, Rodney Metoyer, Jr MS, Zachary M. Swarm, BS, Aaron M. Bray, BS, and Jenn N. Carter, BA

(1) Applied Research Associate, Inc
Raleigh, NC, USA

INTRODUCTION

Baroreceptors are stretch receptors located in the aortic arch and carotid artery. Changes in mean arterial pressure (MAP) trigger the stretch receptor leading to the baroreflex response. The baroreflex response is a negative feedback response that changes the peripheral resistance of the vascular system, the heart rate, and the elastance of the heart to modify the MAP. [1] The response is not only crucial for blood pressure regulation during normal daily function, but also in critical trauma scenarios, such as hemorrhage. During hemorrhage, blood loss causes the blood pressure to drop, triggering a baroreceptor response to attempt to maintain a healthy MAP. [2]

The BioGears physiology engine is a whole body open source physiology model currently used in medical training and teaching protocol and environments. The engine currently lacks a baroreceptor response, which is a significant detriment when teaching trauma care. It is of critical important that the cardiovascular response is accurate and meets validation for these cases to teach correct behaviors in trainees. The lack of the baroreceptor response is a significant limitation in the BioGears engine.

Current work exists in the form of a baroreceptor model in Ottenson, et al [3][4].This model was implemented within a full body physiology model to produce accurate physiologic outputs from the cardiovascular, respiratory, and endocrine systems that currently exist in the BioGears engine.

METHODS

The baroreflex response is calculated from the portion of the response related to the parasympathetic (Eq. 1) and sympathetic response (Eq. 2). .

$$n_p(mpa) = \frac{1}{1+\left(\frac{mpa}{mpa_{sp}}\right)^{-\vartheta}} \quad (1)$$

$$n_s(mpa) = \frac{1}{1+\left(\frac{mpa}{mpa_{sp}}\right)^{\vartheta}} \quad (2)$$

Where mpa is the calculated mean arterial pressure (mmHg), mpa_{sp} is the mean arterial pressure set point (mmHg), ϑ is the slope of the response curve (unitless) and was specified to be 12.0.

The mpa_{sp}must be calculated not just from the healthy patient set point but must also include the changes caused by patient activity, exercise, or drug modifications, such as morphine administration, Eq. 3.

$$mpa_{sp} = mpa_{psp} + \Delta mpa_{drugs} + \Delta mpa_{ex} \quad (3)$$

Where mpa_{psp} is the healthy patient set point (mmHg), Δmpa_{drugs} (mmHg) and Δmpa_{ex} (mmHg) are the change in the set point due to drug effects and exercise, respectively.

This baroreflex model includes changes to peripheral resistance, venous compliance, heart rate, and heart elastance. The time-dependent changes are based on strength of the parasympathetic and sympathetic tone and the time constant for response. Otteson, et al [3] also incorporated an unstressed volume effect, which was not incorporated in the BioGears engine. The current Cardiovascular System does not track unstressed volume, so there was no method for linking these effects. The four effects modeled here are shown in Eq. 4-6.

Copyright 2016 The Organizing Committee for the 2016 Summer Biomechanics, Bioengineering and Biotransport Conference

$$\frac{dx_{HR}}{dt} = \left(\frac{-1}{\tau_{HR}}\right)(-x_{HR} + \alpha_{HR} n_s(mpa) + \beta_{HR} n_p(mpa) + \gamma_{HR} \quad (4)$$

$$\frac{dx_{E,R}}{dt} = \left(-\frac{1}{\tau_{E,R}}\right)(-x_{E,R} + \alpha_{E,R} n_s(mpa) + \gamma_{E,R} \quad (5)$$

$$\frac{dx_C}{dt} = \left(-\frac{1}{\tau_C}\right)(-x_C + \beta_C n_p(mpa) + \gamma_C \quad (6)$$

Where $x_{E,C,R,HR}$, are the elastance (mmHg/mL), venous compliance (mL/mmHg), resistance (mmHg/mL/s), and heart rate (beats/s), respectively, τ is the time constant (s), n_p and n_s are the parasympathetic and sympathetic responses (unitless), respectively, and α and βare the sympathetic and parasympathetic response parameters, and γis the damping parameter. The units for α, β, and γ are the same units as x.

The time-constant values for each variable were used from Otteson, et al [3]: τ_{HR}, τ_E, τ_C, and $\tau_R$were set to 10, 10, 60, and 30 s, respectively. The sympathetic and parasympathetic response parameters and the damping parameter were tuned to achieve the correct response. To validate the responses, a hemorrhage scenario was used. A hemorrhage was applied at a rate of 1000 mL/min for 30 seconds, providing a total blood loss of 500 mL. The heart rate, blood pressure, systemic vascular resistance, and cardiac output were observed over the course of the hemorrhage and during the baroreflex response, and compared to the experimental data.

RESULTS

The tuned parameters for each effect are shown in Table 1.

Table 1: Response and Damping Parameters.

Variable	BioGears
$\alpha_{HR}, \beta_{HR}, \gamma_{HR}$	1.73, 0.25, 0.26
α_E, γ_E	0.1, 0.95
β_C, γ_C	0.6, 0.7
α_R, γ_R	1.2, 0.4

The strength parameters dictate the effect magnitude as MAP changes (Figure 1).

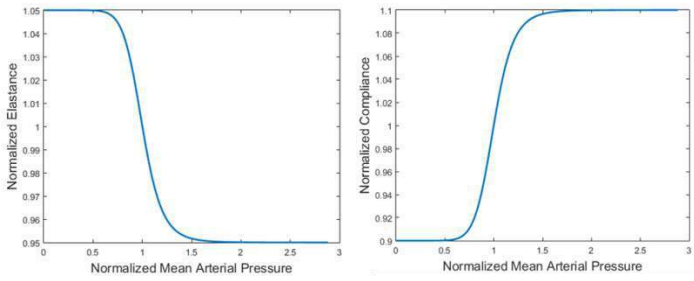

Figure 1: ***The changes to heart elastance and venous compliance as the mean arterial pressure changes.***

The validation case study was based on a 10% hemorrhage (500mL) over 30 seconds. The time dependent data for cardiac output, blood volume, heart rate, and systemic vascular resistance are shown in Figure 2.

There is an expected 30% increase in heart rate, 15-20% decrease in cardiac output and 10-15% increase in systemic vascular resistance [2]. Figure 2 shows that for this blood loss, the baroreflex model integrated with the BioGears engine was able to achieve a 7% increase in systemic vascular resistance and an 18% increase in heart rate. While these fall short of the expected values, they do exhibit the required trends for a baroreflex model.

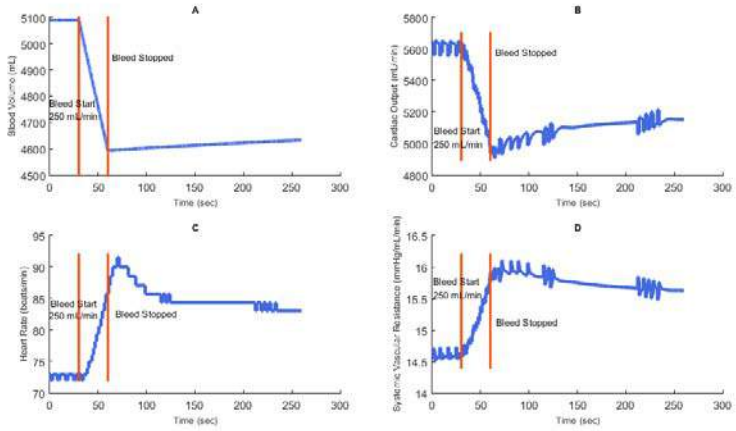

Figure 2: ***The baroreceptor response leads to an increase in heart rate and systemic vascular resistance in an attempt to maintain arterial pressure.***

DISCUSSION

Integration of the Ottenson, et al model was successfully accomplished. The model was a good fit using the constantly changing MAP from the BioGears Cardiovascular System. The tuned parameters were in line with those previously published. The model was further advanced by incorporating the effects of the drug and exercise models in BioGears. Without incorporating these effects, the baroreflex response would override any drug effects in the system causing an inaccurate solution. The addition of the baroreflex model in BioGears creates a more powerful overall model for calculating the physiologic response to trauma on the body.

Two limitations of this model are the lack of any unstressed volume effects and the inability to reach the desired magnitude of the responses for heart rate and systemic vascular resistance. These may both be tied to the over compliant vasculature of the cardiovascular model. The high compliance leads to issues with the central venous pressure when the heart rate and vascular resistance responses were increased. By incorporating unstressed volume in the model, the compliance may be reduced, allowing for a more accurate baroreflex model to be integrated. In addition to addressing these limitations, further nervous system features, such as the chemoreceptor response and general parasympathetic and sympathetic effects should be included in the whole body physiology engine to accurately model trauma to the human body.

ACKNOWLEDGEMENTS

BioGears® is funded by DMRDP JPC-1 and administered by U.S. Army TATRC MMSIC, under USAMRMC award number W81XWH-13-2-0068.

REFERENCES

[1] Guyton, A. C.,et al., "Textbook of medical physiology 11th edition Elsevier Inc." (2006).
[2] Hosomi H. et al *Am. J. of Phys.*, pages H607–H612, 1979.
[3] Ottesen, Johnny T., et al., Siam, 2004.
[4] Ottesen, Johnny T. J. of math. Boil. 36.1 (1997): 41-63.

Copyright 2016 The Organizing Committee for the 2016 Summer Biomechanics, Bioengineering and Biotransport Conference

SB^{3}C2016
Summer Biomechanics, Bioengineering and Biotransport Conference
June 29 –July 2, National Harbor, MD, USA
SB^{3}C2016-889

HEMODYNAMIC EFFECTS OF ASYNCHRONOUS PUMPING OF THE PENN STATE PULSATILE PNEUMATIC PEDIATRIC VAD

Bryan C. Good (1), Keefe B. Manning (1, 2)

(1) Department of Biomedical Engineering
Pennsylvania State University
University Park, PA, USA

(2) Department of Surgery
Penn State Hershey Medical Center
Hershey, PA, USA

INTRODUCTION

Congenital heart disease affects over 1.35 million newborns annually worldwide [1] with heart transplantation the only option for many. The use of mechanical circulatory support devices has been shown to decrease wait list mortality and improve the efficiency of organ utilization in children [2], however, the Berlin Heart EXCOR is currently the only approved pediatric ventricular assist device (PVAD) for use in the United States [3]. In 2004 the National Institutes of Health (NIH) started the National Heart, Lung and Blood Institute (NHLBI) Pediatric Circulatory Support Program and awarded five contracts with the goal of creating mechanical circulatory support devices for children ranging from 2-25 kg [2]. One of those contracts was awarded to Penn State for the development of a pulsatile PVAD based on the adult pneumatic Pierce-Donachy/Thoratec device.

PVADs are most commonly attached via an end-to-side anastomotic graft to the ascending aorta of the patient. One of the long-term failure methods of these grafts, however, is intimal hyperplasia (IH) occurring on the heel and toe of the anastomosis. Good *et al.*, in a computational fluid dynamics study, previously studied the hemodynamics and pulsatility of end-to-side anastomotic graft flow in a pediatric aortic model under both pulsatile and continuous PVAD support conditions [4]. This study showed significantly increased pulsatility with pulsatile support compared to continuous support. Additionally, other studies have shown the benefits of increased pulsatility to improved blood flow to the brain [5], kidneys [5], heart [6] and liver [7] in pediatric and neonate patients. The simulations by Good *et al.* were performed under the assumption of synchronized heart and PVAD beating which is rarely the case, however, with the Penn State PVAD. This device is most often run in "automatic mode" where as soon as the PVAD is filled, the next systolic phase begins after a 30 ms delay. The result is that the diastolic time and PVAD beat rate can vary substantially from beat to beat. Therefore, to fully understand the range of hemodynamics and resultant aortic pulsatility that can occur clinically, a range of asynchronous beating conditions need to be studied.

METHODS

A pediatric patient's aorta (NIH-Georgia Tech Fontan Database ID: CHOP007) is reconstructed using magnetic resonance imaging. To represent the outlet graft of a PVAD, a curved pipe (6 mm diameter) is attached to the ascending aorta in an end-to-side anastomosis configuration. A viscoelastic blood model designed specifically for pediatric blood was previously developed and validated [8] for different physiological hematocrits. For this study, the 40% pediatric hematocrit model is used.

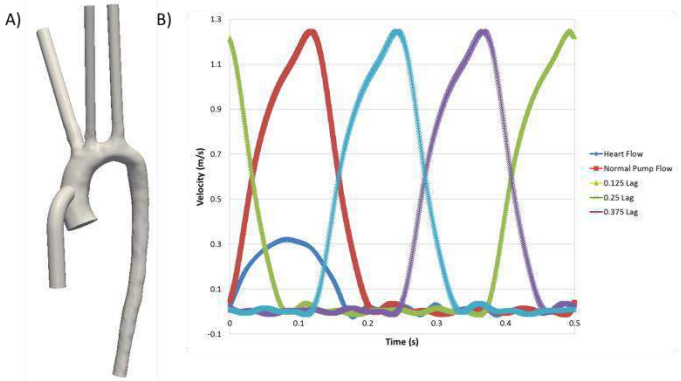

Figure 1: A) Pediatric aortic model with attached PVAD cannula. B) Heart and four PVAD waveforms used in study.

Copyright 2016 The Organizing Committee for the 2016 Summer Biomechanics, Bioengineering and Biotransport Conference

To study the effect of asynchronous heart and PVAD pumping, physiological pediatric waveforms acquired from an *in vivo* study of PVAD function in infant animal models [9] were applied at the inlets of the ascending aorta and PVAD cannula. Both waveforms are scaled to a beat rate of 120 beats per minute and flow rate of 0.5 liters per minute. In the first case, both waveforms are synchronized while in cases 2-4, the PVAD waveform is shifted 90˚ (0.125 s), 180˚ (0.25 s) and 270˚ (0.375 s) out of phase, respectively (Fig. 1).

To compare the pulsatility generated from each of the flow conditions, the surplus hemodynamic energy (SHE, ergs/cm^3) [10] is calculated at each of the inlets and outlets (Table 1). SHE is a measure of the extra energy generation from a flow pulsation (Eq. 1) and is based on the difference between the energy equivalent pressure (EEP, mmHg) (Eq. 2) and time-averaged pressure (TAP, mmHg) (Eq. 3):

$$\mathrm{SHE} = 1332(EEP - TAP) \quad (1)$$

$$\mathrm{EEP} = \frac{\int_0^T p \cdot Q \cdot dt}{\int_0^T Q \cdot dt} \quad (2)$$

$$\mathrm{TAP} = \int_0^T p \cdot dt \quad (3)$$

Where Q is the boundary flow rate (L/min) and p is the boundary pressure (mmHg). The hemodynamic parameters of time-averaged wall shear stress (TAWSS, dyne/cm^2) (Eq. 4) and oscillatory shear index (OSI) (Eq. 5) are important for vascular remodeling and were also compared between the different flow conditions.

$$\mathrm{TAWSS} = \frac{1}{T}\int_0^T WSS \cdot dt \quad (4)$$

$$\mathrm{OSI} = \frac{1}{2}\left(1 - \frac{\left|\frac{1}{T}\int_0^T WSS \cdot dt\right|}{\frac{1}{T}\int_0^T |WSS| \cdot dt}\right) \quad (5)$$

RESULTS

EEP, TAP and SHE are calculated for each inlet and outlet of the pediatric aorta model (Table 1). The highest pulsatilty (SHE) for each boundary occurs during the fully synchronized PVAD flow. For all of the outlets, (brachiocephalic, left common carotid and left subclavian arteries and descending aorta), SHE decreases as the PVAD's systole is shifted further away from the heart's systole. Approximate percent decreases in SHE of 58% are seen between the synchronized and 90˚ phase shift flows, 64% between synchronized and 180˚, and 67% between synchronized and 270˚.

Table 1: Pulsatility Parameters

		Synchronized Flow	90˚ Shift	180˚ Shift	270˚ Shift
Aortic Inlet	EEP	77.59	65.75	65.91	67.03
	TAP	62.74	62.14	61.72	61.82
	SHE	19780.08	4799.05	5572.32	6935.87
Cannula Outlet	EEP	79.46	72.90	68.84	68.30
	TAP	63.93	63.38	62.83	62.93
	SHE	20685.94	12678.62	7999.36	7145.75
Brachiocephalic	EEP	75.64	67.51	66.28	65.90
	TAP	61.75	61.63	61.31	61.40
	SHE	18504.89	7820.60	6626.43	5994.28
Left Common Carotid	EEP	74.73	67.00	65.90	65.51
	TAP	61.38	61.40	61.09	61.20
	SHE	17784.17	7459.01	6408.60	5747.43
Left Subclavian	EEP	73.23	66.12	65.14	64.87
	TAP	60.93	61.08	60.72	60.83
	SHE	16379.04	6718.10	5883.50	5371.88
Aortic Outlet	EEP	60.87	59.50	59.06	59.30
	TAP	58.27	58.38	58.37	58.34
	SHE	3474.38	1491.09	924.79	1279.82

High regions of OSI (> 0.2) indicate flow separation, retrograde flow and are prone to the development of IH. Three primary regions of high OSI are present in all of the PVAD flow conditions: on the floor of the anastomosis, on the toe downstream of the anastomotic graft and between the aortic branches (Fig. 2). All three of the asynchronous cases have higher OSI regions on the anastomotic floor and downstream of the anastomotic toe compared to the synchronized case with the 90˚ shifted flow experiencing the highest at each (0.44 and 0.48), respectively.

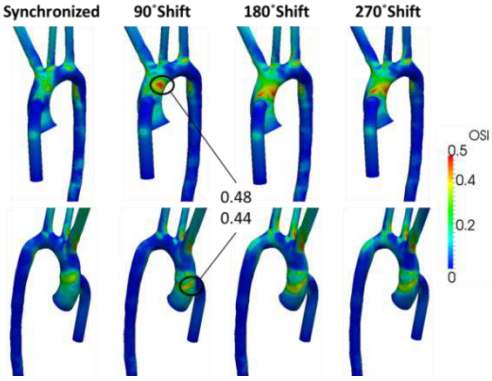

Figure 2: OSI from all four flow conditions.

Anastomotic graft failure has also been linked to increased stress at both the toe and heel. Large differences in TAWSS were seen near the anastomotic junction for all flow conditions with peak TAWSS occurring at the toe region in all cases. The highest TAWSS was during synchronized flow (528 dyne/cm^2) with TAWSS decreasing at the toe region for each of the asynchronous flows: 476, 426, and 432 dyne/cm^2, respectively.

DISCUSSION

Due to the automatic pumping of the Penn State pneumatic PVAD, it is important to study the hemodynamic and pulsatility parameters that can occur over the range of heart and PVAD flow combinations. Previous studies [4][11] have shown that synchronized pulsatile bypass leads to 5-10% decreases in SHE compared to a healthy pediatric patient at the aortic branches. However, due to the more common asynchronicity of the PVAD flow, the decrease in pulsatility is much more significant and could lead to problems in the patient's peripheral organ development. Additionally, the higher regions of OSI in the PVAD asynchronous flows just downstream of the anastomotic toe could lead to even higher rates of long-term graft failure than previously predicted.

ACKNOWLEDGEMENTS

This work was supported through NIH NHLBI HL108123. We also thank Ajit Yoganathan, PhD and Christopher M. Haggerty, PhD from the Georgia Institute of Technology for the pediatric aortic model.

REFERENCES

[1] Van der Linde, et al. *J Am Coll Cardiol*, 58(21):2241-2247, 2011.
[2] Baldwin J, et al. *Circulation*, 113(1), 2006.
[3] Almond C, et al. *Circulation*, 127(16), 2013.
[4] Good B, et al. C*VET*, 2015
[5] Undar A, et al. *Artif Organs*, 26, 2002.
[6] Chiang B, et al. *ASAIO J*, 39, 1993.
[7] Mori A, et al. *J Cardio-vasc Surg,* 28, 1987.
[8] Good B, et al. *ABME*, 2015.
[9] Pantalos G, et al. *ASAIO J*, 53(3), 2007.
[10] Undar A, et al. *Artif Organs*, 23, 1999.
[11] Yang N, et al. *CVET*. 1(1), 2010.

Copyright 2016 The Organizing Committee for the 2016 Summer Biomechanics, Bioengineering and Biotransport Conference

SB^{3}C2016
Summer Biomechanics, Bioengineering and Biotransport Conference
June 29 –July 2, National Harbor, MD, USA
SB^{3}C2016-890

PERFORMANCE EVALUATION OF A DEVELOPED ACOUSTIC IMPEDANCE DEVICE IN TUMOR SCREENING

A. Mohammadabadi (1), Q. Gu (1), A. M. LeBrun (1), M. Younis (2), L. Zhu (1)

(1) Department of Mechanical Engineering
University of Maryland Baltimore County
Baltimore, MD, USA

(2) Dept. of Computer Science & Electrical Engineering
University of Maryland Baltimore County
Baltimore, MD, USA

INTRODUCTION

Piezoceramic transducers (PZTs) have been widely used in industry to evaluate mechanical impedance of materials.[1] Imposing a constant voltage on a PZT exerts a constant force on the transducer, and it causes a PZT to vibrate when the PZT is connected to an alternating electric field. On the contrary, a vibrating PZT can produce output voltage signals; when these signals are analyzed by an I/O electronic circuit board, the impedance of the transducer can then be calculated based on the measured voltage and current. When the PZT is bonded with a testing material specimen, the impedance measured reflects the structural features of the specimen. In industry this is often used as a non-destructive evaluation (NDE) method for defect detection. Compared to other NDE techniques such as ultrasound, acoustic emission, x-ray, and thermography, PZTs have been considered cost-effective and user-friendly because of its simplicity and effectiveness in those applications.

In a previous study,[2] we have developed a low cost acoustic impedance device coupled with an I/O electronic circuit board and software to excite a PZT and record the generated electric signals. This device has been tested in fiberglass epoxy composites, wooden samples, and polymer specimen with an embedded crack. It has been shown that the device can detect the presence, shape and approximate dimension of the defect area.

In this study we test the performance of this device on detecting tumors embedded in agarose gels. Our hypothesis is that the structural and composition difference between the tumor and the gel would sufficiently result in variation in the measured acoustic impedance, and consequently can be used to detect the presence of the tumor located below the gel surface. The surface contour of the normalized impedance is mapped by scanning the device on the surface. The results are compared to the actual locations of the embedded tumors.

METHODS

Figure 1 shows the inner components of the transducer, consisting of: (1) a PZT disk of 10.2 mm in diameter and 2.0 mm in thickness (PZT-5A, American Piezo Ceramics, Mackeyville, PA), (2) a flexible copper clad laminate, (3) a frame manufactured by 3D printing, and (4) coaxial cables connected to an impedance evaluation board (AD5933 board, Analog Device Corporation, Norwood, MA). The board serves as both the actuator and the recorder of the electric signals. The experimental setup is shown in Figure 2.

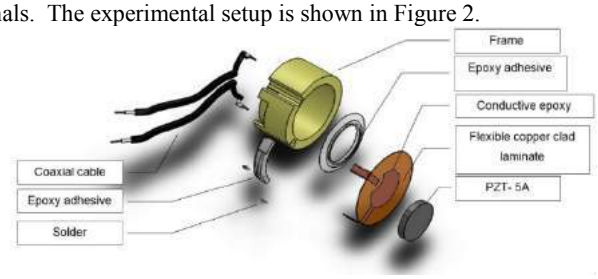

Figure 1: Exploded view of PZT transducer

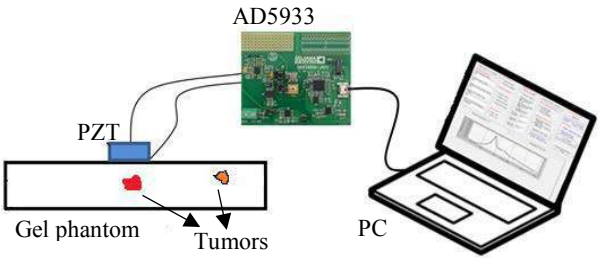

Figure 2: The experiment setup

Copyright 2016 The Organizing Committee for the 2016 Summer Biomechanics, Bioengineering and Biotransport Conference

Typically, the measured impedance is strongly affected by the frequency of the imposed alternating voltage. As shown in Figure 3, a plot of the impedance can be constructed via activating the transducer and recording the responses over a range of the frequency of the voltage. Among all frequencies, there is a peak impedance occurring at the resonance frequency of f_{res}. The impedance at the resonance frequency of the transducer bonded with a specimen (ΔZ in Figure 3) is compared to that of the transducer unloaded, i.e., in air (ΔZ_0 in Figure 3). The bonded specimen will influence the ratio $\Delta Z/\Delta Z_0$, therefore, a surface contour of the ratio can be plotted to show structural variation of a specimen for defect screening.

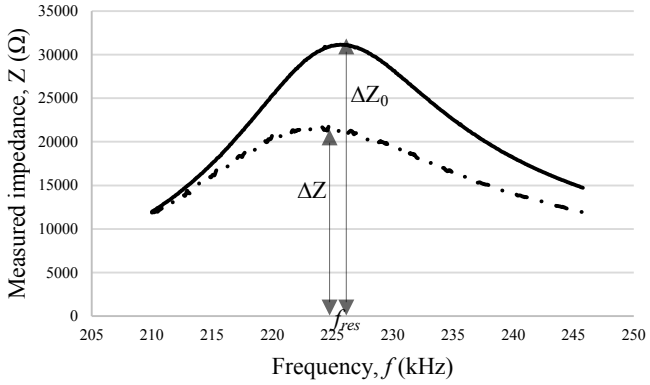

Figure 3: Impedance versus frequency for a loaded (ΔZ) and unloaded transducer (ΔZ_0)

A phantom gel (1% m/m) is prepared by dispersing agarose powder (Sigma-Aldrich, Saint-Louis, MO) in a 10% buffer solution (Tris-Borate EDTA, Gibco BRL, Rockville, MD).[3] The mixture is then heated until the agarose is completely dissolved. After being cooled at room temperature to 60°C, the solution is loaded into a container and cooled further to room temperature (25°C) until solidification. Four prostatic tumors are placed inside the container before the pouring in order to ensure that no bubbles or air gaps are formed in the gel. Tumors 2 - 4 are approximately 10 mm in diameter and tumor 1 is 20 mm in length and 10 mm in width. Tumor 1 is embedded 2 mm beneath the gel surface, tumors 2 and 3 are located deeper in the phantom gel (10 mm), and tumor 4 is the most deeply located in the group (20 mm from the surface). The total surface area to be scanned by the PZT device is 220 mm by 220 mm, gridded in 10×10 mm squares. Note that the actual surface area is much bigger, and we only scan the middle region of the surface to avoid the edge effect. A weight of 50 g is placed on the top of the transducer in order to ensure good and consistent contact between the transducer and the gel surface. The acoustic impedance at the resonance frequency is determined at each gridded square, resulting in a matrix of 22×22 of $\Delta Z/\Delta Z_0$ to cover the gel surface.

RESULTS

Figure 3 also gives the actual experimental recordings of the dependence of the impedance on the imposed frequency. The resonant frequency without loading is identified as 225 kHz. Although the resonant frequency may be affected by the structure of the specimen, the value of f_{res} with the specimen varies slightly in this study (222 kHz – 230 Hz). The impedance magnitude vs frequency curves with or without specimen attachment suggest that the deviation of the ratio of $\Delta Z/\Delta Z_0$ from unity is most evident at the resonant frequency. The ratio at this specific gridded square is 0.7.

The contour of the ratio $\Delta Z/\Delta Z_0$ mapped on the gel surface is presented in Figure 4. $\Delta Z/\Delta Z_0$ varies from approximately 0.70 to 0.86. The ratio at the location without tumor is very uniform, varying slightly as 0.850±0.007, implying repeatability of the sensor. The sensor fails to detect tumor 4; however, it could accurately locate the other three tumors. The gridded squares close to tumor 1 show the lowest ratio of 0.7 - 0.75, while presence of tumors 2 and 3 results in a relatively higher $\Delta Z/\Delta Z_0$ of 0.79, which is still below that of the normal gel of 0.85. The red circles in Figure 4 represent the actual tumor locations and shape. Tumor 4 is not detected because of its depth. Tumor 1 is the most evident; this may be due to the fact that it is located closer to the gel surface and has the largest size in the group.

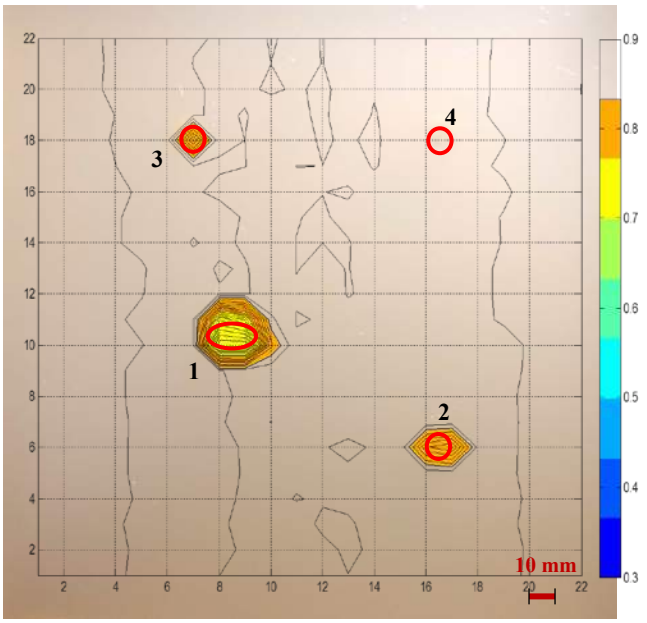

Figure 4: Superimposition of the tumors (red circles) and the contour plot of $\Delta Z/\Delta Z_0$ on the phantom surface.

CONCLUSIONS

In summary, we have developed and prototyped a PZT device for defect screening. The PZT device is tested to evaluate its potential for screening tumors in biomedical applications. In this preliminary study, we could correctly identify three of the four tumors embedded in a gel specimen. The detection fails when the tumor is located more than 10 mm below the gel surface. The results suggest that structural difference between prostatic tumors and normal gels is sufficiently large to generate detectable impedance variation, and demonstrate the feasibility of this approach when the tumor is located close to the surface and/or the tumor is big. Future studies are planned to further improve the device and assess its performance in detecting tumors embedded in actual tissue.

ACKNOWLEDGEMENTS

This study was supported by UMBC.

REFERENCES

[1] Anamdas and Soh, *J Intelligent Material Systems and Structures*, 21:41-59, 2010.

[2] Mohammadabadi A, MS thesis, University of Michigan – Shanghai Jiao Tong University Joint Institute, 2014.

[3] Salloum M, R Ma, D Weeks, and Zhu L, *International Journal of Hyperthermia,* 24(4):337-345, 2008.

Copyright 2016 The Organizing Committee for the 2016 Summer Biomechanics, Bioengineering and Biotransport Conference

SB^{3}C2016
Summer Biomechanics, Bioengineering and Biotransport Conference
June 29 –July 2, National Harbor, MD, USA
SB^{3}C2016-891

MODULATION OF ICE FORMATION CHARACTERISTICS DUE TO ADDITION OF TREHALOSE IN CRYOPROTECTANT

Jason Solocinski, Mian Wang, Quinn Osgood, Aaron Connolly, Nilay Chakraborty

Mechanical Engineering Department
University of Michigan Dearborn
Dearborn, MI, USA

INTRODUCTION

Cryopreservation is an important technology that is important to multitude of biomedical engineering technologies including tissue engineering and biotechnology. It is the only established mechanism to preserve cells and the technique involves subjecting the cellular samples to extremely low temperatures (-180°C), arresting nearly all cellular activity. However, the difficulty in the methodology arises from the fact that unprotected freezing typically results in lethal effect on cellular samples. Therefore cryoprotectants (CPAs), such as glycerol, dimethyl sulfoxide (DMSO), and polyethylene glycol have been used to aid the cells in surviving the cryoprocessing steps. A short review of cryopreservation protocols indicate that a solution of 10% DMSO is frequently used as CPA. However, most CPAs, including DMSO, are natively toxic at non-cryogenic temperatures. Reduction of CPA toxicity is an active area of research in cryobiology. Recently homologous disaccharides such as trehalose have been used as an additive to DMSO to obtain improved cryopreservation outcome. Herein, we study the biophysical effect of addition of such an additive to CPA, with a view to optimize preservation solutions using vibrational Raman microspectroscopy.

The technique of confocal Raman microspectroscopy is a highly sensitive spectroscopic technique, which when combined with hyperspectral imaging techniques can provide great insight of the molecular state and arrangement of a substance under different conditions. Therefore, coupling the techniques of low temperature microscopy with spatially correlated confocal Raman microspectroscopy the effects of addition of trehalose to CPA formulations can be characterized from a molecular point of view. In this study, high-resolution hyperspectral imaging technique was used to quantify and measure the spatial distribution of different contents (ice, DMSO, and trehalose) in freezing media at low temperatures. Special attention was paid to the effect of trehalose concentration on the formation and distribution of ice crystals during the freezing process.

METHODS

A 10% (v/v) DMSO solution was prepared in phosphate buffered saline. 300 mM α,α-trehalose was dissolved in the 10% DMSO solution to study the effect of use of trehalose as an additive.

The Raman measurements were conducted using a high-throughput confocal microscope and Raman microspectrometer combination (WITec GmbH, Germany). Raman spectra were collected using a high-sensitivity EMCCD camera (Andor Scientific, Belfast UK). A 532nm solid-state laser was used for excitation and images were collected using a 10X objective.

A custom-built stage adaptor was used to integrate a freezing stage cooled by liquid nitrogen (Linkam Scientific, Surrey UK) with the microscopy setup. The temperature of the CPA samples (10μL volume) was lowered in a controlled fashion (1°C/min) while collecting the spectral information at either -40°C or at -80°C. Hyperspectral scanning of the CPA solution was performed using a dimension of 50x50μm^2 with a spectral pixel area of 100x100. Each array scan was collected using an integration time of 0.3s. Following background subtraction and processing of the spectral cubes, the hyperspectral images of ice formation were generated by integrating the characteristic spectra of identified ice peaks. Each experiment was repeated 3 times and the confocal Raman images presented here are representative.

RESULTS

A visual analysis of the ice crystals formed in CPAs indicates that the pattern of ice crystal formation depends on both temperature and

Copyright 2016 The Organizing Committee for the 2016 Summer Biomechanics, Bioengineering and Biotransport Conference

CPA composition. At -40°C, the 10% DMSO freezing solution forms large ice crystals [Average area (A_{ave}) =~60μm^2] with sharp and angular boundaries, indicating that the ice crystals are fully developed. However, when 300 mM trehalose was added to 10% DMSO, the ice crystals have extraordinary round boundaries with significantly smaller area (A_{ave}=~22μm^2).

At -80°C, ice crystals have a relatively uniform distribution, and the same decreasing trend of crystal sizes for samples at -40°C. However, for 10%DMSO +300 mM trehalose at -80°C, the structures of ice crystals are more distinguished than the others: the ice crystals are extremely small (A_{ave}=~8μm^2) while forming a characteristic network-like structure.

While Figure 1 shows the hyperspectral images of the ice crystals, Figure 2 shows the distribution of ice and DMSO. Ice and DMSO demonstrate a mutual spatial exclusion. Trehalose, however, exists in both ice and DMSO dominant areas. In order to study the effect of trehalose on ice formation and exclude the influence from DMSO, a detailed spectral analysis was undertaken. The Raman spectra of the red line were collected from the position containing relatively high amounts of both DMSO and trehalose. The Raman spectra of the blue line was collected from the position where is bright in Fig.(2)-Ice, but dark in Fig.(2)-Trehalose, indicating relative high amount DMSO (or Ice) but low amount of trehalose. By comparing the Raman spectra of red line and blue line, it is found that the existence of trehalose did decrease the intensity of ice peak (~3130cm^{-1}), This finding suggestive of a mechanistic inhibition of ice crystal formation by trehalose.

DISCUSSION

It is widely believed that the cellular injury at low temperatures originate from two very different mechanisms that are determined by the rate of cooling [1]. At low cooling rates, the sharp rise of non-physiological extracellular osmotic environment (unfrozen mix) contributes to what is known as 'solution effects injury' [2]. At higher cooling rates the predominant injury mechanism is thought to be due to formation of lethal intracellular ice formation. While the rate of increase of osmolality of the unfrozen mix is a function of ice formation, we believe that the nature and characteristic of ice crystals formed [3, 4] during cooling also has an important role to play to modulate solution effects injury.

While homologous disaccharides such as trehalose are known for their osmoprotective capabilities, herein we demonstrate their ability to actively influence ice formation characteristics of CPAs, which in turn can influence solution effects injury mechanism during cryoprocessing.

Based on Figure 1 and Figure 2, it is suggested that the area of ice crystals decrease for the following two factors: concentration of trehalose increase and decrease of temperature. Furthermore, addition of trehalose results in ice crystals distribution having increased uniformity.

The low temperature microspectroscopic approach described here can provide valuable insights for optimization of the technique of cryopreservation at large. Preliminary research into cellular viability and metabolics suggest that trehalose introduced as an additive to standard CPAs has a beneficial impact over DMSO alone.

Figure 1: Confocal Raman Image of 10% DMSO solution with 0mM and 300mM trehalose separately at two different temperatures; -40 °C and -80 °C. All the images are generated by integrating the ice peak (~3140cm^{-1}) from Raman spectra. The stronger brightness of the area means the higher intensity of ice peak in Raman spectra.

Figure 2: Raman hyperspectral images and corresponding deconvoluted waveforms for ice, DMSO, and trehalose. signatures.

ACKNOWLEDGEMENTS

Authors would like to acknowledge the NSF grant 60157 and startup fund from UM Dearborn.

REFERENCES

[1] Mazur, P et al. *Exp Cell Research,* 71(2): 345-355, 1971
[2] Meryman HT et al. *Cryobiology,* 14(3): 287-302, 1977
[3] Dong, J et al. *Biophys J,* 99(8); 2453–2459, 2010
[4] Karlsson JO et al. 65(6):2524-36, 1993

Copyright 2016 The Organizing Committee for the 2016 Summer Biomechanics, Bioengineering and Biotransport Conference

SB^{3}C2016
Summer Biomechanics, Bioengineering and Biotransport Conference
June 29 –July 2, National Harbor, MD, USA
SB^{3}C2016-892

DISTAL EMBOLI FOLLOWING COVER ASSISTED THROMBECTOMY

Ju-Yu Chueh, PhD, Ajit S. Puri, MD, Matthew J. Gounis, PhD

Department of Radiology
University of Massachusetts Medical School
Worcester, MA, USA

INTRODUCTION

Recent randomized control trials have provided convincing evidence regarding the benefit from sentriever-mediated mechanical thrombectomy for appropriately selected acute ischemic stroke (AIS) patients.[1-3] The latest generation of clot retrieval systems are an effective AIS treatment, however, the use of clot retrievers can cause release of clot fragments. This may help explain why clinical outcomes lag technical success rates.

Our hypothesis is that the safety of thrombectomy devices as indicated by the risk of embolic shower may potentially be altered by the use of adjunctive devices that serve to encapsulate the occlusive clot. The objective of this study is the characterization of distal emboli generated during Solitaire thrombectomy in combination with the Lazarus Cover device (Medtronic Neurovascular, Irvine CA). The Cover is a nitinol braided mesh that inverts over the stentriever as it is extracted and closes around the stent to trap the clot within the device (Figure 1). It is compatible with the smaller and more navigable 5 or 6 Fr access systems, as compared to the stiff and large balloon guide catheters (8 to 9 Fr access) recommended for this procedure.

Figure 1: (A) The Cover device. (B) Clot debris is retained within the Cover device during clot

METHODS

A model system composed of a human vascular replica, clot model, and mock circulation flow loop was used for simulation of mechanical thrombectomy (Figure 2). A small-batch manufacturing process was used to build the vascular replica.[4] The vascular replica was modified to include the internal carotid artery (ICA), posterior communicating artery (PComA), anterior cerebral artery (ACA) and middle cerebral artery (MCA). The MCA had an average of 3mm and two M2 divisions joined distally to form a single output.

A hard, fragment-prone clot model was produced by clotting bovine blood using thrombin (2.5 NIHU thrombin/mL blood) and adding barium sulfate (1g/10mL blood). A 4mm x 5mm clot was injected into the silicone replica to form an MCA occlusion.

The silicone replica was connected into the flow loop with continuous monitoring of flow and pressure in the MCA to ensure that physiologically accurate flow rates were maintained. The flow loop contained a peristaltic pump, which was used to deliver saline via oscillatory throughout the system. Compressor clamps provided peripheral resistance; by adjusting the clamps, baseline flow conditions were matched to normal human phase contrast MR measurements for each vessel. Saline flowing through the MCA and the ACA was collected for particle analysis. Clot fragments greater than 1000μm were manually separated from the sample with a pipette and the number and Feret diameter of each fragment was recorded. Emboli smaller than 1000μm were characterized using a Coulter counter (Multisizer 4; Beckman Coulter, Brea CA).

Apertures with diameters of 400μm and 2000μm were employed in order to provide a complete particle size distribution analysis (8-1000μm). Five bin categories were used for analysis of distal emboli: fragments with diameter >1000μm, 200-1000μm, 100-200μm, 50-100μm, and 8-50μm. Repeat measurements from a single experiment for the smaller particles were reported as average, while the number of clot fragments with size >200μm were summed due to the infrequency of observation.

Three treatment strategies were tested, namely (1) Solitaire thrombectomy through an 8Fr Cello balloon guide catheter (BGC;

Copyright 2016 The Organizing Committee for the 2016 Summer Biomechanics, Bioengineering and Biotransport Conference

Medtronic neurovascular) with the tip placed in the cervical ICA (CONTROL #1); (2) Solitaire thrombectomy through a 6Fr Envoy conventional guide catheter (CGC; Cordis, Miami Lakes, FL) with the tip placed at the cervical ICA (CONTROL #2); and (3) Solitaire thrombectomy with the Lazarus cover device deployed. In both of the control groups, aspiration was performed during thrombectomy using two 25cc syringes connected to a 3-way stopcock through either the BGC or the CGC. Aspiration was not performed in the Cover group. After deployment of the Solitaire, the microcatheter was removed and the rapid-exchange Cover was delivered to the proximal MCA. The Cover device became unsheathed as the guide catheter was withdrawn. Eight experiments were carried out in each group, and the maximum number of thrombectomy attempts was limited to three per experiment.

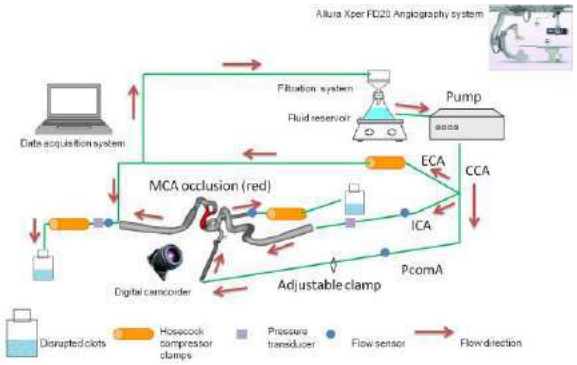

Figure 2: The schematic illustration of the flow loop.

RESULTS

Total number of distal emboli:

Figures 3A shows that, on average, mechanical thrombectomy with the BGC reduced the total embolic particle creation by 2-fold compared to the CGC technique ($p>0.05$, Kruskal-Wallis test). The BGC technique offered a 1.6-fold improvement in the total number of emboli compared to the Solitaire with Cover technique ($p>0.05$, Kruskal-Wallis test). Importantly, it should be noted that 99% of the emboli had a size <200µm (average size: 9.4µm) (Figure 3B).

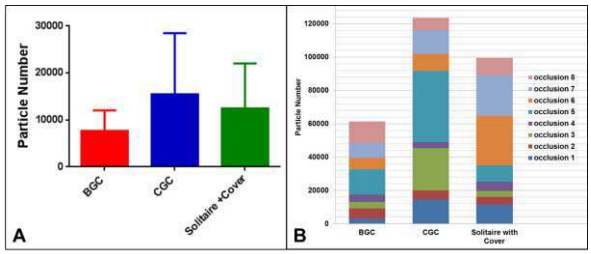

Figure 3: (A) Quantitative measurement of all clot fragments (>8 µm) produced during mechanical thrombectomy. (B) A stacked column graph shows the total number of emboli with size between 8-200µm generated during the procedure.

Number of emboli with size >1000µm:

The rate of forming clot fragments >1000 µm from the hard clot model was increased with the use of the CGC ($p<0.05$, Kruskal-Wallis test) (Figure 4A). Formation of large emboli with size greater than 1000µm occurred in 7 out of 8 cases in the CGC group, versus 2 or 3 out of 8 cases in the other groups. There was no significant difference in the number of large emboli (> 1000µm) between the BGC and the Solitaire with Cover ($p>0.05$, Kruskal-Wallis test). The size of these clot fragments ranged from 1mm to 5mm.

Number of emboli with size between 200-1000µm:

Similarly, in the size range between 200-1000µm, thrombectomy with the use of CGC generated the most number of distal emboli compared to all the other treatment strategies ($p<0.05$, ordinary one-way ANOVA) (Figure 4B). It appeared that for emboli with size between 200-1000µm, the Cover device was comparable to the BGC and superior to the CGC approach. The average size of the clot fragments within this size range was 237.4µm.

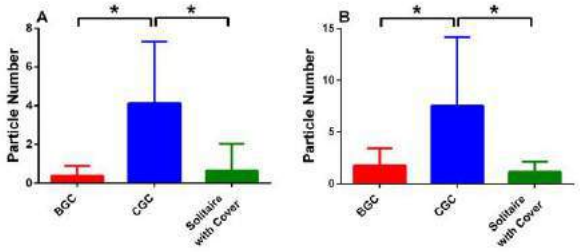

Figure 4: Comparisons of emboli number (Figure 4A: >1000µm, Figure 4B: 200-1000µm) between 3 different clot removal strategies.

Number of emboli with size between 8-50µm, 50-100µm, and 100-200µm:

On average, in the size range between 8-50µm, mechanical thrombectomy via BGC generated the least amount of clot fragments, followed by Cover and CGC ($p>0.05$, Kruskal-Wallis test). The Solitaire/Cover system, as compared to the BGC, was more efficient in reducing the risk of 50-100µm and 100-200µm clot fragmentation ($p>0.05$ in both size ranges, Kruskal-Wallis test).

Distribution of clot fragments:

Approximately half of the disrupted clots with size greater than 1mm were found in the previously unaffected area (ACA, 55%) in the CGC group, versus 40% in the Solitaire with cover group and 33% in the BGC group. On average, 80% of the clot fragments with size between 200-1000µm travelled through the MCA. In the size range between 8-200 µm, the clot fragments were evenly distributed into the MCA and ACA regardless of the treatment approaches (47% in the ACA versus 53% in the MCA).

DISCUSSION

The results of this in-vitro study demonstrate that the new treatment approaches, the Lazarus Cover, is comparable to the BGC technique in terms of risk of distal embolization. The Cover technique is statistically superior to the CGC method in several hard clot subgroups of clinical relevance. If emboli protection with the Cover is translated clinically, this technology could provide a significant advantage to the standard BGC in terms of access size and navigability (current BGC devices are stiff and require 8 or 9 Fr access). Without aspiration, thrombectomy with the Cover allows continuous flow restoration during the clot retrieval procedure. In conclusion, the risk of embolic shower can potentially be altered by the use of adjunctive devices that serve to encapsulate the occlusive clot. When encountering hard clot, the use of the Cover may reduce the risk of distal embolization and may be considered.

REFERENCES

[1] Berkhemer, OA et al., N Engl J Med. 372:11-20, 2015.
[2] Goyal, M et al., N Engl J Med. 372:1019-1030, 2015.
[3] Saver, JL et al., N Engl J Med. 372:2285-2295, 2015.
[4] Chueh, JY et al., AJNR Am J Neuroradiol. 30:1159-1164, 2009.

Copyright 2016 The Organizing Committee for the 2016 Summer Biomechanics, Bioengineering and Biotransport Conference

SB^{3}C2016
Summer Biomechanics, Bioengineering and Biotransport Conference
June 29 –July 2, National Harbor, MD, USA
SB^{3}C2016-893

QUANTIFYING CIRCUMFERENTIAL AND WALL SHEAR STRESS IN A DEVELOPING EMBRYONIC HEART USING NON-INVASIVE TECHNIQUES

David L. Bark Jr. (1,2), Brennan Johnson (2), Deborah Garrity (3), Lakshmi P. Dasi (1,2)

1) Department of Mechanical Engineering
Colorado State University
Fort Collins, CO, United States

(2) School of Biomedical Engineering
Colorado State University
Fort Collins, CO, United States

(3) Department of Biology
Colorado State University
Fort Collins, CO, United Staets

INTRODUCTION

As the first developing organ, the heart produces flow- and pressure-derived mechanical stress that provides critical feedback to cardiovascular cells. Due to the importance of stress to development, *in vivo* cardiovascular flow has been analyzed in a number of embryonic animal models [1]. However, pressure, which produces circumferential stress, has been given much less attention, despite its importance in cardiovascular modeling and remodeling.

Explicit pressure estimates can be used to non-invasively quantify the pressure field based on velocity field data. One approach is to integrate the pressure gradient in the momentum equation [2,3]:

$$\partial_i P = -\rho\left(\frac{\partial u_i}{\partial t} + \partial_j u_j u_i + \nu\left(\partial_k \partial_k u_i\right)\right), \quad (1)$$

where P is pressure, ρ is the fluid density, u_i is the ith component of the velocity vector, and ν is the kinematic viscosity. This method has been proven accurate for moving boundaries in biological flow, but has been primarily used for high Reynolds number (Re) [2].

Here, we use the pressure estimate in Eq. 1 to quantify the wall shear stress (WSS) and circumferential stress in the developing heart based on micro-particle imaging velocimetry (μPIV) data in a zebrafish embryonic model. We apply this technique at 48 hours postfertilization (hpf). This period of mid-cardiogenesis is especially vulnerable to stress because the morphology of the organ is rapidly changing as cardiac looping and chamber ballooning proceed [4].

METHODS

Wild-type zebrafish (Danio rerio) fertilized eggs were collected, incubated, and dechorionated at approximately 24 hpf. Embryos were imaged under a bright-field stereomicroscope (Olympus SZX12). Images were acquired at 1500 fps with a resolution of 1310 pixels/mm using a high speed camera (Photron FASTCAM SA3).

The pressure field for this study is quantified by integrating Eq. 1. Each integration path, extending circumferentially, begins at a node and ends at a fluid-solid boundary, Fig. 1A. Similar to Liu and Katz, we use the mean value of multiple integration paths [3]. The mean value is updated in multiple iterations until the pressure field converges to a solution, as defined by a maximum pressure residual of less than $1x10^{-3}$. A first order upwind spatial integration method is used for the pressure integration. We assume a Newtonian viscosity of 8 mm^2/s after evaluating multiple alternative non-Newtonian models.

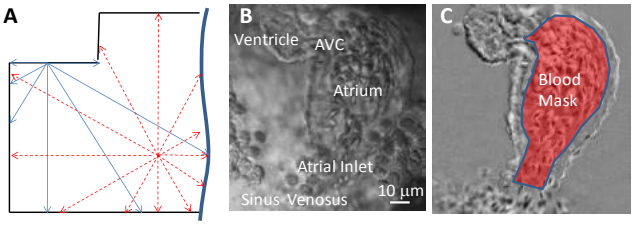

FIGURE 1: A) Pressure integration paths single nodes to a fluid-solid boundary. B) A raw image of the embryonic heart at 48 hpf with anatomical labels. C) Mask applied to the heart image after background subtraction to define a region of fluid.

2D μPIV is used to quantify the entire flow field of the atrium through DaVis 7.2 software (Lavision, Germany), Fig 1B. An ensemble average of the velocity field is taken for 5 cardiac cycles through the cross correlation of 4 image pairs at each cycle. A mask is used to reduce bias error in velocity calculations, Fig. 1C. Cross-correlation vectors are obtained with a 16x16 pixel interrogation

Copyright 2016 The Organizing Committee for the 2016 Summer Biomechanics, Bioengineering and Biotransport Conference

window, followed by an 8x8 interrogation window, both with 50% overlap. The final pass interrogation window approaches the size of erythrocytes, which are used as the seeding particle for the fluid domain. Erythrocytes as a seeding particle can result in an underestimation of the centerline velocity, but are used to minimize the invasiveness of our technique.

Lamé's equation is used to estimate spherical stress in the cardiac wall, assuming an incompressible Hookean material [5]:

$$\sigma = \frac{PR_i^3}{R_o^3 - R_i^3}\left(\frac{2r^3 + R_o^3}{2r^3}\right), \quad (2)$$

where r is the atrial radius, while R_i and R_o are the inside and outside radius respectively. We aim to extend the analysis without the limiting assumption of a Hookean material. Furthermore, we assume that the pressure outside of the heart is approximately equal to pressure at the sinus venosus.

Lastly, we calculate WSS at the atrioventricular canal (AVC) since it may provide a critical cue for valve formation:

$$WSS = \frac{\Delta P}{L}\frac{R_i}{2}, \quad (3)$$

where $\Delta P/L$ is the pressure gradient across the AVC. Eq. 2 is obtained from a basic control volume analysis of flow in the AVC.

RESULTS

Velocity across the atrial inlet and the AVC are shown in Fig. 2A over the course of the cardiac cycle [mapped on a scale of 0-1.0, with 0 representing the onset of atrial systole]. Velocity is calculated through a technique we previously developed [6]. The figure shows an initial increase in velocity across the AVC, which occurs as the atrium contracts. The peak velocity is ~5 mm/s, corresponding to a Re=<v>D/ν of 0.017 and a Womersley number, $\alpha=D(\omega/\nu)^{1/2}$ of 0.014, assuming a viscosity of 8 cP. Subsequently, the AVC closes off, stopping flow across it. Simultaneously, the atrium begins expanding as blood flows through the atrial inlet. The velocity reaches a peak of ~3 mm/s as the atrial inlet, corresponding to a Re of 0.012 and a α of 0.015. Comparatively, velocity vectors obtained through μPIV are shown in Fig. 2B at a time period of 0.2. The peak velocity across the AVC is 4 mm/s, as opposed to 5 mm/s seen through spatiotemporal plot analysis used for Fig. 2A. Pressure contours are also plotted in Fig. 2B, demonstrating that there is a 0.2 mmHg pressure drop across the AVC at a period of 0.2. The plotted pressure is relative to an arbitrary value.

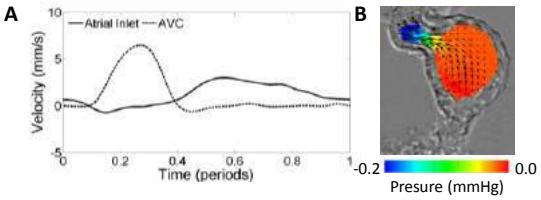

FIGURE 2: A) Velocity with respect to time at the atrial inlet and at the AVC. b) Velocity vectors and pressure contours at a time period of 0.2, corresponding to the beginning of atrial systole.

Pressure is used to estimate circumferential stress and WSS from Eq. 2 and 3 respectively. Circumferential stress is plotted from the endocardium to the myocardium at the middle of the atrium at a period of 0.2 in Fig. 3. Circumferential stress reduces from ~0.3 mmHg at the endocardium to ~0.3 mmHg at the myocardium. Comparatively, the peak WSS from Eq. 3 is 40 dynes/cm^2 or 0.03 mmHg at the AVC.

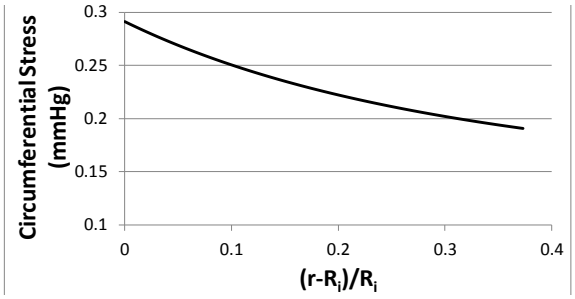

FIGURE 3: Circumferential stress from the endocardium (0) to the myocardium (0.37).

DISCUSSION

This is the first study to our knowledge to estimate stress and pressure in the developing heart through empirical noninvasive imaging. We also show that the atrium appears to contract uniformly creating a uniform pressure in the atrium, thereby creating a bolus of blood that enters the ventricle.

In the current study, we show that the pressure drop across the AVC can reach ~0.2 mmHg during atrial systole. In comparison, the peak pressure drop across the AVC in a chick embryo for a similar stage in development is ~0.2-0.3 mmHg [7, 8]. Therefore, our pressure estimation matches closely with physically measured values. The pressure drop across the AVC is also approximately equal to the gauge pressure in the atrium, justifying its use for Eq. 2.

Our circumferential stress calculation matches well with a computational model from Taber et al. [9]. They approximate the peak circumferential stress as 0.5 mmHg. Also, our WSS value matches well with Jamison et al., who show a value of 40 dynes/cm^2 at 72 hpf [10]. Therefore, our values provide reasonable estimations of circumferential stress and WSS despite the numerous assumptions behind Eq. 2 and 3.

Our study is limited to a 2D analysis. Therefore, there can be an error in our pressure estimation due to out-of-plane flow. We calculated the velocity divergence to determine where this effect is most prominent and we found this to occur at the AVC. Furthermore, we assume highly simplified geometry and simplified conditions for Eq. 2 and 3. Despite this, our results match well with the literature. Also, our μPIV calculation depends on a large seeding particle and viscosity is difficult to define.

The current results can be extended to estimate stress throughout development to relate morphological changes to changes in stress, which is an important step in defining mechanotransduction during cardiac development.

ACKNOWLEDGEMENTS

We acknowledge funding from the National Science Foundation (Award# 1235305), program director Dr. David Fyhrie.

REFERENCES

[1] Hove, JR et al., *Nature*, 421:172, 2003.
[2] Dabiri, JO et al., *J. Exp. Biol*, 217:331, 2014.
[3] Liu, X et al., *Exp. Fluids*, 41:227, 2006.
[4] Johnson, BM et al., *BMMB*, 14:1379, 2015.
[5] Love, AEH, *Cambridge University Press*, 2013
[6] Johnson, BM et al., *J Biomech Eng*, 135:041006, 2013b.
[7] Hu, N et al., *Circ Res*, 65:1665, 1989.
[8] Hu, N et al., *Am J Physiol Heart Circ Physiol*, 269: H1359, 1995.
[9] Taber, L et al., *J Elasticity*, 61:165, 2000.
[10] Jamison, RA et al., *PLOS ONE*, 8: e75722, 2013.

Copyright 2016 The Organizing Committee for the 2016 Summer Biomechanics, Bioengineering and Biotransport Conference

SB^{3}C2016
Summer Biomechanics, Bioengineering and Biotransport Conference
June 29 –July 2, National Harbor, MD, USA
SB^{3}C2016-894

REMODELING BY FIBROBLASTS ALTERS THE RATE-DEPENDENT MECHANICAL PROPERTIES OF COLLAGEN

B. Babaei (1), A. Davarian (2), K.M. Pryse (2), W.B. McConnaughey (2), E.L. Elson (1,2), G.M. Genin (1)

(1) Department of Mechanical Engineering & Materials Science, Washington University in St. Louis, St. Louis, Missouri, USA

(2) Department of Biochemistry & Molecular Biophysics, Washington University School of Medicine, St. Louis, Missouri, USA

INTRODUCTION

Interactions between living cells and their mechanical environments are central to a host of physiologic and pathologic events ranging from development to metastatis to wound healing. Fibroblasts remodel their extracellular neighborhood considerably when activated, stiffening and compressing their extracellular matrix (ECM) environment [1, 2]. During remodeling, fibroblasts secrete ECM proteins, including collagens, proteoglycans, glycoproteins, and proteases, and cross-linking proteins and enzymes [1, 3]. This remodeling changes the tissue as a whole by establishing a network to link and organize individual cells [4]. Rate-dependent mechanical responses underlie the progression of critical pathologies such as fibrotic cardiomyopathy and congestive heart failure. Although several studies have estimated the effects of this remodeling on ECM elasticity, little is known about the viscoelastic effects of ECM remodeling.

The goal of this study was to quantify how fibroblasts modulate ECM viscoelastically and contribute to tissue mechanics viscoelasticity. We studied these effects by performing viscoelastic relaxation tests on engineered tissue constructs (ETCs) at three different time points. ECM viscoelasticity was evaluated by treating ETCs with deoxycholate, a mild detergent which dissolves cell membranes and disperses cytoplasmic structures such as the cytoskeleton. Tests were interpreted using a discrete spectral generalized Maxwell approach [5], which yields both elastic moduli and viscoelastic relaxation finite time constants. Results showed that cells actively adapted the ECM, and that cells relax at multiple timescales, including one that is fast compared to those of the ECM.

METHODS

Engineered tissue construct (ETC) preparation and test protocol. ETCs were synthesized using procedures described in detail elsewhere [6]. ETCs were kept in an incubator for 24, 48 or 72 hours to allow the cells to remodel the collagen. Three specimens were tested at each of the three remodeling times, a total of nine specimens. Tissues were allowed 60 minutes to accommodate to the new media before the stress-relaxation test. Following 10 minutes of force monitoring to establish a baseline, tissues were preconditioned with 5 sequential cycles of 20% axial stretch, followed 30 minutes of recovery. Thereafter, ETC rings were stretched 10% at 20%/s then held isometrically for 3600 s while force was recorded at 50 Hz. Specimens were returned to their baseline configurations and allowed to recover for 30 minutes. To test the contribution of the remodeled ECM to viscoelastic behavior of the ETCs, DMEM+HEPES was replaced with 0.05% w/v deoxycholate in PBS (pH 7.4). After a 60 minute incubation, the stretch-and-hold protocol was then repeated.

Measurement of ETC dimensions and DNA quantification.
Widths and thicknesses of each ETC were measured using confocal microscopy (LSM 510, Zeiss). We synthesized an additional 9 specimens (three each at 24, 48, and 72 hours of incubation) to estimate the final cell concentration in ETCs using a total DNA quantification assay.

Analysis of stress-relaxation data, staining and imaging.
The generalized Maxwell model was used to interpret the relaxation behavior of the specimens tested. We used a discrete spectral implementation described elsewhere [5], based on a large number (n= 1000) of exponential terms. The actin cytoskeletons of the fixed tissues were stained with rhodamine phalloidin (Sigma, St. Louis, MO) and imaged using a Zeiss 510 confocal microscope and a 40x, 1.2 NA, water objective.

Copyright 2016 The Organizing Committee for the 2016 Summer Biomechanics, Bioengineering and Biotransport Conference

RESULTS

Over three days of remodeling, cells proliferated and compressed the ETCs (Fig. 1a), with the initial cross-sectional area decreasing from 13.8×10^{-6} m^2 to 1.01×10^{-6} m^2 during the first 24 hours, and to 0.51×10^{-6} m^2 after 72 hours. The starting population of 250,000 cells (in 0.5 ml of solution) was sustained for 24 hours, and decreased to about 190,000 after 72 hours (Fig. 1b).

The analysis showed subtle but significant transitions in some of the viscoelastic relaxation time constants over the course of ECM remodeling, with a slower finite time constant (~7000 s) emerging between 24 and 48 hours of remodeling, and with some faster time constants (0.5-2 s) merging into a single time constant between 48 and 72 hours of remodeling. As discussed below, these changes were retained following deoxycholate treatment, indicating that the changes occurred in the ECM rather than in the cells. In the deoxycholate treated ETCs, with cells eliminated, the 0.2 s time constant disappeared at all time points. At 24 hours, the ~8 s time constant disappeared with deoxycholate treatment, and at 48 and 72 hours, the 30 s time constant disappeared (only 72-hour-tissue results are presented, fig. 2). The elastic moduli decreased for the deoxycholate treated ETCs with respect to control samples (Figs. (c) and (d)) at finite time constants faster than 100 s. Variance amongst the relaxation spectra was greatest for the 48-hour time point.

Imaging of 24-hour-old-old ETCs showed a disordered collagen fibers (representative image, Fig. 3a. For 48-hour-old ETCs, a transitional state could be observed in which collagen fibers were more organized and began to exhibit a preferred orientation (representative image, Fig. 5b. Finally, a very compact pattern of collagen fibers appeared in 72-hour-old ETCs (representative image, Fig. 3c). This compact pattern could be found at a multitude of locations throughout the ETCs, not only close to the edges.

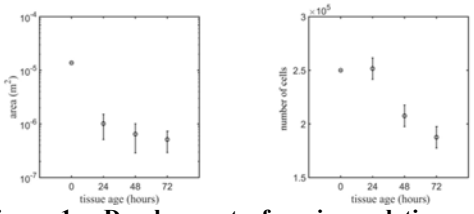

Figure 1: Development of engineered tissue constructs (ETCs) over 72 hours, including variations (a) of their cross-sectional area, (b) of the number of cells within them.

DISCUSSION

Cells reduced ETC cross-sectional area as they collectively remodeled the ECM (Fig. 1). Responses of the tissue constructs to mechanical stretching were quantified using a spectral approach that, through integration with tests involving specific inhibitors, quantified the rheological responses of the cells and extracellular matrix (ECM) over a range of loading time constants. The decrease in the minimum stress of the deoxycholate-treated with respect to non-treated (control) ETCs shows that at least a part of the time-independent (elastic) behavior of tissues, which corresponds to the single spring in the generalized Maxwell model, is due to elastic contributions of the cells. Two of the spectral peaks disappeared following treatment with deoxycholate (those at 0.2 s and 30 s for 48 hour and older specimens; 0.2 s and 8 s for 24-hour-old specimens) indicating that these are attributable to cells or cell-ECM interactions. Many consequences of the interactions between cells and ECM were evident by observing the ETCs. Reflectance mode confocal microscopy, in which collagen fibers of ETCs can be observed directly without staining and with good axial and lateral resolution, showed that collagen fibers remodeled over time into a network showing elements of structural organization (Fig. 3).

The results showed for the first time that cell and ECM viscoelastic contributions to tissue remodeling can be dissected using integrated mechanical testing, spectral analysis, and biochemical treatments. Results further showed that fibroblasts remodel collagen in a way that emphasizes the damping at a frequency associated with heart contraction in humans, suggesting that viscoelastic remodeling associated might play a role in the diastolic filling disorder known to arise with late stage cardiac fibrosis.

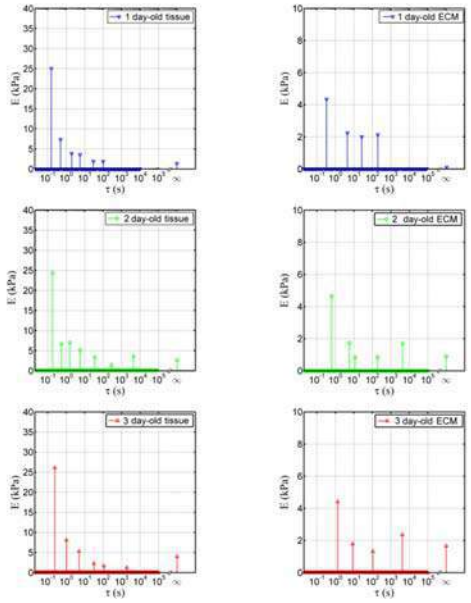

Figure 2: Viscoelastic relaxation spectra of ETCs tested in nutritional medium (left column) or nutritional medium plus deoxycholate to lyse cells (right column).

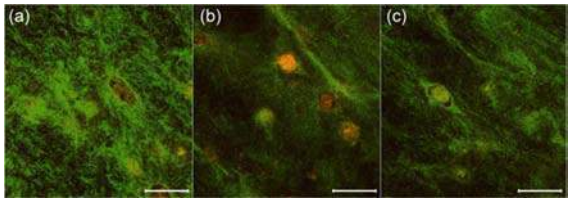

Figure 3: A confocal reflectance microscopy image of collagen fibers (green) superimposed upon images of cells (red) in engineered tissue constructs. During the remodeling, the cells established a connective network, with some clusters of adjacent cells forming ring-like structures. The network appeared to link and organize individual cells in the ECM. Mechanical signals sent to amongst cells over a timescale faster than the fastest time constant in these collagen bundles are not attenuated by the bundles. Scale bar, 50 μm.

REFERENCES

[1] Chiquet M et al., Matrix Biol. 2003;22(1):73-80.
[2] Barocas VH et al., J Biomech Eng. 1995;117(2):161-70.
[3] Prajapati RT et al., Wound Repair Regen. 2000;8(3):238-46.
[4] Wang H et al., Biophys J. 2014;107(11):2592-603.
[5] Babaei B et al., J Mech Behav Biomed Mater. 2015;55:32-41.
[6] Wakatsuki T et al., Biophys J. 2000;79(5):2353-68.

Copyright 2016 The Organizing Committee for the 2016 Summer Biomechanics, Bioengineering and Biotransport Conference

SB³C2016
Summer Biomechanics, Bioengineering and Biotransport Conference
June 29 –July 2, National Harbor, MD, USA
SB³C2016-895

MICROSTRUCTURAL ANALYSIS OF EARLY EMBRYONIC AORTIC ARCH MORHPHOGENESIS

S. Samaneh Lashkarinia, Senol Piskin, Selda Goktas, Kerem Pekkan

Department of Mechanical Engineering
Koc University
Sariyer, Istanbul, Turkey

INTRODUCTION

Embryonic cardiovascular (CV) mechanics is an emerging field that could unravel the interactions between the vessel microstructure and the mechanical loading that govern the prognosis of congenital heart defects (CHD). Unlike mature CV systems, the embryonic vasculature represents a primitive, disorganized but highly dynamic soft tissue microstructure whose mechanical loading and the corresponding microstructural organization are yet to be defined at the key embryonic time-points. Additionally, intervening in the CV flows alters the tissue morphology that correlates well with differences in local shear stress profiles, pressure and CV activity [1].

Recently, embryonic CV tissue growth models attracted attention due to their potential to predict vessel morphology and the physiological vascular stresses simultaneously [2, 3]. For example, Shi et al. suggested that cardiac looping mechanisms based on the computed stresses within the heart tube in early chick embryo [4]. Likewise, Kowalski et al. presented a computational model of aortic arch formation as a function of hemodynamic loading and the outflow tract orientation [5]. In these studies, one key challenge involves the drastic variation of homeostatic growth-equilibrium stress states during CV development.

In our earlier work, we have investigated the hemodynamic wall shear stress (WSS) loading at the major pairs of embryonic aortic arches using subject-specific computational fluid dynamics (CFD) during the three Hamburger Hamilton (HH) stages 18, 21 and 24 [5, 6]. Similar to the WSS dependency, the embryonic soft tissue mechanical stress levels at these stages could also vary significantly and can correlate with the dynamic microstructural configuration of embryonic arch vessels, at an unknown degree. Thus, a finite element solid model will complement our earlier hemodynamic studies and will shed light to the complex growth and remodeling process of the soft tissue in the embryonic aortic arches.

METHODS

The two key embryonic stages of HH 18 and 24, embryonic day 3 and 4 respectively, are investigated. During these stages, arches II, III and IV at HH18 and arches III, IV and VI at stage HH24 exist. Based on the Optical Coherence Tomography (OCT) measurements of vessel diameter and thickness [5], an idealized three-dimensional (3D) finite element method (FEM) (Ansys, Inc.) model of aortic sac is generated for both left and right laterals (Figure 1) separately.

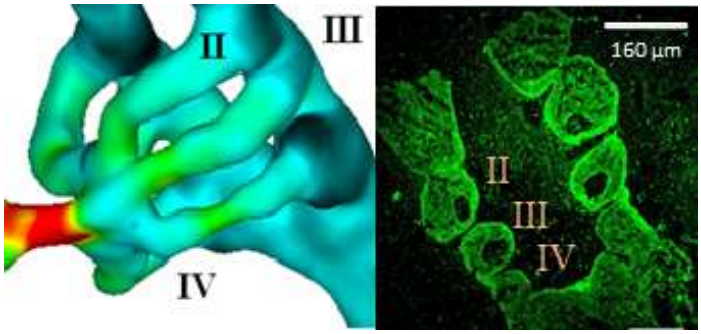

Figure 1: 3D subject specific embryonic arch model (left figure) and the corresponding confocal scan of Collagen type I distribution at HH stage 18 displaying both the left and right arch laterals through the aortic sac (right figure).

FEM model geometries were meshed with 2nd order tetrahedral elements. Fixed support boundary conditions are specified at arches'

Copyright 2016 The Organizing Committee for the 2016 Summer Biomechanics, Bioengineering and Biotransport Conference

connection edges and at the posterior end of arch III for HH18 model, corresponding to arch IV at HH24. While more complex models are investigated for embryonic soft tissue, simple mechanical models can describe embryo mechanics acceptably well [7]. Therefore, a linear elastic material model with a Young's modulus of 1000 Pa and a Poisson's ratio of 0.49 was used [7, 8]. Effect of increased collagen density is simulated by increasing the material parameters (Young's modulus 750 Pa and Poisson's ratio 0.4). Arterial pressure is estimated to be 1 mmHg based on literature measurements in dorsal and vitelline arteries [9, 10] and a recent numerical simulation study of ventricle outflow tract [11].

Using a wide-field of view time-lapsed confocal scanning system (Nikon AZ100-C2+) the fluorescence images of elastin, VEGF and collagen types I, III and IV fiber microstructure and cell number of the chick embryo aortic arch are acquired through immunofluorescence (IF) staining (Figure 1).

RESULTS

Total deformation, equivalent stress (von Misses) and soft tissue shear stress distributions due to pressure loading were calculated by FEA. For comparative purposes, no residual stresses are included. A representative von Misses stress distribution of the right aortic arch model of stage HH24 and the corresponding collagen type I distribution are given in Figure 2. This figure allows us to make a qualitative comparison between stress level and collagen fiber density. Interestingly, first time in literature, we observed that the high tissue stress regions correspond to the high collagen staining intensity. These regions also associated with high VEGF expression and high cell density (data not shown). Stress distribution at other stages showed similar trends but not included due to brevity. Total tissue strains alter between 10 to 15% for different models, which correlated well with our time-lapsed OCT observations.

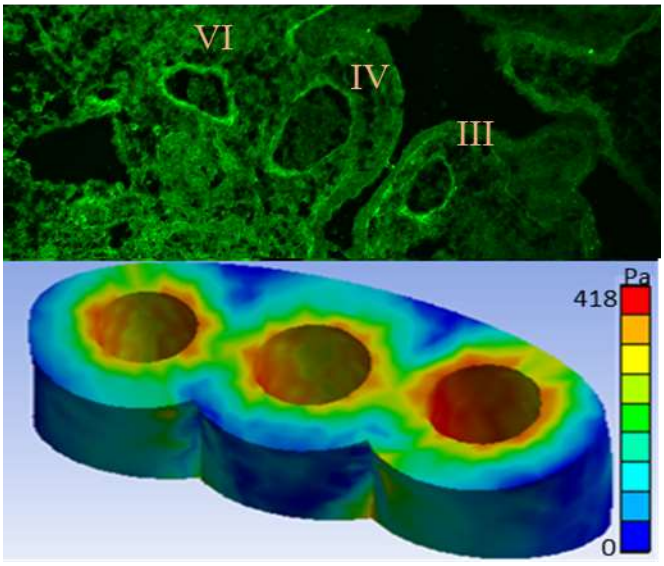

Figure 2: Comparison of stress distribution of the left aortic arches obtained by finite element analysis versus Collagen type I levels on chick embryo right aortic arch at Hamburg Hamilton stage 24.

The maximum von Misses stress, maximum shear stress, total deformation and measured WSS values due to blood flow from our previous work [6] are summarized in Table 1. Finally, aforementioned material remodeling resulted in a 20% decrease in stress levels for the right aortic arch at HH stage 24.

Table 1: Maximum values of stress, deformation and WSS calculations for all four models.

Maximum values	Stage 18		Stage 24	
	Left	Right	Left	Right
Von Misses Stress (Pa)	318	358	309	41
Total Deformation (μm)	3.02	4.04	2.99	6.18
WSS, CFD (Pa)	17.19	16.37	24.51	18.34
Shear Stress (Pa)	15.00	15.75	17.75	19.00

DISCUSSION

In this study, we estimated the stress distribution during the embryonic aortic arch morphogenesis and correlated these findings with immunofluorescence first-time in literature. Our results show that inner walls of arteries have the highest von Misses stresses as expected. Stress level decreases as the distance from the inner wall increases. Interestingly, this stress distribution matched to that of the IF stain intensity of major microstructural proteins. Particularly for collagen fibers, elastin and VEGF, there is a strong relationship with the stress level throughout the tissue. In general high stress levels cause high collagen dense regions at all early stages. Alteration of the material parameters would result changes in stress levels throughout the aortic arch. These changes can be predicted using our FEM model in a noninvasive way (without instrumenting on the chick embryo). Alterations in the ratio of collagen or elastin concentration and its long-term remodeling can be modeled using the present approach.

There are several ways to advance the proposed model. Implementing a hyper-elastic material model constitutes the ongoing effort. Likewise mechanical experiments focusing on the aortic sac tissue would provide experimental stress-strain data that is needed for hyper-elastic material model parameters. Also 3D OCT scans can be used to reconstruct a full 3D model of the aortic sac. Furthermore assigning pulsatile pressure distribution throughout the arteries would allow quantitative comparison of vessel diameter changes obtained from OCT and can correlate with the collagen type I synthesis (Figure 1).

ACKNOWLEDGEMENTS

Funding is through the European Research Council (ERC) Consolidator Grant #307460 (PI: Kerem Pekkan)

REFERENCES

[1] Buskohl, P. R., et al. *Biomech Model Mechanobiol* 11:1205-17.2012
[2] Goenezen, S., et al. *Biomech Model Mechanobiol* 11:1187-204.2012
[3] Rugonyi, S. *J Appl Mech Eng* Suppl 11.2013
[4] Shi, Y., et al. *J Biomech Eng* 136.2014
[5] Kowalski, William J., et al. *PLoS ONE* 8:e60271.2013
[6] Wang, Yajuan, et al. *Annals of Biomedical Engineering* 37:1069-1081.2009
[7] von Dassow, Michelangelo, et al. *PLoS ONE* 5:e15359.2010
[8] Schötz, Eva-Maria, et al. *Journal of the Royal Society Interface* 10:20130726.2013
[9] Hu, N., et al. *Circ Res* 65:1665-70.1989
[10] Clark, E. B., et al. *Circ Res* 51:810-5.1982
[11] Bharadwaj, Koonal N., et al. *Annals of biomedical engineering* 40:2212-2227.2012

Copyright 2016 The Organizing Committee for the 2016 Summer Biomechanics, Bioengineering and Biotransport Conference

SB^{3}C2016
Summer Biomechanics, Bioengineering and Biotransport Conference
June 29 –July 2, National Harbor, MD, USA
SB^{3}C2016-896

FORCES APPLIED TO THE FOOT AND PELVIS IN HIGH RATE VERTICAL ACCELERATIVE LOADING

Jonathan D. Rupp (1,2,3), Carl S. Miller (1), Lauren K. Zaseck, (1), Nichole Ritchie, Anne Bonifas(1), Laura Slykhouse (1) and Matthew P. Reed (1)

(1) University of Michigan Transportation Research Institute
Ann Arbor, MI, USA

(2) Department of Emergency Medicine
University of Michigan
Ann Arbor, MI, USA

(3) Department of Biomedical Engineering
University of Michigan
Ann Arbor, MI, USA

INTRODUCTION

Seated occupants of vehicles exposed to underbody blast sustain inferior to superior loading as a result of high rate vertical accelerations of the seat pan and floor [1]. Previous efforts to reproduce high-rate vertical accelerative loading using whole post mortem human surrogates (PMHS) involved testing with horizontal crash test sleds, impactors that load foot and seat plates, drop towers, and accelerative loading fixtures [e.g., 2,3,4,5]. Efforts to measure forces applied to the body in these tests are needed so that results of tests can be used to help ensure the external biofidelity of human surrogates such as anthropomorphic test devices (ATDs). To data such efforts have been limited such that only a single study has reported forces applied both the pelvis and foot [5] and no studies have reported on load sharing between the hind foot and fore foot and between the sacrum and other parts of the pelvis. This study reports data from a series of PMHS tests that provide new information on load sharing between hind-/fore-foot and the parts of the pelvis.

METHODS

Five whole male post mortem human subjects (PMHS) were tested using a custom designed, single seat drop tower facility that applies a vertical acceleration pulse to the foot and pelvis characterized by a 4 m/s peak velocity and a 5 ms time from the start of loading to peak. The ages, masses, and statures of the PMHS are listed in Table 1. All PMHS were tested in a rigid seat with a horizontal seat pan and vertical seat back. Subjects 1403-1506 were tested while wearing an improved outer tactical vest (IOTV), encumbrances, and a CamelBak.

Aspects of the seat pan and floor that respectively contacted the pelvis and feet were instrumented with custom load plates that measured forces applied to the fore foot and hind foot, the regions of the pelvis containing the sacrum, the left and right ischial tuberosities, and the proximal thigh flesh. Figure 1 shows these load plates. Each load plate contained multiple height-matched load rings (PCB model 202B for the loading plates that measured foot loading and 203B for the plates that measure pelvis loading). Load plates were calibrated by applying quasi static loads at multiple locations on the load plates and then using multivariate linear regression to estimate calibration coefficients for each load cell. A cross validation approach was performed for each seat of calibrations and the maximum resulting error was less than 1.7% at 10 kN for the hind/fore foot load plates and 3.0% at 15kN for the pelvis and thigh flesh load plates.

Table 1: Subject Characteristics

Test ID	Age (yr)	Stature (cm)	Mass (kg)
1401	66	175	98
1403	64	183	78
1504	57	177	88
1505	76	178	75
1506	60	178	78

Copyright 2016 The Organizing Committee for the 2016 Summer Biomechanics, Bioengineering and Biotransport Conference

Inertial compensation factors were estimated for each load plate by dividing the summed forces measured by the load washers by the measured vertical acceleration of the CG of the plate. The resulting values were all slightly larger than the masses of the plates. Force and acceleration data were filtered using a phaseless 4th order lowpass Butterworth filter with a 1650 Hz cutoff frequency.

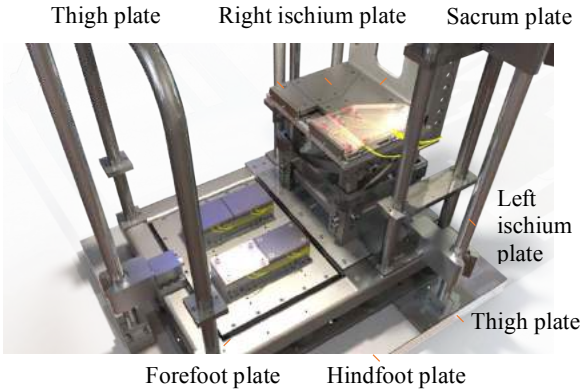

Figure 1. Seat and Foot load plates

RESULTS

Figures 2 and 3 show right foot and seat loads from all five tests. Loads measured by the right fore and hind foot were similar to those measured by to the left foot plate for each test. Loads measured by the plates that load the regions of the pelvis containing the left and right ischial tuberosites also measured similar loads for each test. Responses measured in the test without an IOTV within the range of response measured in test with an IOTV.

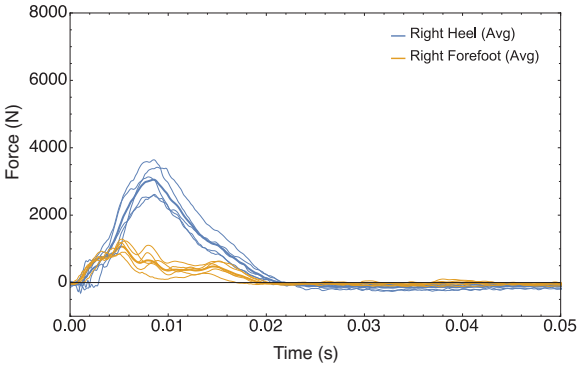

Figure 1: Forces applied to left and right hindfoot and forefoot.

The average peak force applied to the left heel was 2.8 kN while the average force applied to the right heel was 3.1 kN. Approximately 75% of the total force applied to the foot was applied to the hind foot. Peak forces applied to the regions of the pelvis containing the left and right ischial tuberosities were, on average, 5.5 kN and 5.6 kN, respectively. The average force applied to the sacrum at the time of peak pelvis force was 2.4 kN and approximately 17% of the total force applied to the pelvis was transmitted through the sacrum plate. Peak forces applied to the left and right thigh plates averaged to approximately 1.7 kN and 1.8 kN, respectively across the five tests.

Several tests resulted in coccyx and lumbar spine fractures, however, the timing of these fractures was such that they occurred after the time of peak force, around ~20ms.

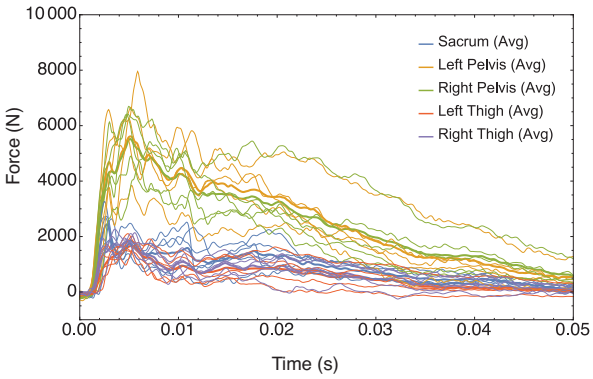

Figure 2: Forces applied to pelvis and proximal thigh

DISCUSSION

This study presents novel information on forces applied to the pelvis and foot and load sharing between different parts of these body regions. Results of these test provide important information for crash test dummy design and can be used to help define the external biofidelity of these devices.

Data presented in this paper were not normalized to account for effects of body size on response. Future work should explore if established methods for normalizing data (e.g., Mertz 1984, Eppinger et al. 1984) reduce scatter in the data. Data were also collected using a single loading condition. Loading at higher rates and longer durations will likely change mass coupling to the pelvis and could therefore change load sharing between the sacrum and ischial tuberosity regions of the pelvis.

ACKNOWLEDGEMENTS

This research was conducted as part of the Biomechanics Product Team led by the Johns Hopkins Applied Physic Laboratory for the WIAMan Project under contract #N00024-13-D-6400, U.S. Army Research, Development and Engineering Command.

REFERENCES

[1] Scherer, R. et al. (2011). "Vehicle and Crash Dummy Response to an Underbelly Blast Event," RDECOM-TARDEC Unclassified Public Release.

[2] Yoganandan et al. (2014) Stapp Car Crash J 58:123-143

[3] Bailey et al. (2015). Comparison of Hybrid-III and Postmortem Human Surrogate Response to Simulated Underbody Blast Loading. J Biomech E 157:051009-1 to 051009-10.

[4] Danelson et al. (2015) Comparison of ATD to PMHS Response in the Under-Body Blast Environment. Stapp Car Crash J 59: 445-520

[5] Reed and Ebert (2014). The Seated Soldier Study: Posture and Body Shape in Vehicle Seats. UMTRI Report 2013-13. University of Michigan Transportation Research Institute, Ann Arbor MI.

[6] Mertz HJ. (1984) A procedure for normalizing impact response data. Society of Automotive Engineers, paper 840084, Warrendale, PA.

[7] Eppinger, R., et a. (1984), "Development of Dummy and Injury Index for NHTSA's Thoracic Side Impact Protection Research Program," SAE Trans., 93(4), pp. 4–359.

Copyright 2016 The Organizing Committee for the 2016 Summer Biomechanics, Bioengineering and Biotransport Conference

SB³C2016
Summer Biomechanics, Bioengineering and Biotransport Conference
June 29 –July 2, National Harbor, MD, USA
SB³C2016-897

ASSESSING KINEMATICS AND KINETICS OF FES-ROWING

Adina E. Draghici (1), Glen Picard (3), J. Andrew Taylor (3, 4), Sandra J. Shefelbine (1, 2)

(1) Department of Bioengineering
Northeastern University
Boston, MA, USA

(2) Department of Mechanical and Industrial Engineering
Northeastern University
Boston, MA, USA

(3) Cardiovascular Research Laboratory
Spaulding Rehabilitation Hospital
Boston, MA, USA

(4) Department of Physical Medicine and Rehabilitation
Harvard Medical School
Boston, MA, USA

INTRODUCTION

In the United States, 11,000 people suffer a spinal cord injury (SCI) each year, resulting in an estimated 276,000 people living with a chronic SCI in the US [1]. The SCI population is at the low end of the fitness spectrum with high risk of cardiovascular disease, diabetes, and profoundly accelerated osteoporosis, with a rapid decrease in bone density to approximately 60% of the normal bone mass [2]. Currently, there is no cure for SCI and most physical therapies to date have focused on only upper body exercises, which limits cardiovascular adaptations [3, 4] and do not apply the mechanical loads to the lower limbs necessary for maintaining bone strength. Hybrid functional electrical stimulation (FES) rowing is a novel training therapy designed to enable the SCI population to exercise both the large muscles of the legs and the upper limbs muscles, leading to increased metabolic responses [5-7]. Previous studies have shown that isolated FES muscle stimulation increases bone mineral density (BMD) in chronic SCI patients [8] and maintains BMD in acute SCI patients [9]. A recent case report suggests that FES-rowing may provide therapeutic benefits for bone [10]. Hybrid FES-rowing can mirror able-bodied rowing, but the specific of the rowing stroke, the loading produced, and the mechanical efficiency of those with SCI who habitually train with FES-rowing remains still unknown [11]. This study provides a biomechanical analysis of FES-rowing in relation to aerobic work to provide guidance for an optimal exercise regime for the SCI population to improve health benefits. The objective of this work was to characterize upper and lower body forces, work produced, and mechanical efficiency (metabolic consumption/mechanical work) during a progressive aerobic capacity tests in SCI FES-rowing vs. able-bodied rowing. We hypothesize that a greater rowing intensity requires greater upper and lower body forces and greater oxygen consumption in both groups.

METHODS

A Concept2 rowing ergometer was adapted to accommodate SCI patients and was instrumented with force transducers (handle, toe and heel of the left and right leg) and string potentiometers (rowing seat position). A biofeedback system was developed using NI LabVIEW software to collect real time forces of the feet and handle and rowing seat position (Fig. 1). Aerobic capacity was determined using on-line computer-assisted open circuit spirometry. Six patients with spinal cord injury (C5-T12, American Spinal Injury Association class A) and six able-bodied individuals were recruited from current patients in the Spaulding Rehabilitation Hospital SCI exercise program for FES-rowing. All subjects performed a progressive aerobic capacity rowing test, increasing wattage every 2 minutes until volition exhaustion. The first three bouts of intensity corresponded to each individual reaching 70%, 80%, and 90% of the maximum age predicted heart rate for able-bodied rowers, and 70%, 80%, and 90% of the maximum heart rate achieved during their last maximal aerobic capacity test for SCI rowers. Force and position data were recorded at 100Hz sampling frequency and a 10Hz low-pass first order Butterworth filter was used to remove unwanted noise. The data was divided into 1-minute intervals for which drive time, recovery time and average stroke rate were obtained. Additionally, each stroke was normalized to 100% rowing stroke to obtain force-time stroke profiles to determine peak force achieved at the handlebar and at the feet during 1-minute intervals. External work produced at the feet and handle was evaluated using a 2D rowing model, as function of the force recorded and rowing seat displacement. The mechanical efficiency of each rowing test was calculated as the ration of the volume of oxygen consumed to the average total external work for the last 30 seconds of each 2-minutes rowing intensity bout. Changes in stroke characteristics (drive time, recovery time and average stroke rate) were assessed via repeated measures ANOVA within group across

Copyright 2016 The Organizing Committee for the 2016 Summer Biomechanics, Bioengineering and Biotransport Conference

relative total workload. Changes in feet and arms forces were assessed using a linear regression model across groups and across average total work. Differences in efficiency between FES-rowers and able-bodied rowers were assessed using a Wilcoxon Rank-Sum test.

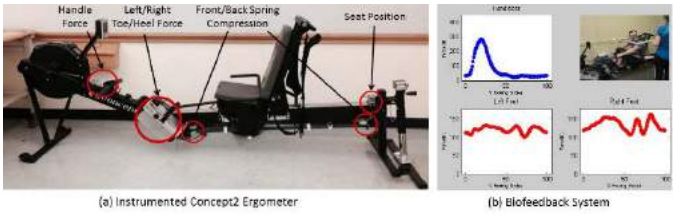

Figure 1: (a) Concept2 ergometer instrumented with force transducers (Handle, L/R Toe/Heel) and string potentiometers (Seat); (b) Biofeedback system for real time data collection.

RESULTS

Differences in kinematics (stroke characteristics: average stroke rate, drive time, recovery time), kinetics (forces applied at the feet and handle), and mechanical efficiency (volume of oxygen consumed/total external work) were compared in able-bodied rowers vs. SCI FES-rowers at each bout of intensity.

With increased rowing intensity, able-bodied rowers increased stroke rate ($p=0.02$) by decreasing recovery time ($p=0.05$) while maintaining a constant drive time. SCI FES-rowers did not increase stroke rate and maintained a constant recovery and drive times even with increasing rowing intensity. Able-bodied rowers spent 53% of the rowing stroke in the drive phase, while FES-rowers spent only 45% of the rowing stroke in the drive phase.

Across all intensities, FES-rowers produced lower magnitudes for both peak forces and work produced by upper and lower body than able-bodied rowers. With increased workload, able-bodied rowers increased foot force ($p<0.01$), while FES-rowers maintained a constant foot force (Fig. 2). For the upper body, peak handle force increased for both groups, but even more so in FES-rowers (both $p<0.01$).

FES-rowers had lower oxygen consumption and produced less external work than able-bodied rowers across all intensities. Oxygen consumption increases in both groups, but more so in able-bodied rowers. The ratio of internal work to external work provided a measure of mechanical efficiency as the volume of oxygen consumption over the total work produced. Our results showed that able-bodied rowers are two times more efficient than SCI FES-rowers.

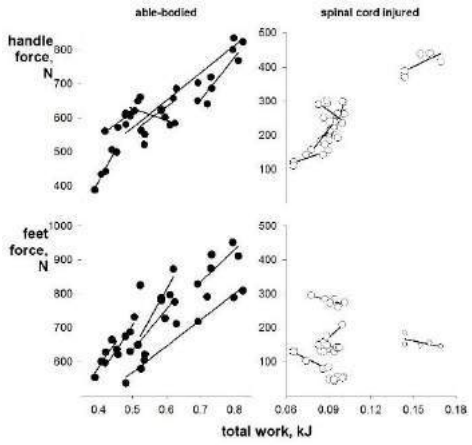

Figure 2: Upper and lower body forces with increased rowing intensity in able-bodied rowing vs. SCI FES-rowing.

DISCUSSION

Even though hybrid FES-rowing mimics able-bodied rowing, the specifics of the rowing stroke, the loading produced and the mechanical efficiency is different in SCI FES-rowing than in able-bodied rowing. FES-rowers demonstrated different rowing stroke kinetics than able-bodied rowers. Able-bodied developed an effective coordination between the upper and lower body movement, the movement pattern being facilitated by the trunk swing predominantly in the sagittal plane. However, the SCI FES-rowers had an altered coordination between the arms and the legs during drive phase; their inability of using the trunk swing resulted in a complete arm pull during the first half of the drive phase, followed by a leg extension during the second half, instead of coordinated arm and leg motion.

Across all intensities, able-bodied rowers produced three times higher peak external forces at arms and legs than FES-rowers. However, while able-bodied rowers increased legs and arms forces with increase in intensity, FES-rowers achieved a higher rowing intensity by only increasing their arm force, while the leg force was maintained constant. The different rowing stroke kinetics and lower magnitudes of peak arms and legs forces of FES-rowers are probably due to both biomechanical and physiological reasons. FES-rowers are not able to use their trunk, limiting an effective coordination between their arms and legs resulting in only very small increases in rowing intensity. Furthermore, the non-physiological recruitment of muscle fibers through electrical stimulation allows engaging the lower body of FES-rowers, but the legs achieve quickly the maximum possible work, without being able to increase the force production. With increased intensity, the oxygen demand is higher in able-bodied rowers than in FES-rowers. This is not surprising given that FES-rowers produced less external work than able-bodied. However, able-bodied rowers not only produce more external work for a higher oxygen demand, they are actually two times more efficient than FES-rowers.

FES-rowing provides a framework that allows exercising. Our results show that FES stimulated muscles are limited in the amount of force produced. Regardless of rowing intensity, the contribution of the legs stays constant and very low in the SCI population. These results imply that the inefficiency of SCI FES-rowing limits the total force output achievable with FES, leading to higher rates of fatigue, limiting the cardiopulmonary exercise possible and the loading applied to the bone. The current work constitutes a benchmark to evaluate FES performance to monitor changes in efficiency during training interventions and to guide the SCI population with respect to an optimal exercise regime, resulting in possible force generation, which will improve cardio-respiratory fitness and bone health.

ACKNOWLEDGEMENTS

This work was funded by a Northeastern University Dean's Scholarship (Adina Draghici).

REFERENCES

[1] University of Alabama at Birmingham. NSCISC National Spinal Cord Injury Statistical Center, *Facts and Figures at a Glance*, 2014.

[2] Jiang, S.-D. et al., *Osteoporos. Int* 17: 180–192, 2006.

[3] Figoni, S.F., *Med. Sci. Sports Exerc.* 25:433–441, 1993.

[4] Gates, P.E. et al., *Med. Sci. Sports Exerc*. 34:1699–1704, 2002.

[5] Hettinga, D.M. et al., *Neuromodulation* 10:291–297, 2007.

[6] Hettinga, D.M. et al., *Sports Med. Auckl. NZ* 38:825–838, 2008.

[7] Taylor, J.A. et al., *PMR* 3: 817–824, 2011.

[8] Bélanger M. et al., *Arch Phys Med Rehabil* 81(8):1090–1098,2000.

[9] Shields R.K. et al., *Spine* 31(5):548–553, 2006.

[10] Gibbons, R.S. et al., *Spinal Cord 52 Suppl 3:*S4–5, 2014.

[11] Halliday, S.E. et al., *Arch.Phys.Med.Rehabil.* 85:1265–1272, 2004.

Copyright 2016 The Organizing Committee for the 2016 Summer Biomechanics, Bioengineering and Biotransport Conference

SB^{3}C2016
Summer Biomechanics, Bioengineering and Biotransport Conference
June 29 –July 2, National Harbor, MD, USA
SB^{3}C2016-898

A ROBUST AND GENERALIZED PROCEDURE FOR GENERATING HUMAN INJURY PROBABILITY CURVES

N. Yoganandan (1), F.S. Gayzik (2), A. Banerjee (1), F. Hsu (2), F. Pintar (1), C.D. Bass (3), H. Cutcliffe (3), J. Rupp (4), F. Tenore (5), J. Zhang (5), L. Voo (5)

(1) Medical College of Wisconsin
Milwaukee, WI, USA

(2) Wake Forest University School of Medicine
Winston-Salem, NC, USA

(3) Duke University
Durham, NC, USA

(4) University of Michigan
Transportation Research Institute
Ann Arbor, MI, USA

(5) Johns Hopkins University
Applied Physics Lab
Laurel, MD, USA

INTRODUCTION

Human injury probability curves (HIPCs) in the automotive safety literature are developed using using post mortem human subjects (PMHS) tests. Logistic regression techniques are generally used for this purpose [1]. The International Standards Organization (ISO) recently released a 12-step methodology to derive HIPCs from retrospective biomechanical data, which has been applied to side impacts and dummy injury curves [2, 3]. Survival analysis was recommended because of its ability to accommodate differing censoring statuses of biomechanical experimental outcomes [4]. The ISO method for foot-ankle injuries produced different results compared to previous logistic regression-based HIPCs [5].

However, the ISO method based on retrospective tests does not accommodate all statistical processes that can be associated with prospective biomechanical experiments. For example, the method uses the Akaike information criterion (AIC) to choose a distribution. The criterion typically over-fits in a statistical model. Parameters such as area under the receiver operator curve (AUROC), Hosmer-Lemeshow (HL) and Kolmogrov-Smirnov (KS) provide more inclusive data, needed to evaluate the best underlying distribution for biomechanical metric(s). Comparing the derived HIPCs based on the least AIC with that based on a non-parametric distribution tends to be qualitative. An updated method is needed for a more generalizable and robust process to derive HIPCs. Thus, the objective of this study is to develop an improved methodology to derive HIPCs that can be used in sub-component and whole body PMHS tests simulating military loading situations such as underbody blast (UBB) events with potential applications in other loading environments as well.

METHODS

The first two steps in the processes focus on preparing data for use in HIPC development. Previously-published Abbreviated Injury Scale (AIS) 3+ injury, average spinal acceleration data from [1] are used to demonstrate the method.

1. Collect the relevant data for the injury assessment. This can include aggregated data for inputs (e.g., biomechanically relevant combinations of forces and moments). Data should include injury types and severities, associated mechanical test values and covariates based on cadaver characteristics (e.g. age, bone mineral content). Injury data should have been properly vetted.

2. Aggregated tests across multiple groups shoul d follow a consistent procedure in terms o f injury categorization or grouping. This is to be done on a component by component basis and driven by observations in component experiments. This is relevant if HIPCs are developed from multiple laboratories. *2a.* It is important that multiple competing injury mechanisms do not confound data, especially with limited experimental samples. This should be biomechanically verified using necropsy and medical imaging data. *2b.* Generally, in the absence of additional information, injury data is left censored or interval censored from zero, and non-injury data is right censored. Additional sensors may be used to produce uncensored data to improve statistical power and confidence interval widths.

3. Estimate the coefficients for the *model chosen.* Coefficients calculated will depend on the model, non-parametric models should also be presented. These estimates should account for the likely limited numbers of experiments in biomechanical tests using PMHS, and should avoid asymptotic large number assumptions whenever possible. Survival analysis is used and distributions evaluated include Weibull, log-normal, and log-logistic to fix zero risk of injury at a zero mechanical parameter value.

Copyright 2016 The Organizing Committee for the 2016 Summer Biomechanics, Bioengineering and Biotransport Conference

4. Identify overly influential observations *in th e data and model.* Like the ISO method, it is suggested to delete one observation at a time using the DFbetas statistic. This corresponds to the difference between the model coefficients when all data has been included vs. the calculated model with one observation excluded scaled by the standard error calculated without the excluded observation. The cutoff is based on sample size, $\frac{2}{\sqrt{n}}$ [6]. The biomechanist should be able to defend any data point identified for potential exclusion.

5. If a parametric distribution is used in the model, choose th e best distribution and check the distribution assumption. This is done using the following techniques. A quintile-quintile plot is used to check distribution percentiles vs percentiles in the data set. If the slope of the line is approximately unity and intercept is approximately zero, then the chosen distribution is appropriate. Three statistical tests are also used to determine the best distribution: AUROC, HL and the KS statistics. The latter is done between each parametric distribution and the non-parametric distribution. Based on these measures, the biomechanist should be able to select the optimal function.

6. Calculate 95% confidence intervals (CI) and a*ssess the Normalized Confidence Interval Size (NCIS) including the validity of the prediction based on the data.* The CI width is normalized by the predictor value from the model at a given level of risk to determine NCIS, which provides a quantitative value for how wide the CIs are compared to the norm.

RESULTS

The result of testing the proposed procedure is presented using a set of biomechanical data (n = 39) described in [1]. Figure 1 shows the results for the log-normal fit with 95% CIs, and the mean with and without overly influential observations flagged by the DFbetas statistic. Table 1 provides the key statistics for each model fit.

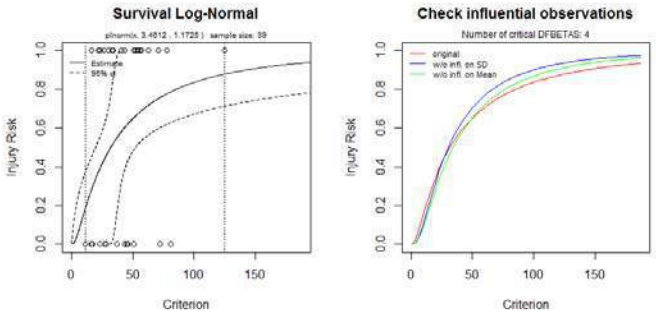

Figure 1: Best fit model shown, with 95% CI. Injury and non-injury data is noted at 0% and 100% risk.

Table 1. Survival Analysis Model fit statistics for sample.

Distribution →	Weibull	Log-normal	Log-logistic
AUROC	0.680	0.680	0.680
H-L	0.017	0.507	0.623
K-S	0.410	0.180	0.205

DISCUSSION

The original ISO suggestions were maintained to the extent possible in this updated procedure while acknowledging that risk curves produced were also applicable for biomechanical experiments using PMHS data. This procedure could be successfully implemented when the biomechanical experiments use prospective experimental designs to control the type and severity of injuries used in obtaining specific HIPCs associated with this outcome dataset, the ability to record multiple parameters of varying sensitivity to peak, and/or derived injury metrics and the ensuing risk curves. Because of its planned broad use, the method is programmed in the freely-available R language. The users will have significant control over the data input and analysis. It is incumbent upon them to select the best distribution given the statistical data from the analysis which is not just AIC, as used in the current ISO method. If the model does not match the non-parametric data, the user should determine if there is an issue with the distribution assumption.

The use of the DFbetas statistic reflects the true sample size in this method. Identification of overly influential (OI) samples was based on the DFbeta calculations although it must be noted that these are a function of the model fit and other parameters such as the standard deviation. The ISO method does not indicate a preference. The updated method relies on the user to make the final determination as to which, if any, observations are omitted. Depending on the type of the biomechanical experiment and sensitivity to a metric(s), the user can choose the type of DFbeta-process to determine OI.

Another aspect is the determination of the quality index, which was proposed to be specific to certain risk levels. In the present study, the methodology allows the user to determine the NCIS not only at discrete probabilities but also one can determine the quality over the entire or partial ranges of the HIPC. While the selection of the underlying distribution is governed by parameters such as AUROC, HL and KS, and evaluations of the tenability of the selected parametric curve is quantitative, the output producing different HIPCs (e.g., log-normal, log-logistic, Weibull) for each biomechanical metric will allow the user to choose the most appropriate HIPC from a biomechanical and practical perspective. For example, the selection may be based on the sensitivity (slope of 'S-curve') of the particular curve for that metric or the length toe region if risks at low levels are of concern. Thus, the expanded methodology consisting of a larger decision tree process, and the provision of multiple curves, associated CIs, and OI plots, has the generalizability and flexibility needed for the user to determine the most optimum HIPC. The process can be used regardless of the type of experimental model (sub-component to whole body) and adaptable to both PMHS and dummy risk curves .

Future work will assess the use of Bayesian survival analysis with the addition of Bayesian priors, which could provide similar levels of CIs for a given risk function, with smaller sample sizes [4].

ACKNOWLEDGEMENTS

This research was conducted as part of the Biomechanics Product Team led by the Johns Hopkins Applied Physics Laboratory for the WIAMan Project under contract #N00024-13-D-6400, U.S. Army Research, Development and Engineering Command. The content included in this work does not necessarily reflect the position or policy of the U.S. government. This material is the result of work supported with resources and the use of facilities at the Zablocki VA Medical Center, W81XWH-12-0041 and Department of Neurosurgery, Medical College of Wisconsin Milwaukee, Wisconsin. NY and FAP are part-time employees of VA Medical Center. Inputs from all members of the HIPC Working Group team including Nicholas Williams of WFU, Klaus Driesslein of MCW, J. O'Bruba, D. Barnes, T. Holdren, T. Melendez, and S. Marsh from the WIAMan program office; and T. Smith and K. Wiley from Dynamic Research Inc., are acknowledged.

REFERENCES

1. Kuppa S et al. (2003) Stapp car crash journal 47:189-210
2. Petitjean A et al. (2012) Stapp car crash journal 56:323-347
3. ISO TS/18506: 2014(E), 1st ed. 2014-03-01
4. Cutcliffe HC et al. (2012) Stapp car crash journal 56:349-386
5. Yoganandan N et al. (2014) Traffic injury prevention 15 Suppl 1:S
6. D. Belsley, et al., Regression diagnostics. New York: Wiley, 1980

Copyright 2016 The Organizing Committee for the 2016 Summer Biomechanics, Bioengineering and Biotransport Conference

SB^{3}C2016
Summer Biomechanics, Bioengineering and Biotransport Conference
June 29 –July 2, National Harbor, MD, USA
SB^{3}C2016-900

A COUNTEREXAMPLE TO ENTROPY—ENTHALPY COMPENSATION IN COLLAGEN DENATURATION

Neil T. Wright

Department of Mechanical Engineering
Michigan State University
East Lansing, MI, USA

INTRODUCTION

The concept of entropy-enthalpy compensation is nearly as old as the Arrhenius description of the relation between temperature and the rate parameter in chemical kinetics. Entropy-enthalpy compensation states that there is a relationship, typically linear, between the activation entropy and activation enthalpy in chemical kinetics. In 1925, Constable [1] wrote of an apparent relationship between the two parameters in the Arrhenius relation for catalysized reactions in alcohols. For biological systems, several authors, for example [2, 3, 4], have noted similar relations. Recently, Qin et al. [5] used this concept to propose that the relationship between temperature and reaction rate can be characterized by activation energy alone.

There is a continuing debate as to whether entropy-enthalpy compensation is an artifact or a bona fide phenomenon. That so wide a variety of chemical reactions can yield such similar relationships between two supposedly independent parameters is surprising. Sharp [6] argued against the compensation effect on the grounds of statistical thermodynamics. Others have noted that uncertainty in measurements could lead to the appearance of a compensation effect. Liu and Guo [7] examined the role that uncertainty in measurements may have on mistaking other phenomena for compensation. Barrie made further analysis to show that random error [8] and systemic error [9] may cause mistaken identification of compensation. Harrington and Wright [10] used scaled sensitivity coefficients to demonstrate the difficulty in estimating both the frequency factor and activation energy over the small range of temperatures that biological specimens can be tested.

Here, published results of the shrinkage of bovine chordae tendineae that is heated while subject to mechanical loading is reexamined to demonstrate a case for which the activation entropy and enthalpy are independent. Thus, the enthalpy and entropy must be separately determined, in general. This agrees with other findings.

METHODS

Consider a first-order reaction

$$dC/dt = -k(T)C \tag{1}$$

where C is the concentration of a substance (e.g., a protein), T is the absolute temperature, t is time, and $k(T)$ is the rate parameter. While this is a great simplification for describing most biological reactions [11], it serves as a model reaction. The relation between $k(T)$ and T is often written in terms of an Arrhenius relation

$$k(T) = Ae^{-E_a/RT} \tag{2}$$

where A is the pre-exponential or frequency factor, R is the ideal gas constant, and E_a is the activation energy. The rate parameter may also be described using transition state theory as

$$k(T) = \kappa \frac{k_b T}{h} e^{S_a/R} e^{-H_a/RT} \tag{3}$$

where k_b is the Boltzmann constant, h is the Planck constant, S_a is the activation entropy, H_a is the activation enthalpy, and $\kappa \approx 1$, typically. In condensed-state matter, $E_a \approx H_a$, and comparing Eqs. (2) and (3), $\ln A \sim S_a$. Similarities in Eqs. (2) and (3) suggest that the compensation effect may be written in terms of E_a and $\ln A$ or H_a and S_a.

Figure 1 shows an example of the apparent compensation effect for tissues (Henriques, Takata, Pearce), cells (Mixter, Moussa, Bhowmick), and proteins (Miles, Chen) from different research studies [3]. The samples presented in Figure 1 share the characteristic of being mechanically unloaded, or at least without specified intentional loading.

RESULTS

Consider the shrinkage during heating of bovine chordae tendineae that have imposed constant uniaxial. Chordae tendineae are nearly cylindrical structures that are predominantly composed of the uniaxially oriented fibrillar type I collagen. Pulling on type I collagen

Copyright 2016 The Organizing Committee for the 2016 Summer Biomechanics, Bioengineering and Biotransport Conference

reduces its conformational entropy as its polymeric chains tend to straighten. Chen et al. [12] measured the change in shrinkage of the bovine chordae tendineae at temperatures of from 65 to 90 °C and subject to first Piola-Kirchhoff stresses of 0 to 650 kPa. They used a characteristic time of the second inflection point τ_2 on the sigmoidal shrinkage curve, which is a clearly identifiable characteristic time.

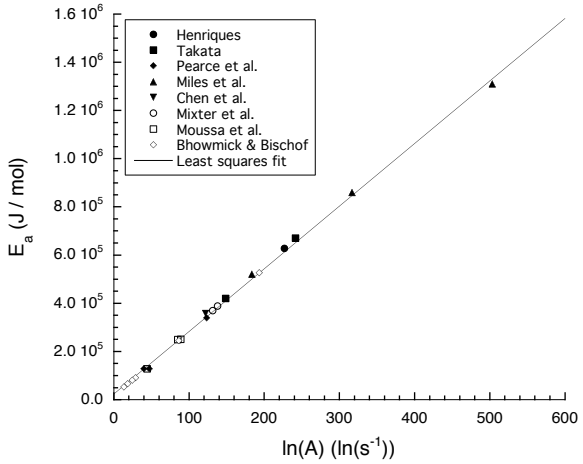

Figure 1: Illustration of entropy-enthalpy compensation from Wright [3]. The ln(A) is proportional to the S_a. (Most papers plot it with E_a on the abscissa, instead of the ordinate as shown here.)

Wright [3] demonstrated that similar scaling results using the half-time for shrinkage τ_{50}, which may be more obviously related to $k(T)$. Figure 2 is an Arrhenius plot of $k(T)$ for the five levels of P. Note that as P increases, greater temperatures are needed for the same $k(T)$, which is to say that increasing P delays shrinkage and increases S_a. Figure 3 shows S_a, as calculated using Eq. (3), as a function of P.

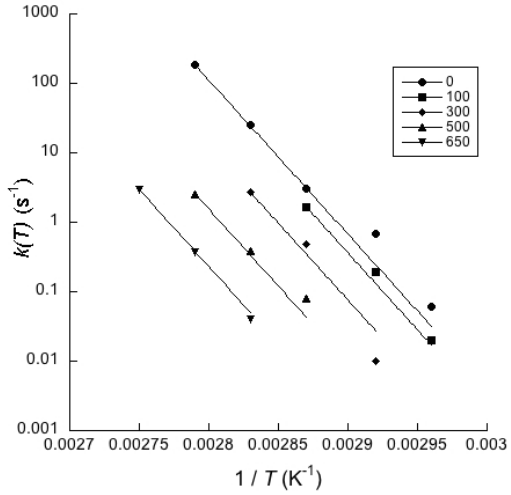

Figure 2: Arrhenius plot for shrinkage of chordae tendineae for first Piola-Kirchhoff stresses of 0 to 650 kPa. Best fit lines with constrained slopes are shown for each level of P.

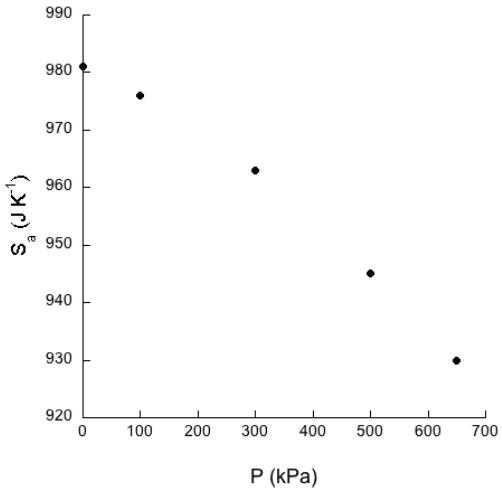

Figure 3: Activation entropy S_a as a function of P for shrinkage of chordae tendineae at temperatures between 65 and 90 °C.

DISCUSSION

The results here for the collagen shrinkage under different mechanical loads follow the time-temperature-load equivalence found by Chen et al. [12]. While a single correlation for shrinkage covering a wide array of imposed conditions was developed in [13], the current analysis uses τ_{50} to calculate $k(T)$, and hence S_a, as a function of P. Miles and Gleshvili [14] used the concept of polymer-in-a-box to propose that the decrease in conformational entropy due to dehydration will increase the thermal stability of type I collagen. Mechanical loading, which also reduces the conformational entropy, increases thermal stability. This is reflected in the decreased S_a for constant H_a. In addition to hydration and mechanical loading, other factors have been cited as changing the entropy of, for example, proteins in a cell, and thus the thermal stability of those proteins [15].

In addition to potential mathematical and thermodynamic arguments against entropy-enthalpy compensation, there are empirical counterexamples. Thus, while the apparent correlation between H_a and S_a can be a useful in some applications, it should be used with caution.

REFERENCES

[1] Constable, FH, *Proc Royal Soc*, 1925.
[2] Rosenberg, B et al., *Nature*, 232:471-473, 1971.
[3] Wright, N, *J Biomech Egr*, 125:300-304, 2003.
[4] He, X, & Bischof, JC, *Crit Rev Biomed Eng,* 31:355–421, 2003.
[5] Qin, ZP et al., *Ann Biomed Engr*, 42:2392-2404, 2014.
[6] Sharp, K., *Protein Sci,* 10: 661-667, 2001.
[7] Liu L & Guo QX, *Chem Rev*, 101, 673−695, 2001.
[8] Barrie, P, *Phys Chem Chem Phys*, 14, 318–326, 2012.
[9] Barrie, P, *Phys Chem Chem Phys*, 14, 327–336, 2012.
[10] Harrington, P & Wright, NT, Proc SBC, 2005.
[11] Pearce, J, *J Biomech E*, 137:121006, 2015
[12] Chen, SS et al., *J Biomech E*, 120:382-388, 1998.
[13] Chen, SS et al., *Trans IEEE Biomed*, 45:1234-1240, 1998.
[14] Miles CA & Ghelashvili, M, *Biophysical J*, 76: 3243–3252, 1999.
[15] Despa F. et al., *Ann NY Acad Sci,* 1066: 54–66, 2005.

Copyright 2016 The Organizing Committee for the 2016 Summer Biomechanics, Bioengineering and Biotransport Conference

SB^{3}C2016
Summer Biomechanics, Bioengineering and Biotransport Conference
June 29 –July 2, National Harbor, MD, USA
SB^{3}C2016-901

BLOOD CLOTTING POTENTIAL AND HEMODYNAMIC ANALYSIS OF A SUPERHYDROPHOBIC BILEAFLET MECHANICAL HEART VALVE

David L. Bark Jr. (1,2), Hamed Vahabi (1), Hieu Bui (2), Sanli Movafaghi (1), Arun K. Kota (1,2), Ketul C. Popat (1,2), Lakshmi P. Dasi (1,2)

1) Department of Mechanical Engineering
Colorado State University
Fort Collins, CO, United States

(2) School of Biomedical Engineering
Colorado State University
Fort Collins, CO, United States

INTRODUCTION

Of the numerous blood-contacting medical devices implanted, 290,000 prosthetic heart valve (PHV) replacements were performed in 2003, which is expected to increase to 850,000 by 2050 [1]. Half of these PHVs are mechanical, which are at high risk of failure through thrombosis and thromboembolism, but are more durable than the alternative bioprosthetic PHVs [2]. To mitigate the risks associated with thrombosis, patients are treated with systemic anticoagulation and antiplatelet drug regimens. These therapies exhibit limited efficacy in high flow environments, while increasing the risk for bleeding. Furthermore, systemic anticoagulation results in the most drug-related deaths occurring from adverse clinical events in the United States [3]. Therefore, less aggressive anticoagulation or antiplatelet therapy due to less thrombogenic biomaterials could provide significant benefits for the numerous patients requiring medical devices.

Superhydrophobic surfaces may provide an effective treatment that significantly reduces thrombus formation on the material surface and may reduce fluid shear stress that can otherwise promote thrombosis. These surfaces are characterized by the degree that water beads on the surface, and are exemplified by the lotus leaf in nature [4]. Here, we report on the potential for these superhydrophobic surfaces to be used as a material treatment for mechanical PHVs. Tests were conducted to quantify hemodynamic improvement, in addition to studying the potential for blood clot formation on the surface.

METHODS

Ultra-Ever Dry (UltraTech International, Inc., Jacksonville, FL) is a commercially available superhydrophobic coating used in this study. The coating was applied as a spray to a 25 mm St. Jude Medical™ standard pyrolytic carbon (PyC) bileaflet mechanical heart valve (BMHV). Due to limitations in obtaining PyC samples, we also applied the coatings to glass for blood studies. This becomes necessary to compare various surface treatments for a given sample of blood. The base material with a sufficient coating thickness, whether pyrolytic carbon or glass, should not contact the blood.

Contact angle goniometry (Ramé-Hart) was used to assess the hydrophilicity. This technique measures the angle between the solid-liquid and liquid-vapor interface of a droplet on the surface. We also study the interaction with blood using two tests, a bouncing and sliding test. In the first test, a FASTCAM SA3 high speed camera (Photron, Inc.) was used to record a 12 μl of blood dropping onto surfaces from a height of 10 mm. In the second, a 30 μl droplet of blood was placed along various surfaces at a 45^o angle to observe the movement of blood.

Shear stress can activate platelets and rupture red blood cells (RBCs). Particle imaging velocimetry (PIV) was performed to assess shear stress for normal physiological aortic flow past a BMHV. Fluid was seeded with 1-20 μm melamine resin particles coated with Rhodamine-B. A Nd:YLF Single Cavity Diode Pumped Solid State High Repetition Rate Laser (Photonics Industries, Bohemia, NY) was used to illuminate a 0.2 mm thick measurement plane. The measurement plane was imaged with a double frame FASTCAM SA3. DaVis (Lavision, Inc.) was used to post-process PIV slices. Instantaneous shear stress was calculated using:

$$\tau_{xy} = \mu\left(\frac{\partial u}{\partial y} + \frac{\partial v}{\partial x}\right), \quad (1)$$

where u and v are the instantaneous velocities in the x (streamwise) and y direction respectively, while μ is the dynamic viscosity.

As a preliminary assessment of hemocompatiblity, whole blood clotting kinetics were evaluated. 5 μL of whole blood was pipetted

Copyright 2016 The Organizing Committee for the 2016 Summer Biomechanics, Bioengineering and Biotransport Conference

onto bare and coated glass samples in a 24-well plate immediately after collection. Samples were incubated with blood at 37 °C. Free hemoglobin concentration was measured at 15, 30, and 60 minutes. For this measurement, RBC were lysed using 500 µL of deionized (DI) water. Absorbance of the sample was then measured at a wavelength of 540 nm, using a plate reader, assuming that RBCs trapped in a clot don't contribute to the measurement.

RESULTS

The addition of the coating changes PyC from a slightly hydrophilic surface with a receding contact angle of 47° to a superhydrophobic surface with a receding contact angle of 160°. Furthermore, with a coating, the contact angle hysteresis is only 4°. With these properties, blood bounces off of the hierarchical surface, while it sticks to PyC, as demonstrated in Fig. 1A. The movement of blood is also visualized by placing a 30 µl droplet of blood on bare and coated glass tilted at 45° relative to the horizontal, Fig. 1B. The droplet slowly slides down bare glass leaving a trail of blood. Conversely, a droplet of blood swiftly slides off of a coated glass slide, leaving no visual trace of blood on the surface.

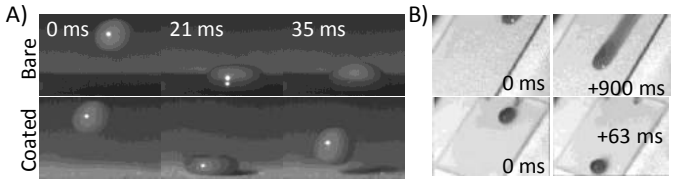

FIGURE 1: A) Blood droplet bouncing on coated and bare PyC and B) blood sliding on coated and bare glass

Instantaneous shear stress is calculated from PIV data to assess potential changes in blood damage with results for peak flow (30 l/min) shown in Fig. 2. Shear stress values are similar for the bare and coated valve, remaining below 10 N/m^2 at peak flow. However, one notable difference between the two valves is that the instantaneous shear stress is higher in the sinus region of the coated valve relative to the bare PyC valve, demonstrating less flow stagnation.

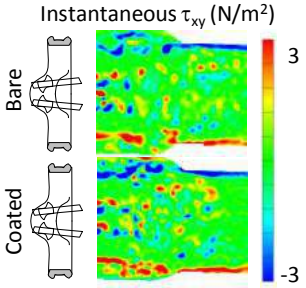

FIGURE 2: Instantaneous shear stress contours for PIV data of bare and coated BMHVs.

Minimizing the thrombotic response from blood is a major goal for the proposed coating. A free hemoglobin assay is used to compare the clotting potential of bare glass with coated glass. In this assay, increased free hemoglobin, corresponding to increased absorbance means that fewer RBCs have been incorporated into a blood clot on the surface. Free hemoglobin is plotted for bare and coated surfaces in Fig. 3. Clotting occurred quickly for glass, demonstrated by a large reduction in absorbance during the first 30 minutes of incubation. Alternatively, free hemoglobin does not exhibit substantial changes for the coated surface.

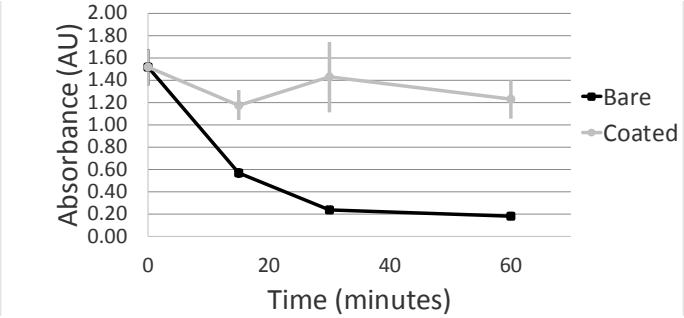

FIGURE 3: Free hemoglobin concentration in terms of absorbance bare and coated glass

DISCUSSION

We show that a superhydrophobic coating reduces surface-blood interactions, while having a minimal impact on the instantaneous shear stress. The latter demonstrates that there is no added hemodynamic damage to blood cells relative to approved PHVs.

Non-physiological hemodynamics, specifically regions of stagnating flow and regions of high shear stress can induce a thrombotic response. Stagnating flow typically corresponds to a fibrin rich blood clot, which is assessed in the current study with the whole blood clotting assay. Resistance to clotting in the current work is likely a result of reduced surface-blood interactions. There also appeared to be a slight increase in washout in the aortic sinus downstream of the coated valve, indicating smaller regions of flow stagnation and therefore a reduced region with the potential for blood clotting. Regions of high shear stress can also cause a thrombotic response, specifically through hemolysis and shear-induced platelet activation. Shear stress values causing these responses remain ill-defined due to variations in studies and due to a dependence on exposure time to a specific shear stress. For a conservative estimation, shear stress must be above 150 N/m^2 to cause hemolysis and above 10 N/m^2 to cause platelet activation [5, 6]. Here, we show that instantaneous shear stress is below 10 N/m^2 for both the PyC BMHV and the coated BMHV, with values similar to Ge et al. [5].

This work provides a preliminary assessment of the thrombotic response of a superhydrophobic BMHV. Additional work will need to be performed to design these valves so that they are durable. Furthermore, there is a need to assess the potential for platelet and plasma protein adhesion to the surface under flow conditions. Lastly, flow analysis is limited to the downstream region of the valve. Additional studies would need to be performed to evaluate the hinge regions and b-datum jet of the valve.

ACKNOWLEDGEMENTS

The authors gratefully acknowledge funding from National Institutes of Health (NIH) under Award Numbers R01HL119824 and F32HL129730. The content is solely the responsibility of the authors and does not necessarily represent the official views of the NIH.

REFERENCES

[1] Yacoub, M & Takkenberg, J, *Nat Clin Pract Card*, 2:60-61, 2005.
[2] Unger, F & Ghosh, P, *Semin Thorac Cardiovasc Surg*, 14:321-323, 2002.
[3] Kutay, V, et al., *J Cardiac Surg*, 21:572-577, 2006.
[4] Leslie, DC, et al., *Nature Biotechnol*, 32:1134–1140, 2014.
[5] Ge, L, et al., *Ann Biomed Eng*, 36:276, 2008.
[6] Hellums, JD, et al., *Ann Biomed Eng*, 22:445, 1994

Copyright 2016 The Organizing Committee for the 2016 Summer Biomechanics, Bioengineering and Biotransport Conference

SB^{3}C2016
Summer Biomechanics, Bioengineering and Biotransport Conference
June 29 –July 2, National Harbor, MD, USA
SB³C2016-902

EXPLORING DIFFERENCES IN THE TENSILE RESPONSE OF THE PREGNANT AND NON-PREGNANT MOUSE CERVIX

Carrie E. Barnum (1), Jennifer L. Fey (1), Brianne K. Connizzo (1,2), Snehal S. Shetye (1), Michal A. Elovitz (3), and Louis J. Soslowsky (1)

(1) McKay Orthopaedic Research Laboratory, University of Pennsylvania, Philadelphia PA, USA

(2) Department of Biological Engineering, Massachusetts Institute of Technology Boston, MA, USA

(3) Maternal and Child Health Research Program, Department OBGYN, University of Pennsylvania, Philadelphia, PA, USA

INTRODUCTION

The cervix is a unique organ able to dramatically change its shape and function from serving as a physical barrier for the growing fetus to dramatic dilation allowing for delivery of a term infant. As a result, the cervix endures changing mechanical forces from the growing fetus [1, 2]. Despite this, only recently have mechanical property changes of the cervix been evaluated throughout pregnancy [3]. There is an emerging concept that the cervix may change or remodel "early" in many cases of spontaneous preterm birth (PTB) [5, 6]. However, the mechanical role of the cervix in the pathogenesis of PTB remains unclear [1, 2]. Therefore, the objective of this study was to measure the biomechanical response of the cervix throughout pregnancy to provide insight into its role in premature cervical remodeling and PTB. We hypothesized that cervical mechanical properties would decrease throughout pregnancy since cervical softening and ripening are essential to a normal pregnancy cycle and parturition.

METHODS

Non-pregnant (NP) and pregnant CD-1 mice at embryonic day (E) E10.5, E12.5, E14.5, E16.5 and E18.5 (n=10-16/group) were sacrificed and frozen until they were prepared for mechanical testing. *Mechanical Testing*: After thawing, the entire reproductive organs (uterus, cervix, vagina) were removed; the bladder was used for orientation and then removed. The vagina and cervix were then cut open on the side opposite to the bladder. The cervix was then dissected free of extra soft tissue and the uterus and vagina were bluntly removed. The cervix was then laid flat to expose the lumen. The ends were affixed between two pieces of sandpaper for gripping, such that a uniaxial tensile load on the grips would simulate dilation of the cervical canal. A custom laser device was used to measure cross sectional area [7]. Tensile properties were measured via a protocol consisting of a preload of 0.005N followed by a hold of 5 minutes and then a ramp to failure at 1mm/minute.

Collagen Re-Alignment: Collagen fiber alignment maps of the cervix were collected throughout the mechanical testing protocol using our established integrated cross-polarizer system, as described [8, 9, 10]. This custom system consists of a linear backlight (Dolan-Jenner, Boxborough, MA), rotating polarized sheets offset by 90° (Edmund Optics), and a camera. Custom software (National Instruments LabVIEW, Austin, TX) synchronized with analog output signals from the Instron triggered alignment maps to image capture at 5 second intervals for NP, E10.5, and E12.5 and at 7.5 second intervals for E14.5, E16.5, and E18.5. Collagen alignment was measured at four points during the mechanical test: (1) start of the toe region, defined by the first map after the hold protocol, (2) at the end of the toe region, determined by the last map before the change of slope to the linear region (3) at 45% of the maximum load, and (4) at 90% of the maximum load. Significant re-alignment was defined as a significant change in circular variance between two time points.

Statistics: One-way ANOVA was used to compare between groups for mechanical parameters with Bonferroni-corrected post-hoc tests when appropriate. Mann–Whitney *U* tests were used to evaluate differences in fiber realignment at each time point. The significance was set at $p < 0.05$ for all statistical comparisons.

RESULTS

Mechanical Testing: Cross-sectional area was significantly reduced in E10.5 pregnant cervices but gradually returned to NP levels by E14.5 (data not shown). Maximum load was significantly smaller in all gestational groups compared to NP samples (Fig.1A). NP and E10.5 samples demonstrated significantly higher ultimate stress values as compared to all other gestational time points (Fig. 1B). Tissue stiffness

Copyright 2016 The Organizing Committee for the 2016 Summer Biomechanics, Bioengineering and Biotransport Conference

was decreased in pregnant samples compared to NP, with the exception of samples at E10.5, which were significantly stiffer compared to all other gestational ages and no different from NP (Fig. 1C). No significant differences were observed in tissue modulus for the NP, E10.5 and E12.5 samples. The NP and E10.5 samples had a significantly higher Young's modulus as compared to the E16.5 and E18.5 samples (Fig. 1D).

Collagen Re-Alignment: Realignment of collagen fibers was observed for all samples between the 'Toe' and '90% maximum load' time points (Fig. 2). E10.5 and E16.5 samples experienced some earlier realignment beginning at the '45% maximum load' time point and '90% maximum load' (Fig. 2B, E). E18.5 samples showed an immediate response to load with collagen fiber re-alignment during all time points (Fig. 2F).

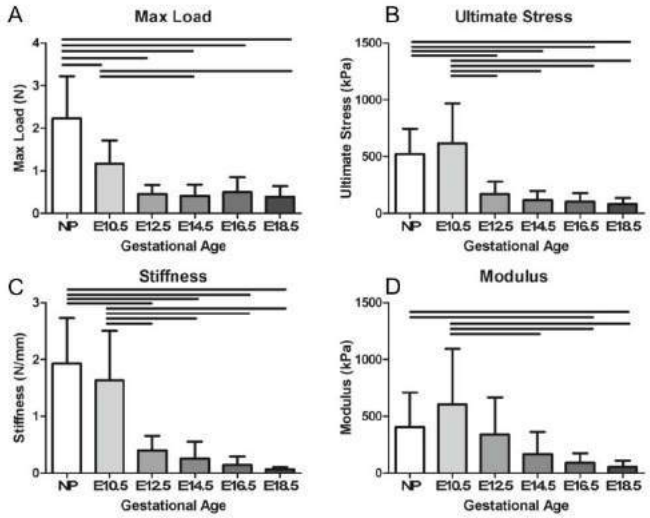

Figure 1: Mechanical properties, such as maximum load (A), ultimate stress (B), stiffness (C) and modulus (D), for NP and gestational ages (n=10-19 for all samples) demonstrate significant changes. Data is presented as mean±standard deviation and significance denoted by a bar spanning two comparison groups represents a p value < 0.05.

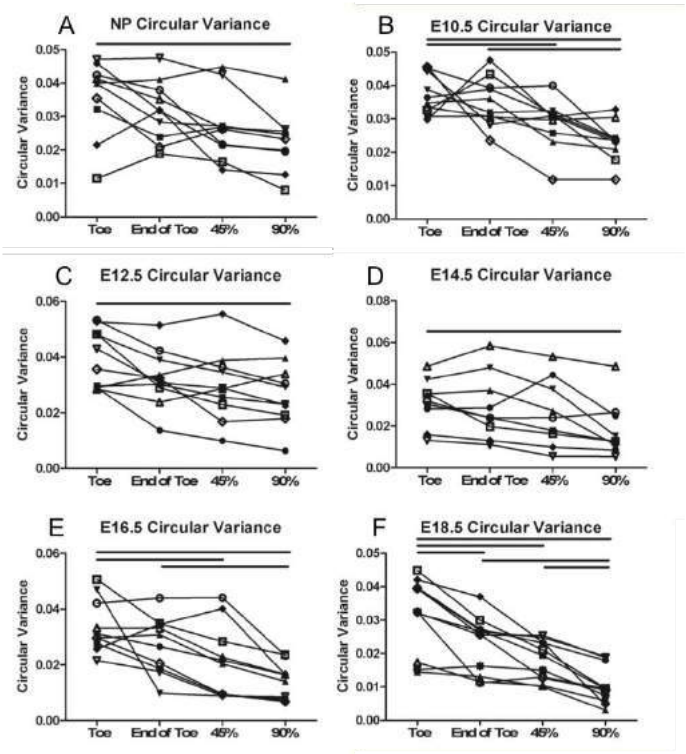

Figure 2: Collagen re-alignment of non-pregnant and pregnant cervix during tensile loading at Toe, End of Toe, 45% of Max Load, and 90% of Max Load for NP (A), E10.5 (B), E12.5 (C), E14.5 (D), E16.5 (E) E18.5 (F) cervix, comparing circular variance of fiber alignment distributions. Each sample represents one line and each point signifies alignment at each part of the mechanical test (n=10 for all samples) demonstrating significant changes. Data is presented as mean±standard deviation and significance denoted by a bar spanning two comparison groups represents a p value < 0.05.

DISCUSSION

Overall, the tensile biomechanical properties of the cervix decrease during pregnancy after E10.5. We showed that both structural (stiffness, and maximum load) and material (ultimate stress and modulus) properties decrease during pregnancy. Specifically, we did not observe changes in tissue stiffness, ultimate stress, and Young's modulus between the NP and E10.5 gestational time points. However, dynamic collagen realignment was observed at the E10.5 gestational time point. These data are consistent with studies showing that the mouse cervix remodels molecularly without loss of mechanical integrity [11, 12]. Significant earlier realignment of the collagen matrix at later gestational time points (E16.5 & E18.5) illustrates that the cervix responds to load dynamically faster at these time points (Fig. 2F). These realignment data, in combination with the significant differences observed in the cervix mechanical properties at the later gestational time points (E14.5, E16.5, and E18.5), provide critical structural insight into the cervical ripening process whereby it has been hypothesized that loosening of the collagen matrix may result in a significant decrease of tissue stiffness and strength well before normal delivery would be expected [4, 12, 13]. Importantly, while the cervix appears "ready" to allow passage of the fetus at this early time from a biomechanical perspective, PTB does not occur in these mice without an inflammatory or other trigger. Further research is necessary to determine mechanisms governing premature cervical remodeling allowing PTB [14]. While correlation of these findings to human pregnancy will be necessary, this work lays a critical foundation for investigating cervical biomechanics and the role of the cervix in PTB.

ACKNOWLEDGEMENTS

This study was supported by the MOD Prematurity Research Center at PENN and the Penn Center for Musculoskeletal Disorders (NIH/NIAMS, P30 AR050950).

REFERENCES

[1]Myers, KM et al., *J Biomech*. 48:1511-23, 2015. [2]Peralta, L et al., *J Biomech.* 48:1557-65, 2015. [3]Yoshida, K et al., *PLoS One.* 9:e112391, 2014. [4]Read CP et al, Reproduction, 134:327–40, 2007. [5]Ghartey, J et al., *Am J Obstet Gynecol.* 212:776.e1-776.e12, 2015. [6]Shah, SJ et al., *J Proteome Res.* 8:2407-17, 2009. [7]Favata M. PhD Thesis. University of Pennsylvania; 2006. [8]Dunkman, AA, et al., *Matrix Biol.* 32:3-13, 2013. [9]Miller, KS et al., *J Biomech Eng.* 134:031007, 2012. [10] Freedman BR et al., *J. Biomech.* 47: 2028–2034, 2014. [11]Akins, ML et al., Biol Reprod. 84: 1053–1062, 2011. [12]Akins, ML et al. J Biomed Opt. 2010 March-April; 15(2): 026020. [13]Zhang Y et al., Proc Natl Acad Sci U S A. 109:12878-83, 2012.

Copyright 2016 The Organizing Committee for the 2016 Summer Biomechanics, Bioengineering and Biotransport Conference

SB³C2016
Summer Biomechanics, Bioengineering and Biotransport Conference
June 29 –July 2, National Harbor, MD, USA
SB³C2016-903

DETERMINING THE RELATIONSHIP BETWEEN THE BIOMECHANICAL AND BIOCHEMICAL PROPERTIES OF ARTICULAR CARTILAGE UTILIZING AN ARTIFICIAL NEURAL NETWORK

Joe T. Rexwinkle (1), Ferris M. Pfeiffer (2,3), Nikki C. Werner (4), Aaron M. Stoker (4)

(1) Mechanical Engineering
University of Missouri
Columbia, MO, USA

(2) Bioengineering
University of Missouri
Columbia, MO, USA

(3) Orthopaedic Surgery
University of Missouri
Columbia, MO, USA

(4) Veterinary Medicine
University of Missouri
Columbia, MO, USA

INTRODUCTION

Articular cartilage is the tissue that forms the interface at joints throughout the body. As an interfacial material, the biomechanical properties are extremely important to the proper function of the joint. Two key properties in modeling the displacement characteristics of articular cartilage are the aggregate modulus and permeability [1,2]. Improper mechanical function in the joint may be indicative of joint disorders or injury.

In the lab, these properties are measured through indentation tests which measure the force-displacement relationship in the tissue [1,2]. Unfortunately, indentation tests cannot be performed clinically. Traditionally, disorders such as osteoarthritis (OA), which is the degradation of articular cartilage over time, are diagnosed after the onset of symptoms (e.g., pain and loss of function) and subsequent imaging to confirm tissue damage [3,4]. This is often at a point where considerable damage has been done and preventative measures can only slow the progression of the disease. For this reason, a relationship between biochemical properties, which can be tested in a clinical setting, and biomechanical properties could be useful in early and accurate diagnosis of various disorders such as OA.

Recent studies have focused on showing the significance between various biomechanical and biochemical properties of the cartilage tissue [4,5]. While these relationships are significant, it does not provide a direct mathematical relationship between these properties making it difficult to apply results from clinical testing to diagnosis. This study will aim to provide an early model for the relationship between biomechanical and key biochemical properties utilizing a neural network.

METHODS

With IRB approval, 121 8mm osteochondral plugs were created from tissues collected from 6 patients that had undergone total knee replacement. The thickness of cartilage tissue on the plug was determined using a needle probe test using a 22g needle. The samples were then subjected to a stress relaxation test on an Instron 8821s using a cylindrical indenter with a diameter of 4 mm where they were compressed to 80% of the original cartilage thickness at a rate of 0.1 mm/s which is a relatively rapid rate which helps to ensure that the full stress relaxation curve is preserved for accurate characterization.. The tissue is then held at a constant strain for 120 seconds. The data was then optimized in order to determine the value of aggregate modulus and permeability that minimized the error between the experimental and simulated data utilizing the following equation produced by Mow et. al in 1980 [1,2]:

$$\sigma_z(t) = H_A\dot{\varepsilon}_0 t_0 - \frac{2\dot{\varepsilon}_0\delta^2}{\pi^2 k_z}\sum_{n=1}^{\infty}\frac{e^{\frac{-n^2 t}{\tau'}} - e^{\frac{-n^2(t-t_0)}{\tau'}}}{n^2} \quad \text{where} \quad \tau' \equiv \frac{\delta^2}{\pi^2 H_A k_z} \quad (1)$$

This equation was selected for its relevance to our testing set up as well as its simplicity and accuracy. The 'fminsearch' function built into the MATLAB optimization toolbox, which uses the Nelder-Mead algorithm, was used due to the lack of constraints on the potential values of the aggregate modulus and permeability.

Copyright 2016 The Organizing Committee for the 2016 Summer Biomechanics, Bioengineering and Biotransport Conference

After indentation testing, the samples were assessed using histological and biochemical measures. The histological analysis determined the structure and quality of the bulk cartilage, chondrocytes, proteoglycans, collagen, and tidemark in the tissue and then valued them on a quantitative scale to be able to use them in the neural network model. The biochemical analysis determined the concentration of a number of known factors (such as collagen content and orientation, proteoglycan content, and many growth factors) that affect the health of articular cartilage. Both the histological and biochemical factors had a simple regression analysis performed on them and all factors that were deemed statistically significant ($P < 0.05$) to the values of the aggregate modulus and permeability were used as inputs for the neural network model. Fifteen histological and biochemical factors were determined to be statistically significant.

The neural network was set up using the neural network toolbox in MATLAB. The values were normalized to be between -1 (minimum) and 1 (maximum) then randomly separated into three categories: training (70%), validation (15%), and testing (15%). The training samples were used to develop the relationship that relates the inputs (biochemical and histological data) to outputs (biomechanical data). The validation samples were plugged into the trained relationship and were used to determine when the program should stop. The testing samples were excluded from all training and provide insight into the performance of the trained system with samples that were not utilized in the development of the model. The most important factor in understanding the performance of the neural network is the R-value of the testing group. The R-value of each group describes the relationship between the experimental data and neural network outputs with a value of 1 representing a perfect match between both sets.

The neural network used the feed-forward back propagation method utilizing the Levenberg-Marquardt algorithm. The neural network used four layers of neurons with the first three layers containing 14, 10, and 3 neurons using a log-sigmoid transfer function. The final layer was a pure linear layer with a single neuron to adjust values to the output.

RESULTS

The results of the neural network model are shown below (Figure 1). The overall R-value is very high at 0.89, representing a strong correlation between the simulated and experimental results. More importantly, the test group R-value is 0.95, which means that this model is able to successfully model samples that were not included in the training of the neural network. One of the drawbacks of a neural network model is the possibility of overfitting the model to the training data. This is observed through a high R-value in the training samples and a much lower value in the test samples. It is clear that this system is well trained from the consistently high R-value across groups.

DISCUSSION

The results achieved in this study provide a very promising first step in developing a mathematical relationship between clinically attainable biochemical data and biomechanical properties. This could provide a tool for monitoring and diagnosis of joint disorders. While the current model has a few dramatic outliers, the R-value in the testing group represents a strong correlation.

The drawback to the neural network to modeling the system is that this is a "black box" approach. This means that the equation relating both sets of properties cannot be taken from the program. However, it is relatively simple to take the data either from an individual patient or to form a generalized model, an approach which is supported by this study, and run later samples through it to determine the mechanical properties of the tissue.

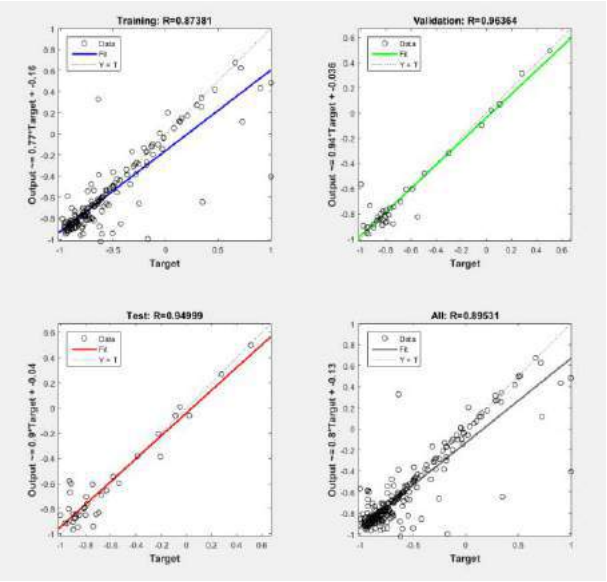

Figure 1: Graphs showing each test group ran through the neural network. The dotted line through each graph represents all points where the experimental and modeled data match perfectly.

Future work will focus upon development of a solid model of the tissue using the properties produced from the neural network for comparison with experimental models and for potential use as a diagnosis and product development tool. A more transparent model may also be created using techniques such as genetic programming. In order to provide a better diagnostic tool, healthy samples can be compared to known diseased tissues through either the neural network or more transparent techniques to allow for specific diagnosis rather than tracking the mechanical properties over time to determine the health of the tissue.

ACKNOWLEDGEMENTS

This study was funded by the Comparative Orthopaedic Lab.

REFERENCES

[1] Mow, V.C. et al, *J Biomech Eng*, 102:73-84, 1980.
[2] Bursać, P.M. et al, *J Biomech*, 32:1125-1130, 1999.
[3] NIAMS, NIH. "What is Osteoarthritis?", Nov. 2014.
[4] Rousseau, J. C., Garnero, P., *Bone*, 51:265-277, 2012.
[5] Lotz, M. et al, *Ann Rheum Dis*, 72:1756-1763, 2013.

Copyright 2016 The Organizing Committee for the 2016 Summer Biomechanics, Bioengineering and Biotransport Conference

SB^{3}C2016
Summer Biomechanics, Bioengineering and Biotransport Conference
June 29 –July 2, National Harbor, MD, USA
SB^{3}C2016-904

VIRTUAL EVALUATION OF SURGICAL REVASCULARIZATION TECHNIQUES IN CORONARY ARTERY BYPASS SURGERY.

Abhay B. Ramachandra (1, 2), Christopher Jensen (3), Andrew B. Goldstone, MD (3), Y. Joseph Woo, MD (3), Jack H. Boyd, MD (3), Andrew Kahn, MD (4), Alison Marsden (2)

(1) Department of Mechanical and Aerospace Engineering
University of California San Diego
La Jolla, CA, USA

(2) Institute for Computational and Mathematical Engineering, Department of Pediatrics Cardiology
Stanford University

(3) Department of Cardiothoracic Surgery
Stanford University
Stanford, CA, USA

(4) Department of Medicine
University of California San Diego
La Jolla, CA, USA

INTRODUCTION

Coronary artery bypass surgery (CABG) is performed to revascularize ischemic myocardium, and is widely accepted as an effective treatment for multivessel coronary artery disease. While arterial grafts are the preferred graft choice, resulting in favorable long-term outcomes, the need for multivessel revascularization and multiple targets necessitates the use of venous grafts in approximately 70% of cases. Venous grafts have high failure rates, with up to 50% of grafts failing within 10 years post-surgery. Further, surgeons are faced with a choice of several different revascularization techniques for venous grafts, including Y-shaped, sequential, or single grafts (Figure 1), with varying long term outcomes.

Decisions regarding the spatial arrangement of grafts, and the locations of anastomoses on target native vessels, rely on retrospective studies, limited geometric guidelines, surgeon's intuition and experience. Prior studies on the efficacy and superiority of each of these techniques [1, 2] report varied results. It is well established that hemodynamics, wall mechanics and geometry play a critical role in the long-term adaptation of grafts. However, numerous questions remain regarding variability across patients and the complex interplay between biology and mechanics. Virtual surgery studies provide a means to perform a controlled experiment in which patient variability can be controlled for, and the mechanics can be examined independent of other factors.

Image-based, patient-specific computational fluid dynamics simulations provide a non-invasive means to obtain finely resolved hemodynamic data, perform virtual surgery, and objectively evaluate these surgeries. Here, we demonstrate the capability of virtual surgery and simulation tools to compare and contrast three different CABG revascularization techniques commonly used in clinical practice today.

METHODS

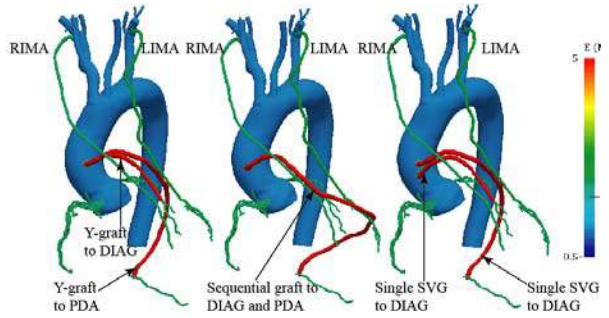

Figure 1: Patient-specific model from CT scan of a patient who had undergone CABG surgery with venous grafts in Y configuration (left); Sequential (middle) and 2 single graft (right) - virtual modifications of the graft geometry. Vessels are colored by their Young's Modulus values.
PDA-posterior descending artery, SVG- Saphenous vein graft, IMA-internal mammary artery, DIAG- Left Diagonal branch

We build patient-specific 3D models of CABG geometries from CT images of a patient who has undergone bypass surgery. We use a customized version of the open source software SimVascular (www.simvascular.org). We discretize the 3D model using linear tetrahedral finite element mesh using MeshSim (Simmetrix Inc, Clifford, New York) and assign vessel specific material properties and thickness, based on values from literature. For regions of the circulation not visible on the CT images we make use of a circuit analogy and design lumped parameter networks (LPN) to mimic the pressure-flow relationships in the systemic circulation, coronary

Copyright 2016 The Organizing Committee for the 2016 Summer Biomechanics, Bioengineering and Biotransport Conference

circulation and the heart. The LPNs are tuned to match non-invasive clinical data, including cuff blood pressure, cardiac output, and empirical data from literature, including coronary flow splits. The flow information in LPNs is coupled with the 3D domain using a modular iterative coupling algorithm [4]. We quantify hemodynamics and wall deformation related quantities in 3D domain by solving the incompressible Navier-Stokes equations for the fluid and linear elasticity equations for the solid, using stabilized finite element methods. The interaction of the fluid and the solid domains relies on the coupled momentum method where the tractions from the solid domain are imposed on a fixed fluid mesh.

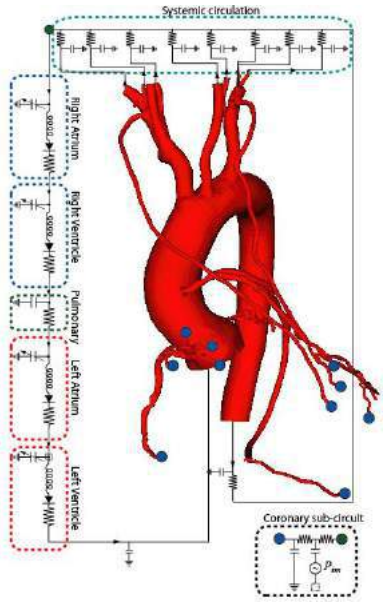

Figure 2: Patient-specific model coupled to a closed loop lumped parameter network (LPN) of circulation. The LPN includes an elastance based heart model, a windkessel model for systemic circulation and coronary-subcircuit.

With input from surgeons on our team, we virtually modify the venous graft geometric configurations to mimic the commonly performed revascularization techniques. In this study, we compare the Y-configuration, sequential anastomosis, and single graft approach, while keeping rest of the simulation parameters, including boundary conditions, material properties, and remaining anatomy, the same. The mechanical quantities correlated with atherogenesis and graft failure are quantified in each of these virtual surgical configurations. The graft regions at potential risk for restenosis or failure are identified.

RESULTS

The framework is able to reproduce clinically observed flow and pressure waveforms from clinical literature, including the out of phase behavior of coronary flow with the systemic circulation. We quantify key mechanical markers that influence endothelial behavior and cell proliferation, including wall shear stress (figure 3), oscillatory shear index, wall shear stress gradients, and wall strain. Preliminary results show that the sequential grafts have lower WSS in segments distal to the first anastomosis, likely making them more prone to atherosclerosis and subsequent failure. Current efforts are directed towards quantifying clinically/biologically relevant quantities in the venous grafts and comparing with clinical data in a cohort of patients.

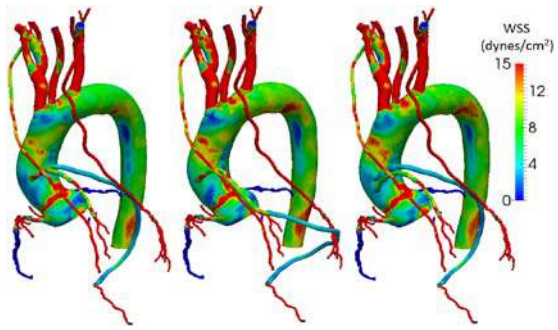

Figure 3: Cardiac cycle time averaged wall shear stress (WSS) distribution in the three venous graft configurations, with rigid wall assumption. Note the distal segment of sequential graft has lower WSS compared to the proximal segment.

DISCUSSION

Cells in the vessel wall sense mechanical stimuli such as stretch, wall shear, and oscillatory components of the flow, and regulate gene expression and turnover of wall constituents. Hence quantifying these stimuli is a necessary step in evaluating and comparing revascularization techniques. Computational simulations provide a non-invasive means to quantify mechanical stimuli on grafts in patient-specific geometries. Patients in this study act as their own control, as only the graft geometry is altered virtually keeping all other parameters fixed. This allows for a controlled comparison of surgical methods that is not possible in the clinical setting.

Our results show that regions distal to the side-to-side anastomosis (SSA) of the sequential graft configuration have lower WSS (3.1 dyn/cm^2) compared to the pre-SSA regions (6.1 dyn/cm^2). Prior studies have reported high failure rates for regions between the SSA and end to side anastomosis (ESA) in a sequential graft, which qualitatively agrees with our results. Additional patients will need to be added to the study cohort before further conclusions regarding clinical application can be drawn. Myriad factors, such as varying local geometry, wall properties and dynamic distal demand, make surgical design decisions non-intuitive, necessitating the use of computational tools, such as those proposed here, to aid in clinical decisions.

There are uncertainties associated with clinical measurements and parameters used to tune lumped parameter networks. Current efforts are being directed towards parameter estimation, identification and uncertainty quantification in these simulations. The models presented in this work lack details at the cellular/sub-cellular level and cannot capture the evolving nature of vessel wall constituents. There is a further need to couple CFD simulations with models of vascular growth and remodeling to gain further insights into the pathophysiology of graft adaptation. Nonetheless, the tools and methods proposed in this paper are a necessary step in that direction.

ACKNOWLEDGEMENTS

This work was supported by an NIH grant (NIH R01-RHL123689A) to A. L. M. and A.K.

REFERENCES

[1] Mehta, R. H., et al., *Circulation,* 124.3: 280-288, 2011

[2] Li, J., et al.,*The Annals of thoracic surgery,* 92.4: 1292-1298, 2011

[3] Sankaran, S., et al., *Annals of biomedical engineering,* 40.10: 2228-2242, 2012

[4] Moghadam, M. E., et al., *Journal of Computational Physics* 244: 63-79, 2013.

Copyright 2016 The Organizing Committee for the 2016 Summer Biomechanics, Bioengineering and Biotransport Conference

SB^{3}C2016
Summer Biomechanics, Bioengineering and Biotransport Conference
June 29 –July 2, National Harbor, MD, USA
SB^{3}C2016-905

IN-VIVO ANALYSIS AND RESIDUAL STRAINS IN SEMILUNAR HEART VALVES

Ankush Aggarwal (1,2), Alison M. Pouch (3), Eric Lai (3), John Lesicko (1), Joseph H. Gorman (3) III^3, Robert C. Gorman (3), and Michael S. Sacks (1)

(1) Center for Cardiovascular Simulation
Institute for Computational Engineering & Sciences
Department of Biomedical Engineering
The University of Texas at Austin, Austin, TX, USA

(2) Zienkiewicz Centre for Computational Engineering
Swansea University, Swansea UK

(3) Gorman Cardiovascular Research Group
Department of Surgery
University of Pennsylvania, Philadelphia, PA, USA

INTRODUCTION

Determining the biomechanical behavior of heart valve leaflet tissues in a non-invasive manner remains an important clinical goal. We have previously developed an inverse modeling framework that would allow us to determine mechanical parameters from clinical imaging modalities, like ultrasound [1]. However, in order to ensure robust results, we need to provide some important information about valve into the inverse model such as valve fiber architecture and its residual strain state. In this work we exploit the advanced in-vivo imaging and segmentation tools and novel technique to calculate strains without using physical markers on the leaflets to quantify in-vivo and residual strains in human aortic valve leaflets. The proposed method is generic and could be applied to any semilunar heart valves.

The information about residual strains is critical to accurate determination of tissue stress state, which in turn is related to pathology development. Yet, the level and functional role of residual strains in heart valves remains an open question. While it is anticipated that some level of residual strains exists in all heart valves, this has not been verified or quantified other than for the mitral valve (MV) [2]. In that study, physical markers were used that limited its clinical applicability and restricted the calculated strains to a sub-region of the leaflet. Thus, the need for valve excision and physical markers in determination of residual strains has rendered it challenging to perform such studies in healthy human subjects. While residual strains are known to exist within the aortic valve (AV) layers [3], it is not known whether, and how much, residual strain exists in the AV tissues in their in-vivo state. We aim to address these questions with a spline-based technique which allows us to determine heterogeneous strains without the need of physical markers. Combining such information into the inverse-modeling tools developed previously would allow us to determine functional properties of heart valves in the least invasive fashion.

METHODS

Five patients with healthy aortic valves were selected and imaged using 3D ultrasound. After their heart transplant, the valve leaflets from randomly selected positions were excised and analyzed to determine their collagen architecture using standard techniques [4]. The in-vivo ultrasound images were segmented at three states – open, just-coapted, and full closed – using a multi-atlas segmentation and deformable modeling technique [5]. The segmented images of the leaflet, both in-vivo and ex-vivo, were parameterized using a spline technique we previously validated [6]. This technique allows us to determine corresponding points in two images of a leaflet within good accuracy. Based upon this, we chose 14 points symmetrically placed on the leaflets as "virtual markers" and determined the strains from them between various states of the leaflet – ex-vivo to in-vivo (open), open to just-coapted, and just-coapted to fully loaded.

Overall leaflet dimensions were compared at various states – their areas and lengths of basal attachment and free edge. Moreover, heterogeneous strains varying of the leaflet were also analyzed. The strains were quantified in terms of the following quantities. The principal stretches λ_1 and λ_2, the stretches in circumferential and radial directions, the area change, the maximum shear, and the shear along circumferential-radial direction. In order to improve the statistical sampling, results from all three AV leaflet types – left coronary, right coronary, and non-coronary – were pooled. For the overall geometrical measurements, such as the total leaflet area and lengths of free edge and basal attachment, the results were averaged and variations were quantified in terms of standard deviation. Furthermore, for regional analysis, the leaflets were considered to follow symmetric deformation patterns, so that the sample sizes were doubled.

Copyright 2016 The Organizing Committee for the 2016 Summer Biomechanics, Bioengineering and Biotransport Conference

RESULTS

The average ratio of leaflet area from ex-vivo to mid-systole was 1.2±0.19 and that from mid-systole to just-coapted configuration was 1.25±0.12. The leaflet areas during just-coapted and fully-loaded states were roughly the same with a 1.025±0.06 ratio (Fig. 1).

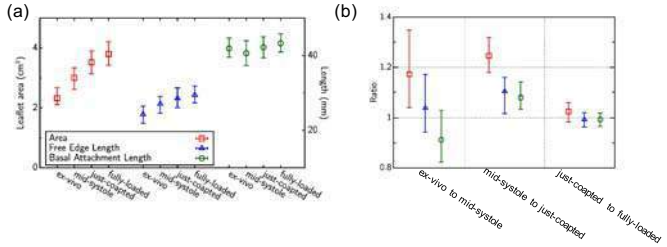

Figure 1: Average leaflet dimensions and areas, and their ratios over four states – ex-vivo, open, just coapted and fully loaded.

Strains over the leaflet varied significantly. The principal stretches for all the mappings were roughly aligned with the circumferential and radial directions, with higher stretch acting radially (Fig. 2). For the just-coapted to fully-loaded deformation, the circumferential stretch was close to one over most of the leaflet, except near the commissure and basal region, where there was 15% stretch in the fiber preferred direction. For the leaflet deformation from open to just-coapted state, the maximum stretch was in 1.3-1.7 range (Fig. 2) and the lower principal stretch varied to a much lesser extent across samples in the 0.8-1 range representing some shrinking. The stretch ratio along the circumferential direction was slightly higher than one, except near the commissure where it was approximately 1.3-1.5. Lastly, for the ex-vivo to in-vivo open state, the leaflet experienced high stretches in the radial direction. The circumferential stretch was usually close to one, whereas the radial stretch varied widely in regions. There was no radial stretch in the basal area, while other areas experienced a stretch of 25-50%. There was some shear deformation (10-30º) in all the cases which varied over the leaflet to some extent.

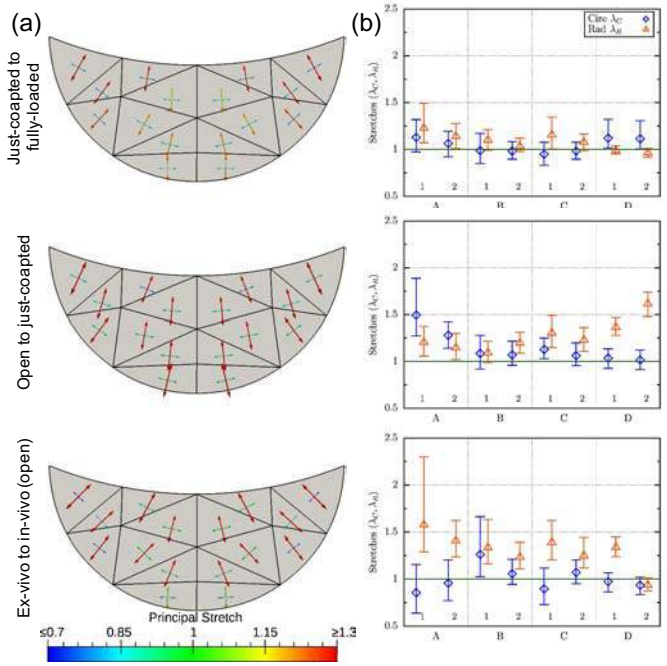

Figure 2: (a) The principal stretches over the leaflet and (b) stretches along circumferential and radial directions.

DISCUSSION

Since reported in the aorta by Fung, residual strain in biological structures has been an active area of research. In spite of their importance, investigation into the residual strains in heart valves is relatively new. This is partly because of the significant difficulty in obtaining the requisite data, including challenges in obtaining in-vivo images and segmentation of the leaflet geometry. In the present work, we utilized the latest imaging and segmentation technology and a novel technique to measure strains in AV leaflets that provided a heterogeneous strain field without the need of physical markers. The leaflets shrank by 17% upon excision on an average, and the deformation was predominantly in the radial direction. These were the first attempt of residual strain measurements on healthy human AV leaflets as per authors' knowledge.

In addition to residual strains, we also calculated the strains experienced in-vivo during valve closure starting with open state and deforming to just-coapted and fully-loaded states. We found that the leaflet area increased by approximately 25% as the valve closed from mid-systole to just-coapted state, even though the valve was not yet supporting any pressure difference. The change in linear dimensions of the leaflets (the free edge and basal attachment lengths) under this deformation was limited to only 3-5%. A heterogeneous analysis revealed that the local area change was highly non-uniform, ranging from almost no change in some parts to more than 50% increase in others, and that the deformation was predominantly in the radial direction.

During the leaflet deformation from just-coapted to fully-loaded, the area change was minimal and circumferential stretch was close to one over most of the leaflet. This indicates that most of the collagen fibers were already recruited in the just-coapted state, making the circumferential direction highly stiff.

For all in-vivo deformations, there was a 10-20º shear present, which was relatively uniform over the leaflet and consistent across samples. For almost all of the cases, the maximum stretch was observed perpendicular to the circumferential direction. This can be expected as the collagen fibers run predominantly along the circumferential direction making it the stiffer one.

Although sufficient for this study, the size of the sample dataset will have to be expanded to establish clear trends between three leaflet types and analyze the asymmetry of leaflet strains. In the future, we would apply this framework to other valves pulmonary valve, as well as pathological valves like bicuspid aortic valve. These results will form the basis of the critical information needed for accurately modeling and predicting biomechanical properties of the healthy human aortic valve leaflets in a non-invasive manner.

ACKNOWLEDGEMENTS

This work was supported by the American Heart Association (14POST18720037 to A.A.), Welsh Government and Higher Education Funding Council for Wales through the Sêr Cymru National Research Network in Advanced Engineering and Materials (F28 to A.A.), and National Institutes of Health (R01 HL108330 to M.S.S.).

REFERENCES

[1] Aggarwal and Sacks, *BMMB*, 2015 (in press).
[2] Amini et al., *ABME*, 40:1455-1467, 2012.
[3] Stella and Sacks, *J Biomech Engg.*, 129:757-766, 2007.
[4] Sacks, Smith, and Hiester, *ABME*, 25:678-689, 1997.
[5] Pouch et al., *Med. Image Anal.*, 26 (1), 217-231, 2015.
[6] Aggarwal et al., *ABME*, 42:986-998, 2014.

Copyright 2016 The Organizing Committee for the 2016 Summer Biomechanics, Bioengineering and Biotransport Conference

SB^{3}C2016
Summer Biomechanics, Bioengineering and Biotransport Conference
June 29 –July 2, National Harbor, MD, USA
SB^{3}C2016-906

THE EFFECT OF SIMULATED ANATOMICAL CONSTRAINTS ON BUCKLING LOADS OF CARDIAC LEADS

Donna L. Walsh (1), Ashok M. Williams (1), Nandini Duraiswamy (1), Oleg Vesnovsky (1), and L. D. Timmie Topoleski (1,2)

(1) Center for Devices and Radiological Health
U.S. Food and Drug Administration
Silver Spring, MD, USA

(2) Department of Mechanical Engineering
University of Maryland, Baltimore County
Baltimore, MD, USA

INTRODUCTION

Perforation of the myocardium is a serious potential adverse event associated with cardiac leads. The load at which a cardiac lead body will bend or buckle is thought to be a factor in whether or not a particular lead design is likely to perforate the heart [1]. The combination of anatomical constraints and natural movement of the cardiac muscle creates forces on the lead that may cause perforation. The flexibility of the lead, which is reflected in its critical buckling force, provides some natural protection against perforation. However, there currently is no standard test method for measuring buckling force or flexibility of pacemaker or implantable cardioverter defibrillator (ICD) leads. Our earlier work incorporated simulated anatomical constraints into a buckling test to show that the load measured at the lead tip is dependent not only on lead design but also on the boundary conditions imposed on the lead during the test [2]. The purpose of this study was to further modify the test setup to continue our investigation of the effect of different boundary conditions on buckling load at the lead tip. The ultimate goal is to further develop a test method to identify characteristics of lead designs that make them more likely to perforate the cardiac muscle.

METHODS

Two pacemaker and two ICD lead models (n=2 each for a total of 8 leads) were subjected to cyclic loading in five test setups (A-E). Test setup A simulated the presence of the superior vena cava (SVC), right atrium (RA), tricuspid valve (TV), and right ventricle (RV) during systole and was previously described in detail [2]. The base plate used in the current study was modified from the previous metal plate [2] to incorporate a conical depression (5.43 mm radius, 3.8 mm depth) for seating the extended helix of the lead tip. The dimensions of the base plate are identical to those specified in a perforation test protocol under development by the AAMI Transvenous Leads Working Group. Setup B was the same as A except that the RV constraint was removed.

In test setup C the lead was fixed 75 mm from the distal tip, with an RV constraint around the distal portion of the lead, and no other simulated anatomical structures. Test setup D used the same fixture as C, without the RV constraint; therefore, D was an unconstrained configuration. Test setup E used the same fixture as C, modified to investigate the potential effects of friction by applying silicone lubricant along the lead body and the interior RV constraint.

Each lead was subjected to multiple cycles under displacement control to determine if the maximum load changed with cycle count. Tests were performed at 0.02 Hz (~50 mm/min) for 50 cycles with the helix extended. The minimum and maximum displacements for each cycle were 3 and 25 mm, with a preload of 1.5 ± 0.5 g.

RESULTS

The different test setups A-E substantially influenced the loading profiles of the leads. In general for pacemaker leads, setups that included the RV constraint (A, C) yielded the highest loads, with peak loads ranging from 30-60 g (Figure 1). Adding the lubricant (E) reduced the peak loads to 15-20 g. Removing the RV constraint (B, D) reduced the loads even further, with peaks less than 10 g.

For the ICD leads, all three setups that included the RV constraint (A, C, E) yielded somewhat similar loading profiles (Figure 2). As with the pacemaker leads, the peak loads for those setups were higher than the peak loads in setups without the RV constraint. The addition of the lubricant had more of an effect in reducing peak loads with pacemaker leads than with ICD leads.

Regardless of test setup, some leads experienced variations in maximum load during the first few cycles of testing, before achieving a steady state max load within 50 cycles (Figure 3, left). In contrast,

Copyright 2016 The Organizing Committee for the 2016 Summer Biomechanics, Bioengineering and Biotransport Conference

maximum loads for other leads were fairly constant for the duration of the test (Figure 3, right).

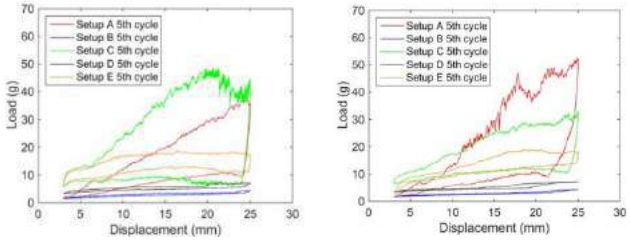

Figure 1. Buckling load vs.displacement for two different representative pacemaker lead models in test setups A-E. The fifth of 50 cycles is shown in each case.

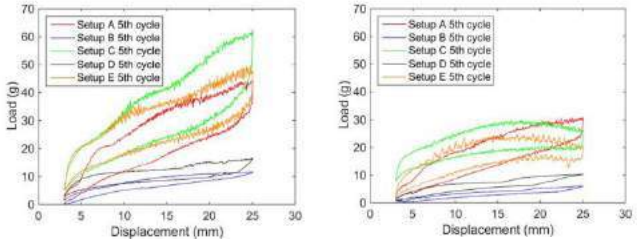

Figure 2. Buckling load vs. displacement for representative ICD lead models in test setups A-E. The fifth of 50 cycles is shown in each case.

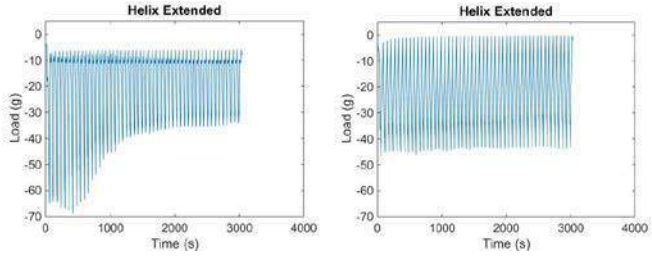

Figure 3. (Left) Compressive load vs. time for one representative pacemaker lead showing variable loads during the first few cycles prior to steady state loading by 50 cycles. (Right) Compressive load vs. time for one representative ICD lead showing fairly constant max load over all 50 cycles.

DISCUSSION

The loading profiles for both pacemaker and ICD leads in setups without the RV constraint (B, D) plateaued after the first few millimeters of displacement, but at the lowest loads (less than 15 g). In contrast, setups with the RV constraint (A, C) generally yielded steadily increasing and much higher loads; this was due to the lead making contact with the wall of the constraint and confirms our previous findings [2].

For all leads, the use of the lubricant in setup E reduced the peak loads compared to those of setup C. (Setup A with the lubricant will be tested at a later date.) For pacemaker leads with lubricant, the load-displacement profiles changed to resemble those of B and D; however, the plateau occurred later in the cycle (after 10-15 mm displacement). Furthermore, the marked difference in peak loads for pacemaker leads with vs. without the lubricant (C vs. E) appears to be due in part to the outer insulation material. Traditionally, silicone and polyurethane are used as outer lead insulation materials [3]. We noticed that the outer insulation of the two pacing lead models had a "sticky" feel (though to different degrees), while the majority of the two ICD leads felt more "slippery." It is our supposition that a greater amount of friction present between the pacemaker lead insulation and the RV constraint allowed a more noticeable decrease in peak load by the addition of the lubricant. In contrast, the ICD leads contacted the RV constraint at the location of the metal defibrillation coil, which provided little friction against the PTFE material of the RV constraint. Therefore, the addition of the lubricant made less of a difference for ICD leads because there was likely already a low coefficient of friction on the lead surface at the point of contact. Additional study of the friction between the various lead components and the RV constraint is necessary to test this supposition.

Despite the addition of the lubricant and the lower friction between the RV constraint and the defibrillation coil, peak loads for some ICD leads with the RV constraint increased steadily with displacement. In this case, lead diameter likely played a role, as the diameters of the ICD leads were up to 30% larger than the pacing leads. A larger lead diameter, combined with a defibrillation coil, and the lead's interaction with the base plate, are some of the factors affecting peak load, which is often construed as a quantitative metric of the lead's ability to bend under load (lead stiffness).

Maximum load varied considerably with cycle count for leads only in setups A and C, indicating that the interaction between the lead and the ventricular wall is a key component in determining peak forces imparted to the tissue by the lead tip. However, the maximum peak load in all setups reached a steady state by the 50th cycle. This steady state behavior provides initial insight on the long-term post-implantation loading conditions between the lead tip and the tissue.

Future research will include testing additional lead models to further determine the effect of simulated anatomical constraints and a "best" model for future testing. Changes in load-displacement behavior (e.g., peak vs. steady state load, loads at specific displacements) during cyclic testing will be analyzed for each individual lead model to explore how these changes might impact pre-clinical perforation assessment of leads. Lead characteristics such as stiffness, insulation materials, and general lead body construction will be examined to gain insight into any variations observed in loading profiles between pacemaker and ICD leads. Another important future consideration will be the interaction of the lead tip (helix) with a tissue substitute gel instead of a metal plate, and longer-term dynamic testing in load control. These tests will ultimately lead to testing conditions that more closely simulate the in vivo environment.

ACKNOWLEDGEMENTS

We thank Biotronik, Boston Scientific, Medtronic, Sorin, and St. Jude Medical for assistance in acquiring test samples for this study.

This project was supported by the FDA Critical Path Initiative [2015CPOSEL04] and by the CDRH Research Participation Program administered by the Oak Ridge Institute for Science and Education.

REFERENCES

[1] Opolski, G.et al., 7th World Symposium on Cardiac Pacing, pp. 423–426, Vienna, Austria, 1983.

[2] Stephen B. et al., *ASME J Med Devices,* 5; 9(1):011001-8, 2015.

[3] Hayes DL et al., ed., Cardiac Pacing, Defibrillation and Resynchronization: A Clinical Approach, 3rd ed., Wiley, 2013.

Disclaimer

The mention of commercial products, their sources, or their use in connection with materials reported herein is not to be construed as either an actual or implied endorsement of such products by the Department of Health and Human Services.

This material is declared a work of the U.S. Government and is not subject to copyright protection in the United States. Approved for public release; distribution is unlimited.

Copyright 2016 The Organizing Committee for the 2016 Summer Biomechanics, Bioengineering and Biotransport Conference

SB^{3}C2016
Summer Biomechanics, Bioengineering and Biotransport Conference
June 29 –July 2, National Harbor, MD, USA
SB^{3}C2016-907

IS SIMPLE GEOMETRIC SCALING TO TRANSFORM CERVICAL SPINE INJURY CRITERIA FROM MALES TO FEMALES ADEQUATE?

N. Yoganandan (1), F. Pintar (1), C.D. Bass (2), M. Ortiz (2), H. Cutcliffe (2), J. Rupp (3), A. Agnew (4), A. Weaver (5) F.S. Gayzik (5), L. Voo (6)

(1) Medical College of Wisconsin
Milwaukee, WI USA

(2) Duke University
Durham, NC, USA

(3) University of Michigan
Transportation Research Institute
Ann Arbor, MI, USA

(4) Ohio State University
Columbus, OH, USA

(5) Wake Forest University School of Medicine
Winston-Salem, NC, USA

(6) John Hopkins University
Applied Physics Lab
Laurel, MD, USA

INTRODUCTION

Current automotive test devices include the mid-size male and small-size female Hybrid III dummies and injury criteria are essentially scaled from one to the other to account for differences between sex and size [1 , 2]. The scaling process is based on geometrical considerations with the assumption that the female spine is a simple scaled-down version of the male. Neck circumference is used as the scaling factor to convert injury metrics from male to obtain female-specific injury criteria. While female spines are smaller and have lower failure forces and moments, the validity of this scaling method and its application to injury criteria are not fully examined. This study presents a synthesis of literature data to examine the efficacy of the process.

METHODS

Methods consisted of examining biomechanical responses from different types of tests on different types of experimental models with male and female specimens from the same study, followed by anatomical studies using cadavers and volunteers to examine the role of injury metrics, patterns, mechanisms, and morphology of female and male human spines.

1. Biomechanical Experimental results

Functional unit tests: Static nondestructive pure moment bending tests under flexion and extension were conducted using the same experimental design to compare male and female responses [3, 4]. Female specimens had greater total range of motion than males. Failure moments in extension and flexion ($p<0.05$) were lower in females for the upper spine. Statistically significant differences were not apparent in the failure moment and angulation when all segments were grouped.

Head-neck complex tests under inertial loading: Dynamic tests simulating responses to whiplash-induced injuries from motor vehicle impacts showed differences in kinematics between male and female spines [5]. Segmental motions in females were greater ($p < 0.05$) at all sub-axial levels with the exception of the middle region. Shear force and extension moment magnitudes at the time of S-curvature were greater ($p < 0.05$) in females [6].

Intact human cadaver tests under tension loads: Distractive forces simulating airbag deployments were simulated using the intact whole body model [7]. Two male subjects sustained tension-related ligamentous injuries at the C1-C2 level while the other and the female subjects sustained injuries at the atlantal-occipital region. Maximum forces and moments showed typical biological variability, measured from the standard deviation (metrics for the female subject were within one standard deviation of the male responses).

Isolated cervical column tests under axial compressive loading: Tests were done using the base of the skull-to-entire osteoligamentous columns using fixed end conditions [8]. Injuries to male specimens consisted of 4 at C1, 1 at C2, 1 at C1 and C2, 1 from C3-C5, and 2 at C5 levels while injuries to female specimens included one each at C1 and C2, C4 and C5 in one, C3 and C6 in one, and an extension failure with unreported level, showing that both groups are susceptible to injuries at all levels. Maximum axial compressive force, deflection and energy of female specimens were lower than male spines.

Isolated cervical column tests under combined loading: Tests were done by applying an eccentric load using a pinned-pinned end condition [9]. The younger male specimen responded with C 4-5-6 anterior and posterior ligament tears and the older spine responded

Copyright 2016 The Organizing Committee for the 2016 Summer Biomechanics, Bioengineering and Biotransport Conference

with wedging of C4-6 bodies associated with C3-4 disc tear, while the female specimen sustained C6-C7 posterior ligament tears. For the younger and older male and female specimens, peak flexion moments were 14.6, 3.4 and 8.7 Nm, and compressive forces were 192, 338 and 214 N. Moment-angulation curves of the female were within the boundaries of two male specimens.

Head-neck complex tests under axial compressive loading: Dynamic compression loading applied to the head simulating automotive and sports events showed differences between male and female head-neck complexes [10]. Compression body fractures to male specimens were concentrated at one level while injuries to female specimens included both body and posterior complex fractures and ligamentous lesions. The mean magnitudes of the axial force, deflection, strain, energy, and acceleration were within one standard deviation from each other. Studies examined the effects of loading rate, age and sex on injury probabilities [11]. Male spines sustained greater failure force (600 N) regardless of rate and age, suggesting that the failure response from a probabilistic perspective depends on these factors. Inverted drop tests were conducted on PMHS head-T1 columns [12]. All specimens sustained multiple level injuries with predominantly ligamentous involvements. Biomechanical data indicated that female metrics for the axial neck force was lower than the male specimens.

2. Cervical spine geometrical analyses

Facet joint-related geometry: Studies aimed to better understand susceptibility of the female population to whiplash associated disorders included the determination of the posterior column morphology [13]. While the facet joint width was greater ($p<0.05$) in the upper cervical spine in both populations, the gap in the dorsal region was greater (reaching significance at 0.06) and the facet cartilage thickness was lower ($p<0.05$) in the upper spine than the lower cervical spine for female specimens. Facet joint angles from 250 males and 173 females using CT scans of 18+ year-old subjects showed greater orientation in females at C2 and C3 (both $p<0.05$) and lower at C6 and C7 levels (both $p<0.05$) [14].

Muscle-related geometry: Human cadavers were used to quantify muscle insertions of C4-C5 and C5-C6 facet capsules [15]. The mean muscle insertion area was greater ($p<0.05$, by 1.8 times) in males (61.4 mm^2 versus 35 mm^2 for females) and mean axial cross sectional capsule area was greater ($p<0.05$, by 1.4 times) in males (14.7 mm^2versus 10.2 mm^2 for females). Estimated mean isometric muscle contraction was greater ($p<0.05$) in males than females (27 versus 15 N). The maximum moment generating capacity during maximum voluntary contractions of neck muscles in females was up to one-half of those in males [16]. Sagittal moments were lower ($p<0.05$) in females.

Vertebra- and disc-related geometries: Sex bias on vertebral geometry was analyzed using CT scans [5, 17]. Independent size-matched subgroups were identified based on sitting height and head circumference [5]. For sitting height-matched subgroup, the disc-facet depth and column height was longer ($p<0.05$) in males. For head circumference-matched subgroup, all vertebral dimensions were greater ($p<0.05$) by 7 to 18% in males.

SUMMARY

The simple scaling process based on neck circumference ignores local, regional and overall differences between male and female spine anatomy, structure/component, injuries, injury mechanisms, injury metrics, and potentially injury tolerance criteria when scaled from male spines. As briefly described above, studies show that differences exist and are statistical. The lack of significance in some studies presumably stems from factors such as sample size and altered focuses, i.e., not designed specifically to investigate female-male differences. The segmented nature coupled with the heterogeneous components of the spine should be given due consideration to derive female injury criteria even when one ignores differences (that might exist) in the head physical and inertial properties, as any added mass due to protective equipment alters the biomechanics and tolerance. As females are increasingly exposed in the military, the present analyses emphasize the need for testing female spines to derive female-specific injury criteria.

ACKNOWLEDGMENTS

This research was conducted as part of the Biomechanics Product Team led by the Johns Hopkins Applied Physic Laboratory for the WIAMan Project under contract #N00024-13-D-6400, U.S. Army Research, Development and Engineering Command. This material is also result of work supported with resources and use of facilities at the Zablocki VA Medical Center, W81XWH-12-0041 and the Department of Neurosurgery, at the Medical College of Wisconsin Milwaukee, Wisconsin Milwaukee, Wisconsin. The authors NY and FAP are part-time employees of the Zablocki VA Medical Center, Milwaukee, Wisconsin. The content included in this work does not necessarily reflect the position or policy of the U.S. Government.

REFERENCES

[1] M. Kleinberger, E. Sun, R. Eppinger, S. Kuppa, R. Saul, in, NHTSA, Washington, DC, 1998, pp. 115 pp. [2] N. Yoganandan, M.W. Arun, F.A. Pintar, Journal of biomechanics, 47 (2014) 1749-1756. [3] R.W. Nightingale, V. Carol Chancey, D. Ottaviano, J.F. Luck, L. Tran, M. Prange, B.S. Myers, Journal of biomechanics, 40 (2007) 535-542. [4] R.W. Nightingale, B.A. Winkelstein, K.E. Knaub, W.J. Richardson, J.F. Luck, B.S. Myers, Journal of biomechanics, 35 (2002) 725-732. [5] B.D. Stemper, N. Yoganandan, F.A. Pintar, D.J. Maiman, M.A. Meyer, J. DeRosia, B.S. Shender, G. Paskoff, Spine, 33 (2008) E44-49. [6] B.D. Stemper, N. Yoganandan, F. Pintar, T.A. Gennarellu, in: IRCOBI, Maastricht, The Netherlands, 2007, pp. 249-260. [7] B. Cheng, K.H. Yang, R.S. Levine, A.I. King, R.M. Morgan, in: Stapp Car Crash Conf, 1982, pp. 1-40. [8] J.H. McElhaney, J.G. Paver, H.J. McCrackin, G.M. Maxwell, in: Stapp Car Crash Conf, San Diego, CA, 1983, pp. 163-177. [9] J.H. McElhaney, B.J. Doughetyt, J.G. Paver, B.S. Myers, L. Gray, in: Stapp Car Crash Conf, Atlanta, GA, 1988, pp. 21-28. [10] N. Yoganandan, F.A. Pintar, P. Arnold, J. Reinartz, J.F. Cusick, D.J. Maiman, A. Sances, Jr., Journal of spinal disorders, 7 (1994) 420-428. [11] F.A. Pintar, N. Yoganandan, L. Voo, Spine, 23 (1998) 1957-1962. [12] R.W. Nightingale, J.H. McElhaney, D. Camacho, M. Kleinberger, B.A. Winkelstein, B.S. Myers, in: Stapp Car Crash Conf, 1997, pp. 451-471. [13] N. Yoganandan, S.A. Knowles, D.J. Maiman, F.A. Pintar, Spine, 28 (2003) 2317-2323. [14] C.S. Parenteau, D. Zuby, K.B. Brolin, M.Y. Svensson, C. Palmertz, S.C. Wang, in: IRCOBI, 2013, pp. 803-817. [15] B.A. Winkelstein, R.E. McLendon, A. Barbir, B.S. Myers, Journal of anatomy, 198 (2001) 455-461. [16] A.N. Vasavada, S. Li, S.L. Delp, Spine, 26 (2001) 1904-1909. [17] N. Yoganandan, F.A. Pintar, B.D. Stemper, J.L. Baisden, R. Aktay, B.S. Shender, G. Paskoff, P. Laud, Bone, 39 (2006) 336-344.

Copyright 2016 The Organizing Committee for the 2016 Summer Biomechanics, Bioengineering and Biotransport Conference

SB^{3}C2016
Summer Biomechanics, Bioengineering and Biotransport Conference
June 29 –July 2, National Harbor, MD, USA
SB^{3}C2016-908

DETECTING OSTEOPOROTIC VERTEBRAL COMPRESSION FRACTURES: BMD VS. ACOUSTIC EMISSION TECHNIQUE

Thomas Mazahery (1), Melanie Pham (2), Ronald Childs (1), Mark Theiss (1), Jihui Li (1)

(1) Department of Orthopedics
Inova Fairfax Hospital
Falls Church, VA, USA

(2) Department of Surgery
Eastern Virginia Medical School
Norfolk, VA, USA

INTRODUCTION

Osteoporosis is a major health problem in the world and affects millions of people. It typically develops unnoticed over many years until a sudden bone fracture occurs. Osteoporosis is also a key cause of vertebral compression fractures (VCF) that influence about 40% of women in their life time [1]. During VCF, cracks accumulate in the vertebral bodies which can be exacerbated by activities of daily living. While medical images such as X-rays and CTs are viewed to evaluate spinal deformities, physicians predominantly use bone mineral density (BMD) to diagnose spinal osteoporosis, estimate the risk of VCF, and determine the appropriate drug dosage. However, BMD was found not a reliable predictor of fracture risk as there is substantial overlap between BMD scores of people who break their vertebra and those who do not [2-4].

Acoustic Emission (AE) is a nondestructive technique that can detect the progression of cracks occurred in a structure in real time. Besides earthquake detection and crack monitoring in oil pipes and bridges, in recent years AE technique has been employed to explore the biomechanical properties of various bone and implant constructs [5-7]. It showed a unique capability of revealing the occurrence time, amplitude and location of microcracks instantly and continuously. The objective of this study is using AE technique to investigate microcrack activities in vertebral bodies and assess its potential in detecting VCF in real patients. We hypothesize: 1) Microcrack signals detected by AE technique correlate to actual damages in a vertebral body; 2) An AE sensor attached posterior to the vertebral body can detect the damage signals occurred in the vertebral body.

METHODS

3 male and 3 female cadaveric lumbar spines (ages from 56 to 94) were collected from a tissue bank. BMD was measured using dual X-ray absorbitometry (DEXA). L2 was separated from each lumbar spine, with cartilaginous end plates resected and soft tissue removed from the anterior side of the vertebral body. Soft tissue posterior to the spinous process (including skin, fat, and muscle) were preserved. Plaster was applied to both end plates to make the surfaces parallel. The construct was mounted onto a Mini Bionix servohydraulic loading machine (MTS Inc. Eiden Prairie, MN), and a quasi-static compression load was applied through a ball joint at a speed of 0.2 mm/min for more than 30 mm displacement (Fig. 1). Yield force, ultimate force and stiffness of the vertebral bodies were monitored on the compression vs. displacement curve. Five small Nano30 AE sensors (MISTRAS Group, Princeton Junction, NJ) were attached directly onto the anterior side of the vertebral body to monitor microcracks that occurred when the vertebral body was loaded. Microcrack occurrence time, number, amplitude, and locations (if a microcrack signal was detected by four or more sensors) were recorded. One large wide band F30a AE sensor (MISTRAS Group) was glued on the skin posterior to the spinous process to examine how often a microcrack detected by Nano30 sensors could also be detected by a wide band sensor (F30a) that was further away from the damages.

The correlation among donor's age, L2's BMD and yield strength, and number of AE microcracks were examined using linear regression method. In statistic analysis a two-sided significance level of 0.05 was selected.

Copyright 2016 The Organizing Committee for the 2016 Summer Biomechanics, Bioengineering and Biotransport Conference

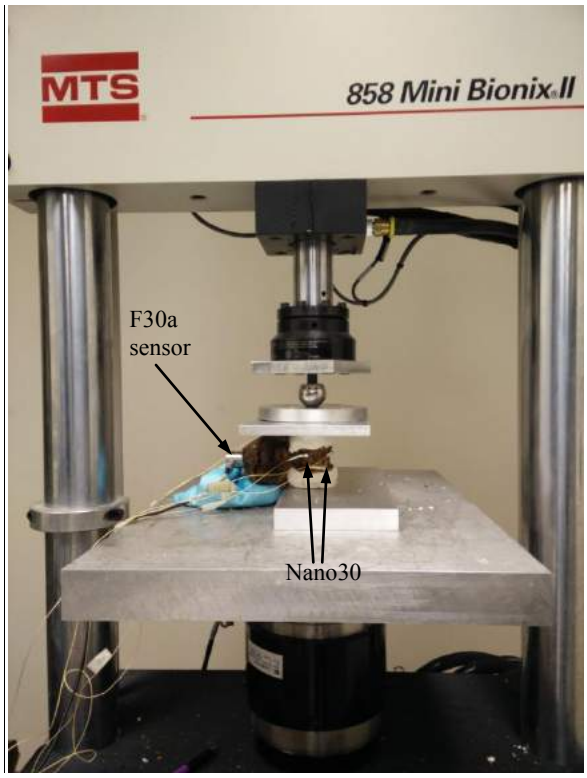

Figure 1. Setup of the biomechanical testing.

RESULTS

BMD of the six L2s ranged from 0.45 to 1.52 (Table 1). BMD negatively correlated to donor's age (R = -0.93) and positively correlated to the vertebral body's yield strength (R = 0.82). The number of AE microcracks did not correlate to either BMD or yield strength. However, the number of microcracks detected by 2 or more sensors (usually indicating a stronger signal and larger damages) was much highly correlated to the body's yield strength (R = -0.91) than BMD (R = -0.59). 71.3% of these multi-sensor microcracks were also detected by the wide band F30a sensor. In the compression tests, all specimens experienced a linear elastic region (recoverable deformation) initially, which was then followed by a plastic region (permanent damages) with no compression increase (Fig. 2). Additionally, AE microcracks were found to initiate around each vertebral body's yield point, and the number of AE microcracks kept increasing further throughout the plastic region (Fig. 2).

DISCUSSION

The compression test results showed that a vertebral body with a higher BMD is not necessarily stronger. The accumulation of AE microcrack in the specimens' plastic region indicated that AE technique can precisely detect ongoing cracks during this permanent damage period. Comparing to the multi-sensor microcracks that highly correlated to specimens' yield strength, those microcracks detected by 1 sensor seemed more random and less indicative. This study demonstrated that AE technique may provide more sophisticated data than the widely used BMD when diagnosing osteoporotic VCF, and allow researchers to reveal VCF from various directions, such as damage time, location, and severity. Additionally, AE technique has a potential to identify VCF patients in the clinical setting, as a wide band AE sensor attached to skin posterior to the vertebral body can successfully detect damages in the vertebral body. However, the potential needs to be further validated in clinic by applying AE technique on actual patients. Also, a fatigue flexion/extension test on cadaveric spines will be helpful to evaluate the performances of AE technique.

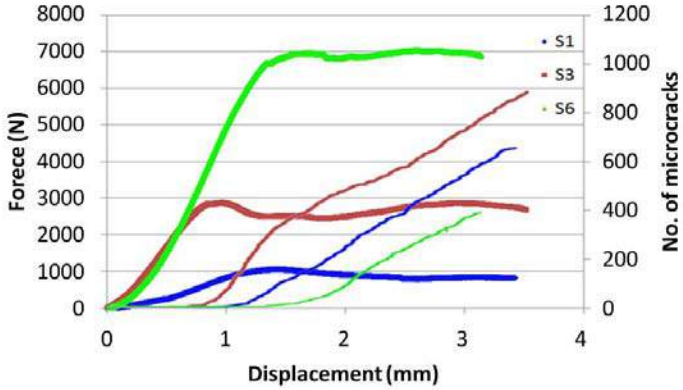

Figure 2. Compression vs. Number of AE microcracks vs. Displacement curves of specimen 1, 3 and 6. Compression force is the thick curve, and number of microcracks is the thin curve.

Table 1. Specimens' condition and testing results.

	Age	BMD	Yield strength (N)	No. of microcracks	Microcracks detected by 2+ sensors
S1	94	0.45	1034	660	463
S2	84	0.713	4508	1235	130
S3	58	1.065	2861	885	340
S4	78	0.832	2739	1058	423
S5	78	0.834	3172	900	392
S6	56	1.522	6675	403	120

ACKNOWLEDGEMENTS

The research fund was provided by Inova Foundation.

REFERENCES

[1] Shen M et al., *Am J Orthop*, 36(5):241-248, 2007. [2] Lehmann R et al., *Calcif Tiss Int,* 56(5):350-354, 1995. [3] Siris E et al., *JAMA,* 286(22):2815-2822, 2001. [4] Kanis J et al., *Osteopo Int,* 16(11):1330-1338, 2005. [5] Lentle B, *United States Patent* 6024711. [6] Hasegawa K et al., *Bone*, 14(5): 737-43, 1993. [7] Li J et al., *J NDT*, 28(1):1-8, 2009.

Copyright 2016 The Organizing Committee for the 2016 Summer Biomechanics, Bioengineering and Biotransport Conference

SB^{3}C2016
Summer Biomechanics, Bioengineering and Biotransport Conference
June 29 –July 2, National Harbor, MD, USA
SB^{3}C2016-909

FLOW FIELD POST-REPAIR IN CRITICAL AORTIC VALVE STENOSIS: IMPLICATIONS TO RECURRING DISEASE STATES

Sana Nasim[1], Glenda Castellanos[1], Angie Estrada[1], Denise Medina[1], Makensley Lordeus[1], Lilliam Valdes-Cruz[2], Steven Bibevski[2], Frank Scholl[2], Benjamin Boesl[3], Arvind Agarwal[3], Sharan Ramaswamy[1]

[1]Biomedical Engineering Department
Florida International University, Miami, FL, USA
[2]Joe DiMaggio's Children's Hospital
Hollywood, FL, USA
[3]Mechanical and Materials Engineering Department
Florida International University, Miami, FL, USA

INTRODUCTION

Heart valve diseases remains an unstudied area in cardiovascular pathologies. Congenital heart defects occur in 4 to 6 out of every 1000 births [1]. Of fundamental interest is the mechanics that regulate the biological environment. One such valve pathology is critical aortic heart valve stenosis (CAHVS). The stenosis is expressed as a severe obstruction to the left ventricular outflow tract due to congenital malformation of structures at the site of the aortic valve leading to abnormal hemodynamics. Currently CAHVS is surgically repaired with balloon aortic valvuloplasty (BAV). Short term results are favorable giving near normal hemodynamic function. However, in many cases the BAV procedure is a temporary solution as the incidence of re-stenosis is high and has been reported to be as much as 50% within 6 months of having undergone BAV repair [2]. This observation leads us to hypothesize that BAV provides a short-term surgical solution to CAHVS but by no means does BAV return the valvular flow environment to normalcy, which the valve endothelial cells (VECs) on the valve surface are not used to.

Our objective here was to identify the flow field under normal and post-BAV environments and subsequent biological responses of VECs.

METHODS

Culture and Expansion of VECs:

Valve endothelial cells (VECs) isolation was previously done from a porcine heart valve by separating the cells from the fibrosa side and the ventricular side in two separate flasks. Approximately 5x10^6 VECs/mL were cultured in T225 vented cell culture flask using DMEM media. Cells were grown in a standard cell culture incubator operating with 5% CO2 at 37°C with 95% humidity. VECs culture expanded to passages 4 to 6 were utilized for subsequent studies.

Computational Fluid Dynamics (CFD):

In order to extract the shear stress from the waveforms, which were obtained from Joe Di Maggio's Children's Hospital (JDCH), Hollywood, FL., CFD (ANSYS Canonsburg, PA) was conducted within the computationally reconstructed aortic structure from a pediatric patient who underwent balloon valvuloplasty and a normal pediatric patient (Fig. 1). The velocity profile was prescribed to the inlet and the pressure profile was specified as the outlet boundary condition (Figs 2 and 3). A transient simulation was conducted with a time step of 0.1 s and specifying a convergence criteria of 1x10-6 for momentum and continuity equations. Finally, blood material properties were used.

Fluid-Induced Mechanobiology Experiment:

VECs isolated from either side of porcine aortic heart valves (Mary's Ranch, Miami, FL) were plated in Collagen Type I (Fisher Scientific) coated microchannels. Side-specific shear stress profiles were obtained from our CFD simulations. Subsequently, side-specific shear stress profiles (fibrosa versus ventricularis) for BAV and normal cases were imparted onto VECs isolated from each corresponding side of the leaflets using (Fluxion Biosciences, San Francisco, CA).

RNA isolation and quantitative real time polymerase chain reaction:

Total RNA was isolated using the Stratagene RNA isolation kit (Agilent Technologies). Reverse transcription was performed with iScript cDNA Synthetic Kit (Bio-Rad). Primer sequence of interest have been complied. PCR was performed with Ssofast Evagreen SyperMix (Bio-Rad) on a C1000 thermal cycler (Bio-Rad)

Copyright 2016 The Organizing Committee for the 2016 Summer Biomechanics, Bioengineering and Biotransport Conference

RESULTS

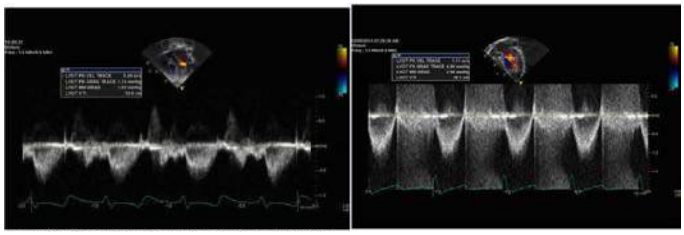

Figure 1. Echocardiography flow profile from normal patient (left) and after balloon valvuloplasty patient (right) obtained from JDCH.

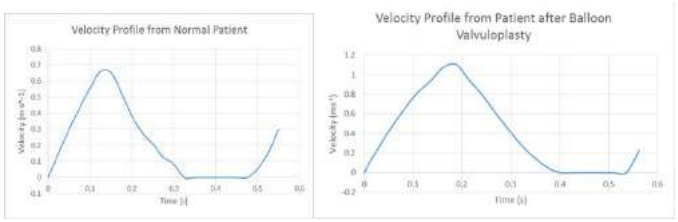

Figure 2. Velocity profile from a normal patient (left) and after balloon valvuloplasty patient (right) fed to the inlet in the CFD simulation

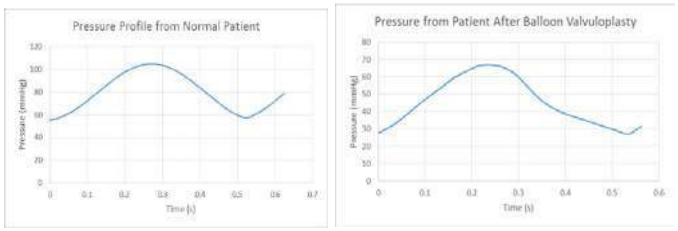

Figure 3. Pressure profile from a normal patient (left) and after balloon valvuloplasty patient (right) fed to the outlet in the CFD simulation

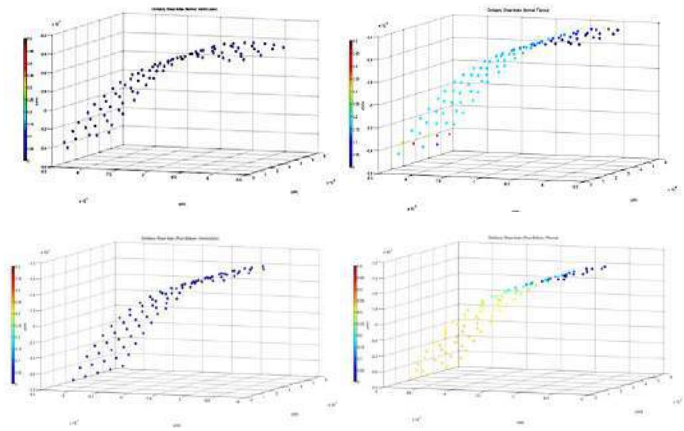

Figure 4. Oscillatory shear stresses from the CFD results of normal ventricularis side (top left), normal fibrosa side (top right), BAV ventricularis side (bottom left) and BAV fibrosa side (bottom right)

DISCUSSION

Critical aortic valve stenosis is considered to be a major source of mortality and morbidity in newborns with congenital heart disease. BAV treatment widens the stenosed valve region using a balloon catheter to increase the effective orifice area and improve the blood flow circulation. Nonetheless, the peak velocity past the heart valve that underwent BAV treatment was 1.11m/s, while the peak velocity observed in the healthy heart valve was 0.66m/s. Moreover, we observed that the fluid-induced shear stress profile on the ventricularis was considerably different compared to the fibrosa side (Fig. 3). We note that the localized hemodynamics is important in maintaining the function of the heart valve via normal valve tissue remodeling events. We found that there were distinct shear stress profiles between the normal and BAV cases which resulted in altered gene expression in the latter case compared to the normal (control) group. We conclude that changes in the local velocity and transvalvular pressure gradient leads to changes in responses at the cellular and molecular scales [3]. These changes may contribute towards rapid re-stenosis post-BAV repair (within 1 year), which has been observed clinically in pediatric patients with critical aortic valve stenosis.

ACKNOWLEDGEMENTS

This work is supported by the NSF FGLSAMP FIU Bridge to the Doctorate award HRD # 1301998

REFERENCES

1. Ferencz, C., J. D. Rubin, R. J. McCarter, J. I. Brenner, C. A. Neill, L. W. Perry, S. I. Hepner, and J. W. Downing. American Journal of Epidemiology. 121(1): 31-36, 1985.
2. Ben-Dor I, Pichard AD, Satler LF, et al., 2010;3(11):1150-1156. doi:10.1016/j.jcin.2010.08.014
3. Gould ST, Srigunapalan S, Simmons CA, Anseth KS. Circ Res. 2013;113(2):186-197.

Copyright 2016 The Organizing Committee for the 2016 Summer Biomechanics, Bioengineering and Biotransport Conference

SB^{3}C2016
Summer Biomechanics, Bioengineering and Biotransport Conference
June 29 –July 2, National Harbor, MD, USA
SB^{3}C2016-910

EFFECTS OF BODY WEIGHT SUPPORTED TREADMILL TRAINING ON BONE AND MUSCLE FOLLOWING SPINAL CORD INJURY

Bridgette Saverine (1), Gabrielle Gehron (1), Brittany King (2), Shania Shaji (1), Jennifer Kadlowec (2), Anita Singh (1)

(1) Biomedical Engineering
Widener University
Chester, PA, USA

(2) Mechanical Engineering
Rowan University
Glassboro, NJ, USA

INTRODUCTION

The incidence of lower extremity fractures has been reported to be as high as 46% post SCI (spinal cord injury), as seen in [1-3]. Body weight-supported treadmill training (BWSTT) has been reported to restore muscle mass and prevent bone loss in SCI patients. While the beneficial effect of this therapy is known, the effect of this training paradigm on varying severity of SCI has not been investigated in a single study. The purpose of this study was to investigate the effects of BWSTT on the muscle mass and biomechanical properties of the bone in transected and contused rats.

HYPOTHESIS

Repetitive BWSTT in SCI animals will: 1) improve behavioral recovery, 2) preserve muscle mass and 3) restore biomechanical properties of bones. Also, the improvements in these various parameters will be greater in contused than in transected animals.

METHODS & MATERIALS

In this experiment 32 female (200-250 g) Sprague-Dawley rats were split up into five groups (Fig. 1A). 16 animals received moderate (25 mm) contusion injury (NYU device) at T9/T10. 12 rats received a complete transection injury at T7. Four normal rats were used as control. At the end of nine weeks post injury, all animals were euthanized and the right soleus muscle and tibial bone was harvested.

Groups: Five groups:
Group 1: No Injury (**Cntl**)
Group 2: Contusion with no BWSTT (**Ctsn**)
Group 3: Contusion with 8 weeks of BWSTT (**Ctsn + BWSTT**)
Group 4: Transection with 8 weeks of BWSTT (**Tx**)
Group 5: Transection with no BWSTT training (**Tx + BWSTT**)

BWSTT Protocol: Animals in the training group received 8 weeks of BWSTT at 75% BWS and 7 cm/sec speed and 500 steps/day for 5 days/week using a robotic device (Robomedica Inc., CA) (Fig 1B).
Locomotor Recovery Tests: Pre-injury and weekly post injury open field Basso, Beattie and Bresnahan (BBB) locomotor test was performed in all animal groups.
Muscle Mass: At the end of the study, the right Soleus muscles was harvested, weighted and calculated against the total body weight.
Biomechanical Testing of the Bone (3-Point Bending): The harvested tibiae bone was subjected to a 3 point bending test. Each bone was placed on the lateral surface on two rounded supporting bars with a distance of 20 mm (Fig. 1C). A constant displacement rate of 5 mm/minute was applied at the medial surface of the diaphysis by lowering a third rounded bar until failure (shampo, Itasca, Illinois) Ultimate failure load (lb) was calculated for each specimen.

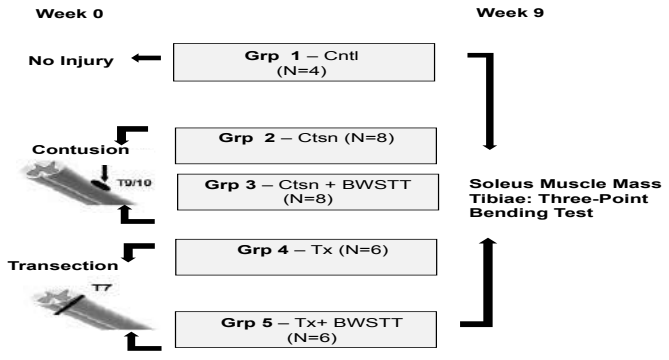

Figure 1: Study Design

Copyright 2016 The Organizing Committee for the 2016 Summer Biomechanics, Bioengineering and Biotransport Conference

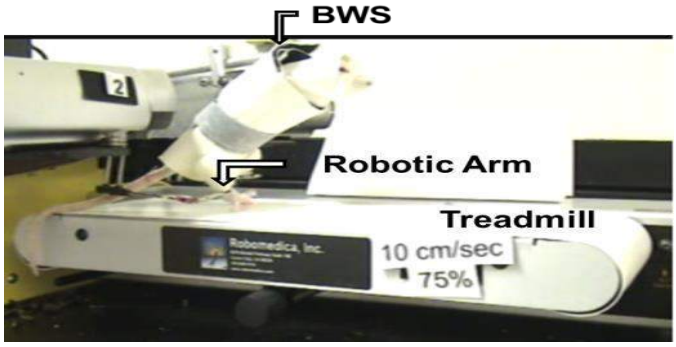

Figure 2: Treadmill Training Device

Figure 2: 3 Point Bending Test Setup

RESULTS

LOCOMOTOR RECOVERY TEST (BBB)

BWSTT resulted in no changes in BBB

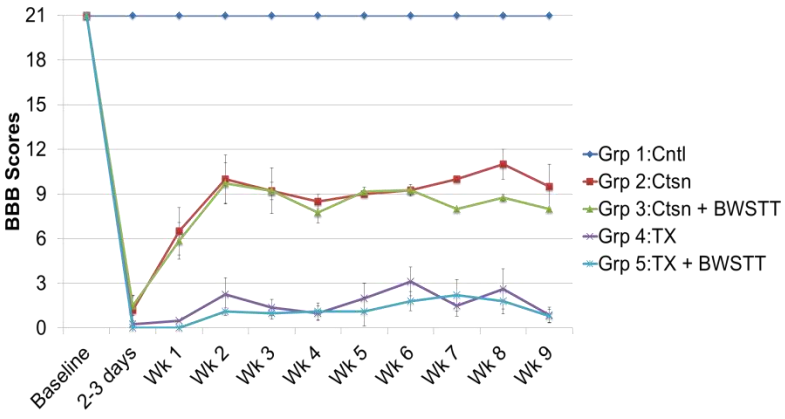

Biomechanical Changes in Bone

BWSTT slightly affects the biomechanical properties of the bone

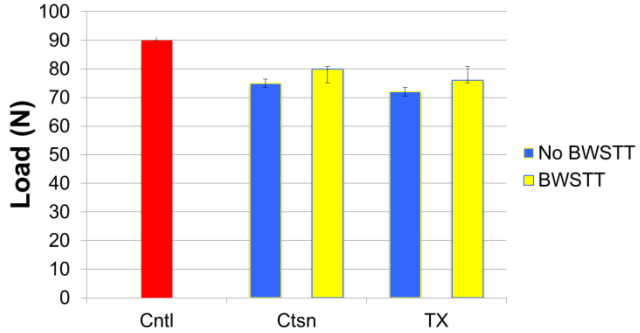

Mean ± SEM of the Ultimate Load.

Muscle Mass

BWSTT restores Soleus muscle weight

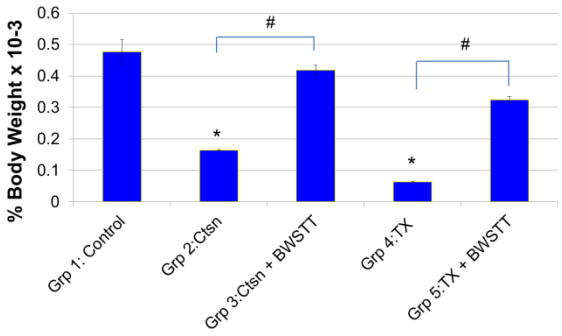

Mean ± SEM of the Soleus Muscle Weight/Body Weight. Asterisks indicate significant difference (p<0.05) from

DISCUSSION

- BWSTT led to significant improvement in the soleus muscle mass when compared to no training in both contused and transected animals.
- Higher Muscle mass was restored with and without training in contused animals than transected animals.
- Higher failure loads were observed in BWSTT groups, however, no significant improvement in the biomechanical property of the tibial bone was observed in the transected and contused rats, with or without training.

We attribute no changes in the bone properties to the severity of contusion injury that results in non-weight supported locomotion in animals in response to injury and also to the 75% BWSTT. Training with lower body weight support might result in significant improvement in the biomechanical properties of the tibial bone. Future studies are needed to investigate the effects of BWS and bone strength in various SCI models.

ACKNOWLEDGEMENTS

This study was partially supported by the New Jersey Commission on Spinal Cord Research – Exploratory Research Grant # CSCR14ERG001 and The Craig Neilson Fellowship Grant.

REFERENCES

[1] Vestergaard P, Krogh K, Rejnmark L, Mosekilde L. Fracture rates and risk factors for fractures in patients with spinal cord injury. Spinal Cord. 1998;36:790-796.

[2] Ashe MC, Craven C, Krasioukov A, Eng JJ. Bone Health Following Spinal Cord Injury. In: Eng JJ, Teasell RW, Miller WC, Wolfe DL, Townson AF, Aubut J et al., editors. Spinal Cord Injury Rehabilitation Evidence. Vancouver, B.C.: SCIRE, 2006: 9.1-9.18.

[3] Craven BC, Robertson LA, McGillivray CF, Adachi JD. Detection and treatment of sublesional ostoeporosis among patients with chronic spinal cord injury: proposed paradigms. Top Spinal Cord Inj Rehabil. 2009;14:1-22.

Copyright 2016 The Organizing Committee for the 2016 Summer Biomechanics, Bioengineering and Biotransport Conference

SB³C2016
Summer Biomechanics, Bioengineering and Biotransport Conference
June 29 –July 2, National Harbor, MD, USA
SB³C2016-911

CONSEQUENCES OF MENISCUS CRACKS IN UNIAXIAL TENSION

John M. Peloquin (1), Julia Pezick (2), Pranita Muralidhar (2), Michael H. Santare(3), Dawn M. Elliott (2)

(1) Department of Bioengineering
University of Pennsylvania
Philadelphia, PA, USA

(2) Department of Biomedical Engineering
University of Delaware
Newark, DE, USA

(3) Department of Mechanical Engineering
University of Delaware
Newark, DE, USA

INTRODUCTION

Meniscus tears are an important knee pathology, causing both immediate dysfunction and, in the long term, increasing the risk of osteoarthritis. Despite the serious consequences of meniscus tears, little is known about how they grow or what effects they have on meniscus mechanics. A tear is essentially a crack and, in principle, should increase stress locally at its tip, causing rupture by crack extension at otherwise safe loads. This process is called fracture. It is fairly well understood in industrial materials, but not in fibrous soft tissues such as the meniscus. Reproducing physiologic crack propagation in controlled laboratory tests has proven difficult, and fracture studies of fibrous soft tissues have produced ambiguous results [1]. The central unknown is whether or not a crack generates a strong enough stress concentration to cause failure by fracture. Since meniscus suffers from both sudden rupture and slow growth of crack-like defects, fracture probably applies to at least some loading conditions. Identifying when fracture applies is important because it determines the meniscus' effective strength. More broadly, it is also important to determine if cracks cause any local mechanical effects, as local overstrain and damage can cause dysfunction even if they do not produce total rupture.

Accordingly, the goal of this study was to measure the consequences of meniscus cracks in uniaxial tension: determine if cracks (1) weaken meniscus and cause fracture, (2) change the sub-failure stress–strain response, or (3) cause local overstrain near their tips. These objectives were met using parameterized stress–strain curve data, inspection of rupture appearance, and continuously recorded strain fields. Loading direction, crack position, and crack orientation were varied. This study introduces the use of specimens with 45° center cracks, which our previous work indicated should produce greater stress concentrations than commonly-used edge crack specimens [2].

METHODS

The uniaxial tensile response of the meniscus was compared between cracked and crack-free control specimens. Specimens were cut from the center of adult bovine meniscus for testing in both the circumferential and radial directions (figure 1). Specimens were cut to ~1.5 mm thickness using a cryomicrotome. Circumferential specimens were cut in an extended tab shape to securely grip the meniscus' circumferential fibers [3]. Three groups of crack & control specimens were cut: circumferential 90° edge cracks (n = 13) and their controls (n = 10), circumferential 45° center cracks (n = 8) and their controls (n = 9), and radial 90° edge cracks (n = 12) and their controls (n = 21) (figure 2). The two separate circumferential control groups were used to ensure anatomical correspondence between the cracked specimens and their controls, since edge and center cracks sever different regions of the meniscus.

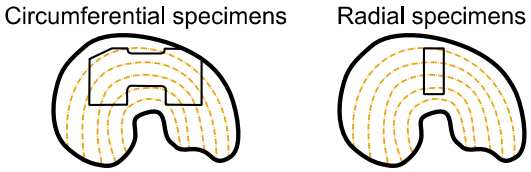

Figure 1: Specimen dissection locations. Dashed lines schematically illustrate the meniscus' circumferential fibers.

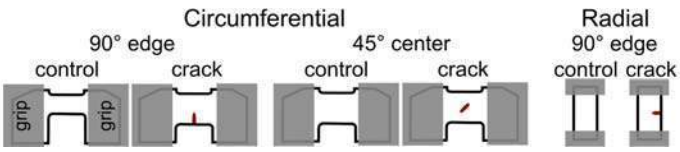

Figure 2: Specimen schematics and groups.

Copyright 2016 The Organizing Committee for the 2016 Summer Biomechanics, Bioengineering and Biotransport Conference

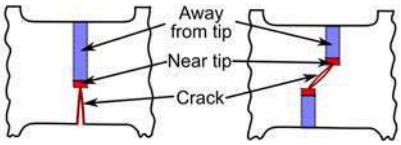

Figure 3: Region of interest definitions for comparing strain near the crack tip to strain away from the crack tip.

Specimens were preconditioned for 10 cycles to 4% strain, then loaded monotonically to failure at 0.5 mm/s. Video was recorded and surface strain fields were measured using digital image correlation. Stress was calculated using the cross-sectional area (at zero strain) not severed by the crack. Ramp to failure stress–strain curves were quantified by yield stretch, yield stress, tangent modulus at yield, peak stretch (at peak stress), and peak stress. Yield was identified using a recently established derivative-based method [3]. To determine if the crack changed the specimen's global mechanics, these stress–strain curve parameters were compared within each of the three control & crack groups shown in figure 2. To determine if the crack caused local overstrain, longitudinal (E_{xx}), shear (E_{xy}), and transverse (E_{yy}) strain components were compared between regions near the crack tip (within 0.5 mm) and away from the crack tip (figure 3). This comparison was made at 70% of the peak stress. All comparisons were done using two-sided Welch's t-tests with significance set at $p < 0.05$. Data were plotted on Tukey boxplots.

RESULTS

Peak stress was not significantly different between control and crack specimens in any of the three cases examined (figure 4). However, yield stress and tangent modulus were greater for both circumferential and radial edge crack specimens than for the corresponding controls (figure 4 *a* and c). No stress–strain curve parameters were significantly different for center crack specimens.

Ruptures tended to occur over a large area, without clear crack propagation. In circumferential specimens, rupture involved widespread inter-fiber sliding. Specimens often ruptured away from the crack.

The strain field analysis showed local effects from the cracks. Circumferential and radial edge cracks produced greater shear strain (E_{xy}) near the crack tip than away from it (figure 5). Radial edge cracks also showed increased transverse compression (negative E_{yy}) near the crack tip. These strain concentrations were readily visible in the strain fields (figure 5). They first appeared at ~25% of peak stress, prior to the yield point. Circumferential 45° center cracks produced no significant strain field alterations. None of the test configurations showed significant crack-associated changes in the longitudinal strain (E_{xx}) field.

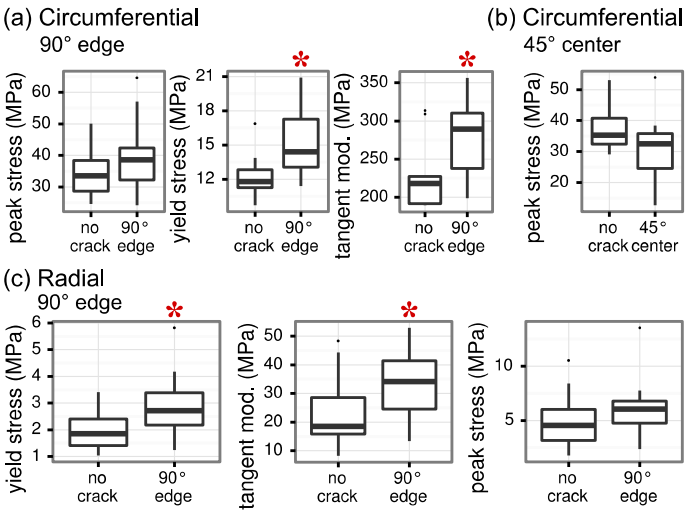

Figure 4: Comparison of stress–strain curve parameters between control (no crack) and cracked specimens. * = $p < 0.05$.

DISCUSSION

Although cracks affected both global and local mechanics, they did not reduce the effective strength of the meniscus in any of the tested configurations. This implies that fracture did not occur. Fracture is likely inhibited by the broad spatial extent of ruptures, as fracture requires progression of local rupture. The observation of ruptures away from the crack indicates that material inhomogeneity (visible in the figure 5 strain fields) trumped crack-induced strain concentrations.

The changes in the sub-failure stress–strain response of 90° edge crack specimens—namely, greater yield stress and tangent modulus—were surprising. They may be caused by load-sharing from the intact cross-section to the severed cross-section, facilitated by fiber dispersion or inter-fiber shear stress. In other words, the effective cross-sectional area of cracked specimens may be greater than measured. However, these load sharing mechanisms must be fairly weak, or they would have similarly caused an increase in apparent peak stress.

Edge cracks affected local mechanics by increasing shear strain near their tips. In circumferential tests, shear strain concentrations extended from the crack tip all the way to the grips, and were probably caused by inter-fiber shear. These strain concentrations could cause problems in vivo by promoting meniscus fragmentation, as in complex (degenerative-type) tears. In our study's test configurations the shear concentration just promotes deflection of the crack towards the grips, and the compressive transverse strain concentration in radial specimens does not facilitate crack propagation at all. Crack propagation across the specimen would instead require increased longitudinal strain.

Since cracks grow in vivo, we attribute our study's lack of crack propagation and fracture to our chosen test configurations. Crack propagation may require multiaxial loading, greater strain rates, cell-mediated degradative processes, or cyclic loading. Deflection of the crack to produce shear overstrain between fiber bundles appears to be an important mechanism by which the meniscus resists fracture and total rupture. As the meniscus is inhomogeneous on the scale of the crack, representing this inhomogeneity in mechanical models is likely necessary for accurately predicting when and how a meniscus will fail.

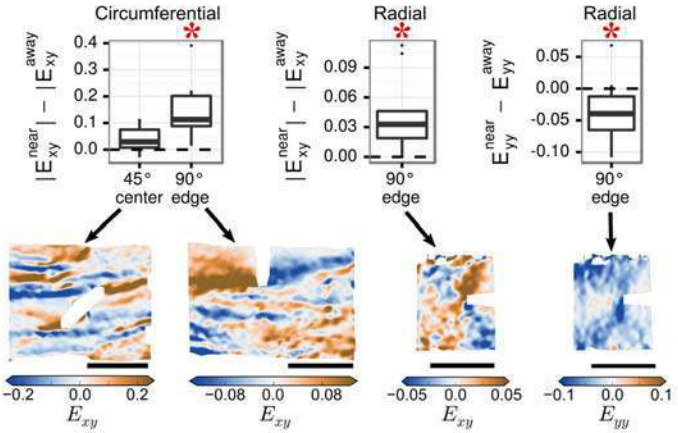

Figure 5: Comparison of strain near the crack tip to strain away from the crack tip. * = $p < 0.05$ for near vs. away. Bars = 5 mm.

ACKNOWLEDGEMENTS

NIH grants R01AR050052 and R01EB002425.

REFERENCES

[1] Taylor, D et al., *JMBBM*, 6:139–147, 2012.
[2] Peloquin, J et al., *JMBBM*, 57:260–268, 2015.
[3] Peloquin, J et al., *J Biomech Eng*, in press [available online], 2016.

Copyright 2016 The Organizing Committee for the 2016 Summer Biomechanics, Bioengineering and Biotransport Conference

SB³C2016
Summer Biomechanics, Bioengineering and Biotransport Conference
June 29 –July 2, National Harbor, MD, USA
SB³C2016-912

FIBRIN GLUE INCREASES THE STRENGTH OF CONDUIT-ASSISTED DIGITAL NERVE REPAIRS

Patrick J. Schimoler (1,2), Jessica Childe (2), Steven Regal (2), Alexander Kharlamov (2), Peter Tang (2), Mark Carl Miller (1,2)

(1) Department of Mechanical Engineering
University of Pittsburgh
Pittsburgh, PA, USA

(2) Department of Orthopaedic Surgery
Allegheny General Hospital
Pittsburgh, PA, USA

INTRODUCTION

Complete digital nerve lacerations require repair to prevent functional or sensory deficits [1]. Ideally, tensionless coaptation of the transected nerve ends is possible. When it is not, autografts, nerve conduits, and glues provide other options for nerve repair: each has strengths and weaknesses. Autografts bridge the gap between nerve ends, but require harvesting of a healthy nerve. Nerve conduits provide a guide and a conducive environment for healing and do no damage to the site where the graft is harvested [2]. Additionally, the use of a conduit may move suture away from the coaptation reducing further damage to the nerve. Finally, nerve glues provide the advantages of reduced damage to the nerve and fast repair [3].

While tensionless repair is ideal, repair strength must still withstand all loading during healing. Researchers have tested the strength of nerve repairs as a function of suture size [4], of number of sutures [4], of suture purchase [4], of number of sutures with conduits [5], and of different glue types [6]. To the best of the authors' knowledge, no one has yet studied the strength of conduit-assisted digital nerve repairs with glue.

The purpose of this study is to determine whether suture configuration or the presence of fibrin glue affects the maximum failure strength of conduit-assisted digital nerve repairs.

METHODS

Ninety digital nerves were removed from seven fresh-frozen cadaveric hands between the proximal bifurcation of the common digital nerve and the distal trifurcation of the proper digital nerve. Specimens of approximately 5 cm in length were assembled. The diameters of the nerve specimens were measured with calipers. The nerves were transected and then repaired with one of five suture configurations and one of two glue configurations; there were nine nerves with each suture and glue configuration. All repairs were conduit-assisted using a nerve protector (Axoguard, Axogen, Alachua, FL) cut to 12mm in length, bathed in saline to increase pliability, formed into a cylinder, and then sutured at its ends with 8-0 nylon suture (Covidien, Medtronic, Minneapolis, MN). The five suture configurations were (4/4), (2/2), (2/0), (1/0), and (0/0) where the first number describes the number of sutures at the coaptation and the second number describes the number of sutures at each end of the conduit connecting it to the nerve's epineurium. The two glue conditions are with and without fibrin glue (Tisseel Duo kit, Baxter, Deerfield, IL).

Tensile testing proceeded after repair. Gauze pads were attached to the ends of nerves with cyanoacrylate. The glued gauze pad / nerve ends were pressed on a flat surface for fifteen minutes with approximately 230 g to ensure even attachment and then the weight was removed for an additional fifteen minutes to ensure the glue fully set. Nerve specimens were loaded to failure in a tensile testing machine (Haake Mars II, Thermo Fisher Scientific, Inc., Waltham, MA) at rate of 0.33 mm/s. Load data was recorded at 10 Hz. Maximum failure load was calculated as the largest tension measured during the trial. A few specimens did not actually fail during testing due to slippage of the nerve in the clamp or due to the stripping of the outer layer of the epineurium in the gauze. In any trial where the nerve specimen did not fail and no damage was visible, the nerve specimen was retested.

A two-way analysis of variance (ANOVA) was performed to determine if suture configuration, glue presence, or their interaction had a significant effect on maximum failure load. Three null hypotheses were considered: first, suture configuration had no significant effect on maximum failure load; second, glue presence had

Copyright 2016 The Organizing Committee for the 2016 Summer Biomechanics, Bioengineering and Biotransport Conference

no significant effect on maximum failure load; and third, the interaction between suture configuration and glue presence had no effect on maximum failure load. P-values less than 0.05 were used to reject the null hypotheses. In the case of significance, the differences within the condition were determined using Tukey's procedure. Finally, a one-way ANOVA was performed to determine if the nerve diameters were significantly different between all ten groups tested (10 groups = 5 suture configurations times 2 glue configurations). The null hypothesis was that there was no significant difference between diameters from one group to another with a p-value less than 0.05 signifying significance.

RESULTS

Both suture configuration and glue presence had significant effects on maximum failure load ($p < 0.01$). Among the suture configurations tested, maximum strength increased with increasing amounts of suture. The addition of the fibrin glue also increased maximum failure load. The interaction between suture configuration and glue presence did not have a significant effect. There was no significant difference in nerve diameters between groups.

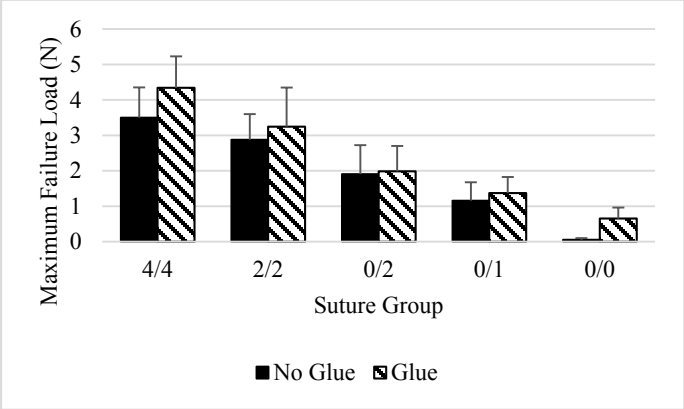

Figure 1: Conduit-assisted digital nerve repair maximum failure strength increases significantly with additional suture and / or the addition of fibrin glue.

Table 1: Average diameter and average maximum failure load by group

Group	Avg. Diameter (mm)	Avg. Max Failure Load (N)
A	1.53±0.16	3.50±0.86
A'	1.52±0.15	4.34±0.89
B	1.52±0.11	2.88±0.72
B'	1.49±0.12	3.25±1.10
C	1.38±0.26	1.91±0.81
C'	1.44±0.26	1.98±0.72
D	1.42±0.17	1.16±0.52
D'	1.50±0.19	1.37±0.45
E	1.52±0.19	0.06±0.04
E'	1.28±0.21	0.65±0.31

DISCUSSION

This study analyzed the effects of fibrin glue and suture configuration on the maximum failure load of conduit-assisted digital nerve repairs. Both the presence of glue and suture configurations with more suture proved to be significant in increasing the maximum failure load of the repairs.

This work was the first to determine the strength of conduit-assisted digital nerve repairs with the addition of fibrin glue. Martins et al. [7] studied the recovery of walking in rats after transection and repair of the sciatic nerve using combinations of fibrin glue and suture, but repair strength was not tested. Goldberg et al. [4] found a significant difference in the strength of digital nerve repairs due to the number of sutures used, but not due to the suture size or the suture purchase. Neither nerve conduits nor glue were used in the study. Schimoler et al. [5] found a significant difference in the strength of conduit-assisted digital nerve repairs as a function of suture configuration, but again did not use a fibrin glue. Isaacs et al. [6] found no difference in the strength of tibial and deep peroneal nerve repairs done with suture or suture plus glue and also did not use conduit-assisted repairs.

The increase in strength due to the fibrin glue in this study has immediate implications. If suture at the coaptation can be reduced by the used of glue while maintaining the same repair strength, damaged nerves will undergo less iatrogenic damage during repair, thereby increasing the chances of functional and sensory recovery.

ACKNOWLEDGEMENTS

We would like to thank Michael Smolinski for his help testing the nerves.

REFERENCES

[1] Mermans, JF, Franssen, BBGM, Serroyen, J, Van der Hulst, RRWJ, Digital Nerve Injuries, *Hand*, 7: 233-241, 2012.

[2] Deal, DN, Griffin, JW, Hogan, MV, Nerve Conduits for Nerve Repair or Reconstruction, *Journal of the American Academy of Orthopaedic Surgeons*, 20: 63-68, 2012.

[3] Narakas, A, The Use of Fibrin Glue in Repair of Peripheral Nerves, *The Orthopaedic Clinics of North America*, 19: 187-199, 1988.

[4] Goldberg, SH, Jobin, CM, Hayes, AG, Gardner, T, Rosenwasser, MP, Strauch, RJ, Biomechanics and Histology of Intact and Repaired Digital Nerves, *The Journal of Hand Surgery*, 32A: 474-482, 2007.

[5] Schimoler, PJ, Kim, H, Kharlamov, A, Veerubhotla, A, Gillman, B, Tang, P, Miller, MC, Conduit-Assisted Primary Nerve Repairs Reduce the Number of Sutures at the Injury Site without Reducing Overall Repair Strength, Orthopaedic Research Society Annual Meeting, Orlando, FL, 2016.

[6] Isaacs, JE, McDaniel, CO, Owen, JR, Wayne, JS, Comparitive Analysis of Biomechanical Performance of Available "Nerve Glues", *The Journal of Hand Surgery*, 33A: 893-899, 2008.

[7] Martins, RS, Siqueira, MG, Da Silva, CF, Plese, JPP, Overall Assessment of Regeneration in Peripheral Nerve Lesion Repair Using Fibrin Glue, Suture, or a Combination of the 2 Techniques in a Rat Model, *Surgical Neurology*, 64: S1:10-S1:16, 2005.

Copyright 2016 The Organizing Committee for the 2016 Summer Biomechanics, Bioengineering and Biotransport Conference

SB^{3}C2016
Summer Biomechanics, Bioengineering and Biotransport Conference
June 29 –July 2, National Harbor, MD, USA
SB^{3}C2016-914

Effect of Mechanical Load on Scaffold-Cartilage Integration: A Computationally Augmented Biological Model

Supansa Yodmuang(1), Hongqiang Guo(1), Tony Chen(1), Caroline Brial(1), Peter A. Torzilli(2), Russell F. Warren(2), Suzanne A. Maher(1)

(1) Department of Biomechanics
Hospital for Special Surgery
New York, NY, USA

(2) Tissue Engineering, Regeneration and Repair Program
Hospital for Special Surgery
New York, NY, USA

INTRODUCTION

Articular cartilage experiences high magnitude, multidirectional, dynamic loads during activities of daily living [1]. Ideally, scaffolds intended for cartilage repair must be able to integrate with the host tissue under these complex loads. While bioreactors have been used to apply mechanical loads to scaffold-tissue explants [2], we have no mechanistic understanding of the relationship between the biological response of the cells at the interface and their mechanical environment. As such, it is impossible to mechanically or structurally optimize scaffolds to enhance scaffold-cartilage integration.

Our goal was to investigate the relationship between the mechanical environment and the biological response of cells at the scaffold-cartilage interface. We hypothesized that the magnitude of micromotion at the scaffold-cartilage interface (i.e. relative movement between cartilage and scaffold) would have a significant effect on interfacial strength (IFS). To test this hypothesis, we developed a computationally driven physical bioreactor cartilage-scaffold explant model in which the following variables were controlled: (i) load magnitude, (ii) degree of confinement of the periphery tissue, and (iii) pre-seeding of cells in the scaffold. The computational model was used to fully characterize the mechanical environment within the scaffold and at the scaffold-cartilage interface, thus allowing for the biological response to a controlled mechanical environment to be assessed.

METHODS

A non-degradable porous scaffold previously developed as a candidate material for cartilage repair [3], poly(vinyl alcohol), was used as a model scaffold to avoid the temporal effects of degradation. Cylindrical disks (5 mm Ø x 2.5 mm thick) were disinfected in 70% ethanol, dehydrated in 100% ethanol and air-dried. The dehydrated scaffolds were then placed into 3.5 mm diameter defects created in 10 mm articular cartilage discs extracted from juvenile bovine knees. The scaffolds, with or without chondrocytes, were rehydrated *in situ* with 50 μl of culture medium to create a press-fit, and cultured for 28 days.

To choose the exact load profiles and degree of confinement within the physical bioreactor, a biphasic finite element model (bFEM) was created: In the axisymmetric model, articular cartilage was modeled as a biphasic material with depth-dependent material properties[4]. The scaffold was modeled as homogeneous biphasic material, with material properties input form unconfined compression tests. In order to mimic different magnitudes of micromotion at the scaffold-cartilage interface, the following conditions were identified from the bFEM for implementation in the physical model: **confined** – where the cartilage disk was confined in a polydimethylsiloxane ring, **unconfined** –the articular cartilage disk could expand peripherally, **low load** –sinusoidal loads of 0.1-1 N (stress 1.27 - 12.7 kPa), and **high load** –sinusoidal loads of 0.6 – 6 N (stress 7.64 - 76.4 kPa). After 28 days of culture, the prescribed loads were applied daily (450 cycle, 0.5 Hz) to confined and unconfined samples, with and without pre-seeding of cells, resulting in 16 groups. To capture the change in properties of the scaffold and at the interface during testing, the bFEM was re-run with D28 scaffold modulus and interface strength values as acquired from physical tests on explants.

Outputs: Scaffold-cartilage interface strength (IFS) was quantified by performing push-out tests. Constructs were then stained by Safranin O for GAG and immunohistochemistry for type II collagen. The scaffold-cartilage interface was visualized using μCT. Two-way ANOVA and Bonferroni post-test were performed and analyzed using GraphPad Prism software (La Jolla, CA), $n \geq 10$ per group, $\alpha = 0.05$. From the bFEM, micromotion at the scaffold-cartilage interface, at peak load, was computed. The distribution of axial stress throughout the scaffold and cartilage was also output.

Copyright 2016 The Organizing Committee for the 2016 Summer Biomechanics, Bioengineering and Biotransport Conference

RESULTS

Physical Model: Unconfined defect models without pre-seeding of scaffolds with chondrocytes (G.1) showed low IFS ranging from 1-3 kPa for all conditions **(Fig. 1)**. The corresponding confined condition (G.2), resulted in a slight, but non-significant increase in IFS, $p > 0.05$. Cell-seeded PVA scaffolds improved IFS in unconfined (G.3) and confined conditions (G.4) compared to their respective non cell-seeded groups (G.1 vs. G.3 and G.2 vs. G.4 at $p < 0.05$) **(Fig. 1)**. Cell-seeded scaffolds in confined conditions (G.4), subjected to 1 N of load had the highest IFS of 50.2 ± 1.0 kPa after 42 days in culture.

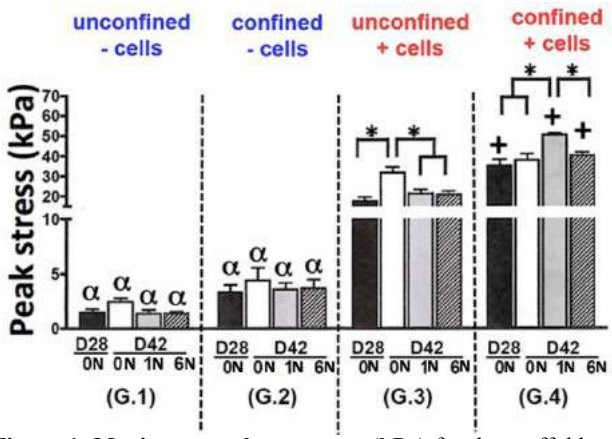

Figure 1. **Maximum push-out stress (kPa)** for the scaffold-cartilage explants as quantified on days 28 and 42. Note: by d28, no mechanical loading had been applied to any group. Applied loads within each condition were 0N (no loading) 1N, or 6N. α significant effects of pre-seeding (G.1 vs. G3 and G.2 vs. G.4). * significant effect of loading within the same group. + significant effect of boundary condition (G.1 vs. G.2 and G.3 vs. G.4)

G. 4 (1N, confined, +cells), which had the highest IFS, showed strong GAG and collagen type II staining at cell clusters within the porous scaffold and extracellular matrix filled the gap between the scaffold and articular cartilage (**Fig. 2**). While the lowest IFS group (G.1: 6N, unconfined, -cells) showed the least abundant staining, the least physically connected interface, and only partial filling of the gap.

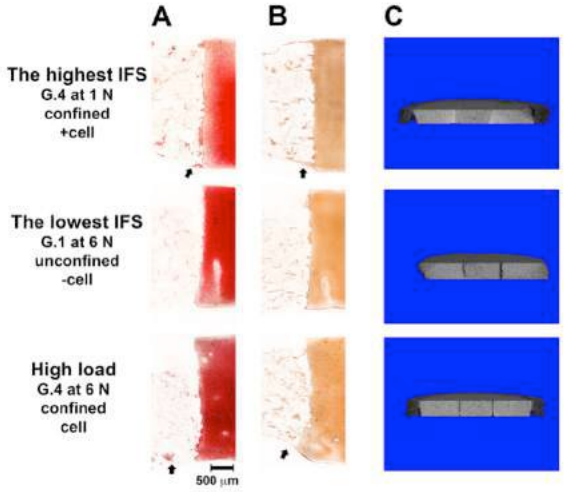

Figure 2. Histology and μCT GAG staining of PVA scaffold and cartilage **(A)**, immunohistochemistry of collagen type II **(B)**, and cross-section of 3D reconstruction of the defect model **(C)**. Arrows indicate cells sediment at the bottom of scaffolds.

Computational Model: Under peak load of 1 N for the confined compression condition, micromotion at the interface of cell-seeded scaffold was not evident (**Fig. 3A and 3B,** *the highest IFS group*). Axial stresses of 3 kPa and 23 kPa were quantified in scaffolds of *the highest IFS* group and *the high load* group, respectively. Peak micromotion of ~90 μm was found for the unconfined compression group at the peak load of 6 N (**Fig. 3B,** *the lowest IFS*). Confinement at the tissue periphery resulted in a decrease of stress within the scaffolds from 11 to 3 kPa at 1 N of load and from 28 to 23 kPa at 6 N of load.

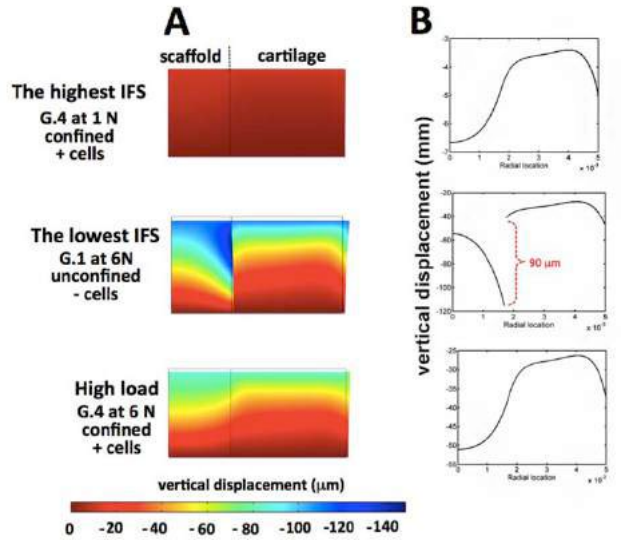

Figure 3. Biphasic finite element models (bFEMs) (A): Distribution of vertical displacement (μm) in the scaffold and cartilage at the peak loading at 1 or 6 N. **(B):** Micromotion between the scaffold to cartilage at the interface at peak load.

DISCUSSION

By way of a computationally augmented bioreactor study, we rejected our hypothesis: both the magnitude of micromotion at the scaffold-cartilage interface and the magnitude of stress within the scaffold had a significant effect on IFS, but only in scaffolds that were pre-seeded with cells. The groups that were not pre-seeded with cells did not respond to changes in interface micromotion or scaffold stress in a robust way: regardless of what variables were altered, low IFS and low cartilaginous matrix production resulted. For the cell-seeded groups, our study suggests that there exists a critical threshold of scaffold-cartilage micromotion combined with a critical level of stress within the scaffold that together are required to encourage robust integration. The magnitude of micromotion was affected not only by the boundary conditions of the explant, but also the integration between the scaffold and articular cartilage: as more matrix is generated at the interface, a corresponding decrease in micromotion occurs. The computationally augmented bioreactor herein described can be used as a model to evaluate the integrative capacity of scaffolds, prior to costly and time consuming animal models.

ACKNOWLEDGEMENTS: The Widgeon Point Charitable Foundation and the Russell Warren Chair in Tissue Engineering are gratefully acknowledged for their support of this study.

REFERENCES : [1] Fox et al., Sports health, 1(6), pp. 461-8. [2] Tognana et al., Osteoarthritis Cartilage. 2005 Oct;13(10):896-905. [3] Ng, et al., 2012, Tissue engineering Part A, 18(11-12), pp. 1273-81. [4] Guo, et al., 2014, Journal of biomechanics, 47(11), pp. 2721-9.

Copyright 2016 The Organizing Committee for the 2016 Summer Biomechanics, Bioengineering and Biotransport Conference

SB^{3}C2016
Summer Biomechanics, Bioengineering and Biotransport Conference
June 29–July 2, National Harbor, MD, USA
SB^{3}C2016-915

UTILIZING BANDWIDTH TO QUANTIFY HUMAN TORSO MOTOR CONTROL CAPABILITY

Shahab Karimi (1), Martin L. Tanaka (1), N. Peter Reeves (2), Sudhir Kaul (1)

(1) Department of Engineering and Technology
Western Carolina University
Cullowhee, NC, USA

(2) Department of Osteopathic Surgical Specialty
Michigan State University
East Lansing, MI, USA

INTRODUCTION

Although the methods used to quantify bandwidth for a simple engineering system are well established [1], the application of bandwidth to complex systems like a human is more challenging. A simple explanation is that higher bandwidth controllers are able to respond to systems that change more quickly. Many different factors influence the human neuromuscular control system, and its response to external inputs. Some of these factors include age, physical health, neurological condition, external environment and body mass distribution. The human neuromuscular control system is further complicated by the fact that it may have different responses to the same input signal. Since there are a large number of confounding factors and since they are inherently coupled with the system, a large amount of experimental data is needed to understand the influence of each factor on bandwidth.

In order to understand the complexity of human motor control, some researchers have used mathematical models to study torso movement. Typically, input commands are presented to the system and the motor control moves the body to track these movement commands.

The ultimate goal of this research is to develop new diagnostic methods that can be used by medical professionals to assess the degree of neuromuscular disease and evaluate the effectiveness of treatment. In this research, methods are developed to calculate the bandwidth of the neuromuscular control system which may be used as a measurable variable to quantify neuromuscular controller capability.

METHODS

The upper body (including the head, arms and torso) was represented as an ellipsoid (Figure 1). The height and width of the ellipsoid were selected based on the values of typical human subjects. A simulated motor was connected to the upper body to control the rotation of the ellipsoid.

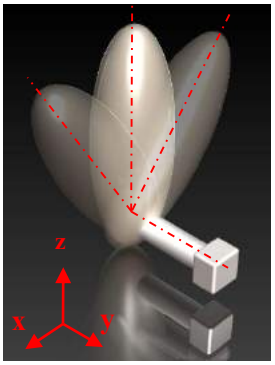

Figure 1: Representation of upper body and controller.

The ellipsoid representing the upper body was assigned a moment fo inertia of I. Torso stiffness due to spinal ligaments, and passive muscle tone of the abdominal and back muscles were assigned a stifness value of k. Viscous damping of the torso during movment was assigned a value of b.

A second order differential equation was used to describe the dynamics of the system. A general rotational dynamic system can be represented by

$$I\ddot{\theta} + b\dot{\theta} + k\theta = u(t) \quad (1)$$

where θ is the angular position about the lumbar spine and $u(t)$ is the torque applied to the system. In this model, $u(t)$ consists of two components.

Copyright 2016 The Organizing Committee for the 2016 Summer Biomechanics, Bioengineering and Biotransport Conference

The first is torque generated by active contractions of the abdominal and back muscles. This torque is controlled by the human motor controller in the brain. The second component is the effect of gravity on the system. A mathematical representation of these torques is given by

$$u(t) = G(\theta_d - \theta) + mgl\ sin(\theta) \quad (2)$$

where G is the gain of the controller. The paremeters m, g and l are the mass of upper body, acceleration due to gravity and the length of the segment to the center of mass, respectively. θ_d is the desired angular position. Using Euler's approximation, the mathematical representation of the system for small angles is

$$I\ddot{\theta} + b\dot{\theta} + \theta(k - mgl) = G(\theta_d - \theta) \quad (3)$$

Representative values for the unknown parameters I, b, k, m, l, and G were selected based on typical human values [2]. These unknown model parameters are stored in the vector $\alpha = (I, b, k, m, l, G)$. The mathematical model was run to generate a system response to a step function. Six step functions were evaluated (±3°, ±2°, ±1°). White Gaussian noise was added to the response curves and the curves were filtered with a band pass filter over the range of 0.01 to 10 Hz. These curves are show as the black lines in Figure 2. Each curve is an average of three separate simulation runs. The curves serve as a surrogate for data that will be collected in future human subject experiments.

Our method uses optimization to determine the unknown parameters in Equation 3. The response of the model is compared to the simulated experimental data. Optimization is carried out by minimizing the cost function shown below,

$$S = \sum(\theta_{s,i} - \theta_{m,i}(\alpha))^2 \quad (4)$$

The values for the parameters in vector α can be determined from the solution of the optimization problem. Variable $\theta_{s,i}$ is the angular position of the simulated experimental data at the i^{th} time step (black line in Figure 2). Variable $\theta_{m,i}(\alpha)$ is the angular position of the model response given parameters α. The optimized curves are shown in Figure 2 (colored lines).

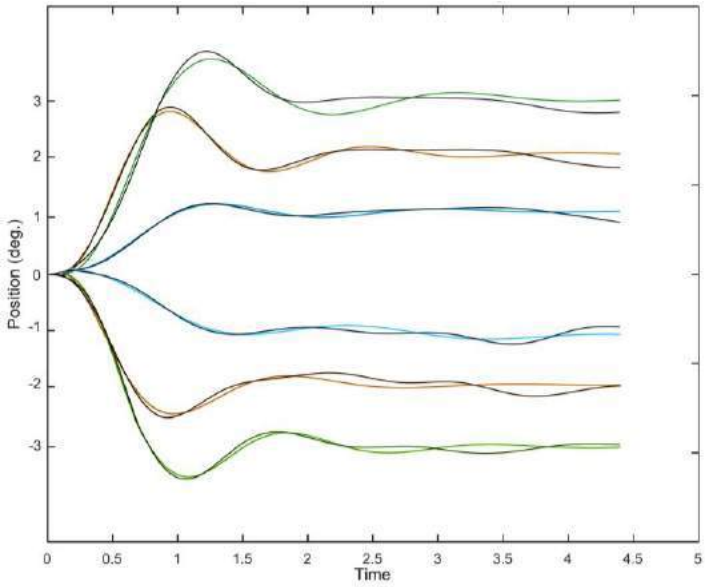

Figure 2: Generated data (black) vs. model (colored).

Now that we have the system response to a step function, we can calculate the bandwidth. A Fourier transform is applied to Equation 3 yielding,

$$\theta_{(j\omega)}(I(j\omega)^2 + b(j\omega) + k - mgl) = G\left(\frac{\theta_d}{j\omega} - \theta_{(j\omega)}\right) \quad (5)$$

where, $\theta_{(j\omega)}$ is the angular position in frequency domain, j is an imaginary number equal to $\sqrt{-1}$, and ω is the frequency. The transfer function, $\theta_{(j\omega)}/\theta_d = Tr_{(j\omega)} = Re(j\omega) + Im(j\omega)$, is determined by manipulating Equation 5. The transfer function has both real and imaginary components. The magnitude response of the Bode plot is given by $mag = \sqrt{Re^2 + Im^2}$, and plotted with respect to frequency (Figure 3).

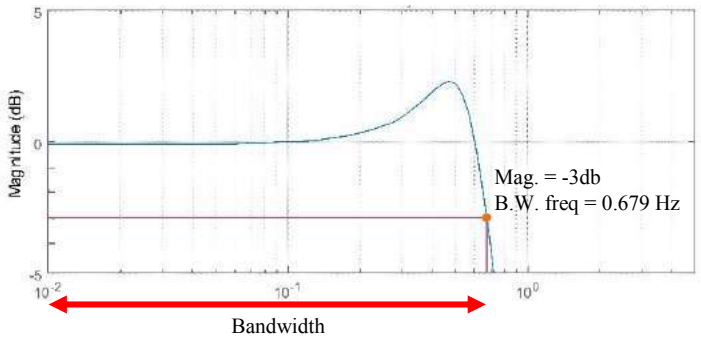

Figure 3: Typical Magnitude Response of Bode Plot.

The bandwidth of a system is defined as the range of frequencies over which the magnitude response of the transfer function drops by 3 dB. This drop in amplitude corresponded to a 50% decrease in power.

RESULTS

The bandwidth frequency was calculated for each of the six step functions and is listed in Table 1. The magnitudes of the step functions were defined as small (1°), medium (2°), and large (3°).

Table 1: Bandwidth frequency (Hz) for different desired positions

		Small	Medium	Large
Direction	Flexion	***0.58***	***0.84***	***0.80***
	Extension	***0.66***	***0.91***	***0.68***

DISCUSSION

Overall, the magnitude of bandwidth frequencies was seen to be fairly consistent, ranging from 0.58 to 0.91 Hz. We see different bandwidth for different input magnitudes and direction. Hence, bandwidth must be a function of magnitude and direction of the motion.

The results of this analysis are promising. The analysis method was applied to surrogate data in the form of a time series. In the future, this method will be used to analyze time series data collected experimentally. This will enable the bandwidth of the human neuromuscular control system to be determined.

REFERENCES

1. Phillips, C., & Harbor, R., 2000. Feedback control systems (4th ed.). Upper Saddle River, N.J.: Prentice Hall
2. Reeves, N., Cholewicki, J., Narendra, K., 2009. Effects of reflex delays on postural control during unstable seated balance. J.Biomech.42,164–170.

Copyright 2016 The Organizing Committee for the 2016 Summer Biomechanics, Bioengineering and Biotransport Conference

SB³C2016
Summer Biomechanics, Bioengineering and Biotransport Conference
June 29 –July 2, National Harbor, MD, USA
SB³C2016-916

KNEE MEDIAL TIBIAL CARTILAGE STRESS ONE AND FIVE YEARS AFTER ANTERIOR CRUCIATE LIGAMENT RECONSTRUCTION

Ashutosh Khandha (1), Kurt Manal (2), Lynn Snyder-Mackler (3), Thomas S. Buchanan (1,2)

(1) Biomedical Engineering
University of Delaware
Newark DE 19713

(2) Mechanical Engineering
University of Delaware
Newark DE 19713

(3) Department of Physical Therapy
University of Delaware
Newark DE 19713

INTRODUCTION

An estimated 400,000 anterior cruciate ligament injuries occur annually in the United States, and at least 100,000 individuals undergo anterior cruciate ligament reconstruction (ACLR) [1, 2]. Premature knee osteoarthritis (OA) after ACLR is a growing concern [3]. Alterations in knee gait mechanics after ACLR have been associated with premature knee OA [3]. In subjects who get knee OA five years post-ACLR, osteophytes are commonly observed near the medial joint margin (region 1 in figure 1). However, it is not clear whether altered gait mechanics result in high stresses specifically near that general region. It is also not clear how cartilage stresses differ over time in subjects who get knee OA, versus those who do not. With that background, the objective of the current study was to evaluate knee gait parameters and medial tibial cartilage stress during gait. The evaluation was conducted one and five years post-ACLR, in subjects who got knee OA, versus those who did not.

METHODS

12 subjects who opted for ACLR participated in gait studies one and five years post-ACLR, per an institutional review board approved protocol. Gait and electromyography (EMG) analysis was performed at self-selected walking speeds using an eight camera video system (Vicon, Oxford Metrics Limited, London, UK), a force platform (Bertec Corporation, Worthington, OH) and surface-EMG recordings (Motion Lab Systems, Baton Rouge, LA). A validated Hill-type EMG-informed musculoskeletal model was used to estimate total and medial compartment force (MCF) [2]. During weight acceptance, peak values for knee gait parameters of interest approximately coincide with the first peak of vertical ground reaction force (vGRF). Hence, quasi-static finite element analysis at the first peak of vGRF was conducted using Open Knee in FEBio ((Musculoskeletal Research Laboratories, Salt Lake City, UT) [4] (figure 1). Subject-specific knee flexion angle (KFA), knee adduction moment (KAM) and total knee joint load were applied to the femur. The central medial tibial cartilage (involved knee) was divided into three regions (figure 1). The stresses in region 3 were negligible, hence peak von Mises stress for regions 1 and 2 are reported here.

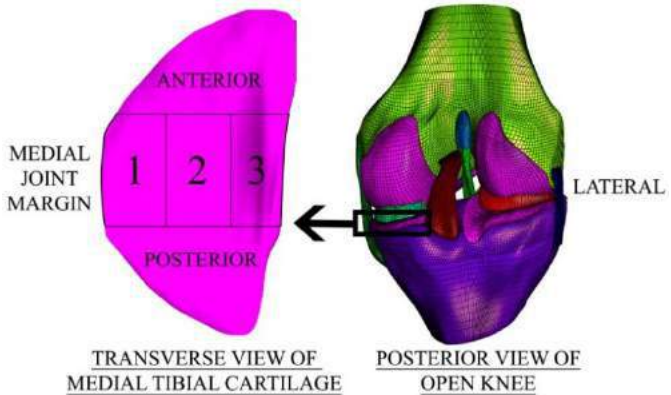

Figure 1: Open Knee finite element model in FEBio [4].

Copyright 2016 The Organizing Committee for the 2016 Summer Biomechanics, Bioengineering and Biotransport Conference

At five years post-ACLR, weight-bearing anterior-posterior radiographs were used to evaluate knee OA (Kellgren-Lawrence grade ≥ 2). Six subjects showed signs of medial compartment knee OA (2 men, 4 women, age = 33 ± 14 years), while six subjects did not have knee OA (4 men, 2 women, age = 32 ±14 years). Students t-tests (α = 0.05) were used to evaluate differences in each parameter between non-OA versus OA groups, at each post-ACLR time point.

RESULTS

In region 1, the OA group demonstrated greater peak von Mises stress at the five year post-ACLR time point (figure 2). Similarly, for region 2, the peak von Mises stress for the OA group was greater at the five year post-ACLR time point (figure 3). For knee gait parameters, the OA group demonstrated lower KFA at the 5 year post-ACLR time point (Table 1).

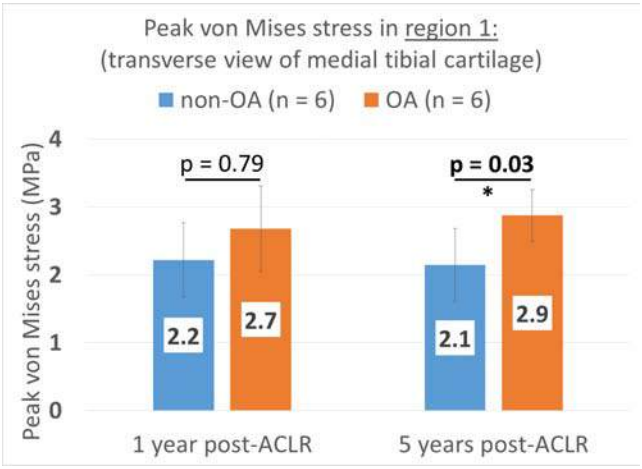

Figure 2: Peak von Mises stress for non-OA versus OA group in region 1 (central medial tibial cartilage region near the medial joint margin)

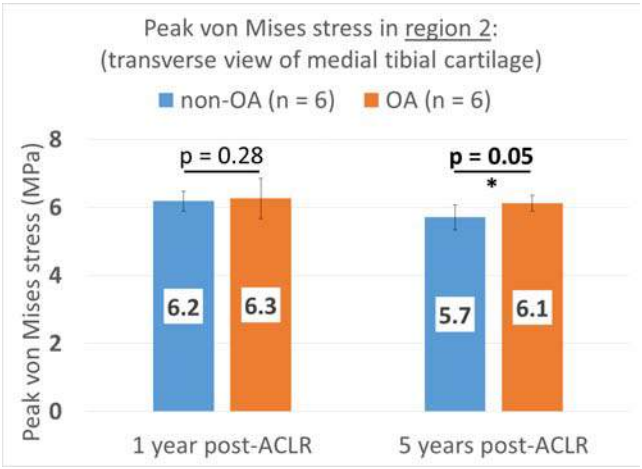

Figure 3: Peak von Mises stress for non-OA versus OA group in region 2 (central load bearing medial tibial cartilage region)

Table 1: Mean ± SD of peak knee gait parameters at the 1st peak of vertical ground reaction force during gait (SD = standard deviation, ACLR = anterior cruciate ligament reconstruction, OA = osteoarthritis, KFA = knee flexion angle, KAM = knee adduction moment, MCF = medial compartment force, BW = body weight, HT = height)

Parameter	1 year post-ACLR			5 years post-ACLR		
	non-OA (n = 6)	OA (n = 6)	p-value	non-OA (n = 6)	OA (n = 6)	p-value
KFA (degrees)	24.6 ± 4.5	20.8 ± 6.5	0.34	25.5 ± 4.4	18.9 ± 2.5	**0.01**
KAM (%BW * HT)	2.0 ± 0.8	2.9 ± 0.4	0.09	2.4 ± 0.9	3.0 ± 0.3	0.15
MCF (BW)	2.7 ± 0.5	2.5 ± 0.2	0.55	2.2 ± 0.3	2.1 ± 0.5	0.58

DISCUSSION

In the current study, the OA group demonstrated a significantly lower knee flexion angle at the five year post-ACLR time point. Also, the differences in knee adduction moment approached significance at both post-ACLR time points, with the OA group demonstrating a higher knee adduction moment. When the combination of knee gait parameters and joint load was used as input for a finite element knee model, the results indicated that subjects with medial compartment knee OA have greater stresses in the medial tibial cartilage, particularly near the medial joint margin, i.e. the region closer to the midline of the body. Five years after ACLR, radiographic signs of medial compartment knee OA were also most commonly observed near the medial joint margin. This is the region where cartilage tends to be thinner (compared to the central region of the joint). Hence, greater stresses in that region may not necessarily be due to abnormally high load magnitudes. A normal load magnitude shifted to the thin cartilage region could be equally detrimental. Studies that utilize both neuromusculoskeletal modeling and finite element analysis can help investigate the combined effect of various knee gait parameters and joint loads on cartilage stress distribution and also help solidify the link between altered gait mechanics and knee OA. Comparing the nature and progression of knee biomechanics in non-OA versus OA ACLR groups may be the key to developing rehabilitation strategies for delaying the progression of the disease.

ACKNOWLEDGEMENTS

Work supported by National Institutes of Health: P30-GM103333, R01-AR046386, R01-AR048212 and R01-HD087459

REFERENCES

[1] Murray, M , *The ACL Handbook,* 2:19-28, 2013.
[2] Gardinier, ES et al., *J Orthop Res*, 31:458-464, 2013.
[3] Fleming, BC et al., *Curr Opin Orthop*, 16:354-362, 2005.
[4] Erdemir, A et al., *Proceedings of ISB*, 2011.

Copyright 2016 The Organizing Committee for the 2016 Summer Biomechanics, Bioengineering and Biotransport Conference

SB³C2016
Summer Biomechanics, Bioengineering and Biotransport Conference
June 29 –July 2, National Harbor, MD, USA
SB³C2016-917

ANATOMICALLY-DRIVEN MULTISCALE MODEL OF ASCENDING THORACIC AORTA, WITH APPLICATION TO MULTIDIRECTIONAL EXPERIMENTS

Rohit Y. Dhume (1), Christopher E. Korenczuk (2), Victor H. Barocas (2)

(1) Department of Mechanical Engineering
University of Minnesota
Minneapolis, MN, USA

(2) Department of Biomedical Engineering
University of Minnesota
Minneapolis, MN, USA

INTRODUCTION

Although only about 15% of the thoracic aorta, the ascending portion is involved in 60% of all thoracic aortic aneurysms [1, 2]. Ascending thoracic aortic aneurysm (ATAA) involves progressive weakening of the aortic wall, which can lead to vessel dissection and/or rupture, often resulting in death. Surgical intervention involves considerable risk, however, and better understanding of aneurysm tissue mechanics would aid in formulating improved surgical guidelines and decision making.

Several theoretical models for ATAA have been described [e.g., 3, 4], but few have addressed failure in the context of microscale structure of the aortic wall. The current work used a multiscale approach to build a unifying model of the ascending thoracic aortic wall, which was compared to a set of multidirectional failure experiments performed on cadaveric porcine tissue.

METHODS

In separate work [5], we performed four different types of experiments on cadaveric porcine aorta. In-plane (uniaxial and biaxial) and out-of-plane (lap and peel) (see Fig. 3 below) tests were performed on aorta tissue to probe its mechanical and failure behavior.

In the current work, a multiscale model was constructed based on a framework developed previously for collagen gel mechanics [6, 7]. The model consisted of two distinct scales: the finite element domain at the millimeter (mm) scale, and the representative volume element (RVE) at the micrometer (μm) scale. The RVE contained a network of fibers in parallel with a nearly incompressible neo-Hookean component (representing non-fibrous material). The structure of the fiber network was selected to represent the lamellar structure and composition observed in the aorta. The final network structure (Fig. 1A) a 2-D sheet of circumferentially aligned collagen fibers embedded in an isotropic elastin network (representing an elastic lamella), attached to an almost isotropic network of inter-lamellar connections (representing components such as smooth muscle cells and fibrillin).

Each finite element (FE) in the model contained eight Gauss points, and each Gauss point was associated with an RVE network (Fig. 1). Displacements at the FE nodes deformed the RVE networks and stresses calculated from the deformed networks were appropriately scaled and used to perform the macroscale force balance, thus fully coupling the microscale behavior to that of the macroscale.

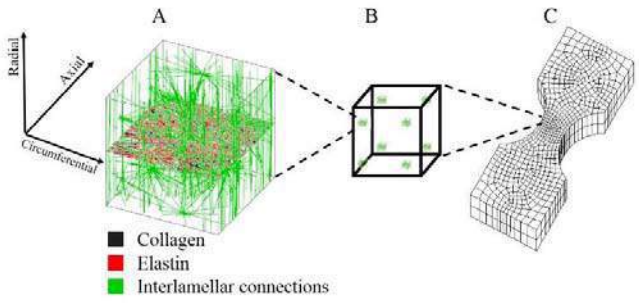

Figure 1: Multiscale scheme included a microscale network (A) at each Gauss point (B) in the macroscopic finite-element model (C).

Fiber constitutive equations were of the form [8, 6]

$$f = \frac{A}{B}\left[e^{B\left(\frac{\lambda^2-1}{2}\right)} - 1\right],$$

Copyright 2016 The Organizing Committee for the 2016 Summer Biomechanics, Bioengineering and Biotransport Conference

where f is fiber force, A controls stiffness, B controls non-linearity, and λ is the fiber stretch. Failure was incorporated into the model by removing a fiber if it was stretched above a critical stretch value λ_c. The nine fiber parameters (A, B and λ_c for each of the three fiber types) and two parameters for the neo-Hookean matrix (bulk and shear moduli) were manually optimized to match the experimental data. All simulations were run using 128 parallel processors; clock times averaged 10 hours per simulation.

RESULTS

Results from the simulation are shown below. Circumferential and axial denote the directions (with respect to the aorta) in which the samples were stretched and stress was calculated. The stresses predicted by the multiscale model (Fig. 3) lay within the 95% confidence interval calculated for the experiments in most cases. The peel simulations ran only a few steps past the start of fiber failure before stopping due to stability issues within the finite element code.

Figure 2 shows the distribution of failed fibers, showing a shift from mostly laminar fibers (collagen and elastin) failing in the uniaxial tests to interlamellar (I.C) fibers failing in the lap shear tests.

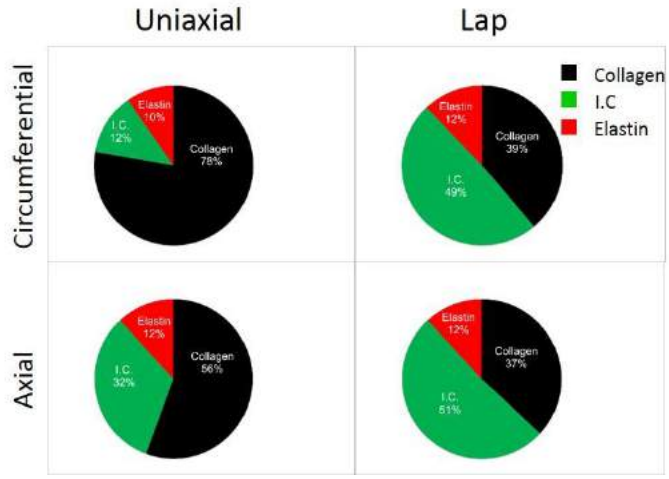

Figure 2: Distribution of failed fibers from simulation

DISCUSSION

A single multiscale model was developed to replicate the failure behavior of aorta tissue seen in multidirectional mechanical tests. A major advantage of this model was the use of anatomically informed networks to capture the microscale mechanics and failure of the aorta in complex three dimensional loading.

The simulation results matched the experimental data quite well. The model also performed well in matching the experimentally observed failure stresses, even for the peel simulations. The stress plots (Fig. 3) along with the simulated distribution of failed fibers (Fig. 2) obtained for the uniaxial and lap tests suggest that the layered structure of the aorta is essential to capture the mechanics and dissection of ATAA. However, lumping the different radial structural components of the aorta into a single type of fiber (inter-lamellar connections) simplifies the actually complex microstructure, which could be a source of some error. That simplification also makes it difficult to distinguish between cell stress and e.g., fibrillin stress, which could be important in a model of vascular remodeling. Furthermore, the instability in the peel test has arisen due to the method employed to simulate fiber failure, i.e., by suddenly reducing fiber stiffness.

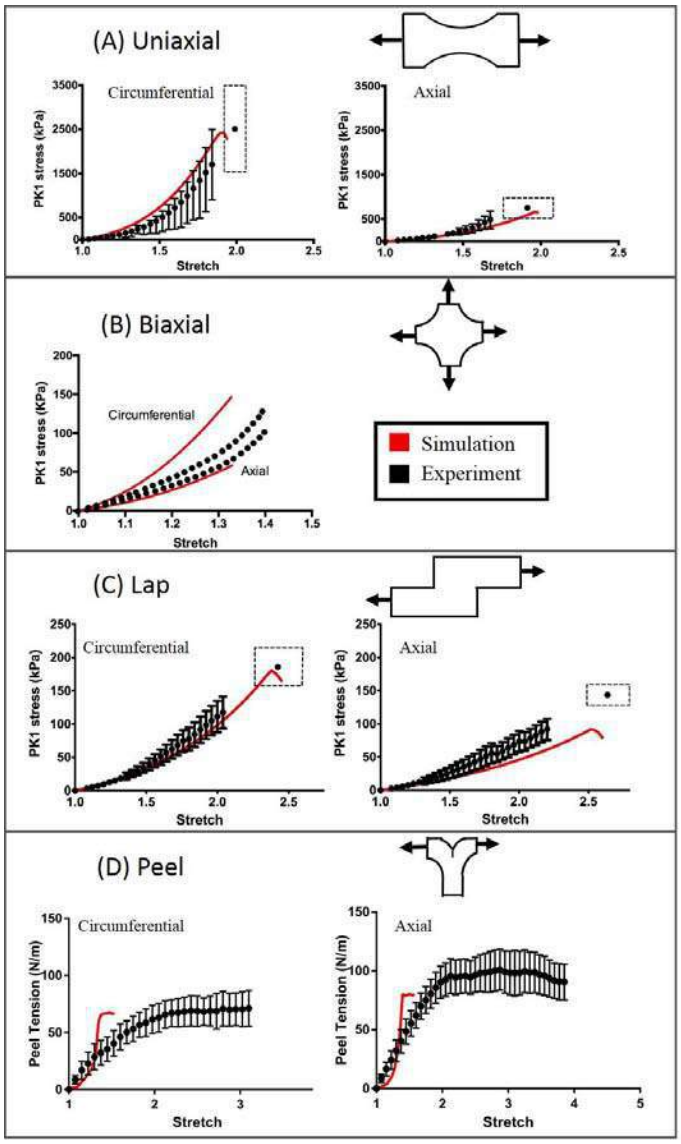

Figure 3: Comparison of multiscale model results (red) with experimental data (black). Error bars for biaxial experiments are not shown. On average, the biaxial error was 36 kPa.

ACKNOWLEDGEMENTS

This work was supported by the National Institutes of Health (R01EB005813) and by the Minnesota Supercomputing Institute at the University of Minnesota. Tissue was graciously provided by the Visible Heart Laboratory at the University of Minnesota.

REFERENCES

[1] Mao, S.S. et al., *Acad. Radiol.*, 15:827-34, 2008.
[2] Gray H., Anatomy of the Human Body, Lea & Febiger, 1918.
[3] Volokh K.Y., *J. Biomech Eng.*, 41:447-53, 2008.
[4] Gasser T.C. et al., *Eur. J. Mech. – A/Solids*, 25:617-633, 2006.
[5] Witzenburg, C.M., Ph.D. dissertation, Dept. Mech. Eng., University of Minnesota, Minneapolis, MN, 2014.
[6] Sander, E.A. et al., *Proc. Natl. Acad. Sci.*, 106:17675-17680, 2009.
[7] Stylianopoulos, T. et al., *J. Biomech Eng.*, 129:611-618, 2007.
[8] Billiar, K.L. et al., *J. Biomech Eng.*, 122:327-335, 2000.

Copyright 2016 The Organizing Committee for the 2016 Summer Biomechanics, Bioengineering and Biotransport Conference

SB³C2016
Summer Biomechanics, Bioengineering and Biotransport Conference
June 29 –July 2, National Harbor, MD, USA
SB³C2016-918

SUBJECT-SPECIFIC VS. AVERAGED STRUCTURAL MODELS OF THE COLLAGEN NETWORK IN THE LUMBAR FACET CAPSULAR LIGAMENT

Vahhab Zarei (1), Amy A. Claeson (2), Chao Liu (2), Taner Akkin (2), Victor H. Barocas (2)

(1) Mechanical Engineering
University of Minnesota, Twin Cities
Minneapolis, MN, USA

(2) Biomedical Engineering
University of Minnesota, Twin Cities
Minneapolis, MN, USA

INTRODUCTION

The lumbar facet capsular ligament (LFCL) surrounds the facet joint in the lumbar spine [1]. The LFCL contains packed aligned collagen fibers as well as mechanoreceptors [1], both of which are embedded in a ground matrix of proteins and water. Collagen fibers are the predominant mechanical component of the LFCL, and their spatially-varying orientation is of particular interest because it leads to concentrated stress regions, and thus, is responsible for both the overall mechanical properties of LFCL and the stresses acting on the innervating nerve fibers. The dense innervation suggests a possible role for the LFCL in chronic low back pain [2] where large stresses in the LFCL could lead to abnormal nerve deformation and to pain.

This study comprises two parts. First, the variability of fiber orientation between samples was studied, and secondly, subject-specific, structure-based models were constructed and examined.

METHODS

Polarization-sensitive optical coherence tomography (PS-OCT) was used to find the fiber orientation of LFCLs on their entire surface. Each sample (n=5), clamped biaxially, was pulled by ~1N force in each direction. The imaging depth was approximately 0.13mm.

To investigate the ***inter-sample variability***, first a 2D average LFCL geometry was constructed. Next, the Shepard morphing method [3] was used to map the orientation field of each sample onto this average geometry. Lastly, an orientation tensor [4] was defined for each point on each orientation field, and the variability of components of this tensor was observed among different samples.

In the second part of this study, ***subject-specific structural models*** were created by using the fiber structure in a multiscale finite element solver [5] to simulate equibiaxial extension tests. Each finite element has fiber networks (representative volume element, RVE), the deformation of which determines the elemental stresses. Each RVE contains an aligned Delaunay network along with a Neo-Hookean material which deforms independently and represents the ground matrix in the LFCL. Fibers follow the phenomenological constitutive equation $F = \frac{A}{B}[\exp(BE) - 1]$ where *F, A, B* and *E* are force, stiffness, nonlinearity parameter and Green strain for fibers [6]. The neo-Hookean matrix was considered nearly incompressible ($v=0.45$).

Each LFCL geometry was constructed and meshed using Abaqus based on an image of the biaxial test. Since the finite element grid is coarse compared to OCT resolution, a proper averaging method was required to specify the fiber orientation for each element. Elemental fiber orientation was obtained by averaging the fiber orientation tensor of its constituent pixels, such that:

$$T_{element} = \frac{\frac{I}{2} + \sum \delta_{pixel} T_{pixel}}{1 + \sum \delta_{pixel}}$$

Where T and δ denote the orientation tensor and retardation respectively. For each element, an aligned fiber network was created based on the obtained fiber orientation, such that the strength of alignment was proportional to the retardation. Fiber orientation and δ can be described by orientation tensor through eigenpairs: If (γ_1, γ_2) and (v_1, v_2) are eigenvalues $(\gamma_2 > \gamma_1)$ and eigenvectors respectively, of T, then $\delta \propto \gamma_2 - \gamma_1$ and v_2 specifies the orientation of fibers.

Fitting parameters were fiber stiffness (A), fiber nonlinearity parameter (B), and Neo-Hookean matrix shear modulus (G_{mat}). Described inputs (fitting parameters, RVEs, sample geometry, and boundary displacements) were used in the multiscale solver to find forces in each direction. To assess the improvement of this OCT-based model over simplified models for LFCLs, a transversely isotropic models with fibers running in the Lateral-Medial (L-M) direction was made and compared to the image-based model.

Copyright 2016 The Organizing Committee for the 2016 Summer Biomechanics, Bioengineering and Biotransport Conference

RESULTS

The OCT-based fiber orientation map for two LFCLs is shown in figure 1. The reference axis (i.e., θ = 0) is from left to right (L-M). Fibers are mainly oriented in the joint direction (L-M). As figure 2 suggests, however, fiber orientation distribution varies considerably between samples.

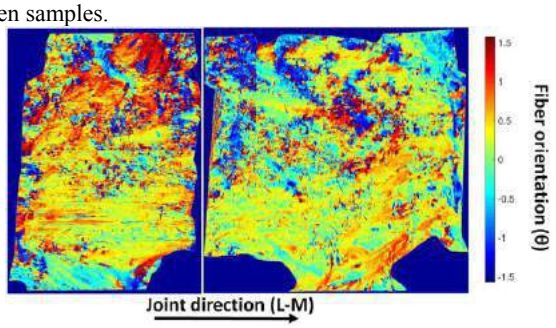

Figure 1. Fiber orientation field for two LFCLs. Fibers are mainly oriented in the joint direction.

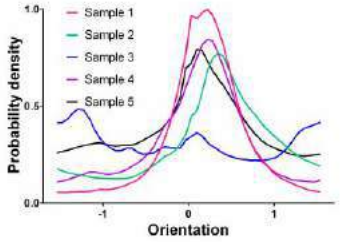

Figure 2. Orientation probability density. Inter-subject variability can be observed.

Force-stretch results for superior-inferior (S-I) and L-M directions are represented in figure 3 (n=5). Experimental average maximum forces in the L-M and S-I directions were 19.5 N and 5.9 N respectively. These values for the OCT-based model were 18.4 N and 8.7 N. Root-mean-square error (RMSE) values for the L-M and S-I directions were 1.03 N and 1.10 N respectively. These values were lower compared to the corresponding values for a transversely isotropic model, which had the RMSE of 1.16 N and 1.19 N for the L-M and S-I directions. The fitting parameters A, B and G_{mat} for the OCT-based simulations are $(10.01 \pm 2.13) \times 10^{-6} N$ $(mean \pm S.D)$, 18.60 ± 2.51, and $28.4 \pm 4.9 KPa$ respectively.

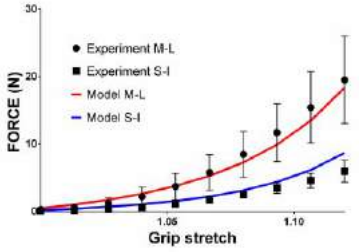

Figure 3. Force-stretch graphs in two normal directions for OCT-based model (mean) and the experiment (mean ± SD)

Figure 4 shows the maximum principal Cauchy stress field for the OCT-based and transverse isotropic models for one LFCL. OCT-based model leads to a more heterogeneous stress field. The heterogeneity was quantified by stress standard deviation and maximum stress to average stress ratio. Average values for these parameters are 588N and 7.6 for the OCT-based model, and 354N and 3.5 for the transverse isotropic model.

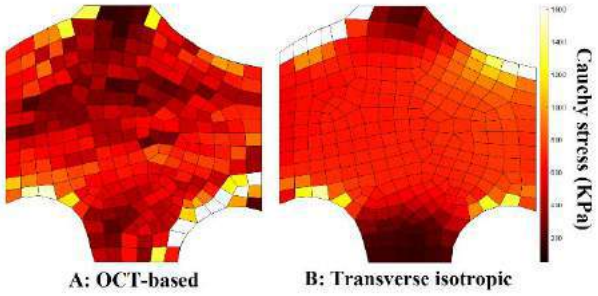

Figure 4. Maximum principal Cauchy stress field for the A: OCT-based and B: transverse isotropic model. OCT-based model generates a more heterogeneous field

DISCUSSION

Fiber structure characterization and improving structural models were two purposes pursued in this study. Fiber orientation over the entire surface of the sample was acquired using PS-OCT. Orientation fields showed that fibers primarily tend to align in the joint direction (L-M). This can also be concluded by observing the higher forces in the L-M direction during equibiaxial extension. Although the maximum probability of orientation belongs to the joint direction, there is a high variation among different locations on each sample. This heterogeneity highlights the need for structural models to capture regions of concentrated stress, which will enable further study microstructural phenomena, such as fiber-nerve interaction.

In addition, orientation fields demonstrated considerable variation between different samples. This variation was observed by the difference in orientation probability distribution as well as difference in relative location of aligned regions on the sample. The importance of sample-specific models in determining the mechanical behavior is the conclusion drawn from this observation.

For each specific sample, the acquired fiber structure was incorporated into a multiscale model and regressed to experimental data to find the best model parameters. The image-based structural model resulted in a roughly 10% reduction in RMSE compared to a transverse isotropic model in which fibers are aligned in the joint direction. In addition, unlike the transverse isotropic model, the structure-based model led to a heterogeneous stress field. Considering the concentration of stress for each sample is particularly important when the microscale behaviors, such as neural is of interest.

In conclusion, fiber structure, which is a significant determinant of overall and microstructural mechanical behavior, varies among samples and is essential to be characterized. Secondly, structure-based models are necessary to describe LFCL mechanical behavior.

ACKNOWLEDGEMENTS

This work was supported by the National Institutes of Health/ National Institute of Biomedical Imaging and Bioengineering [U01EB016638]. The authors acknowledge the Minnesota Supercomputing Institute (MSI) at the University of Minnesota for providing resources that contributed to our research results. We extend our thanks to the UMN Anatomy Bequest program, Mr. Jacob Solinsky, and our collaborator Prof. B. Winkelstein (U of Pennsylvania).

REFERENCES

[1] Cavanaugh J.M. et al. *J biomech* 29, 1117-1129. 1996. [2] Dreyer S. J. et al. Arch. Phys. Med. Rehab. 77, 290-300. 1996. [3] Shepard. D. *Proc. 23rd ACM Natl.* 1968. [4] Sander. E. et al. *J Biomed. Mater. Res* 88, 322-331. 2009. [5] Stylianopoulos T. et al. *J Comput Methods* 196:2981-2990. 2007. [6] Billiar K. L. et al. *J Biomech*, 34:859-871. 2001.

Copyright 2016 The Organizing Committee for the 2016 Summer Biomechanics, Bioengineering and Biotransport Conference

SB^{3}C2016
Summer Biomechanics, Bioengineering and Biotransport Conference
June 29 –July 2, National Harbor, MD, USA
SB^{3}C2016-919

PLACENTA-ON-A-CHIP: A NOVEL PLATFORM IN DRUG TESTING AND TOXICOLOGY APPLICATIONS

Nastaran Hashemi (1)

(1) Department of Mechanical Engineering
Iowa State University
Ames, Iowa, USA

INTRODUCTION

Organ-on-a-chip technology is a relatively new field in which the properties of microfluidics are utilized within a biomimetic cell culture model. They show promise as a novel platform in drug testing and toxicology applications due to several key advantages. First, their large surface area-to-volume ratio ensure that diffusive forces dominate over bulk forces. This has led to a vast increase in popularity over the recent years, as researchers have found them to be a more appealing alternative to other drug testing methods. From this, researchers have split into subjects that focus on a specific organ, including the: lungs, liver, intestines, heart, vasculature, and many others. Contrary to this, however, research regarding a "placenta-on-a-chip" have been few and far between. In the body, the placenta is responsible for nutrient, waste, and gas exchange between the mother and fetus, as well as providing other needs such as endocrine function and important antibodies12. The placental barrier refers to the barrier that separates the maternal blood from the fetal blood. In humans, this barrier is composed of 3 main layers: the vascular endothelium, the extracellular matrix (ECM), and the trophoblast (epithelium). The formation of this barrier starts with the recruiting of trophoblast cells from the uterus. These cells invade the intervillous space and attach to one another to form the chorionic villi. There are two types of trophoblasts prevalent in the placenta: cytotrophoblast and syncytiotrophoblast. The cytotrophoblasts are mononuclear and are responsible for breaking down ECM within the chorionic villi to make the space that will eventually be taken over by the umbilical blood vessels. After completing their function, they are capable of fusing together to form a syncytrotrophoblast layer. This lies in the outermost layer of the chorionic villi and is in contact with the maternal blood, therefore making it extremely important in nutrient/waste exchange applications. The middle layer of the barrier is composed of the extracellular matrix. This matrix is comprised of the "fluff" separating the endothelial and epithelial layers. The ECM provides the cell layers with support, separation, and crosstalk (either cell-cell or cell-ECM).
As stated previously, once the chorionic villi are hollowed out from the cytotrophoblasts, the fetal blood vessels are able to work their way inside of them. Therefore, when considering the barrier between bloodstreams, the layer that will be in contact with the fetal blood is the vascular endothelium of these blood vessels. The vascular endothelium is responsible for controlling particle transfer through the membrane, controlling the blood pressure, and aiding in the repair of damaged tissue.

In this work, these three layers are approximated on a microfluidic organ-on-a-chip platform to create a "placenta-on-a-chip.' Human umbilical vein endothelial cells are used to represent the vascular endothelium, BeWo choriocarcinoma cells are used to represent the trophoblast, and a type 1 collagen solution overlaying a nanoporous polyethylene terephthalate (PETE) membrane is used to represent the ECM.

METHODS

In determining the size and geometry of the design, there are two important considerations that will greatly affect the ability of the chip to diffuse properly: cross-sectional geometry and flow path. The master mold was created using a soft lithography technique on a silicon wafer. PDMS was used as the material of the layers containing microfluidic channels. A nanoporous PETE membrane was placed between the two PDMS layers. The PETE membrane was obtained by cutting the membrane from a Transwell® well plate with membrane insert. The HUVEC cells were chosen to represent the endothelial layer of the device, cultured in an EGM-2 media. The human trophoblast cell line BeWo was chosen to represent the epithelial layer.

Copyright 2016 The Organizing Committee for the 2016 Summer Biomechanics, Bioengineering and Biotransport Conference

The media used for the BeWo cells was F-12K, supplemented with 10% FBS.

RESULTS

After sterilization of the device through ethanol and UV radiation, HUVEC cells were first injected into the top channel of the chip at a seeding density of 5x106 cell/ml. To give the cells sufficient adherence, the chips were brought into an incubator (37°C, 5% CO2) and left for 12 hours to allow for attachment to the membrane. After sufficient time was given, the BeWo cell line was injected into the bottom channel of the chip at a seeding density of 5x106 cell/ml. Before injection, HUVEC cells were stained with CellTrackerTM Green CMFDA fluorescent dye and BeWo cells were stained with CellTrackerTM Orange CMRA fluorescent dye.

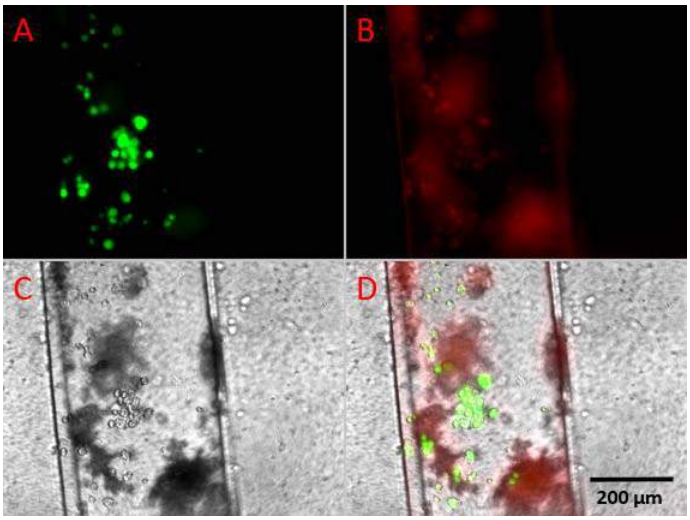

Figure 1: Injected HUVEC (green) and BeWo (red) cells before the start of the trial, seen through: A) GFP filter, B) RFP filter, C) Brightfield, and D) GFP + RFP + Brightfield. Scale bar is at 200 µm.

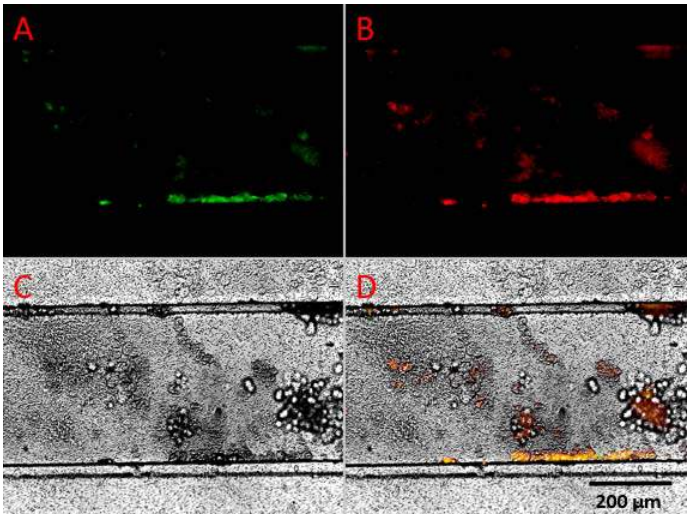

Figure 2: Injected HUVEC (green) and BeWo (red) cells after 5 days of flow, seen through: A) GFP filter, B) RFP filter, C) Brightfield, and D) GFP + RFP + Brightfield. Scale bar is at 200 µm.

Fluorescent and bright field images taken before media flow can be seen in Figure 1. A look through the different filters allows us to key in on the specific cells of interest. For the HUVECs, a green fluorescent protein (GFP) filter is used, and for the BeWo cell line, a red fluorescent protein (RFP) filter is used. The system was observed through an inverted microscope.

Once the cells were attached on the membrane within the chip, constant media flow was administered to the chip via syringes containing the cell media positioned on a double syringe pump. Silicon tubing with an inner diameter of 0.04 inches and outer diameter of 0.085 inches was used to connect the syringes to the inlets of the chip. Tubing was also connected to the outputs of the chip, which directed the media out of the chip to be collected, either as waste or for further analysis. The flow rate used for both channels in this system was 6 µl/hr. Long-term maintenance studies were performed on the chips once it was shown that the cells were able to adhere to the membrane and get nourishment from the media flow. The system was allowed to flow for 5 days. Afterwards, the system was checked under the same filters. Figure 2 shows the resulting images.

DISCUSSION

This technique shows how these pertinent cell lines can be introduced into a microfluidic design in order to create a biomimetic microsystem resembling the placenta. Starting with the basic microfluidic phenomena that control particle density and dispersion, a model was designed the exploit these phenomena in order to create a drug testing platform resembling the placenta. Using this platform, cells were chosen based on their physiological traits and were successfully introduced into the device. This device was then able to be monitored for a significantly long term.

Cells shown after long term maintenance showed some migration, specifically towards the walls of the channels. This may be due to insufficient adherence of the cells or due to the strength of the flow in the channels. The decrease in cell density would suggest the latter, however, cells shown in Figure 1 display weak structural integrity that would suggest that they aren't firmly attached to the membrane. These aspects can be further inspected to improve the functionality of the device. With the successful integration of cells into the microfluidic device, more avenues for analysis can be considered. One aspect to consider is the measurement of markers specific to the placenta. Protein-expressing markers provide a good indication of how well the system is operating and how similar it is to the in vivo environment. For example, E-cadherin, which is known for its role in cell-cell adhesion and epithelial cell signaling, can be found in the placenta at distinctly higher levels in vivo than in vitro. Additionally, an analysis of the impact of various flow rates and cell adhesion times can also be considered.

Another area worth considering for future study is the role of ethanol-induced toxicity for the placenta-on-a-chip. Like the liver-on-a-chip discussed earlier, ethanol contained within the maternal media stream can be representative of the blood alcohol content seen in cases involving fetal alcohol spectrum disorder. This could prove a useful tool in not only being able to use the placenta-on-a-chip in a healthy and functioning placenta, but also in mapping non-ideal scenarios.

ACKNOWLEDGEMENTS

We acknowledge the Lush Prize for support of this work.

REFERENCES

[1] Caplin, J et al., *Adv. Healthcare Mat.*, 4: 1426-1450, 2015.

Copyright 2016 The Organizing Committee for the 2016 Summer Biomechanics, Bioengineering and Biotransport Conference

SB³C2016
Summer Biomechanics, Bioengineering and Biotransport Conference
June 29 –July 2, National Harbor, MD, USA
SB³C2016-920

REGULATION OF VALVE INTERSTITIAL CELL CONTRACTILITY AND METABOLISM BY MESOSCALE ARCHITECTURE

Ishita Tandon (1), Atefeh Razavi (1), Timothy J. Muldoon (1), Narasimhan Rajaram (1), Kartik Balachandran (1)

(1) Department of Biomedical Engineering,
University of Arkansas, Fayetteville AR 72701

INTRODUCTION

Valvular heart disease is the third most common form of cardiovascular disease and is associated with abnormal valve structure and function. *In vivo*, the valves maintain their integrity and function by a complex interplay between the tissue, the cells and the surrounding hemodynamic and mechanical environment. Valve interstitial cells (VICs) exist as a continuum of phenotypes with various physiological roles. Most prior studies have focused on the role of the VIC phenotype in modulating valve function and disease progression. There are, however, relatively few studies that discuss the role of VIC structure in regulating its function or phenotype. Previous publications report that cellular and tissue shape, enforced by constraining the boundary conditions for cell spreading, can result in altered cellular function in various other cell types [1]. We hypothesized that cellular architecture directly affects acute contractile function and metabolism in VICs. To test this hypothesis, we engineered VIC micro-tissue monolayers constrained with control over cellular shape and cell-cell contact density. VIC micro-tissue contractility, phenotype and metabolism was quantified and assessed using the valve thin film assay, western blots and metabolic redox imaging, respectively.

METHODS

1. Valve interstitial cell isolation and culture

Fresh porcine hearts (3-6 months old) were obtained and immediately dissected aseptically. Cells were isolated using collagenase digestion as described in previous protocols [2]. Valve interstitial cells (VICs) were then isolated and cultured in normal and osteogenic media. Cells from passages 2-6 were used in all subsequent experiments.

2 Photolithography, soft lithography and microcontact printing

Photolithographic transparency masks were designed and fabricated in a regular array of line patterns with five different widths (10, 20, 40, 60 and 80μm) spaced 40μm apart. Silicon wafers were then spin coated with Su-8 2005 negative photoresist and exposed to ultraviolet light through the photomask and developed using standard photolithography protocols. Fibronectin was incubated on a polydimethylsiloxane stamp for 1 hour at room temperature, gently blown dry and placed in contact with Ultraviolet-Ozone treated PDMS-coated coverslips for 5 minutes. Coverslips were then blocked with 1% Pluronics, washed three times with dPBS and VICs were seeded at 100,000 cells/cm^2 and cultured at 37°C, 5% CO_2.

3. Quantification of cellular architecture and cell-cell contact density

After 48 hours of culture, cells were fixed andthen labeled with Alexa Fluor 488 phalloidinand 4',6-diamidino-2-phenylindole. Samples were mounted onto a glass slide and imaged and analyzed using custom MATLAB scripts [2].

4. Valve thin film stress measurement assay

Coverslips for valve thin film (vTF) experiments were prepared as previously published [2]. The vTFs were stimulated with 50nM endothelin-1 followed by 100μM HA-1077 while being continually to record changes in the projected length of the film (x) and thus the radius of curvature (r) of the cantilever films. The stress (σ) required to bend the film was then calculated using the modified Stoney's equation. Stress data was then normalized by cell. The thickness of the PDMS layer (t) was measured using stylus profilometry and the cell layer thickness (h) was measured using confocal z-stacks.

5. Two –photon redox imaging

Two Photon microscopy using a custom imaging system was used to image VIC samples at 755nm and 860 nm laser excitation to measure NADH and FAD fluorescence, respectively.[3] Custom MATLAB code was used to quantify FAD/(NADH+FAD) redox ratio.

.

Copyright 2016 The Organizing Committee for the 2016 Summer Biomechanics, Bioengineering and Biotransport Conference

RESULTS

The results shown here correspond to normal DMEM conditions. The experiments with cells cultured in osteogenic media are in progress.

1. In vitro model for altered cell shape and its implications on cell architecture and cell-cell contact density

We induced an elongated, spindle-shaped VIC with low cell-cell contact density with narrower fibronectin pattern widths, and a less elongated VIC with greater cell-cell contact with wider fibronectin patterns. There was a significant positive correlation between actin orientation and cell aspect ratio (Fig. 1A), as well as nuclear aspect ratio and cell aspect ratio (Fig. 1B). There was a significant negative correlation between cell-cell contact density and cell aspect ratio (Fig. 1C - E).

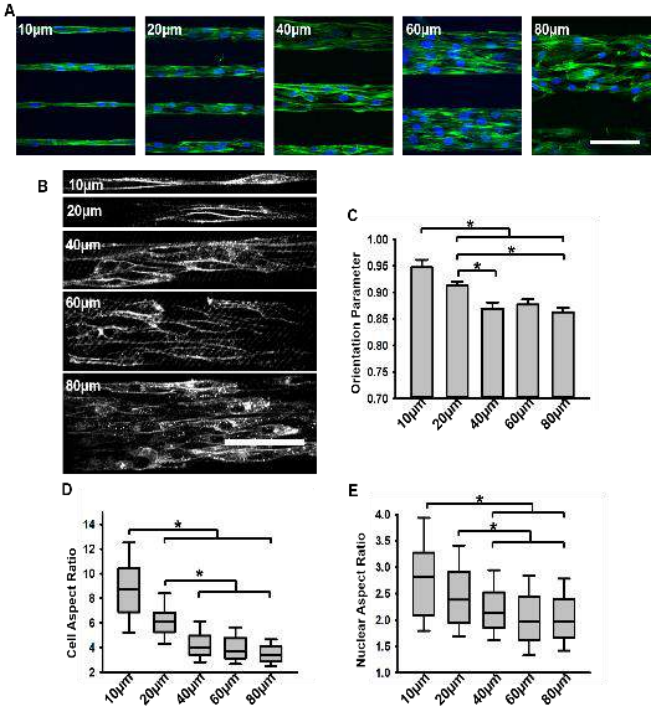

Figure 1: VIC cell architecture data. (A) Phalloidin (green) and DAPI (blue) stained images of VIC micro-tissues constrained to different pattern widths. (Scale bar = 80μm) (B) Di-8 (white) stained VIC micro-tissues. (Scale bar = 80μm). (C) Actin orientation parameter data. (D) Cell aspect ratio data. (E) Nuclear aspect ratio data. (* $p<0.05$)

2. VIC structure and contractile function

Both increases in cell aspect ratio and cell-cell contact density resulted in increased contractile stress response to ET-1 (Fig. 2), resulting in a U-shaped response curve. VIC micro-tissue response to HA-1077 revealed no significant differences in cellular basal tone as a function of VIC micro-tissue width. This result suggested that baseline cellular tension in VICs was independent of cellular architecture or shape.

3. VIC metabolic redox ratio

VIC redox ratio data mimicked the same trends as the contractility data, with minimum redox ratio occurring at 20μm line width, and increasing thereafter. Previous studies reported lower redox ratio values in cells undergoing differentiation and macromolecule synthesis [3]. This result thus suggests VICs in narrower patterns have a greater propensity for differentiation. These studies are currently ongoing.

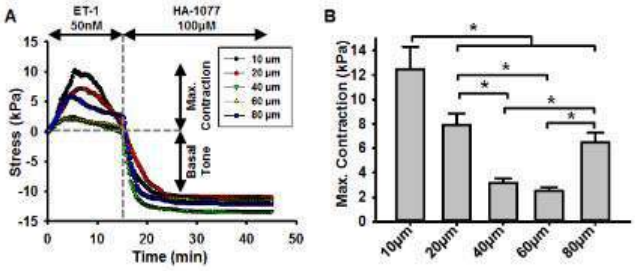

Figure 2: VIC contractility data. (A) Time series data for VIC contractility. (B) Maximum contraction data. (* $p<0.05$)

3. VIC structure and Redox Activity

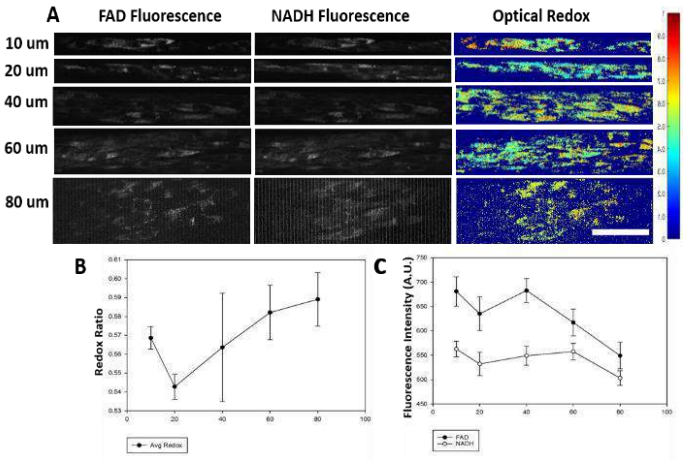

Figure 3: Metabolic redox ratio data. (A) Representative FAD, NADH and redox images. (B) Redox data. (C) FAD and NADH data.

DISCUSSION

We report herein that VIC architecture and shape significantly regulated cellular functional contractile output and metabolism. Our results here also highlight cell-cell contact density as an additional factor that influences VIC function. Redox ratio also mimicked the same trends as that of VIC contractility, suggesting altered glycolysis and oxidative phosphorylation as a result of altering cellular architecture. Taken as a whole, our study implicates VIC cell architecture as a key mediator of function. Studies are ongoing on the role of osteogenic medium in influencing the reported metrics for cell function.

ACKNOWLEDGEMENTS

We acknowledge funding from the National Science Foundation grant CMMI-1452943.

REFERENCES

[1] E. S. Hald, K. E. Steucke, J. A. Reeves, Z. Win, P. W. Alford, Biofabrication 2014, 6, 045005; Z. Win, G. D. Vrla, K. E. Steucke, E. N. Sevcik, E. S. Hald, P. W. Alford, Integrative biology : quantitative biosciences from nano to macro 2014, 6, 1201.

[2] K. Balachandran, P. W. Alford, J. Wylie-Sears, J. A. Goss, A. Grosberg, J. Bischoff, E. Aikawa, R. A. Levine, K. K. Parker, Proceedings of the National Academy of Sciences of the United States of America 2011, 108, 19943.

[3] K. P. Quinn, G. V. Sridharan, R. S. Hayden, D. L. Kaplan, K. Lee, I. Georgakoudi, Sci Rep 2013, 3, 3432.

Copyright 2016 The Organizing Committee for the 2016 Summer Biomechanics, Bioengineering and Biotransport Conference

SB³C2016
Summer Biomechanics, Bioengineering and Biotransport Conference
June 29 –July 2, National Harbor, MD, USA
SB³C2016-921

MULTI-RESOLUTION MODELS OF THE MITRAL VALVE LEAFLETS FOR HIGH FIDELITY BIOMECHANICAL SIMULATIONS

Amir H. Khalighi (1)(2), Andrew Drach (2), Charles H. Bloodworth IV (3), Eric L. Pierce (3) , Ajit P. Yoganathan (3), Robert C. Gorman (4), Joseph H. Gorman III (4), and Michael S. Sacks (1)(2)(5)

(1) Department of Mechanical Engineering, The University of Texas at Austin, Austin, TX, USA

(2) Center for Cardiovascular Simulation, Institute for Computational Engineering and Sciences, The University of Texas at Austin, Austin, TX, USA

(3) Cardiovascular Fluid Mechanics Laboratory, Wallace H. Coulter Department of Biomedical Engineering, Georgia Institute of Technology, Atlanta, GA, USA

(4) Gorman Cardiovascular Research Group, University of Pennsylvania, Philadelphia, PA, USA

(5) Department of Biomedical Engineering, The University of Texas at Austin, Austin, TX, USA

INTRODUCTION

It is strongly believed that the complex Mitral Valve (MV) structure and tissue remodeling play a significant role on the valvular response to MV repair [1]. However, isolating the effect of each factor to study the treatment outcomes is infeasible in the *in vitro* and animal studies. Computational simulations have proven to effectively predict the valvular biomechanical behavior and design of valvular prosthesis [2]. However, due to the complexity of MV structure, computational models are still struggling to account for all the underlying factors that impact the MV response to repair. In fact, most standard biomechanical models of the MV perform suboptimally in predictive simulations of the MV to optimize the repair procedures.

In the current study, we have developed a pipeline to quantitatively characterize the MV leaflet geometry, build personalized models with an adjustable level of detail, and incorporate structural attributes within the geometric models. The developed platform provides the basis to perform high fidelity biomechanical simulation to optimize the annuloplasty ring geometry by allowing linking the internal structure and organ level response. In addition, to the best of our knowledge, this is the first study to develop multi-resolution models for biomechanical simulations.

METHODS

We acquired three data-sets on the MV geometry by imaging ovine heart valves obtained from an USDA approved abattoir (Superior Farms, CA, USA) using micro computed tomography modality as described in [3]. The DICOM images were then segmented in the ScanIP software suite (Simpleware Ltd., Exeter, UK) and labeled in Zbrush sculpting software (Pixologic Inc., CA, USA) (Fig. 1). Next, for each valve, we fitted a superquadric surface model (Eq. 1) to capture the general geometry of the MV through the estimation of size (a_1,a_2,a_3) and shape (ε_1,ε_2) parameters.

$$F(x,y,z)=\left[\left(\frac{x}{a_1}\right)^{2/\varepsilon_2}+\left(\frac{y}{a_2}\right)^{2/\varepsilon_2}\right]^{\varepsilon_2/\varepsilon_1}+\left(\frac{z}{a_3}\right)^{2/\varepsilon_1}-1 \qquad (1)$$

To resolve the surface details, we computed the signed L_2 residual fields of fitting the superquadric surface to the atrial and ventricular surfaces of the MV (Fig. 2). We then applied sparse spectral analysis on the residual fields and reconstructed the fine features of the MV leaflets in the Fourier domain. The sparse spectral analysis was performed using a proximal gradient method in the Lasso optimization framework [4]. This modeling approach enabled us to co-register the MV surfaces and reconstruct them with a customizable level of detail by applying digital filters in the spectral domain.

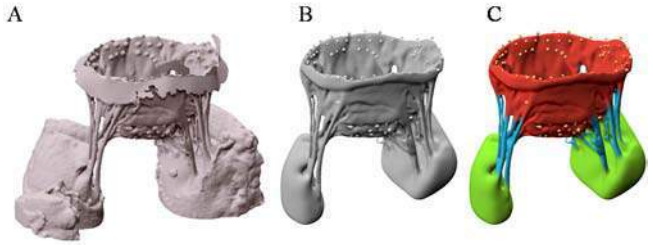

Fig. 1: The segmented micro-CT image of a MV (A) is manually trimmed (B) and the constituent parts are labeled (C).

Copyright 2016 The Organizing Committee for the 2016 Summer Biomechanics, Bioengineering and Biotransport Conference

RESULTS

Here we present both illustrations of our modeling pipeline and the final multi-resolution geometric models of three MVs. First, a unique superquadric surface was computed for each valve to capture the general shape (Fig 2). Then, the surface details were extracted as scalar fields (Fig 3) and reconstructed using spectral analysis. The reconstructed features were then superimposed on the smooth superquadric approximation of the MV geometry (Fig 4A) and the model was trimmed according to MV physical boundaries (Fig 4B) to build a fully detailed parametric model of the MV leaflet structure (Fig 4C). The final models were reconstructed (Fig 5) with an adjustable level of detail through the superposition of the superquadric approximation and surface details.

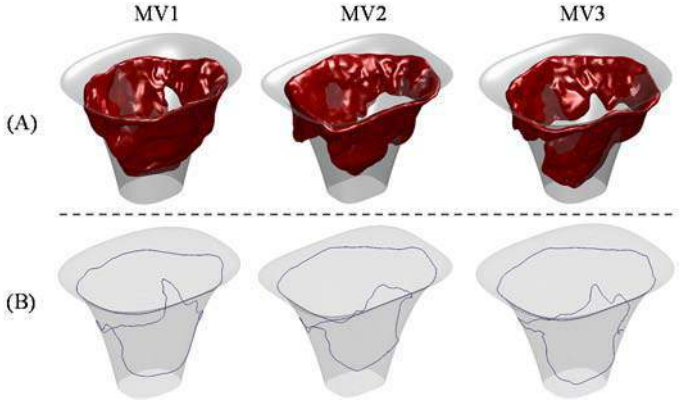

Fig. 2: In (A) the computed superquadric models are shown for three valves. Panel (B) shows the superquadric models and physical boundaries of the MV leaflets.

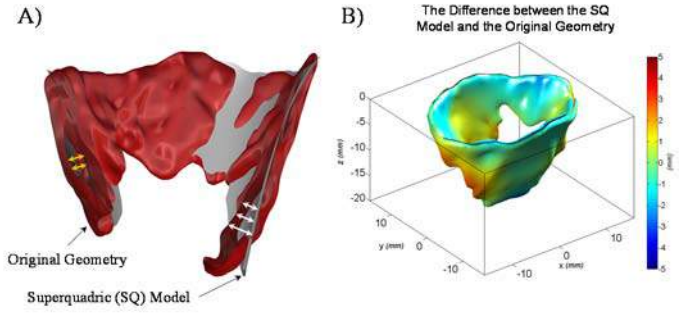

Fig. 3: The geometric details not captured by the superquadric surface (A) are evaluated by projection of original geometry on the superquadric surface fit (B).

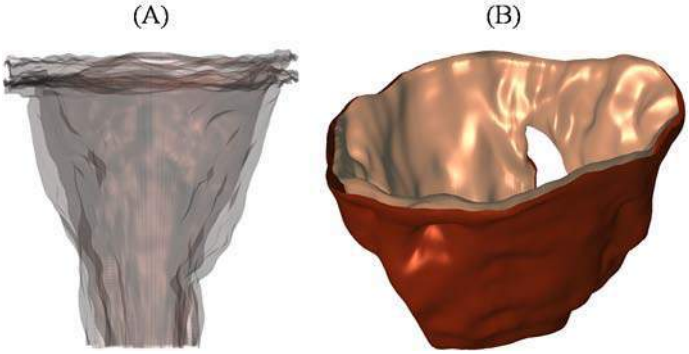

Fig. 4: (A) shows the reconstructed model of the MV in the parametric domain. In (B), the physical boundaries are applied on the parametric reconstruction to recover the true MV geometry.

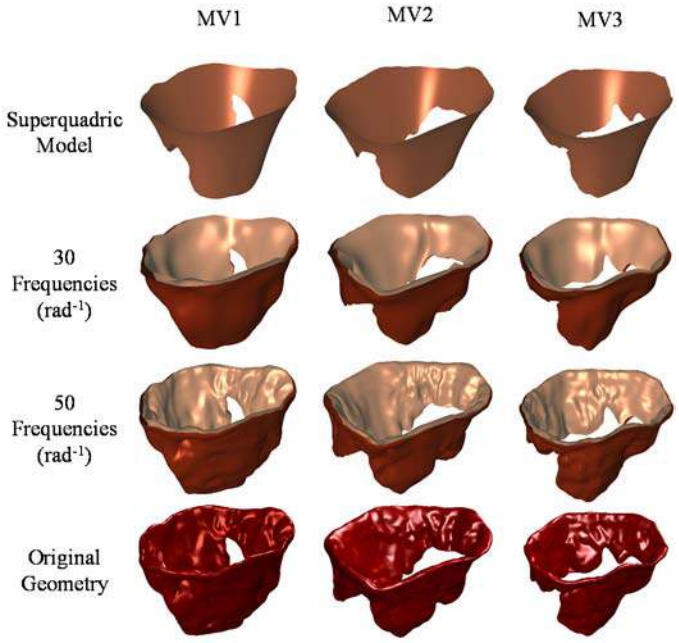

Fig. 5: For three valves, the level of detail in model reconstruction is adjusted by applying filters in the spectral domain. Each frequency corresponds to a range of feature size in the parametric domain of superquadric model.

DISCUSSION

We presented a novel approach to process pre-clinical images into anatomically accurate, detailed geometric models of the MV leaflet. In contrast to the existing geometric models of the MV, we developed models with an adjustable level of detail and controllable spatial resolution. This modeling approach also facilitates the development of a population-averaged geometric model of the MV leaflets through the parametric reconstruction of MV geometry in an objective framework. Furthermore, the results show that a superquadric surface can predict the MV general shape, which can then be enhanced to capture the surface details of the MV 3-D geometry using spectral methods. Other attributes like material properties, multi-layered structure, or internal fiber architecture can be modeled using the same spectral analysis and incorporated with geometric models. This feature of our pipeline is extremely useful for performing finite element simulations of MV behavior since we can adjust the level of detail in terms of geometric details and other physical attributes to develop anatomically accurate, attribute-rich computational models. Our models then provide high fidelity simulation tools for medical device design and surgical treatment planning.

ACKNOWLEDGEMENTS

Research reported in this publication was supported by National Heart, Lung, and Blood Institute of the National Institutes of Health under award number R01HL119297. The content is solely the responsibility of the authors and does not necessarily represent the official views of the National Institutes of Health.

REFERENCES

[1] Flameng, W., et al. *J. Thorac. Cardiovasc. Surg.*, 274-282, 2008.
[2] Chandran, K, et al *Cardiovasc. Eng. Technol., 1*(1), 18-38, 2010.
[3] Khalighi, A et al. *Lecture Notes in Comput. Sci.*, 164-171, 2015.
[4] Tibshirani, R. *J. R. Stat. Soc. Series B,* 267-288, 1996.

Copyright 2016 The Organizing Committee for the 2016 Summer Biomechanics, Bioengineering and Biotransport Conference

SB³C2016
Summer Biomechanics, Bioengineering and Biotransport Conference
June 29 –July 2, National Harbor, MD, USA
SB³C2016-922

BIOMECHANICAL CONSEQUENCES OF SUBCHONDRAL BONE CYSTS – A FINITE ELEMENT ANALYSIS OF THE EQUINE STIFLE JOINT

Lance L. Frazer (1), Elizabeth M. Santschi (2), Kenneth J. Fischer (3)

(1) Bioengineering Graduate Program
University of Kansas
Lawrence, KS, USA

(2) College of Veterinary Medicine
Department of Clinical Sciences
Kansas State University
Manhattan, KS, USA

(3) Department of Mechanical Engineering
University of Kansas
Lawrence, KS, USA

INTRODUCTION

Subchondral cystic lesions (SCL) occur in the medial femoral condyle (MFC) of horses and can cause lameness.[1] They are more common in horses ≤ 2 years of age, but can occur in older horses. The causes of SCL are not well understood, however, trauma and osteochondrosis are most commonly implicated.[2] Serial radiographs of young horses that develop SCL indicate a progression from sclerosis to MFC flattening, and then a defect that enlarges. Treatments are directed at reducing local inflammation and promoting bone and cartilage healing, with approximately 50-75% of horses becoming sound enough for work. However, bone healing after surgery is inconsistent, occurring in <20% of patients.[3] Recently, a treatment of MFC SCL using a lag screw has been reported that improves the rate of lameness resolution and is the first study to report significant and consistent bone healing.[4] This suggests a biomechanical approach can improve the treatment of equine SCL, but very little is known about the stresses within the equine stifle and how the surgical procedure may be optimized. The equine stifle is a complex biological system and direct collection of biomechanical data would be difficult, if not impossible. The objective of this current study is to investigate the stresses in the subchondral femoral bone at different stages of cyst progression using finite element analysis. This information can help us better understand the mechanics associated with SBCs that will allow clinicians to develop and implement rational treatment strategies.

METHODS

Segmentation and Meshing. Using computerized tomography (CT) images of an extended equine stifle joint of a yearling Thoroughbred, 3D geometry was created by manually segmenting structures in ScanIP (Simpleware). This geometry was meshed into 4-node tetrahedral elements (C4D10) and imported into ABAQUS v6.14 (SIMULIA) for finite element analysis (Figure 1). After creation of the original model, five additional models were made to describe cyst progression, resulting in six models analyzed. 1) Intact (unaltered model), 2) Sclerotic (bone moduli elevated by 12.8% in the region of interest), 3) Flat (a small flattening of ~15 mm in diameter of the central MFC, which is a precursor to cyst formation), 4) S1 (stage-one cyst ~.25 cm^3), 5) S2 (stage-two cyst ~0.5 cm^3), and 6) S3 (stage-three cyst ~1.00 cm^3).

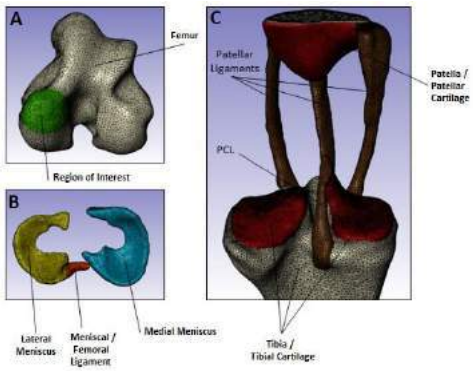

Figure 1: Separate finite element meshes generated in ScanIP prior to reassembly in ABAQUS. Femoral cartilage not shown to highlight the 3.0 cm^3 femoral region of interest (green).

Material Properties. For this study, we were interested in the instantaneous response from an extended stifle joint. Therefore, linear material definitions were suitable for our purposes. Bone moduli was correlated to its mass density using the equations:

$$Mass\ Density = (1.067 * 10^{-3}) * GrayScale \quad (1)$$

$$Young's\ Modulus = (6.0 * 10^{3}) * MassDensity^{2.5} \quad (2)$$

Copyright 2016 The Organizing Committee for the 2016 Summer Biomechanics, Bioengineering and Biotransport Conference

and 20 modulus levels were selected based on an analysis for the appropriate number of bone properties.

Table 1: Material properties used in this study.[5-7]

Structure	Type	E (MPa)	ν
Bone	Iso.	50-21,000	0.3
Menisci	Anis.	Radial, Axial = 20, Circumferential = 120	Radial, Axial = 0.3, Circumferential = 0.45
Cart.	Iso.	25	0.45
Ligs.	Iso.	300	0.3
Cyst	Iso.	0.00001	0.3

Boundary Conditions. To model the kinematics of the stifle joint during loading, a frictionless, non-linear (surface-to-surface) contact formulation was defined for all articulating surfaces. Rotations of the proximal femur were constrained, and the distal tibia was fully constrained. A surface pressure with an equivalent load of 3000 N, the peak force during trot, was placed on the proximal femur. An upward force of 175 N was placed on the proximal patella for joint stability.

Verification and Validation. *A* convergence analysis was performed for all relevant output parameters. Starting with an edge length of 2.00 mm, soft tissue structures and the region of interest were refined by 0.25 mm increments in edge length until a <3% change was observed in each output at an edge length of 1.00 mm. Sensitivity analyses were performed to account for the broad range of material property values found in literature (primarily due to specimen-to-specimen differences). We also investigated the effects of different meniscal/tibial plateau relationships to ensure the most appropriate formulation: a peripheral spring attachment that allowed semi-constrained meniscal translation (k = 20 N/mm).

Analysis. Customized scripts in Matlab (MathWorks) extracted data from the region of interest (Figure 1A). We calculated peak tension as the mean of the top 5% maximum principal stress (σ_{max}), as well as peak shear as the mean of the top 5% maximum shear stresses.

RESULTS

Tensile stress in the ROI altered from Intact in every model (Figure 2). Bone sclerosis generally elevated tensile stress in the ROI, and central MFC flattening caused a further significant increase in subchondral tensile stress at the flat surface. An S1 defect moderately lowered tension but not to intact values. An S2 defect resulted in an additional 45% increase in peak tension compared to S1, with high stress areas lateral and superior to the cyst. Peak shear stress in S2 cysts increased by 20% over S1, primarily medial and posterior to the cyst. Peak tensile and shear stress increased by a further 7% and 1%, respectively, in the ROI with a S3 cyst (Figures 2-4).

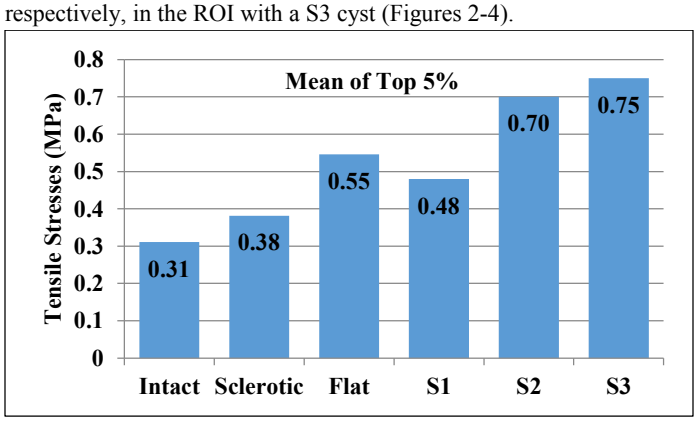

Figure 2: Peak tensile stresses for each model.

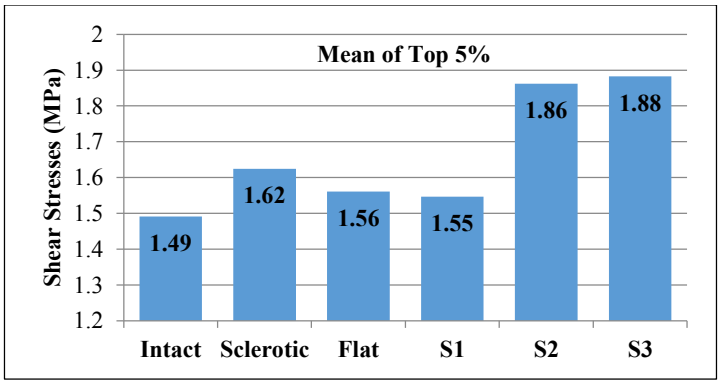

Figure 3: Peak shear stresses for each model.

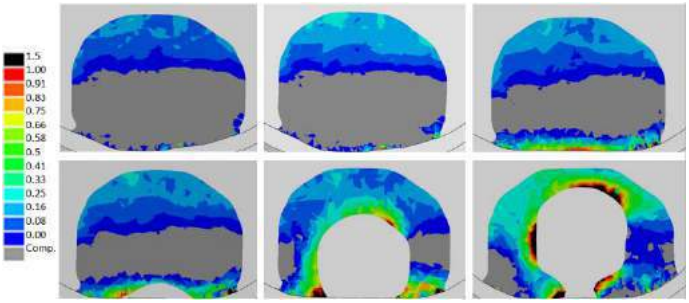

Figure 4: Frontal slice of tested models showing the maximum tensile stresses (MPa). Lateral is to the left and medial to the right. Top row from left to right: Normal, Sclerotic, Flat. Bottom row from left to right: S1, S2, S3.

DISCUSSION

The trabecular bone in the MFC in young horses is susceptible to damage-induced creep (plastic deformation) and is weakest in tension and shear. Focal flattening of the MFC is an early radiographic change that precedes cyst development and is likely the result of this creep. In the flat model, the increased tensile stress occurs where stage one cysts form. At S1 size, peak stress is slightly reduced from the flattened model, but if the defect exposes subchondral bone, joint inflammation will follow and result in further bone destruction and cyst enlargement. As the cyst enlarges to the S2 size, both tensile and shear stresses are substantially elevated, creating an apparent "point of no return." In young horses, when MFC cysts reach this size, spontaneous healing is rare, cysts tend to enlarge to S3 size, and lameness is often observed.

Our results indicate that local MFC mechanics may be a factor in cyst development and progression. These data also support a biomechanical treatment for SBC that addresses the altered stresses in the bone surrounding the cyst. While cyst development is most likely a multifaceted phenomenon, altered MFC biomechanics appear to play a substantial role.

ACKNOWLEDGEMENTS

The authors of this study acknowledge the funding support from the Self Graduate Fellowship that made this research possible.

REFERENCES

1. Jeffcott, LB et al., *Equine Vet J.*, 15(4):304-11, 1983.
2. Jackman et al. JBJS, 83-A: 53-64, 2001.
3. Smith et al., *Equine Vet J.*, 37(2):175-180, 2005.
4. Santschi, E et al., *Vet Surg.*, 10.1111/j.1532-950X, 2014.
5. Donahue, T et al. J Biomech, 36(1), pp. 19-34.
6. Kiapour, A et al. J Biomech Eng, 136(1), pp. 011002.
7. Mootanah, R et al. CMBBE, 17(13), pp. 1502-17.

Copyright 2016 The Organizing Committee for the 2016 Summer Biomechanics, Bioengineering and Biotransport Conference

SB^{3}C2016
Summer Biomechanics, Bioengineering and Biotransport Conference
June 29 –July 2, National Harbor, MD, USA
SB^{3}C2016-923

PATIENT SPECIFIC COMPUTATIONAL MODELS TO OPTIMIZE SURGICAL CORRECTION FOR FLATFOOT DEFORMITY

Brian A. Smith, Robert S. Adelaar, Jennifer S. Wayne

Orthopaedic Research Laboratory
Departments of Biomedical Engineering & Orthopaedic Surgery
Virginia Commonwealth University
Richmond, Virginia USA

INTRODUCTION

Adult Acquired Flatfoot Deformity (AAFD) is a progressive, debilitating disease characterized by the collapse of the medial longitudinal arch most commonly subsequent to posterior tibial tendon (PTT) dysfunction (1,2,3). PTT dysfunction typically results from chronic degradation of the tendon (1). As the PTT serves as the primary invertor of the foot, its degradation leads to arch collapse with subsequent increased strain on the remaining soft tissue structures (4) and gross deformity of the midfoot and hindfoot. Due to the chronic nature of the disorder, AAFD is staged from I to IV as the condition worsens. Similarly, treatments for these stages increase in complexity from singular bony and soft tissue procedures to the fusion of multiple joints. The greatest variety in surgical treatments is associated with stage IIb due to the flexible nature of the foot rendering it able to be corrected via passive mechanisms. In these cases, patients typically receive augmentation of the PTT in either a Flexor Digitorum Longus (FDL) or the Flexor Hallucis Longus (FHL) tendon transfer and a bony correction of the deformity (1,5). The choice then lies in deciding whether to use a hindfoot procedure with the Medializing Calcaneal Osteotomy (MCO), a lateral column lengthening (LCL) procedure with the Evans Osteotomy, Calcaneocuboid Distraction Arthrodesis (CCDA), or the Z Osteotomy, or in rare occasions a combination of both hindfoot and a single LCL procedure (1,5).

The challenge with having multiple surgical combinations available is to select the optimal procedure(s) for a given patient. In hopes to aid this selection, we applied Computer Aided-Design (CAD) modeling approaches to recreate the anatomy and kinematics of the foot and ankle complex to investigate how the surgical procedures correct the flatfoot deformity.

METHODS

In previous work, patient specific models were created from 1 mm MRI scans of the lower extremity of each of six patients with a 1.5 T MRI scanner (GE Healthcare Technologies Waukesha, WI) imported into the software package MIMICS® (v12.0, Materialise's Interactive Medical Imaging Control System, Materialise, Ann Arbor MI) and transformed into three dimensional bodies representing the bones of the lower leg (6). To further define the model, the 3D bones were incorporated within SolidWorks (v2007, Dassault Systèmes SolidWorks Corp., Waltham, MA, USA) and with the addin COSMOSMotion to simulate force and other constraints. The patients' body weight was applied vertically down the shaft of the tibia while linear elements representing the muscle, tendon, and ligament forces were applied throughout the foot and ankle complex providing further support to the anatomical bony constraints (Figure 1). Ligament stiffness and muscle activation values were assigned from the literature and then reduced to replicate the stage of AAFD present in each patient based on MRI signal attenuation. With these features, 3D lower leg models were created solely based on patient specific anatomy and bodyweight without requiring idealized joints (6). The surgically implemented procedures of a tendon transfer and MCO were then simulated as done previously (6).

In order to implement the lateral column procedures, bone cuts were made and wedges inserted at designated locations analogous to the surgical approaches (Figure 1B-D). For the Evans osteotomy, a cut on the anterior neck of the calcaneus was made 10mm from the calcaneocuboid joint surface. A trapezoidal wedge was inserted for a 10mm width at the lateral edge. Similarly, a wedge was inserted into the calcaneocuboid joint after 2mm of subchondral bone was removed to replicate joint surface preparation. Three cuts were made, superiorly, longitudinally, and inferiorly, to create the Z-osteotomy. Two trapezoidal wedges were inserted into the superior and inferior cuts until a 10mm separation was achieved in the superior opening. Osteotomies and wedge insertion created interference in adjacent bones of the forefoot. To eliminate these, three movements (two rotations and one translation) of the overall forefoot were implemented while preserving relative bone relationships. Tension developed in the ligaments during simulation finalized physiological bone positions.

Distance and angular measurements, contact forces between articular surfaces, ground reaction forces, and ligament strains were quantified in each model. In the medial/lateral (ML) view, 5 distance and 5 angular measurements were obtained while 1 distance and 3 angular measurements were obtained in the oblique anterior/posterior

Copyright 2016 The Organizing Committee for the 2016 Summer Biomechanics, Bioengineering and Biotransport Conference

(AP) view, replicating clinical radiographic measures. Values from the six patients were compared to normal and AAFD populations by performing a single sided z-test with differences significant for $p<\alpha=0.05$. Variations among the procedures for each patient in particular were analyzed to distinguish trends in the effectiveness in surgical correction compared to their initial clinical presentation.

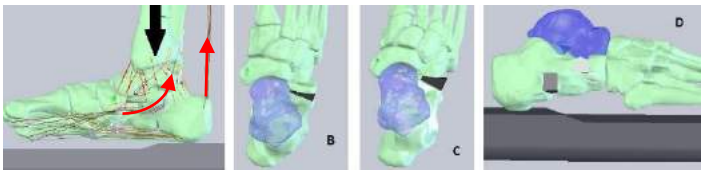

Figure 1: A: Medial exploded view of the computational model showing linear force elements used to replicate the soft tissue constraints and forces applied (shown as arrows for body weight (black), muscles (red)). Superior view of modeled Evans Osteotomy and MCO (B) & CCDA and MCO (C) procedures. Lateral view of modeled Z osteotomy and MCO (D).Translucent talus seen above calcaneus with inserted wedge (black).

RESULTS

Of the seven surgical simulations performed for each patient, the three lateral column and three combination procedures provided significant correction to the heights of the medial column as well as the calcaneal pitch, talar 1st metatarsal angle, talar declination angle, and all three AP angles with the greatest amount of correction coming from the use of the Evans and Z osteotomies with and without the addition of the MCO (Table 1). However, even with the greater amount of correction, these combination procedures also had the greatest occurrence of overcorrection. On a patient to patient basis, the Z osteotomy was the best lateral column procedure for four patients with Evans being the best for the other two. However, the combination MCO & Z procedure was best in three of those cases while the MCO addition had a varying impact on the Evans.

Other measures obtained (data not shown) (7) indicated a redistribution of joint contact force with an increase up to 4 times the patients' body weight between the calcaneus and cuboid. A shift in reaction force off of the medial column and onto the lateral column was also evident. The MCO relieved strain in the spring and deltoid ligaments but increased it in the plantar fascia. The LCL procedures increased strain in the lateral bands of the plantar fascia while relaxing the medial bands. They also relieved strain in the deltoid ligament and the inferiomedial and superiomedial bands of the spring ligament. These effects were amplified when the LCL procedure was combined with the MCO.

DISCUSSION

All procedures provided some form of correction to the flatfoot deformity while reducing strain of soft tissue structures supporting the medial column, with the combination MCO and Evans or Z procedures providing the greatest amount of correction. The Z osteotomy provided better correction when the deformity was more severe which is supported by the work of Vander Griend et al. (8). With the best procedure selected, we were unable to find trends in the pre-op presentation that would indicate which treatment should be chosen similar to the dilemma expressed clinically (9). The significant increase in joint contact and ground reaction forces occurred as reported previously for the Evans and CCDA procedures (9). The force increases for the Z osteotomy are similar to another simulation (10) but contradict the view of Vander Griend et al (8). That clinical study reported no pain increase after the Z osteotomy which should occur with the significant shift in forces onto the lateral column, however, they lacked a long term follow up longer than 1 year (8). Limitations to our study include a small patient population, literature averaged values for ligament stiffness, and only one loading scenario simulated. Our findings indicate that the Z can correct as efficiently as the Evans osteotomy, but special consideration must be taken before adding a lateral column procedure to avoid overcorrection and the significantly increased load on the lateral column.

REFERENCES

[1] Lee MS et al., J Foot Ankle Surg. 44(2): 78-113, 2005.
[2] Key JA. J Bone Joint Surg. 35(4): 1006-1008, 1953.
[3] Goldner JL et al. Orthop Clin North Am. 5(1): 39-51, 1974.
[4] Deland JT et al. Foot Ankle Int. 26(6): 427-435, 2005.
[5] Zaw H et al. Bone & Joint Sur. 2010.
[6] Spratley EM et al. J. Ortho. Research. 31(12): 1861-1868, 2013.
[7] Smith BA. Virginia Commonwealth Univ, M.S. Thesis. 2015.
[8] Vander Griend R. Foot & Ankle Surg. 7(4), 2008.
[9] Ellis SJ et al. Foot Ankle Int. 30(12), 2009.
[10] Roush GC. Univ. of Washington, M.S. Thesis. 2013.

Table 1: Average distance and angle measurements for each surgical procedure (standard deviation). Significant difference from the normal population indicated by * ($p<0.05$). Significant difference from the pre-op model measurements indicated by † ($p<0.05$). Highlighted cells illustrate occurrences of overcorrection.

	Distance (mm)						Angle (°)							
	ML-Tal-h	ML-Nav-h	ML-1CN-h	ML-Cub-h	ML-1CN/5MT-h	TNuncov	ML-CP	ML-T1MT	ML-TC	ML-Tdec	ML-C1MT	AP-TN	AP-T1MT	AP-T2MT
MCO	27.3 (2.9)*	19.8 (5.7)*	12.1 (4.2)*	5.5 (2.1)*†	13.1 (4.7)	12.8 (2.1)	13.1 (3.9)*	8.5 (9.2)	32.4 (3.3)*	25.4 (4.5)	150.0 (7.3)*	9.9 (4.6)†	8.1 (5.1)†	14.8 (6.1)†
Evans	32.7 (2.8)*†	26.2 (5.8)*†	16.9 (4.5)†	10.1 (1.8)†	15.5 (5.6)†	12.7 (1.5)	20.1 (4.8)†	-1.0 (9.9)†	34.4 (4.1)*	21.2 (5.2)*†	137.8 (8.0)†	5.4 (3.1)†	-0.03 (7.6)†	9.4 (8.0)†
CCDA	29.8 (3.4)*†	23.3 (6.4)*†	15.8 (4.6)*†	10.4 (3.0)†	14.1 (5.6)	13.6 (1.2)*	16.1 (3.9)*†	2.4 (9.9)†	32.9 (2.9)*	23.8 (5.0)†	143.1 (8.0)*†	9.7 (6.8)†	7.0 (6.7)†	15.1 (7.4)†
Z	32.5 (2.9)*†	25.6 (5.5)*†	16.4 (4.6)†	10.5 (1.4)†	14.9 (5.7)†	11.9 (2.1)	19.4 (4.2)†	-0.4 (8.8)†	34.4 (3.4)*	20.9 (5.3)*†	138.5 (6.8)*	4.9 (5.8)†	1.6 (7.6)†	11.2 (8.7)†
MCO & Evans	32.5 (1.8)*†	26.5 (5.2)*†	17.3 (4.2)†	9.4 (1.6)*†	17.6 (4.7)†	12.1 (1.6)	20.5 (4.4)†	0.7 (9.0)†	34.2 (3.6)*	20.7 (4.8)*†	138.3 (6.1)*	9.4 (3.2)†	3.2 (5.6)†	13.0 (5.5)†
MCO & CCDA	30.5 (2.5)*†	24.3 (5.9)*†	16.4 (4.2)†	10.2 (2.1)†	15.2 (5.6)†	13.4 (0.8)*	16.6 (3.8)†	1.7 (9.0)†	32.9 (3.4)*	22.8 (4.7)*†	141.4 (7.2)*	10.9 (3.9)†	4.7 (4.3)†	14.7 (5.8)†
MCO & Z	32.5 (1.6)*†	26.1 (4.9)*†	15.9 (5.3)†	10.5 (2.0)†	16.7 (4.9)†	11.5 (1.6)	19.6 (4.2)†	-2.1 (9.3)†	33.3 (4.1)*	20.3 (4.6)*†	138.0 (6.0)*	3.4 (5.2)*†	-0.04 (6.9)†	9.7 (7.0)†

Copyright 2016 The Organizing Committee for the 2016 Summer Biomechanics, Bioengineering and Biotransport Conference

SB^{3}C2016
Summer Biomechanics, Bioengineering and Biotransport Conference
June 29 –July 2, National Harbor, MD, USA
SB^{3}C2016-924

INTEGRATION OF OPENCASCADE AND IMPROVED GLOBAL SURFACE INTERPOLATION ALGORITHMS INTO SIMVASCULAR 2.0

Adam R. Updegrove (1), Nathan M. Wilson (2), Shawn C. Shadden (1)

(1) Department of Mechanical Engineering
University of California, Berkeley
Berkeley, CA, USA

(2) Open Source Medical Software Corporation
Santa Monica, CA, USA

INTRODUCTION

The most common technique for creating imaged-based patient-specific vascular models using the open-source package SimVascular (www.simvascular.org) is to utilize 2-D image segmentation and proprietary, commercial solid modeling kernels [1]. Two primary drawbacks with this approach are the cost of the commercial libraries and limited ability to integrate 3-D image segmentation results into model development, subsequent mesh generation and simulation. To address these issues the authors have previously reported on extending SimVascular to robustly support triangulated surface representations of anatomy [2]. Triangulated surface representations are desirable because they enable the use of direct 3-D image segmentation algorithms, and provide a framework to combine 2-D and 3-D image segmentations results [2].

While the previous reported improvements were useful to many users, there remains significant interest in traditional solid modeling-based techniques. First, some users require CAD packages to manipulate their models (e.g. integrating a medical device design into a patient-specific anatomic model, or optimizing surgical planning). CAD packages today primarily use boundary representation (B-Rep) for solid models where the boundary surfaces of the solid are represented as planes or Non-Uniform Rational B-Spline (NURBS) surfaces. Second, some SimVascular users rely on commercial flow solvers that have poor support for triangulated surface representations and thus require NURBS models that can be incorporated into the pre-processing packages available with these commercial tools. The work described herein extends the open-source version of SimVascular to support users that require NURBS models for their research.

METHODS

The goal of this work is to enable the creation of image-based models that are a collection of planar surfaces and NURBS patches that define a single enclosed volume of interest, and can be used in the SimVascular pipeline. The surfaces will be defined as planes bounded by an ordered boundary edge curve in 3-space. For each NURBS surface, a series of control points and weights will be specified given the following definition:

$$\boldsymbol{S}(u,v) = \sum_{i=0}^{n} \sum_{j=0}^{m} \frac{N_{i,p}(u)\, N_{j,q}(v)\, w_{i,j}}{\sum_{k=0}^{n} \sum_{l=0}^{m} N_{k,p}(u)\, N_{l,q}(v)\, w_{k,l}} \boldsymbol{P_{i,j}} \quad (1)$$

where $N_{i,p}(u)$ are the basis functions in the u parametric direction and $N_{j,q}(v)$ are the basis functions in the v parametric direction. $\boldsymbol{P_{i,j}}$ are the control points in a defined coordinate system and $w_{i,j}$ are the corresponding scalar weighting values for each control point.

Extending the modular SimVascular open source software framework to support NURBS-based solid models required adding a new concrete solid model class with three core capabilities. First, the class needed the ability to create a solid model for an individual object from an ordered set of 2-D image segmentations. The result of this "lofting" operation is a single solid with a NURBS "wall" and planar "caps". Second, the solid modeling class needed to support the standard Boolean operations of union, intersection, and subtraction to be able to create 3-D anatomic models of branching structures by combining separate solid models. Third, the class needed to provide the ability to "tag" individual surfaces so the user can specify boundary conditions or material properties based on the surfaces of individual branches.

Integration of OpenCASCADE: After investigating several open-source alternatives, we integrated OpenCASCADE (www.OpenCASCADE.org) into SimVascular. The primary reasons for selecting OpenCASCADE was its large existing user base,

Copyright 2016 The Organizing Committee for the 2016 Summer Biomechanics, Bioengineering and Biotransport Conference

extensive functionality, lofting operations, Boolean operations, fillets, ability to assign data labels to geometric attributes, data exchange (e.g. saving models in STEP format), and compatibility with the Visualization Tool Kit (VTK). However, we discovered that the existing lofting operations in OpenCASCADE often led to undesirable artifacts in vascular models particularly at the ends of vessels (see Fig. 1). This motivated an investigation into improved lofting operations.

Improved global interpolation methods: Several techniques were explored to address the issues with OpenCASCADE's lofting operation. First, cubic splines were fit to the 2-D segmentation groups along the length of the vessel as is done in the creation of a triangulated surface from 2-D segmentations [2]. The splines were used to create evenly spaced segmentations along the length of the vessel for input into the OpenCASCADE lofting algorithms. While more robust than OpenCASCADE's functions, small ridges still persisted in many test cases. Thus, even additional preprocessing and regularization of the data did not ultimately produce high quality results.

OpenCASCADE enables a developer to explicitly specify the NURBS surface parameters directly and still take advantage of the other required functionality discussed above. Specifically, we resample each 2-D segmentation to the same user-defined number of points. These are "fit points" or points that need to be exactly on the surface $\boldsymbol{S}(u,v)$. The points around the circumference of the 2-D segmentations (n+1 points) become the u parametric direction, and the points along the length of the vessel (m+1 points) become the v parametric direction. These points form the right hand side of a series of linear systems to be solved for the control points, $\boldsymbol{P_{i,j}}$. The left hand side of the linear system is the basis functions, $N_{i,p}(u)$ and $N_{j,q}(v)$, of the desired surface degree. Assuming that all of weightings, $w_{i,j}$, are set to 1, this leads to the equation for a nonrational B-Spline surface used in this work:

$$\boldsymbol{S}(u,v) = \sum_{i=0}^{n} \sum_{j=0}^{m} N_{i,p}(u)\, N_{j,q}(v)\, \boldsymbol{P_{i,j}} \quad (2)$$

The basis functions for the B-Spline surface are the Bernstein polynomials of the desired degree. They are found for each input data point with a corresponding parametric coordinate (u,v), which vary between 0 and 1. The basis functions are evaluated at every fit point to give (n+1) x (m+1) systems that can be solved for the control points. The basis functions and the control points define a formula for the entire B-Spline surface. The method used here also gives the user more flexibility by allowing the specification of the degree, parameterization, knot span type, and end derivatives of the result.

NURBS surfaces from triangulated surfaces: The tools developed in this work provide an additional method to create a vascular CAD model from a triangulated surface created via direct 3-D image segmentation for certain types of anatomy. In particular, the centerlines of the vascular model can be extracted and represented as SimVascular vessel paths. The triangulated model can be sliced by an infinite plane perpendicular to the vessel path at a series of locations along the path. These ordered curves are then used in SimVascular similar to 2-D segmentations as discussed above. The benefits of this technique are twofold. First, it provides the user some ability to resample a direct 3-D segmentation if desired. Second, it enables the straightforward integration of certain classes of triangulated data into CAD-friendly models.

Mesh generation: In addition to the concrete solid modeling class, two other major changes were required. First, the mesh generation classes were updated to support the new solid model type to enable mesh generation with TetGen (www.tetgen.org) and MeshSim (Simmetrix, Inc., Clifton Park, NY, USA). Of note is that special functions in the solid modeling kernel may need to be called to transform surfaces generated in filleting operations to be NURBS surfaces to use MeshSim in the SimVascular pipeline.

RESULTS

Representative results of the improved global interpolation methods are given in Fig. 1. As shown, the techniques developed herein significantly improve on the method available in OpenCASCADE by reducing visible artificial kinks in the surface. Not only is the quality of the model improved, but our method is significantly less computational intensive. For a group of 30 segmentations, it takes approximately 30% of the time it takes to loft the same group of segmentations with the algorithm inside of OpenCASCADE. In addition, because the resultant surface from the improved methods uses fewer control points, the Boolean operations for two typical vessel segments is approximately 50% faster (i.e. 10 seconds instead of 20 seconds). In most practical scenarios, the major timesaving comes by freeing the user from having to fix or manipulate 2D segmentations to achieve an accurate model, which can be highly time-consuming.

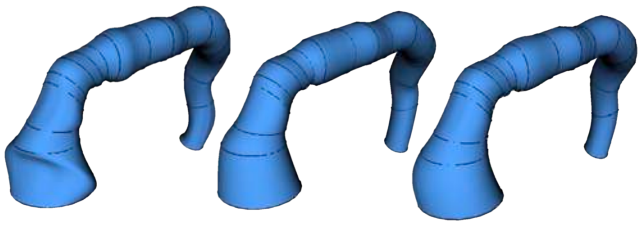

Figure 1: Example of Lofting Artifacts. The techniques integrated into OpenCASCADE 6.9 often create significant artifacts near the end of the vessels (left image). The improved methods described herein produce results without the kinks (middle image) that compare favorably to models lofted using the best-in-class Parasolid 26.1 (right image).

DISCUSSION

Prior to this work, the commercial solid modeling kernel package Parasolid (Siemens PLM Software, Plano, TX, USA) was integrated into SimVascular to provide best-in-class NURBS support and the necessary solid modeling functionality [1]. However, in addition to the expense of the commercial library, the proprietary API of Parasolid prevented the public release of SimVascular source code calling its functionality. This motivated the exploration of open-source alternatives for NURBS solids and the integration of the OpenCASCADE kernel. SimVascular is the only fully open-source project for patient-specific image-based model construction to support solid models with NURBS surfaces. In addition, improved lofting techniques have been implemented that significantly improve upon the existing techniques found in OpenCASCADE. Future work may include testing geometric optimization using the NURBS-based models, improved techniques to directly create NURBS patches from triangulated surfaces, and the integration of isogeometric analysis tools into SimVascular.

ACKNOWLEDGEMENTS

This work was supported by the NSF (award number 1407834) and the NSF GRFP.

REFERENCES

[1] Wilson NM, et al. *Proc MICCAI*, 2001, pp. 449-456.
[2] Updegrove A, et al. Triangulated Surface Boolean Operations for Combining 2-D and 3-D Image Segmentation for Patient-Specific Blood Flow Analysis: SB3C; 2015; Snowbird, Utah

Copyright 2016 The Organizing Committee for the 2016 Summer Biomechanics, Bioengineering and Biotransport Conference

SB³C2016
Summer Biomechanics, Bioengineering and Biotransport Conference
June 29 –July 2, National Harbor, MD, USA
SB³C2016-926

MECHANICAL PROPERTIES OF THE GROWTH PLATE IN A RAT MODEL OF OBESITY

Patrick N. Estep(1), Moriah S. Smoot (2), Shawn R. Gilbert (3), Alan W. Eberhardt (1)

(1) Department of Biomedical Engineering
University of Alabama at Birmingham
Birmingham, AL, USA

(2) Department of Mechanical Engineering
University of Alabama
Tuscaloosa, AL, USA

(3) Division of Orthopaedics
University of Alabama at Birmingham
Birmingham, AL, USA

INTRODUCTION

Obesity is becoming increasingly prevalent, with predictions that up to 51% of the US population will be obese by the year 2030 [1]. The effect of obesity on bone properties is largely controversial; however, studies tend to suggest that obesity increases the risk of fractures, especially in children, and can vastly complicate treatment of skeletal injuries [2]. In particular, obesity in children has been associated with a variety of complex conditions including Blount's disease and slipped capital femoral epiphysis (SCFE) [3,4]. In these two cases, as well as other clinical conditions, excessive compressive forces generated by malalignments and weight act upon the physis (growth plate) [3].

The mechanical environment is a strong regulating factor in the growth and development of long bones [5,6]. Typically, the mechanical properties of the physis are heterogeneous in different layers, such as the reserve and hypertrophic zones, directions with respect to the body, and developmental stage. Starting in the reserve zone and moving through the proliferative, hypertrophic, and calcification zones, the physis becomes significantly less rigid, exhibiting lower stiffness and higher compressive strains [5]. These changes in properties have been hypothesized to be caused by the random organization of collagen fibers in the reserve zone, when compared to more developed zones. Also, the medial and central regions have been found to be weaker and less rigid than the lateral and anterior/posterior regions. In early childhood development, the physis is significantly less stiff than in closure. Also, the physis is viscoelastic by nature due to its largely cartilaginous makeup.

It has long been thought that obesity affects the mechanical properties of the physis and surrounding bone, but no relationships have been established. In the present study, we examine the effects of diet-induced obesity on the shear forces to fracture in rat long bones, as well as local mechanical properties in the physeal region. To date, we have completed shear testing and are beginning to use stress-relaxation methods to assess the exposed cartilaginous surfaces of the failed growth plates.

METHODS

Sprague-Dawley rats were separated into two groups – one control group being fed a control diet consisting of 10% caloric intake of fat with normal drinking water, and one high-fat group being fed a diet consisting of 45% caloric intake of fat with 25% fructose water. Weekly measurements of weight were recorded. Following weaning at 3 weeks, nine 9-week old rats from each group were sacrificed and tibiae were harvested and stored at -20°F in salineated gauze. Tibiae were selected based on the relative flatness of the growth plate on the proximal side.

A custom jig was developed for testing on an MTS 858 MiniBionix (MTS Systems, Eden Prarie, MN) system. All tibiae were thawed at room temperature and potted with bone cement in the jig such that a loading nose would be perpendicular to the bone and approximately parallel to the physis, and acting in the posterior-to-anterior direction (Fig. 1). Shear testing was conducted at a rate of 0.1 mm/s using a 100 N load cell. Data were recorded using MTS Basic Testware at a sampling rate of 100 Hz and were exported to Excel for analysis. The maximum force, stiffness, and energy to max force were calculated. Non-parametric statistical tests (Wilcoxon Ranked Sums and Kruskall-Wallis) were employed due to small sample sizes. Sheared tibiae were stored in PBS and refrozen. One sample per group per time point was submitted for histological sectioning and staining to confirm that shearing occurred at the physis. Bones were decalcified and embedded in paraffin, sectioned into 3 μm segments, and stained using an H&E protocol.

Copyright 2016 The Organizing Committee for the 2016 Summer Biomechanics, Bioengineering and Biotransport Conference

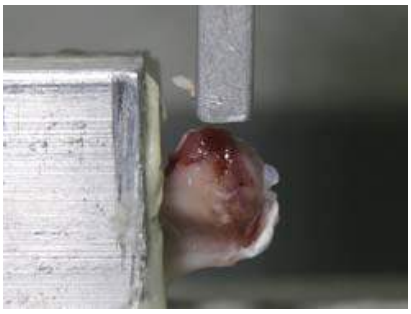

Figure 1: Shear testing of proximal tibia; loading occurs in the downwards direction.

RESULTS

Mean body weight and mean body fat after 9 weeks of the high-fat diet were 9% and 23.6% higher, respectively, than rats undergoing the control diet. The maximum force and the energy to maximum force were decreased, while stiffness was increased in the high-fat group (Fig. 2). Due to small group sizes, these differences did not reach statistical significance ($p = 0.12$, 0.34 and 0.22, respectively).

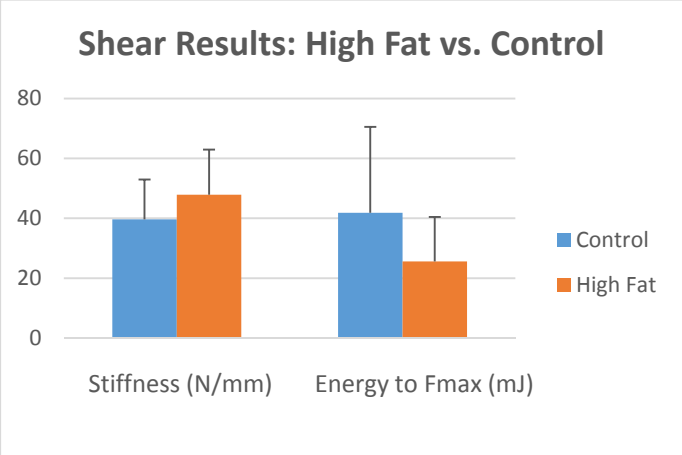

Figure 2: Mean stiffness and energy-to-max-force results from shear testing.

Figure 3 details one histological example of a sheared tibia, which confirmed that shearing occurred at the physis. Among the limited samples examined, it appears that the shear failures occurred through the hypertrophic region of the growth plate.

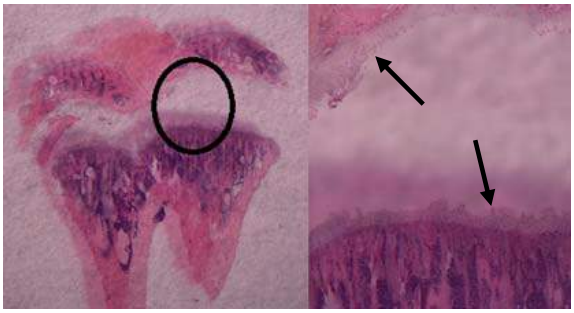

Figure 3: Histology results from samples post-shearing. Left: Macro image of a sheared tibia. Right: Zoomed-in view of encircled region, in which growth plate cartilage can be seen on either side of the shear line (indicated by black arrows).

DISCUSSION

The hypotheses behind this study were that diet-induced obesity in rats would alter both shear forces to fracture the growth plate. Our findings were both consistent with clinical observations, as well as related studies in rat tibiae [7,8], and suggest there are some differences between the growth plates of obese and non-obese rats. Increased stiffness and decreased energy absorbed may indicate that physes in obese rats are less flexible and more brittle than their healthy counterparts, though the differences were not statistically significant. As the increase in weight between the two groups was found to be modest, our findings may also indicate that increased loading due to obesity is not as significant in growth plate alterations as metabolic changes due to obesity. Limitations of this study include variability within groups and small sample sizes.

Ongoing work will focus on shear testing of 5-week old rats, which will be important in characterizing alterations in mechanical properties related to developmental and metabolic alterations. Progressive histological sections may reveal more in-depth information relating to shear fracture patterns through the physes. Lastly, indentation testing will be used to generate the mechanical properties of the growth plate on both sides of the shear fracture line. With these data, we hope to gain new insights into the effects of obesity on the growth plate.

ACKNOWLEDGEMENTS

This study was supported by a grant from the Pediatric Orthopaedic Society of North America and the UAB Division of Orthopedic Surgery.

REFERENCES

[1] Finkelstein, EA et al., *J Prev Med,* 42:563-570, 2012.
[2] Rosen, CJ, Bouxsein, ML. *Nat Clin Pract Rheumatol*, 2:35-43, 2006.
[3] Wearing, SC et al., *Obes Rev*, 7:239-250, 2006.
[4] Manoff, EM, Banffy MB, Winell, JJ. *J Pediatr Orthop*. 25:744-746, 2005.
[5] Villemure, I, Stokes, IA. *J Biomech*. 42:1793-1803, 2009.
[6] Wosu, R, et al,. *Biomech Model Mechanobiol*. 11:303-312, 2012.
[7] Folwarczna, J, Zych M, Nowinska, B, Pytlik, M. *Eur Rev Med Pharmacol Sci*. 18L1937-1947, 2014.
[8] Reimer, RA, LaMothe JM, Zernicke RF. *Int J Obes*. 2012: 1-7, 2012.

Copyright 2016 The Organizing Committee for the 2016 Summer Biomechanics, Bioengineering and Biotransport Conference

SB³C2016
Summer Biomechanics, Bioengineering and Biotransport Conference
June 29 –July 2, National Harbor, MD, USA
SB³C2016-927

A PARAMETERIZED ULTRASOUND-BASED FINITE ELEMENT ANALYSIS OF THE MECHANICAL ENVIRONMENT OF PREGNANCY

Andrea R. Westervelt (1), Michael Fernandez (1), Joy Vink (2), Chia-Ling Nhan-Chang (2), Miaoying Fan (2), Ronald J. Wapner (2), Michael House (3), Kristin M. Myers (1)

(1) Mechanical Engineering
Columbia University
New York, NY, United States

(2) Obstetrics and Gynecology
Division of Maternal Fetal Medicine
Columbia University Medical Center
New York, NY, United States

(3) Obstetrics and Gynecology
Division of Maternal Fetal Medicine
Tufts Medical Center
Boston, MA, United States

INTRODUCTION

Preterm birth (PTB) is defined as delivery between 20 and 37 weeks gestation. Across the globe, PTB affects 15 million babies each year, with 380,000 of those being in the United States [1,2]. Although some PTBs may be medically indicated, approximately 80% of them occur as spontaneous preterm births (sPTB), [3]. Clinically, the majority of sPTBs can be divided into three subcategories: premature cervical remodeling, premature preterm rupture of membranes, and preterm labor. Therapeutic interventions to prevent sPTB (tocolytic agents, progesterone supplementation, mechanical closure of the cervix via a cerclage stitch or silicon pessary) are limited and not always effective [95% of sPTBs are intractable to current therapies, both mechanical and medicinal] [4]. To decrease the rate of sPTB, it is imperative that we improve our understanding of the anatomical and tissue material factors that drive the mechanical environment of pregnancy. Thus, we built a parameterized 3D finite element (FE) model of the pregnant uterus and cervix based on maternal ultrasound measurements.

During pregnancy, the uterus and fetal membranes (FM) (i.e. chorion and amniotic sac) must grow and stretch to accommodate the growing fetus and amniotic fluid. Simultaneously, the cervix must be a mechanical barrier to keep the fetus within the uterus. All three tissues must withstand mechanical forces to support the developing baby. Then, in a reversal of roles, ideally nearing term, the uterus begins to contract and the cervix deforms (softens, shortens and dilates) to prepare for delivery [5,6]. The state of stress and stretch of these soft tissues are thought to contribute to the physiologic processes that regulate tissue growth, remodeling, and contractility. It is generally hypothesized that these mechanical signals are clinical cues for normal labor and sPTB. How these mechanical cues of stress/stretch contribute to the timing of a term or preterm birth remain to be determined.

In a previous finite element study of pregnancy derived from magnetic resonance imaging (MRI) data, we found that the mechanical load on the cervix is influenced by the geometry of the lower uterine segment (LUS) and cervix, the mechanical properties of the cervix, the FM material properties and adhesion, and how these components collectively resist loading from intrauterine pressure (IUP) [7]. In this study, we chose to utilize ultrasound-based CAD models for multiple reasons: lower cost of procedure, improved patient tolerance, and the improved flexibility to conduct a parametric study of input variables.

The goal of this study is to provide a framework for a personalized, parametric computational tool to assess the mechanical loads and tissue stretch of the organs supporting the fetus during pregnancy. Here, we develop a custom computer script to build a parameterized baseline CAD geometry of the uterus and cervix, and we implement FE analyses on various geometries to visualize the impact of cervical angle and cervical length on tissue stretch at the opening of the cervical canal into the uterus (internal os).

METHODS

Maternal Ultrasound Measurements Geometric measurements of the uterus, cervix, and their positions relative to bony reference landmarks were measured via transabdominal and transperineal ultrasound (GE Voluson E8). For the baseline model, uterine diameters, uterine thicknesses, cervical length, cervical diameters, and cervical angle with anterior lower uterine segment (LUS) were measured for a 35 y/o normal patient with no prior pregnancies at 25 weeks gestation (Fig. 1). Based on our group's previous studies, we then chose two parameters to scale individually based on values in the literature to assess each variable's impact on cervical stretch: cervical angle and cervical length [8]. Baseline values of these parameters are a 90° angle and a cervical length of 40 mm.

Copyright 2016 The Organizing Committee for the 2016 Summer Biomechanics, Bioengineering and Biotransport Conference

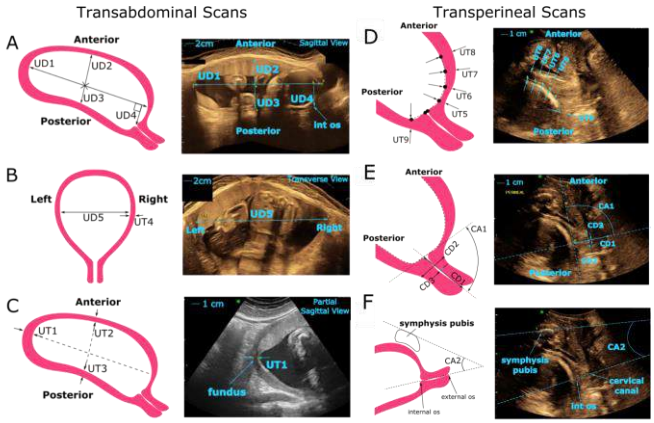

Figure 1: Diagrams of the uterus (left) and cervix based on ultrasound scans and recorded dimensions (right).

Parameterized Model and Finite Element Analysis We generated FE models (FEBio 2.3.1) using a customized computer script (Trelis Pro 15.1.3, csimsoft LLC) based on the ultrasound input parameters. Geometry of the uterus, cervix, FM, and abdomen were generated by Boolean addition and subtraction operations on geometric primitives (Fig. 2). The uterus was built by transforming two spherical surfaces into ellipsoids representing the outer and inner uterine walls. The shells were scaled, translated, and rotated to accommodate differences in uterine wall thickness in the anterior-posterior, superior-inferior, or left-right directions. The cervix was built as a hollow cylinder. Its edges were rounded at both ends to eliminate non-anatomical corners and to match the clinical presentation of the uterocervical connection. The vaginal canal was built by fitting a spline to three points on the outside edge of the cervix at the external os and one point on the approximate location of the vaginal introitus. The FM was generated with uniform thickness in a similar manner to the uterus.

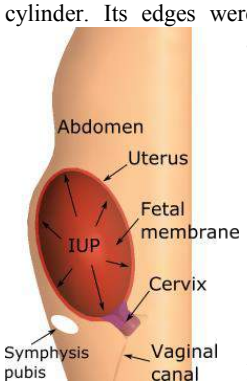

Figure 2: Parameterized CAD model of pregnancy

For FE analysis, the uterus and cervix were modeled as collagenous composite materials meshed using linear tetrahedral elements, based on material fits to passive length-tension curves of pregnant tissue [9], while the FM was modeled as Ogden nonlinear material meshed with hexahedral elements. The FM was prescribed a tied contact to the inner uterine wall and a sliding contact to the cervical internal os. For the FE simulation, IUP was applied over the physiological range for 25 weeks (0 to 0.817 kPa), which was estimated from the following equation:

$$\ln(y+1) = 0.12 + 0.23x - 0.010x^2 + 0.00015x^3 \qquad (1)$$

where y is the amniotic pressure in mmHg and x is the gestation in weeks [10]. The extent of cervical stretch was evaluated as a percentage of entire cervical volume above a 1.05 stretch threshold, and maximum stretch in each case was also calculated.

Parameter Study Multiple dimensions of the uterine and cervical geometries were measured from ultrasound and we chose to sweep the cervical angle with respect to the posterior LUS and the cervical length as input parameters (Fig. 1). After analysis, we measured the right Cauchy-Green stretch in the cervix volume to find the maximum stretch as well as the volume percentage above a 1.05 arbitrary stretch threshold.

RESULTS

The cervical angle of 90° with respect to the anterior LUS has the lowest simulated stretch concentration at the cervix internal os. While maximum tissue stretch does not have a trend, percent volume of cervix above a 1.05 stretch threshold increases directly with cervical angle (Fig. 3).

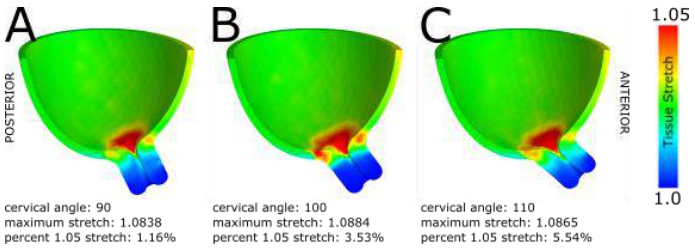

Figure 3: Plane-cut sections of the LUS and cervix showing maximum principal stretch and the corresponding cervical volume percent above 1.05 stretch for A) 90° B)100° and C) 110° cervical angle with the posterior LUS. Stretch increases with increased angle away from the posterior LUS.

The cervical length of 40 mm has the lowest simulated stretch concentration at the cervix internal os. While maximum tissue stretch does not have a trend, percent volume of cervix above a 1.05 stretch threshold increases inversely with cervical length (Fig. 4).

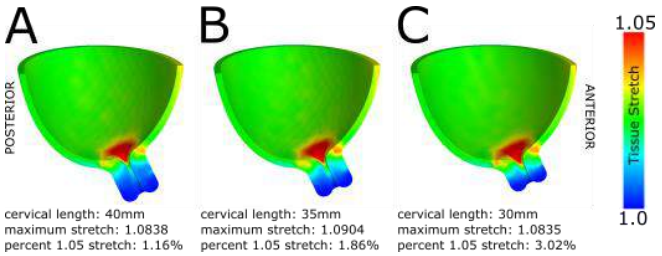

Figure 4: Plane-cut sections of the LUS and cervix showing maximum principal stretch and the corresponding cervical volume percent of stretch above 1.05 for A) 40mm B) 35mm and C) 30mm cervical length. Stretch increases with decreased cervical length.

DISCUSSION

We provided a method to generate a parameterized FE model of the pregnant anatomy using ultrasound-derived geometric parameters and material properties from previous literatures. The results show that the cervix connecting to the uterus at a right angle is the configuration which experiences the least stretch, and any deviation from this angle increases cervical stretch. We are currently exploring the consequence of altered soft tissue properties of the FM, uterus, and cervix on the mechanical environment of pregnancy.

This parameterized FE simulation has potential to be clinically useful due to its flexibility and capacity to model patient-specific geometries at various gestations. In addition, the script may be easily used by obstetricians and sonographers with minimal training, and can provide a detailed analysis for each patient in a timely manner.

ACKNOWLEDGEMENTS

This study was supported in part by the NSF GRF.

REFERENCES

[1] Preterm Birth Fact Sheet. http://www.who.int/mediacentre/factsheets/fs363/en/, 2015.
[2] Premature Babies. http://www.marchofdimes.org/complications/premature-babies, 2013.
[3] Norwitz E. Up To Date. http://www.uptodate.com/contents/prevention-of-spontaneous-preterm-birth, 2015.
[4] Norman, JE et al., *The Lancet*, 381(9862):184–185, 2013.
[5] Cunningham, F et al., *Williams Obstetrics,* 24, 2014.
[6] Martini et al., *Fundamentals of Anatomy & Physiology,* 24, 2014.
[7] Fernandez, M et al., *CMBBE*, 19:404-417, 2015.
[8] House, M et al., *EJOG*, 144S:S65-S69, 2009.
[9] Conrad, J et al., *AJOG*, 96:1055-1059, 1966.
[10] Fisk, NM et al., *BJOG*, 99:18-22, 1992.

Copyright 2016 The Organizing Committee for the 2016 Summer Biomechanics, Bioengineering and Biotransport Conference

SB^{3}C2016
Summer Biomechanics, Bioengineering and Biotransport Conference
June 29 –July 2, National Harbor, MD, USA
SB^{3}C2016-928

A PHENOMONOLOGICAL MODEL OF DAMAGE AND RECOVERY IN THE INTERVERTEBRAL DISC OF THE CERVICAL SPINE DUE TO CYCLIC LOADING

Shruti Motiwale (1), Xianlin Zhou (2), Reuben H. Kraft (1)

(1) Dept. of Mechanical and Nuclear Engineering,
The Pennsylvania State University
University Park, PA, USA

(2) CFD Research Corporation,
Huntsville, Alabama, USA

INTRODUCTION

The purpose of this research is to develop a model for the prediction of damage in the intervertebral disc of the cervical spine due to head supported mass (HSM) applied during military operations. Military personnel wear helmets such as the Advanced Combat Helmet (ACH) for extended periods of time, which may result in severe risk of neck injury. Manoogian et al. report that equipment added to soldiers' helmets can significantly affect head-neck dynamics [1]. In order to predict this damage in the neck, so that preventive measures can be accordingly designed, a damage model is desired for the cervical spine. A number of groups have conducted studies on degeneration of the lumbar spine, but little attention has been given to the cervical spine under cyclic loading. In a previous study, we utilized a whole body musculoskeletal model with detailed neck structures (7 cervical vertebral joints and 24 degrees of freedom on head and neck) [2], [3], in order to simulate the cervical joints during walking and running with a middle-sized army combat helmet (1.43 kg). Fig. 1 shows the compressive loading at C4-C5 joint level during one gait cycle of walking with the US Army Combat Helmet (ACH). In this study, we have proposed a model to predict the evolution of damage and recovery in the intervertebral disc of the cervical spine subjected to repeated cycles of loading for one gait cycle.

METHODS

We have presented a damage evolution model for the disc based on the non-linear damage model proposed by Chaboche and Lemaitre [4]:

$$\delta D = D^{\alpha(\sigma_{max},\sigma_{mean})}\left[\frac{\sigma_a}{M_0(1-b\sigma_{mean})}\right]^{\beta}\delta n \qquad (1)$$

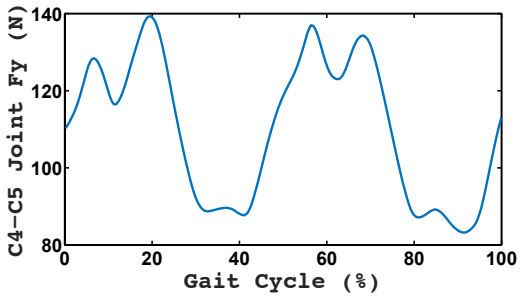

Figure 1: Load pattern on a C4-C5 joint level during one gait cycle of walking with the army combat helmet.

where, σ_a is the alternating stress, σ_{mean} is the mean stress, D is the damage, such that $0 \le D \le 1$, n is the number of cycles, α is a function of the stress σ and M_0 , b, β are material parameters. We calibrated M_0, b and β according to the stress-life data for the discs collected by Green *et al* [5]. For a case of variable loading, the following equations describing damage evolution were obtained from Eq. 1 according to the method proposed by Dattoma et al. [6]:

$$D_i = \left(\frac{n_i^{eff}}{N_{fi}}\right)^{1/(1-\alpha_i)} \qquad (2)$$

$$N_{fi} = \frac{1}{1-\alpha_i}\left[\frac{(\sigma_a)_i}{M_0(1-b(\sigma_{mean})_i)}\right]^{-\beta} \qquad (3)$$

$$n_i^{eff} = n_i + N_{f\,i}\left(\frac{n_{i-1}^{eff}}{N_{f\,i-1}}\right)^{(1-\alpha_i)/(1-\alpha_{i-1})} \qquad (3)$$

Copyright 2016 The Organizing Committee for the 2016 Summer Biomechanics, Bioengineering and Biotransport Conference

$$\alpha_i = 1 - a\,\langle \frac{(\sigma_{\max})_i}{(\sigma_u)_i - (\sigma_{\max})_i} \rangle \quad (4)$$

where, D_i is the damage in the i^{th} iteration, N_{fi} is the number of cycles for failure in the i^{th} iteration, M_0, a, b, β are material parameters, n_i is the number of cycles in the i^{th} iteration and σ_u is the ultimate tensile strength.

It has been shown in the literature that intervertebral discs recover a considerable proportion of damage during rest or recovery periods [7]-[9]. To incorporate this effect in our model, we have proposed an analytical equation describing this effect. We propose a recovery parameter, r, which proportionately reduces the damage as follows:

$$D_i^r = D_{i-1} + (D_i - D_{i-1}) * (1 - r) \quad (5)$$

where, D_i is the damage in the i^{th} iteration without considering recovery, and D^r_i is the damage in the i^{th} iteration after considering recovery. The recovery parameter is a measure of the percentage of damage accumulated during the day that is recovered during the rest period. The value of N_f is modified to incorporate the effect of recovery in the next iteration.

$$N_{fi} = \frac{n_i^{eff}}{(D_i^r)^{1/(1-\alpha_i)}} \quad (6)$$

RESULTS

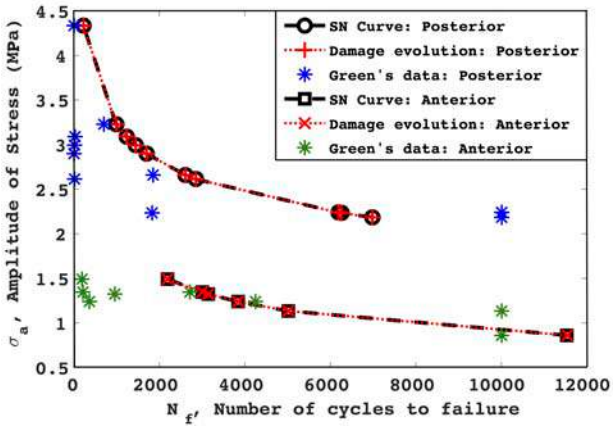

Figure 2: Curve-fitting of Green's data to damage evolution equations.

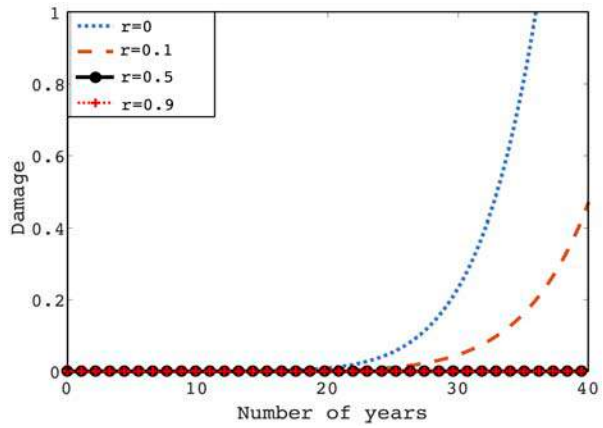

Figure 3: Evolution of damage for a uniaxial cyclically loaded single element in the presence of recovery for varying value of the recovery parameter *r*.

Fig. 2 shows the plots for curve-fitting of Green's data to our non-linear damage model, from which, the material parameters were then determined. Anterior and posterior parts of the disc had different material properties and hence were fitted separately. Fig. 3 shows the plot for evolution of damage for varying values of recovery.

DISCUSSION

We have proposed a non-linear model to study disc degeneration of a cervical spine due to long-term cyclic loads. We also proposed a preliminary recovery model to account for the recovery of damage experienced by the disc during a resting period.

Only 20% of damage was found to occur in 75% of life, after which an exponential increase in damage was observed. The addition of recovery further delays the damage evolution. For a recovery parameter of 0.1, the model predicts a damage value of 0.5 in 40 years. The damage value can be further correlated with pain indicators to predict when the damage becomes severe.

The recovery parameter itself can be a function of many variables, e.g. health status and age of individuals. Youngsters are expected to have a higher recovery parameter than older people. It can also be considered a function of damage - when the disc is already damaged, the recovery capacity of the disc can be assumed to be lower than when the disc is healthy. One aspect that the current recovery model does not consider is lower and upper bounds on the recovery possible during a recovery period. In this paper, the recovery is considered a percentage of damage incurred during the day. This may not be true for certain cases when the damage is too less and the entire damage is recovered during the rest period, or when the damage is too high, and only a small percentage of damage can be recovered. Moreover, this model does not account for disc damage due to any disease, which might accelerate damage growth. Also, this model only considers damage in the annulus part of the disc.

Despite these limitations, this model may provide insight into damage evolution of the intervertebral disc. The two important advancements that this model brings to the area of modeling intervertebral disc degeneration are:

(1) Inclusion of recovery into the damage model that allows the model to resemble the biological phenomenon more accurately than any other pre-existing models.
(2) Consideration of the non-linearity of damage evolution.

The model can be further developed to aid in evaluation of head supported devices and yield recommendations towards better helmet designs and usage scenarios.

ACKNOWLEDGEMENTS

This work was partially supported by US Army under grant W81XWH-14-C-003. This work was also supported in part through instrumentation funded by the National Science Foundation through grant OCI0821527.

REFERENCES

[1] Manoogian S.J. et al., USAARL-CR-2006-01, 2005.
[2] Zhou X. et al., *Int J Hum Factor Mod Sim*, 4(3-4):191-219, 2014.
[3] Vasavada A. N. et al., *Spine*, 23(4):412-422, 1998.
[4] J. Lemaitre and J.L. Chaboche, *Mechanics of solid materials*.
[5] Green et al., *Eur Spine J*, 2(4):209-214,1993.
[6] Dattoma et al., *Int J Fatigue*, 28(2):89-95, 2006.
[7] Johannessen W., *Ann Biomed Eng*, 32(1):70-76, 2004.
[8] Lotz J.C., *Spine*, 29(23):2742-2750, 2004.
[9] Virgin W., *J Bone Joint Surg Br*, 33(4):607-611, 1951.

Copyright 2016 The Organizing Committee for the 2016 Summer Biomechanics, Bioengineering and Biotransport Conference

SB³C2016
Summer Biomechanics, Bioengineering and Biotransport Conference
June 29 –July 2, National Harbor, MD, USA
SB³C2016-929

CLOT INTEGRATION FACTOR FOR IN VITRO QUANTIFICATION OF STENT-RETRIEVER DEPLOYMENT USING CONE-BEAM COMPUTED TOMOGRAPHY

Kajo van der Marel (1), Olivia W. Brooks (1), Robert M. King (1), Ju-Yu Chueh (1), Miklos Marosfoi (1), Erin T. Langan (1), Sarena L. Carniato (2), Raul G. Nogueira (3), Ajay K. Wakhloo (1), Matthew J. Gounis (1), Ajit S. Puri (1)

(1) Department of Radiology
University of Massachusetts Medical School
Worcester, MA, USA

(2) PreClinical Science
Stryker Neurovascular
Fremont, CA, USA

(3) Department of Neurology
Emory University School of Medicine
Atlanta, GA, USA

INTRODUCTION

Stent-retriever technology enables superior endovascular treatment of emergent large vessel occlusions (ELVO) in acute ischemic stroke patients [1]. Mechanical thrombectomy offers high rates of recanalization of the occluded target vessel and subsequent (near-)complete reperfusion of the distal vascular network. Nonetheless, successful angiographic reperfusion after rapid recanalization isn't necessarily followed by good functional outcome [2]. Previous studies have highlighted the dependencies of endovascular treatment efficacy and safety on clot composition and mechanics [3,4]. Importantly, device development and clot retrieval strategies are aimed at maximizing chances of single-pass thrombectomy success with minimal clot disruption.

Intuitively, the stent-retriever should integrate extensively with the clot after deployment at the site of occlusion. To achieve this in clinical practice, the instructions for use of some stent-retrievers include a recommended time to wait before retrieving the device. Additional improvements in functional outcome may be achieved with altered deployment strategies, such as a recently described technique that pushes the Trevo™ stent-retriever out of the retracting microcatheter instead of simple unsheathing [5]. Such varying clinical practices already suggest that the time actually allotted for the clot to integrate into the device may range from 30 seconds to approximately 5 minutes.

Unfortunately, our ability to study the effects and time aspects of clot-device integration in vivo is restricted by poor fluoroscopic clot visibility and limited three-dimensional image resolution. In this study we therefore devised a Clot Integration Factor (CIF) measure that used high-resolution cone-beam CT images to quantitatively capture the integration of the clot into the stent-retriever in an established in vitro vascular model with a reproducible ELVO of the middle cerebral artery (MCA). Our aim was to evaluate the effects of different deployment variations, time, and clot composition on CIF.

METHODS

Deployment variations (pushing vs. unsheathing) of the Trevo™ ProVue/XP stent-retriever (Stryker Neurovascular, Fremont, CA, USA) were tested in an in vitro model system that mimicked a MCA-occlusion with a silicone vascular replica [6] and two contrast-enhanced clot models using 8 trials per group. Hard inelastic clot, representative of the fragmentation-prone cholesterol-rich clots encountered in clinical practice, was generated by thrombin-induced clotting of bovine blood (2.5 NIH U thrombin/ml blood). Soft elastic clot, which is representative of fresh red clots, was obtained by mixing human blood with thrombin (2.5 NIH U thrombin/ml blood).

Under fluoroscopic guidance (Allura Xper FD20, Philips, Best, The Netherlands), the device was positioned across the blood clot and deployed. Before and 5 minutes after deployment, high-resolution cone-beam CT imaging (VasoCT; 617 non-binned projections; 20.4 s rotation; reconstructed at 33% or 50% of the field-of-view, yielding a 24.7 or 34.5 mm cube; 512^3 reconstruction matrix) was performed.

An image processing pipeline was devised by combining existing geometric (vascular) modeling software, including ITK, VTK, and VMTK [7]. The pipeline comprised 1) anisotropic diffusion filtering for spatial noise reduction; 2) manually initialized path tracing using Dijkstra's algorithm to extract the three visible marker wires of the device; 3) smoothing of the wire tracings using cubic B-spline fitting; 4) level-set segmentation of the clot after manual seed point initialization; and 5) Steiner circumellipse fitting to extract and determine the interior volume of the device defined by the three marker wires; 6) CIF was calculated using the device volume V_{device} and clot volume V_{clot} as follows:

Copyright 2016 The Organizing Committee for the 2016 Summer Biomechanics, Bioengineering and Biotransport Conference

$$\frac{V_{\text{device}} \cap V_{\text{clot}}}{V_{\text{clot}}} \quad (1)$$

Separate two-sample t-tests were performed to evaluate the effects of deployment technique and time on CIF for each clot type.

RESULTS

Intensity differences between the contrast-enhanced clot and the marker wires of the device allowed separate segmentation of both structures in all available data sets (see example in Figure 1).

CIF was significantly different for the two deployment variations (pushing vs. unsheathing) when the device engaged a hard inelastic clot (difference between means, 95%CI=[0.004,0.174], p=0.041), but not a soft clot model (95%CI=[-0.138,0.104], p=0.764) (see Figure 2).

Furthermore, it was found that CIF increased significantly over time between the post-deployment (early) and the final (late) time points when the pushing technique was applied in hard inelastic clot models (mean change, 95%CI=[0.006,0.047], p=0.019) (see Figure 3).

Regardless of the delivery technique, we found an overall increase in CIF over time for both hard inelastic clot (mean change=0.032, p=0.004) and soft elastic clot (mean change=0.065, p=0.007).

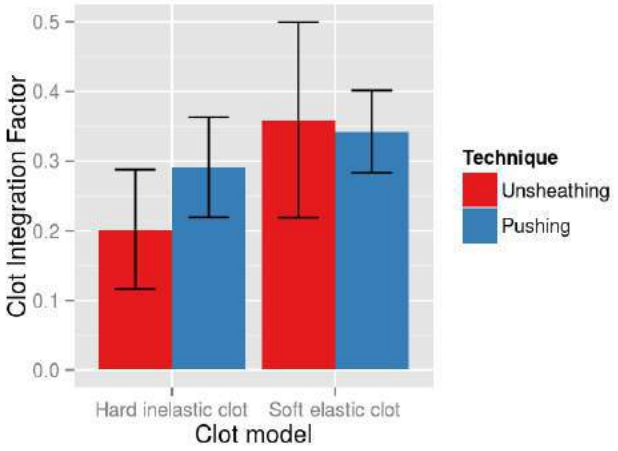

Figure 2: Bar graph showing means and standard deviations of the Clot Integration Factor (CIF) measured just prior to device retraction.

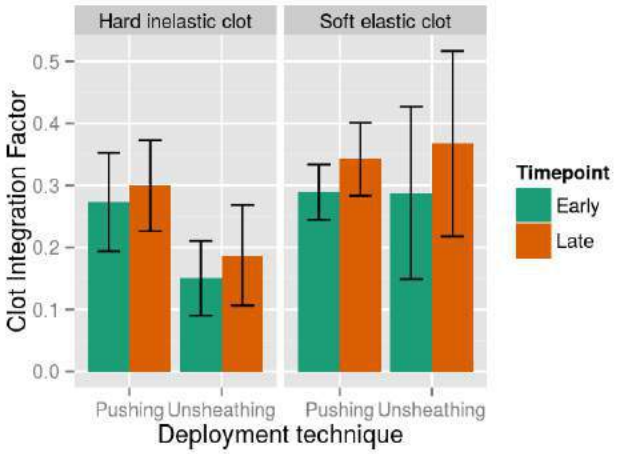

Figure 3: Bar graph showing means and standard deviations of the Clot Integration Factor (CIF) computed immediately post-deployment ("Early") and at 5 minutes after deployment ("Late").

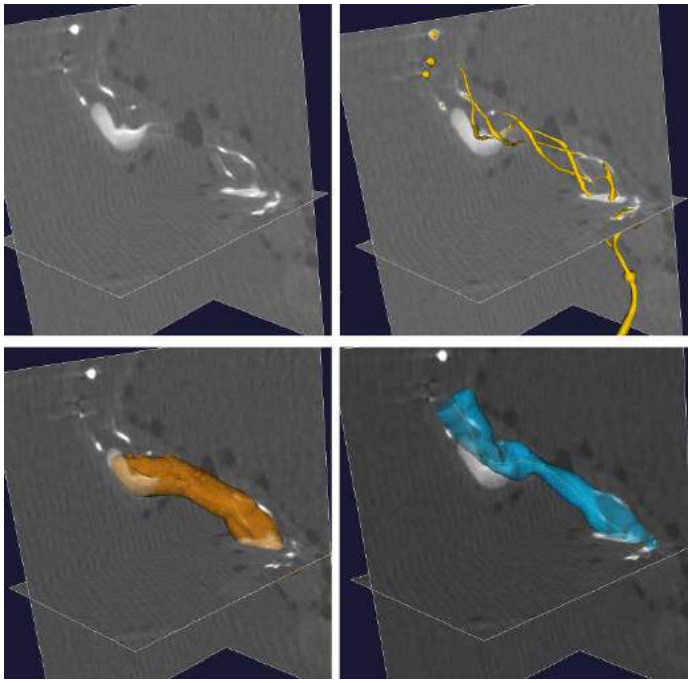

Figure 1: Example views with three orthogonal planes of a reconstructed VasoCT image (top left), the location of the three marker wires (top right), the result of the level-set segmentation of the clot (bottom left), and the determination of the inner volume of the device bounded by the extracted marker wires (bottom right).

DISCUSSION

We described an image-based approach to quantitatively capture the integration of a blood clot into a stent-retriever for evaluation of device and deployment variations in an in vitro model of ELVO.

We found that a recently published deployment strategy that was associated with better functional outcomes was associated with significantly higher CIF values when deployed in our hard inelastic clot models in vitro. However, there was no significant difference between the deployment variations when the device was delivered into a soft elastic clot model.

In clinical practice, and according to the instructions for use of most stent-retrievers, devices are often retrieved only after some time in order to ensure sufficient clot-device integration. Likewise, our CIF measurements showed a tendency to increase over time, regardless of the delivery technique. Nonetheless, when the device was deployed in a hard inelastic clot model, CIF values suggest that the pushing technique may further enhance device-clot integration.

In conclusion, our study shows that in vitro imaging-based quantification of clot integration can detect differences in deployment configuration relative to a clot, which may support procedural and design improvements.

REFERENCES

[1] Berkhemer, OA et al., *N Engl J Med* 372:11-20, 2015.
[2] Almekhlafi, MA et al., *Interv Neuroradiol* 20:21-27, 2014.
[3] Luo, ZH et al., *J Vasc Interv Radiol* 23:1077-1083, 2012.
[4] Chueh, JY et al., *Stroke* 44:1396-1401, 2013.
[5] Haussen, DC et al., *Stroke* 46:2838-2842, 2015.
[6] Chueh, JY et al., *AJNR Am J Neuroradiol* 30:1159-1164, 2009.
[7] Antiga, L et al., *Med Biol Eng Comput* 46:1097-1112, 2008.

Copyright 2016 The Organizing Committee for the 2016 Summer Biomechanics, Bioengineering and Biotransport Conference

SB^{3}C2016
Summer Biomechanics, Bioengineering and Biotransport Conference
June 29 –July 2, National Harbor, MD, USA
SB^{3}C2016-930

CERVICAL SPINE FORCES AND DISC HERNIATION RISK DURING STANDARDIZED REAR-END IMPACT TESTING

Keith D. Button (1), Stephanie M. Rossman (1), Brian T. Weaver (1, 2), Steve A. Rundell (1)

(1) Explico Engineering Company
Novi, Michigan, United States

(2) Orthopaedic Biomechanics Laboratories
Michigan State University
East Lansing, MI, United States

INTRODUCTION

Intervertebral disc herniations account for a major portion of spine-related surgeries. Although temporal consistency between symptomology and a relatively minor automobile collision is a common factor for establishing causation, this may yield a false-negative diagnoses given the prevalence of disc herniations in the asymptomatic population [1]. For example, previous research has demonstrated a temporal relationship of symptomology during placebo rear-end impacts [2]. Therefore, it is imperative that the clinician considers the specifics of an automobile collision as they relate to injury mechanisms prior to establishing causation of objective MRI findings.

Incorrectly associating the presence of a disc herniation with an automobile collision can result in a number of consequences, including somatic symptom disorder, unnecessary procedures, and ineffective treatment. The presence of potential medico-legal proceedings further complicates matters for the treating physician.

Biomechanics provides a valuable tool for quantifiably determining if the necessary mechanism of injury is present. Specifically, several biomechanical studies have previously documented the biomechanical environment associated with disc herniations [3,4]. These studies definitively demonstrate that axial compressive loading is essential in the causation of, or significant contribution to, a disc herniation. Therefore, the objective of the current study was to determine the compressive loading experienced by the upper cervical spine during rear-end collisions, and compare it with benign, non-injurious levels as well as previously reported Injury Assessment Reference Values (IARVs) [5].

METHODS

The Insurance Institute for Highway Safety (IIHS) performs five tests to evaluate passenger vehicle crashworthiness. One of these involves the safety performance of the seat and head restraint. This is performed by simulating rear end collisions with a change in velocity (Delta-V) of 15 kph. Safety performance is determined using an instrumented anthropomorphic test device (ATD). For the current study, ATD data from several IIHS rear-end sled tests, representing a wide range of vehicle types, was evaluated to determine the neck loading experienced during a rear-end collision.

Additionally, the National Highway Traffic Safety Administration (NHTSA) conducts rear impact crash tests to examine the compliance of a passenger vehicle's fuel system integrity (Federal Motor Vehicle Safety Standard 301). The crash tests consist of a stationary motor vehicle impacted in the rear by a flat rigid barrier at speeds up to 48 kph. Delta-V's during these tests were determined from the conservation of linear momentum. Data from Hybrid III ATDs seated in the front occupant seating positions were evaluated to determine the neck loading experienced during these high speed rear-end collisions.

Filtered data from ATDs in ten IIHS test and ten NHTSA crash tests were collected and analyzed for a variety of passenger vehicle types. Trace plots of the z-axis upper neck force were created from filtered ATD data. Additionally, video footage of tests was analyzed to qualitatively assess the loading pattern experienced by ATDs.

RESULTS

A depiction of ATD motion from the IIHS 15 kph rear-end tests is shown in Figure 1. The ATD's cervical spine underwent several phases. Initially, the upper torso was in contact with the seatback with the head not yet in contact with the headrest (Figure 1a). The torso was then accelerated forward due to contact with the forward-accelerating seatback while the head remained stationary (Figure 1b), resulting in tension-extension of the cervical spine. After this, the ATD experienced the "rebound phase," in which the head and torso were

Copyright 2016 The Organizing Committee for the 2016 Summer Biomechanics, Bioengineering and Biotransport Conference

accelerated forward due to the release of stored energy from the seatback, resulting in flexion of the cervical spine (Figure 1c and d).

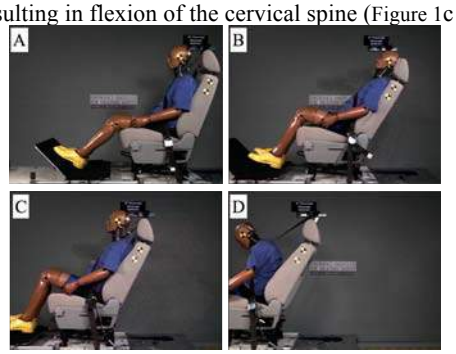

Figure 1: Photographs depicting the response of the ATD to an IIHS rear-end collision. Taken from the 2007 Chevrolet Silverado test.

The maximum tension/compression values from the IIHS and NHTSA tests are shown in Table 1 and Table 2, respectively. The maximum neck tension and compression forces from the IIHS tests were 619.8 N and 148.3 N, respectively. The maximum neck tension and compression forces from the NHTSA tests were 1826.4 N and 118.9 N, respectively. In all tests, the maximum neck tension force exceeded the maximum neck compressive force.

Table 1: Neck Compressive/Tensile Forces from IIHS Testing

Vehicle	Delta-V (kph)	Maximum Tension (N)	Maximum Compression (N)
2005 Suzuki Reno	34.2	1826.4	118.9
2005 Chevrolet Aveo	36.1	1632.2	16.4
2005 Mitsubishi Lancer	35.2	912.9	40.5
2005 Toyota Matrix	34.6	1386.3	21.3
2004 Jeep Liberty	29.3	840.2	50.8
2004 Volkswagen Touareg	25.6	1226.8	36.8
2004 Mitsubishi Endeavor	29.6	1182.3	56.2
2004 Mazda 6	33.1	803.0	72.6
2002 Chevrolet Trailblazer	27.5	1387.4	47.2
2002 Toyota Camry	34.8	476.0	44.0
Average	32.0±3.7	1167 ±412.7	50.51±29.0

Table 2: Neck Compressive/Tensile Forces from NHTSA Testing

Vehicle	Delta-V (kph)	Maximum Tension (N)	Maximum Compression (N)
2007 Chevrolet Silverado	15.5	528.0	85.0
2012 Toyota Camry	15.5	406.1	116.3
2013 Ford Fusion	15.6	619.8	148.3
2013 Honda Accord	15.6	338.4	147.5
2013 Honda Civic	15.7	557.1	60.0
2013 Nissan Altima	15.7	309.2	72.9
2014 Toyota Corolla	15.6	509.2	89.6
2015 Dodge Ram 1500	15.3	526.9	75.2
2015 Ford F150	15.7	419.6	72.7
2016 Honda Pilot	15.4	470.0	73.9
Average	15.6±0.2	468.4±98.8	94.1±32.0

DISCUSSION

The results indicate consistent patterns of loading in the spine across a variety of experimental models, severities, and vehicle seats. Specifically, the primary loading experienced consisted of cervical tension. This type of loading is consistent with the injuries described in cadaveric research in the absence of a head restraint. Specifically, these studies have documented an assortment of osteoligamentous injuries including ligamenta flavum rupture, widening of the facet joint, anterior longitudinal ligament rupture, and chip fracture, but never disc herniations [6].

The causation of intervertebral disc herniations has been previously shown to have two distinct mechanisms. One involves fatigue loading wherein the nuclear material translates through the layers of the annulus as a result of thousands of repetitive compressive loading cycles combined with twisting and bending motions [3]. The other involves a single, traumatic event. In order for this to occur in the absence of bony fracture, a combination of hyper-flexion (forward bending beyond the physiological limit) and a large compressive force must be applied to the cervical spine [4]. It is necessary for both of these loading modes to occur in concert. For example, during pure compressive loading without combined flexion, the pressure in the nucleus will cause fracture of the adjacent bony endplates, and not result in movement of the nucleus into the annular fibers. Hyper-flexion is required to dislodge the nuclear material and stretch the posterior annular fibers, thereby allowing for passage of the nuclear material. The data presented in the current study illustrate that the ATDs did not experiences hyperflexion with simultaneous compression. Therefore, from a general perspective, the necessary injury mechanism for a disc herniation is not present during a rear-end collision.

While the ATDs experienced compressive force in the cervical spine, this was minimal and consistent with everyday activities. Upper neck loading during everyday activities has previously been documented, with compressive values of 171 N, 163 N, 190 N, and 213 N reported for running with an abrupt stop, falling into a chair, skipping rope, and hopping, respectively [7]. These values all exceeded the maximum cervical compressive forces documented in the current study. Additionally, the compressive forces measured in the current study were substantially below IARVs for six month old infants (890 N) through large adult males (4830 N) [5].

The findings from the current study are consistent with research involving cadaveric cervical spine specimens exposed to simulated moderate-to-severe rear-end collisions with and without head restraints [8]. These specimens experienced increased post-collision range-of-motion, but no intervertebral disc herniations. These data, combined wit the results from the current study, indicate that cervical intervertebral disc herniations are not related to rear end automobile collision events, and objective MRI findings following a rear-end collision are more likely associated with some other etiology.

REFERENCES

[1] Matsumoto, M., et al., *J Bone Joint Surg*, 80(1):19-24, 1998.
[2] Castro, W., et al., *Int. J. Leg. Med*, 2001.
[3] Adams, M., et al., *Spine,* 10(6): 524–531, 1985.
[4] Adams, M., et al., *Spine*, 7(3): 184–191, 1982.
[5] Mertz, H., et al., Stapp Car Crash J 47:155-188, 2003.
[6] Yoganandan, N., et al. *Stapp Car Crash J*, 44: 189–204, 2000.
[7] Vijayakumar, et al., *SAE 2006-01-0247*, 2006.
[8] Panjabi, M., et al., *J Biomech*, 38:1694-1701, 2005.

Copyright 2016 The Organizing Committee for the 2016 Summer Biomechanics, Bioengineering and Biotransport Conference

SB^{3}C2016
Summer Biomechanics, Bioengineering and Biotransport Conference
June 29 –July 2, National Harbor, MD, USA
SB^{3}C2016-931

A COUPLED REACTION-DIFFUSION-STRAIN MODEL FOR BONE GROWTH IN THE CRANIAL VAULT

Chanyoung Lee, Reuben H. Kraft

Department of Mechanical and Nuclear Engineering
The Pennsylvania State University
University Park, PA, USA

INTRODUCTION

Bones of the cranial vault are formed by intramembranous ossification due to direct differentiation of mesenchymal cells into osteoblasts. The process is controlled by a cascade of reactions between extracellular molecules and cells. One common approach for modeling the process is the application of a mathematical model for reaction-diffusion controlled by two interacting chemical molecules, first proposed by Alan Turing [1]. The Turing model, commonly referred to as the reaction-diffusion model, shows that through a regulatory loop of interacting molecules the concentration of the molecules forms an inhomogeneous spatial pattern in space. In our previous research [2] we have applied this approach to find locations of the primary centers of ossification in the mouse cranial vault and the pattern of cranial bone growth.

However, mechanical stimuli such as local stress and strain on each cell or organ are not taken account in the Turing's model and have been shown to give important influences on the bone formation by several groups [3, 4]. In this study, we propose an integrated mechanobiological model for the cranial vault bone formation by coupling the reaction-diffusion model for interacting molecules with the biomechanical input in the growing domain.

METHODS

We assume that the behavior of the molecules important to bone formation can be modeled using Turing's reaction-diffusion model which describes the pattern formation driven by two interacting molecules (activator and inhibitor). In addition to the reaction-diffusion model, we hypothesize that mechanical stimuli of the cells due to growth of the underlying brain contribute significantly to the process of cell differentiation in cranial vault development. Distribution of mechanical strain over the surface of the brain on which the ossification process occurs is affected by its geometry that changes over time as the developing brain grows. Material properties of the cells also change according to the stages of cell differentiation. To explore effects of mechanical strain on bone formation in the cranial vault, a structural analysis using the finite element method is conducted in the computational domain that grows with a constant speed which represents the surface of the brain. The strain field at the surface of the brain was estimated at each time step using estimates of the time-evolving material properties for undifferentiated mesenchymal cells and differentiated osteoblasts, whose distribution is predicted using a reaction-diffusion model. The strain field estimated by the structural analysis in turn affects the differentiation of cells again because it is coupled with the reaction-diffusion model.

The mathematical expressions for the coupled reaction-diffusion-strain model are as follows.

$$\frac{\partial a}{\partial t} = \frac{o_s^n}{o^n+o_s^n}\left(\sigma_a + \rho_a \frac{a^2}{h} + D_a\nabla^2 a\right) - \mu_a a + \sigma_o o \qquad (1)$$

$$\frac{\partial h}{\partial t} = \frac{o_s^n}{o^n+o_s^n}(\sigma_h + \rho_h a^2 + D_h\nabla^2 h) - \mu_h h \qquad (2)$$

$$\frac{\partial o}{\partial t} = \eta \frac{o_s^n}{o^n+o_s^n}\frac{a^n}{a^n+a_T^n}\frac{\varepsilon_l^n}{\varepsilon^n+\varepsilon_l^n} \qquad (3)$$

The term a, h and o represent the concentration of activator, inhibitor and differentiated osteoblasts, respectively. The production (σ_a and σ_h), reaction ($\rho_a \frac{a^2}{h}$ and $\rho_h a^2$) and diffusion ($D_a\nabla^2 a$ and $D_h\nabla^2 h$) and of activator and inhibitor are assumed to take place only in mesenchymal cells, not in differentiated osteoblasts and the term $\frac{o_s^n}{o^n+o_s^n}$

Copyright 2016 The Organizing Committee for the 2016 Summer Biomechanics, Bioengineering and Biotransport Conference

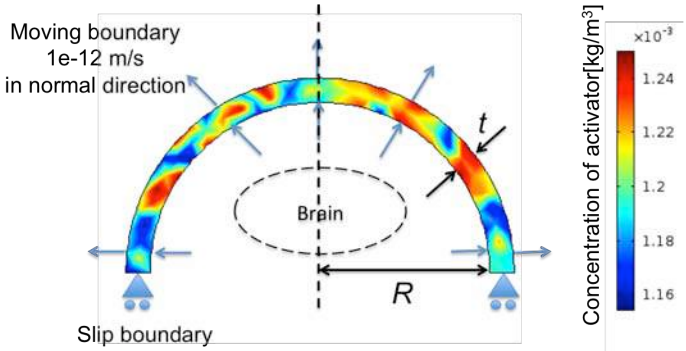

Figure 1: Geometry of the computational domain, initial condition for reaction-diffusion model and boundary condition for structural analysis. The initial activator is randomly distributed. Radius of the inner semicircle R = 7 mm and thickness of the domain t = 0.5 mm.

represents this. o_s represents saturation concentration of osteoblast that sets the upper limit of generation of osteoblast. The terms $\mu_a a$ and $\mu_h h$ quantify degradation of the molecules. The model for the rate of differentiation of mesenchymal cells to osteoblasts ($\frac{\partial o}{\partial t}$) is promoted by activator which has higher concentration than a threshold value (a_T) and is limited by the strain which has a higher magnitude than the limitation value (ε_l). The value n in the terms $\frac{o_s^n}{o^n+o_s^n}$, $\frac{a^n}{a^n+a_T^n}$ and $\frac{\varepsilon_l^n}{\varepsilon^n+\varepsilon_l^n}$ is a constant characterizing how sharply the terms increase or decrease according to the change in variables o, a and ε. Osteoblasts and activator are coupled in the way that osteoblasts enhances activator by the term $\sigma_o o$ and the activator in turn activates differentiation of cells near the osteoblasts, which models the growth of bone.

A commercial software COMSOL Multiphysics was used to solve these mathematical models and to conduct a structural analysis using the finite element method. The computational domain is constructed as a 2-dimensional shell-shaped semicircle (Figure 1), which represents a simplified shape of a cut plane of the space of mesenchymal cells surrounding a brain. To explore the effect of growth of the underlying brain, the inner and outer surface of the semicircle domain move with a constant speed in their normal direction. The bottom surface is free to move with the movement of inner and outer surface. Figure 1 also shows the initial distribution of activator which is random with small perturbation of concentration (±5%)

RESULTS

Figure 2 shows distributions of activator, osteoblast and hydrostatic strain over time. The black solid line represents the initial shape of the domain before it grows over time. Figure 2 (a) shows that distribution of activator, which is nearly homogeneous at initial time, then forms a spatial pattern over time. The distribution of osteoblast (Fig. 2 (b)) follows the distribution of activator as we hypothesize activator activates cell differentiation. Looking at the distribution of osteoblast from 12.5 days to 37.5 days, the region of osteoblast with high concentration expands from several distributed spots (which can be considered as primary centers of ossification) but the separate regions do not fuse with each other, leaving a space of undifferentiated mesenchymal cells between them. This is based on our hypothesis that high strain inhibits cell differentiation. Figure 2 (c) shows that hydrostatic strain increases faster at the region of mesenchymal cells which has a small Young's modulus than at the region of osteoblasts which has large Young's modulus.

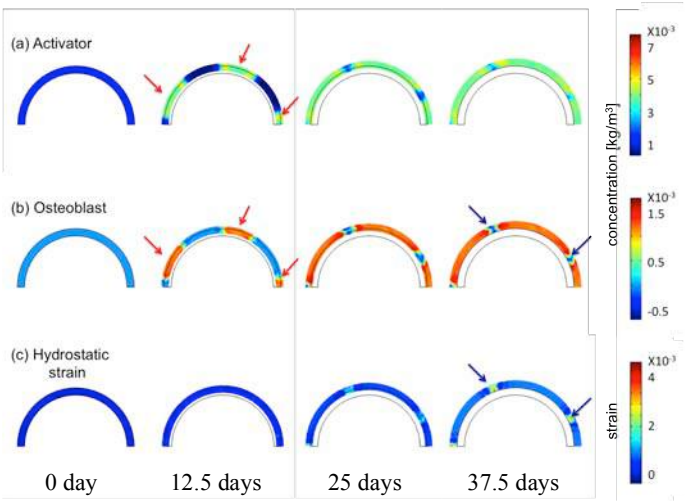

Figure 2: Computational results. Distributions of (a) Activator (b) Osteoblasts and (c) Hydrostatic strain over time. Primary centers of ossification appear according to the distribution of activator (red arrows). Regions of osteoblasts do not fuse leaving a space of undifferentiated mesenchymal cells where the strain rapidly increases (blue arrows)

DISCUSSION

The results show that our mechanobiological model predicts some key features of morphology of cranial vault bone including the emergence of a spatial pattern from nearly homogeneous initial condition, the growth of the pattern over time, and the remaining undifferentiated cell parts between the regions of differentiated osteoblasts, which can be observed as sutures between bones in the cranial vault. From the results, the effect of strain coming from growth of underlying brain can be proposed as one possible explanation of mechanism of suture formation.

Further study is being conducted to apply the coupled reaction-diffusion-strain model to a 3-dimensional domain obtained from real mouse head in experimental research and the model is expected to be more improved to explain the mechanism of bone growth in the cranial vault by comparing the computational results with the experimental data.

ACKNOWLEDGEMENTS

This work was supported in part through instrumentation funded by the National Science Foundation through grant OCI0821527, a Burroughs-Wellcome Fund 2013 Collaborative Research Travel Grant, and by National Institutes of Health grants R01 DE022988 and P01HD078233. The content is solely the responsibility of the authors and does not necessarily represent the official views of the National Institutes of Health.

REFERENCES

[1] Turing, AM, Philosophical transactions of the royal society of LondonSeries B, Biological sciences 237(641):37–72, 1952
[2] Lee, C et al., Frontiers in Bioengineering and Biotechnology 3(2015):24, 2015
[3] Claes, LE et al., Journal of Biomechanics 32(3):255–266,1999
[4] Guevara, J et al., ComputerMethods and Programs in Biomedicine 118(1):59–68, 2015

Copyright 2016 The Organizing Committee for the 2016 Summer Biomechanics, Bioengineering and Biotransport Conference

SB^{3}C2016
Summer Biomechanics, Bioengineering and Biotransport Conference
June 29 –July 2, National Harbor, MD, USA
SB^{3}C2016-932

CONFINED COMPRESSION OF A HYDROGEL COMPOSITE FOR NUCLEUS PULPOSUS TISSUE ENGINEERING

T. Christiani (1), R. Adams (2), E. Signor (3), A. Crudo (4), P. Myers (4), D. Collins (4), K. Wrinn (4), M. Arigot (4), A. Guido (4), J. Vernengo (2), J. Kadlowec (4)

(1) Biomedical Engineering
Rowan University
Glassboro, N.J. U.S.A

(2) Chemical Engineering
Rowan University
Glassboro, N.J. U.S.A

(3) Civil Engineering
Rowan University
Glassboro, N.J. U.S.A

(4) Mechanical Engineering
Rowan University
Glassboro, N.J. U.S.A

INTRODUCTION

Lower back pain (LBP) is a common medical condition that significantly affects the human population [1]. Back pain can be attributed to the degeneration of the intervertebral disc (IVD), a fibrocartilaginous tissue that allows for flexion, extension, lateral bending, torsion, and compression within the vertebral column [2]. Typically, a degenerative cascade begins when the central nucleus pulposus (NP), a soft gel-like tissue, dehydrates and loses its ability to maintain an osmotic swelling pressure [3]. The encompassing concentric rings of collagen, also known as the annulus fibrosus (AF), endure an increased loading and fibers begin to tear. Herniated NP tissue is able to migrate through the annular defect and impinges on adjacent nerve root endings, thus causing radiating discomfort. Discectomy is one of the current available treatments for repairing herniations, however IVD biomechanics become compromised and additional NP material may extrude [4].

Our research aims to replace the NP tissue with an injectable hydrogel during early onset stages of disc degeneration. A novel hydrogel composed of poly (N-isopropylacrylamide) grafted with chondroitin sulfate (PNIPAAm-g-CS) was synthesized and blended with alginate microparticles [5]. The thermally sensitive PNIPAAm forms a miscible solution with water below its lower critical solution temperature (LCST) at approximately 32°C. When heated above the LCST to 37°C, the polymer becomes hydrophobic, expels water from its matrix, and forms a compact gel embedded with localized microparticles. The objective of this study was to construct a confined compression apparatus and characterize the mechanical properties of an injectable, thermally sensitive hydrogel composite.

METHODS

The injectable hydrogel, PNIPAAm-g-CS was synthesized using free radical polymerization [5]. All hydrogel solutions were made by dissolving freeze-dried polymer powder in phosphate buffered saline (PBS) at a concentration of 5% (w/v). Alginate microparticles (≈20 or 100 μm) were crosslinked with calcium in a water in oil emulsion [6]. Freeze-dried microparticles were suspended in the hydrogel solution at a concentration of 25 or 50 mg/mL.

A piston-cylinder apparatus was designed to determine the confined compression properties of various hydrogel formulations, as this is akin to the native *in vivo* environment of NP tissue. The components of the confined compression apparatus were designed and assembled similar to research teams conducting related studies [7,8]. Force and displacement data were recorded using an Instron Model 4442 Universal Testing System and normalized by initial area and height to determine stress and strain. Approximately 300 – 350 μL of the hydrogel composite was injected into the inner cylinder. Distilled water was preheated to 55°C and poured into the water bath. Gel transition and temperature was confirmed and maintained at 37°C both visually and with a thermocouple probe. The piston was slowly lowered into the cylinder and compression tests were performed at a rate of 1 mm/min. Additionally, stress-relaxation tests were performed at 5, 10, 15, and 20% strain at a rate of 50 mm/min with a preload of 0.1% strain. Samples were allowed to relax for 10 minutes in between each strain increment. An average Young's modulus was calculated from 0 to 20% strain for each compression test. Characteristics from the biphasic model such as compressive modulus and hydraulic permeability will be determined from stress-relaxation data.

Copyright 2016 The Organizing Committee for the 2016 Summer Biomechanics, Bioengineering and Biotransport Conference

RESULTS

A confined compression apparatus, seen in Figure 1, was constructed to test the confined mechanical properties of hydrogel hydrogel formulations. A water bath was used to maintain the composite's temperature throughout testing. A thermocouple wire was secured to the bottom of the cylinder containing the composite in order to constantly monitor the temperature. An outer confining cylinder was created using RTV 630 silicone rubber to mimic the material properties of the AF. The piston is coated in Teflon to maintain a low coefficient of friction and tight tolerances along the cylinder wall. A cylindrical filter of sintered metal (Mott U-PXX-002-A-10 0.2 micron pore size) is attached to the bottom of the piston and allows trapped air to escape from the compression chamber.

Compression tests, illustrated in Figure 2, revealed differences in mechanical stress profiles between PNIPAAm-g-CS and PNIPAAm-g-CS with 50 mg/mL of microparticles (≈20 µm). The average Young's modulus for PNIPAAm-g-CS (n=5) and PNIPAAm-g-CS with microparticles (n=3) was 0.607 ± 0.154 MPa and 1.2732 ± 0.092 MPa, respectively. Figure 3 shows preliminary stress-relaxation data for PNIPAAm-g-CS for each incremental strain value.

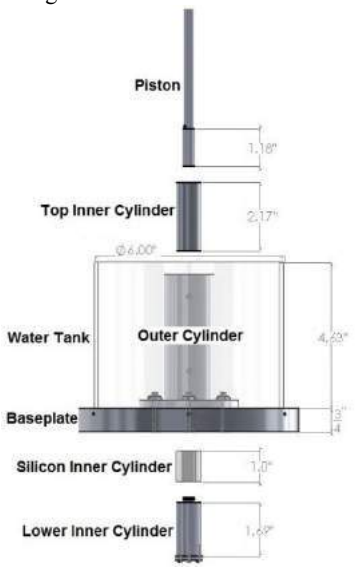

Figure 1: Exploded drawing of the confined compression apparatus.

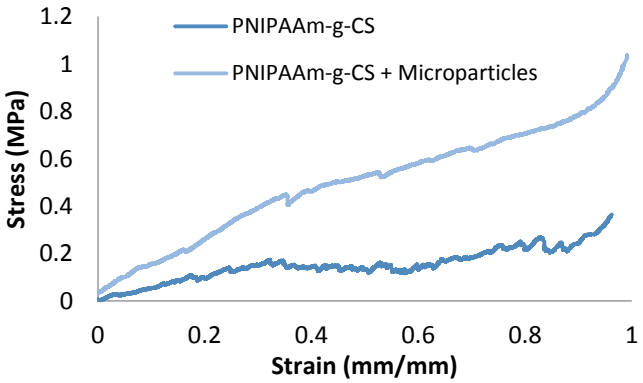

Figure 2: Stress versus strain plot of PNIPAAm-g-CS and PNIPAAm-g-CS with 50 mg/mL of alginate microparticles (≈20 µm) undergoing confined compression.

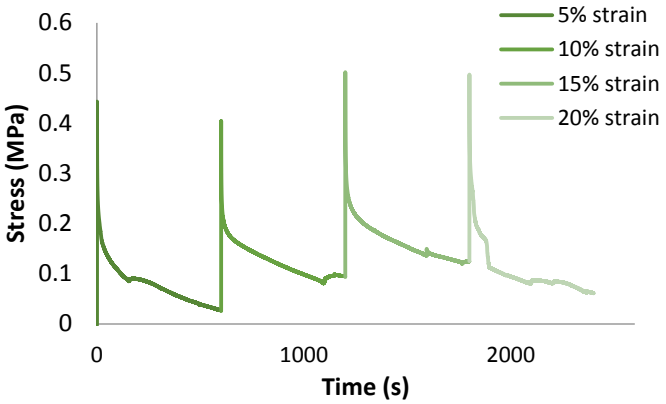

Figure 3: Stress-relaxation plot for PNIPAAm-g-CS at 5, 10, 15, and 20% strain intervals.

DISCUSSION

A thermally sensitive hydrogel composite was formulated for the repair of the NP in the IVD. In our current work, we have built an apparatus to specifically test the confined mechanical characteristics of the composite, while tailoring to its temperature-sensitive property. Confined compression tests revealed a two-fold increase in stiffness for PNIPAAm-g-CS with 50 mg/mL of microparticles compared to PNIPAAm-g-CS alone, yet statistical significance was not confirmed. Alternative microparticle sizes and concentrations will also be explored. Stress-relaxation tests revealed potential gel instability and fracture at 20% strain, while PNIPAAm-g-CS with 50 mg/mL of microparticles withstood higher strains and correspondingly higher stress values. Relaxation time will also be increased beyond 10 minutes. To reiterate, compressive modulus and hydraulic permeability will be determined from stress-relaxation tests using non-linear biphasic modeling. Results will also be compared to the confined compression behavior of native NP tissue extracted from porcine IVDs.

ACKNOWLEDGEMENTS

Research reported in this abstract was supported by the National Institute of Arthritis and Musculoskeletal and Skin Diseases and the National Institute of Biomedical Imaging and Bioengineering of the National Institutes of Health under Award Number 1R15 AR 063920-01. The content is solely the responsibility of the authors and does not necessarily represent the official views of the National Institutes of Health.

REFERENCES

[1] Borges, A. *et al.*, *Acta Biomaterialia*, 7:3412-3421, 2011.
[2] Raj, P., *Pain Practice*, 8: 18-44, 2008.
[3] Leone, G. *et al.*, *J. Biomed. Mat. Research*, 84A2:391-401, 2008.
[4] Jin, D. *et al*., *J. of Spinal Dis. & Tech*., 4:331-337, 2003.
[5] Wiltsey, C. J *et al*., *Acta Biomater*. 16: 71-80, 2013.
[6] Bian, L. *et al*., *Biomaterials*, 27:6425-6434, 2011.
[7] Borges, A. *et al. Composites Sci and Tech*, 7: 1847-1853, 2010.
[8] Perie, J.J *et al*. *Annals of Biomed Eng*, 34: 769-777, 2006.

Copyright 2016 The Organizing Committee for the 2016 Summer Biomechanics, Bioengineering and Biotransport Conference

SB^{3}C2016
Summer Biomechanics, Bioengineering and Biotransport Conference
June 29 –July 2, National Harbor, MD, USA
SB^{3}C2016-933

How Sensitive Are Hemodynamics in Intracranial Aneurysms to Different Blood Flow Waveforms?

Michael J. Durka (1), Isaac H. Wong (1), David F. Kallmes (2), Dario Pasalic (2), Juan R. Cebral (3), Pablo J. Blanco (4), Manoj Jagani (2), Anne M, Robertson (1)

(1) Department of Mechanical Engineering & Materials Science, University of Pittsburgh, Pittsburgh, PA, USA

(2) Mayo Clinic, Rochester, MN, USA

(3) Department of Bioengineering, George Mason University, Fairfax, VA, USA

(4) Laboratório Nacional de Computação Científica, Petrópolis, Brazil

INTRODUCTION

Intra-aneurysm (IA) hemodynamics has been thought to play a key role in aneurysm pathology [1]. Due to the highly limiting difficulties in obtaining hemodynamics in vivo, computational fluid dynamic (CFD) tools have been extensively used to approximate hemodynamics in IAs [2]. It is necessary to prescribe the time-varying waveform of the blood on one or more boundaries of the computational domain used for such studies. This information, however, is often not patient specific and may not be known at or near the boundary of the computational domain [3]. It is thus important to assess the degree of sensitivity of the intra-aneurysmal hemodynamics to the choice of physiological waveform used as boundary conditions. Holdsworth et al. [4] have shown that waveforms from internal carotid arteries of young healthy subjects possess a marked degree of universality. However, this category of individuals is much less likely to possess aneurysms than older patients who have one or more cardiovascular conditions/diseases (e.g. hypertension, coronary artery disease, mitral valve regurgitation)[5],[6],[7]. Therefore, in this work we consider waveforms from 137 older patients with a history of cardiovascular disorders and ages ranging from 19 to 94 (mean age 73 ± 13 years). We first categorized the variability in waveform across this population and then conducted CFD studies to assess the impact of this variability on IA hemodynamics in a representative basilar aneurysm.

METHODS

The left and right internal carotid artery Doppler ultrasounds from 137 elderly patients being treated for cardiovascular disease were analyzed using a custom written MATLAB [Mathworks] script to extract the waveform shape and characteristic metrics. Based on these metrics, waveforms were placed into one of four categories: 1. High resistance, short systolic duration; 2. High resistance, long systolic duration; 3. Low resistance, short systolic duration; 4 High resistance, long systolic duration using a user independent process. Three representative waveforms for each category were chosen for CFD study of the sensitivity of wall shear stress metrics (WSSM) to waveform choice in a basilar bifurcation aneurysm, chosen from our library. In order to distinguish the effects of waveform shape from flow rate, the CFD model for each case was first run with a standardized flow rate (1.81 cm^3/s) and period (1s) based on data reported in [8] and then run with the patient specific flow rate and period. As no corresponding patient specific geometry was available with the waveforms, the flow rates for each patient specific waveform were scaled by a ratio of flow rates reported for basilar and carotid arteries. Blood was modeled as a Newtonian incompressible fluid with a viscosity of 0.0035 Pa·s and having zero velocity at the rigid walls. A time-varying Womersley profile was prescribed at the parent vessel inlet and zero-traction boundary conditions were imposed at the vessel outlets. The model was solved using a custom developed solver [9]. The output metrics considered here are: maximum wall shear stress magnitude (MWSSM), maximum time averaged wall shear stress magnitude (MTAWSSM), and time and space averaged wall shear stress magnitude (TSAWSSM). Collectively, the wall shear stress metrics are denoted as WSSM. For comparison, a similar study was run using the archetypal waveform from Holdsworth.

RESULTS

Representative waveforms for each of the four automatically identified categories are shown in Figure 1. Figure 2 shows the variation in the WSSM arising strictly from variation in shape among 12 waveforms (displayed by waveform group). The variations for the time averaged quantities (TSAWSSM, MTAWSSM) are less than for

Copyright 2016 The Organizing Committee for the 2016 Summer Biomechanics, Bioengineering and Biotransport Conference

the maximum wall shear stress (MWSSM). A one-way ANOVA analysis at the 95% confidence level concludes the group means are statistically different for every metric of WSS ($p_{max} = 0.0350$).

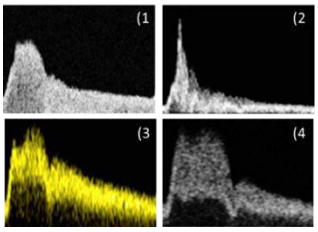

Figure 1: Representative waveform data for each of the four groups: 1) Low Resistance, Short Systole; 2) High Resistance, Short Systole; 3) Low Resistance, Long Systole, 4) High Resistance, Long Systole.

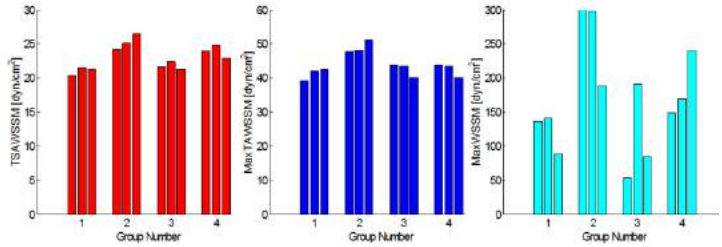

Figure 2: Variation in wall shear stress metrics due solely to waveform shape. Four waveforms considered are grouped by flow group. Q = 1.81 cm^3/s for all cases.

Figure 3 compares the percent differences in WSSM between each patient specific waveform and the reported Holdsworth waveform. One- way ANOVA analysis at the 95% confidence level concludes only the MWSSM group means are statistically different. Shifting focus towards global qualitative characteristics, Figure 4 shows MWSSM contours of the aneurysm lumen for one representative case of each of the four waveform groups having identical flow rates. Despite the significant differences in magnitude among these studies (as seen in difference in contour scales), the qualitative distribution of WSS is quite similar, consistently preserving notable features such as the location, size and shape of the high WSS region (red/pink contour region) in the dome where inflow jet impingement is found.

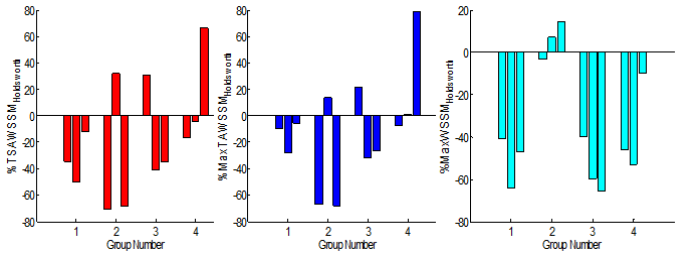

Figure 3. Percent difference in WSSM from patient data and an archetypal waveform.

DISCUSSION

This study sheds insight on the importance of choice of waveforms used as boundary conditions in CFD models of cerebral aneurysms, considering a more clinically relevant older population. It first explores the variation in WSS magnitudes due strictly to choice of waveform shape (identical parent artery flow rates). By selecting an "archetypal" waveform, one inherently assumes these differences to be negligible. In this study, we found that for TSAWSSM (the least sensitive of the three), the range of WSS deviation is 26% of the group average; while the MWSSM range is more than 100% of the average, Table 1. This suggests that obtaining accurate MWSSM without patient specific waveforms could subject the results to significant error, while a much smaller error can be expected if TSAWSSM is of interest.

Table 1. Results for wall shear stress metrics for the 12 waveforms, with Q = 1.81 cm^3/s. Quantities labeled with a (*) are normalized by the average for the column.

[dyn/cm^2]	*TSAWSSM*	*MaxTAWSSM*	*MaxWSSM*
Average	22.98	43.77	169.78
StDev	1.95	4.08	77.40
Range	6.08	12.48	246.50
*StDev**	0.08	0.09	0.46
*Range**	0.26	0.29	1.45

Secondly, the study provides insight on the error produced from assuming the Holdsworth waveform to be a substitute choice for a patient specific waveform and flow rate. The normalized range in WSS variation is in excess of 100% of the average for all measures of wall shear stress used here. This data strongly suggests the need for patient specific flow information for predicting WSS magnitudes. Figure 4 suggests a much more positive message: despite the significant differences in WSS magnitudes, the qualitative features of even the most sensitive WSS metric (MWSSM), are remarkably robust to choice of waveform.

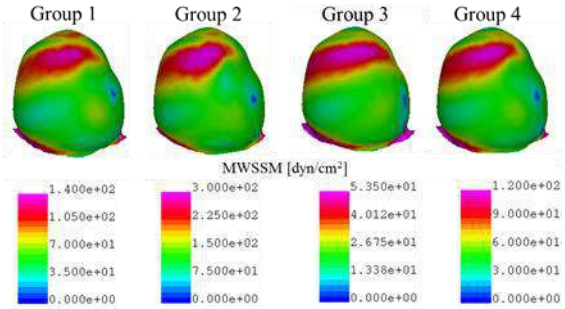

Figure 4. MWSSM contour for a representative case from each waveform group, Q = 1.81 cm^3/s .

Our findings therefore suggest that while quantitative values of WSSM for a particular location in an aneurysm may not be accurately represented without patient specific flow information, patient specific flow rates and waveforms are not a stringent requirement for determining the qualitative WSSM distribution, nor for relative magnitudes within a single aneurysm.

REFERENCES

[1] Frosen, J et al., *ACTA Neurosurgery*, Janurary 2012
[2] Cebral, J.R et al., *Am. J. Neuroradiol*. 26:2550-2559, 2005.
[3] Hoi, Y.et al., *J. Biomechanical Engineering*, July 2010, Vol. 132 / 071006-1
[4] Holdsworth, D.W. et al., *Physiol. Meas.* 20 (1999) 219-240.
[5] Rinkel, G.J.E. et al., *Stroke*. 1998;29:251-256
[6] Wood, M.M. et al., *Ultrasound Quarterly* Vol. 26, No. 2, June, 2010
[7] Madhwal, S. et al, *JACC: Cardiovasculature Imaging*, Vol. 7, No. 2, 2014
[8] Valencia, A., Solis, F., *Computers and Structures* 84 (2006) 1326-1337
[9] Cebral, J.R. et al., *IEEE Transactions on Medical Imaging*, Vol. 24, No. 4, April 2005

Copyright 2016 The Organizing Committee for the 2016 Summer Biomechanics, Bioengineering and Biotransport Conference

SB³C2016
Summer Biomechanics, Bioengineering and Biotransport Conference
June 29 –July 2, National Harbor, MD, USA
SB³C2016-934

QUANTIFICATION AND COMPARISON OF MECHANICAL PROPERTIES OF THE URINARY BLADDER WALL

A. Massafra (1) and S. Roccabianca (1)

(1) Mechanical Engineering Department
Michigan State University
East Lansing, Michigan, U.S.A.

INTRODUCTION

The urinary bladder (UB) is a musculomembranous hollow organ whose main function is to store and periodically void urine in a controlled manner; this is achieved through a regulated cycle of mechanical relaxation and contraction. Alterations to this cycle or obstruction of the urethral outlet can give rise to a number of storage or voiding disorders including underactive and overactive bladder syndromes. Four layers can be identified within the urinary bladder wall (UBW), as shown in Fig.1. From the innermost to the outermost, (1) the mucosa consists of a thin layer of epithelial cells; (2) the submucosa, composed of a matrix of collagen and elastin fibers, endows compliance and strength to the wall; (3) the detrusor, composed of smooth muscle cells (SMC), represents the contractile part; and (4) the adventitia, containing mainly collagen fibers, works as a protective sheet.

Despite the effect that mechanical behaviors have on the physiology of all soft biological tissues, included the UB, the number of models that can be found in literature to describe these behaviors is slim. However, a considerable amount of literature has been devoted in the last decade on developing bio-chemo-mechanical models in the cardiovascular field. The authors see the opportunity of building on these previous works to develop a model of the UB that can describe the interaction between mechanical behavior and biological function. Moreover, a mechanobiological model will also serve as important step towards the development of a growth and remodeling model of the UB.

METHODS

Motivated by the work done in [1], we present a consistent quantification and comparison of uniaxial mechanical properties of the UBW based on five data sets available in the literature and two experimental data sets collected in our laboratory.

Mechanical testing. Two intact pig bladders were collected from the Meat Lab of Michigan State University, then cleaned for luminal contents and adjacent tissues. For the purpose of the biomechanical characterization, samples were harvested along the apex-to-base axis from the lateral region of UB. The samples measured approximately $37.6mm \times 14.3mm$ on average with the longest dimension aligned with the apex-to-base direction. Following isolation, specimens were stored at 4C in Hank's Balances Salt Solution (HBSS). Samples were then subjected to a uniaxial tensile test along the apex-to-base direction. The tissue was first preconditioned for 8 cycles at a displacement rate of 0.3 mm/s reaching a maximum stretch ratio of $\lambda_{precond.} = 1.6$. The stretch ratio has been evaluated as $\lambda = \ell/L$, where ℓ represents the deformed length of the sample throughout the test, and L the length for an unloaded configuration recorded before the test. After preconditioning, a sample-specific stretch ratio λ_{test} was estimated to ensure a maximum stress of at least ~120 kPa. Finally, the tensile test consisted of 5 loading cycles performed at a displacement rate of 0.15 mm/s reaching a stretch of λ_{test}. Figure 2 shows the experimental values of Cauchy stress and stretch, referenced to a 5g preloaded configuration recorded after the test (curves labeled S 1.5 and S 2.1).

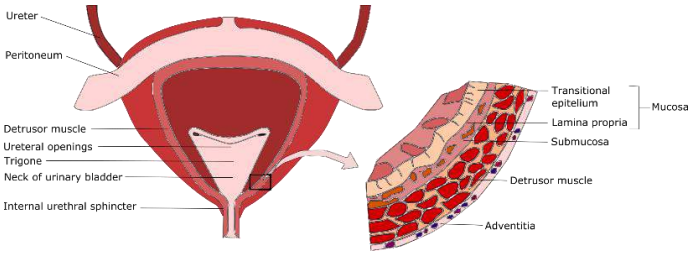

Figure 1. Schematic of the anatomical regions of the human UB.

Copyright 2016 The Organizing Committee for the 2016 Summer Biomechanics, Bioengineering and Biotransport Conference

Constitutive description. The UBW shows a nonlinear mechanical behavior when subjected to large deformations; hence, one must consider an appropriate theoretical framework. The model proposed here builds on the work conducted during the past decade from Humphrey and his coworkers, namely the constrained mixture approach to model the mechanical behavior of soft biological tissues [2]. Specifically, we endowed the amorphous matrix, dominated by randomly distributed elastin fibers, with a neo-Hookean strain energy function (SEF), and we described the behavior of the two families of locally parallel collagen fibers employing a Fung-type exponential. The two-fiber family constitutive model constitutive model is described in terms of a SEF, W, of the form

$$W = \frac{c}{2}(I_C - 3) + \sum_{k=1}^{2} \frac{c_1}{4c_2}(exp[c_2((\lambda^k)^2 - 1)^2] - 1)\,, \qquad (1)$$

where c, c_1, c_2 are material parameters, the first two with the dimension of a stress and the third dimensionless; I_C is the first invariant of the right Cauchy–Green tensor $\boldsymbol{C}$ (i.e., $I_C = tr\boldsymbol{C}$); and λ^k is the stretch experienced by the k^{th} fiber family oriented in direction $\boldsymbol{M}^k = \left[0, sin\ \alpha_0^k, \cos \alpha_0^k\right]$ in an appropriate reference configuration. We let $\alpha_0^1 = 0^\circ$ (apex-to-base family) and $\alpha_0^2 = 90^\circ$(circumferential family).

Simulated uniaxial data. Several experimental data sets describing the mechanical behavior of the UB can be found in literature; most of them, however, have been collected using different types of tests (e.g., uniaxial, equibiaxial, pressure-volume) as well as donors from different species (e.g., human, pig, cat). In order to compare results presented in different studies, we re-created consistent sets of uniaxial data based on nonlinear constitutive relations reported with associated best-fit values of the material parameters found in literature [1]. Specifically all data sets resulted from the same simulated uniaxial loading protocol: stress-controlled tests in the axial direction (i.e., apex-to-base direction) with maximum values of stress of 140 kPa. Assuming the material to be incompressible, the Cauchy stress can be evaluated as $\boldsymbol{t} = -p\boldsymbol{I} + 2\boldsymbol{F}(\frac{\partial W}{\partial \boldsymbol{C}})\boldsymbol{F}^T$, where the Lagrange multiplier p comes from enforcing incompressibility (i.e., $\det \boldsymbol{F} = 1$), $\boldsymbol{C} = \boldsymbol{F}^T\boldsymbol{F}$. We then used nonlinear regression to determine best-fit values of the three model parameters. In this way, we used a consistent means to compare results regardless of the original testing protocols or constitutive relations.

RESULTS

The experimental data of the uniaxial loading tests conducted on the two specimens from different pig bladders are reported in Fig. 2 (square symbols). It is remarkable that they confirm the nonlinear mechanical behavior of the UBW. The difference between the two curves associated with the two samples could be explained by the different percentage of constituents and storage conditions of the two UBW tested. Specifically, prior to testing, one of the bladder was stored in HBSS (i.e., S 1.5), while the other one in the absence of HBSS (i.e., S 2.1). Fig. 2 compares also axial Cauchy stress-stretch responses in uniaxial stress protocol of the five data sets available from the literature. Additionally, the experimental data obtained in our laboratory and the data obtained from the literature are in good agreement. This confirm that we established a reliable uniaxial tensile test protocol to characterize the biomechanical properties of the bladder tissue and guarantee good test repeatability. Table 1 reports best-fit values of the three parameters of our model for each dataset. The goodness of fit is also reported in Table 1 in terms of the percentages of root mean square errors between the experimental data and the associated best-fit.

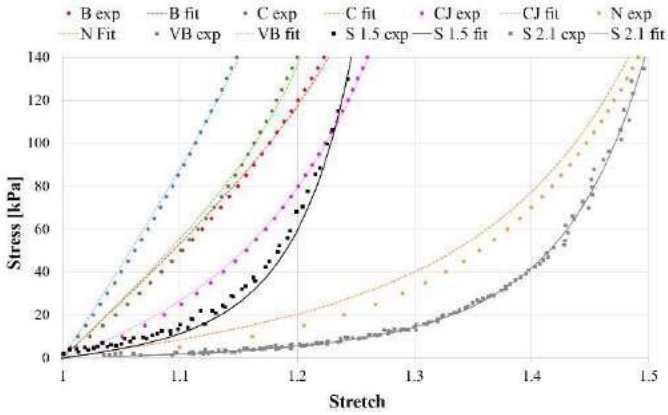

Figure 2. Uniaxial Cauchy stress-stretch data (i.e., apex-to-base direction) recreated from five works available in literature (circles), experimental data from two samples tested in our laboratory (squares), and the associated model prediction (dashed and solid lines). *Data from literature, followed by donor species*: (B) Boubaker et al., human [4]; (C) Chen et al., human [5]; (C-J) Colding-Jorgense et al., human [6]; (N) Natali et al. pig [7]; (VB) Van Beek, cat [8]. *Data from experiments* - Sample 1.5: pig, bladder stored in HBSS prior sample isolation; Sample 2.1: pig bladder stored in absence of HBSS prior sample isolation.

Table 1: Best-fit values of model parameters and root mean square errors (*RMSE %*) for the five datasets available in literature and for the two data sets collected in our laboratory.

	c (kPa)	c_1 (kPa)	c_2	RMSE %
Boubaker et al.	163.69	13.52	3.81	0.03
Chen et al.	164.33	18.07	5.94	0.04
Colding-Jorgense et al.	3.80E-11	99.45	1.17	0.01
Natali et al.	9.98	19.32	0.62	0.11
Van Beek	277.69	11.56	9.82	0.02
Sample 1.5	3.83E-13	35.83	4.95	0.08
Sample 2.1	8.18E-14	6.56	1.33	0.05

DISCUSSION

This work represents the first attempt to collect and then compare diverse results from the literature on the passive uniaxial nonlinear mechanical behavior of the UBW. This work represents the first step toward the development of a growth and remodeling model that will have the capability of describing the changes in the mechanical property of the UBW resulting from changes in the urodynamics.

REFERENCES

[1] Roccabianca S. et al. *J. Mech. Behavior Biomed.*, 19: 618-634, 2014.
[2] Humprey J. D. et al. *Biomech. Model. Mechan.*, 2:109-126, 2003.
[4] Boubaker, M.B. et al. *J. Biomech.*, 42:1862-1868, 2009.
[5] Chen, Z.W. et al. *J. Biomech.,* 48:238-245, 2015.
[6] Colding-Jorgense, M. et al. *Neurourol. Urodynam.*, 15:59-79, 1993.
[7] Natali, A.N. et al. *J. Biomech.,* 48:3088-3096, 2015.
[8] Van Beek, A.J. *A finite element model of the urinary bladder*, ISBN 90-5282-738-9, 1997.

Copyright 2016 The Organizing Committee for the 2016 Summer Biomechanics, Bioengineering and Biotransport Conference

SB³C2016
Summer Biomechanics, Bioengineering and Biotransport Conference
June 19-July 2, National Harbor, MD, USA
SB³C2016-935

VISCOSITY IS A NECESSARY COMPONENT OF MECHANICAL CHARACTERIZATION OF BIOLOGICAL TISSUE

Andres Rubiano, MS
Mechanical and Aerospace Engineering, Gainesville, Florida, USA

Dan Delitto, MD; Song Han, PhD; Steven Hughes, MD
Department of Surgery, Gainesville, Florida, USA

Chelsey S. Simmons, PhD
Mechanical and Aerospace Engineering, Biomedical Engineering, Division of Cardiovascular Medicine
Gainesville, Florida, USA

INTRODUCTION

Mechanical properties of cells and tissues often correlate to physiological and pathological parameters [1]. Fibrosis, for example, has been correlated to an elevated elastic modulus [2] and changes in pathological conditions can be quantified by measuring mechanical properties such as tissue porosity [3], density [4], and elastic modulus [5] in diseased and recovering patients.

Characterization techniques for simple physical parameters such as mass, fluid pressure, and porosity are well developed and are easily and correctly carried out by biologists, physicians, and engineers alike. Quantifying elastic modulus to find a correlation to clinical parameters, and thus evaluate pathologies and therapeutic effects, is slightly more complex.

While many engineering materials such as metals and ceramics can be considered purely elastic, hydrated polymers and biological tissues have entangled polymer chains and high water content. Thus, simple stress-strain models of elastic behavior are not adequate to describe their mechanical behavior.. Furthermore, specifically for tissue, it is important to recognize its micro-structural complexity and likely heterogeneity.

Motivated by dramatic disagreement in the literature for the elastic moduli of heart tissue in rodents, spanning four orders of magnitude, and our success in obtaining consistent values for a wide variety of human subjects and animal pathologies [5], we present a simple and reproducible viscoelastic characterization technique for tissue and other soft matter. Additionally, we demonstrate the importance of incorporating viscous effects through the characterization of viscoelastic properties in pancreatitis and pancreatic cancer patients.

METHODS

Force-displacement quantification with custom indenter. We modified a tool designed to measure friction forces to create a custom Multi-Scale Indenter (MSI, Figure 1) [5]. The cantilever-based probe is displaced vertically using a software-controlled piezoelectric stage. The probe is brought into contact with the tissue sample following a time-dependent displacement profile set by the user in custom LabVIEW code. The reacting normal force of the tissue bends the titanium cantilever, and the relative displacement of the cantilever tip is measured by capacitive probe. The stiffness of the cantilever, calibrated by contact with glass, is utilized by the LabVIEW code to determine the normal load throughout the indentation cycle.

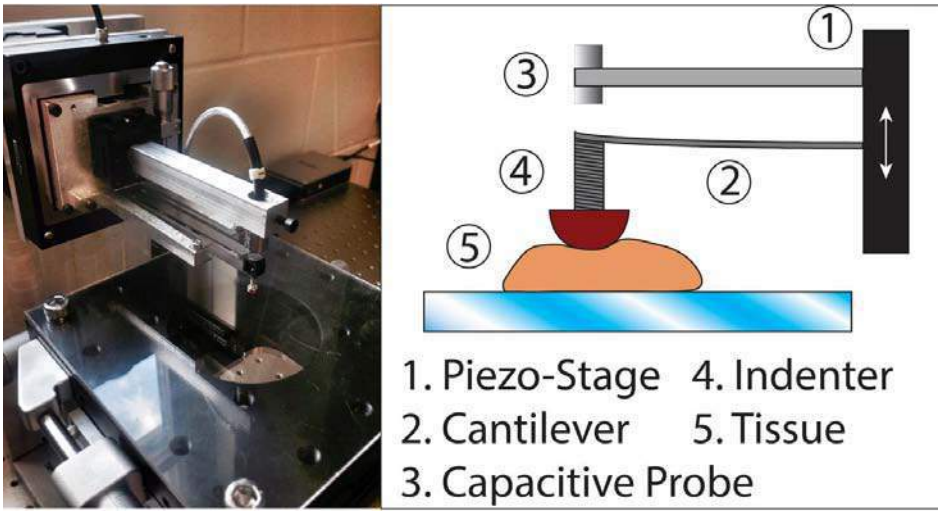

FIGURE 1. MULTISCALE INDENTER (MSI) CHARACTERIZATION TOOL
A rigid probe (4) indents tissue located on top of a glass slide (5). The probe is mounted directly to a cantilevered flexure (2), and capacitance probes (3) measure the displacement of a target (1) mounted on the calibrated flexure, yielding forces.

Copyright 2016 The Organizing Committee for the 2016 Summer Biomechanics, Bioengineering and Biotransport Conference

Tissue Isolation and Characterization. Small samples of pancreas were surgically excised from patients with suspected pancreatitis or pancreatic cancer. The size of the obtained sample for characterization purposes varied based on the size of the tumor and/or extracted fragment of the pancreas. Samples were kept in DMEM-F12 media to maintain hydration and preserve cell and tissue conditions, and indentations were carried out no more than 2 hours after surgery (even though characterization results were found not to vary from one day to the next). Between 7 and 11 indentations were carried out in each sample without indenting the same location twice. The number of indentations was restricted by the size of the tissue fragment; larger tissue samples have a larger area available for indentation. For statistical reliability, the average of the indentation results for a particular sample corresponds with the reported sample properties. Results from pathological analysis of the sample were released 2-3 days after indentation for a semi-blinded study.

Characterization Models. Force-displacement data from the original indentation is converted into Elastic Modulus as a function of time using the Hertz-JKR contact model for flat circular surfaces:

$$E(t) = \frac{F(t)\cdot(1-\nu^2)}{2\cdot R\cdot\delta(t)} \quad (1)$$

where E = elastic modulus, F = force calculated by MSI through LabVIEW, ν = Poisson's Ratio, R = flat punch radius, and δ = indentation depth.

The standard linear solid (SLS) is a common viscoelastic mechanical network model, composed of representative springs (linear elasticity) and a dashpot (viscosity). This simple combination of linear elastic and viscous components has a straightforward physical interpretation, making this model particularly useful for interdisciplinary investigations with collaborators from broad backgrounds. The strain rate-dependent and "liquid-like" properties of the material are represented by viscosity, η, while $E_{ss} + E_a$ is the effective modulus of the tissue during initial compression. As the dashpot η relaxes, E_a trends to zero and E_{ss} can be interpreted as the steady-state or equilibrium modulus.

To determine these parameters, we fit the relaxation portion of the calculated $E(t)$ versus time plot to the following equation[23]:

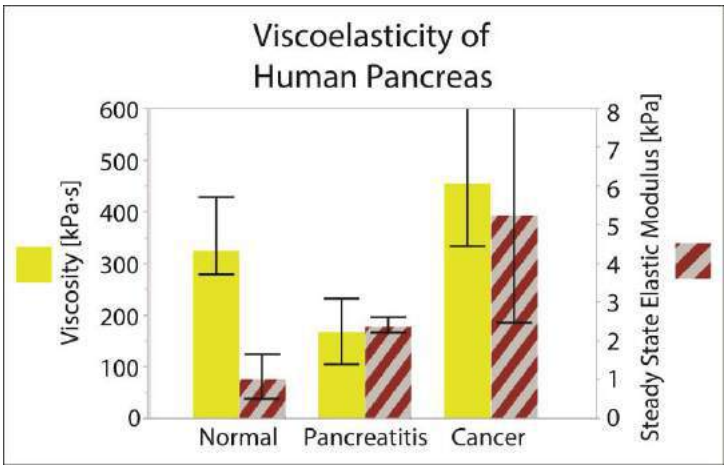

FIGURE 2. VISCOCITY AND ELASTIC MODULUS RESULTS. Strain-rate independent Steady-State Elastic Modulus is reported, as well as the viscosity of the three groups of pancreatic tissue. The bars represent the average of the properties, and the error bars show the range of the results.

$$E_t(t) = E_{ss} + E_a \cdot e^{-t/\tau} \quad (2)$$

where E_t = total effective elastic modulus as a function of time, E_{ss} = steady state elastic modulus after complete relaxation, E_a = apparent strain-rate-dependent contribution to initial elastic modulus, and $\tau = \eta/E_a$ with η = viscosity. Fitting data to the relaxation portion of the curve makes the data less dependent on the depth of the original indentation and rate of indentation compared to other common viscoelastic models and fitting strategies.

RESULTS AND DISCUSSION

Pancreas viscoelasticity shows the importance of considering the viscous nature of biological tissue when quantifying its mechanical properties. By reporting the steady-state elastic modulus, we are eliminating the fraction of the elastic modulus that is test-parameter dependent, which other studies commonly and misguidedly include in their reports. Despite this very important distinction between total and steady-state elastic modulus, the range overlap of steady-state modulus [Figure 2] shows that pancreas from a pancreatitis patient and one with pancreatic cancer could share the same modulus values. However, because the viscosity of pancreatitis is even lower than normal pancreas and their individual values do not overlap, both elastic modulus and viscosity would be an ideal way to differentiate chronic inflammation from malignant tumors.

Since autoimmune pancreatitis is occasionally misdiagnosed as pancreatic cancer and vice versa [6,7], techniques to distinguish the two pathologies are being investigated. Based on our analysis, mechanical approaches could be valuable. While indentation experiments would require access to the tissue through surgery, nonintrusive alternatives such as Magnetic Resonance Elastography and Shear Wave Sound Velocity could estimate viscoelastic properties of tissue with minimal invasion of the patient.

By characterizing viscoelasticity in human pancreas, we demonstrate that the viscous component imparts essential information to evaluate and differentiate tissue condition and disease state. This easily reproducible characterization method can be helpful in a wide variety of applications, from diagnosis to evaluation of treatments in medical studies, as well as finding clearer differences between sample groups.

ACKNOWLEDGEMENTS

The authors acknowledge fellowship support from the Institute for Cell & Tissue Science and Engineering at the University of Florida (AR) and research support from Medtronic (CSS).

REFERENCES

[1] Ford et al. "Designing a fibrotic microenvironment…" Acta Biomater. 2015 Sep;24:220-7.
[2] Tang et al. "Ultrasound Elastography and MR Elastography for Assessing Liver Fibrosis: Part 2…" Am J Roentgenol. 2015;205(1):33-40.
[3] Zhang et al. "In vitro and in vivo evaluation of calcium phosphate …" Mater Sci Eng C Mater Biol Appl. 2016;60:298-307.
[4] Lopez et al. "Correlation of (18)F-fluoroethyl tyrosine positron-emission…" Onco Targets Ther. 2015;8:3803-15.
[5] Rubiano et al. "Stem cell therapy restores viscoelastic properties…" J Mech Behav Biomed Mater. 2015;59:71-77.
[6] Takuma et al. "Strategy to differentiate autoimmune pancreatitis…" World J Gastroenterol. 2012;18(10):1015-20.
[7] Bansal and Sonnenberg. "Pancreatitis is a risk factor for pancreatic cancer." Gastroenterology. 1995;109(1):247-51.

Copyright 2016 The Organizing Committee for the 2016 Summer Biomechanics, Bioengineering and Biotransport Conference

SB³C2016
Summer Biomechanics, Bioengineering and Biotransport Conference
June 29 –July 2, National Harbor, MD, USA
SB³C2016-936

3D CHARACTERIZATION OF CORNEAL DEFORMATION USING ULTRASOUND SPECKLE TRACKING

Keyton Clayson (1,2), Elias Pavlatos (1), Jun Liu (1,2,3)

(1) Department of Biomedical Engineering
The Ohio State University
Columbus, OH, USA

(2) Biophysics Interdisciplinary Group
The Ohio State University
Columbus, OH, USA

(3) Department of Ophthalmology
The Ohio State University
Columbus, OH, USA

INTRODUCTION

The cornea is a highly organized transparent tissue whose shape and biomechanical properties are important for visual acuity [1]. When this tissue is altered or disrupted during disease processes such as keratoconus or from surgical procedures that remove part of the cornea, the cornea's structure and function can change significantly [2].

Although recently developed optical techniques can adequately measure structural details of the cornea, characterization of corneal biomechanical properties remains challenging. Current techniques such as inflation testing [3], strip extensometry [4, 5] and shear wave testing [6] are limited to 1D or 2D visualizations, and the interactions in and out of the corneal plane (the full 3D response) remain largely unknown.

Our laboratory has developed and validated a high-resolution ultrasound speckle tracking method for non-invasive 3D mapping of tissue strains [7, 8]. Using this technique, we investigated the deformation of a volume of the cornea near the apex during inflation for both swelling-controlled and active swelling cases. The objective of this study was to map the 3D strains within the intact cornea during physiological processes including IOP increase and active swelling to better characterize the biomechanical responses of this tissue.

METHODS

Porcine globes were divided into two groups and tested within 72 hours post-mortem. For the swelling-controlled group (n=9), whole globes were first immersed in a 10% dextran solution for 1 hour to reduce corneal swelling [9]. The anterior chamber of the globe was infused with Optisol GS (Bausch and Lomb) via a column to control the intraocular pressure (IOP) and minimize swelling. For the active swelling group (n=8), the globes were not pre-treated with dextran and were infused with 0.9% saline instead of Optisol.

For both groups, the globes were immersed in 0.9% saline with the cornea facing upwards during inflation. The globes were preconditioned with 25 pressure cycles from 10 to 12 mmHg, then equilibrated at a starting pressure of 10 mmHg for 1 hour. Inflation tests were performed with 0.5 mmHg (active swelling) or 1 mmHg (swelling-controlled) steps to ensure proper tracking. After a 15 minute equilibration time at each pressure step, a 55 MHz ultrasound probe (Vevo 660, VisualSonics Inc.) was used to acquire consecutive 2D frames of radiofrequency data (Fig. 1a). The 2D images were acquired in the nasal-temporal direction and the probe was translated at 14 μm steps in the superior-inferior direction over a 2 mm distance to form a 3D volume centered on the corneal apex. (Fig. 1b).

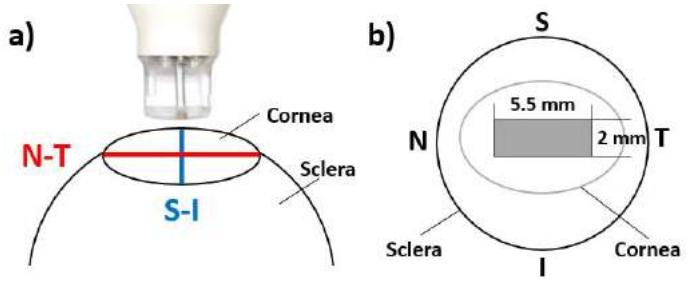

Figure 1: Schematic of a) ultrasound scanning orientations and b) scanning regions (N: nasal, T: temporal, S: superior, I: inferior).

The 3D principal strains (ε_1, ε_2, ε_3), max shear, and volume ratio at each inflation step were calculated using a correlation-based speckle tracking algorithm [7]. Correlation coefficients between pressure steps were evaluated to ensure proper tracking. Two swelling-controlled eyes

Copyright 2016 The Organizing Committee for the 2016 Summer Biomechanics, Bioengineering and Biotransport Conference

were excluded from the final data set due to unsatisfactory tracking (correlation coefficients < 0.6 through majority of volume). Volumetric strain maps and vector plots were visualized in Paraview (Kitware Inc.).

RESULTS

The average 3D principal strains, max shear, and volume ratio for both groups are presented in Table 1. In swelling-controlled cases, the average 3rd principal ε_3 was negative and largest in magnitude, with the average 1st principal ε_1 positive and slightly smaller than ε_3 and the 2nd principal ε_2 very small. In the active swelling group, the average 1st principal ε_1 was positive and largest in magnitude, with a small 2nd principal ε_2 and a negative 3rd principal ε_3. Substantial shear strains were observed in both groups, with the active swelling group having a larger maximum shear than the swelling-controlled group (p=0.001 at 12 mmHg). The volume ratio in the swelling-controlled group was slightly less than 1, while the active swelling group had a volume ratio slightly greater than 1.

Table 1: Average principal strains, max shear, and volume ratios in porcine corneas during inflation with or without active swelling.

Swelling-Controlled (n=7)

IOP (mmHg)	ε_1	ε_2	ε_3	Max Shear	Volume Ratio
11	1.30 ± 0.61%	0.13 ± 0.52%	-2.06 ± 0.71%	1.69 ± 0.47%	0.993 ± 0.014
12	2.35 ± 1.05%	0.24 ± 0.85%	-3.65 ± 1.27%	2.91 ± 0.78%	0.987 ± 0.021

Active Swelling (n=8)

IOP (mmHg)	ε_1	ε_2	ε_3	Max Shear	Volume Ratio
11	3.79 ± 1.20%	0.28 ± 0.60%	-1.30 ± 0.78%	2.48 ± 0.85%	1.026 ± 0.016
12	7.86 ± 2.05%	0.46 ± 0.95%	-2.42 ± 1.39%	4.90 ± 1.67%	1.054 ± 0.027

3D principal strain maps and vector plots are shown in Figure 2. For swelling-controlled corneas, the negative ε_3 was primarily in the through-thickness direction (Fig. 2 c, f), while the positive ε_1 was primarily in-plane (Fig. 2 a, d). In active swelling corneas, the positive ε_1 was primarily in the through-thickness direction (Fig. 2 g, j), showing a larger magnitude in the posterior cornea (Fig. 2 j), while the negative ε_3 was primarily in-plane (Fig. 2 i, l). In both groups, ε_2 was much smaller than the other two principles and did not show a preferred orientation (Fig. 2 b, e, h, k).

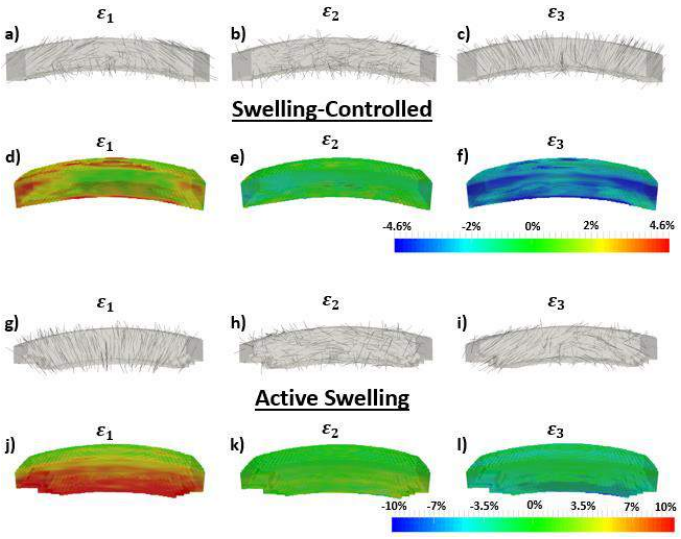

Figure 2: Vector plots and principal strains for swelling-controlled (a-f) and active swelling (g-l) corneas at 12 mmHg.

DISCUSSION

Our study showed that with proper adjustment of data acquisition and analysis, the high-frequency ultrasound method was sufficiently sensitive to successfully track corneal speckles, although they are weaker than speckles from other tissue. The 3D strain data showed that in swelling-controlled eyes, the corneal inflation response was primarily through-thickness compression and in-plane stretch, as expected for a spherical thin shell. The in-plain strains (ε_1 and ε_2) at each measured grid point showed markedly different magnitudes between the two orthogonal directions although there was no perceivable large-scale anisotropy based on the almost random orientation of the vectors (Fig. 2 a, b). A volume ratio slightly less than 1 suggests a small overall volume loss during inflation, confirming that swelling during experimentation was minimized in this group.

The active swelling group of eyes, although inflated at the same pressure levels as the swelling-controlled group, showed a positive strain in the through-thickness direction (Fig. 2 g, j) and a volume ratio slightly greater than 1, which corresponds to an increased thickness consistent with swelling. This swelling response seemed predominant even though the cornea was simultaneously inflated by a small pressure increase. The 3D data showed an anterior-posterior gradient of the through-thickness strains with greater strains in the posterior cornea (Fig. 2 j), consistent with greater swelling reported in the posterior stroma of swollen corneas [10].

The 3D method also allowed quantification of the shear strains, showing substantial shear during corneal deformation induced by inflation or swelling. The pathophysiological relevance of corneal shear is not well understood because this has been difficult to measure, especially in the intact cornea. Three-dimensional ultrasound speckle tracking, among other imaging techniques, provides a tool to fully characterize the biomechanical responses of this unique, highly organized tissue as it deforms under physiological loadings.

One limitation of the current study is that only a small volume of the central cornea was measured, preventing analysis of regional variances. Future work will expand imaging to other regions of the cornea to acquire a complete volume. In addition, we will perform quantitative comparison of the anterior and posterior responses.

In summary, this study showed the feasibility of using ultrasound speckle tracking for 3D mapping of corneal deformation. Our results showed distinct biomechanical responses in swelling-controlled and actively swelling corneas during IOP increase. Three-dimensional characterization of corneal biomechanical responses may help better identify the biomechanical factors involved in corneal pathophysiology and surgical outcomes.

ACKNOWLEDGEMENTS

NIH Grant R01EY020929

REFERENCES

[1] Ethier, CR et al., *Annu Rev Biomed Eng*, 6:249-273, 2004.
[2] Ruberti, JW et al., *Annu Rev Biomed Eng,* 13:269-95, 2011.
[3] Boyce, BL et al., *Biomaterials*, 29(28):3896-3904, 2008.
[4] Hatami-Marbini H, *Ann Biomed Eng,* 42(8):1740-1748, 2014.
[5] Elsheikh, A and Anderson, K, *JR Soc Interface*, 2:177-185, 2005.
[6] Tanter, M et al., *IEEE Trans Med Imaging,* 28(12):1881-1893, 2009.
[7] Cruz-Perez, B et al., *ABME*, Epub ahead of print, Nov. 2015.
[8] Pavlatos, E et al., *JBME*, Epub ahead of print, Dec. 2015.
[9] Terry, MA et al., *Arch Opthalmol*, 112:538-543, 1994.
[10] Meek, KM et al., *Eye*, 17:927-936, 2003.

Copyright 2016 The Organizing Committee for the 2016 Summer Biomechanics, Bioengineering and Biotransport Conference

SB³C2016
Summer Biomechanics, Bioengineering and Biotransport Conference
June 29 –July 2, National Harbor, MD, USA
SB³C2016-937

A MULTI-SCALE MECHANICAL AND CELLULAR ARGUMENT FOR THE DIFFERENTIAL PERFORMANCE OF CORONARY ARTERY BYPASS GRAFTS

David A. Prim (1,2), Boran Zhou (1), Laurel Carter (3), Vinal Menon (2), Jay Potts (2), Tarek Shazly (1,4), John F. Eberth (1,2)

(1) Biomedical Engineering Program
University of South Carolina
Columbia, SC, USA

(2) Department of Cell Biology and Anatomy
USC School of Medicine
Columbia, SC, USA

(3) Research Program for Medical Students
USC School of Medicine
Columbia, SC, USA

(4) Department of Mechanical Engineering
University of South Carolina
Columbia, SC, USA

INTRODUCTION

Each year in the U.S., over 400,000 patients with coronary artery disease undergo bypass grafting [1]. Despite 50 years of surgical advances, approximately 6% of coronary artery bypass grafts (CABGs) fail in the first year at a rate that is strongly dependent upon the source tissue [2]. The ability of a vascular graft to adapt is dependent, in part, upon the degree of mechanical deviation and the capacity of resident vascular cells to enact remodeling processes.

Healthy, mature blood vessels maintain a state of homeostasis whereby stresses are uniformly distributed across the vessel wall and most vascular cells exhibit a quiescent phenotype [3]. Acute changes to a vessel's environment cause contraction or dilation by smooth muscle cells (SMCs) to redistribute mechanical loads. When altered loads persist for days, weeks, and months, quiescent vascular cells shift to metabolically active phenotypes, inducing a number of vascular remodeling pathways: SMC proliferation and migration, extracellular matrix (ECM) protein deposition, and ECM reorganization. Over days, weeks, and months, these pathways give rise to changes in vessel wall thickness, lumen diameter, and vessel composition. Remodeling is not exclusively an SMC dependent process; other mechanocytes including endothelial cells (EC) and fibroblasts (FB) play a major role in restoration of tissue homeostasis.

Intuitively, the vascular remodeling processes described above are imperative to the fate of CABGs, as mechanical deviations between *in situ* and grafted environments provide chronic stimuli that cause vascular remodeling. In most graft vessels, this remodeling is a healthy compensatory process; however, in some graft vessels failures are due to etiologies resulting from maladaptive remodeling. The most common of these etiologies is lumen narrowing (i.e. restenosis) in the form of intimal hyperplasia, whereby smooth muscle cells proliferate in the lumen of the graft vessel, forming a new tissue layer.

Previous studies of clinical outcomes have identified correlations between intimal hyperplasia and patient-specific factors [4]. Furthermore, some of the molecular pathways involved with maladaptive remodeling have been identified [5]. However, at present there is an insufficient understanding of the complex relationship between mechanical loads, cellular mechanisms, and the fate of tissue remodeling as it relates to CABG and other grafting procedures.

Our objectives are to (i) report the mechanical deviation between *in situ* and grafted environments for common CABG tissue and the left anterior descending coronary artery (LAD) [6], and (ii) quantify and compare the capacity of vascular cells from different CABG source tissues for coronary adaptation.

METHODS

Porcine vascular tissue and cells were tested in lieu of human tissue, as it is a readily accessible analog to human vascular tissue. Tissues of interest were the left anterior descending coronary artery (LAD), internal thoracic (or, mammary) artery (ITA), radial artery (RA), great saphenous vein (GSV), and lateral saphenous vein (LSV).

For objective (i) data collection followed a well-established protocol for fitting geometry, histology, and biaxial mechanical testing data to a structure-based constitutive model [7-9]:

$$W = \phi_e c\left[\left(\lambda_\theta^2 + \lambda_z^2 + \left(\lambda_\theta \lambda_z\right)^{-2}\right) - 3\right] + \frac{\phi_c}{4}\sum_{k=1-4}\frac{b_{1k}}{2b_{2k}}\left\{\exp\left[b_{2k}\left(\sqrt{\lambda_\theta^2 \sin^2\alpha_k + \lambda_z^2 \cos^2\alpha_k}^{\,2} - 1\right)^2\right] - 1\right\} \quad (1)$$

Using this constitutive model, we quantified the *in situ* homeostatic stress state for each of the vessels. Also using the model, we predicted the mechanical response of each vessel to the grafted coronary environment (Table 1). Furthermore, we developed a novel metric (Ω)

Copyright 2016 The Organizing Committee for the 2016 Summer Biomechanics, Bioengineering and Biotransport Conference

to quantify the sum of normalized differences between native and grafted states for several important parameters (deformed inner radius, vessel compliance, circumferential and axial stress).

For objective (ii), endothelial cells (ECs), smooth muscle cells (SMCs), and fibroblasts (FBs) were enzymatically isolated from freshly dissected sections of each vessel of interest (LAD, ITA, RA, GSV, and LSV). Cell populations were evaluated temporally (day 0, 7, and 30) using multiple assays (confocal microscopy, qRT-PCR, migration, proliferation) to observe phenotypic properties. Analysis of each tissue at acutely and in early culture allow approximate comparison of cells' *in vivo* properties. Comparisons at the late time point demonstrate the extent to which cell phenotypes change in response to their local environment. Determination of phenotypic difference or convergence was made by synthesizing the results of these assays.

Statistical analyses were conducted using one-way ANOVA with Dunnett's Post Hoc test as well as two-sided paired t-tests at $p<0.05$.

RESULTS

Endowed by unique compositional and structural organization, biaxial mechanical testing identified distinct homeostatic stress states for each vessel (Fig.1 bottom). Using a structure-based constitutive model we found that the ITAs experience the least mechanical deviation between *in situ* native environment and theoretical grafted environment for each of the Ω_θ, Ω_z, Ω_{ri}, and Ω_C categories and is represented by the lowest overall Ω (Fig. 1 top) while GSVs had the highest Ω. [6]

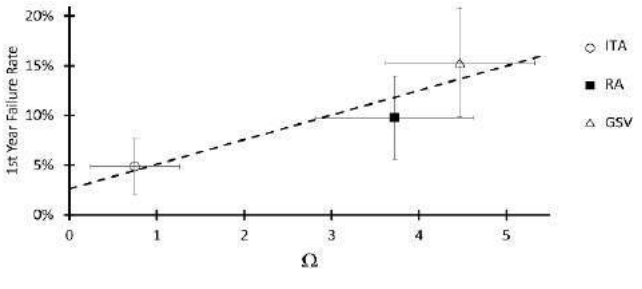

Vessel	C [10-6 m2/kPa]	ri [mm]	<σθ *> [kPa]	<σz * > [kPa]
		Native		
LAD	0.35 ± 0.14	2.3 ± 0.34	68.87 ± 40.78	52.73 ± 24.12
ITA	0.4 ± 0.12	2.24 ± 0.31	70.92 ± 17.53	73.81 ± 17.42
RA	0.15 ± 0.07	1.29 ± 0.6	13.06 ± 3	84.97 ± 96.11
GSV	0.23 ± 0.17	1.47 ± 1.13	3.09 ± 1.01	72.57 ± 109.1
		Grafted		
LAD	0.35 ± 0.14	2.3 ± 0.34	68.87 ± 40.78	52.73 ± 24.12
ITA	0.41 ± 0.14	2.01 ± 0.14	68 ± 12.84	57.45 ± 30.27
RA	0.07 ± 0.03	0.94 ± 0.12	20.54 ± 3.54	101.44 ± 52.43
GSV	0.13 ± 0.03	1.07 ± 0.23	20.6 ± 2.8	89.39 ± 119.47

Figure 1. (Top) Relationship between Ω and clinical 1st year CABG failure rate for each vessel. (Bottom) Values of relevant parameters – compliance (C), deformed inner radius (r_i), circumferential stress (σ_θ), and axial stress (σ_z) – for each vessel in its native and grafted mechanical state. [6]

Concomitant with distinct stress states and functional requirements, resident vascular cells exhibit distinct phenotypic properties. Gene expression profiles (qRT-PCR) suggest significant phenotypic differences between cells isolated from veins (GSV, LSV), muscular arteries (RA), and elastic arteries (ITA, LAD), specifically with respect to genes associated with remodeling processes. Furthermore, these gene expression profiles change temporally within cell populations between early (day 0, day 7) and late (day 30) time points. Confocal microscopy with labeling of specific cell type markers was used to assess cell populations and phenotypes within populations, specifically the proportion of synthetic to contractile SMCs (Figure 2).

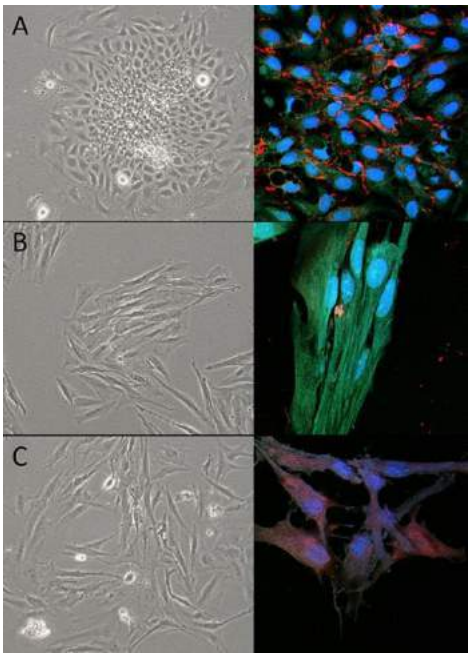

Figure 2. Sample cell populations under phase contrast (200x; left column) and confocal (630x; right column) microscopy: (A) ECs, (B) SMCs, and (C) FBs. For confocal images: Blue=DAPI, Green=Phalloidin, Red=PECAM1/Smoothelin/FSP1 (cell-specific markers).

DISCUSSION

The work represented by objective (i) established the baseline homeostatic stress states for the LAD, ITA, RA, GSV, and LSV. We quantified the mechanical deviation between each vessel's *in situ* and grafted environment using a novel, and clinically relevant, metric (Ω) that can be further applied to other graft candidates, other graft procedures, and tissue engineered blood vessels. These findings motivated further investigation in objective (ii).

The cell studies represented by objective (ii) provide a new perspective toward understand CABG remodeling. By studying the resident cell populations that make up CABGs and are responsible, in part, for remodeling processes, we demonstrate that inherently vessels are not equally capable of vascular remodeling.

In the future, the results of objectives (i) and (ii) will be synthesized to optimize CABG remodeling in an *ex vivo* perfusion bioreactor.

ACKNOWLEDGEMENTS

NIH INBRE for SC (P20GM103499); USC BMEN Provost Graduate Scholarship

REFERENCES

[1] Lloyd-Jones, D., et al., *Circulation*, 121(7), pp. e46-e215, 2010.
[2] Carey, J. S., et al., *J Thorac Cardiov Sur*, 138(5), pp. 1100-1107, 2009.
[3] Fung, Y. C., *Ann Biomed Eng*, 19(3), pp. 237-249, 1991.
[4] Ruengsakulrach, P., et al., *Circulation*, 100(suppl 2), pp. II-139-Ii-144, 1999.
[5] Newby, A. C., et al., *J Pathol*, 190(3), pp. 300-309, 2000.
[6] Prim, D. A., et al., *J Mech Behav Biomed*, 54, pp. 93-105, 2015.
[7] Eberth, J. F., et al., *J Biomech*, 44(14), pp. 2532-2537, 2011.
[8] Holzapfel, G., et al., *J Elasticity*, 61(1-3), pp. 1-48, 2000.
[9] Zhou, B., et al., *J Mech Med Biol*, 14(3), p. 18, 2014.

Copyright 2016 The Organizing Committee for the 2016 Summer Biomechanics, Bioengineering and Biotransport Conference

SB^{3}C2016
Summer Biomechanics, Bioengineering and Biotransport Conference
June 29 –July 2, National Harbor, MD, USA
SB^{3}C2016-938

IN VITRO STUDIES ON NATIVE TO ENGINEERED HEART VALVE TISSUE INTEGRATION

Kristin Comella(1), Danique Stewart(1), Sasmita Rath(1), Sharan Ramaswamy(1)

(1) Tissue Engineered Mechanics, Imaging and Materials Laboratory (TEMIM Lab), Department of Biomedical Engineering, Florida International University, Miami, FL,

INTRODUCTION

Millions of people worldwide suffering from valvular heart disease and the rate of incidence is expected to significantly increase in the future [1]. An inability of prosthetic valves to accommodate somatic growth and practical size limitations of current commercial valves represent specific technical challenges. The field of tissue engineered heart valves holds promise of filling this unmet need. The living, biological heart valve could function in a similar manner as native tissue with normal hemodynamic performance and minimal degeneration. However, an important precursor to successful heart valve engineering lies in the successful integration of engineered to native tissues. Thus, in this study we investigate the morphology of the transition region that forms between native and engineered heart valve tissues after exposure to valve-like mechanical environments.

METHODS

Bone marrow stem cells (BMSCs) were isolated from porcine bone marrow. Bone marrow was collected from the iliac crest and layered using gradient separation media. The buffy coats were collected and seeded in tissue culture dishes to isolate and expand BMSCs. Poly-glycolic acid (PGA) and poly-L-lactic acid (PLLA), nonwoven polymer felt scaffold (Biomedical Structures, Warwick, RI) was seeded with approximately 2 million cells and incubated for 8 days in rotisserie culture.

Scaffolds were sutured to freshly harvested porcine native aortic valve leaflets and then placed in a bioreactor [3] (See figure 1). A custom-built U shape bioreactor connected to a peristaltic pump and an environmentally sealed linear actuator was used to create flex/flow [2]. The experimental set-up consisted of four identical conditioning chambers, with each chamber containing 3 samples. Specimens were fixed with a pin at one end while the other end was attached to a circular moving post. For Flex and Flex-Flow experiments, the moving post was moved linearly in the axial direction to initiate specimen cyclic flexure using the linear actuator (frequency of 1 Hz). A peristaltic pump (Master flex L/S, model # 7523–80, Cole Parmer, model # 7535–04, East Bunker Court Vernon Hills, IL, USA) was used to maintain a continuous flow rate of 850 ml/min.

After 14 days in the bioreactor, samples are subjected to collagen biochemical assays. In addition, histology is completed to measure the presence of key valvular ECM components (collagen, glycosaminoglycans (GAGs) and elastin). Immunofluorescence staining of CD31 and α-SMA cell surface proteins is performed for evidence of endothelial and myofibroblastic phenotypes. CD31 is known to be expressed on the surface of EC and α-SMA in SMC, as well as myofibroblast-like cells in valve interstitial cells. And finally, samples were evaluated for gene expression and quantification of a limited number of valve-related markers in order to verify the immunostaining results was completed using quantitative real time-polymerase chain reaction (QRT-PCR).

RESULTS

We successfully seeded 18 scaffolds with BMSCs and then sutured these scaffolds to native porcine valve leaflets (Figure 2). We also demonstrated that scaffolds placed into the flex-flow mechanical environments support differentiation of BMSCs towards a heart valve phenotype, as evident by cellular distribution and expression of specific gene markers [3]. Figure 3 shows the Russell's Movat pentachrome histological staining of: a) through-thickness section of BMSC-seeded scaffold after 22 days of culture (8 days static + 14 days Flex-Flow conditioning, b) through-thickness section of native porcine aortic valve leaflet (+ve control). GAGs were clearly visible within the tissue engineered construct [3].

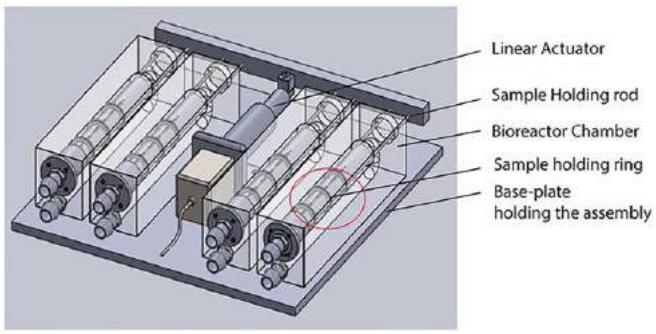

Figure 1: Custom built U shape bioreactor

Copyright 2016 The Organizing Committee for the 2016 Summer Biomechanics, Bioengineering and Biotransport Conference

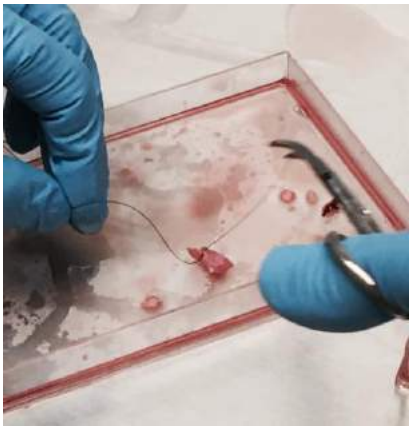

Figure 2: BMSC seeded scaffold sutured to porcine valve

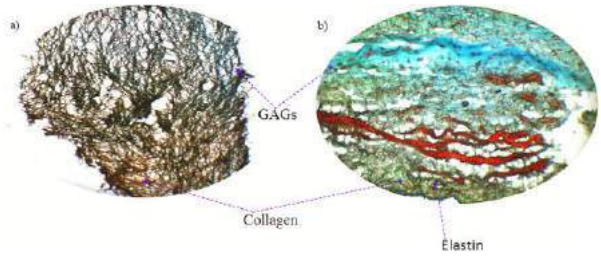

Figure 3: Histological staining of BMSC-seeded scaffold

DISCUSSION

The integration of engineered tissue to native valve tissue is an important component when considering tissue engineered heart valves. transition zone was created between engineered and native valvular tissue constructs. Prior to *in vivo* studies, the current preliminary *in vitro* work provide insights into the nature of integration of engineered heart valve tissues to native tissue structures in a controlled manner.

ACKNOWLEDGEMENTS

Financial support for this study was provided by the College of Engineering and Computing at Florida International University (FIU).

REFERENCES

1. Nkomo VT, Gardin JM, Skelton TN et al. Burden of valvular heart diseases: a population-based study. Lancet 2006;368:1005–11. doi:10.1016/S0140-6736(06)69208-8.
2. Ramaswamy S BS, Schmidt DE, Hobson C, Holmes A, Sacks MS (2014) A novel bioreactor for the study of physiological fluid induced stresses for heart valve tissue engineering;. Journal of Biomechanical Engineering.
3. Rath S, Salinas M, Villegas AG, Ramaswamy S (2015) Differentiation and Distribution of Marrow Stem Cells in Flex-Flow Environments Demonstrate Support of the Valvular Phenotype. PLoS ONE 10(11): e0141802. Poi:10.1371/journal. pone.0141802

Copyright 2016 The Organizing Committee for the 2016 Summer Biomechanics, Bioengineering and Biotransport Conference

SB³C2016
Summer Biomechanics, Bioengineering and Biotransport Conference
June 29 –July 2, National Harbor, MD, USA
SB³C2016-939

A SHAPE OPTIMIZATION APPROACH APPLIED TO INTRALUMINAL THROMBUS DEPOSITION IN ABDOMINAL AORTIC ANEURYSMS

P. Di Achille (1), G. Tellides (2), J.D. Humphrey (1,3)

(1) Department of Biomedical Engineering
Yale University
New Haven, CT, USA

(2) Department of Surgery
Yale School of Medicine
New Haven, CT, USA

(3) Vascular Biology and Therapeutics Program
Yale School of Medicine
New Haven, CT, USA

INTRODUCTION

Over 75% of abdominal aortic aneurysms (AAAs) harbor an intraluminal thrombus (ILT) on their inner wall. Increasing evidence suggests that ILTs contribute to the pathobiology of aneurysms affecting both biomechanically and biochemically the underlying wall [1, 2]. Bioactive effects of ILTs seem to be largely linked to their morphology, with thin thrombi showing a more pronounced proteolytic activity compared to the thick ones, which are more hypoxic. A good predictor of the morphological features of thrombus has thus potential clinical utility since it could help differentiating among lesions that are at a higher/lower risks of developing a thrombus and within the same lesion, among regions of the wall that are more likely to harbor a thin thrombus, a thick one, or no thrombus at all.

Hemodynamics is likely an important player in the formation of ILTs. Blood flow is essential for the transport of components feeding and regulating the dynamic balance between the coagulation cascade and the fibrinolytic process, and exerts friction forces that shape evolving thrombi into their configurations. While computational models can now exploit high-resolution medical images regularly acquired on patients affected by AAA to investigate in fine detail the disturbed hemodynamics, significant challenges are still posed by modeling the complexities of thrombus formation in vivo. At best of the authors' knowledge, no modeling effort has been able to reproduce thrombus configurations as visible in actual CT scans of patients, yet.

In this study rather than attempting to capture all the molecular events that lead to the full formation of a thrombus, we mainly investigate how hemodynamic conditions govern thrombus shaping during propagation by means of complex blood flow transport and erosion patterns. Relying on a phenomenological description of the deposition event, we propose a strategy based on a shape optimization algorithm to predict the final thrombus configuration without requiring full large scale simulations encompassing the several minutes needed for the coagulation to complete and for the thrombus to stabilize. Given the prohibitive computational cost of such simulations, our method is particularly appealing whereas predicting the post-deposition lumen/thrombus morphology is of interest.

METHODS

De-identified CTA scans (n=6) of patients affected by AAAs harboring a thin thrombus (max thickness h_{max} < 1.5 cm) were processed with semi-automated segmentation algorithms to extract lumen boundaries of the abdominal aorta and its main branches. Our models included also large portions of the upstream and downstream vasculature, going from the celiac trunk down to the first bifurcation of the iliac arteries. For each scan we constructed two computational domains: One included only the blood-filled lumen (L), and the other one extended also to the ILT (L+T). Computational fluid dynamic simulations were run for each patient on both geometries using a customized version of the open-source software SimVascular, which employs a stabilized finite element method to compute high resolution time-varying hemodynamic fields characterizing each lesion. Average boundary conditions extracted from literature data were used at the suprarenal inlet, where we imposed a Womersley velocity profile, and at the outlets, where we weakly imposed Windkessel boundary conditions.

Lagrangian particle tracking was used to enrich the Eulerian results output by SimVascular with a macroscopic correlate of shear-induced platelet activation (Figure 1). Following a procedure described in a recent work of ours [3], we combined particle tracking results with wall-shear stress metrics to compute the Thrombus Formation Potential (TFP) index, which is representative of hemodynamic-

Copyright 2016 The Organizing Committee for the 2016 Summer Biomechanics, Bioengineering and Biotransport Conference

induced thrombogenicity on intact endothelium. TFP highlights regions of the aneurysmal wall that might be exposed at the same time to low and oscillatory flow conditions (which are known to reduce the anti-thrombogenic action of the endothelium), and to pro-coagulant agents (e.g. activated platelets) transported by the bulk flow. The concomitance of such events does not seem occur in healthy regions of the vasculature, and it could be one of the reason behind thrombus formation in aneurysms.

Recent findings suggest that other hemodynamic features, specifically low and non-oscillatory flow might contribute (and correlate) to thrombus deposition in growing lesions [4-6]. We thus defined a novel phenomenological index, the Thrombus Deposition Potential or TDP, to describe flow conditions promoting the propagation of thrombus from initiation areas marked by high TFP. In addition to standard WSS-based metrics, the definition of TDP takes into account also wall concentration profiles of plasma-borne proteins such as fibrinogen (FBG). Solving in post-processing an advection-diffusion problem for ten cardiac cycles, we were able, in fact, to differentially locate areas of the aneurysmal wall that were more/less exposed to advection from the upstream bulk flow. We thus considered several definitions for TDP,

$$TDP = f(OSI, TAWSS, [FBG]) \quad (1)$$

where OSI is the oscillatory shear index, TAWSS is time averaged wall shear stress, and [FBG] is fibrinogen concentration.

To choose the best formulation, we then used TDP as the main driver of an optimization procedure aimed at predicting lumen shape at the end of a deposition event. After parameterization of the patient-specific geometries via radial basis functions, we used a derivative-free optimization method based on orthoMADS and the Surrogate Management Framework (SMF) [7] to seek for lumen configurations that minimized TDP absolute values. Assuming that small depositions of thrombus would not affect significantly far-field hemodynamics, we developed a novel strategy to build accurate and continuously updated surrogates of TDP behavior on the parameter space. Specifically, full-scale simulations run on pre-deposition domains were used as a source of boundary conditions for much smaller coupled-simulations focused on updating the near-thrombus hemodynamics. The coupling was performed via a custom solver developed in FEniCS that was able to efficiently read in parallel the results of the large-scale simulations. This allowed us to effectively exploit the flexibility that the SMF gives to users to accelerate convergence towards an optimum.

Outputs of the procedure were predicted post-deposition lumen shapes that we compared to actual geometries segmented from the CT scans.

RESULTS

Comparative analyses of the hemodynamics in the L and L+T domains presented several differences in terms of WSS-based index values. The deposition of thrombus induced, as expected, a general increase in TAWSS, with effects more pronounced in regions where thrombus was thicker. Variations in the OSI index were less coherent, but the index turned out to be very sensitive to changes in shape. Absolute variations were in fact consistent. Finally, [FBG] showed a general tendency towards higher wall concentrations in post-deposition geometries, likely because in these cases the lumen wall was closer to the center of the vessel and therefore more exposed to central flow.

Our approach of combining the TFP and TDP indices proved to be able of successfully locating thrombogenic areas in all the aneurysms that we considered. Despite significant differences in terms of portion of the aneurysmal wall harboring the ILT (e.g. posterior vs anterior side of the AAA), high TDP areas always intersected with regions covered by actual thrombi.

Shape optimization analyses were used to predict final thrombus thickness distributions. Satisfying matches were observed for all the aneurysms, but they were less accurate for lesions harboring thicker thrombi.

DISCUSSION

The primary goal of this work was to develop and validate a phenomenological approach aimed at investigating the changes in hemodynamics that occur during thrombus deposition. ILTs are never fully occlusive suggesting that certain hemodynamic conditions might consistently occur to arrest thrombus growth. We thus sought for a phenomenological metric that could well describe such hemodynamic features combining popular WSS-based indices and other macroscopic descriptions of fluid transport. That is, in contrast to other studies, we did not try to account for all the players intervening in the coagulation cascade, but we opted for simpler metrics better suited to represent the scarce data typically available about patient-specific ILT formation. Our newly proposed TDP index is able to correctly locate areas prone to thrombus propagation. Moreover, when combined to a customized shape optimization procedure, it can be effectively used as a predictor of the final thrombus shape. The reduced number of cardiac cycles that need to be simulated at full-scale to obtain realistic thrombus configurations overcomes many of the limits that have been encountered in modeling intraluminal thrombus formation so far.

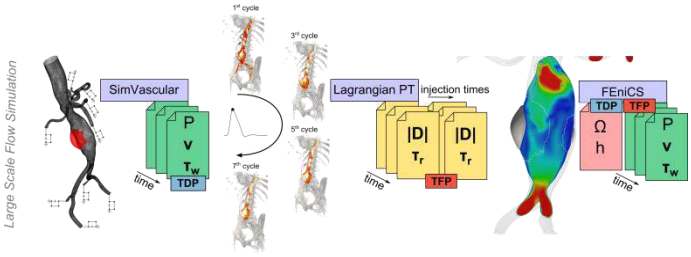

Figure 1: Full characterization of the hemodynamic forces leading to thrombus growth and arrest. Standard CFD computations run in SimVascular were complemented by Lagrangian Particle Tracking analyses. A lumen shape optimization procedure was then used to efficiently explore possible post-deposition configurations.

ACKNOWLEDGEMENTS

This research is funded, in part, by grants from the NIH (R01 HL105297, R01 HL086418, and U01 HL116323) as well as grants from the National Science Foundation that partially funded the acquisition of the computational facilities of the Yale Center for Research Computing (CNS 08-21132) and funded the Extreme Science and Engineering Discovery Environment (XSEDE, ACI-1053575).

REFERENCES

[1] Wilson, JS et al., *J Biomech Eng,* 135(2), 021011, 2013.
[2] Tong, J, Holzapfel GA, *Ann Biomed Eng*, 43(7):1488–1501, 2015.
[3] Di Achille, P. et al., *Proc R Soc A*, 470(2172)163, 2014.
[4] O'Rourke, MJ et al., *Proc Inst Mech Eng H*, 226:548–564, 2012.
[5] Arzani, A et al., *AJP Heart,* 307(12):H1786–H1795, 2014.
[6] Zambrano, BA et al., *Ann Biomed Eng*, online preprint Oct. 2015.
[7] Marsden AL, *Annu Rev Fluid Mech*, 46(1):519–546, 2014.

Copyright 2016 The Organizing Committee for the 2016 Summer Biomechanics, Bioengineering and Biotransport Conference

SB^{3}C2016
Summer Biomechanics, Bioengineering and Biotransport Conference
June 29 –July 2, National Harbor, MD, USA
SB^{3}C2016-940

IMAGING AND QUANTIFYING THE 3D COLLAGEN ARCHITECTURE IN ATHEROSCLEROTIC PLAQUES

Ali C. Akyildiz (1), Lambert Speelman (1), Chen-Ket Chai (2), Cees Oomens (2), Gustav Strijkers (3), Frank Gijsen (1)

(1) Dept. of Biomedical Engineering
Erasmus MC
Rotterdam, the Netherlands

(2) Dept. of Biomedical Engineering
Eindhoven University of Technology
Eindhoven, the Netherlands

(3) Dept. of Biomedical Engineering & Physics
University of Amsterdam
Amsterdam, the Netherlands

INTRODUCTION

Stroke is one of the leading causes of morbidity and mortality in the Western society [1]. The majority of the acute ischemic stroke events are due to the rupture of an atherosclerotic plaque in a carotid artery. Atherosclerosis is a systemic disease of arterial vasculature, primarily characterized by lipid accumulation in arterial walls. The lesion sites are referred to as plaques. Rupture of a plaque triggers thrombus formation in the lumen of the artery, which leads to complete or partial occlusion of the lumen and hence, ischemia downstream of the occlusion site.

Not all atherosclerotic plaques rupture. To judge correctly which plaque to treat surgically, it is of great importance to predict the rupture risk of plaques. As plaque rupture is a mechanical failure, biomechanical models might aid in rupture risk assessment. To obtain reliable results from the biomechanical models, accurate mechanical properties of plaques have to be used in the models.

Atherosclerotic plaques are complex composite structures. Mechanically important structural components of plaques are collagen and elastin fibers, lipid, calcium and smooth muscle cells. Considering the amount and the stiffness, collagen fibers are anticipated to be the major load bearing elements [2]. Hence, quantification of the collagen architecture in atherosclerotic plaques is essential for high-fidelity biomechanical models.

The available data in literature on the collagen distribution in atherosclerotic plaques is incomplete and does not provide the necessary data to feed the 3D biomechanical plaque models. The aim of the current study is to image the 3D collagen architecture in atherosclerotic carotid plaques using diffusion tensor imaging (DTI) and to quantify local collagen fiber orientation.

METHODS

Plaque samples and preperation

Nine carotid plaque samples causing more than 70% stenosis were obtained from patients (all male, age 55-80 years) scheduled for endarterectomy. The samples were snap-frozen and stored at -80º C. After slow thawing, the samples were prepared for DTI by placing them in a cryovial and embedding in 4% agarose, following a previously described protocol [3].

Diffusion tensor imaging (DTI)

DTI was performed with a 9.4 T horizontal MRI scanner (Bruker, Etlingen, Germany) in combination with a dedicated 35 mm diameter quadrature birdcage radiofrequency (RF) coil. DTI was done with a 3D spin echo sequence with unipolar diffusion sensitizing pulsed field gradients placed symmetrically around the 180º RF pulse. Sequence parameter were as follows: echo time=27 ms, repetition time=1000ms, number of averages=1, field of view=30x30x30 mm^3, acquisition matrix=256x96x96, reconstruction matrix=256x256x256, 10 diffusion directions with diffusion weighing b value=1500 s/mm^2. Total acquisition time was about 28 hours. An in-house developed software (http://bmia.bmt.tue.nl/software/viste/) was used to construct and visualize the fiber collagen network from raw DTI data.

Histology

After DTI, agarose medium, in which the plaques were embedded, was removed and plaques were sliced using a crytome to obtain longitudinal cross-sections for histology. Picro Sirius Red staining was applied on the cross-sections to visualize the collagen fibers for qualitative validation of DTI results.

Copyright 2016 The Organizing Committee for the 2016 Summer Biomechanics, Bioengineering and Biotransport Conference

Quantitative assessment of main collagen fiber direction

DTI data acquired contains x-, y-, and z-components of local collagen fiber directions in plaques with respect to a reference Cartesian coordinate system. An in-house developed MATLAB (version R2013a) script was used to convert the data into cylindrical coordinates (radial, circumferential or longitudinal) and to determine the main principal cylindrical direction of the collagen fibers. The radial and circumferential directions were defined with respect to the center of the lumen on the corresponding transversal cross-section. The longitudinal direction in the cylindrical coordinate system coincides with the z-direction of the original Cartesian coordinate system.

RESULTS

Nine human plaque samples from carotid endartaractomy surgeries were obtained and imaged with DTI successfully. DTI data of four out of nine plaques was analysed and main alignment direction of the collagen fibers was determined (Figure 1). The two leftmost samples in figure 1 show a highly organized collagen structure, with a dominant alignment in the longitudinal direction at the luminal side, and in the circumferential direction at the abluminal side. The two rightmost samples are less structured, but longitudinal alignment at the luminal side can still be discerned.

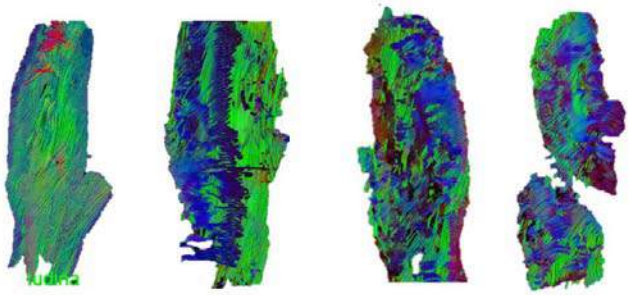

Figure 1: Collagen fiber distribution obtained from DTI in four carotid plaque samples

One sample was further analysed and examined histologically. A representative histological longitudinal cross-section is shown in figure 2. The histology image reveals the presence of a lipid core with a thick fibrous cap (see the zoom-in box in the figure). The collagen fibres clearly demonstrate a longitudinal alignment at the luminal side, qualitatively confirming the findings from DTI.

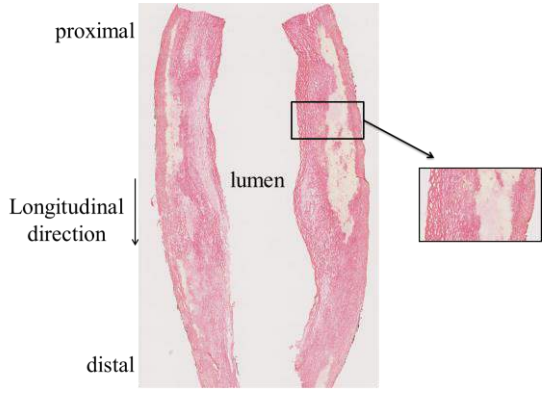

Figure 2: Picro-Sirius Red staining on a longitudinal plaque cross-section

Quantitative assessment of the collagen distribution supported the observations from raw DTI data and histological examinations. The most dominant fiber directions were the longitudinal direction (48% of the total volume) and the circumferential direction (45%). Comparably, the radial alignment of collagen fibers was minimal (6%) (see figure 3). The plaque cross-sections of less advanced stage of atherosclerosis (e.g. bottom two transversal cross-sections in figure 3) showed a clear longitudinal alignment of collagen fibers at the luminal side and circumferential alignment at the abluminal side. For the cross-sections where plaque was larger, this distinction was less clear and in some regions the radial direction was the dominant fiber direction.

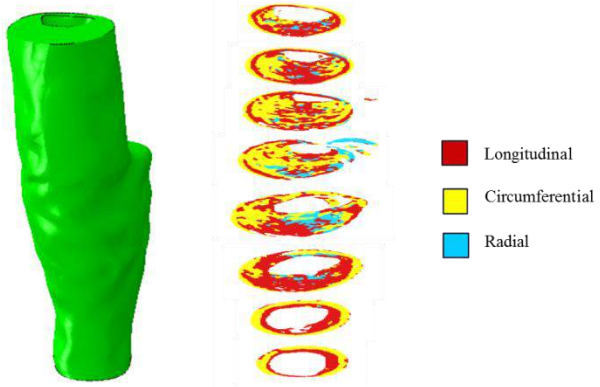

Figure 3: Reconstructed plaque geometry (left) and main direction of collagen fibers on selected transversal cross-sections (right)

DISCUSSION

The presence of collagen fibers in atherosclerotic plaques was demonstrated previously by histological studies, however, as histology provides 2D data, the 3D architecture of the collagen network was not established before. The current study is the first one that images the collagen network in atherosclerotic plaques in 3D.

The findings demonstrated both structured and unstructured fiber alignment in plaques. Hence, isotropy and homogeneity assumptions for plaque material in the biomechanical models might be unrealistic. Longitudinal fiber alignment was observed frequently and this finding was confirmed by histology. This implies that using 2D biomechanical models probably lead to oversimplification and 3D models should be preferred for reliable results. In healthy tissues, under physiological conditions, collagen is aligned in the direction of the maximum principal stress/strain. It seems unlikely that the longitudinal direction is the main stress/strain direction in atherosclerotic plaques. So, it is unclear why collagen is oriented in the longitudinal direction.

In the future, we will analyze the DTI data collected from the other plaque specimens to see whether the current findings are also supported by the rest of the data. Moreover, we will create 3D finite element models of the imaged carotid plaques to investigate the influence of anisotropic and heterogenous mechanical behavior of plaque material on plaque stresses.

ACKNOWLEDGEMENTS

This study is supported by "De Stichting voor de Technische Wetenschappen (STW)".

REFERENCES

[1] Nichols, M et al., *European Cardiovascular Disease Statistics - 2012 Edition*
[2] Akyildiz, AC et al., *J. Biomech.* 47, 773–783 (2014).
[3] Ghazanfari, S et al., *Biochem. Biophys. Res. Commun.* 426, 54–58 (2012).

Copyright 2016 The Organizing Committee for the 2016 Summer Biomechanics, Bioengineering and Biotransport Conference

SB^{3}C2016
Summer Biomechanics, Bioengineering and Biotransport Conference
June 29 –July 2, National Harbor, MD, USA
SB^{3}C2016-941

DTI VOXEL-WISE ANALYSIS OF MILD TBI IN NEONATAL PIGS FOLLOWING NON-IMPACT HEAD ROTATION

Boston C. Terry (1), Gregory G. Scott (2), Osama Abdullah (1), Brittany Coats (2)

(1) Biomedical Engineering Department
University of Utah
Salt Lake City, Utah, USA

(2) Mechanical Engineering Department
University of Utah
Salt Lake City, Utah, USA

INTRODUCTION

Traumatic brain injury (TBI) is a leading cause of death and disability [1]. In mild TBI, the extent of axonal injury damage is challenging to identify. Diffusion tensor imaging (DTI) is commonly used in brain injury research to identify axonal injury [2], and measurements of fractional anisotropy or axial diffusivity are typically averaged over a region of interest where the injury is suspected. However, detection of subtle differences in mild TBI using this method is not feasible as non-injured areas may be included in the averaging process.

We've previously developed a neonatal pig model to simulate pediatric mild TBI induced by non-impact repetitive angular accelerations with and without an added thoracic compression that mimics the physiological increase in intracranial pressure and cerebral blood volume during crying. This model results in various levels of minor axonal injury on histopathology [3].

To determine if this axonal injury can be detected with DTI, we developed an image analysis routine based on one presented by Liu et al. in humans [4]. This routine registered pre- and post-injury images into a single atlas space and statistically compared diffusion metrics for each voxel. Evaluating all locations of the brain increases chances of identifying injury, and improves the region of interest selection for future analysis, making the evaluation of DTI metrics for predicting mild TBI much more effective and accurate.

METHODS

All studies were performed in accordance and approval of the University of Utah Institutional Animal Care and Use Committee. Diffusion weighted images of anesthetized piglets (3-5 days old) were acquired with a 7T Bruker Biospin MRI system using a single-shot echo planar image sequence before and after a repetitive, non-impact inertial head rotation. The head rotation was induced by attaching the anesthetized animal's snout to the biteplate of a mechanical device, and rotating the head in the horizontal plane through a 100° arc at a speed of 45 rad/s. The motion was repeated in both directions at a frequency of 3 Hz for a total duration of 20 seconds.

Animals were divided into three groups. Group 1 (n=4) experienced the cyclic head rotation, was allowed to recover, and then imaged 24 hours post-injury. Groups 2 (n=3) and 3 (n=2) experienced the cyclic head rotation plus had the additional thoracic compression which was applied in increasing increments of 20 mmHg until an increase of CBV and ICP were similar to those found during intense infant crying [5][6]. The compression was applied immediately before rotation. Group 2 was imaged immediately post-injury (acute) and Group 3 was imaged 24 hours post-injury. All animals were imaged prior to injury to provide baseline controls for comparison. During each imaging session, diffusion was measured along 64 independent directions in 2D coronal slices taken every 2 mm (n=15).

For each animal, a non-diffusion weighted image was segmented to create a mask that excluded the skull and extracranial tissues. Diffusion tensors were estimated using a weighted least squares method. Tensor images were then registered using ANTs software [7] into a single atlas space by application of an affine and diffeomorphic registration.

Copyright 2016 The Organizing Committee for the 2016 Summer Biomechanics, Bioengineering and Biotransport Conference

Scalar diffusion metric images, which included fractional anisotropy (FA), mean diffusivity (MD), axial diffusivity (AD), and radial diffusivity (RD) were computed, and a 3x3x3 Gaussian filter was applied to reduce possible registration misalignments. A paired one-tail t-test was performed on each of the spatially corresponding voxels in the baseline and post-injury images, and a p-value map was created for each of the scalar image sets. To reduce the number of false positives potentially arising from registration misalignment and noise, two thresholds were applied. The first used a cross-correlation metric [8] to compute an index of similarity based on the local 2D cross-correlation at each voxel. The second removed any cluster with less than three contiguous voxels with a p-value < 0.05.

To create a numerical means of comparing the levels of significance of post-injury images, a weighted integral measure (WIM) was create for each image (Eq. 1). The area of each significant voxel in a cluster ($area_{ij}$) was divided by the p-value for that voxel ($p\text{-}value_{ij}$) and summed across the cluster. This cluster metric was then summed over all the clusters to create a WIM measurement for each image set.

$$WIM = \sum_{j=1}^{m\ clusters} \sum_{i=1}^{n\ voxels\ per\ cluster} \frac{area_{ij}}{p\text{-}value_{ij}} \qquad (1)$$

To address the statistical problem of multiple comparisons, nonparametric permutation tests were used [9]. Under the null hypothesis, pre- and post-injury image sets can be freely exchanged if the datasets are equal. Therefore, image sets were randomly assigned to either set and statistical tests were performed again. 2^N-1 permutations were performed for each group (N=# image sets available). If the WIM from the real data set was higher than the WIM of all permutated data sets, the statistical significance of that image set was considered real.

RESULTS and DISCUSSION

Significant differences from baseline were detected in all Groups. The average ± SD of the WIM for each group is shown in Figure 1. A higher value indicates that the image set had a larger statistical significance compared to baseline either by a decrease in the p-value, a greater number of clusters, or a larger cluster size. WIM levels in Group 1 were lower than in Groups 2 and 3, suggesting that there is overall less injury in Group 1 compared to Groups 2 and 3. This makes sense given that Groups 2 and 3 had increased ICP and CBV prior to the head rotation. Significant clusters in Group 1 were observed primarily in the internal capsule and corona radiata, which correlate well with locations of positive βAPP staining found in our previous study [4].

Groups 2 and 3, which had the same injury induced, had different DTI responses depending on the timing of imaging. Acute imaging (Group 2) resulted in significant increases in MD and decreases in AD, while longer term imaging (24 hours in Group 3) resulted in greater significant decreases in FA and increases in RD. This data strongly suggests that measurements of DTI metrics for mild TBI will be highly dependent on the time post-injury, and evaluating only one metric may not capture injury. Histology on the brains from this study are currently being processed to correlate positive clusters to axonal injury.

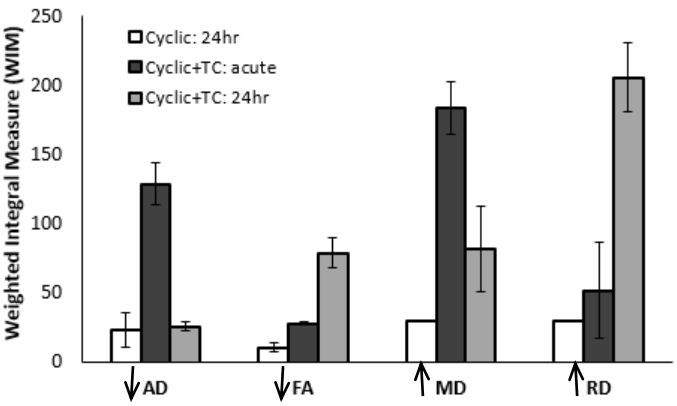

FIGURE 1: Weighted integral measure (WIM) of each diffusion metric for each injury group. Arrow indicates directionality of statistical test.

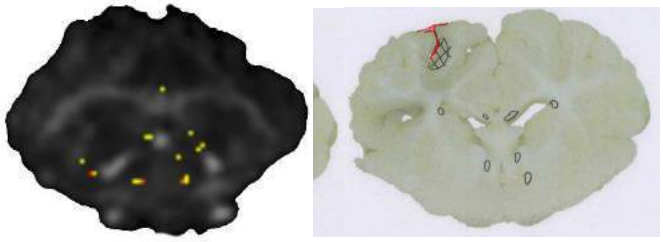

FIGURE 2: P-value map from Group 1 overlaid on an MD image (left). Red: p<0.005; yellow: p<0.01. Axonal injury marked by βAPP (right; open circles) correlated well with locations of significant clusters.

CONCLUSION

DTI is a powerful tool for identifying changes in axonal structure following TBI, but using standard methods of analysis, such as selecting regions of interest and averaging, may not capture subtle changes to axonal architecture. We have created a voxel-wise statistical comparison approach that identified significant differences in DTI measures of axonal injury, dependent on the timing of the imaging. While the results need to be interpreted carefully due to the small sample sizes, there is evidence of axonal injury in each image set, with increased levels of axonal injury due increased ICP and CBV prior to mechanical loading.

AKNOWLEDGEMENTS

We would like to thank the Primary Children's Medical Center Foundation for financially supporting this research. We also thank the University of Utah small animal imaging lab.

REFERENCES

[1] Duhaime, A et al., *N. Engl. J. Med,* 338, 1822–1829, 1998.
[2] MacDonald, C et al,. *Exp Neurol*. 205, 116-131. 2007
[3] Liu, Z et al,. *Proc IEEE Int Symp Biomed Imaging.* 2009.
[4] Coats, B et al., *NNS Meeting. 2011*
[5] Stow P et al., *Br J Anaest.* 60(2):167-70.
[6] Brazy, J., *J Pediatr.* 112(3): 457-61.
[7] Avants, B et al,. *Insight J.* 2009
[8] Avants, B et al,. *Medical Image Analysis,* 12: 30-31. 2008.
[9] Nichols, T et al,. *Hum. Brain Mapping*, 15:1-25. 2001.

Copyright 2016 The Organizing Committee for the 2016 Summer Biomechanics, Bioengineering and Biotransport Conference

SB^{3}C2016
Summer Biomechanics, Bioengineering and Biotransport Conference
June 29 –July 2, National Harbor, MD, USA
SB³C2016-942

SWELLING OF COLLAGEN-HYALURONIC ACID CO-GELS: AN *IN VITRO* RESIDUAL STRESS MODEL

David S. Nedrelow (1), Victor K. Lai (2), Spencer P. Lake (3), Bumjun Kim (1), Emily M. Weiss (1), Robert T. Tranquillo (1, 4), and Victor H. Barocas (1)

(1) Biomedical Engineering
University of Minnesota
Minneapolis, MN, USA

(2) Chemical Engineering
University of Minnesota
Duluth, MN, USA

(3) Mechanical Engineering &
Materials Science
Washington University
St. Louis, MO, USA

(4) Chemical Engineering and
Materials Science
University of Minnesota
Minneapolis, MN, USA

INTRODUCTION

Tissue-equivalents (TEs), simple model tissues with tunable properties, have been used to explore many features of biological soft tissues, including how structural and compositional properties affect mechanical function. To the best of our knowledge, one aspect not previously captured in such formulations is residual stress due to interactions among components with different stress-free states, which has an important functional role in many biological tissues [1, 2]. To create a pre-stressed model system, co-gels were fabricated from a combination of hyaluronic acid (HA) and reconstituted Type-I collagen (Col). When placed in solutions of varying osmolarity, HA-Col co-gels swell as the HA imbibes water, which in turn stretches (and stresses) the collagen network. In this way, co-gels with residual stress (i.e., collagen fibers in tension and HA in compression) were fabricated and evaluated in terms of their mechanical response both experimentally and through a fibril network + non-fibrillar interstitial matrix computational model.

METHODS

Fabrication: Three groups of gels were fabricated: (1) Col, (2) HA, and (3) HA-Col co-gels. For collagen, reconstituted Type-I rat tail collagen (Invitrogen, Carlsbad, CA) was mixed as described previously with 1M HEPES, 1M NaOH, 10X MEM, FBS, Penicillin/Streptomycin, Fungizone, and L-Glutamine, and diluted with deionized, distilled water to a final concentration of 1 mg/mL [3]. HA samples were prepared by mixing thiol-modified HA (Biotime, Inc., Alameda, CA) with a polyethylene glycol based thiol-reactive cross-linker to form a 0.67% (w/v) HA gel (240 +/- 20 kDa). 10-µL aliquots of each gel type were then cast in silicone oil and incubated at 37°C for 24 hours to create spheres of ~2.5 mm diameter, similar to a previously reported procedure [4].

Experiments: After incubation, gel spheres were placed in solutions of 0, 1, 2, 3, 4, 5, 10, 15, 25, 50, 75 or 100%, 1x phosphate buffered saline (PBS; n = 3-4 per solution) for 2 hours. Sphere diameters were either measured by a custom Matlab routine (DOI 10.5281/zenodo.44285) or, for those gels that were highly translucent, measured manually.

Analysis: The fixed-charge density of HA before swelling, c_F^0, was estimated by

$$c_F{}^0 = \frac{|z_{HA}|C_{HA}}{MW_{HA}} \quad (1)$$

where z_{HA} was the charge per HA monomer, C_{HA} was the mass concentration of HA, and MW_{HA} was the molecular weight of an HA disaccharide monomer. Since the HA gels were dilute (0.667% w/v), the fixed charge density after swelling, c_F, was calculated by

$$c_F = c_F{}^0 \left(\frac{D_0}{D}\right)^3 \quad (2)$$

where D_0 and D were the diameters of the HA sphere before and after swelling, respectively. For an HA gel immersed in a solution dominated by monovalent ions (e.g., NaCl) the Donnan osmotic pressure, π_{Donnan}, can be computed as

$$\pi_{Donnan} = RT\left(\sqrt{c_F{}^2 + 4c^{*2}} - 2c^*\right) \quad (3)$$

where R is the universal gas constant, T is the absolute temperature of the system, and c^* is the Na^+ concentration in the external solution, assuming complete ionization and ideal solution behavior [5]. A swollen HA-Col co-gel at equilibrium, under the assumption that the co-gel obeys constrained mixture theory [6], satisfies the following stress balance:

$$\sigma_{HA} + \sigma_{Col} - \pi_{Donnan} = 0 \quad (5)$$

Copyright 2016 The Organizing Committee for the 2016 Summer Biomechanics, Bioengineering and Biotransport Conference

where σ_{HA} is the Cauchy stress in HA estimated from swollen pure HA, σ_{Col} is the Cauchy stress in the collagen network, and π_{Donnan} is calculated using Eq. 1-3.

Experimental results for the collagen pre-stress, σ_{Col}, were compared to computational model predictions obtained from our microscale network model as described previously [7-9]. The mechanical response of each fiber within the network was governed by the non-linear force-strain constitutive equation:

$$F = \frac{A}{B}[\exp(BE_f) - 1] \quad (7)$$

where F is the force exerted by the individual fiber, and A and B are material parameters that characterize the mechanical behavior of the fiber and E_f is the Green strain of each fiber. As the RVE is deformed, the average Cauchy stress in the network, $\langle\sigma_{ij}\rangle$, is given by the summation over all boundary crosslinks

$$\langle\sigma_{ij}\rangle = \frac{1}{V}\sum x_i F_j \quad (8)$$

Where V is the volume of the RVE, x_i is the *i-th* component of the nodal position of a boundary crosslink, and F_j is the *j-th* component of the fiber force exerted on that boundary crosslink. The RVE is scaled to the macroscopic scale to allow computation of the macroscopic-scale stress. From SEM images of acellular collagen gels, an average collagen fiber diameter of 50nm was used.

To obtain material parameters A and B for pure collagen gels, simulations of uniaxial tensile tests on five Voronoi RVE networks were performed, and the stress-strain curves were fitted to previously-obtained experimental tensile test data [8]. Using the fitted parameters (A = 30 nN, B = 4) as inputs for the new computational model, dilatational stretches of the five Voronoi networks were performed to simulate swelling and then compared with σ_{Col} from the swelling experiments.

RESULTS

The results for swelling experiments are shown in figure 1. Swelling occurred only in the pure HA and HA-Col gels. Pure collagen gels did not swell appreciably over 1 hour, and no further data were logged. The pure HA gel, in contrast, swelled the fastest and to the highest degree, as demonstrated by the steep slope and large equilibrium swelling ratio. The HA-col co-gel sphere also exhibited swelling, but not as rapidly as, nor to as great an extent as the pure HA gel.

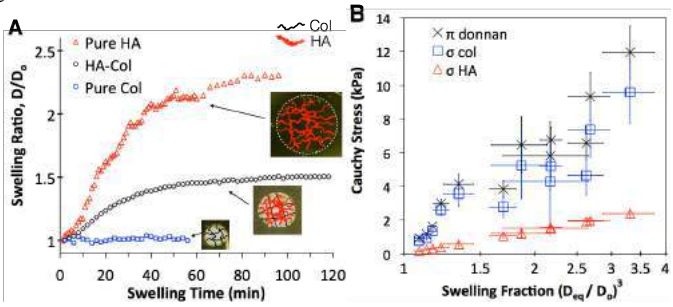

Figure 1. A) Representative swelling behavior exhibited by single-component gel or co-gel spheres immersed in 0%vol PBS. B) The relative magnitude of each stress contribution during swelling in various PBS concentrations (100% is furthest left, and 0% is furthest right)

The stress induced in the collagen network increased nonlinearly with swelling and was the dominant stress resisting the Donnan pressure at large swelling ratios (Fig 1B). Dilatational stretch simulations of pure collagen gels generated collagen stresses similar to those observed in HA-Col co-gel swelling experiments (Fig. 2). It is noteworthy that the curve in Fig. 2 is a prediction based on uniaxial experiments, not a curve fit.

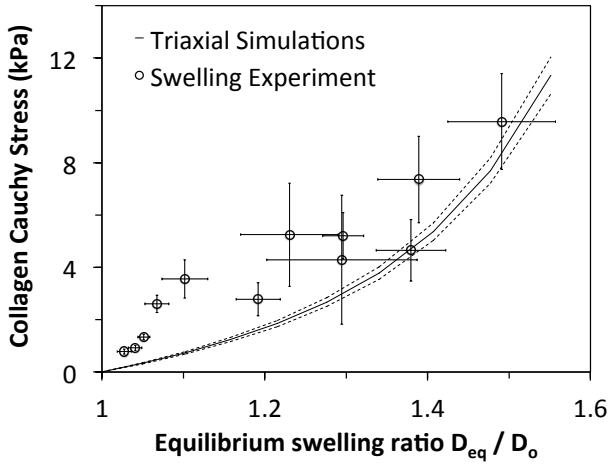

Figure 2. Triaxial simulation with 95% confidence interval bounded by dotted lines. Data points are σ_{Col} calculated from experimental swelling. Both experimental and simulated stretches are presented along one dimension.

DISCUSSION

The simple, *in vitro* HA-Col co-gel model is a candidate system to approximate the residual stresses commonly observed in living tissues. Independent estimates of the collagen stress based on (1) swelling experiments and (2) a computational network model based on uniaxial extension of pure Col gels showed good agreement over the experimental range (Fig 2). The monomer charge, z_{HA}, was assumed to be one, although it is likely to be less due to the larger dissociation constant of thiol monomers, which could improve the agreement between experiment and simulation. Differences between simulation and experiment could be due to HA restricting the conformational space available to collagen network fibers, particularly in the low strain regime, suggesting interaction between the HA and collagen which would further drive the system toward affinity. Such a response was observed previously between collagen-agarose co-gels [10], where the measured strength of collagen fibril alignment (retardation) during uniaxial loading was lessened in the presence of agarose, representing inhibition of the collagen network's microstructural reorganization. It was previously suggested that low concentration HA in HA-Col co-gels does not affect the network structure of collagen [11]. No microstructure characterizations were carried out in this study, but the use of pure HA to estimate σ_{HA} in co-gels, together with good agreement of the computational network simulation implies that interactions between HA and collagen in the co-gel may have negligible mechanical consequences in swelling.

ACKNOWLEDGEMENTS

This work was supported by NIH grant [RO1 EB005813]. We extend our gratitude to the University of Minnesota Supercomputing Institute for making the necessary resources available to complete this study's simulations.

REFERENCES

[1] Lanir Y. *J Biomech Eng*, 131(4):044506, 2009. [2] Ruberti J, Sokoloff J. *J Biomech Eng*, 133(10):104504, 2011. [3] Lai VK et al., *Acta Biomater*. 8(11):4031, 2012. [4] Moon AG, Tranquillo RT, *AIChE J*., 39(1):163, 1993. [5] Donnan FG, *Chem Rev*. 1(1):73, 1924. [6] Barocas VH, Tranquillo RT, *Springer*; 1994. [7] Sander EA, et al., *PNAS*, 106(42):17675, 2009. [8] Lai VK, et al., *J Biomech Eng*, 134(1):011004, 2012. [9] Lake SP et al., *Ann Biomed Eng*, 40(10):2111, 2012. [10] Lake SP, Barocas VH. *Ann Biomed Eng*, 39(7):1891, 2011. [11] Kreger S, Voytik-Harbin S, *Matrix Biol*, 28(6):336, 2009.

SB³C2016
Summer Biomechanics, Bioengineering and Biotransport Conference
June 29 –July 2, National Harbor, MD, USA
SB³C2016-943

A Biomimetic Core-Shell Platform for Miniaturized 3D Cell and Tissue Engineering

Pranay Agarwal (1), Jung K. Choi (1), Haishui Huang (2), Shuting Zhao (1), Jenna Dumbleton (1), Xiaoming He (1,3)

(1) Department of Biomedical Engineering
The Ohio State University
Columbus, Ohio, USA

(2) Department of Mechanical Engineering
The Ohio State University
Columbus, Ohio, USA

(3) Comprehensive Cancer Center
The Ohio State University
Columbus, Ohio, USA

INTRODUCTION

Cells and tissues in their native microenvironment respond to stimuli such as mechanical shear/stress, extracellular matrix (ECM) topography, and rigidity which subsequently determine their morphology, morphology, differentiation, proliferation, development, and function.[1] A number of methods have been developed to control the cell and tissue microenvironment *in vitro*, by patterning adhesive proteins/peptides (e.g., fibronectin/RGD) on two-dimensional (2D) substrates (glass, plastic, polymers) with different physical and chemical properties.[2] Although 2D cultures have proven remarkable in understanding cell/tissue biology, they differ substantially from the *in vivo* microenvironment of most cells/tissues where they are intricately associated with different adherent ligands present on three-dimensional (3D) ECM. Current 3D culture technology mostly require chemical treatment or ultraviolet radiation to crosslink the polymers into insoluble ECM, which may cause damage to the embedded cells/tissues. Moreover, most of the 3D ECMs are macroscale (at least millimeters) scaffolds where the embedded cells/tissues may suffer from deprivation of oxygen and nutrients without the use of complex perfusion/bioreactor systems to maintain cell survival.[2] Here, we describe a method to encapsulate cells/tissues in the collagen ECM of biomimetic microcapsules with an alginate hydrogel shell, which allows precise control of the microenvironment to modulate the cell/tissue proliferation and development. Alginate was used due to its excellent biocompatibility and reversible gelation with divalent cations such as Ca^{2+} or Ba^{2+} under gentle conditions. Further, alginate shell acts as an provides sufficient mechanical strength/structural support to maintain the integrity of the core collagen ECM. Moreover, this biomimetic miniaturized 3D platform 1) ensures effective transport of regulatory molecules (oxygen, nutrients, and cytokines), 2) mediates/regulates cell-cell contacts and autocrine/paracrine signals, and 3) enables control of cell-ECM interactions by changing the properties of core ECM. Using the core-shell microcapsule system, we studied the proliferation, differentiation, and development of mouse embryonic stem cells and mouse preantral follicles.

METHODS

To prepare core-shell microcapsules, 3D non-planar microfluidic device in PDMS was fabricated using standard photolithography and soft lithography techniques.[3,4] Microfluidic device consisted of four inlets I1, I2, I3, and I4 to inject mineral oil infused with aqueous calcium chloride solution (Ca^{2+} oil emulsion), sodium alginate solution, ice-cold collagen solution (with or without cells/tissues), and cellulose solution, respectively. At the flow-focusing junction, the alginate (shell) and collagen (core) solutions were pinched off into spherical droplets by the Ca^{2+} oil emulsion as a result of interfacial tension. Alginate in the outer or shell layer of the spherical droplets was further gelled to form hydrogel when flowing in the serpentine channels by Ca^{2+} in the oil emulsion. Following gelation microcapsules were extracted from oil phase to aqueous phase in the extraction channel.. Microcapsules formed for the purpose of this study have a total and core size of 380.9 ± 33.98 μm and 285.05 ± 80.4 μm in diameter, respectively.

Using this technique we changed the structural and mechanical properties of the core ECM by modulating the concentration of collagen from 0.5-5 mg/ml. In some cases, alginate was also added to the core ECM to increase its mechanical stiffness. We measured the viscoelastic properties including both storage (G`, representing elastic effect) and loss (G``, representing viscous effect) modulus of ECMs made of either single component (0.5-5 mg/ml collagen) or two components (a mixture of 5 collagen and 5 mg/ml alginate) to further increase the mechanical stiffness of the core ECM. In this way, we were able to regulate G` between 0.48 Pa and 429.74 Pa and G`` between 1.14 Pa and 68.45 Pa.

Copyright 2016 The Organizing Committee for the 2016 Summer Biomechanics, Bioengineering and Biotransport Conference

RESULTS

We encapsulated mouse embryonic stem cells (mESCs) in the different core ECMs (0.5-3 mg/ml) to investigate their effect on the cell proliferation and differentiation. Collected microcapsules (containing 48 ± 11 cells/microcapsule) were then cultured in stem cell culture medium for up to 10 days. **Figure 1A-F** shows the typical phase contrast and corresponding live/dead staining images of stem cell aggregates formed on day 10 in different collagen ECMs. As it is evident from the images, we observed the formation of a single massive aggregate (313.1 ± 75.8 µm) in the ECM with lower concentration of collagen (0.5 and 1.5 mg/ml) compared to significantly smaller and multiple aggregates (128.1 ± 51.9 µm) in the ECM with higher concentration of collagen (3 mg/ml). The gene expression data shown in Figure 1H indicate that as the adhesion ligand/elastic modulus of the encapsulating ECM increases, the expression of three pluripotency markers (Sox2, Nanog, and Klf2).

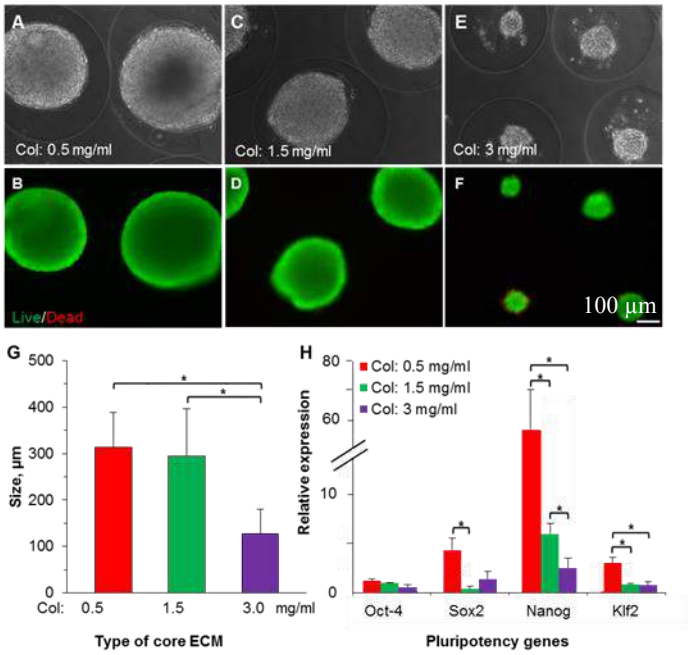

Figure 1: Proliferation of mouse embryonic stem cells in core-shell microcapsules with different ECM properties

We next encapsulated preantral follicles in the core-shell microcapsules to study the effect of ECMs on follicle development. The follicles were encapsulated in three types of core ECMs: 1 mg/ml collagen, 5 mg/ml collagen, and a mixture of 5 mg/ ml collagen and 5 mg/ml alginate. Quantitative data showing proliferation (diameter of follicles) of preantral follicles at 1, 6, 8, and 10 days of culture in the core ECMs **(Figure 2A)** indicates higher proliferation in 5 mg/ml collagen ECM compared to others. The antral follicles obtained after 10 days of culture were typically >300 µm in diameter. Representative DIC and live/dead images showing the morphology and high viability of cells in the encapsulated follicle at day 10 are given in Figure 2B, C, respectively. Figure 2D shows the DIC image of an antral follicle released from the microcapsules together with the oocyte and fluid filled antral cavity in the follicle. We observed 24.4% (11/45) development of preantral follicles to antral stage in 5 mg/ml collagen core ECM (Figure 2E). By contrast, development of follicles to antral stage remarkably decreased to 2.6% (1/38) when the concentration of collagen was lowered to 1 mg/ ml. Interestingly, when the mechanical properties of

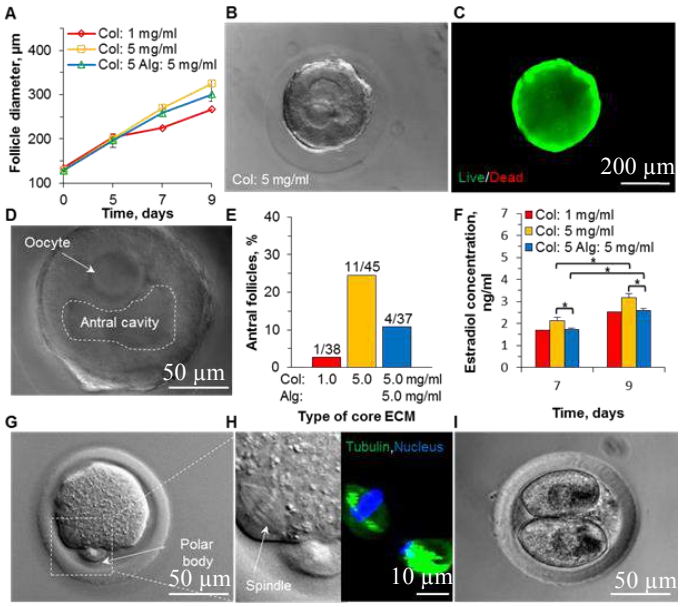

Figure 2: Proliferation and development of preantral follicles in core-shell microcapsules.

the core ECM core was increased while keeping the number of adhesion ligands the same (5 mg/ml collagen by adding 5 mg/ml alginate), we also observed lower (10.8%) development of follicles to the antral. Further, we observed significantly higher production of estradiol in 5 mg/ml collagen ECM compared to other ECMs indicative of better quality of antral follicles. *In vitro* maturation (IVM) of the cumulus-oocyte complex resulted in obtaining 5 (45.45%) Metaphase II (MII) oocytes (Figure 2G-H) . We stained their meiotic spindles and nuclei by tubulin (in microtubules of the spindles) antibody and Hoechst, respectively to show the characterstic chaotic arrangement of tubulin. In addition, 3 out of 5 MII oocytes were used to obtain early embryos by parthenogenetic activation, for which we successfully obtained one 2-cell stage embryo (Figure 2I).[5]

CONCLUSION

We showed the effect of adhesion ligands and stiffness of core matrix in core-shell microcapsules on proliferation, differentiation, and development of mouse embryonic stem cells and mouse ovarian follicles. We anticipate this 3D biomimetic platform will find its potential applications in a variety of fields including but not limited to developmental biology, regenerative medicine, and high throughput drug screening.

ACKNOWLEDGEMENTS

This work was partially supported by grants from NSF (CBET-1033426) and NIH(R01EB012108).

REFERENCES

[1] Engler, A. J. et al, *Cell* 2006, *126*, 677.
[2] Khademhosseini et al, *PNAS* 2006, *103*, 2480.
[3] Choi, J. K. et al, *Biomaterials* 2014, *35*, 5122.
[4] Agarwal, P et al, *Lab on chip* 2013, *13*, 4525.
[5] Agarwal, P et al, *Part Part Sys Char* 2015; 32, 809.

Copyright 2016 The Organizing Committee for the 2016 Summer Biomechanics, Bioengineering and Biotransport Conference

SB^{3}C2016
Summer Biomechanics, Bioengineering and Biotransport Conference
June 29 –July 2, National Harbor, MD, USA
SB^{3}C2016-944

MODIFICATION OF A PARALLEL PLATE FLOW CHAMBER FOR ANALYSIS OF ENDOTHELIAL RESPONSE TO DISTURBED FLOW

Jason M. Sedlak (1), Alisa Morss Clyne (2)

(1) School of Biomedical Engineering, Science & Health Systems
Drexel University
Philadelphia, PA, USA

(2) Department of Mechanical Engineering
Drexel University
Philadelphia, PA, USA

INTRODUCTION

Unidirectional, laminar flow in the straight segments of arteries promotes endothelial cell (EC) survival [1] and production of vasoprotective factors such as nitric oxide and Kruppel-like factor 2 [2,3]. In contrast, recirculating and/or oscillatory flow (collectively, disturbed flow, d-flow) found at arterial bifurcations and sharp turns induces EC turnover [4], compromises barrier function, and promotes an inflammatory EC phenotype [5]. Each of these factors contributes to atherosclerotic plaque formation at points of d-flow [1,3-5].

To date, there are four major methods to study disturbed flow: (1) examine *in vivo* naturally-occurring disturbed flow regions [5,6,7] or modify *in vivo* flow via restrictive cuffs [8-11]; (2) use cone-and-plate devices to rotate the culture dish medium to produce the d-flow pattern, typically using pathological flow waveforms derived from patient data [4,12,13], obstructions in the radial flow path [14], or grooves in the cone [15,18]; (3) modify parallel plate chambers, rectangular chambers with high aspect ratios (length/width:height) typically used for laminar flow, to produce d-flow via step changes [3,17], geometries that induce eddy formation such as a circular flow path [18,19], oscillatory waveforms [7,12], or low shear stress values (~≤0.4 Pa); or (4) custom microfluidic devices that mimic specific physiological geometries such as the impinging flow at the tip of an artery bifurcation [20,21].

Each of these methods to create d-flow has advantages and disadvantages. *In vivo* models provide the most physiologically relevant scenarios, yet conditions cannot be precisely controlled and experiments often prove expensive. Parallel plate flow chambers are simple to build and use. However, when chamber geometry is used to create recirculating flow, the d-flow region may only be several microns in length and therefore not produce enough cells exposed to d-flow for high-cell-demand analysis techniques such as Western blots or flow cytometry. Cone and plate devices efficiently expose a large number of cells to d-flow and can easily apply pathological waveforms, yet they produce sample-wide, homogenous d-flow without precise knowledge of the spatial distribution of recirculating vs. oscillatory flow. Evidence suggests that recirculating and oscillatory flow induced by different geometries *in-vivo* may have distinct pathologically relevant biochemical profiles [10,22,23], so it is critical to be able to resolve these differences. Finally, custom microfluidic devices boast the most pathologically relevant flow but can be challenging to create due to geometry resolution requirements.

Using current devices, researchers must choose whether to have recirculating d-flow with few cells vs. oscillatory d-flow with many cells. We performed a meta-analysis on the usage of high-cell-demand assays, like Western blots or flow cytometry that require millions of cells, in 18 publications that induced d-flow with either a parallel plate chamber (geometry, recirculating) or cone-and-plate device (waveform, oscillatory). Using a one-sided non-parametric sign test for a binomial distribution (α=0.05), we found only ~17% of publications that used geometry-specific d-flow utilized a high-cell-demand assay (p=0.026) compared to ~76% of publications that used pathological waveforms to induce d-flow (p=0.466). These data support the assertion that many current geometry-specific devices do not produce high cell yield [19].

To enable high-cell-content analysis of recirculating d-flow, our lab developed a new gasket for the Glycotech parallel plate chamber with repeating regions of recirculating d-flow. This device produces spatially-consistent eddies that occur uniformly over nearly one-half of the sample total surface area, offering a much higher cell yield than previous recirculating d-flow devices.

Copyright 2016 The Organizing Committee for the 2016 Summer Biomechanics, Bioengineering and Biotransport Conference

METHODS

COMSOL Multiphysics 4.0 was used to model a steady-state flow of culture medium (μ=0.78·10^{-3} Pa·s) at 37°C using the RAN κ-ω turbulence model with a no-slip wall boundary condition. The flow workspace was 10 mm wide x 58 mm long x 0.127 mm high. 9.5 mm x 1 mm baffles extend outward into the flow path, starting 7.5 mm past the inlet and occurring every 5 mm. This design emulates the recirculating flow found in arterial curvature (Fig. 1). Dimensions were chosen such that: 1) the highest shear stress produced in the area following each baffle was below 12 dynes/cm^2, the reported threshold at which flow produces an atheroprotective EC phenotype; and 2) the flow at these locations formed recirculating eddies. Silicone rubber gaskets were molded by Glycotech (Gaithersburg, Maryland).

Figure 1: Completed prototype with vacuum holes for sealing and molded protrusions for gasket alignment with the chamber.

BAECs (passages 4-7, Cell Applications) were cultured in Dulbecco's Modified Eagle's Medium (DMEM) supplemented with 10% fetal bovine serum, 1% L-glutamine, and 1% penicillin–streptomycin. BAEC were seeded at 21,000 cells/cm^2 onto 75x25x1 mm glass microscope slides pre-treated with 10 µg/mL collagen Type I for 3 hours. After 1 day, slides were placed into the parallel plate chamber (n=2 per experiment) with either a disturbed or laminar flow gasket. Additional samples were maintained in static culture as controls. Complete DMEM with 25 mM HEPES buffer (to maintain a pH of 7.2-7.4) was used in all flow experiments. Medium was perfused through the flow chamber via a peristaltic pump at a rate needed to produce 20 dyne/cm^2 shear stress for the laminar flow gasket samples. After 24 hours, samples were removed and imaged via phase contrast microscopy at 10x.

RESULTS

Recirculating eddies consistently appeared behind baffles. Simulated eddy size was 3-4 mm long and 5-6 mm wide. The mean shear stress was 0.97 Pa among all 93,400 computational elements; mean shear stress in the post-baffle pockets was < 0.7 Pa (Fig. 2).

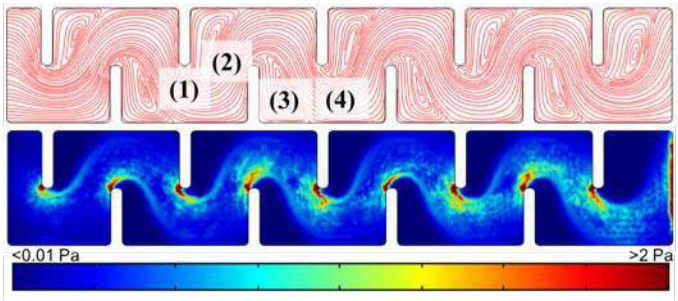

Figure 2: COMSOL simulations of the arterial curvature model gasket. Flow direction is from left to right. (Top): Fluid streamlines with points of interest numbered 1-4. (Middle): shear stress heat map.

Under static conditions, EC maintained a polygonal morphology (Fig 3, A) while cells under 20 dynes/cm^2 (2 Pa) laminar flow elongated in the flow direction (Fig 3, B). Comparatively, cells at point 1 in the d-flow gasket appear elongated in the flow direction, although not as drastically as the laminar samples. Cells in points 2-4 were similarly polygonal to the static control samples.

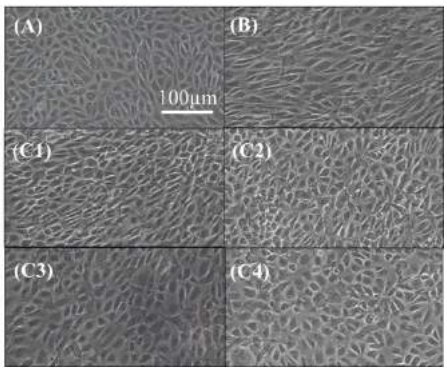

Figure 3: Representative cell morphology in static, laminar, or disturbed flow. Phase contrast microscopy of (A) static sample; (B) laminar flow sample; (C1-4) d-flow samples at locations corresponding with numbers in Fig 2. All images are 10x.

DISCUSSION

83% of the d-flow gasket workspace (480 mm^2) displayed shear stress below 12 dyne/cm^2, meaning that the majority of cells exposed to flow using the d-flow gasket should have an atheroprone phenotype compared to the d-flow surface area of 3.75-265 mm^2 seen in geometry-specific devices that did not use high-cell-content assays. Cells in low shear stress/recirculating zones (points 2-4) had a polygonal shape like the static samples, potentially indicated a disturbed phenotype [4] while cells near the baffle tips at point 1 may be aligning in the small zones of high shear stress. These zones represent a small fraction of the total cell population and would have a negligible effect on protein/RNA analysis.

These preliminary data show a novel parallel plate flow chamber modification for *in vitro* induction of large regions of recirculating d-flow. In the future, we will characterize cells in the d-flow gasket by examining actin structure, cell permeability, and key junctional and inflammatory markers such as β-catenin or ICAM-1/VCAM-1.

ACKNOWLEDGEMENTS

This research was funded by NIH Grant DK102107-01.

REFERENCES

[1]Davies, P. F., *Circ Res,* 101: 10-12, 2001.
[2]Andrews, A.M. et al. *Nitric Oxide* 23(4): 335-42, 2010.
[3]Chien, S., *Ann Biomed Eng,* 36(4): 554-62, 2008.
[4]Davies, P. F. et al., *Proc Natl Acad Sci,* 83: 2114-7, 1986.
[5] Passerini, A. G. et al, *Proc Natl Acad Sci,* 101(8): 2482-7, 2004.
[6] Li, R. et al., *Antioxid Redox Signal,* 23(15): 1207-19, 2015.
[7] Davies, P. F. et al, *Circ Res*, 101: 10-12, 2007.
[8] Van der Heiden, K. et al., *Atherosclerosis,* 196(2): 542-50, 2008.
[9] Cuhlmann, S. et al, *Circ Res,* 108(8): 950-9, 2011.
[10] Jenkins, N. T. et al, *Hypertension,* 61(3): 615-21, 2013.
[11] Lee, D. L. et al, *PNAS,* 109(6): 1967-72, 2011.
[12] Dai, G. et al, *Proc Natl Acad Sci* USA, 101(41): 14871-6, 2004.
[13] Orr, A. W. et al, *J Cell Biol*, 176(5): 719-27, 2007.
[14] DePaola, N.G.J. et al, *ATVB,* 12: 1254-1257, 1992.
[15] Heo, K.-S. et al, *Circulation Journal,* 75(12): 2722-2730, 2011.
[16] Wang, X. Q. et al, *Circ Res,* 110(4): 560-568, 2012.
[17]Patibandla, P. K. et al, *Anal Chem,* 86(21): 10948-10954, 2014.
[18] Brooks, A.R.L. et al, *Physiol Genomics,* 9: 27-41, 2002.
[19] Won, D. et al, *Am J Pathol,* 171(5): 1691-1704, 2007.
[20] Estrada, R. et al, *Biomicrofluidics,* 5(3): 32006-3200611, 2011.
[21] Khan, O. F. et al, *Biomed Microdevices,* 13(1): 69-87, 2011.
[22] Ziegler, T. B. et al, *ATVB*, 18: 686-692, 1998.
[23]Szymanski, M. P. et al, *Ann Biomed Eng,* 36(10): 1681-1689, 2008.

Copyright 2016 The Organizing Committee for the 2016 Summer Biomechanics, Bioengineering and Biotransport Conference

SB^{3}C2016
Summer Biomechanics, Bioengineering and Biotransport Conference
June 29 –July 2, National Harbor, MD, USA
SB^{3}C2016-946

INVESTIGATING COLLAGEN METHACRYLAMIDE, A PHOTOCROSSLINKABLE, THERMOREVERSIBLE, COLLAGEN-BASED HYDROGEL, FOR REGENERATIVE MEDICINE

Kathryn E. Drzewiecki (1), Juilee N. Malavade (1), David I. Shreiber (1)

(1) Department of Biomedical Engineering
Rutgers, the State University of New Jersey
New Brunswick, NJ, USA

INTRODUCTION

As the most ubiquitous protein in the body, type-I collagen has great utility in regenerative medicine. Although collagen is widely utilized as a structural, adhesive network for cell growth *in vitro* and *in vivo*, it is difficult to customize for specific applications in personalized medicine, such as 3D printed collagenous scaffolds, or 3D cell microenvironment design and culture. There are a variety of synthetic materials that potentially fill this void, including poly(ethylene glycol) diacrylate and polylactic acid, but concerns about biocompatibility, release of degradation products, or presence of manufacturing residuals remain [1].

We have synthesized a methacrylate-derivatized collagen, collagen methacrylamide (CMA), which potentially addresses these challenges by imparting two additional properties to collagen while retaining its native bioactive properties. First, CMA is photocrosslinkable: in the presence of a photoinitiator and UV light, CMA can be photocrosslinked to spatially modulate 1) the stiffness through methacrylate coupling in the hydrogel or 2) the bioactive properties through coupling of methacrylated ligands to CMA [2]. CMA is also thermoreversible: CMA rapidly and reversibly self-assembles into a hydrogel at neutral pH when cycled between 37ºC and 10ºC [3]. Additionally, photocrosslinking eliminates thermoreversibility. Herein we will discuss the results of proof-of-principle experiments to use CMA for free-form fabrication, ligand patterning, and 3D culture scaffolds that allow for cell recovery.

METHODS

Collagen Methacrylation

As described in Gaudet et al., the carboxyl group on methacrylic acid was activated with ethyl-3-(3-dimethylaminopropyl) carbodiimide) and N-hydroxysuccinimide and covalently conjugated to free amines on lysine residues on type-I collagen to produce CMA [2]. CMA was dialyzed in acetic acid, lyophilized, and resuspended in 0.02M acetic acid at 3.75 mg/mL for use.

Free-Form Fabrication Studies

Hydrogels were buffered in the following ratio: 10µL HEPES, 68µL 0.15N NaOH, 50µL 10X PBS, 28.5µL PBS, 10µL 10% Irgacure (I2959) in methanol, and 338.5µL CMA (3.75 mg/mL suspension). Hydrogels (100 µm thick) were self-assembled for 1 hour at 37ºC, exposed to UV light (365nm, 50% light, 100 mW/cm^2) through a laser printed transparency for 2 minutes, and were subsequently cold-melted at 4ºC for 30 minutes. Samples were thoroughly washed of cold-melted CMA using PBS, stained using Picrosirius Red, and imaged using a fluorescent microscope.

Ligand Patterning Studies

Hydrogels were buffered as described, however, 28.5µL of ~1 mg/mL Nile Blue Acrylamide (NB) was added in place of PBS as a visible ligand that would couple to methacrylate groups via UV-induced free radicals. Hydrogels (100 µm thick) were self-assembled and exposed to UV through a transparency as described, and imaged using brightfield microscopy. The mechanical properties of samples were assessed using a Kinexus Ultra rotational rheometer with a quartz Peltier-controlled plate to allow for UV exposure during mechanical testing. Samples were loaded onto the rheometer and the temperature was increased to 37ºC and maintained for 10 minutes to allow for self-assembly. Samples were fully exposed to UV for 2 minutes as described. Throughout the measurement, the samples were continuously oscillated (0.5% strain, 1 rad/s) and the resultant torque was measured to acquire mechanical properties of the hydrogel.

Cell Culture and Cell Retrieval Studies

Hydrogel formulations were prepared as follows: 10µL HEPES, 68µL 0.15N NaOH, 50µL 10X MEM, 23.5µL M199, 5µL L-

Copyright 2016 The Organizing Committee for the 2016 Summer Biomechanics, Bioengineering and Biotransport Conference

glutamine, 5µL Pen/Strep, and 338.5µL CMA (3.75 mg/mL suspension). Hydrogels were further diluted by 10% media containing rat dermal fibroblasts (RDFs) at 10^4 or 10^5 cells/mL. Samples were seeded in 48-well plates and allowed to self-assemble at 37ºC for one hour, and then supplemented with media (DMEM with 10% serum, 1% L-glutamine, and 1% Pen/Strep). After 24 hours, samples were cold-melted at 4ºC, diluted with cold media, and centrifuged, and the recovered cells were reseeded in a 25 cm^2 tissue culture flask.

RESULTS

Free-Form Fabrication Studies

CMA hydrogels photocrosslinked through a laser printed transparency patterned with high fidelity when compared to the photomask (Figure 1). Picrosirius Red staining allowed for visualization of the photopattern via fluorescence (Figure 1B and 1C). Areas of the patterned hydrogel that are not sharp as seen in the photomask (Figure 1C and 1A, respectively) are likely the result of excess photocrosslinking and free radical diffusion into unexposed areas of the hydrogel.

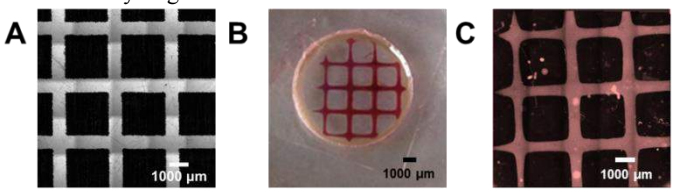

Figure 1: Spatial Patterning of Stiffness in CMA Hydrogels: Photomask (A), Picrosirius Red Stained Hydrogel Macroscale (B), and Microscale (C).

Ligand Patterning Studies

CMA hydrogels can be stiffened through methacrylate-methacrylate coupling or bioactively patterned through coupling of acrylated ligands to methacrylates on CMA. In our study, CMA hydrogels were photopatterned with NB as a representative ligand contrast-agent to visualize photocrosslinking, and to examine the competing effects of coupling on the hydrogel stiffness.

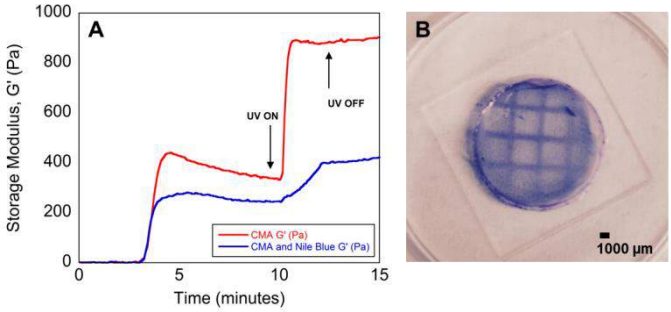

Figure 2: Ligand Patterning of NB in CMA Hydrogels: Effect of Patterning on Hydrogel Mechanical Properties (A) and the Visual Representation of Photopatterning (B).

In rheological studies, CMA prepared with NB demonstrated a lower storage modulus than CMA with only buffers following self-assembly at 37ºC (Figure 2A). Following exposure to UV and Irgacure, hydrogels without NB reached a storage modulus approximately 3-fold higher compared to initial assembly. The storage modulus of hydrogels prepared with NB and fully exposed to UV slowly increased to nearly twice that of the initial measurement due to competing effects of methacrylate coupling within the hydrogel to methacrylate-acrylate interactions between CMA and NB. When the hydrogel was exposed to UV through a photomask, which limits exposure to specific regions of the gel, CMA hydrogels patterned with NB demonstrated precise patterning compared with the photomask (Figure 1A and Figure 2B).

Cell Culture and Cell Retrieval Studies

Following cold-melting, RDFs were difficult to harvest from hydrogels seeded at 10^5 cells/mL, as some hydrogels seeded at this concentration had begun to compact likely due to significant cell remodeling of the matrix. Hydrogels seeded at 10^4 cells/mL were successfully cold-melted, but only ~10% of cells were recovered. Many RDFs were observed to maintain adhesion to small fragments of CMA. Future studies will focus on harvesting alternative cell types, such as those from the neural lineage, which may have weaker adhesion to the collagen hydrogel network.

DISCUSSION

CMA has demonstrated excellent preliminary utility as a tissue engineered scaffold or cell culture substrate. Its properties allow for extensive control over scaffold geometry, and mechanical and/or bioactive properties.

Free-form fabrication and ligand patterning studies demonstrated that CMA hydrogels can be easily patterned in 2D. Initial photopatterning results showed that the fidelity of the pattern was very well maintained, however, excess free radicals led to undesired photocrosslinking. In the future, this may be avoided through the use of a free radical quencher. Ligand patterning had a significant effect on the mechanical properties of the hydrogel. CMA hydrogels with NB were capable of self-assembly, and had a lower modulus in comparison to photocrosslinked CMA scaffolds without ligand. Despite the high ligand concentration, the competing effect of acrylated-ligand-methacrylate and methacrylate-methacrylate coupling resulted in a slight increase in storage modulus.

Studies in cell harvest utilizing CMA as a temporary culture substrate demonstrated preliminary efficacy. CMA hydrogels were capable of disassembly, however, RDFs were highly adherent to the collagen-based substrate, which made detachment procedures difficult. Future studies will focus on utilizing cells from the neural lineage.

The current focus is to combine these three approaches for uses of CMA in regenerative medicine and biotechnology. Customized, 3D tissue engineered scaffolds could be constructed through layer-by-layer self-assembly and photocrosslinking, and subsequent cold-melting of the entire scaffold. Complex, cell-laden CMA hydrogels could be photopatterned with bioactive ligands to influence cell behavior, and if gels are reversible, could allow for cell harvest for further studies. The novel, advantageous properties of CMA described in this work will increase the innovation of collagen-based materials in personalized medicine, cell culture, and biotechnology.

ACKNOWLEDGEMENTS

The authors would like to acknowledge Rutgers Biotechnology Training Program (NIH Grant Number 5T32GM008339-20) and the Philanthropic Educational Organization.

REFERENCES

[1] Abou Neel EA et al., *Adv. Drug Delivery Rev.,* 65: 429–456, 2013.
[2] Gaudet IG et al., *Biointerphases*, 7(1-4):1-9, 2012.
[3] Drzewiecki KE et al., *Langmuir*, 30(37):11204-11211, 2014.

Copyright 2016 The Organizing Committee for the 2016 Summer Biomechanics, Bioengineering and Biotransport Conference

SB^{3}C2016
Summer Biomechanics, Bioengineering and Biotransport Conference
June 29 –July 2, National Harbor, MD, USA
SB^{3}C2016-948

IMPACTS OF MATURATION ON THE NANOSTRUCTURE AND NANOMECHANICS OF THE MENISCUS EXTRACELLULAR MATRIX

Q. Li (1), F. Qu (2), B. Han (1), R. L. Mauck (2,3), L. Han (1)

(1) School of Biomedical Engineering, Science and Health Systems
Drexel University
Philadelphia, PA, United States.

(2) McKay Orthopaedic Research Laboratory
University of Pennsylvania
Philadelphia, PA, United States.

(3) Translational Musculoskeletal Research Center
Philadelphia Veterans Administration Medical Center
Philadelphia, PA, United States.

INTRODUCTION

The unique biomechanical function of the meniscus is endowed by its hierarchically structured extracellular matrix (ECM). The ECM is mainly composed of circumferentially aligned fibers. These fibers are interdigitated by radially aligned "radial tie" fibers [1], and wrapped in a superficial layer, also made of radially aligned fibers [2]. The knee meniscus has very limited self-healing capabilities, especially in the inner avascular, proteoglycan-rich zone [3]. Injuries in the meniscus often lead to the development of post-traumatic osteoarthritis, a prevalent osteoarthritis form among the young population [4]. Interestingly, the meniscus has robust self-repair ability at the fetal stage, but progressively loses this function during maturation [5]. In addition to the reduction in cell density [5], one salient change is the alteration in the ECM modulus and collagen fiber alignment [6]. It is likely such matrix changes increase the impedance of cell migration that is critical for self-healing [7]. In order to provide insights for understanding and improving meniscus regeneration, this study aims to reveal how maturation affects the local nanostructural and nanomechanical properties of the meniscus ECM in an orientation- and region-specific manner.

METHODS

Sample preparation. Menisci were harvested from fetal (mid-gestation) and adult (18-30 months old) cows. The outer one-third (outer zone) and inner one-third (inner zone) tissues of each meniscus were isolated and embedded in Optimal Cutting Temperature (OCT) media. The middle zone is not included here since it is similar to the outer zone. Tissue from each zone was cryo-sectioned transversely and radially onto glass slides to produce ~ 20 μm thick horizontal and vertical sections, respectively (Fig. 1). Samples were stored at -20 °C until AFM nanoindentation.

AFM-nanoindentation (Dimension Icon) was performed with a microspherical tip ($R \approx 5\mu m$, $k \approx 0.6$ N/m, μMasch) following established procedures [8, 9]. For each vertical section, testing locations include the circumferential fiber bundles cross-section, radial tie fibers and superficial layer (Fig. 1a). Within each zone, multiple horizontal sections were taken from the intact surface, superficial layer and circumferential fiber-dominated interior (Fig. 1b). At each location, effective indentation modulus, E_{ind}, was calculated via the finite thickness-corrected Hertz model [10]. After nanoindentation, each section was fixed with Karnovsky's fixative and Hexamethyldisilazane drying to preserve the collagen architecture [11].

Structural analysis. Scanning electron micrographs (***SEM***, Zeiss Supra 50 VP) and tapping mode AFM images were acquired to visualize collagen fibril structure at the nanometer scale.

RESULTS

Significant differences in the modulus, E_{ind}, were detected between fetal and adult menisci in the outer zone. On both the vertical (Fig. 1a) and horizontal sections (Fig. 1b), the adult meniscus exhibits higher E_{ind}. In contrast, in the proteoglycan-rich inner zone, no significant age-related differences were detected among all structural units. Correspondingly, SEM and AFM images showed a higher degree of packing and alignment of collagen fibrils in the circumferential fibers of adult meniscus (Fig. 2).

Fetal and mature tissues also showed different nanomechanical heterogeneity across different units. For example, in the fetal tissue, moduli of the radial tie fibers were much lower than those of the superficial layer in the outer zone ($p < 0.05$), despite both are composed of radially aligned fibrils. In contrast, in mature meniscus, this difference was absent (Fig. 1a).

Copyright 2016 The Organizing Committee for the 2016 Summer Biomechanics, Bioengineering and Biotransport Conference

On the other hand, both adult and fetal tissues also share salient features of heterogeneity and anisotropy, similar to our previously reported results on juvenile meniscus [9]. Nanoindentation along the circumferential fibers (vertical section, along fibril axis) yielded significantly higher moduli ($p < 0.05$) than indentation normal to circumferential fibers (horizontal section, normal to fibril axis). These values are also significantly higher than other structural units.

DISCUSSION

This study underscores how maturation affects the nanostructure and nanomechanical properties of meniscus ECM. In particular, age-associated increase in E_{ind} of the outer zone can be mainly due to the increased packing and alignment of collagen fibrils at the nanoscale (Fig. 2). For nanoindentation along the axis of circumferential fibers (on vertical section, Fig. 1a), higher degree of fibrillar alignment and packing results in increased lateral constraints between adjacent fibrils, and thus, higher modulus. For nanoindentation normal to the fiber axis of circumferential fibers (on horizontal section), a more compliant deformation mode of local fibril uncrimping and realignment is expected to take place. Under this mode, a more organized, densely packed collagen fibril matrix in the adult tissue can provide higher resistance for uncrimping or realignment, and thus, also yield higher modulus.

In contrast to the marked impacts in the outer zone, maturation appears not to influence the properties of the inner zone, which has less organized collagen fibrils and higher proteoglycan content. It is likely that the impacts of maturation are mainly manifested through the organization of collagen fibrils. Interestingly, since the absence of self-healing is most prominent in the inner zone [3], these results suggest the reduced self-healing in meniscus can be, at least partially, attributed to the increased impedance of cell migration through the vascular outer zone near the wound site to reach the avascular inner zone. Manipulation of the outer zone matrix architecture may provide a valuable means to improve the repair of damaged meniscus.

The radial tie fibers also exhibit similar age-dependent changes in the outer zone. These fibers share similar structure of radially oriented fibers with the superficial layer, and similar function of stabilizing circumferential fiber bundles. However, the radial tie fibers appear to be less developed than superficial layer in the fetal stage, as evidenced by much lower modulus on the vertical section (Fig. 1a). This contrast suggests a delayed formation and development of radial tie fibers in accordance with the development of the major structural unit, the circumferential fibers. From fetal to mature ages, the circumferential fibers not only become more organized and packed, but also are interdigitated by stiffer, more aligned radial tie fibers. These trends likely together contribute to the increased impedance for cell migration from the vascular outer zone near the wound site to the avascular inner zone in the mature tissue.

This study delineates the impacts of maturation on the nanoscale structure and mechanical properties of the meniscus ECM in an orientation and region-specific manner. Notably, age-associated changes in the circumferential fiber bundles and radial tie fibers in the outer zone are likely a major factor that determines the increased impedance to cell migration [12, 13]. Study of the maturation dependence and structure-mechanics relationships of native tissue could provide a new path for improving meniscus repair through tuning local matrix mechanical properties.

ACKNOWLEDGEMENTS

This work was supported by the National Institutes of Health AR066824 (LH) and EB002425 (RLM).

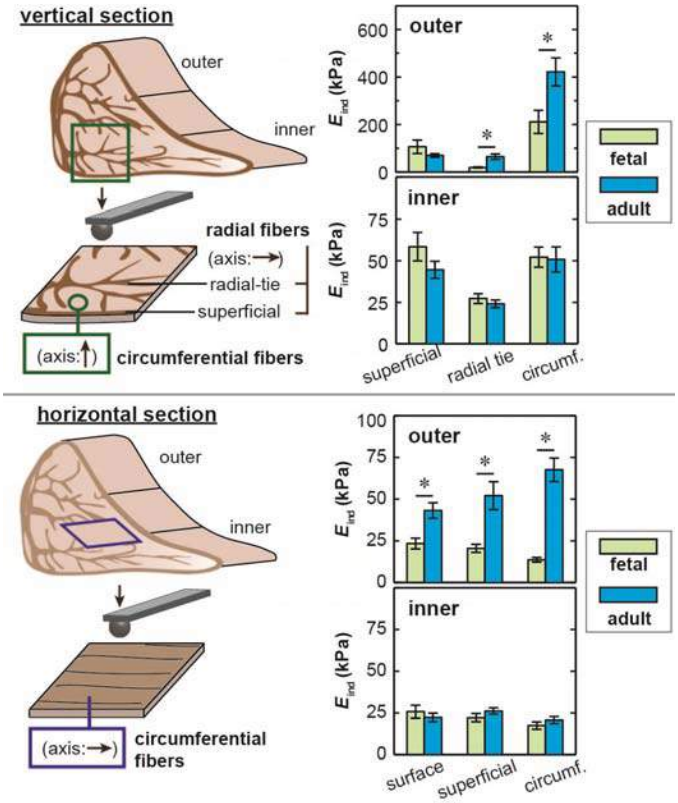

Fig. 1 Nanoindentation modulus of the meniscus ECM on **a** vertical and **b** horizontal sections. (*: $p < 0.05$ between fetal versus adult from Mann-Whitney U test, mean ± SEM of $n \geq 30$ positions from $M = 3$ animals, results of different animals were pooled as no significant differences were detected across animals).

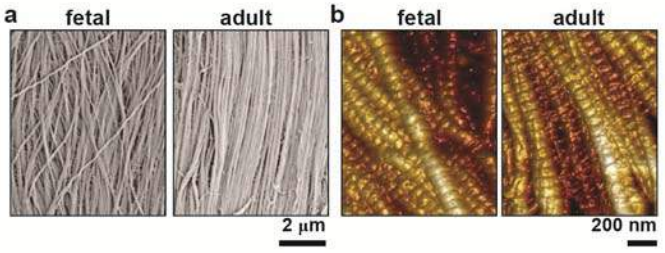

Fig. 2 Nanostructure of outer zone circumferential fibers in the fetal and adult meniscus ECM from **a** SEM and **b** tapping mode AFM.

REFERENCES

[1] Skaggs, DL et al., *J. Orthop. Res.* 12:176-185, 1994.
[2] Petersen, W et al., *Anat. Embryol.* 197:317-324, 1998.
[3] Kawamura, S et al., *Oper. Techn. Sport. Med.* 11:68-76, 2003.
[4] Lotz, MK et al., *Arthritis Res. Ther.* 12:211, 2010.
[5] Ionescu, LC et al., *Tissue Eng. A* 17:193-204, 2011.
[6] Qu, F et al., *Biomaterials* 39:85-94, 2015.
[7] Qu, F et al., *SB^{3}C*, 2015.
[8] Sanchez-Adams, J et al., *J. Orthop. Res.* 31:1218-1225, 2013.
[9] Li, Q et al., *Trans. Orthop. Res. Soc.* 61:1322, 2015.
[10] Dimitriadis, EK et al., *Biophys. J.* 82:2798-2810, 2002.
[11] Bray, DF et al., *Microsc. Res. Tech*. 26:489-495, 1993.
[12] Mauck, R.L. et al., *Ann. Biomed. Eng*. 43(3): 529-542. 2015
[13] Han, W.M., et al., *Nat Mater*, 2016, in press, doi:10.1038/nmat4520.

Copyright 2016 The Organizing Committee for the 2016 Summer Biomechanics, Bioengineering and Biotransport Conference

SB^{3}C2016
Summer Biomechanics, Bioengineering and Biotransport Conference
June 29 –July 2, National Harbor, MD, USA
SB^{3}C2016-949

ACCELERATION OF CRITICAL BONE DEFECT HEALING BY ULTRASOUND RADIATION FORCE IN A RAT TIBIAL MODEL

YX. Qin (1), J. Liu (1), Zhang, D (1), X. Li (1)

(1) Department of Biomedical Engineering
Stony Brook University
Stony Brook, NY 11794, USA

INTRODUCTION

Bone defects, usually caused by trauma, inflammation and tumors, may lead to loss of limb functions and substantially affect the quality of patients' life. When bone is impaired, it undergoes a unique process of self-healing to form new bones, which is regulated by local functional physical stimulation [1]. Therefore, it is essential to find effective methods to accelerate bone healing. Low-intensity Ultrasound radiation force (ARF) or LIPUS, which is a unique form of mechanical energy, can transmit through and into living tissues as acoustic pressure waves, and generate dynamic acoustic radiation force in the local region [2]. Such dynamic stimulation may be able to induce mesenchymal stem cell (MSC) recruitment and differentiation, osteoblast differentiation, extracellular matrix production, endochondral ossification, and mineralization and then may result in biochemical events that accelerate bone formation [3]. Therefore, the objective of this study was to evaluate the effect of ARF induced mechanotransduction in a rat tibial critical bone-defect healing. Following aims will be evaluationed,

1) To create tibial trabecular bone defect model for tissue regeneration.
2) To evaluate ARF ability in acceleration of healing.
3) To evaluate the outcome using μCT, histology, and biomechanical testing.

METHODS

A total of 40 skeletally mature female Lewis rats were used in this study. Bilaterally, the surgical bone defects of 2 mm in diameter were made at proximal tibia. Subsequently, the defects of the left tibia (LIPUS group) received daily treatment of low-intensity pulsed ultrasound, and the defects in the right tibia (Control group) received sham stimulation as the non-treated contralateral control. Sonicator® 740, ultrasound generator with a transducer of 1 cm^2 in cross-sectional area (16 mm in diameter) was used for LIPUS stimulation. A modified repetitive frequency at 100 Hz, and an ultrasound characteristic frequency of 1 MHz and a pulse width of 200 μs at an intensity of 30 mW/cm^2 were used for the stimulation for 20 minutes/day (ISATA). After 2 weeks, the rats were euthanized and the tibias were assessed using micro-CT scanning, histology and mechanical testing. Trabecular bone volume fraction (%, bone volume/total volume, BV/TV), connectivity density (1/mm^3, Conn.D), trabecular thickness (mm, Tb.Th), trabecular separation (mm, Tb.Sp), trabecular number (1/mm, Tb.N), and tissue mineral density (mgHA/cm^3, TMD) were evaluated. After micro-CT scanning, one part of each tibia sample was fixed in 10% phosphate-buffered formalin, dehydrated through graded ethanol, decalcified, and embedded in paraffin. Sections of 5 um were made for hematoxylin & eosin staining. Osteomeasure software was used to evaluate the newly formed trabecular bone in the defections of tibia. BV/TV, Tb.Th, Tb.Sp and Tb.N were measured. The other part of each tibia sample was used for four-point bending to examine the stiffness and strength using a MTS mechanical testing system (585 Mini Bionix II) with a 100 N force transducer (SMT1-100 N, Interface).

Copyright 2016 The Organizing Committee for the 2016 Summer Biomechanics, Bioengineering and Biotransport Conference

RESULTS

2 weeks after surgery, the micro-CT images showed that trabecular bone formed in the defect area of both LIPUS and control group (Fig. 1). Additionally, new bone formed in LIPUS group was more than that in control group. In comparison to control group, LIPUS treated tibia showed increased in BV/TV, Coon.D, Tb.N, and BMD, and significant decrease in Tb.Sp. Osteomeasure analysis showed a similar trend, which is in line with the micro-CT results. As show in Fig. 2, BV/TV and Tb.Th were higher in LIPUS group than those in control group, and Tb.Sp was lower in LIPUS group than that in control group. Four-point bending mechanical testing data showed LIPUS treatment significantly increased the bone stiffness (kN/mm) relative to control group (Fig. 3). Ultimate load (N) at mid-shaft of tibia showed an increasing trend, but no significant increase was observed following the exposure to LIPUS, when compared to control group (t=1.968, *P*=0.056).

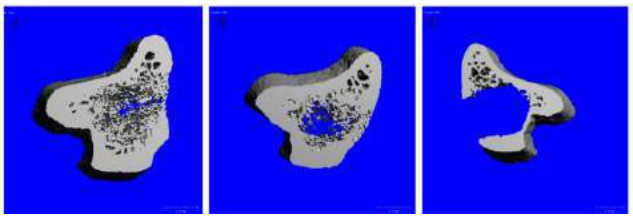

Figure 1: Three-dimensional images of tibia bone defects. (A) LIPUS group. (B) Control group. (C) Micro CT Scan Immediate postoperative.

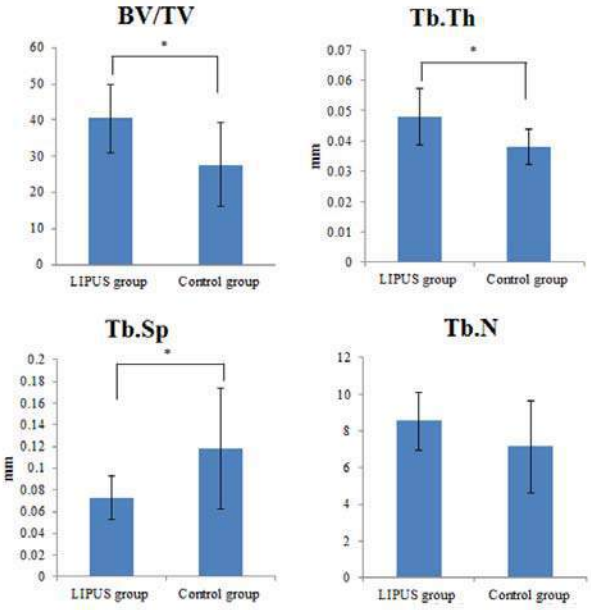

Figure 2: Histomorphometric analysis of newly formed trabecular bone was performed using Osteomeasure. The treatment of ARF promoted bone formation significantly more than control (~33%).

.

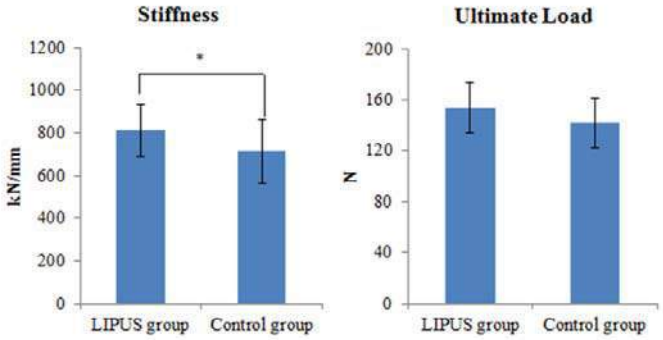

Figure 3: Mechanical testing results at the tibia indicated that stiffness was enhanced in the treatment group.

DISCUSSION

The histological analysis and micro-CT data revealed that new bone formed in both LIPUS therapy and no-therapy groups with tibia bone defect in 2 weeks after bone surgery, and ARF therapy can significantly increase new trabecular bone volume. Moreover, bone stiffness and ultimate load of ARF treated bone were higher than no-therapy group, and LIPUS therapy increased rat bone strength. Two weeks seem to be the key period for bone regeneration after bone defect surgery. During this period, performing ARF therapy on bone defect site could efficiently accelerate bone healing by stimulating trabecular bone formation [2].

SIGNIFICANCE: The data shown in this study provided direct evidence that LIPUS therapy improved bone healing by accelerating the development of newly formed trabecular bone after 2 weeks of bone defect surgery.

ACKNOWLEDGEMENTS

The work is kindly supported by the National Institute of Health (R01 AR52379 and AR61821, YXQ), US Army Medical Research and Materiel Command, and the National Space Biomedical Research Institute through NASA Cooperative Agreement NCC 9-58 (YXQ).

REFERENCES

[1] Qin YX. and Hu M. Biomed Res Int, 2014:863421, 2014.
[2] Uddin SM and Qin YX. BONE, 75:8-17, 2015.
[3] Uddin SM et al.. Ultrasound Med Biol, 39(5):804-12, 2013

Copyright 2016 The Organizing Committee for the 2016 Summer Biomechanics, Bioengineering and Biotransport Conference

SB³C2016
Summer Biomechanics, Bioengineering and Biotransport Conference
June 29 –July 2, National Harbor, MD, USA
SB³C2016-950

STRAIN-RATE DEPENDENT MECHANICAL RESPONSES OF THE AORTIC VALVE INTERSTITIAL CELLS

Yusuke Sakamoto (1), Rachel M. Buchanan (1), Johannah S. Adams (2), Farshid Guilak (3), Michael S. Sacks (1)

(1) Center for Cardiovascular Simulation
Institute for Computational Engineering and Sciences
Department of Biomedical Engineering
Austin, TX USA
The University of Texas at Austin
Austin, Texas USA

(2) Departments of Orthopaedic Surgery and Biomedical Engineering
Duke University Medical Center
Durham, North Carolina USA

(3) Departments of Orthopaedic Surgery, Biomedical Engineering, and Developmental Biology
Washington University, St. Louis USA

INTRODUCTION

Valve interstitial cells (VICs) reside in heart valve tissues and play critical roles in the tissue maintenance, but also the cause of heart valve diseases [1]. VICs are myofibroblast-like cells with tissue remodeling activity due to collagen production and contraction activities mediated by α-smooth muscle actin (α-SMA) stress fibers. The VICs are activated by mechanical stimuli during tissue repair, development, and remodeling, and removed as they complete their role. The VICs are sensitive to their surrounding microenvironments, and excessive and persisting environmental changes cause the improper regulations of VICs, contributing the progression of valve disease. Thus, it is important to characterize how the external mechanical stimuli translate into and activate the VICs, and how the different activation levels affect the VIC's internal mechanics and their mechanical response to the surrounding tissues.

Heart valve leaflets experience dynamic and complex mechanical stress states over the cardiac cycle, including surface shear stress due to blood flow, flexure (opening and closing), and high in-plane tension (closed valve). The resulting forces are translated to the VICs through the complex micromechanical interactions with the extra cellular matrix (ECM) such as collagen stretch with reorientation and fiber compaction. VICs thus interact with the ECM in highly stress-dependent manner in a valve tissue [2, 3, 5]. Recently, the stiffness of mitral heart valve VICs (MVICs) within leaflet tissues under controlled biaxial loading were estimated using finite element simulations [6]. This study found that while the MVIC effective stiffness was quite similar within each of the four leaflet layers, MVICs experienced significantly different mechanical deformations resulting from differing layer microstructures. It is also known that cyclic strain of the Mitral valve leaflet activate the MVICs, and the larger maximum strain activated the MVICs more [2]. These studies indicate that MVICs respond to the mechanical stimuli in strain or strain-rate dependent manner. In fact, the Aortic VICs exhibit viscoelastic responses under micropipette aspiration experiment [3].

The objective of this study is to analyze the strain-rate dependent mechanical properties of the AVICs. The microindentation experiment was carried out on the AVICs with 3 different indentation patterns: slow, fast, and physiological, to assess how the AVICs respond differently to the different strain patterns. Also, the activation states of the AVICs were controlled by treatment with chemical reagents to assess how the AVICs in different activation state behave differently to the indentation.

METHODS

We used a spherical indenter with 5 μm diameter. In the experiment, we controlled the activation states of the aortic VICs (AVICs) with different chemical reagents to alter the biomechanical properties of the stress fibers. Then, using the experimental data from different experimental groups, we studied how the different components of the stress fibers (α-SMA and F-actin) influenced the stress fiber biomechanics, such as their stiffness and contractile strength. We have five experimental groups: Cytochalasin D pretreated group (CytoD), Control groups with 5 mM and 90 mM KCl treatments (C5 and C90 groups, respectively), and Transforming growth factor-beta1 (TGF- β1) pretreated groups with 5 mM and 90 mM KCl treatments (T5 and T90 groups, respectively).

We carried out the microindentation experiment on AVICs cultured on a flat thin-layered collagen substrate over a glass. After 5 days of incubation, the biomechanical properties of control and TGF-β1 treated AVICs were measured using an atomic force microscope (MFP-3D, Asylum Research, Santa Barbara, CA). The TGF-β1 and non-treated AVICs were first tested under normal physiological levels of 5mM KCl at 37°C. The same AVIC sample was then incubated at 37°C

Copyright 2016 The Organizing Committee for the 2016 Summer Biomechanics, Bioengineering and Biotransport Conference

for 10 minutes in hypertensive levels of KCl (90mM) and retested. Finally, the same AVIC sample was treated with 20μM Cytochalasin-D (Sigma-Aldrich, St Louis, MO) for 10 minutes at 37°C to cause complete depolymerization of the actin network and tested using microindentation a third time. To ensure CytoD concentration and incubation time was effective, samples were given CytoD supplemented with 90mM KCl and measured using microindentation. There was no measured increase in stiffness between the 5mM and 90mM controls when delivered with CytoD (data not shown).

Three patterns of microindentation were carried out: slow, fast, and physiological (Figure 1). For the slow and fast indentation patterns, overall time length of indentation were controlled to be around 1000 ms and 100 ms, respectively. For the physiological indentation mode, the indentation pattern was controlled to mimic the deformation pattern of the heart valve tissue in physiological condition [4]. Thus, the physiological indentation mode consists of 50 ms of indentation, 500 ms of hold, and 50 ms of release.

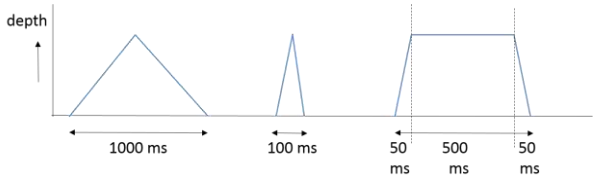

Figure 1: Three modes of indentation patterns: slow (left), fast (middle) and physiological (right).

The indentation depth and force over time were recorded and used to fit the modified Hertz model with thin-layer correction [5] to estimate the stiffness. Also, the standard linear solid model with thin-layer correction was used to determine the viscoelastic properties using the relaxation response of the AVICs during physiological indentation [6].

RESULTS

Generally the AVICs exhibit stronger resistance to the fast indentation than to the slow indentation, especially for TGF-β1 treated groups (Figure 2). The Hertz elastic moduli for different experimental groups were determined by Hertz model with thin-layer correction (Figure 3). The "apparent" stiffness of the AVICs increased as they were activated more with KCl 90mM and/or TGF-β1 treatments. The increase in the apparent stiffness was more pronounced with the fast indentations with TGF- β1 treatments, indicating the strain-rate-sensitivity of the AVICs mechanical responses for these groups.

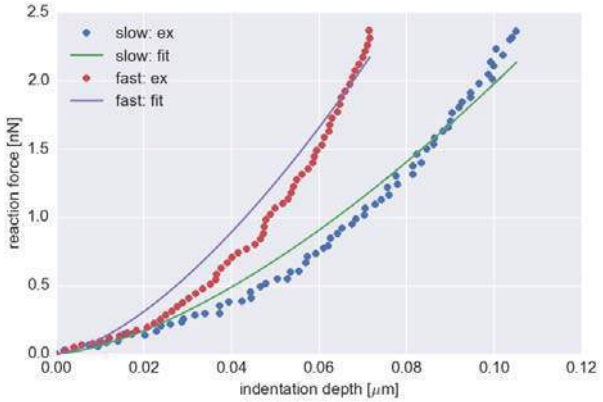

Figure 2: Typical indentation depth vs force curves for slow and fast indentation modes from T90 group.

We then used the relaxation responses of the AVICs from the physiological-pattern indentations to determine their viscoelastic properties under different activation states. We used the standard linear solid model (a spring-dashpot in parallel with another spring). The determined k1 values (the independent spring element) are: 0.16, 2.2, 5.1, 4.7, and 12.8 kPa for CytoD, C5, C90, T5, and T90 groups, respectively. The determined k2 values (the spring element in the spring-dashpot) are: 0.51, 0.94, 2.0, 1.7, and 3.6 kPa for CytoD, C5, C90, T5, and T90 groups, respectively. Finally, the determined μ value (dashpot) are: 0.026, 0.064, 0.10, 0.11, and 0.15 kPa*s for CytoD, C5, C90, T5, and T90 groups, respectively. These results indicate that not only the stiffness of the AVICs increased as they were activated, but also the strain-dependent, viscous response also strengthened for TGF-β1 treated groups. It corresponds to the observation that the apparent Young's modulus increased as the speed of indentation increased (Figure 3).

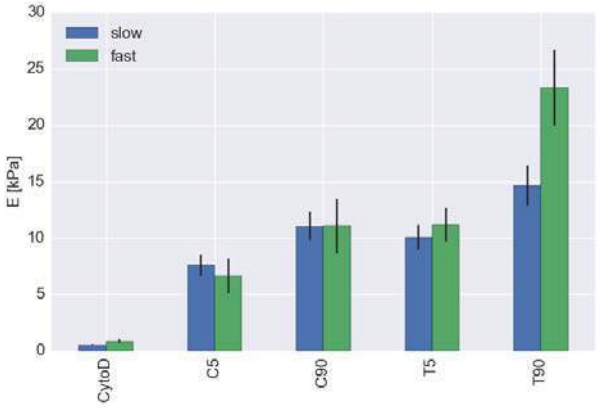

Figure 3: Hertz elastic moduli of AVICs for different experimental groups.

DISCUSSION

In this research, 3 patterns of indentations were applied to the AVICs and their mechanical responses were studied. The primary finding is that the AVICs exhibit strain-rate-dependent mechanical response to external stimuli for TGF-β1 treated groups, where the AVICs resist stronger to the faster indentation than slower indentation. The viscoelasticity of the AVICs were further studied using the standard linear solid model. Again, the TGF-β1 treated groups exhibited larger viscosity values (μ), validating the strain-rate sensitivity. Also, as expected, treatments with KCl and TGF-β1 increased the apparent stiffness of the AVICs. These results indicate the need for a strain-rate-dependent model and analysis for the study of AVICs, as they are under dynamic and rapid loading conditions in the physiological environment.

ACKNOWLEDGEMENTS

- We would like to thank Dr Ferrari at the University of Pennsylvania for donating AVICs used in this study.
- This study was supported by NIH Grant R01 HL-68816-01 and R01 HL119299.

REFERENCES

1. Sacks, M.S., et al. *J Biomech*, 2009. **42**(12): p. 1804-24.
2. Lacerda, C.M., et al. *Am J Physiol Heart Circ Physiol*, 2012. **302**(10): p. H1983-90.
3. Merryman, W.D., et al. *J Biomech Eng*, 2009. **131**(4): p. 041005.
4. Sacks, M.S., et al. *Ann Thorac Surg*, 2006. **82**(4): p. 1369-77.
5. Dimitriadis, E.K., et al. *Biophys J*, 2002. **82**(5): p. 2798-810.
6. Darling, E.M., et al. *Biophysical Journal*, 2007. **92**(5): p. 1784-1791.

Copyright 2016 The Organizing Committee for the 2016 Summer Biomechanics, Bioengineering and Biotransport Conference

SB³C2016
Summer Biomechanics, Bioengineering and Biotransport Conference
June 29 –July 2, National Harbor, MD, USA
SB³C2016-951

WALL SHEAR STRESS AND COMBINED VH-IVUS AND OCT ANALYSIS OF CORONARY PLAQUE COMPOSITION

David S. Molony. Ph.D. (1), Lucas H. Timmins, Ph.D. (2), Udit Joshi (1), Yasir Bouchi (1), Bill D. Gogas (1), Don P. Giddens, Ph.D. (3), and Habib Samady, M.D. (1),

(1) Department of Medicine,
Emory University,
Atlanta, GA, USA

(2) Department of Radiology,
Emory University,
Atlanta, GA, USA

(3) Wallace H Coulter Department of
Biomedical Engineering
Georgia Institute of Technology
Atlanta, GA USA

INTRODUCTION

The most common phenotype associated with coronary plaque rupture is the thin capped fibroatheroma (TCFA) lesion. TCFAs are characterized by a necrotic core with an overlying fibrous cap of <65 μm thickness and a high infiltration of macrophage cells [1]. In-vivo detection of this type of lesion is only possible using intravascular imaging methods such as intravascular ultrasound (IVUS) and/or optical coherence tomography (OCT), though neither of these modalities may be sufficient by themselves. IVUS is an ultrasound based technique capable of penetrating the coronary wall. More specifically, virtual histology (VH) IVUS can assess plaque morphology and is capable of distinguishing plaque components such as necrotic core. On the other hand, OCT is a light based tool with high spatial resolution (10-15 μm) though it is disadvantaged by its poor penetration depth (<2.5 mm) and its inability to see through lipid. Given the lower spatial resolution of IVUS (100 μm) it can be seen that these modalities are complementary if used in conjunction and hence may aid in TCFA detection.

Wall shear stress (WSS) plays a mechanistic role in plaque development, and low WSS has been shown to correlate to increases in plaque area [2, 3]. Further, it has been hypothesized that regions of high WSS may be responsible for transformation to a vulnerable plaque and co-localize with thinning of fibrous caps [3, 4]. Contrarily, another study found that low WSS was correlated with thinner fibrous caps [5]. The previously reported relationships between WSS and both necrotic core size (VH-IVUS) and fibrous cap thickness (OCT) were found in separate patient populations. This work aims to assess the relationship between focal hemodynamics and plaque morphology as assessed by VH-IVUS and OCT in a single patient population. This is achieved by co-registration of VH-IVUS and OCT images and determination of WSS through computational fluid dynamics (CFD).

METHODS

Patients (n=4) who had previously received VH-IVUS and OCT imaging during cardiac catheterization were selected for this study. A fully automatic method involving dynamic time warping and dynamic programming was used to co-register both modalities [6]. Longitudinal/axial co-registration of IVUS and OCT images was achieved by dynamic time warping.

Following one to one image co-registration in the axial direction the images were then co-registered circumferentially using a dynamic programming method. Three features, namely, lumen eccentricity, catheter angle, and calcification, are used to construct a cost matrix. The minimum cost path is then backtracked through the cost matrix. Each value in the minimum cost path corresponds to the co-registration angle between each longitudinally matched IVUS and OCT image. Figure 1 shows an example of co-registered IVUS and OCT images in the longitudinal view along with two co-registered cross-sectional views and their associated cost.

In order to create a 3D model of the coronary arteries VH-IVUS images are combined with the 3D catheter path reconstructed from angiographic images. Side-branches greater than 1mm are added to the 3D reconstruction and a tetrahedral mesh with prismatic boundary layer is created using ICEM-CFD (ANSYS). Patient-specific blood flow velocity is measured by TIMI frame count and applied as an inlet boundary condition. A zero pressure outlet boundary condition was applied to all outlets. Simulations were performed using Fluent 12.0

Copyright 2016 The Organizing Committee for the 2016 Summer Biomechanics, Bioengineering and Biotransport Conference

(ANSYS). WSS is analyzed in 8 sectors in each IVUS image and associated with VH-IVUS plaque composition and OCT plaque composition.

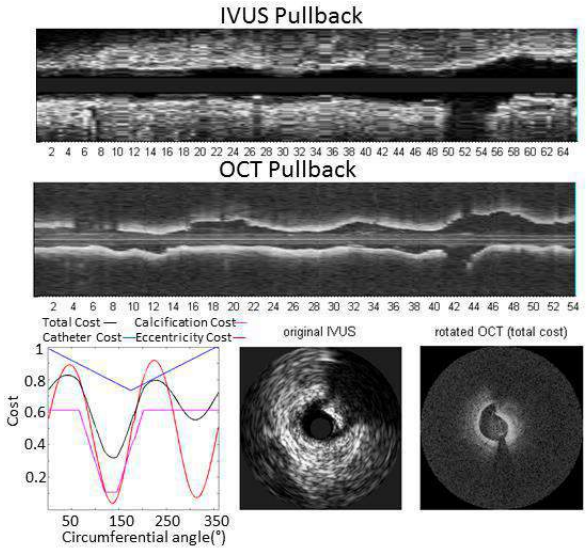

Figure 1: Co-registered VH-IVUS (top row) and OCT (middle row) images displayed in the longitudinal view. Circumferential cost associated with the co-registration of 2 images (bottom row). The lowest cost is found at an angle of 145°, i.e., the OCT image is rotated by 145° to match the orientation of the VH-IVUS image. A calcification in the co-registered images can be identified between 12 and 4 o'clock.

RESULTS

OCT images were successively co-registered to VH-IVUS images (Figure 1). The mean VH-IVUS and OCT pullback lengths were 65.9±22.6 and 70.1±11.9 mm, respectively. The mean co-registered pullback length was 48.8±17.6. Patient-averaged plaque burden as measured by IVUS was 59.3±7%. Contours of WSS for each patient are shown in Figure 2. WSS maps were qualitatively compared with VH-IVUS maps of plaque thickness, necrotic core and OCT maps of calcification. As can be seen in Figure 3 an area of low WSS corresponds to a region of large necrotic core area.

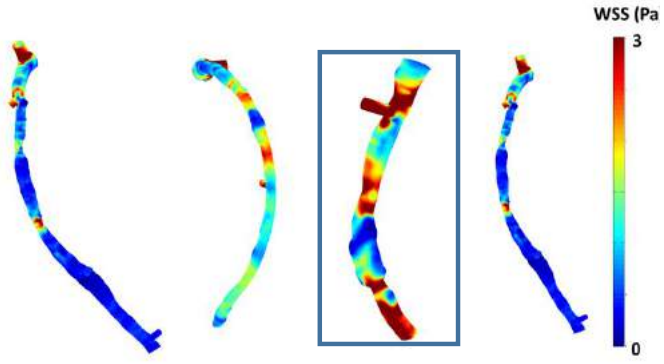

Figure 2: WSS for each patient. Vessels are not shown at the same scale

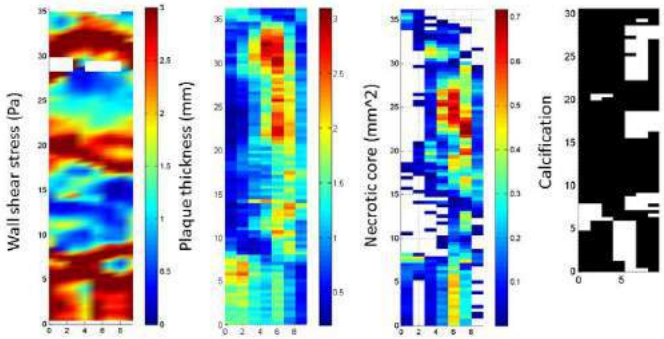

Figure 3: Example (boxed patient in Figure 2) of unwrapped WSS and VH-IVUS defined plaque thickness, necrotic core area and OCT defined calcification. The OCT calcification is displayed as a binary value (1 if present) and has been co-registered longitudinally and circumferentially to the IVUS pullback.

DISCUSSION

In order to further understand the role of WSS in coronary artery disease we developed our methodology using a small number of heavily diseased patients who received both IVUS and OCT imaging. IVUS and OCT images were co-registered automatically providing the ability to conduct a focal analysis of the relationship of WSS and plaque composition. Key determinants of plaque rupture were examined, such as plaque thickness and necrotic core area. Calcifications as observed by OCT were also investigated. While we have shown calcifications as a binary value, it is possible to determine calcification area from OCT whereas because ultrasound does not penetrate calcium IVUS underestimates calcium area [7].

In conclusion, we have developed a framework to analyze the relationship of WSS and plaque morphology through the co-registration of IVUS and OCT images Future work will involve quantitatively analyzing the relationship between WSS and plaque morphology. Further, we will determine fibrous cap thickness and macrophage presence from the OCT images and investigate its co-occurrence with regions of disturbed (low or high) WSS.

ACKNOWLEDGEMENTS

This work was supported by an American Heart Association Postdoctoral Fellowship and by the Georgia Research Alliance Eminent Scholar Program.

REFERENCES

[1] Virmani, R et al., *J Am Coll Cardiol*, 18:C13-18, 2006
[2] Stone, P. et al., *Circulation*, 126:172-181, 2012
[3] Samady, H. et al., *Circulation*, 124:779-788, 2011
[4] Gijsen, F. et al., *Am J Physiol Heart Circ Physiol*, 295:H1608-1614, 2008
[5] Vergallo, R. et al., *Circ Cardiovasc Imaging*, 7:905-911, 2014
[6] Molony, D. et al., SB3C, June 2015
[7] Kostamaa, H. et al., *Am Heart J*, 137:482-488, 1999

Copyright 2016 The Organizing Committee for the 2016 Summer Biomechanics, Bioengineering and Biotransport Conference

SB³C2016
Summer Biomechanics, Bioengineering and Biotransport Conference
June 29 –July 2, National Harbor, MD, USA
SB³C2016-952

ASSESSING THE ABILITY OF HOCKEY HELMETS TO REDUCE CONCUSSION RISK

Bethany Rowson, Steven Rowson, and Stefan M. Duma

Biomedical Engineering and Mechanics
Virginia Tech
Blacksburg, Virginia, United States

INTRODUCTION

Football is often the focal point of concussion research due to its popularity, but the rate of concussion is similarly high in ice hockey [1]. Concerns about the potential long-term effects associated with repeated head injuries emphasize the need to mitigate concussions in sports [2]. Although the reduction in concussion risk may vary greatly between different hockey helmets, there were previously no objective resources available to consumers to enable informed decisions. The purpose of this study was to develop and implement a methodology for evaluating the risk of concussion in different hockey helmets.

METHODS

Development of the Hockey STAR (Summation of Tests for the Analysis of Risk) evaluation system was based on 2 fundamental principles. The first is that each laboratory impact condition is weighted based on how often similar impacts occur during play. The second is that helmets that decrease head acceleration will decrease concussion risk. These principles are the foundation of the Hockey Star equation (Eq. 1), where E is head impact exposure as a function of location (L) and impact energy (θ), and R is concussion risk as a function of linear (a) and rotational (α) head acceleration. Four impact locations (front, side, top, and back) and 3 impact energies (low, medium, and high) result in a total of 12 unique impact conditions.

$$Hockey\ STAR = \sum_{L=1}^{4}\sum_{\theta=1}^{3} E(L,\theta) * R(a,\alpha) \qquad (1)$$

The Hockey STAR value represents the predicted incidence of concussion for a hockey player experiencing a specific head impact exposure over 1 season of play. The main outcomes of the efforts toward developing this methodology were: design and implementation of a custom impact pendulum for laboratory tests, a process for mapping on-ice head impact exposure to laboratory test conditions, and testing of all available helmet models using the methodology.

A pendulum was chosen for its increased repeatability and reproducibility when compared with other head impact systems (Fig. 1) [3]. A rigid nylon impacting face further increases repeatability between tests, and simulates rigid surfaces encountered in hockey such as ice, boards, and glass. The pendulum impacts a helmeted NOCSAE headform mounted on a Hybrid III neck. The head and neck are mounted on a slider table that simulates the effective mass of the torso during impact. To measure the kinematics resulting from impact, the headform is instrumented with a 6 degree of freedom sensor package consisting of 3 linear accelerometers and 3 angular rate sensors. The headform responses from pendulum impacts in the lab were compared to on-ice data by generating corridors from both on-ice player data and ice rink testing with a Hybrid III head. The laboratory impacts proved to be biofidelic when compared with the on-ice data.

Several steps were taken to relate on-ice head impact exposure to laboratory impacts. First, distributions for linear and rotational acceleration data from players were combined into a single bivariate cumulative distribution function (bCDF). The bCDF results in a single percentile output for any combination of linear and rotational acceleration. The next step was to map the bCDF to laboratory impacts by determining the percentiles over a range of pendulum impact energies (arm angles). The result of the mapping was a single cumulative percent of player impacts for each laboratory impact energy. This analysis was performed for all 4 impact locations.

Copyright 2016 The Organizing Committee for the 2016 Summer Biomechanics, Bioengineering and Biotransport Conference

Figure 1: The custom impact pendulum device was used to strike a NOCSAE headform mounted on a Hybrid III 50th percentile neck. The head and neck were mounted on a sliding mass that simulated the effective mass of the torso during impact.

Three impact energies were selected for the Hockey STAR evaluation system to encompass a wide range of head accelerations that included both sub-concussive and concussive impacts. The impact energies selected, in terms of pendulum arm angles, were 40° (low), 65° (medium), and 90° (high). The weighting of each impact in the evaluation system was determined by creating impact energy bins with bounds midway between each impact condition. The cumulative percent of player impacts within each bin, multiplied by the total number of impacts for that location, was used as the exposure weighting for that condition. Both player exposure data and laboratory impacts were divided by impact location. The total number of impacts per player per season, and the percent of impacts by location were taken from the literature [4, 5].

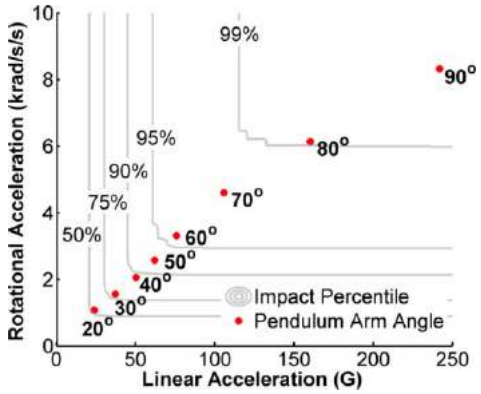

Figure 2: Bivariate cumulative distribution functions (bCDF) were used to determine the cumulative percent of impacts that fell below each pendulum arm angle. This figure shows the bCDF for the front location.

Using the impact pendulum and exposure weightings described above, all commercially available hockey helmets were tested to identify differences in performance between them. For each of the 12 laboratory conditions (4 impact locations and 3 energies), 2 tests per helmet were performed. The peak linear and rotational accelerations were then averaged for repeated tests. The risk of concussion was calculated using the average peak resultant linear and rotational head accelerations for each impact condition [6]. The risk was then multiplied by player exposure to determine incidence of concussion for that condition. The incidences for all 12 conditions were then summed to determine the Hockey STAR value. Two helmets per model were tested, and the Hockey STAR values averaged to a single value per model.

RESULTS

The total number of impacts per player per season was 227. The front, side (right and left combined), and back location each accounted for 30% of the impacts, while the top occurred less frequently at 10%. The head impact exposure of a single player over 1 season for each of the 12 laboratory conditions is shown in Table 1.

Table 1: Player exposure to each impact condition. All conditions together sum to 227 impacts per player per season.

	40°	65°	90°	Total
Front	62.9	4.6	0.6	**68.1**
Side	65.6	2.2	0.3	**68.1**
Top	21.5	1.1	0.1	**22.7**
Back	61.4	4.5	2.2	**68.1**
Total	**211.4**	**12.4**	**3.2**	**227**

All commercially available hockey helmets were evaluated and rated using these methods. A total of 37 available helmet models translated to 1,776 impact tests. The Hockey STAR values ranged from 10.13 to 2.98, with larger values representing a greater risk of concussion. The median Hockey STAR value [25^{th} – 75^{th} percentile] was 6.11 [5.00 – 8.18].

DISCUSSION

The methods outlined here are the first to evaluate the ability of different hockey helmets to reduce concussion risk based on both linear and rotational head accelerations. The testing matrix for each helmet is representative of impacts that hockey players see on the ice, and the evaluation system combines the results from all tests based on how often each condition occurs. Hockey STAR values are greater than on-ice concussion rates because this analysis accounted for the underreporting of injury. The STAR value is inclusive of both diagnosed and undiagnosed concussions.

This work presents a novel methodology for comparing the performance of hockey helmets, and demonstrates differences between helmet types in their ability to reduce concussion risk. The Hockey STAR values were translated to a star rating that could be easily interpreted by consumers, and the results were disseminated online (www.vt.edu/helmet). The Hockey STAR methodology provides a scientific framework for manufacturers to optimize hockey helmet design for injury risk reduction, while providing consumers with a meaningful metric to assess the relative performance of hockey helmets.

REFERENCES

1. Hootman, JM et al., J Athl Train, 2007. **42**(2): p. 311-9.
2. McKee, AC et al., Brain, 2013. **136**(Pt 1): p. 43-64.
3. Pellman, EJ et al., Neurosurgery, 2006. **58**(1): p. 78-96.
4. Mihalik, JP et al., Ann Biomed Eng, 2012. **40**(1): p. 141-9.
5. Wilcox, BJ et al., J Biomech, 2014. **47**(1): p. 109-14.
6. Rowson, S et al., Ann Biomed Eng, 2013. **41**(5): p. 873-82.

Copyright 2016 The Organizing Committee for the 2016 Summer Biomechanics, Bioengineering and Biotransport Conference

SB³C2016
Summer Biomechanics, Bioengineering and Biotransport Conference
June 29 –July 2, National Harbor, MD, USA
SB³C2016-953

DIGITAL MANUFACTURING AND IN SILICO MODELING FOR RATIONAL DESIGN OF DRUG DELIVERY TO THE CENTRAL NERVOUS SYSTEM

Kevin M. Tangen (1), Ted Gabor (2), Lu Lu (2), Yayue Pan (2), Narasimhan Sriram (1), Andreas A. Linninger (1,3)

(1) Bioengineering
University of Illinois at Chicago
Chicago, Illinois, United States

(2) Mechanical Engineering
University of Illinois at Chicago
Chicago, Illinois, United States

(3) Department of Neurosurgery
University of Illinois at Chicago
Chicago, Illinois, United States

INTRODUCTION

Intrathecal drug delivery (IT) is an attractive option to bypass the blood brain barrier for targeting the central nervous system (CNS) through increased drug efficacy, reduction in side effects, and cost-effectiveness. However, due to a lack of knowledge of the driving forces of drug transport in the cerebrospinal fluid (CSF), there are no clear guidelines for clinicians to choose drug infusion parameters. Predictive methods to administer therapeutic compounds to specific regions of the spine or the brain would provide physicians with a tool to improve intrathecal drug delivery treatments.

Computational fluid dynamics is a tool which has been utilized to predict CSF flow fields in global models of the CNS and the resulting drug dispersion [1-2]. These in silico models are reconstructed from medical image data and predicted flow rates are validated with CINE MRI velocity measurements. In addition to computational models, bench-top studies model the relationship between CSF mechanics and drug transport. However to accurately describe the fluid dynamics within the human CSF-filled spaces an anatomically consistent model is needed.

The idea of printing a realistic and functional model of the CNS has never been realized before. Using 3D printing techniques capable of printing complex objects [3-5] and medical image derived geometries, we propose to generate a full-sized, anatomically accurate model of the human central nervous system. This will elucidate the driving forces behind drug transport in the CSF and allow validation between three modalities, MRI measured data, subject-specific in silico predictions, and subject-specific 3D printed bench-top models.

The combination of validated CSF flow measurements and drug transport phenomena will enable the prediction and rational design of IT drug administration protocols for optimal drug delivery for brain cancers, spasticity, and chronic pain.

METHODS

Phase contrast MRI anatomical data of the human cranial and spinal CSF-filled space is acquired. The high resolution images provide information on spinal anatomical dimensions as well as nerve root positions, and volumes of the spinal, cranial, and ventricular CSF spaces. (1,6) Additionally, CSF velocity is acquired at axial planes of interest in the spine using CINE MRI for comparison of flow fields and validation of predictive models.

The high resolution T2 image set was segmented into the CSF domain and the tissue domain containing the spinal cord, nerve roots, and brain parenchyma. The detailed subject-specific computational geometry was reconstructed as an STL file. Then a computational volume mesh is generated using 2M tetrahedral elements covering the CSF filled spaces.

The CSF fluid motion in the model of the entire nervous system with subject-specific anatomical boundaries including nerve roots was simulated by solving the continuity and the Navier-Stokes equations for an incompressible Newtonian fluid, where, ρ, is the density, μ the kinematic viscosity, $\vec{g}$(is gravity, $\vec{u}$ and p are the velocity vector and pressure fields, respectively.

Continuity $$\vec{\nabla} \cdot (\rho \vec{u}) = 0 \quad (1)$$

Momentum $$\frac{\partial \vec{u}}{\partial t} + \vec{u} \cdot \vec{\nabla} \vec{u} = -\frac{1}{\rho} \vec{\nabla} p + \mu \vec{\nabla}^2 \vec{u} + \rho \vec{g} \quad (2)$$

The STL obtained from the human MRI data is used as the input for a novel multi-scale 3D printing system that will be developed by integrating macro stereolithography and micro-stereolithography

Copyright 2016 The Organizing Committee for the 2016 Summer Biomechanics, Bioengineering and Biotransport Conference

(SL) processes. A micro-SL prototype machine has been developed that can fabricate parts with ~10µm resolution, which would capture the complex geometry of the nerve roots in the CNS. [4]

The model will be printed with flexible and transparent acrylic or epoxy photopolymer materials to emulate the mechanical properties of natural SAS tissues. In addition, translucent materials allow for the visualization of injected tracers and drugs. Flow measurements can be taken by Doppler ultrasound and drug tracking by means of structured-optical systems.

RESULTS

Drug distribution in the subarachnoid space is driven by natural pulsatile motion of the CSF. Fig 1A shows temporal plots of CSF flow measured by Cine MRI at axial planes in the cervical (C4), thoracic (T6), and lumbar (L4) spinal regions. During the systolic phase of the cardiac cycle (red) CSF is forced downward into the spine, and during diastole CSF gradually flows cranially. This measurement is compared to the subject-specific computational predictions, Fig. 1B at all three planes. Additionally, the in silico model provides a full spatial flow map along the spine over the cardiac cycle, as shown in Fig 1C. The third model is reconstructed from MRI data and 3D printed to capture anatomical resolution down to 10µm. Velocity flow data from the 3D printed model will be acquired with Doppler ultrasound as indicated in Fig 1D, and velocity plots compared the other two data sets.

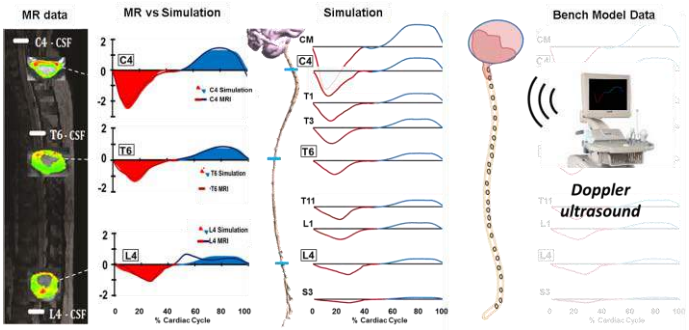

Figure 1: Medical image data for subject anatomy and CSF velocity is extracted for computational and bench-top model validation (A) Anatomical data and CSF flow information is acquired from MRI for the human spinal CSF spaces. (B) CSF flow measurements are compared to in silico predictions at C4, T6, and L4. (C) In silico predictions cover the entire spinal axis. (D) 3D printed model experimental data is extracted with ultrasound to compare to computational and MR measurements.

A magnified view of the cervical spine segment reconstructed from anatomical MR data in the sagittal and axial view is compared in Fig 2, for the computational model and the 3D printed model. The high resolution 3D printing technique easily recreates the complex geometry of the spinal SAS. Geometry-induced mixing has been shown to impact CSF flow and thereby drive drug dispersion.

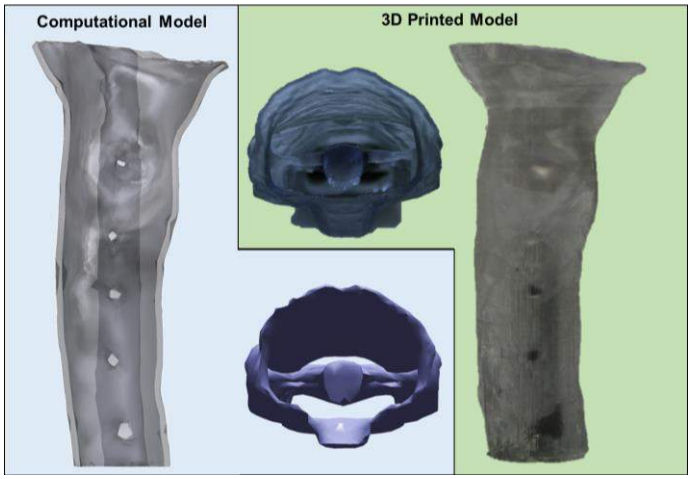

Figure 2: Subject-specific computational model (left) and 3D printed cervical spine segment (right). The Cisterna Magna to the C5 spinal nerve level are reconstructed from MRI data.

DISCUSSION

This research presents for the first time, a subject-specific 3D printed model of the human CSF-filled spaces for comparison to high resolution in silico reconstruction. An anatomically accurate and model of the human CNS can replicate complex fluid flow phenomena in the spinal canal and the brain. These geometry induced mixing vortices are below the resolution capability of MRI but are predicted with computational models. This high fidelity is necessary to accurately predict drug transport in the cerebrospinal fluid to elucidate the driving forces of drug spread.

The bench-top 3D printed model will be anatomically realistic, pulsatile and compliant system of the spinal CNS. This system will allow for detailed and repeatable measurements of the CSF flow. Through validation of a subject-specific CNS test station with computational modeling and MR data this bench-top model will enable the prediction and rational design of IT drug administration protocols for optimal drug delivery for brain cancers, spasticity, and chronic pain.

ACKNOWLEDGEMENTS

The authors would like to gratefully acknowledge the partial support of this project by NSF grants CBET-0756154.

REFERENCES

[1] Tangen, K., Hsu, Y., Zhu, D., Linninger, A., *J Biomechanics,* 48:2144-2154, 2015.

[2] Kuttler, A., Dimke, T., Kern, S., Helmlinger, G., Stanski, D., Finelli, L., *J Pharmacokinetics and Pharmacodynamics*, 37:629-644, 2010.

[3] Pan, Y., Zhao, X., Zhou, C., Chen, Y., *J Manufacturing Processes*, 14:460-470, 2012

[4] Pan, Y., Zhou, C., Chen, Y., *J Manuf Sci Eng*, 134(5), 2012

[5] Song, X., Pan, Y., Chen, Y., *J Manuf Sci Eng*, 137(2), 2015

[6] Hsu, Y., Hettiarachchi, H.D.M., Zhy, D., Linninger, A., *Anesthesia and Analgesia*, 34:859-871, 2001.

Copyright 2016 The Organizing Committee for the 2016 Summer Biomechanics, Bioengineering and Biotransport Conference

SB^{3}C2016
Summer Biomechanics, Bioengineering and Biotransport Conference
June 29 –July 2, National Harbor, MD, USA
SB^{3}C2016-954

A PERMANENT SET CONSTITUTIVE MODEL FOR EXOGENOUSLY CROSS-LINKED COLLAGENOUS TISSUES

Will Zhang(1), Hobey Tam(2), Wei Sun(3), Naren Vyavahare(2) and Michael S. Sacks(1)

(1) Center for Cardiovascular Simulation
Institute for Computational Engineering & Sciences
Department of Biomedical Engineering
The University of Texas at Austin
Austin, TX, USA

(2) South Carolina Bioengineering Center of
Regenerative and Formation of Tissue
Department of Bioengineering
Clemson University
Clemson, SC, USA

(3) Department of Biomedical Engineering
Georgia Institute of Technology
Atlanta, GA, USA

INTRODUCTION

Despite the overall advancements in the treatment of cardiovascular diseases, heart valve surgeries have seen little real improvements in life expectancy since 1985, where the survival rate after 10 years is still 29.7% [1]. The field has been heading in the direction of percutaneous devices to minimize surgical impact and to serve as an alternative for non-surgical candidates. However, the currently technology is still in its early stages, with a 2-year mortality rate of 43.3% for such trans-catheter devices [1]. Biologically-derived exogenously cross-linked (EXL) tissues such as bovine pericardium (BP) is by far the most popular biomaterial used. BHV failure results from leaflet structural deterioration mediated by fatigue and/or tissue mineralization. In general, while mineralization is associated with serious structural deterioration, significant structural damage is known to occur independently from calcification [2]. Most research for BHV devices focus on calcification, but understanding and being able to model and predict the exogenous cross-linking effects on the biomaterials, specifically the permanent set effect that occurs due to scission healing reactions of the exogenously cross-links used to stabilize and suppress immunogenicity, is equally as important. In the present work we developed a structurally-based permanent set constitutive model to help to better understand and predict the change in mechanical property that occurs due to long-term cyclic loading, and aid in the design of new bioprosthetic devices.

METHODS

General Considerations. Mechanical fatigue occurs in the long term due to structural damage and in the short- and mid-term (first 10-20 million cycles) due to permanent set. Whereas structural damage is categorized by the loss of properties due to degradation and physical tearing, permanent set is in no way due to changes in properties of the constituent material, but due to conversion of existing material to new reference states due to persistent loading. To model permanent set, we will make the following assumptions:

1) There is no change in the mechanical properties of the collagen and the matrix; changes in tissue-level mechanical properties are driven completely by the first order scission/healing reaction of the Schiff-base glutaraldehyde polymers.
2) The process is under physiological conditions, thus can be modeled as an isothermal process.
3) There is no strain-level dependence
4) The rate of scission/healing is much slower compared to the cardiac cycle (i.e. days/weeks vs. seconds).
5) The non-collagenous tissue matrix can be modeled as an isotropic hyper-elastic material.

Permanent Set Model. We adopt the permanent set approach previously developed for rubber like materials [4]. As a modification, we allow continuous evolution of reference states where all existing matrix is constantly being remodeling by the first order kinetics of the scission healing process at the macro-level (Fig. 1). The process is entirely governed by one rate constant k_g for scission and healing. The resulting permanent set that occurs, which is a geometrical change described by a deformation gradient, $\mathbf{F}^*$, from the virgin state to the current stress-free state, depends on the proportion of new and old materials and the stress equilibrium.

Mechanical Response of the Matrix under Permanent Set. In a recent study, we developed a model for the EXL bovine pericardium [3]. We now apply a modification to the model to determine its mechanical response under permanent set. The key mechanism of permanent set is a re-expression of the stress of the material with respect to an alternative reference state. Thus solving the resulting chain rule gives the following 2nd Piola Kirchhoff stress:

Copyright 2016 The Organizing Committee for the 2016 Summer Biomechanics, Bioengineering and Biotransport Conference

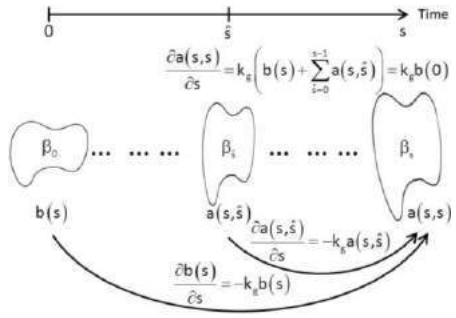

Figure 1: An illustration of the permanent set process, where the original material b(s) is converted to new states a(s,ŝ). The intermediate states are subsequently converted as well.

$$\bar{\mathbf{S}}_m\left(\mathbf{F},\hat{\mathbf{F}}\right)=\left(\mu_\alpha\left(I_1\left(\mathbf{F},\hat{\mathbf{F}}\right)-3\right)^{\alpha-1}+\mu_\beta\left(I_1\left(\mathbf{F},\hat{\mathbf{F}}\right)-3\right)^{\beta-1}\right)\times\left(\hat{\mathbf{B}}^{-1}-\hat{\mathbf{B}}_{33}^{-1}\mathbf{C}_{33}\mathbf{C}^{-1}\right) \quad (1).$$
$$I_1\left(\mathbf{F},\hat{\mathbf{F}}\right)=\mathrm{Tr}\left(\hat{\mathbf{F}}^{-T}\cdot\mathbf{C}\cdot\hat{\mathbf{F}}^{-1}\right)$$

Solving (1) for underlying rate kinetics (Fig. 1) results in the following overall stress of the material

$$\mathbf{S}_m\left(\mathbf{F}(s)\right)=e^{-k_g s}\bar{\mathbf{S}}_m\left(\mathbf{F},\mathbf{I}\right)+\int_0^s k_g e^{-k_g(s-\hat{s})}\bar{\mathbf{S}}_m\left(\mathbf{F},\mathbf{F}\left(\hat{s}\right)\right)d\hat{s} \quad (2).$$

To solve for the permanent set deformation, $\mathbf{F}^*$, a numerical solution is needed. Here, the problem is defined in terms of the number of parameters for $\mathbf{F}^*$, N, and the applied deformation $\bar{\mathbf{F}}$,

$$\mathbf{F}^*=\min_{\mathbf{F}^*\in\mathbb{R}^N}\left\|\mathbf{S}_m\left(\mathbf{F}^*\right)\right\|^2,\qquad k_g=\min_{k_g\in[0,\infty]}\left\|\mathbf{F}^*\left(k_g\right)-\bar{\mathbf{F}}\right\|^2 \quad (3)$$

Permanent Set and Mechanical Studies. First, we measured the permanent set and mechanical properties of glutaraldehyde EXL BP placed under a static strain of 10%, 20% and 30% over the period of 4 weeks; a two state system with only the original and loaded state (Fig. 2A). They were also tested along the preferred fiber direction (PD) and the cross-preferred direction (XD). The tissue strain was quantified using marker tracking [5]. The mechanical properties were determined using a custom built biaxial testing device[6] and analytical method [7]. In addition, we also tested a separate set of specimens where the strain is periodically increased, resulting in a more complex model with multiple states (Fig. 2C). Lastly, we supplemented the results with previous studies done on cyclic strain loading (Fig. 2B)[8] and stress controlled loading (Fig. 2D)[9], which involves a time dependent system for stress loading and the constant increasing strain.

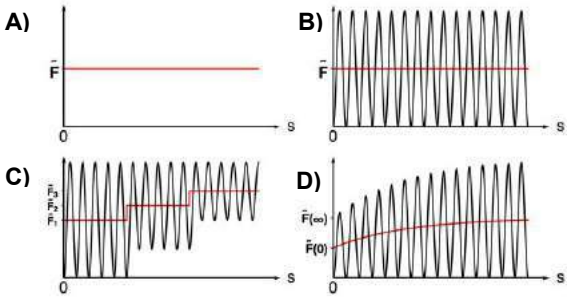

Figure 2: The types of testing that were done showing the actual (Black) and RMS strain (Red). This include a two state system under static (A) and cyclic loading (B), C) multistate system with multistep loading process, and D) a continuous evolution of stats process due to stress loading.

RESULTS

Experimental result shows significantly permanent set in the direction of stretching (Fig. 3A), but not to the full extension ($\lambda = 1.2$). This suggests that the process did not reach completion, and some material still remains in the original state. We also find that this resulted in a stiffening effect along the stretched direction relative to their stress free reference state as predicted (Fig. 3B), significantly limiting the extensibility of the tissue as a result. The resulting rate constant determined from the permanent set stretch shows no statistical difference in the direction of mounting; $k_g = 0.92\pm0.42\times10^{-6}$ s^{-1} and $1.19\pm0.50\times10^{-6}$ s^{-1} for the PD and XD directions respectively ($p = 0.73$). This process is repeated for the multistage data and the stress controlled dataset. Furthermore, the model parameters determined from the PD is used to predict the mechanical response in the XD for validation of the stress loading.

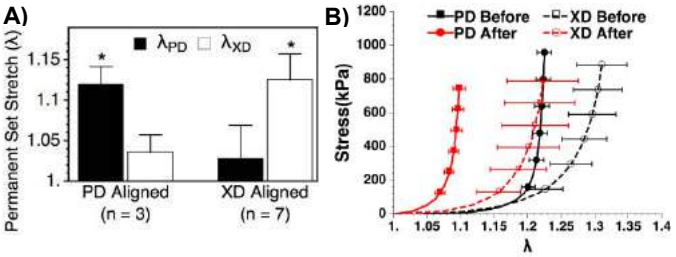

Figure 3: The resulting permanent set stretch for 20% strain is shown in A). B) The results of mechanical testing for the PD aligned group shows that the PD stiffened significantly (Black to Red), corresponding to the significant permanent set stretch in A).

DISCUSSION

In this work, we developed the first permanent set model for exogenously cross-linked tissues based on the underlying scission/healing of the cross-linker. This process does not induce actual structural damage to the tissue, but will nevertheless induce a comparable or larger effect to the mechanical properties. The effective extensibility becomes significantly limited due to the removal of the toe region that occurs. As such, the intended resting geometry of the BHV device is altered, changing the resulting stress distribution, inducing spots with stress concentrations, increasing its wear and tear and ultimately limiting its functionality and durability. Although the effect occurs over a period of 1-2 years, we have observed significant changes in the geometry and mechanical properties after only 4 weeks. Thus proper design of bioprosthetic devices needs to properly account for the permanent set effect to best improve their performance and durability. And computational simulations need to properly consider this effect for predicting the fatigue of tissues.

ACKNOWLEDGEMENTS

This work is supported by NIH grants HL119297, HL108330, HL073021, and HL063964.

REFERENCES

[1] Mozaffarian D et al. Circulation 2015;131:e29-e322.
[2] Sacks MS et al. J Biomed Mater Res 2002;62:359-71.
[3] Sacks MS et al. Interface focus 2016;6.
[4] Rajagopal KR et al. Int. J. Plasticity 1992;8:385-95.
[5] Billiar KL etal. J Biomech Eng-T Asme 2000;122:23-30.
[6] Grashow JS et al. Ann Biomed Eng 2006;34:315-25.
[7] Zhang W et al. J Biomech Eng 2015;137:064501.
[8] Sun W et al. J Biomed Mater Res 2004;69A:658-69.
[9] Sellaro TL et al. J Biomed Mater Res A 2007;80:194-205.

Copyright 2016 The Organizing Committee for the 2016 Summer Biomechanics, Bioengineering and Biotransport Conference

SB^{3}C2016
Summer Biomechanics, Bioengineering and Biotransport Conference
June 29 –July 2, National Harbor, MD, USA
SB^{3}C2016-955

IN SITU ESTIMATION OF AXONAL INJURY STRAIN THRESHOLDS FOLOWING TISSUE-LEVEL TENSILE STRETCH

Sagar Singh (1), Assimina A. Pelegri (2), David I. Shreiber (1)

(1) Department of Biomedical Engineering
Rutgers, The State University of New Jersey
Piscataway, NJ, USA

(2) Department of Mechanical and Aerospace Engineering
Rutgers, The State University of New Jersey
Piscataway, NJ, USA

INTRODUCTION

Primary axonal injury in white matter is a major cause of functional deficits following central nervous system trauma [1]. During trauma, stress and strain are transferred from the tissue-scale to axons at the micro-scale, though the specific translation between the two scales is unclear. We have previously demonstrated that microstructural features such as axon diameter, tortuosity, kinematics, and connectivity to surrounding glia play a role in the transfer [2]. Computational models have been developed to both understand this transfer, and estimate axonal strains following macroscopic stretch, with the ultimate goal of predicting axonal injury strain thresholds [3], [4]. However, it remains difficult to relate these strains to axonal damage or failure, particularly in situ.

In this study, we exposed chick embryo spinal cords harvested at different stages of myelination to controlled tensile stretch. We estimate axon strain using immunostained Caspr as fiducial markers. Caspr is an ideal marker, as it is expressed in pairs at the nodes of Ranvier along axons. We then identified and catalogued broken axons and adapted our kinematic model [5] to estimate an average strain threshold for axon breakage by fitting the predicted proportion of broken axons to experimental results.

METHODS

Experimental Methods: Chick embryonic spinal cords with varying degrees of myelination were excised and exposed to tensile stretch before being fixed and sectioned into 40µm longitudinal slices. Sections were immunostained for neurofilament, and Caspr. Stained sections were imaged via confocal microscopy with a 100x oil immersion objective. Image stacks were obtained in increments of 0.4µm per image through the depth of the section.

Measurements: Axons were traced through the image stacks. End-to-end and pathlength distances between pairs of immunostained

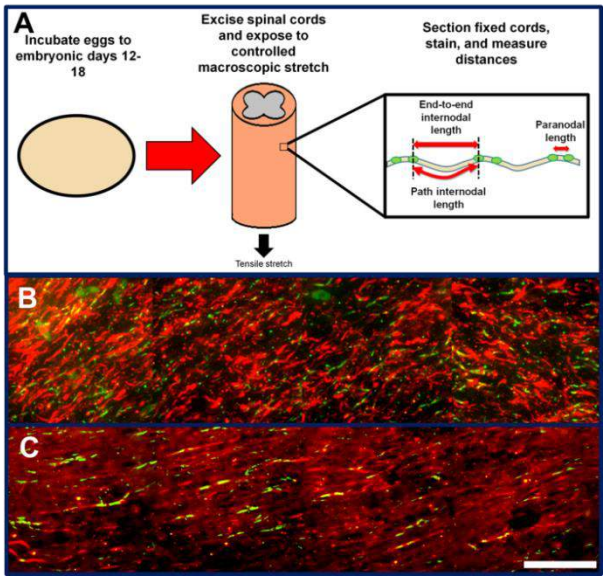

Figure 1: (A) Visual schematic of experimental methods. (B&C) z-projections of imaged longitudinal sections (red = neurofilament, green = caspr) for E18 specimens (B) unstretched, and (C) 20% stretch. (Scale = 50µm)

Caspr (internodal), and individual Caspr proteins (paranodal) along axons were measured (Figure 1A). Broken axons were recorded for different development stages and stretch levels.

Modeling: Kinematic models were adapted from Singh et al. (2015), to predict axon breaking thresholds [5]. Internodal lengths and

Copyright 2016 The Organizing Committee for the 2016 Summer Biomechanics, Bioengineering and Biotransport Conference

tortuosities for unstretched axons were initialized for each development stage. New lengths and tortuosities were calculated as a function of macroscopic stretch. Each axon was individually assigned a breaking strain threshold selected from a normal distribution. When an axon stretched beyond its threshold based on changes in internodal pathlength, the axon was recorded as broken. The predicted proportions of broken axons were fit to the experimental proportions of broken axons. Probability distribution parameters were varied and the model was iterated until parameters reached convergence.

RESULTS

When all axons were included in the analysis, the average end-to-end internodal lengths increased with development stage and stretch level. We observed a strong correlation between tissue-level stretch and changes in individual axon lengths for E12 and E14 specimens. However, results deviated from this trend at later stages (Figure 2A). We then assumed that once broken, an axon no longer experienced stretch and would therefore not increase in length. When lengths from broken axons were not included in the calculation for change in average length, the averaged data moved closer to the 1:1 line for later development stages, suggesting that more axons were breaking at later stages of development.

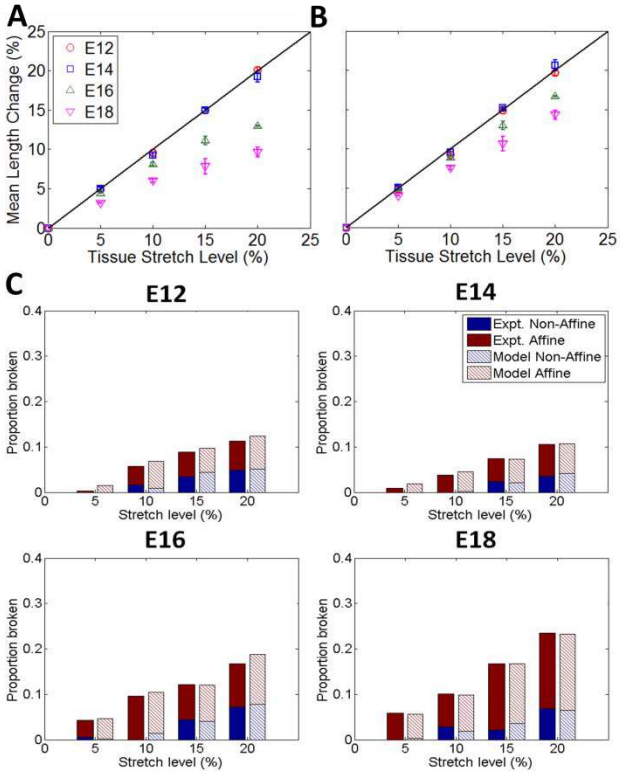

Figure 2: (A) Percentage change in internodal length relative to unstretched tissue was plotted against macroscopic stretch. (B) When lengths from broken axons were not included in the calculation in of average change in length, there was a closer agreement between macroscopic stretch and axon strain. (C) Proportion of broken axons from experiments and model predictions when thresholds were picked from a normal distribution.

By adapting our kinematic model to fit the proportion of broken axons, we determined that individual thresholds picked from a normal distribution provided the best fit (Figure 2C). Thresholds decreased with development stage, from 25% strain to 17% strain (Table 1). When axons were categorized by their predicted kinematic behavior, the estimated thresholds differed, where non-affine axons required more strain to irrevocably injure relative to affine axons.

	Single Threshold	Non-Affine Threshold	Affine Threshold
E12	1.252 ± 0.12	1.291 ± 0.12	1.185 ± 0.13
E14	1.227 ± 0.11	1.284 ± 0.13	1.181 ± 0.14
E16	1.196 ± 0.09	1.269 ± 0.14	1.165 ± 0.09
E18	1.172 ± 0.08	1.270 ± 0.15	1.142 ± 0.10

Table 1: Predicted parameters (mean ± s.d.) for normal distributions of damage thresholds.

DISCUSSION

In this work, we demonstrated a means to estimate axonal strain as a function of macroscopic stretch by measuring changes in internodal end-to-end and pathlengths. We then modeled axon kinematics and fit the proportions of axons predicted to break to experimental results to estimate injury thresholds.

A greater proportion of axons were found to break at later stages of development, which corroborates the lower damage thresholds that were predicted by the model (lower thresholds means axons are easier to break). We examined three distinct regions of the spinal cord (cervical, thoracic, and lumbar) and found no statistically significant difference in proportion of broken axons with regards to region. Along the axon, 96% of axons broke at internodal segments. Examining across the entire cord, we observed no discernible patterns in localization of breaking; axons broke randomly throughout the tissue.

When axons were categorized by their predicted kinematics, and their breaking thresholds calculated, non-affine thresholds were consistently higher than affine thresholds. This correlates well with several findings where *in vitro* preparations of axons, which behave with non-affine kinematics, are able to tolerate up to 75% strain without experiencing injury [6]. In guinea pig optic nerve studies, where nearly all axons are myelinated, coupled to surrounding glia, and are predicted to behave with affine kinematics, these thresholds was closer to 21% [2]. We believe that axons exhibiting affine kinematics experience strain that is commensurate with the macroscopic stretch, whereas in non-affine axons, the macroscopic stretch is initially transferred to straightening tortuous axons, making non-affine axons more resilient to applied tissue-level stretch.

Future work is focusing on characterizing the kinematics of axons once they have broken. We are also investigating methods to snap-freeze tissue immediately following dynamic injury. The results we present provide useful insights into the role of microstructure in injury thresholds, and helps validate predictions made by multi-scale finite element models of central nervous system and axonal injury.

ACKNOWLEDGEMENTS

This work was supported by the NSF CMMI Grant #1000450

REFERENCES

[1] D. H. Smith and D. F. Meaney, *Neurosci.*, vol. 6, no. 6, pp. 483–495, Dec. 2000.

[2] A. Bain and D. Meaney, *J. Biomech. Eng.*, vol. 122, no. December, pp. 615–22, 2000.

[3] R. J. H. Cloots et al., *Biomech. Model. Mechanobiol.*, vol. 12, no. 1, pp. 137–50, Jan. 2013.

[4] Y. Pan et al., *Front. Bioeng. Biotechnol.*, vol. 1, no. December, p. 19, Jan. 2013.

[5] S. Singh et al., *Biomech. Model. Mechanobiol.*, Apr. 2015.

[6] M. D. Tang-Schomer et al., *FASEB J.*, vol. 24, no. 5, pp. 1401–10, May 2010.

Copyright 2016 The Organizing Committee for the 2016 Summer Biomechanics, Bioengineering and Biotransport Conference

SB^{3}C2016
Summer Biomechanics, Bioengineering and Biotransport Conference
June 29 –July 2, National Harbor, MD, USA
SB^{3}C2016-956

DEVELOPMENT OF CLINICALLY RELEVANT CONSTRAINT MEASUREMENT USING MODIFIED TOTAL KNEE REPLACEMENT IMPLANTS

Scott N. Anderson (1), Peter S. Walker (2), Ryan T. Willing (1)

(1) Mechanical Engineering
Binghamton University
Binghamton, NY, USA

(2) Langone Medical Center
New York University
New York, NY, USA

INTRODUCTION

Despite over four decades of development, there is still no established and universal method for the design, evaluation, and comparison of total knee replacement (TKR) designs. The intrinsic constraint of a TKR system is an important metric for determining the stability, and there are standardized techniques for measuring these properties (e.g. ASTM F 1223-14). These standards describe the resistance to anterior-posterior (AP) and medial-lateral (ML) displacements, and internal-external (IE) rotation under an axial load between the femoral and tibial components at discrete flexion angles. Such tests, however, do not necessarily map directly to any physiologically relevant loading scenarios; thus, comparisons of TKR systems based on these techniques may provide misleading results. Recent advancements in the development of force-controlled joint motion simulators have allowed more physiological in-vitro joint loading, including the contributions of virtual soft tissues. We hypothesize that a function-based technique for measuring TKR constraint may yield a different classification of TKR systems in terms of constraint, as compare with the long-standing discrete-angle measurement technique. Therefore, the objective of this study is to develop an alternative, function-based means of assessing TKR constraint.

METHODS

A parametric computer-aided design (CAD) model of the tibial component of an ultra-congruent TKR with asymmetrical medial versus lateral condyles was created, based on an existing commercially available cruciate-sacrificing TKR. The geometry of the ultra-high molecular weight polyethylene (UHMWPE) insert and tibial tray was modelled as a monoblock tibial component, and further modified into three different designs. Each monoblock tibial component featured different sagittal radii, in order to create high, low, and medium-conformity designs when mated with the existing commercially available femoral component. The three designs were printed with acrylonitrile butadiene styrene (ABS) plastic using a uPrint SE Plus fused deposition modeling machine (Stratasys Ltd. Eden Prairie, MN). The femoral component was affixed onto a custom fixture on the upper actuator of the VIVO 6-DOF joint motion simulator (Advanced Mechanical Technology Inc. Watertown, MA) using Bosworth Fastray (Keystone Industries, Gibbstown, NJ) polymethyl methacrylate (PMMA), such that the flexion axis of the femoral component coincided with the flexion axis of the VIVO. Each tibial component was then affixed into a fixture on the lower actuator in a neutral orientation with respect to the femoral component using dental stone. Flexion/extension and abduction/adduction motions were provided by the upper actuator, while all joint displacements and internal/external rotation were provided by the lower actuator. Prior to any force-controlled testing, displacements were applied in the AP, ML, and IE directions with an axial load of 710 N, in order to determine the maximum forces and moments each TKR system could safely withstand without dislocating or achieving clinically unrealistic displacements.

Continuous Flexion Tests: Constraint tests were conducted by applying a continuous flexion/extension motion between 0° and 90°, with 710 N axial load, and all other DOFs unconstrained. The relative motions of the femoral component and tibial components in the AP, ML and IE directions were recorded and defined the "neutral path of motion" of the TKR system. The same loading was repeated, but with a constant anterior, posterior, medial, lateral, internal, or external load applied, equal to 80% of the limit for that TKR system. The relative change in joint motion compared to the neutral path was measured for each superimposed load; this change was defined as the laxity.

Copyright 2016 The Organizing Committee for the 2016 Summer Biomechanics, Bioengineering and Biotransport Conference

Physiological Motion Tests: Knee joint loads and flexion angles during gait have been previously reported in the literature, and were used as inputs for the VIVO joint simulator. The loads were scaled by a constant factor such that the maximum axial load was equal to 710 N to prevent any implant damage. The neutral path of each TKR during gait was determined throughout the simulated gait cycle. Then the laxity was measured by superimposing AP, ML, and IE loads as before, on top of the AP, ML, and IE loads already applied during the simulated gait cycle. The magnitudes of the superimposed loads were adjusted proportionately with the time varying axial force in order to prevent large distracting loads from causing excessive displacements when there is little joint compression.

Soft Tissue Contribution: Additionally, the cruciate and collateral ligaments were simulated as tension-only point-to-point springs incorporated into the control software of the VIVO joint motion simulator. Stiffness characteristics and origin / insertion points were obtained from the MB Knee (simtk.org/home/mb_knee). Table 1 shows the stiffness and original strain values by bundle. To investigate the contributions of soft tissue constraint to implant stability, the continuous flexion and physiological motion tests were performed with (i) all four major ligaments disabled, (ii) all enabled except the ACL, and (iii) the collateral ligaments enabled with cruciate ligaments disabled.

RESULTS

Figure 1 compares the AP laxity of the TKR system with each of the printed tibial components. All three ligament configurations are provided for each TKR. In the ligament model with only the collaterals activated, the percent change in anterior and posterior laxity, compared to the ligament model deactivated, was -0.044% and -22%, respectively. When the PCL was included in the ligament model, the changes in anterior and posterior laxity, compared to all ligaments deactivated, was -7.5% and -44% respectively. Figure 2 shows the AP and IE laxities of the high conformity TKR system as measured using the physiological motion test, comparing three ligament model configurations.

DISCUSSION

The AP laxities of the continuous flexion tests support the validity of modelling knee motion with simulated ligaments. The highest posterior displacements occur with no simulated ligaments. The lowest magnitude posterior laxities occur with a simulated PCL and collateral ligaments, and the ligament model with only collaterals exhibited posterior laxities of magnitudes in between the other two ligament models. Since all of the models represent the clinically relevant scenario of ACL resection, the anterior laxity in each TKR varies less than the posterior laxity.

Similarly, the AP and IE laxity data from the physiological motion tests displayed in Figure 2 highlight the importance of ligament simulation. The collateral ligaments provide considerable restraint to internal-external rotation [1]. The IE laxity of the two ligament models which include collateral ligaments are almost equal, while the model with no simulated ligaments yielded a larger magnitude of IE laxity. The AP laxity supports the model by the same rationality as the continuous flexion tests.

Current knee constraint tests do not correspond to physiologically relevant functional scenarios, and thus it may be misleading to extrapolate results from those tests to in vivo function. An alternative, function-based means of assessing TKR constraint could lead to advancements in design, as well as aid in matching individuals with the most suitable prosthesis for them based on their needs.

ACKNOWLEDGEMENTS

The authors would like to acknowledge AMTI for supporting this research.

REFERENCES

[1] Blankevoort L.& Huiskes R., *J Orthop Res*, 14:676-679, 1996.

Table 1: Ligament stiffness and original strain values

Ligament Bundle	Stiffness (N)	Original Strain (%)
aPCL	9000	-0.11
pPCL	9000	-0.09
aLCL	2000	0.02
sLCL	2000	0.03
pLCL	2000	0.02
aMCL	2750	0.03
iMCL	2750	0.03
pMCL	2750	0.03

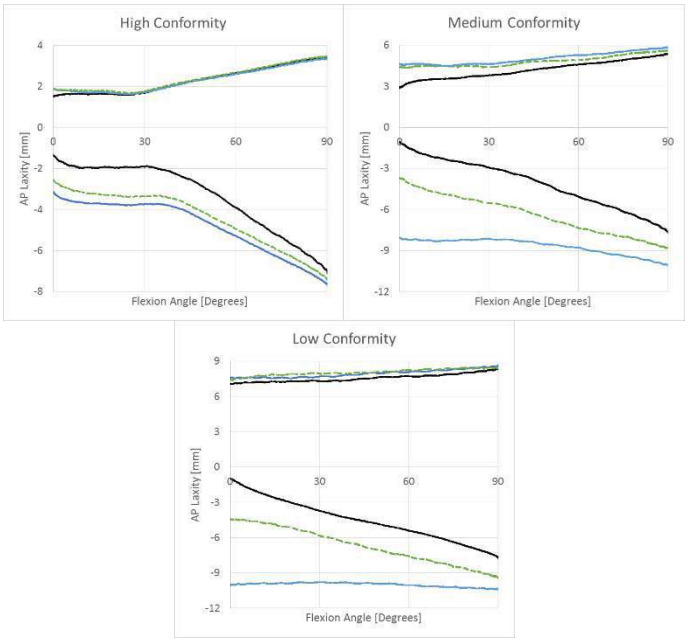

Figure 1: Continuous flexion tests of AP laxity, in three TKR, with simulated PCL and collaterals (black), only collaterals (green-dashed) and without simulated ligaments (blue)

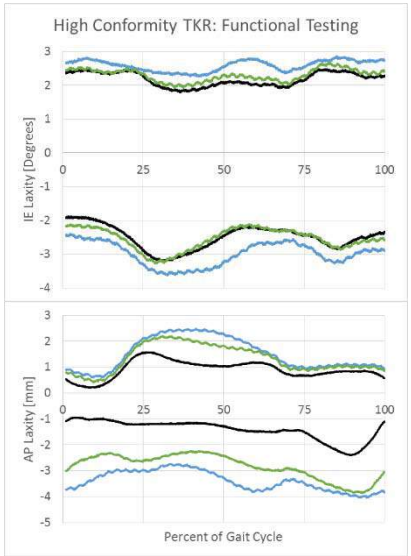

Figure 2: Physiological motion tests of AP and IE laxity with simulated PCL and collaterals (black), only collaterals (green-dashed) and without simulated ligaments (blue)

Copyright 2016 The Organizing Committee for the 2016 Summer Biomechanics, Bioengineering and Biotransport Conference

SB^{3}C2016
Summer Biomechanics, Bioengineering and Biotransport Conference
June 29 –July 2, National Harbor, MD, USA
SB^{3}C2016-958

NONLINEAR BENDING DYNAMICS OF A SEMIFLEXIBLE FILAMENT IN 3D BROWNIAN FLUCTUATION

Jyothirmai J. Simhadri (1), Preethi L. Chandran (1)

(1) Department of Chemical Engineering
Howard University
Washington, DC, USA

INTRODUCTION

Mechanical properties of several biopolymers such as collagen, actin, microtubules, and aggrecan that play a structural role in cells and tissues can be determined from the network of filamentous proteins that constitute them [1]. Depending on the individual filament properties, these filaments behave as semiflexible i.e., because their bending stiffness is on the order of, and resists, the Brownian forces that randomize their conformation [2]. In such semiflexible networks, even though the filament resists the external stresses by storing energy in both bending and stretching modes of deformation, it can still exhibit thermally induced bending. In recent years, much interest has been put into characterizing the mechanics of semiflexible networks due to its importance in understanding the mechanical and rheological properties of complex systems such as cell cytoskeleton and connective tissues.

Several models have been developed to capture the bending in semiflexible filaments. One such model is worm like chain (WLC) model [3], where the biopolymers are modeled as inextensible elastic rods with a continuous description i.e., the chain was considered as a continuous line with no discrete structure. However, only a few properties could be determined due to its analytical limitations. Hence a dynamic simulation presents a way to avoid the mathematical complexities of analytical models.

Chandran and Mofrad [4] had proposed modeling a two-dimensional semiflexible filament as a string of beams that bend continuously under Brownian forces. This idealization not only captures the high-order nonlinear bending of the filament, but it does so at reduced computational cost compared to the string-of-beads idealization or Finite Element simulations. Although at small length scales the discrete nature of the filament becomes important, a major advantage of the beams on string model is that it captures the smooth bending of each beam.

In this work we show how the string-of-beams formulation translates to predict the three-dimensional bending of a fluctuating filament with fourth-order continuity in each bending axis.

MODEL DESCRIPTION

The semiflexible filament is divided into a string of beams or segments that bend, and the Brownian dynamics is determined by solving equations at segment intersections. A beam is geometrically defined as a 3D curve that is tortuous.

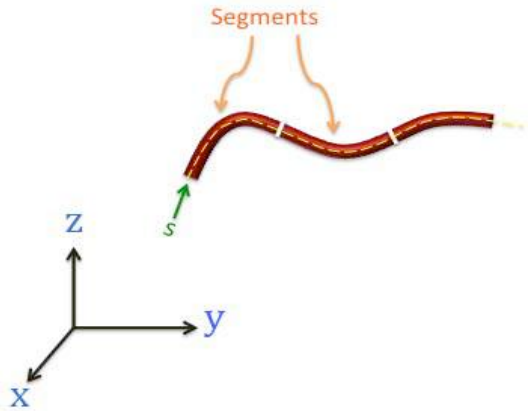

Figure 1: 3D continuous beam

Copyright 2016 The Organizing Committee for the 2016 Summer Biomechanics, Bioengineering and Biotransport Conference

The dynamics of the semiflexible filament is obtained by balancing three forces i.e., Brownian force acting along the length, Drag forces acting along the length, and Shear forces at the ends. In addition to the balance of the forces the filament is assumed to be inextensible.

The governing equations for the filament dynamics are obtained from Langevin equation of motion by summing the external forces acting on the segments (either bead, rod, or beam), i.e.,

$$F^H{}_I(t) + F^S{}_I(t) + F^B{}_I(t) + F^{Br}{}_I(t) = 0, \qquad I = 1, 2, \ldots N \qquad (1)$$

where subscript i refers to the segment number, and F^H, F^S, F^B, F^{Br} are the hydrodynamic drag force, the stretch force, the bending force, and the Brownian force respectively.

SIMULATION PROCEDURE

Simulation procedure consists of the following steps:

1. The semiflexible filament is divided into beam segments. At each of these beam segment intersections the displacements, filament angle, curvature, and shear forces arising as a result of cutting at the intersection or due to the presence of other neighboring beams are calculated.

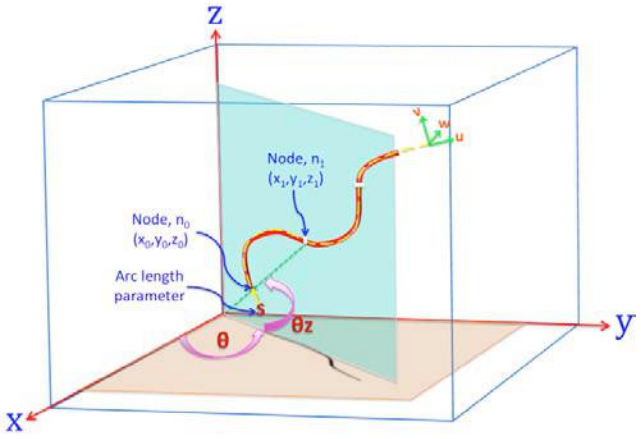

Figure 2: 3D continuous beam having an in-plane rotation angle θ, and out-of-plane rotation angle θ_z.

2. Three forces are balanced: Brownian, Drag, and Shear Forces at ends
   (i) Computation of Brownian forces: Normal and parallel components of Brownian forces are projected in three mutually perpendicular directions and resolved into normal and parallel resultant forces and couples acting at the center of the beam. The variance of the resultant forces and couples are determined by friction coefficients of rigid cylindrical rods.

   (ii) Computation of Drag forces: Normal and parallel components of Drag forces are projected in three mutually perpendicular directions and resolved into normal and parallel resultant forces and couples acting at the center of the beam. The normal and parallel drag forces along the beam are calculated from the displacements along the beam (normal and parallel directions).

   (iii) Computation of Shear forces: Euler beam equations are used to solve for filament curvature, $\frac{d\theta}{ds}$, along a continuous contour s, and shear forces at the ends of the beam segments.

3. Backward Euler time stepping is used to solve for the dynamics of semiflexible filament.

RESULTS

The previous sections provide information on the methodology to solve for the large-deflection Euler beam mechanics in three dimensions. The displacements, and the internal forces are calculated based on in-plane and out-of-plane angles that are approximated by fifth-order interpolation functions.

Filament bending rigidities are also obtained by analyzing the shape fluctuations using a Fourier decomposition technique developed previously [5, 6].

The formulation is validated by comparison against Finite Element simulations of filament bending under similar forces.

DISCUSSION

We present a formulation to model the three-dimensional nonlinear bending of a filament by idealizing it as a string of continuous beams. The idealization reduces the computational cost of modeling semiflexible polymers when compared to string-of-beads models, and is therefore more amenable for modeling large networks and semi-dilute polymer phenomena.

ACKNOWLEDGEMENTS

This work is supported in part by grant 5G12MD007597 from the National Institute on Minority Health and Health Disparities, NIH.

REFERENCES

[1] Mofrad, M.R.K et al., Cytoskeletal Mechanics: Models and Measurements, 2006.
[2] Howard, J. Mechanics of Motor Proteins, 2001.
[3] Kratky, O., and G. Porod, Recueil des Travaux Chim- iques des Pays-Bas 68 (12), 1106, 1949.
[4] Chandran PL, Mofrad MRK. Rods-on-string idealization captures semiflexible filament dynamics. Physical Review E;79:011906, 2009.
[5] Gittes, F., B. Mickey, J. Nettleton, and J. Howard; Flexural rigidity of microtubules and actin filaments measured from thermal fluctuations in shape. J. Cell Biol. 120:923–934, 1993.
[6] Kas, J., H. Strey, J. X. Tang, D. Finger, R. Ezzell, E. Sackmann, and P. A. Janmey; F-actin, a model polymer for semiflexible chains in dilute, semidilute, and liquid crystalline solutions. Biophys. J. 70: 609–625, 1996.

Copyright 2016 The Organizing Committee for the 2016 Summer Biomechanics, Bioengineering and Biotransport Conference

SB^{3}C2016
Summer Biomechanics, Bioengineering and Biotransport Conference
June 29 –July 2, National Harbor, MD, USA
SB^{3}C2016-959

MYOSIN-II MEDIATED CORTICAL CONTRACTILITY REGULATES NUCLEUS PULPOSUS CELL OSMOTIC PROPERTIES AND MORPHOLOGY

Timothy D. Jacobsen (1,2), Paula Hernandez (1), Nadeen O. Chahine (1,2)

(1) Feinstein Institute for Medical Research, Manhasset, NY

(2) Hofstra North Shore LIJ School of Medicine, Hempstead, NY

INTRODUCTION

The highly hydrated nature of the nucleus pulposus (NP) within the intervertebral disc (IVD) induces osmotic forces on NP cells which in addition to forces exerted by the ECM and the contractility of the cell cytoskeleton determine the round morphology of these cells. The regulation of cell volume in response to osmotic changes is important to NP function and alteration of volume regulation parameters may play a crucial role in the loss of cellular function in IVD degeneration (DD) [1]. DD is characterized by elevated levels of pro-inflammatory cytokines [2]; inflammatory stimulation of nucleus pulposus (NP) cells within the disc can lead to a catabolic breakdown of disc ECM and consequentially to a positive feedback of further loss of tissue integrity and further inflammation [3]. Previously we have shown that inflammatory stimulation of isolated NP cells leads to significant and irreversible changes in cellular biomechanical properties, in particular significantly increased hydraulic permeability (Lp) as well as disruption of the actin cytoskeleton [4]. Though actomyosin network contractility regulates cell morphology, the role of cortical contractility in regulation of cellular osmotic properties is unknown. In this study, we investigate the direct relationship between actomyosin contractility, actin cytoskeleton morphology and osmotic properties of NP cells. We hypothesize that inhibition of actomyosin contractility will decrease cellular circularity and increase the hydraulic permeability of NP cells, in a mechanism that mimics mechanobiological disruption due to inflammation. Given that actomyosin contractility is regulated by the Rho/Rock pathway, we evaluated the effects of ROCK inhibitor (Y27632) and a non-muscle myosin-II inhibitor (blebbistatin) on osmotic permeability, actin morphology, circularity, and elastic modulus of NP cells. We also evaluated the effects ML-141, an inhibitor of CDC42, a small GTPase of the Rho/ROCK family that plays a central role in filopodium extension. Effects of cytoskeletal disrupters are also compared to inflammatory (TNFα) stimulated changes.

METHODS

NP Cell Isolation: NP tissue was isolated from young bovine lumbar discs. Cells were expanded for 1-2 passages in DMEM+10% FBS, and cultured in 1.2% alginate beads to promote round morphology. **Treatments:** Cells were exposed to the following treatments for 24h: (1) untreated control, (2) 10ug/ml ROCK inhibitor Y27632, (3) 10ug/ml non-muscle myosin-II inhibitor Blebbistatin, (4) 10ug/ml Cdc42 inhibitor ML141, or (5) 10ng/ml TNF-α inflammatory group. **Immunofluorescence:** Beads were fixed, permeabilized, and stained with Alexa 555-phalloidin (Abcam). After staining, cells were released from beads with sodium citrate, placed in poly-L-lysine coated glass coverslips and mounted with Vectashield. Images were taken with a confocal microscope and processed in ImageJ. Changes in actin cytoskeleton were measured for production of cell extensions and alteration of cell circularity. A circularity of 1 represents a perfectly round object; therefore circularity below 0.45 was considered a loss in cell roundness and indication of cell polarity indicated by visible cellular protrusions. **Osmotic properties:** After treatment cells were released from the alginate beads and seeded into a custom osmotic loading microfluidic chamber [4, 5] where they were allowed to adhere to a Poly-D-Lysine coated slide for 30 minutes and then placed under an inverted microscope for observation. Step hyper- (333 to 466 mOsm/L NaCl) and hypo- (466 to 333mOsm/L NaCl) osmotic loads were applied at room temperature. Volume response was analyzed using multiphasic mixture theory [6,7] to compute material properties: membrane hydraulic permeability (Lp) and osmotically active intracellular water content (φir). **Atomic Force Microscopy:** Force indentation curves were obtained from individual, rounded, live NP

Copyright 2016 The Organizing Committee for the 2016 Summer Biomechanics, Bioengineering and Biotransport Conference

Cells using and Asylum MFP-3D BIO atomic force microscope with spherical tip probes. Obtained curves were fitted to a hertzian mode in order to determine cell elastic modulus. Data was analyzed with 1-way ANOVA and Fisher LSD post-hoc test, with $p<0.05$ significant.

RESULTS

F-actin distribution in control NP cells was found to be mostly cortical, with low to moderate likelihood of observation of short cellular extensions. Cells treated with TNFα show the presence of punctuate F-actin and increased presence of cellular processes resembling neurites or filopodia. Y27632 treated cells exhibited some cell extensions, though a more pronounced effect was observed in blebbistatin treated cells. Treatment with ML141 showed the most pronounced increase in cell roundedness and little to no presence of cellular extensions. Quantitative analysis of extensions and protrusions indicate that a significantly larger proportion of cells in TNFα group have low circularity in comparison to untreated control (Fig 1). Blebbistatin significantly increased % of polarized cells (more extensions, low cellularity). No significant difference between Y27632 treatment and control group was observed. ML141 significantly decreased cellular extensions and improved cell roundedness. Analysis of hydraulic permeability was performed for hyper- and hypo-osmotic loads. Under hyper osmotic loading, treatment with TNFα produced an increase in hydraulic permeability (Fig 2), in agreement with our previous findings [4]. Blebbistatin treatment significantly increased Lp under hyper osmotic loading to similar levels as those produced by TNFα (Fig 2). Y27632 treated cells showed a slight but non-significant increase in Lp (Fig 2). Treatment with ML141 had no significant effect on Lp. All treatments showed trends for increasing Lp under hypo osmotic loading, though none were significant. No group showed a significant change in φir vs. control. TNFα treated cells also exhibited significantly reduced elastic modulus compared to untreated cells (Fig 3). Treatment with both Blebbistatin and Y27632 also lead to significantly reduced modulus akin to that seen with TNFα stimulation (Fig 3).

DISCUSSION

The goal of this study was to examine the role of cytoskeleton cortical contractility in regulating single cell osmotic properties, in particular hydraulic permeability. Our findings confirm that inflammatory stimulation with TNFα increased hydraulic permeability, induced formation of punctate actin extensions, and decreased cell elastic modulus, in agreement with our previous work [4]. Reducing cytoskeletal contractility by inhibiting myosin-II contractility resulted in a significant increase in hydraulic permeability formation of cellular extensions, and decreased modulus akin to that seen with inflammatory stimulation with TNFa. Inhibition of ROCK activity demonstrated similar trends, though the effects were less pronounced than with myosin-II inhibitor. Inhibition of CDC42 decreased formation of extension and had no effect on permeability. These findings indicate that disruption of myosin II cortical contractility can regulate the osmotic response of NP cells. We postulate that inflammatory stimulation disrupts the biomechanical properties of NP cells in a mechanism that is dependent on myosin II contractility. Indeed, measurement of phosphorylated myosin light chain (pMLC) levels confirm that contractile activity is significantly decreased in TNFa treated cells compared to control. This is the first report that directly links cortical contractility with the regulation of cellular osmotic properties in NP or other chondrocyte-like cell, whose cell-ECM interaction are a key regulator of biological and biomechanical function. These findings indicate non-muscle myosin-II cortical contractility plays a key role in how inflammation alters NP cell mechanobiology and consequently in disc degeneration. These findings advance the understanding of how inflammation alters the biomechanical properties and function of disc cells as well as their ability to detect and respond to biomechanical stimuli from surrounding ECM.

ACKNOWLEDGEMENTS

Funded in part by NSF CAREER Award 1151605 (NOC).

REFERENCES

[1] Urban et al., *Spine*, 1989. [2] Le Maitre et al., *Arth Res Ther*, 2005. [3] Millward-Sadler, *Arth Res Ther,* 2009. [4] Maidhof et al., *PLoS ONE*, 2014 [5] Chao et al., *J Biomech*, 2005. [6] Ateshian et al, *J Biomech*, 2006. [7] Albro et al., *Biophys J*, 2009.

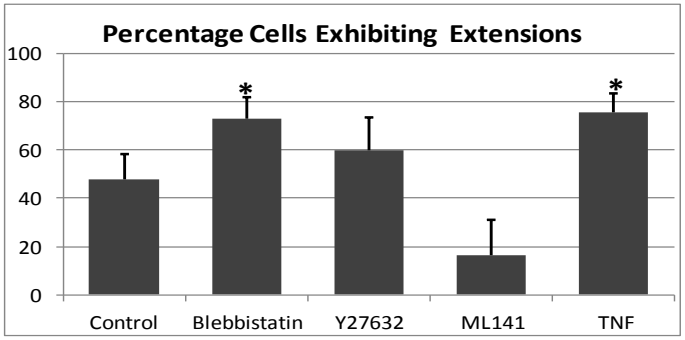

Figure 1: % of cells exhibiting punctate extensions increases with treatment with Blebbistatin or TNFα (*p< 0.05 vs. control)

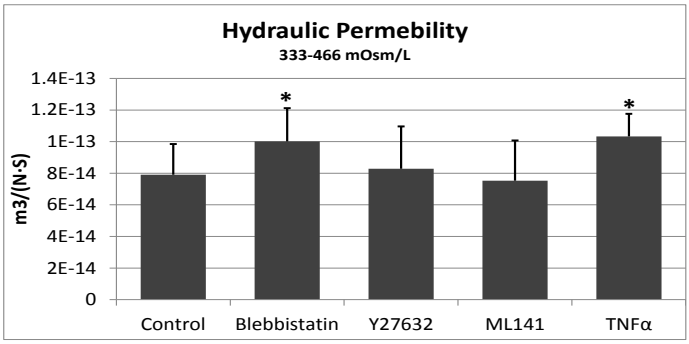

Figure 2: Hydraulic Permeability of NP cells significantly increase with treatment with Blebbistatin or TNFα (*p< 0.05 vs. control)

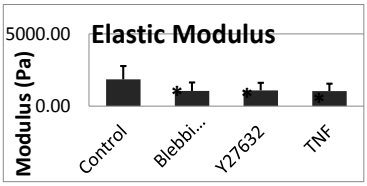

Figure 3: Elastic Modulus of NP cells significantly decreases with treatment with Blebbistatin, Y27632 or TNFα (*p< 0.05 vs. control)

Copyright 2016 The Organizing Committee for the 2016 Summer Biomechanics, Bioengineering and Biotransport Conference

SB³C2016
Summer Biomechanics, Bioengineering and Biotransport Conference
June 29 –July 2, National Harbor, MD, USA
SB³C2016-960

IN SITU MEASUREMENTS OF HYDRAULIC PERMEABILITY IN SKELETAL MUSCLES

Michael Schenk, Lijian Peng, Xingyu Chen, Shaopeng Pei, Xin (Lucas) Lu, Liyun Wang

Mechanical Engineering Department
University of Delaware
Newark, DE, USA

INTRODUCTION

Muscle and bone are known to act as a functional unit and communicate mechanically and biochemically during musculoskeletal development and maintenance [1]. Muscle-derived factors (myokines) have been found to affect bone functions in vitro [2]. However, the transport processes of myokines from muscle to adjacent bone tissue are not well studied. Both pathways through vasculature and interstitium have been proposed [3]. Using confocal microscopy and myokine-mimicking tracers, we found that periosteum, which is involved in the presumed interstitial pathway, behaves as a semi-permeable sieve that allows readily passage of various molecules up to 40kDa [3]. The hydraulic permeability of the periosteum was reported to be 2-5x$10^{-17}$$m^2$ when tested in pre-stressed conditions [4]. However, the permeability of muscle tissue, another important component of the interstitial muscle-bone cross-talk pathway, has not been quantified yet. Our goal was to fill this knowledge gap by measuring hydraulic permeability using murine/bovine skeletal muscles.

METHODS

(i) Indentation Tests: Hindlimbs from 12-week-old (N = 18) and 38-week-old (N = 3) Balb or B6 mice with intact tibial muscles were harvested 5-10 min postmortem, and equilibrated in 1X PBS supplemented with a cocktail of proteinase inhibitors (PBS-PI solution) [5] for 2-6 hours. The samples, immersed in the PBS-PI solution inside a water bath, were subjected to creeping tests on a custom-made indenter (Fig. 1). A porous indentation tip (radius 0.8mm) was brought to contact the tibial lateral gastrocnemius muscle with a small force (~0.4g) by manual adjustments (Fig. 1). After 5 min, the piezo actuator (P602.8SL, Physik Instrumente) was instructed to apply a step load of 0.5g and the load was maintained for a total 90 min. The creeping displacement was recorded using the actuator's internal displacement sensor. The thickness of the muscle (~5mm) was measured using a needle. Bovine (N = 9, 12-24-week-old) gastrocnemius muscle slices (~5mm thick) were sectioned along the muscle fibers from knee samples delivered by a local supplier within 24h of sacrifice. Bovine samples were prepared and tested similarly as described above. (ii) Biphasic Curve-Fitting: To derive transport and mechanical properties of the murine and bovine muscles, a cylinder of muscle tissue indented by a porous cylindrical tip was simulated in FEBio. As the first approximation, a small 1° wedge containing indenter and muscle was meshed to 287 and 2000 penta6/hex8 elements, respectively. The muscle tissue was assumed to be biphasic with the solid phase being a neo-hookean material (Poisson's ratio=0.35) reinforced with radial fibers and the saturated fluid phase being salty water (viscosity of 0.001Pa•Sec). The boundary conditions were shown in Fig.2B. The tissue permeability (k), fibril tensile modulus (E_f) and muscle Young's modulus (E_m) for each muscle sample were obtained by optimizing the predicted displacement-time curves with the experimental data (Fig. 2). A heuristic differential evolution method [6] was adopted for global optimization over a continuous solution space with E_m (2-8kPa), E_f (0.32-2.56MPa), and k (0.1-4*10^{-16} m^2). Typically, a thousand simulations (~100 generations of optimizations) were adequate to achieve convergence and excellent fitting with the experimental data (Fig. 2C). One-way ANOVA with Tukey post-hoc comparisons were performed using Origin (OriginLab Corp., Northampton, MA).

Copyright 2016 The Organizing Committee for the 2016 Summer Biomechanics, Bioengineering and Biotransport Conference

RESULTS

No significant difference was detected in any of the skeletal muscle properties among the three groups (young murine, old murine and cow). The hydraulic permeability from the two species was on the order of 10^{-16} m^2; fibril tensile modulus was on the order of 1.8-2.3 MPa; and the tissue Young's modulus was on the order of 2.2-2.5 KPa (Table 1).

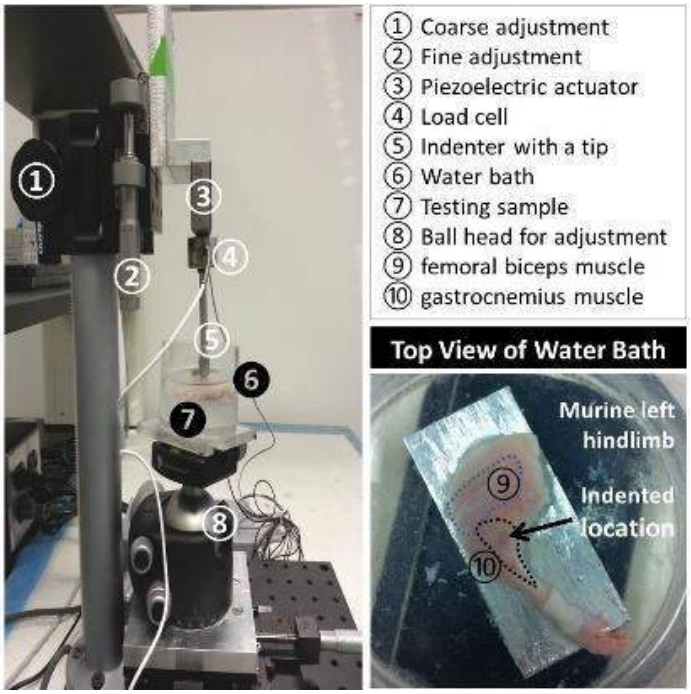

Figure 1: Indentation setup for muscle testing.

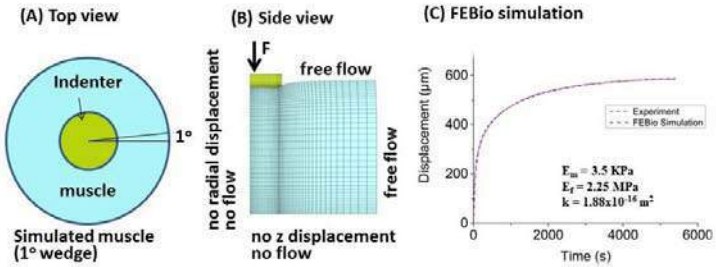

Figure 2: Biphasic curve-fitting of muscle indentation tests. (A) The model consists of a 1^0 wedge of muscle and indenter. (B) Displacement and flow conditions were applied to the boundaries of the model. (C) A representative simulation of murine muscle test showed excellent agreement with experimental data. The optimized parameters (E_m , E_f , and k) for this particular test were derived.

Table 1: Mechanical Properties of Murine and Bovine Skeletal Muscles

Mechanical Property	Murine: Relatively Young (N = 18), Age = 11.9 ± 1.4 weeks	Murine: Relatively Old (N = 3), Age = 38.0 ± 0.0 weeks	Bovine (N = 9), Age = 12-24 weeks	p^1	p^2	p^3
Permeability ($x10^{-16}m^2$)	2.7 ± 1.5	2.3 ± 0.3	1.8 ± 0.8	0.6	0.1	0.3
Fiber Tensile Modulus (MPa)	1.8 ± 0.9	2.3 ± 0.6	2.2 ± 0.8	0.4	0.3	0.9
Matrix Modulus (KPa)	2.5 ± 1.1	2.3 ± 1.0	2.2 ± 0.6	0.8	0.4	0.7

Note: Values are presented as mean ±SD. Pairwise comparisons were performed using one way ANOVA and Tukey tests. p^1: young murine vs. old murine. p^2: young murine vs. bovine. p^3: old murine vs. bovine.

DISCUSSION

We quantified skeletal muscles' hydraulic permeability using indentation and biphasic modeling. Our results showed that the skeletal muscles from two species (murine and bovine) displayed permeabilities on the order of $2x10^{-16}$ m^2, which were 2- to 10-fold higher than that of bone periosteum ($2\text{-}5x10^{-17}$ m^2) [4]. Although the structural and compositional basis for this difference is not known, the highly hierarchical extracellular matrix space formed by the extensively interconnected endo-, peri-, and epi-mysium system [7] may be responsible for the higher permeability detected in muscle, which requires further investigations. Our data suggest that muscle is unlikely to be a major barrier for the interstitial muscle-bone cross talk as is the periosteum. Limitations of the current studies include i) all the muscles were tested postmortem without active muscle contractions typically seen in vivo; ii) structural changes might have occurred during the preparation and testing period (3.5-7.5 hours) despite the use of proteinase inhibitors. Nonetheless, the current study provided the first quantitative estimations of the skeletal muscle permeability, which will help us to understand the physical constrains in muscle-bone cross-talk.

ACKNOWLEDGEMENTS

This study was supported partially by funds from the NIH (RO1AR054385, P30GM103333) and DOD (W81XWH-13-1-0148).

REFERENCES

[1] DiGirolamo, D.J., Kiel, D.P., Esser, K.A., J Bone Miner Res 28, 1509-1518,2013;
[2] Jahn, K., Lara-Castillo, N., et.al., Eur Cell Mater 24, 197-209; discussion 209-110, 2012;
[3] Lai, X., Price, C., Lu, X.L., Wang, L., Bone 66, 82-89, 2014;
[4] Evans, S.F., Parent, J.B., Lasko, C.E., Zhen, X., Knothe, U.R., Lemaire, T., Knothe Tate, M.L., J Bone Miner Res 28, 608-617, 2013;
[5] Lu, X.L., Miller, C., Chen, F.H., Guo, X.E., Mow, V.C., J Biomech 40, 2434-2441, 2007;
[6] Storn, R., & Price, K, Journal of global optimization, 11(4), 341-359,1997;
[7] Trotter, J.A., Purslow, P.P., J Morphol 212, 109-122,1992.

Copyright 2016 The Organizing Committee for the 2016 Summer Biomechanics, Bioengineering and Biotransport Conference

SB^{3}C2016
Summer Biomechanics, Bioengineering and Biotransport Conference
June 29 –July 2, National Harbor, MD, USA
SB^{3}C2016-962

A HIGH THROUGHPUT NUCLEUS PULPOSUS EXPLANT CULTURE SYSTEM PRESERVES TISSUE INTEGRITY

Timothy D. Jacobsen (1,2), Nadeen O. Chahine (1,2)

(1) Feinstein Institute for Medical Research, Manhasset, NY

(2) Hofstra North Shore LIJ School of Medicine, Hempstead, NY

INTRODUCTION

Many intervertebral disc (IVD) research studies utilize either in-vitro isolated cell cultures systems or in-vivo studies. However there is a growing interest and need to perform in-vitro studies on the IVD and nucleus pulposus (NP) in an environment that more closely mimics the native disc, prior to embarking on costly in-vivo experimentation. Cultured in media alone, free swelling NP explants are subject to loss of tissue integrity and ECM content as well as loss of cell viability making them poor representatives of in-situ NP tissue [1]. Explant cultures systems that involve the use balanced osmolarity medium culture or molds and meshes that physically restrict disc swelling, have been recently utilized in order to preserve isolated NP explants and allow for testing of tissue that accurately models in-situ NP. These methods have been shown to address limitations of free swelling explant cultures, however these systems are often time and resource intensive making them relatively low through put systems [2,3]. In the current study we have investigated a new NP explant culture system for its ability to maintain explant integrity, ECM content, and cell viability. The culture system described here provides a benefit over existing systems by maintaining NP explants in cultures at a comparatively lower cost of time and resources, and is easily scalable for higher throughput studies. We hypothesize that restriction of NP explants swelling using an agarose gel culture system will maintain cell viability, ECM content, and tissue integrity of cultured NP explants.

METHODS

NP Explant Isolation: NP explants were isolated from bovine tail segments. The NP region of each disc was exposed and a 4mm punch was used to isolate cylindrical explants. **Agarose Casting and Culture:** Explants were cultured in 24 well-plate and were either cast in 2% agarose (swelling restricted) by suspending the explants in an agarose gel, or they were left unrestricted in the well (free swelling). DMEM+10%FBS+1%AA was added to both explants groups and explants were cultured under standard culture conditions **Live/Dead Staining:** On Day 0 and after either 7 or 14 days in culture, explants were collected and stained with 10 μM Calcein am and 2 μM ethidium homodimer (Sigma) and imaged on a confocal microscope. ImageJ was used to threshold images and quantify the number of live and dead cells. **Size Measurement:** at time of collection explant diameter and height was measured with digital calipers. **NO Assay:** Explant supernatants were assayed for nitrite (NO) concentration by Griess reaction (Promega). **GAG Assay:** Supernatants were also assayed for released GAG content into the media using Blyscan sulfated glycosaminoglycan assay (Biocolor).

RESULTS

Cell viability with live/dead staining showed nearly 100% viability in all groups, with no difference observed in days in culture or relative to Day 0 control explants (Table 1). At day 7, no significant differences in explant diameter were observed between groups. However at day 14, the free swelling explants had a significant greater diameter than swelling restricted samples (Fig 1). Free swelling explants exhibited a significantly higher rate of NO release at day 1 and 3 versus swelling restricted explants. Nitirite levels decreased after day 4 and were comparable in both groups (Fig 2). Free swelling explants also exhibited a burst release of GAGs into the media on day 1 of culture that was significantly higher than GAG release measured in swelling restricted explants. After the initial burst release, free swelling and swelling restricted explants exhibited a similar slow release of GAGs, though the cumulative GAG release was ~ 3X greater in free swelling compared to swelling restricted (Fig 3).

Copyright 2016 The Organizing Committee for the 2016 Summer Biomechanics, Bioengineering and Biotransport Conference

DISCUSSION

The goal of this study was to validate a scalable and cost effective method for culturing NP explants from the IVD, while preserving tissue integrity, ECM content, and cell viability. After 14 days of culture in agarose gel that restricted the swelling of cultured explants, our findings indicate 100% cell viability. Additionally this swelling restricted culture system showed no increase in explant size, as opposed to free swelling explants, indicating a preservation of explant structure and integrity vs. free swelling explants. Explants cultured in agarose also showed low levels of NO release as opposed to free swelling explants which exhibited a high initial rate of NO release, indicating this agarose culture system helps to prevent an initial inflammatory response that is otherwise present in free swelling explants. Lastly explants cultured in agarose showed a lower rate of GAG release compared to free swelling explants indicating a better maintenance of ECM content and explant integrity. Our findings that swelling restriction offers significant preservation of NP integrity is consistent with prior studies that reduced swelling of explants by balancing tissue osmolarity [3] or by physical ring constraints [2]. The use of agarose gel to restrict NP swelling and preserve tissue integrity, not only mitigates inflammatory and tissue fragmentation, but also represents a scalable model for high throughput analysis of NP function in vitro. The scalable explant culture system validated for use with NP tissue can be utilized in future studies in order test injurious and therapeutic stimuli using conditions more representative of in-situ microenvironment than free swelling or single cell culture.

ACKNOWLEDGEMENTS

Funded in part by NSF CAREER Award 1151605 (NOC), New York State Department of Health (ECRIP), and NIH NIA-R41AG050021.

REFERENCES

[1] Urban and Maroudas, *Conn Tis Res*, 1981. [2] Le Maitre et al., *Spine*, 2004. [3] van Dijk et al., *Tissue Engineering*, 2011.

Table 1: Quantified live/dead count for swelling restricted and free swelling explants. No significant differences were found

Average Live/Dead Count			Swelling Restricted	Free Swelling
Day	0	Live	98 ± 12	
		Dead	0 ± 0	
		%Live	**100%**	
	7	Live	97 ± 4.5	127 ± 4.2
		Dead	0 ± 0	0 ± 0
		%Live	**100%**	**100%**
	14	Live	83 ±42.1	161 ± 75.8
		Dead	0 ± 0	0 ± 0
		%Live	**100%**	**100%**

Figure 1: Explant Sizes. Sizes of collected explants are significantly large in free swelling explants as by day 14 (*p< 0.05 vs. respective control)

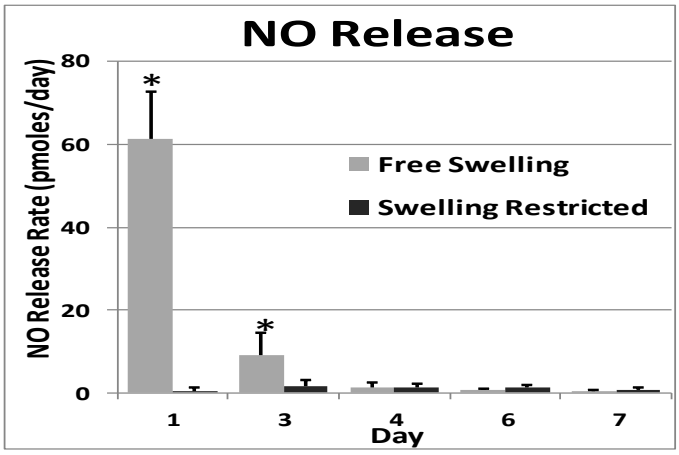

Figure 2: Rate of NO release from explants. Free swelling explants show a significantly higher rate of NO release vs. swelling restricted explants (*p< 0.05 vs. respective control)

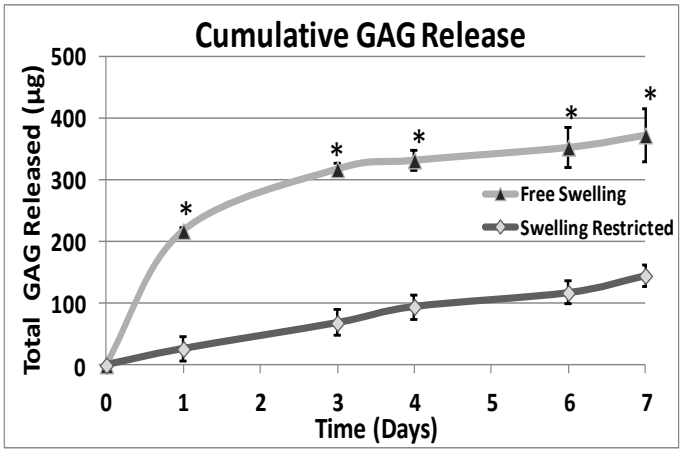

Figure 3: Cumulative GAG release. Free swelling explants show an initial burst release of GAGs that is eliminated in swelling restricted explants(*p< 0.05 vs. respective control)

Copyright 2016 The Organizing Committee for the 2016 Summer Biomechanics, Bioengineering and Biotransport Conference

SB^{3}C2016
Summer Biomechanics, Bioengineering and Biotransport Conference
June 29 –July 2, National Harbor, MD, USA
SB^{3}C2016-963

A MECHANICAL ANALOG MODEL OF ADOLESCENT IDIOPATHIC SCOLIOSIS

Chloe L. Chung (1), Derek M. Kelly (2), Jack R. Steele (3), Denis J. DiAngelo (1)

(1) Department of Orthopaedic Surgery and Biomedical Engineering
University of Tennessee Health Science Center, Memphis, TN, USA

(2) Campbell Clinic Orthopaedics and Le Bonheur Children's Hospital
Memphis, TN, USA

(3) The Center for Orthotics and Prosthetics, Inc.
Memphis, TN, USA

INTRODUCTION

Scoliosis is a three dimensional (3D) skeletal deformity consisting of a combination of spinal axial rotation (AR) and lateral curvature, or Cobb angle (CA), of 10° or greater [1]. Thoracolumbar braces are commonly used to treat Adolescent Idiopathic Scoliosis (AIS) curves between 20° and 50° [2] with the curve apex below T6 in patients who have significant growth remaining (Risser grade ≤ 2).[3] Braces serve to maintain, and, in some cases, reduce [2] the spinal curve to prevent progression of the deformity by applying corrective forces.[4] Until recently, the outcome of bracing treatment has been highly debated. Weinstein et al. conducted a 5-year follow-up study (Bracing in Adolescent Idiopathic Scoliosis Trial [BrAIST]), providing evidence that braces are effective (72% success rate) at treating scoliosis.[5] Scoliosis braces can be rigid, flexible, or composite and can utilize passive or active corrective mechanisms. Many braces use a three-point pressure principle as the method of correction, which involves fixation superior, inferior, and at the apex of the curve.[6] The magnitude and direction of corrective forces applied by a brace to the spine remain unknown and are a common concern for clinicians and orthotists who are tasked with making design alterations to improve fit and comfort for the patient.

Current experimental research of scoliosis bracing mechanics has largely been limited to two-dimensional (2D) and 3D imaging techniques and computational models. To our knowledge, no biomechanical model of a scoliotic spine or testing assembly is available to study bracing mechanics in scoliosis. The objective of this study was to design and validate an analog model of a mid-thoracic, single-curve, scoliotic deformity to quantify brace structural properties and force response on the spine.

METHODS

A mechanically equivalent analog model of the AIS condition was developed and validated (Figure 1a). The Scoliosis Analog Model (SAM) used a linkage-based system to simulate 3D spinal correction of CA and AR deformity of a single-curve scoliotic spine. The model was adjustable to accommodate unique scoliotic deformities and associated braces. The SAM was designed to engage with the interior surface of a scoliosis brace at each of the three levels, superior, inferior, and at the apex, via an adjustable ring between a central linkage assembly and the brace. Tuning of the ring size and variable degree of freedom components allowed for the ring to mate with complex interior surface geometry. Characteristics and dimensions from patient records and EOS images (EOS Imaging, Paris, France) [7, 8] (IRB 14-03110-XP) were used to customize the SAM for use with a Boston brace, including sex (male), age (13), height (1.7m), and weight (570N), "deformed" measures CA (33°) and AR (5°), and "corrected" measures of CA (26°) and AR (0°) (Figure 1b).

The SAM was tested with a robotic testing platform [9] without any input load to ensure the links moved freely. Less than 3 N of

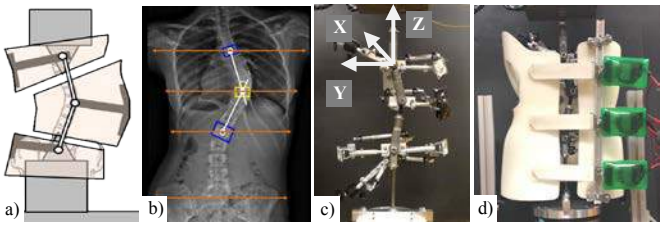

Figure 1: SAM Development and Testing Setup. a) X-Ray Measures, b) SAM Concept, c) SAM Assembly, d) SAM and Brace

Copyright 2016 The Organizing Committee for the 2016 Summer Biomechanics, Bioengineering and Biotransport Conference

vertical force occurred over 40° of linkage rotation (Figure 1c). Validation of the transmission of forces acting on the SAM was performed by applying a series of input forces with varying orientation to the apex point of the SAM during 40° of simulated CA correction. Force components transmitted to the superior connector of the linkage assembly were recorded. Computational model simulations were performed for each respective input force orientation. The percent error relative to the computational results was calculated for each input force orientation. The mean percent error revealed a 6 % force reduction within the SAM over the testing range. This error can be attributed to the frictional losses within the SAM components.

To measure the force response of the brace, three simulations were performed, pure CA correction, pure AR correction, and coupled CA and AR correction (CAAR). The SAM assembly was mounted and the weight of the SAM was zeroed from the load cell. The brace was mounted onto the SAM (Figure 1d) and the Velcro straps were each tightened between 22N and 45N (5-10lbs) as instructed by an orthotist. The testing platform was programmed to either displace downward along the Z (vertical) axis or to rotate about the Z axis. Programmed linear movement caused the SAM to transition from the "corrected" state (26° CA) to the "deformed" state (33° CA), simulating 7° CA change in the spinal curve. Programmed rotation caused the SAM to axially rotate within the brace, which was inferiorly fixed to the platform, effectively simulating AR correction (0° to 5°). Coupled CAAR correction was achieved by executing both protocols simultaneously. Strap tension was monitored to ensure it remained with ± 4.5N (1lb) of the initially set value. The 3D force and moment components, which were generated by the brace as a reaction to the simulated deformity, and the linkage assembly angular displacements were measured at a sampling rate of 25Hz. Brace stiffness properties were calculated both for pure CA/AR and for coupled CAAR simulations, and was expressed as a resistive load relative to the angular change. Linear stiffness properties (X, Y, Z) were derived from the 3D force response relative to CA change. Axial (A) stiffness was derived from the Z-moment relative to AR change.

RESULTS

The 3D force and moment responses are shown in Figure 2a (CA and AR) and in Figure 2b (CAAR). The customized SAM replicated the 7° CA and 5° AR correction observed in the patient's images. In order to simultaneously correct the simulated deformity, a vertical load of 582N and moment of -7Nm were applied to the brace by the model. Calculated brace structural stiffness properties for both correction scenarios are shown in Table 1.

DISCUSSION

Structural properties provide a means to compare and classify bracing technology. Interpretation of the results provides the reader with a basic understanding of the mechanics and structural properties of the particular brace studied. With mean X- and Y-stiffness values between 1.0-4.1N/° and 2.1-3.3N/°, respectively, it can be seen that this brace offers little structural stiffness along those axes. However, with a mean Z-stiffness between 64.8-77.9N/° and A-stiffness between 1.1-1.5Nm/°, the brace has much greater stiffness along the Z axis.

Since this research model and testing methodology are new, directly comparable data are not available. Van den Hout et al. measured the magnitude of direct compressive forces at the body brace interface.[10] The forces exerted by the internal lumbar and thoracic pads of a Boston brace were measured in 16 patients with AIS using an electronic pressure measuring system. The mean forces measured at

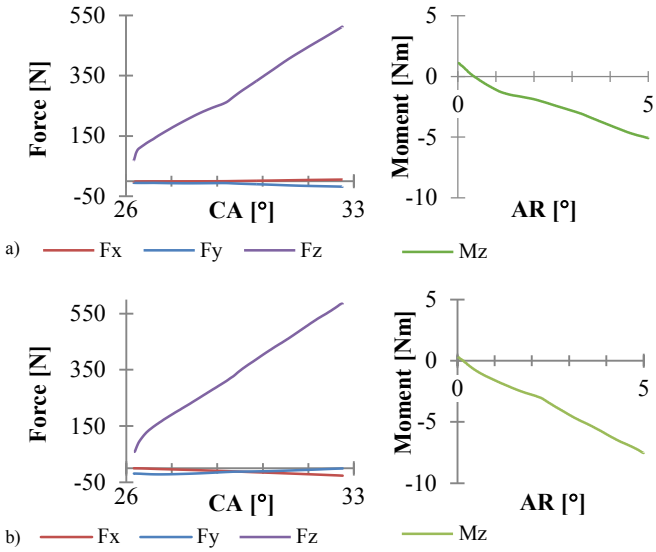

Figure 2: 3D Force and Moment Responses: a) Pure CA and AR, b) Coupled CAAR

Table 1: Brace Stiffness Properties

	Pure (CA or AR)	Coupled (CAAR)
|X-Stiffness| [N/°]	1.0	4.1
|Y-Stiffness| [N/°]	2.1	3.3
|Z-Stiffness| [N/°]	64.8	77.9
|A-Stiffness| [Nm/°]	1.1	1.5

the lumbar brace pad was 214N (range, 0-727N) and at the thoracic brace pad was 66N (range, 4-209N). These force ranges are comparable to the magnitude of the forces measured by the SAM.

The Scoliosis Analog Model and testing methodology enables study of bracing technology. Currently, the model is limited to replicating single curve scoliosis deformities. Future SAM design improvements will permit the 3D study of complex curve types. Future testing may include variable pad and strapping parameters such as orientation, spatial location, size, material, and shape to determine the impact that they have on force transmission. By understanding the effects of removing, adding, or altering the fitting pads and straps, recommended brace design changes may result in improved in-brace correction and treatment outcome.

ACKNOWLEDGEMENTS

The scoliosis brace used in this study was donated by Boston Brace International, Inc.

REFERENCES

[1] Altaf, F et al., *BMJ*, 346:f2508, 2013.
[2] Rinsky, L et al., *Western journal of medicine*, 148:182-191, 1988.
[3] Busscher, I et al., *BMC musculoskeletal disorders*, 11:93, 2010.
[4] Gallo, D et al., *JPO*, 23(2):69-77, 2011.
[5] Weinstein, S et al., *N Engl J Med*, 369(16):1512-1521, 2013.
[6] Boston Brace International I. *Online Manual*, 2015.
[7] Greiner, K et al., *Am. family physician*, 65(9):1817-1822, 2002.
[8] Deschenes, S et al., *Spine*, 35(9):989-994, 2010.
[9] Kelly, B et al., *J of Medical Devices*, 7(3):034502-034502. 2013.
[10] van den Hout JA et al., *Eur Spine J*, 11(4):332-335, 2002.

Copyright 2016 The Organizing Committee for the 2016 Summer Biomechanics, Bioengineering and Biotransport Conference

SB^{3}C2016
Summer Biomechanics, Bioengineering and Biotransport Conference
June 29 –July 2, National Harbor, MD, USA
SB³C2016-964

INDISPENSABLE ROLES OF DECORIN AND BIGLYCAN IN CARTILAGE MECHANICAL FUNCTION DURING MATURATION

B. Doyran (1), Q. Yao (2), S. J. Rozans (1), Q. Li (1), M. F. Young (3), R. V. Iozzo (4), D. E. Birk (2), L. Han (1)

(1) School of Biomedical Engineering, Science and Health Systems
Drexel University
Philadelphia, PA, United States

(2) Department of Molecular Pharmacology and Physiology
University of South Florida
Tampa, FL, United States

(3) Molecular Biology of Bone and Teeth Section
National Institutes of Health
Washington, DC, United States

(4) Department of Pathology, Anatomy and Cell Biology
Thomas Jefferson University
Philadelphia, PA, United States

INTRODUCTION

Decorin and biglycan are two structurally similar, small leucine-rich proteoglycans (SLRPs) that are critical in the development of connective tissues [1, 2]. Decorin has one dermatan sulfate or chondroitin sulfate (DS/CS) glycosaminoglycan (GAG) side chain (~ 45kDa) attached near its N-terminus, while biglycan has two DS/CS GAGs [3]. In vivo, they both regulate the extracellular matrix (ECM) development in various connective tissues through bindings with cytokines to affect cell signaling [4], and with ECM collagen to regulate fibrillogenesis [5, 6]. Specifically, in articular cartilage, they bind to transforming growth factor-β (TGF-β) to inhibit TGF-β-chondrocyte signaling [4], which was recently suggested as a key osteoarthritis (OA) signaling pathway [7]. They also bind to collagens II [8] and VI [9] to regulate ECM assembly (**Fig. 1**). Due to their high structural similarity, the roles of decorin and biglycan could be largely synergistic and complementary. However, the exact mechanisms whereby decorin and biglycan influence the formation and maturation of articular cartilage are not known. In this study, the nanomechanical phenotype of decorin-null and biglycan-null mice was investigated, which can provide direct insights into the regulatory roles of these two SLRPs in the development and maturation of cartilage.

METHODS

Decorin-null ($Dcn^{-/-}$) [5] and wild-type (WT) mice from the C57BL/6 strain were euthanized at 7 to 90 days post-natal (P7, P14, P60 and P90), and biglycan-null ($Bgn^{-/0}/Bgn^{-/-}$) [10] were sacrificed at P14 and P60. Condyle cartilage was harvested from the medial side of right hind legs and stored in PBS (pH = 7.4) with protease inhibitors (Pierce) at 4ºC for < 24 h. Atomic Force Microscopy (AFM)-based nanoindentation (Dimension Icon, BrukerNano) was performed on the intact surfaces of articular cartilage using a microspherical tip ($R \approx 5$ μm, nominal $k \approx 8.9$ N/m, NSC-35 tip A, NanoAndMore), as described previously [11]. For each tissue, at least 10 different indentation locations were tested up to an indentation depth of ~ 1 μm at 10 μm/s rate. Effective indentation modulus, E_{ind} (MPa), was calculated from the loading portion of each indentation force-depth curve via the Hertz model. Mann-Whitney U test or Kruskal-Wallis test followed by Tukey Kramer post-hoc multiple comparison were performed to detect the differences in E_{ind}, across genotypes, where a p-value < 0.05 was considered statistically significant. In addition, histology was performed on all genotypes at P14 and P60, following previously established procedures [12].

RESULTS

Decorin-null mice showed significantly lower E_{ind} compared to WT from P14 ($n \geq 3$) to P90 ($n \geq 4$), but had similar modulus at P7 ($n = 4$) (**Fig. 2**). Furthermore, the expected increase in E_{ind} during skeletal development [13] is observed for WT from P7 to P90, but not for decorin-null mice. For biglycan-null mice tested at P14 and P60 ($n \geq 4$), the cartilage exhibited significantly lower E_{ind} than WT mice. At P60 but not P14, biglycan-null cartilage had higher modulus than decorin-null murine cartilage ($p < 0.05$).

In concert with the lower modulus, histology also showed a markedly lower proteoglycan (PG) staining for decorin-null mice cartilage, at both early development (P14) and young mature (P60) ages (**Fig. 3**). At both ages, while biglycan-null mice also had reduced PG staining, the reduction is more moderate than that for decorin-null mice.

Copyright 2016 The Organizing Committee for the 2016 Summer Biomechanics, Bioengineering and Biotransport Conference

DISCUSSION

The markedly reduced cartilage modulus in both transgenic mice underscores the indispensable roles of decorin and biglycan in the development of cartilage. Noticeably, for decorin-null mice, the modulus difference in comparison to WT progressively increases from early skeletal development (P7) to maturity (P90). This mechanical difference is likely due to several molecular binding activities of decorin during the molecular assembly of cartilage ECM. For example, decorin is known to bind to type II collagen molecules, and thereby, prevent the formation of large fibril or fiber bundles [8] (Fig. 1). In the absence of decorin, cartilage matrix is thus likely characterized by abnormally thick, less organized collagen fibrils, which can contribute to the reduced modulus.

For the first time, our results suggest a critical role of decorin in the structural integrity of proteoglycan in cartilage matrix. We detected a marked reduction in proteoglycan staining by histology as early as the stage of endochondral ossification (P14), and this reduction persists in young, mature cartilage (P60) (Fig. 3). The lower PG concentration is likely a major factor that leads to the reduced modulus in decorin-null cartilage. Several possible scenarios can lead to this phenomenon. In cartilage ECM, the aggrecan-hyaluronan aggregate is entrapped within the collagen network [14]. Given the known regulatory role of decorin in collagen structure [8, 15], it is likely that decorin indirectly affects the retention of aggrecan through influencing collagen structure. Currently, however, it is unclear whether decorin also binds to aggrecan or hyaluronan and therefore plays a direct role in PG structural integrity. Additionally, decorin also sequesters TGF-β signaling [4], which is, less likely to be the major factor for the reduced PG staining, as previous studies have suggested chondrocytes lacking decorin produce similar level of GAGs at the transcriptional level [16].

Biglycan-null mice had a more moderate phenotype in the reduction of both modulus (Fig. 2) and PG staining (Fig. 3). In normal cartilage matrix, decorin is more concentrated in the territorial matrix [17], while biglycan is largely localized in the PCM [18]. It is thus likely that the roles of biglycan are less critical in the formation and function of cartilage ECM fibrillar network. In addition, due to the high structural similarity between decorin and biglycan (57% amino acid sequence homology [3]), we could expect functional compensation between decorin and biglycan when one of them is absent.

Taken together, this study, for the first time, points to potentially indispensable roles of decorin and biglycan in the mechanical function of cartilage. Our ongoing studies are further investigating the underlying molecular mechanisms that contribute to the observed matrix phenotypes. This knowledge will bring decorin and biglycan into the equation of cartilage matrix development, and provide important molecular insights into cartilage regeneration and osteoarthritis pathogenesis.

ACKNOWLEDGEMENTS

This work was supported by the National Institute of Health (AR066824).

REFERENCES

[1] Heinegard, D, *Int. J. Exp. Pathol*. 2009;90:575-86.
[2] Iozzo, RV et al., *The Extracellular Matrix: an Overview*. 2011.
[3] Fisher, LW et al., *J. Biol. Chem*. 1989;264:4571-6.
[4] Hildebrand, A et al., *Biochem. J.* 1994;302:527-34.
[5] Danielson, KG et al., *J. Cell. Biol*. 1997;136:729-43.
[6] Ameye, L et al., *FASEB J*. 2002;16:673-80.
[7] Zhen, G et al., *Nat. Med.* 2013;19:704-12.
[8] Douglas. T et al., *Biomacromolecules*. 2006;7:2388-93.
[9] Wiberg, C et al., *J. Biol. Chem.* 2001;276:18947-52.
[10] Xu, T et al., *Nat. Genet.*1998;20:78-82.
[11] Batista, MA et al., *Matrix. Biol*. 2014;38:84-90.
[12] Pauli, C et al., *Osteoarthr. Cartil.* 2012;20:476-85.
[13] Williamson, AK et al., *J. Orthop. Res*. 2001;19:1113-21.
[14] Hardingham, TE et al., *Biochim. Biophys. Acta*. 1972;279:401-5.
[15] Zhang, G et al., *J. Cell. Biochem*.2006;98:1436-49.
[16] Ferdous, Z et al., *J. Biol. Chem*. 2007;282:35887-98.
[17] Miosge, N et al., *J. Histochem.* 1994;26:939-945.
[18] Wiberg, C et al., *J. Biol. Chem*. 2002;277:49120-6.

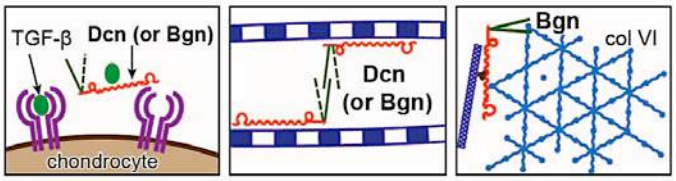

Figure 1: Binding activities of decorin (Dcn) and Biglycan (Bgn) (schematics inspired by Ref. [1]).

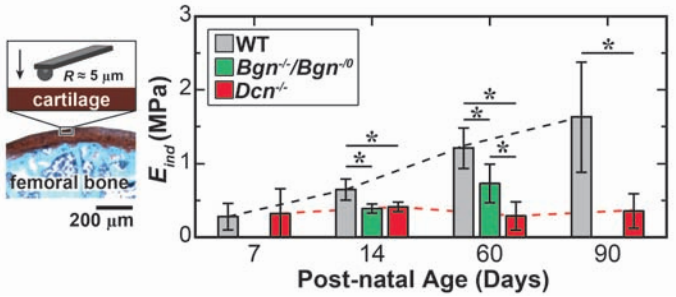

Figure 2: Effective indentation modulus, E_{ind}, of medial condyle cartilage at different ages, days post-natal, P7 (mean ± 95% confidence interval, $n = 4$), P14 (mean ± 95% confidence interval, $n \geq 3$), P60 (mean ± 95% confidence interval, $n \geq 4$) and P90 (mean ± 95% confidence interval, $n \geq 4$, *: $p < 0.05$ via Mann-Whitney U test or Kruskal-Wallis test followed by Tukey Kramer post-hoc test).

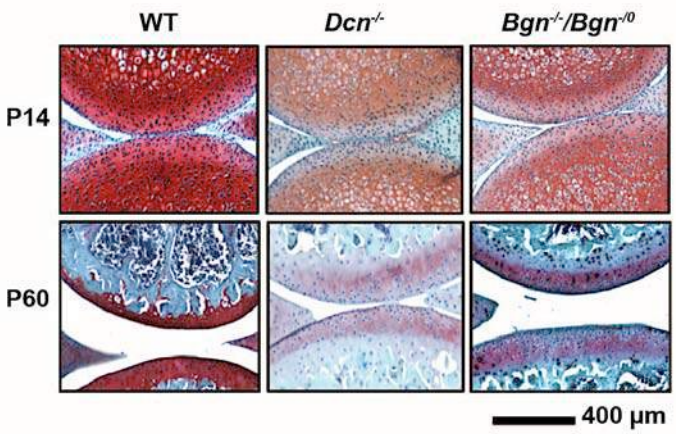

Figure 3: Safranin-O/Fast Green staining of wild-type, decorin-null ($Dcn^{-/-}$) and biglycan ($Bgn^{-/-}/Bgn^{-/0}$) mice at P14 and P60.

Copyright 2016 The Organizing Committee for the 2016 Summer Biomechanics, Bioengineering and Biotransport Conference

SB^{3}C2016
Summer Biomechanics, Bioengineering and Biotransport Conference
June 29 –July 2, National Harbor, MD, USA
SB^{3}C2016-965

THE BIOMECHANICAL EFFECTS OF STRAP OPTIONS ON SCOLIOSIS BRACING MECHANICS

Chloe L. Chung (1), Derek M. Kelly (2), Jack R. Steele (3), Denis J. DiAngelo (1)

(1) Department of Orthopaedic Surgery and Biomedical Engineering
University of Tennessee Health Science Center, Memphis, TN, USA

(2) Campbell Clinic Orthopaedics and Le Bonheur Children's Hospital
Memphis, TN, USA

(3) The Center for Orthotics and Prosthetics, Inc.
Memphis, TN, USA

INTRODUCTION

In Adolescent Idiopathic Scoliosis (AIS), thoracolumbar braces are the gold standard for treatment of moderate curves with 20° to 50° lateral curvature, or Cobb angle (CA), and some axial rotation (AR). [1, 2] Braces serve to maintain, and, in some cases, reduce [2] the spinal curve to prevent progression of the deformity by applying corrective forces.[3] Orthotists are tasked with making patient-specific braces to treat each unique deformity by using design alterations, such as the addition of Velcro straps, extra pads, and section cut-outs, to improve fit and comfort for the patient. However, there is no common understanding of how alterations affect the structural properties or the corrective capacity of a brace. The process is largely subjective and follows best practice, yet these steps can influence brace fit, user compliance, and ultimately treatment outcome.

The Scoliosis Analog Model (SAM) was recently developed and validated.[4] This analog model of a scoliotic deformity enables the study of braces through the measure of brace structural properties and force response on the spine. The objective of this study was to utilize the SAM to investigate the effects of strap-related brace design alterations. Analyzing these braces with various strap configurations would be of clinical importance for orthotists deciding on how many straps to use, where to place the straps, and the type of strap material to ensure proper fitting.

METHODS

A single-curve, thoracolumbar Boston brace (Avon, MA) was tested in nine strapping configurations (configuration) to investigate differences in brace structural properties due to quantity (1, 2, 3, 4) and material (non-backed 38.1mm Velcro and 25.4mm polypropylene webbing with buckle) (Table 1). To assess the full capacity of the brace, the simulated spinal curve correction was across the entire validated SAM range of 40°.[4] The first 20° of correction (i.e. CA 30° to 50°) represented the nondestructive range. The structural stiffness values of the brace were calculated over this loading range. Further correction (i.e., beyond CA of 50°) represented the destructive range. Each brace configuration was tested three times. Before each run, the straps were reset to the original position and orientation with negligible strap tension.

The 3D force components applied by the brace and the linkage assembly angular displacements were measured at a sampling rate of 25Hz. These two variables were plotted in a force-displacement curve (FDC). The slope of the FDC within the nondestructive range represented the structural properties of the brace. IBM SPSS 22 software program (IBM Corp. Released 2013. IBM SPSS Statistics for Windows, Version 22.0, Armonk, NY: IBM Corp.) was used to compare the mean stiffness values. Within the Velcro strap group and buckle strap group, mean stiffness values were compared using a one-

Table 1: Brace Configurations

Label	No.	Mat.	Configuration Description
A	1	Velcro	At apex
B	2	Velcro	Equidistant above apex and below apex
C	3	Velcro	One at apex, one above , and one below
D	4	Velcro	Spaced equidistant along length of brace
E	1	Buckle	At apex
F	2	Buckle	Equidistant above apex and below apex
G	3	Buckle	One at apex, one above , and one below
H	-	-	Rigidly Constrained
I	-	-	Unconstrained

Copyright 2016 The Organizing Committee for the 2016 Summer Biomechanics, Bioengineering and Biotransport Conference

way ANOVA and ranked using Tukey's post hoc test. The Velcro strap group and the buckle strap group mean stiffness values were then each compared to the rigidly constrained and unconstrained groups using a one-way ANOVA and ranked using Tukey's post hoc test. All statistical tests were performed at $\alpha = 0.05$.

RESULTS

The mean FDCs for the nine configurations are shown in Figures 1a and 1b. The slope was calculated for each curve within the nondestructive range. The structural properties of the brace are represented by the vertical and radial stiffness values, and are shown in Figure 2a and 2b. The mean stiffness values for the "I" (unconstrained) configuration are 0.0N/° radially and 1.0N/° vertically. The mean stiffness values for the "H" (rigidly constrained) configuration are 10.9N/° radially and 153.8N/° vertically. For the Velcro strap configuration, a trend of increased radial and vertical stiffness occurred when more straps were added with an optimal brace radial stiffness achieved with three Velcro straps. No statistically significant stiffness was obtained by adding a fourth strap. A similar trend of increased radial and vertical stiffness occurred when more buckle straps were added; however, this was not statistically significant. Use of a rigid strap ("H") significantly increased the radial and vertical stiffness levels well beyond the level achievable using either the Velcro or buckle strap material. The addition of either strap type significantly increased the stiffness values relative to the unconstrained configuration ("I") in all cases, except "A".

DISCUSSION

Braces serve to reduce and prevent progression of the spinal curve by applying corrective forces. Orthotists modify the expected brace force response through alterations in the brace design, such as pad placement and orientation. The force components of 75N radially and 510N vertically (see Figure 1) were measured during testing of "C" (three Velcro straps, 50° CA). These forces correspond to applied brace forces of 150N inward and 510N upward, due to SAM known trigonometric relationship. Theoretically, when the brace applies purely 150N inward, which might occur when a fitting pad is placed at the level of the curve apex, the maximal vertical force component would only be 320N. This difference (i.e., 510N versus 320N) in vertical force suggests that the brace engaged the torso below the curve apex to apply inward and upward corrective forces. The SAM was the first mechanical model to provide evidence of multidirectional force transmission by confirming an upward lifting effect.

The testing of brace configurations showed a measurable difference in brace force response and structural properties between strap material type and quantity. This information proves useful during the fabrication of a brace. An orthotist may desire to change brace structural stiffness to achieve better patient fit or better brace performance. For example, a patient with poor muscle tone and excessive spinal misalignment may require a stiffer brace to achieve and maintain the desired correction, and the addition of Velcro straps could provide the increase in brace stiffness required. Currently, the decision to add straps is made purely based on professional judgment.

For the Boston brace used in this study, optimal brace stiffness was reached after application of three Velcro straps (i.e., there was no significant stiffness gained by adding a fourth strap). Unlike the Velcro material, the addition of two and three buckle straps did not yield statistically significantly differences in brace stiffness. Traditionally, Dacron or cotton webbing is used as backing for the Velcro strap. This testing was performed using basic, non-backed

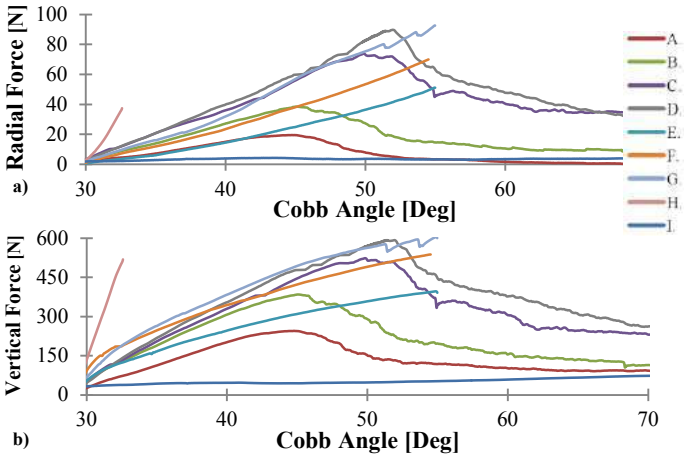

Figure 1: Force Response of Each Strap Configuration. a) Mean Radial FDCs, b) Mean Vertical FDCs.

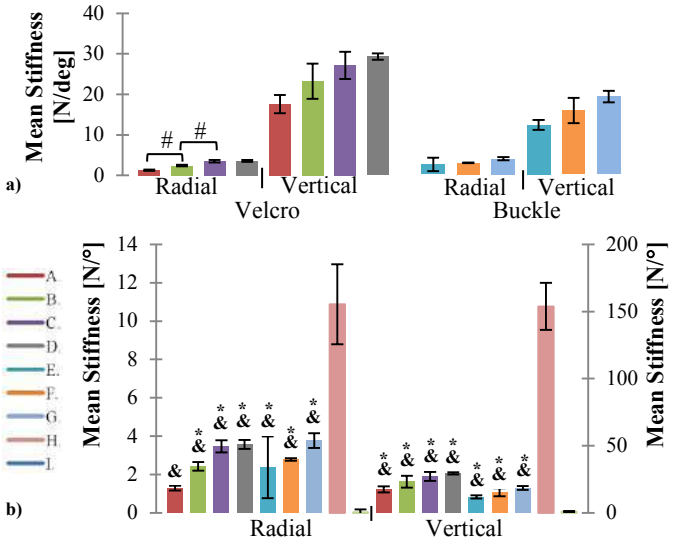

Figure 2: Comparative Studies: Mean Stiffness Values of Strap Configurations. a) Comparison within Each Group, b) Relative to H and I. "#", "&", "*" Denotes a significant difference between the two selected values, with H, and with I, respectively.

Velcro. In the future, the SAM and test assembly can be used to characterize different types of backed Velcro straps, as well as other brace design alterations. These features include brace pads, pad placement, pad geometry, material selection, material cut-outs, rigid components, and other fitting elements. This test assembly could also be used as a design tool and to develop a standard for comparing and classifying braces.

ACKNOWLEDGEMENTS

The scoliosis brace used in this study was donated by the Center for Orthotics and Prosthetics, Inc., Memphis, TN.

REFERENCES

[1] Altaf, F et al., *BMJ*, 346:f2508, 2013.
[2] Rinsky, L et al., *Western journal of medicine*, 148:182-191, 1988.
[3] Gallo, D et al., *JPO*, 23(2):69-77, 2011.
[4] Chung, C, *UTHSC Thesis,* 2015.

Copyright 2016 The Organizing Committee for the 2016 Summer Biomechanics, Bioengineering and Biotransport Conference

SB^{3}C2016
Summer Biomechanics, Bioengineering and Biotransport Conference
June 29 –July 2, National Harbor, MD, USA
SB^{3}C2016-966

SPATIO-TEMPORAL QUANTIFICATION OF CARTILAGE STRUCTURAL CHANGES IN A MURINE MODEL OF POST-TRAUMATIC OSTEOARTHRITIS

Michael A. David (1), Avery T. White (1), Rachael Pilachowski (1), Ryan C. Locke (1), Melanie K. Smith (1), Christopher Price (1)

(1) Biomedical Engineering
University of Delaware
Newark, Delaware, United States

INTRODUCTION

Post-traumatic osteoarthritis (PTOA), an accelerated form of OA, results from traumatic joint injury, e.g., ligament and meniscal tears, and is common in active individuals, e.g., athletes and uniformed service members. Approximately 50% of patients that experience a ligamentous tear will exhibit cartilage damage within 10- to 15-years of the injury [1]. Unfortunately, preventative treatments for PTOA are lacking, potentially due to a preclinical focus on mid-to-end-stage disease, whereas the initial changes precipitating PTOA remain largely unknown [2]. In order to develop prophylactic, chondro-protective therapies it is necessary to understand the natural time-course of cartilage structural degradation within the joint during the progression of PTOA. Knowledge of the spatial and temporal progression of cartilage degeneration across the injured joint, heretofore underappreciated, is critical to defining and interpreting the cartilage biology and pathophysiology underlying PTOA, and whether they are of mechanical or cellular origin. Therefore, the objective of the present study was to provide a detailed spatio-temporal histological quantification of cartilage structural changes from early (3-day) through late-stage (112-days) disease in a surgically-induced, murine joint instability model of PTOA, the destabilization of the medial meniscus (DMM) [3]. We hypothesized that cartilage damage would occur early following a traumatic injury and that the cartilage damage would be preferentially localized to the anterior regions of joint where surgical induced joint-instability results in altered biomechanical contact.

METHODS

Animals and Surgeries: Male C57BL/6 mice (Jackson Labs) at the age of 12-weeks underwent DMM surgery in right limbs with contralateral limbs serving as internal controls (n = 5-10mice/group) were harvested at baseline (0d), 3-, 7-, 14-, 28-, 56-, 84- or 112-days post-injury. *Histological Processing:* Samples were immediately fixed (in a naturally flexed position), decalcified, embedded in paraffin, and serially cut into 5-µm thick coronal sections. Starting at the front of the joint (anterior), two-sections were selected approx. every 100-um and stained with Safranin-O/Fast Green to assess changes in cartilage structure. From these, five sets of sections spanning the cartilage-cartilage contact (~500-µm wide) of the tibial plateau and femoral condyle were selected for scoring. *Scoring:* Scoring was performed across all stages of disease development to establish the natural time-course and spatial distribution of cartilage damage following DMM. Three blinded scorers semi-quantitatively ranked cartilage damage in each section using two separate metrics adapted from prior versions of scoring systems [4-6]. First, the extent of cartilage damage across the width of articular surface (referred to as width-based; Figure 1), and second, the extent of depth-wise articular/calcified cartilage damage (referred to as depth-based; Figure 1). For each metric, cartilage damage was assessed on a 0-6 scale for both the medial and lateral femoral condyles and tibial plateaus, and utilized for both temporal and spatial analysis. For temporal analysis, a single average joint score was aggregated for each specimen based upon each scorer's findings, and used to calculate the group mean and SD for each time point. For spatial analysis, an average score at each section location (anterior to posterior) was aggregated from each scorers findings, and used to calculate a spatial location mean and SD for each location and time point. *Statistical Analysis:* To establish differences in cartilage damage between DMM and contralateral joints at each time point, paired t-tests well as one-way ANOVA with post-hoc and linear regression across location were performed. Statistical significance was set at $p<0.05$. Data is presented as mean ± standard deviation

Copyright 2016 The Organizing Committee for the 2016 Summer Biomechanics, Bioengineering and Biotransport Conference

RESULTS

We found significant, site-specific cartilage damage across the medial compartments of DMM joints. No significant damage was observed in the lateral compartments of DMM joints or in any region of the control joints. Temporally, significant cartilage damage appeared as early as 3-days post-injury in the MTP, observed as a loss of proteoglycan staining (Figure 2). Cartilage structural damage in MTP and MFC continued to increase with time under both scoring methods, with the most damage seen at 112-days post-injury. Spatially, we observed trends of cartilage damage that appeared greater in the anterior region of the tibia compared to posterior (Figure 3); however these findings were only significant at 84- and 112-days post-injury. No differences existed at any time point post-injury within the MFC.

DISCUSSION

By combining two scoring methods with temporal and spatial analyses this study provided a detailed representation of the extent and timing of focal vs. widespread cartilage damage, from anterior to posterior, in the joint following injury. We found early and highly localized cartilage damage within the medial compartments of DMM joints. An initial loss of proteoglycan content (3-d), followed by fibrillations/erosion of articular cartilage (7-d), cumulating in full cartilage loss by 112-days post-injury was observed. When compared to the literature, our observation of cartilage damage from 14-days onward post-DMM is entirely consistent with others findings from DMM models in mouse [7-9], rat [10], and rabbit [11]. However, to the best of our knowledge, no group has investigated cartilage damage from 3-7 days post injury in the murine DMM model of PTOA. Our temporal findings suggest that studies attempting to prophylactically prevent PTOA initiation and progression may require immediate-early interventions (≤ 7d in mice) to be most efficacious.

Moreover, we also observed a spatial localization of cartilage damage in the MTP, but not in the MFC. While a trend for increased MTP damage anteriorly was seen at several time points, statistical significance was only found at the later time points (84 and 112-days). These findings support the idea that the insult of the DMM causes altered loading and presumably increased localized contact stress at the front of the joint (anteriorly). There was no difference in damage spatially in the MFC, which suggests that the MTP and MFC may experience different mechanical loading and articulation patterns following DMM. Importantly, our spatial findings are consistent with qualitative observations made in the pioneering murine DMM study where increased damage was found anteriorly [3]. In addition, other animal DMM models have shown spatially localized changes in cartilage damage (medial to lateral) [10] as well as increased medial compartment peak contact stresses [11]. Non-invasive murine models have also shown localization of cartilage damage and chondrocyte apoptosis that is dependent on magnitude and location of force applied [12]. Taken together, these studies and ours suggest that insult and altered loading may be an important factor in rapid precipitating and progressing cartilage damage post-injury.

Qualitative analysis of the localization of cartilage damage has additionally suggested that temporal- and spatial-localization of damage to the MTP cartilage, and its subsequent cellular response (loss of chondrocytes), may be related to changes in meniscal coverage of the articular surface following DMM (Figure 4). We are presently quantifying this relationship, as well as investigating if spatial-temporal changes in other joint tissues, e.g., synovium, bone, and menisci, occur post-DMM.

This study is significant in that it's the first to provide a detailed analysis of the spatio-temporal cartilage changes within the murine DMM model of PTOA from early (3-day) through late (112-day) stage disease. Overall, our findings establish a baseline for the detailed study of the cellular and molecular pathoetiology of PTOA, as well as its prevention through the use of novel, targeted, prophylactic chondro-protective therapeutics.

ACKNOWLEDGEMENTS

This research was funded by DoD PR120788P1. Special thanks to Brianna Gietter and Fiona Flowerhill for their assistance in this project.

REFERENCES

[1] Gillquist, J. et al., *Sports Med*, 27.3, 143-156, 1999; [2] Anderson, D. D. et al., *JOR*, 29.6, 802-809, 2011; [3] Glasson, S.S. et al., *Osteoarthritis Cart*, 15.9, 1061-1069, 2007; [4] Glasson, S.S. et al., *Osteoarthritis Cart*, 18, S17S23, 2010; [5] Chambers, M.G. et al, *Arth Rheum*, 44.6, 1455-1465, 2001; [6] Poulet, B. et al., *Arth Rheum*, 63.1, 137-147, 2011; [7] Kim, B.J. et al., *Tissue Engineering and Regenerative Medicine*, 10.4, 211-217, 2013; [8] Loeser, R.F. et al., *PloS one*, 8.1, e54633, 2013; [9] Gardiner, M. D. et al., *Osteoarthritis Cart*, 23.4, 616-628, 2015; [10] Iijima, H. et al., *Osteoarthritis Cart*, 22.7, 1036-1043, 2014; [11] Arunakul, M. et al., *JOR*, 31.10, 1555-1560, 2013; [12] Wu, P. et al., *Arth Rheum*, 66.5, 1256-1265, 2014.

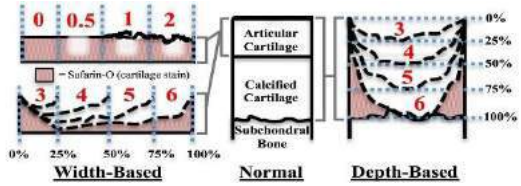

Figure 1: Schematic of width- and depth-based scoring on 0-6 scale (0 normal and 6 being the most cartilage damage). Scoring of 0-2 in both systems are identical. Width is scored irrespective of depth, and vice versa.

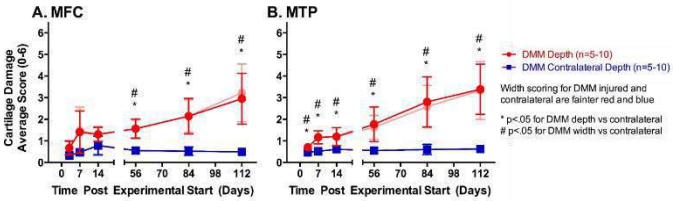

Figure 2: Temporal quantification of cartilage damage width- and depth-wise in the MFC (A) and MTP (B) post-DMM.

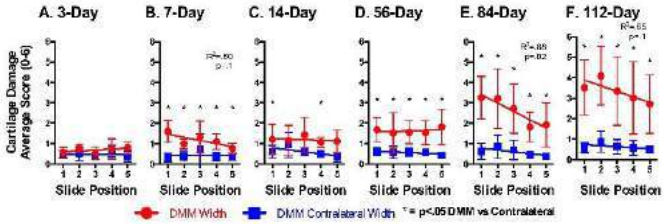

Figure 3: Spatial quantification of cartilage damage, width-wise in MTP post-DMM (A-F) from anterior (position 1) to posterior (position 5) regions of the joint. Regression data only indicated for DMM.

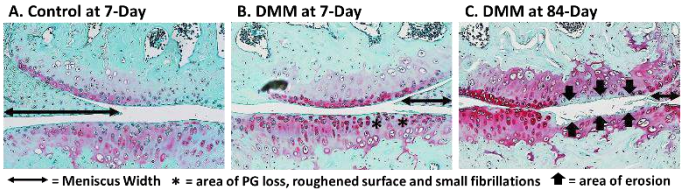

Figure 4: Extrusion of meniscus with medially localized cartilage damage in control (A) & DMM joints at 7- & 84-d (B&C) [position 2 shown].

Copyright 2016 The Organizing Committee for the 2016 Summer Biomechanics, Bioengineering and Biotransport Conference

SB³C2016
Summer Biomechanics, Bioengineering and Biotransport Conference
June 29 –July 2, National Harbor, MD, USA
SB³C2016-967

A FLEXIBLE METHOD FOR PRODUCING F.E.M. ANALYSIS OF BONE USING OPEN-SOURCE SOFTWARE

Abhishektha Boppana (1), Ryan Sefcik (2), Dr. Jerry G. Myers (3)

(1) Department of Biomedical Engineering
Case Western Reserve University
Cleveland, Ohio, USA

(2) Department of Biochemistry
The Ohio State University
Columbus, Ohio, USA

(3) NASA Glenn Research Center
Cleveland, Ohio, USA

INTRODUCTION

Individuals who experience decreases in load-bearing bone densities can be subject to a higher risk of bone fracture during daily activity. Astronauts may lose up to nine percent of their load-bearing bone density for every month they spend in space [1]. Because of this, specialized countermeasures reduce percent loss in bone density and reduce fracture risk upon returning to Earth. Astronauts will typically not be at risk for fracture during spaceflight, because of the lesser loads experienced in microgravity conditions. However, once back on Earth, astronauts have an increased risk for bone fracture as a result of weakened bone and return to 1G conditions [2]. It is therefore important to understand the significance of any bone density loss in addition to developing exercises in an attempt to limit losses in bone strength. NASA seeks to develop a deeper understanding of fracture risk through the development of a computational bone strength model to assess the bone fracture risk of astronauts pre-flight and post-flight. This study addresses the several key processes needed to develop such strength analyses using medical image processing and finite element modeling (F.E.M.).

The model can also be used to help determine contributions to the change in bone fracture risk of individuals as they age. The main objective in determining bone fracture risk is to inform the individual which activities to limit or avoid in order to prevent fracture. In addition, the model allows for the assessment of exercise design intended to strengthen an individual and mitigate bone loss.

METHODS

The tools developed for this model need to successfully segment bone regions from medical images, create a 3D model from the segmented data, and prepare the model for finite element analysis (F.E.A.). A decision was made to develop using only open-source software with the intention of a future public release. Python was chosen as the development language, due to its active open-source community and availability of diverse libraries. The tools have been designed to be highly adaptive and interface with existing software to successfully achieve the necessary tasks, as detailed in the following sections.

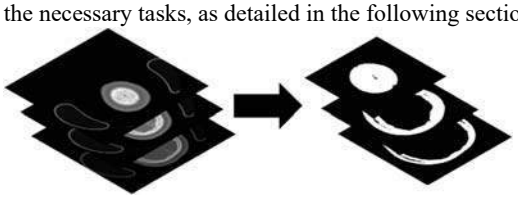

Figure 1: Image segmentation of medical image stack

IMAGE SEGMENTATION SCRIPT: A segmentation technique was developed in Python to allow for the isolation of bone regions of interest. The final script used the visualization toolkit (VTK) library to import and segment the medical images. The library automatically rescales the images' pixel values into Hounsfield units, based of metadata in the image files. This allows for the easy thresholding of the image using known Hounsfield values for bone, as show in in Figure 1. The tool was designed with the ability for the user to input their own threshold values. After segmenting the bone regions from the medical images, the regions are ready to be turned into 3D model.

3D MODEL CREATION: The VTK library also presents the ability to turn the segmented regions into a surface mesh, using a marching cubes algorithm. Compared to the contour reconstruction algorithm, the marching cubes algorithm has shown better performance [5] [6] [7]. The

Copyright 2016 The Organizing Committee for the 2016 Summer Biomechanics, Bioengineering and Biotransport Conference

marching cubes algorithm works by treating each voxel element as a cube, and defining polygons to represent the cube. An isosurface is created along the edge of the segmented region. As a result, a triangle-based surface mesh is constructed over the entire image stack, representing the segmented regions. The VTK library also includes further tools to delete any excess triangles and smooth the surface.

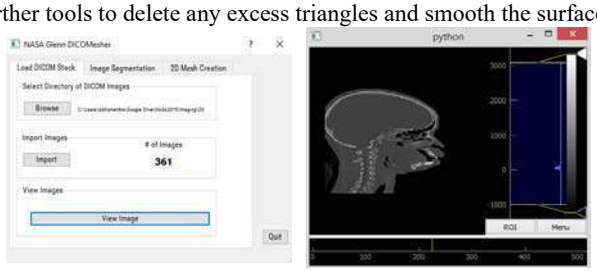

Figure 2: GUI showing image import and viewing capabilities

The surface mesh can be exported as a universal .STL file with the VTK library. A graphical user interface (GUI) has been developed which can provide a centralized location for the image segmentation, surface mesh creation and export. This will allow the user to complete a majority of the steps in one user-friendly program (Figure 2)

After exporting the file, it can be re-meshed in Blender, an open source 3D creation suite, to perform further cleaning. The surface mesh is then exported to Gmsh. Gmsh is a free, open-source 3D finite element mesh generator [8]. Gmsh converts the 2D surface mesh to a 3D volume mesh. An example vertebrae's volume mesh is shown in figure 3.

FINITE ELEMENT ANALYSIS PREPARATION: The chosen finite element solver was the FEBio suite, The model is prepared for finite element analysis by first importing the volume mesh into FEBio, and saving the mesh as a FEBio XML file. This allows for the mesh nodes to be easily identified with the FEBio-friendly node IDs.

The medical images are then reimported into Python as a pixel matrix using the Pydicom library. The pixels are then transformed to Hounsfield values using the image metadata in equation 1:

$$Value_{Hounsfield} = (Value_{Pixel} * slope) - intercept(\quad (1)$$

Where the slope and intercept are values taken from the images' metadata. Previous studies by Kaneko et. al. have shown that a correlation can be found between the Hounsfield units and mechanical material properties [10]. These studies explored the relationship between bone ash material properties, and the density computed from the CT Hounsfield units. Regression curves from these studies were used in the model to extrapolate the mechanical properties based on the Hounsfield units. First, the Hounsfield values were converted to the bone ash density, and the Young's modulus was extrapolated from the regression equations

To assign the material properties to each element in the finite element mesh, the elements' coordinates were found with the data in the FEBio XML file. The centroid of each element was calculated, and mapped to the original location in the medical images. The extrapolated material properties are then assigned to each element based on their location. Finally, the elements, along with their material properties, are written to a new FEBio XML file, ready for finite element analysis in the FEBio suite.

Figure 3: Contour map of effective stress (left) and pressure (right) on vertebrae run through tool

RESULTS

The development of the method resulted in an open-source streamline process designed for the creation of 3-D computational bone models of specific load-bearing regions, such as vertebrae, femurs, and etc. The exported files are FEBio XML files with assigned material properties, ready for finite element analysis in the FEBio suite. Figure 3 shows an example of a contour map of a vertebrae, which was run through the process to create the finite element model. Preliminary work has shown that boundary conditions may be applied to these models and finite element analysis completed, however finite element analysis models for validation have yet to be run.

More results will become available as the validation models are completed and analyzed. In addition, future work includes the compilation of the software streamline into a single, centralized GUI interface for ease of use.

DISCUSSION

The work presented in this paper highlights an exploratory approach to producing models for finite-element creation using open-source methods. Combining Python with available libraries and existing open-source software provided a coding interface which allowed for easy manipulation of image data, and successful segmentation and 3D model creation.

The next big step of this project is validation. Validation will require sending a CT-scan through the workflow, which has mechanical results from clinical experiments. The results from the F.E.A. will be compared to these experiments in order to validate the process. Once validated, the model will be available for use in astronaut bone studies.

The tool can also be extended to use in elderly individuals, who have a tendency to lose bone density as they are aging on Earth. In addition, the model can be used for the study of other soft and hard tissues. Another area of interest in astronaut medicine is muscle atrophy. The model can be extended to muscle studies by changing the thresholding in the initial image segmentation, to segment the muscle. This project serves as an open-source building point for others to contribute and grow the model.

ACKNOWLEDGEMENTS

The authors thank Dr. Beth Lewandowski from NASA Glenn Research Center for her guidance in the beginning stages of the project. Additionally, the authors thank Chris Werner from Zin Technologies for his help in finite element analysis. A. Boppana and R. Sefcik would also like to thank the NASA Space Academy for the opportunity to conduct this research. Lastly, A. Boppana thanks the Ohio Space Grant Consortium for funding his research in the summer of 2015.

REFERENCES

[1] J. Sibonga, et al., *Bone*, 41(6):973-978, 2007.
[2] "Bones in Space", *NASA For Educators*.
[3] M. Harris, et al., *J Orthopaedic Research*, 30(7):1133-1139, 2012.
[4] W. Schroeder, et. al., *Kitware*, 2006.
[5] T. Xu, et. al., *Int Conf Adv Info Engi Edu Sci,* 215-218, 2013.
[6] W. Narkbuakaew, et al., *3rd Int Symp Biomed Eng*, 64-67, 2008.
[7] S. Wijewickrema, et al., *CMBS*, 29-34, 2013.
[8] C. Geuzaine and J.-F. Remacle*, Int J Num Methods Eng,,* 79(11): 1309-1331, 2009.
[9] S. Mass, et al., *J Biomechl Eng*, 2011.
[10] T. S. Kaneko et. al., *J Biomech*, 37:523-530, 2004.

Copyright 2016 The Organizing Committee for the 2016 Summer Biomechanics, Bioengineering and Biotransport Conference

SB^{3}C2016
Summer Biomechanics, Bioengineering and Biotransport Conference
June 29–July 2, 2016, National Harbor, Maryland, USA
SB³C2016-968

AGE DEPENDENT SUSCEPTIBILITY TO INHALED PARTICLES

Jessica M. Oakes[1,2,3], **Irene E. Vignon-Clementel**[2,3], **Céline Grandmont**[2,3], **Shawn C. Shadden**[1]

(1) Department of Mechanical Engineering, University of California, Berkeley, CA, USA
(2) INRIA de Paris, France
(3) UPMC Université Paris 6, Laboratoire Jacques-Louis Lions, France

INTRODUCTION

The airway structure and function changes from birth to adulthood, likely influencing the location and extent of deposited particles. Despite the need to access whether or not children are more susceptible to inhaled particles, very few studies have focused on modeling transport in the juvenile population. Model predictions will provide novel insight on age-dependent particle retentions and will enable the health consequences of toxic airborne particles or delivery efficiency of aerosolized therapeutics to be assessed.

We recently developed a new framework that couples 3D image-based airways to 1D idealized airways to predict aerosol fate throughout the entire lung and respiration cycle [5]. The advantage of this 3D-1D framework is that it enables us to predict particle transport beyond the resolution of imaging data and throughout expiration. The goal of this current study was to apply this framework to predict airflow and aerosol fate in infant, child, and adult human airways to shed light on the relationship between age and deposition fractions. Simulations incorporated subject-specific airway geometry, time-dependent flow waveforms, and several particle sizes.

METHODS

Three-dimensional conducting airway geometries of a three month infant, six year old child, and a 36 year old adult were created from CT images of patients in the Stanford Image Repository, SIRfS. Images only included the thoracic cavity, therefore the extra-thoracic airways could not be created. Model geometry, mesh, and airflow solution were performed with the open source software, SimVascular (http://simvascular.github.io/). Radius-based meshing with boundary layer elements resolved the wide range of airway sizes. Airflow was determined by solving the incompressible Navier-Stokes equations with the finite element solver [1]. Flow waveforms were defined at the trachea entrance as

$$Q = \frac{V_T \pi}{T_B} sin\Big(\frac{2\pi}{T_B} t\Big) \tag{1}$$

where V_T is the tidal volume and T_B is total time for one breath. Resistances (R) were prescribed at the distal faces based on the subtending lobe volume (lobe fractions = 0.20, 0.25, 0.25, 0.09, and 0.21 for the lower left, upper left, lower right, middle right, and upper right lobes, respectively [2]) and the cross-sectional area of the airway. R, V_T, and T_B were determined for each model based on the patient's age, weight, and height [3]. Following the airflow simulations, spherical particles ($d_p = 1, 3, 5\mu m$) were tracked in the 3D models by solving a reduced form of the Maxey-Riley equation [4], including drag and buoyancy forces. Gravity was positioned parallel to the trachea and particles were assumed to be deposited once they penetrated the wall. For the adult model, the time-dependent concentration and air volume exiting each of the models was recorded and passed as a boundary condition for the 1D advection-diffusion trumpet models. All airways distal to the 3D model, defined for each lobe by Yeh et al. [7] were lumped together to solve the trumpet models [6], which included airway evolution throughout the respiration cycle based on mass conservation and a loss term to model deposition in the bronchioles and alveoli. The 1D airway dimensions were scaled to match the lung volume of the adult subject.

RESULTS AND DISCUSSION

Up to 7, 9, and 11 airway generations were extracted from the CT images; model surface areas are presented in Table 1. The mean flow rate and Reynolds number, taken at the trachea is also shown in Table 1. Resistance, defined as the average pressure drop divided by the inhaled flow rate in the 3D geometry, was largest in the infant model (6.0E-3 cmH_2Os/cm^3) compared to the child (1.2E-3 cmH_2Os/cm^3) and adult models (2.7E-4 cmH_2Os/cm^3).

	Model Surface Area, cm^2	Mean Flow Rate cm^3/s	Mean Re	Stk for $d_p = 3\mu m$
Adult	172	250	1077	0.001
Child	60.5	135	1164	0.005
Infant	20.6	65	1143	0.020

Table 1: surface area of the 3D geometries. mean flow rate, reynolds number (Re), and stokes number (Stk) were defined at the trachea.

Deposited particle locations in the each of the 3D models are presented in Figure 1 for $d_p = 3\mu m$. To assess the deposited concentration (C_N) we counted the number of particles to deposit within each surface element relative to the total number of de-

Copyright 2016 The Organizing Committee for the 2016 Summer Biomechanics, Bioengineering and Biotransport Conference

posited particles and normalized that value by the element's surface area fraction. As indicated by relatively large values, the majority of particles deposited at the bifurcation zones and on the gravitational dependent side of the airways (Figure 1).

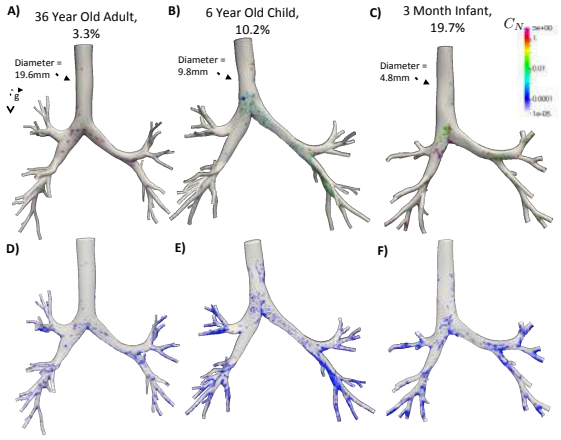

FIGURE 1: Deposition for the 3 μm diameter particles for the adult (A and D), child (B and E), and infant (C and F). panels A, B, and C show C_n, defined as the fraction of deposited particles normalized by the area fraction of the surface element. Individual particle locations are shown in panels D, E, and F. Airways are not shown to scale.

The deposition fractions increased as the subject's age decreased (Table 2). Compared to the adult model, approximately four times more particles deposited in the infant model for all particle sizes. In addition, the total concentration (percent deposition normalized by the model's surface area) was highest in the infant model (Table 2). This enhanced deposition is likely because the airways are much smaller in the juvenile models, resulting in higher Stokes number (Table 1) and a shorter gravitational distance that the particle must travel to deposit. These simulation results suggests that susceptibility to airborne particles is inversely proportional to the subject's age, therefore youth are more prone to health consequences to airborne toxins. However, as few particles deposited in the 3D conducting airways of the adult model, more particles can reach the acinar zone and potentially translocate into the blood stream.

	Adult		Child		Infant	
	%	$\%/cm^2$	%	$\%/cm^2$	%	$\%/cm^2$
1 μm	1.8	0.01	3.7	0.06	4.7	0.23
3 μm	3.3	0.02	10.2	0.17	19.7	0.98
5 μm	12.4	0.07	30.6	0.51	59.0	2.94

Table 2: percent deposition in the 3d model for the adult, child, and infant models and the percent deposition normalized by the surface area of the 3D model.

By solving the 1D trumpet models we are able to determine how many particles deposit in each zone and lobe of the lung. Lobe specific deposition fractions (number of particles deposited divided by the number of particles simulated) for each of the particle sizes are shown in Figure 2A and was largest in the lower right lobe. Calculated by normalizing mass deposited in each zone by the total number of deposited particles, Figure 2B shows the ratio of conducting and acinar deposition for each lobe. As indicated by the relatively small index, the majority of particles deposited in the acinar zone for the $1\mu m$ diameter particles. In contrast, for particles with d_p of $5\mu m$, the majority of particles deposited on the conducting airways.

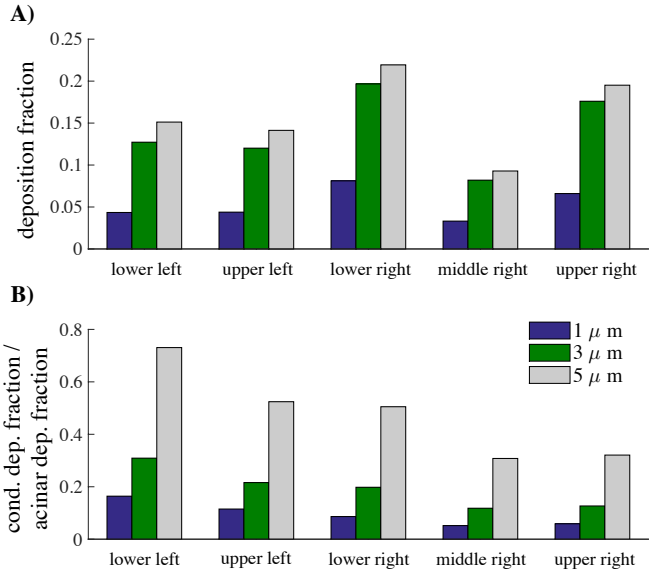

FIGURE 2: total deposition in the adult 3D-1D coupled model for the three different particle sizes. Panel A shows the deposition fraction for each lobe and panel B shows the relationship between deposition in the conducting zone versus the acinar zone.

In conclusion, patient-specific airflow and particle transport simulations indicate that youth are more susceptible to particle deposition in the conducting airways than adults. However, particles may bypass the conducting regions of the adult model and deposit in the deep regions of the lung. As deposition extent and location is highly dependent on the patient's age, it is imperative to calculate or measure age-dependent regional deposition when determining regulations for airborne pathogens or development of aerosol medication.

ACKNOWLEDGMENTS

This work was supported by an ALA Senior Research Training Grant, a University of California Presidential Postdoctoral Fellowship, and an INRIA@SiliconValley Postdoctoral Fellowship. The authors would like to thank Dr. Feinstein for providing the CT images and Adam Updegrove for modeling assistance.

REFERENCES

[1] Esmaily Moghadam, M. et al. *Comp. Mech.*, 52: 1141-1152, 2013.
[2] Horsfield, K. et al. *J. Applied Physiology*, 31: 207-217, 1972.
[3] Nguyen. A. et al. *Pediatric Pulmonology*, 48: 370-380, 2013.
[4] Oakes, J.M. et al. *Annals of Biomed. Eng.*, 42: 899-914, 2014.
[5] Oakes, J.M. et al. *CMBE 2015 Proceedings*, 86-89, 2015.
[6] Taulbee et al. *J. of Applied Physiology*, 38: 77-85, 1975.
[7] Yeh, H. and Schum, G. *Bulletin of Math. Biology*, 42: 461-480, 1980.

Copyright 2016 The Organizing Committee for the 2016 Summer Biomechanics, Bioengineering and Biotransport Conference

SB^{3}C2016
Summer Biomechanics, Bioengineering and Biotransport Conference
June 29 –July 2, National Harbor, MD, USA
SB^{3}C2016-969

INVESTIGATION OF SUPERPOSITION IN MICROCHANNEL GEOMETRY FOR INERTIAL PARTICLE SEPARATION

Utku M. Sönmez (1,2), Samir Jaber (1,2), Levent Trabzon (1,2,3)

(1) Mechanical Engineering Department
Istanbul Technical University
Istanbul, Turkey

(2) ITU-MEMS Research Center
Istanbul Technical University
Istanbul, Turkey

(3) ITUnano Research & Development Center
Istanbul Technical University
Istanbul, Turkey

INTRODUCTION

One of the major fatal diseases, which has been causing a substantial death toll of people worldwide is cancer. In the course of treating this disease, in particular metastatic cancer, early diagnosis plays a crucial role in providing better chances to overcome it[1]. However, due to the intermittence of circulating tumor cells (approximately 1-100 CTCs per 10^9 blood cells)[2], it is quite difficult to characterize and segregate such cells by using conventional microfluidic separation techniques. Recently, research has showed that particles can migrate across the microchannel's cross-section by means of inertial forces which can be adapted for cell separation. Such a microfluidic system can deliver relatively high throughput, resulting in a high process efficiency, and can enable the conveying of cells to post-laboratory analysis with no known ruinous effect on their morphology or vitality. Furthermore, an important aspect that can be associated with this system is its involvement in point of care testing since it has a potential to be manufactured as a portable device with small footprint like pregnancy test tools. Accordingly, we have designed an original microchannel geometry that allows continual size-based separation of cells by means of inertial forces and Dean flow, with no requirement for external forces. This configuration is expected to acquire a notable distinction, as it categorically surpasses its peer microfluidic systems in terms of separation, efficiency, reliability and straightforwardness in use.

METHODS

The microchannel in hand is basically a composite geometry constructed within Polydimethylsiloxane (PDMS), attached to a piece of glass, which serves as the base of the channel. This microchannel was manufactured using soft lithography, and was bonded to the glass using oxygen plasma bonding. The geometry of this microchannel was contemplated by studying the different designs, methodologies and results of two separate configurations, an asymmetric curvilinear pattern[3] and a spiral pattern[4]. By applying the superposition of the two patterns, a new geometry was obtained, which we named the *Sunflower* [Fig. 1].

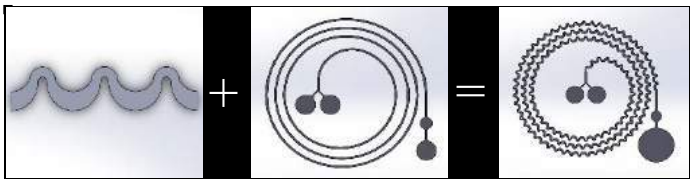

Figure 1: Superposition of the asymmetric curvilinear geometry (left) and the spiral geometry (middle) resulting in the Sunflower geometry (right)

In the course of the separation of cells, the approach towards obtaining this separation is very much similar to that of other deformable particles of equivalent sizes[5]. By taking into consideration this similitude, we performed our separation process on polystyrene particles of dimensions resembling those of cells. This separation procedure is based on inertial focusing, which involves hydrodynamic forces that modify the particle movements, resulting in an equilibrium position for the particles. This equilibrium position, hence, is dependent on the size of the particles. Lift forces tend to push the particles away from the channel boundary and center towards an equilibrium position near the inner sidewall of the microchannel. The net lift force can be justified by a formula derived by Asmolov[6],

$$F_{inertial} = \rho G^2 C_L a_p^4 \; [N] \qquad (1)$$

where ρ is the density of the fluid medium, G is the rate of shear of the fluid $(G = U_{max}/D_H)$, U_{max} being the maximum velocity of the fluid and D_H the hydraulic diameter, C_L is the lift coefficient approximated to an average value of 0.5, and a_p is the particle diameter. This means that the inertial lift force decreases rapidly with decreasing particle size. Moreover, the curvilinear figure of the channel induces a centrifugal acceleration, resulting in two oppositely rotating Dean vortices. This

Copyright 2016 The Organizing Committee for the 2016 Summer Biomechanics, Bioengineering and Biotransport Conference

effect can be rationalized by computing the magnitude of this secondary flow, represented by a dimensionless Dean number

$$De = Re\sqrt{\frac{D_H}{2R}} \quad (2)$$

where Re is the Reynolds number and R is the radius of curvature of the channel. As the particles flow through the channel, they experience a drag force due to the Dean flow crossway. These particles, relying on their sizes, move along the Dean vortices under the effect of this drag force, which can be characterized by

$$F_{drag} = (5.4\times10^{-4})\pi\mu De^{1.63}a_p\ [N] \quad (3)$$

where μ is the dynamic viscosity of the fluid. This shows that the drag force is also proportional to the particle size.

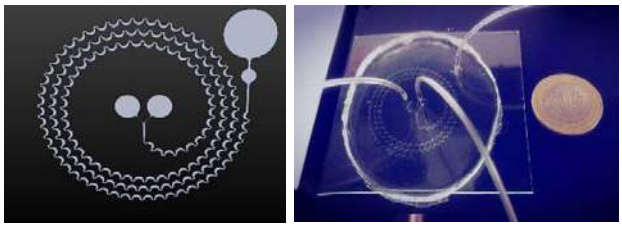

Figure 2

Figure 2: CAD of the microchannel in SolidWorks (left), and the microchannel during operation alongside a Turkish Lira coin to

Several experiments were performed on the Sunflower microchannel [Fig. 2] to examine its separation ability, and the results were compared with those of a spiral microchannel of the same dimensions, radius of curvatures and number of loops. The experiment is done by pumping a particle-carrying fluid from the outer inlet through to the two inner outlets. The fluid delivered to the microchannel is water carrying particles 3 µm (red) and 9.9 µm (green) in diameter. This water was pumped with different flow rates, and the optimum flow rate was selected depending on a brightness analysis performed in *ImageJ*. This analysis was based on a mathematical relation developed with respect to the channel width $W_{channel}$, particle diameter $d_{particle}$, focus width Δx_{focus} and gray values V, resulting in a normalized focus quality q_{focus}. This relation can be written as follows:

$$q_{focus} = \left(\frac{W_{channel}-\Delta x_{focus}}{W_{channel}-d_{particle}}\right)\cdot\left(\frac{\Sigma V_{focus}}{\Sigma V_{all}}\right) \quad (4)$$

RESULTS

The experimental data [Figure 3] shows the of particle focusing at different flow rates. As flow rate increases, the focus line becomes narrower and approaches the inner wall. After a certain flow rate, it starts to move outwards and disperses again. The optimum flow rate was determined by examining fluorescent images taken at the channel outlet. For numerical comparison, the normalized focus quality formula (eq. 4) was developed and used, and the results are shown in Figure 3. The normalized focus quality values are shown for both the spiral geometry (blue) and the Sunflower geometry (red) under various flow rates ranging between 0.3 [ml.min^{-1}] and 2.1 [ml.min^{-1}]. For the sunflower geometry, the best focus quality obtained was 0.93 at 0.9 [ml.min^{-1}], while it was found as 0.81 at 1.5 [ml.min^{-1}] for the spiral geometry. According to the fluorescent image analyses, the Sunflower geometry has a 14.5% advantage compared to the conventional spiral geometry in terms of normalized focus qualities at their optimum operation points. One should keep in mind that our focus quality ratio contains both the enrichment and separation properties of the focus line. Therefore, a focus quality of 0.93 corresponds to a much higher separation ratio which is also compatible with the particle counting analysis. These results clearly show that focus quality can be enhanced by designing such a geometry that superposes the inertial effects of

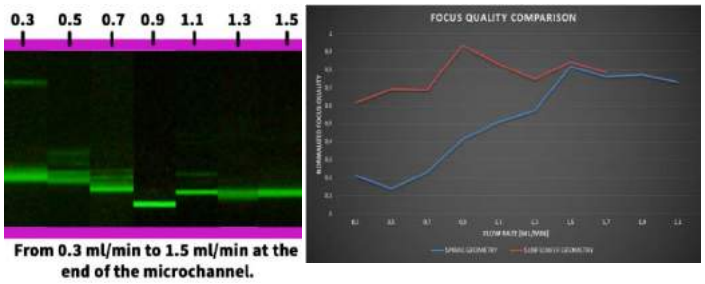

Figure 3: (left) Images of the particles with different focus qualities and locations flowing at increasing flow rates through the Sunflower microchannel; (right) difference in focus quality with respect to various flow rates between the spiral and Sunflower geometries

two different geometries on particles. As the fluorescent image analysis shows, the focus line has a width of only 25 µm (Figure 4), which almost corresponds to two adjacent single particle focus lines of 9.9 µm particles.

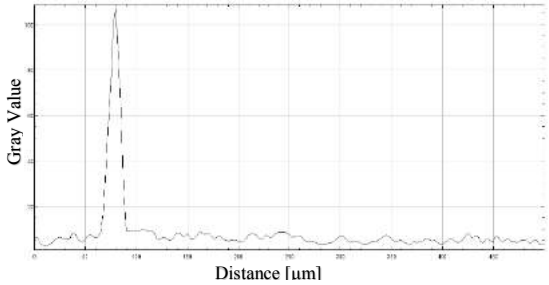

Figure 4: Plot Profile showing the fluorescence intensity along the Sunflower channel width at 0.9 ml.min^{-1}

DISCUSSION

The experimental data shows the superposition of inertial effects of two well-known microchannel geometries resulting in a better separation performance. The formation of the focus lines is consistent with previous research works[7] and theoretical background in terms of focus formation and position. Furthermore, this result implies a potential for the application of superposition principal to other inertial separation geometries (e.g. sudden expansion and contraction, trapezoidal cross-section.). This geometry can be employed to enhance the separation and enrichment of circulating tumor cells in microchannels. For this purpose, experiments with cancer cells should be done to prove the results that we have been presented in this article. One should bear in mind that the optimum conditions for particular size cutoff should be re-determined by altering microchannel height and flow rate. Herein, integration of a micro-pump and cell counter to this geometry is possible, which would result in a completed on-chip diagnostic tool with a very small footprint for cancer patients. On the other hand, multilayered versions of this geometry, which would lead to much higher throughput, can be produced and optimized to accomplish different tasks like water filtration or desalination. Our research on these subjects is currently in progress.

REFERENCES

[1] Cristofanilli, M. et al. *N Engl J Med*, 351: 781-791, 2004.
[2] Hou, H.W. et al. *Sci. Rep.* 3: 1259, 2013.
[3] Di Carlo, D. et al. *M. Phys. Lett*, 102: 94503–4, 2009.
[4] Gregoratto, I. et al. *Proc. SPIE*, 6465: 646503, 2007.
[5] Di Carlo, D. et al. *Anal. Chem.*, 80:2204–2211, 2008.
[6] Asmolov, *J. Fluid Mech*., 381:63–87, 1999.
[7] Di Carlo, D. et al. *PNAS*, 104: 18892–7, 2007.

Copyright 2016 The Organizing Committee for the 2016 Summer Biomechanics, Bioengineering and Biotransport Conference

SB^{3}C2016
Summer Biomechanics, Bioengineering and Biotransport Conference
June 29–July 2, 2016, National Harbor, MD, USA
SB^{3}C2016-970

TOWARDS NON-INVASIVE, COMPUTATIONAL MODELING OF THE TRANSPORT OF THROMBO-EMBOLI AND ATHERO-EMBOLI ALONG ARTERIES

Debanjan Mukherjee and Shawn C. Shadden

Department of Mechanical Engineering
University of California, Berkeley
Berkeley, CA, USA

INTRODUCTION

Floating aggregates of cellular or acellular material (emboli) constitute a leading cause of ischemic stroke. They are also associated with a range of other complications, including deep vein thrombosis, pulmonary embolism, and athero-embolic renal disease. In addition, embolization during endovascular or surgical procedures leads to adverse peri-operative and post-operative effects, reducing treatment efficacy. Emboli causing stroke are mostly fragments of clots (thrombo-emboli), or cholesterol based fragments from ruptured plaques (athero-emboli), originating from heart or valvular diseases, or diseases of the large arteries including the aorta. These emboli are transported to vessels distal to their point of origin by blood flow. Large artery hemodynamics is characterized by unsteady, pulsatile, chaotic flow. Predictive understanding of transport trends for emboli carried by such flows therefore continues to pose challenges. Specifically for stroke, the most prominent diagnosis process relies on the presence of a potential major cardiac source of embolus, with the absence of significant arterial disease [1]. Thus when cardiac and arterial sources of embolism co-exist, identification of stroke etiology becomes difficult. This complication leads to a substantial proportion of stroke cases (30-40%) to be categorized as "Cryptogenic". The identification of embolism source is important for long-term treatment and management of the patient's condition.

In view of the aforementioned complexities and challenges, we describe here a computational framework for investigating the transport of small and medium sized emboli across large arteries. The framework comprises a combination of large artery hemodynamics, discrete particle dynamics, and a sampling-based computational method (Figure 1). The developed tool will serve as a non-invasive probe into anatomically realistic vasculature, and help derive evidence regarding the i) transport mechanics of emboli across chaotic, large artery hemodynamics, ii) size/inertia dependent trends in embolus distribution to the brain (or other potential occlusion sites), and iii) relation between embolism source and embolus destination for stroke etiology. We present here illustrative numerical evidence regarding these objectives, derived from numerical experiments on real patient anatomical models.

METHODS

For our study, four representative patient datasets were selected from a database of Computed Tomography (CT) scan images. Vessel lumen was reconstructed from the images for the entire vasculature from the aortic sinus to the major cerebral arteries connected at the Circle of Willis. These were thereafter translated into a three-dimensional computer model, and discretized into a computational mesh comprised of an unstructured grid of linear tetrahedral elements. Blood was assumed to be a Newtonian fluid with density 1025 kg/m^3, and viscosity 0.004 Pa.s. A Petrov-Galerkin stabilized finite element solver was employed to solve the continuity and Navier-Stokes equations [2], and compute the velocity and pressure fields. A pulsatile, volumetric waveform derived from clinical data was specified at the inlet of the aorta in the form of a cross-sectional plug profile. The outlet boundary conditions were set using single element Windkessel resistors. Resistance values were calculated based on volumetric blood flow to the vessels obtained from measured data, or from proportionality relationship with vessel cross-sectional area. A mean brachial pressure of 93 mm/Hg was assumed.

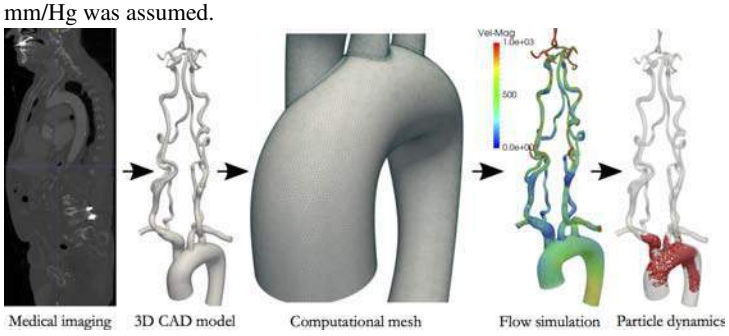

FIGURE 1: Illustration of the overall computational framework.

Individual emboli are modeled as spherical particles with a nominal density of 1100.0 kg/m^3. The particle motion is modeled using a modified form of the Maxey-Riley equation[3], which is derived from a superposition of the steady and unsteady forces on the particle arising from the background flow as well as the disturbed flow around the particle. Near-wall, shear-induced lift forces were considered, and a one-way coupled framework for integrating the particle motion equations based on the obtained velocity and pressure fields from hemodynamics simulations was employed.

Potential sites of embolization were generated by spatially sampling the aorta inlet, and the walls of the ascending aorta and the aortic arch up until the proximal end of the descending aorta. Particles of diameters ranging from 100 - 1000 microns were released across 8 instances during a single cardiac cycle. These ensured that particle sizes were not large relative to the vessel diameters, and could translocate past the M1,A1,P1 segments of the middle, anterior, and posterior cerebral arteries respectively.

RESULTS

The fraction of particles distributed across the six major cerebral arteries connected at the Circle of Willis were scaled by the volumetric blood flow received by these arteries, and compared between cardiogenic and

Copyright 2016 The Organizing Committee for the 2016 Summer Biomechanics, Bioengineering and Biotransport Conference

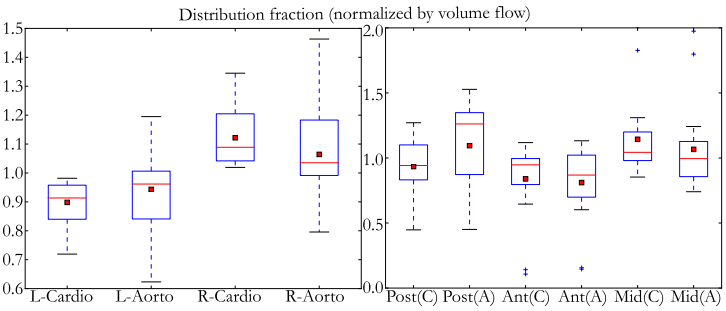

FIGURE 2: Variations in distribution fractions to the cerebral arteries between cardiogenic and aortogenic emboli.

aortogenic cases. Typically, radiological evidences employed in diagnostics involve identifying lesion patterns in the brain vasculature, which is directly related to the cerebral arteries to which the embolic particles travel. Hence, we present the comparison of distribution fractions in terms of the different cerebral vasculature regions in the brain in Figure 2. In terms of left vs right propensity of embolization, a more pronounced right brain preference is observed for cardiogenic emboli, over and above the volumetric blood flow received by the right cerebral arteries. When compared amongst the anterior, middle, and posterior arteries, we observe that while the aortogenic cases have greater variability, the median values (red lines) indicate that aortogenic emboli arrive at the posterior arteries notably in excess of volumetric blood flow as compared to cardiogenic emboli.

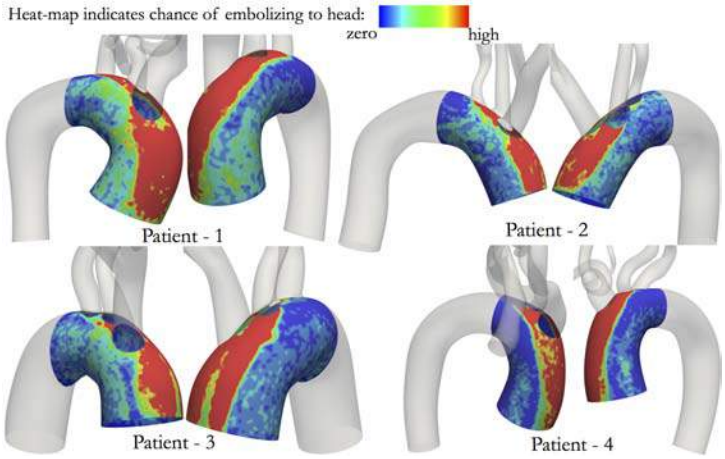

FIGURE 3: Surface map of embolus source and its tendency to send emboli to the head for aortogenic emboli.

Based on the particle trajectories, and the spatial sampling of the aorta inlet and aorta wall, an inverse map can be constructed now to explore the source-destination relationship, and the critical locations along the aorta leading to embolization to the brain. For all the patients considered, this surface heat-map has been compiled in Figure 3. Locations marked red are the ones with highest observed tendency of sending an embolus to the brain, while the locations marked blue are those that never sent any embolus to the brain. Observations indicate that embolization events along the greater curve of the aortic arch have the most potential to send emboli to the brain. The next major location is along the base of the arch or the lesser curve of the aorta. As the arch progresses distal to the left subclavian, there are increasing number of locations which do not send any emboli to the brain.

In our prior studies [4], we have illustrated the effect of particle inertia and its interaction with helical flow in arteries on their distribution across arterial bifurcations. Our computational tool enables further investigations regarding the mechanics of the fluid-particle interactions and their role in embolus transport. As an illustrative example, we present preliminary results from our experiments for assessing the role of shear-driven lift forces in Figure 4. Characteristic unsteady, swirling flow patterns for

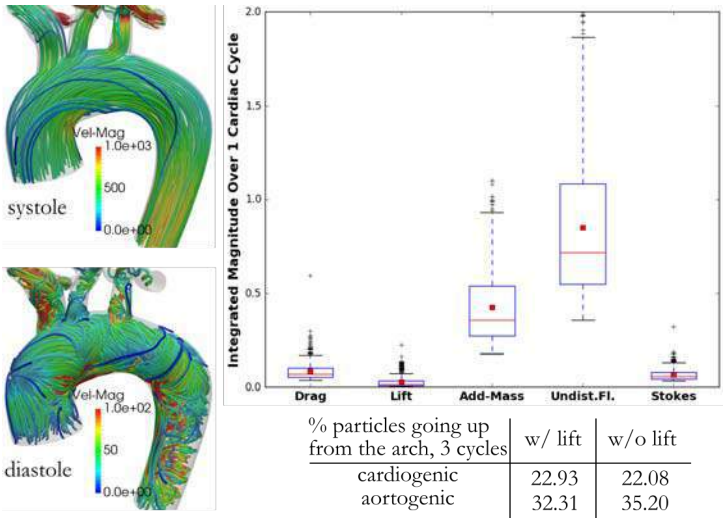

% particles going up from the arch, 3 cycles	w/ lift	w/o lift
cardiogenic	22.93	22.08
aortogenic	32.31	35.20

FIGURE 4: Forces on emboli from their interaction with characteristic unsteady flow, and their role in transport.

one of the patient models has been depicted for peak systole and mid diastole. For this patient, samples of embolic particles were advected with and without the inclusion of shear-driven lift forces, for both aortogenic and cardiogenic cases. The sample statistics for an integrated measure of the various fluid-interaction forces for each particle for one cardiac cycle have been presented. It is seen that cumulative levels of lift and drag are notably smaller in comparison to the unsteady added mass, and stresses from undisturbed flow. However, lift still leads to noticeable difference in transport fractions for aortogenic emboli. This is possibly because of the important role that shear-driven lift plays in drawing aortogenic emboli from the aorta wall into the bulk blood flow and affecting its transport. Further numerical experiments to obtain more detailed numerical evidence on the role of these forces are currently underway.

DISCUSSION

The implications of the developed framework, and the numerical evidence obtained, are multi-fold. Firstly, it enables exploring the difference between cardiogenic and aortogenic emboli in terms of their distribution across the major cerebral arteries. This is valuable for understanding stroke etiology, especially when competing embolus sources exist. Secondly, for aortogenic emboli, exploring the source-destination mapping provides valuable insights into the aspect of site-specificity. Additionally, this has valuable implications for improving treatment outcomes of procedures like percutaneous coronary intervention, for which silent strokes caused by aortic wall trauma and embolization may be more common than recognized [5]. Such a computational tool can thus advance state-of-the-art in terms of understanding complications due to emboli transported along the arteries. Currently, we are continuing investigations in terms of a) extending our experiments to a broader set of patient models, b) including aspects like anatomical variations, and embolus composition in the computations, and c) deriving clinically significant statistics from the computational model.

ACKNOWLEDGMENTS

This research was supported by the American Heart Association, Award No. 13GRNT17070095.

REFERENCES

[1] Ferro, J.M., et al. *Lancet Neurol.*, 9(11):1085-1096, 2010.
[2] Simvascular, `www.simvascular.org`, 2015.
[3] Maxey, M.R., Riley, J.J., *Phys. Fluids*, 26(4):883-889, 1983
[4] Mukherjee, D., et al., *Theor. Comp. Fluid. Dyn.* 2015
[5] Hamon, M.D., et al., *Circulation*, 118(6):678-683, 2008

Copyright 2016 The Organizing Committee for the 2016 Summer Biomechanics, Bioengineering and Biotransport Conference

SB³C2016
Summer Biomechanics, Bioengineering and Biotransport Conference
June 29 –July 2, National Harbor, MD, USA
SB³C2016-971

CORONAL HEAD ROTATION AND RAPID CORPUS CALLOSUM TRACT STRAIN IN SPORTS-RELATED MILD TRAUMATIC BRAIN INJURY

Fidel Hernandez (1), Chiara Giordano (2), Svein Kleiven (2), David B. Camarillo (1,3)

(1) Department of Mechanical Engineering
Stanford University
Stanford, CA, USA

(2) Department of Neuronic Engineering
KTH Royal Institute of Technology
Stockholm, Sweden

(3) Department of Bioengineering
Stanford University
Stanford, CA, USA

INTRODUCTION

Mild traumatic brain injury (mTBI) has been identified by the World Health Organization as a public health threat. Concern for mTBI has heightened due to the recent discovery of early onset, trauma-related neurodegeneration in soldiers and athletes. Public health measures to prevent mTBI are limited because the precise physical mechanism of human injury is unclear. Animal and computational studies previously suggested the brain has direction-dependent tolerance to injury: coronal rotation produced higher severity injuries in primates [1] and larger finite element strain in the corpus callosum [2], a structure responsible for communication between brain hemispheres. Another study found that tract-direction finite element strain in the corpus callosum is predictive of mTBI in laboratory reconstructions of NFL head impacts [3]. Direct rotation measurements of human mTBI were recently published [4] and have now made it possible to extend this analysis and investigate the relationship between coronal rotation and tract-direction corpus callosum strain in sports-related human mTBI.

This study investigated factors relating head accelerations in head impacts to ensuing mTBI diagnosis. We tested the hypothesis that tract-direction strain in the corpus callosum is predictive of mTBI and most associated with rapid coronal rotation using instrumented mouthguard measurements of head accelerations during impact and finite element simulations of brain deformation.

METHODS

Mouthguards instrumented with tri-axis accelerometers and tri-axis gyroscopes previously measured six degree of freedom (6DOF) accelerations in 110 football, boxing, and mixed martial arts video-confirmed head impacts (Fig 1A) [4]. Two of these impacts resulted in mTBI diagnosis, one after the subject suffered loss of consciousness (LOC) (Fig 1B) and one after the subject self-reported (SR) symptoms.

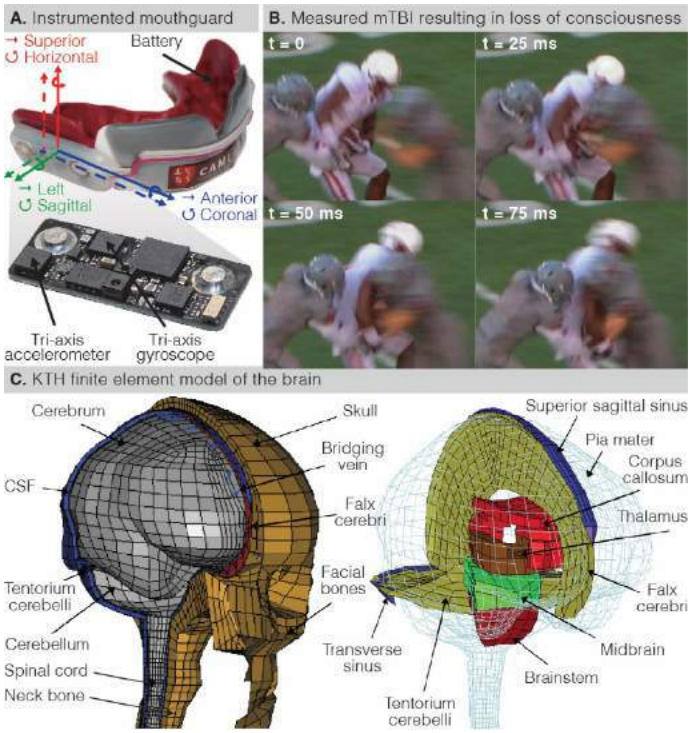

Figure 1: (A) Instrumented mouthguards recorded 110 sports head impacts, including a (B) diagnosed football mTBI resulting in loss of consciousness (LOC), and another that was self-reported (SR). (C) Tract-direction brain strain was estimated using the KTH finite element brain model with mouthguard measurements as input.

Copyright 2016 The Organizing Committee for the 2016 Summer Biomechanics, Bioengineering and Biotransport Conference

Of the remaining 108 impacts, 50 were selected at random to represent typical sports impacts. The remaining 58 impacts exceeded either mTBI in an acceleration component and were selected to represent the highest acceleration impacts and skew the non-injury sample toward those most difficult to distinguish from mTBI. All 110 impacts were simulated using a previously-validated finite element brain model and the mouthguard measurements as input [2]. An average DTI was assumed to determine fiber tract directions in the brain [3]. Cauchy strain tensors extracted from the finite element simulations were then projected in the direction of fiber tracts for individual structures in the brain.

For all measurements, Kolmogorov-Smirnov tests were performed to assess log-normality. Logistic regression for acceleration and strain criteria was performed to assess mTBI prediction. The deviance (D) statistic was calculated to assess the quality of fit of the logistic regression (analogous to r^2 in linear regression) and a null model with no criteria [4]. A smaller deviance suggests higher quality of fit.

RESULTS

For the 110 simulated head impacts, all acceleration measurements passed KS tests for log-normality. The LOC injury produced the highest coronal rotational acceleration (12900 rad s^{-2}), three standard deviations above median (960 rad s^{-2}), that was exceeded in the sagittal plane by 2 impacts that did not result in mTBI diagnosis (Fig. 2A). Peak coronal rotational acceleration and velocity had a strong, unique correlation with peak tract strain in the corpus callosum (both $r^2 > 0.86$) (Fig. 2B). Peak tract strain in the thalamus had the second highest correlation with coronal rotation (both $r^2 > 0.71$), while other brain structures correlated most with sagittal rotation. Peak tract strain in the corpus callosum had the lowest deviance statistic (8.0) among the individually modeled brain structures, followed by peak tract strain in the thalamus (10.4) (Fig. 2C). Peak tract strains in these structures yielded statistically significantly lower deviances than rotational acceleration ($p < 0.05$) and a null model ($p < 0.01$). For the LOC injury, peak tract strain over the duration of measurement was largest in the corpus callosum (0.38) and other proximal structures (Fig. 2D). The SR injury also yielded high tract strains in proximal brain structures, but the average of the 58 highest acceleration non-injury impacts events strained more distal structures.

DISCUSSION

In this study, we tested the hypothesis that tract strain in the corpus callosum is associated with coronal rotation and predicts diagnosed human mTBI better than tract strain in other brain structures. Study observations support this hypothesis. A diagnosed mTBI producing loss of consciousness (LOC) yielded the largest observed coronal rotational acceleration and corpus callosum tract strain among 110 impacts. As a result, tract strain in the corpus callosum had the smallest deviance (highest quality prediction). Two subjects sustained higher rotational accelerations in the sagittal plane without an mTBI diagnosis, suggesting damage to the corpus callosum strain may cause mTBI symptoms and may be sensitive to coronal rotation. Previous studies demonstrated sensitivity of coronal rotation to primate injury [1] and principal strain in the corpus callosum [2]; the present study supports these observations for tract strain with 6DOF human mTBI data [4].

Our results found the strongest correlations between peak coronal rotational acceleration and tract strain produced in the corpus callosum and thalamus. These relationships were unique compared to other brain structures who had stronger correlations with sagittal plane rotation. The corpus callosum and thalamus are proximal structures located around the ventricles. The corpus callosum manages interhemispheric communication and the thalamus is implicated in consciousness. Brain and skull anatomy may expose these structures to strain in coronal plane rotation. Our findings suggest further study of this potential mechanism.

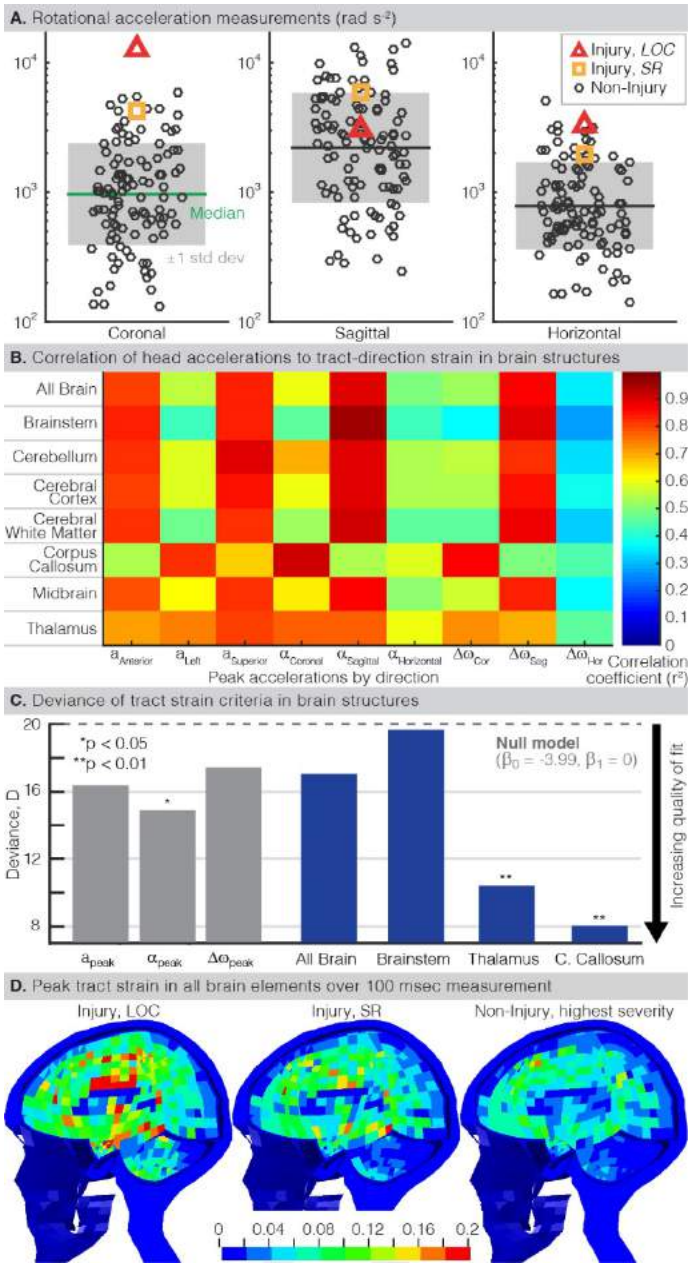

Figure 2: (A) Coronal rotational acceleration distinguishes the loss of consciousness (LOC) mTBI from other measured impacts. (B) Coronal rotation is uniquely correlated with corpus callosum tract strain, which (C) predicted mTBI risk better than other criteria (lowest deviance). (D) Both mTBI impacts yielded higher strains deep in the brain than the average of highest non-injury impacts.

ACKNOWLEDGEMENTS

We thank KTH for their finite element brain model and Stanford Athletics for help with subject enrollment and device deployment. We thank NIH, NSF, David and Lucile Packard Foundation, Stanford Child Health Research Institute, and Ford Foundation for financial support.

[1] Gennarelli, T A et al., *Ann Neurol.* 12(6):564-574, 1982.
[2] Kleiven, S, *Stapp Car Crash J.* 51:81-114, 2007.
[3] Giordano, C et al., *Stapp Car Crash J.* 58:29-61, 2014.
[4] Hernandez, F et al., *Ann Biomed Eng.* 43(8):1918-1935, 2015.

Copyright 2016 The Organizing Committee for the 2016 Summer Biomechanics, Bioengineering and Biotransport Conference

SB³C2016
Summer Biomechanics, Bioengineering and Biotransport Conference
June 29 –July 2, National Harbor, MD, USA
SB³C2016-972

A COMPUTATIONAL STUDY OF THE EFFECTS OF AGE-ASSOCIATED REGIONAL CHANGES IN ARTERY MECHANICS ON SYSTEMIC HEMODYNAMICS

Federica Cuomo (1), Sara Roccabianca (2), Desmond Dillon-Murphy (3), Nan Xiao (3), Jay D. Humphrey (4), C. Alberto Figueroa(1,3)

(1) Department of Biomedical Engineering
University of Michigan
Ann Arbor, MI, USA

(2) Department of Mechanical Engineering
Michigan State University
East Lansing, MI, USA

(3) Department of Biomedical Engineering
King's College London
London, UK

(4) Department of Biomedical Engineering
Yale University
New Haven, CT, USA

INTRODUCTION

Central artery stiffening is an inevitable consequence of aging and of diseases such as Marfan syndrome, diabetes and hypertension. It is recognized that arterial stiffening is both an initiator and indicator of increased cardiovascular, neurovascular, and renovascular risk [1]. Pulse Wave Velocity (PWV) is the speed at which pressure waves move down a compliant vessel and carotid to femoral PWV (cf-PWV) is the clinical standard measurement used to assess arterial stiffness, yet controversy remains over the best clinical metrics for diagnosis and evaluation of treatment efficacy. PWV, indeed, represents an average over a large portion of the arterial tree. The real concern, therefore, is whether *cf-PWV* can detect early regional changes in arterial properties that yet could increase disease risk. Computational modeling is a powerful tool that enables investigating the effects of regional differences in arterial geometry and wall properties on pulse wave propagation and other clinical metrics of arterial stiffening. In this work, we use fluid-structure interaction (FSI) simulations to examine effects of age-associated changes in aortic wall geometry and mechanics on the overall hemodynamics and the impact of arterial stiffening on different biomechanical metrics.

METHODS

In this work we establish a baseline model of a young, healthy human aortic tree and we used averaged population data on geometry and arterial mechanics to virtually age this model. We employed the 3D simulation framework Crimson (www.crimson.software). This is a multi-scale, FSI modeling software that combines a 3D geometric model, a FSI formulation with regionally varying biaxial tissue properties, Windkessel models, and an external tissue support formulation [2]. A 3D geometrical model of the aorta and its main branches was reconstructed from MRI data collected on a 30 year old (yo) volunteer. A multistep approach was used to artificially age the patient-specific 30 yo model to 40, 60 and 75 yo in a controlled manner (Figure 1). First, we increased the length of the aorta to reflect the non-uniform changes observed with aging by Craiem et al. [3]. They noted that per each 10 years aging, the ascending aorta (segment AB in Figure 1) exhibits a 3% increase in length, the aortic arch (segment BC) a 7% increase in length, and the descending aorta (segment CD) a 5% increase in length. We also incorporated the expected slight decrease in subject height due to aging [4] and the reported non uniform changes in diameter along the length of the aorta with aging [5]. A FSI method is essential to capture pulse wave propagation within an arterial network. Here, a coupled momentum method was employed whereby linearized stiffness was assigned to the vessel wall of the 3D model. Specifically, we recreated biaxial data from 6 published studies and we performed consistent nonlinear parameter estimation for a four-fiber family constitutive descriptor [5]. We then computed patient-specific linearized stiffness values informing the four-fiber model with radii, thickness and transmural pressure acting on the vessel wall based on measurements assessed for the 30 years old healthy subject and averaged-population changes with aging. Stiffness values were assigned at locations indicated by the black points in Figure 1 within the ATA, DTA and IAA and linearly interpolated or extrapolated to obtain a continuous distribution, as illustrated colorimetrically on the aortic geometries. A flow waveform measured with phase contrast MRI in the 30 year old volunteer under rest conditions was used as inlet boundary condition. Outlet boundary conditions were prescribed using a multi-domain method whereby three element Windkessel models were

Copyright 2016 The Organizing Committee for the 2016 Summer Biomechanics, Bioengineering and Biotransport Conference

coupled at each outlet of the 3D models representing the distal vasculature to the level of capillaries. The parameters were tuned individually for each age group to ensure appropriate flow splits and to match the arterial pressure considered to calculate the linearized stiffness. We also modeled forces exerted by organs and perivascular tissue on the outer side of the vessel wall as a traction consisting of a viscoelastic term with two parameters: a stiffness coefficient and a damping coefficient. We assigned spatially and temporally variable tissue support coefficients, in order to match the transmural pressure consider to assess the linearized stiffness.

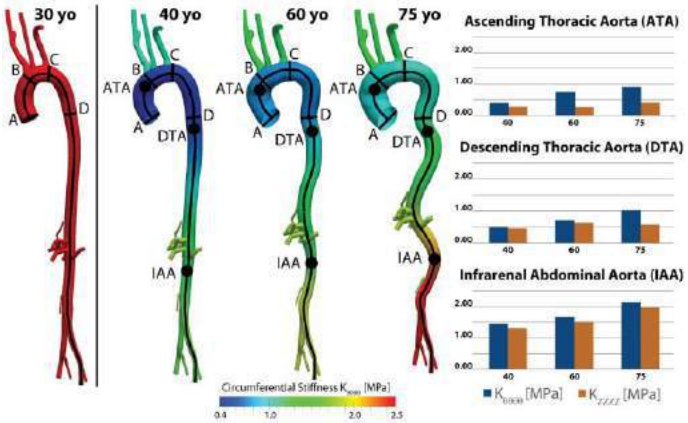

Figure 1: *Left*: Illustrative 3D geometrical models for the based model and the three age groups: 30, 40, 60, and 75 year old (yo) subjects. *Right*: Associated values of segmental circumferential (blue) and axial (orange) material stiffness (MPa) in three regions: ascending thoracic aorta (ATA), proximal descending thoracic aorta (DTA), and infrarenal abdominal aorta (IAA).

RESULTS

Figure 2 compares the distribution of prescribed values of circumferential material stiffness (left) to the spatial distribution of four different metrics of arterial stiffening: pulse pressure (*PP*), distensibility, pulse wave velocity (*PWV*), and changes in elastic energy stored during the cardiac cycle (ΔW) (right). Results are shown in six different anatomical regions along the aorta. Overall, our computed values compared well with data reported in literature for different age groups [5, 6]. We observe amplification of *PP* along the aorta at the youngest age, while the pressure waveforms become more alike in amplitude and contour with aging. We notice that the biggest change in *PP* occurs between 40 and 60 yo; indeed it has been reported that the largest changes in central pulse pressure happen around 50-55 yo [7]. Distensibility was calculated as $D=(d^2_{sys}-d^2_{dia})/(d^2_{dia}\cdot PP)$; as expected, the distensibility decreases distally along the aorta at a given age and it also decreases with aging at each individual location. The pulse wave velocity *PWV* was calculated as the ratio of the distance travelled by the pressure waveform and the transit time between pressure waveforms recorded at two locations of interest. Differently from the other three metrics of interest, the spatial distribution of *PWV* does not follow the prescribed distribution of circumferential stiffness everywhere. This difference arose because *PWV* depends not only from stiffness, but also on geometry (cf. Moens-Korteweg). *PWV* is indeed strongly influenced by arterial tapering and branching. Finally, the change in elastic energy throughout the cardiac cycle was calculated via the work done on the aorta given the assumption of no dissipation. In all regions other than the ATA, this is given by $\Delta W = 0.5(P_{sys}-P_{dia})\cdot(A_{sys}-A_{dia})/A_{dia}$. The distribution of this metric is comparable to the distensibility.

We also obtained good matching between the model predicted values of carotid-to-iliac *PWV* with measured values of *cf-PWV* for different age groups in a population with no risk factors [6, 8].

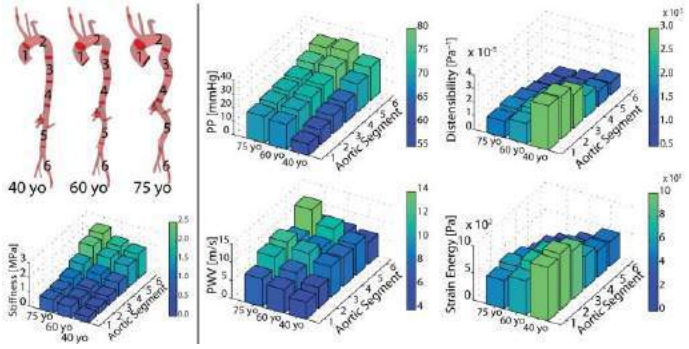

Figure 2: Prescribed values of circumferential material stiffness (MPa) and computed values of local pulse pressure (*PP*, in mmHg), distensibility (Pa^{-1}), pulse wave velocity (*PWV*, in m/s), and change in strain energy storage (ΔW, in Pa x 100) as a function of region (aortic segments 1 to 6) for three different ages: 40, 60, and 75 years old (yo).

DISCUSSION

Based on the best values of arterial stiffness, radii and length found in literature we used computational tools to investigate changes in four different metrics of arterial stiffening with aging. The current gold standard clinical metric is *cf-PWV* which represents an average over a large portion of the arterial tree. We found that differently from the other metrics, *PWV* is not directly related to the prescribed distribution of circumferential stiffness, due to the fact that PWV depends on both arterial geometry and stiffness. The distribution of *PWV* (Figure 2) shows notable differences over age at segment 5, which corresponds to the location of the renal arteries. This work has several limitations: the population-averaged data on anatomy and tissue properties implies that no subject-specific models were considered. Of course, it is not feasible to acquire longitudinal data on anatomy and stiffness for the same individual over a long time span. Furthermore, our FSI method did not taken into account the significant extensibility experienced in the ATA for the younger age groups. Lastly, we did not have flow data at multiple locations down the aorta: this would have allowed us to estimate the Windkessel parameters with more certainty.

ACKNOWLEDGEMENTS

This work was supported by NIH grants (R01 HL086418, R01 HL105297) and by the European Research Council Grant Agreement (n. 307532).

REFERENCES

[1] Mitchell, GF, *J Appl Physiol*, 105:1652–60, 2008.
[2] Xiao, N et al., *J. Comput. Phys*, 244:22-40, 2014.
[3] Craiem, D et al., *Ann Biomed Eng,* 40:1028–38, 2012.
[4] Sorkin, J et al., *Am J Epidemiol*, 150:969–77, 1999.
[5] Roccabianca, S et al., *J Mech Behav Biomed*, 29:618-34, 2014.
[6] Redheuil, A et al., *Hypertension,* 55:319–26, 2010.
[7] O'Rourke, MF et al., *J Am Coll Cardiol,* 50: 1–13, 2007.
[8] Boutouyrie, P, et al., *EurHeart J,* 31:2338–50, 20

Copyright 2016 The Organizing Committee for the 2016 Summer Biomechanics, Bioengineering and Biotransport Conference

SB^{3}C2016
Summer Biomechanics, Bioengineering and Biotransport Conference
June 29 –July 2, National Harbor, MD, USA
SB^{3}C2016-973

NON-SWELLING MICROMOLDED HYDROGELS REVEAL THAT MATRIX DEGRADABILITY CONTROLS MULTICELLULARITY OF CELL INVASION

Brendon M. Baker (1,2), Britta Trappmann (1,2), Jason A. Burdick (3), Christopher S. Chen (1,2)

(1) Deptartment of Biomedical Engineering
Boston University
Boston, MA, USA

(2) Wyss Institute for
Biologically Inspired Engineering
Harvard University
Boston, MA, USA

(3) Department of Bioengineering
University of Pennsylvania
Philadelphia, MA, USA

INTRODUCTION

Synthetic hydrogels are a major class of materials extensively used in biomedical applications ranging from tissue engineering to drug delivery [1]. However, a major drawback to these systems is the significant swelling that occurs with equilibrium hydration. Such swelling not only alters the gross geometry and dimensions of structures, but also leads to changes in hydrogel mechanical properties. We hypothesized that increasing the hydrophobicity of the polymer backbone through the attachment of hydrophobic pendant side chains could be used to modulate and eliminate swelling (Fig 1a), and thus extend the application of hydrogels to settings where swelling is undesirable. We illustrate the utility of this system through integration into a microfluidic device to reveal how endothelial cell invasion into surrounding matrix is modulated by different material properties (e.g., degradability, matrix stiffness).

METHODS

Polymer synthesis: Methacrylated dextran (DexMA) was synthesized by reaction of 86kDa dextran with varying amounts of glycidyl methacrylate. Cell culture: Angiogenic gradient-generating fluidic devices were generated and cultured as previously published [2]. A solution of DexMA (71% methacrylation, 4.4% w/v) and CGRGDS (3 mM) was prepared in M199 media containing sodium bicarbonate (3.5% w/v) and HEPES (10 mM). The pH was adjusted to 8 to couple CGRGDS to DexMA. After 30 min, varying amounts (17 - 44 mM) of crosslinker peptide NCD or LD were added and gels were allowed to polymerize for 1 h prior to seeding with HUVECs. Fluorescent labeling: To examine the organization of the actin cytoskeleton, cells were permeabilized with Triton X-100, blocked in 2% BSA, and stained with phalloidin. Microscopy: Phalloidin/DAPI-stained samples were imaged on a confocal microscope and images are presented as maximum intensity projections. Image analysis was performed with custom Matlab scripts. Statistics: Significance was determined by ANOVA or Student's t-test ($p < 0.05$).

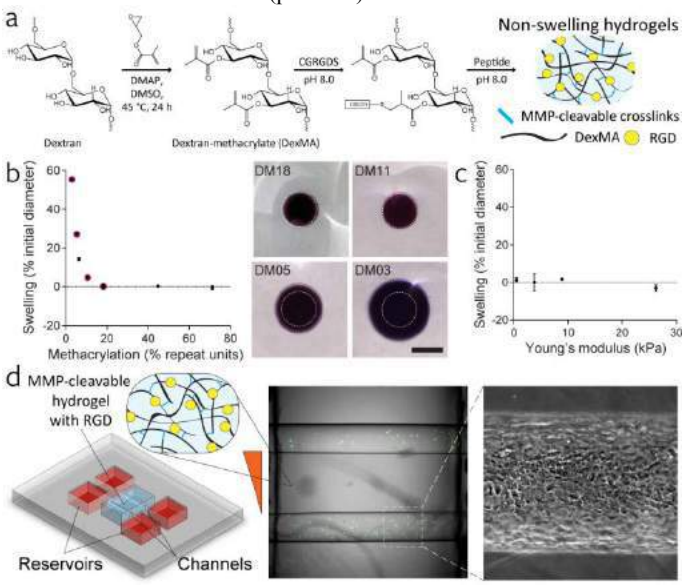

Figure 1: a) Synthetic route to non-swelling hydrogels. b) Swelling behavior as a function of % methacrylation. c) Swelling as a function of Young's modulus. d) DexMA hydrogels incorporated into angiogenic gradient-generating fluidic devices.

RESULTS

Increasing the level of methacrylate functionalization from 3 to 70% decreased DexMA hydrogel swelling from 55 to 0% (Fig. 1b).

Copyright 2016 The Organizing Committee for the 2016 Summer Biomechanics, Bioengineering and Biotransport Conference

Swelling was not affected by the amount of crosslinking, allowing swelling to be controlled independently of hydrogel stiffness (Fig. 1c). Gels were incorporated into a microfluidic device [2] (Fig 1d) to investigate how matrix properties influence angiogenic sprouting. We first examined whether the sprouting response was affected by changing the number of crosslinks via the concentration of MMP labile crosslinker peptides (Fig. 2a). Increasing crosslinking density decreased sprout length and appeared to switch cells from highly collective multicellular sprouting in gels of intermediate crosslinking, to less coordinated single cell migration in lightly crosslinked gels (Fig 2b-c). Fixing samples at different time points to maintain invasion depth constant confirmed that cells primarily invaded alone into matrices of low crosslinking density, whereas intermediate crosslinking densities gave rise to multicellular sprouts and a higher cell density (Fig. 3b-c). Next, hydrogel stiffness was maintained while modulating the degradability of the MMP-cleavable crosslinker sequence by replacing the standard native collagen degradability (NCD) with a lower degradability (LD) sequence. Strikingly, collective invasion was rescued in soft matrices when degradability was lowered, suggesting that high degradability rather than low stiffness drives the single cell migration phenotype observed in lightly crosslinked ECM (Fig. 3d). We posited that high degradability causes cells to degrade the matrix and invade too quickly to maintain cell-cell junctions. Indeed, exposure to a broad spectrum MMP inhibitor slowed cell invasion and rescued multicellular sprout formation even in soft gels crosslinked with the NCD sequence, further supporting the importance of degradability in sprout morphogenesis (Fig. 3e).

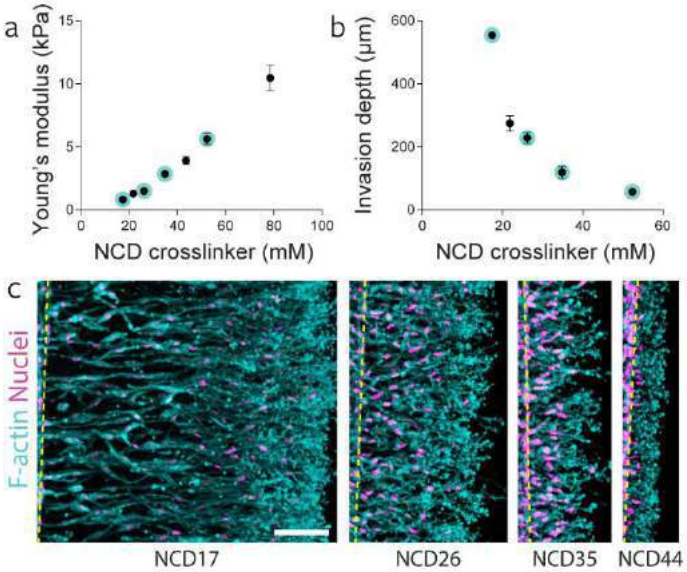

Figure 2: DexMA hydrogel Young's modulus (a) and sprout invasion depth (b) as a function of crosslinker concentration. c) Sprout morphology representative samples. Scale: 100μm.

DISCUSSION

Numerous studies using natural matrices such as fibrin or collagen have suggested that the physical properties of the ECM (e.g. matrix density, ligand density, and matrix stiffness) can regulate angiogenic sprouting. However, because these matrix properties are intrinsically coupled in natural ECMs, it is difficult to isolate the relative contribution of any one of these factors. Using a synthetic hydrogel to tune these properties orthogonally, we found that matrix crosslinking plays a critical role in modulating the extent, morphology, and even multicellularity of cell invasion. Crosslinking of synthetic gels has classically been used to vary the stiffness of a 2D substrate on which cells are seeded; this stiffness has been shown to dramatically impact cell spreading, proliferation, migration and differentiation. However, in 3D settings such as those investigated here, the degree of crosslinking alters not only matrix stiffness but also its degradability – the rate at which cells can cleave through the matrix. Degradability has previously been suggested as a parameter that affects the ability of fully encapsulated single cells to spread into the matrix [3,4]. By tuning degradability independently from matrix stiffness here, we reveal that ECM degradability is a key regulator of the collective nature of multicellular invasion, a critical requirement not only for functional blood vessel formation but also the formation of many other multicellular structures.

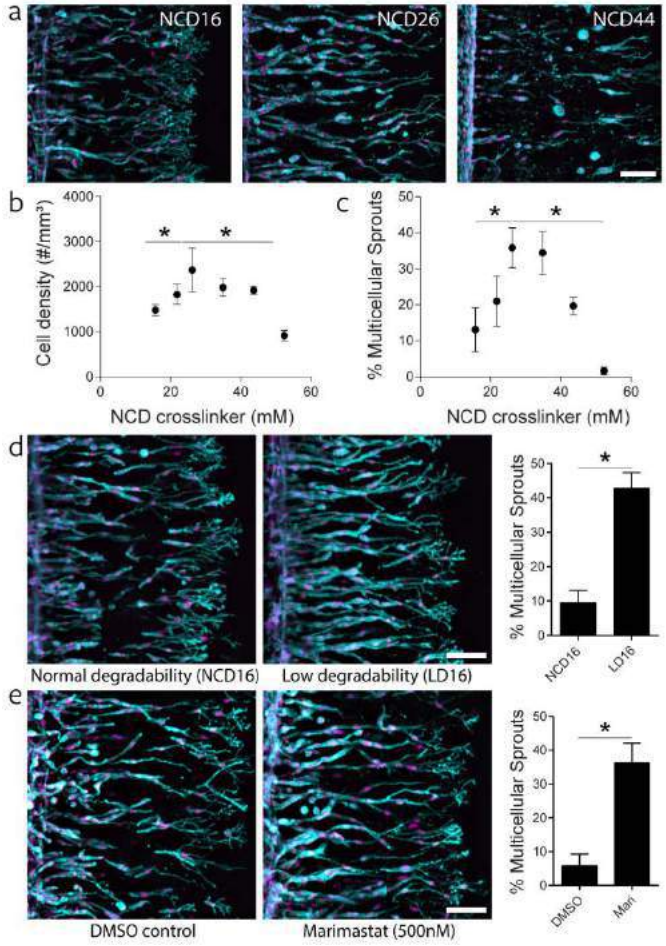

Figure 3: a) Sprout morphology at select crosslinker concentrations. Cell density (b) and sprout multicellularity (c) as a function of crosslinker concentration. Sprout morphology and multicellularity with low degradability crosslinker (d) and in the presence of a broad spectrum MMP inhibitor (e). Scales: 100μm.

ACKNOWLEDGEMENTS

This work was supported by grants from the NIH (EB00262, EB08396, UH3EB017103, 1UC4DK104196), the RESBIO Technology Resource for Polymeric Biomaterials (P41-EB001046), a Kirschstein NRSA (EB014691) and Pathway to Independence Award (HL124322).

REFERENCES

[1] Seliktar, D. *Science,* 336, 1124-1128, 2012. [2] Nguyen, D.H. et al. *Proc Natl Acad Sci U S A,* 110, 6712-6717, 2013. [3] Huebsch, N. et al. *Nat Mater*, 9, 518-526, 2010. [4] Khetan, S. et al. *Nat Mater*, 12, 458-465, 2013.

Copyright 2016 The Organizing Committee for the 2016 Summer Biomechanics, Bioengineering and Biotransport Conference

SB^{3}C2016
Summer Biomechanics, Bioengineering and Biotransport Conference
June 29 –July 2, National Harbor, MD, USA
SB^{3}C2016-974

NOVEL METHOD FOR CHARACTERIZING LOADING PATTERNS OF KNEE STABILIZERS YIELDS NEW INSIGHT INTO THE FUNCTION OF THE ANTEROLATERAL LIGAMENT

Robert N. Kent (1), Thomas L. Wickiewicz (2), Andrew D. Pearle (2), Carl W. Imhauser (1)

(1) Department of Biomechanics
Hospital for Special Surgery
New York, NY, USA

(2) Department of Orthopedic Surgery
Hospital for Special Surgery
New York, NY, USA

INTRODUCTION

Primary stabilizers of the intact knee such as the anterior cruciate ligament (ACL) bear load in concert with surrounding secondary stabilizers to resist multiplanar torques typical of pivoting maneuvers.[1,2] When the ACL is compromised, secondary stabilizers must bear increased load to compensate for the injured primary stabilizer. For example, the lateral meniscus, anterolateral capsule, and iliotibial band are predominately responsible for resisting anterior tibial subluxation characteristic of instability events that occur when the ACL is compromised.[3,4]

The stabilizing role of primary and secondary stabilizers is commonly assessed through serial sectioning studies where changes in primary and coupled motions are measured in response to an applied load following tissue sectioning.[4,5] Another common approach consists of measuring the changes in joint reaction forces before and after sectioning a tissue in response to a known displacement. The changes in joint reaction force represent the load carried by the ligament in response to the applied displacement.[6]

Unfortunately, these previous approaches do not quantify where within the envelope of joint motion these secondary restraints bear load. Knowing where within the envelope of motion ligaments bear load (i.e., their engagement patterns) provides additional information quantifying the function of primary and secondary stabilizers. Such knowledge would provide a framework for understanding the effect of surgical reconstruction of ligaments on knee function. For example, the recently rediscovered anterolateral ligament has been identified as a stabilizer resisting rotatory loads and anterior subluxation events; however, where within the envelope of motion this structure engages has not been determined.[7,8] This hinders formulating surgical reconstruction strategies to restore ligament function and deciding whether a ligament should be reconstructed.

Therefore, a method was developed to assess where within the envelope of motion secondary stabilizers boar load. Then, the following research questions were addressed: Do secondary stabilizers resisting anterior subluxation of the tibia in response to multiplanar rotatory loads such as the anterolateral ligament (ALL), the medial collateral ligament (MCL), and the lateral meniscus engage within the envelope of coupled anterior tibial translation permitted by the ACL-competent knee?

METHODS

With IRB approval, 9 fresh-frozen human cadaveric knees were acquired for testing (mean age: 43 years; range: 20-64 years; 7 male). Specimens were mounted to a robot, which moved the tibia relative to a rigidly grounded femur and was equipped with a universal force-moment sensor. Tibial translation and rotation were described along and about anatomical directions.[9] Valgus torque was increased to 8 Nm and then internal torque was increased to 4 Nm with the knee held at 30° flexion. The position and orientation through which the tibia moved in response to the applied loads were recorded in the ACL-intact and -sectioned conditions. The kinematics were subsequently repeated before and after serially sectioning the ACL, anterolateral ligament (ALL), superficial medial collateral ligament (MCL), posterior oblique ligament (POL), and lateral meniscus; these were likely candidates for bearing load in response to multiplanar torques characteristic of pivoting movements.[3,10] The resultant force borne by these structures was determined via vector subtraction of the forces measured across the knee before and after sectioning each structure.[11]

To quantify the engagement patterns of the aforementioned secondary stabilizers, the following steps were taken. First, each structure was categorized as either load-bearing or non-load-bearing based on whether it carried at least a third of the load seen in the ACL in the same knee. We used the load borne by the ACL as the reference for identifying load-bearing structures since the ACL is a primary stabilizer against multiplanar rotatory loads.[6] This threshold consistently differentiated load-bearing and non-load-bearing structures from knee to knee. If structures did not exceed one third of the load carried by the ACL, they were not analyzed in subsequent steps. Second, load in each structure as a function of coupled anterior translation was used to identify the position of the tibia where the load-bearing secondary stabilizers began to carry load in the ACL-deficient knee. This anterior position was termed the 'engagement point.' More specifically, a secondary stabilizer's 'engagement point' was defined as the anterior tibial translation at which the ligament bore 15% of the load carried by the ACL in response to the combined valgus and internal rotation torques (Fig. 1).

Copyright 2016 The Organizing Committee for the 2016 Summer Biomechanics, Bioengineering and Biotransport Conference

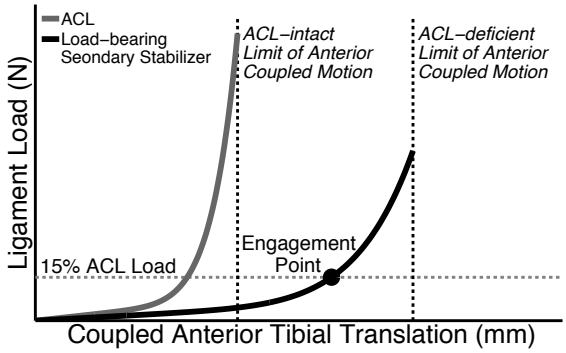

Figure 1: Representative plot of resultant loads in secondary stabilizers as a function of coupled anterior tibial translation in response to combined valgus and internal rotation torques.

Outcome measures, were: (1) the number of knees in which each structure was load-bearing as defined above; and (2) the anterior translation at which secondary stabilizers engaged in the ACL-deficient knee (i.e., the engagement point). The engagement points of the load-bearing secondary stabilizers after the ACL was sectioned were compared to the limit of coupled anterior translation of the ACL-intact knee using paired, two-tailed t-tests ($p < 0.05$).

RESULTS

In the ACL-intact condition, the superficial MCL, lateral meniscus, POL, and ALL were load-bearing in a respective nine, six, two, and zero of the nine knees that were tested. In the ACL-deficient condition, the superficial MCL and lateral meniscus were load-bearing in every knee, and the ALL and POL were load-bearing in a respective seven and one of nine knees. In the ACL-intact and the ACL-deficient conditions, the POL bore 19.7 ± 10.5 N and 14.5 ± 6.2 N, respectively (the average load cutoff was 26.8 ± 8.4 N).

The engagement point of the ALL in the ACL-sectioned knee was 4.3 ± 2.4 mm past the coupled anterior translation that occurred with the ACL intact ($p < 0.005$) with the difference ranging from 0.1 to 7.1 mm (Fig. 2). The engagement points of the MCL and the lateral meniscus were not greater than the coupled anterior translation of the ACL-intact knee on average (both $p > 0.1$) (Fig. 2). These differences ranged from -5.4 to 5.2 mm for the MCL and -5.7 to 7.2 mm for the lateral meniscus (Fig. 2).

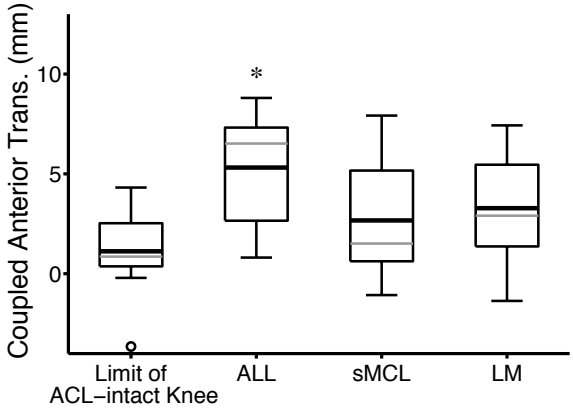

Figure 2: Limit of coupled anterior translation (trans.) of the ACL-intact knee compared to the engagement points of the ALL, superficial MCL, and lateral meniscus after the ACL was sectioned. Black and grey lines denote means and medians, respectively. * indicates $p < 0.05$ compared to the limit of the ACL-intact knee.

DISCUSSION

We established a new method to characterize the function of secondary stabilizers of the knee as a function of combined rotatory loads by assessing where within the passive envelope of motion each structure began to carry load. The major finding of this method was that the ALL consistently engaged (i.e., bore load) beyond the range of coupled anterior translation of the ACL-intact knee. Specifically, the tibia subluxed anteriorly 4.3 mm more on average than the coupled anterior translation of the ACL-intact knee before the ALL engaged. In contrast, the relative engagement positions of the superficial MCL and lateral meniscus were more variable. Each engaged within the limit of coupled anterior translation of the ACL-intact knee in two of nine knees.

One implication of these data is that, although the ALL bore load in seven of nine knees tested in response to multiplanar torques after sectioning the ACL, it does not engage within the envelope of motion permitted by the native knee. Therefore, this tissue resists load after the tibia subluxes anteriorly in response to the combined torques. Interestingly the amount of subuxation occurring with ALL engagement ranged from 0.1 to 7.1 mm, indicating that there is a high degree of variability in the stabilizing role of the ALL. A trend of surgically reinforcing the lateral tissue via lateral extraarticular augmentation as an adjunct to ACL reconstruction has emerged to restore rotational stability. However, use of these combined surgeries remains a subject of debate due to variable outcomes.[7,12] Understanding on a patient-specific basis how and when portions of the anterolateral capsule engage in response to rotatory loads generating anterior tibial subluxation characteristic of a pivot shift may help identify mechanisms driving this variability.

Another key implication involves the high degree of variability seen in the anteroposterior positions of the tibia at which the superficial MCL and lateral meniscus engage. In six knees, the tibia subluxed anteriorly before load had built in either of these structures. Unlike the ALL, these structures are primarily loaded as a result of valgus torque with the superficial MCL in tension and the lateral meniscus in compression. Future work should address anatomical differences across patients that result in engagement of these structures within versus outside of the range of the native knee.

A limitation is the ages of the knees that were tested, which was greater than those typically experiencing ACL injury. However, none of our outcome measures correlated with age (all $R^2 < 0.42$).

In conclusion, we have presented a novel method for characterizing how load builds in stabilizers of the knee in response to multiplanar rotatory loads. By accounting for ligament loads as a function of joint position, this method provides a framework to characterize the stabilizing role of the passive soft tissues of the knee joint. Knowing where within the envelope of motion ligaments bear load may aid establishing patient-specific guidelines for surgical reconstruction of intra and extra-articular stabilizers.

ACKNOWLEDGEMENTS

This work was funded by the Clark and Kirby Foundations, the Institute of Sports Medicine Research, the Surgeon in Chief Fund at Hospital for Special Surgery, and the Gosnell Family Foundation.

REFERENCES

[1] Galway, H et al., *Clin Orthop Relat Res*, 147:45-50, 1980.
[2] Oh, Y et al., *Am J Sports Med*, 40:574-83, 2012.
[3] Tanaka, M et al., *Knee Surg Sports Traumatol Arthrosc*, 20:737-42, 2012.
[4] Monaco, E et al., *Knee Surg Sports Traumatol Arthrosc*, 20:870-7, 2012.
[5] Samuelson, M et al, *Am J Sports Med*, 24:492-7, 1996.
[6] Kanamori, A et al., *Arthroscopy*, 18:394-8, 2002.
[7] Roessler, P et al., *Arch Orthop Trauma Surg*, [Epub], 2015.
[8] Parsons, E et al., *Am J Sports Med*, 43:669-74, 2015.
[9] Grood, E et al., *J Biomech Eng*, 105:136-44, 1983.
[10] Robinson, J et al., *Am J Sports Med*, 34:1815-23, 2006.
[11] Woo, S et al., *The Knee*, 5:267-88, 1998.
[12] Baumfeld, J et al., *Clin Orthop Relat Res*, 473:2619-20, 2015.

Copyright 2016 The Organizing Committee for the 2016 Summer Biomechanics, Bioengineering and Biotransport Conference

SB^{3}C2016
Summer Biomechanics, Bioengineering and Biotransport Conference
June 29 –July 2, National Harbor, MD, USA
SB^{3}C2016-975

QUANTITATIVE COMPARISON OF HUMAN BODY AND ATD OCCUPANT MODELS IN US-NCAP TEST SIMULATIONS

B. Guleyupoglu (1,2), B. Koya (1,2), M. Davis (1,2), F. S. Gayzik (1,2)

(1) Department of Biomedical Engineering
Wake Forest School of Medicine
Winston-Salem, NC, USA

(2) Virginia Tech – Wake Forest
Center for Injury Biomechanics
Winston-Salem, NC, USA

INTRODUCTION

Anthropometric test devices (ATD, aka dummies) are used to evaluate vehicle performance during different crash modes and serve a fundamental role in regulatory and consumer awareness tests. In the virtual testing and research phases, computational models of ATDs are often employed. Recently computational human body models (HBMs) have gained popularity and provide fundamentally different information; human performance in the crash environment. While important data about the effectiveness of the safety systems at protecting the occupant can be derived from HBMs, there are many unanswered questions about the relative performance of these two types of models. Therefore, the objective of this study is to conduct matched pair testing of the validated Global Human Body Models Consortium (GHBMC) 50th percentile HBM male simplified occupant (M50-OS) model and standard ATD models in frontal and lateral US-NCAP crash configurations [1]. We quantitatively compare biomechanical outputs from each model to generate preliminary outcome-based transfer functions between the two in these configurations.

METHODS

The GHMBC M50-OS (v. 1.8, 295k nodes, 357k elements, 79.6 kg), the Humanetics Hybrid-III 50th percentile ATD (v. 7.1.8, 99.5k nodes, 125k elements, 79.9 kg), and the LSTC ES-2Re (v. 0.201, 428k nodes, 515k elements, 72.3 kg) were used in the simulations. The models were gravity settled into the driver position of the National Crash Analysis Center (NCAC) Ford Taurus or simplified occupant compartment (Figure 1). Initial simulations (Neck flexion/extension, chest and knee impacts) were run per certification tests to assess how closely the GHBMC M50-OS compares to the ATD in a laboratory setting. All collision simulations were equipped with an advanced 3 point belt system and frontal or side airbag. Restraint properties were based on literature values [2].

The following simulations were performed: Frontal NCAP, Lateral NCAP with a moving deformable barrier and a side pole impact. The baseline delta-V's were 56.4 kph, 61 kph and 32 kph respectively. In an effort to study model sensitivity, ΔV's were varied by ±20% resulting in 5 simulations per condition and total of 30 simulations. Simulations were run on a Linux cluster using 16 CPUs and MPP LS-DYNA.

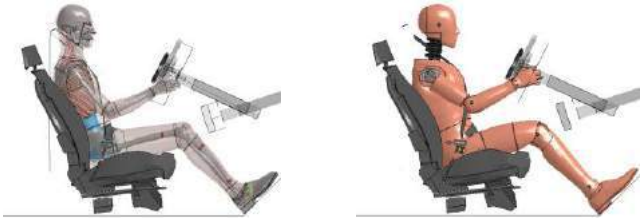

Figure 1: Seated positions of the M50-OS (top) and Hybrid III-50 (bottom) models in the occupant compartment.

RESULTS

Results for frontal impact showed that the human and dummy models predict the same trends in general. Cross plots

Copyright 2016 The Organizing Committee for the 2016 Summer Biomechanics, Bioengineering and Biotransport Conference

of injury criteria can be found in Figure 2. An overlay between the M50-OS and the Hybrid III models can be seen in Figure 3. Cross plots of data demonstrated this trend as being generally linear between the two models for HIC-15, and Chest Deflection. Shoulder and lap belt forces did not follow the same linearity. HIC-15 data shows high linear correlation of 0.929. The last three measures that were examined in this investigation did not linearly correlate well (0.3305 for chest deflection, 0.2111 for shoulder belt forces, and 0.1327 for lap belt forces).

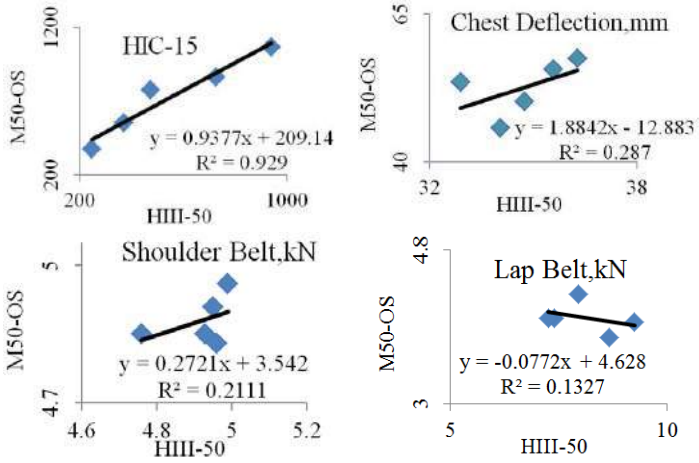

Figure 2: Cross plots of HIC-15, Chest Deflections, Shoulder and Lap belt forces for the M50-OS and HIII-50 models in the Frontal NCAP crash mode. Linear regression for each plot and the R^2 values are given. Plots ordered from highest to lowest R^2.

DISCUSSION

The two models trend similarly for most measures. As the delta-V decreased, the models experienced lower amounts of HIC-15, and chest deflection. Shoulder belt forces, while it did not trend similarly, tended to be within the same range of values for both models with some negligible differences due to belt-body contour interactions. The differences in the lap belt can be attributed to the different designs in the pelvic area for each model. The differences in lap belt forces may also be responsible for the low correlation found for chest deflection values between the two models. Although, another key difference between the two models is that the chest of the M50-OS model is more compliant than the dummy model which will also cause higher chest deflections and possibly lead to a lower correlation between the two models.

While validated, ATDs and human models will have differing biomechanics that arise from their constitutive properties (e.g. ATDs are made of, and modeled as, steel and rubber). As the use of human models proliferate a "transfer function" between virtual humans and ATDs will be a valuable addition to the literature to quantify relative performance. This study is a pilot study towards that aim. These data may be of use in future regulations leveraging virtual human body models. Due to HBM's omnidirectional nature, impact modes in which no specific dummy has been designed (e.g. oblique, roll-over) may benefit from these data.

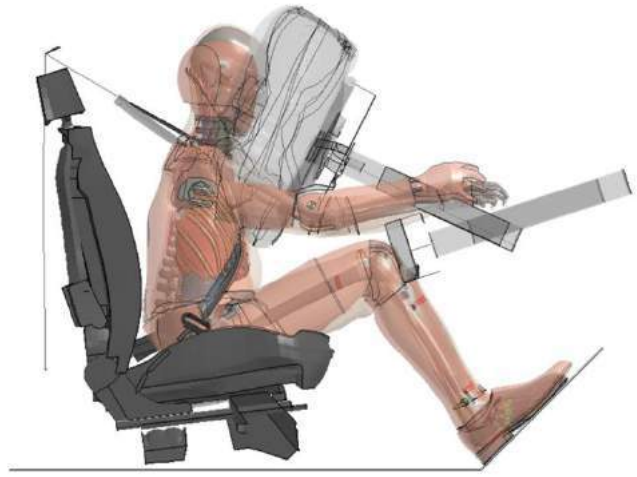

Figure 3: Overlaid image of M50-OS and Hybrid III models at the point of maximal excursion during Frontal NCAP.

ACKNOWLEDGEMENTS

The authors would like to acknowledge the Global Human Body Models Consortium, LLC for funding and support. Wake Forest University is the Integration Center of Expertise of the GHBMC. All simulations were run on the DEAC cluster at Wake Forest University, with support provided by Drs. Timothy Miller and Damian Valles.

Dr. Gayzik is a member of Elemance, LLC., which is the sole licensor and distributor of academic and commercial licenses for use of the GHBMC, LLC. – owned M50 occupant model.

REFERENCES

[1] Vavalle, NA et al., *Ann Biomed Eng*, 2015.
[2] Forman, JL et al., *Stapp Car Crash J*, 53:49-74, 2009.

Copyright 2016 The Organizing Committee for the 2016 Summer Biomechanics, Bioengineering and Biotransport Conference

SB³C2016
Summer Biomechanics, Bioengineering and Biotransport Conference
June 29 –July 2, National Harbor, MD, USA
SB³C2016-976

EVALUATION OF LASER BACTERIAL ANTI-FOULING OF TRANSPARENT NANOCRYSTALLINE YTTRIA-STABILIZED-ZIRCONIA CRANIAL IMPLANT

David L. Halaney (1), Yasaman Damestani (2), Natalie De Howitt (2), Javier E. Garay (1), Santiago Camacho-Lopez (3), Guillermo Aguilar (1,2)

(1) Department of Mechanical Engineering, University of California - Riverside, Riverside, CA 92521, USA

(2) Department of Bioengineering, University of California - Riverside, Riverside, CA 92521, USA

(3) Departmento de Optica
Centro de Investigacion Cientifica y Educacion Superior de Ensenada (CICESE)
Mexico

INTRODUCTION

The development and feasibility of a novel transparent nanocrystalline yttria-stabilized-zirconia (nc-YSZ) cranial implant has been recently established [1]. The purpose of what we now call the "Window to the Brain (WttB)" implant is to improve patient care by providing a technique for delivery and/or collection of light into/from the brain, on demand, over large areas, and on a chronically-recurring basis without the need for repeated craniotomies. WttB holds the transformative potential for enhancing light based diagnosis and treatment of a wide variety of brain pathologies (i.e. cerebral edema, traumatic brain injury, stroke, glioma, and neurodegenerative diseases).

However, bacterial adhesion to cranial implants is the leading factor for biofilm formation (fouling), infection, and treatment failure [2], and further, may limit the use of the WttB for optical imaging and therapy by reducing the transparency of the window. Due to the transparency of the nc-YSZ implant, we hypothesized that medical laser treatment through the implant could reduce the formation of biofilm. However, in order for this approach to be a viable strategy for anti-fouling *in vivo*, it is critical that the temperature of the implant does not exceed an increase of 10°C, the threshold for damage to native tissue [3]. In this study, we investigate continuous wave (CW) and pulsed wave (PW) laser treatments of bacteria underlying the nc-YSZ implant *in vitro*, while monitoring the resulting surface temperature of the nc-YSZ implant.

METHODS

Implant Fabrication and Preparation: Transparent nc-YSZ cranial implants were fabricated with current activated pressure assisted densification (CAPAD), which enables reduction of internal porosity to nanometric dimensions, and thus, reduction of the optical scattering that renders typical YSZ opaque [4]. Transmittance of the implant was measured on a spectrophotometer (Varian Cary 500) and is provided in **Figure 1.** Prior to each experiment, nc-YSZ samples were dry sterilized (Germinator 500) at 250 ºC to remove all preexisting bacteria.

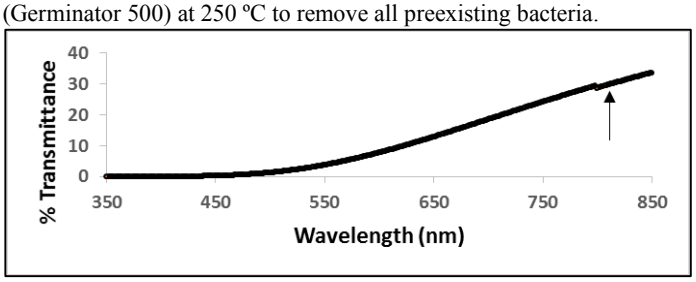

Figure 1: Transmittance of the nc-YSZ implant, including the irradiation wavelength used in this study (810 nm, black arrow).

Bacteria Inoculation: For all experiments, we used genetically engineered bioluminescent BL21 Escherichia coli (CMC0014, Sigma Aldrich) transformed with P. Pyralis luciferase gene using pet28 vector. 0.5 μL of bacteria in media was seeded on agar at 37ºC and the nc-YSZ was placed on top. Bacteria underlying nc-YSZ was treated with selected laser parameters through the nc-YSZ for 20 seconds, and then the nc-YSZ was removed and the culture was incubated for 24 hours at 37ºC. The experimental setup is illustrated in **Figure 2.**

Laser Device: Photo-irradiation was performed using an 810nm laser (Vari-Lase). The laser spot size on the sample was 7mm in diameter ($1/e^2$). The variable laser parameters were power (1-3W) and pulse rate (0.3-5Hz). Control cultures were treated in an identical manner to irradiated cultures, except that the laser was not switched on.

Temperature Measurements: The temperature of the surface of nc-YSZ was measured with a non-contact infrared thermal camera (A325sc, FLIR Systems Inc.) operating in video mode at 60 frames/s. The video was post-processed using ResearchIR software (FLIR

Copyright 2016 The Organizing Committee for the 2016 Summer Biomechanics, Bioengineering and Biotransport Conference

ResearchIR4). According to specifications, the camera measures temperatures with a precision of 50mK, has an accuracy of 2%, and a viewing angle of 5-60 degrees.

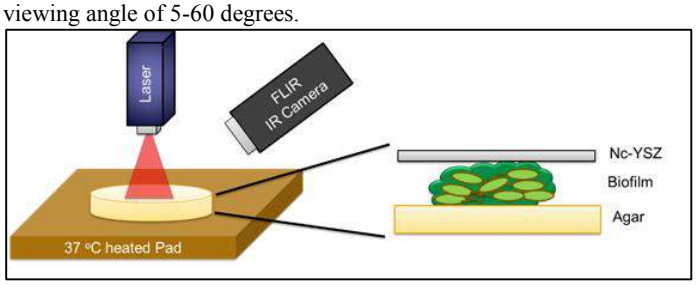

Figure 2: Illustration of the experimental setup used in this study.

Bioluminescence imaging system: 24 hours after laser irradiation, 100µL of the luciferase substrate (D-Luciferin, potassium salt 150µg/ml, Research Products International Corp.) was added at room temperature to evenly cover each culture. Light emission of the bioluminescent bacteria was detected using a Macro Luminescence Dark Box (Stanford Photonics, Inc, Palo Alto, CA). ImageJ software (National Institute of Health) was used to quantify the light emission at the irradiated Regions of Interest (ROIs). The ROIs encompassed a circle equal to the beam spot size on the sample (7mm diameter). The relative luminescence unit (RLU) in the ROI was normalized with respect to the RLU outside of the ROI for each sample.

Statistical Analysis: All statistical comparisons were evaluated using analysis of variance for repeated measurements (ANOVA). When appropriate, post hoc analyses were performed with the Bonferroni's multiple comparisons test. All statistics were calculated using GraphPad Prism 5.01 (GraphPad Software, Inc., San Diego, CA). *$p<0.05$, **$p<0.01$, ***$p<0.001$ relative to control.

RESULTS

Figure 3 shows normalized RLU of biofilm after 24h and the average surface temperature (ΔT) of nc-YSZ at the end of the 20 second laser treatment using CW laser with 1, 2, and 3W of power. The results show that the decrease in the RLU value is statistically significant for all treated groups compared to control ($p<0.05$) and that ΔT for the CW laser powers above 1W is above 10ºC, which is considered the critical threshold for thermal damage.

Figure 4 shows normalized RLU of biofilm after 24h and the average surface temperature (ΔT) of nc-YSZ at the end of the 20 second laser treatment using CW or PW laser with 3W of power. Treatment with all laser parameters except for 0.3Hz leads to a significant reduction of E. coli viability compared to the control group ($p<0.05$). The results indicate that the ΔT is above the 10ºC critical temperature threshold for CW laser and all the PW laser settings exceeding 5J/cm^2 and 1Hz.

DISCUSSION

When CW laser is used, the biofilm reduction seems to follow a linear relationship with ΔT, suggesting an entirely photothermal mechanism of bacterial damage **(Figure 3)**. In the case of PW laser, however, the relationship between temperature and biofilm reduction is less clear. Comparing bar#3, bar#5, bar #6 and bar #7 (frequency of 5, 1, 0.5 and 0.3 Hz) in **Figure 4** indicates that laser treatment with higher frequency results in greater reduction in E. coli biofilm. Comparing bar#4 and bar#5 (10 J/cm^2 400 ms vs. 5 J/cm^2 200 ms) indicates that doubling the energy density per pulse and pulse duration increases the temperature by about 3ºC, while it has negligible effect on the reduction rate of E. coli biofilm.

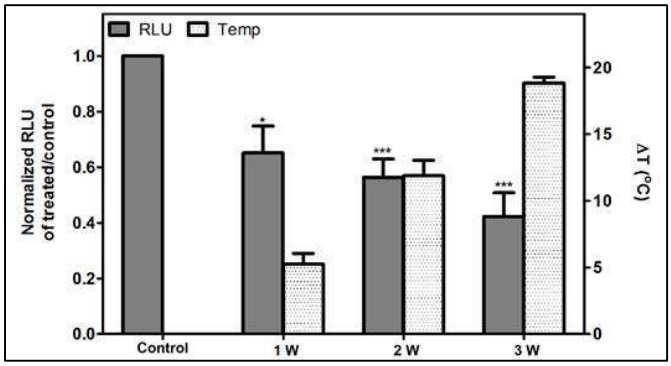

Figure 3: Normalized RLU of biofilm after 24h and the average surface temperature (ΔT) of nc-YSZ after CW laser treatment with 1, 2, and 3W of power. Each bar represent Mean±SEM (n=9).

The results indicate that CW laser has the higher reduction rate of E. coli biofilm compared to PW laser, but also results in the highest temperature increase. In contrast to the linear relationship of temperature and biofilm reduction for CW laser **(Figure 3)**, there is no linear relationship between the differences in temperature change and biofilm reduction for PW laser **(Figure 4).** Lack of correlation between ΔT and RLU suggests that the biofilm disruption mechanism using the PW mode is not entirely due to photothermal effects. This suggests that PW laser may be capable of reducing biofilm formation through the transparent nc-YSZ implant to even greater extent than demonstrated in this study (i.e. more than 40% reduction), without surpassing the thermal damage threshold of 10ºC, if laser parameters are optimized.

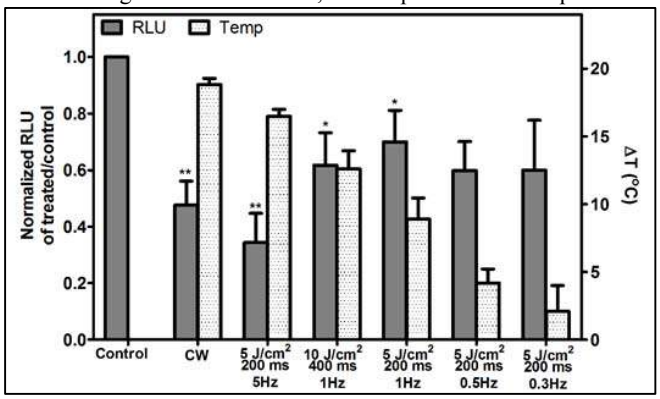

Figure 4: Normalized RLU of biofilm after 24h and the average surface temperature (ΔT) of nc-YSZ after CW or PW laser treatment with 3W of power. Bars represent Mean±SEM (n=9).

In conclusion, this proof-of-concept study demonstrates that an 810nm medical laser can be used to treat biofilm formation through the transparent WttB implant *in vitro* without generating heat above the thermal damage threshold for tissue. Further study is needed to determine if these results can translate into viable *in vivo* approach.

ACKNOWLEDGEMENTS

This study was supported, in part, by the National Science Foundation (NSF) Award No. 1547014 to GA and JEG, a UC-MEXUS Dissertation Research Grant to YD, and an American Society for Lasers in Medicine and Surgery (ASLMS) grant to YD.

REFERENCES

[1] Damestani, Y et al., *Nanomedicine: NBM*, 9:1135-1138, 2013.
[2] Briggs, S et al., *Scand j infect dis,* 36:165-173, 2004.
[3] He, X et al., *Open Biomed Eng J,* 5:47-73, 2011.
[4] Garay, JE, *Annu Rev Mater Res,* 40:445-468, 2010.

Copyright 2016 The Organizing Committee for the 2016 Summer Biomechanics, Bioengineering and Biotransport Conference

SB³C2016
Summer Biomechanics, Bioengineering and Biotransport Conference
June 29 –July 2, National Harbor, MD, USA
SB³C2016-977

AUTOMATED OPTIMIZATION FRAMEWORK FOR CARDIOVASCULAR FLOW SIMULATIONS

A. Verma (1), A. Marsden (2)

(1) Department of Mechanical Engineering
Stanford University
Stanford, CA, USA

(2) Department of Pediatrics
Stanford University
Stanford, CA, USA

INTRODUCTION

In recent years, computational techniques have been used extensively to simulate blood flows in cardiovascular geometries. These simulations provide a key tool for analysis of patient specific cardiovascular geometries. Furthermore, the coupling of design and optimization with high-fidelity blood flow simulations has become a vital asset in medical device design and surgical planning [1]. However, due to noisiness or non-availability of gradient information of the objective function, conventional optimization methods are often unsuitable in such problems. Furthermore, as fluid flow simulations are computationally expensive, the need for efficient methods that limit number of function evaluations becomes paramount.

The objective of this study is to develop a framework that couples components that model and analyze parametrized cardiovascular geometries with a suitable optimization algorithm. The optimization algorithm chosen for this study is the Surrogate Management Framework (SMF), which has been previously used for shape optimization of cardiovascular geometries [2,3] and has an established convergence theory [4]. The performance of the SMF framework deteriorates with the progression of optimization process due to ill-conditioning of the covariance matrix associated with global search step [6]. Variations of the local search in the SMF algorithm are studied in order to improve efficiency under a fixed computational budget. Such a framework can be utilized to design solutions for patient-specific pathologies.

METHODS

A simplified three-dimensional model for an anastomosis over stenosis has been adapted from the clinical study by Ku et al. [5]. The model is parametrized by three design parameters: the angles of graft with vessel upstream and downstream to stenosis (θ_1 and θ_2 respectively) and the radius of the graft (R_a) (Figure 1). The bounds on these parameters are given in Table 1. Regions of pathologically low wall shear stress are typically susceptible to the risk of artherosclerosis and intimal thickening. Hence, the cost function is chosen to be the total area of vessel with wall shear stress magnitude below a threshold wall shear stress magnitude. Equation 1 gives a functional representation of the cost-function where H is the Heaviside function and x is position on the parent vessel.

$$J = \iint_{Parent\ vessel} H\left(2.5 - WSS\left(x\right)\right) dS \qquad (1)$$

SimVascular, an open source software package (www.simvascular.org), was used for constructing the model, generating the mesh and running the three-dimensional finite element flow simulation. The finite element mesh is comprised of tetrahedral elements with refinement at the walls and junctions to accurately resolve wall shear stress. The incompressible Navier-Stokes equations are solved for this study using a finite element method with resistance boundary conditions.

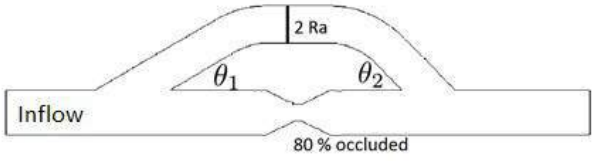

Figure 1: Geometry of model used in the present study. Note the graft parameters under optimization: θ_1, θ_2 and R_a.

Copyright 2016 The Organizing Committee for the 2016 Summer Biomechanics, Bioengineering and Biotransport Conference

Parameter	Lower Bound	Upper Bound
θ_1	30°	81°
θ_2	30°	81°
R_a	$0.5R_v$	$0.9R_v$

Table 1: Bounds on design parameters for the graft. R_v is the radius of the parent vessel.

The SMF is a derivative free optimization method that relies on local search accelerated by a global search step. For forming the surrogate required in the global search, ordinary kriging is utilized. For the local search, MADS pattern search is used with (n+1) vectors that form a positively spanning basis (where n is the dimension of parameter space). Pattern search methods are typically based on a uniform Cartesian grid in the parameter space.

Based on the success of previous search steps, three variations to local search are studied: local search with isotropic coarsening of search grid, anisotropic coarsening of search grid and rotational polling. Isotropic coarsening method increases the grid size in each parameter by a fixed factor whenever the SMF finds an improvement. Anisotropic coarsening method builds on isotropic coarsening, but with a factor of improvement dependent on the previous success direction relative to the current incumbent solution in the event of a successful poll step. Rotational polling refers to the rotation of poll directions based on the directions of previous local (poll step) improvement. A baseline case is also considered which shows the performance of the method without any variation in the poll step.

Figure 2 shows a high level overview of the coupling between components for model generation, meshing, simulation, post-processing, cost-function evaluation and the optimization algorithm.

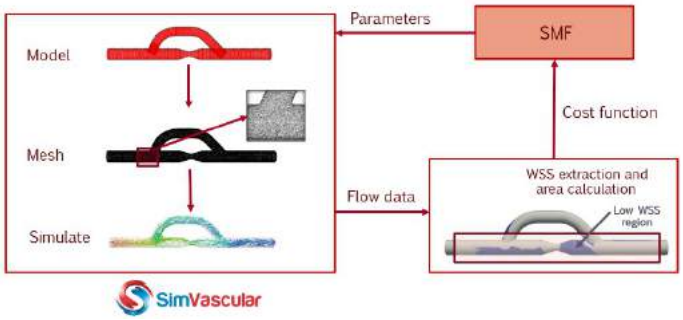

Figure 2: Overview of coupling between the optimization (SMF), modeling, meshing and flow simulation (SimVascular) and cost function evaluation.

RESULTS

Figure 3 displays the overall performance of different variations of the SMF algorithm for steady flow conditions. Each optimization process begins with a common initialization of 13 parameter sets based on Latin Hypercube sampling of the parameter space.

We observe that simple MADS polling (baseline) does not give any improvements beyond the first 20 simulations. On the other hand, all other methods result in further cost function reduction with varying success within a fixed computational budget of a total of 60 simulations. Rotation of the polling directions appears to give the best improvement post-initialization though the performance is closely followed by isotropic coarsening of the grid.

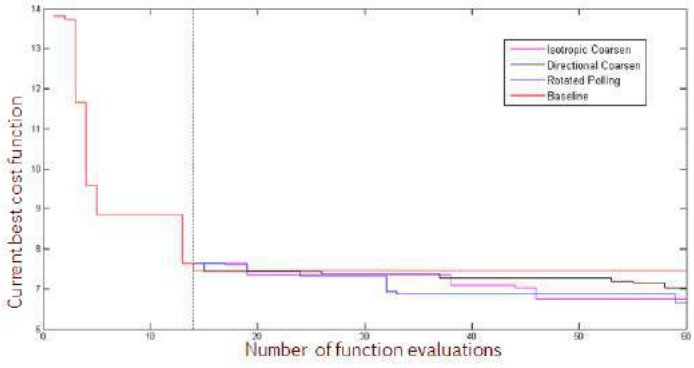

Figure 3: Decrease in cost function with number of function evaluations for different variations of SMF

DISCUSSION

As the number of function evaluations increase, the typical optimization progresses to converge towards a local minimum. However, due to over-refinement of the grid with the lack of a coarsening mechanism, the baseline version of the SMF tends to converge slowly to the minimum when compared to the coarsening aided strategies. Also, the piling-up of several points in a small region in parameter space has been seen to be detrimental to the global search step [6] and hence, coarsening allows for more space between evaluations and a better conditioned covariance matrix for surrogate generation.

We observe that the poll directions may not often align with the direction of steepest descent until the local search grid is very refined. This is due to the Cartesian nature of the local search grid and the use of (n+1) poll directions. In such situations, the rotation of poll directions based on previous improvements allows the selection of the closest path on the discrete grid to the local minimum and hence, a lesser number of evaluations are required.

There have been few studies regarding optimization in cardiovascular geometries in patient-specific models due to the high computational cost of each function evaluation. The proposed automated framework, with suitable acceleration strategies for the optimization procedure, is an important step towards utilizing hemodynamic simulations for designing devices and surgeries in the future.

ACKNOWLEDGEMENTS

This work was supported by a Burroughs Wellcome Fund CASI Award and NSF Career Award (OCI1150184).

REFERENCES

[1] Marsden, A, *Ann Rev Fluid*, 46:519-546, 2013.
[2] Yang, W et al., *CMAME*, 199(33):2135-2149, 2010.
[3] Marsden, A et al., *CMAME*, 197(21):1890-1905, 2008.
[4] Booker, AJ et al., *Struct Optim*, 17(1):1-13, 1999.
[5] Ku, J et al., *Ann Biomedical Engg*, 30:743-752, 2002.
[6] Booker, AJ, *Boeing Tech Rep*, M&CT-TECH-00-002, 2000.

Copyright 2016 The Organizing Committee for the 2016 Summer Biomechanics, Bioengineering and Biotransport Conference

SB^{3}C2016
Summer Biomechanics, Bioengineering and Biotransport Conference
June 29 –July 2, National Harbor, MD, USA
SB^{3}C2016-978

DEVELOPMENT OF A COMBAT HELMET SUSPENSION SYSTEM COMPUTATIONAL MODEL: IMPLICATIONS FOR PAD DESIGN AND INJURY OUTCOME

C. Bradfield (1), Q. Luong(1), B. DeVincentis(1), J. Clark(1), A. Golman(1), C. Carneal(1)

(1) The Johns Hopkins University Applied Physics Laboratory
Laurel, MD, USA

INTRODUCTION

For blunt impact evaluation, current combat helmet standards utilize drop tower tests to measure headform linear acceleration for different impact locations, and apply a simple pass/fail criterion stating that resulting accelerations must not exceed 150 g [1]. These standards do not consider rotational head motion for injury assessments, and weigh all impact directions equally. Therefore, to better protect the warfighter, an improved helmet evaluation process is needed that accounts for probability of head injury. A continuous injury risk metric is beneficial to the helmet design process as it allows for design trade-offs to be properly assessed, whereas the current standards only allow for a binary outcome. An example of such a rating system can be found in the evaluation of collegiate football helmets [2]. The current study explores the advantages of how such an evaluation methodology could be used to assess how suspension pad design features help mitigate head injury. To accomplish this, a Finite Element Model (FEM) of an Advanced Combat Helmet (ACH), retention system and standard seven-pad suspension system was created to simulate a realistic headform response under blunt impact loading. The use of a computational model for this investigation enabled a range of material and design modifications to be evaluated. The purpose of this study is twofold: 1) To develop and validate a FEM of an ACH with a standard seven-pad suspension system for blunt impact loading and 2) to use this model to demonstrate that changes to pad design can influence head injury outcome.

METHODS

To develop realistic material properties for use in the FEM, physical testing was conducted on trapezoidal, oblong and crown pads that comprise the standard seven-pad suspension system. To determine the appropriate stiffness of the trapezoidal, oblong and crown pads, Instron compression tests were performed at loading rates of 2mm/s, 20mm/s, 200mm/s, and 2m/s to 90% strain (n=3 for each loading rate and pad type). Separate stress-strain curves were developed for each of the three pad types for each loading rate.

Previously collected experimental drop tower test data were leveraged to validate model performance in blunt impact loading. In these series of test, a monorail guided freefall drop test system was utilized to measure the acceleration of an EN960 Half Headform outfitted with an ACH and standard seven-pad suspension system upon hitting a hemispherical impact anvil. Average acceleration response corridors were created for impact velocities of 10, 14.1 and 17.3 ft/s to replicate 1x, 2x and 3x the standard kinetic energies [1]. Impact locations consisted of the helmet's front, crown, side, nape and rear locations.

To create the appropriate mesh geometries for the FEM, 3D scans were collected of a large ACH fitted with the standard seven-pad suspension system (Model K610, Nikon, Brighton, MI). The geometries of both helmet and pads were meshed in TrueGrid (XYZ Scientific, Pleasant Hill, CA). Subsequently, pad material properties were defined with the material card *MAT_FU_CHANG_FOAM in LS-DYNA (LSTC, Livermore, CA), which utilized the stress-strain curves from the pad compression testing. The helmet material was defined as a linear elastic material with a Young's modulus of 12.25 GPa, which was based on average values from a previous study [3]. In addition to the helmet and pad meshes, the hemispherical impact anvil, EN960 head form and support arm were meshed and assigned as rigid parts. The helmet, pads, headform and support arm were given an initial velocity of 10, 14.1 or 17.3 ft/s to match the experimental conditions. All simulations were performed with LS-DYNA. Headform accelerations were collected at a sample rate of 100 kHz. Both experimental and computational accelerations were processed

Copyright 2016 The Organizing Committee for the 2016 Summer Biomechanics, Bioengineering and Biotransport Conference

with a CFC1000 standard filter. Percent error was calculated to compare the numerical model and experimental drop tower tests results:

$$\text{Percent Error} = \left|\frac{x_{FEM}-x_{EXP}}{x_{EXP}}\right| * 100 \qquad (1)$$

Where x_{FEM} and x_{EXP} are the peak model and average peak experimental accelerations, respectively.

To provide a proof-of-concept example of how an injury-based rating system could benefit helmet suspension design by readily identifying optimal values for material parameters, two different pad designs were considered. The first pad design utilized the original experimental pad stress-strain curves while the second design used a scaled version in which the stress-values were multiplied by a factor of 10 for a given strain value. This scaling factor was chosen as it was expected to produce a higher chance of injury. To define probability of head injury for a single simulation, a head injury risk function derived from collegiate football impacts was utilized [2]:

$$\text{Probability of Injury} = \frac{1}{1+e^{-(\alpha x+\beta)}} \qquad (2)$$

Where α&and&β are fixed coefficients and x is the peak resultant linear acceleration in g's.

RESULTS

When compared to the experimental headform acceleration responses, the FE acceleration predictions varied in accuracy (Figure 1). The best fit occurred for the 10 ft/s impact scenarios, in which percent errors between model and experiment were under 13% for all impact locations with the exception of the side impact location, which had a percent difference of 89.7%. The side impact location performed the worst for all three impact velocities.

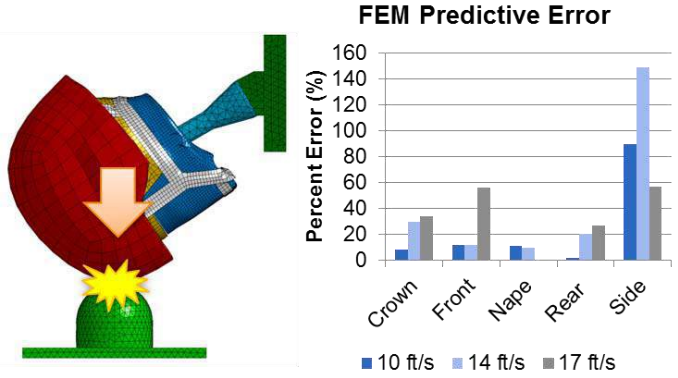

Figure 1: Left – FEM Front Impact Orientation. Right - Peak Acceleration Error between FEM and Experiment

Increasing the FEM pad stiffness from its baseline value to a 10x stiffer value resulted in larger peak accelerations for the front, crown and rear impact locations for all loading rates. However, peak headform accelerations with the artificially stiffer pads were smaller for the nape and side impact locations for the 14.1 ft/s and 17.3 ft/s impact velocities. Furthermore, the probability of injury was small for nape impact simulations at 10 ft/s, with probabilities of injury being <2.5% for both pad stiffness types. When the impact velocity increased to 14.1 ft/s, the stiffer pad type reduced the chance of injury when compared to the baseline material type, with probabilities of 47.5% and 71.4%, respectively (Figure 2).

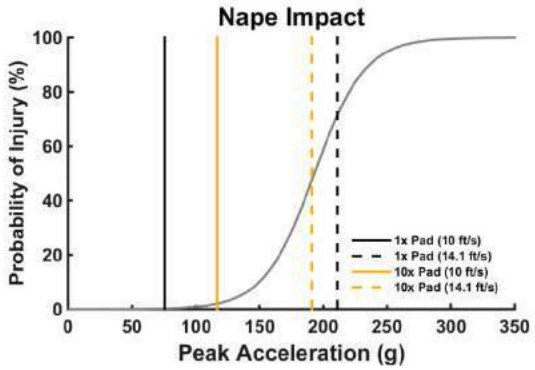

Figure 2: Example of Pad Stiffness Tradeoff for Nape Impact Location. Injury Risk Curve from [2]

DISCUSSION

For simulations with a 10 ft/s impact velocity, the model performed well as 4 out of the 5 impacts locations had errors less than 13%. However, the model did not compare as well to the experimental results for the 14.1 and 17.3 ft/s loading rate, with the exception of the nape. This suggests that the measured material properties measured from the Instron compression tests were sufficient for 10 ft/s impacts, but additional data may be needed to improve model fidelity at higher loading rates.

Drop tower simulations performed with the stiffer pads had mixed results. For 3 out the 5 impact locations, 10x stiffer pads led to a greater chance of head injury. However, when the impact occurred on the nape or side locations, the stiffer pads abated the probability of injury at the 14.1 and 17.3 ft/s impact velocities. While counter-intuitive, the increased pad stiffness reduced nape accelerations by preventing interactions between headform and a bolt in the helmet retention system. This result demonstrates that utilization of a graded injury severity score allows for tradeoff studies across different helmet designs and impact locations. It should be noted that the current results are based on a pre-existing injury risk function to demonstrate model utility. Consequently, further validation of this methodology is needed before accurate assessments of helmet protection can be made. While the current study is a first step in exhibiting the advantages of an updated helmet evaluation system based on a graded metric correlated to injury, it is limited to linear head accelerations. A growing body of evidence suggests that the rotational component of head motion plays a large role in injury outcome [4,5]. Future work should examine combat helmet performance when angular accelerations and velocities are accounted for in the kinematic-based risk function.

ACKNOWLEDGEMENTS

Experimental data provided through the courtesy of the Marine Corps Systems Command PM Infantry Weapon Systems from the Suspension Materials and Retention Technologies Test and Evaluation (SMART-TE) Program Blunt Impact Test (2011)

REFERENCES

[1] McEntire, B et al., USAARL Report No. 2005-12.
[2] Rowson, S et al., Ann Biomed Eng. 2011;39(8):2130-40.
[3] Zhang, L et al., Front Neurol. 2013;4:88.
[4] Rowson, S et al., Ann Biomed Eng. 2013;41(5):873-82.
[5] Takhounts, E et al., Stapp Car Crash J. 2013;57:243-66.

Copyright 2016 The Organizing Committee for the 2016 Summer Biomechanics, Bioengineering and Biotransport Conference

SB³C2016
Summer Biomechanics, Bioengineering and Biotransport Conference
June 29 –July 2, National Harbor, MD, USA
SB³C2016-979

A Study on the Mechanical Response of the Human Head during Single-Collision Car Crashes using Finite Element Analysis

P. Berthelson (1,2), G. Liao (2), J. Liao (1,2), L. Williams (1,2), H. Rhee (2), X. Deng (3), M. Horstemeyer (1,4), R. Prabhu (1,2)

(1) Department of Agricultural and Biological Engineering
Mississippi State University
Mississippi State, MS 39762, USA

(2) Center for Advanced Vehicular Systems
Mississippi State University
Mississippi State, MS 39762, USA

(3) School of Mechanical Engineering and Automation
Xihua University
Chengdu Sichuan, 610039, China

(4) Department of Mechanical Engineering
Mississippi State University
Mississippi State, MS 39762, USA

INTRODUCTION

With approximately 1.7 million cases and 52,000 deaths per year [1], Traumatic Brain Injury (TBI) is a leading cause of injury-related deaths among people under the age of 45 in the United States [2]. TBI is caused by many different forms of trauma including falling and physical violence, but this research primarily focuses on car crash related TBI. A study conducted by the Centers for Disease Control and Prevention found that between the years of 2006 and 2010, vehicular crashes were the cause of 26% of all TBI related deaths in the Unites States [3].

Due to modern breakthroughs in computational engineering, Finite Element (FE) modeling has become a viable alternative to physical testing in a large portion of mechanics based research [4]. Due to the physical limitations of testing collision scenarios, FE modeling allows researchers to more thoroughly investigate the mechanical phenomena behind vehicular impact related TBI without concerns over safety and expenses associated with physically recreating car crash scenarios.

The use of FE simulations allowed Deng *et al.* [4] to conduct a two-step study in which a system-level single collision side crash was simulated between a Dodge Neon, which housed a crash test dummy, and a moving barrier. The data acquired from this simulation was used to determine the Boundary Conditions (BCs) that were later used in the simulations of a high fidelity model of the human head [4]. To allow for a greater understanding of vehicular impact related TBI, the current study expands upon the method presented in the study by Deng *et al.* [4]. to allow for several different points of collision at various impact velocities.

METHODS

As shown in Figure 1, this research consists of two major steps: the car crash simulations and the human brain simulations.

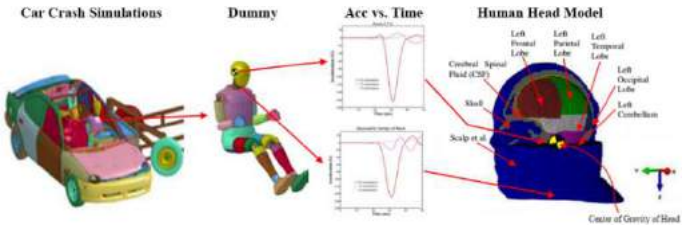

Figure 1. A schematic illustration shows the process of using the data from the Dodge Neon crash simulations as the boundary conditions in the Human Head model (Deng, et. al. [4])

In the first step, an FE model of a Hybrid III 50th percentile male crash test dummy underwent simulated car crash scenarios to determine the BCs that will be used in a more complex FE model of a human head. This began by using LS-Prepost [5], an FE modeling preprocessing software, to configuring the impact scenarios. Each simulation began with the dummy seated in the driver's seat of a FE Dodge Neon model and a moving barrier at one of the 12 starting locations. Once preprocessing was complete, LS-Dyna was used to run each of the simulations. At each of the 12 points of contact, the moving barrier strikes the Dodge Neon at seven different impact velocities: 10, 15, 20, 25, 30, 40, and 50 mph. Upon completion of all of the crash simulations, LS-Prepost will be used to determine the acceleration versus time profiles at the centers of gravity of both the head and the neck of the dummy [4].

In the second step, a high fidelity FE model of the human head will be created, using the model previously developed by Deng *et al.* as the baseline, to determine the mechanical response of the brain during the various car crash scenarios. The updated human head model will have

Copyright 2016 The Organizing Committee for the 2016 Summer Biomechanics, Bioengineering and Biotransport Conference

higher anatomical accuracy than Deng *et al.*'s head model. In order to accurately simulate the movement of the head after impact, LS-Prepost will be used to set the acceleration versus time profiles from the dummy in the car crash simulations as the BCs on the head model. The deformation of the head, due to a car crash scenario, will then be simulated using LS-Dyna to determine the key injury metrics and damage impending on the brain upon impact.

RESULTS

At each of the 12 points-of-impact, the barrier comes into contact with the Dodge Neon at seven different impact velocities. Each of these 84 simulations were analyzed with respect to Pressure and Von Mises stresses, as shown in Figure 2 and Figure 3.

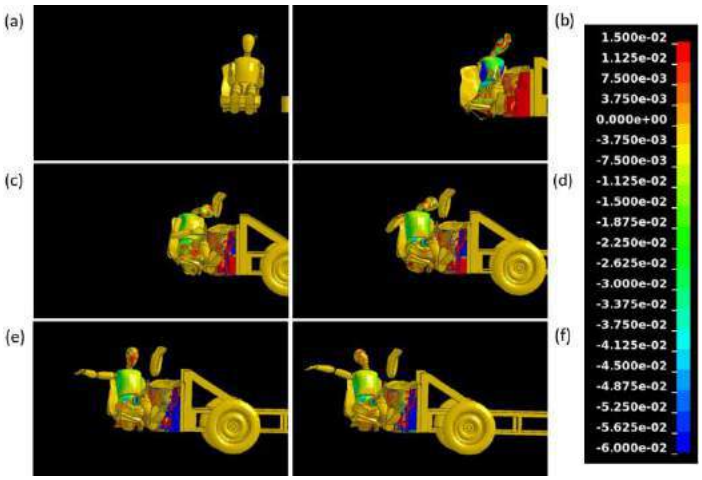

Figure 2. Pressure contour plots of the Hybrid Ⅲ 50th percentile male dummy undergoing a side impact at 50 mph from the 90 degree barrier orientation at (a) 0s (b) 0.3s (c) 0.6s (d) 0.9s (e) 1.2s (f) 1.5s

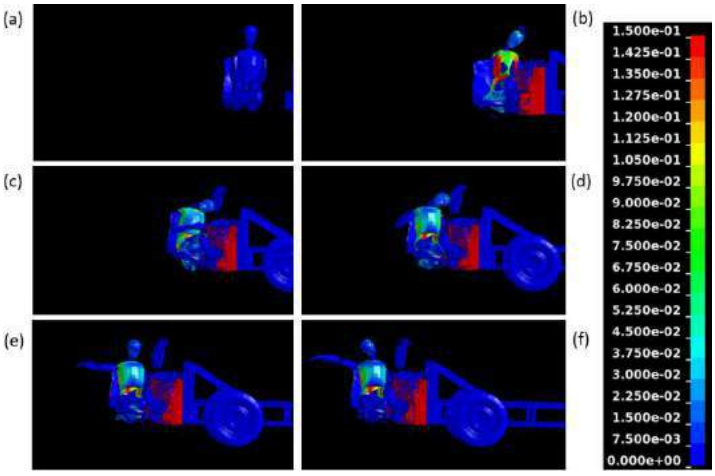

Figure 3. Von Mises contour plots of the Hybrid Ⅲ 50th percentile male dummy undergoing a side impact at 50 mph from the 90 degree barrier orientation at (a) 0s (b) 0.3s (c) 0.6s (d) 0.9s (e) 1.2s (f) 1.5s

As shown in Figure 4, the acceleration results from the simulations showed that for several crash scenarios the peak accelerations, in the dummy's head and neck, were well over the threshold for TBI.

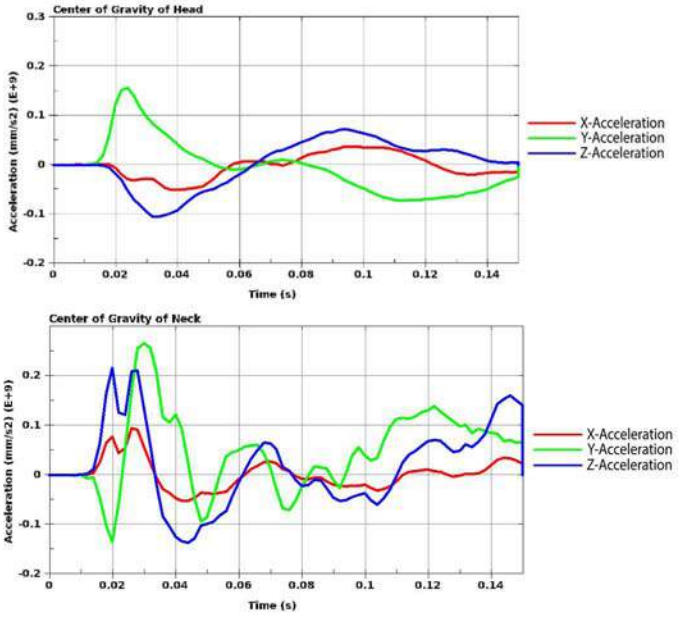

Figure 4. Acceleration versus Time plots at the centers of gravity of the head and neck of the Hybrid Ⅲ 50th percentile male dummy undergoing a side impact at 50 mph from the 90 degree barrier orientation

DISCUSSION

Upon completion of the car crash simulations, the acceleration versus time profiles will be analyzed and used in the configuration of the second step, human head simulations. From these simulations, the locations of the highest pressures, stresses, impulses, and other key injury metrics in the brain will be used to predict the regions where the most significant damage will occur [4]. These FE results will then be used to develop a mathematical surrogate model for brain damage (traumatic brain injury) due to car crashes. This will allow for a better understanding of the relationship between vehicular impact trauma and TBI.

ACKNOWLEDGEMENTS

The authors would like to acknowledge support from the High Performance Computing (HPC) facilities at the Center for Advanced Vehicular Systems (CAVS) and the educational support from the Bagley College of Engineering (BCoE) and Department of Agricultural and Biological Engineering (ABE) staff at Mississippi State University.

REFERENCES

[1] Giordano, C., & Kleiven, S. (2014). Evaluation of Axonal Strain as a Predictor for Mild Traumatic Brain Injuries Using Finite Element Modeling. *Stapp Car Crash Journal, 58*.

[2] Finnie, J., & Blumbergs, P. (2002). Animal Models: Traumatic Brain Injury. *Veterinary Pathology, 39*(6), 679-689.

[3] Traumatic Brain Injury in the United States: Fact Sheet. (2015, January 12). Retrieved October 15, 2015.

[4] Deng, X., An Chen, S., Prabhu, R., Jiang, Y., Mao, Y., & Horstemeyer, M. (2014). Finite Element Analysis of the Human Head Under Side Car Crash Impacts at Different Speeds. *Journal of Mechanics in Medicine and Biology, 14*(6).

[5] LS-Prepost [Computer Software]. (2011). Retreived from http://www.lstc.com/lspp/

Copyright 2016 The Organizing Committee for the 2016 Summer Biomechanics, Bioengineering and Biotransport Conference

SB^{3}C2016
Summer Biomechanics, Bioengineering and Biotransport Conference
June 29 –July 2, National Harbor, MD, USA
SB^{3}C2016-980

NUMERICAL SIMULATION OF MECHANICS OF RUPTURE IN ABDOMINAL AORTIC ANEURYSMS USING FLUID-STRUCTURE INTERACTION METHODS

Tejas Canchi (1, 2), Eddie Y.K Ng (2), Esley C.H Pwee (2), Dinesh K. Srinivasan (1), Sriram Narayanan (3)

(1) Lee Kong Chian School of Medicine, Nanyang Technological University, Singapore

(2) School of Mechanical and Aerospace Engineering, Nanyang Technological University, Singapore

(3) Department of General Surgery, Tan Tock Seng Hospital, Singapore

INTRODUCTION

Abdominal Aortic Aneurysm (AAA) is a vascular condition where the infrarenal aorta dilates to more than 2 times its original diameter [1]. Progressive weakening of the arterial wall results in rupture of the abdominal aorta if the condition is left untreated. The mechanics of AAA have been studied extensively using experimental, analytical, clinical, and computational approaches [2]. Estimation of rupture risk involves calculation of parameters that influence the wall mechanics and the flow physics of the aneurysm lumen. These include patient-specific velocity and intraluminal pressure and material properties of the arterial wall. The resulting wall shear stresses are hypothesized to be indicators of the region of structural failure in the AAA.

The majority of research has looked into modeling the mechanics of rupture of AAA using rigid structural models, due to the complexity of accounting for the arterial wall movement in pulsatile flow conditions. An accurate biomechanical model entails accounting for the wall movement and the interaction between the flow and the arterial wall. This means that a Fluid-Structure Interaction (FSI) model is essential for an accurate estimate of the rupture risk in AAA [3]. In the present work, we carried out an FSI computation with an AAA originated from an Asian patient. The anatomy of the Asian aorta is different from the Caucasian aorta in aspects of aneurysm neck length, common iliac artery diameter and the distance between the caudal renal artery and the common iliac artery bifurcation [4]. This has caused difficulties to clinicians in placing stent grafts during the Endovascular Aneurysm Repair (EVAR) procedure. Hence, the long-term objective of this study is the biomechanical analysis of an Asian patient cohort to understand the effect of the demographics differences leading up to AAA rupture. This will ultimately lead to improved treatment outcomes for AAA patients.

METHODS

The aneurysm geometry was obtained from ethics committee approved patient CT images using itk-SNAP, an open source image segmentation tool [5]. The geometry was cleaned up using MeshLab, a 3D mesh processing tool. Subsequent meshing was done using ICEMCFD, a commercial meshing tool. A 3D model of a patient-specific aneurysm geometry was used for FSI modeling with a fully coupled commercial FSI solver (ANSYS 16.1, Canonsburg, PA). Pulsatile inlet velocity and outlet pressure boundary conditions were applied [6]. Blood was considered to be an incompressible Newtonian fluid with a viscosity of 0.0035 Pa·s and density of 1,060 kg/m^3. The FSI interface was defined at the inner wall of the aneurysm model. The material was assumed to be isotropic with a Young's modulus of 4.5 MPa, density of 1,120 kg/m^3 and a Poisson's ratio of 0.45. Wall thickness was assumed to be constant at 2 mm. The system coupling function in ANSYS Workbench was used to carry out the simulation on a 16 GB RAM machine for 3 pulsatile cycles to damp out any initial transients. No Intraluminal Thrombus (ILT) was considered in the aneurysm model. Validation of the computational solution was carried out by comparing the inlet and outlet intraluminal pressures to those measured prior to surgery. The validation was carried out by considering the aneurysm to be rigid under steady flow conditions. Mesh independence studies determined the optimal size of the structural mesh as 250,000 nodes and the fluid mesh to be 2 million nodes. This was carried out using the assumption that the walls are rigid in both the structural and fluid solutions. The smallest mesh size from each of the domains was used in the final calculation. Wall shear stress (WSS), pressure and velocity distributions at the aneurysm wall were extracted to determine the location of highest WSS so that an estimate of rupture risk can be made.

Copyright 2016 The Organizing Committee for the 2016 Summer Biomechanics, Bioengineering and Biotransport Conference

RESULTS

The deformation, wall shear stress and von Mises stress plots were generated at peak systolic pressure for the third pulsatile cycle. The maximum deformation of the AAA inner wall surface was 0.2 mm. This is seen in the posterior distal location of the aneurysm as shown in Figure 1. This region is seen to have the largest mechanical shear stress (0.16 MPa) in the wall, as seen from Figure 2. The maximum fluid-induced wall shear stress is 15 Pa, as illustrated in Figure 3. The location of the highest stresses at the wall and lumen surface is consistent with the literature [6]. The highest stresses are induced when the pressure in the lumen reaches the systolic peak, in this case being at 15.5 kPa (116 mmHg) in the cardiac cycle. The stress distribution is such that there are a number of areas of high stresses that develop as the flow moves through the AAA. Flow vortices that are formed at the beginning of the cycle due to the geometry of the aneurysm migrate distally as the flow decelerates from peak systolic conditions to diastole. Initially, there is attached flow near the proximal end of the aneurysm but by peak systole there is a separation of the vortices from the wall. This is similar to the flow fields seen in prior FSI simulations [7].

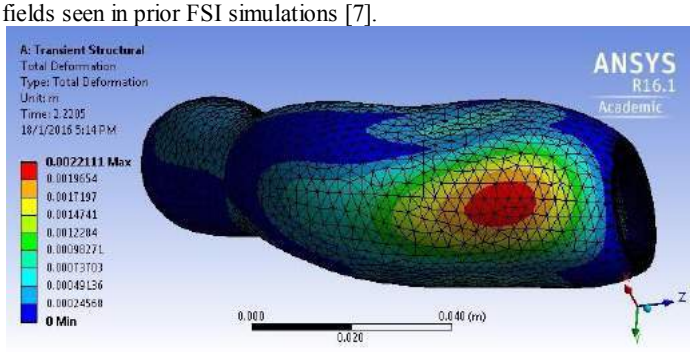

Figure 1: Spatial distribution of the AAA wall deformation (m).

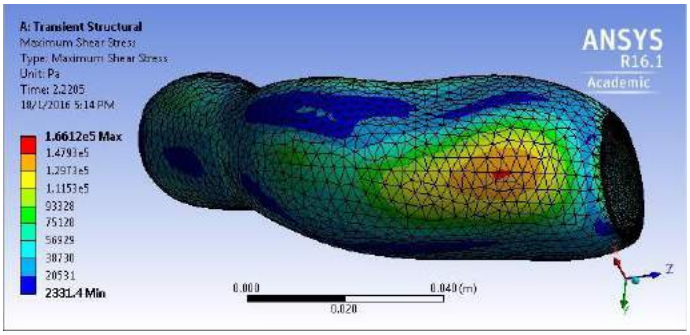

Figure 2: Spatial distribution of mechanical shear stress at the AAA wall (Pa).

DISCUSSION

The study undertaken is an attempt to estimate the mechanics of rupture of AAA using biomechanical methods. The arterial wall being a non-rigid entity is subject to interaction with the fluid flow and vice versa. Hence, this requires a FSI solution in order to investigate the effects of the moving arterial wall in the estimation of rupture risk. As has been seen by clinicians, the geometry of the Asian aorta is different from the Caucasian one. This presents a problem of whether the flow physics and the structural response vary as compared to the Caucasian AAA. This work presents an initial investigation into the analysis of Asian AAA patients, which will eventually help in determining whether an alternate approach is needed when estimating rupture risk in Asian AAA patients. The investigation has shown that

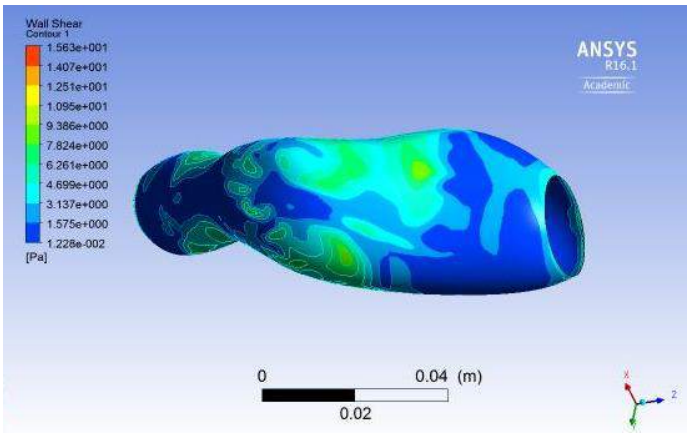

Figure 3: Spatial distribution of the fluid shear stress at the endoluminal surface (Pa).

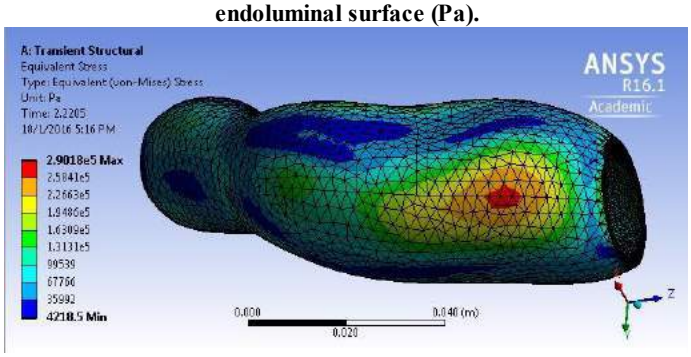

Figure 4: von Mises stress distribution at the AAA wall (Pa).

the location of high shear and induced stresses are at similar sites as of the Caucasian aorta. They provide a measure of the wall stresses that are developed in the arterial wall. However, since the Young's modulus is assumed constant, an improved material model will make the stresses more accurate in the physical sense.

Some of the limitations of this study are the boundary conditions, which have been derived from literature, the constant wall thickness, and the lack of ILT in the model, although there are AAA with no thrombus. Nevertheless, a FSI based solution is an important step towards determining the actual interaction between the arterial wall and blood flow, which will assess rupture risk in an Asian AAA. A more detailed patient-specific model, inclusive of a FSI modeling approach, will further our understanding.

ACKNOWLEDGEMENTS

The first author (Tejas Canchi) acknowledges receipt of the Research Student Scholarship from the Lee Kong Chian School of Medicine, Nanyang Technological University, Singapore. This work has been supported by the Lee Kong Chian School of Medicine, Nanyang Technological University start-up grant awarded to Dinesh K. Srinivasan. The authors would like to thank Prof Ender A. Finol for useful discussions regarding independence studies.

REFERENCES

[1] Raut SS, et al., *Ann Biomed Eng*., 41(7), 1459-1477, 2013.
[2]Vorp DA, *J Biomech*, 40(9), 1887-1902, 2007.
[3] Di Martino ES, et al., *Med Eng & Phy*,23(9), 647-655, 2001
[4] Cheng et al., *J. Endovascular Therapy*, 11:605-612, 2004.
[5] Yushkevich PA et al., *Neuroimage,* 31(3):1116-1128, 2006.
[6] Soudah E et al., *Comp. Math. Methods in Med.*, Art 472564, 2013.
[7] Wolters BJBM, et al., *Med Eng &Phy*, 27, 871-883, 2005.

Copyright 2016 The Organizing Committee for the 2016 Summer Biomechanics, Bioengineering and Biotransport Conference

SB^{3}C2016
Summer Biomechanics, Bioengineering and Biotransport Conference
June 29 –July 2, National Harbor, MD, USA
SB^{3}C2016-982

IS THERE A CRITICAL TIME POINT FOR ANTIHYPERTENSIVE TREATMENT? EMBRYONIC ANTIHYPERTENSIVE TREATMENT ALTERS ARTERIAL STIFFNESS IN ELASTIN HAPLOINSUFFICIENT MICE

Jungsil Kim (1), Victoria Le (2), Robert Mecham (3), Jessica Wagenseil (1)

(1) Dept. of Mechanical Engineering and Materials Science
Washington University
St. Louis, MO, USA

(2) Dept. of Biomedical Engineering
University of Texas
Austin, TX, USA

(3) Dept. of Cell Biology & Physiology
Washington University
St. Louis, MO, USA

INTRODUCTION

Elastin is crucial for cyclic loading in the cardiovascular system to maintain blood circulation throughout the body. The amount, assembly and organization of elastic fibers change with age and determine arterial stiffness. Increased arterial stiffness is associated with cardiovascular disease, including hypertension. Supravalvular aortic stenosis (SVAS), which is characterized by aortic narrowing and hypertension, is a congenital heart defect caused by a heterozygous mutation in the gene encoding elastin (*ELN*). Although hypertension in adults can be managed with pharmacological agents such as diuretics, angiotensin-converting enzyme inhibitors, angiotensin II receptor antagonists, calcium channel blockers, beta-blockers, etc. to decrease physiologic arterial stiffness, typical treatments for congenital aortic stenosis in young patients include catheterization with a balloon and replacement of the aortic valve to prevent the cause of the narrowing. Young SVAS patients that undergo heart surgery often require reoperation [1] with high complication rates. Hemizygous *Eln* mice (*Eln*+/-) have similar features to human SVAS patients, showing hypertension and increased stiffness in large arteries from perinatal period [2] to postnatal period [3]. We hypothesize that there is a critical time point to prevent aortic narrowing and change arterial elasticity in *Eln*+/- mice. To test our hypothesis, we treated mice with captopril, an angiotensin-converting enzyme inhibitor, during embryonic and postnatal development. We found that embryonic captopril treatment in mice alters aortic mechanics, whereas there is not a significant change after postnatal treatment.

METHODS

Animals and samples. *Eln*+/- and wild-type (WT) mice were treated with captopril during two different periods. For embryonic treatment, pregnant female mice were treated by drinking water containing 0.075g/L captopril for the entire gestational period. Pups were sacrificed within 24 hours of birth (postnatal day [P]1). For postnatal treatment, *Eln*+/- pups were treated by drinking water containing 0.075g/L captopril from P7 through their mother's milk, and then directly through drinking water after weaning, and sacrificed at P30. Ascending aortae (AAs) were removed and stored in physiological saline solution (PSS) for mechanical testing. Images of AAs before and after dissection were taken.

Mechanical testing. Inflation tests were performed using a Myograph 110P (DMT). The AAs were tied on stainless steel cannulae with silk suture and mounted horizontally in the test chamber filled with PSS. The AAs were stretched longitudinally to the estimated *in vivo* length for each age (P1 or P30) [3]. The AAs were then incrementally pressurized from 5 to 60 mmHg for P1 and from 0 to 175 mmHg for P30. The AAs were preconditioned before obtaining the data. Outer diameter, longitudinal force, and lumen pressure were recorded. Cross-sectional images of the aortic ring were captured to measure outer diameter and thickness at the unloaded state.

Analysis. Mean circumferential stretch ratios (λ_θ) were calculated by changes in inner (subscript i) and outer (subscript o) radii at the loaded state (r_i, r_o) compared to the unloaded state (R_i, R_o), assuming incompressibility (Eq. 1). Mean circumferential stress (σ_θ) was determined by the internal pressure (P) and inner and outer radii (Eq. 2). Diameter compliance (C_{Pi}) (Eq. 3), a measure of structural properties, was calculated from the derivative of an empirical relationship (Eq. 4) fitted to the outer diameter-pressure curve. Tangent modulus (E_{Pi}) (Eq. 5), a measure of material properties, was calculated from the derivative of a relationship (Eq. 6) fitted to the stress-stretch curve. In Eqs. 3 and 5, constants a_i and b_i (i=1, 2, 3, 4)

Copyright 2016 The Organizing Committee for the 2016 Summer Biomechanics, Bioengineering and Biotransport Conference

Equations:

$$a_{-} = \frac{1}{2}\left(\frac{r_i}{R_i} + \frac{r_o}{R_o}\right) \quad \cdots\cdots (1) \qquad \pm_{-} = \frac{Pr_i}{r_o - r_i} \quad \cdots\cdots\cdots\cdots (2)$$

$$C_{P_i} = \left.\frac{\partial d_o}{\partial P}\right|_{P=P_i} \quad \cdots\cdots (3) \qquad d_o = a_1 + a_2\left\{1 - \exp\left(-\frac{P^{a_3}}{a_4}\right)\right\} \quad \cdots\cdots (4)$$

$$E_{P_i} = \left.\frac{\partial \pm_{-}}{\partial a_{-}}\right|_{P=P_i} \quad \cdots\cdots (5) \qquad \pm_{-} = b_1 + b_2\left\{\exp\left(\frac{a_{-}^{\,b_3}}{b_4}\right)\right\} \quad \cdots\cdots\cdots (6)$$

were determined by nonlinear regression in Matlab. Differences between two groups of interest were compared by using t-tests.

RESULTS

While untreated P1 *Eln*+/- AAs have a normal aortic length, untreated P30 *Eln*+/- AAs are significantly longer than untreated WT. Captopril treatment does not affect *in vivo* aortic length in P1 mice, but it leads to reduced aortic length in P30 *Eln*+/- mice, which becomes similar to WT (Table 1). Unloaded inner and outer diameters in untreated P1 *Eln*+/- AAs are significantly smaller than untreated WT, but no significant difference is found after treatment. Captopril treatment does not alter unloaded inner and outer diameters in P30 *Eln*+/- AAs, which are significantly smaller than untreated WT. Wall thickness of untreated P1 *Eln*+/- AAs is similar to that of untreated WT and captopril treatment does not change the wall thickness at P1, but captopril treatment significantly reduces the wall thickness in both genotypes at P30.

During the inflation test, untreated *Eln*+/- AAs exhibit similar behavior to untreated WT, but captopril treated P1 *Eln*+/- AAs show significantly smaller outer diameters between 5-20 mmHg compared to WT (Fig. 1A). However, the captopril treatment does not affect outer diameter in P30 *Eln*+/- AAs (Fig. 1B). The circumferential stretch ratios in untreated P1 *Eln*+/- AAs are significantly larger than untreated WT between 15-45 mmHg, but after captopril treatment no significant difference is found between *Eln*+/- and WT AAs. Untreated P30 *Eln*+/- AAs show a mild tendency toward larger stretch ratios than untreated WT at medium pressures, and captopril treated *Eln*+/- AAs show significantly larger stretch ratios compared to untreated WT AAs between 75-100mmHg. Circumferential stress does not change with treatment for both P1 and P30 AAs.

Table 1: Unloaded dimensions and *in vivo* length of the untreated and captopril treated AAs in *Eln*+/- and WT mice at P1 and P30. Data are presented as mean ± standard deviation. Symbols indicate significant differences between untreated *Eln*+/- and WT AAs (*), captopril treated *Eln*+/- and untreated WT AAs (#), and captopril treated and untreated WT AAs (&) at P1 and P30.

Age	Genotype & treatment	Number of samples	Outer diameter (μm)	Inner diameter (μm)	Wall thickness (μm)	*In vivo* AA length (mm)
P1	unt *Eln*+/-	7	368 ± 19	187 ± 16	91 ± 6	1.57 ± 0.15
	unt WT	8-9	409 ± 30	233 ± 24	88 ± 8	1.50 ± 0.19
	cap *Eln*+/-	6-7	373 ± 40	202 ± 33	85 ± 8	1.49 ± 0.15
	cap WT	7-9	426 ± 49	258 ± 54	84 ± 7	1.44 ± 0.14
P30	unt *Eln*+/-	14	838 ± 41	580 ± 45	129 ± 8	3.50 ± 0.38
	unt WT	7	936 ± 77	683 ± 70	126 ± 10	2.94 ± 0.37
	cap *Eln*+/-	8	798 ± 28	589 ± 22	105 ± 9	2.91 ± 0.54
	cap WT	4	872 ± 45	663 ± 35	104 ± 11	2.72 ± 0.21
Significant difference			P1*, P30*$^{\#}$	P1*, P30*$^{\#}$	P30$^{\#\&}$	P30*

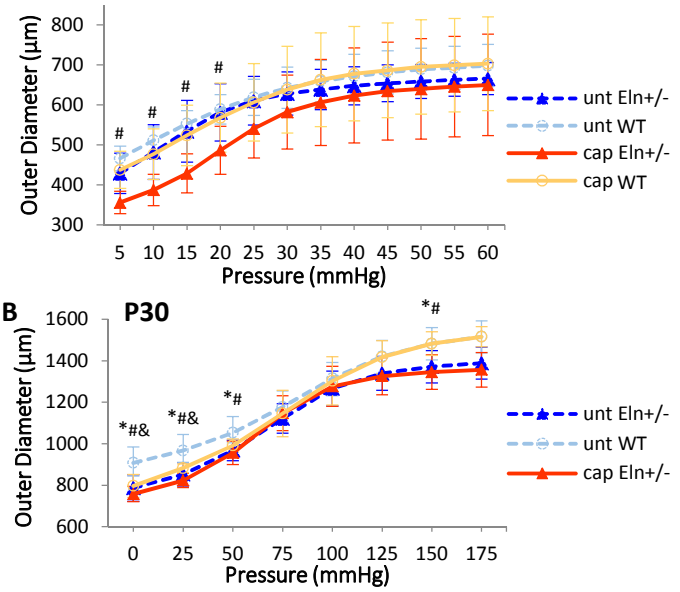

Figure 1: Mean outer diameters with respect to applied pressure during the inflation test for P1 (A) and P30 (B) AAs.

In arterial compliance, there are significant differences between untreated P1 *Eln*+/- and WT AAs between 5-10 mmHg and 35-60 mmHg, but after captopril treatment there are significant differences between 45-60 mmHg only compared to untreated WT. At P30, no significant difference in arterial compliance is found between treated *Eln*+/- and WT AAs, but captopril treatment leads to significantly reduced compliances between 125-150 mmHg in *Eln*+/- AAs. Untreated P1 *Eln*+/- AAs have higher tangent modulus between 5-10 mmHg and 30-60 mmHg compared to untreated WT, but captopril treated P1 *Eln*+/- AAs show significant differences between 5-15 mmHg only. Tangent moduli in untreated P30 *Eln*+/- AAs are similar to those in untreated WT, but after captopril treatment tangent moduli decrease significantly between 0-25mmHg.

In P30 WT mice, captopril treatment leads to a reduced wall thickness at unloaded state and decreased outer diameters between 0-25 mmHg, but other parameters are not affected by captopril at both ages.

DISCUSSION

We found that there are different effects of captopril at different time points (embryonic vs. postnatal). After captopril treatment, P1 *Eln*+/- AAs show significant changes in outer diameter, circumferential stretch, tangent modulus, and unloaded inner and outer diameters, while P30 *Eln*+/- AAs show very minor changes in these parameters. Future work will include embryonic captopril treatment, followed by no treatment up to P30 to determine if the embryonic changes are maintained through maturation.

ACKNOWLEDGEMENTS

This work was supported by National Heart, Lung, and Blood Institute Grants R01-HL-115560 and R01-HL-105314.

REFERENCES

[1] Imamura M et al., *Ann Thorac Surg*, 90:2016-22, 2010
[2] Wagenseil, J et al., *Circ Res*, 104:1217-24, 2009
[3] Wagenseil, J et al., *Am J Physiol Heart Circ Physiol*, 289: H1209-17, 2005

Copyright 2016 The Organizing Committee for the 2016 Summer Biomechanics, Bioengineering and Biotransport Conference

SB^{3}C2016
Summer Biomechanics, Bioengineering and Biotransport Conference
June 29 –July 2, National Harbor, MD, USA
SB^{3}C2016-983

FAILURE PROPERTIES OF ANNULUS FIBROSUS: EFFECTS OF chABC AND STRAIN RATE

Noah Bonnheim*, Benjamin Werbner*, Grace O'Connell, Ph.D.

Department of Mechanical Engineering
University of California, Berkeley
Berkeley, CA, USA

INTRODUCTION

Structural failure of the intervertebral disc (IVD) is a common and painful condition associated with degenerative changes to disc composition [1]. The occurrence of tears in the annulus fibrosus (AF), including radial tears, rim lesions, and circumferential tears, increase with age and degeneration [2,3]. In particular, radial fissures can lead to prolapse of the nucleus, or disc herniation, with impingement of the spinal nerves, leading to lower back and leg pain [4].

The annulus is comprised of collagen fibrils embedded in an extrafibrillar matrix [2]. Negatively charged glycosaminoglycans (GAG) in the extrafibrillar matrix absorb water molecules, providing the tissue with its hyper-viscoelastic mechanical properties [5]. Degeneration is noted by changes in biochemical composition and structure, including a loss in GAG and water content [2]. To date, AF failure mechanics, and the interaction between failure mechanics and biochemical composition, is not well understood. A better understanding of the relationship between biochemical degeneration and failure properties of the AF may help elucidate the mechanisms of disc herniation.

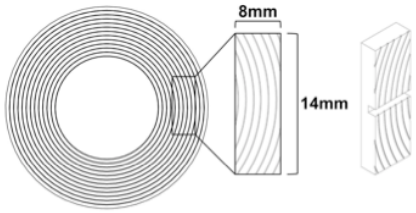

Figure 1. Schematic of test sample orientation (left) and notch geometry (right).

Previous studies [6,7] have used chondroitinase ABC (chABC) to enzymatically digest GAG from disc tissue as an *in vitro* model of disc degeneration. In this study, we examine the effect of chABC digestion on AF failure mechanics. As a decrease in GAG content diminishes the ability of biological tissues to absorb water, it is hypothesized that GAG digestion with chABC will alter both the failure properties and viscoelastic behavior of the AF. Due to the importance of water absorption to AF mechanics, our second objective was to evaluate the effect of strain rate on failure properties.

METHODS

Twelve intervertebral discs were dissected from the first three levels of four bovine caudal spines. Twenty-two circumferentially oriented annulus specimens were isolated from the discs and sliced to a thickness of 2 mm using a freezing stage microtome. To facilitate repeatability with respect to failure dynamics (i.e. avoid failure associated with gripping), samples were horizontally notched midway down their length, such that the un-cracked specimen thickness was 1mm (Figure 1). Sample notching was performed while the samples were frozen (pre-hydration) using a scalpel and depth stop. Samples were randomly divided into four test groups: healthy low strain rate (CTL-low), enzymatic digestion low strain rate (chABC-low), healthy high strain rate (CTL-high), and enzymatic digestion high strain rate (chABC-high; n = 4-8 per group). As annulus mechanical properties are known to vary with hydration state, specimens were soaked for 18 hours at 37 °C in a group specific solution. The healthy group was hydrated in phosphate-buffered saline (PBS, 0.14 M NaCl) while the degenerate group was hydrated in a PBS solution with 0.125 U/mL chABC, as per the digestion protocol described by Isaacs *et al.* [6]. Following hydration or enzymatic digestion, uniaxial tension tests were performed in PBS at room temperature using an Instron 5943 (Norwood, MA). Samples were gripped using 400 grit sandpaper super-glued directly to the specimens.

Copyright 2016 The Organizing Committee for the 2016 Summer Biomechanics, Bioengineering and Biotransport Conference

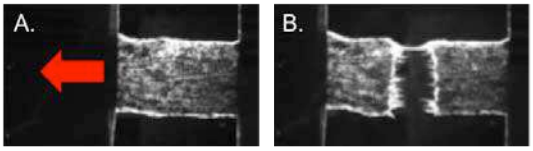

Figure 2. Representative sample (A) before and (B) after failure. Red arrow indicates loading direction.

As AF mechanical behavior in tension is highly dependent on strain rate [8], we evaluated the failure properties at two different strain rates. The high strain rate group was tested at a displacement rate of 50 mm/min, which corresponds to a strain rate of approximately 3.57 min^{-1}, while the low strain rate group was tested at a displacement rate of 0.05 mm/min, or approximately 3.57×10^{-3} min^{-1}. Strain was calculated as the change in displacement divided by the initial gauge length (i.e. grip-to-grip distance). Stress was calculated by dividing measured force by the original cross-sectional area of the notched section. The Young's modulus (E) was calculated using a bilinear fit to the stress-strain response (linear-regression optimization script, Matlab Mathworks Inc.). The stress at failure for each test was defined as the maximum stress recorded during the test, while the strain at failure was defined as the strain at which this maximum stress occurred.

To evaluate the effect of GAG content on failure properties, a two-tailed Student's t-test was performed between healthy and degenerate groups for both strain rates. Similarly, a Student's t-test was performed to determine the effect of strain rate on failure properties. Significance was assumed at $p \leq 0.05$.

RESULTS

The full-width notch resulted in robust failure occurring at the mid-length for all samples (Figure 2). Under quasi-static loading condition (i.e. low strain rate), chABC digestion did not alter the toe- or linear region modulus (Figure 4A – shown for linear-region modulus). However, chABC did significantly decrease failure stress and strain ($p < 0.01$; Figure 4 – blue versus red bar).

An increase in strain rate increased the Young's modulus for both healthy and digested AF groups, as expected ($p \leq 0.05$; Figure 4A – low rate versus high rate). Interestingly, failure properties of chABC digested samples were not significantly different from the control when loaded at a higher strain rate ($p > 0.15$; Figure 4B, 4C). It should be noted that a higher variability in data was observed for the high strain rate cohort, and thus additional testing with a larger sample size is required to further elucidate this phenomenon.

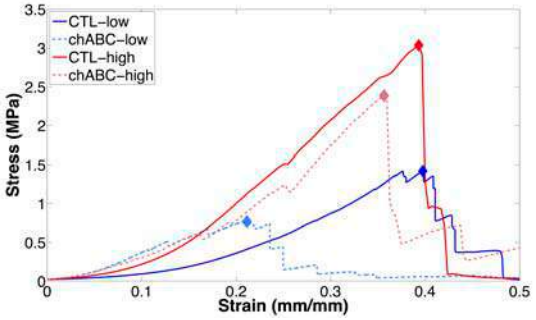

Figure 3. Representative stress-strain curve for each group. Diamond represents failure point.

DISCUSSION

GAG chains are thought to play a dominant role in the mechanical properties of biological tissues including the AF. Due to the high water contribution and the role of water composition on tissue mechanics, we evaluate AF failure mechanics at a low and high strain rates. Our study shows that for quasi-static loading, chABC digestion decreases failure stress and strain; however, these differences are not as pronounced at the higher strain rate. Our results differ from those described by Isaacs *et al.*, who reports no significant change in failure strain for similarly digested AF specimens, which is likely due to difference in strain rate (Isaac's strain rate = 0.30 min^{-1}) [6]. Taken together, these findings suggest that GAGs play an important role in AF failure mechanics that is strain rate-dependent, which is important for understanding loading conditions that may cause disc herniation.

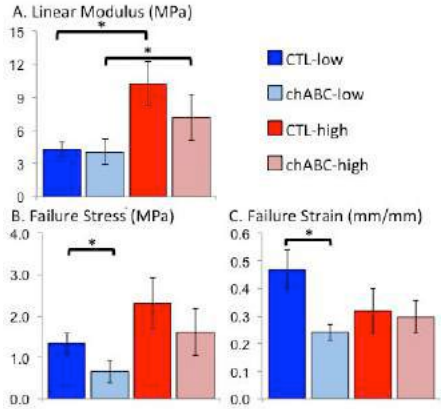

Figure 4. (A) Linear-region modulus, (B) stress and (C) strain at failure. * denotes $p \leq 0.05$.

Enzymatic digestion with chABC has been previosly used to reduce GAG content in biological tissues [6,7]. Ongoing work is focused on quantifying the decrease in GAG composition in our degeneration model. Preliminary data showed significant differences in the water content of control and chABC samples, suggesting that GAG digestion was effective. Furthermore, a strong correlation was found between water content and stress at failure ($R^2 = 0.86$). Future work will focus on correlating GAG composition directly with AF failure properties in tension.

At high strain rates, there was a significant decrease in elastic modulus and a trend for a decrease in the stress at failure. The decrease in Young's modulus with chABC is likely due to fiber-matrix interactions altering tension mechanics at the higher loading rate. For healthy and chABC samples, increasing the strain rate significantly increased the stress at failure and elastic modulus; however, the strain at failure was not altered. Future work will explore whether AF failure mechanics is a strain-driven phenomenon.

GAGs comprise less than 15% of the tissues dry weight [9]. Previous sub-failure AF tensile mechanics is thought to be largely due the collagen fibers [2]; however, the findings here suggest that GAGs may play a larger role in AF failure mechanics.

ACKNOWLEDGEMENTS

* Both authors contributed equally to this work. This work was supported by the Hellman Faculty Fund.

REFERENCES

[1] Adams, M. and Roughley, P., *Spine*, 2006; [2] O'Connell, G. et al., *J Biomech Eng,* 2009; [3] Vernon-Roberts, B. et al. *Spine*, 1997; [4] O'Connell, G. et al, *Bio Research*, 2015; [5] Iatridis, J., et al., *Spine Journal*, 2013; [6] Isaacs, J., et al., JMBBM, 2014; [7] Ando, T., et al., *Clin Orthop Relat Res,* 1995; [8] Gilbert, H., et al., *Arthritis & Rheumatism*, 2010; [9] Antonio et al., *J Clin Invest*, 1996;

Copyright 2016 The Organizing Committee for the 2016 Summer Biomechanics, Bioengineering and Biotransport Conference

SB^{3}C2016
Summer Biomechanics, Bioengineering and Biotransport Conference
June 29 –July 2, National Harbor, MD, USA
SB^{3}C2016-984

AN IMAGED-BASED INVERSE FINITE ELEMENT METHOD TO DETERMINE THE MECHANICAL PROPERTIES OF HUMAN TRABECULAR MESHWORK

Anup D. Pant (1), Lawrence Kagemann (2,3), Ian A. Sigal (2,3), Joel S. Schuman (2,3), Rouzbeh Amini (1)

(1) Department of Biomedical Engineering
The University of Akron
Akron, OH, USA

(2) Department of Ophthalmology
University of Pittsburgh
Pittsburgh, PA, USA

(3) Department of Bioengineering
University of Pittsburgh
Pittsburgh, PA, USA

INTRODUCTION

Glaucoma is a leading cause of irreversible blindness worldwide. It is estimated that by 2020, 79.6 million people will suffer from glaucoma. In the same year, 5.9 and 5.3 million people are expected to be bilaterally blind as a result of open angle and angle closure glaucoma, respectively [1]. Elevated intraocular pressure (IOP) is a risk factor for glaucoma and is generated by the resistance to the aqueous humor outflow. The continuous flow of the aqueous humor is essential for providing the cornea and lens with oxygen and nutrients. In addition, normal IOP maintains the proper shape and the optical properties of the eye. The aqueous humor leaves the eye primarily via the trabecular meshwork (TM) [2]. IOP increases when the aqueous humor production rate is greater than its outflow rate.

Recent studies have shown that in glaucomatous eyes, the TM stiffness is considerably higher than that of normal eyes. It is believed that a higher TM stiffness increases resistance to the aqueous humor outflow and leads to a higher IOP [3]. Therefore, TM mechanical properties play an important role in understanding the pathophysiology of glaucoma and could be a potential risk factor. In this study, using an internally developed inverse finite element model, we aimed to estimate the mechanical properties of the TM in a healthy volunteer. Our model prediction is based on *in-vivo* imaging and estimation of the parameters using a genetic algorithm [4].

METHODS

The temporal limbus of a healthy subject (female, age 26 years) was imaged by optical coherence tomography (OCT, Cirrus, Zeiss, Dublin, CA) at baseline and during IOP elevation (ophthalmodynamometer applying 10g force). IOP was measured at baseline and during IOP elevation. Corresponding Schlemm's canal locations were identified in radial OCT cross-sectional B-scans based on the pattern of limbal vessel crossings [5]. The images was segmented manually using the Gnu Image Manipulation Program (GIMP 2.8.14) into air, cornea/limbus/sclera complex, Schlemm's canal, trabecular meshwork, anterior chamber, iris, supracilliary space, and "deeper structures" (those beyond the limit of penetration of the OCT scan).

An axisymmetric model of TM was constructed based on the following governing equations. The stress balance equation was given by:

$$\nabla.\boldsymbol{\sigma} = \mathbf{0}, \tag{1}$$

where σ represented the Cauchy stress tensor, defined with the assumption of a neo-Hookean material model for TM:

$$\boldsymbol{\sigma} = \frac{\mathbf{G}}{\det \mathbf{F}}(\mathbf{B}-\mathbf{I}) + \frac{2G\nu}{(1-2\nu)\det \mathbf{F}}\ln(\det \mathbf{F})\mathbf{I}, \tag{2}$$

where G was the shear modulus, ν was the Poisson's ratio, **I** was the identity tensor, **F** was the deformation gradient tensor, and **B** was the left Cauchy- Green deformation tensor. **F** and **B** were defined as

$$\mathbf{F} = \frac{d\mathbf{x}}{d\mathbf{X}}, \tag{3}$$

$$\mathbf{B} = \mathbf{F}\mathbf{F}^{\mathbf{T}}, \tag{4}$$

Copyright 2016 The Organizing Committee for the 2016 Summer Biomechanics, Bioengineering and Biotransport Conference

where **x** was the current position of a material point and **X** was its resting position. The finite element meshes were generated based on TM geometry segmented from *in-vivo* images using commercial software Abaqus (Dassault Systèmes, Velizy-Villacoublay, France). A pressure boundary condition with the constant value of IOP (P) was applied along the boundary element of the TM domain (Fig. 1c). The pressure boundary condition was applied to mimic the changes in the IOP *in-vivo*. In particular, since the IOP of the undeformed configuration was 11 mmHg and the IOP of the deformed configuration was 23 mmHg, the difference of 12 mmHg was applied as the pressure boundary condition. The TM boundaries that connect it to its surrounding, much stiffer tissues (Fig 1c), were assumed to have negligible deformation in comparison to the rest of the tissue. Thus, a fixed boundary condition was chosen for these regions. We then used our inverse modeling approach to calculate the shear modulus G from the experimental deformation data. The objective function was defined as absolute value of the difference between the Schlemm's canal area of the experimental measurements SC_{exp} and the genetically driven finite element solution SC_{sim}:

$$SSE = \left\| SC_{exp} - SC_{sim} \right\| . \quad (5)$$

The initial guesses for G were chosen between 10-90 kPa.

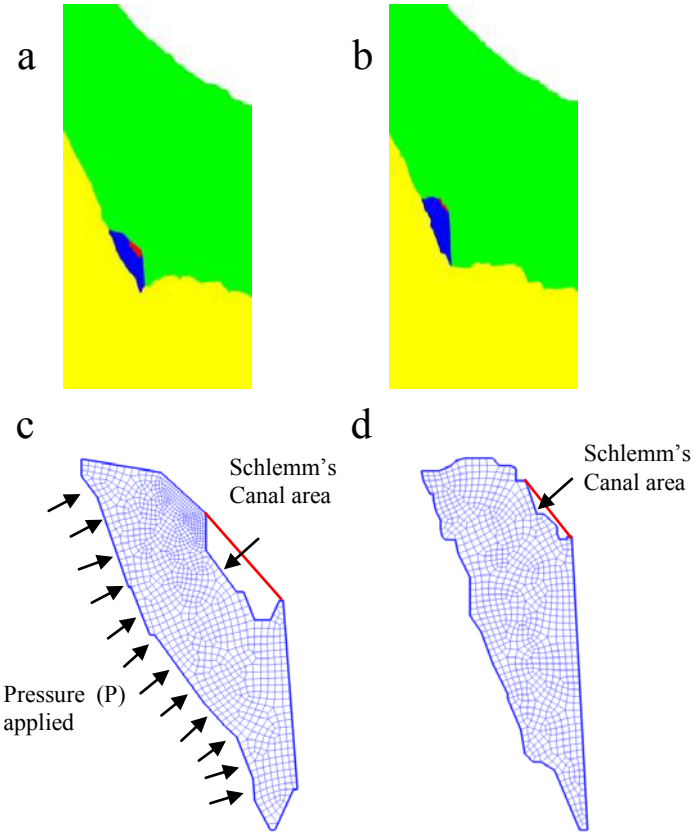

Figure 1: Segmented images of the trabecular meshwork in (a) undeformed and (b) deformed configuration. Finite element meshes of the trabecular meshwork in (c) undeformed and in (d) deformed configuration. The finite element mesh of the deformed configuration is provided only for comparison and was not used in simulation.

The simulations were performed using an HP Intel Xeon machine at the Ohio Supercomputing Center (Columbus, OH).

RESULTS

Figure 2 shows the finite element solution after pressure is applied to the undeformed configuration. Upon applying the pressure and appropriate displacement boundary conditions, the simulated results closely matched the experimental measurements.

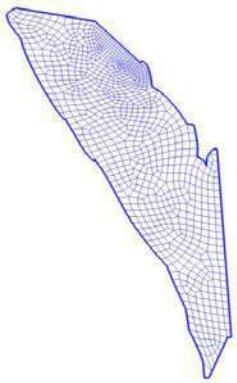

Figure 2: Simulated results of the deformation of the trabecular meshwork

From the optimization technique a value of 2 kPa was obtained for the TM shear modulus, G. We found that the optimization convergence was independent of our initial guess choices and the broader ranges of initial guesses only increased the computational time. The solution process took approximately 120 minutes (~ 30 numbers of generations). The simulated area of the Schlemm's canal (2030 μm^2) was close to 2100 μm^2, the area measured experimentally.

DISCUSSION

We constructed a finite element model of the TM subjected to an IOP. We then calculated the mechanical properties using an inverse optimization approach. Using simplified beam theory, Johnson et al. [6] found the elastic modulus in a living healthy eye to be 128 kPa. Hence, assuming a nearly incompressible material, a shear modulus of 43 kPa could be estimated form their calculation, different form ours. One possible reason is the use of different material models for the calculation. We hope to increase the confidence in our technique by simulating more experiments. Quantification of TM mechanical properties using clinical measurements will help us identify new risk factors for glaucoma.

ACKNOWLEDGEMENTS

Computations were facilitated by a supercomputing resource grant from the Ohio Supercomputer Center.

REFERENCES

[1] Quigley, H.A et al., *Br J Opthalmol*, 90:262-7, 2006
[2] Kaufman, Paul L et al., *Adler's Physiology of the Eye*. Elsevier Health Sciences, 2011. Adler's physiology of the eye.
[3] Last, J.A et al., *IOVS,* 52:2147–2152, 2011
[4] Storn R, Price K., *J. Global. Optim*, 11: 341–359,1997
[5] Kagemann, L et al., IOVS, 55:1805-1809, 2014
[6] Johnson, M et al., *IOVS*, 56:3541, 2015

Copyright 2016 The Organizing Committee for the 2016 Summer Biomechanics, Bioengineering and Biotransport Conference

SB^{3}C2016
Summer Biomechanics, Bioengineering and Biotransport Conference
June 29 –July 2, National Harbor, MD, USA
SB^{3}C2016-985

ADDITIVE MANUFACTURING OF LOCALIZED MICRONEEDLE DRUG-DELIVERY SYSTEM

Sofia Chinchilla (1), Yanfeng Lu (2), Corey J. Schurko (1), Douglas C. Crowder (1), Bum-Joon Park (3) Jae-Won Choi (2), Yang H. Yun (1)

(1) Biomedical Engineering Department
University of Akron
Akron, Ohio, USA

(2) Mechanical Engineering Department
University of Akron
Akron, Ohio, USA

(3) Molecular Biology Department
Pusan National University
Busan, South Korea

INTRODUCTION

Skin cancer affects nearly 82,000 people each year in the United States; the most common and lethal form of skin cancer is melanoma.[1] Roughly 76,000 patients in the U.S. will be diagnosed with melanoma this year.[1] Although the survival rate is excellent when detected early, melanoma accounts for over 10,710 deaths each year.[1] The traditional treatment for cutaneous tumors is surgical removal, but chemotherapy is applied once the skin cancer becomes metastasized. Surgical removal can be emotionally traumatic for the patient and increases the risk of infection. Additional therapy may be required if the initial resection is not completely effective. Alternatively, systemic chemotherapy may be used to treat skin cancers. However, systemic chemotherapy results in considerable side effects that include immune system suppression, sterility, anemia, secondary cancer formation, and hepatic toxicity. As an alternative to systemically delivered chemotherapeutics and surgical removal, localized chemotherapy using a microneedle array could limit these side effects and allow treatment to be administered via an outpatient system. Outpatient systems are preferable because studies have demonstrated that quality of life improves when patients are treated as outpatients.[2]

In collaboration with Jae-Won Choi Ph.D. in the Mechanical Engineering Department at The University of Akron, microneedle arrays have been developed using microstereolithography. Poly(propylene fumarate) (PPF) was mixed with a photoinitiator and cross-linked using ultraviolet rays (Figure 1).[3] By mixing PPF with chemotherapeutics prior to crosslinking, drugs can be encapsulated into the microneedle array. Although dacarbazine is the only FDA approved chemotherapeutic for melanoma, its clinical efficacy is limited.[4] Thus, alternative drugs have to be explored. An attractive chemotherapeutic is 2- 3-[(1,4-dihydro-5,8-dimethoxy-1,4-dioxo-2-naphthalenyl)thio]-propanoic acid (GN25), since all cancers have been linked to mutations of p53, a tumor suppressing gene. A mechanism that inhibits the function of p53 is K-Ras activation through induction of Snail, a protein that binds and eliminates p53 through exocytosis. GN25 blocks the binding of Snail to p53 and allows cancer cells to undergo cellular repair or apoptosis. In this project, the median lethal dosages for GN25 will be determined for a skin cancer cell line and will be loaded into biodegradable microarrays.

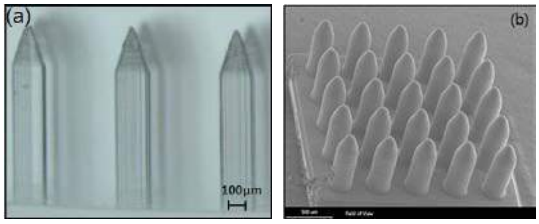

Figure 1. Light and electron scanning micrograph of microneedles

METHODS

The PPF was synthesized using a two-step procedure. In the first step, diethyl fumarate and propylene was reacted in a heated vessel with zinc chloride and hydroquinone. The temperature was gradually increased from 110 °C to 140 °C under a continuous flow of nitrogen gas. In the second step, bis(hydroxypropyl) fumarate was transformed into PPF through a transesterification. This stage of reaction is conducted under vacuum with mechanical stirring and with a gradual increase in temperature from 100 °C to 140 °C. The reaction proceeds until the desired molecular weight of PPF is obtained.

A dynamic mask projection microstereolithography was developed to fabricate the microneedle arrays.[3] A 3D model of the

Copyright 2016 The Organizing Committee for the 2016 Summer Biomechanics, Bioengineering and Biotransport Conference

microneedle array was designed using SolidWorks and then sliced to get the 2D cross-sectional images. Each time, one cross-sectional image was transferred to the digital micro- mirror device of the microstereolithography system, and the patterned light was projected onto the surface of the liquid material, initiating crosslinking. The structure was dipped into the liquid material, cross-linked using light, and stacked to obtain the final microneedle array structured. Each microneedle has a conical tip and a cylindrical shaft and is 1cm tall. The microneedles were tested for shear and tensile strength and have been determined to be strong enough to penetrate the superficial layers of human skin.

The toxicities of dacarbazine and GN25 were determined using the skin cancer cell line A431-H9 as well as human dermal fibroblasts (HDF), The cells were seeded at a fixed concentration of 5,000 cells per well. Then treated with the drug at varying concentrations from 100-0 μM for three days. Finally, metabolic activity of the cells, which is directly correlated with cell viability, was used to determine the efficacy of the drugs and HA conjugates. The median lethal dose (LD_{50}) for the A431-H9 cells will be compared to the LD_{50} for the HDF cells to determine the relative size of the therapeutic window. A small therapeutic window implies that the healthy tissue would see the same toxicity as the cancerous tumor, which is not ideal. Finally, the results from the HA-GN25 will be compared to the results of GN25, HA-R, and dacarbazine.

RESULTS

The resulting microneedles are cylindrical with a height of 0.7 mm and a shaft diameter of 0.2 mm. The points of the microneedles are conical with apex diameters of 0.02 mm and a height of 0.3 mm. Compression testing shows microneedles are strong enough to penetrate into the skin without buckling. Although the elastic modulus decreased from 0.173 to 0.051 and 0.36 GPa for 1 and 2% drug loading, the bucking force is approximately ten times greater then the force needed for insertion into human skin. Confocal studies with quantum dots also show an even distribution within the microneedle's structure.

Dacarbazine loaded into the micro needles shows first-ordered release kinetics with a burst release during the first week (Figure 2). The factors that can alter the release kinetics can be polymer's molecular weight, chemical properties of the drug, amount of drug loading, and geometry of the microneedles. A controlled release is observed after the first week, but the amount of release is incremental.

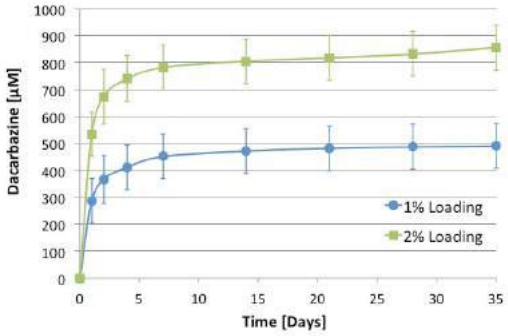

Figure 2. In vitro dacarbazine release kinetics

The toxicities studies show dacarbazine is ineffective against A431-H9 cell line. However, this drug also shows little efficacy against human dermal fibroblasts. At 100 μM concentration of drug, the cellular viability was approximately 78.9 and 86.0% for A341-H9 and human dermal fibroblast, respectively. In contrast, GN25 exhibits LD_{50} at approximately 20 μM for A431-H9. However, human dermal fibroblasts are largely resistant against this drug (LD_{50} at approximately 100 μM). Thus, GN25 seems to be an excellent candidate for further evaluation.

DISCUSSION

The available commercial transdermal drug-delivery systems have experienced considerable growth since the introduction of the scopolamine patch for motion sickness in 1979. An attractive variation of transdermal devices is the microneedle. It has the ability to overcome the drug transport barrier, *i.e.* basal lamina, so that hydrophilic and/or large molecular weight drugs can be diffuse through the skin. Microneedles combine the merits of both the extradermal and intradermal drug-delivery systems. It also could be a pain-free pathway if the needles' size and gauges are carefully selected. Microstereolithography is a convenient process to control printing the desired structure at the microscale. In addition, incorporating the drug prior to printing is straightforward, simple, and flexible.

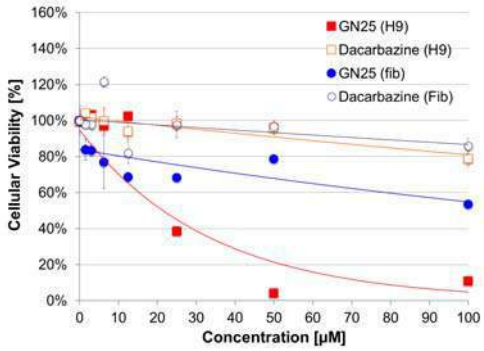

Figure 3. Toxicity of Dacarbazine and GN25

The clinical dosages for dacarbazine range from 300 to 600 mg/m^2. If an average adult has a surface area of 1.7 m^2 and six liters of blood, the dosages ranges from 274.5 to 548.9 μM, respectively. Thus, the release profiles of dacarbazine are within the therapeutic requirements. Diffusion is likely the mechanism of the drug release kinetics, but the degradation could contribute to the zero-order kinetics phase. A first-ordered kinetics is typically observed for non-biodegradable polymer, but PPF degrades slowly by hydrolysis. Approximately 10% of mass loss is expected for PPF during a five-week period. However, the efficacy is relatively poor against certain type of skin cancers, such as A341-H9. Thus a drug that shows more efficacy against this type of cancers but remain relatively nontoxic again normal fibroblast is desired. Thus, GN25, which is an experimental chemotherapeutic, is promising candidate for further studies.

ACKNOWLEDGEMENTS

The authors would like to acknowledge the Ohio Space Grant Consortium and National Science Foundation (CBET-0954360) for providing the funding for this project.

REFERENCES

[1] Siegel, R et al. *CA: A Cancer Journal for Clinicians*. 63: 11–30. 2013.

[2] Reuter, KK et al. *European Journal of Cancer Care*. 16(3): 222-230. 2007.

[3] Lu, Y. et al. *Biofibrcation*. 7: 1-13. 2014.

[4] Bhatia, S et al. *Oncology (Williston Park)*. 23(6): 488–496. 2009.

Copyright 2016 The Organizing Committee for the 2016 Summer Biomechanics, Bioengineering and Biotransport Conference

SB³C2016
Summer Biomechanics, Bioengineering and Biotransport Conference
June 29 –July 2, National Harbor, MD, USA
SB³C2016-986

CHARACTERIZATION OF GLIOBLASTOMA GROWTH USING FIVE DIFFERENT MATHEMATICAL MODELS

Mitra Shabanisamghabady and Martin L. Tanaka

Department of Engineering and Technology
Western Carolina University
Cullowhee, North Carolina, USA

INTRODUCTION

Glioblastoma multiforme is the most common and most malignant primary brain tumor. Optimal therapy results in survival time of 15 months for newly diagnosed cancer and 5-7 months for recurrent disease [1]. Malignant glioma patients demonstrate limited response to conventional therapies which include surgery, radiation, and/or chemotherapy. New and improved methods of therapy are urgently needed. Physiological experiments using animal models are often used to study new chemotherapeutic agents. These studies are quite effective but often expensive and time consuming. Mathematical models are often used to augment physiological experiments. These models can both increase our understanding of tumor growth, as well as aid in the development and preliminary testing of treatment options [2]. In this research five ordinary differential equation models were used determine the cancer growth characteristics. Model parameters for glioblastoma multiforme were determined for each model and the best fitting model was identified.

METHODS

Five classical mathematical models were used to simulate tumor growth, the exponential, logistic, generalized logistic, Gompertz and von Bertalanffy models.

Exponential $$\frac{\mathrm{dV}}{\mathrm{dt}} = aV \quad (1)$$

Logistic $$\frac{dV}{dt} = aV\left(1 - \frac{V}{K}\right) \quad (2)$$

Generalized logistic $$\frac{dV}{dt} = aV\left(1 - \left(\frac{V}{K}\right)^{v}\right) \quad (3)$$

Gompertz $$\frac{dV}{dt} = ae^{-\beta t}V \quad (4)$$

Von Bertalanffy $$\frac{dV}{dt} = aV^{\gamma} - bV \quad (5)$$

For all the models V is the volume of the tumor in mm^3 and t is the time in days. The proliferation rate is a and K is the carrying capacity. In the Gompertz model the proliferation rate changes so a is the initial proliferation rate and β is the rate of exponential decay of this proliferation rate. Each of the ODEs was solved explicitly or using ode45 function in MATLAB.

In order to determine the unknown model parameters the modeled tumor growth behavior was compared to the results of data collected experimentally. An in-vivo experiment was previously conducted at Wake Forest University School of Medicine by one of our collaborators. In this study Luciferase-expressing G48a human GBM tumors were grown in nude mice [3]. Data from the control group (no treatment) was analyzed to determine the tumor growth rate. IVIS imaging data from the experiment is shown in Figure 1.

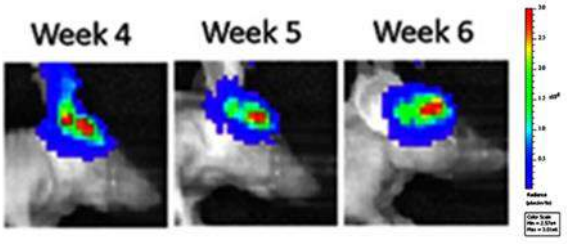

Figure 1: IVIS images of one of the nude mice with xenograft of human GBM tumor [3]

Copyright 2016 The Organizing Committee for the 2016 Summer Biomechanics, Bioengineering and Biotransport Conference

IVIS imaging measures the total photon flux emitted from the tumor. For the cell line used in the experiment there were 6.6 cells per photon, so the number of tumor cells could be estimated. The diameter of a glioblastoma cell was approximated to be $5x10^{-6}$ mm. Using this value, the tumor volume at each time step was calculated.

The tumor growth rate predicted by each mathematical model was compared to the growth rate found experimentally using an optimization cost function,

$$S = \sum (V_{e,i} - V_{m,i})^2$$

The tumor volume determine experimentally, $V_{e,i}$, at each time step, i, was compared to the modeled volume at each time step, $V_{m,i}$.

RESULTS

By minimizing the optimization cost function the unknown model parameters were found for each model. These model parameters characterize the growth rate of glioblastoma multiforme tumors under the conditions described in the experiment [3] and are shown in Table 1. The optimal model parameters were found using the MATLAB optimization tool box functions $lsqcurvefit$ and $fminsearch$. The goodness of fit for each model was also calculated (Table 1). Optimized mathematical models and experimental data are shown for each model type (Figure 2).

Table 1: Characteristic Model Parameter

Mathematical Model	Unknown Parameter	Unit	Parameter Values	Fit %
Exponential	a	[day^{-1}]	0.2265	92%
Logistic	a	[day^{-1}]	0.2655	84%
	K	[mm^3]	1322	
Generalized Logistic	a	[day^{-1}]	1400	86%
	K	[mm^3]	1300	
	υ	-	$4.56*10^{-5}$	
Gompertz	α	[day^{-1}]	0.2409	95%
	β	[day^{-1}]	0.0036	
Von Bertalanffy	a	[mm$^{3(1-\gamma)}$.day^{-1}]	0.7057	90%
	b	[day^{-1}]	0.5774	
	γ	-	0.9664	

DISCUSSION

The result from the optimized mathematical models is consistent with previous research results that modeled the growth of lung and breast cancer [4]. All models fit the experimental data well with fit data ranging from 84% to 95%. The best fitting model for glioblastoma growth was the Gompertz model.

With the characteristic parameters for untreated glioblastoma multiforme known, the next phase of the research will be to model the effects of chemotherapeutic agents on the growth rate. New models are currently being developed that characterize both the tumor growth and decay rates during chemotherapy.

ACKNOWLEDGEMENTS

We thank Dr. Debinski and Ms. Gibo from the Brain Tumor Center of Excellence at Wake Forest School of Medicine for providing the experimental data and valuable information on the interpretation of the physiological experiments.

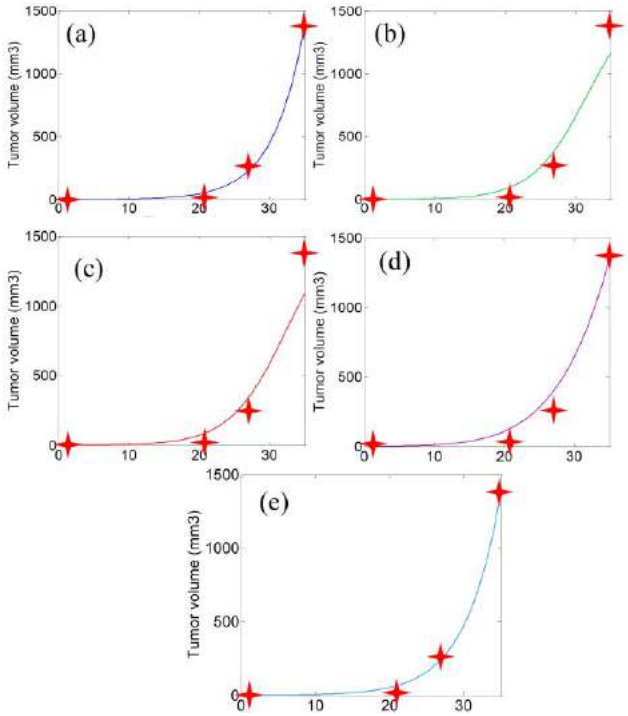

Figure 2: Tumor volume growth (vertical axis) vs. time (horizontal axis): (a) Exponential model (b) Logistic model (c) Generalized Logistic model (d) Von Bertalanffy model (e) Gompertz model, and the experimental data

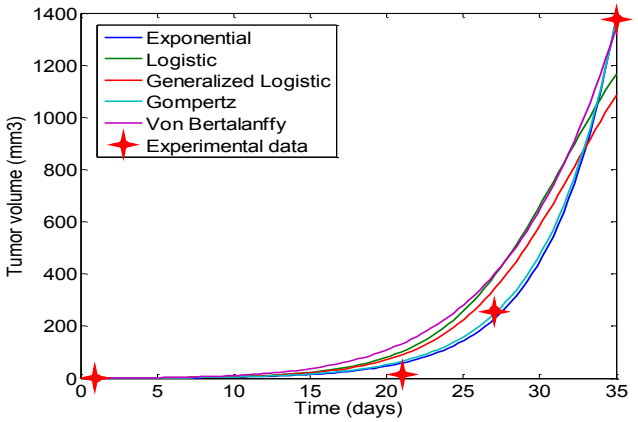

Figure 3: All the mathematical models and the experimental data (stars)

REFERENCES

[1] Henriksson, R., Asklund, T., & Poulsen, H. (2011). Impact of therapy on quality of life, neurocognitive function and their correlates in glioblastoma multiforme: A review. J Neurooncol Journal of Neuro-Oncology, 104, 639-646..

[2] Cooper, M., Tanaka, M., & Puri, I. (2010). Coupled mathematical model of tumorigenesis and angiogenesis in vascular tumours. Cell Proliferation, 43, 542-552.

[3] Gmeiner, W., Lema-Tome, C., Gibo, D., Jennings-Gee, J., Milligan, C., & Debinski, W. (2013). Selective anti-tumor activity of the novel fluoropyrimidine polymer F10 towards G48a orthotopic GBM tumors. J Neurooncol Journal of Neuro-Oncology, 116, 447-454.

[4] Benzekry S, Lamont C, Beheshti A, Tracz A, Ebos JML, Hlatky L, et al. (2014) Classical Mathematical Models for Description and Prediction of Experimental Tumor Growth. PLoS Comput Biol 10(8): e1003800.

Copyright 2016 The Organizing Committee for the 2016 Summer Biomechanics, Bioengineering and Biotransport Conference

SB^{3}C2016
Summer Biomechanics, Bioengineering and Biotransport Conference
June 29 –July 2, National Harbor, MD, USA
SB^{3}C2016-988

THE EFFECT OF LATERALIZING JOINT CENTER OF ROTATION OF REVERSE TOTAL SHOULDER ARTHROPLASTY ON ADDUCTION RANGE OF MOTION AND INITIAL IMPLANT FIXATION: A FINITE ELEMENT STUDY

Josie A. Elwell (1), Joseph Choi (2), Ryan T. Willing (1)

(1) Mechanical Engineering
Binghamton University
Binghamton, NY, United States

(2) Orthopaedic Surgery
Guthrie Clinic
Sayre, PA, United States

INTRODUCTION

Reverse total shoulder arthroplasty (rTSA) for the treatment of conditions associated with a rotator cuff deficiency can yield improvements in range of motion (ROM), namely abduction and forward elevation. The degree of improvement is dependent on several factors relating to both implant design and patient-specific factors, such as scapular topology and morphology. In some patients, an adduction deficit, due to humeral cup impingement on the scapular pillar or the inferior portion of the glenoid, is apparent following the procedure. Repeated impingement is likely the cause of one of the most common complications of the procedure, scapular notching. Although the ramifications of scapular notching are not yet well understood, it has been suggested that lateralizing the joint center of rotation (COR), in reference to the fully medialized COR on the glenoid face suggested in Grammont's original design, can mitigate adduction deficits and decrease the chance of scapular notch development. However, lateralization of the COR away from the glenoid surface may increase the bending moment across the bone-implant interface, leading to excessive micro-motion of the baseplate and preventing osseointegration. Thus, lateralizing the COR has the potential to improve functional outcomes and mitigate the development of complications of rTSA, but may come at a cost of an increased risk of loosening. Therefore, it is important to understand the relationship between lateralization of the COR, adduction deficit, and initial implant fixation (characterized by micro-motion). In this study, finite element (FE) modelling techniques were employed to investigate the aforementioned relationships on a specimen-specific basis.

METHODS

Geometries of four scapulae from three fresh-frozen cadaveric specimens were obtained by segmenting computed tomography (CT) data. Semi-automatic threshold-based segmentation using 3D Slicer was employed to obtain overall scapular geometry as well as the cortical-cancellous bone boundary in the region of the glenoid. Using the solid modeling software Creo, a 42 mm ream was simulated on the glenoid of each scapula after which a 25 mm diameter baseplate with an 8 mm diameter, 15 mm long central post, and four peripheral fixation screws, were implanted. The screws were simplified as 4.5 mm diameter cylinders rigidly attached to the baseplate. The position of the baseplate as well as the lengths and trajectories of the fixation screws were determined on a specimen-specific basis following the guidelines suggested by Humphrey et al. [1] and the surgical guide for the Tornier Aequalis Reversed II [2]. Metaglene and screw placements were verified by a board certified orthopaedic surgeon experienced in rTSA (J.C.).

Each model was meshed with quadratic tetrahedral elements with an average edge length of 1.3 mm; this element size deemed adequate during a prior mesh convergence study. Material properties of the baseplate and central post were assigned as those of Ti6Al4V (E = 113.8 GPa and ν= 0.34). Screws were assigned properties of the same material with a corrected elastic modulus of 57.6 GPa in order to account for simplified thread geometry. All elements in cortical bone regions were assigned corresponding material properties (E = 17.5 GPa, ν= 0.3). Cancellous bone material properties in the region of the glenoid were assigned on an element-by-element basis utilizing CT attenuation data and the following equations [3]:

$$\rho = 0.001 + 0.002 * HU \quad (1)$$

$$E = 1{,}049.45\rho^2 + 0.001 \quad if\ \rho < 0.35 \quad (2a)$$

$$E = 3{,}000\rho^3 \quad if\ 0.35 \leq \rho < 1.8 \quad (2b)$$

Copyright 2016 The Organizing Committee for the 2016 Summer Biomechanics, Bioengineering and Biotransport Conference

where HU represents Hounsfield units, ρ represents density in grams per cubic centimeter, and E represents elastic modulus in MPa.

Zero-displacement boundary conditions were applied to the medial border of each scapula (Fig. 1). Frictional contact with a coefficient of 1.6 was modeled between all bone-implant interfaces. Lateralization of the glenosphere using a metallic spacer was simulated by applying shear loads further from the glenoid surface on an inferior portion of the baseplate (Fig. 1). Lateralization from 0 to 16 mm in 4 mm increments was simulated. Each shear load had a magnitude of 686 N, equating to 1X body weight of a 70 kg individual, and was accompanied by a compressive pressure of the same total magnitude.

Metrics included micro-motion of the baseplate with respect to the glenoid surface and adduction ROM. Micro-motions, both parallel and normal to the reamed glenoid surface of each node on the back surface of the baseplate, were calculated. Subsequently the average and maximum absolute displacements of the baseplate were calculated. Adduction ROM was simulated by revolving a 3D model of a humeral cup in an adduction motion until impingement with any portion of the glenoid side (bone or implant). Adduction was measured as the angle between two planes, one representing the humeral stem with a 155° humeral neck-shaft angle, and one parallel to the glenoid face.

A one-way repeated-measures ANOVA with a Greenhouse-Geisser correction and lateralization as the independent variable was performed. Post Hoc pairwise comparisons with Bonferroni corrections were also performed. A p-value of less than 0.05 was considered statistically significant.

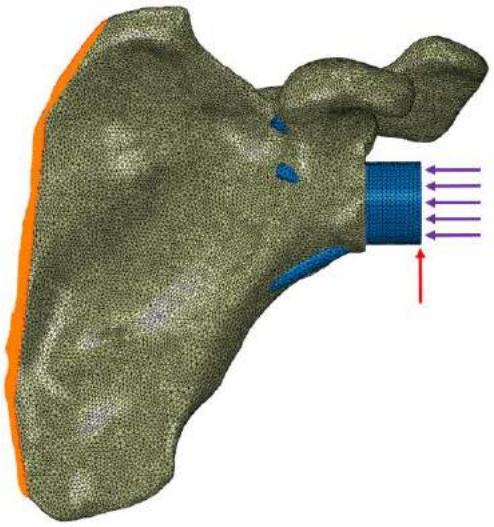

Figure 1. A characteristic meshed FE model where the red arrow is a shear force applied a distance from the glenoid surface, representing lateralization of the COR, the purple arrows represent the accompanying compressive pressure, and orange represents the application of fixed-displacement boundary conditions.

RESULTS

On average, lateralization significantly affected both adduction ROM ($p = 0.001$) and baseplate micro-motion normalized with respect to 0 mm lateralization values ($p = 0.033$). Pairwise comparisons between 0 mm and all other levels of lateralization are shown for adduction ROM and micro-motion (Fig. 2). The average adduction ROM across all specimens with 0 mm lateralization was 0° (range: −7° to 3.5°), where a negative value represents an adduction deficit. Average absolute baseplate micro-motion with 0 mm of lateralization 4.6 μm (range: 2.8 to 6 μm). Maximum absolute displacement averaged across all specimens at 0 mm lateralization was 13.2 μm (range: 6.1 to 21.7 μm).

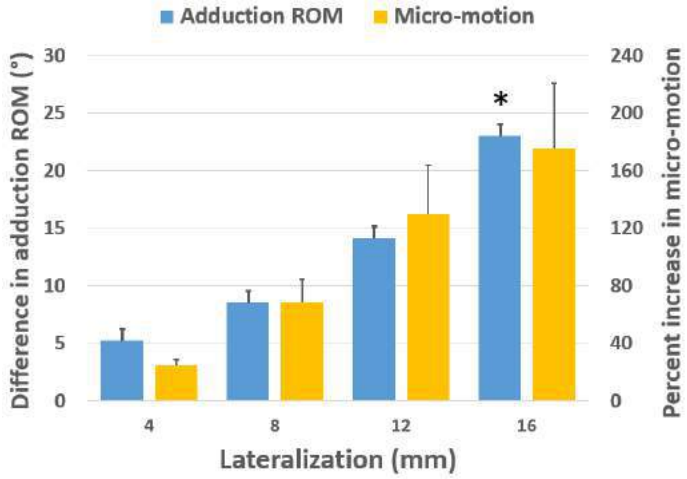

Figure 2. Mean difference in adduction ROM (blue, left scale) and mean percent increase in micro-motion with respect to 0 mm lateralization (yellow, right scale) Note: * indicates statistical significance with respect to 0 mm lateralization

DISCUSSION

Lateralizing the COR of rTSA away from the surface of the glenoid significantly increases ROM in adduction, but also significantly increases micro-motion of the baseplate. Therefore, lateralization can improve upon functional outcomes of the procedure and potentially prevent the development of scapular notching, but also increases the risk of aseptic implant loosening. In this study, none of the baseplates exceeded the 150 μm threshold for osseointegration with any amount of lateralization investigated; however, observed micro-motions in this study are not absolute indications of those that would result from in-*vivo* scenarios. The ability to lateralize to achieve better functional outcomes of rTSA is dependent on initial fixation, which is a function of patient-specific factors such as quality and availability of bone stock.

A limitation of this study is the small sample size of four specimens. However, statistically significant relationships between lateralization and adduction ROM and micro-motion were still observed. Future work will include a greater number of specimens, as well as validation against published experimental data.

ACKNOWLEDGEMENTS

Research reported in this publication was supported by the National Institute Of Arthritis And Musculoskeletal And Skin Diseases of the National Institutes of Health under Award Number R03AR066841. The content is solely the responsibility of the authors and does not necessarily represent the official views of the National Institutes of Health.

REFERENCES

[1] Humphrey, C.S. et al., *J Should & Elbow Surg*, 17:595-601, 2008.
[2] Aequalis®-Reversed II Surgical Technique, www.tornier.com
[3] Ammwenger et al. *Biomed Tech*, 59: 421-430, 2014.

Copyright 2016 The Organizing Committee for the 2016 Summer Biomechanics, Bioengineering and Biotransport Conference

SB^{3}C2016
Summer Biomechanics, Bioengineering and Biotransport Conference
June 29 –July 2, National Harbor, MD, USA
SB^{3}C2016-989

PROBING THE INTERACTIONS BETWEEN MANNOBIOSE MOLECULES, USING ATOMIC FORCE MICROSCOPY (AFM).

Komitige H.Perera (1), Saswati Basu(2), Preethi Chandran (2)

(1) Biochemistry and Molecular Biology
Howard University
Washington DC, United States

(2) Chemical Engineering
Howard University
Washington DC, United States.

(3) Chemical Engineering
Howard University
Washington DC, United States

INTRODUCTION

Carbohydrate-carbohydrate interactions (CCIs) have been recognized to govern a wide range of biological processes including species-recognition, fertilization, embryogenesis, and cell development (1). The goals of our study are to investigate whether mannobiose moieties exhibit CCIs and to determine the solution conditions in which such interactions occur. Mannobiose moieties are disaccharides of mannose sugars. They coat the surfaces of pathogens and immune cells, and are extensively involved in host-pathogen interactions (2). Mannose oligosaccharides are widely used in the design of drug-delivery vehicles for targeting cells that express mannose receptors (e.g., dendritic cells) (2) and for reducing the cytotoxicity induced by the drug-delivery vehicles (4). Our goal is to functionalize α-1,4-mannobiose on gold coated mica (AFM surface) and gold coated AFM tips and measure the adhesive forces between anchored α-1,4-mannobiose moieties, using the force spectroscopy mode of an atomic force microscope. The finding that mannobiose moieties exhibit CCI may impact the field of immunotherapy and the design of drug-delivery vehicles.

METHODS

Attachment of thiolated linkers on gold -coated surfaces.

Excess cysteamine (Sigma-Aldrich Inc., St. Louis, MO) was reacted with 4-azido-2,3,5,6-tetrafluorobenzoate, succinimidyl ester or ATFB, SE (TCI America Inc.,Tokyo) in a 1:1 acetone: HEPES buffer (pH 8.5) solution for 3 hours. The reaction was carried out in a covered ice bath with stirring. The reaction product (ATFB and cysteamine conjugate) was isolated by precipitation with more HEPES buffer and was characterized with ^{1}H NMR spectroscopy and FTIR spectroscopy. The reaction was also monitored via UV absorption spectra of the supernatant, for the appearance of characteristic peak at 270nm, due to the formation of the by-product, hydroxyl succinimide. The ATFB-cysteamine conjugates were then dissolved in a 1:1 DMSO: HEPES buffer solution. Gold-coated mica and AFM tips were incubated in the solution overnight. The ATFB-Cysteamine conjugates self-assembled on the gold surfaces via their thiol end groups.

Linking mannobiose.

Wang et. al, 2009 (5) showed that, irradiation of aryl-azides in the presence of mannobiose can result in the conjugation of mannobiose to aromatic groups. We used the same chemistry to link mannobiose to gold anchored ATFB-cysteamine linkers. Excess of mannobiose dissolved in HEPES buffer was added on top of the ATFB-cysteamine anchored gold surfaces and irradiated with filtered UV radiation (less than 280nm) for 5 minutes.

We tested the mannobiose linking chemistry on gold nanoparticles before carrying out the reactions on gold-coated mica surfaces. Anthrone assay, UV absorption and Dynamic Light Scattering (DLS) were used to verify the mannobiose attachment to gold nanoparticle

Copyright 2016 The Organizing Committee for the 2016 Summer Biomechanics, Bioengineering and Biotransport Conference

RESULTS

The attachment of mannobiose as described in methods section was tested by calorimetric anthrone assay and by the change in hydrodynamic diameters in DLS. When mannobiose attached gold nanoparticles were reacted with anthrone solution, a characteristic green color was produced with a strong UV absorption peak at 627 nm (Figure 1). Positive anthrone test provides strong evidence for the attachment of mannobiose to the gold nanoparticles.

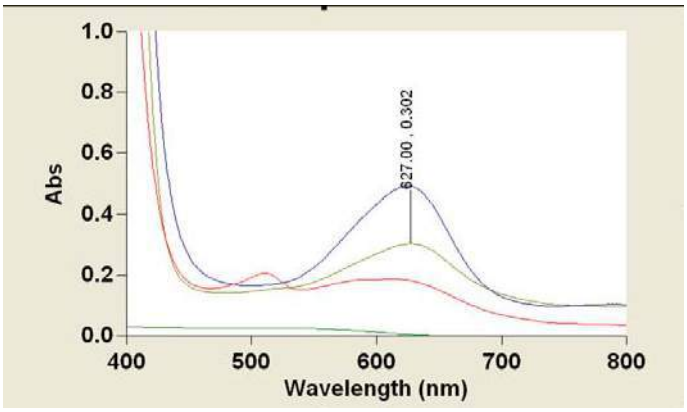

Figure 1: The red line represents the absorption of UV radiation produced by anthrone reaction with gold nanoparticles. The green line represents the absorption produced by the anthrone reaction with gold nanoparticles functionalized with thiolated linker. The blue line is a representation of the anthrone reaction with mannobiose conjugated gold nanoparticles. (The three species of gold nanoparticles were thoroughly washed and resuspended on HEPES buffer before conducting the anthrone assay)

DLS experiments provide means of measuring the hydrodynamic diameter of the suspended particles. Upon conjugation with mannobiose the gold nanoparticle showed a significant increase in the hydrodynamic diameter as shown in Fig.2.

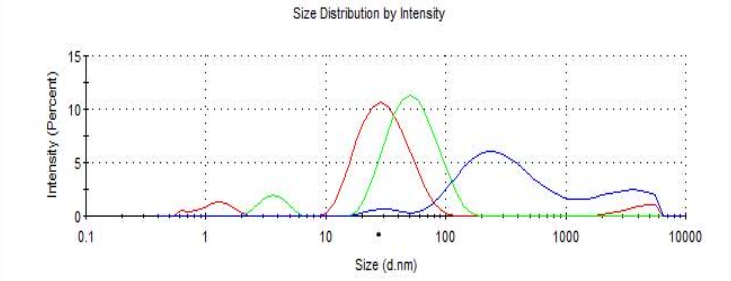

Figure 2: The red line represents the hydrodynamic diameter of the gold nanoparticles ~ 30nm. Green line is the hydrodynamic diameter for the gold nanoparticles conjugated to thiol linkers ~ 50nm. Blue line represents the hydrodynamic diameter of the mannobiose conjugated gold nanoparticles ~300nm. All nanoparticles were suspended on HEPES buffer.

Atomic force spectroscopy was used to measure the mannobiose interactions in a range of solution conditions.

DISCUSSION

Mannobiose moieties were successfully anchored to the AFM mica and tip surfaces. Force spectroscopy is being used to measure mannobiose interactions in different solution conditions. The interaction potential demonstrated by mannobiosylated surfaces can be harnessed for the design of immunotherapies and of drug-delivery vehicles.

ACKNOWLEDGEMENTS

This work is supported by a grant awarded to the principal investigator Dr. Preethi Chandran by the National Science Foundation (Award #1407891).

REFERENCES

1. Rojo, J., Morales, J. C., & Penades, S. (2002). Carbohydrate-carbohydrate interactions in biological and model systems. *Topics in Current Chemistry*, *218*(Host-Guest Chemistry), 45–92.
2. Diebold, S. S., Kursa, M., Cotten, M., Zenke, M., & Wagner, E. (1999). Mannose Polyethylenimine Conjugates for Targeted DNA Delivery into Dendritic Cells Mannose Polyethylenimine Conjugates for Targeted DNA Delivery into Dendritic Cells. *Cell Biology and Metabolism*, *274*(27), 19087–19094.
3. Kennedy, D. C., Orts-Gil, G., Lai, C.-H., Müller, L., Haase, A., Luch, A., & Seeberger, P. H. (2014). Carbohydrate functionalization of silver nanoparticles modulates cytotoxicity and cellular uptake. *Journal of Nanobiotechnology*, *12*(1), 59.
4. Wang, X., Ramström, O., & Yan, M. (2009). A photochemically initiated chemistry for coupling underivatized carbohydrates to gold nanoparticles. *Journal of Materials Chemistry*, *19*(47), 8944.

Copyright 2016 The Organizing Committee for the 2016 Summer Biomechanics, Bioengineering and Biotransport Conference

SB³C2016
Summer Biomechanics, Bioengineering and Biotransport Conference
June 29 –July 2, National Harbor, MD, USA
SB³C2016-990

COMPARISON OF MATERIAL PROPERTIES BETWEEN THE MAIN AND LEFT PULMONARY ARTERIES OF CONGENITAL HEART DISEASE SUBJECTS USING CARDIAC MAGNETIC RESONANCE: A FEASIBILITY STUDY

Gavin A. D'Souza (1), Michael D. Taylor (2), Namheon Lee (2), Rupak K. Banerjee (1)

(1) Department of Mechanical and Materials Engineering
University of Cincinnati
Cincinnati, Ohio, USA

(2) The Heart Institute
Cincinnati Children's Hospital Medical Center
Cincinnati, Ohio, USA

INTRODUCTION

Although surgical outcomes for congenital heart disease (CHD) subjects with complex right heart disease are excellent, subjects are left with residual lesions including pulmonary artery regurgitation and obstruction that result in right ventricular-pulmonary artery (RV-PA) dysfunction [1]. The appropriate timing of re-intervention to correct these residual lesions is difficult to determine due to lack of suitable quantifiable diagnostic techniques.

The PA wall (material) properties contribute significantly to the function of the RV-PA unit as they characterize the mechanical behavior of the arterial wall which has a subsequent effect on the overall RV-PA hemodynamics. Further, these properties are expected to vary between the main PA and branched pulmonary arteries. Therefore, quantification of the properties of each of the pulmonary arteries may provide valuable information on disease status and progression and thus aid in the longitudinal assessment of CHD subjects.

Constitutive modeling of the artery wall using *in vivo* and *in vitro* test data has been previously used to characterize the complex arterial wall properties [2, 3, 4]. However, application of such modeling techniques to the pulmonary arteries of CHD subjects has been limited due to the lack of *in vitro* test data. A previous study proposed a methodology of evaluating the wall properties using only *in vivo* pressure-diameter data coupled with a set of constitutive equations that define a material model [5]. Further, cardiac MRI could be a useful tool for assessing *in vivo* diameter in pediatric subjects. As a first step, we aimed to apply this methodology to characterize the PA wall properties of normal pediatric subjects. Therefore, in this feasibility study, using pressure-diameter data as input to a material model, we quantified and compared the properties of the main PA (MPA) and left PA (LPA) of two CHD subjects with normal RV-PA function and anatomy.

METHODS

Study population. Two CHD subjects (subject N1: age = 13 years, body surface area = 1.57 m^2, subject N2: age = 19 years, body surface area = 2.06 m^2) having a diseased aorta were included for this study. However, both subjects had a normal RV-MPA physiology and normal pulmonary valve function with no PA stenosis. Thus, the two subjects were considered "normal" for this study.

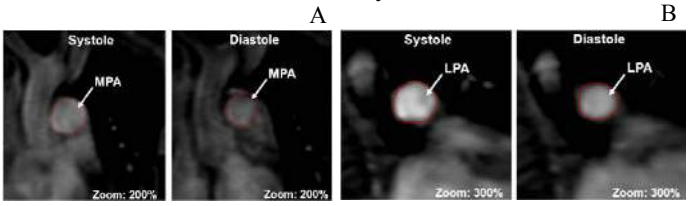

Figure 1: A representative MR image at systole (left pane) and diastole (right pane). A) MPA contour B) LPA contour

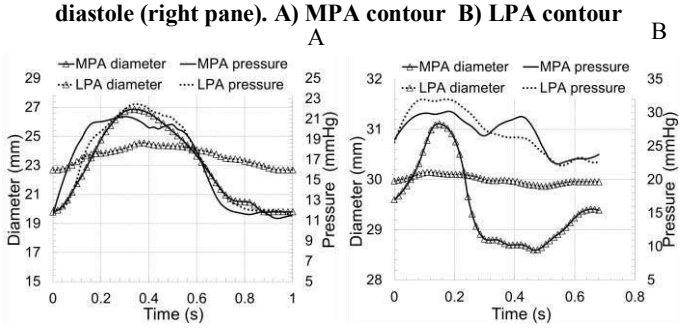

Figure 2: *In vivo* pressure and diameter pulses. A) Subject N1 B) Subject N2

Copyright 2016 The Organizing Committee for the 2016 Summer Biomechanics, Bioengineering and Biotransport Conference

Data acquisition. Cardiac MRI data was acquired using a 3.0 Tesla MRI scanner (Philips Healthcare, Best, The Netherlands). Contours of the MPA and LPA anatomy were obtained on the MRI slice using auto-thresholding (Figure 1) and the diameter (hydraulic) of the vessels was computed. In addition to MRI, cardiac catheterization was conducted and pressure was recorded at 30 time-points over a single cardiac pulse. CMR and cardiac catheterization were both performed in Cincinnati Children's Hospital Medical Center (CCHMC). The pressure and diameter data points, which were measured non-simultaneously, were synchronized using ECG gating. The gated pressure and diameter pulses are shown in Figure 2. The LPA showed smaller variations in diameter over a cardiac cycle in comparison to the MPA. However, a similar pressure pulse was observed in both the vessels.

Material model. A 2D nonlinear and anisotropic hyperelastic model [5] was used to quantify the PA wall properties and predict its mechanical behavior when subjected to bi-axial loading. The principal stresses were modeled using Fung's 2D strain energy function (SEF), $\psi = C(e^{Q} - 1)/2$ where, $Q = c_{\theta\theta}{E_{\theta\theta}}^2 + 2c_{\theta z}E_{\theta\theta}E_{zz} + c_{zz}{E_{zz}}^2$. The principal stretches in the circumferential (θ) and axial (z) directions were defined as $\lambda_\theta = D(A + \pi d^2)/d(A + \pi D^2)$ and $\lambda_z = z/Z$, respectively, where; A is the cross-sectional area of the wall, D and Z represent the inner diameter and length of the vessel, respectively, in the unloaded condition, and d and z represent the inner diameter and length of the vessel, respectively, in the loaded condition. The principal Cauchy stresses (in kPa), predicted by the model, in the circumferential and axial direction were defined as $\sigma_{\theta\theta}^{mod} = \lambda_\theta(\partial\psi/\partial\lambda_\theta)$ and $\sigma_{zz}^{mod} = \lambda_z(\partial\psi/\partial\lambda_z)$, respectively. In order to define the material model for the PA wall and predict the model constants, an equilibrium condition was imposed on the artery wall and the principal theoretical stresses (in kPa) were defined as $\sigma_{\theta\theta} = pd^2\pi/2A$ and $\sigma_{zz} = d^2\pi(4F + pd^2\pi)/4A(A + d^2\pi)$ where p is the pressure and F is the external axial force. The four constitutive parameters, C, $c_{\theta\theta}$, $c_{\theta z}$, and c_{zz} were then evaluated using a least-square error minimization algorithm where the error was defined as the difference between the model and theoretical stresses. An in-house MATLAB® code (MATLAB Inc., Waltham, MA, USA) was developed and used for computing the model constants.

RESULTS

Figure 3 shows the pressure and corresponding diameter recorded *in vivo* (marked by squares and triangles) during the systolic (loading) and diastolic (unloading) phases of the cardiac cycle. Distinct and non-overlapping characteristics were observed for the MPA and LPA.

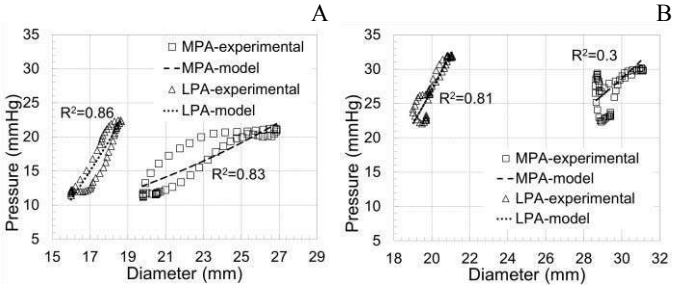

Figure 3: Pressure-diameter characteristics. A) Subject N1 B) Subject N2

Using these characteristics as input to the material model described above, the values of the material model constants which represent the arterial wall properties were obtained for the MPA and LPA of two normal subjects, N1 and N2, and are reported in Table 1. The properties varied between the MPA and LPA for both subjects. This is an expected outcome due to the distinct pressure-diameter characteristics. The C value, which defines the stress level in the artery wall, was observed to be higher for the LPA (16.8% for N1; 45.3% for N2) in comparison to the MPA. A similar trend was observed for the other constants ($c_{\theta\theta}$, $c_{\theta z}$, and c_{zz}) which govern the stress distribution in each loading direction. Further, $c_{\theta\theta}$ values were observed to be greater (absolute difference within 0.092) than c_{zz} (except for Subject N1-MPA) thus indicating a greater stress distribution in the circumferential direction.

Table 1: Values of the material model constants.

	C (kPa)	$c_{\theta\theta}$	$c_{\theta z}$	c_{zz}
Subject N1 - MPA	656	0.025	0.028	0.037
Subject N1 - LPA	766.5	0.175	0.091	0.083
Subject N2 - MPA	400	0.1	0.056	0.054
Subject N2 - LPA	581	0.219	0.159	0.214

In order to determine the accuracy of the material model, the model-predicted pressure-diameter curve (marked by dashed and dotted lines in Figure 3) was computed using the constants in Table 1 and compared against the experimental (*in vivo*) data (Figure 3). A close fit was observed between the model and experiments as can be seen from the R^2 values (ranging between 0.3 to 0.86) reported in Figure 3.

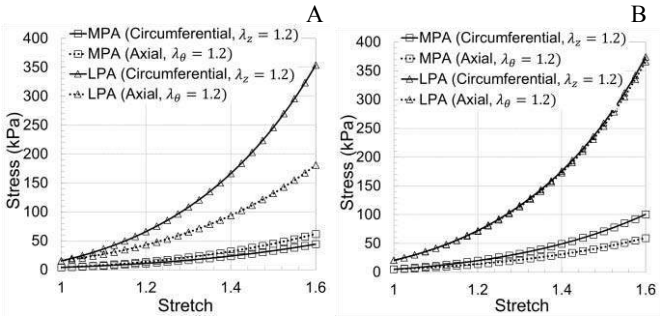

Figure 4: Stress-stretch characteristics. A) Subject N1 B) Subject N2

DISCUSSION

In vivo pressure-diameter characteristics in conjunction with constitutive equations serves as a useful method in quantifying the PA wall properties of CHD subjects. As observed from the results, these properties can quantitatively characterize and differentiate between the MPA and LPA. Further, the PA wall properties may be used to predict the mechanical behavior of the artery under a range of loading conditions, as shown in Figure 4. Circumferential and axial stresses in the MPA and LPA wall were computed at different stretch values. Higher stresses were observed for the LPA in comparison to the MPA for both subjects due to higher C values obtained for the LPA. For example, at a physiologic stretch of 1.2, $\sigma_{\theta\theta}^{mod}$ in the LPA and MPA of subject N1 were 65.9 kPa and 11.2 kPa, respectively. At the same stretch, σ_{zz}^{mod} in the LPA and MPA of subject N1 were 43 kPa and 13.8 kPa, respectively. Also, the LPA and MPA stress values were distinct and non-overlapping over the entire range of stretch values.

Thus, PA wall properties, obtained using cardiac MRI in conjunction with constitutive modeling, may provide valuable information for the longitudinal assessment of the RV-PA dysfunction in CHD patients. Subsequently, this information may aid in determining an appropriate time for re-intervention.

REFERENCES

[1] Lee N, et al., *Biomed Eng Online*, 2014.
[2] Kassab GS, et al., *J R Soc Interface*, 2006.
[3] Holzapfel G, et al., *J Elast Phys Sci Solids*, 2000.
[4] Fung YC, et al., *Am J Physiol*, 1979.
[5] Schulze-Bauer and Holzapfel, *J Biomech*, 2003.

Copyright 2016 The Organizing Committee for the 2016 Summer Biomechanics, Bioengineering and Biotransport Conference

SB^{3}C2016
Summer Biomechanics, Bioengineering and Biotransport Conference
June 29 –July 2, National Harbor, MD, USA
SB^{3}C2016-991

QUANTIFICATION OF DISTAL CEREBRAL VASCULAR BED COLLATERAL RESISTANCES USING 1D HEMODYNAMIC MODEL AND CT PERFUSION

Jeff Pyne (1), Jaiyoung Ryu (1), Jared Narvid (2), Shawn Shadden (1)

(1) Department of Mechanical Engineering
University of California Berkeley
Berkeley, CA, United States

(2) Department of Radiology
UCSF School of Medicine
San Francisco, CA, United States

INTRODUCTION

Within the United States, strokes occur in over 700,000 people each year with costs to the healthcare system in the tens of billions of dollars. Strokes are particularly devastating because of the sudden onset and necessity for rapid diagnosis/treatment in order to save the penumbra (recoverable brain tissue after reperfusion). For the confirmed ischemic stroke patient entering the hospital, the typical workflow includes a cerebral computed tomography angiography (CTA) to look for occlusions within the large carotid, vertebral or circle of willis (CoW) arteries as well as a computed tomography perfusion (CTP) scan to quantify the penumbra size and thus the potential benefit of the treatment. The two stroke treatments, administration of tissue plasminogen activator (tPA) and/or mechanical thrombectomy are options available to the clinician. Since both of these stroke treatments can be hazardous to the patient depending on their situation, it is preferable to do a CTP scan first to determine if the risk is worth the potential benefit of the treatment. It has been shown in recent clinical trials that it is possible to select patients who would benefit most from endovascular treatments from CTP scans.

One important factor in determining eventual patient outcome is their collateral status or redundant circulation between regions in the brain. Most medical standards use a visual technique of identifying blood vessels in multiphase CTA scans to determine collateral status on a numerical scale. By looking at the delay in filling between visual blood vessels on the affected and unaffected side, a scoring system such as the Alberta Stroke Program Early CT Score (ASPECTS) can be used as a treatment outcome predictor. Any improvements upon scores such as ASPECTS with more accurate data, could narrow the selection criterion for patients allowing for better outcomes.

From a computational standpoint, the brain is a complex system due to the complex anatomy structures and autoregulation mechanism that predominately controls the transport of blood throughout the brain. Ryu et al.[1] have built a 1D hemodynamic model with autoregulation capabilities for the purposes of studying intracranial hemodynamics. While major occlusion events could overwhelm the autoregulation mechanism, having this ability allows for the possibility of studying different time points in the ischemic stroke process. While other researchers have used 3D models to study blood flow in the CoW, the 1D model has been validated in studying cerebral hemodynamics and has the additional benefit of being computationally inexpensive facilitating translation to a clinical setting.

The objective of this research is to provide a more quantitative way of quickly classifying collateral status in patients that can fit into the current medical workflow with minimal user interaction in order to improve patient selection for stroke treatment.

METHODS

To analyze and work with de-identified patient data, the STOP stroke database[2], which contains both raw CTA and CTP scans, was used to select a case-study sufficient for this research. Within the database, there exist numerous patient cases of varying stroke severity, occlusion site, and collateral scores so the initial selection was important. The patient selected for this study had a severe RMCA occlusion, had a clear CTA scan which properly showed the non-occluded cerebral vasculature, had one transverse CTP scan done on the upper portion of the cerebral hemispheres (above eye level) and had a separate transverse CTP scan done on the lower portion of the cerebral hemispheres (at eye level).

Beginning with the CTA scan, SimVascular[3] was used to semi-manually segment the vascular anatomy from just after the aorta to just

Copyright 2016 The Organizing Committee for the 2016 Summer Biomechanics, Bioengineering and Biotransport Conference

beyond the CoW. This provides both the anatomy information for the fluid simulation as well as the topology of the CoW that will become important when looking at larger sample sizes. Perfusion Mismatch Analyzer[4] (PMA) was used to generate the cerebral blood volume (CBV) and cerebral blood flow (CBF) maps from the raw CTP datasets. The arterial input function (AIF) was placed within the LMCA for lack of a more proximal artery and since this artery was sufficiently large on the unaffected side. The venous output function (VOF) was placed in the superior sagittal sinus. To generate the perfusion maps, delay-insensitive block-circulant singular value decomposition (bSVD) was the method selected due to validation with single-photon emission CT (SPECT) in conditions similar to AIS. If an algorithm is used that does not account for the significant delay in tracer transport, such as standard SVD (sSVD), CBF values will be significantly reduced. While the absolute CBF (aCBF) values calculated from the bSVD method are not accurate for CTP, the bSVD CBF ratios between affected and unaffected sides are highly correlated with CBF ratios from the gold standard SPECT[5]. Therefore, relative CBF ratios from CTP were used in all further analysis to preserve the accurate relationships between cerebral arteries needed for this research.

In order to quantify the CBF from each major cerebral artery, following Waaijer[6], we selected restrictive cross-sectional ROIs that belonged only to distal branches of each major cerebral vessel. Within each of these ROIs, the average CBF was found with the units of mL per minute per 100 grams of brain tissue. It is important to note that watershed regions were avoided and primarily gray matter was chosen during the ROI selection process. See Figure 1 and Table 1 for the visualization and quantification of CBF for each major cerebral artery on the occluded and contralateral sides. The flow rate ratios, to preserve the accuracy found from the validation of bSVD, were calculated as the specific artery CBF divided by the summation of the 6 major artery CBF values[7]. The CBF ratio within these ROIs, specific to each of the cerebral arteries, will constitute the patient-specific flow rate ratios (FR_i) necessary to feed into the 1D hemodynamics model.

$$FR_i = \frac{CBF_i}{\sum_{j=1}^{6} CBF_j} \qquad (1)$$

Now that relative flow rates for each cerebral artery have been quantified, this acts as the patient-specific outflow boundary conditions within the 1D hemodynamics model[1]. In the context of stroke, consider Q_{in} as leading into the CoW within the arteries and $Q_{regions}$ as that same blood quantity draining in the venous system. Q_{in} is the summation of flow rate of all major cerebral arteries. In this patient case, it can be assumed that $Q_{RMCA_{in}}$ is completely occluded and can be set to zero. Since some blood will be exiting from the RMCA region, this means that collateral flows (q) from neighboring regions are entirely supplying the exit flow rate to this region (Q_{RM}). The other collateral flows will be assumed small in comparison.

$$Q_{RM} = q_{cRAM} + q_{cRMP} \qquad (2)$$

These collateral flows are each determined primarily through collateral resistance values R_{cRAM} and R_{cRMP} that will be set as unknowns to be tuned for this particular patient within a physiological range. The remaining collateral resistances are not as relevant and can be set to literature values[1]. Beginning with an initial guess for the unknown collateral resistances, iterative solves of the system update the resistance values until a tolerance is reached matching the FR outflow ratios[7]. In this particular case, since absolute CBF values are not known, a baseline healthy state will be assumed with literature flow rates at each cerebral artery[1].

RESULTS

The CBF has been quantified for this particular patient with CBF values listed in Table 1 obtained from the PMA bSVD result shown in Figure 1. Equation 1 was used to produce the flow rate ratios seen in Table 2.

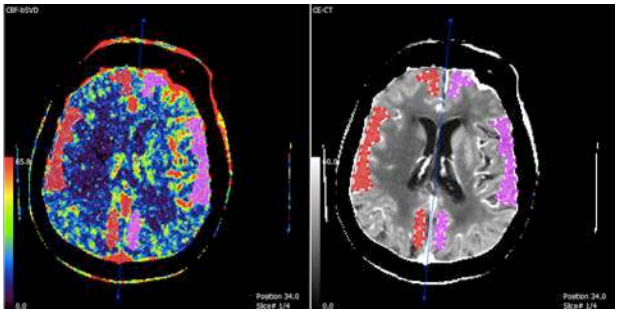

Figure 1: ROIs for average CBF selection for each major cerebral artery perfusion region. Notice the decrease in CBF to the RMCA region. The units on CBF are [mL/(min*100g)].

Region	*CBF Occluded Side* [mL/(min*100g)]	*CBF Contralateral Side* [mL/(min*100g)]	$\frac{CBF_R}{CBF_L}$%
ACA	18.95	35.64	53.17
MCA	19.62	26.55	73.89
PCA	22.63	32.73	69.11

Table 1: CBF values obtained from PMA from bSVD method. The right side has a complete MCA occlusion.

	RA	*RM*	*RP*	*LA*	*LM*	*LP*
FR	.126	.121	.145	.170	.228	.210

Table 2: Flow rate ratios of each major cerebral region. RA refers to RACA region, RM for RMCA region, etc.

DISCUSSION

In this stroke context, it can be seen that the right side of the brain is receiving significantly less flow than the left side with the MCA region having the most relative reduction in flow. Methods are being explored for how to properly design the ROIs to generate robust CBF values that accurately reflect the average CBF for each patient.

This research has the ability to quantify relevant collateral resistances between distal cerebral vascular beds in the context of stroke for the potential to create an improved collateral score.

Further work is needed to create a collateral score from these collateral resistances for clinical translation and this will require more patients to develop. We are continuing work on coupling CTP quantifications with our 1D hemodynamics model for the purposes of stroke assessment. This type of approach provides necessary steps for a score to be adapted to the clinical stroke workflow since it makes use of the CTA and CTP scans necessary for other diagnosis measures.

ACKNOWLEDGEMENTS

The authors graciously acknowledge the Bakar Fellows Program for the funding of this research.

REFERENCES

[1] Ryu, Jaiyoung et al., *J Biomech Eng*, 137(10), 2015.
[2] Smith, W et al., *Stroke*, 40:3834-3840, 2009.
[3] SimVascular web site. <*http://simvascular.github.io*> 2015.
[4] ASIST-Japan web site. <*http://asist.umin.jp/index-e.htm*> 2015.
[5] Sasaki, M et al., *Am J Neuroradiol*, 30:188-93, 2009.
[6] Waaijer, A et al., *Am J Neuroradiol*, 28:927-32, 2007.
[7] Zhang, H et al., *Annals of Biomedical Engineering,* 2015.

Copyright 2016 The Organizing Committee for the 2016 Summer Biomechanics, Bioengineering and Biotransport Conference

SB^{3}C2016
Summer Biomechanics, Bioengineering and Biotransport Conference
June 29 –July 2, National Harbor, MD, USA
SB^{3}C2016-992

INTRODUCTION TO FINITE ELEMENT MODELING IN A GUIDED PROJECT-BASED APPROACH TO BIOMECHANICS RESEARCH

Alexander Kotelsky (1), Amy L. Lerner (1)

(1) Department of Biomedical Engineering
University of Rochester
Rochester, NY, USA

INTRODUCTION

Students in our Biomedical Engineering program often seek opportunities to become involved in research projects, and expect to develop skills with modern computational tools. We have traditionally used a project based learning (PBL) approach in our upper level courses to engage them in real world problems [1]. Motivated by their interests and career goals, students develop a deeper understanding of the material through collaboratively solving challenging questions [2]. As finite element (FE) tools have become more accessible for undergraduate courses, we have adapted our final project to focus on an idealized model of the proximal femur. While the basics of FE software can be taught relatively quickly, it is important to guide students to develop an understanding of the limitations, validation and verification of such models in order to establish confidence in the results [3]. The overall goal of the project is to offer the framework for a research experience while also allowing students to explore an area of personal interest within biomechanics of hip joint. Learning objectives of the project assignment include guiding students to: 1.) develop a testable hypothesis; 2.) apply knowledge of biomechanics; 3.) demonstrate skills in FEM generation; 4.) identify relevant and reasonable input parameters; 5.) develop an understanding of FEM uncertainty; and 6.) communicate research methods and results. Based on three years of implementing this project assignment, we have learned several key points of how to effectively and efficiently offer this experience. In this abstract, we review the structure, key features, challenges and opportunities for learning presented by this project approach.

METHODS

We introduced this FE based final project for a senior / graduate level biomechanics course called BioSolid Mechanics over a three year period. The course includes two lectures each week along with a weekly laboratory period that offers experience with a mix of computation and experimental methods. Class size has ranged from 20 – 30 students, with students generally working in teams of two to complete the project. The emphasis of the course is musculoskeletal solid mechanics, including joint biomechanics, tissue mechanics and mechanical influences on the skeletal system. Thus, projects typically related to topics presented in the course. A graduate teaching assistant (TA) provided significant guidance for the computational modeling, while both TA and faculty instructor offered guidance for key research milestones.

We used the academic version of the finite element software, ABAQUS/CAE (Simulia, Rhode Island, USA), to build and analyze the model. After two laboratory exercises introducing the general methods of finite element modeling, students completed a custom-written tutorial guiding the generation of an idealized finite element model (FEM) of the proximal femur. Specifically, the model was designed using basic geometries, such as cylinders, cones and spheres assembled together, resulting in a 3D model that reasonably represented a human proximal femur. Building the geometry took approximately 1.5 hrs. once students were accustomed to the method. The tutorial guided geometry creation, assignment of boundary conditions and material properties, meshing techniques and guidance to run and interpret results of the simulation. Since the model was geometrically idealized, it allowed for flexibility and parameterization of geometric features included in the model, particularly if such variations were relevant to the hypothesis posed by each student team. Furthermore, the model allowed the students to customize material properties and boundary conditions as appropriate.

Given the model flexibility, parametric study can provide another tool useful for students' projects, either as a method to develop an

Copyright 2016 The Organizing Committee for the 2016 Summer Biomechanics, Bioengineering and Biotransport Conference

understanding of model uncertainty or to test specific hypotheses about model inputs. We include two lectures on design of experiment (DOE) techniques in the course, and associated lab exercises so that this tool is also available to students as they develop and refine their project hypotheses. The implementation of DOE allows students to better understand the sensitivity of model results to various input parameters. For example, students could use a fractional factorial approach with 4 factors (i.e. magnitudes of applied load, the applied load orientation angle, Cortical and Trabecular Modulus values) having 2 levels (the magnitudes of the tested parameters). With the obtained data, the students performed analysis of means (ANOM) and analysis of variance (ANOVA) helped the students to rank the factors according to their importance. The analyses were performed in JMP (Version 11.0, SAS Institute Inc., Cary, NC) statistical software.

In order to provide feedback on different stages of the students' project, several project milestones throughout the semester were implemented into the course. These milestones include the following: 1.) project proposal stating hypothesis and motivation for the study; 2.) critical review of a paper related to the study; 3.) interim progress report presentation; 4.) reality check assignment, where students check the validity of their FEM with initial estimates of boundary conditions and/or material properties in terms of stresses or strains in the reported literature; 5.) final project presentation and report.

RESULTS

With a reasonable amount of guidance, all student teams were successful in generating the femur model and using it to test a wide variety of research hypotheses (Figure 1b-e). These scenarios required FEM modifications in terms of geometries, boundary conditions, material properties and meshing. Representative final project titles for general interest and DOE related studies are listed below.

Examples of general interest related studies:

- The Effect of Sleep Duration on Femoral Neck Fracture Risk during Simulated Falls (Figure1 b).
- Finite Element Model Analysis of the Forces on a Hip Joint during a Squat Exercise.
- Stress Fracture during Military Training.

Examples of DOE related studies:

- Effect of Cement Mantle Thickness on the Fracture Risk of Femoral Neck after Hip Resurfacing (Figure 1c-e).
- Effects of Checking on the Proximal Femur: A Parametric Study.
- The Interplay Between Cortical and Trabecular Moduli, Running Speeds, and Cyclic Loading on Stress at the Femoral Neck.

Observation of students' project progress.

We noted the importance of the project milestones in order to provide guidance in posing reasonable, testable hypothesis, ensuring the identification of appropriate model input parameters (loading conditions and material properties) and assisting in the interpretation of model results. Oral progress reports and final presentations resulted in meaningful interactions between student teams, since projects often shared similar model inputs or related hypotheses. The Academic version of the Abaqus/CAE software presented some limitations in mesh refinement, but did not appear to limit general interpretation of model findings.

DISCUSSION

With three years of refinement, this FE-based project approach offered a novel approach to offer training in both research methods and the appropriate application of computational modeling tools. Initially students routinely assumed that such computational models were more accurate or easier than traditional analysis methods. Through this process, they developed a greater understanding of the critical steps in model building, challenges in capturing realistic conditions and sources of uncertainty. Although generally proud and excited about their projects, they also developed a more realistic view of the models and were able to offer constructive feedback and critiques of other students' models and similar models in the literature. The use of a common model for all student projects offered a more cohesive classroom experience than prior offerings of the course, thus encouraging a more collaborative approach to the research process. As the class size has become larger, it also eased the ability of faculty and TAs to keep up with student questions and offered opportunities to introduce topics in the classroom that were relevant to all projects. Nonetheless, the proximal femur still offered sufficient opportunity for students to explore interests in sports, implants, injuries, and disease.

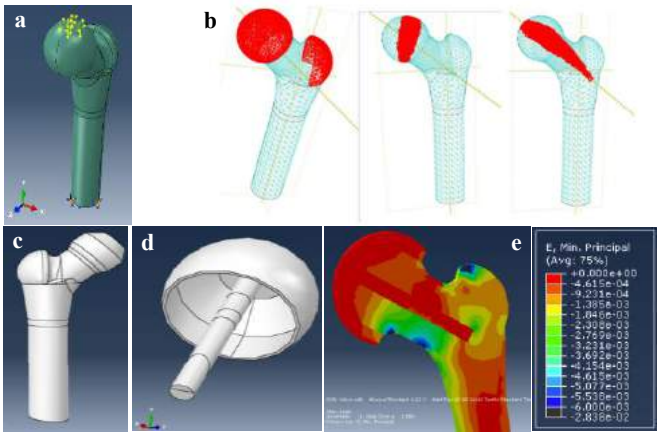

Figure 1. (a) Geometry of FEM given in tutorial; an example of (b) material properties and (c, d) geometry customization. (e) A representative contour map of FEM simulation with modified geometry.

Although the idealized model offered a streamlined educational experience, it also presented several limitations. First, the geometry doesn't represent exact anatomical structure, which may have contributed to model error, and sometimes interfered with assignment of material properties or boundary conditions. This, and a few model-based artifacts occasionally created distractions if they weren't caught early at interim progress reports or the "reality check" assignments. The use of DOE sensitivity studies often helped students to appreciate the relative importance of different model inputs, and they developed greater skill in describing their confidence in model results. In-class progress reports and final presentations offered numerous "teachable moments" that could be shared with the entire class. Based on the successful implementation of this project, we intend to make the tutorial and associated project assignments available online and look forward to further improvements by others.

ACKNOWLEDGEMENTS

The authors would like to acknowledge Jason Inzana, PhD for writing the tutorial for building an idealized proximal femur finite element model. The authors would also like to acknowledge the students who participated in Biosolid Mechanics class in 2011-2013 at the University of Rochester.

REFERENCES

[1] Tseng, K. et al, *Int J Technol Des Educ*, 23:87-102, 2013; [2] Blumenfeld, P. et al., *Educ Psyc*, 26:369-398, 1991; [3] Viceconti, M. et al., *Clin Biomech*, 20:451-54, 2005

Copyright 2016 The Organizing Committee for the 2016 Summer Biomechanics, Bioengineering and Biotransport Conference

SB³C2016
Summer Biomechanics, Bioengineering and Biotransport Conference
June 29 –July 2, National Harbor, MD, USA
SB³C2016-993

A COMPUTATIONAL FRAMEWORK FOR OPTIMIZATION OF TRANSCATHETER AORTIC VALVE LEAFLETS

Kyle Murdock (1), Kewei Li (2), Caitlin Martin (1), Wei Sun (1)

(1) Biomedical Engineering
Georgia Institute of Technology
Atlanta, GA, United States

(2) Biomedical Engineering
Graz University of Technology
Graz, Austria

INTRODUCTION

Transcatheter aortic valve replacement (TAVR) has been established as the standard treatment of aortic stenosis in high-risk populations [1]. Five year outcomes from the hallmark PARTNER trial demonstrated TAVR's non-inferiority to the traditional surgical approach [2]. Since TAVR's introduction, surgical experience and device evolution have improved patient outcomes; however long-term durability has long been postulated as one of TAVR's main concerns. One way to improve the durability during cyclical loading is to reduce the peak stress during each cycle. The role of TAV leaflet geometry, an aspect of TAV design which has been largely unexplored, may provide valuable insight into long-term safety.

In this study, the impact of leaflet geometry on TAV performance was analyzed by employing finite element analysis (FEA) to model valve closure and opening. By parameterizing TAV geometry including the two-dimensional leaflet shape, leaflet free edge, and stent suturing line, a substantial range of designs were generated. TAV design exploration was conducted systematically using an automated process in which the maximum principle stress was examined.

METHODS

Transcatheter aortic valves are typically comprised of three, scallop-shaped leaflets made of glutaraldehyde-treated bovine pericardium, which are sewn along the inside of a rigid stent. In this study, transcatheter valves were generated through a virtual assembly method. Using this technique, simple 2D leaflet shapes are created and transformed into a 3D configuration.

Parametrization of leaflet geometry

A classic, crescent-shape geometry is used as the initial leaflet design point. The characteristic leaflet has a free edge that coapts with the other leaflets and an attachment edge which is sutured onto the stent. The 2D attachment edge and free edge were defined using previously described exponential functions [3]. This description was chosen for the following properties. At a nominal attachment length (SLL), the free edge is simply a straight line connecting the two commissures. When the attachment edge is increased, the free edge exponentially increases toward the commissure from a plateaued height. The height is adjusted an appropriate amount to ensure proper closing. The precise way in which parameters effect the leaflet and valve geometry is shown in Figure 1.

One half of the stent-to-tissue attachment edge is characterized in cylindrical coordinates by the function:

$$z = ae^{b\theta} + ce^{d\theta} \quad (1)$$

where *a, b, c,* and *d* are coefficients controlling the 3D shape. For simplicity, variables *b* and *c* are used to adjust the attachment edge, as illustrated in Figure 1b. Decreasing values of *b* results in a wider attachment curve and increasing values of *c* tends to drive adjacent commissures apart.

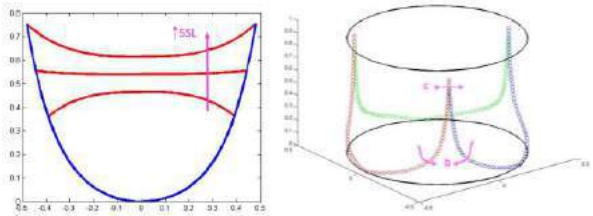

Figure 1: Effect of SSL on 2D leaflet geometry (left) and attachment parameters *b*, *c* on valve shape (right).

Virtual Assembly

Two-dimensional leaflet meshes were generated using a thin plate spline method implemented in Matlab. Using finite element software,

Copyright 2016 The Organizing Committee for the 2016 Summer Biomechanics, Bioengineering and Biotransport Conference

Abaqus\Standard (Dassault Systemes Simulia, Providence, RI), 2D leaflet nodes were displaced to their 3D suturing line positions; very small pressures were applied during this step to facilitate numerical convergence. The other two leaflets were generated via 120° symmetry and the final valve configuration was in a partially-opened, stress-free state.

Finite Element Analysis

Mechanical properties of GLBP tissue have been previously determined using biaxial testing [4]. The experimental data was modelled using a hyperelastic, Fung-type strain energy function:

$$W = \frac{C}{2}[e^{Q} - 1] \quad (4)$$

$$Q = A_1E_{11}^2 + A_2E_{22}^2 + 2A_3E_{11}E_{22} + A_4E_{12}^2 + 2A_5E_{11}E_{12} + 2A_6E_{22}E_{12} \quad (5)$$

Where C and A_i are material constants. Closing simulations were performed by applying a uniform pressure of 120 mmHg to the aortic side of the valve leaflets. Nodes along the attachment edge remain fixed from displacement and rotation in order to mimic the strong contact boundary between the tissue and rigid stent. After completion, the maximum principle stress during closing was output from the analyses in order to determine subsequent design exploration.

Optimization

Process automation software Isight (Dassault Systemes Simulia, Providence, RI) was used to perform an optimization analysis using the Adaptive Simulated Annealing method. Parameters a, b, and SSL were chosen as design inputs and the maximum principle stress was set as the objective function. Inputs a, b, and SSL were assigned ranges of 0.18-0.22 in., 1.3-1.7, and 0.7-0.8 in., respectively. A total of 500 runs were performed.

RESULTS

Each TAV model was generated using the design parameters described above. The modest range of SSL, a, and b resulted in a notable variation in leaflet stress. Figures 2 and 3 illustrate the influence of these design variables on the maximum principle stress, denoted as SMAX. Two instances of closing simulations are presented in Figure 2.

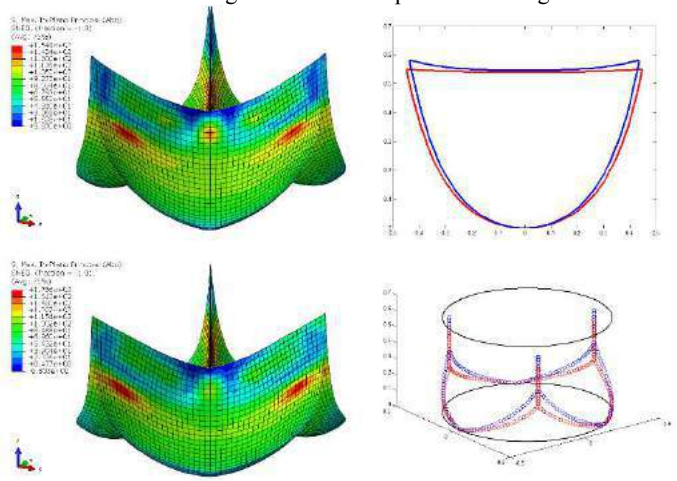

Figure 2: Diastolic loading of an optimal TAV design (top, left) and a representative design (bottom, left). Comparison of input geometry of 2D leaflet shape (top, right) and 3D attachment edge, where blue is the optimized TAV.

The suboptimal valve in Figure 2 has a lower, wider attachment edge than its ideal counterpart. The small geometric modification resulted in higher stress near the commissures and coaptation region. The magnitude of maximum principal stress ranged from ~155-220 PSI and was consistently located near the coaptation zone, a region of considerable bending stress. When comparing the ideal TAV leaflets in this optimization scheme to a TAV design with nominal leaflet geometry, the maximum principle stress was reduced from 181.6 to 154.8 PSI (14.7%).

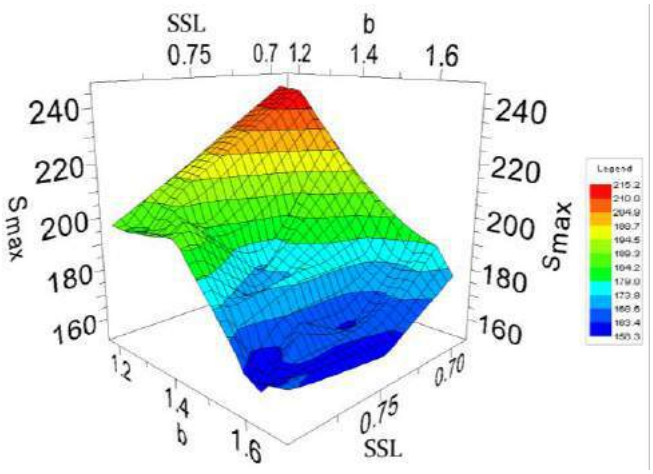

Figure 3: Effect of attachment edge length, SSL and shape, b, on maximum principle stress (PSI).

The 3D surface plot in Fig 3 demonstrates strong correlations between the input parameters and the maximum stress during TAV closure. The optimization process converged on a minimum objective function when the SSL, a, and b approached 0.79 in., 0.219 in., and 1.6, respectively. Two of the three input variables, SSL and a, reached their maximum values, indicating a larger range is required to find a global minimum.

DISCUSSION

The framework developed in this study has established a quantitative method to analyze the influence of geometric design parameters on TAV performance. Computation modeling of TAV biomechanics, like the study presented here, is an important step in developing numerical relationships between design inputs and device performance. By establishing these complex relationships, we are able to optimize certain outputs, for example, minimizing stress during diastole. By minimizing leaflet stress during diastolic loading, we may reduce cyclic fatigue and ultimately increase the durability of TAVs.

Furthermore, modification to the methodology presented could allow for additional, probabilistic-based analyses. For example, the effect of asymmetric leaflet geometries, inhomogeneous material properties, and disproportional attachment edges may be explored to better understand the impact of valve uniformity on TAV performance.

The methodology used in this study is an integration of efficient geometric modeling, rigorous mechanical testing data, and high fidelity simulation. Even though the geometric model of the 2D leaflet and 3D attachment edge is representative of modern TAVs, different free edge shapes, attachment edge shapes, and suturing lines may provide a more robust design space.

REFERENCES

[1] Leon, S et al., *N Engl J Med*, 363(17): 1597-1607, 2010.
[2] Mack, M et al., *Lancet*, 385:2477-84, 2015.
[3] Li, K et al., (Submitted).
[4] Li, K et al., *Ann Biomed Eng*, 38:2690-2701, 2010.
[5] Vesely, I., *Cardiovasc Pathol*, 12(5): 277-286, 2003.

Copyright 2016 The Organizing Committee for the 2016 Summer Biomechanics, Bioengineering and Biotransport Conference

SB^{3}C2016
Summer Biomechanics, Bioengineering and Biotransport Conference
June 29 –July 2, National Harbor, MD, USA
SB^{3}C2016-995

COMPUTATIONAL ANALYSIS OF RIGHT-VENTRICULAR FIBER DISTRIBUTION AS A COMPENSATORY MECHANISM DURING PRESSURE OVERLOAD

Arnold David Gomez (1,2), Huashan Zou (2), Osama M. Abdullah (1), Megan E. Bowen (2), Xiaoquing Liu (2) David A. Bull (2), Edward W. Hsu (1), Stephen H. McKellar (2)

(1) Bioengineering Department
University of Utah
Salt Lake City, UT, USA

(2) Division of Cardiothoracic Surgery
University of Utah
Salt Lake City, UT, USA

INTRODUCTION

Right ventricular failure (RVF) is a deadly deterioration of pump function that can occur in range of etiologies including congenial hearth disease, pulmonary hypertension and indirect pressure-overload from cardiomyopathy [1]. Although research focusing on elucidating progression of left ventricular (LV) failure is plentiful, current knowledge concerning the failing and recovering right ventricle (RV) is limited and insufficient for systematic development of effective treatments [2]. Characterizing patterns of failure and adaptation using preclinical and computational research are important tools for bridging this knowledge gap and for designing and testing of treatments that could have significant impact.

RVF due to pressure overload has been shown to reduce diastolic function associated to hypertrophy and interstitial collagen deposition (in fibrosis). These changes are conceptualized as compensatory mechanisms for limiting the magnitude of internal wall stresses via tissue stiffening [3]. Understanding the effects of structural remodeling in terms of fiber orientation is more difficult, but also of interest, because it relates not only to passive tissue stiffening, but also because fiber orientation has been shown to be a significant contributor to systolic organ function [4].

As in the LV, myocytes in the RV align in fibers following a helical structure quantified in terms of elevation angles with respect to the circumferential direction tangent to the ventricular wall [5]. In the healthy epicardium, the angles are mostly negative resulting in left-handed fiber helices, and the opposite is true in the endocardium. Angles in the mid-myocardium vary from positive to negative almost linearly i.e., the transmural rate of change in helical elevation angles can be approximated by a constant helical angle slope (HAS).

There is some inconsistency on reports regarding hypertension-induced HAS variations due to surgically induced RV pressure overload (RVPO) in animals studies, and there is little information on the precise mechanical consequences of such variation [6], [7]. Therefore, in the present study, we hypothesized that HAS variations caused by surgically induced pressure overload may be associated with a systolic structural compensatory mechanism.

METHODS

Subject-specific biomechanical simulations were constructed to interpret the effect of transmural fiber orientation (quantified by HAS) on cardiac function under elevated RV afterload. To this end, subject-specific finite-element (FE) models (n=3) were constructed from 3D images of the ventricular myocardium at early diastole obtained via multislice CINE MRI. The models were used to generate simulated predictions of RV function quantified by per ejection fraction (RVEF) under 4 conditions depending on RV afterload (normal or RVPO), and transmural fiber orientation (baseline or longitudinally aligned) for a total of 12 simulations. Significance in RVEF was calculated using parried t-tests with a p-value of 0.01

Geometry, structural variation, and intraventricular pressure information was obtained from a group of New Zealand white rabbits (2.0-2.5 kg) including controls (n=3), and RVF (n=6) due to pressure overload obtained via pulmonary artery banding. Band tightness was increased until RV end systolic pressure reached a minimum of 25 mmHg, and maintained until evidence of RVF was observed [8]. Images information was produced using a Bruker Biospec 7T imaging instrument. CINE-MRI was performed *in vivo* in the control group, and DT-MRI was performed *ex vivo in* controls and RVF. All animal protocols were subject to established guidelines and approved by supervisory offices at the University of Utah (protocol #13- 02010).

Pressure boundary conditions were based on interventricular catheter measurements of control animals for normal RV afterload,

Copyright 2016 The Organizing Committee for the 2016 Summer Biomechanics, Bioengineering and Biotransport Conference

and banded animals for RVPO, which was simulated as an increase of 20% on systolic pressure. The RVF group was divided in two groups according to wall thickness, which was interpreted as compensation to increased afterload. In the uncompensated group (n=3), 3D high-resolution DT-MRI scans in the RV wall yielded a quasi-linear variation from -60° in the endocardium to 60° in the epicardium (HAS = *120*°). The compensated group, had a 30% steeper HAS, which was modeled as a longitudinally aligned fiber distribution ranging from -75° to 75°.

The first set of simulations (normal pressure, and baseline fiber orientation) were used to optimize material parameters in a transversely isotropic Fung-type hyperelastic strain energy function so that predicted RVEF matched experimental measurements per CINE MRI observations at systole and diastole. Once optimized, all parameters other than those under study were held constant. A typical FE model and additional boundary conditions and material distribution appear in Figure 1. All simulations were performed using the FEBio Software Suite [9].

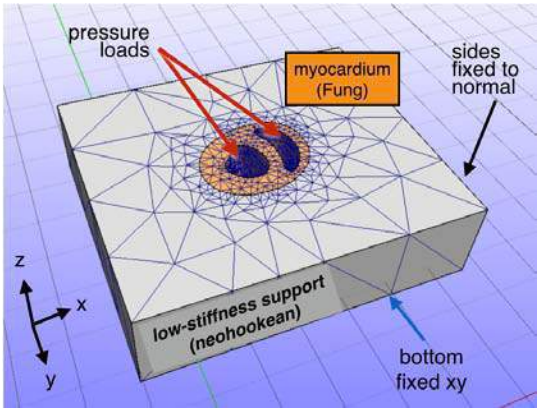

Figure 1: Finite element model of ventricular myocardium. Each subject-specific model (n=3) was modeled in 4 different conditions depending on RV systolic afterload and fiber orientation.

RESULTS

A typical FE model at different stages of the cardiac cycle was illustrated in Figure 2. As expected, end diastole results in dilated chambers, and active contraction results in diminished intraventricular volume development of torsion. Normal pressurization and fiber orientation resulted in volume predictions within 5% of those measured using CINE-MRI *in vivo*. Simulated RVEF calculations for normal and elevated pressure using with baseline or longitudinally aligned fiber are tabulated in Table 1. In RV pressure overload, with other parameters held constant, an increase in helical angle slope (by 30%, which is the high range of DT MRI observations) results in an improvement in ejection fraction of approximately 35%. This gain did not occur in the absence of pressure overload, which remained in the order of 3%.

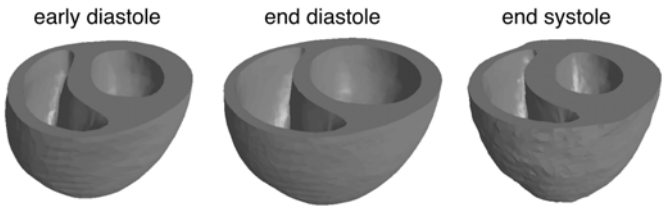

Figure 2: Representative simulation results under normal systolic pressure and baseline fiber orientation.

Table 1: Simulated RV ejection fraction for normal and elevated systolic pressure with or without fiber structure compensation (via HAS increase).

Pressure	*Normal*	*RVPO*
baseline (HAS = 120°)	0.36 ± 0.04	0.20 ± 0.06
longitudinally aligned (+30% HAS)	0.37 ± 0.04	0.27 ± 0.05
difference	*2%*	*35%**

Numerical values are expressed as mean ± (SD). * p =0.01

DISCUSSION

The numerical results show a clear functional consequence associated with structural changes. Increasing transmural helical slope, by an amount similar to that observed in the DT-MRI analysis, results in a remarkable improvement in RVEF under pressure overload. The same increase in HAS was not accompanied by significant changes in RVEF under normal conditions. This result suggests that longitudinal alignment may be particularly beneficial to recover ejection fraction in the presence of pressure overload, and it is consistent with previous studies where longitudinal alignment has been observed as one of the consequences of RVPO [6].

Further, even though all the animals in the RVF group showed clear signs of failure, DT-MRI showed that differences in HAS were observable on hypertrophic RVF hearts, and not on non-hypertrophic RVF, which may explain why previous DT-MRI studies did not report a change [7]. However, due to the relatively low number of animals, the results cannot be uniquely attributed to a biological mechanism without considering fixation or specimen preparation error as a possible disqualifier on the experimental result.

Nevertheless, this study offers numerical evidence that longitudinal fiber alignment could be a compensatory mechanism associated to systolic organ function. Further, mathematical modeling, CINE and diffusion tensor MRI could differentiate between compensated and decompensated forms of RV failure, as limitations associated with non-invasive measurement of fiber orientation can be mitigated by application of in vivo imaging in the sort future.

ACKNOWLEDGEMENTS

Thanks to the Small Animal Imaging Facility, and the Musculoskeletal Research Laboratories at the University of Utah.

REFERENCES

[1] Foegel, M. et al., *Prog Cardiovasc Dis.* Jan; 40(4):343-56. 1998.
[2] Voelkel, N. et al., *Circulation.* Oct 24;114(17):1883-91. 2006.
[3] Gaynor, S. et al., *Circulation.* Aug 30;112(9S):I212-8. 2005.
[4] Nelson, G. et al., *Am. J. Physiol. Heart Circ. Physiol.,* vol. 280, no. 6, pp. H2639–48. 2001.
[5] Streeter, D. et al., *Circ. Res*., 33(6), 656–64. 1973.
[6] Hill, M. et al., *Ann. Biomed. Eng.* 42(12), 2451–2465, 2014.
[7] Nielsen, E. et al., *Anat. Rec.,* 292(5), 640–51, 2009.
[8] McKellar, S. et al. *J Surg Res*. Apr;194(2):327-33. 2015.
[9] Maas, S. et al. *J Biomech Eng.* Jan 134(1):011005. 2012.

Copyright 2016 The Organizing Committee for the 2016 Summer Biomechanics, Bioengineering and Biotransport Conference

SB^{3}C2016
Summer Biomechanics, Bioengineering and Biotransport Conference
June 29 –July 2, National Harbor, MD, USA
SB^{3}C2016-996

SIMULATED BLAST-INDUCED CAVITATION: AN *INVITRO* STUDY

S. Canchi[(1)], Y.Hong [(1)],K. Kelley[(2)], M. A. King[(3,4)],G. Subhash[(1)],M. Sarntinoranont[(1)]

(1) Department of Mechanical & Aerospace Engineering
University of Florida,
Gainesville, FL, USA

(2) ICBR Electron Microscope Facility
University of Florida
Gainesville, FL, USA

(3) Department of Pharmacology & Therapeutics
University of Florida
Gainesville, FL, USA

(4) North Florida/South Georgia VA Medical Center
Gainesville, FL, USA

INTRODUCTION

Exposure to explosive blasts can produce complex brain pathology and debilitating functional outcomes. Blast wave is characterized by rapid rise in amplitude of the pressure (peak overpressure) followed by a swift drop to negative pressure (under pressure / negative phase) with respect to the atmospheric pressure. Aside from the direct interaction of the blast wave with the skull, brain and the cerebrospinal fluid (CSF), multiple secondary events could also transpire one of which includes formation and collapse of bubbles i.e. cavitation. Generation of cavitation which is dependent on fluid properties is considered one of the potential damaging mechanisms upon blast wave loading.

Damage due to cavitation is generally attributed to the large pressure generation inside the collapsing cavity. When a compression wave interacts with a pre-existing bubble, the bubble contracts leading to local increase in surface pressure. The bubble expansion and subsequent collapse leads to a high pressure generated into the surrounding liquid. Additionally, the rebound of the tissue after its deformation during the bubble expansion could cause flattening of the bubble leading to formation of a unidirectional jet. Impact of such a high velocity liquid jet could be associated with cavitation damage.

The extraordinary structural heterogeneity of brain tissue at molecular to gross anatomical scales predicts that it would be highly susceptible to cavitation based tissue damage. Our group has previously developed and dynamically characterized the methodology for blast-induced single bubble cavitation [1]. This study established that realistic simulated blast wave transit was sufficient to induce destructive cavitation. In this study, the use of the *ex vivo* acute brain tissue slice permitted characterization of specific tissue vulnerabilities and anticipates *in vivo* studies that remain technically beyond reach.

METHODS

A customized polymer split Hopkinson pressure bar (PSHPB) [2], was utilized to generate a planar simulated blast waves through a fluid chamber which housed a single brain tissue slice (~350 μm) along with the seed gas bubble (see Fig 1). To maintain cell viability during testing, the brain tissue slices were submerged in artificial cerebrospinal fluid (aCSF), continuously perfused with carbogen gas and maintained at 37^0C. Only one side of the brain (ipsilateral hippocampi) was directly exposed to cavitation events (cavitation side). High speed imaging (100,000 to 500,000 frames/sec) was used to visualize tissue deformation, and strain was calculated using digital image correlation (DIC).

Post testing the tissue slices (n= 40) were fixed in Trump's fixative and processed for electron and confocal microscopy. To assess the viable cellular structural changes beyond the effects of damage due to slicing and handling, the resin embedded samples were sectioned to a depth of 150 μm from the slice surface.

Image analysis software (GNU Image Manipulation Program v2.8.14) was used to superimpose (1) the maximum bubble footprint (2) the collapse jet direction observed in the

Copyright 2016 The Organizing Committee for the 2016 Summer Biomechanics, Bioengineering and Biotransport Conference

video (3) confocal cellular injury zones and (4) calculated strain contours onto a single Paxinos rat atlas image to generate a composite atlas image. This was done to relate the bubble and jet location to corresponding strain and injury.

RESULTS

Maximum von mises strain generally coincided with 45 μs after bubble collapse, and overlapped with the observed injury patterns. Superimposition of the full field von Mises strain at this time point on an anatomical slice image was used to generate composite injury maps (Fig 2).

Distinct injury patterns including separation of normally apposed structures, with some tissue tears and disruption along cell layers were observed on the hippocampal side subjected to cavitation damage as compared to blast wave alone. Despite some localized contralateral strain elevations, structural failures were absent on this side that was exposed to the blast wave without direct cavitation. The observed injury patterns corresponded to instantaneous and early injury immediately after cavitation events.

Within the cavitation injury zone, ultrastructural damage was indicated with a gradual loss in the neuronal contrast with respect to the surrounding neuropil, as well as increased size and indistinguishable soma boundary within the CA3 layer. Sham CA3 neurons exhibited clearly visible Nissl bodies with distinct nuclear membrane and nucleolus. The contralateral neurons showed comparable ultrastructural features as sham with the deviation of dense and shrunken cytoplasm. In contrast, the cytoplasm of the CA3 pyramidal neurons within the cavitation injury zone appeared pale with reduced electron density of the cytoplasm. Frequent discontinuity of the plasma membrane (< 200 nm) was observed throughout the neuronal cell body in the cavitation injury zone.

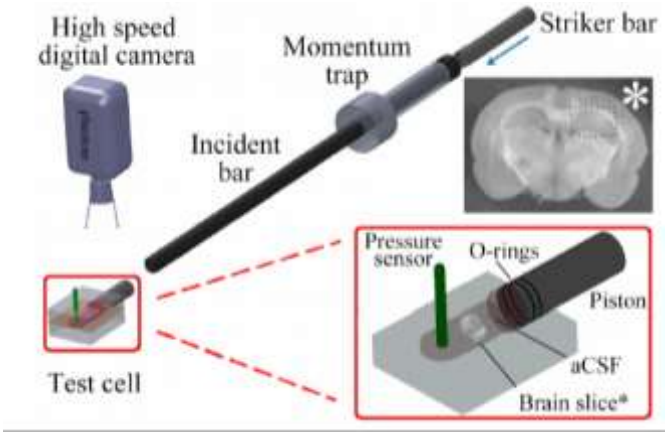

Figure 1: Experimental blast-induced controlled single bubble cavitation system. * Highlights the video frame of the brain tissue slice during growth of the bubble placed under the hippocampus (dotted line).

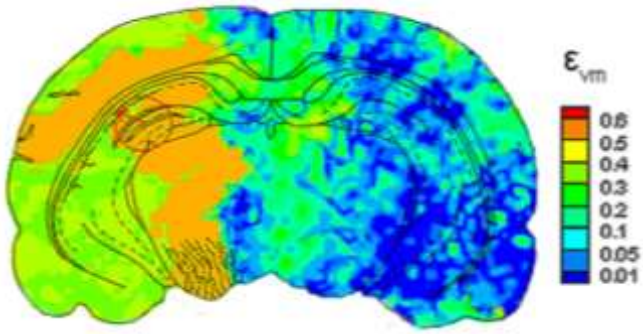

Figure 2: Composite injury map shows the overlap of observed injury (dotted lines) and regions of high strain. The red circle is the trace of maximum bubble diameter and the arrow points to jet direction.

DISCUSSION

By isolating single bubble cavitation events on live slices of mature brain, we were able to associate damage effects (separation of apposed structures, tissue tears and cell layer disruption) due to bubble growth and collapse. Most relevant to injury, we were able to directly measure the high strains created by collapsing bubble jet which overlapped with tissue injury. Data support the strong probability that dynamic cavitation events could directly mediate local structural injury in brain exposed to blast pressure transients. Microbubble formation and collapse, and jet formation, could each mediate unique forms of injuries across a wide spatial scale.

ACKNOWLEDGEMENTS

This research was funded by the Army Research Office award number W911NF-10-1-0276. This work was supported by resources provided by the North Florida/South Georgia Veterans Health System, Gainesville, FL. The contents do not represent the views of the U.S Department of veterans Affairs or the United States Government. The authors would like to thank Ms. Kimberly Backer-Kelly for assistance with SEM, Dr. Yuquing Li for technical assistance with EM data and Dr. Stephen J. Blackband for allowing us to use his laboratory facilities.

REFERENCES

[1] Hong, Y et al., *Exp. Mech*, 1-13, 2015.
[2] Liu, Q and Subhash, G. *Mech Matter, 38:1105-1117, 2006.*

Copyright 2016 The Organizing Committee for the 2016 Summer Biomechanics, Bioengineering and Biotransport Conference

SB³C2016
Summer Biomechanics, Bioengineering and Biotransport Conference
June 29 –July 2, National Harbor, MD, USA
SB³C2016-997

DEVELOPMENT OF AN INTEGRATED MULTI-SCALE SIMULATION SYSTEM WITH MULTI-MODAL DATA FOR CEREBRAL CIRCULATION

M. Oshima (1), H. Zhang (2), M. Kobayashi (1), S. Yamada(3), F.Liang(4), S. Takagi(2)

(1) Interfaculty Initiative in Information Studies
The University of Tokyo
Tokyo, Japan

(2) Department of Mechanical Engineering
The University of Tokyo
Tokyo, Japan

(3) Department of Neurosurgery
Rakuwakai Otowa Hospital
Kyoto, Japan

(4) Department of Naval Architecture
and Ocean Engineering
Shanghai Jiao Tong University
Shanghai, China

INTRODUCTION

Stroke is one of the main causes of death in Japan, and it is strongly associated with carotid stenosis. If the stenosis becomes highly sever, a surgery such as carotid artery stenting (CAS) or carotid endarterectomy (CAE) is performed to prevent the fatal situation. However, the surgery sometimes causes postoperative complications such as cerebral hyperperfusion syndrome (CHS) [1]. Thus, it is important to understand the changes in the distributions of cerebral blood flow and pressure due to the surgery and then to utilize the information to surgery in the preoperative stage.

Since the surgery affects hemodynamics not only in a localized stenotic region but also the entire circulatory system throughout the peripheral areas, it is necessary to develop a simulation system to examine the hemodynamics locally as well as globally in the circulatory system. In addition, the simulation needs to be performed in a reasonable time for case study. Thus, in this paper, a patient-specific one dimensional–zero dimensional (1D-0D) simulation method has been developed taking account of the entire cardiovascular system to obtain the hemodynamics information in the Circle of the Willis (CoW).

The present simulation system consisted of three processes: pre-processing, 2) multi-domain simulation, and 3) post-processing. In order to perform the patient-specific 1D-0D simulation, the information on the radius and the length of CoW was obtained from the 3D vascular geometry constructed from the medical image data such as the computed tomography (CT) or the MRI (Magnetic Resonance Imaging) in the pre-processing process [2]. The 1D-0D simulation was based on the method of Liang F. Y., *et al* with the literature data of vascular geometry and also the vascular parameters such as resistance and compliance [3]. Since there were discrepancies in the results caused by the differences in the vascular geometry between the literature and the patient-specific data, the single photon emission computed tomography (SPECT) data were used as reference to adjust the parameters, i.e. peripheral resistances [4]. In the past-processing process, a visualization system was developed for the 1D domain where the patient-specific geometry was applied. The present simulation system was applied to investigate the blood flow in the CoW. The results of pre- and post-operation were compared to examine the effects of the surgery.

METHODS

Figure 1 summarizes the present integrated simulation system with multi-modal data.

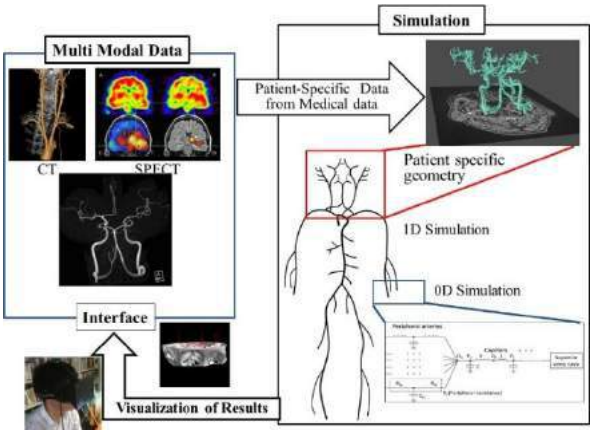

Figure 1: Schematic illustration of the integrated system.

The authors have been developing a vascular geometric modeling system, V-Modeler [2]. The development environment of V-Modeler was based on Visual Studio 2010 Professional (C++ programming

Copyright 2016 The Organizing Committee for the 2016 Summer Biomechanics, Bioengineering and Biotransport Conference

language) on Windows 7 Professional 64bit. The image processing libraries were MIST (Media Integration Standard Toolkit, Nagoya University, Japan) and OpenCV 2.2, visualization library was OpenGL.

The 1D simulation was applied to a total of 83 arteries which consisted of 55 arteries based on Liang model [3] and newly added 27 arteries of cerebrovascular and neck circulations. The governing equations of the 1D simulation are given by:

$$\frac{\partial A}{\partial t}+\frac{\partial Q}{\partial z}=0 \tag{1}$$

$$\frac{\partial Q}{\partial t}+\frac{\partial}{\partial z}\left(\frac{Q^2}{A}\right)+\frac{A}{\rho}\frac{\partial P}{\partial z}+8\pi\frac{\mu}{\rho}\frac{Q}{A}=0 \tag{2}$$

$$P-P_0=\frac{Eh_0}{r_0\left(1-\sigma^2\right)}\left(\sqrt{\frac{A}{A_0}}-1\right) \tag{3}$$

where A, Q and P are the cross-sectional area, the flow rate and the pressure, respectively. In addition, E, h, r, and σ represent the Young's modulus, the wall thickness, the arterial radius, and the Poisson ratio. The subscript 0 denotes a value at the reference state. The Poisson ratio in the paper was taken to be 0.5 because of incompressibility of the artery. The Lax-Wendorff method was used to solve equations (1)-(3).

The 0D simulation comprised two equations for mass and momentum conservation based on the electric circuit analogy. The governing equations were solved using the 4th order Runge-Kutta method. The results of the 0D simulation were given to the 1D simulation at the junction, and vice versa.

The visualization part was incorporated to V-Modeler since the 1D simulation used the information of the radius and length extracted from the medical image data by V-Modeler. V-Modeler had also the information about the centreline of the vascular lumen expressed by a spline-function. First of all, the grid point used for the 1D simulation was allocated in the 3 dimensional coordinates using the information of the centreline in the 3D. Since the radius was obtained from the area resulted from 1D simulation, the pressure and the flow rate were remapped onto the 3D geometry.

RESULTS

The simulation was conducted for a 70 years old male with 73% stenosis at Left Internal Carotid Artery (Lt. ICA).The patient-specific data in this paper used the magnetic resonance angiography (MRA) for the geometry and SPECT for adjustment of the flow rates in the efferent arteries.

Figure 2 summarizes the simulation results of flow rate in each artery at the rest and with ACZ for both the pre- and post- operations.

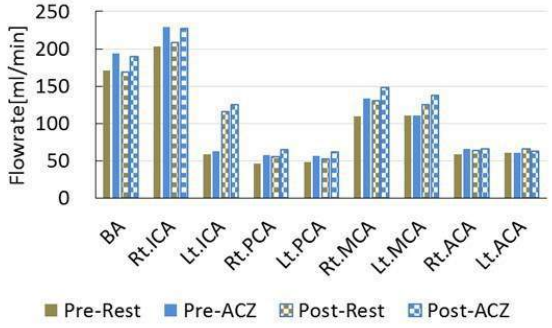

Figure 2: Flow rate of each artery before and after the surgery.

Since the stenosis was located on the left side, the flow rates of the arteries on the left side such as Lt. Middle Cerebral Artery (MCA) and Lt. Anterior Cerebral Artery (ACA) did not change after the ACZ was applied on the pre-operation stage. After the surgery, the flow rates of both afferent and efferent arteries became balanced on both sides.

Figure 3 demonstrates the flow distribution before and after the surgery. The figure on the left is at the rest on the pre-operation stage while one on the right is at one on the post-operative stage. As shown in Figure 3, although the flow rate of Lt. ICA was higher than one of Rt. ICA, both flow rates became the same after the surgery.

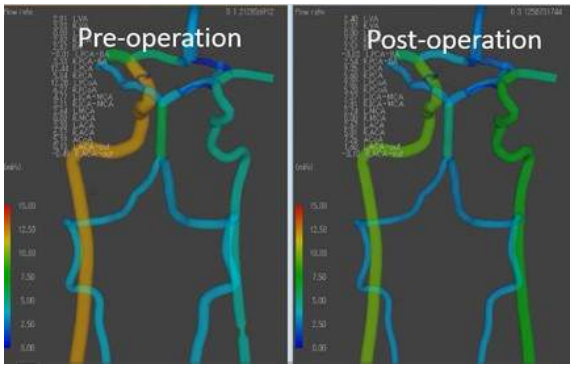

Figure 3: Visualization of flow rates before and after the surgery.

DISCUSSION

In order to investigate the effects of the surgery, the paper presented the integrated numerical system of the 1D-0D simulation for an individual patient by utilizing the patient data from the multi-modal data. In the simulation, the geometric information was obtained from the MRA by V-Modeler while the flow information was obtained from the SPECT.

The averaged computation time for each case in the present 1D-0D simulation was about 50 minutes. It required about 10 cardiac cycles for convergence. In general, the commercial visualization software is available for the 3D simulation but not for the 1D-0D one. Development of the visualization system enabled us to evaluate the detailed difference in the flow distribution between the pre- and post-operative stages.

We found that the flow in the anterior efferent region changes the flow direction before and after the surgery. The flow before the surgery was from MCA to ACA on the right side and then became from ACA to MCA after the surgery. Despite the changes in the flow direction, the overall Cerebral Blood Flow (CBF) before and after the surgery did not show a significant increase for the CHS according to the literature [5]. In addition, the asymmetry index, which is one of the risk factor [5] was improved after the surgery. Those results agreed with the clinical presentation of the patient. In order to examine the applicability of the present method, the further investigation with more case study will be conducted.

ACKNOWLEDGEMENTS

This study is supported by the Grant-in-Aid for Scientific Research (B) (No.24300158) by Ministry of Education, Culture, Sports, Science and Technology in Japan.

REFERENCES

[1] van Mook, W. N. K. A., et al. Lancet Neurology 4:877-888, 2005.
[2] Kobayashi, M. et al. Circulation Journal, DOI: 10.1253/circj.CJ-15-0037, 2015.
[3] Liang, F. Y., K. et al. BioMedical Engineering on Line,10:84, 2011.
[4] Zhang, H., et al. Ann. Biomed Eng. DOI:10.1007/s10439-015-1544-8, 2015.
[5] Kaku, Y. et al, AJNR 25: 1403-1408, 2004.

Copyright 2016 The Organizing Committee for the 2016 Summer Biomechanics, Bioengineering and Biotransport Conference

SB^{3}C2016
Summer Biomechanics, Bioengineering and Biotransport Conference
June 29 –July 2, National Harbor, MD, USA
SB^{3}C2016-998

A REAL–TIME PROGRAMMABLE PULSATILE FLOW PUMP FOR IN-VITRO CARDIOVASCULAR EXPERIMENTATION

Rahul Raj. Mechoor(1), Tyler M. Schmidt(1), Ethan O. Kung(1)

(1) Department of Mechanical Engineering
Clemson University
Clemson, SC, USA

INTRODUCTION

Cardiovascular diseases are one of the leading causes of death around the world. According to the American Heart Association, there were more than 7.6 million cardiovascular procedures performed in the US and total treatment spending exceeded $320.1 billion in 2011 [1]. *In-vivo* studies can be performed to better understand these diseases, but there are challenges due to clinical limitations and ethical considerations. An alternative is bench top cardiovascular experimentation, in which localized vascular conditions are recreated *in-vitro* to better analyze the hemodynamics pertaining to certain defects or surgical conditions. This couples medical imaging with fluid mechanics to recreate physiological conditions on a relatively simple, inexpensive bench top circuit and allows experimental validation of computational models, extensive *in-vitro* testing of medical devices and better overall understanding of vascular hemodynamics without risks or discomfort to any patient.

Accurate replication of the pulsatile blood flow is necessary to study hemodynamics pertaining to any vascular condition. The 'Harvard pump' (Harvard Apparatus, MA) and the 'SuperPump' (Vivitro Labs, Canada) are commercial pumps that can recreate ascending aortic flow but the user must experimentally construct a downstream vascular simulator to obtain the desired flow waveforms at specific anatomic locations. In studies of localized vascular conditions, it is needed to only reproduce the localized flow waveform under consideration. This eliminates unnecessary replication of vascular impedances between the heart and the site of interest. There are experimental systems, such as the dual pump system [2], progressive cavity pump [3], positive displacement pump [4] and the commercial system 'CardioFlow' (Shelley Medical Imaging Technologies, Canada), that are designed to reproduce localized flow waveforms. But these systems are limited by practicality, cost, programmability or accuracy, especially when reproducing multiple waveform shapes with different downstream impedances.

The aim of this study is to design, construct and test a reliable, low cost, fully programmable pulsatile flow pump that can continuously and accurately reproduce localized physiological flow waveforms. The reduced complexity and cost of this design will enable the advancement of cardiovascular medical technologies and improve patient care.

METHODS

Pump Design and Operation*:* A rendering of the bench top cardiovascular pump is shown in Figure 1a. It consists of a piston – cylinder assembly and a stepper motor linear actuator. The cylinder is acrylic, with an internal diameter of 4.75 inches and length of 36 inches. The piston is connected to an actuator (HaydonKerk motion solutions, CT), which has a linear nut and lead screw arrangement driven by the stepper motor, controlled by a driver (HaydonKerk motion solutions, CT). Control signals are generated by LABVIEW and an NI data acquisition system (National Instruments, TX). The cylinder is sealed by end plates on both ends and is divided into two chambers by the piston, making it double-acting. Fluid ports are on the end plates (Figure 1b). Connections from the outlet ports on both ends of the pump are merged using a three way valve to form a single connection to the test section that discharges to the fluid reservoir. A similar pattern of tubing is used to connect the reservoir to pump inlet ports. These connections facilitate switching of active ports from one end of the pump to the other as the piston changes direction. Air release ports are positioned on top of the cylinder's curved surface which is the ideal location for air removal. The actuator velocity and direction are controlled by a counter output and analog voltage signal respectively. The total cost for the pump is less than $1,000 which makes this design considerably cheaper compared to commercial systems that cost around $50,000.

Copyright 2016 The Organizing Committee for the 2016 Summer Biomechanics, Bioengineering and Biotransport Conference

Feedback Mechanism: A feedback mechanism has been implemented to improve accuracy under varying downstream impedances. LABVIEW receives the output flow rates from a clamp-on ultrasonic transit time flow meter (Transonic systems Inc., NY) and averages it over 5 cycles. This flow waveform is compared to the desired waveform and a proportional control is used to rectify any variations. The system executes this process iteratively until the desired waveform is achieved

Test Setup: The pump is connected to a test section with a downstream resistance to create back-pressure. Flow waveform data is supplied as input to the pump-control program, which then runs the pump, collects flow values averaged over five cycles and uses this for feedback calculations. When the system attains the user's desired level of accuracy, corresponding control data is stored for later use. The counter frequency is set to vary in timesteps of 20 ms, providing the operator with 50 data points per second for the input. For this particular test case, a general infra-renal abdominal aortic flow waveform with a peak flow of 110mL/s [5] is used under varying downstream conditions to demonstrate the pump performance. A 40% glycerin solution is used as the blood mimic. Pressure is measured using a pressure transducer (Argon Medical Devices Inc., TX).

RESULTS & DISCUSSION

Figure 2 shows the flow and pressure waveforms produced by the pump (averaged over five cycles) compared to the actual desired waveforms. The mean absolute percentage error in flowrate is 2.46% and the maximum absolute percentage error is 5.7%. Pump accuracy is comparable to that of commercial models (±3% for 'CardioFlow 5000'). Shape of the recreated pressure waveform resembles that of physiologic waveforms. The coincidence of the peak of pressure curve with that of flow waveform and the large difference between maximum and minimum pressure is due to the absence of a compliance chamber downstream.

Figure 3 shows the averaged recreated flow waveforms under varying levels of back-pressure. The same input waveform is tested under different peak pressure conditions. Results show that pump performance is independent of downstream impedances until the back-pressure reaches 180 mmHg, which is beyond physiological pressures. Pump performance degrades as the abnormally high back-pressure pushes the power requirements beyond the actuator's limit, especially at higher flow rates. This shows that the pump is powerful enough to recreate any physiological pressure given the peak flow rate is within limits.

The maximum flow rate of the current prototype is limited to 160 mL/s due to limitations of the stepper motor. For higher flow rates the use of a servo motor might be necessary. The pump has been designed so that it can be modified for continuous use for medical device testing by automating inlet and outlet manifold valve control. Future work in these areas could result in useful refinement of the current system.

Through this study we have successfully designed and tested a versatile computer controlled pulsatile flow pumping system that produces repeatable flow waveforms under various downstream conditions with an accuracy comparable to commercial systems at 2% of the cost.

ACKNOWLEDGEMENTS

This study is supported by funding from the Mechanical Engineering department of Clemson University. We also acknowledge Michael Justice, Jamie Cole and Stephen Bass for their assistance in the pump construction.

REFERENCES

[1] D. Mozaffarian, et al., Circulation vol. 131:4. 2014.
[2] W. Tsai, et al., *Med. Biol. Eng. Comput.*, 48:2, 197–201, 2010.
[3] A. Eriksson, et al., *Rev. Sci. Instrum.*, 71:1, 235–242, 2000.
[4] R. Frayne, et al., *J. Magn. Reson. Imaging*, 2:5, 605–612, 1992.
[5] E. O. Kung, et al., *J. Biomech. Eng.*, 133:4, 041003, 2011.

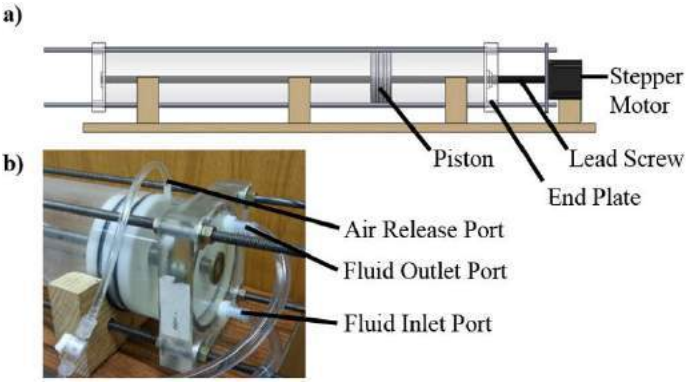

Figure 1: Pulsatile Pump a) Side view rendering b) Open end plate with fluid ports

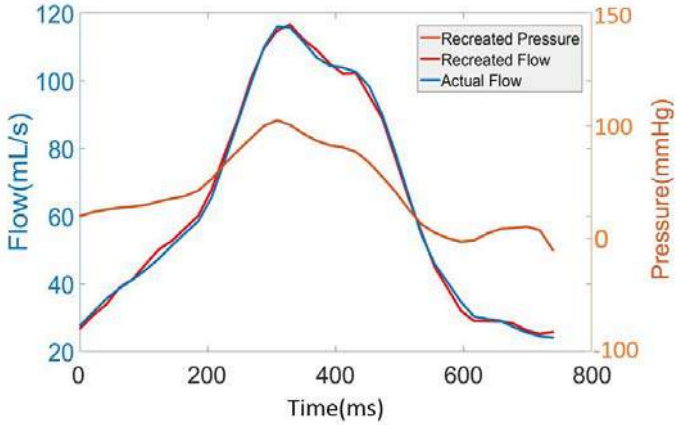

Figure 2: Comparison of actual and recreated flow waveforms

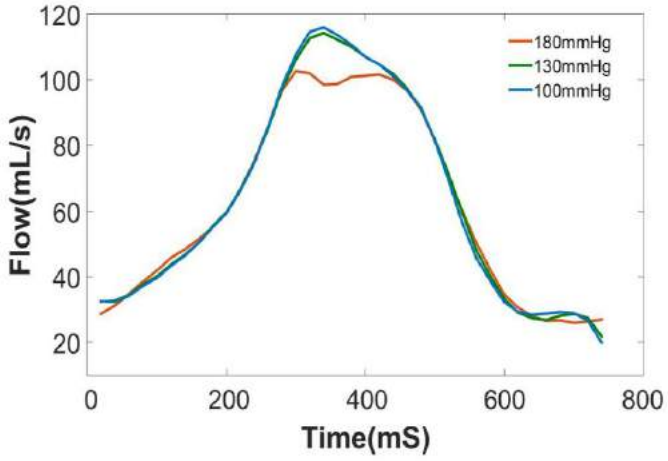

Figure 3: Pump performance under different peak values for back-pressure

Copyright 2016 The Organizing Committee for the 2016 Summer Biomechanics, Bioengineering and Biotransport Conference

SB³C2016
Summer Biomechanics, Bioengineering and Biotransport Conference
June 29 –July 2, National Harbor, MD, USA
SB³C2016-999

CHONDRO-PROTECTIVE EFFECT OF ZOLEDRONATE ON IN SITU CHONDROCYTES DAMAGED BY INTERLEUKIN-1

Mengxi Lv(1), Yilu Zhou(2), Shongshan Fan(2), Olivia Smith(3), Liyun Wang(2), X. Lucas Lu(2)

(1) Center for Bioinformatics & Computational Biology
University of Delaware
(2) Department of Mechanical Engineering
University of Delaware
(3) Department of Biomedical Engineering
University of Delaware

INTRODUCTION

Interleukin (IL)-1 is one of the inflammatory cytokines that could be elevated after traumatic joint injuries. IL-1 can mediate articular cartilage tissue degradation, induce chondrocyte apoptosis, and lead to post-traumatic osteoarthritis (PTOA) of the joint [1]. Our recent studies found that zoledronic acid (ZA), an FDA-approved drug for the treatment of osteoporosis, can suppress the development of OA in the DMM (destabilization of medial meniscus) mouse model (Fig. 1) [2]. Using cartilage explant model, we further showed that zolendronic acid could improve the mechanical integrity of cartilage explants during long-term *in vitro* culture. However, it is not clear whether zolendronic acid can directly rescue the chondrocytes from the injuries from inflammatory attack. In this study, we tested the following two hypotheses: (1) Zolendronic acid can prevent the GAG loss in cartilage explants and protect the viability of chondrocytes in the presence of IL-1β. (2) The chondro-protective effect of ZA is related to the intracellular calcium ($[Ca^{2+}]_i$) signaling of chondrocyte.

METHODS

Bovine cartilage explant model Cylindrical cartilage explants (diameter = 3 mm, thickness = 2 mm) were harvested from fresh calf knee joints within 24 hours of slaughter (Green Village, NJ) and cultured in chemically defined medium (DMEM, 1% ITS, 50 μg/mL L-proline, 0.9 mM sodium pyruvate, and 50 μg/mL ascorbate 2-phosphate) [1]. After 3-day balance in culture medium, IL-1β and/or ZA were introduced into the culture for extra 8 days (see below for details).

Mechanical properties and sGAG release GAG contents in the culture medium and the cartilage explants were measured using DMMB dye-binding assay. The accumulative GAG loss was defined as the total GAG released into the medium divided by the sum of GAG contents in both explant and culture medium. Young's modulus and dynamic modulus of cartilage explants on day 8 were determined by unconfined compression tests [4].

Cell viability Cells in cartilage explant were stained using LIVE/DEAD Viability/Cytotoxicity Kit (Thermo Fisher Scientific) and imaged using a confocal fluorescent microscope (Zeiss LSM 510).

In situ Spontaneous Calcium Signaling Cartilage explants were cut into two halves and cultured in 5 μM Fluo-8AM dye medium for 40 minutes. Calcium images of *in situ* chondrocytes resided in cartilage were taken every 2 s for 16 minutes without alien stimuli using a confocal microscope. The spontaneous responsive percentage of cells was calculated as the fraction of cells with calcium spikes over the number of total cells. A set of spatiotemporal parameters of the $[Ca^{2+}]_i$ peaks were also reported as described in our previous studies [4]. Calcium is a universal second messenger in cell activities and functions as the upstream of many metabolic activities of chondrocytes.

Statistical analysis Tukey's Honestly Significant Difference test was performed following the one-way ANOVA to compare the GAG loss and mechanical properties among groups (data shown as mean ± standard deviation). For the parameters related to $[Ca^{2+}]_i$ signaling, nonparametric Mann-Whitney U test was utilized to detect the significant difference (data shown as mean±SEM).

RESULTS

ZA inhibits the IL-1β-induced GAG loss in cartilage explant

Cartilage explants treated with IL-1β released sGAG in a dosage- and time-dependent manner (Fig. 2A). 1ng/ml IL-1β induced ~50% total sGAG loss in cartilage after 8 days (~6% per day), significantly lower than those of 10 or 25 ng/ml treatment. Thus the 1ng/ml IL-1β treatment was chosen for all the following experiments to mimic a moderately aggressive inflammation injury. In the second study, zolendronic acid, at 0.5 μm, 1 μm, 2.5 μm or 5 μm, was added together

Copyright 2016 The Organizing Committee for the 2016 Summer Biomechanics, Bioengineering and Biotransport Conference

with 1ng/ml IL-1β during the 8-day culture, and sGAG loss were measured (Fig. 2B). ZA treatment at 1 μm showed the optimal inhibitory effect on sGAG loss, and thus ZA at 1 μm was chosen for all following experiments.

During 8 days culture, GAG release from cartilage treated with ZA alone is close to that of control group (Fig. 3A), with ~1.5% per day at an almost constant rate. However, ZA significantly reduced the GAG release when cartilage was exposed to IL-1β (36% vs. 47% of IL-1β alone, p=0.03). A similar trend was also observed when comparing the Young's modulus and dynamic modulus of the samples in four groups (Fig. 3B-C) (Young's modulus of IL-1β + ZA vs. IL-1β alone: 0.15 vs. 0.08 MPa, p = 0.04).

ZA maintained bovine chondrocyte viability in the presence of IL-1β

After 8 days exposure to IL-1β, increased cell death was observed (Fig. A-B) in explants, while the addition of ZA in the treatment greatly reduced the number of dead cells (Fig. 4 B-C).

Spontaneous calcium signaling of in situ chondrocytes

Spontaneous $[Ca^{2+}]_i$ signaling of *in situ* chondrocytes in cartilage was recorded after 2-day culture. IL-1β treated samples showed significantly dampened $[Ca^{2+}]_i$ signaling in chondrocytes, lower than half of that in control group (Fig. 5A). Treatment of ZA preserved the $[Ca^{2+}]_i$ signaling of chondrocytes injured by IL-1β in term of the responsive percentage (Fig. 5A). ZA and IL-1β also modified the frequency and rising speed of $[Ca^{2+}]_i$ peaks (Fig. 5B-C).

DISCUSSION

Using an *in vitro* long-term explant culture model, this study showed that zoledronic acid, an FDA approved medicine, could protect the chondrocytes and mechanical integrity of cartilage from the damage of IL-1β. The chondro-protective function of zoledronic acid is correlated with the spontaneous $[Ca^{2+}]_i$ signaling of chondrocytes. As ZA or bisphosphonates are believed without anti-inflammatory functions, our future study will investigate the detailed chondro-protective mechanisms of ZA.

REFERENCES: [1] Tan AR., et al., Arthritis Res Ther, 2015. [2] Matos MA., et al., Eur J Orthop Surg Traumatol, 2010. [3] Bian, L., et al., J Biomech, 2008. [4] Lu, X.L., et al., J Bone Miner Res, 2012.

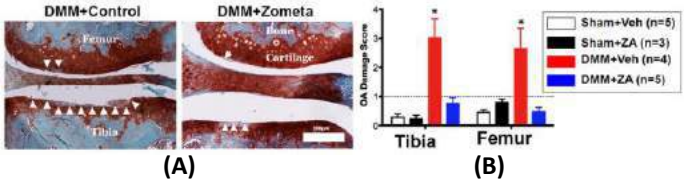

Figure1. Continuous administration of zolendronic acid (ZA) suppressed the development of post-traumatic OA in a DMM mouse model (destabilization of the medial meniscus). A, Histological analysis and B, Cartilage Damage Scoring of DMM and ZA treated mouse knees. (Veh: Vehicle control group)

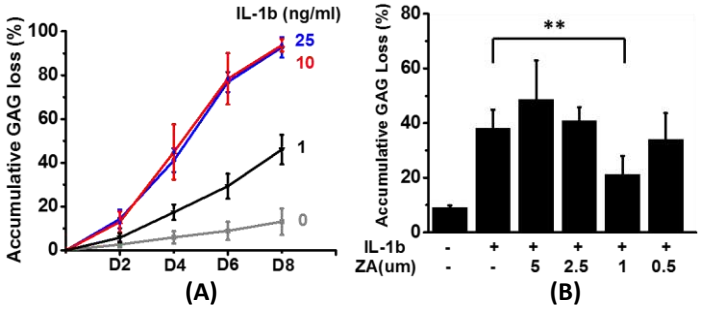

Figure2. Percent sGAG loss from IL-1β damaged explants that are rescued by ZA treatment: A, Kinetics of sGAG loss from cartilage in response to 8-day treatment with different doses of IL-1β; N=5 disks from 3 animals. B, Accumulative sGAG loss from cartilage in an 8-day time response experiment. Explants were subjected to different doses of ZA in the presence of IL-1β (1ng/ml); N=4 disks from 2 animals. *: P < 0.05, and **: P < 0.01.

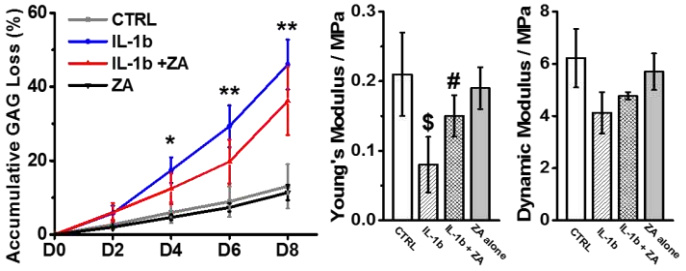

Figure 3: Treatment groups are control, IL-1β (1 ng/mL), IL-1β + ZA (1 nM) and ZA (1um) alone. A, Kinetics of sGAG loss from cartilage in response to 8-day treatment. B, Mechanical property of explants: Equilibrium Young's modulus and dynamic modulus; N=5 disks from 3 animals. $ vs. CTRL and # vs. IL-1β: P < 0.05.

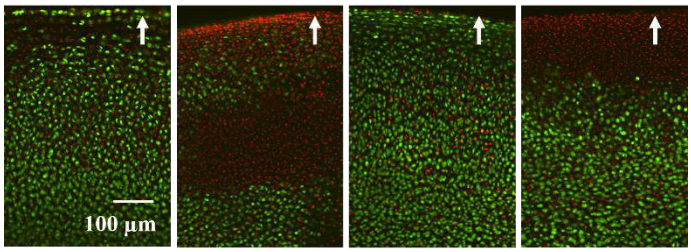

(A) CTRL **(B)** IL-1β **(C)** IL-1β + ZA **(D)** ZA alone

Figure 4: Bovine chondrocyte viability evaluated on Day 8 after treatments. Viable cells were labeled with calcein-AM (green) and non-viable cells with ethidium homodimer-1 (red). White arrow: intact superficial surface of cartilage.

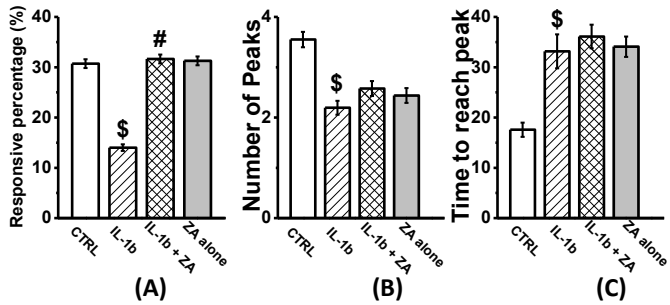

Figure 5: Responsive rate of $[Ca^{2+}]_i$ signaling and other spatiotemporal characteristics of each responsive cells for in situ chondrocytes after 2-day culture. Treatment groups are control, IL-1β (1 ng/mL), IL-1β + ZA (1 nM) and ZA (1um) alone. N=5 disks from 3 animals. $ vs CTRL and # vs IL-1β: P < 0.05.

Copyright 2016 The Organizing Committee for the 2016 Summer Biomechanics, Bioengineering and Biotransport Conference

SB^{3}C2016
Summer Biomechanics, Bioengineering and Biotransport Conference
June 29 –July 2, National Harbor, MD, USA
SB^{3}C2016-1000

CONTRACTILE ACTIVITY IN BRANCHED LYMPHATIC VESSELS

Samira Jamalian (1), Michael J. Davis (2), James E. Moore Jr. (1)

(1) Department of Bioengineering
Imperial College London
London, United Kingdom

(2) Department of Pharmacology and Physiology
University of Missouri School of Medicine
Columbia, MO, USA

INTRODUCTION

The lymphatic system is a branched network of vessels that is present in all of the tissues of the body. To maintain the fluid balance, the system has to transport viscous fluid (lymph) against gravity and adverse pressure difference. Lymph flow is maintained by contraction of individual vessel segments (via contraction of muscle cells in their wall) as well as lymphatic valves that prevent back flow. Consistent lymph flow is essential for tissue homeostasis and prevention of edema.

In situ observations of rat mesenteric lymphatic vessels have shown that adjacent lymphagions (vessel segments between two valves) contract with the same frequency and a small time delay. Contraction propagation in both orthograde and retrograde directions has been previously observed in bovine, guinea-pig, and rat lymphatic vessels in vivo, in situ as well as in isolated vessel experimental set ups. These experiments were mostly performed on short segments of lymphatic vessels without branching points. It is expected that pumping coordination and propagation would be much more complex in a branched network arrangement [1−4].

In this study, we have quantified determinants of lymphatic contractility in isolated rat mesenteric lymphatic vessels containing one branch point, with at least one valve in each vessel. Our experimental set up permits us to control inlet and outlet pressures of the system. We can track the diameter of the vessel in real time and quantify contractile activity throughout the length of the branched segment. To our knowledge, this is the first isolated vessel experiment performed on lymphatic branches. We have developed computational models of lymphangions in series and in branched network arrangement closely tied to available experimental data. The novel findings of these experiments will be used to inform our computational model and improve its physiological relevance [5−7].

METHODS

Mesenteric lymphatic vessels with one branch point and at least one valve in each vessel were isolated from male Sprague-Dawley rats and cannulated with glass micropipettes. The cannulated vessels were then transported to an inverted microscope. The pressures p_{in} and p_{out} of the reservoirs beyond the pipettes were controlled with servo controllers. Vessels were imaged continuously throughout the experiment for diameter tracking. Animal protocols were approved by the Institutional Animal Care and Use Committee at the University of Missouri-Columbia and conducted in accordance with the NIH Guide for the Care and Use of Laboratory Animals. An image of one of the isolated and cannulated vessels is presented in Figure 1.

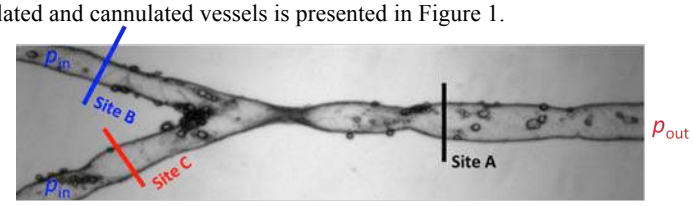

Figure 1. Cannulated lymphatic vessel segment with one branch point. Site A, site B, and site C are diameter tracking sites in each vessel. p_{out} is the pressure of the outlet reservoir. Both vessels upstream of the branch point are connected to the inlet reservoir. (p_{in})

RESULTS

Lymphatic contractions were modulated by transmural pressure. Figure 2 shows diameter tracings at sites A, B, and C during a 0.4 min period at each pressure step as inlet and outlet pressures increased from 3 to 10 cmH_2O, with steps of 1 cmH_2O (p_{in} = p_{out}). Amplitude, frequency, and coordination of contractions varied with transmural

Copyright 2016 The Organizing Committee for the 2016 Summer Biomechanics, Bioengineering and Biotransport Conference

pressure. External pressure (p_e = 0.5cmH_2O) remained constant.

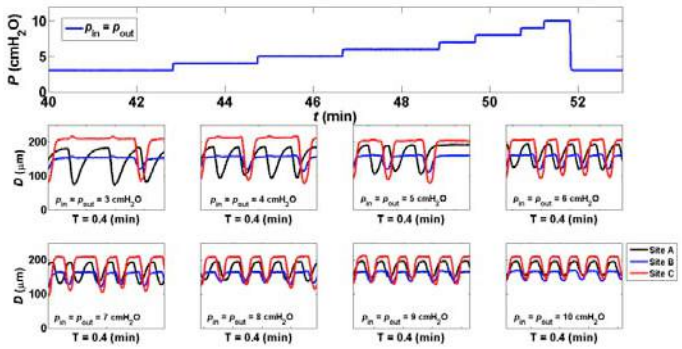

Figure 2. Top: Step increase in p_{in} and p_{out} ($p_{in} = p_{out}$, blue). Bottom: Diameter tracings of the vessel in figure 1 at sites A (black), B (blue), and C (red) during a 0.4 min period at each pressure step. Amplitude, frequency, and coordination of lymphatic contractions were modulated by transmural pressure.

Contraction frequency (f) increased with transmural pressure, with maximum increase occurring at lower pressure values. For example, average contraction frequency 2.3× increased for vessels B and C when inlet and outlet pressures increased from 3 to 5 cmH_2O. Importantly, vessels B and C contracted with similar frequencies at all pressure differences, while vessel A initially had a higher contraction frequency. All three vessels eventually synchronized and reached a 0.25 Hz contraction frequency at $p_{in} = p_{out}$ = 10 cmH_2O. However, contractions at sites B and C were synchronized in all pressure steps.

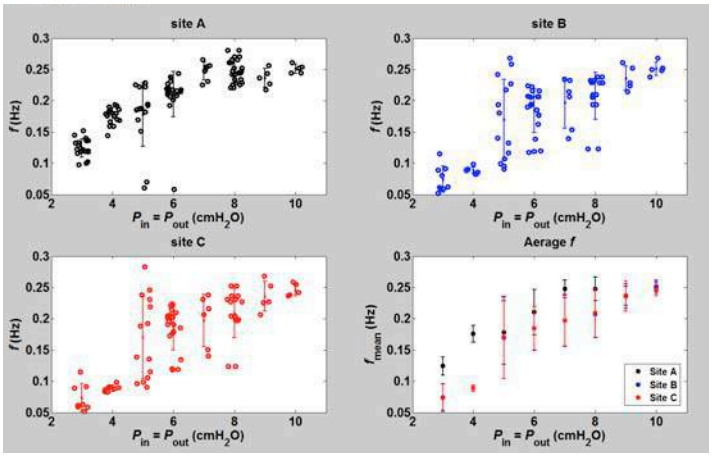

Figure 3. Frequency of contractions at sites A, B, and C at each pressure step. Contractions at sites B and C were synchronized with equal frequencies. Thus, average frequency of site C (red) overwrites the data for site B (blue) (Bottom right).

Diameter amplitude (D_{amp} = D_{max} − D_{min}) decreased as transmural pressure increased from 4 to 10 cmH_2O. This is due to larger minimum diameters (D_{min}) at higher transmural pressures while maximum diameter (D_{max}) of vessels (during their relaxed and non-contracted state) remained relatively unchanged. It should be noted that on the first rising of pressures (from 3 to 4 cmH_2O), diameter amplitude increased by 6 and 3.5% at site A and B, respectively. Overall, at the highest tested pressure (10 cmH_2O), D_{amp} dropped by 47, 62, and 37% (of its initial value at 3 cmh_2O), at sites A, B, and C, respectively.

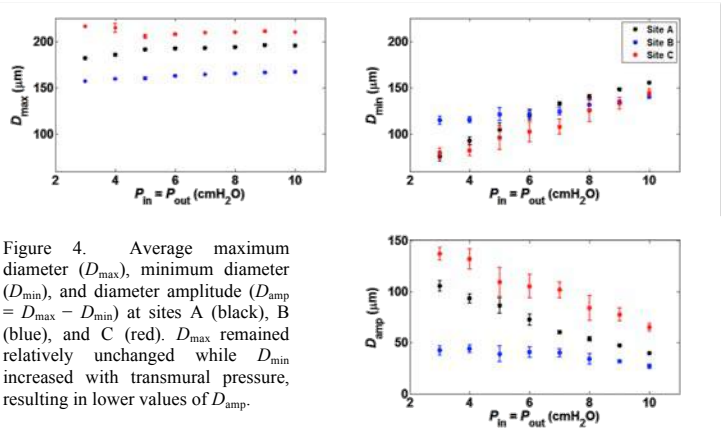

Figure 4. Average maximum diameter (D_{max}), minimum diameter (D_{min}), and diameter amplitude (D_{amp} = D_{max} − D_{min}) at sites A (black), B (blue), and C (red). D_{max} remained relatively unchanged while D_{min} increased with transmural pressure, resulting in lower values of D_{amp}.

DISCUSSION

Diameter measurements in isolated branched lymphatic vessels from rat mesentery demonstrated that diameter amplitude, contraction frequency and coordination are modulated by transmural pressure. Contractions at sites B and C were synchronized with equal frequency at all pressure steps. This may be attributed to the fact that the two sites were connected to the same pressure reservoir (p_{in}) and were located upstream of the branch point. At $p_{in} = p_{out}$ =10 cmH_2O, all sites contracted synchronously, suggesting that this might be the optimum pumping condition at high transmural pressures. Contraction frequency increased while diameter amplitude dropped as inlet and outlet pressures increased. This is due to vessel wall stiffening at higher transmural pressures, which prevents the vessels from reducing their diameter as much during maximum contraction, resulting in higher minimum diameters, while peak diameter remains unchanged. In this study we report the first measurement of contractility in branched segments of isolated lymphatic vessels. These findings will be used to inform our computational model of lymphatic networks to improve the physiologic relevance of our modeling framework.

ACKNOWLEDGEMENTS

This research was funded by NIH grants R01-HL094269, U01-HL123420, and R01-120867. JEM gratefully acknowledges the support of The Royal Society and The Royal Academy of Engineering.

REFERENCES

[1] Zawieja, DC et al., *Am J Physiol*, 264: H1283–H1291, 1993.
[2] McHale, NG et al., *J Physiol*, 450: 503–512, 1992.
[3] Crowe, MJ et al., *J Physiol*, 500: 235–244, 1997.
[4] Davis, MJ et al., *Lymphatic Research and Biology*, 4: 3–10, 2006.
[5] Jamalian, S et al., *Am J Physiol*, 305(12):H1709-H1717, 2013.
[6] Bertram, CD et al., *Am J Physiol*, In press.
[7] Jamalian, S et al., *Proceedings of ASME 2013 SBC*, 2013

Copyright 2016 The Organizing Committee for the 2016 Summer Biomechanics, Bioengineering and Biotransport Conference

SB³C2016
Summer Biomechanics, Bioengineering and Biotransport Conference
June 29 –July 2, National Harbor, MD, USA
SB³C2016-1001

ACOUSTIC VISUALISATION OF FLOW-SOUND IN THE RESPIRATORY AIRWAY

Gabriel P. Saputra (1), Kazunori Nozaki (2), Satoshi Ii (1), Chizu Habukawa (3), Shigeo Wada (1)

(1) Department of Biomechanical Science and Bioengineering
Osaka University
Osaka, Japan

(2) Division of Dental Informatics
Osaka University Dental Hospital
Osaka, Japan

(3) Department of Pediatrics
Minami Wakayama Medical Center
Wakayama, Japan

INTRODUCTION

Detection of early stage lung diseases is still a challenging field for physician and engineers. Practice of radiology or magnetic resonance imaging technique provides advantages to observe the condition of the inner organ, however, the risk of the radiation and the high cost of magnetic resonance imaging technique cannot be neglected. On the other hand, the usage of lung sound for diagnosing the lung condition may offer a solution for this setback. Importance of the lung sound detection appeared a long time ago since the invention of stethoscope, yet the practice of listening to the patient's lung sound are still performed until today. Recently, the development of the respiratory acoustic measurement technique results in the improvement of the ability of acoustic analysis to be implemented in continuous respiratory observation which is important especially in treating young children, the elderly people, and people with disability.

The diagnosis method using lung sound measurements demonstrates a promising future, but has practical limitations. It is well known that the sound measured on the chest surface by the stethoscope laid between 100-5000 Hz with sharp decrease at 800 Hz and low strength at 1500 Hz [1]. Nevertheless, the fundamental phenomena of the sound generation and the sound propagation from the source to the chest surface are unsatisfactorily known. This study examines the generation of the sound caused by the flow inside an airway model. Frequency analysis of the recorded sound was performed in aiming better understanding of the acoustic characteristics generated by the flow in the respiratory system.

METHODS

A lung silicone model was prepared based on a set of CT scan images of an 11 years old boy with a stable, non-asthmatic condition. The CT images were segmented using in-house segmentation code based on multidirectional segmentation method [2]. The segmentation method was able to extract the airways up to 8th generation airway branch. A total of 39 airway bronchi was successfully obtained.

A silicone model size of 185×115×60 mm^3 was constructed based on the segmented image. As shown in Figure 1A, the trachea end was connected to 15 mm diameter rubber hose which is connected to a 3D printed connector, while the bronchi was connected with 2 mm (5 bronchi) and 1 mm (34 bronchi) silicone tube. The silicone tubes were collected in an acrylic flow distributor and all open-ended silicone tube were located outside the measurement box to prevent the sound generation at the edge of the tubes. Air with constant flow rate of 500 mL/s corresponds to a Reynolds number of 4500 at the trachea was employed in order to simulate the flow condition at peak velocity of tidal breaths. Both the inspiration and expiration direction were studied.

The sound generated by the air flowing through the airways was measured by using a microphone array system consists of 4 microphones (GRAS 40PH, GRAS Sound and Vibration, Holte, Denmark) calibrated to a standard pressure calibrator. The microphone array measured at 20 locations on horizontal direction and 34 locations on vertical direction so that in total 680 measurement points were obtained to map the sound pressure distribution of the silicone model. Distance between each measurement points was kept constant at 5 mm. All microphones were located at a distance of 3 mm from the surface of the silicone model to the microphone tip. All measurements were performed inside an anechoic room to reduce the background noise level.

Copyright 2016 The Organizing Committee for the 2016 Summer Biomechanics, Bioengineering and Biotransport Conference

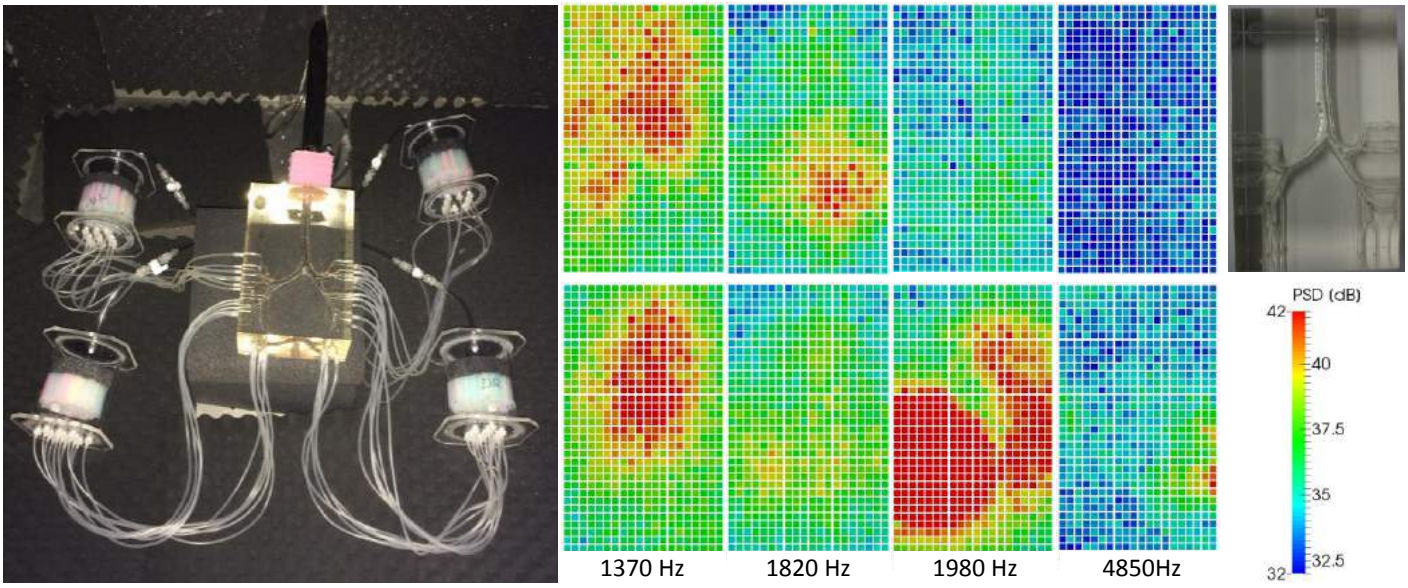

(A) **(B)**

Figure 1: (A) Setup of the airflow from the air tank to the model. Each bronchi was connected to a silicone tube. (B) Color-graph of the sound pressure power spectral density (PSD) at 1368 Hz, 1818 Hz, 1984 Hz, and 4848 Hz at inspiration (top), and expiration (bottom) direction.

The sound was recorded using a National Instrument Data Acquisition system with a sampling frequency of 20000 Hz. The length of each measurement was three providing enough number of samples for the 50 times ensemble averaging in the frequency analysis. All data processing calculations were performed using MATLAB® R2012a.

RESULTS

Power spectral density of the sound generated from the silicone airway model at 680 points are shown in Figure 1. The results show the main feature of the airways shape at frequency of 1370 Hz, 1820 Hz, 1980 Hz, and 4850 Hz. In these figures, red color indicates locations with high sound pressure, while blue color indicates low sound pressure detected by the microphone. Air flowing in the inspiration direction majorly produce sound on frequency less than 2000 Hz on the larger airways such as trachea and main bronchus. In the expiration direction, a wide frequency band sound was generated between 1000-8000 Hz. At frequency range between 1000 Hz and 2000 Hz, the sound was produced mainly on the trachea and main bronchus, while at range 2000-8000 Hz the sound mainly generated at small airways.

DISCUSSION

Characteristics of the sound may be determined by the frequency component and the magnitude of the sound pressure. Current results showed us that the frequency component generated by the air flowing inside the silicone model is different between the inspiration and expiration direction. Low frequency components (around 1000 Hz) was majorly generated in the large airways such as trachea and main bronchus. High frequency components (2000 Hz and more) were generated mainly in the smaller airway, especially those close to the outlet of the silicone model.

Lung sound analysis has been performed since a long time ago, and physician believe that the information contained in the lung sound laid in the lower frequency region less than 3000 Hz. In our results, it is clearly shown that the information contained in the frequency range less than 3000 Hz was successfully obtained although in the frequency range of less than 1000 Hz our model did not show a good frequency feature.

On the other hand, our measurement showed some locations with frequency component sound. It is not clear how the sound is generated at these locations. This new information is important since many airway disease encompass remodeling and inflammation of the airway [3] and the appearance of bronchoconstriction [4].

In this study, the manner of the sound propagation affected by anatomical tissues e.g. skin, bon, fat, etc. was not discussed yet. Those features may influence the propagation characteristics and lead to some differences between the sound characteristics generated in the airways and the sound measured on the chest surface. In our future work, an evaluation of the sound propagation as a function of the surrounding tissues must be performed computationally in order to result a better understanding of lung sound analysis.

ACKNOWLEDGEMENTS

This work was supported in part by JSPS Grants-in Aid for Scientific Research No. 24240073.

REFERENCES

[1] Bohadana, A et al., *N Engl J Med,* 370(8):744-751, 2014.
[2] Nakamura, M et al., *J Physiol Sci*, 58:493-498, 2008.
[3] Elias, J A et al., *J Clin Inves*, 104(8):1001-1006, 1999.
[4] Grainge, C L et al., *N Engl J Med*, 364(21):2006-2015, 2011.

Copyright 2016 The Organizing Committee for the 2016 Summer Biomechanics, Bioengineering and Biotransport Conference

SB^{3}C2016
Summer Biomechanics, Bioengineering and Biotransport Conference
June 29 –July 2, National Harbor, MD, USA
SB^{3}C2016-1002

NUMERICAL CONSTRAINT FOR TRACKING TAGGED MAGNETIC RESONANCE IMAGES IN BIOMECHANICAL SIMULATIONS

Arnold David Gomez (1), Chan Deva (2), Yuan-Chiao Lu (2), Dzung Pham (2), Philip Bayly (3), Jerry Prince (1)

(1) Electrical and Computer Engineering Dept.
Johns Hopkins University
Baltimore, MD, USA

(2) Center for Neuroscience and Regenerative Medicine, Henry Jackson Foundation,
Bethesda, MD, USA

(3) Mechanical Engineering Department
Washington University in St. Louis
St. Louis, MO, USA

INTRODUCTION

Tissue deformation is plays a fundamental role in many vital organs, including cardiac function, and displacement during impact leading to traumatic brain injury [1-2]. Motion estimation using tagged MRI has had an expanding role as a functional biomarker in clinical practice, and as method for providing experimental validation of mechanical simulations [1,3]. Harmonic phase (HARP) analysis is a popular approach to track tagged images by extracting phase vector images, which effectively become conserved material properties associated to a reference configuration i.e., values that travel with the tissue as it deforms [4]. However, generation 3D displacement fields requires volumetric data acquired over multiple repetitions, which, given experimental inconsistency, magnify the effects of motion, partial volume, and other artifacts. To reduce these effects, estimation of 3D is often accompanied by regularization and filtering, but these strategies often elicit additional parameters that are difficult or impossible to measure experimentally, and thus may induce additional uncertainty and error to the estimation.

This study describes the HARP tracking process as enforcing conservation of an additional material property—the phase vector at each material location. This novel description enables embedding the tracking process into finite element (FE) simulations, and including mechanical features inherent to numerical biomechanical analysis such as realistic boundary conditions, and material properties. Because these features can be measured or inferred experimentally, FE-based HARP tracking (HARP-FE) produces accurate and representative 3D strain fields. To illustrate these ideas, HARP-FE was derived and deployed to: (1) calculate the principal stress distribution of a pre-strained incompressible tissue sample using synthetic image data, and (2) estimate motion of a brain phantom subject to rotational acceleration using experimental MRI data.

METHODS

Theory—A harmonic phase vector field, $\boldsymbol{\phi}$, is typically extracted from complex MRI by applying a band-pass filter centered at the tagging frequency [4]. HARP tracking consists of finding spatial coordinates, $\boldsymbol{x}$, with the same phase values as those in a set of initial material points, $\boldsymbol{X}$, i.e., $\boldsymbol{x}(\boldsymbol{X})$ such that $\boldsymbol{\phi}(\boldsymbol{X}, t_0) = \boldsymbol{\phi}(\boldsymbol{x}(\boldsymbol{X}), t)$. This relationship is equivalent to a mass transport expression stemming from the weak formulation of conservation of the phase density field $\boldsymbol{\phi}$ in a control volume [5]. In a mass-conservative field, it can be shown that

$$\frac{\mathrm{D}(\boldsymbol{X}, t_0)}{\mathrm{D}t} = \frac{\partial \boldsymbol{\phi}(\boldsymbol{x}, t)}{\partial t} + \nabla \boldsymbol{\phi}(\boldsymbol{x}, t) \cdot \boldsymbol{v}(\boldsymbol{x}, t) = 0, \qquad (1)$$

where $\boldsymbol{v}$ is velocity. The spatial terms above represent a phase version of the familiar *optical flow* equation used for motion estimation via image registration [6]. With the Lagrange multiplier, λ, the material term yields the HARP-FE tracking constraint,

$$\boldsymbol{f}_{harp} = \lambda(t)[\boldsymbol{\phi}(\boldsymbol{x}(\boldsymbol{X}), t) - \boldsymbol{\phi}(\boldsymbol{X}, t_0)], \qquad (2)$$

which is directly applied (as an additional phase-based body force) to the virtual work equation from conservation of momentum, or

$$\delta \mathrm{W} = \int_{\mathcal{R}} \boldsymbol{P} : \delta \dot{\boldsymbol{F}}\, dV - \int_{\mathcal{R}} \boldsymbol{f} \cdot \delta \boldsymbol{v}\, dV + \oint_{\mathcal{S}} \boldsymbol{t} \cdot \delta \boldsymbol{v}\, dV dS = 0, \qquad (3)$$

where $\boldsymbol{P}$ is the material-dependent 2nd Piola-Kirchhoff stress tensor, $\boldsymbol{F}$ is the deformation gradient, $\boldsymbol{t}$ represents external loads, and $\boldsymbol{f}$ represents all internal forces, including tracking $\boldsymbol{f} = \boldsymbol{f}_o + \boldsymbol{f}_{harp}$. The HARP-FE constraint was implemented as a plug-in extension for the FEBio Software Suite [7] using (2), and tangent stiffness contribution defined by the linearization of (3), i.e,

Copyright 2016 The Organizing Committee for the 2016 Summer Biomechanics, Bioengineering and Biotransport Conference

$$\mathrm{D}\delta W_{harp}(\boldsymbol{x}, \delta\boldsymbol{v})[\mathrm{u}] = \int_{\mathcal{R}} \lambda(t)\nabla\boldsymbol{\phi}(\boldsymbol{X}, t_0)\ \delta\boldsymbol{v}\cdot\delta\boldsymbol{u}\ dV, \qquad (4)$$

where $\mathrm{D}f(\mathrm{x})[\mathrm{u}]$ is the directional (or Gateaux) derivative.

Approximation of Stress Distribution—The goal this experiment was to demonstrate compatibility and benefits of including mechanical analysis along with motion estimation. An incompressible tissue sample was modeled as a rectangular, pre-stretched (10% in the x-direction), Veronda-Westmann solid (C_1= 0.5 kPa, C_2= 2.5), subject to force at its center (Fig. 1a). Synthetic tagged images in each direction (64×64×2 px, 0.2×0.2mm, complementary spatial modulation of magnetization, or C-SPAMM, 12 px spacing) were generated before and after the application of the force for the reference and deformed configurations. These images were decomposed into magnitude and phase to define $\boldsymbol{\phi}$ [4], and used as input for HARP-FE, which was performed first without any constraints, then with added boundary conditions at the ends, and, finally, with boundary conditions as well as pre-stretching. The multiplier $\lambda(t)$ was set to <0.05 rad mean tracking error. Combined grid images (x and y) appear in Fig. 1b-c.

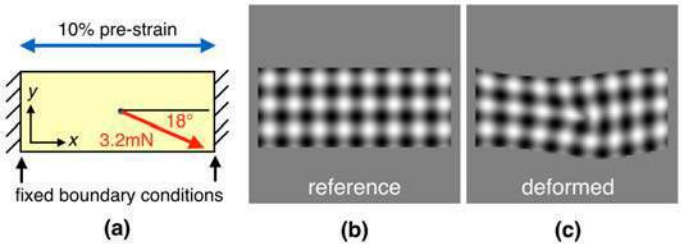

Figure 1: Displacement information from a model (a) was used to create synthetic images (b-c) and stress estimation via HARP-FE.

Experimental Motion Estimation of Brain Phantom—This experiment was designed to evaluate the HARP-FE using actual MRI data against a conventional tracking approach. A gelatin phantom was mounted in a MRI-compatible rotational apparatus (Fig 2a) and subsequently imaged while experiencing sudden angular acceleration (Siemens 3.0T mMR Biograph scanner, 13 axial slices, 160×24 zero padded to 160×160 px, 1.5×1.5mm, 15×15mm, SPAMM sequence, 12 px spacing, see [8] for more information). The images were interpolated into a 160×160×130 volume, and decomposed for tracking as described. Phase images were tracked with conventional 3D-HARP [4] and with HARP-FE, which was performed in the geometry shown in Fig. 2b. $\lambda(t)$ was set to <0.25 rad mean tracking error.

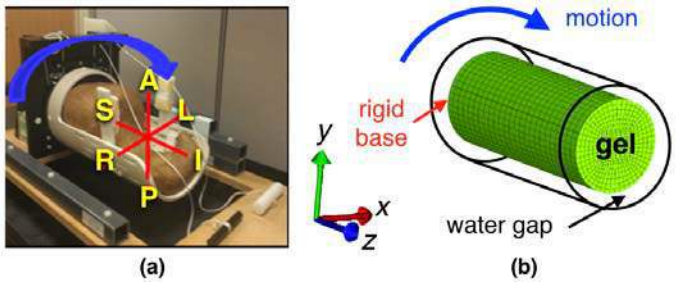

Figure 2: An MRI-compatible rotation apparatus (a) was used to image a gel phantom [8]. The bottom of the phantom was affixed to the container and other surfaces were surrounded by water (b). The gel volume was discretized into a FE domain for tracking. The letters indicate standard imaging directions, and the 3D arrows indicate the FE coordinate system.

RESULTS

Figure 3 shows stress approximations using different variations of HARP-FE. Although material and tracking parameters are constant, the unconstrained solution allows small differences in deformation (labeled with arrows), which have little effect on kinematics, but yield large changes in stress due to the exponential nature of the material. Incorporation of boundary conditions improves the solution, but the most notable differences occur with inclusion of pre-strain.

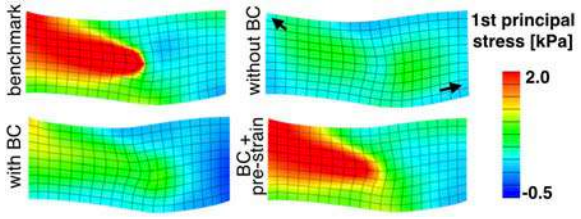

Figure 3: Adding boundary conditions (BC) reduces but does not eliminate visible discrepancies in stress distribution (arrows). Pre-strain with BCs allows excellent agreement with the benchmark.

Figure 4 shows a comparison between conventional 3D-HARP, and HARP-FE. Because the former does not include regularization, it is susceptible to error in areas with imaging artifacts, such as the boundaries, producing intractable deformations. The deformation via HARP-FE is subject to elastic regularization minimizing the artifacts.

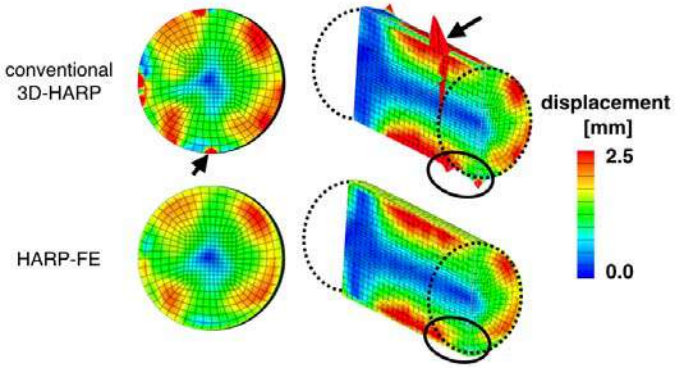

Figure 4: Radial (left), and axial (right) views of magnitude displacement maps show artifacts (arrows and circles) that eliminated via continuum mechanics regularization.

DISCUSSION

Although FE-based HARP tracking requires mesh generation, it offers unique advantages that enable calculation of stress as well as kinematics and exhibits improved tolerance to imaging artifacts. Because it can be performed simultaneously with physical loads, or as a stand-alone driver of deformation, this technique is well suited for different applications, including inverse parameter identification.

ACKNOWLEDGEMENTS

This research was funded with NHI grant R01-NS055951 and support by the Center for Neuroscience and Regenerative Medicine.

REFERENCES

[1] Gotte, M. et al. *J Am Coll Cardiol.* Mar 1;37(3):808-17. 2001.
[2] Coats, et al. NNS Meeting. 2011
[3] Bayly, P. et al. *Annu Rev Biomed Eng*. 14: 369–396. 2012.
[4] Osman, N. et al. Magn Reson Med. Dec; 42(6): 1048–1060. 1999.
[5] Spencer, A. J. M. *Continuum Mechanics.* Dover. 2004.
[6] Horn, B. et al. *Artificial Intelligence* 59 (1993) 81-87.
[7] Maas, S. et al. *J Biomech Eng.* Jan 134(1):011005. 2012.
[8] Knutsen, A. et al. J Biomech. 2014 Nov 7;47(14):3475-81.

Copyright 2016 The Organizing Committee for the 2016 Summer Biomechanics, Bioengineering and Biotransport Conference

SB³C2016
Summer Biomechanics, Bioengineering and Biotransport Conference
June 29 –July 2, National Harbor, MD, USA
SB³C2016-1003

A ROBUST FRAMEWORK FOR BUILDING ATTRIBUTE-RICH FE MODELS OF MITRAL VALVE FROM IMAGING DATA

Andrew Drach (1), Amir H. Khalighi (1,2), Robert C. Gorman (3), Joseph H. Gorman III (3), Ajit P. Yoganathan (4), Michael S. Sacks (1,2,5)

(1) Center for Cardiovascular Simulation
Institute for Computational Engineering and Sciences
The University of Texas at Austin
Austin, TX, USA

(2) Department of Mechanical Engineering
The University of Texas at Austin
Austin, TX, USA

(3) Gorman Cardiovascular Research Group
University of Pennsylvania
Philadelphia, PA, USA

(4) Cardiovascular Fluid Mechanics Laboratory
Wallace H. Coulter Department of Biomedical Engineering
Georgia Institute of Technology
Atlanta, GA, USA

(5) Department of Biomedical Engineering
The University of Texas at Austin
Austin, TX, USA

INTRODUCTION

Mitral Valve (MV) is the dual-flap atrioventricular heart valve, which regulates the blood flow between the left atrium and left ventricle. The structure of MV apparatus is comprised of two leaflets (anterior and posterior), chordae tendineae, and papillary muscles. Heart diseases associated with abnormalities in MV structure and/or function are among the most common cardiovascular disorders, affecting over 2 million people in the United States [1]. Treatment procedures include heart valve repair and prosthetic valve replacement, with the former considered more effective [2]. The quality of clinical care and treatment outcomes may be improved by using predictive computational models for surgical planning and medical device design.

Kunzelman et al. [3] performed the first Finite Element (FE) simulation of the MV's biomechanical behavior using post-mortem geometry and tissue properties. Since then, the fidelity of FE models have significantly improved to build models based on *in vivo* geometries [4], patient-specific information [5], and also internal structure [6]. However, the complex geometry and strong heterogeneity in structural properties of the MV require fast and robust methodologies for building FE models from imaging data.

Here, we propose a novel, robust pipeline to build high-fidelity, attribute-rich FE models of the complete mitral heart valve from imaging data. In the sections to follow, we describe the major steps of the proposed framework, including the generation of geometric models and registration of structural properties.

METHODS

Five ovine MV sample were obtained from an USDA approved abattoir (Superior Frams, CA, USA), instrumented with fiducial markers, and imaged using micro-computed tomography (μCT) to acquire geometry with high resolution, as described in [7]. We first simulated the end-systolic state of the valve in the Georgia Tech Cylindrical Left Heart Simulator (CLHS) [8] to collect geometric data from the fully closed state. In this state, the branching details of the MV chordae tendineae are much clearer. Next, we dripped a solution of 0.5% glutaraldehyde over the valves for two hours in a vertical fixation loop to simultaneously unfurl and spread the leaflet surfaces while stiffening the tissue at the end-diastolic state. We then imaged the valves and acquired the information to build geometric models of the MV leaflets.

The acquired images from open and closed states were segmented in ScanIP software suite, labeled and trimmed in ZBrush 3D sculpting software (ZBrush Inc., CA, USA), and analyzed using customized Python scripts. Open-state imaging data was used to reconstruct the high-resolution geometry of the leaflets using median surface representation. Closed-state data was used to reconstruct the chordae tendineae using the centerline representation. Fiducial markers were extracted from both imaging datasets for landmark registration.

Collagen fiber architecture (CFA) data was collected from flattened leaflets using the small-angle light scattering (SALS) technique [9]. The CFA images of flattened leaflets were mapped using landmark registration to the reconstructed leaflet median surface unfolded into 2D plane using cylindrical projection.

RESULTS

The major steps of processing open state images and building the leaflet median surface representation are illustrated in Figure 1. The volumetric data was segmented (once for leaflet tissue, next for fiducial markers), trimmed, labeled and analyzed to obtain the median surface geometry and project the markers onto the median surface.

Copyright 2016 The Organizing Committee for the 2016 Summer Biomechanics, Bioengineering and Biotransport Conference

The major steps in obtaining the chordae tendineae geometry are shown in Figure 2. The closed state scan was segmented, trimmed, and labeled in the same way as the open state data. The processed volumetric data was analyzed using the feature thinning method to obtain centerline representation with pointwise cross-sections. Having a geometric model

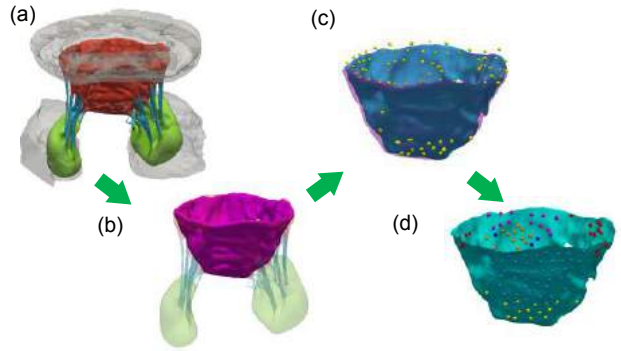

Figure 1: Data processing steps for open state MV images: (a) trimmed and labeled geometry with original data overlaid in gray; (b) trimmed leaflet tissue surface (purple); (c) reconstructed median surface and fiducial markers; (d) labeled and projected markers onto the median surface.

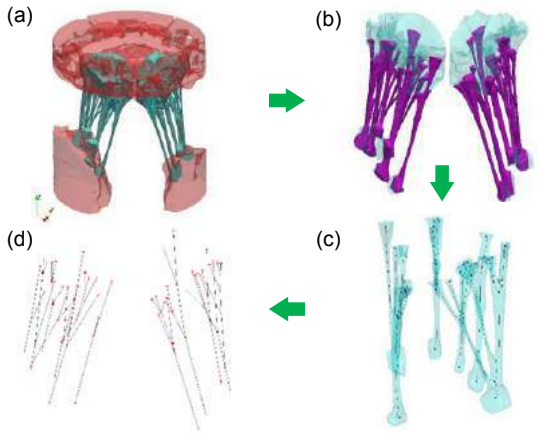

Figure 2: Data processing steps for closed state MV images: (a) trimmed geometry with original data overlaid in red; (b) trimmed chordae tendineae geometry (purple); (c) centerlines with volumetric data overlaid in cyan; (d) reconstructed chordae tendineae in the closed state.

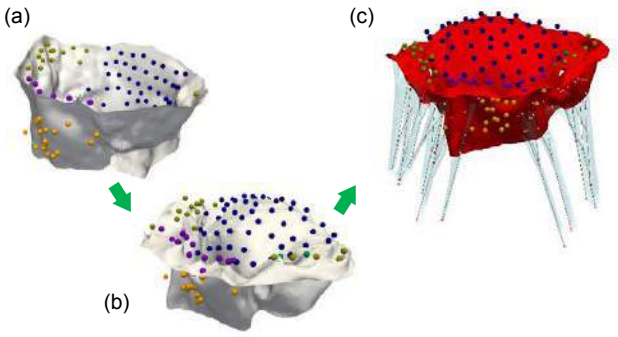

Figure 3: Landmark registration and the reconstruction of the full MV in closed state: leaflets with mapped markers (a) in the open state and (b) in the closed state after registration; (c) reconstructed MV leaflets with chordae tendineae.

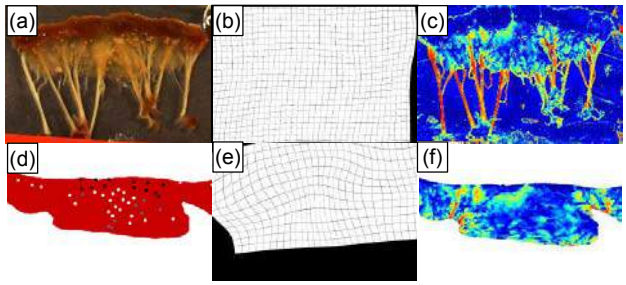

Figure 4: Registration procedure for mapping CFA onto the leaflet surface: (a) flattened posterior leaflet with fiducial markers; (b) deformation grid for mapping markers onto the CFA image; (c) image of CFA with registered markers; (d) reconstructed leaflet surface after cylindrical projection; (e) deformation grid for mapping the leaflet surface onto the CFA image; (f) CFA mapped onto the leaflet surface.

of the leaflets in the open state, and fiducial markers in both open and closed states, we performed landmark registration between the two to reconstruct the leaflet surfaces in the closed state. The major steps, including the final reconstruction of leaflets and chordae tendineae in the closed state, are presented in Figure 3.

The registration of CFA data onto the reconstructed leaflet geometry was performed using landmark registration algorithm. The original images, deformation grids, final mapped CFA data are illustrated in Figure 4.

DISCUSSION

The proposed pipeline was successfully used to build high-fidelity attribute-rich finite element (FE) models of ovine mitral valves from μCT imaging datasets. Our approach allows for a robust segmentation, reconstruction, geometric analysis, and mapping of tissue attributes of the full MV apparatus (leaflets & chordae tendineae). One of the important advantages of this framework is the parametric representation of the geometry and embedded attributes. This allows to adjust the level of detail of the geometric and attribute variations independently of the required level of discretization for FE simulation. This is an important feature for the practical use of the FE models for medical device design and surgical planning, because it allows to easily simplify the model for the preliminary simulations / case studies, and then switch back to the high-fidelity simulations in the final stage of design or planning. Another important feature of the proposed framework is that it can be easily modified to incorporate statistical analysis of patient-specific models, and build representative population-averaged FE models.

ACKNOWLEDGEMENTS

Research reported in this publication was supported by National Heart, Lung, and Blood Institute of the National Institutes of Health under award number R01HL119297. The content is solely the responsibility of the authors and does not necessarily represent the official views of the National Institutes of Health.

REFERENCES

[1] Enriquez-Sarano, M. et al., *Lancet*, 373(9672):1382-1394, 2009.
[2] Fedak, P. W. et al., *Circulation*, 117(7):963-974, 2008.
[3] Kunzelman, K. et al., *J Heart Valve Dis* 2.3: 326-340, 1993.
[4] Lim, K. et al., *J Heart Valve Dis* 14.3: 386-392, 2005.
[5] Wang, Q., & Sun, *Ann. Biomed. Eng.* 41(1), 142-153, 2013.
[6] Lee, CH. et al. *Biomech Model Mechanobiol,* 1-22, 2015.
[7] Rabbah, JP. et al., *Ann. Biomed. Eng.* 41.2: 305-315, 2013.
[8] Khalighi, A. et al., *Lecture Notes in Comput. Sci.*, 164-171, 2015.
[9] Sacks, MS. et al., *Ann. Biomed. Eng.* 25:678–689, 1997.

Copyright 2016 The Organizing Committee for the 2016 Summer Biomechanics, Bioengineering and Biotransport Conference

SB³C2016
Summer Biomechanics, Bioengineering and Biotransport Conference
June 29 –July 2, National Harbor, MD, USA
SB³C2016-1004

IMAGE-BASED ANALYSIS FOR INVERSE ESTIMATION OF MUSCLE FIBER FORCES IN THE TONGUE

Narihiko Koike (1), Tsukasa Yoshinaga (1), Kazunori Nozaki (2), Satoshi Ii (1), Shigeo Wada (1)

(1) Graduate School of Engineering Science
Osaka University
Toyonaka, Osaka, Japan

(2) Division of Dental Informatics
Osaka University Dental Hospital
Suita, Osaka, Japan

INTRODUCTION

The tongue has an ability to deform its shape largely by contracting the muscle fibers which are broadly distributed in the tongue. This mechanical deformation of tongue creates a complex and subtle movement for speech. The muscle consists of three types of extrinsic muscle fibers and four types of intrinsic muscle fibers. It is known that the extrinsic muscle fibers contribute to move and deform the tongue largely since the muscle is connected to a fixed bone. On the other hand, it is considered that the intrinsic muscles inside the tongue undertake the role to control the subtle movement and deformation of tongue. In the past studies, in order to understand the mechanism of tongue deformation, the action potentials of extrinsic muscles during pronunciation were measured with electromyogram [1], and the orientation of extrinsic muscle fibers was investigated by using diffusion MRI [2]. However it is not clear how the tongue is deformed by contraction of the multiple muscle fibers distributed in it.

Image-based simulation has a potential to investigate the effect of muscle fiber contraction in a continuum tissue on the deformation of tongue. Recently, Buchaillard et al. conducted a computational analysis of the tongue deformation and the acoustic propagation in the oral cavity for the utterance of French vowels under *a priori* given parameter for the muscle contraction [3]. However, due to lack of the experimental data of muscle contraction, such a direct analysis has a limitation to represent the actual deformation of the tongue and consequently estimate the muscle contraction.

In this study, we propose an image-based analysis for inverse estimation of muscle fiber contraction in the tongue. In this proceeding, we show a basic concept of the formulation and the results for validation, and discuss a feasibility of the proposed approach.

METHODS

Muscle fiber orientation The shape of tongue at a rest position was obtained from the MRI image of a subject (Fig. 1). The muscle fibers were classified into three types of extrinsic tongue muscles: genioglossus (GG), hyoglossus (HG), and styloglossus (Sty), and four types of intrinsic tongue muscles: superior longitudinal (SL), inferior longitudinal (IL), transversal (Trans), and vertical (Vert). The orientation of each muscle fiber was determined based on the anatomical data [4]. The volume model was divided into 59,502 tetrahedral elements including the muscle fibers which produce the contraction stress in the direction of orientation.

Governing equation The deformation of tongue can be expressed by the law of conservation of mass and the motion equation,

$$\rho_0 = \rho J, \quad \rho d_t \boldsymbol{v} + \eta \boldsymbol{v} = \nabla \cdot \boldsymbol{\sigma} \tag{1}$$

where ρ_0 and ρ are an initial density and a current density, respectively, J is a volume change, $\boldsymbol{v}$ is a velocity vector, η is a viscous dumping coefficient, $\boldsymbol{\sigma}$ is a stress tensor. The stress involves the elastic stress for an isotropic part of the tissue ($\boldsymbol{\sigma}_{\mathrm{elas}}$) and anisotropic part of the muscle fiber ($\boldsymbol{\sigma}_{\mathrm{fiber}}$),

$$\boldsymbol{\sigma} = \boldsymbol{\sigma}_{\mathrm{elas}} + \boldsymbol{\sigma}_{\mathrm{fiber}}. \tag{2}$$

In this study, the tissue of muscle was assumed to be a hyperelastic body which can be expressed as a 2nd-order Mooney-Rivlin model. The strain energy density function is described as

$$W = \sum_{p,q=0}^{2} C_{pq}(\bar{I}_1 - 3)^p(\bar{I}_2 - 3)^q + \frac{K}{2}(J-1)^2 \tag{3}$$

where C_{pq} is the material constant, I_1 and I_2 are the first and the second invariant of the right Cauchy-Green deformation tensor, respectively, K is a bulk modulus. The second term is a penalty term for the constraint of a constant volume. The elastic stress tensor $\boldsymbol{\sigma}_{\mathrm{elas}}$ was calculated by the partial differentiation of W with respect to Green

Copyright 2016 The Organizing Committee for the 2016 Summer Biomechanics, Bioengineering and Biotransport Conference

strain tensor. The values of material constant obtained by experiments were C_{10} =1037 Pa, C_{20} =486 Pa and $C_{01} = C_{11} = C_{02}$ =0 Pa [5].

The stress tensor of muscle fiber $\boldsymbol{\sigma}_{\text{fiber}}$ produced by contraction of muscle fibers can be represented by

$$\boldsymbol{\sigma}_{\text{fiber}} = f_a(\boldsymbol{e}_a^* \otimes \boldsymbol{e}_a^*) \quad (4)$$

where f_a is a magnitude of the contraction stress produced by the muscle fiber, $\boldsymbol{e}_a^*$ is a unit vector of fiber orientation in a current arrangement.

Inverse analysis The contraction stress of muscle fibers was estimated from the deformation of tongue by solving the minimizing problem with respect to the magnitude of contraction stress f_a,

$$\min\ E(f_a) = \frac{1}{2}\sum_l \left(\boldsymbol{x}_l^{\text{ref}} - \boldsymbol{x}_l(\boldsymbol{v}_l)\right)^2 + \frac{w}{2}\sum_i (\Delta t \delta \boldsymbol{v}_i)^2 \quad (5)$$

subject to Eq. (1) and $f_a \geq 0$

where $\boldsymbol{x}^{\text{ref}}$ and $\boldsymbol{x}$ are the corresponding nodal position on the surface of a reference model and a current model, respectively, $\delta \boldsymbol{v}$ is a time variation of velocity, Δt is a time step for iteration, w is a weighting factor, l and i are the node number on the surface and the whole region, respectively. A primal-dual interior point method [6] was used to solve the minimizing problem with respect to the contraction stress f_a. The second term in the right side in Eq. (5) was introduced to stabilize the convergence of f_a in the explicitly interactive calculation.

RESULTS AND DISCUSSION

To validate the inverse analysis of the muscle fiber contraction stress, three reference shapes of the deformed tongue were prepared by solving the governing equation (1) with a finite element method as a direct problem under a given contraction stress. In the direct analysis, the contraction stress f_a was set to 3 kPa at each extrinsic muscle fibers, GG, HG, or Sty and 0 Pa at the other muscles. Here we call them the GG, HG, and Sty model, respectively. Furthermore, the surface displacement was fixed to zero at the site where the tongue attached to the bone. The initial density, viscous coefficient, bulk modulus used for the calculation were $\rho_0 = 1.04 \times 10^3$ kg/m^3, $\eta = 1.0 \times 10^4$ kg/m^3·s, K =1.0×10^4 Pa, respectively.

Figure 2 shows the change in error of surface geometry, E in Eq. (5), during the iteration for inverse analysis using three reference shapes of GG, HG, and Sty models. The error was normalized by the initial value, E_0. It was found that the error in surface geometry of tongue between the reference and simulated models were decreased monotonically after taking the maximum and successfully converged to a negligible small value.

Figure 3 shows the change of contraction stress f_a at three extrinsic muscle fibers of GG, HG, and Sty, and four intrinsic muscle fibers of SL, IL, Trans, and Vert during the error converging of surface geometry. The final values of contraction stress converged at seven muscles are listed in Table 1. In the case of HG and Sty model (Fig. 3(b) and (c)), the contraction stress once generated at all muscles but finally dissipated except at the HG or Sty muscle where the contraction stress was given. The contraction stress f_a estimated by the inverse analysis was close to the preset value of 3 kPa (Table 1).

On the other hand, in the case of GG model (Fig. 3(a)), the contraction stress remained at the Sty and HG muscles in the error convergence although the contraction stress at the GG muscle closed to the preset value. This indicates the difficulty to identify the contraction stress only from the surface geometry of the tongue. In order to improve the accuracy in the estimation of contraction stress by the inverse analysis, it would be necessary to consider the physiological nature of tongue muscle obtained by experiments.

ACKNOWLEDGEMENT

We acknowledge Prof. Yoshikawa, Associate Prof. Murakami, Assistant Prof. Uchiyama from Graduate School of Dentistry Osaka University and Associate Prof. Tamakawa from Osaka University Dental Hospital for their contribution to MRI image. This research was partially supported by the flagship 2020 project using Post-Kei computer, MEXT, Japan.

REFERENCES

[1] Baer, T. et al., *Ann Bull RILP*, 22:7-19, 1988.
[2] Gaige, T. A. et al., *J Magn Reson Imag*, 26:654-661, 2007.
[3] Buchaillard, S. et al., *J Acous Soc Am*, 126(4):2033-51, 2009.
[4] Miyawaki, K., *Res Inst Logoped Phoniat Univ Tokyo Ann Bull*, 8:23-50, 1974.
[5] Gerard, J. M. et al., *Med Eng Phys*, 27:884-892, 2005.
[6] Yamashita, H., *Tech Rep*, *Math Sys*, *Inc*., *Tokyo*, *Japan*, 1994.

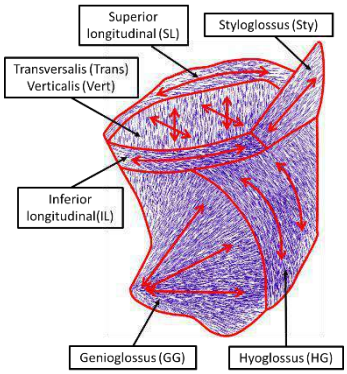

Figure 1: The configuration of tongue and the muscle fiber orientation. The red arrows indicate the overall direction of muscle fibers.

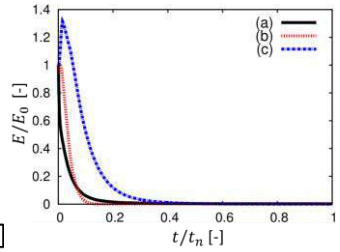

Figure 2: Convergence of the error in surface geometry for three reference shapes of (a) GG, (b) HG and (c) Sty model.

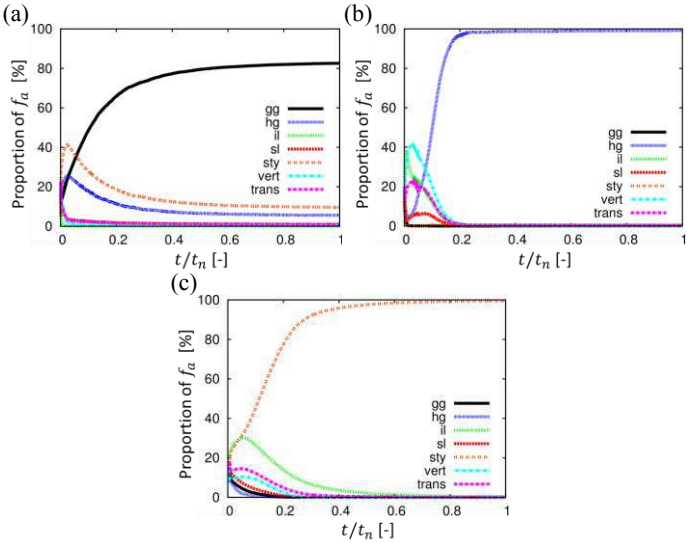

Figure 3: Convergence of f_a at the seven muscles in tongue for three reference shapes of (a) GG, (b) HG and (c) Sty model.

Table 1: Estimated f_a by inverse analysis for three reference shapes of (a) GG, (b) HG and (c) Sty model. [Pa]

	GG	HG	IL	SL	Sty	Trans	Vert
Case (a)	2977	201	0	36	346	33	15
Case (b)	2	3115	1	11	3	12	2
Case (c)	0	0	14	0	2975	2	1

Copyright 2016 The Organizing Committee for the 2016 Summer Biomechanics, Bioengineering and Biotransport Conference

SB^{3}C2016
Summer Biomechanics, Bioengineering and Biotransport Conference
June 29 –July 2, National Harbor, MD, USA
SB^{3}C2016-1005

ANCHORAGE-INDEPENDENT PRIMING INCREASES CHONDROGENIC POTENTIAL OF HUMAN MESENCHYMAL STEM CELLS

Andrea R. Tan (1), Daniel S. Donovan (2), Gerard A. Ateshian (1), J. Chloe Bulinski (3), Clark T. Hung (1)

(1) Department of Biomedical Engineering
Columbia University
New York, NY, USA

(2) Department of Orthopaedic Surgery
Mt. Sinai-Roosevelt Hospital
New York, NY, USA

(3) Department of Biological Sciences
Columbia University
New York, NY, USA

INTRODUCTION

Stem cells derived from patients can be differentiated into a variety of cell types, offering great potential for regenerative and personalized medicine. In particular, mesenchymal stem cells (MSCs) have been explored as an attractive alternative cell source to the limited chondrocytes for tissue engineering of articular cartilage. Unfortunately, like native terminally differentiated cells, MSCs exhibit cell-to-cell variability that translates to poor homogenous matrix development (Figure 1A) and represents a significant challenge to their optimization for cell-based therapies. While some heterogeneity may be due to contaminant cell populations, even in cases where cells are pre-selected, enriched subpopulations, variation still remains. We hypothesize that this variability may be due to cells being in different phases of the cell cycle (Figure 1B) and that these differences may hinder the efficacy with which cells can respond to exogenous factors such as growth factors to produce functional tissue. As such, to increase their predisposition to respond to cues, we have focused on the use of cell synchronization to selectively obtain cells in desired phases.

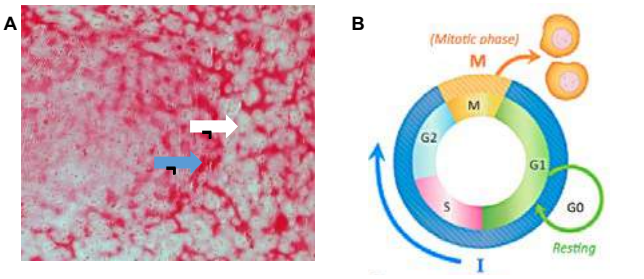

Figure 1. A) Picrosirius red staining for collagen in chondrocyte-seeded agarose constructs showing heterogeneity of cell elaborated matrix. White arrow: cells with little collagen; blue arrow: cells with rich collagen halo. B) schematic of cell cycle, which can be modulated to optimize cell differentiation and matrix production. G0: quiescent, G1: growth and synthesis, S: synthesis.

Classical cell biology studies investigating the effect of cell synchronization have typically utilized techniques untenable for tissue engineering, including S-phase inhibitors and physical detachment of less adherent mitotic cells, both of which result in limited cell yield [1,2]. We, and others, have recently explored the use of methylcellulose suspension to synchronize cells in the G1 phase [3,4], the growth phase believed to be responsible for differentiation [5]. Toward this end, we have previously shown that chondrocytes can be induced to produce greater and more uniform cartilage-like tissue when the cells have been synchronized during 2D expansion prior to 3D micropellet formation [3]. Here, we look to expand this technique to undifferentiated cells; we envision that modulation and manipulation of the cell cycle in this manner may provide a platform technology for optimization of cell differentiation and priming for a number of tissue regeneration goals. We hypothesize that synchronization of undifferentiated MSCs to G1 phase will prime them to be more chondrogenic in 3D culture.

METHODS

Tissue harvest and cell isolation MSCs were isolated from fresh unprocessed bone marrow (Lonza) of a 22 year-old male donor. Following separation via Percoll gradient, mononucleated cells were plated (5 x 10^3 cells/cm^2); adheredMSCs were expanded in high glucose DMEM supplemented with FBS until passage 4. Flow cytometry At desired timepoints, cells were harvested from monolayer culture by trypsinization and fixed in a 1:1 mixture of ethanol and PBS. Cells were stained with propidium iodide and analyzed on a flow activated cell

Copyright 2016 The Organizing Committee for the 2016 Summer Biomechanics, Bioengineering and Biotransport Conference

sorting (FACS) machine to determine cell cycle phase time and characterize the population of cells in each phase for each synchronization technique described below.

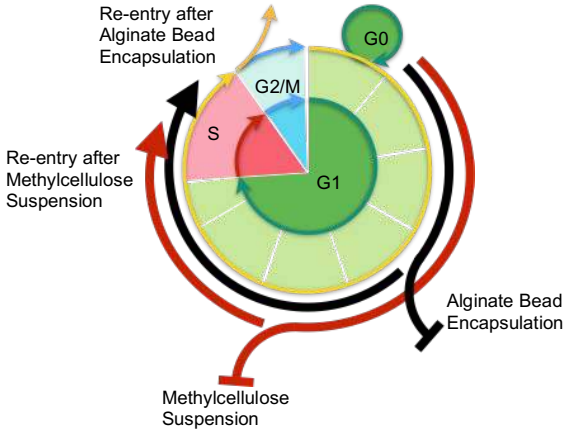

Figure 2. Representative cell cycle for human mesenchymal stem cells (total cell cycle time = 56.3 hr) with schematic of experimental synchronized groups (cells synchronized to G1 or triggered to re-enter the cell cycle toward S).

Cell Synchronization Various cell synchronization methods were employed to explore the individual phases (Figure 2); in particular, two distinct and established techniques were used to synchronize cells to the **G1 phase** and investigate whether triggered re-entry into the cell cycle **(toward S phase)** is necessary. *Asynchronous control*: as a control, one subset of cells was trypsinized at 90% confluence, maintaining an **asynchronous population** of cells. *G1 phase synchronization:* Cells were synchronized to the G1 phase via two adhesion removal techniques. (1) Alginate bead encapsulation*:* At 90% confluence, one subset of cells was trypsinized and encapsulated in 1% wt/vol alginate beads (seeding density: 4 x 10^6 cells/mL). After 48 hours, cells were extracted from the alginate beads with a depolymerization solution (55 mM sodium citrate, 0.15M sodium chloride). (2) Methylcellulose suspension: At 90% confluence, one subset of cells was trypsinized and resuspended in 1% wt/vol methylcellulose solution (seeding density: 1 x 10^6 cells/mL) for 48 hours. Cells were then extracted from solution through centrifugation. *Re-entry into cell cycle:* Following alginate bead encapsulation or methylcellulose suspension, cells from each group were reintroduced to FBS and plated at low seeding density to induce re-entry into the cell cycle toward S phase. Micropellet Formation For each group, following trypsinization, cells were counted and 0.5mL of 0.5 x 10^6 cell suspension was aliquotted into 1.5 mL sterile screw-top tubes. The tubes were spun in a microcentrifuge at 37°C and 2500 rpm for 20 minutes to form a visible cell pellet at the base of the tube. Micropellets were cultured in chondrogenic medium (dexamethasone, ascorbic acid TGFβ-3) and harvested on days 4 and 28. Biochem Analysis Each micropellet was dried and digested in proteinase K solution overnight at 56°C, with one aliquot used to quantify GAG content via the 1,9 dimethylmethylene blue dye-binding assay and a second aliquot used to determine collagen content via orthohydroxyproline assay, scaled for microplates. Total double stranded DNA content was assessed by the Picogreen assay. Statistics Statistical analyses were performed using one-way analysis of variance (ANOVA) with Tukey's Honest Significant Difference post hoc tests (Statistica), with α=0.05 and statistical significance set at $p \leq 0.05$ to compare groups across synchronization method. Data is reported as the mean and standard deviation of 4-5 samples per time point and group.

RESULTS

Experimental determination of the cell doubling time in combination with flow cytometry was used to calculate the time for each cell cycle phase (G1 = 41.40 hrs, S = 10.19 hrs, G2/M = 4.70 hours). Synchronization of cells to the G1 phase was generally successful across both anchorage-independent techniques, with cell phase population distributions found to be significantly different from asynchronous cell populations (Table 1, chi-squared test: $p<0.0001$). In response to differentiation cues (TGF-β3) in 3D, cells exhibited an elevated biosynthetic capacity (GAG/DNA, Figure 3, $p<0.05$). When methyl- cellulose suspended cells were induced to re-enter the cell cycle toward the S phase, cells were even more prolific in GAG production (Figure 3, $p=0.03$). In contrast, when alginate bead encapsulated cells were retriggered to enter the cell cycle to the S phase, cells exhibited reduced biosynthetic capacity, similar to asynchronous cells (Figure 2, $p=0.01$).

Table 1. Percent of human mesenchymal stem cells in each cell cycle phase as determined by flow cytometry.

	G1	G2	S
Asynchronous	73.54	8.35	18.10
Methylcellulose	94.52	1.63	3.84
Alginate Bead Encapsulation	82.48	17.52	0.00
Re-entry after Methylcellulose	79.30	11.21	9.49
Re-entry after Alginate Beads	77.47	8.86	13.67

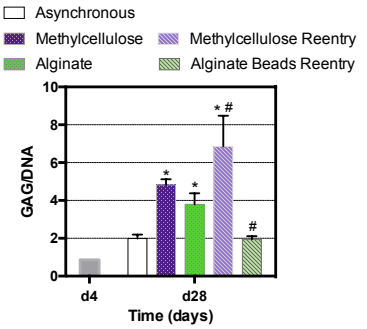

Figure 3. Normalized GAG/DNA biosynthetic output over 28 days in culture. *p<0.05 vs. asynchronous. #p<0.05 vs. respective G1 synchronized state.

DISCUSSION

Contrary to literature reports [5,7], but in line with our previous findings [3], the maximal benefit is observed when methylcellulose-suspended cells are induced to re-enter the cell cycle toward the S phase rather than staying arrested in the G1 phase, rejecting our initial hypothesis. Interestingly, alginate encapsulated cells induced to re-enter the cell cycle fail to exhibit similar behavior, suggesting that the particular technique of synchronization is of importance. Further work is ongoing to identify the differential effects produced by each synchronization technique to understand the factors that may be manipulated for engineered tissue optimization. Nevertheless, we have shown here that the use of methylcellulose synchronization produces a pure population of MSCs and maximizes the downstream effectiveness of cells to respond to differentiation cues and increase their biosynthetic output, a direct clinical translation of our previous finding.

A major limitation in using stem cells as a clinical source is their inefficient conversion to desired cell fates. Future work will build on this platform technology by examining the role of synchronization in modulating osteogenic and adipogenic differentiation from MSCs to identify which cell cycle phases may be most responsive to exogenous cues.

ACKNOWLEDGEMENTS

This work was supported in part by The Coulter Foundation and Columbia Technology Ventures (WHCF CU12-0369).

REFERENCES

[1] Kurose, A et al, *Cell Prolif*, 2006. [2] Merrill, GF et al, *Methods Cell Biol*, 1998. [3] Tan, A et al., *Trans ORS 2015*. [4] Sachidanandan, C et al., *J Cell Sci*, 2002. [5] Jovic, D et al., *J Biotechnol Biomaterial*, 2011. [6] Miller, J et al., *Cell Cycle*, 2007. [7] Roccio, M et al., *Development*, 2013.

Copyright 2016 The Organizing Committee for the 2016 Summer Biomechanics, Bioengineering and Biotransport Conference

SB³C2016
Summer Biomechanics, Bioengineering and Biotransport Conference
June 29 –July 2, National Harbor, MD, USA
SB³C2016-1006

EFFECTS OF SEATED SOLDIER POSTURE ON PELVIC FORCE TRANSMISSIBILITY

Brandon J. Perry (1), Kyvory A. Henderson (1), E. Meade Spratley (1), JiangYue Zhang (2), Andrew C. Merkle (2), Robert S. Salzar (1)

(1) Center for Applied Biomechanics
University of Virginia
Charlottesville, VA, United States

(2) Applied Physics Laboratory
Johns Hopkins University
Baltimore, Maryland, United States

INTRODUCTION

Pelvic response and injury due to underbody blast (UBB) has become a topic of interest in injury biomechanics since recent conflicts Operation Iraqi Freedom and Operation Enduring Freedom. One study reported that out of 608 casualties, 36% sustained pelvic injuries as a result of underbody blast [1].

Evans (1955) tested 22 denuded component pelves statically and dynamically with the goal of studying fracture [2]. The authors did not report pelvic angles or any data other than fracture patterns. Kemper 2008 tested six component pelves denuded of all soft tissue except the sacroiliac ligaments [3]. Pelves were tested with a sacrum angle of 25 degrees relative to the transverse plane and an input velocity of 2m/s. Pelvic angles were not reported.

Pelvis response due to high-rate axial impacts, such as in UBB, is not yet well known. Given the variability in deployed military vehicles seats and the resulting ranges of pelvic angle, a definitive relationship between seated posture and pelvic response is not feasible [4]. However, as a preliminary investigation, a set of nominally sub-injurious cadaveric experiments were developed to determine the posture effects on pelvic response.

METHODS

With institutional review board approval, ten (10) fresh-frozen post-mortem human subjects (PMHS) were acquired for this study. All specimens were screened for infectious disease and pre-existing pathology that may alter the specimen properties. Each specimen was sectioned between the L3 and L4 vertebral bodies and was disarticulated from its femurs. Abdominal contents were removed and replaced with ballast masses of ballistics gel in order to preserve inertial loading within the interior of the pelvic girdle. Pelvic angle was measured from a plane comprised of the bilateral anterior superior iliac spines (ASIS) and the pubic symphysis, relative to the coronal plane. Specimens 1-6 and 7-10 were potted with a target pelvic angle of 40° and 28°, respectively. Specimens were positioned in a custom made potting fixture, including a potting cup in which the lumbar spine is placed. Fixation was further bolstered with two six inch screws secured axially and four to six screws secured transversely through the vertebral bodies. Once the proper pelvic angle was achieved, FastCast® (Model FC-891, Goldenwest Manufacturing) urethane resin was used to envelop the specimen from the lumbar spine to the junction at S1-S2.

The pelvis potting block was rigidly affixed to the carriage of the test rig. (Figure 1) The carriage, which included a six degree-of-freedom load cell (Denton® Model 3868), was constrained to translate in the SAE-Z direction only. The inferior aspects of the pelves were allowed to rest against the seat platen, which was also constrained only to SAE-Z translate. All pelves were preloaded to the equivalent of the weight of a 50th percentile male torso. A suite of six axial accelerometers (Endevco® Model 7270A) were mounted on the carriage at the boundaries above and below the pelves in order to provide rig response and allow for load cell mass compensation. A pneumatically-driven transfer mass was used to provide input at the seat platen, such that a peak ΔV of 2m/s with a 10ms rise time was achieved. All data were baseline shifted and filtered with a four-pole phase-less low pass filter with a 3000Hz cutoff frequency.

Copyright 2016 The Organizing Committee for the 2016 Summer Biomechanics, Bioengineering and Biotransport Conference

RESULTS

Axial construct stiffness (SAE-Z) was assessed at each posture using force-displacement plots (Figure 2). Force was derived from the mass-compensated load cell attached to the potting and displacement was derived from the differential displacement of the input and reaction rig motions. Linear regressions of the force-displacement traces resulted in a mean axial stiffnesses of 323.42 N/mm (±47.14 N/mm) and 468.68 N/mm (±183.36 N/mm) for the 40° and 28° postures, respectively.

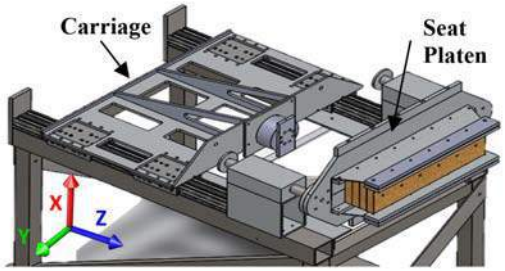

Figure 1. Pelvis testing rig.

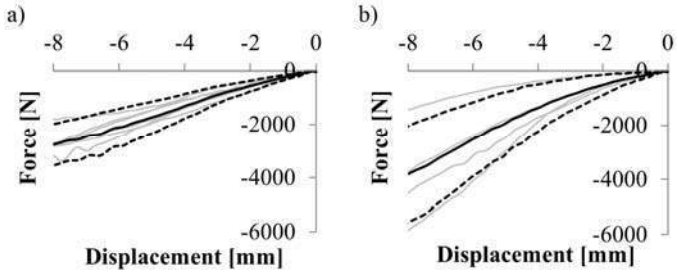

Figure 2. Reaction force-displacement curves for a) 40 degree and b) 28 degree pelvic angle. Gray lines represent individual tests, solid black lines are the average of the gray lines, and the dashed black lines are the mean ± the standard deviation.

Reaction moments (about the SAE-Y) were assessed using moment time history plots (Figure 3). Pelvic reaction moment was transposed from the potting load cell to the center of the L5-S1 joint in accordance with prior work [5]. Moment data was mass normalized by a factor proportional to the quotient of a reference mass and individual specimen mass [6]. Mean peak reaction moments of 118.18 Nm (±52.84 Nm) and 136.19 Nm (±42.29 Nm) were observed for the 40° and 28° postures, respectively.

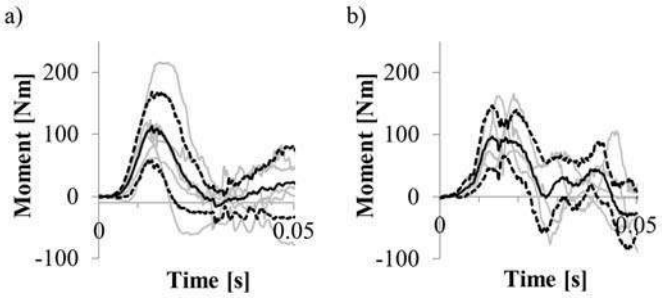

Figure 3. Reaction moment curves for a) 40 degree and b) 28 degree pelvic angle. Gray lines represent individual tests, solid black lines are the average of the gray lines, and the dashed black lines are the mean ± the standard deviation.

DISCUSSION

The pelvis is a highly complex shape with numerous articulations that provide for substantial compliance under load. Of these articulations, the most pertinent to axial response is the sacroiliac joint. The broad flat nature of this articulation allows for axial slipping as well as sagittal rotation resulting in the anterior pelvis being swept forward and superior during an impact. Given this arrangement, it was expected that the more vertical 28° construct would be stiffer in axial stiffness but produce a lower peak reaction moment, and indeed, this more upright posture produced a 45% larger axial pelvic stiffness but a 15% larger peak moment. However, the means of these groups were not statistically different (Axial: p=0.094; Moment: p=0.586).

One justification for the increase in reaction moment with the more vertical construct is the normalization factors (Figure 4). Normalized moment is directly proportional to the normalization factor, thus, specimens 8 and 10 moments were amplified by more than 75%. Non-normalized moments produced a mean of 108.01 Nm (±36.44 Nm) and 94.19 Nm (±26.03 Nm) for the 40° and 28°, respectively, resulting in a 13% decrease in the more vertical construct (p=0.534).

Given these apparent differences in construct response in the more upright versus more slouched posture, it is likely that different postures will correlate to different levels of risk for pelvic injury during UBB. Future efforts will investigate additional postures as well as acceleration and strain response within the pelvis in order to better describe its response to axial loading. Ultimately, it is hoped that through robust characterization of this response, better predictions and consequently better mitigation technologies maybe employed to decrease the incidence of pelvis injury from UBB.

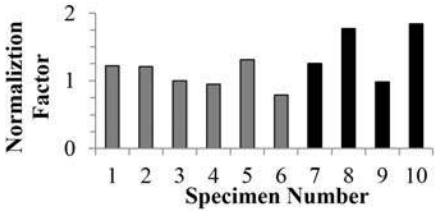

Figure 4. Specimen number and normalization factor (Gray: 40°, Black: 28°).

ACKNOWLEDGEMENTS

The authors of this study would like to thank the United States Army under contract# N00024-13-D-6400. This work and its conclusions do not necessarily reflect the position or policies of the U.S. Government.

REFERENCES

[1] Alvarez, J, *A Survey of Blast Injury across the Full Landscape of Military Science,* 2011: Keynote KN1, 2011.

[2] Evans, F et al., *The Anatomical Record*, 121:141-165, 1955.

[3] Kemper, A et al., *Rocky Mountain Bioengineering Symposium &International ISA Biomedical Sciences Instrumentation Symposium,* 472:150-155, 2008.

[4] Reed, M, *RDECOM-TARDEC Unclassified Public Release*, 2014.

[5] Rudd, R et al., *SAE Technical Paper,* 2006.

[6] Eppinger, R et al., *SAE Technical Paper,* 1984.

Copyright 2016 The Organizing Committee for the 2016 Summer Biomechanics, Bioengineering and Biotransport Conference

SB³C2016
Summer Biomechanics, Bioengineering and Biotransport Conference
June 29 –July 2, National Harbor, MD, USA
SB³C2016-1007

MATHEMATICAL MODELLING OF OXYGEN TRANSPORT IN THE RETINA

Wouter J. Thijssen, Emilie Lunddahl, Andris Piebalgs, Xiao Y. Xu

Department of Chemical Engineering
Imperial College London
London, United Kingdom

INTRODUCTION

The retina is known for being one of the most metabolically active tissues in the human body which makes it especially vulnerable to conditions of insufficient oxygen supply. Ischemia in the retina, as can be caused by diabetic and glycemic retinopathy, is perceived to be one of the most common causes for visual impairment in the developed world [1]. Therefore, an in-depth understanding of retinal oxygenation is necessary. However, multiple factors complicate the prediction of retinal oxygenation, amongst other features the localized placement of the mitochondria and the retinal microcirculation [2].

Many attempts have been made to improve the understanding of retinal oxygenation. This has been done experimentally by measuring oxygen tension as a function of retinal thickness via intrusive animal studies, as well as by developing empirical and mathematical models. Of particular interest is the 4-layer model developed by Roos [3] as shown in Fig. 1, where the outer retina is divided into 3 separate regions. Oxygen moves through these regions under diffusion-limited transport and is consumed only in region 2 which contains photoreceptors' mitochondria. The inner retina is assumed to have uniform oxygen diffusion, consumption and supply.

Roos' model is limited to 1D analysis and contains parameters that have only been readily measured in animals. This work critically evaluates the model to assess the importance of these parameters towards oxygen distribution in the retina by performing a global sensitivity analysis. Ranking these potentially unsuitable parameters in order of sensitivity can help guide which are in most need of more accurate empirical measurement in humans, as well as guide treatment forms which leverage this sensitivity.

Furthermore, the model has been extended into 2D to analyze the effect that the tissue geometry may have on oxygen distribution. By enhancing mathematical modeling of oxygen distribution in the retina, we hope to better understand the factors that affect the disease progression of retinopathy.

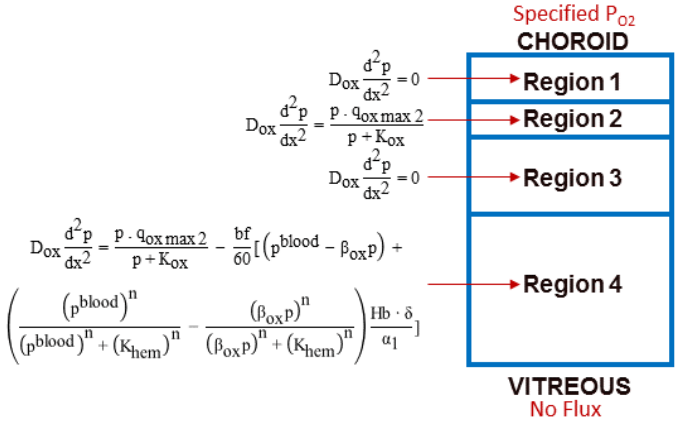

Figure 1: Illustration of Roos' model with the retina divided into 4 regions, with their respective equations

METHODS

A global sensitivity analysis using the Morris one-step-at-a-time method [4] was used to critically evaluate Roos' model and rank its parameters in order of sensitivity. The model's parameters for which this analysis was conducted on can be seen in Table 1.

Roos' model employs a uniform retinal thickness of 251μm, and therefore does not consider its variation along the arc of the retina. The effect of varying this parameter between 150μm and 300μm, both 'in

Copyright 2016 The Organizing Committee for the 2016 Summer Biomechanics, Bioengineering and Biotransport Conference

range' values for retinal thickness across the retinal arc [5], was analyzed by comparing their respective 1D oxygen profiles.

To extend into 2D, the model was set up in ANSYS Fluent using a mesh representing a quarter of the retina which spans from the back of the eye to the top of the eye. To explore the spatial heterogeneity a 2D model allows for, non-uniformity was incorporated into the inner-retinal supply term in two different ways. Firstly, a localized region was set to be completely ischemic, simulating a section of the vascular tree network becoming completely ischemic, a potential result of retinopathy. Secondly, non-uniformity of inner-retinal supply was set up across the arc in a linearly decreasing fashion to study non-uniformity's implications. This approach serves to evaluate the need of measuring and incorporating the non-uniformity of inner-retinal supply to build a more representative model for retinal oxygenation.

RESULTS

Parameters were ranked in decreasing order of importance following the global sensitivity analysis (Table 1).

Table 1: Parameter sensitivity ranking (decreasing order)

Hb	Hemoglobin concentration in blood
K_{hem}	P_{O2} at which haemoglobin is 50% saturated with oxygen
α_1	Solubility of oxygen in blood
α_2	Solubility of oxygen in the retina
D_{ox}	Diffusion coefficient of oxygen
n	Hill coefficient
K_{ox}	Michaelis-Menten constant of oxygen
δ	Oxygen carrying capacity of haemoglobin

A separate investigation into the retinal thickness' sensitivity is displayed in Fig. 2.

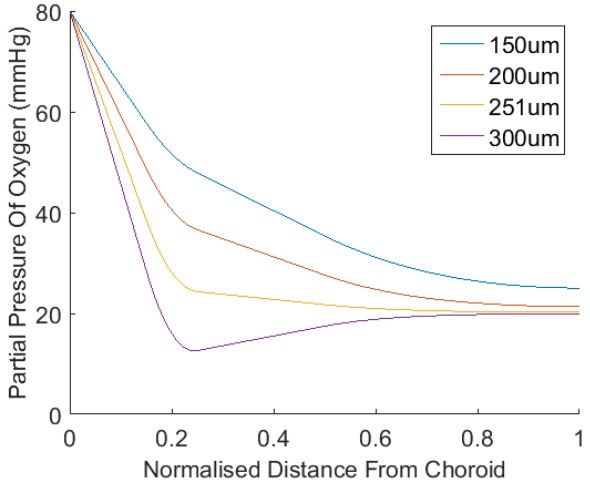

Figure 2: Oxygen profiles of retinal thicknesses at 150, 200, 251 and 300µm, normalized to allow for comparison.

The implications on 2D retinal oxygenation from applying a linear inner-retinal supply profile are summarized in Fig. 3. This profile applied along the arc has its maximum at the back of the retina (at theta = 90°, where the retina was set to be thicker) and linearly decreases to zero at the top of the retina (where the retina was set to be thinner).

DISCUSSION

Developing techniques to attain accurate measurements of the more sensitive parameters (Table 1) at the human retina is of high importance to further develop Roos' model. The implication of the most sensitive parameter, the hemoglobin concentration in blood, on the oxygen profile can also be significant towards clinical interests. At its upper bound typically seen in adult males of 170g/L, retinal oxygenation is sufficient, whereas at a value of 100g/L typically seen in anemic patients there is a much stronger risk of oxygen deficiency in the inner retina.

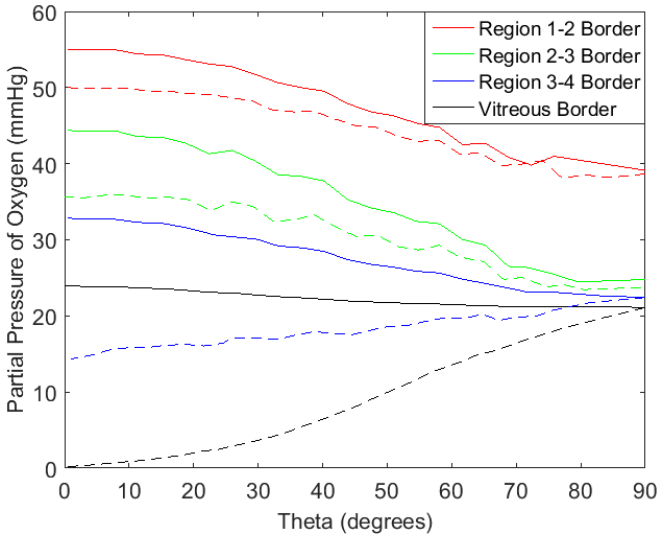

Figure 3: Oxygen profiles along retinal arc. Solid lines: uniform supply case; dashed lines: linear inner-retinal supply case.

The need to develop a 2D model is highlighted in Fig. 2, which shows significant discrepancies in the oxygen profiles as the thickness is varied. As the thicknesses plotted are within the range seen across the arc of the retina in 2D, there is a strong incentive to model this non-uniformity as part of a 2D model.

From this extended 2D model with linear inner-retinal supply applied, an interesting relationship between retinal thickness and inner-retinal supply can be seen (Fig. 3). Closer towards the border between regions 1 and 2, retinal thickness heterogeneity controls the oxygen profile, where the thinner end of the retina has a higher value for the partial pressure of oxygen. However, further towards the vitreous border, the effect of non-uniform inner-retinal supply becomes increasingly apparent. At the vitreous border, this effect is such that the oxygen profile effectively mirrors that of the applied linear supply term. As this is a region particularly vulnerable to oxygen deficiency, further developing an understanding of how the retinal vasculature, and thereby the inner-retinal supply profile, varies along the arc of the retina is of great importance to further development of the model.

For future studies, a 2D/3D model complemented with more accurate empirical measurements of the various parameters as identified in this work's sensitivity analysis can model clinical conditions more accurately and allow for clinically relevant conclusions to be drawn. With this, our work helps set the pace for improved modelling of retinal oxygenation to address the increasing problem of retinopathy.

REFERENCES

[1] Osborne, N et al., (2004). Retinal ischemia: mechanisms of damage. *Progress in Retinal and Eye Research*, 23(1), pp.91-147.

[2] Wangsa-Wirawan, N. and Linsenmeier, R. (2003). Retinal Oxygen. *Archives of Ophthalmology*, 121(4), p.547.

[3] Roos, M. (2004). Theoretical estimation of retinal oxygenation during retinal artery occlusion. *Physiol. Meas*., 25(6), pp.1523-1532

[4] Morris, Max D. "Factorial Sampling Plans for Preliminary Computational Experiments". *Technometrics* 33.2 (1991): 161–174.

[5] Sigelman, J. and Ozanics, V. (1982). In: F. Jokobiec, ed., Ocular anatomy, embryology and teratology., 1st ed. Philadelphia: Harper and Rowe, pp.441-485.

Copyright 2016 The Organizing Committee for the 2016 Summer Biomechanics, Bioengineering and Biotransport Conference

SB^{3}C2016
Summer Biomechanics, Bioengineering and Biotransport Conference
June 29 –July 2, National Harbor, MD, USA
SB^{3}C2016-1008

HEMODYNAMICS IN DEVELOPING STAGES OF CEREBRAL ANEURYSMS USING SPECTRAL-ELEMENT SIMULATIONS AND COMPARISON WITH PIV EXPERIMENTS

Tanvi K. Kaushik, Yulia T. Peet

School for Engineering of Matter, Transport and Energy
Arizona State University
Tempe, AZ, USA

Priya Nair, David H. Frakes

School of Biological and Health Systems Engineering
Arizona State University
Tempe, AZ, USA

INTRODUCTION

Aneurysms are pathological dilations of arteries; cerebral aneurysms are among the most dangerous ones and are commonly located in or near the circle of Willis [1][2]. The factors responsible for initiation, growth and eventual rupture of aneurysms have been identified as hemodynamics, wall biomechanics, mechano-biology and the peri-aneurysmal environment [1][2]. The rupture of this abnormality causes intra-cranial hemorrhagic strokes [1][2].

To compare the risks associated with surgery and the rupture of an untreated aneurysm, it is imperative to study the progression of its growth. In this paper we investigate the changes in hemodynamic quantities of three developing stages of aneurysm models through CFD simulations.

METHODS

Simulations were performed in an open source spectral element based CFD solver [3] Nek5000. Higher order spectral element methods with hexahedral mesh provide a better accuracy than the conventionally used finite volume codes that employ tetrahedral mesh [4]. The three developing stages of aneurysm models investigated in this paper are the advanced, mid and early stages. The advanced stage model was segmented and reconstructed from a patient-specific CT angiography dataset at the School of Biological and Health Systems Engineering (SBHSE) at ASU. This model was virtually modified to produce the early and mid stage models. Outlets and inlets for all the three models were extended to 10-15 times the diameter to allow for a better flow development and less interference with boundary conditions. The computational model of the advanced stage aneurysm with extended inlet and outlet is shown in Fig. 1. Hexahedral meshes were generated in the HyperMesh Software using mesh morphing tools. The numbers of elements in the early, mid and advanced stage models are 12760, 13946 and 15156 respectively, with 8 GLL points per element per direction in all the three directions. The numbers of nodes present in the three developing stages are 6533120, 7140352 and 7759872 respectively. Steady Poiseuille inflow conditions were applied at the inlet of all the three models. Simulations were executed for 0.7 seconds (600,000 time steps) with Reynolds number (based on mean inlet velocity and inlet diameter) equal to 653.21.

PIV experiments were performed at the SBHSE using a mixture of aqueous sodium iodide, glycerin and water. This blood analog was seeded with 8μm fluorescent microspheres.

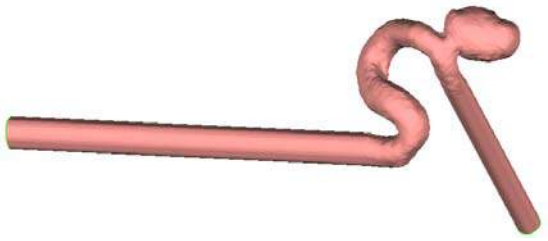

Figure 1: Advanced stage aneurysm model with extended inlet and outlet

RESULTS

Results from the PIV experiment and CFD simulation on the advanced stage aneurysm are compared in Table. 1. The center plane velocity profiles of the CFD and PIV models are shown in Fig. 2. The

Copyright 2016 The Organizing Committee for the 2016 Summer Biomechanics, Bioengineering and Biotransport Conference

velocity magnitude scale is non-dimensional, where 0.41 corresponds to 18 cm/s.

Table 1: Comparison of CFD and PIV root mean square velocity magnitude

Aneurysmal Quantity	CFD (cm/s)	PIV (cm/s)	Error (%)
Vrms	18.577	23.528	21.04

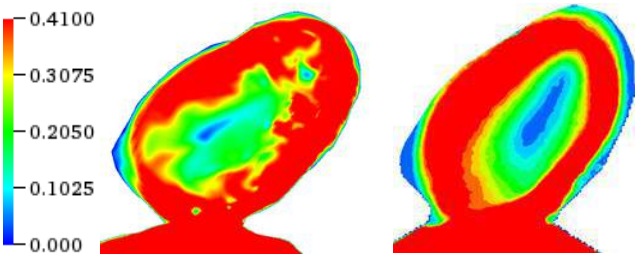

(a) CFD (b) PIV

Figure 2: Center plane velocity magnitude plot of the advanced stage aneurysm model

The following results have been obtained from CFD simulations. Center plane velocity vector plot of the early, mid and advanced stage aneurysm models are displayed in Fig. 3.

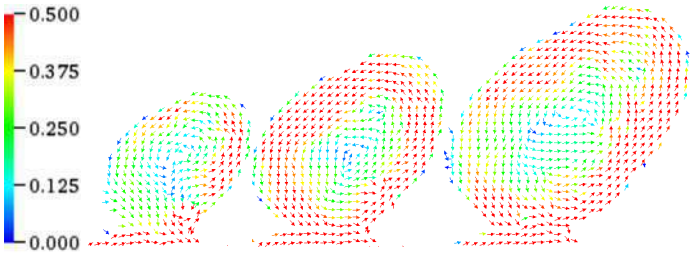

(a) Early (b) Mid (c) Advanced

Figure 3: Center plane velocity vector plot of the early, mid and advanced stage aneurysm models

Distribution of wall shear stress in the three stages is presented in Fig. 4

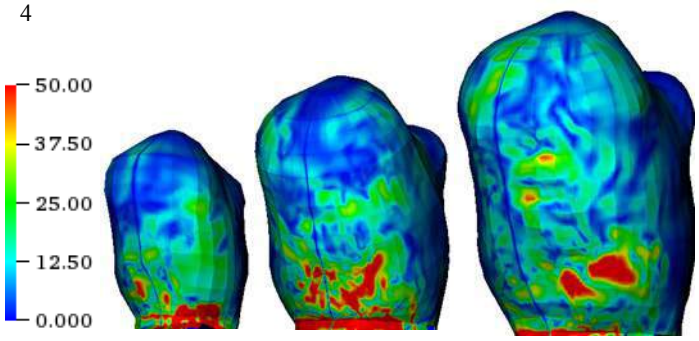

(a) Early (b) Mid (c) Advanced

Figure 4: Wall shear stress (Pa) in the developing stages

The weighted average values of hemodynamic quantities have been compared between the stages in Table. 2.

Table 2: Comparison of aneurysmal hemodynamic quantities in the three stages

Aneurysmal Quantities	Early Stage	Mid Stage	Advanced Stage
Vrms (cm/s)	14.192	20.524	18.577
WSS (Pa)	7.037	10.79	8.487
Pressure (Pa)	267.05	276.13	185.23

DISCUSSION

Local distribution of wall shear stress (wss) is governed by the swirling flow along the arterial walls. Circulation of fluid inside the curving geometry of the three models is noticeable in Fig. 3, although it is more distinct in the advanced and mid stages. Volume-averaged hemodynamic quantities in Table. 2 are seen to first increase between early-mid stages and then decrease between mid-advance stages. The initial increase could signify very early stages of aneurysm formation and flow development [1]. Reduction in values in the advanced stage is a consequence of wall enlargement, which is an adaptive response of the tissues to high blood flow [1]. Studies have shown that high wss regions initiate aneurysm formation as a response to the impact of inflow jets, and low wss regions are responsible for further remodeling and progression due to blood stagnation [1] and endothelial dysfunction [5]. Therefore it is important to identify both these regions, as seen in Fig. 4.

Results presented in this paper give us an insight into the flow dynamics in anatomically realistic aneurysm models. The two hurdles faced by such studies are, the necessity to perform these simulations at a time rate suitable for clinical decision making [6] and the requirement of physically-based parameters for predicting precise flow dynamics[6][7]. Also, further analysis of interaction among the aforementioned factors responsible for the growth and rupture is essential to gain a more comprehensive understanding of the disease.

REFERENCES

[1]Sforza, D. M., Putman, C. M., & Cebral, J. R., *Annual review of fluid mechanics*, *41*:91-107, 2009.

[2]Cebral, J. R., Putman, C. M., Alley, M. T., Hope, T., Bammer, R., & Calamante, F., *Journal of engineering mathematics*, *64*(4):367-378, 2009.

[3]Deville, M., Fischer, P., & Mund, E., "High-Order Methods for Incompressible Fluid Flow." *Cambridge University Press*, 2002.

[4]De Santis, G., et al., *Medical & biological engineering & computing*, 48(4):371-380, 2010.

[5]Boussel, L., et al., *Stroke,* 39(11): 2997-3002, 2008.

[6]Steinman, D. A., Milner, J. S., Norley, C. J., Lownie, S. P., & Holdsworth, D. W., *American Journal of Neuroradiology*, 24(4): 559-566, 2003.

[7]Castro, M. A., Putman, C. M., & Cebral, J. R., *Academic radiology*, 13(7):811-821, 2006.

Copyright 2016 The Organizing Committee for the 2016 Summer Biomechanics, Bioengineering and Biotransport Conference

SB^{3}C2016
Summer Biomechanics, Bioengineering and Biotransport Conference
June 29 - July 2, 2016, National Harbor, Maryland, USA
SB³C2016-1009

DESIGN OF A CARDIOVASCULAR FLOW MIMICKING PUMP

Chris F. Brake (1), Clifton R. Johnston (1)

(1) Mechanical Engineering
Dalhousie University
Halifax, Nova Scotia, Canada

INTRODUCTION

In vitro testing is an important part of the development of new cardiovascular prosthesis designs. One important aspect of simulating the cardiovascular system is properly modeling the pulsatile flow created by the heart. To test prosthesis' effect on the blood flow and the vessels themselves, it must be possible to reproduce the complex, time varying flow generated by the heart. Therefore, there is a need for a pump that is capable of delivering complex, time varying flows that can be easily adapted to mimick waveforms in a range of vessels.

A novel pump has been developed that can output a wide variety of complex pulsatile waveforms at physiologically relevant flows. The design uses a linear actuator to drive a piston pump, as illustrated in Figure 1. With closed loop velocity reference tracking of a piston head, the flow can be accurately controlled. A prototype pump was constructed as a proof of concept for the design. The prototype showed that basic linear control theory is insufficient to achieve accurate velocity control. The friction characteristics of the pump are the main source of nonlinearity in the system. The next step was to apply a LuGre model based friction compensator. Since the pulsatile flow in cardiovascular systems frequently oscillates around the zero velocity point, adequate friction compensation is critical to achieve accurate flow control.

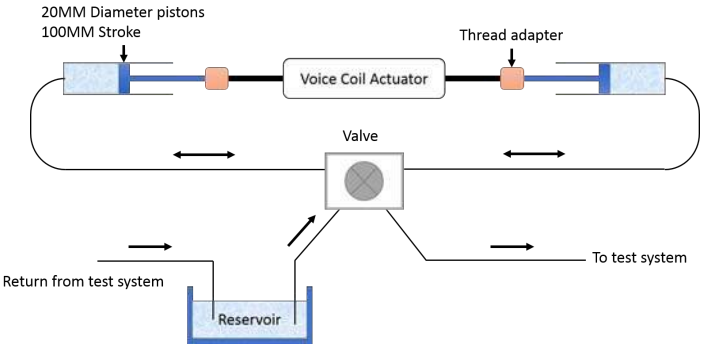

Figure 1: Block diagram of pump setup

METHODS

This project started with the desire to build a pump to mimic cardiovascular flow with the specific design challenge of using a voice coil type actuator to drive a piston.

The valve serves to rectify the flow from the two pistons. Without the valve the fluid will oscillate back and forward with no net positive displacement. By having the valve switch between the two pistons after every pulse, flow is always going in the same direction in the test section.

To validate the control, parameter identification, and design of the pump, the measured flow should closely match the desired profile. Particle image velocimetry (PIV) was used to measure the complex waveform created by the

Copyright 2016 The Organizing Committee for the 2016 Summer Biomechanics, Bioengineering and Biotransport Conference

pump.

RESULTS

Figure 2 shows the 10 cycle average for the PIV flow measurement. The dashed lines in Figure 2 show the bounds of the standard deviation.

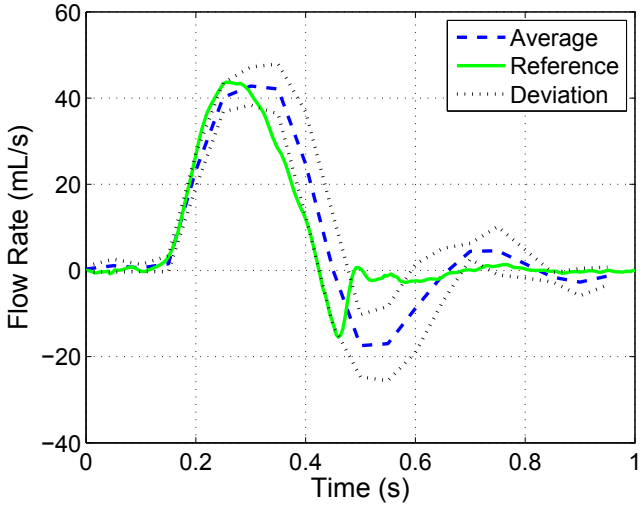

Figure 2: PIV measurement 10 cycle average

While the rising edge of the pulse matches quite well, after the peak and during the change in flow direction pump lags behind the reference waveform. Tsai [1] also had results where their pump tracked the reference well during constant acceleration. While the general shape of the produced waveform is pulsatile, and could be used to approximate some cardiovascular flow, its ability to accurately match the reference waveform is poor. Figure 3 shows the PIV measurement along with with the encoder feedback from the pump.

The other feedback worth analysing is the flow based on encoder measurements from the pump. The flow calculated based on the encoder measurements is shown in Figure 3 alongside the PIV measurements. When the encoder is near zero flow, the PIV measurement still records some small flow oscillations. These oscillations are likely caused by the compliance of the tubing that was used. Additionally, the inertia of the moving fluid also contributes to the oscillations when the pump should be at zero flow. It is not really possible for the controller to eliminate the oscillations since that would require in the loop flow feedback.

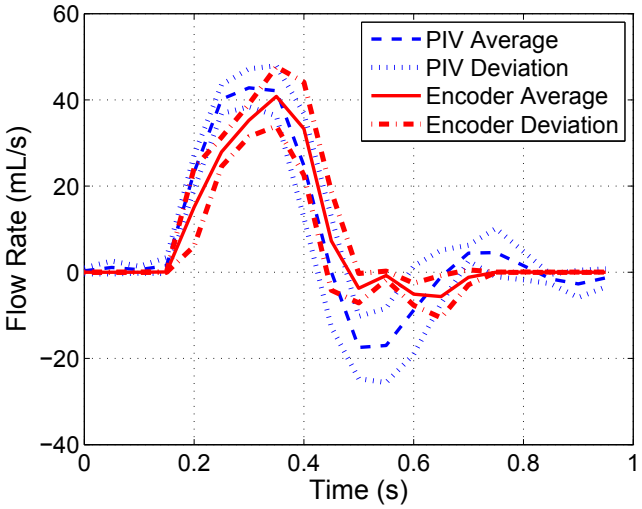

Figure 3: PIV and encoder measurement comparison

So the two measurements clearly do not agree well. This is not a good result as it means that the encoder cannot be relied on to accurately calculate the flow. This also means that using the encoder for feedback wont be accurate when trying to reproduce these kinds of pulsatile waveforms. This also means that using the encoder feedback to try and tune the pump to accurately match the reference probably wont produce a good match when measured with the PIV system.

DISCUSSION

Comparing the different measurements to the reference is useful, but so is comparing the two measurements to each other. Figure 3 shows the two flow measurements averaged over 10 cycles along with the standard deviation for each measurement method. Looking at the encoder measurement it can be seen that the PIV measurement is slow to respond to the pistons displacement. This is slow response can be attributed to fluid inertia.

ACKNOWLEDGEMENTS

This work has been supported by a grant from the Natural Sciences and Engineering Research Council of Canada.

REFERENCES

[1] William Tsai and Omer Savas. “Flow pumping system for physiological waveforms”. In: *Medical and Biological Engineering and Computing* 48.2 (2010), pp. 197–201. ISSN: 01400118. DOI: 10.1007/s11517-009-0573-6.

Copyright 2016 The Organizing Committee for the 2016 Summer Biomechanics, Bioengineering and Biotransport Conference

SB^{3}C2016
Summer Biomechanics, Bioengineering and Biotransport Conference
June 29 –July 2, National Harbor, MD, USA
SB^{3}C2016-1010

DIRECT OSMOTIC PRESSURE MEASUREMENTS IN ARTICULAR CARTILAGE DEMONSTRATE NON-IDEAL AND CONCENTRATION-DEPENDENT PHENOMENA

B. K. Zimmerman (1), R. J. Nims (2), C. T. Hung (2), G. A. Ateshian (1,2)

(1) Mechanical Engineering
Columbia University
New York, NY, USA

(2) Biomedical Engineering
Columbia University
New York, NY, USA

INTRODUCTION

Despite the critical role of osmotic pressure in biological tissue mechanics, the precise magnitude and concentration dependence of the osmotic pressure within osmotically active tissues remains elusive. In articular cartilage, the negatively charged glycosaminoglycan (GAG) chains enmeshed within the collagen network give rise to the well-known fixed charge density (FCD) of cartilage. The abundance of fixed charges produces a swelling pressure within the tissue, which is balanced by tensile forces in the collagen network. An early sign of osteoarthritis is swelling of cartilage accompanied by an increase in water content, as damaged collagen loses its ability to restrain swelling forces [1]. A more complete understanding of such complex interactions in extracellular matrix mechanics is crucial in understanding mechanically mediated diseases.

Over the past few decades, Donnan osmotic pressure of polyelectrolyte solutions has been adopted to model cartilage swelling [1-3]. Donnan law is strongly dependent on empirical coefficients describing deviations from chemically ideal conditions, and several notable efforts to quantify this behavior have been made. An early study by Maroudas calculated activity coefficients in 0.15 M NaCl, but concluded that ideal Donnan behavior was a good approximation for cartilage [4]. The same group later equilibrated cartilage samples against polyethylene glycol solutions and obtained values of osmotic pressure [1]. However, due to the general non-equivalence between mechanical and osmotic loading [5], it is unclear how such results are to be interpreted. Others have examined the osmotic pressure of individual constituent proteoglycans of cartilage in solution [6,7], with some results suggesting ideal Donnan may over-predict swelling pressure by up to a factor of two [6]. These results do not consider the complex environment within the tissue, nor the interactions between the collagen network and GAGs. In response to this lack of consensus, most models assume ideal conditions [3].

Another active question is the effect of salt concentration on material properties of cartilage, including the modulus and permeability. Theoretical correspondence principles have been proposed to include the effect of external salt concentration on tissue moduli [3, 8], but currently lack experimental validation.

The aims of this study were to: 1) isolate and quantify the magnitude of cartilage swelling pressure in situ; and 2) identify the effect of salt concentration on material parameters. To address these aims, we measured the swelling pressure of cartilage in confined compression in solutions with different osmolarities.

METHODS

Ten cylindrical cartilage explants were harvested from calf femoral condyles and both superficial and middle zones were removed by sledge microtome. The resulting specimens were cylindrical plugs of deep zone tissue (∅5 mm × 0.70 ± 0.18 mm) which were frozen at -20 °C until the day of testing. Each sample was placed inside a smooth confining cylindrical chamber with impervious sidewalls and bottom surface. The entire chamber was immersed in a bath containing a prescribed concentration of NaCl supplemented with 0.5 mM ethylenediamine tetra-acetic acid, 35 mM sodium phosphate monobasic, and an isothialozone based biocide (Sigma-Aldrich #46878-U). The top surface of the tissue was loaded in compression with a rigid porous indenter in series with a load cell and LVDT. Confined-compression stress-relaxation tests were performed on each sample while immersed in six different external baths (c^*=2, 0.6, 0.15, 0.03, 0.006, and 0.001 M NaCl), in the order listed. The first test, in 2 M NaCl, was used to determine a baseline response for the tissue.

In this initial configuration, a 500 kPa pre-conditioning load was applied for 60 s and then removed, to securely seat the sample in the confining chamber, followed by a 50 kPa tare creep load until equilibrium (~ 5 min). The sample was defined to be in its nominal zero-strain reference configuration under this tare load. Following stress relaxation the porous indenter was lifted, the bathing solution was replaced with the next NaCl concentration, and the sample was allowed to equilibrate to a new swelling state (~ 1 h). The porous indenter slowly (1 μm s^{-1}) applied a prescribed displacement to return the sample to the defined zero-strain reference configuration, where it was again allowed to equilibrate (~ 10 min). This procedure ensured each stress-relaxation test began at the same reference configuration. The stress $\sigma_0(c^*)$ required to return each sample to its nominal zero-

Copyright 2016 The Organizing Committee for the 2016 Summer Biomechanics, Bioengineering and Biotransport Conference

strain configuration from its swelled state was measured and used to evaluate the swelling pressure.

In each stress-relaxation test displacement of the sample was prescribed in the form of a linear ramp to 20% engineering strain at a rate of 0.25 μm s^{-1}, and then held constant until the stress reached an equilibrium value $\sigma_1(c^*)$ (~ 1 h). All testing for each individual sample was conducted on a single day. After testing, the fixed charge density for each sample was obtained by use of the dimethylmethylene blue assay [9].

RESULTS

For each sample, a series of six stress-relaxation curves were obtained (Fig. 1). The equilibrium stress $\sigma_1(c^*)$ at 20% compression rose monotonically but nonlinearly as c^* decreased, from 0.12 ± 0.01 MPa in 2 M NaCl to 0.66 ± 0.06 MPa in 0.001 M NaCl (Fig. 2). It plateaued at the two lowest concentrations.

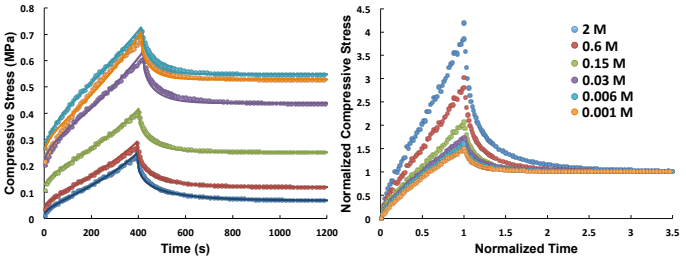

Figure 1: (Left) Stress-relaxation curves obtained for the same sample as c^* was varied. Smooth lines are triphasic curve-fits. (Right) The normalized curves, displaying concentration-dependent transient stress-relaxation behavior.

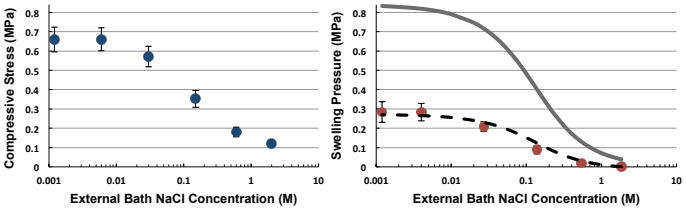

Figure 2: (Left) Mean equilibrium stress as a function of c^*. (Right) Mean swelling pressure at zero strain as a function of c^*. The solid line is the prediction from ideal Donnan law and the dashed line is ideal Donnan multiplied by Φ=0.34.

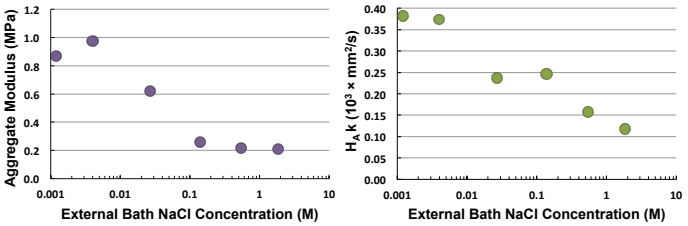

Figure 3: (Left) Aggregate modulus obtained by triphasic curve-fitting the transient data in Fig. 1. A neo-Hookean constitutive model was assumed for the solid matrix. (Right) The product of aggregate modulus and permeability $H_A k$, which is inversely related to the relaxation time.

The swelling pressure $\pi(c^*)$, evaluated at the nominal zero strain configuration using $\pi(c^*) = \sigma_0(c^*) - \sigma_0(2M)$, decreased monotonically with increasing c^*. As in the case of $\sigma_1(c^*)$, $\pi(c^*)$ was sigmoidal in shape; it plateaued at 0.28 MPa in NaCl concentrations below 0.006 M. The dependence of π on c^* followed the trend of ideal Donnan law, but its magnitude was about one-third of the ideal response (Fig. 2). A regression analysis $\pi = \Phi\, \pi_{ideal}$ produced an osmotic coefficient Φ=0.34±0.05 with a regression coefficient R^2=0.87. The fixed-charge density determined from the GAG assay was c^F = 344 ± 34 mEq/L.

By normalizing all stress-versus-time relaxation curves for a single sample to their respective equilibrium stress $\sigma_1(c^*)$ and ramp time, it becomes evident that the relaxation time increases with increasing c^* (Fig. 1). For the specimen shown in Fig. 1, stress-relaxation responses were fitted to the triphasic theory [2] in FEBio [10], using non-ideal Donnan behavior with the above value of Φ. The aggregate modulus obtained from the curve-fitting showed a strong dependence on c^* (Fig. 3), rising from 0.21 MPa in 2 M NaCl to 0.86 MPa in 0.001 M NaCl.

DISCUSSION

This study presents, for the first time, isolated values of the osmotic swelling pressure in articular cartilage explants as a function of c^*, as well as demonstrating the dependence of the mechanical response of cartilage on c^*. These results strongly suggest that the material properties of articular cartilage are a function of c^*, which may necessitate new constitutive relations to fully describe such behavior. In addition, cartilage displays strongly non-ideal swelling, in contrast to the typical assumption of ideality. Although able to qualitatively describe the swelling behavior of cartilage, ideal Donnan law is unable to offer quantitative predictions of osmotic pressure. The disparity between π and π_{ideal} (Fig. 2) suggests incorporation of non-ideal osmotic and activity coefficients is necessary to accurately characterize and model cartilage swelling.

By performing identical testing procedures on the same sample as c^* varied, encompassing the full range from hypertonic to hypotonic, this study is able to provide support for previous hypotheses regarding the dependence of cartilage material properties on c^* [3, 8]. Normalized stress-relaxation profiles (Fig. 1) clearly indicate the relaxation time increases with c^*. The product $H_A k$ is inversely related to the relaxation time, and decreases as c^* increases (Fig. 3), indicating decreasing interstitial fluid diffusivity with greater salt concentrations. Furthermore, the ramp phase of the curves at higher NaCl molarities (2 M and 0.6 M) displays the transient response characteristic of strain-dependent permeability [11], while this effect vanishes as c^* decreases. The ratio of peak to equilibrium stress, which changes by a factor of 3, has also been linked to nonlinear permeability parameters [11]. The tissue aggregate modulus also depends on c^*, increasing nonlinearly as c^* decreases (Fig. 3). The trend of increasing modulus with decreasing c^* is very similar to results obtained by Eisenberg and Grodzinsky [12] in an earlier experimental study. Those authors found the aggregate modulus to increase by ~ 0.9 MPa as c^* decreased from 1 M to 0.005 M, in close agreement with the results of the present study.

Models of the mechanical interactions between extracellular matrix constituents in biological tissues may benefit from the non-ideal osmotic behavior suggested here. A more complete understanding of swelling behavior in articular cartilage will provide a valuable tool for computationally modeling complex electrokinetic phenomena in cartilage.

ACKNOWLEDGEMENTS

The authors acknowledge support from NSF GRFP DGE-11-44155.

REFERENCES

[1] Maroudas, A and Bannon, C, *Biorheology*,, 1981. [2] Lai, W+, *J Biomech Eng*, 1991. [3] Lu, X+, *J Biomech*, 2007. [4] Maroudas, A, *Biorheology*, 1975. [5] Lai, W+, *J Biomech*, 1998. [6] Ehrlich, S+, *Biorheology*, 1998. [7] Chahine, N+, *Biophys J*, 2005. [8] Ateshian, G+, *J Biomech*, 2004. [9] Farndale, R+, *Biochim Biophys Acta*, 1986. [10] Maas, S+, *J Biomech Eng*, 2012. [11] Holmes, M+, *Ann Biomed Eng*, 1985. [12] Eisenberg, S and Grodzinsky, A, *J Orthop Res*, 1985.

SB^{3}C2016
Summer Biomechanics, Bioengineering and Biotransport Conference
June 29 –July 2, National Harbor, MD, USA
SB^{3}C2016-1011

MECHANICAL PROPERTIES OF PREGNANT CERVIX FROM MOUSE MODELS OF INFECTION-MEDIATED AND HORMONE-MEDIATED PRETERM BIRTH

Kyoko Yoshida (1), Alexandra Willcockson (2), Shanmugasundaram Nallasamy (2), Mala Mahendroo (2), Kristin Myers (1)

(1) Mechanical Engineering
Columbia University
New York, New York, USA

(2) Obstetrics and Gynecology
UT Southwestern Medical Center
Dallas, Texas, USA

INTRODUCTION

The timely remodeling of the uterine cervix from a rigid into a compliant structure is essential for the safe delivery of a term baby. We have quantified this dramatic remodeling as a four orders of magnitude decrease in cervical stiffness within a 19-day gestation in a normal mouse pregnancy [1]. Preterm birth (PTB) is a leading cause of neonatal death and affects 15 million babies worldwide every year [2]. Premature softening and dilation of the cervix is often the final common pathway to many preterm births. The physiology of normal and premature cervical remodeling, however, remains unclear.

The objective of this study is to investigate the mechanical properties of pregnant cervices from two distinct mouse models of PTB and to compare these properties with cervices from normal term remodeling. Here, we conduct mechanical tests on normal pregnant mouse cervices at gestation days (d) 15 and term d18 and cervices from two mouse models of PTB: (1) infection-mediated via lipopolysaccharide (d15+LPS) and (2) premature withdrawal of progesterone (d15+RU486).

Histologic evidence of cervical samples from these term and preterm models suggest that the ECM mechanisms responsible for cervical remodeling are different between the two PTB models. In a normal mouse pregnancy, collagen fibers become less organized and more undulated from d15 to d18 [3]. In a recent study, electron microscope (TEM) images showed compromised elastic fibers but normal collagen fibril organization in the d15+LPS compared to d15 while d15+RU486 cervices had collagen fibril morphology similar to d18 tissue [3,4]. The consequences of these ECM profiles on the mechanical properties of the different mouse models of PTB remain to be determined. In this study we utilize load-to-break and load-unload-recover tests to investigate the contributions of the cervical collagen and elastin to tissue stiffness, strength, hysteresis, and recoverability.

METHODS

Mouse models: Mice were generated and maintained at the University of Texas Southwestern Medical Center. Wild-type 2-6 month old nulliparous pregnant females were used in all experiments. Normal pregnant mice were sacrificed on gestation d15 and d18, where term delivery usually occurs between 6PM on d18 to 12 PM on d19 of pregnancy. For the infection-mediated PTB model (d15+LPS), 150ug of lipopolysaccharide was injected into the uterus of pregnant d15 female mice between 7-9 AM and sacrificed 6 hours later. Under this condition, PTB occurs 7-8 hours after injection. For the hormone-mediated PTB model (d15+RU486), a progesterone receptor antagonist, RU486, was used to stimulate premature progesterone withdrawal by subcutaneous injection late on d14. Pregnant mouse was sacrificed 12h later on d15 (d15+RU486). Under this condition, PTB occurs 13-16h after injection. For all mouse samples, the cervix was isolated with uterine horns and surrounding vaginal tissue immediately after sacrifice, flash frozen, shipped overnight to Columbia University on dry ice, and stored at -80°C until testing.

Mechanical testing: On the day of testing, the cervix was carefully removed from the uterine horns and the surrounding vaginal tissue. Two surgical sutures (Ethicon, Silk 2-0) were threaded through the inner canal of the cervix, attached to custom tensile grips, and tensioned [1]. Samples were positioned onto a universal testing

Copyright 2016 The Organizing Committee for the 2016 Summer Biomechanics, Bioengineering and Biotransport Conference

machine (Instron 5948 MicroTester, 10N load cell) inside a bath filled with phosphate buffered saline+2mM EDTA (protease inhibitor). Before tensile testing, samples were allowed to equilibrate in the solution (2-4 hours) while two calibrated perpendicular CCD cameras (Point Grey GRAS-50S5M-C 75 mm, f/4 lens) tracked tissue geometry. After swelling equilibrium, samples were subjected to either a load-to-break test or a cyclic load-unload-recover test. Throughout testing, samples were kept hydrated in PBS and time, grip-to-grip displacement, force, and tissue geometry were continuously recorded.

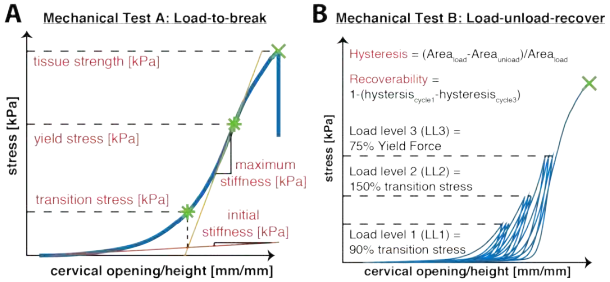

Figure 1: Mechanical test loading curves for A) load-to-break and B) load-unload-recover test with calculated parameters in red.

Load-to-break: Whole, intact cervices (n=5 per group) were subjected to load-to-break tensile testing to determine stiffness and strength for each group (Fig.1A). Tensile grips were pulled apart at a constant rate of 0.1mm/s until the sample broke. Stress [kPa] was calculated by normalizing the force [N] by the stress-free reference sample cross-sectional area [mm^2] defined as the product of width [mm] and length [mm]. Cervical opening [mm], defined as the suture-to-suture distance, was normalized by the stress-free sample height [mm] to calculate the normalized cervical opening [mm/mm]. For each sample, a loading curve (normalized cervical opening [mm/mm] vs. stress [kPa]) was generated and the parameters *initial slope* [kPa], *maximum slope* [kPa], *transition stress* [kPa], *yield stress* [kPa], and *tissue strength* [kPa] were calculated as shown (Fig.1A).

Load-unload-recover: Whole, intact cervical samples (n=3-4 per group) were subjected to cyclic load-unload-recover tensile testing to measure sample hysteresis and recoverability (Fig.1B). To account for differences in the loading curves between sample groups in the load-to-break test, three load levels were selected based on the group averages of transition stress and yield stress. The first load level (LL1) was selected as 90% of the average transition stress, within the toe region of the loading curve. The second load level (LL2) was selected as 150% of the average transition stress, past the toe region. The third and highest load level (LL3) was selected as 75% of the average yield force, just before the sample begin to yield and break. Samples were loaded at a grip-to-grip rate of 0.1mm/s to LL1, immediately unloaded at the same rate to a stress-free state and allowed to recover for 20 mins. This cycle was repeated twice more for a total of 3 cycles (cycles 1-3). The cycles were repeated for LL2 (cycles 4-6) and LL3 (cycles 6-9) for a grand total of 9 load-unload-recover cycles.

Hysteresis was calculated as the area between the loading and unloading curves for each cycle. This measurement represents the dissipated energy due to both viscous and unrecoverable permanent deformations. To determine the extent of unrecoverable permanent damage, *recoverability* was calculated as 1 minus the change in *hysteresis* between the 1st (cycles 1,4,7) and 3rd cycle (cycles 3,6,9) at each load level.

RESULTS

In general, d15+LPS cervices exhibited similar mechanical behavior to d15 samples while d15+RU486 cervices exhibited similar mechanical behavior to d18 samples in the load-to-break tests. Normal d15 and d15+LPS cervices tended to be stiffer and stronger compared to d18 and d15+RU486 cervices (Fig.2A). However, these differences were not statistically significant.

Hysteresis was consistently higher in d15 cervices compared to all other groups (Fig.2B). Hysteresis was higher in d15 compared to d15+LPS and d18 cervices for all loading levels and compared to d15+RU486 only for LL1. Recoverability was consistently higher in d15 cervices compared to all other groups. Significant differences, however, were found only between d15 and d15+LPS at LL3.

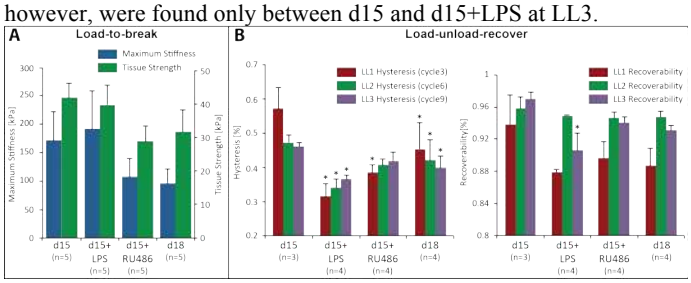

Figure 2: A) Load-to-break: d15+LPS and d15 cervices are stiffer and stronger compared to d15+RU486 and d18 cervices, but differences were not significant. B) Load-unload-recover: d15 cervices exhibit higher hysteresis and recoverability compared to d15+LPS. *'s indicate significantly different parameters compared to d15 (One way ANOVA, $p<0.05$).

DISCUSSION AND CONCLUSIONS

The objective of this study was to investigate the mechanical behavior of pregnant cervices from mouse models of two different models of PTB: infection-mediated PTB via LPS and premature hormone-withdrawal via RU486. Our load-to-break results agree with our histological studies, where more organized collagen in the d15+LPS and d15 cervices lead to stiffer and stronger tissue compared to d15+RU486 and d18 cervices. These differences, however, were not significant. The higher hysteresis in the d15 cervices in our load-unload-recover tests suggests that more energy is dissipated during a load-unload cycle in the d15 cervix. Recoverability tended to be higher in d15 cervices compared to all other groups, especially d15+LPS samples, indicating viscous deformations in the d15+LPS samples were less recoverable. This result agrees with histologic studies, where compromised elastic fibers in the d15+LPS cervices may result in tissues with lower recoverability. The overall trends in this study suggest that the biomechanical signatures between the two mouse models of PTB are distinct and that infection and progesterone withdrawal facilitate distinct mechanisms of cervical remodeling where both lead to a compromised cervix and thus PTB.

A limitation of this study is the assumption of a homogeneous deformation state in our tensile tests. Our previous modeling study shows that ring tests induce a complex combined loading on the cervix. To fully characterize the material properties, we are currently conducting inverse finite element studies. The results in this study will be used to help inform and extend our current material model for the cervix to include time dependence. This extension to the model will help us to better understand normal and abnormal cervical remodeling in pregnancy.

ACKNOWLEDGEMENTS

This study was supported in part by the NSF Graduate Research Fellowship and the March of Dimes Prematurity Research Initiative.

REFERENCES

[1] Yoshida, K et al., *Acta Biomat*, under review, 2016.
[2] WHO, http://www.who.int/mediacentre/factsheets/fs363/en/
[3] Akins, M et al., *J Biomed Opt*, 15(2):026020, 2010.
[4] Holt, R et al., *Endocrinology*, 152(3):1036-46, 2011.
[5] Willcockson, A et al., *SRI Annual meeting poster*, 2016.

Copyright 2016 The Organizing Committee for the 2016 Summer Biomechanics, Bioengineering and Biotransport Conference

SB^{3}C2016
Summer Biomechanics, Bioengineering and Biotransport Conference
June 29 –July 2, National Harbor, MD, USA
SB^{3}C2016-1012

DEVELOPMENT AND VALIDATION OF A BRAIN PHANTOM FOR THERAPEUTIC COOLING DEVICES

Ryan D.M. Packett, Philip J. Brown, Gautam V. Popli, F. Scott Gayzik

Department of Biomedical Engineering
Wake Forest University School of Medicine
Winston-Salem, NC, USA

Department of Neurology
Wake Forest Baptist Medical Center
Winston-Salem, NC, USA

INTRODUCTION

Individuals with medically refractory epilepsy currently have no reliable treatment to control seizures and make up about 30% of the approximately 3 million Americans with epilepsy [1]. In these cases, the most promising course of action is to surgically remove the portion of the brain responsible for the seizures, an approach with only a 60% success rate [2]. This limited success is due to the difficulty in correctly identifying the exact location and scope of seizure onset. Current technology and methods are somewhat limited in the precision of locating the zone of seizure onset. If the entire epileptogenic zone is not successfully removed, seizures continue in the patient after surgery.

Research suggests that cooling the affected brain tissue can reduce the rate of activity, thus reducing or eliminating seizures. It has been determined that tissue at a depth of 5 mm below the surface of the brain must be cooled by 12 degrees Celsius to reach a temperature of 25 ^{o}C to slow or terminate seizure activity [3]. The present study analyzes the viability of obtaining such cooling using a device operating on the cortical surface of the brain two ways. First, a pre-test prediction is conducted, using mathematical modeling of the brain tissue to determine if an achievable convective coefficient can be used to obtain such cooling. Next, we introduce a novel instrumented phantom which can be used to test concept cooling devices. The phantom will be used to investigate various cooling strategies on the benchtop. Ultimately, the goal of the research program is to determine a method to more precisely identify the epileptogenic zone, thereby increasing the rate of success of surgery.

METHODS

The mathematical model calculates the transient temperature response along a single dimension. The aim of this part of the study was to conduct a pre-test prediction. We sought to determine if the desired temperature drop could be achieved by using surface convection that could be achieved in a concept device. Temperature vs. time data are output at depths of 5, 10 and 15 mm. This code utilizes a finite-difference method, material properties of human tissue are used, and boundary conditions, and an initial temperature profile [4] of the brain were set. The model is represented schematically in Figure 1.

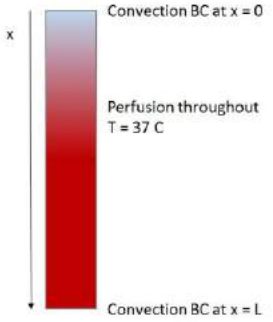

Figure 1: The mathematical model includes material properties and boundary conditions in a single dimension.

The cooling phase of this simulation was created by setting the surface boundary temperature to 0 °C (ice water) with an appropriate heat transfer coefficient correlated to the flow of ice water through the device (h = 75 W/m^2*K). The model was set to mimic human circulation at a temperature of 37 °C at the deep boundary of the spatial domain using a convection coefficient of h =200 W/m^2*K and thoughout the spatial domain using a perfusion term of 3300 W/m^3*K. A thermal recovery phase was introduced as well to model the removal of the cooling device. In this phase, the surface boundary was returned to 37 °C to once again match biologic conditions. The model is based upon the Pennes bioheat equation, which is given in Equation I. Properties used in the equation are provided in Table 1. The model is programmed in Matlab (The Matworks, Natick, MA).

$$\rho C_{p,tis}(T)\frac{\partial T}{\partial t} = k\nabla T + \omega_{bl}\left(\rho C_p\right)_{bl}(T - T_{bl}) \quad \text{(I)}$$

The second part of the work involved developing a phantom for use as a device test bed, in which the goal is to mimic the temperature drop

Copyright 2016 The Organizing Committee for the 2016 Summer Biomechanics, Bioengineering and Biotransport Conference

observed in the model. Table 1 below, summarizes and compares the key material properties associated with the model and the experiment.

Table 1: Paraffin wax serves as a readily-available, inexpensive representation of brain tissue.

	Model	Experiment
Medium	Brain parenchyma	Paraffin wax
Density,)ρ) (kg/m^3)	1039	900
Thermal conductivity, k (W/m*C)	.515	.24
Specific heat, C_p (J/kg*C)	3680	2890

We introduce a benchtop test configuration which involves pumping water through two isolated loops, as depicted in Figures 2 and 3.

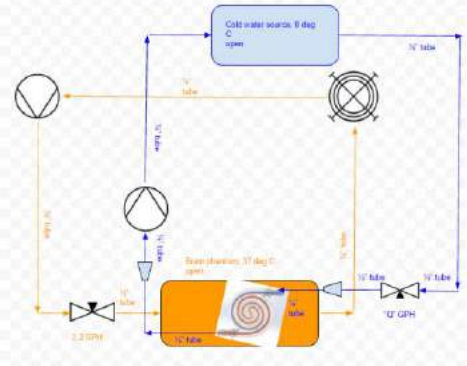

Figure 2: The warm loop represents circulation while the cool loop simulates the therapeutic device.

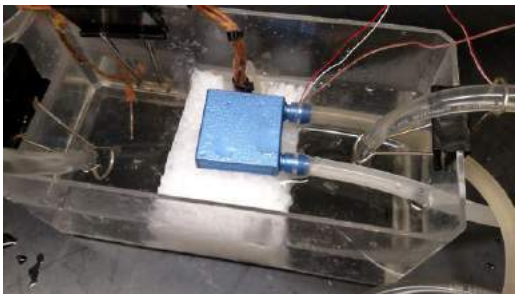

Figure 3: A molded block of wax beads represents a human brain in the lab.

One loop consists of warm water, which, when circulated at 37 °C, simulates human blood circulation. This water flows through a brain phantom made of paraffin wax beads formed into an 90 x 65 x 45 mm block. Three embedded thermocouples at depths of 5, 10 and 15 mm read out temperature at 1 Hz. The second loop includes the cooling device, which is placed on top of the phantom, directly above the thermocouples. Ice water at 0 °C, cycles through this loop, including the device, in order to cool the brain phantom. The cooling device used in this pilot study is a 41 x 41 mm anodized aluminum cooling block. The embedded thermocouples obtain temperature information which is plotted over time. The system is allowed to reach a steady state condition in which the ambient warm water remains constant at 37 °C before the cooling device is place atop the phantom. The cooling phase persists for 45 minutes, after which the device is removed and the phantom allowed to return to its original warm state.

RESULTS

Figure 4 depicts the results of the one dimensional brain model. The graphs of the cooling phase and recovery phase are superimposed next to one another to demonstrate both phases of the process. Data from the benchtop phantom also yielded promising results, shown in Figure 3.

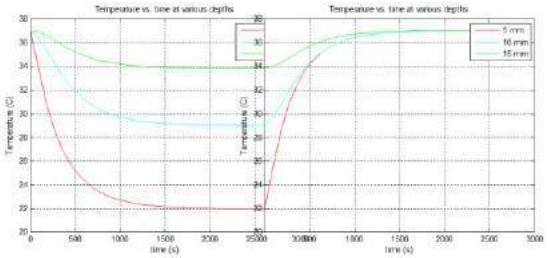

Figure 4: Mathematical simulation using MatLab suggests that a 12-degree C temperature drop is possible at 5 mm deep.

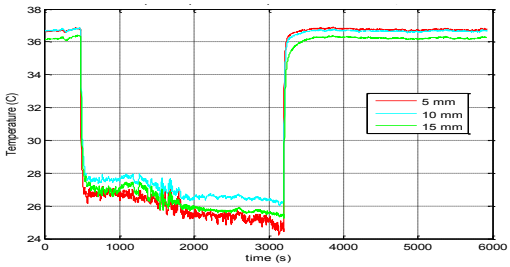

Figure 5: Benchtop brain phantom simulation suggests that a 12-degree C temperature drop is possible at 5 mm deep.

DISCUSSION

The predicted temperature drop at a depth of 5 mm was within 2 degrees of the computational model. However the benchtop experiment exhibited a much tighter distribution of temperature and faster temperature recovery time. The two modeling methods developed in this study serve complimentary roles. The mathematical model creates a pre-test prediction which gives confidence in the convective cooling method as well as a temperature recovery target for the phantom.

The near term goal is improved biofidelity of the physical phantom. Based on pretest predictions, a phantom with greater depth sensitivity and slower temperature recovery is needed.

In summary, with a temperature reduction of approximately 12 °C at a depth of 5 mm, both techniques indicated viability for the testing platform and convective cooling approach. Future work on the model will involve a prediction of a porous paraffin wax structure. Future efforts on the phantom will seek to reduce in porosity of the paraffin wax block to develop a greater distraction of temperature within it, and develop more non-directional flow. Both of these alterations should more closely replicate the effects of non-directional perfusion on heat transfer within the cortex.

ACKNOWLEDGEMENTS

Pilot funding was provided by Wake Forest Innovations and Wake Forest University School of Medicine Dept. of Biomedical Engineering.

REFERENCES

1. Kwan, P. and M.J. Brodie, *Early identification of refractory epilepsy.* N Engl J Med, 2000. **342**(5): p. 314-9.
2. Rothman, S.M., et al., *Focal cooling for epilepsy: an alternative therapy that might actually work.* Epilepsy Behav, 2005. **7**(2): p. 214-21.
3. Fujii, M., et al., *Application of focal cerebral cooling for the treatment of intractable epilepsy.* Neurol Med Chir (Tokyo), 2010. **50**(9): p. 839-44.
4. Gayzik et al., *Experimental validation of an inverse heat transfer algorithm for optimizing hyperthermia treatments.* Journal of Biomechanical Engineering, 2006.

Copyright 2016 The Organizing Committee for the 2016 Summer Biomechanics, Bioengineering and Biotransport Conference

SB^{3}C2016
Summer Biomechanics, Bioengineering and Biotransport Conference
June 29 –July 2, National Harbor, MD, USA
SB^{3}C2016-1013

THE QUANTIFICATION OF BLOOD FLOW PATTERNS INDUCED BY ENDOVASCULAR STENT GRAFTS: AN EXPERIMENTAL INVESTIGATION OF THE EFFECTS OF OVERSIZING AND COMPLIANCE

Amanda Colella-Centazzo (1), Clifton R. Johnston (1)

(1) Department of Mechanical Engineering
Dalhousie University
Halifax, NS, Canada

INTRODUCTION

In current medical practice endovascular stents are the most common treatment used in the management of arterial disease, particularly to bridge blood flow through aneurysmal vessels. Despite their relative ease of implantation they have been shown incite harmful secondary issues long-term that negate these benefits, with additional interventions occurring at higher rates as compared to open repair surgery [1], while showing no significant difference in survival after 2 years [2]. The alterations to the fluid dynamic forces that are incited by the stent play an important role in tissue healing, stent migration and by extension stent efficacy.

More specifically, areas of low wall shear stress (WSS) have been shown to affect the progression of atherosclerosis, the proliferation of intimal hyperplasia and the formation of thrombi [3]. These fluid dynamic considerations directly affect the long-term patency of stent grafts and have therefore prompted investigation into how the presence of the stent alters the local hemodynamic environment.

An environment representing that of the human femoral artery was constructed with optical access to the blood analog as it exits an implanted stent graft. Using Particle Image Velocimetry (PIV) the flow patterns were imaged and the changes to the peak velocity and WSS induced by stent implantation were quantified for several stent-vessel cases, specifically examining the effect of stent sizing and the compliance of the treated vessel. Tests were conducted in a rigid acrylic test section and an elastic mock artery with a compliance within the clinically observed range.

METHODS

A closed flow loop was designed and constructed for visualization and measurement of flow through a 10 mm inner diameter tube, representing a simplified geometry of the femoral artery. A common non-Newtonian blood analog representative of physiological hemodynamic parameters and comprised of a mixture of glycerol (40%), xantham gum (0.04%) and water, was circulated through the test section [4]. The mixture was exposed to a 1Hz pulsatile flow profile typical of the human femoral artery (Figure 1) with a peak velocity of 47 cm/sec, the mean peak forward velocity in the femoral artery reported by Fronek et al. [5]. This corresponds to a Reynolds number at peak flow of 1033.5, which is within the physiologically observed range [6].

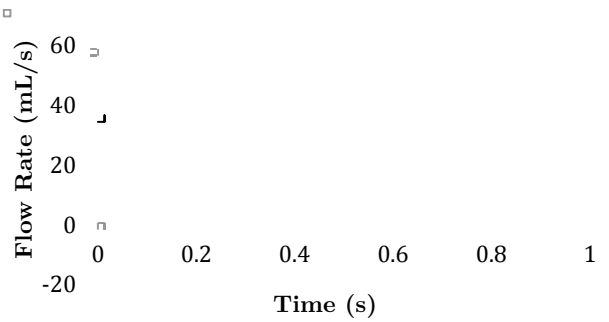

Figure 1 - 1 Hz Input waveform representing pulse profile typical of the human femoral artery.

Using PIV, cross-sectional velocity and wall shear stress immediately downstream of a Gianturco Zenith stent graft (Cook Medical, Inc., Bloomington, IN, USA) were quantified. The compliance of the elastic tube was tested in a modified PIV set-up and was found to be 7.77 % mm Hg^{-1x} x 10^{-2}, which is representative of a healthy human male femoral artery. The two stents of 20% and 40% oversizing were deployed in the test section and an identical test was performed in a rigid acrylic tube for comparison.

The test section was embedded in an acrylic flow chamber, which was filled with 100% glycerol to correct for the refraction index differences between the circulating fluid and the surrounding vessel and allow the laser sheet to reach the test area unaffected. The fluid was seeded using 10 µm silver coated hollow glass spheres, which were illuminated using a 1 mm thick laser sheet. Image frames were collected using a Photron mini UX100 at 4000fps with 20 image pairs collected per pulse, over 10 pulses.

RESULTS

Oversizing: Introduction of a full stent (3 wires in a polyester cover) had a substantial effect on flow velocities, particularly at peak pulse. The flow observed followed an asymmetric pattern due to variations in the folding and pillowing of the fabric between the stent wires. This

Copyright 2016 The Organizing Committee for the 2016 Summer Biomechanics, Bioengineering and Biotransport Conference

asymmetry was more pronounced in the 12 mm stent. This appears to be due to the fact that the 12 mm stent has seven wire peaks, while the 14 mm stent has eight. Although both were installed in the tube such that their wires were symmetric in the plane of the camera, the seven peaks allowed more intra-wire spacing and therefore allowed the fabric sheath and wires to deploy asymmetrically.

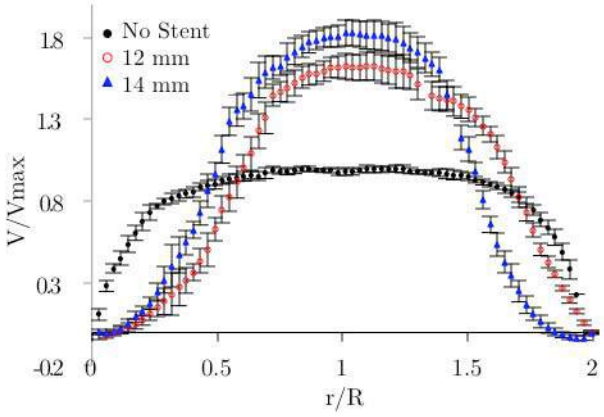

Figure 2 - Velocity profiles at peak pulse at x/R=0.5 downstream of a 12 mm and 14 mm Gianturco stent compared to the same acrylic vessel with no stent.

Both stents caused a considerable reduction in velocity close to the wall accompanied by an accelerated core flow (Figure 2). At 20% and 40% oversizing (12 mm and 14 mm stents) the centerline velocities at x/R=0.5 increased by 65.4% and 86.2%, respectively, as compared to the non-stented condition. At peak pulse, the 12 mm stent caused a velocity reduction from the wall to r/R = 0.5776 and r/R=0.7040 to the far wall, with flow reversal noted between the wall and r/R= 0.08664. A similar pattern was observed with the 14 mm stent, with reduced velocities occurring between the wall and r/R = 0.4621 and r/R= 1.5306. The largest absolute change for both stents occurred at r/R=0.2310 and was a decrease of 35.60 cm/s (85.0%) and 31.72 cm/s (75.8%) for the 12 mm and 14 mm stents, respectively

The wall shear stress saw a decrease upon introduction of both stents across the pulse cycle, with the most substantial changes in WSS occurring during acceleration of the fluid (Figure 4-11). Due to the asymmetry in the vessel, the WSS drop varied between the two walls. For comparison, the most severe case is considered. The drop observed at peak flow was found to be 82.1% for the 12 mm stent. The 14 mm stent saw a 120.7% in the WSS due to the flow reversal noted at the wall.

The cycle averaged WSS decreased from 0.920 Pa in the non-stented case to -0.832 Pa and -1.2675 Pa for the 12 mm and 14 mm stent. The change in sign of the cycle averaged WSS indicates a substantial flow reversal over the course of the pulse at the near wall. The OSI, surprisingly, decreased upon stent introduction from 0.4385 to 0.4182 and 0.3642 for the 12mm and 14mm stent, respectively. This is due to the fact that the flow was already pulsatile and therefore highly oscillatory to begin with, which is an important characteristic of flow in the peripheral arteries. The lowering of the WSS in both positive and negative flow direction, led to an overall WSS approaching zero, in turn lowering the OSI.

Compliance: Tests conducted in the compliant vessel showed similar trends to those in acrylic, however changes were more pronounced. Cross-sectional velocity profiles downstream of a single stent wire (Figure 3) showed a larger drop in velocities at the vessel periphery compared to the acrylic values (5.306 cm/s and 8.77 cm/s respectively). The centerline velocities increased more in the SYLGARD at 11.7%, compared to 4.65% in the acrylic. The WSS saw a drop at the peak with a 22.0% decrease in the acrylic and a 26.9% decrease in the SYLGARD.

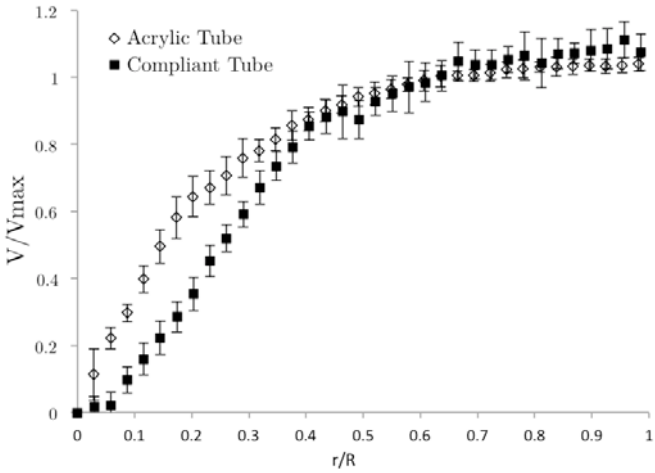

Figure 3 - Velocity profiles at peak pulse downstream of a Gianturco stent wire in acrylic and compliant vessels

DISCUSSION

The effect of oversizing was consistent across vessel compliances, with the larger 14 mm stent causing more substantial changes to the flow profiles as compared to the smaller 12 mm. The stents both caused an increase in the centerline velocities, accompanied by a drop at the vessel periphery. This incited a drop in the WSS, a feature that has been shown to promote re-stenosis. Oversizing of the stent is common practice clinically to ensure proper adhesion of the graft and to minimize stent migration, however this convention has important implications on the degree of disturbance introduced into the blood flow. These findings suggest that a graft with a diameter closer to the native vessel could be helpful in reducing the instances of stent re-occlusion.

Additionally the rigid tube was shown to lessen the velocity disturbances induced by the stents introduction, with centerline velocity increases more than double in the compliant vessel. This would imply that in more compliant vessels where the compliance mismatch is greater the stent has a larger effect on the fluid flow.

REFERENCES

[1] Greenhalgh, RM, *The Lancet*, 364: 843-848, 2004.

[2] De Bruin et al., *NEJM*, 362:1881-1889, 2010.

[3] Chiu and Chien, *Physiological Reviews*, 91: 327–387, 2011.

[4] Brookshields, K.A. et al., *J of Bioreheology*, 30:107-116, 1994.

[5] Fronek, A et al., *Circulation*, 53:957-960, 1976.

[6] C. Caro, *The Mechanics of the Circulation*, 2012.

Copyright 2016 The Organizing Committee for the 2016 Summer Biomechanics, Bioengineering and Biotransport Conference

SB³C2016
Summer Biomechanics, Bioengineering and Biotransport Conference
June 29 –July 2, National Harbor, MD, USA
SB³C2016-1014

DEVELOPMENT AND PARAMETRIC STUDY OF A 3-YEAR-OLD CHILD ABDOMINAL FINITE ELEMENT MODEL

Haiyan. Li(1), Ruirui. Lu(1), Shijie. Ruan(1), Shihai. Cui(1), Chunxiang. Wang(2)

(1) College of Mechanical Engineering
Tianjin University of Science and Technology
Tianjin, China

(2) Department of Radiology
Tianjin Children's Hospital
Tianjin, China

INTRODUCTION

Abdomen injury is a significant cause of mobility for children. Understanding its biomechanical mechanism is urgent. So far, numerous injury criteria have been proposed, such as energy-based blunt criterion [1], abdominal pressure [2]. However, no consensus has been reached on the performance of the injury criteria. This may be because those injury criteria do not inform tissue-level mechanical responses. Crash dummies play an important role in vehicular safety design. One limitation is that crash dummies do not export strain or stress, which is believed to damage internal organ [3].

To break this limitation, finite element (FE) modeling becomes a significant approach. For example, Mizuno et al. developed a finite element model of a 3-year-old child abdomen by scaling from a 50th percentile adult FE counterpart [4]. Because a significant difference in the simulation results was found between 3-year-old child and the corresponding dummy [5], this may have substantial effect in injury assessment. Therefore, the aim of this study is to establish a finite element model of a 3-year-old child abdomen, and to parametrically investigate the directional sensitivity of tissue-level responses of internal organs to blunt impact.

METHODS

Model Development

The model geometry was extracted from CT scans of a 3-year-old female healthy child volunteer by Tianjin Children's hospital. Importing these CT images using Mimics (Materialise Inc., Leuven, Belgium). The surface of each critical anatomical component was converted into non-uniform rational basis spline (NURBS) using Geomagic Studio(Geomagic, Inc., Research Triangle Park, NC, USA). FE modeling was performed using a combination of TrueGrid and Hypermesh. The FE model of a 3-year-old child abdomen consists of 273322 nodes, 194684 hexahedral solid elements and 118549 shell elements (Fig. 1).

Bones and internal organs were models by elastic and linear visco-elastic materials, respectively. Contacts were defined self-contacts among the abdominal viscera to allow interfacial sliding. Computation was performed using Pam-Crash (Pam-Crash, Inc., Paris, FR).

Model Validation

The post mortem human subjects of 3-year-old children are rarely used for biomechanical experiments due to regulatory and ethical concerns. In this research, a simulation test was implemented to validate the FE model according to the child cadaver tests conducted by Ouyang et al. [6]. A cylindrical impactor with 5 cm diameter, 2.5kg mass was designed to impact the FE model. The impact location was selected as the position one third the distance from the umbilicus to the bottom of the sternum. The model was kept free [7]. The impactor with an initial velocity of 6m/s was applied to the finite element model.

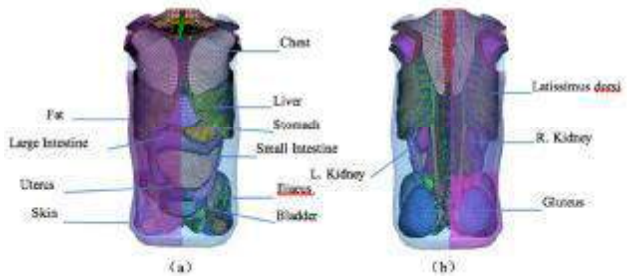

Figure 1 Finite element model of a 3-year-old child abdomen (a) Front view (b) Rear view

The impact lasted for 40ms. In the Pam-Crash, we defined sets of the contacts. There were not only the defined self-contacts between internal organs finite elements components, but also the surface to surface contact between the impactor and the skin of the finite element model.

Parametric Study

In the vehicle frontal collision study, it generally used three different degrees to study the vehicle safety. It was 0 degree, the left 30 degree and the right 30 degree [8]. In the tests, the impactor was rotated 30 degrees clockwise (minus 30 degrees) and counterclockwise (plus 30 degrees) respectively along the vertical direction of its velocity. The other conditions were designed as same as model validation. The simulation state was shown in Figure 2.

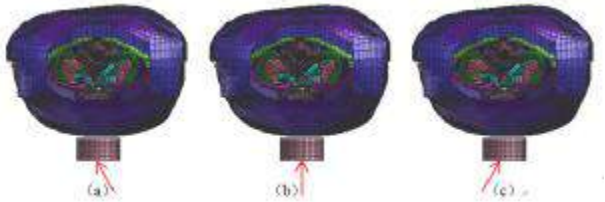

Figure 2 Top view of the impact at different angles (a)The plus 30 degrees impact (b) The 0 degree (head-on) impact (c) The minus 30 degrees impact

RESULTS

In the 3-year-old child abdominal finite element model validation test, the impact force-time curve and abdominal deformation-time curve were output by Pam-Crash. The FE model impact force-abdominal deformation curve was shown in the Figure 3, which was obtained by the data from the curves of the FE model impact force-time and abdominal deformation-time. In the figure 3, the +1 and -1 standard deviation corridor boundary were given by cadaver tests data analysis conducted by Ouyang et al. It was obvious that the simulation curve of the impact force-abdomen deformation fell inside the corridor obtained from cadaveric experiment, which suggests a validity of FE simulation results.

Copyright 2016 The Organizing Committee for the 2016 Summer Biomechanics, Bioengineering and Biotransport Conference

The Figure 4 showed the curves of children's abdominal impact force-abdomen deformation when the crash by the impactor happened head-on or from the rotating angle of plus and minus 30 degrees (that is, the impactor crashes the same position from different angles). As was shown in the figure, when the impactor crashed the same position on the abdomen from different angles, there were obviously more big differences. In three kinds of degrees simulation results, the visceral peak strains were shown in Table1. In consideration that the peak strain may be caused by a much distorted element, we calculated the elements' mean strain around the element which happened the peak strain.

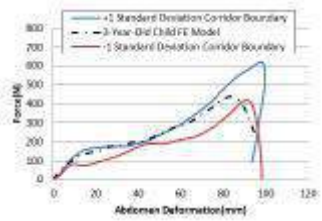

Figure 3

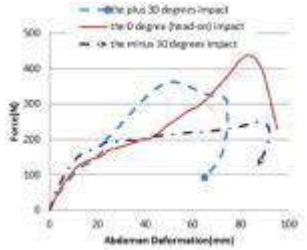

Figure 4

Figure 3 Impact force-abdomen deformation curves

Figure 4 The impact force-abdomen deformation curve from different angles for the impact

To directly compare the strains of different viscera organs and analyze their injury threshold when the crash by the impactor happened head-on or from the rotating angle of plus and minus 30 degrees, the bar chart is shown in Figure 5.

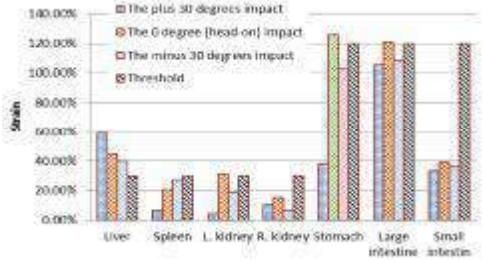

Figure 5 The peak strain of child's viscera form different angles for impactor

Table 1 The peak strain of child's viscera at different degrees for impacting

Part	The plus 30 degrees impact	The 0 degree (head-on) impact	The minus 30 degrees impact	Threshold
Liver	58.85%	44.77%	39.96%	30%
Spleen	6.62%	20.75%	27.29%	30%
L. kidney	4.59%	31.13%	18.65%	30%
R. kidney	10.63%	15.64%	6.75%	30%
Stomach	38.32%	126.01%	103.22%	120%
Large intestine	105.36%	120.84%	108.79%	120%
Small intestin	33.48%	38.94%	36.23%	120%

DISCUSSION

In this study, a finite element model of 3-year-old child abdomen with high biofidelity was developed. The FE model was validated against a cadaveric experiment. The parametric study based on the FE model is used to analyze the sensitivity of internal organs to blunt impact.

As Figure 3 shows, the simulation curve is not absolutely in the corridor of cadaver test. It may due that the FE model was slightly fatter than the cadaver specimens. The 3-year-old FE model was constructed by the specimen child whose mass was 15.6kg. And the cadaver specimens of Ouyang tests were 10.5~13.5kg.

Generally researchers estimated abdominal and visceral injury by its internal strain. This study carried out the injury analysis by adoption of adults visceral injury threshold. Due to the asymmetry of children's abdominal viscera, even if the same position at different impact angle, visceral injury situations were not same. As was shown in Figure 5, compared with the impactor form the different crash directions, the visceral strains had the obvious difference. The strain of the stomach became bigger and the strain of the liver became smaller when the impact direction rotated an angle of -30 °. And when the impact rotated the angle of +30 °, most of the overlap part was located in the liver. So the strain of the liver became bigger and the strain of the stomach became smaller. In addition, from three groups of visceral strain, we could also conclude that the position which the impactor impacted also affected children's abdominal visceral injury. Children's abdominal viscera were more vulnerable at the position of the impactor contact compared to others.

This study provided a high biofidelity FE model of a 3-year-old child abdomen and it could be used to parametrically study the injury mechanism. This is very valuable to develop protection devices of children.

ACKNOWLEDGEMENTS

This work was supported by the National Natural Science Foundation of China (81201015，81371360，81471274).

REFERENCES

[1] Larry M. Sturdivan, David C. Viano, Howard R. Champion. Analysis of Injury Criteria to Assess Chest and Abdominal Injury Risks in Blunt and Ballistic Impacts. The Journal of TRAUMA Injury, Infection, and Critical Care, 56(3): 651-663, 2004

[2] Heiko Johannsen, Xavier Trosseille, Philippe Lesire, et al. Estimating Q-Dummy Injury Criteria Using the CASPER Project Results and Scaling Adult Reference Values. IRCOBI Conference 2012, 580-596

[3] Kapoor T, Altenhof W, Wang Q, et al.. Injury potential of a three-year-old Hybrid III dummy in forward and rearward facing positions under CMVSS 208 testing conditions. Accident Analysis & Prevention, 38(4): 786-800. 2006

[4] Mizuno, K., Iwata, K., Deguchi, T., Ikami, T., Kubota, M.,. Development of a three-year-old child FE model. Traffic injury prevention, 6(4), 361-371, 2005

[5] Koizumi, T., Tsujiuchi, N., Taki, N., Forbes, P. A., Lange, R. D., 2007. Development and impact analysis of 3-year-old child FE human model.

[6] Jun Ouyang, Qingan Zhu, et al.. Abdominal impact study on pediatric cadaveric subjects. Proceedings of the 11th International Forum of Automotive Traffic Safety, 2014:303-310, 2014

[7] Jun Ouyang, et al.. Thoracic impact testing of pediatric cadaveric subjects. Journal of Trauma and Acute Care Surgery 61.6: 1492-1500, 2006

[8] Kaiwang Zhang, Jide Zhuang, Cheng Cheng, et al., 2006. Automotive technical regulations and legal services. China machine press.

Copyright 2016 The Organizing Committee for the 2016 Summer Biomechanics, Bioengineering and Biotransport Conference

SB³C2016
Summer Biomechanics, Bioengineering and Biotransport Conference
June 29 –July 2, National Harbor, MD, USA
SB³C2016-1015

ANALYSIS OF CELL SPREADING ON MICROPATTERNED SUBSTRATES USING A THERMODYNAMICALLY CONSISTENT NON-LOCAL ACTIVE FORMULATION

Eóin McEvoy (1), Tommaso Ristori (2), Sandra Loerakker (2), Vikram S. Deshpande (3), Patrick McGarry (1)

(1) Department of Biomedical Engineering, National University of Ireland Galway, Galway, Ireland

(2) Department of Biomedical Engineering, Eindhoven University of Technology, Eindhoven, The Netherlands

(3) Department of Engineering, University of Cambridge, Cambridge, United Kingdom

INTRODUCTION

Several experimental studies demonstrate that control of cell spreading using substrate micro-patterning has a significant impact on cell behavior. A study by McBeath *et al.* [1] reveals that stem cell differentiation can be controlled by limiting cell spread area. It has also been shown that the contractility of smooth muscle cells increases with increasing cell area (Tan *et al.* [2]). Lamers *et al.* [3] show the spread geometry and stress-fibre (SF) distribution of osteoblasts on grooved surfaces is highly dependent on groove spacing. Wide grooves result in polarized cells with SFs aligned along the grooves. Narrow groove spacing leads to randomly oriented cells and SFs. Finally, a study by Théry *et al.* [4] has shown that cells spread on V-shaped fibronectin patches exhibit SFs align along the free edge of the cell.

The bio-mechanisms underlying such experimental observations are not fully understood. In the current study we propose a new approach to the analysis of the spreading of cells on micro-patterned substrates. We demonstrate that a non-local thermodynamically consistent active cell model explains several of the key phenomena observed experimentally.

MODEL DEVELOPMENT

The thermodynamically consistent kinetic equation for SF formation/dissociation proposed by Vigliotti *et al.* (2015) [5] reduces to

$$\hat{\eta} = \left(\hat{N}_u/\pi\hat{n}\right)exp[\hat{n}(\mu_u - \mu_b)/kT] \qquad (1)$$

under steady state conditions in a representative volume element (RVE) within the cell. $\hat{\eta}$ is the SF concentration per unit surface area of the RVE, $\hat{n}$ is the number of actin-myosin contractile units along the length of the RVE, μ_b is the free energies of the bound contractile units in a stress fibre, μ_u is the free energy of unbound SF proteins, while k and T are the Boltzmann constant and absolute temperature. $\hat{N}_u$ is the number of unbound SF proteins. Here we implement non-local conservation of the total number of SF proteins within the cell, $\hat{N}_T$, under the assumption that the diffusion of unbound proteins through the cytoplasm is infinitely fast relative to the timescale of SF remodeling. The number of unbound proteins in the whole cell is therefore given as

$$\hat{N}_u = \hat{N}_T - \int_{V_c} \int_{-\pi/2}^{+\pi/2} \hat{\eta}\,\hat{n} d\phi dV \qquad (2)$$

where the inner integral computes the number of bound proteins in a RVE, and the outer integral provides a summation over all the RVEs in the entire cell volume V_c. At steady state, $\hat{n}$ in a SF at orientation ϕ is given as

$$\hat{n} = \left(1 + \varepsilon_n(\phi)\right)/(1 + \tilde{\varepsilon}_{ss})(\qquad (3)$$

where ε_n is the SF nominal axial strain. When a SF is extended, contractile units are added, with the effect that the internal strain in the SF is reduced until a steady state value $\tilde{\varepsilon}_{ss}$ is achieved. Conversely, when a SF shortens, functional units are removed. In both cases, the internal fibre steady state strain is different from the axial material strain in the direction of the fibre, $\varepsilon_n(\phi)$.

The formulation is completed by the addition of a non-linear hyperelastic formulation (Ogden, N=8) in parallel with the SF model in order to represent the passive components of the cell.

SIMULATIONS AND RESULTS

The model described above is used to simulate two separate cell spreading experiments:

Experiment 1. As shown in Fig. 1, cells spreading across a series of parallel grooves and fibronectin adhesion patches, both of width L_r , is simulated. In order to spread on N grooves the cell must deform from

Copyright 2016 The Organizing Committee for the 2016 Summer Biomechanics, Bioengineering and Biotransport Conference

its reference configuration in the x-direction by a stretch λ_x, after which it may spread along the groves by deforming in the y-direction by a stretch λ_y.

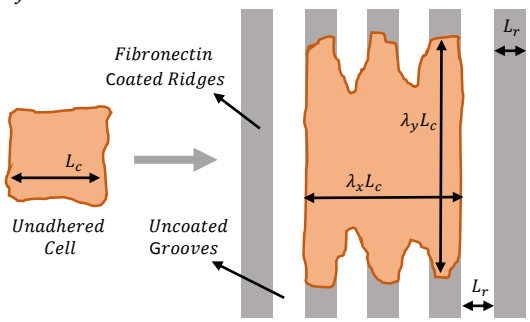

Figure 1: Schematic of parametric study of cell spreading across a series of parallel grooves and fibronectin adhesion patches.

A parametric study is conducted for a range of spread states (λ_x and λ_y). For each spread state the free energy of the system $\bar{G}$ is computed from

$$\bar{G} = W_{elas} + (\rho kT) ln(\hat{N}_u) \qquad (4)$$

where W_{elas} is the elastic free energy due to deformation of the passive components of the cytoplasm during cell spreading. The second term is the cytoskeleton free energy, where ρ is the density of cytoskeletal proteins. Eqn.(4) can be interpreted as a competition between the elastic free energy, which increases with cell spreading, and the cytoskeleton free energy, which decreases with cell spreading (in accordance with eqns.(1-3)).

As shown in Fig. 2(a), results reveal that when the groove spacing is wide (L_c/L_r=3) $\bar{G}$ is minimized when the cell extends along the grooves in the y-direction ($\lambda_y = 1.5$) while spanning only one grove (N=2 and $\lambda_x = 0$). Such spreading in the y-direction, coupled with the global conservation of cytoskeletal proteins, dictates that SFs align primarily in the direction of the grooves. Spreading in the x-direction is discouraged by the high elastic penalty, as shown for the case of N=4.

Fig.2(b) considers the case of a small groove spacing (L_c/L_r=12). Here $\bar{G}$ is minimized when $\lambda_x \approx \lambda_y \approx 1.55$ and an isotropic distribution of stress fibres is obtained. Notably, global conservation of cytoskeletal proteins dictates that the SF concentration in any given direction, $\eta(\phi)$, in Fig.2(b) is lower than the concentration of SFs along the grooves in Fig.2(a).

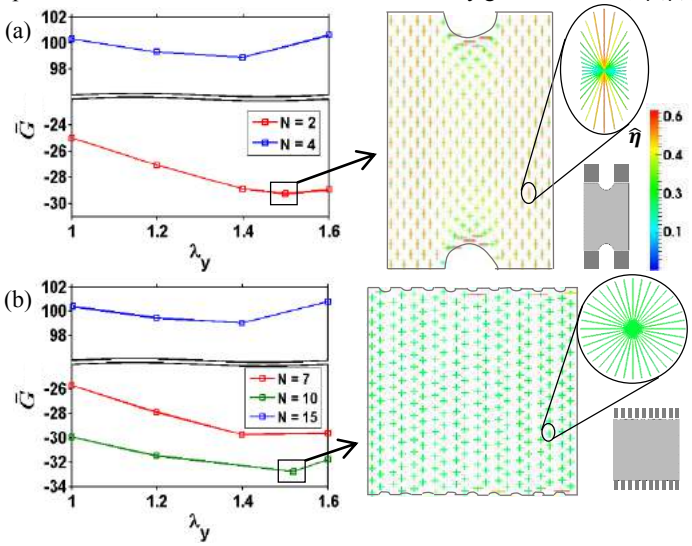

Figure 2: Free energy of the system ($\bar{G}$) and vector plot of SF concentration ($\hat{\eta}$) for: (a) Cell is spread on wide (L_c/L_r = 3) ridges and grooves; (b) Cell spread on thin (L_c/L_r=12) ridges and grooves

Experiment 2: In a second series of simulations, a circular unadhered cell spreads on a V-shaped adhesion patch of length L_a, as shown in Fig. 3. For a cell of radius r_c , the spreading process is parameterized in terms of the proportion of the cell perimeter ωr_c that adheres to the patch. The stretch along the patch is therefore given as $\lambda_p = L_a/\omega r_c$. The influence of the ratio of initial cell size to groove length is also considered.

For the longest adhesion patch ($r_c/L_a = 0.38$) $\bar{G}$ is high due to high levels of elastic deformation required for spreading. For the shortest adhesion patch ($r_c/L_a = 0.44$), $\bar{G}$ is high due to the low levels of SF formation associated with limited cell spreading. The minimum free energy spread state, characterized by λ_p, is dependent on the length of the adhesion patch. The lowest value of $\bar{G}$ is computed for $r_c/L_a = 0.40$, with $\lambda_p = 1.24$. In this configuration highest strains occur in the region of the free unadhered edge of the cell. Global conservation of cytoskeletal proteins therefore dictates that the SFs form predominantly parallel to the free edge.

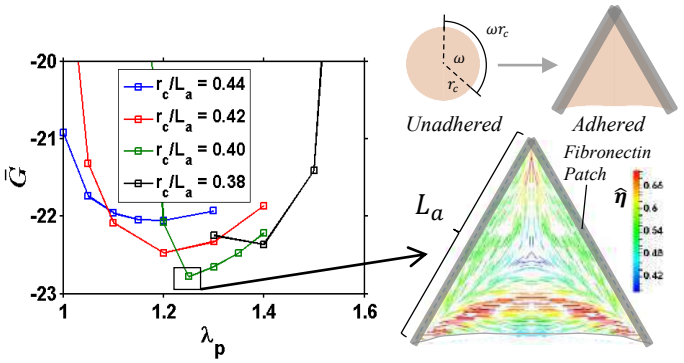

Figure 3: Free energy of the system ($\bar{G}$) and vector plot of SF concentration ($\hat{\eta}$) for cell spreading over V-shaped adhesion patch.

DISCUSSION

The modelling framework presented here captures the key trends reported in the studies by Lamers *et al.* [3] and Théry *et al.*[4], suggesting that cells tend to assume a minimum free energy ($\bar{G}$) spread state. This minimum free energy state is determined by competition between the elastic free energy due to deformation of the passive cytoplasm and the cytoskeleton free energy, subject to a non-local conservation of cytoskeletal proteins throughout the cell. Simulations suggest that the evolving strain distribution during spreading is a critical determinant of the SF distribution. This model represents a significant advance on recent phenomenological approaches to the analysis of cell spreading and SF remodeling [6, 7].

ACKNOWLEDGEMENTS

Funding for this research was provided by the Irish Research Council (RCS1434) and the National University of Ireland Galway Hardiman Scholarship.

REFERENCES

1. McBeath, R *et al. Developmental Cell*, 6:483-95, 2004
2. Tan, J *et al. PNAS*, 100(4):1484-89, 2003
3. Lamers, E *et al.*, *Biomaterials*, 31(12):3307-16, 2010
4. Théry, M et al., *Cell Motil Cytoskeleton,* 63(6):341-55, 2006.
5. Vigliotti, A *et al.*, *Biomech Model Mechanobiol*, [Epub ahead print], 2015.
6. Ronan, W *et al.*, *J Mech Behav Biomed Mater,* 14:143-57, 2012.
7. Reynolds, N *et al.*, *Biomaterials,* 35(13):4015-25, 2014.

Copyright 2016 The Organizing Committee for the 2016 Summer Biomechanics, Bioengineering and Biotransport Conference

SB³C2016
Summer Biomechanics, Bioengineering and Biotransport Conference
June 29 –July 2, National Harbor, MD, USA
SB³C2016-1016

VALIDATION AND UNCERTAINTY ANALYSIS OF A CLINICAL CFD TOOL– AVIEW–FOR INTRACRANIAL ANENURYSM FLOW SIMULATION

Jianping Xiang (1,2,3), Nikhil Paliwal (1,3), Nicole Varble (1,3), Adnan H. Siddiqui (2,3), Hui Meng (1,2,3)

(1) Department of Aerospace and Mechanical Engineering
State University of New York at Buffalo
Buffalo, NY, USA

(2) Department of Neurosurgery
State University of New York at Buffalo
Buffalo, NY, USA

(3) Toshiba Stroke and Vascular Research Center
State University of New York at Buffalo
Buffalo, NY, USA

INTRODUCTION

With the FDA approval of HeartFlow®, CFD tools are making their way to clinical management of cardiovascular diseases. All these tools need to be validated before being applied into clinical workflow. Intracranial aneurysm (IA) is one challenging cardiovascular disease, since their rupture is catastrophic, but not often, and treatment complication can be significant. Utilizing image-based computational fluid dynamics (CFD), detailed flow dynamics can help neurosurgeons make better treatment plans. However, currently no such modeling tools allow routine integration of flow dynamics in clinical workflow.

To this end, we have developed AView, a clinician-oriented, integrated computation tool for aneurysmal flow dynamics, morphology, and risk and data management to support clinical management of IAs.[1] At the heart of this tool is the CFD solver, Gnuid.[2] In this study, following the ASME V&V20,[3] we aim to validate AView based on the intended use, a patient-specific IA under physiological flow using particle image velocimetry (PIV) system.

METHODS

AView is employed to simulate the hemodynamics in a typical patient-specific internal carotid artery (ICA) aneurysm. A physical model (phantom) of this aneurysm is fabricated and placed in an *in vitro* flow loop, which is operated under a range of physiological flow conditions (flow rate of 189-360 *mL/min*, heart rate of 60-90 *bpm*). The CFD settings match these experimental conditions. To measure the flow fields under each of the experimental flow conditions, we employ planar PIV and acquired 40 instantaneous flow fields in each cardiac cycle, continuously for 50 cycles to obtain averaged peak systole, end-diastolic and mean flow fields at middle coronal and transverse planes. The working fluid is a mixture of water, glycerin, and sodium iodine (density=1.23 g/cm^3, viscosity=4.03 *cP*) to mimic the blood properties.

Validation

We present the validation results at three levels: a) Qualitative comparison; b) Quantitative comparison; c) Uncertainty analysis of PIV, CFD and their comparison, following their definition in ASME V&V20.[3]

Qualitative Comparison

To validate the aneurysmal flow patterns from CFD simulations, we plot 2D velocity contours and velocity vectors on the time-averaged flow field and on the peak and end-diastolic time points on the middle planes, and compare them against PIV measurements.

Quantitative Comparison

We quantitatively compare the velocity magnitude on the intersecting line (100 discretized points) of coronal and transverse planes and plotted the velocity magnitude from both CFD and 3 sets of PIV measurements. Furthermore, we apply two commonly used parameters to quantify the differences in point-wise velocity vectors between CFD and PIV flow field data.[4] The first variable, angular similarity index (ASI), measures the similarity of the directions of the velocity vectors between CFD and PIV results and was defined as:

$$ASI = \frac{u_{CFD}.u_{PIV}}{|u_{CFD}|\,|u_{PIV}|} \quad (1)$$

The range of ASI is [-1, 1], with 1 being the highest similarity. The second variable, magnitude similarity index (MSI), quantifies the similarity in the *magnitudes* of the vectors and was defined as:

$$MSI = 1 - \left|\frac{|u_{CFD}|}{max(|u_{CFD}|)} - \frac{|u_{PIV}|}{max(|u_{PIV}|)}\right| \quad (2)$$

The variable MSI varies in the range [0, 1], with 1 being the value with the highest similarity in the magnitude.

Uncertainty Analysis

The model form uncertainty represents the best estimation of the model form error, which lies within the range

Copyright 2016 The Organizing Committee for the 2016 Summer Biomechanics, Bioengineering and Biotransport Conference

$$u_{model} = E \pm u_{val} \quad (3)$$

where u_{model} is the model form uncertainty, E is the comparison error between simulation and experimental outputs, and u_{val} is the combined uncertainty of the errors in the overall validation.[3]

The combination of the errors that arise during code validation is estimated in the form of a validation uncertainty, u_{val}. These errors combine in the form of uncertainties as

$$u_{val} = \sqrt{u_{num}^2 + u_{input}^2 + u_D^2} \quad (4)$$

where u_{num}, u_{input}, and u_D are numerical uncertainty, input parameter uncertainty and experimental uncertainty, respectively.[3]

RESULTS

Qualitative Comparison

As one example, Figure 1 shows qualitative comparison between CFD simulations and 3 sets of PIV measurements on the middle coronal plane under the flow condition of 256 *mL/min* and 70 *bpm* for the mean flow field. We observe that the flow patterns of CFD and PIV are very similar to each other, showing aneurysmal flow going through the distal end of wall and forming a vortex inside the sac.

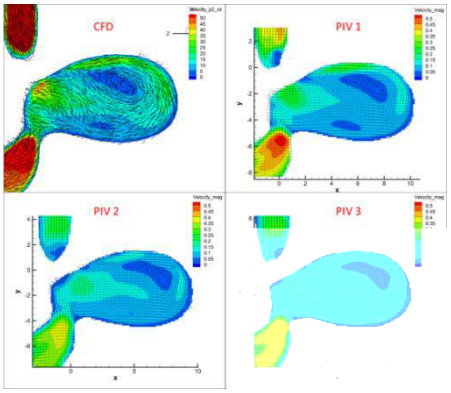

Figure 1: Qualitative comparison between CFD and 3 sets of PIV.

Quantitative Comparison

We perform quantitative comparison and subsequent uncertainty analysis on the intersecting line (100 points) between the middle coronal and transverse planes. Figure 2 plots the velocity on the line from CFD and PIV (mean ± sd). In general, the velocity has the similar trend, but different magnitudes, especially at the high flow region close to the aneurysmal distal wall. Furthermore, the calculated high average ASI and MSI values of 0.84 and 0.83 demonstrate decent agreement between CFD and PIV.

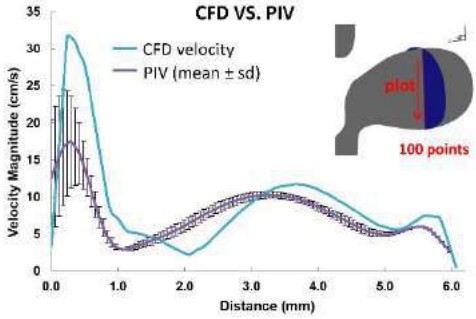

Figure 2: Quantitative comparison between CFD and PIV.

Uncertainty Analysis

Following V&V20 guidance, we calculate numerical uncertainty $u_{num,}$ input parameter uncertainty u_{input}, and experimental uncertainty $u_{D.}$ Figure 3 shows the CFD plot with combined numerical and input parameter uncertainty as error bars against the PIV velocity mean with the experimental uncertainty as error bars. Figure 4 shows estimated error with error bars indicating validation uncertainty, where we observe small errors in most regions, except for the high velocity region near the aneurysm wall. Furthermore, the average relative error is calculated to be 22.7%. However, if we exclude the near wall region (20% points), the average relative error is 13.6%.

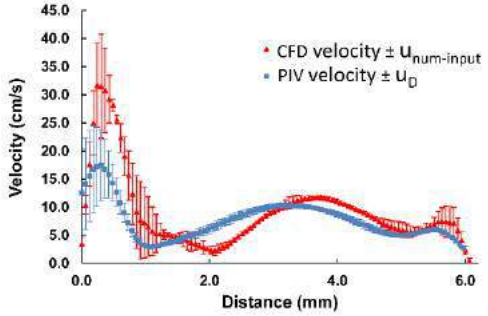

Figure 3: PIV and CFD velocity along the intersecting line with error bars indicating combined numerical and input parameter uncertainty, and experimental uncertainty, respectively.

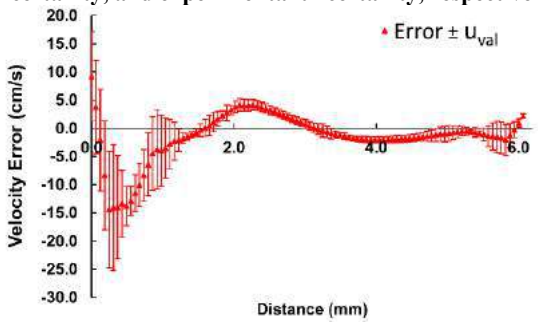

Figure 4: Estimated comparison error along the intersecting line with error bars indicating validation uncertainty.

DISCUSSION

Clinically imaged-based CFD has high potential to be used in the clinical world, provided that they are accurate and validated. In this study, we demonstrate that CFD results from AView match with PIV measurements under different physiological flow conditions in a typical aneurysm (in this abstract we only report results under one flow condition). At the same time, we also observe that the CFD-derived velocity has different magnitude as from PIV measurements (Figure 1), and location of the vortex from CFD and PIV are not at the exact same location. We believe this is due to the non-rigid material property of silicone phantom model used in PIV measurement, while in CFD the wall is assumed as rigid. During the PIV experiment, we observe noticeable movement for the aneurysm wall, probably causing lower velocity magnitude from PIV and that the vortex in PIV is closer to the aneurysm tip wall (Figure 1).

CONCLUSION

ASME V&V20 has been applied to perform the uncertainty analysis for an integrated, clinical modeling tool for IA blood flow dynamics. Our validation and uncertainty analysis demonstrate that AView has a reliable CFD solver to calculate aneurysm flow field.

ACKNOWLEDGEMENTS

This work was funded by Toshiba Medical System Corp and NIH grant (R03 NS090193).

REFERENCES

[1] Xiang, J et al., *ABME*, Jun 23, 2015. [Epub ahead of print]
[2] Botti, L et al., *JCP*, 230(3), 572-585.
[3] V&V 20, *ASME Guide on Verification in CFD*. 2009.
[4] Raschi, M et al., *IJNMBE*, 28:214-228, 2012.

Copyright 2016 The Organizing Committee for the 2016 Summer Biomechanics, Bioengineering and Biotransport Conference

SB³C2016
Summer Biomechanics, Bioengineering and Biotransport Conference
June 29 –July 2, National Harbor, MD, USA
SB³C2016-1017

INTERNAL-EXTERNAL ROTATION AXIS LOCATES LATERALLY OUTSIDE OF STIFLE JOINTS IN THE DOG

Tetsuya Takagi (1), Nobuo Kanno (2), Masakazu Shimada (2), Yasushi Hara (2)
Satoshi Yamakawa (1), Richard E. Debski (3), Glen A. Livesay (4), Hiromichi Fujie (1)

(1) Faculty of System Design
Tokyo Metropolitan University
Tokyo, Japan

(2) Division of Veterinary Surgery
Department of Veterinary Science
Faculty of Veterinary Medicine
Nippon Veterinary and Life Science University
Tokyo, Japan

(3) Bioengineering department
Faculty of Engineering
University of Pittsburgh
Pittsburgh, PA, USA

(4) Department of Biology & Biomedical Engineering
Rose-Hulman Institute of Technology
Terre Haute, IN, USA

INTRODUCTION

Three-dimensional motions of the knee joint are usually described with respect to the knee joint coordinate system originally developed by Grood and Suntay [1]. Previous studies indicated that the flexion-extension axis of the coordinate system passes near the femoral insertions of the collateral ligaments [2], while the internal-external axis is located close to the center of the tibial axis in the human knee joints [3]. This coordinate system has been widely accepted in biomechanical research and has been utilized for the mechanical testing of the human knees [4-6]. Recently, this coordinate system has been also used for the biomechanical tests of porcine [7] and canine stifle joints [8], although detailed information as regard to the relative location of the coordinate system remain unclear in these joints. Therefore, the present study was undertaken to determine the relative location of the knee joint coordinate system axes with respect to porcine and canine stifle joints using a robotic system. With a novel geometrical representation of the helical axis devised in the present study, the 3-dimensional position and orientation of the rotational axes of these animal joints were assessed.

METHODS

Novel geometrical representation of the helical axis

It is well known that any 3-dimensional motion of a rigid body can be expressed by a translation along and a rotation about a unique axis, the so-called helical axis. Although mathematical formulae for the helical axis have been proposed in previous studies, here we present a novel, geometrical representation of the axis which can be easily understood. Consider a rigid body locating at A expressed with a position and orientation described by a [4x4] homogeneous transformation matrix, T, with respect to the reference coordinate system. If the rigid body moves to another location, B expressed with the position and orientation described by another homogeneous transformation matrix, T', the relative motion of the rigid body, H, can be calculated as follows.

$$H = T'\,T^{-1} = \begin{bmatrix} n_x & o_x & a_x & d_x \\ n_y & o_y & a_y & d_y \\ n_z & o_z & a_z & d_z \\ 0 & 0 & 0 & 1 \end{bmatrix} \quad (1)$$

The rotation angle, θ and orientation, $\boldsymbol{k}$, of the helical axis that translates T to T' can be described as follows [9].

$$\theta = \tan^{-1}\left(\frac{\sqrt{(o_z-a_y)^2+(a_x-n_z)^2+(n_y-o_x)^2}}{(n_x+o_y+a_z-1)}\right) \quad (2)$$

$$\boldsymbol{k} = \begin{bmatrix} k_x \\ k_y \\ k_z \end{bmatrix},\ k_x = \frac{o_z-a_y}{2\sin\theta},\ k_y = \frac{a_x-n_z}{2\sin\theta},\ k_z = \frac{n_y-o_x}{2\sin\theta} \quad (3)$$

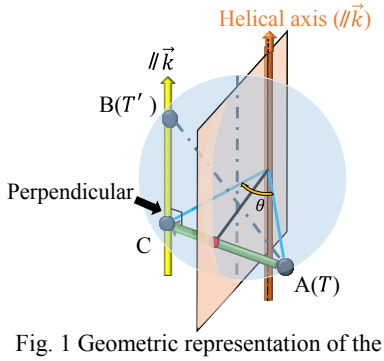

Fig. 1 Geometric representation of the HA

Copyright 2016 The Organizing Committee for the 2016 Summer Biomechanics, Bioengineering and Biotransport Conference

Since the rigid body located at A is rotated around the helical axis to a new location C, and then translated to B along this axis, the angle ACB is always 90 degree (Fig.1). Therefore, the transit location C is on a sphere that has the line AB as a diameter. The transit location C can be determined as the intersection between the sphere and a line parallel to $\boldsymbol{k}$ that passes through B. Imagine a flat plane perpendicular at the midpoint of the line AC. The helical axis is determined as the line in this flat plane with the orientation $\boldsymbol{k}$ where the angle A-axis-C is θ, as shown in Figure.1.

Determination of the rotation axes of animal and human knees

Porcine stifles (n=3), canine stifles (n=3), and a human knee (n=1) were used and each knee was fixed to the robotic system (FRS2015, Technology Service, Japan) [10]. First, flexion-extension rotation was applied to the joint at about 1.5 degree/s to 90 degree of flexion by setting the other 5 DOFs - except the flexion-extension DOF - under force control with prescribed force/moment at 0. After the joint was extended to the initial orientation, internal-external rotation was applied to the joint at about 1 degree/s up to 1 N-m in canine stifles, 2 N-m in porcine stifles, and 5 N-m in human knees. During the application of internal-external rotation, all DOFs except the internal-external and flexion-extension DOFs were set under force control with prescribed force/moment at 0.

The kinematic data collected during the tests were analyzed to determine the homogeneous transformation matrices of the tibia as a function of rotation angle. A matrix, T, at a rotation angle and another matrix, T' at the angle plus 10 degree were substituted to equation (1), and the helical axis of the animal and human joints during the tests were determined following the above-indicated procedure.

RESULTS

The helical axis representation of the flexion-extension rotation axis of the stifles and knees were similar to those previously determined for the human knees [2], with no significant difference observed between porcine, canine, and human joints. However, a significant difference was found in the helical axis representation of the internal-external rotation in these species. In porcine stifles and human knees, the axis was located at the center of the joint in the frontal plane (Fig. 2(a)), while the axis was slightly tilted in the sagittal plane (Fig. 2(b)) possibly because of nominal flexion at extension. In contrast, the helical axis representation of the internal-external rotation axis of canine stifles was located laterally outside of the joint in the frontal plane, as shown in Fig. 2(c), while the axis was slightly tilted in the sagittal plane, similar to the porcine and human joints (Fig. 2(d)).

DISCUSSION

In the present study, a novel representation of the helical axis was developed in which the axis can be described geometrically. The authors ensured that the developed geometrical representation of the helical axis is mathematically identical to a vector representation of the helical axis previously reported [11]. It is beneficial to use the currently developed representation because the geometrical features of the axis can be easily recognized with a minimum of mathematical calculations. Using the developed representation of the helical axis, the flexion-extension rotation and internal-external rotation axes were determined in porcine and canine stifles as well as human knees. It is worth noting that the internal-external rotation axis was located more than 2 cm laterally outside of the canine joints (Fig. 3) while no difference was observed in the flexion-extension axes in the animal and human joints. Thus far, the authors have found no valid reason for the distinct characteristic of the internal-external axis in the dog stifle joint, though it may be attributed to the mechanical role of the joint that assumes a half-bent posture during standing and normal gait. Further experimental and analytical studies are required to determine the helical axis of stifle joints in various activities and to clarify the biomechanical functions of these joints.

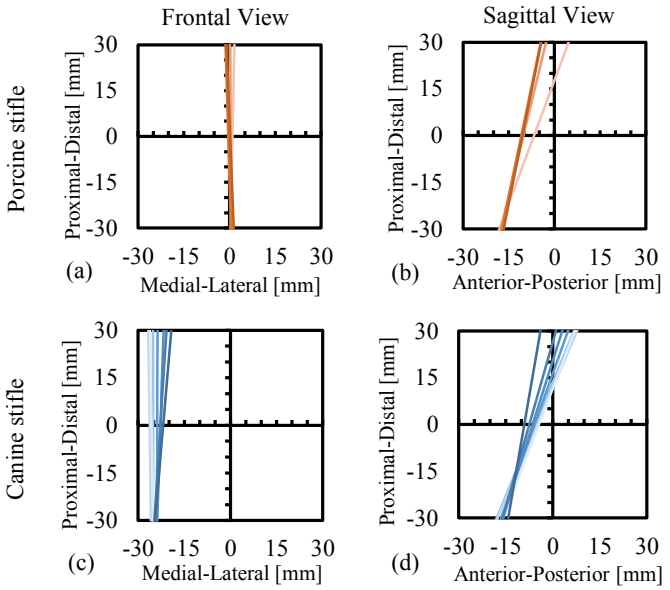

Fig.2 HA of porcine stifle during IE test (a, b) and canine stifle (c, d). Coronal view (a, c) and sagittal view (b, d)

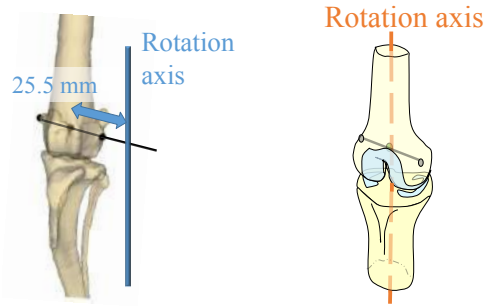

Fig.3 Schematic representation of the HA of canine stifle (Left) in comparison with that of porcine stifle (Right)

ACKNOWLEDGEMENTS

The present study was financially supported by the Grant-In-Aid for Scientific Research B (#25252134) and Challenging Exploratory Research (#26560218) both from the MEXT, Japan.

REFERENCES

[1] Grood, ES and Suntay, WJ., *JBME* 105: 136-144, 1983.
[2] Blankevoort, L et al., *J Biomech* 23: 1219-1229, 1990.
[3] Fujie, H et al., *J Biomech Eng (ASME)* 126: 54–61, 2004.
[4] Grood, ES et al., *JBJS* 70: 88-97, 1988.
[5] Fujie, H et al., *J Biomech Eng (ASME)* 115: 211-217, 1993.
[6] Kadaba, M P et al., *J Orthop Res* 8: 383-392, 1990.
[7] Kevin, M Bell et al., *J Biomech* 48: 3728-3731, 2015.
[8] Cinti, F et al., *JSAP* 56: 389-406, 2015.
[9] Richard, P Paul, *The MIT press*, USA, 1981.
[10] Fujie, H et al., *SB3C (ASME)*, 2015.
[11] Spoor, C W and Veldpaus, F E., *J Biomech* 13: 391-393, 1980.

Copyright 2016 The Organizing Committee for the 2016 Summer Biomechanics, Bioengineering and Biotransport Conference

SB^{3}C2016
Summer Biomechanics, Bioengineering and Biotransport Conference
June 29 –July 2, National Harbor, MD, USA
SB^{3}C2016-1018

EFFECT ON OLIGOSACCHARIDE GRAFTING ON THE POLYELECTROLYTE AND PROTONATION DYNAMICS OF POLYETHYLENIMINE

Saswati Basu, Danielle N. Miller, Stacy N. Apugo, P. L. Chandran

Chemical Engineering Department
Howard University
Washington, DC, USA

INTRODUCTION

Polyethylenimine (PEI) is one of the most commonly used polymers for condensing DNA in cell-transfection and gene-therapy applications (1). The 2.5kDa polymer backbone is intrinsically hydrophobic, semiflexible, and contains closely-spaced amine groups which are charged when protonated. As a result, the polymer exhibits unusual polymer dynamics. Our studies indicate that the backbone protonation occurs discontinuously with increasing pH, and a clustered phase exists in equilibrium with free polymers at conditions of high inter-chain and low intra-chain repulsion. Mannobiosylated PEI is commonly used for targeting DNA to immune cells and to lower drug induced toxicity (2). Our goal is to understand how the grafting of a hydrophilic moiety alters the semiflexibility, protonation, and clustering dynamics of the PEI backbone; and if these alterations significantly affected the interaction with DNA to form condensed nanoparticles.

METHODS

Solutions of PEI (Polysciences Inc., Warrington, PA) and mannobiosylated PEI (Polyplus Transfection Inc., 67400 Illkirch-Graffenstaden, France) were prepared at different polymer and salt concentrations, and at varying pH. The protonation profile of the polymer was obtained by pH titration with the polymer-less solution as reference in order to control for CO_2 dissolution and other artifacts. The free polymer extensibility was assessed from hydrodynamic diameter measurements of the polymer in Dynamic Light Scattering (DLS) experiments. AFM images of surface-trapped polymers were used to corroborate the trends in polymer extensibility. The dynamic interchange between free and clustered polymers was investigated by studying the multiple relaxation times evident in DLS autocorrelation data. Osmotic experiments were used to affirm the clustering effects. DNA nanoparticles were made by incubating the solution of DNA, PEI, and salt overnight. Atomic Force Microscopy (AFM) images of the particles were used to assess changes in the DNA condensation pattern.

RESULTS

The distribution between the free and clustered phase was investigated as a function of salt. 2.5 kDa PEI shows an unusual phenomenon of salt-dependent clustering; the formation of clusters decreases as salt concentration is increased to physiological levels, but then increases at higher salt concentrations. This phenomenon can be attributed to the balance between inter- and intra- chain charge repulsion.

pH changes affect the protonation of the polymer, which appears to occur in characteristic regimes (Fig. 1). Interestingly, the protonability is not affected by the presence or absence of a clustered phase.

The extensibility (i.e. the persistence length) of the free 2.5kDA polymer increases with intra-chain repulsion and decreases with inter-chain repulsion; and varies with both pH and salt conditions.

The grafting of mannobiose to the PEI backbone significantly changes the polymer extension, and its clustering and protonation dynamics.

We investigated if the changes in PEI clustering, protonation, and oligosaccharide grafting altered its interaction with DNA and the subsequent condensation into nanoparticles. AFM images are

Copyright 2016 The Organizing Committee for the 2016 Summer Biomechanics, Bioengineering and Biotransport Conference

presented showing the condensation pathway of the nanoparticle for different states of the PEI polymer.

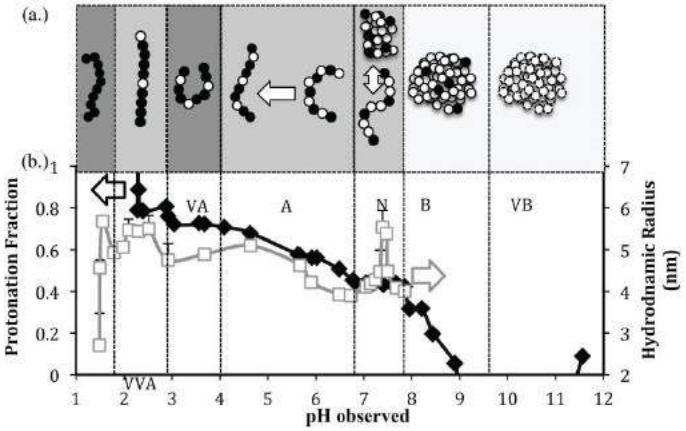

Figure 1. pH dependent protonation-polyelectrolyte interplay in 4.08mM PEI solution with 150mM NaCl. (a) Schematic depicting the protonation and polyelectrolyte dynamics of the polymer in different regions. Charged PEI monomers are shown as black beads and uncharged monomers as white beads. (b) Simultaneous tracking of PEI protonation and backbone extension state in different pH regimes.

DISCUSSION

2.5kDa PEI is the simplest model of a hydrophobic semiflexible polyelectrolyte. Our studies indicate that the polymer is richly sensitive to the solution conditions, and that the polymer dynamics is altered by the grafting of hydrophilic moieties. Understanding the polymer dynamics will allow scientists to design DNA drug delivery vehicles with tailored organization and interaction specificity (3).

ACKNOWLEDGEMENTS

This work is supported by the NSF Award #1407891 to Dr. Chandran. We are grateful to the NSF HU-Crest center for facilities support.

REFERENCES

[1] L. M. Santhakumaran, A. Chen, C. K. S. Pillai, T. Thomas, H. He and T. J. Thomas, Nanotechnology in Nonviral Gene Delivery, Wiley-VCH Verlag GmbH & Co. KGaA, 2005.
[2] J. Lisziewicz, J. Trocio, L. Whitman, G. Varga, J. Xu, N. Bakare, P. Erbacher, C. Fox, R. Woodward, P. Markham, S. Arya, J. P. Behr and F. Lori, *J. Invest. Dermatol*., 124, 160–169, 2005
[3] J. M. Irache, H. H. Salman, C. Gamazo and S. Espuelas, *Expert Opin. Drug Delivery*, 5, 703–724, 2008.

Copyright 2016 The Organizing Committee for the 2016 Summer Biomechanics, Bioengineering and Biotransport Conference

SB³C2016
Summer Biomechanics, Bioengineering and Biotransport Conference
June 29 –July 2, National Harbor, MD, USA
SB³C2016-1019

A CT BASED MODEL OF THE FRACTURE OF CALCIFIED ATHEROSCLEROTIC PLAQUES

Brían L. O'Reilly (1), Peter E. McHugh (1), Patrick McGarry (1)

(1) Biomedical Engineering
National University of Ireland, Galway
Galway, Ireland

INTRODUCTION

Atherosclerosis is a major cause of cardiac disease and strokes worldwide. This occurs due the blockage of an artery by a lesion of atherosclerotic plaque. The experimental characterization of plaque tissue mechanical behavior is distinctly lacking in the literature in comparison to the extensive experimental characterization of healthy arterial tissue. Advances in current understanding of plaque biomechanics can potentially guide the design of angioplasty devices and assist in the planning of clinical intervention.

This study investigates the delamination of calcified particles from the fibrous matrix of the plaque. This mode of material damage may play an important role in plaque rupture, leading to the onset of adverse clinical consequences, e.g. strokes [1].

METHODS

Excised human atherosclerotic plaque samples were acquired from University College Hospital Galway as approved by the hospital's ethical research committee. The plaque samples were scanned using computed topography (CT) to generate accurate 3D images for calcifications present in the plaque. CT scans were used to generate bi-phasic finite element models consisting of hard calcifications embedded in a soft fibrous matrix (Figure 1).

The fibrous matrix of the plaque samples were isolated and subjected to biaxial testing. Results reveal that the plaque fibrous matrix is significantly stiffer in the circumferential direction than in the axial direction. A compressible form of the HGO anisotropic hyperelastic model [2, 3] is calibrated using the biaxial test results, whereby the stress tensor is given as

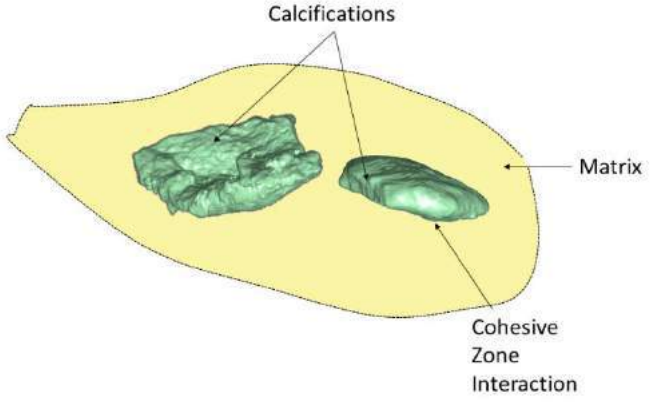

Figure 1: CT generated 3D calcification geometries embedded in a fibrous matrix. A cohesive zone fracture model is implemented at the interface between the calcifications and the matrix.

$$\boldsymbol{\sigma} = \kappa_0(J-1)\mathbf{I} + \mu_0 J^{-1}\left(\overline{\mathbf{B}} - \frac{1}{3}\bar{I}_1\mathbf{I}\right) + 2J^{-1}k_1\sum_{i=4,6}(I_i-1)\exp[k_2(I_i-1)^2](\boldsymbol{a_i}\otimes\boldsymbol{a_i}) \quad (1)$$

where κ_0 is the isotropic bulk modulus, μ_0 is the isotropic shear modulus, k_1 and k_2 are the anisotropic material constants, $\boldsymbol{a_i}$ is the fibre directional vector, J is the determinant of the deformation gradient, $\bar{I}_1$ is the first invariant of the right Cauchy-Green tensor and

Copyright 2016 The Organizing Committee for the 2016 Summer Biomechanics, Bioengineering and Biotransport Conference

I_4 and I_6 are the anisotropic invariants describing the deformation of reinforcing fibres.

Stress relaxation testing was performed on the fibrous matrix in both the circumferential and axial directions and results were used to calibrate Prony series parameters to represent the tissue viscoelasticity.

The CT generated plaque finite element mesh is embedded in an idealized artery geometry. Again the anisotropic hyperelastic formulation (Eqn. 1) is used to model the artery wall. Angioplasty is simulated by expanding a balloon in the artery lumen with contact surfaces being defined between the balloon and the outer surface of the plaque/artery.

A cohesive zone fracture model is applied the interface between the plaque calcifications and the fibrous matrix. A mixed mode cohesive zone model proposed by McGarry et al. [4] is used, whereby the work of separation is given as

$$\phi(\Delta_n, \Delta_t) = \phi_0 + \sigma_{max} \exp(1) \left(1 + \sqrt{\frac{\Delta_n^2}{\delta_n^2} + \frac{\Delta_t^2}{\delta_t^2}}\right) \exp\left(-\sqrt{\frac{\Delta_n^2}{\delta_n^2} + \frac{\Delta_t^2}{\delta_t^2}}\right) \quad (2)$$

The mode I and mode II interface strengths are assumed to be equal and values of the characteristic lengths δ_n and δ_t are chosen so that the interface is several orders of magnitude stiffer than the surrounding materials. A parametric study of the interface strength (σ_{max}) is performed whereby the angioplasty balloon is expanded until the calcified particles debond from the surrounding fibrous matrix.

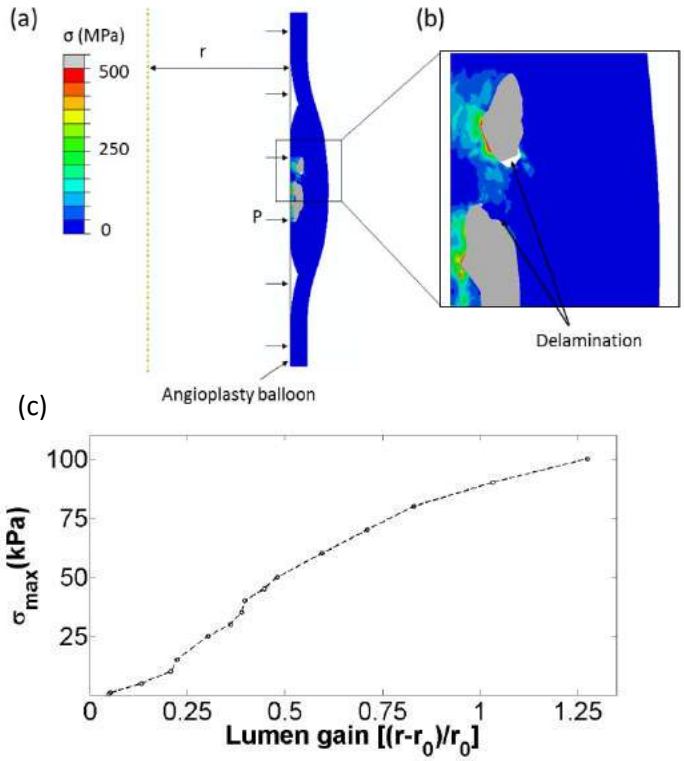

Figure 2: (a) Contour plot of the maximum principal stress of the angioplasty model. (b) Magnified section showing the presence of separation in the cohesive interface. (c) Graph demonstrating of the relationship of lumen gain at calcification delamination and the interface strength.

RESULTS

The computed deformation of the artery and plaque is shown in Figure 2(a) following balloon expansion from an initial lumen radius r_0=5.25mm to a radius r=7.59mm, i.e. a lumen gain of 45%. The expanded balloon contacts both the plaque and the artery, resulting in significant localized deformation of the plaque.

The distribution of maximum principal stress is also shown in Figure 2. Stress concentration occurs in the fibrous plaque near the calcified particles.Ssuch stress concentrations result in mixed mode delamination of the fibrous matrix from the calcifications, as detailed in Figure 2(b).

The relationship between the matrix-calcification interface strength and the lumen gain at the onset of delamination is shown in Figure 2(c). A non-linear relationship is observed. A lumen gain of 1.0 requires an interface strength of 98.4kPa in order to avoid delamination of plaque calcifications.

DISCUSSION

This study presents the first investigation into the delamination of calcifications during balloon angioplasty using patient specific calcification geometries derived from CT scans. The relationship between lumen gain during angioplasty and the onset of delamination for a range of interface strengths is uncovered. Experimental studies are currently being conducted to characterize σ_{max} for calcified excised plaques. The experimental and computational methodologies developed in this study can potentially be used for planning of patient specific clinical interventions and device design.

ACKNOWLEDGEMENTS

The authors would like to thank the clinicians at the Western Vascular Institute in University College Hospital Galway for provision of plaque samples. BOR acknowledges a NUIG College of Engineering and Informatics PhD Scholarship.

REFERENCES

[1] Mulvihill, J et al., *Acta Materialia*, 9:9021-9035, 2013.
[2] Holzapfel, GA et al., *J. Elasticity*, 61:1-48, 2000.
[3] Nolan, DR et al., *J. Mech. Behav. Biomed.*, 39:48-60, 2014
[4] McGarry, JP et al., *J. Mech. Phys. Solids.*, 63:336-362, 2014

Copyright 2016 The Organizing Committee for the 2016 Summer Biomechanics, Bioengineering and Biotransport Conference

SB³C2016
Summer Biomechanics, Bioengineering and Biotransport Conference
June 29 –July 2, National Harbor, MD, USA
SB³C2016-1020

MODELING THE VISCOELASTIC PROPERTIES OF PULMONARY VESSELS IN A HYPERTENSIVE RAT

Erica R. Pursell (1), Daniela Vélez-Rendon (1), Daniela Valdez-Jasso (1)

(1) Bioengineering Department
University of Illinois at Chicago
Chicago, IL, USA

INTRODUCTION

Pulmonary arterial hypertension (PAH) is a disease of the heart and pulmonary vessels characterized by elevated blood pressure. To adjust for elevated blood pressures, pulmonary vessels undergo remodeling. This remodeling changes the pulmonary arteries' (PA's) ability to store and deliver the entire stroke volume of the right ventricle (RV) which then hinders the heart's ability to pump blood *with heart failure as an end stage of the disease*[1].

One way of quantifying the arteries' ability to store and deliver blood is determining the mechanical properties of the vessels. There have been studies on the mechanical properties of human and ovine vasculature using either Voigt [2, 3] or Kelvin [4, 5] viscoelastic models. Alastruey *et al*. assumed material properties of human vessels to be similar to those of silicone [2] while Valdez-Jasso *et al.* found the parameter η (time dependent coefficient) for ovine vessels to be location specific [4].

To elucidate our understanding of the disease progression, we propose to develop mechanistic models that can incorporate important vascular mechanical properties. Our goal is to establish a constitutive equation that accurately portrays vessel behavior in normo- and hypertensive animal.

METHODS

The experimental protocols used for this study were approved by University of Illinois at Chicago Animal Care and Use Committees. PA segments were harvested from two 12-week-old male Sprague-Dawley rats weighing 350 grams (Charles River Laboratories). At 8 weeks of age, one rat was treated with a subcutaneous monocrotaline (MCT) injection to induce PAH while the other was injected with a placebo solution. The animals were then left for four weeks to allow the PAH to reach a severe state.

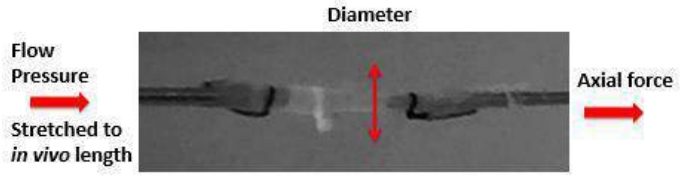

Figure 1: Schematic of the tubular biaxial mechanical testing set-up. Flow and pressure measured *in vivo* are used as inputs, axial stretch is prescribed, and diameter and axial force measured

Post invasive hemodynamic measurements confirmed the normotensive state of the placebo and hypertensive state of the MCT animal before the arterial segments were harvested from left pulmonary arteries. Segments were cannulated on each end and underwent tubular biaxial testing using a Bose biodynamic chamber (Figure 1). The vessels were tested at three axial stretches, *in vivo* and ± 5% where *in vivo* stretch was taken to be 40% of the *ex vivo* length. Pressure and flow were prescribed (and recorded) to simulate values measured *in vivo* and diameter was measured using a laser micrometer during the experiment.

Copyright 2016 The Organizing Committee for the 2016 Summer Biomechanics, Bioengineering and Biotransport Conference

Two viscoelastic models were used for modeling of our data: the Voigt (Equation 1) and the Kelvin (Equation 2) viscoelastic models.

$$P = kA + \eta \frac{dA}{dt} \quad (1)$$

$$\frac{d\epsilon}{dt} = \frac{\frac{k_2}{\eta}\left(\frac{\eta}{k_2}\frac{dP}{dt} + P - k_1\epsilon\right)}{k_1 + k_2} \quad (2)$$

$$A = 2\pi\left(\frac{d}{2}\right)^2 \quad ; \quad \epsilon = \frac{A - A_{min}}{A_{min}} \quad (3)$$

These models are derived from a mechanical body with one spring and one dashpot in parallel (Voigt) and another spring in series with the dashpot (Kelvin model). In these relations, P is representing blood pressure, k the spring constant, η the dashpot constant, A the vessel cross-sectional area, d the measured diameter, and ϵ the circumferential strain. For the Voigt model, area was fitted using a 7 term Fourier approximation and used to predict pressure. In the Kelvin model, the pressure was fitted with a 7 term Fourier approximation to predict a change in strain over time, which was then solved using MATLAB's ODE solver and fminsearch and converted to area. Pressure and area are plotted for comparison (Figure 2).

RESULTS

The Voigt model produced a good initial estimate for our pressure, but it was not able to characterize all of the features in the data waveform. The Voigt model closely predicted the oval shape of the placebo data, but not it's J-shape (Figure 2, left column). The MCT data waveforms show different and unique features. In this case, the Voigt model was not sufficient to predict the leaf shape of the pressure-area relation (Figure 2, right column). Here the predicted hysteresis was greater than the measured, and the slope of the pressure-area plot was not large enough. In contrast, the Kelvin model was able to more closely represent the more complex behaviors of both vessel types. It accurately reflected the J-shape in the placebo data and for *in vivo* stretch of the MCT data, expressed the lower hysteresis and increased slope. However, this was not true when the axial stretch was changed in the MCT-treated vessel. The parameters of the Kelvin model are shown in Table 1 with relatively low error values contrasted with much larger error in the Voigt model (Table 2).

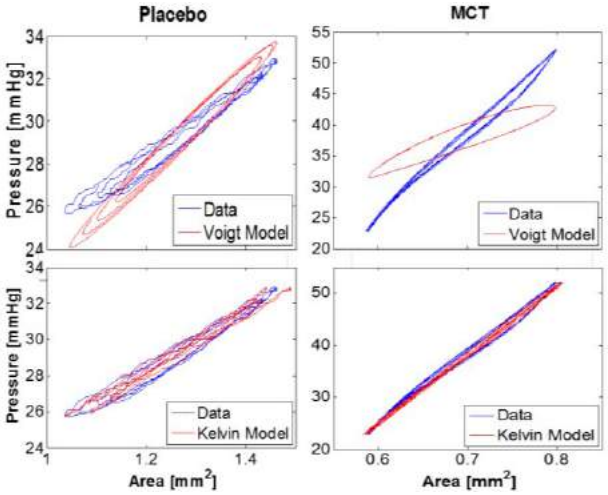

Figure 2: Pressure-area relation in a placebo (left column) and PAH (right column) left-pulmonary artery. As shown, the cross-sectional area prediction is improved from the Voight model (top panels) to the Kelvin model (bottom panels).

Table 1: Results for placebo data using Kelvin model. Top row are the initial values fed into the optimizer. Lower rows show optimized parameters for each respective axial stretch. Right column is the 2-norm error between prediction and measurement.

	$\eta\left[\frac{mmHg*s}{mm^2}\right]$	$k_1\left[\frac{mmHg}{mm^2}\right]$	$k_2\left[\frac{mmHg}{mm^2}\right]$	Error [mm²]
Guess	0.1	1	20	----
35% Stretch	0.194	-0.0002	18.044	2.50
40% Stretch	0.133	0.0006	0.647	0.64
45% Stretch	0.235	-0.0011	18.035	1.34

Table 2: Optimal parameter values found using the Voigt and Kelvin models in placebo and MCT-treated animals. Right column is the 2-norm error between prediction and measurement. Note that error has different units, depending on model used.

	$\eta\left[\frac{mmHg*s}{mm^2}\right]$	$k_1\left[\frac{mmHg}{mm^2}\right]$	$k_2\left[\frac{mmHg}{mm^2}\right]$	Error
Placebo (Voigt)	-1.82	----	23.07	514.24 [mmHg]
Placebo (Kelvin)	0.13	0.0006	0.65	0.65 [mm²]
MCT (Voigt)	-16.50	----	49.68	545.62 [mmHg]
MCT (Kelvin)	0.06	0	78.24	0.17 [mm²]

DISCUSSION

This study compared the Voigt and Kelvin viscoelastic models in the *in vivo* stretch values of the placebo and MCT treated animals. One limitation in comparing these two models is that the results are time series with different units, posing difficulty in computing a standardized error. While the Voigt model proved to be a good initial point, especially for the placebo data, the model failed to reflect more complex vessel waveform features and gave an overall larger error between predicted and measured values. Although the Kelvin model predicted vessel behavior more accurately than the Voigt model, the model was unable to match the behavior exactly in the MCT data. Hence, we propose to increase the number of animals in our study and explore a more complex viscoelastic model.

ACKNOWLEDGEMENTS

Funded in part by UIC Graduate College Abraham Lincoln Fellowship. We would also like to acknowledge the experimental and computational assistance from Julie Wagner and Gregory Roytman, respectively.

REFERENCES

[1] Stenmark KR., *et al., Circulation Research* 99, 7: 675-691, 2006.
[2] Alastruey, J et al., *J Biomech*, 44:2250-2258, 2011.
[3] Bia, D et al., *Proceedings of the 29th Annual International Conference of the IEEE EMBS*, 29:3986-3989, 2007.
[4] Valdez-Jasso, D et al., *IEEE Transactions on Biomedical ENgineering*, 56:2250-2258, 2009.
[5] Valdez-Jasso, D et al., *Annals of Biomedical Engineering*, 39:1438-1456, 2011.

Copyright 2016 The Organizing Committee for the 2016 Summer Biomechanics, Bioengineering and Biotransport Conference

SB^{3}C2016
Summer Biomechanics, Bioengineering and Biotransport Conference
June 29 –July 2, National Harbor, MD, USA
SB^{3}C2016-1021

HEMODYNAMIC ANALYSIS ON CORRELATIONS BETWEEN BICUSPID AORTIC VALVE AND ANEURYSM PROGRESSION WITH AN INTEGRATED MODEL OF LEFT VENTRICLE AND AORTA

T. Fujiwara (1), F. Liang (2, 3), K. Sughimoto(4), H.Liu (1, 3)

(1) Graduate School of Engineering
Chiba University
Chiba, Japan

(2) School of Naval Architecture, Ocean & Civil Engineering
Shanghai Jiao Tong University
Shanghai, China

(3) Shanghai Jiao Tong University-Chiba University International Cooperative Research Center (SJTU-CU ICRC)
Shanghai, China

(4) Kitazato University Hospital
Kanagawa, Japan

INTRODUCTION

Bicuspid aortic valve (BAV) is one of the common congenital heart diseases and said to be associated with progression of aortic aneurysms[1]. The incidence of BAV is not very high (1~2% of population), but higher incidence of aortic aneurysm in BAV patients often matters and attracts the interest of clinicians. Hemodynamic forces and genetic inheritance are thought as potential pathological causes [1].

Due to these clinical facts, some conventional studies were conducted to elucidate the association and consequently some prominent characteristics were found. For example, Hope and his colleagues[2] employed four dimensional phase-contrast magnetic resonance images (4D PC-MRI) and clarified that aortic systolic jet in BAV patient was helical. Schaefer and his colleagues[3] found that the shape of BAV affected the location of aneurysm progression. Furthermore, a numerical study[4] implies that BAV leads to increased wall shear stress at ascending aorta. However, the relation between BAVs and aortopathy is still not clearly explained in terms of hemodynamics.

In this study, we aim at finding some typical hemodynamic characteristics seen in BAV and presuming dominant factors triggering off aortic aneurysms. MRI studies are useful to observe the blood flow in aorta and its outcome is qualitatively reliable. On the other hand, computational approaches enable us to predict blood flow assuming various kinds of situations. Therefore, we use a computational approach to investigate the effects of BAV and its phenotypes on aortic hemodynamics. We construct three-dimensional left ventricle-aorta coupling model and conduct numerical simulation with several kinds of aortic valve model. A lumped-parameter model is also involved to take into account the effects of a whole circulatory system.

METHODS

CT angiography and ultrasound images provided by Funabashi Municipal Medical Center (Chiba, Japan) were employed for construction of three-dimensional models of left ventricle and aorta, respectively. First, we derived the coordinates of centerline and diameter of aorta with equally spaced intervals. The aorta model was then constructed by assuming elliptic cross-sectional shape. The left ventricle model was also constructed in almost the same way but using 11 images to reproduce periodical dilatation and contraction over a cardiac cycle.

In numerical analysis, we employed *in-house* solver built by Liu[5]. Governing equations were three-dimensional, unsteady, incompressible Navier-stokes equation and equation of continuity with the pseudo-compressibility method. These equations were discretized by the finite volume method. We employed pressure waveforms in left atrium, left ventricle and ascending aorta as boundary conditions. These waveforms were derived from a lumped parameter model.

The opening and closing of mitral and aortic valve were two-dimensionally modeled by manipulating boundary conditions at valve orifice; non-slip and free flow conditions were imposed on closed and opened parts, respectively. Particularly, we prepared four kinds of valve phenotypes for aortic valve: tricuspid aortic valve (TAV: the normal), LR-BAV, AP-BAV and asymmetrical AP-BAV (See Figure 1). TAV and asymmetric BAV patterns were modeled based on previous studies whereas completely symmetric pattern was assumed for the other two valves.

Left ventricle and aorta were coupled by spatially overlapping interface. Velocity and pressure at overlapped interface were mutually interpolated at each computational time step since flow in left ventricle and aorta was solved separately. Reynolds number and Strouhal number are 1042 and 0.1, respectively. To evaluate the results, we see

Copyright 2016 The Organizing Committee for the 2016 Summer Biomechanics, Bioengineering and Biotransport Conference

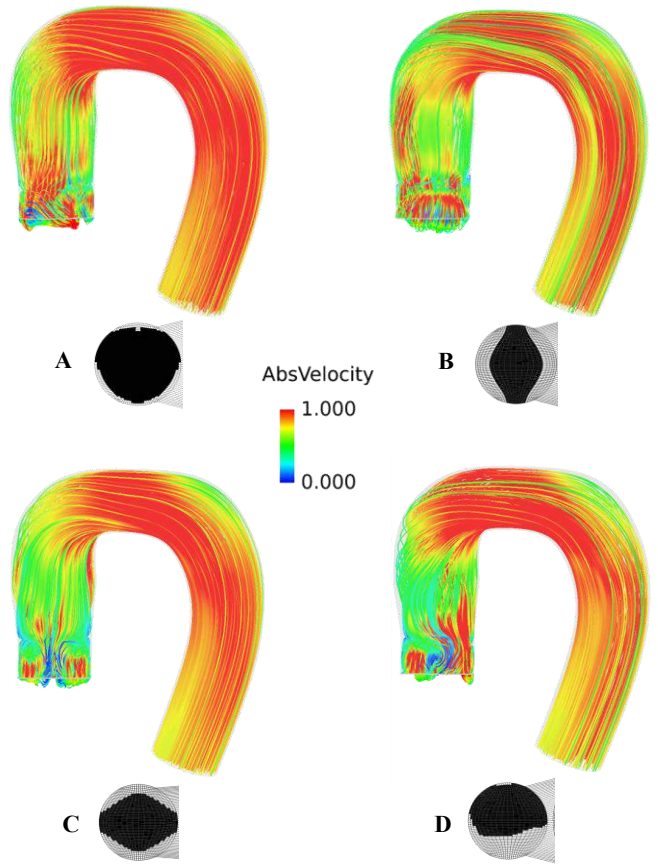

Figure 1: Streamlines of four valve models. A: TAV; B: LR-BAV; C: AP-BAV; D: Asymmetrical BAV.

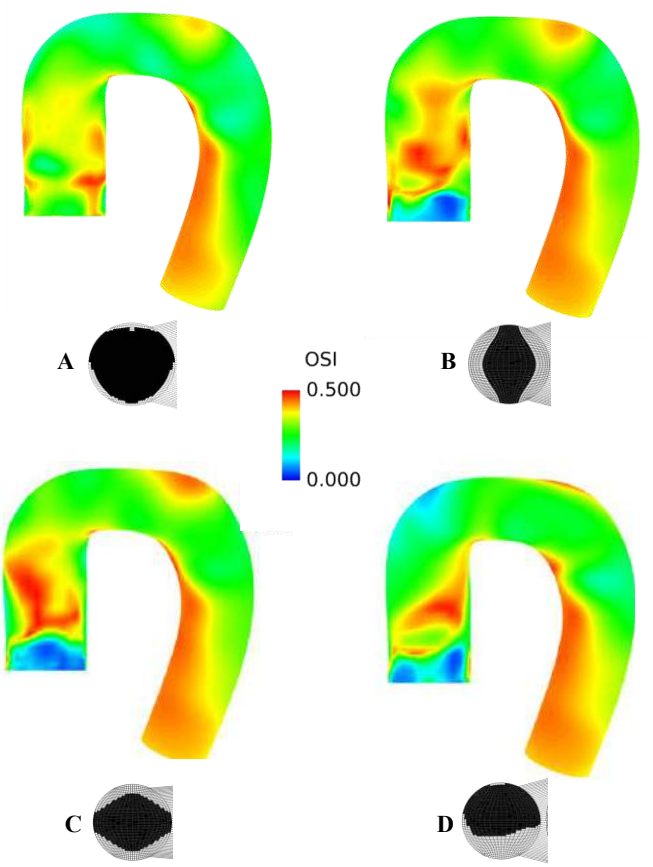

Figure 2: OSI distribution of four valve models. The symbols correspond to those in Figure 1.

oscillatory shear index (OSI) in addition to ordinary physical quantities. OSI is defined as

$$\mathrm{OSI} = \frac{1}{2}\left(1 - \frac{\tau_{mean}}{\tau_{abs}}\right), \tag{1}$$

$$\tau_{mean} = \frac{1}{T}\left|\int_0^T \tau dt\right|, \ \tau_{abs} = \frac{1}{T}\int_0^T |\tau|\, dt, \ \tau = \mu\frac{\partial \mathbf{u}}{\partial \zeta}, \tag{2}$$

where ξ is grid coordinate system along the vessel wall, $\mathbf{u}$ velocity vector, τ wall shear stress, μ viscosity, T cardiac duration. Larger OSI is associated with directionally fluctuating wall shear stresses over a cardiac cycle hence with aortic abnormalities.

RESULTS

Some significant differences are found in streamlines (Figure 1) and OSI distribution (Figure 2). In BAV models, systolic jet migrates toward the vessel wall while comparatively uniformly distributed flow was observed in TAV model (Figure 1). Furthermore, the direction of systolic jet is different among three BAV models. OSI distribution shows not only significantly different distribution at ascending aorta but also slightly larger OSIs at outer curvature of aortic arch in BAV model. (Figure 2)

DISCUSSION

Deviation of systolic jet seen in the BAV models was also observed in previous study [4]. However, we cannot see helical flow and increased wall shear stresses at ascending aorta in the BAV models, which was seen in the some studies[2,4]. This is probably because some physiological conditions are not taken into account in the present study such as valve motion due to the dilatation and contraction of heart and three-dimensional shape of valve. We can see the difference in OSIs at aortic arch. Since a previous clinical observation [3] pointed out that the location of progression of aortic aneurysms varied according to BAV phenotypes, this characteristic may be one of the factors predicting the aneurysm development.

ACKNOWLEDGEMENTS

This work is partly supportedby Research and Development of the Next-Generation Integrated Simulation of Living Matter, JST, a part of the Development and Use of the Next-Generation Super-computer Project of the MEXT, Japan.

REFERENCES

[1] Verma, S et al., *N Engl J Med*, 370:1920-1929, 2014.
[2] Hope, M et al., *Radiology*, 255:53-61, 2010.
[3] Schaefer, B et al., *Am J Cardiol*, 99:686-690, 2007.
[4] Faggiano, E et al., *Biomech model mechanobiol*, 12: 801-813, 2013.
[5] Sughimoto, K et al. *Heart Vessels*, 29: 404-412, 2014.

Copyright 2016 The Organizing Committee for the 2016 Summer Biomechanics, Bioengineering and Biotransport Conference

SB^{3}C2016
Summer Biomechanics, Bioengineering and Biotransport Conference
June 29 –July 2, National Harbor, MD, USA
SB^{3}C2016-1022

TGF-BETA 1 AND ADIPOSE-DERIVED MESENCHYMAL STEM CELL SECRETED FACTORS AID IN THE ORGANIZATION OF DEPOSITED ELASTIN WITHIN 3D FIBROBLAST AND SMOOTH MUSCLE CELL CONSTRUCTS

Aneesh K. Ramaswamy[1] MS, Justin S. Weinbaum[1,5] PhD, and David A. Vorp[1,2,3,4,5] PhD

(1) Department of Bioengineering
University of Pittsburgh
Pittsburgh, PA, USA

(2) Department of Cardiothoracic Surgery
University of Pittsburgh
Pittsburgh, PA, USA

(3) Department of Surgery
University of Pittsburgh
Pittsburgh, PA, USA

(4) Center for Vascular Remodeling and Regeneration
University of Pittsburgh
Pittsburgh, PA, USA

(5) McGowan Institute for Regenerative Medicine
University of Pittsburgh
Pittsburgh, PA, USA

INTRODUCTION

Abdominal aortic aneurysms (AAA) are enlargements of the abdominal aorta, diagnosed among 12.5% of men and 5.2% of women over age 75 [1]. AAA progression and rupture is biomechanically explained by a homeostatic imbalance within the ECM; as patients age, elastin levels decrease as overall collagen levels rise, resulting in increased vascular stiffness and AAA [2]. Currently, patients with AAA diameters dilated from the typical 2cm to larger than 5.5cm are treated with endovascular aneurysm repair. Treatments for AAA between 3 and 5.5cm are limited, so most clinicians move forward with increased screening in lieu of an interventional treatment option.

Enhancing the secretion, coacervation, and cross-linking of the elastin precursor tropoelastin is a promising regenerative strategy for AAA therapy. Preliminary work by our group has shown that mesenchymal stem cell (MSC) delivery to a growing elastase-induced AAA prevents further elastin degradation and/or stimulates new elastin synthesis, as evidenced by maintenance of elastic lamellae. Treated animals also exhibit halted AAA growth. Our *in vitro* work confirms that factors secreted by MSCs upregulate elastin deposition by smooth muscle cells (SMCs) within 3D fibrin gels. However, assembly of elastic fibers involves a cadre of ECM accessory proteins that are needed for proper tropoelastin processing and assembly, and these proteins have not been monitored in the regenerative context.

This project aims to establish a non-invasive elastin reporter gene (ERG), validated within a 3D fibrin gel model, to construct time-elapsed elastin transcription reports within varying stimulation conditions without necessitating scaffold digestion. Elastogenesis response will be monitored in response to chemical (TGF-β1, MSC secreted factors) and mechanical (stretching) stimulation. After ERG-RFL-6 validates the activity of ERG, transfection will move forward within vascular SMCs for AAA-targeted experiments.

METHODS

Fibrin gel constructs were fabricated [4, 5] using 3.7mg/mL fibrinogen, 0.21U/mL thrombin, and cell seeding density of $5x10^5$ cells/mL. 200μL gels were cultured with 15mM ε-aminocaproic acid (ACA), a fibrinolysis inhibitor halting construct breakdown. 400 μL fibrin gels for dynamic loading were seeded onto FlexCell Uniflex culture plates (FlexCell Int'l, Burlington, NC). The FlexCell FX-4000T strain unit induced a cyclic, uniaxial loading condition (10% stretch, 1Hz). A biochemical elastin protein quantification assay, Fastin Elastin (Accurate Chem, Westbury, NY), solubilized elastin in oxalic acid, quantified using a colormetric absorbance reading.

All fibrin gels were fixed using a 4% paraformaldehyde. RFL-6 cells were stained for elastin using rabbit anti-mouse recombinant tropoelastin (a donation from Dr. Robert Mecham's lab at Washington University in St Louis), goat anti-rabbit polyclonal AlexaFluor 488, and nuclear DAPI stain. Images were obtained using an Olympus FluoView FV1000 confocal microscope (20x oil, NA=0.85 objective).

Multiphoton elastin images (using 400μL fibrin gels) were collected on an Olympus FV10 (XLPlanN 25x water, NA=1.05 objective), and laser wavelength of 830nm. All obtained images (2D and 3D cultures) were processed through an established Matlab script [3], written to identify collagen/elastin fibril networks.

To develop ERG, an elastin promoter sequence was excised from a validated plasmid [6], with a mutation made at the start site to allow downstream luciferase translation [7]. This ELN promoter was ligated onto pGL4.14 (Promega) and verified via DNA sequencing. Transfection into RFL-6 and SMCs has been completed using a ERG:TransIT-LT1 (Mirus) ratio of 1ug:6μL. Luminescence measurements, reflective of elastin production, were taken by immersing gels in a 1mM Luciferin-EF (Promega) solution under an IVIS Lumina imaging system.

Copyright 2016 The Organizing Committee for the 2016 Summer Biomechanics, Bioengineering and Biotransport Conference

RESULTS

Stacked confocal immunofluorescence images, shown in Figure 1A, display elastin fiber development in static conditions under varying culture time lengths and dosing concentrations of TGF-β1. Figures 1B-E show the quantified results of the immunofluorescence imaging performed. Fiber concentration uniformly increases as culture length progresses (Figure 1A), but no significant differences can be seen between TGF-β1 dosing concentrations and unsupplemented F12 culture media. Mean fiber diameter does not significantly change (Figure 1B), but some TGF-β1 concentrations show statistically significant decreases as harvest day progresses. Similar results are seen in average segment length (Figure 1D), as the trends were mirrored between Day 7 and Day 10 harvests. Tortuosity remained constant throughout the culture conditions (Figure 1E), except for a significant increase in the Day 10, 1ng/mL TGF-β1 culture.

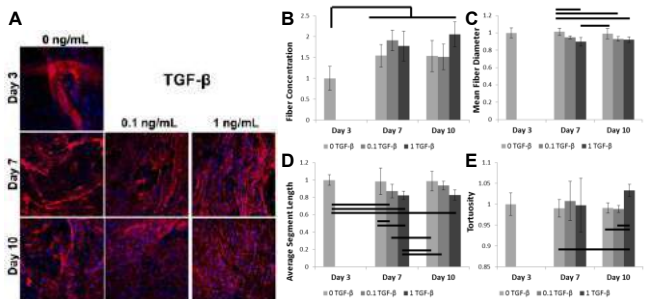

Figure 1: TGF-β1 treated 3D RFL-6 constructs.
A) Elastin (red) and nuclear (blue) immunostaining.
B-E) 3D image quantification using custom Matlab script [3], normalized to Day 3. n = 2, 3 images each, α = 0.05 per Fisher's LSD.

Elastin fibers expressed by unstimulated RFL-6 cells embedded within fibrin gels and grown (with 15mM ACA media), in either static (constrained) or dynamic cultures (Figure 2A), are mature enough to appear clearly during multiphoton microscopy. Multiphoton images of both RFL-6 cells and SMC-loaded fibrin gels (not shown) treated with TGF-β1 or MSC secreted factors are currently being quantified.

Elastin content increased as the RFL-6 loaded fibrin gels were exposed to a cyclic uniaxial strain, visible 7 days after culture seeding (Figure 2B). TGF-β1 treatment on these dynamic RFL-6 fibrin gels, however, did not yield any significant increases (Figure 2C). Rather, elastin content was decreased at both 7 and 14 day time points when compared to the untreated 7 day culture.

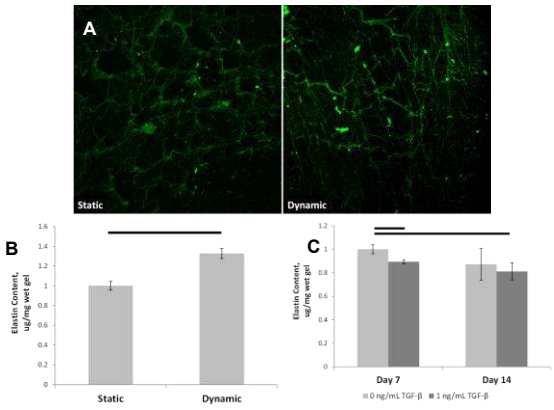

Figure 2: 3D RFL-6 constructs under cyclic uniaxial loading.
A) Multiphoton images of elastin fibers (green) after 7 days of culture.
B-C) Fastin Elastin protein assay for: B) 7 day unstimulated cultures, and C) 7 or 14 days, with and without TGF-β1. α = 0.05, as per Fisher's LSD.

DISCUSSION

Previously collected 2D image analysis of RFL-6 elastin fibers (not shown) illustrate that porosity decreases and segment length increases steadily, but both measurements experience a dramatic switch after 15 days in culture. This seems to suggest that the cells force an organization into distinct patterns when a spatial limit is reached, and that the elastin monomers seemed to disperse into more evenly-distributed fibrils as they received more time to develop. These results are muted in 3D cultures, as seen in Figure 1, possibly due to a significant increase in physical culture space available to express elastin. RFL-6 cells do continue to produce elastin throughout the culture window, as evidenced by the increasing fiber concentration measurements, but never reach the upper limit seen in 2D.

Currently, we are confirming that factors secreted by MSCs upregulate elastin deposition by SMCs within 3D fibrin gels, using both ERG and the image quantification software shown here to identify changes in elastic fiber deposition. However, assembly of elastic fibers involves a cadre of ECM accessory proteins that are needed for proper tropoelastin processing and assembly, and these proteins have not been monitored in the regenerative context. A fibulin-5 treatment could be useful within 3D fibrin vascular constructs, as, the cultures do not reach a self-organizing stage if given no stimulation. Fibulin-5 treatments would not wait for a cell-induced signal to reorganize the elastic fibers as they were being produced, as shown in 2D cultures.

Cells within a dynamic culture (Figure 2) decreased elastin production when treated with TGF-β1, suggesting that TGF-β1 only induces a remodeling phenotype in RFL-6 cells when a physically constraining stress is placed upon them as well. The dynamic culture did produce increased elastin production when compared to static cultures with no TGF-β1 treatment, meaning that any combination therapy with fibulin-5 might have to be staggered to induce the quickest amount of remodeling and organization for a AAA treatment.

Future work is focused on one elastic fiber accessory protein, fibulin-5, which is expressed by many elastogenic tissues and may be critical for enabling AAA elastin organization. Fibulin-5 mediates the initial interactions between tropoelastin and the microfibrillar scaffold, allowing for alignment and crosslinking of tropoelastin after secretion. If successful, this work will lay the foundation for an innovative combination therapy using fibulin-5 and MSC secreted factors for sub-surgical AAA, wherein elastogenesis would be organized through increased activity of naturally secreted fibulin-5.

ACKNOWLEDGEMENTS

We would like to acknowledge funding through the Angiopathy Training Program (T32HL094295) (AKR), an NIH training grant awarded through the University of Pittsburgh's Department of Bioengineering.

REFERENCES

1. Go, A.S., et al., *Circulation*, 2013. **127**(1): p. e6-e245.
2. Zannettino, A.C., et al., *J Cell Physiol*, 2008. **214**(2): p. 413-21.
3. Koch, R.G., et al., *J Biomech*, 2014. **47**(5): p. 935-943.
4. Weinbaum, J.S., J. Qi, and R.T. Tranquillo, *Tissue Eng Part C Methods*, 2010. **16**(3): p. 459-67.
5. Ahmann, K.A., et al., *Tissue Eng Part A*, 2010. **16**(10): p. 3261-70.
6. Pierce, R.A., C.H. Moore, and M.C. Arikan, *Am J Physiol-Lung Cell Mol Physiol*, 2006. **291**(3): p. L391-L399.
7. Quinteiro, C., et al., J Pediatr Endocrinol Metab, 2002. **15**(7): p. 1041-1045.

Copyright 2016 The Organizing Committee for the 2016 Summer Biomechanics, Bioengineering and Biotransport Conference

SB^{3}C2016
Summer Biomechanics, Bioengineering and Biotransport Conference
June 29 –July 2, National Harbor, MD, USA
SB^{3}C2016-1023

MODAL ANALYSIS OF HUMAN BRAIN DYNAMICS IN CONTACT SPORTS

Mehmet Kurt* (1), Kaveh Laksari* (1), David Camarillo (1, 2)

(1) Department of Bioengineering
Stanford University
Stanford, CA, USA

(2) Department of Mechanical Engineering
Stanford University
Stanford, CA, USA

* Equal contribution as first authors.

INTRODUCTION

Traumatic brain injury (TBI) is a major cause of death and disability in the United States, contributing to about 30% of all injury-related deaths. Every year, an estimated 1.7 million people are diagnosed with TBI in the US alone. Of these cases, 80% are categorized as mild, with much higher statistics for undiagnosed cases. Until recently, mild TBI (mTBI) was generally regarded as a minor health issue and its effects were thought to disappear after a short recovery period. However, emerging evidence suggests that this injury is by no means mild and even a single insult to the brain could lead to chronic neurodegeneration[1].

Fundamental dynamical behavior of brain as a sudden motion of the head is still unknown for the most part. Efforts to model the brain's physics date back to World War II when rotational acceleration was hypothesized as the main cause of trauma, not linear acceleration. However, only few studies have studied both the magnitude and frequency content of the rotational acceleration pulse to determine the dynamic effects on brain injury and deformation. In a recent study, we showed that frequency-dependence of human brain's mechanical response may play an important role in whether a given loading scenario could lead to injury[2]. In this study, it was shown that, contrary to current standards that is mainly concerned with high frequency components, low-frequency dynamics could be more devastating as far as the motion and deformation of brain is concerned.

To study the temporal behavior of brain tissue, we utilized Dynamic Mode Decomposition (DMD). Also known as the method of snapshots, DMD is a multi-variate method that gives a compact representation of the original data from experiment or simulation, while reducing a large number of interdependent variables to a much smaller number of independent temporal modes and retains as much as possible of the variation in the original variables. This method has been successfully applied to modal analysis of fluid flows and solid structures[3]. DMD can extract relevant dynamic information from snapshots without explicit knowledge of the dynamical operator. It is based on considering the sequence of snapshots of a physical phenomenon and directly gives the system's characteristics, e.g. decay rate or energy and uniquely associates a frequency to each mode.

Our goal in this study is to investigate the modal behavior of brain tissue under various impact conditions in terms of loading amplitude and direction, and to test our hypotheses that (1) Head impacts in sports consistently excite a small set of principal displacement modes, which indicates a low-order system, and (2) brain's motion and deformation is governed low-frequency dynamics. We will then provide new insights into design requirements for protective headgear.

METHODS

First, we investigated the behavior of brain tissue under mild loading regimes by analyzing tagged MRI data from two different experimental protocols: sagittal and axial rotation[4,5]. We used Dynamic Mode Decomposition (DMD), which is a multi-variate method for data compression, to extract the modal behavior of brain tissue. By showing similarities between brain's modal behaviors in these two studies, we motivated our study that brain's deformation due to external loading inputs on the head, can be captured by a set of displacement modes that exist regardless of the input loading.

In a previous study, we had collected head motion kinematics due to head impacts in football[2]. We used a detailed finite element model[7] of the head to simulate the motion and deformation of brain tissue under these impact conditions, and used the resulting relative motion of the brain nodes as a separate dataset for our modal analysis. We

Copyright 2016 The Organizing Committee for the 2016 Summer Biomechanics, Bioengineering and Biotransport Conference

then used DMD to extract the most important displacement modes and brain's fundamental modal behavior.

We validated our results by comparing the reconstructed strains calculated from the modes with original strain data. To study the implications of our results on helmet design, we used previously conducted cadaver drop test experiments at 2 ft with barehead, airbag, EPS, football helmets and measured the head kinematics. Using these kinematics, we then ran DMD analysis on the resultant FE brain simulations.

RESULTS

DMD analysis on 110 simulations, randomly selected from over 500 football impact simulations, revealed that the most dominant displacement modes concentrate around 30-50 Hz range (Figure 1A). Here, each point on the graph represents the dominant behavior of the brain in a single simulation. This observation was consistent with our previously published study on tagged MRI experiments [2]. Each mode we find has an associated frequency and decay rate. By using these quantities, we calculated each mode's contribution to the overall energy of brain dynamics and discovered that 90% of energy of brain displacement can be captured by modal frequencies up to 60 Hz (Figure 1B).

By studying the orthogonality and independence of these modes, we also showed that brain's dynamic motion and deformation is governed by a small number of modes, i.e. brain-meninges-skull system constitutes a low-order dynamic system. In our analysis we found that 99% of responses from 110 football impacts and 2 independent MRI experiments can be reconstructed by only 21 independent modes (out of approximately 1000 modes initially extracted for all cases). We also compared the contributions of individual modes to the overall strain pattern in the brain tissue and found that by using the first 7 dominant modes in each football impact case, one can explain the peak principal strain with less than 10% error. We studied the effect of frequency and decay rate of each DMD mode on the peak principal strain and strain rate in the brain tissue. We found out that higher peak principal strains are observed for lower frequency modes; whereas higher decay rates cause higher strain rates.

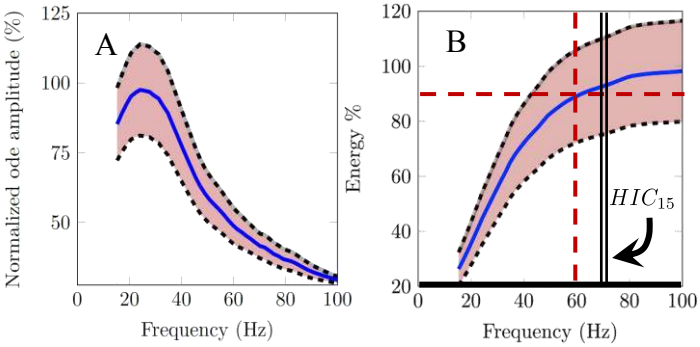

Figure 1: Frequency spectrum of DMD modes in football impacts. A) Overall normalized mode amplitude curve for DMD modes as a function of frequency. B) Cumulative energy contribution of DMD modes as a function of frequency.

Finally, analyzing the FE simulations of the cadaver drop test experiments, we discovered that current EPS bicycle helmets and football helmets fail to eliminate the most energetic brain displacement modes, which are usually lower than 100 Hz, whereas using a softer medium such as an airbag can filter brain dynamics up to 60 Hz (Figure 2A). A similar story can be seen for decay rates: In analyzing the time constants of two most dominant DMD modes from these experiments, we found that EPS and football helmets have almost the same time constants as barehead whereas a softer medium such as an airbag can increase the time constants almost 10 times, which is an indication of a significant drop for modal decay rates (Figure 2B).

DISCUSSION

In this study, we introduced a dynamic approach to explain brain injury mechanism. We argue that dynamical characteristics of relative brain motion can be helpful in understanding the reasons that lead to brain injury.

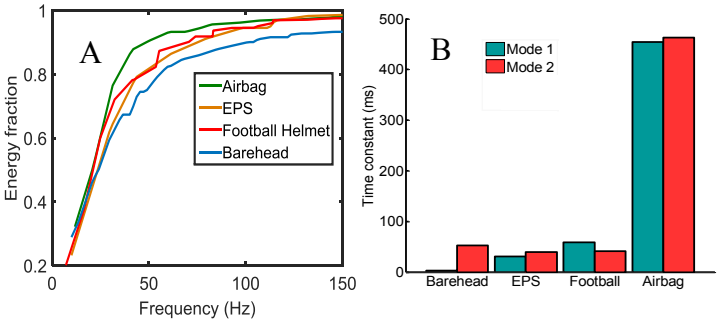

Figure 2: DMD analysis of cadaver drop test experiments with different helmets. A) Cumulative energy contribution of DMD modes as a function of frequency. B) Time constants associated with two most dominant DMD modes for each helmet (and barehead).

We first showed that impacts on the skull lead to displacement and deformation in brain tissue that can be captured by only a few independent displacement modes, and therefore concluded that brain is a low-dimension system. Second, this system's behavior mostly revolves around low frequency range (<60Hz). We went on to show that exciting certain relative displacement modes will result in higher strain and strain rates, which is potentially dangerous and may result in neurocognitive deficits. These results bring up an important question in terms of head protective gear design: Can current helmets successfully eliminate relative brain displacement modes that have low frequencies and high decay rates? We show that conventional helmets in fact fall short and we might need new approaches in helmet design.

ACKNOWLEDGEMENTS

The study was supported by the National Institutes of Health (NIH) National Institute of Biomedical Imaging and Bioengineering (NIBIB) 3R21EB01761101S1, David and Lucile Packard Foundation 38454, Child Health Research Institute - Transdisciplinary Initiatives Program, and NIH UL1 TR000093 for biostatistics consultation. We also thank Dr. Svein Kleiven and KTH for providing the FE head model.

REFERENCES

[1] Faul, M et al., National Center for Injury Prevention and Control, 2010.
[2] Laksari, K et al., *J Royal Society Interface*, 2015.
[3] Schmid, P, *J Fluid Mechanics*, 2010.
[4] Feng, A et al., *J Royal Society Interface*, 2010.
[5] Knutsen, A et al., *J Biomechanics*, 2014.
[6] Camarillo, D et al., *Annals Biomed Eng*, 2013.
[7] Kleiven, S, *Stapp Car Crash J*, 2007.
[8] Kuo, K et al., *BMES* 2015.

Copyright 2016 The Organizing Committee for the 2016 Summer Biomechanics, Bioengineering and Biotransport Conference

SB³C2016
Summer Biomechanics, Bioengineering and Biotransport Conference
June 29 –July 2, National Harbor, MD, USA
SB³C2016-1024

SIMULATION OF CENTRIFUGAL PUMP THROMBOSIS IN VITRO

S. Hastings (1), S. Desphande (2), S. Wagoner (2), K. Maher (2), D. Ku (1)

(1) GWW School of Mechanical Engineering
Georgia Institute of Technology
Atlanta, GA, USA

(2) Department of Pediatrics
Children's Healthcare of Atlanta
Emory University School of Medicine
Atlanta, GA, USA

INTRODUCTION

Extracorporeal membrane oxygenation (ECMO) provides mechanical life support for patients suffering from cardiac and/or pulmonary failure. The majority of ECMO patients are neonatal (≤30 days old), though the adult patient population experienced a marked increase in 2009 due to H1N1 and has remained steady [1]. ECMO is burdened by both hemorrhagic and thrombotic complications [1-3]. Original concerns with hemolysis due to centrifugal pumps have kept the roller head pump in use over the past two decades, however there has been a strong shift to centrifugal pumps from roller head pumps due to recent technological improvements [3-6].

Thrombosis is ECMO circuits is difficult to study. There are multiple factors influencing the formation of clot or inhibition of the same within a clinical circuit. Variables related to flow dynamics, rheological properties as well as effect of anticoagulation have complex interactions and warrant creation of a valid in-vitro setup for the study. Here, we present our development of an *in vitro*, benchtop, recirculating system that is capable of reproducing centrifugal pump thrombosis as seen in clinical ECMO circuits.

METHODS

ECMO circuits (N=16) were collected after use by pediatric and neonatal patients, facilitated by our collaborators at Emory University School of Medicine (Atlanta, GA). Circuits were analyzed for adherent thrombi, and if any were found, the location and macroscopic sample morphology was recorded. In some cases pictures were taken and/or samples were excised and preserved in 10% formalin for histology.

Benchtop *in vitro* loops were constructed using a Revolution ® centrifugal pump (Sorin Group USA, Arvada CO), a Better Bladder ™ (Circulatory Technology, Inc., Oyster Bay, NY), and tubing and connectors (Medtronic, Minneapolis, MN). Porcine blood (N=5) was collected into a minimal amount of heparin at a local abattoir. The blood was treated with glucose, L-glutamine, and an antibiotic/antimycotic solution (Sigma-Aldrich, St. Louis, MO). The loop was circulated for 48 hrs, with heparin dosing every 12 hrs, and the RBC health was monitored using blood smears. After circulation, the loop was examined for adherent thrombi, and if any were discovered, the location and macroscopic morphology of the thrombus was recorded. In some cases, pictures were taken and/or samples were excised and preserved.

Histological analysis was performed after 48 hrs of fixation in formalin using Carstairs' stain for fibrin and platelets, which stains platelets blue-gray to navy, fibrin red, red blood cells clear to yellow, and collagen bright blue [7].

Copyright 2016 The Organizing Committee for the 2016 Summer Biomechanics, Bioengineering and Biotransport Conference

RESULTS

Centrifugal pumps exhibited clinical thrombosis in 100% of cases. The Revolution ® is not a levitated pump, and thus has a shaft. The shaft has an exposed piece of metal near the flow entrance. An adherent thrombus over the metal shaft was observed in all circuits ig 1, A). In some cases, large thrombus had formed, appearing to grow from the exposed steel shaft (Fig 1, B).

Macroscopic morphological recreation of centrifugal pump thrombosis was accomplished successfully in the *in vitro* flow loop (Fig 2). The clot shape and extent is similar to the clinical thrombus seen in Figure 1, B.

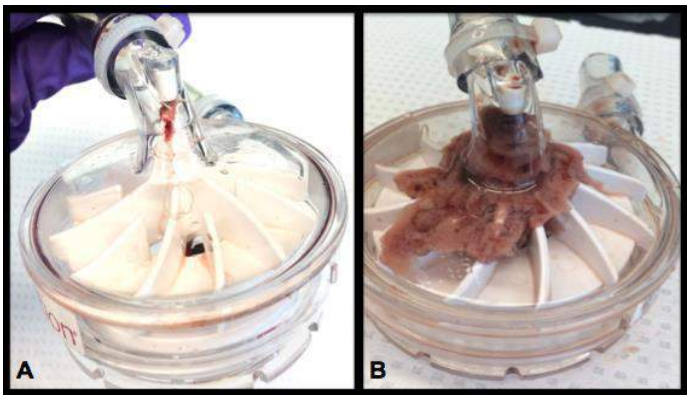

Figure 1: (A) Small thrombus coverage of the exposed metal shaft seen in 100% of clinical ECMO circuits. (B) Large thrombus growth seen in some clinical circuits.

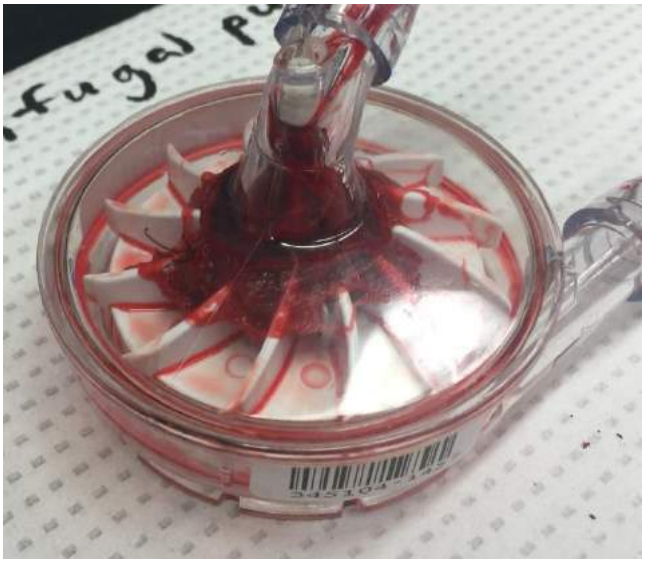

Figure 2: Large thrombus growth example seen in *in vitro* loop after a 48 hr run.

Histological analysis of clinical samples revealed mixed composition with platelet-rich regions alongside fibrinous regions, suggesting some platelet thrombosis involvement.

DISCUSSION

Adherent thrombus formation was observed in 100% of clinical centrifugal pumps. Typically the exposed shaft of the Revolution ® pump exhibited thrombus coverage, but in some cases excessive thrombus growth covered the pump head. Histological analysis of clinical thrombi revealed distinct regions of platelet-rich thrombi and red clot, suggesting some platelet thrombosis involvement.

An *in vitro* flow loop was constructed to recreate the clinical thrombosis. Whole porcine blood was perfused for 48 hrs through a simplified system consisting of a Revolution ® centrifugal pump, a Better Bladder™, connectors, and tubing. At 48 hrs, large thrombus was formed which was morphologically consistent with clinical thrombosis.

Here we demonstrate a promising system to study centrifugal pump design *in vitro*. Successful recreation of clinical thrombosis leads the way for trial methods to prevent thrombus formation using our benchtop system. Further microscopic and histological characterization, as well as fluid mechanics analyses of the pump head, will help to understand the mechanism behind thrombus formation in the Revolution ® centrifugal pump and thus indicate how to prevent it.

ACKNOWLEDGEMENTS

We would like to express our gratitude to the clinical staff that assisted with the circuit collection. This work was funded by a grant from the Center for Pediatric Innovation (Ga Tech – Children's Healthcare of Atlanta, Atlanta, GA).

REFERENCES

[1] Paden, ML et al., *ASAIO J*, 29:202-210, 2013.
[2] Haines, NM et al., *ASAIO J*, 55:111-116, 2009.
[3] Halaweish, I et al., *ASAIO J*, 61:496-501, 2015.
[4] Lawson, S et al., *J Extra Corpor Technol*, 43:236-244, 2011.
[5] Byrnes, J et al., *ASAIO J*, 57:456-461, 2011.
[6] Lequier, L et al., *Pediatr Crit Care Med*, 14:S7-S12, 2013.
[7] Carstairs, KC. *J Path Bact* 90:225-231, 1965.

Copyright 2016 The Organizing Committee for the 2016 Summer Biomechanics, Bioengineering and Biotransport Conference

SB^{3}C2016
Summer Biomechanics, Bioengineering and Biotransport Conference
June 29 –July 2, National Harbor,MD, USA
SB^{3}C2016-1025

DESIGN OF FATIGUE TEST FOR EX-VIVO MOUSE VERTEBRA

Megan M. Pendleton (1), Joshua S. Alwood (2), Grace D. O'Connell (1), Tony M. Keaveny (1)

(1) Mechanical Engineering
University of California Berkeley
Berkeley, California, USA

(2) Space Biosciences Division
NASA Ames Research Center
Moffett Field, California, USA

INTRODUCTION

Exposure to ionizing radiation increases degeneration, risk of fracture, and decreases long-term bone quality. The complications related to high levels of ionizing radiation impact both astronauts and radiotherapy (RT) patients. Astronauts embarking on deep-space missions outside the Earth's protective magnetosphere, such as lunar, Mars, or near-Earth asteroid missions, will be exposed to high-energy ionizing radiation from cosmic or solar sources. Bones neighboring radiotherapy treatment are exposed to high doses of gamma radiation.

Previous studies have demonstrated significant changes in bone mechanics and quantity with radiation. Women with cervical, rectal, or anal cancer and treated with RT were 1.7 - 3.2 times more likely to suffer a pelvic fracture than patients who did not receive RT [1]. Animal studies of low to high dose radiation (2 – 20 Gy) have shown decreased trabecular bone volume fraction [2], bone embrittlement [3], and altered tissue composition, such as collagen cross-linking [4].

Understanding changes in bone mechanics is important for identifying increased risk of fracture with radiation exposure. In particular, fatigue, or cyclic load testing provides insight into changes at the molecular level that are not apparent in a monotonic test. Changes to the organic matrix can decrease energy dissipation mechanisms intrinsic to bone and manifest in a decreased fatigue life.

The mouse model is the IACUC preferred and most common mammalian model for experimental testing. However, mechanical testing of mouse vertebrae is not trivial due to its geometry and small scale. Thus, the purpose of this work was to develop a protocol, including sample preparation and test methodologies, for testing mouse vertebrae in fatigue. Fatigue testing of human bone was used for validation of the methods presented here. This work can be widely applied to investigations on the effect of musculoskeletal disuse, drug treatment, or genetic modification on bone mechanics.

METHODS

Sample Collection and Preparation

Mice were euthanized and the lumbar spine was dissected using IACUC approved protocols. The vertebra (L5) was extracted from the spine via cuts through the adjacent intervertebral discs. Surrounding musculature and soft tissues were removed with kimwipes and rubber-tipped surgical tools to protect the bone during preparation.

The cranial endplate of the mouse lumbar vertebral body is at an angle with respect to the caudal endplate. Planoparallel surfaces are critical for reliable uniaxial compression testing; however, the small specimen size makes this a challenging and arduous task. To ensure parallel surfaces for uniaxial compression testing, we modified the methods reported by Tommasini *et al*. for mouse vertebrae to improve repeatability [5]. All tasks done by hand were automated to remove human error in endplate removal and as such decreased scatter in the data.

First, the vertebral posterior process was potted in polymethyl methacrylate (PMMA). The vertebra is housed in a 3D-printed, custom-made jig designed with a pin through the spinal canal to ensure alignment (Fig. 1) and to fit within a SP1600 Leica microtome (Leica Biosystems, Nussloch, Germany). PMMA is slowly applied to the posterior process via a syringe to avoid getting PMMA on the vertebral body. Then, the jig was placed into the microtome and two parallel cuts were made, under constant irrigation. The height of the microtome arm was adjusted with respect to the blade to make the second parallel cut (1 μm resolution), resulting in a final sample height of between 2.0 to 2.5 mm. The specimen was removed from the PMMA with a scalpel, leaving the posterior process embedded in the jig. Samples were wrapped in saline-soaked gauze and stored at -20˚C until testing.

Copyright 2016 The Organizing Committee for the 2016 Summer Biomechanics, Bioengineering and Biotransport Conference

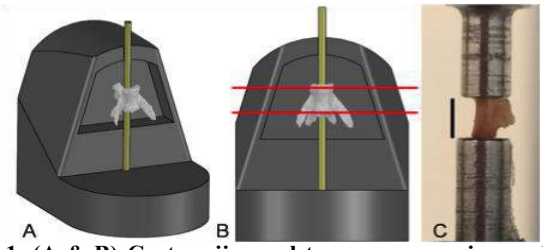

Figure 1. (A & B) Custom-jig used to prepare specimens. Yellow cylinder represents the pin used for alignment, and red lines represent parallel cuts. (C) Specimen in mechanical testing device (saline bath not shown). Bar = 2.25 mm.

Imaging & Mechanical Testing

Samples were imaged using microcomputed tomography (μCT, resolution = 10 μm/voxel; SCANCO Medical AG, Brüttisellen, Switzerland). Images from the caudal-end of the vertebral body were used to calculate minimum cross-sectional area (ImageJ; Fig. 2).

Our fatigue methods are similar to those used previously for human and bovine trabecular bone [6-8]. The specimen was compressed between two concentric, stainless-steel plattens and tested at room temperature in a saline-water bath to maintain hydration (Fig. 3). The test was conducted in load control (ELF 3200, Bose Corp., Framingham, MA, USA). Fatigue loading was initiated by applying 0.35% strain. To determine the amount of force needed to apply 0.35% strain, the initial modulus, E_0, was determined by applying ten cycles of .1% strain at 2 Hz. E_0 was defined as the slope of the stress-strain response during the last cycle.

A cyclic uniaxial compressive load was applied in a sinusoidal waveform at 2 Hz. The load applied to each specimen (i.e. input amplitude) was calculated as $F = E_0 * \varepsilon_0 * A$, where the ε_0 was set to 0.35% and A represents the bone area measured from μCT images. Normalizing the applied load by the specimen modulus was important for minimizing scatter in the data due to differences in specimen porosity. Failure was defined as a ten-percent reduction in modulus (Eqn. 1).

Figure 2. Representative uCT image of mouse vertebrae (area = 0.74 mm^2). Bar = 1.20 mm.

$$\varepsilon_{\text{failure}} = \frac{\sigma}{(0.9)(E_0)} \qquad (1)$$

Force and displacement data were collected throughout the experiment (750 Hz). The maximum strain during a cycle was plotted with respect to cycle number to determine fatigue properties.

RESULTS

Maximum strain per cycle was plotted for the duration of the test resulting in a tertiary curve (Fig. 4; red). The primary phase shows a sharp increase in strain, followed by a secondary phase characterized by nearly constant strain that spans more than 85% of the total fatigue test. Finally, in the tertiary phase, there is a sharp increase in strain, as the specimen approaches failure. The same trend for strain versus cycles is reported in Lambers *et al*. for fatigue testing of cylindrical cores of cancellous bone from human vertebra (Fig.4; blue)[6]. The transition point between the secondary and tertiary phase was defined as the intersection of two lines that make a bi-linear fit for this region of data. The strain at the transition point between the secondary and tertiary phase was 0.98% for mouse vertebra and 1.12% for human vertebra. The percentage of cycles to failure (N/N_f) at the transition point between secondary and tertiary phase was 84% for mouse vertebra and 93% for human vertebra. The slope of the secondary phase for mouse was 0.0041 and for human was 0.0055.

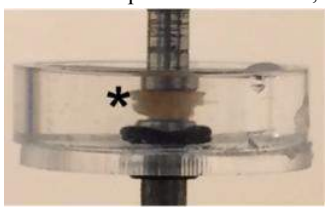

Figure 3. Mouse vertebrae (*) tested in saline bath.

DISCUSSION

Human vertebrae are characterized by a thin cortical shell surrounding a cancellous bone core with trabeculae of similar thickness to the shell. This geometry has been shown to affect load distribution between cortical and trabecular bone [10]. As such, it is important to use animal models with similar bone structure to compare to human vertebral mechanics. The geometry of mouse lumbar vertebra (Fig. 2) and intervertebral disc are comparable to the human vertebra and disc geometry, making the mouse an ideal animal model for understanding effects of degeneration, radiation, or injury on the lumbar spine [11].

In this study, we compared mouse fatigue behavior with human data available. We observed a tertiary response during fatigue, which has been previously reported for human, bovine, and rat cancellous and cortico-cancellous tissue [7-9]. The slope and length of the secondary phases have similar values. Also, the strain percentage for mouse and human at the inflection point of the secondary and tertiary phases show the values within 0.28%. These findings support the use of the mouse model for understanding the effect of radiation, degeneration or injury on human vertebra mechanics.

We have developed and validated testing procedures to use mouse vertebra for mechanical testing, which allows for reasonable inferences about human bone. On-going work is using this method to investigate dose and type of radiation. However, these methods can be applied for understanding the bone mechanics with respect to musculoskeletal disuse, drug treatment, or genetic modification.

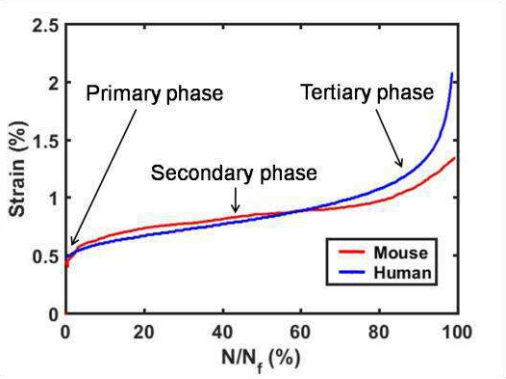

Figure 4. Strain versus number of cycles to failure (N_f) response for a representative mouse vertebra and human vertebrae (adapted from Lambers *et al.*)[6].

ACKNOWLEDGEMENTS

This work was supported by NASA Science and Technology Research Fellowship NNX14AM56H.

REFERENCES

[1] Baxter, J et al., *JAMA*, 2005; [2] Kondo, H et al., *Radiation Research*, 2009; [3] Wernle, J et al., *J Biomech*, 2010; [4] Gong, B et al., *Bone*, 2013; [5] Tommasini, S et al., *J Bone Miner Res*, 2005; [6] Lambers, F et al., *PLoS One*, 2013; [7] Haddock, S et al., *J Biomech*, 2004; [8] Bowman S et al., *J Biomech*, 1998.[9] Kummari, S et al., *CalcifTissue Int*, 2009; [10] Eswaran, S et al., *J Bone Miner Res*, 2006; [11] O'Connell, GD et al, *Spine*, 2007.

Copyright 2016 The Organizing Committee for the 2016 Summer Biomechanics, Bioengineering and Biotransport Conference

SB^{3}C2016
Summer Biomechanics, Bioengineering and Biotransport Conference
June 29 –July 2, National Harbor, MD, USA
SB^{3}C2016-1026

A SIMPLE AND RATIONAL APPROACH TO OUTFLOW CONDITIONS IN CEREBROVASCULAR CFD MODELS

Christophe Chnafa (1), Kristian Valen-Sendstad (2), Olivier Brina (3), Vitor Mendes Pereira (3), David A. Steinman (1)

(1) Mechanical and Industrial Engineering
University of Toronto
Toronto, ON, Canada

(2) Centre for Biomedical Computing
Simula Research Laboratory
Lysaker, Norway

(3) Department of Medical Imaging
Toronto Western Hospital
Toronto, ON, Canada

INTRODUCTION

Computational fluid dynamics (CFD) is now widely used to characterize cerebrovascular hemodynamics and their role in aneurysm initiation, growth, rupture and treatment outcome [1]. Nevertheless, there remains skepticism about the fidelity of aneurysm CFD models, in part owing to the various modelling assumptions and uncertainties [2], one of them being the outflow conditions.

Owing to the difficulty of obtaining patient-specific flow measurements, the vast majority of the published CFD on intracranial aneurysm hemodynamics relies on "*do nothing*" boundary conditions, i.e., stress-free or zero pressure (**p0 method**). Such an approach is not justified physiologically, and leaves the flow division at the outlets uncontrolled, governed mainly by user-dependent choices in terms of the model segmentation, number of branches retained, their lengths and, potentially, artificially added outlet flow extensions. This is becoming increasingly problematic, as aneurysm CFD models are including more of the cerebrovasculature, owing to advances in imaging and computation, and the recognition that flow disturbances in proximal vessels like the internal carotid artery (ICA) can propagate downstream into distal e.g., middle cerebral artery (MCA) aneurysms [3].

An alternative to the p0 method is to assume that outflow rates scale with a Power-Law (**PL method**) using a square or cube relation with the outlet radii. Still, the flow rates are dependent upon the often-arbitrary decisions about which branches to include in the CFD model (see **Figure 1**). In this abstract, we present a novel extension of this power law approach (**PL* method**) that determines flow divisions independently at each bifurcation along the CFD model. Using a cohort of 70 realistic MCA aneurysm cases, we demonstrate that our method provides both more physiologically plausible flow rates and relative independence from model extents compared to the other methods, especially the popular "do nothing" approach.

METHODS

We recently developed a novel lumped parameter approach for fast and accurate prediction of flow divisions in 3D CFD models [4], and applied it here for the three types of boundary conditions (p0, PL, PL*). For each 3D CFD model in our cohort, a 0D model is derived in two steps: (i) the centerlines of the model are computed using the Vascular Modelling Toolkit library (www.vmtk.org) and (ii) these centerlines are decomposed in a network of straight and rigid segments parametrized by their mean radius, length and bifurcation angles.

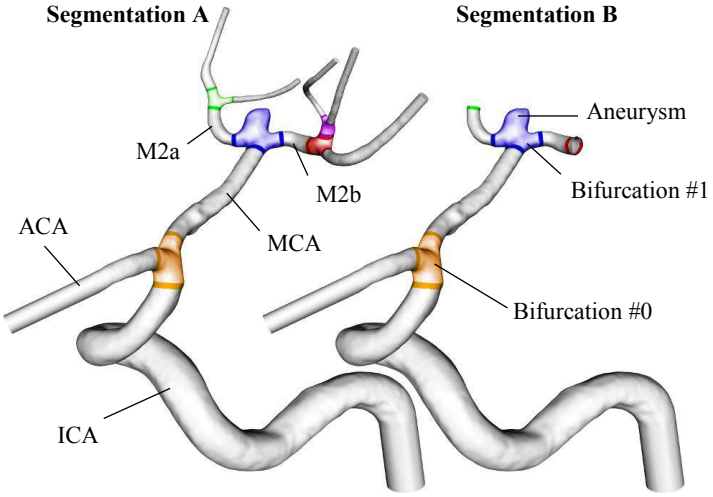

Figure 1: Representative case showing original segmentation (A), and a truncated version (B) used to demonstrate sensitivity of outflow rates to model extent for the three different BC methods.

Copyright 2016 The Organizing Committee for the 2016 Summer Biomechanics, Bioengineering and Biotransport Conference

In these networks, we assumed a steady state and a fully developed, pressure-driven Poiseuille flow with a no-slip boundary condition at the wall. For each segment, the flow rate is proportional to the pressure gradient along the vessel and the inverse of its resistance. Novel to our approach is the use of additional resistances to account for pressure drops at bifurcations [5]. By applying an analogue of Kirchhoff's current law to satisfy segment-to-segment mass conservation, equations for all segments are assembled and solvable by an iterative process [6].

The method was validated against 70 pulsatile 3D CFD simulations that prescribed only ICA inflow, and used the p0 method for outflow [4]. Although momentum balance is not fully accounted for, and the geometry idealized, 0D-predicted outflow rates were on average within 4% of the actual 3D CFD model outflow rates. Using this 0D tool with prescribed ICA inflow, branch flow rates were anticipated using the three different outlet boundary conditions: **p0 method**, as a zero pressure on all the outlets *j*; **PL method**, for which at each outlet *j* the flow rate Q_j is set as

$$Q_j = (A_j / \sum_i A_i) Q_{inlet} \qquad (1)$$

where A_i is the area of the *i*-th outlet and Q_{inlet} is the inlet flow rate imposed to the model at the ICA; and our proposed **PL* method**, defined *locally* for each bifurcation as

$$Q_j = \alpha_{j,b}\, Q_{supplier} \qquad (2)$$

where $\alpha_{j,b}$ is the fraction of flow coming through the outlet *j* at the b^{th} bifurcation. $\alpha_{j,b} = \tilde{A}_j / \sum_c \tilde{A}_{c,b}$ with $\tilde{A}_{c,b}$ the mean area of the c^{th} collector branch of the considered bifurcation *b* and $Q_{supplier}$ the flow rate coming in the bifurcation. When all bifurcations in a model have two collectors (e.g., as in **Figure 1**), Q_j can be computed *globally* as

$$Q_j = [(1-\alpha_{0,0}) \dots (1-\alpha_{j-1,b-1})\alpha_{j,b}]\, Q_{inlet} \qquad (3)$$

RESULTS

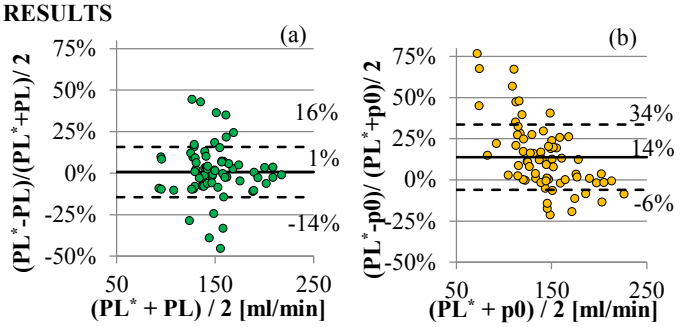

Figure 2: Bland-Altman plots comparing MCA flow rates predicted using our novel PL* method against those predicted by the PL method (a) and p0 method (b) for the 70 cases.

Figure 2 shows that MCA flow rates predicted by PL* and PL methods agree to within about ±15%, albeit with some notable outliers. Relative to PL*, the p0 method underestimates MCA flow rates by 14% on average, but up to 75% for some cases. **Table 2** confirms that methods PL* and PL give similar results, remarkably close to *in vivo* measurements from a separate cohort, while the p0 method diverts too much flow to the ACA, and overestimates interindividual variance.

Table 1: Descriptive statistics (mean ± SD) for the flow rates (in mL/min) into the ACA and MCA for 70 cases using the three different outflow boundary conditions, compared against in vivo measurements from Zarrinkoob et al. [7].

Vessels	p0	PL	PL*	In vivo [7]
ACA	98.8 ± 38.7	77.3 ± 27.2	82.1 ± 25.3	82.0 ± 18.0
MCA	134.0 ± 40.2	148.5 ± 29.4	149.3 ± 28.3	146.0 ± 31.0

DISCUSSION

As we do not know the "true" flow rates for our cohort we can only comment on the flow rate divisions induced by the choice of the boundary conditions, and not the accuracy of the estimated flow rates for individual cases. Nevertheless, flow rates obtained with the PL and PL* method were shown to produce flow divisions closer, in terms of means and standard deviations, to in vivo measurements compared to the popular p0 method. While PL and PL* show consistent results with respect to one another, PL* has the advantage to show little influence from the segmentation choices of the 3D models. For large or multicenter cohort studies such differences may balance out; however, for smaller cohorts and especially individual case studies, such sensitivity to outflow conditions could have significant impact on the 3D CFD results.

This is demonstrated in **Table 2**, which shows that the choice of outflow extent (segmentation A vs. B in **Figure 1**) can have a dramatic impact on flow entering the aneurysm (i.e., fraction of prescribed ICA inflow going to MCA vs. ACA) and aneurysm outflow (M2a:M2b) division. For the p0 method, segmentation extent clearly affects MCA inflow rate, by more than 60%, and more than 40% for the PL method, whereas the PL* method is unaffected by the downstream truncation, by virtue of its 'local' calculations of flow divisions upstream. Regarding aneurysm outflow, p0 and PL methods both predict unbalanced outflows, which would undoubtedly serve to bias the aneurysm inflow jet and hence intra-aneurysm flow patterns, whereas the PL* method predicts a more physiologically plausible balanced outflow.

Table 2: Flow divisions at the ACA/MCA bifurcation and at the aneurysmal sac for segmentations A vs. B shown in Figure 1.

Flow division	MCA:ACA		M2a:M2b	
Segmentation	**A**	**B**	**A**	**B**
p0 method	30:70	49:51	27:73	22:78
PL method	45:55	64:36	29:71	35:65
PL* method	54:46	54:46	42:58	42:58

In summary, the PL* method demonstrates a more physiologically plausible range of flow rates over the 70 cases studied, and is less dependent on the segmentation or extent of the CFD models. We also stress that, although here the PL* method employed a square law for dividing the flow at branchings, one could easily use a cube law, or some combination (e.g., square law for larger branches, cube law for smaller). Current work is aimed at confirming the impact of the choice of outflow boundary conditions on intra-aneurysmal flow and wall shear stress patterns. It is also worth noting that our 0D tool is based on open-source libraries, and our intent is to release it similarly, with the aim of encouraging a better understanding and standardization of cerebrovascular CFD outflow boundary conditions.

ACKNOWLEDGEMENTS

Grant and salary awards from the Heart & Stroke Foundation of Canada are gratefully acknowledged.

REFERENCES

[1] Meng, H. et al., A*JNR Am J Neuroradiol*, 35:1254-62, 2014.
[2] Kallmes, D.F., A*JNR Am J Neuroradiol*, 33:395-96, 2012.
[3] Valen-Sendstad, K. et al., *J Biomech*, 47:3210-16, 2014.
[4] Chnafa, C. et al., *Ann Biomed Eng,* submitted.
[5] Mynard, J. et al., *Int J Numer Meth Biomed Eng*, 31:e02717, 2015.
[6] Manini, S. et al., *Comp Meth Biomech Biomed Eng*, 17:1358, 2014.
[7] Zarrinkoob, L. et al., *J Cereb Blood Flow Metab* 35:648-54.2015.

Copyright 2016 The Organizing Committee for the 2016 Summer Biomechanics, Bioengineering and Biotransport Conference

SB^{3}C2016
Summer Biomechanics, Bioengineering and Biotransport Conference
June 29 –July 2, National Harbor, MD, USA
SB^{3}C2016-1027

SENSITIVE INJURY DETECTION IN THE CERVICAL SPINE USING ACOUSTIC EMISSION

Jay K. Shridharani (1), Brian R. Bigler (1), Courtney A. Cox (1), Maria A. Ortiz-Paparoni (1), Anna E. Knight (1), Cameron R. 'Dale' Bass (1)

(1) Biomedical Engineering
Duke University
Durham, NC, USA

INTRODUCTION

Current techniques for detecting failure in biological tissues often rely on observing discontinuities or inflection points in a material's force-displacement curve. While these characteristics suggest material failure, they may result from the underlying material geometry (e.g. cervical spine buckling). Acoustic emissions provide a method of sensitively detecting injuries with minimal influence from non-injury events. Currently, an extensive characterization of acoustic emissions from osteoligamentous injuries does not exist. Therefore, injury detection typically assumes every acoustic emission indicates injury. However, external factors exist that may cause acoustic emissions without causing injury (e.g. test apparatus vibration). This study presents a characterization of spectral content in acoustic emissions from cortical bone failure and a technique to determine timing of cortical bone injury in complex geometries.

METHODS

Three human cortical bone specimens were excised from thoracic vertebral bodies and placed in a custom test apparatus designed to apply compressive loading without introducing artifacts in microCT images. Pre-test material structure was visualized using microCT images, then acoustic sensors were adhered to the specimens. Specimens were loaded until an acoustic emission was measured, at which time loading was automatically suspended. MicroCT images were recaptured to validate the existence of material fracture *in vitro*. If no tissue damage was observed, the procedure was repeated until there was positive confirmation of injury. The spectral content was analyzed using a Welch power spectrum density estimate.

Three whole cervical spines were loaded in compression to displacements previously determined to cause injury. The acoustic emission response was measured using an array of acoustic sensors on multiple vertebral bodies. The timing of cortical bone failure for the whole spine was determined by the moment at which the frequency content of cortical bone failure occurred in the time domain.

RESULTS

The acoustic emissions from cortical bone failure showed wideband spectral response from 20 kHz to 901 kHz with multiple peaks and a dominant frequency of 60.4 kHz (Figure 1). Cervical spine tests showed the frequency content occurred in bursts containing wideband frequency content from 35 kHz to 603 kHz and centered at 63 kHz. The timing of cortical bone injury was calculated with resolution of 20 μs (Figure 2).

DISCUSSION

The presence and timing of cortical bone failure can be difficult to assess in complex loading scenarios where acoustic emissions may not be from injury. By first identifying the characteristic frequency of cortical bone failure alone, the presence and timing of cortical bone failure in a whole cervical spine can be identified based on the presence of this characteristic frequency centered around 60.4 kHz.

Copyright 2016 The Organizing Committee for the 2016 Summer Biomechanics, Bioengineering and Biotransport Conference

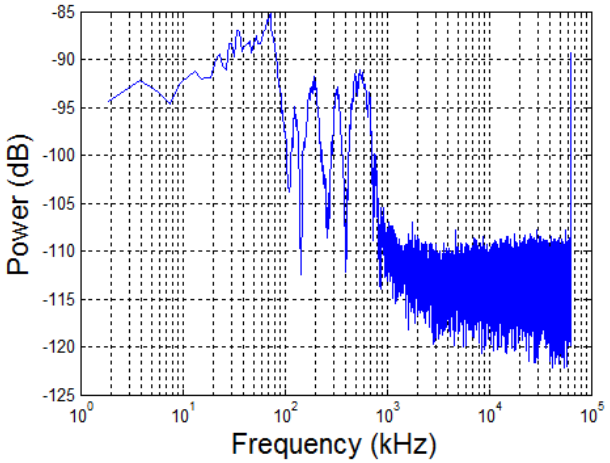

Figure 1. Welch power spectrum density of purely cortical bone sample loaded in compression, showing peak in response around 60 kHz.

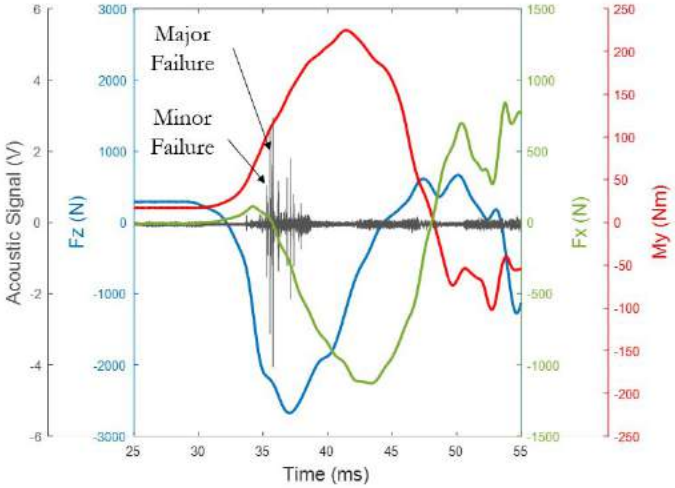

Figure 2. Full loading profile (Fx, Fz, and My) and resulting acoustic signal on C4 vertebra of an observed break in full cervical spine specimen.

ACKNOWLEDGEMENTS

This research was conducted as part of the Biomechanics Product Team led by the Johns Hopkins Applied Physic Laboratory for the WIAMan Project under contract #N00024-13-D-6400, U.S. Army Research, Development and Engineering Command. The content included in this work does not necessarily reflect the position or policy of the U.S. Government.

Copyright 2016 The Organizing Committee for the 2016 Summer Biomechanics, Bioengineering and Biotransport Conference

SB³C2016
Summer Biomechanics, Bioengineering and Biotransport Conference
June 29 –July 2, National Harbor, MD, USA
SB³C2016-1028

EFFECTIVE REMODELING OF WALL CONTENT IN CEREBRAL ANEURYSMS

Xinjie Duan (1), Juan R. Cebral (2), Khaled M. Aziz (3), Simon C. Watkins (4), Anne M. Robertson (1)

(1) Department of Mechanical Engineering & Materials Science, University of Pittsburgh, Pittsburgh, PA, USA

(2) Department of Bioengineering, George Mason University, Fairfax, VA, USA

(3) Department of Neurosurgery, Allegheny General Hospital, Pittsburgh, PA, USA

(4) Department of Cell Biology, University of Pittsburgh, Pittsburgh, PA, USA

INTRODUCTION

Rupture of intracranial aneurysms (IAs) causes 80% of subarachnoid hemorrhages and occurs when the local stress exceeds the local strength of the wall. In order to avoid rupture, an aneurysm must maintain its structural integrity even under extreme physiological loading The factor of safety (FoS) is a frequently used engineering metric for estimation of structural integrity, and is defined as ratio of structural capacity to the applied loads. To avoid rupture, aneurysm walls must have the capacity to maintain their structural integrity overtime despite repeated loading and abnormal flows.

In a previous work [1], we estimated the FoS for two aneurysm cases, chosen from our bank of resected domes (labelled CA-25 and CA-26) using stresses estimated from finite element studies of the intramural load distribution. We found both cases have FoS higher than 4.8. Here, we further investigate those two cases, focusing on remodelling of collagen fibers responsible for the structural integrity and the intramural cells that maintain these fibers. We compare the quantity and distribution of these cells and fibers in the aneurysm wall to those in a control basilar artery. A third unruptured aneurysm (CA-09) from a young patient (27 years old) is also considered due to its unique collagen structure compared with other aneurysm tissue in our data base [2].

METHODS

In order to better understand the wall structure of the aneurysm wall, immunofluorescent staining of collagen type I, collagen type III, αSMA on cross sections of aneurysms and control arteries were imaged under confocal microscopy. Specimens were dissected from 3 aneurysm samples and 1 basilar artery, and then fixed in an unloaded condition in 2% paraformaldehyde for 2h. Cross sections were obtained by freezing the specimen in liquid nitrogen and cutting 8 um thick slices using a cryostat (HM 505E, Microm). Sections were stained with antibodies against collagen type I, collagen type III and alpha smooth muscle actin (αSMA). Sections were permeabilized with 0.1% Triton X-100 in PBS for 10 min, and then blocked in 2% BSA for 45 min. Subsequently, sections were incubated with the primary antibody of collagen type I (ab34710, Abcam), collagen type III (ab7778, Abcam) or αSMA (ab7817, Abcam) for 60 min, washed 5 times with PBB, incubated with fluorescent secondary antibody (Cy3, CBI) for 60 min. DAPI was added to stain nuclei and then a cover slip was adhered for imaging. All sections were imaged using Olympus Fluoview 1000 confocal microscopy (Olympus Imaging America, Melville, NY).

Image analysis was used to determine the thickness fraction of positive αSMA, collagen type I and collagen type III as well as nuclei count per wall area. To quantify the thickness fractions of these components, a custom image analysis program was developed in Matlab to identify the wall thickness, αSMA, collagen I and collagen III layer thickness. The RGB image was enhanced and thresholded to a binary image to define the wall boundary using an edge detection algorithm. Similarly, the red channel images (αSMA, collagen I and collagen III labeled with Cy3) were used to identify the boundary of αSMA, collagen I and collagen III layers. The shortest distance from a point on the luminal boundary to any point on the abluminal boundary was calculated as wall thickness. Wall thickness was measured at 20 locations on the image and averaged. The normalized thickness was defined as the thickness of positive fluorescence layer divided by the total wall thickness. Cell nuclei counts were determined by identifying objects according to size and intensity threshold on the blue channel (DAPI). Cell density was calculated as cell count divided by the wall area, which is the area between the wall boundaries. T test was used to test whether the mean values of layer thicknesses between aneurysms and control artery were statistically different. Differences were

Copyright 2016 The Organizing Committee for the 2016 Summer Biomechanics, Bioengineering and Biotransport Conference

considered statistically significant if the p values were less than 0.05 (95% confidence).

RESULTS

In the wall of the control basilar artery, collagen type I was mostly confined to the adventitia and collagen type III was distributed across the wall. CA-25 and CA-26 displayed a similar layered collagen structure to that of the control artery, with collagen I confined to an outer layer on the abluminal side and collagen III distributed across the wall. In contrast, collagen type I is shown across the entire aneurysm wall for CA-09, which is consistent with the adventitial type collagen seen in both luminal and abluminal sides on MPM images in a previous study [2]. CA-09 was the only aneurysm tissue that displayed this distribution under MPM in a study of 16 IAs. Collagen III in CA-09 was also distributed across the wall, similar to the other two aneurysms and the control artery. The existence of a band of collagen I on the abluminal side in all of three aneurysms as well as in the control artery is consistent with a prior study of four aneurysms imaged using polarized light microscopy [3].

Quantitatively, the average normalized collagen I layer thickness are 1.0 ± 0.01 for CA-09, 0.14 ± 0.03 for CA-25, 0.17 ± 0.01 for CA-26 and 0.22 ± 0.02 for control artery. Compared to the control artery, CA-25 and CA-26 have significantly thinner collagen I layers (p=0.011 and p=0.01), while CA-09 has a significantly thicker collagen I layer (p=0.0001), Figure 1. In summary, the existence of two layers in CA-25 and CA-26, is similar to that of the basilar artery. However, CA-09 displays a qualitatively different remodeled wall. It may be important that this aneurysm came from the only young patient in our study (27 years old). The two layered wall found in CA-25 and CA-26 is consistent with the existence of luminal and abluminal layers in aneurysms found by Mimata et al. [4].

αSMA in the control artery is largely restricted to the medial layer, Figure 1. Similar to the control artery, an αSMA layer on the luminal side was observed in all three aneurysms. Thickness of the αSMA layer was normalized to the total wall thickness. Remarkably, the normalized wall thickness was quite similar for CA-09, CA-25 and CA-26: 0.69 ± 0.034, 0.79 ± 0.033 and 0.82 ± 0.054, respectively. Differences between normalized αSMA layer thickness of these aneurysms and the control artery (0.78 ± 0.070) are not statistically significant (p=0.19, 0.81 and 0.49).

CA-09 and CA-25 have average cell densities of 5231 ± 490 /mm^2 and 6854 ± 686 /mm^2 respectively, both of which are higher than that of basilar artery 4540 ± 805 /mm^2 (p=0.057 and p=0.01), Figure 2. The cell density of CA-26 (3273 ± 659 /mm^2) is lower than that of control artery. However, the difference between cell density of CA-26 and control artery was not statistically significant (p=0.13).

DISCUSSION

In engineering practice, as well as in the current study, we can only project the expected capacity of the wall to continue to maintain a suitable FoS. Unlike classical engineering materials such as steel, biological tissues are endowed with cells that have the capacity for maintenance and adaptation over time. In particular, the passive load bearing components of the vascular wall, elastin and collagen fibers, are maintained and manufactured by vascular cells including vascular smooth muscle cells, fibroblasts and even endothelial cells [5]. In this case study, we found robust aneurysm walls both had cell densities comparable with the control artery and were endowed with a substantial αSMA layer, suggesting these walls have the capacity to maintain the ECM structure over time. Moreover, two of the aneurysm walls had two wall layers that were similar in collagen type and αSMA content to the media and adventia of the control artery. A third aneurysm wall from a young patient displayed a new type of wall structure with both collagen I and III distributed across the wall.

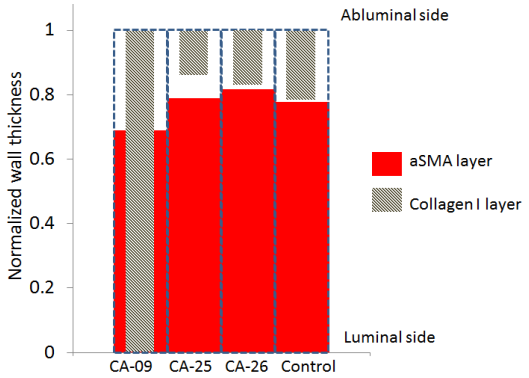

FIGURE 1. Normalized collagen type I and αSMA layer thickness in aneurysms (CA-09, CA-25, CA-26) and control artery.

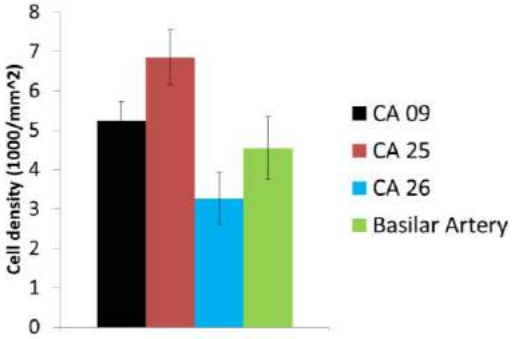

FIGURE 2. Cell density for CA-09, CA-25, CA-26 and basilar artery with standard deviation. Cell density was determined from counts of cell nuclei as visualized from DAPI signal.

ACKNOWLEDGEMENTS

This work was supported by a grant from the National Institute of Neurological Disorders and Stroke of the National Institute of Health (1R21NS080031-01A1). The authors wish to thank the Alzheimers Disease Research Center (ADRC) of the University of Pittsburgh and Dr. Julia K. Kofler, Director of the Neuropathology Core of the ADRC for providing the cadaveric human cerebral vessels.

REFERENCES

[1] X Duan, B Chung, JR Cebral, K. Aziz, AM Robertson, Effective Remodeling in Cerebral Aneurysm: A Case Study, 2015 Summer Biomechanics, Bioengineering and Biotransport Conference (SB3C2015), Snowbird, Utah, June 17-20, 2015, SB3C2015-1159.

[2] Robertson AM, Duan X, Aziz KM, Hill MR, Watkins SC, Cebral JR. Diversity in the strength and structure of unruptured cerebral aneurysms. Annals of Biomedical Engineering. 2015 Jan 30:1-4.

[3] MacDonald DJ, Finlay HM, Canham PB. Directional wall strength in saccular brain aneurysms from polarized light microscopy. Annals of Biomedical Engineering. 2000 May 1;28(5):533-42.

[4] Mimata C, Kitaoka M, Nagahiro S, Iyama KI, Hori H. Differential distribution and expressions of collagens in the cerebral aneurysmal wall. Acta Neuropathologica. 1997 Aug 1;94(3):197-206.

[5] Hu, Y., & Xu, Q. (2011). Adventitial Biology Differentiation and Function. Arteriosclerosis, Thrombosis, and Vascular Biology, 31(7), 1523-1529.

Copyright 2016 The Organizing Committee for the 2016 Summer Biomechanics, Bioengineering and Biotransport Conference

SB^{3}C2016
Summer Biomechanics, Bioengineering and Biotransport Conference
June 29 –July 2, National Harbor, MD, USA
SB^{3}C2016-1029

COMPUTATIONAL MODELING OF COILED CEREBRAL ANEURYSMS: COMPARING HOMOGENEOUS POROUS MEDIUM AGAINST MICRO-CT RECONSTRUCTED COIL VOLUME IN ANEURYSMAL SAC HEMODYNAMICS

Michael C. Barbour (1), Patrick McGah (1), Christian Geindreau (2), Sabine Rolland du Roscoat (2), Kurt Sansom(1), V. Keshav Chivukula (1), Ryan P. Morton (3), John D. Nerva (3), Basavaraj V. Ghodke (4), Laligam N Sekhar (3), Michael R. Levitt (3), Louis J. Kim (3), Alberto Aliseda (1)

(1) Mechanical Engineering
University of Washington
Seattle, Wa, USA

(2) 3SR
Université Grenoble Alps
Grenoble, France

(3) Neurological Surgery
University of Washington
Seattle, WA, USA

(4) Dept. of Radiology
Harborview Medical Center
Seattle, WA, USA

INTRODUCTION

Endovascular treatment methods for cerebral aneurysm, e.g. flow diverting stents and coils, are designed to reduce flow into the aneurysmal sac, promoting flow stasis, thrombosis, and reducing the risk of rupture. While these methods pose significantly less risk to the patient than invasive surgical techniques, up to 30% of aneurysms treated with an endovascular device remain patent at mid-term angiographic follow-up[1].

The hemodynamic environment inside the aneurysmal sac and in the parent vessel is widely considered to play a crucial role in aneurysm remodeling. Recently, computational fluid dynamic (CFD) simulations have been used to study the aneurysmal hemodynamic environment post-treatment in the hopes of understanding what fluid mechanics factors affect treatment outcome[2-4]. However, there are a number of strategies for simulating post-treatment cerebral aneurysm hemodynamics with a wide range of fidelities and computational costs. On one end of the spectrum is the homogeneous porous media approximation, where the coil mass is modeled as a homogenous porous volume that fills the entire aneurysmal sac[5]. This method is attractive due to the low computational cost, but over-simplifies the aneurysmal hemodynamics. On the other end of the spectrum, the full geometry of the coil volume inside the sac is included in the CFD simulation. The coils are often "virtually deployed" inside the aneurysmal sac via an FEA computational model[6-7]. These virtually-coiled simulations are able to capture small-scale flow features induced by the presence of a coil mass but are orders of magnitude more computationally expensive, and it is uncertain to what degree the location of the numerically-deployed coils accurately mimics the *in vivo* configuration.

In this study, we compare the hemodynamic environment computed by CFD simulations that model the entire coil geometry with simulations that approximate the sac as a homogeneous-porous-medium. However, rather than rely on a numerical deployment of the coil treatment, the geometry is acquired from µCT scans of treated *in vitro* models of patient-specific aneurysms. By better understanding the differences in the two modeling approaches, we aim to understand to which degree they can accurately represent the hemodynamics and therefore be appropriate for studying aneurysmal hemodynamics and treatment outcome.

METHODS

Patients enrolled in this IRB-approved study are prescribed coil embolization for a cerebral aneurysm as the standard of care. Three-dimensional rotational angiography is obtained pre- and post-treatment. Blood velocity and pressure measurements are gathered using a dual-sensor pressure and Doppler velocity guidewire and analysis workstation (ComboWire and ComboMap, Volcano Corp, San Diego, CA)[8]. Pressure and velocity measurements are taken every 5 ms at four peri-aneurysmal locations. These measurements are made pre- and post- treatment and used to establish patient-specific boundary conditions in the computational simulations[9]. Three-dimensional vessel reconstruction is done using the Vascular Modeling Toolkit (VMTK v1.2).

In vitro models of the patients are created using a four-stage wax casting procedure. A physical 'positive' model made of acrylonitrile butadiene styrene (ABS) is first created at 1:1 scale by 3D printing. This model is coated, casted and converted to one made of wax, which is finally cast in a clear polyester resin to produce the *in vitro* flow phantom (Clear-Lite, TAP Plastics, San Leandro, CA). The wax is melted away leaving the final 'negative' model of the aneurysm and parent vessel lumen. The *in vitro* model is then treated by an experienced clinician with the same treatment received by the patient

Copyright 2016 The Organizing Committee for the 2016 Summer Biomechanics, Bioengineering and Biotransport Conference

(coil number and size). Synchrotron radiation μCT scans of the treated *in vitro* models are carried out using the ID19 beamline at the European Synchrotron Radiation Facility (ESRF). From these images, a computational reconstruction of the vessel lumen and treatment surface is generated and then meshed for CFD simulations.

To create the porous media model, the portion of the aneurysm sac filled with coils is determined from post-treatment angiographic data and differentiated from the parent vessel reconstruction. The coiled aneurysmal sac is numerically filled with a porous medium approximation that adds a sink term to the momentum equation that depends on the fraction of coils to aneurysmal sac volume. The number, length and diameter of the coils used in the patient's treatment are used to estimate the packing density, which informs the model parameters. The packing density of the porous media model is validated with the actual packing density of the μCT-generated model.

Finite-volume fluid simulations of both models are performed using ANSYS FLUENT (Release 14.1, ANSYS, Inc.). Blood flow is assumed to be incompressible and Newtonian. At the inlet boundary, the time-dependent Womersley velocity profile based on *in situ,* wire-measured, centerline velocity is imposed. At distal outlets, pressures are prescribed using the unsteady *in situ* wire pressure measurements.

RESULTS

Preliminary results show significant differences between the porous medium simulation and the μCT-derived simulation. Shown in figure 1 are oscillatory shear index (OSI) and time-averaged wall shear stresses (TAWSS) for both simulations. The μCT-derived simulation has significant variation in aneurysmal OSI, indicating non-homogenous flow patterns, while the porous media simulation predicts minimal fluctuation in the aneurysm dome. The TAWSS maps suggest similar quantitative patterns, but values of TAWSS integrated over the aneurysm dome are significantly different as pointed out in Table 1. Summarized in this table are various hemodynamic variables integrated over the aneurysm dome from both simulations. The μCT-derived simulations predict higher energy dissipation, OSI, and wall shear stress gradient (WSSG), but lower WSS values.

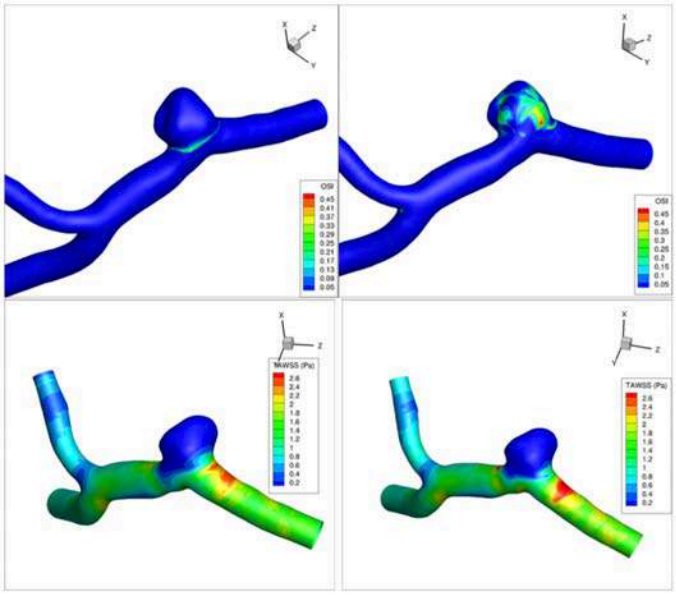

(a) Porous Media (b) μCT

Figure 1:OSI (top row) and TAWSS (bottom row) in a mid basilar, coil-embolized cerebral aneurysm. Flow is from left to right. The treatment geometry is modeled by a porous media approximation (left column) and fully resolved using μCT (right column).

Table 1: Hemodynamic parameters averaged over the aneurysmal sac for both simulations.

	Porous Media	μCT
TAWSS [Pa]	0.0792	0.0487
Sys. WSS [Pa]	0.139	0.09227
OSI [•]	0.0192	0.07228
WSSG (TA)[Pa/m]	192	492
Eng. Dissipation (TA) [mW]	$1.98\ 10^{-3}$	$2.75\ 10^{-3}$

DISCUSSION

The variation in flow parameters seen in Table 1 is caused by the different hemodynamic environments as modeled by the two simulation methods. These preliminary results suggest that the porous medium approximation oversimplifies the flow-damping phenomenon, as it is unable to resolve the small-scale flow features that develop as blood moves through the coil structure. As a direct link between hemodynamic parameters and treatment outcome has not yet been established, and taking into consideration the numerous sources of additional error introduced when simulating cerebral aneurysm hemodynamics, it remains unknown how important this oversimplification may be. However, it is clear that the porous medium model may over or under estimate certain hemodynamic parameters, and caution should be exercised when attempting to correlate porous medium-derived flow parameters to treatment outcomes.

In the quest to determine how hemodynamics impact treatment success, large cohort CFD studies are necessary. While modeling the full geometry of an aneurysmal intervention strategy for every patient would be ideal, it is not practical from a computational resource perspective. Furthermore, if CFD simulations are to be used in a prospective framework to predict the outcome of future interventions, full-scale simulations become even more unrealistic

The need for an intermediate modeling approach is clear. After compiling μCT scans of multiple treated *in vitro* models, the next goal of this study is to develop an improved model of endovascular coiling based on the heterogeneity and anisotropy of the resulting coil structures that develop inside the sac. This model will include aneurysm geometry and location, packing density, etc. The goal is to develop a computational model that captures the key hemodynamics inside and around the sac with sufficient fidelity to be used in treatment predictions, but computationally-efficient enough to be used in a large cohort study of cerebral aneurysm treatment outcomes.

ACKNOWLEDGEMENTS

This work has been financially supported by the NIH/NINDS (grant 1R03NS078539 and 1R01NS088072) and by an unrestricted grant from Volcano Corporation, San Diego CA.

REFERENCES

[1] Crobeddu et all, *AJNR* 34:266-270, 2013
[2] Zhang, Y et al. *Med Eng Phy* 35:608-615,2013
[3] Zulcsar, Z et al. *Acta Neurochir* 33:2010;2016, 2012
[4] Levitt, MR et al. *AJNR* 35:143-148 2013
[5] Muschenborm, A et al. *Biomed Engr. Online* 12:103-116, 2013
[6] Damiano, R et al. *J of Biomechanics* 48:3332-3340, 2015
[7] Morales HG et al. *AJNR 3*2:1935–941, 2011
[8] McGah PM et al. *Physiol. Meas*. 36:2301:2316, 2015
[9] McGah PM et al. *Ann. Biomed Engr.* 42:503-514,2013

Copyright 2016 The Organizing Committee for the 2016 Summer Biomechanics, Bioengineering and Biotransport Conference

SB^{3}C2016
Summer Biomechanics, Bioengineering and Biotransport Conference
June 29 –July 2, National Harbor, MD, USA
SB^{3}C2016-1030

STUDY OF LAYER DEPENDENT RECRUITMENT OF COLLAGEN FIBERS DURING LOADING OF URINARY BLADDER TISSUE

Jack Hornsby (1), Fangzhou Cheng (2), Lori A. Birder (3), F. Aura Kullmann (3), Donna Daly (4), Paul Watton (5), Mark Thompson (1), Anne M. Robertson (2)

(1) Department of Engineering Science, University of Oxford, Oxford, UK

(2) Department of Mechanical Engineering & Materials Science, University of Pittsburgh, Pittsburgh, PA, USA

(3) Department of Pharmacology & Cell Biology, University of Pittsburgh, Pittsburgh, PA, USA

(4) Department of Biomedical Science, University of Sheffield, Sheffield, UK

(5) Insigneo Institute of in silico Medicine, University of Sheffield, Sheffield, UK

INTRODUCTION

Bladder dysfunction occurs frequently in older people, with an estimated 15-30% of people over the age of 60 affected. Disorders such as lower urinary tract symptom (LUTS), indicative of bladder obstruction and urinary incontinence, can dramatically lower the quality of life. The incidence of bladder disorders has been shown to increase with age in both men and women. Since the two working phases of bladder function, filling and voiding, largely depend on its mechanical properties, understanding age-related changes in bladder wall structure is extremely important.

From a mechanical point of view, the bladder is a complex layered composite with passive structural components (elastin and collagen fibers) as well as active components (smooth muscle cells), Figure 1. The inner most surface of the bladder is the urothelium (UT) a transitional epithelium that provides a barrier to protect underlying bladder tissue from urine as well as other deleterious factors [1]. More recently, its sensory and signaling roles have been recognized and received increasing attention, motivated in part by the possible changes in these roles with disease and age [2]. In addition to sensing chemical signals, the UT is responsive to mechanical loads. Hence the mechanical properties and structure of the adjacent lamina propria likely play an important role in its function. The ECM of the lamina propria is composed mainly of collagen types I, III and IV interspersed with some elastin. For this work, we designed and employed a planar biaxial testing device compatible with multiphoton microscopy (BA-MPM) to visualize the collagen fibers and lamina propria during mechanical loading.

METHODS

Male aged (24 month) rats were used in this study. The bladders were cut open and trimmed into square pieces with width varying from 5mm to 7mm. Samples were immersed in HBSS media with 0mM external calcium with thapsigargin to deplete and block smooth muscle calcium stores and prevent contraction. Four strain markers were glued on the bottom surface of each sample using a protocol developed to minimize artifacts associated with marker attachment. Mechanical testing was performed using a custom biaxial system coupled with a multiphoton microscope (Olympus FV1000 MPE), Figure 2. A mirror system consisting of a CCD camera and a 45 degree offset mirror was designed to image displacement of strain markers from beneath the mounted tissue. During testing, the tissue was first preconditioned by 5 consecutive cycles of varying stretch ratios in principal directions, using a protocol decribed in [3]. After preconditioning, the sample was extended until a tare load of 0.02N. Dimensions and initial marker

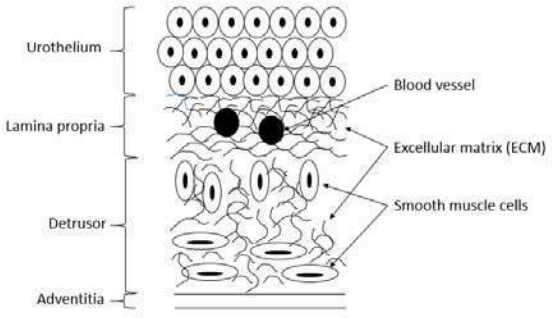

Figure 1. Schematic of the layers of the bladder.

Copyright 2016 The Organizing Committee for the 2016 Summer Biomechanics, Bioengineering and Biotransport Conference

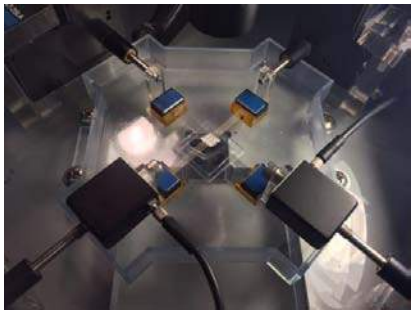

Figure 2: Photograph of biaxial system with mounted tissue. Four linear actuators control the stretch level. Two loadcells measure the force in the principal directions.

coordinates were measured in the preconditioned and load tared configuration and used for stress and strain calculations. Cyclic equibiaxial strain was imposed for 5 cycles at a strain rate of $1\%s^{-1}$ to a maximum stretch of 2.0 as estimated from end to end distance. Tissue was MPM imaged from the UT side at fixed strain levels during the loading cycle. Fiber orientation as a function of depth was measured using a previously developed protocol [4]. The lamina propria layer was identified by scan depth and presence of blood vessels.

RESULTS

MPM imaging of collagen in the lamina propria indicated two distinct layers of fibers with qualitatively different fiber architecture. Representative images from the inner and outer layer are shown in Figure 3. The layer closer to the urothelium (termed inner) is approximatley 20 microns thick and likely associated with the basal membrane. This layer was comprised of fine fibers with a large distribution of orientations. These fibers maintained a distributed orientation under increasing equi-biaxial load. The second layer (termed outer) was imaged across 100 microns of depth and consisted of larger diameter fibers that were wavy in the absence of stretch. When the tissue was stretched, these fibers straightened and reoriented.

Mechanical and MPM imaging data were combined to assess the relationship between collagen recruitment and the stress strain loading curve. In the toe region of the curve, collagen fibers in both layers were wavy, consistent with low stiffness in this region, Figure 3. As strain increased beyond 0.3, the loading curve in the longitudinal direction transitioned to a region of high stiffness. This transition strain was consistent with partial recruitment of outer fibers at a strain of 0.33 and nearly complete recruitment by 0.37. In contrast, the circumferential response showed only modest steepening, consistent with the more moderate recruitment of collagen fibers in that direction over this range.

DISCUSSION

While the physiology of the bladder is a subject of intense investigation, less is known about the biomechanics of the bladder wall [3], and even less about the relationship between the mechanics and biological activities of the wall. Such knowledge is of vital importance as the phenotype and biological activity of the intramural cells that produce and remodel the ECM are responsive to the magnitude and direction of loads on the ECM. Further the cells lining the bladder in the UT, are sensitive to the mechanics of the underlying wall. Here, we have used a custom planar biaxial-MPM system to identify two types of collagen architectures within the lamina propria and investigated the relationship between structure and function in the lamina propria. We found the recruitment of collagen fibers in the outer layer coincides with strains at which the loading curve transitioned to high stiffness, suggesting the two layers in the lamina propria play different mechanical roles during bladder filling.

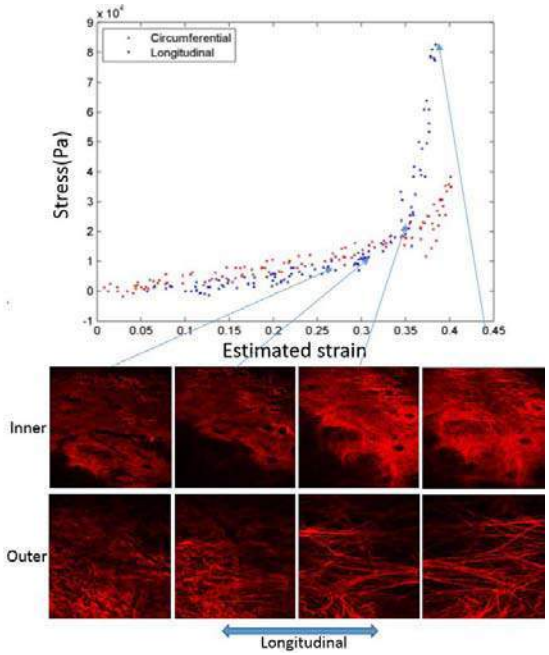

Figure 3. Strain vs. Stress curve and MPM images of the two fiber layer structure taken at increasing strains. From left to right the strains are 0.27, 0.31, 0.33, 0.37.

In the future, collagen recruitment and reorientation will be imaged and quantified across the bladder wall, including the detrusor and adventitia layers, enabling the development of a microstructurally motivated mechanobiological model of the bladder wall [4]. This modeling framework, coupled with biological data will enable us to develop a mechanistic model of the bladder wall that will be used to understand how disease and aging impact the bladder mechanobiology and hence bladder function. For example, changes in fiber architecture with disease or age would be expected to impact urothelial-neural signaling. This in turn could lead to changes in bladder compliance, or, for example, increased spontaneous activity in aged populations.

ACKNOWLEDGEMENTS

We would like to acknowledge support from the NIH for this work, through grants R56 AG050408 and R37 DK54824. We would also like to acknowledge Dr. Xinjie Duan, and Mr. Chao Sang for their contributios to the experiments.

REFERENCES

[1] Campbell, MF, AJ Wein, and LR Kavoussi, Campbell-Walsh Urology. 9th Ed. Philadelphia: W.B. Saunder. 4 v. (xlii, 3945, cxv), 2007.

[2] Birder, L and Andersson, K-E,Urothelial Signaling, *Physiol Rev* 93(2):653–680, 2013.

[3] Toosi, KK, J Nagotomi, MB Chancellor, and MS Sacks, The effects of long-term spinal cord injury on mechanical properties of the rat urinary bladder. *Ann Biomed Eng* 36:1470-80, 2008.

[4] Hill, MR., X Duan, GA Gibson, S Watkins, and AM Robertson. "A theoretical and non-destructive experimental approach for direct inclusion of measured collagen orientation and recruitment into mechanical models of the artery wall. *J Biomech* 45:762-771, 2012.

Copyright 2016 The Organizing Committee for the 2016 Summer Biomechanics, Bioengineering and Biotransport Conference

SB³C2016
Summer Biomechanics, Bioengineering and Biotransport Conference
June 29 –July 2, National Harbor, MD, USA
SB³C2016-1031

THREE-ELEMENT WINDKESSEL MODEL TO DESCRIBE PULMONARY VASCULATURE CHANGES IN HYPERTENSIVE RAT

Jesse W. Gerringer (1), Daniela Vélez-Rendon (1), Daniela Valdez-Jasso (1)

(1) Department of Bioengineering
University of Illinois at Chicago (UIC)
Chicago, Illinois, USA

INTRODUCTION

Pulmonary arterial hypertension (PAH) is characterized by a rise in blood pressure in the pulmonary circulatory system. Vascular lesions are found in the autopsy of advanced PAH patients. However, to date, the mechanisms leading to these lesions and remodeling of the vasculature are unknown. To ascertain how the disease progresses, we propose to determine the resistive and compliant properties of the vascular wall in a rat animal model of PAH. Four different stages of PAH are evaluated in a monocrotaline (MCT) PAH animal model. Flow measurements from the main pulmonary artery (MPA) obtained *in vivo* are used as the input signal into a three-element Windkessel model. Blood pressure is predicted and compared to the *in vivo* measured data. Through this inverse problem, a set of parameters related to the distal and proximal vascular resistance and compliance are obtained and are used to characterize the effects of PAH in the vasculature as a function of the disease stage.

METHODS

Pressure and flow data were acquired during open chest surgery on a normotensive (placebo – PL) and a MCT-treated animal for each week (Figure 1). The *in vivo* measurements were obtained using a pressure catheter inserted into the right ventricle and placed in the MPA, and an ultrasonic flow probe was wrapped around the MPA. For each animal, four single cardiac cycles were assessed. In order to derive resistance and compliance from the data, a circuit analogy is used (Figure 2). This Windkessel circuit is composed of three elements: a resistor in series and a capacitor and resistor in parallel. The analogy is that blood pressure is equivalent to voltage and blood flow equivalent to flow of electricity, or current. The alternating current source is the heart beat that generates flow. The resistor in parallel, R_d, represents the total vascular resistance and the series resistor, R, is referred to as the characteristic impedance, primarily affecting the proximal vasculature.

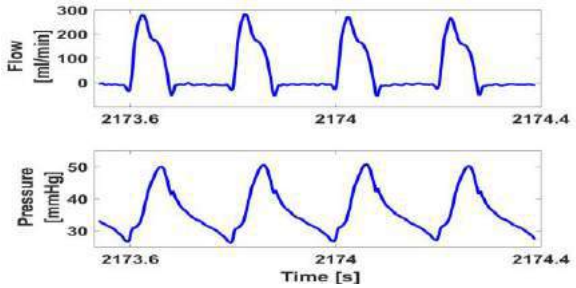

Figure 1: Blood flow (top panel) and blood pressure (bottom panel) measured simultaneously in the rat MPA.

Initial values of R_d and R are determined using Fourier analysis. Each harmonic of impedance is calculated from the ratio of the amplitudes of pressure and flow at the respective harmonic. R_d is obtained from the ratio of mean pressure and flow, and R from the average of the higher impedance frequencies. Thus, characteristic impedance is the impedance in absence of wave reflection. The parameter C represents the compliance of the vessel walls and is arbitrarily set to 0.15 ml/mmHg as an initial guess based on the trends previously seen in our data. Based on conservation principles, or Kirchhoff's law, Equation 1 is derived to represent the pressure and flow relation.

$$\frac{dP}{dt}RR_d + P = \frac{dQ}{dt}RR_dC + Q(R + R_d) \quad (1)$$

Copyright 2016 The Organizing Committee for the 2016 Summer Biomechanics, Bioengineering and Biotransport Conference

Using blood flow as the input signal, blood pressure is predicted. A set of optimal parameters is determined by minimizing the difference between measured and computed pressure signals using a Nedler-Mead simplex algorithm in Matlab (Mathworks, Natick, Massachusetts, USA). The goodness of fit of our prediction is evaluated using residual mean squared error RMSE=$\sqrt{\sum(P_{data}-P_{model})^2/(N-1)}$ in mmHg, where N is number of data points. Intergroup comparison was done using the Student *t-test* with the assumption of unequal variance and considering $p<0.05$ to be significant.

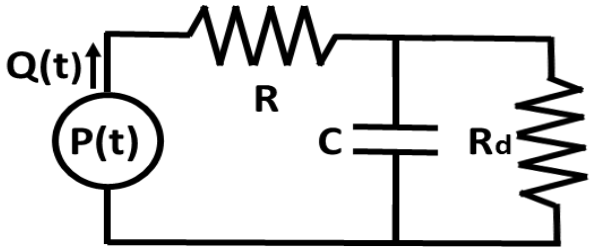

Figure 2: Three-element Windkessel circuit model with a resistor *R*, a resistor R_d, and compliance *C*. *P(t)* represents blood pressure and *Q(t)* blood flow as a function of time.

RESULTS

Here we compare the early and acute/advanced stages of the disease, or week 1 and week 4 post-MCT injections. Plotting the measured against the predicted pressure (Figure 3), we can visually determine a good fit for our model. The RMSE ranges between 0.55 mmHg and 2.65 mmHg, with values near 0.55 mmHg being the better fit. The difference between the prediction and measured pressure is plotted in red and ranges between -4 and 4.3 mmHg.

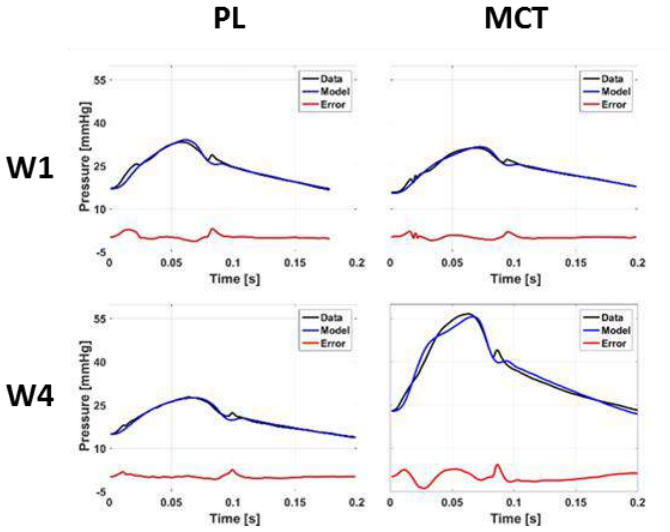

Figure 3: MPA pressure waveforms measured (black line) and predicted of a three-element Windkessel model (blue line). Pressure difference (red line) for PL and MCT groups from weeks 1 and 4.

In the MCT group, R_d and R increased as the disease progressed. This increase was found to be statistically significant from early to acute PAH stage. However, the parameter of compliance C decreased significantly in the progression of the disease. The parameters of resistance in the PL group show no change in the distal vessels (Rd), and no statistical significant change in the proximal vessels (R). Finally, our results show a statistically significant increase in compliance C. The summary statistics of these parameters are illustrated in Figure 4.

DISCUSSION

Our study indicates that the parameters of distal resistance and proximal resistance remain constant in the PL group, whereas in the MCT group we find a statistically significant increase in these parameters as the disease progresses. Based on these results, it is evident that age (4 weeks) does not play a role in vascular resistance, while in the MCT group significant remodeling is occurring. As the MCT injection induces constriction in the pulmonary arteries, a decrease in compliance and an increase in total resistance are to be expected and are in accordance with the work reported by Nishikawa *et al.* [1]. Our findings, and the work by Segers *et al.* using a four-element Windkessel model, are consistent with this notion in that constriction of blood vessels are manifested through the change in these parameters [2, 3]. In week 1 the RMSE values were consistently under 1 mmHg^2, while week 4 MCT had values greater than 2 mmHg^2. This indicates the fitting procedure had a larger error but this goes in hand with the larger pressure ranges in the advanced PAH stage. Through the error plots (Figure 3), one can trace where along the cardiac cycle the fitting is poor. Particularly, we find that our model is unable to fit the physiological characteristic of the pulmonic valve closing, or the dichotic notch. Nevertheless, the prediction of flow is remarkably good, and in our near future, we will explore variations of the Windkessel model to address this physiological marker. Finally, other optimization algorithms will be explored to address the robustness and uniqueness of the parameters.

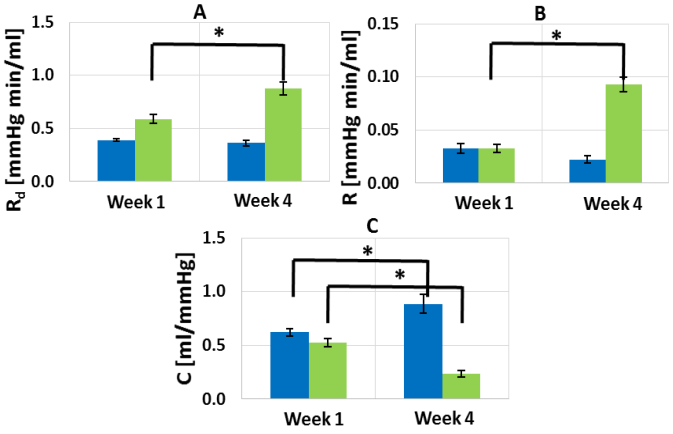

Figure 4: Change in resistance and compliance elements over the course of the four disease stages. A) Total vascular resistance R_d, B) Characteristic impedance *R, and* C) Compliance *C. *p<0.05.* PL is shown in blue and MCT in green.

ACKNOWLEDGEMENTS

This work was supported by UIC Honors College Undergraduate Research Grant (JWG) and College of Engineering Seed Fund (DVJ).

REFERENCES

[1] Nishikawa, T et al., *Circulation*, 132: A17109, 2015.
[2] Segers, P et al., *Am J Physiol*, 288:H1157-H1164, 2005.
[3] Segers, P et al., *Hypertension*, 36:760-765, 2000.

Copyright 2016 The Organizing Committee for the 2016 Summer Biomechanics, Bioengineering and Biotransport Conference

SB^{3}C2016
Summer Biomechanics, Bioengineering and Biotransport Conference
June 29 –July 2, National Harbor, MD, USA
SB^{3}C2016-1032

MICROFLUIDIC-FABRICATION OF BUNDLED CELLULAR SCAFFOLDS BY PHASESEPARATED POLYMER SOLUTION

Y.T. Matsunaga (1), Y.J. Kim (1)

(1) CIBiS, Institute of Industrial Science, The University of Tokyo, Tokyo, Japan

INTRODUCTION

Fibrous structures have been widely developed with a diverse range of geometries, from simple fibres, core-shell structures, to yarns. They are used in filters, electronic devices, and in biomaterial[1]. In particular, bundles of thin, multiply parallel fibres are widely seen in nature such as plant matter, notably in xylems, and human protein assemblies and muscle tissue. Because of their hierarchical structure, they have superior toughness and strength relative to single fibres, and have been a key research focus in artificial tissue engineering. To construct artificial tissues in vitro, soft matter such as polymers, proteins, or colloids have been used because of the ease of fabrication and handling, as well as for the ability to design and manipulate complex, unique structures with two or more components[2]. Thus, biomimetic bundled fibrous structures of soft matter could be used for soft tissue engineering.

Here, we discuss fabrication of biomimetic bundle-structured gel fibres using a microfluidic device and rapid cross-linking of a phase-separated polymer blend solution.

METHODS

Materials

Sodium alginate (Na-Alg) was kindly provided by Kimica Corporation (Tokyo, Japan). The HPC (average MW: 100 kDa) and divinyl sulfone (DVS) were obtained from Sigma-Aldrich (Tokyo, Japan) and Tokyo Chemical Industry (TCI, Tokyo, Japan), respectively.

Fabrication of bundled gel fiber

To generate HPC bundled gel fibre, we used aqueous solutions of HPC and Na-Alg at 28 °C. Phase-separated polymer solution to generate the bundled gel fibres was prepared as follows. H5A1 solution consisting of HPC (5.0 wt%) and Na-Alg (fixed at 1 wt%) polymer blend solution, was prepared by dissolving in Milli-Q water and stirring for 24 hours at pH 13. The co-flow microfluidic device[3] used to fabricate bundled gel fibre was reported previously. H5A1 solution as inner flow and $CaCl_2$ aq. (100 mM) as outer flow was injected into the co-flow microfluidic device. The flow rates were fixed at 300 µL/min and 2,500 µL/min for the H5A1 and $CaCl_2$ solutions, respectively. The fibres were immersed in DVS solution (2.0 wt%, pH 13) for HPC cross-linking for 12 hours under agitation (84 rpm). Citric acid was added to remove un-reacted Alg molecules.

Fabrication of bundled gel fiber

A universal testing machine (UTM, EZ-SX, Shimadzu, Kyoto, Japan) was used to characterize the mechanical properties of the all gel fibres. Each specimen was placed so that the chuck-to-chuck spacing was 20 mm, and pulled at a 10 mm/min load cell rate at 25 or 64 °C in a humid environment.

Cell culture

HPC bundled gel fibres were pre-incubated with PLL-g-PEG-RGD for enhanced cell attachment. Suspended NHDFs (normal human dermal fibroblasts) in Dulbecco's modified Eagle's medium with 10% fetal bovine serum and 1% antibiotics were seeded on the bundled gel fibres at 7,000 cell/mL, and incubated in a 5% CO_2 atmosphere at 37 °C. After 3 and 6 days, immunofluorescence images of F-actin and nuclei were also acquired. To this, the cells were fixed in 4% paraformaldehyde, then the F-actin and the nuclei were respectively stained with Alexa568-conjugated phalloidin and Hoechst33342 (Molecular Probe, Invitrogen, Carlsbad, CA, USA). The stained cells were imaged with CLSM.

RESULTS

Bundled gel fibres and morphologies

Copyright 2016 The Organizing Committee for the 2016 Summer Biomechanics, Bioengineering and Biotransport Conference

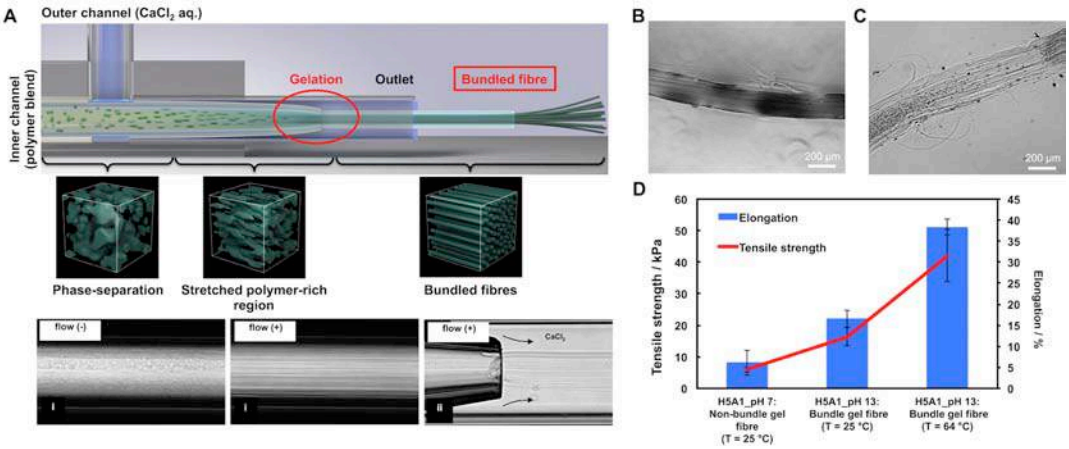

Fig. 1 Fabrication of biomimetic bundled gel fibres using dynamic microfluidic gelation of phase-separated polymer solutions. (A) Microscopic views of phase-separated polymer solution in the microfluidic channel. (B, C) Fabricated bundled gel fibres. (D) Tensile test of the bundled and non-bundled gel fibres.

We generated bundled gel fibres with the co-flow microfluidic device at 28 °C. The aqueous HPC/Na-Alg polymer blend solution (H5A1) and the aqueous $CaCl_2$ solution were injected respectively into the inner and outer channels at respective flow speeds of 300 µL/min and 2,500 µL/min. As shown in Fig. 1A, The phase-separated polymer networks of the H5A1 in the inner channel were stretched by applying shear stress, and were immediately fixed by cross-linking Alg with calcium ions in the co-flow region. We thus obtained bundled gel fibres and non-bundled gel fibres with long lengths and extremely high aspect ratios. The fibre bundles were 200 ~ 400 µm in a diameter and consisted of approximately 10^2 ~ 10^4 small fibres that were 1 ~ 3 µm in a diameter (Fig. 1B and C).

Mechanical properties of bundled gel fibre

We investigated the mechanical properties of the bundled gel fibres with a tensile tester (Fig. 1D). The tensile strength and elongation of the non-bundled gel fibres (H5A1 at pH7) and the bundled gel fibres (H5A1 at pH 13) were 5.9 ± 0.7 kPa, 6.0 ± 2.9%, 16.3 ± 2.9 kPa, and 16.6 ± 2.0%, respectively. These results can be understood by the structure of bundled gel fibres, which can disperse tensile forces among all the constituent small parallel fibres, and inhibit fibre breakage[4]. Furthermore, because the bundled gel fibres were fabricated from cross-linking concentrated polymer domains after phase separation, they have a higher polymer density and enhanced entanglement than do normal gel fibres after gelation. By increasing the temperature above the lower critical solution temperature (LCST) of HPC, the tensile strength can be increased further (42.1 ± 8.2 kPa) because of the strong entanglements in HPC molecules induced by dehydration and shrinking. There was also a much greater elongation (38.3 ± 1.9%) than that observed for temperatures lower than the LCST. Tensile strength and elongation are generally inversely related. However, they both increased with temperature because the residual cross-linked Alg molecules deep in the bundled gel fibres contributed to the elongation instead of condensed HPC molecules above the LCST.

Cell culture of bundled gel fibres

The bundled gel fibres were used as a substrate for culturing NHDFs. After 3 days of cultivation, most of cells were still alive. By immunostaining, we confirmed actin stress fibres in the cells after 3 and 6 days of cultivation. The cells did not fully cover the surface of the bundled gel fibre after 3 days of culturing. However, after 6 days, the fibres were fully covered with cells that expressed actin stress fibres. Most of the cells were aligned parallel to the micro fibres, forming a cylinder-like structure along the fibre bundle. In contrast, no cell orientation was observed on non-bundled gel fibre surfaces; instead they were randomly spread.

DISCUSSION

HPC was the primary material for the gel fibres because it is (i) thermo-sensitive, (ii) easy to acquire in various molecular weights, and (iii) biocompatible. In particular, HPC has a LCST at 45 °C in aqueous solution and thus undergoes a reversible hydrated-to-dehydrated phase-transition with temperature. The polymer Na-Alg blends well with HPC, is rapidly cross-linked, and maintains the string-like structure of the phase-separated solution formed by shear stress. By adding Na-Alg and NaOH to the HPC aqueous solution, a salting-out effect reduces the polymer blend solubility. The phase-separation, therefore, occurs at pH 13 and a lower temperature than the LCST of HPC. Consequently, the polymer blend solution exhibits: (i) an isotropic phase below 25 °C; (ii) an initial formation of droplets via spinodal decomposition at 25 °C; and (iii) droplet growth and network formation above 28 °C. These results demonstrate that the phase-separated state of polymer-rich and polymer-poor regions is key to bundle formation. The bundled gel fibre was an effective scaffold for NHDFs cultures. While spreading along the bundled fibre, the cells fully covered the surface and formed a cylinder-like structure with cell orientations that mimicked vascular, muscle, tendon, and nerve tissues. Given its unique properties, such temperature-responsive property, biocompatibility and ease of manipulation near room temperature, HPC and its blends with the other polymers is an excellent candidate for soft tissue engineering..

ACKNOWLEDGEMENTS

This work was partly supported by PRESTO, Japan Science and Technology (JST), Japan. This work was also supported by a JSPS Grant-in-Aid for Young Scientists (A) (No. 25706010 to Y.T.M.).

REFERENCES

[1] Y.-J. Kim, M. Ebara and T. Aoyagi, *Adv. Funct. Mater.*, 2013, **23**, 5753-5761.

[2] Y. T. Matsunaga, Y. Morimoto and S. Takeuchi, *Adv. Mater.*, 2011, **23**, H90-H94.

[3] Y.J. Kim Y. Takahashi, N. Kato and Y.T. Matsunaga, *J of Mater Chem B*, 2015, **3**, 8154-8161.

Copyright 2016 The Organizing Committee for the 2016 Summer Biomechanics, Bioengineering and Biotransport Conference

SB³C2016
Summer Biomechanics, Bioengineering and Biotransport Conference
June 29 –July 2, National Harbor, MD, USA
SB³C2016-1033

INHOMOGENEITY OF THE MATERIAL PROPERTIES OF THORACIC AORTA IN THREE DIMENSIONS

G. Kermani (1), A. Hemmasizadeh (1), S. Assari (1), M. Autieri (2), K. Darvish (1)

(1) Biomechanics Laboratory, Department of Mechanical Engineering
(2) Department of Physiology, School of Medicine
Temple University
Philadelphia, PA 19122

ABSTRACT
Characterizing the biomechanical behavior of arterial walls is of paramount importance in understanding the local mechanisms of deformation, progression of vascular diseases, and the underlying mechanisms of Traumatic Aortic Rupture (TAR). Current finite element (FE) models of aorta generally consist of simplistic material models with the assumptions of isotropy and homogeneity that are in contradiction with the inhomogeneous microstructure of aortic tissue. This study investigates the inhomogeneity and anisotropy of porcine descending thoracic aorta (DTA) viscoelastic behavior using a custom-made nano-indentation technique. The results showed that in the radial direction, distinct anatomical features had significantly different instantaneous Young's modulus E with the outer media being stiffer than the inner media. Also, E was significantly lower in mid-DTA and in the medial side. In terms of anisotropy, the axial direction had the lowest modulus, and the circumferential direction showed the least relaxation. Overall, our results suggest that under identical mechanical loading, the medial side of the inner media in the axial direction would experience larger strains compared to other regions. This can party explain why aortic ruptures predominantly initiate from the lumen side and propagate in the transverse direction.

INTRODUCTION
TAR is the 2nd leading cause of morbidity and mortality in motor vehicle crashes only after traumatic brain injury [1]. Consequently, mitigation and prevention of TAR is of paramount importance. Experimental reproductions of complex states of loading and deformation in cadaveric surrogate tests are inconclusive[2], hence FE modeling is the preferred method to gain better insight into the mechanisms of TAR. In current FE models, aorta is assumed to be isotropic and homogeneous; however studies show that aorta has an inhomogeneous microstructure with preferred fiber directions.

The function and mechanical response of aortic tissue depend on its structure and composition. The main components of aortic microstructure are elastin, collagen, and smooth muscle cells. Elastin is a highly elastic protein contributing to the resilience and flexibility of aorta and is responsible for its passive elastic behavior under low stretch. Collagen is the load bearing component, at medium to large stresses, and avoids permanent deformation of aorta. The aortic wall can be divided into three main layers with different structures: intima, media and adventitia. Moreover, the DTA structure changes from proximal to distal sections [3]. The proximal sections contain more elastin content and less collagen content compared with the distal sections. Characterizing the anisotropy and inhomogeneity of aortic tissue is necessary to improve the TAR FE models and in gaining better insight into the local mechanisms of deformation, force transmission, and failure.

METHODS
Fresh porcine aorta specimens were excised from seven pigs. Transverse rings with the length of approximately 9 mm were excised after cleaning the aortas. The specimens were divided into upper-DTA, mid-DTA, and lower-DTA sections along the aortic tree (z direction). In order to study the effect of circumferential location (θ direction) on the mechanical behavior, anterior, posterior, medial, and lateral regions were marked on the specimens. Custom-designed nano-indentation tests were performed in the axial direction (A-Dir.) moving across the aorta thickness (r direction) from the inner wall to the outer wall for each of the mentioned regions. Afterwards, cubic samples were cut at the medial and lateral regions and indentation tests in the circumferential (C-Dir.) and radial (R-Dir.) were conducted at various points across the thickness of the aorta, and on the lumen side of the specimens, respectively. The indenter displacement was ramp and hold with 60 μm depth, 25 ms ramp time, and 20 s hold time. A

Copyright 2016 The Organizing Committee for the 2016 Summer Biomechanics, Bioengineering and Biotransport Conference

Quasi-Linear Viscoelastic (QLV) model was used to describe the relationship between the indenter force, $P(t)$, and the indentation depth, h:

$$P(t) = \int_0^t G(t-\tau)(\partial P^e(h)/\partial h)(\partial h)/\partial \tau)d\tau \qquad (1)$$

in which $P^e(h)$ is the instantaneous elastic force and $G(t)$ is the reduced relaxation function assumed to be of the following forms:

$$G(t) = G_\infty + \sum_{i=1}^{4} G_i \exp(-\beta_i t) \qquad (2)$$

in which G_i and $\beta_{1..4} = 0.1,1,10,100\ s^{-1}$ are the reduced relaxation amplitudes and decay rates, respectively [4]. The total load needed to achieve h for a conical indenter is [5]:

$$P^e = (1/\alpha)\{2Ecot(\beta)/\pi(1-\nu^2)\}h^2 \qquad (3)$$

where $\beta = 62.5^\circ$ is the semi-vertical angle of the indenter, E is the instantaneous Young's modulus, and ν is the Poisson's ratio which was assumed to be 0.49 (almost incompressible) for fresh aorta. The correction factor, α, accounts for the imperfect geometry of the indenter and contact surface and was evaluated as 3, for h = 60 μm [4].

RESULTS

The QLV material parameters (Eqs. 2 and 3) were determined by optimizing for G_i and E to match the experimental data. Fig. 1 shows the variation of E (determined in A-Dir.) with z direction (error bars represent the standard error). There is an increase in E from proximal to distal sections where the lower-DTA is about 15% stiffer than the upper-DTA (p<0.0001). Comparison between the values of E (A-Dir.) in different regions in the θ direction shows that the medial side is significantly more compliant (p<0.0001) compared to other locations (Fig. 2). Fig. 3 shows relatively large variations in E in the r direction, where $r = 0$ and 1 represent the innermost and outermost layers, respectively. Fig. 4 shows the anisotropy of E as this parameter is significantly higher in R-Dir. compared with A-Dir. (p<0.0005). G_∞ was significantly different in tests conducted in A-Dir., C-Dir., and R-Dir. (p<0.0002). Also, G_∞ was about 30% which confirmed that significant anisotropic viscoelasticity (stress relaxation) exists in the tissue.

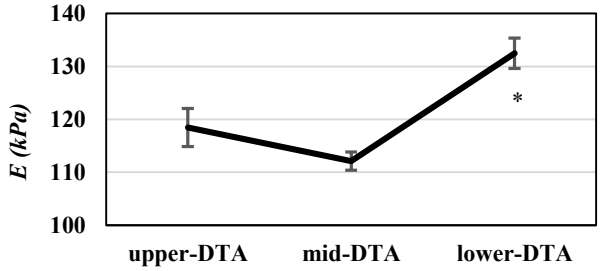

Figure 1: Variation of E in the z (longitudinal) direction.

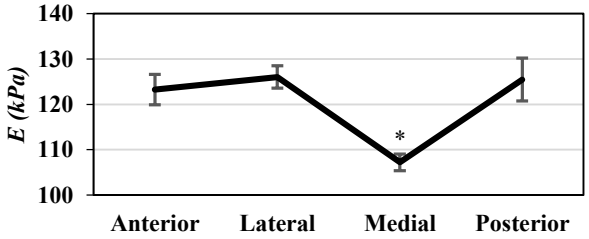

Figure 2: Variation of E in the θ (circumferential) direction.

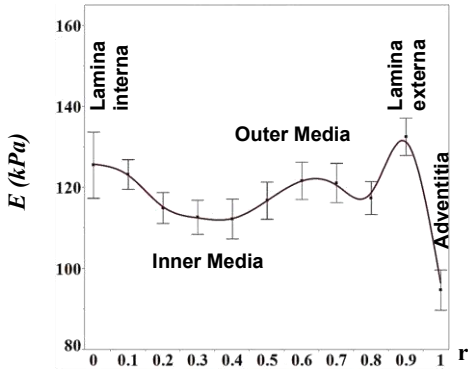

Figure 3: Variation of E in the r direction (across the thickness).

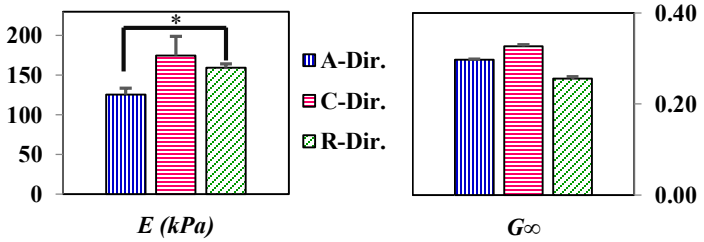

Figure 4: Three-dimensional anisotropy of E and G_∞.

DISCUSSION

The results showed that the assumption of viscoelastic behavior for aorta is valid and the characterized QLV model could sufficiently describe the experimental data. The statistical analysis showed there were regional variations in aorta, where E was significantly higher in the distal sections compared to the proximal ones. This is in agreement with previous study of Sokolis et al. [3] in which they showed these variations were due to changes in aorta micro-structure, i.e., a decrease in the elastin content, and an increase in the collagen content. The variation of E in the r direction showed five distinct regions which approximately corresponded to the micro-structural organization of fibers including lamina interna, inner media, outer media, lamina externa, and the adventitia, respectively.

The porcine DTA showed anisotropy both in terms of the elastic and relaxation characteristics. The A-Dir. showed the least stiff behavior and the C-Dir. showed the least relaxation.

The proximal sections and the medial region of aorta were more compliant and therefore experience higher strains in identical loading conditions. Based on previous studies [7] aortic failure is strain based. Therefore, our results suggest that the medial region, closer to the aortic arch, can be more prone to rupture in an axial loading.

ACKNOWLEDGEMENTS

The work reported herein was partially supported by AHA under Grant Number 15PRE25090213 (SA) and NHLBI under Grant numbers K25 HL086512-05 and R21 HL088159-02 (KD).

REFERENCES

[1] Richens, D., Eur. J. Cardio-Thoracic Surg., 23(2):143–148, 2003.
[2] Nahum, M. J. W. et al., Accidental Injury, 2nd ed., Springer NY, 2002.
[3] Sokolis, D. P. et al., Hellenic J. Cardiol., 49(3):145–154, 2008.
[4] Hemmasizadeh, A. et al., J. Mech. Beh. Biomed. Mat., 15:199–207, 2012.
[5] Sneddon, I. N., Int. J. Engng Sci, 3:47–57, 1965.
[6] D. Mohan and J. Melvin, J. Biomech., 16:31-44, 1983.

Copyright 2016 The Organizing Committee for the 2016 Summer Biomechanics, Bioengineering and Biotransport Conference

SB³C2016
Summer Biomechanics, Bioengineering and Biotransport Conference
June 29 –July 2, National Harbor, MD, USA
SB³C2016-1034

STUDY OF THE CONSISTENCY OF WALL SHEAR STRESS IN HEALTHY MAJOR HUMAN CEREBRAL ARTERIES

K. Takanishi (1), T. Yagi (1), T. Murayoshi (1) K. Suto(1), M. Umezu (1), H. Yoshida (2), K. Nishitani (2), Y. Okada (2), S. Kitahara (2), A.Yamamoto (3), H.Iida (3), H.Kataoka (3),

(1) Center for Advanced Biomedical Science (TWIns), Waseda University
2-2 Wakamatsu-cho, Shinjuku-ku, Tokyo

(2) Kitahara International Hospital
Oowada-cho, Hachioji-shi, Tokyo

(3) National Cerebral and Cardiovascular Center
5-7-1 Fujishirodai, Suita-shi, Osaka-fu

1. INTRODUCTION

One of the problems with the cerebral bypass surgery is a high rate of postoperative complications such as cerebral hyperperfusions, cerebral ischemia, and strokes[1]. These complications occur because the adaptation mechanisms of the cerebral arteries are yet unknown to predict the blood flow condition after the surgery. As a well-known arterial adaptation mechanism, it is widely recognized that endothelial cells control the diameter of the artery along with the change of blood flow by sensing the wall shear stress (WSS)[2]. It has been also postulated that the mean wall shear stress (MWSS) is maintained at a constant value in the arterial system[3]. However, there are not many studies that have discussed about the consistency of the MWSS in the major cerebral arteries where brain surgeons are interested. Therefore, this study investigates the consistency of the MWSS for the major cerebral arteries around the circle of Willis to further understand the adaptation mechanism of the cerebral arteries.

2. METHODS

2.1 Subjects

12 healthy volunteers were examined for the phase-contrast magnetic reasoning imaging (PC-MRI) and the blood viscosity measurement. The PC-MRI examinations were carried out at Kitahara Internnational Hospital and the blood viscosity were measured at Waseda University. Of 12 subjects proceeded to MRI examination, 4 subjects were excluded due to technical problems. 1 subject was excluded from the blood viscosity measurement because the blood sample could not draw from the subject. In total the study population consisted of 7 healthy subjects (average age 26.3 years; 6 men, 1 woman).

2.2. Measurement of blood flow rate and diameter

PC-MRI method was conducted for noninvasive measurement of cerebral blood flow rate and arterial diameter. Phase contrast data have been acquired using GE Signa HDxt (3.0T). Specifications of the MR imaging conditions were as follows: FOV = 128mm, number of pixels = 256 × 256, Resolution = 0.5 mm, slice thickness = 5 mm, velocity encoding = 150 cm/s, bandwidths = 64 kHz, 20 images per beat, and NEX = 4. Major cerebral arteries examined for the study includes: basilar artery (BA), both sides of internal carotid arteries (ICA), middle cerebral arteries (MCA), anterior cerebral arteries (ACA), posterior cerebral arteries (PCA), and superior cerebellar arteries (SCA).

2.3. Blood Viscosity Measurement

The Blood samples from each of the subjects were anticoagulated with heparin for 50 to 1 ratio (blood to heparin). A rotating viscometer (TPE-100, Toki-Sangyo, Japan) was used to measure the viscosity of the blood. The maximum shear rates of the viscometer (383 s^{-1}) were recorded as blood viscosity.

2.4. Acquisition of MWSS Characteristics

MWSS (τ_w) were calculated assuming that the Hagen Poiseuille flow is established in the major cerebral arteries. According to the Hagen Poiseuille formula, WSS can be calculated as shown below:

$$\tau_w = \frac{32\mu Q}{\pi d^3} \qquad (1)$$

where μ (mPas) is the viscosity of blood measured, Q is the blood flow (mL/min), and d is the diameter (mm). To calculate and investigate the consistency of MWSS, the results were plotted on a graph with the third power of the diameter as an x-axis and the blood flow rate as a y-axis. The MWSS was calculated from the coefficients of the linear approximated lines constructed from the graph assuming the blood viscosity is unchanged anywhere within the cerebral arterial system. The level of a correction coefficient of the linear approximations represents the level of consistency of the MWSS.

3. RESULTS

Copyright 2016 The Organizing Committee for the 2016 Summer Biomechanics, Bioengineering and Biotransport Conference

Total of 80 cerebral arteries, 10 to 13 cerebral arteries per a subject, were successfully analyzed and plotted on the graph with the third power of the diameters as x-axis against blood flow rates as y-axis (see Figure.1). Table.1 shows correlation coefficients, MWSSs, and blood viscosity for each of seven volunteers examined with this study.

3.1. Consistency of MWSS in each subject

For all the subjects, correlation coefficients of linear approximation lines were ranged from 0.419 to 0.898 with the average value of 0.659 ±0.187 (see Table.1). The bold trend line in Figure.1 displays the linear approximation line for all the 80 arteries analyzed. The overall correlation coefficient was confirmed as 0.514.

3.2. MWSS Value

WSSs for each subjects were ranged from 1.20 Pa to 2.77 Pa with the average WSS of 1.92 ±0.53 Pa.

3.3. Blood Viscosity

Blood viscosities were ranged from 3.77 mPas to 4.81 mPas with the average value of 4.24 ±0.35 mPas.

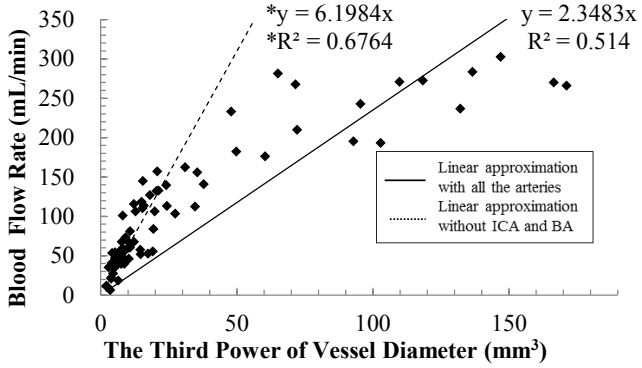

Figure 1: Blood flow rate vs. the third power of vessel diameter for all 80 arteries analyzed in this study. The solid line shows the linear approximation with all the arteries. *The dotted line shows the linear approximation excluding ICA and BA.

Table 1: Correlation coefficients, MWSSs, and blood viscosities for each of seven subjects. * Correlation coefficient and MWSS calculated excluding ICA and BA.

Subject ID	Correlation Coefficient (R^2)	MWSS (Pa)	Blood Viscosity (mPas)	*Correlation Coefficient (R^2)	*MWSS (Pa)
#1	0.419	1.60	4.09	0.678	4.11
#2	0.812	1.74	4.47	0.325	3.76
#3	0.586	1.81	4.81	0.898	6.50
#4	0.677	1.91	4.13	0.887	4.04
#5	0.898	2.77	3.77	0.692	5.28
#6	0.434	1.20	3.98	0.733	3.88
#7	0.788	2.45	4.45	0.900	4.10
Average Value	0.659 ±0.187	1.92 ±0.53	4.24 ±0.35	0.730 ±0.204	4.52 ±1.01

4. DISCUSSION

4.1. MWSS Values

The former studies have shown that the range of human CCA's MWSS are reported to be 0.50 Pa to 1.52 Pa[4,5,6]. In this study, the MWSS value for cerebral arteries is 1.92 Pa. It can be said that the value of this study is considerably similar to the former studies.

4.2. Consistency of WSS

A linear relationship between the third power of the vessel diameters and the blood flow rate represents the consistency of the MWSS within the arterial system. The consistencies of MWSS were somewhat observed because the linear relationship ($R^2 > 0.42$) were confirmed in all seven healthy volunteers. However, judging from the shape of plots in Figure.1, the linear approximation might not be the best fitting curve for the data. It seems that arteries with smaller diameters fit in a linear approximation, but not for the arteries with larger diameters including ICAs and BAs.

4.3. Consideration of the Wormersley number

In the cardiovascular system, the parabolic velocity profile cannot be assumed if the inertial force induced by the pulse is stronger than the viscous force of the blood. Thus, the non-establishment of the Poiseuille flow in the region with larger diameters might be the reason for ICAs and BAs to be deviated from a linear approximation. In order to investigate the establishment of the Poiseuille flow, the Wormerley numbers (α) are examined with a formula below:

$$\alpha = \frac{D}{2}\sqrt{\frac{\omega\rho}{\mu}} \qquad (2)$$

where angular frequency (ω) as 1.083 (assuming a general human heart beat as 65 BPM), a blood density(ρ) as 1060 kg/m^3, a blood viscosity (μ) and the arterial diameter (D) as measured values. The average Wormersley number for ICAs was 3.06 and 2.20 for BAs. It suggests that the Poiseuille's equation is questionable in the regions of ICAs and BAs. The correlation coefficients and MWSSs were re-calculated excluding ICAs and BAs, and the results were also shown in Table.1 and Figure.1. Strong linear relationship (R^2=0.73) was confirmed with a higher MWSS value of 4.52 Pa by excluding ICAs and BAs. The difference between the MWSS of 1.92 Pa and 4.52 Pa were because of the assumption of Poiseuille's equations. The Wormersley numbers calculated for ICAs and BAs suggested that the Poiseuille's flow cannot be is established in those large arteries. Therefore, the MWSS for the larger arteries might have been underestimated. Furthermore, S.K. Samijo[7] have calculated the MWSS using the actual velocity profile of CCA of male in the age of 20 to 29, and the MWSS and the peak WSS (PWSS) was found to be 1.39 Pa and 3.59 Pa, respectively. The values of the PWSS by Samijo and our MWSS (excluding ICAs and BAs) are quite similar; thus, it can be inferred that the actual WSS "sensed" by the endothelial cells may be constant around 4.50 Pa throughout the cerebral arterial systems.

5. CONCLUDSION

The consistency of WSS in cerebral arteries was studied for healthy volunteers to further understand the blood flow regulation mechanism of cerebral arteries. The result of this study suggests that establishment of Poiseuille flow must be considered for calculating MWSS. In addition, by considering the establishment of the Poiseuille flow, the MWSS of the cerebral arteries are constant in a healthy volunteer.

ACKNOWLEDGEMENTS

This research was supported by Grant-in-Aid for Scientific Research (C) from Japan Society for the Promotion of Science.

REFERENCES

[1]. F.McDowell, E.S. Flamn, EC/IC bypass Study. Stroke, Vol.17, No.1, 1986

[2]. D.P.Giddens, et al., The role of fluid mechanics in the localization and detection of atherosclerosis. Journal of Biomechanical Engineering, Vol.115/ 593, 1993

[3]. C.K.Zarins, et al., Shear stress regulation of artery lumen diameter in experimental atherogenesis. Journal of Vascular Surgery, Vol.5, No.3, pp.413-420, 1987

[4] A.Gnasso, et al., Association between intima-Media Thickness and Wall Shear Stress in Common Carotid Arteries in Healthy Male Subjects. Circulation, 94:3257-3262, 1996 [5] R.Dammers, et al., Shear stress depends on vascular territory: comparision between carotid and branchial artery. J Appl Physiol 94:485-489, 2003

[6] S.Oyre, Accurate Noninvasive Quantitation of Blood Flow, Cross-Sectional Lumen Vessel Area and Wall Shear Stress by Three-Dimensional Paraboloid Modeling of Magnetic Reasonance Imaging Velocity Data. JACC Vol.32, No.1, 1998

[7] S.K.Samijo, Wall shear stress in the human common carotid artery as function of age and gender. Cardiovascular Research 39,512-522, 1998

Copyright 2016 The Organizing Committee for the 2016 Summer Biomechanics, Bioengineering and Biotransport Conference

SB^{3}C2016
Summer Biomechanics, Bioengineering and Biotransport Conference
June 29 –July 2, National Harbor,MD, USA
SB^{3}C2016-1035

LONGITUDINAL ASSESSMENT OF MOUSE BONE MICROSTRUCTURE BY IN VIVO μCT IMAGING WITH MINIMAL RADIATION EFFECTS

Hongbo Zhao, Chih-Chiang Chang, Youwen Yang, Wei-Ju Tseng, Chantal M de Bakker, X Sherry Liu*

McKay Orthopaedic Research Laboratory,
University of Pennsylvania,
Philadelphia, PA, USA

INTRODUCTION

In the last decade, development of the *in vivo* micro-computed tomography (μCT) imaging techniques has enabled assessment of longitudinal changes in bone mass and bone microstructure in small rodents, such as rats and mice [1]. However, there are concerns associated with *in vivo* μCT due to its exposure of tested animals to ionizing radiation. This side effect may cause damage to bone cells, thus affecting bone quality. Therefore, it is important to understand the radiation effects associated with *in vivo* μCT imaging protocols of different settings. However, to date only a limited number of studies have addressed this subject. Laperre *et al.* tested radiation effects of μCT protocols with a high (9μm) and low (18μm) image resolution on mouse tibia after3 repeat scans with 2-week interval. They reported minor radiation effects for low image resolution protocol. However, the high resolution protocol caused significant bone loss in the irradiated tibia [2]. Another study by Klinck *et al.* tested radiation effects of a weekly scan protocol on multiple mouse strains and showed a significant decrease in bone volume fraction (BV/TV) in the irradiated tibia at 10.5 μm voxel size [1]. The above studies suggested that different scan settings, such as image voxel size, scan frequency, and scan intervals, may have different effect on bone. The purpose of this study was to develop a low dose, *in vivo* μCT protocol for imaging mouse femur and vertebrae and to test the radiation effects of this protocol on bone quality and bone cell activities. The new protocol, in which mice are scanned at 10.5μm (femur) and 15μm (vertebra) with 3-week interval, was tested on both the tissue level and cellular level for the first time. We hypothesized that a well designed *in vivo* scanning protocol can assess longitudinal changes in mouse bone microstructure with minimized radiation effects.

METHODS

All animal studies performed in this research were approved by the Institutional Animal Care and Use Committee (IACUC) at the University of Pennsylvania. Eight female C57BL/6J (BL6) mice were scanned at the right femur and the 4th lumbar vertebra (L4) by an *in vivo* μCT system (VivaCT40, Scanco Medical, Switzerland). For the distal femur, 212 slices were scanned at 10.5 μm voxel size. For the L4, 212 slices at the center of L4 were scanned at 15μm voxel size. The scanner was operated at 55 kVp energy, 145 μA intensity, and 200 ms integration time and the average time for each scan was about 10 minutes. This scan protocol induced a radiation dose of 639 mGy on femoral bone and 310 mGy on vertebral bone. Baseline scans occurred when mice reached age 12 weeks, and 2 follow-up scans were performed at 3 and 6 weeks after the baseline scan. All animals were sacrificed 3 weeks after the last scan when they reached age of 21 weeks. Left (non-radiated) and right (radiated) femur, L3 (non-radiated) and L4 (radiated) vertebra were harvested from each mouse for further analysis.

All the harvested bone samples underwent *ex vivo* scans at 6 μm isotropic voxel size in a μCT system (MicroCT35, Scanco Medical, Switzerland). In each scan, 227 slices in the region that was covered in the *in vivo* μCT scan were acquired. Images were smoothened using a Gaussian filter (sigma = 0.6, support = 1), followed by a segmentation threshold corresponding to 450.7 mgHA/cm^3 and semi-automatic contouring to extract the trabecular bone for microstructural analysis. Bone volume fraction (BV/TV), connectivity density (Conn.D), structure model index (SMI), trabecular number (Tb.N), trabecular thickness (Tb.Th), and trabecular spacing (Tb.Sp) were calculated by three dimensional (3D) standard microstructural analysis software provided by the manufacturer. Bone microstructure was also evaluated

Copyright 2016 The Organizing Committee for the 2016 Summer Biomechanics, Bioengineering and Biotransport Conference

for all baseline scans. Percent changes over 9 weeks were quantified by comparisons between the baseline and endpoint scans.

Both left and right femurs were processed for methylmethacrylate embedding. Five μm thick plastic sections were cut using a Polycut-S motorized microtome (Reichert, Heidelberg, Germany) and stained with Goldner's trichrome stain (Fig.1) [3]. Histomorphometric measurements were performed in the metaphyseal bone region that was scanned by *in vivo* μCT using Bioquant Osteo Software (Bioquant Image Analysis, Nashville, TN). Osteoblast number (Ob.N/BS), osteoclast number (Oc.N/BS), osteoblast surface (Ob.S/BS), and osteoclast surface (Oc.S/BS) were evaluated.

Paired Student's t-tests were performed to compare radiated and non-radiated bone microstructure and bone cell activities. A p value below 0.05 was considered to indicate significant radiation effect.

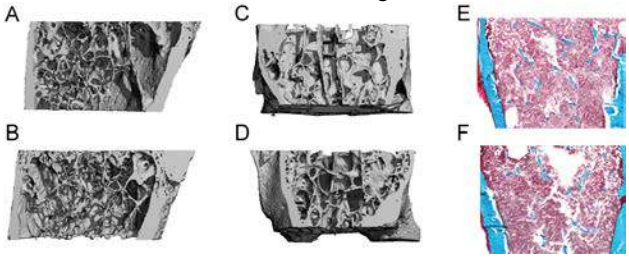

Figure 1. Representative μCT images of (A) non-radiated left femur *vs.* (B) radiated right femur; (C)non-radiated L3 *vs.* (D)radiated L4; and representative Goldner trichrome staining images of (E) non-radiated left femur *vs.* (F) radiated right femur.

RESULTS

Comparisons between radiated L4 and non-radiated L3 showed no significant difference in BV/TV, Tb.Th, SMI, or Conn.D. However, radiated L4 had 10.0% lower Tb.N and 14.1% greater Tb.Sp than non-radiated L3 ($p<0.05$). As for the femur, there was no difference in BV/TV, Tb.N, or Tb.Sp between radiated right femur and non-radiated left femur. However, radiated right femur had 28.8% lower Conn.D, 16.8% greater SMI, and 12.8% greater trabecular thickness (Tb.Th) than non-radiated left femur (Fig 2). Bone histomorphometry analysis showed no difference in Ob.N/BS, Oc.N/BS, Ob.S/BS or Oc.S/BS between the non-radiated and radiated femurs (Fig 2).

Comparisons between the baseline and endpoint scans suggested significant bone loss in mice from age of 12 to 21 weeks, as shown in Table 1.

Table 1. % change in bone microstructure in mice from age of 12 to 21 weeks. * indicates significant change ($p<0.05$).

% change over time	Distal Femur	Lumbar Vertebra
BV/TV	-31.3 ± 22.6*	-12.4 ± 10.6*
Tb.N	-21.7 ± 6.4*	-22.2 ± 8.9*
Tb.Th	2.3 ± 11.3	-19.6 ± 4.7*
Tb.Sp	31.9 ± 9.6*	29.6 ± 14.5*
SMI	-3.7 ± 12.1	-64.7 ± 8.9*
Conn.D	26.6 ± 68.6	23.9 ± 43.9

DISCUSSION

In this study, we developed and tested a low dose, *in vivo* μCT scan protocol of the mouse femur and vertebra with image voxel size of 10.5 μm and 15 μm, respectively. Minimal radiation effects were found on trabecular bone mass and microstructure while no radiation effect was observed in number and surface of osteoblasts and osteoclasts.

Despite minimal radiation effect on BV/TV, significant differences found in Tb.N and Tb.Sp of the vertebra, and Conn.D, SMI, and Tb.Th of the femur suggested that radiation effect by *in vivo*μCT can lead to deteriorations in trabecular bone micro architecture. Nevertheless, aging also plays a significant role in trabecular bone loss. Results from our study is consistent with those reported by Glatt*et al.*, which showed that female mice had significant bone loss in the distal femur and vertebra from age of 3 to 5 months [4]. Comparing with aging effect, our study suggested that ionizing radiation associated with *in vivo* μCT exerted significant but negligible effect on some of trabecular bone microarchitecture parameters. Therefore, we conclude that the low dose *in vivo* μCT imaging protocols developed for the mouse femur and vertebra can assess longitudinal changes in bone mass and microstructure with minimal radiation effects.

ACKNOWLEDGEMENTS

This study is supported by NIH/NIAMS P30-AR050950, and NIH/NIAMS K01-AR066743.

REFERENCES

[1] Klinck, R. J.*et al.*, Medical Engineering & Physics, 30(7):888-895, 2008.[2] Laperre, K*et al.*, Bone, 49(4): 613–622, 2011.[3] Chandra, A*et al.*, Bone, 55(2): 449–457, 2013.[4] Glatt, V*et al.*, Journal of Bone and Mineral Research, 22(8):1197–1207, 2007.

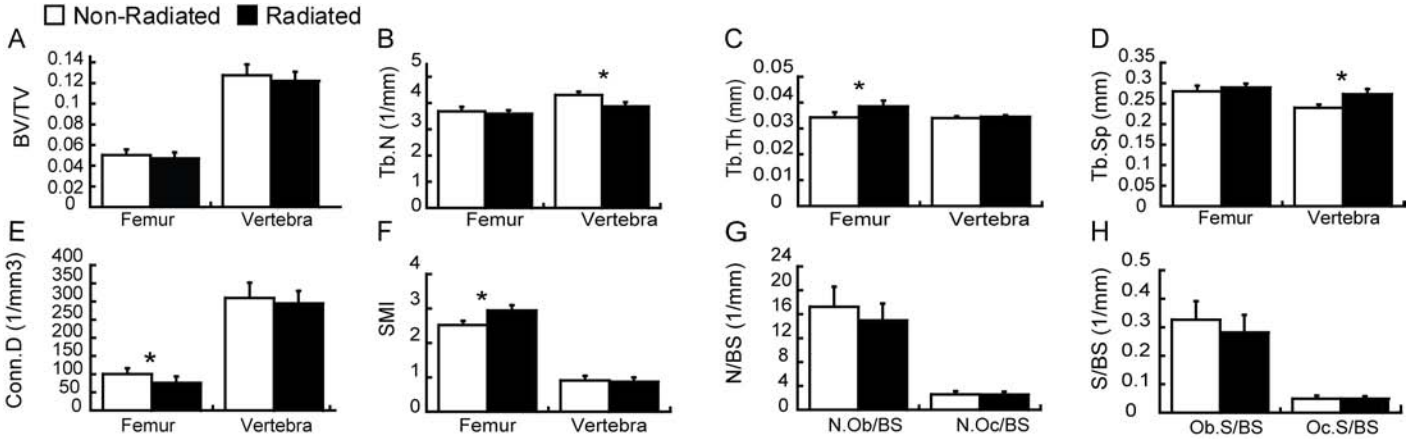

Figure 2. Differences of (A) BV/TV, (B) Tb.N, (C) Tb.Th, (D) Tb.Sp, (E) Conn.D, (F) SMI, (G) N.Ob/BS, N.Oc/BS and (H) Os.S/BS, Oc.S/BS between non-radiated and radiated bone.

Copyright 2016 The Organizing Committee for the 2016 Summer Biomechanics, Bioengineering and Biotransport Conference

SB^{3}C2016
Summer Biomechanics, Bioengineering and Biotransport Conference
June 29 –July 2, National Harbor, MD, USA
SB^{3}C2016-1036

ASSESSMENT OF ANALYSIS METHODS TO EVALUATE THE ASSOCIATION BETWEEN WALL SHEAR STRESS AND CORONARY ARTERY DISEASE PROGRESSION IN THE CLINICAL SETTING

Lucas H. Timmins (1,2), David S. Molony (2,3), Parham Eshtehardi (3), Michael C. McDaniel (3), John N. Oshinski (1,2), Habib Samady (3), Don P. Giddens (2)

(1) Department of Radiology and Imaging Sciences
Emory University School of Medicine
Atlanta, GA, USA

(2) Department of Biomedical Engineering
Georgia Institute of Technology
Emory University School of Medicine
Atlanta, GA, US

(3) Division of Cardiology
Department of Medicine
Emory University School of Medicine
Atlanta, GA, USA

INTRODUCTION

Computational hemodynamics have been investigated as a clinical tool to aid in identifying rapidly progressing coronary artery disease (CAD) and the potential for lesions to acquire high-risk characteristics (i.e., vulnerable plaque). Prospective clinical investigations have evaluated the prognostic value of wall shear stress (WSS) in determining the characteristics of CAD progression [1,2]. However, the evaluation methods to quantify the association between these spatially heterogeneous data are varied. For example, studies have employed analysis techniques that average the hemodynamic data over 3-mm segments [2] or around the artery circumference [1] and associate these data with intravascular ultrasound (IVUS) defined CAD progression. Moreover, we recently developed a framework that allows for examination of the focal association between WSS and CAD progression [3]. Although each of these studies has merit in investigating the complex association between hemodynamics and CAD progression, the accurate and specific identification of vulnerable plaques has direct clinical implications in long-term prognostication of patients with CAD.

Therefore, the aim of this investigation was to examine differences in hemodynamic characterization and resulting associations with CAD progression between the previously employed evaluation methods. We present data from patients with moderate CAD and note distinct differences in CAD progression patterns, for example, in areas of low and oscillatory WSS.

METHODS

Clinical Data Patients (n = 20) enrolled in a prospectively study evaluating the association between WSS and VH-IVUS defined CAD progression were included in this investigation. Enrollment criteria and acquired clinical data have been previously described in detail [1]. Briefly, patients presenting with an abnormal non-invasive stress test of stable angina and determined to have non-obstructive disease were enrolled. Patients underwent baseline and 6-months follow-up catheterizations to collect
biplane coronary angiography, end-diastolic gated virtual histology-IVUS (VH-IVUS) images, and Doppler derived velocity data. The Emory University Institutional Review Board approved the study, and each patient provided informed consent.

Computational Modeling The patient-specific computational fluid dynamics (CFD) modeling techniques employed have been previously described in significant detail [1,4]. Briefly, the 3-dimensional (3D) lumen geometries were reconstructed from biplane angiography and segmented VH-IVUS images. A volume was created from the reconstruction (Geomagic Studio 11, Geomagic, Inc.), discretized with an unstructured tetrahedral mesh (ICEM CFD 15.0, ANSYS, Inc.), and imported into a commercial solver FLUENT (ANSYS, Inc.). Patient-specific pulsatile velocity values were applied at the inlet of the computational domain as a series of uniform profiles. Outlets were assumed traction-free, and a no-slip boundary condition was applied at the rigid wall. Following simulation convergence, WSS vectors were extracted at each node across the cardiac cycle. Vector magnitudes were averaged across the cardiac cycle yielding time-averaged (WSS) values. Furthermore, the WSS angle deviation (WSSAD, ϕ), which quantifies the temporal angular variation between the TAWSS vector and instantaneous WSS vectors at each node, was calculated at time points (n) throughout the cardiac cycle as,

Copyright 2016 The Organizing Committee for the 2016 Summer Biomechanics, Bioengineering and Biotransport Conference

$$\phi_n = \arccos\left(\frac{\vec{\tau}_i \cdot \vec{\tau}_j}{|\vec{\tau}_i| \cdot |\vec{\tau}_j|}\right) \quad (1)$$

where τ_i and τ_j are the TAWSS and instantaneous WSS vectors, respectively. The maximum WSSAD value in the cardiac cycle was determined to characterize the oscillatory hemodynamic environment.

Plaque Progression Quantification Longitudinal VH-IVUS images were co-registered in the axial and circumferential direction with the aid of fiduciary anatomical landmarks and a developed multivariate cross-correlation algorithm [1,5]. Changes in total plaque and constituent areas (fibrous, FT; fibro-fatty, FF; necrotic core, NC; dense calcium, DC) were quantified in focal regions (i.e., sectors) by comparing co-registered baseline and 6-month follow-up image data.

Data Analysis Baseline hemodynamic were evaluated in 3-mm segments, circumferentially, and sectors. Briefly, hemodynamic data were extracted over 3-mm segments, which encompassed 6 VH-IVUS images (0.5mm between images) or at the spatial location of each VH-IVUS image. Data were either averaged within the 3-mm segment, around the artery circumference, or within defined sectors (Fig. 1). To allow for comparison between the analysis techniques, sectors for a given paired VH-IVUS image set were assigned a segment, circumferential, or sector defined TAWSS and WSSAD value. Thus, while there were 8 values for change in total plaque and each VH-IVUS defined plaque constituent areas, the same spatially (circumferentially) averaged hemodynamic values were assigned to each sector for the circumferential method. Moreover, the same segmental average of hemodynamic values were assigned in all sectors across the 6 images within each defined segment.

We classified TAWSS values into three groups: low (< 10 dynes/cm^2), intermediate (10-25 dynes/cm^2), and high (> 25 dynes/cm^2) [1,4]. Similarly, WSSAD values were classified as low (< 45°), intermediate (45°-90°), or high (>90°) oscillation [3]. Finally, sectors were identified that exhibited both low TAWSS < 10 dynes/cm^2 and high WSSAD > 90°, herein low and oscillatory WSS.

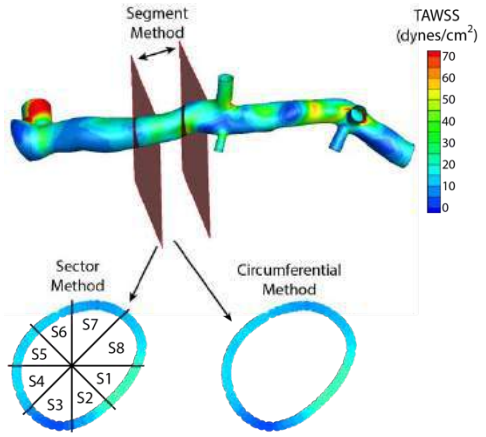

Figure 1: Evaluation methods to characterize hemodynamic environment. TAWSS and WSSAD values were averaged within defined regions (e.g., 3-mm segment, circumference, sector) and associated with VH-IVUS defined CAD plaque progression.

RESULTS

Examination of the hemodynamic data revealed a significant reduction in data count and range by increasing the dimension over which data were spatially averaged. Employing the sector analysis (n = 14,235) resulted in TAWSS values ranging from 1.0 – 363.3 dynes/cm^2, whereas the circumferential analysis (n = 1,846) led to a range from 2.1 – 117.7 dynes/cm^2 and the segment method (n = 307) from 2.6 – 100.6 dynes/cm^2. Furthermore, WSSAD values ranged from 0.2° – 178.4°, 0.6° – 124.6°, and 0.8° – 69.9° for the sector, circumferential, and segment method, respectively. Observed variations in the characterized hemodynamic environment between the analysis methods resulted in noticeable differences in the association between hemodynamics and 6-month VH-IVUS defined plaque progression. Most notably, distinct differences in progression patterns were observed in the low and oscillatory WSS environment (Fig. 2). Employing the sector method, we observed regression of total plaque, fibrous, and fibrofatty tissue area, but progression of necrotic core and dense calcium; however, we observed regression of total plaque, fibrous, necrotic core, and dense calcium tissue, but progression of fibrofatty tissue utilizing the circumferential method. Notably, there were no 3-mm segments that exhibited a (spatially averaged) low and oscillatory WSS environment.

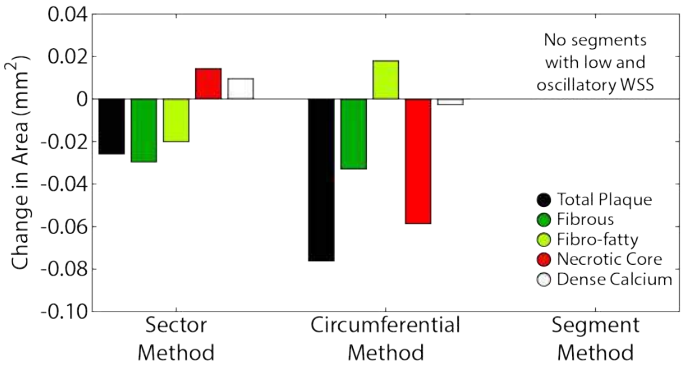

Figure 2: Association between CAD and low and oscillatory WSS employing the sector, circumferential, or segment method. Note that no segments had a spatially averaged hemodynamic environment characterized by low TAWSS (< 10 dynes/cm^2) and high WSSAD (>90°).

DISCUSSION

Our investigation highlights the importance of analysis methods when examining the complex association between hemodynamics and CAD progression, and the dependence of progression patterns on these analysis methods. We report a significant reduction in hemodynamic variable data range when the size of spatial averaging is increased, and these reductions led to definitive differences in associations with CAD progression patterns (Fig. 2). It cannot be overemphasized that CAD progression and plaque rupture are focal pathologic events [5], and associations with variables that influence these events should be analyzed at a similar length scale. Thus, the (spatial) reduction of hemodynamic data and masking of complex hemodynamic environments should be limited to avoid misinterpreting resulting associations. Future clinical studies that rigorously evaluate the hemodynamic environment and CAD progression at a focal length scale will provide insight on the long-term prognostication of WSS in the early identification of high-risk coronary lesions.

ACKNOWLEDGEMENTS

This research was supported by the National Institutes of Health (LT) and the Georgia Research Alliance (DM, DPG).

REFERENCES

[1] Samady, H et al., *Circulation*, 124:779-788, 2011.
[2] Stone, PH et al., *Circulation*, 126:172-181, 2012.
[3] Timmins, LH et al., *Ann Biomed Eng*, 43:94-106, 2015.
[4] Timmins, LH et al., *IEEE Trans Med Imag*, 32:1989-1996, 2013.
[5] Virmani, R et al., *Arterioscl Thromb Vasc Biol*, 20:1262-1275, 2000.

Copyright 2016 The Organizing Committee for the 2016 Summer Biomechanics, Bioengineering and Biotransport Conference

SB^{3}C2016
Summer Biomechanics, Bioengineering and Biotransport Conference
June 29 –July 2, National Harbor, MD, USA
SB^{3}C2016-1037

LONG-TERM EXPOSURE TO BUFFER SOLUTION ALTERS TENDON STRUCTURE AND MECHANICS – IMPLICATIONS FOR FATIGUE STUDIES

Babak N. Safa (1,2), Kyle D. Meadows (2), Spencer E. Szczesny (3), Dawn M. Elliott (2)

(1) Department of Mechanical Engineering
University of Delaware
Newark, DE, USA

(2) Department of Biomedical Engineering
University of Delaware
Newark, DE, USA

(3) Department of Orthopaedic Surgery
University of Pennsylvania
Philadelphia, PA, USA

INTRODUCTION

The water content of soft connective tissues strongly influences their mechanical properties. Mechanical tests are usually performed in a buffer solution to regulate the tissue water content. Phosphate buffered saline (PBS, 0.9% w/v (0.15 M)) is the most common solution. The concentration of isotonic 0.9% PBS solution closely corresponds to the physiological concentration of the interstitial fluid. However, fibrous tissues become over-hydrated and swell in PBS, decreasing their modulus [1]. In addition, over time the buffer's solutes can diffuse into the tissue, altering both the structure and mechanics. These two effects, swelling and solute diffusion, are time-dependent so the apparent mechanical properties are different depending on the duration over which the tissue is exposed to the buffer solution. Thus, a short mechanical test would have consistent properties through the course of the experiment. However, a longer mechanical test, such as a fatigue test lasting several hours, can be problematic because the mechanical effects of fatigue loading and of hydration and solute diffusion may confound each other. As a result, it is important to identify and minimize the effect of the buffer solution on tissue mechanics.

Alternative solutions to PBS have been used, such as sucrose [3] and poly(ethylene) glycol (PEG) [4], which is a hydrophilic polymer. However, it is not known how PBS or alternative buffers affect the tissue for long-term tests (hours to days). The objective of this study was to measure the effect of exposure to buffer solution on tendon structure and mechanics and suggest an appropriate buffer for long-term mechanical tests.

METHODS

Sprague-Dawley rat tail tendons from 7-13 month old animals were used in this study. Fascicles were harvested from the proximal end of the tail and 60 mm long samples were incubated for 8 hours at room temperature in a range of concentrations of sodium chloride (NaCl) or PEG (20kDa molecular weight). The solutions of varying concentrations were buffered with Tris (0.01M) to pH=7.6. Additional samples were incubated in 0.9% NaCl, 25% NaCl, or 8% PEG for only 15 min to represent the duration of a short mechanical test. Each sample was then weighed (W_{wet}), dehydrated at 40˚C in an oven for 20 hours, and weighed (W_{dry}). The apparent water content (φ_{app}) was calculated as:

$$\varphi_{app} = \frac{W_{wet} - W_{dry}}{W_{wet}} \qquad (1)$$

The tendon is permeable to buffer solutes, especially in high concentrations. In order to measure the solute diffusion into tendon, which can artificially lower the apparent water content, true water content was measured in a separate group of samples (n=5/group). The sample was initially dehydrated, weighed ($W_{dry,i}$), incubated for 8 hours, weighed (W_{wet}), dehydrated a final time, and weighed ($W_{dry,f}$). The true water-content (φ_{true}), which excluded solutes that diffused into the tissue, was calculated as:

$$\varphi_{true} = \frac{W_{wet} - W_{dry,f}}{W_{wet} - (W_{dry,f} - W_{dry,i})} \qquad (2)$$

The percent difference between the apparent and true water content was calculated as $100(\varphi_{true} - \varphi_{app})/\varphi_{app}$.

Uniaxial tensile mechanical tests were performed in 0.9% NaCl and concentrations that, based on hydration curves for each solution (Fig. 1), maintain the fresh-frozen apparent water content after 8 hours of incubation (25% NaCl and 8% PEG). The 60 mm tendon was cut into equal proximal and distal portions, randomly assigned to non-treated (fresh-frozen) and treated groups (8 hours incubation prior to test). All tendons were tested in a bath of the 'treatment' buffer, such that the exposure time of non-treated samples to buffer solution during

Copyright 2016 The Organizing Committee for the 2016 Summer Biomechanics, Bioengineering and Biotransport Conference

the test was 15 min, while the treated samples were in a buffer for 8 hours and 15 min. For the mechanical test the sample was preloaded to 0.01 N, preconditioned for 5 cycles of 2.5% grip-to-grip strain (ref. length = 10.9 ± 0.8 mm), and loaded to 5% strain at 1%.s^{-1}. This strain was maintained during a 10 min stress-relaxation. The tangent modulus was measured and averaged between 1.5%-4% strain, and the percent stress relaxation was measured. One-way ANOVA and a post-hoc Tukey's test were used to compare across different solutions. Paired t-tests were used to compare non-treated to treated groups within the same solution. Significance was set at $p<0.05$.

To observe the change in microstructure due to the buffer treatment, fascicle cross-sectional images were obtained using transmission electron microscopy (TEM) for fresh-frozen tissue and after 8 hours of incubation in 0.9% NaCl and 8% PEG solutions (n=1/group, 3 month old rat).

RESULTS

The fresh-frozen water content was 52.9 ± 1.6% (n = 58) (Fig 1, dashed line). The apparent water content for both NaCl and PEG decreased with an increase in solute concentration, with 25% NaCl and 8% PEG closely matching the fresh-frozen water content (Fig 1). The apparent water content after 15 min and 8 hours was unchanged for 0.9% NaCl and 8% PEG (Fig 1). However, 25% NaCl has a dramatic drop in the apparent water content at 15 min that increases to the equilibrium value at 8 hours (Fig 1). The true water content was higher than the apparent water content for NaCl, but there is no difference for PEG (Fig 2), demonstrating solute diffusion into the sample for NaCl concentrations above 5%.

The modulus of the 8% PEG group was unchanged compared to the untreated group, however the modulus of the 0.9% and 25% NaCl groups decreased by 27% and 23%, respectively, with treatment ($p<0.05$, Fig 3). The percent relaxation decreased by a small amount (4%, $p=0.04$) for the PEG group and was unchanged for the NaCl treatments (Fig 3). When comparing the non-treated groups across the solutions, the 25% NaCl modulus was higher and the percent relaxation was lower than the 8% PEG and 0.9% NaCl groups ($p<0.05$), perhaps related to the initial apparent dehydration at 15 min (Fig 1).

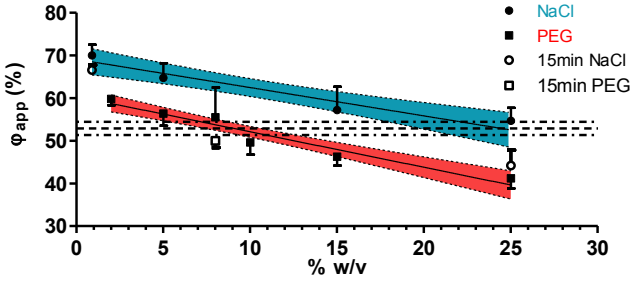

Figure 1: Apparent water content at equilibrium (8 hours) or 15 min (hollow marker) incubation in NaCl (n=17) and PEG (n=44). Dashed lines = fresh frozen water content mean ± CI (95%). Error bars indicate mean ±

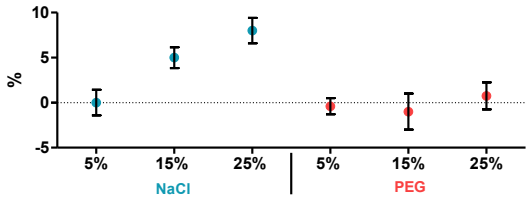

Figure 2: Percent difference between true and apparent water content. The bars indicate mean ± SD.

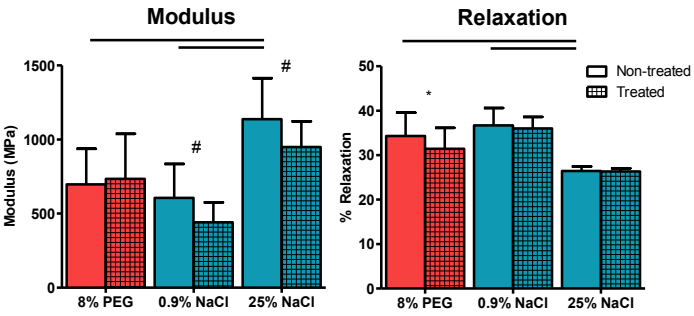

Figure 3: Modulus and percent relaxation following short and long-term exposure to different solutions. #p<0.05 *p=0.04.

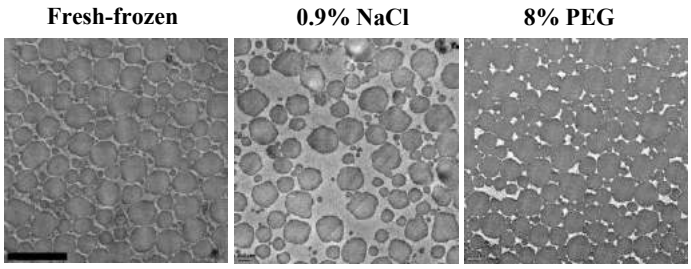

Figure 4: TEM images from cross section of the fascicles after 8 hours of incubation. Scale bar indicates 1um.

Spacing between fibrils increased after incubation in 0.9% NaCl compared to the fresh-frozen, while fibril spacing after incubation in 8% PEG was qualitatively identical to the fresh-frozen (Fig 4).

DISCUSSION

This study finds that 8% PEG maintains hydration (Fig 1,2), tensile modulus (Fig 3), and microstructure (Fig 4) of the fresh-frozen state. It is thus an appropriate buffer solution for long mechanical tests such as fatigue. The slight change in relaxation is probably due to lack of ionic content in the buffer, which causes entropic diffusion of ionic tissue constituents into the buffer. Using small ionic content in the buffer solution might help overcome this issue. Nonetheless, use of PEG solution for long-term mechanical fatigue tests is recommended.

In contrast to PEG, normal saline (0.15M = 0.9% NaCl) swells the tissue considerably and rapidly (Fig 1), which increases the spacing between collagen fibrils (Fig 4) and lowers the modulus (Fig 3) compared to fresh-frozen samples. This is consistent with previous work in meniscus [1]. A higher concentration of 25% NaCl maintains the apparent water content to the fresh-frozen level (Fig 1). However, at this concentration solutes diffuse into the tissue (Fig 2), demonstrating that the true water content is actually greater than the fresh-frozen level. These behaviors are problematic because the rapid initial dehydration causes an elevated "untreated" modulus (with 15 min in solution) for the 25% NaCl compared to the other untreated solutions (Fig 3). With additional time in solution, solutes diffuse into the tissue, the apparent water content increases (Fig 1) and the modulus decreases (Fig 3). There is likely a mechanical effect due to the large influx of NaCl into the tendon that would confound fatigue studies of long duration. Thus NaCl-based buffers, whether normal saline or increased concentration, are not suitable for long tests.

ACKNOWLEDGEMENTS

This study was funded by NIH grant R01 EB002425.

REFERENCES

[1] Han et al., *Ann. Biomed. Eng.* 40:1610–21. 2012. [2] Mehta et al., *Colloids Surf. B. Biointerfaces*, 117:376–82, 2014. [3] Wang et al., *J. Exp. Biol.*, 198: 847–52, 1995. [4] Lujan et al., *Appl. Physiol.*, 106:423–31, 2009.

Copyright 2016 The Organizing Committee for the 2016 Summer Biomechanics, Bioengineering and Biotransport Conference

SB³C2016
Summer Biomechanics, Bioengineering and Biotransport Conference
June 29 –July 2, National Harbor, MD, USA
SB³C2016-1038

PROJECT-BASED BIOMECHANICS LABORATORIES: THEORY AND PRACTICE

Kristen L. Billiar and Glenn R. Gaudette

Department of Biomedical Engineering
Worcester Polytechnic Institute
Worcester, MA, USA

INTRODUCTION

Problem-based instruction offers one of the most effective means of facilitating learning by compelling students to solve authentic problems through a self-discovery process. In biomedical engineering (BME), there has been intense activity in problem-based learning instruction in the educational literature [1-4]. When there are multiple solutions to a problem and teamwork is required to solve the problem, we term the process project-based learning. Problem-based learning appears to be especially well suited for BME laboratories where quantitative measurements of complex and variable biological systems are required [3].

In particular, the biomechanics laboratory provides an authentic context for students to attack their problems and an opportunity to observe how the physical world compares to the theoretical descriptions taught in the classroom [3]. Use of biological test specimens and industry-standard test machines introduces the students to the difficulty in sample preparation and gripping and the complexity of dealing with non-linearity, non-homogeneity, and variability inherent in biomechanical measurements. The variability of biological specimens naturally leads to the necessity of statistical treatment of the data for hypothesis testing.

The goal of this work was to develop a structured problem-based learning experience for junior-level biomedical engineering undergraduate students to facilitate self-directed learning of solid biomechanics theory while developing practical mechanical testing skills. There was also a strong focus on aiding each student in making progress in problem identification, fitting data to mathematical models, testing hypotheses statistically, communicating the results and conclusions of experiments, and working in teams.

METHODS

Over the past 10 years, we approached our educational challenge in various ways within the unique, fast-paced 7-week term structure at our institution. Here, we focus on our latest and most successful iteration which aligns well with a standard 14-week semester. In the Discussion, comparisons with previous iterations are provided along with practical advice for incorporation into existing curricula.

Biomechanical analysis theory and practice

For the first half of the learning experience, the students review stress analysis and learn how to use a uniaxial materials test frame (Instron 5544). To aid the students in reviewing stress analysis theory, with a focus on biological tissues, we provided the students with lectures (often online) and reading materials once per week. Topics include analysis of non-linear stress-strain curves, viscoelasticity, and beam-in-bending. In parallel, demonstrations of how to operate the equipment safely are provided during class time (once per week), and pre-recorded videos covering the same material are provided as written instructions and as videos online (Figure 1a) so that the students can review the methods at their own speed. Access to the videos is facilitated by QR-codes (Figure 1b) which link to the YouTube channel. Detailed videos demonstrating the use of the industry-standard Bluehill software are also provided (Figure 2). The third class period each week is dedicated to data analysis in Matlab.

The student learning is assessed with individual and team homework assignments focused on analyzing mechanical data that they generate from samples of plastic, leather, and wood. In the seventh week, the students complete a final practicum and report involving testing and analyzing tendon or bone material properties. Throughout

Copyright 2016 The Organizing Committee for the 2016 Summer Biomechanics, Bioengineering and Biotransport Conference

the term, instruction in effective communication is provided including comments on formative drafts and presentations.

a) b)

Figure 1: a) Video tutorials detailing how to use the equipment safely are provided via a YouTube channel. b) QR-codes linking to the videos are posted in the lab for quick smartphone access.

Figure 2: Video tutorials for using the software are also posted.

Project-based approach

At the beginning of the second half of the course (which, at WPI is a new term), a potential design to solve an authentic clinical problem is posed, and the students are tasked with determining the mechanical feasibility of the design. For example, students were given decellularized aortas and asked to determine if they have sufficient mechanical properties to warrant further development as a vascular graft material. To solve the challenges, the students work in 3- or 4-person teams to research the problem in medical and engineering literature and develop a testing protocol. They then complete experiments to test their hypotheses and/or validate the designs. The majority of class time is used to discuss the proposal, experimental design, report and poster in various draft stages and to provide formative feedback. In the final week of the term, they present their findings to their peers both orally and in writing.

RESULTS AND DISCUSSION

Overall, the students learned how to mechanically characterize a biological tissue, and efficiently perform uniaxial mechanical testing (Figure 3) to complete a controlled experiment (including statistical analysis). They also progressed substantially in their ability to communicate their goals, means, and conclusions. This project-based course is writing and teamwork intensive by necessity which benefited the students greatly, but also required a large amount of time from both the students and instructor. However, the video tutorials helped reduce the amount of time required for training during class time, and the recorded mini-lectures also allowed class time to be used for discussion and working through problems (a.k.a., flipped format).

The students reported that the homework assignments in the first half of the class were very helpful in clarifying how the theory could be utilized to analyze experimental data. These assignments facilitated progressively more complex use of the testing software and Matlab analysis tools.

The grading of the written assignments was made as objective as possible by using a set of grading rubrics (based on Newstetter [2]) which also served to clarify the requirements of each assignment for the students. The students appreciated learning how to write a range of professional formats.

Figure 3: Picture of a ring of aortic tissue being tested.

Based on student feedback and our personal observations, the current iteration of the course is the most successful. In the first iteration, two separate challenges were assigned to the students to solve in a single 7-week course. Although this offering was an intensive 5-day-a-week course worth a full 3 credits, the students felt too rushed to propose a solution, complete the testing, and communicate the solution all in 3 ½ weeks, then do it all over again in the next 3 ½ weeks. In response, we created a semester-long offering, consisting of two 1.5 credit 7-week courses, each with a separate challenge posed (one regarding bone, the other blood vessels). Students were able to solve two separate authentic challenges, but they reported that they did not get enough practice with using software on machine to be able to use it on their own in the future (e.g., for senior design projects or undergraduate research). In the current format of the course sequence, the student report that they become sufficiently skilled in using the industry-standard equipment and software in the first half of the course to solve an authentic challenge in the second half of the course (and in their senior design projects as well).

CONCLUSION

We have created a laboratory course which reinforces biomechanical engineering theory with authentic problem-based experimentation, and provides a scaffolded, mentored experience for learning. The breadth of subject matter that could be covered was less than in a standard didactic course, and some students wanted more lectures rather than learning the theory on their own from the posted materials. However, we found that when working in the laboratory in teams without the instructor present where they have to learn from their failures and re-engineer solutions for their setback, the student learn more effectively, as shown previously [5].

ACKNOWLEDGEMENTS

Special thanks to Dr. John Wixted, M.D., University of Massachusetts Medical School (currently at Harvard Medical School) and Nicholas Deangelis, University of Massachusetts Memorial Hospital, for posing the challenges orthopaedic-themed challenges.

REFERENCES

[1] Harris T, et al., Ann Rev BME;, 4:29-48, 2002
[2] Newstetter W. Whitaker Educational Summit; 2005.
[3] Perreault E, et al., Whitaker Educational Summit, 2005.
[4] Roselli R, Brophy S. IEEE Eng Med Biol Mag 22(4):66-70; 2003
[5] Feisel L, Rosa A. J Engr Education; 94(1):121-130, 2005.

Copyright 2016 The Organizing Committee for the 2016 Summer Biomechanics, Bioengineering and Biotransport Conference

SB³C2016
Summer Biomechanics, Bioengineering and Biotransport Conference
June 29 –July 2, National Harbor, MD, USA
SB³C2016-1039

BAYESIAN APPROACH TO MODEL SELECTION AND SURROGATE MODELING: APPLICATION TO TRAUMATIC BRAIN INJURY SIMULATIONS

Sandeep Madireddy, Kumar Vemaganti

Department of Mechanical and Materials Engineering
University of Cincinnati
Cincinnati, Ohio 45221-0072

INTRODUCTION

Traumatic brain injury simulations are complex and computationally challenging. Among the challenges are the large uncertainty in the material testing data, uncertainty in the material constitutive model parameters, high strain rates and the short time scales of the impact loading, and the complex geometry of the human brain model.

We propose a Bayesian approach to objectively selecting a constitutive model for the brain tissue, taking into account the nonlinear visco-hyperelastic and rate-dependent effects. This approach also provides a probabilistic method to material parameter evaluation in order to obtain the uncertainty associated with them.

The uncertainty in the material model parameters is propagated using the SIMon finite element head model [1] to obtain the uncertainty in the maximum principal strain-based brain injury criterion. As the finite element model is computationally expensive, we resort to a Gaussian process surrogate model for the injury criterion as a function of the material model parameters.

Our results show that the proposed method can be used for material model selection and parameter estimation in a quantitative manner. Also the surrogate model based uncertainty propagation provides a probabilistic approach to calculating injury criteria. We provide a framework to report the probability that the injury tolerance is reached for a given impact loading.

MATERIALS AND METHODS

Brain tissue is assumed to be an isotropic and nonlinear visco-hyperelastic. The constitutive relations are obtained using the formulation described in [2] where the hyperelastic behavior, short-term viscoelastic behavior, and long-term viscoelastic behavior are all modeled explicitly:

$$\sigma(t) = \sigma_e(\mathbf{C}(t)) + \sigma_v(\dot{\mathbf{C}}(t), \mathbf{C}(t)) + \mathbf{F}(t)\mathcal{G}\{t-s, \mathbf{C}(s)|_{s=\delta}^{s=\infty}\}\mathbf{F}(t)^T \quad (1)$$

where σ_e, σ_v are the hyperelastic and short-term viscoelastic contributions to the Cauchy stress respectively given by:

$$\sigma_e(\mathbf{C}(t)) = 2\mathbf{F}(t)\frac{\partial \Psi_e}{\partial \mathbf{C}}\mathbf{F}(t)^T,$$

$$\sigma_v(\dot{\mathbf{C}}(t), \mathbf{C}(t)) = 2\mathbf{F}(t)\frac{\partial \Psi_v}{\partial \dot{\mathbf{C}}}\mathbf{F}(t)^T$$

where ψ_e, ψ_v are the elastic strain energy and short-term viscoelastic dissipation potentials and $\mathbf{F}$ is the deformation gradient, $\mathbf{C}$ is the right Cauchy-Green deformation tensor and $\dot{\mathbf{C}}$ is its time derivative.

The function ψ_e in this study is selected from among

$$\Psi = \sum_{i=1}^{N} \frac{2\mu_i}{\alpha_i^2}(\lambda_1^{\alpha_i} + \lambda_2^{\alpha_i} + \lambda_3^{\alpha_i} - 3)$$

$$\Psi = B_1(\exp(B_2(I_1 - 3)) - 1) \qquad \Psi = C_1(I_1 - 3) + C_2(I_2 - 3)$$

where I_k are invariants of $\mathbf{C}$. The dissipation potential ψ_v used in this study is

$$\Psi_v = \eta J_2(I_1 - 3)$$

where J_2 is the second invariant of $\dot{\boldsymbol{C}}$. The third term in (1) is the long-term viscoelastic contribution given by:

$$\mathcal{G}\{t-s, \mathbf{C}(s)|_{s=\delta}^{s=\infty}\} = \int_{\delta}^{\infty} \mathcal{G}(t-s, s, \mathbf{C}(s))\, ds$$

The relaxation function is chosen to a 3-term Prony series whose parameters are obtained by using the relaxation test data from [3]. The hyperelastic model form is selected using experimental response at a constant strain rate of 1/s. Four candidate models are considered for model selection: Ogden (N=1,2), exponential, Mooney-Rivlin. Model selection is done using the nested sampling-based Bayesian model selection approach outlined in [4]. The parameters in the selected hyperelastic model, short term viscoelastic model and their uncertainties are obtained using the Bayesian approach outlined in [5]. The unconfined compression test data at strain rates of 1/s, 10/s and 50/s are used to to obtain the parameter distributions.

Further, this material model is implemented into LS-Dyna [6] finite element software using a UMAT subroutine. This material model is used to model the soft tissue in the SIMon model. The loading corresponds to a frontal impact vehicle crash test.

The Bayesian Gaussian process model is used to fit a surrogate model:

$$\mathbf{Y(s)} = \boldsymbol{\mu(s)} + \mathbf{w(s)} + \boldsymbol{\epsilon(s)} \quad (2)$$

where $\mathbf{Y}$ is the response (injury criterion), $\mathbf{s}$ is the input parameter vector, $\boldsymbol{\mu}(\mathbf{s}) = \mathbf{X}^T(\mathbf{s})\boldsymbol{\beta}$ is the mean surface, and $\mathbf{w}(\mathbf{s}) = \mathrm{N}(\mathbf{0}, \mathbf{C}(\theta))$ is the spatial correlation represented by a multivariate normal distribution and $\boldsymbol{\varepsilon}(\boldsymbol{s}) = N(\mathbf{0}, \tau^2\mathbb{I})$ is the nugget term.

The input parameters used for the surrogate are the material parameters corresponding to the hyperelastic and short-term viscoelastic contributions. The parameters in long-term viscoelasticity are neglected under the assumption that their effect is not significant in an impact loading. The response is the maximum principal strain-based injury criterion. The data for the surrogate model fitting are obtained by Latin hypercube sampling 104 points, using 90 for fitting and 14 for validating the surrogate. The parameters are obtained using the same procedure as the calibration of material model parameters.

The uncertainty in the material parameters is non-intrusively propagated to the injury criterion using the surrogate model. This is done using the Monte Carlo approach.

RESULTS AND DISCUSSION

The model selection statistics, and the model ranks for the four hyperelastic model forms considered in this study is shown in Table 1. The exponential model is seen to describe the hyperelastic response with

Copyright 2016 The Organizing Committee for the 2016 Summer Biomechanics, Bioengineering and Biotransport Conference

highest Bayesian evidence. Hence we choose this model with parameters B_1, B_2 hereafter to describe hyperelasticity. However, the traditional least squares approach (equivalent to log-likelihood) prefers the Ogden (N=2) model, which is found to over-fit the data.

Material model	Max log-likelihood	log-evidence	Model-Rank
Mooney-Rivlin	2.644	-9.502	Rank 3
Exponential	2.162	-6.078	Rank 1
Ogden ($N=1$)	2.529	-7.476	Rank 2
Ogden ($N=2$)	2.955	-13.282	Rank 4

Table 1: Model selection statistics and ranks for the hyperelastic material model forms

The maximum likelihood estimate (MLE) of the Prony series parameters obtained are shown in Table 2.

G_1	$\tau_1(s)$	G_2	$\tau_2(s)$	G_3	$\tau_3(s)$
4.168	1.512 E-02	0.828	2.833 E-01	0.606	1.732

Table 2: MLE of the Prony series parameter distributions

The posterior distributions of the material parameters B_1, B_2, η are obtained by fixing the Prony series parameters are shown in Fig. 1.

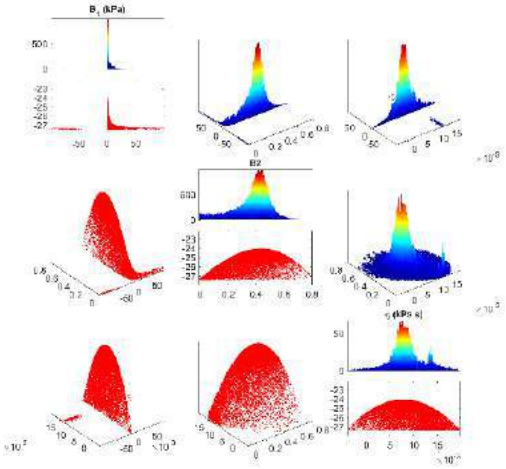

Figure 1: Material model parameters and their uncertainties.

In order to simulate traumatic brain injury, the angular velocity about y-axis is given as the load (see Fig. 4), because of its contribution to brain injury in frontal impact, and our interest in studying the correlation between the loading and the injury criteria.

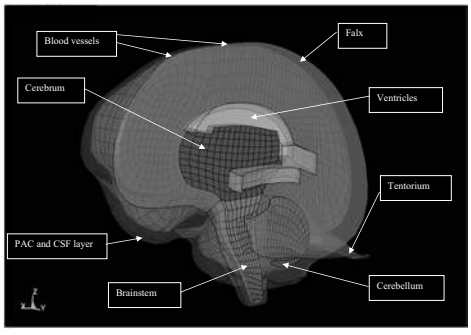

Figure 2: Simon finite element head model [1]

The maximum principal strain (MPS) as a function of time for the original SIMon finite element model (Fig. 2) and the one with MLE of visco-hyperelastic material parameters is shown in Fig. 3. This is for the element with the maximum principal strain over the duration of impact. The peaks in the MPS are the same for both models and they correspond to the peaks in the Y angular velocity. The reason for the differences in the responses can be attributed to the material properties.

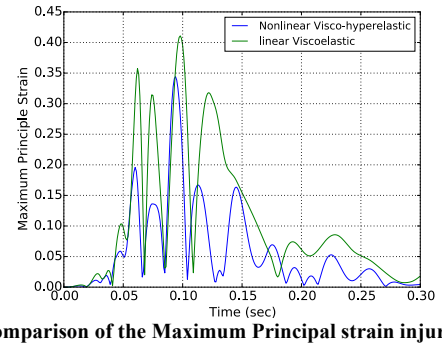

Figure 3: Comparison of the Maximum Principal strain injury criteria for the SIMon model with linear viscoelastic and nonlinear visco-hyperelastic material properties for the soft tissue

In order to build the surrogate, deterministic finite element simulations are run using the SIMon finite element head model for all the 104 samples described in the previous section. The parameter ranges used for sampling are within the bounds of the uncertainties seen in Fig. 1. The Gaussian process surrogate is built using the data and the uncertainty in the material parameter distributions (Fig. 1) is propagated to the injury criterion. The uncertainty in the injury criteria is shown in Fig. 4.

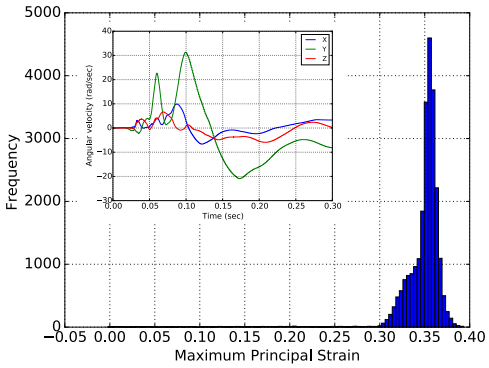

Figure 4: Uncertainty in maximum principal strain-based injury criterion.

This enables us to calculate the probability that an injury tolerance is reached for a given impact loading. This probabilistic method can be used to further simulate injury and calculate injury criteria with higher fidelity.

ACKNOWLEDGEMENTS

We are grateful to the UC Simulation center for providing financial support for this work.

REFERENCES

[1] Takhounts, EG, et al., Stapp Car Crash journal, 2008.
[2] Pioletti, DP et al., European J Mechanics A-solids,, 2000.
[3] Tamura, A et al., J Biomech. Sci. and Engg., 2007.
[4] Madireddy, S et al., Comp. Meth. in Applied Mech & Engg., 2015.
[5] Madireddy, S et al., J. Mech Behavior Biomed Matl., 2016.
[6] Hallquist, JO et al. LS-Dyna theory manual, LSTC, 2006.

Copyright 2016 The Organizing Committee for the 2016 Summer Biomechanics, Bioengineering and Biotransport Conference

SB³C2016
Summer Biomechanics, Bioengineering and Biotransport Conference
June 29 –July 2, National Harbor, MD, USA
SB³C2016-1040

SITE- AND FORCE-DEPENDENT STRAIN BEHAVIOR IN THE PORCINE ANTERIOR CRUCIATE LIGAMENT

Satoshi Yamakawa (1), Richard E. Debski (2), Hiromichi Fujie (3)

(1) Division of Human Mechatronics Systems,
Graduate School of System Design,
Tokyo Metropolitan University
Tokyo, Japan

(2) Bioengineering Department,
Faculty of Engineering,
University of Pittsburgh
Pittsburgh, PA, USA

(3) Department of Intelligent Mechanical
Systems, Faculty of System Design,
Tokyo Metropolitan University
Tokyo, Japan

INTRODUCTION

Quantitative data on the strain behavior of the anterior cruciate ligament (ACL) in response to knee loads are necessary for better understanding of biomechanics of the ACL and the improvement of ACL reconstruction. Although important data were obtained in previous studies[1, 2], physiological knee motion and loading were not simulated due to experimental limitations. Therefore, the objective of the present study was to apply both a robotic system for mechanical testing of biological joints and a motion tracking system based on the image correlation method to the determination of site-dependent strain in the ACL, specifically in the attachment area on the femur and tibia, during anterior translation of the knee.

METHODS

A 6-DOF robotic system consisting of a custom-made 6-axis manipulator with a 6-DOF universal force/moment sensor (UFS)[3] was used. In the system, a LabView-based control program runs on a windows PC to control the displacement of, and force/moment applied to, the cadaveric knees with respect to the knee joint coordinate system[4]. Porcine knees (n=8) were dissected down to the joint capsule and fixed to the robotic system, and were subjected to the anterior drawer test up to 50 N at full extension. During the test, the anterior-posterior DOF was translated under displacement control at a rate of 0.1 mm/s while all the DOFs except the AP and flexion-extension DOFs were set under force control with prescribed force/moment at zero. After the lateral condyle was removed for the observation of the ACL the intact knee motions were reproduced. The medial view of the ACL surface during the test was recorded with a CCD camera. Using a motion tracking system based on the image correlation method (VW-9000, KEYENCE, Osaka, Japan), the surface deformation of the ACL including the attachment area to the femur and tibia was analyzed. In the recorded image, the ACL was transversely divided into 5 portions; 0-10%, 10-20%, 20-80%, 80-90% and 90-100% of the length from the femoral attachment, and was longitudinally divided into 5 portions from anterior to posterior fibers (Figure 1). Multiple markers were placed at the anterior and posterior edges in each portion on the recorded image, and length change between the markers were calculated to analyze local strains. Using the same method as for the surface layer, the strain distributions of the middle and deep layers were determined after the removal of the medial and the middle layers. Note that zero strains (no deformations) were defined for the knee located at full extension with 1.0 Nm of extension moment.

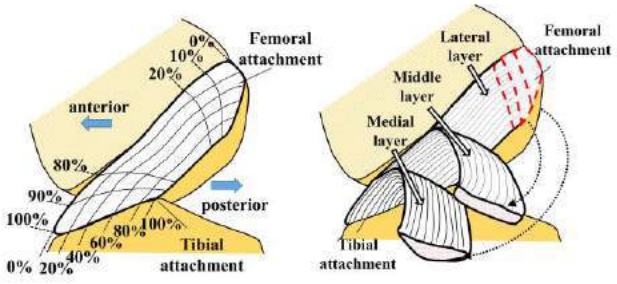

Fig.1 Twenty five portions on the ACL surface layer for the calculation of strain distribution, and sequential removal of the surface and middle layers for the measurement of 3-D strain distribution

In the present study, the behavior of the ACL surface in sub-ligament level was observed using a light microscope (VHX-1000, KEYENCE, Osaka, Japan). The porcine ACL with bone fragments (n=3) was carefully dissected and was fixed to a metal stage under the application of 0.1 N of tensile force. The ACL surface was observed at 0.1 N (unloading condition), 20 N and 40 N (loading condition). By

Copyright 2016 The Organizing Committee for the 2016 Summer Biomechanics, Bioengineering and Biotransport Conference

tracking distinctive features of the structure pattern, ACL strain in sub-ligament level in the medial layer was analyzed.

RESULTS

Result revealed that the tensile strain was larger in the ACL attachments (0-20% and 80-100%) than in the mid-substance (20-80%) in all the layers. In the medial layer, the largest strain was 8.0% observed in the tibial attachment on the posterior fiber (Fig.2). Strain distributions in the middle and lateral layers were similar to that in the medial layer, with the largest strain observed on the posterior fiber in the tibial attachment area in the middle layer (6.4%) and on the anterior fiber in the femoral attachment area in the lateral layer (7.7%). Strain on the anterior fiber in the medial layer as a function of applied anterior force is indicated in Fig.3. In the femoral and tibial attachment areas, strain increased rapidly up to 6-8% by the inflection points around 20 N and 30 N of anterior force, then increased slowly thereafter. In contrast, strain increased slowly and gradually without distinct inflection point in the mid-substance area. This force-dependent change in strain increase was observed in all the fibers in all the layers.

Microscopic observation in the present study indicated that the periodic patterns (crimp structure) at a right angle to the fiber direction were recognized in unloaded condition. The ACL strains were 8.8% and 13.8% in the femoral attachment area, and 2.6% and 5.2% in the mid-substance at 20 N and 40 N of tensile force, respectively (Fig.4).

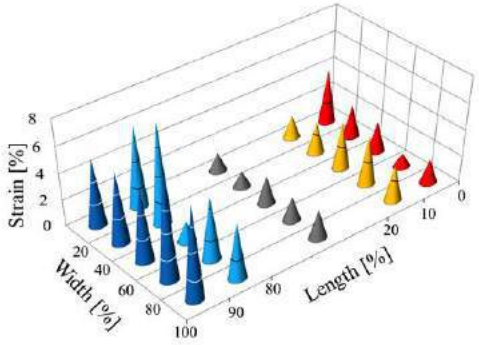

Fig.2 Strain distribution in the medial layer in response to 50 N of anterior force to the knee

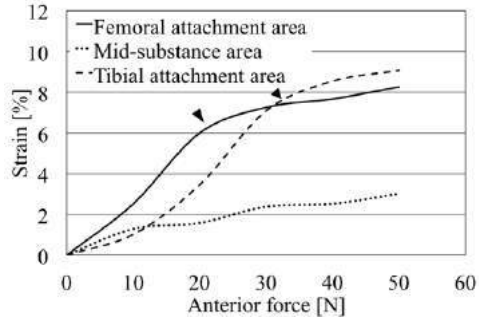

Fig.3 Strain on the anterior fiber in the medial layer as a function of anterior force. Inflection points are indicated by triangles around 20 N and 30 N of anterior force in the femoral and tibial attachment areas.

DISCUSSION AND SUMMURY

The 3-D strain distribution in the ACL in response to anterior drawer force to the knee was determined in the present study using the 6-DOF robotic system and the motion tracker. We succeeded to obtain a detailed 3-D map of site-dependent strain data in the ACL. In previous studies, video tracking systems were often involved to measure deformation and strain in soft tissues. Although high resolution measurement was possible with the system, there was limitations in position and number of markers. It was also problematic in video tracking systems that marker motion relative to tissues affect experimental results. These problems are solved in the present study by the use of the motion tracking system. Since it is possible with the method to select unlimited arbitrary points for tracking after video recording without marker on the surface, detailed and precise analysis of local strain in the ACL surface is possible under physiological conditions.

Results revealed that ACL strain is site-dependent in all the fibers in all the layers; it is higher in the attachment area than in the mid-substance. Results also revealed that there are two phases in ACL strain change in the femoral and tibial attachment areas; a rapid increase to approximately 6-8% at the beginning of force application followed by a slow increase thereafter. Interestingly, such force-dependent strain change is not observed in the mid-substance. It is well known that ligament and tendon tissues have the crimp structure at the sub-ligament and sub-tendon level. Franchi et al reported that the crimp structure is more located in both ends of ligaments and tendons than in mid substance[5]. Weiss et al reported that a wavy crimp structure was found in the proximal one quarter of the ACL[6]. Microscopic observation in the present study indicated that crimp structures exist in all areas of the ACL, while change in crimp strain is site- and force-dependent in the same way as macro ACL strain; a rapid increase in the attachment areas while a gradual increase in the mid-substance at the beginning of force application. These results suggest that the 3-D strain in the ACL is site- and force-dependent probably due to unevenness in both distribution and property/function of crimp structures. In addition, it is suggested that the ACL crimp structure plays more important role in ACL behavior and function in the femoral and tibial attachment areas than in the mid-substance. Because of the behavior and function of the ACL attachment, the contribution of the ACL to knee stability is probably maintained at any physiological knee postures.

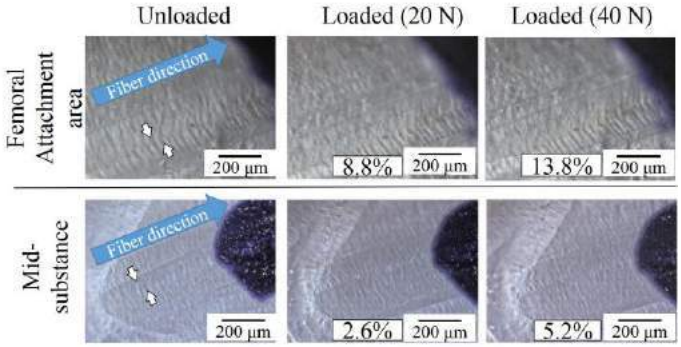

Fig.4 Observation of the crimp structures in the femoral attachment area and the mid-substance of the porcine ACL with crimp strain magnitude observed at 20 N and 40 N of tensile force. Typical periodic pattern of the crimp structure is indicated by white arrows.

ACKNOWLEDGEMENTS

The present study was financially supported by the Grant-In-Aid for Scientific Research B (#25252134) and Challenging Exploratory Research (#26560218) both from the MEXT, Japan.

REFERENCES

1) Yamamoto K., et al., Medical Engineering & Physics, 1998
2) Spalazzi J.P., et al., Wiley InterScience, 2006
3) Fujie H., et al., J. Biomech. Eng. (ASME), 2004
4) Grood, E.S. and Suntay, W.J., J. Biomech. Eng. (ASME), 1983.
5) Franchi M., et al., Connect Tissue Res., 2012.
6) Weiss M., et al., Knee Surg. Sports Traumatol Arthrosc., 2012.

Copyright 2016 The Organizing Committee for the 2016 Summer Biomechanics, Bioengineering and Biotransport Conference

SB^{3}C2016
Summer Biomechanics, Bioengineering and Biotransport Conference
June 29 –July 2, National Harbor, MD, USA
SB^{3}C2016-1041

COMPUTATIONAL FLUID DYNAMICS PREDICTIONS OF PRESSURE LOADING ON THE HUMAN HEAD IN A LABORATORY-BASED BLAST TEST METHODOLOGY

Rubbel Kumar (1), Ashish Nedungadi (1), Catherine M. Carneal (1), Marina Carboni (2), Jonathan Cyganik (2), Michael A. Maffeo (2)

(1) Johns Hopkins University, Applied Physics Lab
Laurel, MD, USA

(2) United States Army
Natick Soldier Research Development and Engineering Center
Natick, MA, USA

INTRODUCTION

A laboratory blast simulator is being established to mimic the primary overpressure magnitude and impulse loading on the head surface, in a manner representative of free-field explosive events selected to isolate the primary shock front. A validated Computational Fluid Dynamics (CFD) model has been established as a design tool to aid the understanding of flow within the ABS system, and characterize the applied pressure loading to a bare headform. Ultimately this model will be used to augment experimental findings to fully understand the influence of headborne systems on pressure applied to the human head, and to support the design of optimized laboratory test methodologies for helmet evaluation which are accurately representative of a broad range of free-field blast events [1].

METHODS

An existing experimental shock tube design, the Advanced Blast Simulator, has been modified to achieve a 3 foot cross-sectional test area capable of evaluating a helmeted headform internal to the system [2] with minimal effects from sidewall reflections. This system consists of driver, transition, test, and diffuser sections [3], with a membrane material inserted between the driver and downstream components. The driver section is pressurized with gas (air or helium) until diaphragm rupture. Gas escapes and forms a shock front that generates the representative pressure signature upon striking the model in the test section. Concurrently, a human surrogate headform representative of an average male surface geometry was fabricated and instrumented with surface sensors to experimentally measure the pressure loading applied to the headform when tested in the modified ABS system. A simplified schematic of the ABS with headform is shown in Figure 1.

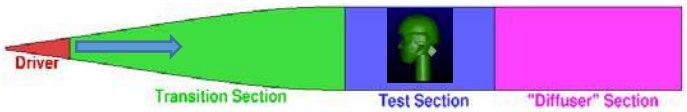

Figure 1: Advanced Blast Wave Simulator

To support the current study objectives, Computer-Aided Design (CAD) models for the shock tube and human head surrogate were used to generate computational meshes. Time accurate CFD simulations with 2nd order spatial accuracy were run using a time-step of 1 microsecond in Metacomp's commercial code, CFD++. Simulations of the ABS operations were implemented with the diaphragm modeled as an ideal rupture [4]. Experimental test data at diaphragm burst pressure was used to initiate the simulations. Pressure-time traces were qualitatively compared between the experiment tests and CFD models both without headform (two-dimensional or 2D model) and with headform (three-dimensional or 3D model) in the test section.

RESULTS

A comparison plot between the 2D CFD model and experiment with an empty test section is shown in Figure 2. This model was subsequently expanded to include the headform for this study, and CFD predictions for 188 psi burst pressure compared with experimental data (Figure 3). The verified model was then used to depict the maximum pressure experienced on the discretized head surface for each local point at any given time (Figure 4).

Copyright 2016 The Organizing Committee for the 2016 Summer Biomechanics, Bioengineering and Biotransport Conference

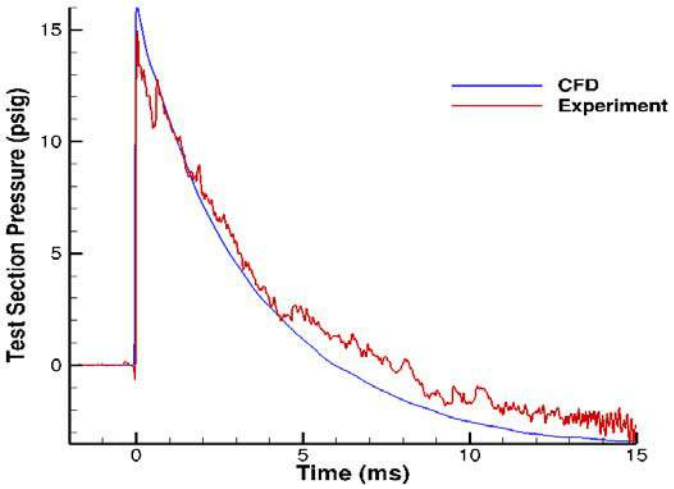

Figure 2: 2D CFD Model Comparison with Experimental Data

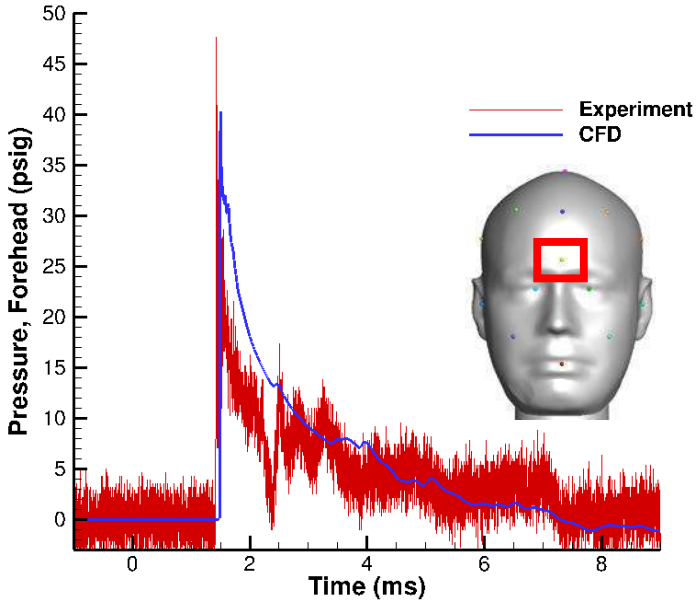

Figure 3: 3D CFD Model Comparison with Experimental Data

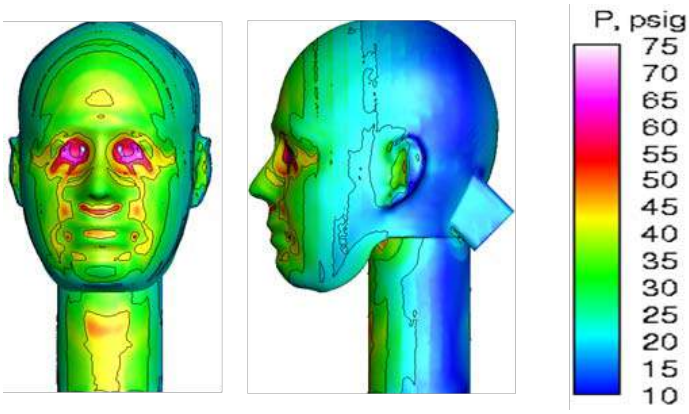

Figure 4: Maximum Pressure Isosurface Map on Head Geometry

DISCUSSION

The 2D CFD model was verified with experimental data using pressures observed in the test section. This model was tailored to replicate the experimental set-up by applying a curvature to the diaphragm to simulate a bulging diaphragm prior to rupture. This allowed the model to capture the true energy level of the driver section of the shock tube immediately before the diaphragm ruptures. Despite this, it is important to note that the CFD still models an ideal and immediate diaphragm rupture.

The results of the 3D CFD model with the headform were in good agreement with experimental data. The maximum pressure envelope plot indicates the eyes experience the largest pressures by a significant margin – more than double the pressure on the nose. This is likely due to the curvature of the head, which encourages pressure build-up in the eye socket. The relatively lower pressures elsewhere are justified because the local geometry would encourage the flow to move past the area. Local valleys in the front-facing geometry of the head are areas corresponding to higher pressure build up. These results indicate what areas of the human head may be most vulnerable for a frontal overpressure exposure.

Helmets are worn by ground troops in combat situations, so it is important to understand the pressure loading for different orientations of overpressure exposure. Ongoing work includes the implementation of a helmet system into the model, and the assessment of pressure loading on the human head in multiple orientations. The model will be used to aid the comparison of blast loading on the head with and without personal protective equipment, and supplement insights from experimental data to fully assess the influence of helmet systems.

ACKNOWLEDGEMENTS

The authors would like to thank the United States Army Natick Soldier Research Development and Engineering Center for sponsoring this effort.

REFERENCES

[1] Ganpule S. et al., *Computer Methods in Biomechanics and Biomedical Engineering,* 15:1233-1244 , 2011

[2] Ritzel, D. V., and Steven Parks. SHOCK TUBE APPARATUS FOR BLAST WAVE SIMULATION. ORA, INC., assignee. Patent 2013/0042665. 2013.

[3] Reneer, D. V. et al., *Journal of Neurotrauma,* 28:95–104, 2011

[4] Chandra N. et al., *Shock Waves,* 22:403-415, 2012

Copyright 2016 The Organizing Committee for the 2016 Summer Biomechanics, Bioengineering and Biotransport Conference

SB^{3}C2016
Summer Biomechanics, Bioengineering and Biotransport Conference
June 29 –July 2, National Harbor, MD, USA
SB³C2016-1042

DYNAMIC IMAGING OF TENDON TISSUE STRESS

Jack A. Martin (1)
Alexander C. Ehlers (2), James R. Hermus (2), Matthew S. Allen (3,4), Daniel J. Segalman (3*)
Darryl G. Thelen (1,2,4)

(1) Materials Science Program
University of Wisconsin-Madison
Madison, WI, USA

(2) Department of Biomedical Engineering
University of Wisconsin-Madison
Madison, WI, USA

(3) Department of Engineering Physics
University of Wisconsin-Madison
Madison, WI, USA

(4) Department of Mechanical Engineering
University of Wisconsin-Madison
Madison, WI, USA

*Currently professor of mechanical engineering at Michigan State University, East Lansing

INTRODUCTION

An understanding of tendon tissue loads is critically important for investigating musculoskeletal disorders. However, it remains very challenging to assess tendon stress during functional movement. Modeling approaches rely on assumptions regarding musculoskeletal geometry, tissue morphology, and muscle coordination [1]. Further, current measurement approaches are highly invasive [2], and thus are not practical for widespread use. We are exploring the potential of noninvasive wave propagation measurements for assessing tendon tissue stress under dynamic loading conditions. Such an approach could dramatically extend our ability to characterize functional tissue loads that are relevant to the diagnosis and treatment of tendon injury and disease. The specific objectives of the current study are twofold:

1) To characterize the theoretical relationship between shear wave speed (SWS), material properties, and normal stress in axially loaded, transverse isotropic tissue. In current clinical shear wave elastography (SWE) systems [3], SWS (v) is assumed to be strictly dependent on tissue shear modulus (μ) and density (ρ):

$$v = \left(\frac{\mu}{\rho}\right)^{1/2} \quad (1)$$

Recent work would suggest that this simple relationship is invalid in tendon, where SWS increases significantly with tendon stretch [4].

2) To empirically test the theoretical relationship between wave speed, material properties, and tissue stress. To accomplish this, a novel ultrasound-based imaging method was used to track waves induced via impulsive mechanical excitation of a mechanically loaded *ex vivo* tendon. The use of ultrasound provides a basis to extend the approach to *in vivo* conditions, which would allow for the characterization of tendon tissue loads during functional movement.

METHODS

Wave Propagation Model – Tendon was modeled as a tensioned Timoshenko beam with constant cross-sectional area. The Timoshenko beam accounts for both shear elasticity and rotational inertia effects. Transverse isotropic elastic material properties and negligible bending stiffness were assumed. With these assumptions, SWS (v) is dependent on shear elastic modulus (μ), effective density (ρ_{eff}), a shear correction factor (k'=0.9), and importantly, axial stress (σ):

$$v = \left(\frac{k\,\mu+\sigma}{\rho_{eff}}\right)^{1/2} \quad (2)$$

Equation 2 assumes small motion about the stressed state, such that μ is defined as the tangential shear modulus. For this study, we assumed a constant shear modulus (μ=150kPa) based on values for ligament under moderate shear strain [5].

Based on a classical result [6], the effective mass per unit length of a beam vibrating in a viscous fluid can be approximated as,

$$\frac{m_{eff}}{L} = \rho_t A + \rho_f \left(\frac{\pi}{4} b^2\right) \Gamma_r \quad (3)$$

where ρ_t (=1200g/cm^3) is the density of the tendon tissue, ρ_f (=1200g/cm^3) is the fluid density, b is the width of the tendon perpendicular to the direction of motion, A is the cross-sectional area of the tendon, and Γ_r is the real part of the hydrodynamic function (=1.01 to 1.04 over the frequencies of interest for tendon). Rearrangement of equation 3 yields an effective density, ρ_{eff} :

$$\rho_{eff} = \rho_t + \frac{\pi b^2 \Gamma_r}{4A} \rho_f \quad (4)$$

The ratio, $\pi b^2\,\Gamma_r/4A$, was set at a constant value based on the average ratio measured in the tendons tested ($= 0.62$).

***Ex Vivo* Validation** – The model was tested by measuring wave speeds in 12 porcine digital flexor tendons axially loaded using a

Copyright 2016 The Organizing Committee for the 2016 Summer Biomechanics, Bioengineering and Biotransport Conference

mechanical test system (MTS Acumen 3). Tendons were immersed in physiological saline and gripped at each end using stainless steel waveform grips (Test Resources G240KSS). Tendons were loaded sinusoidally from 10 to 300N at 1Hz. Tendon stress was calculated by dividing applied force by initial cross-sectional area. Tendons were assumed to be elliptical in cross-section and area was calculated based on the width of the major and minor axes at 3 locations spaced evenly along the length of the unloaded tendon.

Shear waves were generated using a piezoelectric actuator (Thorlabs PK4JQP1, 19.8μm motion) housed in a 3D printed mechanical tapping device (Fig. 1A). Tendons were tapped at 25Hz with a 1ms pulse width. A linear array ultrasound transducer (Ultrasonix L14-5/38) was mounted to visualize the tendon longitudinally through an acoustic window in the bath (Fig. 1B). M-mode ultrasound radiofrequency (RF) data was collected at 14000 frames/second from a single transducer element located 10mm from the tapper. RF data was recorded for 2 seconds (2 loading cycles) after 5 preconditioning cycles.

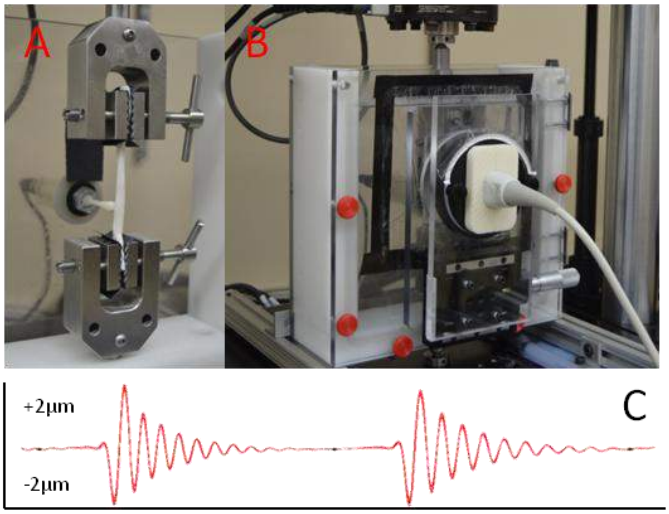

Figure 1: Mechanical testing setup. A) Tapping device contacting tendon. B) Ultrasound transducer fixed to front of bath. C) Transverse tendon motion pattern.

A speckle tracking algorithm was used to calculate the transverse frame-to-frame motion (Fig. 1C) of kernels positioned over the tendon tissue. FFT analysis was performed on the transverse motion trajectories to determine the frequency of the induced wave in the tendon. Based on the frequency, $\boldsymbol{f}$, and the known tendon grip-to-grip length, $\boldsymbol{L}$, SWS was calculated as:

$$\boldsymbol{v = 2fL} \quad (5)$$

SWS was calculated during the period of time after each tendon tap, so that SWS was measured at 25Hz, or 50 times per 2-second trial. A total of 58 trials were analyzed for this study, such that approximately 2900 data points were analyzed. The fit of the wave propagation model was assessed based on the correlation between applied stress and predicted stress from measured SWS for each trial. Additionally, the fit of the model was assessed based on its coincidence with mean values of SWS within 0.5MPa bins.

RESULTS

SWS increased with tendon loading, averaging 19.3m/s at 0.44MPa and increasing to 61.7m/s at 7.75MPa. As predicted by the model, SWS was non-linearly dependent on tendon stress, increasing most rapidly at low loads (Fig. 2). Stress estimated based on the wave propagation model was highly correlated with actual stress in the tendon (mean r^2=0.981, range: 0.930-0.997). Additionally, it was found that the model predicted SWS within one standard deviation of experimentally determined mean values across the whole range of stresses for which there was a complete data set (Fig. 2).

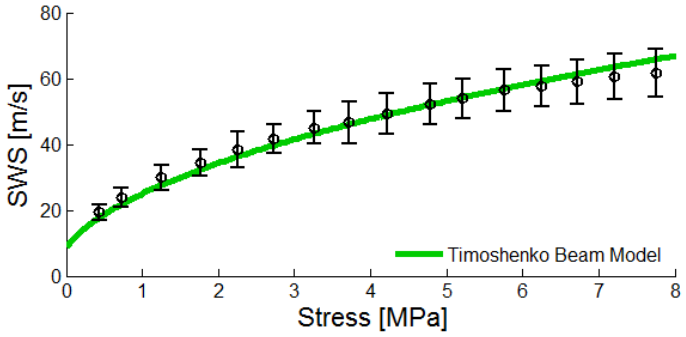

Figure 2: Shear wave speed vs. tendon stress. Experimental data plotted as means and standard deviations within 0.5MPa bins.

DISCUSSION

This study demonstrates the exciting potential to noninvasively measure tendon wave propagation, and to use that information to estimate the stress within the tissue. The most salient insight of the model is the need to account for the direct influence of axial loading on SWS. Clinical SWE systems presume that wave speed is only dependent on material properties, and further, can only track wave speeds up to 16.3m/s. Our data shows that SWS in lightly loaded tendon can exceed 20m/s, and increases with stress in a manner predicted by a tensioned beam model. Thus, results from previous and future studies using clinical SWE in loaded tendon must be interpreted with caution.

Our work sets the stage for measuring and interpreting tendon SWS under physiological conditions. The method of SWS measurement presented here is particularly well suited to *in vivo* applications. The ability to measure SWS values of magnitudes up to 100m/s will allow us to measure tissue stresses during functionally relevant activities. Future work will focus on advancing our wave propagation model in two important ways. First, the influence of variations in tendon cross-section must be considered. This will be especially important as we transition to complex musculotendon structures *in vivo*. Second, the added mass effects of surrounding tissues will add complexity to the *ex vivo* case, and must be well understood to provide a meaningful interpretation of *in vivo* SWS.

In conclusion, a promising new approach for noninvasively assessing tendon tissue stress is demonstrated. Embodiment of this technology for *in vivo* application would provide valuable quantitative tissue loading data relevant to the diagnosis and treatment of tendon disorders.

ACKNOWLEDGEMENTS

This material was based upon work supported by the National Science Foundation Graduate Research Fellowship Program under Grant No. DGE-1256259. This research was additionally supported by the National Institutes of Health Grant No. EB015410.

REFERENCES

[1] Erdemir, A et al., *Clin Biomech*, 22:131-154, 2007.
[2] Fleming BC & Beynnon BD, *Ann Biomed Eng*, 32:318-328, 2004.
[3] Bercoff, J et al., *IEEE Trans. Ultrason., Ferroelect., Freq. Control*, 51:396-409, 2004.
[4] DeWall, RJ et al., *J Biomech*, 47:2685-2692, 2014.
[5] Weiss, JA et al., *J Biomech*, 35:943-950, 2002.
[6] Sader, JE et al., *J Appl Phys*, 84:64-76, 1998.

Copyright 2016 The Organizing Committee for the 2016 Summer Biomechanics, Bioengineering and Biotransport Conference

SB^{3}C2016
Summer Biomechanics, Bioengineering and Biotransport Conference
June 29 –July 2, National Harbor, MD, USA
SB^{3}C2016-1043

HETEROGENEITY OF VISCOELASTIC BEHAVIOR OF RAT BRAIN

S. Assari (1), G. Kermani (1), A. Hemmasizadeh (1), Mary Barbe (2), K. Darvish (1)

(1) Biomechanics Laboratory, Department of Mechanical Engineering
(2) Department of Anatomy and Cell Biology
Temple University
Philadelphia, PA 19122

ABSTRACT
Characterizing the biomechanical behavior of brain tissue is critically important for developing more realistic finite element (FE) models of the brain that can be used in better understanding the mechanisms of traumatic brain injury (TBI) and improving neurosurgical procedures among other applications. In most FE models, brain tissue is assumed to be homogeneous or consist of distinct white matter and gray matter regions and its local inhomogeneity is ignored. In this study, the local heterogeneous viscoelastic behavior of rat brain tissue was characterized using a custom-designed micro-indentation setup. The results showed that the heterogeneity of brain tissue was more pronounced in longer term shear moduli. The gray matter exhibited stiffer response than the white matter.

INTRODUCTION
Characterizing of the heterogeneity of the mechanical properties of brain tissue is a fundamental step in improving our evaluations of brain deformation and tissue stresses and strains during high-rate events that lead to TBI. Recent advances in FE models of brain tissue with sub-millimeter resolution have brought forth more attention to the heterogeneity of brain material properties. Although rat brain has been frequently used in *in vivo* neurotrauma studies and its heterogeneous injury patterns are well characterized, little is known about its regional viscoelastic material properties. The goal of this study was to determine the local mechanical behavior of several anatomical regions of rat brain using a custom-designed micro-indentation device. The results of this study can contribute to developing a heterogeneous constitutive model for brain tissue and improving the predictability of TBI FE models.

METHODS
Brains of four adult Sprague-Dawley rats were harvested shortly after euthanasia, and 2-mm coronal slices were cut using a brain matrix. Slices were kept in artificial cerebrospinal fluid to maintain their viability. A slice including the hippocampus was selected from each brain for this study. Gray matter regions were divided into Inner, Middle and Outer Cortex (OC), Thalamus (T), Hippocampus (CA1, CA2, CA3, and DG) and white matter regions were divided into Corpus Callosum (CC), Alveus (Alv) (Fig. 1). These regions were consisted with another recent study [1].

A custom-designed micro-indentation test setup [2] was used, consisting of Z-axis nano-positioner with resolution of 0.2 nm and 100 µm range (Nano-Z100, MCL,WI), and an XY positioner with resolution of 0.02 mm. A spherical indenter (1.5 mm diameter) was attached to a force transducer (Aurora Scientific, Ontario, Canada, Model 406A) with resolution of 10 nN (1 µg) and range of 0.5 mN (50 mg). The setup was equipped with a horizontally positioned 300x Stereo Microscope (Olympus SZX7) for contact visualization and the whole setup was mounted on an active vibration isolation table (TMC 63-533 Peabody, MA).

Rapid ramp and hold displacement was applied to the specimen with ~10-ms ramp time, 20s hold time, and penetration depth of 40 µm (~200-µm diameter indentation contact area). A Quasi-Linear Viscoelastic (QLV) model was used to describe the indentation force history $P(t)$ in terms of the indentation depth h:

$$P(t) = \int_0^t G(t-\tau)(\partial P^e(h)/\partial h)(\partial h)/\partial \tau) d\tau \quad (1)$$

in which $P^e(h)$ is the instantaneous elastic force that is generally a nonlinear function of h. For a spherical indenter we have [3]:

Copyright 2016 The Organizing Committee for the 2016 Summer Biomechanics, Bioengineering and Biotransport Conference

$$P^e = \left\{\frac{8\mu\sqrt{R}}{3(1-\nu)}\right\} h^{3/2}((\quad (2)$$

in which μ, R, and ν are the shear modulus, the indenter radius, and the Poisson's ratio respectively. ν was assumed to be 0.49 (almost incompressible). $G(t)$ is the reduced relaxation function and was assumed to be a Prony series:

$$G(t) = (G_\infty + \sum_{i=1}^{4} G_i \exp(-\beta_i t)(\quad (3)$$

in which β_i are the decay rates and $\beta_{1..4} = 0.1, 1, 10, 100 s^{-1}$ were chosen to represent the time scales of the ramp and hold. G_i are the relaxation amplitudes that together with μ were obtained using an optimization algorithm written in MATLAB.

RESULTS

The QLV material parameters (Eqs. 2 and 3) were determined by optimizing for G_i and μ to match the experimental data. Figure 2 shows representative force and displacement time history curves of typical indentation tests and provides a comparison between the experimental data and the corresponding QLV model. The comparison of experimental force curves with the theoretical model demonstrated that the application of the QLV model was valid.

To compare the tissue heterogeneity, the shear moduli at relaxation times of 10 ms, 100 ms, 1s, and 10 s were compared ($\mu_{10\text{ms}}$, $\mu_{100\text{ms}}$, $\mu_{1\text{ms}}$, and μ_{10s} respectively). The results showed that several anatomical regions had significantly different material properties. Generally, the brain tissue showed more compliant behavior moving from Cortex (surface) toward Thalamus (core) (Fig. 3). Table 1 lists the overall range of shear modulus with regions that had the highest and the lowest shear moduli and their differences. Comparison between the average values of the shear moduli indicated that the gray matter was generally stiffer than the white matter for all time scales (Table 2).

DISCUSSION

The current study showed that brain tissue is heterogeneous. More difference was observed in longer term shear moduli between the anatomical regions which would be particularly important in modeling applications with low loading rates, e.g., neurosurgery, hydrocephalus, and tumor growth. Since the core regions were found to be more compliant than the outer layers, it is expected that the inner regions would be more susceptible to injury due to higher shear strain levels under uniform shear loading.

The gray matter showed generally stiffer behavior than the white matter which is in agreement with the results reported by Elkin et al [1]. The shear moduli reported in our study are slightly smaller than the results reported by Elkin et al., which could be due to the higher strain levels in their experiments (nonlinear response) and the use of a flat indenter.

The heterogeneous brain properties characterized in this study is a step toward implementing more accurate brain constitutive models in TBI FE models which would improve the predictions of such models.

ACKNOWLEDGEMENTS

The work reported herein was partially supported by the American Heart Association under Grant Number 15PRE25090213 (SA).

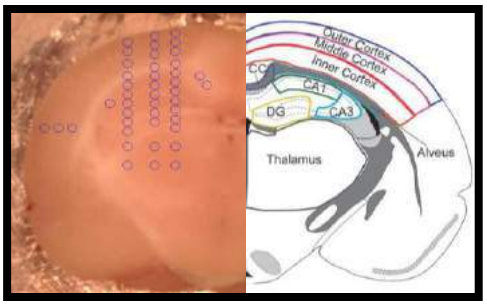

Figure 1: Indentation locations on a coronal section of rat brain

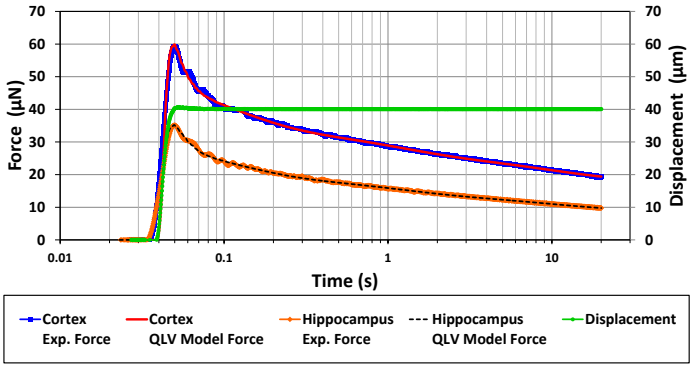

Figure 2: Representative indentation force and displacement vs time curves.

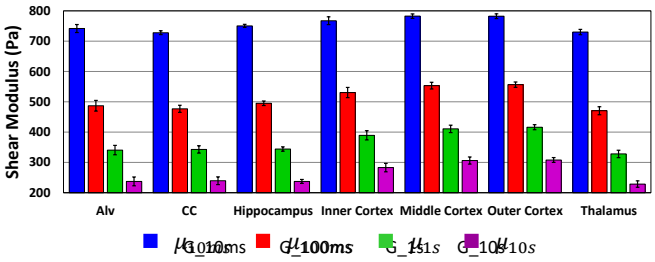

Figure 3: Heterogeneity of shear moduli at different time scales in different anatomical regions.

Table 1: Overall Ranges of the Shear Moduli (Pa)

	μ_{10ms}	μ_{100ms}	μ_{1s}	μ_{10s}
Min	CC 728±6	T 470±13	T 328±12	T 229±11
Max	OC 783±8	OC 556±9	OC 416±8	OC 308±8
Diff	8%	18%	27%	25%

Table 2: Average Shear Moduli in White and Gray Matter (Pa)

	μ_{10ms}	μ_{100ms}	μ_{1s}	μ_{10s}
White Matter	735±10	482±15	342±14	239±14
Gray Matter	763±8	521±11	378±11	273±10
Diff	4%	8%	11%	14%

REFERENCES

[1] Elkin, Benjamin S., Ashok I. Ilankovan, and Barclay Morrison III. "A detailed viscoelastic characterization of the P17 and adult rat brain." Journal of neurotrauma 28.11 (2011): 2235-2244.

[2] Hemmasizadeh, Ali, Michael Autieri, and Kurosh Darvish. "Multilayer material properties of aorta determined from nanoindentation tests." Journal of the mechanical behavior of biomedical materials 15 (2012): 199-207.

[3] Sneddon, I. N., Int. J. Engng Sci, 3:47–57, 1965.

Copyright 2016 The Organizing Committee for the 2016 Summer Biomechanics, Bioengineering and Biotransport Conference

SB³C2016
Summer Biomechanics, Bioengineering and Biotransport Conference
June 29 –July 2, National Harbor, MD, USA
SB³C2016-1044

HISTOLOGICAL AND BIOMECHANICAL ANALYSES OF HUMAN ABDOMINAL AORTIC ANEURYSMS

Mirunalini Thirugnanasambandam (1), Karthik Mikkineni (2), Satish Muluk (2), Oluwaseun R. Adeyinka (1), Ender Finol (1)

(1) Department of Biomedical Engineering
University of Texas at San Antonio
San Antonio, Texas, USA

(2) Division of Vascular Surgery
Allegheny Health Network
Pittsburgh, Pennsylvania, USA

INTRODUCTION

Abdominal Aortic Aneurysms (AAA) have been studied extensively over the past decade from different perspectives. While the mechanobiology of AAAs is important in studying its pathogenesis and the evolution of its composition, AAA mechanics is important in evaluating its growth and predicting rupture risk. The positive feedback loop involving both the microbiological changes and biomechanical changes aggravates AAA growth and hastens rupture risk. Hence, in the present work, we studied both of these factors in unison while evaluating their effect on each other. Isolating the biological factors that contribute significantly toward increasing the biomechanical index of rupture risk helps to narrow down the key biological markers of AAA rupture.

METHODS

Five patients with AAA underwent open abdominal repair at Allegheny General Hospital (Pittsburgh, PA). CT angiography scans of the abdominal region were acquired prior to the surgery. A portion of the AAA anterior wall and the intraluminal thrombus (ILT) were harvested during the surgery and shipped to University of Texas at San Antonio. The wall tissue was cleaned in 70% isopropyl alcohol and then cut into one square inch specimens. The ILT was separated into three layers (inner bright red luminal layer, white medial layer and outermost reddish brown abluminal layer). Each layer was processed similar to the wall tissue and cut into one square centimeter specimens. The tissues were put in cassettes and submerged in 70% isopropyl alcohol, ready to be fixed for histological analysis.

2.1 Histological analysis

The specimens were fixed and embedded in paraffin blocks. The sections were stained with Hematoxylin and Eosin (H&E) stain and Verhoff Van Gieson stain. The H&E stain was used to recognize different tissue types and to identify the morphological changes due to pathology. Verhoff stain was mainly used for differential staining of elastin. Eleven quantitative and qualitative variables were evaluated from the images of the stained specimens, as follows:

- Medial elastin present in the vessel wall as a % of normal
- Area fraction of inflammatory cells present in the vessel wall
- Presence of smooth muscle cell calcification in the vessel wall
- Presence of vasa vasorum in the vessel wall
- Volume % of the media occupied by elastin
- Volume % of the media occupied by collage/ground substance
- Volume % of the media occupied by smooth muscle cells
- Presence and severity of medionecrosis
- Presence and severity of cystic medial necrosis
- Presence and severity of fibrosis
- Degree of change in cell orientation

2.2 Biomechanical analysis

The clinical images were acquired immediately prior to surgery and were used as input to AAAVASC, an in-house segmentation and geometry quantification code. The output of the segmentation was binary masks comprising three domains – wall, lumen and thrombus. These masks were then used as input to AAAMesh, an in-house mesh generation software to generate a volume and surface mesh of the AAA. Finite element analysis was performed using these meshes in the solver ADINA (Adina R&D Inc., Watertown, MA), while applying an endoluminal pressure of 120 mmHg. The results were post-processed using Ensight (CEI Inc., Apex, NC) to obtain the principal stress distributions on the AAA wall. Since the wall tissue was harvested from the anterior region of the AAA, the mean wall stress in that region was also calculated.

Copyright 2016 The Organizing Committee for the 2016 Summer Biomechanics, Bioengineering and Biotransport Conference

2.3 Statistical analysis

The mean wall stress on the anterior AAA wall was regressed on the 11 histological variables using Lasso regression in SAS (SAS Institute Inc., Cary, NC). Lasso is a method of variable selection, which reduces the residual sum of squares subject to the sum of the absolute values of the coefficients being less than a constant. This method is especially useful when the number of subjects is low compared to the number of variables.

RESULTS

The histological stains of the wall tissue were obtained and the regions of interest isolated. The chronic inflammatory cells and smooth muscle cells were identified in the H&E stain images, and the elastin and collagen fibers were identified in the Verhoff stain images, as shown in Figure 1.

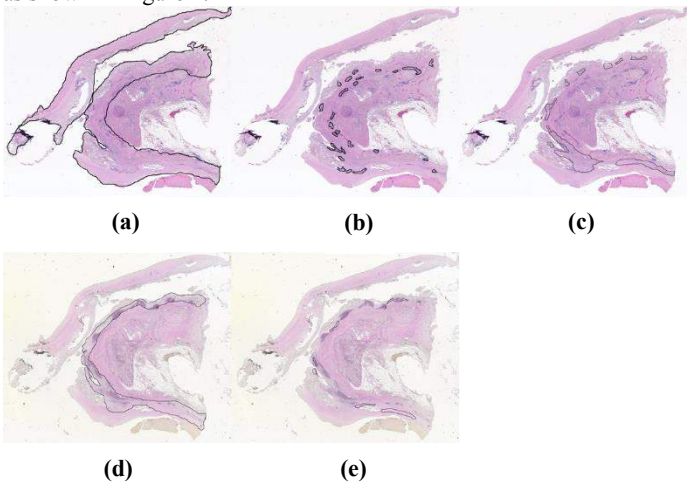

Figure 1: Identification of vessel wall (a), chronic inflammatory cells (b) and smooth muscle cells (c) from H&E stain; medial layer of the wall (d) and collagen fibers (e) from Verhoff stain. The purple patches in the medial layer in (d) are the elastin fibers.

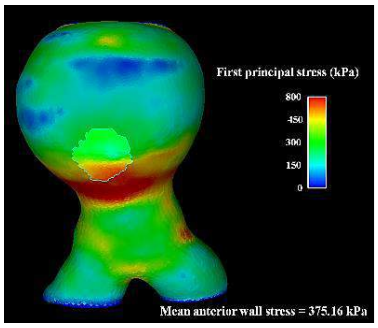

Figure 2: Distribution of first principal stress at the AAA wall in kPa. The highlighted region shows the anterior portion of an AAA from which a tissue specimen was analyzed histologically.

The distribution of first principal stress on the AAA wall was obtained for each AAA as shown in Figure 2 for an exemplary aneurysm. The anterior region was isolated and the mean wall stress in this region evaluated. The Lasso regression of the histological variables on the mean stress in the anterior wall region resulted in the following significant variables:

- Presence of vasa vasorum (vasa_1);
- Interaction between area fraction of chronic inflammatory cells and presence of vasa vasorum (CIC*vasa_1);
- Interaction between volume % of media contributed by collagen, volume % of media contributed by smooth muscle cells and presence of vasa vasorum (volcoll*volsmc* vasa_1);
- Interaction between volume % of media contributed by collagen, volume % of media contributed by smooth muscle cells and presence of grade 3 fibrosis (volcoll*volsmc* fibr_3).

The evolution of coefficient progression with each regression step is presented in Figure 3.

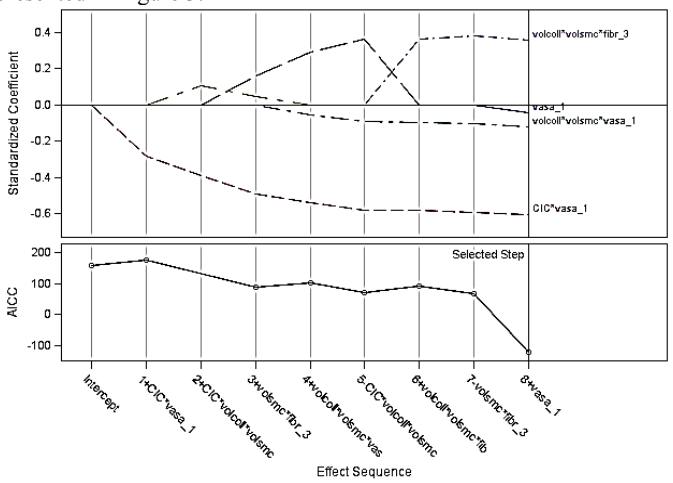

Figure 3: Effect of Lasso regression step number on the normalized coefficients of the significant variables.

DISCUSSION

The biomechanical parameter considered in this study (wall stress) has been used to assess rupture risk of AAAs. From Figure 3, it can be observed that the coefficient of regression for the presence of vasa vasorum is negative, implying that an increase in vasa vasorum reduces the mean wall stress. Since the vasa vasorum serves as the secondary supply of nutrients to the aortic wall while luminal diffusion fails [1], it follows logically that its presence would contribute towards homeostasis and hence lower wall stress. The presence of chronic inflammatory cells in the aortic wall is a result of an atherosclerotic intima which enables their direct recruitment through neovascularization. The cytotoxic mediators secreted by these cells lead to a weakened aortic wall by inducing smooth muscle apoptosis. Fibrosis is defined as an increase in interstitial collagen. If the increase in collagen is in an area comprising more than two thirds of the total width of the media, it was classified in this study as grade 3 fibrosis [2]. An increase in fibrosis of the AAA wall may lead to compression of the blood vessel by the fibrotic mass, which in turn increases blood pressure and sets off the positive feedback loop involving further recruitment of inflammatory cells. Thus, in this work, the key components involved in the mechanobiology of the evolution of AAAs, as identified in literature, have been found to affect the biomechanics of AAAs. The limitation of this work is the small sample size of AAA subjects and tissue.

ACKNOWLEDGEMENTS

This work was supported in part by award No. 1012763 of the Burroughs Wellcome Fund.

REFERENCES

[1] Jones, Gregory T., *INTECH Open Access Publisher*, (2011): 53-74.

[2] de Sa, Mauro, et al., *The Journal of Thoracic and Cardiovascular Surgery*, 118, 4 (1999): 588-596.

Copyright 2016 The Organizing Committee for the 2016 Summer Biomechanics, Bioengineering and Biotransport Conference

SB³C2016
Summer Biomechanics, Bioengineering and Biotransport Conference
June 29 –July 2, National Harbor, MD, USA
SB³C2016-1046

METHODS TO DETERMINE RIGHT VENTRICULAR PERFORMANCE IN A RAT ANIMAL MODEL OF PULMONARY ARTERIAL HYPERTENSION

Daniela Velez-Rendon (1), Jesse Gerringer (1), Gizzel Gomez (1), Erica Pursell (1), Daniela Valdez-Jasso (1)

(1) Department of Bioengineering
University of Illinois at Chicago
Chicago, IL, USA

INTRODUCTION

Pulmonary arterial hypertension (PAH) is defined as the increase in mean arterial pressure in the vasculature of the lungs. Measurement of pulmonary arterial pressure, however, is limited to invasive techniques due to the location of the pulmonary system. In PAH, the immediate organ affected by this pressure overload is the right ventricle (RV), whose response is to become hypertrophic. As the condition persists, the RV performance is compromised and can lead to cardiac failure. Since PAH is typically diagnosed when it has started compromising other organs, it is not caught on the early onset. The mechanisms underlying PAH remain unknown and heart and lung transplant remains the only cure [1, 2].

One method to assess ventricular contractility clinically is through right heart catheterization to obtain pressure-volume signals in the steady state of a patient. Since this method only requires one cardiac cycle of these measurements, it is called the single-beat method (SBM). The other method is the multi-beat method (MBM), which is the gold standard. However, this method requires occlusion of the inferior vena cava or a Valsalva maneuver. To our knowledge, no RV contractility has been studied in rats, which is a widely used animal to study PAH. Therefore, our goal is to compare the predictions of the single- and multi-beat method at an early and acute/advance stage of PAH.

METHODS

To study PAH, 8 Sprague Dawley rats were injected with a doses of 60mg/kg of monocrotaline (MCT, Sigma-Aldrich) dissolved in hydrogen chloride (HCl) and studied the disease progression for four weeks. A normotensive or placebo group was included to account for any aging effects (PL, N= 8). This group was only injected with HCl. Open chest surgeries were performed every week for four weeks on one animal of each treatment group. Once the RV was exposed through a thoracotomy, a 1.9F admittance pressure-volume (PV) catheter (Transonic Science, Ontario, Canada) was inserted. After obtaining reproducible steady state PV data, the IVC was slowly occluded to study the afterload effect and determine ventricular contractility using MBM. Following the PV measurements in the RV, the catheter is exchanged by a 1.6F dual pressure sensor catheter, and placed passed the pulmonic valve, allowing for simultaneous measurements of the pressure in the RV and pulmonary artery (PA). Once reproducible data are recorded, a flow probe (Transonic Science, Ontario, Canada) is placed on the PA for blood flow measurements. The data are collected and pre-processed in Labchart Software (ADInstruments Inc. Colorado Springs, CO). A schematic of the hemodynamics measurements is summarized in Figure 1. The cardiac parameters (heart rate (HR), cardiac output (CO), stroke volume (SV), dP/dt_{max}, dP/dt_{min}, ejection fraction (EF) and relaxation coefficient ($\tau()$) are obtained from the RV and reported to assess cardiac performance.

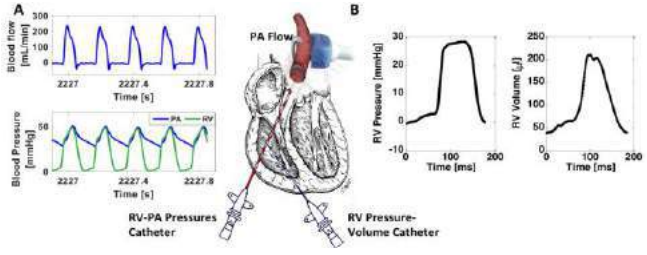

Figure 1. *In-vivo* hemodynamic measurements. A: simultaneous RV-PA pressure (bottom) and PA blood flow (top) time series. B: RV pressure-volume time series

To determine ventricular contractility, we computed the end-systolic elastance (E_{es}) using two different methods. E_{es} in MBM was

Copyright 2016 The Organizing Committee for the 2016 Summer Biomechanics, Bioengineering and Biotransport Conference

computed as the slope of the end-systolic pressure-volume relationship of the decreasing PV loop [3]. In contrast, in SBM, E_{es} was calculated as the slope of the line passing through P_{max} and the end-systolic PV point. P_{max} is found by interpolating the pressure curve over time in the RV from the $dP/dt_{max,min}$ points. For both methods, the effective arterial elastance (E_a) was computed as the ratio of the end-systolic pressure and SV [4, 5].

Comparisons of the cardiac performance between the groups and stages of PAH are done via an ANOVA analysis and considering $p<0.05$ to be significant.

RESULTS

The early and advanced stages of PAH, or results from week 1 and 4 are presented. The summary statistics of RV performance are based on the total cohort of 8 animals, and the comparison of the SBM and MBM is based on 6 animals. As shown in the summary statistics in Figure 2, the cardiac performance of the PL group overall remained constant, indicating no effect due to aging and/or injection of HCl. The cardiac performance in the MCT group changed from week 1 to 4. Particularly, the time decaying constant τ had a statistically significant increase with the advance of PAH. Ventricular relaxation, or dP/dt_{min}, was statistically significantly different between normo- and hypertensive animals in week 1, and ejection fraction, EF, statistically significantly decreased from normotensive to hypertensive in week 4.

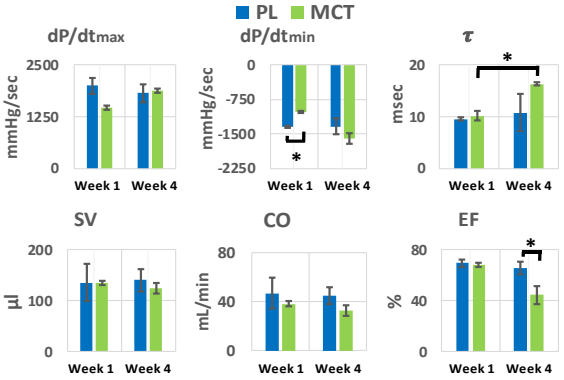

Figure 4. Summary statistics of *in vivo* hemodynamic measurements from the PL and MCT groups for week 1 and week 4. dP/dt_{max}; dP/dt_{min}; τ; SV; CO and EF. *$p<0.05$*

A comparison of the ventricular and vascular parameters E_{es} and E_a is shown in Figure 4. E_{es} tends to remain constant when comparing between week 1 and week 4 in SBM. However, MBM predicts a decrease in Ees values from week 1 to week 4 in both normo- and hypertensive groups. E_a predictions are, however, close and the trend of E_a to be larger in the PL group is preserved independently of the method used.

DISCUSSION

Cardiac performance of the PL group was maintained and did not change as a function of the animal aging. In addition, our cardiac performance values resemble the reported parameters for a normotensive rat [6]. On the other hand, the RV performance during diastole changed in the MCT group. The increase in τ indicates the loss of elasticity of the RV. The decrease in ejection fraction from week 1 to week 4, while stroke volume remained constant, indicates that the RV has increased in size (due to hypertrophy) and also its resting volume. These adaptations of the RV are in line with an overloaded ventricle.

Our predictions of E_{es} through the SBM and MBM are significantly different. With the MBM we find a decrease of E_{es} as the disease

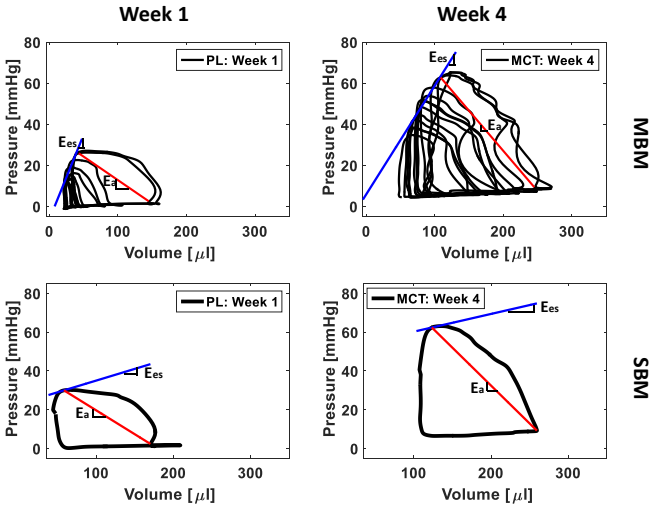

Figure 2. Left column: data from week 1 and right column: data from week 4. Top to bottom: MBM (steady state & IVC occlusion), SBM.

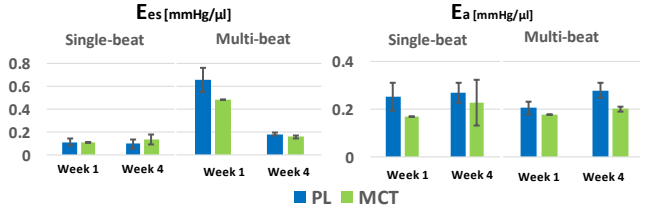

Figure 3. Computed E_{es} and E_a via the single-beat and multi-beat methods for PL and MCT groups in week 1 and week 4.

progresses, while the SBM predicts no change in RV contractility. This comparison has only been reported in the RV of humans [7]. In addition, Lambermont *et al.* found that the SBM overestimates E_{es}. This was an unexpected result that we are looking forward to addressing. The method, however, does predict similar E_a values and the same trend from week 1 to week 4. The only E_a values that have been reported are in the left ventricle in rats (0.5-1.1 mmHg/µL), therefore we are unable to compare our results of 0.18-0.3 mmHg/µL [6].

As the E_{es} values computed using the SBM are not close to the values given by the gold standard, it is necessary to determine the origin of this discrepancy and modify, if needed, the SBM in our animal model for clinical purposes. To our knowledge, no studies have been performed in the rat RV using the SBM. Therefore, it is essential to increase the number of animals in our study and fully characterize RV contractile properties using the SBM in the rat.

ACKNOWLEDGEMENTS

We would like to acknowledge the UIC College of Engineering Seed Fund (DVJ), Honors College Undergraduate Research Grant (JWG), and Lincoln Graduate Student Fellowship (EP).

REFERENCES

[1] M. George et al., *Pulmonary Circulation,* vol. 1, no. 2, pp. 298-305, 2011.

[2] R. Benza and et al., *CHEST,* vol. 142, no. 2, pp. 448-56, 2012.

[3] W. Zhijie and et al., *Physiological Reports,* vol. 1, no. 7, 2013.

[4] R. Naeije and et al. Humana Press, 2015, pp. 19-40.

[5] A. Bellofiore et al., *Ann Biom. Eng,* vol. 41, no. 7, pp. 1384-98, 2013.

[6] P. Pacher et al., *Nat Protoc.,* vol. 3, no. 9, pp. 1422-34, 2008.

[7] B. Lambermont et al., *Crit Care Med,* vol. 32, no. 9, pp. 1886-90, 2004.

Copyright 2016 The Organizing Committee for the 2016 Summer Biomechanics, Bioengineering and Biotransport Conference

SB^{3}C2016
Summer Biomechanics, Bioengineering and Biotransport Conference
June 29-July 2, National Harbor, Maryland, USA
SB^{3}C2016-1047

INTRAHOSPITAL ASSISTIVE TRANSPORTATION DEVICE FOR MECHANICALLY VENTILATED PEDIATRIC PATIENTS

Allison E. Fetz
Biomedical Engineering,
University of Memphis
Memphis, TN, USA

Elysia A. Masters
Biomedical Engineering,
University of Memphis
Memphis, TN, USA

Ravi M. Patel
Biomedical Engineering,
University of Memphis
Memphis, TN, USA

Ameen Z. Ozrail
Biomedical Engineering,
University of Memphis
Memphis, TN, USA

Faculty Advisor(s)

Dr. John Williams
Biomedical Engineering,
University of Memphis
Memphis, TN, USA

Dr. Gary Bowlin
Biomedical Engineering,
University of Memphis
Memphis, TN, USA

Clinical Advisor

Maris Brown, TN
Regulatory Readiness Manager,
LeBonheur Children's Hospital
Memphis, TN, USA

INTRODUCTION

In 2012, 3,200 patients under the age of 1 year required long-term mechanical ventilation [1]. The leading cause of long-term ventilation in pediatric patients is respiratory distress syndrome (RDS) which occurs in approximately 50% of neonates born at 26-28 weeks of gestation [2]. Preterm infants diagnosed with RDS are predisposed for the development of bronchopulmonary dysplasia (BPD) and become dependent on ventilator support. After intensive physical and occupational therapy, infants with BPD are discharged from the hospital on a portable ventilator to continue building strength and eventually become ventilator independent.

Children's hospitals across the United States currently adapt pediatric wheelchairs, wagons, strollers, and medical stands to transport patients with BPD from the hospital room to therapy sessions. The current methods involve haphazardly placing medical equipment and cords wherever they fit which introduces high risk to the transportation process. Furthermore, the process requires assistance from multiple caretakers and takes an unnecessary amount of time.

Clinical Problem: Intrahospital transport of patients aged 6 to 18 months who require continuous respiratory support is inefficient because the equipment used to transport patients does not allow for deliberate placement of medical devices and their cords in relation to the patient, therefore increasing time of transport and risk of harm to the patient.

Need Statement: There is a need to improve the clinical transportation efficiency of pediatric patients who require continuous respiratory support and better accommodate for medical devices and their cords in order to minimize the risk of harm to the patient as well as the time and staff required for transportation.

Here we present the design of a compact, assistive transportation device to be used in conjunction with a common, lightweight stroller. The device houses a portable ventilator, humidifier, pulse oximeter, oxygen cylinder, and emergency supply kit. It aims to improve transportation efficiency to enhance the safety of the transportation process. Our device will increase frequency of therapy sessions and allow for the hands-on involvement of family members to promote confidence in caring for their child. Ultimately, this will speed discharge from the hospital, improve the transition to a home-setting, and facilitate weaning from the ventilator, thereby improving quality of life for BPD patients across the United States. Because the number of BPD patients is increasing each year as a result of medical technologies' ability to save the lives of preterm infants, there is a growing and substantial need for our device.

PRODUCT DESIGN

The compact, assistive transportation device is intended to house the all of the medical equipment supporting ventilated patients, including a ventilator, pulse oximeter, oxygen cylinder, humidifier and emergency supply kit. It sits on 360° rotating and braking caster wheels for easy maneuverability on solid surfaces and over elevator gaps. With a total height of 3 feet, the device can be comfortably managed by one caretaker. Ultimately, our device better addresses the needs than current solutions because it is designed to be compact, organized, and easy to use to increase safety during patient transport. Our team is the first to specifically address this problem with systematic organization of equipment and efficiency in mind.

Our assistive transportation device is a three-tiered structure with designated places for each piece of medical equipment (Figure 1). The top level is fitted with a basket for storage and easy access to an emergency supply kit containing an Ambu bag and emergency tracheostomy tubes. This level was designed as a basket rather than a shelf for versatility. The pulse oximeter is placed below the emergency supplies on the middle tier, designed for a standard pulse oximeter. The pulse oximeter controls and monitor can be easily seen when placed in our device and are secured with an anti-slip gripping surface. The bottom tier is designed to house the patient's ventilator. Our device is compatible with both the Philips Respironics Trilogy 202 Ventilator as well as the Carefusion LTV 1150 Ventilator because both of these ventilators are commonly used with pediatric patients. The organization also allows the ventilators' circuit tubes to extend comfortably to the humidifier, mounted at the front of our device, and then directly to the patient. The humidifier is attached to the vertical support using a mounting feature that is compatible with Fisher & Paykel humidifiers. Furthermore, the ventilator connects to the oxygen cylinder located at the rear of the device. The oxygen cylinder mount is located closest to the caretaker during transport to increase cylinder safety and limit potential bumping or knocking of the cylinder. The cylinder is supported with a rigid y-shaped beam from beneath, a rigid ring at the

Copyright 2016 The Organizing Committee for the 2016 Summer Biomechanics, Bioengineering and Biotransport Conference

base, and an adjustable strap at the top of the cylinder in compliance with compressed gas transport regulations defined by the Occupational Safety and Health Administration, the Compressed Gas Association, and the Uniform Fire Code. In addition, the device is equipped with clip features that quickly and securely attach to a variety of lightweight strollers. Together, this configuration reduces the risk of cord entanglement and circuit tube dislodgement while providing continuous, visual monitoring of the equipment, ultimately increasing ease and improving safety of the transportation process.

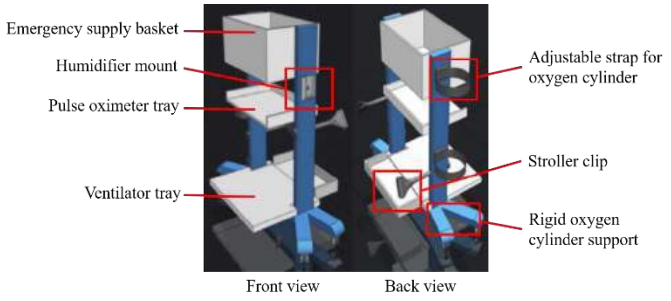

Figure 1. Computer Aided Drafting (CAD) model of the assistive transportation device.

Medical personnel should use our device by loading the equipment onto the device in the patient's room, attaching a lightweight portable stroller to the device with clips, placing the patient in the stroller, and pushing the single unit down the hallway as they would a normal stroller. Upon arriving at therapy or the final destination, the device can be detached from the stroller and left free standing with the medical equipment while therapy occurs or the patient is examined. Afterwards, it is simply reattached to the stroller, and the unit is transported back to the patient's room.

Transportation by one caretaker, easy loading and movement of medical equipment, and increased safety for the patient were the top needs that inspired our design. Patients with BPD require rigorous physical and occupational therapy to build strength and become ventilator independent. Without our device, these patients remain in their rooms 99% of the time, miss critical therapy time outside of the hospital room, and experience limited interaction with their families.

Our team has developed a working, wooden prototype (Figure 2) that serves as a preliminary test. We are in the process of building a working prototype with slight modifications using 304 stainless steel and high density polyethylene. These materials were chosen because they are lightweight, durable, and easily sanitized in a clinical environment. Since this prototype, we have redesigned our wheel configuration in order to mitigate the risk of turnover. We also plan to add a push handle to the top of our device for transportation independent from the stroller as well as improve the quality and safety of device-to-stroller attachment by redesigning our clip features.

BUDGET & MARKET ANALYSIS

Pediatric patients age 6 to 18 months treated in hospital with mechanical ventilation have the longest average length of stay and largest aggregate charges of all pediatric age groups receiving this treatment [1]. In 2013, there were 3,137 patients below 1 year of age diagnosed with a respiratory condition requiring long-term mechanical ventilation in the United States, representing 46% of the total amount of pediatric patients with this condition [3].

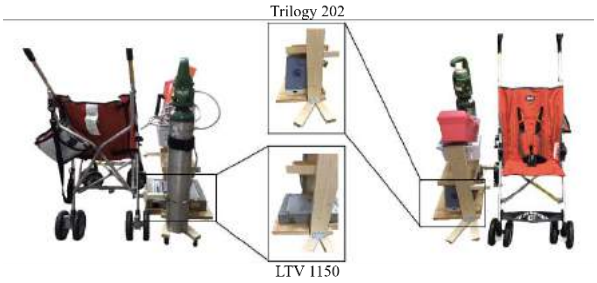

Figure 2. Wooden prototype attached to a Chicco stroller, displayed housing the Trilogy 202 and LTV 1150 ventilators.

According to 2013 Tennessee health statistics, mechanically ventilated patients under 1 year of age resulted in nearly $9,000,000 of aggregate charges [4]. That equates to an average of over $180,000 per patient, which provides an extensive market landscape for devices like ours. The market for devices designed specifically for the intrahospital transportation of ventilation equipment in conjunction with pediatric patients is currently unestablished. Hospitals throughout the country are adapting what is available to them because a solution does not yet exist. Therefore, our first-of-its-kind device will acquire the majority of this market.

Our working prototype, built with the intended product materials, costs approximately $150 excluding bulk purchase pricing and manufacturing labor costs. In consideration of bulk purchasing prices, we believe that our device could be mass manufactured for roughly $100 and sold for $400 per unit, equating to a 400% markup. When conservatively targeting only specialized children's hospitals, we expect to sell 500 units within our first year of production. With an investment of $250,000 we will be able to acquire all essential manufacturing equipment and establish initial inventory build. Approximately one year into sales we will be cash flow positive, net profiting $100,000 and predict to break even with profit and loss 18 months into sales. Once our market in a children's hospital is established, we plan to expand to general hospitals and facilities that care for ventilated pediatric patients across the country and ultimately at-home use by parents and caregivers. Thus, considering an early stage 50% market penetration we anticipate total sales to be $2,500,000 over the first 5 years with continued growth and improvement as the market evolves.

ACKNOWLEDGEMENTS

Our team would like to acknowledge all of the clinical staff at LeBonheur Children's Hospital. In particular, we would like to thank Susan Anderson, PTA/Adaptive Equipment Specialist-LEAD, Ginny Burbank, RN, IMCU, and Maris Brown, MHA, Regulatory Readiness Manager, for the invaluable information they shared with our team. We would also like to acknowledge our faculty mentors, Dr. Gary Bowlin and Dr. John Williams, for mentoring our team through the development of our device.

REFERENCES

[1] Healthcare Cost and Utilization Project (HCUPnet), *AHRQ,* 2013.
[2] Effgen SK, *Meeting the Physical Therapy Needs of Children*, 2012.
[3] Centers for Disease Control and Prevention (CDC), *Births and Natality,* 2015.
[4] Overman AE, & Liu M, *Pediatrics*, 131:5, 1491-96, 2013.

Copyright 2016 The Organizing Committee for the 2016 Summer Biomechanics, Bioengineering and Biotransport Conference

SB^{3}C2016
Summer Biomechanics, Bioengineering and Biotransport Conference
June 29 –July 2, National Harbor, MD, USA
SB^{3}C2016-1049

NOVEL IRREVERSIBLE CHEMISTRY PRODUCES STRUCTURALLY MORE STABLE TISSUE BASED BIOMATERIALS

H. Tam (1), W. Zhang (2), D. Infante (1), N. Parchment (1), M. Sacks (2), N. Vyavahare (1)

(1) Bioengineering
Clemson University
Clemson, SC, USA

(2) Biomedical Engineering
University of Texas, Austin
Austin, TX, USA

INTRODUCTION

Bioprosthetic heart valves (BHVs) are used to replace stenotic and regurgitant heart valves [1]. BHVs do not require long-term anticoagulant therapy and also have more optimal hemodynamics, thus making them the preferred option for valve replacements [1]. BHVs are fabricated out of two types of xenogeneic tissues: (1) Porcine aortic valve (PAV) leaflets or (2) bovine pericardium (BP) sheet. Both are crosslinked with glutaraldehyde (GLUT). Commercially available BHVs fail due to structural degradation and/or calcification [1].

BP is the most commonly used material to fabricate BHVs and contains a high amount of layered structural proteins (collagen and elastin with proteoglycans) to impart viscoelastic properties into the tissue composite [2]. BP patches are selected based on thickness (0.5 mm) but it is not common industry practice to select for any type of preferred orientation despite previous literature suggesting there are preferred orientations of isotropy [2] that may result in different biomechanical behavior. Tears and structural degradation account for half of BHV failures [3].

Because GLUT crosslinked biomaterials have previously been demonstrated to exhibit permanent geometric deformation from cyclic mechanical deformation resulting in deviated biomechanics [3], there is motivation to search for a more stable crosslinking chemistry that produces a structurally more stable biomaterial. Previously, we have demonstrated a novel crosslinking method (TRI) that utilizes carbodiimide, neomycin trisulfate, and pentagalloyl glucose to stabilize tissue based biomaterials [4]. Here, we demonstrate that BP sections treated with TRI are structurally more durable and retain similar viscoelastic properties required of a compliant biomaterial.

METHODS

Fabrication of tissue based biomaterials

Bovine pericardium (BP) was sourced from Animal Technologies, Inc. (Erwin Tyler, TX) delivered on 0.9% saline and ice to the laboratory. BP sacs were cut into flat sheets and were washed in 0.9% saline. BP sheets were then treated with two different chemical treatment techniques: (1) GLUT – industry standard control and (2) TRI – novel, more irreversible crosslinking technique.

GLUT: BP sheets were treated with 0.6% glutaraldehyde in 50 mM 4-(2-hydroxyethyl)-1-piperazineethanesulfonic acid (HEPES) buffered saline (pH 7.4) at room temperature with gentle shaking for 24 hours, solution decanted, and replaced with 0.2% glutaraldehyde in 50 mM HEPES buffered saline (pH 7.4) and the crosslinking was continued for at least six days.

TRI: BP sheets were treated with 0.5 mM neomycin trisulfate solution in 2-(N-morpholino) ethanesulfonic acid (MES) buffer for 1 hour. The solution was decanted and leaflets were then incubated in a 30 mM *1-ethyl-3-(3-dimethylaminopropyl) carbodiimide* (EDC) and 6 mM *N-hydroxysuccinimide* (NHS) / 0.05% PGG solution in 50 mM MES buffered saline (pH 5.5) for twenty-four hours. The solution was decanted and then the leaflets were then crosslinked further in 30 mM EDC and 6 mM NHS solution in 50mM MES buffered saline (pH 5.5) for 24 hours. Following fixation, sheets were placed in 20% isopropanol in 50 mM HEPES buffer (pH 7.4) for at least six days.

Biaxial Mechanical Testing

Tissue specimens were tested under biaxial tension using a custom-built biaxial device. Roughly 2 cm by 2 cm sections were cut from preselected BP sheets for fiber orientation and mounted on the device

Copyright 2016 The Organizing Committee for the 2016 Summer Biomechanics, Bioengineering and Biotransport Conference

with the circumferential and radial directions along the device axes. The specimens were then loaded to a maximum membrane tension of 60 N/m over a period of 15s following a preconditioning step. The strain was determined via four fiducial markers were glued to the central region of the specimen. All mechanical testing were performed in PBS at room temperature. Samples were preselected by looking at collagen fiber alignment and quantifying biomechanics using biaxial testing to confirm preferred (PD) and non-preferred (XD) fiber orientation.

Stretch Test

After preselection process and biaxial testing, GLUT or TRI BP were held stretched in the PD or XP orientation at 20% past their nominal gauge length for 4 weeks in a custom built clamp system at Clemson University. Reference photos before and after stretching were taken with a high definition camera. Photos were also taken with scale references every week. Photos were also taken immediately following, 1 day, and 1 week after release from clamps to observe both short and long term behaviors of the material to return to gauge length in both the PD and XD directions.

Suture Pull-out Test

BP patches were evaluated for structural integrity and its ability to resist tearing. GLUT and TRI BP patches were cut with a die in rectangular 40 mm x 4.0 mm sections. Sections were then treated with collagenase, GAGase (combination of enzymes to degrade GAGs), porcine pancreatic elastases, or no enzyme treatment (8 groups, n = 8). One side of tissue samples was attached to a bottom clamp in a tensile tester (MTS, Minneapolis, MN). A single suture (Polypropylene blue monofilament 4-0 P-3 Ethicon™, San Lorenzo, Puerto Rico) was pierced through the sample a third of the way down the sample and was clamped to the top clamp. Samples were tensile tested at 12 mm/min to determine the amount force it took to pull the suture out of the sample. With the peak load, thickness of the sample and width were used to calculate cross sectional area to determine stress.

RESULTS

After stretch testing for 4 weeks, GLUT BP patches exhibited significant permanent set effects in both the PD and XD directions while TRI BP patches did not exhibit these effects (Figure 1). A lambda value of 1 is ideal in which there are no permanent set effects. After suture pull-out testing, it was found that TRI BP patches took significantly more stress to cause rupture than GLUT suggesting TRI is the more durable material with improved structural integrity (Figure 2). Enzymatic degradation does not affect either tissue in terms of point stress required to cause rupture. It is also important to note that biaxial testing shows that TRI BP is the more compliant biomaterial than GLUT BP before and after stretch testing (not shown). Furthermore, GLUT and TRI BP both exhibit similar denaturation temperatures ($81 \pm 1.2^{o}C$ or $82 \pm 0.9^{o}C$, respectively).

DISCUSSION

Previous studies have shown permanent set effects affect the biomechanics and function in explanted [5] and *in vitro* cyclically fatigue tested BHV materials [2, 3]. We hypothesize that this is due to the reversibility of GLUT crosslinking and replacing GLUT with chemistry that is more irreversible will provide more stable bonds to prevent permanent set. This study has demonstrated that using TRI on BP, the commercially preferred raw material for BHV fabrication, produces a very durable material that retains increased compliancy over GLUT even after mechanical deformation over a long period of time. Coupled with this material's ability to resist calcification [4], more irreversible chemistries such as TRI should be considered for BHV fabrication. Therefore, using TRI in lieu of GLUT may significantly suppress the two modes of BHV failure thereby increasing implant life and patient quality of life.

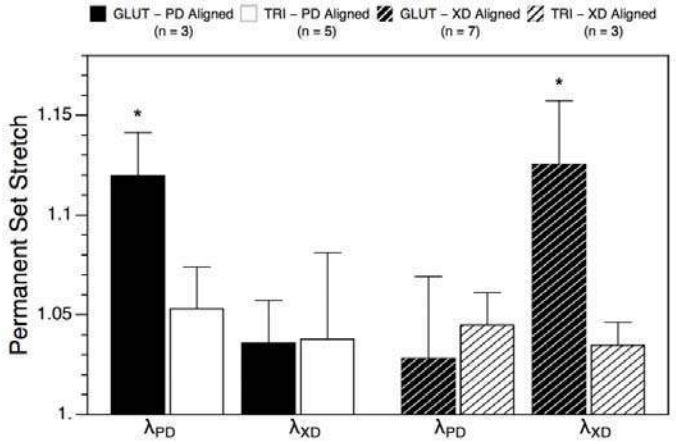

Figure 1: Permanent set effects in GLUT or TRI BP patches. *Indicates significant difference from TRI.

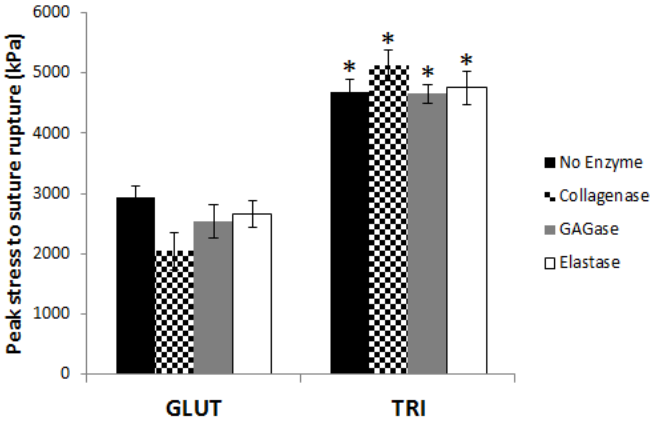

Figure 2: Peak stress to cause rupture in GLUT or TRI treated BP patches. *Indicates significant difference from GLUT.

CONCLUSION

A novel and irreversible crosslinking chemistry, TRI, for BHV fabrication was shown to have significantly more structural durability than the industry standard use of GLUT. TRI crosslinked material was able to retain higher compliancy before and after sustained mechanical deformation while GLUT materials exhibited permanent set effects resulting in deviations in biomechanical behavior. Future investigation will focus on accelerated wear testing of BHV biomaterials to discern the action of mechanism behind structural degradation. This will revolutionize the future of BHV design by introducing a core biomaterial that better fits patient needs and enables better quality of life.

ACKNOWLEDGEMENTS

NIH Grant R01HL108330 and NSF GRFP.

REFERENCES

[1] Schoen. Ann Thorac Surg 2005;79:1072–80.
[2] Sun et al. J Biomed Mater Res A. 2004 Jun 15;69(4):658-69.
[3] Smith et al. J Heart Valve Dis. 1997 Jul;6(4):424-32.
[4] Tam et al. Biomaterials. 2015 Oct; 66:83-91.
[5] Sacks, Schoen J Biomed Mater Res. 2002 Dec 5;62(3):359-71.

Copyright 2016 The Organizing Committee for the 2016 Summer Biomechanics, Bioengineering and Biotransport Conference

SB^{3}C2016
Summer Biomechanics, Bioengineering and Biotransport Conference
June 29 –July 2, National Harbor, MD, USA
SB^{3}C2016-1050

THE DEVELOPMENT OF A "FUZZY" YIELD ENVELOPE FOR TRABECULAR PORCINE SKULL BONE USING NUMERICAL SIMULATIONS

Allison N. Ranslow (1), Reuben H, Kraft (1)

(1) Department of Mechanical & Nuclear Engineering
The Pennsylvania State University
University Park, PA USA

INTRODUCTION

Typically, trabecular bone failure is characterized under uniaxial tension or compression loading, and sometimes even biaxial loading. While this information is valuable, it leaves gaps in determining the multiaxial failure surface of trabecular bone, which is important to describe the mechanical response of the skull during complex loading scenarios- especially those with loads in all three directions.

In addition, there is a lack of knowledge concerning the changes in yielding behavior in trabecular bone as a result of variations in porosity. That is, as the porosity and bone architecture changes from one spatial location in the skull to the next, the failure responses may change as well. With current advances in finite element programs and the availability of high performance computing, numerical methods give us the power to analyze and characterize these changes in properties. By running simulations on numerous trabecular microstructure models, each with a different level of porosity, the changes in response can be easily captured without having to run mechanical testing or prepare physical bone samples.

Furthermore, due to the lack of quantitative data on the multiaxial failure response of trabecular bone, it is not clear exactly how microstructural architecture influences the anisotropy of failure. Simulations may provide a means to understand and connect mechanisms of failure, such as trabecular ligament fracture, with the resulting failure envelope. Insight into these physical mechanisms will elucidate the mechanical response of trabecular bone.

To address these gaps and gain a better understanding, the aim of this study is to develop a multiaxial yield surface for trabecular skull bone. To achieve this, we use finite element analysis to examine hundreds of multiaxial loading conditions with both normal and shear loads each applied to 12 different microstructural trabecular bone samples (with a goal of eventually analyzing 30). The final result is a three-dimensional yield surface plotted in both principal stress and principal strain space. We used an approach similar to one that has been previously published [1], but considered a different bone (skull), additional microstructure models, and completed a statistical analysis of yield points in relation to porosity. The resulting compilation of yield points from thousands of simulations gives an overall characterization of the yielding behavior for trabecular bone.

METHODS

Trabecular bone microstructure models were derived from microCT scans of the skull of a six-month old Gottingen minipig. The full skull was cropped to smaller 3.15mm^3 volumes to create the 30 microstructures of interest. Each was taken from a different location in the skull, and thus has a different level of porosity. Volume meshes of these models were then created in Ansys with roughly 400-500 thousand elements per microstructure. Figure 1 shows 5 of the thirty microstructure meshes.

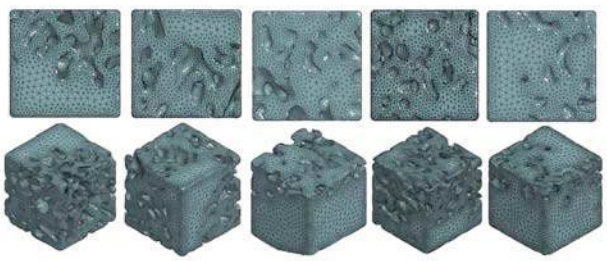

Figure 1: 5 of the 30 microstructure models used in this study

Copyright 2016 The Organizing Committee for the 2016 Summer Biomechanics, Bioengineering and Biotransport Conference

To set up simulations and span all areas of stress space, a systematic approach was used to determine displacement boundary conditions. Boundary conditions of two types were simulated. The first was normal loading where displacement loads were applied uniaxially, biaxially or triaxially normal to the face of the microstructure. And the second was a combination of normal and shear loading where displacement loads were applied uniaxially normal to one of the microstructure's faces along with a shear load parallel to one of the microstructure faces. The equation of a sphere was used to systematically determine the ratios of x, y and z displacements, for each boundary condition type, to ensure all areas of stress and strain space (uniaxial, biaxial, triaxial, tension and compression) were covered. In total, each of the 30 microstructures was subjected to 457 simulations, each with unique boundary conditions.

So far, 12,796 of the 13,710 total simulations were completed. In order to semi-automate and standardize this process, an algorithm was written to automatically set-up, submit and analyze all simulations for each model by setting up the LS-Dyna input files, submitting the simulations to run in parallel on Penn State's supercomputing cluster, extracting the results, and determining the yield points from each simulation using a variation of the 0.2% offset method. Simulations were run at a strain rate of roughly $60s^{-1}$ using an elastic perfectly plastic material model with material properties taken both from the literature and from physical experiments (Young's Modulus = 7.5GPa, Yield Stress = 20.3 MPa). After all simulations were complete, yield points were plotted in three-dimensional principal stress and principal strain space to compare the differences between different simulations loading conditions, as well as between each of the microstructures in order to determine how porosity plays a role in the results.

RESULTS

Yield points were plotted to compare results between microstructures and simulations. Although each microstructure was subjected to the exact same boundary conditions, their resulting yield points from those simulations were rather different. Points generally populated a surface of the same shape (a diagonally oriented modified ellipsoid) but the radii and curvatures were different depending on the porosity of the model. Figure 1 shows the span of yield points for the microstructures in stress space for simulations that had biaxial loading in the x and y-directions. Results are similar for the other two biaxial directions, as well as for simulations were loads were applied triaxially.

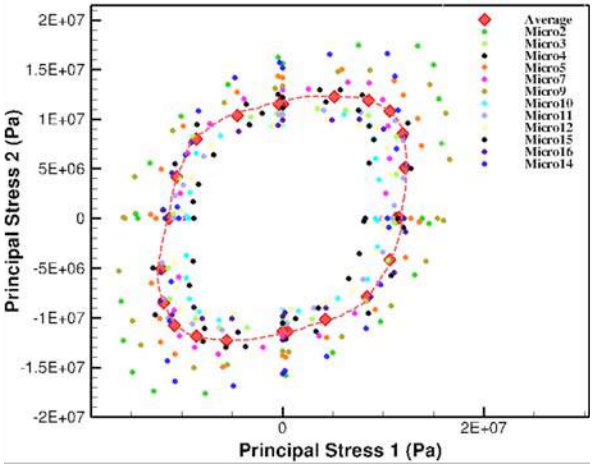

Figure 2: Yield stresses for biaxial XY simulations for 12 of the 30 microstructures. Average yield points shown in red.

To get a more overall response for trabecular bone, all yield points were averaged between the microstructure models for each of the loading conditions (red triangles in Figure 1). When looking at these averaged yield points in the three biaxial planes (xy, yz, xz), the results are nearly identical- showing that, for these chosen samples, trabecular bone displays isotropic yielding behavior-despite some other studies that have stated otherwise[2].

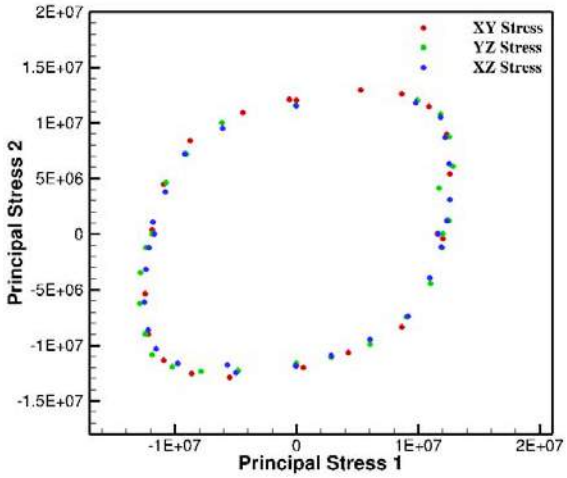

Figure 3: Average Biaxial yield stresses are identical in each plane (XY, YZ, XZ) - proving isotropy for these trabecular bone samples

DISCUSSION

The primary objective of this research was to develop a three-dimensional yield surface in both stress and strain space and investigate the effect of porosity on the failure of trabecular bone. The equation for the three-dimensional porosity-based yield surface derived from the resulting yield points can be used in new material models to govern the failure behavior of trabecular bone under a certain stress/strain state.

This dependence on porosity is clear when looking at the spread of yield points in Figure 1. For the same loading condition, each microstructure produces a different yield point. In light of this, porosity must be included in models in order to obtain an accurate response. Some efforts have said that volume fraction (porosity) plays a minimal role in yielding behavior [3], however, here, we see the opposite-where porosity greatly affects the resulting yield points, as noted by the spread in the data. Trabecular bone comes in many levels of porosity. In fact, in porcine skull bone, it has been shown that there is a gradient of porosity throughout its thickness. Thus, when developing an equation for a yield surface, this variation in porosity must be reflected so the material model governing the behavior of trabecular bone is accurate.

ACKNOWLEDGEMENTS

This work was supported by the Army Institute for Soldier Nanotechnology at MIT as well as the United States Army Research Laboratory.

REFERENCES

1. Bayraktar, H.H., et al., *The modified super-ellipsoid yield criterion for human trabecular bone.* Journal of biomechanical engineering, 2004. **126**(6): p. 677-684.
2. Keaveny, T.M., et al., *Differences between the tensile and compressive strengths of bovine tibial trabecular bone depend on modulus.* Journal of biomechanics, 1994. **27**(9): p. 1137-1146.
3. Niebur, G.L., M.J. Feldstein, and T.M. Keaveny, *Biaxial failure behavior of bovine tibial trabecular bone.* Journal of Biomechanical Engineering, 2002. **124**(6): p. 699-705.

Copyright 2016 The Organizing Committee for the 2016 Summer Biomechanics, Bioengineering and Biotransport Conference

SB³C2016
Summer Biomechanics, Bioengineering and Biotransport Conference
June 29 –July 2, National Harbor, MD, USA
SB³C2016-1051

DIRECT QUANTIFICATION OF SOLUTE DIFFUSIVITY IN POROUS, VISCOELASTIC MATERIALS USING CORRELATION SPECTROSCOPY

Janty Shoga (1), Christopher Price (1, 2)

(1) Biomechanics and Movement Science
University of Delaware
Newark, DE, USA

(2) Department of Biomedical Engineering
University of Delaware
Newark, DE, USA

INTRODUCTION

Osteoarthritis (OA) is a debilitating disease affecting millions of Americans. OA progression is slow and cumulative, and patients typically do not present symptoms until late-stage time points, leaving clinicians with limited treatment options. Earlier diagnosis of OA may allow for improved outcomes through proactive treatment strategies.

One of the earliest signs of OA is proteoglycan loss in the articular cartilage [1]. The negatively charged proteoglycans are essential for cartilage's characteristic water retention, which modulates the tissue's low friction properties and fluid load support [2]. Solute-matrix interactions and interstitial fluid flow in articular cartilage are also affected by the loss of proteoglycans [3]. Thus, changes in solute-matrix interactions may be useful as markers of early OA.

Recently, Fluorescence Correlation Spectroscopy (FCS) has been used to quantify the diffusivity of various solutes in healthy and chemically degraded cartilage [4]. While FCS is a well-established technique, it is somewhat limited by its use of a stationary, confocal observation volume. Raster Image Correlation Spectroscopy (RICS) is a confocal laser scanning microscope-based extension of correlation spectroscopy that can determine the diffusivity of solutes within images [5]. However, RICS has not been used to quantify solute diffusion in solid media. The goal of this study was to use FCS and RICS to quantify the diffusion of fluorescent solutes in strained and unstrained plugs of agarose and cartilage.

METHODS

A. Agarose

Agarose plugs (3-mm diameter, 1.5-mm thick, n = 55) were prepared at 1, 3, and 5% wt/vol. Plugs were equilibrated for 24 hours in 10 nM solutions of either fluorescein isothiocyanate (FITC, MW = 389 Da), AlexaFluor (AF) 488-Conjugated 3K Dextran (MW = 3,000 Da), or AF488-10K Dextran (MW = 10,000 Da). Correlation spectroscopy was performed at 3 locations within each sample to obtain an average diffusivity value. Samples were quantified at 0 and 10% equilibrium strain, applied via unconfined compression.

B. Cartilage

Articular cartilage plugs (3-mm diameter) were harvested from juvenile bovine medial femoral condyles (< 1 year old; n = 3). Each plug was cut into three 1-mm thick sections (n = 35), with each section corresponding to a cartilage zone (i.e. superficial, middle, or deep). Section were stained with DAPI followed by 24-hour equilibration in 10 nM of FITC or AF488-3K Dextran. Correlation spectroscopy was performed at three locations within each sample to obtain an average diffusivity value. Samples were observed under 0, 10, 20, and 30% equilibrium strain, applied via unconfined compression.

C. Correlation Spectroscopy

Diffusivity was quantified via FCS and RICS, following previously described protocols [5-7]. FCS is an Eulerian measurement technique, in which fluorescent intensity fluctuations due to transits through a 1-fL observation volume are analyzed via autocorrelation, and fit to a diffusion model to calculate diffusivity. RICS is an image-based method, which exploits the time lags between consecutively captured pixels in a raster-scanned image to quantify the diffusivity of the particles in the system under observation. Autocorrelations are performed on these images, and fit to a 3-D diffusion model that contains scanning parameters to obtain a diffusion coefficient. This analysis was performed using custom MATLAB scripts.

D. Microscopy

All experiments were performed at room temperature using a 40X water-immersion lens on a Zeiss LSM780 or LSM880 microscope. A

Copyright 2016 The Organizing Committee for the 2016 Summer Biomechanics, Bioengineering and Biotransport Conference

488-nm laser was used to excite all fluorescent dyes. RICS images (256 x 256 or 512 x 512 pixels) were captured at 200-320x (spatially oversampled) according to established protocols [8]. All data was captured at a depth of 20-μm into the sample.

Point spread function (PSF) size calibrations, which are required to calculate diffusivity using FCS and RICS, were performed using an aqueous FITC solution and standard diffusivity of 450-$\mu m^2/s$. Experimental diffusivity measurements of the other solutes and conditions were quantified using the calibrated PSF parameters, and are reported with reference to FITC.

E. Statistical Analysis

Two-way ANOVA, with replication, was performed on all data sets. One-way ANOVA with Tukey's post-hoc test was used to determine significance between groups. For all tests, $p < 0.05$ indicated significance.

RESULTS

A. Agarose

The diffusivity of fluorescent solutes in agarose was dependent upon the solute size and agarose concentration. As expected, the effects of gel concentration were dependent upon the effects of solute size, and vice versa (two-way ANOVA). Diffusivity decreased with both increased solute molecular weight and increased agarose concentration. FCS and RICS measures demonstrated similar trends (Fig. 1). Solute diffusion also decreased with compressive strain (not shown).

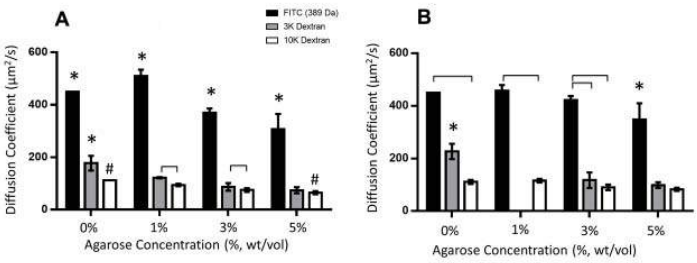

Figure 1: Diffusion coefficients of FITC, 3K dextran, and 10 K dextran determined by FCS (A) and RICS (B) in 0, 1, 3, and 5% agarose. Bars signify mean ± SD. Groups marked by * are significantly different from all other groups ($p < 0.05$, One-way ANOVA, Tukey post-hoc). Brackets and # indicate groups that are significantly different from each other. (n = 5 for each group)

B. Cartilage

Both FCS and RICS data showed that axial strain significantly affected solute diffusivity (two-way ANOVA, $p < 0.05$). We observed that solute diffusivity decreased between 0% and 10% compressive strain in superficial zone cartilage (Fig.2). No trends were apparent at higher levels of strain or in the deeper zones of cartialge. Diffusion coefficients determined by RICS tended to be slightly lower than those found via FCS. The diffusivity of FITC and 3K Dextran were also compared in zonally matched cartilage samples. As expected, the diffusivity of FITC was found to be greater than that of the 3K Dextran (not shown).

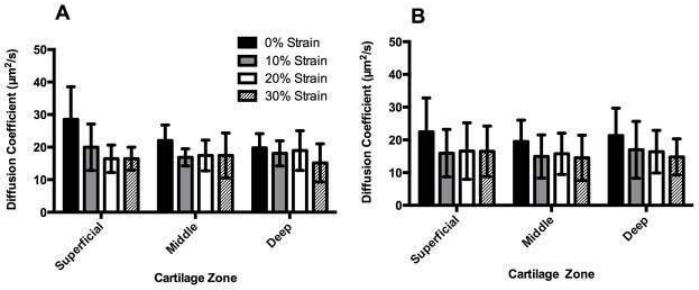

Figure 2: Diffusion coefficients of 3K dextran determined by FCS (A) and RICS (B) in the superficial, middle, and deep zones of bovine calf cartilage under 0, 10, 20, and 30% strains. Bars signify Mean ± SD. (n = 12 for each group)

DISCUSSION

FCS and RICS demonstrated similar accuracy in determining solute diffusivity in agarose and cartilage. Greater precision was observed in the measurement of diffusivity in agarose than in cartilage, potentially due to the fact that agarose is a more homogeneous material. Inhomogeneity may influence correlation spectroscopy sensitivity due to the effects of spatial averaging. Presently, we are developing spatial windowing analysis technique for RICS to increase its spatial sensitivity and to enable diffusivity mapping within an observation sub-region.

Articular cartilage structure and function has been shown to be heterogeneous through the joint [9], which could explain the variability in diffusivity observed experimentally. Similar trends, demonstrating no difference in solute diffusivity between the middle and deep zones of articular cartilage, but differences between the superficial and middle/deep zones have been reported previously [10]. Ongoing work is investigating the quantification of matrix porosity based upon these diffusion data, in order to better understand the influence of matrix structure on solute-matrix interactions and diffusivity.

Future work will extend these analysis techniques to the study of osteoarthritic human cartilage in order to determine if pathophysiological changes in solute-matrix interaction can be detected via correlation spectroscopy.

ACKNOWLEDGEMENTS

This work was supported by funding from the NIH R21 AR062738.

REFERENCES

[1] Rizkalla, G et al. (1992) J Clin. Invest.
[2] Armstrong, C.G et al. (1982) J Bone Joint Surg Am.
[3] Kwan, M.K et al. (1984) Ann Biomed Eng.
[4] Lee, J. I. et al. (2011) J. BMC Biotechnology.
[5] Elson, E. L. et al. (1974) Biopolymers.
[6] Brown, C. M., et al. (2008). Journal of Microscopy.
[7] Hendrix, J et al. (2013). Biophys J.
[8] Digma, M. A et al. (2005). Biophys J.
[9] Moore, A.C et al. (2015). Osteoarthritis and Cartilage.
[10] Leddy, H et al. (2003). Annals of Biomedical Engineering.

Copyright 2016 The Organizing Committee for the 2016 Summer Biomechanics, Bioengineering and Biotransport Conference

SB^{3}C2016
Summer Biomechanics, Bioengineering and Biotransport Conference
June 29 –July 2, National Harbor, MD, USA
SB^{3}C2016-1052

NOVEL GROWTH AND REMODELING MECHANISMS MAY EXPLAIN THE UNIQUE EXPANSION PATTERNS AND EVOLVING MECHANICAL BEHAVIOR OF ABDOMINAL AORTIC ANEURYSMS

J.S. Wilson (1), C.J. Cyron (2), J.D. Humphrey (3)

(1) Department of Radiology
Emory University
Atlanta, GA, USA

(2) Department of Mechanical Engineering
Technical University of Munich
Garching, Germany

(3) Department of Biomedical Engineering, Department of Surgery, and Vascular Biology and Therapeutics Program
Yale University / Yale School of Medicine
New Haven, CT, USA

INTRODUCTION

The optimal timing of surgical intervention for abdominal aortic aneurysms (AAAs) remains a significant challenge as a clinician attempts to weigh surgical risk versus rupture risk for each unique case. There has been significant interest in using computational models of aortic mechanics to estimate this rupture risk, but classic stress analyses are unable to account for the evolving nature of these complex lesions. Thus, growth and remodeling (G&R) models that attempt to capture the evolution of the primary biomechanical constituents of the aortic wall have increasingly been explored to gain insight and identify key factors governing AAA progression and outcomes. Nevertheless, these models have yet to capture the full range of AAA expansion patterns observed clinically, notably including the propensity for stepwise increases of maximum diameter [1], nor have they reproduced the wide range of mechanical behaviors observed experimentally from in vitro tissue testing [2]. One possible reason for this shortcoming may be the failure to include the biochemomechanics of intraluminal thrombus (ILT), a heterogeneously evolving and biologically active structure present in the majority of AAAs, which has only recently begun to be incorporated into G&R models [3]. We have previously hypothesized that dissection of the ILT could destabilize an AAA [4]. Herein, we explored the potential for intermittent thrombus deposition and dissection, combined with evolving collagen G&R parameters, to explain the observed clinical and mechanical behavior of AAAs.

METHODS

A previously described axisymmetric G&R membrane model of AAAs [5] was modified (with only key changes noted here) to capture phenomenologically the biological effect of the deposition and evolution of ILT on the underlying aortic wall. Briefly, an AAA was initiated by prescribing elastin loss from a normal aorta endowed with best-fit material properties derived from published data [6]. Following stabilization of the lesion as a result of G&R, space-filling thrombus deposition was prescribed. Since the luminal layer of ILT possesses the greatest amount of proteolytic enzymes [7], a gamma-like function was used to define an evolving half-life of collagen ($t^c_{1/2}$) in the wall as a function of adjacent normalized ILT thickness ($\bar{h}_{ILT}$) according to

$$t^c_{1/2}(\tau) = \left(t^{lum}_{1/2} - t^{c,h}_{1/2}\right)\bar{h}_{ILT}(\tau)\exp\left(1 - \bar{h}_{ILT}(\tau)\right) + t^{c,h}_{1/2} \quad (1)$$

where $t^{lum}_{1/2}$ is the minimum collagen half-life induced by luminal ILT and $t^{c,h}_{1/2}$ represents the homeostatic half-life of collagen. Idealized dissections of ILT (which bring 'luminal' properties to the ILT-wall interface) were simulated at prescribed times by resetting the half-life to $t^{lum}_{1/2}$ before a first order decay to $t^c_{1/2}(\tau)$ to simulate re-thrombosis.

To account for the increase in material stiffness in AAA tissue, the stiffness parameter within the Fung exponential (c^c_2) describing the strain energy function for collagen was increased by a factor α following complete elastolysis. However, we also hypothesized that stiffness would decrease for newly deposited collagen fibers when collagen half-life was significantly reduced since activated proteases and associated rapid turnover may inhibit cross-linking and the formation of thicker fibers. Thus, for AAA tissue c^c_2 was equal to its homeostatic value below a prescribed half-life $t^{c,*}_{1/2}$ and was equal to αc^c_2 for half-lives above $t^{c,*}_{1/2} + \Delta t$, with a linear transition across Δt.

Also differing from our previous G&R models, we allow the pre-stretch of collagen (G^c) to decrease from 1.05 to 1.01 following complete elastolysis. Physiologically, this change may be explained by contractile cells that produce collagen (e.g., smooth muscle cells and myofibroblasts) locally contracting the surrounding matrix, inserting a new collagen fiber, and then releasing the matrix to induce a pre-stress

Copyright 2016 The Organizing Committee for the 2016 Summer Biomechanics, Bioengineering and Biotransport Conference

in the new fiber. Thus, as the local matrix stiffens due to loss of elastin and increased cross-linking, pre-stretch decreases as the cells cannot compress the matrix to the same degree (cf. Figure 3 in [8]). Since the degree of cross-linking before the cells release the matrix will determine the pre-stress in each new fiber, we introduce a multiplication factor β to increase pre-stress that varies with c_2^c. The final collagen stiffness parameter (c_1^c) can then be calculated to ensure the new pre-stress.

RESULTS

Figure 1 demonstrates the stepwise expansion at the apex of the AAA as a result of robust growth and remodeling punctuated by four destabilizing events (initial elastolysis, deposition of thrombus, first ILT dissection, second ILT dissection). Spikes in circumferential (and axial) Cauchy stress coincide with periods of expansion and decreased wall thickness (not shown). Peak stress increased as the lesion expanded with the exception of the initial peak stress when almost all elastin and smooth muscle were lost to initiate the lesion.

Simulated equibiaxial stress-stretch plots in Figure 2 before, during, and immediately after the second ILT dissection demonstrate the evolving mechanical behavior of the aortic wall. Previous cycles are similar, and the curves shift left before the cycle repeats during the next expansion. Comparison is provided to three representative equibiaxial curves from two AAA subgroups (1 stiff and 2 moderate) described in [9] based on data from testing excised AAA samples [2].

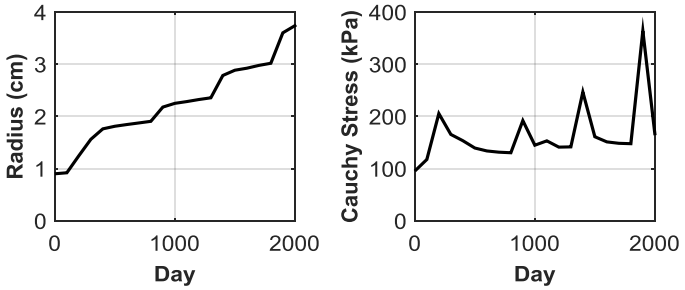

Figure 1: Evolution of radius and circumferential Cauchy stress at the apex of the AAA.

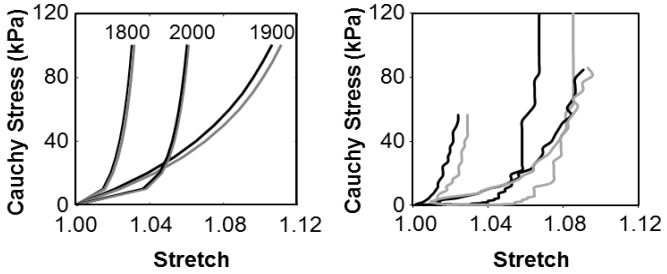

Figure 2: (Left) Simulated equibiaxial stress-stretch behavior at the apex of AAAs before, during, and immediately after expansion (1800-2000 days). (Right) Representative AAA equibiaxial data from [2]. (Circumferential = black, Axial = gray)

DISCUSSION

Stepwise AAA expansion requires intermittent destabilization events followed by robust G&R capable of arresting further expansion (often within as little as a few months [1]). This G&R can take the form of increased collagen production or altered mechanical properties such as material stiffness and pre-stretch. Herein, we demonstrate that deposition of a biologically active ILT can destabilize a previously stable AAA until the active luminal layer (~2mm) is displaced from the underlying wall as the ILT thickens. Furthermore, we propose that dissection of fresh blood and inflammatory cells deep within the ILT can lead to punctuated periods of expansion. Such ILT dissections have been visualized clinically as the 'crescent sign' on CT imaging with contrast [10], and are further supported by evidence of iron accumulation and inflammatory cells embedded deep within the ILT of experimental rat AAAs with thick thrombi [11] and by increased uptake of USPIO nanoparticles in focal regions of deep ILT in expanding human AAAs [12]. Importantly, these results suggest that rupture risk may not monotonically increase, but rather peak during destabilization events. Thus, prediction of these events may be as important, if not more, than predicting exact failure stresses.

The wide variation and increased stiffness of AAA material behavior reported in [2] was further analyzed and sub-categorized according to circumferential stiffness and anisotropy in [9]. Increasing the collagen material stiffness allowed a better fit to the steep stress-strain curves from experimental data and may be a result of increased cross-linking. Capturing the stiffest behavior also required a reduction in collagen pre-stretch. The assumption that the stiffness of new collagen decreases with half-life (which drops during destabilization events) allowed rapid expansion until half-life normalized. The resulting cycle of predicted material behavior observed in Figure 2 suggests that periods of expansion may be 'encoded' in the material behavior of the aortic wall, with the moderately stiff behavior indicating current or recent rapid expansion. Furthermore, this cyclic evolution of simulated behavior suggests that much of the variation in the experimental data may reflect random sampling of common AAA evolution patterns as opposed to unrelated patient variability.

This model is currently limited by the need to prescribe the times of ILT deposition and dissection, as well as the use of elastin mass as a proxy for gross matrix stiffness. Future fluid-solid-growth models that include metrics determining thrombus formation, the mechanics and failure of fibrin, and a direct relationship between pre-stretch and evolving matrix stiffness would be beneficial. Further data and computational analysis regarding AAA expansion and mechanics apart from the apex is also needed. Nevertheless, the current model has provided insight.

In conclusion, the novel G&R mechanisms of thrombus-induced destabilization, matrix-dependent pre-stretch, and cyclically evolving material behavior qualitatively reproduce the best available data regarding human AAA expansion and mechanics at the apex of these complex lesions. In vitro and in vivo experiments to confirm these findings are recommended and are under development.

ACKNOWLEDGEMENTS

This work is supported by AHA award 13PRE14130007 and NIH training grant T32HL007745 (JSW), the Emmy Noether grant CY 75/2-1 of the German Research Foundation (CJC), and NIH grants R01 HL086418 and U01 HL116323 (JDH).

REFERENCES

[1] Kurvers, H et al. *J Am Coll Surg*, 199:709-15, 2004.
[2] Vande Geest, JP et al. *J Biomech*, 39:1324-34, 2006.
[3] Virag, L et al. *Ann Biomed Eng*, 43:2852-67, 2015.
[4] Wilson, JS et al. *J Biomech Eng*, 135:021011, 2013.
[5] Wilson, JS et al. *J Royal Soc Interface* 9 (74), 2047-2058, 2012.
[6] Vande Geest, JP et al. *J Biomech Eng*, 126: 815-22, 2004.
[7] Houard, X et al. *Cardiovasc Res*, 82: 532-41, 2009.
[8] Hinz, B. *Periodontol 2000*, 63:14-28, 2013.
[9] Wilson, JS et al. *J Biomech*, 47:2995-3002, 2014.
[10] Roy, J et al. *J Vasc Surg*, 48:1108-13, 2008.
[11] Nchimi, A et al. *Eur Radiol*, (in print), 2015.
[12] Richards, JM et al. *Circ Cardiovasc Imag*ing, 4:274-81, 2011.

Copyright 2016 The Organizing Committee for the 2016 Summer Biomechanics, Bioengineering and Biotransport Conference

SB³C2016
Summer Biomechanics, Bioengineering and Biotransport Conference
June 29 –July 2, National Harbor, MD, USA
SB³C2016-1053

SYNTHESIS AND CHARACTERIZATION OF MESOPOROUS FORSTERITE POWDER FOR BIOMEDICAL APPLICATION

S.M. Mirhadi (1), F. Tavangarian (2)

(1) Department of Materials Engineering, Shahreza Branch, Islamic Azad University, 86145-311, Shahreza, Isfahan, Iran

(2) Department of Engineering and Technology Management, Morehead State University, Morehead, KY 40351, United States

INTRODUCTION

Forsterite with the chemical formula Mg_2SiO_4 has attracted the attention of many scientists as a bioceramic in the recent decades [1]. Si and Mg components of forsterite play a vital role in the growth and mineralization of the bones in human bodies [2]. In some studies performed by Carlisle [3,4] it was found that silicon (more than 5 wt.%) was uniquely localized in the active growth areas in the bones of young rats (when the Ca/P ratio was 0.7) and involved in the early stage of bone calcification in physiological conditions. Similar studies showed that the growth rate of rats was increased by adding silicon to their diets. Furthermore, it was found that silicon deficiency in rats resulted in skull deformations [5].
Magnesium also plays a significant role in the bone fragility, bone-growth, osteoblastic activities and degradation of hydroxyapatite crystals [6]. In clinical experiments, it is proven that Mg-containing materials such as diopside [7], bredigite [8] and merwinite [9] can be promising candidates for bone tissue engineering at load bearing applications.

Forsterite has been synthesized by various techniques such as the polymer precursor method [10], heat treatment of the mixed powders prepared by alkoxymethod [11], the sol–gel method [12] and ball milling method [13]. During the synthesis of forsterite, it is very difficult to avoid the formation of enstatite (MgSiO3) or/and periclase (MgO). Annealing up to 1200–1600 °C is reported to be necessary to obtain single phase forsterite structure.

In this paper mesopore forsterite powder was synthesized at much lower temperature, regarding to the conventional synthesis method, by a sol-gel method. mesoporous structure can boost the cell growth, bioactivity, and biological fixation in bone defect. The forsterite formation mechanism was studied as well.

METHODS

Forsterite powder was synthesized according to the following steps: sol-gel method and subsequent annealing at 600 to 1000 °C for 1h. In order to prepare the forsterite powder, proper amount of magnesium nitrate and silica were dissolved in deionized water utilizing magnetic stirrer to result stoichiometric forsterite structure with Mg:Si molar ratio of 2:1. A solution of sucrose with the molar ratio of sucrose to metal equal to 4:1 was prepared. Then this solution was added gently to nitrate solution while it was stirring. Subsequently a solution of polyvinyl alcohol with PVA to metal molar ratio of 0.5:1 was added to the obtained sucrose and nitrate solution and then the pH was adjusted to 1 utilizing nitric acid. Subsequently, the solution was heated at 200 °C for 24h. Heat treatment of ball milled powders was carried out from 600 to 1000 °C for 1 h in air.

To evaluate the thermal behavior of the ball milled powder, thermogravimetry (TG) test was performed up to 1200 °C at a heating rate of 10 °C/min. Phase transformation of the obtained powders after heat treatment was investigated by X-ray diffractometry (XRD) using a Philips X'PERT MPD diffractometer with Cu Kα radiation (λ=0.154056 nm). The XRD patterns were recorded with a step size of 0.04° and a time per step of 1 s. The morphology of powder particles was studied by field emission scanning electron microscopy (SEM) (Quanta3D FEG, FEI Company, USA) at acceleration voltages between 20 kV.

Copyright 2016 The Organizing Committee for the 2016 Summer Biomechanics, Bioengineering and Biotransport Conference

RESULTS

Fig. 1 shows the thermal gravimetric (TG) and differential thermal gravimetric (DTG) analyses curves of RS. Three main stages were observed in the TG curve. The first stage (5%) belonged to the region below 200 °C, accompanied with an endothermic peak at around 130 due to the removal of free water. The second stage of weight loss (47%) was observed from 200 to 600 °C which is accompanied with two exothermic peaks at around 320 and 500 °C can be assigned to the decomposition of precursor, burning of carbon and formation of magnesium oxide, respectively [14]. The third stage of weight loss (7%) accompanied with an exothermic peak at around 715 °C is due to the formation of forsterite powder [15]. Forsterite forms through diffusion-controlled mechanism. Hence the exothermic peak assigned to the formation of forsterite structure is spread from 650 to about 800 °C.

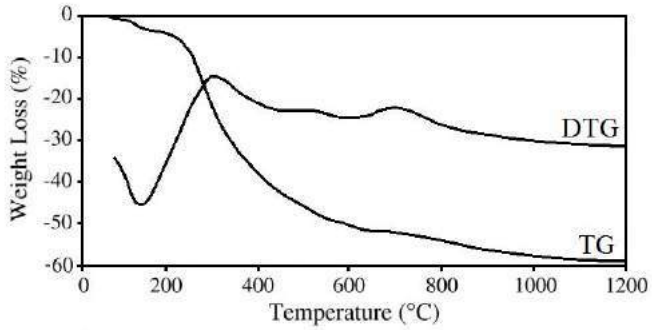

Fig. 1. The TGA evaluation of the obtained powder from sol gel method.

Based on the results obtained from thermal analysis, powders were annealed at various temperatures and the produced powders were characterized by X-ray diffraction method to reveal the phase transformations occur during heat treatment. The XRD patterns of the prepared powders after sintering at 610 °C for 6h are shown in Fig. 2.

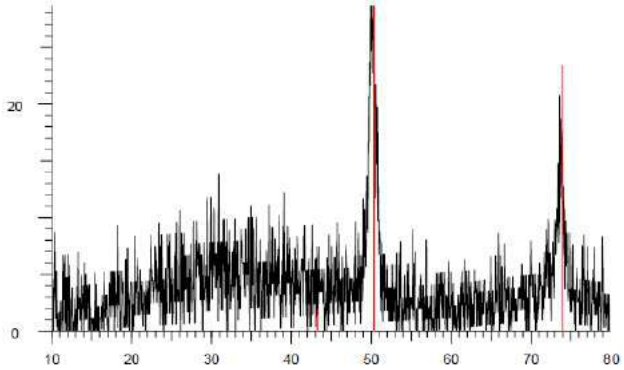

Fig. 2. XRD patter of the heat treated sample at 610 °C for 6 h.

An amorphous structure was observed on the XRD pattern of powder. Annealing of powder at 610 for 6h led to the formation of MgO (XRD JCPDS data file No. 43-1022) in the structure. With increasing the annealing temperature to 750 °C, forsterite peaks (XRD JCPDS data file No. 34-0189) were observed in the XRD pattern. Forsterite formation mechanism was investigated in our previous study [16]. Initially magnesium oxide forms in the structure and then the produced MgO reacts at the surface of SiO_2 to form enstatite. Subsequently, MgO diffuses through the enstatite layer and form forsterite phase. Decreasing the diffusion distances through producing smaller particles and formation of a homogenous powder cause the faster formation of forsterite structure at lower temperatures.

The morphology of the obtained forsterite powders after sintering at 610 °C for 6 h is shown in Fig. 3, respectively. As can be seen, the obtained powders consist of agglomerates with almost uniform particle size distribution. Image tool analysis was used to measure the particle size of forsterite nano-powder. It was found that the mean particle size of obtained forsterite structure after sintering at 610 was 10 µm, respectively.

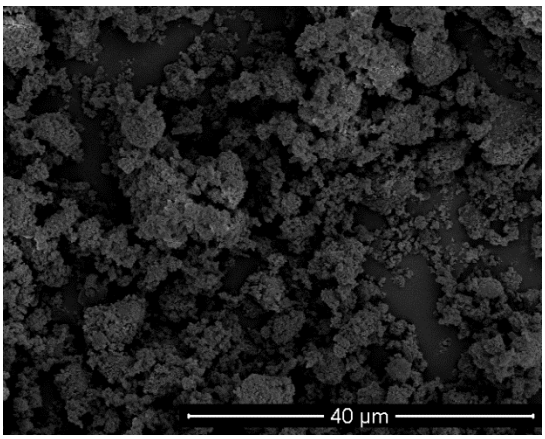

Fig. 3. Forsterite powder structure obtained after sintering at

DISCUSSION

The results of this paper showed that single-phase nanostructure forsterite powder can be obtained after sintering the obtained powders from sol gel method at 610 °C for 1h. The absence of other phases such as $MgSiO_3$, MgO and SiO_2 in the final product disclosed the beneficial effects of utilizing sol-gel procedure. The mean agglomerate size of the obtained nanostructure forsterite were 10 µm.

ACKNOWLEDGEMENTS

This investigation was partially supported by Kimiya Darou Co. Ltd. under the contract number 2896.

REFERENCES

[1] Ni, S, et al., Ceram. Int. 33:83–88,2007.
[2] Carlisle, EM, Nutr. Rev. 40:193–198:1982.
[3] Carlisle, EM, J. Nutr. 110:1046–1055,1979.
[4] Carlisle, EM, Sci. Total. Environ. 73:95–106,1988.
[5] Schwarz, K, Proc. Natl. Acad. Sci. 70:1608–1612,1973.
[6] Sojka, JE, et al. Nutr. Rev. 53:71-74,1995.
[7] Wu, C, Acta Biomater. 6:820-829,2010.
[8] F. Tavangarian, et al., Matter. Lett. 65:2354-2356,2011.
[9] M. Hafezi-Ardakani, et al., Ceram. Inter. 37:175-180,2011.
[10] Martin, MHE, et al. J. Am. Ceram. Soc. 75:1831–1838,1992.
[11] Yamaguchi, O, Chem. Lett. 5:401–404,1976.
[12] Kazakos, A, et al. Mater. Lett. 10:405–409,1990.
[13] Emadi, R, et al., J. Ceram. Proc. Res. 12:538-543,2011.
[14] Saberi, A, et al., Mater. Res. Bull. 42:666-673,2007.
[15] Tavangarian, F, et al., J. Alloys Compd. 485:648-652,2009.
[16] Tavangarian, F, et al., Powder Technol. 198:412-416,2010.

Copyright 2016 The Organizing Committee for the 2016 Summer Biomechanics, Bioengineering and Biotransport Conference

SB^{3}C2016
Summer Biomechanics, Bioengineering and Biotransport Conference
June 29 –July 2, National Harbor, MD, USA
SB^{3}C2016-1054

CHARACTERIZATION OF THE MECHANICAL BEHAVIOR OF THE OPTIC NERVE SHEATH

J. Raykin (1), R. Wang (1), T.E. Forte (1), A. Feola (1), B. Samuels (2), J.G. Myers (3), E.S. Nelson (3), R.L. Gleason (1), C.R. Ethier (1)

(1) Department of Biomedical Engineering, Georgia Institute of Technology/Emory University, Atlanta, GA

(2) Department of Ophthalmology, U. Alabama at Birmingham, Birmingham, AL

(3) NASA Glenn Research Center, Cleveland, OH

INTRODUCTION

A major priority in current space medicine research is to characterize the mechanisms underlying Visual Impairment and Intracranial Pressure (VIIP) syndrome, a group of ophthalmic changes that occur in some astronauts following long-duration spaceflight [1]. It is hypothesized that microgravity-induced cephalad fluid shifts lead to increases in intracranial pressure (ICP), which drives maladaptive remodeling of the optic nerve sheath (ONS). In this study, we investigated the effects of mechanical loading on the porcine ONS to better understand the mechanical response of the ONS to increased ICP.

METHODS

Porcine optic nerves (n=6) were obtained immediately after death from a local abattoir. The ONS was isolated from the optic nerve proper and was used for mechanical characterization. A custom mechanical testing system was developed that allowed for unconfined lengthening, twisting, and circumferential distension of the porcine ONS during inflation and axial loading. The distal end of the ONS (the end furthest from the eye) was cannulated and connected to tubing connected a pressure control system consisting of a syringe pump, a pressure transducer, and a LabVIEW program. The ONS was filled with phosphate-buffered saline and the proximal end was plugged with a small screw to create an "end cap." The sample was then hung vertically in a saline bath and subjected to six constant rate (~0.5 mmHg/s) quasi-static pressurization cycles (0-60-0 mmHg), while changes in diameter and length were simultaneously recorded. These tests were performed under variable axial loads (4.9 mN – 48 mN) by attaching increasing weights to a loop attached to the end cap.

Collagen organization in unpressurized ONSs was visualized at an axial stretch of 20% using second harmonic generation (SHG) microscopy. Image stacks were processed using a previously described fast Fourier transform (FFT) algorithm [2] to obtain fiber angle distributions. The distributions were fit to a von Mises distribution to obtain the mean fiber angle at each location of the ONS wall.

RESULTS

Despite large sample-to-sample variations between individual ONSs, there appeared to be a characteristic pattern in their mechanical response (Figure 1a). The circumferential stress was nearly constant between samples and axial loading, despite large variations in strain (Figure 1b-c). SHG imaging revealed helical and axial orientation of the collagen fibers (Figure 2a). Variations in the predominant fiber angle at different locations of the wall were observed (Figure 2b-c).

DISCUSSION

In this study, we have presented a comprehensive assessment of the mechanical response of the porcine ONS to variations in ICP. Particularly interesting was the existence of a "cross-over point" at a pressure of approximately 11 mmHg (Figure 1a). At this pressure, the same diameter was obtained for all axial loads applied to the tissue; i.e., as the axial load was varied, the diameter of the ONS remained constant. This cross-over in the pressure-diameter curves occurred in all ONSs that were tested and appears to correspond with *in vivo* ICP levels for pigs [3]. Taken together our data suggest that the ONS is a complex mechanical structure in which the bulk behavior is determined by the underlying microstructural properties. The presence of a cross-over point and the preservation of a nearly constant circumferential stress between the tested samples could suggest a homeostatic target for the ONS, such as the one found in arterial remodeling processes [4]. Given the similar geometry, microstructure, and nonlinear response found in this study between the ONS and blood

Copyright 2016 The Organizing Committee for the 2016 Summer Biomechanics, Bioengineering and Biotransport Conference

vessels, we believe many of the fundamental arterial growth and remodeling concepts can be applied to the ONS to better understand the mechanisms involved in VIIP.

ACKNOWLEDGEMENTS

This work was supported by the National Space Biomedical Research Institute through NCC 9-58, by NASA's Human Research Program through the Digital Astronaut Project (DAP) and NASA grant number NNX13AP91G (CRE), and by the Georgia Research Alliance. We would like to thank DeVon Griffin, Beth Lewandowski, and Paula Dempsey for administrative support. Porcine eyes were generously provided by Holifield Farms (Covington, GA).

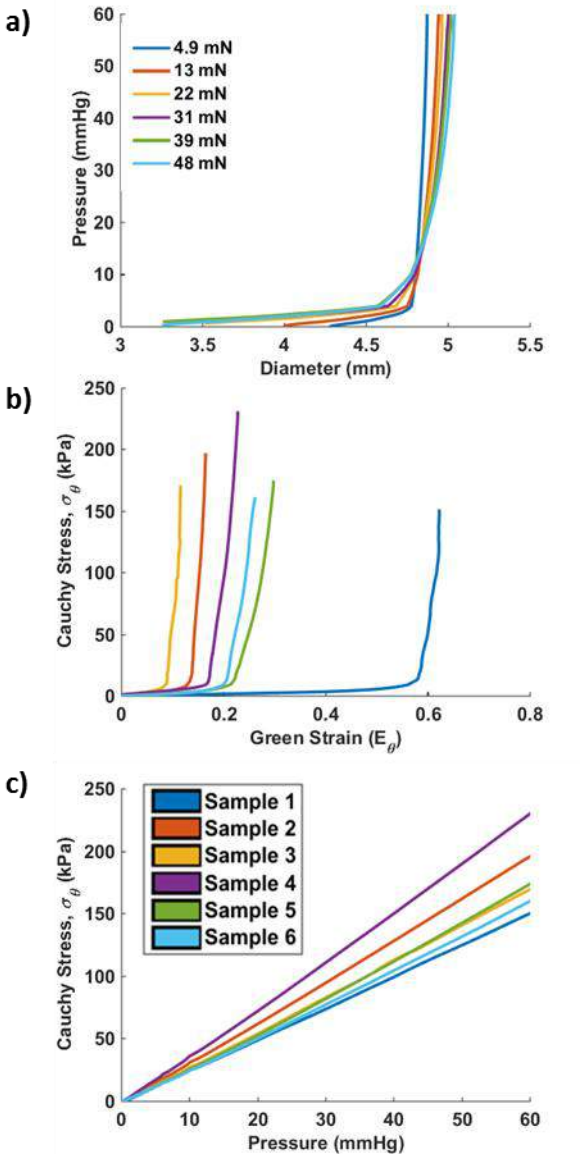

Figure 1: a) Representative pressure-diameter response of one ONS. b-c) Mechanical response of 6 porcine ONSs at an axial load of approximately 4.8 mN. b) Stress-strain response. c) Variation in the Cauchy stress in response to luminal pressure. Note that large sample-to-sample variations in the circumferential Green strain were seen, while only modest variations in the circumferential Cauchy stress were observed.

REFERENCES

[1] Alexander, DJ, et al., Evidence Report: Risk of spaceflight-induced intracranial hypertension and vision alterations. NASA, 2012.

[2] Wang, R., et al., Differential mechanical response and microstructural organization between non-human primate femoral and carotid arteries. Biomechanics and modeling in mechanobiology, 2014: p. 1-11.

[3] Kaiser, G.M., et al., Method of intracranial pressure monitoring and cerebrospinal fluid sampling in swine. Laboratory animals, 2007: 41(1):p. 80-85.

[4] Matsumoto, T. and Hayashi, K., Stress and strain distribution in hypertensive and normotensive rat aorta considering residual stress. Journal of Biomechanical Engineering, 1996: 118:62-73.

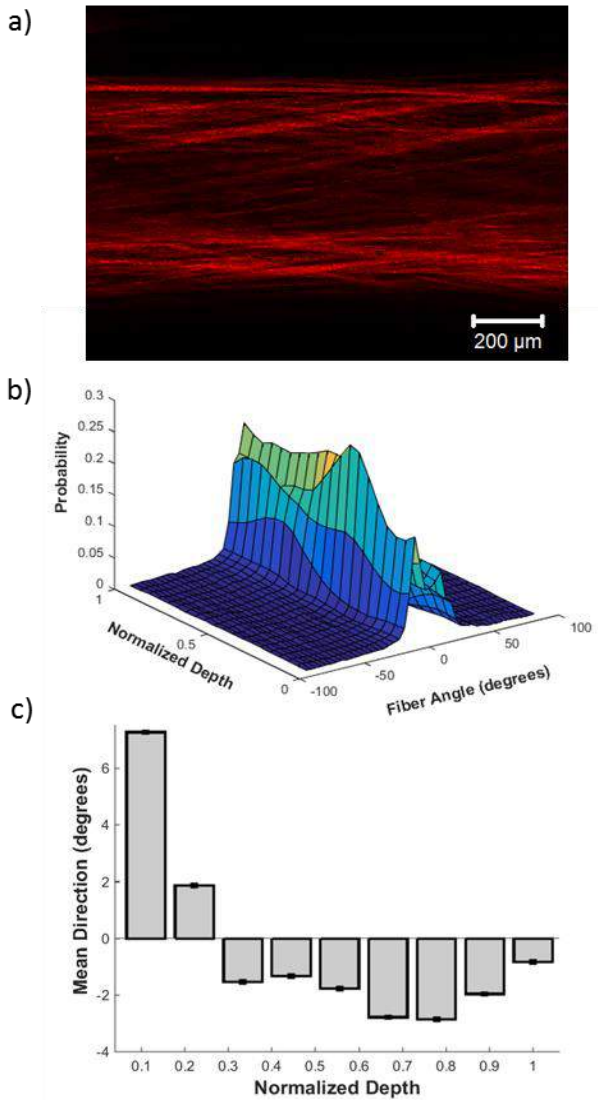

Figure 2: a) Second harmonic generation microscopy of a single, unpressurized porcine ONS at an axial stretch ratio of λ_z=1.2. b) Fiber distributions of the same ONS taken at various locations across the wall. A normalized depth of 0 corresponds to the inner surface and 1 corresponds to the outermost surface. c) Mean fiber alignment angle (mean of the von Mises distribution). 0° and 90° correspond to the axial and circumferential directions, respectively. Error bars indicate the mean ± one standard deviation.

Copyright 2016 The Organizing Committee for the 2016 Summer Biomechanics, Bioengineering and Biotransport Conference

SB³C2016
Summer Biomechanics, Bioengineering and Biotransport Conference
June 29 –July 2, National Harbor, MD, USA
SB³C2016-1055

APPLICATION OF A NOVEL BIOMECHANICAL FIBER MODEL TO TISSUE ENGINEERING FOR IMPROVED CLINICAL OUTCOMES

Andrew B. Robbins (1), Silvia Minardi (3), Ennio Tasciotti (3), Alan D. Freed (1,2), Michael R. Moreno (1,2,3)

(1) Biomedical Engineering
Texas A&M University
College Station, TX, United States

(2) Mechanical Engineering
Texas A&M University
College Station, TX, United States

(3) Methodist Research Hospital
Houston, TX, United States

INTRODUCTION

Tuning the mechanical properties of engineered tissues to match those of the native tissue they are designed to replace has become a widespread practice in the tissue engineering community (1,2,3). However, since many if not most biological materials are anisotropic, viscoelastic, and non-linear, determining their mechanical properties is highly non-trivial. The current paradigm for matching mechanical properties of tissues uses models more suited to engineering materials like steel and concrete; using just two parameters, a s tiffness and a strength measure taken from a traction stretch plot. This is not to say that there has not been extensive work done in the mechanics community creating material models that are appropriate for more complicated materials, including biological materials. But rather that there is a huge gulf between the state of the art in tissue mechanics, and the practice in the tissue engineering community. Some of this is likely due to a lack of awareness on the part of tissue engineers, but the greater hurdle is the extreme difficulty in using many of the more sophisticated material models in practice, especially in comparing native tissue to tissue engineered constructs. Models are needed that:

1) Provide a more robust description of the mechanical behavior of tissues than the current paradigm,
2) Have parameters that can be determined with simple experiments.

Freed and Rajagopal (4) have developed a novel biological fiber model that is rigorously derived from thermodynamics and the implicit theory of elasticity. This model describes not only terminal stiffness in the linear region (the current standard), but also an initial (lower) stiffness, and a heel region defined by a maximum crimp. In one dimension this results in three parameters that can be easily measured from stress strain plots. By applying this model to native tissue as well as a synthetic collagen elastin scaffolds, we can show that the behavior of materials are strongly influenced by these other parameters and two materials that have the same terminal stiffness can have very different behavior.

METHODS

Uniaxial tensile testing was performed on excised rat abdominal wall, as well as artificial tissue grafts designed for use in hernia repair consisting of porous collagen and elastin scaffolds. All samples were tested in wet conditions at 37 C. The samples were sized approximately 2x2 cm. and the samples were tested using a constant stretch rate of 5% per minute on a standard load frame (Test Resources R Controller).

The fiber model used, having been derived from implicit elasticity by Freed and Rajagopal, results in a relationship as follows, with stress and strain being the Cauchy stress and true strain respectively:

$$\varepsilon = \frac{\sigma}{E^C} + \frac{1}{\beta}\left[1 - \frac{1}{\left(1+(\beta-1)\frac{\sigma}{E^E}\right)^{\frac{\beta}{\beta-1}}}\right] \quad (1)$$

Where E^C is the stiffness in the final linear region (here denoted as the terminal stiffness), E^E is the initial stiffness, and β is the max crimp determined by the inverse of the intersection of the lines fitting the two linear regions. The current practice is to determine a single stiffness in the linear region, often called the modulus, or Young's Modulus (although this is a misnomer in most cases).

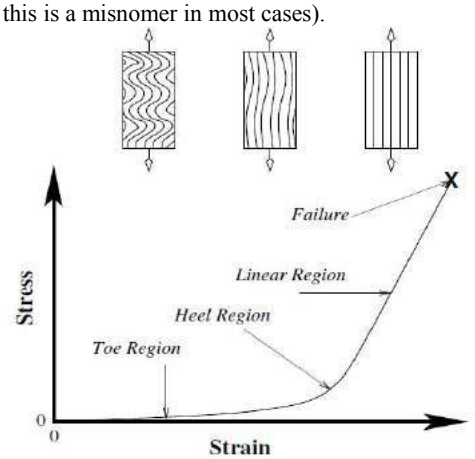

Figure 1: Diagram showing collagen fibers uncramping throughout the stress strain curve. Taken from Freed and Rajagopal (4)

Copyright 2016 The Organizing Committee for the 2016 Summer Biomechanics, Bioengineering and Biotransport Conference

RESULTS

Figure 2 shows the stress strain relationship from the rat abdominal wall. We can clearly see that there is a large initial linear region of very low modulus, a transitionary heel region, and then a much stiffer terminal region.

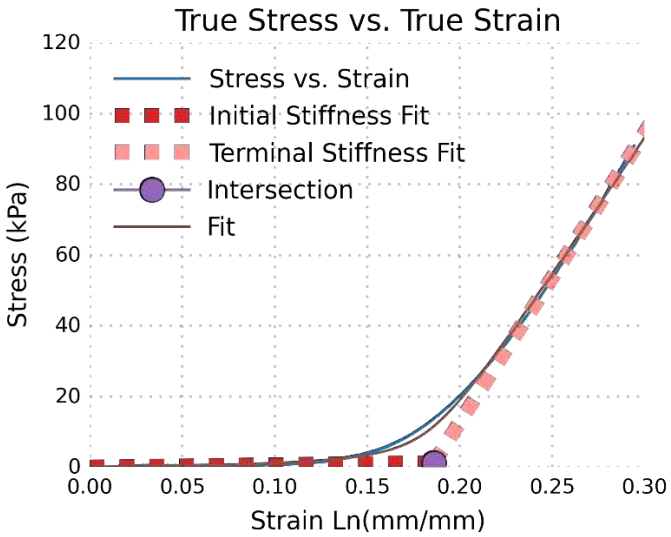

Figure 2: Example of the fiber model applied to rat abdominal wall tissue. Initial Stiffness = 5.5 kPa, Terminal Stiffness = 782 kPa, Max Crimp (Beta) = 5.5

After the native tissue, we consider hypothetical materials that match the terminal stiffness, but that do not match the initial stiffness or the max crimp. Even though the terminal stiffness is the same we can see in Figure 3 that the actual behavior of the hypothetical materials is very different. **Under the current paradigm, these materials would be said to be the same** despite the very different behavior.

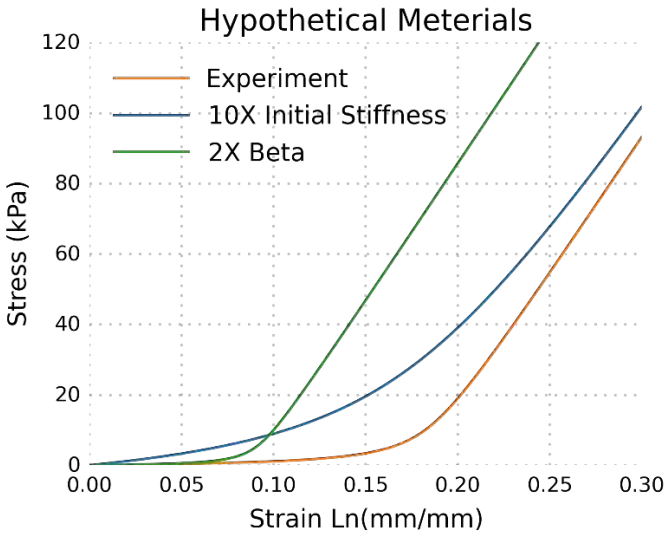

Figure 3: Even though the terminal stiffness is the same for all three models and could be said to be 'tuned' to match, we can see that the materials have very different behavior.

Finally, we compare a porous collagen elastin scaffold tuned to mimic the mechanical properties of the native tissue in Figure 4. Just like the hypothetical materials, we can see that despite the reasonable matching of the terminal stiffness, the total behavior is very different from the native tissue.

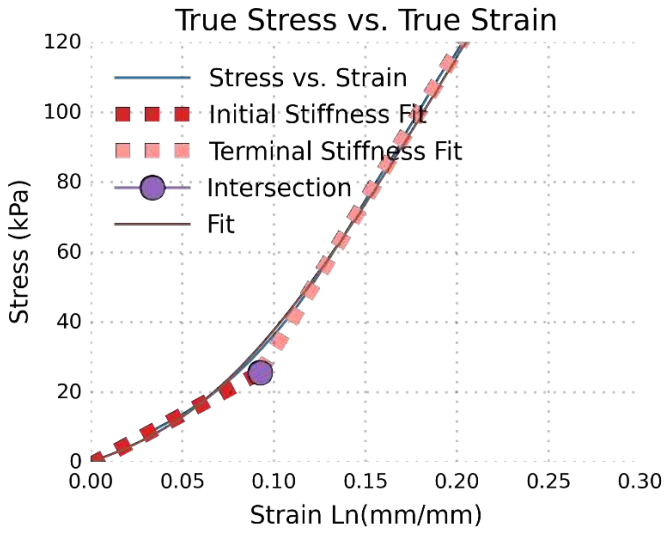

Figure 4: Example of the fiber model applied to collagen elastin porous scaffold. Initial Stiffness = 214 kPa, Terminal Stiffness = 941 kPa, Max Crimp (Beta) = 11

DISCUSSION

As we noted previously, the terminal stiffness is an important measure of the behavior of the material, but that the initial stiffness and the maximum crimp also have strong influence on the total behavior. For example, there have been indications that cells are sensitive to the smaller strains achieved in the toe region (5), and these strains may not be produced in a material with a higher initial stiffness such as the synthetic material above, even though the current paradigm would call the material well-tuned to the native tissue.

ACKNOWLEDGEMENTS

Mechanical testing of abdominal wall tissue assisted by Hunter Storaci

REFERENCES

[1] Chen, H et al., *J Biomaterials,* 76:261-272, 2016
[2] Fang, J et al., *Langmuir*, 28:8260-8265 2012
[3] Martinez, A et al., *J Carbpol,* 132:606-619, 2015
[4] Freed A et al., *Acta Mechanica*, To Appear
[5] Rubbens, M et al., *Tissue Eng Part A*, 15:841-849, 2008 (strain)

Copyright 2016 The Organizing Committee for the 2016 Summer Biomechanics, Bioengineering and Biotransport Conference

SB^{3}C2016
Summer Biomechanics, Bioengineering and Biotransport Conference
June 29 –July 2, National Harbor, MD, USA
SB^{3}C2016-1056

THERMAL CONTRAST AMPLIFICATION (TCA) READERS IMPROVE THE LIMIT OF DETECTION FOR INFLUENZA AND MALARIA LATERAL FLOW ASSAYS

Yiru Wang (1), Zhenpeng Qin (1)*, David Boulware (2), Iveth J. González (3), David Bell (3), Warren Chan (4), Peter Chiodini (5), Roxanne Rees-Channer (5), and John C. Bischof (1)**

(1) Department of Mechanical Engineering
University of Minnesota – Twin Cities
Minneapolis, Minnesota, USA

(2) Department of Medicine
Infectious Diseases and International Medicine
University of Minnesota – Twin Cities
Minneapolis, Minnesota, USA

(3) Foundation for New Innovative Diagnostics (FIND)
Geneva, Switzerland

(4) Department of Chemistry
University of Toronto
Toronto, Ontario, Canada

(5) Hospital for Tropical Disease
University College London
London, UK

(*) Current Address:
University of Texas at Dallas
Richardson, Texas, USA

(**) Current Address:
Global Good Fund (Intellectual Ventures Lab)
Bellevue, Washington, USA

INTRODUCTION

There is an increasing need for quick, easy and cheap detection and quantification of diseases such as influenza and malaria at the point-of-care (POC). For instance, influenza can cause epidemics and typically affects 5 – 20% of the population, leads to 200,000 hospitalizations and causes on average 35,000 deaths a year in the US alone [1]. In the case of malaria, there were an estimated 198 million cases worldwide and an estimated 584 000 deaths in 2013, 90% of all deaths occurring in Africa [2]. For both cases, rapid and precise detection of disease can help control epidemics (i.e. influenza) and disease eradication (i.e. malaria). To help achieve this goal we present a new reader based on technology called "thermal contrast amplification" (TCA) that improves the sensitivity and quantification of influenza and malaria in lateral flow assays (LFAs).

Lateral flow assays employ *indirect detection* of a chemical reaction to identify the target and a physical contrast (i.e. a gold nanoparticle - GNP) to visually indicate the result. The chemical reaction is based on a sandwich assay of an antibody anchored at the test line of the LFA that binds the antigen from the patient specimen as it flows by. After antigen test line binding, a GNP bound to another antibody will sandwich bind the antigen attached to the first antibody at the test line. The GNP then provides a physical contrast at the test line (i.e. red color due to plasmon resonance). By irradiating these gold nanoparticles with a visible laser that further exploits the plasmon resonance, TCA provides heat generation and a thermal signal which we have demonstrated is vastly more sensitive than visual detection alone in CrAG LFAs [3,4,5].

There are several other technologies under development to increase indirect disease detection and quantification. While typically more sensitive than LFAs, these approaches (i.e. RT-PCR or microscopy) are slower, more expensive and require training and specialized laboratory equipment. In the case of LFAs, new contrast through fluorescence molecules, magnetic beads and "readers" are also under development to replace visual gold nanoparticle based LFAs [6]. Importantly, visual readers of GNP LFAs such as the BD Veritor do not increase the visual LOD, but can reduce human error (unpublished result). Other assays (i.e. fluorescence) can be more sensitive but are subject to degradation and cannot quantify disease burden. Magnetic bead LFAs are an interesting alternative, but are not widely used and require further testing and translation for broad impact [9]. TCA, on the other hand, simply adds a reading step to existing gold nanoparticle based LFA tests. In short, the GNP based lateral flow assay (LFA) is among the cheapest, simplest and fastest possible approaches for point-of-care use, but they suffer from low detection performance (i.e. sensitivity). Here then we present a reader based on "thermal contrast amplification" (TCA) to increase sensitivity and provide quantitation. We show the reader can improve the limit of detection (LOD) over visual alone thereby improving the sensitivity and quantification of existing influenza and malaria gold nanoparticle based LFAs.

METHODS

TCA readers are based on existing GNP LFAs but instead of visual contrast, they evoke a new heat contrast under laser (Figure.1). The basic components of TCA reader are a green light source (LRS-0532-PFM-00200-03, LaserGlow, work for ~30 nm GNPs), an Infrared sensing unit (ThermoVision^{TM} A20 IR camera, FLIR), and a sample holding unit. Control software was written in LabVIEW [7]. LFAs were tested with the same protocol but slighted modified by laser output power. A second test was applied if the first was unclear.

Specifically, when irradiated with green laser (532 nm) GNPs are stimulated by surface plasmon resonance and generate heat [5],

Copyright 2016 The Organizing Committee for the 2016 Summer Biomechanics, Bioengineering and Biotransport Conference

$$Q = N \cdot I \cdot C_{abs} \quad (1)$$

This heat (Q, W/m^3) is the product of GNP concentration (N, GNPs/m^3), GNP absorption cross-section (C_{abs}, m^2), and laser intensity (I, W/m^2). The thermal contrast signal (temperature rise) is collected along a cross line of the nitrocellulose membrane [7]. TCA signal is proportional to GNP concentration as the absorption cross-section and laser intensity remain the same. In order to assess the operation of a TCA reader for detection and quantification of influenza and malaria, serial dilutions were prepared with existing LFAs.

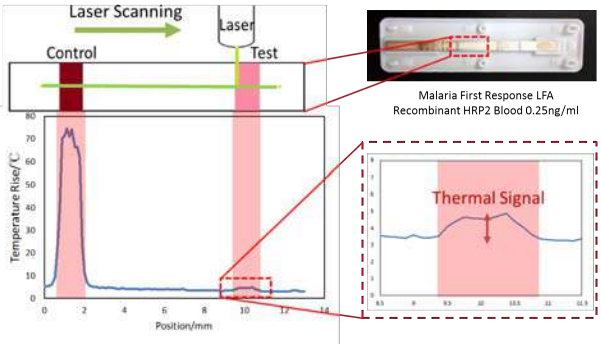

Figure 1: Thermal contrast test shows positive signal on a visual false negative malaria LFA (Rec HRP2 0.25 ng/mL in blood)

Serial Dilutions and LFA selection:

Influenza. BD Veritor Reader and LFAs were purchased directly. The system was CLIA-waived for Rapid Detection of Flu A+B. Flu A positive control swabs were used to create 1:2 serial dilution sets. The BD Veritor visual reader was used to assess the flu strips followed directly by TCA reader.

Malaria. First Response Malaria Ag. pLDH/HRP2 Combo Card Test was used. HRP2 protein (P.f parasites antigen) dilution sets were prepared by FIND and sent blind to UM collaborators. Two technicians evaluated the LFA results in FIND.

RESULTS

Quantitative thermal results for flu and malaria recombinant HRP2 in blood are shown in Figures 2 and 3 respectively with linear fitting (dashed lines). The LOD of TCA is 8 times lower than the visual reader for flu, and the visual appearance in malaria [8]. Furthermore, the signal is shown to be linear suggesting the ability to also quantify disease burden.

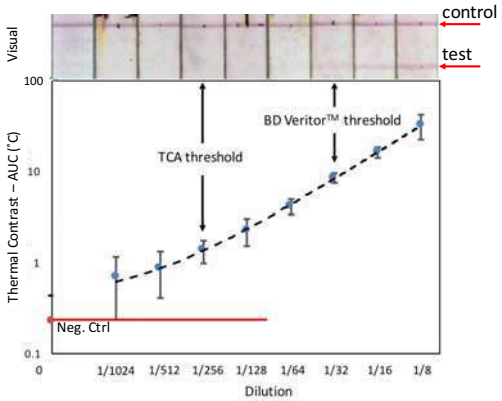

Figure 2: Quantitative TCA signal in BD Veritor flu A dilution study and scanned LFAs

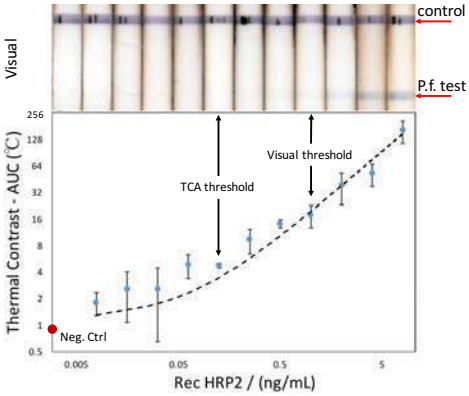

Figure 3: Quantitative TCA signal in malaria recombinant HRP2 in blood dilution study and scanned LFAs

DISCUSSION

Thermal contrast improves the performance of existing LFAs by interpreting them with the TCA reader after the test. The results show an 8-fold improvement in the LOD for both flu and malaria (Figs. 2 and 3). Previous work in Cryptococcus shows up to 32-fold improvement in a patient cohort [3,4]. The difference in the results is thought to be mainly due to the different construction of the LFAs and blood hemoglobin thermal noise in the case of malaria. For instance, the antibodies used are critical to the LFA design and their ultimate specificity and sensitivity with visual or thermal contrast. A high specificity LFA with lower sensitivity appears to offer the optimum performance increase with TCA. We got 2/19 false positives in malaria study (no false positives in influenza) which we believe due primarily to blood staining in the background. In short, sensitivity is expected to improve with TCA, while the specificity remains roughly unchanged in well-designed GNP LFAs with low background.

TCA can be further improved by careful LFA design and TCA algorithm development. For instance, the thermal signal can be improved by selecting different GNPs (larger size and/or Cabs, and more efficient matching of laser power and spectrum to the GNP). Further, the LFA can be designed to decrease background signal (i.e. noise) by changing LFA materials. In the case of malaria LFAs using blood, there may be new ways to minimize hemoglobin staining (i.e. noise) or avoiding it entirely. Finally, a new algorithm is under development leveraging improved heat transfer physics in the TCA that can improve the speed with which the LFA is read.

ACKNOWLEDGEMENTS

UM NIH CTSI seed grant, UM Mayo grant and NSF # 1066343. We thank FIND for help with the malaria LFAs in the study. John C. Bischof is Carl and Janet Kuhrmeyer Chair in Mechanical Engineering.

REFERENCES

[1] http://www.cdc.gov/flu/about/season/
[2] "WHO malaria report 2014." Geneva, Switzerland: WHO (2014).
[3] Qin, Z., Angew. Chem. Int. Ed. 2012. 51: p. 4358–4361
[4] Boulware, DR Emerging infectious diseases 20.1 (2014): 45.
[5] Qin Z. Chemical Society Reviews, 2012, 41(3): 1191-1217
[6] Posthuma-Trumpie, G. A., Anal and Bioanal Chem 393.2 (2009): 569-582.
[7] W. Scheychon, master thesis (Leibniz U. Hannover), 2012
[8] Loock, HP. Sensors and Actuators B: Chemical 173 (2012): 157-163.
[9] Xu, Q. Materials Science and Engineering C 29 (2009) 702–707

Copyright 2016 The Organizing Committee for the 2016 Summer Biomechanics, Bioengineering and Biotransport Conference

SB³C2016
Summer Biomechanics, Bioengineering and Biotransport Conference
June 29 –July 2, National Harbor, MD, USA
SB³C2016-1057

THE CHARACTERIZATION OF THE BONE MARROW MECHANICAL ENVIRONMENT USING POROELASTIC MODELS WITH MATERIAL PROPERTIES DETERMINED FROM MICRO-FINITE ELEMENT MODELING

Jason A. Shar (1), Thomas A. Metzger (2), Tyler Kreipke (3), Glen L. Niebur (2,3), Joshua A. Gargac (1)

(1) Mechanical Engineering
University of Mount Union
Alliance, OH, USA

(2) Bioengineering Graduate Program
University of Notre Dame
Notre Dame, IN, USA

(3) Aerospace and Mechanical Engineering Department
University of Notre Dame
Notre Dame, IN, USA

INTRODUCTION

Bone marrow is naturally composed of many mechanosenstive cells which may signal adaptation cascades [1] in response to fluid shear stresses resulting from whole bone loading. However, the determination of the *in situ* mechanical environment of these cells is difficult, since bone has a complex geometry and the relevant features span multiple length scales. Little is known about the mechanical environment of the bone marrow, because it is encased in the opaque bone, making observation and measurement difficult.

Finite element (FE) models can determine stress in complex geometries when generated from computed tomography (CT) images [2]. Recently, poroelasticity theory was incorporated in such models to estimate the marrow mechanics during whole porcine femur mechanical loading [3]. In the absence of density-modulus relationships for porcine bone, these models used published relationships from human bone [4].

The objectives of this study were to 1) use microscale-FE models of trabecular bone to determine the density-modulus relationship for porcine femurs, 2) develop poroelastic models of whole porcine femurs using this new material model, and 3) quantify the effect of the material model on the calculated whole bone stiffness, surface strains, pressure gradients, and fluid shear stresses.

METHODS

Five porcine femurs from five animals 6-8 months of age were procured at the time of slaughter (Martin's Custom Butchering, Wakarusa, IN), and testing was completed within 8 hours post-mortem to minimize storage effects on marrow. Miniature pressure transducers (Precision Measurements Inc., Ann Arbor, MI) were inserted in four holes drilled approximately 5 mm apart along the curvature of the femoral neck. Strain gage rosettes were fixed to the anterior and posterior aspects of the lesser trochanter for validation of finite element models. The instrumented femurs were loaded in cyclic compression, from approximately 600 to 2000 N sinusoidally at 1 Hz while submerged in 37°C water bath. Pressure, load, and strain data were monitored at 100 Hz (LabVIEW, National Instruments, Austin, TX). The data were filtered using a 5 Hz third-order Butterworth filter.

Whole femurs were imaged using a spiral *in vivo* μCT system (Bioscan, Paris, France) at 70 kVp, 100 mA, and reconstructed with a 0.143 mm cubic voxel size using a Hanning filter. Strain gages remained in place during scanning in order to identify their locations on the final models. The locations of the pressure transducers were identified from the drill holes in the μCT images. Following the scan, the femoral neck was sectioned from the femurs, and high resolution μCT scans were performed at 20 μm resolution, 70 kVp, 114 mA and 400 ms integration (μCT-80, Scanco Medical AG, Brüttisellen, Switzerland). Subsections of the neck located between the insertion of the pressure transducers were reconstructed as cubic volumes with edge length of 5 mm, and an in-plane voxel size of 40 μm (Fig. 1). Micro-FE models were generated by directly converting voxels into elements.

To determine the stiffness matrix, three uniaxial compressive strain boundary conditions and three shear boundary conditions were applied to each cube [5]. The tissue modulus was assumed to be 7500 MPa. The full 6x6 stiffness matrix was calculated was inverted to find the compliance matrix, and the moduli were extracted as the inverse of the diagonal terms (Fig. 1).

The outer boundaries of the femurs were traced on each image slice of the whole femur scans using Analyze Visualization Workshop (AVW, BIR, Mayo Clinic) and imported into a general-purpose FE program (ADINA 9.0.1, Watertown, MA). A 10-node tetrahedral mesh was generated, and displacement boundary conditions were applied to mimic the experimental loading conditions.

Copyright 2016 The Organizing Committee for the 2016 Summer Biomechanics, Bioengineering and Biotransport Conference

Elastic moduli were assigned using both the micro-FE (Fig. 1) and the relationship for human bone used previously (Wirtz) [3,4]. Transverse orthotropic material properties were applied assuming the material aligns with the principal stress directions calculated from the first iteration of the FE models [6]. A poroelastic constitutive model was applied assuming the pore bone marrow is incompressible and that the pores in trabecular bone were fully saturated with marrow.

Permeability, k, was applied spatially based on a relationship between bone mineral density (BMD) and permeability determined from computational fluid dynamics models at three locations within the proximal femur. To account for marrow viscosity, the intrinsic permeability was divided by the measured viscosity of 85 Pa*s [7]. A zero-pressure boundary was defined on the periosteal surface and at the distal end of the model.

The calculated whole bone stiffness and principal strains at the gage locations were compared to the experimental results (Fig. 2). Pressure gradients (Fig. 3b) were calculated within each element of the models. A Darcy flow model was used to estimate the shear stress (Fig. 3c) in the pores by idealizing the pores as simple parallel tubes aligned in the flow direction, where R was the hydraulic radius of the pores, k is the permeability in the axial direction calibrated from the 15 µCT images, and Φ was the porosity.

$$R = \sqrt{\frac{8k}{\phi}} \qquad \tau_{max} = \frac{1}{2}\frac{\partial P}{\partial X} * R$$

RESULTS

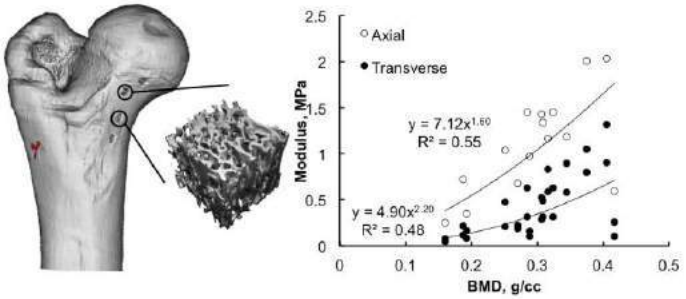

Figure 1: High resolution CT imaging was performed on three subsections to acquire the geometric data used create microscale models. Microscale models were used to determine the density-modulus relationship for the femurs.

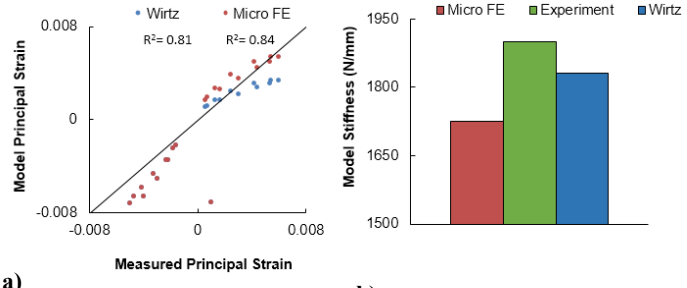

a) b)

Figure 2: The principal strain was correlated to the measured data at the anterior surface for both material models (R^2 = 0.84). The model was 9.2% less stiff than the measured value.

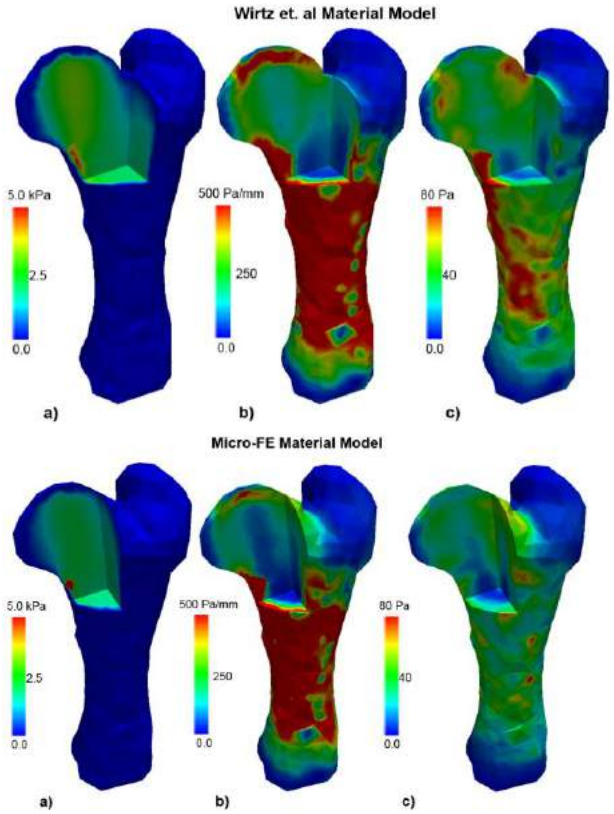

Figure 3: Pore pressure (a), pressure gradient (b), and maximum shear stress (c) were calculated for the Wirtz and µFE models

DISCUSSION

This study incorporated micro-FE models to determine the relationship between BMD and elastic modulus in porcine femurs. Assigning moduli based on the micro-FE models resulted in a 9.2% reduction in the stiffness compared to the Wirtz models (Fig. 2b). Principal strain on the surface of the models better represented the measured data (R^2=0.84; Fig.2a). Lower magnitudes of pressure, pressure gradient, and shear stress were also observed (Fig. 3).

These poroelastic models enabled the investigation of the mechanical environment of the bone marrow. The calculated pressure was well below the mechanostimulatory threshold of 200 kPa for mesenchymal stem cells, but the estimated maximum shear stress was well above this threshold of 0.5 Pa [8]. This may suggest that physiologic loading may impart biomechanical signals to marrow cells which influence mesenchymal stem cell regulation.

ACKNOWLEDGEMENTS

The National Science Foundation: NSF-1100207

REFERENCES

1. Duncan R et al., *Calcif Tissue Int,* 57(5):344-58, 1995.
2. Taddei, F et al., *Med Eng Phys*, 26(1): 61-9, 2004.
3. Gargac, J et al., *SB3C conf. proceedings,* 2015.
4. Wirtz, D et al., *J Biomech*, 33(10): 1325-30, 2000.
5. van Rietbergen, B et al., *J Biomech,* 27(4): 433-444, 1994
6. Marangalou J et al., *Bone*, 60:213-220, 2014.
7. Metzger T et al., *JMBBM*, 40:307-13, 2014.
8. Castillo, A et al., *Curr Osteoporos Rep*, 8:98-104 2010

Copyright 2016 The Organizing Committee for the 2016 Summer Biomechanics, Bioengineering and Biotransport Conference

SB^{3}C2016
Summer Biomechanics, Bioengineering and Biotransport Conference
June 29 –July 2, National Harbor, MD, USA
SB^{3}C2016-1058

INVESTIGATION OF FORCES AND MOMENTS DURING MINIMALLY INVASIVE TOTAL HIP ARTHROPLASTY AND THE LIKELIHOOD OF INTRAOPERATIVE FRACTURE

Pooyan Abbasi (1), Dustin Greenhill (2), Andrew Star (2), Kurosh Darvish (1)

(1) Biomechanics Laboratory
Department of Mechanical Engineering
Temple University
Philadelphia, Pennsylvania, 19122

(2) Department of Orthopaedic Surgery
& Sports Medicine
Temple University Hospital
Philadelphia, Pennsylvania, 19140

ABSTRACT
This study evaluates three-dimensional broaching forces and moments brought about by specialized curved implantation handles designed to be used during total hip replacement via the direct anterior approach. For this purpose, finite element (FE) models of broach handle and bone assembly were developed and studied.

These forces and moments were compared to those from conventional handles as a possible explanation for the increased intraoperative fracture rates that have been reported for these procedures.

As broach handle offset increased, the percentage of vertically directed force (down the medullary canal) decreased. Thus, more force was directed outward toward cortical bone. We also found that varying the hammering location on the broach handle surface resulted in significantly different force ratios that change with handle design. Furthermore, variable impact locations on the double offset broach handle produced vertical to horizontal force ratios between -71% and 37%, thus suggesting that an impact location in which off-plane force distribution is the most hazardous (0%) may exist.

Our data also proves that there are optimal locations of impact that vary with broach handle design. By contrast, impacting a broach handle surface at suboptimal locations can magnify the effect of forces that contribute to intraoperative fracture.

INTRODUCTION
Total hip arthroplasty is being performed through a minimal incision with increasing popularity. Several authors have reported an increased rate of intraoperative fracture with this method [1, 2]. These fractures most often occur during femoral canal preparation. In order to safely perform "less invasive" total hip arthroplasty, manufacturers have developed various new broach handle designs [3-5]. However, the dynamic effects of these handles on the proximal femur have not been widely investigated.

METHODS
Four handles were studied that covered a wide range of shapes and are commonly used including AK0405 as Base (H1), Depuy NB18161 (H2), Depuy J0807 (H3), and ABC 3326 Left (H4) (Fig. 1). Each handle was attached to a #10 broach and the assembly, in vertical position, was scanned using Romer Arm RA-7330 SI with 0.05 mm resolution. Based on the scanned point clouds, a solid model was developed for each assembly using Rhinoceros software (Robert McNeel & Assoc.).

The top surface of the handles and the broach lateral sides were modeled as rigid materials with shell elements (LS-Dyna, LSTC). Having the orientations of these surfaces the same as when they are used in practice was critical for this study. The bone surrounding the broach was modeled as a deformable 5-mm thick layer with solids elements. The bone material properties were selected similar to trabecular bone to account for osteoporosis that is common in total knee replacement (ash density = 0.21, Young's modulus E = 1 GPa). The applied force was 133 kN point load at different locations on the handle top surface. This force is equivalent to a 500g hammer hitting the surface at 4 m/s.

In addition to the central point of the handle top surface that is the recommended impact point, impact points lateral and medial to the center point were also studied to account for variability in the hitting location that may occur during practice. Five impact points were considered for each handle including Central (C), Lateral Anterior (LA), Lateral Posterior (LP), Medial Anterior (MA), and Medial Posterior (MP). For H2, a Lateral Center (LC) point was also considered that was at the same location as H1-C. For H3, a Lateral

Copyright 2016 The Organizing Committee for the 2016 Summer Biomechanics, Bioengineering and Biotransport Conference

Center (LC) point was considered that was aligned with H1-C. For H4, a Lateral Center (LC) point was considered that was between H4-LP and H4-LA (Fig. 2).

For comparison of the handles, the following mechanical quantities were considered. a) The average and range (maximum and minimum) of Von-Mises (or effective) stress (in MPa) and strain (in %) in bone. These quantities describe the likelihood of bone failure. b) Ratio of force in the Z direction (downward) to the resultant force in three sections that were considered in upper (Section 1), middle (Section 2), and lower (Section 3) regions of the bone (Fig. 2). This quantity describes how much the applied impact is transferred into a downward force. A downward force is desirable, as the goal of broaching is to move the broach downward into the femur medullary canal. Ideally, this number should be -1.0 to indicate a 100% downward force. c) Ratio of resultant moment to resultant force in the three sections (in N.m/kN). This measure describes how much moment is generated per unit force. The more moment is generated, it generally means that the stress distribution in bone becomes non-uniform (some regions in tension and some regions in compression) and as a result the chance of failure in tension (which usually has a lower threshold than compression) is increased. d) Ratio of resultant rotational displacement to resultant linear displacement (in deg/mm). This measure describes how much the broach rotates for a unit displacement. The more the broach rotates, its contact area with bone becomes non-uniform (some regions are pressed harder into the bone and some regions are released) and as a result the risk of local failure is increased. Ideally, the last two quantities should be zero.

RESULTS

The results show that generally for curved handles, the average and range of Von-Mises stress and strain are increased (maximum about 4 and 3 times respectively). This shows that bone undergoes more non-uniform deformation and the risk of failure is increased.

The magnitude of ratio of Z force in the curved handles (H3 and H4), approximately -0.7 to 0.4, is significantly less compared to the almost -1 value for straight handles (H1 and H2). It is important to note that in H3 and H4, there are impact points that can make the Z force ratio more acceptable than others. H4-MA gave the best force transmission for H4 (about -0.6 for sections 2 and 3), and H3-C and H3-LP gave the best force transmission for H3 (about -0.6).

Moment transmission is generally higher for the curved handles. It is important to note that in the case of H4, three impact points (H4-LA, H4-LC, and H4-LC) resulted in dramatically less moment transmission that other impact points. H3 had the highest moment transmission.

Broach rotation was higher in other three handles compared to H1. Some impact points resulted in slightly higher rotations (H2-MA, H2-MP, H4LC, and H4-LP) that would indicate more risk of non-uniform contact surface between the broach and bone.

DISCUSSION

Broach handle design is a critical determinant of resultant forces transmitted to the bone during total hip arthroplasty. Curved handles (H3 and H4) generally cause more out of plane forces than straighter handles (H1 and H2), especially in the proximal femur. These unanticipated out of plane forces may play a role in the increased rate of fractures seen during "minimally invasive" procedures. When surgeons use different broach handles in order to accommodate the anatomic constraints, even small changes in design can potentially lead to poor outcomes.

Our data also proves that there are optimal locations of impact that vary with broach handle design. By contrast, impacting a broach handle surface at suboptimal locations can magnify the displacements and forces that contribute to intraoperative fracture.

ACKNOWLEDGEMENTS

Authors thank the Center for Applied Biomechanics at the University of Virginia for providing the Romer Scanner.

REFERENCES

[1] Nicholas E. Ohly, Michael R. Whitehouse, Clive P. Duncan. (2014). Periprosthetic femoral fractures in total hip arthroplasty. *Hip Int*; 24 (6): 556-567

[2] Hans Lindahl. (2007). Epidemiology of periprosthetic femur fracture around a total hip arthroplasty. *Injury, Int. J. Care Injured* 38, 651—654

[3] David Putzer, Eckart Mayr, Christian Haid, Wiliam Hozack, Michael Nogler. (2012). Force transmission in offset broach handles used for hip replacement: comparison of three different designs. *Hip Int*; 23 (2) : 187 - 192

[4] Michael Nogler, Martin Krismer, William J. Hozack, Philip Merritt, Franz Rachbauer, Eckart Mayr. (2006). A double offset broach handle for preparation of the femoral cavity in minimally invasive direct anterior total hip arthroplasty. *The Journal of Arthroplasty* Vol. 21 No. 8

[5] Benjamin Bender, Michael Nogler, WilliamJ. Hozack, (2009). Direct anterior approach for total hip arthroplasty. *Orthop Clin N Am* 40 321–328

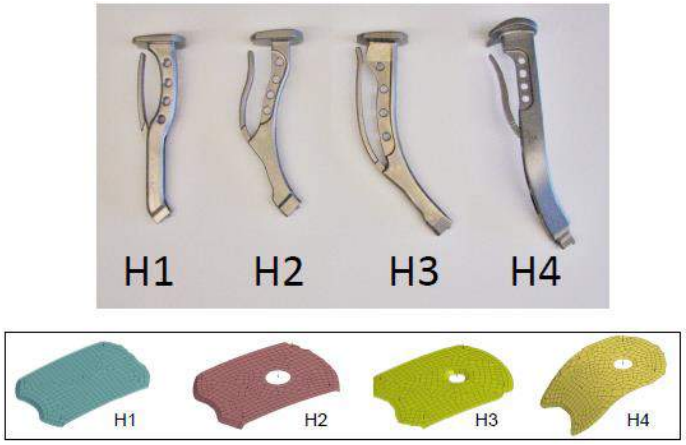

Figure 1: Four different handles used and their corresponding scanned top surfaces.

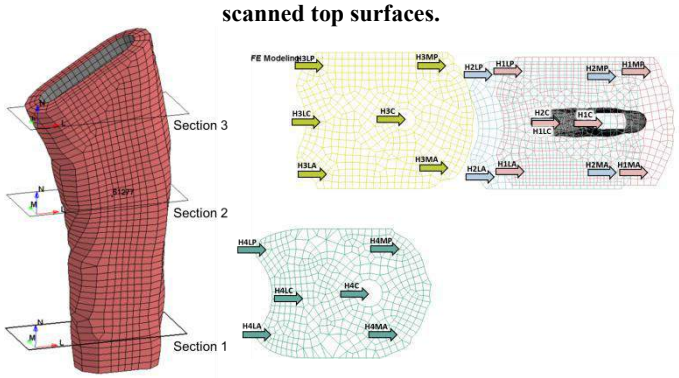

Figure 2: Left) Three sections along the cortical shaft where the forces and moments were measured. Right) Loading configurations on the axial view of broach handles.

Copyright 2016 The Organizing Committee for the 2016 Summer Biomechanics, Bioengineering and Biotransport Conference

SB^{3}C2016
Summer Biomechanics, Bioengineering and Biotransport Conference
June 29 –July 2, National Harbor, MD, USA
SB^{3}C2016-1060

ANALYZING EFFECTS OF CHEMOTHERAPEUTIC DRUGS FOR THE PREVENTION OF CHEMOTHERAPY-INDUCED ALOPECIA

Likitha Somasekhar (1), Kunal Mitra (1), Carlos Martino (1)

(1) Department of Biomedical Engineering
Florida Institute of Technology
Melbourne, Florida, United States

INTRODUCTION

Alopecia that is promoted due to chemotherapy treatment in patients continues to be the most traumatic side effect. Reducing the temperature of the scalp during administration of cytotoxic drugs can prevent hair loss. The results of scalp cooling have shown that it is a promising method to reduce hair loss. However, the efficiency varies due to a large number of factors which affects the outcome. The effects of scalp cooling are based on the function of temperature, cooling duration and the drug type and its dosage. Temperature affects blood perfusion and cellular metabolism during delivery of chemotherapy drugs to the scalp tissue. It also affects the mass-transfer, drug transport and cellular uptake of the chemotherapeutic agent over time. Mathematical models have been developed to study the scalp cooling procedure by quantifying the relationship between temperature and blood perfusion in the scalp [1, 2]. But effects on cellular metabolism have not yet been entirely characterized in order to minimize the cytotoxic effect of the drug concerning the hair-forming cells and preventing hair loss. This characterization must also be drug-specific because these processes are different for each chemotherapeutic agent. For example, the best hair preservation along with scalp cooling has been achieved for taxanes or anthracyclines when they are not given in combination [3]. Along with chemotherapy characteristics, patient characteristics also affect the outcome of this procedure. To differentiate the effects of reduced perfusion and metabolism independently, *in vivo* model would be challenging. Due to reduced temperatures during scalp cooling, cellular drug uptake and damage will be lower and therefore hair follicles are thought to be less susceptible to cytotoxic drugs. Therefore, the goal of this paper is to analyze the cellular metabolism due to uptake of different chemotherapeutic agents by cooling *in vitro*.

METHODS

A controlled in vitro experiment is conducted using cultured human epidermal keratinocytes (obtained from Promo Cell) to quantify the effects of reduced cell metabolism on the hair preservative effect during scalp cooling along with reduced perfusion. The effects of temperature and concentration of chemotherapeutic agent, doxorubicin on cell damage is determined from cell viability. Cell viability measurements such as MTT assay and Amplex Red assay are conducted to study the effects of temperature and doxorubicin on cell damage. Furthermore, cell mito stress test is conducted to test the amount of mitochondrial function in cells and glycolysis test is conducted to measure the amount of glycolytic function in cells. This will facilitate to assess the damage exerted by the chemotherapeutic agent on human epidermal keratinocytes for a range of chemotherapy concentrations and exposure temperatures [4]. The level of hypothermia is varied by testing temperatures in the range of 24°C to 37°C. This is primarily because it has been suggested by various studies that a scalp temperature of 22°C or less is required for hair preservation [5]. The drug dosage is varied from 0.01µg per ml to 10µg per ml. The exposure time for the chemotherapeutic drugs is also varied in the range of 30 minutes to 2 hours. Cells are cultured at a seeding density of $5x10^5$ cells cm^{-2} under an atmosphere of 95% air and 5% CO_2 at 37°C, using keratinocyte basal media supplemented with keratinocyte growth kit components. The cells are harvested and centrifuged when the cells reach 70%-80% confluence. Consequent passage cells are plated in two 24-well plates, after which the plates are incubated at 37°C and 5% CO_2 for 24 hours before the drug is introduced [4].

MTT is prepared at 5:1 dilution and is added to the cells. Similarly, Amplex Red/Horse radish peroxidase (HRP) is prepared wherein, Amplex Red is diluted at 1:1000 and Horse radish peroxidase (HRP) at 1:100 dilutions. The absorbance is read at 570nm for MTT and at 530-590nm for AUR assay. For the cell mito stress test and glycolysis test [4], the cells are plated in the XFp Cell Culture Miniplate and incubated for 24 hours. The cells are then exposed to appropriate drug concentration. The respective assay media and the drug compounds are prepared wherein, three tubes containing oligomycin, FCCP and rotenone/ antimycin A are resuspended in respective tubes with prepared assay media for cell mito stress test. For glycolysis test the stock compounds are prepared which comprises of a vial of oligomycin, glucose and 2-DG which are resuspended in assay media. The compounds are loaded into hydrated sensor cartridge and the assay is started using the XFp analyzer. The same steps are repeated for both the plates with two different temperature conditions [4].

RESULTS

A significant decreasing effect on keratinocyte cell viability is observed when the doxorubicin concentrations is increased and a

Copyright 2016 The Organizing Committee for the 2016 Summer Biomechanics, Bioengineering and Biotransport Conference

significant increasing effect on keratinocyte cell viability is seen when the temperature is reduced in Figure 1 and Figure 2 for MTT assay and Amplex Red assay.

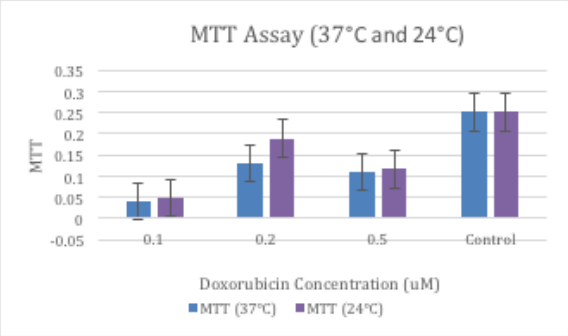

Figure 1: Mitochondrial Respiration for 24°C

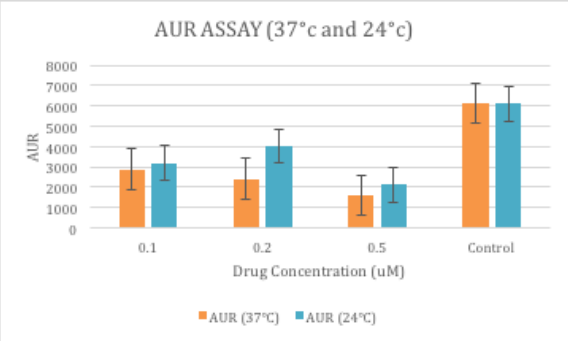

Figure 2: Mitochondrial Respiration for 24°C

A higher cell viability for every concentration of doxorubicin is observed in 24°C than the 37°C group. At the lower range of doxorubicin concentration (0.1µM), the effect of reduced temperature is more distinct than in the higher values of doxorubicin concentration. This observation validates a strong correlation between doxorubicin concentration and exposure temperature. For the stress test, the oxygen consumption rate in Figure 3 is reduced due to cell death when compared to the control wherein, the oxygen consumption rate is not affected and there is steady respiration rate. The ATP production is less compared to the control since the cell metabolism is reduced and not much ATP is produced. The spare respiratory capacity when compared between the two temperatures is nil in the 24ºC due to the amount of cell metabolism when compared to 37ºC which indicates that the fitness of the cell is better [4].

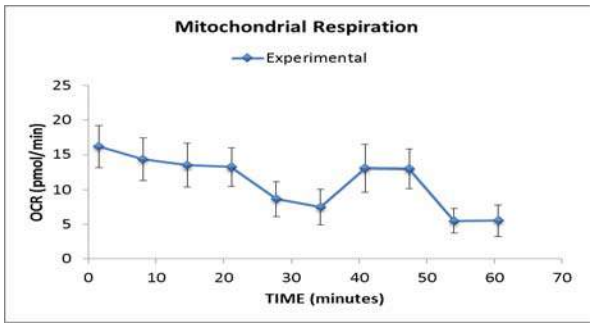

Figure 3: Mitochondrial Respiration for 24°C at 0.1µM

The extracellular acidification rate (ECAR) measured in glycolysis test in Figure 4 is greater when compared to the control group since the cell viability is greater due to the amount of glycolysis that occurs in the cells. It is also observed that glycolytic activity for the control and the 24ºC group is greater than 37ºC group due to the shutdown of oxidative phosphorylation which drives the cell to use glycolysis to its maximum capacity. This also results in the group 24°C to show greater ECAR rate than the 37°C group [4].

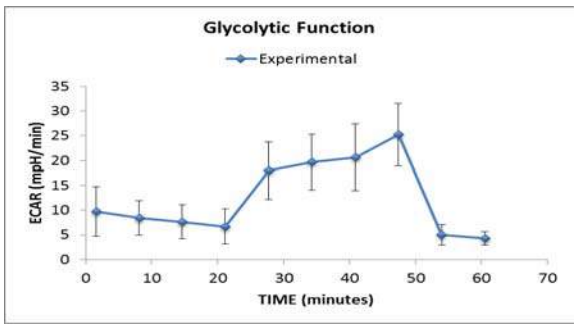

Figure 4: Glycolytic function for 24°C at 0.1µM

DISCUSSION

The relationship obtained for cell viability as a function of chemotherapeutic agent concentration and exposure temperature, in combination with the value obtained for critical viability measurement is used to determine the optimal scalp cooling temperature at different doses and exposure time for doxorubicin. The results will provide indication of what temperatures should be reached during scalp cooling before administering the treatment dose.

The role of reduced metabolism on the hair preservative effect of scalp cooling is investigated wherein, the two temperatures show that 24°C group has decrease cell cytotoxicity at the same doxorubicin concentration. This observation shows that there is a presence of an interaction between doxorubicin concentration and exposure temperature that is significant. The results of the experiment relate to the idea of scalp cooling wherein, reduced temperature due to scalp cooling results in lower perfusion rate and lower cellular metabolism. It is also noted that the in vitro experiments signify that the reduction in both temperature and concentration may increase cell survival. To relate drug concentration and exposure temperature to cell survival in the experiments conducted, only two temperatures that are representative for scalp cooling is considered wherein the transition point in the effect of temperature needs to be determined for better understanding of cell viability conditions. Although the cells used in vitro experiments are characteristic of the cells that produce the hair shaft, in vitro experiments that were conducted are not able to replicate the interaction that occurs between these cells. In vitro experiments on a complete hair follicle is required to better understand the effect of cooling the scalp and the distribution of doxorubicin in the hair follicle and subsequent cell damage need to be studied.

REFERENCES

(1) Janssen, F. E. M. et al., Physics in medicine and biology, 50(17), 4065, 2005.

(2) Pliskow, B. et al, *Summer Biomechanics, Bioengineering, and Biotransport, Snowbird Resort (Utah),* June17-20 (2015).

(3) Breed, W. P et al, Presentation, impact and prevention of chemotherapy-induced hair loss: scalp cooling potentials and limitations 109-125 (2011).

(4) Somasekhar, L., "Analyzing Effects of Chemotherapeutic Drugs for the Prevention of Chemotherapy-induced Alopecia and Multi-Physics Drug Transport Modeling", Thesis 2015.

(5) Komen, M. M. et al., *The oncologist*, *18*(7), 885-891. 2013.

Copyright 2016 The Organizing Committee for the 2016 Summer Biomechanics, Bioengineering and Biotransport Conference

SB^{3}C2016
Summer Biomechanics, Bioengineering and Biotransport Conference
June 29 –July 2, National Harbor, MD, USA
SB^{3}C2016-1061

MYOCARDIAL WALL STIFFENING IN A MOUSE MODEL OF PERSISTENT TRUNCUS ARTERIOSUS

Christine Miller Buffinton (1), Kerra R. Mercon (1), Alyssa K. Benjamin (2), Asena Abay (3), Elise M. Buffinton (4), Roberta K. Blaho (3), Ashley N. Firment (5), Anne M. Moon (5)

(1) Department of Mechanical Engineering
(2) Department of Biology
(3) Department of Biomedical Engineering
Bucknell University
Lewisburg, PA USA

(4) School of Civil and Environmental Engineering
Cornell University
Ithaca, NY USA

(5) Weis Center for Research
Geisinger Medical Center
Danville, PA USA

INTRODUCTION

The most common single chromosomal defect associated with congenital cardiovascular malformation is 22q11 deletion syndrome (DiGeorge syndrome), which often includes ventricular septal defect, tetralogy of Fallot, and persistent truncus arteriosus (PTA). The truncus arteriosus is an embryological structure, a common vessel conveying blood outflow from both the left and right ventricles, which are joined by a ventricular septal opening. In normal development, the truncus arteriosus divides into the pulmonary trunk and ascending aorta. This septation fails to occur in PTA, allowing harmful mixing of oxygenated and deoxygenated blood in the systemic circulation.

The structural abnormality in PTA is usually repaired with surgery during the first months of life [1]. Despite the structural repair, however, other long-term problems may persist. We hypothesized that the altered hemodynamic and mechanical loading patterns created by the PTA structural defect during development will also affect the passive mechanical properties of the ventricles and outflow tract. This hypothesis was tested with a mouse model of PTA. This model includes a hypomorphic allele for fgf8 expression, which has been shown to recapitulate the PTA defect seen in human 22q11 deletion syndrome [2, 3].

One goal of this research was to develop an imaging and reconstruction procedure to allow comparison of anatomical measurements and 3D reconstructions of the ventricles and outflow tract from whole-mount embryonic day (ED) 12.5 mouse hearts, both control (wild-type) and with PTA (fgf8-deficient). This then provided a framework for the second goal, to measure passive myocardial stiffness in control and fgf8-deficient embryonic mice hearts with a recently developed pipette aspiration system.

METHODS

Control (wild-type) and fgf8-deficient (mutant) embryos were obtained at embryonic day (ED) 12.5 from the Moon lab. Hearts were harvested in accordance with Geisinger IUCAC-approved procedures. For imaging and reconstruction, hearts were arrested with verapamil, treated with a red blood cell lysis solution, fixed in paraformaldeyde, and dehydrated in an ascending series of EtOH. Groups of hearts were prepared with either (1) glycerol clearing, (2) no clearing with phalloidin-Alexa488 labeling, and (3) BABB (2:1 benzyl alcohol: benzyl benzoate) clearing. Imaging took place on a Leica TCS SP5 inverted confocal microscope in specially designed chambers. The BABB-cleared specimens, which were completely transparent in solution, required the design of custom pipettes and transfer chambers and use of epifluorescent illumination for transfer. Scans, requiring 3-5 hr each, used a dry 10X objective with an argon laser and maximum combined blue excitation of 458, 476, and 488 nm at 45%. The stacks of 200-400 tiff files were segmented, reconstructed, and measured using various tools in Amira v6.0 (FEI Visualization Sciences Group). All images were processed with a contrast-limited adaptive histogram equalization routine to compensate for variations in signal intensity. Metrics were developed to compare dimensions of ventricles, outflow tract, and developing cushions. Further thresholding and surface rendering created volumetric representations of each ventricle.

For mechanical testing, hearts were extracted and arrested in diastole with 4% verapamil. Hearts were positioned in PBS in a small glass chamber on micromanipulator stage. Under microscopic viewing, a 100-µm-ID glass pipette was lowered perpendicular to the tissue surface until a seal was accomplished, aided by the natural adhesion of the tissue to the glass. Negative pressure applied to the pipette then aspirated a small amount of myocardial wall (Fig. 1), while video and pressure were recorded at 15 Hz [4]. Locations on the

Copyright 2016 The Organizing Committee for the 2016 Summer Biomechanics, Bioengineering and Biotransport Conference

left ventricle (LV), right ventricle (RV), and outflow tract (OFT) were tested in turn. Images were analyzed in MaxTRAQ to obtain aspirated length L, which was normalized to pipette inner radius r_i (Fig. 1). Aspirated pressure Δp was plotted versus L/r_i and various functional forms of the relationship were tested.

A strain energy density measure was calculated as the area under the Δp vs. L/r_i curve for two ranges of strain: $L/r_i = 0 – 0.2$ and $0 – 0.4$. Statistical significance was assessed with t-tests between the control and mutant strain energy values for each range at each of the three locations. The mechanical tests were also analyzed with a finite element model to assess the effect of wall structure on measured pipette aspiration behavior.

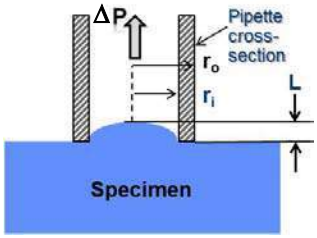

Figure 1. Schematic of pipette aspiration procedure. The glass pipette had internal radius r_i of 50 μm and external radius r_o of 85 μm. Heart walls were loaded to strain ratios L/r_i of 0.4 with maximum aspiration pressures ranging from 1-10 kPa.

RESULTS

Hearts cleared with BABB allowed the best laser penetration and tissue detail as opposed to the other methods, with good penetration up to 2 mm (Fig. 2). Calculated volumes were .095 (.035) and .071 (.044) mm^3 for control and mutant right ventricle and .085 (.017) and .090 (.066) mm^3 for control and mutant left ventricle (mean (standard deviation)). Measurements of length and width of ventricular chambers and conotruncal cushions showed no significant differences between mutant and control. Mutant hearts had greater conotruncal cushion separation and a thicker right compact wall.

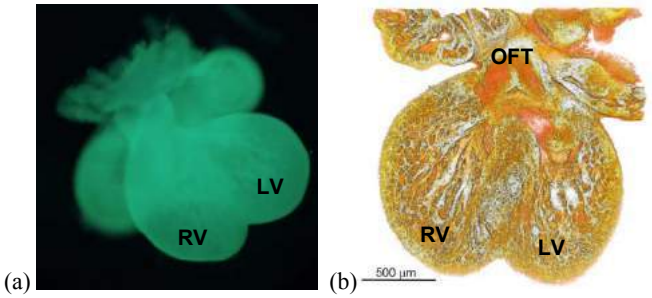

Figure 2: (a) Control ED12.5 heart under epifluorescent illumination; (b) Reconstruction of ED12.5 heart with the Volren module in Amira. RV: right ventricle, LV: left ventricle, OFT: outflow tract.

The Δp vs L/r_i relationship was highly linear for L/r_i from 0-0.4 at each of the three locations, LV, RV, and OFT (R^2 = .96-.98). The maximum aspiration pressures in control and mutant mouse ventricles were 6 and 10 kPa, respectively. The area under the Δp vs L/r_i curve, a measure of material elastic stiffness, was significantly higher ($p<0.05$) in the RV of fgf8-deficient mice, i.e., those with deficient septation of the truncus arteriosus, compared to control in both strain ranges, L/r_i of 0-0.2 and 0-0.4 (Fig. 3), while that in the LV of fgf-8 deficient mouse was more than double that in control from 0-0.2 L/r_i ($p=0.08$).

Finite element mechanical analysis of pipette aspiration based on the geometry from the reconstructed 3D images showed no significant differences between control and mutant when assuming equivalent material properties, indicating the measured difference in mechanical stiffness represents a material property difference rather than a structural difference.

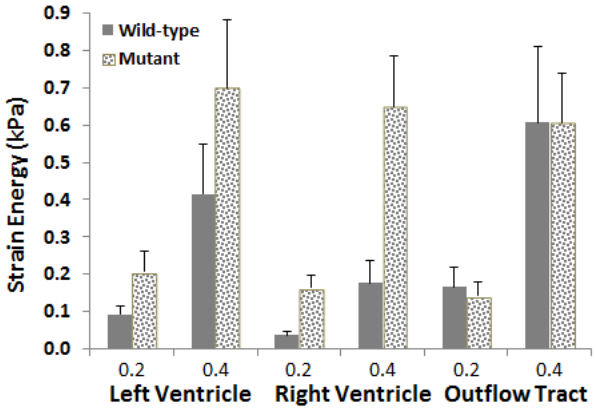

Figure 3. Mean strain energy in the ranges of L/r_i=0-0.2 and 0-0.4 for control (wild-type) and fgf8-deficient mutant mouse at ED12.5. Error bars show standard error.

DISCUSSION

This is the first demonstration that hearts developing PTA show early changes in ventricular tissue properties. The embryonic time frame studied here is crucial, as it is the latter stage of chamber and valve formation. In humans, the effects of PTA on tissue stiffness may cause lasting problems, even after early surgical repair. The stiffer walls may be a result of the excessive force needed or resistance encountered when pumping blood in the presence of the structural abnormality, or of the abnormal fluid flow patterns. We have begun studies in histology and gene expression to help elucidate the mechanism.

This study has also demonstrated that confocal microscopy can be extended to capture the entire volume of the mm-scale ED12.5 mouse heart (ventricles and outflow tract), an extension to its usual use at the cellular and small tissue level. The 3D models created will form the geometrical basis for studies in blood flow modeling and fluid-elastic interaction in models of the mouse embryonic heart.

ACKNOWLEDGEMENTS

RKB and AKB were supported by the Bucknell Presidential Fellows Program. KRM was supported by the Bucknell University Program for Undergraduate Research. A grant from the Bucknell-Geisinger Research Initiative provided funding for RKB, AKB, ANF, AMM, and CMB.

REFERENCES

[1] Sojak, V. et al., *Multmedia Manual Cardio-Thoracic Surgery,* 10.1093/mmcts/mms011, 2012.
[2] Frank, D. et al., *Development*, 129:4591-4603, 2002.
[3] Park, E. et al., *Development,* 133: 2419–2433, 2006.
[4] Buffinton, C. et al., *J Mechanical Behavior Biomedical Materials*, 51:367-379, 2015.

Copyright 2016 The Organizing Committee for the 2016 Summer Biomechanics, Bioengineering and Biotransport Conference

SB^{3}C2016
Summer Biomechanics, Bioengineering and Biotransport Conference
June 29 –July 2, National Harbor, MD, USA
SB^{3}C2016-1062

CEREBRAL BLOOD FLOW SIMULATION FOR THE WHOLE MOUSE BRAIN

Ben C. Schneller (1), Mahsa Ghaffari (1), Sahar Ghanavati (3,4), John G. Sled (3,4), Andreas A. Linninger (1,2)

(1) The Richard and Loan Hill Department of Bioengineering
University of Illinois at Chicago
Chicago, Illinois, USA

(2) Department of Neurosurgery
University of Illinois at Chicago
Chicago, Illinois, US

(3) Mouse Imaging Centre
The Hospital for Sick Children
Toronto, Ontario, Canada

(4) Department of Medical Biophysics
University of Toronto Toronto, Ontario, Canada

INTRODUCTION

Cerebral hemodynamics is a complex phenomenon involving a hierarchy of vessels over multiple length scales including large arteries, pial arteries, capillary networks and draining veins. Due to the vast distribution of vessels of different size and density, direct methods of observation cannot capture all details of the perfusion process. In order to gain a more complete knowledge of cerebral blood distribution we propose to perform massive computer simulations on anatomically accurate models obtained from high resolution micro-CT images. This approach allows for quick acquisition of reproducible results at all length scales, and provides a mechanism to assess blood flow in normal and disease states (i.e. stroke).

We used imaging data acquired from multiple modalities covering the macro- and micro-scale to build a complete and closed cerebral vasculature of a mouse brain. High resolution micro-CT images were used to generate anatomically correct models of the arteries and veins, and two-photon images were used to reconstruct the microvasculature include penetrating arterioles, capillaries and draining veins [1,2]. We assembled these data to generate an in-silico model of the entire cerebral angioarchitecture in the mouse. We present results on the anatomical features as well as steady state blood flow predictions.

METHODS

The raw imaging data was acquired using a contrast enhanced μCT procedure [3]. The vasculature of anesthetized C57BL/6 mice was injected with a radio opaque silicone rubber, Microfil. After polymerization the skulls were dissected and decalcified with 8% formic acid. Images were acquired with a micro-CT (SkyScan 1172 high-resolution micro-CT, Bruker micro-CT, Belgium) at an isotropic voxel size of 20 μm.

The original data is processed using our multi-scale vessel enhancement filter that increases the intensity of tubular objects in order to create a probability map of vessel location along all length scales [4]. A threshold is selected to create a binary map of the vascular network. From the binary map a skeletonized image and distance map are generated in order to acquire centerline trajectories and the corresponding diameters. From this we then generate a network file composed of vertices and edges. Each edge has an associated diameter that is used in the computational flow simulations.

Boundary conditions must be applied at all inlets and terminal nodes for the simulations. Hemodynamic measurements of different regions of the mouse brain have shown a range of flow rates in the arterioles. In order to assign these variable flows at the terminal branches a spectral clustering method was used for grouping functional territories. This allows a programmatic approach to assigning inlet flow boundary conditions at the vertebral and carotid arteries as well as the appropriate flow rates at the terminal branches.

Blood flow simulations on the network are performed using continuity equation, eq 1, and the Hagen-Poiseuille flow model, eq 2, where Q is flow rate, P is pressure, μ is the viscosity, L is length, and r is the vessel radius.

$$\nabla Q = 0 \tag{1}$$

$$\Delta P = \frac{8\mu L Q}{\pi r^4} \tag{2}$$

Copyright 2016 The Organizing Committee for the 2016 Summer Biomechanics, Bioengineering and Biotransport Conference

RESULTS

Vascular network creation is a multi-step process (Figure 1). The initial processing of the raw image data (a) with the vessel enhancement filter greatly increases the contrast between the vessels and the background while also decreasing the noise (b). The increased contrast allows us to make a clean binary image that includes only tubular structures (c). From the binary image a skeleton (d) and distance map (e) are computed to find the vessel centerlines and diameters. This information is then used to construct the vessel network to be used for simulation (f).

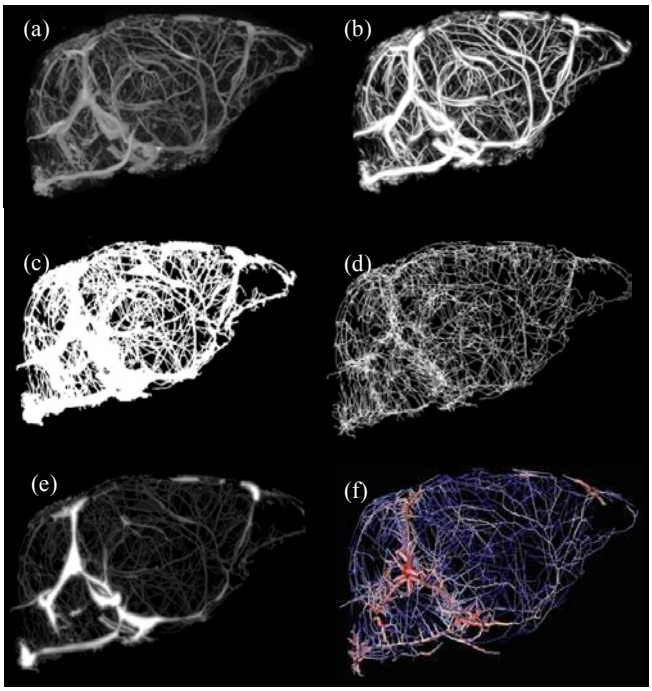

Figure 1: Segmentation procedure for creating vascular network from raw imaging data. a) Raw image data is acquire from contrast-enhanced μ-CT, b) Filtered vasculature, using the vessel enhancement filter, c) Binary vessel image, d) Centerline extraction, e) Distance map, f) and network of connected vertices with associated diameters.

The functional grouping of the arterial tree is displayed (Figure 2) showing the distribution to the olfactory bulb, the left and right regions of the neortex, the left and right regions of the cerebellum, the vertebral arteries and the Circle of Willis. Also displayed are results of hemodynamic simulations showing color maps of the flow velocities (center), and the arterial pressure distribution (right).

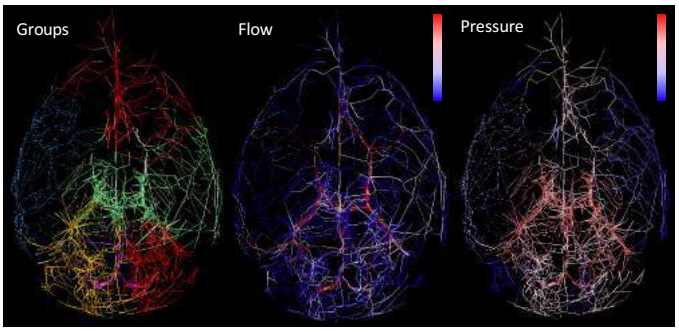

Figure 2. Arterial territory groups (left) were obtained by automatic labeling. Preliminary results of flow (center) and pressure simulations (right) by solving the flow equations for the entire arterial tree. As boundary conditions, known inflows were assumed. Territorial perfusion, and pressure field emerge.

DISCUSSION

The segmentation of the high-resolution micro-CT images show that a large portion of a subject-specific arterial network can be recovered using the techniques described. The steps involved in the segmentation, as well as the grouping, are fully automated. Using experimental values to establish the inlet and outlet boundary conditions of the network allow one to observe trends across the entire vascular network. Upon validation of the obtained results these can be used as a baseline case to explore the effects of cerebrovascular diseases on the distribution of blood to the entire brain.

Closing the whole brain vascular network involves connecting the terminal branches of the arterial trees to the capillary networks and then drain these networks through the venous system. To do so, the terminal ends of the vessel network, (Figure 3a), will be used as inlets to the capillary bed, (Figure 3b). Regional perfusion maps can then be assessed using a mouse cortical model separated by functional regions, (Figure 3c).

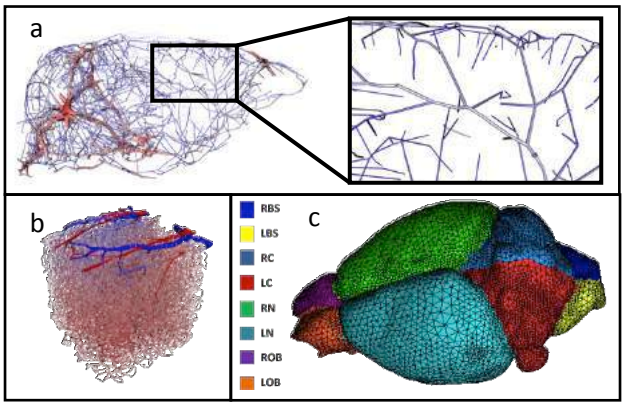

Figure 3. Schematic of the whole-brain simulation of blood flow in mouse. a) Full pial network and inset showing penetrating arteries from micro-CT, b) detailed image of the microvasculature in a 1 mm^3 subsection of the cortex showing penetrating arterioles the capillary bed and draining veins, c) mouse cortex grouped into functional areas to assess blood perfusion in each region.

ACKNOWLEDGEMENTS

The authors would like to gratefully acknowledge the partial support of this project by NSF grants CBET-0756154 and CBET-1301198.

REFERENCES

[1] Schaffer C B, Friedman B, Nishimura, N, Schroeder LF, Tsai PS, Ebner, FF, Lyden PD, Kleinfeld D. "Two-photon imaging of cortical surface microvessels reveals a robust redistribution in blood flow after vascular occlusion." PLoS biology 4.2 (2006): 258.

[2] Gould IG, Tsai, PS, Kleinfeld D, Linninger AA. Complex cerebral angioarchitechiture and neuronal metabolism lead to wide variations of hematocrit RBC saturation in the capillary bed. 27th International Symposium of Cerebral Blood Flow, Metabolism and Function.

[3] Ghanavati S, Yu LX, Lerch JP, Sled JG. A perfusion procedure for imaging of the mouse cerebral vasculature by X-ray micro-CT. J Neurosci Methods. 2014;221:70–7.

[4] Hsu CY, Schneller B, Ghaffari M, Alaraj A, Linninger A. Medical Image Processing for Fully Integrated Subject Specific Whole Brain Mesh Generation. Technologies. 2015; 3(2):126–41.

Copyright 2016 The Organizing Committee for the 2016 Summer Biomechanics, Bioengineering and Biotransport Conference

SB^{3}C2016
Summer Biomechanics, Bioengineering and Biotransport Conference
June 29 –July 2, National Harbor, MD, USA
SB^{3}C2016-1063

EXPERIMENTAL BIOMECHANICS OF THE ANTERIOR CRUCIATE LIGAMENT: HYPERELASTICY AND VISCOELASTICITY

Kaitlyn Mallett (1), Ellen M. Arruda (1,2,3)

(1) Mechanical Engineering
University of Michigan
Ann Arbor, MI, USA

(2) Biomedical Engineering
University of Michigan
Ann Arbor, MI, USA

(3) Program in Macromolecular Science and Engineering
University of Michigan
Ann Arbor, MI, USA

INTRODUCTION

Anterior cruciate ligament (ACL) replacements are among the most common knee ligament invasive procedures. It is estimated that the combination of ACL and meniscal injuries can lead to the development of osteoarthritis in up to 48% of patients with replacements [1]. Within the dynamic model of the knee, the ACL is primarily responsible for preventing anterior translation of the tibia with respect to the femur, and is particularly challenging to experimentally characterize. In its anatomically relevant state, it is twisted and partially extended regardless of knee flexion angle [2–5]. The tissue structures that make up the ACL also exhibit mechanical heterogeneity. The ACL is primarily comprised of two sections of tissue, the anteromedial and the posterolateral bundles (AM and PL respectively). These bundles are not simultaneously unloaded under any configuration, and are oriented so that regardless of the angle of extension of the knee, one bundle is always in a state of tension, further complicating the overall tissue biomechanics [6,7]. These complications pose a major challenge to health care professionals, and there is a pressing need to understand the mechanics of the ACL in physiologically relevant loading states in order to develop accurate constitutive models and select appropriate replacement options.

METHODS

The complex insertions of both the AM and PL bundles at the femur and tibia make performing experiments and accurately modelling the properties of the tissue difficult. At the femur, both bundles insert tangentially to the curved surface of the lateral femoral condyle. In addition, at the tibia, the AM bundle inserts along the anterior aspect of the medial tibial spine, while individual fibrils of the PL splay before inserting into the tibial plateau. A novel grip device has been designed to orient the individual ACL bundles in uniaxial tension, taking into account the complex bundle insertions. We have performed experiments on the individual bundles of the ACL in uniaxial tension from their unloaded reference configurations to characterize them, as well tests of the full ACL in a physiologically relevant loading condition (i.e. anterior tibial translation or ATT). Using digital image correlation (DIC) and our tension testing techniques, we are able to obtain quantitative grip-to-grip stress and time data, as well as average and region-specific strain information over the surface of the test specimens. Uniaxial load-unload experiments have been conducted up to 8% grip-to-grip strains at several strain rates. The viscoelastic response of the tissue has been quantified by performing stress relaxation tests and load-unload tests at several strain rates.

RESULTS

This work provides quantitative data for constitutive modelling of the heterogeneous bundles of the ACL, using a custom-designed gripping fixture optimized for uniaxial tension testing. **Figure 1** shows the strains and displacements of the AM bundle at 8% grip-to-grip strain. The E_{yy} longitudinal

Copyright 2016 The Organizing Committee for the 2016 Summer Biomechanics, Bioengineering and Biotransport Conference

strain shows the relative homogeneity of the AM bundle strain response within the mid-region of the tissue, while the E_{xy} shear images shows little shear in this same region. **Figure 1** shows the vertical (V) and horizontal (U) displacement contours of the AM bundle, along with the, vertical (E_{yy}), horizontal (E_{xx}) and shear (E_{xy}) strain contours. The lateral displacement field, **Figure 1B**, shows extensive lateral motion of the AM bundle within the mid-substance region, demonstrating lateral expansion of the bundle due to the splaying of individual fibrils under uniaxial tension loading. **Figure 2** shows the homogeneity of the stress v. strain response of the AM bundle in a load-unload test to 8% grip-to-grip strain. The stress v. strain response within the mid-substance region outlined in Figure **1E** is relatively homogeneous. In addition, the grip-to-grip measurement over predicts actual tissue level strains by 47% due to system compliance.

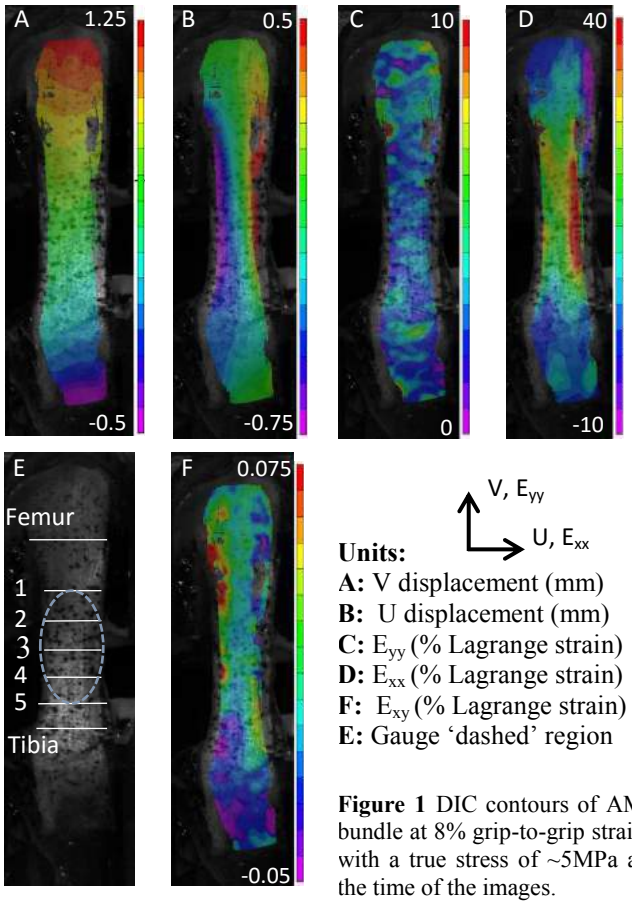

Units:
A: V displacement (mm)
B: U displacement (mm)
C: E_{yy} (% Lagrange strain)
D: E_{xx} (% Lagrange strain)
F: E_{xy} (% Lagrange strain)
E: Gauge 'dashed' region

Figure 1 DIC contours of AM bundle at 8% grip-to-grip strain with a true stress of ~5MPa at the time of the images.

DISCUSSION

The data from these experiments is used in a constitutive model that captures the response of the ACL experimentally. In addition, the patterning technique is capable of generating the pseudo-random, high density and high-contrast pattern necessary for obtaining accurate high resolution strain data of the surface strains of soft biological tissue. We demonstrate that the posterolateral bundle of the ACL is linear viscoelastic up to 10% initial strain, whereas the anteromedial bundle is non-linear viscoelastic after about 8% strain. In addition, the AM bundle is homogeneous within the midsection of the tissue, allowing for constitutive modelling using well-understood boundary conditions in this region.

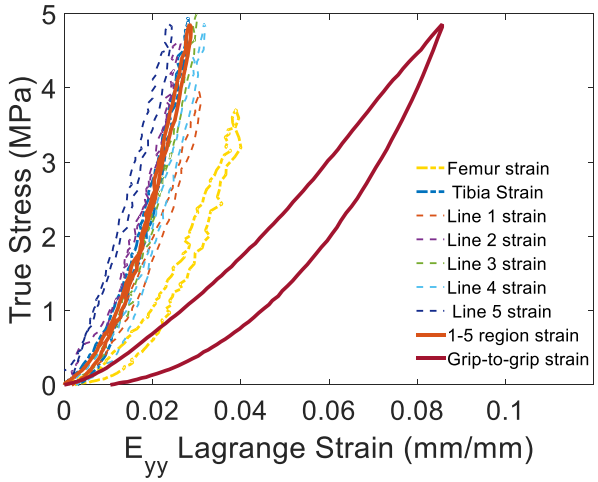

Figure 2 Stress v. strain response of the AM bundle using local DIC strains along horizontal lines within the 'gauge' mid-substances region, and global grip-to-grip strains.

With the non-linear viscoelastic responses of the two bundles characterized via tension testing in the manner described, we implement the models into a finite element environment in which we start with each bundle in its reference configuration, reassemble the bundles, twist them to their physiological state, apply a knee flexion angle matching that in our ATT experiments, and simulate the ATT response. The approach is predictive of the strain fields in the ACL during the ATT test. Our computational model is able to predict the location of ACL tears in the proximal third of the tissue. Moreover it may be used with full knee models to simulate the ACL tissue response to diverse knee injury situations.

ACKNOWLEDGEMENTS

This material was based upon work supported by the National Science Foundation Graduate Research Fellowship Program under Grant No. DGE1256260.

REFERENCES

[1] Øiestad B. E., Engebretsen L., Storheim K., Risberg M. A.: *Am. J. Sports Med.* **37**(7): 1434–43, 2009.
[2] Butler D. L., Kay M. D., Stouffer D. C.: *J. Biomech.* **19**(6): 425–432, 1988.
[3] Norwood L. A., Cross M. J.: *Am. J. Sports Med.* **7**(1): 23–26, 1979.
[4] Girgis F., Marshall J. L., Monajem A.: *Clin Orthop* **106**: 216–231, 1975.
[5] Butler D. L.: *J. Orthop. Res.* **7**(6): 910–21, 1989.
[6] Arnoczky S. P., Warren R. F., Ashlock M. A.: *J Bone Jt. Surg [Am]* **68**(3): 376–385, 1986.
[7] Odensten M., Gillquist J., *J-Bone-Joint-Surg-Am* **67**(2): 257–9355, 1985.

Copyright 2016 The Organizing Committee for the 2016 Summer Biomechanics, Bioengineering and Biotransport Conference

SB^{3}C2016
Summer Biomechanics, Bioengineering and Biotransport Conference
June 29 –July 2, National Harbor, MD, USA
SB^{3}C2016-1064

BIOMECHANICAL EVALUATION OF GELATIN/FIBRINOGEN ELECTROSPUN CYLINDRICAL SCAFFOLDS SEEDED WITH 3T3 MOUSE FIBROBLASTS AND PORCINE SMOOTH MUSCLE CELLS

Ehab Tamimi (1), Jamie L. Hernandez (2), Corina MacIsaac (2), Catalina Ardila (1), Jonathan P. Vande Geest (3)

(1) Graduate Interdisciplinary Program of Biomedical Engineering, The University of Arizona, Tucson, AZ, USA, 85721

(2) Department of Biomedical Engineering, College of Engineering, The University of Arizona, Tucson, AZ, USA, 85721

(3) Department of Bioengineering, University of Pittsburgh, Pittsburgh, PA, USA, 15260

INTRODUCTION

Heart disease is the major cause of death in the United States, with an estimated 83.6 million Americans with one or more type of cardiovascular disease (CVD). Mortality data from 2010 shows that CVD is the underlying cause of death for 1 out of every 3 Americans [1]. There is an increasing demand for affordable, compatible and more easily accessible coronary vascular grafts. Tissue-engineered vascular grafts (TEVGs) offer an alternative source of grafts that can be developed to be nonthrombogenic, biocompatible, nonimmunogenic, resistant to infection, and compliance-matched to the native vessel. Since compliance mismatch is a major cause of restenosis and graft failure, it's important that the mechanical properties of the TEVG be comparable to that of native vessel.

Our resesarch group has recently shown that it is possible to create native vessel compliance-matched TEVGs by modulating the mechanical properties of electrospun acellular gelatin/fibrinogen TEVGs via changing glutaraldehyde (GLUT) vapor crosslinking time [2]. We have also shown that porcine aortic smooth muscle cells (PSMCs) proliferated and migrated within gelatin/fibrinogen electrospun sheets [3]. In addition, transforming growth factor beta 2 (TGFβ2) was shown to have a significant effect on the proliferation and collagen deposition of the PSMCs, which suggests that seeded cell lines could have the ability to modify the mechanical properties of cylindrical constructs over time [3]. The purpose of this study was to better understand the mechanisms of biomechanical changes that non-synthetic TEVGs undergo when seeded with 3T3 mouse fibroblasts (3T3FB) and PSMCs cultured *ex vivo* in a custom bioreactor.

METHODS

Gelatin/fibrinogen cylindrical constructs were fabricated by electrospinning a 10% (w/v) of gelatin/fibrinogen (80:20) in HFP onto a rotating translating mandrel. The constructs were suspended inside a 25% GLUT chamber and exposed to the GLUT vapor phase for 2 hours. The constructs were then dried, sterilized and seeded with a normalized concentration of either cultured 3T3MF or a mixture of 3T3MF and PSMCs by using a custom-built vacuum lumen seeding device and by pipetting cellularized media onto the constructs. The seeded constructs were then transferred into custom-built bioreactors for culturing.

Three bioreactors were machined out of Teflon in accordance with a custom, in-house design. Each bioreactor has a LinMot electromagnetic actuated linear motor, a 1-pound submersible FUTEK load cell to induce axial load, and a Harvard Apparatus pressure regulation system to induce circumferential load. The bioreactors' dynamic loading system can be controlled by a custom written LabVIEW program in conjunction with proprietary software by Harvard Apparatus. The experimental setup is shown in Figure 1. The bioreactors have the capacity to hold cannulated constructs (mechanically stimulated) and non-cannulated constructs (not mechanically stimulated). The experimental groups, shown in Table 1, were cultured in the bioreactors for 3 weeks. In an attempt to encourage collagen deposition, the culture media for one bioreactor was injected with TGFβ2 at a concentration of 5 ng/ml in the last week of the experiment. Non-seeded controls were placed in media in a petri dish for the same time duration.

After the experimental culture time, the constructs were removed from the bioreactors, sectioned and prepared for further analysis. Cell proliferation was evaluated using a cell proliferation assay. To determine the mechanical properties of the constructs, a custom-made microbiaxial optomechanical device was used [4]. A collagen assay was

Copyright 2016 The Organizing Committee for the 2016 Summer Biomechanics, Bioengineering and Biotransport Conference

used to measure the concentration of deposited collagen. Multiphoton imaging was used to analyze fiber alignment and determine the distribution of collagen deposition via the detection of second harmonic signal and finally histology sections were prepared to visualize cell phenotype and distribution.

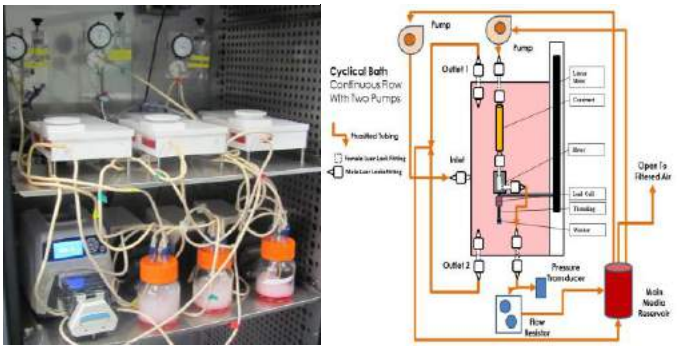

Figure 1. Experimental setup showing three bioreactor, flow resisters (top), three media reservoirs and three peristaltic pumps (bottom) and bioreactor flow diagram (right)

Bioreactor	A		B		C		Control
Cell Type	3T3FB + PSMC		3T3FB + PSMC		3T3FB		None
TGFβ2	Yes		No		No		No
Stimulation	Yes	No	Yes	No	Yes	No	No
Replicates	3	3	3	3	3	3	3

Table 1. Summary of experimental groups in this study

PRELIMINARY RESULTS

The cell proliferation assay indicated large cell proliferation while in the bioreactors. The assay also suggested that constructs that were seeded with only 3T3FB cells proliferated better than those of the mixed culture. The proliferation cell concentration results for bioreactors A, B and C are shown in Figure 2. The mechanical testing indicated that there were some experimental groups that became slightly more compliant than the control. In addition, many of the construct experimental groups were able to achieve higher axial strains than that of the controls, suggesting more mechanical integrity and higher deformability.

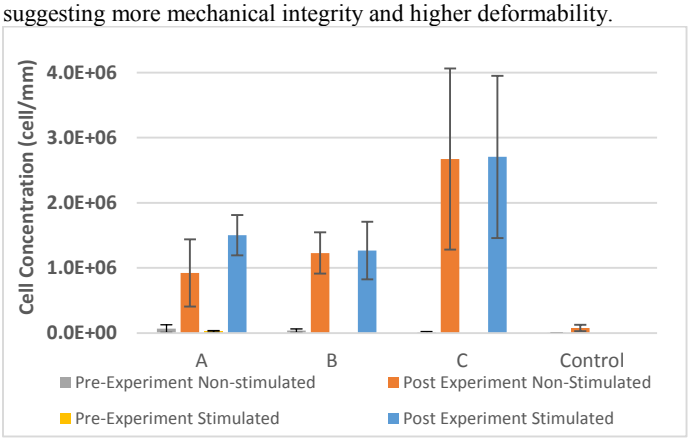

Figure 2. Cell proliferation results before and after cell culture

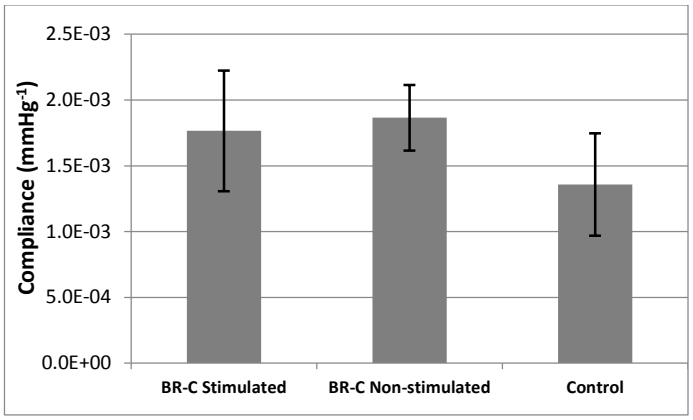

Figure 3. Compliance values of stimulated and non-stimulated constructs from Bioreactor C compared to control constructs

DISCUSSION

Preliminary results show that cells were able to grow well on the gelatin/fibrinogen construct cylindrical geometry. Also, the mechanical data suggests that the cells may have had an effect on the mechanical behavior of the seeded constructs. Further tests are necessary to determine if these are significant changes. The collagen assay and multiphoton imaging will provide information related to the cell deposition of matrix that could possibly explain the increase in compliance and deformability of the seeded constructs.

Previous studies have shown that GLUT crosslinking has a biaxial stiffening effect on the gelatin/fibrinogen construct that decreases the compliance of the constructs [2]. If cell culture is shown to have a softening effect, it may be possible to further modulate the mechanical properties of non-synthetic conduits, which would allow more custom development of durable and biocompatible TEVGs. Furthermore, the current *ex vivo* bioreactor study may provide information related to the *in vivo* durability and biocompatibility of these TEVGs.

ACKNOWLEDGEMENTS

The authors acknowledge funding from the NIH (1R21HL111990 to JPVG, Co-I Doetschman and Slepian). The authors would also like to acknowledge the help of David Maestas, Joshua Alan Uhlorn and Timothy Leach.

REFERENCES

1. Go, A.S., et al., *Heart disease and stroke statistics--2014 update: a report from the American Heart Association.* Circulation, 2014. **129**(3): p. e28-e292.
2. Tamimi, E., et al., *Biomechanical Comparison of Glutaraldehyde-Crosslinked Gelatin Fibrinogen Electrospun Scaffolds to Porcine Coronary Arteries.* J Biomech Eng, 2016. **138**(1).
3. Ardila, D.C., et al., *TGFbeta2 differentially modulates smooth muscle cell proliferation and migration in electrospun gelatin-fibrinogen constructs.* Biomaterials, 2015. **37**: p. 164-73.
4. Keyes, J.T., et al., *Deformationally dependent fluid transport properties of porcine coronary arteries based on location in the coronary vasculature.* J Mech Behav Biomed Mater, 2013. **17**: p. 296-306.

Copyright 2016 The Organizing Committee for the 2016 Summer Biomechanics, Bioengineering and Biotransport Conference

SB^{3}C2016
Summer Biomechanics, Bioengineering and Biotransport Conference
June 29 –July 2, National Harbor, MD, USA
SB^{3}C2016-1065

MODELLING THE EVOLUTION OF SMOOTH MUSCLE CELL STRESS FIBRES FOLLOWING STENT DEPLOYMENT IN AN ARTERY

Catherine A. O'Connor (1), Noel H. Reynolds (1), Patrick McGarry (1)

(1) Department of Biomedical Engineering
National University of Ireland, Galway
Galway, Ireland

INTRODUCTION

Alterations in the biomechanical environment of arterial tissue post stent implantation commonly results in the proliferation of smooth muscle cells (SMC) and remodelling of the collagen extracellular matrix (CECM) [1, 2]. The restenosis rates post stent implantation can be as high as 60% [3], where restenosis is defined as >50% reduction of the lumen diameter [3, 4]. It is reported that stents with thinner struts reduce the occurrence of restenosis [5]. This suggests that a reduction in compliance of a section of artery may result in SMC proliferation.

In an attempt to understand the relationship between effective vessel compliance post-stent implantation and the biomechanical behavior of SMC's in the artery wall, an active modelling framework is developed in the current study. Cell behavior in healthy arterial walls, arteriosclerotic arterial walls and in stented arterial walls is analyzed.

METHODS

A finite element model is developed using an idealized artery and the stent geometry [6] shown in Figure 1. The stent is deployed through contact with a radially expanding balloon. The balloon is then removed to simulate recoil. Following stent deployment a pulsatile lumen pressure ranging from 80mmHg to 120mmHg is applied at a frequency of 1Hz.

A novel approach to the modelling of the artery wall is implemented whereby actively contractile SMC's are simulated using a fading memory formulation [7, 8]. The passive matrix surrounding the SMC's is modelled using an anisotropic hyperelastic constitutive model [9].

Fading Memory Model

Active contractility of SMC's is modelled in Abaqus 6.13 (Simula, Providence, RI, USA) using a user defined material subroutine (UMAT) which implements a fading memory [8] into a constitutive model for the contractility of the actin cytoskeleton [7]. The SF activation level is determined using a first order kinetic equation originally proposed in [8] which incorporates SF formation and dissociation:

$$\frac{d\eta(\phi,\omega)}{dt} = [1-\eta(\phi,\omega)]Ck_f - \left[1-\frac{\sigma_f(\phi,\omega)}{\sigma_0(\phi,\omega)}\right]\eta(\phi,\omega)k_b \quad (1)$$

The first term on the right governs SF formation and is initiated by an exponentially decaying signal C:

$$C = exp\left(-\frac{t_s}{\theta}\right) \quad (2)$$

where θ is the decay constant, t_s is the time measured since the most recent signal, η is the dimensionless SF activation level ($0 \leq \eta \leq 1$), k_f is forward reaction rate constant and k_b is the backward reaction rate constant. The term on the right governs SF dissociation. This occurs when the tension in the SF drops below the isometric fiber tension. The fiber tension is determined using a fading memory strain rate given as:

$$h_f = \sum \int_{-\infty}^{t} Ae^{-\infty(t-\tau)}\dot{\varepsilon}_m(\tau)d\tau \; \dot{\varepsilon}_m = \begin{cases} \dot{\varepsilon}_f & \dot{\varepsilon}_f \leq 0 \\ 0 & \dot{\varepsilon}_f > 0 \end{cases} \quad (3)$$

This time integrated strain rate is inserted into a Hill type contractility equation to determine the fiber tension:

$$\frac{\sigma_f}{\sigma_0} = 1 + \frac{\overline{k}_v}{\eta}\frac{h_f}{\dot{\varepsilon}_0}; \; -\frac{\eta}{\overline{k}_v} \leq \frac{h_f}{\dot{\varepsilon}_0} \leq 0 \quad (4)$$

At each integration point the equations 1-4 are solved in 240 discrete directions allowing for the prediction of the spatial evolution

Copyright 2016 The Organizing Committee for the 2016 Summer Biomechanics, Bioengineering and Biotransport Conference

of SMC SF distributions throughout the artery wall. The active stress tensor is obtained by integrating the tension in the individual fibers over the volume:

$$\boldsymbol{\sigma}^{Active} = \sigma_{ij}^{A} = \frac{1}{V}\int_{v} \sigma_f(\omega,\phi) m_i m_j dV \quad (5)$$

Passive Anisotropic Matrix Model

The matrix surrounding the SMC's is modelled using a compressible form of the HGO anisotropic hyperelastic model [9, 10] and is calibrated using the biaxial test results of descending ovine aorta, whereby the stress tensor is given as:

$$\boldsymbol{\sigma} = \kappa_0(J-1)\mathbf{I} + \mu_0 J^{-\frac{5}{3}}\left(\mathbf{B} - \frac{1}{3}I_1\mathbf{I}\right) + 2J^{-1}k_1\sum_{i=4,6}(I_i - 1)\exp[k_2(I_i - 1)^2](\boldsymbol{a_i}\otimes\boldsymbol{a_i}) \quad (6)$$

Whereby κ_0 is the isotropic bulk modulus, μ_0 is the isotropic shear modulus, $k_1$and k_2 are the anisotropic material constants, $\boldsymbol{B}$ is the left Cauchy-Green tensor, $\boldsymbol{a_i}$ is the fiber directional vector, J is the determinant of the deformation gradient, $\boldsymbol{I}$ is the identity matrix, I_1 is the first invariant of the right Cauchy-Green tensor and I_4 and I_6 are the full anisotropic invariants describing the deformation of reinforcing fibers.

The total stress tensor is obtained by the addition of the active and passive stress tensors:

$$\boldsymbol{\sigma}^{Total} = \boldsymbol{\sigma}^{Passive} + \boldsymbol{\sigma}^{Active} \quad (7)$$

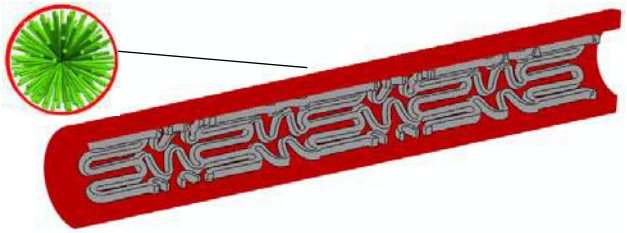

Figure 1: Closed-cell stent geometry in an artery [6] showing the 240 discrete directions equations 1-4 are solved for [8].

RESULTS

Biaxial tests reveal aortic material is highly anisotropic as shown in Figure 2 and that it is approximately 2 times stiffer in the circumferential direction than in the axial direction.

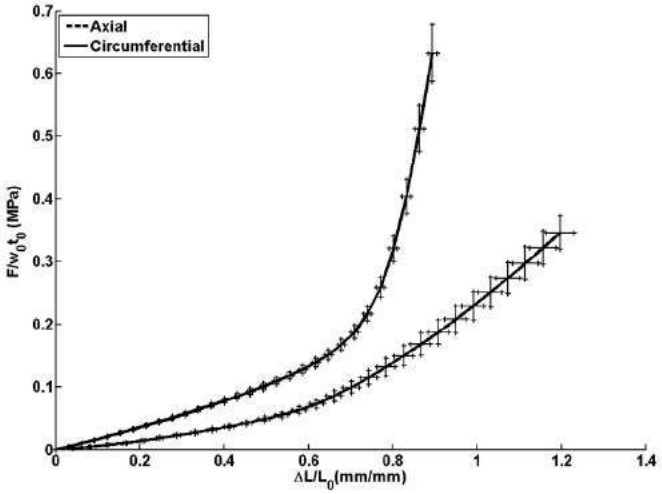

Figure 2: Biaxial test results clearly showing the anisotropy of arterial tissue.

Simulations reveal that the maximum circumferential strain rate during physiological loading of a healthy artery is 0.3738 s^{-1}.

Figure 3 shows the computed SF activation level in the circumferential direction for a healthy artery. Slight fluctuations occur during a cardiac cycle but SF levels are approximately constant. If a stent is deployed in the artery at time t=0, the circumferential strain rate in the artery wall reduces to 0.0004s^{-1}. This dramatically reduces tension in the diastolic part of the cardiac cycle, and thus inhibits dissociation of SFs. A gradual increase in SF activation in the circumferential direction is computed following stent deployment, with the final steady state value being significantly greater than that for a healthy artery. Finally, Figure 3 also shows that SF levels for stented arteries are significantly higher than for an arteriosclerotic artery, in which the compliance has been reduced by a factor of 2 [11].

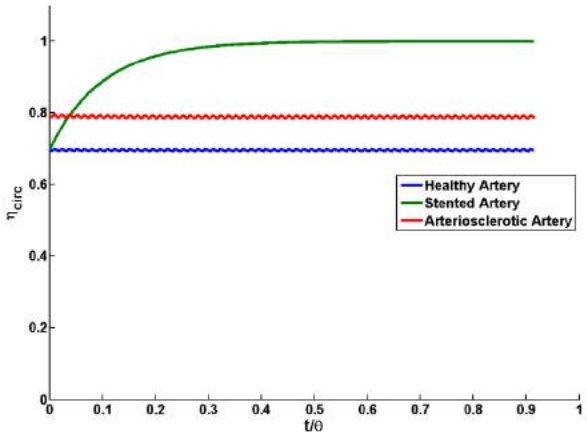

Figure 3: Circumferential stress fiber activation level for cyclic loading at 1 Hz for a healthy, arteriosclerotic and stented artery.

DISCUSSION

Simulations suggest that decreased cyclic strain rates of in the artery wall following stent deployment lead to a significant increase in circumferentially oriented SFs in smooth muscle cells. This finding is supported by an animal study which reports circumferential organization of smooth muscle cells in the artery wall at day 14 post stent implantation in porcine coronary arteries [12]. A companion experimental study is currently being conducted to further characterize the relationship between the applied strain rate, SF formation, and SMC proliferation.

ACKNOWLEDGEMENTS

The authors would like to acknowledge funding from Science Foundation Ireland (SFI-12/IP/1723).

REFERENCES

[1] Marx SO et al. *Circ Cardiovasc Interv*, 4:104-11, 2011.
[2]. McGarry JP et al, *Philos Trans A Math Phys Eng Sci*, 367:3477-97, 2009.
[3] Mitra, AK et al., *J Clin Pathol*, 59:232-239, 2006.
[4] Teirstein PS et al., *N Engl J Med*, 336:1697-1703, 1997
[5] Pache, J et al., *J Am Coll Cardiol*, 41:1283-1288, 2003.
[6] Conway, C et al., *Cardiovasc Eng Technol*, 3:374-387, 2012.
[7] Deshpande, VS et al., Proc R Soc, 463:787-815, 2007.
[8] Reynolds, NH et al., *Acta Biomater,* 27:251-263, 2015.
[9] Nolan, DR et al., *J Mech Behav Biomed Mater*, 39:48-60, 2014
[10] Holzapfel, GA et al., *J. Elasticity*, 61:1-48, 2000.
[11] Carter, AJ et al., *J Am Coll Cardiol*, 24:1398-1405, 1994.
[12] Gates, PE et al., *Br J Sports Med*, 40:897-899, 2006.

Copyright 2016 The Organizing Committee for the 2016 Summer Biomechanics, Bioengineering and Biotransport Conference

SB³C2016
Summer Biomechanics, Bioengineering and Biotransport Conference
June 29 –July 2, National Harbor,MD, USA
SB³C2016-1066

DETERMINATION OF HIFU INDUCED TEMPERATURE RISE AT FOCAL LOCATION USING NUMERICAL APPROACH

Sai Sameer Paruchuri[1], Surendra B. Devarakonda[1], Seyed Ahmad Reza Dibaji[1], Matthew R. Myers[2], Rupak K. Banerjee[1]

(1) Department of Mechanical Engineering, University of Cincinnati, Cincinnati, OH, USA

(2) Division of Applied Mechanics, Center for Devices and Radiological Health, US Food and Drug Administration, Silver Spring, Maryland, USA

INTRODUCTION

High Intensity Focused Ultrasound (HIFU) is a hyperthermia therapy that deposits high amount of acoustic energy at a point resulting in a high temperature rise. It is used in treatment of uterine fibroids, prostate and other cancers where the diseased tissue is heated to a specific temperature. Thus, accurate prediction of temperature rises during such scenarios is extremely important. Measurement of temperature rises with experiments is challenging. In addition, errors due to artifacts are possible during temperature measurements [1]. Therefore, it is advantageous to perform numerical studies to estimate the temperature rise.

The *objective* of this study is to predict the HIFU induced temperature rise in a tissue phantom for different acoustic powers using the software PZFlex and compare that with experimental results.

METHODS

Numerical model: The computational model involves a HIFU transducer and a 2D axisymmetric nonlinear tissue mimicking material (TMM). The TMM was surrounded by water. The default values for the initial temperature of TMM and the surrounding water were 37 °C and 25°C, respectively. The transition distance or the distance between the transducer and the material was maintained at 15 mm (Fig. 1). The computations were performed for an ultrasound frequency of 3.3 MHz, for different input powers of 5, 10, 20, 30, 40, 50 and 60 W.

The governing equations used for simulation of ultrasound in tissue models are the conventional momentum and constitutive equations. Taking into account, the first two terms of pressure expansion in power series, we obtain the 'B/A' model.

$$p = -K\left(\nabla.u + \frac{1}{2}\frac{B}{A}(\nabla.u)^2\right) \quad (1)$$

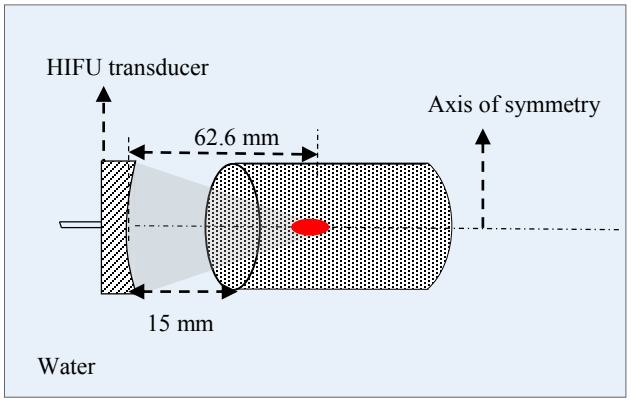

Figure 1: Geometry of the HIFU model

where p is the pressure (Pa), K or ρc^2 is the bulk modulus of the tissue material (Pa), ρ is the TMM density (Kg/m^3), c is the bulk velocity of sound (m/s) and u is the displacement vector (m), B/A is the parameter of nonlinearity (dimensionless) [2].

$$I = < p^2 > / \rho c \quad (2)$$

$$Q = \sum_{n=1} 2\alpha I_n \quad (3)$$

Heat source, Q (W/m^3) can be calculated using intensity, I (W/m^2) which is obtained from acoustic pressure. α is the acoustic absorptivity (dB/m).

Copyright 2016 The Organizing Committee for the 2016 Summer Biomechanics, Bioengineering and Biotransport Conference

The thermal transient response was obtained by solving the Pennes bioheat transfer equation [3]. The perfusion term was neglected because of the absence of microvasculature in the TMM:

$$\rho C \frac{\partial T}{\partial t} = k(\nabla^2 T) + Q \quad (4)$$

where T is the temperature (°C), C is the specific heat of the TMM (J/Kg.°C), k is the thermal conductivity of the TMM in (W/m.°C).

Computations for the seven different applied acoustic powers were conducted keeping the sonication time as 30 s. The calculated pressure values at the transducer surface for each of the applied powers were used as the input along with the transducer properties (Table 1) to obtain the focal temperature rise. The difference between the peak temperature of the material and the initial temperature was used as the value for temperature rise. The properties of the nonlinear TMM used in the computations are presented in Table 2.

Table 1: Transducer properties and setup

Diameter	64 mm
Focal length	62.6 mm
Transition distance	15 mm
Sonication time	30 s

Table 2: TMM material properties

Density	1040 Kg/m^3
Bulk velocity	1534 m/s
Bulk attenuation	46 dB/MHz/m
B/A	7
Specific heat capacity	3780 J/Kg.°C
Thermal conductivity	0.58 W/m.°C

Experimental setup: Experiments were performed to estimate the focal temperature rises in a TMM for similar scenarios as in numerical method. The TMM was prepared as per the protocol presented in King et al [4]. The TMM was mixed in liquid form and poured into a cylindrical fixture of diameter 8 cm. The fixture was embedded with eight thin wire thermocouples (TCs) [5], positioned in four separated layers, with two TCs in each layer. The TCs in the same layer were placed 4 mm apart, while the adjacent layers were separated by a distance of 3 mm.

The HIFU beam was positioned inside the TCs array and away from the TCs junction to avoid any errors due to the artifacts. In order to evaluate the focal temperature rise using the remote TCs measurements, a localization algorithm [5] was first implemented to determine the location of beam focus inside the TCs array. After finding the relative location of the beam focus, the focal temperature prediction was made using an estimating function [5]. The estimating functions can be developed from common fitting functions where the unknown parameters can be determined based on the TCs measurements. Here, assuming that the heat production has Gaussian profile in radial direction (with no axial variation), the estimating function was written in terms of exponential integral as shown by Dillon et al [6]. The focal temperature estimation using the exponential integral was performed for the acoustic powers of 30, 40 and 50 W.

RESULTS

The values shown in the Fig. 2 correspond to the maximum focal temperature rise attained numerically for the sonication period of 30 s. The focal temperature rise values obtained numerically were 6.8 ºC, 13.6 ºC, 27.2 ºC, 40.8 ºC, 54.6 ºC, 68.1 ºC and 81.9 ºC for the input acoustic powers of 5, 10, 20, 30, 40, 50 and 60 W, respectively. The nonlinearity in the peak temperature rise at higher powers (40 W, 50 W and 60 W) cannot be observed and further investigation is required.

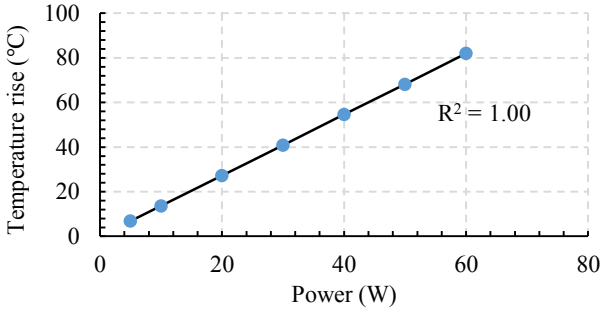

Figure 2: Variation of temperature rise with input power

Comparison of the computational results with the experimental [5] values shows a deviation of 13.2 % for 30 W, 1.0% for 40 W, and 2.6 % for 50 W of input power (Fig.3), while the average deviation for the three powers is 5.7%.

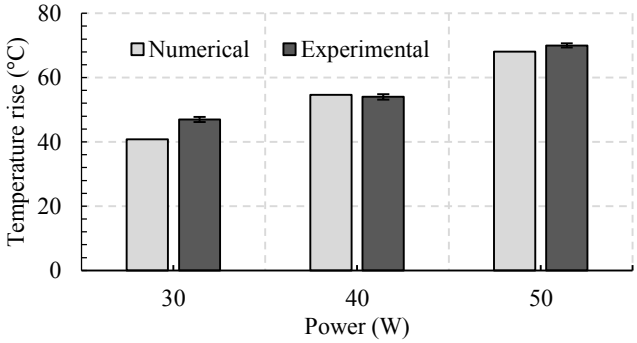

Figure 3: Comparison of numerical and experimental values of temperature rise

DISCUSSION

The temperature rise values achieved for various power inputs based on computations for nonlinear TMM have been presented in this study. The numerical temperature rises show good agreement with experimental temperature rises for 30 W, 40 W and 50 W. Numerical results match within 5.7% of the experimental values when averaged for all the three powers. Hence, numerical methods can provide reliable estimates of focal temperatures when conducting experiments is difficult.

Assumptions and limitations. All the computations have been performed assuming that the tissue properties are uniform. Nonlinear temperature rise at higher power needs further assessment.

Future scope. The current study will be extended to estimate the temperature rise by incorporating different TMM properties. A comparison of the numerically obtained results will be made with *in-vivo* experimental temperature values.

ACKOWLEDGEMENTS

Financial support from National Science Foundation (Grant no.: 1403356) is gratefully acknowledged.

REFERENCES

[1] Dasgupta, S., et al., Ultrasonics, 2011. **51**(2): p. 171-80.
[2] Wojcik L. Gregory., et al., International Mechanical Engineering Conference and Exposition Proceedings, 1999.
[3] Pennes, H.H., J Appl Physiol, 1948. **1**(2): p. 93-122.
[4] King et al, IEEE tran. Ultrason. Vol. 58, no. 7, 2011
[5] Hariharan., et al., IEEE Tran. on Ultrasonics, 2014;61(12):2019-31
[6] Dillon et al., Phys. Med. Biol., vol. 57, no. 14, 2012

Copyright 2016 The Organizing Committee for the 2016 Summer Biomechanics, Bioengineering and Biotransport Conference

SB^{3}C2016
Summer Biomechanics, Bioengineering and Biotransport Conference
June 29 –July 2, National Harbor, MD, USA
SB^{3}C2016-1067

INCREASED CAPTURE OF MAGNETIC MICROBEADS DUE TO SWITCHING OF ELECTROOSMOTIC FLOW

Samuel A. Miller (1), William R. Heineman (2), Rupak K. Banerjee (1)

(1) Department of Mechanical and Materials Engineering, University of Cincinnati Cincinnati, Ohio, USA

(2) Department of Chemistry University of Cincinnati Cincinnati, Ohio, USA

INTRODUCTION

Detection and isolation of bio-molecules for immunoassays is crucial to efficient and accurate performance of micro total analysis systems (μTAS). To accomplish this, magnetophoretic separation techniques are commonly used in these microfluidic platforms. This technique utilizes magnetic microbeads coated with epitomes targeted to specific pathogens as part of an antigen-antibody binding complex to tag specific bio-molecules [1]. Separation is then accomplished through the application of a magnetic field to isolate the microbeads/bio-molecule complex from the continuous flow in the device. The continuous flow in microfluidic devices can be either pressure driven or electrokinetically driven. Electrokinetically driven mechanisms, such as electroosmotic flow (EOF) has advantages over pressure driven flow due to the absence of mechanical pumps, which can be inefficient [2], as well as the ability to operate at atmospheric pressure.

The difficulty with magnetophoretic immunoassays is producing a reliable and efficient capture of microbeads to ensure accurate results with the highest possible sensitivity using dilute samples. The capture efficiency (CE), or ratio of number of particles captured to number of particles injected into the channel, relies on the attractive magnetic force overcoming the viscous forces of the liquid moving the particles with the flow. However, previous studies have shown that magnetic beads can escape the area with high magnetic field strength [3], resulting in uncaptured beads and decreased sensitivity. Thus, a switching method is implemented to increase the bead residence time in the area of higher magnetic field strength. This switching is accomplished by alternating the external voltage driving the electroosmotic flow through the microchannel. The goal of this study is to assess increase in capture efficiency using the switching flow mechanism as compared to the constant flow mechanism.

METHODS

The microchannel device used during testing is shown in Fig. 1. The channel is produced using standard soft lithography with the final device made from PDMS bonded to a glass slide, resulting in a channel that is 50mm long with a cross section of 50 μm x 50 μm. A 1/8" x 1/8" x 3/8" tall neodymium (NdFeB) magnet is placed above the channel, 25 mm from either well. The channel is pre-treated with NaOH to induce surface charge on the walls and then PBS with Tween20 to prevent the microbeads from sticking to the wall when not captured.

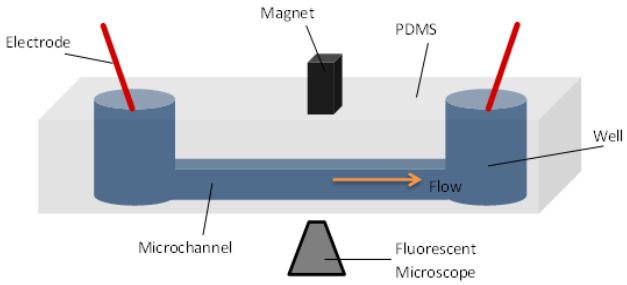

Figure 1: Schematic of microchannel device.

The beads used were Dynabead® M280 Sheep anti-Rabbit IgG tagged with Alexa Fluor® 488 Rabbit anti-Mouse IgG by slow tilt mixing for 24 hours at 8°C. The beads were suspended in PBS buffer to achieve the desired concentrations for the experiments (C1 = 2×10^6, C2 = 4×10^6 beads/mL).

The capture zone was determined for the device by running tests at the lowest flow rate followed by immediately running the buffer to clear out any uncaptured beads before determining the distance from

Copyright 2016 The Organizing Committee for the 2016 Summer Biomechanics, Bioengineering and Biotransport Conference

the front and far edge of the magnet beads were visualized. The electroosmotic flow is governed by equations 1 and 2

Poisson's equation: $\nabla^2\phi = 0$ (1)

Helmholtz-Smoluchowski equation: $U_e = \varepsilon\zeta E/\mu$ (2)

These two equations are coupled so that the EOF velocity, U_e corresponds to the applied potential, ϕ. For the experiments, voltage was applied for 20 min total, with the time breakdown shown in Table 1.

Table 1: Applied voltage conditions as function of time. V for case 1 is 650 volts; V for case 2 is 750 volts.

Time (min)	Steady State		Switching	
	Inlet	Outlet	Inlet	Outlet
0-8	+V	Ground	+V	Ground
8-11	+V	Ground	**-V**	Ground
11-14	+V	Ground	+V	Ground
14-17	+V	Ground	**-V**	Ground
17-20	+V	Ground	+V	Ground

The beads were visualized and images were captured using inverted fluorescent microscopy, with example images of captured beads shown in Fig. 2. A calibration curve of fluorescence as a function of concentration is shown in Fig. 3. Beads located in the starting well or before the capture zone were not considered, those located in the capture zone were considered captured, and those located in the channel after the capture zone or in the ending well were considered uncaptured.

Figure 2: Fluorsecent images of beads captured under switching protocol at concentration of 4×10^6 beads/mL and 750 V (left) and 650 V (right).

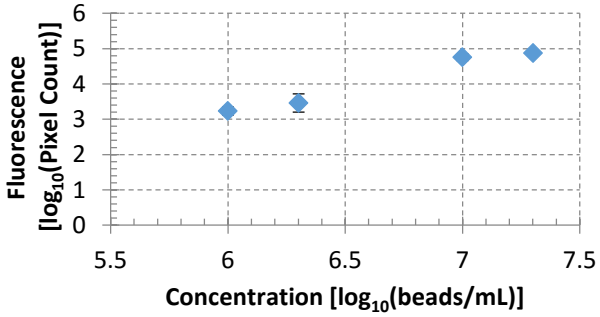

Figure 3: Calibration curve of fluorescence as function of bead concentration.

The images were analyzed using MATLAB to determine the fluorescent intensity based on Red-Green-Blue (RGB) values to determine percentage of beads captured based on pixel count (PC) of captured and uncaptured beads according to

$$Capture\% = \frac{PC_{captured}}{PC_{captured} + PC_{uncaptured}} * 100\% \quad (3)$$

The relative percentage difference between switching and constant flow capture was determined by

$$Rel\%Diff = \frac{Capture\%_{Switch} - Capture\%_{Constant}}{Capture\%_{Constant}} * 100\% \quad (4)$$

RESULTS

Capture percentage for both switching and constant flow as well as relative percentage difference for voltages of 750 V and 650 V and concentrations of 2×10^6 beads/mL and 4×10^6 beads/mL are shown in Table 2.

Table 2: Capture percentage for switching and constant flows and the relative percentage difference.

Concentration (beads/mL)	Voltage (V)	Switching Capture %	Constant Capture %	Relative % Diff
2×10^6	650	85.0 ± 5.8	41.7 ± 5.5	99.2 ± 30.0
2×10^6	750	83.6 ± 6.7	37.6 ± 6.6	122.5 ± 42.1
4×10^6	650	80.6 ± 4.1	37.3 ± 4.6	112.6 ± 29.5
4×10^6	750	71.1 ± 6.2	31.7 ± 5.8	122.8 ± 44.7

The main result is seen in the difference between capture percentages of the switching and constant flow protocols. The drastic increase in capture percentage in the switching situation, around 2 times the capture percentage, is due to the increased residence time in the higher magnetic field capture zone. The different concentrations and voltages had very little effect on the capture percentages. There was a relative difference of less than 20% for each permutation in voltage or concentration, keeping all variables (voltage, concentration, and switching versus constant flow) constant. This difference is insignificant compared to the drastic improvement in capture percentage when incorporating the switching protocol.

The maximum capture zone was determined to be 12 mm before the front of the magnet and 15 mm beyond the back of the magnet.

DISCUSSION

The change in capture efficiency as a result of the switching flow protocol was examined and compared to the capture efficiency using constant flow. The major finding of this study shows that switching causes a relative difference of 2 times the capture percentage for all cases as compared to the constant flow protocol. This is due to the switching function returning beads that would be lost under constant flow conditions back to the capture zone and the influence of the higher magnetic field strength.

Future examination of this device through variation of the exact switching protocol could optimize the capture efficiency and residence time in the capture zone. In addition, varying the switching protocol could also result in more beads entering the capture zone, potentially increase the sensitivity. Further studies consisting of beads capturing bio-molecules would also provide vital information concerning the performance of the device in its intended application as a portable magnetophoretic immunoassay.

ACKNOWLEDGEMENTS

This research study was supported by the National Institute for Occupational Safety and Health Grant #1011206.

REFERENCES

[1] McCloskey, KE et al., *Anal Chem*, 75.24:6868-6874, 2003.

[2] Comandur, KA et al.., *J Micromech and Microeng* 20.3:035017, 2010.

[3] Das, D et al., *ASME 2012 Summer Bioengineering Conference*, 821-822, 2012.

Copyright 2016 The Organizing Committee for the 2016 Summer Biomechanics, Bioengineering and Biotransport Conference

SB³C2016
Summer Biomechanics, Bioengineering and Biotransport Conference
June 29 –July 2, National Harbor, MD, USA
SB³C2016-1068

DIFFERENCES IN PELVIC BLOOD FLOW MEDIATE DIFFERENCES IN ABDOMINAL WALL SHEAR STRESS BETWEEN MEN AND WOMEN

E. Iffrig (1), JN. Oshinski (1,2), WR. Taylor (1,3)

(1) Department of Biomedical Engineering
Georgia Institute of Technology
& Emory University
Atlanta, GA, USA

(2) Department of Radiology & Imaging Services
Emory University
Atlanta, GA, USA

(3) Department of Medicine – Division of Cardiology
Emory University & Atlanta VA Medical Center
Atlanta, GA, USA

INTRODUCTION

Abdominal aortic aneurysms (AAA) are more prevalent in men than they are in women with an increased frequency of 4 or 5 to 1.[1] While it has been proposed that hormonal regulation, specifically estrogen, plays a role in this discrepancy, women provided with hormone replacement therapy (HRT) following menopause are not any more protected from AAA than women without HRT.[2] It is possible, therefore, that a difference exists in the biomechanics rather than the biology of the aorta that results in a difference in the development or outcome of AAA. Given the relationship between vascular inflammatory processes (atherosclerosis and aneurysms in particular) and low and oscillatory wall shear stress, it is possible that men are exposed to wall shear stress profiles that increase their risk for developing AAA while women are prtoected.[3] For this study we compared the abdominal aortic wall shear stress (WSS) profiles of healthy men and women using phase contrast MRI.

In addition to quantifying any differences in the shear stress, we tested a possible cause for why WSS differences exist. Previous studies have shown that parous women (who experience an increase in uterine flow) are protected against AAA when compared with non-parous women.[4] Therefore, we compared flow in the internal and external iliac arteries (also measured by phase contrast MRI) to test the hypothesis that differences in pelvic blood flow (mediated by the uterus in women and supplied by the internal iliac artery) could cause a difference in aortic hemodynamics.

METHODS

We recruited 12 men and 15 women aged 30-42 with no history of cardiovascular disease under an Emory University IRB approved protocol to participate in the study. In each of these volunteers we acquired between 3 and 10 phase contrast image sets taken at evenly spaced locations along the length of the aorta. All phase contrast sequences were ECG-gated 2D axial image sets encoded to measure through plane velocity (Venc=150 cm/s). Thirty time frames were acquired over the cardiac cycle and final voxel resolution of 1.33x1.33x5 mm. Using a method developed in our lab, we quantified the wall shear stress at 80 locations around the circumference for each of the acquired slices.[5] We then evaluated the oscillatory shear index in which τ^* is the portion of the shear wave that is in the opposite direction of the average shear vector (towards the head in the abdominal aorta) and τ is the shear stress wave:

$$OSI = \frac{\int \tau^* dt}{\int \tau dt} \quad (1)$$

The location of each slice was normalized to the total length of the aorta for each volunteer and placed one of 10 normalized bins. For any volunteers lacking data in one of these bins it was filled in using a validated two dimensional interpolation method. This allowed us to create a 10x80 matrix of the averaged results among all volunteers in which each row corresponds to a different longitudinal location in the aorta and each column to circumferential positions. This matrix normalized to the size of the vessel in both the radial and axial directions and allowed for a direct comparison of the sexes at each of the elements in the array.

In addition to phase contrast images in the abdominal aorta, we also acquired PCMR image sets for both the internal and external artery and quantified the flow through these vessels. We compared the average reverse flow, forward flow and oscillatory flow ratio in which Q_{rev} is the flow wave in the cranial direction and Q_{for} is the flow wave in the caudal direction:

Copyright 2016 The Organizing Committee for the 2016 Summer Biomechanics, Bioengineering and Biotransport Conference

$$OFR = \frac{\int Q_{rev} dt}{\int Q_{for} dt} \quad (2)$$

This parameter allows us to assess the extent of flow reversal normalized to the forward flow which controls for any discrepancies that exist as a result of differences in size between men and women.

RESULTS

Figure 1 shows the results of our comparison our OSI between the healthy men and women. Globally, the average OSI value for men was significantly higher than women (0.40±0.00040 vs 0.35±.00039, $p<0.0001$).

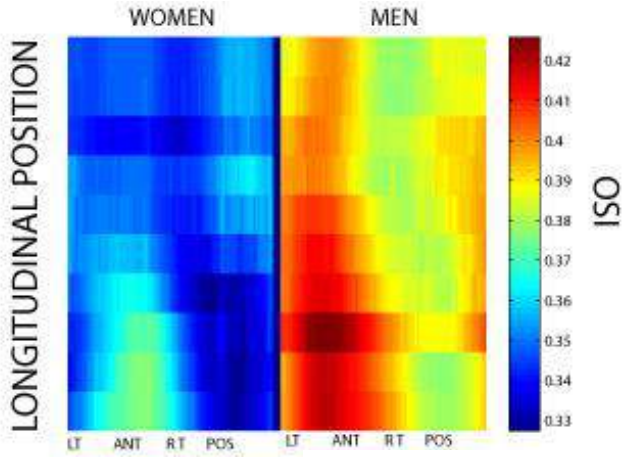

n=15 women, 13 men

Figure 1

Figure 2 shows the average external and internal iliac arteries' OFR values for men and women. When looking at the values of forward and reverse volume it was found that only the internal reverse flow volume was significantly higher in men when compared with women using a two tail t-test (1.2 ± 0.26 mL in men vs 0.22 ± 0.075 mL in women, $p<0.05$).

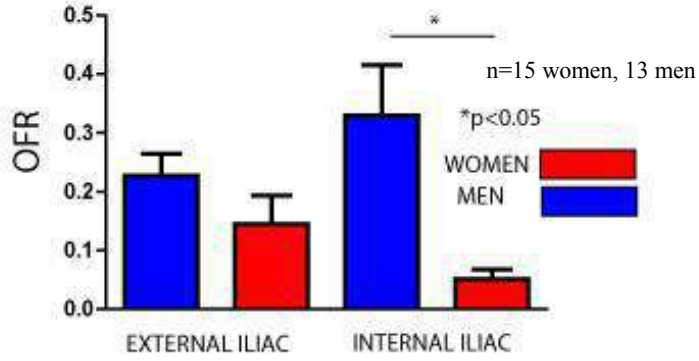

Figure 2

DISCUSSION

Our results demonstrate a significant reduction in the extent of oscillatory shear in women when compared with men in this age group. This observation supports the hypothesis that differences in abdominal aortic aneurysm incidence in the two populations may be explained by a difference in the biomechanics prior to onset of the disease. Specifically that women of this age are protected from harmful oscillatory shear in the abdominal aorta that is known to incite atherosclerosis lesions and underscore aneurysm development.

Further, our results show that this difference in OSI is, at least in part, most likely mediated by a difference in peripheral resistance. More specifically that women have less flow reversal in the internal iliac artery when compared with men. This observation can be explained physiologically by the differences in pelvic anatomy which is the recipient of internal iliac artery blood. That this same reduction is not seen in the external iliac artery confirms that a decrease in oscillatory flow is not a global phenomenon in women but is specific to the internal artery and consequently the aorta.

While peripheral arterial resistance of the iliacs may contribute to the differences in hemodynamics that are seen in men and women, it is likely that it is not the only contributing factor. We are also evaluating differences in geometry such as aortic size, length and curvature as well differences in tissue mechanics such as compliance and strain to evaluate the influence of these factors on wall shear stress measurements.

ACKNOWLEDGEMENTS

This work was funded in part by a PreDoctoral Fellowship from the American Heart Association

REFERENCES

Sample Reference:

[1] Starr JE et al, *J Vasc Surg*, 57:3S-10S, 2013.
[2] C Main et al, *Coch Data Sys Rev*, 4, 2013.
[3] Pedersen EM et al, *Eur J Vasc Surg*, 18:328-333,1999.
[4] Villard C et al, *J Vasc Surg*, 54:341-345, 2011
[5] Iffrig E et al, *SB3C,* Session 2015

Copyright 2016 The Organizing Committee for the 2016 Summer Biomechanics, Bioengineering and Biotransport Conference

SB^{3}C2016
Summer Biomechanics, Bioengineering and Biotransport Conference
June 29 –July 2, National Harbor, MD, USA
SB^{3}C2016-1069

MATHEMATICAL MODELING OF FLUID-STRUCTURE INTERACTION IN BIOPROSTHETIC HEART VALVES: NUMERICAL APPROXIMATION AND EXPERIMENTAL VALIDATION

David Kamensky (1), Ming-Chen Hsu (2), John G. Lesicko (1), Mitchell A. Katona (1), Jordan L. Graves (1), Samuel J. Petter (1), Thomas J.R. Hughes (1), Michael S. Sacks (1)

(1) Center for Cardiovascular Simulation
University of Texas at Austin
Austin, Texas, USA

(2) Department of Mechanical Engineering
Iowa State University
Ames, Iowa, USA

INTRODUCTION

Bioprosthetic heart valve (BHV) design has remained nearly static over the past 10 years. Current BHVs frequently require replacement 10-15 years after implantation [1]. Mechanical stresses have been shown to drive the degradation of BHVs [2]. Convenient and accurate predictive modeling of BHV mechanics could therefore accelerate the design of more durable valves. The forces driving BHV leaflets are due to surrounding blood flow. Thus a complete mechanical model of a BHV must include fluid-structure interaction (FSI). The purpose of this work is to develop a robust framework for modeling and simulation of BHV FSI. This effort can be divided into two broad tasks:

- Devising a mathematical model that accurately describes BHV FSI.
- Developing numerical methods to compute approximate solutions to this mathematical model.

The mathematical model must be *validated*: we must compare the predictions of the model with experimental results, to ensure that the mathematical description of reality is adequate for our purposes. The numerical method must be *verified*: we must take measures to ensure that computational results accurately approximate solutions to the desired mathematical model. For more on these concepts, see [3].

The starting points for our mathematical model are continuum descriptions of BHV leaflets and blood flow that have been previously validated in the contexts of static pressure loading of valves and flow through large arteries. However, mathematical models are only valid under limited ranges of conditions, which may or may not include BHV FSI. Very little work has been done on validating mathematical models of BHV FSI.

Numerical approximation of mathematical models for fluids, structures, and FSI are well-studied topics, but the problem of BHV FSI introduces challenges that make it at best inconvenient to study using "off-the-shelf" technologies. Aspects that make the problem especially difficult include similarity of fluid and structure densities, large structure deformations, and changes in fluid domain topology. Due to these difficulties, we participate in an interdisciplinary research effort, collaborating with applied mathematicians and computational engineers to develop and verify novel numerical methods for FSI analysis that combine immersed boundary [4] concepts and isogeometric analysis [5] to allow for maximal flexibility in simulation workflow, without sacrificing modeling capabilities.

METHODS

We propose to model the structure displacement and fluid velocity fields as solutions to coupled partial differential equations (PDEs), using the framework of continuum mechanics. We model the fluid (be it blood or the working fluid of an *in vitro* experiment) as incompressible and Newtonian. We model the BHV leaflets using Kirchhoff-Love thin shell theory. These sub-problems are coupled by standard kinematic and dynamic compatibility conditions. Aside from the use of continuum mechanical assumptions widely held to be valid for predicting macroscopic deformation of bulk materials, we have introduced the following (possibly invalid) assumptions:

- The BHV leaflets are modeled geometrically as surfaces of co-dimension one to the surrounding fluid domain.
- The BHV leaflet mechanics are represented using Kirchhoff-Love thin shell assumptions and a hyperelastic constitutive model.
- All fluids of interest are assumed to be incompressible and Newtonian.

The validity of these modeling assumptions needs to be tested. To this end, we have constructed a flow loop to pump water through an

Copyright 2016 The Organizing Committee for the 2016 Summer Biomechanics, Bioengineering and Biotransport Conference

artificial aortic valve. The flow loop is instrumented to collect ventricular and aortic pressures, volumetric flow rate and time-stamped images of the valve.

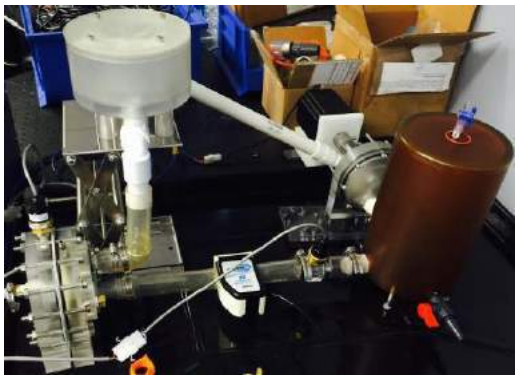

Figure 1: Photograph of the validation flow loop

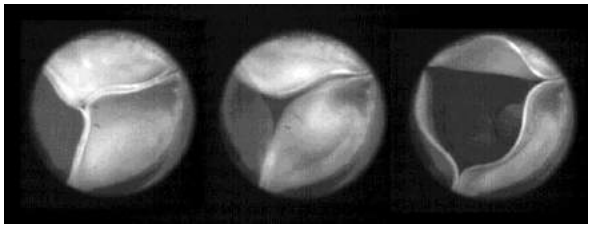

Figure 2: View of artificial valve in flow loop (contrast enhanced)

The measured flow rate can be prescribed as a boundary condition on the mathematical model and an approximate solution can be computed using a numerical method. Then the computed deformations of the leaflets and the computed pressure drop across the valve can be reasonably compared with the time-stamped images and measured aortic and ventricular pressures. Assuming that the numerical method has been sufficiently verified, this comparison tests the validity of the modeling assumptions itemized above, in the context of predicting leaflet deformation and net resistance to fluid flow.

Our numerical approach was introduced in [6]. In summary, we immerse a discretization of the structure into a non-matching fluid discretization. This allows for great freedom in the choice of fluid and structure discretizations and avoids the difficulties associated with generating discrete solution spaces that conform to FSI kinematics. Unlike the earliest immersed boundary methods [4], which used a spring network as a placeholder for the structure, we apply isogeometric analysis to the structure sub-problem, allowing for accurate treatment of shell structure mechanics with hyperelastic constitutive behavior [7].

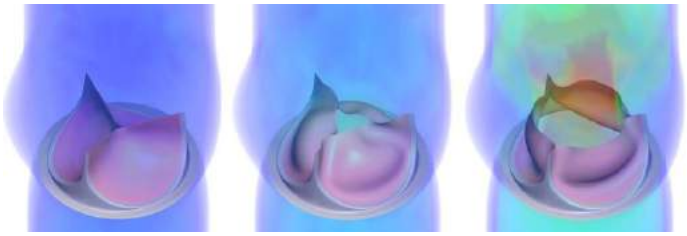

Figure 3: Example simulation results (reproduced from [9])

RESULTS

The validation study remains a work in progress. The majority of complete results contribute to the verification of the numerical method. In [6] we demonstrated that the numerical method could match solutions to benchmark problems computed using previously-verified methods. More recent, ongoing work on verification aims to derive *a priori* error estimates for linearized model problems and test convergence to analytical solutions.

As a preliminary validation, we can make comparisons between computations and existing experimental results from the literature, e.g. [8]. Many of the free parameters of our present model (e.g. the valve geometry, constitutive properties, flow boundary conditions, etc.) cannot be reliably determined from publications describing prior experiments, so no precise quantitative correspondence is expected. We nonetheless find that the qualitative features of the BHV dynamics are reproduced in approximate solutions to our mathematical model. Some of these features are conspicuously absent from models that employ only structural dynamics. In [9], we compared FSI computations, structural dynamics computations, and experimental results from the literature.

DISCUSSION

As noted in the previous section, preliminary comparisons of computational and experimental results indicate that our model of BHV FSI provides more accurate representations of BHV leaflet kinematics than models considering structural dynamics alone. We are, at present, conducting more rigorous verification and validation studies. Further verification will improve our confidence that computational results approximate solutions to the desired PDEs. New validation experiments will allow for more accurate estimation of the free parameters of these PDEs. These advances will render observed correspondences and/or discrepancies between computational and experimental results more meaningful.

ACKNOWLEDGEMENTS

D. Kamensky was supported by the CSEM Graduate Fellowship at UT Austin. This research was supported by NIH grant R01 HL108330.

REFERENCES

[1] R.F. Siddiqui et al., *Histopathology*, 55:135-144, 2009.

[2] M.J. Thubrikar et al., *J. Thorac. Cardiovasc. Surg.*, 86(1):115-125, 1983.

[3] I. Babuska and J.T. Oden, ICES Report 03-52, 2003.

[4] C.S. Peskin, *J. Comput. Phys.*, 10(2):252-271, 1972.

[5] T.J.R. Hughes et al., *Comput. Meth. Appl. Mech. Eng.*, 194:4135-4195, 2005.

[6] D. Kamensky et al., *Comput. Meth. Appl. Mech. Eng.*, 284:1005-1053, 2015.

[7] J. Kiendl et al., *Comput. Meth. Appl. Mech. Eng., 291:280-303, 2015.*

[8] A.K.S. Iyengar et al., *Ann. Biomed. Eng.*, 29(11):963-973, 2001.

[9] M.-C. Hsu et al., *Comput. Mech.*, 55(6):1211-1225, 2015.

Copyright 2016 The Organizing Committee for the 2016 Summer Biomechanics, Bioengineering and Biotransport Conference

SB³C2016
Summer Biomechanics, Bioengineering and Biotransport Conference
June 29 –July 2, National Harbor, MD, USA
SB³C2016-1070

COMPARISON OF HUMERAL HEAD OSTEOTOMY USING ANATOMIC AND GUIDE-ASSISTED CUTS

Emily A. West (1,2,3), Nikolas K. Knowles (1,2,3), Louis M. Ferreira (1,2,3), George S. Athwal (2)

(1) Biomedical Engineering
Western University
London, Ontario, Canada

(2) Roth|McFarlene Hand and Upper Limb Clinic
London, Ontario, Canada

(3) Lawson Health Research Institute
London, Ontario, Canada

INTRODUCTION

Shoulder arthroplasty is used to treat several common pathologies of the shoulder, including osteoarthritis, post-traumatic arthritis, and avascular necrosis [1]. In replacement of the humeral head, modular components allow for natural variability in shoulder anatomy, including retroversion and head-neck angles. Surgical options include anatomic cut or guide-assisted cut at a fixed retroversion and head-neck angle. The purpose of this study was to determine the variability between head height and anteroposterior (AP) and superoinferior (SI) diameters using anatomic and guide-assisted humeral head cuts.

METHODS

Computed tomography (CT) scans of 10 cadaveric shoulder specimens (5 male, 5 female; mean age 71 ± 14 years; 7 left) were converted to 3D models using medical imaging software. An anatomic humeral head cut plane was placed at the anatomic head–neck junction, maintaining the posterior cuff insertion for all shoulders by a fellowship trained shoulder surgeon. Cut planes were generated for each of the standard implant head neck angles (125°,130°,135°, and 140°) and retroversion angles (20°,30°, and 40°) in commercially available cutting guides, for a combination of 12 repeated virtual cut conditions per specimen. The humeral head height and the cut head diameter were measured in the AP and the SI planes for the anatomic and guide-assisted osteotomy planes. Differences were compared using a separate two-way repeated measures ANOVA for each dependent variable.

RESULTS

Guide-assisted cuts showed no significant effect on head height due to head-neck angle ($p=0.205$) or retroversion angle ($p=0.190$). These results persisted by gender (male: head-neck $p=0.659$ and retroversion $p=0.386$; female: head-neck $p=0.204$ and retroversion $p=0.190$).

SI head diameter increased by 1.3 mm with increasing head-neck angle ($p<0.001$), but there was no effect due to retroversion ($p=0.148$). A head-neck angle of 125° caused the greatest decrease in SI diameter of -2.8 mm compared to the anatomic cut, averaged over the retroversion range. The greatest reduction of SI diameter, -3.4 mm compared to anatomic, occurred with 125° head-neck angle and 20° retroversion. By gender, males showed a significant effect from head-neck angle ($p=0.008$), but females did not ($p=0.077$). There was no significant difference from retroversion in either gender group (male $p=0.792$; female $p=0.057$).

There was no significant difference in AP diameter by head-neck angle ($p=0.192$) or retroversion angle ($p=0.168$). These results persisted in the males (head-neck $p=0.420$ and retroversion $p=0.780$). In females, there was no effect from head-neck angle ($p=0.232$); however, retroversion angle trended toward significance ($p=0.050$).

Copyright 2016 The Organizing Committee for the 2016 Summer Biomechanics, Bioengineering and Biotransport Conference

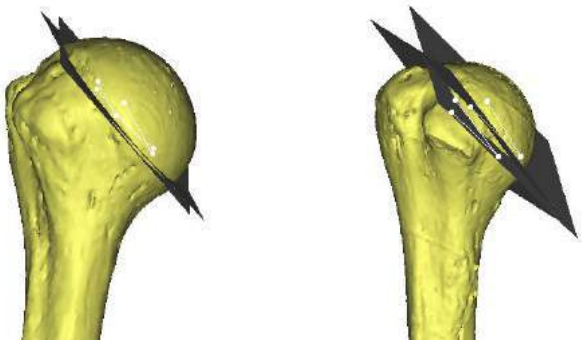

Figure 1: Three dimensional models created from CT scans to show comparison of the optimized anatomic cut and guide-assisted cut at the average cut plane (135 head-Neck angle and 30 Retroversion) between a patient with average anatomy (left) and anatomy falling outside the range of normal values (right) (125 Head-Neck angle and 60 Retroversion)

DISCUSSION

For patients whose natural anatomy falls outside the range of the commercial cut guides, resection according to the template may result in deviation from natural dimensions of the humeral head. Due to the large variability in anatomic retroversion and head-neck angles in the subjects of this study, further study with a larger sample size is needed to investigate if the observed trends persist. These preliminary results have implications for manufacturers to create guides to represent a larger segment of the population, and surgeons' choices in intra-operative planning

ACKNOWLEDGEMENTS

Emily is partially supported by Western University's collaborative training program in musculoskeletal health research.

REFERENCES

[1] Caniggia, M et al., *Panminerva Medica*, 41:341-349, 1999.

Copyright 2016 The Organizing Committee for the 2016 Summer Biomechanics, Bioengineering and Biotransport Conference

SB^{3}C2016
Summer Biomechanics, Bioengineering and Biotransport Conference
June 29 –July 2, National Harbor, MD, USA
SB^{3}C2016-1071

PRINCIPAL COMPONENT ANALYSIS OF FRICTION FORCE HYSTERESIS CURVES FOR DETECTING FATIGUE FAILURE AND GENERATING FRICTIONAL S-N CURVES FOR ARTICULAR CARTILAGE

Krista M. Durney (1), Robert J. Nims (1), James F. Boorman-Padgett (2), Jason T. Suh (1), Hyeon Jin Koo (1), Polina V. Smirnova (1), Gregory T. Salamone (1) Brian K. Jones (2), Sevan R. Oungoulian (2), Clark T. Hung (1), Gerard A. Ateshian (1,2)

(1) Department of Biomedical Engineering
Columbia University
New York, NY, USA

(2) Department of Mechanical Engineering
Columbia University
New York, NY, USA

INTRODUCTION

Osteoarthritis (OA) is a degenerative joint disease resulting in damage and eventual loss of articular cartilage. Cartilage swelling and collagen fiber realignment are well-characterized early hallmarks of OA, but OA etiology remains poorly understood and therefore early-stage treatments target pain management rather than underlying mechanisms. Other than in the case of blunt injury, causative factors for the *mechanical initiation* of cartilage damage and wear in OA remain unknown. Weakening of the collagen matrix may be attributable to the number of cycles cartilage endures in its lifetime, or fatigue failure [1], and may cause the tissue to fail in shear at the middle zone due to its low shear modulus [2]. In this investigation, we hypothesize that the onset of fatigue failure can be detected by examining the principal components of frictional hysteresis curves and that frictional stress correlates with the number of cycles to damage. This mechanical study utilized devitalized full-thickness articular cartilage to preclude the reparative or inflammatory action of chondrocytes.

METHODS

Sliding experiments were performed in which cartilage strips were tested against a glass lens in either synovial fluid (SF) or phosphate buffered saline (PBS) (Fig. 1). A range of loads and test durations were selected to elucidate the combined effect of lubricant, stress, and number of cycles on frictional force and cartilage damage.

Specimen Preparation: Cartilage strips (10 × 30 mm) were harvested from the tibial plateaus of knee joints of immature bovine calves (4-8 weeks old). Forty separate sliding experiments were performed on tissue collected from fifteen knees. Specimens were trimmed on a freezing stage sledge microtome to a final thickness of 1.5 mm ± 0.2 mm, removing underlying bone. Samples were stored in filtered PBS supplemented with biocide and a cocktail of protease inhibitors and frozen at −20 °C for no more than 3 weeks prior to testing. On the day of testing, samples were aligned and affixed via adhesive to the translating stage. Sliding Friction: A custom two-axis loading device with a six-degrees-of-freedom load cell was used for continuous measurements of specimen motion, deformation, and reaction loads as described previously [3,4]. Reciprocal sliding motion (±2.0 mm at 1 mm/s) under a range of applied loads (F_n, 4.5 – 35.6 N) was prescribed for a range of test durations (4 – 24 h). The radius of curvature of the glass lens was selected to best match the femoral condyle (12.7 mm).

Determination of Cycles to Failure: Tangential force (F_t) measurements were collected for each cycle and plotted against strip position (U_x), generating a family of hysteresis curves representing the frictional force at each reciprocating strip location. Principal Component Analysis (PCA) was performed on a per cycle basis by computing the covariance matrix of the F_t vs. U_x data and calculating its eigenvalues and eigenvectors. Magnitudes of the first and second eigenvalues were recorded and during post-hoc analyses a threshold was selected to identify the onset of damage and extract the parameter: number of cycles to damage, N. The threshold identifies an increase in the rate of change of the first eigenvalue relative to steady-state (cycles 10-20), and labels the earliest occurrence of this change as cycle N. To validate the

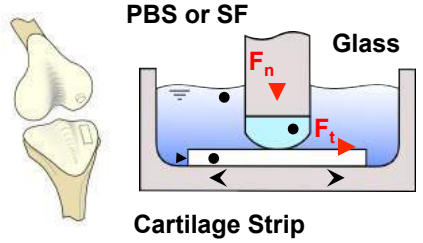

Figure 1: Cartilage strips are tested against a glass lens counterface in a bath of either PBS or SF. F_n is the applied normal force and F_t is the measured tangential force

Copyright 2016 The Organizing Committee for the 2016 Summer Biomechanics, Bioengineering and Biotransport Conference

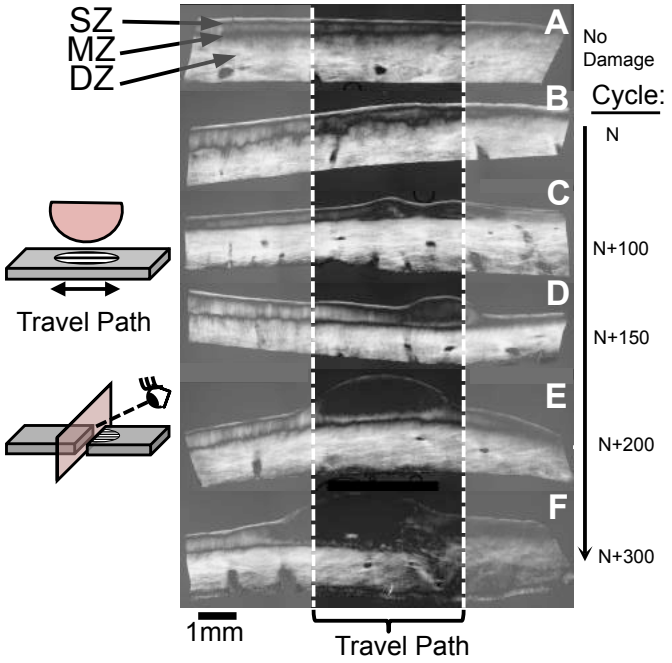

Figure 2: Polarized light microscopy depicting damage onset and damage progression in cross-sections taken through the travel paths of six strips halted mid-test at spaced intervals (*N*+*M*): (A) no damage (F_z = 4.4 N, SF, 2800 cycles) (B-F) damage (F_z = 4.4 N in PBS). Illuminated regions indicate collagen fiber alignment (SZ, surface zone; DZ, deep zone); dark regions indicate isotropic collagen organization (MZ, middle zone).

identification of damage onset, a subset of sliding experiments were halted mid-test at either *N* or at subsequent cycles, *N*+*M,* using real-time visualization of the hysteresis data. This was done in order to capture corresponding images of mid-test damage progression. Strips were sectioned (120 μm thick) and imaged under polarized light microscopy (PLM). Frictional S-N curve: Friction data were pooled from the experimental groups that resulted in visual damage to the strips (32 of 40 strips). The cycle friction coefficient μ was calculated from the ratio: avg. tangential force (F_t) / avg. normal force (F_n), for each reciprocating cycle. To encompass the entire response prior to damage, μ was averaged over the range: cycle 10 – cycle *N*. This average 'pre-damage' μ was then multiplied by the applied stress (F_n/A) to obtain the frictional shear stress, *S*.

RESULTS

The average contact area, *A*, between the glass lens and cartilage strip varied from 8.7 – 19.9 mm^2 for different loading conditions (yielding contact stresses over the range from 0.5 – 0.9 MPa). Experimental conditions that did not result in visual damage to the cartilage strip generated hysteresis curves that maintained their shapes over the course of the test (Fig. 3A). When visual damage to the strip was observed, hysteresis curves progressively rotated and elongated, with corresponding increases in magnitude of associated eigenvalues (Fig. 3B,D,F). Fig. 2 depicts corresponding snapshots of damage progression, which indicate that damage occurs via delamination of the middle zone. Strip B in Fig. 2B was stopped at cycle *N*, and though this strip showed no macroscopic signs of damage, PLM revealed a jagged MZ-DZ transition within the travel path. These results are complemented by the correlation found between frictional shear stress and *N* (R^2=0.33) (Fig. 4), which is in good agreement with the observed mode of failure. No other parameter (e.g. contact stress) was found to correlate with *N* ($R^2 < 0.12$).

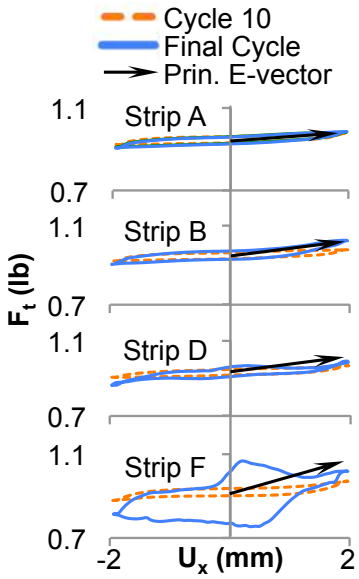

Figure 3: Hysteresis curves for four strips (A,B,D,F) depicting two cycles: cycle 10 (baseline) and the cycle at which the test was halted (final cycle). The final cycle corresponds to the respective strip in Fig. 2. The vectors represent the first principal eigenvectors of the final cycle which determined *N*.

DISCUSSION

The damage progression visualized in Fig. 2 was predicted using our method of hysteresis curve examination. This confirms the hypothesis that variations in principal components of hysteresis curves correspond to physical disruption of the tissue. At the earliest indication of damage (at *N*), strip B had no visible damage (Fig. 2B, 3B). This suggests that PCA of the frictional hysteresis curves detects not only visual tissue damage, but early mechanical breakdown of the sub-surface collagen network prior to the onset of macroscopic damage, highlighting the sensitivity of this method of determining *N*. On close examination of the strips (Fig. 2), there is an intensified bright signal in the fatigued MZ coincident with dark spindles extending into the deep zone, perhaps indicating the recruitment of fibers from the highly organized DZ to resist shearing and swelling of the MZ. The ability to accurately identify *N* for various cartilage loading configurations allows for improved fatigue failure characterization and more complete *S*-*N* curves that could serve as tools for predicting fatigue-life estimates. In separate, more physiologically representative experiments, cartilage plugs of different diameters are slid against strips and tested to damage in both PBS and SF. Determining both the *N* and *S*-*N* characteristic for this testing configuration are currently under development.

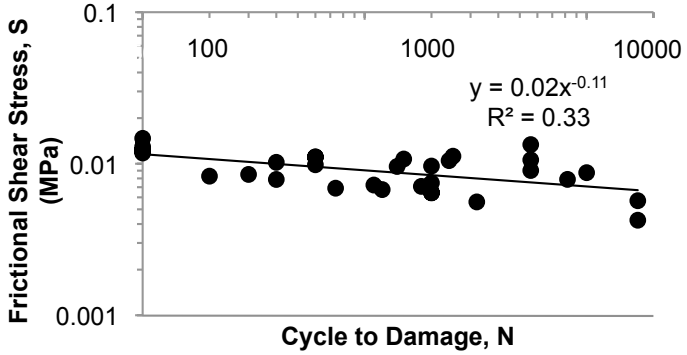

Figure 4: Fatigue curve (S-N) correlating frictional shear stress with cycle to damage. Data for thirty-two damaged strips is shown.

ACKNOWLEDGEMENTS

NIH AR043628. We thank Dr. X.E. Guo (Columbia) for PLM support.

REFERENCES

[1] Freeman, *J Orthop Res*, 17:3-8, 1999. [2] Buckley et al., *J Biomech Eng*, 135:31002, 2013. [3] Krishnan et al., *J Biomech*, 38:1665-1673, 2005. [4] Schmidt et al., *Arthritis Rheum*, 56:882-91, 2007.

SB^{3}C2016
Summer Biomechanics, Bioengineering and Biotransport Conference
June 29 –July 2, National Harbor, MD, USA
SB^{3}C2016-1073

BIOMECHANICS OF MUSCLE-TENDON JUNCTION AND TENDON-BONE INSERTIONS

Sandhya Chandrasekaran (1), Ashle J. Saltzman (2), HY Shadow Huang (3)

(1) Mechanical and Aerospace Engineering
North Carolina State University
Raleigh, NC, USA

(2) Mechanical and Aerospace Engineering
North Carolina State University
Raleigh, NC, USA

(3) Mechanical and Aerospace Engineering
North Carolina State University
Raleigh, NC, USA

INTRODUCTION

The muscle-tendon-bone unit transmits contractile loads, developed in the muscle, through the tendon as a tensile load, into the bone to produce motion. The myotendinous junction (MTJ) connects the muscle to the tendon through a series of interdigitated extensions of the microstructure. The last collagen fibrils of the tendon extend into invaginations in the myofibers of the muscle and transmit loads through lateral contractions [1, 2]. The tendon-to-bone insertion is a functionally graded tissue that varies in collagen types, collagen orientation, and mineralization [3-8].

The tendon is a hierarchical tissue starting at the nanoscale with collagen molecules which aggregate into microfibrils which aggregate into fibrils which form fibers which collect to form fascicles which aggregate to form the tendon [8]. It is composed of collagen, proteoglycans, glycoproteins, water and cells [9]. The study of the muscle-tendon-bone unit is of importance because injuries of these tissues are common and they tend to heal slowly. Additionally, biomechanical properties are not restored to their original value after healing [9].Most studies focus on the uniaxial tendon properties aligne d with the primary load direction. There are few studies that consider the biaxial properties of the tendon [10, 11]. However, these studies consider one longitudinal and one transverse direction. To the best of the authors' knowledge, no previous studies have been conducted on the biomechanical properties of a cross-section of the tendon.

In this study we report stress-strain data for the tendon cross-section in various locations and relate the findings back to the biochemical composition.

METHODS

Porcine forelimbs of large sows were obtained from the local abattoir. The skin and fatty tissue surrounding the muscle-tendon-bone unit was carefully cleared away from the deep digital flexor tendon of the third digit. The tendon is removed via a cut near the tendon-to-bone insertion and a cut near the muscle-tendon junction (MTJ) (tendon branches for other digits are severed near the main tendon stem).

Biaxial Testing From each of these tendons, three cross-sections for biaxial testing were removed with two razor blades fixed together. One cross-section is extracted from the tendon proximal to the junction of flexor tendons (muscle-end, n=8), one cross-section from the middle of the third digit tendon (mid-tendon, n=9), and one cross-section from the distal end of the removed sample (bone-end) (n=6). Samples that were not large enough to mount in the testing apparatus were thrown out. The average thickness of the cross-sections was 0.79±0.20 mm. After removal from the forelimb, all cross-sections were stored in Hanks' Balanced Salt Solution (HBSS) at 4° C between dissection and testing.

The BioTester 5000 (CellScale Biomaterials Testing, Waterloo, ON, Canada) biaxial testing apparatus, equipped with a 0.5 N load cell in each axis of loading, was used to measure the force and displacement of the tissue samples. The built-in CCD camera is synchronized with the load cells and actuators and collected 1280 x 960 px images at a rate of 1 Hz. Force and displacement data were collected at a rate of 5 Hz and were used to compute stress and strain data. Each tested sample was mounted to the BioTester with four BioRakes each consisting of five tungsten tines spanning 4 mm in width. Testing was performed in a room temperature bath of HBSS. The dorsopalmar axis of the tendon cross-section was aligned with the x-axis of the BioTester and the mediolateral axis was aligned with the y-axis. A pre-load of 10mN was applied in both axes and this state was defined as the zero strain state. Each sample was pre-conditioned

Copyright 2016 The Organizing Committee for the 2016 Summer Biomechanics, Bioengineering and Biotransport Conference

equibiaxially with five successive triangular waveform to 10% true strain at a medium strain rate of 2%/s [12]. After pre-conditioning samples were rested at zero strain for 30 seconds to allow the tendon to relax. This rest duration was determined during preliminary testing to allow the tendon samples to return to a zero stress state. Finally, each sample was strained equibiaxially at 2%/s to a peak of 20% true train. Stress and strain curves are prepared from the collected force and displacement data. These curves are broken into three strain regions: 0-7.5% (low strain), 7.5-15% (medium strain), and 15-20% (high strain). An effective elastic modulus in each strain region was computed. **Statistical Analysis** All data are presented as the means ± the standard deviations. Differences in collagen concentration are tested using a single factor ANOVA. A Bonferroni multiple comparisons test with $p < 0.05$ was performed to compare the elastic modulus of the tendon samples between location and direction to determine if there is a variation in biomechanical property along the length of the tendon or any anisotropy within the cross-section. All statistical analysis was conducted using GLM in SAS 9.4 (SAS Institute Inc, Cary, NC, USA). A value of $p < 0.05$ was considered significant.

RESULTS

The biaxial testing results for the three locations (bone end, mid tendon, and muscle end) were used to produce stress versus strain curves presented in **Figure 1**. Maximum stresses at 20% true strain for the muscle end were 35.2±34.2 kPa in the x-direction and 36.9±51.9 kPa in the y-direction, for the mid tendon were 83.8±34.4 kPa in the x-direction and 92.0±52.1 kPa in the y-direction, and for the bone end were 142.2±85.7 kPa in the x-direction and 110.6±77.6 kPa in the y-direction. From these data, effective elastic moduli were computed for each of the previously mentioned strain ranges. Using a Bonferroni multiple comparisons test with $p < 0.05$, it was determined that the bone end of the tendon is stiffer in all regions of strain than the muscle end of the tendon. No differences between the bone end of the tendon and the mid tendon were detected. And the muscle end of the tendon was only more compliant in the larger strain range (15-20%). No differences were detected between the x- and y-direction stiffnesses in any strain range or location.

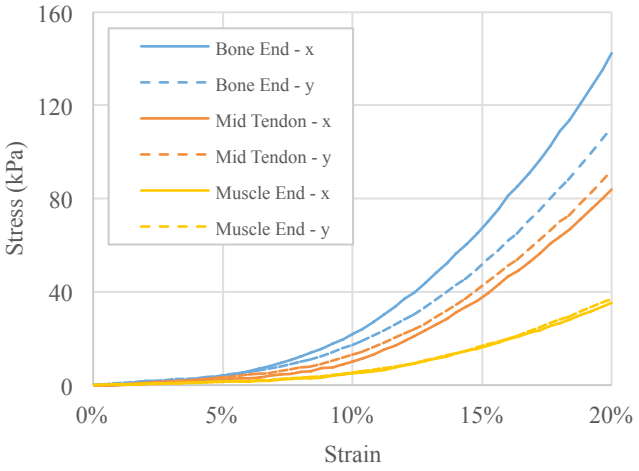

Figure 1: Average stress versus strain response for tendon cross-sections collected from the bone end (blue, n=6), the mid tendon (red, n=9) and the muscle end (purple, n=8). The tendon cross-section tends to be more stiff toward the bone end and more compliant toward the muscle end. No dramatic transverse anisotropy is apparent.

CONCLUSION

The current study, to the best of the authors' knowledge, is the first to provide stress-strain data for the cross-section of the tendon. This equibiaxial testing was performed at three locations along the porcine deep digital flexor tendon and a variation in stiffness was observed. Additionally, we report the collagen concentration in these same three regions, however, observed no variation. The result of this study will be furthered by expanding the locations and orientations tested along the muscle-tendon-bone unit in an effort to improve the understanding of its unique structure and to aid in tissue engineering repair techniques.

ACKNOWLEDGEMENTS

This work is supported by the NSF CMMI 1400018.

REFERENCES

[1] Trotter J., 2002, "Structure – function considerations of muscle-tendon junctions," Comparative Biochemistry and Physiology Part A, 133 pp. 1127-1133

[2] Finni T., 2006, "Structural and functional features of human muscle-tendon unit," Journal of Applied Physiology, 98 pp. 1328-1333

[3] Thomopoulos S., Williams G., Gimbel J., Favata M., and Soslowsky L., 2003, "Variation of biomechanical, structural, and compositional properties along the tendon to bone insertion site," Journal of Orthopaedic Research, 21(3) pp. 413-419

[4] Thomopoulos S., Genin G., and Galatz L., 2010, "The development and morphogenesis of the tendon-to-bone insertion – what development can teach us about healing -," Journal of Musculoskeletal and Neuronal Interactions, 10(1) pp. 35-45

[5] Wang J., 2006, "Mechanobiology of tendon," Journal of Biomechanics, 39(9) pp. 1563-1582

[6] Killian M., Cavinatto L., Galatz L., and Thomopoulos S., 2012, "The role of mechanobiology in tendon healing," Journal of Shoulder and Elbow Surgery, 21(2) pp. 228-237

[7] Benjamin M., Kumai T., Milz S., Boszczyk B., Boszczyk A., and Ralphs J., 2002, "The skeletal attachment of tendons – tendon 'entheses'," Comparative Biochemistry and Physiology Part A: Molecular & Integrative Physiology, 133(4) pp. 931-945

[8] Genin G., Kent A., Birman V., Wopenka B., Pasteris J., Marquez P., and Thomopoulos S., 2009, "Functional grading of mineral and collagen in the attachment of tendon to bone," Biophysical Journal, 97(4) pp. 976-985

[9] Dourte L.M., Pathmanathan L., Jawad A.F., Iozzo R.V., Mienaltowski M.J., Birk D.E., and Soslowsky L.J, 2012, "Influence of decorin on the mechanical, compositional, and structural properties of the mouse patellar tendon," Journal of Biomechanical Engineering, 134(3)

[10] Szczesny S.E., Peloquin J.M., Cortes D.H., Kadlowec J.A., Soslowsky L.J., and Elliott D.M., 2012, "Biaxial tensile testing and constitutive modeling of human supraspinatus tendon," Journal of Biomechanical Engineering, 134(2)

[11] Azizi E., and Roberts T.J., 2009, "Biaxial strain and variable stiffness in aponeuroses," Journal of Physiology, 587(17) pp. 4309-4318

[12] Gregory D.E., and Callaghan J.P., 2010, "An Examination of Strain Rate on Subfailure Mechanical Properties of the Annulus Fibrosus," Journal of Biomechanical Engineering, 132(9):091010-091010-8.

SB^{3}C2016
Summer Biomechanics, Bioengineering and Biotransport Conference
June 29 –July 2, National Harbor, MD, USA
SB^{3}C2016-1074

ERROR AND UNCERTAINTY QUANTIFICATION OF A COMMERCIAL CFD SOLVER IN AN INTRACRANIAL ANENRUSYM

Nicole Varble (1, 2), Nikhil Paliwal (1, 2), Jianping Xiang (2, 3), Kristian Debus (4), Hui Meng (1, 2, 3, 5)

(1) Department of Mechanical and Aerospace Engineering
SUNY University at Buffalo
Buffalo, NY, USA

(2) Toshiba Stroke and Vascular Research Center
SUNY University at Buffalo
Buffalo, NY, USA

(3) Department of Neurosurgery
SUNY University at Buffalo
Buffalo, NY, USA

(4) CD-adapco
Melville, NY, USA

(5) Department of Biomedical Engineering
SUNY University at Buffalo
Buffalo, NY, USA

INTRODUCTION

Although medical image-based computational fluid dynamics (CFD) has been extensively used as a research tool for years, it was not until recently that CFD has finally come to the crucial point of rapidly growing into a clinical tool. In an increasingly wider range of medical applications, various home-grown and commercial CFD packages are finding themselves having the potential of becoming either a clinical diagnostic tool, as in the case of HeartFlow® [1], or as a validation tool of new medical devices as outlined by the FDA "Critical Path Initiative" [2]. However, before such potential can be realized, it is critical that the CFD solver be thoroughly verified and validated. Still, a big hurdle in the CFD solvers making this historic transition is the lack of systematic guidelines for proper validation.

Therefore in this study we present an application of the guidelines from the ASME Verification and Validation 20 (V&V 20) document [3] to systematically validate CFD solvers. The CFD solver used for research at our center is the commercially available package STAR-CCM+ (v10.02, CD-adapco, Melville, NY), which is a widely used software that allows seamless access to all the components of the CFD model under a single integrated platform. We use 2D Particle Image Velocimetry (PIV) on an intracranial aneurysm (IA) model to collect experimental data and demonstrate the validation procedure.

METHODS

We used a patient-specific internal carotid artery aneurysm geometry reconstructed from a three-dimensional digital subtraction angiographic image for experimental and computational calculations. For experimental analysis, the flow field of a transparent silicone phantom model was analyzed under a physiologic pulsatile waveform using PIV. The fluid had blood mimicking properties with density and viscosity of 1234 kg/m^3 and 4.03 cP respectively. The index of refraction of 1.42 of the fluid matched that of the phantom so that there was no optical distortion. The fluid was comprised of 47% water, 37% glycerol and 16% NaI by weight and was seeded with neutrally buoyant particles.

The phantom was placed in a pulsatile flow loop with flow rate of 256 mL/min. Velocity magnitude in two orthogonal central planes was calculated using a LaVision system with a Nd:YAG laser with a wavelength of 532 nm. Data was acquired on these 2D planes at 40 time-points in a cardiac cycle which was monitored and triggered using an in-house LabView code (National Instruments, Austin, TX).

For computational analysis, the experimental phantom was imaged using Toshiba Infinix C-arm machine and a 3D model was reconstructed. The reconstructed geometry was volumetrically meshed using polyhedral elements with four prism layers at the wall using STAR-CCM+. The fluid density, viscosity, flow rate, and the pulsatile inlet waveform were all taken from the experimental data. We assumed a no slip boundary and rigid walls. Second-order temporal and spatial discretization schemes were used to solve the transient Navier-Stokes equations.

As shown in Figure 1, following the ASME V&V 20 guidelines, the model error, δ_{model} was calculated as:

$$\delta_{model} = E \pm u_{val} \quad (1)$$

where E is the difference between experimental, D, and simulation, S results:

$$E = S - D \quad (2)$$

and the model uncertainty, u_{val} is:

$$u_{val} = \sqrt{u_{num}^2 + u_{input}^2 + u_D^2} \quad (3)$$

Copyright 2016 The Organizing Committee for the 2016 Summer Biomechanics, Bioengineering and Biotransport Conference

the root sum square of u_{num}, the numerical uncertainty, u_{input}, the input parameter uncertainty, and u_D, the uncertainty in the experimental data.

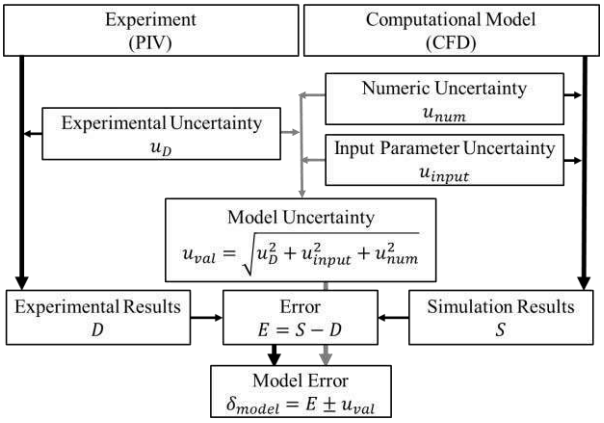

Figure 1: Workflow for calculation of model error and uncertainty adopted from ASME V&V 20.

Briefly, u_{num} , the uncertainty of the simulation due to spatial and temporal discretization, is calculated based on a series of systematically refined grids. We tested a series of four simulations with meshes ranging from 54k to 842k elements. The input parameter uncertainty, u_{input}, is the error of the simulation due to the uncertainties in measurement of input parameters. We analyzed the uncertainty due to the input parameters density, viscosity, flow rate, and period, where the systematic uncertainty was derived from experimental measurements. We also evaluated the fractional contribution of each parameter to input uncertainty by calculating Importance Factor (*IF*) [3], which is defined as the reciprocal of ${u_{input}}^2$. Experimental uncertainty, u_D, was quantified from PIV experiments and was dependent on several factors including background noise, out-of-plane particle motion, camera focus, and non-homogenous particle seeding density. The uncertainty calculation was based on the correlated statistics [4], and calculated in the LaVision software.

In both computational and experimental analyses, the quantification of uncertainty was based on velocity magnitude and evaluated on a 1D line at the intersection of two orthogonal planes.

RESULTS

Figure 2 shows a comparison of PIV and CFD results. The flow patterns for cycle-averaged velocity magnitude contours and vectors match remarkably well as both the location of the impingement jet (in the right of the aneurysm domain) and vortex (center) are captured by CFD and PIV analyses.

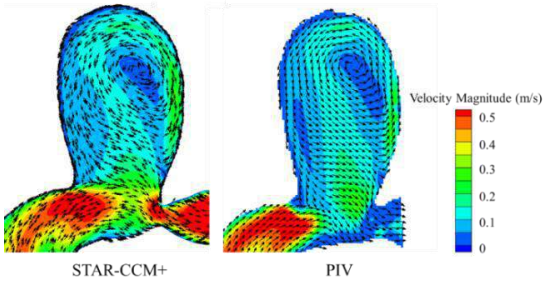

Figure 2: Cycle-averaged velocity magnitude contours with velocity vectors on the center plane of the IA for CFD simulations from STAR-CCM+ (left) and PIV experiment (right).

Figure 3 shows the computational and the experimental results of velocity magnitude along the 1D line. The uncertainty is represented by the error bars. The average numerical uncertainty and input parameter uncertainty along the 1D line was found to be 8.8% of the velocity magnitude. The largest contribution to input parameter uncertainty was from flow rate with an *IF* of 2.38 x10^{-2}, which was three orders of magnitudes higher than other input parameters. Additionally, the average experimental uncertainty was found to be 9.8% of the velocity magnitude. This resulted in the culminating model error, δ_{model} to be 2.0 ± 1.0 cm/s on average. The highest uncertainty and error occurred nearer to the impingement jet (normalized distance = 0.9).

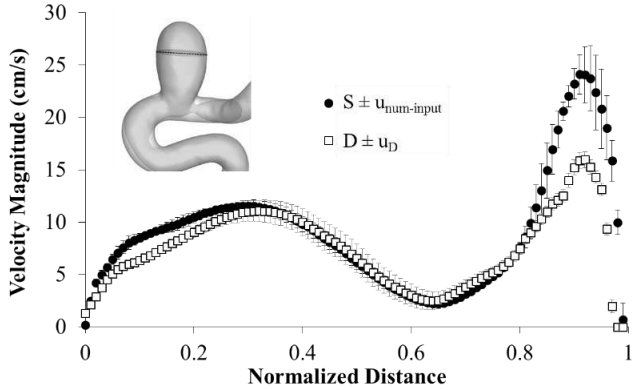

Figure 3: Quantitative results of computational (S, black) and experimental (D, white) results and uncertainty of velocity magnitude. Uncertainty is indicated by the error bars.

DISCUSSION

In this study, we have shown a comprehensive approach for the validation of commercial CFD solver STAR-CCM+ by utilizing the guidelines of ASME V&V 20. Through the analysis of PIV and CFD datasets we have assessed error and quantified uncertainty for flow in an IA model. The value of model error shows that the range of error in velocity in the model is 1-3 cm/s in the IA model, which is small as compared to the average velocity in the flow domain. This indicates that STAR-CCM+ CFD solver performed very well in this context.

To the best of our knowledge, this is the first study to validate a CFD solver in the vein of IAs. The framework in this study has validated a CFD solver by quantifying errors and uncertainties. This quantification of uncertainty can potentially dictate the context of use of the CFD solvers in medical application in the future.

ACKNOWLEDGEMENTS

This work was partially funded by the National Institutes of Health (R01 NS 091075) and a grant from Toshiba Medical Systems Corp.

REFERENCES

[1] Taylor CA, et al. Computational fluid dynamics applied to cardiac computed tomography for noninvasive quantification of fractional flow reserve: Scientific basis. *J Am Coll Cardiol.* 2013;61:2233-2241

[2] Stewart SF et al. Results of FDA's first interlaboratory computational study of a nozzle with a sudden contraction and conical diffuser. *Cardiovascular Engineering and Technology.* 2013;4:374-391

[3] ASME V&V 20-2009, Standard for Verification and Validation in Computational Fluid Dynamics and Heat Transfer.

[4] Wieneke, B., PIV uncertainty quantification from correlation statistics. *Measurement Science and Technology*, 26(7), 2015.

Copyright 2016 The Organizing Committee for the 2016 Summer Biomechanics, Bioengineering and Biotransport Conference

SB³C2016
Summer Biomechanics, Bioengineering and Biotransport Conference
June 29 –July 2, National Harbor, MD, USA
SB³C2016-1075

ANALYSIS OF THE EFFECT OF SALIVA ON THE DEGRADATION OF ABSORBABLE SUTURES

Luke E. Riexinger (1), Jenna W. Briddell (2), Donna M. Ebenstein (1)

(1) Biomedical Engineering
Bucknell University
Lewisburg, PA, USA

Otolaryngology
Geisinger Medical Center
Danville, PA, USA

INTRODUCTION

Surgical sutures are thread-like pieces of material which hold tissue together so a wound will heal properly. Absorbable sutures are designed to degrade in the body as the tissue heals, eliminating the need to have sutures removed.[1] The location of a suture within the body and the type of suture influence the rate at which the suture dissolves. Three common types of absorbable sutures are Monocryl, a monofilament synthetic (poliglecaprone 25) fiber, Vicryl, a braided multifilament synthetic (polyglactin 910) fiber, and Chromic Gut, a natural monofilament fiber. Absorbable sutures are regularly used in oral and pharyngeal surgery where they are exposed to saliva which contains enzymes to break down food. However, little is known about how these digestive enzymes affect suture dissolution. The goal of this study was to compare the degradation of suture strength in saline and artificial saliva to help doctors make more informed decisions when selecting sutures for use in oropharyngeal surgery.

METHODS

Samples of Monocryl (n=90), Vicryl (n=90), and Chromic (n=90) 3-0 sutures were tied with a surgeons knot into loops approximately 10 cm long by the same head and neck surgeon. The loops were connected into groups of six in series using c-clips, so that one set could be easily removed and tested at each time point. Each group of sutures was woven between six nylon rods on a custom-built apparatus and held in tension with a 100g weight, such that each suture had an equivalent load. Each apparatus was loaded with seven groups of sutures of each type and submerged in an aquarium containing either phosphate buffered saline (median pH 7.25) or artificial saliva[2] (median pH 6.24) at 37° C. The artificial saliva was a salt solution containing α-amylase, a d igestive enzyme, lysozyme, a b acteriocidal enzyme, acid phosphatase and lubricating mucins to simulate the oral environment. Solutions were changed every 3-4 days.

Six samples were removed from the solution at regular time intervals (every 3 days for Monocryl, every 4 days for Vicryl and Chromic) for testing. The breaking force was determined by pulling samples to failure using an Instron machine at 30 mm/min.[3] The diameter and the dry mass of each suture were also measured after failure. Six samples of each suture type were pulled to failure after knotting but before being submerged as a control group to provide baseline values for comparison. Percent strength at each time point was then calculated by dividing the average breaking force at each time point by the average breaking force of the control group for each suture type. A two sample t-test was performed between the breaking force of sutures soaked in saline and sutures soaked in saliva at each time point, with a significance level of 0.05.

RESULTS

Monocryl degraded the fastest, reaching 50% of its original breaking strength after 11 days in both environments (Fig. 1a). Vicryl and Chromic, when soaked in saliva, reached 50% of their initial breaking strength after 18 and 26 days, respectively (Fig. 1bc). In saline neither Vicryl nor Chromic reached 50% within

Copyright 2016 The Organizing Committee for the 2016 Summer Biomechanics, Bioengineering and Biotransport Conference

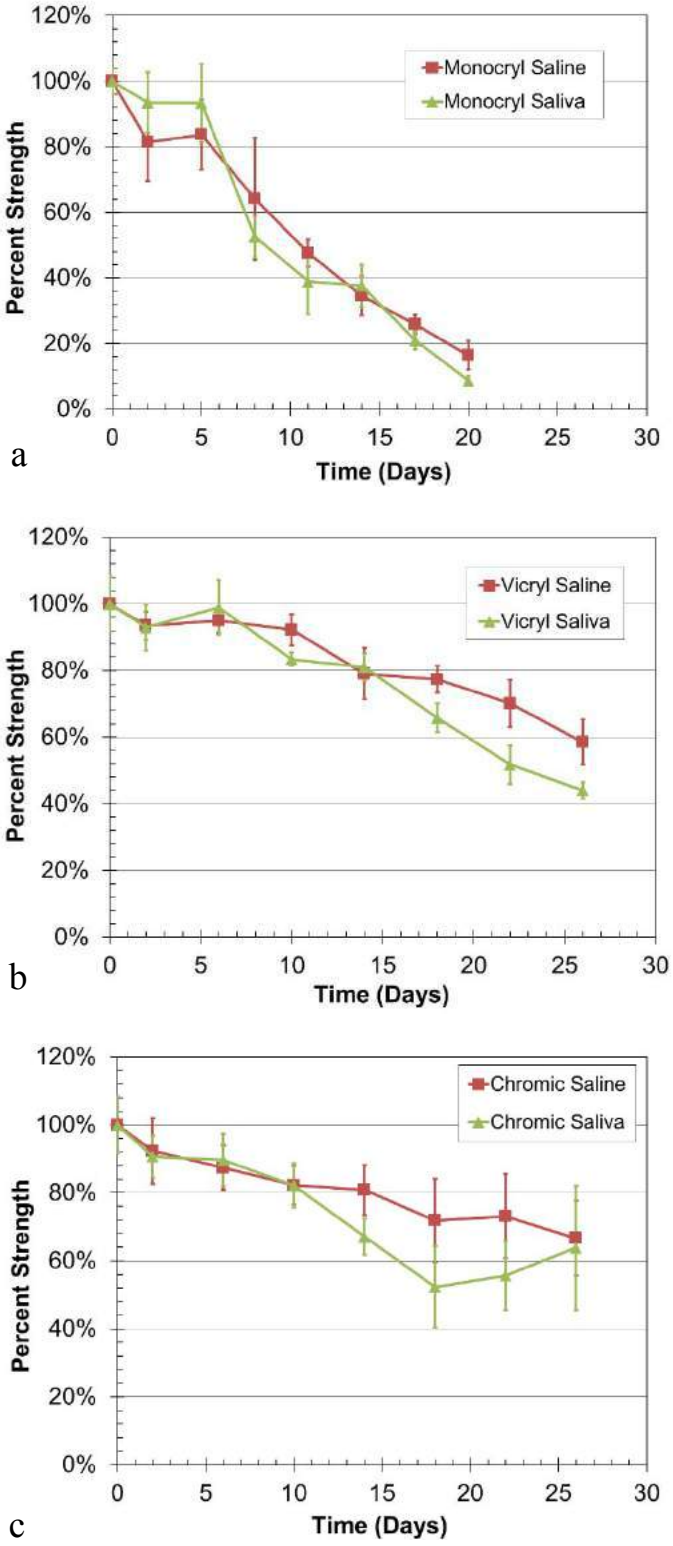

Figure 1: Average percent of initial breaking force of knotted (a) Monocryl, (b) Vicryl, and (c) Chromic sutures illustrating the decrease in knot strength relative to the control over 26 days.

the 26 day testing period. The saliva did not cause degradation to begin at an earlier time, but rather enhanced the amount of degradation once the suture strength began to decrease. The average breaking strength of Monocryl and Vicryl in saliva was significantly less than in saline (by 18-47% and 15-26%, respectively) for time points greater than 10 days (except day 14). The average breaking strength of Chromic in saliva was significantly less than in saline (by 17-27%) for days 14-22, but not day 26 (the final testing date).

DISCUSSION

All three types of absorbable sutures lost strength at a faster rate in saliva than in saline (which is assumed to simulate a normal physiological environment). There have been limited previous studies of suture degradation in saliva, and those studies did not load the sutures and used different saliva formulations.[4-5] Despite the differences in testing methods, the results of those studies also showed significant increases in degradation rate of sutures in saliva versus saline, although they also showed greater degradation in saliva at earlier time points.

The results of this study could influence surgeon selection of sutures for use in the oral environment to ensure that the suture degrades at an appropriate rate to allow effective healing of the wound. Further investigation will include identifying which saliva components are responsible for increasing the suture degradation rate.

ACKNOWLEDGEMENTS

This project was funded by a Bucknell-Geisinger Research Initiative Grant. LER was funded by the Bucknell Program for Undergraduate Research. The authors would like to thank Dr. David Schoepf in the Physics Department at Bucknell University for providing the weights used to load the sutures in this study.

REFERENCES

[1] Pillai, C, and Charma, C. Absorbable Polymeric Surgical Sutures: Chemistry, Production, Properties, Biodegradability, and Performance. *Journal of Biomaterial Applications*, 25: 291-366, 2010.

[2] Chou, C and Hee, S. Bioassay-Driven Analysis of Chewing Tobacco Extracts. *Environmental Toxicology and Chemistry*, 13: 1177-1186, 1994.

[3] ASTM International *F1635 Standard Test Method for in vitro Degradation Testing of Hydrolytically Degradable Polymer Resins and Fabricated Forms for Surgical Implants,* 2004.

[4] Khiste, SV, et al. Evaluation of tensile strength of surgical synthetic absorbable suture materials: an in vitro study. *Journal of Periodontal and Implant Science,* 43: 130-13, 2013.

[5] Ferguson, R, et al. The effect of saliva and oral intake on the tensile properties of sutures. *Annals of Plastic Surgery*. 58: 268-272, 2007.

Copyright 2016 The Organizing Committee for the 2016 Summer Biomechanics, Bioengineering and Biotransport Conference

SB³C2016
Summer Biomechanics, Bioengineering and Biotransport Conference
June 29 –July 2, National Harbor, MD, USA
SB³C2016-1076

DIAGNOSTIC POTENTIAL OF KIRSCHNER (K-) WIRE AND REFERENCE PROBE INDENTATION FOR THE PREDICTION OF BONE MINERAL DENSITY (BMD)

Eric A. Kennedy (1), Sarah C. Denning (1), Donna M. Ebenstein (1), Thomas R. Bowen (2)

(1) Department of Biomedical Engineering
Bucknell University
Lewisburg, PA, USA

(2) Department of Orthopaedic Surgery
Geisinger Health System
Danville, PA, USA

INTRODUCTION

Fragility fractures due to osteoporosis stand as the most frequent cause of hospitalization and death in the US population for adults over age 65. One of every two women will sustain a fragility fracture after age 50 and the most common and often debilitating fracture is in the femoral neck [1]. During hip fracture fixation surgery, a Kirschner (K-) wire is used as a guide for a permanent screw (Figure 1). Anecdotal surgical evidence suggests that K-wire extraction force may be indicative of bone health at the site of repair; however, the correlation of this force metric to bone quality has not been explored. Another recently developed technique for mechanical assessment of local bone quality is reference probe indentation (RPI), where a small probe is cyclically pressed into the bone surface in vivo [2]. The current clinical approach for quantifying bone health is bone mineral density (BMD) inferred from DEXA scans. The goal of this study is to evaluate screw extraction and RPI as potential clinical measures of local bone quality during hip fixation surgery by investigating correlations between these mechanical measures of bone health and BMD.

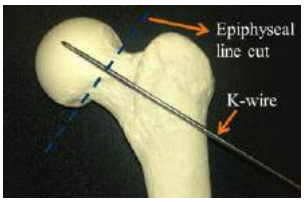

Figure 1: Location of cut to prepare for K-wire insertion into central-femoral head for pullout force testing.

METHODS

Trabecular bone samples from the femoral head (hip) and medial knee condyle (knee) of three bovine and ten porcine femur specimens and from the hip of eighteen excised human specimens from hip arthroplasty were tested. K-wires were inserted at five locations in each trabecular bone sample (Figure 2) and the peak screw extraction force was measured during extraction using the Screw Pullout Testing (SPOT) device modeled in Figure 3.

Each sample was then tested using reference probe indentation (Active Life BioDent Hfc; 25 indents, 10 indentation cycles at 2Hz with 2N peak load) (Figure 4). Loading slope (LS, measure of stiffness) and indentation distance increase (IDI, measure of fracture resistance) were determined for each indent.

Bone samples were then cut into the largest possible rectangular prism, measured to determine volume, dried, and ashed in an oven at 800ºC for 8 hours [3] to physically measure the BMD. The correlations between peak screw extraction forces, as well as indentation parameters of LS and IDI, to BMD were then determined.

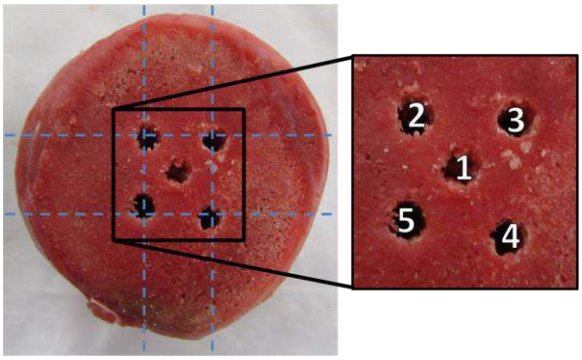

Figure 2: Each specimen was tested in five locations including the center of the bone as well as corners intersected by a superimposed 3 x 3, nine-quadrant grid.

Copyright 2016 The Organizing Committee for the 2016 Summer Biomechanics, Bioengineering and Biotransport Conference

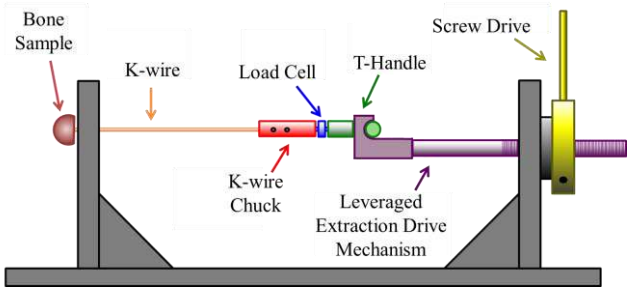

Figure 3: The K-wire was manually extracted from the bone specimen using a SPOT device. The peak extraction force could be used as a measure of bone quality.

Figure 4: Active Life BioDent Hfc reference probe micro-indenter (left) with indenter positioned on trabecular bone for testing (right).

RESULTS

The porcine, bovine, and human bone samples covered a range of BMD from 0.19 to 0.58 g/cm^3, which covers the healthy range of human trabecular bone (0.2 to 0.4 g/cm^3) [4]. Median peak extraction force values range from 250 to 1360 N. A very strong positive correlation (r = 0.88) was observed between median extraction force and BMD, suggesting that extraction force may be related to localized bone density (Figure 5). In contrast, IDI and LS exhibited only moderate correlations with BMD (r = -0.55 and 0.56 respectively) (Figure 6), possibly because micro-indentation is influenced more by bone quality at the indentation site than the overall architecture of the sample which has been shown to have significant influence in bone's resistance to fracture [5]. Currently there is no direct, mechanical method to quickly assess bone quality at a particular anatomical location like at a site of fracture. While DEXA is the most common means to measure BMD, these scans often fail to account for the overall quality of the bone [6], which may better predict fracture risk, and are not able to look locally at a fracture site.

DISCUSSION

This study investigated two potential direct measures of bone health which could be deployed in the operating room, in vivo, to measure bone health directly at the site of fracture, potentially affording the option to influence post-operative or other follow-up care. K-wire extraction forces showed much stronger correlation to BMD than reference probe indentation parameters, suggesting that K-wire extraction force may be a more useful measure of bone quality at the site of femoral neck fracture which is already known to correlate to fracture risk [7]. A similar experiment of the extraction vertebral pedicle screws also supports the validity of such testing, though K-wire extraction is already a harmless component of a fracture repair [8]. However, the variation in measurements within each sample must be further investigated to enhance the clinical value of a single screw extraction force to assess localized bone quality.

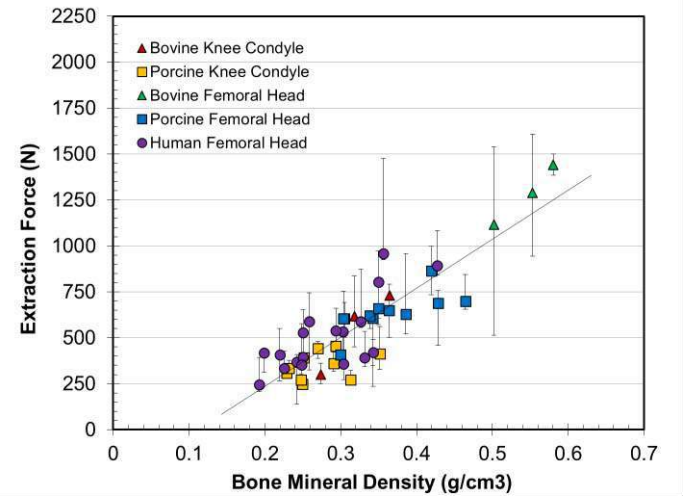

Figure 5: Median K-wire extraction force vs. BMD for all bone specimens with interquartile range error bars.

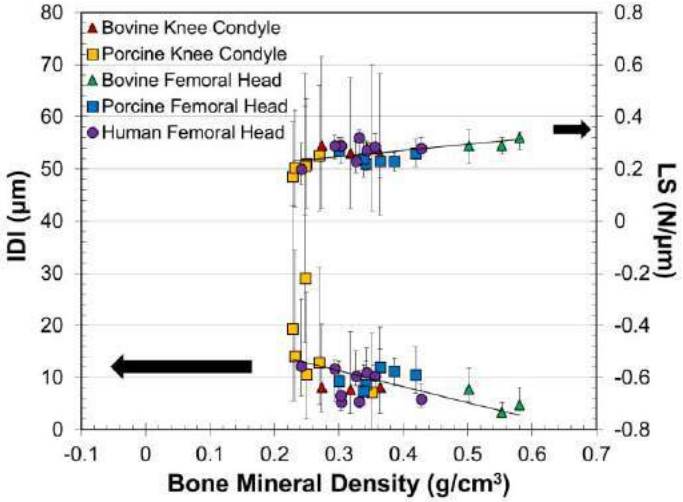

Figure 6: IDI and LS vs. BMD with interquartile range error bars.

The knowledge of localized bone quality could then help to determine how best to proceed with therapy after surgery and reduce overall complications. Additionally, future work will concentrate on investigating relationships between the mechanical metrics and BMD within osteoporotic bone to determine the best mechanical measure of bone quality with clinical relevance in predicting future fracture risk.

ACKNOWLEDGEMENTS

The authors wish to thank the Bucknell-Geisinger Healthcare Research Initiative for funding this study.

REFERENCES

[1] AAOS (2008) Burden of Musculoskeletal Diseases in the US
[2] Gullberg B (1997) Osteoporosis Int 7: 407-413
[3] Scafoglieri A (2010) Medicon IFMBE Proceedings 29: 549-553.
[4] Kaplan FS (1994) Orthopaedic Basic Science, Simon SR, ed.
[5] Yu Y (2015) SB3C 2015-242
[6] Weaver A (2015) SB3C 2015-236
[7] Rivadeneira F (2007) J Bone Miner Res 22(11): 1781-90
[8] Solitro G (2015) SB3C 2015-186

Copyright 2016 The Organizing Committee for the 2016 Summer Biomechanics, Bioengineering and Biotransport Conference

SB³C2016
Summer Biomechanics, Bioengineering and Biotransport Conference
June 29 –July 2, National Harbor, MD, USA
SB³C2016-1077

ELECTROMECHANICAL COUPLING BEHAVIOR OF ENDOTHELIAL CELL

Khashayar Teimoori[1], Richard Khalily[2], Ali M. Sadegh[3], Marom Bikson[4]

[1,3] Department of Mechanical Engineering
The City College of the City University of New York
New York, NY 10031, USA

[2,4] Department of Biomedical Engineering
The City College of the City University of New York
New York, NY 10031, USA

INTRODUCTION

The Blood-Brain Barrier (BBB) is formed by the endothelial layers, in which there are tight junctions that allow minimal transport from the blood to the extracellular fluid. To investigate the primary source of LDL transport, one study compared contributions of vesicles by examining paracellular transport through "breaks" in the tight junction and "leaky" junctions found in dying or dividing cells as illustrated in Figure 1.

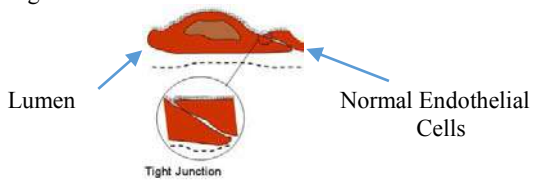

Figure 1: Tight junction break between Endothelial Cells (ECs)

This examination was accomplished by measuring water, albumin and LDL fluxes through Bovine Aortic Endothelial Cell (BAEC) monolayers in vitro. Tarbell et al. [1], assessed that the majority of transendothelial transport was accomplished through leaky junctions in dying or dividing cells. Bingmei Fu et al. [3], created a model to analyze time dependent intermediate-size solute transport in the interendothelial cleft of frogs, in an effort to interpret tracer labeling in this region. They variated the pressure in the vessel lumen from 0 cm to 30 cm H_2O. Concentration distribution was analyzed in three cases: in the cleft, along the cleft exit, and along the cleft exit with a varying ratio of diffusivity in the tissue to free solute diffusivity. The first case only allowed them to conclude that the model does not preserve upstream profiles, but the second case showed concentration levels at Δp= 30 cm H2O almost three times that of when Δp= 0 cm H2O, yet there is no visible HRP trail. In the third case, at Δp= 0 cm H2O, trails of HRP that contained 30 percent of the perfusate is not detectable. Cheng Wang et al. [2], details the electroosmosis effect in pressure-driven two phase fluid-flow microchannels containing aqueous NaCl and aqueous glycerol. A varying electric field was applied to the NaCl side, and using the fluorescence imaging technique, the interface position between the two fluids was examined. Afterwards they implemented the micro-PIV technique to measure the velocity field. Under normal pressure-driven flow in the microchannel, NaCl occupies a smaller portion of the channel because it is less viscous. When a negative electric field is applied, causing the NaCl to flow against the pressure driven flow, the aqueous NaCl moves slower and thus occupies a larger width in the channel; likewise, when a positive field is applied in the direction of the pressure driven flow, the NaCl moves faster, occupying a smaller width [2]. The present study hypothesizes that the use of transcranial Direct Current Stimulation (tDCS), a stimulation technique that energizes the extracellular fluid, and possibly other electrical stimulations could aid in transendothelial transport through electro-osmosis. Using modeling software from COMSOL 5.2, a basic localized model of the endothelial layer was created to mimic the passage of blood through a vessel and to investigate the effect of applying an electric field across this layer. The simulated model and the geometry used in this study are depicted in Figure 2 in order for better understanding on what is going on the present study.

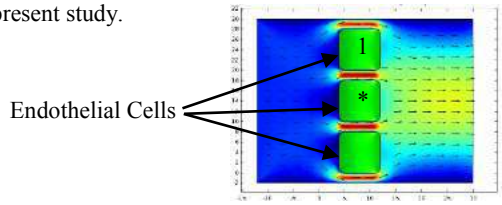

Figure 2: Geometry and simulation of the ECs and the fluid flow

Copyright 2016 The Organizing Committee for the 2016 Summer Biomechanics, Bioengineering and Biotransport Conference

METHODS

This study uses a very first electro-Fluid-Structure-Interaction, simply called (eFSI) model to inspect the behavior of the BBB under an applied electric field and compare it to the case when there no electric field applied. We examined the localized model in two cases: fluid-pressure flow, and fluid-pressure flow with an accompanying electric field. First, by applying an induced velocity profile as an inlet, we measured flow and Von Mises stress applied to the cells without any applied electric field. Here, the fluid flow is described by an incompressible Navier-Stokes equations for the velocity field, where $\mathbf{u} = (u, v)$, $\mathbf{u}_m = (u_m, v_m)$, and the pressure, p, in the spatial (deformed) moving coordinate system is stated in equations (1) and (2), respectively.

$$\rho\frac{\partial \mathbf{u}}{\partial t} - \nabla.[-p\mathbf{I} + \eta(\nabla\mathbf{u} + (\nabla\boldsymbol{u})^T)] + \rho\big((\mathbf{u} - \mathbf{u}_m).\nabla\big)\mathbf{u} = \mathbf{F} \quad (1)$$

$$-\nabla \cdot \mathbf{u} = 0 \quad (2)$$

Where, $\mathbf{I}$ denote the unit diagonal matrix and $\mathbf{F}$ is the volume force affecting the CSF flow. It is assumed that there is no gravitation or other volume forces affect the axoplasm, so that $\mathbf{F} = 0$. At the channel entrance on the left, the flow has fully developed laminar characteristics with a parabolic velocity profile but its amplitude changes with time. At first, flow increases rapidly, reaching its peak value at 0.3s as depicted in Figures 3 and 4; thereafter it gradually decreases to a steady-state value of 0.005cm/s. The velocity in the x direction, u_{in} with the steady-state amplitude U comes from the equation (3);

$$\boldsymbol{u}_{in} = \frac{U.t^2}{\sqrt{(0.04-t^2)^2+(0.1t)^2}} \quad (3)$$

Where, t is the time expressed in seconds and U is the mean velocity at steady state and is equal to 0.3[cm/s] due to a very small movement of the fluid inside the model. Afterwards, we applied both electric field and the velocity profile induced flow as an inlet. An electroosmotic induced flow was simulated by using COMSOL Muliphysics 5.2 (Palo Alto, CA 94304 USA) Software. Therefore, a very first novel steady state electro-Fluid-Solid-Interaction (eFSI) numerical analysis performed in order to investigate the effects of the applied electric field on the axoplasm fluid and thereby the stress as well as FSI interactions between MTs and the tau connections. The geometry is meshed using extremely fine mesh for the fluid dynamics analysis and the process of simulation was done within 11min and 4 secs in order to get the final eFSI results. The dimensions of each part of the model is illustrated in Table 1 and the final results are depicted in Figures 3 and 4 to be scrutinized in the Results section as well as discussed properly in the discussion section, respectively.

Dimension	Width (μm)	Height (μm)
Endothelial Cells (Squares)	8	8
Channel	42	32
Fillet Radius on ECs	r =0.1 (μm)	

Table 1: Information of the model [1,3]

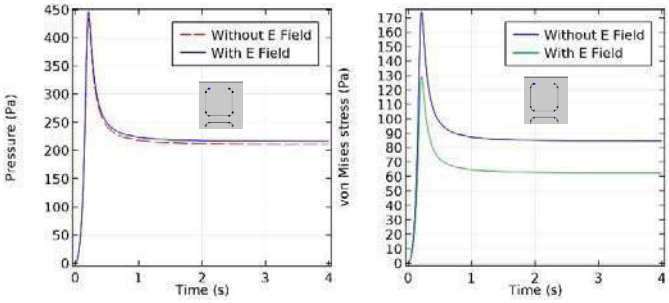

Figure 3: **Pressure and Von Mises stress changes of the upper EC as labeled in Figure 2 by 1**

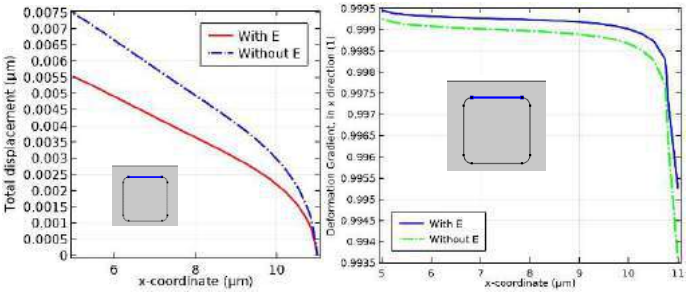

Figure 4: **Total displacement and deformation gradient changes of the middle EC as labeled in Figure 2 by** *

RESULTS

The results demonstrated that the applied electric field in conjunction with the induced velocity affect the endothelial cells. The results of this study also revealed that the pressure and Von Mises stresses on the ECs are reduced when the whole channel is subjected to an applied electric field as depicted in Figure 3. The analysis of this paper was based on the coupling of electromechanical and FSI in direct relation with fluid mechanics' theories. Specifically, by looking at Figure 4, where the deformation gradient on the middle EC is significantly influenced by the applied electric field, it can be found that the applied electric field decreased the amount of the total displacements of the cells while significantly reduces its total deformation gradients.

Finally, by looking at both ECs and the fluid flow through the endothelial cells, this study showed that an applied Electric field can affect the BBB.

DISCUSSION

This study was the analysis of a simplified and localized model of the endothelial monolayer and the passage of fluid through tight junctions, yet it was the very first of its kind. In the analysis of both regular fluid flow and fluid flow with an applied electric field, we found conclusive results suggesting that electrical stimulation may aid in transendothelial transport. To further the applications of this investigation, it is essential to build a more accurate and comprehensive model, even if that requires greater localization. As shown in Figure 1, the endothelial layer is composed in more irregular shaping than the model used in this study. Therefore, the model would benefit from the use of slightly more trapezoidal endothelial cells in order to mimic the tight junctions. Furthermore, this study would benefit from the scrutiny of transendothelial solute transport aided by an electric field, rather than speculating simply the fluid flow. While aided fluid flow provides the possibility of the electric field contributing to solute transport, it is important to more closely examine the effects on solute transport in order to begin using tDCS for transendothelial permeation.

REFERENCES

[1] Cancel, Limary M., Andrew Fitting, and John M. Tarbell. "In vitro study of LDL transport under pressurized (convective) conditions." American Journal of Physiology-Heart and Circulatory Physiology 293, no. 1 (2007): H126-H132.

[2] Wang, Cheng, Yandong Gao, Nam-Trung Nguyen, Teck Neng Wong, Chun Yang, and Kim Tiow Ooi. "Interface control of pressure-driven two-fluid flow in microchannels using electroosmosis." Journal of Micromechanics and Microengineering 15, no. 12 (2005): 2289.

[3] Fu, Bingmei, Fitz-Roy E. Curry, Roger H. Adamson, and Sheldon Weinbaum. "A model for interpreting the tracer labeling of interendothelial clefts." Annals of biomedical engineering 25, no. 2 (1997): 375-397.

Copyright 2016 The Organizing Committee for the 2016 Summer Biomechanics, Bioengineering and Biotransport Conference

SB^{3}C2016
Summer Biomechanics, Bioengineering and Biotransport Conference
June 29 –July 2, National Harbor, MD, USA
SB^{3}C2016-1078

VALIDATION OF A HIGH THROUGHPUT HYDROSTATIC PRESSURE BIOREACTOR ON THE NUCLEUS PULPOSUS BIOSYNTHESIS

Bhranti S. Shah (1), Farzana Chowdhury (1), Nadeen O. Chahine (1,2)

(1) The Feinstein Institute for Medical Research, North Shore LIJ Health System, Manhasset, NY
nchahine@northwell.edu

(2) Hofstra North Shore LIJ School of Medicine, Hempstead, NY

INTRODUCTION

Application of physical loading, such as compression, tension and pressure for tissue engineering of replacement tissues has been widely investigated in many tissues/organs. However, one challenge to these cultures is the relatively low-throughput nature of loading bioreactors. Intervertebral disc (IVD) experiences tensile and compressive loads and hydrostatic pressure during locomotion. This dynamic hydrostatic loading has been shown to stimulate cellular biosynthesis [1], and may be essential for disc tissue maturation [2]. On the other hand, non-physiological levels of loading have been implicated as a contributing factor to alterations in tissue biology and biomechanics, leading to IVD degeneration (DD) [1, 3]. Therefore, a need exists to develop high throughput hydrostatic pressure bioreactors that can optimally simulate the proliferation and biosynthetic activity of disc cells *in vitro* for tissue regeneration. Culturing disc cells in a 3D environment has been shown to be crucial for cell mechano-transduction and simulate extracellular matrix (ECM) remodeling [4]. Static hydrostatic pressure in magnitude of 0.1-0.35 MPa inhibits proteoglycan synthesis but stimulates collagen synthesis in NP cells [5], whereas, application of dynamic pressure led to increased proteoglycan and collagen synthesis [6]. The goal of this study is to examine the effects of dynamic HP on bovine nucleus pulposus cells cultured in alginate beads using a novel high throughput bioreactor, where individual beads in multiwall plates are exposed to controlled dynamic HP. We hypothesize that both hydrostatic pressure treatment and 3D environment will promote disc like ECM expression and synthesis.

METHODS

NP Cell Isolation: NP tissue was isolated from young bovine lumbar discs. Cells were expanded for 1-2 passages in DMEM+10% FBS, and cultured in 1.2% alginate beads to promote round 3D morphology. **Hydrostatic loading:** During the loading regime, NP alginate beads from static and HP treated group were cultured in a 12 well tissue culture plate, though the system allows for 96-well or 384-well plate formats. The HP treated group plate was placed in Instron TGT hydrostatic pressure chamber (Figure 1) attached to an Instron servo hydraulic tension/compression system (Instron). Briefly, the bioreactor device is a sealed aluminum chamber that fits standard tissue culture multi-well plates. In order to apply hydrostatic pressure to samples within the bioreactor chamber, incubator air is compressed using a continuously running scroll compressor and, subsequently, pumped into the bioreactor chamber via a temperature controller that maintains the temperature of the compressed air at 37°C, creating a gas–liquid interface with a pressurized gas phase on top of a liquid medium phase [7]. A vacuum is generated to remove the gas phase from the bioreactor chamber and direct the air back into the incubator where it is reused for the stimulation process. The stimulation regime is controlled by system accompanying software (GrowthWorks, Instron TGT) that enables the application of sinusoidal waveforms with frequencies between 0.0001 and 2 Hz and a pressure range between 0 and 600 kPa. In addition, this software also enables continuous stimulation regimes. For this study, static group was placed in the same incubator as the HP treated group. The HP treated group pressure ranged from 0 to 0.1 MPa at 0.1 Hz for 2 hours daily for 7 days. All the samples were placed in a cell culture incubator for rest of the time. Mechanical stimulation was not applied until 24 h of culture to allow the cells to acclimate to their environment. **Live/Dead Staining:** On Day 8, the cell culture beads were collected and stained with 10 µM Calcein AM and 2 µM ethidium homodimer (Sigma) and imaged on a confocal microscope. **Viability assay:** On Day 8, cell viability was assessed for static and HP treated cell culture beads based on quantification of the ATP present, using CellTiter Glo 3D viability

Copyright 2016 The Organizing Committee for the 2016 Summer Biomechanics, Bioengineering and Biotransport Conference

assay (Promega). **RT-PCR:** On Day 8, mRNA was extracted from static and HP treated cell culture beads and analyzed for ECM genes: aggrecan, collagen II, collagen I and GAPDH as housekeeping gene.

RESULTS

Cell viability with live/dead staining showed nearly 100% viability in both static and HP treated groups, as observed in Figure 2. Assessment using the CellTiter Glo assay demonstrated no significant changes in ATP activity in both static and HP treated groups (Figure 3). Relative mRNA of HP treated group exhibited a statistically significant up-regulation of matrix protein, aggrecan on day 8 relative to static group (Figure 4). In both, HP treated and static groups, collagen II and I levels did not change significantly.

Figure 1: Instron TGT hydrostatic bioreactor chamber

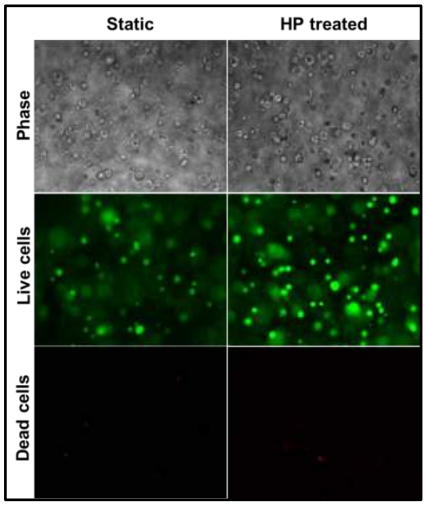

Figure 2: Viability was assessed using Live/dead staining and showed no significant differences between groups, with the majority of the cells stained green indicating high viability.

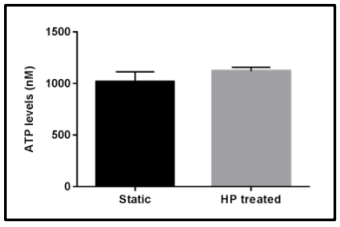

Figure 3: ATP activity was assessed using CellTiter Glo 3D viability assay and showed no significant differences between groups, showing that HP treatment does not affect cell viability.

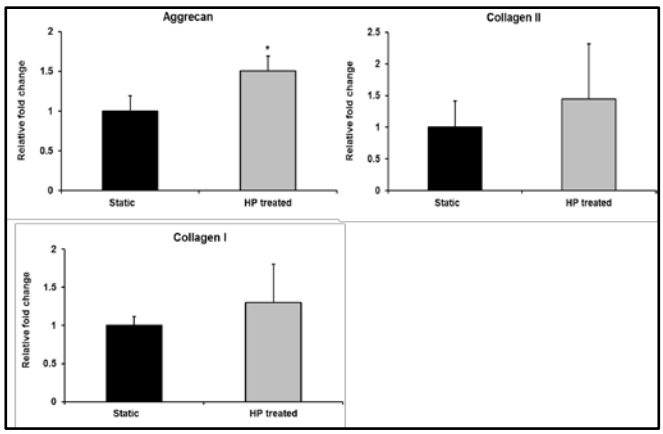

Figure 4: Quantitative RT-PCR was performed to assess fold-changes in gene expression between the groups. No significant changes were observed in Coll II and I, but there was a significant increase in Aggrecan expression between the two groups.

DISCUSSION

Dynamic pressurization has long been known to regulate disc cell phenotype and have beneficial effects, increase production of ECM macromolecules, including Col II and glycosaminoglycans (GAGs) [3]. The prior art for application of HP was through the use of piston driven pressurization chamber. This study evaluated a novel high throughput bioreactor, where individual cell containing alginate beads in multiwall plates were exposed to controlled dynamic HP. Application of dynamic pressure did not affect cell viability and enhanced ECM gene expression. In this study, hydrostatic pressurization did not translate into clear quantitative differences in coll II by mechanically stimulated cells over static, although there was a trend for increased Col II gene. Similar gene expression pattern was observed by Ganteinbein et al., in their study utilizing dynamic hydrostatic bioreactor to mechanically load an *in vitro* disc organ culture [3]. GAG content of NP cells in beads were also measured using Blyscan assay. Results indicate that while aggrecan gene expression increased, the GAG content was down-regulated under the application of dynamic HP (not shown). Optimization of conditions for enhancement of ECM deposition is warranted. Based on our findings, application HP may be a beneficial method of modulating cellular phenotype for high throughput tissue engineering applications, where evaluation of interactions between biologic factors and loading may be evaluated in repeatable and expedited modality. Future studies will concentrate on assessing the functionality of the ECM produced in response to HP via mechanical testing to determine of the increase in ECM correlates to enhanced mechanical properties. Additionally, future work will investigate the expression of other anabolic (GAG) and catabolic (MMP-3, -13) involved in ECM remodeling.

ACKNOWLEDGEMENTS

Funded in part by NSF CAREER award 1151605.

REFERENCES

[1] Ishihara, H et al., *J Appl Physiol (1985)*, vol. 80, pp. 839-46, 1996.
[2] Purmessur D et al., *Arthritis Res Ther*, vol. 15, pp. R122.
[3] Gantenbein B et al., *Spine (Phila Pa 1976)*, pp. 2665-73, 2006.
[4] Harjanto D et al., *PLoS One*, vol. 8, pp. e52509.
[5] Hutton W et al., Clin Biomech (Bristol, Avon), vol. 16, pp. 728-34
[6] Kasra M et al., *JOR*, vol. 21, pp. 597-603, 2003
[7] Reinwald Y et al., *Tissue Engineering Part C Methods*, vol. 21, pp. 1-14, 2015

Copyright 2016 The Organizing Committee for the 2016 Summer Biomechanics, Bioengineering and Biotransport Conference

SB^{3}C2016
Summer Biomechanics, Bioengineering and Biotransport Conference
June 29 –July 2, National Harbor, MD, USA
SB^{3}C2016-1079

THE DETERMINATION OF FREE TORQUE ON ATHLETIC TURF SURFACES USING INSOLE PRESSURE DATA

Brian T. Weaver (1,2), Jerrod E. Braman (1), Roger C. Haut (1)

(1) Orthopaedic Biomechanics Laboratories
Michigan State University
East Lansing, MI, USA

(2) Explico Engineering Co.
Novi, MI, USA

INTRODUCTION

Rotational traction at the shoe-surface interface may be directly related to the development of high ankle sprains due to internal rotation of the body on a planted foot. Although it is generally accepted that low levels of rotational traction are more desirable than high levels from a lower extremity injury risk perspective, currently there are no engineering standards or accepted thresholds to be used for turf and/or shoe design. The majority of research has been focused on investigating rotational traction between the shoe's outsole and the athletic turf. This has been accomplished with material's testing machines and/or mechanical devices fitted with surrogate ankles [1,2]. Yet, these methods may not represent real world athletic kinematics. Consequently, use of live human subjects may provide the most accurate method for investigating injury potential as it might relate to various shoe-surface characteristics. One advantage live human subjects afford is the ability to employ inverse dynamics calculations to estimate joint reaction forces. These calculations necessitate ground reaction forces and moments in conjunction with motion tracking data. Ground reaction data are measured by a force plate, which needs to be located underneath the test surface. Yet, this may alter the integrity of the surface and puts restrictions on the size of the test area.

To help address these limitations in current methodology, one recent study has proposed the use of pressure insole technology and linear regression analyses to determine free torques generated at the shoe-surface interface during internal rotation of the body relative to a planted foot [3]. These regression variables are both subject and shoe specific [3,4]. It is, however, currently unknown if these regression models are surface specific. The goal of the current study was to investigate the feasibility of developing linear regression variables from a single "calibration" surface in the lab that can be used to predict free torques on various athletic turfs. The hypothesis of the current study was that a subject and shoe specific linear regression equation developed on an anti-fatigue mat could accurately predict the free torque that develops on grass and an artificial turf.

METHODS

Six subjects wore a size 11 Nike Vapor cleated shoe (Nike, Beaverton, OR, USA) fitted with a Pedar plantar pressure insole (Novel, Munich, Germany). A 0.3 mm thick non-slip material (Dycem®, Warwick, RI, USA) was placed between the insole and the shoe to prohibit potential insole motion during the tests. Plantar pressure data were collected at 100 Hz. Concurrent ground reaction data was collected at 1000 Hz with an AMTI force plate (Advanced Mechanical Technology, Inc., Watertown, MA, USA).

Three surfaces were selected for this study; anti-fatigue floor matt (AFM) (Crown, Fremont, OH, USA), natural grass (NG), and an artificial turf (AT) (AtroTurf RootZone®, Dalton, GA, USA). The matt was cut to the approximate size of the force plate and adhered with industrial adhesive tape, which prohibited its motion during testing. The grass turf was obtained from the Michigan State University Hancock Turfgrass Research Center. Square sections were placed into a metal tray that matched the approximate dimensions of the force plate. The artificial turf was also placed into a tray with a mixture of sand and crumb rubber according to manufacturer specifications. A 0.3 mm thick non-slip material (Dycem®, Warwick, RI, USA) was placed between the trays and the force plate to prohibit motion of the trays on the force plate during testing. Subjects stood with both feet planted on the ground approximately shoulder-width apart. Only the right foot was on the force plate. Their left foot was placed on the AT if testing NG and vice versa to insure both feet were at the same height (Figure 1). Subjects performed an internal rotation of their body relative to their right, planted foot. The subjects were

Copyright 2016 The Organizing Committee for the 2016 Summer Biomechanics, Bioengineering and Biotransport Conference

instructed to exert maximum effort and not to move either foot. Trials were rejected if either foot lifted off the surface or translated. Subjects performed each motion until ten successful trials per surface were collected for a total of 30 trials. Force plate data were re-sampled to match the plantar pressure sampling frequency. Data were synchronized utilizing peak vertical force as the common datum. Each trial was trimmed to only consider motion onset to peak torque.

Pearson's Product correlation coefficients were calculated between each of the 99 insole pressure sensors and the free torque developed on each surface. Sensors having positive correlations greater than 0.80 between insole pressure and the free torque measured by the force plate (actual-Tz) were used to develop a sensor mask.

For each subject, one trial from each surface was removed at random. The remaining 9 trials from each surface were used to develop the surface-specific linear regression models. The slope and intercept were determined between the sensor mask and actual-Tz. The linear regression models developed from natural grass (NG) and artificial turf (AT) were used to self-predict their respective randomly removed trial. The linear regression model developed from the anti-fatigue mat (AFM) was used to cross predict the same NG and AT trial. Root Mean Square error (RMS error) and predicted peak free torques were used to measure the accuracy of each model. Statistical differences between these parameters were measured with two-tailed t-tests ($p < 0.05$).

RESULTS

The sensors with the highest correlation with actual Tz were located in the medial forefoot. There were no statistical differences in any measure across all six subjects (Table 1). This indicates that both the NG and AT models accurately predicted their own respective data. Additionally, the AFM model accurately predicted both the NG and AT data. All three models had a relatively low RMS error (less than 13% of peak torque) indicating that each was able to predict the temporal data well. Most of the error occurred at the beginning and end of the motion (Figure 2).

Figure 1: Illustration of the set-up for NG testing.

Table 1: Data from NG and AT models performing self-prediction and the AFM model performing a cross prediction (mean ± stdev).

Regression Model	Correlation	RMS Error (Nm)	Error Predicting Peak (%)	RMS/Peak (%)
NG	0.98 ± 0.02	2.15 ± 0.93	10.30 ± 11.73	9.60 ± 1.52
AFM	0.98 ± 0.02	2.98 ± 0.80	3.38 ± 13.02	10.74 ± 7.81
AT	0.99 ± 0.01	3.07 ± 0.83	2.76 ± 6.51	8.89 ± 4.35
AFM	0.99 ± 0.01	2.87 ± 1.48	2.51 ± 8.38	12.72 ± 5.55

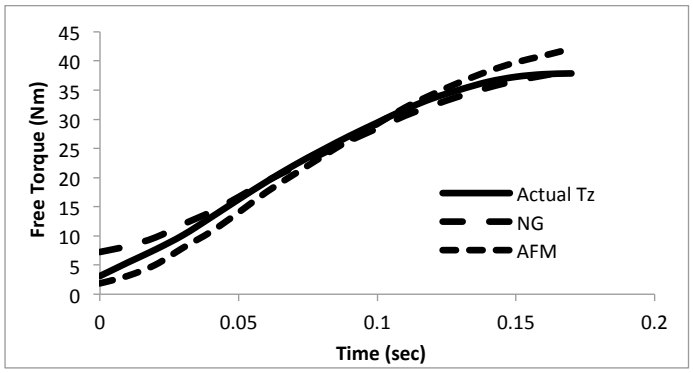

Figure 2: Typical plot for NG data.

DISCUSSION

The results support the hypothesis that subject and shoe specific linear regression models developed from insole pressure data allow for the accurate prediction of free torque on NG and AT surfaces during internal rotation of the body relative to a firmly planted foot. This may indicate that subject and shoe specific linear regression models can be developed in the laboratory using an AFM as the interface between a cleated shoe and the force plate for testing outside the laboratory on athletic surfaces comprised of NG and/or AT. This may allow for research utilizing live human subjects on actual fields of play without the need for an embedded force plate in order to better understand the kinetics and kinematics associated with traumatic injury.

Epidemiological data suggest that eversion ankle injury rates are 31% higher on artificial/synthetic turf compared to natural grass [5]. It has been suggested that rotational traction is a key factor in predicting injury risk because artificial/synthetic turf has been shown to have higher rotational traction compared to natural grass [2]. Yet, in the current study there were no measurable differences in the peak torque developed on NG and AT. The disparity may, in large part, be a result of methodological differences. The subjects in the current manuscript were instructed not to rotate their foot relative to the turf surface. Research that documents differences in rotational traction between turf surfaces utilize mechanical devices fitted with a surrogate ankle that drag the foot through a set rotation. The torque required to move the foot through this displacement is then reported. However, ligament injuries in the ankle have been shown to occur during excessive internal rotation of the body relative to a planted foot [6]. Therefore, having the foot move relative to the surface with the lower extremity and upper body is inconsistent with the known mechanism of injury.

In summary, the methodology presented in the current study accurately predicted the free torques developed on NG and AT during internal rotation of the body relative to the foot. The use of pressure insoles to predict the free torque on various surfaces, in conjunction with motion capture data, may better be able to assess potential injury mechanisms on actual athletic field turfs using human subjects.

REFERENCES

[1] Galbusera, F., et al., *Sports Biomech* 12(3):293-301, 2013.
[2] Villwock, M., et al., *Am J Sports Med*, 37:518-25, 2009.
[3] Weaver, B., et al., *Sports Eng & Tech*, 227(4):219-225, 2013.
[4] Weaver, B., et al., *Sports Biomech*, In Review.
[5] Hershman, E., et al., *Am J Sports Med*, 40:2200-5, 2012.
[6] Wei, F., et al., *J Biomech Eng*, 091001, 2010.

SB³C2016
Summer Biomechanics, Bioengineering and Biotransport Conference
June 29 –July 2, National Harbor, MD, USA
SB³C2016-1080

CADHERIN-11 EXCACERBATES MALADAPTIVE REMODELING AFTER MYOCARDIAL INFARCTION

Alison K. Schroer (1) and W. David Merryman (1)

(1) Biomedical Engineering
Vanderbilt University
Nashville, TN, USA

INTRODUCTION

Over one million Americans experience a myocardial infarction (MI) every year, and the resulting scar impairs heart function and stresses the remaining cardiac muscle, leading to cardiac fibrosis and progressive cardiac failure in many patients. The cells primarily responsible for scar formation and cardiac fibrosis are cardiac fibroblasts (CFs), which differentiate into myofibroblasts in response to increased transforming growth factor β1 (TGF-β1) and mechanical strain and stress. Myofibroblasts secrete extracellular matrix (ECM) proteins and actively contract the ECM to create a dense collagen scar, further increasing tissue stiffness. One of the proteins that allow myofibroblasts to effective coordinate this contraction is cadherin-11 (CDH11), a mechanosensitive intercellular adhesion protein. CDH11 has recently been shown to play key roles in the progression of both arthritis and pulmonary fibrosis, but its function in infarct healing has not been studied.

CDH11 engagement promotes the expression of the inflammatory cytokine IL-6 as well as profibrotic signaling factors and myofibroblast markers in joints, lungs, and heart valves [1]. Established fibrosis in the lungs has been reversed by treatment with functional blocking antibody against CDH11 [2]. Mechanosensitive signaling through CDH11 affects both inflammation and fibrosis, two key phases of remodeling after MI, but the details of this signaling are still poorly understood. CDH11 junctions are stabilized by p120-catenin, which modulates signals through downstream Rho/Rac pathways and can regulate cell migration and contractility [3]. The objective of this work is to clarify the role and function of CDH11 in the dynamic chemical and mechanical context of myocardial remodeling. We hypothesize that preventing CDH11 adhesion in CFs will reduce inflammation-driven infarct expansion and fibrotic scar formation after MI and improve cardiac outcomes.

METHODS

MI was induced in mice by coronary artery ligation and the resulting changes in cardiac function were monitored with echocardiogram. The effect of MI was compared between littermate wild type (WT) and CDH11 null (CDH11-/-) mice, and between C57 B6 mice treated with a functional blocking antibody against CDH11 (CAb) or a control IgG. Following dissections at 3, 7, and 21 days post-MI, we assessed changes in protein transcription, expression, and localization by qPCR, western blot, and immunohistochemistry, respectively. To complement and inform our *in vivo* studies, we isolated CFs from WT and CDH11-/- mice and measured their contractility in collagen gels. We also measured IL-6 transcription and p120-catenin expression changes when plated with CAb and treated with TGF-β1 for 24 hours. Finally, we used atomic force microscopy (AFM) to measure the stiffness of scar tissue and collagen gels.

RESULTS

Echo analysis showed a less significant reduction of ejection fraction and less significant increase in ventricular systolic volume after MI in the CDH11-/- animals relative to WT animals (**1A**). In addition, a larger fraction of the CDH11-/- population survived to day 21, when the hearts were collected for histological assessment (**1B**). Masson's trichrome stained revealed a thicker, less compact scar in the null animal, which was much less stiff than both the WT scar and the WT cardiac tissue opposite the infarct (**1C-D**). *In vitro* collagen gel contraction data complemented these findings, revealing a significant reduction in contraction by CDH11-/- cells relative to WT cells (**1E**), and a corresponding decrease in gel stiffness, measured by AFM (**1F**).

Mice receiving CAb treatment maintained higher ejection fractions relative to the control group (**2A**). Furthermore, increasing dilation of the left ventricle observed in the control was curtailed in the

Copyright 2016 The Organizing Committee for the 2016 Summer Biomechanics, Bioengineering and Biotransport Conference

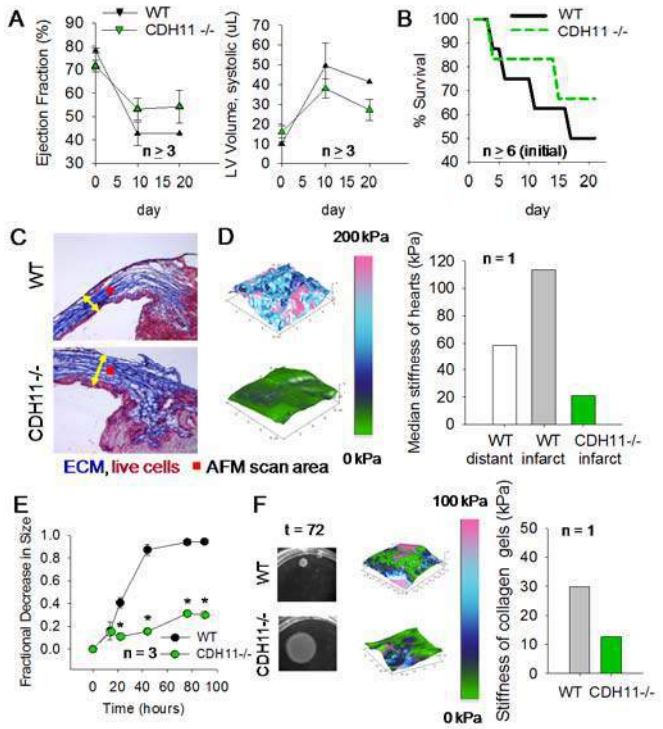

Figure 1: Heart function is better maintained (A,B) and scar contraction and stiffness is decreased (C,D) in CDH11-/- hearts relative to WT. AFM analysis (D, F); representative scan of elastic modulus over surface, median value of modulus plotted on right.

animals receiving the blocking antibody, resulting in significantly reduced total ventricle volume at 21 days post-MI (**2B-C**). This reduced remodeling coincided with increased survival (**2D**) and reduced induction of IL-6 transcription (**2E**). CAb treatment of WT CFs *in vitro* effected a similar reduction in IL-6 transcription (**2F**). CDH11-/- CFs transcribed significantly lower amounts of IL-6 than WT CFs, regardless of treatment.

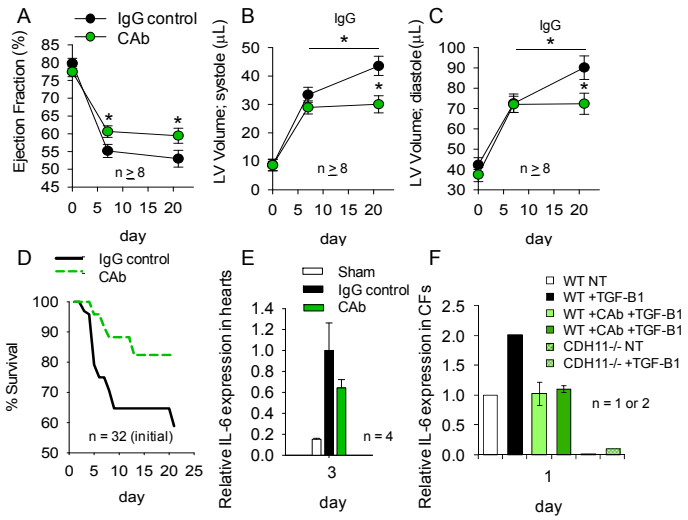

Figure 2: Cardiac function and survival improved with CDH11 blocking antibody treatment (A-D). * indicates $p < 0.05$. IL-6 transcription reduced in CAb treated hearts after MI and CF.

Immunostaining and western blot analysis show that overall expression of p120 is increased in CAb treated hearts relative to NT at both 21 (**3A**) and 7 days (**3B**) post-MI. Immunostaining of cells shows higher cytoplasmic p120 localization with CAb treatment (**3C**), with a modest increase in overall expression in both CAb treated and CDH11-/- CFs (**3D**).

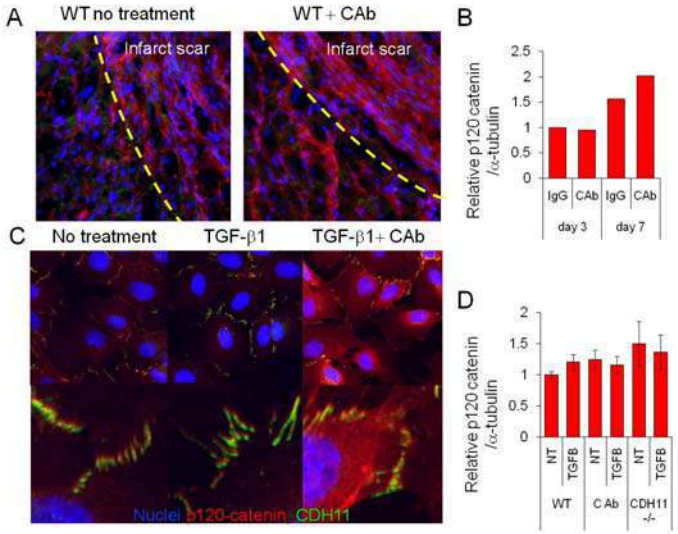

Figure 3: Immunostaining (A, C) and western blot densitometry (B, D) show p120 catenin expression and localization in the heart 21 days post MI (A,B) and in CFs (C,D).

DISCUSSION

Our findings suggest that CDH11 plays a key role in the process of fibrosis after MI, and that targeting CDH11-expressing myofibroblasts limits inflammation and remodeling while preserving cardiac function. Our initial results highlight intrinsic differences in contractile ability of WT and CDH11-/- CFs and establish a link between CF contractility and mechanical stiffness that is relevant to infarct healing.

We have shown that blocking CDH11 adhesion after MI maintains cardiac function and prevents ventricle expansion, especially between 7 and 21 days post-MI (**2B-C**). The reduction of IL-6 transcription demonstrates that CDH11 significantly regulates IL-6 expression after MI and supports a key role for CDH11-expressing CFs regulating inflammation and myocardial remodeling.

Finally, we have identified one potential mechanism for CDH11 signaling. Increased immunostaining of p120-catenin in the peri-infarct zone and in the cytoplasm of CFs suggest that CAb treatment may disrupt the association of CDH11 and p120 catenin. This may prevent mechanically induced Rac1 activation known to increase IL-6 expression.

This work characterizes CDH11-dependent phenotypic changes and tissue remodeling throughout the course of infarct healing, providing new biological insights and highlighting a potential new treatment strategy for improving outcomes after MI.

ACKNOWLEDGEMENTS

This work was funded by the NSF (1055384 and DGE-0909667), the AHA (15PRE25710333), and the NIH (R01-HL115103).

REFERENCES

[1] Schroer, A. et al., *J Cell Science*, 128:1865-1875, 2015.
[2] Schneider, D. et al., *FASEB Journal*, 26:1-10, 2011.
[3] Yanagisawa. et al., *J Cell Biology*, 174(7):1087-1096, 2006.

Copyright 2016 The Organizing Committee for the 2016 Summer Biomechanics, Bioengineering and Biotransport Conference

SB^{3}C2016
Summer Biomechanics, Bioengineering and Biotransport Conference
June 29 –July 2, National Harbor, MD, USA
SB^{3}C2016-1081

ANEURYSMAL FLOW MODIFICATIONS BY COILS AND FLOW DIVERTERS AND LONG-TERM TREATMENT OUTCOME

Robert J. Damiano (1,2), Nicole Varble (1,2), Rahul Sanal (1,2), Jason M. Davies (2,4), Adnan H. Siddiqui (2,4), Hui Meng (1,2,3,4)

(1) Department of Mechanical and Aerospace Engineering
State University of New York at Buffalo
Buffalo, NY

(2) Toshiba Stroke and Vascular Research Center
State University of New York at Buffalo
Buffalo, NY

(3) Department of Biomedical Engineering
State University of New York at Buffalo
Buffalo, NY

(4) Department of Neurosurgery
State University of New York at Buffalo
Buffalo, NY

INTRODUCTION

Coil embolization and flow diversion are the primary endovascular strategies for treatment of intracranial aneurysms (IAs). Coils, which are deployed into the IA sac, are intended to promote thrombotic occlusion of the IA through blood stasis and reactivity with their metallic surfaces. Flow diverters (FDs), on the contrary, are deployed across the ostium of the IA and are intended to promote IA occlusion and neointimal healing of the parent artery through flow reduction into the IA. Unfortunately, these strategies are not always effective, and adverse treatment outcomes have been reported. According to several systematic reviews of endovascular treatment outcomes, 20.8% of coiled IAs recanalize, 10.3% require retreatment [1], and 24% of FD-treated IAs remain patent at 6-month follow-up [2].

Since these devices inherently affect intra-aneurysmal blood flow, post-treatment hemodynamics may play a critical role in treatment outcome. Considering that IA hemodynamics cannot currently be assessed *in vivo*, computational tools can be utilized to simulate IA treatment cases *in silico*. We previously used our validated finite element method (FEM)-based stenting method, in conjunction with computational fluid dynamics (CFD), to recreate three patient-specific FD-treated cases and compared the resulting hemodynamic modifications to their long-term treatment outcomes [3]. We found that in general, faster IA occlusion rates are associated with larger hemodynamic modifications post-treatment. In the current preliminary study, we propose that this same trend may also apply to coiled IA cases. To test this, we virtually recreated four patient-specific coiled IA cases using our validated FEM-based coiling method [4]. We then simulated and assessed pre- and post-treatment hemodynamics for each case using CFD and compared with their long-term treatment outcomes. Based on our preliminary results, the IA cases which had adverse treatment outcomes were associated with larger post-treatment flow modifications. This interesting finding is opposite of our previous results for FDs [3]. In the future, more clinical cases will be assessed to confirm or deny this trend.

METHODS

Patient-Specific Aneurysm Cases

Four patient-specific IA cases were selected for this preliminary study. The inclusion criteria for the IAs were as follows: (1) location in the internal carotid artery, (2) un-ruptured at initial treatment, and (3) treated with only coils. We collected retrospective image and clinical data for each case from the Gates Vascular Institute (Buffalo, NY) under IRB-approval. Based on 12-month follow-up data, two of the IA cases completely occluded and two IAs had a poor treatment outcome by this time point. A poor outcome was defined to be either reccurance of the IA which required retreatment or recanalization of the IA after having been completely occluded.

FEM Modeling of Coil Deployments

We simulated each patient-specific treatment using our FEM-based coil deployment method [4]. For each case, we modeled the specific coil types, sizes, shapes, and material properties as close to their manufactured specifications as possible. We assessed the post-treatment angiographic images of these cases before conducting simulations to determine where the coils resided and how they were distributed in the IA sac in the actual treatments.

CFD Simulations

Pre- and post-treatment hemodynamics were simulated using the CFD software Star CCM+ v.10 (CD-adapco, Melville, NY). Computational grids for each case were generated following our previously described meshing strategy [4]. The flow governing Navier-Stokes equations were solved under the assumptions of incompressible, steady-state, and laminar flow. Constant velocities were prescribed at each IA inlet whose values were calculated from physiologic flow rates for each IA

Copyright 2016 The Organizing Committee for the 2016 Summer Biomechanics, Bioengineering and Biotransport Conference

location. At the outlet boundaries, the ratios of the total mass flux were calculated and prescribed from Murray's Law for branching vasculature. Both the IAs and deployed coils were assumed rigid and assigned as no-slip boundaries. Blood was modeled as a Newtonian fluid with constant density and viscosity of 1056 kg/m^3 and 3.5 cP respectively. We qualitatively assed blood flow velocities and quantitatively calculated spatially-averaged velocity and wall shear stress (WSS) inside each IA sac.

RESULTS

Deployment Results

Images of the post-treatment angiography and the corresponding virtual deployment for each IA case are shown in Figure 1A. Qualitatively, the virtually deployed coils exhibit similar complex configurations and distributions in the IA sac as those observed in the angiographic images.

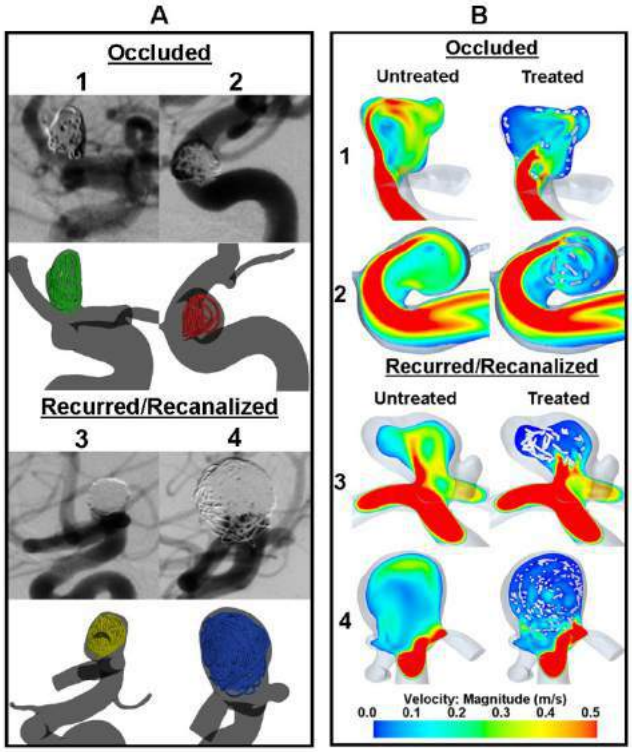

Figure 1: A. Side-by-side images of post-treatment angiography and the corresponding virtual deployments for each IA case. IA cases are labeled 1-4 and are segregated into two groups: occluded or recurred/recanalized. B. Intra-aneurysmal velocity magnitude for the four IA cases plotted on each IA mid-plane. The blank spaces in the velocity contours in the treated cases represent the intersection of the mid-plane and the deployed coils.

Hemodynamic Results

To visualize the flow, we plotted velocity magnitude contours on the IA mid-planes for each case, shown in Figure 1B. In the untreated cases, inflow jets are observed, which create "vortex"-like flow patterns in each IA sac. After coil deployment however, these inflow jets appear to be blocked from entering each IA sac. However, higher velocities are observed post-treatment in the occluded IA group compared to the recurred/recanalized IA group. Aneurysm-averaged velocity and wall shear stress (WSS), shown in Figure 2A, reveal that reductions in these values were greater post-treatment in the recurred/recanalized group compared with the occluded group.

DISCUSSION

Our results in this preliminary study appear to be opposite of those found in our previous FD study [3]. Whereas faster occlusion times were associated with larger hemodynamic modifications post-treatment in FD-treated IAs (Figure 2B), we found that coiled IAs which recurred or recanalized had larger hemodynamic modifications post-treatment compared to those which occluded successfully. This interesting finding suggests that post-treatment hemodynamic modifications may not be as important for coil embolization as for flow diversion for successful IA treatment, or that there may be additional factors to consider. Since FDs are deployed across the ostium of an IA, their mechanism of action is independent of the size or morphology of the IA. On the contrary, coils are deployed into the IA sac and thus their treatment effect is more likely affected by IA morphology such as dome and neck size, or even the type of coils used for treatment [5]. We will expand this study in the future to more cases in order to clarify the current results or potentially uncover new mechanisms of coil embolization that could explain these contradictory findings.

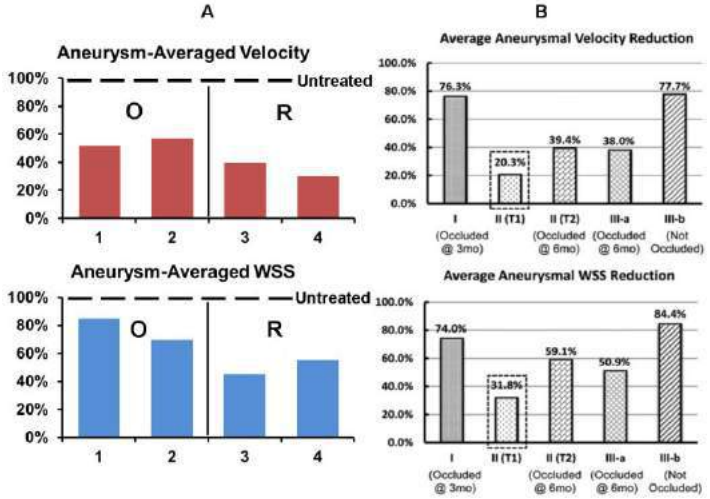

Figure 2: A. Hemodynamic parameters for the coil-treated IA cases. Values for each parameter are represented relative to a 100% baseline in the untreated case, designated by the dashed lines. The letters O and R designate the IAs in the occluded and recurred/recanalized groups, respectively. B. Hemodynamic results from our previous FD study [3].

ACKNOWLEDGEMENTS

This ongoing research is funded by the National Institutes of Health (R01 NS 091075). Computational resources were provided by the Center for Computational Research at the University at Buffalo. We would like to thank Nikhil Paliwal for technical assistance.

REFERENCES

[1] Ferns, Sandra P., et al. "Coiling of intracranial aneurysms a systematic review on initial occlusion and reopening and retreatment rates." Stroke 40.8 (2009): e523-e529.

[2] Brinjikji, Waleed, et al. "Endovascular treatment of intracranial aneurysms with flow diverters a meta-analysis." Stroke 44.2 (2013): 442-447.

[3] Xiang, Jianping, et al. "High-fidelity virtual stenting: modeling of flow diverter deployment for hemodynamic characterization of complex intracranial aneurysms." Journal of neurosurgery 123.4 (2015): 832-840.

[4] Damiano, Robert J., et al. "Finite element modeling of endovascular coiling and flow diversion enables hemodynamic prediction of complex treatment strategies for intracranial aneurysm." Journal of biomechanics 48.12 (2015): 3332-3340.

[5] Ishida, Wataru, et al. "The significant impact of framing coils on long-term outcomes in endovascular coiling for intracranial aneurysms: how to select an appropriate framing coil." Journal of neurosurgery (2016): 1-8.

Copyright 2016 The Organizing Committee for the 2016 Summer Biomechanics, Bioengineering and Biotransport Conference

SB^{3}C2016
Summer Biomechanics, Bioengineering and Biotransport Conference
June 29 –July 2, National Harbor, MD, USA
SB^{3}C2016-1082

NUCLEOTOMY ALTERS INTERNAL STRAIN DISTRIBUTION OF THE HUMAN LUMBAR INTERVERTEBRAL DISC

Amy A. Claeson (1), Brent L. Showalter (2), Edward J. Vresilovic (3)
Alexander C. Wright (4), James C. Gee (4), Neil R. Malhotra (4), Dawn M. Elliott (1)

(1) Department of Biomedical Engineering
University of Delaware
Newark, DE, USA

(2) Department of Bioengineering
University of Pennsylvania
Philadelphia, PA, USA

(3) Department of Orthopaedics and Rehabilitation
Pennsylvania State University
Hershey, PA, USA

(4) Department of Radiology
University of Pennsylvania
Philadelphia, PA, USA

INTRODUCTION

Nucleotomy is a surgical procedure following herniation and also simulates the reduced nucleus pulpousus (NP) pressure that occurs with disc degeneration. Internal disc strains are an important factor in disc function, yet it is unclear how internal strains are affected by nucleotomy. We previously developed a technique to acquire internal disc strains within the lamellae of the annulus fibrosus (AF) using MRI and image registration techniques [1]. Following techniques in neuroimaging [2], strains were then transformed to an anatomical template to minimize the effects of individual variability, and the strain components across several disc regions were determined for physiological axial compression loading [3]. Here, we use these techniques to explore the internal strain following partial nucleotomy for compressive axial loading, evaluating both on the incision side and uninjured side. Findings from this study could inform the residual effects of the nucleotomy procedure as a surgical intervention and the degenerative changes in the disc linked to loss of NP pressure.

METHODS

Specimen Preparation: Grade II L3-L4 human cadaveric discs (n=6) were analyzed intact and after a partial nucleotomy that removed 30-50% (by weight) of the NP through a left posterolateral incision. Specimens were rehydrated in 1X PBS overnight at 4ºC before mechanical testing commenced. Figure 1 shows a mid-sagittal image of a disc after partial nucleotomy with a left posterolateral incision (incision) while the right side is intact (uninjured). Remaining NP material reconstituted during rehydration, filling the disc space.

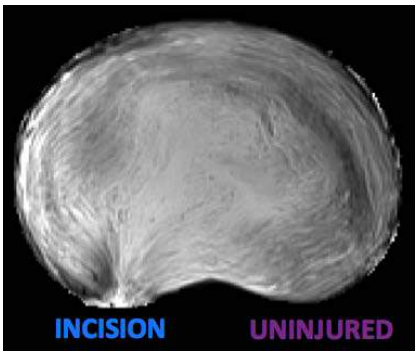

Figure 1. Mid-transverse view of a cadaveric disc post-nucleotomy procedure through a left incision leaving the right side intact.

Mechanical Testing and Image Acquisition: Two cycles of stress-relaxation testing were performed for reference and loaded configurations. For the reference configuration, axial displacement increased until an instantaneous compressive load of 50 N was obtained, and this reference displacement was then held for a 3 hour relaxation period. The loaded configuration followed, where axial displacement increased until an instantaneous 0.7 MPa load was obtained. Then, this loaded displacement was held for an 8 hour relaxation period. After each relaxation period, the reference and loaded discs were imaged separately at 0.3 mm isotropic resolution in a 7T MRI scanner. Only the lateral half of the disc closest to the radiofrequency coil was used for analysis because the signal-to-noise ratio decreased with increasing distance from the coil. Thus, the uninjured and incision sides of the disc were scanned separately to ensure sufficient MR signal for analysis.

Copyright 2016 The Organizing Committee for the 2016 Summer Biomechanics, Bioengineering and Biotransport Conference

Data Analysis: Advanced Normalization Tools (ANTs) were used to register the reference and loaded images prior to calculating internal strain within the AF lamellae. The discs were spatially normalized (averaged) to create separate anatomical templates for each condition: intact, uninjured and incision. Circumferential (E_C), radial (E_R) and axial (E_Z) strains for each individual disc were transformed to their respective templates. Each template was divided into thirds through the transverse plane, and five regions were defined within the middle third: anterior (A), anterolateral (AL), lateral (L), posterolateral (PL), and posterior (P). The effect of nucleotomy was compared on the uninjured and incision sides, and intact [3] using a repeated measure ANOVA with a Holm-Sidak post-hoc test. All marked results have $p < 0.05$ significance.

RESULTS

Disc nucleotomy with a left posterolateral incision site altered disc strains on both the incision and uninjured sides from the intact state as viewed from the strain templates of circumferential (E_C), radial (E_R), and axial (E_Z) strains (Figure 2). Strain fields were inhomogeneous through the five regions shown qualitatively in Figure 2 for a representative sample and quantitatively in Figure 3 with pooled data (n=6).

Mean Circumferential Strain varied from 3.5 to 5.8% throughout the intact AF and was unaffected by nucleotomy on the uninjured side. Circumferential strain decreased on the incision side, ranging from 1.6 to 2.4% and was significantly lower in all regions except posterolateral.

Mean Radial Strain varied from 3.8% and 6.5% in the intact AF and there was no difference with nucleotomy on either the uninjured or incision side. While not significant, the strain did decrease to approximately 3% in the anterior, anterolateral, and lateral AF on both sides.

Mean Axial Strain varied between -13% and -20% in the intact AF. Following nucleotomy, the strains in the uninjured side increased in magnitude to approximately -24% in all regions except anterior. The incision side exhibited similar strains to intact.

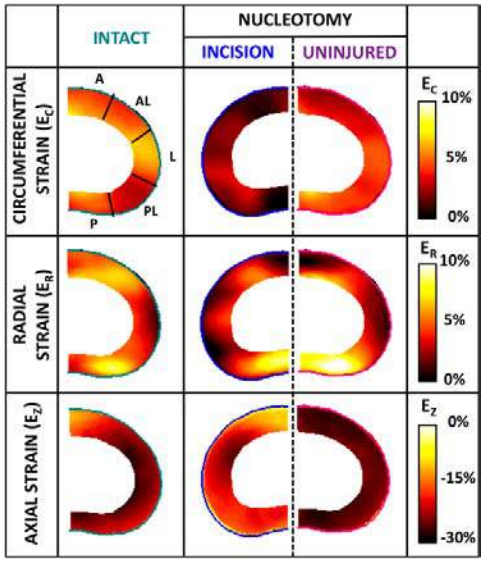

Figure 2. Strain templates for intact, uninjured and incision sides show changes in circumferential (E_C), radial (E_R) and axial (E_Z) strains. Strains, divided into five regions, are more heterogeneous in the incision and uninjured discs compared to intact.

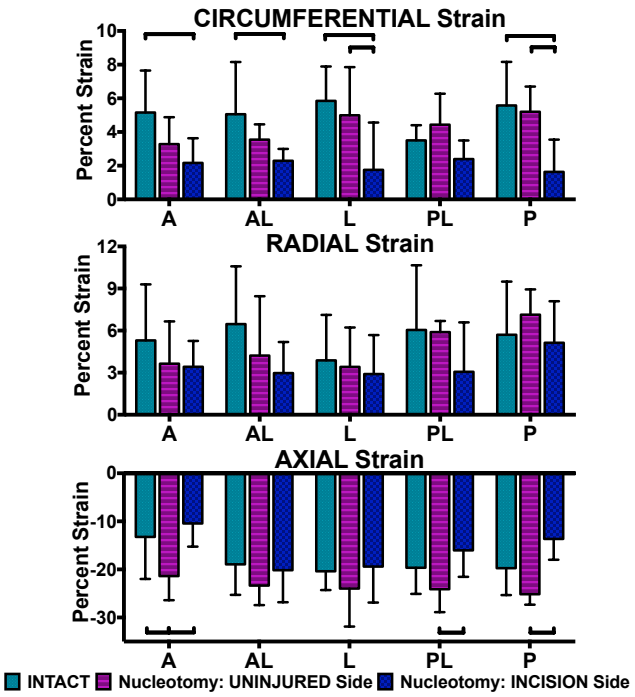

Figure 3. Mean circumferential, radial and axial strains of intact, uninjured and incision discs (n=6/group) with 95% confidence intervals. Circumferential and axial strains were most affected by partial nucleotomy treatment.

DISCUSSION

The effects of nucleotomy on discs undergoing axial compression were successfully determined using templates of internal disc strain through the AF lamellae. We found nucleotomy intervention alters disc structural and mechanical states compared to intact discs and these changes were different depending on the side with the incision. Axial strains were greater on the uninjured side of the AF. Tools used in nucleotomy procedures allow easier NP removal from the side opposite the incision; thus, this lack of NP material on the uninjured side may leave only the AF to resist the compressive load. Circumferential strains were lower on the incision side of the AF, where the large AF defect likely prevented the AF from supporting hoop stresses.

This study used a partial nucleotomy procedure, which reduced NP pressure, to measure alterations in disc mechanics with regards to (1) degenerative changes in the disc and (2) the AF incision inherent to the intervention. These findings are important to address etiology and progression of degeneration, and to develop and evaluate therapeutic interventions

ACKNOWLEDGEMENT

Study was funded by NIH R01AR05005.

REFERENCES

[1] Yoder, JH et al., *J Biomech Eng*, 136(11):10.1115, 2014. [2] Lancaster JL, et al., *Hum Brain Mapp*, 28(11):1194-205, 2007. [3] Showalter, BL et al., *J Orthop Res*, *published online 01/08/2016*, doi:10.1002/jor.23137.

Copyright 2016 The Organizing Committee for the 2016 Summer Biomechanics, Bioengineering and Biotransport Conference

SB³C2016
Summer Biomechanics, Bioengineering and Biotransport Conference
June 29 –July 2, National Harbor, MD, USA
SB³C2016-1085

CHANGES OF TOTAL FINGER FORCES DUE TO EMULATING FINGER AMPUTATIONS USING A CYLINDER HANDLE DEVICE

Diego F. Villegas (1), Jorge H. Escobar (1), Ricardo A. Quiros (1), Edna R. Buitrago (2), Ivan D. Quintero (2)

(1) Department of Mechanical Engineering
Universidad Industrial de Santander
Bucaramanga, Santander, Colombia

(2) School of Medicine
Universidad Industrial de Santander
Bucaramanga, Santander, Colombia

INTRODUCTION

Hands are strongly associated with sense of touch. They are vital for humans because fingers allow the hand to perform many different activities. Therefore, losing part of a finger will modify the biomechanics of the grip [1]. Finger amputation is a surgical procedure used to remove the phalanx involve in a trauma which can be the consequence of work-related accidents, congenital deformities or other incidents. The motivation for this study was to the difficulty of finding a group of finger amputees with different types of finger amputation. Basically, the present study seeks to establish what finger amputations are more critical in terms of the reduction of due to different finger amputations. Whole finger amputation as well as thumb amputation was not considered in this study.

METHODS

Handgrip force equipment

A 38-mm diameter cylindrical mechanical device was designed and built to emulate different finger amputations. The device has a load cell at the bottom of the cylinder to measure handgrip force. In addition, the device has eight gates which open by means of a motorized gear depending of what combinations will be used to emulate amputated phalanges. Each gate has three force sensors in order to obtain the force on each of the three finger phalange (distal, medial, and proximal).

Subjects

A total of ten adult subjects (five women, five men), right-handed, average height and weight, palm length less than 112 mm were used for this study. Subjects with muscular lessons, amputations, or any physical problems in hands or forearm did not participate on this study. Handgrip force measurement protocol was followed according to previous studies [2]

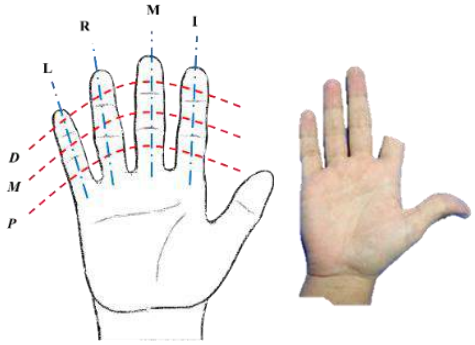

Figure 1: a) Matrix to determine combinations for amputations b) Example for an amputation I:*D*+*M*

Statistical Analysis

Eleven combinations of finger amputations were obtained by eliminating finger phalanges according to most common finger amputations. Analysis of variance was assessed in order to find differences in total handgrip force between gender and dominant hand. Also, two-way ANOVA was done in order to obtain significantly differences with combinations

Total force were determined summing the forces obtained by twelve sensors -three phalanges on each finger (P: Proximal, M: Middle, D: Distal) and four fingers (I: Index, M: Middle, R: Ring, L: Little).

Copyright 2016 The Organizing Committee for the 2016 Summer Biomechanics, Bioengineering and Biotransport Conference

RESULTS

Although several studies have found the force on each phalanx, none had emulated a finger amputation by means of a mechanical device. The device is able to measure the handgrip force and also obtain the forces on each phalange for each finger (except thumb) of the hand. Our results were validated in two ways: 1) Comparison of the handgrip force values with previous studies, 2) Comparison of phalange forces with a male adult with a congenital deformity in his Ring and Little fingers.

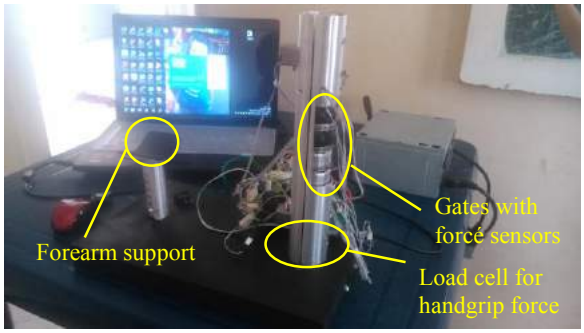

Figure 2: Handgrip force and pdevice.

Our results of the handgrip force strongly agree with those found by Kong [3] where handgrip force of men was found to be greater than women. ANOVA test showed that handgrip force was significantly different between men and women. On the contrary, dominance of the hand was not significantly different; although, it was shown that the 10% rule was fulfilled [4]

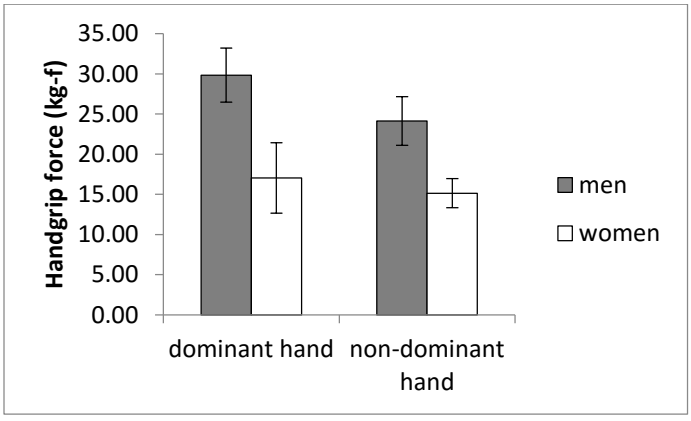

Figure 3: Handgrip force for hand dominance and gender.

On the other hand, it was found differences between combinations for amputations in men total finger force. Nonetheless, there were not significantly differences in the total finger force for amputations in women. It was observed that men total finger force is reduced in 62% for combination #11, and women total finger force showed a reduction of 48.55% for the same combination. The less reduction was noted on combination #2 for men, and combination #12 for women.

	MEN		WOMEN	
# of Combi-nation	**Total finger force (kg-f)**	**Loss of grip force (%)**	**Total finger force (kg-f)**	**Loss of grip force (%)**
1: No-amputation	18,56	0.0	10,58	0.0
2 [I:*D*]	16,52	10,99	9,22	12,84
3 [M:*D*]	12,86	30,73	8,82	16,59
4 [R:*D*]	12,27	33,86	7,96	24,74
5 [L:*D*]	14,47	22,02	8,67	18,01
6 [I:*M+D*]	15,02	19,07	9,50	10,23
7 [M:*M+D*]	10,09	45,61	7,47	29,34
8 [R:*M+D*]	12,29	33,78	7,49	29,24
9 [I+M:*D*]	11,26	39,31	8,55	19,18
10 [R+L:*D*]	11,68	37,08	8,46	20,06
11 [I+M:*M+D*]	6,93	**62,64**	5,44	**48,55**

Table 1. Percentage of loss of grip force with respect to the total finger force without finger amputations. Combinations [Fingers : *Phalanges*] Fingers (I: Index, M: Middle, R: Ring, L: Little, T: Thumb) Phalanges (*P*: Proximal, *M*: Middle, *D*: Distal).

DISCUSSION

It was expected that handgrip force for men be greater than women. Also, the reduction of total finger force for men was more critical than women because men reduce about 20% more than women for the same #11 combination. On the other hand, the difference between # of combinations in the less reduction (#2 for men, # 12 for women) could be due to the differences in hand morphology for both. The results of this study will help to rehabilitation therapists to understand how much of grip force they could expect for a patient with a specific finger amputation, and also will aid to the development of finger prosthesis.

ACKNOWLEDGEMENTS

We would like to thank to Universidad Industrial de Santander for all supports on this study.

REFERENCES

[1] Smith, D., *inMotion,* 17: 1, 2007.

[2] Roberts, H et al., *Age and Ageing,* 40:423-429, 2011.

[3] Kong, Y.K. and Lowe, B.D., *Int J of Ind Erg,* 35:495-507, 2005.

[4] Petersen, P. et al., *The Am J of Occup Therapy,* 43: 444-447, 1989.

Copyright 2016 The Organizing Committee for the 2016 Summer Biomechanics, Bioengineering and Biotransport Conference

SB^{3}C2016
Summer Biomechanics, Bioengineering and Biotransport Conference
June 29 –July 2, National Harbor, MD, USA
SB^{3}C2016-1086

MUSCLE ACTIVATION IN CYCLIC LIFTING WITH TRAINED LUMBAR-PELVIC COORDINATION

Timothy D. Craig (1), Alice E. Riley (1), Neena K. Sharma (2), Sara E. Wilson (1)

(1) Department of Mechanical Engineering
University of Kansas
Lawrence, KS, USA

(2) Department of Physical Therapy and Rehabilitation Science
University of Kansas Medical Center
Kansas City, KS, USA

INTRODUCTION

The National Institute for Occupational Safety and Health has identified repetitive lifting and trunk flexion as risk factors for low back disorders [1]. In previous investigations by our laboratory and others, experienced lifters were observed to have an altered lumbar-pelvic coordination and reduced lumbar flexion during cyclic lifting tasks as compared to novice lifters [2-3]. It was speculated that experienced lifters select such strategies to avoid low back injuries. As such, there is an interest in examining the effects of training lumbar-pelvic coordination as a means to prevent low back injuries. The goal of this study was to examine muscle activity during such training in order to better understand the effects of such training.

METHODS

Seventeen subjects provided informed consent and participated in this study approved by the human subjects committee at the University of Kansas Medical Center. There were nine men and eight women with an average age, height, and weight of 24.1±4.2 years, 1.70±0.1 meters, and 66.4±12.7 kilograms. The subjects were divided into two groups based on weight lifting experience. Subjects having lifted weights three times per week for the previous year were considered experienced and individuals who had not lifted weights regularly in the previous year were considered novice. The experienced group (EXP) had a total of 8 subjects with 3 females and 5 males while the novice group (NOV) had 5 females and 4 males for a total of 9 NOV lifters. Subjects performed a repetitive lifting task to examine three different lumbar pelvic coordination strategies. The three strategies examined included a self selected strategy, a highly kyphotic (HK), and a neutral (NU) strategy.

The lifting strategies were performed using a repetitive lifting task. The task involved lifting a milk crate from the ground to waist level and then returning to near ground height. The crate held a small amount of weight normalized to 3% of a single max lift. The crate was never released and held throughout the trial that lasted approximately 4 minutes. A metronome controlled the rate of lifting by beeping at 1Hz with each lift cycle (ground-waist-ground) lasting four seconds.

Two angles, lumbar angle (LA) and trunk flexion angle (FA), were measured using three electromagnetic sensors (MotionStar, Ascension Technology, VT) collecting position and orientation data at 100Hz using MotionMonitor Software (Innsport, IL). The sensors were located at T10, S1, and the manubrium. The FA was defined as the angle between T10-S1 and vertical and the LA was the difference in angular tilt of the sensors at T10 and S1 to describe the spinal curvature.

The LA was normalized using individual subjects range of motion (ROM) by collecting the maximum and minimum kyphotic postures at 0, 30, 60, and 80 degrees of flexion. A ROM envelope expanded the ROM using linear interpolation to calculate a normalized LA at any given FA. Biofeedback displayed an XY-plot with the FA on the x-axis and normalized LA on the y-axis for visual feedback. A target box was displayed to control for the lifting strategy. The target box ranged between normalized LA of 42% and 58% ROM for the NU strategy and 80% to 95% ROM for the HK strategy. For both trained strategies, the FA range for the target was between 20 and 70 degrees. Prior to introducing the biofeedback program, subjects completed the lifting task using a self selected strategy without visual feedback. During the trained strategies, subjects were instructed to make the cursor pass through the target box during the extension (lifting) phase of the lift.

Copyright 2016 The Organizing Committee for the 2016 Summer Biomechanics, Bioengineering and Biotransport Conference

Integrated electromyograhic data (EMG) for the right side erector spinae was examined during these cyclic lifting tasks. The data was filtered, demeaned, rectified, and integrated using a 100 point Hanning window. Following the filtering, all EMG data was normalized to the average peak value for the first four cycles of lifting during the self selected lifting strategy. An EMG curve was then interpolated based on flexion angle to get EMG as a function of flexion angle. The EMG data was examined over flexion angles between 10 and 70 degrees for both the flexion and extension phases of the lift.

RESULTS

During self-selected lifting, NOV lifters were found to have a lumbar-pelvic coordination pattern that reached high lumbar flexion during extension, while the EXP lifters were found to have a lumbar-pelvic coordination pattern that are more neutral. This was consistent with previous studies [2-3].

Examining the erector spinae EMG patterns, it was found that both groups generally had higher EMG during extension than during flexion as would be expected. Over time, during the self-selected strategy, NOV lifters transitioned to a pattern of lower EMG levels at high trunk flexion.

During the trained strategies, it was expected that the NU trained strategy was most different from self-selected for the NOV group. Examining the EMG it was found that the NOV group again exhibited a pattern of lower EMG at high trunk flexion that increased over time. For the HK trained strategy, both the NOV and EXP groups exhibited this lower EMG at high trunk flexion over time.

DISCUSSION

While the lumbar-pelvic coordination patterns (and thus trunk motion) remained relatively consistent when subjects were practicing trained lumbar-pelvic coordination patterns, the changes in EMG patterns suggest that muscular coordination is changing. As these patterns were more pronounced for NOV lifters, it suggests that fatigue and task difficulty (during trained strategies) may be the cause of this change in muscle activation. At high trunk flexion, subjects could be relying more on the passive elements of the spine (such as ligaments) rather than the musculature. They could also be changing their velocity of trunk extension, which has not been examined yet.

Future work will further examine these observed patterns and their relationship to the lumbar-pelvic motion. Additionally, other muscles, including the antagonist trunk muscles, should be examined to see if changes in co-contraction may be a component of these changes in erector spinae muscle activation.

ACKNOWLEDGEMENTS

Research reported in this publication was supported by National Institute of Arthritis and Musculoskeletal and Skin Diseases of the National Institutes of Health under award number 1R03AR061597-01. The content is solely the responsibility of the authors and does not necessarily represent the official views of the National Institutes of Health.

REFERENCES

[1] Bernard, B, *DHHS (NIOSH) Publication Number 97-141*, 1997.
[2] Maduri, A et al., *J Electromyogr Kinesiol,* 18: 807-14, 2008.
[3] Plamondon A et al., *Ergonomics*, 53(10):1239-1253, 2010.

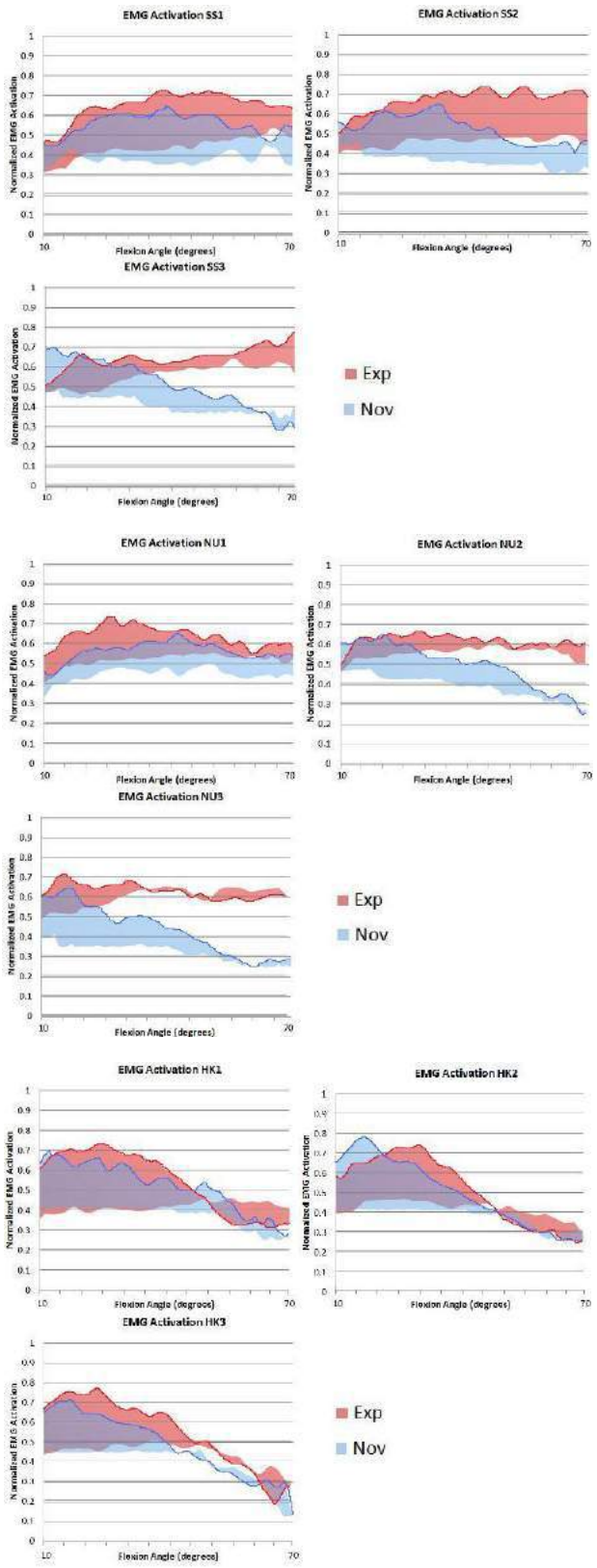

Figure 1. Average EMG patterns of erector spinae activation are shown for self-selected (SS) and trained lifting strategies (NU, neutral, and HK, highly kyphotic). These are shown at 3 time intervals (1:50-80s, 2:80-110s, and 3:110-140s). Trunk extension is illustrated by the dark edge while flexion is illustrated by the light edge.

Copyright 2016 The Organizing Committee for the 2016 Summer Biomechanics, Bioengineering and Biotransport Conference

SB³C2016
Summer Biomechanics, Bioengineering and Biotransport Conference
June 29 –July 2, National Harbor, MD, USA
SB³C2016-1087

EVALUATION OF DESIGN PARAMETERS FOR A NOVEL PERSONAL AIR PURIFICATION METHOD TO MITIGATE PARTICLE ASPIRATION

Christopher R. Idelson (1), Christopher G. Rylander (1)

(1) Department of Mechanical Engineering
The University of Texas at Austin
Austin, TX, USA

INTRODUCTION

Airborne transmission of pathogens and allergens represent a prominent medical issue in the healthcare industry. In recent years, respiratory acquired conditions such as tuberculosis (TB), pneumonia, and influenza have accounted for direct medical costs at an estimated $435 million, $3.7 billion, and $10.4 billion in the United States, respectively [1-3]. Respiratory allergies present a global problem, with the illness known as allergic rhinitis affecting roughly 60 million adults in the US alone, and further accounting for about $3.5 billion in direct medical costs in 2011 [4, 5]. TB affects roughly 9 million people worldwide, with a death toll around 1.5 million each year [6]. These and many other afflictions are still prominent in today's world, and seen in virtually all populations. More so, human occupancy density has been identified as another factor for increased exposure to bacteria, consequentially labeling such environments as offices, schools, and clinics as centralities for the spread of numerous illnesses [7, 8].

While masks which cover the mouth and nose are effective at preventing aspiration of pathogens and allergens, current reports show low user compliance with these devices [9, 10]. Therefore, we have identified the need for a device to promote high user compliance while achieving effective results for personal air purification, with the ultimate goal of reducing aspiration of detrimental air contaminants. Our intended design concept is a wearable device that blows purified air toward the human breath area without obstructing the face.

METHODS

The objective of our study was to examine which parameters of our conceptual design most influence pnuematic purification of sampled (inhaled) air. Data was acquired using a system emulating a typical breathing envinroment (Figure 1). A clean air input port and sampling port (diameters= ¾") simulated an air purifier prototype device and a human mouth, respectively. Three parameters were experimentally tested to determine feasibility for air purification via the flow of clean air directed at the sample port in a dirty-air environment: (1) distance between ports, (2) flow rate of clean air input, and (3) angle between ports. First, 1.5933±0.0796 grams of aerosolized glycol particles (400W Metal Fog Blaster, 1byone Inc), simulating "dirty air," were dispersed into a sealed chamber. Controlled flow of clean room air was introduced into the chamber. Excess intake/exhaust filters were included, allowing for mass conservation in/out of the chamber.

Sample filter (In-Line Bacteria Filter, Kinship Comfort Brands) mass measurements were made using a Mettler Toledo XS104 balance with 0.1 mg resolution. A GAST 1023-101Q vacuum pump pulled the chamber air through the filters (99.2% efficiency of 0.3 µm particles) collecting glycol particles, allowing for subsequent calculation of

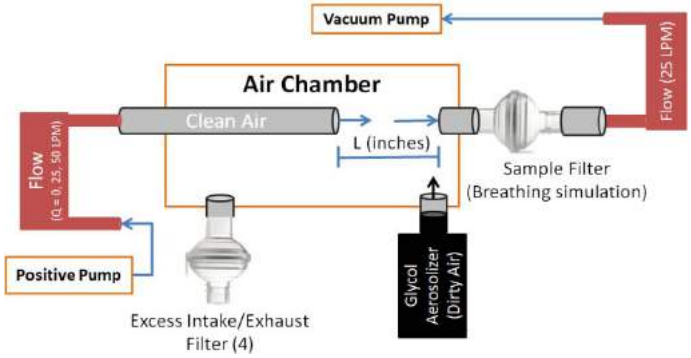

Figure 1. Experimental chamber setup for particle sampling.

Copyright 2016 The Organizing Committee for the 2016 Summer Biomechanics, Bioengineering and Biotransport Conference

collected glycol mass. Particle size and distribution were not controlled variables in these experiments.

Experiment 1- *Distance between clean air port and sample port ("L")*. Distances (L) were set at 1/8, 1, 5, and 12 inches. L=1/8" simulated the best case purification scenario. L=12" represented the worst case scenario. The sample port flow rate was set to 25 LPM, simulating a typical adult male breathing rate [11, 12]. Clean air input flow rate was set to 50 LPM. Three trials were repeated for each distance (N=12).

Experiment 2 – *Clean air input flow rate ("Q")*. Flow rates were tested at 0, 25, and 50 LPM. 50 LPM represented a best case purification scenario and 0 LPM represented a worst case scenario. Sample port flow rate remained at 25 LPM. L was set at both 1" and 12". Three trials were repeated for all flow rate and distance combinations (N=18).

Experiment 3 - *Angle of approach of clean air input*. Two angles of approach were tested: 0º (concentric alignment), as seen in *Experiments 1 & 2*, and 90º (perpendicular alignment). Sample port flow rate remained at 25 LPM, and L was set to 1" and 12". Clean air input flow rate was set to 50 LPM. L at 90° was measured from the end of the input port to the center of the sample port. Three trials were repeated for each angle and distance (N=12).

RESULTS

For *Experiment 1*, an order of magnitude more mass was collected in the sample filter for the worst case scenario (L=12") when compared to L=1" (Figure 2A). Results from *Experiment 2* at L=1" showed that a clean air input flow rate of Q=50 LPM decreased the average amount of glycol particles collected by more than 2 orders of magnitude when compared to Q=0 LPM, and more than 1 order of magnitude when compared to Q=25 LPM (Figure 2B). For *Experiment 3*, altering the angle of approach for the input flow to 90° increased particle mass collected by more than an order of magnitude when compared to 0°, at L=1" (Figure 2C).

DISCUSSION

Experiment results showed that each variable played a key role in purifying sampled air. All 3 factors appeared to affect air purification by at least an order of magnitude when comparing extreme levels of each parameter for each experiment. It is worth noting that *Experiment 3* results at L=12" and a 90° angle of approach still provided purification by more than a factor of ~2 when compared to values at Q=0 LPM in *Experiment 2* (i.e. where no purification method is implemented). This establishes an initial design baseline point with effective purification levels above typical environmental conditions. It will also be noted that the worst case scenario (Experiment 2, Q=0 LPM) collected the highest mass of all the experiments, yet was only ~1/3 of the input glycol mass supplied by the aerosolizer. This is likely explained by glycol particles that escaped via exhaust filters in addition to particles settling on the inner surface of the chamber. For *Experiment 1*, some trials displayed an interesting phenomenon, ultimately losing initial filter mass compared to pre-experiment values. One explanation for this might be that close proximity of input and high flow caused any pre-existing particles/humidity droplets to dry from the filter. It would be beneficial to explore whether there is interaction between the tested parameters. Future efforts will include refining the current protocol to incorporate biological agents, in addition to computational fluid dynamic modeling. It is crucial to recognize that augmenting user compliance via ergonomic device design will possibly require performance tradeoffs. In conclusion, all 3 tested parameters appear to warrant further consideration for the intended device design.

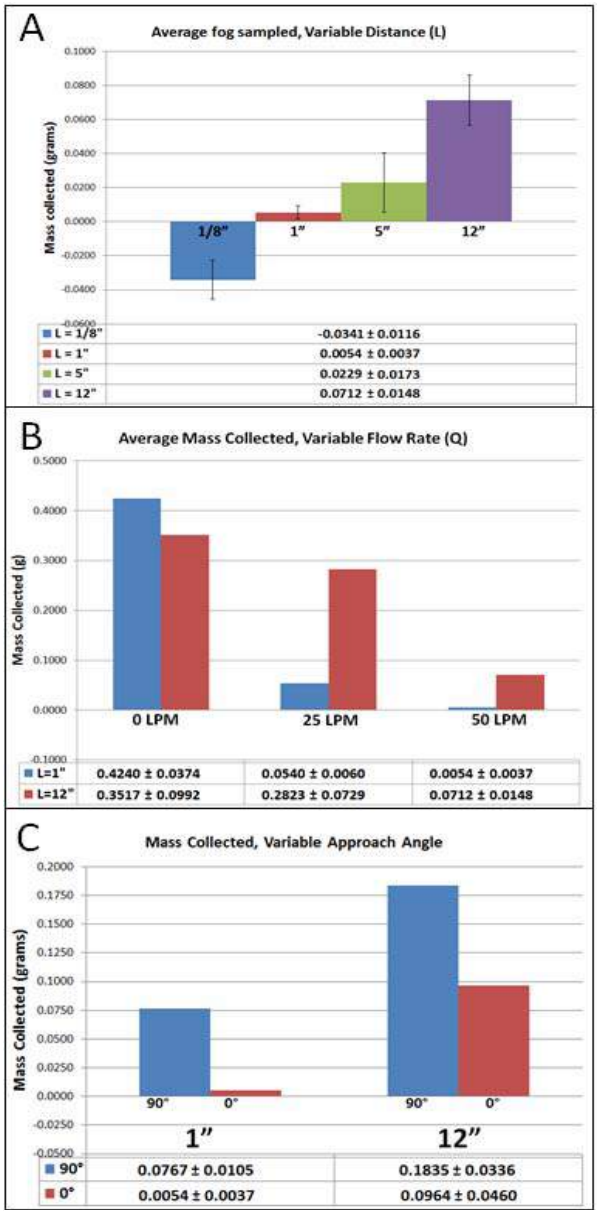

Figure 2. Results for experiments testing (A) distance between ports, (B) input flow rate (C) angle of approach.

ACKNOWLEDGEMENTS

Research supported by the Wallace Coulter Foundation.

REFERENCES

[1] CDC, *Department of Health and Human Services*, 2015.
[2] Huang, S et al., *Vaccine*, 2011. **19**(18): p. 3398-3412.
[3] Molinari, N, et al., *Vaccine*, 2007. **25**(27): p. 5086-5096.
[4] Meltzer, E et al., *Aller and Asth Pro*, 33(1): S113-S141, 2012
[5] Meltzer, E, Bukstein, D, *An of Al, Asth, & Im*, 106: S12-S16, 2011.
[6] WHO, *Global Tuberculosis Report 2014*. WHO, 2015.
[7] Qian, J et al, *Indoor Air*, 2012. (22): p. 339-351.
[8] D, H., et al., *PLOS ONE*, 2012. **7**(4): p. e34867.
[9] Cowling, B et al., *Ann of Internal Med*, 2009. **151**: p. 437-446.
[10] Cowling, B et al., *PLOS ONE*, 2008. **3**(5): p. e2101.
[11] Morton, D et al., *The Williams and Wilkins Co*, 1952.
[12] Fisher, L et al., *Ann of Rhuem Dis*, 1990. **49**: p. 921-925.

Copyright 2016 The Organizing Committee for the 2016 Summer Biomechanics, Bioengineering and Biotransport Conference

SB³C2016
Summer Biomechanics, Bioengineering and Biotransport Conference
June 29 –July 2, National Harbor, MD, USA
SB³C2016-1088

DELETION OF CADHERIN-11 INCREASES SMOOTH MUSCLE ACTIN EXPRESSION BUT PREVENTS CONTRACTION IN VALVE FIBROBLASTS

Meghan A. Bowler (1) and W. David Merryman (1)

(1) Biomedical Engineering
Vanderbilt University
Nashville, TN, USA

INTRODUCTION

Calcific aortic valve disease affects 25% of the Western population over 65. The only current treatment is total valve replacement, which necessitates open-chest surgery – a particularly traumatic procedure for the affected population. Alternative therapies remain scarce mainly because the mechanism of calcification is largely unknown. Two proposed hypotheses for the development of calcific nodules (CNs) are widely studied. Dystrophic calcification is initiated by TGF-β-mediated myofibroblastic differentiation of resident aortic valve interstitial cells (AVICs), which exhibit increased cell contractility and a subsequent imbalance of intercellular tension that are speculated to lead to apoptosis of AVICs. Osteogenic calcification proceeds when myofibroblasts spontaneously transdifferentiate into osteoblast-like cells and actively deposit mineralized material. In a study of human valves, 83% had evidence of dystrophic calcification and 13% of those contained mature lamellar bone and evidence of active remodeling [1]. While it is unclear whether these processes occur simultaneously or sequentially, we focus on elucidating the more prevalent pathway: dystrophic calcification.

We define CNs as round aggregates with a 100 μm minimum diameter that contain a ring of apoptotic cells around a necrotic core. In dystrophic calcification, transforming growth factor-β1 (TGF-β1) mediates the activation of AVICs into myofibroblasts, characterized by expression of vimentin, α-smooth muscle actin (αSMA), and cadherin-11 (CDH11). CDH11, a mechanosensitive transmembrane protein involved in cell-cell adhesion, is thought to be responsible for mediating much of the intercellular tension integral to the dystrophic pathway [2], whereas αSMA is involved in cell motility and contractile machinery [3]. When these proteins are upregulated in the diseased state, individual AVICs experience uneven and increased tension and contraction, resulting in membrane tearing and apoptosis-mediated calcification. This cell death provides increased imbalance in cellular forces and a local increase in substrate stiffness, acting as a nucleation event in the formation of a CN.

Both CDH11 and αSMA are overexpressed in diseased human valves, though previous *in vitro* work suggests they have an inverse relationship [4]. While cadherins are known to complex with catenins intracellularly, downstream signaling is poorly understood. A better understanding of the role of αSMA and especially CDH11 in calcific aortic valve disease could uncover potential therapeutic targets.

METHODS

Murine aortic and pulmonary valves were excised from immortalized WT, $CDH11^{+/-}$ and $CDH11^{-/-}$ mice and digested in 500 μL 600 U/mL collagenase for 30 minutes at room temperature. They were seeded on 0.1% gelatin and expanded in DMEM supplemented with 10% FBS and 1% PenStrep. Cardiac fibroblasts (CFs) were isolated from the ventricles.

WT AVICs were infected with pLL-CDH11-mCherry and processed via fluorescence-assisted cell sorting to create a pure population of AVICs overexpressing CDH11 tagged with mCherry.

Strain experiments were performed using the Flexcell FX-4000 Tension System. Cells were plated onto the flexible bottom of Flexcell plates coated with pronectin and then exposed to 30 minutes or 24 hours of 10% equibiaxial strain to recapitulate the mechanical environment of the valves. Samples were analyzed for CDH2, CDH11, αSMA, β-catenin, p120-catenin, RhoA, pp38, and pERK protein expression via western blot or mRNA levels via qPCR.

AVICs were seeded on collagen gels at 40,000/gel, treated with 1 ng/mL murine TGF-β1 every 24 hours, and imaged at least every 24 hours for 4 days to assay contractility.

Copyright 2016 The Organizing Committee for the 2016 Summer Biomechanics, Bioengineering and Biotransport Conference

WT+CDH11-mCherry AVICs, WT AVICs, CDH11$^{-/-}$ AVICs, and WT pulmonary valve interstitial cells (PVICs) were plated on coverslips and stained for CDH11 (Cell Signaling), αSMA (Sigma), and/or myosin light chain II (MLC II) (Cell Signaling).

RESULTS

Loss of CDH11 in AVICs results in a dramatic increase in αSMA both from *in vivo* sources and *in vitro* experiments (**1A**). This is conserved across cardiac cell type; WT CFs have less αSMA than CDH11$^{-/-}$ CFs (**1B**). We observe reduced contractility in response to TGF-β1 in AVICs that lacked CDH11 (**1C**). Probing related proteins reveals a compensatory increase in CDH2, a mesenchymal cadherin (**1D**). Increases in β-catenin and p120-catenin expression indicate dramatic changes in intracellular cadherin signaling (**1E**). qPCR shows a decrease in RhoA transcription (**1F**), and immunofluorescence shows a decrease in MLC II (**1G**).

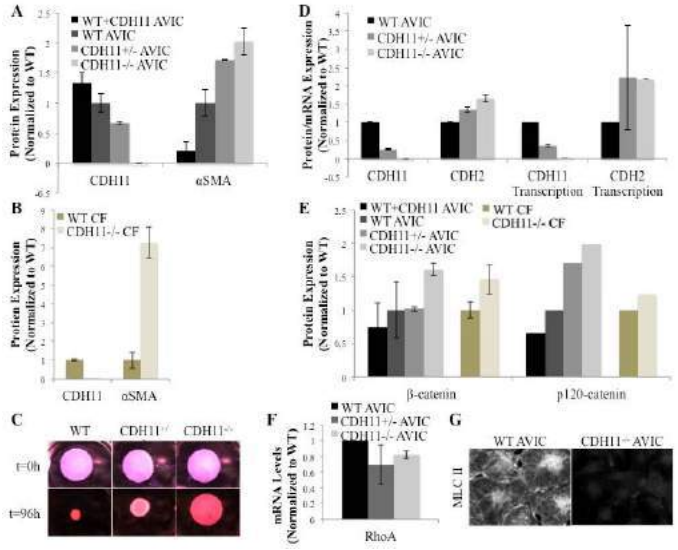

Figure 1: Loss of CDH11 increases αSMA expression (A) across cell types (B), but reduces TGF-β1-induced contraction (C). CDH11 loss increases CDH2 and catenin expression (D-E), but decreases RhoA (F) and MLC II (G).

Subjecting AVICs to physiological strain causes transcriptional decrease of CDH11, increase of CDH2, decrease or no change of αSMA, and increase of RhoA only in WT AVICs (**2A**). Analysis of phosphorylation events after strain in WT, CDH11$^{+/-}$ and CDH11$^{-/-}$ AVICs suggests a decreasing dependence on pERK and an increasing dependence on p38 (expression was normalized within cell type) (**2B**). Treatment of the WT+CDH11-mCherry (**2C**) and WT AVICs with 5 ng/ml TGF-β1 resulted in slight increases in p120-catenin and β-catenin expression and a significant increase in WT pp38 at 30 minutes (**2D**). At 24 hours, CDH11 and αSMA increased to the same level across multiple cell types (**2E**), suggesting TGF-β1 induces maximal expression of these proteins.

Preliminary investigation of WT PVICs demonstrated increased expression of CDH2, CDH11, αSMA, over animal-matched AVICs (**3A**). qPCR data suggests less transcription of RhoA in WT PVICs than AVICs (**3B**).

DISCUSSION

Loss of CDH11 may prevent TGF-β1-induced contraction by either preventing linkage between contractile AVICs or preventing MLC II and RhoA expression. Preventing the excessive contraction of AVICs would lessen the forces experienced by the cells and decrease the probability of apoptosis-mediated calcification.

Interestingly, the increased expression of CDH2 and αSMA in PVICs does not correspond with increased contractility (data not shown), but does exhibit decreased RhoA transcription, as in the CDH11$^{-/-}$ AVICs. Pulmonary valves are much less likely to develop calcification than aortic valves, supporting the hypothesis that CN formation in valve cells is RhoA-dependent.

Here, we have investigated the role of CDH11 in calcific aortic valve disease and provided insight into its mechanism of action. This has revealed surprising information about the role of αSMA in contractility (that its expression does not correlate with contraction) and identified effectors of contractility in AVICs, providing novel potential therapeutic targets.

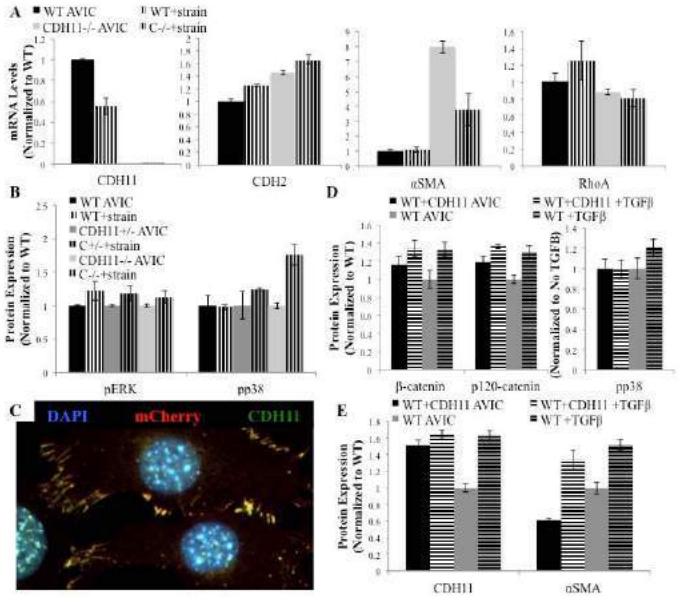

Figure 2: Effects of physiological strain on WT and CDH11$^{-/-}$ AVICs (A-B). CDH11 and associated proteins affected by TGF-β1 treatment (D-E) in overexpression model (C) and WT AVICs.

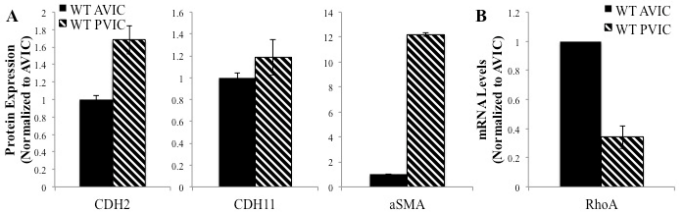

Figure 3: WT PVICs display higher expression of cadherins and αSMA (A) but decreased RhoA transcription (B).

ACKNOWLEDGEMENTS

This work was supported by the NIH (R01-HL115103) and the NSF: Graduate Research Fellowship (2013170175) and CAREER Award (1055384).

REFERENCES

[1] Mohler, ER et al., *Circulation*, 103:1522-8, 2001.
[2] Hutcheson, JD et al., *ATVB*, 33:114-20, 2013.
[3] Walker, GA et al., *Circ Res*, 95:253-60, 2004.
[4] Wang, H et al., *FasebJ*, 28:4551-62, 2014.

Copyright 2016 The Organizing Committee for the 2016 Summer Biomechanics, Bioengineering and Biotransport Conference

SB³C2016
Summer Biomechanics, Bioengineering and Biotransport Conference
June 29 –July 2, National Harbor, MD, USA
SB³C2016-1089

NANOWARMING OF ARTERIES

Navid Manuchehrabadi (1,2), Zhe Gao (1,3), Jinjin Zhang (4), Hattie L. Ring (3,4), Qi Shao (1), Feng Liu (1), Yung Chung Chen (6), Michael McDermott (3), Alex Fok (6), Kelvin G.M. Brockbank (8,9), Michael Garwood (4,5), Christy L. Haynes (3), John Bischof (1,2)

(1) Department of Mechanical Engineering, University of Minnesota
(2) Department of Biomedical Engineering, University of Minnesota
(3) Department of Chemistry, University of Minnesota
(4) Center for Magnetic Resonance Research, University of Minnesota
(5) Department of Radiology, University of Minnesota
(6) Minnesota Dental Research Center for Biomaterials and Biomechanics
(7) Department of Surgery, University of Minnesota
(8) Department of Bioengineering, Clemson University
(9) Tissue Testing Technologies LLC

INTRODUCTION

Transplantation addresses a tremendous societal need for donor tissues for patients with diseased tissues requiring replacement due to failure or disease. In short, there are far too few fresh donor tissues and organs available, and the short-term preservation methods currently available allow only hours between procurement and transplantation. Thus, long-term banking of these systems continues to be a critical and unmet enabling technology for the transplantation medicine community [1,2]. Thus, a method for long term cryopreservation or "banking" of organs and tissues such as arteries, veins, skin, heart valves and cartilage would revolutionize the way organs are recovered, allocated, and used in transplantation.

One of the most attractive approaches to achieving long-term banking of biomaterials is by a technique known as cryopreservation by vitrification, which allows cooling and storage of tissues at temperatures close to liquid nitrogen (-160 °C) for indefinite time periods. Typical freezing processes cause significant damage to biomaterials through ice crystal formation and cellular dehydration. However, with the aid of cryoprotective solutions (CPAs), biospecimens can be stabilized in the vitreous (i.e. "glassy" or "amorphous") state, allowing for long-term cryopreservation. While this is not trivial, a number of groups have employed successful techniques for cooling bulk systems to the vitreous state (including entire rabbit kidneys). Unfortunately, rewarming these vitrified biomaterials is an even greater engineering challenge, as the warming rates to avoid crystallization during the thawing phase of the thermal protocol are typically an order of magnitude higher (hundreds of °C/min) than the required cooling rates (tens of °C/min), even with the aid of CPAs. In addition, temperature non-uniformity may produce thermal stresses that can cause fracture cracks within the biomaterial. Hence, speed and uniformity of warming are essential, and have not yet been achieved in bulk.

Here we present new physical, chemical, computational and biological data using "nanowarming" to address this limitation. We have already demonstrated that this approach can match or exceed the current best approach for rewarming by convection in small 1 ml samples[3]. We are also able to physically generate heating rates sufficiently rapid to avoid devitrification (≥ 200°C/min) in larger 60ml samples where convection rewarming fails.

METHODS

Specifically, we deploy 10 mg Fe/ml biocompatible mesoporous silica-coated iron oxide magnetic nanoparticles (msIONPs) in a cryoprotective agent (VS55) which, when exposed to an appropriate RF field, improves the uniformity and speed of rewarming from the vitrified state. The msIONPs are comprised of a 10 nm Fe_3O_4 core and 50 nm mesoporous silica shell (by TEM) co-modified with PEG and trimethylsilane with -38 zeta potential[4]. As a proof of principle human dermal fibroblasts (HDF) and porcine carotid arteries (inner diameter of ~ 3 mm; wall thickness of ~1 mm and length: ~3-5 mm) were chosen as the systems of study. Protocols were optimized to step load the nanoparticle impregnated VS55 into the HDF and artery systems with negligible toxicity. The systems were then vitrified at roughly 10 °C/min by methods previously described[5].

RESULTS

Copyright 2016 The Organizing Committee for the 2016 Summer Biomechanics, Bioengineering and Biotransport Conference

Micro computed tomography (μCT) was used as a quality control tool to demonstrate both the loading and vitrification of the VS55 into the arteries. Rewarming was carried out in a low frequency (20KA/m, 360 KHz) RF field achieving warming rates > 55 °C/min (a critical rate to avoid devitrification of VS55) or by less optimal rates (< 10 °C/min).

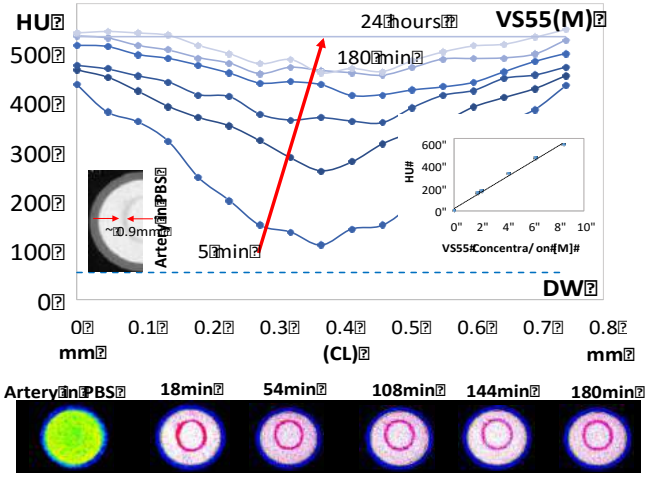

Figure 1: Vs55 loading of an artery (0.9 mm thick) visualized and quantified by micro Computed tomography (μCT).

Thermal measurements and modeling verified the rates of freezing and heating in the systems tested. Further mechanical modeling verified that the thermal stress remained below a 2 MPa yield stress of the tissue during nanowarming and no cracks were identified in histology[6]. The presence and washout of msIONPs in cells and luminal structure of arteries was verified by TEM and sweep imaging with Fourier transform (SWIFT) MRI, respectively by an established technique[7]. The viability of HDFs and arteries 1 day after nanowarming were assessed by Hoechst-PI assays and alamarBlue®[8] and shown to remain ≥ 85% of controls vs. ≤ 30% of control when less optimal warming was used[8].

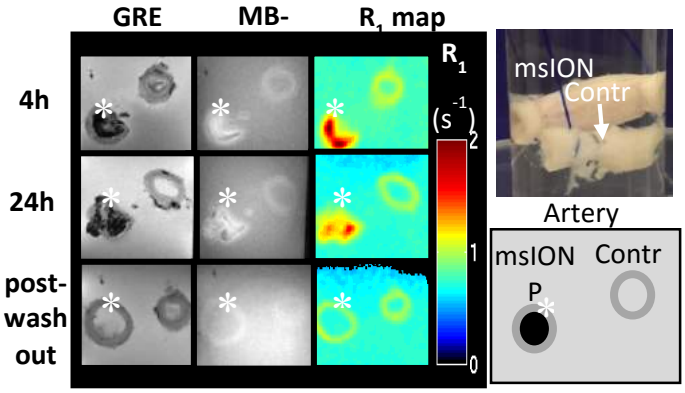

Figure 2: An artery loaded with 1.0 mg Fe/mL of msIONPs was compared to a control artery in V55. GRE and SWIFT MR images were acquired and the R_1 map was generated from the SWIFT data. The colorbar indicates the R_1 in 1/s. Images were taken at 4 and 24h after msIONP loading and post-wash out. These images demonstrate how easily msIONPs are washed out after 24h of incubation.

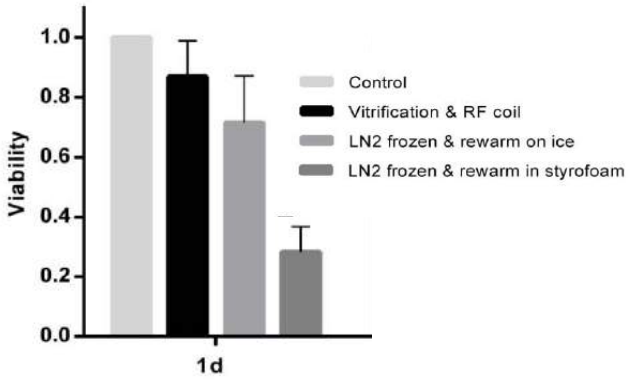

Figure 3: Artery viability post RF rewarming using alamarBlue® assay.

DISCUSSION

This study provides the first evidence that nanowarming can provide both the uniformity and speed necessary to successfully return cells and tissues from the vitrified state. Importantly, nanowarming is the first warming technology to match convective warming for small artery systems[8] and unlike convection should successfully scale with larger size systems. Thus, using this approach, we anticipate successful nanowarming of other vitrified tissues (i.e. heart valves, cartilage, skin)[9]. Future studies will use nanowarming to thaw vitrified organs and other large biomaterial systems that cannot at present be successfully thawed due to slow and non-uniform rates within the sample.

ACKNOWLEDGEMENTS

Funding from NSF CBET 1336659, NIH R43HL123317, NIH P41EB015894, the MN Futures grant (UM), and the Kuhrmeyer Chair to JCB are gratefully acknowledged. We also thank the Visible Heart Lab (Iaizzo) Charles Soule (7) and Tinen Healy (7) for access to porcine arteries and Connie Chung for help with initial cell culture experiments.

REFERENCES

1. UNOS. United Network for Organ Sharing Web page., www.unos.org, 2007.
2. McBride, MA et al., *Clin Trans,* 53-64, 2003.
3. Fahy, G, *Cryo*, 21(4):407-26, 1984.
4. Hurley KR et al., *Chem of Mat*, *25* (9), 1968–1978, 2013.
5. Etheridge, LE et al., Tech (b), 2(3), 229 – 242, 2014b.
6. Rios, J et al., Cryo, 52, 269–283, 2006.
7. Zhang, J et al., *Mag Res Med*, 71, 1982–1988, 2014.
8. Baicu, S et al., *Cell Pres Tech*, 4(4), 236-244, 2006.
9. Brockbank, KGM *MOJ Cell Science and Report*, 1(2), 2014.

Copyright 2016 The Organizing Committee for the 2016 Summer Biomechanics, Bioengineering and Biotransport Conference

SB³C2016
Summer Biomechanics, Bioengineering and Biotransport Conference
June 29 –July 2, National Harbor, MD, USA
SB³C2016-1090

DIFFERENCES IN THE ABILITY OF BICYCLE HELMETS TO REDUCE RISK OF HEAD INJURY

Megan L. Bland and Steven Rowson

Biomedical Engineering and Mechanics
Virginia Tech
Blacksburg, VA, USA

INTRODUCTION

According to the U.S. Consumer Product Safety Commission (CPSC), cycling was the number one activity responsible for sports-related head injuries treated in U.S. emergency rooms in 2009, accounting for over 85,000 of the 446,800 total that year [1]. The actual number of injuries is likely much higher, as many go unreported. Bicycle helmets, which can help prevent injury, must pass a CPSC Safety Standard to be sold in the U.S. This standard mandates that in all specified impact tests, a helmet must prevent linear accelerations exceeding 300 g (a value associated with risk of skull fracture [2]).

While the CPSC standard requires helmet design to minimize severe head injury risk, no data are available to consumers on relative impact performance between helmets. The standard also does not test lower accelerations, such as those associated with concussion (around 100 g [3]). Helmet damage replication studies have shown that the most common impacts are around 100 g [4], and also that the majority of impacts are to the front and side of the helmet and often at the rim, which is below the impact test line specified by the standard [4-5].

The objective of this study was to investigate differences in the ability of bicycle helmets to attenuate impact accelerations associated with both mild brain injuries (by testing common impact conditions) and severe head injuries (by testing according to the standard).

METHODS

A twin-wire drop rig with a flat anvil was used to replicate CPSC standard impact tests. Ten helmet models were selected based on their varied design parameters (Table 1), and a total of 160 tests were conducted using four samples of each model and four impact conditions per sample. These conditions included two velocities: 3.4 and 6.2 m/s, and two locations: frontal-temporal (referred to as frontal in the remainder of the text) at the rim and temporal above the CPSC test line (Fig. 1). The lower velocity and rim location are not in accordance with the CPSC standard but were chosen to reflect common impact conditions found in literature [4]. Locations were a minimum of 120 mm apart (in accordance with the standard) and were mirrored on the helmet using a laser positioning system. Order of testing conditions was randomized between samples to avoid bias.

Table 1. Helmet models. Soft shells are made of a thin layer of polycarbonate, while hard shells are made of ABS or thicker polycarbonate. *MIPS: multidirectional impact protection system.

Helmet	Abbreviation	Shell Style	Weight [g]
Bell Solar Flare	BSF	Soft	312
Bell Star Pro	BSP	Soft	296
Bell Super 2 MIPS*	BMIPS	Hard	360
Catlike Whisper	CW	Soft	283
Giro Sutton MIPS*	GMIPS	Hard	370
Giro Synthe	GS	Soft	250
Nutcase Watermelon	N	Hard	465
Smith Optics Overtake	SOO	Soft	250
Schwinn Thrasher	ST	Soft	340
S-Works Evade	SWE	Soft	317

For each impact, linear acceleration data were collected and filtered according to SAE J211 with a CFC-1000 low pass filter. Average peak acceleration was determined per impact configuration by helmet. Risk of skull fracture and concussion for each test was calculated using previously published risk curves [2-3]. Results were compared using ANOVA and Tukey HSD post hoc tests.

Copyright 2016 The Organizing Committee for the 2016 Summer Biomechanics, Bioengineering and Biotransport Conference

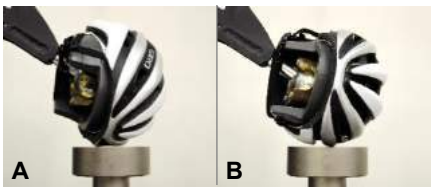

Figure 1. (A) Frontal (below CPSC test line) and (B) temporal (above CPSC test line) impact locations. Locations were mirrored on the helmet and were a minimum of 120 mm apart. Drop tests were performed at both locations at 3.4 and 6.2 m/s.

RESULTS

Figure 2 shows average peak linear accelerations at each impact configuration by helmet. For every helmet at 3.4 m/s and for seven helmets at 6.2 m/s, the temporal location yielded higher accelerations than the frontal location. Visual observation post-testing showed that the frontal area of each helmet appeared to experience more liner crushing than the temporal area. Overall, this sample of ten models produced average accelerations of 105.0 ± 22.4 g at 3.4 m/s and 226.8 ± 45.5 g at 6.2 m/s. Each impact configuration revealed significant differences between helmet models, most notably at the temporal location. The trends in relative impact performance between helmets appeared to be consistent between the two velocities at the temporal location, but produced more variance at the frontal location.

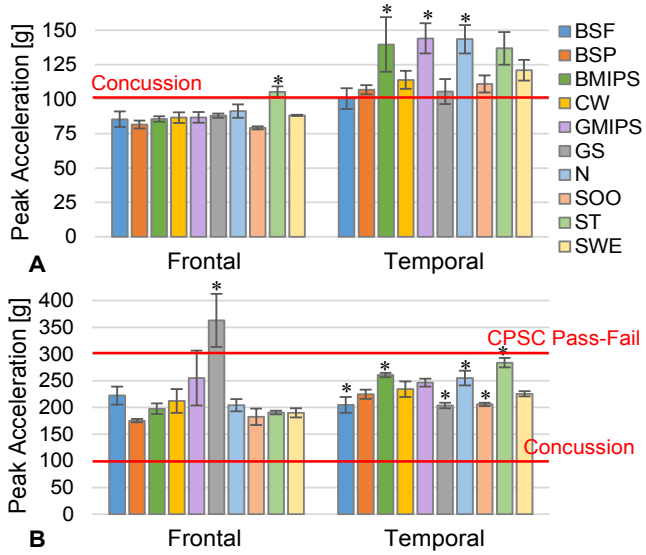

Figure 2. Peak acceleration per helmet type and location for 3.4 m/s (A) and 6.2 m/s (B). Error bars are standard deviations, and stars signify helmets that were significantly different than at least five other helmets ($p<0.05$). The red lines represent the CPSC threshold (300 g) and an average concussive acceleration (100 g).

Because accelerations were well below the CPSC threshold at 3.4 m/s (Fig. 2A) and well above the concussive level at 6.2 m/s (Fig. 2B), skull fracture risk only varied at 6.2 m/s and concussion risk at 3.4 m/s. These risks are shown in Figure 3. At 3.4 m/s (Fig. 3A), concussion risk at the frontal location was minimal and consistent, ranging from 2.7 to 17.7%. Risks varied more at the temporal location, with four models having over 60% risk and four models having less than 30% risk. At 6.2 m/s (Fig. 3B), skull fracture risks reflected concussion risk trends at the temporal location, although the differences were less extreme. Skull fracture risk at the frontal location was not as uniform as concussion risk at this location; seven models had low risks (<17%), but the other three were relatively high, with GS resulting in a risk of 95.0 ± 6.0%.

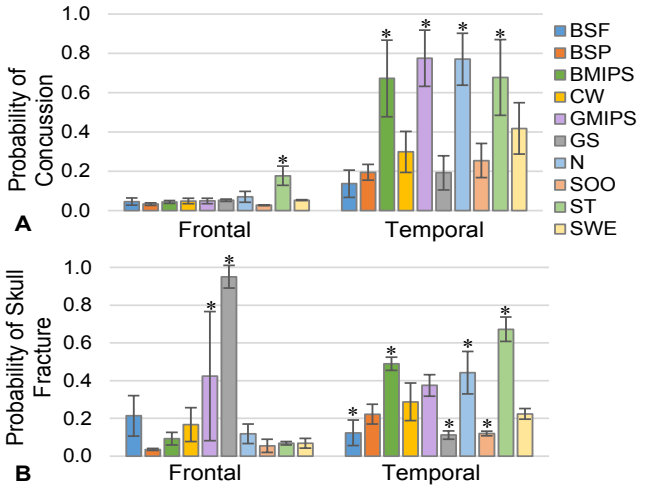

Figure 3. Concussion risk at 3.4 m/s (A) and skull fracture risk at 6.2 m/s (B) per helmet type and location. Error bars are standard deviations, and stars signify helmets that were significantly different than at least five other helmets ($p<0.05$).

DISCUSSION

The present study shows that significant and clinically relevant differences exist in the ability of helmets to attenuate impacts. These differences were more apparent and consistent at the temporal location. Frontal impact accelerations were generally lower than that of temporal impacts. This may suggest that the temporal part of the helmet experiences a larger contact area upon impact, increasing effective liner stiffness and reducing likelihood of crushing (the mechanism of energy absorption). This corroborates what was visually observed.

The high skull fracture risks for GS and GMIPS at the frontal location (Fig. 3B) may point to local weak points in helmet design, which would have been exacerbated at this higher impact energy. Because this location is below the CPSC impact test line, it would not have been considered in the homologation process. However, this is a very common location in accident reconstructions [4-5], so testing of helmets at this location would provide valuable safety information.

At the temporal location, BMIPS, GMIPS, N, and ST generally yielded higher risk values. Interestingly, these were the four heaviest helmets, and each had a hard shell except for ST (Table 1). This suggests that hard shell helmets may offer inferior impact protection compared to traditional bicycle helmets, but more testing is needed to confirm this.

Helmets that pass the CPSC standard are effective in reducing risk of severe head injury, but considerable variation in their ability to attenuate impact accelerations exists. Adding lower severity tests could improve ability to prevent milder injuries such as concussion, and expanding the impact area could ensure that helmets are effective at minimizing injury risk at all locations. Furthermore, disseminating objective impact data to the public would enable consumers to make informed decisions when purchasing helmets.

ACKNOWLEDGEMENTS

The authors would like to acknowledge the Insurance Institute for Highway Safety for their funding and support.

REFERENCES

[1] AANS, “Sports-related Head Injury,” 2014.
[2] Mertz, H.J. et al, *Stapp Car Crash Journal*, 47:155-188, 2003.
[3] Rowson, S et al., *Ann of Biomed Eng*, 41:873-882, 2013.
[4] Williams, M, *Accid Anal and Prev*, 23:119-131, 1991.
[5] Bourdet, N, *Proc IMechE P: J Sports Eng & Tech*, 226:282-289, 2012.

Copyright 2016 The Organizing Committee for the 2016 Summer Biomechanics, Bioengineering and Biotransport Conference

SB^{3}C2016
Summer Biomechanics, Bioengineering and Biotransport Conference
June 29 –July 2, National Harbor, MD, USA
SB^{3}C2016-1091

IMPLEMENTATION OF THE ASSISTED BIDIRECTIONAL GLENN IN AN IDEALIZED SINGLE VENTRICLE MODEL

Jessica K. Shang (1), Mahdi Esmaily-Moghadam (2), Tigran Khalapyan (3), Richard Figliola (4), Olaf Reinhartz (3), Tain-Yen Hsia (5), Alison L. Marsden (1)

(1) Dept of Pediatrics
Stanford University
Stanford, CA, USA

(2) Center for Turbulence Research
Stanford University
Stanford, CA, USA

(3) Dept of Cardiothoracic Surgery
Stanford University
Stanford, CA, USA

(4) Dept of Mechanical Engineering
Clemson University
Clemson, SC, USA

(5) Dept of Cardiothoracic Surgery
Greater Ormond Street Hospital
London, UK

INTRODUCTION

For neonates born with single ventricle physiology, a series of three surgical procedures are typically undertaken to bypass the deficiencies caused by the missing ventricle. An initial palliation is performed soon after birth to provide oxygenated blood flow. Neonates with single ventricle heart defects are often treated with a modified Blalock-Taussig (mBT) shunt that connects a carotid or subclavian artery with the pulmonary artery to provide flow to the lungs. The mBT is not sustainable in the long term; the ventricle still operates at a high load and the shunt is prone to failure due to thrombosis, leading to high mortality rates [1, 2]. Ideally, a more stable cavopulmonary connection such as the bidirectional Glenn procedure (BDG) could be executed without the initial mBT. The bidirectional Glenn routes half of the deoxygenated blood through the superior vena cava (SVC) directly to the pulmonary arteries to be oxygenated by the lungs, reducing ventricular load. However, clinical studies have historically shown that the BDG had unacceptably high mortality rates in infants less than a month old, and so cannot be used in neonates [3].

A major cause of death for single ventricle patients is inadequate pulmonary circulation. Recently, a novel procedure called the assisted bidirectional Glenn (ABG) was proposed which addresses the inadequate pulmonary flow of the BDG and may permit implementation in neonates [4]. Based on the principle of an ejector pump, a constricted shunt between the innominate artery and the superior vena cava (SVC) acts as a nozzle to inject higher-energy flow into the SVC and elevate pulmonary pressure (Fig. 1). Multiscale modeling has shown that the ABG has benefits such as higher systemic oxygen saturation and delivery, higher pulmonary blood flow, and lower ventricular workload than the mBT for both neonatal and infant physiologies. SVC pressures also increased, which may lead to SVC syndrome, a potential cause of death with BDG.

In the current study, we apply the ABG to a single ventricle physiology in the originally proposed iteration (ABG-SVC), and consider an alternate configuration where the shunt is between the innominate artery and the innominate junction (ABG-IJ). The second iteration could offer potential benefits over the first by increasing the alignment of the injected jet with the direction of the bulk SVC flow and minimizing momentum loss.

METHODS

Multiscale simulations are used to compare the clinical performance of the ABG in two configurations against that of the BDG and the mBT shunt. A 3D anatomical model of the relevant physiology of a single-ventricle, pre-BDG patient was coupled to a 0D lumped parameter network (LPN) describing the closed loop circulation using an implicit coupling algorithm [5]. The 3D model represents an idealized patient at the pre-BDG, post-mBT stage. The LPN was derived from a prior study that aggregated clinical catheterization and angiographic data from 28 Norwood patients [6]. The pulmonary vascular resistance was set to 2.3 Wood units-area. In the mBT shunt model, the shunt is 3.5mm in diameter. In the ABG model, the shunt is 2.5mm in diameter with a 25% area reduction near its distal end. The heart rate was 120 BPM.

The local hemodynamics are solved with an in-house finite element solver, assuming rigid walls and a Newtonian fluid with density of 1.06 g/cm^3 and dynamic viscosity of 0.04 dyn s/cm^2. The model was constructed with an open-source cardiovascular modeling software (SimVascular, simvascular.org). The mesh consisted of 1.2 to 1.5 million tetrahedral elements generated by commercial meshing software (MeshSim, Simmetrix) with a maximum edge length of

Copyright 2016 The Organizing Committee for the 2016 Summer Biomechanics, Bioengineering and Biotransport Conference

0.6mm. The time step of the solver was set to 0.5 ms and at least 6 cycles were simulated to allow convergence to a steady state.

RESULTS

Clinical performance targets such as oxygen delivery and oxygen saturation are calculated using the oxygen transport model and parameters derived for the Norwood patients in [6]. A comparison of outcomes of each surgical procedure is shown in Table 1. The BDG and ABG procedures offer superior oxygen delivery and saturation compared to the mBT shunt and significantly decreased ventricular load. Both ABG configurations increase oxygen delivery and saturation and pulmonary pressure as desired, but also increase the ventricular load and venous pressure as measured in the innominate junction.

The two ABG configurations are comparable to each other, and the ABG-IJ does not offer any significant benefits over the originally proposed ABG-SVC configuration. For the ABG design and placement used in this study, the ABG-IJ performs slightly worse. The instantaneous flow fields (Figure 1) illustrate potential disadvantages to the ABG-IJ approach. While the jet leaving the ABG shunt is more aligned with the bulk flow, the greater distance between the jet and the pulmonary artery junction potentially reduces the pressure gradient through the SVC. Further, the jet must also mix with the converging flows in the innominate junction, reducing its momentum.

DISCUSSION

In this study we have presented a preliminary comparison of two possible configurations of the assisted bidirectional Glenn procedure. In practice, due its higher placement in the jugular region and its shorter shunt length, the ABG-IJ may be more difficult to execute. Consequently, the ABG-SVC configuration may be more relevant for future investigation since the performance of both configurations is comparable. Current work is underway to simulate the ABG in patient-specific models to verify that the benefits found in the idealized model will be observed with realistic circulatory parameters. Future work is also necessary to optimize the placement, shape, and size of the ABG shunt to maximize oxygen delivery, pulmonary flow rates, and saturation while maintaining low venous pressures and heart load.

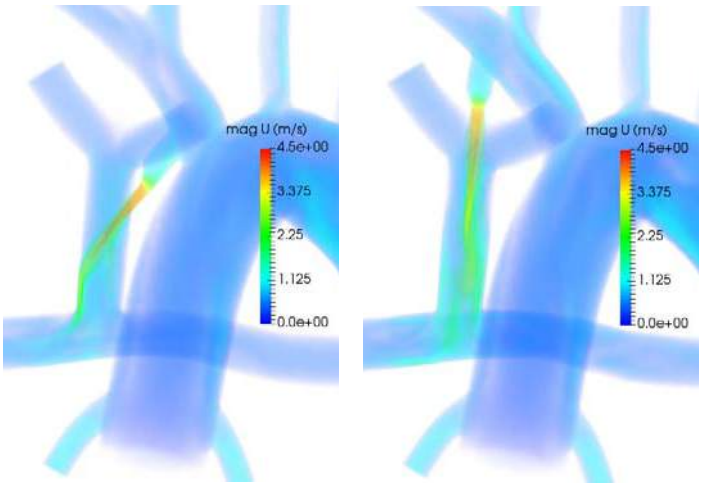

Figure 1: Instantaneous snapshot of velocity magnitudes in the ABG-SVC (left) and ABG-IJ (right) configurations in the vicinity of the SVC.

	mBT	BDG	ABG-SVC	ABG-IJ
OD (mL O_2/s)	2.87	3.08	3.54	3.36
OD_{cor} (mL O_2/s)	0.221	0.227	0.266	0.257
OD_{ub} (mL O_2/s)	1.25	1.32	1.49	1.39
HL (Nm/min)	29.9	11.5	15.4	14.5
CO (L/min)	2.05	1.14	1.37	1.32
Q_p/Q_s	1.03	0.40	0.58	0.57
P_{ao} (mmHg)	50.9	54.9	57.6	56.1
P_{ven} (mmHg)	3.70	6.56	8.70	9.2
P_{pulm} (mmHg)	9.85	4.48	6.40	6.06
Q_{pulm} (L/min)	1.04	0.454	0.678	0.638
Sat ao (%)	75.6	72.3	80.8	79.7
Sat svc(%)	49.2	48.4	57.1	54.7
Sat ivc (%)	55.2	54.3	63.5	62.0

Table 1: Results of the different surgical procedures. mBT, BDG, and ABG denote modified Blalock-Taussig shunt, bidirectional Glenn, and assisted bidirectional Glenn, respectively; -SVC and –IJ specify the endpoint of the ABG nozzle shunt. OD, OD_{cor}, OD_{ub}: systemic, coronary, upper body oxygen delivery; HL: ventricle load, CO: cardiac output; Q_p/Q_s: pulmonary to systemic flow rates; P_{ao}: average aortic pressure, P_{ven}: average pressure in innominate junction, P_{pulm}: pulmonary arterial pressure; Sat ao, Sat svc, Sat ivc: aortic, SVC, IVC oxygen saturations.

ACKNOWLEDGEMENTS

This work has been developed with the assistance and expertise of Jeff Feinstein and Weiguang Yang (Stanford University), and has been made possible by funding support from the Burroughs Wellcome Fund, the National Science Foundation, the Leducq Foundation, and the Stanford Cardiovascular Institute.

REFERENCES

[1] Tamisier, D et al., *Ann Thorac Surg*, 49:797-801, 1990.
[2] Bartram, U et al., *Ann Thorac Surg*, 64: 1795-1802, 1997.
[3] Glenn, W et al., The Heart and Circulation in the Newborn and Infant, Circulatory bypass of the right side of the heart: cavopulmonary artery shunt indications and results (report of a collected series of 537 cases), 1966.
[4] Esmaily-Moghadam, M et al., *J Thorac Cardiovascular Surg*, doi: 10.1016/j.jtcvs.2014.10.035, 2014.
[5] Esmaily-Moghadam, M et al., *J Comp Phys*, 224:63-79, 2013.
[6] Migliavacca, F et al., *Am J Phys-Heart and Circulatory Phys,* 280: H2076-H2086, 2001.

Copyright 2016 The Organizing Committee for the 2016 Summer Biomechanics, Bioengineering and Biotransport Conference

SB^{3}C2016
Summer Biomechanics, Bioengineering and Biotransport Conference
June 29 –July 2, National Harbor, MD, USA
SB³C2016-1092

AN INVESTIGATION OF HUMAN LONG BONE FRACTURE PATTERNS DURING TRAUMATIC AMPUTATIONS FROM MOVING RAILROAD EQUIPEMNT

Brian T. Weaver (1,2), Mark Davison (1), Steve Rundell (1), Eric Meyer (3)

(1) Explico Engineering Co.
Novi, MI, USA

(2) Orthopaedic Biomechanics Laboratory
Michigan State University
East Lansing, MI, USA

(3) Biomedical Engineering
Lawrence Technological University
Southfield, MI, USA

INTRODUCTION

The Federal Railroad Administration (FRA) reported that 1,844 trespassing pedestrians (non-railroad employees) were struck and injured by moving railroad equipment between the years of 2012 and 2014 [1]. A common injury associated with these types of accidents is Traumatic amputation [2]. Specifically, these injuries occur as a result of interaction between a pedestrian's limb, the rail equipment, and the rail [3]. The circumstances surrounding the injury are often in question. Determining the exact manner and circumstances of the injuries can be challenging when no eyewitness or video evidence is available. In these circumstances, the injury pattern may provide key information in determining what the pedestrian was doing moments before the incident. This information is essential in the implementation of best practices regarding pedestrian safety around moving rail equipment.

Emergency Room nurses and/or physicians assess the injuries and document the findings in the medical records. These often include x-rays of the amputated limb. Currently, there is no research available that document the mechanism of injury associated with contact from a railroad wheel. In the absence of carefully controlled experiments that associate specific fracture patterns with limb position, these x-rays provide very little useful information beyond the location of the amputation. The fracture pattern of the amputated limb might provide details regarding the orientation of the limb at the moment of the incident. This information could assist the investigator in determining the sequence of events that led to the injury.

The current study investigated the mechanism associated with traumatic amputations to human femurs caused by contact with a moving railroad wheel. The objective of the current study was to carefully characterize long bone fracture patterns during a variety of relative positions to moving rail equipment. The current study hypothesized that distinct positioning of a pedestrian's limb would result in distinct and specific bony fracture patterns.

METHODS

Testing was performed at the Henry Ford DT&M Roundhouse in Dearborn, MI. A section of track was blue flagged for safety. Twelve 4th-generation composite femur bones (Sawbones®, Vashon island, WA, USA) were utilized to simulate human femur bones. The proximal and distal ends of each femur were potted into 4-inch and 3-inch schedule 40 PVC couplings, respectively, using room temperature curing epoxy resin (Fiber Strand™, Martin Senior Corp., Cleveland, OH, USA). Approximately 12 inches of composite bone was exposed between each pot. The exposed portion of each bone was covered with ordnance/ballistic gelatin (Gelatin Innovations, Shiller Park, IL, USA) to simulate soft tissue.

Each leg was secured on top of, and perpendicular to, the rail by fastening each pot to wooden blocks located on either side of the rail (Figure 1). These blocks were rigidly fixed to a railroad tie so the proximal end of the femur was 9 inches from the gauge side (i.e. inside) of the track (Figure 2). Each pot was fastened to the wooden blocks via hinges to allow the specimen to swing away from the locomotive after bone fracture occurred. Each bone was run over by the leading wheel of a locomotive (GE B-B-100/100-2GE733) traveling approximately 5 mph. The orientation of the legs was precisely controlled. Testing included two orientations (supine/prone) and two locomotive directions (medial/lateral). Fracture patterns were recorded and analyzed following each test.

Copyright 2016 The Organizing Committee for the 2016 Summer Biomechanics, Bioengineering and Biotransport Conference

Figure 1: Illustration of test setup

RESULTS

All 12 specimens fractured as a result of contact from the railroad wheel. The fracture of all 12 specimens was located on the gauge side the rail as a result of contact from the flange on the railroad wheel (Figure 2). None of the specimens were crushed. The most common fracture pattern was a butterfly wedge (n=6) (Figure 3). Interestingly, the other cases (comminuted; n=3, oblique; n=2, transverse; n=1) produced similar "Y" shaped crack propagation patterns, but the wedge fracture was incomplete (Figure 3). The fracture pattern was dependent on the orientation of the femur and direction of locomotive movement. Specifically, the "Y" shaped fracture pattern opened up towards the flange in all 12 specimens (Figure 3).

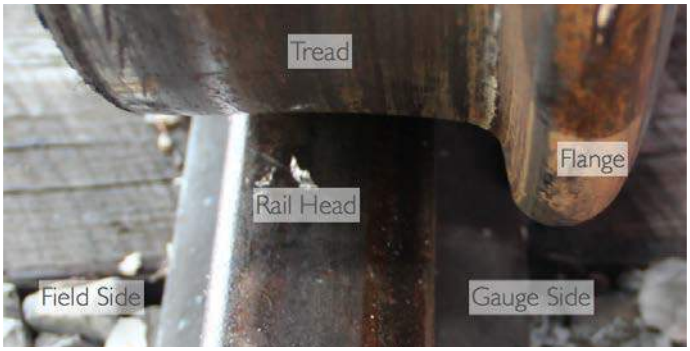

Figure 2: Illustration of a typical railroad wheel and rail

DISCUSSION

The results of the current study support the hypothesis that human bones contacted by moving railroad equipment develop a distinct fracture pattern that is dependent on the direction and impact location of the wheel on the limb/bone. Additionally, results demonstrated that the fracture patterns were all indicative of bending failure.

The results presented here are similar to previous experimental studies involving bending of human cadaveric long bones, which also generated similar patterns of fracture, including the typical butterfly, oblique and transverse fractures [4]. During bending, the fracture initiates on the tensile side and propagates to the neutral axis before bifurcating on the compression side to form the characteristic "Y" shape [5]. In the current study, the flange contacted the bone and attempted to push the bone out of the way resulting in 3 point bending.

This study shared the limitations inherent in utilizing composite bones. However, the use of cadaveric specimens was not possible given the nature and location of testing. Regardless, the 4th generation composite femur bones have been validated for use as a surrogate to healthy human bones for biomechanical testing [6]. The flexural rigidity has been shown to be less than 8% of the biological range of healthy adult bones and the failure modes closely match published findings of human bones [6]. It is also noteworthy that intra-specimen variations are under 10%, which permit greater experimental control, greater repeatability, and more meaningful comparisons between different scenarios.

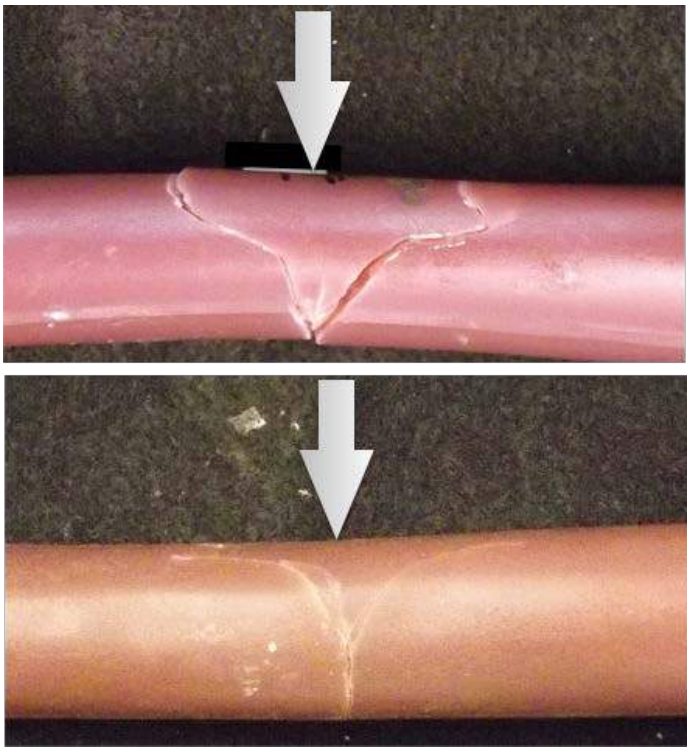

Figure 3: Illustration of the typical fracture patterns observed. Top: Butterfly wedge pattern; Bottom: Oblique / incomplete wedge pattern. Arrow indicates direction of impact

This study contradicts the conventional wisdom in forensic biomechanics that bones are crushed when run over by rail equipment. These results indicate that a bending fracture mechanism occurs. Therefore, it may be possible to determine the orientation of a body that was stuck and run over by moving railroad equipment. This is an important finding that will assist investigators when analyzing the circumstances surrounding a trespasser or railroad worker that sustained a traumatic amputation as a result of being run over by moving rail equipment.

ACKNOWLEDGEMENTS

The authors would like to thank Mr. Matthew Goodman from the Henry Ford DT&M Roundhouse for serving as our railroad engineer and allowing access to the facility and equipment.

REFERENCES

[1] Safetydata.fra.dot.gov
[2] Shapiro, M., et al., *Am J Emerg Med*, 12(1):92-3, 1994
[3] Thompson, G., et al., *J Ped Orth*, 3:443-8, 1983
[4] Porta, D., *Forensic Science and Medicine*, 279-310, 2005
[5] Sharir, A., et al., *Vet J*, 177:8-17, 2008
[6] Gardner, M. et la., *Ann Biomed Eng*, 38(3):613-20, 2010

Copyright 2016 The Organizing Committee for the 2016 Summer Biomechanics, Bioengineering and Biotransport Conference

SB^{3}C2016
Summer Biomechanics, Bioengineering and Biotransport Conference
June 29 –July 2, National Harbor, MD, USA
SB^{3}C2016-1093

STRESS-RELAXATION BEHAVIORS OF DISEASED HEART VALVE TISSUES

Kaitlyn B. Barbour (1), Siyao Huang (2), HY Shadow Huang (3)

(1) Biomedical Engineering
North Carolina State University
Raleigh, NC, USA

(2) Mechanical and Aerospace Engineering
North Carolina State University
Raleigh, NC, USA

(3) Mechanical and Aerospace Engineering
North Carolina State University
Raleigh, NC, USA

INTRODUCTION

Heart valve tissue with collagenous ECM is regarded as a load-adapting biomaterial. Mechanical forces have significant influence for stimulating biomechanical regulation of heart valve cells that modulate tissue remodeling through collagen fibers, such as homeostasis, synthesis, or degradation of collagen. Generally, coordinated collagen synthesis and degradation are processes of matrix remodeling under physiological conditions. However, severe collagen depletion caused by matrix metalloproteinases (MMPs) pathologically induces matrix destruction, changes viscoelastic properties of the heart valve, further affects cellular regulations mediated by heart valve cells, and even leads to heart valve diseases. Moreover, during disease, it has been observed that the mechanical force enables the heart valve leaflet to retain structural strength via accumulation of collagen fibers and prevents deterioration or tissue destruction from collagen cleavage mediated by cellular activities.

The impact of collagen degradation on the biochemical regulation of heart valves in matrix and at cellular levels has been demonstrated comprehensively in previous studies. In this study, therefore, to understand the mechanical behavior in stress and the viscoelastic properties of the heart valve as they vary with collagen degradation, a tissue-level investigation of collagen-deficient heart valve tissue responding to its mechanical environment was conducted via testing of stress relaxation. Collagenase was applied to simulate collagen degradation by MMPs in matrix remodeling. A series of stress relaxation tests under different strain levels and with application of collagenase solution were performed to test the sensitivity of collagen fibers to proteolytic degradation. Further, the quantity of collagen released from the heart valve tissue was also measured to verify the relationship among collagenase concentrations, strain levels, and amounts of collagen remaining in heart valve tissues, corresponding with stress drops under different conditions.

METHODS

Preparation of specimens and collagenase solutions: Eight porcine hearts (sows, eight months to one year old) were dissected in the Nahunta Pork Center (Pikeville, NC) and returned to the laboratory within 60 minutes. Twenty-four AVs and 24 PVs were dissected axially along the aorta and pulmonary artery in each heart, and then square specimens (10 mm × 10 mm) were cut from all AV and PV leaflets [1]. To better maintain the physiological functions of the tissues in a biomimic environment, all 48 leaflet specimens were immediately immersed in HBSS solution (Lonza, Walkersville, MD) at 37°C. Meanwhile, three concentrations (0.2 mg/ml, 0.5 mg/ml, and 1.0 mg/ml) of collagenase solution (Worthington, Lakewood Township, NJ) were prepared for collagen degradation and then stored in the refrigerator at 4°C.

Biaxial Tissue Tester: Our laboratory's biaxial testing system and protocols have been described in detail previously [1]. In brief, a biaxial tissue tester (BioTester 5000, CellScale, Canada) equipped with two load cells (500 mN) for two perpendicular axes of loading was used for measuring the force and displacement of the semilunar heart valve tissue leaflets. The measured values were used to further obtain stress–strain curves and to calculate the parameters of the material stiffness. Synchronized time lapse video for real-time monitoring and postprocess analysis was performed with the charged-couple device (CCD) camera, which acquired images with a pixel resolution of 1280×960 at an acquisition rate of 15 Hz, with a lens focal length of 75 mm. A temperature-controlled saline chamber with data logging capability provided a physiological environment for testing soft tissue specimens. BioRakes provided fast and accurate

Copyright 2016 The Organizing Committee for the 2016 Summer Biomechanics, Bioengineering and Biotransport Conference

sample mounting: each BioRake consisted of five tungsten tines used to anchor one edge of the specimen. Four rakes provided uniform attachment across the edges of the samples and evenly distributed load spanning 4 mm in length on each side of the sample.

Stress Relaxation: Stress relaxation is a viscoelastic property of soft tissue which involves a decrease in stress under a constant strain. It is known that the magnitude of stress relaxation changes with variation of external mechanical stretching or the tissue structure. Here two groups were tested: 18 AV and 18 PV specimens were assigned to the collagenase-treated group (experimental group) and other fresh specimens were defined as the untreated group (control group). Six conditions where three different collagenase concentrations combined with two strain levels were applied to each AV or PV experimental group while two strain levels but no application of collagenase were set for each control group. Three AV or PV specimens were tested under each condition. Moreover, in order to avoid rapidly tearing the tissue sample during stretching before stress relaxation, 10 cycles of pre-conditioning stretching under 10% of strain and step increasing the strain rate at 2.5% per second were applied [2]. When the strain reached 37% or 50%, respectively, the specimen was held for 10,000 seconds to mimic comparable levels of relaxation [3-4]. For each AV or PV collagenase-treated group, during stress relaxation testing the specimens were immersed in the fluid chamber filled with 37°C HBSS for the first 3,000 seconds, and then HBSS was replaced immediately with collagenase solution. HBSS was gently removed from the chamber and collagenase solution was added using a Powerpette controller (VWR, Radnor, PA). However, solution replacement was not applied to each AV or PV untreated group. At the end of the testing, each specimen was gently removed from the biorakes and stored in individual centrifuge tubes filled with HBSS at 37°C for collagen assay.

Normalization of Data for Stress Relaxation: The stress relaxation responses at the various strain levels and collagenase solutions varied in magnitude. Higher strain level led to higher peak stress at the beginning of testing, and a lower state of stress relaxation resulted from smaller applied strain. To understand how applied strain and collagenase concentration affected stress relaxation, normalization of the stress relaxation that was exhibited by each stress drop relative to the peak stress was performed, which was beneficial for observing whether the patterns of all the curves were consistent. Therefore, normalization of stress relaxation was applied so as to more easily observe the mechanical behaviors of all specimens under different conditions.

RESULTS

The average AV responses to stress relaxation versus time at each condition are shown in **Figure 1**. Over a time period of 3,000 seconds (t = 0 ~ 3,000), the stress drops rapidly at the beginning of stress relaxation and then decreases more slowly to a constant value at each condition. The normalized stresses in the control group under all conditions remain between 0.4 and 0.5 after 3,000 seconds until the end of testing. However, after adding collagenase solution (t = 3,000 s), each stress-time curve for the collagenase-treated group starts to decline again until t = 10,000 s. At the end of testing, circumferential and radial normalized final stresses were below 0.1 for both conditions at 37.5% and 50% of strain when the 0.5 mg/ml or 1.0 mg/ml collagenase solution is applied. The smallest collagenase concentration (0.2 mg/ml) apparently has a smaller influence on stress drops, and the final normalized stresses in two directions are close to 0.2 and 0.15 under the strain conditions at 37.5% or 50%, respectively. Up to 98% of circumferential and radial normalized stresses drop under the condition of highest concentration of collagenase (1.0 mg/ml) for both strain levels. Further, it shows that only about 80% to 87% of the normalized stress relaxation in two directions occurs under the condition of lowest concentration of collagenase (0.2 mg/ml) for 37.5% or 50% of strain, respectively.

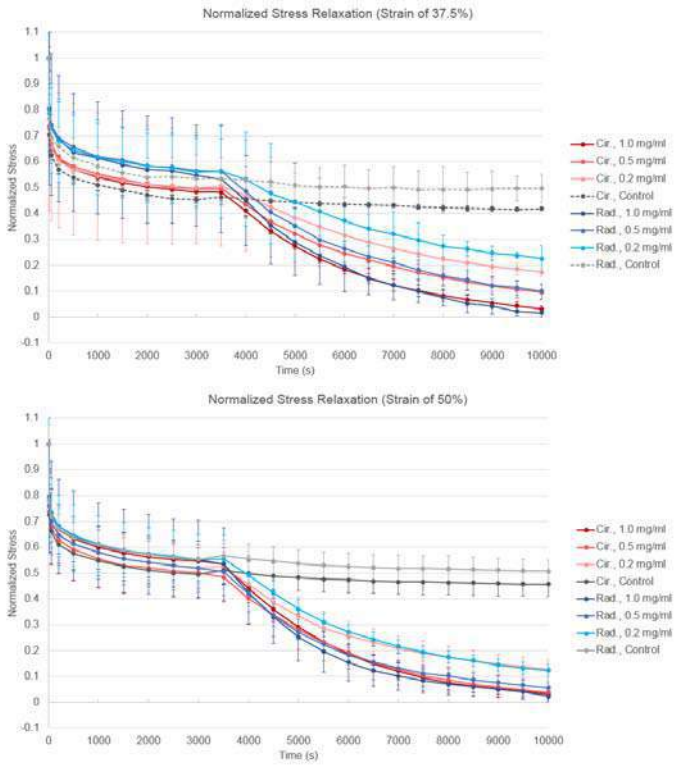

Figure 1: Average AV responses for stress relaxation versus time at two strain levels, 37.5% and 50%. Specimens immersed in HBSS are stretched under 37.5% or 50% of the strain control and holds for 10,000 seconds. For the collagenase-treated groups, HBSS is replaced with the 0.2 mg/ml, 0.5 mg/ml, or 1.0 mg/ml collagenase solution, respectively, after 3,000 seconds. For the control group, HBSS in the chamber is not changed. The circumferential direction of the specimen is denoted "Cir.," while the radial direction is "Rad."

REFERENCES

[1] Huang, H. S., Balhouse, B. N., and Huang, S., 2012, "Application of Simple Biomechanical and Biochemical Tests to Heart Valve Leaflets: Implications for Heart Valve Characterization and Tissue Engineering," Proceedings of the Institution of Mechanical Engineers, Part H: Journal of Engineering in Medicine, 226(H11) pp. 868-876.

[2] Duncan, A., Boughner, D., and Vesely, I., 1996, "Dynamic Glutaraldehyde Fixation of a Porcine Aortic Valve Xenograft: 1. Effect of Fixation Conditions on the Final Tissue Viscoelastic Properties," Biomaterials, 17(19) pp. 1849-1856.

[3] Stella, J. A., Liao, J., and Sacks, M. S., 2007, "Time-Dependent Biaxial Mechanical Behavior of the Aortic Heart Valve Leaflet," Journal of Biomechanics, 40(14) pp. 3169-3177.

[4] Grashow, J. S., Sacks, M. S., Liao, J., 2006, "Planar Biaxial Creep and Stress Relaxation of the Mitral Valve Anterior Leaflet," Annals of Biomedical Engineering, 34(10) pp. 1509-1518.

Copyright 2016 The Organizing Committee for the 2016 Summer Biomechanics, Bioengineering and Biotransport Conference

SB^{3}C2016
Summer Biomechanics, Bioengineering and Biotransport Conference
June 29 –July 2, National Harbor, MD, USA
SB^{3}C2016-1094

MAGNETICALLY LEVITATED SHEAR INDUCING DEVICE FOR THE TESTING OF CELL FRAGILITY

Ramnath Raghunathan (1), Oyuna Myagmar (1), Steven W. Day (1,2)

(1) Department of Mechanical Engineering
Rochester Institute of Technology
Rochester, NY, USA

(2) Department of Biomedical Engineering
Rochester Institute of Technology
Rochester, NY, USA

INTRODUCTION

Most blood pumps are designed to boost the pumping abilities of the heart by mechanical energy transfer using a rotor. Due to the nature of blood contacting devices, the various components of blood are subjected to shear stresses caused by the device. The accurate analysis and prediction of blood damage during the design phase of a device has been difficult to achieve. This has been complicated by both the inaccuracy of computer tools used to model the blood flow and the large uncertainty in the reported values of stress that damage blood components. Different components of blood, such as red blood cells, platelets and VWF (Von Willebrand Factor), have different sensitivities to shear stress. Further, the damage to blood components has been correlated to both the magnitude of the shear stress and duration of time that the components are exposed to that stress (exposure time).

Several studies have presented measurements of red cell fragility and many of these are based on a shear flow created by a rotating element [1]. Unfortunately, in all of these devices, the suspension system of the rotor, whether a fluid or mechanical bearing, creates additional stress and may generate heat so that the bearings could be causing an additional and unknown shear on the fluid and suspended elements.

We developed a device that uses cylindrical Couette flow called the Maglev (Magnetic Levitation) shearing device. This device has a magnetically suspended rotor thus reducing a major amount of friction when compared to pumps with mechanical bearings. The device is intended to have a single region of laminar Couette flow (between an inner rotating cylinder and a stationary housing) that exposes the fluid to stress. The two primary goals of this work are to fabricate a functional magnetically levitated shearing device to induce stress in blood and other fluids using the new fluid path design and to determine the damage done to bovine blood at different exposure time and stress levels.

Myagmar [4] designed a fluid flow path built around the magnetic suspension from the RIT left ventricular assist device (LVAD) [2] that could be used to create the Maglev shearing device. Her work included design iterations of the rotor in order to achieve the desired range of shear stress and exposure time. For the first order approximation, it is assumed that the Maglev shearing device has a Couette flow condition that creates a constant shear stress and CFD results prove this to be true. Her work shows that the region 1 (gap region) provides a uniform shear stress throughout the region and, in region 2, the impact of shear stress is negligible (shear stress is inversely proportional to the gap).

METHODS

Experimental Apparatus: The goal of this work was to fabricate a device that exposes blood to varying shear stresses for known amounts of exposure time. We modified the magnetic suspension system of a fully magnetically levitated axial blood pump so that there are no regions of heat generation or high shear stress other than the single Couette flow region designed to have a constant shear stress. The base structure consists of the pump like assembly with the five major parts kept together in sequence with appropriate distances from each other. This design refers back to the initial design of the LVAD. The major parts of the shearing device, including the active components such as the motor, magnetic bearings, and position sensors, are shown using the cross sectional view of the shearing device; magnets are shown in color.

Copyright 2016 The Organizing Committee for the 2016 Summer Biomechanics, Bioengineering and Biotransport Conference

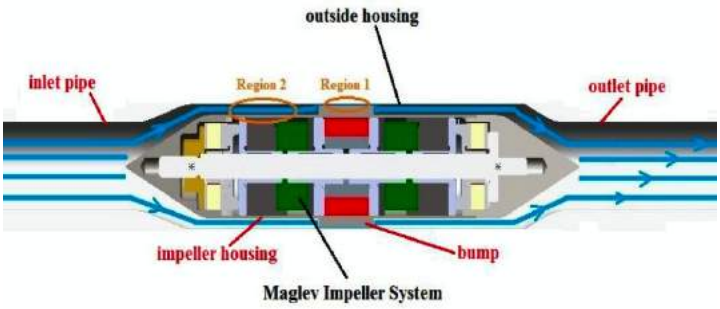

Figure 1: Maglev shearing device cross sectional view [4]

Blood Measurements: Whole citrated blood was pumped through the device at a controlled rate. The shear stress and exposure time are controlled and varied by adjusting the rotational speed and flow rate of the pump, respectively. Samples are to be collected for several combinations of shear stress and exposure time.

The samples were centrifuged in centrifuge tubes, stored in cuvettes, and then analyzed using the Cripps method [3], an optical technique to determine the quantity of free hemoglobin (fHB). The results of Cripps method, fHb in units of mg/dL,was converted to Index of Hemolysis (I.H) (%) assuming a total hemoglobin of 12,000 mg/dL (mean of the reported range of 9500 mg/dL to 13500 mg/dL).

Before the blood damage measurement, the blood samples were passed to a centrifuge tube using the syringe pump, tubes, and tube fittings () without passing through the device. After which centrifuge tube underwent the Cripps method and I.H was determined. The results showed that the samples experienced negligible damage (low I.H value) of 0.002%. This experiment was conducted 3 times and all results showed similar I.H value.

RESULTS

To date, we have only one trial and preliminary results, but they do indicate a dependence on exposure time for shear levels (0-125 Pa), as shown in Figure 2.

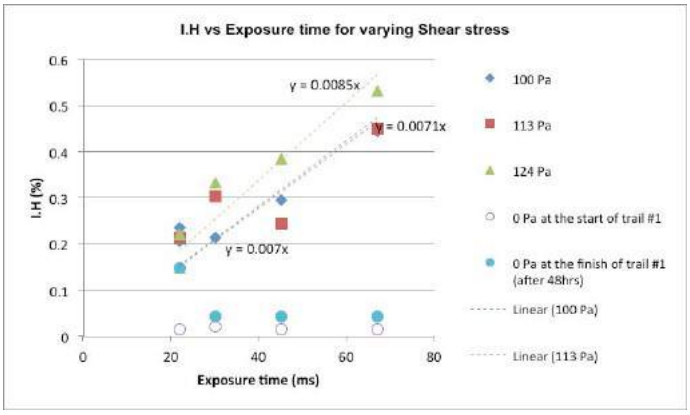

Figure 2: Preliminary data showing the amount of damage, Index of Hemolysis (IH) as a function of exposure time at three different levels of stress.

DISCUSSION

The use of a magnetic suspension for a blood shearing device has promise to create a method of exposing blood to a uniform shear field over a range of physiologically relevant stress magnitudes and exposure times. Although the data shown is limited for one trial and over a limited range of shear magnitudes, the feasibility of the apparatus and general method of I.H prediction is presented in this paper.

ACKNOWLEDGEMENTS

The authors wish to acknowledge the support and guidance from Richard Malinauskas, FDA CDRH. We are currently collaborating on an improved version of this device.

REFERENCES

[1] Paul, R.; Apel, J.; Klaus, S.; Schugner, F.; Schwindke, P.; Reul, H., Shear stress related blood damage in laminar Couette flow. *Artificial Organs* 2003, *27* (6), 517-529.

[2] Cheng, Shanbao, Mark W Olles, Don B. Olsen, Lyle D Joyce, and Steven W Day. 2010. "Miniaturization of a Magnetically Levitated Axial Flow Blood Pump." *Artificial Organs* 34 (10). Wiley Online Library: 807–15. doi:10.1111/j.1525-1594.2010.01077.x.

[3] Cripps, C. M. (1968). Rapid method for the estimation of plasma haemoglobin levels. Journal of Clinical Pathology, 21(1), 110–2.

[4] Myagmar, Oyungerel, and Steven W Day. 2015. "The Evaluation of Blood Damage in a Left Ventricular Assist Device." In *Journal of Medical Devices*, 9:20914. American Society of Mechanical Engineers.

Copyright 2016 The Organizing Committee for the 2016 Summer Biomechanics, Bioengineering and Biotransport Conference

SB³C2016
Summer Biomechanics, Bioengineering and Biotransport Conference
June 29-July 2, National Harbor, Maryland, USA
SB³C2016-1095

WIRELESS INSTRUMENTED CANE

Me'Lanae Garrett
Mississippi State University
Cruger, Mississippi, USA

Binod Shilapakar
Mississippi State University
Bhaktapur, Nepal

Joel A. Whitney
Mississippi State University
Philadelphia, Mississippi, USA

Jon T. Williams
Mississippi State University
Memphis, Tennessee, USA

Faculty Advisor(s)

Radhakrishnan Srinivasan
Mississippi State University
Starkville, Mississippi, USA

Lakiesha Williams
Mississippi State University
Starkville, Mississippi, USA

INTRODUCTION

More than six million Americans use assistive mobility devices such as walkers, canes, or crutches to increase their limited mobility each year. Of this six million, around 4.8 million use canes specifically to aid their movement [1,2]. A person's reason for using a cane can vary, but one of the more common reasons is for balance assistance during rehabilitation therapy. For many people, insurance covers the cost of rehabilitation therapy, but the insurance company will only continue to provide coverage if the patient is showing improvement [3]. Currently, there are devices that can quantitatively measure and record patient data, but the devices are not portable. They are bulky, and many times, they are confined to one particular area. These devices are usually wired to the clinician's computer and require the use of special cameras, reflective markers, and a special mat used to measure the force. This type of set-up limits maneuverability about the room, and the trailing wires are often inconvenient. We propose to build an attachment for a cane that will be more portable and user-friendly. The current prototype for this design is an attachment for the removable end of a standard adjustable cane. This position was chosen to allow the patient to use a cane that may be more familiar to the patient. The other key point of this design is that any data recorded during the therapy session is wirelessly transmitted and can be accessed remotely through a website. This type of design allows the clinician to test the patient in a more comfortable environment without dealing with various inconveniences such as trailing cords.

PRODUCT DESIGN

The proposed prototype has been designed to eliminate the use of trailing wires and the supplemental camera system. In this model, a force transducer measures the amount of reliance that the user has on the cane, and an inclinometer measures the angle at which the user holds the cane relative to the floor. A magnetic proximity sensor in conjunction with a permanent magnet inside an adjustable ankle strap measures how close the patient holds the cane to his body when using the cane. The force transducer is placed on the removable fitting at the bottom of the cane so that it can be fitted to different canes. The force transducer, the magnetic proximity sensor, and the inclinometer are connected to a breadboard and controlled by an Arduino Yún microcontroller. The data from each sensor are communicated to a central computer wirelessly with a web interface. The Arduino microcontroller contains a removable SD card for data storage.

Figure 1: Current Prototype

The Arduino microcontroller, the inclinometer, the magnetic proximity sensor, and the breadboard, to which each of the sensors are connected, are enclosed in a case attached to the removable end of the cane with a screw and bracket. This set up will restrict the movement of the housing case so that each measurement is accurate and not affected by any excess movement. Since the housing and electric components are affixed to the removable bottom of the cane, the patient can use

Copyright 2016 The Organizing Committee for the 2016 Summer Biomechanics, Bioengineering and Biotransport Conference

the handle that is most comfortable for them. This type of device can help make it easier for the clinician to accurately test the patient while maintaining patient comfort.

BUDGET & MARKET ANALYSIS

The design budget shown in Table 1 displays the cost of the components used in the current prototype design. As testing continues, some elements may be substituted or changed. The miscellaneous materials will cover the expenses of batteries and other materials that may be changed during the testing process. Many of the materials used in this design are currently unavailable for bulk ordering which limits the amount of cost reduction. The projected budget cost for 100 units is also shown in Table 1, along with the expected pricing for each component of the design. The miscellaneous category is expected to cover the production costs, such as labor and equipment, for producing the 100 units. Some production costs can be reduced by purchasing parts in bulk, which can decrease the price per unit from $510 to $451.

Table 1: Budget

Component	Cost (1 Unit)	Cost (100 Units)
Arduino YUN	$80	$8,000
Cane	$20	$1,500
Load Cell*	$60	$6,000
Inclinometer	$20	$2,000
Magnetic Proximity Sensor	$5	$75
Magnets	$5	$25
SD Card	$20	$1,500
Misc. Materials	$200	$20,000
Shipping and Handling	$100	$6,000
Total	**$510**	**$45,100**

This product is designed to be used by any patient requiring rehabilitation services using canes. Over 4.8 million patients use canes for consistent or rehabilitative use. With this type of design, patients undergoing physical therapy will have definitive proof of improvement for insurance purposes. The design may be altered for use in a home setting so that the clinician can remotely monitor the patient without having to bring the patient into a clinical setting. Currently, the projected sale cost for this design is $550, which can allow for a profit margin of around $100 per unit when produced in the 100-unit bulk size.

ACKNOWLEDGEMENTS

This project would not have been possible without the contributions from the faculty and staff of the Agricultural and Biological Engineering Department at Mississippi State University, with special acknowledgments going to Dr. Filip To, Dr. Radhakrishnan Srinivasan, and Dr. Lakiesha Williams for their support and guidance during the design process. We would also like to thank the Methodist Rehabilitation Center in Jackson, Mississippi, for concept generation.

REFERENCES

[1] Kaye, S. Et al., *Disability Statistics Report*, 14: 8-10, 2000.
[2] Bernstein, R., *United States Census Bureau*, 2012.
[3] n.d., *Center for Medicare Advocacy,*2013.
[4] n.d., *American Physical Therapy Association,* 2015.

Copyright 2016 The Organizing Committee for the 2016 Summer Biomechanics, Bioengineering and Biotransport Conference

SB^{3}C2016
Summer Biomechanics, Bioengineering and Biotransport Conference
June 29 –July 2, National Harbor, MD, USA
SB^{3}C2016-1096

BIOINSPIRED SIMULATION OF POLYCRYSTALLINE MATERIALS

Liqiang Lin (1), Xiaodu Wang (2), Xiaowei Zeng (3)

(1) Department of Mechanical Engineering
University of Texas at San Antonio
San Antonio, Texas, US

(2) Department of Mechanical Engineering
University of Texas at San Antonio
San Antonio, Texas, US

(3) Department of Mechanical Engineering
University of Texas at San Antonio
San Antonio, Texas, US

INTRODUCTION

Biological materials, such as fish scale, bone and nacre, exhibit outstanding strength and toughness with high contents of brittle minerals due to their ingenious design of microstructure. In the microstructure of these biological materials, the universal feature is that the brittle mineral tablets are bonded by relative soft organic interface. Thus, although the minerals are brittle, the organic interfaces could deflect the crack propagation and provide addition energy dissipation path along the interfacial surfaces. To investigate how the interface properties will determine the mechanical performance of bulk materials, various experimental tests were conducted, it was found out that the toughness and strength of bulk materials can be improved through the interface shear deformation [1], interlocking of nano-asperities and micro-scale waviness [2], as well as fracture of mineral bridges [3]. In the meanwhile, several theoretical models have also been proposed to study the transfer of stress through tablets and interfaces under the tension loading [4], the effects of interface stiffness and volume fraction on the stiffness and toughness response of bulk materials [5]. In addition, several numerical models were applied to study the effects of mineral-collagen interfacial behavior on microdamage accumulation in lamellar bone tissues [6], the independent roles of enzymatic and non-enzymatic cross-linking on the mechanical behavior of a mineralized collagen fibril [7]. Despite broad studies have been conducted to study the effects of these interfaces in high mechanical performance of biological materials, it still has not been fully elucidated how the interfaces' properties, such as interface toughness, strength and modulus, independently influences the mechanical response of bulk materials.

Since the mechanical performance of bionanocomposite material such as bone extrafibrillar matrix is strongly influenced by organic interface properties and behavior, it is necessary to provide a comprehensive interfacial model to describe different interfacial interactions and study the bulk material response from different interface behaviors. In this work, we developed an interfacial interaction model to characterize difference material interface behaviors and predict the mechanical response of extrafibrillar matrix in bone with wet and dry interface condition through modeling interface interaction. Through the study, the significant different mechanical behaviors of extrafibrillar matrix in bone were observed with dry and wet interface.

METHODS

Bionanocomposites, e.g. bone or nacre, consisting of brittle minerals bonded with low volume fraction of organic interface have high mechanical macroscopic properties. Due to the existing of organic interface, when fracture happened in bone, the mineral will slide along interface and dissipate more energy. During the interface deformation and debonding process, the interface will open along normal direction or shear along tangential direction. To predict the failure behavior of biological material related to interface properties, such as interface stiffness ($K_n \; or \; K_t$), interface strength ($\sigma_c \; or \; \tau_c$) and interface toughness ($\phi_n \; or \; \phi_t$), a generalized interfacial interaction model was proposed to model different interface behaviors. The traction-separation relations in normal and shear direction was used to govern the interface behavior as shown in Figure 1, which include four deformation stages in normal traction-separation law: compressive contact stage ($0 \sim \delta_0$), elastic stage ($\delta_0 \sim \delta_{dn}$), damage stage ($\delta_{dn} \sim \delta_{fn}$) and complete failure stage ($\delta_{fn} \sim +\infty$). In the shear traction-separation law, it has all the deformation stages except compressive contact stage. The interface toughness is the area under the traction-separation curve and the normal and shear interface toughness are respectively defined as:

Copyright 2016 The Organizing Committee for the 2016 Summer Biomechanics, Bioengineering and Biotransport Conference

$$\emptyset_n = \int_{\delta_0}^{\delta_{fn}} \mathbf{T}\, d\boldsymbol{\delta} \quad (1)$$

$$\emptyset_t = \int_{0}^{\delta_{ft}} \mathbf{T}\, d\boldsymbol{\delta} \quad (2)$$

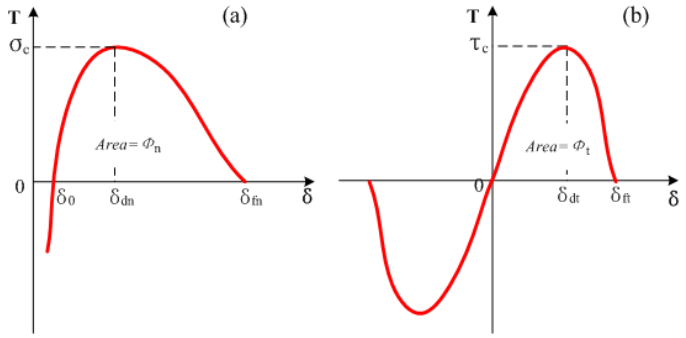

Figure 1: Generalized traction-separation relation used to characterize interface behavior:(a) normal direction, (b)tangential direction

From the experiment results, we observed that bone has brittle behavior when it is dry. However, the bone has softening process when it is in wet condition [8]. In Figure 2, it shows the variation of traction-separation relation with respect to dry and wet interface conditions. For dry interface condition, we assume that the organic interface has the brittle properties, that is, after passing the damage position, the interface completely fails in both normal and shear direction. For wet interface condition, we assume that the organic interface has the softening properties. After passing the damage position, the interface shows softening behavior and the interface tractions gradually decrease with the increase of separation after damage position in both normal and shear direction.

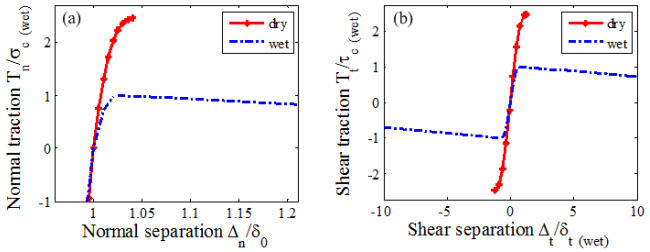

Figure 2: The traction-separation relations with respect to dry and wet interface conditions in: (a)normal direction, and (b)shear direction

RESULTS

In this study, we have run six simulation cases with random polycrystalline grain distribution in the extrafibrillar matrix specimen. The deformation process from one of the simulation cases with wet interface condition under compression loading is shown in Figure 3. The stress distribution, shear band and crack propagation are captured from the simulation. In addition, different mechanical response of extrafibrillar matrix with wet and dry organic interface conditions were captured in the simulation results. It was also found that the bulk material properties are strongly influenced by the interface properties in extrafibrillar matrix of bone.

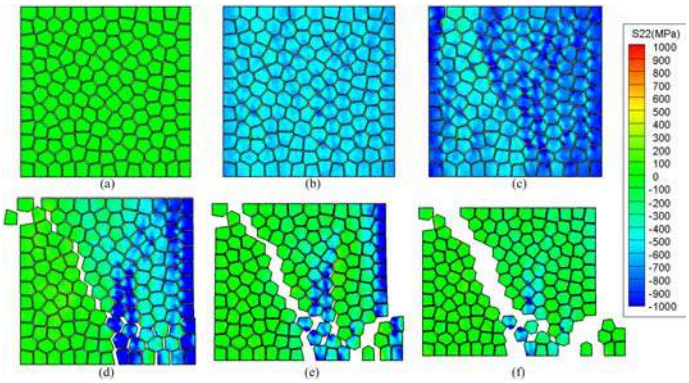

Figure 3: Snapshot of stress distribution(σ_{22}) under compression loading

DISCUSSION

Through the study of mechanical behavior of extrafibrillar matrix in bone, it was verified that the interface properties strongly influence the mechanical response of bulk materials. Additionally, by modeling the interface properties with interfacial interaction model, it provides a possible to independently study the effects of different interfacial interaction on the mechanical response of bulk material and bulk material behavior prediction through the interface properties and behavior. More importantly, it is possible to provide preliminary framework for artificial super material design.

ACKNOWLEDGEMENTS

This work is supported by a grant from NIH (Grant No. R21AR066925) and a grant from NSF (Grant No. CMMI-1538448).

REFERENCES

[1] Barthelat, F., Espinosa, H., Experimental mechanics 47: 311-324, 2007.

[2] Espinosa, H. D. et al., Nature communications 2: 173, 2011.

[3] Smith, B. L. et al., Nature 399: 761-763, 1999.

[4] Gao, H. et al., Proceedings of the national Academy of Sciences 100: 5597-5600, 2003.

[5] Okumura, K., De Gennes, P.-G., The European Physical Journal E 4: 121-127, 2001.

[6] Luo, Q. et al., Journal of the mechanical behavior of biomedical materials 4: 943-952, 2011.

[7] Siegmund, T. et al., Journal of biomechanics 41: 1427-1435, 2008.

[8] Samuel, J. et al., Journal of the Mechanical Behavior of Biomedical Materials, 2015.

Copyright 2016 The Organizing Committee for the 2016 Summer Biomechanics, Bioengineering and Biotransport Conference

SB^{3}C2016
Summer Biomechanics, Bioengineering and Biotransport Conference
June 29 –July 2, National Harbor, MD, USA
SB^{3}C2016-1097

THE EFFECT OF SOFT TISSUE ARTIFACT ON KINEMATIC MEASUREMENT – AN EVALUATION OF OPTICAL MARKER MOTION USING BIPLANE FLUOROSCOPY

Joseph M. Iaquinto (1,2), Matthew W. Kindig (1), David R. Haynor (3), William R. Ledoux (1,2,4)

(1) Center for Limb Loss Prevention and Prosthetic Engineering
VA Puget Sound Health Care System
Seattle, WA, USA

Departments of Mechanical Engineering (2), Radiology (3) and Orthopaedics & Sports Medicine (4)
University of Washington
Seattle, WA, USA

INTRODUCTION

Optical motion capture is the current standard in kinematic analysis. This technology typically uses infra-red light, a dispersed cloud of cameras, and lightweight retro-reflective markers which are attached to a subject. While providing the ability to measure dynamic activities with minimal disturbance to the subject's typical movements, there are several known limitations of this technology. Optical markers are typically attached to the skin or clothing of a subject, and thus move with the skin/clothes, not the underlying bone; this phenomenon is known as soft tissue artifact (STA). STA induces errors at the individual marker level, which propagates into assumptions about bone or segment rigidity, and ultimately creates errors in measured joint kinematics. In the lower extremity, these issues are further compounded by the numerous small and closely neighboring joints of the foot and ankle, causing marker occlusion and interference.

The nature and extent of STA has been studied in the foot using both ultrasound [1] and with subcutaneous bone pins (a highly invasive method) [2]. An X-ray based imaging modality, biplane fluoroscopy, is also capable of directly capturing bone motion, and is non-invasive. This technique uses two fluoroscope units to image a common 3D volume while a subject's joint of interest moves through that volume. This method is ideal for evaluating STA due to its higher accuracy than optical methods [3].

We imaged the foot and ankle of non-pathological subjects during gait, while those subjects were instrumented with modified optical motion capture markers. Our objectives were to evaluate (A) movement of the skin markers relative to the bone, (B) the rigidity of bone marker sets, and (C) the error imparted to joint motion due to STA. At the time of this abstract submission, we present data for the hallux and first metatarsal.

METHODS

Our biplane fluoroscopy system (biplane system) is comprised of two BV Pulsera fluoroscopes (Philips Medical Systems; Best, The Netherlands), disarticulated and positioned around an imaging walkway [3]. A pair of high-speed video cameras (Phantom v12, Vision Research, Wayne NJ) captured dynamic fluoroscope images at 1000 frames/sec. An 8-camera optical motion capture system (Vicon Motion Systems Ltd., UK) was also installed around the walkway.

Tantalum beads (1.6mm) were inserted into the center of a set of 6.4mm optical motion capture markers – with care taken to not damage any of the optical surfaces of the marker. Three healthy subjects (VA IRB approved) were instrumented with optical markers based on a validated foot model [4]. Each subject was imaged in quiet stance, and during gait until three forefoot and three hindfoot trials were captured. For this preliminary data, we did not identify heel strike and foot off, and thus only show gait duration. Subjects also received a CT scan of their feet and distal legs.

We used custom software to extract the 3D geometry of each bone from the CT scans, and then tracked the 3D trajectory of the hallux and first metatarsal in the fluoroscopic videos [5]. A bead-tracking algorithm was developed to determine the position of the bead inside of the optical markers, in the fluoroscope images; this bead position was then converted to a 3D trajectory for comparison with the bone data. The markers tracked are: proximal phalanx (hallux), PM; and the first metatarsal head, FMH and base, FMB.

To determine (A) the movement of the skin mounted markers relative to bone, we transformed the position of the optical markers PM, FMH and FMB from global space to a local embedded coordinate

Copyright 2016 The Organizing Committee for the 2016 Summer Biomechanics, Bioengineering and Biotransport Conference

system for the bone (hallux or first metatarsal respectively) that they are "attached" to in the static image. We compared this static location to each subject's dynamic marker position during the gait trials. For (B), we considered only the FMH and FMB markers as they are assumed to be a rigid single bone segment. The change in the distance between FMH and FMB during gait, relative to the static position of these markers was calculated. For (C), we determined the joint angles of the hallux coordinate system, relative to the local coordinate system of the first metatarsal. The first metatarsal coordinate system was then used to evaluate the motion of PM relative to FMH and FMB.

RESULTS

The magnitude of the RMS error (including all three components) across all three subjects was 1.46 mm for the PM marker, 1.90 mm for the FMH marker, and 1.62 mm for FMB marker. It should be noted that while subjects S1 and S3 had similar walking speeds on average (0.88 m/s and 0.89 m/s), S2 was markedly faster (1.43 m/s). No clear trends in the errors were observed (Figure 1). For each subject, the RMS change in first metatarsal segment length (Figure 2) was 0.87 mm, 2.69 mm, and 1.63 mm, this error varied over time, indicating effective compression/lengthening of the FMB-FMH segment.

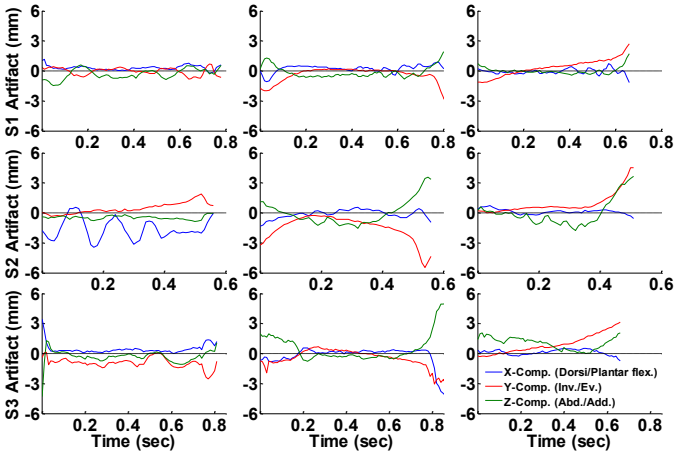

Figure 1: Soft tissue artifact average for PM, FMH, and FMB markers of subjects 1-3 (S1-3). The motion artifact is the difference between the static and dynamic coordinates of the markers (i.e., zero artifact indicates that the marker perfectly tracked the underlying bone throughout the trial). Coordinates are given in the coordinate system of the relevant bone (i.e., the hallux for PM; the first metatarsal for FMH and FMB).

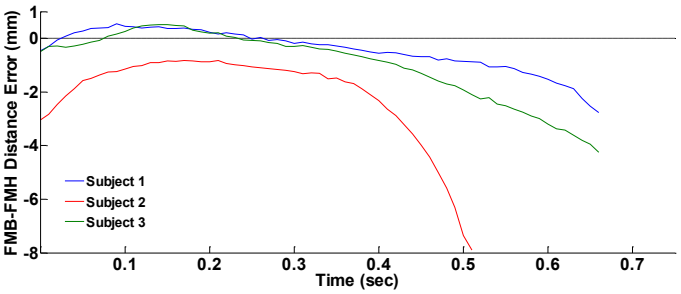

Figure 2: Marker-to-marker distance error between the markers at the two extremities of the first metatarsal (i.e., FMB and FMH markers) at a given time during the gait trial. Zero error indicates that the marker-to-marker distance is identical to the distance during the static pose.

The hallux joint angle varied markedly between the bone-based tracking and the markers, especially for subject S3 (Figure 3). The joint angles calculated directly from the bones tended to be markedly larger than their analogous angles calculated from the markers, with the bone data often giving joint angles that are frequently twice or more greater than the marker data. This resulted in the marker data exhibiting a RMS error of 8.63° in X (dorsiflexion/plantar flexion), 7.06° in Y (inversion/eversion), and 5.97° in Z (abduction/adduction) across all subjects.

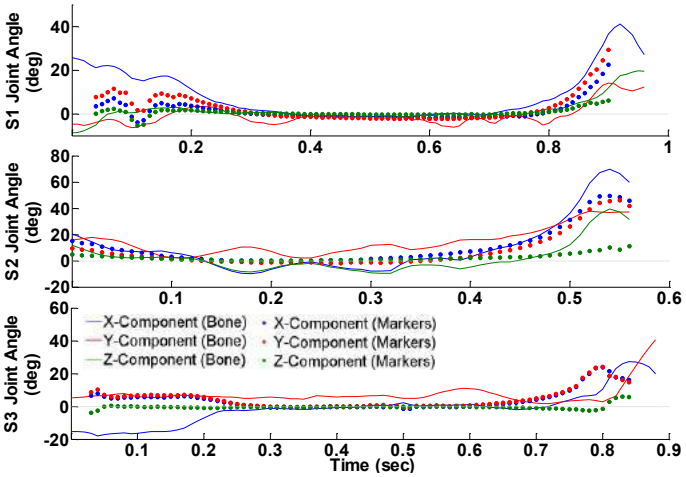

Figure 3: Joint kinematics derived from the bone-based tracking (solid lines) and from the angle between PM-FMH and FMH-FMB marker segments, in the first metatarsal coordinate system. Note that the Z-component was not available for the S3 bone tracking.

DISCUSSION

The objectives of this work were to evaluate how STA arises and ultimately affects measures of joint kinematics. We have demonstrated the error in skin markers motion due to soft tissue deformation during gait. This data, particularly the segment rigidity evaluation, also suggests that such errors vary in magnitude during gait, and increase with joint speed. Lastly, the propagation of these errors into joint kinematics, with typical errors of ~6-9°, identifies how such errors compound in the final measurement of interest.

This work aims to inform investigators and clinicians about the sources and magnitudes of errors present in optical motion capture of the foot and ankle. Such information can aid investigators in designing new optical marker models, and in compensating for errors that currently are undetectable in these systems.

Processing of the other bones of the foot and ankle, as well as the optical motion capture data is currently underway.

ACKNOWLEDGEMENTS

We wish to acknowledge the Department of Veterans Affairs grant number A1442-P for supporting this work, and to Jan Pecoraro for her assistance with recruitment.

REFERENCES

[1] Telfer S et al., *J Biomech,* 47:1225-8, 2014
[2] Nester C et al., *J Biomech,* 40:3412-23, 2004
[3] Iaquinto J et al., *Med. Eng. & Phys,* 36(3):391-6, 2012.
[4] Leardini A et al., *Gait Posture.* 25:453-62, 2007.
[5] Iaquinto, J et al., *Med. Eng. & Phys*, In Review, Nov 2015

Copyright 2016 The Organizing Committee for the 2016 Summer Biomechanics, Bioengineering and Biotransport Conference

SB³C2016
Summer Biomechanics, Bioengineering and Biotransport Conference
June 29 –July 2, National Harbor, MD, USA
SB³C2016-1098

PHOTOCLICKABLE PEPTIDE MICROARRAYS FOR HIGH THROUGHPUT SCREENING AND DISCOVERY IN REGENERATIVE MEDICINE AND DISEASE MODELS

Michael L. Floren (1), Sadhana Sharma (2), Stephanie J. Bryant (2), Wei Tan (1)

(1) Department of Mechanical Engineering
University of Colorado Boulder
Boulder, CO, USA

(2) Department of Chemical & Biological Engineering
University of Colorado Boulder
Boulder, CO, USA

INTRODUCTION

Stem cell (SC) therapy promises to revolutionize the treatment of various diseases with the potential to regenerate functional tissues *in vitro* or *in vivo*. Several recent studies have demonstrated that cellular microenvironments such as ligand-activated cell-matrix interactions and/or matrix physical properties such as elasticity and geometry have significant role in directing the differentiation processes in stem cells (1, 2). Microarrays have emerged as an important tool for studying stem cell processes in a high-throughput manner (3). Nevertheless, most of the existing ECM arrays being either 2-D or shallow 3-D are not able to capture the effects of biophysical and chemical cues on stem-cell fate completely. Here, we report the development of a microarray platform based on electrospun nanofibrous hydrogels of photoclickable thiol-ene poly(ethylene glycol) (PEG) hydrogels. Thiol- ene polymerizations proceed by an orthogonal, step-growth mechanism where one thiol reacts with one ene leading to a highly homogenous distribution in crosslinks, thus imparting tunable substrate stiffness with high fidelity (4). Furthermore, it allows for the subsequent covalent post-modification of PEG thiol-ene hydrogel substrates with small engineered peptides with high reactivity and specificity. Taken together, the manipulation of the matrix properties, such as stiffness and geometry, in concert with engineered peptides will facilitate the interrogation of multiple and distinct SC microenvironments. To this end, we demonstrate the potential application of this high-throughput technology for screening of a variety of engineered 3D microenvironments with applications in stem cell fate optimization and disease model progression.

METHODS

Substrate Preparation: Four-arm poly(ethylene glycol) norbornene (PEGNB, 5 kDa, 10wt%), poly(ethylene glycol) dithiol (1 kDa), poly(ethylene oxide) (5 wt%, 400 kDa), and I2959 (0.1 wt%) were dissolved in DI water, electrospun (16 kV, 20 cm, 0.8 ml/hr), and collected as fibers (647.6 ± 81.4 nm) on a glass slide previously modified with 3-(mercaptopropyl) triethoxysilane. Substrates were subsequently exposed to UV (352 nm, 5 mW/cm2) light for specific time points to achieve elastic modulus ranging from 1-20 kPa.

Microarray Fabrication: Microarrays were prepared using a 2470 Aushon arrayer (Fig 1A). Fluorescent dye (Alexa Fluor® 488/546 -C5 maleimide) or peptide (CRGDS, CRGES, YRGDS, CGDEAK-A568) in buffer (1% glycerol, 0.2% Triton X-100, 0.1% I2959) were printed and exposed to UV light.

Cell Culture: Cell studies were conducted using primary bovine pulmonary arterial smooth muscle cells (PASMCs). Following cell culture, substrates were fixed and subsequently stained with DAPI (cell nuclei) and A488-phallodin (F-actin cytoskeleton) to observe cell adhesion and spreading.

RESULTS

Characterization of 3-dimensional fibrous PEG thiol-ene hydrogel matrix: Fibrous, PEG thiol-ene hydrogels were prepared by an electrospinning process similar to our previous method (5). We thiolated conventional glass slides to allow covalent attachment of the PEG thiol-ene matrices which improves sample handling and longevity for cell studies. We examined the fibrous architecture of electrospun PEG thiol-ene substrates using SEM in both hydrated and dry states.

Copyright 2016 The Organizing Committee for the 2016 Summer Biomechanics, Bioengineering and Biotransport Conference

Microscopy revealed a highly fibrous hydrogel structure with average fiber diameter of 647.6 ± 81.4 nm.

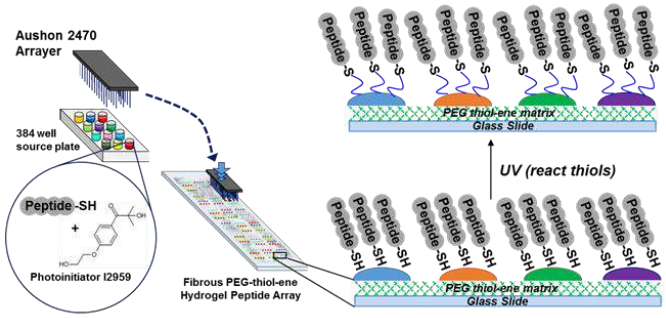

Figure 1. Fibrous PEG-thiol-ene hydrogel peptide array fabrication. Schematic of microarray contact printer used to spot different peptide solutions onto electrospun PEG-thiol-ene coated glass slide. Crosslinking is achieved via UV light initiated thiol-ene reactions of di-thiol and norbornene groups on 4-armPEGNB.

Engineered Peptide Synthesis and Array Fabrication: The deposition of peptide microdots is illustrated in Figure 1. Following the preparation of PEG thiol-ene matrices, peptide printing is achieved using a contact style arrayer (Ashon 2470) and subsequently post stabilized via a second UV step. Post functionalization of our PEG thiol-ene matrices allows for the covalent incorporation of a diversity of biological ligands or other engineered biomolecules. To illustrate this, printing optimization strategies employing a fluorescently labelled control (CDGEA 488/546) are depicted in Figure 2. Post functionalization of engineered biomolecules is obtained via a secondary UV exposure, see Figure 2A. Deposition size was found to be approximately 200μm in diameter which is in agreement with our previous work utilizing ECM proteins (5).

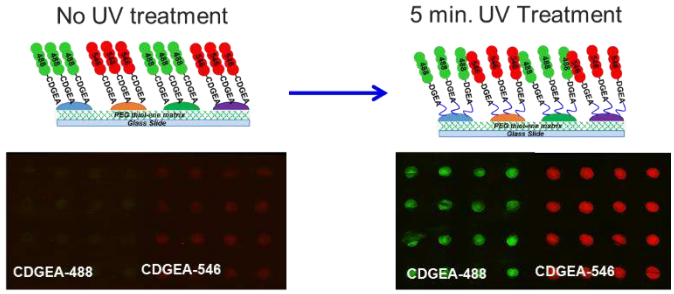

Figure 2. Representative example of fluorescently labeled CDGEA with and without UV stabilization.

Primary Cell Adhesion and Spreading within Peptide Functionalized PEG thiol-ene Matrices: To further demonstrate the utility of our peptide arrays, we investigated the influence of the adhesive ligand (RGD) post functionalized within the PEG thiol-ene matrices, as shown in Figure 3. As depicted from the confocal microscope images in Figure 3, the cells only attached to RGD deposited spots with no attachment outside the printing deposition, i.e. neat PEG thiol-ene substrate. In contrast, covalent attachment of CRGES peptide (scrambled sequence) to the PEG thiol-ene matrices did not facilitate cell adhesion (Figure 3D). We varied CRGD dilution range from 0.1 to 15 mM and observed cell attachment of PASMCs after 24 h (Figure 3C, single cellular island) with cell attachment positively correlated with CRGDS printing concentration (data not shown). The prepared PEG thiol-ene peptide arrays were amenable to extended culture period of up to 72 h (Figure 3E). The precision of robotic array spotting allows for complex array layout and design over large areas (Figure 3C). The utility of these complex depositions are further supported by localized cellular attachment on CRGDS functionalized complex array as shown in Figure 3F. We can conclude from these results that advanced peptide array designs can be prepared, with cellular recognition at modest peptide concentrations (< 1 mM), as well as potential for more complex

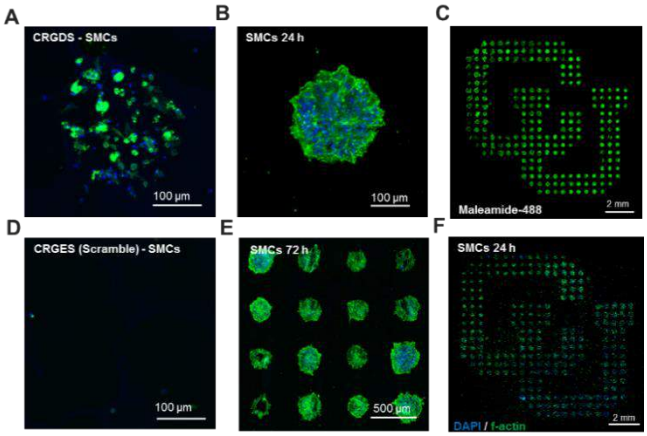

Figure 3. Cells selectively attach to engineered peptides. Confocal images of initial attachment of PASMCs cultured on fibrous PEG thiol-ene hydrogels functionalized with CRGDS (A), CRGES (scramble) (D), cellular island prepared from PASMCs after 24 h (B) and 72 h respectively (E). Custom array layout represented by fluorescent control (maliamide)(C) and analogous PASMC culture using CRGDS functionalized deposition (F).

combinatorial array designs.

DISCUSSION

Similar to our previous work using ECM proteins (5), we find contact-style array technology to represent a reliable and reproducible method to prepare complex array designs using engineered peptides, which may be further functionalized via UV stabilization post array printing. Here we demonstrated the potential to exploit the adhesive ligand (RGD) to influence cell attachment and spreading of PASMCs within 24 or 72 h. While we only investigated the role of RGD ligand on cell behavior, we note that post functionalization of our PEG thiol-ene matrices can be achieved with any molecule with thiol-ene reactivity, i.e. cysteine residues. Collectively, these results highlight the diverse properties of our substrates, whereby stiffness, geometry, and functionalized molecules (biological or chemical) can be tuned with high specificity. Future work will be focused on designing combinatorial peptide studies, whereby, the integration of several biological ligands of interest with tunable physical properties can instruct stem cell differentiation in a highly specific manner.

REFERENCES

[1] Engler, J.A., S. Sen, H.L. Sweeney, and D.E. Discher. *Cell*, 126:677-689, 2006.
[2] Wingate, K., W. Bonani, Y. Tan, S. Bryant, W. Tan. *Acta Biomater*, 8:1440-1449, 2012.
[3] Gobaa, S., S. Hoehnel, M. Roccio, A. Negro, S. Kobel, and M.P. Lutolf. *Nat Meth*, 8:949-955, 2011.
[4] Hoyle, C.E., and C. N. Bowman. *Angew. Chem. Int. Ed.*, 49:1540-1573, 2010.
[5] Floren, M., Tan, W. *Biomaterials*. 59:39-52, 2015.

Copyright 2016 The Organizing Committee for the 2016 Summer Biomechanics, Bioengineering and Biotransport Conference

SB³C2016
Summer Biomechanics, Bioengineering and Biotransport Conference
June 29 –July 2, National Harbor, MD, USA
SB³C2016-1099

STUDY OF GANCICLOVIR PERMEABILITY THROUGH BOVINE, RABBIT AND HUMAN ALZHEMEIR EX-VIVO OCULAR TISSUES

Anita N. Penkova(1,2), Komsan Rattanakijsuntorn (1), Satwindar Singh Sadhal (1,2)

(1) Aerospace and Mechanical Engineering Department
University of Southern California
Los Angeles, CA, USA

(2) Saban Research Institute
Children's hospital Los Angeles
Los Angeles, CA, USA

INTRODUCTION

Ganciclovir is a hydrophilic drug used as antiviral medicine in form of eye drops, gel ointment and as a surgically-inserted implant in the eye. For patients having serious conditions such as cytomegalovirus (CMV) retinitis with immune deficiency syndrome (AIDS), one of the preferred treatment options is ganciclovir implant insertion in the eye. To improve and effectively apply Ganciclovir for ocular treatment, knowledge of the transport properties (permeability, diffusion) is required. This information is also necessary for mathematical modeling of the drug transport processes.

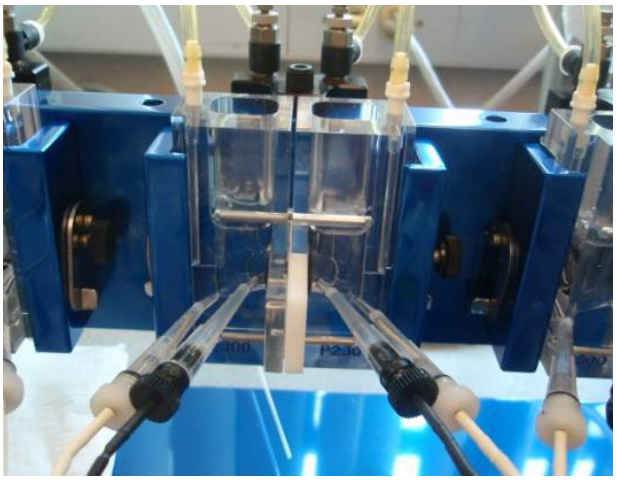

Figure 1: Ussing chamber apparatus for permeability measurement.

METHODS

For osmotically-driven permeability measurements, conventional Ussing chamber (Figure1) was used. In our experimental model various ocular tissues of interest have been isolated from "ex-vivo" bovine, rabbit and Alzheimer human eyes. These membranes were inserted between the two chambers (donor and acceptor) of the apparatus. DMEM with 4.5 g/L glucose (4ml) was added to both sides of the diffusion chamber, while Ganciclovir is injected into donor side only. Samples of 100 μL were taken from donor and acceptor sides at different time points (30, 60, 90, 120, 150, 180, 210, and 240 minutes. During the experiment, oxygen was bubbled through both chambers to keep the tissue healthy for as long as possible. HPLC (High Performance Liquid Chromatography) was utilized to measure Ganciclovir concentration. The change in concentration due to sample extraction was allowed for in the calculation of the net permeation of Ganciclovir across the membrane.

RESULTS

Our preliminary results (Table 1) showed that for bovine eyes, the RPE has the highest value of P_{app} (4.273±0.706 x10^{-5} cm/s) followed by sclera (3.463±0.532 x10^{-5} cm/s) and iris (2.540±0.137 x10^{-5} cm/s). For rabbit eyes the P_{app} across RPE is 4.332 x10^{-6} cm/s) and RPE-choroid-sclera is 4.375 x10^{-6} cm/s. For ex-vivo human eyes the permeability across cornea is 0.684 x x10^{-5} cm/s.

Linear plots of total accumulation of the drug versus time were obtained. The flux values were obtained from the slopes (Figure 2). The plots do not pass through the origin because of some degree of hysteresis with the tissue absorbing the Ganciclovir at the start of the experiment. The net flow rate per unit area, J, of Ganciclovir across the membrane was obtained from the plots of sample concentration

Copyright 2016 The Organizing Committee for the 2016 Summer Biomechanics, Bioengineering and Biotransport Conference

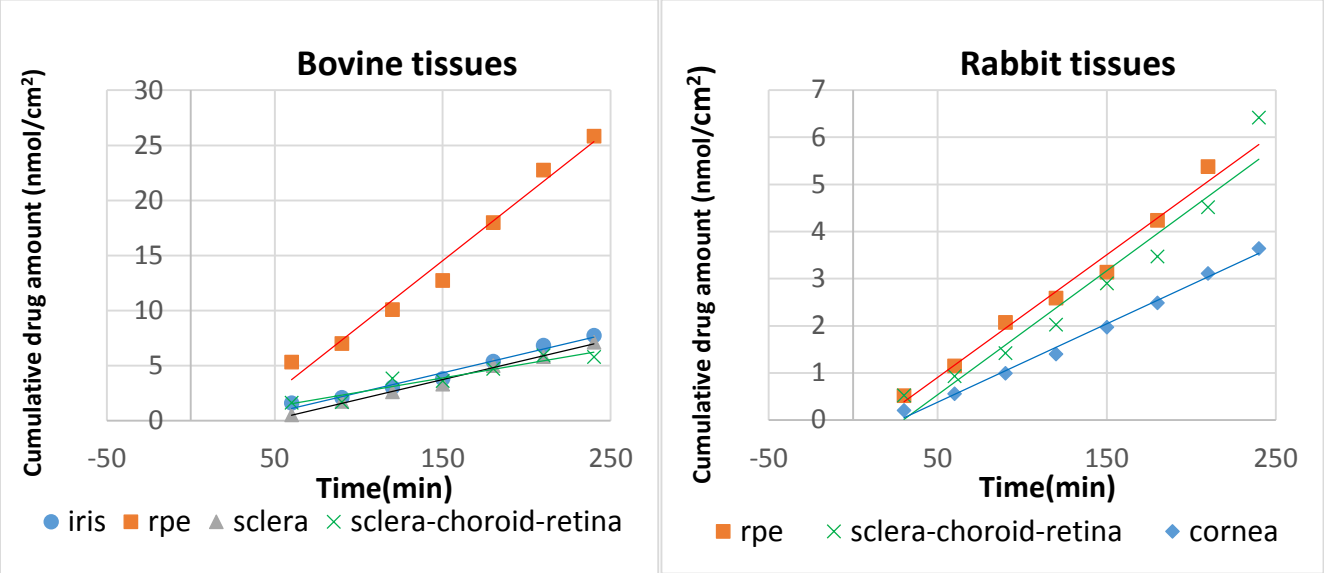

Figure 2: Transient accumulation of ganciclovir for the bovine and rabbit tissues (scaled with tissue area).

Tissue	Bovine	Rabbit
	P_{app} (cm/s)	P_{app} (cm/s)
Iris	$(2.540 \pm 0.137)\times10^{-5}$	
RPE	$(4.273 \pm 0.706)\times10^{-5}$	$(4.332 \pm \text{N/A})\times10^{-6}$
Cornea		$(3.883 \pm 0.165)\times10^{-6}$
Sclera	$(3.463 \pm 0.532)\times10^{-5}$	
Sclera-choroid	$(2.467 \pm \text{N/A})\times10^{-5}$	
Sclera-Choroid-Retina	$(1.523 \pm 0.457)\times10^{-5}$	$(4.375 \pm \text{N/A})\times10^{-6}$

Table 1: Apparent permeability coefficient values of ganciclovir through bovine and rabbit tissues.

measurements at the different time points. The concentration measurements were used to calculate the total accumulation of Ganciclovir on the receiver side.

With making some assumptions that:

- the concentration profile is linear in time after initial hysteresis;
- the Ganciclovir concentration in the donor side is nearly constant;
- the concentration in the receiver chamber is close to zero;

the permeability (called also apparent permeability) can be found using following equation:

$$P_{app} = \frac{J}{C_{donor}}$$

where P_{app} is apparent permeability, J is the flux of the drug from the donor to the receptor side and C_{donor} is the concentration of the drug in the donor chamber. While we are able to see the time-varying accumulation of Ganciclovir, the relative concentration changes on the donor side is quite small, and the receiver side remains very small as compared with the donor, thus justifying the above assumptions.

DISCUSSION

The apparent permeability of Ganciclovir through RPE and RPE-choroid-sclera are very similar for both rabbit and bovine eyes (Table 1). However, the apparent permeability through bovine RPE is ten times higher in comparison with the rabbit RPE.

We compared our data with the existing ones in the literature and found that the permeability through the rabbit cornea is very close to the permeability of the same drug in the cornea reported by Majumdar [1].

We are presently working on conducting more experiments and collecting more samples for bovine, rabbit and human tissues to build a mathematical predictive model for transport mechanisms of Ganciclovir, and thus improve drug delivery techniques.

ACKNOWLEDGEMENTS

This work is supported by a research grant from Allergan, Inc., Irvine, California.

REFERENCES

[1] Majumdar, S, PhD Thesis, 2005 Pharmaceutical Sciences and Pharmacology University of Missouri-Kansas City, MO, USA.

Copyright 2016 The Organizing Committee for the 2016 Summer Biomechanics, Bioengineering and Biotransport Conference

SB³C2016
Summer Biomechanics, Bioengineering and Biotransport Conference
June 29 –July 2, National Harbor, MD, USA
SB³C2016-1100

DEVELOPMENT OF A TISSUE ENGINEERED 3D MICROFLUIDIC TUMOR PLATFORM TO STUDY NANOPARTICLE TRANSPORT

Manasa Gadde (1), Matthew R. DeWitt (2), Marissa Nichole Rylander (3)

(1) Biomedical Engineering
University of Texas at Austin
Austin, TX, USA

(2) Virginia Tech-Wake Forest SBES
Virginia Tech
Blacksburg, VA, USA

(3) Mechanical Engineering
University of Texas at Austin
Austin, TX, USA

INTRODUCTION

Nanoparticle based therapy is a new mode of cancer therapy that offers a solution to barriers of current treatment approaches such as untargeted and insufficient delivery of drugs. The goal of nanoparticle based therapy is to deliver a concentrated amount of drug to a targeted tumor site resulting in less systemic toxicity with high treatment efficacy[1]. Nanoparticle systems are unique in that they allow for both passive and active targeting of tumors while maintaining multi-functionality. The proangiogenic behavior present in tumors results in formation of leaky blood vessels with abnormal architecture. The tumor mass also has poor lymphatic drainage, allowing for accumulation of macromolecules. Nanoparticles exploit this feature known as the enhanced permeability and retention (EPR) effect, to target solid tumors.[2] Particles that are too small will be cleared by the kidneys, preventing accumulation into the tumor site, and particles that are too large will not adequately penetrate the tumor vasculature and interstitial space.[2]

Many novel therapeutic and diagnostic nanoparticles have been developed and optimized using *in vitro* studies; however there has been relatively less success in their *in vivo* translation. Nanoparticles face many barriers *in vivo* before they successfully reach the target site such as crossing the endothelium or penetrating through a dense extracellular matrix. Traditional models used to study nanoparticle enhanced therapy transport consist of monolayer cell culture or animal models. Monolayer models are static and are unable to reproduce the transport and uptake conditions nanoparticles undergo *in vivo*. While animal models provide a more physiologically representative environment, the interplay of many different variables such as growth factor, immune reaction, and cellular interactions result in an uncontrollable environment making it difficult to isolate the effect of a specific stimulus on cell response without enormous expense. Due to these limitations, 3D microfluidic models provide a good alternate.

3D microfluidic tumor models are able to reproduce the native tumor microenvironment in a controllable system. These models commonly utilize a small number of cells making it hard to perform assays that require large amount of cell matter. Also, the flow rate present in these systems is much lower than physiological flow. Additionally, it is vital that the 3D *in vitro* model be capable of recapitulating key dynamic nanoparticle transport processes including transvascular transport, diffusion and interaction with the extracellular matrix, and cellular uptake, along with presenting a physiologically relevant tumor microenvironment.

We have developed a 3D microfluidic tumor engineered platform that recreates the tumor microenvironment through the incorporation of an endothelialized microchannel within a collagen 3D matrix containing human cancer cells. The optically clear platform allows for high imaging resolution and dynamic monitoring of nanoparticle transport and angiogenic vessel sprouting.

METHODS

Collagen was extracted using a protocol developed by Buchanan et. al. [3]. Briefly, collagen was extracted from rat tail tendons and dissolved in 0.01 M HCl overnight, centrifuged, and lyophilized. The lyophilized collagen was resuspended in HCl to create a collagen stock solution of 14 mg/mL. For the tumor platforms, human breast adenocarcinoma cells, MDA-MB-231 (ATCC) and telomerase immortalized human microvascular endothelial cells (TIME) which stably express GFP or mKate respectively were used in this study. To create the perfusable tumor platform, 14 mg/ml collagen stock solution was mixed with 10x DMEM, 1N NaOH to neutralize the HCl, and supplemented with DMEM containing MDA-MB-231 cells to bring the final solution to 7 mg/ml collagen. The mixture was then injected into

Copyright 2016 The Organizing Committee for the 2016 Summer Biomechanics, Bioengineering and Biotransport Conference

cylindrical FEP tubing with a 22G needle inserted to create a vessel lumen in the center as shown in Fig. 1. TIME cells were then added to the inner vessel lumen and a 72 hr graded flow rate protocol previously developed [3] was utilized in order to maintain endothelial integrity and establish a confluent monolayer. To determine the ability of the 3D microfluidic system to be used to measure nanoparticle transport, polystyrene nanoparticles ranging from 20-1000nm (Fluor-Max , Thermo Scientific) at 0.05 mg/ml were introduced into the system at a rate of 26 µl/min. Vessel permeability was quantified by flowing the channel with 10ug/ml fluorescently labeled 70 kDa dextran at a rate of 26 µl/min. Nanoparticle uptake was assessed by treating the platform with collagenase to isolate the cells and then performing flow cytometry.

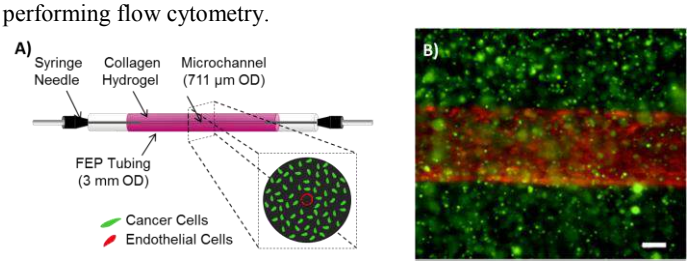

Fig. 1: A. Microfluidic tumor platform setup. B. Co-culture of MDA-MB-231 cells (green) in collagen with an endothelialized (red) inner lumen.

RESULTS

Vessel permeability was determined by flowing green fluorescently labeled dextran through the channel at 2 time points: 24 hr and 72 hr [Fig. 2]. Vessel permeability was lower at 72 hr time which allowed for the formation of a confluent endothelium [Fig 2A] compared to leaky endothelium present at the 24 hr time point [Fig 2B].

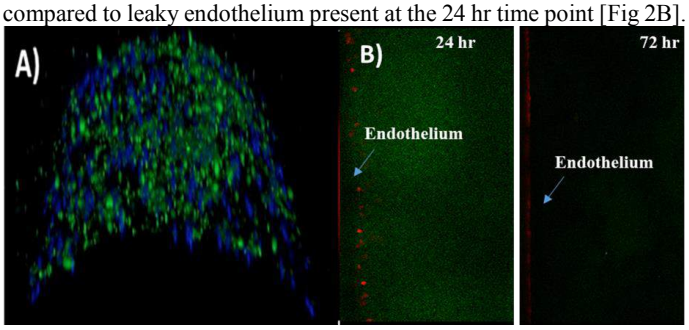

Fig. 2: A) Microfluidic platform with a confluent layer of endothelium. B) Permeability of dextran (green) across the endothelium (red) at 24 and 72 hrs

We had previously shown that nanoparticles aggregate at the endothelium and extravastion of nanoparticles into the collagen matrix increases over time using the 50 nm particle. In this study, we compared the transport of 2 different sized particles: 20 nm, and 1000 nm as shown in Fig 3. The 20 nm particles crossed the endothelium and extravasated into the collagen matrix as shown in Fig 3 where the white lines depict the boundaries of nanoparticle (shown in red) extravasation at 0 hr [Fig 3A] and 3 hrs [Fig 3B]. In contrast, the 1000 nm particles were unable to extravasate into the collagen matrix as shown in the front view [Fig 3C] and a cross sectional view [Fig 3D] of the channel. The 1000 nm particles aggregated at the endothelium which is revealed by the intensity of the nanoparticle signal (red) being concentrated at the endothelium and lack of red signal in the collagen matrix with the MDA-MB-231 cells (green cells in Fig 3C). Although tumor endothelial pore size has been measured to be as large as 2 microns, the results from this study imply that nanoparticles need to be significantly smaller than the pore size of the endothelium to ensure the delivery of the drug to the target site.

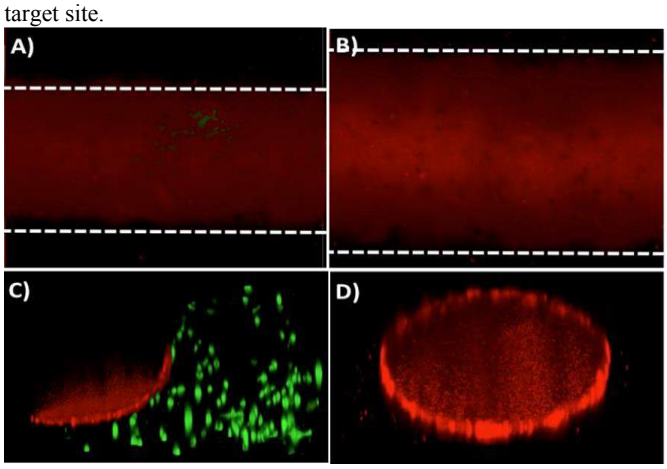

Fig. 3: Confocal Imaging of size dependent transport of nanoparticles. The transvascular transport of 20 nm particles at 0h (A) and 3h (B). 1000 nm particles show no extravasation after 12h (C) in co-culture setup and accumulation of particles along the lumen is seen in (D).

Cellular uptake studies as shown in Fig. 4 revealed that the uptake increased over time [Fig. 4B] and the aggregation of particle along the endothelium resulted in uptake of the nanoparticle by both the endothelial and the cancer cells [Fig. 4A].

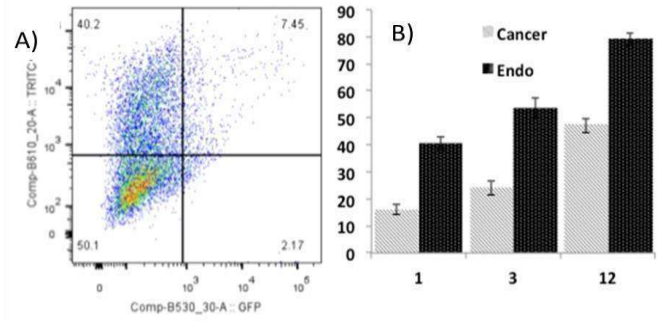

Fig. 4: A) FACS Analysis of Uptake of 50nm Particles by Cancer and Endothelial cells at 12h. B) Summary of results

DISCUSSION

The development of tissue engineered platforms to study key events of nanoparticle transport will lead to optimized nanoparticle treatments of cancer. In this study, we developed a microfluidic device that recapitulates many of the barriers nanoparticles face during tumor transport including transvascular transport, diffusion and interaction with an extracellular matrix, and nanoparticle uptake. Nanoparticle penetration and uptake studies showed the versatility of the system, confirmed a particle size cutoff for efficient nanoparticle delivery deep into the extracellular matrix and the need for modification to ensure uptake of particles by the appropriate cells. This platform can be utilized to study and understand nanoparticle features such as size and shape and to test the efficacy of tumor cell active targeting to result in greater uptake by cancer cells. Future studies will include incorporation of stromal cells and studying transport in abnormal vessel geometries.

ACKNOWLEDGEMENTS

Funding was granted by NSF Early CAREER Award CBET 0955072 and NIH R21 CA156078 and CA135230 and the NSF-GRFP.

REFERENCES

[1] Cho, K et al., *Clin Cancer Res,* 14: 1310-1316, 2008.
[2] Ediriwickrema, A et al., *ACS Biomater Sci Eng*, 1(2): 64–78, 2015.
[3] Buchanan, C et al., *Tissue Eng C*, 20:64-75, 2013.

Copyright 2016 The Organizing Committee for the 2016 Summer Biomechanics, Bioengineering and Biotransport Conference

SB³C2016
Summer Biomechanics, Bioengineering and Biotransport Conference
June 29 –July 2, National Harbor, MD, USA
SB³C2016-1101

THE ROLE OF IGF-1 IN THE CYTOSKELETAL REGULATION OF GATING OF TRPV4 CHANNELS IN ARTICULAR CHONDROCYTES

Victor DeBarros (1), Joseph D. Gardinier (3), Lauren Hurd (1,2), Mary E. Boggs (1), Randall L. Duncan (1,4)

(1) Department of Biological Sciences
University of Delaware
Newark, Delaware, USA

(2) Molecular Diagnostics Laboratory
Nemours/Alfred I. duPont Hospital for Children
Wilmington, Delaware, USA

(3) Orthopedics/bone and Joint Center
Henry Ford Health System
Detroit, Michigan, USA

INTRODUCTION

Osteoarthritis (OA) is characterized by the degradation of the articular cartilage that provides load support and smooth articulation for diarthrodial joints. This disease is the leading cause of disability among American adults that impacts over 50 million adults in the US, with 54% of adults over 65 afflicted (1). Both biochemical and biomechanical stimuli regulate the functional behavior of articular chondrocytes. IGF-I is key for regulation of chondrocyte function, stimulating anabolic, anti-catabolic and mitogenic chondrocyte functions (2). Mechanical stimulation is also necessary for regulation of articular chondrocyte function (3) and physical exercise is essential to articular cartilage integrity (4). The transient receptor potential vanilloid 4 (TRPV4) channel is central to chondrocyte mechano-transduction *in vitro* (5) and *in vivo* (6). Loss of TRPV4 activation through inhibition or knockout of the channel results in a loss of mechanosensitivity and the development of OA in male mice (6).

The gating mechanism through which TRPV4 is mechanically activated has yet to be determined. We have previously shown that regulation of mechanically-sensitive channel gating in osteoblasts is mediated by the actin cytoskeleton (7). Here, we propose that insulin-like growth factor 1 (IGF-1) modulates TRPV4 channel activity similarly, by altering the actin cytoskeleton to protect chondrocytes from extensive loading.

METHODS

Cell Culture - ATDC5 mouse chondrocyte-like cells were cultured in Dulbecco's Modified Eagle Medium, 10% FBS, 100 U/ml penicillin G, and 100 µg/ml streptomycin and buffered to pH 7.35 with 26 mM $NaHCO_3$ and maintained at 37°C with humidified 5% CO_2, 95% air and passaged once cells reached 75% confluence. Human chondrocytes were purchased from Lonza and cultured in Chondrocyte Basal Medium (Lonza) supplemented with Chondrocyte Growth SingleQuots (Lonza) containing R3-IGF-1, bFGF, transferrin, insulin, 5% FBS, 30 mg/ml gentamicin and 15 µg/ml amphotericin until 50% confluent, then placed in serum/supplement free medium. For FSS testing, cells were seeded at 1×10^3 cells/cm^2 on 75 mm x 25 mm x 1 mm glass slides coated with chicken-derived type II collagen (150 µg/ml in 0.02N acetic acid). Once cells reached 80-90% confluence, they were serum starved for 24 hours prior to testing with serum free medium.

Intracellular Calcium Measurement - Chondrocytes were loaded with 10µM of the fluorescent Ca^{2+} chelator, Fluo-4, for 15 minutes at 37°C. Cells were washed with HBSS with Ca^{2+} and Mg^{2+} and allowed to equilibrate for 10 minutes. $[Ca^{2+}]_I$ was visualized on a Zeiss LSM 510 high speed confocal microscope with a 10x C-Apochromat water immersion lens with a 488nm excitation laser and changes in fluorescent intensity were measured over time. Baseline calcium values were established then stimulated with hypotonic medium (HTS:150mOsm). Images were analyzed using Zeiss Zen Physiology 2012 software. Response to stimulation was measured as change in intensity from average baseline to peak response.

Electrophysiological recordings: Pipettes were manufactured by pulling 100 µL capillary tubes to a tip diameter of ~0.5 micron (tip resistance = 1-5 MΩ) using a dual-stage pipette puller (Narishige). ATDC5 cells were plated on 15mm round coverglass and bathed in an extracellular-like solution (ECF) while pipettes were filled with an intracellular-like solution (ICF). Whole cell recordings were performed with an Axopatch 200B amplifier (Axon Instruments) equipped with a Digidata 1332A A/D converter. Recordings were performed using a ramp protocol that clamped the cell from -80mV to +80mV over a 1s period. Cells were then challenged with HTS and changes in whole cell current recorded using the same ramp protocol as described above.

Copyright 2016 The Organizing Committee for the 2016 Summer Biomechanics, Bioengineering and Biotransport Conference

RESULTS

We examined the effects of pretreatment of cells from the rat chondrocyte-like cell line, ATDC-5, with 100ng/ml IGF-1 and how this pretreatment altered TRPV4 channel activity and the corresponding $[Ca^{2+}]_i$ response to HTS. We found that IGF-1 increased actin stress fiber formation within three hours of stimulation that resulted in a 3-4 fold increase in ATDC-5 cell stiffness that could be attenuated with depolymerization of actin with CytoD. We also observed that treatment of ATDC5 cells with either the non-specific TRPV channel blocker, ruthenium red (RR) or the specific TRPV4 blocker, RN1734 (RN) significantly attenuated the increase in $[Ca^{2+}]_i$ in response to HTS and the number of cells responding to HTS. This response could be significantly reduced by addition of 100 ng/ml IGF-1 prior to HTS. To determine if IGF-1 suppressed the TRPV4 channel activity through either actin polymerization or cell stiffening, we treated the cells with CytoD following IGF-1 pretreatment, but 30 min before HTS. We found that CytoD partially restored the $[Ca^{2+}]_i$ response to HTS (Fig. 1). Using patch clamp techniques, we used a whole cell configuration to measure whole cell TRPV4 currents during application of HTS in chondrocytes (Fig. 2). Using a ramp protocol that clamps the voltage progressively from -80mV to +80mV over a 1 sec time period, we forego any activation of voltage-activated currents that have introduced current rectification observed in previous studies. However, some rectification was still seen in the representative trace. No whole cell currents were observed in static cells at room temperature. However, within 5 min of application of HTS, whole cell currents increased. The effects of IGF-1 on TRPV4 channel activity was confirmed in these patch studies where we saw that pre-treatment of chondrocytes with 100 ng/ml IGF-1 three hours prior to patch completely attenuated TRPV4 channel activity to hypotonic challenge.

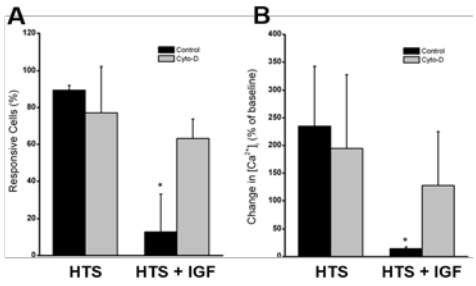

Fig. 1. Addition of 100 ng/ml IGF-1 3 hr prior to HTS challenge significantly suppressed (A) the number of cells responding to HTS and (B) the peak $[Ca^{2+}]_I$. Depolymerization of actin with cytochalasin D (5μM) rescued this response. * denotes p< 0.05

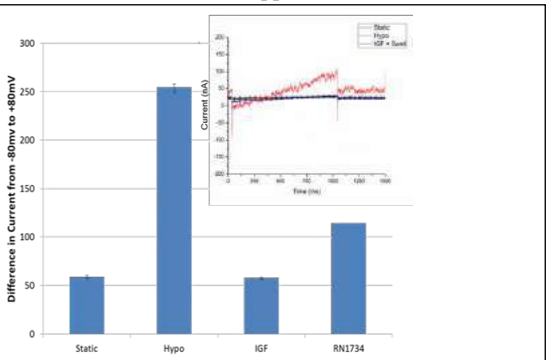

Figure 2. Inset: Representative trace of whole cell currents from static cells (untreated conditions; black line) or subjected to hypotonic swelling (red line) or IGF+hypotonic swelling (blue line). Bar graph: Summary of chondrocyte peak currents in conditions of static, hypotonically swelled, IGF-1-treated cells with HTS or inhibited by RN1734. (n=2)

We next examined the role of the cytoskeleton in regulation of TRPV4 mechanical gating in human chondrocytes. Interestingly, both depolymerization of actin with cytochalasin D and disruption of the microtubule network with vincristine significantly decreased the response of human chondrocytes to mechanical load, suggesting that both are involved in the regulation of TRPV4 gating in human cells (Fig.3)

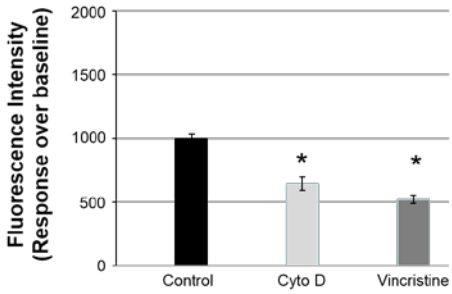

Fig. 3. HTS response of human chondrocytes to depolymerization of the actin cytoskeleton with 5μM cytochalasin D or microtubule destabilization with 5μM vincristine. Both cytoskeletal disrupting agents significantly decreased the peak $[Ca^{2+}]_I$ response to HTS. * denotes p<0.001.

DISCUSSION

Previous studies have shown that, individually, both IGF-1 treatment and activation of TRPV4 can elicit anabolic responses in chondrocytes. However, the data presented here would suggest that IGF-1 may tonically suppress TRPV4 channel activity by increasing cell stiffness through increased polymerization of the actin, and perhaps the microtubule, network. This is not particularly surprising since IGF-1 stimulation of chondrocytes has been shown to activate small Rho-GTPases that control actin polymerization. (8, 9). A potential explanation is that increased loading of chondrocytes can result in release of inflammatory factors that could be caused by TRPV4 activation and ultimately lead to OA. OA may not proceed in younger adults due to the relatively high levels of IGF-1. However, the same amount of load in older adults, where IGF-1 is very low, could result in OA due to overactivity or hypersensitivity of the TRPV4 channel.

ACKNOWLEDGEMENTS

This work was supported by the Nemours Foundation, Delaware INBRE grant number 5P20GM103446 and private donations from Dr. Jeremie Axe.

REFERENCES

1. Barbour, K et al., *MMWR* **62**, 869-873, 2013.
2. Fortier L. et al., *Clin Orthop Relat Res* **469**, 2706-2715, 2011.
3. Leong D et al., *FASEB J* **25**, 182-191 2011
4. Racunica T, et al., *Arthritis Rheum* **57**, 1261-1268, 2007.
5. Phan, M et al., *Arthritis Rheum* **60**, 3028-3037, 2009
6. Clark, A et al., *Arthritis & Rheumatism* **62**, 2973-2983, 2010.
7. Zhang, J et al., *J. Bone Miner. Res.* **21**, 1729-1737, 2006
8. Fortier, L et al., *J. Bone Joint Surg. Br.* **84**, 276-288, 2004
9. Novakofski, K et al., *J. Orthop. Res.* **27**, 58-64, 2009

Copyright 2016 The Organizing Committee for the 2016 Summer Biomechanics, Bioengineering and Biotransport Conference

SB³C2016
Summer Biomechanics, Bioengineering and Biotransport Conference
June 29 –July 2, National Harbor, MD, USA
SB³C2016-1102

DYNAMIC BENDING RESPONSE OF THE UNRESTRAINED FEMUR IN UNDERBODY BLAST LOADING

Joshua G. Chen[1], Gwansik Park[1], E. Meade Spratley[1], Robert S. Salzar[1]

(1) Center for Applied Biomechanics
University of Virginia
Charlottesville, VA, United States

INTRODUCTION

Occupants of military vehicles exposed to underbody blast (UBB) have endured high percentages of lower extremity trauma, including greater than 50% prevalence of fractures. Among these, femur injuries represent a small but debilitating cohort, accounting for approximately 13% of all UBB injuries.[1] UBB loading through the femur creates a load path that is thought to be distinct from other high-rate injuries, such as are observed in automotive collisions. Unlike automotive intrusion injuries, entrapment is not thought to be responsible for the observed UBB femur fractures as the occupant knees are unrestrained. Instead, one hypothesized mechanism of injury is the dynamic anteroposterior bending of the femur wherein the high-rate vertical displacement of the distal condyles results in a significant thigh soft-tissue load on the anterior femur and results in a bending fracture along the mid-shaft. However, given the extremely high loading rates involved in UBB, laboratory recreation of this mechanism is difficult.

One tool available to begin investigating the bending response to high-rate UBB loading is the finite element model (FEM). Numerous models of the human body have been developed for use in the automotive safety industry with extensive validation at automotive crash rates. Of these, the Global Human Body Model Consortium (GHBMC) models represent some of the most advanced, detailed, and well-validated efforts available.

The objective of this study is to determine the input conditions that produce peak moments and peak strains associated with femur bending fractures. We then intend to parametrically investigate the effects of peak ΔV and rise-time on these tolerances.

METHODS

For this study, we developed a template thigh FE model based on the geometry of the Global Human Body Model Consortium-owned GHBMC M50 Seated Model (version 4.3). This template thigh model was used to simulate an anteroposterior displacement of the distal femur at rates within the realm of those seen in UBB. A total of 18 simulations of the femur were recorded wherein the distal condyles were subjected to input velocities of 5, 10, 15, 20, 25, and 30m/s with 5, 10, and 15ms peak times. The proximal end of the femur was constrained to zero translation, but free rotation in all three directions, analogous to a spherical joint. Distally, the impacting plate was constrained in all rotation axes and in two translational dimensions, allowing only one-dimensional linear motion. The impactor plate began in contact with the rectangular potting cup, the plate then prescribed a symmetric triangular shaped velocity curve defined by peak velocity and time-to-peak, causing the femur and potting to rotate anteriorly and superiorly away from the impactor.

Three planes were defined *a priori* at the proximal third, center, and distal third where section force, stress, strain, and moment time-histories were recorded for each simulation.

Within the GHBMC femur, bone was represented using a piecewise elastic-plastic material model. Soft tissue was represented using a hyperelastic constitutive model including rate effects. To avoid potential instabilities within the model at such high-rates, failure criteria such as element deletion were disabled. Instead, thresholds for fracture relative to peak moment and peak strain derived from the existing automotive literature were used to assess the likelihood fracture within the model.[2,3]

Copyright 2016 The Organizing Committee for the 2016 Summer Biomechanics, Bioengineering and Biotransport Conference

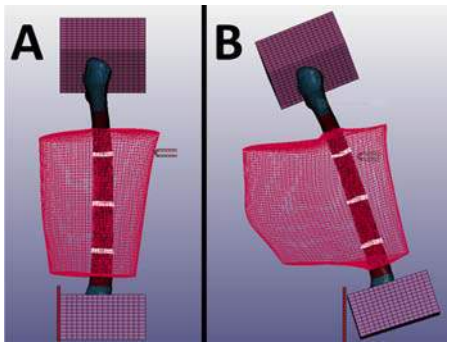

Figure 1: Femur model with A) Impactor Plate at rest B) Impactor Plate undergoing Prescribed Motion

RESULTS

The largest moments in all three sections were observed in the sagittal plane about the positive x-axis defined in the LS-Dyna workspace. [Figure 1B] As expected, the distal section typically developed its peak moment and peak strain earlier, and at a higher magnitude, than did the more proximal sections. Increasing velocity input and decreasing time-to-peak resulted in higher magnitude responses for all measures such that 30m/s in 5ms was the most severe impact tested.

Peak moments exceeded the existing dynamic failure criteria of 387 Nm for 10/18 simulations. These represented all velocities cases except 5m/s for the 5ms time-to-peak group; the 20, 25, and 30m/s velocities for the 10ms time-to-peak group; and 25 and 30m/s velocities for the 15ms group. However, peak strains exceeded the existing ultimate strain threshold of 1.60% in fewer total simulations, 4/18. [3]

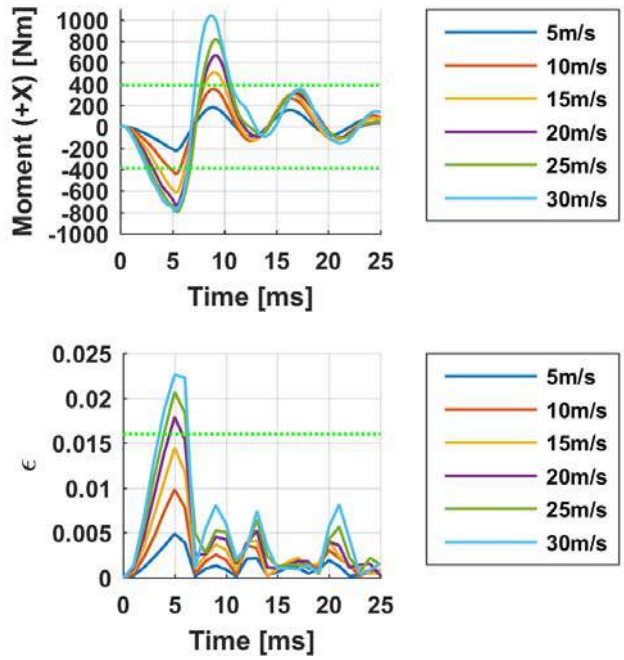

Figure 2. Moment versus time (A) and Strain versus time plots for the 5ms rise time group. Dotted green line indicates existing failure threshold of 387Nm and 1.60% ε, respectively.

DISCUSSION

As expected, the simulations with the highest loading rates produced the largest magnitude moment and strain responses and that by lowering the input energy (by decreasing ΔV) or by elongating the pulse by increasing the rise-time, the model response could be made less severe. Additionally, by design, the model did not fail, but instead allowed for an elastic response beyond the typical automotive failure levels set for the GHBMC bone. This allowed for the investigation of how loading rate effected changes in material response. In general, the models predicted a trend of higher sensitivity to moment versus strain for all three rise-time groups. This may be noteworthy as the two criteria investigated were derived from very similar automotive-rate testing of femurs in three-point bending at a ΔV of 1.5m/s, thus suggesting that the two criterion may not be interchangeable at very high rates. [2,3] Future characterization work should include human surrogate testing at loading rates greater than 10 m/s and shorter rise times in order to fully characterize the strain and moment tolerances of the femur.

This study artificially excluded failure and the corresponding element deletion within the mesh in order to explore the sensitivity of the GHBMC model to high-rate loading. Consequently, moment and strain responses for elements with stresses beyond the typical yield stress of bone will be over predicted, making interpretation of the long-time response of the model difficult. Additionally, the input pulses prescribed here do not account for injuries that would be incurred by loading the distal femur through the lower extremity. Such injuries would very likely disrupt load transmission through the limb and reduce the likelihood of a bending-type fracture of the femur. Thus, it is unclear if loading rates associated with femur bending failure are indeed possible under the inertia-only force of the thigh soft-tissue.

These simulations provide insight for designing laboratory experiments around bending-type femur fractures in vertically loaded, inertial-only situations. Future work will focus on collecting and incorporating sufficiently high-rate human surrogate data to more fully validate this model and provide further understanding of the human tolerance to this mechanism of injury.

Table 1: Predicted fracture risk. (M) denotes moment threshold exceeded; (S) denotes ultimate strain threshold exceeded.

		Rise Time		
		5ms	10ms	15ms
Input Velocity	5m/s			
	10m/s	M		
	15m/s	M		
	20m/s	M,S	M	
	25m/s	M,S	M	M
	30m/s	M,S	M,S	M

REFERENCES

[1] Alvarez, RTO-MP-HFM-207—a survey of blast injury across the full landscape of military science NATO: Halifax Canada. *J. Epidemiol. Blast. Inj. Curr. Oper.* KN1-10. 2011

[2] Kerrigan, Jason Robert. *A computationally efficient mathematical model of the pedestrian lower extremity.* Vol. 68. No. 12. 2008.

[3] Funk et al., 2004. Dynamic Bending Tolerance and Elastic-Plastic Material Properties of the Human Femur. *48th Annual Proceedings of the Association for the Advancement of Automotive Medicine.*

Copyright 2016 The Organizing Committee for the 2016 Summer Biomechanics, Bioengineering and Biotransport Conference

SB³C2016
Summer Biomechanics, Bioengineering and Biotransport Conference
June 29 –July 2, National Harbor, MD, USA
SB³C2016-1103

COMPARISON OF VALIDATION DATA FOR FINITE ELEMENT MODELS OF THE HUMAN HEAD

Logan E. Miller (1,2), Jillian E. Urban (1,2), Joel D. Stitzel (1,2)

(1) Center for Injury Biomechanics
Virginia Tech-Wake Forest University
School of Biomedical Engineering and Sciences
Winston-Salem, NC, USA

(2) School of Medicine
Wake Forest University
Winston-Salem, NC, USA

INTRODUCTION

Each year, approximately 1.7 million people in the United States suffer from traumatic brain injury (TBI) [1]. TBI is a major public health concern as it is a leading cause of disability and injury-related death - accounting for nearly one third of all injury-related deaths [2]. To prevent and treat these types of injuries, the fundamental injury mechanisms need to be well-characterized and understood. There are various theories about what causes brain injury, but there is still a great deal that we do not know about the fundamentals of brain injury, as well as injury thresholds. Various methods have been used over the years to investigate and gain a deeper understanding of brain injury mechanisms, including animal tests, cadaver studies, anthropomorphic test devices (ATDs), and computational models [7]. Finite element (FE) models are powerful tools because they can provide spatial and temporal distributions of stresses and strains over the problem domain. The quality of a model's predictions, however, is dependent on the accuracy of the modeled geometry and the model's ability to describe complex mechanical behavior and material response.

FE models with varying degrees of anatomical accuracy, element size and material properties, have been developed. The process typically employed in current model development begins with image segmentation of medical images, such as computed tomography (CT) and magnetic resonance imaging (MRI), to define 3D surfaces of desired structures, followed by a surface-based mesh generation process. During the mesh generation process, complex anatomical features are frequently simplified and 'smoothed' to allow faster development and simple contact definitions. One feature of particular importance that is over-simplified in many brain FEMs is the gyral folds on the surface of the brain. The brain surface is typically modeled as a smooth surface, but this simplification and reduction in geometrical accuracy could significantly impact the model's local brain response and prediction of injury. Various studies have indicated that the intricate folding patterns on the surface of the brain greatly affect both the distribution and magnitude of stress and strain throughout the brain [11].

The experimental validation of FE models is a critical step in model development and the application of such models to fields such as injury prediction and automotive safety. Many currently used FEMs have only been validated intracranial pressure (ICP) experiments, but there is some controversy about whether validating against only pressure data is sufficient, since some brain injuries (e.g., diffuse axonal injury) are found to be dependent on strain [30]. This motivates validation using the more robust displacement data set that captures the strain field that develops in the brain, which is examined in the current investigation. The objective of the current study is to present localized brain motion validation data for three experimental configurations for six validated brain FE models and use an objective rating method for a quantitative comparison between models.

METHODS

Three cadaver impact tests (C755-T2, C383-T1, C291-T1) conducted by Hardy et al. (2001, 2007) are presented in the current study and validation data for the following six FE models are examined and compared: Atlas-Based Brain Model (ABM), Simulated Injury Monitor (SIMon), Global Human Body Models Consortium (GHBMC) head model, Total Human Model for Safety (THUMS) head model, Kungliga Tekniska Högskolan (KTH) model, and the Dartmouth Head Injury Model (DHIM). The ABM, a high-resolution FE model derived from the International Consortium for Brain Mapping (ICBM) brain atlas was developed in our lab and multi-objective optimization was

Copyright 2016 The Organizing Committee for the 2016 Summer Biomechanics, Bioengineering and Biotransport Conference

performed to identify the ideal parameters for the brain material model.

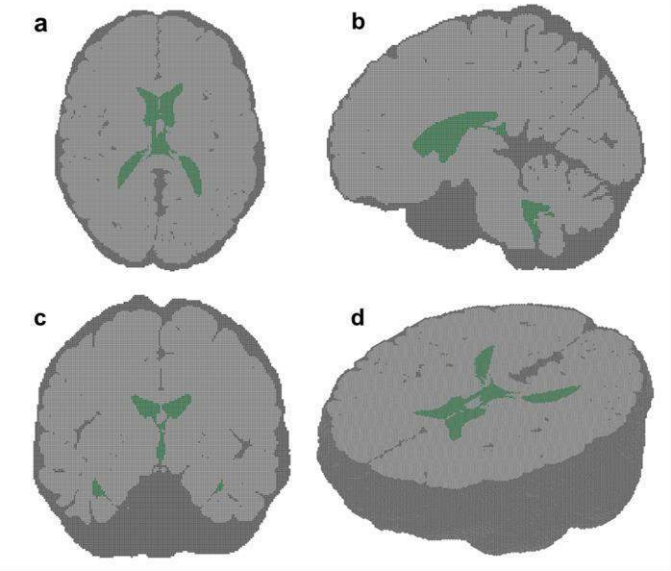

Figure 1: Axial (a), sagittal (b), coronal (c), and isometric views of the ABM.

The impact conditions were simulated using LS-DYNA for the ABM, SIMon, GHBMC, and THUMS models and localized brain motion quantified using nodal displacements. Results for the remaining models were obtained from published literature. To evaluate model performance for each impact condition, the error between experimental and predicted displacements for each NDT was quantified using a powerful metric called CORA (CORrelation and Analysis) [44]. CORA evaluates the similarity of two curves by calculating a rating using two methods: the corridor method and the cross-correlation method. Both ratings range from 0 to 1 and are averaged to determine a total CORA score (1 corresponds to a perfect match). The corridor method computes a rating based on where the comparison curve falls in relation to corridors around the reference curve. The cross-correlation method is based on ratings for the phase shift, size and progression of time-shifted curves.

RESULTS

CORA scores were computed for each model for each NDT curve and averaged to compute an average CORA score for each experimental configuration for each model (Table 1).

Table 1: Average CORA scores

	C755-T2	C383-T1	C291-T1	Average
ABM	0.445	0.421	**0.412**	**0.426**
SIMon	0.342	0.411	0.393	0.382
GHBMC	0.433	0.386	0.241	0.353
THUMS	0.418	0.302	0.343	0.354
KTH	**0.476**	0.419	0.355	0.417
DHIM*	0.316	**0.432**	-	0.374

DISCUSSION

Looking at model response in the C755-T2 impact, we see that all models perform relatively well, with the KTH model scoring the highest average CORA rating of 0.476. Most of the models considered score the highest CORA rating under this impact configuration. This is likely because it is the lowest severity impact with the simplest experimental curves (i.e. few local maxima and minima). In the C383-T1 test, the DHIM has the highest CORA score. It should be noted, however, that this CORA rating is based on the response of only 4 of the 12 total NDTs, so it may not be representative of the response of the DHIM in general. Considering the remaining models, whose performance is based on the response of all 12 NDTs, the ABM performs best with a CORA score of 0.421. Considering the response in the C291-T1 parietal configuration, which was the most severe impact simulated, the ABM scores the highest CORA rating (0.412). Additionally, looking at each model's average CORA score between the three impacts, the ABM again scores the best CORA rating. This result indicates that of the models considered, the ABM demonstrates the strongest ability to predict local brain deformations under a range of impact severities and directions.

ACKNOWLEDGEMENTS

Funding for this project is provided by the National Institutes of Health (R01 NS082453). All simulations were run on the DEAC Cluster at Wake Forest University. The authors would like to thank the ANSIR lab for providing the ICBM labelmaps, the THUMS and GHBMC teams at Wake Forest University for providing the respective head models, and Elizabeth Lillie for her work on the MATLAB code to produce the ABM from the ICBM labelmaps.

REFERENCES

[5] Bergmann, G et al., *J Biomech*, 34:859-871, 2001.

Copyright 2016 The Organizing Committee for the 2016 Summer Biomechanics, Bioengineering and Biotransport Conference

SB³C2016
Summer Biomechanics, Bioengineering and Biotransport Conference
June 29 –July 2, National Harbor, MD, USA
SB³C2016-1104

ENHANCING BIOMECHANICAL ENGINEERING EDUCATION THROUGH PROBLEM BASED LEARNING

Alisa Morss Clyne

(1) Mechanical Engineering
Drexel University
Philadelphia, PA, USA

INTRODUCTION

A critical lag between bioengineering bench discovery and clinical implementation delays lifesaving therapies from reaching patients. Biomechanical engineering courses often do not focus on translating research into consumer devices. Through a N ational Science Foundation Transforming Undergraduate Education in STEM grant, we redesigned MEM 304: Introduction to Biomechanical Systems into a problem-based learning course focused on current biomechanical research challenges. Course modules included medical device design, cellular and tissue biomechanics, biomanufacturing, bio-microfluidics, and bio-inspired robotics. Each module was inspired by a real-world problem, and students completed hands-on laboratory projects as part of each module's learning progression. We hypothesized that problem-based learning can be successfully integrated into a cooperative education curriculum to produce engineers who bridge the gap between research and development.

METHODS

Problem (or challenge)-based learning is ideal for integrating biomechanical engineering classroom, laboratory, and cooperative education. In problem-based learning, the process is student-centered within small student groups with the professor serving as a facilitator or guide. Students encounter authentic problems which are then used as a tool through which the students direct their own learning [1]. While many active and collaborative teaching strategies are more effective than traditional lecture formats in enhancing student knowledge and retention, studies suggest that problem-based learning enhances students' abilities to apply their knowledge both immediately and in the long term [2-4]. Thus the problem-based learning approach will help integrate classroom learning, research and design projects, and co-op, as well as improve student performance in these experiences.

Improvements in engineering education largely come not from research on new educational techniques but rather from implementation of proven techniques. Therefore, we adopted the challenge-based instruction methods pioneered by the VaNTH Engineering Research Center, an NSF-funded collaboration in improving biomedical engineering education among Vanderbilt, Northwestern, the University of Texas, and the Harvard/MIT Health Sciences and Technology Program. The VaNTH model recognized that the rapidly developing bioengineering industry requires engineers who can expand and adapt their knowledge and skills [5]. Therefore, students need to build "adaptive expertise," the ability to apply engineering knowledge to solve new problems [6].

The VaNTH model integrates conceptual and innovation knowledge development through the STAR.Legacy cycle [7]. The STAR.Legacy cycle begins by posing exploratory challenges. Students then generate initial ideas about how to solve these challenges. In the "Multiple perspectives" phase, students take into account ideas by other people familiar with these or similar challenges (e.g., industry professionals, end users). Students then base their learning on questions prepared from these initial experiences. Research is instructor-supported and can take the form of online or in-class lectures, discussions, and demonstrations among many others. Students then "Test their mettle" by applying the new knowledge to an assessment technique

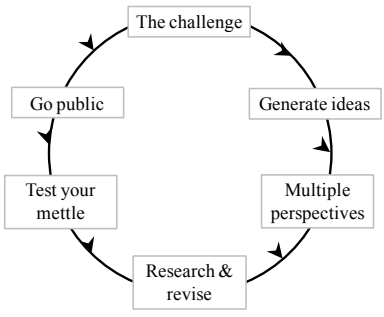

The VaNTH STAR.Legacy Cycle

Copyright 2016 The Organizing Committee for the 2016 Summer Biomechanics, Bioengineering and Biotransport Conference

such as a quiz or problem set. This allows students to return to the research phase if needed to enhance their knowledge. Finally, the students "Go public" by synthesizing their newly acquired knowledge to solve either the original or an analogous challenge (e.g., exam, presentation, report).

A primary obstacle to implementation of active and challenge based learningwas that face-to-face class time was limited. We used cyberlearning, specifically online lectures, assignments, assessments, and journals, to support the STAR.Legacy cycle. Review lectures on mechanical engineering, biology, physiology, and disease were provided to students through Drexel's Blackboard Vista (Bb Vista) system. In addition, at the end of each week, students completed online journal entries to assess their opinion of the class and their depth of knowledge. Cyberlearning's significant advantages include that it allows students to proceed at their own pace, rewind and repeat material they may have missed, and open up in-class time for questions, discussions, and active learning.

RESULTS

The four faculty members and their graduate student teaching assistants all participated in a problem-based learning workshop led by faculty from the University of Delaware the summer prior to course implementation. During the workshop, each faculty member created a problem for his/her module. These modules were then integrated into the course. 25 students enrolled in the course (23 from mechanical engineering, 2 from electrical engineering). The 5 problem-based learning modules from the course were:

1. Medical Devices: In this module, students first received an overview of physiological systems and we visited the human anatomy lab at Drexel Medical School to provide students with a physical understanding of the human body. Student teams then received the problem, in which they were an engineer tasked with pitching a new medical device idea to their company's CEO. Students delivered a practice elevator pitch, followed by a final pitch one week later.
2. Lung Biomechanics: This module took a real life problem—a highly- publicized lung transplant in a pediatric patient with cystic fibrosis—and tasked students with determining how to measure lung function decline in patients with cystic fibrosis before and after lung transplantation. A pulmonologist from Drexel College of Medicine taught students the basics of cystic fibrosis and lung function testing, allowing the students to practice reading real patient lung function tests. For the laboratory component, we acquired pig lungs from the slaughterhouse and treated them in various ways to replicate obstructive and restrictive lung diseases. Students then inflated the lungs and measured pressures/volumes to determine which lung represented which disease. The students completed an executive summary describing which lung function test they selected, and the pig lung lab data analysis was included as supplementary material.

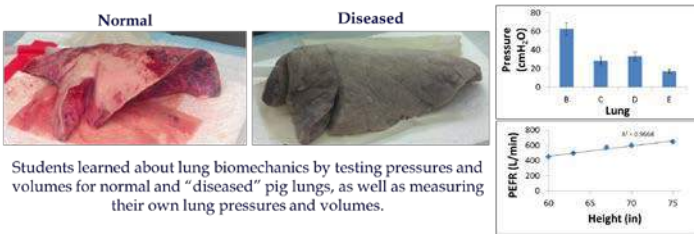

Students learned about lung biomechanics by testing pressures and volumes for normal and "diseased" pig lungs, as well as measuring their own lung pressures and volumes.

3. Lung Biomanufacturing: This module continued the cystic fibrosis case, but now the students were tasked with developing a system to tissue engineer new lungs for transplantation. Students learned about tissue culture and tissue engineering from Professor Clyne. They then analyzed current journal articles on how cell migration changes on scaffolds of different stiffness as preparation for their lab experience. In the lab, students measured cell migration speed on polyacrylamide gels of varied stiffness. Since the lab time was not adequate to complete each section in series, we had one student from each team complete each section of the lab. Student teams then designed a lung tissue engineering system, using the lab data as supplemental materials.
4. HIV Lab on a Chip: In this module, student teams created new microfluidic devices to either diagnose HIV or perform HIV monitoring. Students learned about microfluidics from Dr. Noh, and received an excellent overview of HIV/AIDS and the state of the art in disease detection/monitoring from an infectious disease specialist from Drexel College of Medicine. In the laboratory components, students observed microchip/microfabrication demonstrations in Dr. Noh's lab. The students then designed a lab-on-a-chip device for HIV detection or monitoring, and their final deliverable was a Powerpoint presentation of their devices. An infectious disease specialist from Drexel College of Medicine observed and commented on their final designs.
5. Biologically derived prosthetics: In the final module, student teams designed a new athletic prosthetic leg. Students learned about animal locomotion and musculoskeletal modeling from Dr. Tangorra, and then experimented with designing new systems using Animatlab (a free computational dynamics program). The student team deliverable was a Powerpoint presentation of their new prosthetic design.

DISCUSSION

Overall, engineering students enjoyed the hands-on nature of the course. Initial student deliverables often did not meet quality and depth expectations; however, deliverables improved dramatically with faculty critique followed by student revision. Faculty did not feel that the problem based learning format significantly increased their workload, after problem formulation.

Quantitative and qualitative course assessment provided by an external reviewer showed that the students learned to transform their learning into new ways to focus on problem and come to new ideas and discoveries. Through analysis of pre/post evaluations, interview/focus groups, journals, and modules it became evident that the students embraced both problem solving and cooperative groups. One student stated, "*I learned what it really meant to be an engineer. In this class, just as the real world, we were given a problem to solve, and step by step, worked up until we had a right design and specification that we could present.*" The impact this course had on students' ability to synthesize information from many content areas and come up with a design plan solution was a wonderful bridge between knowledge and application. One student summed it up this way, "*It prepared me to function in a work environment, and helped to see what it would really mean to be an engineer in the field.*"

ACKNOWLEDGEMENTS

This research was funded by NSF grant 1141186.

REFERENCES

[1] Bringing problem-based learning to higher education, 1996.
[2] Gijbels, D *et al*., *Rev Educ Res*, 75(1): 27-61, 2005.
[3] Kuh, G *et al*., Student success in college: Creating conditions that matter. 2005.
[4] Pascarella, E *et al.*, How college affects students, 2005.
[5] Harris, TR *et al.*, *Annu Rev Biomed Eng,* 4: 29-48, 2002.
[6] Harris, TR *et al.*, *Med Eng Phys*, 27(7): p. 617-24, 2005.
[7] Schwartz, DL *et al*., *ETR&D-Educ Tech Res*, 47(2): 39-59, 1999.

Copyright 2016 The Organizing Committee for the 2016 Summer Biomechanics, Bioengineering and Biotransport Conference

SB^{3}C2016
Summer Biomechanics, Bioengineering and Biotransport Conference
June 29 –July 2, National Harbor, MD, USA
SB^{3}C2016-1105

MECHANICAL REGULATION OF CELL BEHAVIORS DURING CONVERGENT EXTENSION OF THE XENOPUS LAEVIS NEURAL PLATE

Deepthi S. Vijayraghavan (1), Emily E. Kieffer (1), Joseph H. Shawky (1), Lance A Davidson (1,2,3)

(1) Department of Bioengineering
University of Pittsburgh
Pittsburgh, PA, USA

(2) Department of Developmental Biology
University of Pittsburgh
Pittsburgh, PA, USA

(3) Department of Systems and Computational Biology
University of Pittsburgh
Pittsburgh, PA, USA

INTRODUCTION

The formation of the vertebrate neural tube, the primordial structure of the central nervous system, is one of the earliest morphogenetic events during embryonic development. Failure of neurulation leads to congenital defects that affect nearly 3000 pregnancies in the US annually.[1] Despite progress being made in understanding genetics of these defects, it remains unclear how and when they will manifest due to the multifactorial nature of their etiology. Establishing a better knowledge of the physical principles guiding this process will expand our understanding on how these defects occur.

Neurulation entails several coordinated cell movements and shape changes that turn a planar epithelial neural plate into an elongate tubular structure. At the onset of this process, the lateral edges of the neural plate, converge towards the dorsal midline while the neural plate elongates along the anterior-posterior axis. Previous studies of epithelial convergence extension have described planar directed cell rearrangements that are thought to actively drive these movements.[2] Neural epithelial cells display preferential localization of actomyosin at cell-cell boundaries that remodel junctions and facilitate directional rearrangement. By contracting junctions in the mediolateral direction, epithelial cells form unstable "high-order" vertices that contain 4 or more cells. These vertices then resolve in the perpendicular, anterior-posterior direction driving mediolateral neighbor exchanges. Coordinated contraction and resolution of junctions cause local arrays of cells to directionally intercalate, narrowing along the mediolateral direction while lengthening anterior-posteriorly. Mutant analysis in chick and mouse neural tube morphogenesis reveals that the Planar Cell Polarity (PCP) pathway enables polarized cell behaviors and cell intercalation, which together with apical constriction drive neural plate bending.[3,4] It remains unclear whether PCP directs polarized behaviors or transduces tissue polarity cues from other patterning systems.[5,6] Mechanical patterning processes can provide an alternative source of tissue polarity, for instance, anisotropic mechanical stresses and tensional forces have been shown to polarize cell behaviors and epithelial tissue patterning in other systems.[7] Tissues may also adapt to altered mechanical environment in order to maintain programmed behaviors which allows for robustness. For example, converging and extending tissues in *Xenopus laevis* increase their force production when facing larger mechanical resistance. [8] Thus we would suggest that cells might also alter their behaviors to accommodate such changes in mechanical loads and maintain morphogenetic programs.

In this study, we first described cell morphological and behavioral changes that accompany neural plate convergent extension in *Xenopus laevis* embryos. We then tested whether externally imposed patterns of mechanical stresses are able to regulate polarized cell behaviors during this process. Finally, we investigated how altering cell size affected cell behaviors and tissue morphology.

METHODS

Embryo Handling Eggs are obtained from female *Xenopus laevis* and fertilized *in vitro*. Fertilized eggs are dejellied in 2% cysteine and cultured in 1/3× Modified Barth's Solution (MBS).

Spatiotemporal Cell Morphology To observe temporal differences in apical cell shape and arrangement in the neuroepithelium, embryos were fixed at 4 time points between the end of gastrulation and the end of the flat neural plate stage. Embryos were stained for f-actin using Bodipy-phallacidin. Apical cell outlines on dorsal surface of the embryo were imaged using confocal laser scanning microscope (Leica SP5, mounted on an inverted compound microscope DMI6000, Leica Microsystems, Inc.). To confirm spatial differences in cell identity, embryos were stained for cytokeratin, an epidermal ectoderm marker or Sox3, a neural ectoderm marker.

Copyright 2016 The Organizing Committee for the 2016 Summer Biomechanics, Bioengineering and Biotransport Conference

Live Cell Dynamics Dorsal tissue isolates containing all three embryonic germ layers were excised from the dorsal anlagen of embryos expressing utrophin-GFP or membrane-GFP. Time-lapse image sequences of the neural ectodermal apical surface were collected during early neural plate morphogenesis.

Cell Shape and Rearrangement Z-projected images of cell boundaries within the dorsal surface of the embryos or dorsal isolates were segmented using SeedWater Segmenter software. Morphological parameters describing cell shape and orientation as well as vertex order, an indicator of junctional remodeling, were quantified via custom written ImageJ macros. This analysis was performed on both live time-lapses image sequences as well as static images of fixed embryos. In live images, duration of high-order multi-cell vertices were additionally quantified.

Dorsal Isolate Confinement To alter the strain field within the neural plate, polyester blockades were placed on the anterior and posterior ends of dorsal tissue explants. The blockades prevented the explants from elongating. Stereoscopic time-lapse images were collected of confined and unconfined isolates to obtain tissue convergence and extension strain rates. Explants were fixed at stage 15 and the F-actin labeled apical surface was imaged to detect alterations in cell shape or rearrangement due to confinement. Live imaging was also performed to reveal changes in cell kinematics.

Cell Size Alteration During early development *Xenopus* embryos undergo reductive cleavage, where total embryo volume is conserved even as cells divide. Thus, during early rounds of division cells become progressively smaller. Arresting the cell cycle within embryos inhibits this reduction in cell size compared to carrier-treated control embryos that undergo normal rates of cell division. The cell cycle inhibitor cocktail of hydroxyurea and aphidicolin (HUA) has been previously used successfully in *Xenopus* embryos causing no visible defects in neural tube closure.[9] We cultured embryos in media containing 20 mM hydroxyurea and 150 μM aphidicolin in 1/3x MBS from the start of gastrulation until the late neural plate stage at which point embryos were fixed and stained for F-actin. Control embryos were cultured in DMSO carrier in 1/3x MBS. During these stages, cells in the neural plate normally undergo between 1 and 2 rounds of cell division.

RESULTS

As the neural plate matures the apical surface of cells at the neural plate midline become isodiametrically constricted whereas cells at the border of the plate become elongated and aligned with the AP axis. Neural epithelial cells increasingly form high order junctions, indicative of increased cell rearrangement. These high order junctions are seen at the beginning of neurulation. Live imaging confirmed the occurrence of cell rearrangement and the transient nature of these high order vertices that resolved within an hour of formation. Live imaging of actin reveals a dense and highly contractile apical cortex with bursts of actin flares occurring at cell-cell junctions.

Blocking extension of dorsal tissues altered tissue strain. Unconstrained control explants elongated at a rate of ~15% per hour and converged at ~10% per hour whereas as confined explants elongated at a rate of 0.2% per hour and converged at a rate of 2% per hour. Comparing cell shapes within unconfined to confined explants revealed no changes at the tissue midline; however cells at the border were on average 20% less elongate and 15° less aligned with the AP axis in confined explants ($p<0.05$; nested ANOVA). Confined explants showed a slight but not significant decrease in percentage of high-order junctions

HUA treated embryos showed a 2-fold increase in apical area at all locations within the neural plate. Compared to controls, a similar pattern of cell shapes was seen. There was a significant decrease in the percentage of high-order vertices within HUA treated embryos compared to control ($p<0.01$, Student's t-test). The width of the neural plate remains the same in control and HUA treated embryos as confirmed through immunofluorescent staining of cytokeratin.

DISCUSSION

Our description of cell rearrangement within the *Xenopus* neural plate complements similar findings of studies performed in later stages of chick and mouse neurulation and in other experimental models of convergent extension such as *Drosophila* germband elongation.[3,4,1] Thus, cell rearrangement appears to be a conserved behavior during convergent extension across species and tissue types. The contractile actin network within the apical cortex and at the junctions of the cells potentially facilitates rearrangement.

Interestingly, neuroepithelial cells demonstrate differential regulation of apical shape based on their location within the neural plate. Cells near the midline actively constrict and remain relatively isodiametric while cells at the periphery of the plate elongate anterior-posteriorly possibly reflecting a passive deformation guided by the overall tissue strain field. Our tissue confinement experiments corroborate this hypothesis, as border cells within confined tissues fail to elongate and align to the same extent as in unconfined tissues. The confinement experiments indicate no overall difference in apical shape or area of cells near the midline. Confinement also does not disrupt formation of high order junctions. However, further studies on live tissues must be performed to confirm that the polarized formation and resolution of these junctions are not affected. Tissues with larger cells show a decrease in high-order vertices possibly due to reduction in rearrangement. Given that no observable defects were observed in overall tissue strain, larger cells may reduce the required amount of rearrangement since each net intercalation of larger cells contributes greater tissue strains compared to smaller cells.

Taken together, cell rearrangement through junctional remodeling appears to be a timed program that coincides with convergent extension at the start of neurulation. Cells may be able to adapt these behaviors to maintain overall tissue strain rates. Because the tissue strain field does alter apical shape of a population of cells near the border of the neural plate, alterations of the tissue mechanical environment *in vivo* may make neural tube closure more susceptible to failure. Thus, linking genetic mutations to mechanical aberrations may give further insight into neural tube defects.

ACKNOWLEDGEMENTS

The members of the Davidson Lab. This work has been supported by grants from the NIH (R01 HD044750 and R21 ES019259) and the NSF (CAREER IOS-0845775 and CMMI-1100515). DV additionally supported by NIBIB BiRM T32 EB003392-01

REFERENCES

[1] Williams J, et al., *CDC MMWR* 64:1-5, 2015.
[2] Blankenship JT et al., *Dev Cell*, 11: 459–470, 2006.
[3] Nishimura, T. *Cell,* 149: 1084–1097, 2012.
[4] McGreevy EM, et al ., *Biol Open*., 4(2):186-96, 2015.
[5] Kim, HY et al., *J. Cell Sci,* 124(4):635-46, 2011.
[6] Lawrence PA and Casal J, *Dev Biol,* 377(1):1-8, 2013.
[7] Chien YH et al., *Curr. Biol*, 25(21):2774-84., 2015.
[8] Zhou J et al., *Development,* 142(4):692-701 2015
[9] Harris WA and Hartenstein V, *Neuron*, 6:499-515, 1991.

Copyright 2016 The Organizing Committee for the 2016 Summer Biomechanics, Bioengineering and Biotransport Conference

SB^{3}C2016
Summer Biomechanics, Bioengineering and Biotransport Conference
June 29 –July 2, National Harbor, MD, USA
SB^{3}C2016-1106

INVESTIGATION OF FLOW INSTABILITY WITH VASCULAR GEOMETRY AT THE BIFURCATION OF MIDDLE CEREBRAL ARTERIES FROM HEALTHY VOLUNTEERS

T. Murayoshi (1), T. Yagi (1, 2), Y.Tobe (1), K.Takanishi (1),K.Suto (1), M. Umezu (1)
H. Yoshida (3), K. Nishitani (3), Y. Okada (3), S. Kitahara (3)

(1) Center for Advanced Biomedical science (TWIns), Waseda University
2-2 Wakamatsu-cho, Shinjuku-ku, Tokyo, Japan

(2) EBM corporation
Ohmoriminami, Ohtaku, Tokyo, 143-0013
Japan

(3) Kitahara International Hospital
Oowada-cho, Hachioji-shi, Tokyo
Japan

INTRODUCTION

The initiation of cerebral aneurysms has been considered to be related with wall shear stress (WSS). More specifically, the temporal and spatial variations of WSS at that site have been focused in an attempt to find out the relationship with aneurysmal initiation[1,2]. Although there have been numbers of proposed correlation parameters, the basic principle of aneurysmal initiation still awaits further researches. The bifurcation of cerebral arteries is known to be a favorite site of aneurysmal initiation, and the geometry is also known to be deformed due to atherosclerosis from aging. Understanding the relationship between the flow and geometry motivated the present research. The objective of this research is to investigate the relationship of flow instability on vascular geometry at the bifurcation of middle cerebral arteries from healthy volunteers.

METHODS

Choice of case

20 healthy volunteers were examined for the magnetic resonance imaging (MRI). The MRI examinations were carried out at Kitahara International Hospital. Out of 20 subjects, 2 subjects were excluded due to the inability of constructing cerebral arterys. In total the study consisted of 18 healthy subjects (average age 28.8 years; 16 men, 2 women). Three-dimentional vascular models were constructed using ziostation® (Ziosoft inc, Japan) based on MRI images.

CFD analysis

CFD software hemoscope® (EBM corporation, Japan) was used for meshing, hemodynamic analysis and visualization of analysis results. Each case was simulated pulsatile condition. The blood was defined as Newtonian fluid with the density of 1050 kg/m^3 and the viscosity of 0.004 PaS. The inlet boundary condition used an average pressure of 100 mmHg. The outlet boundary conditions were set velocity boundary based on the constant shear stress theory and Hagen-Poiseuille flow.

WSS vector variation

An index to quantify the WSS vector variation is shown in the following equation. WSS vector variation τ was defined as total accumulation of an instantaneous relative angle between a pair of wall shear stress vector over time during one cardiac cycle .

$$\tau = \sum_{i=1}^{T} \arccos\left(\frac{\tau_i \bullet \tau_{i+1}}{|\tau_i||\tau_{i+1}|}\right)\frac{180}{\pi} \qquad (1)$$

Measuring method bifurcation and inclination angle

A conceptual diagram of the bifurcation and inclination angles are shown in Fig. 1. The bifurcation and the inclination angles were measured by ImageJ®. The bifurcation angle was defined as the angle between the daughter vessels[3]. The inclination angle was defined as the angle between 2 planes of parent vessel and both daughter branches[3].

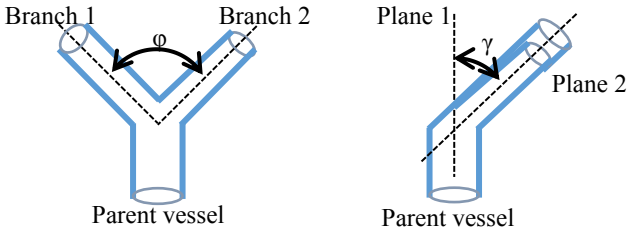

(a) Bifurcation angle (b) Inclination angle

Fig.1 Conceptual diagram for shape of parameter

Copyright 2016 The Organizing Committee for the 2016 Summer Biomechanics, Bioengineering and Biotransport Conference

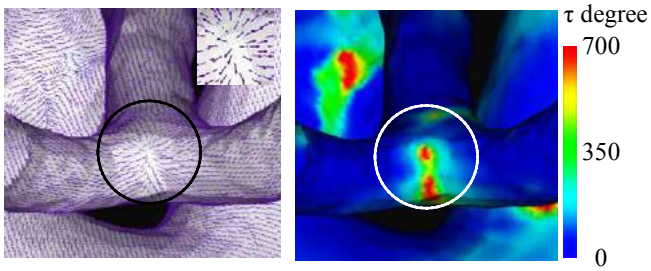

(a) WSS vector (b) WSS vector variation

Fig. 2 Hemodynamics with MCA bifurcation

RESULTS

An example of hemodynamics with MCA bifurcation is shown in Fig. 2. Impinging flow was confirmed at the top of the MCA bifurcation because full-divergence of WSS vector was observed. At that point, high WSS vector variation was confirmed. The value of WSS vector variation was 700degree.

Fig. 3, Fig. 4, and Fig. 5 represent the relationship between WSS vector variation degree and bifurcation angle, inclination angle, and Reynolds number, respectively. It confirmed that the relationship of the bifurcation angle with the WSS vector variation gave a correlation of R=0.5156, while that of inclination angle gave R=0.3541. Also, it confirmed that the relationship of Reynolds number with the WSS vector variation gave a correlation of R=0.4747.

DISCUSSION

The former study has shown that the bifurcation angle and the inclination angle gave an average of 92.1 degree (mix/max of 76.2 to 97.7 degree) and 15.4 degree (min/max of 5.2 to 33.7 degree)4). In this study, the average of bifurcation angle was 90.2 degree, and the average of inclination angle was 19.4 degree, which confirmed the reproducibility of angle measurements with former studies.

The present data showed that the flow instability at the bifurcation of middle cerebral arteries from healthy volunteers gave the highest correlation with bifurcation angle rather than inclination angle or Reynolds number. This result implied that the instability of flow at the bifurcation may be affected by the change of bifurcation angle which may be related with the risk of aneurysm initiation.

The former study has shown that MCA bifurcations harboring aneurysms have significantly larger branching angles[3]. The study, however, left a question of branching angles increase as the result of aneurysm formation or branches with high angles result in aneurysm formation. Considering the average age difference of subjects between the two studies and CFD analysis results from this study, results suggested that the widening of bifurcation angles may be due to morphological change by aging which may increase the WSS vector variation at the bifurcation and result in aneurysm formation.

CONCLUSION

This study examined the effects of bifurcation angle, inclination angle, and Reynolds number on flow instability. Results showed that the bifurcation angle have stronger correlation with WSS vector variations from impinging flow than inclination angle or Reynolds number.

ACKNOWLEDGEMENTS

This study is a research of project commissioned to EBM , Inc. by the 2014 Fukushima medical equipment development subsidies.

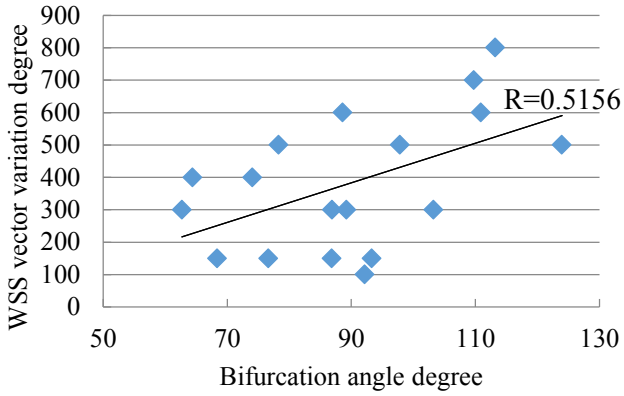

Fig. 3 The correlation between bifurcation angle and WSS vector variation

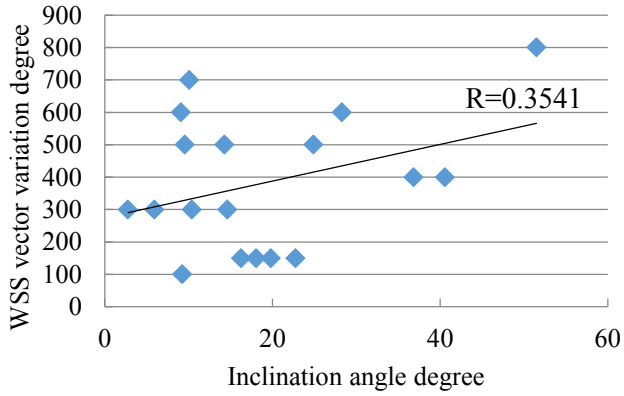

Fig. 4 The correlation between inclination angle and WSS vector variation

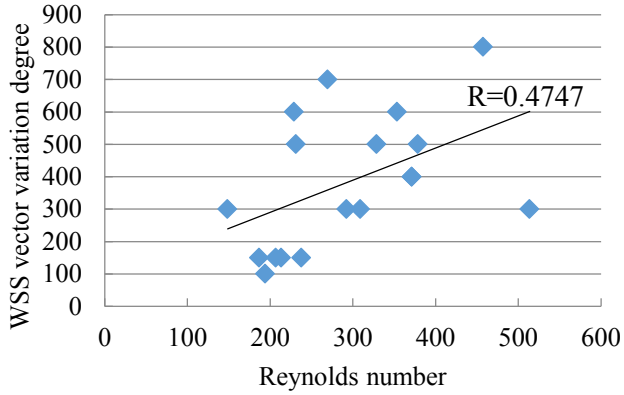

Fig. 5 The correlation between Reynolds number and WSS vector variation

REFERENCES

[1] A. Mantha, et al, AJNR, 27, pp1113-1118, 2006.
[2] Y. Shimogonya,et al,Journal of Biomechanics, pp550-554, 2009.
[3] Merih I. Baharoglu, et al, Stroke. 2014;45: 2649-2655.

Copyright 2016 The Organizing Committee for the 2016 Summer Biomechanics, Bioengineering and Biotransport Conference

SB^{3}C2016
Summer Biomechanics, Bioengineering and Biotransport Conference
June 29 –July 2, National Harbor, MD, USA
SB^{3}C2016-1107

A REACTIVE VISCOELASTIC CONTINUUM DAMAGE MODEL FOR TENDON

Babak N. Safa (1,2), Andrea H. Lee (2), Michael H. Santare (1), Dawn M. Elliott (2)

(1) Department of Mechanical Engineering
University Delaware
Newark, DE, USA

(2) Department of Biomedical Engineering
University of Delaware
Newark, DE, USA

INTRODUCTION

Tendons become structurally and mechanically damaged due to overload and/or overuse, frequently resulting in clinical disorders such as tendinopathy or tendon rupture. Tendon damage includes non-recoverable degradation in mechanical properties such as elongation or decreased modulus. Such changes in mechanics are clear signs of damage; however, they do not provide insight into the mechanism of damage. A damage model that includes key tendon mechanical behaviors of nonlinearity (strain stiffening until yield, continued with strain softening after) and viscoelasticity (relaxation, creep, and hysteresis) is needed to elucidate mechanisms of damage across a full strain range. While models that separately address these individual mechanical behaviors have been proposed, a single model that can simultaneously address all of these behaviors is still needed.

Ateshian [1] recently developed "reactive viscoelasticity" framework for cartilage, which was conceptually based on elastomer scission and crosslinking [2,3]. This framework includes a mixture of different bond types, categorized as strong and weak. This framework, applied to tendon, has the potential of not only describing nonlinearity, viscoelastity, and damage, but also being used to elucidate damage mechanisms. The first step in this process, and thus the objective of this study, was to develop and apply a reactive viscoelastic continuum damage model to the post-yield loading and relaxation of tendon.

METHODS

Reactive viscoelasticity for tendon*:* The model consists of a mixture of two bond types that are categorized as strong and weak (Fig 1 top, thick and thin lines, respectively). The strong bonds govern the elastic response, and "reacting" weak molecular bonds govern the viscous response [1]. The weak bonds repeatedly break and reform via chemical kinetics of molecular bonds. For a Heaviside step, breaking

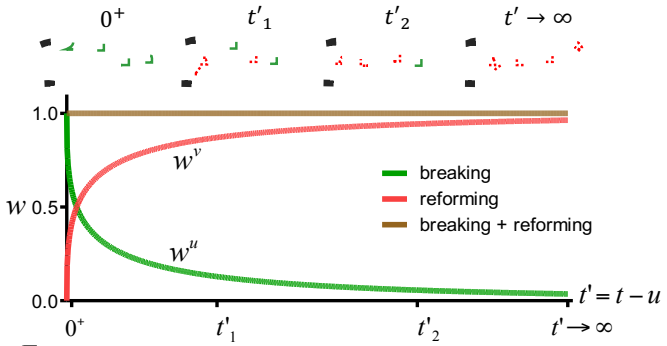

Figure 1: Schematic of strong elastic bonds (thick) and weak reactive bonds (thin) that are initially unloaded. With a Heaviside step at $t = u$, the strong (black) and weak (green) bonds support load. Weak bonds break (green) and reform (dashed, red). Reforming weak bonds bear no load. Because the tissue is held at constant strain, all the weak bonds eventually reform, bearing no load ($t \to \infty$).

weak bonds number fraction (w^u) and carried load is constantly decreasing according to an asymptotic decay function g(t) (Fig 1, green). However, reforming weak bonds number fraction (w^v) increases, but they do not carry load because their strain energy is based on the relative deformation since reforming, and no additional deformation has yet been applied (Fig 1, red). The weak bonds are simultaneously breaking and reforming over time, however, the sum of their number fraction is one (i.e., $w^u + w^v = 1$). The relative populations of breaking and reforming bonds, therefore, change over time, which governs the viscoelastic response.

All bonds are assumed to be inherently hyperelastic. The strain energy of the system for a Heaviside step load at time u is:

Copyright 2016 The Organizing Committee for the 2016 Summer Biomechanics, Bioengineering and Biotransport Conference

$$\Psi(\boldsymbol{F}(t), D, w) = (1-D)\Psi^e(\boldsymbol{F}(t)) + w^u(\mathrm{t})\Psi^b(\boldsymbol{F}(t)) + w^v(\mathrm{t})\Psi^b(\boldsymbol{F^u}(t)) \quad (1)$$

Superscripts e and b refer to strong and weak bonds. $\boldsymbol{F}$ is the deformation gradient tensor and $\boldsymbol{F^u}$ is the deformation relative to $t = u$ (i.e. $\boldsymbol{F}(t) = \boldsymbol{F}(u).\boldsymbol{F^u}(\boldsymbol{t})$), where $\boldsymbol{F^u} = \boldsymbol{I}$ for a Heaviside step. Finally, D is an internal state variable representing damage (defined later).

For general loading ($u_{i+1} = u_i + du$) of a continuous, linearized, one dimensional system, Cauchy stress $\left(\boldsymbol{T} = \frac{1}{\mathrm{J}}\frac{\partial \Psi}{\partial \boldsymbol{F}}\boldsymbol{F}^T\right)$ is (see [1]):

$$\mathrm{T}(\varepsilon(t), D) = (1-D)\mathrm{T}^e(\varepsilon(t)) + g(t)\mathrm{T}^b(\varepsilon(t)) - \int_{0^+}^{t} \dot{g}(t-u)\,\mathrm{T}^b(\varepsilon(t) - \varepsilon(u))du \quad (2)$$

Here $\varepsilon(t)$ is the infinitesimal strain. The function $g(t)$ is assumed to be of the form $g(t) = \exp\left[-\left(\frac{t}{\tau}\right)^{\beta}\right]$ in which τ is a time constant, and β is a positive constant number.

Damage: Damage is used to account for softening at high strains. Here damage is only applied to strong bonds, but can also be applied to weak bonds [4]. The damage is non-recoverable and history dependent (i.e. $\dot{D} \geq 0$ and $D(t) = \max\{D(\tau) \in [0,1]: \tau \in [0,t]\}$). The damage space is defined as $\varphi = \varepsilon - r \leq 0$, where r indicates the range of admissible strains and expands as damage evolves. The strain at which damage initiates, r_0, was selected to be the experimental yield point [5]. Damage accumulation is assumed to be a stochastic process [6] and Weibull distribution function was selected to represent the damage accumulation $D = \int_0^{\varepsilon} f(\varepsilon^*; k, l)\, d\varepsilon^*$, where, $f(\varepsilon; k, l)$ is the Weibull PDF, k is the shape parameter and l is the scale parameter. Note that $D = 0$ corresponds to a non-damaged state, and $D = 1$ corresponds to complete failure of the strong bonds.

Hyperelastic constitutive relations: The stress response of the strong bonds was defined based on established nonlinear models as:

$$\mathrm{T}^e(\lambda) = \begin{cases} {C_1}^e\,[\exp({C_2}^e\varepsilon) - {C_2}^e\varepsilon - 1] & 0 < \varepsilon \leq \varepsilon_c \\ {C_3}^e\varepsilon + {C_4}^e & \varepsilon_c < \varepsilon \end{cases} \quad (3)$$

where the behavior in the toe-region is exponential up to uncrimping strain ε_c, after which the behavior is linear. Continuity and smoothness at ε_c, constrain the modulus ${C_3}^e$ and the stress at the end of the toe region ${C_3}^e\varepsilon_c + {C_4}^e$. The stress response of the weak bonds was defined as exponential, following Eq (3) top row.

Experimental methods and results: Tendon fascicles (n=14) were dissected from the tail of Sprague-Dawley rats and tested in tension in a PBS bath. The mechanical test consisted of 5 mN preload, 5 cycles of preconditioning to 4% strain, a ramp load at 1%/sec to 8% strain, and a relaxation for 15 smin. The stress-strain-time data for all samples were averaged (Fig 2 dotted red line) and a smoothing spline fit to the ramp data. The first inflection point of the ramp, defined as the yield and the initiation of damage, occurred at 4.3% strain.

Model parameter optimization to data: A built-in Matlab function for constrained optimization of nonlinear multivariable functions was used to fit the model to averaged experimental data. First, the relaxation response was used to solve $g(t)$ for $\boldsymbol{\tau}$ and $\boldsymbol{\beta}$. Next, the entire loading and relaxation response was fit to the full model and solved for the remaining parameters: strong bond constitutive (${C_1}^e$, ${C_2}^e$, ε_c), weak bond constitutive (${C_1}^b$, ${C_2}^b$) and damage (k,l). The root mean square of error (RMSE) of the fit was calculated.

RESULTS

The reactive viscoelastic damage model was able to describe the nonlinearity, time-dependence, and damage behaviors of the tendon as seen by comparing the red experimental and black model fits (Fig 2A). The RMSE was 1.9 MPa, which is 5% of the maximum experimental stress. The optimization result for the model parameters is summarized in Table 1.

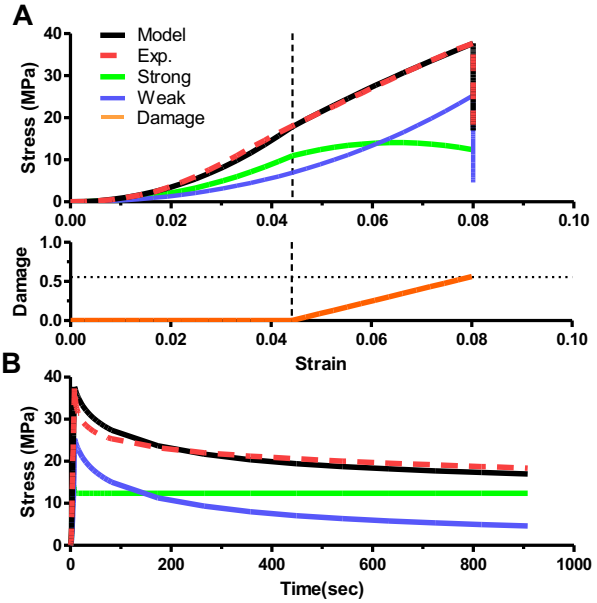

Figure 2: Experimental (red) and model fit (black), with model decomposed into contribution of strong (green) and weak (blue) bonds. (A) Stress-strain, and damage-strain (B) Strain-time.

Table 1: Results of optimization

${C_1}^e$(Mpa)	${C_2}^e$	ε_c	${C_1}^b$(Mpa)	${C_2}^b$	k	l	τ(sec)	β
194.2	7.1	0.04	47.4	12.7	5.8	0.02	90.1	0.38

During the ramp loading, the strong (green) and weak (blue) bonds contributed a similar amount to the total stress, until yield at 4.3% strain, where damage initiated (Fig 2A). Damage increased to 0.56 by the end of the ramp at 8% strain. This damage prevented an increase of strong bond contributions, while the weak bond load continued to increase (Fig 2A).

During the relaxation phase (Fig 2B), the stress contribution of strong bonds was constant (12.4 MPa), as they were defined as elastic. The weak bonds continued to relax to about 5 MPa at the end of the 15 min period. Equilibrium, where weak bonds stress eventually reduces to zero, was not achieved.

DISCUSSION

This model provides a non-linear and reactive viscoelastic framework to study tendon damage. One of the advantages of the model is the ability to describe softening and relaxation at post yield strains, which cannot be achieved by conventional hyperelastic models. Secondly, the model constituents can be varied individually to address time-dependence and damage. Future improvements, using this framework of bond kinetics, could extend the model to multiple types of bonds, each with damage, time dependency, or both, to elucidate damage mechanisms in tendon.

ACKNOWLEDGEMENTS

National Institutes of Health grants R01EB02425 and R01AR050052.

REFERENCES

[1]Ateshian, *J. Biomech.*, 48(6), 2015. [2] Tobolsky, "Properties and structure of polymers," 1960. [3] Wineman, *Int. J. Adv. Eng. Sci. Appl. Math.*, 1(2–3), 2010. [4] Nims, *Interface Focus*, 6(1), 2015. [5] Peloquin, *J. Biomech. Eng.*, 2015. [6] Schmidt, *Comput. Methods Appl. Mech. Eng.*, 278, 2014.

Copyright 2016 The Organizing Committee for the 2016 Summer Biomechanics, Bioengineering and Biotransport Conference

SB³C2016
Summer Biomechanics, Bioengineering and Biotransport Conference
June 29 –July 2, National Harbor, MD, USA
SB³C2016-1108

MODELING CALCIUM TRANSIENTS IN HUMAN PLURIPOTENT STEM CELL-DERIVED CARDIOMYOCYTES

Kevin M. Beussman (1), Marita L. Rodriguez (1), Adam Rakla (1), Ashley Emery(1), Nathan J. Sniadecki (1,2)

(1) Department of Mechanical Engineering
University of Washington
Seattle, WA, USA

(2) Department of Bioengineering
University of Washington
Seattle, WA, USA

INTRODUCTION

Recent advances in cardiovascular therapy have indicated that cardiomyocytes derived from pluripotent human stem cells (hPSC-CMs) have the potential to be used to repair the damage due to myocardial infarction or other cardiovascular diseases. Currently, these hPSC-CMs are immature when compared with adult cardiomyocytes: they exhibit a smaller, round morphology with unaligned myofibrils, and generally have inferior calcium handling ability [1]. The combination of these factors leads to a weaker contractile output from hPSC-CMs when compared to their adult counterparts.

The driving mechanism of cardiomyocytes is excitation-contraction (EC) coupling: the interaction between an ionic action potential and sarcomeric contraction. Calcium ions (Ca^{2+}) are stored in the sarcoplasmic reticulum (SR) and released via a calcium-induced calcium release process. The role of the SR in immature hPSC-CMs is still unclear, but some evidence shows that they do in fact have a functional SR with ryanodine receptors capable of producing cardiac-like action potentials [2].

In this work, we examine a proposed model to study Ca^{2+} propagation in immature cardiomyocytes. The model includes dynamics for both cytosolic and sarcoplasmic Ca^{2+} based on diffusion equations. We then compare this model with experimental Ca^{2+} transients for hESC-CMs.

METHODS

Modeling Calcium Dynamics

A 2D model governing calcium dynamics is adapted from [3]. In this model, cytosolic and sarcoplasmic calcium concentrations are defined and balanced by taking into account Ca^{2+} into and out of the sarcolemma and SR. The governing partial differential equations are:

$$\partial_t w_c = \mathrm{div}(\mathbf{D}\nabla w_c) + K(w_c, w_s) \quad (1)$$
$$\partial_t w_s = L(w_c, w_s) \quad (2)$$

Where w_c is the concentration of cytosolic Ca^{2+}, w_s is the concentration of sarcoplasmic Ca^{2+}, and the diffusivity tensor is $\mathbf{D} = \mathrm{diag}(D_f, D_s)$, where $D_f$and D_s are the anisotropic diffusivities in the orthogonal directions. Initially, we set the diffusivity in the myofibril direction D_f = 60 μm^{2}s^{-1} and the diffusivity in the transverse direction D_s = 30 μm^{2}s^{-1}. Finally, the terms K and L are given by:

$$K(w_c, w_s) = \nu_1 - \frac{\nu_2 w_c^2}{k_2 + w_c^2} + \frac{\nu_3 w_c^4 w_s^2}{(k_3 + w_c^4)(k_4 + w_s^2)} - \nu_4 w_c \quad (4)$$
$$L(w_c, w_s) = \frac{\nu_2 w_c^2}{k_2 + w_c^2} + \frac{\nu_3 w_c^4 w_s^2}{(k_3 + w_c^4)(k_4 + w_s^2)} - \nu_5 w_s \quad (5)$$

The constant ν_1 (1.58 μMs^{-1}) represents the influx of Ca^{2+} into the cytosol, ν_2 (16 μMs^{-1}) is the uptake of Ca^{2+} into the SR, ν_3 (91 μMs^{-1}) represents the CICR of Ca^{2+} from the SR into the cytosol, ν_4 (2 s^{-1}) represents the passive rate of Ca^{2+} leaving the cytosol through the cell membrane due to a concentration gradient, and ν_5 (0.2 s^{-1}) represents the passive rate of Ca^{2+} leaving the SR to the cytosol. The terms k_2 (1 μM), k_3 (4 μM^2), and k_4 (0.7481 μM^4) are constants determined through experimental fitting. These values are determined for experimental data for adult cardiomyocytes [3]. This model may be stimulated by a local increase in ν_1, after which point it spontaneously beats.

Together, these governing partial differential equations (PDEs) are solved using a parabolic nonlinear PDE solver in MATLAB. For our simulations, we use the initial conditions w_c = 0.1 μM, w_s = 1.6 μM as well as an insulated boundary condition on all cell boundaries.

Experimental Procedure

To observe Ca^{2+} transients *in vitro*, we derived cardiomyocytes from GCaMP3-expressing RUES2 hESCs. The cardiomyocyte differentiation procedure was based on previously published methods [4]. Briefly, undifferentiated RUES2 hESCs were plated in a monolayer on Matrigel. On day 0, the media was switched to RPMI supplemented with B-27 minus insulin, activin-A, and BMP-4. In the proceeding days, the monolayer was sequentially supplemented with Wnt agonist CHIR 99021 and Wnt antagonist Xav 939 to promote cardiomyocyte differentiation. After approximately 7 days, the cardiomyocytes begin spontaneously beating. After 20 days, the cardiomyocytes were lifted from the monolayer and reseeded onto the experimental substrates at a density of approximately 250,000 cells/cm^2 to promote single-cell culture.

Prior to cell seeding, experimental substrates were created with patterned extracellular matrix (ECM) protein. A soft PDMS substrate is created by mixing quantities of 10:1 (base : curing agent) Sylgard-184 and 1:1 Sylgard-527 and curing onto a thin glass substrate. Using a mixture of 10% Sylgard-184 and 90% Sylgard 527, we achieve a substrate stiffness of approximately 21 kPa. Using a stamp-off procedure, laminin was patterned onto the surface of the soft PDMS substrate. The pattern consists of parallel lines ranging between 12 and 24 um in width, promoting various degrees of elongation of the hESC-CMs. Data was collected using a 60X objective on a fluorescence microscope with a high-speed camera allowing for video capture of up to 100 frames per second.

Copyright 2016 The Organizing Committee for the 2016 Summer Biomechanics, Bioengineering and Biotransport Conference

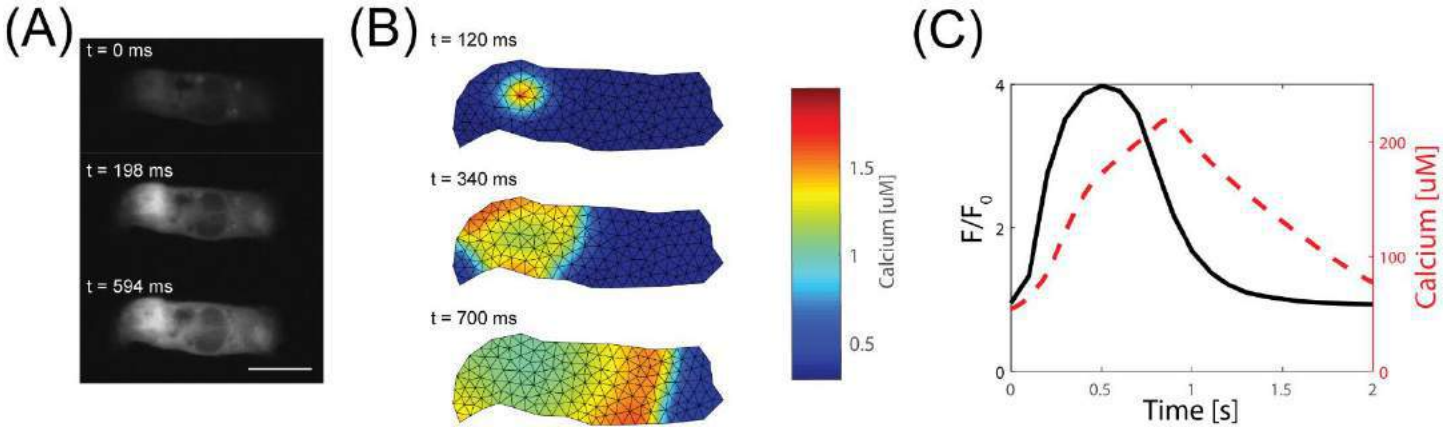

Figure 1: (A) Typical cytosolic Ca^{2+} fluorescence in GCaMP3-expressing hESC-CMs. Scale bar is 20 µm. (B) Simulation using adult parameter values with a stimulus near the earliest activation point determined from (A). (C) Total Ca^{2+} levels obtained from experimental images (black solid line) and simulation (red dashed line).

RESULTS

Figure 1A shows typical GCaMP fluorescence for a patterned hPSC-CM. We determine the activation point of the calcium wave by creating an activation map in which each pixel's activation is calculated based on its time to peak fluorescence. Using this map, the model is solved with a stimulus at the initial point of activation, shown in Figure 1B. The Ca^{2+} propagates from the activation point throughout the cell following the governing Ca^{2+} dynamics.

To obtain characteristic properties of the patterned hESC-CMs, we average the fluorescence within the cell boundary for each frame and divide it by the basal fluorescence, resulting in the solid curve in Figure 1C. Performing a similar averaging for the simulated data, we generate the red dashed line in Figure 1C and compare it with the experimental data. The model predicts a Ca^{2+} peak near 0.9 seconds, while the experimental data shows that the GCaMP fluorescence peaks at around 0.5 seconds. Additionally, the rise of Ca^{2+} in the model begins with an exponential increase that levels off to a linear rise, followed by a relatively linear decay, drastically differing from the rapid, yet smooth rise and fall of the experimental fluorescence.

DISCUSSION

It is easy to see that the calcium transients in Figure 1C do not closely follow the experimental results. We attribute this to the fact that the model constants (ν_1 - ν_5) are determined for adult cardiomyocytes which exhibit greatly matured calcium handling and SR. However, at any single point in the model the calcium transient closely resembles that of adult cardiomyocytes: a sharp increase in Ca^{2+} from the SR followed by a slower uptake back into the SR. This is evident in Figure 1B by the sharp "shockwave" of Ca^{2+} spreading throughout the cell. Nevertheless, the total cytosolic Ca^{2+} in Figure 1C shows a much slower transient than that of a typical experimental hPSC-CM.

To properly model hPSC-CMs, our focus is to improve the model to account for the diminished role of the SR. One such way to alter the model is to tune the model constants; for example, ν_2 and ν_3 account for Ca^{2+} entering and leaving the SR, respectively. By reducing the influence of these sources, the model will more appropriately reflect the fact that much of the Ca^{2+} in immature hPSC-CMs comes from extracellular sources. However, the terms in equations (1) and (2) are highly coupled and balanced; the alteration of one constant can wildly imbalance the Ca^{2+} and prevent systolic activity. Once properly tuned for the properties of hPSC-CMs, we can appropriately model the calcium dynamics for hPSC-CMs.

The proposed model includes differing diffusivities along and transverse to the myofibrils. For aligned cells, we can assume that the myofibrils run along the major axis of the cell. For unaligned hPSC-CMs, however, this assumption is not enough to properly describe the dynamics. One remedy is to assume that diffusion is isotropic, but a more physiological approach may be to assume a somewhat random orientation of myofibrils within the immature cardiomyocyte. Experimental images of myofibrils could also serve as inputs in a more physiological model.

Finally, the question of maturation with respect to excitation-contraction coupling is not yet answered. The coupling between mechanical strain and calcium dynamics is vital to the full understanding of cardiomyocyte function. We are actively pursuing the development of a model that includes the calcium dynamics described here coupled with mechanical strain, which may be used to study the development and maturation of hPSC-CMs.

ACKNOWLEDGEMENTS

This research is funded by NIH grant 5T32EB001650.

REFERENCES

[1] Yang, X. L. *et al.*, 2014, "Engineering Adolescence Maturation of Human Pluripotent Stem Cell-Derived Cardiomyocytes," Circulation Research, 114(3), pp. 511-523.
[2] Satin, J. *et al.*, 2008, "Calcium handling in human embryonic stem cell-derived cardiomyocytes," Stem Cells, 26(8), pp. 1961-1972.
[3] Ruiz-Baier, R. *et al.*, 2014, "Mathematical modelling of active contraction in isolated cardiomyocytes," Mathematical Medicine and Biology-a Journal of the Ima, 31(3), pp. 259-283.
[4] Laflamme, M. A. *et al.*, 2007, "Cardiomyocytes derived from human embryonic stem cells in pro-survival factors enhance function of infarcted rat hearts," Nat Biotechnol, 25(9), pp. 1015-1024.

Copyright 2016 The Organizing Committee for the 2016 Summer Biomechanics, Bioengineering and Biotransport Conference

SB^{3}C2016
Summer Biomechanics, Bioengineering and Biotransport Conference
June 29 –July 2, National Harbor, MD, USA
SB^{3}C2016-1110

PATHOLOGICAL ENGINEERING STUDY OF HUMAN CEREBRAL ANEURYSMS: THREE-DIMENSIONAL ACCUMULATION OF FOAM CELLS VERSUS HEMODYNAMICS

K. Suto (1), T.Yagi (1, 2), Y.Tobe (1), T.Murayosi (1), K.Takanisih (1), M. Umezu (1)
H. Yoshida (3), K.Nishitani (3), Y.Okada (3), S. Kitahara (3)

(1) Center for Advanced Biomedical science (TWIns), Waseda University
2-2 Wakamatsu-cho, Shinjuku-ku, Tokyo, Japan

(2) EBM corporation
Ohmoriminami, Ohtaku, Tokyo, 143-0013 Japan

(3) Kitahara International Hospital
Oowada-cho, Hachioji-shi, Tokyo
Japan

INTRODUCTION

Cerebral aneurysms are lesion at cerebral artery that is known to cause subarachnoid hemorrhage (SAH). Cerebral aneurysm initiation, growth, and rupture mechanisms are still not clear. Although causes of aneurysm rupture is debated to be related to the hemodynamic stress, there have not been any studies which directly compared pathological and blood flow analysis of human cerebral aneurysms. Recently, relationship between rupture and lipid consumption in aneurysm wall have been reported[1].The relationship between rupture mechanism and foam cells, however, are not been discussed Foam cells are known to exist in the plaques of atherosclerosis and they are reported to cause fragility in the artery wall[2]. The relationships between hemodynamic stress and plaque formation have been also reported[3]. From these previous reports, it can be hypothesized that foam cells may be involved in the remodeling of aneurysms wall and aneurysm rupture. The purpose of this study is to investigate the relationship between foam cells accumulation and hemodynamic stress in four unruptured cerebral aneurysms.

METHODS

Choice of case

Four aneurysms were harvested from three patients after microsurgical clipping. The clinical summary of the tissues were listed in the Table 1.

Histological analysis

Harvested tissues were then fixed in 4% paraformaldehyde, embedded in paraffin, sliced in semi serial sections of 2 μm thicknesses, and stained with hematoxylin-eosin (HE) method. This research was accepted by the ethical committee of Waseda University and Kitahara International Hospital.

Definition of foam cells

Two types of mural cells were distinguished (Fig.2). Foam cells (a) were defined as foam-like morphology cells and without foam cells (b) were defined as mural cells tight extracellular matrix. If more than six consecutive semi-serial sections contained foam cells, it was defined as foam cell region.

Table 1 Detailed patient information

ID	#1	#2	#3	#4
Age/Sex	74/F	72/F		44/M
Location	Rt.MCA	Lt.MCA	Acom	Rt.MCA
Size	7mm	10mm	2.5mm	3.5mm

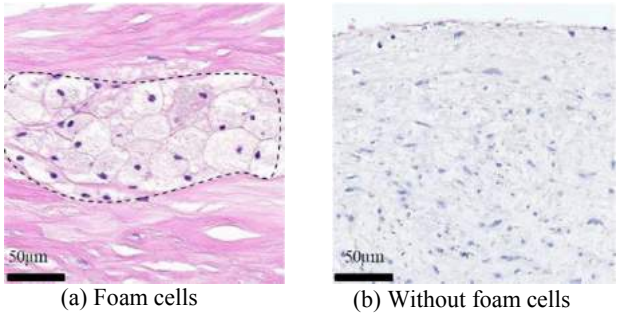

(a) Foam cells (b) Without foam cells

Fig.2 Two types of mural cells

CFD analysis

Three-dimensional vascular models were constructed based of magnetic resonance imaging and digital subtraction angiogram images. These models were created using 3D image processing workstation

Copyright 2016 The Organizing Committee for the 2016 Summer Biomechanics, Bioengineering and Biotransport Conference

(Ziostation; Ziosoft Inc, Tokyo, Japan). CFD software (hemoscope; EBM Inc, Tokyo, Japan) was used for meshing, hemodynamic analysis and visualization of analysis results. Each case was simulated with pulsatile simulation. The blood was defined as Newtonian fluid with the density of 1050 Kg/m^3 and the viscosity of 0.004 Pas. The inlet boundary condition used an average pressure of 100mmHg. The outlet boundary conditions were set as velocity boundary based on the constant shear stress theory and Hagen-Poiseuille flow.

RESULTS

Histological analysis and CFD analysis

Fig.3 (a-c) shows two examples of HE staining and CFD results. Fig.3 (a) represented the region of foam cells which was painted yellow in three dimension map. Fig.3 (b) represented the time average wall shear stress (WSS) mapping of the aneurysm. Fig.3 (c) represented the time average WSS vector mapping of the aneurysm.

In #1, foam cells were located at low WSS region (Fig. 3b-1), (Fig.3b-2). Divergence of WSS vector showed that the parallel flow (Fig. 3c-1), and rotation flow (Fig. 3c-2) were observed at foam cell region. In #2, foam cells were located at low WSS region (Fig. 3b-3), and merging flow was observed at foam cell region (Fig. 3c-3).

DISCUSSION

Relationship between foam cells, WSS and WSS vector

Out of four aneurysms, six foam cell regions were observed. 83% of foam cell region were located at low WSS region. The median value of the WSS observed at foam cell region was 0.38 Pa (Fig.4). This suggests that the foam cells tended to accumulate in the region with low WSS. When comparing the WSS vector result with the histological analysis, there were no relationships between WSS vector and foam cell region (Table 2). The WSS vector at foam cell region was 50 percent stagnant (e.g. Merging flow, Rotation flow). Foam cells are involved in atherosclerosis[2] and several studies have reported that low WSS is one of the factors that cause atherosclerosis[3-4]. Therefore this result suggested that atherosclerosis derived by foam cells are generated in the cerebral aneurysm. Atherosclerosis is known to induce unstable plaques[2], so it can be concluded that the atherosclerosis derived by foam cells may have a role in the degeneration of the cerebral aneurysm wall and it may be associated with low WSS from the blood flow.

CONCLUSION

Comparison of the Histological analysis and CFD analysis of four unruptured cerebral aneurysms suggested a relationship between foam cells and low WSS region. Since the behavior of the foam cells is similar to the cause of atherosclerosis, the result indicated that the foam cells may play an important role in the aneurysm rupture mechanisms.

ACKNOWLEDGEMENTS

This study is a research of project commissioned to EBM , Inc. by the 2014 Fukushima medical equipment development subsidies.

REFERENCES

[1]. Kataoka, et al., Structural fragility and inflammatory response of ruptured cerebral aneurysms: a comparative study between ruptured and unruptured cerebral aneurysms. Stroke 39:1396-1401

[2]. Ross, et al., The pathologenesis of atherosclerosis: a perspective for the 1990s. NATURE, vol 362, 29, 1993

[3]. Adel M. Malek, et al., Hemodynamic Shear Stress and Its Role in Atherosclerosis. JAMA , vol 282, No.21, 1999

[4]. Yiannis S.Chatzizisis, et al., Role of Endothelial shear stress in the Natural history of coronary atherosclerosis and vascular remodeling, JACC, 49, 2379-2393, 2007

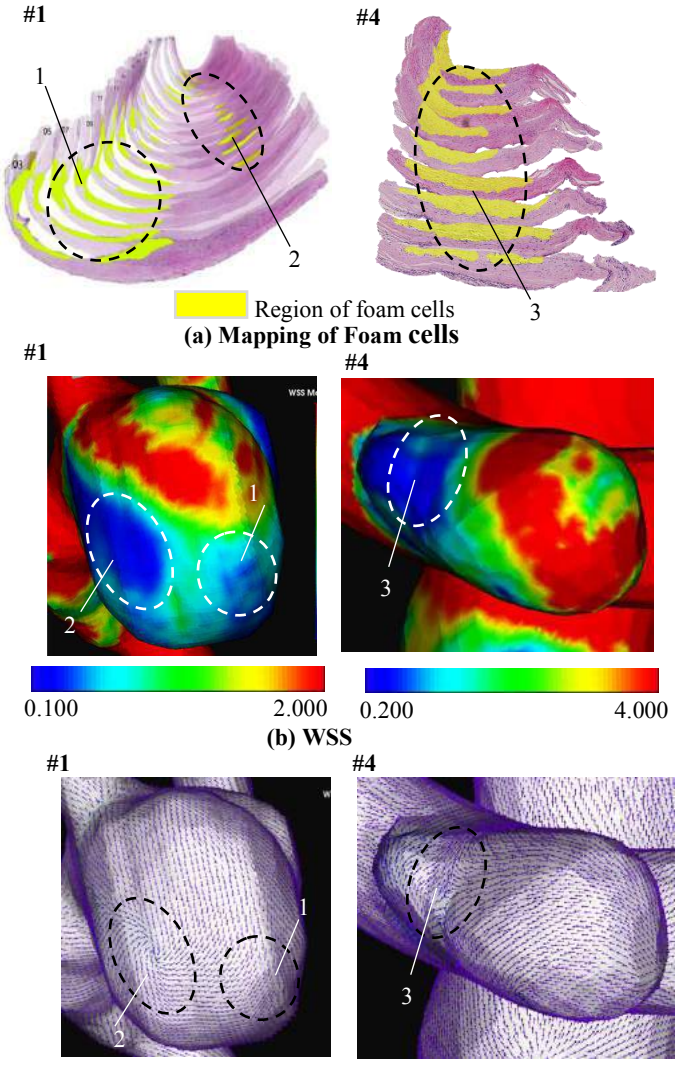

Fig.3 (a-c) Comparison of histological analysis and CFD analysis results of two aneurysms.

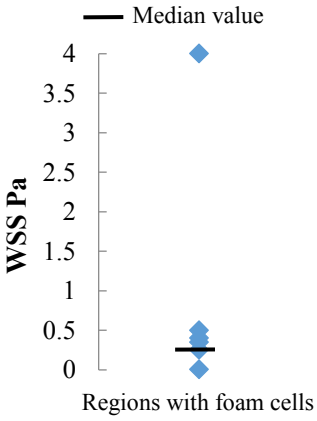

Table 2 Results all of the CFD at region of foam cells

Magnitude of WSS	
High	0
Mid	1
Low	5
Direction of WSS vector	
Pararell	2
Merging	2
Rotation	1
Divergence	1

Fig.4 Range of WSS at foam cell regions

Copyright 2016 The Organizing Committee for the 2016 Summer Biomechanics, Bioengineering and Biotransport Conference

SB³C2016
Summer Biomechanics, Bioengineering and Biotransport Conference
June 29 –July 2, National Harbor, MD, USA
SB³C2016-1111

AN INNOVATIVE METHOD FOR MEASURING ADHESION AT THE VITREORETINAL INTERFACE

Christopher J. Creveling (1), Dr. Brittany Coats (1)

(1) Mechanical Engineering
University of Utah
Salt Lake City, Utah, USA

INTRODUCTION

Retinal hemorrhage and detachment from abusive head trauma in infants is believed to be caused by traction between the retina and vitreous during rapid head rotation [1]. The mechanisms of adhesion between the vitreous and the retina, and the amount of force required to disrupt the interface are currently unknown. Previous studies have measured adhesion between the retinal pigment epithelium (RPE) and choroid in adult eyes by extracting rectangular strips of the eye and peeling the retina while holding the choroid with a vacuum [2]. This method is highly destructive, drying of the tissues, and is not practical when one side of the adhesion is a gel (vitreous). Others have measured adhesion between the choroid and RPE by inflating a small bubble in-between the layers [3]. This method resulted in higher forces than the previous method, but would be challenging on a gel-membrane interface.

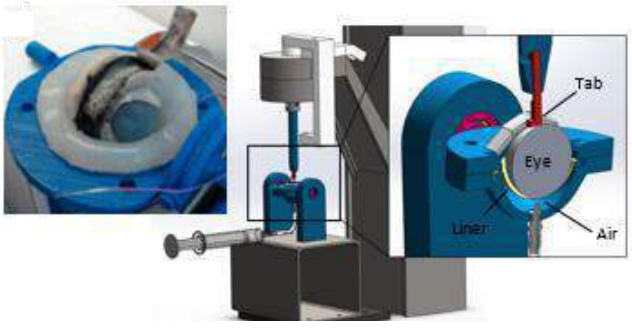

Figure 1. Sclera is dissected away from the retina prior to testing and the eye is placed in the fixture. The eye is raised toward the testing window by inflating the liner with air.

In this study, we develop a unique method for measuring adhesion force at the vitreoretinal interface that maintains the general structure of the eye. We then use this method to measure vitreoretinal adhesion in sheep eyes based on developmental age (neonatal, adolescent, and adult) and region (posterior, equator). The specific objectives of this study are to (1) measure the maximum and steady-state peel force of the retina from the vitreous and (2) identify age and region effects on peel force.

METHODS

Adult (N=7), adolescent (5 months, N=8) and neonatal (3 days, N=9) sheep eyes were obtained from existing non-ocular animal studies on campus and refrigerated until tested (~2 hours). Muscle and surrounding fatty tissue was removed from the eye, and the optic nerve was dissected from the globe. Using this dissection as a starting point, scissors were used to separate and cut the sclera, creating a retinal window approximately 1cm x 4cm (Fig. 1). The eye is then placed in a spherical eye-holder and inserted into a rotating fixture. Retinal peeling from the vitreous is achieved by gently scoring the retina along the edges of the window, and adhering a plastic tab (Fig. 2A) with adhesive. Optical coherence tomography images of the peel retina indicate that the adhesive does not penetrate into the retina (Fig. 2B). The tab is connected to a 5N uniaxial load cell (2530,

Copyright 2016 The Organizing Committee for the 2016 Summer Biomechanics, Bioengineering and Biotransport Conference

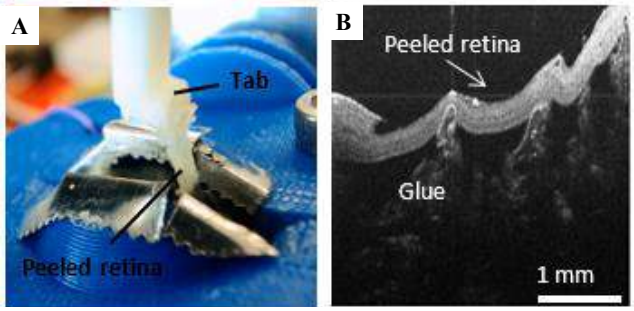

Fig. 2 (A) An L-shaped tab is glued to the retina and used to peel it from the vitreous while measuring force. (B) OCT imaging of the peeled retina shows that separation is at the vitreoretinal interface and glue penetration is minimal.

Instron, Norwood, MA) attached to the crosshead of an electromechanical testing frame. As the crosshead displacement initiates the peel test, it simultaneously applies a controlled rotation of the device at the same rate as the peel. This ensures a consistent 90° peel relative to the retinal surface.

Using ASTM D6862-04 as a guideline, the crosshead was displaced at a constant rate of 0.02 mm/min. Maximum peel force was defined as the peak of the resulting force-time curve. Steady-state peel was defined as the average force of the steady-state region (Fig. 3). After testing was completed, the eye was rotated, and a different region was tested. Preliminary evaluation found no significant effect of test order on peel adhesion.

To validate the rotating peel adhesion device, peel tests were performed with tape adhered to a steel ball bearing, and compared to conventional peel tests of the same tape adhered to a flat aluminum plate. The strips of tape were cut to the same dimensions of the retina and peeled according the same methods described above.

RESULTS

The tape peel tests performed with the rotating device were not different than the standard linear tape peel tests (Fig. 4), validating the innovative device design and methodology. Using the validated device, there was a higher maximum peel force for the neonatal age group compared to the adolescent and adult groups, but this trend did not reach significance (Fig. 5, p=0.08). There was no significant difference between the posterior and equator regions for any of the age groups tested.

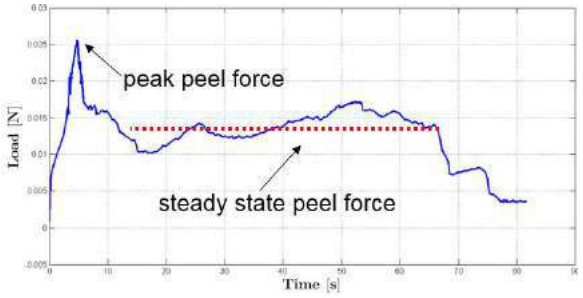

Fig. 3 Peak and steady state peel force extracted from a vitreoretinal peel test on an adult sheep eye.

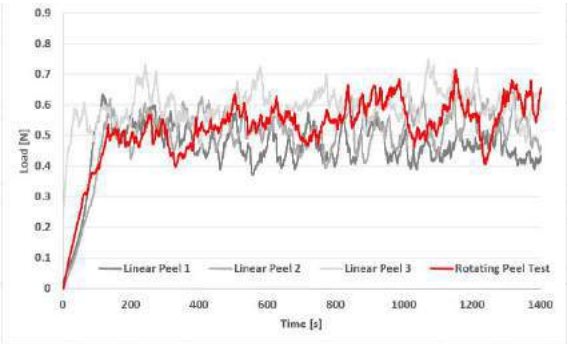

Fig. 4 No difference was found between peel force from linear (grey) and rotating (red) tape peel tests, validating device design and methods.

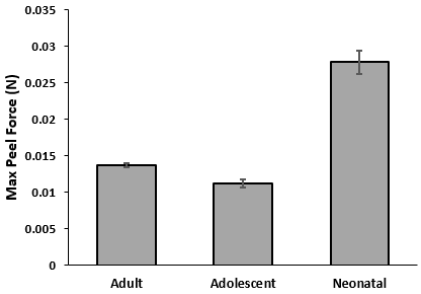

Fig. 5 Maximum peel force at the neonatal vitreoretinal interfaces was larger than adolescent or adult, but this difference did not quite reach significance (p=0.08). Errors bars indicate standard error.

DISCUSSION

On average, neonatal eyes had greater initial vitreoretinal adhesion compared to adolescent or adult eyes. Neonatal eyes are known to have more collagen at the vitreoretinal interface compared to adults, and some hypothesize that collagen fibers tethering the vitreous to the retina are responsible for adhesion. Our results support this hypothesis and warrant further investigation into collagen as the mechanism of vitreoretinal adhesion. Collagen is also known, however, to significantly differ between the equator and posterior regions of the eye. We found no significant differences in regional adhesion, which may be a result of peel strips spanning regional boundaries or differing collagen distributions in the ovine eye compared to the human. Studies are underway to investigate these aspects and to increase sample size for each of the age groups evaluated.

ACKNOWLEDGEMENTS

The authors would like to thank the financial support from the University of Utah Research Foundation.

REFERENCES

[1] Rangarajan, N et al., *J AAPOS* 13:364-369, 2009
[2] deGuillebon, H et al., *Arch Ophthal*, 86:679-684, 1971.
[3] Kita, M et al., *J Investigative Ophthalmology & Visual Science*, 31:624-628, 1990.

Copyright 2016 The Organizing Committee for the 2016 Summer Biomechanics, Bioengineering and Biotransport Conference

SB³C2016
Summer Biomechanics, Bioengineering and Biotransport Conference
June 29 –July 2, National Harbor, MD, USA
SB³C2016-1112

A COMPARATIVE STUDY OF THE MECHANICAL RESPONSE AND FIBER STRUCTURE IN AN ELASTASE INDUCED ANEURYSM MODEL IN RABBITS AND HUMAN CEREBRAL ANEURYSMS

Chao Sang (1), Xinjie Duan (1), David F. Kallmes (2), Ram Kadirvel (2), Yonghong Ding (2), Daying Dai (2), Khaled M. Aziz (3), Juan R. Cebral (4), Anne M. Robertson (1)

(1) Department of Mechanical Engineering & Materials Science, University of Pittsburgh, Pittsburgh, PA, USA

(2) Department of Radiology, Mayo Clinic, Rochester, MN, USA

(3) Department of Neurosurgery Allegheny General Hospital, Pittsburgh, PA, USA

(4) Department of Bioengineering George Mason University, Fairfax, VA, USA

INTRODUCTION

An intracranial aneurysm (IA) is a saccular enlargement in the wall of a cerebral artery. As the IA grows there is a greater risk of rupture – an event that can lead to severe hemorrhage, and other complications, including sudden death. Due to the risks associated with treatment, it is important from a clinical perspective to identify which aneurysms are at risk for rupture, so these aneurysms can be treated and risky procedures can be avoided in others. Currently, the most reliable indicator of risk is IA size. However, while larger IAs are more likely to rupture than small IAs, due to the large number of small IAs, most aneurysms that rupture are small. Hence, size is insufficient for risk stratification. There is a pressing need to better understand disease progression in order to identify a clinically useful metric for improving risk assessment. Further such knowledge will be critical for the rational development of alternate treatment strategies.

While IA samples can be obtained following treatment by surgical clipping, this tissue only represents one time point in the pathology. Animal models for IAs provide a means of studying multiple time points in disease progression. However, it is vital to prove the relevance of these models. Here, we compare the mechanical and wall properties for a commonly used elastase induced saccular aneurysm model in rabbits [1] with those in 8 human IAs [3-5]. We include an assessment of the structural changes during loading, obtained using multiphoton imaging. In earlier work, we have shown the relevance of the aneurysm geometry and flow field found in this model to human IAs [2].

METHODS

Nine human aneurysms, 5 rabbit aneurysms, 6 human basilar arteries and 2 rabbit left common carotid arteries were included in this study. The elastase aneurysms were created as described in [1] and harvested 8 weeks after creation. Rabbit aneurysms and control rabbit vessels were harvested at the Mayo Clinic and transported overnight on ice to the University of Pittsburgh where they were mechanically tested and simultaneously imaged under multiphoton microscopy. Uniaxial data for 8 human aneurysms and 6 human basilar arteries that were previously obtained [3,5] were used in the current study.

All aneurysms and control arteries were mechanically tested to failure using a custom-built uniaxial loading system compatible with the multiphoton microscope (MPM, Olympus FV1000 MPE, Tokyo, Japan) [4], enabling simultaneous mechanical testing and MPM imaging of elastin and collagen fibers. Aneurysm samples were cut into rectangular strips and subjected to uniaxial extension at a speed of 0.02mm/s, controlled by a linear actuator (ANT-25LA, Areotech, Pittsburgh, PA). Force was recorded with a 5 lb. load cell (MDB-5, Transducer Techniques, Rio Nedo Temecula, CA). The zero strain point was defined as that under 0.005 N load, which is consistent with previous work [3,5]. The samples were tested to failure to obtain the mechanical response and ultimate strength. Assuming an isochoric motion, current cross sectional areas were calculated from stretch and unloaded cross sectional area. The Cauchy stress was then calculated from external load and current area.

Collagen fibers were imaged using the SHG signals from stacks of MPM images. From these stacks, fiber orientation and recruitment stretch was assessed as a function of depth in the aneurysm wall for chosen stretch levels. Fiber orientation was computed using an edge detection algorithm in substacks of five images [5].

RESULTS

Mechanical Response: The loading curves for the uniaxial failure tests of all rabbit and human IA samples are shown in Figure 1. As elaborated in [3], even these unruptured human IAs display

Copyright 2016 The Organizing Committee for the 2016 Summer Biomechanics, Bioengineering and Biotransport Conference

heterogeneity in the mechanical behavior. Of importance, a weaker group of aneurysms was identified within the unruptured human population [1], Fig. 1. IAs with strong (solid lines) and weak (dashed) response can be seen. A weak rabbit aneurysms was also found with ultimate strength of 0.65 MPa, similar in magnitude to that of the weak human IAs (average of 0.59 MPa). The shape of the mechanical response for the rabbit aneurysms is well fit by an exponential model with an R^2 value of 0.85 or higher, similar to findings in all robust human IAs, [3]. The high strain stiffness in the rabbit model ranges from 5.22 MPa to 12.36 MPa with a mean of 8.18 MPa, falling within the range found for the human IAs where the high strain stiffness ranged from 3.42 MPa to 25.06 MPa with a mean value of 12.38 MPa. In Figure 2, the response of the control arteries is shown for comparison for both rabbit and human vessels. In both human and rabbit aneurysms, the toe region is substantially shorter (rabbit mean = 1.14, human mean = 1.19) than for the respective control arteries (rabbit mean = 1.7, human mean = 1.78). The shortened toe region is consistent with the lack of internal elastic lamina in the aneurysm tissue for both human IAs [1] and current results for elastase induced aneurysms.

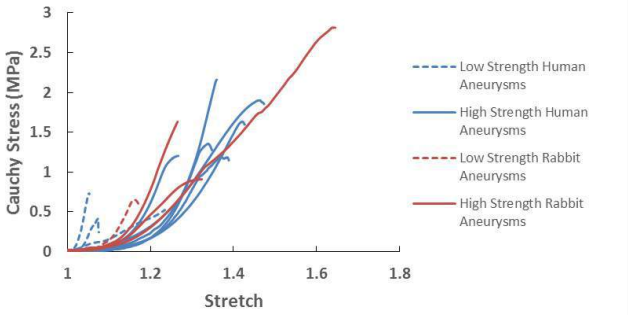

Figure 1: Results for Cauchy stress versus stretch for uniaxial failure testing of human and rabbit aneurysm samples.

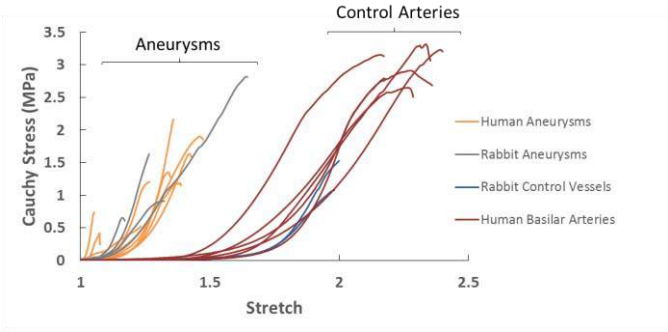

Figure 2: Comparison of unaxial testing to failure for aneruysm tissue versus control arteries for humans and rabbits.

Collagen Architecture and Layered Structure: The changing collagen reorientation and recruitment during mechanical loading can be imaged using the UA-MPM system as shown for a representative case in Figure 3. Projected stacks of MPM images obtained from the luminal side are shown below the loading curve for chosen levels of stretch. Fiber orientation as a function of position across the wall is shown below the MPM images. In the unloaded state, the collagen fibers showed a broad distribution of fibers angles, (a). With increasing axial load (meridional direction left to right in Fig. 3), collagen fibers can be seen to reorient and straighten with prominent orientation nearly symmetric about the loading axis (b and c), the layered nature of fiber orientation can be seen by the abrupt change in dominant orientation with depth in the colored contours of fiber distribution. At stretches of 1.3 and higher, the fibers are highly aligned in the loading direction. These results are consistent with the shift to a single dominant orientation for points d and e.

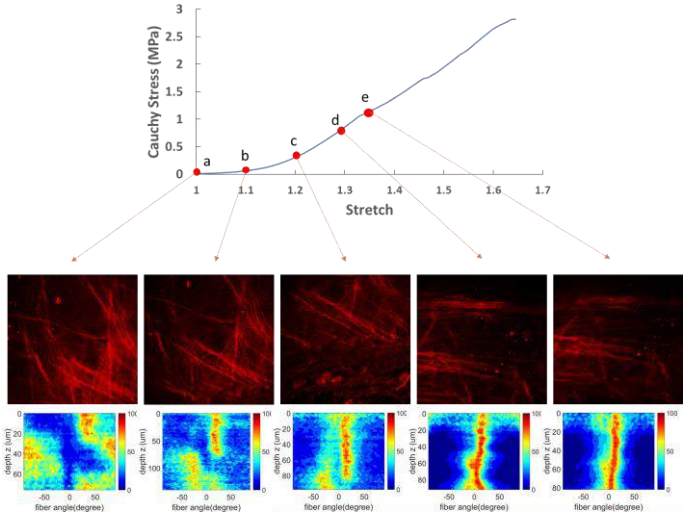

Figure 3: Recruitment of collagen fibers during uniaxial loading of H552 obtained at stretches of (a) 1.0 (b) 1.1 (c) 1.2 (d) 1.3 (e) 1.35 and the corresponding fiber orientation plots.

DISCUSSION

In this work, we have demonstrated the elastase induced aneurysm model in rabbits has similar stiffness and failure properties to human cerebral aneurysms. Further the weak and robust categories found in human IAs are also seen in the rabbit model. This finding, which will be confirmed in a larger study, suggests the rabbit model may be useful for studying differences in ineffective and effective remodeling in the aneurysm wall, a subject we are currently exploring in human IAs [3].

ACKNOWLEDGEMENTS

This work was supported by the National Institute of Health (1R21NS080031-01A1). We wish to thank the Alzheimers Disease Research Center (ADRC) of the University of Pittsburgh and Dr. Julia K. Kofler, Director of the Neuropathology Core of the ADRC for providing the cadaveric human cerebral vessels used in this study.

REFERENCES

[1] Bouzeghrane, F, Naggara, O Kallmes, DF, Berenstein, A Raymond, J (2010), *AJNR. Am J Neuroradiol*, 31(3). 418–23.
[2] Zeng, Z, Kallmes DF, Durka, MJ, Ding, Y, Lewis, D, Kadirvel, R, Robertson, AM (2011), *AJNR Am J Neuroradiol,* 32(3), 595–601.
[3] Robertson, AM, Duan, X, Aziz, KM, Hill, MR, Watkins, SC, Cebral, JR (2015). *Annals of Biomedical Engineering*, 43(7), 1-14.
[4] Hill, MR, Duan, X, Gibson, GA, Watkins, S., Robertson, AM, (2012). *Journal of biomechanics*, *45*(5), 762-771.
[5] Duan, X. (2016). Doctoral dissertation). University of Pittsburgh, (2016).
[6] Robertson, AM, Hill, MR, Li, D (2012). Structurally motivated damage models for arterial walls. Theory and application. In *Modeling of Physiological Flows,* 143-185. Springer.
[7] Austin, G, Fisher, S, Dickson, D, Anderson, D, Richardson, S (1993). *Annals of Clinical & Laboratory Science*, *23*(2), 97-105.

Copyright 2016 The Organizing Committee for the 2016 Summer Biomechanics, Bioengineering and Biotransport Conference

SB^{3}C2016
Summer Biomechanics, Bioengineering and Biotransport Conference
June 29 –July 2, National Harbor, MD, USA
SB^{3}C2016-1113

A COMPARISON OF PHENOMENOLOGICAL AND THERMODYNAMICALLY CONSITENT APPROACHES FOR THE MODELLING OF CELLS SUBJECTED TO DYNAMIC LOADING

Patrick McGarry (1), Vikram S. Deshpande (2)

(1) College of Engineering and Informatics
National University of Ireland Galway
Galway, Ireland

(2) Dept. of Engineering,
University of Cambridge,
Cambridge, United Kingdom

INTRODUCTION

In the dynamic loading experiments of Wille et al. [1] fibroblast cells are seeded into a collagen scaffold and the resultant synthetic tissue construct is attached to a mechanical test machine. Displacement controlled cyclic stretching is applied to the tissue and cells are shown to align in the direction of cyclic stretching. Force measurements reveal that active cell force is very sensitive to strain rate but not sensitive to strain magnitude. Dynamic experiments performed by Weafer et al. [2] on single osteoblasts also reveal that active cell force is not sensitive to changes in strain magnitude, but highly sensitive to strain rate. A study by Mitrolosis [3] reveals that under static conditions cell contractility follows a Hill type tension-strain rate relationship.

Motivated by empirical observations of cardiac tissue under dynamic conditions [4], a fading memory type contractility formulation is first proposed to simulate cell forces measured in the experiments of Wille et al. [1] and Weafer et al. [2].

It is then shown that the fading memory formulation does not correctly predict stress fibre alignment in the direction of loading for cells embedded in collagen gels, as observed experimentally. A thermodynamically consistent model for stress fibre formation/dissociation and remodeling [5] is then investigated. When implemented in conjunction with a non-local conservation of cytoskeleton proteins within a cell this framework predicts the correct alignment of stress fibres in addition to capturing transient changes in active force during dynamic loading.

FADING MEMORY MODEL

The fading memory formulation is based on the empirical observation that under dynamic conditions tension is a function of the linear superposition of previous length changes, with current tension being more influenced by recent length changes than earlier length changes [4]. Therefore we express the "fading memory" weighted accumulated strain for a fibre at an angle ϕ as

$$h(\phi) = \sum_{i=1}^{n} A_i \int_{-\infty}^{t} e^{-\alpha_i (t-\tau)} \dot{\varepsilon}_m(\phi)\, d\tau \tag{1}$$

where α_i are exponential rate constants and A_i are weighting coefficients (where $\sum A_i = 1$). It should be noted that, unlike the formulation of Hunter et al. we do not include positive strain rates (fibre lengthening) in the accumulated strain. Following from the approach of Hunter et al. (1998) we insert a fading memory strain rate $\bar{\alpha} h(\phi)$ in a Hill-type equation such that

$$B^h(\phi) = \frac{1 - \bar{k}_v \bar{\alpha} h(\phi)/\dot{\varepsilon}_o \eta(\phi)}{1 + k_k h} \tag{2}$$

and

$$\frac{T(\phi)}{T_o} = \begin{cases} 0 & B^h(\phi) < 0 \\ B^h(\phi) & 0 \le B^h(\phi) \le 1 \\ 1 & 1 < B^h(\phi) \end{cases} \tag{3}$$

where $\bar{\alpha}$ is a rate constant, the parameters k_k and $\bar{k}_v$ control the curvature of the tension-strain rate. The parameter $\dot{\varepsilon}_o$ is a reference strain rate, so that the quantity $\bar{\alpha} h(\phi)/\dot{\varepsilon}_o$ is a non-dimensional fading memory strain rate for a stress fibre at an angle ϕ, and $\eta(\phi)$ is the stress fibre activation level. If $k_k = 0$ and $\alpha_i \to \infty$ the static Hill equation is recovered.

For the constant strain rate experiments of Wille et al. [1] and Weafer et al. [2] a closed form solution can be obtained for equation 1:

Copyright 2016 The Organizing Committee for the 2016 Summer Biomechanics, Bioengineering and Biotransport Conference

$$h(\phi) = A\dot{\varepsilon}_U(\phi)\int_{P/2}^{P} e^{-\alpha(t-\tau)}\,d\tau + A\dot{\varepsilon}_U(\phi)\int_{3P/2}^{2P} e^{-\alpha(t-\tau)}\,d\tau$$
$$= \frac{A\dot{\varepsilon}_m(\phi)}{\alpha}\left\{e^{-\alpha(t-P/2)} - e^{-\alpha(t-P)} + e^{-\alpha(t-3P/2)} - e^{-\alpha(t-2P)}\right\} \quad (4)$$

The predicted fore-strain loops at steady state are shown in Figure 1. It can clearly be observed that the curve shapes bear a strong resemblance to the experimentally observed force strain loops [1, 2].

When the fading memory formulation is implemented in conjunction with a phenomenological kinetic equation for stress fibre remodeling a dependence on predicted force on applied strain rate is correctly computed. However, this formulation fails to correctly predict the alignment of stress fibres in the direction of stretching.

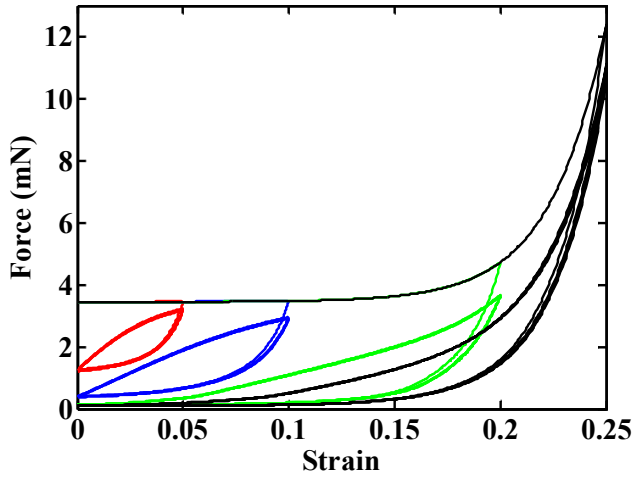

Figure 1. Fading memory prediction of active cell force as a function of applied strain rate. A loading frequency of 0.1Hz in all cases.

THERMODYNAMICALLY CONSISTENT MODEL

In an effort to correctly predict cell alignment in a dynamically loaded 3D environment we use a thermodynamically consistent model (Viglotti et al. []) for stress fibre formation/dissociation and remodeling in conjunction with a non-local conservation of cytoskeleton proteins within a cell.

The rate of stress fibre formation and dissociation is given as

$$\dot{\hat{\eta}} = \frac{\hat{N}_u}{\pi\hat{n}}\omega_n \exp\left[-\hat{n}\frac{\mu_a - \mu_u}{k_B T}\right] - \hat{\eta}\omega_n \exp\left[-\hat{n}\frac{\mu_a - \mu_b(\phi)}{k_B T}\right] \quad (5)$$

where $\hat{\eta}$ is the SF concentration per unit surface area of a representative volume element (RVE), $\hat{n}$ is the number of actin-myosin contractile units along the length of the RVE, μ_b is the free energies of the bound contractile units in a stress fibre, μ_u is the free energy of unbound SF proteins, while k_B and T are the Boltzmann constant and absolute temperature. $\hat{N}_u$ is the number of unbound SF proteins in the RVE.

Here we implement non-local conservation of the total number of SF proteins within the cell, $\hat{N}_T$, under the assumption that the diffusion of unbound proteins through the cytoplasm is infinitely fast relative to the timescale of SF remodeling. The local number of unbound proteins in an RVE is therefore given as

$$\hat{N}_u = \hat{N}_T - \int_{V_c}\int_{-\pi/2}^{+\pi/2} \hat{\eta}\,\hat{n}\,d\phi\,dV \quad (6)$$

where the inner integral computes the number of bound proteins in a RVE, and the outer integral provides a summation of the number of bound proteins throughout the entire cell volume V_c. The kinetic law for stress-fiber remodeling is given as

$$\dot{\hat{n}} = \begin{cases} -\frac{1}{\hat{n}}\left(\frac{\hat{N}_u}{\hat{\Pi}}\right)^2\left[\psi(\tilde{\epsilon}_n) - \frac{\delta\psi}{\delta\tilde{\epsilon}_n}(1+\tilde{\epsilon}_n)\right]\frac{\alpha}{\mu_{b0}} & if\ \frac{\delta\Psi}{\delta n} \le 0 \\ -\frac{\hat{n}}{4}\left[\psi(\tilde{\epsilon}_n) - \frac{\delta\psi}{\delta\tilde{\epsilon}_n}(1+\tilde{\epsilon}_n)\right]\frac{\alpha}{\mu_{b0}} & otherwise \end{cases} \quad (7)$$

Contractility is implemented via a Hill-type tension strain rate law, without the requirement of introducing the phenomenological fading memory formulation. The model correctly predicts transient changes in active cell stress as a function of applied strain rate. Importantly, the model predicts stress fibre alignment in the direction of loading, as shown in Figure 2. Stress fibres form only in the general direction of applied stretching ($\phi = 0$), with no fibres forming perpendicular to the loading direction.

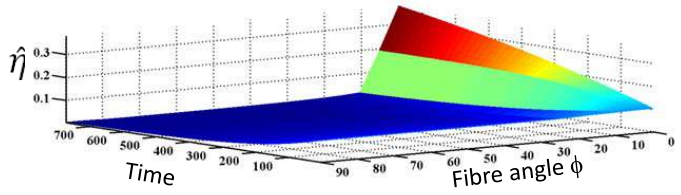

Figure 2. Evolution of stress fibre concentration $\hat{\eta}$ as a function of fibre angle ϕ.

DISCUSSION

A fading memory formulation correctly captures the transient changes in stress fibre tension during applied dynamic loading. However, alignment of stress fibres in the direction of loading is not correctly predicted when a phenomenological kinetic equation is used for stress fibre evolution. In contrast, a thermodynamically consistent formulation with non-local conservation of cytoskeleton proteins within a cell correctly predicts both transient changes in fibre tension, and alignment of fibres in the stretching direction. A simple hill model for contractility is sufficient when stress fibre formation and remodeling is correctly described. This suggests that the "fading memory" type strain rate really represent the "catching-up" of the apparent stress fibre strain rate with the applied strain rate as contractile actin-myosin units are added or removed from the stress fibre in response to external loading.

ACKNOWLEDGEMENTS

PMCG acknowledge funding from Science Foundation Ireland (SFI-12/IP/1723).

REFERENCES

[1] Wille et al. *Ann.Biomed. Eng*., 34: 1678-1690, 2006.
[2] Weafer et al., *Acta Biomaterialia* 27: 236–250, 2015.
[3] Mitrossilis et al., *Proc Natl Acad Sci U S A* 2009;106:18243-8.
[4] Hunter et al., *Prog. Biophys. Molec. Biol.* 69:289-331, 1998.
[5] Vigliotti, A *et al.*, *Biomech Model Mechanobiol*, in press, 2015.

Copyright 2016 The Organizing Committee for the 2016 Summer Biomechanics, Bioengineering and Biotransport Conference

SB³C2016
Summer Biomechanics, Bioengineering and Biotransport Conference
June 29 –July 2, National Harbor, MD, USA
SB³C2016-1114

POINT-OF-CARE DIAGNOSIS BY NANOPARTICLE AGGREGATION: TUNING THE SENSITIVITY BY NANOPARTICLE SIZE AND CONCENTRATION

Peiyuan Kang (1), Zhenpeng Qin (1, 2)

(1) Department of Mechanical Engineering
University of Texas at Dallas
Richardson, TX, USA

(2) Department of Bioengineering
University of Texas at Dallas
Richardson, TX, USA

INTRODUCTION

POC diagnosis of infectious diseases requires a fast assay time, minimal infrastructure, and sufficient sensitivity and specificity. Among the various infectious disease biomarkers, the amplification and detection of pathogen's nucleic acid sequence has been shown to be highly sensitive and specific. To detect the target nucleic acid sequence, a gold nanoparticle (GNP)-based aggregation assay has shown great promise to meet the POC requirements. For this assay, GNPs were conjugated with two different DNA sequences that are complementary to target nucleic acid sequence to create "probes". The probes hybridize with the target to form GNP aggregates which induce a color change due to the altered plasmon resonance (Figure 1). Previous work has reported the optimized reaction conditions and detection methods [1-2]. However, the effects of GNP probe concentration and size on the assay performance are not clearly understood.

In this work, we investigated the effects of the nanoparticle probe's concentration and size on the assay performance. Preliminary results suggest that higher GNP probe concentration shifts the assay dynamic range to be less sensitive, and increasing GNP probe size increases the sensitivity (30 – 50nm versus 15nm). Our work presents guidelines to design this nanoparticle assay to meet sensitivity needs.

METHODS

Malaria parasite genus *Plasmodium* was chosen as a clinically relevant target [1]. A poly A-tail was included in the probes to increase flexibility of the sequence. The HPLC-purified probes were synthesized and purchased from Bio Basic Canada Inc. GNPs were prepared by reducing gold chloride by sodium citrate. To conjugate DNA probes to GNPs, we followed a pH-assisted and surfactant-free method reported earlier [3]. The complementary target was then hybridized with GNP probes for 30 min at room temperature in the presence of a hybridization buffer which consisted of 20 % Formamide, 16% dextran sulfate and 0.6 M NaCl. The optical spectrum was measured using a Beckman Coulter UV-Vis spectrophotometer (model DU800).

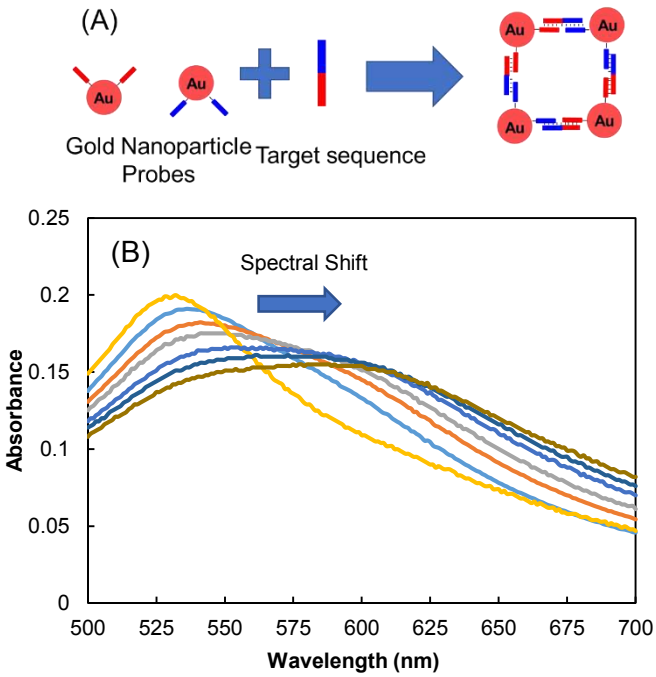

Figure 1. Schematic of the nanoparticle aggregation assay (A) and example spectral shift (B).

Copyright 2016 The Organizing Committee for the 2016 Summer Biomechanics, Bioengineering and Biotransport Conference

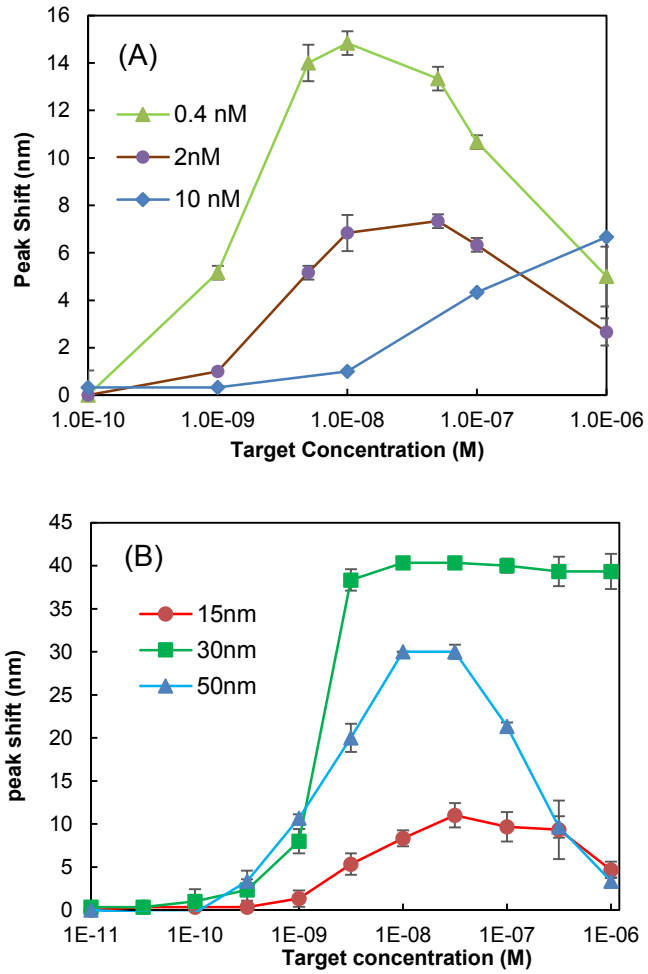

Figure 2 (A) Effect of GNP probe concentration on the aggregation sensitivity and dynamic range (15nm). (B) Effect of GNP size on the aggregation sensitivity and dynamic range (OD=0.75 for all cases).

RESULTS

15nm GNP probe was used to test the effect of nanoparticle concentration. The probe nucleic acid conjugation on GNP leads to plasmon resonance peak shift from 518 to 524 nm and hydrodynamic diameter increase by 9 nm. Within the concentration range studied here, increasing the GNP probe concentration shifts the dynamic range of the assay to higher target sequence concentrations and thus leads to higher limit of detection (i.e. less sensitive, Figure 2A). For instance, a low probe concentration (0.4nM) can detect down to 0.1nM while a higher probe concentration (10nM) can only detect down to ~10nM. We hypothesize that the large excess of non-aggregated GNPs (thus background) for higher probe concentration explains the less sensitive detection.

The effect of nanoparticle size on the assay performance was investigated by varying GNP size including 15nm, 30nm, and 50nm. While changing the GNP size, we kept the peak OD value the same for all samples. The result is shown in Figure 2B. Larger GNP size decreases the limit of detection (i.e. more sensitive to detect lower target concentrations). For example, 50nm GNP probe can detect down to 0.1nM while a smaller probe size (15nm) can only detect 1nM. Interestingly 30nm gives a highest spectral shift in all the three sizes. Careful examination of the assay kinetics shows that the reaction and peak shift of 30nm GNP probe is faster than the cases for 15nm and 50nm (data not shown). One possible explanation is the balance between the peak shift and Brownian motion. While the larger GNP gives a larger signal and thus higher signal, larger GNP also has a slow Brownian motion thus reducing the speed of the reaction. As a result, 30nm may be an optimal balance between the two factors, giving the highest peak shift.

DISCUSSION

Optimization of the assay performance is an important first step towards the development of a reliable and highly sensitive point-of-care diagnostic platform. In this study, we carefully evaluated the effects of the nanoparticle probe parameters including the concentration and size, and the results suggest that lower GNP concentration and larger size improve the ability to detect lower target concentration. The current nanoparticle aggregation assay can detect nucleic acid targets in the pM to nM range, and future work is needed to further improve sensitivity.

ACKNOWLEDGEMENTS

Z. Q. thanks Kyryl Zagorovsky in Dr. Warren Chan's group at University of Toronto for helpful discussions and suggesting the pH-assisted conjugation approach. This study is supported by the Texas Medical Research Collaborative (TexasMRC) program.

REFERENCES

[1] M.S. Codray, M. Amdahl and R.R. Richards-Kortum, "Gold nanoparticles aggregation for quantification of oligonucleotides: optimization and increased dynamic range" *Anal. Chem.* 2012, vol 431, pp. 99-105.

[2] J.J. Storhoff, A.D. Lucas, V. Garimella, Y.P. Bao and U.R. Muller, "Homogeneous detection of unamplified genomic DNA sequences based on colorimetric scatter of gold nanoparticle probes" Nat. Biotechnol. 2004, vol 22, pp. 883-887

[3] X. Zhang, M.R. Servos and J. Liu, "Instantaneous and quantitative functionalization of gold nanoparticles with thiolated DNA using a pH-assisted and surfactant-free route" *J. Am. Chem. Soc.* 2012, vol 134, pp. 7266-7269.

Copyright 2016 The Organizing Committee for the 2016 Summer Biomechanics, Bioengineering and Biotransport Conference

SB³C2016
Summer Biomechanics, Bioengineering and Biotransport Conference
June 29 –July 2, National Harbor, MD, USA
SB³C2016-1115

AGE-DEPENDENT DIFFERENCES IN MECHANICAL PROPERTIES OF CHEMICALLY TREATED BOVINE PERICARDIUM

A.D. Caballero (1), F. Sulejmani (1), W. Sun (1)

(1) The Wallace H. Coulter Department of Biomedical Engineering
Georgia Institute of Technology and Emory University
Atlanta, GA, USA

INTRODUCTION

The pericardium, a collagen extracellular meshwork, is the connective tissue sac surrounding the heart. Adult and calf bovine pericardium (BP) are widely used as biomaterials for tissue engineering applications, including the construction of vascular grafts and patches, as well as for manufacturing bioprosthetic heart valves (BHVs) [1]. A critical parameter of BHVs designed to be implanted percutaneously is the BP thickness, since the collapsed valve should be able to be delivered in a small diameter catheter so that it can be threaded through the arterial system.

It has been suggested that neonatal BP is significantly thinner and has superior strength than adult BP [2], making it a potential candidate tissue for percutaneous BHV manufacturing. These findings, however, are limited by the use of simplistic uniaxial loading, given that pericardial tissue is considered to be mechanically anisotropic. Moreover, it is still unclear whether the age of the animals has an impact on the mechanical behavior of the BP. Therefore, the objective of the present study was to investigate and compare the age-dependent mechanical properties of fetal, calf and adult BP by means of multi-axial mechanical testing and structural analysis.

METHODS

Fresh pericardial sacs were obtained from 10 adult (12-24 months old), 11 calf (6-12 months old) and 11 fetal (third trimester of gestation) cattle from Animal Technologies, Inc. (Tyler, TX, USA). Tissue fixation was performed in 0.625% glutaraldehyde in a two-step procedure. Due to the fact that there is a structure-function- relationship between collagen alignment and mechanical strength, two-photon microscopy was used to determine the collagen fiber orientation of the BP samples. Quantification of a preferred fiber orientation of the samples was done semi-automatically using an in-house ImageJ/Matlab code.

Biaxial mechanical testing was carried out according to the methods presented by Sacks and Sun [3]. Briefly, four graphite markers placed in the central region of the samples were used for optical strain measurements. Samples were then mounted in a trampoline fashion and tested in saline solution at 37 °C. The preferred fiber orientation was aligned with the X11 direction of the loading axis of the biaxial device. Seven stress-controlled test protocols were utilized and preconditioning was performed to reduce tissue hysteresis. Constitutive modeling was carried out from the multi-protocol biaxial mechanical data, and the tissue responses were fitted with the anisotropic hyperelastic Holzapfel-Gasser-Ogden model.

Uniaxial test samples adjacent to the biaxial samples were cut into a “dog-bone” shape to ensure failure in the center region and to minimize grip effects. Each sample was cut in a way to insure that the preferred fiber orientation was parallel to the device loading axis. Graphite optical markers were placed on the narrow portion of the samples for optical strain measurements. After preconditioning, samples were loaded until failure and an in-house LabVIEW/Maltab program was used to obtain the stress–strain curves.

Finally, the fibrous structure of the BP was examined via histological analysis. Samples were cut into strips parallel to the X11 direction of the biaxial test fixture, and fixed in 10% formalin prior to paraffin processing and sectioning. The sections were then stained with Picrosirius red and imaged with circularly polarized light. Images were analyzed with an automated in-house Matlab code to quantify the maturity of the collagen fibers. All measurements are presented as a mean ± standard deviation. For all statistical considerations, a p-value

Copyright 2016 The Organizing Committee for the 2016 Summer Biomechanics, Bioengineering and Biotransport Conference

< 0.05 was considered to be statistically significant (indicated by *, while ** indicates high statistical significance with p < 0.001).

RESULTS

The mean thickness was 0.451 mm for adult BP (ABP), 0.321 mm for calf BP (CBP), and 0.231 mm for fetal BP (FBP). There was a high statistically significant difference between the three age groups (p < 0.001). Quantification of the angular distribution of the collagen fibers allowed us to measure the anisotropy of the samples in a systematic way (Figure 1).

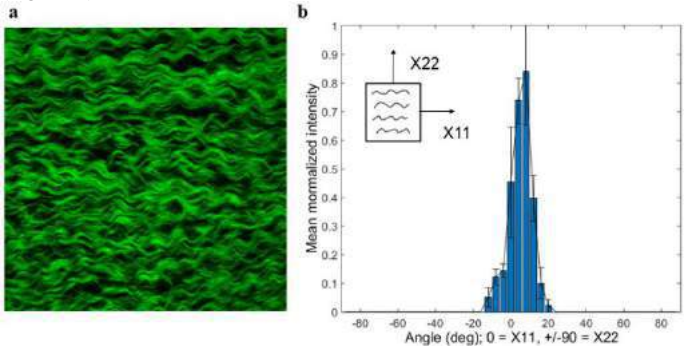

Figure 1: (a) Representative second-harmonic generation image slice of FBP sample, (b) Distribution of fiber alignment through the thickness for FBP sample

Regarding the biaxial mechanical response, the tissue stiffness was quantified at three equibiaxial stress values: 60 kPa, 250 kPa and 600 kPa (Figure 2). ABP and CBP demonstrated a higher stiffness than FBP in both directions. This difference was statistically significant in the cross-fiber direction (X22) direction at all stress values. On the other hand, FBP showed a higher extensibility than ABP and CBP, with a statistically significant difference in the X22 direction (Figure 3a). The modified Holzapfel model successfully captured the BP biaxial response with a mean R^2 value of 0.95 for all age groups (Figure 3b).

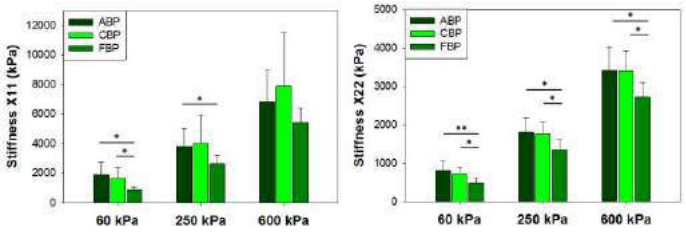

Figure 2: Tissue stiffness at 60 kPa, 250 kPa and 600 kPa of ABP, CBP and FBP in the X11 and X22 directions

The ultimate tensile strength (UTS) of ABP and CBP was found to be much greater than for FBP, with a high statistically significant difference (p < 0.001) (Figure 4a). On the other hand, the strain at failure was significantly greater for FBP than for ABP and CBP (p < 0.001) (Figure 4b). Also, when the extensibility for each age group was compared, the strain was significantly larger in the X22 direction than in the X11 direction for ABP, CBP and FBP, confirming the anisotropic properties of the tissue. There was no statistically significant difference in mechanical properties between the ABP and CBP groups. Quantitative collagen color (hue) analysis of the histological samples indicated statistically significant differences in the percentage of green (thin) fibers between ABP and FBP, and between CBP and FBP (p < 0.001), where the proportion of thin newly synthesized fibers decreased with age.

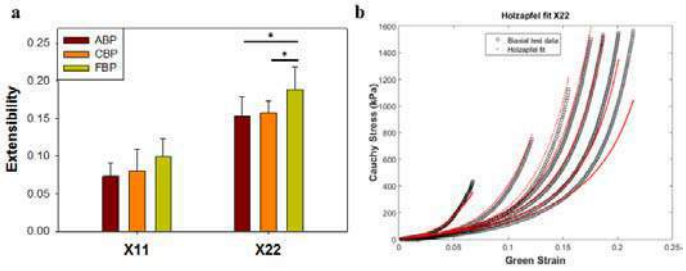

Figure 3: (a) Tissue extensibility of ABP, CBP and FBP in the X11 and X22 directions, (b) Representative multi-protocol biaxial test data for one ABP sample (black) with modified Holzapfel model fit (red) in the X22 direction

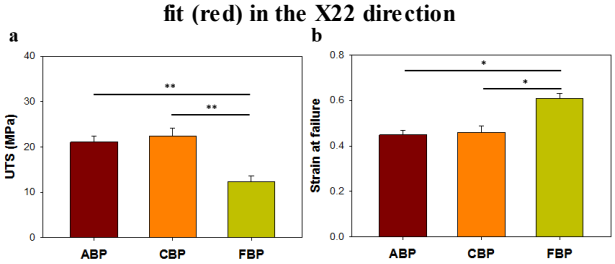

Figure 4: (a) UTS of ABP, CBP and FBP, (b) Strain at failure of ABP, CBP and FBP

DISCUSSION

Overall, ABP and CBP demonstrated a markedly higher stiffness and a higher tensile strength than FBP. However, FBP was significantly thinner and presented a higher extensibility and strain at failure than ABP and CBP. Results suggest that BP is more compliant during the fetal stage and then stiffens and strengthens during young adulthood. The significant difference in thin collagen fibers between ABP, CBP and FBP supports the idea that the newly synthesized collagen fibers found in younger tissue are not as strong as the thick mature collagen fibers.

In contrast to the results of Sizeland et al. [2], our fetal BP did not show a higher stiffness and a higher ultimate tensile strength than the older tissue. This variance may be due to differences between juvenile and fetal tissues. In conclusion, a deeper understanding and utilization of the BP mechanical and structural properties may ultimately result in BHV designs with more predictable performance and improved durability, as well as would enable percutaneous valve technologies to develop the minimal profile size required to reduce adverse events at the vascular access site.

ACKNOWLEDGEMENTS

Research for this project was funded in part by the R21HL108240 grant. Andres Caballero is also supported by a Fulbright-Colciencias fellowship. The authors would also like to thank Michael Moon for his help in collecting experimental data.

REFERENCES

[1] Rémi, E., et al., Pericardial processing: challenges, outcomes and future prospects. *INTECH Open Access Publisher*, 2001.

[2] Sizeland, K. H., et al., Age Dependent Differences in Collagen Alignment of Glutaraldehyde Fixed Bovine Pericardium. *BioMed research international*, 2014.

[3] Sacks, M. S., and Sun, W., Multiaxial mechanical behavior of biological materials. *Annual review of biomedical engineering*, 5(1), 251-284, 2003.

Copyright 2016 The Organizing Committee for the 2016 Summer Biomechanics, Bioengineering and Biotransport Conference

SB³C2016
Summer Biomechanics, Bioengineering and Biotransport Conference
June 29 –July 2, National Harbor, MD, USA
SB³C2016-1116

STUDENT LEARNING OF BIOMECHANICS TOPICS BY EMBEDDING "QUANTIFIED SELF" MOTIVATED PROBLEM BASED LEARNING MODULES IN BIOMEDICAL ENGINEERING COURSES

Eric G. Meyer, Mansoor Nasir

Biomedical Engineering Department
Lawrence Technological University
Southfield, MI, USA

INTRODUCTION

Traditional undergraduate courses in engineering have followed the deductive pedagogy of proposing a concept, explaining the principles and demonstrating the theoretical framework of the concept [1]. The student is expected to memorize the material or work many examples and their mastery is then evaluated during an exam. This teaching method lacks important student learning opportunities, such as; the reason why these concepts or mathematics are important, what is their real-world relevance and how this will impact the students' future career in engineering. Project Based Learning (PBL) is an alternative method that is an inductive pedagogy, which is more student-centered [2]. These techniques begin with a real-world problem or observation that is introduced to the students and can lead to deeper student learning when properly implemented [3].

The "Biomechanics" sub discipline of Biomedical Engineering (BME) is taught in various forms in most undergraduate programs. The BME curricula at Lawrence Technological University requires that students take semester long courses covering "Statics", "Biomechanics" with "Biomechanics Lab", and "Tissue Mechanics". There are also opportunities to develop interest and experience with biomechanical applications in non-technical or elective courses, such as the freshman-level "Introduction to Biomedical Engineering" or senior-level "Engineering Applications in Orthopedics" courses.

"Quantified Self" (QS) is a trend in the consumer electronics and digital health industries that have introduced many devices with new sensors and data logging systems to allow individuals to understand their personal health and wellness through quantification and tracking a variety of physiologically relevant parameters. The QS theme can be related to a variety of topics in many engineering and science disciplines (Figure 1). Besides companies' excitement over QS devices, it is increasingly common to find students that own these devices, such as the Fitbit activity trackers, Withings smart scales, or Apple smart watch. Many popular QS devices are based on biomechanics concepts using kinematics (e.g. Microsoft Kinect and Nintendo Wii Remote) or the kinetics (e.g. Wii Balance Board). Other examples like the electromyography based Myo Gesture and pressure based Nike in-shoe sensors do not have wide customer base yet.

Figure 1: Representation of the broad diversity of topics that can be related to Quantified Self devices.

The goal of this project was to develop and implement learning modules and associated resources that use the QS theme to motivate biomechanics topics in a range of BME courses. By spreading the modules into a variety of courses at the freshman, sophomore, junior and senior levels, the students may be repeatedly exposed to QS devices with an increasing levels of difficulty and expectations throughout their degree program. This not only promotes a deeper understanding of the fundamental biomechanics concepts but also allows the students to

Copyright 2016 The Organizing Committee for the 2016 Summer Biomechanics, Bioengineering and Biotransport Conference

develop experience and confidence in working with these types of devices.

METHODS

In this project, we developed and implemented QS theme based PBL modules to teach biomechanics topics in four BME courses following a similar pedagogical technique from modules developed for other topics in a range of disciplines [5]. The PBL modules were organized as a combination of short Active Collaborative Learning (ACL) activities that were completed in class and partner/group based design project homework assignments. The modules combined several open-ended tasks that build sequentially, following previously completed work and the topics that were covered in class. Student learning outcomes during a pilot implementation of the modules were measured with direct (formal design report and/or group presentations) and indirect (student survey) assessments. The instructors also maintained close observation of student groups in class and during office hours to reflect and improve the implementation of the module.

RESULTS

Detailed assignments and instructor guides for the biomechanics modules were developed and implemented for at least one pilot test prior to being shared with other BME faculty through teaching workshops and a website [6]. Generally, these modules required 1-3 partial class periods to introduce the theme, develop understanding of the QS devices, and conclude with a final project wrap-up with the groups. The modules were scheduled to coincide with the appropriate technical concepts that were covered in the course.

Course: BME 1002 "Introduction to Biomedical Engineering"
Module: Product Concept Development based on the Nike+ Shoe Sensors

The project started with an introduction of the engineering design process. Then groups were formed to practice opportunity recognition through the "Painstorming" technique [7]. Finally, the groups were asked to develop a new application for the Nike+ Shoe Sensor system. They produced a device concept, a simple business model and evaluated the market potential. The assessment was concluded with a student produced elevator pitch video on economic and social benefits of their proposed application. Most students understood the importance of design in engineering and were able to communicate their product concept in terms of technical capability, customer value and economic viability. The sensors for this project were functional prototypes manufactured by Nike but are not currently commercially available.

Course: BME 3303 "Introduction to Biomechanics"
Module: Sensing Angular Kinematics of a Baseball Swing with Arduino

The scenario was a call for assistance from the university's baseball coach to help improve the team's batting performance. Students worked together during class to investigate baseball swing kinematics. Guided homework questions walked the students through the design process steps of; identifying customer needs, brainstorming, determining specifications, analyzing solutions. Next, students were introduced to open-source electronics like Arduino and sensor platforms (SEEED Grove) to use for the prototype development phase of the project. Next, the student teams developed a calibration method for the sensors and recorded the motions during a baseball bat swing. Finally, they developed a formal design report that refined their concept into a commercial product that could be marketed to the baseball coach and potential investors. Although most students had no prior experience with Arduino, they enjoyed the hands-on aspects of building a prototype. The hardware kits cost approximately $50/group, but can be reused in future course offerings.

Course: BME 4313 "Tissue Mechanics"
Module: Mimicking Muscle Optimization Strategies with Myo Gesture

In this course, students learn how to predict muscle contraction patterns using static optimization of various performance criteria. These same patterns can be directly measured with new QS sensors like the Myo Gesture armband. Students used the sensors to record forearm electromyography during everyday activities like using tools, typing, playing music or video games, sports, etc. They compared muscle contraction patterns between two different activies. Finally, they had to suggest ways that this information might be used for human-computer interface applications like active prosthetics control. The Myo Gesture devices cost approximately $200 per unit, and can be synced with a computer or mobile device running a variety of applications. The package includes a software development kit that allows access to raw EMG data.

Course: BME 5093 "Engineering Applications in Orthopedics"
Module: Surrogate Head Impact Measurement with Triax Headband

Impact biomechanics uses surrogate human devices like crash test dummies to assess injury risk and the effectiveness of safety systems to prevent injury. Students built their own surrogate head and neck to simulate the anthropometry and biofidelity of a human. Then they used the Triax headband sensors to quantify impacts for different scenarios and with various helmets. Hands on use with head impact sensors allowed the students to understand differences between linear acceleration and angular velocity and how those motions might lead to different injury patterns. The Triax SIM-G sensors cost approximately $200 per unit, but can be shared and/or reused for other projects.

DISCUSSION

Students were able to create product concepts, to collect and calibrate sensor data and relate this information to various biomechanical topics that were being studied in the BME courses. Although most students had no prior experience with the QS devices prior to the modules, they enjoyed the hands-on aspects of these PBL modules. Other positive reflections included the open-ended and real world aspect of these projects. On the other hand, some students expressed confusion during the projects, due to a lack of understanding of how the module was introduced and what was expected. These course modules were part of a larger project to implement Entrepreneurial Minded Learning into a variety of engineering courses so that students will be repeatedly exposed to this mindset with the ultimate goal of improving students' preparation and skills for their senior capstone projects and as professionals in the real-world.

ACKNOWLEDGEMENTS

The authors would like to acknowledge the support of Lawrence Technical University, Provost Dr. Maria Vaz, and funding from a Kern Entrepreneurship Education Network Topical Grant to support this project.

REFERENCES

[1] Froyd, JE et al., *Proc IEEE*, 100:1334-1357, 2012.
[2] Smith, KA et al., *J Eng Ed*, 94(1):87-101, 2005.
[3] Prince, M. *J Eng Ed*, 93(3):223-231, 2004.
[4] quantifiedself.com
[5] Meyer, EG and Nasir, M. ASEE Conf Proc, 2015.
[6] qs4eml.ltu.edu
[7] Weaver, J et. al. J Eng. Ent., 2(1): 10-27, 2010.

Copyright 2016 The Organizing Committee for the 2016 Summer Biomechanics, Bioengineering and Biotransport Conference

SB³C2016
Summer Biomechanics, Bioengineering and Biotransport Conference
June 29 –July 2, National Harbor, MD, USA
SB³C2016-1117

POTENTIAL INVOLVEMENT OF ENDPLATE PURINERGIC SIGNALING IN LOW BACK PAIN

Mary E. Boggs (1), John F. DeLucca (2), Dawn M. Elliot (2), Randall L. Duncan (1,2)

(1) Department of Biological Sciences
University of Delaware
Newark, DE, USA

(2) Department of Biomedical Engineering
University of Delaware
Newark, DE, USA

INTRODUCTION

Low back pain (LBP) can occur from nerve irritation or physical impingement caused by trauma. However, the most common type of LBP results from nonspecific causes lacking trauma or specific pathology. It has been postulated that up to 84% of people will experience lower back pain at some point during their life, and 23% will experience chronic LBP (1). Nonspecific LBP is often difficult to treat as the underlying pain mechanism is not well understood. Degeneration of the disc and surrounding tissue may be involved in spinal pain transmission. It is hypothesized that load-induced degeneration of the disc is preceded by degeneration of the cartilage endplate (CEP), a thin, hyaline-cartilage tissue located between the disc and the vertebrae that regulates diffusion of solutes across the disc (2). During endplate load-induced degeneration, cells within the endplate may undergo changes including release of TGF-β and apoptosis (3, 4). Additionally, degeneration leads to increased innervation of the tissue, and it has been suggested this change can modulate LBP (5, 6). A molecule that has been described as being released by mechanical stimulation and inducing pain is ATP (7, 8), however release of ATP from endplate chondrocytes has not been described. We propose that cartilage endplate cells release soluble factors in response to mechanical load, such as ATP, that activate nociceptors in the CEP in particular in load-induced degeneration contributing to LBP. We demonstrate here that ATP released by mechanically stimulated murine long-bone osteocyte-like cells (MLO-Y4) activate neurons through the purinergic receptor, $P2X_3$. We propose that communication between CEP chondrocytes and local nerves is through similar mechanisms. Understanding the exact cellular and mechanical mechanisms behind LBP will enhance therapeutic treatment of this debilitating condition.

METHODS

Dorsal Root Ganglia Culture

Primary mouse single-cell dorsal root ganglia (DRG) were isolated and cultured as described by Malin et al (Malin et al. 2007). Briefly, adult C57BL/6 mice (Jackson Lab, Bar Harbor, ME) were humanely euthanized by CO_2 and cervical dislocation according to IACUC approved protocol. DRG at locations L3-L5 were removed from both sides of the animal and held in cold Dulbecco's modified eagle medium: Nutrient mixture F-12 (50:50; DMEM-F12; Mediatech, Manassas, VA) with 1% [v/v] penicillin/streptomycin (Mediatech). Ganglia were washed in DMEM-F12 with penicillin (100IU)/streptomycin (100µg/mL)and transferred to Hank's balanced salt solution (HBSS; Mediatech) with Ca2+ and Mg2+ containing papain (20 units/mL; Worthington, Lakewood, NJ) with L-cysteine (0.33 mg/mL; Sigma-Aldrich, St. Louis, MO) for 10 min at 37ºC. The ganglia were then centrifuged at 160xg for 1 min. Papain solution was removed and replaced with HBSS with Ca2+ and Mg2+ containing collagenase Type II (1440 units/mL; Worthington) and dispase (4.7 mg/mL; BD Biosciences, San Diego, CA) and incubated for 10 min at 37ºC. Ganglia were then centrifuged at 160xg for 1 min and collagenase/dispase solution was removed. Collagenase was inactivated with serum. Ganglia were triturated with a flame-polished pipette 10 to 20 times to mechanically break up the ganglia. The cells were plated onto glass coverslips coated with poly-D-lysine (100µg/mL; Sigma) and Laminin Type 1 (20µg/mL; BD Biosciences). Complete media was supplemented with Nerve growth factor (NGF 50ng/mL; Sigma) and cells were grown at 37ºC in a 95% air/5% CO2 atmosphere. Cells were used no later than 48 hours after culture.

MLO-Y4 Cell Culture

Copyright 2016 The Organizing Committee for the 2016 Summer Biomechanics, Bioengineering and Biotransport Conference

MLO-Y4 cells (kindly provided by Dr. Lynda F. Bonewald, Department of Oral Biology, University of Missouri at Kansas City School of Dentistry, Kansas City, MO), were cultured on Col1 (BD Biosciences, San Jose, CA) coated dishes. MLO-Y4 cells were cultured on prepared plates at 37ºC in a humidified atmosphere of 5% CO2 in alpha Minimal Essential Medium (αMEM; Mediatech) supplemented with fetal bovine serum (2.5% [v/v]) (FBS; Hyclone, Logan, UT) and penicillin (100IU)/streptomycin (100µg/mL) (Invitrogen, Carlsbad, CA).

Calcium Imaging

DRG neurons were cultured in 8-well Nunc™ Lab-Tek™ dishes coated with LN. After being in culture for 18-24h, DRG neurons were loaded with the calcium indicator Fluo-4 acetoxymethyl ester (5µM; Invitrogen, Carlsbad, CA). Cell loading was performed by washing wells 3-times with HBSS and then adding HBSS with Ca2+ and Mg2+ containing Pluronic acid in DMSO (20% v/v; Fisher Scientific, Pittsburg, PA) and Fluo-4 AM. Cells were incubated with Fluo-4 for 30 min at 37ºC. Cells were washed with HBSS and allowed to recover for 30 min at 37ºC. The dishes were immediately imaged on a Zeiss 5 LIVE DUO under the Plan-Apochromat 10X water objective (filters 495-555) and images were taken every 50ms for 4.6 min. ATP (Sigma), ATP antagonists and conditioned media were added to cells by pipetting into bath solution. Treatments were applied approximately 20-30 s after initiation of imaging. Drugs remained in the bath solution for the remainder of the experiment. For TNP-ATP treatment, drug was added to cells during recovery period and remained on the cells throughout experiment.

MLO-Y4 Conditioned Media

Conditioned media from MLO-Y4 cells was collected by placing cells in hypotonic solution in order to induce swell and release of ATP. MLO-Y4 cells were cultured in 100mm polystyrene cell culture dishes (Corning) in αMEM containing 2.5% FBS, 2.5% FCS and penicillin (100IU)/streptomycin (100µg/mL) to ~80% confluence. Cells were serum-starved overnight. Prior to hypotonic swelling, media was removed from plates and 3 mL of HBSS with Ca2+ and Mg2+ was added to each dish and placed back at 37ºC for 1 h. Plates were then removed from the incubator and 1 mL of media was removed and stored at - 80ºC. This was retained as control media. Cells were then swelled by gently adding 2 mL of deionized water reducing osmolarity to 143 mOsm. Hypotonic solution remained on the cells for 15 min. After swelling, 1 mL of media was removed and frozen at - 80ºC.

RESULTS

Initial studies focus on nerve activation by ATP and identification of pain-associated purinergic receptors. Data indicates that DRG increase intracellular calcium at even nanomolar concentrations of ATP (Fig 1). This response can be inhibited with the addition of the $P2X_3$ specific antagonist, TNP-ATP. Additionally, application of conditioned media from MLO-Y4 cells on DRG neurons results in an increase in intracellular calcium. This response is blocked by pre-incubation with TNP-ATP (Fig 2). Taken together, these data indicate that puringeric signaling plays a role in neuronal activation through binding of $P2X_3$ receptor.

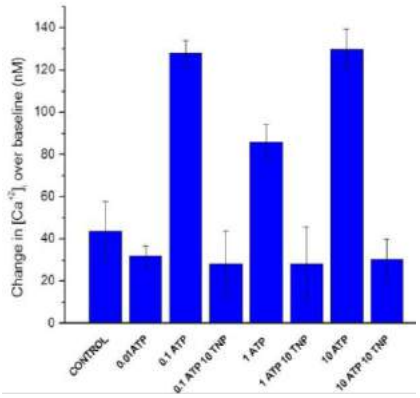

Figure 1. Application of ATP (0.1, 1 and 10 µM) to DRG results in increased intracellular calcium. This response is blocked with application of 10µM TNP-ATP which specifically inhibits $P2X_3$ receptors.

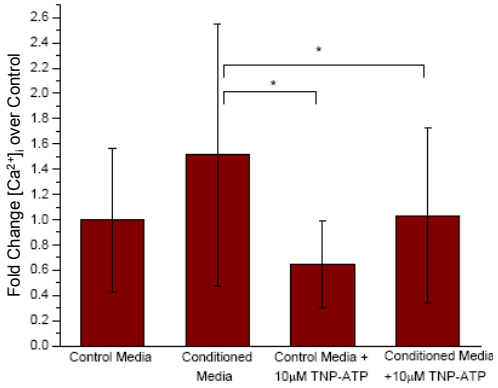

Figure 2. Application of MLO-Y4 conditioned media on DRG results in increased intracellular calcium. Intracellular calcium release is significantly reduced by blocking with the $P2X_3$ antagonist TNP-ATP. * Tukey-Kramer test $p<0.05$.

DISCUSSION

We propose that a potential mechanism for transduction of nonspecific LBP is release of ATP from CEP cells. We show here that ATP, which is released by bone cells during mechanical stimulation, activates neurons and thus presents as a potential pain signal in LBP. As described previously, mechanical load results in soluble factor release, potential cell apoptosis and degeneration of CEP tissue. Degeneration is often preceded by increased innervation leading to a potential mechanism for increased pain sensation. However, how these mechanisms together contribute in nonspecific LBP are not clear. ATP has been shown to be released by cells with mechanical stimulation and is a potent stimulator of pain. It is likely that CEP cells, similarly to bone cells and chondrocytes in articular cartilage, release ATP in response to mechanical stimulation (8,9). If this is the case, then ATP presents as a likely candidate for pain sensation in LBP. As $P2X_3$ is the main purinergic receptor associated with pain, it is a likely candidate for pain associated with nonspecific LBP. Future studies will focus on communication between CEP chondrocytes and DRG. Identification of a molecular mediator of nonspecific LBP will provide an invaluable therapeutic target for those affected by this debilitating condition.

ACKNOWLEDGEMENTS

This work has been supported through NIH/NIAMS award EB002425-09A1.

REFERENCES

[1] Airaksinen, O et al., European Section of the Cervical Spine Research Society, 15 Suppl 2:S192-300, 2006.
[2] Moon SM, et al., European Section of the Cervical Spine Research Society. 22(8):1820-8, 2013.
[3] Ariga, K et al., *Spine*. 28(14):1528-33, 2003.
[4] Xu, H et al., *Mol med rep*. 4(5):831-5, 2011.
[5] Krock, E et al., *J cell mol med*. 18(6):1213-25, 2014.
[6] Pezet S and McMahon SB, *Ann rev neurosci*. 29:507-38, 2006.
[7] Bele T and Fabbretti E, *Cur med chem*. 22(7):845-50, 2015.
[8] Genetos, D et al., *J cell phys*. 212(1):207-14, 2007.
[9] Garcia M and Knight M, *J Anat* 214(2):275-83, 2010.

Copyright 2016 The Organizing Committee for the 2016 Summer Biomechanics, Bioengineering and Biotransport Conference

SB³C2016
Summer Biomechanics, Bioengineering and Biotransport Conference
June 29 - July 2, National Harbor, MD, USA
SB³C2016-1118

THERMODYNAMIC FLUCTUATIONS DETERMINE THE KINETICS OF SWELL-BURST CYCLES OF GIANT UNILAMELLAR VESICLES UNDER OSMOTIC STRESS

Morgan Chabanon [(1)], James Ho [(2)], Atul N. Parikh [(2,3)], Padmini Rangamani [(1)]

(1) Department of Aerospace and Mechanical Engineering
University of California San Diego
La Jolla, CA, USA

(2) School of Materials Science and Engineering
Nanyang Technological University
Singapore, Singapore

(3) Departments of Applied Science, Biomedical Engineering, and Chemical Engineering & Materials Science
University of California Davis
Davis, CA, USA

INTRODUCTION

Osmolarity is a key parameter of cell microenvironment, having implications in numerous cellular activities ranging from gene expression to cancer metastasis [1-3]. Two biophysical aspects of the plasma membrane determine the entire subsequent cell responses to osmotic stress: (i) its transport properties for water and osmolytes, (ii) its mechanical behavior related to variations in cellular volume. In this work, we use giant lipid vesicles as a model system to study the response of the cell membrane to osmoregulation, and combine experimental characterization and mathematical modeling to reveal the dynamics of vesicle under osmotic stress.

When subject to hypotonic conditions, giant unilateral vesicles (GUVs) exhibit a swell-burst cycle behavior, driven by osmotic flux through the membrane, increasing the membrane tension until a pore is open and releases part of the content of the GUV. Once the membrane tension decreases, the pore reseals, and a new cycle begins (Fig. 1). Moreover, when the membrane is composed of a phase separating lipid mixture, domains of distinct composition and organization appear due to the osmotically induced stretching of the membrane. Although these behaviors have been observed [4,5], the relations between membrane deformation, pore formation/resealing, tension dependent phase separation, and transport properties are still unknown.

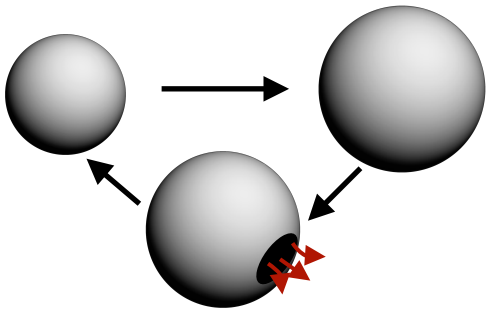

Figure 1: Schematic of a swell-burst cycle of a single lipid giant unilamellar vesicle (GUV) under hypotonic conditions. Red arrows represent leak-out through the transient pore.

Starting with single lipid vesicles, we experimentally quantify the swell-burst cycles of GUVs, and develop a theoretical model capturing the physical features of the system. We show the importance of membrane fluctuations, due to thermal and mechanical solicitations, in the determination of the dynamics of GUV in hypotonic conditions.

METHODS

The experimental methods for the GUVs preparation has been described in [5,6]. In brief, GUVs (100% POPC + 1mol% Rho-DPPE) containing 200, 600 or 1000 mM of sucrose were prepared by electro-formation, yielding radii ranging from 7 to 20µm. GUVs were then placed in a bath of deionized water at room temperature, inducing hypotonic stress proportional to the inner sucrose concentration. The kinetics of GUVs were recorded by time-laps microscopy at 1/150 images/ms. Note that for practical reasons, observations started about one minute after the GUVs were put in hypotonic conditions. For each frame, the GUV radius was measured with a homemade image analysis code built in Matlab, which fits the GUVs contour to a circle, based on intensity gradient contour detection. The evolution of the GUV radius with time was obtained, with a precision of about 0.1µm. Pore opening events were identified as sudden drop of GUV radius, and confirmed by direct observation.

In order to understand the observed swell-burst cycles, we propose a theoretical description of the system which couples mass conservation of the solvent (including osmotic influx, and leak-out through the pore), mass conservation of the solute (including diffusive and convective flux through the pore), and dynamics of the membrane (including elastic energy, membrane folding and unfolding, pore edge energy, and viscous dissipation) [7-10]. Based on the idea that pore nucleation event under membrane tension is a critical phenomenon of the cycle dynamics, we incorporate thermal fluctuations which drive the formation of stochastic nano-pore at the origin of large pore opening [11,12]. The full model is formulated in terms of three coupled stochastic differential equations, one for the GUV radius, one for the pore radius, and one for the amount of solute. These equations are solved numerically in Matlab® (Mathworks, Natick, MA) through a Euler-Maruyama scheme.

Copyright 2016 The Organizing Committee for the 2016 Summer Biomechanics, Bioengineering and Biotransport Conference

RESULTS

Single lipid GUVs in 200mM sucrose hypotonic conditions exhibit cyclic behavior, characterized by the formation of large transient pores, as illustrated in Fig. 2A. Interestingly, GUVs show irregular contours during the pore opening event and for a short time after, where "nodules" are observed at the opposite side from the pore (middle and right panels).

The typical evolution of a GUV radius with time is depicted in Fig. 2B. Swelling phases are characterized by a quasi-linear increase of the GUV radius, while pore openings produce a sudden decrease of the vesicle radius. The periods of the swell-burst cycles increase with the cycle number, or in other words, the deformation rate (therefore also stress rate) decreases with each cycle. Incidentally, the maximum vesicle radii also decrease with time. Maximum membrane deformations are measured to range between 10 and 20%. Direct observations of the pore opening/resealing events, yields an estimate of the pore life time of the order of 100 milliseconds.

Numerical results for a 13µm radius GUV under 200mM hypotonic stress are presented in Fig. 2C, and show an overall agreement with the experimental dynamics. The stochastic nature of the pore nucleation events allows a stress rate dependence of the rupture stress, in agreement with our experimental results and previews studies [13,14].

At 600 and 1000mM sucrose hypotonic conditions, the observed GUVs do not show measurable time variations in size.

DISCUSSION

In all our experiments, the maximum membrane deformation is at least twice larger than the 4% deformation to rupture usually reported for elastic deformation [15]. This suggests that, during the observed cycles, the GUV's projected area (measured areas) are not always equal to the true membrane area (actual area occupied by the lipid). Indeed, at low tension, microscopically unresolved folds may be present, serving as membrane reservoir to allow the larger range of deformation observed. This hypothesis is supported by the presence of membrane "nodules" after pore resealing (Fig 2A right panel), which indicates accumulation of membrane material. The (un)folding of the membrane is taken into account in our model through a stress-strain relationship of an exponential form in the membrane folded regime, and linear form in the elastic regime [16,17].

Another striking experimental observation is the size of the pore which can be as large as the GUV radius itself. Previews studies suppose the vesicle to remain spherical during the pore event [7-10]. This assumption does not hold for large vesicles in the conditions presented in here. Therefore our model has been built in order to take into account the influence of the pore on the vesicle shape, making it more general, and allowing to match experimentally observed GUV swell-burst cycles.

One of the main feature of our model, is to include thermal fluctuations inducing pore nucleation. Although many studies have focused on the physics of pore nucleation in lipid bilayer membranes [11,12], to our knowledge, none have been applied to vesicle systems with multiple swell-burst cycles. Here we fill this gap, and show that thermal fluctuations trigger pore nucleation, and therefore determine the subsequent swell-burst cycle dynamics. Importantly, the stochastic basis of thermal fluctuations naturally induce a dependence of the pore opening tension to the stress rate, which is a characteristic property of lipid membranes [13,14].

The behavior of GUVs at 600 and 1000 mM sucrose hypotonic conditions suggests that a fast equilibrium is reached, before any observation is made (there is about a minute between the application of the osmotic stress and the beginning of the observations). Such fast events are not yet well represented by our model, and will be the subject of future efforts. Moreover, different dynamic regimes (e.g. long lived pore, catastrophic rupture) will be examined theoretically through linear analysis, in order to explore possible parameter spaces where such behavior may be observed.

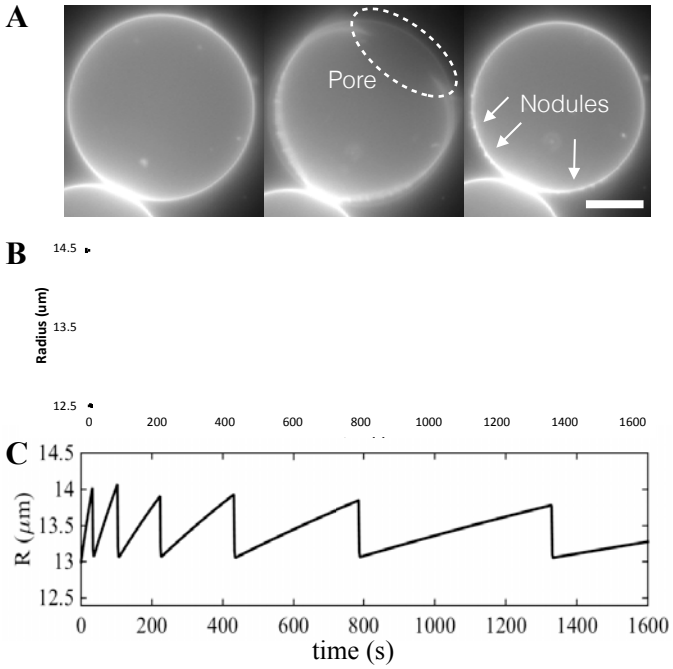

Figure 2: (A) Micrographs of a swelling (left), bursting (middle) and resealed (right) GUV. Scale bar represents 10µm. (B) Typical experimentally measured radius of a GUV in 200mM sucrose hypotonic conditions. Each drop of vesicle radius correspond to a pore opening/closing event. (C) Typical model result for a the radius of a GUV in the same conditions as in (B)

Finally, GUVs composed of phase separating lipid mixtures will be studied by coupling mixing/segregation energy of different types of lipids in our model.

The impact of this work is two-fold — it provides us with a fundamental understanding of mechanics and pore dynamics of biological membranes and the results from our study can also shed light on the mechanisms of cellular osmotic regulation.

ACKNOWLEDGEMENTS

This work was supported by AFOSR, award number FA9550-15-1-0124.

REFERENCES

[1] Burg M. et al., *FASEB J*, 10:1598-1606, 1996.
[2] Hoffmann E. et al., *Physiol. Rev.*, 89:193-277, 2009.
[3] Porta C. A. et al., *Eur. Phys. J. Plus.*, 130:1-15, 2015.
[4] Oglęcka K. et al., *Front. Physiol.*, 3:120, 2012.
[5] Oglęcka K. et al., *eLife Sciences*, 3:e03695, 2014.
[6] Angelova M. I. et al., Trends in Colloid and Interface Science VI, 89:127-131, 1992.
[7] Koslov M. M. et al., *J. Theor. Biol.*, 109:17-39, 1984.
[8] Brochard-Wyart F. et al., *Physica A*, 278:32-51, 2000.
[9] Idiart M. A. & Levin Y. et al., *Phys. Rev. E*, 69:061922, 2004.
[10] Ryham R. et al., *Biophys. J.*, 101:2929-2938, 2011.
[11] Ting C. L. et al., *Phys. Rev. Lett.*, 106:168101, 2011.
[12] Bicout D. J. & Kats E. et al., *Phys. Rev. E*, 85:031905, 2012.
[13] Evans E. et al., *Biophys. J.*, 85:2342-2350, 2003.
[14] Evans E. & Smith B. A., *New J. Phys.*, 13:095010, 2011.
[15] Citation needed
[16] Helfrich W. & Servuss R.M., *Il Nuovo Cimento D*, 3(1):137-51, 1984.
[17] Umeda T. et al., *Biosystems*, 93:15-119, 2008.

Copyright 2016 The Organizing Committee for the 2016 Summer Biomechanics, Bioengineering and Biotransport Conference

SB^{3}C2016
Summer Biomechanics, Bioengineering and Biotransport Conference
June 29 –July 2, National Harbor, MD, USA
SB^{3}C2016-1119

ADIPOSE-DERIVED MESENCHYMAL STEM CELLS STIMULATE ELASTIN PRODUCTION BY ADULT HUMAN SMOOTH MUSCLE CELLS IN A 3D FIBRIN SCAFFOLD

Kory J. Blose (1), Justin S. Weinbaum (1,5), David A. Vorp (1,2,3,4,5)

(1) Department of Bioengineering
University of Pittsburgh
Pittsburgh, PA, United States

(2) Department of Cardiothoracic Surgery
University of Pittsburgh
Pittsburgh, PA, United States

(3) Department of Surgery
University of Pittsburgh
Pittsburgh, PA, United States

(4) Center for Vascular Remodeling and Regeneration
University of Pittsburgh
Pittsburgh, PA, United States

(5) McGowan Institute for Regenerative Medicine
University of Pittsburgh
Pittsburgh, PA, United States

INTRODUCTION

Adult human vascular smooth muscle cells (SMCs) do not normally produce elastin in vivo, but do so in vitro with external stimuli such as transforming growth factor beta-1 (TGF-β1). As human adipose-derived mesenchymal stem cells (hADMSCs) are known to produce TGF-β1 and other growth factors [1-5], we hypothesized that adult SMCs co-cultured with hADMSCs would produce elastin.

METHODS

Constructs (n=3 per group) were made by embedding $6x10^4$ commercially sourced SMCs in fibrin gels. After two days, $9x10^5$ commercially sourced hADMSCs embedded in fibrin gels were added on top of the constructs. Additional experimental constructs were made without hADMSCs but were treated with hADMSC conditioned media (CM). Positive and negative control constructs lacking hADMSC were treated with or without TGF-β1, respectively. After 28 days of culture at incubator conditions, constructs were imaged with an Olympus multiphoton microscope to visualize elastin via its intrinsic autofluorescence, and total elastin content was measured using a ninhydrin assay [6].

RESULTS

All cellular groups showed elastin production via ninhydrin assay (Figure 1). From a qualitative standpoint, the hADMSC/SMC co-culture experimental group (Figure 2A) produced a similar elastin network as the TGF-β1 treated positive controls (Figure 2B). The CM group (Figure 2C) showed a less developed elastin network than the hADMSC/SMC co-culture group (Figure 2A) and positive control group (Figure 2B). While the negative control group (Figure 2D) did show elastin production in the ninhydrin assay, a developed elastin network was non-existent in the autofluorescent images.

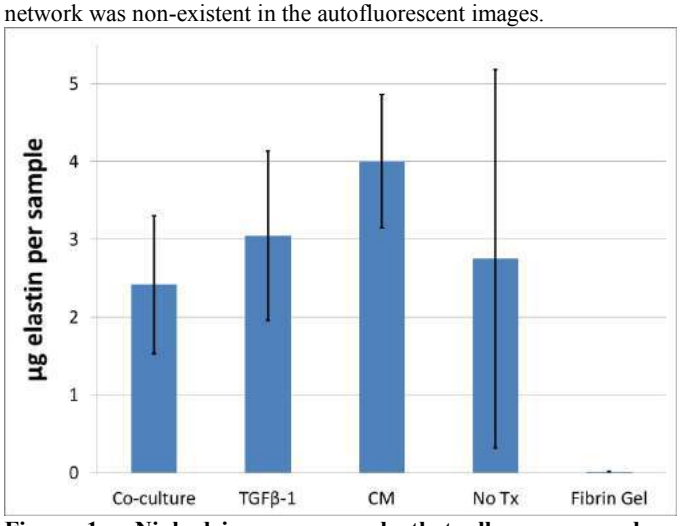

Figure 1: Ninhydrin assay reveals that all groups produced elastin, and fibrin gel alone shows negligible amounts of elastin.

DISCUSSION

The results of this study show promise for using hADMSCs as a possible elastogenic therapy, stimulating new elastin production by adult SMCs in vivo - ideally in the context of elastolytic diseases such as aneurysms. Interestingly, the underdeveloped elastin network seen

Copyright 2016 The Organizing Committee for the 2016 Summer Biomechanics, Bioengineering and Biotransport Conference

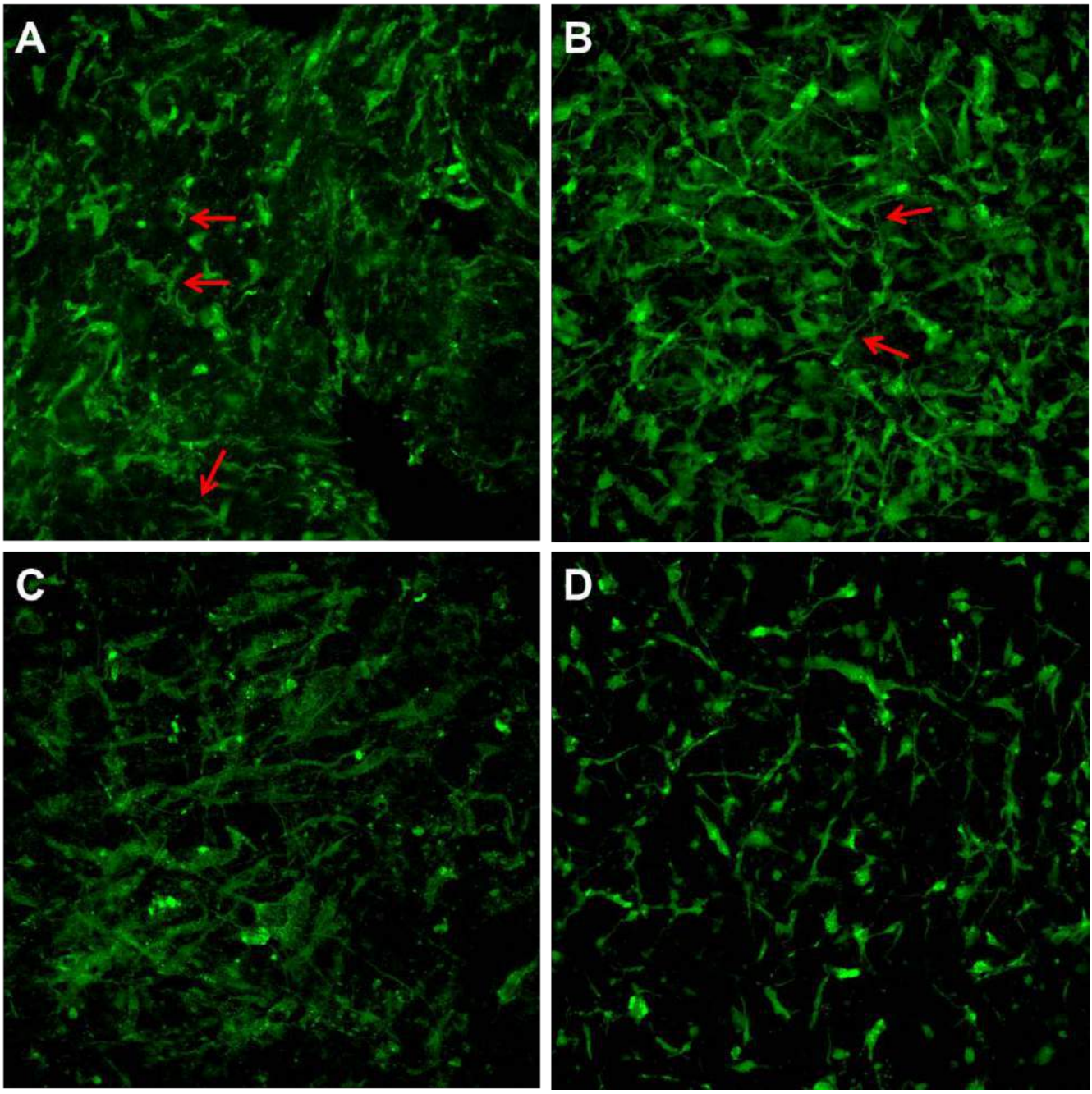

Figure 2: Elastin autofluorescence images reveal a developed elastin network with elastic fibers (red arrows) in the hADMSC/SMC co-culture experimental group (A) and TGF-β1 treated positive control group (B), a less developed network in the CM group (C), and no network (merely glowing cell outlines) in the untreated negative control group (D).

in the conditioned media group may indicate that the co-culture of hADMSCs and SMCs allow the cells to communicate and better form an elastic network compared to growth factor treatment alone.

ACKNOWLEDGEMENTS

The authors would like to disclose funding support by the National Institutes of Health (Cardiovascular Bioengineering Training Program T32HL076124 and Biomechanics in Regenerative Medicine T32 EB000392 to KJ Blose).

REFERENCES

[1] Davidson JM, et al., J Cell Phys. 1993;155(1):149-56.
[2] Kinnaird T, et al., Circulation Res.. 2004;94(5):678-85.
[3] Lin S, et al., Tissue Eng Pt A. 2011;17(11-12):1561-71.
[4] Liu J, et al., Biochem. Biophys. Res.Commun.1988;154(3):895-901.
[5] Rehman J, et al., Circulation. 2004;109(10):1292-8.
[6] Starcher B, Anal. Biochem.. 2001;292(1):125-9.

Copyright 2016 The Organizing Committee for the 2016 Summer Biomechanics, Bioengineering and Biotransport Conference

SB^{3}C2016
Summer Biomechanics, Bioengineering and Biotransport Conference
June 29 –July 2, National Harbor, MD, USA
SB^{3}C2016-1120

ROLE OF P_2R-ER CA^{2+} SIGNALING IN CA^{2+} OSCILLATIONS OF *IN SITU* OSTEOCYTES IN RESPONSE TO MEDIUM INTENSITY FOCUSED ULTRASOUND

M. Hu (1), J. Jiao (1), D.E. Gibbons (1), Yi-Xian Qin (1)

[1]Department of Biomedical Engineering, Stony Brook University,
Stony Brook, NY 11794-5281

INTRODUCTION

Current clinical evidences have shown that osteocyte mechanotransduction is critical in bone remodeling related to tissue regeneration. Elevation of $[Ca^{2+}]i$ has been observed as one of the earliest biochemical events in bone cells under external physical signals. While the biological effect of ultrasound on bone healing has been well documented, the underlying mechanism is currently unknown. Our previous study elucidated the mechanobiological modulation of cytoskeleton and Ca^{2+} influx in *in vitro* osteoblastic cells by short-term focused acoustic radiation force [1]. In greater relation to the physiological setting, our current study aimed to visualize and quantify Ca^{2+} oscillations of *in situ* osteocytes in real-time response to Medium Intensity Focused Ultrasound (MIFU), and moreover, the roles of various Ca^{2+} signaling pathways in this process.

METHODS

All animal protocols were approved by Stony Brook University IACUC. Three-month-old Black6 mice were used to obtain fresh calvaria samples immediately after euthanasia by CO_2 inhalation. The bone samples were incubated in DMEM with 5% FBS and 1% penicillin/streptomycin till ready for incubation in specific Ca^{2+} signaling blockers: 1) Amlodipine (L-type VGCC antagonist; n=4), 2) 18alpha-glycyrrhetinic acid (18alpha-GA, reversible intercellular GJ blocker; n=5), 3) thapsigargin (TG, inhibitor of Ca^{2+}-ATPase pump of the ER; n=5), 4) NNC 55-0396 (T-type Ca^{2+} channel inhibitor; n=5), 5) pyridoxalphosphate-6-azophenyl-2',4'-disulfonic acid (PPADS, nonselective P2R blocker; n=2), 6) ICG-001 (antagonist of Wnt/beta-catenin-TCF-mediated transcription; n=3), and control (n=5) with 6W MIFU energy power. Other experimental groups were included to test the energy powers of 1W (n=5), 3W (n=8), 9W (n=9) and 12W (n=7) to be compared to the 6W group. The samples were stained with Fluo-8 AM for Ca^{2+} fluorescent label and subjected to MIFU stimulation for 30sec (Figure 1). Real-time confocal imaging (40X, 488-nm, 2 frames/sec) was performed to capture the Ca^{2+} signals. For data analysis, the fluorescent intensity of each cell body was extracted as a function of time. By normalization to the baseline, the responsive percentage, number of spikes, normalized spike magnitude, and the initiation time were quantified.

RESULTS

MIFU stimulation at 6W, 9W and 12W lead to significant Ca^{2+} oscillations - 85±16% (p<0.01 vs. 1W; p<0.05 vs. 3W), 80±18% (p<0.01 vs. 1W; p<0.05 vs. 3W) and 84±17% (p<0.01 vs. 1W; p<0.05 vs. 3W) of responsive cells, respectively (Figure 2). MIFU at >6W energies lead to a higher number of Ca^{2+} spikes and larger spike magnitudes compared to the lower energies. The initiation time to the first Ca^{2+} spike seemed to be relatively the same for all the energy levels (~18sec). The MIFU-induced Ca^{2+} oscillations at 6W were completely abandoned by PPADS (p<0.01 vs. control) (Figure 3). TG significantly lowered the number of Ca^{2+} spikes and spike initiation time; NNC 55-0396 also significantly lowered the spike initiation time (p<0.05 vs. control). We concluded that the P_2R-ER pathway played a major role in the *in situ* MIFU-induced Ca^{2+} oscillations.

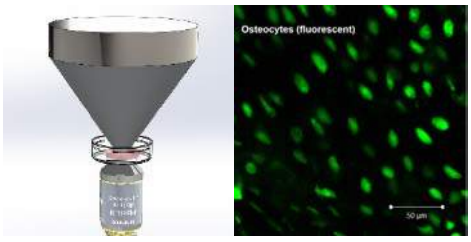

Figure 1. *Experimental setup of an ex vivo mouse calvaria under MIFU loading and Ca^{2+} imaging.*

Copyright 2016 The Organizing Committee for the 2016 Summer Biomechanics, Bioengineering and Biotransport Conference

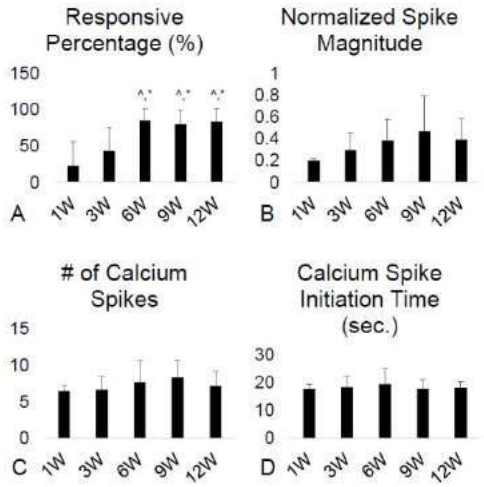

Figure 2. *Ca^{2+} response to MIFU at various energy powers. ^p<0.05 vs. 1W; *p<0.05 vs. 3W.*

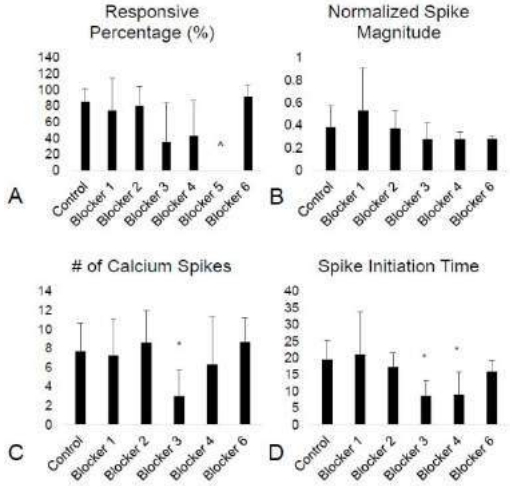

Figure 3. *Investigation of the roles of various Ca^{2+} signaling pathways in 6W MIFU-induced Ca^{2+} oscillations. ^p<0.01 and *p<0.05 vs. control.*

DISCUSSION

This study provided insights into the interactions between acoustic mechanical stress and *in situ* osteocyte Ca^{2+} oscillations, which aids further exploration of the mechanosensing mechanism triggered by noninvasive acoustic radiation force. This study provided promising findings on the signaling mechanisms involved in the interactions between acoustic mechanical stress and *in-situ* osteocytic Ca^{2+} oscillations, which provides future exploration of the ultrasound triggered mechanosensing mechanism.

ACKNOWLEDGEMENTS

This research is kindly supported by the National Institute of Health (R01 AR52379 and AR61821, YXQ), the US Army Medical Research and Materiel Command, and the National Space Biomedical Research Institute through NASA Cooperative Agreement NCC 9-58 (YXQ).

REFERENCES

[1] Zhang et al., *PLoS One*, 2012.

Copyright 2016 The Organizing Committee for the 2016 Summer Biomechanics, Bioengineering and Biotransport Conference

SB³C2016
Summer Biomechanics, Bioengineering and Biotransport Conference
June 29 –July 2, National Harbor, MD, USA
SB³C2016-1121

FSI SIMULATION OF INTRAVENTRICULAR FLOW IN A PATIENT-SPECIFIC LEFT VENTRICULAR MODEL WITH BOTH MITRAL AND AORTIC VALVES

A.D. Caballero (1), W. Mao (1), W. Sun (1)

(1) The Wallace H. Coulter Department of
Biomedical Engineering
Georgia Institute of Technology and
Emory University
Atlanta, GA, USA

INTRODUCTION

In recent years, computational modeling of cardiac flow has emerged a viable approach to study cardiac function in healthy and diseased states [1]. The study of left ventricular (LV) function requires a combination of methods for both the intraventricular fluid mechanics, and the valvular and ventricular solid mechanics. Although fluid-structure interaction (FSI) studies on heart valves and the LV have been reported [2,3], many groups have used fictitious FSI methods or have adopted an approach more conducive to fundamental analysis of cardiac flows. Thus, results have been restricted to simplified flow regimes, simplified material models, or idealized models of the LV and the heart valves due to computational challenges. Inherent simplifications, however, raise the question of the relevance of the findings for clinical decision making or medical device design.

The aim of the present study was to develop a fully-coupled FSI LV model with the aortic valve (AV) and the mitral valve (MV) that could capture the patient-specific LV hemodynamics and valve structural responses during the cardiac cycle. In this work, smoothed particle hydrodynamics (SPH) method was used to model the LV flow. In SPH, a continuum medium, such as fluid, is discretized as a set of particles distributed over the solution domain without the need of a spatial mesh.

For the validation of our hemodynamic flow solver, we compared the flow dynamics of the LV without the valves to the computed blood flow using a well-known CFD approach. The main goal of this work was to enhance the understanding of cardiac blood flow, by means of the development and validation of a patient-specific LV computational model that accommodated detailed anatomical, structural and flow data.

METHODS

Full phase de-identified cardiac MSCT scans were collected from patients at Hartford Hospital (Hartford, CT), from which a 72-year-old female with normal LV function was selected for the study. The MSCT examination was performed on a GE LightSpeed 64-channel volume CT scanner. 10 phases were obtained for one cardiac cycle and images were imported into Avizo software (VSG, Burlington, MA) for 3D reconstruction. The LV model developed in this study captures the LV internal structure and motion in great detail, including the patient-specific AV and MV geometries, mitral annulus and proximal left atrium motion during the cardiac cycle, and an anatomically realistic dynamic approximation of the papillary muscles (Figure 1).

To generate the 3D LV wall motion needed for the numerical simulations, the LV wall mesh and its known displacements were obtained by creating a unique structured mesh for all 10 MSCT phases in Hypermesh (Altair Engineering, Inc., MI). In this fashion, the 10 LV surface grids maintained the same number of nodes across all the phases, thus ensuring one-to-one connectivity. As numerical simulations typically involve much smaller time steps than the time separating two MSCT acquisitions, cubic-splines were used to interpolate the LV wall motion between phases.

The structural mechanics of the fully-coupled LV model were modeled by the finite element method (FEM) using ABAQUS/Explicit (SIMULIA, Providence, RI). The mechanical behavior of the heart valves were characterized using the anisotropic hyperelastic Holzapfel-Gasser-Ogden model. The LV blood flow was modeled by SPH method. The coupling of FEM and SPH method was implemented in ABAQUS/Explicit by using a contact algorithm, i.e., the fluid particles impact the surfaces of finite elements. The Lagrangian nature associated

Copyright 2016 The Organizing Committee for the 2016 Summer Biomechanics, Bioengineering and Biotransport Conference

with the absence of a fixed mesh for fluid makes this method well suited for dealing with complex flows and large deformations.

To minimize the influence of the boundary conditions on the intraventricular flow field, the boundary location was moved upstream from the MV and downstream from the AV plane by two straight tubes (not shown in Figure 1). Two rigid plates were used to apply velocity and pressure boundary conditions in the mitral and aortic orifices, respectively.

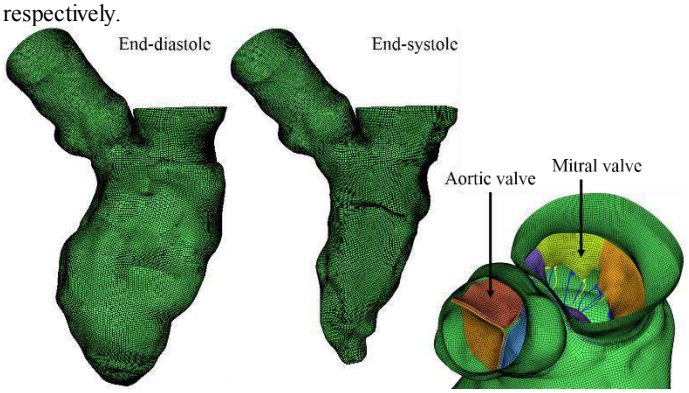

Figure 1: LV model including AV, MV, mitral annulus, proximal left atrium and approximation of the papillary muscles

RESULTS

The end-systolic and end-diastolic volumes were 47 ml and 111 ml, respectively, which are well within the physiological range [4]. The resulting stroke volume, ejection fraction and cardiac output were 64 ml, 58% and 4.8 L/min, respectively, which are also within normal values [4].

Using the LV model without the valves, cross-sectional velocity vectors during systole were compared between a CFD simulation using StarCCM+ (CD-adapco, Melville, NY) and the FSI simulation developed in this study (Figures 2a and 2b, respectively). A qualitative comparison of the two sets of data indicated that the hemodynamic flow solver of our FSI method reproduces all the key features of the intraventricular flow reasonably well. Similarly, Figures 2b and 2c show cross-sectional velocity vectors during systole for the FSI LV model without and with the AV, respectively.

DISCUSSION

The flow patterns clearly demonstrated the expected blood flow dynamics during systole, with regular laminar flow directed towards the aorta due to LV contraction. The results were consistent with in vivo measurements [5] and other FSI studies [6]. For the three LV models, the velocity reached its peak value at $t = 0.1$ ms. However, the maximum velocity for the FSI model with the AV (Figure 2c) is considerably higher than the peak velocity without the AV (Figure 2b). This difference in velocity is due to the interaction between the blood flow and the AV leaflets during systole, and reinforces the crucial role that heart valves have on the detailed cardiac flow structure.

Although many FE studies have been performed to investigate the structural responses of AV opening and closing at various configurations [7], the kinematics of the valves cannot be fully evaluated using FE models alone. In this study, the use and coupling of the anisotropic hyperelastic Holzapfel-Gasser-Ogden model allowed us to obtain detailed and realistic AV and MV opening and closing dynamics. A fully integrated model is a promising tool for understanding the overall heart function. This study provides motivation for continued advancements in computational modeling that could eventually facilitate patient-specific modeling of cardiac hemodynamics.

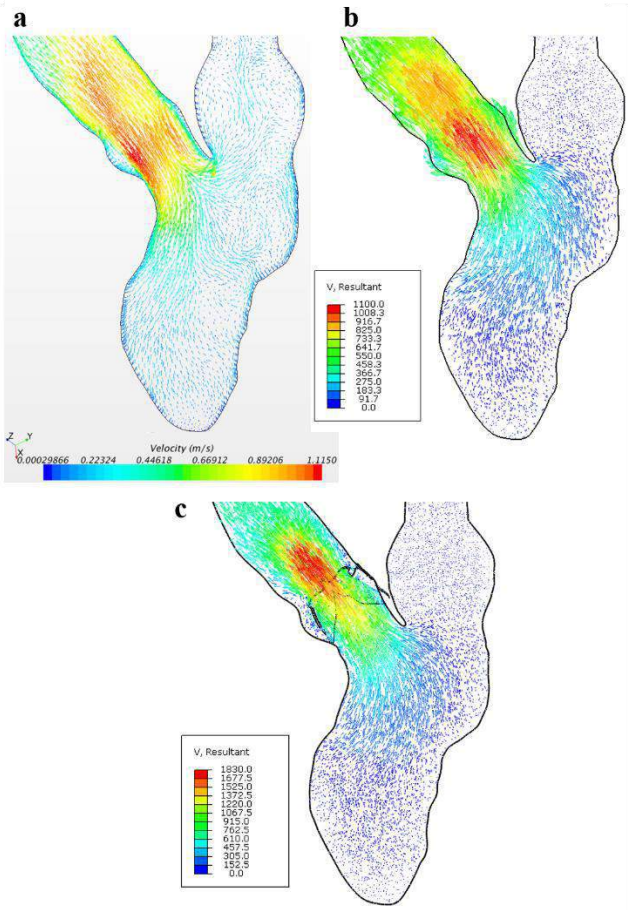

Figure 2: Velocity contours during systole for (a) CFD-LV model, (b) FSI-LV model without the AV, (c) FSI-LV model with the AV

ACKNOWLEDGEMENTS

Research for this project was funded in part by NIH HL104080 and HL108240 grants. Andres Caballero is also supported by a Fulbright-Colciencias fellowship.

REFERENCES

[1] Khalafvand, S. S., Ng, E. Y. K., and Zhong, L., CFD simulation of flow through heart: a perspective review, *Computer Methods in Biomechanics and Biomedical Engineering*, 14(01), 113-132, 2011.

[2] De Hart, J., Peters, G.W., et al., A three-dimensional computational analysis of fluid–structure interaction in the aortic valve. *Journal of Biomechanics*, 36 (1), 103–112, 2003.

[3] Einstein, D.R., Del Pin, F.,et al., Fluid–Structure Interactions of the mitral valve and left heart: comprehensive strategies, past, present and future. *International Journal for Numerical Methods in Engineering,* 26 (3–4), 348–380, 2010.

[4] Bronzino J.D., The Biomedical Engineering Handbook, second ed., CRC Press, Boca, Raton, 1999.

[5] Sengupta, P. P., et al., Emerging trends in CV flow visualization. JACC: Cardiovascular Imaging, 5(3), 305-316, 2012.

[6] Sturla, F., et al., Impact of modeling fluid–structure interaction in the computational analysis of aortic root biomechanics. *Medical engineering & physics*, 35(12): p. 1721-1730, 2013.

[7] Capelli C, et al., Patient-specific simulations of transcatheter aortic valve stent implantation. *Med Biol Eng Comput*, 50(2):183-92, 2012.

Copyright 2016 The Organizing Committee for the 2016 Summer Biomechanics, Bioengineering and Biotransport Conference

SB³C2016
Summer Biomechanics, Bioengineering and Biotransport Conference
June 29 –July 2, National Harbor, MD, USA
SB³C2016-1122

RELATIONSHIP BETWEEN FORCE APPLIED AND VELOCITY OF CONTRACTION OF AIR MUSCLES.

Aniruddha Sudhir Phatak

Department of Mechanical Engineering
Rochecter Institute of Tecnology
Rochester, NY, USA

INTRODUCTION:

An air muscle is a simple pneumatic device which was developed by J.L. Mckibben in the 1950's. It was primarily developed for polio patients as an orthotic appliance according to Baldwin [2, 3]. Initially these muscles were made up of pure latex rubber. As they closely resemble the natural muscle when actuated by air, they are known as air muscles. Mckibben Air muscle consists of rubber bladder surrounded by braided mesh shell which is attached to air fitting on one end and two mechanical fittings at either ends. As the internal bladder is pressurized, it expands and pushes it against the mesh to increase its volume. Due to high non-extensibility of the threads in braided mesh shell, when activated its diameter increases and produces tension if coupled to a mechanical load, producing a contractive force.

Currently the main application areas of air muscles are to produce a dexterous robotic hand having good control on all the fingers in order to fulfill basic hand operations like catching, picking, pulling and placing of objects. Another important application is to make an artificial leg which is able to walk, run and jump like a human. For all these applications it is very essential to study the force and velocity characteristics of air muscles.

My research question primarily asks, what is the exact relationship between the force acting on the air muscle and the corresponding velocity of its contraction for varying air pressures? Hence we can achieve desired movement of the fingers or the legs to perform the required operations by knowing the mathematical equation force and velocity. And thereby my objective consists of building a test rig which can calculate the velocity of contraction of air muscles when different loads are applied to it at varying pressures, in order to know the relation between force and velocity of the air muscles and to propose a theoretical model to quantify relationship between force applied and velocity of contraction.

METHODS:

1. Theoretical Modeling:

Novel Approach to find relation between force and velocity is the proposed theoretical Model. The first step of my research was the detailed study of theoretical modeling of air muscles. As per the equation for the pulling force applied by the air muscle by Chou [1], I derived the theoretical relation between force and the velocity of the contraction of the air muscle. The force equation is given by

$$F = \frac{\pi {D_0}^2 P'}{4}(3cos^2\theta - 1) \quad (1)$$

Initially θ i.e. angle between braided thread is substituted by length, in order to find the respective diameter for corresponding force and pressure.

By substituting

$$\theta = \cos^{-1} L/b \quad (2)$$

Therefore

$$L = \left(\sqrt{\frac{\frac{4F}{\pi {D_0}^2 P\prime}+1}{3}}\right) * b \quad (3)$$

First approach consists of taking a derivative of length w.r.t time is taken into account to find the velocity of contraction of the air muscle.

Second theoretical approach consists of calculating diameter for the respective force and pressure.

$$D = \frac{\left(\sqrt{1-\frac{\frac{4F}{\pi {D_0}^2 P\prime}+1}{3}}\right)*b}{\pi n} \quad (4)$$

With the help of length and diameter volume is calculated. For the modeling, pressures ranging from 30 to 80 psi were taken into account. Force was varied from 0 to 5 Kgs.

Copyright 2016 The Organizing Committee for the 2016 Summer Biomechanics, Bioengineering and Biotransport Conference

Assumptions: n = 3.5, θ = 45°, b = 16, D_0= 1.6. Finally, by using the ideal gas law equation, density for respective pressures was calculated by the formula-

$$\rho = \frac{P}{(R*T)} \quad (5)$$

The theory of Integral Relations for a Control Volume and formula for Rate of change of mass within an air muscle were used to eventually derive the velocity of change in length of the air muscle.

$$\left(\left(\frac{dm}{dt}\right)_{system} = \frac{d}{dt}\left(\int_{CS} \rho dV\right) + \int_{CS} \rho(V_r.n)dA \quad (6)$$

$$\left(\frac{dm}{dt}\right)_{system} = \frac{d}{dt}(\rho_b * \pi R^2 L) - \rho_1 V_1 A_1 \quad (7)$$

By the law of conservation, rate of change of system mass is equal to zero. Hence by substituting the change in density, diameter, velocity at inlet and area, calculation of velocity of contraction i.e. derivative of length w.r.t time is approached.

2. Experimental Modeling:

A vertical experimental test rig functioned with the Lab View program was designed to calculate the velocity of contraction for different and varying pressures. The main parameters monitored during the tests are load, pressure and the linear displacement and the data acquisition is done through Lab View Program.

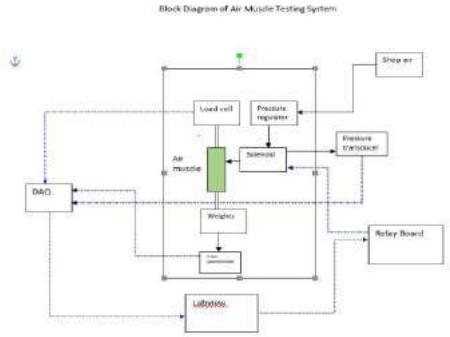

Fig:1 Block Diagram of Working of Test Rig

ANALYSIS OF READINGS:

With the help of linear potentiometer readings, saved in the excel file, actual position displacement is calculated by taking into account the voltage scale of the potentiometer. As the displacement is plotted against time, actual velocity is calculated by finding the slope of the graph. From the velocity readings, maximum velocity and average velocity are calculated for one of the contraction cycles observed by the air muscle. This process is carried out for different set of loads and pressures mentioned above. Also 95% velocity, (velocity of the air muscle at 95% of its total contraction) was calculated by noting the time at the point where contraction cycle starts and the time at which contraction of the muscle has reached 95%. Corresponding displacements are noted down, to find the velocity. Set of each type of velocity is plotted against loads ranging from 0 to 5.3 kg at two different pressures namely 40 psi and 60 psi. Change in length at 95% contraction (delta L) and time to reach 95 % of contraction are respectively plotted against the load to conferee upon the velocity and load plots. The load applied is rightly considered as the force applied.

RESULTS AND DISCUSSION:

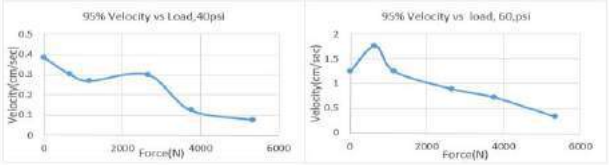

Fig:2 Comparison of 95%Velocity Vs Force Plots a.40psi b. 60psi

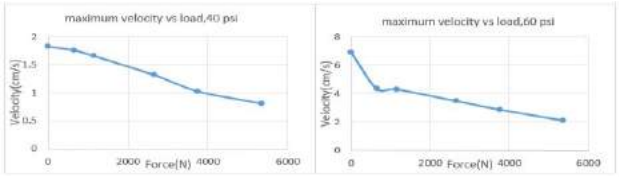

Fig:3 Comparison of Maximum Velocity Vs Force Plots a.40psi b.60psi

Here we can see that as the applied load increases i.e., the force increases, the velocity of the air muscle decreases. Hence we can definitely observe an inversely proportional relation between force and velocity of contraction of the muscle. We can also observe that as the air pressure is increased the velocity is increased. Some outlier points are observed and the reasons can be the noise due the jerk applied on the linear potentiometer during contraction. The second reason might be the inbuilt variation in the linear potentiometer. Also for specific load and pressure conditions the volume flow rate may have varied and so velocity might have hampered. The outliers were tested second time, however same results were obtained. (40 psi/ 2650 kg, no load and 650 kg/ 60 psi).

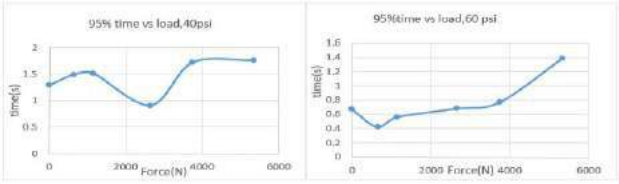

Fig:4 Comparison of 95%-time Vs Force Plots a.40psi b. 60psi

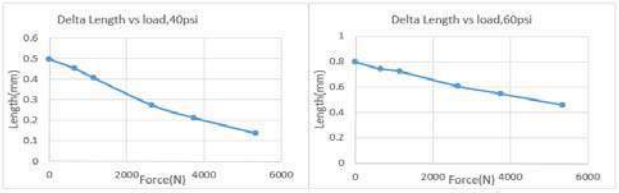

Fig:5 Comparison of 95%Contracted L Vs Force Plots a.40psi b. 60psi

Here in both these graphs we can clearly observe that as the load increases time to reach 95% of the its contraction in increased, which supports that velocity of contraction decreases as the load increases.

Also, we can observe that the displacement of the muscle i.e., the change in length at 95% of the contraction is decreased as the load increases.

From the above graphs plotted with the help of tests performed over uniquely designed test rig, we can clearly observe the relation between velocity of contraction of air muscles and force applied to it.

ACKNOWLEDGEMENTS:

First of all, I would like to extend my sincere thanks to my advisor, Dr. Steven Day, for his guidance in the development of this thesis proposal. I am very much thankful to Dr. Wayne Walter for providing linear potentiometer because of which I could measure the linear displacement of my Air Muscle.

REFERENCES:

1. Chou, Ching-Ping, and Blake Hannaford. "Measurement and modeling of McKibben pneumatic artificial muscles." Robotics and Automation, IEEE Transactions on 12.1 (1996): 90-102.
2. Ranjan, Ranjeet, P.K Upadhyay, Dr. Arbind Kumar, and Dr. Praveen Dhyani. "Theoretical and Experimental Modeling of Air Muscle."International Journal of Emerging Technology and Advanced Engineering 2.4 (2012). 1504-150.
3. Baldwin H. A. 1969. “Realization models of muscle function”. Proceedings of the Furdt rock Biomechanics Symposium, pp. 139-148.

Copyright 2016 The Organizing Committee for the 2016 Summer Biomechanics, Bioengineering and Biotransport Conference

SB³C2016
Summer Biomechanics, Bioengineering and Biotransport Conference
June 29 –July 2, National Harbor, MD, USA
SB³C2016-1123

DIRECTING ANGIOGENESIS WITH FLUID MECHANICS AT VESSEL BIFURCATIONS

Ehsan Akbari (1), Kaushik K. Rangharajan (1), Shaurya Prakash (1), & Jonathan W. Song (1, 2)

(1) Department of Mechanical and Aerospace Engineering
The Ohio State University
Columbus, OH, 43210

(2) Comprehensive Cancer Center,
The Ohio State University
Columbus, Ohio, 43210

INTRODUCTION

Providing a functional vascular network is essential for sustaining human tissue *in vivo* [1]. Therefore, a fundamental understanding of the factors that regulate the expansion or extension of vascular networks by sprouting angiogenesis is critical for advancing progress in the fields of tissue engineering, oncology [2], and regenerative medicine.

On the arteriole side of the vascular microcirculation, an upstream parent vessel branches or bifurcates into two downstream smaller daughter vessels [3]. The resulting hemodynamics of this vascular geometry are stagnation of impinging flow at the base of the vessel bifurcation compared to constant laminar shear stress (LSS) exerted tangential to the luminal surface of endothelial cells in the downstream daughter vessels. Although previous research has described how LSS coordinates angiogenesis with signals from the local biochemical environment [4-7], the effect of impinging flow that stagnates at vessel bifurcations is not well- understood. One challenge to study angiogenesis coordinated by stagnation point flow is designing a model system that reconstitutes the flow dynamics of a bifurcating vessel while also producing the correct vessel/extracellular matrix (ECM) geometry that is necessary for observing the tissue remodeling associated with angiogenesis.

In this study, we overcome this challenge by applying principles from microfluidic design and microfabrication, which enables reproduction of the vascular structure and the subsequent unique flow dynamics of the bifurcation point in vitro. Using this approach, we directly compare the effects on sprouting angiogenesis mediated by the mechanical forces associated with impinging stagnation point flow at the vessel bifurcation versus LSS in the downstream daughter branches within the same flow circuit.

METHODS

The microfluidic model of angiogenesis at bifurcation point (MMABP) was fabricated out of polydimethylsiloxane (PDMS) using soft lithography [8] (Fig.1, a). The MMABP model contains monolithic microfluidic features that were $50\mu m$ in height with a $1300\mu m$ wide inlet parent channel that branches into two $500\mu m$ wide daughter channels. The two daughter channels were separated by a 3-D ECM gel region ($400\mu m$ wide), which is localized using surface tension and capillary forces as previously described [4], and comprised of a Type I collagen/fibronectin mixture to reproduce the tissue space between two bifurcating vessels at the region. (Fig. 1, c) The flow dynamics of the MMABP are such that flow is perfused into the parent channel, impinges upon the base of the bifurcation, and then separates into the two daughter channels. The characteristics of the flow patterns were verified using a finite volume method (FVM) based model that was generated using COMSOL in order to predict the hemodynamics dominant throughout the perfusion microchannel and inside the collagen. (Fig. 1, b). The governing equations based on which the computational model was stablished consist of Navier-Stokes equation for the perfusion region coupled with Brinkman equation for the fluid flow throughout the collagen matrix.

The parent and daughter microchannels were fully-lined with mouse aortic endothelial cells (MAECs) and were laterally adjacent to the 3-D collagen gel channel. MAECs were selected for this study in part because the MMABP mimics the flow dynamics that occur at vessel bifurcations in the arteriole region of the microcirculation. We perfused our MMABP using two different media conditions, high serum media condition supplemented with 20% fetal bovine serum (FBS) versus low serum media condition supplemented with 2% FBS, at $5(dyn/cm^2$ LSS. Each experimental setup was repeated 4 times and the sprouting area of MAECs into the collagen gel channel was monitored up to 48

Copyright 2016 The Organizing Committee for the 2016 Summer Biomechanics, Bioengineering and Biotransport Conference

hours and quantified using ImageJ. The statistical significance was tested using two sample t-test.

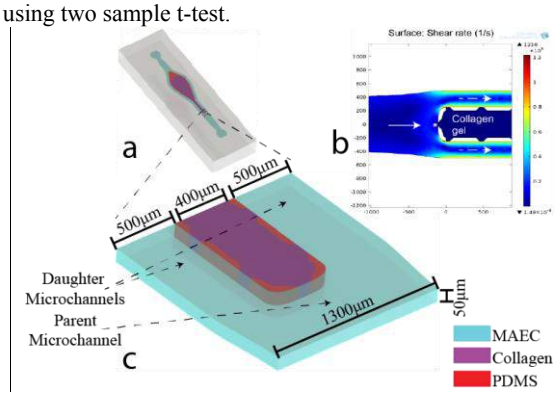

Fig. 1. MMABP composed of the parent microchannel branched into two daughter microchannels, which resemble pre-formed vasculature, and adjacent collagen gel channel, which functions as the ECM analog. (a) The MMABP overview (b) The constructed computational model predicting the shear distribution. Impinging flow (solid arrow) stagnated upon contact with the semi-permeable collagen gel (star) followed by flow separation into two laminar shear regions (dashed arrows) (c) The magnified illustration of the MMABP at the vicinity of the bifurcation point.

RESULTS

The fluid dynamics predicted by our computational model was zero shear stress local to the bifurcation point compared to the uniform LSS ($5(dyn/cm^2$) throughout the two branching daughter channels (Fig. 1. b). When evaluating angiogenesis in response to these fluid dynamic conditions, the MAECs exposed to LSS inside the two daughter channels prominently invade into the adjacent collagen gel as sprouts for both high and low serum media conditions (Fig. 2. a, c, e). In contrast, at the bifurcation point, the rate of sprouting area of MAECs is significantly greater for the high serum compared to the low serum media conditions after 36 hours of perfusion ($P<0.02$ based on two sample t-test) (Fig. 2. b, d, f).

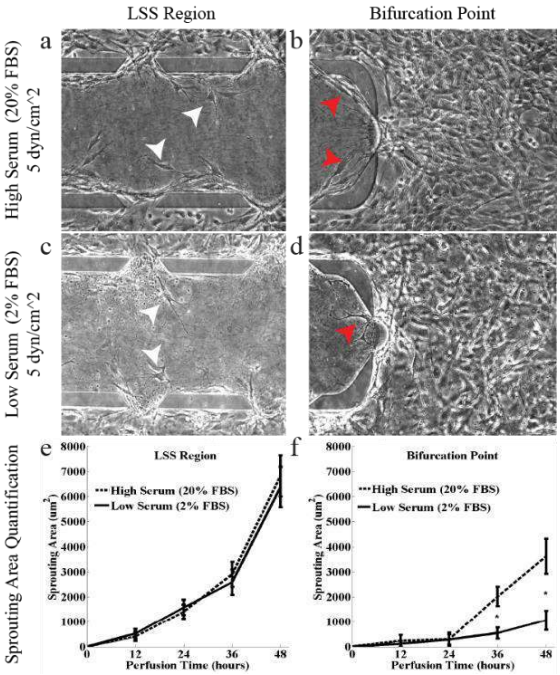

Figure 2. The hemodynamic forces created by the impinging flow on a branching vessel regulates sprouting angiogenesis. (a, b) Sprouting angiogenesis in MMABP perfused with the high serum media condition for 48 hours (red arrow heads). (c, d) Sprouting angiogenesis in MMABP sheared with the low serum media condition for 48 hours (white arrow heads). (e) Quantitatively comparable developmental angiogenesis for the MAECs constantly sheared with $5(dyn/cm^2$ LSS over the course of 48 hours. (f) The sprouting angiogenesis progression at the bifurcation point over the course of 48 hours of perfusion is depicted. The enhancing effect of the level of serum supplementation is statistically evident after 36 hours of perfusion.

DISCUSSION

These results are amongst the first reports on the effect of the hemodynamics created by the impinging flow in a bifurcating vessel on sprouting angiogenesis *in vitro*. Our results indicate a previously reported enhancing effect of LSS on sprouting angiogenesis [5, 6]. Furthermore, while the angiogenic activity of the MAECs at the bifurcation point is dependent on the local biochemical micro environment, the enhancement in sprouting angiogenesis under the effect of $5(dyn/cm^2$ LSS is independent of the level of serum the perfusion media is supplemented with. One possible explanation for the aforementioned observation can be attributed to the locally stagnated flow at the bifurcation point which increases the efficacy of potential pro-angiogenic factors to activate the quiescent endothelium to start to sprout into the 3D collagen matrix. The relatively larger convective flux at the two daughter microchannels, on the other hand, decreases the dwell time for the serum biochemical components, which in turn prevents these growth factors from interacting with the quiescent endothelium.

Future steps include inspecting how the streamlines inside the collagen can be utilized to predict/control the sprouting extension inside the collagen gel. Furthermore, we need to investigate the potential pro-angiogenic factors responsible for the observed dependence of sprouting angiogenesis at the bifurcation point on perfusion media condition.

In summary, our MMABP accurately mimics the effect of the hemodynamics created by the impinging flow in a bifurcating vascular network on sprouting angiogenesis in vitro. By utilizing the principles of microfluidics, our designed MMABP provides a fundamental understanding of how blood hemodynamics cooperates with the biochemical microenvironment to regulate bifurcating vascular network expansion and extension.

ACKNOWLEDGEMENTS

We are grateful to the laboratory of Dr. M. Ostrowski's for providing the MAECs. Funding was provided by American Heart Association (15SDG25480000) and the American Cancer Society (IRG-67-003-50).

REFERENCES

[1] Griffith, L. G. et al., Science, 295 (5557), 1009-+, 2002.
[2] Hanahan, D. et al., Cell, 144 (5), 646-674.5, 2011.
[3] Lipowsky, H. H. et al., Microcirculation, 12 (1), 5-15.9, 2005.
[4] Song, J. W. et al., PNAS, 108 (37), 15342-15347, 2011.
[5] Galie, P. A. et al., PNAS, 111 (22), 7968-7973.3, 2014.
[6] Jung, B. et al., Developmental Cell, 23 (3), 600-610.6, 2012.
[7] Ghaffari, S. et al., Development, 142 (23), 4151-4157.4, 2015.
[8] Duffy, D. C. et al., Analytical Chemistry, 70 (23), 4974-4984.2, 1998.

Copyright 2016 The Organizing Committee for the 2016 Summer Biomechanics, Bioengineering and Biotransport Conference

SB^{3}C2016
Summer Biomechanics, Bioengineering and Biotransport Conference
June 29 –July 2, National Harbor, MD, USA
SB^{3}C2016-1125

INVITRO TESTING OF HYDROGEL DELIVERY FOR POTENTIAL TREATMENT FOR PANCREATIC CANCER LESIONS

Nesrine Bouhrira (1), Steve Michetti (1), Denise R. Merrill (2), Jennifer Mitchell (2)
Thomas L. Merrill (1,2)

(1) Department of Mechanical Engineering
Rowan University
Glassboro, NJ, USA

(2) FocalCool, LLC
Mullica Hill, NJ, USA

INTRODUCTION

Locally advanced pancreatic cancer (LAPC) has a devastating prognosis[1]. Treating LAPC is challenging. Looking at the physical makeup of lesions we have discovered that they are hypovascular, have a high interstitial pressure, and have a dense extracellular matrix[2]. While localized intratumoral (IT) injection of liquid Gemcitabine is currently under clinical trial, lesion physical attributes make drug leakage into surrounding tissues likely.

We are developing a new drug delivery platform that involves endoscopic ultrasound (EUS) and injecting a drug-encapsulated hydrogel. EUS fine needle injection (EUS-FNI) is emerging as a promising treatment method to provide direct treatment of tumors via IT injection[3]. We hypothesize that encapsulating the drug in a thermally reversible hydrogel will allow the drug to be injected as a liquid (at room temperature or colder), and then transition to a gel in-situ (at body temperature), creating a drug reservoir for a sustained drug release. The hydrogels mechanical properties will reduce drug leakage, providing extended drug release for weeks, reducing the number of necessary treatments.

This work shares an initial exploration looking at the ability to inject and retain a thermosensitive hydrogel into a controlled mock lesion environment with physical properties simulating pancreatic lesions. Temperature and pressure were controlled. Using distilled liquid water injection for comparison, the hydrogel retention was significantly greater.

METHODS

Before testing the injection and retention qualities of thermosensitive hydrogel, a mock lesion was created (Fig.1). There were three mock cancer lesion parameters fixed: 1) the volume of the mock lesion, 2) the mechanical properties of the mock lesion, and 3) the volume of a cavity or void inside the mock lesion. The volume of the cancer lesion was approximately 15 ml. The mechanical properties of the mock lesion were determined based on 1% Agarose, Type 1A low EEO (FMC, Newark DE). This provides a Young's Modulus, a measure of material elastic quality, of approximately 20 kPa.[4] This value, while less than the Young's Modulus of many pancreatic lesions, provided a reasonable balance between sufficient rigidity and the ability to transmit external pressures into the internal void. A urethane medical balloon (#04001000CA) from Vention Medical (South Plainfield, NJ) enabled cavities of approximately 1ml inside the agarose mock lesion.

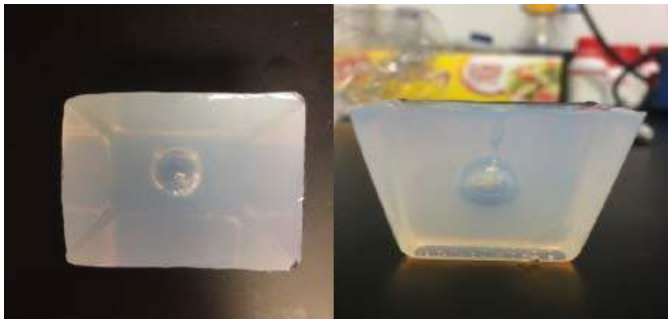

FIGURE 1: Top and side views of the mock cancer lesion showing a 1ml void for hydrogel injection. A void is necessary to allow the hydrogel to enter and solidify inside the mock cancer lesion. Void creation can take place clinically using biopsy needles like the EchoTip ProCore®.

Copyright 2016 The Organizing Committee for the 2016 Summer Biomechanics, Bioengineering and Biotransport Conference

A schematic of the mock loop is shown in Figure 2. From left to right, a computer and data acquisition system record flow rates, temperatures, and pressures (National Instruments, Austin, TX). Hydrogel is pumped with a syringe pump through a 19 gauge needle (#Z219347, Sigma Aldrich, St. Louis, MO). The agarose gel mock cancer lesion was placed inside a pressurized box with a heated pouch or IV bag to maintain normal body temperature at 37˚C conditions. Internal and external pressures were measured (ColeParmer, Vernon Hills, IL). Building or wall pressure was regulated to the pressurized box.

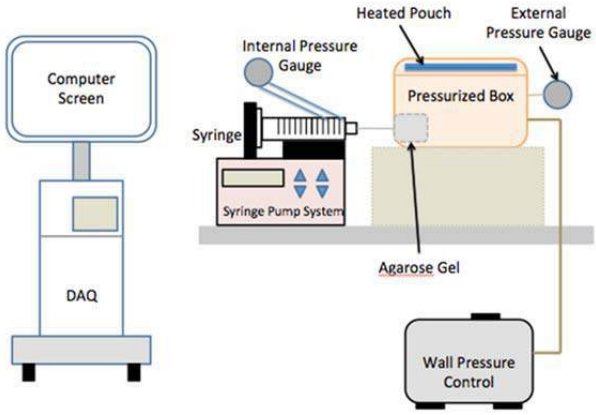

FIGURE 2: Fluid injection and retention testing setup. A syringe pump is used to deliver ~ 1 ml of hydrogel into a mock cancer lesion with void that is both externally pressurized and temperature controlled. External pressure created internal void pressure.

Two injection fluids were tested: (1) distilled water and (2) 30% (w/v) Pluronic F127 (Sigma Aldrich, St Louis, MO). The 30% Pluronic mixture is a hydrogel with a liquid-to-gel transition temperature of 14ºC. Viscosity values transition from <1 Pa-s at 4˚C to 3000 Pa-s at 37˚C. A 5 mL syringe of each test fluid was prepared and stored at 4ºC. Both fluids were pumped at 0.5 ml/min for 2 minutes using a syringe pump (Harvard Apparatus, Holliston, MA). **Two** internal void pressures were explored. Pilot testing showed that an external applied pressure of 100.5 ±1.9 mmHg translated to an internal pressure inside the void of 78.9 ± 3.8 mmHg. After the injection process retention in the void was measured after two minutes. Gravimetric analysis of the syringe and the exterior of the mock cancer void provided the mass delivered to the void, Eqs. (1) and (2).

$$m_{box} = m_{syringe@before} - m_{syringe@after} \quad (1)$$

$$m_{void} = m_{box} - m_{exterior} \quad (2)$$

Test conditions are described in Table 1.

TABLE 1: Test Conditions

Temperature Inside the Pressurized Box	37.5˚C ± 0.5˚C
Pressure Inside the Pressurized Box	0 mmHg or 100 mmHg gauge
Temperature of Test Fluid Inside Syringe	< 10˚C
Pump Setting	0.5 mL/min for 2 min
Each test was conducted 3 times.	

RESULTS

Figure 3 shows the mass of the void retained (Eq.2) for distilled water and 30% (w/v) hydrogel testing at two pressures 0 mmHg and 78.9 ± 3.8 mmHg. In each case a total of approximately 1.0 grams of fluid was injected via the syringe pump. Final gravimetric measurements were taken after 4 minutes (2 minutes injection + 2 minutes post-injection). At the 4 minute mark no significant flow was observed for either fluid.

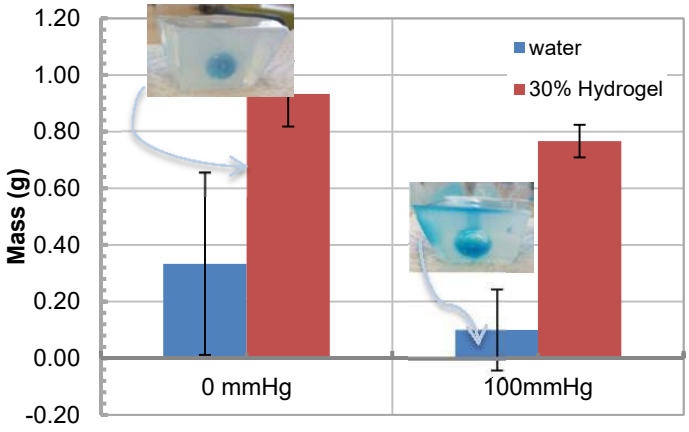

FIGURE 3: Injected mass retention results with photos of each fluid colored with blue dye.

DISCUSSION

Our testing shows that 30% (w/v) hydrogel injection provides superior mass retention over distilled water for a mock cancer void with and without internal void pressure. While elevated internal void pressure reduces retention for both fluids, its impact is significantly less for the hydrogel. With an applied pressure of approximately 80 mmHg we explored the lower range of expected pancreatic lesion interstitial pressure[5,6].

Testing also revealed that the hydrogel transitioned to gel rapidly once inside the mock cancer void. Liquid on the other hand immediately spills out and stops flowing out from the void at approximately 2 minutes.

Future work will focus on higher internal void pressures and different hydrogel concentrations. All of this work will provide insight for future in vivo testing and drug delivery parameters with a KPC mouse model for pancreatic cancer. In particular this work and future work will guide the selection of the optimal void volume and hydrogel concentration, setting the stage for first-in-man clinical testing.

ACKNOWLEDGEMENTS

Our work was supported by NIH's National Heart, Lung and Blood Institute (NHLBI). Grant Number: 1R43HL117403-01. The content is solely the responsibility of the authors and does not necessarily represent the official view of NHLBI or NIH.

REFERENCES

[1] NCI. *Surveillance, Epidemiology, & End Results Program (SEER)* 18 2004-2010. Available at: http://seer.cancer.gov/. Accessed 05/20, 2014.

[2] Jain RK. *Sci.Am*. 310(2):46-53. Feb 2014

[3] M. J. Levy, S. R. Alberts, S. T. Chari, M. B. Farnell, M. G. Haddock, M. L. Kendrick, D. Mukhopadhyay, G. M. Petersen, and N. Takahashi, "EUS Guided Intra-Tumoral Gemcitabine Therapy for Locally Advanced and Metastatic Pancreatic Cancer," Gastrointest. Endosc., vol. 73, no. 4, pp. AB144–AB145, 2011.

[4] Ahearne M, Yang Y, El Haj AJ, Then KY, Liu K-K. Characterizing the viscoelastic properties of thin hydrogel-based constructs for tissue engineering applications. *Journal of th e Royal Society Interface*. 2005;2(5):455-463. doi:10.1098/rsif.2005.0065.

[5]. Bo Rööser, Anders Rydholm & Björn M. Persson (1986) Internal pressure in soft-tissue tumors, Acta Orthopaedica Scandinavica, 57:5, 444-446

[6] Provenzano PP, Hingorani SR. Hyaluronan, fluid pressure, and stromal resistance in pancreas cancer. *British Journal of Cancer* . 2013;108(1):1-8. doi:10.1038/bjc.2012.569.

Copyright 2016 The Organizing Committee for the 2016 Summer Biomechanics, Bioengineering and Biotransport Conference

SB^{3}C2016
Summer Biomechanics, Bioengineering and Biotransport Conference
June 29 –July 2, National Harbor, MD, USA
SB^{3}C2016-1126

NUMERICAL INVESTIGATION OF CELL MIGRATION

Xiaowei Zeng (1), Liqiang Lin (2)

(1) Department of Mechanical Engineering
University of Texas at San Antonio
San Antonio, Texas, USA

(2) Department of Mechanical Engineering
University of Texas at San Antonio
San Antonio, Texas, USA

INTRODUCTION

Cell migration is a fundamental biological process throughout all the stage of animal life, from its commencement to its end[1]. A variety of complex mechanisms, such as embryonic morphogenesis and wound healing, in development, health and disease depend on the cell motion. For instance, in the human immune system, the movement and circulation of white blood cells (leukocytes) on the endothelial layer is highly coordinated with the disease and inflammatory response[2]. To accomplish certain physiological tasks, cell motion must occur in a defined direction. The failure of cells to migrate or migration to inappropriate locations can result in abnormities and diseases, e.g. tumor formation and metastasis. To explain such biological and biophysical phenomenon has been the focus of cell research as well as cell mechanics research. In this study, we will present our latest results on computational modeling and simulation of cell migration. And we have simulated the fluid driven monocyte rolling process in flow channel and studied the collective epithelial cell migration behaviors.

METHODS

In this research, we have built a cell model with internal structures to capture the essential features of cell membrane, cytoskeleton and cell nucleus. We are using soft materials to model the major cell components [3-4].

In the fluid driven monocyte rolling study in flow channel, the forces controlling the cell motion includes the flow shear driven force, the cell-microchannel adhesion force, and the resistant force. The numerical simulations are conducted by using Meshfree methods[5]. A total Lagrangian Meshfree formulation has been developed and a related Galerkin weak formulation has been derived for numerical computation. The main advantage of adopting a meshfree Lagrangian formulation is its ability to avoid remeshing and easy-tracking of cell surface and interface.

In the collective epithelial cell migration study, the forces control the collective cell migration can be modeled as adhesion force between cell and ECM, protrusion force at the cell leading edge due to actin polymerization, the drag force arising from viscous resistance to cell movement, and the cell-cell adhesion force for collective cell migrations:

$$\boldsymbol{f} = \boldsymbol{f}_{adhesion} + \boldsymbol{f}_{protrusion} + \boldsymbol{f}_{resistance} + \boldsymbol{f}_{cell-cell}$$

A cohesive interface zone model has been developed to model the cell-cell interaction and an advanced Finite Element Simulation package has been developed for the numerical simulation.

RESULTS

For the monocyte rolling in flow channel, the rolling process was shown in Figure 1. The position of one node was highlighted by elliptical shape to mark the monocyte rotation. From Figure 1, we can see the monocyte starts to deform upon tethering. The contact area between the monocyte and the substrate surface becomes flat and increases with time (c.f. Figure 1(a)-(c)). Then, the rear bonds of monocyte and substrate break and the monocyte starts to roll over substrate surface (c.f. Figure 1(d)). In the meanwhile, the contact area reduces. Subsequently, the monocyte is tethered again and the cell is firmly adhesive over the substrate (c.f. Figure 1(e)-(f)).

For the collective epithelial cell migration study, we have observed the collective cell migration behavior through cell-cell interactions, the

Copyright 2016 The Organizing Committee for the 2016 Summer Biomechanics, Bioengineering and Biotransport Conference

stress distribution in the epithelial cells during cell migration. The arrow is the velocity and the direction of motion in Figure 2.

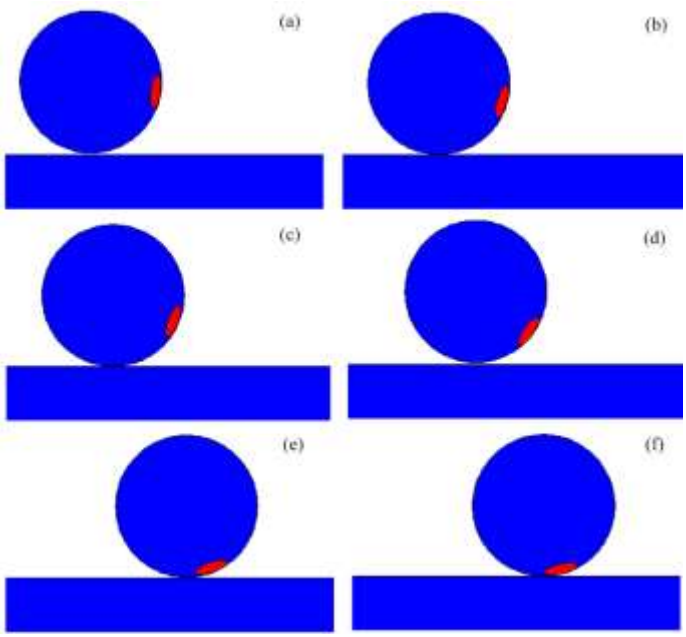

Figure 1: Snapshots of cell rolling process in the fluid channel (the highlighted red point is the mark point to detect the cell rolling behavior)

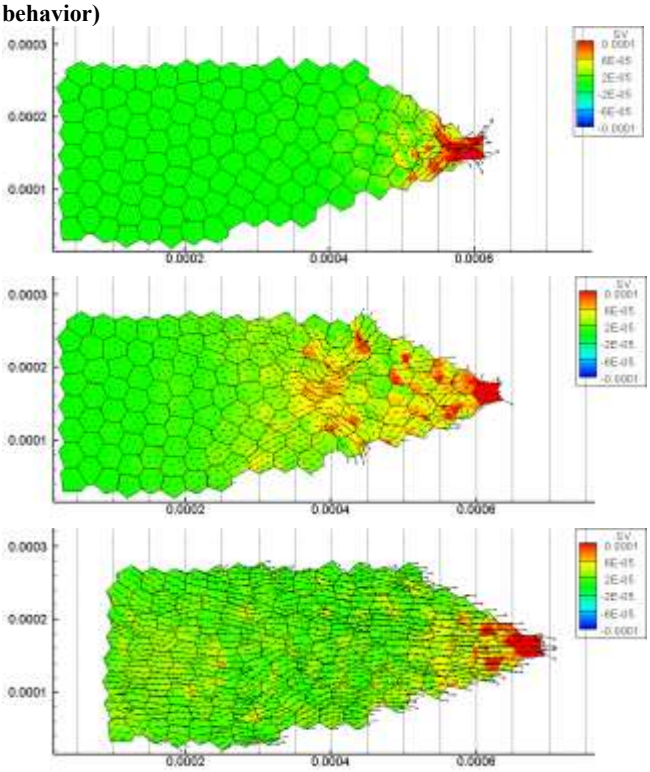

Figure 2: The migration motion of collective epithelial cells

DISCUSSION

Our long-term goal is to develop a generic multiscale numerical simulation tool that may possibly simulate tumor cell migration and invasion in more realistic setting. The current research is the most important step towards that goal by contributing prototype simulation software to set a benchmark on future commercial software of cell modeling and simulations.

ACKNOWLEDGEMENTS

This work is supported by a grant from NIH (Grant No. SC2GM112575).

REFERENCES

[1] Li, B., Sun, S. X., Biophysical journal 107: 1532-1541, 2014.

[2] Simon, S. I., Green, C. E., Annu. Rev. Biomed. Eng. 7: 151-185, 2005.

[3] Zeng, X., Li, S., Journal of the mechanical behavior of biomedical materials 4: 180-189, 2011.

[4] Zeng, X., Li, S., Soft Matter, 8: 5765-5776, 2012.

[5] Li, S., Liu, W. K., Meshfree Particle Methods, Springer, Berlin, 2004.

Copyright 2016 The Organizing Committee for the 2016 Summer Biomechanics, Bioengineering and Biotransport Conference

SB³C2016
Summer Biomechanics, Bioengineering and Biotransport Conference
June 29 –July 2, National Harbor, MD, USA
SB³C2016-1127

BUILDING A BETTER QUARTERBACK: USING BIOMECHANICS TO OPTIMIZE THROWING MECHANICS

Hunter W. Storaci (1), Andrew B. Robbins (1), Michael R. Moreno (2,1)

(1) Biomedical Engineering
Texas A&M University
College Station, Texas, United States

(2) Mechanical Engineering
Texas A&M University
College Station, Texas, United States

INTRODUCTION

A professional football quarterback must learn several techniques for throwing the ball to be successful. All techniques must be mastered to high level of precision and accuracy. The technique employed depends on the route of the receiver. Some throws require high release angle trajectories ("air under the ball"), while others require flat trajectories. Some require high velocity, while others require a low velocity ("touch"). Other variables that are adjusted depending on the play call include shoulder alignment, release point, posture, and stance. Shorter routes require quick releases and more economical arm motion. Longer routes require more torque and lower body contribution to force generation. In addition, lower body concerns include but are not limited to throwing from 1, 3, 5, or 7 step drops (for example), or a designed "roll out" where the throw must be made on the run. None of these concerns addresses the tactical adjustments that must be made to account for defensive pursuit or action to stop the pass from occurring. Even the most basic pass, requires highly technical coordination of body motion. However, relatively little biomechanical analysis has been performed with respect to the optimization of this motion.

Beginning as early as 5 years of age, a child may be coached in a Pop Warner league (for example) on a method to throw a football. As the athlete progresses, he will continue to be coached on a "proper" technique, which will likely be primarily based on qualitative assessment of empirical observations. Though coaches may agree on some general principles, there is no formal consensus on what constitutes "proper" technique. Moreover, there is very little quantitative data to support the development of such a consensus or the acceptance of diversity as a basis to yield to an individual's unique but effective form.

We worked with 6 quarterbacks from age 12 to age 23 and used an 8 camera Vicon motion capture system to study the biomechanics of the throwing motions employed for a simple 10 yard pass from a three step drop. Reflective markers were placed on the subjects at specific anatomical landmarks; the motion capture system tracks these marker positions throughout the throwing motion. Vicon Nexus software was then used to determine marker positions as well as force data from four AMTI force plates and was fed into a full body biomechanical model (Vicon Full-Body Plugin Gait). We worked with local high school coaches to generate a list of "coaching points" which were used to assess the performance. Coaching points of interest included but were not limited to: hip versus shoulder angles throughout the throwing motion, ball release point, and weight distribution throughout the throwing motion.

METHODS

Using an 8 camera Vicon motion capture system (4MP, 120fps, T-Series), and 4 AMTI 6-axis force plates (OR6-6-1000), we acquired throwing data from 6 quarterbacks, ranging from 12 to 23 years in age. Reflective markers were placed on the subjects according to the Vicon Full-Body Plugin Gait model. Subjects were directed to perform a simple 10-yard pass, from a three-step drop.

Local middle school and high school coaches were interviewed to identify "coaching points" that were used to assess quarterback execution. Data was acquired based on the prescribed coaching points and plotted to give a visual interpretation of the throwing performance. All data was analyzed and plots were generated using a custom Python script.

RESULTS

Preliminary results showed fundamental differences in the throwing motion of a trained quarterback (high school athlete) versus an untrained quarterback (middle school athlete). Figures 2 and 3 show the hand trajectory, and forward movement of the body throughout the pass. We found that the trained quarterback had a much higher release point on the pass, and had far less forward body motion while throwing, leading us to conclude that the throwing power was being generated through the rotation of the hips and snapping of the arm, rather than through the forward momentum of the body, as we saw in the untrained quarterback.

Figures 4 and 5 show the hip and shoulder angles of each quarterback throughout the throw. Some differences that we noticed were the smoothness of the motion in the trained quarterback's throw compared to the much choppier motion of the untrained athlete. The untrained quarterback also had a much more abrupt follow through, compared to the gradual slowdown of the motion in the throw of the trained quarterback. The trained quarterback also tended to release the ball at approximately the moment where the hip leading angle had returned to 0. Meaning that the hips and shoulders were approximately square to each other at the point of ball release. The untrained quarterback tended to release the ball much later into the motion, when the hip leading angle had already passed the 0-point.

Copyright 2016 The Organizing Committee for the 2016 Summer Biomechanics, Bioengineering and Biotransport Conference

Figure 1: View of a quarterback in the system using Vicon Nexus

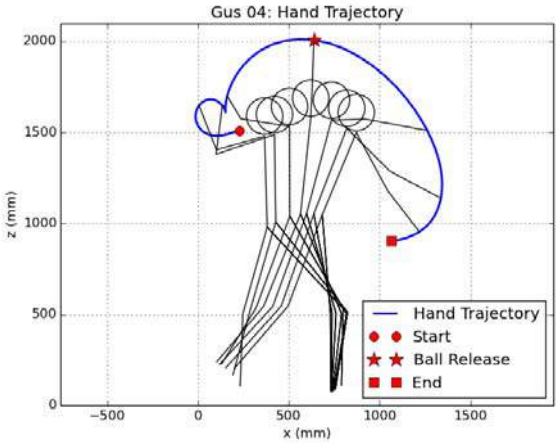

Figure 2: Trained Quarterback. Hand trajectory, release point, and body motion throughout the throwing motion

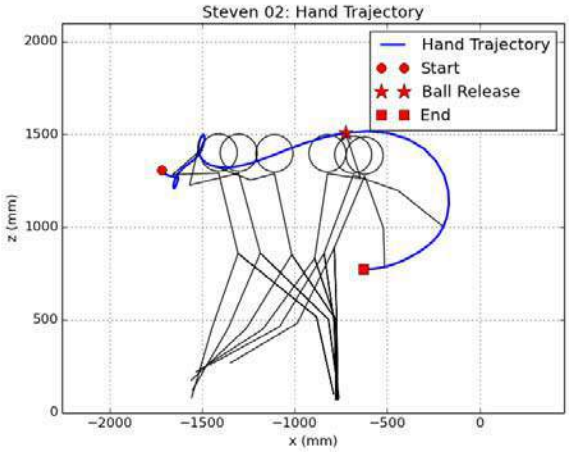

Figure 3: Untrained Quarterback. Hand trajectory, release point, and body motion throughout the throwing motion

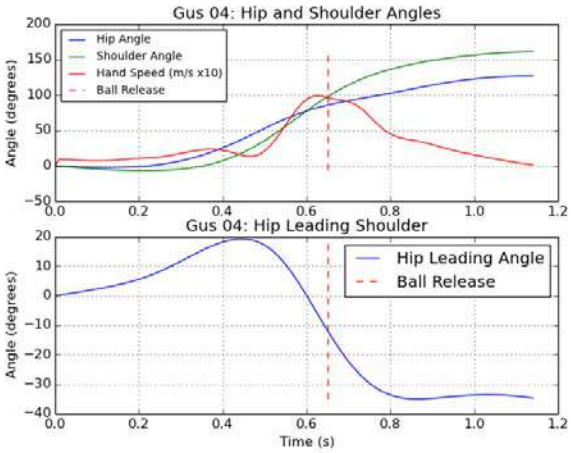

Figure 4: Trained Quarterback. Plot of hip and shoulder angles, as well as hand speed. Plot of the relative angle between the hips and the shoulder (hip leading angle).

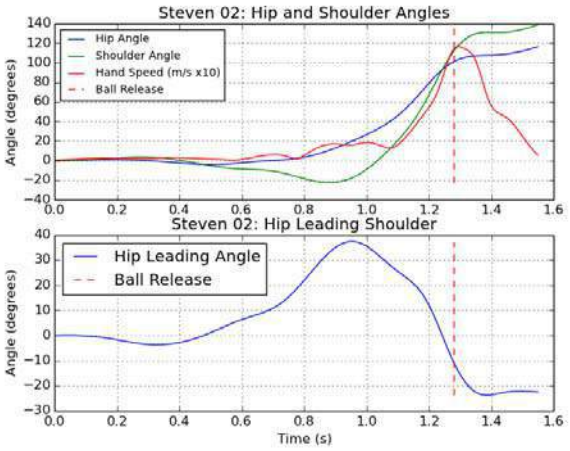

Figure 5: Untrained Quarterback. Plot of hip and shoulder angles, as well as hand speed. Plot of the relative angle between the hips and the shoulder (hip leading angle).

DISCUSSION

With the variation in levels of training and proficiency, we are able to quantify some of the differences between less experienced and more experienced (and more highly coached) players. We identified several trends associated with each group. More highly trained athletes (1) tend to better incorporate their lower body in the throwing motion, leading with the hips to generate torque, (2) tend to turn their hips completely through the throwing process and follow-through, (3) tend to release the ball at the highest point in the throwing motion, and (4) exhibit smoother better coordinated body motion overall.

Future work on this study will be focused on expanding the work to incorporate athletes from a broader range of levels of development, e.g. from Pop Warner through professional level athletes. The research goals are to (1) investigate natural development of athletic performance with age, (2) quantify differences in performance attributable to coaching that is focused on technique development, and (3) identify mechanical principles that contribute to improved performance outcome, (4) acquire throwing data from different types of throws (i.e. 1 step drop, throwing on the run, etc.).

Copyright 2016 The Organizing Committee for the 2016 Summer Biomechanics, Bioengineering and Biotransport Conference

SB^{3}C2016
Summer Biomechanics, Bioengineering and Biotransport Conference
June 29 –July 2, National Harbor, MD, USA
SB^{3}C2016-1128

NONLINEAR MULTIFACTORIAL INFLUENCE OF LIGAMENT PROPERTIES ON ROTATORY KNEE STABILITY: NOVEL APPLICATION OF BAYESIAN SENSITIVITY ANALYSIS

Mohammad Kia (1), Po-Hsu Chen (3), Thomas L. Wickiewicz (2), Andrew D. Pearle (2), Thomas Santner (3), Carl W. Imhauser (1)

(1) Department of Biomechanics
Hospital for Special Surgery
New York, NY, USA

(2) Department of Orthopedic Surgery
Hospital for Special Surgery
New York, NY, USA

(3) Department of Statistics
The Ohio State University
Columbus, OH, USA

INTRODUCTION

The anterior cruciate ligament (ACL) acts together with secondary stabilizers of the knee to resist complex combinations of rotatory loads encountered during challenging athletic activities involving pivoting and cutting. For example, the medial collateral ligament (MCL) and the posterior oblique ligament (POL) work in concert with the ACL to resist combined valgus and internal rotation loads[1]. However, untangling how these structures interact to control knee stability is difficult considering the number of ligaments, the interplay of ligament properties such as slack and stiffness, and the tremendous variability in ligament properties.[2] Knowledge of the unique stabilizing mechanisms of the knee may improve predictability of treatment for ACL injury, which remains suboptimal as indicated by inability to return to sports[3] and revision rates of up to 15%.[4]

Integrating multibody dynamic simulator models of the knee with sensitivity analyses of the model inputs holds promise for quantifying how ligaments interact to provide knee stability. Previous studies have integrated such models with Monte Carlo methods to quantify uncertainties in ligament properties such as slack length and stiffness.[5, 6]. However, these models excluded important knee stabilizers including the menisci. Moreover, relationships between ligament properties and knee kinematics were assessed using linear correlations of a single variable and a single outcome measure[6]. This approach is unable to identify nonlinear relationships between ligament properties and knee kinematics, and interactions between ligament properties.

This study integrated a sensitivity analyses based on a kriging predictor of a multibody knee model that included menisci[7]. This predictor automatically allows nonlinear relationships between ligament properties and knee kinematics, as well as interactions between ligament properties. The research questions were: 1) what ligament properties control anterior-posterior (AP) translation of the medial and lateral compartments in response to rotatory loads; 2) are there interaction between ligament properties that explain variations in the AP compartmental translations; and 3) are any of these relationships nonlinear?

METHODS

A computational model of the tibiofemoral joint of a 20 year-old male cadaver was developed within the multibody dynamics framework (ADAMS) (Fig. 1). The model consisted of subject-specific bone, articular cartilage, and meniscal geometries obtained using computed tomography (CT). Ligament insertions were identified from bony landmarks on the CT scans and visual inspection. The collaterals, cruciates, capsule, and meniscal horns and their coronary attachments were represented with 42 force elements using mean structural properties and a tension-only, nonlinear load-displacement response. Meniscal geometries were discretized radially and a linear stiffness matrix connected neighboring elements to represent a deformable geometry[8]. Rigid body contact was defined between the meniscal geometries and the femoral and tibial cartilage as a non-linear function of penetration depth and velocity.[8]

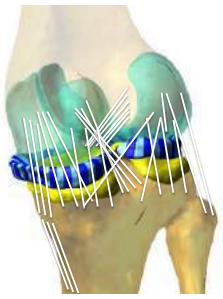

Figure 1: Multibody model of the tibio-femoral joint with 42 ligament fibers and discretized menisci.

Clinical tests of rotatory stability were simulated because of their importance in diagnosing ACL injury and their ability to predict clinical outcome and function based on the magnitude of tibial subluxation[9]. To assess rotatory stability, the femur was rigidly fixed and the tibia was maintained in 15° flexion, leaving it with five degrees of freedom. Multiplanar torques were applied in three phases: 1) 10 N compression; 2) increasing the valgus moment to 8 Nm; and 3) increasing the internal rotation moment to 4 Nm while the axial load and valgus moment remained constant. The coupled AP translations of the medial and lateral compartments of the tibia in each phase of loading were measured to assess knee stability.

The training data for the sensitivity analysis consisted of model simulation runs in which the model inputs consisting of slack length, toe region, and linear stiffness of the ACL, MCL, and POL were varied by at least ±2 standard deviations of their mean values reported in the literature. This range captured the variability observed in these parameters across a population.[2, 10] To fully explore the entire space of ligament properties, the inputs for the runs were selected to form a maximin Latin Hypercube design[7] consisting of 105 total runs of the multibody knee simulator.

The effect of variations in the model inputs (described above) on AP translation of the medial and lateral compartments during the three

Copyright 2016 The Organizing Committee for the 2016 Summer Biomechanics, Bioengineering and Biotransport Conference

loading phases were determined by calculating main effect and total effect sensitivity indices (SI) for each input as well as main effect and 2-way interaction plots. The main effect SI for a given input and output is the estimated proportion of the total variation in the outputs (AP translation of the medial and lateral compartments) due to changes in that input. The total effect SI is the sum of estimated proportions of the total variation in AP translation due to changes in the input alone or its interactions with other inputs. Inputs where the total effect SI is greater than the main effect SI tell the researcher that this input interacts with other input variables. The main effect curve is the estimated average AP compartmental translations vs an input when that input is fixed at a given value and the other inputs are varied. Similarly the 2-way interaction plots fix two inputs and average over the remaining ones. The main effect and total effect SIs were calculated using a Bayesian method based on flexible non-parametric kriging predictors[7] as were the main effect and interaction plots.

RESULTS

With an axial load of 10 N, ACL slack was responsible for 98% of the variation in the AP position of the lateral compartment (Table 1). This corresponded to anterior translation of 14 mm over the range of ACL slack (Fig. 2a). Both ACL and POL slack were responsible for a respective 63% and 34% of the variation in the AP position of the medial compartment during this first loading phase. This corresponded to changes of 6 mm anteriorly with increasing ACL slack and 4 mm posteriorly with increasing POL slack (Fig. 2b).

Table 1: Main Effect and Total Effect Sensitivity Indices

			ACL			POL			MCL		
Load Phase	Compartment	Effect	Slack (%)	Toe (%)	Linear (%)	Slack (%)	Toe (%)	Linear (%)	Slack (%)	Toe (%)	Linear (%)
Compression	Lateral	Main	98	0	0	2	0	0	0	0	0
		Total	98	0	0	2	0	0	0	0	0
	Medial	Main	63	0	0	34	0	0	0	0	0
		Total	66	0	0	36	0	1	0	0	0
Valgus	Lateral	Main	56	0	0	7	0	0	0	0	0
		Total	91	0	2	42	0	3	0	1	1
	Medial	Main	17	0	0	41	1	0	0	2	0
		Total	50	1	2	72	3	3	6	11	0
Valgus + Internal Rotation	Lateral	Main	17	1	2	3	0	2	0	1	0
		Total	89	2	4	74	2	5	0	5	0
	Medial	Main	17	0	1	44	0	13	0	2	0
		Total	27	1	2	64	1	26	0	6	1

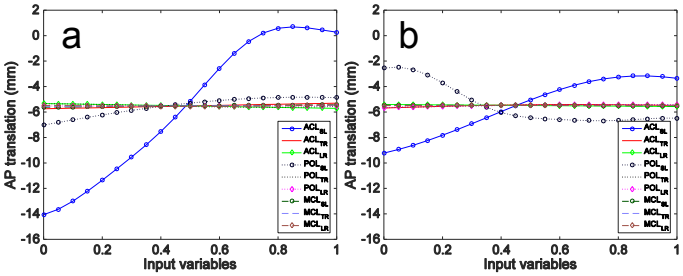

Figure 2: Main effect curves of anterior-posterior (AP) translation of the (a) lateral compartment and (b) medial compartment with 10 N axial load in response to 9 input variables: slack length (SL), toe region (TR), and linear region (LR) of the ACL, MCL, and POL. Anterior translation is indicated by increasing magnitudes.

With an isolated valgus moment, ACL slack was responsible for 56% of the variation in AP translation of the lateral compartment. Differences between main effect and total effect SI's of ACL slack and POL slack were 35% (Table 1). Interactions between ACL slack and POL slack were nonlinear; the most lateral compartment translation occurred with maximum ACL and POL slack (Fig. 3a).

With combined valgus and internal rotation moments, the isolated effect of ACL and POL slack on AP translation of the lateral compartment was small with main effect SIs of 17% and 3%, respectively (Table 1). The differences between main effect and total effect SIs were 72 and 71% for ACL and POL slack, respectively. Interaction between ACL and POL slack was nonlinear with the most lateral compartment translation occurring with maximal ACL slack and minimal POL slack (Fig. 3b).

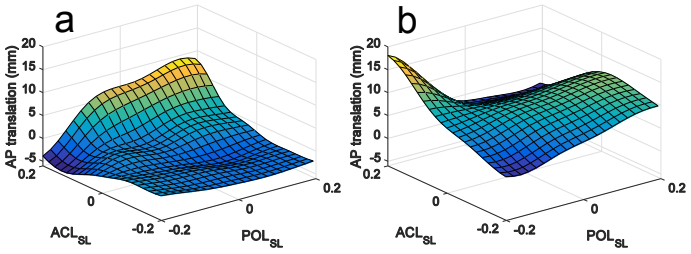

Figure 3: Interaction between ACL slack (SL) and POL slack affect anterior-posterior (AP) translation of the lateral compartment nonlinearly with (a) applied valgus load, and with (b) applied valgus and internal rotation loads. Anterior translation is indicated by increasing magnitudes.

AP translation of the medial compartment in response to the combined moments was influenced by POL slack with a main effect SI of 44% (Table 1). POL slack also interacted with ACL slack and POL linear stiffness to control AP translation of the medial compartment in response to the combined moments indicated by the 20% difference between total and main effect SI's (Table 1). Neither ACL stiffness nor the toe region of any ligament explained more than 11% of the variation in AP compartmental translations.

DISCUSSION

ACL and POL slack exert strong, monotone but nonlinear, influence on AP translation of the medial and lateral compartments. In contrast, ACL and MCL stiffness and the toe region of the ACL, MCL and POL had minimal effect on compartmental translations. ACL slack also exhibits powerful control of the initial AP positon of the lateral compartment and to a lesser extent the medial compartment, while POL slack influences the initial AP position of the medial compartment.

Our findings have important implications for ACL reconstruction because ligament slack can be manipulated at the time of surgery to achieve desired knee behavior. For example the slack in an ACL graft can be adjusted based on the flexion angle at which the graft is fixed. Moreover, the findings suggest that close assessment of the POL is warranted during surgery as knowledge of its mechanical integrity would help more predictably understand the effect of ACL reconstruction. Our findings of the important role of ACL slack in knee kinematics agrees with previous work indicating that setting the slack length of an ACL graft plays a critical role in controlling knee stability[11] and function during gait[10]. The current study has limitations. Namely, the applied loads represent clinical loading scenarios; additional compressive load should be applied to better represent function pivoting events.

In conclusion, Bayesian statistical methods based on flexible non-parametric kriging predictors have the power to identify two-way, highly nonlinear interactions between ligament properties, a fact that is not true of uncertainty analysis based on linear regression. Thus, the described approach is an important tool to identify sources of variability in knee function, and ultimately to develop subject-specific treatment of knee injuries.

ACKNOWLEDGEMENTS

The Clark, Kirby, and Gosnell Family Foundations

REFERENCES

[1] Schafer KA. *Am J Sports Med*, Accepted, 2016. [2] Butler DL. *J Biomech*, 25: 511-8, 1992. [3] McCullough KA. *Am J Sports Med*, 40: 2523-9, 2012. [4] Bach BR, Jr., *Arthroscopy*, 19 Suppl 1: 14-29, 2003. [5] Baldwin MA. *Comput Methods Biomech Biomed Engin*, 12: 651-9, 2009. [6] Smith CR. *J Knee Surg*, 2015. [7] Santner TJ. The Design and Analysis of Computer Experiments. New York: Springer, 2003. [8] Guess TM. *Med Eng Phys*, 32: 505-15, 2010. [9] Leitze Z. *Clin Orthop Relat Res*, 229-36, 2005. [10] Robinson JR. *J Biomech*, 38: 1067-74, 2005. [11] Amis AA. *Bone Joint Surg Br*, 71: 819-24, 1989.

Copyright 2016 The Organizing Committee for the 2016 Summer Biomechanics, Bioengineering and Biotransport Conference

SB^{3}C2016
Summer Biomechanics, Bioengineering and Biotransport Conference
June 29 –July 2, National Harbor, MD, USA
SB^{3}C2016-1129

POST-OPERATIVE COMPLICATIONS OF COMPUTER ASSISTED TOTAL KNEE ARTHROPLASTY IN OSTEOPOROTIC FEMURS AND TIBIAS: A FINITE ELEMENT STUDY

R. Solomon (1), A. Sori (1), S, Asfour (1), L. Latta (2), A. Alhandi (2), F. Travascio (1)

(1) Industrial Engineering
University of Miami
Coral Gables, FL, USA

(2) Max Biedermann Institute for Biomechanics
Mount Sinai Medical Center
Miami Beach, FL, USA

INTRODUCTION

Total knee arthroplasty (TKA) is commonly used to relieve pain and restore function in severely arthritic and injured knees. Computer assisted surgery is often used to provide better positioning of implants during total knee arthroplasty, with several studies showing reduced component malpositioning, while providing the benefit of reproducibility in determining component size, kinematics, and ligament balancing.[1] However, a recent study determined that computer assisted TKA of osteoporotic knees (with a T-score of -2.5 or less in the femoral neck/lumbar spine) resulted in more valgus position placement of the coronal tibial component (1.2 ± 3.4° valgus) than in non-osteoporotic bones (0.7± 1.8° varus).[2] Malalignment may cause off-axis loading, polyethylene wear, result in implant loosening, and lead to postoperative complications that may require revision surgery.[1, 3, 4] Therefore, when considering an osteoporotic total knee arthroplasty, it is important for the surgeon to determine if the benefits of computer assisted surgery are enough to outweigh the additional cost and duration of surgery time required. The objective of this study is to perform computational analysis on a generic bone model in order to compare the distribution of stresses on a valgus osteoporotic tibia and femur with a properly aligned tibia and femur. The resulting stresses will also be compared to those of corresponding nonosteoporotic bones.

METHODS

A CT scan of a generic femur bone model was converted into a 3D geometry comprised of both cortical and cancellous bone via Mimics Innovation Suite (Materialise, Belgium). The femur was fitted with a modeled total knee arthroplasty implant, and with the help of a surgeon, aligned with a tibia implant of corresponding size (see fig. 1). Both implant and bone mechanical properties were found in literature.[5-7]

The base of the tibia implant was fixed, and a static load of approximately 500N was applied to the top of the femur. A tied contact was applied at the tibial-femoral implant interface. Two scenarios were simulated on both a healthy bone and an osteoporotic bone: (1) proper alignment; (2) 4.6 degree valgus alignment (one standard deviation for computer navigated osteoporotic alignment).[2] The computational analysis was performed using FEBio (University of Utah) to determine effective stresses on the femoral bone. Stress distributions were examined on the lateral and medial condyles, the anterior cortex, and the intercondyloid fossa (see fig. 2).

RESULTS

When a valgus alignment was applied, the peak effectrive stress in the lateral condyle of the osteoporotic femur was 221 MPa, twice as high as the peak effective stresses in the aligned knees at 114 MPa, while the speak stresses in the valgus aligned normal knee were four times as high as the aligned knees at 431 MPa (see fig. 3). Additionally, the anterior cortex of the knee had a peak stress 75.5 MPa higher in the osteoporotic knee and 91.1 MPa higher in the normal knee for the valgus tibia implant compared to their aligned counterparts. Peak effective stresses in the medial condyle and intercondyloid fossa were similar for both the properly aligned and valgus implants at 391 Mpa and 2118 MPa respectively.

The osteoporotic and healthy knees resulted in similar peak stresses for all regions of the distal femur for both tibia implant alignments, with the exception of stresses at the lateral condyle; the rotated normal bone experienced stresses at 430 MPa, while the rotated osteoporotic, aligned osteporotic, and aligned normal experienced stresses at 220, 112, and 116 MPa respectively.

Copyright 2016 The Organizing Committee for the 2016 Summer Biomechanics, Bioengineering and Biotransport Conference

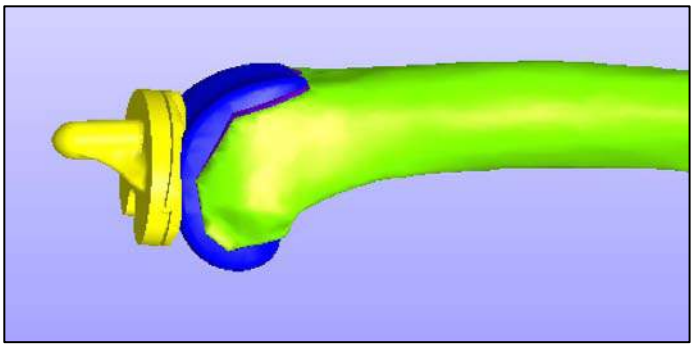

Figure 1: Femur (green) with femoral implant (blue) in alignment with the tibia implant (yellow).

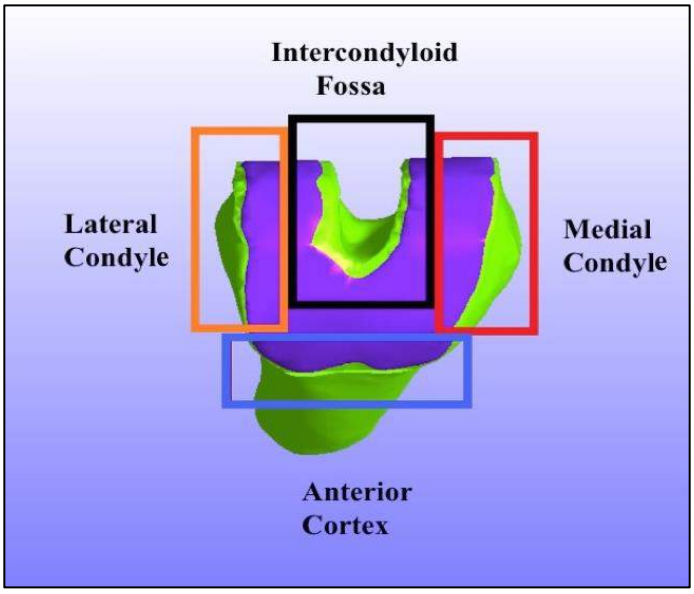

Figure 2: Schematic showing the regions investigated in the computational analysis. Cortical bone is shown in green; cancellous bone is shown in purple.

DISCUSSION

Valgus tibia implant alignment has been shown to result in osteoporotic total knee arthroplasties when computer aided surgery is used.[4] The results of this study indicate that this valgus alignment leads to higher peak stress values in the lateral condyle and anterior cortex of the distal femur. This information may be necessary when considering whether or not to use computer navigated surgery when conducting a total knee arthroplasty in osteoporotic patients, as larger peak stresses may result in polyethylene wear or an increased prominence of femoral fracture. Additionally, similar peak stresses resulted in both osteoporotic and healthy knees, with the exception of the lateral condyle in a valgus alignment. This may be an indication that osteoporosis does have a large impact on the long term success of a total knee arthroplasty.

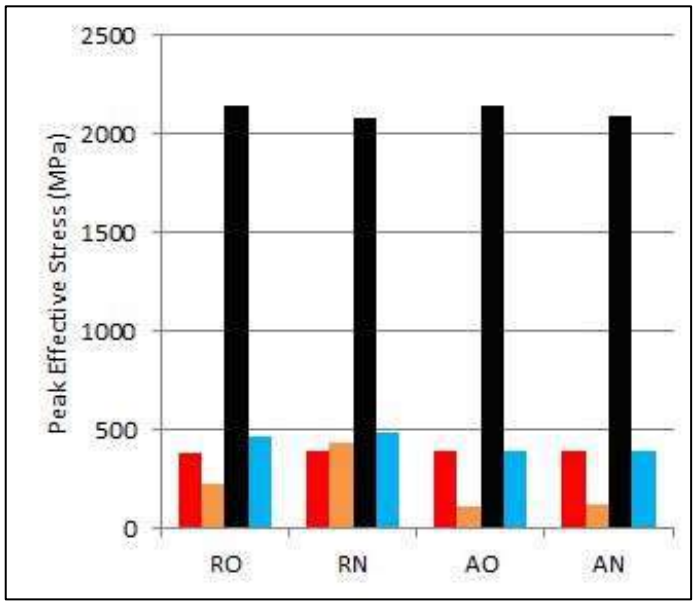

Figure 3: Peak values of effective stress on the medial condyle (red), lateral condyle (orange), intercondyloid fossa (black) and anterior cortex (blue) of the distal femur after a load is applied. Values are shown for when the tibia implant is properly aligned with the femur in a normal (AN) and osteoporotic knee (AO) in addition to when the knee is rotated 4.6 degrees valgus in a normal (RN) and osteoporotic (RO) knee.

ACKNOWLEDGEMENTS

Please acknowledge any grant or other funding support or the assistance of others as appropriate.

REFERENCES

1. Bae, D.K. and S.J. Song, *Computer Assisted Navigation in Knee Arthroplasty.* Clin Orthop Surg, 2011. **3**(4): p. 259-267.
2. Lee, D.-H., et al., *Osteoporosis affects component positioning in computer navigation-assisted total knee arthroplasty.* The Knee, 2012. **19**(3): p. 203-207.
3. Mahfouz, M.R., et al., *A New Method for Calculating Femoral Anterior Cortex Point Location and Its Effect on Component Sizing and Placement.* Clinical Orthopaedics and Related Research, 2015. **413**(1): p. 126-132.
4. Page, S.R., et al., *Profile of the distal femur anterior cortex -- a computer-assisted cadaveric study.* Orthopaeics & Traumatology: Surgery & Research, 2011. **97**(8): p. 821-825.

Copyright 2016 The Organizing Committee for the 2016 Summer Biomechanics, Bioengineering and Biotransport Conference

SB³C2016
Summer Biomechanics, Bioengineering and Biotransport Conference
June 29 –July 2, National Harbor, MD, USA
SB³C2016-1131

BEARING SURFACE DAMAGE ANALYSIS OF ANATOMICAL AND REVERSE TOTAL SHOULDER REPLACEMENTS: RETRIEVAL ANALYSIS ACROSS FIXATION DESIGNS AND UHMWPE COMPOSITION

L. Malito, MS (1), N. Bonnheim, BS (1), L. Li (1), T. Lee (1), S. Gunther, MD (2), T. Norris, MD (3), M. Ries, MD (4), L. Pruitt, PhD (1)

(1) Department of Mechanical Engineering
University of California, Berkeley
Berkeley, CA, USA

(2) Department of Orthopedic Surgery
Martha Jefferson Hospital
Charlottesville, VA, USA

(3) San Francisco Shoulder, Elbow & Hand Clinic
San Francisco, CA, USA

(4) Tahoe Fracture and Orthopaedic Clinic
Carson City, NV, USA

INTRODUCTION

Osteolysis due to polyethylene wear debris has been well documented across total joint replacements (TJRs) [1-3]. Retrieval studies examining the surface damage of polymeric bearings have focused on knee and hip components, while comparatively little attention has been given to devices used in the shoulder [4,5]. This work presents an analysis of the mode and geometric extent of surface damage for conventional total shoulder replacement (TSR) and reverse shoulder replacement (RTSR) retrievals. The cohort of retrievals spans more than 20 years of device designs with different bearing fixation types and UHMWPE formulations. A better understanding of the relationship between material behavior and damage mechanics can inform implant designs which better resist *in vivo* damage.

METHODS

Conventional TSR: Twenty-six retrieved glenoid components with different fixation designs and UHMWPE formulations were analyzed. Fixation designs were categorized as either all-polyethylene backed or metal-backed. The UHMWPE glenoids were of Hylamer, conventional (2.5 Mrad gamma-air), and modern cross-linked (2.5-5 Mrad gamma-inert) formulations. Glenoids used in this study were implanted between 1987 and 2011, with an average patient age at implantation of 61 years and an average time *in vivo* of 4.7 years (**Table 1)**. Each glenoid bearing surface was divided into 17 regions of equal area via a grid, and all regions were photographed at 249 dpi using a Nikon 1 J1 camera and an Infinivar Video Microscope lens under an AMScope LED ring light. The presence, severity, and extent of 11 damage modes (**Figure 1)** were noted using Image J (Bethesda, MD, v1.48) image processing software. The 11 damage modes used were based on implant classification methodology described by the Hood technique and further expanded upon by other authors [4,5,6,7,8]. Each implant was scored by at least two observers, and inter-observer agreement was evaluated by calculating the average percent agreement for damage mode identification, geometric extent, and severity.

TABLE 1: SUMMARY OF CLINICAL INFORMATION FOR TWENTY-SIX RETREIVED GLENOIDS

	TSA Glenoids (n=26)					
Clinical Information	**All TSA**	**Poly-Backed (n=20)**	**Metal-Backed/ Gamma Air (n=6)**	**Hylamer (n=8)**	**Moderately Cross-Linked (n=3)**	**Lightly Cross-Linked (n=8)**
Age at Surgery	60.8 ± 9.4 years	61.4 ± 9.9 years	59 ± 7.6 years	62 ± 12.1 years	62 ± 6.8 years	59.1±9.2 years
In vivo duration	4.7 ± 5.6 years	2.9 ± 3.0 years	13 ± 7.4 years	5.4 ± 3.7 years	2.3 ± 1.1 years	1.4 ± 1.0 years

Copyright 2016 The Organizing Committee for the 2016 Summer Biomechanics, Bioengineering and Biotransport Conference

Figure 1: EIGHT OF THE 13 PRIMARY DAMAGE MODES OBSERVED ON UHMWPE GLENOIDS. DELAMINATION, EMBEDDED DEBRIS, RIM EROSION, ADHESION, WEAR THROUGH, SUBSURFACE CRACKING, AND BURNISHING NOT SHOWN.

Reverse TSR: Eighteen retrieved UHMWPE humeral cups were analyzed for mode and geometric extent of surface damage. UHMWPE components were of conventional (2.5-4 Mrad gamma-air) and lightly cross-linked (2.5-4 Mrad gamma-inert) formulations. The humeral cups used in this study were implanted between 2004 and 2014, with an average patient age at implantation of 61 years and an average time *in vivo* of 3.2 years (**Table 2)**. The bearing surfaces of the humeral cups were divided into four regions of equal area, similar to the method reported by Nam [9]. Six observers noted damage modes through visual inspection of each quadrant.

TABLE 2: SUMMARY OF CLINICAL INFORMATION FOR EIGHTEEN RETREIVED HUMERAL CUPS

	RSA Humeral Cups (n=18)		
Clinical Information	**All RSA**	**Gamma Air (n=3)**	**Lightly Cross-Linked (n=15)**
Age at Surgery	61.2 ± 6.1 years	70.0 ± 4.0 years	57.0 ± 7.0 years
In vivo duration	3.2 ± 3.0 years	4.0 ± 3.0 years	3.0 ± 3.0 years

RESULTS

All TSA components demonstrated instances of scratching, striation, pitting, and surface deformation regardless of fixation design and UHMWPE formulation. At least one TSA glenoid for each material formulation and fixation type had fractured (**Table 3**). The group of cross-linked glenoids had the shortest time in vivo and exhibited scratching, striation, pitting, surface deformation, and abrasion in all of the samples, in line with damage modes in components made from non cross-linked UHMWPE formulations. Twelve RSA samples (67%) demonstrated abrasion on the rim of the humeral cup in the inferior quadrant. The most common damage modes in the reverse RSA cohort were scratching and striations, which in occurred in all quadrants on 10 (56%) of the samples.

TABLE 3: SUMMARY OF GLENOID AND HUMERAL CUP DAMAGE MODES

Glenoids and Humeral Cups With Each Damage Mode Present							
Damage Mode	**Poly-Backed Glenoids (n=20)**	**Metal-Backed/ Gamma Air Glenoids (n=6)**	**Hylamer Glenoids (n=8)**	**Moderately Cross-Linked Glenoids (n=3)**	**Lightly Cross-Linked Glenoids (n=8)**	**Gamma Air Humeral Cups (n=3)**	**Lightly Cross-Linked Humeral Cups (n=15)**
Scratching	100%	100%	100%	100%	100%	67%	67%
Striations	100%	100%	100%	100%	100%	33%	73%
Pitting	100%	100%	100%	100%	100%	66%	53%
Surface Deformation	100%	100%	100%	100%	100%	33%	47%
Abrasion	72%	100%	74%	89%	65%	100%	13%
Delamination	61%	75%	88%	61%	35%	100%	33%
Embedded Debris	23%	67%	26%	17%	25%	66%	7%
Fracture	52%	83%	83%	33%	33%	0%	7%

DISCUSSION

To the authors' knowledge, this is the only study that assesses the presence of damage modes on shoulder components for both conventional and reverse designs across fixations types and UHMWPE compositions. The reduction in fatigue crack growth resistance for cross-linked UHMWPE may have contributed to the early incidence of significant fracture observed in one of the cross-linked glenoids (less than three years in vivo). Some lightly cross-linked glenoids, exhibited fracture but at a much smaller degree and at shorter in vivo times (1.8 years). The observed damage on these implants is likely associated with some degree of oxidative embrittlement as there was no work up of the material post gamma-inert sterilization. Damage (including fracture) on the re-melted implants indicate that surface damage is not solely attributable to oxidative embrittlement and that cross-linked implants in general are showing damage modes at short in vivo times.

The high frequency and severity of inferior rim damage observed in the RSA cohort likely indicates a high prevalence of scapular notching; a finding in line with other investigations [10]. Damage modes including scratching, striations, pitting, and surface deformation are present on implants with short in vivo durations, suggesting that damage can occur shortly after implantation. While the clinical relevance remains uncertain, changes in shoulder component design and UHMWPE formulation (including modern RSA designs and cross-linked UHMWPE) have not prevented against certain damage modes in shoulder arthroplasty.

REFERENCES

[1] Raiss et al. *J Bone Joint Surg Am.* 2014; 96(e54): 1-9.
[2] Alidousti et al. *J Mech Behav Biomed Mater.* 2014; 32: 225-244.
[3] Naudie et al. *J Am Acad Orthop Surg*. 2007; 15(1): 53-64. [4] Hood. *J Bio Mat Res*. 1983; 17: 829-42.
[5] McKellop. *Biomat*. 2007; 28: 5049-57.
[6] Harman et al. *J Mat Sci-Mater M*. 2011; 22(5): 1137-1146. [7] Gunther et al. *J Athroplasty. 2002*; 17(1): 95-100
[8] Scarlat et al. *J Athroplasty. 2001*; 16(6): 795-801
[9] Nam, et al. *J Shoulder Elb Surg*. 2010; 19(7): 1003-1012.
[10] Le´vigne, et al. *Clin Orthop Relat Res.* 2011; 469: 2512–2520.

Copyright 2016 The Organizing Committee for the 2016 Summer Biomechanics, Bioengineering and Biotransport Conference

SB^{3}C2016
Summer Biomechanics, Bioengineering and Biotransport Conference
June 29 –July 2, National Harbor, MD, USA
SB^{3}C2016-1132

EFFECT OF STENT OVERSIZING ON IN-STENT RESTENOSIS IN THE SECOND PART OF THE POPLITEAL ARTERY

A. Lotfi (1), R. Varcoe (2), A. Simmons (1), T. Barber (1)

(1) Department of Mechanical and Manufacturing Engineering
University of New South Wales
Sydney, NSW, Australia

(2) Department of Surgery
Prince of Wales Hospital
Sydney, NSW, Australia

INTRODUCTION

Stents are commonly used by vascular surgeons to reduce atherosclerotic lesions and restore the blood flow within the stenosed blood vessels. All stents are frequently being deployed to the diameter greater than that of the native vessel to securely anchor the device against the arterial wall [1]. Due to variations in target vessel wall, different stent-to-artery ratios are being considered for implantation. However, it has been found that 20% of the patients having undergone the stent surgeries annually develop restenosis due to intimal thickening within 6 month after the operation. Studies show that the geometric differences caused by stent over-expansion can be one of the causative factors leading to this problem, further limiting the effectiveness of stent [2]. Our previous study [3] highlighted the effect of various stent-to-artery expansion ratios ranging from 1:1 up to 2:1 on the vascular damage and the underlying mechanism involved in this phenomenon. In this study, the combined Computational Fluid Dynamics (CFD) and clinical evidence were used to examine the hypothesis that correlates the alteration of local hemodynamics with in-stent restenosis in the oversized stented artery. The likelihood of restenosis was assessed by using wall shear stress (WSS) and wall shear stress gradient (WSSG) as a determinant within the second part of the popliteal artery stented to the expansion ratio of 2. The results of this study give insight into the understanding of the mechanisms that may contribute to in-stent restenosis when over-expanded, and can provide a guideline for vascular surgeons to find a technique for reducing or avoiding such post-stenting vascular damages.

METHODS

The geometry of an idealized oversized model with rigid walls [4] was reproduced in SolidWorks base on the dimensions obtained from the patient specific angiogram. The model is a second part of the popliteal artery with 2.8-3.2mm in diameter and the flow rate of 480 ml/min. The stent struts was excluded from the geometry of the patient angiogram as the primary sites of stenosis occurred around stent struts are shown to be independent of expansion ratio and the degrees of oversizing seemed to outweigh the small flow disturbances produced by stent struts [3]. The mesh independence study was performed according to our previous study [5] using fully structured hexahedral elements.

For CFD calculations, blood density was prescribed as 1060 kg/m^3 and dynamic viscosity of 0.0035 Pa.s. All simulations were carried out for steady flow conditions at a Reynolds number of 970 calculated based on the inlet velocity and diameter. Zero pressure boundary condition was set at the downstream outlet while velocity inlet was used as an inlet condition. Blood was defined as an incompressible, homogenous and Newtonian fluid [6]. Residual reduction to 10^{-6} of the primary value was set as a convergence criterion. ANSYS Fluent 14.5 (Fluent Inc., Lebanon, NH) was used to solve the Reynolds Averaged Navier-Stokes equations while k-ω SST turbulence model was employed to capture the flow properties.

The threshold for comparing the distribution of low WSS was defined at 0.5 Pa as the values slightly less than this value is known to affect the shape and alignment of the endothelial cells that causes excessive Neointimal Hyperplasia (NH) [7]. In contrast, endothelial cells that perform as a barrier to NH progression are shown to be pushed away from high WSSG regions of above 5000 Pa/m [8].

RESULTS

The effect of WSS on the formation of in-stent restenosis is shown in Figure 1. Regions of low WSS (<0.5 Pa) localized at the proximal segment of the oversized artery as well as within the oversized part of the artery (indicated in dark blue) is clearly visible in this Figure.

Copyright 2016 The Organizing Committee for the 2016 Summer Biomechanics, Bioengineering and Biotransport Conference

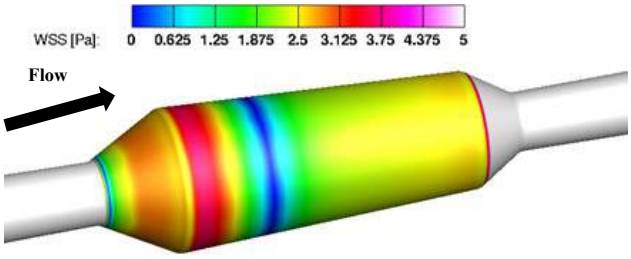

Figure 1: WSS distribution along the oversized artery

It has been widely known that the injury due to the localization of low and high WSS is highly dependent on the local hemodynamics particularly the near-wall condition. The velocity pattern within the artery is depicted in Figure 2 for clarification. As shown, some breakups are found at the proximal segment of the oversized artery that pushes the near-wall stagnation point from the proximal part to further downstream along the artery, resulting in the lower near-wall velocity at where the low WSS (<0.5 Pa) values were obtained previously in Figure 1.

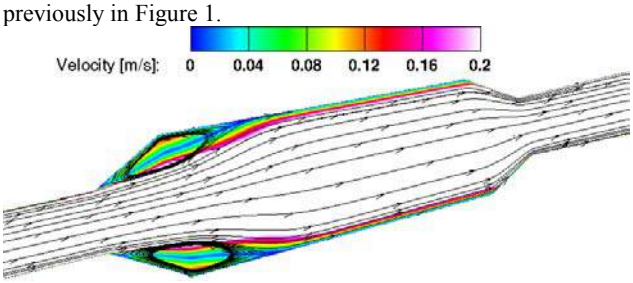

Figure 2: Velocity contour projected on the mid-longitudinal plane

Regions of elevated WSSG (>5000 Pa/m), the relevant parameter responsible for the biological response of arteries to the over-expansion, are recognizable at both proximal and distal parts of the oversized area.

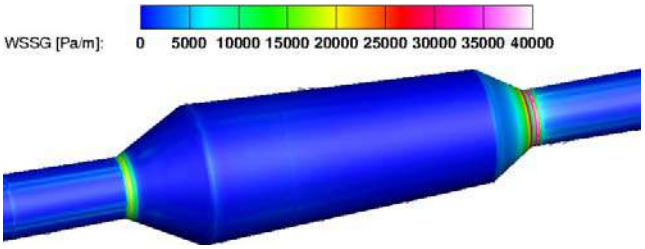

Figure 1: WSS gradient distribution along the oversized artery

The angiographic luminal change due to in-stent restenosis in the second part of the oversized popliteal artery is shown in Figure 3. As expected, stenosis is more pronounced at the inlet and outlet of oversized segment, as well as within the oversized part proximally to the inlet (white arrows).

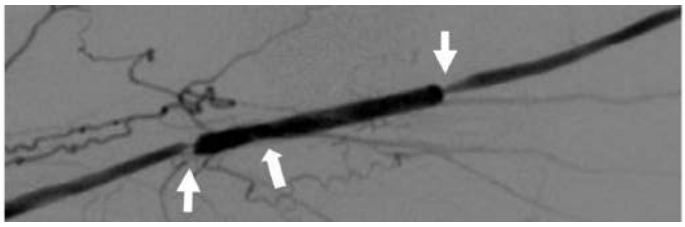

Figure 3: Angiographic image acquired after implementing oversized stent with deployment ratio of 2

DISCUSSION

Our previous study [3] showed that increasing the expansion ratio has an adverse hemodynamic effect, resulting in the exposure of larger areas of arterial surface to the distribution of low WSS which is known to correlate with the development of in-stent restenosis. It has also been demonstrated that there is an increased risk of vascular injury and thrombotic events at the stent-artery transition region [9] due to the localization of high WSS values. Consistent with the previous work [3], small area of low WSS is found in this study at the inlet of the oversized section due to the near-wall stagnation point. The recirculating vortices formed at the over-expanded area pushed this low velocity from the inlet of the oversized segment to the near-wall at where the low WSS region is obtained within the artery. However, the extent and level of these low WSS areas is not similar to the previous work model, most probably due to the considerable change in the geometrical configuration.

The present CFD results on the location of restenosis exposed to the low WSS values is shown to be in a great agreement with the clinical data, confirming the high vulnerability of low WSS regions to the NH and restenosis.

Although many theories have been used high WSS or high WSSG as an indicator of NH and restenosis, the exact mechanism of NH prone to these regions remains uncertain as both mechanical and biological factors are involved in this phenomenon [10, 11]. The present findings well demonstrated the consequence of oversizing while supporting the hypothesis that the location of restenosis is not limited to the to the low WSS regions. In addition, the high WSSG values are shown to be responsible for the formation and progression of NH (Figure 2) as restenosis has also been found at these locations in the current clinical study (Figure 3).

.Comparing the CFD and clinical data, the extent to which the low WSS and the elevated WSSG regions can contribute to restenosis and their significance is not yet clear. However, in this study, the regions exposed to elevated WSSG are found to be more critical as they are localized at the inlet and outlet of the oversized segment which can result in the complete occlusion of the artery if not treated.

The results also revealed that the constraint of rigid wall did not have a considerable effect on the prediction of restenosis in this case of study as the CFD results match well with the clinical study. The rigid wall can be a reasonable assumption as the elasticity of the arterial wall reduces and the artery stiffens due to the further development and accumulation of plaque built ups.

REFERENCES

[1] Zhao, HQ et al., Cardiovasc Interv Radiol, 32:720-726 , 2009.
[2] La Disa, JF et al., J Appl Physiol, 97: 424-430 , 2004.
[3] Lotfi, A et al., 19th AFMC Conference, 2014.
[4] Back, M et al., J. Vasc. Surg., 19: 905-911 , 1997.
[5] Lotfi, A et al., J Biomech Eng, In Press , 2016.
[6] Marossy, A et al., Clin Hemorheol Microcirc, 42: 239-58 , 2009.
[7] Malek, AM st al., J Am Med Assoc, 282: 2035-2042, 1999.
[8] DePaola, N et al., Arter Throm, 12: 1254-1257, 1992.
[9] Chen, HY et al., J Appl Physiol, 106:1686-1691 , 2009.
[10] Poon, EKW et al., J Biomech, 47: 2843-2851, 2014.
[11] Keynton, RS et al., J J Biomech Eng, 123: 464-473, 2001.

Copyright 2016 The Organizing Committee for the 2016 Summer Biomechanics, Bioengineering and Biotransport Conference

SB³C2016
Summer Biomechanics, Bioengineering and Biotransport Conference
June 29 –July 2, National Harbor, MD, USA
SB³C2016-1133

DETERMINING IMPEDANCE IN PULMONARY VESSELS USING FOUR-ELEMENT WINDKESSEL MODELS

Julie C. Wagner (1), Jesse W. Gerringer (1), Daniela Valdez-Jasso (1)

(1) Department of Bioengineering
University of Illinois at Chicago (UIC)
Chicago, IL, USA

INTRODUCTION

Pulmonary arterial hypertension (PAH) is characterized by an increase in blood pressure and remodeling of the pulmonary vasculature, modifying the pulmonary hemodynamics. PAH is difficult to diagnose in a routine medical exam and is often hard to determine the location to target. In addition, it is an aggressive disease: within the first year of diagnosis, patients have a 68% chance of survival, which drops to 34% after five years, with the only known cure being a heart-lung transplant (Wexner Medical Center, Ohio State University).

Impedance takes into account the resistive and compliant properties of the vasculature, which can then be used to characterize physical properties of pulmonary arteries and can help elucidate where in the vasculature the disease is affecting. Previous studies used Windkessel models to study pressure-flow relationships by evaluating impedance [1]. The four-element Windkessl model utilizes an inertial term (*L*), the total resistance (*Rd*), characteristic impedance (*R*), and compliance (*C*), to fit hemodynamic data. Through a minimization algorithm, pressure can be predicted and a set of parameters describing vascular changes in the disease can be obtained [1]. In this study we will describe the effects of PAH in normotensive (placebo – PL) and monocrotaline (MCT) treated rats using three versions of the four-element Windkessel model.

METHODS

Pulmonary arterial (PA) pressure and flow data were collected during open chest surgery on PL and MCT rats. Each week (up to four) related to a different stage of PAH, the 4th week being the acute stage. Pressure measurements were collected using a pressure catheter inserted through the right ventricle. In order to obtain simultaneous flow data, a flow probe was placed around the main PA. These data were analyzed using three variations of the four-element Windkessel models: series, parallel, and viscoelastic (Figure 1).

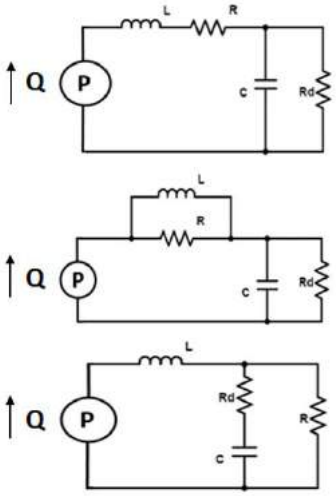

Figure 1: Four-element Windkessel models with resistors *R* and *Rd*, capacitor *C*, and inductance *L*. Inductance is (A) in series (B) in parallel (C) and the viscoelastic model.

For each Windkessel model, the pressure is analogous to voltage and the flow to electronic current in an electrical circuit. Each model can be represented based on the parameter combinations in relation to pressure and flow according to the positioning of the inductor as seen in Equation (1-3) for the series, parallel, and viscoelastic models respectively. For each model, blood flow (*Q*) is used as an input to predict PA pressure (PAP). Each parameter, *R*, *Rd*, *C*, and *L*, is

Copyright 2016 The Organizing Committee for the 2016 Summer Biomechanics, Bioengineering and Biotransport Conference

optimized using a Nedler-Mead simplex algorithm in Matlab, which minimizes the difference between measured and computed values.

$$\frac{dP}{dt} + \left(\frac{1}{R_d C}\right) P = L\frac{d^2Q}{dt^2} + \left(R + \frac{L}{R_d C}\right)\frac{dQ}{dt} - \left(\frac{1}{C} + \frac{R}{R_d C}\right) Q \quad (1)$$

$$\frac{d^2P}{dt^2} + \left(\frac{1}{R_d C} + \frac{R}{L}\right)\frac{dP}{dt} + \left(\frac{R}{R_d CL}\right) P = R\frac{d^2Q}{dt^2} + \left(\frac{R}{R_d C} + \frac{1}{C}\right)\frac{dQ}{dt} - \left(\frac{R}{CL}\right) Q \quad (2)$$

$$\frac{dP}{dt} + \left(\frac{R}{R_d C(R + R_d)} + \frac{1}{R_d C}\right) P = L\frac{d^2Q}{dt^2} + \left(\frac{RR_d}{R+R_d} + \frac{RL}{R_d C(R+R_d)} - \frac{L}{R_d C}\right)\frac{dQ}{dt} - \left(\frac{R}{C(R+R_d)}\right) Q \quad (3)$$

The optimization routine for the resistance parameters (R, R_d) is initiated with the ratios of the amplitude of PAP and Q that were determined via Fourier analysis in the frequency domain. The overall vascular resistance (Z_o) is the impedance at the 0th order harmonic and is the R_d in the four-element Windkessel models. The characteristic impedance, or the average of the higher order harmonics R, is a parameter representing the contribution of the proximal vessels. For our case, we chose the harmonics from the 6th – 10th order to determine initial value of R. The capacitance C and inductance L parameters were chosen arbitrarily. Goodness of fit of the predicted pressure is computed via the residual mean squared error (RMSE). ANOVA test is used to determine if the models are statistically different one from each other. The comparison is done for PL and MCT during week 1 and week 4 where $p<0.05$ is considered to be significant.

RESULTS

In the impedance spectrum, (Figure 2) computed for up to the 10th harmonic, the MCT-treated animals at week 4 have a higher overall vascular resistance (close to 1.2 mmHg/ml/min) as compared to the same aged normotensive animals (0.5 mmHg/ml/min). The characteristic impedance however, displays no apparent difference.

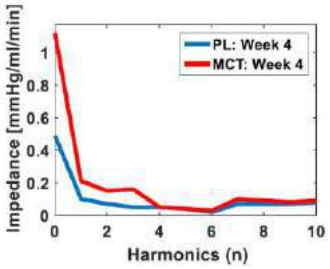

Figure 2: Impedance spectrum for up to the 10th order harmonic.

The time-series of the computed and measured pressure are compared for the PL and MCT data (Figure 3). Each row shows the prediction of pressure using a different model (from top to bottom: series, parallel, and viscoelastic). The data from the placebo animal is qualitatively best fitted by the parallel model (RSME = 1.13 mmHg). In the MCT-treated data, however, the series model provides the best fit (RSME = 1.51 mmHg). All the parameters were initialized with the same initial guess, but their optimal values differ according to the model used (Table 1). The *p*-values reveal that there is at least one model different from the other two. Based on the computed fit (Figure 3) and optimized parameters (Table 1) the viscoelastic model differs the most from the series and parallel models.

DISCUSSION

The positioning of the inductor in the Windkessel model has a major effect when used to predict pressure. Studies done by Burattini *et al.* have used these models in various applications with notable success [1-2]. They were able to optimize the parameters and fit the pressure data in humans, ferrets, and dogs including the dicrotic notch [1-2]. Another study by Segers *et al.* used just the parallel model to fit mice aortic data [3]. Even though our parallel model fits the PL pressure and the series model fits the MCT pressure very well, the models are unable to mimic the dicrotic notch in the pressure waveform with high accuracy. Therefore, there is substantial work to be done with these models. We need to further explore the optimization algorithms and to refine our fitting. With a larger cohort of animals we will also be able to determine a confidence interval for the model parameters to better represent this population.

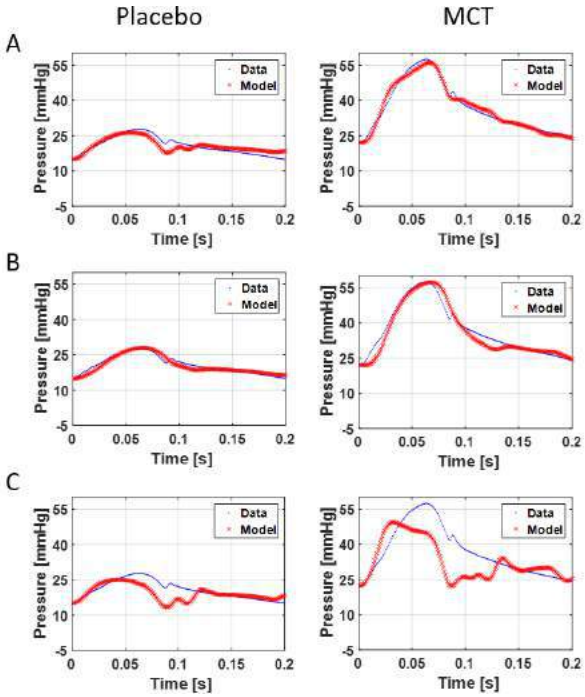

Figure 3: Pressure prediction and measured for the PL (left) and MCT (right) at week 4. (A) Series (B) Parallel (C) Viscoelastic.

Table 1: Optimized parameters for each model PL and MCT.

Placebo Week 4

	Series	Parallel	Viscoelastic
R	0.02	0.01	0.04
Rd	0.37	0.05	0.66
C	0.89	0.57	1.34
L	0.00	0.15	0.00

MCT Week 4

	Series	Parallel	Viscoelastic
R	0.08	0.02	0.14
Rd	0.70	0.20	1.13
C	0.30	0.13	0.68
L	0.00	-0.03	0.00

ACKNOWLEDGEMENTS

This work was supported by the College of Engineering Seed Fund and Honors College Undergraduate Research Grant (DVJ, JG).

REFERENCES

[1] Burattini, R and Di Salva, P., *Journal of Applied Physiology*, 103:66-79, 2006 [2] Burattini, R et al., *Medical Engineering & Physics*, 33:739-754, 2011. [3] Segers, P et al., *Am J Physiol*, 288:H1157-H1164, 2005.

Copyright 2016 The Organizing Committee for the 2016 Summer Biomechanics, Bioengineering and Biotransport Conference

SB³C2016
Summer Biomechanics, Bioengineering and Biotransport Conference
June 29 –July 2, National Harbor, MD, USA
SB³C2016-1135

A MECHANICAL ANALYSIS OF COMPRESSIBLE COLLAGEN HYDROGELS

Brooks A Lane (1), Tarek Shazly (1,2), John F Eberth (1,3)

(1) Biomedical Engineering Program
University of South Carolina
Columbia, SC, USA

(2) Mechanical Engineering
University of South Carolina
Columbia, SC, USA

(3) Cell Biology & Anatomy
University of South Carolina School of Medicine
Columbia, SC, USA

INTRODUCTION

Collagen hydrogels are a biphasic material system composed of a collagen fiber matrix and varying amounts of water (97-99%). Collagen, the most abundant structural extracellular matrix (ECM) constituent in the body, provides a biologically compatible platform for cellular attachment, proliferation, and remodeling. These hydrogels are generally weak but can be modified mechanically through methods such as ultraviolet (UV) exposure and chemical cross-linkers. Collagen hydrogels are routinely polymerized via pH neutralization and can easily be cast in molds enabling a wide-assortment of shapes and sizes. Numerous applications exist for these materials within the biomedical engineering field.

Although collagen hydrogels have been used extensively as cellular test beds over the years, contemporary research lacks specific information linking cellular behavior and the mechanical environment within a collagen hydrogel. Certain cell types are 'programmed' to actively maintain an unknown yet quantifiable homeostatic stress state, most notably vascular smooth muscle cells and fibroblasts. This phenomenon is observed experimentally when these cell types are incorporated within, or on the surface of, collagen hydrogels and cultured (e.g. cell contraction assays). The cells attempt to achieve a favorable mechanical environment through contraction and compression of the collagen hydrogel scaffold. During this period, cells rearrange collagen fibers and apply traction forces to the hydrogel to regain their specific homeostatic stress state. It has become increasingly clear that the local mechanical environment, defined by stresses and strains, provide cellular cues that are key for maintaining optimal functionality via mechano-sensitive cellular pathways. Therefore, relating continuum mechanics-based descriptors of the local mechanical environment to cellular behavior can reveal crucial information about cell-collagen hydrogel interactions.

The mechanics of collagen hydrogels are commonly characterized through rheology and tensile/compression testing, often with the assumption that the response is linearly elastic. Evidence suggests that these hydrogels are actually highly compressible and nonlinearly elastic. For instance, in the presence of surface or embedded mammalian cells, hydrogels undergo dramatic compression and distortion of the matrix [1]. Thus, to encompass these features into a mechanical model, we apply a (hyper)elastic compressible material strain-energy function developed by Blatz and Ko in 1962 to a series of collagen hydrogels with different mechanical characteristics [2].

METHODS

Theoretical Framework

The Blatz-Ko strain energy function for homogeneous isotropic elastic materials [3] is given as $W = W\left(I_C, II_C, III_C\right)$ with the principal invariants of the right Cauchy-Green strain tensor defined as

$$I_C = tr(\boldsymbol{C}),\ II_C = (tr\boldsymbol{C})^2 - tr\boldsymbol{C}^2,\ III_C = \det(\boldsymbol{C}). \qquad (1)$$

The generalized strain energy function is thus

$$W = \frac{\mu\alpha}{2}\left(I_C - 1 - \nu^{-1} + \left(1-2\nu\right) III_C^{-\frac{\nu}{1-2\nu}}\nu^{-1}\right) + \frac{\mu\left(1-\alpha\right)}{2}\left(\frac{II_C}{III_C} - 1 - \nu^{-1} + \left(1-2\nu\right) III_C^{\frac{\nu}{1-2\nu}}\nu^{-1}\right), \qquad (2)$$

The three material parameters are: $\mu > 0$ the shear modulus, $0 \le \alpha < 1$ the void fraction, and $0 < \nu < 0.5$ the Poisson's ratio.

Material particles originally at (R, Θ, Z) in an unloaded reference

Copyright 2016 The Organizing Committee for the 2016 Summer Biomechanics, Bioengineering and Biotransport Conference

configuration are mapped to (r,θ,z) in a finitely extended axisymmetric configuration according to (Figure 1):

$$r = \lambda R\,,\ \theta = \Theta\,,\ z = \Lambda Z\,. \quad (3)$$

The deformation gradient is

$$\mathbf{F} = \begin{bmatrix} \lambda & 0 & 0 \\ 0 & \lambda & 0 \\ 0 & 0 & \Lambda \end{bmatrix}, \quad (4)$$

and the right Cauchy-Green strain tensor is $\mathbf{C} = \mathbf{F}^T\mathbf{F}$. The Cauchy stress tensor is defined

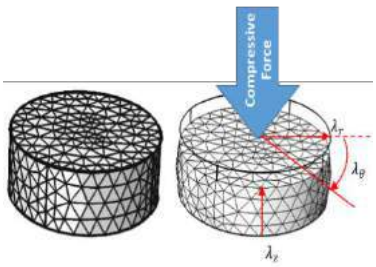

Figure 1: Experimental layout of collagen disc compression

$$\boldsymbol{\sigma} = \frac{2\mathbf{F}\left(\partial W/\partial \mathbf{C}\right)\mathbf{F}^T}{\det \mathbf{F}}, \quad (5)$$

where, by using the chain rule [4], we have

$$\frac{\partial W}{\partial \boldsymbol{C}} = \frac{\partial W}{\partial I_C}\frac{\partial I_C}{\partial \boldsymbol{C}} + \frac{\partial W}{\partial II_C}\frac{\partial II_C}{\partial \boldsymbol{C}} + \frac{\partial W}{\partial III_C}\frac{\partial III_C}{\partial \boldsymbol{C}} \quad (6)$$

and by definition $\partial I_C/\partial \boldsymbol{C} = \boldsymbol{I}$, $\partial II_C/\partial \boldsymbol{C} = I_C\boldsymbol{I} - \boldsymbol{C}^T$, and $\partial III_C/\partial \boldsymbol{C} = III_C\boldsymbol{C}^{-T}$. Using simple uniaxial compression while measuring active changes in cross-sectional area we let $\lambda = \Lambda^{-\nu}$ (per the ad hoc assumption of [2]). Evaluating the remaining derivatives of (6) yields an expression for σ_z

$$\sigma_z = 0.5\lambda_z\mu\left(\Lambda^{2\nu}\alpha - 2\Lambda^{4\nu-2} + 2\Lambda^{4\nu-2}\alpha - \Lambda^{2\nu-2}\alpha\left(\Lambda^{-4\nu+2}\right)^{\frac{\nu}{2\nu-1}} - 2\Lambda^{2\nu-4} + \Lambda^{2\nu-2}\left(\Lambda^{-4\nu+2}\right)^{\frac{\nu}{2\nu-1}} + 2\Lambda^{2\nu-4}\alpha - \Lambda^{2\nu-2}\alpha\left(\Lambda^{-4\nu+2}\right)^{-\frac{\nu}{2\nu-1}}\right). \quad (7)$$

Collagen Isolation and Preparation

Type I collagen was isolated from bovine corium through mechanical separation of the dermis and epidermis. Hair follicles and non-collagenous proteins were removed with a $Ca(OH)_2$ and NaHS solution. The remaining collagen proteins were enzymatically treated with pepsin and grinded with ice to form a collagen gel. The resultant gel was forced through a mesh filter in order to remove large undigested pieces of dermis. The gel was then diluted with acetic acid and collagen proteins were salted out with the addition of NaCl. Collagen was collected via centrifugation and dialyzed against dH_2O. The resultant gel pH was adjusted to 5.5 and desired concentrations (2-3%) were obtained via dilution or centrifugation

A 3D printed mold was designed in order to fabricate dimensionally uniform (d = 10 [mm], h = 3.5 [mm]) discs. Non-polymerized collagen hydrogel was loaded into the mold and subsequently polymerized via pH neutralization using a HEPES buffer (pH = 7.4). Collagen hydrogel discs were then either exposed to a series of UV cross-linking energies or t reated with a 4 nM matrix metalloproteinase-2 (MMP-2) solution for 1 hour at body temperature.

Collagen hydrogel discs were compressed using a MARK-10 mechanical testing device at a s train rate of 10 [mm/min]. Displacements were recorded using video calipers. Cauchy stress was then calculated from

$$\sigma_z^{\exp} = f/A \quad (8)$$

where f is the force and A deformed cross sectional area.

RESULTS

Unconfined uniaxial compression of collagen hydrogels was used to generate experimental stress-strain curves as shown in Figure 2.

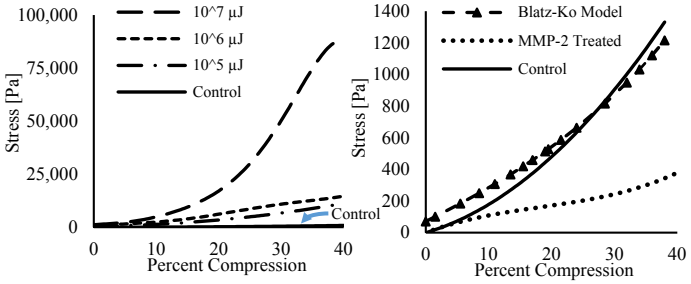

Figure 2: Representative compressive stress-strain results using 3% collagen hydrogels (left) when exposed to UV radiation (n=3) and (right) when incubated with a 4 nM MMP-2 solution (n=3). Piola-Kirchhoff (engineering) stress is shown.

Parameter fitting was performed for the control discs by minimizing the error between the modeled (7) and measured (8) stresses. Note that the value of the void fraction α was determined from the % aqueous solution in the hydrogel while Poisson's ratio ν was found as an average at any discrete measurement. With these two parameters, and the known stress-strain relationship, the shear modulus μ was found.

Table 1: Blatz-Ko Material Parameters for Collagen Hydrogel

	μ (Pa)	α (..)	ν (..)	error
Control	1,588	0.97	0.170	0.139

DISCUSSION

Collagen hydrogels have the capability of being mechanically tuned to improve or decrease mechanical properties depending on the desired outcome. Exposure to UV energy results in a marked increase in mechanical stiffness. UV exposure provides energy for cross-link formation between collagen fibrils within the hydrogel and thus improved mechanical stability (Figure 2). In contrast collagen hydrogels incubated with MMP-2 show a marked decrease in material stiffness (Figure 2). MMP-2 is a w ell characterized gelatinase enzyme responsible for ECM remodeling through collagen degradation. MMP incubation not only serves as a method for a ltering collagen hydrogel mechanical properties but further highlights the effects of upregulation of MMP-2 in certain disease states, especially in aneurysms, where protein integrity is compromised. This also reinforces the potential for collagen hydrogels to be used as an *in vitro* model to investigate the effects of weakened collagen structures on c ellular activities or to simulate proteases common in the inflammatory response.

A Blatz-Ko constitutive model is presented and an initial set of material parameters determined. These parameters can be used to estimate cell traction forces based upon measurable strains or applied to finite element analysis to determine the behavior of complex but biologically relevant collagen hydrogel geometries.

ACKNOWLEDGEMENTS

NIH South Carolina INBRE. *IDeA Networks of Biomedical Research Excellence* P20GM103499

REFERENCES

[1] Gourdie RG et al. 2012 *Microsc. Microanal.* 1-8
[2] Blatz PJ, Ko WL. 1962. *Trans. Soc. Rheol.* VI:223–251.
[3] Horgan CO. 1995. *J. Elasticity*. 42: 165-176
[4] Humphrey JD. 2002. Cardiovascular Solid Mechanics

Copyright 2016 The Organizing Committee for the 2016 Summer Biomechanics, Bioengineering and Biotransport Conference

SB³C2016
Summer Biomechanics, Bioengineering and Biotransport Conference
June 29 –July 2, National Harbor, MD, USA
SB³C2016-1136

ORIENTATION DEPENDENT STRAIN CHARACTERIZATION OF THE ULTRASTRUCTURE IN BONE

Jitin Samuel (1), Jun-Sang Park (2), Jonathan D. Almer (2), Xiaodu Wang (1)

(1) Mechanical Engineering Department
University of Texas at San Antonio
San Antonio, TX, United States

(2) Advanced Photon Source
Argonne National Laboratory
Lemont, IL, United States

INTRODUCTION

Bone is a highly hierarchical material with different structural features over several length scales ranging from macro to the ultrastructure length scales. Bone toughness is understood to originate at the ultrastructural level where the primary architectural feature is one resembling a hybrid nano-composite of an organic matrix comprised mainly of type-I collagen and mineral crystals intertwined with non-collagenous proteins in the presence of water. Understanding the fundamental features of bone at the ultrastructure and their contributions to the bulk behavior is imperative in the explanation of the mechanistic origins of bone fragility in conditions where the ultrastructural features as altered such as disease, age etc.

Bone minerals are also highly textured most likely due to the functional adaptations of the bone tissue under load as the mineral crystals are the primary load bearing components at the ultrastructure. Texture contributes to anisotropy in polycrystalline materials. Another interesting feature of the ultrastructure is that the mineral crystals can be distinctive based on their spatial location in the matrix. Minerals occurring inside collagen fibrils have been reported as staggered plate-like structures and highly oriented whereas the minerals occurring outside the fibrils have been reported to possess very limited spatial correlation. It is unclear how the minerals occurring in distinct locations in bone influence the bulk level deformation based on their differences in orientation distribution.

The ultrastructural stress states in bone minerals and collagen may not be representative of the bulk stress state of bone. Mineral crystals are inherently anisotropic and the contribution of each crystal to the bulk deformation is orientation dependent. The intrafibrillar and extrafibrillar differences exacerbate the difficulty in explaining the mechanistic origins of bone toughness at the ultrastructure level.

The aforementioned complexity of bone architecture makes a detailed experimental characterization a challenging task. So far, the work in this field has been limited to computational modeling based approaches or to experimental characterization using highly simplified strain gauge rosette models. Such models fail to capture the anisotropy and micromechanical differences in the intrafibrillar and extrafibrillar deformations. In this study we propose a detailed stress-strain characterization in bone using high energy x-ray diffraction measurements of mechanically loaded bone specimens along with optimization based texture analysis and strain characterization techniques.

The proposed method would enable us to obtain the following information;

- Detailed stress-strain characterization of bone and an understanding of the orientation dependent micromechanical stress states of the ultrastructure constituents and their contribution to the bulk deformation.
- A means to differentiate the micromechanical stress states of minerals which have possibly distinct orientation distributions such as the intrafibrillar and extrafibrillar minerals
- The evolution of micromechanical stress states in response to bulk deformation characteristics such as elastic deformation and post-yield plastic deformation.
- A detailed investigation of ultrastructural changes in bone owing to conditions such as disease, age and hydration status and their effect on the micromechanical stress states and their contribution to the overall bulk deformation.

Thus, this study aims at providing a tool for experimentally characterizing the orientation and location dependent ultrastructural

Copyright 2016 The Organizing Committee for the 2016 Summer Biomechanics, Bioengineering and Biotransport Conference

deformation of bone mineral crystals and collagen fibrils. This tool can be exploited to provide insights into the ultrastructural origins of bone toughness and the role of the ultrastructure in bone fragility under different conditions such as disease, age and hydration status.

METHODS

Cylindrical compressive specimens (Φ3.0x5.0mm) were harvested from the mid-diaphysis of male human cadaveric femurs. A monochromatic high-energy X-ray beam was irradiated to the center of the specimen WAXS (Wide Angle X-ray Scatter) patterns were recorded sequentially for every steps of the progressive loading scheme.

Strain Characterization: aggregate mineral strain using Dolle-Hauk method.

$$\varepsilon_{\phi\psi} = \frac{d_{\phi\psi} - d_0}{d_0} = \varepsilon_{11}\cos^2\phi\sin^2\psi + \varepsilon_{22}\sin^2\phi\sin^2\psi + \varepsilon_{33}\cos^2\psi \quad (1)$$
$$+ \varepsilon_{12}\sin 2\psi\sin^2\psi + \varepsilon_{13}\cos\phi\sin^2\psi + \varepsilon_{23}\sin\phi\sin 2\psi$$

Assuming ε_{13} and ε_{23} terms are zero the above equation becomes linear for a fixed ϕ

$$\varepsilon_{\phi\psi} = \frac{d_{\phi\psi} - d_0}{d_0} = \sin^2\psi[\varepsilon_{11}\cos^2\phi + \varepsilon_{22}\sin^2\phi + \varepsilon_{12}\sin 2\phi - \varepsilon_{33}] \quad (2)$$
$$+ \varepsilon_{33}$$

Non-linearity represent anisotropy in the aggregate deformation.

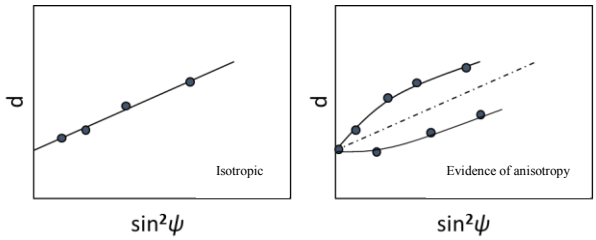

Figure 1: d spacing vs. $sin^2\psi$ for isotropic and anisotropic mineral deformation. A straight line indicates isotropic behavior whereas a "psi-splitting" is typically observed in anisotropic deformation.

Representation of Crystal Orientation: Orientation can be defined as a rotation operator C relating the crystallographic orientation [c] with a reference orientation [s].

[c]= [C]*[s]. A probability density function of all orientations is the Orientation Distribution Function (ODF)

In this study, we have used a quaternion rotation scheme and represented the orientations on Rodrigues-Frank space.

An optimization based pole figure inversion technique was used to determine the ODF of mineral crystals and analogously strain pole figures were inverted using spherical harmonic approximations for strain fields to obtain orientation dependent stress-strain tensors. The inversion formulation is described in detail by Barton et al. [1]

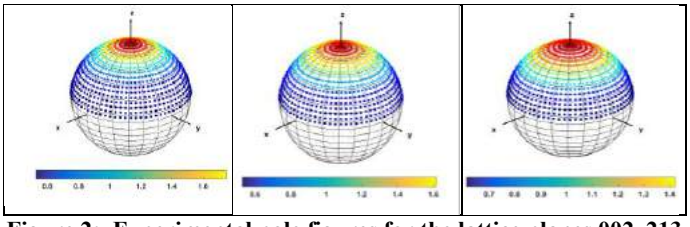

Figure 2: Experimental pole figures for the lattice planes 002, 213 and 113.

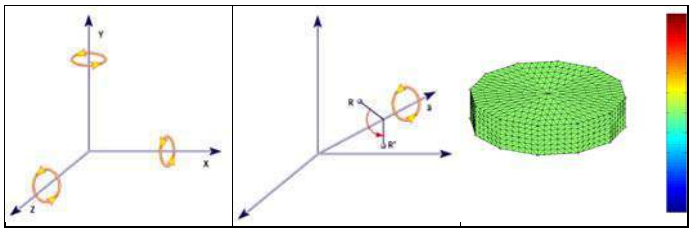

Figure 3: Representation of orientations using Euler scheme, using angle axis pairs and the fundamental region to represent ODF and stress fields for Hexagonally symmetric configurations.

RESULTS

Results from conventional strain characterization techniques show presence of anisotropy in bone, ODF was obtained following pole figure inversion techniques [2].

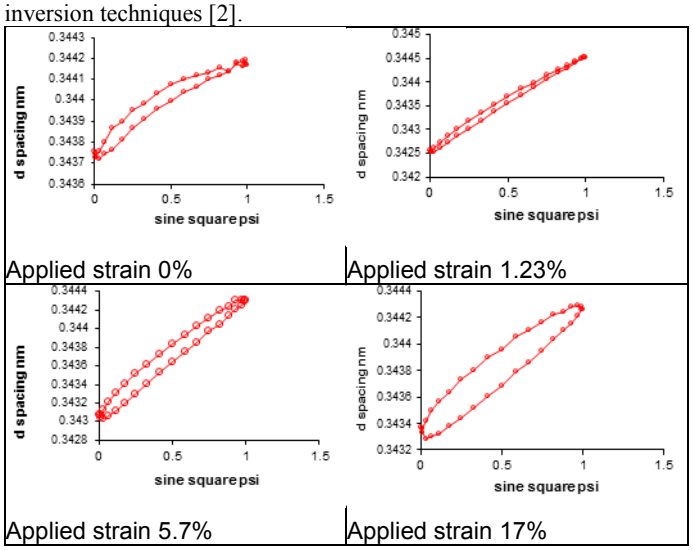

Figure 4: "psi-splitting" indicative of anisotropy observed in bone at different strain levels.

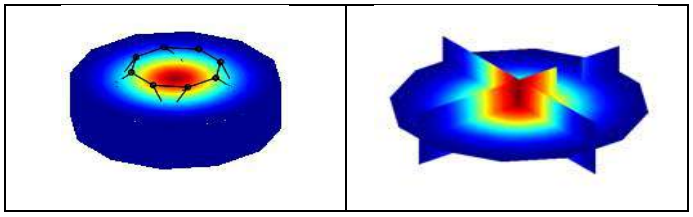

Figure 5: Orientation distribution function of bone crystals obtained from pole figure inversion.

DISCUSSION

The pole figure inversion technique was able to provide accurate orientation distribution function, this technique will be extended to obtain orientation dependent stress-strain tensors. Further deconvolution of intrafibrillar and extrafibrillar deformation will be attempted by considering experimental techniques to distinguish the volume fraction/distribution of intrafibrillar and extrafibrillar minerals followed by using the aggregate strain response for deconvolution of the intrafibrillar and extrafibrillar strains and subsequently stress.

ACKNOWLEDGEMENT: NSF grant (CMMI-1266390). Advanced Photon Source, DOE contract DE-AC02-06CH11357.

REFERENCES [1] N. R. Barton et al. *Textures Microstruct.*, vol. 35, no. 2, pp. 113–144, 2002. **[2]**J. V. Bernier et al. *J. Appl. Crystallogr.*, vol. 39, no. 5, pp. 697–713, 2006.

Copyright 2016 The Organizing Committee for the 2016 Summer Biomechanics, Bioengineering and Biotransport Conference

SBC^{3}C2016
Summer Biomechanics, Bioengineering ans Biotransport Conference
June 29 - July 2, 2016, National Harbor, MD, USA
SB³C2016-1137

TRANSLATING 4D-FLOW MRI TO CLINICAL PRACTICE: SEQUENCE DEVELOPMENT, IN-VITRO VALIDATION, NUMERICAL AND EXPERIMENTAL FRAMEWORK

Kurt R. Sansom (1), Haining Liu (2), Chun Yuan (2), Alberto Aliseda (1), Gador Canton(1,2)

(1) Dept. of Mechanical Engineering
University of Washington
Seattle, Washington 98195

(2) Vascular Imaging Laboratory
University of Washington
Seattle, Washington 98109

INTRODUCTION

Use of magnetic resonance Imaging (MRI) in understanding cardiovascular physiology and pathology diagnosis has undergone tremendous developments in the past decade and provides expanding potential of evaluating cardiovascular function in the clinical setting [1]. Historically, MRI has enjoyed acceptance by clinicians as an anatomic imaging modality for diagnosing cardiac and vascular disease, and assessing patient response to treatment [2]. More recently, comprehensive acquisition and analysis of blood flow dynamics has been developed to provide functional information on cardiac perfusion, myocardial viability, and blood supply [3]. Quantitative assessment of cardiovascular disease with more in-depth understanding of the pathophysiology requires this functional information. Time-resolved, three-dimensional velocity encoding and anatomic coverage Phase Contrast-MRI (PC-MRI 4D-Flow) is one such tool that has been developed to assess blood flow quantitatively. 4D-Flow velocity encoding is based on signal phase changes along a magnetic field gradient which are directly related to blood flow velocity. Two acquisitions are acquired with different velocity-dependent signal phase and subtraction of the resulting phase images removes the background and provides a means to calculate three components of the velocity in each imaging voxel. Standard MRI is to slow to capture real-time spatio-temporal information, and requires ECG cardiac cycle gating over multiple heartbeats. The challenge, however, is that 4D-Flow acquisition sequences have not yet been optimized for clinical applications and are limited by the trade-off between acquisition time and spatial and temporal resolution. Clinical relevance of 4D-Flow depends on the optimization of the image acquisition sequence to make it adequate to the realistic constraints presented by the patient care environment. The optimization of this imaging sequence entails the development of a framework that provides a rapid and efficient feedback loop between the sequence measurements and benchmarked data. This work presents the development of new assessment metrics for 4D MRI flow sequences. First, 4D-MRI flow in a subject's carotid bifurcation is compared to a patient-specific CFD simulation. Second, Particle Image Velocimetry in a patient-specific phantom is used as a benchmark to compare the 4D-MRI in vivo measurements and CFD simulations under the same conditions. Comparison of measureable flow parameters such as velocity and vorticity, and estimated, such as wall shear stress, is used to determine the accuracy of the 4D flow as a function of scan time by connecting them to their biomechanics relevance and the insights they can provide on the pathophysiology of arterial disease: atherosclerosis and intimal hyperplasia. Lastly, the framework is applied to a new sequence development and a quantitative assessment is provided.

METHODS

Patient specific data of the carotid artery was collected from a healthy volunteer. Both 3D-MERGE [4] and 4D-Flow sequences were executed to acquire geometry and flow information. The anatomical information from the 3D-MERGE sequence was segmented with ITK-SNAP. From the voxel-based image segmentation, a surface mesh representation was extracted and post processed to add inlet vessel extensions with Vascular Modeling Toolkit(VTMK v1.2). Meshmixer (Autodesk Meshmixer v3.0) was used to add additional geometrical features required to create a 3D-printable flow phantom. The 1 : 1 scaled flow phantom positive was printed by a Fused Deposition Modeling (FDM) printer. A transparent polydimethylsiloxane (PDMS, Dow Corning Slygard 184) was used to create the negative of the

Copyright 2016 The Organizing Committee for the 2016 Summer Biomechanics, Bioengineering and Biotransport Conference

3D-printed object. Once the mold was cured the, 3D printed positive was manually extracted. The flow phantom was connected to a pulsatile pump (Harvard Apparatus Inc., Holliston, MA) with long tubes to accommodate the separation from the MRI machines magnetic field. The pump flow rate matched velocities from the 4D-Flow acquisition at the inlet to the flow phantom. For the PIV setup, an ultrasonic flowmeter (Atrato, Titan Enterprises) was placed in the CCA inlet just upstream of the flow phantom to provide a comparison with an average physiological carotid artery waveform [5] and the waveform extracted from the 4D-Flow data. Three needle valves were used to control the flow rate at the Common Carotid Artery (CCA), Internal Carotid Artery (ICA) and External Carotid Artery (ECA) while maintaining the percent systolic (37.5%) and average flow rate. A 60 : 40 by weight water:glycerin mixture was used to mimic the viscosity of blood, $3.2cP$ at a temperature of 25° and match the index of refraction of the PDMS, 1.41. The water-glycerin mixture was seeded with lycopodium particles, illuminated with pulsed laser plane and the light scattered by the particles collected by a high-speed camera (Phantom V12, Vision Research Inc., Wayne NJ.) oriented perpendicular to the laser plane. PIV processing was done with an in-house MATLAB (MATLAB 8.6, The MathWorks Inc., Natick, MA, 2015) wrapper that combines Fiji and MatPIV to pre-process, calculate velocity vectors from the cross correlation of sequential images within the region of interest, and post-process the velocity fields. The waveform data collected from the ultrasonic flow meter at the CCA was used as the inlet boundary condition of a CFD simulation of the segmented carotid artery. The CFD volume meshes were generated in Star-CCM+ (Release 10.02, CD-adapco) and finite volume fluid simulations were performed using ANSYS FLUENT (Release 14.7, ANSYS, Inc.).

RESULTS

The velocity field along the carotid artery phantom was computed from the PIV for the straight inlet CCA segment and the carotid bulb and bifurcation region as depicted in figure 1. The CFD simulations of the unsteady hemodynamics are quanttatively compared with the post processed PIV data. CFD provides easy access to accurate wall shear stress that cannot be accurately provided by PIV, while the PIV provides high temporal and spatial resolution velocity measurements in-vitro to validate the resolution limited 4D Flow MRI. This data combined provides a foundation to assess the different 4D-Flow sequences. Wall Shear Stress was chosen as a biomechancis marker because of the relevance to cardiovascular disease [6]. 4D-Flow combined with CFD could provide a more accurate assessment of the Wall Shear Stress and have the potential to become a clinical tool for predicting disease progression.

DISCUSSION

This preliminary data is a solid foundation on which to build a new framework for PC-MRI development. The next steps include creating the hemodynamics metric objective function to use the PIV velocity and the CFD wall shear stress to optimize the 4D-Flow sequence, taking into account the accuracy of the time-resolved velocity, vorticity and shear fields (with different positive mutlipliers), and the scanning time (with a strong negative multiplier).

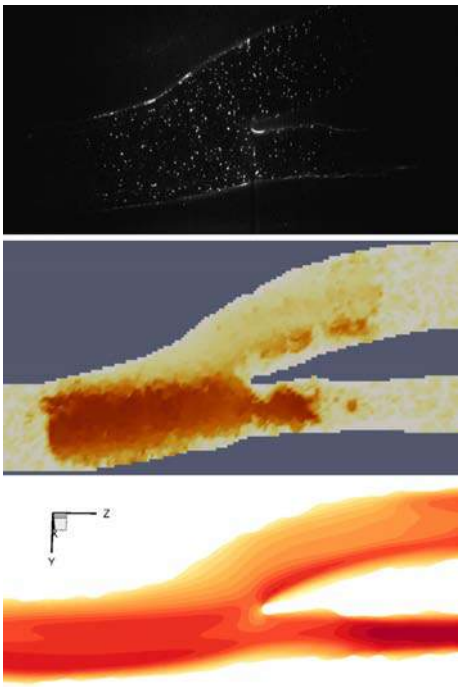

FIGURE 1. Comparison between the raw PIV images (top), Post processed PIV Z Velocity (middle), and the CFD Z Velocity contours (bottom) at the peak inlet velocity.

ACKNOWLEDGMENT

This work has been financially supported by a Department of Education GAANN fellowship, and NINDS R01 grant (1R01NS088072-01A1) and an NIBIB R43 grant (2 R42 EB018124 02).

REFERENCES

[1] Markl, M., Frydrychowicz, A., Kozerke, S., Hope, M., and Wieben, O., 2012. "4d flow MRI". *Journal of Magnetic Resonance Imaging,* **36**(5), Nov., pp. 1015–1036.

[2] Tempany, C. M., and Zerhouni, E. A., 1990. "Clinical magnetic resonance imaging of the vascular system". *Topics in magnetic resonance imaging: TMRI,* **2**(2), Mar., pp. 13–30.

[3] Stankovic, Z., Allen, B. D., Garcia, J., Jarvis, K. B., and Markl, M., 2014. "4d flow imaging with MRI". *Cardiovascular Diagnosis and Therapy,* **4**(2), Apr., pp. 173–192.

[4] Martin, N., Malfair, D., Zhao, Y., Li, D., Traboulsee, A., Lang, D., and Vertinsky, A. T., 2012. "Comparison of MERGE and axial T2-weighted fast spin-echo sequences for detection of multiple sclerosis lesions in the cervical spinal cord". *AJR. American journal of roentgenology,* **199**(1), July, pp. 157–162.

[5] Holdsworth, D. W., Norley, C. J., Frayne, R., Steinman, D. A., and Rutt, B. K., 1999. "Characterization of common carotid artery blood-flow waveforms in normal human subjects". *Physiological Measurement,* **20**(3), Aug., pp. 219–240.

[6] Peiffer, V., Sherwin, S. J., and Weinberg, P. D., 2013. "Does low and oscillatory wall shear stress correlate spatially with early atherosclerosis? A systematic review". *Cardiovascular Research,* **99**(2), July, pp. 242–250.

Copyright 2016 The Organizing Committee for the 2016 Summer Biomechanics, Bioengineering and Biotransport Conference

SB^{3}C2016
Summer Biomechanics, Bioengineering and Biotransport Conference
June 29 –July 2, National Harbor, MD, USA
SB^{3}C2016-1138

INTRA ANEURYSMAL ANGIOGRAPHIC ANALYSIS IN PATIENTS TOWARDS DETERMINATION OF FLOW DIVERSION EFFICACY

Ronak J. Dholakia, Chander Sadasivan, David J. Fiorella, Henry H. Woo, Baruch B. Lieber

Department of Neurological Surgery
Stony Brook University
Stony Brook, NY, USA

INTRODUCTION

Endovascular treatment of brain aneurysms by flow diversion was recently approved by the FDA for complicated aneurysm geometries such as large/giant sized, wide-necked, or fusiform aneurysms not amenable to coiling. Efficacy of flow diverters depends on porosity and pore density, or permeability, of the device as well as the anatomic configuration and position of the aneurysm relative to the oncoming flow as well as the flow rate in the parent artery. At Present, quantitative assessment of the long term efficacy of flow diversion at time of treatment is not available. Clinicians estimate adequacy of treatment by visual inspection of contrast transport and its residence time within the aneurysm immediately post implantation. Angiographic image analysis on data acquired at a high frame rate in patients can be used to quantify the alteration in contrast transport mechanics post flow diversion. This study evaluated angiographic analysis in clinical patients to establish parameters that can predict flow diverter treatment efficacy.

METHODS

Following IRB approval, consent for high speed angiograms was obtained from patients scheduled for flow diversion treatment. High speed angiograms were acquired in 40 aneurysms from 32 patients before and after flow diverter implantation using an Artis zee biplane angiography unit (Siemens Medical Solutions, Erlangen, Germany). Contrast injections were performed at 6 ml/sec for 1 second duration following a 2.5 second injection delay through a 5Fr catheter. The catheter tips were maintained at the same position in each patient. Contrast injections were performed using a power injector (Medrad Warrendale, Pennsylvania) coupled electronically to the angiography unit. Angiograms were acquired in either single- or dual-plane as determined by the neurointerventionalist. The selection of the plane was done based on the orientation of the aneurysm.

A variable frame rate (VFR) protocol was incorporated in collaboration with Siemens to reduce radiation exposure. Through VFR angiograms are acquired at high frame rate (15 fps) during the early portion of the angiogram when contrast transport high while a low frame rate (7.5 fps) is used for the rest of the angiogram when contrast transport in minimal. Follow up imaging was acquired in the patients at 6 months.

Angiographic image analysis

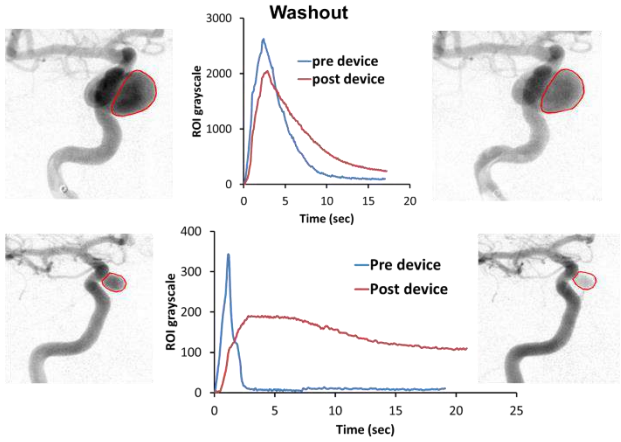

Figure 1: Aneurysm region of interest segmentation in large cavernous internal carotid artery aneurysm (top) and ophthalmic segment aneurysm (bottom) and pre and post washout curves quantified.

Copyright 2016 The Organizing Committee for the 2016 Summer Biomechanics, Bioengineering and Biotransport Conference

The angiograms acquired during the patient treatment was anonymized and exported from the Siemens angiographic unit. The aneurysm region of interest (ROI) was segmented and the contrast concentration-time curve within the region of interest was recorded. Angiographic image segmentation and washout curve generation are demonstrated for two patients in Figure 1. The angiograms were corrected for venous contrast overlay and catheter leakage.

The corrected washout curves were normalized and fitted to a mathematical model that differentiates between convective and diffusive contrast transport. The model was fit to the data by minimizing the sums of squares differences between the data and the model using a library function available within the optimization toolbox in MATLAB.

$$f(t)/\delta = \rho_{conv} \int_0^t \frac{1}{\sigma\sqrt{2p}} e^{-\frac{(\eta-\mu)^2}{2\sigma^2}} \times \frac{1}{\tau_{conv}} e^{-\frac{t-h}{\tau_{conv}}} d\eta + \rho_{diff} \left[\int_0^t \frac{1}{\sigma\sqrt{2p}} e^{-\frac{(\eta-\mu)^2}{2\sigma^2}} d\eta - \left(1 - e^{-\frac{t}{\tau_{diff}}}\right) \right]$$

Here, ρ_{conv} and ρ_{diff}: represent the proportions of convective and diffusive transport, respectively. τ_{conv} and τ_{diff} are the convection and the diffusion time constants, respectively. σ and μ: are related to the method and profile of contrast injection.

RESULTS AND DISCUSSION

Follow up angiograms of 34 aneurysms in 27 patients have been acquired so far. Twenty five aneurysms were selected for angiographic analysis (3 giant, 9 large, 13 small/medium) based on their size (>4mm). Aneurysms less than 4mm could not delineate any change in contrast transport through angiographic analysis. So far analysis has been completed on 19 of the 25 selected aneurysms. Of the 19 aneurysms analyzed, 11 occluded at follow up.

Figure 2 presents an example of mathematical model fit to angiographic washout curve in a patient where the aneurysm did not occlude at follow up. The washout curves appeared almost identical pre and post flow diversion showing very little difference in intra-aneurysm contrast transport.

For the sample set analyzed, post flow diversion angiographic washout parameters were significantly different (p=0.0016 for amplitude δ and p = 0.0001 for convective time constant) than the pre washout parameters as determined from the paired test comparisons shown in Figures 3 and 4. Thus, flow diversion significantly reduced the concentration of contrast in the aneurysm, represented by washout amplitude, and increased the residence time of the contrast in the aneurysm. Comparison was made between the occluded and non-occluded groups to determine parameters what parameters, if any, can predict treatment efficacy.. The scatter plots demonstrate similar spread for the pre device values for the patients from both occluded and non-occluded groups. However the range for the occluded group is reduced post flow diversion. The study, however, did not reach statistical significance because of a low sample size. However, trends in the washout parameters appears to occur indicating that angiographic analysis can help in obtaining a perioperative diagnostic tool for flow diversion efficacy.

This work was partly supported by Siemens.

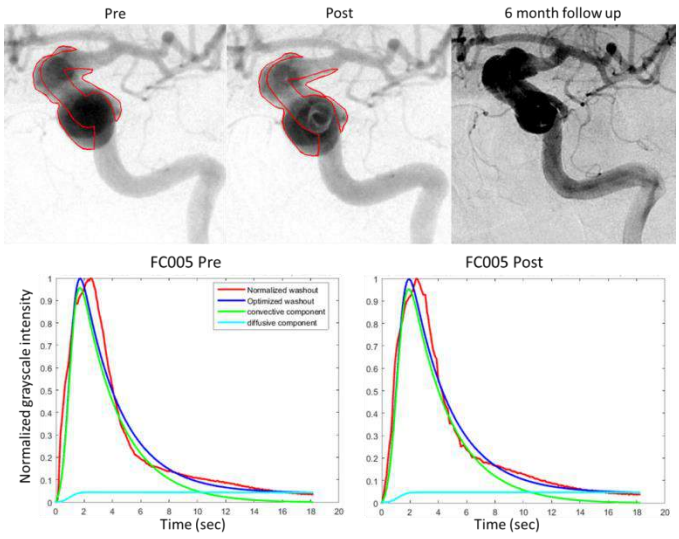

Figure 5: Angiographic image analysis for patient with giant fusiform ICA aneurysm. Top panel represents the aneurysm ROI segmented pre and post device angiographic images and 6month follow up angiogram showing aneurysm filling. Bottom panel shows the mathematical model fitted on the washout curves obtained from angiographic image analysis.

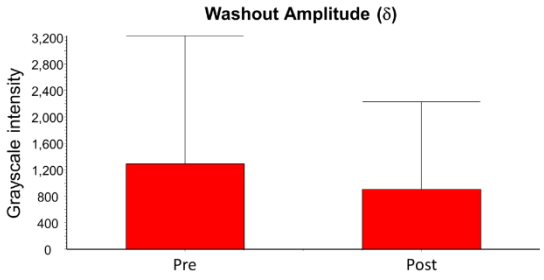

Figure 2: Comparison of the contrast concentration washout mean amplitude pre and post flow diverter implantation (p=0.0016)

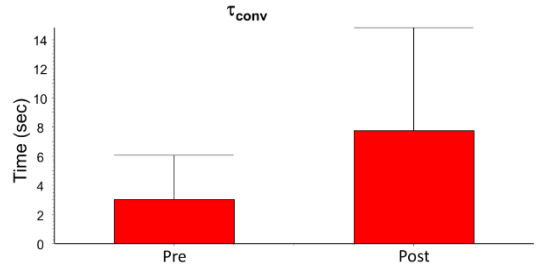

Figure 3: Comparison of mean convective time coefficient obtained from mathematical model fitting of the contrast concentration time curves pre and post flow diverter implantation (p<0.0001).

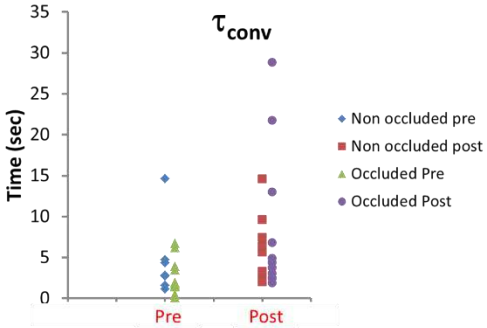

Figure 4: Scatter plot comparison of convective decay time coefficient among the occluded and non-occluded aneurysm groups pre and post.

Copyright 2016 The Organizing Committee for the 2016 Summer Biomechanics, Bioengineering and Biotransport Conference

SB^{3}C2016
Summer Biomechanics, Bioengineering and Biotransport Conference
June 29 –July 2, National Harbor, MD, USA
SB^{3}C2016-1139

PATIENT-SPECIFIC ASSESSMENT OF PRE-TPVR ANGIOPLASTY CORONARY COMPRESSION USING THE FINITE ELEMENT METHOD

S. Amendola (1), D. McElhinney(2), P. Bhatla (3), V. Flamini(1)

(1) Tandon School of Engineering
New York University
New York, NY, United States

(2) Stanford University Medical Center
Stanford, CA, United States

(3) Langone Medical Center
New York University
New York, NY, United States

INTRODUCTION

The incidence of congenital heart disease, referring to a problem in the structure of the heart that is present at birth, varies from about 4/1,000 to 50/1,000 live births [1].

Approximately 20% of babies born with congenital heart disease have anomalies that involve the right ventricular outflow tract (RVOT) and the pulmonary valve.

Children that are born with this type of congenital heart disease have to undergo multiple surgeries already within the first two years of life in order to restore the regular physiological circulation of the heart [2].

The Melody Transcatheter Pulmonary Valve Replacement therapy (TPVR) is frequently considered in patients with right ventricle outflow tract (RVOT) conduit obstruction [2], as an alternative to the open-heart surgery. In fact, this procedure is minimally invasive.

However, even though this method has many advantages compared to traditional open-heart surgery, it is also related to some risks. In fact, depending on the specific geometry of the patient, a compression of the coronary artery (CA) may happen during the stent expansion [3].

Therefore, prior to TPVR procedure, dynamical testing is performed to evaluate CA compression. Dynamical testing is accomplished by performing an angioplasty with a balloon having the same diameter as the valve to be implanted. However, this procedure exposes patients to CA compression risk and for many patients it will represent an unnecessary procedure: if dynamical testing fails they will be referred to traditional open heart surgery.

The aim of this work is to provide an alternative and safe way to evaluate non-invasively the risk of CA compression in pediatric patients. This method requires building a patient-specific 3D model of the RV and the CA, and a Finite Element simulation of the balloon angioplasty inside the RVOT conduit.

METHODS

Patients who attempted TPVR were included in the study (n=4). Patient-specific models are shown in figure 1 A.

Patient-specific models were segmented from pre-procedural Magnetic Resonance Images (MRI) or Computational Tomography (CT) scans, using Mimics (Materialize, Belgium). The segmented models were further edited using Meshmixer (Autodesk, California) and meshed using Cubit (CSimSoftware, Utah) software.

Each model was constituted by the components of the cardiovascular system that would be affected by the pre-TPVR angioplasty procedure, which are: pulmonary artery (PV), aorta, RVOT, conduit, and left and right CAs. Tetrahedral elements where used for the mesh. In average, the number of elements used was 14406 ± 5875. In order to evaluate the accuracy of the solution obtained with the chosen mesh density, the results were compared to those obtained with a mesh density 20% denser than the one chosen, and the error difference was less than 0.03%.

The balloon model was created in ABAQUS (Dassault Systèmes, RI) and was chosen to be a deformable 3D cylinder of 20 mm length, 1 mm of external diameter and 0.2 mm thickness, thus mimicking the angioplasty balloons used in clinical practice. For this balloon a mesh of 630 quadrilateral elements was generated with reduced integration and a large-strain formulation. Since models for simulation of angioplasty balloon are a current research topic, the deformable model was compared with a balloon model composed by 5 analytical rigid surfaces representing the balloon folds [5,8].

Human vessel tissues were modeled as linear-elastic isotropic materials with Young modulus of 2.7 MPa, Poisson ratio of 0.49 and mass density of 1000 m^3/kg [4]. The balloon was modeled as an isotropic, linear-elastic material, with a Young's modulus of 900 MPa and Poisson's ratio of 0.3 [5,6].

Copyright 2016 The Organizing Committee for the 2016 Summer Biomechanics, Bioengineering and Biotransport Conference

For each patient model, FE simulations of balloon conduit angioplasty were implemented in ABAQUS.

The finite element model generated was nonlinear and the equilibrium equation obtained by discretizing the virtual work equation in terms of the variables of the nonlinear equation can be symbolically written as:

$$F^N(u^M) = 0$$

Where F^N is the force component non-conjugate to the N^{th} variable in the problem and u^M is the value of the M^{th} variable. The method used to solve the nonlinear equation system was the Newton's method. Static general time steps were chosen and nonlinear effects were included [7].

Two contact pairs were identified. Surface-to-surface frictionless hard contact was imposed between the external surface of the balloon model and the internal surface of the conduit and between the external PA surface and the external surface of the aorta and the CA. The direct method was chosen as contact constraint enforcement method.

Balloon expansion was modeled as deformable body dilation to a dimension related to the original RVOT conduit diameter conforming to clinical guidelines as shown in Table 1.

Patients	Conduit Diameter (mm)	Balloon Diameter (mm)
1	23	22
2	20	22
3	22	18
4	23	18

Table 1: Patients clinical data.

For both the deformable and the rigid balloon model, radial displacements were imposed to the nodes of the balloon, which was positioned at the center of mass at the narrowest point of the conduit lumen. Encastre was imposed as boundary condition at both edges of PA and aorta and on the nodes at the extremities of the CAs.

RESULTS

This work successfully identified a method to simulate pre-TPVR procedure. Results in terms of stress and displacement were obtained for all the 4 patients; see Figure 1 and Tables 2 and 3. The stress analysis in the stenotic site is in accordance with literature data (max stress 1.98 ± 0.25 MPa) [8]. Coronary bending and distortion was identified and compared in all the 4 patients. For patients III and IV the results in terms of stress and displacement are respectively 88% and 99% higher than the ones of patients I and II for which there is no compression.

Simulations were more robust when a deformable balloon model was used as opposed to a balloon described by analytically rigid surfaces. Comparing the results obtained between the two balloon models the difference in stress results was < 0.8\%.

Table 2: Displacement results for the 4 patients.

Patients	Balloon Diameter (mm)	Conduit Displacement (mm)	Coronary artery Displacement (mm)
1	22	7.733	0.4087
2	22	6.609	0.3825
3	18	5.719	2.372
4	22	5.667	3.323

Table 3: Stress results for the 4 patients.

Patients	Balloon Diameter (mm)	Conduit Stress (MPa)	Coronary artery Stress (MPa)
1	22	2.203	0.06696
2	22	1.809	0.04123
3	18	2.126	0.3753
4	22	1.231	0.6214

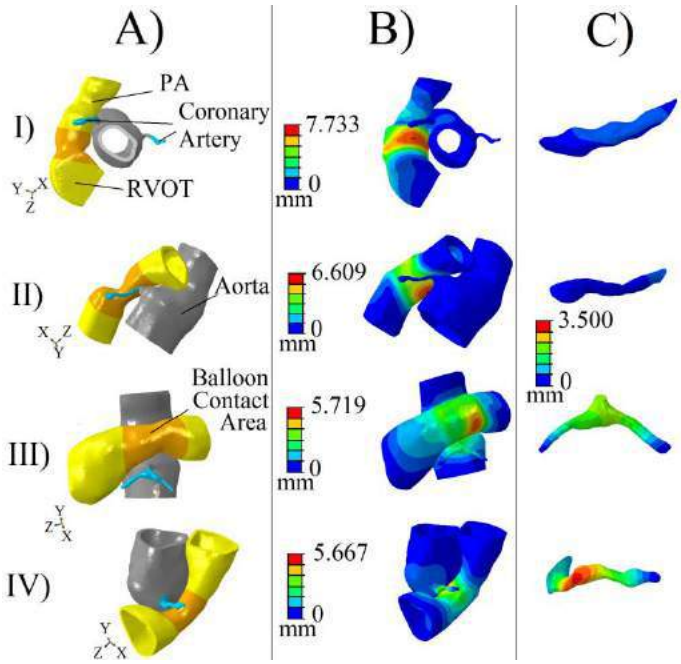

Figure 1: A) Patient specific 3D models used in the study; B) Displacement results of the FE pre-TPVR angioplasty simulations; C) Detail of the results of the simulations on the CAs.

DISCUSSION

The developed models enabled the investigation of important parameters that could play a role in the determination on the angioplasty procedure outcome in terms of CA compression.

The results of the four expansion simulations presented similar values of the maximum Von Mises stresses on the pulmonary arteries, however they present different results in terms of displacement and stresses in the coronary arteries. Moreover, ours results show that coronary compression is strictly dependent on the specific geometry on the specific patient.

ACKNOWLEDGEMENTS

We gratefully acknowledge the KiDs of NYU Foundation and H^2CU, Honors Center of Italian Universities.

REFERENCES

[1] Hoffman, E, *J Am Chem Soc,* 39:1890-900, 2002.
[2] McElhinney, D B, *Ann. N. Y. Acad. Sci*, 1291, 77-85, 2013.
[3] McElhinney, B, *Circulation,* 122:507-516, 2010.
[4] Choudhury, N, *J. Car. Path.,* 18, 83-91, 2009.
[5] Zahedmanesh, H, *Journal of Biomechanics,* 43: 2126-2132, 2010.
[6] Gervaso, F, *Journal of Biomechanics,* 41: 1206-1212, 2008.
[7] Nikishkov, G, *University of Aizu*, 1-70, 2004.
[8] Capelli, C, *EuroIntervention*, 6, 638-642, 2010.

Copyright 2016 The Organizing Committee for the 2016 Summer Biomechanics, Bioengineering and Biotransport Conference

SB^{3}C2016
Summer Biomechanics, Bioengineering and Biotransport Conference
June 29 –July 2, National Harbor, MD, USA
SB^{3}C2016-1140

A FLUID DYNAMICS ANALYSIS OF THE MANIFESTATION OF EBSTEIN'S ANOMALY IN THE RIGHT VENTRICLE

Alyssa L. Niquette (1), Shelly Lo (1), Adam Shore (2), Vittoria Flamini (1), Puneet Bhatla (2)

(1) Mechanical Engineering Department
New York University Tandon School of Engineering
Brooklyn, NY, USA

(2) Cardiothoracic Surgery Department
New York University School of Medicine
New York, NY, USA

INTRODUCTION

The right ventricle (RV) is a high volume, low pressure pump which is responsible for moving all of the blood from the body to the lungs, where the adverse pressure is relatively low [1]. Ebstein's anomaly presents itself in a wide range of deformities of the right heart [2]. Most commonly affected by the anomaly is the tricuspid valve of the RV. In some cases of Ebstein's anomaly, the flow rate through the RV is so reduced that the resulting pressure is insufficient to open the pulmonary valve. The main goal of this research is to create a computational fluid dynamic (CFD) analysis of the right ventricle function, as affected by Ebstein's anomaly, which may be compared to several current studies with 4D echocardiography [3]. The goal of this and similar computational models is to predict the severity and extent of the anomaly without invasive methods or procedures.

METHODS

Ultrasound images were used to determine the dimensions of the RV to simulate the blood flow patterns within. The computational domain was idealized from medical data, and parameters such as typical dimensions, pressures, and velocities were determined from literature. Variables known to affect the RV flow field as a result of the Ebstein's anomaly include modifications to the angle and dimension of the tricuspid valve.

Therefore, a parametric CFD study was implemented with COMSOL Multiphysics (Stockholm, Sweden) in which inlet RV conditions are varied to represent different presentations of the anomaly. In the time-dependent model of the RV function, inlet flow rates were related to outlet pressure values through use of the two-element Windkessel model [4].

Simultaneously, work was done to develop a three-dimensional (3D) model from two-dimensional (2D) ultrasound images. This involved mapping certain known 3D points between MRI and ultrasound data to orient the coordinate system, and create a verifiable 3D model from the stacked 2D ultrasound images, using MATLAB (MathWorks, Ma).

RESULTS

A 2D model was initially created with an RV shape defined by the plane cut through points at the center of the tricuspid valve, pulmonary valve, and apex of the right ventricle. The results of parametric variation of inlet valve dimension and angle are shown in Figure 1A. In this study, mass flow rate was the constant inlet condition, and the outlet was characterized by an average pulmonary artery pressure. Reduced flow velocities through the model RV were observed, consistent with the characteristic response of Ebstein's anomaly. However, steps were taken to create a time-dependent study, with outflow pressure values determined by the Windkessel model and inlet flow rates.

When creating a 3D model, several methods were used. The points from the ultrasound image were plotted in

Copyright 2016 The Organizing Committee for the 2016 Summer Biomechanics, Bioengineering and Biotransport Conference

MATLAB, and edited using Meshmixer (Autodesk, CA), as seen in Figure 1B and 1C.

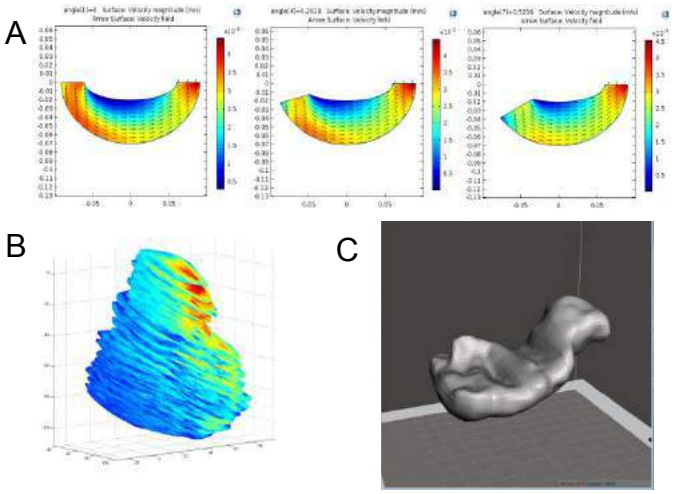

Figure 1: (A) Results of parametric CFD study of inlet angle ranging from 0 to 0.5236 radians (0-30 degrees) with constant mass flow rate and outlet pressure conditions (B) MATLAB representation of 2D images of RV mapped onto 3D model (C) 3D model of RV in Meshmixer.

DISCUSSION

By attempting to model the flow through the right ventricle, a better understanding of the effects and the severity of Ebstein's anomaly can be obtained. The problem faced in the CFD analysis with creating an imaginary plane in which to simulate cardiac function is that the results are very difficult to reproduce through alternate imaging methods. In addition, the shape is highly idealized, and measurements are approximated from literature.

The results obtained from the creation of the 3D right ventricle model may be able to combat these issues, by ensuring that the data set is functional in our applications. This will allow for increased flexibility in the orientation of the 2D plane of study and a greater understanding of how the blood flow through the chosen 2D plane affects the volume as a whole.

Future work includes a more complete analysis of the 3D flow field in order to predict the effect of tricuspid valve modification and create effective treatment techniques.

REFERENCES

[1] L.J. Dell'Italia. Anatomy and physiology of the right ventricle, 2012. pp. 167-87.
[2] C.M. Lee et al. The shape and function of the right ventricle in Ebstein's Anomaly, 2013. pp. 704-10.
[3] A.G. Fredriksson et al. 4-D blood flow in the human right ventricle, 2011. pp. 2344-50.K.B.
[4] Chandran, et al. Biofluid Mechanics: The Human Circulation, 2006. pp. 192-5.

Copyright 2016 The Organizing Committee for the 2016 Summer Biomechanics, Bioengineering and Biotransport Conference

SB^{3}C2016
Summer Biomechanics, Bioengineering and Biotransport Conference
June 29 –July 2, National Harbor, MD, USA
SB^{3}C2016-1141

STUDY ON THE BIOSOLUBILITY OF CALCINED BOVINE BONE SCAFFOLD FOR BONE TISSUE ENGINEERING

Shigeo. M. Tanaka (1), Naoki. Hirooka (2)

(1) Institute of Science and Engineering
Kanazawa University
Kanazawa, Ishikawa, Japan

(2) Graduate School of Natural Science and Technology
Kanazawa University
Kanazawa, Ishikawa, Japan

INTRODUCTION

Currently, various types of artificial and synthetic materials such as hydroxyapatite (HA), β-tricalcium phosphate (β-TCP), and titanium alloy are clinically utilized as bone substitute material. Although they have good biocompatibility, however, have some limitations in usage for tissue-engineered bone scaffold, due to poor mechanocompatibility, bioabsorbability, and high cost in manufacturing. Calcined bovine trabecular bone is attractive scaffold material able to solve these problems. Although, the mechanical properties are deteriorated by calcination process, we found that they could be improved by giving physical stimulation to osteoblasts seeded into the scaffold [1]. On the other hand, its bioabsorbability is not understood enough. Bioabsorption is crucial for complete tissue replacement, and realized by osteoclastic matrix resorption and chemical dissolution to body fluid. In this study, to evaluate the biosolubility of calcined bovine bone, change in calcium amount released from calcined bovine bone in simulated body fluid was investigated, additionally the microscopic structure of the bone surface was observed after immersing in the fluid. The results were compared with those of HA and β-TCP.

METHODS

Calcined compact bone disks

Compact bone of freeze-preserved bovine femur was machined cylindrical shape (ϕ5 mm ×L100 mm) in parallel to the bone axis using a lathe (Fig.1a). The cylindrical bone was sliced using a diamond blade with a thickness of 1.6 mm in perpendicular to the axis (Fig.1b). The surface of the bone disk was polished on a sandpaper (#1000) to give identical roughness to the surface. Finally, bone disks were calcined in an electric furnace for 22 hours at 600 or 900°C. Organic components such as collagen were confirmed to be burned out over 600°C by thermal analysis in our previous study [2]. Finally, five types of sample were prepared, i.e., bovine compact bone disk (BCB), compact bone disks calcined at 600°C, and 900°C, additionally, HA and β-TCP disks, which have the same shape and size as those of the compact bone disk, purchased from the company (TDB, USA) as references

Evaluation of biosolubility

The biosolubility of samples was evaluated by measuring calcium (Ca) concentration of simulated body fluid (SBF) after immersing samples in it. Here, lactated Ringer's solution (Otsuka Pharmaceutical, Japan) was used as SBF. A sample was placed into a well of 96-well plate with 300 μl SBF and incubated at 37°C, 5%CO2, 95%RH.

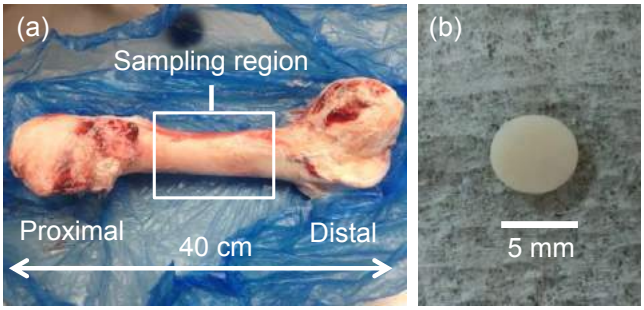

Figure 1: Sampling of bovine compact bone disks from the midshaft of a bovine femur. (a) Sampling region. (b) Close-up picture of a compact bone disk before calcination

Copyright 2016 The Organizing Committee for the 2016 Summer Biomechanics, Bioengineering and Biotransport Conference

Calcium measurement was performed at 10 min, 30 min, 1 hour, 3 hours, on 1 day, and 3 days after the start of the incubation. At each observation time point, 25 μl of SBF was taken from a well, and Ca concentration was measured by a colorimetric method using a kit (Wako, Japan) and a photometer (Hitachi U-1900, Japan) according the manufacturer's instruction. A calibration line was made using the lactated Ringer's solution in this measurement.

Scanning electron microscopic (SEM) observation

On day 7, samples were taken out of wells and naturally dried. The surfaces of sample were coated with Pd and Au by sputter deposition process (Hitachi E-1030, Japan, treatment time: 120s, distance 30 mm, ultimate vacuum: 6 Pa) to give them conductivity. A field emission-type scanning electron microscope (FE-SEM) was used for the observation of sample surfaces.

RESULTS

Fig.2 shows changes in Ca concentration in SBF for the samples. The changes are represented as a ration to Ca concentration at the starting time of incubation (0 min). BCB, HA, and β-TCP did not show any obvious changes in Ca concentration at time points until 3 hours of incubation. However, the concentrations increased on day 1 and 3, representing Ca releases from these materials due to their biosolubility. On the other hand, bone samples calcined at 600°C and 900°C demonstrated time-dependent decreases in Ca concentration from 30 min or 1 hour incubation, exhibiting Ca adsorption to these samples. This tendency was more remarkable in 600°C rather than in 900°C sample, showing higher Ca adsorptive ability of 600°C sample.

FE-SEM images of each sample surface on 7 days are shown in Fig.2. Comparing surfaces before incubation, the surfaces become rougher in BCB, more granular in HA, and more porous in β-TCP, which seems to be results of dissolution of the surfaces. On the other hand, deposition matter was observed on the surfaces of calcined bone samples, supporting the results of Ca concentration measurement.

DISCUSSION

Our results suggest that calcined bovine bones lack bioabsorbability, because of their low biosolubility. On the other hand, strong osteoconductivity would be expected for the bones. Calcination process for bone tissue changes the mineral structure and composition of the tissue. We previously found that the mineral of bovine trabecular bone still keeps carbonate apatite structure after calcination at 600°C, but became hydroxyapatite like at 900°C by FT-IR analysis [2]. Synthetic carbonate apatite has been reported to be superior in bioabsorbability by osteoclasts over hydroxyapatite [3]. This suggests that calcined bovine bone also has better osteoclast-related absorbability than hydroxyapatite, although with low biosolubility in body fluid. The above discussion should be validated by cell culture studies with osteoblasts and osteoclasts on a calcined bone sample, as well animal studies to see tissue replacement after implantation.

Bone-like apatite could be spontaneously formed on the surface of osteoconductive biomaterial such as bioglass by repeatedly providing Ca^{2+} and PO_4^{2-} to the surface in SBF [4]. In this study, lactated Ringer's solution was used as SBF. However, this solution does not include PO_4^{2-}, meaning that the observed deposition on the surface may not be bone apatite, but crystalized calcium.

In conclusion, calcined bovine compact bones are insoluble in SBF, rather than bio-adsorptive.

ACKNOWLEDGEMENTS

This study was partially supported by the Ministry of Education, Science, Sports and Culture, Grant-in-Aid for Scientific Research (B), 15H03890.

REFERENCES

[1] Tanaka, S.M., et al., *Proceedings-Book of SB3C2015*, 2015
[2] Tanaka S.M., et al., *Proceedings of Life Engineering Symposium*, 312-313, 2014
[3] Nakamura, M., et al., *J Biomed Mater Res A*, 101: 3141-3151, 2013.
[4] Kim, H-M., et al., *Biomaterials*, 26: 4366-4373, 2005

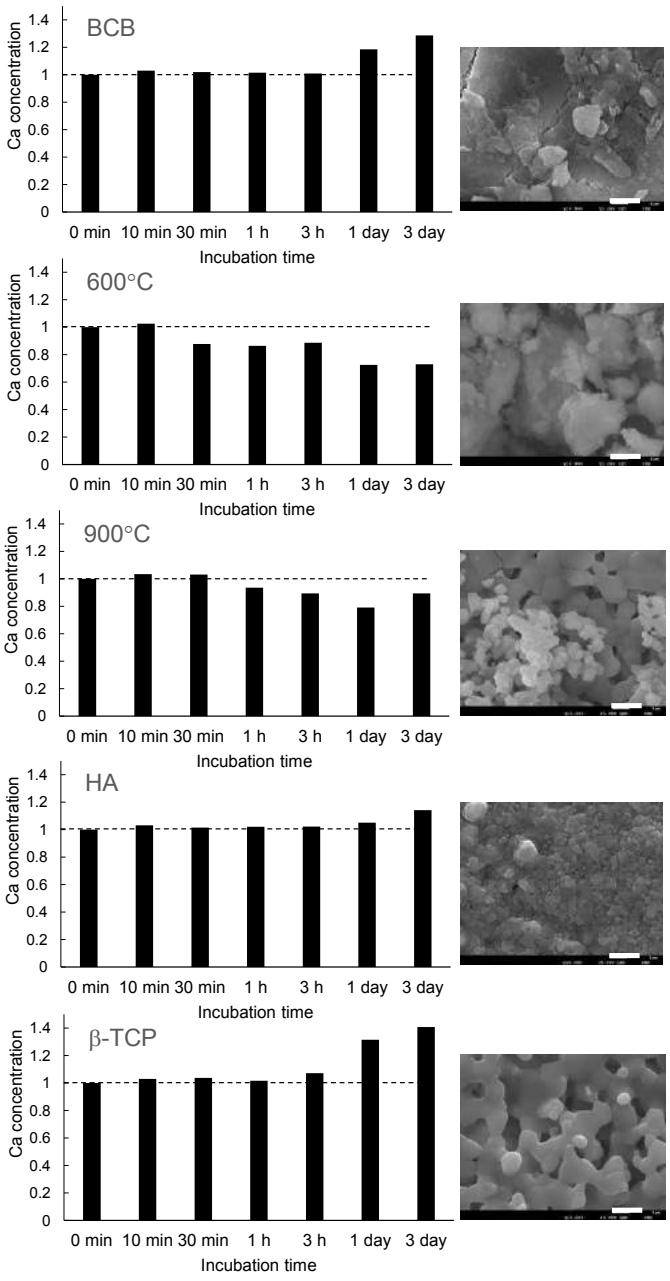

Figure 2 Changes in calcium concentration in Ringer's lactate solution with incubation time (left) and FE-SEM images after incubation for 7 days (right). Data are represented as a ratio of the value at 0 min.

Copyright 2016 The Organizing Committee for the 2016 Summer Biomechanics, Bioengineering and Biotransport Conference